EDITORIAL: Thanks to Our Editorial Advisory Board and Reviewers

We welcome the following distinguished scientists as *new members* of the Editorial Advisory Board, and we look forward to working with them to take the journal in new directions.

Christine Allen, University of Toronto
David Andreu, Pompeu Fabra University
You Han Bae, University of Utah
Santanu Bhattacharya, Indian Institute of Science
Marcel P. Bruchez, Carnegie Mellon University
Jari Hovinen, PerkinElmer
Lee Josephson, Harvard University
Rudy Juliano, University of North Carolina
Hisataka Kobayashi, National Institutes of Health
Felix Kratz, University of Freiburg
Igor L. Medintz, U.S. Naval Research Laboratory
Dario Neri, ETH Zurich
Ravindra K. Pandey, Roswell Park Cancer Institute
William M. Pardridge, University of California Los Angeles
Theresa M. Reineke, Virginia Tech
Molly S. Shoichet, University of Toronto
Arne Skerra, Technische Universitat Muenchen
Gang Zheng, University of Toronto

We are thankful to the following *outgoing members* of the Editorial Advisory Board for their service during the past years, and we wish them well in their future endeavors.

Carolyn J. Anderson, Mallinckrodt Institute of Radiology
Darryl Bornhop, Vanderbilt University
Sylvia Daunert, University of Kentucky
Ruth Duncan, Cardiff University
Philip R. Hamann, Wyeth Research
Allan S. Hoffman, University of Washington
Michael R. Lewis, University of Missouri—Columbia
Helmut R. Mäcke, University Hospital Basel
Sheri L. Morrison, University of California Los Angeles
Glenn D. Prestwich, University of Utah
Keith Rose, University of Geneva
John E. Shively, City of Hope
Caroline J. Springer, CRC Centre for Cancer Therapeutics
Suresh Srivastava, Brookhaven National Laboratory
M. Graca H. Vicente, Louisiana State University
Eric Wickstrom, Thomas Jefferson University
John R. Yates III, The Scripps Research Institute

These scientists have played a significant role in advising, reviewing, and guiding the journal, and the effects of their contributions will persist.

The *continuing members* of the Editorial Advisory Board, whose service to the journal is gratefully acknowledged, are as follows:

Jacqueline K. Barton, California Institute of Technology
Jean-Paul Behr, University of Strasbourg
Cynthia J. Burrows, University of Utah
Chien-Hsing Ken Chang, Immunomedics, Inc.
Xiaoyuan (Shawn) Chen, National Institutes of Health
Patrick Couvreur, Université de Paris-Sud
Mark E. Davis, California Institute of Technology
Peter B. Dervan, California Institute of Technology
Gene M. Dubowchik, Bristol-Myers Squibb
David Filpula, Enzon Pharmaceuticals, Inc.
M. G. Finn, The Scripps Research Institute
Shiroh Futaki, Kyoto University
David A. Goodwin, Stanford University (Emeritus)
Anna Grandas, Universitat de Barcelona
Anne Gruaz-Guyon, Inserm
M. Frederick Hawthorne, University of Missouri Columbia
John E. Hearst, University of California Berkeley (Emeritus)
Ned D. Heindel, Lehigh University
W. E. Hennink, Utrecht University
Greg T. Hermanson, Thermo Fisher Scientific
Donald J. Hnatowich, University of Massachusetts
Dr. Kenneth A. Jacobson, National Institutes of Health
Alexander V. Kabanov, University of Nebraska Medical Center
Kazunori Kataoka, University of Tokyo
John A. Katzenellenbogen, University of Illinois
Sung Wan Kim, University of Utah
Thomas Kissel, Philipps University Marburg
Kenji Kono, Osaka Prefecture University
Jindrich Kopecek, University of Utah
Robert Langer, Massachusetts Institute of Technology
Christopher P. Leamon, Endocyte Pharmaceuticals, Inc.
Shuang Liu, Purdue University
Hiroshi Maeda, Sojo University
Thomas J. Meade, Northwestern University
Oleg Melnyk, CNRS/Universite de Lille
Peter E. Nielsen, University of Copenhagen
Jong-sang Park, Seoul National University
Tae Gwan Park, KAIST
Tariq Rana, Burnham Institute for Medical Research
Steven L. Regen, Lehigh University
Ralph Reisfeld, Scripps Clinic and Research Foundation
Steve Roffler, Academia Sinica
P. August Schubiger, ETH - Zurich
Peter G. Schultz, The Scripps Research Institute
Francis C. Szoka, Jr., University of California San Francisco
David H. Thompson, Purdue University
David A. Tirrell, California Institute of Technology
Donald A. Tomalia, Dendritic Nanotechnologies, Inc.
Vladimir P. Torchilin, Northeastern University
Eishun Tsuchida, Waseda University
Pierre Vierling, Universite de Nice Sophia-Antipolis
Ernst Wagner, Ludwig-Maximilians-University
Ralph Weissleder, Massachusetts General Hospital
Michael J. Welch, Washington University in St. Louis
D. Scott Wilbur, University of Washington
Meir Wilchek, The Weizmann Institute of Science
Karen L. Wooley, Washington University in St. Louis
Anna Wu, University of California Los Angeles
Samuel Zalipsky, Intradigm, Inc.
Michael Zalutsky, Duke University Medical Center

10.1021/bc900575s © 2010 American Chemical Society
Published on Web 01/20/2010

Thanks to Our Reviewers

It is a pleasure to acknowledge the contributions of the reviewers of manuscripts submitted in 2009 for publication in *Bioconjugate Chemistry*. Their unselfish service has been essential in the shaping of the twentieth volume of the journal. The scientific community is fortunate that its members are willing to share their time and specialized knowledge in this way. The reviewers are as follows:

Samuel Achilefu	Dennis Benjamin	Hak Soo Choi	Kazuhisa Fujimoto
Catalina Achim	Steven Benner	Francisco Ciruela	Toshiaki Furuta
William E. Acree	Paul D. Benny	Gary Cline	Shiroh Futaki
Hidetaka Akita	David Eric Benson	Chris E. Cooper	Detlef Gabel
Kazunari Akiyoshi	Kristian Berg	David Reid Corey	Hans-Joachim Gabius
Fernando Albericio	Debora Berti	Eain Cornford	Laurie Gahan
Roger A. Alberto	Silvia Bertuglia	Patrick Couvreur	Lea Gainkam
Roger Alberto	Michael Best	James A. Cowan	Michael Gait
Markus Albrecht	Michael Bienert	Gabriella Csik	Hariprasad Gali
Janice R. Aldrich-Wright	Gary Bignami	Louis Cuccia	Jean Gariepy
Frank Alexis	Galia Blum	James N. Culver	Sveltlana Gelperina
Matthew J. Allen	Jozsef Bodi	Masad Jose Damha	Jason Gestwick
Stephen Charles Alley	Otto Boerman	Jeffery T. Davis	Hamid Ghandehari
Carmen Alvarez-Lorenzo	Jean-Marie Boeynaems	Mark E. Davis	Indraneel Ghosh
Andreja Ambriovic-Ristov	Alexei A. Bogdanov	Anton I. de Kroon	Michael F. Giblin
Carolyn J. Anderson	Robert D. Bolskar	Jason Dearling	Mauro Ginanneschi
David Andreu	Dennis Bong	Clemens Decristoforo	Todd D. Giorgio
Kristi Anseth	Guy M. Bormans	Eric Defrancq	Edith Caroline Glazer
Ichio Aoki	Darryl J. Bornhop	Vincent F. Degroot	Peter M. Glazer
Sadahito Aoshima	Alexandre Y. Borovkov	Marie-Helene Delville	Edie Goldsmith
Yasushi Arano	Szilvia Bosze	Attila Demeter	Wayne Gombotz
Paola Barbara Arimondo	Viktor Brabec	Sapna Deo	Shinya Goto
Bruce Alan Armitage	Martin W. Brechbiel	Mahendra Deonarain	Michael Gottschaldt
Ulrich Arnold	John David Brennan	Michael R. Detty	Duncan Graham
Jeffrey B. Arterburn	Rui M. M. Brito	Michael Diehl	David W. Grainger
Andrey Arzumanov	Roland Brock	Chaitanya Divgi	Anna Grandas
Tomohiro Asai	Christian Brueckner	Christian Dohmen	Francesca Greco
Hiroyuki Asanuma	Merlin Bruening	Chikara Dohno	Mark A. Green
Shoichiro Asayama	Bruno Bujoli	Pavlina Dolashka-Angelova	Hans Joerg Griesser
Ulysse Asseline	Uwe Bunz	Svetlana O. Doronina	Mark Grinstaff
Didier Astruc	Patrick J. Burke	Adriano Duatti	Ernest V. Groman
You Han Bae	Carmen Burtea	Mitsuhiro Ebara	Hermann J. Gruber
Sandor Bajusz	Michael Daro Buschmann	Gene Michael Dubowchik	Zhongwu Guo
Scott Banta	Weibo Cai	Todd Shannon Emrick	Rainer Haag
Ande Bao	Paolo Caliceti	Ramon Eritja	Georg Hacker
Janina Baranowska-Kortylewicz	James W. Canary	Emanuel Escher	Heike Hall
Mihai Barboiu	Peter Caravan	Tarek Fahmy	Itaru Hamachi
Gabriel Luis Barletta	Chien-Hsing Ken Chang	Neil Fairweather	Kimberly Hamad-Schifferli
Gillian Barratt	Ravi J. Chari	Andreas Faust	Henri Handel
Stefan Barth	Arabinda Chaudhuri	Laszlo Fesus	Robert Haner
Philippe Antoine Barthelemy	Gong Chen	David Ray Filpula	Robert N. Hanson
Serge L. Beaucage	Xiaoyuan Chen	Peter M. Fischer	Hideyoshi Harashima
Annette Beck-Sickinger	Ying-Hua Chen	Simone Fishburn	Eva Marie Harth
Patrick J. Bednarski	Laura Chiarantini	Warren Ford	Frederick R. Haselton
Gerd Bendas	Ashutosh Chilkoti	Keith R. Fox	Jun Hatazawa
Ettore Benedetti	Marco Chinol	Katherine Franz	Mary Hefford
Itai Benhar	Chong-Su Cho	Wolfgang Fritzsche	Ritva Heljasvaara

Stefan W. Hell
Lothar Helm
Wim E. Hennink
Vitor Renaux Hering
Greg T. Hermanson
Jacobus Herscheid
Robert Hider
Scott Alan Hilderbrand
Ole Hindsgaul
Donald Hnatowich
Ralf Hoffmann
Jari Juhani Hovinen
Jeff Hrkach
Guanggan Hu
Robert H. E. Hudson
L. Hunyady
Yoshiya Ikawa
Asparouh Iliev
Toshiro Inubushi
T. Ishida
Kazuhiko Ishihara
Yoshihiro Ito
Bela Ivan
Hiroo Iwata
Gopal Iyer
Dowdy Jackson
Kenneth A. Jacobson
Tamas Janaky
Scott Charles Jeffrey
Raz Jelinek
Rongchao Jin
Seongbong Jo
Paul Johnson
Arwyn Tomos Jones
Lee Josephson
Lokesh Joshi
Rudolph L. Juliano
Kazuaki Kakehi
Nazila Kamaly
Jan Kamps
Koji Kano
Kazunori Kataoka
Yoshiki Katayama
John A. Katzenellenbogen
Hiroyoshi Kawakami
Shigeru Kawakami
Brian Kay
Gyorgy Keglevich
Toshiyuki Kida
Satoru Kidoaki
Akihiko Kikuchi
Byeang Hyean Kim
Jong-Man Kim
Akio Kishida
Yoshiaki Kiso
Eva Kiss
Thomas H. Kissel
Hisataka Kobayashi
Kazukiyo Kobayashi
Akio Kobori
Teruyuki Komatsu
Makoto Komiyama
Burkhard Konig
Kenji Kono
Roland E. Kontermann
Jindrich (Henry) Kopecek
Pavla Kopeckova
Kostas Kostarelos
Lajos Kovacs
Jiri Kozelka
Felix Kratz
Kenneth Krohn
David L. Kukis
Hank F. Kung
Glen S. Kwon
Young Jik Kwon
Majid Laassiri
Kit S. Lam
Twan Lammers
Norbert Lange
Ulo Langel
Olivier Laurent
Benedict Law
Christopher Paul Leamon
Bernard Lebleu
Doo Sung Lee
Kang Choon Lee
Minhyung Lee
Robert Lee
Seulki Lee
Marcia Levitus
Jason S. Lewis
Michael Robert Lewis
Shyh-Dar Li
Pi-Hui Liang
Jonathan Sidney Lindsey
Rob Liskamp
Chuan-Fa Liu
Dongsheng Liu
Guozheng Liu
Shuang Liu
Pui-Chi Lo
Harri Lonnberg
Loren Looger
Yan Lu
Zheng-Rong Lu
Hendrik Luesch
Konstantin A. Lukyanov
Dangshe Ma
Robert H. Mach
Helmut Maecke
Yasushi Maeda
Stefano Maiorana
Yoshie Maitani
Alexander Makarov
Marilena Manea
Muthiah Manoharan
Giuseppe Mantovani
Atsushi Maruyama
Andreas Marx
Steve Mather
Hiroshi Matsui
Michiya Matsusaki
Laszlo Matyus
Heather Dawn Maynard
Jason R. McCarthy
Michael Thomas McMahon
Thomas J. Meade
Claude F. Meares
Igor L. Medintz
Oleg Melnyk
Andre E. Merbach
John Mertens
Damon Meyer
Yubin Miao
Jason Micklefield
Patrick Midoux
Mingshe Zhu
Tamara Minko
Chad A. Mirkin
Takashi Miyata
Shin Mizukami
Mike Modo
Mariko Morishita
Janet Ruth Morrow
Chung-Yuan Mou
Willem J. M. Mulder
Russell Mumper
Takeharu Nagai
Takeshi Nagasaki
Natalie Naim
Hiroyuki Nakamura
Jun Nakanishi
Tamaki Nakano
Ikuhiko Nakase
Masamichi Nakayama
Ravin Narain
Stephen Neidle
Dario Neri
Klaas Nicolay
Peter E. Nielsen
Christof Niemeyer
Takuro Niidome
Makiya Nishikawa
Shin-Ichiro Nishimura
Nobuhiro Nishiyama
Takahiro Ochiya
Johannes Oehlke
Akiya Ogawa
Yu-Kyoung Oh
Yuichi Ohya
Akimitsu Okamoto
Subhani M. Okarvi
Barry O'Keefe
Nicole Okeley
Naoto Oku
Mike Olive
Kenneth Wayne Olsen
Chris Orvig
Masaki Otagiri
David Oupicky
Richard Owczarzy
Mark D. Pagel
Monica M. Palcic
Renato Palumbo
Huaizhong Pan
Ravindra K. Pandey
Virendra N. Pandey
Jayanth Panyam
Anna Maria Papini
William Pardridge
Jong-sang Park

Ki-Dong Park
Kinam Park
Tae Gwan Park
Pascale Ondoa
Gianfranco Pasut
M. S. Patankar
Laszlo Patthy
James C. Paulson
Teresa Pellegrino
Valerie Christine Pierre
H. J. Pietzsch
David Piwnica-Worms
Michael Ploug
Nicola Lucia Brendel Pohl
Andrew Polson
Richard T. Pon
Mirco Ponzoni
Margus Pooga
Marcel Popa
Michel R. Popoff
Danny Porath
James C. Powers
Glenn D. Prestwich
Michael Przybylski
Suzie Hwang Pun
David Putnam
Xiaozhong Qu
Thomas P. Quinn
T. Shantha Raju
Gary Rankin
Jianghong Rao
Horst Recum
Steven Louis Regen
Raymond M. Reilly
Gary Rhodes
Art A. Rodriguez
Gerard Roelfes
Daniela Roethlisberger
Steve R. Roffler
Ewa Rogalska
Steve Rokita
Paolo Rovero
David B. Rozema
Floris P. J. T. Rutjes
Xavier Saelens
Hideo Saji
Hiromi Sakai
Maria Sakarellos-Daitsiotis
Yogesh S. Sanghvi
Paul Bennett Savage
Roger Schibli
James W. Schneider
Carsten Schultz
David Schwartz
Francesco Scopinaro
Frank Seela
Paul R. Selvin
Mathias O. Senge
Peter Senter
Jai Woong Seo
Doron Shabat
Ajit Sharma
Heather Sheardown
A. Dean Sherry
Hisanori Shinohara
Kazuo Shinozuka
Kouichi Shiraishi
Molly Shoichet
Eric Shusta
Jerson L. Silva
Eric Edward Simanek
Alexandr Sinyakov
Masahiko Sisido
Bradley D. Smith
Stavroula Sofou
Soo-Chang Song
Carissa M. Soto
Alexandre Specht
Caroline J. Springer
Dmitry A. Stetsenko
Vladimir Subr
Yasuo Suda
Helga Suli-Vargha
Brent S. Sumerlin
Kathy A. Suprenant
C. Raman Suri
May Sutherland
Sonke Svenson
Harold M. Swartz
Mark Thomas Swihart
Csaba Szabo
Francis C. Szoka
Maryam Tabrizian
Jonathan F. Tait
Yuuki Takashima
Naoya Takeda
Shigeori Takenaka
Shinji Takeoka
Daniel R. Talham
Hirokazu Tamamura
Kazuhito Tanabe
Kazuo Tanaka
Lutz Tautz
John-Stephen Taylor
F. Akif Tezcan
Mathew L. Thakur
T. J. Thomas
Thommey P. Thomas
David H. Thompson
David Thonon
Philip Thorpe
David A. Tirrell
Werner Tjarks
Jose Luis Toca-Herrera
Brian Toki
Vladimir Tolmachev
Donald A. Tomalia
Kenneth Beamer Tomer
Michael Torgov
Eva Toth
Nicolas Tsapis
Andrew Tsourkas
Ching-Hsuan Tung
Karel Ulbrich
Katalin Uray
Naoki Utoguchi
Oscar Vadas
Ganesan Vaidyanathan
John F. Valliant
Maria Vamvakaki
Mike van Brunt
Serge Van Calenbergh
A. van der Vliet
Jan Cornelis Maria Van Hest
Johan E. van Lier
Peter C. M. Van Zijl
Karen M. Vasquez
Irina Velikyan
Maria Jesus Vicent
M. Graca Henriques Vicente
Pierre Vierling
Chris Vlahos
John Wade
David Hennessey Waldeck
Chunru Wang
Dong Wang
Jun Wang
Peng George Wang
Qian Wang
Shu Wang
Yun-Ming Wang
Thomas R. Ward
Marcus Weck
Klaus H. Weisz
Michael J. Welch
Han Wendel
Eric Wickstrom
D. Scott Wilbur
Meir Wilchek
Itamar Willner
Paul Winnard
You-Yeon Won
Mark Woods
Karen L. Wooley
Tetsuji Yamaoka
Ichiro Yamashita
Mingdi Yan
Kevin J. Yarema
Paul J. Yazaki
Duyun Ye
Yoon Yeo
Hyunmin Yi
Jun Yin
Masayuki Yokoyama
Ryo Yoshida
Samuel Zalipsky
Dimitrios I. Zeugolis
George Zhang
Yue Zhao
Qi-Huang Zheng
Su Zhiguo
Zhiyuan Zhong
Guonian Zhu
Guy Zuber

Claude F.Meares
Editor-in-Chief

BC900575S

REVIEWS

Antibody−Drug Conjugates: Linking Cytotoxic Payloads to Monoclonal Antibodies

Laurent Ducry* and Bernhard Stump

Lonza Ltd, CH-3930 Visp, Switzerland. Received May 4, 2009; Revised Manuscript Received July 7, 2009

Antibody−drug conjugates (ADCs) combine the specificity of monoclonal antibodies (mAbs) with the potency of cytotoxic molecules, thereby taking advantage of the best characteristics of both components. Along with the development of the mAbs and cytotoxins, the design of chemical linkers to covalently bind these building blocks is making rapid progress but remains challenging. Recent advances have resulted in linkers having increased stability in the bloodstream while allowing efficient payload release within the tumor cell.

INTRODUCTION

After cardiovascular diseases, cancer represents the second most common cause of death in the Western world and is a major area of focus for the pharmaceutical industry. Surgery and radiotherapy are generally used when a tumor is localized to a certain tissue, but chemotherapy is needed when metastasis has occurred. Despite extensive research, most anticancer drugs have nonspecific toxicity. By targeting the cell cycle and thereby killing rapidly proliferating cells, they do not explicitly discriminate between healthy and tumor tissues and only gain a limited selectivity for malignant cells. Such cytotoxic drugs have a narrow therapeutic window, which limits their efficacy and results in severe side effects. Due to a lack of selectivity, drug concentrations that would eradicate the tumor can often not be used. In addition, tumors can develop resistance against anticancer drugs after prolonged treatment. Therefore, achieving improved tumor selectivity through targeting of cytotoxic drugs to the cancer cells is needed.

A promising approach to achieving a more selective treatment is targeted prodrug therapy (*1*). Antibody−drug conjugates (ADCs) are ideal candidates for such prodrugs. ADCs are monoclonal antibodies (mAbs) linked to cell-killing drugs. Thanks to their high binding specificity for tumor-specific antigens, mAbs can be used as vehicles to target cell-killing payloads to tumor cells. Unique or overexpressed, tumor-specific antigens can be found in a wide range of human tumor cells (*2*). Some mAbs have the ability to recognize and specifically bind to these tumor-associated antigens. They can be used as single agents for the treatment of cancer through binding to cancer-cell-specific antigens and induction of an immunological response against the target cancer cell (*3*). However, therapeutic efficacy is often limited by the extent to which the antibody leads to cell death. Monoclonal antibodies are extremely discriminating for their targets but sometimes therapeutically ineffective on their own. The insufficient efficiency of most naked mAbs in cancer therapy has been circumvented by arming the immunoglobulin with radioactive isotopes (*4*) or cytotoxic drugs (*5*−*7*) (Figure 1), yielding highly specific ADCs.

ADCs can be viewed as sophisticated delivery systems for antitumor cytotoxic drugs. The mAb guides the toxin precursor to the target cancer cell, where the prodrug can be converted chemically and/or enzymatically to the parent drug and unfold its cytotoxic activity. The ADC is exposed to different conditions on its journey from the blood vessels to the molecular target in the tumor tissue. The mode of action at cellular or molecular level is complex, with each step bringing its own challenges:

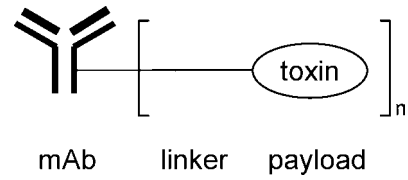


Figure 1. Schematic representation of an antibody−drug conjugate.

a. Circulation. The ADC must behave like a naked antibody when circulating in the plasma. In particular, the linker must be stable in the bloodstream to limit the damage to healthy tissue. Decomposition or decay would release the cytotoxin before being delivered to the target site.

b. Antigen Binding. It is necessary that the conjugated mAb retains high immunoaffinity. Attaching the cytotoxic compound to the mAb must thus not disturb its binding specificity.

c. Internalization. A sufficient intracellular concentration of the drug must be achieved. This is challenging because antigen targets on cell surfaces are often present in limited numbers and the internalization process for antigen−antibody complexes is frequently inefficient.

d. Drug Release. Once internalized, the ADC has to efficiently release the original cytotoxic drug in its active form inside the tumor cell.

e. Drug Action. The inherent potency of the released drug must be sufficient to kill the tumor cell, even at low concentration. To achieve significant cytotoxicity, use of very potent drugs with subnanomolar IC_{50} (as free drug) becomes necessary. It has been shown that compounds found to be too toxic when tested as a stand-alone chemotherapy agent are suitable candidates for ADC payloads. These toxins can be 100 to 1000 times more cytotoxic than traditional anticancer agents.

The molar loading of the drug on the mAb can be tuned to achieve the desired potency. Because of points (c) and (d), linkage of several drugs is generally necessary to achieve significant cytotoxicity. However, if too many cytotoxic molecules are attached

* laurent.ducry@lonza.com.

10.1021/bc9002019 © 2010 American Chemical Society
Published on Web 09/21/2009

Chart 1

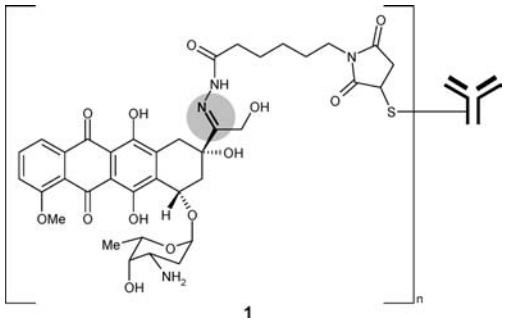


Chart 2

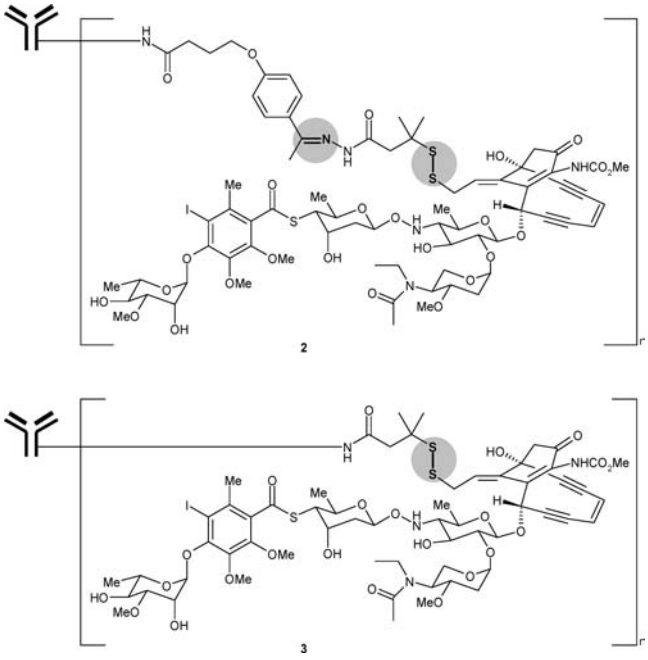
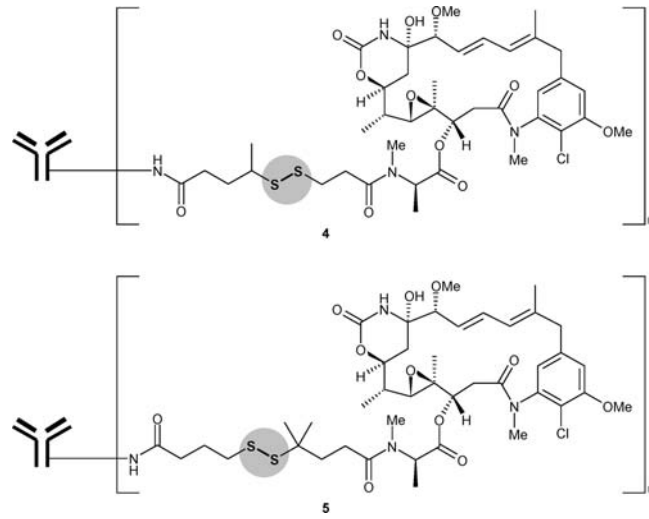


Chart 3



to the antibody, the body may recognize the conjugate as a damaged form of the protein and quickly clears it from the system, proving points (a) and/or (b) to be problematic. The extent of drug substitution may also affect pharmacokinetics, so that most of the time 2−4 drugs per antibody give the best therapeutic window (*8, 9*). To avoid the interference with the antigen recognition, the drugs are ideally linked at the Fc or constant region of the mAb that does not participate in binding to the antigen (point (b)). To regain the full cytotoxic potential of the drugs, cleavable linkers releasing the drug molecule at the target site in unmodified form were developed to address point (d), although these also affect the stability of the construct. Therefore, the right balance between plasma stability and efficient drug release at the target cell has to be found.

The insights gained during ADC development within the past decade have resulted in a number of new strategies and drugs (*4*−*7*). This review focuses on linker technologies used to attach low molecular weight cytotoxic drugs to mAbs. The linker is a small but central part of ADCs and as such accounts for stability in circulation, favorable pharmacokinetic properties, and efficient release of toxic agent at the tumor site.

CHEMICALLY LABILE LINKERS

Selective linker cleavage and payload release is based upon the differential properties between the plasma and some cytoplasmic compartments. Linkers were chosen that were stable in the blood's neutral pH environment but were getting cleaved once the ADC entered the lower pH environment found inside a cell. The focus in the early days of ADC development was on acid-cleavable hydrazone linkers that were relatively stable at neutral pH (bloodstream pH 7.3−7.5), but were undergoing hydrolysis once internalized into the mildly acidic endosomes (pH 5.0−6.5) and lysosomes (pH 4.5−5.0).

In the 1990s, Bristol-Myers Squibb scientists covalently linked doxorubicin, an intercalating agent that blocks DNA replication and is used as chemotherapeutic agent, to the humanized mAb BR96 (*10*). Doxorubicin was connected over a (6-maleimidocaproyl)hydrazone linker to cysteine residues of the Lewis-Y specific mAb. The preclinical activities of BR96-doxorubicin (**1**, Chart 1) were remarkable, but despite the use of eight drugs per mAb molecule, the amount of conjugate needed to achieve these effects *in vivo* were high (>100 mg/kg). This was presumably due to the relatively low potency of doxorubicin (IC_{50} of 0.1−0.2 μM for human carcinoma lines (*11*), whereas subnanomolar activities are now typically seen for ADC payloads). Moreover, the half-life of the drug in the blood was approximately 43 h, which is short compared to the half-lives of several days to weeks of the naked BR96 mAb in humans. The compound later failed to show sufficient clinical efficacy.

The first and so far sole mAb linked to a cytotoxic payload that has been given regulatory approval is Wyeth's gemtuzumab ozogamicin (**2**, Mylotarg; Chart 2) (*12*−*14*). The drug was approved by the US Food and Drug Administration (FDA) in 2000 for use in patients over 60 suffering from relapsed acute myelocytic leukemia (AML), the most common form of leukemia in adults. Gemtuzumab ozogamicin (**2**) consists of *N*-acetyl-γ-calicheamicin (an enediyne antibiotic that binds to the minor groove of DNA and causes double-strand breaks leading to apoptosis) covalently attached to humanized anti-CD33 IgG4 κ antibody (hP67.6) via a bifunctional linker. The 4-(4-acetylphenoxy)butanoic acid moiety allows for attachment to surface-exposed lysines of the antibody over an amide bond and forms an acyl hydrazone linkage with *N*-acetyl-γ-calicheamicin dimethyl hydrazide. Upon internalization of the ADC, the calicheamicin prodrug is released by hydrolysis of the hydrazone in lysosomes of the CD33-positive target cells. The hydrolyzability of an unconjugated intermediate at 37 °C over 24 h increased from 6% at pH 7.4 to 97% at pH 4.5 (*15*). The enediyne drug then gets activated by reductive cleavage of the disulfide bond. This disulfide linkage has been stabilized by two methyl groups to prevent premature release of calicheamicin by circulating reduced thiols, such as glutathione. In most preclinical models, the hydrazone linkage produced ADCs with higher potency than the corresponding amide-bearing conjugate **3**, providing evidence that with this mAb the disulfide alone is insufficient for

Scheme 1. Presumed Release Mechanism of MMAE (7) from ADC 6 Incorporating a Valine-Citrulline Peptidic Linker

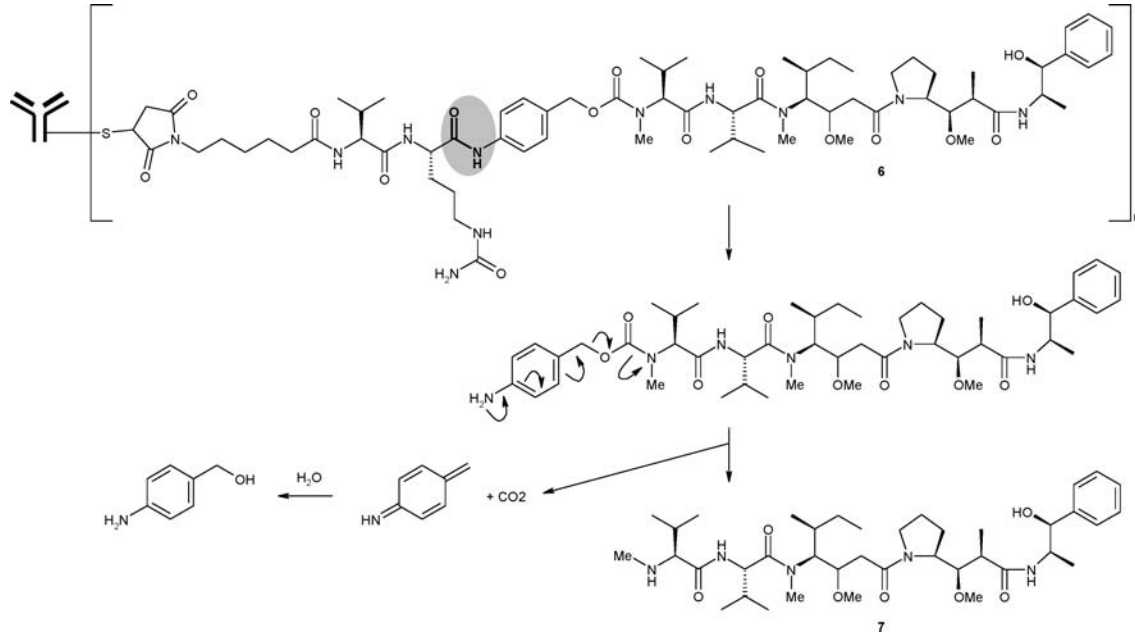
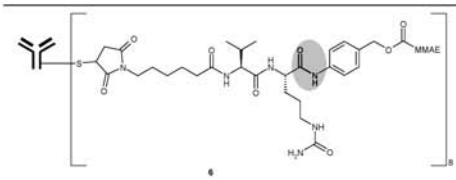
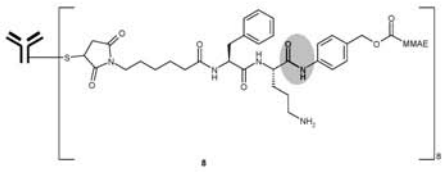
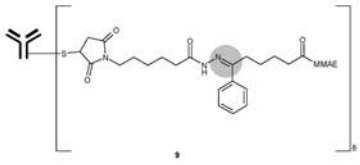


Table 1. Compared Stabilities of Enzyme-Labile and Chemically Labile Linkers in ADCs with MMAE Conjugated to cBR96 mAb

ADC	Linker	Half-live mouse plasma	Half-live human plasma	Maximum tolerated dose
	Valine-citrulline	30 days*	230 days*	30 mg/kg
	Phenylalanine-lysine	12.5 days*	80 days*	n/a
	Hydrazone	2.1 days	2.6 days	15 mg/kg

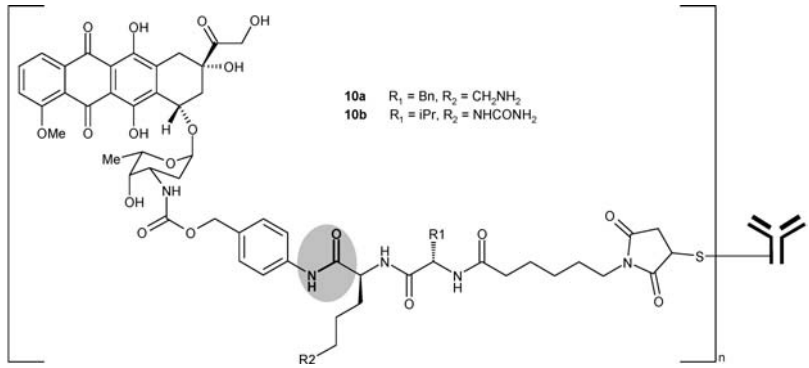
* projected half-life

efficient release of the drug in the target cell. Interestingly, with the murine mAb CTM01, ADC **3** showed activities equal to or even greater than that of the corresponding hydrazone conjugate **2** in several *in vitro* and *in vivo* tumor models, revealing that this conclusion is not general (*16*). In clinical trials, however, compound **3** had only limited evidence of activity.

Mylotarg has met limited successes due to a narrow therapeutic window. The linker technology based on pH-dependent release mechanism is possibly not sufficiently stable and too much of the drug is being released in the bloodstream, as pharmacokinetic data have shown that the mean half-life of Mylotarg is 72 h (*15*). Nonetheless, the development of CMC-544 (inotuzumab ozogamicin), which is a humanized anti-CD22 mAb identically attached to *N*-acetyl-γ-calicheamicin dimethyl hydrazide via the acid-labile 4-(4′-acetylphenoxy)butanoic acid linker is ongoing at Wyeth. Although this ADC is closely related to Mylotarg, good stability was shown in both human plasma and serum (rate of hydrolysis of 1.5−2%/day over 4 days) (*17, 18*).

Disulfide bonds can be an alternative to acid-labile hydrazone linkers. In this case, the release is attributed to the high intracellular concentration of glutathione. This thiol-containing tripeptide is present in micromolar concentrations in the blood, whereas its concentration in the cytoplasma is in the millimolar range (up to 1000-fold higher). This is especially true for tumor cells, where irregular blood flow leads to hypoxic state (decreased oxygen level), resulting in enhanced activity of reductive enzymes and therefore even higher glutathione concentrations. In the absence of sulfhydryl groups, disulfide

Chart 4



bonds are thermodynamically stable and provide reasonably good stability in the bloodstream.

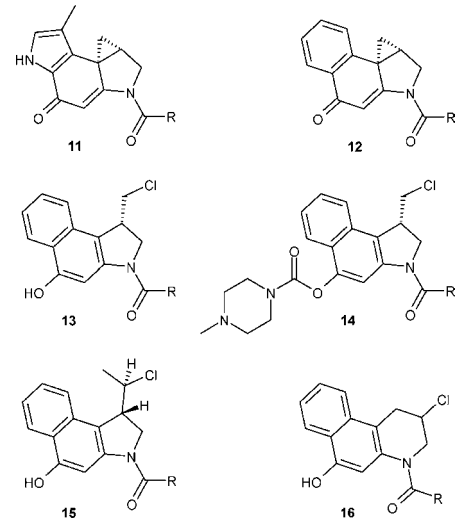
An example of an intracellularly cleavable disulfide-based linker was already discussed above (see "amide" conjugate **3**). Other examples are taxoid ADC payloads, conjugated via a disulfide-bearing 4-mercaptopentanoate linker to mAbs directed against the epidermal growth factor receptor (*19*). However, the most significant examples are ADCs where the immunoglobulin is connected over the same type of linker to ImmunoGen's drugs DM1 or DM4 (*20*−*22*). These potent thiol-containing maytansine analogues are antimitotic agents that bind to tubulin and inhibit microtubule assembly. After internalization of the ADC via antigen-mediated endocytosis and delivery to lysosomes by vesicular trafficking, the mAb is believed to be degraded, affording lysine derivatives linked to the toxin (*22*). Further intracellular modifications like cleavage of the disulfide linker through a disulfide exchange, and finally thiol methylation presumably catalyzed by intracellular methyltransferases, generate potent derivatives of DM1 or DM4 (*22*). These methylated drugs are uncharged, enabling them to pass back out through cell membranes to broaden their attack; the drug not only kills from inside the cell, but also knocks out adjacent cells within the tumor that are not targeted by the antibody (*23*). The linker of compound **4** (Chart 3) nevertheless proved to be relatively unstable *in vivo* (half-life of 47 h in mice) (*24*). Replacement of DM1 by DM4 structurally leads to the introduction of two methyl substituents on the carbon atom geminal to the disulfide bond, thereby limiting the accessibility for reducing agents. Consistent with these considerations, ADC **5** exhibits an increased half-life of 102 h in mice.

ENZYME-LABILE LINKERS

Chemically labile linkers often suffer from limited plasma stability. An alternative approach to achieve better control of the drug release involves linking a drug to an antibody via a peptide linkage. The free drug can be specifically cleaved from the carrier by the action of lysosomal proteases (e.g., cathepsin or plasmin) present at elevated levels in certain tumor tissues (*25*). Peptidic bonds are expected to have good serum stability, as proteases are normally not active outside cells because of unfavorable pH conditions and inhibition by serum protease inhibitors.

Seattle Genetics is using a maleimido-containing dipeptide linker to conjugate cysteine residues of mAbs with monomethyl auristatin E (MMAE, **7**) and F (MMAF), two auristatin derivatives that bind to tubulin and inhibit microtubule assembly. A valine-citrulline linker was designed to provide high plasma stability (half-lives in mice and monkey of 6.0 and 9.6 days, respectively) as well as a cleavage site for proteases (*26*). Efficient hydrolysis of the dipeptide linker by cathepsin B has been established *in vitro*. After enzymatic cleavage, 1,6-elimination of the strongly electron-donating 4-aminobenzyl group will occur, releasing MMAE in its active form (Scheme 1). This self-eliminating spacer is needed to spatially separate the drug from the site of enzymatic cleavage (*27*). Otherwise, the bulky payload has a negative influence on the kinetics of the peptide hydrolysis, as the access to the enzyme's active site can be affected.

Chart 5

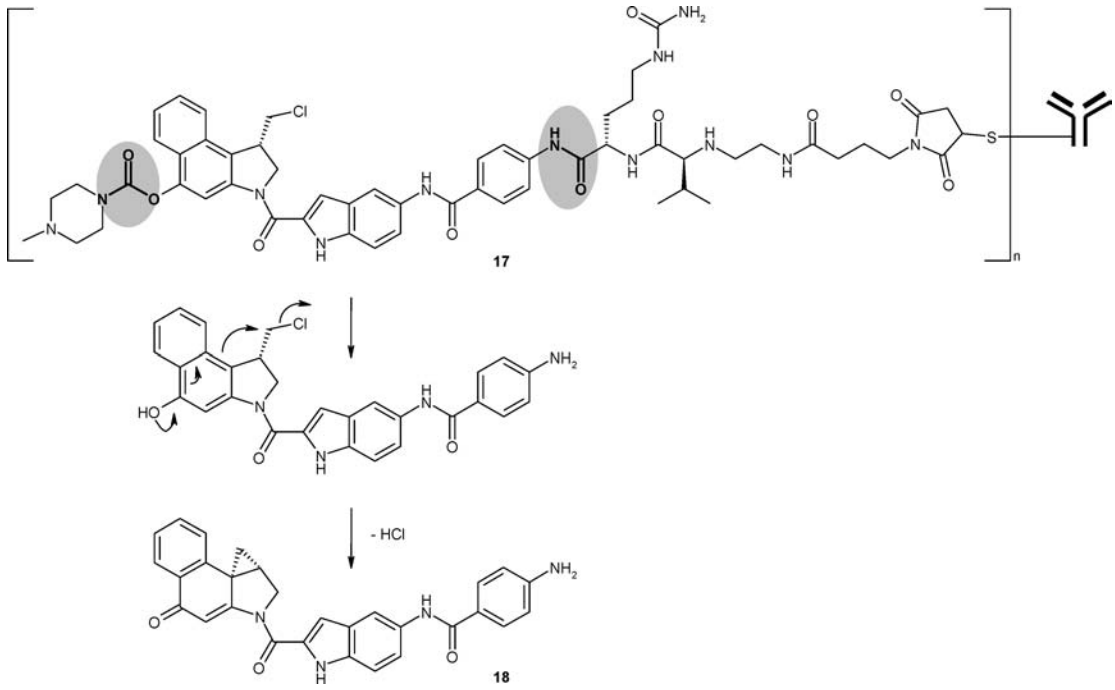


Comparison of plasma stabilities of ADCs bearing enzyme-labile valine-citrulline or phenylalanine-lysine linkers (**6** and **8**, respectively) with ADC **9** equipped with a chemically labile hydrazone linker connecting MMAE with the cBR96 mAb showed impressively the advantage of the peptide linkage (Table 1): in human plasma, the ADC **6**, featuring a peptidic valine-citrulline-derived linker, exhibits an almost 100-fold increased stability compared to its hydrazone relative **9** and the *in vitro* specificity was increased (*26*). The peptidic linker has a half-life of 6 days in mice compared to 2 days for the hydrazone linker (3-fold improvement), resulting in a lower *in vivo* toxicity (*28*). Several ADCs incorporating a peptidic linker are in clinical development, with the most advanced being cAC10-vcMMAE (SGN-35) for CD30-positive hematologic malignancies (*26, 29, 30*).

In addition to *N*-terminus linked MMAE and MMAF, attachment of dipeptide linkers at the *C*-terminus was studied as a way to vary the rate of drug release and thus ADC potency and tolerability (*26, 31*). For MMAF, it could be shown that linking the mAb over a dipeptide linker to the C-terminus of the drug can lead to further improvement of the therapeutic window.

The superiority of enzyme-labile linkers was also shown for doxorubicin derivatives conjugated to mAbs (*11, 32*). With this

Scheme 2. Presumed Release Mechanism of CBI-Containing Drug 18 from ADC 17



strategy, the immunological specificity of BR96 mAb−peptide−doxorubicin conjugates **10a** and **10b** (Chart 4) was significantly improved compared to that of the corresponding hydrazone-based conjugate **1** (*11*), demonstrating again the importance of the linker structure for the ADC properties.

Peptide-containing linkers have been successfully used with CC-1065-derived toxins. CC-1065, duocarmycins, and other cyclopropapyrroloind-4-one (CPI, **11**; Chart 5) derivatives are potent minor-groove binding DNA alkylating agents. According to Boger et al., cyclopropabenzindol-4-one analogues (CBI, **12**) are chemically more stable, biologically more potent, and synthetically more accessible than their parent compounds incorporating the natural CPI alkylation subunit (*33*). In analogy to a duocarmycin prodrug (*34*), the seco-CBI precursor **13** was developed. This compound, which was postulated to show improved pharmacokinetics, will provide the CBI analogue **12** via Winstein cyclization (*35*). A further improvement was achieved by protecting the phenolic hydroxyl group with an enzyme-labile carbamate, as in derivative **14**, decreasing the toxicity of the prodrug while increasing its water solubility by introduction of an additional basic nitrogen (*36*).

Using their UltiMAb technology, Medarex conjugated compound **14** to a mAb via a peptidic linker (*37*). Conceptually, this approach is a double prodrug strategy. It does not only improve the drug's therapeutic efficacy by conjugating it to a tumor-specific mAb, but additionally employs a prodrug of the cytotoxic agent that has reduced potency and thus minimizes side effects before being released intracellularly by carboxyesterases. The two activating steps needed to trigger the release of the active drug (Scheme 2) may lead to an enlarged therapeutic window.

Tietze et al. have reported that the CBI prodrugs **15** and **16** exhibit lower toxicities due to the reduced reactivity of the secondary chloride compared to the primary chloride present in **13** and **14** (*39*−*41*). Such derivatives with secondary chlorides (see, for example, ADC **19**; Chart 6) are used in Syntarga's SpaceLink conjugation technology (*42*). To our knowledge, no data are yet published on the linker stability.

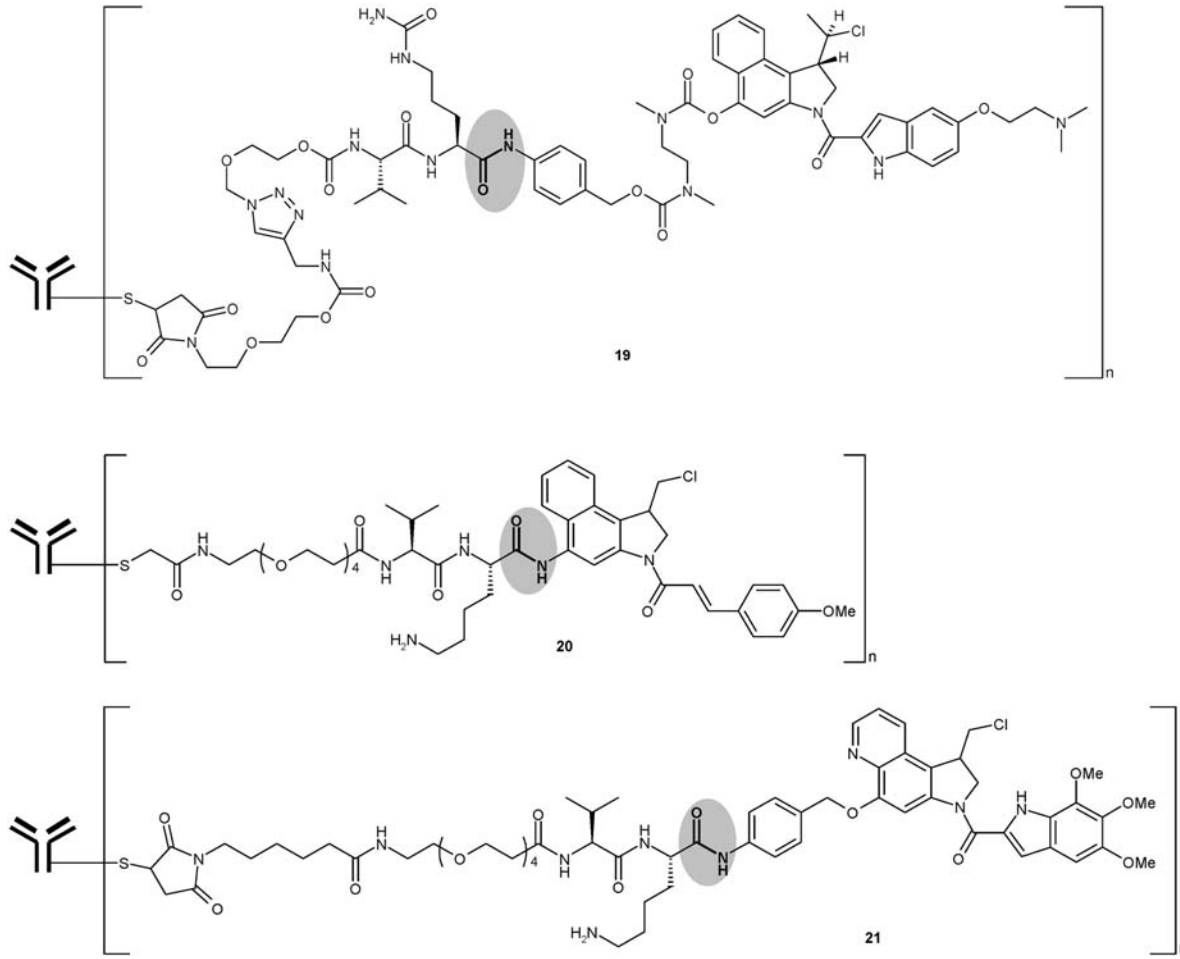
To extend its ADC technology to drugs with a complementary mode of action, Seattle Genetics has developed ADCs **20** and **21** (Chart 6) containing an amino-CBI and a hydroxy aza-CBI payload, respectively (*43*). Because of the hydrophobicity of this class of molecules, attention was focused on developing hydrophilic peptide-linker derivatives that prevented aggregation. This was achieved by use of a more hydrophilic valine-lysine sequence (compared to valine-citrulline as in ADC **6**) and incorporating a tetra(ethylene glycol) unit between the mAb and the peptide linker. The direct attachment of the linker to the amine of the CBI building block (as in **20**) or over a self-immolative *p*-aminobenzyl spacer to the corresponding hydroxyl group of the aza-CBI toxin (as in **21**) prohibits the spontaneous formation of the active toxin in the plasma. Only the enzymatic cleavage of the linker after internalization of the ADC into the cancer cell triggers the release of the prodrug that can now be transformed into the DNA-alkylating cyclopropyl derivative via a Winstein cyclization.

Another type of enzyme-labile linker was recently reported by Seattle Genetics (*44*). In this case, a carbohydrate moiety serves as the cleavage site. Its hydrophilic nature should limit aggregation. Interestingly, the β-glucoronide moiety in ADC **22** is not directly linking the ADC with the payload. Nevertheless, cleavage by β-glucuronidase triggers the 1,6-elimination of the spacer liberating the free drug **23** (Scheme 3). This carbohydrate motif was also used in ADCs bearing Camptothecin analogues (*45*).

NONCLEAVABLE LINKERS

ImmunoGen has reported the fortuitous discovery of a noncleavable thioether bond to link DM1 to mAbs (*22, 46*). Derivative **24** was actually prepared as a control experiment, but surprisingly, this noncleavable thioether linked ADC also proved very potent. The release mechanism is believed to occur via internalization of the ADC followed by degradation of the mAb component in the lysosome, resulting in the release of the maytansinoid drug **25** still attached via the linker to a lysine residue. This chemical modification of the drug did not diminish its cytotoxic potential. This form of the drug is, however, charged and presumably not able to diffuse into neighboring cells. Hence, it cannot kill adjacent tumor cells

Chart 6

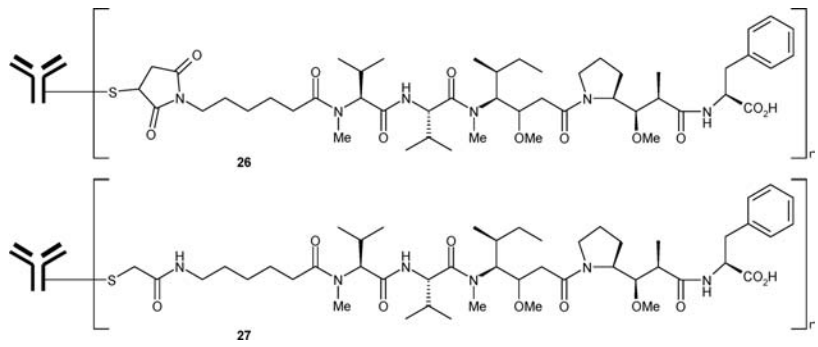


that do not express the target antigen (antigen-negative cells). Besides this by-stander effect (*23*), there is an additional reason why cleavable linkers may have a broader efficacy. Although internalization is often the common initial activation process for both cleavable and noncleavable linkers (*22*), ADCs with cleavable linkers may also be active even when they are poorly internalized (*47*). One possible explanation is that, when the linker is cleaved in extracellular space, the free drug subsequently permeates the cell to reach its target. This mechanism is not operating for ADCs incorporating noncleavable linkers, which must be internalized and degraded within the cell to become active. They are thus dependent on the biology of the target cell.

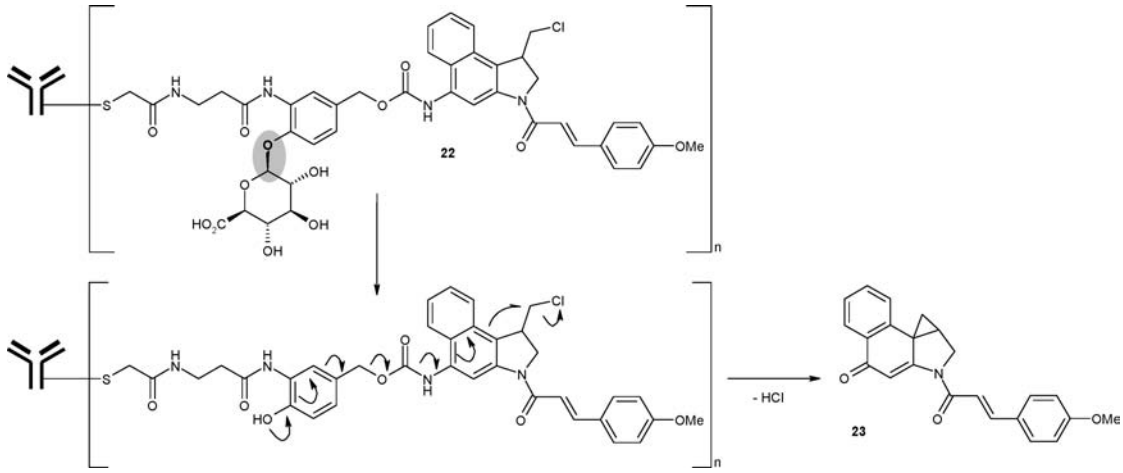
The *in vivo* stability of the thioether-linked ADC **24** proved, with a half-life of 134 h in mice, superior to that of compounds **4** and **5** (47 and 102 h, respectively). ADCs with noncleavable linkers were found to be better tolerated (*47*), presumably resulting in an improved therapeutic index. The use of noncleavable linkers has thus become an important feature of ImmunoGen TAP (tumor-activated prodrug) conjugation technology. This is best exemplified by the promising clinical results obtained by Genentech's trastuzumab-DM1 (T-DM1) for HER2-positive metastatic breast cancer (*48*).

Seattle Genetics made the same finding with MMAF, namely, that the cleavable dipeptide linker (as in **6**) could be replaced by a noncleavable thioether bond (as in ADC **26**; Chart 7) while retaining the *in vivo* activity (*49*). Mass spectrometry showed that the released drug was a cysteine-adduct of MMAF, presumably resulting from mAb degradation within lysosomes as proposed for maytansinoid conjugate **24**. MMAE, although closely related structurally, was not

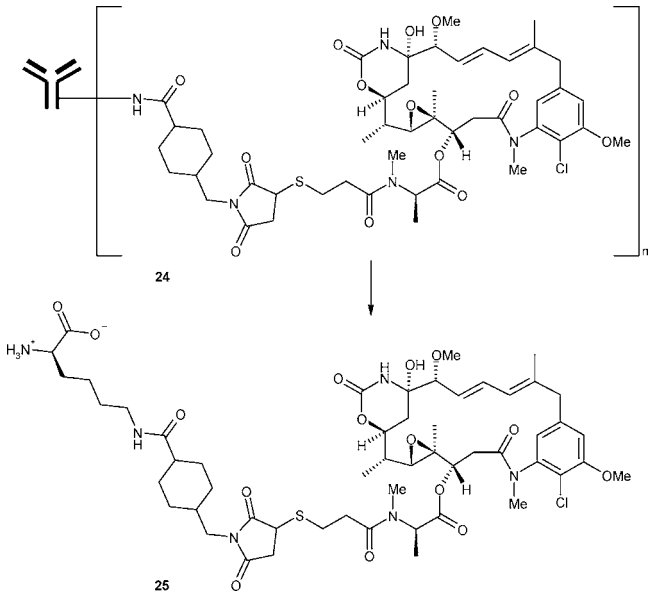
Chart 7



Scheme 3. Postulated Release Mechanism of CBI-Containing Drug 23 from ADC 22



Scheme 4. Release of Maytansine Drug-Derivative 25 through Lysosomal Degradation of ADC 24



active when attached in this manner. Only MMAF can sustain significant modification to the *N*-terminal position and still retain its potency. Recently, it was shown that a slow transfer of the drug from the ADC to albumin cysteines in the plasma occurs with alkyl-maleimide ADCs (*50*). To counteract this effect, the linker stability was enhanced by replacing the maleimide (as in ADC **26**) with an acetamide functionality (as in ADC **27**). This type of ADC led to no apparent degradation in the bloodstream for up to 14 days.

CONCLUSION

A promising approach to improve the potency of antibody-based cancer therapies is to conjugate the mAb with cytotoxic chemotherapeutic drugs. In the foreseeable future, ADCs will eventually fulfill the promise of specific delivery of cytotoxic drugs to tumor cells (targeted therapy), thus avoiding the dose-limiting toxicity of chemotherapy that occurs as a result of its effects on normal cells. The linker technology profoundly impacts ADC potency, specificity, and safety. Early ADC linkers were commonly derived from acid-labile hydrazones, which were designed to be cleaved inside target cancer cells, but inevitably underwent cleavage at nontarget sites. Newer linkers feature hindered disulfides and peptidic moieties that have achieved greater *in vivo* stability. To spare nontarget tissues from chemotherapeutic damage, noncleavable linkers were recently developed. They are thus far the most stable linkers used in ADCs. This recent development may shift some of the future challenge in ADC development from the linker technology toward finding cytotoxic drugs that retain their potency when bearing a covalently attached linker. The improved linker stability and reduced toxicity, however, come together with greater target dependence than in the case of cleavable linkers. ADCs with noncleavable linkers must be internalized and degraded within the cell, whereas compounds with cleavable linkers may be active against targets that are poorly internalized through extracellular drug release and drug entry into tumor cells. Similarly, killing of bystander antigen-negative cells through targeting of antigen-positive cells (collateral toxicity) is presumably only possible with cleavable linkers. The Lonza ADC-team thus believes that no general linker design exists for all ADCs or cancer types. Despite significant progress, each mAb must be examined separately in order to optimize a specific delivery system.

LITERATURE CITED

(1) Kratz, F., Müller, I. A., Ryppa, C., and Warnecke, A. (2008) Prodrug strategies in anticancer chemotherapy. *ChemMedChem 3*, 20–53.

(2) Panchal, R. G. (1998) Novel therapeutic strategies to selectively kill cancer cells. *Biochem. Pharmacol. 55*, 247–252.

(3) Zangemeister-Wittke, U. (2005) Antibodies for targeted cancer therapy - technical aspects and clinical perspectives. *Pathobiology 72*, 279–286.

(4) Monoclonal antibodies conjugated with radioisotopes do not have to release their payload at the target site and need thus completely different linkers that mAb conjugated with cytotoxins. They are not reviewed in this article. For a review, see Wu, A. M., and Senter, P. D. (2005) Arming antibodies: Prospects and challenges for immunoconjugates. *Nat. Biotechnol. 23*, 1137–1146.

(5) Ricart, A. D., and Tolcher, A. W. (2007) Technology insight: Cytotoxic drug immunoconjugates for cancer therapy. *Nat. Clin. Pract. Oncol. 4*, 245–255.

(6) Carter, P. J., and Senter, P. D. (2008) Antibody-drug conjugates for cancer therapy. *Cancer J. 14*, 154–169.

(7) Rohrer, T. (2008) New weapons for the oncology arsenal. *Chem. Rundschau 9*, 26–28.

(8) Hamblett, K. J., Senter, P. D., Chace, D. F., Sun, M. M. C., Lenox, J., Cerveny, C. G., Kissler, K. M., Bernhardt, S. X., Kopcha, A. K., Zabinski, R. F., Meyer, D. L., and Francisco, J. A. (2004) Effects of drug loading on the antitumor activity of

a monoclonal antibody drug conjugate. *Clin. Cancer Res. 10*, 7063–7070.

(9) McDonagh, C. F., Turcott, E., Westendorf, L., Webster, J. B., Alley, S. C., Kim, K., Andreyka, J., Stone, I., Hamblett, K. J., Francisco, J. A., and Carter, P. (2006) Engineered antibody-drug conjugates with defined sites and stoichiometries of drug attachment. *Prot. Eng. Des. Sel. 19*, 299–307.

(10) Trail, P. A., Willner, D., Lasch, S. J., Henderson, A. J., Hofstead, S., Casazza, A. M., Firestone, R. A., Hellström, I., and Hellström, K. E. (1993) Cure of xenografted human carcinomas by BR96-doxorubicin immunoconjugates. *Science 261*, 212–215.

(11) Dubowchik, G. M., Firestone, R. A., Padilla, L., Willner, D., Hofstead, S. J., Mosure, K., Knipe, J. O., Lasch, S. J., and Trail, P. A. (2002) Cathepsin B-labile dipeptide linkers for lysosomal release of doxorubicin from internalizing immunoconjugates: Model studies of enzymatic drug release and antigen specific *in vitro* anticancer activity. *Bioconjugate Chem. 13*, 855–869.

(12) Hamann, P. R., Hinman, L. M., Beyer, C. F., Lindh, D., Upeslacis, J., Flowers, D. A., and Bernstein, I. (2002) An anti-CD33 antibody-calicheamicin conjugate for treatment of acute myeloid leukaemia. Choice of linker. *Bioconjugate Chem. 13*, 40–46.

(13) Hamann, P. R., Hinman, L. M., Hollander, I., Beyer, C. F., Lindh, D., Holcomb, R., Hallett, W., Tsou, H.-R., Upeslacis, J., Shochat, D., Mountain, A., Flowers, D. A., and Bernstein, I. (2002) Gemtuzumab ozogamicin, a potent and selective anti-CD33 antibody-calicheamicin conjugate for treatment of acute myeloid leukemia. *Bioconjugate Chem. 13*, 47–58.

(14) Hollander, I., Kunz, A., and Hamann, P. R. (2008) Selection of reaction additives used in the preparation of monomeric antibody-calicheamicin conjugates. *Bioconjugate Chem. 19*, 358–361.

(15) van der Velden, V. H. J., te Marvelde, J. G., Hoogeveen, P. G., Bernstein, I. D., Houtsmuller, A. B., Berger, M. S., and van Dongen, J. J. M. (2001) Targeting of the CD33-calicheamicin immunoconjugate Mylotarg (CMA-676) in acute myeloid leukemia: *in vivo* and *in vitro* saturation and internalization by leukemic and normal myeloid cells. *Blood 97*, 3197–3204.

(16) Hamann, P. R., Hinman, L. M., Beyer, C. F., Lindh, D., Upeslacis, J., Shochat, D., and Mountain, A. (2005) A calicheamicin conjugate with a fully humanized anti-MUC1 antibody shows potent antitumor effects in breast and ovarian tumor xenografts. *Bioconjugate Chem. 16*, 354–360.

(17) DiJoseph, J. F., Dougher, M. M., Kalyandrug, L. B., Armellino, D. C., Boghaert, E. R., Hamann, P. R., Moran, J. K., and Damle, N. K. (2006) Antitumor efficacy of a combination of CMC-544 (inotuzumab ozogamicin), a CD22-targeted cytotoxic immunoconjugate of calicheamicin, and rituximab against non-Hodgkin's B-cell lymphoma. *Clin. Cancer Res. 12*, 242–249.

(18) DiJoseph, J. F., Khandke, K., Dougher, M. M., Evans, D. Y., Armellino, D. C., Hamann, P. R., and Damle, N. K. (2008) CMC-544 (inotuzumab ozogamicin): A CD22-targeted immunoconjugate of calicheamicin. *Hematology Meeting Reports 5*, 74–77.

(19) Ojima, I., Geng, X., Wu, X., Qu, C., Borella, C. P., Xie, H., Wilhelm, S. D., Leece, B. A., Bartle, L. M., Goldmacher, V. S., and Chari, R. V. J. (2002) Tumor-specific novel taxoid-monoclonal antibody conjugates. *J. Med. Chem. 45*, 5620–5623.

(20) Ranson, M., and Sliwkowski, M. X. (2002) Perspectives on anti-HER monoclonal antibodies. *Oncology 63* (suppl. 1), 17–24.

(21) Widdison, W. C., Wilhelm, S. D., Cavanagh, E. E., Whiteman, K. R., Leece, B. A., Kovtun, Y., Goldmacher, V. S., Xie, H., Steeves, R. M., Lutz, R. J., Zhao, R., Wang, L., Blättler, W. A., and Chari, R. V. J. (2006) Semisynthetic maytansine analogues for the targeted treatment of cancer. *J. Med. Chem. 49*, 4392–4408.

(22) Erickson, H. K., Park, P. U., Widdison, W. C., Kovtun, Y. V., Garrett, L. M., Hoffman, K., Lutz, R. J., Goldmacher, V. S., and Blättler, W. A. (2006) Antibody-Maytansinoid conjugates are activated in targeted cancer cells by lysosomal degradation and linker-dependent intracellular processing. *Cancer Res. 66*, 4426–4433.

(23) Kovtun, Y. V., Audette, C. A., Ye, Y., Xie, H., Ruberti, M. F., Phinney, S. J., Leece, B. A., Chittenden, T., Blättler, W. A., and Goldmacher, V. S. (2006) Antibody-drug conjugates designed to eradicate tumors with homogeneous and heterogeneous expression of the target antigen. *Cancer Res. 66*, 3214–3221.

(24) Xie, H., Audette, C., Hoffee, M., Lambert, J. M., and Blättler, W. A. (2004) Pharmacokinetics and biodistribution of the antitumor immunoconjugate, cantuzumab mertansine (huC242-DM1), and its two components in mice. *J. Pharmacol. Exp. Ther. 308*, 1073–1082.

(25) Koblinski, J. E., Ahram, M., and Sloane, B. F. (2000) Unraveling the role of proteases in cancer. *Clin. Chim. Acta 291*, 113–135.

(26) Doronina, S. O., Toki, B. E., Torgov, M. Y., Mendelsohn, B. A., Cerveny, C. G., Chace, D. F., DeBlanc, R. L., Gearing, R. P., Bovee, T. D., Siegall, C. B., Francisco, J. A., Wahl, A. F., Meyer, D. L., and Senter, P. D. (2003) Development of potent monoclonal antibody auristatin conjugates for cancer therapy. *Nat. Biotechnol. 21*, 778–784.

(27) Toki, B. E., Cerveny, C. G., Wahl, A. F., and Senter, P. D. (2002) Protease-mediated fragmentation of *p*-amidobenzyl ethers: A new strategy for the activation of anticancer prodrugs. *J. Org. Chem. 67*, 1866–1872.

(28) Sanderson, R. J., Hering, M. A., James, S. F., Sun, M. M. C., Doronina, S. O., Siadak, A. W., Senter, P. D., and Wahl, A. F. (2005) In vivo drug-linker stability of an anti-CD30 dipeptide-linked auristatin immunoconjugate. *Clin. Cancer Res. 11*, 843–852.

(29) Francisco, J. A., Cerveny, C. G., Meyer, D. L., Mixan, B. J., Klussman, K., Chace, D. F., Rejniak, S. X., Gordon, K. A., DeBlanc, R., Toki, B. E., Law, C.-L., Doronina, S. O., Siegall, C. B., Senter, P. D., and Wahl, A. F. (2003) cAC10-vcMMAE, an anti-CD30-monomethyl auristatin E conjugate with potent and selective antitumor activity. *Blood 102*, 1458–1465.

(30) Bartlett, N., Forero-Torres, A., Rosenblatt, J., Fanale, M., Horning, S. J., Thompson, S., Sievers, E. L., and Kennedy, D. A. (2009) Complete remissions with weekly dosing of SGN-35, a novel antibody-dug conjugate (ADC) targeting CD30, in phase I dose-escalation study in patients with relapsed or refractory Hodgkin lymphoma (HL) or systemic anaplastic large cell lymphoma (sALCL). *J. Clin. Oncol. 27*, 8500.

(31) Doronina, S. O., Bovee, T. D., Meyer, D. W., Miyamoto, J. B., Anderson, M. E., Morris-Tilden, C. A., and Senter, P. D. (2008) Novel peptide linkers for highly potent antibody-auristatin conjugate. *Bioconjugate Chem. 19*, 1960–1963.

(32) Jeffrey, S. C., Nguyen, M. T., Andreyka, J. B., Meyer, D. L., Doronina, S. O., and Senter, P. D. (2006) Dipeptide-based highly potent doxorubicin antibody conjugates. *Bioorg. Med. Chem. Lett. 16*, 358–362.

(33) Boger, D. L., Boyce, C. W., Garbaccio, R. M., Searcey, M., and Jin, Q. (1999) CBI prodrug analogs of CC-1065 and the duocarmycins. *Synthesis* 1505–1509, and references cited therein.

(34) Nagamura, S., Kanda, Y., Kobayashi, E., Gomi, K., and Saito, H. (1995) Synthesis and antitumor activity of duocarmycin derivatives. *Chem. Pharm. Bull. 43*, 1530–1535.

(35) Baird, R., and Winstein, S. (1963) Neighboring carbon and hydrogen. LI. Dienones from $Ar_1\theta-3$ participation. Isolation and behavior of spiro(2,5)octa-1,4-diene-3-one. *J. Am. Chem. Soc. 85*, 567–578.

(36) Wang, Y., Li, L., Tian, Z., Jiang, W., and Larrick, J. W. (2006) Synthesis and antitumor activity of CBI-bearing ester and carbamate prodrugs of CC-1065 analogue. *Bioorg. Med. Chem. 14*, 7854–7861.

(37) Chen, L., Gangwar, S., Guerlavais, V., Lonberg, N., Zhang, Q. Chemical linkers with single amino acids and conjugates thereof, international patent application, WO 2008/103693 A2.

(38) Longberg, N. (2008) Medarex '2008 R&D Day', New York City.

(39) Tietze, L. F., Feuerstein, T., Fecher, A., Haunert, F., Panknin, O., Borchers, U., Schuberth, I., and Alves, F. (2002) Proof of principle in the selective treatment of cancer by antibody-directed enzyme prodrug therapy: The development of a highly potent prodrug. *Angew. Chem., Int. Ed. 41*, 759–761.

(40) Tietze, L. F., Herzig, T., Feuerstein, T., and Schuberth, I. (2002) Synthesis and biological evaluation of novel analogues and prodrugs of the cytotoxic antibiotic CC-1065 for selective cancer therapy. *Eur. J. Org. Chem.* 1634–1645.

(41) Tietze, L. F., Major, F., Schuberth, I., Spiegl, D. A., Krewer, B., Maksimenka, K., Bringmann, G., and Magull, J. (2007) Selective treatment of cancer: Synthesis, biological evaluation and structural elucidation of novel analogues of the antibiotic CC-1065 and the duocarmycins. *Chem.—Eur. J. 13*, 4396–4409.

(42) Beusker, P. H., de Groot, F. M. H., Tietze, L. F., Major, F., Joosten, J. A. F., Spijker, H. J. Water-soluble CC-1065 analogs and their conjugates, international patent application, WO 2007/089149 A2.

(43) Jeffrey, S. C., Torgov, M. Y., Andreyka, J. B., Boddington, L., Cerveny, C. G., Denny, W. A., Gordon, K. A., Gustin, D., Haugen, J., Kline, T., Nguyen, M. T., and Senter, P. D. (2005) Design, synthesis, and in vitro evaluation of dipeptide-based antibody minor groove binder conjugates. *J. Med. Chem. 48*, 1344–1358.

(44) Jeffrey, S. C., Nguyen, M. T., Moser, R. F., Meyer, D. L., Miyamoto, J. B., and Senter, P. D. (2007) Minor groove binder antibody conjugates employing a water soluble β-glucuronide linker. *Bioorg. Med. Chem. Lett. 17*, 2278–2280.

(45) Burke, P. J., Senter, P. D., Meyer, D. W., Miyamoto, J. B., Anderson, M., Toki, B. E., Manikumar, G., Wani, M. C., Kroll, D. J., and Jeffrey, S. C. (2009) Design, synthesis, and biological evaluation of antibody-drug conjugates comprised of potent Camptothecin analogues. *Bioconjugate Chem. 20*, 1242–1250.

(46) Chari, R. V. J. (2008) Targeted cancer therapy: Conferring specificity to cytotoxic drugs. *Acc. Chem. Res. 41*, 98–107.

(47) Polson, A. G., Calemine-Fenaux, J., Chan, P., Chang, W., Christensen, E., Clark, S., de Sauvage, F. J., Eaton, D., Elkins, K., Elliott, J. M., Frantz, G., Fuji, R. N., Gray, A., Harden, K., Ingle, G. S., Kljavin, N. M., Koeppen, H., Nelson, C., Prabhu, S., Raab, H., Ross, S., Stephan, J.-P., Scales, S. J., Spencer, S. D., Vandlen, R., Wranik, B., Yu, S.-F., Zheng, B., and Ebens, A. (2009) Antibody-drug conjugates for the treatment of non-Hodgkin's lymphoma: Target and linker-drug selection. *Cancer Res. 69*, 2358–2364.

(48) Vogel, C. L., Burris, H. A., Limentani, S., Borson, R., O'Shaughnessy, J., Vukelja, S., Agresta, S., Klencke, B., Birkner, M., and Rugo, H. (2009) A phase II study of trastuzumab-DM1 (T-DM1), a HER2 antibody-drug conjugate (ADC), in patients (pts) with HER2+ metastatic breast cancer (MBC): Final results. *J. Clin. Oncol.* 27:15s (suppl; abstr 1017).

(49) Doronina, S. O., Mendelsohn, B. A., Bovee, T. D., Cerveny, C. G., Alley, S. C., Meyer, D. L., Oflazoglu, E., Toki, B. E., Sanderson, R. J., Zabinski, R. F., Wahl, A. F., and Senter, P. D. (2006) Enhanced activity of monomethylauristatin F through monoclonal antibody delivery: Effects of linker technology on efficacy and toxicity. *Bioconjugate Chem. 17*, 114–124.

(50) Alley, S. C., Benjamin, D. R., Jeffrey, S. C., Okeley, N. M., Meyer, D. L., Sanderson, R. J., and Senter, P. D. (2008) Contribution of linker stability to the activities of anticancer immunoconjugates. *Bioconjugate Chem. 19*, 759–765.

BC9002019

COMMUNICATIONS

Binding Affinity and Kinetic Analysis of Targeted Small Molecule-Modified Nanoparticles

Carlos Tassa, Jay L. Duffner, Timothy A. Lewis, Ralph Weissleder, Stuart L. Schreiber, Angela N. Koehler, and Stanley Y. Shaw*

Center for Systems Biology Massachusetts General Hospital and Harvard Medical School, Boston, Massachusetts, Broad Institute of Harvard and MIT, Cambridge, Massachusetts, and Howard Hughes Medical Institute Department of Chemistry and Chemical Biology, Harvard University, Cambridge, Massachusetts. Received October 7, 2009; Revised Manuscript Received November 9, 2009

Nanoparticles bearing surface-conjugated targeting ligands are increasingly being explored for a variety of biomedical applications. The multivalent conjugation of targeting ligands on the surface of nanoparticles is presumed to enhance binding to the desired target. However, given the complexities inherent in the interactions of nanoparticle surfaces with proteins, and the structural diversity of nanoparticle scaffolds and targeting ligands, our understanding of how conjugation of targeting ligands affects nanoparticle binding remains incomplete. Here, we use surface plasmon resonance (SPR) to directly and quantitatively study the affinity and binding kinetics of nanoparticles that display small molecules conjugated to their surface. We studied the interaction between a single protein target and a structurally related series of targeting ligands whose intrinsic affinity varies over a 4500-fold range and performed SPR at protein densities that reflect endogenous receptor densities. We report that even weak small molecule targeting ligands can significantly enhance target-specific avidity (by up to 4 orders of magnitude) through multivalent interactions and also observe a much broader range of kinetic effects than has been previously reported. Quantitative measurement of how the affinity and kinetics of nanoparticle binding vary as a function of different surface conjugations is a rapid, generalizable approach to nanoparticle characterization that can inform the design of nanoparticles for biomedical applications.

Targeted nanoparticles are an exciting class of materials that are undergoing clinical development as diagnostics, molecular imaging probes, and therapeutic delivery vehicles (*1*). Targeting is typically achieved through the surface display of multiple high affinity ligands, such as antibodies, peptides, or natural products. Multivalent interactions between the nanoparticles and their targets can increase the affinity of target binding (avidity) (*2*), much as multivalency in Nature facilitates the attachment of pathogens to host cells, or circulating cells to vascular endothelium (*3, 4*). More recently, investigators have used synthetic, non-natural product small molecules as targeting ligands on the surface of nanoparticles (*5, 6*). This approach allows a much more diverse range of chemical matter to be used for targeting and enables libraries of small molecule modified nanoparticles to be rapidly screened for the desired binding properties. Non-natural product small molecules generally have much weaker affinity for their targets (e.g., micromolar K_D), so their use as targeting ligands assumes that multivalent avidity effects will enhance the binding affinity. This notion is supported by the observation that multivalency enhances the avidity as well as recognition specificity of weak interactions between carbohydrates and their protein partners (*7–9*) and increases the biologic activity of a weakly binding therapeutic (*10*). However, given the complexities inherent in interactions of nanoparticle surfaces with proteins (*11, 12*), we sought to develop an approach that could quantitatively describe the binding of a surface-conjugated nanoparticle to its target, and that was sufficiently rapid and generalizable to be widely applicable to the development and characterization of targeted nanoparticles.

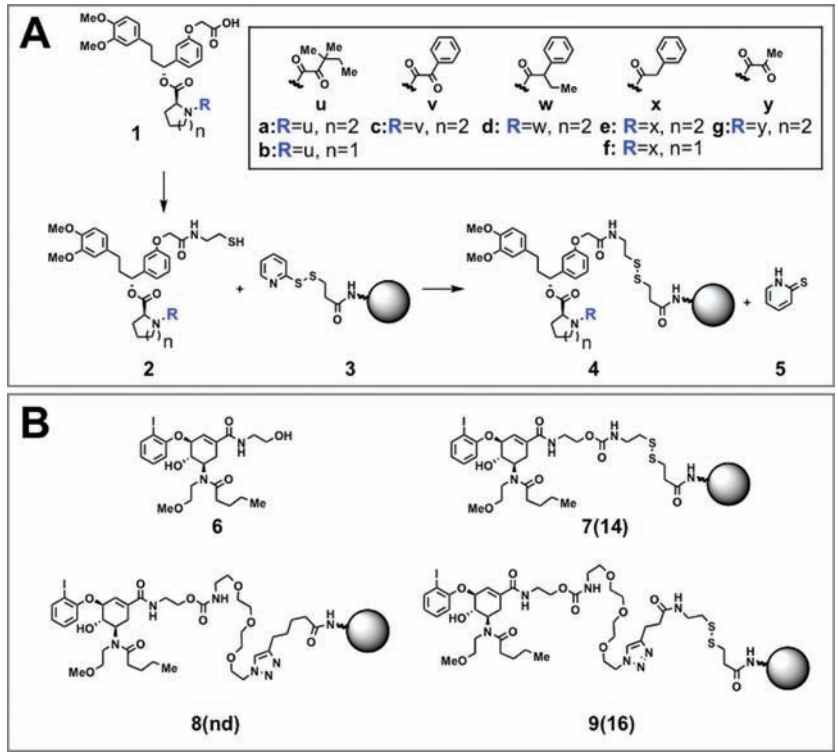
Here, we use surface plasmon resonance (SPR) to directly and systematically study the affinity and binding kinetics (*13*) of nanoparticles that display targeting small molecules conjugated to their surface. To enable direct comparisons, we study a series of structurally related ligands to the same protein, whose intrinsic K_D varies over a 4500-fold range. Importantly, we perform SPR measurements at target protein densities that are comparable to those reported for known cellular targets. These studies demonstrate that even weak small molecule ligands can increase the avidity of nanoparticle target interactions, but also reveal unanticipated effects on binding kinetics. As targeted nanomaterials move toward clinical application, a quantitative understanding of the structure−activity relationships underlying their avidity and kinetics would inform the future design of targeted nanoparticles.

We chose the well-studied interaction between synthetic derivatives of the natural product FK506 and its target protein, FK506-binding protein 12 (FKBP12). A series of structurally related synthetic FK506 analogues possessing K_Ds that range from 24 nM to 110 μM (*14*) (Scheme 1A) were individually conjugated to a dextranated magnetic nanoparticle (cross-linked iron oxide, or CLIO) originally developed for MR imaging (*15*)

* Corresponding author. Stanley Y. Shaw Simches Research Center, 185 Cambridge St., Boston, MA 02114. Fax: 617-643-6133, E-mail: shaw.stanley@mgh.harvard.edu.

10.1021/bc900438a © 2010 American Chemical Society
Published on Web 12/22/2009

Scheme 1. Conjugation of Small Molecules to Nanoparticles[a]



[a] A. Conjugation of a series of synthetic derivatives of FK506 (**1**) by sulfhydryl exchange. B. Small molecule that binds aurora A kinase (**6**) and nanoparticle conjugates obtained by sulfhydryl exchange and Huisgen 1,3-dipolar cycloaddition.

and biosensor applications (*16*). This nanoparticle has a diameter of approximately 38 nm in aqueous solutions. We conjugated small molecule ligands to sulfhydryl reactive groups on the nanoparticle using sulfhydryl exchange, and ultraviolet quantitation of the amount of released pyridine-2-thione (**5**) allowed calculation of the average number of small molecules conjugated to each nanoparticle (*17*) (Scheme 1A). (For ligands of class **1**, our conjugation linkers utilized the same carboxylic acid moiety that has been previously used to modify this class of compounds while preserving their affinity for FKBP12 (*18–21*).) Nanoparticles with low and high small molecule valency (approximately 3−5 vs 13−18 small molecules per nanoparticle, respectively) were selected for further study; the number of small molecules conjugated per nanoparticle is depicted in parentheses (e.g., **4a(17)** corresponds to particle **4a** with 17 conjugated small molecules).

Binding of small molecule conjugated nanoparticles to their target protein is specific and exquisitely sensitive to the density of protein immobilized onto the SPR sensor chip. Since our target protein is immobilized to the sensor chip as an FKBP12-GST (glutathione S-transferase) fusion protein, we tested nanoparticles for nonspecific binding to GST and saw no binding to either unmodified or small molecule conjugated nanoparticles (Figure 1A,B). In contrast, at protein densities commonly used for SPR experiments, targeted nanoparticles remain bound to an FKBP12-GST surface (hereafter called an FKBP12 surface) with no appreciable dissociation even after more than 12 min (Figure 1C). At lower protein densities (e.g., 100 response units, corresponding to approximately 1 protein per 648 nm^2), we observe a measurable (but still slow) off-rate that allows calculation of dissociation kinetics (Figure 1C). Of note, this low protein density is still the same order of magnitude at which physiologically relevant receptors are expressed on cell surfaces. For instance, the HER2 receptor is expressed in SKBR-3 breast cancer cells at a density of $\sim 1 \times 10^6$ receptors per cell (*22*); assuming a single-sided disk 15 μm in diameter, this corresponds to a HER2 receptor every 707 nm^2. An analogous calculation for folate receptors on KB cells ($\sim 2.5 \times 10^6$ receptors per cell (*23*)) corresponds to a receptor every 283 nm^2.

We measured the association rate k_a, dissociation rate k_d, and dissociation constant K_D (k_d/k_a) for the interaction of FKBP12 with each small molecule (**1a**−**1g**), as well as with those same small molecules conjugated to CLIO nanoparticles (**4a**−**4g**) (Scheme 1A). For each experiment, small molecules or nanoparticles were flowed in parallel over a reference sensor bearing GST (see Supporting Information); the minimal signal arising from GST interaction is then subtracted out to yield SPR tracings that reflect specific interactions with FKBP12 (Figure 1D,E). Small molecule and nanoparticle sensorgrams were analyzed with a Langmuir 1:1 binding kinetic analysis, using software provided by the instrument manufacturer (Biacore). $K_{D(free)}$ for all free ligands are in excellent agreement with previously published values, ranging from 24 nM to 110 μM (Table 1). By comparison, the conjugated nanoparticles show profound changes in both association and dissociation kinetics, with only the weakest free ligand, compound **1g**, failing to bind FKBP12 when conjugated to a nanoparticle. As expected, k_d for the multivalent nanoparticles are all markedly decreased relative to the corresponding free ligand (up to 3400-fold slower for **4a(17)** vs **1a**). (Dissociation of FKBP12-GST from the surface is negligible during the time course of these experiments; see Supporting Information.) In contrast, k_a for different nanoparticles show widely divergent effects. For instance, nanoparticle **4a(17)** has a 400-fold slower k_a compared to the free ligand **1a**, while nanoparticle **4f(20)** has a 39-fold faster k_a compared to the free ligand **1f**.

$K_{D(multivalent)}$ (calculated from k_d and k_a) for all of the nanoparticles is in the single digit nanomolar range. To relate $K_{D(multivalent)}$ to $K_{D(free)}$ in cases where the precise number of ligand−target interactions is not known, Whitesides and colleagues defined an enhancement factor β, which increases as the relative affinity of a multivalent interaction increases: $\beta =$

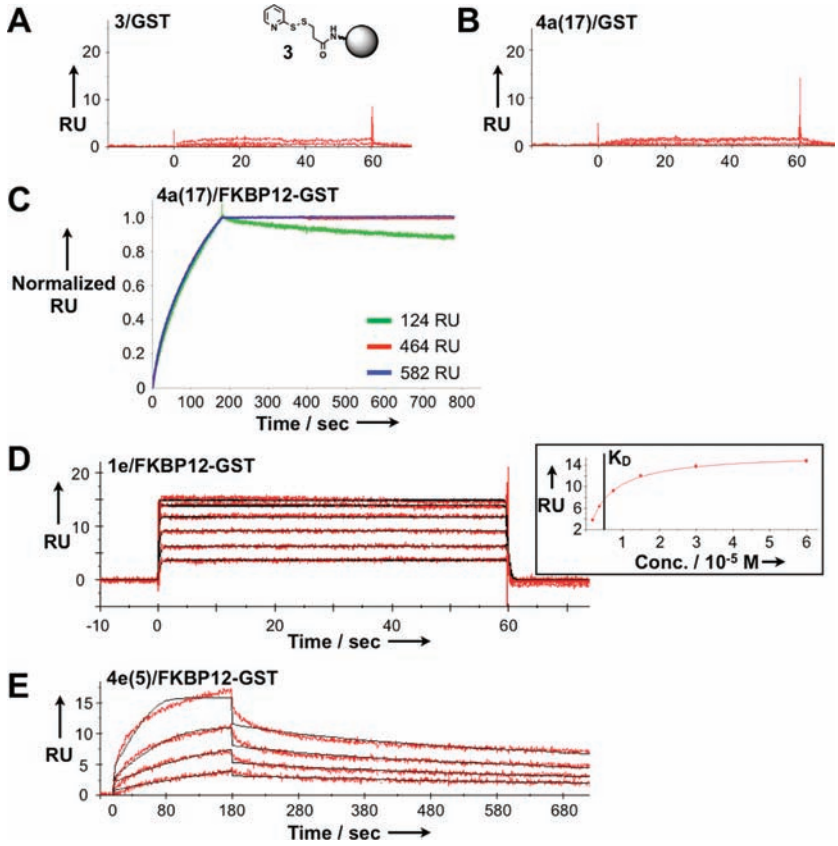


Figure 1. Specific protein−nanoparticle binding documented in SPR sensorgrams. A. Nanoparticle intermediate **3** does not bind to a control surface of GST. B. Targeted nanoparticle **4a(17)** does not bind to a GST surface. C. Sensorgrams for targeted nanoparticle **4a(17)** at different immobilization densities of FKBP12-GST. Significant binding occurs; appreciable dissociation only occurs at the lowest protein density tested. D. Representative sensorgram for a free small molecule (**1e**) flowed over an FKBP12-GST surface. Inset: Depiction of calculating K_D from steady-state affinity studies. E. Representative sensorgram for multivalent nanoparticle **4e(5)**. In parts D and E, red curves depict experimental data at different analyte concentrations; fitted curves modeled to describe a 1:1 binding event are overlaid in black.

Table 1. Equilibrium Affinity and Rate Constants Derived from a Langmuir 1:1 Binding Kinetic Analysis[a]

analyte (valency)	k_a (M^{-1} s^{-1})	k_d (s^{-1})	K_D (M) multivalent	β	K_D (M) ligand	χ^2 (RU^2)
1a	2.31×10^7	0.557	--	--	2.41×10^{-8}	0.11
4a(5)	4.88×10^4	2.78×10^{-4}	5.68×10^{-9}	4	--	0.45
4a(17)	5.76×10^4	1.64×10^{-4}	2.84×10^{-9}	8	--	0.60
1b	1.04×10^6	0.812	--	--	7.85×10^{-7}	0.17
4b(4)	6.64×10^5	2.86×10^{-3}	4.30×10^{-9}	182	--	0.17
4b(9)	6.62×10^5	2.08×10^{-3}	3.14×10^{-9}	250	--	0.40
1c	1.11×10^6	0.117	--	--	1.05×10^{-7}	0.37
4c(4)	1.13×10^5	7.64×10^{-4}	6.77×10^{-9}	16	--	0.29
4c(13)	1.21×10^5	3.58×10^{-4}	2.96×10^{-9}	36	--	0.33
1d	1.70×10^4	0.0500	--	--	2.94×10^{-6}	0.29
4d(6)	2.19×10^5	1.62×10^{-3}	7.39×10^{-9}	398	--	0.05
1e	5.23×10^5	2.67	--	--	5.11×10^{-6}	0.35
4e(5)	3.46×10^5	2.15×10^{-3}	6.20×10^{-9}	824	--	0.19
4e(18)	7.29×10^5	4.43×10^{-3}	6.09×10^{-9}	840	--	0.26
1f	5.62×10^4	2.21	--	--	3.94×10^{-5}	0.61
4f(20)	2.17×10^6	9.01×10^{-3}	4.15×10^{-9}	9498	--	0.72
1g	1.90×10^4	2.08	--	--	1.10×10^{-4}	0.58
6	1.79×10^4	0.0775	--	--	4.33×10^{-6}	0.37
8(nd)	2.13×10^6	8.32×10^{-3}	3.91×10^{-9}	1107	--	0.64
9(16)	4.20×10^5	3.82×10^{-3}	9.08×10^{-9}	477	--	0.58

[a] Corresponding groups of free ligand and conjugated nanoparticles are listed in alphabetical order (**a**−**g**). Nanoparticle names have the measured number of small molecules conjugated per nanoparticle (valency) in parentheses. $\beta = K_{D(free)}/K_{D(multivalent)}$. Valency was not determined for nanoparticle **8(nd)**.

$K_{D(free)}/K_{D(multivalent)}$ (*3*). For the multivalent nanoparticles tested here, β ranges from approximately 4 to 9500; the largest β is for ligand **1f**, with a K_D of 39 μM as a free ligand and a $K_{D(multivalent)}$ of 4.15 nM as nanoparticle **4f(20)**. Thus, nanoparticles bearing ligands with weak intrinsic affinity demonstrate greater β and increased affinity (avidity).

The rate map in Figure 2 graphically summarizes several features of the data: (i) A series of multivalent nanoparticles, all binding to the same protein target with approximately the same $K_{D(multivalent)}$, can nonetheless display markedly different kinetics. (ii) Conjugating free ligands (open symbols) to form the corresponding multivalent nanoparticles (closed symbols) has dramati-

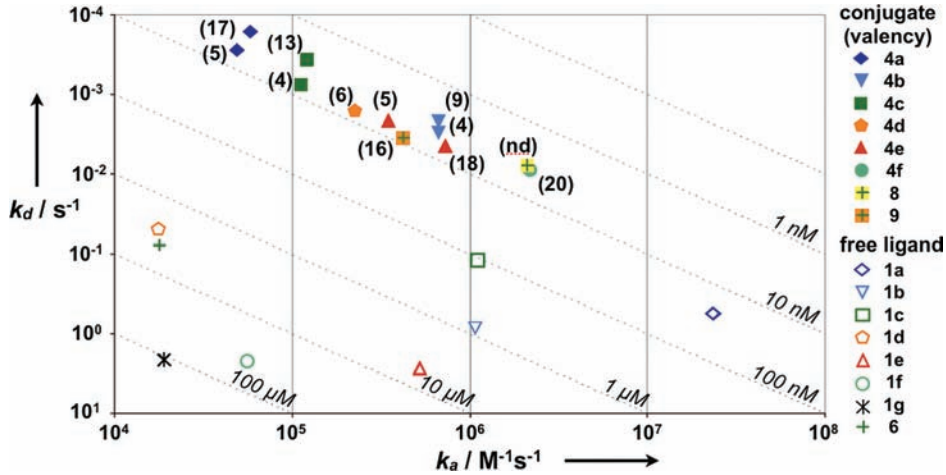


Figure 2. Rate maps summarizing binding affinity and kinetics. Different combinations of k_a and k_d that result in the same K_D are indicated by dashed lines. Data for free ligands are depicted by open symbols; for each ligand, the corresponding nanoparticles are depicted by a solid symbol of the same shape, with conjugation valency listed in parentheses next to the solid symbol. Valency of **8(nd)** was not determined.

Table 2. Equilibrium Affinity and Rate Constants Derived from a Tertiary Interaction (Bivalent) Kinetic Analysis[a]

analyte	k_{a1} (M^{-1} s^{-1})	k_{d1} (s^{-1})	k_{a2} (M^{-1} s^{-1})[b]	k_{d2} (s^{-1})	K_{D1} (M)	K_{D2} (M)	K_{D1}/K_{D2}	χ^2 (RU^2)
4a(5)	2.61×10^4	3.41×10^{-4}	4.88×10^4	0.106	1.31×10^{-8}	2.17×10^{-6}	6.03×10^{-3}	0.40
4a(17)	3.15×10^4	2.31×10^{-4}	1.03×10^5	0.109	7.33×10^{-9}	1.06×10^{-6}	6.91×10^{-3}	0.44
4b(4)	7.88×10^4	2.33×10^{-2}	2.70×10^4	1.23×10^{-3}	2.95×10^{-7}	4.69×10^{-8}	6.28E+00	0.08
4b(9)	2.17×10^5	3.09×10^{-3}	8.35×10^3	6.43×10^{-6}	1.42×10^{-8}	7.70×10^{-10}	1.84×10^1	0.3
4c(4)	2.95×10^4	7.99×10^{-4}	2.09	1.17×10^{-3}	2.71×10^{-8}	5.62×10^{-4}	4.82×10^{-5}	0.37
4c(13)	5.95×10^4	3.67×10^{-4}	5.26	1.04×10^{-3}	6.16×10^{-9}	1.98×10^{-4}	3.11×10^{-5}	0.35
4d(6)	6.10×10^4	3.98×10^{-2}	8.05×10^4	3.92×10^{-4}	6.52×10^{-7}	4.87×10^{-9}	1.33×10^2	0.05
4e(5)	2.24×10^4	3.49×10^{-2}	6.55×10^3	4.64×10^{-4}	1.56×10^{-6}	7.08×10^{-8}	2.20×10^1	0.08
4e(18)	4.66×10^4	3.91×10^{-2}	7.26×10^3	6.93×10^{-4}	8.39×10^{-7}	9.55×10^{-8}	8.78	0.11
4f(20)	1.62×10^5	1.56×10^{-1}	6.41×10^3	1.75×10^{-3}	9.63×10^{-7}	2.73×10^{-7}	3.52	0.27
9(16)	1.89×10^4	2.57×10^{-3}	1.91×10^3	1.30×10^{-5}	1.36×10^{-7}	6.84×10^{-9}	1.99×10^1	0.34

[a] Bivalent interactions between A (analyte) and B (immobilized ligand) are described by the following equations: (1) A + B $\leftrightarrows$ AB (with rate constants k_{a1} and k_{d1}, and $K_{D1} = k_{d1}/k_{a1}$), (2) AB + B $\leftrightarrows$ AB_2 (with rate constants k_{a2} and k_{d2}, and $K_{D2} = k_{d2}/k_{a2}$). [b] k_{a2} (RU^{-1} s^{-1}) was converted approximately to k_{a2} (M^{-1} s^{-1}) as follows: k_{a2} (M^{-1} s^{-1}) = k_{a2} ($RU^{-1}s^{-1}$) × MW × 100.

cally diverse effects on interaction kinetics; $k_{d(multivalent)}$ decreases to a variable extent, and $k_{a(multivalent)}$ can increase, decrease, or remain largely unchanged. (iii) Under the tested protein densities, adding more small molecule ligands to each nanoparticle has a modest effect on both kinetics and affinity.

We also extended our analysis to a relatively uncharacterized synthetic small molecule screening "hit". Compound **6** (Scheme 1B), discovered through a biochemical affinity screen, binds aurora A kinase with $K_{D(free)} = 4\ \mu M$ (*24*). We conjugated **6** to CLIO using sulfhydryl exchange (conjugates **7(14)** and **9(16)**) or Cu(I)-catalyzed Huisgen 1,3-dipolar cycloaddition ("click" chemistry, conjugate **8**) (Scheme 1B). (Conjugation of **6** to CLIO utilized the same primary alcohol that was used to immobilize **6** in the affinity screen that led to its discovery (*19, 24*).) Nanoparticle **7(14)** does not bind to immobilized aurora A kinase (data not shown). In contrast, nanoparticles **9(16)** (with a similar but longer linker than the inactive **7(14)**) and **8** both show significantly increased avidity, with $K_{D(multivalent)} = 9$ and 4 nM, and $\beta = 480$ and 1100, respectively (Table 1 and Figure 2). Thus, in this second model system, multivalent attachment of a weakly binding screening "hit" results in large β factors and enhanced avidity toward the compound's target. The rate map in Figure 2 illustrates how different methods of conjugating the same molecule (e.g., in nanoparticles **9(16)** and **8**) can result in significantly divergent effects on binding kinetics (especially with regard to k_a) (Figure 2).

Because it is not possible to precisely determine the number of interactions each nanoparticle makes with immobilized ligands, all of the above sensorgrams used a simple binary interaction model (similar to one used for other nanoparticle studies (*23*); full details in Supporting Information). In fact, a binary model fits the data quite well with very small residual differences (between experimental and fitted curves; residual curves are shown in Supporting Information) and small χ^2 values (minimized sum of the squared residual difference). This is consistent with our choice of relatively sparse protein densities to mimic physiologic receptor densities. To estimate the contribution of higher-order interactions, we reanalyzed the data using a tertiary interaction model (i.e., corresponding to a bivalent interaction between the nanoparticle and protein) as follows (the full binding model is described in Supporting Information):

(1) A + B $\leftrightarrows$ AB (with rate constants k_{a1} and k_{d1}, and $K_{D1} = k_{d1}/k_{a1}$)

(2) AB + B $\leftrightarrows$ AB_2 (with rate constants k_{a2} and k_{d2}, and $K_{D2} = k_{d2}/k_{a2}$).

For the conjugated nanoparticles **4a**−**4f** and **9**, the ratio of K_{D1}/K_{D2} correlates with $K_{D(ligand)}$, the dissociation constant for the free ligand ($R^2 = 0.57$; Table 2 and Figure 3A). That is, the bivalent mode of binding contributes more to the overall nanoparticle interaction (greater K_{D1}/K_{D2} ratio) for nanoparticles bearing ligands of weaker intrinsic affinity (larger $K_{D(ligand)}$). This is consistent with our finding that nanoparticles bearing weaker ligands also exhibit the greatest β and enhancement of avidity. Interestingly, the avidity effect for weaker ligands appears to be mediated primarily by the dissociation rate of the bivalent interaction. The dissociation constant for the free ligand ($K_{D(ligand)}$) shows a strong correlation with k_{d1}/k_{d2} ($R^2 = 0.76$; for weaker free ligands, $k_{d1} \gg k_{d2}$) but no correlation with k_{a1}/k_{a2} ($R^2 = 0.01$) (Table 2 and Figure 3B,C). While it is uncertain

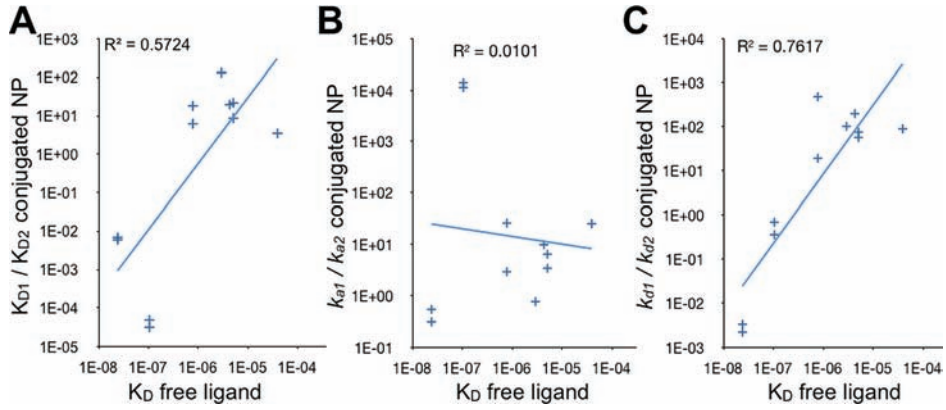


Figure 3. Relative contribution of monovalent vs bivalent reaction terms to nanoparticle binding as a function of the intrinsic K_D of the free ligand. A. As the intrinsic affinity of the free ligand becomes weaker, K_{D1}/K_{D2} increases ($R^2 = 0.57$). B. No correlation between k_{a1}/k_{a2} and intrinsic affinity of the free ligand. C. As the intrinsic affinity of the free ligand becomes weaker, k_{d1}/k_{d2} increases ($R^2 = 0.76$).

whether the nanoparticles interact through bivalent or higher-order interactions, this analysis confirms that multivalent interactions make important contributions to nanoparticle avidity.

Predicting the structure−activity relationships (SAR) for multivalent ligands has not been straightforward, even for relatively small systems such as dimers of the antibiotic vancomycin (*25*). This problem is exacerbated as functionalized nanoparticles increasingly utilize chemically and structurally diverse scaffolds (e.g., dextranated nanoparticles, dendrimers, albumin, liposomes) and targeting ligands (e.g., antibodies, peptides, aptamers, or low-affinity small molecules). Here, we have performed SPR on relatively sparse but physiologic protein surfaces (*22, 23*) to very sensitively detect how subtle variations in targeting ligands can affect binding kinetics and affinity. Our target protein densities are approximately 100-fold sparser than those used to document very large avidity effects for folate-targeted dendrimers (*23*), and our findings provide a complementary view of avidity at a distinct, physiologically relevant regime of protein concentrations. Using even slightly denser (e.g., 4-fold) protein surfaces, we observed essentially no dissociation of nanoparticles (Figure 1C), which suggests that our results may underestimate the maximal avidity obtainable with these particles, as well as the contribution of higher ligand valencies. Other factors, such as deformable and fluid membranes that could facilitate close apposition of cellular receptors, could further increase avidity.

We demonstrate strong avidity effects (β of up to 4 orders of magnitude) for nanoparticles conjugated to relatively weak (micromolar K_D) small molecule ligands, including "hits" from a high-throughput screen. We observed a dramatic decrease in k_d for the nanoparticles relative to the free ligand, consistent with other reports (*23*); however, we observed a much wider variety of effects on k_a than has been reported previously, including markedly increased, markedly decreased, or unchanged k_a relative to the free ligands. These unanticipated effects on binding kinetics were revealed because of the deliberate constraints of our experiment (a common protein target, shared nanoparticle scaffold, similar valency, and identical conjugation chemistry), which were imposed to allow detailed comparisons of multivalent binding. The kinetic differences displayed by our series of related functionalized nanoparticles could translate into functional differences. For instance, nanoparticle affinity and association and dissociation rates can all affect how deeply an intravascular circulating agent penetrates into tissue before its target sites become effectively saturated (*26*); the relative contribution of these variables depends on several in vivo factors, including capillary permeability, particle size, and target density.

Overall, this approach can be generalized rapidly to a variety of ligand−target combinations, as it does not require de novo development of a cell-based assay for each target. Systematic application of this approach could reveal principles that guide nanoparticle design. For instance, our studies suggest that a view in which nanoparticles are largely modular assemblies of scaffold, linker, and targeting ligand may be too simplistic; instead, SPR studies could clarify how different structural components collaborate to determine binding kinetics and affinities. Our data also suggest testable hypotheses about how nanoparticles with distinct binding and kinetic properties will behave in complex in vitro and in vivo systems. This in turn has broad implications for the design and synthesis of functionalized nanoparticles for the imaging, diagnosis, and treatment of disease.

ACKNOWLEDGMENT

This work has been supported by the National Institutes of Health, National Heart Lung Blood Institute (HL077186 to S.Y.S., HL80731 to S.Y.S., S.L.S., and R.W.), and National Cancer Institute (CA119349 to R.W.); and the Broad Institute of Harvard and MIT (to S.Y.S., R.W., and S.L.S.). The authors acknowledge Dr. Kara Herlihy for SPR support, and Jason Fuller, Katie Doud, Dr. Ralph Mazitschek, Dr. Eric Yi Sun, Dr. Lee Josephson, Dr. Greg Thurber, Dr. Karl Münger, and Dr. Hiroyuki Hayakawa for reagents and comments.

Supporting Information Available: Experimental procedures, characterization data, and NMR spectra for all novel compounds, as well as sensorgrams for small molecules and nanoparticles.This material is available free of charge via the Internet at http://pubs.acs.org.

LITERATURE CITED

(1) De, M., Ghosh, P. S., and Rotello, V. M. (2008) Applications of nanoparticles in biology. *Adv. Mater. 20*, 4225–4241.
(2) Montet, X., Funovics, M., Montet-Abou, K., Weissleder, R., and Josephson, L. (2006) Multivalent effects of RGD peptides obtained by nanoparticle display. *J. Med. Chem. 49*, 6087–6093.
(3) Mammen, M., Choi, S. K., and Whitesides, G. M. (1998) Polyvalent interactions in biological systems: Implications for design and use of multivalent ligands and inhibitors. *Angew. Chem., Int. Ed. 37*, 2754–2794.
(4) Mulder, A., Huskens, J., and Reinhoudt, D. N. (2004) Multivalency in supramolecular chemistry and nanofabrication. *Org. Biomol. Chem. 2*, 3409–3424.

(5) Weissleder, R., Kelly, K., Sun, E. Y., Shtatland, T., and Josephson, L. (2005) Cell-specific targeting of nanoparticles by multivalent attachment of small molecules. *Nat. Biotechnol. 23*, 1418–1423.

(6) Kelly, K. A., Shaw, S. Y., Nahrendorf, M., Kristoff, K., Aikawa, E., Schreiber, S. L., Clemons, P. A., and Weissleder, R. (2009) Unbiased discovery of *in vivo* imaging probes through *in vitro* profiling of nanoparticle libraries. *Integr. Biol. 1*, 311–317.

(7) Mortell, K. H., Weatherman, R. V., and Kiessling, L. L. (1996) Recognition specificity of neoglycopolymers prepared by ring-opening metathesis polymerization. *J. Am. Chem. Soc. 118*, 2297–2298.

(8) Kiessling, L. L., Gestwicki, J. E., and Strong, L. E. (2000) Synthetic multivalent ligands in the exploration of cell-surface interactions. *Curr. Opin. Chem. Biol. 4*, 696–703.

(9) Carlson, C. B., Mowery, P., Owen, R. M., Dykhuizen, E. C., and Kiessling, L. L. (2007) Selective tumor cell targeting using low-affinity, multivalent interactions. *ACS Chem. Biol. 2*, 119–127.

(10) Bowman, M. C., Ballard, T. E., Ackerson, C. J., Feldheim, D. L., Margolis, D. M., and Melander, C. (2008) Inhibition of HIV fusion with multivalent gold nanoparticles. *J. Am. Chem. Soc. 130*, 6896–6897.

(11) Cedervall, T., Lynch, I., Lindman, S., Berggard, T., Thulin, E., Nilsson, H., Dawson, K. A., and Linse, S. (2007) Understanding the nanoparticle-protein corona using methods to quantify exchange rates and affinities of proteins for nanoparticles. *Proc. Natl. Acad. Sci. U.S.A. 104*, 2050–2055.

(12) Lundqvist, M., Stigler, J., Elia, G., Lynch, I., Cedervall, T., and Dawson, K. A. (2008) Nanoparticle size and surface properties determine the protein corona with possible implications for biological impacts. *Proc. Natl. Acad. Sci. U.S.A. 105*, 14265–14270.

(13) Myszka, D. G. (1997) Kinetic analysis of macromolecular interactions using surface plasmon resonance biosensors. *Curr. Opin. Biotechnol. 8*, 50–57.

(14) Keenan, T., Yaeger, D. R., Courage, N. L., Rollins, C. T., Pavone, M. E., Rivera, V. M., Yang, W., Guo, T., Amara, J. F., Clackson, T., Gilman, M., and Holt, D. A. (1998) Synthesis and activity of bivalent FKBP12 ligands for the regulated dimerization of proteins. *Bioorg. Med. Chem. 6*, 1309–1335.

(15) Nahrendorf, M., Jaffer, F. A., Kelly, K. A., Sosnovik, D. E., Aikawa, E., Libby, P., and Weissleder, R. (2006) Noninvasive vascular cell adhesion molecule-1 imaging identifies inflammatory activation of cells in atherosclerosis. *Circulation 114*, 1504–1511.

(16) Perez, J. M., Josephson, L., O'Loughlin, T., Hogemann, D., and Weissleder, R. (2002) Magnetic relaxation switches capable of sensing molecular interactions. *Nat. Biotechnol. 20*, 816–820.

(17) Zhao, M., Kircher, M. F., Josephson, L., and Weissleder, R. (2002) Differential conjugation of tat peptide to superparamagnetic nanoparticles and its effect on cellular uptake. *Bioconjugate Chem. 13*, 840–844.

(18) MacBeath, G., and Schreiber, S. L. (2000) Printing proteins as microarrays for high-throughput function determination. *Science 289*, 1760–1763.

(19) Bradner, J. E., McPherson, O. M., Mazitschek, R., Barnes-Seeman, D., Shen, J. P., Dhaliwal, J., Stevenson, K. E., Duffner, J. L., Park, S. B., Neuberg, D. S., Nghiem, P., Schreiber, S. L., and Koehler, A. N. (2006) A robust small-molecule microarray platform for screening cell lysates. *Chem. Biol. 13*, 493–504.

(20) Wang, X., Imber, B. S., and Schreiber, S. L. (2008) Small-molecule reagents for cellular pull-down experiments. *Bioconjugate Chem. 19*, 585–587.

(21) Ong, S. E., Schenone, M., Margolin, A. A., Li, X., Do, K., Doud, M. K., Mani, D. R., Kuai, L., Wang, X., Wood, J. L., Tolliday, N. J., Koehler, A. N., Marcaurelle, L. A., Golub, T. R., Gould, R. J., Schreiber, S. L., and Carr, S. A. (2009) Identifying the proteins to which small-molecule probes and drugs bind in cells. *Proc. Natl. Acad. Sci. U.S.A. 106*, 4617–4622.

(22) Nielsen, U. B., Kirpotin, D. B., Pickering, E. M., Drummond, D. C., and Marks, J. D. (2006) A novel assay for monitoring internalization of nanocarrier coupled antibodies. *BMC Immunol. 7*, 24–38.

(23) Hong, S., Leroueil, P. R., Majoros, I. J., Orr, B. G., Baker, J. R. J., and Banaszak Holl, M. M. (2007) The binding avidity of a nanoparticle-based multivalent targeted drug delivery platform. *Chem. Biol. 14*, 107–115.

(24) Miao, H., Tallarico, J. A., Hayakawa, H., Munger, K., Duffner, J. L., Koehler, A. N., Schreiber, S. L., and Lewis, T. A. (2007) Ring-opening and ring-closing reactions of a shikimic acid-derived substrate leading to diverse small molecules. *J. Comb. Chem. 9*, 245–253.

(25) Griffin, J. H., Linsell, M. S., Nodwell, M. B., Chen, Q., Pace, J. L., Quast, K. L., Krause, K. M., Farrington, L., Wu, T. X., Higgins, D. L., Jenkins, T. E., Christensen, B. G., and Judice, J. K. (2003) Multivalent drug design. Synthesis and in vitro analysis of an array of vancomycin dimers. *J. Am. Chem. Soc. 125*, 6517–6531.

(26) Thurber, G. M., Schmidt, M. M., and Wittrup, K. D. (2008) Factors determining antibody distribution in tumors. *Trends Pharmacol. Sci. 29*, 57–61.

BC900438A

ARTICLES

Inhibiting Tumor Growth by Targeting Tumor Vasculature with Galectin-1 Antagonist Anginex Conjugated to the Cytotoxic Acylfulvene, 6-Hydroxylpropylacylfulvene

Ruud P. M. Dings,[†] Emily S. Van Laar,[‡] Melissa Loren,[†] Jeremy Webber,[‡] Yan Zhang,[§] Stephen J. Waters,[‡] John R. MacDonald,[‡] and Kevin H. Mayo*,[†]

Departments of Biochemistry, Molecular Biology, and Biophysics, and Biostatistics Core, University of Minnesota, and MGI PHARMA Inc, Bloomington, Minnesota. Received July 2, 2009; Revised Manuscript Received November 11, 2009

Targeted delivery of therapeutic drugs promises to become the norm to treat cancer. Here, we conjugated the cytotoxic agent 6-hydroxypropylacylfulvene (HPAF) to anginex, a peptide that targets galectin-1, which is highly expressed in endothelial cells of tumor vessels. In a human ovarian cancer model in mice, the conjugate inhibited tumor growth better than equivalent doses of either compound alone. Immunofluorescence on tumor tissue demonstrated that the conjugate, like parent anginex, selectively targeted tumor vasculature and inhibited tumor angiogenesis. Increased activity from the conjugate further suggests that HPAF retains at least some of its normal cytotoxic activity when linked to anginex. More importantly perhaps is the observation that the conjugate abrogates apparent systemic toxicity from treatment with HPAF. This work contributes to the development of tumor vascular targeting agents against cancer in the clinic.

INTRODUCTION

When used at optimal doses, chemotherapeutic agents can result in considerable systemic toxicity. Recently, it was demonstrated in the clinic that chemotherapy at doses below maximally tolerated doses can be very effective when used in combination with the antiangiogenic agent, Avastin (Genentech) (*1*). In fact, a number of antiangiogenic agents have been developed and used in a similar fashion in various preclinical animal models (*2*−*4*). The most promising of these appear to be those that act directly on endothelial cells (EC) (*5*), because they are effective against a broad spectrum of tumors and less prone to induce drug resistance (*5*). Moreover, such EC-specific agents are also being used as tumor targeting moieties to increase specificity of chemotherapeutics (*6*) and to deliver contrast agents for magnetic resonance imaging (MRI) (*7*). For example, the α_v integrin-binding RGD tripeptide has been coupled to the chemotherapeutic drug doxorubicin, and shown in tumor-bearing mice to prolong survival, decrease the optimal effective dose, and reduce toxicity (*6*).

Another EC specific antiangiogenic agent, anginex (*8, 9*), targets galectin-1 (gal-1) (*10*), a cell surface glycan binding protein that is highly upregulated in tumor-activated EC (*10*−*12*). Differential stromal elevation of gal-1 over the tumor parenchyma has been reported in several cancers, including cancer of the breast (*13*), colon (*14*), prostate (*15*), and ovary (*16*). By weakly binding to "carrier protein" plasma fibronectin (*17*), anginex is transported through the cardiovascular system to the tumor vasculature where the peptide binds gal-1 (*10*). Anginex binding to gal-1 disrupts tumor EC adhesion and migration, thereby inducing EC apoptosis and resulting in the inhibition of tumor angiogenesis (*10, 18*). Because gal-1 is likely expressed in most tumor types at relatively high levels, using anginex as a tumor vasculature homing device should be widely applicable.

The acylfulvenes are a semisynthetic class of compounds derived from illudin S, a toxin from the *Omphalotus illudens* mushroom, that demonstrate broad spectrum antitumor activity in studies conducted in vitro and in vivo. Irofulven (MGI-114; 6-hydroxymethylacylfulvene) is a leading member of the acylfulvene analogues and has shown clinical activity against a variety of cancers, either as a monotherapy or in combination with other chemotherapeutic agents (*19*). Similar to other alkylating agents, dose-limiting toxicities, such as myelosuppression, neutropenia, thrombocytopenia, nausea, vomiting, and fatigue, are observed when therapeutic concentrations of irofulven are used in patients (*20, 21*). At higher doses, ocular disturbances and symptoms of renal tubular acidosis have been observed (*20, 21*). Conjugating acylfulvenes to a vascular targeting agent, like anginex, has the potential not only to reduce the chemotherapeutic's toxicity profile and maintain, or even improve, efficacy in the clinic, but also to be employed against a broader spectrum of tumors. In this report, we conjugated an irofulven analogue, 6-hydroxypropylacylfulvene (HPAF) to anginex and investigated the ability of anginex to act as a tumor vasculature homing device. In human tumor xenograft studies, we found that the conjugate indeed targeted the tumor vascu-

* To whom correspondence should be addressed. Dr. K. H. Mayo, Dept. of Biochemistry, 6-155 Jackson Hall, University of Minnesota Health Sciences Center, 321 Church Street, Minneapolis, Minnesota 55455, USA, Phone: 612-625-9968; Fax: 612-624-5121; E-mail: mayox001@tc.umn.edu.

[†] Departments of Biochemistry, Molecular Biology, and Biophysics, University of Minnesota.

[‡] MGI PHARMA Inc.

[§] Biostatistics Core, University of Minnesota.

10.1021/bc900287y © 2010 American Chemical Society
Published on Web 12/18/2009

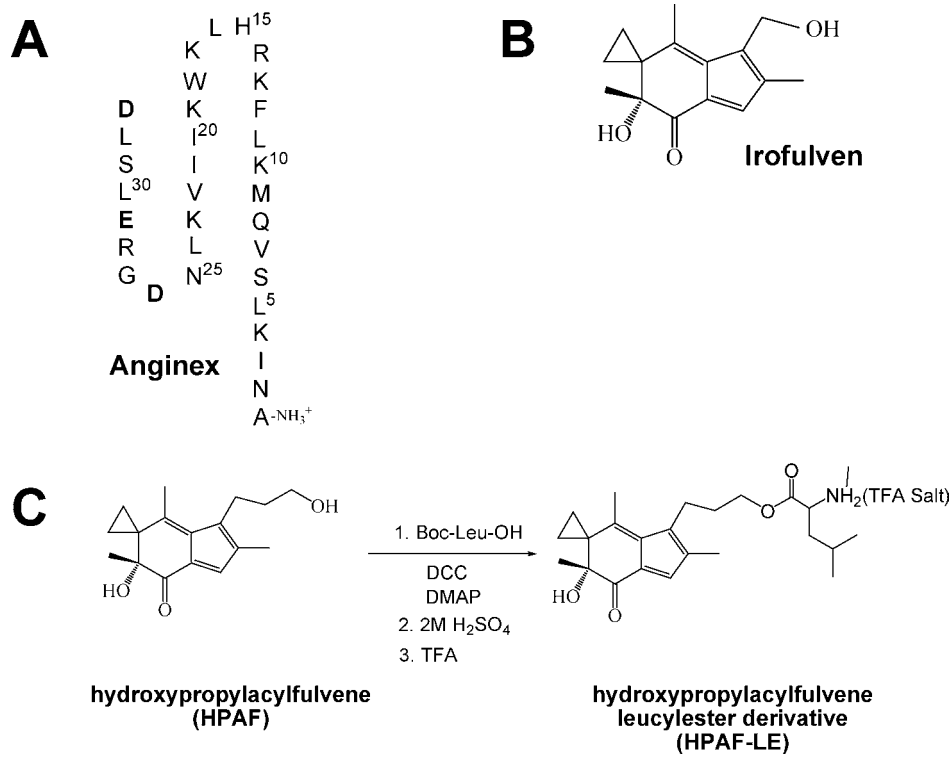


Figure 1. Synthesis of the HPAF-LE-anginex conjugate. (A) The amino acid sequence of anginex with the three possible sites for coupling of HPAF-LE, with the side-chain carboxylates D26, E29, and D33 depicted in bold. (B) The chemical structure of irofulven is shown. (C) Schematic representation of the leucylester derivative of hydoxypropylacylfulvene synthesis, starting with HPAF, is shown.

lature and was more efficacious than either agent alone, without systemic toxicity.

EXPERIMENTAL PROCEDURES

Synthesis of 6-Hydroxypropylacylfulvene Conjugated to Anginex. The irofulven analogue, 6-hydroxypropylacylfulvene, was conjugated to amino acid side-chain carboxylate groups on the peptide anginex (MW = 3941 Da) via a leucyl ester linkage as shown schematically in Figure 1. For convenience, we refer to the leucyl ester derivative of HPAF as HPAF-LE (MW = 380 Da) throughout this paper. Chemical linkage was performed manually using Fmoc chemistry. Coupling was performed by dissolving an excess (1.2 mol equiv) of HPAF in Activator 1 (HATU in DMF). This solution was cooled on ice, and then Activator 2 (DIPEA in DMF) was added. The reaction mixture remained on ice for 5 min before it was added to a solution of anginex and DMF and allowed to react overnight. The next morning, a mixture of acetonitrile and water was added to the reaction mixture, which was then lyophilized.

Because the C-terminal carboxylate of anginex is amidated, there are three possible sites for coupling of HPAF-LE to the anginex side-chain carboxylates: D26, E29, and D33 (Figure 1). To favor coupling to one site per anginex molecule, the molar ratio of HPAF-LE/anginex was adjusted to 1.2:1 during the coupling reaction. Mass spectrometry (MS) analysis on the crude conjugate indicated that the desired products were obtained, with 3941 Da for unreacted anginex and 4353 Da for the 1:1 conjugate. No 2:1 conjugate (4688 Da) was detected.

The crude conjugate was purified by HPLC (CH semiprep column) using a water/ACN gradient running from 25% to 100% ACN. For this procedure, 10 mg of crude material was dissolved in 1 mL ACN/9 mL water, sonicated for 10 min, and centrifuged. Five mL was injected per HPLC run. Although unreacted anginex (about 10% by analytical HPLC) could be separated from the reaction products by HPLC, the three 1:1 (HPAF/anginex) conjugates could not be separated, and biological studies were performed on this mixture of single adduct conjugates.

To prevent possible compound instability, we prepared fresh working solutions on the day of administration. For in vitro studies, the conjugate, e.g., was dissolved in a stock solution of 100% ethanol (30 mg/mL), aliquoted out, and kept frozen at −80 °C. On the day of use, a work solution was prepared by diluting the stock solution in media, such that the ethanol content was reduced to 3% at the highest concentration tested in vitro (20 μM). No decline in activity was observed in repeated experiments, suggesting that the compound was stable when prepared in this fashion. Similarly, in animal studies, the conjugate was made fresh on the initial day of treatment, first dissolved in pure ethanol and then diluted in PBS to reduce ethanol content (3% in the 50 mg/kg and 0.6% in the 10 mg/kg treatment group). To check for degradation, samples were routinely submitted for MS analysis, including following in vitro studies for material remaining in solution.

Antibodies. Antianginex antibody was made and used in our lab as previously described (*10*). Antigal-1 antibodies were purchased from Santa Cruz Biotechnologies, and react with both human and murine galectin-1. Galectin-1 is highly conserved intra- and interspecies, being 90% identical between human and murine amino acid sequences (*26*).

Cell Culture. Human umbilical vein derived EC (HUVEC)[1] were harvested and cultured as described earlier (*22*). Human epithelial ovarian carcinoma MA148, murine melanoma B16F10, and human alveolar epithelial carcinoma A549 cells were cultured, as described previously (*22*−*24*).

Proliferation Assay. HUVEC were seeded in a 96-well culture plate coated with 0.2% gelatin (2 h at 20 °C). MA148

[1]Abbreviations: EC, endothelial cell; HUVEC, human umbilical vein EC; PBS, phosphate buffered saline; BSA, bovine serum albumin; VTA, vascular targeting agent.

cells were seeded in noncoated 96-well plates. Both cell types were seeded at a concentration of 3000 cells per well and allowed to adhere overnight at 37 °C in 5% CO_2/95% air before treatments were initiated. Cells were then exposed to complete medium supplemented with 10 ng/mL bFGF, 0.4% Endo-Gro (VEC technologies Rensselaer, NY), 10 ng/mL VEGF, or 20% FBS, with or without various concentrations of anginex, HPAF, anginex−HPAF conjugate, or gal-1 antibody (1/1000; Santa Cruz Biotechnologies, CA) for 72 h. Cell Counting Kit (CCK-8; Dojindo, Japan) was used to assess cell proliferation rates relative to untreated cells, as described previously (*23, 25*). All measurements were done in triplicate, and each experiment was performed at least three times.

Cell Adhesion Assay. HUVEC suspended in complete medium, with or without anginex-HPAF conjugate or anginex (both 10 μM), were seeded at a concentration of 10 000 cells in a 96-well culture plate as described above and allowed to adhere for 2 h on gelatin (0.2% w/v; 50 μL) or gal-1 (1 mg/mL; 50 μL). Subsequently, the wells were aspirated and washed with PBS carefully to discard the nonadherent cells, and complete media were added to the cells. Cell Counting Kit (CCK-8) was used to calculate the number of adherent cells (*23, 25*). All measurements were done in triplicate, and each experiment was performed at least three times.

MA148 Ovarian Carcinoma Mouse Model. Female athymic nude mice (nu/nu, 5−6 weeks old) were purchased from the National Cancer Institute and allowed to acclimate to local conditions for at least 1 week. Animals were given water and standard chow ad libitum and were kept on a 12 h light/dark cycle. Experiments were approved by the University of Minnesota Research Animal Resources ethical committee. Exponentially growing human ovarian MA148 epithelial carcinoma cells were cultured, harvested, suspended in serum free RPMI (2.0×10^6 cells/mouse), and inoculated subcutaneously (s.c.) into the right flank of the mouse, as described previously (*3, 25*). Studies were carried out in a therapeutic intervention model with established tumors to test the capacity of the conjugate to inhibit or reduce tumor growth. Tumors were allowed to grow to the size of approximately 75 mm^3 prior to randomization and initiation of treatment (all treatments were administered q3d×4 IP in 3% v/v ethanol/PBS). When tumors reached the size of about 1500 mm^3, animals were euthanized as per the approved protocol. As an indirect measurement of general toxicity, body weights of mice were monitored twice weekly, using a digital balance (Ohaus Florham, NJ).

Tumor volume was determined by measuring the size of the tumors on the flanks of the mice. The diameters of tumors were measured using calipers (Scienceware, Pequannock, NJ), and the volume was calculated using the equation to determine the volume of a spheroid: $(a^2 \times b \times \pi)/6$, where a is the width of the tumor and b is the length of the tumor. A complete response was defined as tumor regression to less than 15 mm^3 (3 mm in diameter), and a partial response was defined as a smaller tumor than at the start of treatment. Stable disease was defined as tumor volume less than 100 mm^3.

Immunohistochemistry. We used immunohistochemistry on MA148 tumor tissue from mice to demonstrate that the conjugate, like parent anginex, targets gal-1. For this work, similarly sized tumors were embedded in tissue freezing medium (Miles Inc.; Elkart, IN), snap-frozen in liquid nitrogen, and subsequently cut into 5 μm sections. Preparation and procedures for the frozen tumor sections were performed as described previously, with slight modifications (*23*). Briefly, sections of tissue were fixed for 10 min in acetone, and then incubated for 30 min in PBS/5%BSA/3%FBS to saturate aspecific binding sites. After washing with PBS, the slide was incubated with 10 μg of conjugate per slide, and followed by a washing step, tissue was incubated with antianginex and antigalectin antibodies (1:50) (*10*). Following overnight incubation, slides were washed with PBS and respective secondary antibodies were added: fluorescein isothiocyanate (FITC)-conjugated for conjugate detection and phycoerythrin (PE) for gal-1 detection (Sigma Chemical; St. Louis, MO) (*10*).

Microvessel density was detected using a 1:50 dilution with phycoerythrin (PE)-conjugated antibody to mouse CD-31 (PECAM-1; Pharmingen; San Diego, CA) or FITC conjugated antibody to mouse αSMA (alpha smooth muscle actin; Pharmingen; San Diego, CA) (*24*). A minimum of 10 randomly chosen images per treatment group were acquired using an Olympus BX-60 microscope at 200× magnification and digitally analyzed and differentially quantified by morphometric analysis (*24*).

Statistical Analyses. Tumor volume was analyzed using general linear mixed models (*27*). During the process of model selection, the likelihood ratio test was used to determine random effects and variance−covariance structures. The final general linear mixed model of tumor volume on the original scale contained interaction terms of treatment with both time and time^2, while that of tumor volume on a natural log scale, i.e., ln(tumor volume +1), contained the interaction of treatment with time only. The variance−covariance structure of random effects was unstructured, whereas that of random errors was first-order autoregression. Using derived parameters, model-based tumor growth curves for raw data were drawn, and the integral from day 1 to day 26 for each curve was estimated from the area under the curve. This area-under-the-curve integral provided estimates of percentage inhibition in tumor growth for treatment versus control groups over the time course of the study, rather than just on a single day. We also performed nonparametric and postcomparison tests, i.e., Kruskal−Wallis and Wilcoxon Rank-Sum, as well as Student's t test to validate differences between control and treatment data sets.

RESULTS AND DISCUSSION

Initially, we assessed the ability of conjugate to inhibit proliferation of various cells in culture. Anginex inhibited endothelial cell (EC) proliferation (Figure 2A) with an IC_{50} value of 5 μM, consistent with previous results (*8, 18, 22, 23*). In comparison, both the conjugate and HPAF-LE at 5 μM exhibited greater than 90% inhibition of EC proliferation, with IC_{50} values of 1.4 μM and 0.6 μM, respectively. Results were the same whether medium was supplemented with 10 ng/mL bFGF, 10 ng/mL VEGF, 0.4% Endo-Gro, or 20% FBS. Although anginex was essentially inactive against human ovarian carcinoma MA148, murine melanoma B16F10, and human alveolar epithelial carcinoma A549 cells, HPAF-LE and conjugate were quite effective, with respective IC_{50} values of 11 μM and 14 μM against MA148 (Figure 2B), 7 μM and 23 μM against B16F10 (Figure 2C), and 0.1 μM and 0.6 μM against A549 (Figure 2D).

These results suggest that conjugation to the peptide anginex does not substantially modify the effectiveness of HPAF-LE as a chemotherapeutic agent. This is interesting because acylfulvenes are known to function intracellularly by forming DNA adducts (*28*), and for this to occur, the conjugate should be internalized by these cells. At least with EC, anginex is known to be rapidly internalized upon binding to the cell surface (*10*). Nevertheless, demonstration that the acylfulvene-based anginex conjugate can still promote formation of acylfulvene−DNA adducts requires further investigation.

To demonstrate that the conjugate still targets gal-1 like parent anginex (*10*), we employed cell adhesion and competition assays, as well as ex vivo double immunostaining (Figure 3). As illustrated in Figure 3A, conjugate and anginex significantly ($p < 0.05$) block EC adhesion on gal-1-coated surfaces, whereas

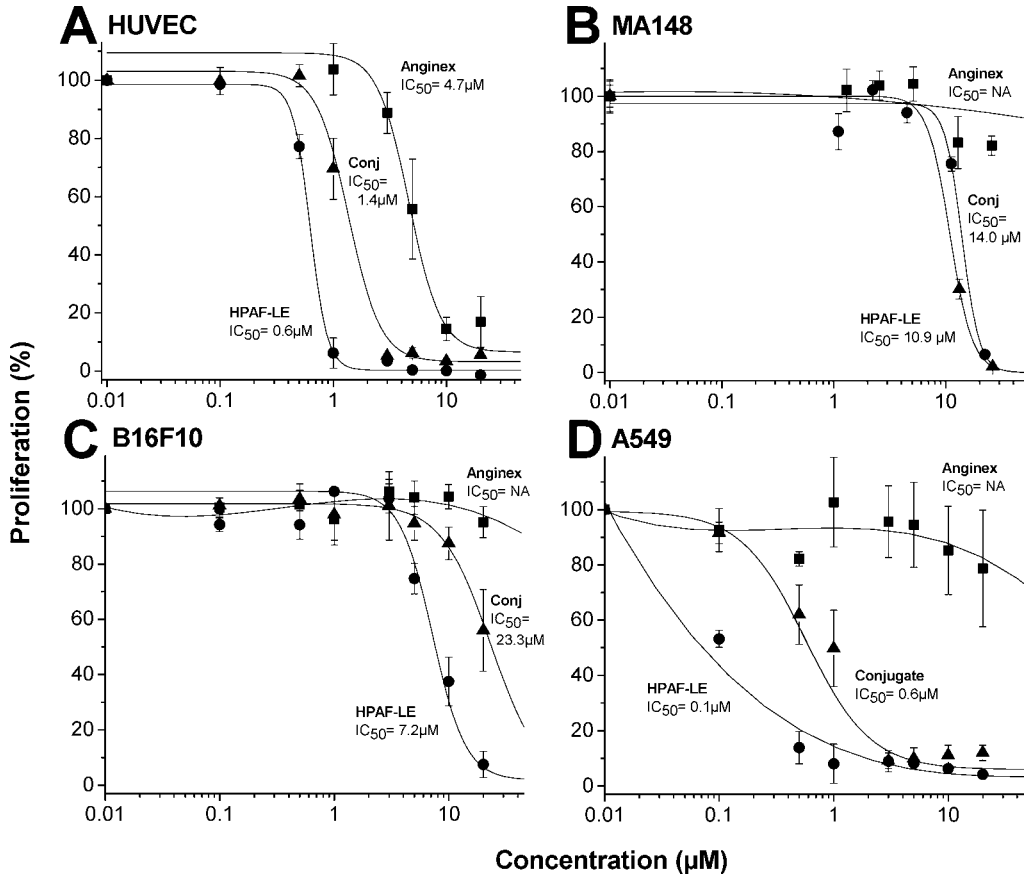


Figure 2. Differential inhibition of EC and MA148 cell proliferation by HPAF-LE, anginex, and conjugate. Concentration response curves of HPAF-LE, anginex, and conjugate on HUVEC (A), MA148 proliferation (B), B16F10 (C), and A549 (D). Average values for quantification of at least three separate experiments are shown ± SEM.

both conjugate and anginex could not block adhesion of EC to gelatin-coated surfaces. In addition, the inhibitory proliferation by both compounds was diminished by the presence of anti-gal-1 antibody (Figure 3B).

Using double immunostaining of cross sections from untreated MA148 xenograft tumors, we first showed that the antianginex antibody cross-reacted with the conjugate, indicating that the epitopes on anginex peptide were not blocked by the presence of the conjugated irofulven analogue (Figure 3D, middle panel). Then, we showed that gal-1 is present in the stroma of MA148 tumor tissue (Figure 3C,D upper panel), confirming earlier reports (*27*), and that gal-1 and conjugate could be identified by immunofluorescence (Figure 3D). The merged images, which illustrate the morphology of tumor blood vessels, demonstrate colocalization of gal-1 and conjugate (Figure 3D, lower panel). This in turn allows us to conclude that the conjugate indeed targets gal-1, and that conjugation of HPAF-LE to the peptide does not interfere with its ability to target gal-1.

Next, we compared the in vivo activity of HPAF-LE (5 and 10 mg/kg) to that of irofulven (1.5 and 3 mg/kg) and carboplatin (32.5 mg/kg) in the MA148 human ovarian carcinoma model (IP administration on a q3d×4 schedule, Figure 4A). Carboplatin was used as the standard comparator in this model because platinum agents are the most widely used drugs in first-line defense against ovarian cancer (*3, 29*). Our study demonstrated a dose response in both irofulven and HPAF-LE treated mice. Although HPAF-LE at 5 mg/kg or 10 mg/kg inhibited MA148 tumor growth to a similar degree to irofulven at 1.5 mg/kg or 3 mg/kg, respectively, irofulven was about 3-fold more effective than HPAF-LE at the same dose (Figure 4B). On the other hand, HPAF-LE at 10 mg/kg had essentially the same effect as carboplatin at 32 mg/kg, which amounts to a 3-fold improvement in dose over this platinum agent. The toxicity profiles of all compounds tested appeared to be very similar, with body weight gains being somewhat suppressed compared to those in vehicle-treated mice (Figure 4C).

To assess the effect of the conjugate on tumor growth, we treated MA148 tumor-bearing mice with the conjugate (10 mg/kg and 50 mg/kg), along with several control groups (vehicle treatment, and stand-alone treatments with anginex (10 mg/kg and 50 mg/kg) and HPAF-LE (5 mg/kg)). Figure 5A shows tumor growth curves for all groups. Even though the time course for the study is shown out to day 28, mice received treatment only during the first 10 days and were euthanized when tumors reached the size of about 1500 mm^3. Overall, tumor growth was inhibited in all treated groups compared to that in the vehicle-treated control group, and both anginex and the conjugate showed a dose response. On the day when control mice had to be sacrificed (day 23), Student's *t*-test indicated that the conjugate at 50 mg/kg inhibited tumor growth by 94% ± 1.6% compared to vehicle-treated control mice ($p = 0.02$), whereas equimolar doses of anginex (50 mg/kg) and HPAF-LE (5 mg/kg) inhibited tumor growth by 76% ± 7.3% ($p = 0.03$) and 82% ± 5.0% ($p = 0.03$), respectively (Figure 5B). Analysis of data on day 23 using Kruskal−Wallis and Wilcoxon Rank-Sum nonparametric and post-comparison tests showed that, while there were no significant differences between anginex (10 and 50 mg/kg), HPAF-LE (5 mg/kg), and conjugate (10 mg/kg) groups, there was a significant ($p = 0.003$) difference between conjugate (50 mg/kg) and HPAF-LE treated groups. This was supported by statistical analysis over the time course of the study using general linear mixed models, which showed significant differences between the control group and all other groups (anginex 10 mg/kg, $p < 0.01$; anginex 50 mg/kg and conjugate

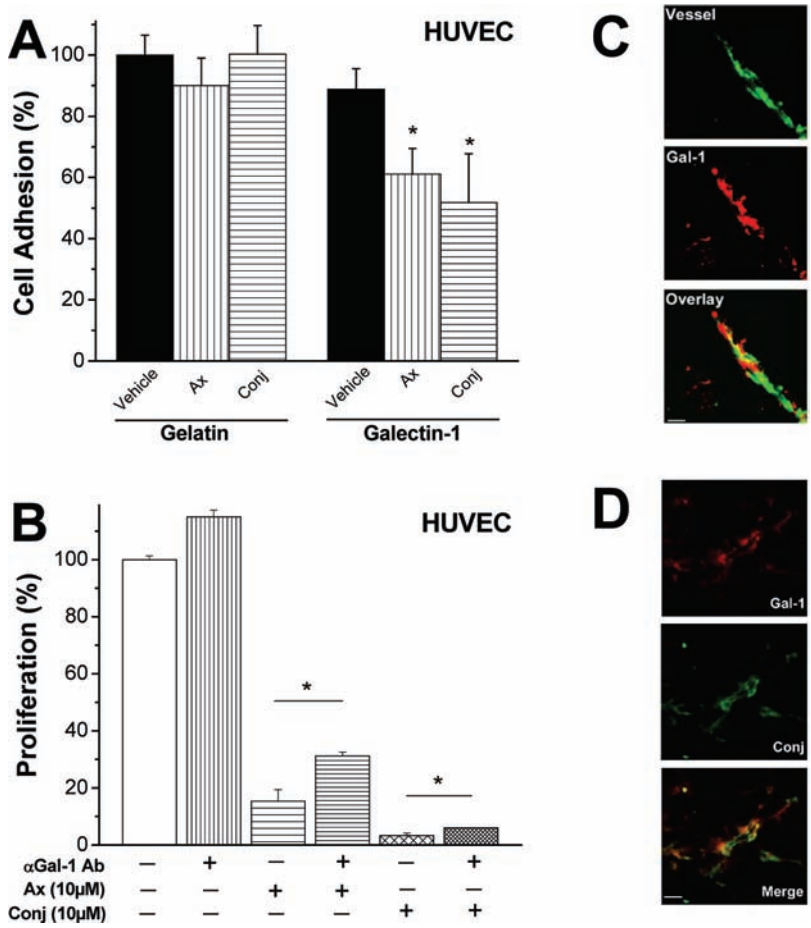


Figure 3. (A) EC adhesion to gal-1 coated surface, but not to gelatin-coated surface, is inhibited by conjugate (10 μM) or anginex (10 μM). (B) Conjugate (10 μM) or anginex (10 μM) EC proliferation inhibition is significantly reduced by anti-gal-1 antibody (1/1000). (C) Immunohistochemistry staining of mouse vessels, pericytes (green; αSMA), gal-1 expression (red); co-localization of gal-1 and mouse vessels (yellow; CD31). (D) Immunohistochemistry staining of mouse vessels, showing that HPAF-LE anginex conjugate targets gal-1 in MA148 tumors: gal-1 expression (red); conjugate binding (green); co-localization of gal-1 and conjugate (yellow). Original magnification 200×; scale bar = 50 μm.

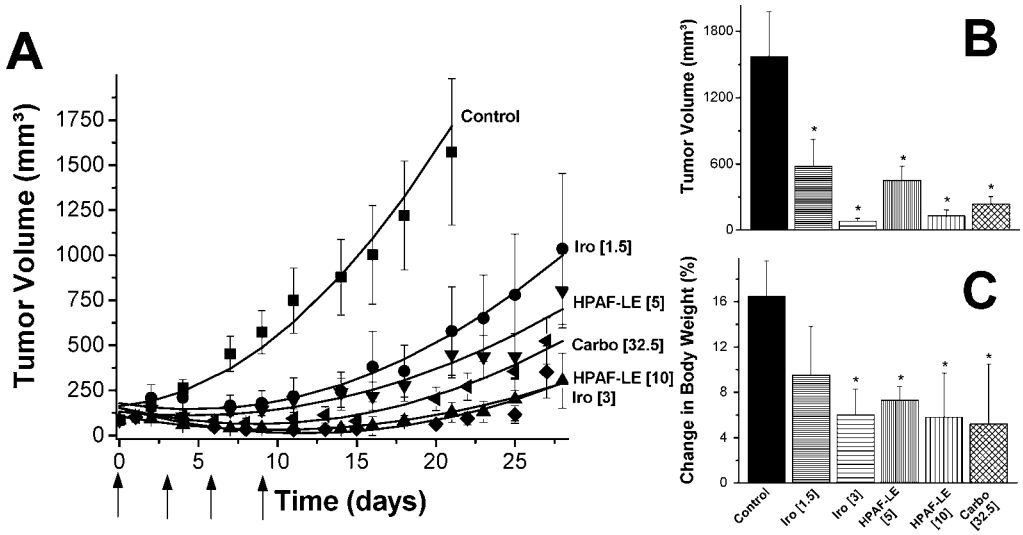


Figure 4. MA148 tumor growth inhibition by HPAF-LE, irofulven, and carboplatin. (A) Six groups of mice were studied (treatments were all administered IP q3d×4): two HPAFLE groups (5 mg/kg, $n = 7$, and 10 mg/kg, $n = 7$), two irofulven groups (1.5 mg/kg and 3 mg/kg, each $n = 8$), one carboplatin group (32.5 mg/kg, $n = 8$), and one control group (vehicle, $n = 7$), as indicated. Tumors were allowed to grow to the size of approximately 75 mm^3 prior to initiation of treatment. Tumor volumes are plotted as mm^3 (± SEM). (B) MA148 tumor growth inhibition by the individual treatments derived from the growth curves in panel A. Data represent means ± SEM on day 21 after the initiation of treatment. (C) The average gain in body weight (in %) for the experimental groups indicated. Data represent means ± SEM on day 21 after the initiation of treatment.

10 mg/kg, $p = 0.001$; HPAF-LE and conjugate 50 mg/kg, $p < 0.001$), as well as, e.g., between conjugate (50 mg/kg) and HPAF-LE treated groups ($p = 0.04$). Furthermore, at the end of the study on day 37 (absent control group due to sacrifice),

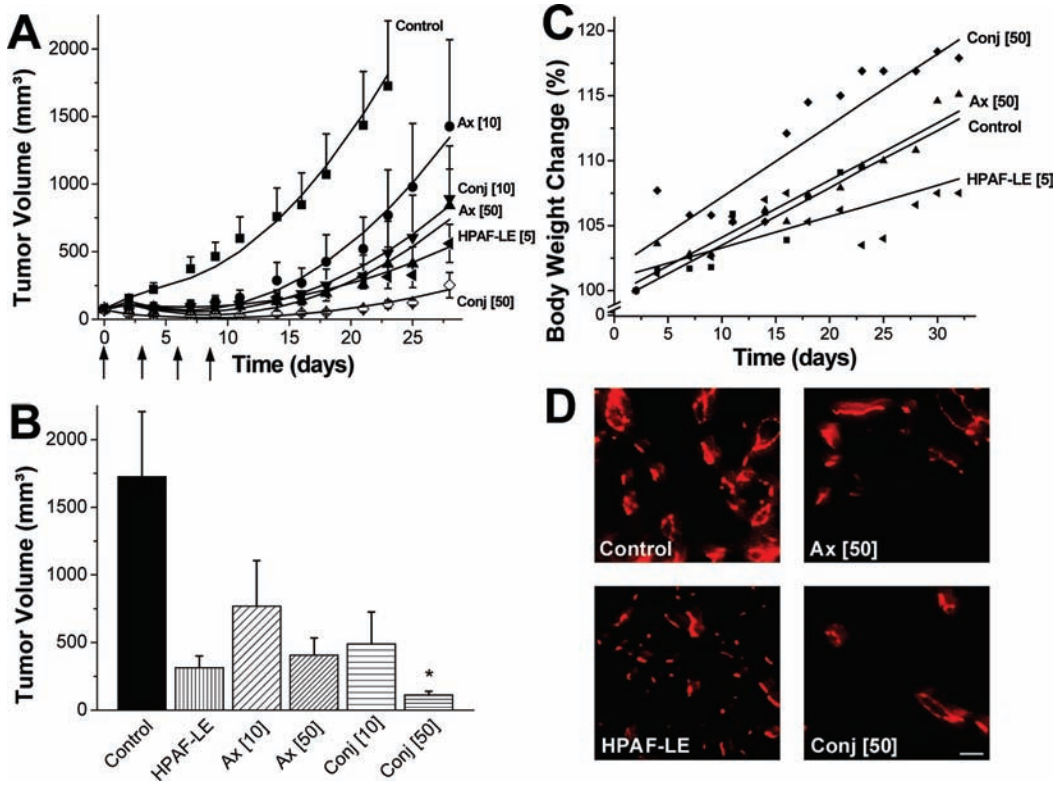


Figure 5. MA148 tumor growth inhibition by HPAF-LE-anginex conjugate. (A) Six groups of mice were studied (treatments were all administered IP q3d×4): two conjugate groups (10 mg/kg and 50 mg/kg), two anginex groups (10 mg/kg and 50 mg/kg), one HPAF-LE group (5 mg/kg), and one control group (vehicle), as indicated. Tumors were allowed to grow to the size of approximately 75 mm^3 prior to initiation of treatment (n = 10−12 animals per treatment). (B) MA148 tumor growth inhibition by the individual treatments derived from the growth curves in panel A. Data represent means ± SEM on day 23 after the initiation of treatment. *$p < 0.003$ for conjugate compared to other treatment groups. (C) The average change in body weight, normalized to individual weights at the start of treatment (in %) for the experimental groups indicated, are plotted over time with linear line fitting (no significant differences $p < 0.9$). (D) Representative images illustrate the average amount of vessel density staining on tumor tissue from control, anginex (50 mg/kg), HPAF (5 mg/kg), and conjugate (50 mg/kg) treated groups. Original magnification 200×; scale bar = 50 μm.

conjugate treated mice had an average tumor size of 600 mm^3, whereas the average tumor size of HPAF-LE treated mice reached this value on day 32, amounting to a tumor growth delay time of about 5 days in mice treated with conjugate compared to HPAF-LE.

This improvement in efficacy from the conjugate was also reflected in the level of individual tumor responses (Table 1). On day 11, analysis of individual mice showed that administration of conjugate at 50 mg/kg resulted in 20% complete remissions, 60% partial responders, and 20% stable diseases, whereas the HPAF-LE treated group (5 mg/kg) had 8% complete and partial responders and 17% stable diseases. At the lower dose of conjugate (10 mg/kg), 17% of the mice had either a complete or partial remission, or stable disease. In the anginex-treated groups, administration of 50 mg/kg caused 17% partial responders and 67% stable diseases, whereas at 10 mg/kg, there was 50% stable diseases. At the end of the study, more than 2 weeks after the last treatment, tumors relapsed in conjugate-

Table 1. Tumor Responses after Different Treatment Regimens[a]

treatment	stable (%)	response partial (%)	complete (%)
Control	0	0	0
HPAF-LE [5]	16.6	8.3	8.3
Anginex [10]	50	0	0
Anginex [50]	66.7	16.7	0
Conjugate [10]	16.7	16.7	16.7
Conjugate [50]	20	60	20

[a] Tumor response rates were evaluated on day 11, two days after the last treatment. n = 10−12 animals per treatment.

Table 2. Immunofluorescent Analysis of Microvessel Density

	vessel density[a]	end points[b]	branch points[c]	vessel length[d]
Control	17398 ± 1068	58.8 ± 7.5	9.8 ± 1.1	14.8 ± 0.9
HPAF-LE [5]	14099 ± 1009[e]	76.9 ± 6.1[e]	5.6 ± 0.9[e]	11.0 ± 0.9[e]
Anginex [10]	11221 ± 1124[e]	30.0 ± 7.1[e]	6.0 ± 1.3[e]	7.1 ± 1.1[e]
Anginex [50]	9819 ± 874[e]	41.1 ± 7.5[e]	3.6 ± 0.8[e]	7.2 ± 0.9[e]
Conjugate [10]	10302 ± 1330[e]	22.2 ± 3.4[e]	3.8 ± 1.0[e]	6.0 ± 0.6[e]
Conjugate [50]	8471 ± 612[e,g]	11.0 ± 2.2[e,f,g]	2.3 ± 0.7[e,g]	4.8 ± 0.8[e,g]

[a] Following binarization of images (magnification 200×), microvessel density was estimated by scoring the total number of white pixels per field. Results show the mean white pixel count per image ± standard error. At least 3 different tumors per treatment group were analyzed with a total of 10 or more images. [b] Mean number of vessel end points ± standard error as determined after skeletonization of the images. [c] Mean number of vessel branch points/nodes per image in pixels ± standard error as determined after skeletonization of the images. [d] Mean total vessel length per image in pixels ± standard error as determined after skeletonization of the images. [e] $p < 0.001$. Experimental group compared to vehicle (Kruskal−Wallis Test). [f] $p < 0.01$. Conjugate group (50 mg/kg) compared to molar equivalent Anginex (50 mg/kg) Wilcoxon Rank-Sum Test. [g] $p < 0.03$. Conjugate group (50 mg/kg) compared to molar equivalent HPAF-LE group (5 mg/kg) Wilcoxon Rank-Sum Test.

treated animals. The control group showed no responders and no stable diseases.

Although we found that the effective concentration of conjugate in vitro is lower than its effective dose in vivo, we realize that such differences are not always readily explainable, since in vivo exposure is multifaceted and would require complete pharmacokinetic and dynamic studies. Nevertheless, a dose of 50 mg/kg is not that unusual for a protein/peptide-based therapeutic in mouse studies (*30*), and we did observe the absence of apparent toxicity from the conjugate or anginex at either dose (10 mg/kg or 50 mg/kg) in any of the mice. Apparent lack of toxicity is based on normal weight gain (Figure 5C) and normal behavior in mice during the study. Trend line fitting ($R^2 > 0.8$) revealed that the rate of weight gain in the HPAF-LE (5 mg/kg) treated animals was reduced 3-fold as compared to the conjugate (50 mg/kg) treated animals, i.e., 0.19% vs 0.58% weight gain per day (Figure 5C). This is consistent with dose limiting toxicities usually observed from agents of this class of alkylating chemotherapeutics (*20*).

To demonstrate changes in microvessel density, we used immunohistochemistry (CD31 staining) on cryosections of MA148 tumor tissue from treated and untreated mice (Table 2 and Figure 5D). Morphometric analysis of viable tissue showed that microvessel density in treated groups was reduced in comparison to that in control tumor tissue. General morphology of tumor tissue showed that mice treated with higher doses of anginex or conjugate had regional antivascular effects, resulting in necrotic centers and surviving rims. At either dose, effects from conjugate and anginex are comparable, whereas there is a significantly ($p < 0.03$) smaller effect from HPAF-LE at a molar equivalent dose. These data indicate that conjugation of HPAF-LE to anginex does not affect the ability of anginex to function as an antiangiogenic agent. On the other hand, MA148 tumor growth inhibition (Figure 5A) is significantly ($p = 0.01$) greater from treatment of mice with the conjugate (50 mg/kg) compared to that from anginex (50 mg/kg), and this enhancement should result from the presence of HPAF-LE on targeting peptide anginex.

Although the precise mechanism by which anginex-conjugated HPAF-LE functions in situ remains unknown, it may be that improved efficacy is attributable to increased in vivo exposure of the acylfulvene moiety at the target site, i.e., targeting and sequestering within the tumor, and/or greater serum half-life. Moreover, although it is indirect evidence, it appears that conjugation of HPAF-LE to anginex reduces the inherent toxicity from the acylfulvene moiety. Body weight gain was normal during the course of the treatment with the conjugate (5.5% weight gain compared to 5.6% weight gain for control animals, Figure 5C), whereas it was significantly ($p = 0.03$) lower (3.2%) in HPAF-LE treated mice. Taken together, this study suggests that HPAF-LE can be made more effective when conjugated to anginex as a tumor targeting agent.

ACKNOWLEDGMENT

This research was supported by a research grant from the National Institutes of Health (NIH CA-96090) to KHM, and by MGI Pharma, Inc., Bloomington, MN.

LITERATURE CITED

(1) Hurwitz, H., Fehrenbacher, L., Novotny, W., Cartwright, T., Hainsworth, J., Heim, W., Berlin, J., Baron, A., Griffing, S., Holmgren, E., Ferrara, N., Fyfe, G., Rogers, B., Ross, R., and Kabbinavar, F. (2004) Bevacizumab plus irinotecan, fluorouracil, and leucovorin for metastatic colorectal cancer. *N. Engl. J. Med. 350*, 2335–42.

(2) Teicher, B. A., Sotomayor, E. A., and Huang, Z. D. (1992) Antiangiogenic agents potentiate cytotoxic cancer therapies against primary and metastatic disease. *Cancer Res. 52*, 6702–4.

(3) Dings, R. P., Yokoyama, Y., Ramakrishnan, S., Griffioen, A. W., and Mayo, K. H. (2003) The designed angiostatic peptide anginex synergistically improves chemotherapy and antiangiogenesis therapy with Angiostatin. *Cancer Res. 63*, 382–385.

(4) Griffin, R. J., Molema, G., and Dings, R. P. (2006) Angiogenesis treatment, new concepts on the horizon. *Angiogenesis 9*, 67–72.

(5) Griffioen, A. W., and Molema, G. (2000) Angiogenesis: potentials for pharmacologic intervention in the treatment of cancer, cardiovascular diseases, and chronic inflammation. *Pharmacol. Rev. 52*, 237–68.

(6) Arap, W., Pasqualini, R., and Ruoslahti, E. (1998) Cancer treatment by targeted drug delivery to tumor vasculature in a mouse model. *Science 279*, 377–80.

(7) Mulder, W. J., Strijkers, G. J., Habets, J. W., Bleeker, E. J., van der Schaft, D. W., Storm, G., Koning, G. A., Griffioen, A. W., and Nicolay, K. (2005) MR molecular imaging and fluorescence microscopy for identification of activated tumor endothelium using a bimodal lipidic nanoparticle. *Faseb J. 19*, 2008–10.

(8) Griffioen, A. W., van der Schaft, D. W., Barendsz-Janson, A. F., Cox, A., Struijker Boudier, H. A., Hillen, H. F., and Mayo, K. H. (2001) Anginex, a designed peptide that inhibits angiogenesis. *Biochem. J. 354*, 233–42.

(9) Dings, R. P., and Mayo, K. H. (2007) A journey in structure-based drug discovery: from designed peptides to protein surface topomimetics as antibiotic and antiangiogenic agents. *Acc. Chem. Res. 40*, 1057–65.

(10) Thijssen, V. L., Postel, R., Brandwijk, R. J., Dings, R. P., Nesmelova, I., Satijn, S., Verhofstad, N., Nakabeppu, Y., Baum, L. G., Bakkers, J., Mayo, K. H., Poirier, F., and Griffioen, A. W. (2006) Gal-1 is essential in tumor angiogenesis and is a target for antiangiogenesis therapy. *Proc. Natl. Acad. Sci. U.S.A. 103*, 15975–80.

(11) Camby, I., Le Mercier, M., Lefranc, F., and Kiss, R. (2006) Gal-1: a small protein with major functions. *Glycobiology. 16*, 137R–157R.

(12) Rabinovich, G. A. (2005) Gal-1 as a potential cancer target. *Br. J. Cancer 92*, 1188–92.

(13) Gabius, H. J., Brehler, R., Schauer, A., and Cramer, F. (1986) Localization of endogenous lectins in normal human breast, benign breast lesions and mammary carcinomas. *Virchows Arch. B. Cell. Pathol. Incl. Mol. Pathol. 52*, 107–15.

(14) Lotan, R., Matsushita, Y., Ohannesian, D., Carralero, D., Ota, D. M., Cleary, K. R., Nicolson, G. L., and Irimura, T. (1991) Lactose-binding lectin expression in human colorectal carcinomas. Relation to tumor progression. *Carbohydr. Res. 213*, 47–57.

(15) Clausse, N., van den Brule, F., Waltregny, D., Garnier, F., and Castronovo, V. (1999) Gal-1 expression in prostate tumor-associated capillary endothelial cells is increased by prostate carcinoma cells and modulates heterotypic cell-cell adhesion. *Angiogenesis 3*, 317–25.

(16) Allen, H. J., Sucato, D., Woynarowska, B., Gottstine, S., Sharma, A., and Bernacki, R. J. (1990) Role of galaptin in ovarian carcinoma adhesion to extracellular matrix in vitro. *J. Cell. Biochem. 43*, 43–57.

(17) Akerman, M. E., Pilch, J., Peters, D., and Ruoslahti, E. (2005) Angiostatic peptides use plasma fibronectin to home to angiogenic vasculature. *Proc. Natl. Acad. Sci. U.S.A. 102*, 2040–5.

(18) Dings, R. P., van der Schaft, D. W., Hargittai, B., Haseman, J., Griffioen, A. W., and Mayo, K. H. (2003) Anti-tumor activity of the novel angiogenesis inhibitor anginex. *Cancer Lett. 194*, 55–66.

(19) Baekelandt, M. (2002) Irofulven (MGI Pharma). *Curr. Opin. Invest. Drugs 3*, 1517–26.

(20) Eckhardt, S. G., Baker, S. D., Britten, C. D., Hidalgo, M., Siu, L., Hammond, L. A., Villalona-Calero, M. A., Felton, S., Drengler, R., Kuhn, J. G., Clark, G. M., Smith, S. L., MacDonald, J. R., Smith, C., Moczygemba, J., Weitman, S., Von Hoff, D. D., and Rowinsky, E. K. (2000) Phase I and pharmacokinetic study of irofulven, a novel mushroom-derived cytotoxin, administered for five consecutive days every four weeks in patients with advanced solid malignancies. *J. Clin. Oncol. 18*, 4086–97.

(21) Alexandre, J., Raymond, E., Kaci, M. O., Brain, E. C., Lokiec, F., Kahatt, C., Faivre, S., Yovine, A., Goldwasser, F., Smith, S. L., MacDonald, J. R., Misset, J. L., and Cvitkovic, E. (2004) Phase I and pharmacokinetic study of irofulven administered weekly or biweekly in advanced solid tumor patients. *Clin. Cancer Res. 10*, 3377–85.

(22) Dings, R. P., Williams, B. W., Song, C. W., Griffioen, A. W., Mayo, K. H., and Griffin, R. J. (2005) Anginex synergizes with radiation therapy to inhibit tumor growth by radiosensitizing endothelial cells. *Int. J. Cancer 115*, 312–9.

(23) Dings, R. P., Chen, X., Hellebrekers, D. M., van Eijk, L. I., Zhang, Y., Hoye, T. R., Griffioen, A. W., and Mayo, K. H. (2006) Design of nonpeptidic topomimetics of antiangiogenic proteins with antitumor activities. *J. Natl. Cancer Inst. 98*, 932–6.

(24) Dings, R. P., Loren, M., Heun, H., McNiel, E., Griffioen, A. W., Mayo, K. H., and Griffin, R. J. (2007) Scheduling of radiation with angiogenesis inhibitors Anginex and Avastin improves therapeutic outcome via vessel normalization. *Clin. Cancer Res. 13*, 3395–402.

(25) Mayo, K. H., Dings, R. P., Flader, C., Nesmelova, I., Hargittai, B., van der Schaft, D. W., van Eijk, L. I., Walek, D., Haseman, J., Hoye, T. R., and Griffioen, A. W. (2003) Design of a partial peptide mimetic of anginex with antiangiogenic and anticancer activity. *J. Biol. Chem. 278*, 45746–52.

(26) Kadoya, T., and Horie, H. (2005) Structural and functional studies of gal-1: a novel axonal regeneration-promoting activity for oxidized gal-1. *Curr. Drug Targets 6*, 375–83.

(27) Dings, R. P., Van Laar, E. S., Webber, J., Zhang, Y., Griffin, R. J., Waters, S. J., MacDonald, J. R., and Mayo, K. H. (2008) Ovarian tumor growth regression using a combination of vascular targeting agents anginex or topomimetic 0118 and the chemotherapeutic irofulven. *Cancer Lett. 265*, 270–80.

(28) Wang, J., Wiltshire, T., Wang, Y., Mikell, C., Burks, J., Cunningham, C., Van Laar, E. S., Waters, S. J., Reed, E., and Wang, W. (2004) ATM-dependent CHK2 activation induced by anticancer agent, irofulven. *J. Biol. Chem. 279*, 39584–92.

(29) Tattersall, M. H. N. (2002) Ovarian cancer chemotherapy: carboplatin as standard. *The Lancet 360*, 500–1.

(30) Lee, T. Y., Tjin Tham Sjin, R. M., Movahedi, S., Ahmed, B., Pravda, E. A., Lo, K. M., Gillies, S. D., Folkman, J., and Javaherian, K. (2008) Linking antibody Fc domain to endostatin significantly improves endostatin half-life and efficacy. *Clin. Cancer Res. 14*, 1487–93.

BC900287Y

Thiol-Modified Chitosan Sulfate Nanoparticles for Protection and Release of Basic Fibroblast Growth Factor

Yi-Cheng Ho,[‡] Shao-Jung Wu,[§] Fwu-Long Mi,*[,†,‡,⊥] Ya-Lin Chiu,[||] Shu-Huei Yu,[#] Nilendu Panda,[||] and Hsing-Wen Sung*[,†,||]

Department of Biotechnology, Nano Materials R&D Center, and Department of Polymer Materials, Vanung University, Chung-Li, Taiwan, ROC, Department of Chemical Engineering, MingChi University of Technology, Taipei, Taiwan, ROC, and Department of Chemical Engineering, National Tsing Hua University, Hsinchu, Taiwan, ROC. Received May 8, 2009; Revised Manuscript Received November 20, 2009

A series of chitosan (CS) derivatives, the 6-*O*-carboxymethylchitosan (6-O-CC), 2-*N* sulfated 6-*O*-carboxymethylchitosan (N-SOCC) and the 2-*N* and 3,6-*O* sulfated 6-*O*-carboxymethyl chitosan (N,O-SOCC) were synthesized in this study. The chemical structures and the degrees of substituted carboxymethyl and sulfate groups of the synthesized compounds were respectively determined by FT-IR spectra and elemental analysis. N,O-SOCC displayed the highest protective efficiency for basic fibroblast growth factor (bFGF) as examined by the L929 fibroblast culture test and docking simulation. N,O-SOCC-4-thio-butylamidine (TBA) conjugates prepared by modification of N,O-SOCC with 2-iminothiolane were in situ cross-linkable. The degrees of thiol substitution of the 2-iminothiolane modified N,O-SOCC polymers were determined to be in the ranges of 45.9 ± 3.7 and 415.6 ± 12.5 μmol SH/g SOCC by quantifying the amount of thiol groups on the thiolated polymers with Ellman's reagent. The 2-iminothiolane modified N,O-SOCC and CS complex could be used for preparing nanoparticles by a polyelectrolyte self-assembly method, and the release of bFGF from the nanoparticles was successfully controlled. L929 fibroblast culture tests showed that the thiol modified N,O-SOCC/CS nanoparticles could effectively protect bFGF from inactivation over a 120 h period. The results of this study suggest that the thiol modified N,O-SOCC/CS nanoparticles may be useful as novel materials for specific delivery of bFGF with mitogenic activity.

INTRODUCTION

Heparin and heparan sulfate (HS) are members of the glycosaminoglycan family possessing higher negative charge density than other known biological macromolecules. Heparin/HS is able to establish ionic interactions with a variety of proteins including enzymes, extracellular-matrix proteins, various cytokines, and members of the family of fibroblast growth factors (FGFs), epidermal growth factor (EGF), and the transforming growth factor (TGF) (*1, 2*). Such interactions especially control specified polysaccharide−protein interactions and possess biological potential in relation to cell growth, wound healing, and tissue regeneration, as well as thrombin inhibition (*3*).

Basic fibroblast growth factor (bFGF) is a heparin/HS-binding growth factor and has shown therapeutic potential to enhance angiogenesis, soft tissue formation, re-epithelialization, and collagen maturation, as well as to accelerate bone fracture healing (*4, 5*). Heparin/HS can stabilize an active conformation of bFGF and enhance interaction with specific cellular receptors (*6, 7*). On the basis of these reasons, many studies have reported the development of heparin-functionalized materials for the purpose of delivering bFGF to enhance tissue regeneration (*8*−*10*). Besides, preparations of conjugates of bFGF and polymer-based gene delivery vectors became potential targets for cancer gene therapy because fibroblast growth factor receptors (FGFRs) are highly expressed on a variety of human cancer cells (*11, 12*).

In recent years, significant advances in the modification of polysacchsarides with specific structures or synthesis of polymers with pendent saccharides offer one biomimetic strategy to obtain heparin-like materials. For example, acrylamide with alkene-derivatized mono- and disaccharides can be polymerized to yield glycopolymers with biologically active, sulfated *N*-acetyl-D-glucosamines on the side chains (*13*). Chemical modifications of biological macromolecules such as dextran, colominic acid, poly(γ-glutamic acid), and alginate with sulfate or sulfonate groups have been shown to bind various growth factors and protect them from inactivation (*14, 15*).

Chitosan (CS) and its derivatives have been used for the purpose of biomedical applications, such as gene delivery (*16*). A series of chitosan derivatives, the 6-*O*-carboxymethylchitosan (6-O-CC), 2-*N* sulfated 6-*O*-carboxymethylchitosan (N-SOCC) and the 2-*N* and 3,6-*O* sulfated 6-*O*-carboxymethylchitosan (N,O-SOCC) were synthesized in this work. The structures of 6-O-CC, N-SOCC, and N,O-SOCC were characterized by FT-IR spectra analysis. The studies of L929 cell proliferation and docking simulation were used to investigate the growth factor protective effects of these chitosan derivatives with carboxymethyl and sulfate groups substituted in different position. 2-Iminothiolane as a prethiomer was reacted with N,O-SOCC to prepare the thiol-modified N,O-SOCC polymers, and the degrees of thiolation were determined by a colorimetric assay using Ellman's reagent. The 2-iminothiolane modified N,O-SOCC polymers displayed in situ cross-linking properties due to the oxidation of substituted thiol groups. Basic fibroblast

* Correspondence to Fwu-Long Mi, PhD, Professor, Department of Biotechnology, Vanung University, Chung-Li, Taiwan 320, ROC, Fax: 886-3-4333063, E-mail: flmi530326@vnu.edu.tw. Dr. H.W. Sung: hwsung@che.nthu.edu.tw.

† The contributions by the two collaborating parties are equal.

‡ Department of Biotechnology, Vanung University.

§ MingChi University of Technology.

|| National Tsing Hua University.

⊥ Nano Materials R&D Center, Vanung University.

Department of Polymer Materials, Vanung University.

10.1021/bc900208t © 2010 American Chemical Society
Published on Web 12/14/2009

growth factor (bFGF) were readily immobilized in the 2-iminothiolane modified N,O-SOCC/chitosan (CS) nanoparticles, and the immobilized bFGF could be released in a sustained manner with mitogenic activities. The novel materials prepared from the thiol-modified N,O-SOCC polymer may be useful to deliver bFGF for biomedical applications.

EXPERIMENTAL PROCEDURES

Materials. Monochloroacetic acid, isopropyl alcohol, and sodium carbonate were purchased from ACROS Chemical Co. (USA). Chitin powder was acquired from Tokyo Chemical Industry Co., Ltd. Oleum ($H_2SO_4 \cdot SO_3$), dithiothreitol (DTT), and trimethylamine sulfur trioxide were purchased from Sigma-Aldrich Chemical Co., Ltd. (USA). 2-Iminothiolane was from Aldrich Chemical Co. (Milwaukee, WI). CS (MW 60 kDa) with a degree of deacetylation of approximately 85% was acquired from Koyo Chemical Co. Ltd. (Japan). Recombinant human bFGF and enzyme-linked immunosorption assay (ELISA) kit were obtained from R&D Systems (Minneapolis, MN, USA).

Synthesis of 6-O-CChitin and 6-O-CC. 6-O-CChitin was prepared according to the method described in the previous literature with some modification (*17*). 8.16 g of chitin powder was suspended in 40 mL sodium hydroxide solution (0.4 g/mL) including 0.2% sodium dodecyl sulfate (SDS) at 4 °C, and the slurry was kept in a freezer at −20 °C overnight. The frozen alkali-chitin was suspended in 200 mL isopropyl alcohol at room temperature, and 11.34 g of monochloroacetic acid was added in portions with mechanical stirring until the reaction mixture was neutralized. The product was filtered and washed with ethanol. The residue was extracted with water, and the water extract was slowly added to acetone to precipitate the crude product. The crude product was extensively dialyzed against deionized water and finally freeze−dried to obtain 6-O-CChitin. 9.65 g of 6-O-CChitin was placed in 40 mL NaOH/isopropyl alcohol aqueous solution (0.4 g/mL) and refluxed for 3 h under purging with nitrogen. The gel-like product was dissolved in water and precipitated by slowly adding acetone to the aqueous solution. The precipitation was dissolved in water and lyophilized after thorough dialysis against deionized water to remove the salt. The final product was 6-O-carboxymethylchitosan (6-O-CC).

Synthesis of N-Sulfated 6-O-CC. 6-O-CC was N-sulfated according to the method developed by Holme and Perlin (*18*). 6-O-CC (0.23 g) was suspended in 60 mL of an aqueous solution of sodium carbonate (0.33 g), stirred at 65 °C, and trimethylamine sulfur trioxide complex (0.62 g) was added. The reaction was carried out for 20 h. The media became clear and homogeneous at the end of the reaction. At the determined reaction time, the mixture was cooled to room temperature, extensively dialyzed against deionized water, and finally freeze−dried to obtain N-sulfated 6-O-CC (N-SOCC).

Synthesis of N,O-Sulfated 6-O-CC. N-SOCC was further sulfated for the preparation of N,O-Sulfated 6-O-CC (N,O-SOCC), according to the method developed by Vikhoreva et al. (*19*). Sulfation of N-SOCC was conducted in a reaction vessel by adding of small portions of oleum to a dimethylformamide (DMF) excess (0.53 g oleum and 2.12 g DMF per 0.29 g N-SOCC). The mixture was stirred vigorously at 5 °C, and then N-SOCC was added to the mixture for sulfation reaction. By stirring for 2 h, the reaction mixture was cooled to 20 °C, and a solid fraction was separated by filtration through a glass filter. Crude N,O-SOCC was precipitated from solution in 5-fold acetone volume and washed with acetone twice, then dissolved in distilled water with simultaneous neutralization with a 20% NaOH solution. Sodium salts of N,O-SOCC were extensively dialyzed against deionized water, and finally freeze−dried to obtain purified N,O-SOCC. Degrees of carboxymethylation and sulfation of the chitosan derivatives were determined by elemental analysis. The schematic procedure for the synthesis of 6-O-CChitin, 6-OCC, N-SOCC, and N,O-SOCC were shown in Figure 1.

Characterization of the Synthesized Compounds. The synthesized 6-O-CChitin, 6-OCC, N-SOCC, and N,O-SOCC products were characterized by FT-IR (Perkin-Elmer Spectrum RX1 FT-IR System, Buckinghamshire, England). The substitutions of carboxymethyl groups and sulfated groups were determined by elemental analysis (Elementar vario EL □) of the content ratios of C, H, O, N, and S in the synthesized 6-O-CChitin, 6-OCC, N-SOCC, and N,O-SOCC polymers. Molecular weights of chitin and its derivatives were measured by gel permeation chromatography (GPC), which incorporated a TSK G3000-PW column and a RI 150 refractive index detector with 0.1 M aq NaCl eluent flowing at 1.0 mL/min at 30 °C (*20*).

Protection of Mitogenic Activity of bFGF Using 6-OCC, N-SOCC, and N,O-SOCC Polymers. The mitogenic activity of the bFGF protected by the synthesized polymers, under acidic condition, was assessed in vitro by determining its ability to stimulate the proliferation of L929 fibroblast cells cultured in serum-free Eagle's MEM medium, according to the method reported by Akashi et al. (*21*). The bFGF solution (5 μg/mL) was dissolved in phosphate buffered saline (PBS) containing the synthesized 6-OCC, N-SOCC, and N,O-SOCC polymers. The mixture was adjusted to pH 4.0 with HCl. After 30−120 min of incubation, the solutions were diluted with Eagle's MEM containing 10% FCS, and then these solutions added to chlorate-treated L929 fibroblasts which had been preincubated 24-well multiplates at 1×10^4 cells/well for 24 h at 37 °C. The final concentration of bFGF in the medium was 250 ng/mL, whereas the concentration of all synthesized polymers was 10 μg/mL. Cell viability is determined in percent by comparison to control cell cultures uisg a MTT cell viability assay kit (Biotium, Inc. USA). The bFGF protective activity was evaluated as relative cell proliferation respectively in polymer treated groups, at pH 4.0, as compared with the control group (in PBS, pH 7.4). Percent cell number = (cell number in treated bFGF and polymer treated groups)/(cell number in the control). The control (100%) consists of cells incubated with bFGF and polymers under normal conditions (37 °C, 5% CO2, pH =7.4).

Docking Simulation. Molecular modeling was performed with the program AutoDock using parameters adapted from the AMBER force field. The dimer units of 6-OCC, N-SOCC, and N,O-SOCC polymers and heparin were used for molecular docking in Sybyl mol2 format. A heparin-binding site of bFGF was obtained from X-ray crystallography as reported in the literature (*22*). The structural data of bFGF were obtained from the Protein Data Bank (entry code 1BFC). The flexible torsions of ligands were calculated with AutoTors, which docked a flexible ligand into a rigid receptor. To carry out docking simulations, a grid box was defined to enclose the heparin binding site with dimensions of $60 \times 60 \times 60$ Å^3 and a grid spacing of 0.375 Å. Docking was performed using the Lamarckian genetic algorithm (LGA) and Solis and Wets algorithm, where the number of GA is 10, the population size is 50, the maximum number of energy evaluations is 250 000, and the size of local search space to sample is 1.0 will perform at most 300 interactions. The simulation results were shown by figures displaying atomistic pictures of the molecules generated using the molecular graphic program UCSF Chimera.

Thiolation of N,O-SOCC. Thiolated N,O-SOCC was prepared by reacting 2-iminothiolane with amino groups bestows SH groups to N,O-SOCC (*23*). Initially, 500 mg of N,O-SOCC was dissolved in 50 mL of DI water and different amounts of 2-iminothiolane (200−600 mg) was added with 1 mL of 2% DTT. The pH value was adjusted, respectively, with 0.1 M

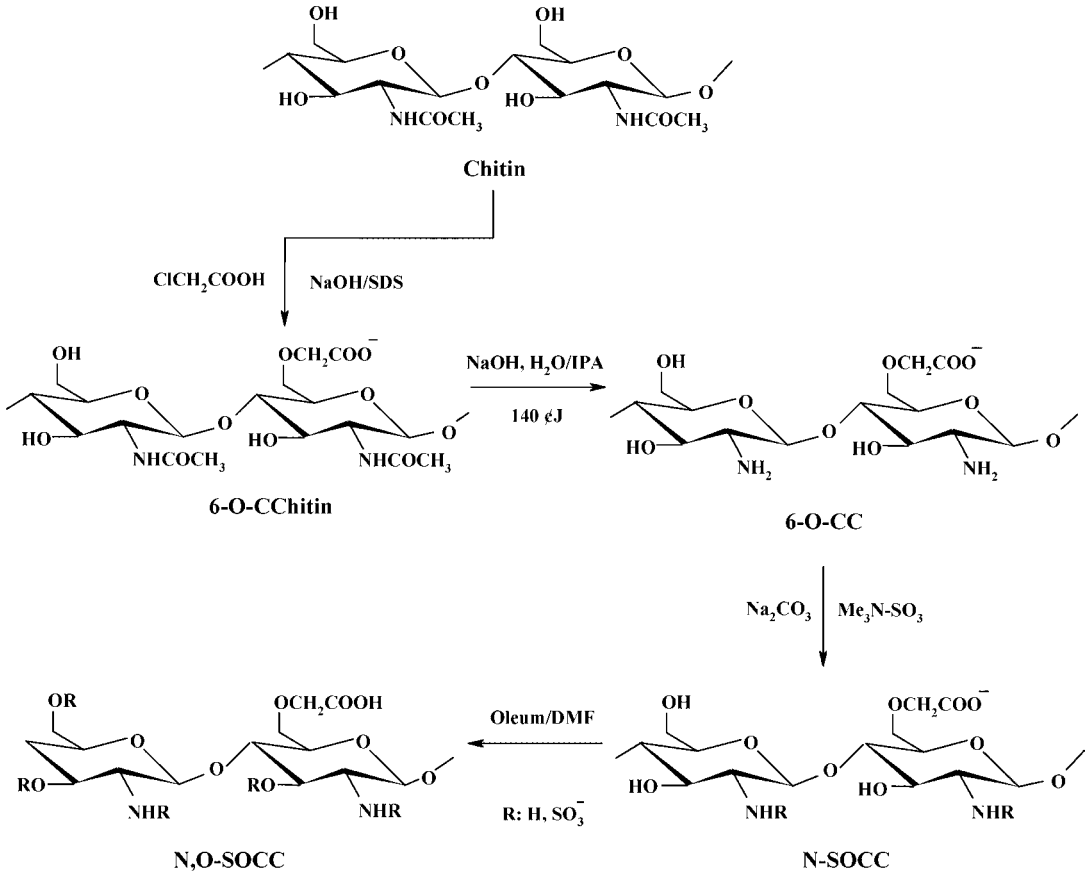


Figure 1. Schematic illustration of the procedures for synthesis of 6-O-CC, N-SOCC, and N,O-SOCC. SDS, sodium dodecyl sulfate; IPA, isopropanol; Oleum, fuming sulfuric acid; DMF, dimethylformamide.

NaOH and HCl to pH 5.0 or 7.0. The coupling reaction was allowed to proceed for 24 h at room temperature under continuous stirring. For purification, the resulting polymer conjugate was dialyzed against 5 mM HCl containing 1% NaCl, against 5 mM HCl and finally against 1 mM HCl to obtain a final pH of 3. Thereafter, the reaction mixtures were dialyzed to remove unreacted 2-iminothiolane at 10 °C and obtain the new kind of thiolated polymer, the 2-iminothiolane modified N,O-SOCC.

Determination of the Thiol Group Content. The degree of modification was determined by quantifying the thiolated N,O-SOCC polymers with 5,5′-dithiobis(2-nitrobenzoic acid) (DTNB, Ellman's reagent) (*24, 25*). DTNB working reagent was prepared by add 50 μL of the DTNB solution and 100 μL Tris solution into 840 μL deionized water. First, 5 mg of thiolated N,O-SOCC polymers was dissolved in 2.5 mL of deionized water. Afterward, 10 μL sample solution was mixed with 990 μL of DTNB reagent and incubated 5 min at 37 °C. The absorbance values of the samples were immediately measured at 415 nm using PowerWave X340 (Bio-TEK Instrument, Inc., Winooski, VT, USA) plate reader. The amount of thiol moieties was calculated from an standard curve obtained by the 2-iminothiolane modified N,O-SOCC solutions with increasing amount of cysteine.

Thiol Oxidation. The 2-iminothiolane modified N,O-SOCC was then dissolved in 100 mM acetate buffer pH 5.0, 100 mM phosphate buffer pH 6.0, or PBS (phosphate buffered saline) buffer pH 7.4, in a final concentration of 0.5% (w/v) at 4 °C. After dissolution, the samples were incubated at 37 °C under permanent shaking. At predetermined time points, aliquots of 500 μL were withdrawn and 50 μL of 1 M HCl was added in order to quench any further reaction. The amount of remaining thiol groups was determined with Ellman's reagent as described above.

Preparation of Polyelectrolyte Complex Nanoparticles. The 2-iminothiolane modified N,O-SOCC/CS nanoparticles were prepared using a polyelectrolyte complex method under magnetic stirring at room temperature. In brief, an aqueous 2-iminothiolane modified N,O-SOCC (1.0 mg/mL, 2 mL, pH 7.4) was added by flush mixing with a pipet tip into aqueous CS at various known concentrations (0.15, 0.30, 0.60, 0.90, or 1.20 mg/mL, 8 mL, pH 6.0). The polyelectrolyte complex nanoparticles were collected by centrifugation at 12 000 rpm for 20 min. Supernatants were discarded, and nanoparticles were resuspended in DI water for further studies. The mean particle sizes and zeta potential values of nanoparticles were measured using a Zetasizer (3000HS, Malvern Instruments Ltd., Worcestershire, UK).

bFGF Entrapment. For preparing the bFGF-loaded nanoparticles, 1 mL of bFGF stock solution (1 μg/mL) was added to the dissolved N,O-SOCC or 2-iminothiolane modified N,O-SOCC solutions (2.0 mg/mL, 1 mL) with continuous stirring at 4 °C. After dissolution of bFGF, the mixed N,O-SOCC or 2-iminothiolane modified N,O-SOCC solution was respectively added into an aqueous CS (1.2 mg/mL, 8 mL) as described before. Afterward, the bFGF-loaded nanoparticles were collected by centrifugation and the amounts of bFGF in the supernatants were analyzed to determine the free bFGF content. The bFGF loading efficiency was calculated by dividing the weight of the loaded bFGF (subtract free bFGF from total amount of bFGF) by the total amount of bFGF (*26*).

The amounts of bFGF were measured by enzyme-linked immunosorption assay (ELISA) kit (Human bFGF Duoset; R&D Systems, Minneapolis, MN, USA). ELISA plates (NUNC; Polylabo, Strasbourg, France) were coated with capture monoclonal antibodies and blocked with 1% BSA (w/v) for 1 h. After adding the appropriately diluted samples to the ELISA plates,

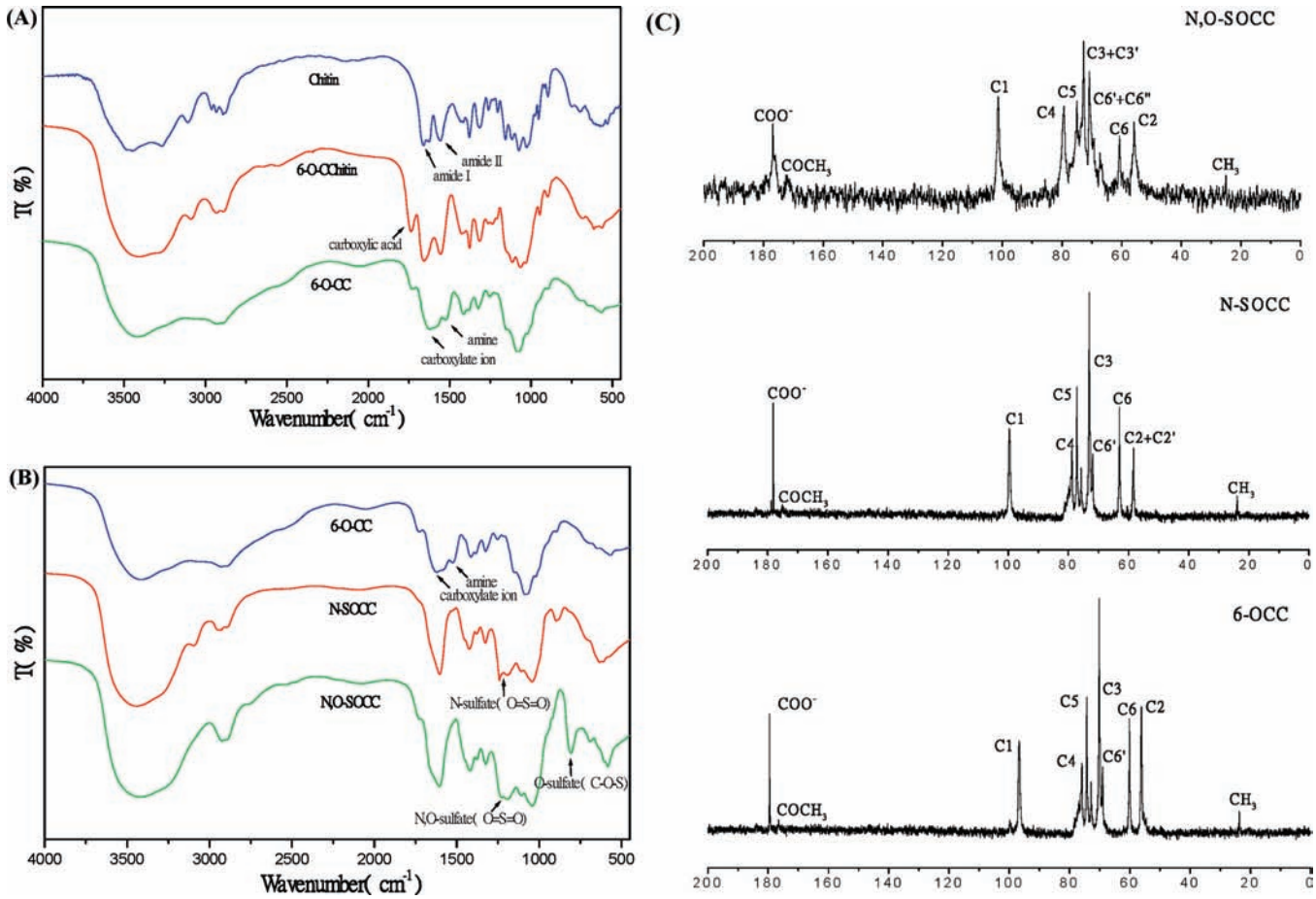


Figure 2. FT-IR spectra of (A) chitin, 6-O-CChitin, and 6-O-CC; (B) 6-O-CC, N-SOCC, and N,O-SOCC; and (C) ^{13}NMR spectra of 6-O-CC, N-SOCC, and N,O-SOCC.

released bFGF was detected using antihuman bFGF polyclonal antibodies. Then, streptavidin-conjugated horseradish peroxidase was added to the plates. The enzyme substrate (tetramethylbenzidine and peroxide) was added and incubated for color development for 20 min. The enzyme reaction was stopped by adding an acidic solution. The absorbance of the samples was read at 450 nm using PowerWave X340 (Bio-TEK Instrument, Inc., Winooski, VT, USA) plate reader. All of the experiments were repeated six times.

Long-Term Release of Protected bFGF for Cell Proliferation. The release profiles of bFGF from the 2-iminothiolane modified N,O-SOCC/CS nanoparticles were determined to study the effects of the in situ cross-linkable thiolated N,O-SOCC on long-term release of protected bFGF. The samples were incubated at 37 °C under continuous agitation, in 5 mL of PBS (pH 7.4) or PBS containing 5.0 mM glutathione (GSH) (*27*). At various time points, the release medium was collected and centrifuged at 12 000 rpm for 20 min, and the supernatant was withdrawn and fresh buffer was replenished. The amounts of bFGF in the supernatants were determined with the above-mentioned method of ELISA assay. All of the experiments were repeated four times.

Long-term protection of the mitogenic activity of the growth factor was assessed by proliferation of L929 fibroblasts cultured in serum-free Eagle's MEM medium with 250 ng/mL of bFGF either in solution or equivalent weight bFGF in nanoparticles. Cell cultured in serum-free Eagle's MEM medium without adding bFGF was used as a control. The cell proliferation was measured using a hemocytometer at different time points over a period of 5 days post-treatment.

Statistical Analysis. Statistical analysis for the determination of differences in the measured properties between groups was accomplished using one-way analysis of variance and determination of confidence intervals, performed with a computer statistical program (*Statistical Analysis System*, v 6.08, SAS Institute Inc., Cary, NC). All data are presented as a mean value with its standard deviation indicated (mean ± SD). Differences were considered to be statistically significant when the p values were less than 0.05.

RESULTS AND DISCUSSION

Synthesis and Characterization of 6-O-CC, N-SOCC, and N,O-SOCC. 6-O-CC was synthesized from its original compound—chitin. Figure 2A showed the FT-IR spectrum of chitin, 6-O-CChitin and 6-O-CC polymers. The characteristic absorption at 1580 cm^{-1} and 1620−1660 cm^{-1} was respectively assigned to the amide I (N—H) and amide II (C═O) stretch of chitin (*18*), while the characteristic absorption at 1710−1715 cm^{-1} was assigned to the carboxylic acid groups on 6-OCChitin. After deacetylation of 6-OCChitin in alkali solution, the carboxylic acid groups were converted into carboxylate ions (∼1650 cm^{-1}), which were partially overlapped with the amine groups (∼1560 cm^{-1}) on 6-O-CC.

Figure 2B showed the FT-IR spectrum of 6-O-CC, N-SOCC, and N,O-SOCC polymers. N-SOCC demonstrated a significant decrease of N—H absorption bands around 1560 cm^{-1} as compared with 6-O-CC. The characteristic absorption bands in the area of 1160−1260 cm^{-1} (O═S═O asymmetric stretch) indicated the presence of sulfamate groups (N-sulfation) (*18*). N-SOCC was further sulfated with oleum, leading to the final

Table 1. Substitution Degrees of 6-O-CChitin, 6-O-CC, N-SOCC, and N,O-SOCC

	DDA[a]	DC[b]	DS[c]	M_w[d]
Chitin	—	—	—	—
6-O-CChitin	—	0.46	—	1.54×10^5
6-O-CC	0.92	0.46	—	1.38×10^5
N-SOCC	0.92	0.46	0.51	8.75×10^4
N,O-SOCC	0.92	0.46	1.13	5.73×10^4

[a] DDA means the degree of deacetylation. [b] DC means the degree of carboxymethylation. [c] DS means the degree of sulfation. [d] M_w means the weight-average molecular weights determined by GPC.

product, N,O-sulfated 6-O-CC (N,O-SOCC) with nonselective sulfate groups at the 2-N, 3-O, and 6-O positions (*19*). The additional characteristic band of N,O-SOCC observed at 800 cm^{-1} representing the C—O—S stretch, suggesting the formation of sulfate ester linkage via the O-sulfation reactions with hydroxyl groups (*20*).

Figure 2C showed the ^{13}C NMR spectra of 6-O-CC, N-SOCC, and N,O-SOCC polymers of chitosan and carboxymethylchitosan. In the spectrum of 6-O-CC, the signals observed at 176.5 and at 23.6 ppm were assigned to the carbonyl carbon of $COCH_3$ and the methyl carbon (CH_3), respectively. The signal at 96.7 ppm was assigned to carbon C-1 of 6-O-CC, and those signals at 56.3, 70.1, 75.9, 74.3, and 60.2 ppm were assigned to carbons C-2, C-3, C-4, C-5, and C-6, respectively. The signal observed at 179.5 ppm is assigned to the carbonyl carbons of carboxymethyl groups (*28*). The spectrum of N-SOCC showed split signals at 58.1 ppm corresponding to N-sulfation, though it was not completely sulfated because the unsulfated signal of C-2 could still be observed (C2+C2′) (*18*). The ^{13}C NMR spectrum of N,O-SOCC indicated that in additional to the N-sulfation, the C-6 and C-3 hydroxyl groups were both partly sulfated (O-sulfation) because of the existence of sulfated and unsulfated signals (C6+C6′+C6″ and C3+C3′) (*19, 20*). The degrees of carboxymethylation and sulfation estimated from elemental analysis, and the molecular weights determined by GPC were shown in Table 1.

bFGF Protective Efficiency and Docuking Simulation. Figure 3A shows the effect of the substituted carboxymethyl and sulfate groups of the synthesized 6-O-CC, N-SOCC, and N,O-SOCC on the retention of bFGF activity. At pH 4.0, the L929 cells proliferated well in serum-free medium containing bFGF and N-SOCC or N,O-SOCC. Dextran sulfate and (1→6)-α-D-mannopyranan sulfate having sulfate groups have been reported to interact with FGFs and mimic heparin effects on the biological activities of FGFs (*29, 30*). Interestingly, N,O-SOCC showed higher bFGF-protective effect compared with its N-SOCC counterpart under the tested pH condition ($p < 0.05$), suggested that the interaction between the sulfated polymer and bFGF requires not only N-sulfate groups, but also the O-sulfate groups. In contrast, 6-O-CC without the sulfate groups could not significantly protect bFGF, and the bFGF-induced cell growth in serum-free Eagle's MEM medium was not observed.

It is noted that binding of bFGF and heparin is mediated by ionic interaction between both N- and O-sulfate groups of heparin molecules and certain lysine (R) and arginine (K) cations in bFGF (*31*). In the study of docking simulation, four docking ligand molecules, respectively, correlating with the dimer units of 6-O-CC, N-SOCC, N,O-SOCC, and heparin were designed (Figure 4A), and their docking energies were computed (Table 2). The N,O-SOCC ligand with the lowest docked energy structure showed sulfate-mediated interactions between bFGF and the ligand involving 2-*N*-sulfate, 3-*O*-sulfate, and 6-*O*-sulfate groups of the ligand and R121, K126, and K136 residues of bFGF (Figure 4B). The interactions between K120, K126 residues and the N,O-SOCC ligand are also mediated via 6-*O*-carboxymethyl groups (Figure 4B). The sulfate groups appeared to predominantly bind to basic amino acid residues, while the carboxymethyl groups complement sulfate groups to contribute in stabilizing the binding structure (*14*). N,O-SOCC substituted with 6-*O*-carboxymethyl groups and 2-N, 3-O, and 6-O sulfate groups may have well-balanced steric and electrostatic structures that can stably interact with bFGF to protect the growth factor against acidic inactivation.

The results of docking simulation and cell proliferation reveal that N,O-SOCC shows the lowest computed docking energy and is the most effective ligand in the retention of bFGF activity (Table 2). Although the N,O-SOCC ligand might have higher affinity to bFGF than heparin, N,O-SOCC is still less effective in the retention of bFGF activity for cell proliferation, as

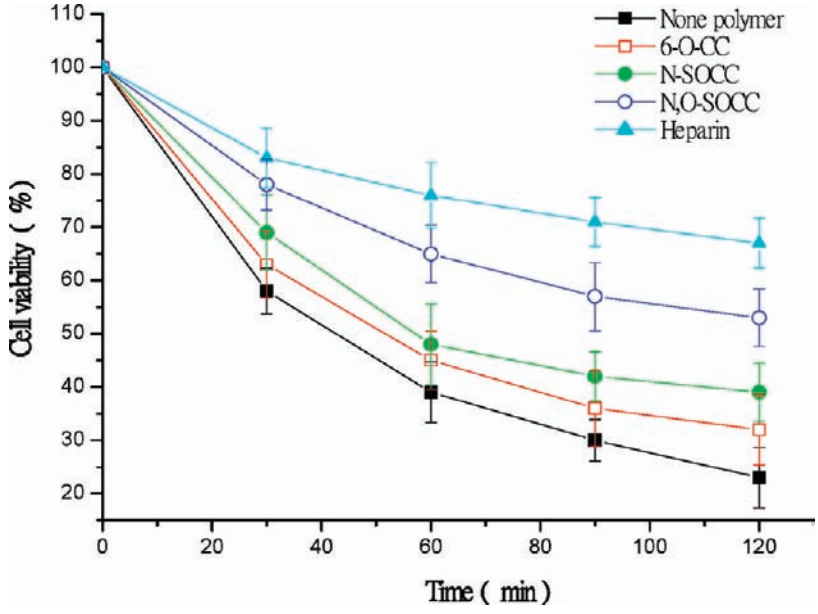


Figure 3. Comparison of the bFGF-protective effect of 6-O-CC, N-SOCC, N,O-SOCC, and heparin polymers under acidic condition (bFGF in pH 4.0 medium, 30−120 min of incubation). Chlorate-treated L929 fibroblasts proliferated in serum-free culture medium with bFGF (250 ng/mL) and polymers (10 μg/mL) for 96 h.

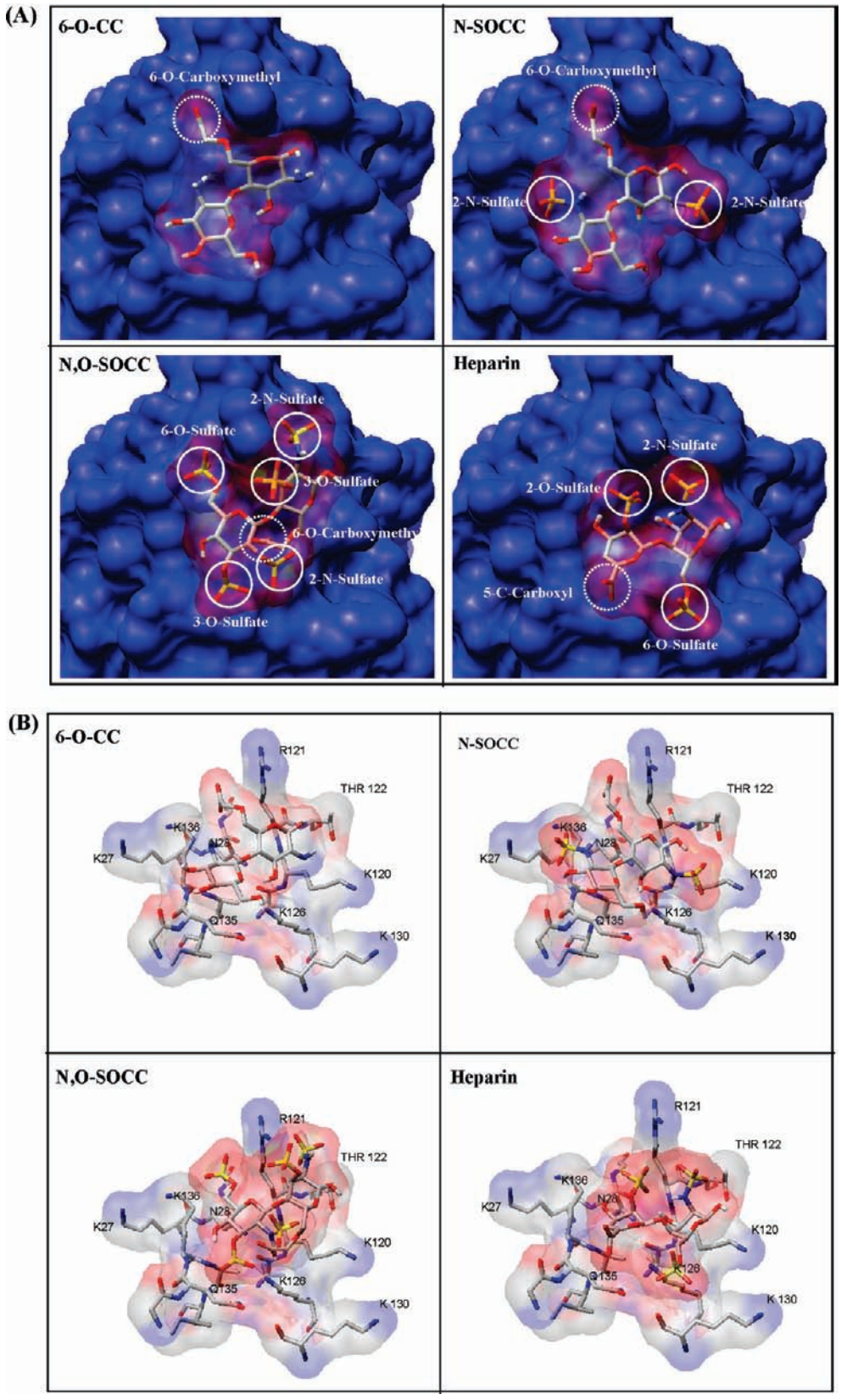


Figure 4. Molecular modeling of docking simulation. (A) Docking conformations of 6-O-CC, N-SOCC, N,O-SOCC, and heparin docking ligands after binding to the heparin-binding site of bFGF. (B) Interaction of 6-O-CC, N-SOCC, N,O-SOCC, and heparin with the amino acids residues at the heparin-binding site of bFGF.

compared with its heparin counterpart (Figure 4A). This will be attributed to heparin not only demonstrating high affinity to FGF family growth factors but also binding to its receptor that facilitates FGF-receptor dimerization and activation (*32*).

Synthesis and Characterization of Thiolated N,O-SOCC. In situ gelling systems based on chitosan derivatives have been developed for glucose-sensitive, pulsatile delivery of insulin (*33*). Thiol-functionalized polymeric micelles or nanoparticles

Table 2. Docked Energy of 6-O-CC, N-SOCC, N,O-SOCC, Thiolated N,O-SOCC, and Heparin

	F[a]	INTM[b]	INTN[c]	Dk[d]
6-O-CC	−5.02	−5.02	0.62	−4.40
N-SOCC	−5.60	−5.60	0.77	−4.83
N,O-SOCC	−5.29	−5.29	−1.19	−6.48
Thiolated N,O-SOCC[e]	−4.24	−4.24	0.56	−3.69
Heparin	−4.63	−4.63	−0.52	−5.15

[a] F means the free energy (kcal/mol). [b] INTM means the intermolecular energy (kcal/mol). [c] INTN means the internal energy (kcal/mol). [d] DK means the docked energy (kcal/mol). [e] Thiolated N,O-SOCC means the 2-iminothiolane modified N,O-SOCC.

have also been investigated for molecular recognition, tumor immunotargeting, or intracellular DNA delivery in response to glutathione (*28, 34, 35*). In this work, N,O-SOCC was selected for thiolation because the correlated ligand has the lowest docking energy. The thiolated N,O-SOCC polymer prepared by modification of N,O-SOCC with 2-iminothiolane was in situ cross-linkable. Apart from a sulfhydryl group, a cationic moiety is also introduced in the form of an amidine substructure resulting in a N,O-SOCC-4-thio-butylamidine (TBA) conjugate (*23*). The schematic procedure for the synthesis of 2-iminothiolane modified N-SOCC and the formation of its disulfide compound is shown in Figure 5. The modification of N,O-SOCC with 2-iminothiolane can be performed under inert condition to avoid the oxidation of thiol groups. The low reactivity of 2-iminothiolane in acid has also been reported (*23*). Therefore, we synthesized the thiolated N,O-SOCC in acidic (pH 5) and neutral (pH 7) conditions, and the reactants were purged with nitrogen. The amount of covalently attached thiol groups on the thiolated polymers was shown in Table 3.

The docking ligand molecule correlates with the 2-iminothiolane modified N,O-SOCC displayed a higher docking energy as compared with its original N,O-SOCC counterpart, revealing a lower thiolated N,O-SOCC affinity of bFGF (Table 2). The steric hindrance of the conjugated thiomer (TBA) resulted in the shift of 2-N, 3-O, and 6-O sulfate groups to the region far from the heparin-binding residues, such as R121, K126, and

Table 3. Substituted Thiol Moieties on the 2-Iminothiolane Modified N,O-SOCC Polymers

polymer N,O-SOCC	2-iminothiolane (g)	pH	conjugated thiol groups (μmol/g polymer)
500 mg	200 mg	5.0	45.2 ± 3.7
500 mg	400 mg	5.0	67.5 ± 7.9
500 mg	600 mg	5.0	298.4 ± 9.8
500 mg	200 mg	7.0	97.3 ± 7.1
500 mg	400 mg	7.0	258.4 ± 8.6
500 mg	600 mg	7.0	415.6 ± 12.5

K136 (Figure 6A). This simulated result suggested that bFGF protective efficiency of the thiolated N,O-SOCC might be decreased with the increase of the substituted thiomer degree. Therefore, we selected a 2-iminothiolane modified N-SOCC product with mediate thiol substitution [258.4 ± 8.6 (μmol/g polymer)] for the following studies.

Thiol Oxidation of 2-Iminothiolane Modified N,O-SOCC. At pH 7.4, in the presence of oxygen, the thiol groups on the 2-iminothiolane modified N,O-SOCC can be easily oxided to disulfide bonds (Figure 6B), forming an in situ cross-linked network structure. Depending on the pH value, the thiol groups of 2-iminothiolane modified N,O-SOCC were oxidized, thereby forming inter- as well as intramolecular disulfide bonds. At pH 5.0, the thiol groups of 2-iminothiolane modified N,O-SOCC remained stable toward oxidation, whereas at pH 6.0, a decrease of 56% in the thiol moieties was observed, within 6 h of oxidation in air. Raising the pH value from 6.0 to 7.4 led to a higher concentration of negative thiolate anions, representing the reactive form for oxidation, finally resulting in a significant decrease of thiol moieties due to the formation of disulfide bonds (*23, 25*). These results revealed that thiolated N,O-SOCC could be used as an in situ cross-linkable polymer to entrap peptide or protein drugs for specific drug delivery purpose.

Characterization of 2-Iminothiolane Modified N,O-SOCC/CS Nanoparticles. 2-Iminothiolane modified N,O-SOCC and CS complex could be used for preparing nanoparticles by a polyelectrolyte self-assembly method. The particle sizes and the zeta potential values of the thiol-modified N,O-SOCC/CS

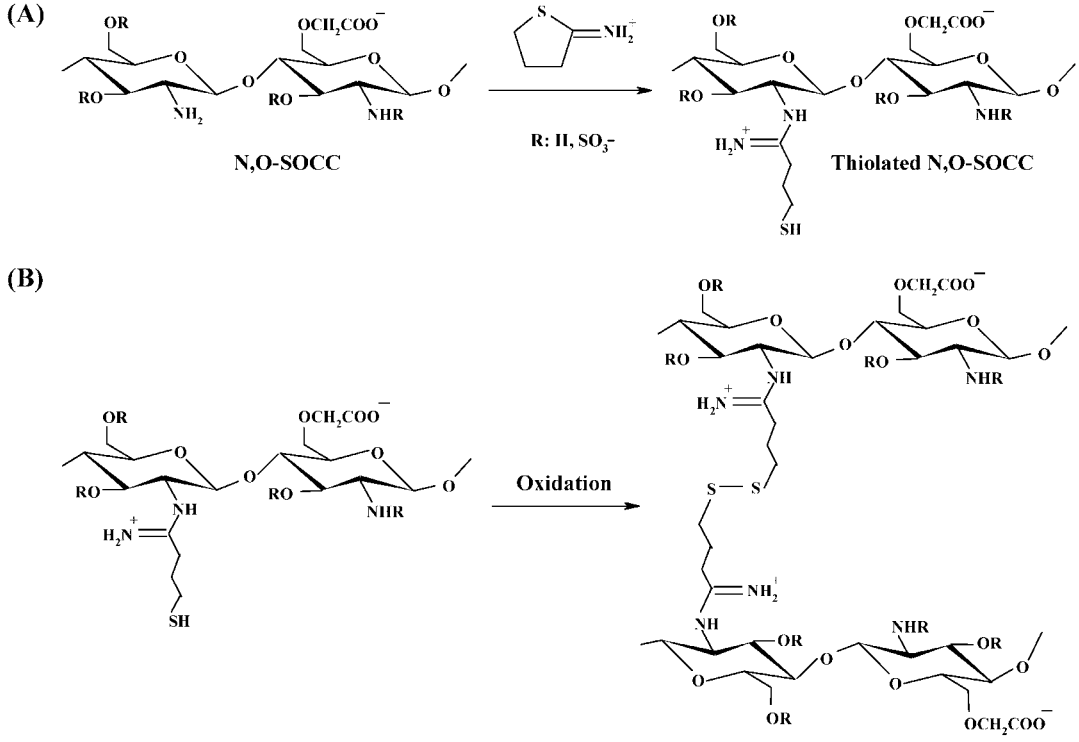


Figure 5. Schematic procedures for the synthesis of 2-iminothiolane modified N,O-SOCC (A) and the formation of its disulfide compound (B).

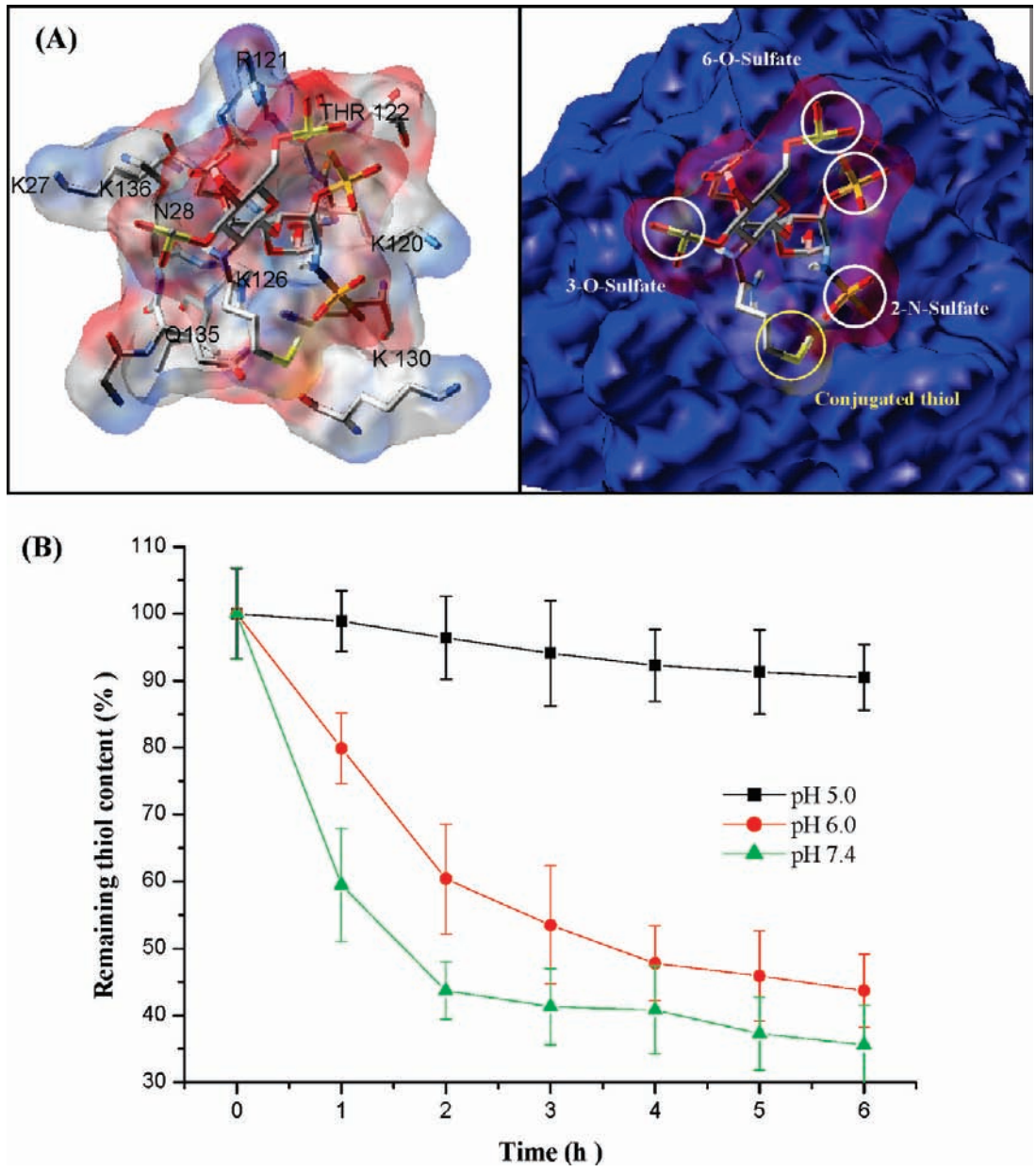


Figure 6. (A) Docking conformation of the 2-iminothiolane modified N,O-SOCC ligand after binding to the heparin binding site of bFGF and the interaction of the 2-iminothiolane modified N,O-SOCC with the amino acid residues of bFGF. (B) Decrease in thiol groups of 1.0% (w/v) 2-iminothiolane modified N,O-SOCC at pH values 5.0, 6.0, and 7.4. The thiol content of the 2-iminothiolane modified N,O-SOCC was 258.4 ± 8.6 μmol/g polymer.

nanoparticles, prepared at varying concentrations of the thiolated N,O-SOCC and CS, were determined, and the results are shown in Table 4. It was found that the particle size values of the prepared nanoparticles were mainly determined by the relative amount of the local concentration of the 2-iminothiolane modified N,O-SOCC in the added solution to the surrounding concentration of CS in the sink solution. At a fixed concentration of CS, an increase in the CS concentration allowed the thiolated N,O-SOCC molecules interacting with more CS molecules and thus formed a larger-sized nanoparticle. The formed nanoparticles had CS exposed on the surfaces and thus had a positively charged zeta potential.

In contrast, as the amount of local 2-iminothiolane modified N,O-SOCC molecules sufficiently exceeded that of surrounding CS molecules, the formed nanoparticles had the thiolated N,O-SOCC exposed on the surfaces and thus had a high negative charge of zeta potential. Therefore, the particle size and the zeta potential value of the prepared thiolated N,O-SOCC/CS nanoparticles can be controlled by their constituted compositions. The nanoparticles shelled with 2-iminothiolane modified N,O-SOCC were unstable, while those shelled with CS remained

Table 4. Effects of Various Weight Ratios (or charge ratios) of Chitosan to 2-Iminothiolane Modified N,O-SOCC on Mean Particle Size and Zeta Potential of Nanoparticles

2-iminothiolane N,O-SOCC/CS (w/w)	2-iminothiolane N,O-SOCC/CS charge ratio	mean particle size (nm)	zeta potential (mV)
1/0.6	1.00/0.48	218.4 ± 8.6	−21.8
1/1.2	1.00/0.95	[c]	[c]
1/2.4	1.00/1.90	242.6 ± 6.9	20.3
1/3.6	1.00/2.86	262.8 ± 3.4	28.1
1/4.8	1.00/3.81	289.9 ± 4.5	32.8

[a] Prepared in deionized water (pH 6.0, $n = 5$). [b] Ratio of positively charged $-NH_3^+$ groups on CS to negatively charged $-COO^-$ and $-SO_3^-$ groups on 2-iminothiolane modified N,O-SOCC. [c] Precipitation of aggregates was observed after 1 h.

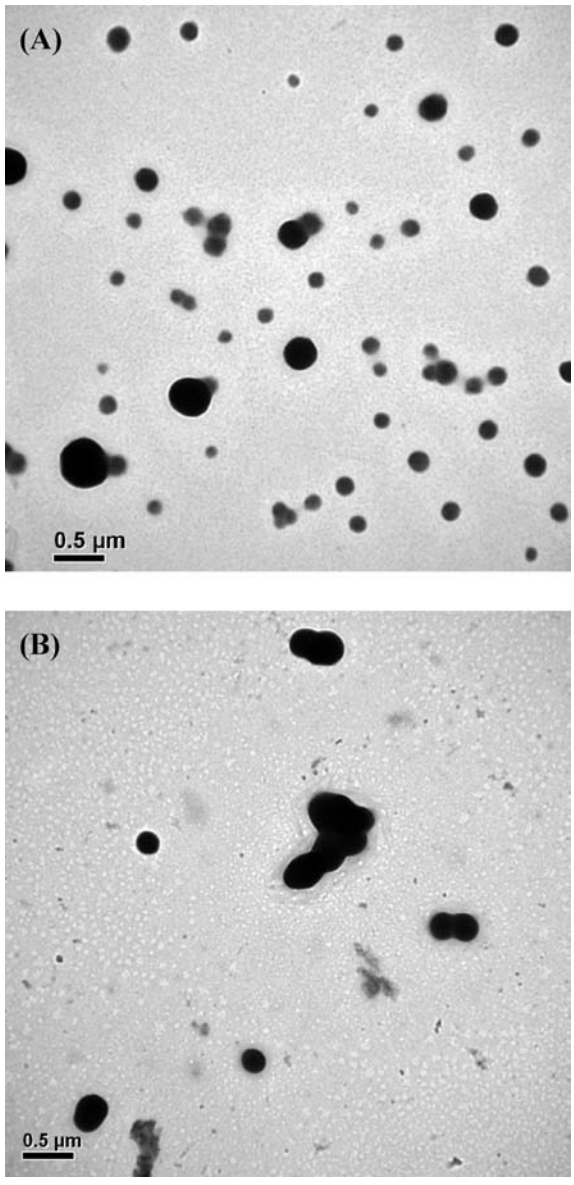


Figure 7. TEM micrographies of the 2-iminothiolane modified N,O-SOCC/CS nanoparticles shelled with (A) CS (1.0 mg/mL thiolated N,O-SOCC: 1.2 mg/mL CS) and (B) 2-iminothiolane modified N,O-SOCC (1.0 mg/mL thiolated N,O-SOCC: 0.30 mg/mL CS).

intact in PBS buffer. Even a minute amount of free thiolated N,O-SOCC in the medium could react with the thiol groups shelled on nanoparticles to form disulfides and finally resulted in the aggregation of nanoparticles. The results obtained by the TEM examination showed that the morphology of the prepared nanoparticles shelled with CS (1.0 mg/mL thiolated N,O-SOCC: 1.2 mg/mL CS) was spherical in shape with a smooth surface, while the nanoparticles shelled with 2-iminothiolane modified N,O-SOCC (1.0 mg/mL thiolated N,O-SOCC: 0.30 mg/mL CS) were aggregated due to the oxidation of surface thiol groups to disulfide bonds between the nanoparticles (Figure 7). Therefore, the CS shelled nanoparticles (1.0 mg/mL thiolated N,O-SOCC: 1.2 mg/mL CS) was selected for the following studies of bFGF entrapment and release.

In body fluids and extracellular matrixes, a relatively low concentration of GSH (approximately 2−20 μM) could be found. In contrast, inside cells the concentration of GSH is 0.5−10 mM. The variation of particle size in simulated physiological condition (pH 7.4 with 10 mM glutathione) was determined to study the stability of nanoparticles. As shown in Table 5, the mean particle size of GSH-treated nanoparticles gradually increased, reaching about 480 nm within 120 h. However, without GSH treatment, the nanoparticles in PBS solution showed negligible size variation within the same period of time. This result suggested that the cleavage of disulfide linkage in the presence of GSH led to swelling of the nanoparticles.

Table 5. Variation of Mean Particle Size of Thiolated N,O-SOCC/CS Nanoparticles in GSH-Containing PBS Solution

time (h)	pH 6.0 (in DI water)	pH 7.4 (in PBS)	pH 7.4 (in PBS/GSH medium)
0	289.9 ± 4.5	289.9 ± 4.5	289.9 ± 4.5
24	293.7 ± 7.8	307.4 ± 7.3	425.4 ± 7.3
48	298.2 ± 5.9	309.5 ± 5.8	447.8 ± 8.6
72	301.6 ± 6.7	307.6 ± 7.1	462.1 ± 6.8
96	299.1 ± 8.5	308.4 ± 6.5	471.5 ± 7.9
120	298.9 ± 6.9	309.1 ± 7.7	480.6 ± 8.4[a]

[a] The concentration of GSH is 10 mM.

bFGF Entrapment and Release. Chitosan and its derivative-based nanoparticles have been previously investigated for delivery of bioactive reagents, including proteins and genes (*36*−*38*). In this study, the thiolated N,O-SOCC, as an in situ cross-linkable polymer, has the advantage of entrapping bFGF without leading to the decrease in bioactivity of the peptide drug. The encapsulation of bFGF does not seem to significantly change the size and zeta potential of the nanoparticles. We have found that nanoparticles prepared only by CS and N,O-SOCC (the N,O-SOCC/CS nanoparticles), without modification with thiol groups, were very unstable and disintegrated rapidly in PBS buffer due to the balance of electrostatic charges by phosphate salts. Owing to the formation of covalently disulfide bonds, the 2-iminothiolane modified N,O-SOCC/CS nanoparticles with a positive surface charge (1.0 mg/mL thiolated N,O-SOCC: 1.2 mg/mL CS) could be used for bFGF entrapment and were kept stable in PBS buffer. The bFGF loading efficiency for N,O-SOCC/CS and 2-iminothiolane modified N,O-SOCC/CS nanoparticles were 61.4% ± 5.8% and 54.9% ± 3.6%, respectively.

Figure 8A shows the release profile of bFGF from the nanoparticles of N,O-SOCC/CS and 2-iminothiolane modified N,O-SOCC/CS nanoparticles in PBS buffer and the buffer containing glutathione. The N,O-SOCC/CS nanoparticles were unstable in PBS and could disintegrate rapidly to release the growth factor quickly. In contrast, the 2-iminothiolane modified N,O-SOCC introduced the disulfide bonds could assembled with CS into stable nanoparticles, coinciding with a slower release rate. The thiolated N,O-SOCC/CS nanoparticles shelled with CS suggested that bFGF-binding N,O-SOCC could be incoporated in the core of nanoparticles. Glutathione can reduce the covalent disulfide bonds to thiols leading to a quicker release of the growth factor from the nanoparticles.

Cell Proliferation. The mitogenic activity of bFGF released from the 2-iminothiolane modified N,O-SOCC/CS nanoparticles after 5 days of incubation was evaluated by L929 cell culture in serum-free Eagle's MEM medium (Figure 8B). The cell number of L929 fibroblasts does not seem to increase in the serum-free basal medium (control), indicating no additional cell growth in the medium without bFGF. The addition of bFGF in a free form to the basal medium stimulated the growth of L929 fibroblasts at day 2, and the growth increase of cells is significant as compared with that of the control group. The cells in the medium added with the bFGF-loaded, N,O-SOCC/CS nanoparticles showed increased cell proliferation comparable to the group of cells cultured with a free-form bFGF, because the nanoparticles disintegrate rapidly to release the growth factor quickly. Conversely, cells treated with bFGF-loaded, thiol modified N,O-SOCC/CS nanoparticles demonstrated a sustained significant increase in the cell proliferation activity ($p < 0.05$).

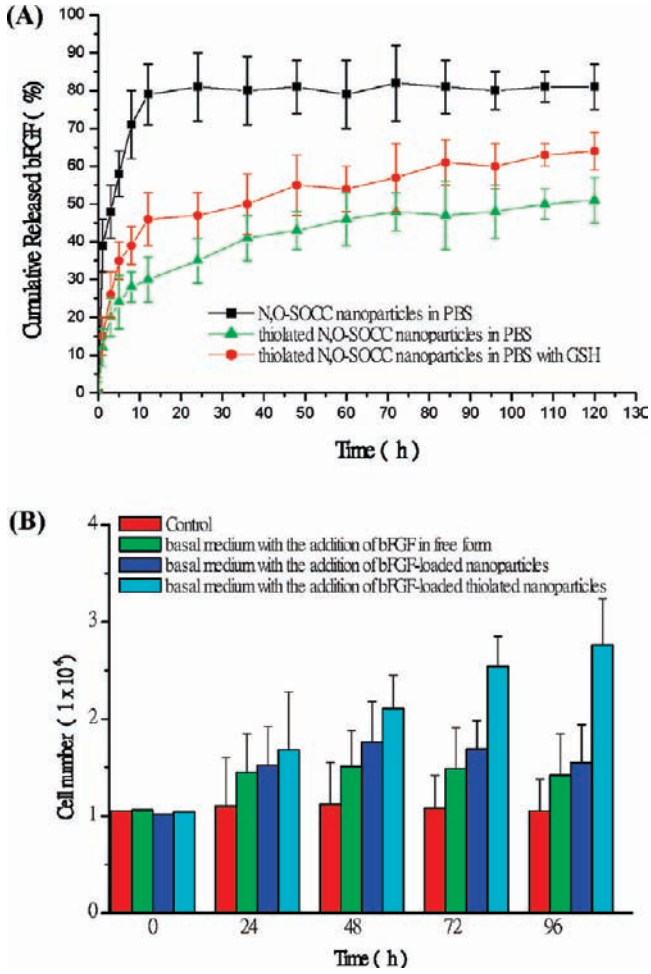


Figure 8. (A) Release profiles of bFGF from N,O-SOCC/CS and 2-iminothiolane modified (thiolated) N,O-SOCC/CS nanoparticles at 37 °C in 10 mL of PBS (pH 7.4) or PBS containing 5.0 mM glutathione (GSH). The thiol content of the 2-iminothiolane modified N,O-SOCC was 258.4 ± 8.6 μmol/g polymer. (B) The growth kinetics of L929 fibroblasts cultured in serum-free culture medium (basal medium), basal medium with the addition of bFGF in free form, and the N,O-SOCC/CS and 2-iminothiolane modified (thiolated) N,O-SOCC/CS nanoparticles loaded with bFGF.

This result indicates that only the thiol modified N,O-SOCC/CS nanoparticle is able to protect bFGF from inactivation over the long term.

Due to the protective effect of the nanoparticles, mitogenic activity of bFGF could be retained for a long time, without evident denaturation. The released growth factor could effectively bind to the cellular bFGF receptor for cell growth. It was encouraging to find that the nanoparticles could be easily mixed with several biological components such as alginate, chitosan, collagen, gelatin, and hyaluronic acid to be reshaped into nanoparticle-containing hydrogels or 3-D scaffolds. As reported in the literature, the therapy of ischemic disease and "in advance angiogenesis" for cell transplantation are two important objectives of angiogenesis in tissue engineering. In tissue repairing applications, therapeutic strategies of injecting bFGF-containing nanoparticles to stimulate arteriogenesis in animal models suffering from occlusive vascular disease received significant benefit from improved targeting, less invasiveness, better growth-factor stability, and more sustained growth-factor release (*39*).

Other studies reported that prolonged retention of activity of the growth factors and controlled release of the signal proteins at the site of action with reduced burst effect became possible by encapsulating the factors in micro- or nanoparticles before being incorporated with hydrogels or 3-D scaffolds (*40*). The results of this study suggest that the thiol modified N,O-SOCC/CS nanoparticles may be useful as novel materials for tissue engineering and might yield interesting future work.

CONCLUSIONS

In conclusion, we have synthesized a heparin-like chitosan derivative, N,O-sulfated, 6-O-carboxymethylchitosan (N,O-SOCC). N,O-SOCC demonstrated high affinity to bFGF and could protect mitogenic activity of bFGF as investigated by cell proliferation and docking simulation. Thiol modified N,O-SOCC was assembled with CS to form thiolated N,O-SOCC/CS nanoparticles. The thiolated N,O-SOCC/CS nanoparticles enhance the bFGF-stimulated cell growth through protecting the released growth factor from inactivation. It may be useful as a new biomaterial for the controlled release of bFGF for tissue-engineering applications.

ACKNOWLEDGMENT

The financial support for this research was provided by the National Science Council (NSC 95-2120-M-007-010 and NSC 96-2221-E-238-010), Taiwan, R.O.C.

LITERATURE CITED

(1) Burgess, W. H., and Maciag, T. (1989) The heparin-binding (fibroblast) growth factor family of proteins. *Annu. Rev. Biochem. 58*, 575–606.
(2) Ruoslahti, E., and Yamaguchi, Y. (1991) Proteolglycans as modulators of growth factor activities. *Cell 64*, 867–869.
(3) Gospodarowicz, D., Neufeld, G., and Schweigerer, L. (1986) Fibroblast growth factor. *Mol. Cell. Endocrinol. 46*, 187–204.
(4) DiGabriele, A. D., Lax, I., Chen, D. I., Svahn, C. M., Jaye, M., Schlessinger, J., and Hendrickson, W. A. (1998) Structure of a heparin-linked biologically active dimer of fibroblast growth factor. *Nature 393*, 812–817.
(5) Langer, R., and Vacanti, J. P. (1993) Tissue engineering. *Science 260*, 920–926.
(6) Abrahma, J. A., Mergia, J., Whang, L., Tumolo, A., Friedman, J., Hjerrild, K. A., Gospodarowicz, D., and Fiddes, J. C. (1986) Nucleotide sequence of a bovine clone encoding the angiogenic protein, basic fibroblast growth factor. *Science 233*, 545–548.
(7) Schreiber, A. B., Kenney, J., Kowalski, J., Friesel, R., and Mehlman, T. (1985) Interaction of endothelial cell growth factor with heparin: characterization by receptor and antibody recognition. *Proc. Natl. Acad. Sci. 82*, 6138–6142.
(8) Pike, D. B., Cai, S., Pomraning, K. R., Firpo, M. A., Fisher, R. J., Shu, X. Z., Prestwich, G. D., and Peattie, R. A. (2006) Heparin-regulated release of growth factors in vitro and angiogenic response in vivo to implanted hyaluronan hydrogels containing VEGF and bFGF. *Biomaterials 27*, 5242–5251.
(9) Chung, Y. I., Tae, G. , and Yuk, S. H. (2006) A facile method to prepare heparin-functionalized nanoparticles for controlled release of growth factors. *Biomaterials 27*, 2621–2626.
(10) Nillesen, S. T. M., Geutjes, P. J., Wismans, R., Schalkwijk, J., Daamen, W. F., and van Kuppevelt, T. H. (2007) Increased angiogenesis and blood vessel maturation in acellular collagen-heparin scaffolds containing both FGF2 and VEGF. *Biomaterials 28*, 1123–1131.
(11) Fisher, K. D., Ulbrich, K., Subr, V., Ward, C. M., Mautner, V., Blakey, D., and Seymour, L. W. (2000) A versatile system for receptor-mediated gene delivery permits increased entry of DNA into target cells, enhanced delivery to the nucleus and elevated rates of transgene expression. *Gene Ther. 7*, 1337–1343.
(12) Li, D., Yu, H., Huang, H., Shen, F., Wu, X., Li, J., Wang, J., Cao, X., Wang, Q., and Tang, G. (2007) FGF receptor-mediated gene delivery using ligands coupled to polyethylenimine. *J. Biomater. Appl. 22*, 163–180.

(13) Baskaran, S., Grande, D., Sun, X. L., Yayon, A., and Chaikof, E. L. (2002) Glycosaminoglycan-mimetic biomaterials. 3. Glycopolymers prepared from alkene- derivatized mono- and disaccharide-based glycomonomers. *Bioconjugate Chem. 13*, 1309–1313.

(14) Matsusaki, M., and Akashi, M. (2005) Novel functional biodegradable polymer IV: pH-sensitive controlled release of fibroblast growth factor-2 from a poly(γ-glutamic acid)-sulfonate matrix for tissue engineering. *Biomacromolecules 6*, 3351–3356.

(15) Freeman, I., Kedem, A., and Cohen, S. (2008) The effect of sulfation of alginate hydrogels on the specific binding and controlled release of heparin-binding proteins. *Biomaterials 29*, 3260–3268.

(16) Kim, T. H., Jiang, H. L., Jere, D., Park, I. K., Cho, M. H., Nah, J. W., Choi, Y. J., Akaike, T., and Cho, C. S. (2007) Chemical modification of chitosan as a gene carrier in vitro and in vivo. *Prog. Polym. Sci. 32*, 726–753.

(17) Mi, F. L., Chen, C. T., Tseng, Y. C., Kuan, C. Y., and Shyu, S. S. (1997) Iron(III)- carboxymethylchitin microsphere for the pH-sensitive release of 6-mercaptopurine. *J. Controlled Release 44*, 19–32.

(18) Holme, K. R., and Perlin, A. S. (1997) Chitosan N-sulfate. A water soluble polyelectrolyte. *Carbohydr. Res. 302*, 7–12.

(19) Vikhoreva, G., Bannikova, G., Stolbushkina, P., Panov, A., Drozd, N., Makarov, V., Varlamov, V., and Gal'braikh, L. (2005) Preparation and anticoagulant activity of a low-molecular- weight sulfated chitosan. *Carbohydr. Polym. 62*, 327–332.

(20) Huang, R, Du, Y., Yang, J., and Fan, L. (2003) Influence of functional groups on the in vitro anticoagulant activity of chitosan sulfate. *Carbohydr. Res. 338*, 483–489.

(21) Matsusaki, M., Serizawa, T., Kishida, A., and Akashi, M. (2005) Novel functional biodegradable polymer II: bFGF stabilizing activity of poly(γ-glutamic acid) sulfonate. *Biomacromolecules 6*, 400–407.

(22) Faham, S., Hileman, R. E., Fromm, J. R., Linhardt, R. J., and Rees, D. C. (1996) Heparin structure and interactions with basic fibroblast growth factor. *Science 271*, 1116–1120.

(23) Bernkop-Schnurch, A., Guggi, D., and Pinter, Y. (2004) Thiolated chitosans: development and in vitro evaluation of a mucoadhesive, permeation enhancing oral drug delivery system. *J. Controlled Release 94*, 177–186.

(24) Masuko, T., Minami, A., Iwasaki, N., Majima, T., Nishimura, S., and Lee, Y. C. (2005) Thiolation of chitosan. Attachment of proteins via thioether formation. *Biomacromolecules 6*, 880–884.

(25) Vanderhooft, J. L., Mann, B. K., and Prestwich, G. D. (2007) Synthesis and characterization of novel thiol-reactive poly(ethylene glycol) crosslinkers for biomaterials. *Biomacromolecules 8*, 2883–2889.

(26) Mi, F. L., Wu, Y. Y., Lin, Y. H., Sonaje, K., Ho, Y. C., Chen, C. T., Juang, J. H., and Sung, H. W. (2008) Oral delivery of peptide drugs using nanoparticles self-assembled by poly(gamma-glutamic acid) and a chitosan derivative functionalized by trimethylation. *Bioconjugate Chem. 19*, 1248–1255.

(27) Kommareddy, S., and Amiji, M. (2005) Preparation and evaluation of thiol-modified gelatin nanoparticles for intracellular DNA delivery in response to glutathione. *Bioconjugate Chem. 16*, 1423–1432.

(28) de Abreu, F. R., and Campana-Filho, S. P. (2009) Characteristics and properties of carboxymethylchitosan. *Carbohydr. Polym. 75*, 214–221.

(29) Kajio, T., Kawahara, K., and Kato, K. (1992) Stabilization of basic fibroblast growth factor with dextran sulfate. *FEBS 306*, 243–246.

(30) Kunou, M., and Hatanaka, K. (1995) Effects of heparin, dextran sulfate, and synthetic (1→6)-α-D-mannopyranan sulfate and acidic fibroblast growth factor on 3T3-L1 fibroblasts. *Carbohydr. Res. 28*, 107–112.

(31) Rusnati, M., Coltrini, D., Caccia, P., Dell'Era, P., Zoppetti, G., Oreste, P., Valsasina, B., and Presta, M. (1994) Distinct role of 2-O-, N- and 6-O-sulfate groups of heparin in the formation of the ternary complex with basic fibroblast growth factor and soluble FGF receptor-1. *Biochim. Biophys. Res. Commun. 203*, 450–458.

(32) Spivak-Kroitzman, T., Lemmon, M. A., Dikic, I., Ladbury, J. E., Pinchasi, D., Huang, J., Jaye, M., Crumley, G., Schlessinger, J., and Lax, I. (1994) Heparin-induced oligomerization of FGF molecules is responsible for FGF receptor dimerization, activation, and cell proliferation. *Cell 79*, 1015–1024.

(33) Kashyap, N., Viswanad, B., Sharma, G., Bhardwaj, V., Ramarao, P., Kumar, M. N. V., and Ravi. (2007) Design and evaluation of biodegradable, biosensitive in situ gelling system for pulsatile delivery of insulin. *Biomaterials 28*, 2051–2060.

(34) Nobs, L., Buchegger, F., Gurny, R., and Alle′mann, E. (2006) Biodegradable nanoparticles for direct or two-step tumor immunotargeting. *Bioconjugate Chem. 17*, 139–145.

(35) Dufresne, M. H., Gauthier, M. A., and Leroux, J. C. (2005) Thiol-functionalized polymeric micelles: from molecular recognition to improved mucoadhesion. *Bioconjugate Chem. 16*, 1027–1033.

(36) Mi, F. L., Wu, Y. Y., Chiu, Y. L., Chen, M. C., Sung, H. W., Yu, S. H., Huang, M. F., and Shyu, S. S. (2007) Synthesis of a novel antennary type of galactosylated chitosan and preparation of its derived nanoparticles for targeting HepG2 cells. *Biomacromolecules 8*, 892–898.

(37) Lee, P. W., Peng, S. F., Su, C. J., Mi, F. L., Chen, H. L., Wei, M. C., Lin, H. J., and Sung, H. W. (2008) The use of biodegradable polymeric nanoparticles in combination with a low-pressure gene gun for transdermal DNA delivery. *Biomaterials 29*, 742–751.

(38) Lin, Y. H., Sonaje, K., Lin, K. M., Juang, J. H., Mi, F. L., Yang, H. W., and Sung, H. W. (2008) Multi-ion-crosslinked nanoparticles with pH-responsive characteristics for oral delivery of protein drugs. *J. Controlled Rel. 132*, 141–149.

(39) Tabata, Y. (2005) Significance of release technology in tissue engineering. *Drug Discovery Today 10*, 1639–1646.

(40) Biondi, M., Ungaro, F., Quaglia, F., and Netti, P. A. (2008) Controlled drug delivery in tissue engineering. *Adv. Drug Delivery Rev. 60*, 229–42.

BC900208T

Peptide Conjugation at the 5′-End of Oligodeoxynucleotides Abrogates Toll-Like Receptor 9-Mediated Immune Stimulatory Activity

Mallikarjuna Reddy Putta, Fu-Gang Zhu, Daqing Wang, Lakshmi Bhagat, Meiru Dai, Ekambar R. Kandimalla, and Sudhir Agrawal*

Idera Pharmaceuticals, Inc., 167 Sidney Street, Cambridge, Massachusetts 02139. Received June 4, 2009; Revised Manuscript Received November 30, 2009

Bacterial and synthetic DNA containing unmethylated CpG motifs act as ligands of Toll-like receptor 9 (TLR9). Our earlier studies showed that 5′-accessibility of synthetic oligodeoxynucleotides containing CpG motif (ODN) is required for TLR9-mediated immune stimulatory activity. Blocking the 5′-end of ODN through conjugation to a variety of moieties reduces immune stimulatory activity (*Bioconjugate Chem.* **2002**, *13*, 966−974). In the present study, we conjugated a model peptide, a 28-amino-acid-long β-amyloid peptide, to either the 5′- or the 3′-end of an ODN via C3 and C6 alkyl linkers. We compared the immune stimulatory activity of the resulting conjugates with that of a parent ODN without conjugation in TLR9-transfected cells, mouse spleen cell cultures, and in vivo in mice. ODN with the peptide conjugated at the 3′-end via C3 and C6 linkers had immune stimulatory activity similar to that of the parent ODN in both in vitro and in vivo in mice. On the contrary, conjugation of peptide at the 5′-end of the ODN significantly abrogated immune stimulatory activity. In conclusion, the results presented here demonstrate that peptide/protein conjugation to ODN is optimal at the 3′-end with either C3 or C6 linker and conjugation at the 5′-end leads to significant loss of TLR9-mediated immune stimulation.

INTRODUCTION

Toll-like receptor 9 (TLR9) belongs to a family of conserved pathogen-associated molecular pattern recognition receptors and is predominantly expressed in the endosomal membranes of human B cells and plasmacytoid dendritic cells (pDCs). Synthetic oligodeoxynucleotides containing unmethylated CpG motifs (ODNs) act as ligands of TLR9 (*1*). Stimulation of TLR9 with ODN leads to the activation of MyD88-dependent NF-κB and MAPK pathways, resulting in Th1-type immune responses (*2, 3*). Agonists of TLR9 are currently at various stages of clinical evaluation for the treatment of cancers, allergies, and infectious diseases and as adjuvants with vaccines (*1–4*).

Agonists of TLR9 (ODNs) induce potent Th1-type immune responses and show encouraging results as adjuvants when coadministered with DNA/protein/peptide vaccines (*5–12*). In addition to coadministration of ODN with vaccines/antigens (proteins), studies have been carried out to deliver both protein and ODN to the same antigen-presenting cell (APC) either by coformulation of both agents in liposomes or by conjugating proteins to ODN to increase immune responses (*13*). Some of the peptides/proteins conjugated to ODNs include Amb a 1, OVA, β-galactosidase, and HIV gp120 (*14–17*). Proteins and peptides are commonly conjugated to the 5′-end of ODN, because the chemical modifications required for conjugation reactions at the 5′-end are easily accomplished during the solid-phase synthesis (*18*). Recently, a conjugate of Amb a 1-ODN failed to meet the end points in a clinical study, prompting us to perform the present study to further elucidate the impact of 5′-conjugation of peptide to ODN on immune stimulatory activity.

Our extensive structure−activity relationship studies of ODNs have identified critical structural features in the pentose sugar (*19–22*), phosphate backbone (*23*), nucleobases (*24, 25*), and nucleosides (*26*) required for TLR9 stimulation. Our previous studies showed that the 5′-end of an ODN must be accessible for TLR9-mediated immune stimulatory activity. Modifications such as conjugation of di-, tetra-, or longer oligonucleotide, a fluorescein molecule or hairpin structures at the 5′-end block 5′-accessibility, resulting in significant abrogation of TLR9-mediated immune stimulatory activity (*27, 28*).

In the present study, we synthesized 5′- and 3′-conjugates of ODN and a model 28-mer β-amyloid peptide using C3 and C6 linkers and compared their immune stimulatory activity with that of the parent ODN in TLR9 transfected HEK293 and J774 cell lines, mouse spleen cell cultures, and in vivo in mice.

EXPERIMENTAL PROCEDURES

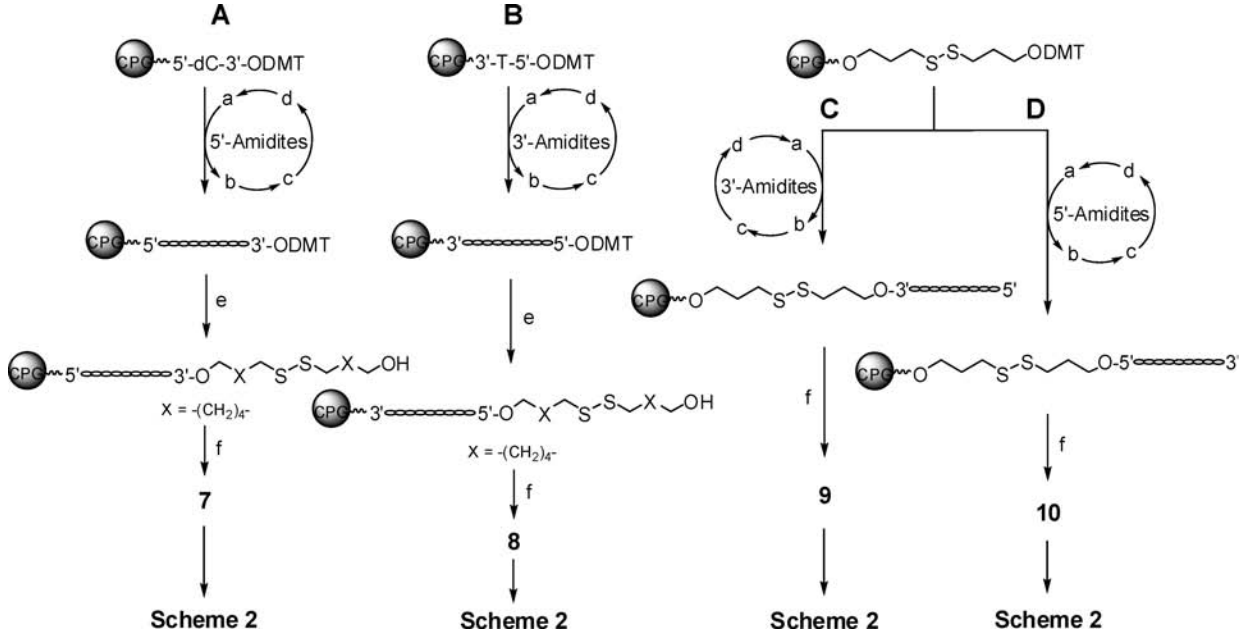
Reagents. Bromoacetyl-β-amyloid peptide (BrAc-DAEFRHDSGYEVHHQKLVFFAEDVGSNK-OH) was purchased from AnaSpec (San Jose, CA). Disulfide functionalized ODNs 5′-CTATCTGACGTTCTCTGT-3′-$(CH_2)_6$S-S$(CH_2)_6$OH (**7**), HO-$(CH_2)_6$S-S$(CH_2)_6$-5′-CTATCTGACGTTCTCTGT-3′ (**8**), 5′-CTATCTGACGTTCTCTGT-3′-$(CH_2)_3$S-S$(CH_2)_3$OH (**9**), and HO$(CH_2)_3$S-S$(CH_2)_3$-5′-CTATCTGACGTTCTCTGT-3′ (**10**) and unmodified ODNs **1** and **6** were synthesized as described below. DTT was obtained from Sigma-Aldrich (St. Louis, MO). Illustra NAP-25 columns were purchased from GE Healthcare (Piscataway, NJ). Thiol-modifier C6 S-S phosphoramidite and C3 S-S controlled-pore glass solid support were obtained from ChemGenes (Wilmington, MA) and Glen Research (Sterling, VA), respectively. Regular 5′-O−DMT-3′-phosphoramidites and reverse 3′-O-DMT-5′-phosphoramidites of dA, dC, dG, and T were obtained from Applied Biosystems (Foster City, CA) and ChemGenes (Wilmington, MA), respectively.

Synthesis and Purification of Disulfide-Functionalized ODNs. Both 3′- and 5′-disulfide functionalized ODNs **7**−**10** (Scheme 1) as well as unmodified ODNs **1** and **6** (Table 1) with phosphorothioate (PS) backbone were synthesized on a MerMade 6 DNA synthesizer (Bioautomation, Inc., Plano, TX) using β-cyanoethylphosphoramidite chemistry. Synthesis was carried out on a 10-μmol scale as DMT-off in either 3′ → 5′ or

* Tel.: 617-679-5501, Fax: 617-679-5572; e-mail: sagrawal@iderapharma.com.

10.1021/bc900425s © 2010 American Chemical Society
Published on Web 12/18/2009

Scheme 1. Schematic Representation of the Synthesis of 3′- and 5′-Linker-Disulfide Functionalized ODNs 7−10[a]



[a] Reagents and conditions used on automated DNA synthesizer: (a) Detritylation: with 3%TCA in DCM; 2 min. (b) Coupling: with 0.05 M phosphoramidite in acetonitrile and 0.25 M ethylthiotetrazole (ETT), 6 min. (c) Capping: with Cap A (acetic anhydride/pyridine/THF) and Cap B (*N*-methylimidazole in THF), 3 min. (d) Oxidation: with 3% Beaucage reagent in acetonitrile, 6 min. (e) Coupling: with 0.05 M thiol-modifier C6 S-S phosphoramidite in acetonitrile and 0.25 M ETT in acetonitrile, 6 min. (f) Cleavage and deprotection off the synthesizer: with 28−30% NH_4OH solution at 56 °C, 16 h. CPG stands for controlled-pore glass solid support.

Table 1. Oligodeoxynucleotide Sequences and Analytical Data of TLR9 Agonist and Its Peptide Conjugates

		accessibility		mol. wt.[b]		purity (% FLP)[c]	
ODN number	sequence[a]	3′-end	5′-end	calcd	obsd	HPLC	CGE
1	5′-CTATCTGACGTTCTCTGT-3′	free	free	5705	5706	98	97
2	5′-CTATCTGACGTTCTCTGT-3′-$CH_2(CH_2)_4CH_2$S-**P**	conjugated	free	9219	9218	98	92
3	**P**-$SCH_2(CH_2)_4CH_2$-5′-CTATCTGACGTTCTCTGT-3′	free	conjugated	9219	9217	92	95
4	5′-CTATCTGACGTTCTCTGT-3′-$CH_2CH_2CH_2$S-**P**	conjugated	free	9177	9178	99	94
5	**P**-$SCH_2CH_2CH_2$-5′-CTATCTGACGTTCTCTGT-3′	free	conjugated	9177	9174	94	90
6	5′-CTATCTCACCTTCTCTGT-3′	free	free	5624	5625	98	98

[a] All are oligodeoxynucleotides with phosphorothioate backbone; **P** = β-amyloid (1−28) peptide. [b] Molecular weights as determined by MALDI-ToF mass spectrophotometer; calcd and obsd indicate calculated and experimental values, respectively. [c] FLP = full length product; CGE = capillary gel electrophoresis.

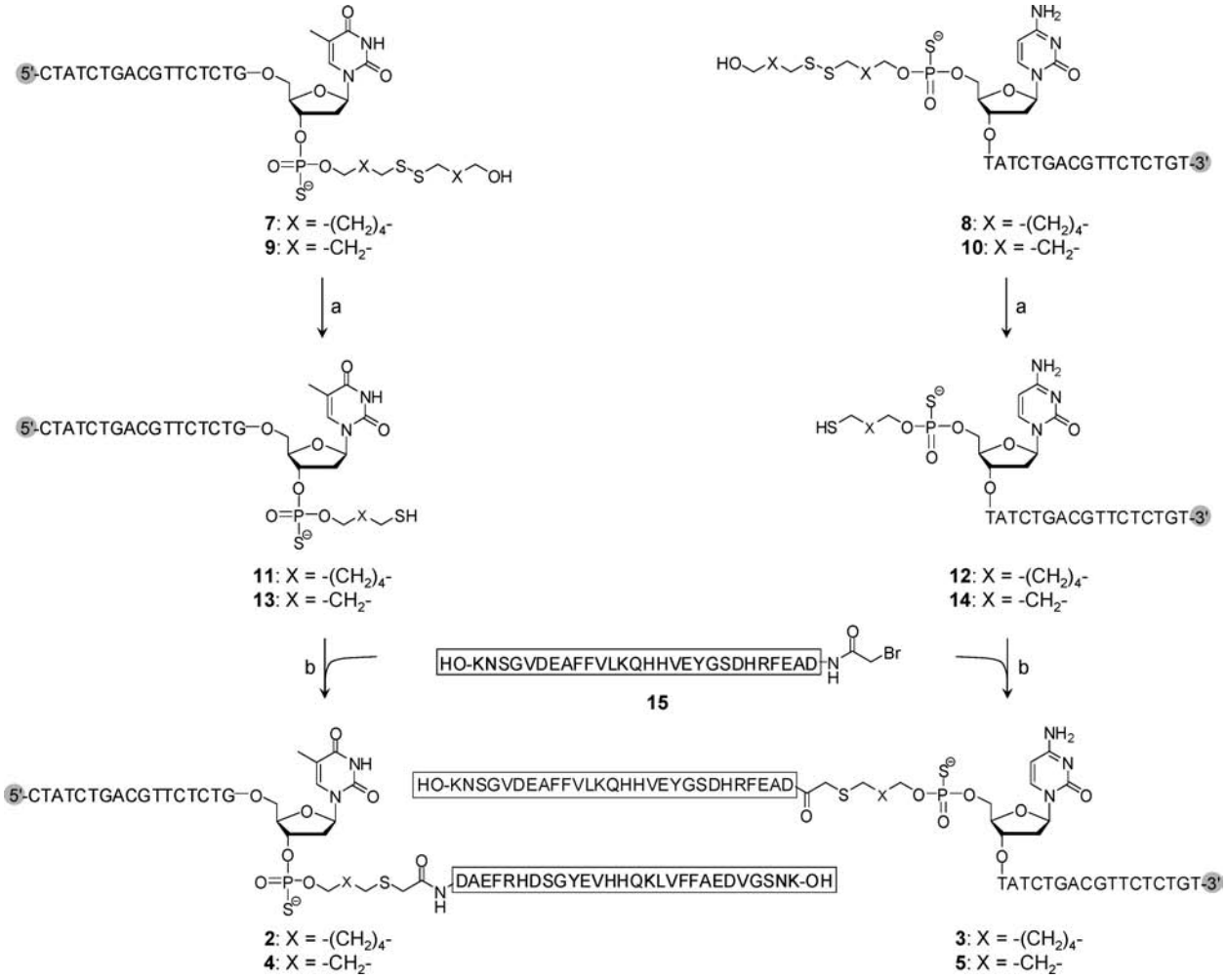
5′ → 3′ direction as needed. Beaucage sulfurizing agent was used as an oxidizing agent to obtain the PS backbone modification (*29*). ODN **7** with C6 linker disulfide modification at 3′-end was achieved using 5′-dC solid support and 5′-phosphoramidites followed by final coupling with C6 S-S linker phosphoramidite (Sheme 1A). On the other hand, ODN **8** with C6 linker disulfide modification at the 5′-end was achieved using 3′-dT solid support and 3′-phosphoramidites followed by final coupling with C6 S-S linker phosphoramidite (Scheme 1B). Conversely, ODNs **9** and **10** with C3 linker disulfide modification at 3′- and 5′-ends were achieved using 3′- and 5′-phosphoramidites, respectively, on C3 S-S thiol-modifier solid support (Scheme 1C,D). After the synthesis, ODNs were cleaved from the solid support and deprotected using 28−30% ammonium hydroxide solution at 56 °C for 16 h. Solid support was removed by filtration; excess ammonia was removed under vacuum.

The remaining solution was diluted with 5 vol equiv of distilled water, and crude ODNs were purified on a Waters (Milford, MA) 600 HPLC system using a Source 15Q resin (GE Healthcare Biosciences, Piscataway, NJ) column (20 cm × 250 mm) at 85 °C. A 25 mM Tris−HCl, pH 7.5 buffer containing 20% acetonitrile was used as buffer A and 2.5 M NaCl in buffer A was used as buffer B. HPLC purification was performed at a flow rate of 10 mL/min running100% buffer A for 2 min, and then increasing buffer B from 0% to 30% in 10 min then 30% to 70% in 40 min. The major absorbance peak detected at 260 nm was collected, solvent was evaporated by rotoevaporation, and the residue was redissolved in RNAase-free water and desalted as following.

Then ODNs were desalted on a C18 reverse-phase HPLC column and dialyzed against United States Pharmacopea-quality sterile water for irrigation (Braun). All ODNs synthesized were lyophilized and reconstituted in distilled water, and the concentrations were determined by measuring UV absorbance at 260 nm. The purity of all ODNs was determined by analytical anion-exchange HPLC (DNA Pack100 column) and capillary gel electrophoresis (P/ACE MDQ, Beckman Coulter, Fullerton, CA). The sequence integrity was characterized by matrix-assisted laser desorption/ionization-time-of-flight (MALDI-ToF) mass spectrometry (Micro MX, Waters, USA).

Preparation of Free Thiol-Functionalized ODNs 11−14 (Scheme 2). About 2.5 mg of each of the 3′- or 5′-disulfide functionalized ODNs **7**−**10** were dissolved separately in 2.25 mL of 100 mM sodium phosphate, pH 7.2 buffer and treated with 0.25 mL of 1 M DTT solution in 100 mM sodium phosphate, pH 7.2 buffer at room temperature. The mixture was vortexed, centrifuged, and the reaction progress monitored by MALDI/ToF mass spectral analysis. The reaction was completed in about 3.5 h, and the mixture was purified on Illustra NAP-

Scheme 2. Schematic Showing the Synthesis of 3′- and 5′- ODN-β-Amyloid Peptide Conjugates[a]



[a] Reagents and conditions: (a) 100 mM DTT in 100 mM sodium phosphate buffer pH 7.2, rt, 3.5 h; (b) DMSO/100-mM sodium phosphate buffer pH 7.2, rt, 24 h. Free 3′- and 5′-ends are highlighted.

25 column using water by following the supplier's protocol. Thiol-functionalized ODNs **11**−**14** obtained from ODNs **7**−**10**, respectively, were stored frozen immediately after elution and lyophilized to avoid dimerization. The purity and sequence integrity of ODNs were determined by analytical anion-exchange HPLC (DNA Pack100 column), capillary gel electrophoresis, and MALDI-ToF mass spectrometry.

Synthesis and Purification of ODN−Peptide Conjugates (2−5) (Scheme 2). About 2 mg of bromoacetyl-β-amyloid peptide **15** in 0.1 mL of DMSO was treated with 2.5 mg of 3′- or 5′-thiol functionalized ODN (**11**−**14**) in 0.9 mL of 100 mM sodium phosphate, pH 7.2 buffer, vortexed and centrifuged, and the mixture was allowed to react at room temperature. The reaction progress was monitored by analytical anion-exchange-HPLC and MALDI/ToF mass spectral analysis. After 24 h, ODN−peptide conjugates (**2**−**5**) were purified on an anion exchange HPLC equipped with Source 15Q column at 85 °C using a gradient of solvent B (25 mM Tris−HCl, pH 7.5 buffer containing 20% acetonitrile and 2.5 M NaCl) over solvent A (25 mM Tris−HCl, pH 7.5 buffer containing 20% acetonitrile). Pure fractions were desalted on a C18 cartridge, dialyzed, and lyophilized to get conjugate as a white fluffy solid. Conjugates were reconstituted in distilled water, and concentrations were determined by measuring UV absorbance at 260 nm. The purity of ODNs **2**−**5** was determined by analytical anion-exchange HPLC (DNA Pack100 column), capillary gel electrophoresis, and denaturing PAGE. The sequence integrity of ODNs was characterized by MALDI-ToF mass spectrometry.

HEK293 Cell Assays. HEK293 cells stably expressing mouse TLR9 (Invivogen, San Diego, CA) were cultured and transiently transfected with secreted form of human embryonic alkaline phosphatase (SEAP) reporter plasmid (pNifty2-Seap) (Invivogen) as described previously (*30*). After transfection, medium was replaced with fresh culture medium, ODNs were added to the cultures, and the cultures were continued for 18 h. At the end of ODN treatment, culture supernatants were harvested and used for measuring SEAP activity by the QuantiBlue method following the manufacturer's protocol (Invivogen). The data are shown as fold increase in NF-κB activity over PBS control.

J774 Cell Cultures, Preparation of Nuclear Extracts, and EMSA. For NF-κB activation studies, murine J774 macrophage cells (ATCC) were plated at a density of 5×10^6 cells/well in 6-well plates and cultured as described previously (*31*). Cells were treated with ODNs at 1 μg/mL concentration for 1 h. Nuclear extracts were prepared using the nuclear extraction kit (Sigma) according to the manufacturer's instructions, and protein concentrations were determined by Bradford assay. Samples were either used immediately or stored frozen at −70 °C. NF-κB activation in the nuclear extracts was monitored by electrophoretic mobility shift assay (EMSA) as described previously (*31*).

Mouse Spleen Cell Cultures. Spleen cells from C57BL/6 mice were prepared and cultured in RPMI complete medium consisting of RPMI 1640 with 10% fetal bovine serum, 100 U/mL penicillin, 100 μg/mL streptomycin, and 2 mM L-glutamine. Mouse spleen cells were plated in 96-well plates at

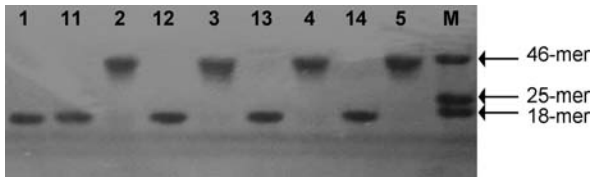


Figure 1. Denaturing PAGE analysis of purified ODNs **1**−**5** and **11**−**14** (lane numbers correspond to ODN numbers used in the text). Lane M is marker ODNs of defined length.

5×10^6 cells/mL and incubated with different concentrations of ODNs. Culture supernatants were collected after 24 h. The levels of cytokines and chemokines in the culture supernatants were measured using a mouse multiplex kit on an Applied Cytometry Systems Luminex 100 or 200 instrument, and the data were analyzed using *StarStation* software version 2.0. The required reagents were purchased from Invitrogen (Carlsbad, CA).

In Vivo Studies in Mice. Four-to-six-week-old female C57BL/6 mice were obtained from Taconic Farms, Germantown, NY. The animal studies reported in the paper were carried out following Idera's IACUC guidelines and approved protocols. Mice ($n = 3$) were injected subcutaneously (s.c.) with 20 μg of ODN (1 mg/kg). Blood was collected by retro-orbital bleeding 2 h after ODN administration, and serum IL-12 levels were determined by sandwich ELISA.

RESULTS

Synthesis of ODN-β-Amyloid Peptide Conjugates. We have synthesized ODN−peptide conjugates by covalently attaching N_α-(bromoacetyl)peptide (amino acids 1−28 fragment of the β-amyloid protein) to 5′- or 3′-thiol modified 18-mer phosphorothioate ODNs with C6 or C3 linkers. In this approach, first we synthesized ODNs functionalized with C6- and C3-linker disulfide moieties at 3′- and 5′-ends as shown in Scheme 1 (ODNs **7**−**10**). ODNs **7**−**10** were converted to activated-thiol-functionalized ODNs **11**−**14** by cleaving the disulfide bridge with DTT (Scheme 2). Then, ODN−peptide conjugates **2**−**5** (with thioether linkages) with C6 and C3 linkers were obtained by adding the bromoacetyl peptide **15** to ODNs **11**−**14** with an activated thiol function at either the 3′- or 5′-end (Scheme 2). ODN **1** served as a parent immune stimulatory agent without peptide conjugation. ODN **6** was a control that had the same length and structure as that of ODN **1** but lacked an immune stimulatory motif.

All ODNs were characterized by MALDI/ToF mass spectral analysis for their sequence integrity, and the purities were checked by HPLC and capillary gel electrophoresis (Table 1). All ODNs were also analyzed by denaturing slab gel polyacrylamide gel electrophoresis (PAGE). Figure 1 shows PAGE profiles of ODNs **1**−**5** and **11**−**14**. ODNs **11**−**14** (with a thiol functional group at the 3′- or 5′-end) had mobility similar to that of ODN **1**, which is an 18-mer. ODN-β-amyloid peptide conjugates **2**−**5** moved slower as that of a 46-mer ODN marker, suggesting the formation of peptide conjugates (Figure 1).

Activity of ODNs in TLR9-Expressing HEK293 Cells. TLR9 agonists activate immune signaling pathways, including the NF-κB pathway (*32*). To determine the effects of 3′- and 5′-conjugation of peptide to ODN, as well as the linker length between ODN and peptide, HEK293 cells transfected with mouse TLR9 and SEAP reporter gene were stimulated with ODNs **1**−**6** and examined for NF-κB activation. The results of dose-dependent NF-κB activation over PBS control are shown in Figure 2. The control ODN **6** (lacking a stimulatory motif) exhibited no activity. ODNs **1**−**5** showed activation of NF-κB to different levels for 3′- and 5′-conjugates (Figure 2). ODNs **2** and **4** (with peptide conjugated at the 3′-end) induced levels of NF-κB activation similar to that of parent ODN **1**, suggesting that conjugation of peptide at the 3′-end has minimal effect on TLR9-mediated immune stimulatory activity of ODN (Figure 2). Additionally, spacer length between ODN and peptide (**2** with C6-linker vs **4** with C3 linker) has insignificant effect on immune stimulation. In contrast, ODNs **3** and **5** (with peptide conjugated at the 5′-end) induced lower levels of NF-κB than ODNs **1**, **2**, and **4** (Figure 2). These results support our previous observations that an accessible 5′-end is required for TLR9 recognition and stimulation and that blocking of the 5′-end of an ODN by conjugation of a bulkier ligand abrogates immune stimulation (*27, 28*).

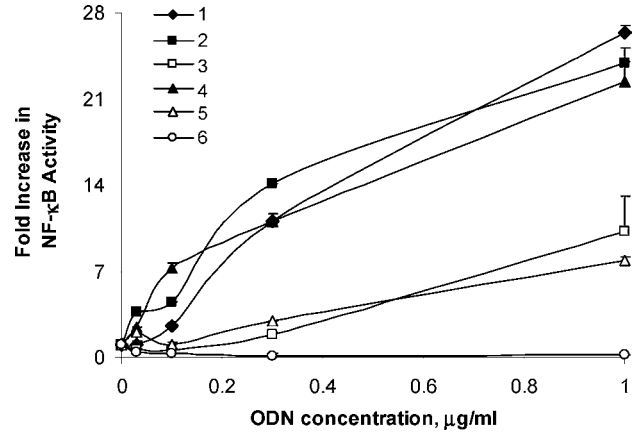


Figure 2. Dose-dependent activation of NF-κB in HEK293 cells expressing mouse TLR9 by ODNs **1**−**6**. Data shown are representative of three independent experiments.

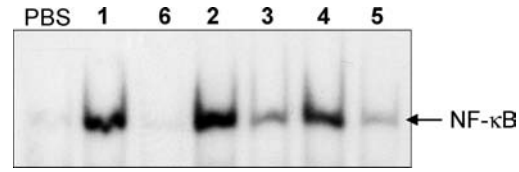


Figure 3. Activation of NF-κB in J774 murine macrophages upon treatment with ODNs. Autoradiogram showing NF-κB activation at 1 μg/mL concentration of indicated ODNs. Lane numbers correspond to ODN numbers used in the text. Experiments were carried out as described in the Experimental Section. Data shown are of one representative experiment of three independent experiments.

Activity of ODNs in J774 Cells. To further study the effects of 3′- and 5′-conjugation of peptide to ODN and the role of linker length on NF-κB activation, J774 mouse macrophage cells, which express TLR9 (*32*), were stimulated with 1 μg/mL ODNs **1**−**6** and the nuclear extracts were examined for NF-κB activation by EMSA. The results are presented in Figure 3. The presence of bands corresponding to NF-κB with ODNs **1**, **2**, and **4** suggest that the transcription factor NF-κB was activated (Figure 3). In contrast, the band intensity with ODNs **3** and **5** was minimal, suggesting that conjugation of peptide at the 5′-end of ODN results in the loss of TLR9-mediated immune activation (Figure 3).

Activity of ODNs in Mouse Spleen Cell Cultures. To study the impact of peptide conjugation with different linker lengths at the 3′- or 5′-end of ODN in primary cells, we evaluated ODN-induced production of cytokines in C57BL/6 mouse spleen cell cultures. The induction of IL-12, IL-6, MIP-1α, and TNF-α at 10 μg/mL concentration of ODN in spleen cell cultures is shown in Figure 4. The response was dependent on the dose of ODN (Supporting Information Figure 1). Control ODN **6** (lacking a stimulatory motif) induced no or insignificant levels of IL-12, IL-6, MIP-1α, and TNF-α in mouse spleen cell cultures. ODNs

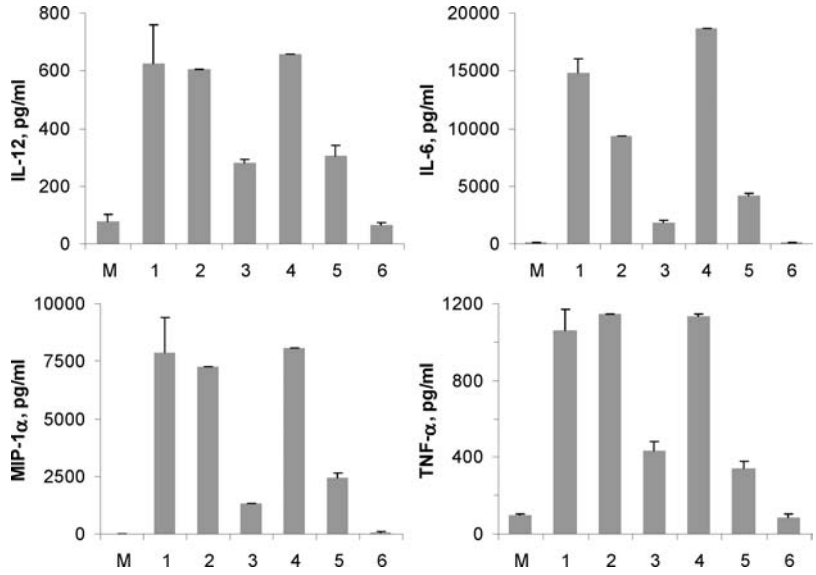


Figure 4. IL-12, IL-6, MIP-1α, and TNF-α induction profiles of ODNs **1**−**6** (10 μg/mL concentration) in C57BL/6 mouse spleen cell cultures. Spleen cells were cultured in the presence of ODNs for 24 h, and the levels of secreted cytokines in culture supernatants were measured by multiplex luminex assay as described in the Experimental Section. Each value is an average of three replicate wells, and the results are of one representative experiment of three independent experiments.

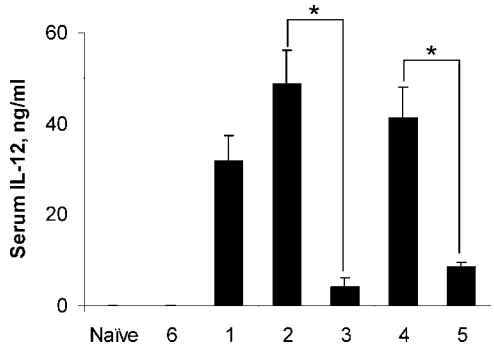


Figure 5. In vivo IL-12 induction by ODNs **1**−**6** administered s.c. to C57BL/6 mice at 1 mg/kg dose. Blood was collected 2 h post-ODN administration, and serum IL-12 levels were determined by ELISA as described in the Experimental Section. Data shown are representative of three independent experiments. * $p < 0.001$.

2 and **4** (peptide conjugated with C6 and C3 linkers at the 3′-end) induced similar levels of IL-12, IL-6, MIP-1α, and TNF-α to that of parent ODN **1** (Figure 4). In contrast, ODNs **3** and **5** (peptide conjugated with C6 and C3 linkers at the 5′-end) induced lower levels of IL-12, IL-6, MIP-1α, and TNF-α than did ODNs **1**, **2**, and **4** (Figure 4). These results are consistent with HEK293 and J774 cell culture results and further confirm that blocking the 5′-end of ODN results in decreased TLR9-mediated immune stimulatory activity.

Activity of ODNs In Vivo in Mice. We then examined the in vivo IL-12 induction profiles of ODNs **1**−**6** in mice to further understand the effects of site of peptide conjugation. ODNs were administered subcutaneously to C57BL/6 mice at a dose of 1 mg/kg, and serum IL-12 levels were determined by sandwich ELISA 2 h post-ODN administration. As shown in Figure 5, control ODN **6** induced no IL-12, whereas ODN **1** induced higher levels of IL-12 compared with ODN **6** suggesting that the stimulatory motif is required for immune responses. ODNs **2** and **4** (peptide conjugated with C6 and C3 linkers at the 3′-end) induced slightly higher levels of IL-12 than did ODN **1** (Figure 5). In contrast, ODNs **3** and **5** (peptide conjugated with C6 and C3 linkers at the 5′-end) induced significantly lower levels of serum IL-12 than did ODNs **1**, **2**, and **4** (Figure 5). These in vivo data are in agreement with the results observed in cell-based assays.

DISCUSSION

While coadministration of ODN and vaccine candidates has yielded promising results (*11, 12*), attempts are being made to deliver both antigen (protein/peptide) and ODN to the same APC to enhance cross-presentation and cross-priming (*17*). Liposomal formulations and conjugation of protein/peptide antigen to ODN are commonly employed to deliver both of the components to the same APC (*17*).

Our previous studies showed that an accessible 5′-end of an ODN is required for TLR9-mediated immune responses and blocking the 5′-end results in loss of immune stimulatory activity (*27, 28*). In the present study, we have conjugated a 28-mer β-amyloid peptide that is not immunogenic to distinguish ODN-mediated TLR9 activation from peptide/protein-induced immune responses and study the role of 5′-accessibility of ODN for TLR9-mediated immune responses. In vitro studies carried out in TLR9 transfected cell line, mouse macrophage J774 cell line, and mouse primary splenocytes showed that conjugation of peptide at the 5′-end of ODN significantly reduces TLR9-mediated immune responses. Conjugation of peptide at the 3′-end of ODN resulted in similar activity to that of parent ODN.

Moreover, we have also examined whether the proximity of peptide to the 3′- or 5′-end of the ODN would have an effect on TLR9-mediated immune stimulation of 3′- and 5′-conjugates by synthesizing and studying peptide−ODN conjugates using C3- and C6-linkers. ODN conjugated with peptide at the 3′-end through C3- and C6-linkers showed similar TLR9-mediated immune responses to that of the parent ODN, suggesting that the effects observed in these studies are not dependent on the proximity of peptide to the 3′- or 5′-end of ODN, but because an accessible 5′-end of ODN is required for TLR9-mediated immune stimulation. These results were further confirmed in acute administration studies in vivo in mice, in which the parent compound without peptide conjugation and the two conjugates that have peptide attached at the 3′-end of ODN either via C6- or C3-

linker (**2** and **4**) are significantly more immune stimulatory than those with peptide conjugated at the 5′-end (**3** and **5**).

Our previous studies have demonstrated that differences in immune stimulatory activity of 3′- and 5′-conjugates is due to the requirement of 5′-end accessibility for TLR9-mediated immune responses, but not as a result of their differences in cellular uptake, as both types of conjugates are taken up by cells to the same extent (*28*). Further, these studies have shown that conjugation of a mono, di, tetra, or oligonucleotide through 5′−5′ linkage or a fluorescein moiety, but not a phosphorothioate group, at the 5′-end significantly reduces TLR9-mediated immune responses (*28*). These results together with the present studies with a peptide conjugated at the 5′- and 3′-end of ODN suggest that an accessible 5′-end of ODN is required for TLR9-mediated immune responses and conjugation of bulkier moieties like peptides/proteins at the 5′-end of ODN results in loss of TLR9-mediated immune responses.

Several peptide/protein−ODN conjugates are currently at various stages of preclinical and clinical evaluation for the treatment of various disease indications (*13–17, 33–37*). These studies have utilized conjugation of peptides at the 5′-end of ODN due to ease of incorporation of chemical modifications required for conjugation. The present studies described above suggest that conjugation of peptides or proteins at the 5′-end of ODN does not benefit the TLR9 agonist-mediated immune responses to the full extent. A ragweed allergen, Amb a 1, conjugated at the 5′-end of an ODN has been the most extensively studied and evaluated in human clinical trials (*15, 33, 34*). However, the clinical trial results have failed to achieve the end points.

We have also conjugated other peptides of 23 and 28 amino acids to ODN and observed a loss of TLR9-mediated activity with 5′-, but not 3′-, conjugates (data not shown). Taken together, the present results clearly demonstrate that conjugation of large molecules such as peptides/proteins at the 5′-end of an ODN could lead to significant loss of TLR9-mediated immune stimulatory activity, thereby compromising the advantage provided by TLR9-mediated adjuvant activity. Therefore, conjugation of peptides/proteins at the 3′-end of ODN would be beneficial.

Supporting Information Available: A figure showing concentration-dependent cytokine induction in mouse spleen cell cultures is available. This material is available free of charge via the Internet at http://pubs.acs.org.

LITERATURE CITED

(1) Hemmi, H., Takeuchi, O., Kawai, T., Kaisho, T., Sato, S., Sanjo, H., Matsumoto, M., Hoshino, K., Wagner, H., Takeda, K., and Akira, S. (2000) A Toll-like receptor recognizes bacterial DNA. *Nature 408*, 740–745.

(2) Yamamoto, S., Yamamoto, T., Nojima, Y., Umemori, K., Phalen, S., McMurray, D. N., Kuramoto, E., Iho, S., Takauji, R., Sato, Y., Yamada, T., Ohara, N., Matsumoto, S., Goto, Y., Matsuo, K., and Tokunaga, T. (2002) Discovery of immunostimulatory CpG-DNA and its applications to tuberculosis vaccine development. *Jpn. J. Infect. Dis. 55*, 37–44.

(3) Agrawal, S., and Kandimalla, E. R. (2005) Role of Toll-like receptors in antisense and siRNA. *Nat. Biotechnol. 22*, 1533–1537.

(4) O'Neill, L. A., Bryant, C. E., and Doyle, S. L. (2009) Therapeutic targeting of Toll-like receptors for infectious and inflammatory diseases and cancer. *Pharmacol. Rev. 61*, 177–197.

(5) Klinman, D. M., Currie, D., Gursel, I., and Verthelyi, D. (2004) Use of CpG oligodeoxynucleotides as immune adjuvants. *Immunol. Rev. 199*, 201–216.

(6) McCluskie, M. J., and Davis, H. L. (1998) CpG DNA is a potent enhancer of systemic and mucosal immune responses against hepatitis B surface antigen with intranasal administration to mice. *J. Immunol. 161*, 4463–4466.

(7) Oxenius, A., Martinic, M. M. A., Hengartner, H., and Klenerman, P. (1999) CpG-containing oligonucleotides are efficient adjuvants for induction of protective antiviral immune responses with T-cell peptide vaccines. *J. Virol. 73*, 4120–4126.

(8) Schneeberger, A., Wagner, C., Zemann, A., Luhrs, P., Kutil, R., Goos, M., Stingl, G., and Wagner, S. N. (2004) CpG motifs are efficient adjuvants for DNA cancer vaccines. *J. Investig. Dermatol. 123*, 371–379.

(9) Zhu, F. G., Kandimalla, E. R., Yu, D., and Agrawal, S. (2007) Oral administration of a synthetic agonist of Toll-like receptor 9 potently modulates peanut-induced allergy in mice. *J. Allergy Clin. Immunol. 120*, 631–637.

(10) Aurisicchio, L., Peruzzi, D., Conforti, A., Dharmapuri, S., Biondo, A., Giampaoli, S., Fridman, A., Bagchi, A., Winkelmann, C. T., Gibson, R., Kandimalla, E. R., Agrawal, S., Ciliberto, G., and La Monica, N. (2009) Treatment of mammary carcinomas in HER-2 transgenic mice through combination of genetic vaccine and an agonist of Toll-like receptor 9. *Clin. Cancer Res. 15*, 1575–1584.

(11) Cooper, C. L., Davis, H. L., Morris, M. L., Efler, S. M., Krieg, A. M., Li, Y., Laframboise, C., Al Adhami, M. J., Khaliq, Y., Seguin, I., and Cameron, D. W. (2004) Safety and immunogenicity of CPG 7909 injection as an adjuvant to Fluarix infleuenza vaccine. *Vaccine 22*, 3136–3143.

(12) Halperin, S. A., Dobson, S., McNeil, S., Langley, J. M., Smith, B., McCall-Sani, R., Levitt, D., Van Nest, G., Gennevois, D., and Eiden, J. J. (2006) Comparison of the safety and immunogenicity of hepatitis B virus surgace antigen co-administered with an immunostimulatory phosphorothioate oligonculetide and a licensed hepatitis B vaccine in healthy young adults. *Vaccine 24*, 20–26.

(13) Krishnamachari, Y., and Salem, A. K. (2009) Innovative strategies for co-delivering antigens and CpG oligonucleotides. *Adv. Drug Delivery Rev. 61*, 205–217.

(14) Tighe, H., Takabayashi, K., Schwartz, D., Marsden, R., Beck, L., Corbeil, J., Richman, D. D., Eiden, J. J., Spiegelberg, H. L., and Raz, E. (2000) Conjugation of protein to immunostimulatory DNA results in a rapid, long-lasting and potent induction of cell-mediated and humoral immunity. *Eur. J. Immunol. 30*, 1939–1947.

(15) Tighe, H., Takabayashi, K., Schwartz, D., Van Nest, G., Tuck, S., Eiden, J. J., Kagey-Sobotka, A., Creticos, P. S., Lichtenstein, L. M., Spiegelberg, H. L., and Raz, E. (2000) Conjugation of immunostimulatory DNA to the short ragweed allergen Amb a 1 enhances its immunogenicity and reduces its allergenicity. *J. Allergy Clin. Immunol. 106*, 124–134.

(16) Heit, A., Maurer, T., Hochrein, H., Bauer, S., Huster, K. M., Busch, D. H., and Wagner, H. (2003) Toll-like receptor 9 expression is not required for CpG DNA-aided cross-presentation of DNA-conjugated antigens but essential for cross-priming of CD8 T cells. *J. Immunol. 170*, 2802–2805.

(17) Daftarian, P., Sharan, R., Haqa, W., Ali, S., Longmate, J., Termini, J., and Diamonda, D. J. (2005) Novel conjugates of epitope fusion peptides with CpG-ODN display enhanced immunogenicity and HIV recognition. *Vaccine 23*, 3453–3468.

(18) Agrawal, S., Christodoulou, C., and Gait, M. J. (1986) Efficient methods for attaching non-radioactive labels to the 5′ ends of synthetic oligodeoxyribonucleotides. *Nucleic Acids Res. 14*, 6227–6245.

(19) Zhao, Q., Yu, D., and Agrawal, S. (1999) Site of chemical modifications in CpG containing phosphorothioate oligodeoxynucleotide modulates its immunostimulatory activity. *Bioorg. Med. Chem. Lett. 9*, 3453–3458.

(20) Zhao, Q., Yu, D., and Agrawal, S. (2000) Immunostimulatory activity of CpG containing phosphorothioate oligodeoxynucleotide is modulated by modification of a single deoxynucleoside. *Bioorg. Med. Chem. Lett. 10*, 1051–1054.

(21) Yu, D., Kandimalla, E. R., Zhao, Q., Cong, Y., and Agrawal, S. (2002) Immunostimulatory properties of phosphorothioate CpG DNA containing both 3′-5′- and 2′-5′-internucleotide linkages. *Nucleic Acids Res. 30*, 1613–1619.

(22) Agrawal, S., and Kandimalla, E. R. (2001) Antisense and/or immunostimulatory oligonucleotide therapeutics. *Curr. Cancer Drug Targets 1*, 197–209.

(23) Yu, D., Kandimalla, E. R., Zhao, Q., Cong, Y., and Agrawal, S. (2001) Immunostimulatory activity of CpG oligonucleotides containing nonionic methylphosphonate linkages. *Bioorg. Med. Chem. 9*, 2803–2808.

(24) Yu, D., Kandimalla, E. R., Zhao, Q., Cong, Y., and Agrawal, S. (2001) Modulation of immunostimulatory activity of CpG oligonucleotides by site-specific deletion of nucleobases. *Bioorg. Med. Chem. Lett. 11*, 2263–2267.

(25) Yu, D., Kandimalla, E. R., Zhao, Q., Bhagat, L., Cong, Y., and Agrawal, S. (2003) Requirement of nucleotide bases proximal to a CpG-motif for immunostimulatory activity of synthetic oligonucleotides. *Bioorg. Med. Chem. 11*, 459–464.

(26) Yu, D., Kandimalla, E. R., Cong, Y., Tang, J., Tang, J. Y., Zhao, Q., and Agrawal, S. (2002) Design, synthesis, and immunostimulatory properties of CpG DNAs containing alkyl-linker substitutions: role of nucleosides in the flanking sequences. *J. Med. Chem. 45*, 4540–4548.

(27) Yu, D., Zhao, Q., Kandimalla, E. R., and Agrawal, S. (2000) Accessible 5′-end of CpG-containing phosphorothioate oligodeoxynucleotides is essential for immunostimulatory activity. *Bioorg. Med. Chem. Lett. 10*, 2585–2588.

(28) Kandimalla, E. R., Bhagat, L., Yu, D., Cong, Y., Tang, J., and Agrawal, S. (2002) Conjugation of ligands at the 5′-end of CpG DNA affects immunostimulatory activity. *Bioconjugate Chem. 13*, 966–974.

(29) Iyer, R. P., Egan, W., Regan, J. B., and Beaucage, S. L. (1990) 3H-1,2-Benzodithiole-3-one 1,1-dioxide as an improved sulfurizing reagent in the solid-phase synthesis of oligodeoxyribonucleoside phosphorothioates. *J. Am. Chem. Soc. 112*, 1253–1254.

(30) Putta, M. R., Zhu, F. G., Li, Y., Bhagat, L., Cong, Y., Kandimalla, E. R., and Agrawal, S. (2006) Novel oligodexoynucleotide agonists of TLR9 containing N^3-Me-dC or N^1-Me-dG modifications. *Nucleic Acids Res. 34*, 3231–3238.

(31) Kandimalla, E. R., Bhagat, L., Wang, D., Yu, D., Zhu, F. G., Tang, J., Wang, H., Huang, P., Zhang, R., and Agrawal, S. (2003) Divergent synthetic nucleotide motif recognition pattern: design and development of potent immunomodulatory oligodeoxyribonucleotide agents with distinct cytokine induction profiles. *Nucleic Acids Res. 31*, 2393–2400.

(32) Stacey, K. J., Sweet, M. J., and Hume, D. A. (1996) Macrophages ingest and are activated by bacterial DNA. *J. Immunol. 157*, 2116–2122.

(33) Creticos, P. S., Schroeder, J. T., Hamilton, R. G., Balcer-Whaley, S. L., Khattignavong, A. P., Lindblad, R., Li, H., Coffman, R., Seyfert, V., Eiden, J. J., and Broide, D. (2006) Immunotherapy with a ragweed-toll-like receptor 9 agonist vaccine for allergic rhinitis. *N. Engl. J. Med. 355*, 1445−1455.

(34) Broide, D. H. (2005) Immunostimulatory sequences of DNA and conjugates in the treatment of allergic rhinitis. *Curr. Allergy Asthma Rep. 5*, 182–185.

(35) Heit, A., Huster, K. M., Schmitz, F., Schiemann, M., Busch, D. H., and Wagner, H. (2004) CpG-DNA aided cross-priming by cross-presenting B cells. *J. Immunol. 172*, 1501–1507.

(36) Heit, A., Schmitz, F., O'Keeffe, M., Staib, C., Busch, D. H., Wagner, H., and Huster, K. M. (2005) Protective CD8 T cell immunity triggered by CpG-protein conjugates competes with the efficacy of live vaccines. *J. Immunol. 174*, 4373–4380.

(37) Suzuki, M., Ohta, N., Min, W. P., Matsumoto, T., Min, R., Zhang, X., Toida, K., and Murakami, S. (2007) Immunotherapy with CpG DNA conjugated with T-cell epitope peptide of an allergenic Cry j 2 protein is useful for control of allergic conditions in mice. *Int. Immunopharmacol. 7*, 46–54.

BC900425S

Fluorescence-Based Liver Microsomal Assay for Screening of Pharmaceutical Reactive Metabolites Using a Glutathione Conjugated 96-Well Plate

Xiang Ma[†,‡] and Eric Chun Yong Chan*[,†]

Department of Pharmacy, Faculty of Science, National University of Singapore, 18 Science Drive 4, Singapore 117543, and Department of Chemical and Biomolecular Engineering, Faculty of Engineering, National University of Singapore, 4 Engineering Drive 3, Singapore 117576. Received July 3, 2009; Revised Manuscript Received November 16, 2009

The purpose of our paper is to develop and validate a fluorescence-based mouse liver microsomal (MLM) assay in screening pharmaceutical reactive metabolites (RMs) using a glutathione (GSH)-conjugated 96-well plate. Poly(2-hydroxyethylmethacrylate) (pHEMA) polymeric membrane was coated on 96-well plates to provide a functional support for GSH conjugation. Oxidized GSH (GSSG) was conjugated on a cyanogen bromide (CNBr)-activated pHEMA surface. The conjugated GSH was regenerated after the reduction of GSSG using D,L-dithiothreitol (DTT). X-ray photoelectron spectroscopy, Ellman's, and fluorescence assays were applied to validate the chemistry and optimize the processes of GSH conjugation. The performance of the 96-well assay was further cross-validated using *N*-acetyl-*p*-benzo-quinone imine (NAPQI), a RM of acetaminophen (APAP), and the *in vitro* MLM assay of APAP. Finally, the developed method was applied to screen a batch of marketed drugs and chemicals on the formation of RMs. Our results indicated that optimum conditions were obtained for pHEMA loading, CNBr activation of pHEMA, and GSSG coupling and reduction. The detection limit of the assay for NAPQI was 500 nM with good specificity. *In vitro* MLM assay of APAP demonstrated a positive trapping index (TI) of 19.3%. The subsequent RM screening of a series of marketed drugs and chemical compounds resulted in a range of TI values (1.0−25.7%) that corroborated with their capacity in generating RMs. The differences of TI values are statistically significant between the compounds which are known to produce RMs and those that do not generate reactive intermediates. In conclusion, we successfully developed a fluorescence-based GSH-conjugated 96-well plate platform for the screening of RMs using MLM.

INTRODUCTION

Drug discovery and development is a time-consuming and expensive enterprise (*1*). It has been estimated that only 1 in 5000 compounds makes it to the market from drug discovery (*2*). Major contributors to the high attrition rate in drug development, other than poor clinical efficacy, are serious adverse drug reactions, undesired side effects, and unfavorable drug metabolism and pharmacokinetics (DMPK) properties (*3*). Because of the inherent high failure rates related to drug development, a recent trend in the pharmaceutical industry is to front-load drug absorption, distribution, metabolism, elimination, and toxicity (ADMET)[1]screening to an early stage in parallel with the optimization of pharmacological efficacy (*4*). Among the ADMET properties, the metabolic profile of a new chemical entity (NCE) is a pertinent characteristic to be elucidated during its development (*5*).

Metabolism is a biotransformation process that occurs in liver and other organs by which endogenous compounds and xenobiotics are converted into water-soluble derivatives that are more readily excreted via the kidney (*6*). Cytochrome P450 enzymes play a primary role in the metabolism of a diverse range of xenobiotics, including therapeutic agents. Although the major roles of drug metabolism are elimination and detoxication, metabolism may also result in toxicological outcomes. Some therapeutic agents can undergo biotransformation to electrophilic reactive metabolites (RMs) that have intrinsic chemical reactivity to bind covalently to cellular macromolecules, such as lipids, nucleic acids, and proteins. There is a substantial amount of evidence that RMs are critical cellular mediators of liver toxicity (*6*−*8*). Acetaminophen (APAP) was among the first set of drugs to be extensively studied on its relationship of hepatotoxicity to the covalent binding of cellular proteins by *N*-acetyl-*p*-benzoquinone imine (NAPQI), a RM of APAP (*9, 10*). Presently, there is an emerging consensus in drug discovery and development that formation of RMs is not a desirable characteristic of a drug candidate because of the potential safety concern, especially hepatotoxicity. Therefore, in order to reduce the attrition rate in drug development, both screening and structural characterization of RMs have been integrated into the ADMET-guided lead optimization process of some pharmaceutical companies (*11, 12*).

Direct measurement of the levels of covalent binding of RMs to liver microsomal proteins *in vitro* was often adopted as an early screening tool several years ago (*11*−*13*). This experiment requires the use of radio-labeled drug candidate and such a low-throughput method is currently reserved during the late stage of drug discovery. A more common approach for the identifica-

* To whom correspondence should be addressed. Assistant Professor Eric Chun Yong Chan, phone: +65 65166137. Fax: +65 67791554. E-mail: phaccye@nus.edu.sg.

† Department of Pharmacy, Faculty of Science.

‡ Department of Chemical and Biomolecular Engineering, Faculty of Engineering.

[1]**Abbreviations:** ADMET, absorption, distribution, metabolism, elimination, and toxicity; 1,5-I-AEDANS, *N*-(iodoacetylamino-ethyl)-1-naphthylamine-5-sulfonic acid; APAP, acetaminophen; CNBr, cyanogen bromide; CNL, constant neutral loss; DTT, DL-dithiothreitol; ESI, electrospray ionization; GSH, glutathione reduced; GSSG, glutathione oxidized; HTS, high-throughput screening; LC/MS/MS, liquid chromatography/tandem mass spectrometry; MLM, mouse liver microsomes; NAPQI, *N*-acetyl-*p*-benzo-quinone imine; pHEMA, poly(2-hydroxyethylmethacrylate); PI, precursor ion; RMs, reactive metabolites; TI, trapping index; UPLC/MS/MS, ultraperformance liquid chromatography/tandem mass spectrometry; UPLC/QTOF/MS/MS, ultraperformance liquid chromatography/quadrupole time-of-flight tandem mass spectrometry; XPS, X-ray photoelectron spectroscopy.

10.1021/bc900289m © 2010 American Chemical Society
Published on Web 12/03/2009

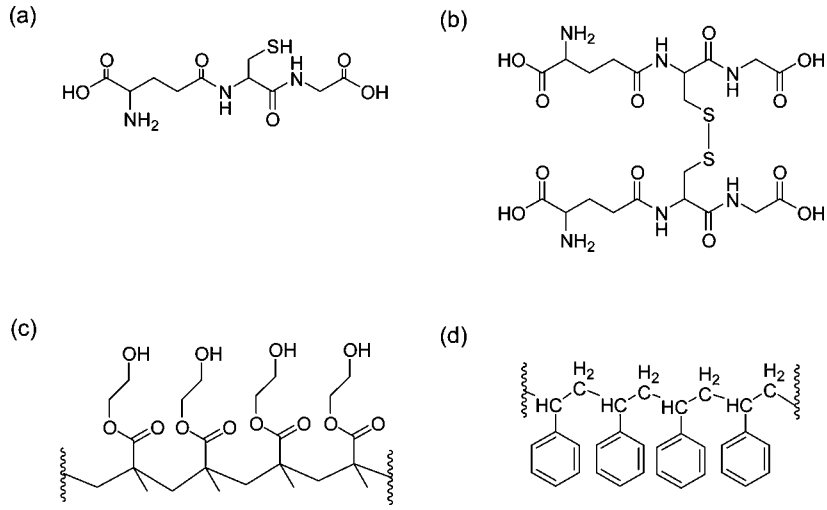


Figure 1. Chemical structures of (a) glutathione reduced (GSH), (b) glutathione oxidized (GSSG), (c) poly(2-hydroxyethylmethacrylate) (pHEMA), and (d) polystyrene.

tion of RMs nowadays is to trap them with an established nucleophile that is structurally smaller and easier to work with compared to proteins. One of the techniques includes the conjugation of pharmaceutical RMs with glutathione (GSH) via reaction with the latter's nucleophilic thiol group. GSH is an endogenous tripeptide that contains cysteine glutamate glycine amino acids (Figure 1a). It is used commonly to evaluate the potential of drug candidates in generating thiol-reactive species upon oxidative metabolic activation in incubations with liver microsomes. Endogenously, GSH is an antioxidant and protects cells from toxins such as free radicals and RMs. In the RM-trapping assay by GSH, the stable RM−GSH adducts are typically characterized by liquid chromatography/tandem mass spectrometry (LC/MS/MS). Traditionally, a constant neutral loss (CNL) scanning experiment in the electrospray ionization positive mode (ESI+) has been employed to screen and characterize the RM−GSH adducts (*14*). Since some GSH adducts such as thioester-linked GSH adducts may not afford the neutral loss of 129 Da (*15, 16*), a precursor ion (PI) scanning experiment in the electrospray ionization negative mode (ESI-) was developed as an alternative for the screening of RM−GSH conjugates (*17*). While the RM-trapping assay using GSH and LC/MS/MS has proven to be an effective and reliable approach, the application of both CNL and PI scanning experiments in the screening of RMs is not suitable for high-throughput screening (HTS) of hit compounds. Hence, in the early stage of the drug discovery especially after HTS of drug candidates on the biological activity, the availability of a relatively high-throughput and low-cost screening method for the profiling of RMs would be desirable (*18, 19*).

The pharmaceutical industry has adopted 96- and 384-well microtiter plates with liquid-dispensing and plate-handling robotics as the standard platform for HTS. The vast majority of HTS techniques are focused on bioactivity testing of compounds using biochemical or cellular screens (*20*). However, HTS is comparatively less commonly applied in toxicity testing especially in the profiling of RMs (*21*). The goal of our work was to develop and optimize a novel HTS platform for RM profiling using the liver microsomal system. In this paper, we investigated the immobilization of oxidized GSH (GSSG, Figure 1b) on a 96-well plate after poly(2-hydroxyethylmethacrylate) (pHEMA) (Figure 1c) polymeric membrane coating and functional group activation of pHEMA for GSSG conjugation. We also investigated the GSSG reduction to GSH for the subsequent trapping reaction with RMs. With the use of an optimized fluorometric assay, the performances of our RM profiling strategy were evaluated using the NAPQI standard, *in vitro* mouse liver microsomal (MLM) assay of APAP and *in vitro* MLM assay of a series of marketed drugs and chemical compounds.

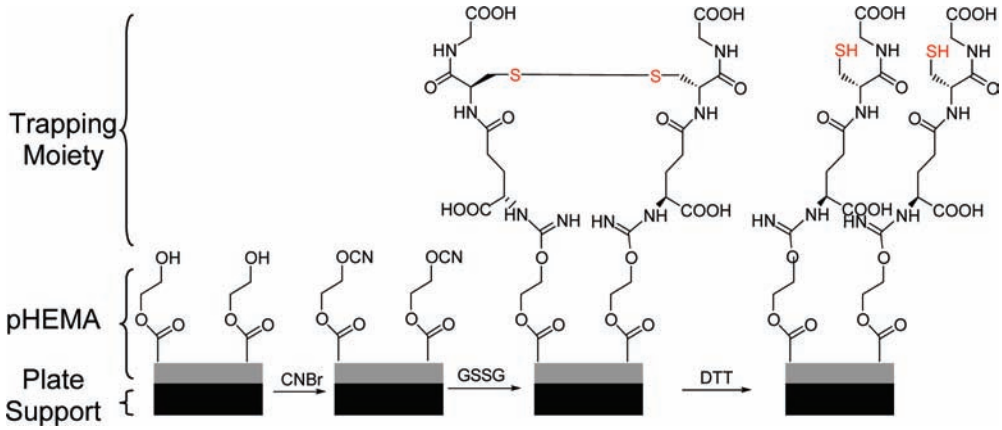
EXPERIMENTAL PROCEDURES

Materials. Glutathione oxidized (GSSG), glutathione reduced (GSH), cyanogen bromide (CNBr), poly(2-hydroxyethylmethacrylate) (pHEMA), DL-dithiothreitol (DTT), acetaminophen (APAP), *N*-acetyl-*p*-benzoquinone imine (NAPQI), *N*-(iodoacetylaminoethyl)-1-naphthylamine-5-sulfonic acid (1,5-I-AEDANS), 5,5′-dithio-bis-(2-nitrobenzoic acid) (DTNB; Ellman's reagent), mitomycin C, 3-acetamidophenol, sulfanilamide, procainamide hydrochloride, amodiaquine, deiquat monohydrate, zomepirac sodium salt, tolmetin sodium salt dehydrate, diclofenac sodium salt, acetaminophen, verapamil donepezil, galantamine, memantine, cimetidine, pilocarpine, and streptomycin were purchased from Sigma-Aldrich (Singapore). NADPH regenerating system solutions A and B and pooled mouse liver microsomes (MLM) were purchased from BD Gentest (Woburn, MA). All solutions were prepared with Milli-Q water obtained from a Millipore Direct-Q3 UV water purification system (Millipore S.A.S, Molsheim, France). The 96-well plates were Corning 96-well black flat bottom polystyrene nontreated microplates (Corning, NY). All other reagents used were of analytical grade.

Instrumentation. The 96-well plates were washed on a Tecan HydroFlex Platform (Tecan, Austria) while fluorescence intensity was measured using a TECAN Infinite M200 plate reader (Tecan, Austria). The X-ray photoelectron spectroscopy (XPS) measurements were performed using an AXIS His spectrometer (Kratos Analytical Ltd., England) equipped with a monochromatized A1 Kα X-ray source (1486.6 eV photons). A constant dwell time of 100 ms and a pass energy of 40 eV were used throughout the experiments. NAPQI-GSH conjugate generated using MLM incubation was analyzed using an ACQUITY UPLC system (Waters, Milford, MA) interfaced with a quadrupole, orthogonal acceleration time-of-flight tandem mass spectrometer (QTOFMS) equipped with an ESI source (Q-Tof Premier, Waters, Manchester, U.K.). The UPLC/QTOFMS system was controlled by MassLynx 4.1 software (Waters).

Conjugation of GSH on pHEMA Coated Surfaces. During early method development, pHEMA was coated on glass Petri dishes using the appropriate proportion of the reagents to investigate the immobilization of GSH (Scheme 1). pHEMA (5 mg/mL, 5 mL) was casted on each glass Petri dish at 23 ±

Scheme 1. Schematic of the Immobilization of the GSH via the Activation of Hydroxyl Functional Groups on pHEMA Support (Activated by CNBr)



1 °C overnight to allow evaporation of the alcoholic casting solvent. CNBr (2 mg/mL, pH 11.5) was then freshly prepared in aqueous solution and added in 5 mL of solution to the pHEMA precoated dish. To allow for sufficient activation, a 1 h incubation time was applied. After the reaction time, the dish was washed with 10 mL of sodium bicarbonate solution (0.1 M) for one time and subsequently water for two times. GSSG solution (2 mM) was then prepared in sodium carbonate buffer (0.1 M, pH 9.5) and added in 5 mL of solution to the CNBr-activated dish. Coupling of GSSG to CNBr-activated supports preceded quite efficiently between pH 8.0 and 9.5. Amine containing buffers such as Tris and other nucleophiles were avoided due to potential competition for coupling sites. An overnight incubation at 23 ± 1 °C was used to ensure a high extent of GSSG immobilization on pHEMA. The elemental contents of carbon, oxygen, nitrogen, and sulfur of the pHEMA-coated, CNBr-activated and GSSG-conjugated glass chips were measured using XPS.

GSH was formed by subsequent reduction of conjugated GSSG using DTT. In our study, DTT solution (2 mM, 10 mL) was freshly prepared in phosphate buffer (0.1 M, pH 8) and incubated with the GSSG-conjugated pHEMA dish for 1 h at 23 ± 1 °C. The dish was tested using Ellman's assay for free thiol group determination (*22*) after washing with copious amount of water. The procedure is based on the reaction of the thiol group with Ellman's reagent 5,5′-dithio-bis(2-nitrobenzoic acid) (DTNB) to generate the 2-nitro-5-thiobenzoic acid (TNB) which is quantified subsequently by measuring the absorbance of the anion (TNB^{2-}) at 412 nm.

Conjugation of GSH to pHEMA on 96-Well Plates. To determine the optimal thickness of pHEMA layer on the surface of the 96-well plates, serial dilutions of the alcoholic pHEMA solution were introduced into each well of the 96-well plates at a constant volume of 100 μL, resulting in decreasing thickness of the polymeric membrane (3, 1, 0.5, and 0.25 mg/well). Considering that different evaporation rate of casting solvent might also have an effect on the morphology of the polymer on the surface, casting temperature was also evaluated from 23 to 70 °C. Immobilization and subsequent reduction of GSSG were performed on each well of the plates, and the conjugated GSH density was measured fluorometrically using 1,5-I-AEDANS as the probe molecule. 1,5-I-AEDANS (0.1 mM, 100 μL) was added into DTT pretreated and nontreated wells that were regarded as test and blank, respectively. The optimized conditions (concentration of pHEMA and casting temperature) were adopted to prepare pHEMA-coated plates for the next stage of our optimization experiments.

After determination of the optimal thickness and casting temperature of pHEMA, the activation of pHEMA, and conjugation and reduction of GSSG were also optimized. As shown in Scheme 1, three steps of the chemical reaction were used to immobilize GSH onto the polymer support, namely, CNBr activation, GSSG conjugation, and DTT reduction. In each step of the reaction, optimization of the reaction time and reagent concentration were explored while maintaining other variables unchanged. The CNBr activation time and concentration were varied between 0 and 60 min and 0−10 mg/mL, respectively. GSSG conjugation time and concentration were experimented between 0−6 h and 0−4 mM, respectively. Finally, DTT reduction time and concentration were investigated between 0 and 150 min and 0 and 4 mM, respectively.

For the determination of the quantity of conjugated GSH in all optimization experiments, a solution (100 μL) of 1,5-I-AEDANS (0.1 mM) in phosphate buffer was transferred to each well and incubated at 23 ± 1 °C for 1 h. The plate was then washed three times with Milli-Q water and subjected to fluorescence measurement using the Tecan plate reader. Conjugated GSH−1,5-AEDANS was excited at 360 nm (9 nm bandwidth), and fluorescence emission was recorded simultaneously at 490 nm (20 nm bandwidth).

Determination of Nucleophilic Potential of Conjugated-GSH. NAPQI, a commercially available RM of APAP, was employed as a standard to determine the nucleophilic potential of the conjugated GSH. The GSSG-conjugated plate was charged with 100 μL of freshly prepared DTT (2 mM) solution per well and incubated at 25 °C for 1 h. NAPQI solution was prepared in a series of concentrations at 100, 10, 5, 1, 0.5, 0.1, and 0.05 μM using Milli-Q water. The DTT pretreated plate was then incubated with NAPQI solutions (100 μL per well) at 23 ± 1 °C. After a 1 h incubation, the plate was washed with Milli-Q water three times and subsequently incubated with 1,5-I-AEDANS (100 μL, 0.1 mM) in phosphate buffer at 23 ± 1 °C for 1 h. The plate was washed three times with Milli-Q water and subjected to fluorescence measurement as described earlier.

Ultra Performance Liquid Chromatography−Quadrupole Time-of-Flight Tandem Mass Spectrometry (UPLC/QTOF/MS/MS) Analysis of NAPQI−GSH. For the confirmation of the *in vitro* generation of NAPQI, a sample consisting of 800 μM APAP incubated in MLM with GSH for 60 min at 37 °C was analyzed. Chromatographic separations were performed on an AQUITY UPLC BEH C_{18} 1.7 μm, 50 mm × 2.1 mm i.d. column (Waters). The column heater and autosampler were kept at 60 and 4 °C, respectively. The mobile phases consisted of solvent A (0.1% formic acid in water) and solvent B (0.1% formic acid in acetonitrile). The optimized elution conditions were gradient of 0.1−10.0% solvent B (0−1.80 min), 10.0−95.0% solvent B (1.80−1.81 min), isocratic at 95.0% solvent B (1.81−2.14 min), and isocratic at 0.1% solvent B (2.15−2.50

min). The flow rate was 0.7 mL/min. The eluent was split postcolumn (ratio of 2:1 between waste and MS) into the ESI source using a T-splitter so as to enhance the MS sensitivity.

The QTOFMS system was tuned for optimum sensitivity and resolution in electrospray positive ionization mode (ESI+) mode using leucine enkephalin (50 pg/uL infused at 5 μL/min). The QTOF/MS/MS analysis was operated in "V" mode, and the optimized conditions were as follows: capillary voltage 3400 V, sampling cone 24 V, source temperature 100 °C, desolvation temperature 350 °C, cone gas flow 0 L/h, desolvation gas flow 500 L/h, collision energy 15 eV, MCP detector voltage 1800 V, pusher voltage 915 V, pusher voltage offset −0.70 V, and puller voltage 640 V. The precursor mass was set at 457.1 Da, and continuum data were acquired for each sample from 50 to 600 Da with a 0.2 s scan time and a 0.02 s interscan delay. Prior to analysis, the system was calibrated in ESI+ mode using 0.5 M sodium formate solution infused at a flow rate of 4 μL/min. All analyses were acquired using an independent reference spray via the LockSpray interface to ensure high mass accuracy and reproducibility; the $[M + H]^+$ ion of leucine enkephalin (2 ng/μL infused at 3 μL/min) was used as the reference lock mass (*m*/*z* 556.2771). The LockSpray was operated at a reference scan frequency, reference cone voltage, and collision energy of 10 s, 30, and 18 V, respectively.

MLM Assay of APAP Using a GSH-Conjugated 96-Well Plate. The test compound APAP solution (50 mM) mixed with MLM proteins in potassium phosphate buffer (50 mM, pH 7.4) was prewarmed at 37 °C for 5 min. The reaction was then initiated by the addition of a NADPH A and B regenerating system to give a final volume of 1 mL in eppendorf tubes. The final reaction mixtures contained 1 mM APAP and 1 mg/mL microsomal protein, respectively. The solution (100 μL) was added subsequently into each well of a DTT pretreated plate and incubated at 37 °C for 1 h. After the incubation, the reaction was terminated by washing the plate with Milli-Q water three times. Immediately after washing, 100 μL of 1,5-I-AEDANS (0.1 mM) solution in phosphate buffer (0.1 M, pH 8) was added and the plate was incubated for 1 h. After the reaction period, the plate was then washed again and subjected to fluorescence measurement. Positive controls consisted of incubations with only NAPQI solution (100 μM) while negative controls were incubations that lacked in APAP substrate. Blank wells were not subjected to DTT treatment. The performance of the plate was quantified as the trapping index, TI%, which was calculated using the following equation where F_t, F_{pc}, and F_{nc} are the fluorescence intensities of test wells, positive control wells, and negative control wells, respectively.

$$\mathrm{TI\%} = \frac{(F_t - F_{pc})}{(F_{nc} - F_{pc})} \times 100\%$$

RM Screening of Marketed Drugs and Chemical Compounds Using a GSH-Conjugated 96-Well Plate. The marketed drugs used to evaluate the RM profiling strategy were verapamil, donepezil, galantamine, memantine, cimetidine, pilocarpine, streptomycin, zomepirac, procainamide, amodiaquine, tolmetin, sulfanilamide, diclofenac, and mitomycin C. The two chemical compounds are 3-acetomidopgenol and deiquat. These substrates (including APAP) in stock aqueous solution (50 mM) were loaded on DTT pretreated 96-well plates. A solution of NADPH A and B mixed with MLM proteins in potassium phosphate buffer was prewarmed at 37 °C for 5 min. A total of 98 μL of the solution was then transferred to each well of the drug loaded 96-well plate. Each final reaction mixture contained 1 mM of the test drug substrate and 1 mg/mL of microsomal protein with a total volume of 100 μL. The plate was incubated at 37 °C for 1 h. After the incubation, the reaction was terminated by washing the plate with Milli-Q water three times. Immediately after washing, 100 μL of 1,5-I-AEDANS (0.1 mM) solution in phosphate buffer (0.1M, pH 8) was added and the plate was further incubated for 1 h. After the reaction period, the plate was then washed again and subjected to fluorescence measurement. The TI % was determined based on the method above.

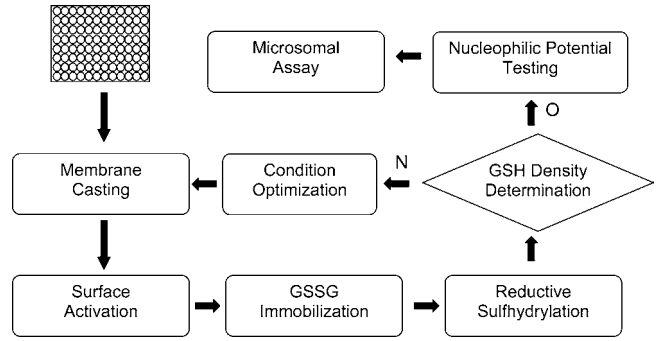


Figure 2. Workflow of the immobilization of GSH on a 96-well plate (O and N refer to optimum and nonoptimum, respectively).

Table 1. Surface Element Analysis by XPS for GSSG-Conjugated pHEMA

	percentage (%)		
elements	pHEMA	CNBr-activated pHEMA	GSSG-conjugated pHEMA
O	36.43	33.55	30.74
C	63.57	66.44	68.91
N		0.01	0.26
S			0.09

Data Analysis. A one-way analysis of variance (ANOVA) was conducted to determine statistical significance between the TI values of compounds which are known to produce RMs and those that do not generate reactive intermediates using the MLM system. The statistical test was performed using GraphPad Prism 4 software (GraphPad Software, San Diego, CA), and a *P*-value of <0.05 was considered statistically significant.

RESULTS

Conjugation of GSH on pHEMA Coated Surfaces. Before performing the development work using 96-well plates as shown in the summary flowchart (Figure 2), it was essential to confirm the feasibility of the various reactions leading up to the conjugation of GSH on pHEMA-coated surfaces. For this purpose, elemental analysis of the polymeric surfaces was conducted by XPS and the results are shown in Table 1. pHEMA consists of oxygen and carbon elements (Figure 1c) which were analyzed by XPS yielding the respective percentages of 36.43 and 63.57%. After CNBr activation, the percentage of carbon content was found to be increased with an associated decline in the percentage of oxygen, indicating cyanogen attachment on the surface of pHEMA. The untraceable nitrogen content in XPS was possibly due to the relatively lower contribution of nitrogen in the polymer. After GSSG was conjugated on the surface of pHEMA, the percentage of nitrogen atoms was found to increase to 0.26% due to its higher nitrogen content in the GSSG molecule (Figure 1b). XPS further confirmed the coupling of GSSG based on the 0.09% of sulfur atom detected. In addition, the percentage of oxygen atoms also dropped substantially due to the lower content of oxygen in the GSSG molecule. Our results further indicated that the ratios of the respective elements were not significantly different when the incubation time was increased. This was possibly due to the fact that the surface modification reaction was already saturated using the reaction conditions mentioned above.

Table 2. Fluorescence Intensity and Signal-to-Noise (S/N) Ratio of Each Well Using Different Casting Conditions

			fluorescence intensity[a] (SD)		
no.	pHEMA (mg per well)	casting temperature (°C)	DTT-treated	nontreated	S/N ratio
1	3	25	12200 (1010)	2247 (450)	5.4
2	3	70	OL[b]	2175 (520)	
3	1	25	1301 (121)	876 (232)	1.5
4	1	30	2937 (533)	821 (225)	3.6
5	1	40	4557 (344)	336 (18)	13.6
6	1	50	5706 (309)	409 (61)	14.0
7	1	60	5918 (403)	432 (46)	13.7
8	1	70	6181 (393)	360 (45)	17.1
9	0.5	70	3474 (312)	323 (19)	10.8
10	0.25	70	1377 (78)	167 (20)	8.2
11	0.20	70	1010	171 (17)	5.9

[a] Values were average of intensity ± SD of 6 replicates. [b] The reading was over limit (OL) based on the instrument settings.

On the basis of the results of the Ellman's assay (*22*) for free thiol group determination, we confirmed the presence of free thiol groups in the DTT-treated GSSG-conjugated pHEMA-coated Petri dish. The positive color change from light yellow to brown confirmed the presence of free thiol groups. Our XPS and Ellman's assay data demonstrated collectively that GSSG was successfully conjugated on pHEMA, and the free thiol groups were regenerated in the DTT-treated dish. Using these conditions, we proceeded to apply the methodology to the 96-well plate system and further optimized the conditions for the screening of RMs *in vitro* (Figure 2).

Conjugation of GSH to pHEMA on 96-Well Plates. Sensitivity was a key consideration for the detection of trace levels of RMs. Therefore, a sensitive detection method for free thiol group of GSH using fluorometric assay was necessary. 1,5-I-AEDANS has been extensively used in labeling cysteine in protein analysis because it has an advantage that it reacts rather specifically with the thiol group and spares other nucleophilic functional groups of proteins. This specificity renders 1,5-I-AEDANS particularly useful in our study where the level of emission from the fluorescence probe was inversely proportional to the amount of trapped RMs. In this study, 5-I-AEDANS was used in all our optimization experiments to determine the density of the conjugated GSH on pHEMA-coated 96-well plates.

Regarding the optimization of the casting temperature and concentration of pHEMA, the testing conditions and results are summarized in Table 2. Our results suggest that both the concentration of pHEMA and casting temperature played an important role in determining the fluorescence signal. When the loaded pHEMA amount was reduced, the density of the conjugated GSH was also decreased as expected. Similarly, it was found that higher temperature gave higher fluorescence emission which represented a higher density of conjugated GSH. The best signal/noise ratio (S/N = 17.1) was obtained when 1 mg of pHEMA was casted on each well of the plate at 70 °C. However, the density of the conjugated GSH based on the fluorescence emission under this condition was found to be too high for obtaining sufficient sensitivity to detect trace levels of RM. Thus, the optimum density of GSH was achieved by further reducing the loading amount of pHEMA to 0.25 mg per well at 70 °C where the approximate S/N ratio and absolute fluorescence emission value were 8.2 and 1377 ± 78, respectively. Further decreasing the loading amount of pHEMA only resulted in a lower S/N ratio of less than 6 (Table 2). For the next phase of optimization, pHEMA (125 mg) was dissolved in ethanol (95%, 50 mL) to make up a 2.5 mg/mL solution. The pHEMA solution was casted onto each 96-well plate by pipetting 100 μL of the above solution into each well of the plate using a multichannel pipettor. The solution in the plate was allowed to dry in an incubator at 70 °C overnight. A thin, hard film of optically clear polymer was tightly bound to the plastic surface after the alcohol evaporated.

The results of the optimization of CNBr activation, GSSG conjugation, and DTT reduction are presented in Figure 3. In each step of the reaction, optimization of the reaction time and reagent concentration were investigated while maintaining other variables unchanged. As shown in Figure 3a, the activation of the hydroxyl group by CNBr was fast, and the maximal fluorescence value was attained at 20 min of reaction duration. Another important parameter was the concentration of CNBr. As reported in Figure 3b, the use of 1 mg/mL of CNBr was determined to be optimum to obtain a high activation level of the pHEMA polymer. In the second step, both the increases in the duration of the GSSG immobilization (Figure 3c) and GSSG concentration (Figure 3d) were found to strongly improve the immobilization efficiency. The optimum reaction time and GSSG concentration were 2 h and 2 mM, respectively. In the DTT reduction step (Figure 3f), 2 mM of reductive DTT reagent was optimum in reducing the conjugated GSSG into GSH to expose the free thiol group. The reaction time for achieving the target fluorescence intensity of approximately 1400 was achieved at 1 h (Figure 3e).

For the subsequent validation assay, the pHEMA-coated plates were rehydrated using 100 μL per well of Milli-Q water during which the polymer swelled without dissolving. An aqueous solution of CNBr (1 mg/mL) was freshly prepared in Milli-Q water, and the solution was adjusted to pH 11.5 with 0.2 M NaOH. The CNBr solution (100 μL) was then transferred into each well of the plates and reacted on pHEMA for 20 min at 25 °C. After the reaction period, the CNBr-activated plates were washed once with 0.1 M $NaHCO_3$ and then three times with Milli-Q water using a Tecan plate washer. Subsequently, an aqueous solution of GSSG (100 μL, 2 mM) in carbonate buffer (0.1 M, pH 9.5) was added and allowed to react for 2 h at 25 °C. After the coupling reaction, the GSSG-conjugated plates were washed again as described above and stored dry at 4 °C before the reduction reaction.

GSH was formed by reduction of conjugated GSSG using DTT as described (Scheme 1). Phosphate buffer (0.1 M) was prepared, and the pH was adjusted to 8.0 using 1 M NaOH. DTT (2 mM) was freshly prepared in phosphate buffer and was added (100 μL) into each well of the plate. The reduction was carried out for 1 h, and the plate was washed with Milli-Q water three times. These plates were used for the subsequent *in vitro* assays.

Determination of Nucleophilic Potential of Conjugated-GSH. NAPQI, a RM of APAP, was used to determine the nucleophilic potential of conjugated GSH. The GSH-conjugated plate was prepared based on the optimized conditions as discussed above. Different concentrations of NAPQI were added into the wells and incubated at 23 ± 1 °C for 1 h. The plate was then subjected to fluorometric assay based on 1,5-I-AEDANS to determine the amount of free unbound GSH. Wells without treatment by DTT were included in the assay as blanks. The negative controls were the DTT-treated wells where only vehicle solution was incubated. The nucleophilic activity of conjugated GSH toward NAPQI was significant and concentration-dependent as shown in Figure 4. At the concentration of 10 μM or more of NAPQI, about 90% of the conjugated GSH bound to NAPQI while the remaining 10% bound to the fluorescence probe. The detection limit for NAPQI was approximately 500 nM where the TI% was 11.2%. However, when the concentration was further reduced to 100 nM or lower, the trapping of NAPQI was not reproducibly detected. Nonetheless, the detection limit of 500 nM of NAPQI was potentially

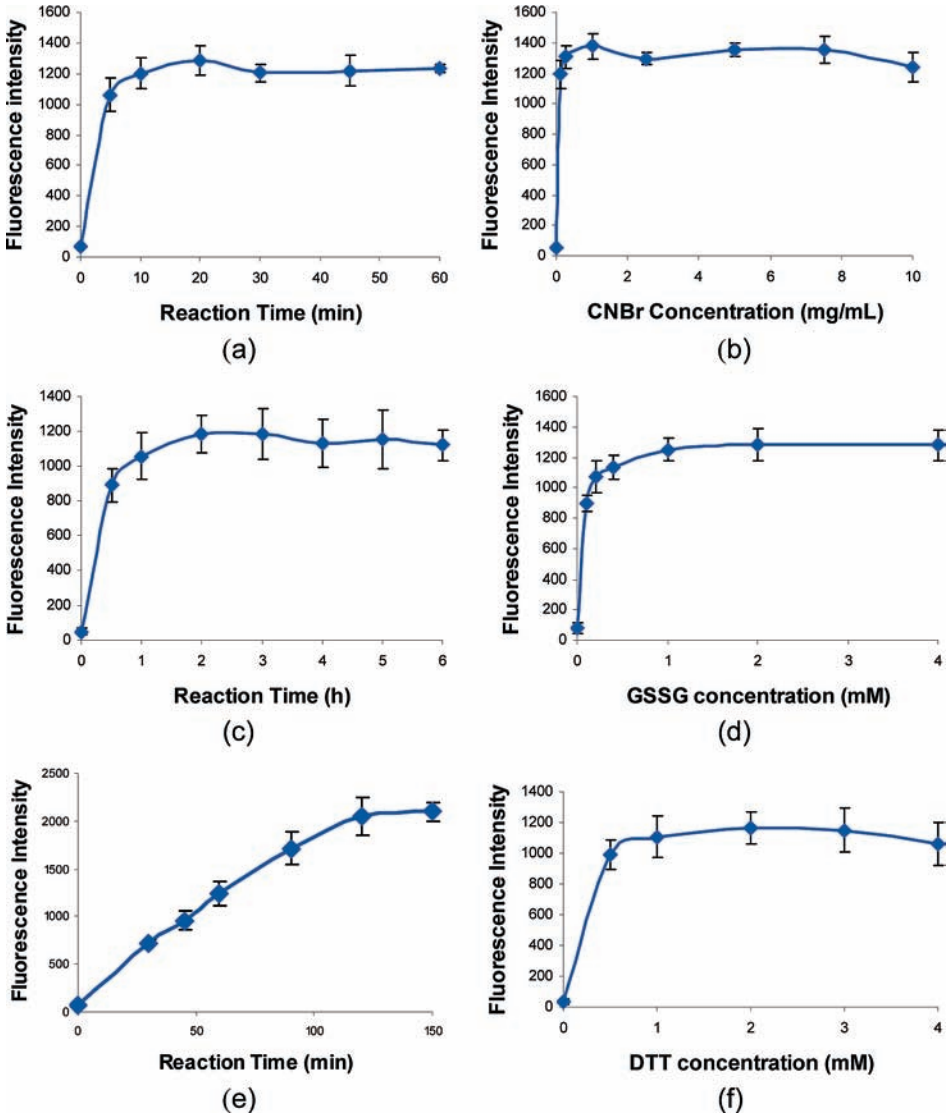


Figure 3. Reaction optimization of CNBr activation (a) time and (b) concentration; GSSG immobilization (c) time and (d) concentration; DTT reduction (e) time and (f) concentration.

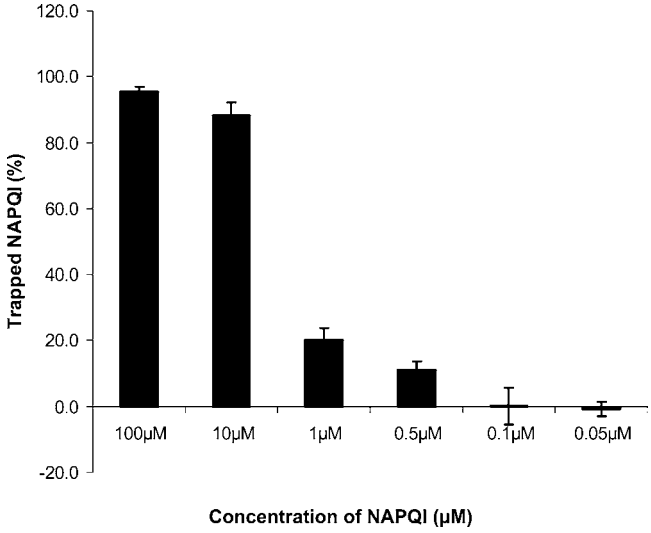


Figure 4. Plot of percentages of trapped NAPQI using the 96-well plate against concentration of NAPQI (micromolar).

sensitive to be explored for the *in vitro* profiling of RM using the MLM assay of 1 mM APAP.

UPLC/QTOF/MS/MS Analysis of NAPQI−GSH. With the use of MassLynx, the theoretical calculated masses, mass accuracy (millidaltons (mDa) and parts per million (ppm)), i-FIT (the likelihood that the isotopic pattern of the elemental composition matches a cluster of peaks in the spectrum) values, and elemental compositions associated with NAPQI−GSH and its fragments were generated and studied. With the use of a mass tolerance of 10 ppm, the experimentally determined masses/mDa/ppm/i-FIT/elemental composition of NAPQI−GSH ($[M + H]^+$) was 457.1383/−1.0/−2.2/ 0.0/$C_{18}H_{25}N_4O_8S$ and its fragments were (i) $[M - 75]^+$: 382.1070/−0.3/−0.8/5.7/$C_{16}H_{20}N_3O_6S$; (ii) $[M - 129]^+$: 328.0961/−0.6/−1.8/0.2/$C_{13}H_{18}N_3O_5S$; (iii) $[M - 146]^+$: 311.0707/0.5/1.6/3.6/$C_{13}H_{15}N_2O_5S$; (iv) $[M - 188]^+$: 269.0606/1.0/3.7/7.9/$C_{11}H_{13}N_2O_4S$; (v) $[M - 232]^+$: 225.0704/0.6/2.7/0.7/$C_{10}H_{13}N_2O_2S$; (vi) $[M - 249]^+$: 208.0428/−0.4/−1.9/0.9/$C_{10}H_{10}NO_2S$; and (vii) $[M - 275]^+$: 182.0279/0.3/1.6/0.2/$C_8H_8NO_2S$, respectively (Figure 5). On the basis of the accurate mass measurement of the parent and product ions and the fragmentation pattern of the NAPQI−GSH adduct, we confirmed the formation of NAPQI *in vitro* using the MLM assay of APAP.

MLM Assay of APAP Using a GSH-Conjugated 96-Well Plate. In order to validate that NAPQI produced *in situ* could be trapped by our GSH-conjugated 96-well plates, a standard *in vitro* MLM assay with APAP as a substrate was

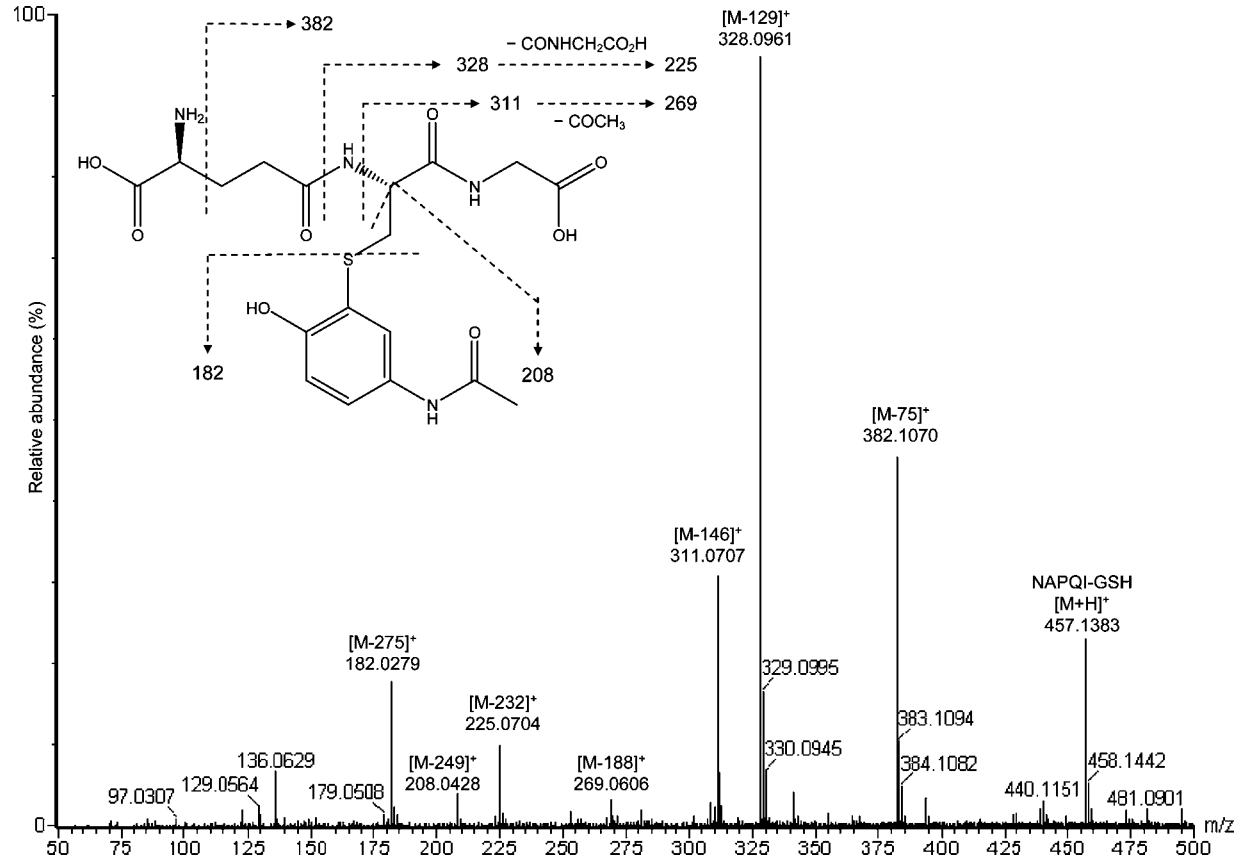


Figure 5. Extracted UPLC/QTOF/MS/MS ion spectrum of NAPQI−GSH. The CID pathways of NAPQI−GSH and its respective fragments are shown.

Table 3. Mouse Liver Microsomal Assay of APAP on a GSH-Conjugated 96-Well Plate

	fluorescence intensity		
wells	NAPQI (p)	negative control (nc)	test (t)
W1	194	1103	1010
W2	182	1244	1147
W3	191	1451	1014
W4	179	1398	1260
W5	188	1439	1119
W6	190	1309	1080
mean	187	1324	1105
SD	5.7	134	94
trapping index (TI%)			19.3%

adopted. The results are shown in Table 3. The TI% of the APAP was determined to be 19.3%. Assuming NAPQI was the main reactive species, our data suggested that approximately 19% of conjugated GSH reacted with NAPQI, while the remaining unbound GSH was detected using the fluorescence probe.

RM Screening of Marketed Drugs and Chemical Compounds Using MLM. Zomepinac, procainamide, 3-acetomidophenol, amodiaquine, tolmetin, deiquat, sulfanilamide, diclofenac, mitomycin C, and APAP were selected for the RM screening experiment. These drugs and chemicals were selected as they had been reported to generate reactive metabolite in previous microsomal study (*23*−*27*). Verapamil, donepezil, galantamine, memantine, cimetidine, pilocarpine, and streptomycin were tested as negative controls as they are known not to produce any electrophilic species metabolically. On the other hand, NAPQI at 100 μM was used as a positive control as it was believed to block all the trapping GSH moieties and set the TI at 100%. As shown in Figure 6, after incubation with MLM, these substrates exhibited different degrees of trapping

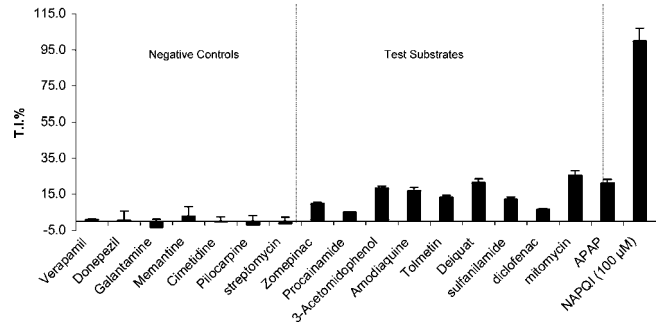


Figure 6. Plot of TI% values of selected marketed drugs and chemical compounds screened by the mouse liver microsomal assay using the fluorescence-based GSH-conjugated 96-well.

index (−3.2 to 25.7%). The highest TI% was attributed to mytomycin C, a chemotherapeutic agent, with a TI of 25.7%. Accordingly, the TI values of negative control substrates were marginally low at −3.2 to 2.8%. The differences in TI values between the negative control substrates (verapamil, donepezil, galantamine, memantine, cimetidine, pilocarpine, and streptomycin) and test substrates (zomepinac, procainamide, 3-acetomidophenol, amodiaquine, tolmetin, deiquat, sulfanilamide, diclofenac, mitomycin C, and APAP) were found to be statistically significant for the MLM system ($P < 0.05$). The data also indicated that the background signal related to the reoxidation of free GSH was minimal during the microsomal incubation.

DISCUSSION

In this study, we aimed to develop a HTS 96-well plate platform with conjugated GSH for the screening of pharma-

ceutical RMs. The most challenging part of our study was the conjugation of GSH trapping molecule on 96-well plates. Most commercially available 96-well plates are made of polystyrene (Figure 1d). Unmodified polystyrene normally has no active sites or functional groups available for the direct immobilization of ligands. For this reason, the hydrophobic character of a polystyrene surface was often exploited to noncovalently immobilize ligands through passive adsorption (*28*−*30*). However, for coupling of small molecules, such as the tripeptide GSH, the technique of simple adsorption may not work. In many instances, hydrophilic substances do not adhere very well to the hydrophobic polystyrene surface. Direct aryl functionalities may be useful for covalent ligand attachment via an electrophilic aromatic substitution (*31, 32*). However, the conditions of such a reaction are normally harsh and somewhat difficult to execute on polystyrene microtiter plates because the latter would be clouded, colored, or deformed. Another direct covalent linking method was also available using chemical attachment by a UV-catalyzed free radical reaction (*33*−*35*). This approach might result in a covalent linkage and maintain the critical optical clarity necessary for enzyme-linked immunosorbent assays (ELISA). However, the photoreactive cross-linking agents are generally costly and the resulting yield of conjugated ligand is also low.

In this paper, we developed a novel approach to provide a covalent link between the plate surface and GSH ligand where the intermediate noncovalent coating of a polymer that contains functional group was exploited. The polymeric membrane coating would provide a reactive site for chemical modification. The preferable functional group for subsequent activation and attachment of an affinity ligand was the primary hydroxyl group. Primary hydroxyls are amenable to a wide assortment of activation procedures but do not contribute to nonspecific binding of nontargeted molecules. Although many classical organic reactions may be used to modify the hydroxyl group, care was taken in choosing our method, since some required solvents may also dissolve the polymeric membrane. pHEMA (Figure 1c) attracted our interest because it has been traditionally used as an agent to coat a 96-well plate so as to reduce cell adhesivity in cell culture. pHEMA is also a hydrophilic hydrogel of neutral charge with the preferable hydroxyl functional group. After conversion of the hydroxyl group into an amine active functional group, it could be used to immobilize the GSSG on the plate surface. Another important property of this support material is that it has a hydrolyzable ester group. After trapping of RM, pHEMA offers the potential to cleave away the RM−GSH conjugate for LC/MS/MS analysis.

GSH (Figure 1a) contains two nucleophilic groups, namely, the amino and thiol groups. The thiol group was targeted for trapping pharmaceutical RMs during the *in vitro* liver microsomal assay. However, the thiol group is highly reactive and prone to auto-oxidation to GSSG (Figure 1b) by oxygen in the atmosphere during the workup process (*36*). In our study, we exploited the unique redox property of the GSH−GSSG pair as a strategy for thiol protection during the conjugation process. The linked disulfide group of GSSG would not compete with its amino group for the CNBr-activated electrophiles during the conjugation process (*37*). The use of GSSG would also circumvent challenges related to auto-oxidation of GSH. After the immobilization, the free thiol group of GSH was regenerated via a reductive thiolation reaction (*38*) (Scheme 1). On th basis of the results of XPS and Ellman's assay, we confirmed the feasibility of this chemical strategy and applied it for coupling GSH to pHEMA-coated surfaces.

During of coupling of excess GSH to precoated functional pHEMA polymeric membrane, it was pertinent to ensure that the thiol trapping group of GSH was intact and active for subsequent conjugation with RMs. As the density of conjugated GSH influenced the sensitivity of the assay in detecting trace levels of RMs produced by the *in vitro* liver microsomal system, it became important to optimize the immobilization conditions so as to achieve the best S/N ratio and sensitivity for the assay. A density determination step was also essential to control the quality of the plate. The structure of polymeric pHEMA as a coating material is dominated by the presence of primary hydroxyl groups sticking out from a polyvinyl backbone (Figure 1c). The chains are held together and stabilized by periodic cross-links formed by the ethylene dimethacrylate monomer. The chemical structure of pHEMA forms numerous tertiary α-carbonyl esters of pivalic acid, one of the most stable and least hydrolyzable esters known (*39*). Once dissolved in ethanol and casted onto a 96-well plate surface, it formed a thin, hard, and optically clear membrane which remained tightly bonded to the polystyrene surface after the alcohol was evaporated. The film was stable in aqueous solution within the pH range of 2−12 but was dissolvable in organic solvent. This latter physicochemical property posed great challenge in selection of suitable reagents and conditions for membrane activation and GSSG immobilization. In our study, the projected hydroxyl groups in pHEMA were preferentially activated to be reactive toward the amino group of GSSG in an aqueous environment (Scheme 1). Among amine reactive chemistries, CNBr has grown to be the most prevalent method for the activation of hydroxyl groups of polysaccharide matrixes (*40*). The CNBr-activated support could subsequently be used to couple to small ligands as well as to high molecular weight biopolymers containing primary amine moiety. In this study, we successfully optimized the conditions in the activation of pHEMA surfaces using CNBr, coupling of GSSG to CNBr-activated surfaces, and subsequent reduction of GSSG to GSH to obtain optimal GSH density for the trapping of RMs.

As the objective of this paper was to develop a 96-well plate platform for the profiling of RM, we further validated our optimized assay using commercially available NAPQI to determine the detection limit and optimum density of GSH. Our data demonstrated the detection limit of the trapped NAPQI was 500 nM, which was near the estimated trace levels of RM produced by 1 mM of APAP *in vitro* using the liver microsomal system. Before validating our RM profiling strategy using the MLM assay of APAP, it was essential to confirm the biotransformation of APAP to NAPQI electrophilic species *in vitro* using the standard microsomal assay. This was important to ensure that the subsequent binding to the conjugated-GSH was related to NAPQI and not other forms of nonspecific binding. With the use of UPLC/QTOF/MS/MS with GSH trapping, the high mass accuracies of the parent and product ion and the characteristic fragmentation pattern of the NAPQI−GSH conjugate supported strongly that NAPQI was generated *in vitro* using our MLM assay. Our results obtained for the RM profiling assay of APAP (TI of 19.3%) confirmed that the GSH-conjugated 96-well plates could be applied for the profiling of NAPQI generated from APAP *in vitro* in addition to standard NAPQI. Finally, we subjected our RM profiling strategy to the screening of a series of marketed drugs and chemical compounds. Importantly, for the compounds that are known to generate electrophilic metabolites (*21*−*25*), our assay identified them positively with a range of TI ranging from 5.1 to 26.0% in MLM. As expected, the TI value of verapamil was close to 0% since this compound did not generate electrophilic metabolites *in vitro*. This confirmed that our experiment was selective toward reactive species and nonspecific binding was maintained at a minimal. Similar observations were made with regards to the other negative control substrates.

Currently, there is a growing demand in the pharmaceutical industry for an efficient method that can be used to screen a large volume of compounds for the formation of pharmaceutical RMs. Hit and lead compounds that show the propensity in forming RMs may be eliminated at an early stage of drug development. This "fail early, fail cheap" approach renders the drug discovery process more cost-effective. Furthermore, the information gleaned from the structural elucidation of RMs is important for the drug development team. Medicinal chemists will become more mindful of specific functional groups that are liable for the generation of RMs and should be avoided in the design of the next generation of drug candidates. Direct detection and characterization of RMs have been proven to be extremely difficult. A widely utilized strategy is to trap reactive metabolites generated by cytochrome P450 enzymes with a capture molecule such as GSH, and resulting stable GSH adducts can be subsequently characterized by tandem mass spectrometry (LC/MS/MS). This method is sensitive and reliable but is time-consuming and unsuitable for high-throughput screenings. While there has been a recent report that challenged the use of *in vitro* covalent binding data to prospectively predict toxicity (*41*), it was determined in a separate study (*42*) that there is a general trend between the extent of thiol adduct formation and the potential for drug-induced toxicity. The latter study suggested that screening of thiol adduct formation is a pertinent part of an overall discovery optimization paradigm. The present study describes a novel approach that demonstrates good sensitivity and reliability, as well as suitability for the high-throughput screening of RMs. High sensitivity is critical for the current method to detect less abundant RMs. In a quantitative term, sensitivity of a given analytical method is normally assessed by the S/N ratio of a designated benchmark compound. For the present method, trapping of RMs was not measured directly, However, identification of GSH adducts by the our method was largely based on unbound GSH which was covalently bound to a fluorescence moiety that was subsequently measured. Therefore, the density of the GSH immobilized on the plate was a pertinent factor to ensure sufficiently high sensitivity of our assay. We optimized the amount of GSH conjugated on the 96-well plate extensively and achieved an optimal balance to ensure high S/N ratio and sensitivity as well as low assay variability. The amenability of our method for high-throughput screening of RMs is another important attribute. Although only 18 compounds were involved in our validation study, the throughput of our assay was clearly improved because of its high efficiency using a 96 well plate and suitability for screening RMs at an unprecedented speed. Therefore, fully automated identification of RMs can be accomplished in a high-throughput fashion if large libraries of compounds are screened.

In conclusion, we presented a novel and feasible conjugation method of GSH for the fast profiling of pharmaceutical RM. The detection of a fluorescence signal with 1,5-I-AEDANS enables semiquantitative and reciprocal measurement of RM−GSH formation and renders it possible for the broad screening of drugs described in our study without the use of radio-labeled materials. In this study, we have not completely optimized the sensitivity of the assay and investigated sufficiently the TI% for compound rejection. Future research should further improve the sensitivity of our assay so that RM may be detected at micromolar level of drug incubation. At the same time, more marketed drugs should be screened using our platform so that the correlation of TI values with established toxicities may be established.

ACKNOWLEDGMENT

This work was supported by the National University of Singapore grant (Grant R-279-000-249-646) for the initiative on advanced membranes for pharmaceutical and biomedical applications. The authors are grateful to Professor Neal Chung and Associate Professor Chan Sui Yung for facilitating the grant support. The assistance by Ms. New Lee Sun in the UPLC/MS/MS analysis of reactive metabolite is also acknowledged.

LITERATURE CITED

(1) DiMasi, J. A., Hansen, R. W., and Grabowski, H. G. (2003) The price of innovation: new estimates of drug development costs. *J. Health Econ. 22*, 151–185.

(2) Kraljevic, S., Stambrook, P. J., and Pavelic, K. (2004) Accelerating drug discovery. *EMBO Rep. 5*, 837–842.

(3) Frank, R., and Hargreaves, R. (2003) Clinical biomarkers in drug discovery and development. *Nat. Rev. Drug Discovery 2*, 566–580.

(4) Sugiyama, Y. (2005) Druggability: selecting optimized drug candidates. *Drug Discovery Today 10*, 1577–1579.

(5) Li, P., Wang, G. J., Li, J., Hao, H. P., and Zheng, C. N. (2006) Simultaneous determination of tanshinone IIA and its three hydroxylated metabolites by liquid chromatography/tandem mass spectrometry. *Rapid Commun. Mass Spectrom. 20*, 815–822.

(6) Nelson, S. D. (1982) Metabolic activation and drug toxicity. *J. Med. Chem. 25*, 753–765.

(7) Park, B. K., Kitteringham, N. R., Maggs, J. L., Pirmohamed, M., and Williams, D. P. (2005) The role of metabolic activation in drug-induced hepatotoxicity. *Annu. Rev. Pharmacol. Toxicol. 45*, 177–202.

(8) Walgren, J. L., Mitchell, M. D., and Thompson, D. C. (2005) Role of metabolism in drug-induced idiosyncratic hepatotoxicity. *Crit. Rev. Toxicol. 35*, 325–361.

(9) Dahlin, D. C., and Nelson, S. D. (1982) Synthesis, decomposition kinetics, and preliminary toxicological studies of pure N-acetyl-p-benzoquinone imine, a proposed toxic metabolite of acetaminophen. *J. Med. Chem. 25*, 885–886.

(10) Streeter, A. J., Dahlin, D. C., Nelson, S. D., and Baillie, T. A. (1984) The covalent binding of acetaminophen to protein. Evidence for cysteine residues as major sites of arylation in vitro. *Chem.−Biol. Interact. 48*, 349–366.

(11) Caldwell, G. W., and Yan, Z. (2006) Screening for reactive intermediates and toxicity assessment in drug discovery. *Curr. Opin. Drug Discovery Dev. 9*, 47–60.

(12) Evans, D. C., Watt, A. P., Nicoll-Griffith, D. A., and Baillie, T. A. (2004) Drug-protein adducts: an industry perspective on minimizing the potential for drug bioactivation in drug discovery and development. *Chem. Res. Toxicol. 17*, 3–16.

(13) Day, S. H., Mao, A., White, R., Schulz-Utermoehl, T., Miller, R., and Beconi, M. G. (2005) A semi-automated method for measuring the potential for protein covalent binding in drug discovery. *J. Pharmacol. Toxicol. Methods 52*, 278–285.

(14) Yan, Z., and Caldwell, G. W. (2004) Stable-isotope trapping and high-throughput screenings of reactive metabolites using the isotope MS signature. *Anal. Chem. 76*, 6835–6847.

(15) Baillie, T. A., and Davis, M. R. (1993) Mass spectrometry in the analysis of glutathione conjugates. *Biol. Mass Spectrom. 22*, 319–325.

(16) Grillo, M. P., Hua, F., Knutson, C. G., Ware, J. A., and Li, C. (2003) Mechanistic studies on the bioactivation of diclofenac: identification of diclofenac-S-acyl-glutathione in vitro in incubations with rat and human hepatocytes. *Chem. Res. Toxicol. 16*, 1410–1417.

(17) Dieckhaus, C. M., Fernandez-Metzler, C. L., King, R., Krolikowski, P. H., and Baillie, T. A. (2005) Negative ion tandem mass spectrometry for the detection of glutathione conjugates. *Chem. Res. Toxicol. 18*, 630–638.

(18) Baillie, T. A. (2008) Metabolism and toxicity of drugs. Two decades of progress in industrial drug metabolism. *Chem. Res. Toxicol. 21*, 129–137.

(19) Prakash, C., Sharma, R., Gleave, M., and Nedderman, A. (2008) In vitro screening techniques for reactive metabolites for

minimizing bioactivation potential in drug discovery. *Curr. Drug Metab. 9*, 952–964.
(20) Fox, S., Farr-Jones, S., Sopchak, L., Boggs, A., and Comley, J. (2004) High-throughput screening: searching for higher productivity. *J. Biomol. Screen. 9*, 354–358.
(21) Ansede, J. H., and Thakker, D. R. (2004) High-throughput screening for stability and inhibitory activity of compounds toward cytochrome P450-mediated metabolism. *J. Pharm. Sci. 93*, 239–255.
(22) Ellman, G. L. (1959) Tissue sulfhydryl groups. *Arch. Biochem. Biophys. 82*, 70–77.
(23) Lang, W., Caldwell, G. W., and Masucci, J. A. (2005) Evaluation of the effect of oxygen exposure on human liver microsomal metabolism of mitomycin C in the presence of glutathione using liquid chromatography-quadrupole time of flight mass spectrometry. *Anal. Biochem. 343*, 268–276.
(24) Zhu, M., Ma, L., Zhang, H., and Humphreys, W. G. (2007) Detection and structural characterization of glutathione-trapped reactive metabolites using liquid chromatography-high-resolution mass spectrometry and mass defect filtering. *Anal. Chem. 79*, 8333–8341.
(25) Elton, R. C., Garle, M. J., and Fry, J. R. (2000) Glutathione depletion in a liver microsomal assay as an in vitro biomarker for reactive metabolite formation. *Biomarkers 5*, 285–294.
(26) Chen, Q., Doss, G. A., Tung, E. C., Liu, W., Tang, Y. S., Braun, M. P., Didolkar, V., Strauss, J. R., Wang, R. W., Stearns, R. A., Evans, D. C., Baillie, T. A., and Tang, W. (2006) Evidence for the bioactivation of zomepirac and tolmetin by an oxidative pathway: identification of glutathione adducts in vitro in human liver microsomes and in vivo in rats. *Drug Metab. Dispos. 34*, 145–151.
(27) Mutlib, A., Lam, W., Atherton, J., Chen, H., Galatsis, P., and Stolle, W. (2005) Application of stable isotope labeled glutathione and rapid scanning mass spectrometers in detecting and characterizing reactive metabolites. *Rapid Commun. Mass Spectrom. 19*, 3482–3492.
(28) Backer, M. V., Patel, V., Jehning, B. T., Claffey, K. P., and Backer, J. M. (2006) Surface immobilization of active vascular endothelial growth factor via a cysteine-containing tag. *Biomaterials 27*, 5452–5458.
(29) Loomans, E. E., Gribnau, T. C., Bloemers, H. P., and Schielen, W. J. (1998) Adsorption studies of tritium-labeled peptides on polystyrene surfaces. *J. Immunol. Methods 221*, 131–139.
(30) Pyun, J. C., Cheong, M. Y., Park, S. H., Kim, H. Y., and Park, J. S. (1997) Modification of short peptides using epsilon-aminocaproic acid for improved coating efficiency in indirect enzyme-linked immunosorbent assays (ELISA). *J. Immunol. Methods 208*, 141–149.
(31) Mukul Biswas, S. C. (1982) Chemical modification of polystyrene. I. Electrophilic substitution of polystyrene with aromatic anhydrides. *J. Appl. Polym. Sci. 27*, 3851–3857.
(32) Migonney, V., Lacroix, M. D., Douzon, C., and Jozefowicz, M. (1992) Chemical modifications of insoluble polystyrene derivatives. *J. Appl. Polym. Sci. 46*, 1151–1158.
(33) Guire, P. E. (1990) Biocompatible coating for solid surfaces U.S. Patent 4,979,959.
(34) Guire, P. E. (1990) Method of improving the biocompatibility of solid surfaces. U.S. Patent 4,973,493.
(35) Guire, P. E., Dunkirk, S. G., Josephson, M. W., Swanson, M. J. (1991) Preparation of polymeric surfaces via covalently attaching polymers, U.S. Patent 5,002,582.
(36) New, L. S., and Chan, E. C.Y. (2008) Evaluation of BEH C18, BEH HILIC, and HSS T3 (C18) column chemistries for the UPLC-MS-MS analysis of glutathione, glutathione disulfide, and ophthalmic acid in mouse liver and human plasma. *J. Chromatogr. Sci. 46*, 209–214.
(37) Kohn, J., and Wilchek, M. (1982) A new approach (cyano-transfer) for cyanogen bromide activation of Sepharose at neutral pH, which yields activated resins, free of interfering nitrogen derivatives. *Biochem. Biophys. Res. Commun. 107*, 878–884.
(38) Cleland, W. W. (1964) Dithiothreitol, a New Protective Reagent for Sh Groups. *Biochemistry 3*, 480–482.
(39) Zainuddin, Barnard, Z., Keen, I., Hill, D. J., Chirila, T. V., and Harkin, D. G. (2008) PHEMA hydrogels modified through the grafting of phosphate groups by ATRP support the attachment and growth of human corneal epithelial cells. *J. Biomater. Appl. 23*, 147–168.
(40) Ruegg, U. T., and Rudinger, J. (1977) Reductive cleavage of cystine disulfides with tributylphosphine. *Methods Enzymol. 47*, 111–116.
(41) Obach, R. S., Kalgutkar, A. S., Soglia, J. R., and Zhao, S. X. (2008) Can in vitro metabolism-dependent covalent binding data in liver microsomes distinguish hepatotoxic from nonhepatotoxic drugs? An analysis of 18 drugs with consideration of intrinsic clearance and daily dose. *Chem. Res. Toxicol. 21*, 1814–1822.
(42) Gan, J., Ruan, Q., He, B., Zhu, M., Shyu, W. C., and Humphreys, W. G. (2009) In Vitro Screening of 50 Highly Prescribed Drugs for Thiol Adduct FormationComparison of Potential for Drug-Induced Toxicity and Extent of Adduct Formation. *Chem. Res. Toxicol. 22*, 690–698.

BC900289M

Nanotubes Functionalized with Lipids and Natural Amino Acid Dendrimers: A New Strategy to Create Nanomaterials for Delivering Systemic RNAi

Joshua McCarroll,[§,†,||] Huricha Baigude,[§,†,‡] Chao-Shun Yang,[§,†,‡] and Tariq M. Rana*[,†,‡]

Department of Biochemistry and Molecular Pharmacology, University of Massachusetts Medical School, Worcester, Massachusetts 01605, and Program for RNA Biology, Sanford Children's Health Research Center, Burnham Institute for Medical Research, 10901 North Torrey Pines Road, La Jolla, California 92037. Received July 7, 2009; Revised Manuscript Received November 13, 2009

Single-walled carbon nanotubes (SWNT) have unique electronic, mechanical, and structural properties as well as chemical stability that make them ideal nanomaterials for applications in materials science and medicine. Here, we report the design and creation of a novel strategy for functionalizing SWNT to systemically silence a target gene in mice by delivering siRNA at doses of <1 mg/kg. SWNT were functionalized with lipids and natural amino acid-based dendrimers (TOT) and complexed to siRNA. Our model study of the silencing efficiency of the TOT-siRNA complex showed that, in mice injected at 0.96 mg/kg, an endogenous gene for apoliproprotein B (ApoB) was silenced in liver, plasma levels of ApoB decreased, and total plasma cholesterol decreased. TOT-siRNA treatment was nontoxic and did not induce an immune response. Most (80%) of the RNA trigger molecules assembled with TOT were cleared from the body 48 h after injection, suggesting that the nanotubes did not cause siRNA aggregation or inhibit biodegradation and drug clearance *in vivo*. These results provide the first evidence that nanotubes can be functionalized with lipids and amino acids to systemically deliver siRNA. This new technology not only can be used for systemic RNAi, but may also be used to deliver other drugs *in vivo*.

INTRODUCTION

Single-walled carbon nanotubes (SWNT) have unique electronic, mechanical, and structural properties as well as chemical stability that make them ideal nanomaterials for applications in materials science and medicine. However, native SWNT have poor solubility and biocompatibility, which has stimulated approaches to functionalize them by conjugating molecules such as peptides, nucleic acids, and polymers (*1, 2*). The potential of SWNT has recently been investigated in the cellular delivery of DNA plasmids and of small interfering RNAs (siRNAs) for gene silencing (*2, 3*). To date, however, the potential of designing, creating, and applying SWNT for systemic delivery of nucleic acids or drugs has not been investigated.

RNA interference (RNAi), a gene-silencing mechanism whereby double-stranded RNA (dsRNA) induces the sequence-specific degradation of homologous mRNA (*4*), has been widely used to identify gene functions and holds great potential to provide a new class of therapeutic agents (*5*). During RNAi, long dsRNA is processed by Dicer into short-interfering RNAs (siRNAs) and incorporated into the RNA-induced silencing complex (RISC) (*6*), a multiturnover enzyme complex that cleaves the target mRNA. The RNAi machinery can also be programmed in cells by introducing duplexes of siRNAs (*7, 8*) that are assembled into siRISC containing Dicer, Argonautes and other proteins (reviewed in ref *9*). Therefore, new siRNA-based therapeutic agents could be designed to lower concentrations of disease-causing gene products.

* To whom correspondence should be addressed: trana@burnham.org.

[§] These authors contributed equally to this work.

[†] University of Massachusetts Medical School.

[‡] Burnham Institute for Medical Research.

[||] Present address: Children's Cancer Institute Australia for Medical Research, Randwick, NSW 2031, Australia.

However, the development of such siRNA-based therapies faces two barriers: (1) identification of chemically stable and effective siRNA sequences, and (2) efficient delivery of these sequences to *in vivo* targets using siRNA amounts that can be translated to clinically feasible doses for humans. Recent advances in understanding the rules for chemically modifying siRNA sequences without compromising their gene-silencing efficiency (*10*−*12*) have allowed the design and synthesis of therapeutically effective siRNA molecules that can silence target genes *in vivo* (*13, 14*). Furthermore, siRNAs have recently been delivered *in vivo* to successfully inhibit various gene functions. This delivery has been facilitated by conjugating cholesterol to siRNA (*14*) or to oligonucleotide inhibitors of miRNA (*15*), by forming stable nucleic acid−lipid particles (SNALP) of siRNA (*13, 16*), and by assembling lipid−siRNA complexes (*17, 18*). In addition, a protamine−antibody fusion protein has been used to deliver siRNAs to HIV-infected cells (*19*). Recently, application of nanotubes to successfully deliver siRNA in cells has been reported (*3, 20*−*22*).

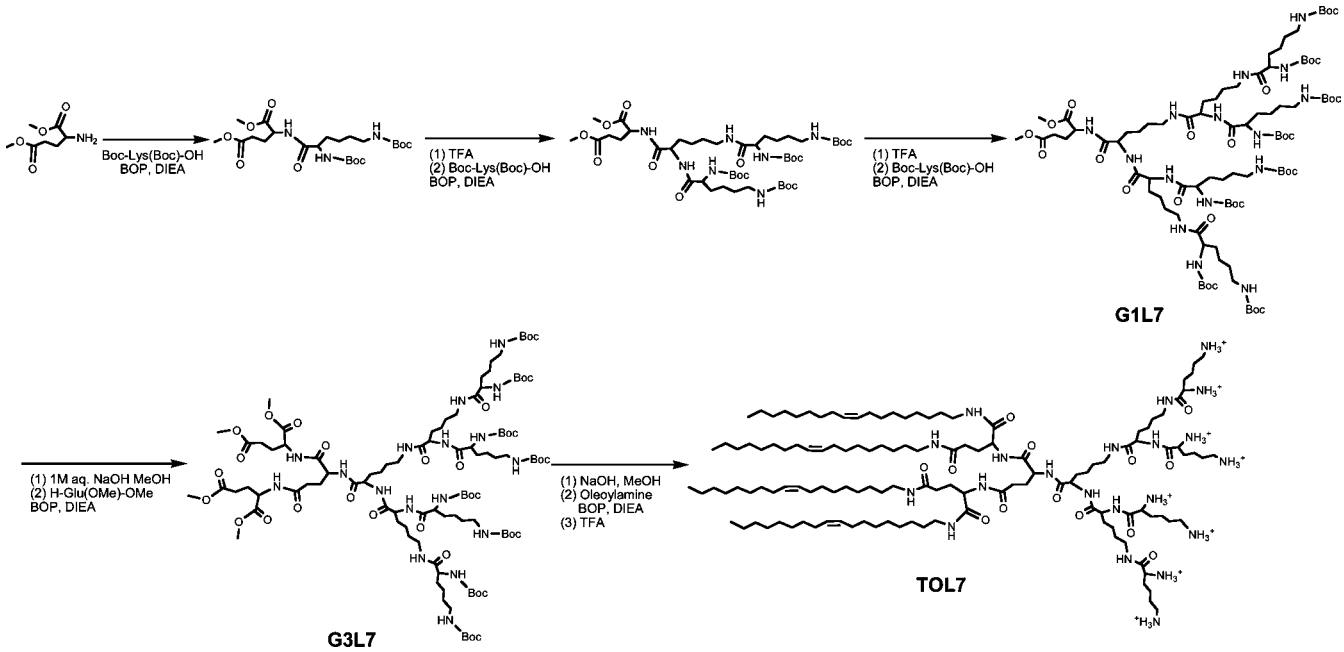
Despite this progress, new chemistry and delivery approaches are greatly needed to systematically silence disease-causing genes in a tissue-specific manner with high efficiencies and at clinically achievable doses. Here, we report the design and creation of novel nanotubes (TOT) functionalized with lipids and natural amino acid-based dendrimers. We used these TOT to systemically silence a target gene in mice at siRNA doses of <1 mg/kg. Moreover, this treatment did not induce an immune response and showed favorable pharmacokinetics.

EXPERIMENTAL PROCEDURES

Synthesis of Nanotubes Functionalized with Lipids and Lysine Dendrimers (TOT). To create functionalized new nanomaterial, single-walled carbon nanotubes (SWNT) were oxidized and cut by suspending 20 mg of SWNT in 40 mL of

10.1021/bc900296z © 2010 American Chemical Society
Published on Web 12/03/2009

Scheme 1. Synthesis of Tetra-Oleoyl Lysine Dendrimer Generation 3 (TOL7)



a mixture of concentrated H_2SO_4/HNO_3 (3:1) and sonicating at 40 to 50 °C for 3 h (*23*). The resulting suspension was poured into 350 mL water and filtered through a 100 nm pore membrane. The resulting solid was washed repeatedly with water, resuspended in water, and centrifuged (5000 rpm, 10 min) to remove large particles.

Synthesis of Glutamic Acid−Lysine Dendrimer Generation 1 (G1L1). A mixture of H-Glu(OMe)-OMe hydrochloride (0.50 g, 2.4 mmol), Boc-lysine(Boc)-OH dicyclohexylamine salt (1.24 g, 2.4 mmol), and DIEA (0.80 mL, 4.72 mmol) was suspended in 30 mL DMF under nitrogen atmosphere (*24, 25*). After the suspension was cooled to 0 °C in an ice bath, BOP reagent (1.1 g, 2.4 mmol) was added. The reaction was performed at 0 °C for 30 min and then at room temperature for 24 h. Then, the solvent was removed by evaporation, and the resulting syrup was dissolved in ethyl acetate, followed by washing with 5% citric acid, 5% sodium bicarbonate, and water. After the solution was dried over anhydrous sodium sulfate, the target compound was purified by silica gel chromatography using ethyl acetate and hexane (4:1) as eluent. The purity of the compound was confirmed by TLC, and G1L1 was obtained as a white powder (1.01 g) in 91% yield.

^{1}H NMR (DMSO-d_6, ppm): 1.17−1.57 (m, 24H, −C(CH_3)$_3$, −CH_2−), 2.23−2.31 (m, 4H, −CH_2−), 3.01 (m, 2H, −CH_2−), 3.84 (m, 2H, −C(NH−)HCH_2−), 3.68 (s, 6H, −CH_3), 6.61−6.65 (m, 2H, −CONH−), 7.65 (t, 1H, −CONH−). MS (ESI) *m*/*z* 526.48 (M + Na)$^+$.

Synthesis of Glutamic Acid−Lysine Dendrimer Generation 2 (G1L3). *Deprotection of G1L1.* G1L1 was dissolved in a mixture of dichloromethane and trifluoroacetic acid. After vigorously stirring at room temperature for 30 min, the solvents were evaporated, and the syrup was washed with anhydrous ethyl ether.

Synthesis of G1L3. Deprotected G1L1 was reacted with Boc-lysine(Boc)-OH in a similar method described above to give G1L3 in 88% yield. ^{1}H NMR (DMSO-d_6, ppm): 1.17−1.57 (m, 54H, −C(CH_3)$_3$, −CH_2−), 2.23−2.31 (m, 4H, −CH_2−), 3.01 (m, 6H, −CH_2−), 3.84 (m, 2H, −C(NH−)HCH_2−), 4.14 (m, 2H, −C(NH−)HCH_2−), 3.68 (s, 6H, −CH_3), 6.61−7.65 (m, 7H, −CONH−). MS (ESI) *m*/*z* 982.95 (M + Na)$^+$.

Synthesis of Glutamic Acid−Lysine Dendrimer Generation 3 (G1L7). G1L3 was deprotected and reacted with Boc-lysine(Boc)−OH in a similar method described above to give G1L7 in 82% yield.

^{1}H NMR (DMSO-d_6, ppm): 1.17−1.57 (m, 118H, −C(CH_3)$_3$, −CH_2−), 2.23−2.31 (m, 4H, −CH_2−), 3.01 (m, 14H, −CH_2−), 3.84 (m, 4H, −C(NH−)HCH_2−), 4.14 (m, 4H, −C(NH−)-HCH_2−), 3.68 (s, 6H, −CH_3), 6.61−7.65 (m, 15H, −CONH−). MS (ESI) *m*/*z* 1896.84 (M + Na)$^+$.

Synthesis of Glutamic Acid−Lysine Dendrimer Generation 4 (G2L7). G1L7 (0.36 g, 0.19 mmol) was stirred in a mixture of methanol (15 mL) and 1 M NaOH solution (15 mL) at room temperature. The demethylation process was monitored by TCL (DCM/methanol, 10: 1). After the reaction was complete, the suspension was neutralized by adding dilute hydrochloric acid, followed by evaporation, extraction with chloroform, and washing with dilute HCl solution. Then, the solution was dried and the solvent was removed to give demethylated G1L7 as oil.

The oil was dissolved in 5 mL DMF. To this solution was added H-Glu(OMe)-OMe hydrochloride (0.163 g, 0.77 mmol), DIEA (0.164 mL), and BOP reagent (0.34 g, 0.77 mmol). The reaction was performed at 0 °C for 30 min and at room temperature for 24 h. Then, a mixture of ethyl acetate and hexane (4:1, 100 mL) was poured into the reaction flask, and the resulting precipitate was collected by filtration. The solid was suspended in 10 mL methanol and reprecipitated by adding ethyl acetate and hexane to give a white powder (0.31 g) in 75% yield. ^{1}H NMR (DMSO-d_6, ppm): 1.17−1.57 (m, 118H, −C(CH_3)$_3$, −CH_2−), 2.23−2.31 (m, 12H, −CH_2−), 3.01 (m, 14H, −CH_2−), 3.84 (m, 6H, −C(NH−)HCH_2−), 4.14 (m, 4H, −C(NH−)HCH_2−), 3.68 (s, 12H, CH_3), 6.61−7.65 (m, 17H, −CONH−). MS (ESI) *m*/*z* 2183.06 (M + Na)$^+$.

Synthesis of Tetra-Oleoyl Lysine Dendrimer Generation 3 (TOL7) (Scheme 1). Demethylated G2L7 (0.09 g, 0.05 mmol), oleoylamine (0.14 g, 0.54 mmol), and DIEA (0.15 mL) were dissolved in DMF. BOP (0.24 g, 0.54 mmol) was added, and the solution was stirred at r.t. for 24 h. After workup, a white powdery TOL7 (0.12 g) was obtained in 80% yield.

^{1}H NMR (DMSO-d_6, ppm): 0.81 (t, 12H, −CH_3), 1.21−1.62 (m, 154H, −CH_2−), 1.93−1.99 (m, 16H, −CH_2CH═CHCH_2−),

2.73, 2.96−3.03 (m, 22H, $-CH_2NH-$, $-CH_2NH_2$), 3.59, 4.18 (m, 10H, $-OCCH(NH-)CH_2-$), 5.28 (m, 8H, $-CH{=}CH-$), 7.75−8.48 (m, 25H, $-CONH-$, $-NH_2$). MS (MALDI-TOF) *m*/*z* 2322.91 $(M + Na)^+$.

Conjugation of TOL7 to Oxidized SWNT (TOT). To a solution of TOL7 (0.5 mL, 24 mg/mL) in water was added SWNT stock solution (2 mL). EDC (80 mg) was added, and the suspension was stirred at r.t. After 2 h, the mixture was filtered through a polycarbonate filter, rinsed, and resuspended in water, followed by dialysis against pure water for 3 days. The larger particles were removed by centrifuge at 7000 rpm for 5 min. The final concentration of TOT was 0.2 mg/mL. The concentration of TOL7 on SWNT was determined by quantitative Kaiser assay (*26*). The structure of TOT was characterized by transmission electron microscopy (Core Electron Microscopy Facility, UMASS Medical School) and dynamic light scattering (Department of Food Science, Umass Amherst).

Preparation of TOT-siRNA Complexes. All siRNAs used in these studies were chemically synthesized using silyl ethers to protect 5′-hydroxyls and acid-labile orthoesters to protect 2′-hydroxyls (2′-ACE) (Dharmacon, Lafayette, CO, USA). After deprotection and purification, siRNA strands were annealed as described (*11*): ApoB siRNA (ORF position 10049−10071): Unmodified (UM) sense 5′-GUCAUCACACUGAAUACCAAU-3′, antisense 5′-AUUGGUAUUCAGUGUGAUGACAC-3′; chemically modified (CM) sense 5′-$G^SU^FC^FAU^FC^FACACU$-$GAAUAC^{FS}C^FAA^SU^F$-propylamine-3′, antisense 5′-PAU^FU^FG-$GUAUUCAGUGUGAU^FGAC^{FS}A^SC$; UM mismatch (mm) siRNA sense 5′-GUGAUCAGACUCAAUACGAAU propylamine-3′, antisense 5′-AUUCGUAUUGAGUCUGAUCACAC-3′; CM mm sense 5′-$G^SU^FGAU^FC^FAGACUCAAUAC^FGAA^SU^F$ propylamine-3′, antisense 5′-$AU^FU^FCGUAUUGAGUCUG$-$AU^FCAC^{FS}A^SC$. The superscript letters F and S represent 2′-O-F and HS-backbone modifications, respectively. TOT-siRNA complexes were prepared by mixing siRNA and TOT in Hepes saline or Opti-MEM culture medium (Invitrogen) and incubating at room temperature for 20 min (see below).

***In Vitro* Assay for RNAi Activity of TOT-siRNA.** FL83B (mouse hepatocyte) cells were maintained at 37 °C with 5% CO_2 in F12 Khangians modified culture medium (ATCC, USA) supplemented with 10% fetal bovine serum (FBS), 100 U/mL penicillin and 100 μg/mL streptomycin. Cells were regularly passaged and plated in 96-well and 6-well culture plates 16 h before transfection at 70% confluency. Cells were transfected with 1 mL/well of complex (siRNA-TOT) for 2.5 h at 37 °C. Medium was removed and replaced with complete medium without antibiotics and incubated for an additional 24 h. Cell viability was assessed using a CellTiter 96 AQ_{ueous} One Solution cell proliferation assay by colorimetric analysis of the MTS tetrazolium compound according to the manufacturer's instructions (Promega, USA). Total RNA was extracted using RNeasy minispin columns and treated with DNase I (Qiagen, USA) before quantitation. To assess levels of ApoB mRNA, real-time quantitative PCR (qPCR) was performed using SYBR Green (Qiagen USA) with forward (5′-TTCCAGCCATGGGCAACTT-TACCT-3′) and reverse (5′-TACTGCAGGGCGTCAGTGA-CAAAT-3′) ApoB primers. ApoB mRNA levels were normalized against the housekeeping gene GAPDH using forward (5′-ATCAAGAAGGTGGTGAAGCAGGCA-3′) and reverse (5′-TGGAAGAGTGGGAGTTGCTGTTGA-3′) GAPDH primers.

***In Vivo* Assay for RNAi Activity of TOT-siRNA.** Six- to eight-week-old male C57BL/6 mice (Charles River laboratories, USA) were maintained under a 12 h light/dark cycle in a pathogen-free animal facility. Mice were injected via the lateral tail vein with phosphate buffered saline pH 7.4 (PBS) or TOT-siRNA complexes of chemically modified (CM) ApoB siRNA or its mismatched (mm) siRNA. At 48 h after injection, liver tissue levels of ApoB mRNA, plasma levels of ApoB protein, and total plasma cholesterol were measured. For pharmacokinetic studies, liver tissue levels of ApoB mRNA were analyzed at various time intervals (48−144 h) after the injection.

Measurement of *in Vivo* ApoB mRNA and Protein Levels. To determine ApoB mRNA levels in liver tissue after siRNA treatment, small uniform tissue samples were collected from three regions of the liver. Total RNA was extracted with Trizol and treated with DNase I before quantification. ApoB mRNA levels were determined by qPCR as described above. ApoB protein levels were determined by Western blot using a polyclonal goat anti-ApoB100/48 antibody (Santa Cruz, USA). ApoB protein levels were then detected by enhanced chemiluminescence (PerkinElmer Life Sciences, USA). As a control, fibronectin was visualized by immunoblot using a polyclonal rabbit antifibronectin antibody (Sigma, USA).

Measurement of Total Cholesterol Levels. Plasma cholesterol was measured by a commercial enzyme assay according to the manufacturer's instructions (Biodesign International, USA).

***In Vivo* Interferon Induction.** To assess for any nonspecific immune response to injected TOT-containing siRNA, mouse liver tissue was assessed for expression of two interferon (IFN)-inducible genes, IFN-induced protein with tetratricopeptide repeats 1 (IFIT1), and signal transducer and activator of transcription 1 (STAT 1). Liver tissue was obtained from mice treated with PBS (control) and TOT-ApoB siRNA. Expression of IFIT1 and STAT1 were measured by qPCR as described above using the following primers: IFIT1 forward, 5′-AAAC-CCTGAGTACAACGCTGGCTA-3′; IFIT1 reverse, 5′-AAAC-CCTGAGTACAACGCTGGCTA-3′; STAT 1, forward: 5′-CAGCTGCAAAGCTGGTTCACCATT-3′; STAT 1 reverse, 5′-AGGTTCGATCTGACAACACCTGCT-3′. IFIT1 and STAT 1 mRNA levels were normalized against the housekeeping gene GAPDH. In addition, plasma IFN-α levels were quantified 24 h after the final injection using sandwich ELISA according to the manufacturer's instructions (PBL Biomedical Laboratories, USA). As a positive control for both assays, C57BL/6 mice were injected via the lateral tail vein with 250 μg polyinosinic−polycytidylic acid (Poly IC, total volume 0.125 mL). Six hours after the injection, liver and plasma samples were collected.

RESULTS AND DISCUSSION

To create a novel SWNT-based nanomaterial for efficient systemic siRNA delivery, we hypothesized that SWNT should be functionalized with at least two moieties: (1) a positive charge for siRNA binding, and (2) lipid chains to modify the hydrophilic properties of siRNA-SWNT and make contacts with cellular membranes (Figure 1a,b). Thus, we constructed TOL7, a lysine-based dendrimer with covalently attached oleoyl lipid chains. The MALDI-TOF mass spectrum (Figure 1a) shows a major peak at 2322.91, which matches the calculated molecular mass of TOL7 ($2300.47 + Na^+$). Although the spectrum also shows some other minor peaks due to the lower purity of starting material (oleoylamine contains 60% C18 chain), nonetheless, the MS and ^1H NMR confirms the successful synthesis of the target molecule. The lipid moieties on TOL7 bind to the hydrophobic wall of the nanotube upon mixing a solution of TOL7 and oxidized SWNT. However, we found that adding EDC to the mixture during the coupling increases the loading of TOL7 to the nanotube, suggesting that a covalent attachment occurred through amide bonds between carboxyl groups of SWNT and amines on the surface of TOL7, which facilitated the TOL7-SWNT interaction. Quantitative analysis by performing Kaiser assay showed that in the presence of EDC the loading was 1.35 mg TOL7 to 1.0 mg SWNT, higher than in the absence of EDC (1.0 mg TOL7 to 1.0 mg SWNT). SWNT modified

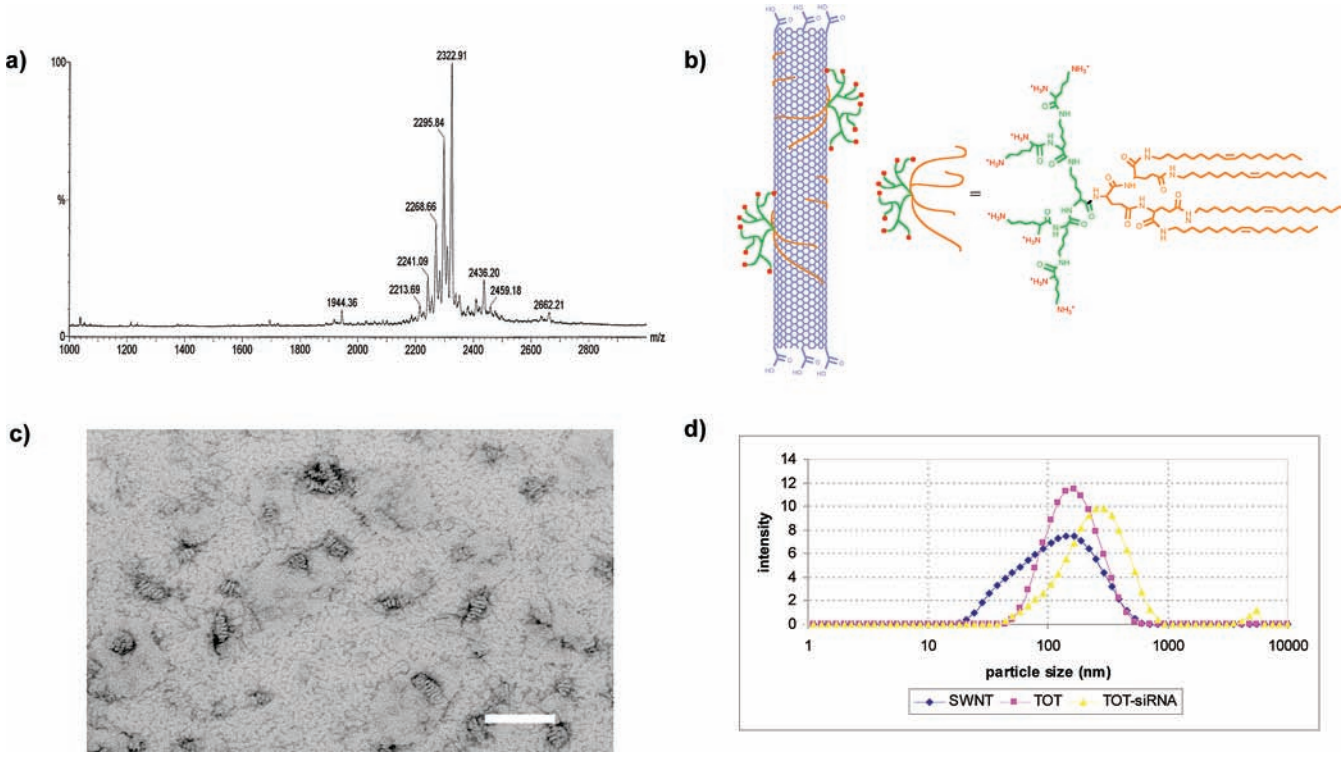


Figure 1. Structural analysis of lysine dendrimers TOL7 and functionalized nanotube TOT. (a) MALDI-TOF MS spectrum of TOL7. (b) Chemical structure of TOL7 and schematic illustration of TOT. (c) Electron micrograph of TOT complex and (d) particle size distribution of oxidized single-walled nanotube (blue), TOT (pink), and TOT-siRNA (yellow) complex by dynamic light scattering. Scale bar = 200 nm.

with TOL7 (see Experimental Procedures for details) is denoted here as TOT (Figure 1). Electron microscopic images of TOL7 assembled on the surface of SWNT reveal regular lateral striations on the surface of 80- to 150-nm nanotubes (Figure 1c). These striations suggest that TOL7 molecules are coupled to SWNT by forming half-cylinders on the nanotube surface, consistent with a previous report (*27*) showing supramolecular self-assembly of lipid derivatives on carbon nanotubes.

To test the efficacy of TOT for systemic RNAi, we chose as model system the endogenous mouse gene, apolipoprotein B (ApoB). ApoB, a large protein that exists in two forms, ApoB100 and ApoB48 (*28*), is a ligand for the low-density lipoprotein (LDL) receptor and is involved in cholesterol metabolism. Mouse ApoB contains 4515 amino acids and is predominantly expressed in the liver and intestine. In mice, both ApoB100 and ApoB48 are expressed in the liver, whereas ApoB48 is predominantly expressed in the intestine. Heterozygous knockout mouse models for ApoB show a 20% decrease in serum cholesterol levels and resist diet-induced hypercholesterolemia (*29*).

In humans, serum levels of ApoB have been strongly correlated with increased risk of coronary artery disease (*28, 30*). Because ApoB is a large protein for which no three-dimensional structural data are available, it is not a suitable target for small molecule development to treat hypercholesterolemia. An alternative therapy that has recently been explored in a mouse model is to silence ApoB with siRNA chemically modified by conjugation to cholesterol (*14, 31*). These studies were very encouraging in providing proof of the concept for developing RNAi-based therapeutics (*14*), but the amounts of siRNA used (50 mg/kg) would translate to unfeasible doses for clinical application in humans (*31*). Furthermore, the delivery of siRNA required cholesterol conjugation, which might increase risk factors in patients who cannot tolerate higher levels of cholesterol. Lower doses of siRNAs have recently been used by encapsulating them in SNALP to efficiently silence ApoB in nonhuman primates (*16*), but this approach requires a sophisticated SNAPL assembly. Therefore, we planned to develop a new nanomaterial that can be used to easily assemble siRNA for systemic delivery. To test our approach for systemic siRNA delivery and to achieve ApoB silencing with siRNA doses in animals that are clinically relevant for RNAi-based therapy in humans, we chose ApoB silencing in mice as an animal model system.

To determine whether TOT could deliver active siRNA to its target and silence ApoB mRNA levels *in vitro*, we treated FL83B (mouse hepatocyte) cells with TOT-siRNA complexes and analyzed ApoB mRNA levels by quantitative PCR (qPCR). TOT-siRNA containing ApoB siRNA almost completely silenced ApoB mRNA expression (>80%) in FL83B cells relative to that in controls or cells treated with TOT containing mismatched siRNA (Figure 2a). Notably, the efficiency of ApoB mRNA silencing using TOT to transport siRNA was similar to that of cells transfected with Lipofectamine 2000 complexed to siRNA (Figure 2a), although we observed slightly lower RNAi with TOT as compared with L2K. Similar to unmodified siRNA, TOT containing our chemically modified siRNA directed against ApoB efficiently silenced ApoB mRNA (Figure 2a). These results therefore show that our modifications to siRNA did not negatively influence its RNAi activity (Figure 2a). Furthermore, these reduced levels of ApoB mRNA levels in FL83B cells were not due to TOT-siRNA induced cell toxicity, as confirmed by cell viability assays (Figure 2b). Taken together, these results demonstrate that TOT-siRNA is nontoxic and efficiently transports siRNA into cells.

To determine the effect of TOT on the uptake and localization of siRNA in FL83B cells, we used Lipofectamine 2000 (L2K) or TOT as described above to deliver Cy3-labeled siRNA to cells. The localization of Cy3-SS/AS-3′N3 siRNA was first established by transfecting it into cells using L2K. In both live and 4′,6-diamidino-2-phenylindole (DAPI)-stained transfected cells (*32*), Cy3-labeled siRNA delivered by L2K was localized

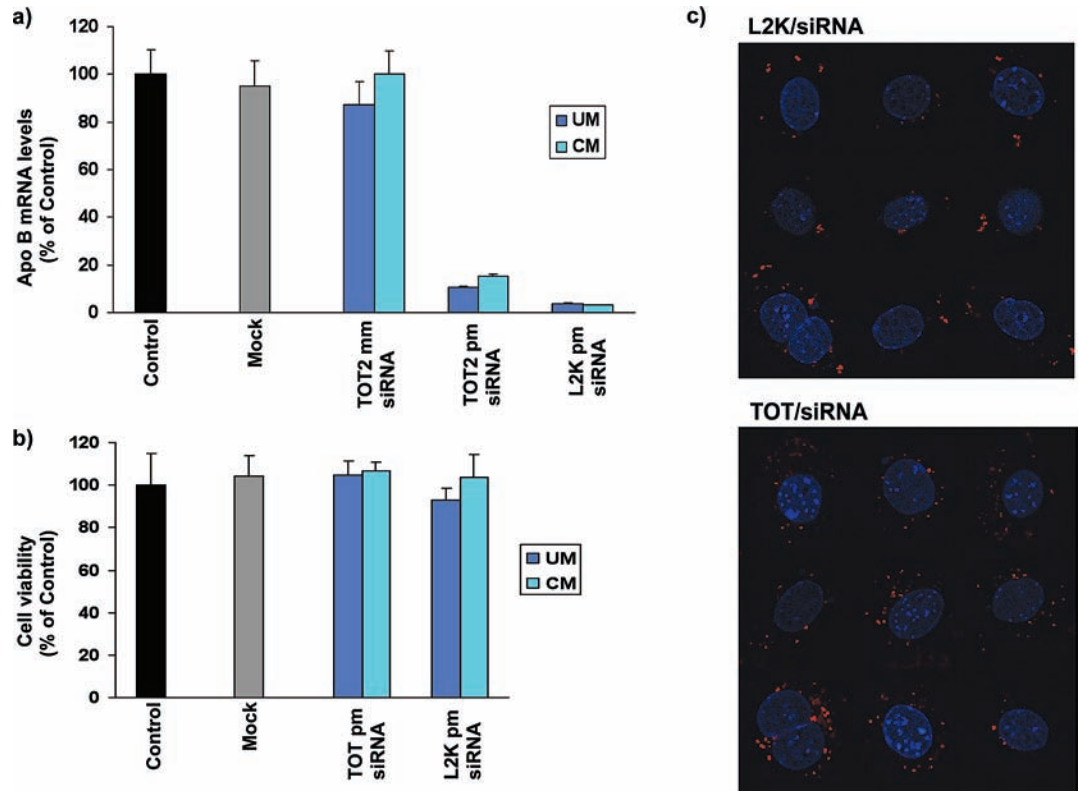


Figure 2. *In vitro* silencing of ApoB by TOT-siRNA. (a) TOT-siRNA complex specifically silences ApoB in mouse hepatocyte cells. FL83B cells were treated for 24 h with TOT without siRNA (Mock) or with TOT-siRNA complex containing unmodified (UM) siRNA, chemically modified (CM) siRNA, or their respective mismatches (mm). As a control, Lipofectamine 2000 (L2K) was used to transfect chemically modified or unmodified siRNA. ApoB mRNA levels are expressed as percent of control (no transfection). Each value represents the mean ± SD of duplicate cultures from two representative experiments. (b) FL83B cells remain viable after 24 h treatment with TOT-siRNA complex. Cells were treated with TOT without siRNA (Mock) or with TOT-siRNA complex containing unmodified (UM) or chemically modified (CM) siRNA. Cell toxicity levels are expressed as percent of control (no transfection). Each value represents the mean ± SD of duplicate cultures from two representative experiments. (c) Localization of siRNA. Cells were transfected with Cy3-labeled siRNA using Lipofectamine 2000 (L2K) or with siRNA-TOT complex. Localization of the duplex siRNA after 24 h was monitored by confocal microscopy. Overlay images of siRNA and nuclear DNA (4′,6-diamidino-2-phenylindole [DAPI] stained) are shown.

to the cytoplasm around the periphery of the nucleus (Figure 2c). To determine the effect of TOT on localization of Cy3-SS/AS-3′N3 siRNA, cells were transfected with the Cy3-labeled siRNA-TOT complex. Similar to the siRNA delivered into cells by L2K, siRNA delivered by TOT localized to perinuclear regions of the cytoplasm (Figure 2c). This localization pattern is typical for siRNA transfection because siRNA duplexes are first localized to cytoplasm, which are not P bodies, and then released to form RISC assembly for RNAi functions and localization to P bodies together with argonaute proteins (*9, 32, 33*). Due to low fluorescence intensity and higher backgrounds, it is quite difficult to quantify the amount of RNA released and subsequent assembly into RISC in cells. Nonetheless, this result indicates that siRNA delivery by TOT did not affect cellular localization of the RNA and did not cause any aggregate formation or nuclear translocation of siRNA.

We next determined the ability of TOT to deliver siRNA to its target and to silence ApoB expression *in vivo*. To determine if chemical modifications in the siRNA sequence are necessary for *in vivo* RNAi, we verified that injecting mice with cholesterol-conjugated unmodified siRNA did not significantly knock down ApoB expression (data not shown), consistent with a previous report (*14*). Therefore, our *in vivo* experiments focused on TOT containing chemically modified siRNA. After mice were injected via tail vein with TOT complexed to either chemically modified ApoB-targeted siRNA or its mismatch, samples of liver and plasma were analyzed (see Experimental Procedures for details). To quantify ApoB mRNA silencing throughout the liver, separate regions were analyzed for ApoB mRNA levels. ApoB mRNA decreased in a dose-dependent manner in liver tissue from mice treated with TOT-siRNA relative to that in liver tissue from control mice and mice treated with TOT containing mismatched siRNA (Figure 3a).

The maximum silencing effect of TOT-siRNA was reached at 0.96 mg/kg, resulting in 56 ± 4% reduction in ApoB mRNA ($n = 5$ animals). Increasing the siRNA dose did not enhance the *in vivo* RNAi efficiency (data not shown).). We reasoned that applying multiple doses would not enhance the silencing efficiency of TOT-siRNA, since our previous work showed that a nanoparticle created from similar dendrimer (iNOP) did not increase the RNAi efficiency when injected multiple times in animals (*34*). To quantify the amount of ApoB siRNA in livers of mice injected with varying doses of TOT-siRNA, total RNA was isolated from liver 48 h after treatment and guide strand ApoB siRNA was identified by Northern blot analysis. Interestingly, the amount of guide strand in mouse liver decreased with decreasing doses of injected siRNA (Figure 3b). It was not clear why higher concentrations of TOT-siRNA did not increase RNAi efficiency. Nonetheless, these observations show a clear correlation between *in vivo* RNAi efficiency and amount of guide strand delivered.

To determine if silencing of ApoB mRNA correlated with reduced plasma levels of ApoB protein, we used immunoblot analysis to measure levels of ApoB100 and ApoB48. Both ApoB100 and ApoB48 serum levels decreased to >60% of control (Figures 3c,d) in mice injected with 0.96 mg/kg TOT-siRNA, while fibronectin levels were unaffected. These results show that TOT-siRNA complex efficiently silenced ApoB

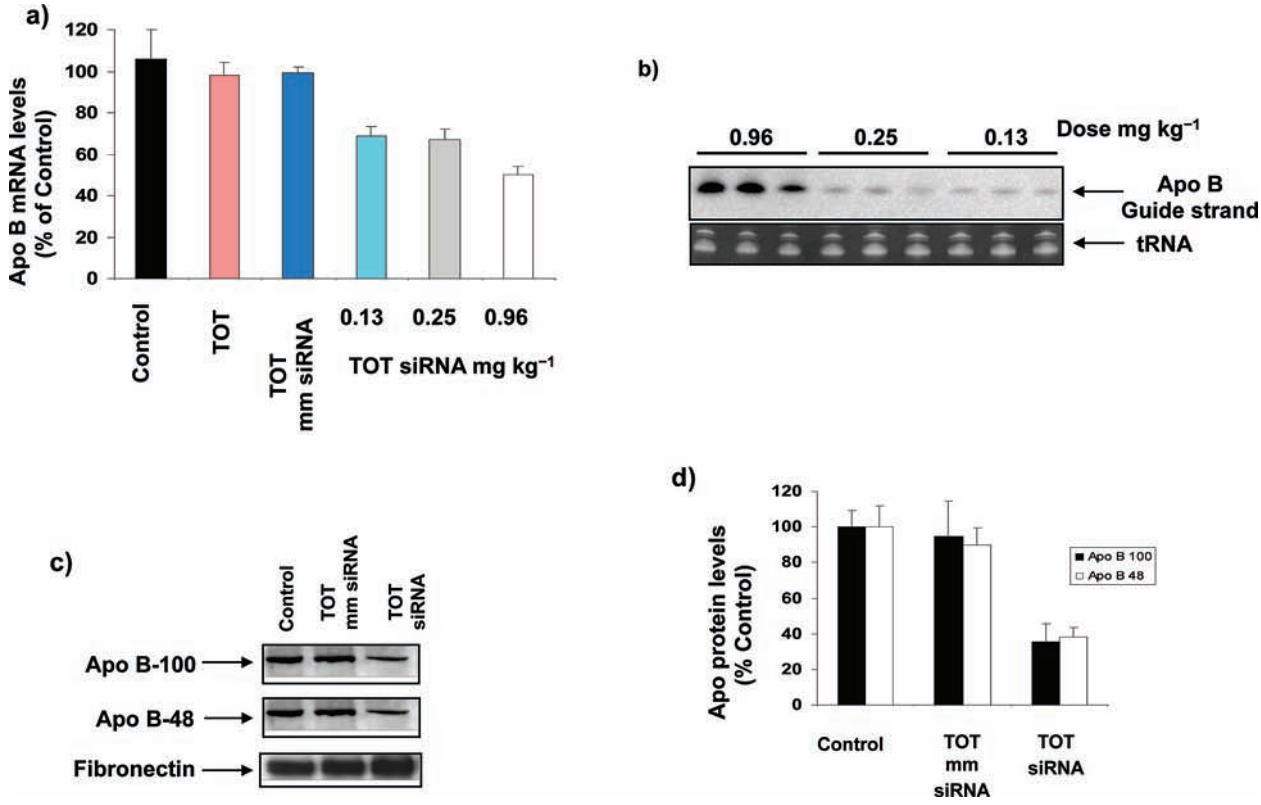


Figure 3. *In vivo* silencing of ApoB by TOT-siRNA. (a) ApoB is specifically silenced in livers of mice injected with TOT-siRNA complex. ApoB mRNA levels were reduced in livers of mice treated 48 h earlier with varying doses of TOT complexed to chemically modified (CM) siRNA or its mismatch (mm). Values represent the mean ± SD of tissue samples from three liver regions ($n = 3-5$ animals). Data are expressed as percent of control. (b) ApoB siRNA content in mouse liver varies with TOT-siRNA dose. Total RNA was isolated from livers of mice treated with varying doses (a) of TOT complexed to unmodified (UM) or chemically modified (CM) siRNA, and was identified by Northern blot analysis. A representative Northern blot shows the presence of the ApoB guide strand siRNA in mouse liver 48 h after the treatment. tRNA was identified as a positive control. (c) ApoB protein plasma levels are reduced in mice injected with TOT-siRNA. Mice were injected with TOT-siRNA containing chemically modified (CM) siRNA or its mismatch (mm), and 48 h later, plasma was analyzed for ApoB100 and ApoB48 protein levels by Western blot analysis with anti-ApoB100 or anti-ApoB48. Total protein loading was confirmed by assessing plasma fibronectin levels. (d) Quantification of reduced ApoB plasma levels after TOT-siRNA treatment. Western blots for mouse plasma levels of ApoB100 and ApoB48 (d) were analyzed by densitometry. Data are expressed as percent of control ($n = 3-5$ animals).

expression *in vivo*. Remarkably, this TOT-mediated silencing required only 0.96 mg/kg siRNA, a clinically feasible dose for RNAi therapeutic applications.

To investigate the physiological effects of ApoB mRNA silencing on cholesterol metabolism, we measured total plasma cholesterol levels in mice 48 h after a single injection of 0.96 mg/kg TOT-siRNA. As shown in Figure 4a, TOT-siRNA-mediated silencing of ApoB expression in liver and plasma samples was correlated with a reduction of total cholesterol (33 ± 10%). However, cholesterol levels were unchanged in mice treated with PBS TOT (control) or with TOT containing mismatched siRNA (Figure 4a). Together, these findings demonstrate that TOT-siRNA-mediated targeting of ApoB could provide a clinically significant new approach to reducing cholesterol levels in patients with hypercholesterolemia.

siRNA-based therapies could have at least two major side effects: (1) activation of an immune response (*35, 36*) and (2) toxic effects. To address the concern that a nonspecific immune response could be elicited by injecting mice with TOT-CM siRNA, their liver tissue RNA was assessed by qPCR for induction of the interferon (IFN)-inducible genes, IFN-induced protein with tetratricopeptide repeats 1 (IFIT1) and signal transducer and activator of transcription 1 (STAT 1), and plasma IFN-α levels were measured by ELISA. Our results show that injecting mice with TOT-siRNA did not alter the expression of IFLT1 and STAT 1 genes in the liver (data not shown), nor did it induce the release of IFN-α in plasma relative to controls (Figure 4b). To address concerns about TOT-siRNA toxicity, all mice were monitored daily for overall health, food intake, and weight changes. At the end of TOT-siRNA treatment, mice were sacrificed and necropsied. Histological sections of liver, our target tissue for ApoB silencing, were prepared and independently examined for toxic effects by a board-certified animal pathologist. No histological differences were noted between tissues from control (no treatment or TOT only) mice and from those treated with TOT-siRNA complex (data not shown). These results demonstrate that TOT-siRNA treatment may not induce an immune response in animals and caused no apparent toxic effects.

One concern about applying nanotechnology in medicine is its safety. Nanomaterials used to deliver a drug could cause undesired effects by inhibiting the drug's biodegradation and clearance, thus prolonging its half-life *in vivo*. To address this question, we determined the *in vivo* pharmacokinetics of TOT-siRNA by injecting mice with 0.96 mg/kg of TOT-siRNA via tail vein, isolating liver tissues at various times after injection, and analyzing different regions for ApoB mRNA levels. The maximum knockdown of ApoB mRNA was observed 48 h after injecting TOT-siRNA, and the ApoB mRNA levels increased to ~80% after 72 h and remained at that level until 144 h (Figure 5a). To determine the amount of ApoB siRNA in mouse liver, total RNA was isolated from livers at various times after injecting mice with TOT-siRNA, and guide strand ApoB siRNA was identified by Northern blot analysis. The amount of guide strand found in mouse liver was greatest at 48 h after TOT-siRNA injection and decreased with time (up to 144 h) (Figure

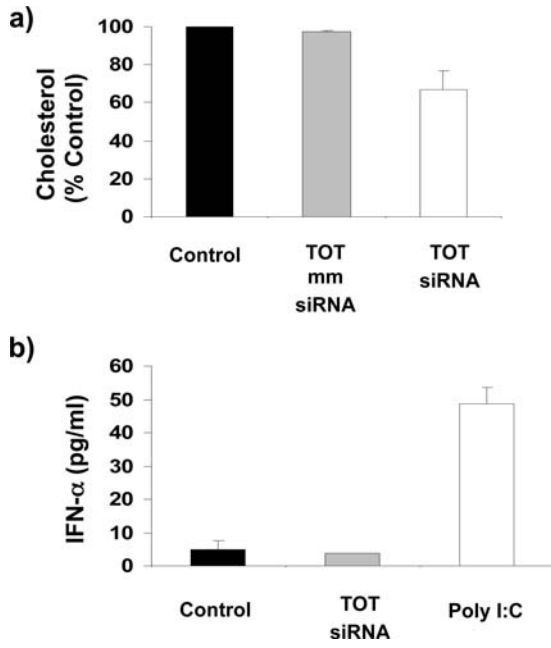


Figure 4. (a) TOT-siRNA therapeutically reduces cholesterol levels. Plasma cholesterol levels were measured 48 h after injecting mice with 0.96 mg/kg TOT-siRNA complex. (b) TOT-siRNA treatment does not induce interferon response in mice. IFN-α plasma levels were measured 48 h after injecting mice with 0.96 mg/kg TOT without siRNA (Mock) or with 0.96 mg/kg TOT-CM siRNA. As a positive control, IFN-α plasma levels were measured after injecting mice with 250 μg Poly IC. Each value represents the mean ± SD of 5 plasma samples from each treatment group.

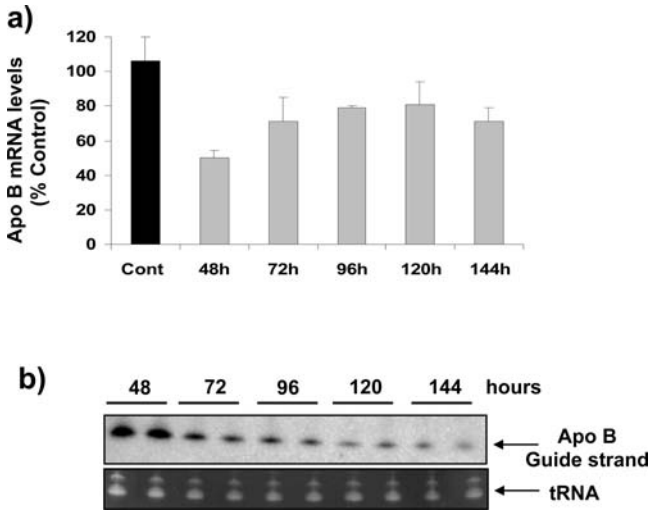


Figure 5. Pharmacokinetics of TOT-siRNA. (a) Mice were injected with 0.96 mg/kg of TOT-siRNA, and ApoB mRNA levels were measured in liver at various times after injection. Values represent the mean ± SD of tissue samples from 3−5 animals. (b) ApoB siRNA decreases with time in livers of mice injected with TOT-siRNA. Mice were injected with TOT-siRNA (a), total RNA was isolated from their livers at various times after injection, and ApoB siRNA guide strand was identified by Northern blot analysis. A representative Northern blot shows that the amount of ApoB guide strand siRNA decreased over the time range shown. tRNA was identified as a positive control.

5b). Taken together, these results show a correlation between *in vivo* RNAi efficiency at various times after TOT-siRNA treatment and amount of guide strand present in mouse liver. Although these findings do not directly demonstrate the half-life of nanomaterial *in vivo*, however, these results suggest that the RNA trigger molecules in the siRNA-TOT complexes were not trapped in liver and were cleared quite rapidly from the body.

Nanomedicine has recently emerged as a new branch of science that explores applications of nanotechnology for diagnosing, monitoring, treating, and controlling biological functions (*37*). However, the questions of physiological toxicity and favorable pharmacology of nanomaterials remains unanswered. Here, we present evidence that a new approach to designing nanotubes can be used to create nanomaterials for *in vivo* delivery of siRNA to silence endogenous disease-related genes at clinically acceptable and therapeutically affordable doses. Injecting mice with only 0.96 mg/kg siRNA in complex with TOT (SWNT functionalized with lipids and natural amino acid-based dendrimers) silenced ApoB mRNA and reduced protein levels in liver, decreased plasma levels of ApoB, and lowered total plasma cholesterol. Moreover, TOT treatment was nontoxic and did not induce an immune response. Most of the RNA molecules (80%) assembled with TOT were cleared from the body 48 h after treatment, indicating that the nanotubes did not inhibit siRNA biodegradation and clearance, ensuring a short half-life for siRNA *in vivo*. These results provide the first evidence that nanotubes can be safely and effectively used to systemically deliver siRNA, thus offering a new technology for systemic RNAi and potentially for delivering other drugs *in vivo*.

ACKNOWLEDGMENT

We thank Michael Czech, Craig Mello and members of the Rana lab for helpful discussions, and Dr. David Garlick for histological examination of slides. We also thank Dr. Gregory Hendricks and his group at the Core Electron Microscopy Facility, UMASS Medical School for their advice and help with the electron microscopy experiments. This work was supported in part by a grant from the NIH to T.M.R.

LITERATURE CITED

(1) Star, A., Stoddart, J. F., Steuerman, D., Diehl, M., Boukai, A., Wong, E. W., Yang, X., Chung, S. W., Choi, H., and Heath, J. R. (2001) Preparation and properties of polymer-wrapped single-walled carbon nanotubes. *Angew. Chem., Int. Ed. Engl. 40*, 1721–1725.

(2) Singh, R., Pantarotto, D., McCarthy, D., Chaloin, O., Hoebeke, J., Partidos, C. D., Briand, J. P., Prato, M., Bianco, A., and Kostarelos, K. (2005) Binding and condensation of plasmid DNA onto functionalized carbon nanotubes: toward the construction of nanotube-based gene delivery vectors. *J. Am. Chem. Soc. 127*, 4388–96.

(3) Kam, N. W., Liu, Z., and Dai, H. (2005) Functionalization of carbon nanotubes via cleavable disulfide bonds for efficient intracellular delivery of siRNA and potent gene silencing. *J. Am. Chem. Soc. 127*, 12492–3.

(4) Fire, A., Xu, S., Montgomery, M. K., Kostas, S. A., Driver, S. E., and Mello, C. C. (1998) Potent and specific genetic interference by double-stranded RNA in Caenorhabditis elegans. *Nature 391*, 806–11.

(5) Hannon, G. J., and Rossi, J. J. (2004) Unlocking the potential of the human genome with RNA interference. *Nature 431*, 371–8.

(6) Hammond, S. M., Bernstein, E., Beach, D., and Hannon, G. J. (2000) An RNA-directed nuclease mediates post-transcriptional gene silencing in Drosophila cells. *Nature 404*, 293–6.

(7) Caplen, N. J., Parrish, S., Imani, F., Fire, A., and Morgan, R. A. (2001) Specific inhibition of gene expression by small double-stranded RNAs in invertebrate and vertebrate systems. *Proc. Natl. Acad. Sci. U.S.A. 98*, 9742–7.

(8) Elbashir, S. M., Harborth, J., Lendeckel, W., Yalcin, A., Weber, K., and Tuschl, T. (2001) Duplexes of 21-nucleotide RNAs

mediate RNA interference in cultured mammalian cells. *Nature 411*, 494–8.
(9) Rana, T. M. (2007) Illuminating the silence: understanding the structure and function of small RNAs. *Nat. Rev. Mol. Cell Biol. 8*, 23–36.
(10) Amarzguioui, M., Holen, T., Babaie, E., and Prydz, H. (2003) Tolerance for mutations and chemical modifications in a siRNA. *Nucleic Acids Res. 31*, 589–95.
(11) Chiu, Y. L., and Rana, T. M. (2003) siRNA function in RNAi: a chemical modification analysis. *RNA 9*, 1034–48.
(12) Chiu, Y. L., and Rana, T. M. (2002) RNAi in human cells: basic structural and functional features of small interfering RNA. *Mol. Cell 10*, 549–61.
(13) Morrissey, D. V., Lockridge, J. A., Shaw, L., Blanchard, K., Jensen, K., Breen, W., Hartsough, K., Machemer, L., Radka, S., Jadhav, V., Vaish, N., Zinnen, S., Vargeese, C., Bowman, K., Shaffer, C. S., Jeffs, L. B., Judge, A., MacLachlan, I., and Polisky, B. (2005) Potent and persistent in vivo anti-HBV activity of chemically modified siRNAs. *Nat. Biotechnol. 23*, 1002–7.
(14) Soutschek, J., Akinc, A., Bramlage, B., Charisse, K., Constien, R., Donoghue, M., Elbashir, S., Geick, A., Hadwiger, P., Harborth, J., John, M., Kesavan, V., Lavine, G., Pandey, R. K., Racie, T., Rajeev, K. G., Rohl, I., Toudjarska, I., Wang, G., Wuschko, S., Bumcrot, D., Koteliansky, V., Limmer, S., Manoharan, M., and Vornlocher, H. P. (2004) Therapeutic silencing of an endogenous gene by systemic administration of modified siRNAs. *Nature 432*, 173–8.
(15) Krutzfeldt, J., Rajewsky, N., Braich, R., Rajeev, K. G., Tuschl, T., Manoharan, M., and Stoffel, M. (2005) Silencing of microRNAs in vivo with 'antagomirs'. *Nature 438*, 685–9.
(16) Zimmermann, T. S., Lee, A. C., Akinc, A., Bramlage, B., Bumcrot, D., Fedoruk, M. N., Harborth, J., Heyes, J. A., Jeffs, L. B., John, M., Judge, A. D., Lam, K., McClintock, K., Nechev, L. V., Palmer, L. R., Racie, T., Rohl, I., Seiffert, S., Shanmugam, S., Sood, V., Soutschek, J., Toudjarska, I., Wheat, A. J., Yaworski, E., Zedalis, W., Koteliansky, V., Manoharan, M., Vornlocher, H. P., and MacLachlan, I. (2006) RNAi-mediated gene silencing in non-human primates. *Nature 441*, 111–4.
(17) Palliser, D., Chowdhury, D., Wang, Q. Y., Lee, S. J., Bronson, R. T., Knipe, D. M., and Lieberman, J. (2006) An siRNA-based microbicide protects mice from lethal herpes simplex virus 2 infection. *Nature 439*, 89–94.
(18) Santel, A., Aleku, M., Keil, O., Endruschat, J., Esche, V., Fisch, G., Dames, S., Loffler, K., Fechtner, M., Arnold, W., Giese, K., Klippel, A., Kaufmann, J. (2006) A novel siRNA-lipoplex technology for RNA interference in the mouse vascular endothelium. *Gene Ther.*
(19) Song, E., Zhu, P., Lee, S. K., Chowdhury, D., Kussman, S., Dykxhoorn, D. M., Feng, Y., Palliser, D., Weiner, D. B., Shankar, P., Marasco, W. A., and Lieberman, J. (2005) Antibody mediated in vivo delivery of small interfering RNAs via cell-surface receptors. *Nat. Biotechnol. 23*, 709–17.
(20) Krajcik, R., Jung, A., Hirsch, A., Neuhuber, W., and Zolk, O. (2008) Functionalization of carbon nanotubes enables noncovalent binding and intracellular delivery of small interfering RNA for efficient knock-down of genes. *Biochem. Biophys. Res. Commun. 369*, 595–602.
(21) Liu, Z., Winters, M., Holodniy, M., and Dai, H. (2007) siRNA delivery into human T cells and primary cells with carbon-nanotube transporters. *Angew. Chem., Int. Ed. Engl. 46*, 2023–7.
(22) Wang, X., Ren, J., and Qu, X. (2008) Targeted RNA interference of cyclin A2 mediated by functionalized single-walled carbon nanotubes induces proliferation arrest and apoptosis in chronic myelogenous leukemia K562 cells. *ChemMedChem 3*, 940–5.
(23) Liu, J., Rinzler, A. G., Dai, H., Hafner, J. H., Bradley, R. K., Boul, P. J., Lu, A., Iverson, T., Shelimov, K., Huffman, C. B., Rodriguez-Macias, F., Shon, Y. S., Lee, T. R., Colbert, D. T., and Smalley, R. E. (1998) Fullerene pipes. *Science 280*, 1253–6.
(24) Baigude, H., Katsuraya, K., Okuyama, K., Tokunaga, S., and Uryu, T. (2003) Synthesis of sphere-type monodispersed oligosaccharide-polypeptide dendrimers. *Macromolecules 36*, 7100–7106.
(25) Shao, J., and Tam, J. P. (1995) Unprotected peptides as building blocks for the synthesis of peptide dendrimers with oxime, hydrazone, and thiazolidine linkages. *J. Am. Chem. Soc. 117*, 3893–3899.
(26) Gao, L., Nie, L., Wang, T., Qin, Y., Guo, Z., Yang, D., and Yan, X. (2006) Carbon nanotube delivery of the GFP gene into mammalian cells. *ChemBioChem 7*, 239–42.
(27) Richard, C., Balavoine, F., Schultz, P., Ebbesen, T. W., and Mioskowski, C. (2003) Supramolecular self-assembly of lipid derivatives on carbon nanotubes. *Science 300*, 775–8.
(28) Olofsson, S. O., and Boren, J. (2005) Apolipoprotein B: a clinically important apolipoprotein which assembles atherogenic lipoproteins and promotes the development of atherosclerosis. *J. Intern. Med. 258*, 395–410.
(29) Farese, R. V., Jr., Veniant, M. M., Cham, C. M., Flynn, L. M., Pierotti, V., Loring, J. F., Traber, M., Ruland, S., Stokowski, R. S., Huszar, D., and Young, S. G. (1996) Phenotypic analysis of mice expressing exclusively apolipoprotein B48 or apolipoprotein B100. *Proc. Natl. Acad. Sci. U.S.A. 93*, 6393–8.
(30) Brown, M. S., and Goldstein, J. L. (1986) A receptor-mediated pathway for cholesterol homeostasis. *Science 232*, 34–47.
(31) Rossi, J. J. (2004) Medicine: a cholesterol connection in RNAi. *Nature 432*, 155–6.
(32) Chiu, Y. L., Ali, A., Chu, C. Y., Cao, H., and Rana, T. M. (2004) Visualizing a correlation between siRNA localization, cellular uptake, and RNAi in living cells. *Chem. Biol. 11*, 1165–75.
(33) Chu, C. Y., and Rana, T. M. (2006) Translation repression in human cells by microRNA-induced gene silencing requires RCK/p54. *PLoS Biol. 4*, e210.
(34) Baigude, H., McCarroll, J., Yang, C. S., Swain, P. M., and Rana, T. M. (2007) Design and creation of new nanomaterials for therapeutic RNAi. *ACS Chem. Biol. 2*, 237–41.
(35) Marques, J. T., and Williams, B. R. (2005) Activation of the mammalian immune system by siRNAs. *Nat. Biotechnol. 23*, 1399–405.
(36) Robbins, M. A., and Rossi, J. J. (2005) Sensing the danger in RNA. *Nat. Med. 11*, 250–1.
(37) Wagner, V., Dullaart, A., Bock, A. K., and Zweck, A. (2006) The emerging nanomedicine landscape. *Nat. Biotechnol. 24*, 1211–7.

BC900296Z

A Doubly Labeled Penetratin Analogue as a Ratiometric Sensor for Intracellular Proteolytic Stability

Rainer Fischer,*[,†,‡,||] Hansjörg Hufnagel,[†,‡,⊥] and Roland Brock[‡,§]

Interfaculty Institute for Cell Biology, University of Tübingen, Auf der Morgenstelle 15, 72076 Tübingen, Germany, and Department of Biochemistry, Nijmegen Centre for Molecular Life Sciences, Radboud University Nijmegen Medical Centre, P.O. Box 9101, 6500 HB Nijmegen, The Netherlands. Received July 8, 2009; Revised Manuscript Received November 12, 2009

Endocytosis has been shown to play a major role in the cellular import of cationic cell-penetrating peptides (CPPs) and CPP conjugates. Considering the presence of proteolytic activities inside the endolysosomal compartment, it is necessary to assess the consequences of the import mechanism on the intracellular integrity of the vector and the cargo. In this work, a penetratin analogue terminally labeled with two different fluorophores was synthesized and used as a sensor to quantitatively dissect the contribution of intracellular proteolytic activities on the breakdown of this specific CPP. Using a panel of lysosomal protease inhibitors, the endocytic compartment was identified as the major site of degradation. In contrast, an inhibitor of the proteasome had little effect on intracellular peptide integrity. Very remarkably, inhibitors of endolysosomal proteolysis also affected the intracellular distribution of fluorescence, leading to a reduction of fluorescein fluorescence in the cytoplasm. This change in fluorescence distribution was very similar to the one observed after incubation of cells with inhibitors of endosomal acidification. These results indicate that cytoplasmic fluorescence, typically interpreted as CPP entering the cytosol, may originate from proteolytic breakdown products.

INTRODUCTION

The lipid bilayer of the plasma membrane protects the intracellular content from entry of pathogens and molecules that may interfere with cellular functions. Only molecules within a narrow range of molecular size, net charge, and polarity are able to directly cross the plasma membrane (*1*). On the other hand, the introduction of membrane-impermeable molecules into mammalian cells has important applications in biomedical (*2*) as well as in fundamental research (*3, 4*). Applications include the import of siRNAs interfering with gene expression (*5*) or peptides that disrupt molecular interactions in cellular signal transduction (*6*).

Peptide-mediated import has attracted growing attention as a delivery technology during the past decade (for reviews, see *refs* 7−9). Cell-penetrating peptides (CPPs) represent a group of functional peptides with little cell-type specificity. These peptides mediate the noninvasive import of cargo molecules into cells *ex vivo* as well as in animals (*10, 11*). Peptides (*6, 12*), proteins as large as 120 kDa (*11, 13*), oligonucleotides (*14*), plasmids (*15*), siRNA (*16*), peptide nucleic acids (PNAs) (*17*), and even nanoparticles (*18*) have been used as cargo for intracellular delivery. The majority of these types of cargo exert their biological activity inside the cytoplasm or the nucleus of the treated cells.

The amphiphatic and basic penetratin peptide, derived from the third helix of the homeodomain of the *Drosophila* Antennapedia[1]transcription factor, has been widely used as a CPP (*19*). Despite its broad acceptance as a molecular carrier, the mechanism of internalization and intracellular trafficking of the penetratin peptide is still not fully understood. Earlier data demonstrated transfer of penetratin across a pure lipid bilayer (*20*) without forming pores (*20, 21*) independent of endocytosis, but more recently published data have indicated endocytosis as an uptake mechanism for the internalization of the penetratin peptide (*22, 23*).

However, for cationic CPPs taken up by endocytosis, the mechanism by which these molecules are actually released into the cytoplasm still needs to be addressed, as well as the question to which degree proteolytic breakdown occurs during endocytic uptake. So far, only evidence was presented that endosomal acidification is involved in the release into the cytosol (*23, 24*).

The investigation of cellular trafficking and cellular distribution of CPPs has greatly benefited from the incorporation of fluorophores as reporter moieties providing the possibility to follow the fluorescently labeled CPPs in living cells (*25, 26*). Problems associated with the fixation and labeling of CPP-

* Corresponding author. Dr. Rainer Fischer, Wacker Polymer Systems GmbH & Co. KG, Hanns-Seidel-Platz 4, 81737 München, Germany, Rainer.Fischer@wacker.com, Ph.: +49 - 89 - 6279-1966 Fax: +49 - 89 - 6279-2294.

† These authors contributed equally.

‡ University of Tübingen.

§ Radboud University Nijmegen Medical Centre.

|| Current Address: Wacker Polymer Systems GmbH & Co. KG, Hanns-Seidel-Platz 4, 81737 München, Germany.

⊥ Current Address: Department of Biochemistry, University of Cambridge, 80 Tennis Court Road, Cambridge CB2 1TA, United Kingdom.

[1]Abbrevations: Penetratin, Antennapedia; CLSM, confocal laser scanning microscopy; CPP, cell-penetrating peptide; Boc, *tert*-butyloxycarbonyl; DCM, dichloromethane; Dde, 1-(4,4-dimethyl-2,6-dioxocyclohexylidene)ethyl; DHAP, 2,5-dihydroxyacetophenone; DIC, *N*,*N*′-diisopropyl carbodiimide; DIPEA, *N*,*N*′-diisopropylethylamine; DMF, *N*,*N*′-dimethylformamide; DMSO, dimethylsulfoxide; EDTA, ethylene diamine tetraacetic acid; Fluo, 5(6)-carboxyfluorescein; Fmoc, 9-fluorenylmethoxycarbonyl; FRET, fluorescence resonance energy transfer; HOBt, 1-hydroxybenzotriazol; HPLC, high-performance liquid chromatography; MALDI-MS, matrix-assisted laser desorption ionization mass spectrometry; MeOH, methanol; Mtt, 4-methyltrityl; PBS, phosphate-buffered saline; RP, reversed phase; RT, room temperature; SPPS, solid-phase peptide synthesis; Tamra, 5(6)-carboxytetramethylrhodamine; tBu, *tert*-butyl; tBuOH, *tert*-butyl alcohol; TFA, trifluoroacetic acid; TIS, triisopropylsilane; Trt, trityl.

10.1021/bc900301k © 2010 American Chemical Society
Published on Web 12/03/2009

loaded cells (*25*) can be avoided and loading efficiencies can be compared quantitatively by live cell flow cytometry (*23, 25*).

In order to further address molecular details of intracellular trafficking and breakdown, we synthesized a penetratin analogue that was amino- and carboxy-terminally labeled with 5,6-carboxy-fluorescein (Fluo) and carboxytetramethylrhodamine (Tamra), respectively. Peptides incorporating two different fluorescent dyes have served as sensors for conformational changes (*27, 28*) and proteolytic breakdown (*29, 30*). Förster (Fluorescence) resonance energy transfer (FRET) (*31*) provides a sensitive readout for molecular events affecting the proximity of the reporter groups.

In a former contribution, we applied a doubly labeled cell-penetrating cathepsin substrate to determine proteolytic selectivity (*23*). In this contribution, we have extended this approach to a doubly labeled penetratin. On the basis of a ratiometric protocol, we developed a protocol for flow cytometry to monitor peptide breakdown within living mammalian cells.

By incubating mammalian cells with the doubly labeled peptide in the presence of a variety of protease inhibitors, we were able to assess the contribution of different post-endocytic proteolytic activities from different cellular compartments after endocytic uptake for the penetratin CPP.

EXPERIMENTAL PROCEDURES

Materials. Standard chemicals for peptide chemistry were obtained from Fluka (Deisenhofen, Germany) and Merck (Darmstadt, Germany); solvents were p.a. grade. Fluorenylmethoxycarbonyl (Fmoc)-amino acids were purchased from Novabiochem (Heidelberg, Germany), Senn Chemicals (Dielsdorf, Switzerland), and Orpegen Pharma (Heidelberg, Germany). Fmoc-Lys(Dde)-OH was purchased from Novabiochem (Läufelfingen, Schweiz). Rink amide resin was purchased from Rapp Polymere (Tübingen, Germany). The isomeric mixtures of 5(6)-carboxyfluorescein (Fluo) and 5(6)-carboxytetramethylrhodamine (Tamra)-*N*-succinimidyl ester were supplied by Fluka. Bafilomycin A1 was from Tocris Biotrend (Bristol, UK), chloroquine diphosphate from Fluka, the furin inhibitor (Dec-RVKR-CMK) from Calbiochem (Bad Soden, Germany), lactacystin from Professor Corey (Harvard, University), E-64d from Serva (Heidelberg, Germany), and leupeptin from Bachem (Bubendorf, Switzerland).

Peptide Synthesis. Automated peptide synthesis was performed on an automated peptide synthesizer (RSP5032, Tecan, Hombrechtlikon, Switzerland) using solid-phase Fmoc/tBu-chemistry in 2 mL syringes according to the following protocol: Fmoc-amino acids (12-fold excess) were coupled by *in situ* activation using *N*,*N*′-diisopropylcarbodiimide (DIC)/HOBt in dimethylformamide (DMF) for 90 min followed by removal of the Fmoc-protecting group by treatment with piperidine/DMF (1:4, v/v) twice for 8 min. The resin was washed with DMF (6×) after each coupling and deprotection step. Side chains of Asn and Gln were Trityl (Trt)-protected, the side chains of Lys and Trp were *tert*-butyloxycarbonyl (Boc)-protected, and the side chain of Arg was 2,2,4,6,7-pentamethyldihydrobenzofuran-5-sulfonyl (Pbf)-protected. Peptides were cleaved off the resin by treatment with trifluoro acetic acid (TFA)/triisopropylsilane (TIS)/ethanedithiole/H_2O (92.5:2.5:2.5:2.5, v/v/v/v) for 4 h. Crude peptides were precipitated by adding cold diethyl ether (−20 °C). The precipitated peptides were collected by centrifugation and resuspended in cold diethyl ether. This procedure was repeated twice. Finally, peptides were dissolved in *tert*-butyl alcohol/H_2O (4:1, v/v) and lyophilized 3 times.

Reverse-Phase High-Performance Liquid Chromatography (RP-HPLC). Peptides and conjugates were analyzed by analytical RP-HPLC using a water (0.1% TFA) (solvent A)/ACN (0.1% TFA) (solvent B) gradient on a Waters 600 System (Eschborn, Germany) with detection at 214 nm. The samples were analyzed on an analytical column (Nucleosil 100, 250 × 2 mm, C18 column, 5 μm particle diameter; Grom, Herrenberg, Germany), using a linear gradient from 10% B to 100% B within 30 min (flow rate: 0.3 mL/min). All peptides were purified by preparative RP-HPLC (Nucleosil 300, 250 × 20 mm, C18 column, 10 μm particle diameter; Grom, Herrenberg, Germany) on a Gilson preparative HPLC system (Bad Camberg, Germany), equipped with a 321 Pump and a 156 UV/vis detector, flow rate: 10 mL/min. Gradients were adjusted according to the elution profiles and peak profiles obtained from the analytical HPLC chromatograms. Purities of peptides used in this study were >98% (214 nm, HPLC).

Matrix-Assisted-Laser-Desorption/Ionization−Time-of-Flight-Mass-Spectrometry (MALDI-TOF MS) of Synthetic Peptides. One microliter of 2,5-dihydroxyacetophenone (DHAP) matrix (20 mg of DHAP, 5 mg of ammonium citrate in 1 mL of isopropyl alcohol/H_2O (4:1, v/v)) was mixed with 1 μL of each sample (dissolved in ACN/water (1:1) at a concentration of 1 mg/mL) on a gold target. Measurements were performed using a MALDI-TOF system (G2025A, Hewlett-Packard, Waldbronn, Germany). For signal generation, 20−50 laser shots were added up in the single-shot mode.

Solid-Phase Synthesis of Tamra-Penetratin-Fluo. The doubly labeled peptide Tamra-Penetratin-Fluo was synthesized according to our previously described protocol (*29*) using Fluo(Trt)-Lys-Rink amide resin. The peptide RQIKIWFQNRRMKWKK was assembled on this resin in a 15 μmol scale as described above (*32*). A small fraction of this peptide was cleaved off and analyzed (H-RQIKIWFQNRRMKWKK-εLys-(Fluo)-NH_2 (purity 80% (HPLC, 214 nm), calcd $[M+H]^+$ = 2733.3 Da, found $[M+H]^+$ = 2733.3 Da, determined by MALDI-TOF MS)). Five micromoles of the resin-bound and side chain protected peptide was then reacted with 5(6)-carboxytetramethylrhodamine-*N*-succinimidyl ester (10 μmol, 5.3 mg) in DMF (200 μL) containing DIPEA (25 μmol, 4.3 μL). After 16 h, the resin was thoroughly washed with DMF to remove excess of Tamra. Cleavage and deprotection of the doubly labeled peptide amide were performed as described above. The peptide was dissolved in ACN/water (1:1), lyophilized, and analyzed using RP-HPLC and MALDI-TOF MS. Methionine sulfoxide reduction was performed as described (*33*). The peptide was then purified as described by preparative RP-HPLC (Figure 1).

Peptide Stock Solutions. Peptides were dissolved in DMSO to concentrations of 10 mM. These stock solutions were further diluted 1:20 in ddH_2O. Peptide concentrations were determined on the basis of absorption of the rhodamine label by UV/vis spectroscopy of a further 1:100 dilution in methanol. Absorptions of these solutions were measured at 540 nm (ε = 95 000 L/ (mol·cm)).

Cell Culture. The adherent MC57 fibrosarcoma cell line was grown in a 5% CO_2 humidified atmosphere at 37 °C in RPMI 1640 medium with stabilized glutamine and 2.0 g/L $NaHCO_3$ (PAN Biotech, Aidenbach, Germany) supplemented with 10% fetal calf serum (PAN Biotech), 100 U/mL penicillin, and 100 μg/mL streptomycin (Biochrom, Berlin, Germany). Cells were passaged by trypsinization with trypsin/ethylenediaminetetraacetic acid (EDTA) (0.05/0.02% (w/v)) (Biochrom) in PBS every third to fourth day.

Confocal Laser Scanning Microscopy (CLSM). Confocal laser scanning microscopy was performed on an inverted LSM510 laser scanning microscope (Carl Zeiss, Göttingen, Germany) fitted with a Plan-Apochromat 63× 1.4 N.A. lens. All measurements were performed with living, nonfixed cells.

MC57 cells were seeded at a density of 10 000/well in 8-well chambered cover glasses (Nunc, Wiesbaden, Germany). Two

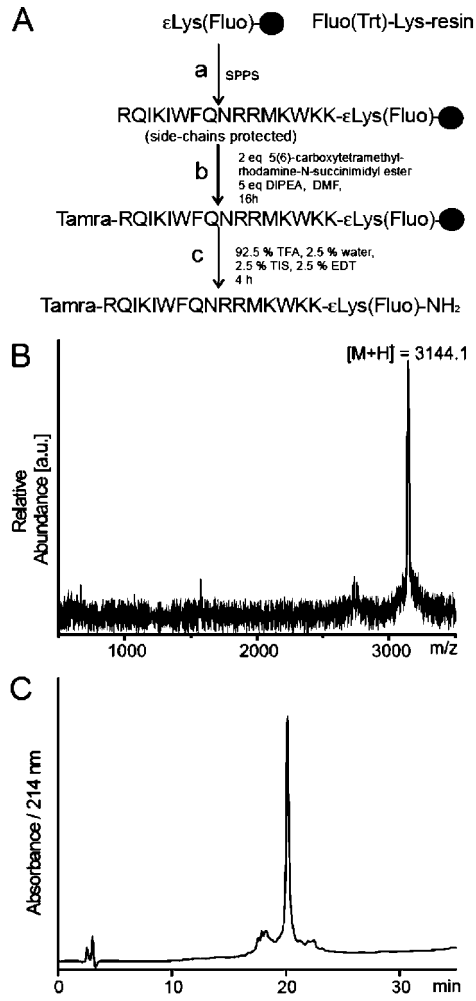


Figure 1. Scheme for the synthesis and analytical data for Tamra-Penetratin-Fluo. (A) Scheme for the synthesis of the doubly labeled penetratin peptide amide Tamra-RQIKIWFQNRRMKWKK-εLys(Fluo)-NH_2 (=Tamra-Penetratin-Fluo). The penetratin peptide is assembled by automated solid-phase peptide synthesis (a) on the free ε-amino group of the N^{α}-carboxyfluorescein-labeled lysyl-Rink amide resin followed by (b) introduction of the second fluorophore at the N-terminus of the solid-phase bound peptide, and (c) cleavage of the peptide amide off the resin and side-chain deprotection. In order to further increase the purity of the raw product, the methionine sulfoxide was subsequently reduced as described previously. (B) MALDI-TOF mass spectrum (theor. $[M+H]^+ = 3145.7$ Da). (C) HPLC elution profile of the crudeTamra-RQIKIWFQNRRMKWKK-εLys(Fluo)-N_2 peptide.

days later, before addition of inhibitors and peptides, cells were washed once with serum-free RPMI 1640. The indicated inhibitor was added in 200 μL serum-free RPMI 1640 30 min before addition of peptides. After 2 h incubation with peptides, images were acquired immediately at RT with excess peptide in the medium.

For double detection of fluorescein and Tamra, the 488 nm line of an argon-ion laser and the light of a 543 nm helium−neon laser were directed over an HFT 488/543 beam splitter, and fluorescence was detected using an NFT 545 beam splitter in combination with a BP 505−530 band-pass filter for fluorescein detection and an LP 560 long-pass filter for Tamra detection.

Fluorescence Emission Spectra. Fluorescence emission spectra were recorded at RT using an LS50B spectrofluorometer (Perkin-Elmer, Norwalk, CT, USA). The excitation and emission bandwidths were set to 10 nm.

Fluorescence Emission Measurements in Cell Lysates and Ratiometric Measurements. MC57 cells were seeded in 6-well plates (Sarstedt, Nümbrecht, Germany) in serum-containing RPMI 1640. Two days later, the confluent cell layer was washed with serum-free RPMI 1640 and incubated with 500 μL serum-free RPMI 1640 (with/without the indicated inhibitor) for 30 min. Then, Tamra-Penetratin-Fluo was added, and after 2 h incubation, cells were washed twice with PBS, detached using EDTA (5 mM)/PBS (10 min at 37 °C), transferred into a fresh tube, and washed twice with 1 mL ice-cold PBS. A small fraction of the cells were used for analysis by flow cytometry. Cell suspensions were then resuspended in 1 mL PBS and split into half. Both suspensions were then transferred into a fresh tube and spun down (14 000 rpm).

Supernatants were removed, and one-half of the cells was lysed in 200 μL NP-40 lysis buffer (0.5% (v/v) NP-40, 150 mM NaCl, 5 mM EDTA, 50 mM TRIS, pH 7.0, containing protease inhibitor cocktail (Roche Diagnostics, Mannheim, Germany)). The lysates were then sonicated and centrifuged for 30 min at 4 °C and 14 000 rpm. Fluorescence emission spectra of the supernatants were recorded immediately (excitation at 492 nm). These lysates were always stored on ice.

The second half of the cells was lysed in 180 μL NP-40 lysis buffer (0.5% (v/v) NP-40, 150 mM NaCl, 5 mM EDTA, 50 mM TRIS, pH 7.0). The lysates were then also sonicated and centrifuged for 30 min at 4 °C and 14 000 rpm. Twenty microliters of proteinase K-solution (10 mg/mL, Sigma, Taufkirchen) were then added to the supernatants. After 16 h digestion, fluorescence emission spectra of the supernatants were recorded (excitation 492 nm) (see Figure 4A).

In order to quantify the absolute amounts of digested Tamra-Penetratin-Fluo in cell lysates, we performed fluorescence emission measurements in lysis buffer as described above based on a standard solution containing different amounts of intact and digested peptide. The ratios (520 nm/575 nm) obtained by this procedure were used to calculate relative amounts of intact and digested substrate.

To prepare standard solutions, Tamra-Penetratin-Fluo (100 nM) was digested at 37 °C with proteinase K (20 μg/mL) in NP-40 lysis buffer (containing 0.5% (v/v) NP-40, 150 mM NaCl, 5 mM EDTA, 50 mM TRIS, pH 7.0). After 5 h, the reaction was stopped by adding PMSF (final concentration 500 μM). Different amounts of this solution and fresh undigested Tamra-Penetratin-Fluo (100 nM in NP-40 lysis buffer, including 500 μM PMSF) were mixed, and fluorescence emission spectra of the solutions were recorded (excitation at 492 nm).

To account for the influence of other constituents of the cell lysates and postlysis proteolysis, we lysed cells that had not been incubated with any peptide or inhibitor in lysis buffer containing various ratios of intact and digested substrate. Different amounts of solutions containing fresh, undigested Tamra-Penetratin-Fluo (100 nM, in NP40 lysis buffer containing 500 μM PMSF) and completely digested Tamra-Penetratin-Fluo according to above-mentioned procedure were mixed (ratios 0/100, 25/75, 50/50, 75/25, 100/0). Protease inhibitor cocktail was then added to all five solutions. Then, these solutions were used for the preparation of cell lysates essentially as described above, and fluorescence emission spectra of the solutions were recorded (excitation at 492 nm). All measurements were performed in duplicate and ratios (520 nm/575 nm) were calculated and plotted. These data were fitted using a linear function. Complete inactivation of proteinase K using PMSF at the indicated concentration was verified in a different experiment (data not shown).

Flow Cytometry. Flow cytometry was performed on a FACS-Calibur (Becton Dickinson, Franklin Lakes, USA). Vital cells were gated on the basis of sideward scatter and forward

Table 1. (A) Sequence of the Tamra-Penetratin-Fluo Sensor and (B) Used Inhibitors to Study Intracellular Proteolytic Breakdown

(A) sensor sequence	
Tamra-RQIKIWFQRNRMKWKK-εLys(Fluo)-NH_2	(Tamra-Penetratin-Fluo)
(B) inhibitor	**site of action**
bafilomycin A1	inhibits endosomal acidification(*39, 41*)
chloroquine	inhibits endosomal acidification(*40, 41*)
lactacystin	20S proteasome(*44*)
furin inhibitor	furin(*45, 46*)
leupeptin	(endosomal) cysteine proteases(*47*)
E-64d	(endosomal) cysteine proteases(*48*)

scatter. For calculating the fluorescence emission ratios, the median fluorescence intensities of 5000 vital cells were taken.

RESULTS

***In Vitro* Proteolytic Digestion of Tamra-Penetratin-Fluo.** In order to address the intracellular proteolytic breakdown of penetratin (Table 1 A), the peptide was N- and C-terminally labeled with Tamra and fluorescein, respectively (Figure 1A). In previous studies, both fluorophores were demonstrated to be compatible with the uptake of penetratin by mammalian cells (*29, 34*). Assembly of the peptide on a carboxyfluorescein-preloaded resin, followed by N-terminal labeling of the peptide with Tamra-*N*-hydroxy-succinimidyl ester yielded the final product in high purity (85%, Figure 1B,C). The fluorescence of both dyes within the Tamra-Penetratin-Fluo peptide was almost completely quenched (Figure 2A,B). This loss of fluorescence in both channels is most likely attributed to a mechanism involving dimer formation (*28*). As expected, digestion of the peptide by proteinase K enhanced the fluorescence emission of both fluorophores significantly (Figure 2A,B). In order to rule out that the differences in fluorescence emission were caused by the adhesion of the intact peptide to plastic and glass (*35*), the ratio of fluorescein (520 nm) versus rhodamine emission (575 nm) upon excitation at 492 nm was calculated (Figure 2C). This experimental approach renders the detection of changes in the fluorescence spectra robust toward changes in concentration (*36*). The ratio was almost doubled upon proteinase K digestion in HBS buffer from about 1.7 to 3.0. The ratiometric difference between intact and digested peptide was even more pronounced when using NP 40 buffer. Here, the ratio was about 0.3 for the intact peptide and 2.8 for the completely digested peptide and might be due to secondary structure induced by NP 40. Both results validate that, next to a dequenching of both fluorophores, digestion of the peptide also led to a more pronounced increase of fluorescein fluorescence due to a loss of FRET.

Confocal Fluorescence Microscopy of Tamra-Penetratin-Fluo-Incubated Cells. The *in vitro* spectral characteristics demonstrate that Tamra-Penetratin-Fluo can serve as a sensitive sensor for probing the proteolytic integrity of this peptide inside mammalian cells. We therefore performed live cell confocal fluorescence microscopy of murine MC57 cells pulsed with Tamra-Penetratin-Fluo. In these cells, our data indicated that penetratin accesses the cytoplasm in an endocytosis- and acidification-dependent way (*23*). The Tamra-Penetratin-Fluo peptide was taken up efficiently in MC57 cells (Figure 3). A high degree of colocalization for the fluorescence of both fluorophores could be observed in vesicular structures. Little Tamra fluorescence was detectable within the cytoplasm and the nucleus. In contrast, pronounced fluorescein fluorescence was present in these compartments. Furthermore, some vesicular structures contained either Fluo fluorescence or Tamra fluorescence. Similar to the cell-penetrating Cathepsin D substrate, this differential localization indicates proteolytic breakdown within the endocytic compartment and preferential release of fluorescein-labeled fragments into the cytoplasm (*29*).

Endolysosomal Acidification Plays a Major Role in Intracellular Peptide Integrity. The results indicated that penetratin is subject to proteolytic degradation. We therefore intended to determine in more detail the extent of breakdown and the proteases involved in the intracellular degradation of the peptide. For this purpose, we followed our previously developed protocol for the incubation of cells with inhibitors of cellular proteases and quantification of intact peptides in cell lysates (*29*). Generally, there is a concern that, in intact cells, the reduction of fluorescein fluorescence by the acidic conditions in the endosomes (*37*) and concentration quenching set a limit to the quantitative assessment of the proteolytic breakdown using a microscopy approach (*38*).

First, a set of four different inhibitors was selected that affect proteolytic activity in different cellular compartments (Table 1B). Bafilomyin A1 (*39*) and chloroquine (*40*) are widely used inhibitors of endosomal acidification (for review, see *41*). Endolysosomal proteases have an acidic pH optimum. For this reason, these inhibitors also efficiently inhibit endolysosomal proteolysis (*42, 43*). The bacterial metabolite lactacystin was chosen as an inhibitor of peptide degradation within the cytosol by blocking the 20S proteasome (*44*). Furthermore, an inhibitor of the protease furin was included. Furin is ubiquitously expressed and mainly localized in the trans-Golgi network, although some portion of the protease cycles between this compartment and the cell surface. Furin cleaves proteins and peptides within cationic stretches (*45*), and more importantly, furin was demonstrated to cleave the HIV-1 Tat protein, which contains the cationic CPP Tat in its sequence, inside cells (*46*).

MC 57 cells were pulsed with the Tamra-Penetratin-Fluo peptide in the absence and presence of these different inhibitors. After incubation, the cell suspensions were split in half (Figure 4A). One-half of the cell population was lysed in the presence of protease inhibitors to prevent postlysis proteolysis, and fluorescence emission spectra of the cell lysates with excitation of fluorescein were recorded immediately (Figure 4B, left panel). The second half of the cell suspensions were lysed in lysis buffer. Aliquots of the lysates were then digested with proteinase K in order to cleave all peptides present in the lysates before recording emission spectra (Figure 4B, right panel).

For all samples, digestion with proteinase K led to fluorescence emission ratios (520 nm/575 nm) very similar to the value of 2.8 observed for completely digested Tamra-Penetratin-Fluo in NP-40 lysis buffer (Figure 2C). For cells pulsed with peptide in the absence of inhibitor, the ratio was 2.3 indicating degradation of the major part of the peptides inside the cells. Bafilomycin A1 and chloroquine showed the strongest inhibitory effects on peptide degradation. The emission ratios decreased in both cases to about 0.9. Lactacystin and the furin inhibitor showed little, albeit significant, effect on the emission ratios (Figure 4C). These results indicate that the endosomal passage has a major impact on the integrity of the peptide inside the cell, while the proteasome seems to degrade only a rather small fraction of the intracellular peptide.

The Endolysosomal Compartment Is the Major Site of Degradation of Penetratin. Even though bafilomycin A1 and chloroquine are expected to reduce the activity of endolysosomal proteases, at this stage it could not be concluded whether the increased integrity of the peptides caused by both drugs was due to the inhibition of endolysosomal proteases or due to the inhibition of an acidification-dependent entry of intact peptide into the cytoplasm, followed by degradation inside the cytosol (*23*). In the latter case, lactacystin-insensitive cytoplasmic proteases would contribute significantly to the breakdown of the peptide. In order to resolve this issue, peptide-pulsed cells

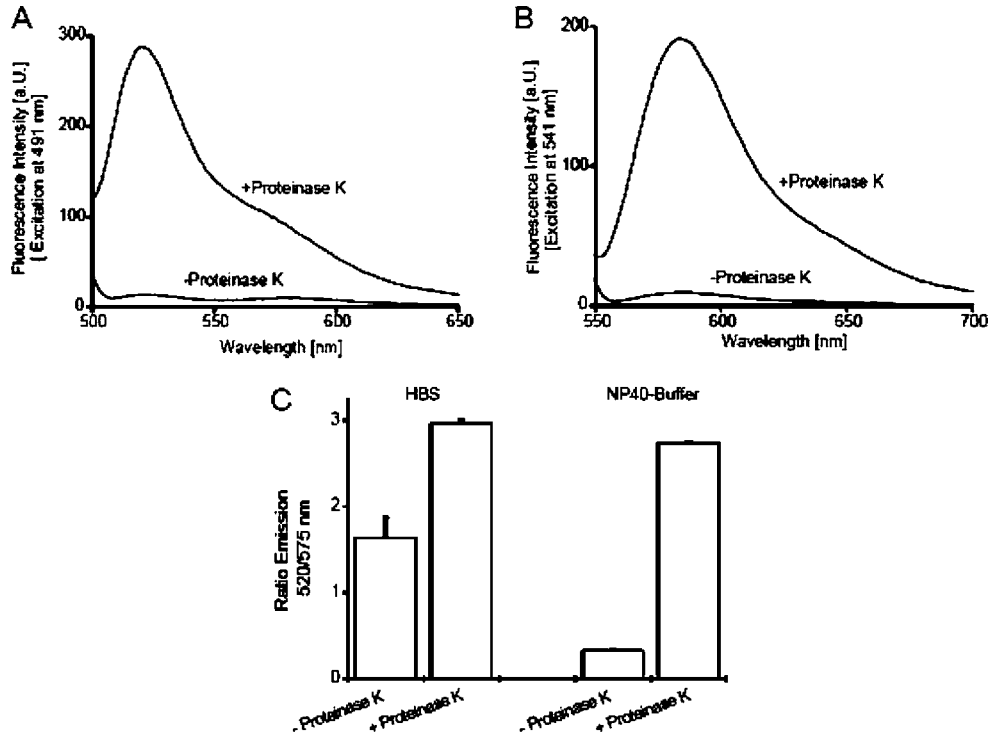


Figure 2. Tamra-Penetratin-Fluo as a proteolytic sensor. Fluorescence emission spectra of Tamra-Penetratin-Fluo (100 nM) in HBS with excitation at (A) 492 nm and (B) 541 nm with (upper curves) and without (lower curves) digestion with proteinase K (100 μg/mL, 1 h). (C) Fluorescence ratios were calculated for the data shown in A (digest in HBS, first two columns) and for an identical digest in NP-40 lysis buffer. Each condition was tested in duplicate; error bars represent the absolute deviations from the mean value.

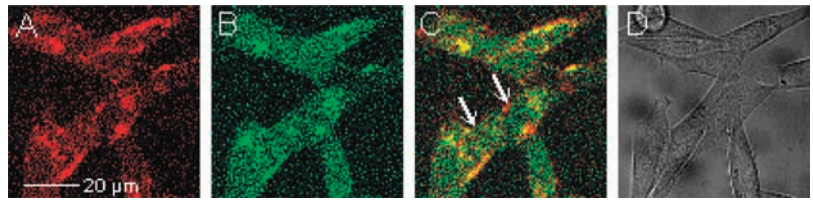


Figure 3. Endocytic uptake and intracellular localization of Tamra-Penetratin-Fluo in MC57 cells. MC57 cells were incubated with serum-free medium containing Tamra-Penetratin-Fluo (3 μM) for 30 min and were then analyzed by multichannel CLSM. Panel A shows the Tamra fluorescence and Panel B the fluorescein fluorescence of the substrate. Panel C shows the overlay of these two channels. Panel D shows the transmission channel.

were incubated with the broadband cysteine protease inhibitors leupeptin (*47*) and E-64d (*48*). Inside the endolysosomal compartment, members of the aspartic and cysteine proteases comprise the major part of protease activity. Most mammalian lysosomal cysteine proteases are cathepsins, although not all cathepsins are cysteine proteases (*49*). Both leupeptin and E-64d reduced the proteolytic degradation of Tamra-Penetratin-Fluo significantly, albeit not as significantly as bafilomycin A1 (Figure 5A).

Finally, we intended to confirm the relevance of these results for intact cells. For this purpose, flow cytometry was employed. Fluorescein was excited with the 488 nm line of the argon ion laser, and the fluorescence of fluorescein and rhodamine was detected in two channels. Especially for the testing of a large number of different conditions, flow cytometry is superior to microscopy-based measurements of intact cells. In this case, different concentrations of E-64d and leupeptin were tested. In cell lysates, for both compounds an increase in inhibitor concentration increased the fraction of intact peptide (Figure 5B). We compared these results to data obtained from flow cytometry using intact cells instead of lysates (Figure 5C). Differences in the ratios determined by both techniques are due to different sizes of the spectral windows and, second, to concentration- and pH-dependent quenching effects of the fluorophores inside the cells. Still, both sets of values exhibited a strong linear correlation (Figure 5D), when the ratios of the FL1 and FL2 emission (corresponding to the intensity of the fluorescein and tamra channel) obtained from flow cytometry were plotted against the corresponding ratios of fluorescence of emissions at 520 and 575 from cell lysates, confirming the applicability of both experimental approaches.

Live Cell Microscopy to Determine the Impact of Inhibitors on the Intracellular Localization of Fluorescence. To further confirm that E-64d and leupeptin exerted their activity on lysosomal proteases, live cell confocal microscopy was performed in the absence and presence of different inhibitors. If the degradation was mediated primarily by endolysosomal cysteine proteases, the colocalization of both fluorophores should increase inside endosomal compartments. Incubation of cells with E-64d increased the degree of colocalization within endocytic vesicles and reduced the cytoplasmic fluorescein fluorescence (Figure 6B). Since bafilomycin A1 had a profound effect on breakdown, we included this inhibitor in this experiment, as well. Bafilomycin A1 also led to a strong reduction in cytoplasmic fluorescence (Figure 6C). Still, the E-64d-induced phenotype was different from the one induced by bafilomycin A1. Instead of being localized in the cell periphery, for

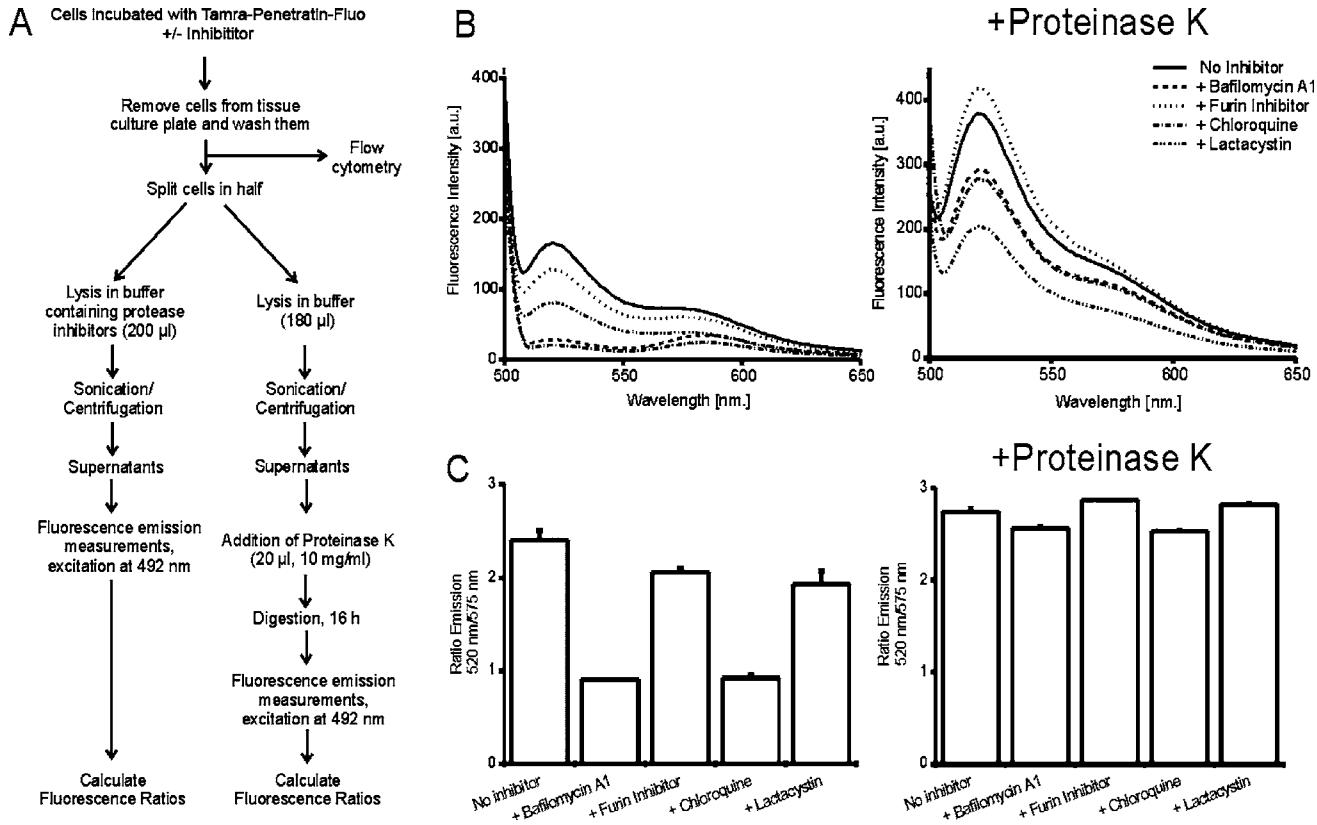


Figure 4. Ratiometric fluorescence emission spectroscopy in cell lysates. (A) Experimental workflow for the measurement of fluorescence emission ratios in cell lysates including the detection of fluorescence by flow cytometry (Figure 5). (B) MC57 cells were incubated with Tamra-Penetratin-Fluo (3 μM) for 2 h in serum-free medium in the absence or presence of different inhibitors (300 nM bafilomycin A1, 50 μM furin inhibitor, and 100 μM chloroquine or 50 μM lactacystin). The inhibitors were added 30 min prior to the peptide. Cells were then washed and removed from the tissue culture plate using EDTA/PBS. Cell lysates were then prepared as described in the Experimental Section. In brief, one-half were lysed in NP-40-lysis buffer containing protease inhibitors. After sonication and centrifugation, fluorescence emission spectra were recorded immediately with excitation at 492 nm (left panel). The other half of the peptide-pulsed cells were lysed in NP-40-lysis buffer. After sonication and centrifugation, proteinase K was added. Lysates were digested for 16 h at 37 °C. Fluorescence emission spectra were then recorded with excitation at 492 nm (right panel). (C) Fluorescence ratios were calculated from the data shown in A. Each condition was tested in duplicate; error bars represent the absolute deviations from the mean value.

bafilomycin A1 peptide-loaded vesicles were concentrated in a region next to the nucleus.

Quantification of Intracellular Breakdown. Our analyses demonstrate that the endocytic uptake has a major impact on peptide integrity. In order to convert the emission ratios into absolute concentrations, we employed solutions containing known fractions of intact and degraded peptide for calibration. By a combination of results obtained for the effects of bafilomycin A1, chloroquine, leupeptin, and E-64d, the amount of peptide in an intact form can be estimated to be around 40% of the total peptide entering the cell (Figure 7).

DISCUSSION

The results presented in this paper provide a quantitative account of the intracellular fate of the cell-penetrating peptide penetratin by a combination of fluorescence microscopy, fluorescence emission spectroscopy, and flow cytometry. The investigation of intracellular proteolysis of proteins and peptides is of high general interest for the cellular import of bioactive molecules. The endolysosomal pathway is the major route of entry and processing of antigens to be presented by antigen-presenting cells. Analysis of the processing of peptides and proteins in the endolysosomal compartment is therefore of major significance, both for understanding the basis of antigen-presentation and for the development of new biologicals as drugs such as immunotherapeutics (*49*).

For CPP, analysis of the intracellular proteolytic fate is of great relevance for understanding the molecular mechanisms by which these peptides mediate uptake and to which extent the uptake mechanism may compromise the activity of these peptides. In the original contribution on penetratin, it was found that this peptide is mainly found in its intact form inside the cell (*19*), but the assay was based on a detection of biotinylated peptides using Western Blot analysis and did not address distribution in different cellular compartments. We cannot exclude that conjugation with two fluorophores affected the trafficking pathway (*50*). However, for their application as mediators of cellular uptake, an analysis of CPP-conjugates may be more relevant than analysis of a CPP alone.

A major advantage of the doubly labeled peptide is that the same molecule can be applied to different fluorescence-based techniques. Therefore, the results can then be cross-validated. We demonstrate that the measurements in the cell lysates strongly correlate with live cell techniques, i.e., flow cytometry and live cell fluorescence microscopy. The strong positive correlation of the flow cytometry measurements with the measurements in cell lysates indicates that, at least for relative comparisons of different conditions, concentration quenching and acidification is less of a concern than initially assumed.

Our results confirm the rather small impact of cytoplasmatic peptide degradation in comparison to endosomal peptidases on the fate of the Tamra-Penetratin-Fluo construct. The amount of intact peptide (Figure 7A) was calculated on the basis of fluorescence ratios (data not shown) and a calibration curve (Figure 7B). Nevertheless, the impact of furin inhibitor that increased the amount of intact peptide by 20% and the 5%

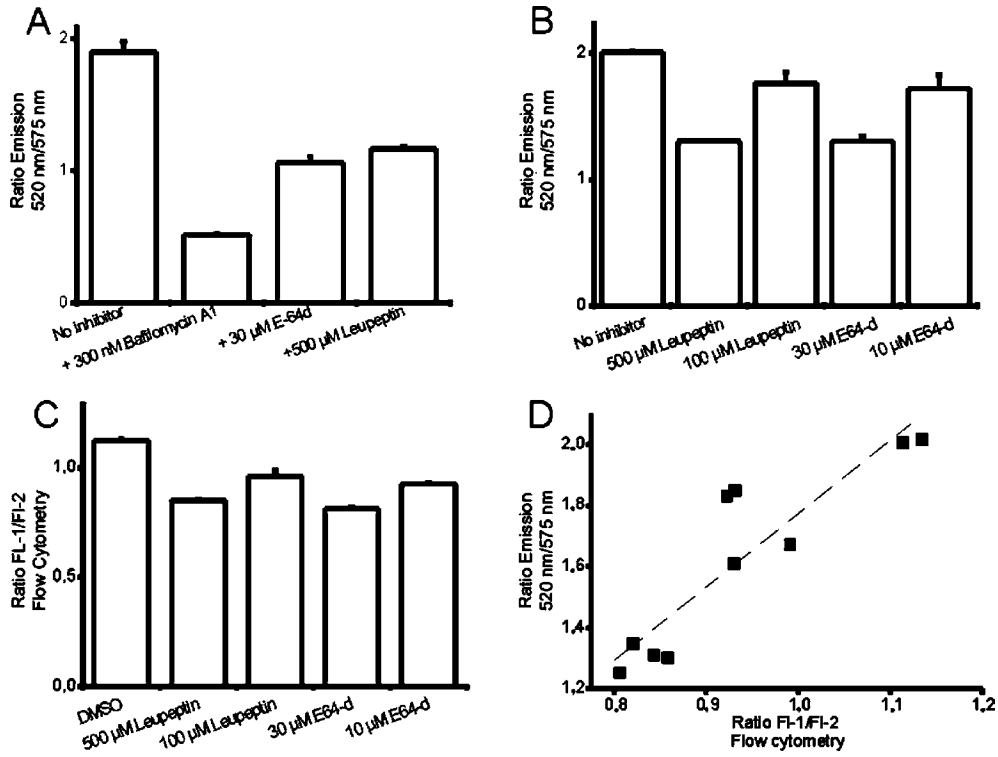


Figure 5. Involvement of cysteine proteases in the cellular degradation of Tamra-Penetratin-Fluo. (A) MC57 cells were incubated with Tamra-Penetratin-Fluo (4 μM) for 2 h in serum-free medium in the absence or presence of different inhibitors, as indicated. The inhibitors were added 30 min prior to the peptide. Cells were then washed, removed from the tissue culture plate using EDTA/PBS. Cells were then washed once more and lysed in NP-40-lysis buffer containing protease inhibitors. After sonication and centrifugation, fluorescence emission spectra were recorded immediately with excitation at 492 nm, and fluorescence ratios were calculated from the data. (B) The same experiment as in (A) was performed applying different concentrations of cysteine proteases inhibitors. Shown are fluorescence ratios in cell lysates; each condition was tested in duplicate; error bars represent the absolute deviations from the mean value. (C) A small fraction of the cells from experiment 5B were subjected to analysis by flow cytometry before lysis and ratios of FL-1 channel vs FL-2 channel were calculated. Each condition was tested in duplicate; error bars represent the absolute deviations from the mean. (D) For each condition, the different ratios obtained in B (measurements in cell lysates) and C (flow cytometric data) were plotted. Here, the individual data points instead of the means of the duplicates are shown.

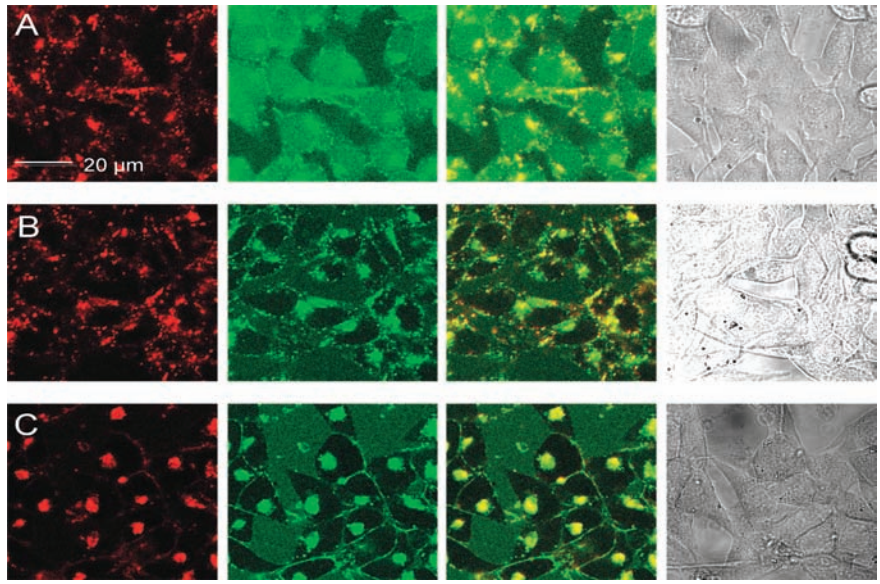


Figure 6. Impact of bafilomycin A1 and a cysteine protease inhibitor on the subcellular distribution of Tamra-Penetratin-Fluo. MC57 cells were incubated with Tamra-Penetratin-Fluo (4 μM) for 2 h in serum-free medium in the absence or presence of different inhibitors (panels A, no inhibitor; panels B, 30 μM E-64d; panels C, 300 nM bafilomycin A1). The inhibitors were added 30 min prior to the peptide. Left panels show the Tamra fluorescence, followed by the fluorescein channel, and the superposition of both fluorescence channels. Right panels show the transmission images.

increase yielded by lactacystin indicate that at least 20−25% of the penetratin analogue leave the endosomal compartment and reach the cytosol and/or the Golgi network where furin is mainly located. The impact of an inhibitor of the furin protease supports an involvement of retrograde transport in the intracellular fate of cationic CPPs such as penetratin (*23*). For the 40% of intact peptide found in the absence of any inhibitor, the origin cannot be resolved. It will be interesting to further investigate

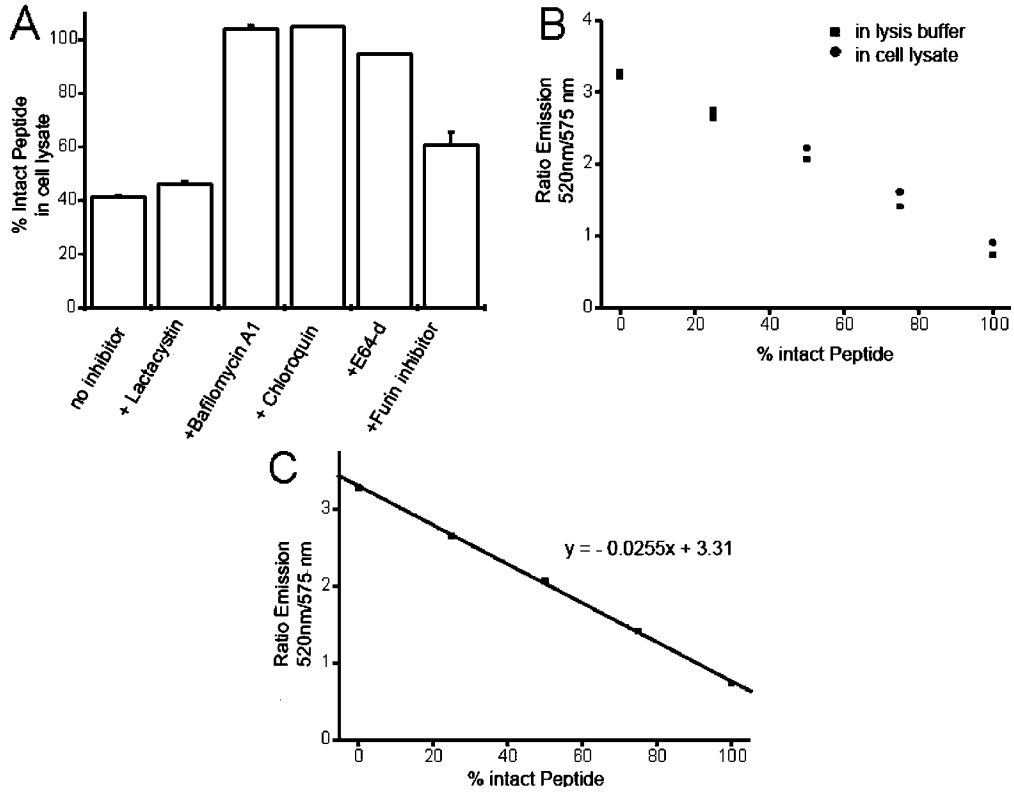


Figure 7. Absolute quantification of intracellular breakdown. For quantification, all experiments were performed in 12-well plates (previous ones were performed in 6-well plates). Ratiometric values obtained in an inhibitor experiment (data not shown) were transformed into percentage of intact peptides (A) using the parameters shown in the equation in (C). (B) A solution containing 100 nM of Tamra-Antp-Fluo was digested with proteinase K in lysis buffer. After blocking protease activity by addition of PMSF, different amounts of this solution and a 100 nM Tamra-Penetratin-Fluo solution were mixed to yield the indicated fractions of digested peptide and fluorescence emission spectra were recorded upon excitation at 492 nm. These solutions were also used to lyse cells in 12-well plates, and emission spectra were recorded and ratios calculated again to show the value of measurements in cell lysates. (C) Linear regression for the ratiometric values obtained for the internal standard solutions in lysis buffer.

whether this material was located in endosomes, still associated with the plasma membrane, or released into the cytoplasm and nucleus.

The results obtained for the doubly labeled penetratin analogue also demonstrate that one needs to be cautious about interpreting results obtained for peptides carrying only one label. Unless, inside the cytoplasm selective dequenching of fluorescein but not rhodamine occurred, the distribution of fluorescein did not reproduce the localization of the intact peptide. Instead, elimination of cytoplasmic fluorescein fluorescence upon incubation with leupeptin and E-64d indicates that this fluorescence rather originated from fluorescein-labeled peptide fragments released into the cytoplasm.

The similarity of effects observed for bafilomycin A1 and the inhibitors of endosomal proteases warrants further investigation into the role of endosomal acidification in endosomal peptide release. In the absence of inhibitors, cytoplasmic fluorescence may originate from fluorescein-labeled fragments released into the cytoplasm and from intact peptide that was released in an acidification-dependent manner. However, in this case, more cytoplasmic rhodamine signal had been expected. Bafilomycin A1 should inhibit both release and degradation, while E-64d and leupeptin should only interfere with degradation. Nevertheless, the role of endosomal acidification has been validated for proteolytically stable (*51*) cell-penetrating β-peptides (*24*) and in a functional assay for the cell-penetrating HIV-Tat protein (*52, 53*).

The calibration of ratiometric measurements by flow cytometry with measurements in cell lysates is a specific strength of the approach described here for defining the intracellular fate of CPPs. It will therefore be highly interesting to extend this approach to further CPPs and their analogues. By using the same pair of fluorophores, differences in proteolytic profiles will allow valuable conclusions about differences in trafficking routes.

ACKNOWLEDGMENT

We gratefully acknowledge the technical assistance of Nicole Sessler in peptide synthesis and thank Günther Jung for providing excellent facilities in peptide chemistry and instrumental analytics. This work was supported by the Volkswagen Foundation ("Nachwuchsgruppen an Universitäten", I/77 472). H.H. was supported by Stiftung der Deutschen Wirtschaft (Foundation of German Business) as an undergraduate scholar.

LITERATURE CITED

(1) Lipinski, C. A., Lombardo, F., Dominy, B. W., and Feeney, P. J. (2001) Experimental and computational approaches to estimate solubility and permeability in drug discovery and development settings. *Adv. Drug Delivery Rev. 46*, 3–26.

(2) Foerg, C., and Merkle, H. P. (2008) On the biomedical promise of cell penetrating peptides: Limits versus prospects. *J. Pharm. Sci. 97*, 144–162.

(3) Stephens, D. J., and Pepperkok, R. (2001) The many ways to cross the plasma membrane. *Proc. Natl. Acad. Sci. U.S.A. 98*, 4295–4298.

(4) Kersemans, V., Kersemans, K., and Cornelissen, B. (2008) Cell penetrating peptides for in vivo molecular imaging applications. *Curr. Pharm. Des. 14*, 2415–2427.

(5) Chiu, Y.-L., Ali, A., Chu, C.-y., Cao, H., and Rana, T. M. (2004) Visualizing a correlation between siRNA localization, cellular uptake, and RNAi in living cells. *Chem. Biol. 11*, 1165–1175.

(6) Prochiantz, A. (1996) Getting hydrophilic compounds into cells: lessons from homeopeptides. *Curr. Opin. Neurobiol. 6*, 629–634.

(7) Fischer, R., Fotin-Mleczek, M., Hufnagel, H., and Brock, R. (2005) Break on through to the other side-biophysics and cell biology shed light on cell-penetrating peptides. *ChemBioChem 6*, 2126–2142.

(8) Fischer, P. M., Krausz, E., and Lane, D. P. (2001) Cellular Delivery of Impermeable Effector Molecules in the Form of Conjugates with Peptides Capable of Mediating Membrane Translocation. *Bioconjugate Chem. 12*, 825–841.

(9) Langel, U. (2002) *Cell Penetrating Peptides: Processes and Applications*, CRC Pres, Boca Raton, FL.

(10) Schutze-Redelmeier, M.-P., Gournier, H., Garcia-Pons, F., Moussa, M., Joliot, A. H., Volovitch, M., Prochiantz, A., and Lemonnier, F. A. (1996) Introduction of exogenous antigens into the MHC class I processing and presentation pathway by Drosophila antennapedia homeodomain primes cytotoxic T cells in vivo. *J. Immunol. 157*, 651–655.

(11) Schwarze, S. R., Ho, A., Vocero-Akbani, A., and Dowdy, S. F. (1999) In vivo protein transduction: Delivery of a biologically active protein into the mouse. *Science 285*, 1569–1572.

(12) Hawiger, J. (1999) Noninvasive intracellular delivery of functional peptides and proteins. *Curr. Opin. Chem. Biol. 3*, 89–94.

(13) Rojas, M., Donahue, J. P., Tan, Z., and Lin, Y.-Z. (1998) Genetic engineering of proteins with cell membrane permeability. *Nat. Biotechnol. 16*, 370–375.

(14) Astriab-Fisher, A., Sergueev, D., Fisher, M., Shaw, B. R., and Juliano, R. L. (2002) Conjugates of antisense oligonucleotides with the Tat and Antennapedia cell-penetrating peptides: effects on cellular uptake, binding to target sequences, and biologic actions. *Pharm. Res. 19*, 744–754.

(15) Singh, D., Bisland, S. K., Kawamura, K., and Gariepy, J. (1999) Peptide-based intracellular shuttle able to facilitate gene transfer in mammalian cells. *Bioconjugate Chem. 10*, 745–754.

(16) Muratovska, A., and Eccles, M. R. (2004) Conjugate for efficient delivery of short interfering RNA (siRNA) into mammalian cells. *FEBS Lett. 558*, 63–68.

(17) Pooga, M., Soomets, U., Hallbrink, M., Valkna, A., Saar, K., Rezaei, K., Kahl, U., Hao, J.-X., Xu, X.-J., Wisenfeld-Hallin, Z., Hokfelt, T., Bartfai, T., and Langel, U. (1998) Cell penetrating PNA constructs regulate galanin receptor levels and modify pain transmission in vivo. *Nat. Biotechnol. 16*, 857–861.

(18) Lewin, M., Carlesso, N., Tung, C.-H., Tang, X.-W., Cory, D., Scadden, D. T., and Weissleder, R. (2000) Tat peptide-derivatized magnetic nanoparticles allow in vivo tracking and recovery of progenitor cells. *Nat. Biotechnol. 18*, 410–414.

(19) Derossi, D., Joliot, A. H., Chassaing, G., and Prochiantz, A. (1994) The third helix of the Antennapedia homeodomain translocates through biological membranes. *J. Biol. Chem. 269*, 10444–50.

(20) Thoren, P. E. G., Persson, D., Karlsson, M., and Norden, B. (2000) The Antennapedia peptide penetratin translocates across lipid bilayers - the first direct observation. *FEBS Lett. 482*, 265–268.

(21) Persson, D., Thoren, P. E. G., Herner, M., Lincoln, P., and Norden, B. (2003) Application of a novel analysis to measure the binding of the membrane-translocating peptide penetratin to negatively charged liposomes. *Biochemistry 42*, 421–429.

(22) Drin, G., Cottin, S., Blanc, E., Rees, A. R., and Temsamani, J. (2003) Studies on the internalization mechanism of cationic cell-penetrating peptides. *J. Biol. Chem. 278*, 31192–31201.

(23) Fischer, R., Koehler, K., Fotin-MLeczek, M., and Brock, R. (2004) A stepwise dissection of the intracellular fate of cationic cell-penetrating peptides. *J. Biol. Chem. 279*, 12625–12635.

(24) Potocky, T. B., Menon, A. K., and Gellman, S. H. (2003) Cytoplasmic and nuclear delivery of a TAT-derived peptide and a b-peptide after endocytic uptake into HeLa cells. *J. Biol. Chem. 278*, 50188–50194.

(25) Richard, J. P., Melikov, K., Vives, E., Ramos, C., Verbeure, B., Gait Mike, J., Chernomordik, L. V., and Lebleu, B. (2003) Cell-penetrating peptides. A reevaluation of the mechanism of cellular uptake. *J. Biol. Chem. 278*, 585–90.

(26) Waizenegger, T., Fischer, R., and Brock, R. (2002) Intracellular concentration measurements in adherent cells: a comparison of import efficiencies of cell-permeable peptides. *Biol. Chem. 383*, 291–299.

(27) Geoghegan, K. F., Rosner, P. J., and Hoth, L. R. (2000) Dye-pair reporter systems for protein-peptide molecular interactions. *Bioconjugate Chem. 11*, 71–77.

(28) Wei, A.-P., Blumenthal, D. K., and Herron, J. N. (1994) Antibody-mediated fluorescence enhancement based on shifting the intramolecular dimer.dblarw. monomer equilibrium of fluorescent dyes. *Anal. Chem. 66*, 1500–6.

(29) Fischer, R., Bachle, D., Fotin-Mleczek, M., Jung, G., Kalbacher, H., and Brock, R. (2006) A targeted protease substrate for a quantitative determination of protease activities in the endolysosomal pathway. *ChemBioChem 7*, 1428–1443.

(30) Cummings, R. T., Salowe, S. P., Cunningham, B. R., Wiltsie, J., Park, Y. W., Sonatore, L. M., Wisniewski, D., Douglas, C. M., Hermes, J. D., and Scolnick, E. M. (2002) A peptide-based fluorescence resonance energy transfer assay for Bacillus anthracis lethal factor protease. *Proc. Natl. Acad. Sci. U.S.A. 99*, 6603–6606.

(31) Clegg, R. M. (1995) Fluorescence resonance energy transfer. *Curr. Opin. Biotechnol. 6*, 103–10.

(32) Fischer, R., Mader, O., Jung, G., and Brock, R. (2003) Extending the applicability of carboxyfluorescein in solid-phase synthesis. *Bioconjugate Chem. 14*, 653–660.

(33) Beck, W., and Jung, G. (1994) Convenient reduction of S-oxides in synthetic peptides, lipopeptides and peptide libraries. *Lett. Pept. Sci. 1*, 31–7.

(34) Fischer, R., Waizenegger, T., Kohler, K., and Brock, R. (2002) A quantitative validation of fluorophore-labelled cell-permeable peptide conjugates: fluorophore and cargo dependence of import. *Biochim. Biophys. Acta, Biomembr. 1564*, 365–374.

(35) Chico, D. E., Given, R. L., and Miller, B. T. (2003) Binding of cationic cell-permeable peptides to plastic and glass. *Peptides 24*, 3–9.

(36) Miyawaki, A., Llopis, J., Heim, R., McCaffery, J. M., Adams, J. A., Ikura, M., and Tsien, R. Y. (1997) Fluorescent indicators for Ca^{2+} based on green fluorescent proteins and calmodulin. *Nature 388*, 882–7.

(37) Sjoeback, R., Nygren, J., and Kubista, M. (1995) Absorption and fluorescence properties of fluorescein. *Reservoir Evaluation and Engineering Spectrochimica Acta, Part A 51A*, L7–L21.

(38) Chen, R. F., and Knutson, J. R. (1988) Mechanism of fluorescence concentration quenching of carboxyfluorescein in liposomes: energy transfer to nonfluorescent dimers. *Anal. Biochem. 172*, 61–77.

(39) Bowman, E. J., Siebers, A., and Altendorf, K. (1988) Bafilomycins: a class of inhibitors of membrane ATPases from microorganisms, animal cells, and plant cells. *Proc. Natl. Acad. Sci. U.S.A. 85*, 7972–6.

(40) Kozak, S. L., Kuhmann, S. E., Platt, E. J., and Kabat, D. (1999) Roles of CD4 and coreceptors in binding, endocytosis, and proteolysis of gp120 envelope glycoproteins derived from human immunodeficiency virus type 1. *J. Biol. Chem. 274*, 23499–23507.

(41) Mellman, I., Fuchs, R., and Helenius, A. (1986) Acidification of the endocytic and exocytic pathways. *Annu. Rev. Biochem. 55*, 663–700.

(42) Turk, B., Turk, D., and Turk, V. (2000) Lysosomal cysteine proteases: more than scavengers. *Biochim. Biophys. Acta, Protein Struct. Mol. Enzym. 1477*, 98–111.

(43) Dash, C., Kulkarni, A., Dunn, B., and Rao, M. (2003) Aspartic peptidase inhibitors: Implications in drug development. *Crit. Rev. Biochem. Mol. 38*, 89–119.

(44) Dick, L. R., Cruikshank, A. A., Grenier, L., Melandri, F. D., Nunes, S. L., and Stein, R. L. (1996) Mechanistic studies on the inactivation of the proteasome by lactacystin. A central role for clasto-lactacystin b-lactone. *J. Biol. Chem. 271*, 7273–6.

(45) Nakayama, K. (1997) Furin: a mammalian subtilisin/Kex2p-like endoprotease involved in processing of a wide variety of precursor proteins. *Biochem. J. 327*, 625–635.

(46) Tikhonov, I., Ruckwardt, T. J., Berg, S., Hatfield, G. S., and Pauza, C. D. (2004) Furin cleavage of the HIV-1 Tat protein. *FEBS Lett. 565*, 89–92.

(47) Vidard, L., Rock, K. L., and Benacerraf, B. (1991) The generation of immunogenic peptides can be selectively increased or decreased by proteolytic enzyme inhibitors. *J. Immunol. 147*, 1786–91.

(48) Tamai, M., Matsumoto, K., Omura, S., Koyama, I., Ozawa, Y., and Hanada, K. (1986) In vitro and in vivo inhibition of cysteine proteinases by EST, a new analog of E-64. *J. Pharmacobio-Dyn. 9*, 672–7.

(49) Honey, K., and Rudensky, A. Y. (2003) Lysosomal cysteine proteases regulate antigen presentation. *Nat. Rev. Immunol. 3*, 472–482.

(50) Dupont, E., Prochiantz, A., and Joliot, A. (2007) Identification of a signal peptide for unconventional secretion. *J. Biol. Chem. 282*, 8994–9000.

(51) Frackenpohl, J., Arvidsson, P. I., Schreiber, J. V., and Seebach, D. (2001) The outstanding biological stability of b- and g-peptides toward proteolytic enzymes: an in vitro investigation with fifteen peptidases. *ChemBioChem 2*, 445–455.

(52) Rayne, F., Vendeville, A., Bonhoure, A., and Beaumelle, B. (2004) The ability of chloroquine to prevent Tat-induced cytokine secretion by monocytes is implicated in its in vivo anti-human immunodeficiency virus type 1 activity. *J. Virol. 78*, 12054–12057.

(53) Vendeville, A., Rayne, F., Bonhoure, A., Bettache, N., Montcourrier, P., and Beaumelle, B. (2004) HIV-1 tat enters T cells using coated pits before translocating from acidified endosomes and eliciting biological responses. *Mol. Biol. Cell 15*, 2347–2360.

BC900301K

Synthesis and In Vitro Testing of New Potent Polyacridine−Melittin Gene Delivery Peptides

Nicholas J. Baumhover, Kevin Anderson, Christian A. Fernandez, and Kevin G. Rice*

Divisions of Medicinal and Natural Products Chemistry and Pharmaceutics, College of Pharmacy, University of Iowa, Iowa City, Iowa 52242. Received July 14, 2009; Revised Manuscript Received October 28, 2009

The combination of a polyacridine peptide modified with a melittin fusogenic peptide results in a potent gene transfer agent. Polyacridine peptides of the general formula $(Acr\text{-}X)_n$-Cys were prepared by solid-phase peptide synthesis, where Acr is Lys modified on its ε-amine with acridine, X is Arg, Leu, or Lys and n is 2, 3, or 4 repeats. The Cys residue was modified by either a maleimide−melittin or a thiolpyridine-Cys-melittin fusogenic peptide resulting in reducible or non-reducible polyacridine−melittin peptides. Hemolysis assays established that polyacridine−melittin peptides retained their membrane lytic potency relative to melittin at pH 7.4 and 5. When combined with plasmid DNA, the membrane lytic potency of polyacridine−melittin peptides was neutralized. Gene transfer experiments in multiple cell lines established that polyacridine−melittin peptides mediate expression as efficiently as PEI. The expression was very dependent upon a disulfide bond linking polyacridine to melittin. The gene transfer was most efficient when X is Arg and n is 3 or 4 repeats. These studies establish polyacridine peptides as a novel DNA binding anchor peptide.

INTRODUCTION

An important element of many polyplex nonviral gene delivery systems is a releasable fusogenic peptide that can effect endosomal lysis (*1*). The endosomal escape of DNA is especially essential for receptor-targeted gene delivery systems to avoid polyplex degradation by the lysosome (*2*−*4*).

To improve the endosomal escape of DNA, several prior studies have incorporated fusogenic peptides, including GALA, KALA, HA2, JTS-1, and melittin, into a nonviral gene delivery system (*5*−*11*). Most applications in gene delivery have utilized melittin because of its relative ease of chemical synthesis and because its mechanism of membrane lysis has been extensively studied (*12*−*14*). Melittin has been covalently attached to polylysine, PEI, and cationic lipids and even self-polymerized by terminal disulfide bonds and demonstrated to increase in vitro gene transfer efficiency (*4, 10, 11, 15, 16*).

While DNA anchoring polymers such as PEI, polylysine, dendrimers, and chitosan are known to bind ionically to the phosphate backbone of plasmid DNA, this strategy leads to the formation of cationic polyplexes that favor in vitro gene transfer, but to a much lesser degree in vivo gene transfer (*17*). This is partly because positively charged polyplexes bind non-specifically to proteins and cells (*18*). Attempts at masking the charge with PEG still results in a residual positive charge as measured by zeta potential (*19, 20*). The non-specific binding of PEGylated cation polyplexes in vivo complicates strategies that attempt to combine a receptor ligand and releasable fusogenic peptide into a non-viral delivery system (*21, 22*). Consequently, it would be beneficial to reversibly bind fusogenic peptides, receptor ligand, and PEG to DNA while simultaneously controlling the charge of polyplexes. Likewise, it would be advantageous if the DNA binding anchor were sufficiently small in size to allow for its chemical manipulation and specific functionalization with PEG, targeting ligand, and fusogenic peptide (*22*).

Polyacridine peptides have been shown to reversibly bind with high affinity by intercalating into double-stranded DNA (*23*). An early study by Szoka demonstrated the synthesis of a divalent acridine neoglycopeptide for delivery of DNA to the cells expressing the asialoglycoprotein receptor (*24*). More recently, polyacridine-nuclear localization sequences (NLS) possessing up to three acridines were shown to improve in vitro gene transfer (*25, 26*).

However, to date, a polyacridine DNA binding peptide has not been substituted with a fusogenic peptide. The new strategy described herein demonstrates the synthesis of polyacridine−melittin as a DNA binding peptide and establishes its efficacy as a potent in vitro gene transfer agent. The results demonstrate that short polyacridine anchor peptides bind to plasmid DNA with sufficient affinity to deliver melittin in vitro and have the potential to control DNA polyplex charge to allow improved in vivo gene delivery.

MATERIALS AND METHODS

Unsubstituted Wang resin for peptide synthesis, 9-hydroxybenzotriazole, Fmoc-protected amino acids, *O*-(benzotriazole)-*N*,*N*,*N*′,*N*′-tetramethyluronium hexafluorophosphate (HBTU), 1,3-diisopropylcarbodiimide (DIC), Fmoc-Lysine-OH, and *N*-methyl-2-pyrrolidinone (NMP) were obtained from Advanced ChemTech (Lexington, KY). *N*,*N*-Dimethylformamide (DMF), trifluoroacetic acid (TFA), and acetonitrile were purchased from Fisher Scientific (Pittsburgh, PA). Diisopropylethylamine, piperdine, acetic anhydride, tris(2-carboxyethyl)-phosphine hydrochloride (TCEP), 9-chloroacridine, maleic anhydride, 2,2′-dithiodipyridine (DTDP), and thiazole orange were obtained from Sigma Chemical Co. (St. Louis, MO). Polyethylene amine (PEI 25 KDa) was purchased from Aldrich (Milwaukee, WI). D-Luciferin and luciferase from *Photinus pyralis* were obtained from Roche Applied Science (Indianapolis, IN). HepG2, CHO, and 3T3 cells were acquired from the American Type Culture Collection (Manassas, VA). Inactivated qualified fetal bovine serum (FBS) was from Life Technologies, Inc. (Carlsbad, CA). BCA reagent was purchased from Pierce (Rockford, IL). pGL3 control vector, a 5.3 kb luciferase plasmid containing a SV40 promoter and enhancer, was obtained from Promega (Madison,

* To whom correspondence should be addressed. E-mail kevin-rice@uiowa.edu. tel: 319-335-9903; fax: 319-335-8766.

10.1021/bc9003124 © 2010 American Chemical Society
Published on Web 12/07/2009

WI). pGL3 was amplified in a DH5α strain of *Escherichia coli* and purified according to manufacturer's instructions.

Synthesis of 9-Phenoxyacridine and Fmoc Lysine (Acridine). 9-Phenoxyacridine was synthesized with modification from the methods of Tung et al. (*27*). Briefly, 12 g of phenol (127.5 mmol) and 0.72 g of sodium hydroxide (18 mmol) were heated to 100 °C. To the liquefied phenol, 2.8 g of 9-chloroacridine (13.105 mmol) was added and stirred vigorously for 1.5 h. The reaction was quenched by the addition of 100 mL of 2 M sodium hydroxide, then allowed to sit at RT overnight. A yellow precipitate was filtered, washed with water, and dried in vacuo (3.4822 g, 12.835 mmol, 97.9%, m.p. 123−124 °C, TLC 15:5:1:0.5 ethyl acetate/methanol/hexane/acetic acid, $R_f = 0.18$). ^{1}H NMR (DMSO-d_6) δ 8.23 (d, 2H), 8.04 (d, 2H), 7.88 (t, 2H), 7.59 (t, 2H), 7.32 (t, 2H), 7.08 (t, 1H), 6.88 (d 2H).

Fmoc-Lysine(Acridine)-OH was prepared by adding 2.18 g of Fmoc-Lys-OH (5.91 mmol) in liquid phenol (6.781 g, 73.01 mmol) to 9-phenoxyacridine (3 g, 11.06 mmol), then heated at 60 °C for 4 h under an argon atmosphere. Diethyl ether (80 mL) was then added while stirring vigorously until a yellow precipitate formed that was immediately recovered by filtration and washed repeatedly with diethyl ether. The product was allowed to dry overnight under vacuum (2.90 g, 5.32 mmol, 90%), m.p. 135−140 °C, TLC 1:1, 0.1 v/v % TFA/acetonitrile, $R_f = 0.75$). MS: $(M + H^+)^{1+} = 545.5$ *m/z*. ^{1}H NMR (DMSO-d_6) δ 6.7−7.8 (m, 17H), 3.6−3.95 (m, 2H), 3.25−3.53 (br, 3H), 2,06 (m, 1H), 0.8−1.5 (m, 6H).

Synthesis of Maleimide Glycine (Mal-Gly-OH). Glycine (5 g, 66.6 mmol) and maleic anhydride (6.6 g, 66.6 mmol) were suspended in 80 mL of acetic acid and allowed to react for 3 h at RT. The resulting white precipitate was collected by filtration, washed with cold water, and dried (10.95 g, 63.3 mmol, 95%, m.p. 187−189 °C, TLC 2:1:1:1 isopropyl alcohol/acetic acid/ethyl acetate/water, $R_f = 0.5$). The glycine maleic acid intermediate was characterized by proton NMR (300 MHz, DMSO-d_6): $\delta = 9.2$ (s, 1H), 6.397 (d, 1H, $j = 8.57$ Hz), 6.310 (d, 2H, $j = 12.86$ Hz), 2.0 (d, 2H, $j = 6.86$ Hz).

Glycine maleamic acid (5.2 g, 30.04 mmol) and 2.1 equiv of triethylamine (6.37 g, 63 mmol) were refluxed for 3 h in 500 mL toluene with removal of water with a Dean−Stark apparatus. Upon reaction completion, the toluene solution was decanted and dried. The resulting solid was acidified with 2 M HCl, extracted with ethyl acetate, dried with $MgSO_4$, and evaporated to yield Mal-Gly-OH (1.7 g, 11 mmol, 36.5%, m.p. 99−110 °C, TLC 2:1:1:1 isopropyl alcohol/acetic acid/ethyl acetate/water, $R_f = 0.72$). The product was characterized by proton NMR (300 MHz, DMSO-d_6): $\delta = 7.108$ (s, 2H), 4.105 (s, 2H) (*28*).

Synthesis and Characterization of Polyacridine−Melittin Analogues. Melittin analogues, polyacridine peptides, and control peptides were prepared by solid-phase peptide synthesis using standard Fmoc procedures with 9-hydroxybenzotriazole and HBTU double couplings on a 30 μmol scale on an Advanced ChemTech APEX 396 synthesizer. Mal-melittin was prepared by coupling Mal-Gly-OH to the N-terminus of sidechain protected full-length melittin on resin utilizing a 6-fold excess of Mal-Gly-OH, DIC, and HOBt, reacted for 4 h while stirring. The resin was filtered; washed with DMF, DCM, and methanol; then dried. Peptides were removed from resin and sidechain deprotected using a cleavage cocktail of TFA/triisoproylsilane/water (95:2.5:2.5 v/v/v) for 3 h followed by precipitation in cold ether. Precipitates were centrifuged for 10 min at 4000 rpm at 4 °C and the supernatant decanted. Peptides were then reconstituted with 0.1 v/v % TFA and purified to homogeneity on RP-HPLC by injecting 0.5−2 μmol onto a Vydac C18 semipreparative column (2 × 25 cm) eluted at 10 mL/min with 0.1 v/v % TFA with an acetonitrile gradient of 20−45 v/v % over 30 min while monitoring tryptophan (Abs 280 nm) or acridine (Abs 409 nm). The major peak was collected and pooled from multiple runs, concentrated by rotary evaporation, lyophilized, and stored at −20 °C. Purified peptides were reconstituted in 0.1% v/v TFA and quantified by absorbance (tryptophan $\varepsilon_{280nm} = 5600$ M^{-1} cm^{-1}, thiolpyridine, and tryptophan $\varepsilon_{280nm} = 10\,915$ M^{-1} cm^{-1}, or acridine $\varepsilon_{409nm} = 9266$ M^{-1} cm^{-1}) to determine isolated yield. Purified peptides were characterized by LC-MS by injecting 2 nmol onto a Vydac C18 analytical column (0.47 × 25 cm) eluted at 0.7 mL/min with 0.1 v/v % TFA and an acetonitrile gradient of 10−55 v/v% over 30 min while acquiring ESI-MS in the positive ion mode.

Cys-melittin was reacted with 10 equiv of DTDP in 2-propanol/2 N acetic acid (10:3) for 8 h at RT to generate the thiolpyridine protected peptide. The reaction mixture was concentrated by rotary evaporation and applied to a Sephadex G-10 column eluted (2.5 × 50 cm) with 0.1 v/v % TFA while monitoring absorbance at 280 nm to remove excess DTDP. The peptide peak fractions were pooled, concentrated, lyophilized, and purified to homogeneity by RP-HPLC as described previously.

Poly(Acr-X)$_n$-SS-melittin and poly(Acr-X)$_n$-Mal-melittin peptides were synthesized on a 2 μmol scale based on melittin, using 1.7 equiv (3.4 μmol) of the reduced poly(Acr-X)$_n$-Cys, where X equals Arg, Lys, or Leu. Mal-melittin (2 μmol) was prepared in 8 mL of 10 mM ammonium acetate pH 5 and added to poly(Acr-X)$_n$-Cys and 2 mL of methanol to facilitate solubility. The reaction occurred over 12 h at RT as determined by analyzing aliquots by LC-MS. At completion, the reaction mixture was concentrated by rotary evaporation and lyophilized prior to purification of poly(Acr-X)$_n$-Mal-melittin by RP-HPLC eluted with 0.1 v/v % TFA and acetonitrile gradient (35−45% over 30 min) while detecting at 409 nm.

Alternatively, thiolpyridine-Cys-melittin (2 μmol) was prepared in 8 mL of 10 mM ammonium acetate pH 6 and added to 3.4 μmol poly(Acr-X)$_n$-Cys in 2 mL of methanol. After 24 h, poly(Acr-X)$_n$-SS-melittin was purified and characterized by LC-MS as described above.

Polyacridine−Melittin Hemolysis Assay. Whole blood was obtained from male ICR mice by heart puncture with heparinized 22G needles and collected in conical tubes containing 10 mL of 0.15 M PBS (pH 7.4) prewarmed to 37 °C. Erythrocytes were immediately separated from plasma by centrifugation at 2000 rpm for 2 min, washed three times with 10 mL of PBS, and then diluted to 1.5 × 10^8 cells/mL. Peptides were prepared at 15 μM and serially diluted to 10−0.01 μM, after which 100 μL was pipetted in triplicate into a MultiScreenHTS BV 96-well plate. Erythrocytes (50 μL, 7.5 × 10^6 cells) were added to the peptides and incubated at 37 °C for 1 h followed by filtration on a Multiscreen vacuum manifold (Millipore Corporation, Billerica, MA). The filtrate was measured for abs$_{410nm}$ on a Biotech plate reader (Biotech Instruments Incorporated., Winooski, VT) and compared to the 100% hemolysis caused by replacing PBS with water. Peptide DNA polyplexes (1.5 nmols and 7.5 μg pGL3) were also assayed for hemolysis as described above.

Formulation and Characterization of Polyacridine−Melittin Polyplexes. The relative binding affinity of peptides for DNA was determined by a fluorophore exclusion assay (*29*). pGL3 (200 μL of 4 μg/mL in 5 mM Hepes pH 7.5 containing 0.1 μM thiazole orange) was combined with 0, 0.05, 0.1, 0.25, 0.35, 0.5, 1, and 2 nmols of peptide in 300 μL of Hepes and allowed to bind at RT for 30 min. Thiazole orange fluorescence was measured using an LS50B fluorometer (Perkin-Elmer, U.K.) by exciting at 498 nm while monitoring emission at 546 nm with the slit widths set at 10 nm. A fluorescence blank of thiazole

orange in the absence of DNA was subtracted from all values before data analysis. The data are presented as nmol of peptide per μg of DNA versus the percent fluorescence intensity plus/minus the standard deviation determined by three independent measurements.

Particle size and zeta potential were determined by preparing 2 mL of polyplex in 5 mM Hepes pH 7.5 at a DNA concentration of 30 μg/mL with 15 nmols/mL of peptide (0.5 nmol of peptide per μg of DNA). Particle size was measured by quasi-elastic light scattering (QELS) at a scatter angle of 90° on a Brookhaven ZetaPlus particle sizer (Brookhaven Instruments Corporation, NY). The zeta potential was determined as the mean of ten measurements immediately following acquisition of the particle size.

Polyacridine−melittin DNA polyplexes were prepared at 0.5 nmol of peptide per μg of DNA at a concentration of 100 μg per mL of DNA and directly deposited on a freshly cleaved mica surface and allowed to bind for 10 min prior to washing with deionized water (*30*). Alternatively, naked DNA (100 μg pGL3 per mL) was prepared in 10 mM Tris, 1 mM EDTA pH 8, then diluted to 1 μg per mL in 40 mM Hepes 5 mM nickel chloride pH 6.7, and deposited on a fresh cleaved mica surface for 10 min followed by washing with deionized water. An Asylum atomic force microscope (AFM) MFP3D (Santa Barbara, CA) was operated in the AC-mode in order to image either naked DNA or DNA polyplexes using a silicon cantilever (Ultrasharp NSC15/AIBS, Mikro Masch).

Polyacridine−Melittin Polyplex Toxicity. The in vitro toxicity of polyacridine−melittin polyplexes was evaluated by MTT assay (*31*). CHO, HepG2, and 3T3 cells were plated on 6 × 35 mm wells at 5 × 10^5 cells/well and grown to 40−70% confluency. The media was replaced with 2 mL of fresh MEM supplemented with 2% FBS and the cells treated with 10 μg of DNA polyplex (0.5 nmol peptide/μg DNA) in HBM (HBM; 5 mM Hepes, 0.27 M mannitol, pH 7.5). After 6 h, the media was replaced with fresh culture media and grown an additional 18 h. Alternatively, cells were treated with DNA polyplexes for 24 h. The media was replaced with 2 mL of fresh media and 500 μL of 0.5% (w/v) 3-(4,5-dimethylthiazole-2-yl)-2,5-diphenyl tetrazolium bromide (MTT) in PBS solution and allowed to incubate at 37 °C for 1 h to let formazan crystals form. The media containing MTT was removed, and the crystals dissolved by the addition of 2 mL of dimethyl sulfoxide (DMSO) and 250 μL Sorenson's Glycine Buffer, then measured by absorbance 595 nm on a microplate reader. The percent viability was determined relative to untreated cells.

In Vitro Gene Transfer of Polyacridine−Melittin DNA Polyplexes. HepG2 cells (5 × 10^5) were plated on 6 × 35 mm wells and grown to approximately 50% confluency. Transfections were performed in MEM supplemented with either 2% or 10% FBS, sodium pyruvate (1 mM), and penicillin and streptomycin (100 U and 100 μg/mL). Polyplexes were prepared at a DNA concentration of 30 μg/mL and a stoichiometry of 0.5 nmol peptide per μg of DNA in HBM (HBM; 5 mM Hepes, 0.27 M mannitol, pH 7.5). Polyplexes (10 μg of DNA in 0.3 mL of HBM) were added dropwise to wells in triplicate and incubated 24 h. After 24 h, the cells were washed twice with 2 mL of ice-cold phosphate-buffered saline (Ca^{2+}- and Mg^{2+}-free) and then treated with 0.5 mL of lysis buffer (25 mM Tris chloride, pH 7.8, 1 mM EDTA, 8 mM magnesium chloride, and 1% Triton X-100) for 10 min at 4 °C. Cell lysates were scraped, transferred to 1.5 mL microcentrifuge tubes, and centrifuged for 10 min at 13,000 *g* at 4 °C to pellet cell debris. Lysis buffer (300 μL) and sodium-ATP (4.3 μL of a 165 mM solution at pH 7, 4 °C) were combined in a test tube, mixed briefly, and immediately placed in the luminometer. Luciferase relative light units were measured by a Lumat LB 9501 (Berthold Systems, Germany) with 10 s integration after automatic injection of 100 μL of 0.5 mM D-luciferin. The relative light units were converted to fmol using a standard curve generated by adding a known amount of luciferase to 35 mm wells containing 50% confluent HepG2 cells. The resulting standard curve had an average slope of 2.6 × 10^4 RLU/fmol enzyme. Protein concentrations were measured by a BCA assay using bovine serum albumin as a standard (*32*). The amount of luciferase recovered in each sample was normalized to mg of protein and reported as the mean and standard deviation obtained from triplicate transfections. PEI pGL3 polyplexes were prepared by mixing 35 μg of DNA in 525 μL of HBM with 43.8 μg PEI in 525 μL of HBM while vortexing to create DNA complexes possessing a charge ratio (NH_4^+/PO_4^-) of 9:1. Cells were transfected with 10 μg PEI−DNA polyplexes as previously described. CHO and 3T3 (5 × 10^5) cells were plated on 6 × 35 mm wells and grown to ca. 50% confluency and then transfected as described above.

RESULTS

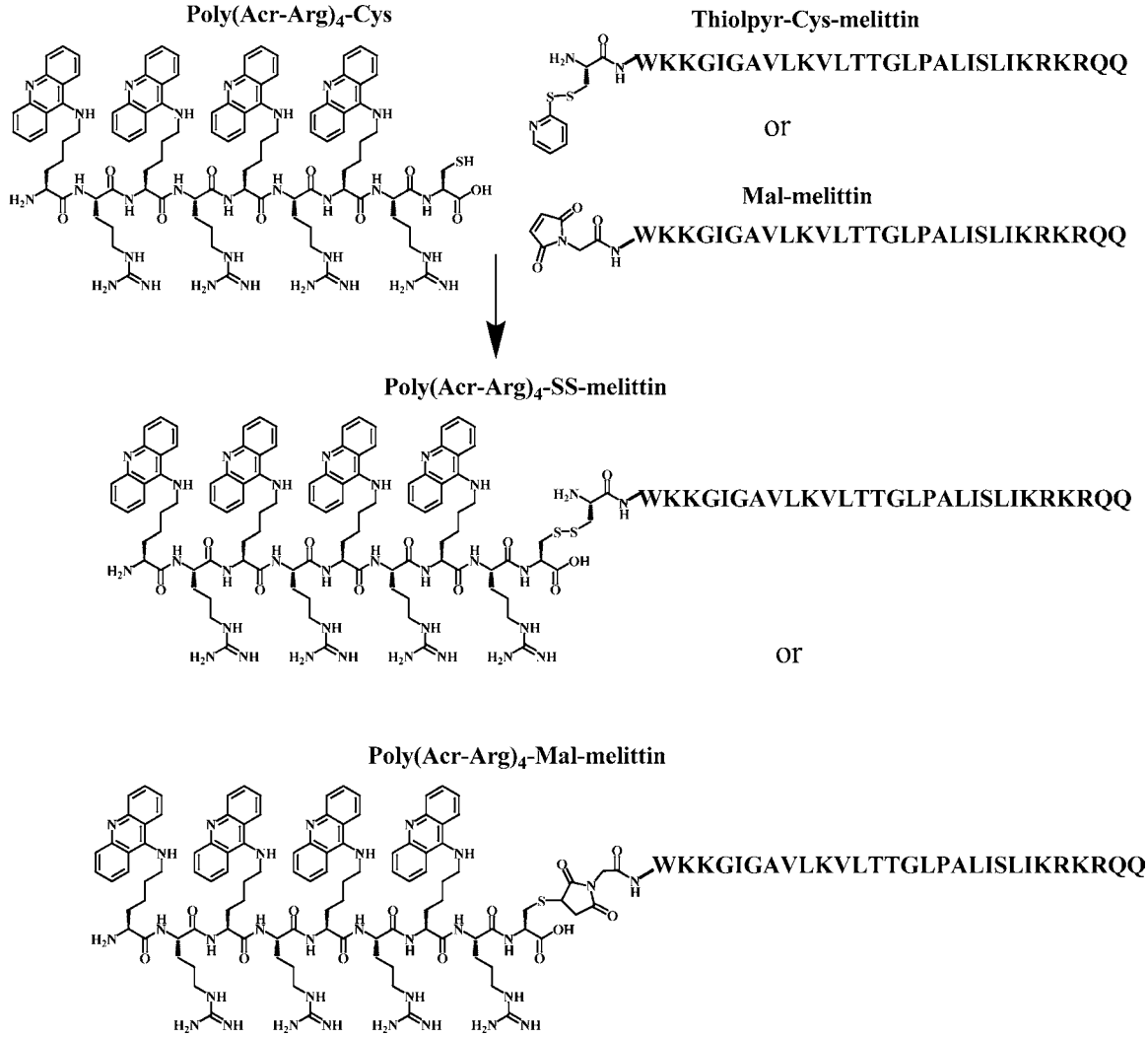
Synthetic Strategy for Polyacridine−Melittin. Naturally occurring melittin isolated from bee venom is a 26 amino acid peptide amide composed of two α-helices conjoined through an interrupting proline (*12*−*14*). Numerous studies have been conducted to investigate the mechanism and sequence specificity of melittin's membrane lytic activity.

Natural melittin contains a single aromatic Trp at residue 8 and does not contain a Cys residue. To improve the synthesis of polyacridine−melittin, we replaced Trp 8 with Leu, and reinstalled a single Trp near the N-terminus in Cys-Trp-Lys-Lys. The reactivity of the Cys residue was increased by flanking Lys residues. This also allowed selective chromatographic detection of full-length melittin at 280 nm. These modifications resulted in a Cys-melittin analogue, CWKKGIGAVLKVLTTGLPALISLIKRKRQQ, that SOPMA analysis (*33*) predicted to maintain α-helical character. A similar Mal-melittin analogue (Mal-GWKKGIGAVLKVLTTGLPALISLIKRKRQQ), possessing an N-terminal maleimide-glycine (Mal-G) in place of Cys, was also prepared.

Polyacridine and melittin peptides were synthesized using HBTU/HOBt with increased coupling efficiency compared to DIC. Early attempts to synthesize polyacridine peptides using DIC resulted in heterogeneous mixtures of truncated peptides with minimal recovery of full-length peptide. The identity of the spacing amino acid between Lys-acridine residue significantly influenced the synthetic yield. Bulky amino acid side chains and protecting groups such as Lys-Boc, Phe-Trt, Leu, Glu-OBut, and Arg-Pbf were well-tolerated, whereas Gly surprisingly was not. Polyacridine peptides possess a C-terminal Cys to accommodate bioconjugation to Cys-melittin or Mal-melittin. Polyacridine peptides possessing an alternating Lys-Acr (Acr) spaced by Arg, Lys, or Leu were designed to influence the charge character of the anchor peptide (Scheme 1 and Table 1). The lengths of polyacridine peptides were systematically varied to possess 2−4 Acr-Arg repeats to examine the influence of affinity. Polyacridine nona-peptides were routinely obtained in 30−35% purified yield with >95% purity.

Polyacridine−melittin peptides were designed to possess either a reducible dithiol or a nonreducible maleimide linkage (Scheme 1 and Table 1). The most expedient synthetic route proved to be cleavage of Cys-melittin from the resin, followed by modification with dithiol dipyridine to produce a thiolpyr-melittin. The RP-HPLC monitoring of the reaction of thiolpyr-melittin with poly(Acr-Arg)$_4$-Cys is illustrated in Figure 1A and B. The desired poly(Acr-Arg)$_4$-SS-melittin product is formed with complete consumption of thiolpyr-melittin, along with formation of a poly(Acr-Arg)$_4$-Cys$_2$ byproduct (Figure 1B). This

Scheme 1. Synthesis of Polyacridine−Melittin Peptides



Thiolpyr-melittin is reacted with the DNA binding anchor peptide poly(Acr-Arg)$_4$-Cys at pH 6 to yield poly(Acr-Arg)$_4$-SS-melittin as a reducible gene transfer polyacridine melittin peptide. Alternatively, Mal-melittin is reacted with poly(Acr-Arg)$_4$-Cys at pH 5 to yield a non-reducible poly(Acr-Arg)$_4$-Mal-melittin gene transfer peptide. In each case, Acr refers to a Lys substituted on its ε-amine with acridine. The Arg was substituted with Lys and Leu to produce DNA binding anchor peptides with different affinity. The poly(Acr-Arg)$_n$ was also varied from $n = 2-4$ repeats.

synthetic route resulted in poly(Acr-X)$_n$-SS-melittin in 35−50% purified yield at >95% purity as illustrated by LC-MS analysis of purified poly(Acr-Arg)$_4$-SS-melittin (Figure 1C). ESI-MS was used to establish structure based on the triple and quadruple charged positive ions corresponding to the calculated mass of the desired polyacridine−melittin peptide (Figure 1C, inset). The release of melittin from poly(Acr-Arg)$_4$-SS-melittin was established by reaction with TCEP to regenerate poly(Acr-Arg)$_4$-Cys and Cys-melittin peptide peaks (Figure 1D).

Poly(Acr-X)$_4$-Mal-melittin peptides, where X is Arg, Lys, or Leu, were synthesized to compare their gene transfer properties with poly(Acr-Arg)$_4$-SS-melittin (Scheme 1 and Table 1). The synthetic strategy utilized Gly-maleimide that was coupled to the N-terminus of the fully protected melittin peptide on resin (Scheme 1). Upon workup, this yielded Mal-melittin that was then directly conjugated to poly(Acr-X)$_n$-Cys peptides. The conjugation of Mal-melittin with poly(Acr-Arg)$_4$-Cys was monitored by RP-HPLC resulting in the complete consumption of Mal-melittin and the formation of poly(Acr-Arg)$_4$-Mal-melittin. Purification of poly(Acr-Arg)$_4$-Mal-melittin was achieved with a final yield of 35% and >95% purity. Reducible and nonreducible polyacridine−melittin peptides with Acr-Arg repeat of 2 and 3 were synthesized with similar yield and purity, and characterized by LC-MS (Table 1).

Physical Properties of Polyacridine−Melittin DNA Polyplexes. The binding of polyacridine−melittin peptides to pGL3 was investigated using a thiazole orange exclusion assay (*29*). Polyacridine−melittin peptides were found to compete for intercalation and displace thiazole orange resulting in a decrease in fluorescence intensity. When titrated at increasing concentration, the fluorescence decreased until an asymptote was reached at an equivalence point (Figure 2A). Analysis of the DNA binding affinity of poly(Acr-Arg)$_4$-Cys established an equivalence point at approximately 0.4 nmol peptide per μg of DNA. By comparison, Cys-melittin demonstrated weaker binding and was not able to fully exclude thiazole orange, only approaching an equivalence point at approximately 0.5 nmol of peptide per μg of DNA (Figure 2A). Alternatively, poly(Acr-Arg)$_4$-SS-melittin demonstrated higher affinity resulting in an equivalence point at approximately 0.25 nmol of peptide per μg of DNA. This affinity is comparable to that afforded by a Cys-Trp-Lys$_{18}$ peptide using the same assay (*29*).

Comparison of poly(Acr-Arg)$_{2-4}$-SS-melittin demonstrated nearly equivalent affinity for Acr-Arg repeats of 3 and 4, but

Table 1. Sequence and Hemolytic Potency of Peptide Conjugates

		mass[a] (calc/obs)	HL_{50} (μM)[b] pH 7.4: 5.0
Polyacridine Anchor Peptides (Acr) = Lys-ε-acridine, Ac = acylated ε-amine)			
poly(Acr-Arg)$_2$-Cys		1044.3/1044.2	N.D.[c]
poly(Acr-Arg)$_3$-Cys		1505.8/1505.6	N.D.
poly(Acr-Arg)$_4$-Cys		1967.4/1967.0	>10/>10
poly(Acr-Lys)$_4$-Cys		1855.3/1855.0	N.D.
poly(Acr-Leu)$_4$-Cys		1795.3/1795.1	N.D.
Trp-(Lys(Ac)-Arg)$_4$-Cys		1612.9/1612.7	N.D.
Melittin Analogues (thiolpyr = thiol pyridine, Mal = maleimide)			
Melittin	GIGAVLKVLTTGLPALISWIKRKRQQ	2847.5/2847.4	0.9/2.3
Cys-melittin	CWKKGIGAVLKVLTTGLPALISLIKRKRQQ	3320.1/3320.4	1.0/0.7
Dimeric-melittin	(CWKKGIGAVLKVLTTGLPALISLIKRKRQQ)$_2$	6638.2/6637.6	1.0/1.2
Thiolpyr-melittin	C(tp)WKKGIGAVLKVLTTGLPALISLIKRKRQQ	3429.2/3428.4	N.D.
Mal-melittin	(m)GWKKGIGAVLKVLTTGLPALISLIKRKRQQ	3354.0/3454.0	3.84/4.8
Polyacridine−Melittin (SS = reducible, Mal = nonreducible)			
poly(Acr-Arg)$_2$-SS-melittin	(Acr-Arg)$_2$-C−CWKKGIGAVLKVLTTGLPALISLIKRKRQQ	4359.5/4362.3	2.5/3.9
poly(Acr-Arg)$_3$-SS-melittin	(Acr-Arg)$_3$-C−CWKKGIGAVLKVLTTGLPALISLIKRKRQQ	4823.9/4823.2	1.4/2.2
poly(Acr-Arg)$_4$-SS-melittin	(Acr-Arg)$_4$-C−CWKKGIGAVLKVLTTGLPALISLIKRKRQQ	5285.5/5285.2	1.7/1.9
poly(Acr-Arg)$_4$-Mal-melttin	(Acr-Arg)$_4$-C(m)GWKKGIGAVLKVLTTGLPALISLIKRKRQQ	5321.4/5320.8	2.1/1.7
poly(Lys(Ac)-Arg)$_4$-SS-melttin	W(Lys(Ac)-Arg)$_4$-C−CWKKGIGAVLKVLTTGLPALISLIKRKRQQ	4931.0/4930.4	5.6/7.7
poly(Acr-Lys)$_4$-SS-melittin	(Acr-Lys)$_4$-C−CWK KG IGAVLKVLTTGLPALISLIKRKRQQ	5173.4/5173.2	1.0/2.8
poly(Acr-Lys)$_4$-Mal-melittin	(Acr-Lys)$_4$-C(m)GWKKGIGAVLKVLTTGLPALISLIKRKRQQ	5209.4/5208.8	1.5/1.9
poly(Acr-Leu)$_4$-SS-melittin	(Acr-Leu)$_4$-C−CWK KG IGAVLKVLTTGLPALISLIKRKRQQ	5113.4/5112.8	2.2/1.6
poly(Acr-Leu)$_4$-Mal-melittin	(Acr-Leu)$_4$-C(m)GWKKGIGAVLKVLTTGLPALISLIKRKRQQ	5149.3/5149.2	2.4/1.2

[a] Calculated and observed mass as determined by ESI LC-MS. [b] RBC hemolysis at pH 7.4 and 5.0. [c] N.D. = not determined.

less affinity afforded for a repeat of 2 (Figure 2B). Direct comparison of the DNA binding affinity of poly(Acr-Arg)$_4$-SS-melittin with poly(Acr-Lys)$_4$-SS-melittin and poly(Acr-Leu)$_4$-SS-melittin established that there was a negligible difference, with each producing fully complexed polyplexes at 0.3 nmol per μg of pGL3 (Figure 2C).

The particle size and zeta potential of polyacridine−melittin polyplexes were determined by QELS analysis (Table 2). Poly(Acr-Arg)$_4$-SS-melittin and poly(Acr-Arg)$_4$-Mal-melittin produced polyplexes of 79−84 nm average diameter, respectively. Comparison of the size of polyplexes prepared with poly(Acr-Arg)$_3$-SS-melittin (126 nm) and poly(Acr-Arg)$_2$-SS-melittin (737 nm) established that shorter repeats produced larger particle size (Table 2). This result is consistent with earlier findings that indicated that shorter, low-affinity polylysine peptides (<13 residues) produced larger polyplexes, whereas polylysine of 18 repeats or longer produced polyplexes of approximately 80 nm in diameter.

Substitution of the spacing Arg for Lys or Leu in Acr-Arg repeats resulted in a minimal change in particle size (Table 2). This supports the hypothesis that polyintercalation, and not ionic binding, is primarily responsible for the binding affinity to DNA. To test this hypothesis, an analogue was prepared that replaced the acridine modified Lys with an acetyl on the ε-amine of lysine resulting in poly(Lys(Ac)-Arg)$_4$-SS-melittin. This analogue produced polyplexes of average diameter of 177 nm, suggesting a significantly lower affinity (Table 2).

To further validate the change in particle size determined by QELS, polyplexes were analyzed by atomic force microscopy (AFM) (*30*). Analysis of pGL3 by AFM demonstrated an open structure occupying 0.5−1 μm with no single morphology (Figure 3A). Polyplexes prepared with poly(Acr-Arg)$_2$-SS-melittin appeared to form clusters composed of several individual particles that account for the larger size determined by QELS (Figure 3B). In contrast, the AFM images for polyplexes prepared with poly(Acr-Arg)$_4$-SS-melttin (Figure 3C), poly(Acr-Leu)$_4$-SS-melittin (Figure 3D), and poly(Acr-Lys)$_4$-SS-melittin (Figure 3E) all appeared to be less aggregated resulting in overall smaller particle size. It is interesting to note that the zeta potentials of polyacridine−melittin polyplexes containing a spacing Arg, Lys, or Leu were approximately +25 mV (Table 2). This result indicated that the charge on melittin strongly influenced the overall charge of polyplexes prepared with different anchoring peptides.

Biological Activity of Polyacridine−Melittin DNA Polyplexes. The membrane lytic potency of polyacridine−melittin peptides were investigated using a RBC hemolysis assay (*9*). As anticipated, poly(Acr-X)$_4$-Cys anchor peptides alone were inactive in membrane lysis. Alternatively, modification of the N-terminus of natural melittin with Cys-Trp-Lys-Lys and substitution of Leu for Trp 8 to generate Cys-melittin, resulted in retention of RBC hemolytic (HL_{50}) potency at pH 7.4 relative to natural melittin (Figure 4A). Likewise, the hemolytic potency of poly(Acr-Arg)$_4$-SS-melittin was comparable to Cys-melittin, indicating the attachment of the polyacridine anchor had a negligible influence on the membrane lytic activity of Cys-melittin. The results for polyacridine−melittin peptides possessing either a reducible or non-reducible linkage are summarized in Table 1, establishing their nearly equivalent hemolytic potency at pH 7.4.

The hemolytic potency of polyacridine melittin peptides was also determined at pH 5 to simulate the pH of the endosome. In contrast to an earlier finding that C and N-terminal modification of natural melittin with Cys-(Lys)$_4$ resulted in the complete loss of hemolytic activity at pH 5 (*9*), Cys-melittin possessed an improved pH 5 RBC lytic potency relative to that of natural melittin (Figure 4B). Consequently, poly(Acr-Arg)$_4$-SS-melittin and poly(Acr-Arg)$_4$-Mal-melittin both possess potent hemolytic activity at pH 7.4 and 5 (Table 1). When combined with pGL3, Cys-melittin and Mal-melittin maintained their hemolytic activity at pH 7.4, demonstrating their weak association with DNA (Figure 4C). In contrast, the hemolytic activity of poly(Acr-Arg)$_4$-SS-melittin DNA polyplexes was completely neutralized due to the strong binding of the polyacridine peptide with DNA (Figure 4C). Reduction of the disulfide bond would decrease the binding affinity to DNA and thereby release hemolytic Cys-melittin.

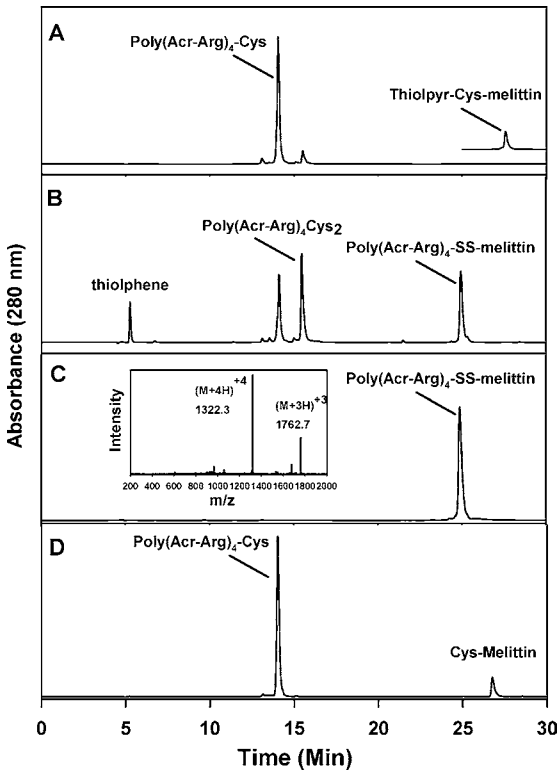


Figure 1. RP-HPLC analysis of polyacridine-melittin peptide synthesis. The reaction monitoring of poly(Acr-Arg)$_4$-Cys with thiolpyr-Cys-melittin at time 0 at 1.7:1 mol ratio is illustrated in panel A. The RP-HPLC chromatograms were produced by injecting 2 nmol then eluting with 0.1% TFA (v/v) and an acetonitrile gradient of 10−55% over 30 min while monitoring absorbance at 280 nm. The reaction monitoring at 12 h established the complete consumption of thiolpyr-Cys-melittin with formation of the product poly(Acr-Arg)$_4$-SS-melittin and by-products of dimeric poly(Acr-Arg)$_4$-Cys$_2$ and thiolphene (panel B). LC-ESI-MS of purified poly(Acr-Arg)$_4$-SS-melittin produced ions of 1762.7 *m*/*z* and 1322.3 *m*/*z*, respectively (inset), corresponding to a mass of 5285.2 amu (panel C). Reduction of poly(Acr-Arg)$_4$-SS-melittin with TCEP resulted in formation of equimolar amounts of poly(Acr-Arg)$_4$-Cys and Cys-melittin (panel D).

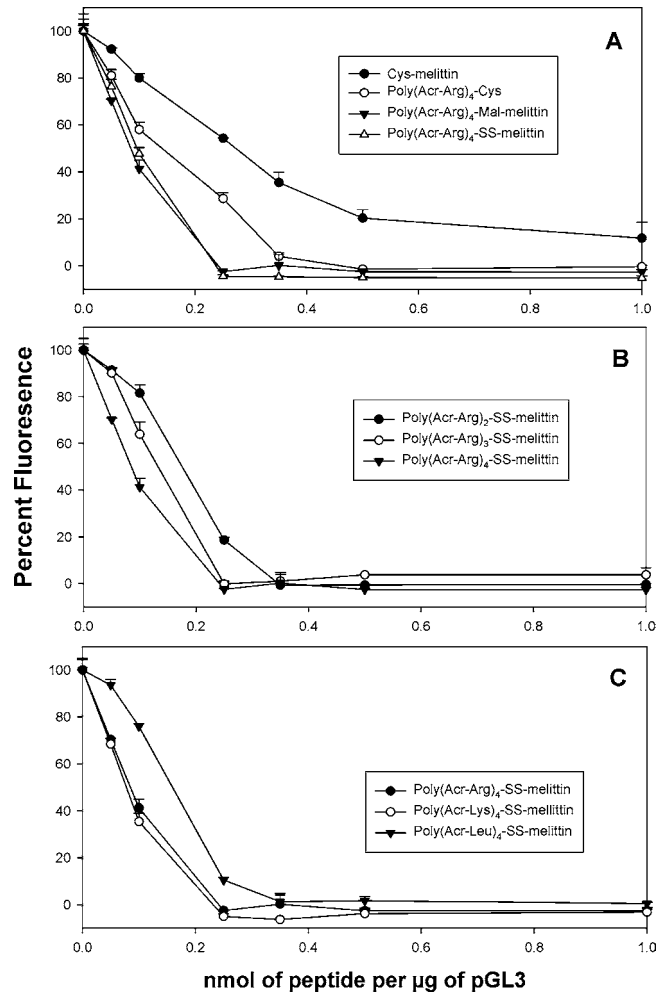


Figure 2. Relative binding affinity of polyacridine-melittin peptides to DNA. The concentration-dependent displacement of the thiazole orange from DNA by polyacridine−melittin peptides was used to establish relative affinity. Cys-melittin bound weakly to DNA resulting in an asymptote in the fluorescence intensity at approximately 0.5 nmol of peptide per μg of DNA, compared to 0.35 for (Acr-Arg)$_4$-Cys and 0.25 for poly(Acr-Arg)$_4$-SS-melittin (panel A). Comparison of poly(Acr-Arg)$_{2-4}$-SS-melittin established that poly(Acr-Arg)$_2$-SS-melittin was the weakest binding resulting in an asymptote at 0.35 nmols of peptide per μg of DNA, whereas poly(Acr-Arg)$_{3and4}$-SS-melittin were nearly equivalent in displacing thiazole orange (panel B). An equal DNA binding affinity was demonstrated for poly(Acr-Arg)$_4$-SS-melittin, poly(Acr-Leu)$_4$-SS-melittin, and poly(Acr-Lys)$_4$-SS-melittin, each resulting in polyplex formation at 0.25 nmol of peptide per μg of DNA (panel C).

To establish a relationship among peptide anchor length, reducibility, and peptide DNA stoichiometry, CHO cells were transfected with polyplexes formed with poly(Acr-Arg)$_2$-SS-melittin, poly(Acr-Arg)$_3$-SS-melittin, poly(Acr-Arg)$_4$-SS-melittin, and poly(Acr-Arg)$_4$-Mal-melittin while varying the peptide to DNA ratio from 0.1, 0.3, 0.5, and 0.75 nmols of peptide per μg of DNA (Figure 5). Luciferase reporter gene expression for polyplexes formed with 0.1 nmol of peptide per μg DNA resulted in expression comparable to a WK$_{18}$/DNA control polyplex. Increasing the stoichiometry to 0.35 nmols of peptide per μg of DNA or higher increased the gene expression approximately 100-fold relative to 0.1 nmol of peptide per μg of DNA. Within this series, poly(Acr-Arg)$_4$-SS-melittin produced the highest expression at a stoichiometry of 0.3 and 0.5. The expression mediated by poly(Acr-Arg)$_4$-SS-melittin was approximately 1000-fold greater than that of poly(Acr-Arg)$_4$-Mal-melittin, which differed only by the reducibility of the linkage between the anchor and melittin (Figure 5).

A broader panel of polyacridine−melittin peptides were combined with pGL3 at a fixed stoichiometry of 0.5 nmol per μg of pGL3 and used to mediate gene expression in HepG2, 3T3, and CHO cells. As illustrated in Figure 6, polyacridine−melittin peptides of the poly(Acr-Arg)$_{2-4}$-SS-melittin series produced the highest gene transfection in all three cell lines, with levels similar to that of PEI (9:1 N:P) when performed with either 2% or 10% FBS. By comparison, poly(Acr-Lys)$_4$-SS-melittin and poly(Acr-Leu)$_4$-SS-melittin were approximately 10−100-fold less active in gene transfer than poly(Acr-Arg)$_4$-SS-melittin in all three cell lines. Reducible poly(Acr-Arg)$_{2-4}$-SS-melittin peptides were 100−1000-fold more active in gene transfer compared to poly(Acr-Arg)$_4$-Mal-melittin in all three cell lines. The importance of the reductive release of melittin was also determined for poly(Acr-Lys)$_4$-SS-melittin and poly-(Acr-Leu)$_4$-SS-melittin in all three cell lines.

To establish the contribution of poly-acridine to DNA binding affinity and gene transfer, the ε-amine of lysine was modified with an acetyl group to prepare poly(Lys(Ac)-Arg)$_4$-SS-melittin. Gene transfer mediated by poly(Lys(Ac)-Arg)$_4$-SS-melittin was approximately 100−1000-fold less relative to poly(Acr-Arg)$_4$-SS-melittin in all three cell lines (Figure 6). To further establish the importance of the anchor peptides, Cys-melittin and dimeric-melittin were used to mediate gene transfer (Figure 6). Both mediated gene transfer that was 10−100-fold lower than poly(Acr-Arg)$_{2-4}$-SS-melittin, demonstrating the importance of the polyacridine anchor in this gene transfer system. Alterna-

Table 2. Physical Properties and Toxicity of DNA Polyplexes

peptide	particle size (nm)[a]	zeta potential (+mV)[b]	MTT assay[c]		
			CHO	HepG2	3T3
poly(Acr-Arg)$_2$-SS-melittin	737 ± 46.8	25 ± 2.2	99 ± 7	92 ± 7	85 ± 2
poly(Acr-Arg)$_3$-SS-melittin	126 ± 4.5	29 ± 4.5	103 ± 7	97 ± 13	91 ± 2
poly(Acr-Arg)$_4$-SS-melittin	84 ± 2.0	29 ± 2.6	70 ± 5	67 ± 9	58 ± 4
poly(Acr-Arg)$_4$-Mal-melittin	79 ± 1.3	28 ± 2.5	69 ± 5	88 ± 13	82 ± 1
poly(Lys(Ac)-Arg)$_4$-SS-melittin	177 ± 6.2	20 ± 2.9	55 ± 4	64 ± 9	33 ± 4
poly(Acr-Lys)$_4$-SS-melittin	89 ± 3.5	23 ± 1.6	76 ± 5	66 ± 5	72 ± 6
poly(Acr-Lys)$_4$-Mal-melittin	86 ± 2.4	26 ± 2.0	87 ± 8	79 ± 6	82 ± 2
poly(Acr-Leu)$_4$-SS-melittin	119 ± 1.4	20 ± 2.9	46 ± 4	49 ± 4	50 ± 4
poly(Acr-Leu)$_4$-Mal-melittin	121 ± 2.5	22 ± 2.1	90 ± 3	117 ± 5	74 ± 3

[a] Mean particle size of peptide-DNA polyplex (0.5 nmol of peptide per μg of DNA) as determined by QELS. [b] Mean zeta potential determined in 5 mM Hepes, pH 7.4. [c] Percent viability of peptide-DNA polyplexes determined by MTT assay in CHO, HepG2, and 3T3 cells at 10 μg DNA dose (0.5 nmol of peptide per μg DNA) applied to 5×10^5 cells for 6 h.

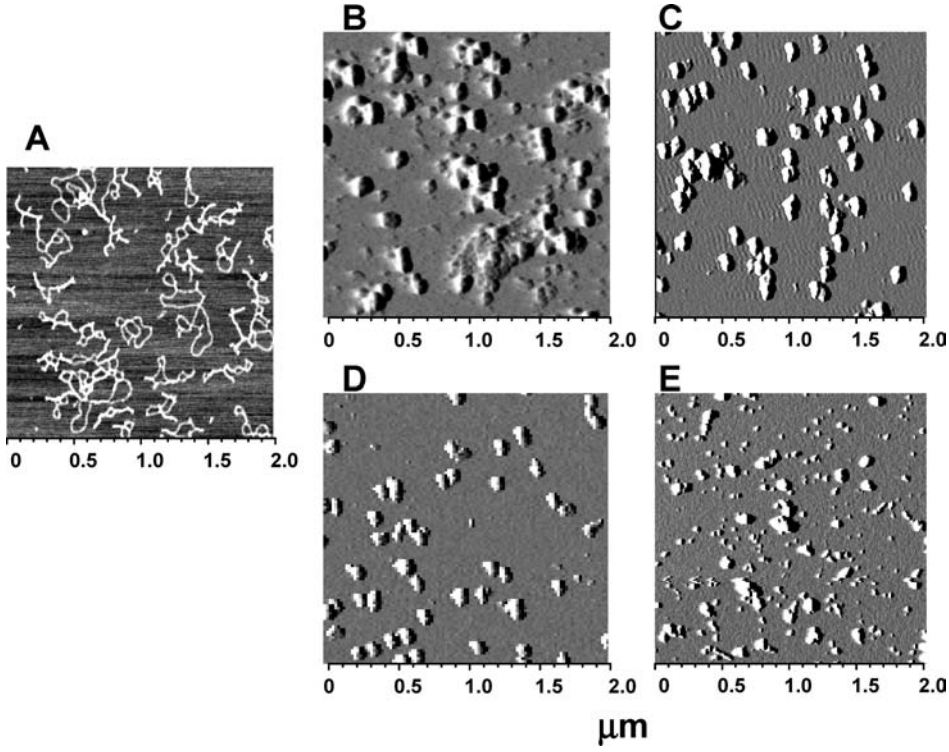


Figure 3. Atomic force microscopy of polyacridine−melittin polyplexes. The size and shape of pGL3 (A) or polyacridine−melittin DNA polyplexes (B−E) were determined by atomic force microscope. Poly(Acr-Arg)$_2$-SS-melittin (B), poly(Acr-Leu)$_4$-SS-melittin (C), poly(Acr-Arg)$_4$-SS-melittin (D), and poly(Acr-Lys)$_4$-Mal-melittin (E) pGL3 polyplexes are compared. The results establish that the weaker DNA binding of poly(Acr-Arg)$_2$-SS-melittin results in aggregated polyplexes.

tively, poly(Acr-Arg)$_n$Cys peptides produced negligible gene transfer on their own, establishing the importance of both the anchor peptide and melittin.

The toxicity of polyacridine DNA polyplexes was assessed by MTT assay on CHO, HepG2, and 3T3 cells (Table 2). Poly(Acr-Arg)$_{2-3}$-SS-melittin DNA polyplexes display very little toxicity in all three cell lines. However, poly(Acr-Arg)$_4$-SS-melittin and poly(Acr-Arg)$_4$-Mal-melittin polyplexes resulted in approximately 70% cell viability whereas control peptide poly(Lys(Ac)-Arg)$_4$-SS-melittin polyplexes were more toxic, resulting in 55% viability. Treatment of CHO, 3T3, and HepG2 cells with 10 μg of poly(Acr-Lys)$_4$-SS-melittin and poly(Acr-Lys)$_4$-Mal-melittin polyplexes for either 6 or 24 h resulted in the same degree of toxicity, whereas lowering the DNA polyplex dose to either 1 or 5 μg resulted in 100% viability. Despite its lower gene transfer efficiency, poly(Acr-Leu)$_4$-Mal-melittin polyplexes were less toxic compared to poly(Acr-Leu)$_4$-SS-melittin polyplexes, which produced approximately 50% viability (Table 2).

DISCUSSION

The endosome has been proposed as one of the major barriers that limits the gene transfer efficiency of nonviral gene delivery systems (*34*). To increase the endosomal escape of plasmid DNA, many prior studies have incorporated fusogenic peptides into experimental delivery systems (*4, 8, 16, 35−40*). Most often, a fusogenic peptide is linked to a PEI or polylysine to allow for multivalent reversible ionic binding with the phosphate backbone of DNA (*4, 10, 11*). While this approach often leads to significant increases in gene transfer efficiency in vitro, ionic interactions are relatively weak leading to premature dissociation of the carrier in vivo and degradation of the DNA (*41*). To overcome weak binding, higher molecular weight polycations are used. These can be prepared with reducible linkages that revert to low molecular weight, lower affinity polycations and

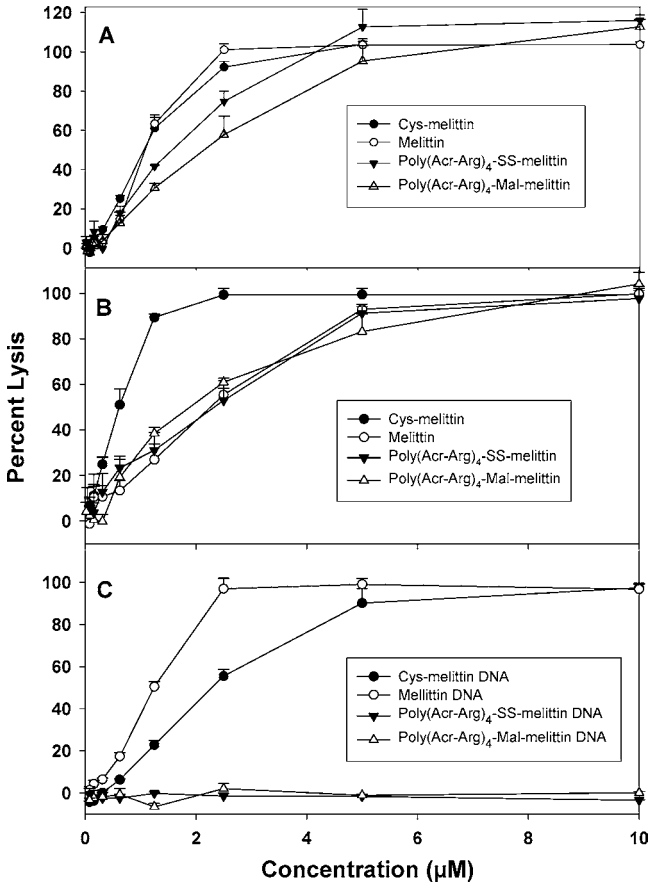


Figure 4. Membrane lytic potency of polyacridine−melittin peptides. The hemolytic activity of melittin and polyacridine−melittin peptides were compared at pH 7.4 and 5 using a RBC hemolysis assay. The results establish Cys-melittin is equally potent as natural melittin at pH 7.4 (panel A), but more potent at pH 5 (panel B). In comparison, poly(Acr-Arg)$_4$-SS-melittin retains nearly full hemolytic potency at pH 7.4 (panel A) but is less potent at pH 5. However, when combined with pGL3, the pH 7.4 hemolytic activity of both Cys-melittin and melittin is nearly unchanged, whereas poly(Acr-Arg)$_4$-SS-melittin is non hemolytic (panel C). These results establish the masking of poly(Acr-Arg)$_4$-SS-melittin membrane lytic activity while bound to DNA.

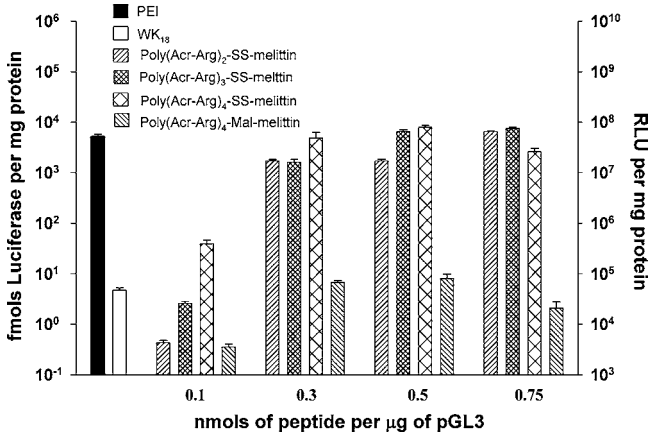


Figure 5. Comparative in vitro gene transfer potency of polyacridine−melittin polyplexes. CHO cells were transfected with increasing amounts of peptide (0.1, 0.35, 0.5, and 0.75 nmol peptide per microgram DNA) combined with 10 μg pGL3. The luciferase expression determined at 24 h represents the mean and standard deviation for three independent transfections.

trigger the release of DNA inside the cell (*21, 22, 42*−*45*). However, despite numerous attempts, i.v. dosed polycationic

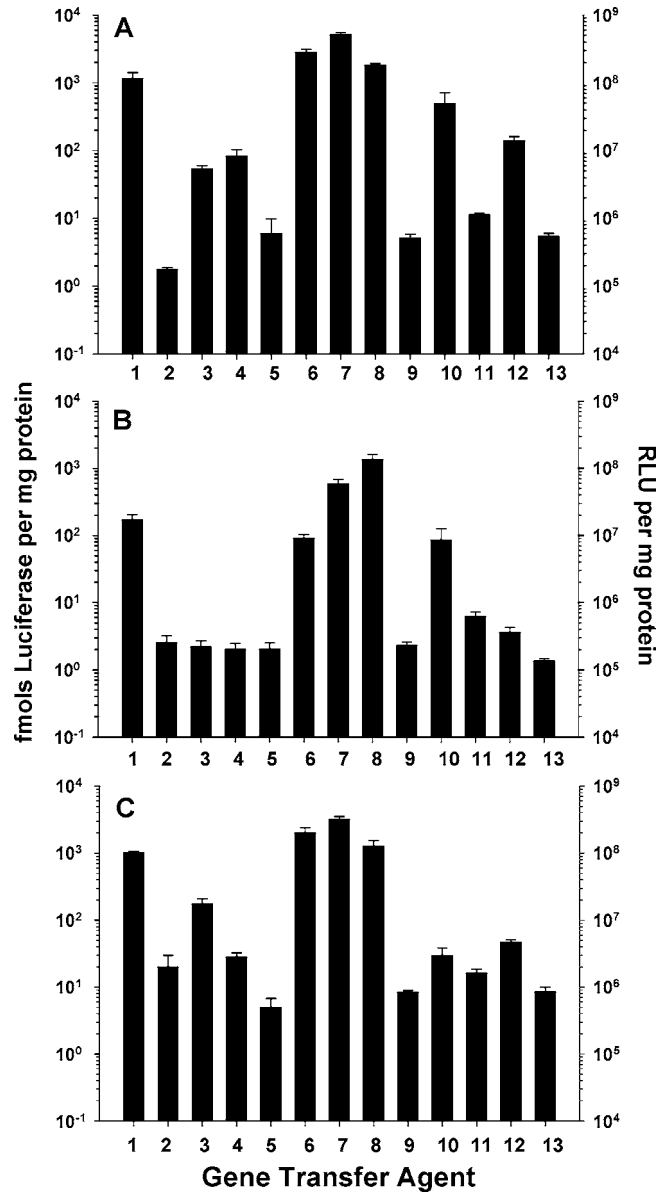


Figure 6. Cell-dependent in vitro gene transfer potency of polyacridine−melittin polyplexes. The relative gene transfer efficiency of DNA polyplexes was determined in CHO (A), 3T3 (B), and HepG2 (C) cells. Transfections were performed with 10 μg of pGL3 polyplex prepared with 0.5 nmol of peptide per μg of DNA. The gene transfer efficiency mediated by polyacridine−melittin peptides was compared to PEI (N/P 9:1) DNA polyplexes and WK$_{18}$ DNA polyplexes. The bars indicate transfection pGL3 combined with (1) PEI, (2)WK$_{18}$, (3) dimeric-melittin, (4) Cys-melittin, (5) poly(Lys(Ac)-Arg)$_4$-SS-melittin, (6) poly(Acr-Arg)$_2$-SS-melittin, (7) poly(Acr-Arg)$_3$-SS-melittin, (8) poly-(Acr-Arg)$_4$-SS-melittin, (9) poly(Acr-Arg)$_4$-Mal-melittin, (10) poly(Acr-Lys)$_4$-SS-melittin, (11) poly(Acr-Lys)$_4$-Mal-melittin, (12) poly(Acr-Leu)$_4$-SS-melittin, and (13) poly(Acr-Leu)$_4$-Mal-melittin. The luciferase expression was determined at 24 h. The results represent the mean and standard deviation for three independent transfections.

DNA polyplexes are unable to produce therapeutic levels of gene expression (*22*).

We have therefore explored an alternative method of binding fusogenic peptides to plasmid DNA by reversible intercalation. Preliminary studies suggested that a single acridine binds to DNA through intercalation but with relatively weak affinity. Consequently, we sought to increase the binding affinity by preparing polyacridines. Considering the pioneering studies of Szoka who developed a synthetic scheme to prepare a diacridine glycopeptide (*24*), Vierling with a single acridine modified nuclear localizing peptide (*26*), and Nielsen who prepared and

tested di and triacridine nuclear localization peptides (*25*), we sought a simplified approach that would allow us to extend the valency of polyacridine to four or more acridine units and control the charge of polyacridine DNA polyplexes. We therefore adopted a strategy reported by Ueyama et al. (*23*), who demonstrated that polyacridine peptides could be prepared from Fmoc-Lys(Acr) using solid-phase synthesis. Several early attempts at synthesis established that polyacridine peptides could be prepared in good yield (>30%) provided that coupling was conducted with HBTU and that a spacing amino acid was used that had a bulky side chain or protecting group. Using Gly as a spacing amino acid resulted in poor yields.

The synthetic design of polyacridine peptides took into account the relative DNA binding affinity by varying polyacridine repeat, the influence of the spacing amino acid on gene transfer and linkage between polyacridine and a melittin fusogenic peptide. As indicated in Figures 5 and 6, there is a strong dependency on the nature of the linkage between polyacridine and melittin in relationship to the gene transfer efficiency. A reducible disulfide bond provided a means for the triggered release of melittin either at or inside the cell. The reduction of the disulfide bond greatly diminishes the affinity of melittin for DNA, releasing it and unmasking its membrane lytic activity (Figure 2C). The released melittin apparently enhances gene transfer by lysis of endosomal membranes that then allows the DNA to more efficiently reach the cytosol and the nucleus, resulting in gene expression that equals or surpasses that of PEI in multiple cell lines (Figure 6). In support of this mechanism, polyacridine linked to melittin by a non-reducible maleimide is 1000-fold less active in gene transfer, despite its equivalent membrane lysis potency against RBCs (Table 1). These results agree with previously observed improved gene transfer mediated by a reductively triggered release of a fusogenic peptide from a gene delivery system (*10, 46*).

The length of the polyacridine repeat appears to be less important for in vitro gene transfer, since repeats of 2, 3, and 4 poly(Acr-Arg)-SS-melittin all produced nearly equivalent gene transfer in three cell lines (Figure 6). However, it is clear that poly(Acr-Arg)$_2$-SS-melittin has lower affinity for DNA as indicated by its ability to displace an intercalator dye (Figure 2B). The lower affinity results in larger DNA polyplexes as determined by QELS (Table 2) and AFM (Figure 3B). However, larger polyplexes also sediment more efficiently, facilitating in vitro gene transfer.

The spacing amino acid of Arg, Lys, or Leu within a poly(Acr-X)$_4$-SS-melittin only slightly influences their affinity for binding DNA (Figure 2C). Each of the resulting polyplexes possessed comparable size, charge, and shape as determined by QELS, zeta potential, and AFM (Table 2, Figure 3). However, the gene transfer efficiency was influenced significantly by the identity of the spacing amino acid in the order Arg > Lys > Leu (Figure 6). In each case, and in each cell line, the reducible polyacridine−melittin peptide mediated greater expression than the nonreducible analogue. The mechanism by which the spacing amino acid influences gene transfer efficiency is unclear. We speculate that the polyacridine and spacing amino acid collaborate to provide DNA binding affinity. It is likely that, following disulfide bond reduction to release the melittin, the anchoring peptide binds to DNA with less affinity, and the charge character of the polyplex changes significantly.

Nonetheless, it is clear that polyacridine is necessary to mediate significant gene transfer. This is further established with a control peptide, poly(Lys(Ac)-Arg)$_4$-SS-melittin, that was fully active in membrane lysis but proved to be approximately 1000-fold less active than poly(Acr-Arg)$_4$-melittin in mediating gene transfer (Figure 6).

The lytic potency of melittin on cells in culture has been well documented (*12, 14*). However, this toxicity can be overcome by polymerization of melittin through disulfide bonds resulting in its neutralization due to high-affinity binding to DNA (*9*). It is apparent that even dimeric-melittin can bind to DNA and mediate moderate gene transfer (Figure 6). The MTT assay did establish that polyacridine−melittin peptides are moderately toxic (approx 50−70% viable) when added to DNA at 0.5 nmol of peptide per microgram of DNA or higher (Table 2). However, this toxicity is the result of saturation of the DNA with polyacridine peptide resulting in unbound peptide that can lyse cells. Lower stoichiometries of 0.3 nmol of peptide per microgram of DNA or lower DNA doses of 5 and 1 μg result in negligible toxicity on all three cell types.

In conclusion, we have described a new polyacridine DNA binding anchor that, when linked with melittin through disulfide bond, produces potent in vitro gene transfer. The polyacridine anchor is designed to be optimized for either in vitro or in vivo gene transfer by controlling the binding affinity to DNA and charge of resulting DNA polyplexes. Furthermore, the Cys residue allows coupling of fusogenic peptides, ligands, and PEG. These attributes should allow polyacridine several unique advantages compared to other polycationic DNA binding peptides and polymers.

ACKNOWLEDGMENT

We gratefully acknowledge support for this work from the NIH Grant DK066212.

LITERATURE CITED

(1) Mahato, R. I. (1999) Non-viral peptide-based approaches to gene delivery. *J. Drug Targeting 7*, 249–268.
(2) Plank, C., Oberhauser, B., Mechtler, K., Koch, C., and Wagner, E. (1994) The influence of endosome-disruptive peptides on gene transfer using synthetic. *J. Biol. Chem. 269*, 12918–12924.
(3) Van Dyke, R. W. (1996) Acidification of lysosomes and endosomes. *Sub-Cell. Biochem. 27*, 331–60.
(4) Ogris, M., Carlisle, R. C., Bettinger, T., and Seymour, L. W. (2001) Melittin enables efficient vesicular escape and enhanced nuclear access of nonviral gene delivery vectors. *J. Biol. Chem. 276*, 47550–47555.
(5) Parente, R. A., Nadasdi, L., Subbarao, N. K., and Szoka, F. C., Jr. (1990) Association of a pH-sensitive peptide with membrane vesicles: role of amino acid sequence. *Biochemistry 29*, 8713–9.
(6) Parente, R. A., Nir, S., and Szoka, F. C., Jr. (1990) Mechanism of leakage of phospholipid vesicle contents induced by the peptide GALA. *Biochemistry 29*, 8720–8.
(7) Wyman, T. B., Nicol, F., Zelphati, O., Scaria, P. V., Plank, C., and Szoka, F. C. (1997) Design, synthesis and characterization of a cationic peptide that binds to nucleic acids and permeabilizes bilayers. *Biochemistry 36*, 3008–3017.
(8) Gottschalk, S., Sparrow, J. T., Hauer, J., Mims, M. P., Leland, F. E., Woo, S. L. C., and Smith, L. C. (1996) A novel DNA-peptide complex for efficient gene transfer and expression in mammalian cells. *Gene Ther. 3*, 448–457.
(9) Chen, C.-P., Kim, J.-S., Steenblock, E., Liu, D., and Rice, K. G. (2006) Gene transfer with poly-melittin peptides. *Bioconjugate Chem. 17*, 1057–62.
(10) Boeckle, S., Wagner, E., and Ogris, M. (2005) C- versus N-terminally linked melittin-polyethylenimine conjugates: the site of linkage strongly influences activity of DNA polyplexes. *J. Gene Med. 7*, 1335–1347.
(11) Boeckle, S., Fahrmeir, J., Roedl, W., Ogris, M., and Wagner, E. (2006) Melittin analogs with high lytic activity at endosomal pH enhance transfection with purified targeted PEI polyplexes. *J. Controlled Release 112*, 240–8.
(12) Goto, Y., and Hagihara, Y. (1992) Mechanism of the conformational transition of melittin. *Biochemistry 31*, 732–8.

(13) Subbalakshmi, C., Nagaraj, R., and Sitaram, N. (1999) Biological activities of C-terminal 15-residue synthetic fragment of melittin: design of an analog with improved antibacterial activity. *FEBS Lett. 448*, 62–6.

(14) Terwilliger, T. C., and Eisenberg, D. (1982) The structure of melittin. II. Interpretation of the structure. *J. Biol. Chem. 257*, 6016–22.

(15) Legendre, J. Y., Bohrmann, T. B., Deuschle, U., Kitas, E., and Supersaxo, A. (1997) Dioleoymelittin as a novel serum-insensitive reagent for efficient transfections of mammalian cells. *Bioconjugate Chem. 8*, 57–63.

(16) Rozema, D. B., Ekena, K., Lewis, D. L., Loomis, A. G., and Wolff, J. A. (2003) Endosomolysis by masking of a membrane-active agent (EMMA) for cytoplasmic release of macromolecules. *Bioconjugate Chem. 14*, 51–7.

(17) Read, M. L., Logan, A., and Seymour, L. W. (2005) Barriers to gene delivery using synthetic vectors, in *Advances in Genetics* (Hall, J. C., Dunlap, J. C., Friedmann, T., and van Heyningen, V., Eds.) pp 19−46, Academic Press, London.

(18) Dash, P. R., Read, M. L., Barrett, L. B., Wolfert, M. A., and Seymour, L. W. (1999) Factors affecting blood clearance and in vivo distribution of polyelectrolyte complexes for gene delivery. *Gene Ther. 6*, 643–650.

(19) Burke, R. S., and Pun, S. H. (2008) Extracellular barriers to in vivo PEI and PEGylated PEI polyplex-mediated gene delivery to the liver. *Bioconjugate Chem. 19*, 693–704.

(20) Kwok, K. Y., McKenzie, D. L., Evers, D. L., and Rice, K. G. (1999) Formulation of highly soluble poly(ethylene glycol)-peptide DNA condensates. *J. Pharm. Sci. 88*, 996–1003.

(21) Kwok, K. Y., Park, Y., Yongsheng, Y., McKenzie, D. L., and Rice, K. G. (2003) In vivo gene transfer using sulfhydryl crosslinked PEG-peptide/glycopeptide DNA co-condensates. *J. Pharm. Sci. 92*, 1174–1185.

(22) Chen, C. p., Kim, J. s., Liu, D., Rettig, G. R., McAnuff, M. A., Martin, M. E., and Rice, K. G. (2007) Synthetic PEGylated glycoproteins and their utility in gene delivery. *Bioconjugate Chem. 18*, 371–378.

(23) Ueyama, H., Takagi, M., Waki, M., and Takenaka, S. (2001) DNA binding behavior of peptides carrying acridinyl units: First example of effective poly-intercalation. *Nucleic Acids Symp. Ser. (Oxf.) 1*, 163–164.

(24) Haensler, J., and Szoka, J. F. C. (1993) Synthesis and characterization of a trigalactosylated bisacridine compound to target DNA to hepatocytes. *Bioconjugate Chem. 4*, 85–93.

(25) Shiraishi, T., Hamzavi, R., and Nielsen, P. E. (2005) Targeted delivery of plasmid DNA into the nucleus of cells via nuclear localization signal peptide conjugated to DNA intercalating bis- and trisacridines. *Bioconjugate Chem. 16*, 1112–1116.

(26) Boulanger, C., Di Giorgio, C., and Vierling, P. (2005) Synthesis of acridine-nuclear localization signal (NLS) conjugates and evaluation of their impact on lipoplex and polyplex-based transfection. *Eur. J. Med. Chem. 40*, 1295–306.

(27) Tung, C., Zhu, T., Lackland, H., and Stein, S. (1992) An acridine amino acid derivative for use in Fmoc peptide synthesis. *Peptide Research 5*, 115–8.

(28) Rich, D. H., Gesellchen, P. D., Tong, A., Cheung, A., and Buckner, C. K. (1975) Alkylating derivatives of amino acids and peptides. Synthesis of N-maleoylamino acids, [1-(N-maleoylglycyl)cysteinyl]oxytocin, and [1-(N-maleoyl-11-aminoundecanoyl) cysteinyl]oxytocin. Effects on vasopressin-stimulated water loss from isolated toad bladder. *J. Med. Chem. 18*, 1004–1010.

(29) Wadhwa, M. S., Collard, W. T., Adami, R. C., McKenzie, D. L., and Rice, K. G. (1997) Peptide-mediated gene delivery: influence of peptide structure on gene expression. *Bioconjugate Chem. 8*, 81–8.

(30) Bezanilla, M., Drake, B., Nudler, E., Kashlev, M., Hansma, P. K., and Hansma, H. G. (1994) Motion and enzymatic degreadation of DNA in the atomic force microscope. *Biophys. J. 67*, 2454–9.

(31) Mosmann, T. (1983) Rapid colorimetric assay for cellular growth and survival: application to proliferation and cytotoxicity assays. *J. Immunol. Methods 65*, 55–63.

(32) Smith, P. K., Krohn, R. I., Hermanson, G. T., Mallia, A. K., Gartner, F. H., Provenzano, M. D., Fujumoto, E. K., Goeke, N. M., Olson, B. J., and Klenk, D. C. (1985) Measurement of protein using bicinchoninic acid. *Anal. Biochem. 150*, 76–85.

(33) Combet, C., Blanchet, C., Geourjon, C., and Deleage, G. (2000) Network protein sequence alignment. *TIBS 25*, 147–150.

(34) Legendre, J. Y., and Szoka, F. C., Jr. (1993) Cyclic amphipathic peptide-DNA complexes mediate high-efficiency transfection of adherent mammalian cells. *Proc. Natl. Acad. Sci. U.S.A. 90*, 893–7.

(35) Wagner, E., Plank, C., Zatloukal, K., Cotten, M., and Birnstiel, M. L. (1992) Influenza virus hemagglutinin HA-2 N-terminal fusogenic peptides augment gene transfer by transferrin-polylysine-DNA complexes: Toward a synthetic virus-like gene-transfer vehicle. *Proc. Natl. Acad. Sci. U.S.A. 89*, 7934–7938.

(36) Midoux, P., Kichler, A., Boutin, V., Maurizot, J. C., and Monsigny, M. (1998) Membrane permeabilization and efficient gene transfer by a peptide containing several histidines. *Bioconjugate Chem. 9*, 260–267.

(37) Schuster, M. J., Wu, G. Y., Walton, C. M., and Wu, C. H. (1999) Multicomponent DNA carrier with a vesicular stomatitis virus G-peptide greatly enhances liver-targeted gene expression in mice. *Bioconjugate Chem. 10*, 1075–1083.

(38) Nishikawa, M., Yamauchi, M., Morimoto, K., Ishida, E., Takakura, Y., and Hashida, M. (2000) Heptocyte-targeted *in vivo* gene expression by intraveneous injection of plasmid DNA complexed with synthetic multi-functional gene delivery system. *Gene Ther. 7*, 548–555.

(39) Rittner, K., Benavente, A., Bompard-Sorlet, A., Heitz, F., Divita, G., Brasseur, R., and Jacobs, E. (2002) New basic membrane-destabilizing peptides for plasmid-based gene delivery in vitro and in vivo. *Mol. Ther. 5*, 104–14.

(40) Li, W., Nicol, F., and Szoka, F. C., Jr. (2004) GALA: a designed synthetic pH-responsive amphipathic peptide with applications in drug and gene delivery. *Adv. Drug Delivery Rev. 56*, 967–985.

(41) Collard, W. T., Yang, Y., Kwok, K. Y., Park, Y., and Rice, K. G. (2000) Biodistribution, metabolism, and in vivo gene expression of low molecular weight glycopeptide polyethylene glycol peptide DNA co-condensates. *J. Pharm. Sci. 89*, 499–512.

(42) McKenzie, D. L., Kwok, K. Y., and Rice, K. G. (2000) A potent new class of reductively activated peptide gene delivery agents. *J. Biol. Chem. 275*, 9970–9977.

(43) Park, Y., Kwok, K. Y., Boukarim, C., and Rice, K. G. (2002) Synthesis of sulfhydryl crosslinking poly (ethylene glycol) peptides and glycopeptides as carriers for gene delivery. *Bioconjugate Chem. 13*, 232–239.

(44) Read, M. L., Bremner, K. H., Oupicky, D., Green, N. K., Searle, P. F., and Seymour, L. W. (2003) Vectors based on reducible polycations facilitate intracellular release of nucleic acids. *J. Gene Med. 5*, 232–45.

(45) Zhou, Q.-H., Wu, C., Manickam, D., and Oupický, D. (2009) Evaluation of pharmacokinetics of bioreducible gene delivery vectors by real-time PCR. *Pharm. Res. 26*, 1581–1589.

(46) Meyer, M., Philipp, A., Oskuee, R., Schmidt, C., and Wagner, E. (2008) Breathing life into polycations: functionalization with pH-responsive endosomolytic peptides and polyethylene glycol enables siRNA delivery. *J. Am. Chem. Soc. 130*, 3272–3.

BC9003124

Tumor Delivery and In Vivo Processing of Disulfide-Linked and Thioether-Linked Antibody−Maytansinoid Conjugates

Hans K. Erickson,* Wayne C. Widdison, Michele F. Mayo, Kathleen Whiteman, Charlene Audette, Sharon D. Wilhelm, and Rajeeva Singh

ImmunoGen, Inc., 830 Winter Street, Waltham, Massachusetts 02451. Received July 15, 2009; Revised Manuscript Received October 5, 2009

Antibody−drug conjugates (ADCs) are designed to eradicate cancer cells that express the target antigen on their cell surface. A key component of an ADC is the linker that covalently connects the cytotoxic agent to the antibody. Several antibody−maytansinoid conjugates prepared with disulfide-based linkers such as those targeting the CanAg antigen have been shown to display more activity in preclinical mouse xenograft models than corresponding conjugates prepared with uncleavable thioether-based linkers. To investigate how the linker influences delivery and activation of antibody−maytansinoid conjugates, we isolated and characterized the [^{3}H]maytansinoids from CanAg-positive tumor tissues following a single intravenous administration of 300 μg/kg (based on maytansinoid dose) of anti-CanAg antibody (huC242)-^{3}H-maytansinoid conjugates prepared with cleavable disulfide linkers and an uncleavable thioether linker. We identified three target-dependent tumor metabolites of the disulfide-linked huC242-SPDB-DM4, namely, lysine-N^{ε}-SPDB-DM4, DM4, and *S*-methyl-DM4. We found similar metabolites for the less hindered disulfide-linked huC242-SPP-DM1 conjugate with the exception that no *S*-methyl-DM1 was detected. The sole metabolite of the uncleavable thioether-linked huC242-SMCC-DM1 was lysine-N^{ε}-SMCC-DM1. The AUC for the metabolites of huC242-SMCC-DM1 at the tumor over 7 d was about 2-fold greater than the corresponding AUC for the metabolites of the disulfide-linked conjugates. The lipophilic metabolites of the disulfide-linked conjugates were found to be nearly 1000 times more cytotoxic than the more hydrophilic lysine-N^{ε}-linker-maytansinoids in cell-based viability assays when added extracellularly. The cell killing properties associated with the lipophilic metabolites of the disulfide-linked conjugates (DM4 and *S*-methyl-DM4, and DM1) provide an explanation for the superior in vivo efficacy that is often observed with antibody−maytansinoid conjugates prepared with disulfide-based linkers in xenograft mouse models.

INTRODUCTION

Antibody−drug conjugates (ADC[1]) are targeted anticancer agents that utilize the specificity of a monoclonal antibody (mAb) to deliver potent cytotoxic agents to cancer cells that express the target antigen. Several ADCs are currently showing promise in clinical trials, and one, gemtuzumab ozogamicin, has been approved for the treatment of acute myeloid leukemia (*1*). It employs a derivative of the potent DNA-damaging agent calicheamicin γ^1 linked to an anti-CD33 antibody. Other ADCs under clinical evaluation utilize derivatives of the potent antimitotic agents, auristatin and maytansine (*2, 3*), linked to antibodies targeting different cancer-antigens such as the anti-HER2 mAb-maytansinoid conjugate, trastuzumab-DM1, that recently advanced to phase III evaluation for the treatment of metastatic breast cancer (*4*), and the anti-CD30 mAb-auristatin conjugate, SGN-35, that has demonstrated significant activity in patients with relapsed or refractory CD30-positive lymphomas (*5*).

A key design feature of ADCs is the chemical nature of the linker that connects the cytotoxic agent to the antibody (*4, 6*−*12*). Several ADCs utilize "uncleavable" linkers that contain no sites for chemical or enzymatic cleavage in biological systems (*8, 10*). Since the release of the free cytotoxic agent from these ADCs requires complete hydrolysis of the polypeptide backbone of the antibody component in the lysosomes of cells (*10, 11*), these conjugates have the advantage of minimizing the release of the cytotoxic agent during circulation in plasma. Indeed, the clearance of these conjugates from plasma following administration to mice is similar to the clearance of the unmodified antibody used to prepare the ADC (*13*). Other ADCs that utilize "cleavable" linkers with disulfide, hydrazone, or peptide moieties, which are cleaved by chemical or enzymatic processes in the tumor, may have somewhat lower stability during circulation in plasma than their uncleavable counterparts, depending on the specific chemical structure of the linker (*7*).

During the preclinical development of IMGN242 (huC242-SPDB-DM4), several disulfide linkers with varying susceptibility toward cleavage by thiol−disulfide exchange reactions were prepared by changing the steric hindrance adjacent to the disulfide bond (*12*). For example, IMGN242 has a sterically hindered disulfide linkage with two methyl groups on the carbon adjacent to the maytansinoid side of the disulfide bond, while the huC242-SPP-DM1 conjugate has a relatively less hindered disulfide linkage with one methyl group on the carbon adjacent to the antibody side of the

* To whom correspondence should be addressed. Tel.: 781-895-0734; fax:781-895-0611, E-mail address: hans.erickson@immunogen.com.

[1]Abbreviations: ADC, antibody−drug conjugate; NEM, *N*-ethylmaleimide; TFA, trifluoroacetic acid; BSA, bovine serum albumin; HPLC, high performance liquid chromatography; mAb, monoclonal antibody; LSC, liquid scintillation counting; WST-8, 2-(2-methoxy-4-nitrophenyl)-3-(4-nitrophenyl)-5-(2,4-disulfophenyl)-2*H* tetrazolium, monosodium salt; SPDB, *N*-succinimidyl 4-(2-pyridyldithio)butyrate; SPP, *N*-succinimidyl 4-(2-pyridyldithio)pentanoate; SMCC, *N*-succinimidyl 4-(*N*-maleimidomethyl)cyclohexane-1-carboxylate; DM1, $N^{2'}$-deacetyl-$N^{2'}$-(3-mercapto-1-oxopropyl)-maytansine; DM4, $N^{2'}$-deacetyl-$N^{2'}$-(4-mercapto-4-methyl-1-oxopentyl)-maytansine; AMC, antibody−maytansinoid conjugate; DM4-NEM, *S*-(*N*-ethylsuccinimid-2-yl)DM4; DM1-NEM, *S*-(*N*-ethylsuccinimid-2-yl)DM1.

10.1021/bc900315y © 2010 American Chemical Society
Published on Web 11/05/2009

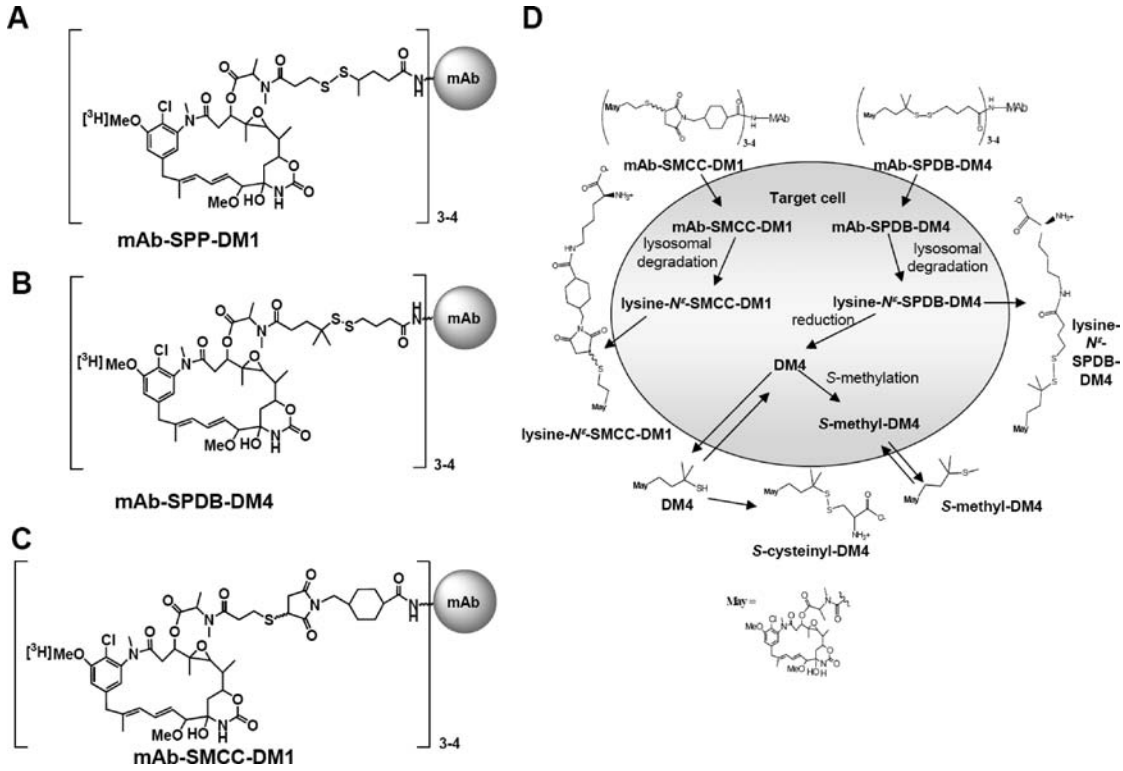


Figure 1. (A,B,C) Structures for the three antibody−maytansinoid conjugates used in this study. (D) Model for the activation of huC242-maytansinoid in targeted cancer cells (*10*). The activation of the disulfide-linked huC242-SPP-DM1 conjugate (not shown) is similar to the activation of huC242-SPDB-DM4 with the exception that the DM1 metabolite is not S-methylated.

disulfide bond (Figure 1A,B). Other disulfide-linked conjugates with varying degrees of steric hindrance and an uncleavable thioether-linked version were evaluated in mouse xenograft models (*12, 14*). The disulfide-linked conjugate, IMGN242, was found to have the most antitumor activity and the widest therapeutic window in vivo as defined by the difference between the maximum tolerated dose and the minimally effective dose in mouse xenograft models. Similar preclinical observations have led to the selection of other disulfide-linked antibody−maytansinoid conjugates (AMC's) for further clinical development (*15*−*17*). In addition, several disulfide-linked AMCs targeting B-cell antigens were recently shown to display significantly more activity in mouse xenograft models than the corresponding uncleavable versions (*18*). However, an uncleavable linker was found to yield more antitumor activity in preclinical models for a trastuzumab−maytansinoid conjugate targeting the HER2 antigen when compared with disulfide-based linkers (*4*), suggesting that there are properties unique to the target antigen (or cancer cell) that influence the observed antitumor activity of AMCs.

We previously identified the major target-cell metabolites of the disulfide-linked huC242-SPDB-DM4 and the uncleavable huC242-SMCC-DM1 conjugate and found that both conjugates were processed to lysine-linker-maytansinoids following antigen-mediated internalization and lysosomal processing. However, only the disulfide-linked lysine-linker-maytansinoid underwent further intracellular processing to yield the liphophilic metabolites, DM4 and *S*-methyl-DM4 (Figure 1) (*10*). We proposed that "bystander" effects associated with these metabolites could enhance the potency of disulfide-linked conjugates in vivo if the processing of the conjugates within tumors was the same as those observed in vitro. This would explain why disulfide-linked AMCs for certain targets such as CanAg display more activity than uncleavable versions in preclinical models. However, the relationship between the in vitro and in vivo target-cell processing of the conjugates is unclear and other possibilities such as better processing and tumor delivery for disulfide-linked conjugates in vivo could also explain the observed efficacy results. In the current study, we examined the in vivo processing and delivery by isolating the ^{3}H-maytansinoid metabolites from tumor tissue following the treatment of mice bearing CanAg positive COLO 205 tumors with the thioether-linked huC242-SMCC-[^{3}H]DM1, and the two hindered disulfide-linked conjugates huC242-SPDB-[^{3}H]DM4 and huC242-SPP-[^{3}H]DM1. Our findings support our previous proposal that the superior activity of the disulfide-linked huC242-maytansinoid conjugates over the uncleavable huC242-SMCC-DM1 conjugate is likely due to the unique cell-killing properties associated with the metabolites derived from the disulfide-linked conjugates.

EXPERIMENTAL PROCEDURES

Cell Lines and Reagents. All cells were obtained from the American Type Culture Collection and grown in the recommended culture medium. Ultima Flo M scintillation fluid and solvable were from PerkinElmer life and analytical sciences. All chemicals were obtained from Sigma-Aldrich. The HPLC 10 μm C-18 column (0.46 × 25 cm, Vydac) was obtained from the Nest Group. The ULTRA-TURRAX T8 dispersing instrument was obtained from IKA Works Inc.

Preparation of Conjugates. Both tritium-labeled DM1 and DM4 were prepared from tritium-labeled ansamitocins P-3 by methods that were previously described for the synthesis of unlabeled DM1 and DM4 (*12*). The tritium-labeled ansamitocin P-3 was prepared as follows. First, the C20-OMe methyl group of ansamitocins P-3 was removed by incubation with the bacterial strain *Streptomyces platensis* to give ansamitocins PDM-3 (*19*). The C-20-OH moiety of ansamitocins PDM-3 was then methylated using tritium-labeled methyl iodide by a method described by Iwaskai (*20*). AMCs were prepared as described elsewhere (*12*) using the tritium-labeled DM1 and DM4. The humanized anti-CanAg monoclonal antibody, huC242, and

isotype-matched nonbinding human IgG_1 antibodies, mAb with similar pharmacokinetic properties as huC242, were isolated at ImmunoGen. Neither huC242 or any of the nonbinding control antibodies bind to any antigen in mice. In this report, conjugates are described by including the abbreviation for the linkers used in conjugation. The average ratio of maytansinoid molecules-DM1 or DM4-linked per antibody molecule (D/A) for each conjugate was as follows: huC242-SPP-DM1 (3.9 D/A), huC242-SMCC-DM1 (3.3 D/A), huC242-SPDB-DM4 (3.4 D/A), huC242-SPP-[^{3}H]DM1 (4.0 D/A), huC242-SMCC-[^{3}H]DM1 (4.1 D/A), huC242-SPDB-[^{3}H]DM4 (3.9 D/A), nontargeting mAb-SMCC-[^{3}H]DM1 (4.3 D/A), nontargeting mAb-SPDB-[^{3}H]DM4 (3.7 D/A).

Mouse Xenograft Models. Female CB-17 severe combined immunodeficient mice (SCID mice; Taconic Laboratories, Germantown, NY) bearing COLO 205 tumor xenografts were used for both the in vivo efficacy and metabolism studies. Mice were inoculated with 3×10^6 COLO 205 cells in 100 μL serum-free medium by subcutaneous injection in the area under the right shoulder. CB-17 SCID mice were randomized into four groups ($n = 6$ for efficacy, $n = 2$ for metabolism studies) by tumor volume, 12 days post inoculation of COLO 205 cells. The tumor volumes ranged from 165.6 to 413.4 (296.5 ± 80.5, mean $\pm$ SD) mm^3. Treatments began on the same day. The tumor volumes were measured as described previously (*12*). Log_{10} cell kill was calculated as described elsewhere (*21*). For the metabolism studies, the systemic circulation of mice was flushed by injecting 5 mL PBS into the left ventricle and draining through an incision in the inferior vena cava immediately following sacrifice. Whole tumor tissues were collected, frozen in liquid nitrogen, and stored at -80 °C.

In Vitro Cell Proliferation Assays. The cytotoxic potencies of the maytansinoids toward human cancer cell lines were assessed using a WST-8 cell viability assay as described previously (*12*). For controls to assess the antigen dependence on the activity of the huC242-maytansinioid conjugates, 1 μM unconjugated huC242 was added to the cells 30 min prior to the addition of the conjugate.

Extraction of [^{3}H]maytansinoid Metabolites from Tumor Tissue. Tumor tissue was thawed on ice and immediately cut into small pieces. Five volumes (v/w) of ice-cold 10 mM Tris−HCl, pH 7.5, containing 5 mM NEM was added, and the tissue was homogenized with a Ultra-Turrax T8 dispersing instrument with a S8N dispersing tool (IKA Works Inc.). The homogenate was then placed on ice for 2 h to allow complete alkylation of any free thiols with *N*-ethyl-maleimide (NEM), trapping any intratumoral DM1 or DM4 thiol metabolites as the respective NEM adducts. The alkylation also eliminates the possibility of DM1 or DM4 release from intact conjugate during the workup through thiol disulfide interchange. A portion of the homogenate (0.4 mL) was extracted three times with a solution (3.4 volumes) of ethyl acetate/methanol (7.5:1, v/v), and the extracts were evaporated to dryness in an evacuated centrifuge. The samples were then dissolved in 0.12 mL 20% aqueous acetonitrile containing 0.025% TFA and analyzed by HPLC.

Determination of Total Radiolabeled Maytansinoid Associated with Tumor Tissue. Homogenate of the entire tumor tissue was prepared as described above. The homogenates were solubilized using solvable (PerkinElmer) as described by the manufacturer, and radioactivity was determined by liquid scintillation counting (LSC).

Analytical Methods. Maytansinoids were separated on an analytical C-18 column (Vydac, 0.46 × 25 cm) (*10*). The effluent was collected in 0.5 or 1 mL fractions, and the radioactivity associated with each fraction was determined by mixing each vial with 4 mL Ultima Gold liquid scintillation cocktail before counting for 5 min in a Tri-Carb 2900T liquid scintillation counter. LCMS analysis was performed as described previously (*10*).

RESULTS

The Uncleavable huC242 Antibody−Maytansinoid Conjugate Displays Similar Cytotoxic Activity to Disulfide-Linked Conjugates in Vitro but Lower Antitumor Activity in Vivo. The two disulfide-linked conjugates—huC242-SPDB-DM4 and huC242-SPP-DM1—and the uncleavable conjugate huC242-SMCC-DM1 were assayed for their cytotoxic potency against antigen-positive COLO 205 cells using a cell viability assay. All three conjugates displayed similar cytotoxic potencies (IC_{50} 50−90 pM) upon a 4-day exposure of the cells to the conjugates (Figure 2A). These observed cytotoxicities were reduced over 100-fold ($IC_{50} > 5$ nM) when the assay was repeated in the presence of excess unconjugated huC242 antibody demonstrating that cell killing by the conjugates was antigen-specific.

We then investigated the antitumor activities of the conjugates against established COLO 205 xenografts in SCID mice. A single intravenous administration of 300 μg/kg based on DM1 or DM4 (equivalent to ~15 mg/kg based on antibody dose) of the three conjugates was administered once the tumors had reached a relatively large size of 300 mm^3. The same treatment conditions were selected for the metabolism studies described in the following sections. The antitumor responses are displayed in Figure 2B. A single administration of huC242-SPDB-DM4 was found to be more active than huC242-SPP-DM1 (log cell kill 0.9 vs 0.5, respectively), while huC242-SMCC-DM1 was inactive under these conditions. Although treatment with huC242-SMCC-DM1 elicited no measurable tumor regression for the 300 mm^3 established tumors in this study, previous studies have demonstrated significant antitumor activity when smaller established COLO 205 xenografts (100 mm^3) were treated with a greater total dose (750 μg/kg of conjugated DM1, ~38 mg/kg based on antibody dose administered as five daily injections of 150 μg/kg/d) (*14*).

Accumulation of ^{3}H-maytansinoid in Tumor Tissue. DM1 and DM4 were tritium-labeled at the C-20 methoxy group (Figure 1A,B) and conjugated to the huC242 antibody as described previously (*10, 14*). The [^{3}H]AMCs were found to exhibit in vitro cytotoxicities similar to non-radiolabeled AMCs (data not shown). SCID mice bearing COLO 205 tumors were treated with single intravenous injections of 300 μg/kg based on DM1 or DM4 (~15 mg/kg antibody dose) of the three [^{3}H]AMCs and tumor tissues were analyzed for total radioactivity to determine the percentage of the administered conjugate (based on DM1 or DM4) that had accumulated per gram of tumor tissue (%ID/g). Figure 2C shows the %ID/g over time following the administration of the conjugate. The AUC for the %ID/g associated with the huC242-SMCC-[^{3}H]DM1 was nearly 2-fold greater than the AUC associated with the two disulfide-linked conjugates, huC242-SPP-[^{3}H]DM1 and huC242-SPDB-[^{3}H]DM4. Next, we investigated the relationship between the administered dose of the conjugate and tumor localization. SCID mice bearing COLO 205 xenografts (2 animals per dose group) were treated with single bolus injections of 100 μg/kg, 200 μg/kg, and 300 μg/kg (based on maytansinoid) of huC242-SMCC-[^{3}H]DM1 or huC242-SPDB-[^{3}H]DM4 and the tumor localization after 2 days was calculated as described above (Figure 2D). The %ID/g associated with both conjugates changed little in the dose range of 100−300 μg/kg based on DM1 or DM4 (~5−15 mg/kg antibody dose). In addtion, at all doses, the %ID/g localized with the uncleavable huC242-SMCC-DM1 conjugate (10−12%ID/g) was 1.5- to 2-fold greater than the %ID/g associated with the cleavable huC242-SPDB-[^{3}H]DM4 conjugate (6−8%ID/g).

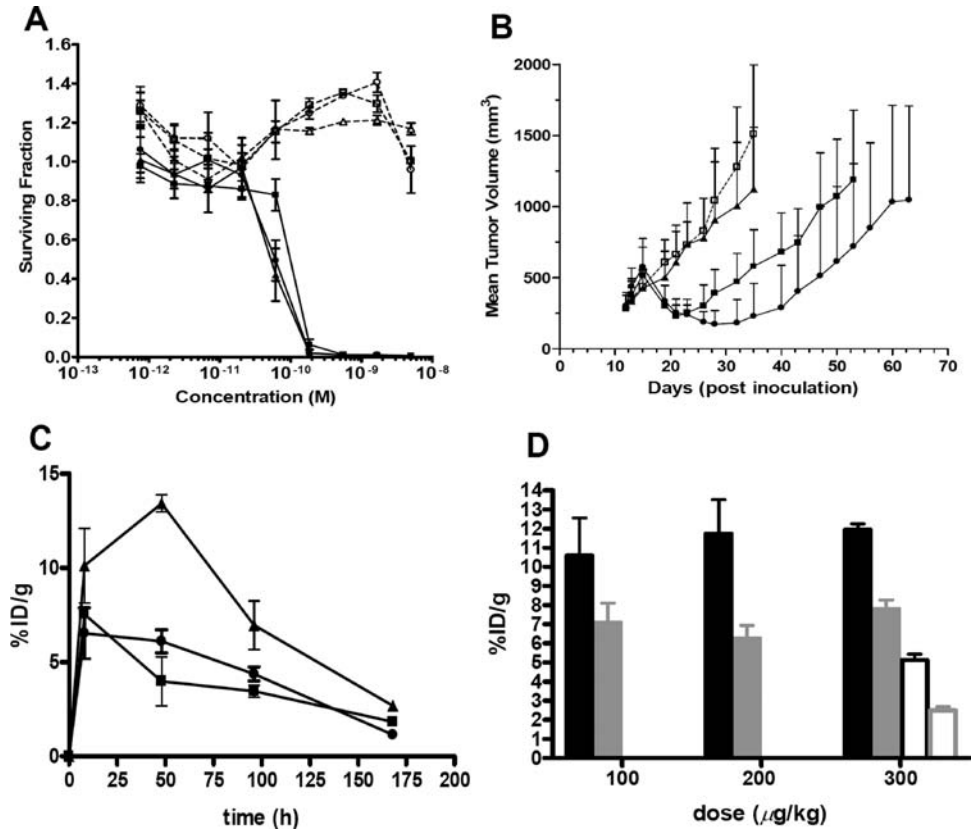


Figure 2. Targeted activity and tumor localization of huC242-maytansinoid conjugates. (A) In vitro activities of huC242-SMCC-DM1, huC242-SPDB-DM4, and huC242-SPP-DM1. COLO 205 cells were exposed to different concentrations of huC242-SMCC-DM1 (▲), huC242-SPDB-DM4 (●), and huC242-SPP-DM1 (■) in the presence (△,○,□) or absence (▲,●,■) of 1 μM huC242 for 4 d. Surviving fraction is plotted vs concentration (based on mAb). (B) Antitumor activities in SCID mice bearing subcutaneous COLO 205 xenografts. A single bolus injection of a vehicle control (□), huC242-SMCC-DM1 (▲), huC242-SPDB-DM4 (●), and huC242-SPP-DM1 (■) were each administered at a dose of 300 μg/kg once tumors reached sizes of 300 mm^3. Dosage is based on the amount of conjugated DM1 or DM4 and is approximately equivalent to 15 mg/kg of antibody. (C) Tumor localization of huC242-SMCC-[^{3}H]DM1, huC242-SPDB-[^{3}H]DM4, and huC242-SPP-[^{3}H]DM1conjugates. The percentage of the injected dose of [^{3}H]DM1 or [^{3}H]DM4 accumulated per gram of tissue (%ID/g) at 8 h, 2 d, 4 d, and 7 d from mice treated with single bolus injections of huC242-SMCC-[^{3}H]DM1 (▲), huC242-SPDB-[^{3}H]DM4 (●) and huC242-SPP-[^{3}H]DM1 (■). Conjugates were administered at a dose of 300 μg/kg (based on DM1 or DM4 concentration) once tumors reached sizes of 300 mm^3. The radioactivity accumulated in tumor tissues was determined by LSC of solubilized tumor homogenates and divided by the total CPM of tritium administered. (D) The effect of dose and antigen targeting on accumulation. Tumor accumulation (%ID/g) at 2 d following single bolus injections of 100 μg/kg, 200 μg/kg, and 300 μg/kg (based on DM1 or DM4 concentration) of huC242-SMCC-[^{3}H]DM1 (black), huC242-SPDB-[^{3}H]DM4 (gray) once tumors reached sizes of 300 mm^3. Tumor localization for the nontargeting mAb_1 SMCC-[^{3}H]DM1 (open black bars) and mAb_2-SPDB-[^{3}H]DM4 (open gray bars) was also determined at the 300 μg/kg dose.

To investigate the antigen specificity of maytansinoid localization at the tumor, two nontargeting conjugates were prepared, mAb-SPDB-[^{3}H]DM4 and mAb-SMCC-[^{3}H]DM1, each using antibodies that do not bind to COLO 205 cells (data not shown). The %ID/g of these nontargeting conjugates was determined at the 300 μg/kg dose in mice bearing COLO 205 tumors (Figure 2D) two days following administration of the conjugates. The %ID/g for the nontargeting conjugates was approximately 3-fold lower than the respective targeting huC242 conjugates at the same dose (Figure 2D). As was observed for the targeting conjugates, the tumor accumulation of the uncleavable nontargeting conjugate was greater than the tumor accumulation of nontargeting disulfide-linked mAb-SPDB-[^{3}H]DM4 conjugate.

Extraction of ^{3}H-maytansinoid Metabolites from Tumors. To determine the amount and nature of the released maytansinoids, the conditions for the extraction of protein-free ^{3}H-maytansioids from tissue homogenates were first optimized by spiking tissue homogenates with synthetically prepared ^{3}H-maytansinoids and measuring the recovery by HPLC. We found the highest (80%) recoveries for all of the metabolites using a mixture of ethyl acetate and methanol (data not shown). To ensure that maytansinoids were not released from the intact conjugate during the ex vivo homogenization and extraction steps, radiolabeled conjugates were added to freshly prepared COLO 205-tumor homogenates and extracted following the optimized procedure. The extracts were analyzed for ^{3}H-metabolites by reverse-phase HPLC and found to contain no metabolites (data not shown).

Once the conditions for the extraction of protein-free maytansinoids were optimized, portions of the tumor homogenates collected 2 d after treatment with 300 μg/kg of the conjugates in Figure 2B were extracted and analyzed for ^{3}H-maytansinoid metabolites by reverse-phase HPLC and LSC (Figure 3A,B). Three major tumor metabolites were observed with retention times identical to those of the synthetic standards lysine-N^{ε}-SPDB-DM4, *S*-(*N*-ethylsuccinimid-2-yl)DM4 (DM4-NEM), and *S*-methyl-DM4 for both the targeting huC242-SPDB-[^{3}H]DM4 and the nontargeting mAb-SPDB-[^{3}H]DM4 conjugates (Figure 3A). DM4-NEM is the protected form of the DM4 metabolite that arises from alkylation of DM4 in the tissue homogenates with NEM. In separate experiments, mass spectral analysis of the isolated [^{3}H]maytansinoid metabolites showed the expected masses (DM4-NEM, M + Na^+ = 927; lysine-N^{ε}-SPDB-DM4, M + Na^+ = 1048.4; *S*-methyl-DM4, M + Na^+ = 816.4, M + K^+ = 832.5). The sole tumor metabolite from mice treated with huC242-SMCC-[^{3}H]DM1 and the nontargeting mAb-SMCC-

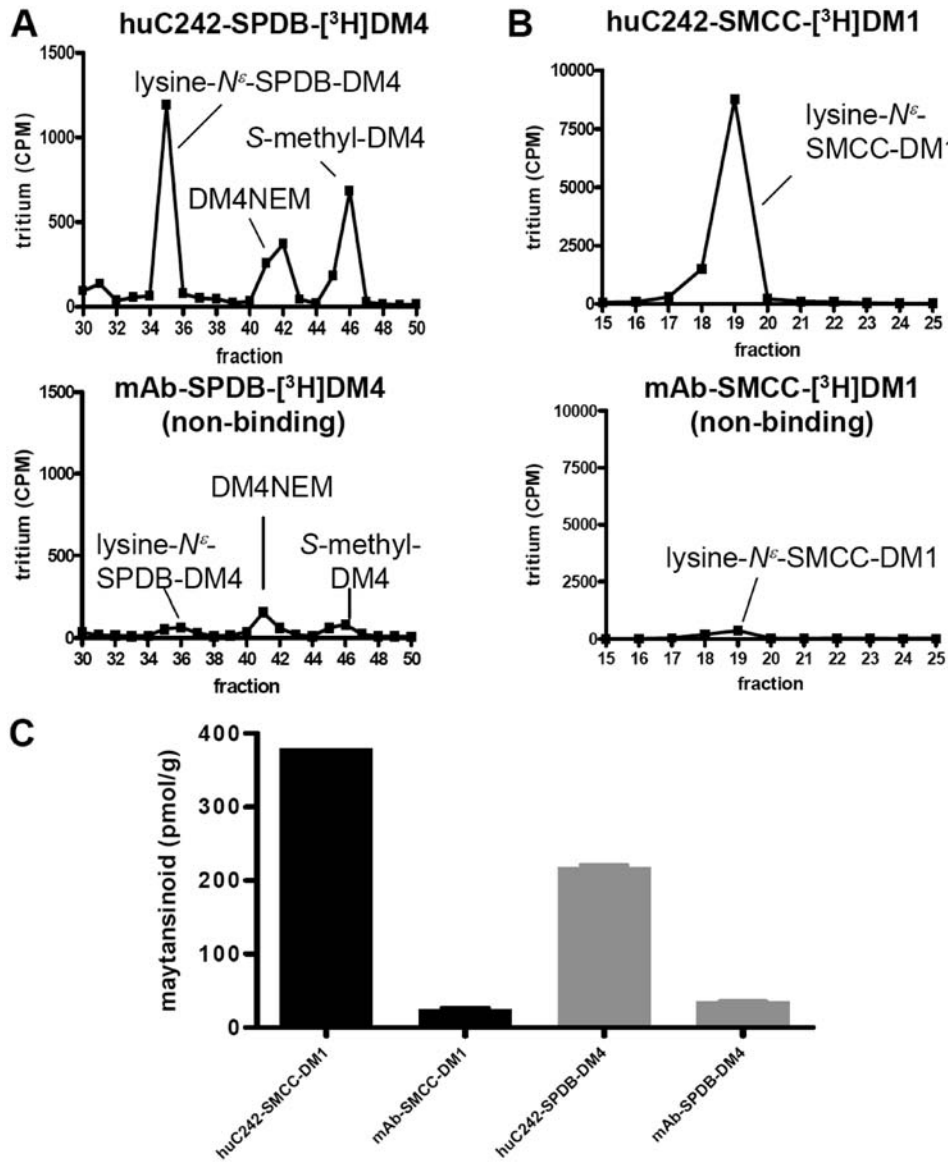


Figure 3. [^{3}H]Maytansinoid metabolites in tumor tissues 2 d following treatment of COLO 205-bearing SCID mice with antibody-[^{3}H]maytansinoid conjugates. (A) Chromatograms associated with tumor metabolites of huC242-SPDB-[^{3}H]DM4 and nontargeting control mAb-SPDB-[^{3}H]DM4, and (B) huC242-SMCC-[^{3}H]DM1 and nontargeting mAb-SMCC-[^{3}H]DM1. Portions of the tumor homogenates analyzed in Figure 2B were extracted, and the extracts were analyzed for metabolites by HPLC. The effluent from the samples associated with the uncleavable conjugate, and the disulfide-linked conjugates were collected in 1 and 0.5 mL fractions, respectively. The radioactivity in each effluent fraction was determined by LSC. The chromatograms show the fraction number on the abscissa and counts per minute of tritium on the ordinate. (C) Total metabolites. The peaks of radioactivity from the chromatograms in A and B were converted to pmol of maytansinoid metabolites, and the sum of the metabolites from each chromatogram was divided by the weight of tumor tissue analyzed to calculate the pmol/g.

[^{3}H]DM1 was lysine-N^{ε}-SMCC-DM1 (Figure 3B). In separate experiments, the lysine-N^{ε}-SMCC-DM1 metabolite was found to have the expected mass ($M + Na^+ = 1125.5$). The radioactivity associated with each of the metabolites in Figure 3A,B were converted to picomole of maytansinoid per gram of tumor tissue (pmol/g) using the specific radioactivities associated with the [^{3}H]AMCs and the weight of the corresponding tumors (Figure 3C). The data revealed a specific effect of antigen binding on accumulation of maytansinoid metabolite(s). The tumor accumulation for the targeting huC242-SPDB-DM4 conjugate was 6-fold higher than the corresponding accumulation from the nontargeting mAb-SPDB-DM4, while the accumulation of maytansinoid metabolites from the targeting huC242-SMCC-DM1 was 16-fold greater than the accumulation from nontargeting mAb_1-SMCC-DM1.

The time course for the accumulation of maytansinoid metabolites was assessed in tumor tissues collected at 8 h, 2 d, 4 d, and 7 d following administration of the huC242-[^{3}H]maytansinoid conjugates for which the tumor localization data was described in Figure 2. The HPLC chromatograms in Figure 4 display the peaks of radioactivity associated with the tumor metabolites isolated from each sample. The sole metabolite of huC242-SMCC-[^{3}H]DM1 at all time points was lysine-N^{ε}-SMCC-[^{3}H]DM1 (Figure 4A). The major metabolite of huC242-SPDB-[^{3}H]DM4 observed at the first time point (8 h) was lysine-N^{ε}-SPDB-[^{3}H]DM4 (72% of total metabolites) (Figure 4B). However, DM4-NEM (24% of total metabolites), representing intratumoral release of DM4, and a small amount of *S*-methyl-DM4 (4% of total metabolites) were also evident by 8 h.

Figure 4C displays the signals for the amount of radioactivity associated with the tumor metabolites from mice treated with huC242-SPP-[^{3}H]DM1. Peaks of radioactivity with retention times identical to the synthetic standards, lysine-N^{ε}-SPP-DM1 and *S*-(*N*-ethyl succinimid-2-yl)DM1 (DM1-NEM), were ob-

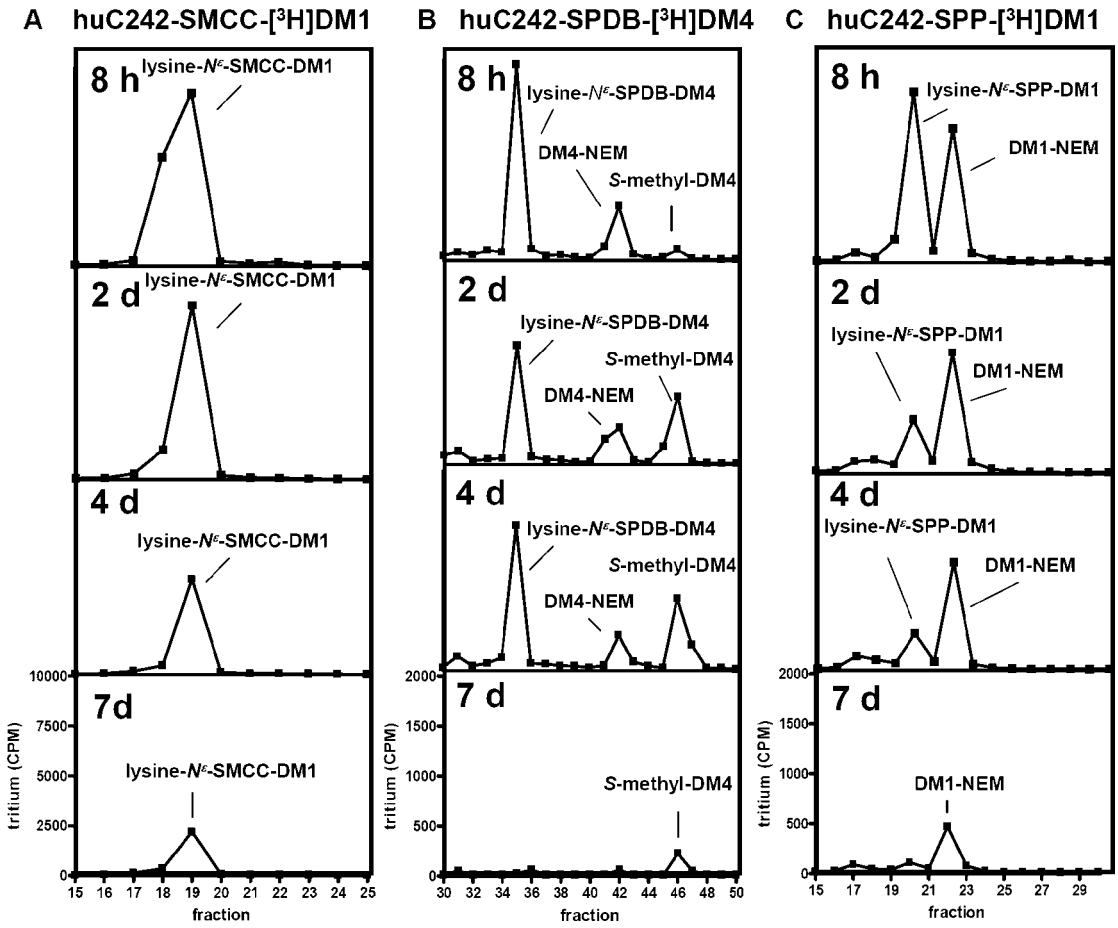


Figure 4. Maytansinoid metabolites formed in tumor tissues over time. Chromatograms associated with tumors collected from mice 8 h, 2 d, 4 d, and 7 d following administration of huC242-SMCC-[^{3}H]DM1 (A), huC242-SPDB-[^{3}H]DM4 (B), and huC242-SPP-[^{3}H]DM1 (C). Portions of the tumor homogenates from the COLO205 bearing SCID mice treated with a single dose of 300 μg/kg (DM1 or DM4 dose/ ~15 mg/kg antibody dose) described in Figure 2C were analyzed for metabolites described in Figure 3. The chromatograms show the fraction number on the abscissa and counts per minute of tritium on the ordinate.

served in the tumor tissues from the first three time points. The identities of the two metabolites were confirmed in separate experiments by LC-MS (DM1-NEM, M + Na^+ = 885.3; lysine-N^ε-SPP-DM1, M + Na^+ = 1020.3 and M + K^+ = 1036.4). The major difference between metabolites of huC242-SPP-[^{3}H]DM1 and huC242-SPDB-[^{3}H]DM4 was the absence of *S*-methyl-[^{3}H]DM1 in the tumor tissues from the mice treated with huC242-SPP-[^{3}H]DM1, suggesting that the DM1 thiol is a poor substrate for the *S*-methyltransferase in tumor cells. Nearly 45% of the total metabolite at 8 h was associated with DM1−2-fold higher than the percentage of DM4 and *S*-methyl-DM4 in the corresponding 8 h tumors treated with huC242-SPDB-[^{3}H]DM4, consistent with its less hindered and more readily reducible disulfide linker.

The radioactivity associated with the metabolites generated from the three ^{3}H-conjugates in tumor tissues from Figure 4 was converted to picomoles per gram of tumor tissue (pmol/g). Figure 5 shows the accumulation of the maytansinoid metabolites per gram of tumor tissue over time following administration of each conjugate to the mice. The AUC over seven days associated with the lysine-N^ε-SMCC-[^{3}H]DM1 metabolite was about 2-fold greater than the corresponding AUCs of the total extractable metabolites from either of the two disulfide-linked conjugates. We further demonstrate that the observed metabolites account for the majority of the radioactivity at the tumors (Supporting Information Figure S1).

Cytotoxic Potency of Maytansinoid Metabolites Identified in Vivo. Maytansinoids bind to the same vinca alkaloid binding domain of tubulin as the antimitototic drug vinblastine. Maytansine was found to be about 3- to 10-fold more cytototoxic than vinblastine toward several cell lines (*22*). The major maytansinoid metabolites identified in vivo were prepared synthetically, and their cytotoxic potencies were assayed against several human carcinoma cell lines using a cell viability assay. The IC_{50} values for each of the maytansinoids are displayed in Table 1. The *S*-methyl-DM4 and *S*-methyl-DM1 (the latter not identified in significant quantities in vivo) display the highest potency with IC_{50} values of between 0.01 and 0.03 nM, 2- to 3-fold higher than the potency of maytansine. All of the lysine derivatives are 100- to 1000-fold less potent than *S*-methyl-DM1 and *S*-methyl-DM4, likely due to the inability of these charged maytansinoids to diffuse into cells (*10*). The two thiol-bearing metabolites, DM1 and DM4, were not tested in the assay because their potencies measured in vitro assays are variable, and less than that of the reference compound, maytansine, likely due to the formation of mixed disulfides via thiol/disulfide exchange reactions with cystine and protein disulfides in the cell culture medium.

Efflux of Maytansinoid Metabolites from Cells. Previously, we speculated that the more lipophilic maytansinoid metabolites (DM1, DM4, and *S*-methyl-DM4) generated within the target cells could diffuse out of the cells and into and kill neighboring cells (bystander effect), providing additional activity for disulfide-linked conjugates (*14*). To estimate whether the concentrations of the metabolites were high enough within the tumor cells to reach levels where efflux would be expected, we first determined those levels in vitro. Cultures of COLO 205 cells (2×10^6 cells/mL) were treated with varying concentrations of

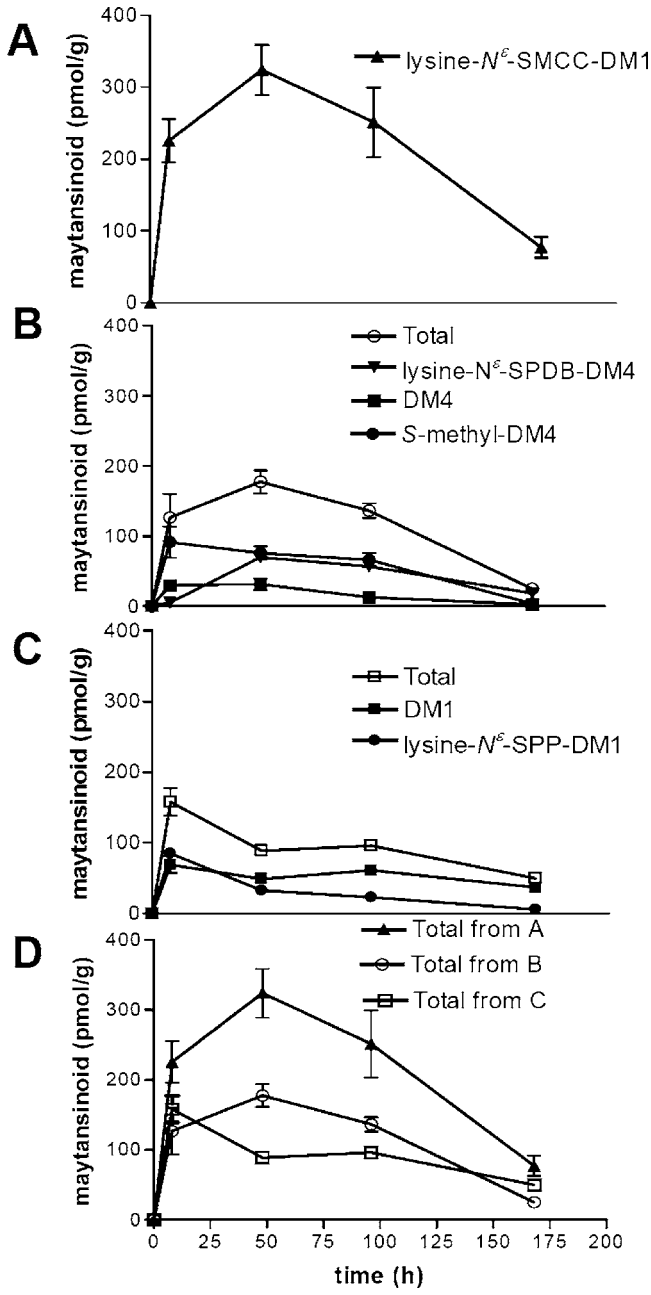


Figure 5. Kinetics of tumor processing. The amounts of maytansinoid metabolites in tumor tissue at 8 h, 2 d, 4 d, and 7 d following a single intravenous administration of 300 μg/kg (DM1 or DM4 dose/ ~15 mg/kg antibody dose) of (A) huC242-SMCC-[^{3}H]DM1; lysine-N^{ε}-SMCC-DM1(▲), (B) huC242-SPDB-[^{3}H]DM4; lysine-N^{ε}-SPDB-DM4 (▼), DM4 (■), *S*-methyl-DM4 (●), total metabolites (○), (C) huC242-SPP-[^{3}H]DM1; lysine-N^{ε}-SPP-DM1 (●), DM1 (■), total metabolites (□), (D) total metabolites from A−C. The radioactivities associated with each of the metabolites (Figure 4) were divided by the amount of tumor tissue analyzed to calculate the pmol/g. The relative pmol/g data differs slightly from the relative peak areas in Figure 4 due to differences in tumor weights.

huC242-SPDB-[^{3}H]DM4 (50 nM, 5 nM, or 0.5 nM) for 24 h, and the cells and medium were analyzed for metabolites as described previously (*10*). The amount of metabolites, as quantified by radioactive measurements, was used to calculate the number of maytansinoid molecules per cell. Exposure of cells to 5 nM and 50 nM huC242-SPDB-[^{3}H]DM4 resulted in an intracellular accumulation of 590 000 and 5 100 000 maytansinoid molecules per cell, respectively, and significant accumulation of maytansinoids in the medium via efflux from the cell (an amount corresponding to about 60% of the intracellular accumulation). Exposure of cells to 0.5 nM conjugate for 24 h resulted in accumulation of 39 000 molecules per cell and no detectable efflux (Supporting Information Figure S2 and Supporting Information Table 1).

We next estimated the average number of maytansinoid molecules per cell localized in the tumors from the current study. The C_{max} for the total maytansinoid metabolites of huC242-SPDB-[^{3}H]DM4 in tumor tissue in the current study was 180 pmol/g (Figure 5A). Assuming the cell density in COLO 205 tumor xenografts is in the range $(2-4) \times 10^8$ cells/mL (*23*), an average value of 300 000−600 000 molecules/cell of maytansinoid metabolites was observed in the tumor tissue. Since we observe significant efflux from COLO 205 cells that have accumulated this level of metabolite in vitro, the results displayed in Figure 5 suggest that it is very likely that cellular efflux of the metabolites also occurred within the tumors of the current study.

DISCUSSION

The major maytansinoid metabolites of the disulfide-linked and uncleavable thioether-linked huC242-maytansinoid conjugates isolated from tumor tissue imply an in vivo activation pathway similar to the one described previously from our in vitro studies (Figure 1) (*10*). A major metabolite observed in the tumor tissue from mice treated with all three conjugates is the lysine-linker-maytansinoid metabolite, presumably formed by the degradation of each conjugate in the lysosomes of the targeted cancer cells (*10*). The lysine-N^{ε}-SMCC-DM1 metabolite is the only maytansinoid metabolite observed in the tumor tissue of mice treated with the uncleavable huC242-SMCC-DM1 conjugate, reflecting the stability of the thioether linker. By contrast, analysis of tumor tissues from the mice treated with the cleavable disulfide-linked huC242-SPDB-DM4 and huC242-SPP-DM1 conjugates reveal the additional lipophilic metabolites, DM4 and *S*-methyl-DM4, and DM1, respectively. In vitro, we found that the DM4 and *S*-methyl-DM4 metabolites of huC242-SPDB-DM4 were formed within target cells from lysine-N^{ε}-SPDB-DM4 following reduction and *S*-methylation steps. The observed tumor metabolites suggest similar tumor cellular processing steps in vivo. Similarly, the lysine-N^{ε}-SPP-DM1 metabolite of huC242-SPP-DM1 appears to be reduced in vivo to yield DM1; however, the released DM1 does not appear to be further *S*-methylated. In separate experiments, we found that DM1 was less readily *S*-methylated than DM4 by the endogenous *S*-methyl-transferase(s) of COLO 205 cells, as well as several other human carcinoma cells in vitro (data not shown).

In vitro, the maytansinoid metabolites were all found to be released from the target cells into the medium where the readily diffusible DM1, DM4, and *S*-methyl-DM4 metabolites retain their cell killing potency, while the lysyl derivatives lose their cell killing potency, presumably because the charged lysyl moiety hinders diffusion across the plasma membrane of cells and thus inhibits re-entry into neighboring cells (*10*). We have speculated previously that the potential for bystander killing of neighboring cells by diffusible metabolites may partially explain why the disulfide-linked huC242-SPP-DM1 was found to eradicate mixed tumor xenografts consisting of antigen-positive and antigen-negative cells as previously reported and why—as observed in this study—the cleavable disulfide-linked huC242-maytansinoid conjugates have more antitumor activity than the uncleavable thioether-linked conjugate toward COLO 205 cells that express the target antigen homogeneously (*10, 14*). In the study described herein, we estimate that the levels of the tumor metabolites accumulated in vivo are high enough to allow for the metabolites to diffuse from the target cells

Table 1. Cytotoxic Potencies of Maytansine and Metabolites of Antibody−Maytansinoid Conjugates Towards Human Carcinoma Cell Lines in Vitro (4 d Exposure).

	in vitro IC_{50} (nM)				
maytansinoid	A375 (melanoma)	BJAB (B-cell)	COLO205 (colon)	KB (cervix)	MOLT-4 (T-cell)
maytansine	0.05	0.03	0.08	0.05	0.09
lysine-N^{ε}-SPP-DM1	10	50	60	10	>100
lysine-N^{ε}-SPDB-DM4	2	7	20	3	16
lysine-N^{ε}-SMCC-DM1	8	8	17	10	16
S-methyl-DM1	0.02	0.01	0.03	0.02	0.03
S-methyl-DM4	0.02	0.01	0.03	0.03	0.03

within the solid tumors, providing support for the hypothesis that bystander killing contributes significantly to tumor eradication in vivo upon treatment with cleavable disulfide-linked conjugates. Such bystander killing may explain why the disulfide-linked conjugates are more active than the uncleavable conjugate despite the fact that the levels for the tumor metabolites of the disulfide-linked conjugates were about 2-fold lower than the corresponding levels for the uncleavable conjugates. The relative tumor accumulation does not appear to correlate with the serum half-lives of the conjugates determined in separate experiments (unpublished data). One explanation for this may be that the lipophilic metabolites of the disulfide-linked conjugates—implicated in the bystander effect—may diffuse out of the tumor tissue more readily than the lysine-N^{ε}-SMCC-DM1 metabolite of the huC242-SMCC-DM1 conjugate. Previously, we have shown that the rates of processing of both disulfide-linked conjugates and uncleavable conjugates are similar in vitro (*10*), and the in vivo results from this study suggest that the mechanism of processing is the same as that determined in the in vitro experiments (Figure 1). Thus, it appears that the very property that allows penetration of the small-molecular-weight lipophilic cytotoxic agent throughout the tumor, resulting in higher antitumor activity, may also result in the maytansinoid metabolites being more readily cleared from the tumor. Despite yielding the highest concentration of tumor metabolites, the huC242-SMCC-DM1 conjugate displayed no detectable antitumor activity at the dose tested in the current study, yet in vitro, the huC242-SMCC-DM1 conjugate and the disulfide-linked conjugates all displayed similarly high cytotoxic potencies. This suggests an uneven uptake and metabolism of the conjugates within COLO 205 tumor xenografts. In another preclinical study, the uncleavable trastuzumab-SMCC-DM1 conjugate was found to have more antitumor activity than the disulfide-linked trastuzumab-SPP-DM1 conjugate in mice bearing HER2-positive tumor xenografts (*4*), suggesting that distribution and delivery of maytansinoid metabolites is sufficient in the trastuzumab-DM1/HER2 system without the need for bystander killing. Thus, the selection of the optimal linker for a given tumor-specific antibody−maytansinoid conjugate requires preclinical experimentation and may depend upon many factors including the biology of the antigen and the biology of the tumor.

Treatment of mice with nontargeting mAb-SMCC-[^{3}H]DM1 and mAb-SPDB-[^{3}H]DM4 resulted in levels of metabolites that were 6-fold and 16-fold lower than the levels observed in mice treated with the targeting huC242-SMCC-[^{3}H]DM1 and huC242-SPDB-[^{3}H]DM4 conjugates, respectively. These results indicate that the tumor metabolites of the targeting huC242−maytansinoid conjugates were formed primarily through a CanAg antigen-mediated mechanism. We were intrigued by the fact that low levels of metabolites are formed from nontargeting conjugates, because it may explain why, in some xenograft mouse models, the nontargeting conjugates at high doses have been found to display significant antitumor activity, albeit significantly lower than that of the corresponding targeting conjugates. The concentration of the nontargeting conjugates in the tumor tissue at the dose used in this study (15 mg/kg) reached 40 nM for mAb-SPDB-[^{3}H]DM4 and 80 nM for mAb-SMCC-[^{3}H]DM1 at 2 d (approximated from the data shown in Figure 2D). At these concentrations, some antigen-independent uptake, for example, by pinocytosis, is likely. The nontargeted processing was more efficient for the disulfide-linked conjugate than for the uncleavable conjugate as shown in Figure 3 suggesting that the release of maytansinoids by thiol/disulfide exchange mechanisms in a nonlysosomal compartment (or extracellularly) may be relatively more significant for antigen-independent metabolism.

Our data are consistent with the proposal (*10, 14*) that disulfide-linked huC242-maytansinoid conjugates are more active than the uncleavable huC242-SMCC-DM1 conjugate in mouse xenograft models due to "bystander" killing. We identified and characterized the major maytansinoid metabolites of the conjugates and estimate that they are produced at levels that would allow for their efflux from targeted cancer cells. Diffusion of the lipophilic metabolites of the disulfide-linked conjugates within the tumor may possibly overcome the numerous barriers that serve to limit access of antibody-based therapeutics to solid tumor targets (*24−26*). We are currently applying the methods developed here to investigate how the target antigen and tumor type influence the delivery and metabolism of AMCs.

ACKNOWLEDGMENT

We thank John Lambert and Ravi Chari for their many helpful suggestions and their careful reading of the manuscript, and Rabih Gabriel and Barbara Leece for the reagents and assistance.

Supporting Information Available: An assessment of the radioactivity associated with tumor tissues (mass balance) is provided. In addition, an analysis of the dose-dependent efflux of metabolites following treatment of target COLO 205 cells in vitro with huC242-SPDB-[^{3}H]DM4 is also provided. This material is available free of charge via the Internet at http://pubs.acs.org.

LITERATURE CITED

(1) Bross, P. F., Beitz, J., Chen, G., Chen, X. H., Duffy, E., Kieffer, L., Roy, S., Sridhara, R., Rahman, A., Williams, G., and Pazdur, R. (2001) Approval summary: gemtuzumab ozogamicin in relapsed acute myeloid leukemia. *Clin. Cancer Res. 7*, 1490–6.

(2) Wu, A. M., and Senter, P. D. (2005) Arming antibodies: prospects and challenges for immunoconjugates. *Nat. Biotechnol. 23*, 1137–46.

(3) Lambert, J. M. (2005) Drug-conjugated monoclonal antibodies for the treatment of cancer. *Curr. Opin. Pharmacol. 5*, 543–9.

(4) Lewis Phillips, G. D., Li, G., Dugger, D. L., Crocker, L. M., Parsons, K. L., Mai, E., Blattler, W. A., Lambert, J. M., Chari, R. V., Lutz, R. J., Wong, W. L., Jacobson, F. S., Koeppen, H., Schwall, R. H., Kenkare-Mitra, S. R., Spencer, S. D., and Sliwkowski, M. X. (2008) Targeting HER2-positive breast cancer with trastuzumab-DM1, an antibody-cytotoxic drug conjugate. *Cancer Res. 68*, 9280–90.

(5) Younes, A., Forero-Torres, A., Bartlett, N. L., Leonard, J. P, Lynch, C., Kennedy, D. A., and Sievers, E. L. (2008) Multiple

complete responses in a Phase 1 dose-escalation study of the antibody-drug conjugate SGN-35 in patients with relapsed or refractory CD30-positive lymphomas. *Blood (ASH Annual Meeting Abstracts 112*, 1006. 2008) in ASH.

(6) Xie, H., Audette, C., Hoffee, M., Lambert, J. M., and Blattler, W. A. (2004) Pharmacokinetics and biodistribution of the antitumor immunoconjugate, cantuzumab mertansine (huC242-DM1), and its two components in mice. *J. Pharmacol. Exp. Ther. 308*, 1073–82.

(7) Chari, R. V. (2008) Targeted cancer therapy: conferring specificity to cytotoxic drugs. *Acc. Chem. Res. 41*, 98–107.

(8) Doronina, S. O., Bovee, T. D., Meyer, D. W., Miyamoto, J. B., Anderson, M. E., Morris-Tilden, C. A., and Senter, P. D. (2008) Novel peptide linkers for highly potent antibody-auristatin conjugate. *Bioconjugate Chem. 19*, 1960–3.

(9) Hamann, P. R., Hinman, L. M., Beyer, C. F., Lindh, D., Upeslacis, J., Flowers, D. A., and Bernstein, I. (2002) An anti-CD33 antibody-calicheamicin conjugate for treatment of acute myeloid leukemia. Choice of linker. *Bioconjugate Chem. 13*, 40–6.

(10) Erickson, H. K., Park, P. U., Widdison, W. C., Kovtun, Y. V., Garrett, L. M., Hoffman, K., Lutz, R. J., Goldmacher, V. S., and Blattler, W. A. (2006) Antibody-maytansinoid conjugates are activated in targeted cancer cells by lysosomal degradation and linker-dependent intracellular processing. *Cancer Res. 66*, 4426–33.

(11) Doronina, S. O., Mendelsohn, B. A., Bovee, T. D., Cerveny, C. G., Alley, S. C., Meyer, D. L., Oflazoglu, E., Toki, B. E., Sanderson, R. J., Zabinski, R. F., Wahl, A. F., and Senter, P. D. (2006) Enhanced activity of monomethylauristatin F through monoclonal antibody delivery: effects of linker technology on efficacy and toxicity. *Bioconjugate Chem. 17*, 114–24.

(12) Widdison, W. C., Wilhelm, S. D., Cavanagh, E. E., Whiteman, K. R., Leece, B. A., Kovtun, Y., Goldmacher, V. S., Xie, H., Steeves, R. M., Lutz, R. J., Zhao, R., Wang, L., Blattler, W. A., and Chari, R. V. (2006) Semisynthetic maytansine analogues for the targeted treatment of cancer. *J. Med. Chem. 49*, 4392–408.

(13) Stephan, J. P., Chan, P., Lee, C., Nelson, C., Elliott, J. M., Bechtel, C., Raab, H., Xie, D., Akutagawa, J., Baudys, J., Saad, O., Prabhu, S., Wong, W. L., Vandlen, R., Jacobson, F., and Ebens, A. (2008) Anti-CD22-MCC-DM1 and MC-MMAF conjugates: impact of assay format on pharmacokinetic parameters determination. *Bioconjugate Chem. 19*, 1673–83.

(14) Kovtun, Y. V., Audette, C. A., Ye, Y., Xie, H., Ruberti, M. F., Phinney, S. J., Leece, B. A., Chittenden, T., Blattler, W. A., and Goldmacher, V. S. (2006) Antibody-drug conjugates designed to eradicate tumors with homogeneous and heterogeneous expression of the target antigen. *Cancer Res. 66*, 3214–21.

(15) Chen, Q., Millar, H. J., McCabe, F. L., Manning, C. D., Steeves, R., Lai, K., Kellogg, B., Lutz, R. J., Trikha, M., Nakada, M. T., and Anderson, G. M. (2007) Alphav integrin-targeted immunoconjugates regress established human tumors in xenograft models. *Clin. Cancer Res. 13*, 3689–95.

(16) Al-Katib, A. M., Aboukameel, A., Mohammad, R., Bissery, M. C., and Zuany-Amorim, C. (2009) Superior antitumor activity of SAR3419 to rituximab in xenograft models for non-Hodgkin's lymphoma. *Clin. Cancer Res. 15*, 4038–45.

(17) Ikeda, H., Hideshima, T., Fulciniti, M., Lutz, R. J., Yasui, H., Okawa, Y., Kiziltepe, T., Vallet, S., Pozzi, S., Santo, L., Perrone, G., Tai, Y. T., Cirstea, D., Raje, N. S., Uherek, C., Dalken, B., Aigner, S., Osterroth, F., Munshi, N., Richardson, P., and Anderson, K. C. (2009) The monoclonal antibody nBT062 conjugated to cytotoxic Maytansinoids has selective cytotoxicity against CD138-positive multiple myeloma cells in vitro and in vivo. *Clin. Cancer Res. 15*, 4028–37.

(18) Polson, A. G., Calemine-Fenaux, J., Chan, P., Chang, W., Christensen, E., Clark, S., de Sauvage, F. J., Eaton, D., Elkins, K., Elliott, J. M., Frantz, G., Fuji, R. N., Gray, A., Harden, K., Ingle, G. S., Kljavin, N. M., Koeppen, H., Nelson, C., Prabhu, S., Raab, H., Ross, S., Stephan, J. P., Scales, S. J., Spencer, S. D., Vandlen, R., Wranik, B., Yu, S. F., Zheng, B., and Ebens, A. (2009) Antibody-drug conjugates for the treatment of non-Hodgkin's lymphoma: target and linker-drug selection. *Cancer Res. 69*, 2358–64.

(19) Asai, M. N., K.; and Izawa, M. Demethyl Maytansinoids, U.S. Patent 4,307,016, December 22, 1981.

(20) Sawada, T., Kato, Y., Kobayashi, H., Hashimoto, Y., Watanabe, T., Sugiyama, Y., and Iwasaki, S. (1993) A fluorescent probe and a photoaffinity labeling reagent to study the binding site of maytansine and rhizoxin on tubulin. *Bioconjugate Chem. 4*, 284–9.

(21) Bissery, M. C., Guenard, D., Gueritte-Voegelein, F., and Lavelle, F. (1991) Experimental antitumor activity of taxotere (RP 56976, NSC 628503), a taxol analogue. *Cancer Res. 51*, 4845–52.

(22) Gupta, R. S. (1985) Species-specific differences in toxicity of antimitotic agents toward cultured mammalian cells. *J. Natl. Cancer Inst. 74*, 159–64.

(23) Lyng, H., Haraldseth, O., and Rofstad, E. K. (2000) Measurement of cell density and necrotic fraction in human melanoma xenografts by diffusion weighted magnetic resonance imaging. *Magn. Reson. Med. 43*, 828–36.

(24) Jain, R. K. (1999) Transport of molecules, particles, and cells in solid tumors. *Annu. Rev. Biomed. Eng. 1*, 241–63.

(25) Thurber, G. M., Schmidt, M. M., and Wittrup, K. D. (2008) Antibody tumor penetration: transport opposed by systemic and antigen-mediated clearance. *Adv. Drug Delivery Rev. 60*, 1421–34.

(26) Beckman, R. A., Weiner, L. M., and Davis, H. M. (2007) Antibody constructs in cancer therapy: protein engineering strategies to improve exposure in solid tumors. *Cancer 109*, 170–9.

BC900315Y

Fluorescent Nanoprobes as a Biomarker for Increased Vascular Permeability: Implications in Diagnosis and Treatment of Cancer and Inflammation

Britto S. Sandanaraj,*,† Hans-Ulrich Gremlich,† Rainer Kneuer,*,† Janet Dawson,‡ and Stefan Wacha†

Global Imaging Group and Department of Autoimmunity, Transplantation and Inflammation, Novartis Institutes for Biomedical Research, Basel, Switzerland. Received July 15, 2009; Revised Manuscript Received September 27, 2009

This article describes the use of a fluorescent nanoprobe as a functional biomarker for the identification of increased vascular permeability in cancer/arthritis disease models. Synthesis of the fluorescent nanoprobe was achieved by passive loading of a fluorophore inside the nanoparticle using thin film hydration method. The outer layer of the nanoprobe was decorated with poly(ethylene glycol) arms to increase the bioavailability of the fluorophore. Stability studies of the nanoprobe showed that the particles were stable up to 70 days. The uptake and internalization of the fluorescent nanoprobe inside target cells was confirmed by fluorescence microscopy studies. Co-localization of the probe with the target tissue *in vivo* was unambiguously identified using intravital microscopy. Results from *in vivo* imaging studies showed that the particles had a long half-life in the circulation and passively targeted tumor or arthritic tissue. The increased and specific uptake of the fluorescent nanoprobe in tumor/arthritic tissue is attributed to an enhanced permeation and retention (EPR) effect. Use of an optical method to validate anti-inflammatory drugs in an arthritis disease model is demonstrated in this study. In general, this methodology could be used for detection of leaky vasculature in different pathological states.

INTRODUCTION

Biomarkers play a crucial role in both preclinical and clinical evaluation of drugs (*1–7*). In particular, imaging-based biomarkers can speed up drug discovery by supplementing or replacing preclinical and clinical pharmacokinetic and pharmacodynamic assessment, including target selection and modulation. In addition, imaging-based biomarkers could be used for diagnosis, staging, prognosis, and treatment selection (*8–10*).

Presence of leaky vasculature is a classical biomarker for some diseases which include cancer (*11*), inflammation (*12, 13*), and diabetes (*14, 15*). The intrinsic biological processes that drive the formation of leaky blood vessels can vary depending on various disease conditions. However, leaky blood vessels present in different disease conditions share some unique properties that could be used as biomarkers for the identification of pathological states. Dynamic contrast-enhanced MRI (DCE-MRI) (*16, 17*), positron-emission tomography (PET) (*18*), dynamic contrast-enhanced CT (DCE-CT) (*19–21*), and contrast enhanced ultrasound (CEUS) (*22*) have been routinely used as functional biomarkers for measuring the vascular leakiness in various disease conditions. Although these techniques have clearly paved the way for the use of imaging based biomarkers as a routine tool in both preclinical and clinical settings, they are not optimum in their performance: for example, DCE-MRI suffers from quantification and reproducibility, use of DCE-CT might be a problem because of the high exposure to X-ray radiation, and requirement for in-house cyclotron is a limitation in the case of PET. Therefore, there is a need for new functional biomarkers to overcome these issues.

Fluorescence microscopy and near-infrared fluorescence (NIRF) imaging are important research tools in the area of *in vivo* imaging applications (*10, 23–28*) These techniques provide information at a molecular level, thus offering a distinct advantage over other imaging modalities such as magnetic resonance imaging and computer tomography. The use of light in the near-infrared range (NIR; 650−950 nm) is well suited for *in vivo* studies due to the reduced absorbance and scattering of endogenous substances (especially water, oxyhemoglobin, and melanin). The low cost and high sensitivity of this imaging modality has increased the widespread use of this technique in diagnostics (*29*), preclinical drug discovery (*30, 31*), and, to some extent, clinical settings (*32, 33*).

The use of optical methods to assess vascular leakiness is an attractive imaging based biomarker to speed up drug discovery in preclinical settings. As a "proof of concept", we have shown that "optical imaging combined with fluorescent nanoprobes" can be used effectively as a functional biomarker for the identification of increased vascular leakiness. The versatility of this method is demonstrated by using this technique for diagnosis and monitoring of two different disease conditions where vascular leakiness exists. In general, this methodology can be extended to any disease model where leaky blood vessels exist. This technology can be translated easily to clinical settings since all the components used for formulation of fluorescent nanoprobes are clinically approved for different applications (*34*). By encapsulating a clinically approved fluorescent dye (e.g., indocyanine green (*35, 36*) (ICG)) inside a nanoprobe, this nanoparticle can be used as a biomarker for functional imaging in clinical settings. The preclinical studies described here were carried out with a nanoparticle-ICG formulation for one such application in a mouse model (*vide infra*). We have used sterically shielded liposome (SSL) (*37*) based nanoparticulates as a delivery vehicle to carry our fluorescent probes to their target location. The reason for using a delivery vehicle is twofold; first, it increases the bioavailability of the probe in *in vivo* conditions, second, it increases the targeting efficiency of this nanoparticle toward leaky vasculature (*11, 38*), thus reducing the signal/noise ratio. Since all the components of the formula-

* Email: sandanaraj.selvaraj@novartis.com, rainer.kneuer@novartis.com.

† Global Imaging Group.

‡ Department of Autoimmunity, Transplantation and Inflammation.

10.1021/bc900311h © 2010 American Chemical Society
Published on Web 12/03/2009

tion are already used in clinics, we do not anticipate any toxicity from the delivery vehicle. Apart from *in vivo* validation of the probe, we have also validated the performance of the probe at the cellular level.

EXPERIMENTAL PROCEDURES

Reagents. Egg phosphaditylcholine, cholesterol, 1,2-disteroyl-*sn*-glycero-3-phosphoethanolamine-*N*-methoxy(poly(ethylene glycol))-2000) were purchased from Avanti Polar Lipids, Inc. Cyanine 5.5 and indocyanine green (ICG) were purchased from Fluka. Hoechst, Phalloidin, and CM-DiI were purchased from Molecular Probes. RPMI medium and fetal bovine serum were purchased from Invitrogen.

Synthesis and Characterization of Fluorescent Nanoprobes. Liposomes were prepared at defined molar ratio of individual lipids to give a predetermined total lipid concentration of 7.6 mg/mL. Egg phosphaditylcholine, cholesterol, 1,2-disteroyl-*sn*-glycero-3-phosphoethanolamine-*N*-methoxy-(poly(ethylene glycol))-2000) (2:1:0.2 molar ratio) and fluorescent probe (Cy5.5 or ICG) were dissolved in 5 mL chloroform, and the resulting mixture was evaporated on a rotary evaporator under room temperature. The resulting lipid film was again subjected to high vacuum to remove residual solvent. Finally, the lipid film was hydrated at 50 °C with 5 mL 10 mM PBS buffer (pH 7.4) to give liposome solution. The hydrated mixture was frozen at liquid nitrogen temperature and heated to 50 °C. This treatment was repeated 3 times for the preferential encapsulation of Cy5.5 or ICG inside the nanoprobe. After this, the solution was passed through a 0.2 μM filter (3 times) to get rid of larger particles. The unbound probe molecules present in the bulk solution were separated by passing solution through a Sephadex G-25 M column. Percentage encapsulation efficiency of Cy5.5 and ICG was 5% and 50%, respectively. Liposomes were lysed by the addition of methanol, and the encapsulation efficiency was calculated from the amount of released dye, which is determined from the UV−vis calibration curve. Size of nanoprobes was characterized by dynamic light scattering using a Zetasizer Nano ZS over a time period of 70 days at 4 °C.

Spectroscopic Measurements. The UV−vis absorption spectra were recorded on a PerkinElmer spectrophotometer using plastic cells. Fluorescence spectra were recorded on a Varian fluorimeter. The spectra were recoded using a 1 mL disposable plastic cell. Excitation and emission bandwidth was kept at 2.5 and 5 nm, respectively, for Cy5.5 nanoprobe and for ICG nanoprobe bandwidth was kept at 10 and 20 nm, respectively. Cy5.5 nanoprobe was excited at 660 nm and the emission was recorded from 670 to 900 nm. For ICG-nanoprobe, the excitation wavelength was 770 nm and emission was recorded from 770 to 900 nm.

Cell Studies and Imaging with IN Cell Analyzer 3000. Prostate cancer cells (PC3, passage number 12) were cultured at 37 °C under 5% CO_2 in RPMI supplemented with 10% heat-inactivated fetal bovine serum, 2% glutamine, and 0.1% penicillin−streptomycin solution. For passaging, cells were detached with 0.25% trypsin/1 mM EDTA, counted with nucleocounter (ChemoMetec, Allerød, Denmark), and the required number of cells were seeded in T75 cell culture flasks. For imaging plates, Cells were seeded on black Corning 384-well plates using multidrop, 10 000 cells/well in 100 μL, and incubated for 24 h. After 24 h, 16.6 μL nanoprobes (PEGylated nanoprobe 1: size = 73 nm, Cy5.5 concentration = 50 μg/mL. PEGylated nanoprobe 2: size = 120 nm, Cy5.5 concentration = 43 μg/mL. Naked nanoprobe: size = 106 nm, Cy5.5 concentration = 24 μg/mL. Control nanoprobe: size = 106 nm, Cy5.5) were added and incubated for required time. The cells were fixed by adding 100 μL 8% PFA which contained 50 ng/well Hoechst (a nuclear stain). Thus, the end concentration of PFA was 4% and that of Hoechst was 25 ng/well. Cells were incubated with PFA and Hoechst for 15 min at RT. Then, the PFA-Hoechst solution was aspirated. The cells were washed once with PBS. The cells were washed twice with 20 μL PBS, which was aspirated, and the wells were filled with 20 μL PBS. The plates were sealed with silverseal aluminum tape and kept at 4 °C in the dark until imaging with the IN Cell Analyzer 3000. Images were acquired using the IN Cell Analyzer 3000 (GE Biosciences, Piscataway, NJ) automated cell imager. Flat field correction was done using a plate with various mixtures of Oregon Green (Molecular Probes, Carlsbad, CA), Cy5 calibration reagent (GE Biosciences), and Alexa Fluor 350 carboxylic acid (Molecular Probes). Images for the nuclear stain Hoechst and Cy5.5 were taken on 2 different channels with 2 CCD cameras simultaneously. Cy5.5 was excited with the 647 nm krypton laser, and a 695/BP55 emission filter was used to collect the emitted light. Hoechst was excited with 350 nm line of the argon laser, and a 450/BP50 emission filter was used to collect the emitted light. Exposure time for both the channels was 1.7 ms.

Intravital Imaging and Preparation of DiI mice. Two weeks before the experiment, 2×10^6 PC3 prostate cancer cells were labeled *in vitro* with DiI and implanted subcutaneously into nude mice. Twenty-four hours before imaging, the Cy5.5-labeled nanoprobe (size = 120 nm, Cy5.5 concentration = 43 μg/mL) was injected via tail vein injection 5 min before imaging, FITC-dextran (M_W = 500 000; 5 μL of 1 mg/mL stock diluted into 95 μL NaCl 0.9%) was applied via tail vein injection as well, and then mice were anesthetized with Ketamin/Xylasol and a skin-flap was performed in order to get access to the subcutaneously implanted tumor. Images were taken using the IV100 intravital microscope from Olympus using 4× and 20× objectives as well as a 27× stick lense for highest resolution. A stock solution of 1 mg/mL CM-DiI (Molecular Probes) was prepared in dimethyl sulfoxide (DMSO) and stored at −20 °C. For labeling of cells, the stock solution was diluted in cell culture medium to achieve a concentration of 10 μg/mL. One million cells were suspended per milliliter and incubated for 30 min at 37 °C. Cells were gently resuspended every 5 min. Afterwards, cells were washed twice in PBS (centrifugation for 10 min at 400 *g* at room temperature) and resuspended in cell culture medium at 750 000 cells per 100 μL.

Mouse Tumor Model and NIRF Imaging. 3×10^6 PC-3 human prostate adenocarcinoma (ATCC: CRL-1435) cells in 100 μL HBSS (1 mg/mL Matrigel) were injected under Forene inhalation narcosis on the right flank of 6−8 week old female athymic nude mice for generation of subcutaneous tumors.

The Siemens BonSAI Imager was used (Siemens AG, Medical Solutions, and Erlangen, Germany). NIRF imaging started at day 14 after inoculation of the tumor cells, and NIRF images were recorded 6, 24, 48, 72, and 96 h after i.v. administration of the 100 μL Cy5.5 nanoprobe (size = 73 nm, Cy5.5 concentration = 50 μg/mL). For NIRF measurements, the animals were anaesthetized using 1.5% Isoflurane (Abbott, Cham) in nitrous oxide/oxygen 2:1 administered via a face mask. The duration of the anesthesia was 3 min. All experiments have been carried out in adherence to the Swiss laws of animal protection. For fluorescence excitation, three laser diodes at 660 nm with a power of 10 mW/cm^2 were used. The fluorescent light emitted from the sample (mouse) was detected by a charge-coupled device (CCD) camera (Hamamatsu) equipped with a focusing lens system (macro lens 60 mm, 1:2.8, Nikon). The CCD features low noise and

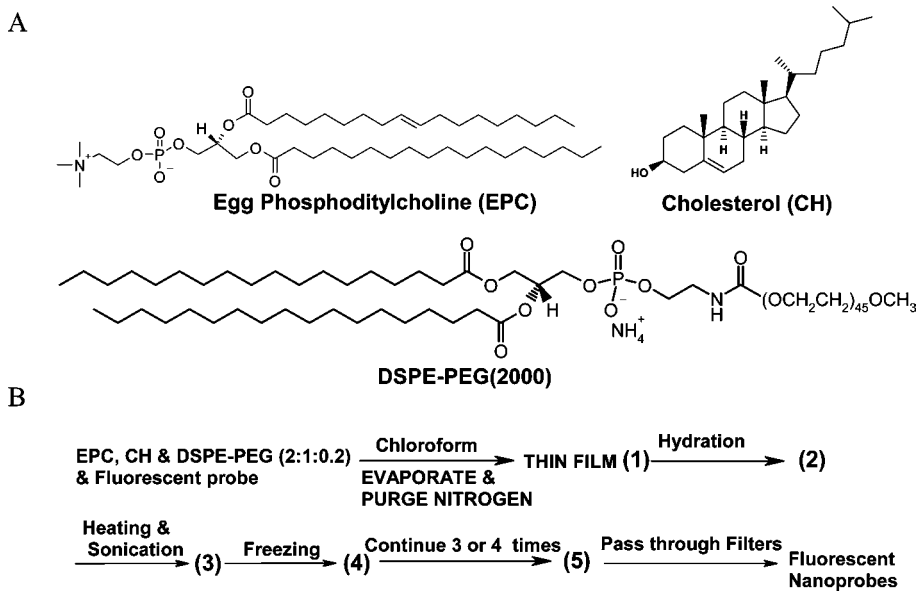


Figure 1. (A) Chemical constituents of fluorescent nanoprobe. (B) Schematic representation of formulation procedure.

low dark signal enabling low light level detection as well as long integration times. The matrix size of the images is 532 × 256 pixels. A hard filter was used for detection wavelength selection (700 nm). Data acquisition (i.e., integration) times ranged from 0.5 to 2.0 s depending on the intensity of fluorescence. The experiment was controlled by a PC using the Siemens SYNGO software. NIRF images have been analyzed quantitatively on a ROI basis using the same SYNGO software.

Mouse Antigen Induced Arthritis Model and NIRF Imaging. Ten female OF-1 mice, 12−14 weeks of age, were used. They were housed under standard conditions with a 12 h light/dark cycle, and water was provided *ad libitum*. During the 14 days before imaging experiments, the animals were fed a low-pheophorbide diet to reduce autofluorescence. Arthritis was induced in all 10 mice. The phase of systemic immunization proceeded as follows. Mice were sensitised intradermally on the back at two sites to methylated bovine serum albumin (mBSA) homogenised 1:1 with complete Freund's adjuvant on days −21 and −14 (0.1 ml containing 1 mg/ml mBSA). On day 0, the mice were anaesthetised using a 5% isoflurane/air mixture and maintained using isoflurane in a face mask for the intra-articular injections. The right knee received 10 μl of 10 mg/ml mBSA in 5% glucose solution (antigen injected knee), while the left knee received 10 μl of 5% glucose solution alone (vehicle injected knee). From day 0 to 7, the animals were treated with dexamethasone (NVP-AFC572-AB-2; 1 mg/kg, p.o.) or vehicle (A. dist). Arthritis development was monitored by measuring the lateral joint diameter with an Oditest vernier caliper on days 0, 2, and 4.

Using a GE eXplore Optix small animal imager (GE Healthcare, London, England), NIRF images for arthritis studies were recorded 6 h after i.v. injection of the ICG nanoprobe (size= 120 nm, ICG concentration = 151 μg/mL). For NIRF measurements, the animals were anaesthetized using 1.5% Isoflurane (Abbott, Cham) in nitrous oxide/oxygen 2:1 administered via a face mask. The duration of the anesthesia was 3 min, the time needed to scan 1 animal. All experiments have been carried out in adherence to the Swiss laws of animal protection. A pulsed laser at 670 nm with a power of 4.4 mW at 80 MHz repetitive rate and pulse durations of 60 ps was used for fluorescence excitation. The fluorescent light emitted from the sample (mouse) was detected by a photomultiplier tube (TD-

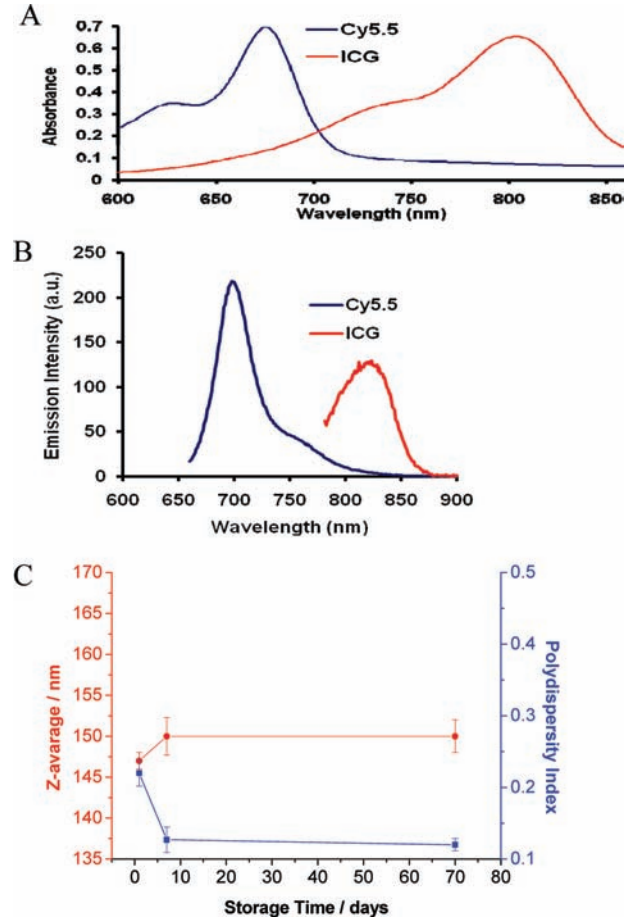


Figure 2. (A) UV−vis spectra of Cy 5.5 or ICG inside nanoprobe. (B) Fluorescence spectra of Cy 5.5 or ICG inside nanoprobe. Cy5.5 nanoprobe was excited at 660 nm, and the emission was recorded from 670 to 900 nm. For ICG-nanoprobe, the excitation wavelength was 770 nm and emission was recorded from 770 to 900 nm. (C) Stability studies of nanoprobe formulation: average size and polydispersity index of liposomes with respect to time.

detector) at 700 nm. The experiment was controlled by a PC using the GE eXplore Optix acquisition software. NIRF images have been analyzed quantitatively on a ROI basis using the same software tool.

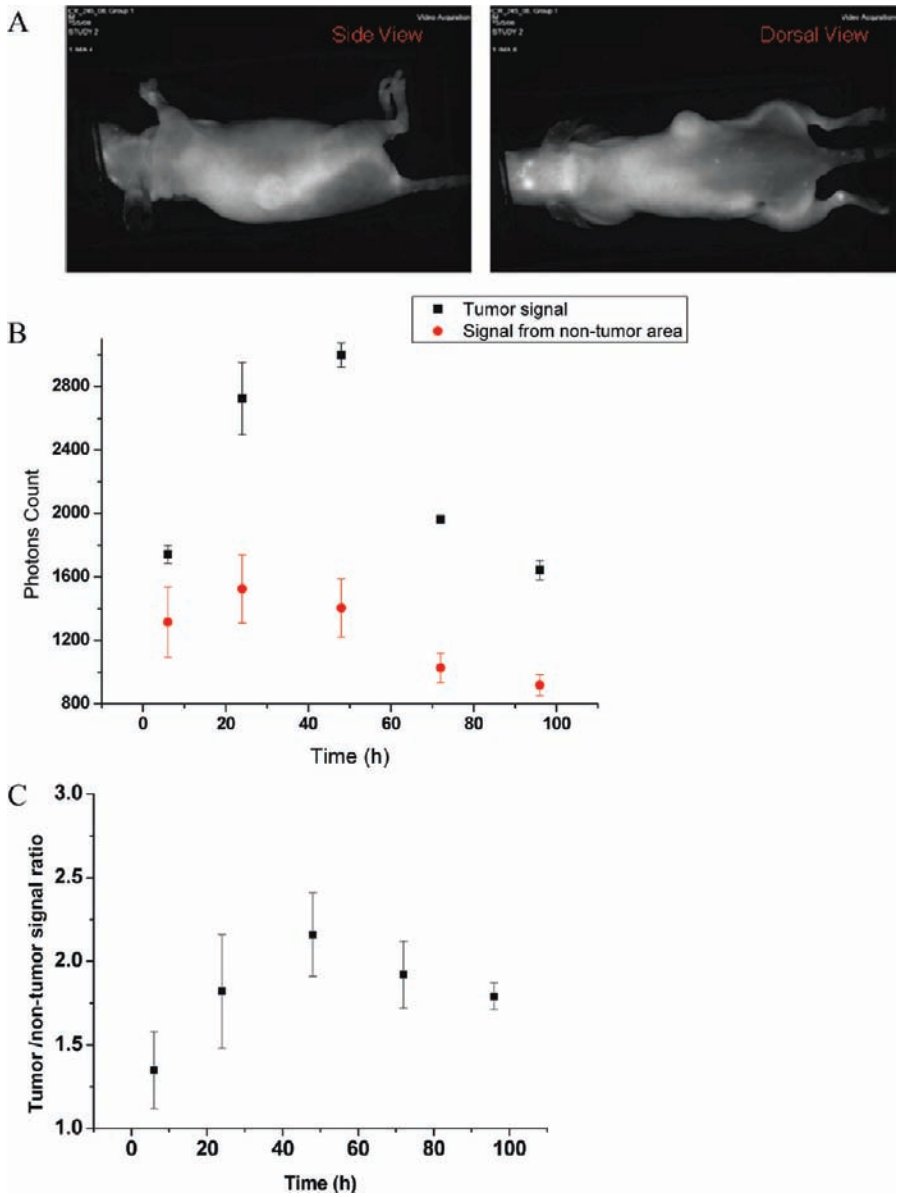


Figure 3. NIRF imaging started at day 14 after inoculation of the tumor cells, and NIRF images were recorded 6, 24, 48, 72, and 96 h after i.v. administration of the 100 μL Cy5.5 nanoprobe (size = 73 nm, Cy5.5 concentration = 50 μg/mL). (A) A representative NIRF whole body image at 24 h time point. (B) Fluorescence signal from tumor and nontumor area. (C) Ratio of tumor to nontumor signal ratio. Each data point represents the mean ± SEM of 3 animals.

Statistical Analysis. All results are expressed as mean ± SEM (n = number of animals).

RESULTS AND DISCUSSION

Formulation and Characterization of Fluorescent Nanoprobes. Formulation of sterically shielded liposomes (SSL) was achieved by thin film hydration method. Egg phosphatidylcholine, cholesterol, 1,2-disteroyl-*sn*-glycero-3-phosphoethanolamine-*N*-methoxy(poly(ethylene glycol))-2000) (2:1:0.2 molar ratio) and Cy5.5 or ICG were mixed together and subjected to repeated freeze−thaw cycles and filtration through polycarbonate membranes and finally passed through a Sephadex column (Figure 1A). The size and polydispersity index (PDI) of the synthesized nanoprobes were estimated using dynamic light scattering (DLS) technique. Scanning electron microscopy studies showed that the particles are spherical and about the size of 100−150 nm, which is consistent with the results from DLS studies (data not shown). The liposome particles are decorated with poly(ethylene glycol) (PEG) arms in order to improve the pharmacokinetics/pharmacodynamics *in vivo* and avoid particle phagocytosis by macrophages (*39*).

As the probe molecules can be hydrophilic or hydrophobic depending on the nature of chemical functionality, it is crucial that delivery vehicles can encapsulate all types of compounds irrespective of their hydrophilic/hydrophobic index. The advantage of using liposomes is twofold: (i) they have an aqueous interior where hydrophilic compounds can be dissolved in the nanoscale dimension; (ii) second, they also have lipid bilayers made up of phosphatidylcholine and cholesterol that can be exploited to encapsulate hydrophobic probe molecules. Therefore, we consider that liposome-based nanoparticulates are ideal delivery vehicles for *in vivo* and cell-based applications. In order to demonstrate that our delivery vehicles can indeed encapsulate all types of probe molecules, we have tested the encapsulation ability of these particles with both hydrophobic (indocyanine green, ICG) and hydrophilic (Cy5.5) fluorescent probes. As expected, the liposomes can dissolve both hydrophilic and hydrophobic probe molecules (Figure 2). We also carried out

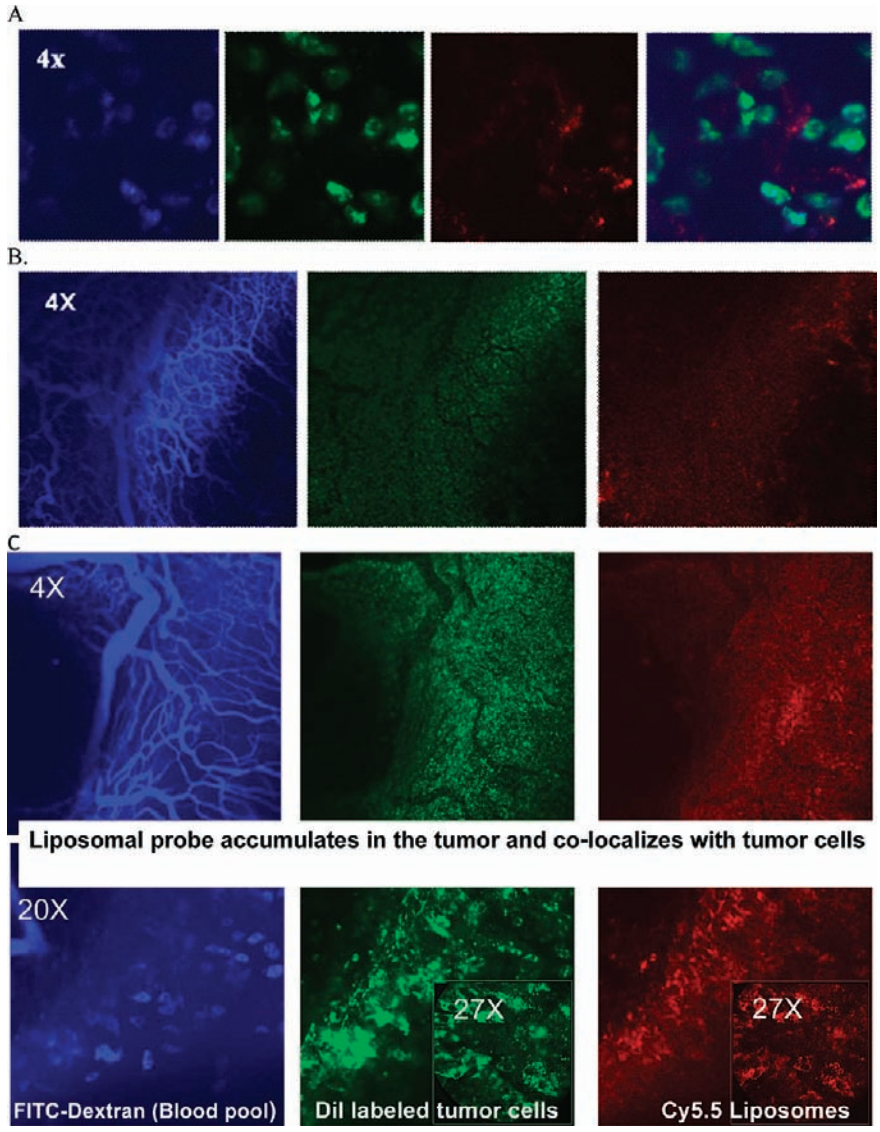


Figure 4. Cy5.5-labeled nanoprobe (size = 120 nm, Cy5.5 concentration = 43 μg/mL) was injected via tail vein injection 5 min before imaging, FITC-dextran (M_W = 500 000; 5 μL of 1 mg/mL stock diluted into 95 μL NaCl 0.9%) was applied via tail vein injection. (A) 30 min; (B) 6 h; (C) 24 h.

fluorescence measurements to determine that the dye inside the nanoscale compartment of liposomes resembles a dye in bulk solution. This is important because it has been shown that increased local concentration of a fluorophore inside the aqueous interior of the liposome might result in fluorescence quenching, thus complicating any analysis of the results. We have also performed stability studies of liposome formulation for 70 days and found that the particles were exceptionally stable. There was no problem of particle aggregation with long-term storage (Figure 2C).

***In Vivo* Studies of Fluorescent Nanoprobes in Tumor Model.** In order to test the passive targeting efficiency of these particles toward leaky vasculature, we chose tumor and arthritis disease models in mice. These two diseases share a common feature, which is the leaky vasculature nature of tumor/arthritic tissue (*11*) where the fluorescent liposome particles can be trapped and retained for longer time periods through the process called enhanced permeation and retention (EPR) effect (*11, 38*). The first *in vivo* studies of fluorescent nanoprobes were carried out in mice bearing PC3 tumors. PC3 tumor cells were subcutaneously implanted in nude mice and allowed to grow for 2 weeks until tumors achieved size of 150 mm^3. The nanoprobe containing Cy5.5 dye was injected i.v. via the tail vein of the mice and the particles tracked at different times. The 6 h time point revealed that the particles were circulating uniformly throughout the body. There was no preferential accumulation of particles in the tumor tissue/region at this time point, and the nanoprobe was distributed uniformly throughout the body. However, at 24 h, we could differentiate between tumor area and other parts of the body because of the enhanced fluorescence signal from the tumor region. We continued the studies to the next day, and the third reading was taken at the 48 h time point. The fluorescence signal intensity from the tumor area further increased, but the fluorescence signals from other parts of the body remained the same as previous time points. The studies were continued for another two days; the fluorescence signal at the 72 h time point started to decrease gradually and attained the base level at the 96 h time point (Figure 3a). Another interesting feature is that the fluorescence signal from a nontumor area remained the same during the entire study period (Figure 3b). In addition to that, we did not observe any adverse side effects in the animals due to nanoparticle toxicity and they were healthy throughout the study period. The above studies reiterate the point that these nanoprobes have good bioavailability and there are no toxicity issues associated with these delivery vehicles.

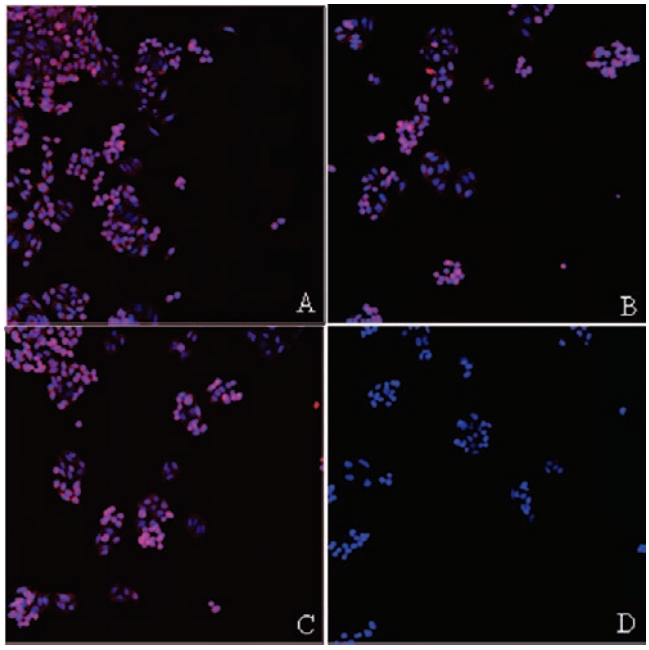


Figure 5. Intracellular uptake studies of nanoprobes in PC3 cell line: (A) PEGylated nanoprobe 1, size ~120 nm; (B) PEGylated nanoprobe 2, size ~73 nm; (C) naked nanoprobe (without PEG coating), size ~106 nm; (D) control nanoprobe (empty liposomes), size ~106 nm.

Intravital Microscopy Studies. The results from *in vivo* studies gave us only the macroscopic picture of the targeting nature of our nanoprobe toward tumor tissue but did not reveal information about the localization of our probe inside tumor cells. In order to look more closely at the cellular level, we have used intravital microscopy (IVM) for our studies. IVM has the ability to provide insight into various molecular and cellular processes *in vivo* with high spatial and temporal resolution down to the subcellular level (*40*). More recently, IVM was used to study the architecture and physiology of tumor neovasculature (*41*). For our studies, nude mice were implanted with DiI-labeled (green channel) PC-3 cells 2 weeks before nanoprobe infusion. The study involved 6 mice total, 2 mice/group, 3 time points (20 min, 6 h, and 24 h). The blood vessels were stained with FITC-labeled dextran (blue channel). Cy5.5-labeled nanoprobe (red channel) was injected in the tail vein and measurements were taken at time points similar to tumor studies in order to compare the results. At the 20 min time point, the fluorescent nanoprobe did not extravasate from intact blood vessels to the tumor tissue. After 6 h, Cy5.5-labeled nanoprobes were taken up by some of the tumor cells, which is in contrast to the *in vivo* imaging study results where fluorescence signal from the tumor area remained the same as the background signal (Figure 4). The inherent difference between fluorescence signal intensities from these two methods is attributed to the high sensitivity of IVM. However, the IVM results at the 24 h time point resembled *in vivo* studies in which fluorescent particles are retained in the tumor region for extended period. The colocalization of the nanoprobes and tumor cells at the 24 h time point suggests that the nanoprobe might be internalized by the tumor cells. In summary, the biodistribution and pharmacokinetics trends of liposome particles in *in vivo* studies are supported by the intravital microscopy results.

Intracellular Uptake of Nanoprobes in Tumor Cells. The results from intravital microscopy results suggest that nanoprobes might be internalized by tumor cells, but it is not definitive evidence. Therefore, we have focused our attention on *in vitro* cellular characterization of the nanoprobes through fluorescence microscopy. The uptake of custom-designed nanoparticles or microparticles inside a living cell depend on size, shape, and the particle surface potential (*42, 43*). In a classical example, DeSimone et al. showed that positively charged microparticles were taken up by the live cells more readily compared to negatively charged particles. In our studies, we

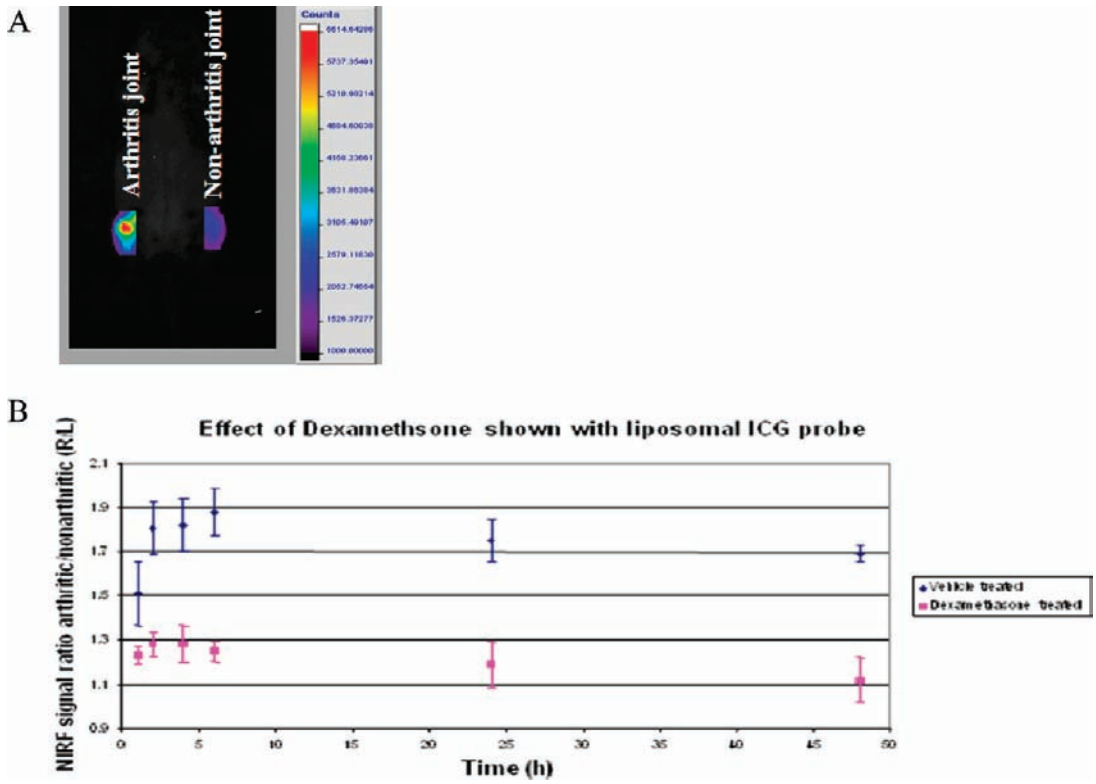


Figure 6. (A) NIRF images for arthritis studies were recorded 6 h after i.v. injection of the ICG nanoprobe (size ~120 nm, ICG concentration = 151 μg/mL). (B) Effect of drug treatment. Each data point represents the mean ± SEM of 10 animals.

have used PEG-coated nanoprobes to increase the circulation time and bioavailability of the fluorescent cargo. In order to demonstrate that PEG-coated nanoprobes have the same ability to get into the cells as nanoprobes without PEG coating, we incubated PEG-coated nanoprobes and naked nanoprobes with PC3 cells, and the particle internalization was analyzed. Results from fluorescence microscopy show that both particles were indeed internalized by the PC3 cells irrespective of their surface charge. We also studied the effect of particle size on the internalization process; however, it does not have any effect. The reason for the above phenomenon may be the small difference in the nanoparticle size (73 nm vs 120 nm) that we tested in this study (Figure 5).

Inflammation Imaging. Encouraged by the results in the tumor model, we wanted to extend this methodology to another disease model. We have chosen an arthritis model, antigen-induced arthritis (AIA), because of the presence of leaky vasculature in arthritic tissue (*44, 45*). We encapsulated indocyanine green (ICG), a clinically approved fluorescent dye (*36*), inside the nanoprobe. Arthritis was induced in the right knee of mice by the injection of mBSA into the joint in mice previously sensitized to mBSA systemically. The nanoprobes were injected i.v. via the tail vein and the NIRF measurements taken at different time points (Figure 6). There was no preferential accumulation of particles in the arthritis joints at initial time points. However, at the 24 h time point, we saw 2-fold increases in fluorescence signal from arthritic joint compared to the nonarthritic joint. These studies indicate that the nanoparticles can passively target leaky vasculature and can be trapped in arthritic joints for a longer time. The extension of this methodology in an arthritic disease model has shown the versatile nature of this methodology. The effects of drugs on vascular leakiness were subsequently investigated using fluorescent nanoparticles. Animals were treated orally with vehicle or dexamethasone at a dose of 0.3 mg/kg. Dexamethasone is an anti-inflammatory steroid from a class of drugs frequently used to treat human rheumatoid arthritis (RA) (*46–48*). Nanoprobes were injected i.v. after the administration of dexamethasone or vehicle, and the fluorescence signal was measured for these two groups of animals. The fluorescence signal from arthritic joint of the dexamethasone-treated animals was similar to the signal from nonarthritic joints. In contrast, the signals from the arthritic joints of vehicle-treated animals were 2-fold higher than the nonarthritic joints. This result indicates that treatment with dexamethasone can inhibit the vascular leakiness associated with the inflammation in the arthritic joints. The above results indicate that this method could be used as a tool to screen the efficacy of anti-inflammatory compounds in preclinical settings.

Preclinical and Clinical Implications of the Present Findings. The immediate question that one might ask is, how is this biomarker different from existing optical biomarkers for the detection of vascular leakiness? How could it be used to identify different stages of cancer or arthritis? Is it possible to translate this biomarker from preclinical to clinical use?

Use of near-infrared fluorescent probes for the detection of arthritis has previously been reported in the literature (*29, 49*). However, these small molecule fluorescent probes suffer from severe limitations that arise due to poor pharmacokinetics and biodistribution properties (*50*). In addition, these probes nonspecifically bind to various blood proteins (*51*). Fluorophore-labeled antibodies were also explored for these kinds of applications (*49*). However, no specific biomarker for arthritis is known. The significance of our finding is the elegant combination of delivery vehicle (*34*) (PEGylated liposomes) and the fluorescent probe (ICG), as both are clinically approved for use in humans for different applications. By encapsulating ICG inside liposomes, the half-life time of this probe is increased from minutes (*50*) to several hours. Second, the size range of liposome particles (100−200 nm) favors the targeting efficiency of these particles toward leaky vasculature. Out of all, the most important finding of this report is the use of an optical method to screen anti-inflammatory drugs in *in vivo* conditions in preclinical settings. The utility of this method goes beyond the present findings. This tool also could be used to detect at least two stages of antigen-induced arthritis in mouse model, since the vascular leakiness drastically differs between acute and chronic phase of inflammation (*52*). The extravasation of fluorescent liposomes during acute-phase inflammation is expected to be higher compared to chronic phase, and therefore, the NIRF signal during acute phase should be higher compared to chronic phase. With respect to tumor imaging, the limitation of this probe is the detection of tumors with sizes less than 1−2 mm^3, as neovascularization starts only after tumor reaches size of about ∼2 mm^3, which results in leaky vasculature of tumor tissue (*53–56*). On the positive side, this method could be used as a tool to screen the efficacy of various antiangiogenic agents in various tumor models based on the notion that the treatment with antiangiogenic compounds should result in normalization of abnormal blood vessels that should result in decreased extravasation of fluorescent liposomes to tumor tissue (*57*).

CONCLUSION

We have shown the design, synthesis, and characterization of fluorescent nanoprobes. Stability studies of nanoprobe solutions show that these particles are stable for long periods of time. These nanoparticles are decorated with poly(ethylene glycol) for the enhanced circulation and passive targeting of tumor/arthritis tissue. Apart from the validation of probes with near-infrared fluorescence imaging studies, the probes have also been validated in intravital and fluorescence microscopy studies. Results from our studies show that optical imaging combined with appropriate nanoparticles could be used as functional biomarkers for the presence of increased vascular leakiness in pathological conditions. The concept behind the application of this new technology is demonstrated in two different disease models.

ACKNOWLEDGMENT

We thank Mr. Fritz Wenger and Ms. Alexandra Suter for preparing the animals for the *in vivo* imaging studies. We also thank members of Gabriel Lab for their support and assistance. This work was funded by Novartis Institutes for Biomedical Research, Education Office, and Global Imaging Group.

Supporting Information Available: Fluorescence spectra of Cy5.5 in liposome and PBS. This material is available free of charge via the Internet at http://pubs.acs.org.

LITERATURE CITED

(1) Severino, M. E., Dubose, R. F., and Patterson, S. D. (2006) A strategic view on the use of pharmacodynamic biomarkers in early clinical drug development. *IDrugs. 9*, 849–853.

(2) Kuhlmann, J., and Wensing, G. (2006) The applications of biomarkers in early clinical drug development to improve decision-making processes. *Curr. Clin. Pharmacol. 1*, 185–191.

(3) Bakhtiar, R. (2008) Biomarkers in drug discovery and development. *J. Pharmacol. Toxicol. Methods 57*, 85–91.

(4) Frank, R., and Hargreaves, R. (2003) Clinical biomarkers in drug discovery and development. *Nat. Rev. Drug Discovery 2*, 566–580.
(5) Colburn, W. A. (2003) Biomarkers in drug discovery and development: from target identification through drug marketing. *J. Clin. Pharmacol. 43*, 329–341.
(6) Colburn, W. A. (2000) Optimizing the use of biomarkers, surrogate endpoints, and clinical endpoints for more efficient drug development. *J. Clin. Pharmacol. 40*, 1419–1427.
(7) Hargreaves, R. J. (2008) The role of molecular imaging in drug discovery and development. *Clin. Pharmacol. Ther. 83*, 349–353.
(8) Rudin, M. (2009) Noninvasive structural, functional, and molecular imaging in drug development. *Curr. Opin. Chem. Biol. 13*, 360–371.
(9) Rudin, M. (2007) Imaging readouts as biomarkers or surrogate parameters for the assessment of therapeutic interventions. *Eur. Radiol. 17*, 2441–2457.
(10) Rudin, M., and Weissleder, R. (2003) Molecular imaging in drug discovery and development. *Nat. Rev. Drug Discovery 2*, 123–131.
(11) Maeda, H., Fang, J., Inutsuka, T., and Kitamoto, Y. (2003) Vascular permeability enhancement in solid tumor: various factors, mechanisms involved and its implications. *Int. Immunopharmacol. 3*, 319–328.
(12) Andersson, S. E., Lexmuller, K., and Ekstrom, G. M. (1998) Physiological characterization of mBSA antigen induced arthritis in the rat. I. Vascular leakiness and pannus growth. *J. Rheumatol. 25*, 1772–1777.
(13) Andersson, S. E., and Ekstrom, G. M. (1997) Changes in vascular porosity and joint blood flow during development of collagen induced arthritis in the rat. Modulation by indomethacin and L-NAME. *J. Rheumatol. 24*, 2188–2195.
(14) Medarova, Z., Castillo, G., Dai, G., Bolotin, E., Bogdanov, A., and Moore, A. (2007) Noninvasive magnetic resonance imaging of microvascular changes in type 1 diabetes. *Diabetes 56*, 2677–2682.
(15) De Paepe, M. E., Corriveau, M., Tannous, W. N., Seemayer, T. A., and Colle, E. (1992) Increased vascular permeability in pancreas of diabetic rats: detection with high resolution protein A-gold cytochemistry. *Diabetologia 35*, 1118–1124.
(16) Muruganandham, M., Lupu, M., Dyke, J. P., Matei, C., Linn, M., Packman, K., Kolinsky, K., Higgins, B., and Koutcher, J. A. (2006) Preclinical evaluation of tumor microvascular response to a novel antiangiogenic/antitumor agent RO0281501 by dynamic contrast-enhanced MRI at 1.5 T. *Mol. Cancer Ther. 5*, 1950–1957.
(17) Demsar, F., van Dijke, C. F., Kirk, B. A., Kapila, S., Peterfy, C. G., Roberts, T. P., Shames, D. M., Tomazic, S., Mann, J., and Brasch, R. C. (1996) Mapping abnormal synovial vascular permeability in temporomandibular joint arthritis in the rabbit using MRI. *Br. J. Rheumatol. 35*, 23–25, Suppl 3.
(18) Kaplan, J. D., Trulock, E. P., Anderson, D. J., and Schuster, D. P. (1992) Pulmonary vascular permeability in interstitial lung disease. A positron emission tomographic study. *Am. Rev. Respir. Dis. 145*, 1495–1498.
(19) Kruger, E. F., Puchalski, S. M., Pollard, R. E., Galuppo, L. D., Hornof, W. J., and Wisner, E. R. (2008) Measurement of equine laminar blood flow and vascular permeability by use of dynamic contrast-enhanced computed tomography. *Am. J. Vet. Res. 69*, 371–377.
(20) Roberts, H. C., Roberts, T. P., Lee, T. Y., and Dillon, W. P. (2002) Dynamic, contrast-enhanced CT of human brain tumors: quantitative assessment of blood volume, blood flow, and microvascular permeability: report of two cases. *Am. J. Neuroradiol. 23*, 828–832.
(21) Terada, T., Nambu, K., Hyotani, G., Miyamoto, K., Tsuura, M., Nakamura, Y., Nishiguchi, T., Itakura, T., Hayashi, S., and Komai, N. (1992) A method for quantitative measurement of cerebral vascular permeability using X-ray CT and iodinated contrast medium. *Neuroradiology 34*, 290–296.
(22) Heppner, P., and Lindner, J. R. (2005) Contrast ultrasound assessment of angiogenesis by perfusion and molecular imaging. *Expert Rev. Mol. Diagn. 5*, 447–455.
(23) Jaffer, F. A., Kim, D. E., Quinti, L., Tung, C. H., Aikawa, E., Pande, A. N., Kohler, R. H., Shi, G. P., Libby, P., and Weissleder, R. (2007) Optical visualization of cathepsin K activity in atherosclerosis with a novel, protease-activatable fluorescence sensor. *Circulation 115*, 2292–2298.
(24) Pande, A. N., Kohler, R. H., Aikawa, E., Weissleder, R., and Jaffer, F. A. (2006) Detection of macrophage activity in atherosclerosis in vivo using multichannel, high-resolution laser scanning fluorescence microscopy. *J. Biomed. Opt. 11*, 021009.
(25) Wunder, A., Tung, C. H., Muller-Ladner, U., Weissleder, R., and Mahmood, U. (2004) In vivo imaging of protease activity in arthritis: a novel approach for monitoring treatment response. *Arthritis Rheum. 50*, 2459–2465.
(26) Weissleder, R., and Ntziachristos, V. (2003) Shedding light onto live molecular targets. *Nat. Med. 9*, 123–128.
(27) Petrovsky, A., Schellenberger, E., Josephson, L., Weissleder, R., and Bogdanov, A., Jr. (2003) Near-infrared fluorescent imaging of tumor apoptosis. *Cancer Res. 63*, 1936–1942.
(28) Weissleder, R., Tung, C. H., Mahmood, U., and Bogdanov, A., Jr. (1999) In vivo imaging of tumors with protease-activated near-infrared fluorescent probes. *Nat. Biotechnol. 17*, 375–378.
(29) Hansch, A., Frey, O., Hilger, I., Sauner, D., Haas, M., Schmidt, D., Kurrat, C., Gajda, M., Malich, A., Brauer, R., and Kaiser, W. A. (2004) Diagnosis of arthritis using near-infrared fluorochrome Cy5.5. *Invest. Radiol. 39*, 626–632.
(30) Hickson, J. (2009) In vivo optical imaging: preclinical applications and considerations. *Urol. Oncol. 27*, 295–297.
(31) Wong, D. F. (2008) Imaging in drug discovery, preclinical, and early clinical development. *J. Nucl. Med. 49*, 26N–28N.
(32) Kiesslich, R., Gossner, L., Goetz, M., Dahlmann, A., Vieth, M., Stolte, M., Hoffman, A., Jung, M., Nafe, B., Galle, P. R., and Neurath, M. F. (2006) In vivo histology of Barrett's esophagus and associated neoplasia by confocal laser endomicroscopy. *Clin. Gastroenterol. Hepatol. 4*, 979–987.
(33) Kiesslich, R., Burg, J., Vieth, M., Gnaendiger, J., Enders, M., Delaney, P., Polglase, A., McLaren, W., Janell, D., Thomas, S., Nafe, B., Galle, P. R., and Neurath, M. F. (2004) Confocal laser endoscopy for diagnosing intraepithelial neoplasias and colorectal cancer in vivo. *Gastroenterology 127*, 706–713.
(34) Torchilin, V. P. (2005) Recent advances with liposomes as pharmaceutical carriers. *Nat. Rev. Drug Discovery 4*, 145–160.
(35) Zhu, L., Zheng, Y., von Kerczek, C. H., Topoleski, L. D., and Flower, R. W. (2006) Feasibility of extracting velocity distribution in choriocapillaris in human eyes from ICG dye angiograms. *J. Biomech. Eng. 128*, 203–209.
(36) Ishigami, Y., Masuzawa, M., Miyoshi, E., Kato, M., Tamura, K., Kanda, M., Awazu, K., Taniguchi, K., Kurita, M., and Hayashi, N. (1993) Clinical applications of ICG Finger Monitor in patients with liver disease. *J. Hepatol. 19*, 232–240.
(37) Klibanov, A. L., Maruyama, K., Torchilin, V. P., and Huang, L. (1990) Amphipathic polyethyleneglycols effectively prolong the circulation time of liposomes. *FEBS Lett. 268*, 235–237.
(38) Maeda, H., Sawa, T., and Konno, T. (2001) Mechanism of tumor-targeted delivery of macromolecular drugs, including the EPR effect in solid tumor and clinical overview of the prototype polymeric drug SMANCS. *J. Controlled Release 74*, 47–61.
(39) Harasym, T. O., Tardi, P., Longman, S. A., Ansell, S. M., Bally, M. B., Cullis, P. R., and Choi, L. S. (1995) Poly(ethylene glycol)-modified phospholipids prevent aggregation during covalent conjugation of proteins to liposomes. *Bioconjugate Chem. 6*, 187–194.
(40) Jain, R. K., Schlenger, K., Hockel, M., and Yuan, F. (1997) Quantitative angiogenesis assays: progress and problems. *Nat. Med. 3*, 1203–1208.
(41) Brown, E. B., Campbell, R. B., Tsuzuki, Y., Xu, L., Carmeliet, P., Fukumura, D., and Jain, R. K. (2001) In vivo measurement of gene expression, angiogenesis and physiological function in

tumors using multiphoton laser scanning microscopy. *Nat. Med. 7*, 864–868.

(42) Gratton, S. E., Napier, M. E., Ropp, P. A., Tian, S., and DeSimone, J. M. (2008) Microfabricated particles for engineered drug therapies: elucidation into the mechanisms of cellular internalization of PRINT particles. *Pharm. Res. 25*, 2845–2852.

(43) Gratton, S. E., Ropp, P. A., Pohlhaus, P. D., Luft, J. C., Madden, V. J., Napier, M. E., and DeSimone, J. M. (2008) The effect of particle design on cellular internalization pathways. *Proc. Natl. Acad. Sci. U.S.A. 105*, 11613–11618.

(44) Levick, J. R. (1981) Permeability of rheumatoid and normal human synovium to specific plasma proteins. *Arthritis Rheum. 24*, 1550–1560.

(45) Kushner, I., and Somerville, J. A. (1971) Permeability of human synovial membrane to plasma proteins. Relationship to molecular size and inflammation. *Arthritis Rheum. 14*, 560–570.

(46) Yamaki, K., Uchida, H., Li, X., Yanagisawa, R., Takano, H., Hayashi, H., Mori, Y., and Yoshino, S. (2005) Effect of varying types of anti-arthritic drugs on Th1 and Th2 immune responses in mice. *Int. J. Immunopathol. Pharmacol. 18*, 133–144.

(47) Takeshita, M., Sugita, T., and Takata, I. (1997) Pathological evaluation of effect of anti-rheumatic drugs on type II collagen-induced arthritis in Lewis rats. *Exp. Anim. 46*, 165–169.

(48) Ueno, M., Imaizumi, K., Sugita, T., Takata, I., and Takeshita, M. (1995) Effect of a novel anti-rheumatic drug, TA-383, on type II collagen-induced arthritis. *Int. J. Immunopharmacol. 17*, 597–603.

(49) Hansch, A., Frey, O., Sauner, D., Hilger, I., Haas, M., Malich, A., Brauer, R., and Kaiser, W. A. (2004) In vivo imaging of experimental arthritis with near-infrared fluorescence. *Arthritis Rheum. 50*, 961–967.

(50) Desmettre, T., Devoisselle, J. M., and Mordon, S. (2000) Fluorescence properties and metabolic features of indocyanine green (ICG) as related to angiography. *Surv. Ophthalmol. 45*, 15–27.

(51) Mordon, S., Devoisselle, J. M., Soulie-Begu, S., and Desmettre, T. (1998) Indocyanine green: physicochemical factors affecting its fluorescence in vivo. *Microvasc. Res. 55*, 146–152.

(52) Hansch, A., Sauner, D., Hilger, I., Frey, O., Haas, M., Malich, A., Brauer, R., and Kaiser, W. A. (2003) Noninvasive diagnosis of arthritis by autofluorescence. *Invest. Radiol. 38*, 578–583.

(53) Naumov, G. N., Folkman, J., and Straume, O. (2009) Tumor dormancy due to failure of angiogenesis: role of the microenvironment. *Clin. Exp. Metastasis 26*, 51–60.

(54) Naumov, G. N., Folkman, J., Straume, O., and Akslen, L. A. (2008) Tumor-vascular interactions and tumor dormancy. *APMIS 116*, 569–585.

(55) Naumov, G. N., Akslen, L. A., and Folkman, J. (2006) Role of angiogenesis in human tumor dormancy: animal models of the angiogenic switch. *Cell Cycle 5*, 1779–1787.

(56) Folkman, J. (2002) Role of angiogenesis in tumor growth and metastasis. *Semin. Oncol. 29*, 15–18.

(57) Jain, R. K. (2005) Normalization of tumor vasculature: an emerging concept in antiangiogenic therapy. *Science 307*, 58–62.

BC900311H

Strategies and Limitations in Dendrimeric Immunogen Synthesis. The Influenza Virus M2e Epitope as a Case Study

Wioleta Kowalczyk, Beatriz G. de la Torre, and David Andreu*

Department of Experimental and Health Sciences, Pompeu Fabra University, Barcelona Biomedical Research Park, Dr. Aiguader 88, 08003 Barcelona, Spain. Received July 27, 2009; Revised Manuscript Received December 3, 2009

Dendrimeric platforms such as multiple antigen peptides (MAPs) are regarded as one of the most efficacious approaches for antigenic presentation. Originally described as available by stepwise solid-phase peptide synthesis (SPPS), MAPs have also been prepared by chemical (thioether, oxime, hydrazone) ligation of appropriately functionalized tetra- or octavalent polylysine scaffolds with the peptide antigen to be multiply displayed. In this work, the advantages and limitations of two of the most frequent methods of MAP preparation, namely, chemoselective thioether ligation in solution, and all-solid-phase synthesis, have been tested in the case of a particularly troublesome epitope model, the ectodomain of protein M2 from influenza virus (M2e). The strong tendency of M2e to self-associate is a serious inconvenient for conjugation in solution, which as a result fails to produce the target MAPs with the specified number of M2e copies. In contrast, the fully stepwise SPPS approach is shown to be quite practical, especially when 6-aminohexanoic acid spacer units providing increased internal flexibility are inserted at each branching point.

INTRODUCTION

The usually low immunogenicity of short peptide epitopes, which precludes their use in free form for purposes such as raising antisera or candidate vaccine trials, has been addressed by various strategies, chiefly conjugation to carrier proteins (for an exhaustive treatment, see ref *1*), but also lipidation (*2, 3*) or association to particulate systems such as liposomes (*4, 5*) or immunostimulating complexes (*6*). One particularly successful approach has been multimerization, either by simple polymerization (*7*) or by chemically better defined strategies such as conjugation to sequential oligopeptide carriers (*8, 9*), display on lysine scaffolds (*10, 11*), or, last but not least, incorporation into dendrimeric systems such as the multiple antigenic peptides (MAPs) pioneered by Tam in the 1980s (*12*). MAPs are based on a small immunologically inert core of radially branching lysine dendrites onto which a number of peptide epitopes are attached. The result is a large macromolecule with a high molar ratio of peptide antigen to core molecule that usually does not require further conjugation to a carrier protein (though it may benefit from it; see, e.g., *refs* 13, 14). MAPs were originally described as available by standard stepwise solid-phase peptide synthesis (SPPS) (*12*), but have later also been produced in solution through various forms of chemical ligation (*15*−*17*). As the ligation reactions usually involve the combination of prepurified peptide modules, they can purportedly produce chemically more unambiguous materials (*16*) than SPPS methods, where minute but cumulative synthetic errors (deletions, truncations, etc.) become amplified by multimerization and may predictably lead to relatively heterogeneous immunogens. While the fairly extensive literature on, e.g., the immunological and microbiological applications of MAP and similarly dendrimeric platforms, highlights their value as candidate vaccines (*18*) or antimicrobial agents (*19, 20*), it is not always informative enough on the chemical specifications of the constructs at hand. In particular, and to the best of our knowledge, the literature on immunopeptides, MAPs, and similar bioconjugates lacks comparative studies where the potential merits and flaws of each synthetic (solution or stepwise SPPS) approach are evaluated in adequate chemical detail. In this work, we have investigated these aspects as they apply to a synthetically demanding peptide epitope (see below), then selected and improved the synthetic route leading to MAP platforms with optimal specifications.

The epitope chosen for this study is based on the N-terminal ectodomain (M2e) of influenza type A virus matrix protein 2 (M2). The M2 protein forms a pH-activated proton channel on the surface of the virion that mediates the uncoating of the viral particles in endosomes of the infected cell (*21*). The importance of the M2 protein in viral replication has been demonstrated by the ability of the antiviral drug amantadine and M2 specific antibodies to reduce viral propagation *in vitro* and *in vivo* (*22*−*24*).

M2 is made up of three main regions: the N-terminal, 24-residue ectodomain (M2e), the ensuing 19-amino acid transmembrane region that tetramerizes to form the pore of the proton channel (*25*), and the 54-residue cytoplasmic tail. While M2 is expressed abundantly on infected cell surfaces, in virus particles only a few M2 copies are displayed (*24*), in contrast to the other two major viral surface proteins hemagglutinin (HA) and neuraminidase (NA) (*26*−*29*). M2 is also weakly immunogenic relative to HA and NA (*30*) and highly conserved among human influenza virus strains (*31*). Table 1 lists (nonexhaustively) the M2e sequences from different influenza strains. It can be seen that, despite a high number of outbreaks up to the present 2009 pandemic, M2e has experienced minimal sequence alterations since 1933 (*32*), when the first human influenza strain was isolated. This remarkable lack of genetic variability, plus its relatively small size and the fact that antibodies to M2e protect mice from influenza A mortality, have made M2e a very popular epitope, not only for general immunogenicity studies but also as a potential vaccine candidate (*26, 31, 33*−*37*). M2e-based vaccines have been mostly obtained by either chemical conjugation to carrier proteins such as keyhole limpet hemocyanin, bovine serum albumin, or outer membrane protein complex or

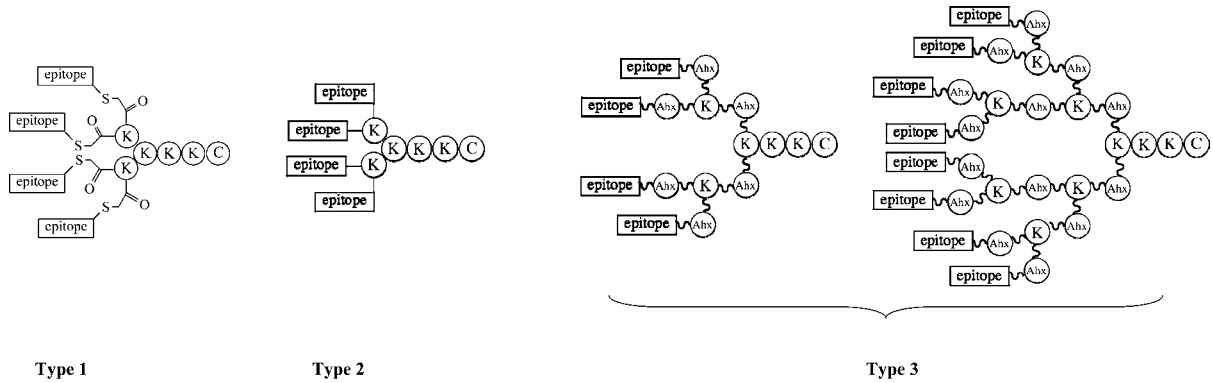
* To whom correspondence should be addressed. Professor David Andreu, Department of Experimental and Health Sciences, Pompeu Fabra University, Barcelona Biomedical Research Park, Dr. Aiguader 88, 08003 barcelona, Spain; Phone: (+34) 933 160 868, Fax: (+34) 933 160 901, E-mail: david.andreu@upf.edu.

10.1021/bc9003316 © 2010 American Chemical Society
Published on Web 12/21/2009

Table 1. M2 Ectodomain (M2e) Sequences Are Highly Conserved Across Multiple Strains of Influenza

Representative virus	Subtype	Amino acid sequences *
A/Wilson-Smith/1933	H1N1	MSLLTEVETPIRNEWGCRCNDSSD
A/Puerto Rico/8/34	H1N1	MSLLTEVETPIRNEWGCRCNGSSD
A/Wisconsin/3523/88	H1N1	MSLLTEVETPIRNEWGC**K**CNDSSD
A/California/04/2009	H1N1	MSLLTEVETP**T**R**S**EW**E**CRC**S**DSSD
A/Aichi/470/68	H3N1	MSLLTEVETPIRNEWGCRCNDSSD
A/Hebei/19/95	H3N2	MSLLTEVETPIRNEW**E**CRCNGSSD
A/Viet Nam/1203/2004	H5N1	MSLLTEVETP**T**RNEW**E**CRC**S**DSSD
A/Chicken/Nakorn-Patom/Thailand	H5N1	MSLLTEVETP**T**RNEW**E**CRC**S**DSSD
A/Thailand/1(KAN-1)/04	H5N1	MSLLTEVETP**T**RNEW**E**CRC**S**DSSD
A/Hong Kong/156/97	H5N1	MSLLTEVETL**T**RN**G**WGCRC**S**DSSD
A/Duck/1525/81	H5N1	MSLLTEVETP**T**RN**G**W**E**C**K**C**S**DSSD
A/Chicken/New York/95	H7N2	MSLLTEVETP**T**RN**G**W**E**C**K**C**S**DSSD
Consensus		**MSLLTEVETPTRNEWE<u>S</u>R<u>S</u>SDSSD**

* Highlighted in bold are variant residues relative to the A/Wilson-Smith/1933 (H1N1) sequence. The two underlined Ser residues in the consensus sequence were introduced as an isosteric replacement for Cys, to avoid synthetic problems.



Epitope	Sequence
M2e	MSLLTEVETPTRNEWESRSSDSSD(C)
sM2e	EVETPTRNEWES(C)

Figure 1. General structures of the different MAPs in this study. For type 1, the tioether linkage between the peptide epitope and the tetra-acetylated Lys core is shown. For type 2, the line between the epitope and the Lys core indicates a peptide bond. For type 3, the wavy lines around every Ahx residue emphasize the flexibility provided by this residue.

by genetic insertion into hepatitis B virus core antigen or papaya mosaic virus (PapMV) vaccine platforms (*26, 31, 38*−*40*).

As mentioned above, the goal of this study was to evaluate the advantages and limitations of chemical (thioether) ligation vs SPPS approaches for producing MAP dendrimeric peptides, and M2e was judged to be an interesting epitope not only for its above-mentioned biological relevance but also for the fact that despite its apparent (24 amino acid) simplicity it turns out to be synthetically nontrivial. Thus, three different types of MAP constructs (Figure 1) have been designed and prepared by either chemical ligation or SPPS methods, and the product composition of each synthetic trial has been analyzed in considerable detail. The study reveals how some structural peculiarities of the chosen M2e epitope, mainly its tendency to self-associate, entail considerable difficulties for the chemical ligation approach. In such an unfavorable context for conjugation in solution, the SPPS-based MAP synthetic strategy, especially fine-tuned in the present case to prevent sequence aggregation, emerges as the preferred route to MAP platforms displaying the M2e epitope.

EXPERIMENTAL PROCEDURES

Chemicals and Biologicals. Fmoc-protected amino acids were obtained from Senn Chemicals (Dielsdorf, Switzerland). Fmoc-Ser(tBu)-Ser($\Psi^{Me,Me}$pro)OH and Fmoc-Rink-amide (MBHA) resin were from Novabiochem (Läufelfingen, Switzerland). ChemMatrix resin, 2-(1*H*-benzotriazol-1-yl)-1,1,3,3-tetramethyluronium hexafluorophosphate (HBTU), and *N*-hydroxybenzotriazole (HOBt) were from Matrix Innovation (Montreal, Canada). HPLC-grade acetonitrile, and peptide synthesis grade *N*,*N*-dimethylformamide (DMF), dichloromethane (DCM), *N*,*N*-diisopropylethylamine (DIEA), and trifluoroacetic acid (TFA) were from SDS (Peypin, France). Anti-influenza A virus M2 protein monoclonal antibody 14C2 and rabbit polyclonal antibody to mouse IgG were from Abcam plc (Cambridge, UK). SIGMA*FAST p*-nitrophenyl phosphate tablets were from Sigma (Saint Louis, MO, USA). 96 well microplates were from Corning Inc. (Corning, NY, USA). All other reagents were of the highest quality available commercially.

General SPPS Protocols. Automated syntheses were performed in an ABI433 peptide synthesizer (Applied Biosystems, Foster City, CA) running standard Fmoc (FastMoc) protocols (*41*) at 0.1 mmol scale on Fmoc-Rink-amide ChemMatrix resin. Eight-to-10-fold excesses of Fmoc-L-amino acids and HBTU/HOBt, in the presence of double the molar amount of DIEA, were used for the coupling steps, with DMF as solvent. All side-chain functions were protected with TFA labile groups. In the longer M2e epitope, the two pairs of consecutive Ser residues were introduced as the pseudoproline dipeptide Fmoc-Ser(tBu)-Ser($\Psi^{Me,Me}$pro)-OH using a manual coupling with 4-fold excess

Table 2. Chemical Characteristics of Different Dendrimeric Presentations of the M2e Epitopes

MAP type[a]	n° copies	epitope	synthetic approach	composition	MW calculated (mo/av)	MW found
1	1−4	M2e	ligation	$C_{160}H_{263}N_{46}O_{57}S_4Cl_3$	3977.73/3973.71	3977.91
				$C_{275}H_{446}N_{80}O_{104}S_6Cl_2$	6800.32/6794.98	6794.11
				$C_{390}H_{629}N_{114}O_{151}S_8Cl_1$	9622.91/9616.25	9607.10
				$C_{505}H_{812}N_{148}O_{198}S_{10}$	12445.50/12437.53	12460.40
1	1−4	sM2e	ligation	$C_{110}H_{178}N_{31}O_{35}S_3Cl_3$	2697.36/2694.13	2691.51
				$C_{175}H_{276}N_{50}O_{60}S_4Cl_2$	4239.57/4235.84	4237.26
				$C_{240}H_{374}N_{69}O_{85}S_5Cl_1$	5781.79/5777.54	5813.82
				$C_{305}H_{472}N_{88}O_{110}S_6$	7324.00/7319.24	7341.23
2	4	sM2e	SPPS	$C_{281}H_{432}N_{80}O_{102}S$	6591.07/6595.05	6596.28
3	4	sM2e	SPPS[b]	$C_{317}H_{498}N_{86}O_{108}S_1$	7269.58/7273.99	7269.52
3	4	M2e	SPPS[b]	$C_{517}H_{838}N_{146}O_{196}S_5$	12387.86/12395.50	12387.80
3	8	sM2e	SPPS[b]	$C_{637}H_{998}N_{170}O_{216}S_1$	14517.21/14525.97	14515.89
3	8	M2e	SPPS[b]	$C_{1037}H_{1678}N_{290}O_{392}S_9$	24753.78/24768.97	not found

[a] As described in Figure 1. [b] MAPs with flexible spacers.

of dipeptide and HATU in the presence of DIEA (8-fold excess) in DMF. For manual synthesis operations, the peptide resin was placed in a syringe reactor fitted with a porous polyethylene disk. After synthesis completion, peptide resins were N-deblocked with piperidine/DMF (20% v/v) prior to full deprotection and cleavage with TFA/H_2O/EDT/TIS (94:2.5:2.5:1 v/v, 90 min, RT). Peptides were precipitated by addition of chilled methyl *tert*-butyl ether, taken up in aqueous AcOH (10% v/v), and lyophilized.

Analysis and Purification. Analytical reversed-phase HPLC was performed on C_{18} or C_8 columns (4.6 × 50 mm, 3 μm, Phenomenex, Torrance, CA) in a model LC-2010A system (Shimadzu, Kyoto, Japan). Solvent A was 0.045% (v/v) TFA in water, solvent B was 0.036% (v/v) TFA in acetonitrile. Elution was done with linear gradients of solvent B into A over 15 min (see chromatograms for further details) at 1 mL/min flow rate, with UV detection at 220 nm. Preparative HPLC was performed on C_{18} (21.2 × 250 mm, 10 μm, Phenomenex) or on C_8 column (10 × 250 mm, 10 μm, Phenomenex) in a Shimadzu LC-8A instrument. Solvents A and B were 0.1% TFA (v/v) in water and acetonitrile, respectively, and elution was again with linear gradients of solvent B into A over 35 min, at 25 or 5 mL/min flow rate for C_{18} or C_8 separations, respectively, with UV detection at 220 nm. Preparative fractions of satisfactory purity (>95%) by analytical HPLC were pooled and lyophilized. The purified peptides and MAPs were characterized for identity by MALDI-TOF MS in a Voyager DE-STR instrument (Applied Biosystems), using either sinapinic or α-hydroxycinnamic acid matrixes. MS spectra were in the reflector mode for the two linear peptide epitopes and the tetravalent Lys core; for larger-sized analytes, the linear mode was used. For even larger sized MAPs (e.g., the last two entries in Table 2), spectra were acquired in an LTQ-Orbitrap XL instrument (Thermo Fisher, San José, CA).

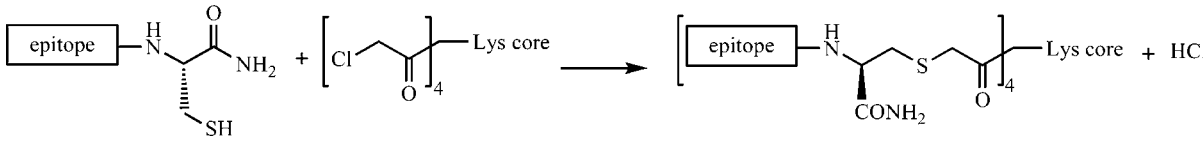
Type-1 MAPs by Thioether Ligation. The peptide epitopes M2e and sM2e to be conjugated to the tetravalent branched Lys core (see Figure 1) were prepared by the above SPPS protocols and, after significant optimization, particularly for M2e (see Results below), were characterized by analytical HPLC and MALDI-TOF MS (see Table S1, Supporting Information). In all cases, the purified peptides were obtained in free thiol form, with no disulfide detected by MS. The tetravalent [$(Lys)_2$LysLysLysCys(S-*t*Bu)] core was also assembled by SPPS in the ABI433 instrument at 0.1 mmol scale. For the first two Lys residues (from the C-terminus), the conventional Fmoc-Lys(tBu) derivative was used; branching was then achieved by introducing Fmoc-Lys(Fmoc) at the following two synthetic cycles. After this, the synthesis was switched to the manual mode (see above) for deprotection with piperidine/DMF (20% v/v) for 5 and 15 min and chloroacetylation with 4 mmol of chloroacetic acid in the presence of an equivalent amount of diisopropylcarbodiimide in dichloromethane. Cleavage with TFA/H_2O/TIS (95:2.5:2.5 v/v/v, 1 h, RT) and preparative RP-HPLC purification led to the target branched peptide in analytical HPLC-homogeneous form and with the expected mass by MALDI-TOF MS (see Figure S1 and Table S1, Supporting Information).

For the thioether ligation reaction, 1.16 mg (1 μmol) of the tetra-chloroacetylated Lys core was dissolved in 5 mL of 20 mM Tris, 2 M guanidinium chloride buffer, pH 7.6, at 50 °C, then 12 μmol (12-fold molar excess) of either M2e or sM2e peptide epitope were added portionwise to the solution, adjusting the pH as required. Aliquots of the mixture were taken for analytical HPLC and MALDI-TOF MS, and when no further changes in the HPLC profile were observed (usually after 15−20 h), the reaction product was separated by preparative RP-HPLC. Fractions representative of different degrees of epitope incorporation (Table 2, first entry) were characterized by analytical HPLC and MALDI-TOF MS. For further details, see the Results section below.

Full Stepwise SPPS of Type-2 and Type-3 MAPs. The different MAP constructs (see Figure 1 for details) were assembled mostly by automated procedures in an ABI433 synthesizer running the FastMoc protocols discussed above on Fmoc-Rink-amide ChemMatrix resin at 0.02 mmol scale. 10-fold excesses of Fmoc-protected L-amino acids and HBTU/HOBt in the presence of DIEA (20-fold excess) were routinely used throughout. Branching was achieved at the appropriate points by incorporation of the Fmoc-Lys(Fmoc) derivative. As above, the two Ser-Ser dipeptides of the full-length M2e epitope were introduced in the manual mode as the pseudoproline dipeptide Fmoc-Ser(tBu)-Ser($\Psi^{Me,Me}$pro)-OH. Deprotection and cleavage were as described in the general SPPS protocols above. The synthetic crudes were purified by preparative HPLC and characterized by analytical HPLC and MALDI-TOF MS. Analytical data on the different MAPs are given in Table 2.

ELISA. Peptide stock solutions (either the single M2e sequence or tetravalent type-3 MAP) were initially made up at 25 μM concentration in PBS (pH 7.4), then serially diluted so that 0.8, 0.6, 0.4, and 0.2 nmol peptide aliquots in 50 μL PBS were placed in triplicate in the wells of a microtiter plate for overnight coating at 4 °C. Wells were then washed three times with PBS containing 0.05% Tween-20, and the remaining sites on the wells were blocked by 3% BSA in PBS/Tween-20 at 37 °C for 2 h. After another three washes, 200 μL of a 1:10 000 dilution of mouse monoclonal 14C2 was added to wells and incubated for 2 h at 37 °C. The wells were washed three times

Scheme 1. Thioether Ligation Route to Type-1 MAPs



with PBS/Tween-20 to remove unbound antibody, then incubated with a 1:5000 dilution of the alkaline phosphatase conjugate of rabbit polyclonal antimouse IgG in 1%BSA/PBS/Tween-20 for 2 h at 37 °C. Wells were next washed three times with PBS/Tween-20, and 50 μL of a 1.0 mg/mL solution of *p*-nitrophenyl phosphate in 0.2 M Tris, 5 mM $MgCl_2$ was added to each well. After 30 min incubation, the plate was read at 405 nm in an ELx808 microplate reader (Bio-Tek Instruments Inc., Winooski, VT).

RESULTS

Ligation Approach to M2e Dendrimers. The different types of MAP structures produced and examined in this study are shown in Figure 1, along with the sequences of full-length (M2e) and shortened (sM2e) versions of the M2 ectodomain epitope. An influenza H5N1 M2e peptide sequence was used in this study in which the two internal Cys residues were changed to Ser to prevent disulfide bond formation which would complicate the synthetic work (see Table 1). Table 2 provides detailed molecular structures and analytical data to help the reader through the following description and discussion.

The M2e peptide initially used in the ligation approach to type-1 MAP contained a Cys residue in free thiol form required for the thioether ligation reaction with the tetra-chloroacetylated branched lysine core (Scheme 1), which in turn was made with a C-terminal Cys orthogonally protected with a temporary *tert*-butylthio group ensuring temporary protection during the ligation step and eventually enabling, after deprotection, either dimerization of the MAP or further conjugation onto a higher-order carrier. Another feature of this type-1 MAP (see Figure 1) was the two Lys residues adjacent to the first Lys branching point. The purpose of this Lys-Lys motif was to define a cathepsin-like cleavage site (*7*) which might favor the in vivo processing of the dendrimeric moiety.

An unforeseen problem of the ligation approach was that the 25-residue-long M2e peptide turned out to be a relatively challenging synthetic target, requiring considerable optimization. A first synthesis on standard Rink-amide by the typical Fmoc methodology resulted in a complex, unpromising product vis-à-vis its subsequently expected use (Figure 2A). Use of the demonstrably superior Rink-amide ChemMatrix resin (*42*) and double coupling at some positions (Glu residues 16 and 14, plus the entire Glu8-Ser2 stretch, based on MS analysis of the crude from the initial trial, and on prediction of difficult sequences with the Peptide Companion program) ameliorated only partially the situation (Figure 2B). In a third, successful trial, the above improvements plus replacement of the two pairs of consecutive Ser residues in the M2e sequence with the pseudoproline dipeptide Ser(tBu)-Ser($\Psi^{Me,Me}$pro)-OH (*43*−*45*) led to a more acceptable product that could be purified and characterized as the desired M2e peptide in free thiol form (Figure 2C; see also Figure S1 and Table S1, Supporting Information). The chemoselective ligation of this purified, sparingly soluble peptide to the $ClAc_4$-Lys core was carried out in Tris-Cl buffer at pH 7.6 and 50 °C, using a 10−12-fold molar excess of M2e peptide in order to drive the reaction into completion. Addition of chaotropic agents (e.g., guanidinium chloride) to multimer-building reactions of this type has been predicated as preventing aggregation and favoring maximal substitution (*46, 47*), but in our case, it did not have any positive effect. Analytical RP-HPLC of the ligation process revealed quite a complex reaction mixture (Figure 3), which by MALDI-TOF MS analysis (Figure S3,

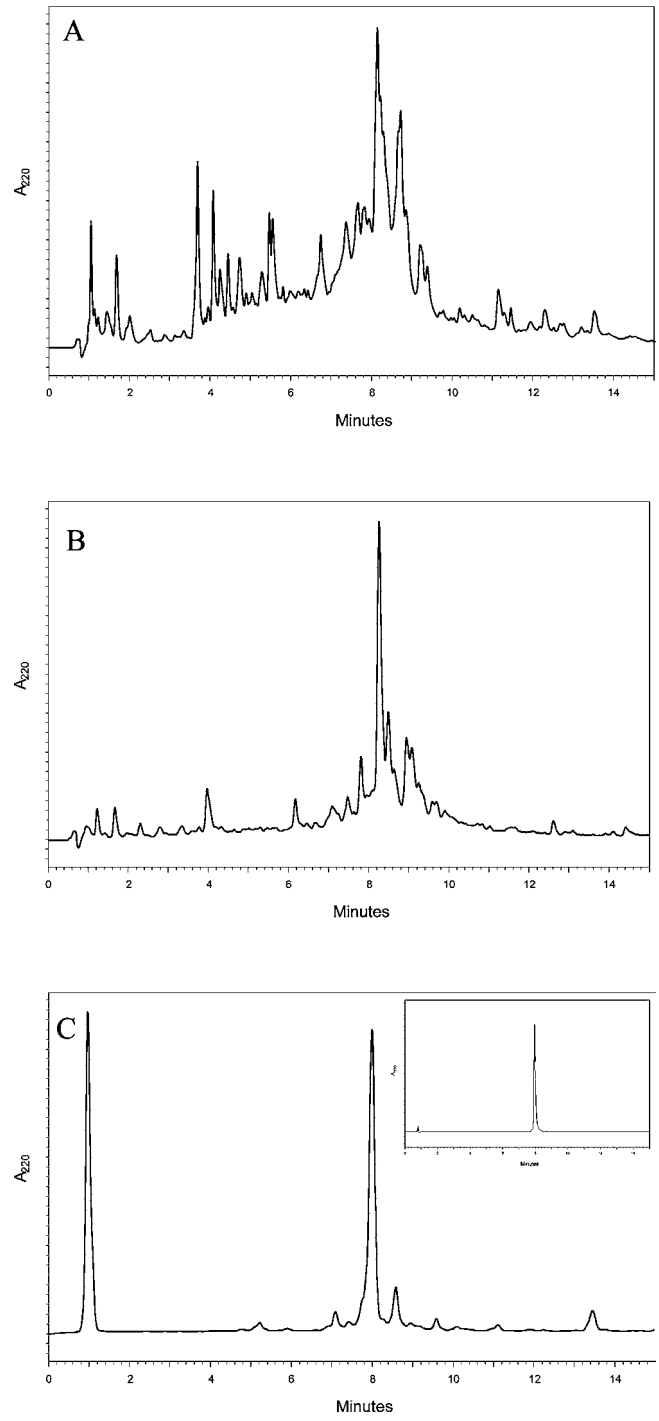


Figure 2. HPLC of crude M2e peptide made by different Fmoc synthesis strategies. A: Rink amide MBHA resin. B: Rink-amide ChemMatrix resin, double couplings at selected positions. C: as in B, with pseudo-Pro dipeptide replacements. 5−50% linear gradient of eluent B into A over 15 min. Analytical C_{18} column. Inset: HPLC of purified M2e, same elution conditions. See Experimental Procedures (Analysis and Purification section) in the main text for further details.

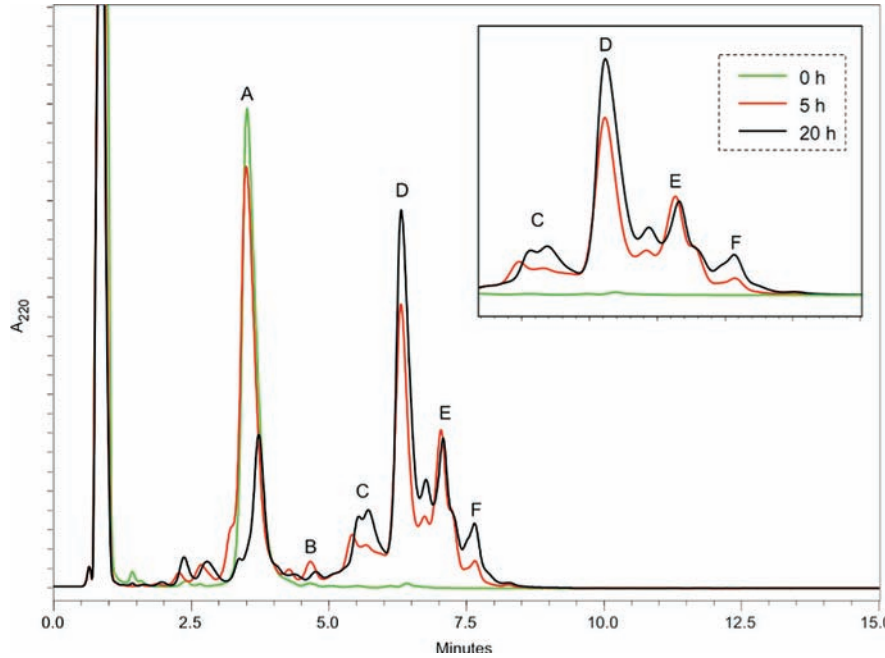


Figure 3. Progress of the chemical ligation of M2e to $ClAc_4$-Lys core monitored by HPLC at 0, 5, and 20 h reaction time (green, red, and black traces, respectively). 20−35% linear gradient of eluent B into A over 15 min. Analytical C_{18} column. Peaks labeled A−F correspond to M2e peptide, 1-copy MAP, mixture of 1- and 2-copy MAP, M2e dimer and tetramer, 3-copy MAP, mixture of 3- and 4-copy MAP, respectively.

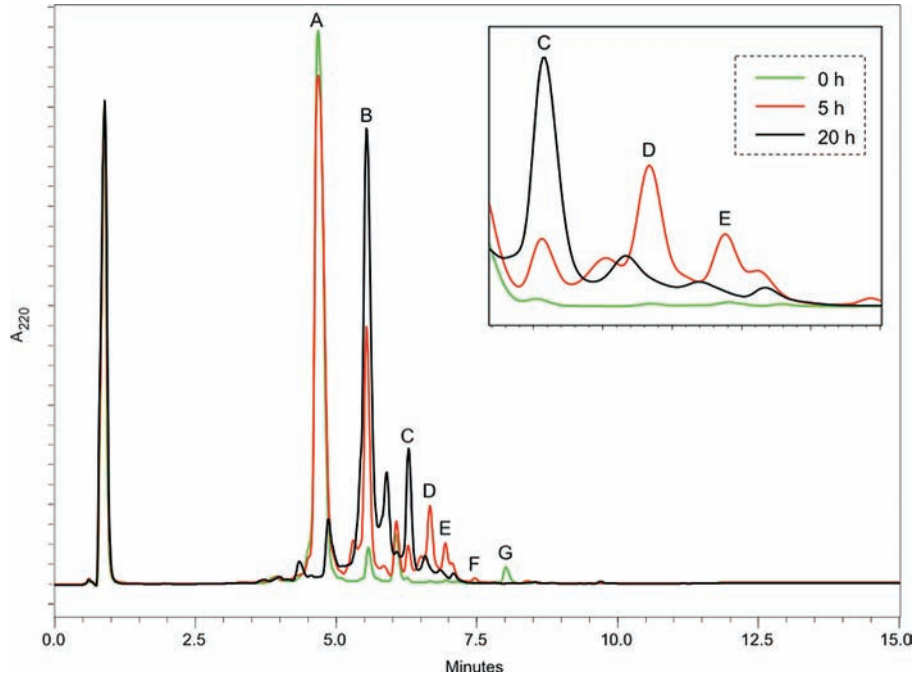


Figure 4. Progress of the chemical ligation of sM2e to $ClAc_4$-Lys core monitored by HPLC at 0, 5, and 20 h reaction time (green, red, and black traces, respectively). 10−40% linear gradient of eluent B into A over 15 min. Analytical C_{18} column. Peaks labeled A−G correspond to sM2e peptide, sM2e dimer, 4-copy MAP, 3-copy MAP, 2-copy MAP, 1-copy MAP, and unreacted $ClAc_4$-Lys core, respectively.

Supporting Information) was shown to include type-1 MAPs containing different numbers of copies of the M2e epitope (Table 2, first entry). HPLC resolution of these MAP products was poor (Figure 3), even using rather shallow gradients. Coeluting with the MAP products, substantial levels of the disulfide dimer of M2e were found (Figure 3), and quite unexpectedly, sizable amounts as well of a species that by MALDI-TOF and MS/MS analysis was identified as a tetramer of M2e (Figures S3A and S4, Supporting Information), i.e., the aggregate of two M2e (disulfide) dimers.

Since the aggregation tendency of the 25-residue M2e epitope posed unanticipated complications in the ligation approach, a shorter version of M2e (sM2e) was prepared (Figure S2 and Table S1, Supporting Information). This peptide was much simpler to make and gave no evidence of multimerization. Using the above reaction conditions, the ligation of the $ClAc_4$-Lys core and sM2e proceeded smoothly, as monitored by analytical RP-HPLC (Figure 4). MALDI-TOF MS analysis (Figure S5, Supporting Information) showed the target dendrimer (four copies of the sM2e peptide) as the main outcome, although byproducts with two or three copies of sM2e were also present in the reaction mixture. Results are summarized in Table 2.

Solid-Phase Approach to M2e Dendrimers. Since the chemoselective ligation described above fell short of expecta-

tions as an efficient route to M2e dendrimeric constructs, we turned our attention to the originally reported SPPS method of MAP synthesis. The two MAP varieties made by this approach, types 2 and 3 (Figure 1), similarly to type 1 contained a Cys residue at the C-terminus, to be used for dimerization, attachment of an additional peptide epitope (e.g., a T-cell epitope), or conjugation to carrier proteins (KLH or BSA), all with a view to further increasing the immunogenicity of the constructs.

Given the difficulties observed during the synthesis of the M2e peptide (see above), the shortened sM2e sequence was initially chosen to optimize the synthetic methodology. As shown in Figure 1, the first MAP attempted by SPPS was of the classical, type 2 variety, displaying four copies of sM2e (Table 2, third entry). This dendrimer was obtained rather straightforwardly by stepwise SPPS on a Rink amide ChemMatrix resin using standard Fmoc chemistry (Figure S6, Supporting Information) with double couplings throughout the sequence of the epitope. Next, and in anticipation of the difficulties that a full-length M2e epitope might pose to MAP synthesis, it was decided to enhance the overall flexibility of the MAP skeleton by introducing 6-aminohexanoic acid (Ahx)[1] spacer units at each branching point. This modification defined a novel architecture, type-3 MAP (Figure 1), first tested in tetravalent fashion with the uncomplicated sM2e epitope (Table 2, fourth entry). Again, this dendrimer was readily accessible, basically trouble-free, through stepwise SPPS (Figure S7, Supporting Information). With such favorable results in hand, it seemed appropriate to take on the potentially challenging synthesis of the MAP with four copies of the full-length M2e epitope (Table 2, fifth entry). The same tactics that had significantly improved the synthesis of the single-chain M2e, namely, replacement of the two Ser-Ser pairs by pseudoproline dipeptides (Fmoc-Ser(tBu)-Ser($\Psi^{Me,Me}$pro)OH), were again applied in a stepwise Fmoc SPPS on Rink amide ChemMatrix resin, again using double couplings throughout the entire M2e epitope sequence. Once more, the SPPS approach turned out a rather clean, easily purifiable and satisfactorily characterized end product (Figures S8 and S9, Supporting Information). Encouraged by this positive result, the strategy was pushed one step further in the synthesis of a type-3 octavalent sM2e MAP (Table 2, sixth entry). Remarkably, the end product was again readily accessible and characterized (Figure S10, Supporting Information). The logical extension of the all-SPPS approach was the octavalent version of the M2e MAP (Table 2, last entry). Unfortunately, application of the so-far successful combination of improvements (i.e., Ahx spacers, ChemMatrix resin, double couplings, pseudoproline dipeptide mimics) completely failed this time to provide any discernible trace of the desired MAP product.

Immunological Evaluation of M2e Presentations. After having proven the feasibility of obtaining a multimeric version of M2e in a relatively trouble-free way, it remained to be ascertained whether the enhanced epitope display provided by the tetravalent MAP platform translated into an equivalent increase in antigenic recognition (*48, 49*). This point was investigated by means of an ELISA where the monovalent M2e peptide and its tetravalent version (Table 2, fifth entry) were tested against the M2e-specific monoclonal 14C2. Lack of specific antibodies prevented a similar evaluation with sM2e-displaying MAPs. Figure 5 shows that the antigenic response obtained with the single M2e peptide was indeed amplified with the MAP, with a 3-to-4-fold increased response that was in good agreement with the multimerization level provided by the MAP.

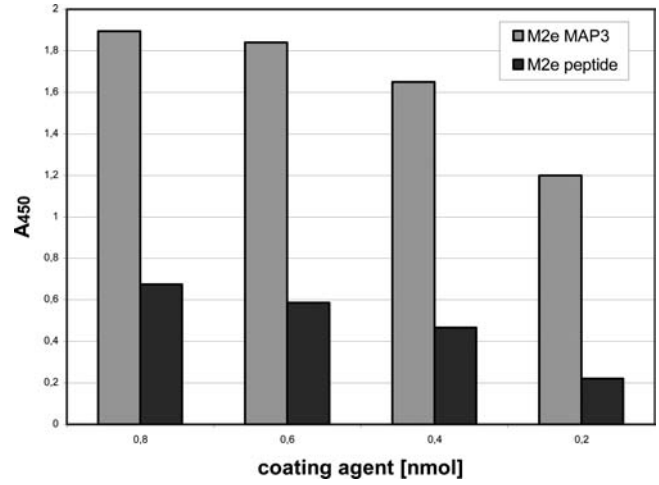


Figure 5. ELISA of M2e peptide in monomer (black columns) and type-3 MAP (gray columns) presentations against 14C2 monoclonal antibody.

DISCUSSION

The goal of this study was to examine the relative advantages and limitations of the two main approaches to MAP constructs, namely, chemical ligation in solution (*16, 50, 51*) or fully stepwise SPPS (*12*). As a backdrop for such an endeavor, there was an intuition, partially grounded on our own previous experience in the field, that a nontrivial fraction of the synthetic attempts on MAPs by either of the above approaches had met with problems such as insolubility of the final product, sluggish progress of chemical ligation, and so forth, all leading to unsatisfactory results that either went unreported or were published with minimal, if any, chemical documentation.

In principle, the former (ligation) method would appear to be conducive to superior results, since purification of the intermediates (peptide epitope and branched Lys core) would yield an end product devoid of the minute but inevitable impurities (truncations, deletions) accumulated over a stepwise process, where the simultaneous growth of four—or even eight—peptide chains on a single molecular platform may, in some cases, promote aggregation, and in general have an amplifying effect on side reactions and thus the heterogeneity of the final product. These theoretical benefits of the ligation approach, however, can be severely challenged by experimental facts, as the above results on the incomplete conjugation of both M2e and sM2e epitopes on type-1 MAP scaffolds show. The most likely cause for our failure to obtain type-1 MAPs with the maximum number of epitope copies as a major final product is that, as successive epitope units are incorporated onto the $ClAc_4$-Lys scaffold, they generate a certain steric hindrance that may seriously hamper the access of (the Cys nucleophilic sulfur atom of) any incoming peptide epitope to the remaining unreacted ClAc groups. In the particular case of the present study, the nature of one of the peptide epitopes chosen, i.e., the full-length M2e, posed even additional difficulties for the chemoselective ligation approach (see below), exceeding in complexity any other similar reaction within our own expertise (*18*). It is indeed known from structural studies that the ion channel-forming transmembrane domain of M2 protein exists as a homotetramer (*21, 25, 52*−*57*). The present results would appear to suggest that, beyond the transmembrane region, an

[1]Abbreviations: Ahx, 6-aminohexanoic acid (residue); ClAc, chloroacetyl; DIEA, *N*,*N*-diisopropylethylamine; EDT, ethanedithiol; ESI, electrospray ionization; Fmoc, 9-fluorenylmethoxycarbonyl; HBTU, 2-(1*H*-benzotriazole-1-yl)-1,1,3,3-tetramethyluronium hexafluorophosphate; HPLC, high performance liquid chromatography; MALDI-TOF, matrix-assisted laser desorption ionization time-of-flight; LTQ, linear trap quadrupole; MS, mass spectrometry; SPPS, solid phase peptide synthesis; TFA, trifluoroacetic acid; TIS, triisopropylsilane.

aggregation propensity is also inherent (or somehow relayed) to the ectodomain as well.

Yet, even when this latter inconvenient was dealt with appropriately (i.e., by switching to a shorter sM2e epitope), solution ligation remained a less rewarding approach to MAP constructs than originally anticipated. In assessing the evidently complex outcome of this synthetic route (see especially Figure 3, also Figure 4), it is worth noting that, of all the possible products (final and intermediate) of such a ligation reaction, only the 4-copy MAP has a univocal chemical constitution; other intermediates (i.e., those with 1−3 epitope copies) may exist as slightly similar but constitutionally nonequivalent (though isobaric) isomers, depending on which positions in the branched Lys scaffold are occupied by the epitopes. Therefore, and despite very careful collection, HPLC fractions representative of a given M2e epitope multiplicity (n= 2, 3, 4) were not strictly homogeneous.

The alternative approach to MAPs, namely, fully stepwise SPPS, was for its part not devoid of difficulties either. While the relatively simple type-2 MAP with four copies of the sM2e epitope was viable, the known propensity to aggregate of the biologically more relevant M2e epitope (see Ligation approach to M2e dendrimers, Results section) might pose synthetic trouble for the corresponding MAP. As a safeguard against interchain association, it seemed to us that augmenting the global flexibility of the growing MAP construct by insertion of Ahx spacing units might be beneficial. This was indeed proven so in the syntheses of the tetravalent type-3 MAPs of both sM2e and M2e, as well as for the octavalent MAP of sM2e. However, extension of the approach to an octavalent M2e MAP did not meet with success, and its synthetic viability remains an open question.

In sum, depending on the targeted level of multiplicity and on the size and aggregation potential of the epitope to be displayed, MAP synthesis can range from facile to outright impracticable. The theoretical advantage that chemoselective ligation of prepurified components offers is seriously offset by slow reaction rates (possibly due to steric hindrance) and, in aggregation-prone peptide epitopes such as M2e, by additional adverse effects. This appears to give an edge to the original SPPS approach, which can be even further improved—especially in the case of potentially problematical epitopes such as M2e—by an enhancement of the internal flexibility of the construct such as that provided by the insertion of Ahx spacing units at the different branching points of the MAP dendrimer. While this appears to have a positive effect on synthetic viability and general quality (e.g., yield, solubility) of the end product, it cannot be regarded as a failsafe solution, as our results on the octavalent M2e show. All in all, our data suggest that, as for other similarly complex biomolecules, careful fine-tuning of synthetic conditions is essential if chemically well-defined MAPs, e.g., suitable for drug registry, are desired. In studies currently underway, we continue to explore the validity of the above and other approaches for other MAP platforms where sequence-specific features of the peptide epitope may again translate into synthetic complications.

ACKNOWLEDGMENT

Work supported by the Spanish Ministerio de Educación y Ciencia (grants BIO2005-07592-CO2-02 and BIO2008-04487-CO3-02 to D.A.), by the regional government of Catalunya (SGR2005-00494), and by Chimera Pharma SLU (Tres Cantos, Madrid, Spain). W.K. is a fellow in the Juan de la Cierva Program of the Spanish Ministry of Science and Innovation. We thank Drs. Thomas Zürcher and Cayetano von Kobbe of Chimera Pharma for fruitful discussions and critical reading of the manuscript.

Supporting Information Available: HPLC traces and MALDI-TOF spectra of peptides and MAPs. This material is available free of charge via the Internet at http://pubs.acs.org.

LITERATURE CITED

(1) Van Regenmortel, M. H. V., and Muller, S. (1999) Synthetic Peptides as Antigens, in *Laboratory techniques in biochemistry and molecular biology* (van der Vliet, P. C., Ed.) Elsevier, Amsterdam.

(2) Chua, B. Y., Zeng, W., Lau, Y. F., and Jackson, D. C. (2007) Comparison of lipopeptide-based immunocontraceptive vaccines containing different lipid groups. *Vaccine 25*, 92–101.

(3) BenMohamed, L., Wechsler, S. L., and Nesburn, A. B. (2002) Lipopeptide vaccines--yesterday, today, and tomorrow. *Lancet Infect. Dis. 2*, 425–431.

(4) Gregoriadis, G. (1994) Liposomes as immunoadjuvants and vaccine carriers: antigen entrapment. *Immunomethods 4*, 210–216.

(5) Nagata, T., Toyota, T., Ishigaki, H., Ichihashi, T., Kajino, K., Kashima, Y., Itoh, Y., Mori, M., Oda, H., Yamamura, H., Taneichi, M., Uchida, T., and Ogasawara, K. (2007) Peptides coupled to the surface of a kind of liposome protect infection of influenza viruses. *Vaccine 25*, 4914–4921.

(6) Lovgren, K., and Larsson, M. (1994) Conjugation of synthetic peptides to carrier iscoms: factors affecting the immunogenicity of the conjugate. *J. Immunol. Methods 173*, 237–243.

(7) Borras-Cuesta, F., Fedon, Y., and Petit-Camurdan, A. (1988) Enhancement of peptide immunogenicity by linear polymerization. *Eur. J. Immunol. 18*, 199–202.

(8) Tsikaris, V., Sakarellos, C., Cung, M. T., Marraud, M., and Sakarellos-Daitsiotis, M. (1996) Concept and design of a new class of sequential oligopeptide carriers (SOC) for covalent attachment of multiple antigenic peptides. *Biopolymers 38*, 291–293.

(9) Mezo, G., de Oliveira, E., Krikorian, D., Feijlbrief, M., Jakab, A., Tsikaris, V., Sakarellos, C., Welling-Wester, S., Andreu, D., and Hudecz, F. (2003) Synthesis and comparison of antibody recognition of conjugates containing herpes simplex virus type 1 glycoprotein D epitope VII. *Bioconjugate Chem. 14*, 1260–1269.

(10) Kragol, G., and Otvos, L., Jr. (2001) Orthogonal solid phase synthesis of tetramannosylated peptide construct carrying three independent branched epitopes. *Tetrahedron 57*, 10.

(11) Mozdzanowska, K., Feng, J., Eid, M., Kragol, G., Cudic, M., Otvos, L., Jr., and Gerhard, W. (2003) Induction of influenza type A virus-specific resistance by immunization of mice with a synthetic multiple antigenic peptide vaccine that contains ectodomains of matrix protein 2. *Vaccine 21*, 2616–2626.

(12) Tam, J. P. (1988) Synthetic peptide vaccine design: synthesis and properties of a high-density multiple antigenic peptide system. *Proc. Natl. Acad. Sci. U.S.A. 85*, 5409–5413.

(13) Cruz, L. J., Iglesias, E., Aguilar, J. C., Cabrales, A., Reyes, O., and Andreu, D. (2004) Different immune response of mice immunized with conjugates containing multiple copies of either consensus or mixotope versions of the V3 loop peptide from human immunodeficiency virus type 1. *Bioconjugate Chem. 15*, 1110–1117.

(14) Cruz, L. J., Iglesias, E., Aguilar, J. C., Gonzalez, L. J., Reyes, O., Albericio, F., and Andreu, D. (2004) A comparative study of different presentation strategies for an HIV peptide immunogen. *Bioconjugate Chem. 15*, 112–120.

(15) Rose, K., Zeng, W., Brown, L. E., and Jackson, D. C. (1995) A synthetic peptide-based polyoxime vaccine construct of high purity and activity. *Mol. Immunol. 32*, 1031–1037.

(16) Tam, J. P., Yu, Q., and Miao, Z. (1999) Orthogonal ligation strategies for peptide and protein. *Biopolymers 51*, 311–332.

(17) Fitzmaurice, C. J., Brown, L. E., Kronin, V., and Jackson, D. C. (2000) The geometry of synthetic peptide-based immunogens affects the efficiency of T cell stimulation by professional antigen-presenting cells. *Int. Immunol. 12*, 527–535.

(18) Cubillos, C., de la Torre, B. G., Jakab, A., Clementi, G., Borras, E., Barcena, J., Andreu, D., Sobrino, F., and Blanco, E. (2008) Enhanced mucosal immunoglobulin A response and solid protection against foot-and-mouth disease virus challenge induced by a novel dendrimeric peptide. *J. Virol. 82*, 7223–7230.

(19) Pini, A., Giuliani, A., Falciani, C., Runci, Y., Ricci, C., Lelli, B., Malossi, M., Neri, P., Rossolini, G. M., and Bracci, L. (2005) Antimicrobial activity of novel dendrimeric peptides obtained by phage display selection and rational modification. *Antimicrob. Agents Chemother. 49*, 2665–2672.

(20) Pini, A., Falciani, C., and Bracci, L. (2008) Branched peptides as therapeutics. *Curr. Protein Pept. Sci. 9*, 468–477.

(21) Stouffer, A. L., Acharya, R., Salom, D., Levine, A. S., Di Costanzo, L., Soto, C. S., Tereshko, V., Nanda, V., Stayrook, S., and DeGrado, W. F. (2008) Structural basis for the function and inhibition of an influenza virus proton channel. *Nature 451*, 596–599.

(22) Treanor, J. J., Tierney, E. L., Zebedee, S. L., Lamb, R. A., and Murphy, B. R. (1990) Passively transferred monoclonal antibody to the M2 protein inhibits influenza A virus replication in mice. *J. Virol. 64*, 1375–1377.

(23) Hay, A. J., Wolstenholme, A. J., Skehel, J. J., and Smith, M. H. (1985) The molecular basis of the specific anti-influenza action of amantadine. *EMBO J. 4*, 3021–3024.

(24) Zebedee, S. L., and Lamb, R. A. (1988) Influenza A virus M2 protein: monoclonal antibody restriction of virus growth and detection of M2 in virions. *J. Virol. 62*, 2762–2772.

(25) Schnell, J. R., and Chou, J. J. (2008) Structure and mechanism of the M2 proton channel of influenza A virus. *Nature 451*, 591–595.

(26) Neirynck, S., Deroo, T., Saelens, X., Vanlandschoot, P., Jou, W. M., and Fiers, W. (1999) A universal influenza A vaccine based on the extracellular domain of the M2 protein. *Nat. Med. 5*, 1157–1163.

(27) Slepushkin, V. A., Katz, J. M., Black, R. A., Gamble, W. C., Rota, P. A., and Cox, N. J. (1995) Protection of mice against influenza A virus challenge by vaccination with baculovirus-expressed M2 protein. *Vaccine 13*, 1399–1402.

(28) Frace, A. M., Klimov, A. I., Rowe, T., Black, R. A., and Katz, J. M. (1999) Modified M2 proteins produce heterotypic immunity against influenza A virus. *Vaccine 17*, 2237–2244.

(29) Okuda, K., Ihata, A., Watabe, S., Okada, E., Yamakawa, T., Hamajima, K., Yang, J., Ishii, N., Nakazawa, M., Okuda, K., Ohnari, K., Nakajima, K., and Xin, K.-Q. (2001) Protective immunity against influenza A virus induced by immunization with DNA plasmid containing influenza M gene. *Vaccine 19*, 3681–3691.

(30) Feng, J., Zhang, M., Mozdzanowska, K., Zharikova, D., Hoff, H., Wunner, W., Couch, R. B., and Gerhard, W. (2006) Influenza A virus infection engenders a poor antibody response against the ectodomain of matrix protein 2. *Virol. J. 6*, 102.

(31) Fan, J., Liang, X., Horton, M. S., Perry, H. C., Citron, M. P., Heidecker, G. J., Fu, T. M., Joyce, J., Przysiecki, C. T., Keller, P. M., Garsky, V. M., Ionescu, R., Rippeon, Y., Shi, L., Chastain, M. A., Condra, J. H., Davies, M. E., Liao, J., Emini, E. A., and Shiver, J. W. (2004) Preclinical study of influenza virus A M2 peptide conjugate vaccines in mice, ferrets, and rhesus monkeys. *Vaccine 22*, 2993–3003.

(32) Smith, W., Andrews, C. H., and Laidlaw, P. P. (1933) A virus obtained from influenza patients. *Lancet 2*, 66–68.

(33) Liu, W., Zou, P., and Chen, Y. H. (2004) Monoclonal antibodies recognizing EVETPIRN epitope of influenza A virus M2 protein could protect mice from lethal influenza A virus challenge. *Immunol. Lett. 93*, 131–136.

(34) De Filette, M., Martens, W., Roose, K., Deroo, T., Vervalle, F., Bentahir, M., Vandekerckhove, J., Fiers, W., and Saelens, X. (2008) An influenza A vaccine based on tetrameric ectodomain of matrix protein 2. *J. Biol. Chem. 283*, 11382–11387.

(35) Huleatt, J. W., Nakaar, V., Desai, P., Huang, Y., Hewitt, D., Jacobs, A., Tang, J., McDonald, W., Song, L., Evans, R. K., Umlauf, S., Tussey, L., and Powell, T. J. (2008) Potent immunogenicity and efficacy of a universal influenza vaccine candidate comprising a recombinant fusion protein linking influenza M2e to the TLR5 ligand flagellin. *Vaccine 26*, 201–214.

(36) De Filette, M., Martens, W., Smet, A., Schotsaert, M., Birkett, A., Londoño-Arcila, P., Fiers, W., and Saelens, X. (2008) Universal influenza A M2e-HBc vaccine protects against disease even in the presence of pre-existing anti-HBc antibodies. *Vaccine 26*, 6503–6507.

(37) De Filette, M., Min Jou, W., Birkett, A., Lyons, K., Schultz, B., Tonkyro, A., Resch, S., and Fiers, W. (2005) Universal influenza A vaccine: optimization of M2-based constructs. *Virology 337*, 149–161.

(38) Ionescu, R. M., Przysiecki, C. T., Liang, X., Garsky, V. M., Fan, J., Wang, B., Troutman, R., Rippeon, Y., Flanagan, E., Shiver, J., and Shi, L. (2006) Pharmaceutical and immunological evaluation of human papillomavirus viruslike particle as an antigen carrier. *J. Pharm. Sci. 95*, 70–79.

(39) Jegerlehner, A., Tissot, A., Lechner, F., Sebbel, P., Erdmann, I., Kündig, T., Bächi, T., Storni, T., Jennings, G., Pumpens, P., Renner, W. A., and Bachmann, M. F. (2002) A molecular assembly system that renders antigens of choice highly repetitive for induction of protective B cell responses. *Vaccine 19*, 3104–3112.

(40) Denis, J., Acosta-Ramirez, E., Zhao, Y., Hamelin, M. E., Koukavica, I., Baz, M., Abed, Y., Savard, C., Pare, C., Lopez Macias, C., Boivin, G., and Leclerc, D. (2008) Development of a universal influenza A vaccine based on the M2e peptide fused to the papaya mosaic virus (PapMV) vaccine platform. *Vaccine 26*, 3395–3403.

(41) Fields, G. B., and Noble, R. L. (1990) Solid phase peptide synthesis utilizing 9-fluorenylmethoxycarbonyl amino acids. *Int. J. Pept. Protein Res. 35*, 161–214.

(42) Garcia-Martin, F., Quintanar-Audelo, M., Garcia-Ramos, Y., Cruz, L. J., Gravel, C., Furic, R., Cote, S., Tulla-Puche, J., and Albericio, F. (2006) ChemMatrix, a poly(ethylene glycol)-based support for the solid-phase synthesis of complex peptides. *J. Comb. Chem. 8*, 213–220.

(43) White, P., Keyte, J. W., Bailey, K., and Bloomberg, G. (2004) Expediting the Fmoc solid phase synthesis of long peptides through the application of dimethyloxazolidine dipeptides. *J. Pept. Sci. 10*, 18–26.

(44) Garcia-Martin, F., White, P., Steinauer, R., Cote, S., Tulla-Puche, J., and Albericio, F. (2006) The synergy of ChemMatrix resin and pseudoproline building blocks renders RANTES, a complex aggregated chemokine. *Biopolymers 84*, 566–575.

(45) von Eggelkraut-Gottanka, R., Machova, Z., Grouzmann, E., and Beck-Sickinger, A. G. (2003) Semisynthesis and characterization of the first analogues of pro-neuropeptide Y. *ChemBioChem 4*, 425–433.

(46) Neugebauer, J. M., and Murray, P. D. (1990) Detergents: An overview. *Methods Enzymol. 182*, 239–253.

(47) Marston, F. A. O., and Hartley, D. L. (1990) Solubilization of protein aggregates. *Methods Enzymol. 182*, 264–276.

(48) Liu, W., and Chen, Y. H. (2005) High epitope density in a single protein molecule significantly enhances antigenicity as well as immunogenicity: a novel strategy for modern vaccine development and a preliminary investigation about B cell discrimination of monomeric proteins. *Eur. J. Immunol. 35*, 505–514.

(49) Liu, W., Peng, Z., Liu, Z., Lu, Y., Ding, J., and Chen, Y. H. (2004) High epitope density in a single recombinant protein molecule of the extracellular domain of influenza A virus M2 protein significantly enhances protective immunity. *Vaccine 23*, 366–371.

(50) Lu, Y. A., Clavijo, P., Galantino, M., Shen, Z. Y., Liu, W., and Tam, J. P. (1991) Chemically unambiguous peptide immunogen: preparation, orientation and antigenicity of purified peptide conjugated to the multiple antigen peptide system. *Mol. Immunol. 28*, 623–630.

(51) Spetzler, J. C., and Tam, J. P. (1995) Unprotected peptides as building blocks for branched peptides and peptide dendrimers. *Int. J. Pept. Protein Res. 45*, 78–85.

(52) Sugrue, R. J., and Hay, A. J. (1991) Structural characteristics of the M2 protein of influenza A viruses: evidence that it forms a tetrameric channel. *Virology 180*, 617–624.

(53) Lamb, R. A., Zebedee, S. L., and Richardson, C. D. (1985) Influenza virus M2 protein is an integral membrane protein expressed on the infected-cell surface. *Cell 40*, 627–633.

(54) Holsinger, L. J., and Lamb, R. A. (1991) Influenza virus M2 integral membrane protein is a homotetramer stabilized by formation of disulfide bonds. *Virology 183*, 32–43.

(55) Holsinger, L. J., Nichani, D., Pinto, L. H., and Lamb, R. A. (1994) Influenza A virus M2 ion channel protein: a structure-function analysis. *J. Virol. 68*, 1551–1563.

(56) Nishimura, K. K. S., Zhang, L., and Cross, T. A. (2002) The closed state of a H+ channel helical bundle combining precise orientational and distance restraints from solid state NMR. *Biochemistry 41*, 13170–13177.

(57) Li, C., Qin, H., Gao, F. P., and Cross, T. A. (2007) Solid-state NMR characterization of conformational plasticity within the transmembrane domain of the influenza A M2 proton channel. *Biochim. Biophys. Acta 1768*, 3162–3170.

BC9003316

Controlled Synthesis of Camptothecin−Polylactide Conjugates and Nanoconjugates

Rong Tong and Jianjun Cheng*

Department of Materials Science and Engineering, University of Illinois at Urbana−Champaign, Urbana, Illinois 61821.
Received August 11, 2009; Revised Manuscript Received November 4, 2009

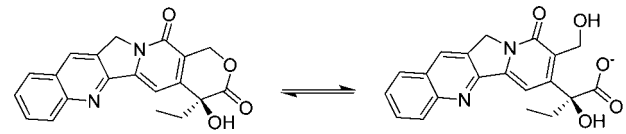
We report here a unique method of formulating camptothecin−polylactide (CPT-PLA) conjugate nanoparticles, termed nanoconjugates (NCs), through CPT/(BDI)ZnN(TMS)$_2$ [(BDI) = 2-((2,6-diisopropylphenyl)amido)-4-((2,6-bisalkyl)-imino)-2-pentene] mediated polymerization of lactide (LA) followed by nanoprecipitation. When CPT was used as the initiator to polymerize LA in the presence of (BDI)ZnN(TMS)$_2$, the polymerization was completed within hours with nearly 100% CPT loading efficiency and 100% LA conversion. CPT loading as high as 19.5% can be achieved for the CPT-polylactide (CPT-PLA) conjugate prepared at a LA/CPT ratio of 10. The steric bulk of the chelating ligands and the type of metals used had a dramatic effect on the initiation of the LA polymerization and the tendency of the ring-opening of the CPT lactone. The CPT/(BDI)ZnN(TMS)$_2$-mediated LA polymerization yielded CPT-PLA conjugates with well-controlled molecular weights and narrow molecular weight distributions (1.02−1.18). The nanoprecipitation of CPT-PLA led to the formation of NCs around 100 nm in size with narrow particle size distributions. Sustained release of CPT from CPT-PLA NCs was achieved without burst release. CPT-PLA NCs were toxic to PC-3 cells with tunable IC_{50} possible by adjusting the drug loading of the CPT-PLA NCs.

INTRODUCTION

20(S)-Camptothecin (CPT), a topoisomerase II inhibitor isolated from the Chinese tree *Camptotheca acuminate* in the 1960s, exhibits a broad range of anticancer activity in various animal models (*1, 2*). CPT has low aqueous solubility in its therapeutically active lactone form. Once placed in an aqueous solution at physiological pH, the lactone form of CPT is quickly transformed to its carboxylate form, which is highly toxic and therapeutically inactive (*3*−*5*). Serum albumin preferentially binds to the carboxylate form of CPT and serves as the driving force of shifting the lactone−carboxylate equilibrium (shown in Scheme 1) toward the formation of the carboxylate (*3*−*5*). These pharmacological properties of CPT result in rapid deactivation and fast clearance of CPT from the circulation after it is intravenously administered. To overcome these drawbacks, CPT has been conjugated to various polymeric carriers for improved solubility, enhanced stability of its lactone form and reduced renal clearance (*6*−*14*).

Polymer−CPT conjugates prepared with conventional coupling chemistry have various heterogeneities that may impact their pharmacological and pharmacokinetic properties *in vivo*. For instance, various polymers used for the conjugation of CPT were prepared via condensation reaction with molecular weight distributions (MWDs) over the range 1.5−2.5 (*6, 8*). It is also difficult to control the site of CPT conjugation to polymers with pendant functional groups. Furthermore, the direct conjugation of CPT through its C20-hydroxyl groups involves complex, multi-step reaction; the CPT must first be converted to a CPT-amino ester and then conjugated to a polymer that contains carboxylate groups via the amine end group of the CPT-amino ester (*12, 15*).

Scheme 1. Equilibrium of CPT Lactone and Carboxylate Forms



Here, we report a simple, unique chemistry that allows for one-step conjugation of CPT to the terminal carboxylate group of polylactide (PLA). Instead of using coupling chemistry, we developed a ring-opening polymerization method to facilitate the incorporation of CPT to PLA. Through a living polymerization, both the initiation (drug incorporation) and the chain propagation proceed in a well-controlled manner and result in materials with predefined drug loadings and MWDs in the range 1.02−1.18. The resulting CPT−PLA conjugate was nanoprecipitated to form CPT−PLA conjugate nanoparticles, termed nanoconjugates (NCs), around 100 nm in size with narrow polydispersities and controlled antitumor toxicities.

EXPERIMENTAL PROCEDURES

General. D,L-Lactide (LA) was purchased from TCI America (Portland, OR), recrystallized three times in toluene, and stored at −30 °C in a glovebox prior to use. All of the anhydrous solvents were purified by alumina columns and kept anhydrous by using molecular sieves. CPT was purchased from LC Laboratories (Woburn, MA), dried, and stored at −30 °C in a glovebox. Triethylamine (TEA) was dried with 4 Å molecular sieves overnight, transferred by a cannula under nitrogen to a dry flask that contained CaH_2, refluxed overnight, distilled and collected under nitrogen, and stored in a glovebox over activated 4 Å molecular sieves. All other chemicals were purchased from Sigma-Aldrich (St Louis, MO) and used as received unless otherwise noted. The molecular weights (MWs) of PLA were determined by gel permeation chromatography (GPC also

* To whom correspondence should be addressed. E-mail: jianjunc@illinois.edu. Tel: (217) 244-3924. Fax: (217) 333-2736. Address: Department of Materials Science and Engineering, University of Illinois at Urbana−Champaign, Urbana, Illinois 61801.

10.1021/bc900356g © 2010 American Chemical Society
Published on Web 12/10/2009

known as size exclusion chromatography (SEC)) equipped with an isocratic pump (model 1100, Agilent Technology, Santa Clara, CA), a Dawn Heleos 18-angle laser light scattering detector and an Optilab rEX refractive index detector (Wyatt Technology, Santa Barbara, CA). The wavelength of the Heleos detector was set at 658 nm. The size exclusion columns (Phenogel columns 100 Å, 500 Å, 10^3 Å and 10^4 Å, 5 μm, 300 $\times$ 7.8 mm, Phenomenex, Torrance, CA) used for the analysis of polymers or polymer−drug conjugates were serially connected on the GPC. The GPC columns were eluted with THF (HPLC grade) at 40 °C at 1 mL/min. HPLC analyses were performed on a System Gold system equipped with a 126P solvent module and a System Gold 128 UV detector (Beckman Coulter, Fullerton, CA). An analytical reverse-phase (RP) column was utilized to separate CPT, CPT-succinic acid (CPT-SA), and other CPT derivatives. The NMR studies were conducted on a Varian UI500NB system (500 MHz). The sizes and the polydispersities of the PLA-CPT NCs were determined on a ZetaPALS dynamic light scattering (DLS) instrument (15 mW laser, incident beam = 676 nm, Brookhaven Instruments, Holtsville, NY). The lyophilization of the NCs was carried out on a benchtop lyophilizer (FreeZone 2.5, Fisher Scientific, PA). The BDI ligands (BDI-1 (*16*), BDI-2 (*16*), BDI-3 (*16*), and BDI-4 (*17*)) were synthesized by following the procedures previously reported. Synthesis and characterization of the corresponding metal complexes of these ligands were also previously reported (*16*−*19*). The low-resolution electrospray ionization mass spectrometry (LR-ESI MS) experiments were performed on a Waters Quattro II mass spectrometer. The high-resolution electrospray ionization mass spectrometry (HR-ESI MS) experiments were performed on a Micromass Q-TOF Ultima system. The PC-3 cells (ATCC, Manassas, VA) used in the MTT (3-(4,5-dimethylthiazol-2-yl)-2,5-diphenyltetrazolium bromide) assay (*20*) were cultured in Ham's F12K medium containing 10% fetal bovine serum, 1000 units/mL aqueous penicillin G, and 100 μg/mL streptomycin. The SEM analysis of NCs was conducted on a Hitachi-S4700 high-resolution scanning electron microscope.

General Procedures for the Preparation of CPT−PLA Conjugate via CPT-Mediated Ring-Opening Polymerization of LA. (BDI-3)ZnN(TMS)$_2$ (5.5 mg, 8.9 μmol) was dissolved in anhydrous THF (300 μL). The solution was added to a vial containing CPT (3.0 mg, 8.6 mmol), and the mixture was stirred for 15 min until the CPT was completely dissolved in THF. LA (124 mg, 0.86 mmol) was dissolved in a vial containing THF (940 μL), and the resulting solution was added to the mixture of CPT/(BDI-3)ZnN(TMS)$_2$ ([LA]$_0$ = 0.69 M). FT-IR was used to follow the conversion of the LA in the polymerization solution by monitoring the intensity of the lactone band at 1772 cm^{-1}. After the LA was completely consumed, the polymerization was quenched with ice-cold methanol (10 mL). The precipitate (CPT−PLA) was collected by centrifugation and then dried under vacuum. The resulting CPT−PLA conjugate was denoted as CPT-LA$_n$ where n is the monomer/initiator (LA/CPT) molar ratio.

Reaction of CPT with Succinic Anhydride (SA) Mediated by Zn or Mg Catalysts. In a glovebox, (BDI-3)ZnN(TMS)$_2$ (6.2 mg, 0.01 mmol) was dissolved in anhydrous THF (200 μL). The solution was added to a clean vial containing CPT (3.5 mg, 0.01 mmol) and THF (300 μL) and stirred for 15 min until the CPT was completely dissolved. SA (1.1 mg, 0.011 mmol) in THF (600 μL) was added and the vial was tightly sealed. It was then immediately taken out of the glovebox and stirred for 4 h at 40 °C. The reaction was quenched with ice-cold methanol (1 mL). An aliquot of this solution was analyzed by HPLC equipped with an analytical C18 column (Luna C18(2), 250 $\times$ 4.6 mm, 5 μ, Phenomenex, Torrance, CA). The mobile phase for the HPLC analysis was a solvent mixture containing equal volumes of acetonitrile and water (0.1% TFA). All HPLC spectra were recorded and analyzed by a UV detector at 370 nm. The areas of the HPLC peaks of CPT and the CPT-SA were integrated and used for the quantification of their concentrations as compared to corresponding standard curves. An aliquot of the reaction mixture was also used for the MS analysis.

The CPT-SA used for NMR analysis was collected by preparative thin-layer chromatography (prep-TLC, silica gel with a fluorescent indicator (254 nm), 1.5 mm thickness, Aldrich), and developed by ethyl acetate/methanol (v/v = 10/1). The R_f values of CPT and CPT-SA were 0.7 and 0.1, respectively. The silica gel was removed from the glass plate and the CPT-SA was extracted with methanol (2 $\times$ 30 mL). The methanol solution was then removed under vacuum; the resulting CPT-SA was analyzed by ^{1}H NMR. ^{1}H NMR (CD_3OD, 500 MHz): δ 8.63 (s, 1H, 7-H), 8.21 (d, J = 8.5 Hz, 1H, 12-H), 8.07 (d, J = 8.0 Hz, 1H, 9-H), 7.87 (td, J_t = 8.5 Hz, J_d = 1.5 Hz, 1H, 11-H), 7.71 (td, J_t = 8.0 Hz, J_d = 1.0 Hz, 1H, 10-H), 7.43 (s, 1H, 14-H), 5.57, 5.44 (AB, J_{AB} = 17.0 Hz, 2H, 17-H), 5.35 (s, 1H, 5-H), 2.81 (t, J = 7.5 Hz, 2H, $-CH_2-$COOH), 2.55 (t, J = 7.5 Hz, 2H, $-CH_2-CH_2-$COOH), 2.24 (m, 2H, 18-H), 0.99 (t, J = 8.0 Hz, 19-H). MS (LR-ESI, positive mode): calculated for $C_{24}H_{20}N_2O_7$ $[M + H]^+$ m/z 449.1; found m/z 449.1. MS (HR-ESI, positive mode): calculated for $C_{24}H_{20}N_2O_7$ $[M + H]^+$ m/z 449.1349; found m/z 449.1355.

General Procedure for the Formation and Characterization CPT−PLA Nanoconjugates (NCs). A DMF solution containing the CPT-LA$_{10}$ conjugate (100 μL, 5 mg/mL) was added dropwise to nanopure water (4 mL). The resulting CPT-LA$_{10}$ NCs were collected by ultrafiltration (15 min, 3000 $\times$ g, Ultracel membrane with 10 000 NMWL, Millipore, Billerica, MA) and were characterized by DLS and SEM for particle sizes and by HPLC for drug loading and release kinetics.

Hydrolysis of CPT-LA$_{10}$ NCs. The CPT-LA$_{10}$ NC in water (1 mL, 1 mg/mL) was treated with a NaOH solution (1 M, 1 mL) for 12 h. The solution was then tuned to pH 2 by phosphoric acid addition, which resulted in a yellow solution. The solvent was removed by rotary evaporation. The resulting residue was then dissolved in acetonitrile/water (0.1% TFA) (v/v = 1/1) and injected into a semiprep HPLC column (Jupitor Proteo 90 A, 250 $\times$ 21.20 mm, 10 μ, Phenomenex, Torrance, CA). The fraction that had the identical elution time to the authentic CPT was collected. After the solvent was removed by vacuum, the resulting yellow, oily residue was dissolved in phosphoric acid/methanol at a volume ratio of 1:1. The solution was tuned to pH 3−4 by 0.1 M NaOH and then extracted with chloroform (5 $\times$ 100 mL). The organic phase was combined and dried with $MgSO_4$. After the $MgSO_4$ was removed by filtration and the solvent was removed under vacuum, the resulting pale yellow solid was analyzed by ^{1}H NMR. The ^{1}H NMR spectrum of the CPT released from CPT−PLA NCs was identical to that of the authentic CPT (see Figure 6B) (*21*).

Release Kinetics of the CPT-LA$_n$ NCs and the CPT/PLA Nanoparticle (NP). CPT/PLA NPs were prepared through nanoprecipitation of CPT and PLA (MW = 1.5 $\times$ 10^4 g/mol) by following the procedures reported in literature (*22*). The CPT-LA$_{10}$ NCs were prepared with CPT-LA$_{10}$ conjugate by following the standard nanoprecipitation procedure described above. The NCs (or NPs) were collected and washed three times with nanopure water by ultrafiltration (Ultracel membrane 10 000 NMWL, Millipore, Billerica, MA). The NCs (or NPs) collected from the ultrafiltration device were dispersed in 1$\times$ PBS solution (pH = 7.4) (1 mg/mL) and incubated at 37 °C. At selected time intervals, an aliquot of NCs (or NPs) ($\sim$1 mL) was taken out of the incubator and centrifuged at 10 000 rpm for 10 min. The

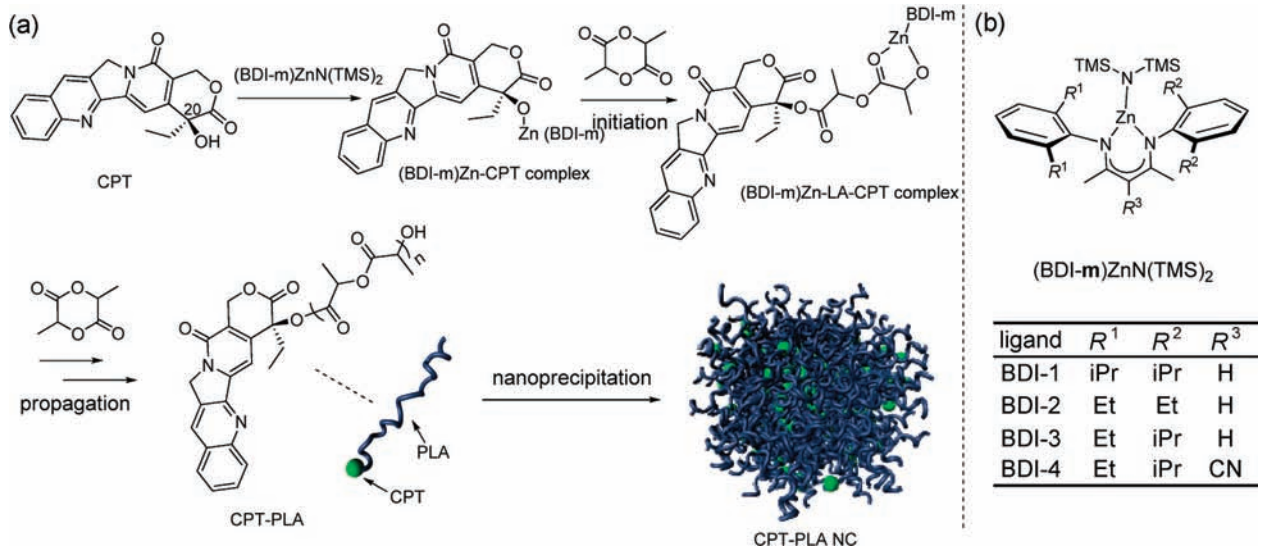


Figure 1. (a) Schematic illustration of (BDI-m)ZnN(TMS)$_2$/CPT mediated ring-opening polymerization of LA to make CPT−PLA conjugates followed by nanoprecipitation of the resulting CPT−PLA conjugates for the preparation of CPT−PLA nanoconjugates; (b) The structure of (BDI-m)ZnN(TMS)$_2$ (m = 1−4).

supernatant (500 μL) was carefully transferred to an Eppendorf tube using a micropipet without disturbing the precipitates (NCs or NPs). The solution was tuned to pH 2 with phosphoric acid (85%), and the resulting solution was directly injected into HPLC equipped with an analytical pentafluorophenyl RP-column (Curosil-PFP, 250 × 4.6 mm, 5 μ, Phenomenex, Torrance, CA). A mixture of acetonitrile and water (containing 0.1% TFA) at a volume ratio of 1:1 was used as the mobile phase. The flow rate was set at 1 mL/min. The area of the HPLC peak of the released CPT was intergraded for the quantification of CPT as compared to the standard curve for this drug.

Determination of the Cytotoxicity of CPT-LA$_n$ NCs. PC-3 cells were placed in a 96-well plate for 24 h (10 000 cells per well). Cells were washed with 100 μL of prewarmed PBS. Freshly prepared CPT-LA$_{10}$, CPT-LA$_{25}$, and CPT-LA$_{50}$ NCs (prepared in 1× PBS, 100 μL) were added to the cells. CPT was used as a positive control. Untreated cells were used as a negative control. PLA NPs without CPT being conjugated or encapsulated were prepared via the nanoprecipitation of the PLA with a MW of 14 kDa (*22, 23*) and were subsequently used as a negative control in the MTT study. The PLA-NPs were applied to PC-3 cells at a concentration up to 0.5 μg/mL. The cells were incubated for 72 h in a 5% CO_2 incubator at 37 °C. The standard MTT assay protocols were followed thereafter (*20*).

RESULTS AND DISCUSSION

(BDI)MN(TMS)$_2$/CPT (M = Zn, Mg)-Mediated Polymerization of Lactide. By mixing a hydroxyl-containing compound (ROH) with a metal-amido complex, M-OR, a highly active metal alkoxide can be generated *in situ* and can be subsequently used to initiate a controlled polymerization of LA (*24−26*). Many well-designed M-ORs can quantitatively incorporate OR to the PLA termini with 100% monomer conversions (*18, 19, 27−31*). Recently, we demonstrated that hydroxyl-containing therapeutic agents with complex structures, such as paclitaxel and doxorubicin, can form coordination complexes with metal catalysts and subsequently initiate controlled LA polymerizations with the drug molecules being covalently attached to the PLA through ester linkers (*32, 33*). Both paclitaxel and doxorubicin have complex molecular structures that contain multiple hydroxyl groups. By using rationally designed metal catalysts, we were able to control the polymerization to be initiated at one of the specific hydroxyl groups of these complex therapeutic molecules (*32, 33*). In the context of expanding this drug-initiated ring-opening polymerization technique to other therapeutic molecules, we studied CPT-initiated LA polymerization.

We first tested the feasibility of forming CPT-metal complex. (BDI-1)MgN(TMS)$_2$ (Figure 1), a catalyst that we previously used in paclitaxel- and doxorubicin-mediated ROP of LA (*32, 33*), was dissolved in THF. A colorless solution was obtained. We then added this solution to a vial containing CPT powder (1 equiv relative to (BDI-1)MgN(TMS)$_2$). After the mixture was stirred for 20 min, it was noted that CPT was completely dissolved and the solution color gradually became orange. In the absence of (BDI-1)MgN(TMS)$_2$, however, CPT remained insoluble in THF and the solution stayed colorless. The sharp contrast of the solubility of CPT in the presence versus in the absence of (BDI-1)MgN(TMS)$_2$ as well as the color change after CPT was mixed with (BDI-1)MgN(TMS)$_2$ suggest possibly a coordination reaction between CPT and the (BDI-1)MgN(TMS)$_2$. (BDI-1)Mg-CPT alkoxide through the C20-OH of CPT is presumably the complex formed *in situ* via the coordination of (BDI-1)MgN(TMS)$_2$ and CPT (Figure 1).

We next examined whether the mixture of (BDI-1)MgN(TMS)$_2$/CPT could initiate LA polymerization. After LA (100 equiv) in THF was added dropwise to the (BDI-1)MgN(TMS)$_2$/CPT mixture, the polymerization proceeded rapidly and was completed within 10 h with 100% LA conversion; the monomer conversion was followed by monitoring the intensity of the lactone band of LA at 1772 cm^{-1} on a FT-IR. One interesting observation was that the orange color of the polymerization solution gradually faded away during the course of polymerization, which indicated the segregation of the (BDI-1)Mg from CPT. This observation was in good agreement with the proposed reaction mechanism as shown in Figure 1a. After 100% LA conversion was achieved, the polymerization solution was analyzed by HPLC, which showed that CPT was completely incorporated to PLA with no detectable free CPT in the polymerization solution (data not shown). This observation was similar to what we observed in paclitaxel- and doxorubicin-initiated LA polymerization, both of which gave 100% drug incorporation efficiency in corresponding drug-initiated polymerization (*32, 33*). The incorporation efficiency is also the initiation efficiency, which is the percent of therapeutic agent utilized in the initiation of LA polymerization and is equivalent to the encapsulation efficiency utilized in making NPs via

Table 1. CPT/(BDI)MN(TMS)$_2$ Mediated LA Polymerization (M = Zn or Mg)[a]

entry	catalyst	temp	IE (%)[b]	CV (%)[c]	M_n ($\times 10^4$g/mol)	MWD (M_w/M_n)
1	(BDI-1)MgN(TMS)$_2$	r.t.	>99	>99	1.13	1.31
2	(BDI-1)ZnN(TMS)$_2$	r.t.	61	>99	2.83	1.07
3	(BDI-2)ZnN(TMS)$_2$	r.t.	>99	>99	2.01	1.20
4	(BDI-3)ZnN(TMS)$_2$	r.t.	>99	>99	1.73	1.18
5	(BDI-4)ZnN(TMS)$_2$	r.t.	0	0	ND	N.D
6	(BDI-4)ZnN(TMS)$_2$	40 °C	>98	>98	1.12	1.32

[a] All reactions were performed at a LA/CPT/catalyst ratio of 100:1:1.01 in anhydrous THF for 12 h ($[LA]_0$= 0.69 M). The expected M_n of CPT−PLA conjugate = 1.47 × 10^4 g/mol. Abbreviations: LA = lactide; CPT = camptothecin; temp = temperature; IE = incorporation efficiency or initiation efficiency, which is the percent of therapeutic agent utilized in the initiation of LA polymerization; the IE is equivalent to the encapsulation efficiency utilized in making nanoparticles via noncovalent, encapsulation strategy; CV = conversion of LA; ND = not determined. [b] Determined by the HPLC measurement of the unreacted CPT in the polymerization solution. [c] Determined by monitoring the IR band of the LA lactone at 1772 cm^{-1}.

Table 2. CPT/(BDI-3)ZnN(TMS)$_2$ Mediated LA Polymerization at Various LA/CPT Ratios[a]

entry	[LA]/[CPT]	IE (%)[b]	CV (%)[c]	M_{nCal} ($\times 10^3$g/mol)	M_n ($\times 10^3$g/mol)	MWD (M_w/M_n)
1	75	>99	>99	11.1	10.4	1.02
2	100	>99	>99	14.7	17.3	1.18
3	200	>99	>99	29.1	26.6	1.13
4	300	>99	>99	43.5	40.1	1.11
5	400	>99	>99	57.9	48.0	1.16

[a] All reactions were performed in anhydrous THF for 12 h at room temperature ($[LA]_0$= 0.69 M). Abbreviation: LA = lactide; CPT = camptothecin; IE = incorporation efficiency or initiation efficiency, which is the percent of therapeutic agent utilized in the initiation of LA polymerization; the IE is equivalent to the encapsulation efficiency utilized in making nanoparticles via noncovalent, encapsulation strategy. [b] Determined by the HPLC measurement of the unreacted CPT in the polymerization solution. [c] Determined by monitoring IR band of LA lactone at 1772 cm^{-1}.

noncovalent, encapsulation strategy. The M_n of the resulting CPT−PLA conjugate was 1.13 × 10^4 g/mol, which was in good agreement with the expected M_n (1.47 × 10^4 g/mol) (entry 1, Table 1). The molecular weight distribution (MWD) of the CPT−PLA conjugate, however, was relatively broad (M_w/M_n = 1.31) due in part to the chain transfer during polymerization (*18*). In our previous studies of paclitaxel- and doxorubicin-initiated LA polymerization, only the primary or the secondary hydroxyl groups of these drugs could efficiently initiate the polymerizations of LA (*32, 33*). The present study demonstrated for the first time that the C20-OH of CPT, a tertiary hydroxyl group, could also be activated by (BDI-1)MgN(TMS)$_2$ to initiate LA polymerization.

In order to achieve better controlled polymerization, we next tested (BDI-1)ZnN(TMS)$_2$, a Zn analogue of (BDI-1)MgN(TMS)$_2$. As reported by Coates and co-workers, Zn catalysts in general out-perform Mg catalysts for LA polymerization (*18*). After (BDI-1)ZnN(TMS)$_2$ and CPT were mixed and stirred for 20 min, a light yellow solution was obtained. This (BDI-1)ZnN(TMS)$_2$/CPT complex mediated LA polymerization at an M/I ratio of 100 and gave CPT−PLA conjugate with a very narrow MWD (M_w/M_n = 1.07, entry 2, Table 1). However, the CPT incorporation efficiency was only 61% based on the HPLC analysis, indicating the poor efficiency of forming Zn-CPT complex during the initiation step. The actual M/I ratio in this reaction was 163 (calculated based on the LA/CPT ratio of 100:0.61). It was therefore not surprising that the obtained M_n (2.83 × 10^4 g/mol) was substantially higher than the M_n calculated based on the LA/CPT ratio of 100:1 (expected M_n = 1.47 × 10^4 g/mol, entry 2, Table 1,). The poor efficiency of the coordination of CPT with (BDI-1)ZnN(TMS)$_2$ was due in part to the relatively low activity of Zn as compared to Mg as well as the steric bulk of BDI-1 ligand surrounding the coordination site (Figure 1b). We next studied whether enhanced incorporation efficiency of CPT could be achieved by using a Zn catalyst with a BDI ligand with reduced steric bulk and/or altered electronic property.

It has been reported that subtle change of BDI ligands can significantly affect the activity of (BDI)ZnN(TMS)$_2$ and its capability of controlling the polymerizations of cyclic esters or carbonates (*16, 34*−*38*). Specifically, the 2,6-substituents of the aryl groups (at the R^1 and R^2 positions) and the substitute at the R^3 position were found to have profound effects on the activity of the catalysts (Figure 1b) (*17*). We synthesized a series of zinc catalysts containing BDI ligands with variable 2,6-aryl substituents and R^3 group (Figure 1b) and then used these catalysts in CPT-initiated LA polymerizations. We first checked the effect of the steric bulk of BDI on the LA polymerization. BDI-2 is an analogue of BDI-1 whose isopropyl (iPr) groups at both R^1 and R^2 position were replaced by ethyl (Et) groups, while BDI-3 is an analogue of BDI-1 whose iPr groups were replaced by Et groups only at both R^1 position. Both ligands were synthesized and used to prepare the corresponding (BDI)ZnN(TMS)$_2$ catalysts. As expected, the steric bulk of the BDI at its R^1 and R^2 positions had a profound effect on the capability of the Zn catalysts to form coordination complexes with CPT during the initiation step. As compared to the 61% of incorporation efficiency observed with the use of (BDI-1)ZnN(TMS)$_2$, 100% incorporation efficiencies were observed in both (BDI-2)ZnN(TMS)$_2$/CPT and (BDI-3)ZnN(TMS)$_2$/CPT mediated polymerizations. The corresponding M_n values (2.01 × 10^4 g/mol and 1.73 × 10^4 g/mol, entries 3 and 4, Table 1) were much closer to the expected M_n than that of the PLA−CPT obtained from the (BDI-1)ZnN(TMS)$_2$/CPT mediated LA polymerization (entry 2, Table 1). Narrow MWDs (M_w/M_n < 1.2) were obtained for the CPT−PLA conjugates derived from (BDI-2)ZnN(TMS)$_2$/CPT and (BDI-3)ZnN(TMS)$_2$/CPT mediated polymerizations (entries 3 and 4, Table 1). BDI-4, an analogue of BDI-3 with a cyano group at the R^3 position (Figure 1b), was also prepared and studied. However, CPT remained insoluble in THF containing 1 equiv (BDI-4)ZnN(TMS)$_2$, indicating the poor efficiency of forming (BDI-4)ZnN(TMS)$_2$/CPT coordination complex at room temperature. Thus, it was not surprising that the mixture of CPT and (BDI-4)ZnN(TMS)$_2$ could not initiate LA polymerization at room temperature (entry 5, Table 1). When this mixture of CPT and (BDI-4)ZnN(TMS)$_2$ was incubated at 40 °C for 20−30 min, CPT was completely dissolved, suggesting that the formation of (BDI-4)ZnN(TMS)$_2$/CPT coordination complex requires higher temperature. The CPT−PLA conjugate derived from (BDI-4)ZnN(TMS)$_2$/CPT-mediated LA polymerization had a high loading efficiency (98%) and a M_n very close to the expected molecular weight (entry 6, Table 1), but its MWD (M_w/M_n = 1.32, Table 1) was broader than that of the CPT−PLA conjugate derived from the (BDI-3)ZnN(TMS)$_2$/

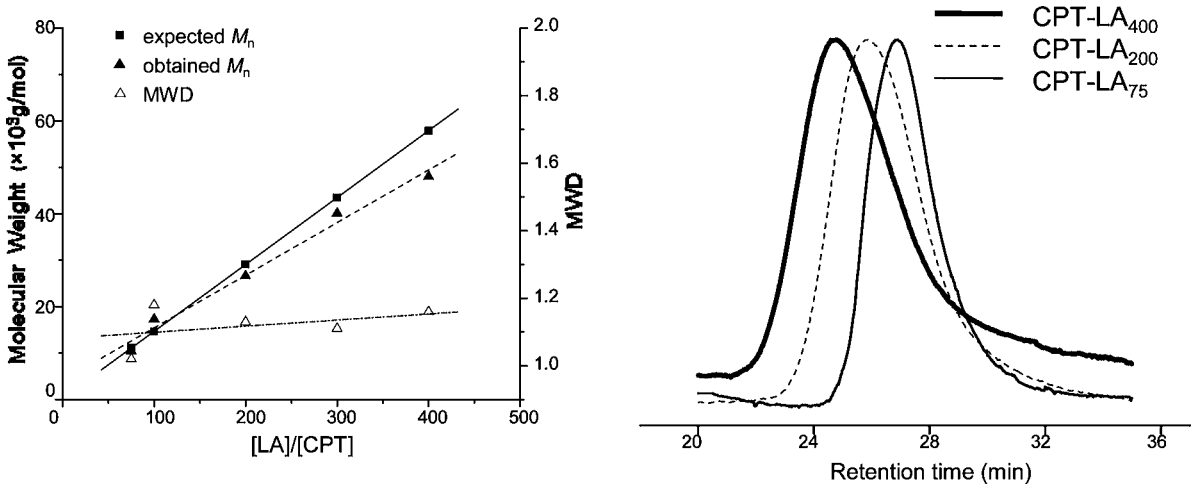
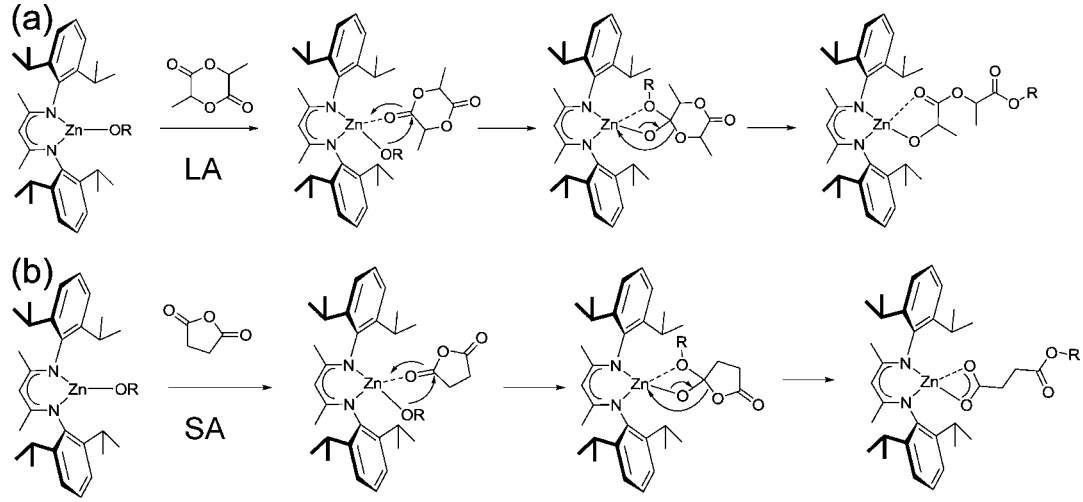


Figure 2. (a) (BDI-3)ZnN(TMS)$_2$/CPT mediated ring-opening polymerization of LA at various LA/CPT ratios. (b) Overlay of the GPC trace of CPT-LA$_{75}$, CPT-LA$_{200}$, and CPT-LA$_{400}$ prepared by (BDI-3)ZnN(TMS)$_2$/CPT mediated LA polymerizations.

Scheme 2. Suggested Insertion-Coordination Mechanism of (BDI)Zn-OR Mediated Ring-Opening of (a) LA and (b) SA



CPT-mediated polymerizations. On the basis of these preliminary studies, (BDI-3)ZnN(TMS)$_2$ was found to be the overall best catalyst with respect to control over CPT incorporation and polymerization. (BDI-3)ZnN(TMS)$_2$ was therefore selected for further investigation for its capability to control polymerization of LA at various LA/CPT ratios.

Excellently controlled polymerizations were observed over a broad range of LA/CPT ratios from 75 to 400 when the LA polymerizations were mediated by (BDI-3)ZnN(TMS)$_2$/CPT (Table 2). Quantitative CPT incorporation efficiencies and very narrow MWDs (M_w/M_n = 1.02−1.18) were observed in all experiments performed. The obtained MWs of the CPT−PLA conjugates were in excellent agreement with the expected MWs (Table 2), which followed a linear correlation with the LA/CPT ratios (Figure 2a). Monomodal GPC MW distribution curves were observed in all CPT−PLA conjugates prepared with various LA/CPT ratios (Figure 2b). The well-controlled polymerization mediated by (BDI-3)ZnN(TMS)$_2$ likely proceeded through the widely accepted insertion-coordination mechanism (Scheme 2a).

Control of Initiation by (BDI)ZnN(TMS)$_2$ Catalysts. As mentioned earlier, the lactone ring of CPT should be preserved in order to maintain the antitumor activity of CPT. However, it is known that the lactone ring of CPT is unstable and subject to ring-opening in the presence of a nucleophile. We next studied how the initiation could be specifically controlled at the C20-OH of CPT with negligible CPT lactone ring-opening during (BDI)ZnN(TMS)$_2$/CPT initiated LA polymerizations.

In the initiation step, LA first reacts with (BDI)Zn-CPT alkoxide and then is inserted between the CPT and Zn to generate (BDI)Zn-lactide-CPT alkoxide, the new chain-propagating end group (Scheme 2a). CPT does not involve the subsequent chain propagation. Apparently, the most critical step determining whether the lactone ring of CPT is opened or remains closed is the initiation step. As LA is subject to rapid polymerization and the resulting CPT−PLA conjugate is difficult to be precisely characterized, we used succinic anhydride (SA) as the model monomer to study (BDI)ZnN(TMS)$_2$/CPT mediated initiation. Such a reaction led to the formation of CPT-succinic acid (CPT-SA), a small molecule instead of a polymer, whose structure can be easily determined by routine characterization methods.

When just CPT and SA were mixed without addition of other reagents, no reaction occurred (entry 1, Table 3). Triethylamine (TEA), a non-nucleophilic base, has been used previously to facilitate the ring-opening of SA by an alcohol (*39*). When TEA was added to the mixture of CPT and SA, the reaction was very slow and generated CPT-SA with a yield of 10.6% after the reaction mixture was incubated at 40 °C for 12 h (peak z, Figure 3a−i; entry 2, Table 3). A substantial amount of CPT in its carboxylate form was also detected (peak x, Figure 3a−i), indicating that the lactone ring of CPT was unstable in the

Table 3. Ring Opening of Succinic Anhydride (SA) by CPT in the Presence of TEA, EDC/DMAP, or (BDI)MN(TMS)$_2$ (M = Mg or Zn)[a]

entry	temp (°C)	catalyst	solvent	time (h)	yield (%)[c]
1	r.t	/	THF	24	0
2	40	TEA	THF	12	10.6
3	40	EDC/DMAP[b]	pyridine	12	12.8
4	40	(BDI-1)MgN(TMS)$_2$	THF	4	59.5
5	40	(BDI-1)ZnN(TMS)$_2$	THF	4	18.8
6	40	(BDI-3)ZnN(TMS)$_2$	THF	4	89.1
7	40	(BDI-4)ZnN(TMS)$_2$	THF	4	71.7

[a] All reactions were performed at a SA/CPT/catalyst ratio of 1.1:1:1 ([SA]$_0$ = 0.01 M). Abbreviations: SA = succinic anhydride; CPT = camptothecin; TEA = triethylamine; temp = temperature; EDC = *N*-(3-dimethylaminopropyl)-*N*′-ethylcarbodiimide; DMAP = dimethylaminopyridine. [b] [EDC]/[DMAP] = 4/1. [c] Determined by the HPLC measurement of the CPT-succinic ester (CPT-SA) generated in the reaction solution.

presence of TEA. In a control study, when naphthalene ethanol, an alcohol with a primary −OH group that is supposed be more reactive for nucleophilic reaction than the tertiary C20-OH of CPT, was used for the conjugation with SA in the presence of TEA, the yield of naphthalene-SA was 86.8% (data not shown).

N-(3-Dimethylaminopropyl)-*N*′-ethylcarbodiimide (EDC), in conjunction with 4-(dimethylamino)-pyridine (DMAP), has been used previously for the conjugation of CPT with SA (*40*). When the reaction of CPT and SA was performed in the presence of EDC and DMAP at 40 °C for 12 h, the yield of CPT-SA was only 12.8% (entry 3, Table 3), which was in good agreement with the previously reported result (*40*) and further confirmed the low activity of the tertiary C20-OH group of CPT.

We next studied the ring-opening of SA by CPT in the presence of Mg or Zn catalysts. (BDI-1)MgN(TMS)$_2$ mediated conjugation of CPT and SA resulted in CPT-SA conjugates (Scheme 2b) with 59.5% yield when the reaction was carried out at 40 °C for 4 h (entry 4, Table 3). CPT in carboxylate form was also detected (peak x, Figure 3a−ii), indicating that the CPT lactone ring was opened in the presence of (BDI-1)MgN(TMS)$_2$ and that it may function not only as a ROP catalyst, but also as a strong base. The mechanism of ring opening remains elusive. When such a reaction was mediated by (BDI-1)ZnN(TMS)$_2$, a weaker base and a less reactive ROP catalyst compared to its Mg analogue, CPT-SA in 18.8% yield was obtained (entry 5, Table 3). Formation of small amount of CPT in its carboxylate form was also detected (peak x, Figure 3a−iii).

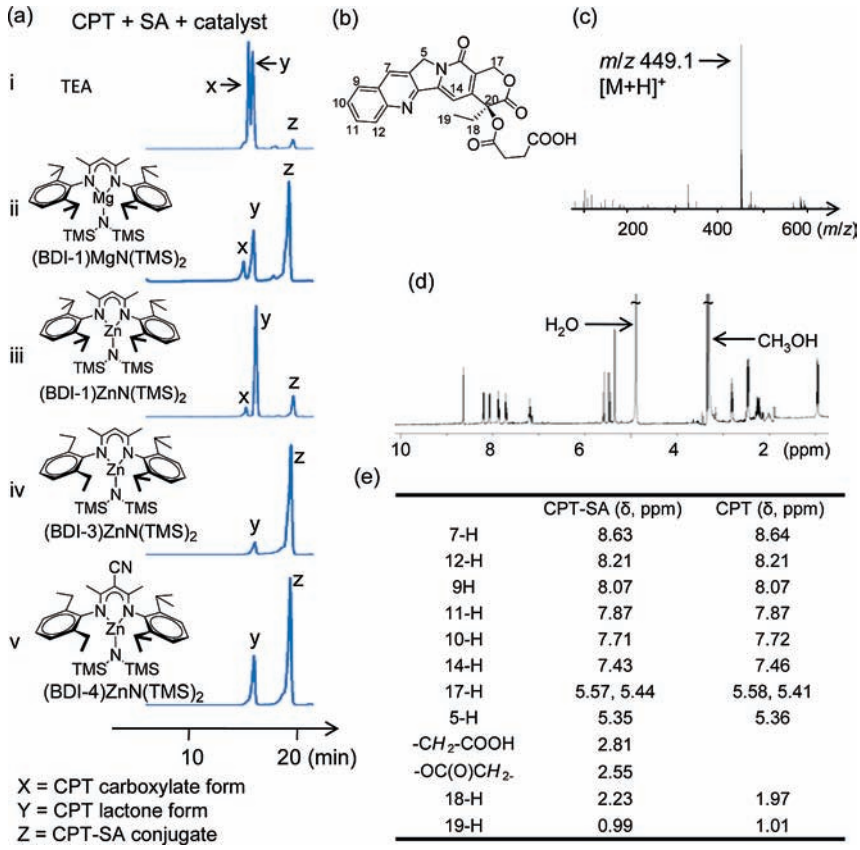
As shown in the polymerization study mentioned above (Table 1), the chelating BDI ligands have a significant impact on the activity of the BDI-metal complexes for LA polymerization. We tested (BDI-3)ZnN(TMS)$_2$, which was previously identified to be the best catalyst for CPT-initiated LA polymerization, in this CPT/SA conjugation reaction. CPT-SA in 89.1% yield was obtained when the reaction of CPT and SA was carried out at 40 °C for 4 h in the presence of (BDI-3)ZnN(TMS)$_2$ (entry 6, Table 3). The substantially increased yield of CPT-SA in this experiment indicated that (BDI-3)ZnN(TMS)$_2$ activated the tertiary C20-OH group of CPT very effectively to allow for facile nucleophilic ring opening of SA. Very interestingly, CPT-SA was the only product formed; no carboxylate form of CPT was detected (Figure 4a−iv). Excellently controlled ring opening of SA by CPT with no detectable CPT carboxylate was also observed with the use of (BDI-4)ZnN(TMS)$_2$ (Figure 3a−v), although the yield of the CPT-SA (71.7%, entry 7, Table 3) was not as high as that derived from the (BDI-3)ZnN(TMS)$_2$-mediated reaction (entry 6, Table 3).

The CPT-SA (peak z, Figure 3a−iv) was collected by preparative thin-layer chromatography and analyzed by MS (Figure 3c) and ^{1}H NMR (Figure 3d,e). The high-resolution MS analysis showed that the CPT-SA has a $[M + H]^+$ m/z= 449.1355, which was in excellent agreement with the expected $[M + H]^+$ m/z= 449.1349. To determine whether the SA ring was opened by the C17-OH (formed after the opening of the lactone ring of CPT) or by the C20-OH (Figure 3b), we compared the ^{1}H NMR spectra of CPT-SA and CPT (Figure 3e). If C17-OH mediated the ring opening of SA, the chemical shift of the C17-H of CPT-SA should change to some extent. However, as shown in Figure 3e, the chemical shift of the C17-H of CPT-SA was nearly identical to that of the authentic CPT (with a change of less than 0.03 ppm, Figure 3e), indicating that the lactone ring of CPT is well-preserved in CPT-SA. In fact, the only major change of the chemical shifts among all the protons of CPT was the C18-H, which was shifted downfield from 1.97 ppm for CPT to 2.23 ppm for CPT-SA (Figure 3e). The only possible explanation is that the SA ring was opened by the C20-OH by CPT (Figure 3b). The high yield of CPT-SA obtained in this experiment indicated that (BDI-3)ZnN(TMS)$_2$ was capable of efficiently activating the C20-OH of CPT to facilitate the ring-opening reaction with SA. The CPT/SA ring-opening conjugation mediated by BDI-Zn catalyst appeared to be a versatile method for converting the C20-hydroxyl group of CPT to a carboxylic acid end group with a degradable ester linker, which can be further used for conjugation to various drug delivery vehicles through the conventional carboxylate−amine coupling chemistry.

Controlled Formation of CPT−PLA Nanoconjugates and Their *in Vitro* Evaluation. CPT−PLA conjugated nanoparticles, termed nanoconjugates (NCs) in this study to differentiate them from the NPs prepared by coprecipitating drugs and polymers, were readily prepared through the nanoprecipitation of CPT−PLA conjugates (Figure 1a) after the metal and the BDI ligand were removed by solvent extraction. NCs of less than 100 nm in size with narrow, monomodal particle distributions were readily obtained (Table 4 and Figure 4). The narrow size distributions and monomodal size distribution of NCs were in sharp contrast to the multimodal particle distributions frequently observed in the NPs prepared by the coprecipitation of polymers and drugs (*22, 23*). It is not clear why NCs derived from the nanoprecipitation of PLA−CPT conjugates have such narrow size distributions (Figure 4a). As the multimodal particle distributions in conventional NPs were attributed in part to the self-aggregation of the nonencapsulated drugs (*22*), the unimolecular structure of polymer−drug conjugates with reduced heterogeneities (low polymer polydispersities, controlled site of conjugation on CPT and PLA, absence of free CPT) may contribute to the formation of NCs with low particle polydispersity.

DLS can give quick assessment of the NP size and size distribution; however, the data should be treated with caution and compared with data collected by other techniques. When the same CPT−PLA NC was dried and analyzed by SEM (Figure 4b), the NC size distribution was found to be not as narrow as that observed in DLS (Figure 4a). As the particle sizes were assessed under different conditions using these two different techniques, the impact of the drying process for the SEM sample preparation on the particle size distribution is unclear. It should be noted, however, that both SEM and DLS analyses showed that there were no large aggregates (over 300−500 nm) as observed frequently in NPs prepared through the coprecipitation of polymers and drugs (*22, 23*).

Because both monomer conversion and drug incorporation were quantitative (Table 4), the drug loadings of CPT−PLA NCs can be predetermined by adjusting LA/CPT feeding ratios. At a low M/I ratio of 10, the drug loading of CPT−PLA NC can be as high as 19.5% (CPT-LA$_{10}$, Table 4). To our



	CPT-SA (δ, ppm)	CPT (δ, ppm)
7-H	8.63	8.64
12-H	8.21	8.21
9H	8.07	8.07
11-H	7.87	7.87
10-H	7.71	7.72
14-H	7.43	7.46
17-H	5.57, 5.44	5.58, 5.41
5-H	5.35	5.36
-CH_2-COOH	2.81	
-OC(O)CH_2-	2.55	
18-H	2.23	1.97
19-H	0.99	1.01

Figure 3. (a) HPLC analysis of the reaction of SA and CPT in the presence of (i) TEA, (ii) (BDI-1)$MgNTMS_2$, (iii) (BDI-1)$ZnNTMS_2$, (iv) (BDI-3)$ZnNTMS_2$, or (v) (BDI-4)$ZnNTMS_2$. (b) Structure and H-assignment of CPT-SA. (c) ESI-MS of CPT-SA (positive mode). $[M+H]^+$: *m/z* 449.1. High-resolution ESI-MS for $[M+H]^+$: obtained *m/z* 449.1355; calculated *m/z* 449.1349. (d) ^1H NMR of CPT-SA (CD_3OD, 500 MHz). (e) The chemical shift values of CPT and CPT-SA derived from the corresponding ^1H NMR spectra.

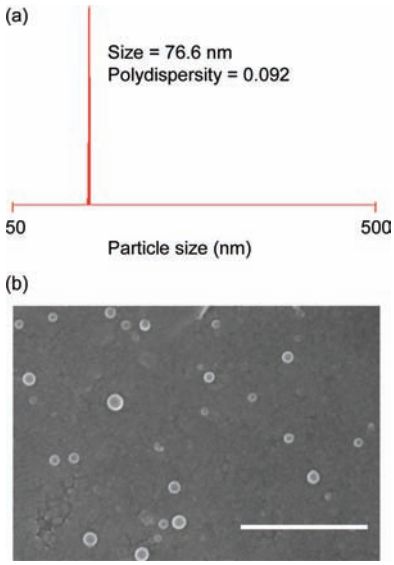


Figure 4. (a) Analysis of the particle size and size distribution of CPT-LA_{25} NC by DLS. (b) Scanning electron microscope (SEM) image of CPT-LA_{25} NC. Scale bar = 1.0 μm.

knowledge, this CPT−PLA NC has by far one of the highest loadings of CPT ever reported (*2, 8*).

We then studied the release kinetics of CPT from CPT−PLA NCs in PBS solution (pH = 7.4) at 37 °C. Even at drug loading as high as 20%, sustained release of CPT from CPT-LA_{10} NC was observed through the hydrolysis of the ester linker that connects the CPT and the PLA (Figure 5a); roughly 40% of CPT was released from CPT-LA_{10} NC in 7 days with no burst release of CPT being observed (Figure 5a). This observation was in sharp contrast to the burst release of PLA/CPT NP that was prepared by the coprecipitation of CPT and PLA. In the latter system, the release of CPT depends entirely on diffusion of the drug from polymer matrices; as much as 97.1% of the encapsulated CPT was released from CPT/PLA NP when the NP was incubated in PBS for 24 h at 37 °C (Figure 5a). The released CPT (in PBS, pH = 7.4, 37 °C) has an HPLC elution time identical to that of authentic CPT (Figure 6a) and was confirmed to have identical molecular structure to that of authentic CPT after it was isolated and characterized by ^1H NMR (Figure 6b).

Cheng and co-workers have previously reported the synthesis and development of IT-101 (*10−13*), a CPT−cyclodextrin polymer conjugate with the drug molecule being conjugated to the polymeric carrier via a triglycinyl ester linker. IT-101 has been evaluated in numerous preclinical studies and a phase-I human clinical study (*41−43*). Roughly 25% of the CPT in IT-101 was released in 24 h when the release kinetics study was performed in PBS (pH = 7.4) at 37 °C (*12*), whereas 15% of CPT was released from CPT-LA_{10} NC under similar condition (Figure 5). In CPT-LA_{10} NC, CPT is connected to PLA through a lactic ester bond, a linker with similar hydrophobicity and size to the glycinyl ester linker of IT-101. Because PLA is hydrophobic, the water and ions (H^+, OH^-) may not have easy access to the lactic ester linker in CPT−PLA NC as to the glycinyl ester of IT-101 in which CPT is conjugated to hydrophilic cyclodextrin polymers. It is therefore not surprising to observe decreased CPT release rate in CPT-LA_{10} NC compared to that of IT-101. It is anticipated that the release rate of CPT may further decrease when the pH value surrounding CPT−PLA NCs decreases from 7.4 to 5. This pH range is

Table 4. Preparation and Characterization of CPT−PLA NCs[a]

NC	[LA]/[CPT]	LD (%)	CV (%)	IE (%)	NC sizes ± SD(nm)	PD ± SD
CPT-LA_{100}	100	2.36	>99	>99	80.6 ± 0.8	0.083 ±0.016
CPT-LA_{50}	50	4.61	>99	>99	70.7 ± 0.7	0.096 ± 0.007
CPT-LA_{25}	25	8.82	>99	>99	76.6 ± 0.9	0.092 ± 0.006
CPT-LA_{10}	10	19.48	>99	>99	72.5± 0.7	0.056 ± 0.015

[a] Abbreviations: NC = nanoconjugates; LD = CPT loading in wt %; CV = conversion of LA; IE = incorporation efficiency or initiation efficiency, which is the percent of therapeutic agent utilized in the initiation of LA polymerization; the IE is equivalent to the encapsulation efficiency utilized in making nanoparticles via noncovalent, encapsulation strategy; PD = polydispersity of NCs; STD = standard deviation.

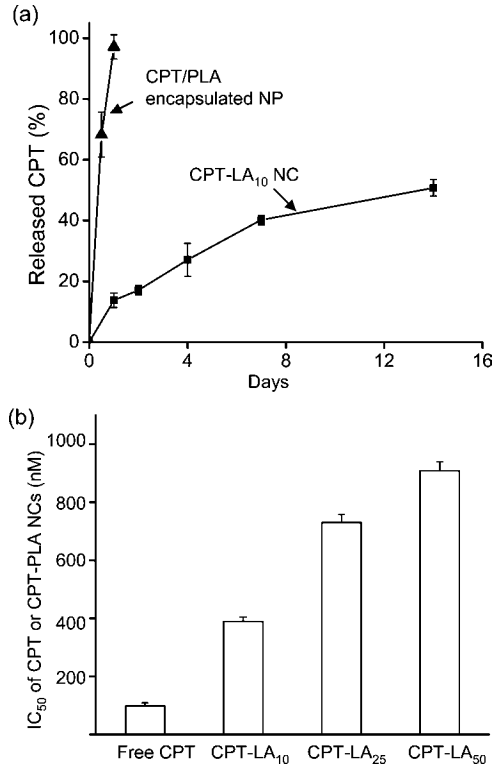


Figure 5. (a) Release of CPT from the CPT-LA_{10} NC (■) and the CPT/PLA NP prepared by encapsulation (▲, CPT/PLA = 5/95 (w/w)). (b) MTT assay to evaluate the cytotoxicity of CPT-LA_{10}, CPT-LA_{25}, CPT-LA_{50} NCs, and CPT in PC-3 cell (37 °C, 72 h).

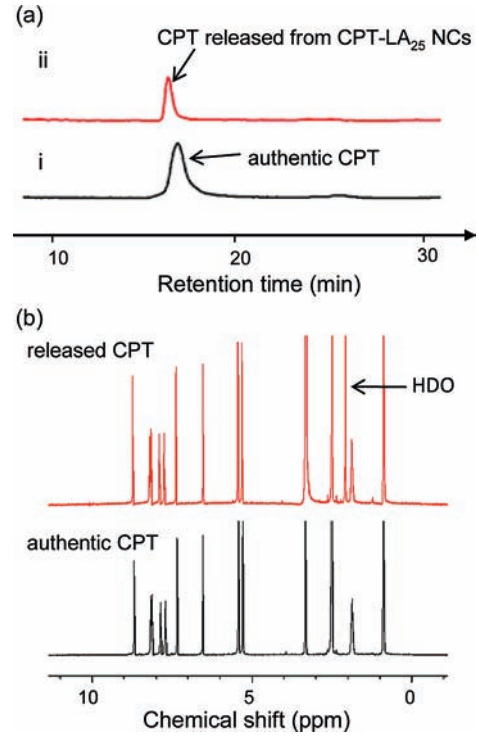


Figure 6. (a) Overlay of the HPLC spectrum of (a) authentic CPT and (b) CPT released from CPT-LA_{25} NC (incubated in PBS for 2 days at 37 °C. (b) ^{1}H NMR spectrum (DMSO-d_6) of the CPT released from CPT-LA_{25} and collected on a preparative RP HPLC, and compared with the ^{1}H NMR spectrum of the authentic CPT.

of particular importance and interest because it is well-known that the cancerous tissues and the endosomes, where the NPs will be located following endocytosis, show pH changes in this range. The decreased hydrolysis rate of ester linkers may contribute to the antitumor efficacy *in vivo*. For instance, we found that a trace amount of CPT in conjugated form in the harvested tumor tissues of mice could be detected by HPLC 109 days after the administration of IT-101 (data not reported). Very surprisingly, the amount of CPT detected in tumor tissue was inversely proportional to the tumor size at day 109. It is yet to be confirmed for the correlation of long-term tumor inhibition with the reduced release rates of CPT drug delivery system in slightly acidic environment.

The *in vitro* toxicities of CPT−PLA NCs were determined by MTT assays in PC-3 cells (Figure 5b). The IC_{50} values of CPT-LA_{10}, CPT-LA_{25}, and CPT-LA_{50} NCs with similar sizes (50−100 nm) were 389, 730, and 908 nM, respectively. The MTT studies revealed that the toxicity of the CPT-PLA NC, which was directly related to the release kinetics of CPT, could be tuned by the CPT loading in the NCs (Figure 5b). In general, NCs with higher drug loadings released drug more rapidly (*32, 33*) and therefore showed higher toxicities (Figure 5b). This observation was presumably due to the fact that the NCs derived from the nanoprecipitation of the higher-loading (lower MW) CPT−PLA conjugates have more loosely packed structures, as compared to the NCs derived from the lower-loading (higher MW) CPT−PLA conjugates. Therefore, the ester linkers between CPT and PLA in the NCs with higher drug loadings were more accessible to the aqueous phase and were subject to faster hydrolysis. PLA NPs without CPT were used as a negative control and were found to show negligible toxicity to the PC-3 cells. The cell viability was 0.956 ± 0.003 when the PC-3 cells were incubated with the PLA NPs at a concentration of 0.5 μg/mL for 72 h at 37 °C.

Conventional polymeric NPs prepared via coprecipitation of polymers and drugs have several formulation challenges that remain to be addressed (*44−47*). NPs typically exhibit a "burst" drug release in aqueous solution; as much as 80−90% of the encapsulated drugs are rapidly released during the first few to tens of hours (*48*). The rapid dose dumping may cause severe systemic toxicities (*49*). In addition, drug loadings in conventional NPs can be very low, typically in the range 1−5% in most NPs studied (*48, 50, 51*). Drug loading of a delivery vehicle has been a critical measure of its utility in clinical settings (*52, 53*). At lower drug loadings, a larger amount of delivery vehicles is needed. Due to the limited body weight and blood volume of animals, the administered volumes are usually fixed. For instance, the volume of a solution intravenously administered to mice with 20 to 30 g body weights should be controlled to below 100 μL (*11*). Intravenous administration of NPs with 1 wt % drug loading in a 100 μL

solution at a dose of 50 mg/kg to a nude mouse with 20 g body weight requires the formulation of a concentrated, 1 g/mL NP solution, which is too viscous to formulate and inject intravenously. The third major challenge presented by NPs prepared via the encapsulation approach is the lack of a general strategy to achieve quantitative drug encapsulation. Depending on the amount of drug used, the hydrophobicity and hydrophilicity of the drug and the compatibility of the drug and polymer, the encapsulation efficiencies vary drastically over the range 10−90% (*48, 54*). Non-encapsulated drugs may self-aggregate (*48*) and can be very difficult to remove from the NPs. These formulation challenges significantly impact the processability and clinical translation of NP delivery vehicles prepared by drug/polymer coprecipitations.

PLA/CPT NPs prepared by the coprecipitation method have been previously reported to give low drug loading (0.1−1.5%), low loading efficiency (2.8−38.3%), and poorly controlled release kinetics (*55*). Depending on the formulation method, 20−90% of the encapsulated CPT was released within 1 h after the NP was exposed to the PBS solution. The ring-opening polymerization method that we developed allows for the incorporation of CPT to PLA with a tunable drug loading as high as 20% and 100% loading efficiency (Table 4), which is in line with the high drug loading reported in polyglutamate−CPT conjugates (*2, 8*). The unique conjugation technique allows for formation of CPT-containing PLA NCs with superbly controlled formulation parameters, which makes PLA−CPT NCs potentially useful agents for sustained treatment of cancer *in vivo*.

CONCLUSION

Preparation of PLA−drug conjugates with controlled drug loading and release profiles has been previously reported using conventional coupling chemistry (*56−60*). In this study, we report a unique conjugation method that allows for CPT conjugation to PLA via CPT-initiated ROP of LA. This method allows for facile incorporation of CPT to PLA and forms PLA−CPT conjugates with low polydispersities, predetermined drug loadings (as high as 20%), and 100% loading efficiencies. By controlling the metal and the chelating ligands of the catalysts, the initiation of LA polymerization can be specifically controlled at the C20-OH of CPT with negligible lactone ring opening in CPT. CPT conjugated to PLA should maintain its lactone form (the therapeutically active form). The BDI-metal chelating complexes do not have deleterious effects on CPT and can be easily removed by solvent extraction. Because both Zn and Mg ions are biocompatible (as key elements in our dietary mineral supplements), there should not be significant safety concerns regarding the use of these two metal catalysts for the ROP and formulation of NCs for potential clinical applications. Multigram scale of PLA−CPT conjugates can be readily prepared within hours using this one-pot polymerization approach. Because CPT molecules are covalently conjugated to PLA, the postreaction formulation process (nanoprecipitation, purification, sterilization, lyophilization, shipping and handling, transportation, etc.) can be much more readily handled with a minimum change of sample property, in contrast to drug/polymer NPs prepared via encapsulation methods that struggle to prevent drug release during the formulation process. Given that the lack of a controlled formulation for nanoparticulate drug delivery vehicles presents bottlenecks to their clinical translation, this unique, ROP-mediated conjugation methodology may contribute to the development of clinically applicable CPT and CPT-analogue based nanomedicines.

ACKNOWLEDGMENT

This work is supported by the National Science Foundation (Career Program DMR-0748834), the National Institute of Health (R21 grant 1R21CA139329-01), and the Siteman Center for Cancer Nanotechnology Excellence (SCCNE, Washington University)-the Center for Nanoscale Science and Technology (CNST, University of Illinois at Urbana−Champaign). R.T. acknowledges a student fellowship from SCCNE. We would like to thank Professors Martin Burke and Jeffrey Moore for providing the anhydrous solvents.

Note Added after ASAP Publication: This manuscript was released ASAP on December 10, 2009 with errors in the structures of Scheme 2. The revised version was released on December 15, 2009.

LITERATURE CITED

(1) Muggia, F. M., Dimery, I., and Arbuck, S. G. (1996) Camptothecin and its analogs. *Ann. N.Y. Acad. Sci. 803*, 213–223.

(2) Liehr, J. G., Giovanella, B. C., and Verschraegen, C. F. (2000) *The Camptothecins: Unfolding Their Anticancer Potential (Annals of the New York Academy of Sciences)*, New York Academy of Sciences, New York.

(3) Hertzberg, R. P., Caranfa, M. J., and Hecht, S. M. (1989) On the mechanism of topoisomerase-I inhibition by camptothecin-evidence for binding to an enzyme DNA complex. *Biochemistry 28*, 4629–4638.

(4) Mi, Z., and Burke, T. G. (1994) Differential interactions of camptothecin lactone and carboxylate forms with human blood components. *Biochemistry 33*, 10325–10336.

(5) Mi, Z., and Burke, T. G. (1994) Marked interspecies variations concerning the interactions of camptothecin with serum albumins: a frequency-domain fluorescence spectroscopic study. *Biochemistry 33*, 12540–12545.

(6) Greenwald, R. B., Pendri, A., Conover, C., Gilbert, C., Yang, R., and Xia, J. (1996) Drug delivery systems 0.2. Camptothecin 20-O-poly(ethylene glycol)ester transport forms. *J. Med. Chem. 39*, 1938–1940.

(7) Dharap, S. S., Wang, Y., Chandna, P., Khandare, J. J., Qiu, B., Gunaseelan, S., Sinko, P. J., Stein, S., Farmanfarmaian, A., and Minko, T. (2005) Tumor-specific targeting of an anticancer drug delivery system by LHRH peptide. *Proc. Natl. Acad. Sci. U.S.A. 102*, 12962–12967.

(8) Bhatt, R. L., de Vries, P., Tulinsky, J., Bellamy, G., Baker, B., Singer, J. W., and Klein, P. (2003) Synthesis and in vivo antitumor activity of poly(L-glutamic acid) conjugates of 20(S)-camptothecin. *J. Med. Chem. 46*, 190–193.

(9) Cabral, H., Nakanishi, M., Kumagai, M., Jang, W. D., Nishiyama, N., and Kataoka, K. (2009) A photo-activated targeting chemotherapy using glutathione sensitive camptothecin-loaded polymeric micelles. *Pharm. Res. 26*, 82–92.

(10) Schluep, T., Cheng, J., Khin, K. T., and Davis, M. E. (2006) Pharmacokinetics and biodistribution of the camptothecin-polymer conjugate IT-101 in rats and tumor-bearing mice. *Cancer Chemother. Pharmacol 57*, 654–662.

(11) Cheng, J., Khin, K. T., and Davis, M. E. (2004) Antitumor activity of beta-cyclodextrin polymer-camptothecin conjugates. *Mol. Pharmacol. 1*, 183–193.

(12) Cheng, J. J., Khin, K. T., Jensen, G. S., Liu, A. J., and Davis, M. E. (2003) Synthesis of linear, beta-cyclodextrin-based polymers and their camptothecin conjugates. *Bioconjugate Chem. 14*, 1007–1017.

(13) Schluep, T., Hwang, J., Cheng, J., Heidel, J. D., Bartlett, D. W., Hollister, B., and Davis, M. E. (2006) Preclinical efficacy of the camptothecin-polymer conjugate IT-101 in multiple cancer models. *Clin. Cancer Res. 12*, 1606–1614.

(14) Schluep, T., Hwang, J., Hildebrandt, I. J., Czernin, J., Choi, C. H. J., Alabi, C. A., Mack, B. C., and Davis, M. E. (2009) Pharmacokinetics and tumor dynamics of the nanoparticle IT-101 from PET imaging and tumor histological measurements. *Proc. Natl. Acad. Sci. U.S.A. 106*, 11394–11399.

(15) Greenwald, R. B., Pendri, A., Conover, C. D., Lee, C., Choe, Y. H., Gilbert, C., Martinez, A., Xia, J., Wu, D. C., and Hsue, M. (1998) Camptothecin-20-PEG ester transport forms: the effect of spacer groups on antitumor activity. *Bioorg. Med. Chem. 6*, 551–562.

(16) Moore, D. R., Cheng, M., Lobkovsky, E. B., and Coates, G. W. (2003) Mechanism of the alternating copolymerization of epoxides and CO_2 using beta-diiminate zinc catalysts: Evidence for a bimetallic epoxide enchainment. *J. Am. Chem. Soc. 125*, 11911–11924.

(17) Jeske, R. C., DiCiccio, A. M., and Coates, G. W. (2007) Alternating copolymerization of epoxides and cyclic anhydrides: An improved route to aliphatic polyesters. *J. Am. Chem. Soc. 129*, 11330–11331.

(18) Chamberlain, B. M., Cheng, M., Moore, D. R., Ovitt, T. M., Lobkovsky, E. B., and Coates, G. W. (2001) Polymerization of lactide with zinc and magnesium beta-diiminate complexes: Stereocontrol and mechanism. *J. Am. Chem. Soc. 123*, 3229–3238.

(19) Cheng, M., Moore, D. R., Reczek, J. J., Chamberlain, B. M., Lobkovsky, E. B., and Coates, G. W. (2001) Single-site beta-diiminate zinc catalysts for the alternating copolymerization of CO2 and epoxides: Catalyst synthesis and unprecedented polymerization activity. *J. Am. Chem. Soc. 123*, 8738–8749.

(20) Martin-Kleiner, I., Svoboda-Beusan, I., and Gabrilovac, J. (2006) PMA and doxorubicin decrease viability, MTT activity and expression of CD10 marker on NALM-1 leukemic cells. *Immunopharm. Immunotox. 28*, 411–420.

(21) Conover, C. D., Greenwald, R. B., Pendri, A., and Shum, K. L. (1999) Camptothecin delivery systems: the utility of amino acid spacers for the conjugation of camptothecin with polyethylene glycol to create prodrugs. *Anti-Cancer Drug Des. 14*, 499–506.

(22) Cheng, J., Teply, B. A., Sherifi, I., Sung, J., Luther, G., Gu, F. X., Levy-Nissenbaum, E., Radovic-Moreno, A. F., Langer, R., and Farokhzad, O. C. (2007) Formulation of functionalized PLGA-PEG nanoparticles for in vivo targeted drug delivery. *Biomaterials 28*, 869–876.

(23) Farokhzad, O. C., Cheng, J., Teply, B. A., Sherifi, I., Jon, S., Kantoff, P. W., Richie, J. P., and Langer, R. (2006) Targeted nanoparticle-aptamer bioconjugates for cancer chemotherapy in vivo. *Proc. Natl. Acad. Sci. U.S.A. 103*, 6315–6320.

(24) Dechy-Cabaret, O., Martin-Vaca, B., and Bourissou, D. (2004) Controlled ring-opening polymerization of lactide and glycolide. *Chem. Rev. 104*, 6147–6176.

(25) Coulembier, O., Degee, P., Hedrick, J. L., and Dubois, P. (2006) From controlled ring-opening polymerization to biodegradable aliphatic polyester: Especially poly(beta-malic acid) derivatives. *Prog. Polym. Sci. 31*, 723–747.

(26) Okada, M. (2002) Chemical syntheses of biodegradable polymers. *Prog. Polym. Sci. 27*, 87–133.

(27) Kuran, W. (1998) Coordination polymerization of heterocyclic and heterounsaturated monomers. *Prog. Polym. Sci. 23*, 919–992.

(28) Chisholm, M. H., and Eilerts, N. W. (1996) Single-site metal alkoxide catalysts for ring-opening polymerizations. Poly(dilactide) synthesis employing {HB(3-Bu(t)pz)(3)}Mg(OEt). *Chem. Commun.* 853–854.

(29) O'Keefe, B. J., Hillmyer, M. A., and Tolman, W. B. (2001) Polymerization of lactide and related cyclic esters by discrete metal complexes. *J. Chem. Soc., Dalton Trans.* 2215–2224.

(30) Williams, C. K., Breyfogle, L. E., Choi, S. K., Nam, W., Young, V. G., Hillmyer, M. A., and Tolman, W. B. (2003) A highly active zinc catalyst for the controlled polymerization of lactide. *J. Am. Chem. Soc. 125*, 11350–11359.

(31) O'Keefe, B. J., Monnier, S. M., Hillmyer, M. A., and Tolman, W. B. (2001) Rapid and controlled polymerization of lactide by structurally characterized ferric alkoxides. *J. Am. Chem. Soc. 123*, 339–340.

(32) Tong, R., and Cheng, J. (2008) Paclitaxel-initiated, controlled polymerization of lactide for the formulation of polymeric nanoparticulate delivery vehicles. *Angew. Chem., Int. Ed. 47*, 4830–4834.

(33) Tong, R., and Cheng, J. (2009) Ring-opening polymerization-mediated controlled formulation of polylactide-drug nanoparticles. *J. Am. Chem. Soc. 131*, 4744–4754.

(34) Allen, S. D., Moore, D. R., Lobkovsky, E. B., and Coates, G. W. (2002) High-activity, single-site catalysts for the alternating copolymerization of CO_2 and propylene oxide. *J. Am. Chem. Soc. 124*, 14284–14285.

(35) Coates, G. W., and Moore, D. R. (2004) Discrete metal-based catalysts for the copolymerization CO_2 and epoxides: Discovery, reactivity, optimization, and mechanism. *Angew. Chem., Int. Ed. 43*, 6618–6639.

(36) Rieth, L. R., Moore, D. R., Lobkovsky, E. B., and Coates, G. W. (2002) Single-site beta-diiminate zinc catalysts for the ring-opening polymerization of beta-butyrolactone and beta-valerolactone to poly(3-hydroxyalkanoates). *J. Am. Chem. Soc. 124*, 15239–15248.

(37) Rowley, J. M., Lobkovsky, E. B., and Coates, G. W. (2007) Catalytic double carbonylation of epoxides to succinic anhydrides: Catalyst discovery, reaction scope, and mechanism. *J. Am. Chem. Soc. 129*, 4948–4960.

(38) Moore, D. R., Cheng, M., Lobkovsky, E. B., and Coates, G. W. (2002) Electronic and steric effects on catalysts for CO_2/epoxide polymerization: Subtle modifications resulting in superior activities. *Angew. Chem., Int. Ed. 41*, 2599–2602.

(39) Spivey, A. C., and Andrews, B. I. (2001) Catalysis of the asymmetric desymmetrization of cyclic anhydrides by nucleophilic ring-opening with alcohols. *Angew. Chem., Int. Ed. 40*, 3131–3134.

(40) Lu, H., Lin, H. X., Jiang, Y., Zhou, X. G., Wu, B. L., and Chen, J. M. (2006) Synthesis and antitumor activity of 20-O-linked succinate-based camptothecin ester derivatives. *Lett. Drug Des. Discov. 3*, 83–86.

(41) Yen, Y., Synold, T., and Schluep, T. (2007) First-in-human phase I trial of a cyclodextrincontaining polymer-camptothecin nanoparticle in patients with various solid tumors. *J. Clin. Oncol. 25* (Suppl. 18), 14078.

(42) Heath, J. R., and Davis, M. E. (2008) Nanotechnology and cancer. *Annu. Rev. Med. 59*, 251–265.

(43) Davis, M. E., Chen, Z., and Shin, D. M. (2008) Nanoparticle therapeutics: an emerging treatment modality for cancer. *Nat. Rev. Drug Discovery 7*, 771–782.

(44) Tong, R., and Cheng, J. (2007) Anticancer polymeric nanomedicines. *Polym. Rev. 47*, 345–381.

(45) Tong, R., Christian, D. A., Tang, L., Cabral, H., Baker, J. R., Kataoka, K., Discher, D. E., and Cheng, J. J. (2009) Nanopolymeric Therapeutics. *MRS Bull. 34*, 422–431.

(46) Teply, B. A., Tong, R., Jeong, S. Y., Luther, G., Sherifi, I., Yim, C. H., Khadernhosseini, A., Farokhzad, O. C., Langer, R. S., and Cheng, J. (2008) The use of charge-coupled polymeric microparticles and micromagnets for modulating the bioavailability of orally delivered macromolecules. *Biomaterials 29*, 1216–1223.

(47) Cheng, J. J., Teply, B. A., Jeong, S. Y., Yim, C. H., Ho, D., Sherifi, I., Jon, S., Farokhzad, O. C., Khademhosseini, A., and Langer, R. S. (2006) Magnetically responsive polymeric microparticles for oral delivery of protein drugs. *Pharm. Res. 23*, 557–564.

(48) Musumeci, T., Ventura, C. A., Giannone, I., Ruozi, B., Montenegro, L., Pignatello, R., and Puglisi, G. (2006) PLA/PLGA nanoparticles for sustained release of docetaxel. *Int. J. Pharm. 325*, 172–179.

(49) Matsumura, Y., Hamaguchi, T., Ura, T., Muro, K., Yamada, Y., Shimada, Y., Shirao, K., Okusaka, T., Ueno, H., Ikeda, M., and Watanabe, N. (2004) Phase I clinical trial and pharmacokinetic evaluation of NK911, a micelle-encapsulated doxorubicin. *Br. J. Cancer 91*, 1775–1781.

(50) Mu, L., and Feng, S. S. (2003) A novel controlled release formulation for the anticancer drug paclitaxel (Taxol(R)): PLGA

nanoparticles containing vitamin E TPGS. *J. Controlled Release 86*, 33–48.

(51) Avgoustakis, K. (2004) Pegylated poly(lactide) and poly(lactide-co-glycolide) nanoparticles: preparation, properties and possible application in drug delivery. *Curr. Drug Delivery 1*, 321–333.

(52) Hamblett, K. J., Senter, P. D., Chace, D. F., Sun, M. M. C., Lenox, J., Cerveny, C. G., Kissler, K. M., Bernhardt, S. X., Kopcha, A. K., Zabinski, R. F., Meyer, D. L., and Francisco, J. A. (2004) Effects of drug loading on the antitumor activity of a monoclonal antibody drug conjugate. *Clin. Cancer Res. 10*, 7063–7070.

(53) Barenholz, Y. (2003) Relevancy of drug loading to liposomal formulation therapeutic efficacy. *J. Liposome Res. 13*, 1–8.

(54) Missirlis, D., Kawamura, R., Tirelli, N., and Hubbell, J. A. (2006) Doxorubicin encapsulation and diffusional release from stable, polymeric, hydrogel nanoparticles. *Eur. J. Pharm. Sci. 29*, 120–129.

(55) Kunii, R., Onishi, H., and Machida, Y. (2007) Preparation and antitumor characteristics of PLA/(PEG-PPG-PEG) nanoparticles loaded with camptothecin. *Eur. J. Pharm. Biopharm. 67*, 9–17.

(56) Lee, C. C., Gillies, E. R., Fox, M. E., Guillaudeu, S. J., Frechet, J. M. J., Dy, E. E., and Szoka, F. C. (2006) A single dose of doxorubicin-functionalized bow-tie dendrimer cures mice bearing C-26 colon carcinomas. *Proc. Natl. Acad. Sci. U.S.A. 103,* , 16649–16654.

(57) Yoo, H. S., Lee, K. H., Oh, J. E., and Park, T. G. (2000) In vitro and in vivo anti-tumor activities of nanoparticles based on doxorubicin-PLGA conjugates. *J. Controlled Release 68*, 419–431.

(58) Yokoyama, M., Miyauchi, M., Yamada, N., Okano, T., Sakurai, Y., Kataoka, K., and Inoue, S. (1990) Polymer micelles as novel drug carrier - adriamycin-conjugated poly(ethylene glycol) poly(aspartic acid) block copolymer. *J. Controlled Release 11*, 269–278.

(59) Sengupta, S., Eavarone, D., Capila, I., Zhao, G. L., Watson, N., Kiziltepe, T., and Sasisekharan, R. (2005) Temporal targeting of tumour cells and neovasculature with a nanoscale delivery system. *Nature 436*, 568–572.

(60) Zhang, Z. P., and Feng, S. S. (2006) Nanoparticles of poly(lactide)/vitamin E TPGS copolymer for cancer chemotherapy: Synthesis, formulation, characterization and in vitro drug release. *Biomaterials 27*, 262–270.

BC900356G

New Nucleotide Analogues with Enhanced Signal Properties

Dmitry Cherkasov,*,† Thorsten Biet,‡ Englbert Bäuml,‡ Walther Traut,§ and Michael Lohoff†

Institute for Medical Microbiology, BMFZ, Philipps University of Marburg, Hans-Meerweinstrasse 2, 35043 Marburg, Germany, and Institute of Chemistry and Institut für Biologie, Zentrum für Medizinische Strukturbiologie, Universität Lübeck, Ratzeburger Allee 160, 23538 Lübeck, Germany. Received August 16, 2009; Revised Manuscript Received October 31, 2009

We describe synthesis and testing of a novel type of dye-modified nucleotides which we call macromolecular nucleotides (m-Nucs). Macromolecular nucleotides comprise a nucleotide moiety, a macromolecular linear linker, and a large macromolecular ligand carrying multiple fluorescent dyes. With incorporation of the nucleotide moiety into the growing nucleic acid strand during enzymatic synthesis, the macromolecular ligand together with the coupled dyes is bound to the nucleic acid. By the use of this new class of modified nucleotides, signals from multiple dye molecules can be obtained after a single enzymatic incorporation event. The modified nucleotides are considered especially useful in the fields of nanobiotechnology, where signal stability and intensity is a limiting factor.

INTRODUCTION

Nucleotides conjugated with fluorescent dyes have been widely used to label nucleic acids for different techniques in molecular biology, e.g., FISH, microarray, or Sanger sequencing, for over 20 years. The state of the art structure of these nucleotides comprises a nucleotide moiety, a short linker arm, and a low molecular weight fluorescent dye moiety, e.g., fluorescein or a cyanine dye. Regarding signal strength, this structure has been sufficient for most analytical purposes. The presence of a large population of identically labeled nucleic acid molecules used for signal generation not only contributed to the required strength of the signal, but also compensated for photophysical phenomena of individual molecules like blinking and spectral drift. Recent developments in analytical science opened new frontiers down to the level of nanoscale and single molecules (*1–6*). Here, the detection of fluorescent signals is increasingly influenced by peculiarities in the photophysical behavior of individual fluorophores, e.g., blinking (*7, 8*), which result in uncertainties and instability of signal detection. Thus, the development of new technologies may benefit from the redesign of dye-labeled nucleotides.

In particular, single molecule sequencing technologies hold great promise regarding cost and time reduction, compared to methods which require bulk populations of DNA molecules for sequencing (*9–13*). Since the late 1990s, several techniques for single molecule sequencing have been under development by academic groups (*14–16*) and commercial vendors (e.g., www.helicosbio.com, www.genovoxx.com, www.visigenbio.com, www.pacificbiosciences.com, www.nanoporetech.com); two newly published approaches (*17, 18*) use differently labeled nucleotides during the primer extension reaction to translate the sequence content into specific light signals that can be detected. The raw data accuracy in both procedures ranges from 80% to 95% in a single run. In comparison, sequencing methods based on the analysis of bulk populations achieve about 99% (www.illumina.com). One of the reasons for the relatively high error rate in those novel approaches is the use of a single fluorophore molecule as the source of the light signal. During sequencing, each fluorophore is excited only for a short period of time (tens to hundreds of milliseconds). During this period of time, several photophysical phenomena, e.g., blinking, quenching, spectral shift, and photobleaching (*3, 6, 8*), can lead to a hindrance of signal detection, resulting in a loss of sequence information. Further augmentation of sequencing speed during single molecule sequencing will most likely require even shorter illumination periods, resulting in a further increase of the error rate. Taken together, single molecule sequencing technologies should address signal stability issues in order to overcome such limitations.

In this paper, we present a new type of nucleotide analogues—collectively called m-Nucs (macromolecular nucleotides) here—that may solve the problem of signal instability. We assumed that ideally each nucleotide should carry several dye molecules. By using such nucleotides during sequencing, incoporation of only one nucleotide molecule into the growing strand will result in an accumulated signal produced from a bunch of molecules instead of only one fluorophore. Such nucleotides could have several advantages compared to conventionally labeled nucleotides. First, because each dye molecule is functioning as an individual light generator independent from others, the probability of nonemitting states in one particular nucleotide decreases with the number of dye molecules in this nucleotide. Second, the strength of the fluorescent signal from multiple dye molecules is greatly increased compared to that of only one dye molecule. Thus, the crucial parameters signal stability and signal strength could be dramatically improved by multiple labeling of nucleotides with fluorescent dyes. In the present study, we report on the development of such nucleotides and their labeling technology.

In the following, we describe the new nucleotide analogues, their synthesis, and their suitability as substrates in solid-phase primer extension assays. The synthesis was conducted by coupling of a long PEG (poly(ethylene glycol)) linker carrying a biotin moiety to nucleotide analogues, the 5-allylamine-dUTP and the 5-propargylamine-dCTP. Subsequently, streptavidin or its derivatives were coupled to the biotin moiety of the PEG linker. The resulting compounds contain the nucleotide moiety, a long PEG linker, and streptavidin, which can be modified with multiple dye molecules. The incorporation of such new nucle-

* E-mail: cherkasovd07@yandex.ru.
† Philipps University of Marburg.
‡ Institute of Chemistry, Universität Lübeck.
§ Zentrum für Medizinische Strukturbiologie, Universität Lübeck.

10.1021/bc900364f © 2010 American Chemical Society
Published on Web 01/04/2010

otides into the growing strand by several DNA polymerases was shown using a solid-phase primer extension assay.

MATERIAL AND METHODS

Materials. Chemical reagents and solvents were purchased from Sigma-Aldrich (Seelze, Germany), oligonucleotides from MWG Biotech (now Eurofins MWG Operon, Ebersberg, Germany). All DNA polymerases were from New England Biolabs (Frankfurt a. Main, Germany). Silica gel 60 F254 TLC (thin layer chromatography) plates were purchased from VWR International (Darmstadt, Germany), SA (streptavidin) and paramagnetic beads from Promega (Mannheim, Germany), and premixed 30% acrylamide−bisacrylamide solution from Bio-Rad Laboratories (Munich, Germany). Ultrafiltration vials (Microcon MWCO 50 kD and 100 kD) were purchased from Millipore (Schwalbach, Germany). We used dUTP-16-Biotin and Fluorescein-12-dUTP from Roche Applied Science (Mannheim, Germany); Fluorescein-12-dCTP from Perkin-Elmer (Offenbach a. Main, Germany); dUTP-AA (5-aminoallyl-dUTP) and dCTP-PA (5-propargylamino-dCTP) from Jenabiosciences (Jena, Germany); and NHS-PEG-Fluorescein (*N*-hydroxysuccinimidyl ester−poly(ethylene glycol)−fluorescein, M_w 5000) and NHS-PEG-5000-biotin (*N*-hydroxysuccinimidyl ester−poly(ethylene glycol)−biotin, M_w 5000) from Nektar Therapeutics (San Carlos, CA, USA). SA-PE (streptavidin-R-phycoerythrin) was from Invitrogen (Karlsruhe, Germany). HPLC was conducted on TSKgel DEAE-2SW columns from Sigma-Aldrich.

Synthesis of Compounds. *General Considerations.* The components of the m-Nucs synthesized in this study are a nucleotide moiety, a water-soluble linker (PEG-linker), and streptavidin or its derivatives, e.g., dye-labeled streptavidin. An overview of the composition of nucleotide conjugates is given in Table 2. Synthetic schemes are shown in the Supporting Information Supplement 1 and Figure 1.

First, we coupled PEG-biotin to the nucleotides to generate precursors of the m-Nucs (compounds **1** and **2**). Next, dNTP-PEG-biotin (abbreviated as dNTP-PEG-B) was coupled to streptavidin (SA) or its phycoerythrin (PE)-modified derivative (compounds **3** to **5** and **7**). To produce dye-labeled streptavidin derivatives, NHS-PEG-fluorescein was coupled to SA (compound **6**). In all protocols, separation of the resulting m-Nucs from unbound dNTP-PEG-biotin or other compounds with a molecular weight of less than 50 kDa was performed via ultrafiltration and repetitive washes.

Synthesis of Compounds **1** *and* **2.** To generate compound **1**, dUTP-PEG-B, NHS-PEG-5000-biotin (20 mg) was added to a solution of dUTP-AA (500 μL, 20 mM, in 50 mM borate buffer, pH 8.5) and the reaction was allowed to proceed for 1 h at room temperature. After that, compound **1** was isolated by DEAE-HPLC in a salt gradient (0.0 to 0.5 M NaCl in Tris−HCl buffer, 50 mM, pH 8.0). Compound **1** was eluted from the DEAE-HPLC column at around 0.3 M NaCl. Fractions were collected and analyzed by UV−vis and TLC (silica gel 60 F254) in an ethanol−water mixture (70:30, v/v) for the presence of dUTP-AA (retention factor $R_f = 0.4$) and dUTP-PEG-B ($R_f = 0.05$). The fractions of dUTP-PEG-B with no detectable contaminations of dUTP-AA were combined and stored at −20 °C.

Compound **2**, dCTP-PEG-B, was synthesized in a similar way, but exchanging dCTP-PA for dUTP-AA.

Synthesis of Compounds **3** *and* **4.** To produce compound **3**, (dUTP-PEG-B)$_1$-SA, 1 mg of streptavidin was dissolved in 1 mL of 50 mM Tris−HCl buffer, pH 8.0, and an equimolar amount of compound **1** (as a 0.17 mM solution in 0.1 mL of 50 mM Tris−HCl buffer, pH 8.0) was added to the streptavidin-containing solution. The resulting solution was kept at room temperature for 1 h. After that, compound **3** was separated from compounds with lower molecular weight by repetitive ultrafiltration using Microcon MWCO 50 kDa filters according to manufacturer's instructions, using 50 mM Tris−HCl buffer, pH 8.0.

Compound **4**, (dCTP-PEG-B)$_1$-SA, was synthesized in a similar manner, using dCTP-PEG-B, however, instead of dUTP-PEG-B.

Synthesis of Compounds **5***,* **7***, and* **8.** For the synthesis of compound **5**, (dUTP-PEG-B)$_4$-SA, 0.5 mg streptavidin was dissolved in 0.5 mL of 50 mM Tris−HCl, pH 8.0, and a 5-fold excess of dUTP-PEG-B (as 0.1 mM solution in 0.5 mL of 50 mM Tris-HCl buffer, pH 8.0) was added. The resulting solution was kept at room temperature for 1 h. After that, compound **5** was separated from compounds with lower molecular weight as described for compound **3**.

Compound **8**, (dUTP-16-B)$_4$-SA, was synthesized in a similar way to compound **5**, but using dUTP-16-biotin instead of dUTP-PEG-B.

Compound **7**, (dUTP-PEG-B)$_n$-SA-PE, was synthesized in a similar way as described for compound **5**: a solution of 0.2 mg SA-PE conjugate (streptavidin-R-phycoerythrin) was added to an excess of dUTP-PEG-B (as 0.1 mM solution in 0.2 mL of 50 mM Tris−HCl buffer, pH 8.0). The resulting mixture was kept at room temperature for 1 h. Thereafter, compound **7** was separated from compounds with lower molecular weight by repetitive ultrafiltration via Microcon MWCO 100 kDa filters according to the manufacturer's instructions, using 50 mM Tris−HCl buffer, pH 8.0. R-phycoerythrin is a naturally occurring large fluorescent protein with a molecular weight of about 240 kDa. Therefore, the streptavidin-R-phycoerythrin conjugate has a size of more than 240 kDa. In this conjugate, some biotin binding sites may have been inactivated during coupling of PE to SA, or the access to the binding site may be hindered by PE. Therefore, (dNTP-PEG)$_n$-SA-PE represents a mixture of compounds, where the number of dNTP-PEG-molecules per SA-PE can be in the range 1−4.

Synthesis of Compound **6***, (dUTP-PEG-B)$_4$-SA-(PEG-Fluorescein).* To obtain compounds with a ratio of 5 dye molecules to 1 nuc-macomolecule, compound **5** was subjected to additional labeling of SA by NHS-PEG-fluorescein according to the manufacturer's recommendations. NHS-PEG-fluorescein was dissolved in DMSO (100 mg/mL), while 0.1 mg of compound **5** was dissolved in 100 μL of 50 mM phosphate buffer, pH 7.5. Labeling was conducted at room temperature by stepwise addition of the NHS-PEG-fluorescein solution to the compound **5** containing solution until a final NHS-PEG-fluorescein concentration of 0.5 mM was reached. After labeling, compound **6** was separated from byproduct of the reaction by ultrafiltration with MWCO 50 kDa and repeated washes with 50 mM phosphate buffer, pH 7.5, until no more dye was detected in the waste wash. The colored substance with >50 kDa was collected. Calculation of the average number of fluorescent dye molecules per one molecule of streptavidin in compound **6** was conducted using the known starting amount of compound **5** and molar extinction coefficient for PEG-fluorescein ($\varepsilon_{490} = 80.000$ M^{-1} cm^{-1} in a buffer solution, pH 9). It was concluded that, on average, compound **6** was labeled by five fluorescein molecules per molecule of compound **6**. The labeled compound **6** was dissolved in 50 mM Tris−HCl buffer, pH 8.0, and stored at 4 °C until needed. Measurements of excitation and emission spectra were conducted in 50 mM Tris−HCl buffer pH 8.5 at RT.

Solid-Phase Primer Extension Assay. To test m-Nucs in an enzymatic reaction, a solid-phase primer extension assay was chosen. Modified nucleotides were incorporated into the primer in a template-dependent reaction and, being attached to the solid phase, could be easily separated from the reaction mixture after

Table 1. Oligonucleotides Used in the Study

no.	laboratory name	3′ modification	5′ modification	sequence (from 5′to 3′)[a]
1	Primer T7−19			TAATACGACTCACTATAGG
2	Primer T7−19-Cy3		Cy3	TAATACGACTCACTATAGG
3	Template Oligo 87			$(dA)_{50}$TCCTTAGTCCTATAGTGAGTCGTATTA
4	dT-48−3′-Biotin	biotin		$(dT)_{48}$

[a] Primer binding site of the template is underlined.

the incorporation reaction. After that, extended primers were separated by gel electrophoresis and visualized by detection of signals from the fluorescent labels coupled to the nucleic acid strands (fluorescently labeled primers or incorporated fluorescently labeled nucleotides).

All DNA polymerases were tested in an incorporation buffer consisting of 50 mM Tris−HCl pH 8.0, 50 mM NaCl, 5 mM $MgCl_2$, 10% glycerol, and 0.2 mM EDTA. The washing buffer for the magnetic beads was 50 mM Tris−HCl pH 8.0, 50 mM NaCl, 10% glycerol, and 0.2 mM EDTA. The stop-buffer used to terminate the enzymatic reaction consisted of 50 mM Tris−HCl pH 8.0, 50 mM NaCl, 10% glycerol, and 20 mM EDTA.

Primer and template (Table 1) were annealed by incubation in incorporation buffer (0.2 mL, 1 μM each) at 80 °C for 2 min followed by cooling to RT for 10 min. The combinations of primer and template for each experiment are described in the Results section; the sequences are listed in Table 1.

To prepare the solid phase with bound template−primer complex, an oligo dT_{48}-3′-biotin-anchor was bound to streptavidin which was immobilized on paramagnetic beads, and the template−primer complex was bound to this anchor. The following protocol was used: Streptavidin beads (600 μL) were washed twice with washing buffer, then 5 μL of 100 μM oligo dT_{48}-3′-biotin was added and incubated for 5 min at RT. After that, the beads were washed twice with washing buffer to remove unbound oligo dT_{48}-3′-biotin. The anchor-containing magnetic beads were used immediately or stored at 4 °C for several weeks until use.

The solution with annealed template primer was added to the anchor-containing beads and incubated for 5 min at 37 °C. Then, beads loaded with the template−primer pairs were rinsed with washing buffer, suspended in 100 μL of this buffer, and used immediately or stored in washing buffer at 4 °C for maximally one week. Immediately prior to use in the primer-extension reaction, loaded beads were briefly rinsed with washing buffer containing 1 μM biotin to saturate all free biotin binding sites on the beads and twice with washing buffer to remove unbound biotin. For each primer extension reaction, 10 μL of the bead suspension was used.

To conduct the primer extension reaction, beads with attached template−primer complexes were combined at room temperature with m-Nucs and other components of the reaction to yield a final volume of 19 μL per reaction. For the enzymatic reactions, dNTPs, commercially available modified nucleotides, or m-Nucs were used at final concentrations of 1 μM or higher as indicated. Each reaction was initiated by the addition of 1 μL of a particular polymerase (i.e., 5 units of Klenow Fragment (exo -) DNA polymerase, or 5 units of *Taq* DNA polymerase, or 2 units of *Vent* (exo-) DNA polymerase) and incubated at 37 °C for 15 min. The incorporation reaction was limited to the first two to five bases starting from the 3′-OH of the primer, because at least one dNTP necessary for further extension was omitted from the reaction. The reaction was stopped by addition of 200 μL of stop buffer. After that, the nucleic acid strands bound to the beads were washed several times to remove the unincorporated nucleotides. In the last step, the suspension of beads with bound nucleic acid strands was concentrated to a volume of 10 μL and loaded directly onto the vertical slab gel (10% polyacrylamide) or stored at 4 °C until analysis.

Electrophoretic Analysis. The primer extension products were analyzed on 10% polyacrylamide−bisacrylamide gels, prepared from 30% of the Bio-Rad stock solution (acrylamide/bisacrylamide, 19.5:0.5% w/w). Gel electrophoresis was conducted at 120 V on a BioRad Miniprotean in 50 mM Tris−HCl Buffer pH 8.0 at 60 °C for 3 min and after that for 10 to 25 min at 40 °C. The 60 °C step served to dissociate the extended nucleic acid strands from the template and, hence, disconnect them from the magnetic beads. After the run, the gel was exposed to UV illumination, and fluorescence images were taken with a CCD camera. Signal intensities were compared using the software Bio-Profile Bio 1D (Vilber Lourmat GmbH). The signal from the extension product obtained from compound **6** was taken as a standard for comparison to other signals. Its relative fluorescent intensity was arbitrarily set to 5 fluorescence units according to the number of the fluorescein molecules bound to the single streptavidin molecule of compound **6**.

RESULTS

Synthesis. To evaluate substrate properties of m-Nucs, several different compounds were synthesized (synthetic schemes are shown in the Supporting Information Supplement 1, Figure 1). These nucleotide conjugates comprise differences in nucleotide moieties (dUTP or dCTP), composition and size of the macromolecular ligands (streptavidin, streptavidin-(PEG-fluorescein)$_5$, streptavidin-phycoerythrin), and linker size. Since there was a potential for binding of more than one nucleotide moiety to one macromolecular ligand, compounds comprising one or several nucleotide moieties were synthesized.

To synthesize the nucleotides modified with NHS-PEG-biotin (compounds **1** or **2**, Table 2), the strategy of Giller et al. 2003 (*19*) for modification of dUTP-AA and dCTP-PA by Dye-NHS was adopted. We replaced Dye-NHS with a NHS-PEG-biotin derivative. The nucleotide analogues, dUTP-AA and dCTP-PA, contain a side chain at the 5 position of the pyrimidine base, allylamine in dUTP-AA, and propargylamine in dCTP-PA. Each side chain includes a primary amino group, which can be further modified. The coupling of NHS-PEG-biotin to the dUTP-AA and dCTP-PA was performed in an aqueous solution. The course of the reaction was followed by TLC analysis, and the products were subsequently purified by HPLC. TLC and UV-analysis indicated a successful modification of nucleotides (altered R_f and nonaltered UV absorption spectrum). As described for the nucleotide analogues dUTP-AA and dCTP-PA (*19*), the covalent binding of a given NHS-conjugated ligand (e.g., a dye) to the nucleotide occurs only at the primary amino group of the allylamine or propargylamine side chain. Accordingly, we assumed the structure depicted in Figure 1 for the new nucleotide analogues. To the best of our knowledge, this is the first time that coupling of such a long linker to a nucleotide moiety is described.

Streptavidin has four binding sites for biotin and a potential to bind up to four dNTP-PEG-B molecules. To synthesize further derivatives carrying streptavidin or its modifications, compound **1** or **2** or commercially available dUTP-16-biotin was added to solutions containing streptavidin or its modifications, so that a range of compounds could be formed (Table 2).

To account for the possible effects of multiple binding of dNTP-PEG-B or the presence of free biotin binding sites within

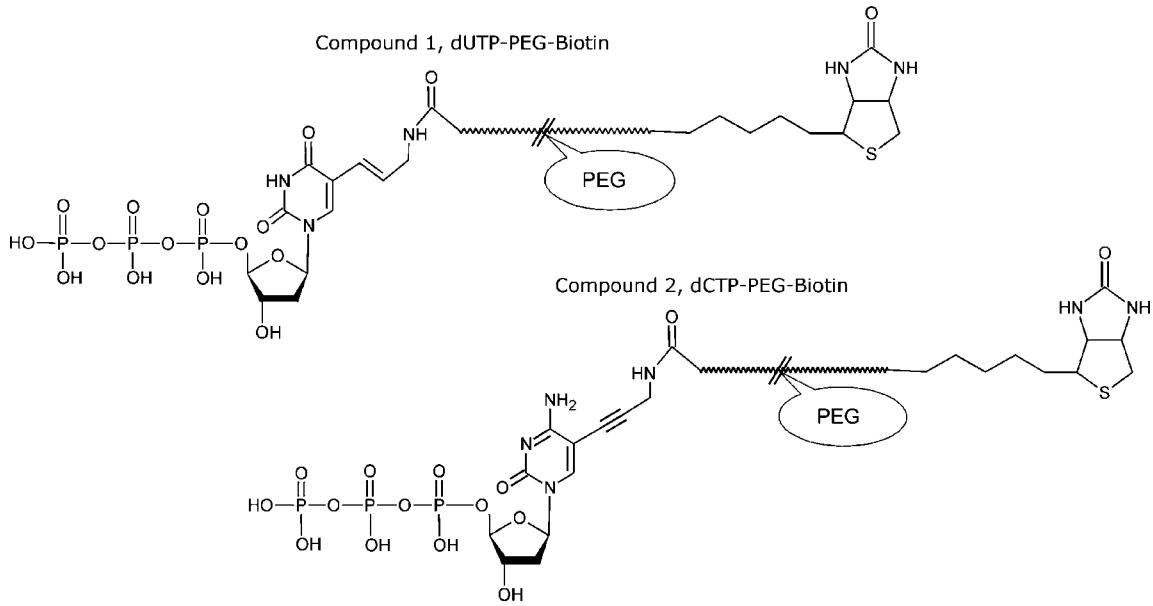


Figure 1. Structure of compounds **1** and **2**.

Table 2. Composition of Synthesized Compounds and Abbreviations[a]

compound no.	name	dNTP/SA ratio	nucleotide moiety	PEG-linker	macromolecular moiety
1	dUTP-PEG-B	-	dUTP	PEG5000	PEG
2	dCTP-PEG-B	-	dCTP	PEG5000	PEG
3	$(dUTP\text{-}PEG\text{-}B)_1$-SA	1:1	dUTP	PEG5000	PEG/SA
4	$(dCTP\text{-}PEG\text{-}B)_1$-SA	1:1	dCTP	PEG5000	PEG/SA
5	$(dUTP\text{-}PEG\text{-}B)_4$-SA	4:1	dUTP	PEG5000	PEG/SA
6	$(dUTP\text{-}PEG\text{-}B)_4$-SA-$(PEG\text{-}Fluor)_5$	4:1	dUTP	PEG5000	PEG/SA-PEG-Fluor
7	$(dUTP\text{-}PEG\text{-}B)_n$-SA-PE	*n*:1	dUTP	PEG5000	PEG/SA-PE
8	$(dUTP\text{-}16\text{-}B)_4$-SA	4:1	dUTP	none	SA

[a] $n = 1, 2, 3$ or 4. Abbreviations: Biotin is indicated as "B", e.g., dUTP-PEG-B is dUTP-PEG-biotin; PEG-fluorescein is indicated as "PEG-Fluor", streptavidin as "SA", poly(ethylene glycol) as "PEG", R-Phycoerythrin as "PE".

one m-Nuc, we synthesized m-Nucs with ratios of 1:1 and 4:1 between dNTP-PEG-B and streptavidin. By setting up the reaction with equimolar amounts of compound **1** (or **2**) and streptavidin, compounds **3** and **4** were synthesized. Approximately 25% of the available biotin binding sites were occupied by dUTP-PEG-B in compound **3** or by dCTP-PEG-B in compound **4**, corresponding to a 1:1 ratio. The 4:1 ratio corresponds to the occupation of all four binding sites of streptavidin by dNTP-PEG-B moieties. To obtain the 4:1 ratio between dNTP-PEG-B and streptavidin (compound **5**), we used saturating amounts of dUTP-PEG-B in the binding reaction.

M-Nucs with and without fluorescent labels were synthesized. Compounds **3**−**5** and compound **8** contained no additional fluorescent dyes and therefore had no fluorescent signal properties in the visible spectrum. They were used in further steps to synthesize fluorescently labeled compound **6**, and in enzymatic reactions to monitor the electrophoretic mobility of the extended nucleic acids or for testing different DNA polymerases. The fluorescently labeled compounds were synthesized in two ways. (1) The low molecular weight dye fluorescein was coupled to the streptavidin moiety of compound **5**, resulting in compound **6**. (2) A streptavidin-R-phycoerythrin conjugate was used in the coupling reaction, resulting in compound **7**. The two ways represent general cases of the synthetic procedures to obtain m-Nucs: first, nonfluorescent m-Nucs are synthesized and thereafter modified by fluorescent dyes or, on the contrary, a large fluorescent structure is first assembled and then coupled to the dNTP moiety.

When we generated the fluorescently labeled m-Nuc compound **6**, we found that direct coupling of fluorescein to streptavidin resulted in a decrease of fluorescence from fluorescein dyes (data not shown). This phenomen can be partially explained by self-quenching effects of fluorescein molecules if placed in close proximity to each other and by the influence of the streptavidin itself (*20*–*22*). Gruber et al. (*20*) circumvented the last phenomenon by introduction of a PEG spacer between fluorescein and streptavidin. Similar to their procedure, we used a commercially available fluorescein derivative containing a PEG spacer, NHS-PEG-fluorescein, to covalently bind fluorescein to compound **5**. After chemical coupling and purification, a quantification of the number of coupled fluorescein molecules per one molecule of compound **6** was conducted using UV−vis spectroscopy. Knowing the amount of compound **5** in the reaction and measuring the absorption at 490 nm of compound **6**, we calculated an average number of about 5 fluorescein molecules per molecule of compound **6**. Excitation and emission spectra of compound **6** are shown in the Supporting Information Supplement 2, Figure 2.

Substrate Properties of dUTP-PEG-B and $(dUTP\text{-}PEG\text{-}B)_1$-SA. DNA polymerase Klenow Fragment (exo-) was tested for its capacity to use the nucleotide analogues. For this purpose, we performed primer extension assays using natural dNTPs (dATP, dCTP), synthesized nucleotide analogues, Klenow fragment (exo-), and fluorescently labeled primer annealed to a template which was immobilized on magnetic beads. Incorporation of the nucleotides occurred in a single round of reactions. According to the template sequence, the order of the incorporation was A, C, T, A, A, and then stopped since dGTP was omitted from the reaction mix. In this series of experiments, dUTP-PEG-B or $(dUTP\text{-}PEG\text{-}B)_1$-SA (compounds **1** and **3**) replaced dTTP. A reaction mix containing $(dUTP\text{-}PEG\text{-}B)_1$-SA but omitting the Klenow fragment (exo-) served as a negative

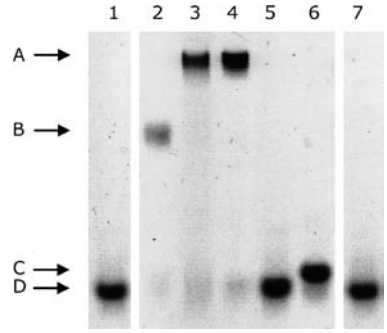


Figure 2. Fluorescent gel image of electrophoretically separated Cy3 labeled primer and extension products. Standard primer extension assays were performed using the Cy3-labeled primer T7−19-Cy3, the template oligo 87, dATP, dCTP, Klenow Fragment (exo-), adding or omitting the following components. Lane 1: with $(dUTP\text{-}PEG\text{-}B)_1$-SA but without Klenow Fragment (exo-). Lane 2: with dUTP-PEG-B. Lane 3: as in lane 2 but strepavidin was added after the reaction and before electrophoresis. Lane 4: with $(dUTP\text{-}PEG\text{-}B)_1$-SA. Lane 5: with $(dUTP\text{-}PEG\text{-}B)_1$-SA but EDTA added to suppress incorporation by the polymerase. Lane 6: with $(dUTP\text{-}PEG\text{-}B)_1$-SA and 50 μM dTTP as a competitor. Lane 7: with $(dUTP\text{-}PEG\text{-}B)_1$-SA but without dCTP, to test misincorporation. A: Extended primer after incorporation of dUTP-PEG-biotin and subsequent binding of exogenous streptavidin (lane 3) or after incorporation of $(dUTP\text{-}PEG\text{-}B)_1$-SA (lane 4). B: Extended primer after incorporation of dUTP-PEG-B in the absence of SA (lane 2). C: Extended primer after incorporation of five unmodified nucleotides ACTAA (lane 6). D: primer T7−19-Cy3 only (lane 1). Abbreviations for nucleotide conjugate structures: Streptavidin (SA), poly(ethylene glycol) (PEG), biotin (B).

control (Figure 2, lane 1). In the presence of polymerase, the primer was extended and dUTP-PEG-B incorporated, seen as a drastic shift in mobility (Figure 2, lane 2). The incorporation of dUTP-PEG-B was verified by incubation of the extended primer with saturating amounts of streptavidin before electrophoresis. This led to a further increase in molecular weight and electrophoretic retardation (Figure 2, lane 3). When $(dUTP\text{-}PEG\text{-}B)_1$-SA (which already contains streptavidin) was used instead of dUTP-PEG-B in the extension assay, the extended primer showed the same mobility in electrophoresis (Figure 2, lane 4). The result demonstrates that $(dUTP\text{-}PEG\text{-}B)_1$-SA was indeed incorporated during the extension assay by Klenow fragment (exo-) DNA polymerase. Three more controls tested the correct enzymatic incorporation of $(dUTP\text{-}PEG\text{-}B)_1$-SA into the growing DNA strand. When EDTA was added to suppress the Mg^{2+}-dependent polymerase activity, no incorporation was detected (Figure 2, lane 5). Incorporation of $(dUTP\text{-}PEG\text{-}B)_1$-SA was outcompeted when dTTP (50 μM final concentration) was added to the extension reaction (Figure 2, lane 6). To test the ability of polymerase to discriminate complementary and noncomplementary base pairing of $(dUTP\text{-}PEG\text{-}B)_1$-SA, the extension reaction was performed with dATP and $(dUTP\text{-}PEG\text{-}B)_1$-SA, but without dCTP and dGTP. In this reaction, for $(dUTP\text{-}PEG\text{-}B)_1$-SA to be incorporated, the polymerase would have to incorporate it opposite the guanosine base, i.e., noncomplementary base, but no incorporation was seen (Figure 2, lane 7).

Two other DNA polymerases, *Taq* and *Vent* (exo -), were also able to use compound **3** in the incorporation reaction (results not shown). In similar assays, compounds dCTP-PEG-B, $(dCTP\text{-}PEG\text{-}B)_1$-SA, and $(dUTP\text{-}PEG\text{-}B)_4$-SA (compounds **2**, **4**, and **5**) were tested and also found to be incorporated into the primer (results not shown). In contrast, $(dUTP\text{-}16\text{-}B)_4$-SA (compound **8**) was not incorporated at all. It contained a short linker between the nucleotide and streptavidin and, therefore, probably was not a suitable substrate for the Klenow fragment (exo-) DNA polymerase in the primer extension assay (Supporting Information Supplement 3, Figure 3, lanes 1 to 3). Two other DNA polymerases, *Taq* and *Vent* (exo-), were also unable to use $(dUTP\text{-}16\text{-}B)_4$-SA in the incorporation reaction (Supporting Information Supplement 3, Figure 3, lanes 4 to 9).

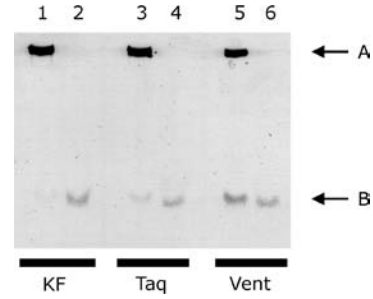


Figure 3. Fluorescent gel image of electrophoretically separated Cy3 labeled primer and extension products with $(dUTP\text{-}PEG\text{-}B)_n$-SA-PE. Standard primer extension assays were performed with Klenow fragment (exo-), "KF", lanes 1 and 2; *Taq* Polymerase "Taq", lanes 3 and 4; and *Vent* (exo-) Polymerase "Vent", lanes 5 and 6. Controls contained EDTA to suppress the incorporation (lanes 2, 4, 6). A: extended primer after incorporation of $(dUTP\text{-}PEG\text{-}B)_n$-SA-PE (lanes 1, 3, and 5). B: primer T7−19-Cy3 (lanes 2, 4, 6). Abbreviations for nucleotide conjugate structures: Streptavidin (SA), poly(ethylene glycol) (PEG), biotin (B), R-Phycoerythrin (PE).

The shift of electrophoretic mobility of strands extended by a single m-Nuc was considerable, compared to those extended by natural nucleotides (Figure 2). Upon incorporation of compound **1**, the mobility of the extended oligonucleotide with the length of only 22 nucleotides corresponded to that of nucleic acid fragments with 100 to 150 nucleotides in length (Supporting Information Supplement 4, Figure 4, lane 2). After incorporation of the even larger compound **3**, the mobility of the extended oligonucleotide corresponded to that of fragments with 500 to 700 nucleotides (Supporting Information Supplement 4, Figure 4, lane 3). The relative mobility of the molecules in the gel is influenced by charge, shape, and size of a molecule. All of them may have caused the mobility shift seen in m-Nuc extended oligonucleotides. Similar changes in mobility are known from the electophoretic mobility shift assays (EMSA) often used in the characterization of protein−nucleic acid interactions (*23*).

Acceptance of m-Nucs with a Size of over 200 kDa. To test the influence of a ligand with an even larger size than that of streptavidin, a commercially available streptavidin-R-phycoerythrin conjugate (SA-PE) was used in the synthesis of a m-Nuc ($(dUTP\text{-}PEG\text{-}B)_n$-SA-PE, compound **7**). Standard primer extension assays were set up with $(dUTP\text{-}PEG\text{-}B)_n$-SA-PE and Klenow fragment (exo-). The control reaction contained EDTA to suppress the Mg^{2+}-dependent polymerase primer extension under exposure to UV illumination, fluorescent signals from Cy3 labeled primer as well as fluorescent signal from PE were used to detect the position of the reaction products. As shown in Figure 3, lane 1, $(dUTP\text{-}PEG\text{-}B)_n$-SA-PE was successfully used as a substrate by Klenow Fragment (exo-) but not incorporated in the presence of EDTA (Figure 3, lane 2). Because $(dUTP\text{-}PEG\text{-}B)_n$-SA-PE has its own strong fluorescence due to PE, the success of its incorporation by the Klenow fragment (exo-) was established by the appearance of a strong fluorescent signal in the top of the gel (lane 1, band A) and disappearance of the signal from the fluorescently labeled primer at the bottom of the gel (compare with lane 2, band B). This means the primer was consumed during the extension reaction.

Acceptance of m-Nucs by Polymerases from Different Families. Because size, shape, and geometry of the polymerase itself, as well as differences in the nucleotide binding sites and enzymatic coupling rate may play a critical role in the acceptance of m-Nucs, two further polymerases, *Taq* polymerase (a member of the DNA polymerase family A), and *Vent* (exo-) polymerase (belonging to DNA polymerase family B) were

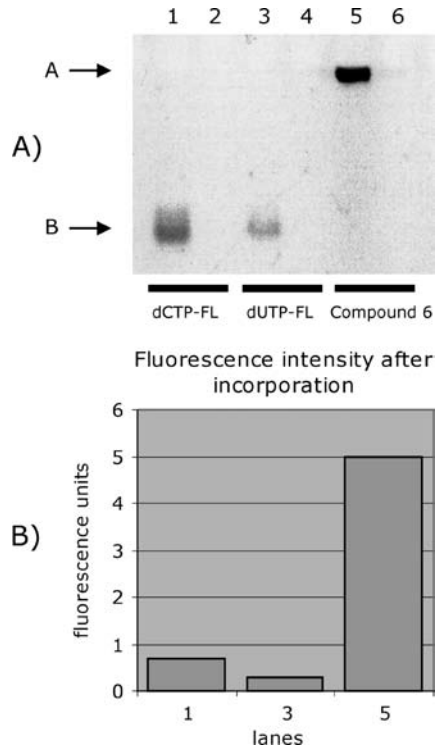


Figure 4. Signal intensities after primer extension with Fluorescein-12-dUTP, Fluorescein-12-dCTP and (dUTP-PEG-B)$_4$-SA-(PEG-Fluor)$_5$. (A) Gel image of electrophoretically separated primers extended by fluorescently labeled nucleotides. Lane 1: Fluorescein-12-dCTP (dCTP-FL). Lane 2: Fluorescein-12-dCTP and EDTA. Lane 3: Fluorescein-12-dUTP (dUTP-FL). Lane 4: Fluorescein-12-dUTP and EDTA. Lane 5: (dUTP-PEG-B)$_4$-SA-(PEG-Fluor)$_5$. Lane 6: (dUTP-PEG-B)$_4$-SA-(PEG-Fluor)$_5$ and EDTA. A: Extended primer after incorporation of (dUTP-PEG-B)$_4$-SA-(PEG-Fluor)$_5$. B: Extended primer after incorporation of Fluorescein-12-dCTP or Fluorescein-12-dUTP. (B) Relative fluorescence intensities of primer extension products from lanes 1, 3, and 5 in (A). Abbreviations for nucleotide conjugate structures: Streptavidin (SA), poly(ethylene glycol) (PEG), biotin (B), R-Phycoerythrin (PE), PEG-fluorescein (PEG-Fluor).

tested for their ability to use (dUTP-PEG-B)$_n$-SA-PE (compound **7**), the largest of all m-Nucs synthesized in this study.

Standard primer extension assays were set up as described above. While most protocols recommend a temperature regime around 60−70 °C for optimal extension reaction by thermostable polymerases, it is known that *Taq* polymerase is active also at 37 °C (*24*). (dUTP-PEG-B)$_n$-SA-PE contained protein (SA and PE). To avoid possible denaturation effects at elevated temperatures around 70 °C, the reactions were performed at 37 °C as for Klenow fragment (exo-). As a control for enzymatic incorporation, parallel reactions were set up with EDTA as described above. Both types of polymerases accepted (dUTP-PEG-B)$_n$-SA-PE as a substrate, as shown by the bright fluorescent bands at the top of the gel (Figure 3, lanes 3 and 5). The incorporation of (dUTP-PEG-B)$_n$-SA-PE was suppressed by EDTA (Figure 3, lanes 4 and 6). The extent of primer consumption, however, differed between *Taq* and *Vent* (exo-) polymerases. While almost all primer was used up in the reaction with *Taq*, a fraction of the primer had not been extended in the reaction with *Vent* (exo-). The difference may by explained by a lower activity of *Vent* (exo-) polymerase at lower temperatures. We have not yet investigated this effect further.

Comparison of Signal Intensities. To compare signal intensities of the new nucleotides with conventional fluorescein modified nucleotides, primer extension reactions were conducted with m-Nuc (dUTP-PEG-B)$_4$-SA-(PEG-Fluorescein)$_5$ (compound **6**), which had been labeled with fluorescein, and compared to extension reactions with commercially available Fluorescein-12-dUTP or Fluorescein-12-dCTP. The primer extension reactions were set up similarly to those described before with the exceptions that the primer used in these experiments was not labeled and specific combinations of nucleotides were used. The reaction mixes contained dATP and Fluorescein-12-dCTP (Figure 4A, lanes 1 and 2), dATP, dCTP, and Fluorescein-12-dUTP (Figure 4A, lanes 3 and 4), or dATP, dCTP, and (dUTP-PEG-B)$_4$-SA-(PEG-Fluorescein)$_5$ (Figure 4A, lanes 5 and 6). No fluorescent signal was observed in lanes with reactions containing EDTA (Figure 4A, lanes 2, 4, and 6), used as control to suppress enzymatic reaction. This means that wash steps were effective and no unspecific co-isolation of the fluorescently labeled nucleotides with magnetic beads occurred. As can be seen in Figure 4A, (dUTP-PEG-B)$_4$-SA-(PEG-Fluorescein)$_5$, as well as the commercially available fluorescently labeled nucleotides, was incorporated into the growing strand of DNA by the Klenow fragment (exo-). Due to the large size of the (dUTP-PEG-B)$_4$-SA-(PEG-Fluorescein)$_5$, the position of the fluorescent band was shifted toward the top of the gel (Figure 4A, lane 5) compared to the position of bands with the low molecular weight nucleotide analogues (Figure 4A, lanes 1 and 3).

Since, according to the template sequence, only one fluorescently labeled nucleotide was incorporated in each growing DNA strand in the three primer extension reactions, the fluorescent signals were comparable. The signal intensity generated by incorporation of (dUTP-PEG-B)$_4$-SA-(PEG-Fluorescein)$_5$ (Figure 4B, lane 5) was about 7-fold stronger than the signal from Fluorescein-12-dCTP (Figure 4B, lane 1) and 15-fold stronger compared to the Fluorescein-12-dUTP signal (Figure 4B, lane 3). Besides this, we detected a difference in signal intensity between the two conventionally labeled nucleotides (Fluorescein-12-dCTP, lane 1, and Fluorescein-12-dUTP, lane 3) in this particular setting. Although we did not investigate this difference in detail, the signal heterogeneity between commercial dCTP and dUTP analogues may be explained by the remarkable sensitivity of fluorescein to the DNA microenvironment, particulary to the DNA sequence content (*25, 26*).

DISCUSSION

The aim of this study was the synthesis and applicability testing of a novel kind of modified nucleotide which were labeled with several fluorescent dyes molecules per nucleotide. We describe here the design of such nucleotides and call them m-Nucs (for macromolecular nucleotides). The general structure comprises one or several nucleotide moieties, a large, macromolecular ligand labeled with dyes, and a macromolecular linear linker, which connects each nucleotide moiety with the macromolecular ligand. Using this new class of modified nucleotides in enzymatic incorporation reactions, signals from multiple dye molecules are obtained when only one nucleotide molecule is incorporated, thus considerably enhancing the signal strength of this nucleotide.

For the construction of such nucleotides, several general aspects have to be taken into consideration. First, the individual dye molecules have to have sufficient distance from each other in order to achieve a strong fluorescent signal from each of them. To this end, dyes should be coupled to a larger structure, e.g., a polymer. In this study, streptavidin (SA) was used as a polymer and the dyes were coupled to its reactive surface groups via a PEG-linker. A second aspect refers to the fact that the large structure may impede the incorporation of nucleotides coupled to such macromolecular ligands. The solution found to overcome this limitation was a long hydrophilic linker, in this study, PEG, to separate the nucleotide moiety from the bulky streptavidin molecule. As a third aspect, the positioning of the linker on the

nucleotide itself is an important factor affecting the function of the nucleotide. Here, we used the 5-position of pyrimidines as acceptor sites for the linker, because its modifications are known to be tolerated by DNA polymerases (*27, 28*). Therefore, the pyrimidines 5-Allylamino-dUTP and 5-Propargylamino-dCTP were used by us as starting compounds to couple the PEG-linker to the nucleotide moiety.

Once the m-Nucs were generated, their functionality had to be tested. Specifically, it had to be proven that coupling to a large molecule did not interfere with the substrate properties of the nucleotides during an incorporation reaction. Using dUTP-PEG-B for a test, we showed that the modified nucleotides preserved their ability to be incorporated into the growing strand by the polymerases. This finding encouraged us to test whether a further modification, namely, coupling of either streptavidin modified by dyes or another even larger ligand like PE, would still result in conservation of substrate properties. In this paper, we demonstrate that this is indeed the case: the nucleotide moiety coupled to a macromolecular ligand via a long hydrophilic linker preserves its substrate properties. It can be incorporated into the growing nucleic acid chain by a number of DNA polymerases in a template-dependent manner. Therefore, such m-Nucs can be used in primer extension reactions.

The ability to be incorporated proves that the nucleotide moiety preserves its accessibility to the nucleotide binding center of the polymerase. Usually, PEG-linkers influence the interaction of two compounds, providing a shielding effect that decreases the binding strength of a potential partner. Apparently, in the situation discussed here, PEG does not shield the nucleotide moiety, at least not completely, and allows an interaction between nucleotide and polymerase. Further, PEG apparently leaves sufficient mobility for the nucleotide moiety in the solution, thus preserving the substrate properties of a low molecular weight ligand. In contrast, a simple combination of a nucleotide carrying a convential short linker, dUTP-16-Biotin, with streptavidin led to an inhibition of incorporation of the nucleotide into the growing strand (Supporting Information, Supplement 3, Figure 3). We attribute this effect to steric hindrance by the large streptavidin molecule, brought about by the close proximity to the nucleotide moiety (linker length of only 16 atoms). This apparently repelled the polymerase and inhibited the polymerase−nucleotide interaction.

The use of m-Nucs with a long linker and an increased number of dye molecules instead of conventionally labeled nucleotides with only short linker and one dye molecule offers several advantages. First, according to theoretical assumptions, the cumulative strength of fluorescent signal from m-Nuc should increase. This is supported by our findings that m-Nucs carrying multiple dye molecules indeed created increased fluorescent signal when compared to those from conventional fluorescently labeled nucleotides (see Figure 4). Second, because each fluorophore bound to m-Nuc can emit light independently from the others bound to the same m-Nuc, the effect of disturbing events such as blinking and bleaching, which lead to reduced visibility of a given dye molecule, should be minimized. Third, the long linker itself plays an important role by separating the fluorophores from the DNA strand. This feature is interesting because not only the pecularities of a single fluorophore introduce uncertanties in signal detection as discussed in the introduction, but also local DNA sequence content may have a strong influence on signal intensity of fluorophores. Several studies have analyzed those effects on commonly used fluorescent dyes like fluorescein, Cy3, and rhodamines, conjugated to the oligonucleotides via short linkers (*25, 26, 29–34*). Particularly, fluorescein is known to be sensitive to the local DNA sequence content (*25, 26*). We chose fluoresein as a fluorophore to label m-Nucs, in order to challenge the structure of m-Nucs for such potentially detrimental effects. Indeed, there was a difference in fluorescent signal intensity even between incorporated commercial nucleotide analogues. The difference may be explained by quenching of fluorescence caused by DNA (see Figure 4). On the other hand, the fluorescence intensity of compound **6** exceeded the fluorescence of fluorescein modified dCTP and dUTP by more than five times, i.e., by a factor larger than a simple addition of fluorescence intensities of individual dyes would have predicted. We attribute this effect to the structure of m-Nucs. Apart from the number of dye molecules (e.g., in compound **6**), the larger distance between the fluorophores in an incorporated m-Nuc and the nucleic acid strand may have contributed to the increase of fluorescence intensity. When placed in close proximity of a fluorochrome, guanosine bases are supposed to have a quenching effect on some commonly used fluorochromes (*25, 33*). Altogether, effects of the nucleic acid bases on the dye molecules of a particular incorporated m-Nuc may be minimized due to introduction of a long linker between the nucleotide moiety and the dyes, thus leading to a more uniform fluorescence and its independence from the sequence content.

As pointed out in the Introduction, limitations in signal detection are one of the obstacles in the field of nanobiotechnology, especially in the field of DNA analysis on the single molecule level. We believe that m-Nucs may reveal a new perspective in this field. Until now, only a limited numbers of fluorophores, such as Rhodamine 6G, TAMRA, Cy3, Cy5, and several Alexa-dyes or Atto-dyes had sufficiently high quantum yields and stability for analyzing single fluorescent molecules in biological applications (*2, 3, 6–8, 35*). Because, within a m-Nuc, a large number of dyes can be coupled to the nucleotide, one can now use a larger variety of dyes of different nature and spectral properties.

One particular application which may be considerably influenced by our novel m-Nucs, is single molecule nucleic acid sequencing. Here, the current technology deals with considerable limitations in part due to the use of conventionally labeled nucleotide structures including sequencing errors in the range 5−20% (*17, 18*). We anticipate that this error rate can be considerably decreased by the use of m-Nucs. Different additional requirements need to be met to use the m-Nucs for the sequencing at the single molecule level. In particular, it is desirable to have m-Nucs capable of supporting reversible termination for the sequencing by synthesis scheme and m-Nucs labeled with different fluorophores, e.g., with four different dyes corresponding to each nucleic base. To meet these requirements, we are presently adopting m-Nucs for reversible termination and sequencing reaction of nucleic acid strands (Cherkasov et al. manuscript in preparation).

ACKNOWLEDGMENT

We thank Genovoxx GmbH for financial support and would like to thank the staff of Genovoxx GmbH for constructive discussions. We would also like to thank the reviewers of the manuscript for helpful criticism.

Supporting Information Available: Additional related figures. This material is available free of charge via the Internet at http://pubs.acs.org.

LITERATURE CITED

(1) Ha, T. (2001) Single-molecule fluorescence methods for the study of nucleic acids. *Curr. Opin. Struct. Biol. 11*, 287–92.
(2) Joo, C., Balci, H., Ishitsuka, Y., Buranachai, C., and Ha, T. (2008) Advances in single-molecule fluorescence methods for molecular biology. *Annu. Rev. Biochem. 77*, 51–76.

(3) Roy, R., Hohng, S., and Ha, T. (2008) A practical guide to single-molecule FRET. *Nat. Methods 5*, 507–16.
(4) Shi, J., Dertouzos, J., Gafni, A., and Steel, D. (2008) Application of single-molecule spectroscopy in studying enzyme kinetics and mechanism. *Methods Enzymol. 450*, 129–57.
(5) Walter, N. G., Huang, C. Y., Manzo, A. J., and Sobhy, M. A. (2008) Do-it-yourself guide: how to use the modern single-molecule toolkit. *Nat. Methods 5*, 475–89.
(6) Weiss, S. (1999) Fluorescence spectroscopy of single biomolecules. *Science 283*, 1676–83.
(7) Gensch, T., Bohmer, M., and Aramendia, P. F. (2005) Single molecule blinking and photobleaching separated by wide-field fluorescence microscopy. *J. Phys. Chem. A 109*, 6652–8.
(8) Sabanayagam, C. R., Eid, J. S., and Meller, A. (2005) Long time scale blinking kinetics of cyanine fluorophores conjugated to DNA and its effect on Forster resonance energy transfer. *J. Chem. Phys. 123*, 224708.
(9) Gupta, P. K. (2008) Single-molecule DNA sequencing technologies for future genomics research. *Trends Biotechnol. 26*, 602–11.
(10) Marguerat, S., Wilhelm, B. T., and Bahler, J. (2008) Next-generation sequencing: applications beyond genomes. *Biochem. Soc. Trans. 36*, 1091–6.
(11) Pettersson, E., Lundeberg, J., and Ahmadian, A. (2009) Generations of sequencing technologies. *Genomics 93*, 105–11.
(12) Shendure, J., and Ji, H. (2008) Next-generation DNA sequencing. *Nat. Biotechnol. 26*, 1135–45.
(13) Shendure, J. A., Porreca, G. J., and Church, G. M. (2008) Overview of DNA sequencing strategies. In *Current Protocols in Molecular Biology*; Chapter7, Unit 7 1, John Wiley & Sons, New York, NY.
(14) Braslavsky, I., Hebert, B., Kartalov, E., and Quake, S. R. (2003) Sequence information can be obtained from single DNA molecules. *Proc. Natl. Acad. Sci. U.S.A. 100*, 3960–4.
(15) Krieg, A., Ruckstuhl, T., and Seeger, S. (2006) Towards single-molecule DNA sequencing: assays with low nonspecific adsorption. *Anal. Biochem. 349*, 181–5.
(16) Sauer, M., Angerer, B., Ankenbauer, W., Foldes-Papp, Z., Gobel, F., Han, K. T., Rigler, R., Schulz, A., Wolfrum, J., and Zander, C. (2001) Single molecule DNA sequencing in submicrometer channels: state of the art and future prospects. *J. Biotechnol. 86*, 181–201.
(17) Eid, J., Fehr, A., Gray, J., Luong, K., Lyle, J., Otto, G., Peluso, P., Rank, D., Baybayan, P., Bettman, B., Bibillo, A., Bjornson, K., Chaudhuri, B., Christians, F., Cicero, R., Clark, S., Dalal, R., Dewinter, A., Dixon, J., Foquet, M., Gaertner, A., Hardenbol, P., Heiner, C., Hester, K., Holden, D., Kearns, G., Kong, X., Kuse, R., Lacroix, Y., Lin, S., Lundquist, P., Ma, C., Marks, P., Maxham, M., Murphy, D., Park, I., Pham, T., Phillips, M., Roy, J., Sebra, R., Shen, G., Sorenson, J., Tomaney, A., Travers, K., Trulson, M., Vieceli, J., Wegener, J., Wu, D., Yang, A., Zaccarin, D., Zhao, P., Zhong, F., Korlach, J., and Turner, S. (2009) Real-time DNA sequencing from single polymerase molecules. *Science 323*, 133–8.
(18) Harris, T. D., Buzby, P. R., Babcock, H., Beer, E., Bowers, J., Braslavsky, I., Causey, M., Colonell, J., Dimeo, J., Efcavitch, J. W., Giladi, E., Gill, J., Healy, J., Jarosz, M., Lapen, D., Moulton, K., Quake, S. R., Steinmann, K., Thayer, E., Tyurina, A., Ward, R., Weiss, H., and Xie, Z. (2008) Single-molecule DNA sequencing of a viral genome. *Science 320*, 106–9.
(19) Giller, G., Tasara, T., Angerer, B., Muhlegger, K., Amacker, M., and Winter, H. (2003) Incorporation of reporter molecule-labeled nucleotides by DNA polymerases. I. Chemical synthesis of various reporter group-labeled 2′-deoxyribonucleoside-5′-triphosphates. *Nucleic Acids Res. 31*, 2630–5.
(20) Gruber, H. J., Marek, M., Schindler, H., and Kaiser, K. (1997) Biotin-fluorophore conjugates with poly(ethylene glycol) spacers retain intense fluorescence after binding to avidin and streptavidin. *Bioconjugate Chem. 8*, 552–9.
(21) Lakowicz, J. R., Malicka, J., Huang, J., Gryczynski, Z., and Gryczynski, I. (2004) Ultrabright fluorescein-labeled antibodies near silver metallic surfaces. *Biopolymers 74*, 467–75.
(22) Marme, N., Knemeyer, J. P., Sauer, M., and Wolfrum, J. (2003) Inter- and intramolecular fluorescence quenching of organic dyes by tryptophan. *Bioconjugate Chem. 14*, 1133–9.
(23) Hellman, L. M., and Fried, M. G. (2007) Electrophoretic mobility shift assay (EMSA) for detecting protein-nucleic acid interactions. *Nat. Protoc. 2*, 1849–61.
(24) Kermekchiev, M. B., Tzekov, A., and Barnes, W. M. (2003) Cold-sensitive mutants of Taq DNA polymerase provide a hot start for PCR. *Nucleic Acids Res. 31*, 6139–47.
(25) Nazarenko, I., Pires, R., Lowe, B., Obaidy, M., and Rashtchian, A. (2002) Effect of primary and secondary structure of oligodeoxyribonucleotides on the fluorescent properties of conjugated dyes. *Nucleic Acids Res. 30*, 2089–195.
(26) Sjoback, R., Nygren, J., and Kubista, M. (1998) Characterization of fluorescein-oligonucleotide conjugates and measurement of local electrostatic potential. *Biopolymers 46*, 445–53.
(27) Held, H. A., and Benner, S. A. (2002) Challenging artificial genetic systems: thymidine analogs with 5-position sulfur functionality. *Nucleic Acids Res. 30*, 3857–69.
(28) Roychowdhury, A., Illangkoon, H., Hendrickson, C. L., and Benner, S. A. (2004) 2′-deoxycytidines carrying amino and thiol functionality: synthesis and incorporation by Vent (exo-) polymerase. *Org. Lett. 6*, 489–92.
(29) Cuppoletti, A., Cho, Y., Park, J. S., Strassler, C., and Kool, E. T. (2005) Oligomeric fluorescent labels for DNA. *Bioconjugate Chem. 16*, 528–34.
(30) Kurata, S., Kanagawa, T., Yamada, K., Torimura, M., Yokomaku, T., Kamagata, Y., and Kurane, R. (2001) Fluorescent quenching-based quantitative detection of specific DNA/RNA using a BODIPY((R)) FL-labeled probe or primer. *Nucleic Acids Res. 29*, E34.
(31) Neubauer, H., Gaiko, N., Berger, S., Schaffer, J., Eggeling, C., Tuma, J., Verdier, L., Seidel, C. A., Griesinger, C., and Volkmer, A. (2007) Orientational and dynamical heterogeneity of rhodamine 6G terminally attached to a DNA helix revealed by NMR and single-molecule fluorescence spectroscopy. *J. Am. Chem. Soc. 129*, 12746–55.
(32) Sanborn, M. E., Connolly, B. K., Gurunathan, K., and Levitus, M. (2007) Fluorescence properties and photophysics of the sulfoindocyanine Cy3 linked covalently to DNA. *J. Phys. Chem. B 111*, 11064–74.
(33) Torimura, M., Kurata, S., Yamada, K., Yokomaku, T., Kamagata, Y., Kanagawa, T., and Kurane, R. (2001) Fluorescence-quenching phenomenon by photoinduced electron transfer between a fluorescent dye and a nucleotide base. *Anal. Sci. 17*, 155–60.
(34) Vamosi, G., Gohlke, C., and Clegg, R. M. (1996) Fluorescence characteristics of 5-carboxytetramethylrhodamine linked covalently to the 5′ end of oligonucleotides: multiple conformers of single-stranded and double-stranded dye-DNA complexes. *Biophys. J. 71*, 972–94.
(35) Luong, A. K., Gradinaru, C. C., Chandler, D. W., and Hayden, C. C. (2005) Simultaneous time- and wavelength-resolved fluorescence microscopy of single molecules. *J. Phys. Chem. B 109*, 15691–8.

BC900364F

Genetically Engineered Clostridial C2 Toxin as a Novel Delivery System for Living Mammalian Cells

Jörg Fahrer,[†] Rainer Plunien,[†] Ulrike Binder,[†] Torben Langer,[†] Hartmut Seliger,[‡] and Holger Barth*[,†]

Institute of Pharmacology and Toxicology, University of Ulm Medical Center, Albert-Einstein-Allee 11, and Research Group on Chemical Functions in Biosystems, University of Ulm, Albert-Einstein-Allee 47, D-89081 Ulm, Germany. Received August 17, 2009; Revised Manuscript Received November 30, 2009

The C2 toxin of *Clostridium botulinum* is a binary bacterial protein toxin, comprising the enzyme component C2I and the separate binding/translocation component C2IIa. C2IIa mediates the transport of C2I into the host cell cytosol. The N-terminal domain of C2I (C2IN) is enzymatically inactive but essential for C2IIa-mediated internalization of C2I. Here, we exploit the C2IIa/C2IN system to generate a recombinant C2IN−streptavidin fusion protein allowing for the delivery of biotinylated molecules into the cytosol of mammalian cells. C2IN−streptavidin overproduced in *E. coli was* affinity-purified and capable of binding biotinylated proteins in a concentration-dependent manner. Real-time surface plasmon resonance confirmed the biotin-mediated interaction yielding a K_D-value of ~0.75 μM. Internalization of C2IN−streptavidin into the cytosol of epithelial cells and macrophages was demonstrated by immunoblot analysis and confirmed by confocal microscopy. Cell viability studies showed no cytotoxic effects of the novel transporter. Furthermore, Vero cells treated with biotin−fluorescein or biocytin−Alexa488 as model cargo displayed a specific C2IN−streptavidin/C2IIa-dependent uptake, providing proof-of-principle for the functionality of this novel delivery system.

INTRODUCTION

C2 toxin produced by *C. botulinum* is the archetype of binary actin-ADP-ribosylating toxins, comprising the two nonlinked proteins C2I and C2II (*1*). The enzyme component C2I harbors ADP−ribosyltransferase activity, whereas C2II represents the binding/translocation moiety. C2II is converted by proteolytic cleavage into its biologically active form C2IIa (*2*), which directs the uptake of C2I into the host cell cytosol. C2IIa forms ring-shaped heptamers, also referred to as prepores, and binds to complex carbohydrate receptors on the cell surface of eukaryotic cells (*3, 4*). Subsequently, cell-surface bound C2IIa serves as a docking platform for C2I, allowing toxin assembly on the cell surface, which in turn triggers receptor-mediated endocytosis (*5*). Acidification of early endosomes results in a structural change of C2IIa heptamers to the so-called pore conformation, triggering their insertion into the endosomal membrane and subsequent pore formation (*6*). Translocation of C2I through this pore is driven by a pH gradient between the cytosol and the endosomal lumen. This process is facilitated by the host cell factors Hsp90 and cyclophilin A, as recently demonstrated (*7, 8*). In the cytosol, C2I catalyzes the covalent modification of actin with ADP-ribose, inducing the depolymerization of the actin cytoskeleton (*9*).

The N-terminal domain of C2I (C2IN) is enzymatically inactive but essential for C2IIa-mediated internalization of C2I (*10*). The adaptor domain C2IN has been successfully used for the cellular import of various proteins, such as the virulence factor SpvB from *S. enterica* (*11*) or dihydrofolate reductase (*12*). Furthermore, C2IN has been genetically fused to bacterial C3 ADP-ribosyltransferases, which are selective inhibitors of Rho GTPases. This allowed the delivery of C3 proteins into numerous eukaryotic cell lines to study Rho-mediated signaling and turned out to be a powerful pharmacological tool (*10, 13*).

Streptavidin, produced by *Streptomyces avidinii*, is a tetrameric protein which exhibits an extraordinary affinity for biotin ($K_D = 10^{-15}$ M) (*14*). In addition, streptavidin is an exceptionally stable protein, showing a high resistance against heat, denaturants, or extreme pH values. Owing to these properties, it has been used in a wide range of applications including life sciences, (nano-) medicine, and drug delivery (*15*−*17*). Streptavidin and its chicken homologue avidin have recently been used as cellular delivery systems in conjunction with molecular Trojan horses. These systems comprise monoclonal antibodies directed against cell-surface receptors, such as the transferrin receptor, that induce receptor-mediated endocytosis, thus enabling the passage through biological membranes (*18, 19*). In this approach, avidin or streptavidin are either genetically fused to the respective monoclonal antibody or covalently linked by chemical means. Previously, a bioconjugate consisting of streptavidin and an antibody to the human insulin receptor was applied for the intracellular delivery of radiopharmaceuticals in vivo (*20*). Streptavidin was also fused to the cell-penetrating peptide TAT and demonstrated to promote the internalization of a biotinylated cargo into mammalian cells (*21, 22*). Moreover, an antitransferrin receptor−avidin fusion protein was used to deliver biotinylated molecules in myeloma and T cell lymphoma cells (*23*). Recently, streptavidin mutants have been generated allowing for a reversible biotin binding due to a decreased affinity. Sano and co-workers described the construction of a dimeric streptavidin, which is capable of biotin binding, however, with reduced affinity ($K_D = 1.5 \times 10^{-7}$ M) (*24*).

In the present study, we exploit the transport mechanism of the clostridial C2 toxin in conjunction with dimeric streptavidin allowing for the delivery of exogenous biotinylated molecules into mammalian cells. We report the generation, functional characterization, and application of a chimeric C2IN−streptavidin fusion protein. Notably, C2IN−streptavidin applied in combina-

* Corresponding author. Dr. Holger Barth, Institute of Pharmacology and Toxicology, University of Ulm Medical Center, Albert-Einstein-Allee 11, D-89081 Ulm, Germany, Tel.: +49-731-50065503; Fax: +49-731-50065502; E-mail: holger.barth@uni-ulm.de.

[†] University of Ulm Medical Center.

[‡] University of Ulm.

10.1021/bc900365b © 2010 American Chemical Society
Published on Web 12/23/2009

tion with the binding/translocation component C2IIa was detected in the cytosol of various tested mammalian cell types, emphasizing its versatility as a delivery system. We provide proof-of-principle for this novel transport system using biotin−fluorescein or biocytin−Alexa488 as cargo.

EXPERIMENTAL PROCEDURES

Cloning of C2IN−Streptavidin. Plasmid pGEX2T-C2I (*10*), harboring a GST-tagged version of C2I, was digested with *Bam*HI to remove the C-terminal part of C2I and religated yielding pGEX2T-C2IN. Streptavidin cDNA was amplified by PCR from plasmid TSA43 (*24*) using the primers StrepI (5′-GAATTCAGATCTGGCATCACCGGCACC-3′) and StrepII (5′-GAATTCGGATCC CTACACCTTGGTGAA-3′) to introduce a *Bgl*II and a *Bam*HI site, respectively. The PCR product was ligated in the pCR-Blunt vector using the Zero Blunt PCR cloning kit (Invitrogen, Karlsruhe, Germany) and transformed in competent *E. coli* DH5α cells. Isolated pCR−streptavidin was then digested with *Bgl*II and *Bam*HI, ligated with *Bam*HI-digested pGEX2T-C2IN, and transformed in competent *E. coli* cells. Subsequently, the C2IN−streptavidin construct was sequenced with the pGEX2T 5′- and 3′-sequencing primers. In addition, the C2IN−streptavidin boundary was analyzed with the sequencing primers 5′-SeqI (5′-TTAGATAGGGATGC-TATAGGC-3′) corresponding to position 280−300 and 3′-SeqII (5′-GTCACGATGAAGGTCGAGCC-3′) mapping to position 709−728 of the C2IN−streptavidin construct.

Expression and Purification of Recombinant Fusion Protein. C2IN was overproduced in *E. coli* BL21 and purified as described previously (*10*). C2IN−streptavidin was overexpressed as GST-tagged fusion protein in *E. coli* BL21 and isolated by affinity chromatography. Briefly, *E. coli* BL21 transformed with pGEX2T-C2IN-streptavidin was grown at 37 °C in Luria−Bertani (LB) medium supplemented with 100 μg/mL ampicillin to an optical density of 0.6−0.8. To induce protein expression, isopropyl-β-D-thiogalactopyranoside (IPTG) was added to a final concentration of 0.2 mM, and cultures were incubated at 29 °C for 6 h. Bacteria were harvested by centrifugation for 10 min at 4 °C at 4400 *g*, resuspended in buffer containing 0.1% Triton X-100, and disrupted by sonication. Cellular debris was sedimented for 15 min at 4 °C at 20 000 *g*, and the clear supernatant was incubated with glutathione−agarose beads (Macherey-Nagel, Düren, Germany) for 2 h at room temperature. After centrifugation for 5 min at 1000 *g*, the beads were washed 2 times with lysis buffer and 2 times with PBS pH 7.4. To remove the GST-tag, the immobilized protein was incubated with thrombin (15 NIH units/L culture) for 1 h at room temperature, and supernatant containing C2IN−streptavidin was obtained by centrifugation at 10 000 *g* for 1 min. To eliminate thrombin, the supernatant was further incubated with benzamidine beads (GE Healthcare, München, Germany) for 10 min and collected. Isolated C2IN−streptavidin was analyzed for homogeneity by SDS-PAGE followed by Coomassie staining. Protein identity was confirmed by Western blot analysis with an anti-streptavidin antibody (Abcam, Cambridge, UK) and an anti-C2IN antibody raised in rabbits (*25*), respectively.

To monitor the time-dependent expression of C2IN−streptavidin, 300 μL aliquots of the suspension culture were collected and analyzed by SDS-PAGE and Coomassie staining. In addition, the GST-tagged protein was detected on a nitrocellulose membrane using an anti-GST antibody (BD Biosciences, Heidelberg, Germany).

SDS-PAGE and Immunoblot Analysis. Proteins were separated by SDS-PAGE on 12.5% gels according to the method of Laemmli (*26*). For immunoblot analysis, the proteins were transferred onto a nitrocellulose membrane (Whatman, Dassel, Germany) by electroblotting using a semidry system (PeqLab, Erlangen, Germany) or alternatively with a wet-blot chamber (GE Healthcare, München, Germany). The membranes were blocked for 1 h at room temperature with 5% nonfat dry milk in PBS containing 0.1% Tween 20 (PBS-T) followed by 1 h incubation with the respective antibodies in blocking solution. After washing the membranes with PBS-T, the blots were probed with the appropriate secondary antibodies coupled to horseradish peroxidase (1:2000), and proteins were detected by enhanced chemiluminescence.

Overlay Blot Assay. Biotinylation of proteins was carried out using the EZ-Link Micro Sulfo-NHS-Biotinylation Kit (Pierce, Bonn, Germany). To assess the biotin-binding properties of the generated fusion protein, increasing amounts of C2IN−streptavidin as well as the negative control C2IN (each protein 1−50 pmol) were subjected to SDS-PAGE. After separation, the proteins were transferred on a nitrocellulose membrane by wet blotting and the membrane was blocked. Subsequently, the membrane was incubated with biotinylated BSA in PBS-T (5 μg/mL) or biotinylated C3bot (1 μg/mL). To disrupt unspecific binding, the membrane was washed with PBS-T containing 500 mM NaCl followed by three washing steps in PBS-T. Bound biotin-labeled BSA or C3bot were detected with streptavidin-POD (Roche, Mannheim, Germany) diluted 1:2000 in PBS-T.

Surface Plasmon Resonance. All SPR experiments were performed with a Biacore 2000 system equipped with a CM5 sensor chip (GE Healthcare). C2IN−streptavidin in sodium acetate buffer (pH 4.5) was immobilized onto a CM5 sensor chip using the amine coupling procedure to obtain a final response level about 2500 RU. An activated reference cell without immobilized ligand was used to subtract buffer refractive effects and as a control for unspecific binding. The following concentrations of biotin-labeled C3bot protein from *Clostridium botulinum* were injected at room temperature: 750 nM, 1 μM, 2.5 μM, 5 μM, 7.5 μM, 10 μM. Flow rate was set to 30 μL/min with the following parameters: 130 s contact time, 1800 s dissociation time. Dissociation was carried out in HBS buffer pH 7.4 without a regeneration step. Baseline levels were stable throughout all cycles. Data evaluation was carried out using *BIAevaluation* software v 3.2.

Cell Culture and Cytotoxicity Assays. HeLa and Vero cells were cultured at 37 °C and 5% CO_2 in Minimum essential medium (MEM), and CHO cells were maintained in a 1:1 mixture of Ham's F12/ Dulbecco's modified Eagle medium (DMEM), containing 10% heat-inactivated fetal calf serum (FCS), L-glutamate (2 mM), 100 U/mL penicillin, and 100 μg/mL streptomycin. Cells were routinely trypsinized and reseeded three times per week. J774A.1 cells (a kind gift of Dr. Singh Chhatwal, Braunschweig, Germany) were cultured at 37 °C and 5% CO_2 in DMEM, containing 10% heat-inactivated FCS, L-glutamate (4 mM), penicillin (100 U/mL), and streptomycin (100 μg/mL). Cells were routinely scraped off and reseeded three times per week.

Cell viability was determined by trypan blue exclusion. Briefly, Vero cells were seeded in a 12 well plate (4×10^4 cells/well) and grown overnight. Subsequently, varying concentrations of C2IN−streptavidin and C2IIa were added in serum-free medium. As a positive control, cells were exposed to 1 μM staurosporine. After 2 h, the medium was removed and the cells were incubated for another 3 h with MEM supplemented with FCS. Thereafter, cells were collected by trypsination and mixed 1:1 with 0.4% trypan blue solution. Viable and nonviable (i.e., blue) cells were counted with a hemocytometer permitting the calculation of the cell viability. In addition, cell proliferation was assessed over a period of 48 h using the Cell Titer 96 Aqueous nonradioactive cell proliferation

assay (Promega, Mannheim, Germany). Briefly, Vero cells were seeded in 96 well plates at a density of 5×10^3 cells per well. The next day, cells were incubated with different combinations of C2IN−streptavidin and C2IIa, as well as 0.5 μM staurosporine as a positive control. Cell viability was determined after 5, 24, and 48 h, respectively, by measuring absorbance at 490 nm in an ELISA reader.

Cell Fractionation by Digitonin Treatment. To obtain the cytosolic fraction of cultured Vero cells, digitonin-based cell fractionation was performed according to the method described by Sørensen and co-workers (*27*).Vero cells grown in 12 well plates were preincubated at 37 °C in serum-free medium for 30 min. Subsequently, a combination of C2IN−streptavidin (2 μg/mL) and C2IIa (4 μg/mL) was added to the medium and cells were incubated for up to 4 h with the complex. As a control, cells were left untreated or incubated without the binding/translocation component C2IIa. Cells were then washed twice with PBS to remove unbound toxin from the surface. Thereafter, cells were incubated in the presence of digitonin (20 μg/mL in PBS) for 5 min at 25 °C to permeabilize the cell membrane and for additional 25 min at 4 °C to allow the cytosol to diffuse into the buffer. The supernatant was carefully collected and adherent extracted cells were scraped off in Laemmli loading buffer. The samples were then subjected to SDS-PAGE and transferred to a nitrocellulose membrane by wet blotting, and C2IN−streptavidin was detected with a polyclonal anti-C2IN antibody as described before. Thereafter, the blot membrane was stripped, and the identity of the cytosolic fraction was confirmed by immunoblot analysis of cytosolic marker protein Hsp90, using a monoclonal anti-Hsp90 antibody (Santa Cruz Biotechnology, Heidelberg, Germany). Importantly, the absence of early endosomes in this fraction was verified in immunoblot with an antibody directed against rab5 (BD Biosciences, Heidelberg, Germany), a marker protein for early endosomes.

Immunofluorescence Microscopy of C2IN−Streptavidin-Treated Cells. For immunocytochemical analysis of C2IN−streptavidin uptake, cells were seeded on sterile coverslips at a density of 3.5×10^4 per well and incubated in 12-well culture dishes overnight. Cells were then treated with a combination of 1 μg C2IN−streptavidin and 2 μg C2IIa in serum-free medium for 2 h. Medium was exchanged and cells were incubated for another 2 h. As controls, cells were left untreated or incubated with the single components, i.e., C2IN−strepavidin or C2IIa. Subsequently, cells were fixed with 4% paraformaldehyde, permeabilized with 0.4% Triton X-100, and blocked with 5% dry milk powder in PBS-T. C2IN−streptavidin was then visualized with an α-streptavidin antibody (1:1000 in PBS) in conjunction with a secondary antibody−Alexa488 conjugate (1:400 in PBS). Finally, nuclei were counterstained with Hoechst 33342 (1:20 000 in PBS), and coverslips were mounted with ProLong Gold antifade reagent (Invitrogen, Karlsruhe, Germany). Confocal microscopy was performed with a Zeiss Axiovert 200 M microscope equipped with a LSM510 Meta laser scanning device (Zeiss, Oberkochen, Germany). 1-μm-thick sections were recorded with LSM Image Examiner and processed with *ImageJ* software (NIH, USA).

Confocal Microscopy to Monitor Biotin−Fluorophor Uptake into Vero Cells. To analyze the uptake of biotin−fluorescein (Sigma, Deisenhofen, Germany) or biocytin−Alexa488 (Invitrogen, Karlsruhe, Germany), Vero cells were grown overnight on sterile coverslips. After preincubation of 2 μg C2IN−streptavidin and an excess of fluorescein−biotin or biocytin−Alexa488 for 30 min, the mixture was supplemented with 4 μg C2IIa, and complex formation was allowed to occur for 30 min at 4 °C. Subsequently, the complex was added to the cells and incubated for 2 h. Untreated cells, cells incubated with biotinylated fluorophor alone or with the complex omitting C2IIa, served as controls. After 2 h, the medium was replaced by serum-containing MEM, and cells were further incubated for 2 h. Cells were then processed for immunofluorescence as described above. After fixation and permeabilization, cells were blocked and early endosomes were stained with a primary antibody directed against EEA1 (Novus Biologicals, Littleton, USA) in conjunction with an Alexa 647-labeled secondary antibody. Cells embedded in ProLong Gold antifade reagent were visualized using a LSM510 Meta confocal system connected to a Zeiss Axiovert 200 M microscope (Zeiss, Oberkochen, Germany). *z*-Stack images were recorded in 1 μm confocal sections using LSM Image Examiner and processed with *ImageJ* software.

Reproducibility of the Experiments and Statistics. All experiments were performed independently at least twice. Results from representative experiments are shown in the figures. Values ($n \geq 3$) are calculated as mean ± standard deviation (S.D.) using the GraphPad *Prism4* software.

RESULTS

Cloning, Expression and Purification of C2IN−Streptavidin. To generate a recombinant C2IN−streptavidin fusion protein, dimeric streptavidin was cloned in frame to C2IN, yielding the expression vector pGEX-2TGL-C2IN-streptavidin. The fusion construct features the N-terminal domain of C2I, which mediates the interaction with C2IIa to trigger cellular uptake, and a dimeric streptavidin, thus providing a versatile adaptor for biotinylated molecules (Figure 1A). The GST-tagged fusion protein was overproduced in *E. coli* BL21, and time-dependent expression was monitored. Western blot analysis with a monoclonal α-GST antibody revealed maximum expression 6 h post induction (p.i.), whereas longer expression times resulted in degradation of the fusion protein (Figure 1B). Thus, bacterial cultures were harvested after an expression period of 6 h. Then, C2IN−streptavidin was purified using glutathione−agarose affinity chromatography and analyzed by an immunoblot with a polyclonal α-streptavidin antibody (Figure 1C). After immobilization on the beads, the GST-tag was removed by thrombin cleavage releasing C2IN−streptavidin into the supernatant (Figure 1C, elution). C2IN−streptavidin was not completely soluble, as it could still be detected in the bacterial pellet. However, genetic fusion to C2IN markedly enhanced the solubility compared to the expression of dimeric streptavidin, which has to be purified under denaturing conditions (*24*). The purified protein was then checked for homogeneity by SDS-PAGE and Coomassie staining and revealed about 85% purity as calculated by *ImageJ* (Figure 1D, left panel). In addition, protein identity was confirmed by Western blot analysis with a polyclonal α-C2IN antibody (Figure 1D, right panel).

Biotin Binding Properties of the Novel C2IN−Streptavidin Fusion Protein. In order to characterize the binding of biotin-labeled macromolecules to C2IN−streptavidin, an overlay blot technique was employed. To this end, we have selected three biotinylated proteins differing in size and origin: bovine serum albumine (BSA), the ADP-ribosyltransferase C3bot from *Clostridium botulinum*, and calf alkaline phosphatase, Increasing amounts of the fusion protein and C2IN as negative control were subjected to SDS-PAGE and transferred onto a nitrocellulose membrane. Following incubation with 5 μg/mL biotinylated BSA, unspecifically interacting biotinylated protein was removed by high-salt washes, and bound BSA was detected using streptavidin−POD. Biotinylated BSA specifically interacted with C2IN−streptavidin in a concentration-dependent manner, whereas the negative control C2IN did not show any signal (Figure 2A). In addition, C2IN−streptavidin was incubated with streptavidin−POD omitting biotinylated BSA. Here, no signal was

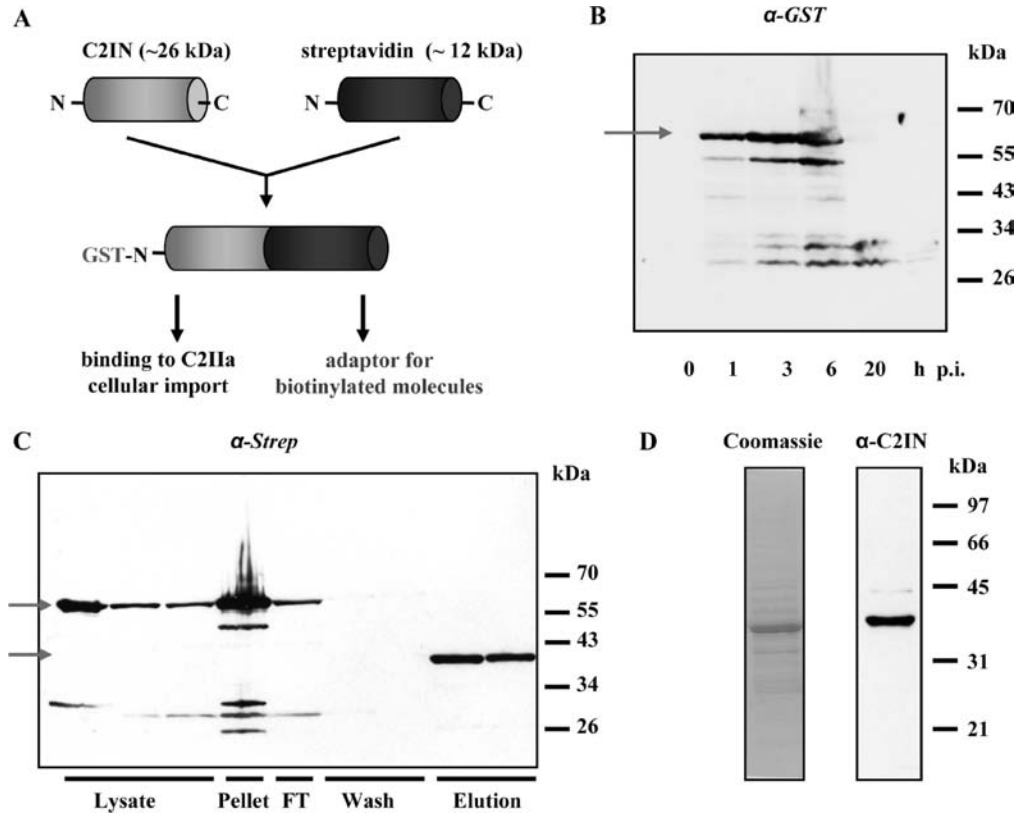


Figure 1. Cloning, expression, and purification of C2IN−streptavidin. (A) Cloning strategy to generate the novel fusion protein C2IN−streptavdin. (B) Time-course of C2IN−streptavidin expression in *E. coli* BL21. Aliquots of the suspension culture were removed after the time points post induction (p.i.) as indicated and analyzed by Western blotting with a monoclonal α-GST antibody. The arrow highlights the GST-C2IN-streptavidin fusion protein (C) Purification of GST-C2IN-streptavidin by affinity chromatography. Fractions obtained during the purification process were collected and C2IN−streptavidin was detected using a polyclonal α-streptavidin antibody. The upper arrow indicates the GST-tagged C2IN−streptavidin. The GST tag was removed by specific thrombin cleavage, yielding the 37 kDa fusion protein (designated by the lower arrow). (D) Characterization of isolated C2IN−streptavidin. 2.5 μg of the fusion protein was subjected to SDS-PAGE and visualized by Coomassie staining (left panel). Moreover, protein identity was confirmed by Western blot analysis with a polyclonal α-C2IN antibody (right panel).

observed, thus excluding a direct interaction of both streptavidin conjugates (data not shown). Next, biotinylated C3bot was shown to bind to immobilized C2IN−streptavidin with an affinity comparable to biotinylated BSA (Figure 2B), which was also demonstrated for biotin-coupled alkaline phosphatase (data not shown). To obtain more quantitative information on the biotin−streptavidin mediated interaction, binding kinetics were assessed by real-time surface plasmon resonance (*28, 29*). C2IN−streptavidin was covalently immobilized on a Biacore CM5 sensor chip, and biotinylated C3 was injected in HBS buffer pH 7.4 at various concentrations ranging from 750 nM to 10 μM. Concentration-dependent binding was monitored and allowed the determination of binding kinetics resulting in a K_D value of 7.57×10^{-7} M (Figure 2C and Table 1). Signal was corrected for unspecific binding and buffer changes using an activated reference cell. Taken together, the fusion protein C2IN−streptavidin is functionally active with regard to biotin binding. As expected, the binding affinity was clearly reduced in comparison to wild-type streptavidin, but is in the range reported for dimeric streptavidin (*24*).

Specific Internalization of C2IN−Streptavidin into the Cytosol of Epithelial Cells and Macrophages. As a next step, the time-dependent uptake of C2IN−streptavidin in living Vero cells was monitored after cell fractionation by digitonin. C2IN−streptavidin and the translocation/binding component C2IIa were preincubated on ice and then added to the culture medium. At the time points indicated, cells were permeabilized with digitonin to extract the cytosolic proteins. The cytosolic fraction as well as the remaining extracted cells were then subjected to SDS-PAGE and analyzed by Western blotting using a polyclonal α-C2IN-antibody (Figure 3A). Increasing amounts of C2IN−streptavidin were observed in the cytosolic fraction in a time-dependent manner, reaching a maximum after 4 h, which was confirmed by time course experiments over a period of 8 h (data not shown). However, the majority of the fusion protein was detected in the extracted cells representing cell-bound or vesicular-internalized C2IN−streptavidin. Treatment of cells with C2IN−streptavidin in the absence of C2IIa resulted in weak nonspecific binding or uptake, which could only be observed after long exposure times. The identity of the cytosolic fraction was attested by immunoblot analysis of cytosolic marker protein Hsp90 (Figure 3B), showing approximately 50% of Hsp90 in the extracted cytosolic fraction, which is in line with previous studies applying digitonin extraction (*30*). Importantly, Rab5 as endosomal marker protein was found exclusively in extracted cells, ruling out a contamination of the cytosolic fraction by early endosomes (Figure 3C). Consistent with this observation, EEA1 as another marker for endosomes was only detected in extracted cells (data not shown). Furthermore, the specific internalization of C2IN−streptavidin into the cytosol of other mammalian cells was demonstrated for human epithelial HeLa cells, hamster epithelial CHO cells, and murine macrophage-like J774A.1 cells (Figure 3D). The uptake kinetic of C2IN−streptavidin into the cytosol of HeLa cells was similar to Vero cells, culminating 4 h after treatment (Figure 3D, upper panel). CHO cells exhibited the most efficient internalization of C2IN−streptavidin into the cytosol, whereas incubation of cells without the transport component C2IIa resulted in a weak background signal of C2IN−streptavidin (Figure 3, middle panel). Compared to the epithelial cell lines,

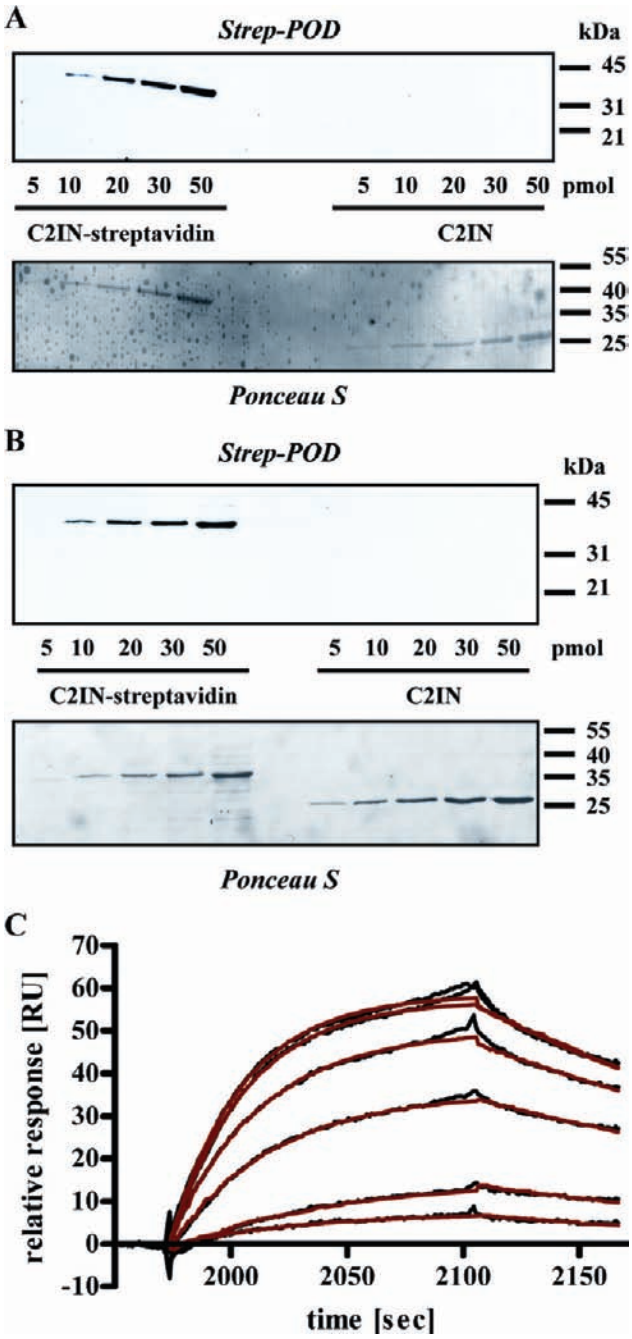


Figure 2. Characterization of C2IN−streptavidin with regard to biotin binding. (A) Overlay blot using biotinylated BSA. Increasing amounts of C2IN−streptavidin and C2IN as negative control were separated by SDS-PAGE and transferred onto a nitrocellulose membrane stained with Ponceau S. Following incubation with 5 μg/mL biotinylated BSA, unspecifically interacting biotinylated protein was removed by high-salt washes and bound BSA was detected using streptavidin−POD. (B) Overlay blot using biotinylated C3bot protein. This experiment was performed as describe above, except that 1 μg/mL C3bot protein was applied. (C) Real-time SPR analysis. C2IN−streptavidin was immobilized on a Biacore CM5 sensor chip and increasing concentrations of biotinylated C3bot protein were injected (750 nM up to 10 μM). Black lines show experimentally obtained data, whereas red lines indicate the calculated curve fit according to a Langmuir 1:1 model.

Table 1. Binding Kinetics of C2IN-Streptavidin and Biotinylated C3bot Obtained from Real-Time SPR Analysis

k_a (M^{-1} s^{-1})	k_d (s^{-1})	K_D (M)	χ^2
6.75×10^3	5.11×10^{-3}	7.57×10^{-7}	0.174

J774A.1 macrophages displayed a pronounced nonspecific binding/internalization of the fusion protein in the absence of C2IIa, most likely due to pinocytosis (Figure 3D, lower panel). Unlike the other cell types tested, lower amounts of C2IN−streptavidin were detected in the cytosol of J774A.1 cells.

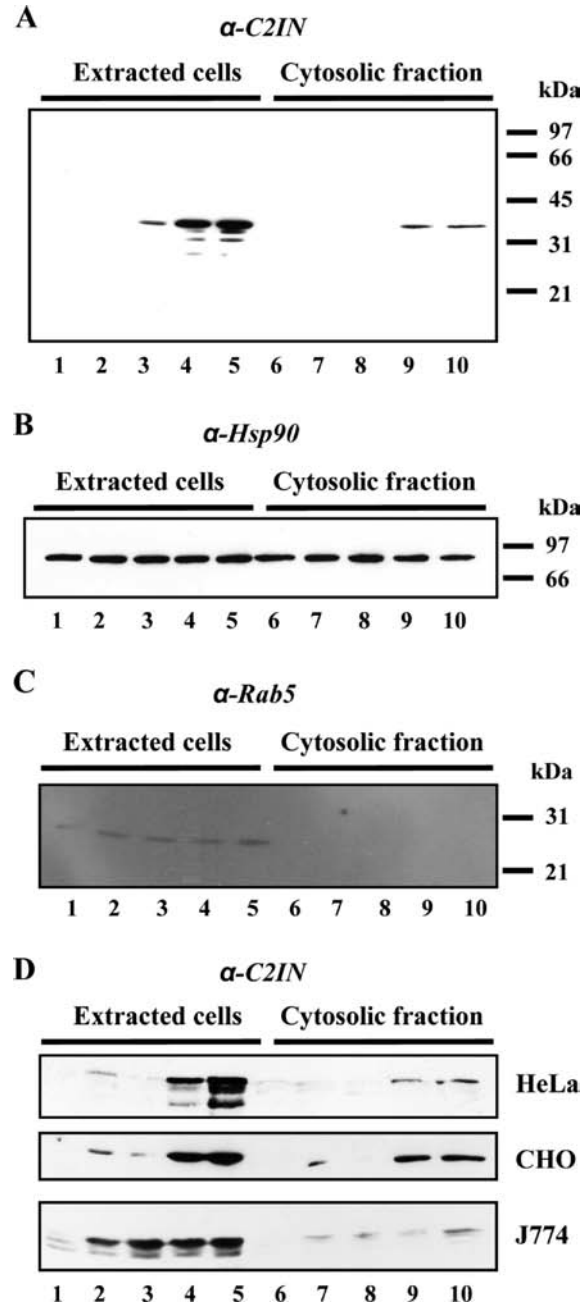


Figure 3. Uptake of C2IN−streptavidin into the cytosol of Vero cells. (A) Vero cells were treated with a combination of C2IN−streptavidin and C2IIa. As control, cells were left untreated or exposed to C2IN−streptavdin alone. After 0.5, 2, or 4 h, respectively, the cells were permeabilized by digitonin treatment to extract cytosolic proteins. The cytosolic supernatant was collected, and the remaining extracted cells were lysed. Both fractions were subjected to SDS-PAGE and analyzed by immunoblotting with a polyclonal α-C2IN-antibody. Lanes 1 and 6: control cells, 4 h. Lanes 2 and 7: cells treated with C2IN−streptavidin alone, 4 h. Lanes 3−5 and 8−10: cells treated with C2IN−streptavidin and C2IIa, 0.5, 2, and 4 h. Equal protein loading was confirmed by Ponceau S staining (data not shown). (B) Immunodetection of Hsp90, a cytosolic marker protein, on the same blot. (C) Visualization of Rab5, a marker protein for early endosomes, by Western blotting to exclude a possible contamination of the cytosolic fraction with early endosomes during digitonin treatment. (D) Treatment of HeLa, CHO, and J774 cells with a combination of C2IN−streptavidin and C2IIa as described under (A).

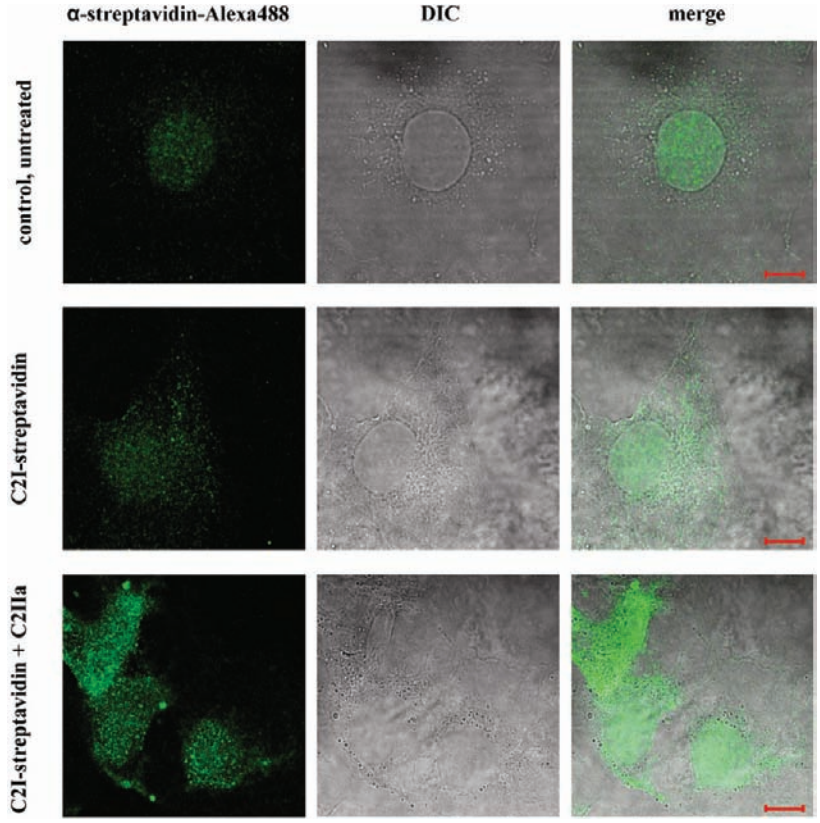


Figure 4. Confocal microscopy of internalized C2IN−streptavidin. Vero cells grown on coverslips were incubated with C2IN−streptavidin and C2IIa (1 + 2 μg). After 4 h, cells were fixed and C2IN−streptavidin was visualized by an α-streptavidin antibody and a secondary antibody coupled to Alexa488. Cells embedded in ProLong Gold antifade reagent were then analyzed by confocal microscopy and optical thin layer sections obtained were processed with *ImageJ*. Representative pictures thereof are shown. Scale bars correspond to 10 μm.

In addition, confocal laser-scanning microscopy was performed to analyze the intracellular localization of C2IN−streptavidin in more detail. Vero cells grown on coverslips were incubated with C2IN−streptavidin and C2IIa. After 4 h, cells were fixed and C2IN−streptavidin was visualized by an α-streptavidin antibody together with a secondary antibody coupled with Alexa488. Strikingly, confocal microscopy showed the uptake of the novel fusion protein as revealed by bright intracellular foci and diffuse staining (Figure 4). In contrast, untreated cells and cells treated with C2IN−streptavidin alone displayed weak diffuse background staining. In conclusion, we demonstrated the specific, i.e., C2IIa-dependent, uptake of C2IN−streptavidin into the cytosol of different mammalian cell types, which underscores the versatility of this novel delivery system.

Absence of Cytotoxic Effects of the Novel Transporter C2IN−Streptavidin/C2IIa. To reveal any possible cytotoxic effect of the fusion protein generated, Vero cells grown overnight were incubated with different combinations of C2IN−streptavidin and C2IIa for 5 h. Staurosporine, a well-known inducer of apoptosis, was used as positive control. Cell viability was determined by trypan blue assay, which is based on the selective uptake of trypan blue dye in dead cells, whereas living cells exclude the dye (Figure 5A). No effect was observed even at high concentrations (1 μg/mL C2IN−streptavidin + 2 μg/mL C2IIa), whereas the positive control staurosporine markedly decreased the cell viability to 60%. To monitor long-term effects on cell proliferation, cells were seeded in 96 well plates and treated with increasing concentrations of C2IN−streptavidin and C2IIa ranging from 100 ng/mL + 200 ng/mL up to 2.5 μg/mL + 5 μg/mL. After 5, 24, and 48 h, respectively, cell viability was assessed using the MTS proliferation assay. No cytotoxicity of the novel transporter could be recorded (Figure 5B). It should be noted that full-length C2I induces delayed caspase-dependent apoptosis after 24 h due to its intrinsic and persistent ADP-ribosyl-transferase activity (*31*), which has been removed in the novel fusion protein. In contrast to C2IN−streptavidin, staurosporine dramatically reduced the cell viability to about 25% after 48 h of incubation. Moreover, putative adverse effects of C2IN−streptavidin on the actin cytoskeleton were analyzed by immunofluorescence microscopy using the actin-specific probe phalloidin-Alexa 594, but no alterations were observed compared to control cells (data not shown).

C2IN−Streptavidin/C2IIa-Mediated Uptake of Biotin−Fluorescein in Vero Cells. Finally, biotin−fluorescein was used as model cargo to test the functionality of the novel transport system. Vero cells grown on coverslips were treated with a complex of biotin−fluorescein and the transporter C2IN−streptavidin/C2IIa. After 4 h, cells were fixed and permeabilized with Triton X-100. To visualize the endosomal marker protein EEA1, cells were stained with a polyclonal α-EEA1 antibody in conjunction with an Alexa647-coupled secondary antibody. Confocal laser scanning microscopy showed several bright foci in cells treated with the transporter together with fluorescein-labeled biotin (Figure 6A). These spots were obviously localized in the cytosol and did not overlap with early endosomes as evidenced by the vesicular EEA1 staining. In contrast, cells exposed to biotin−fluorescein alone or with the transporter omitting C2IIa revealed no signal, demonstrating the specific uptake mediated by the transport system. Since the acidification of early endosomes may diminish the fluorescence signal of fluorescein, we used the polar tracer biocytin−Alexa488, which is cell-impermeant and shows enhanced pH stability. As observed for biotin−fluorescein, the C2IN−streptavidin/C2IIa delivery system mediated the uptake of biocytin−Alexa488 in

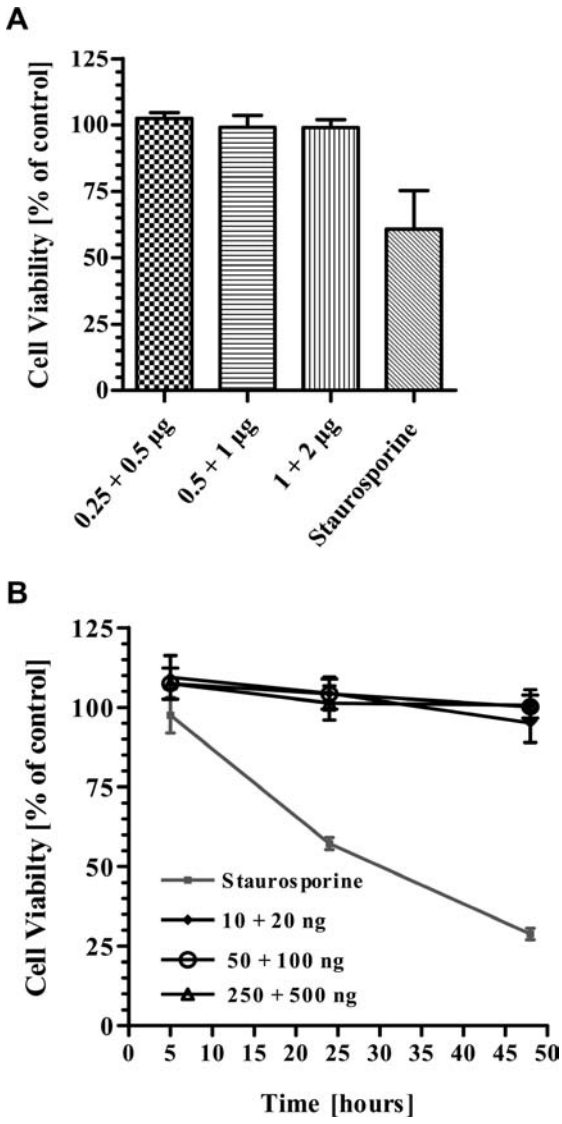


Figure 5. Determination of putative cytotoxic effects caused by C2IN−streptavidin. (A) Trypan blue exclusion. To reveal putative adverse effects on cell viability, Vero cells grown overnight were incubated with different combinations of C2IN−streptavidin and C2IIa for 5 h at 37 °C. Staurosporine, a well-known inhibitor of protein kinases and inducer of apoptosis, was used as a positive control. Subsequently, cell viability was determined by trypan blue assay using phase contrast microscopy. (B) To monitor long-term effects, cells were seeded in 96 well plates and treated with increasing concentrations of C2IN−streptavidin and C2IIa. After 5, 24, and 48 h, respectively, cell viability was assessed using the MTS proliferation assay. As above, staurosporine treatment was included as positive control. Data in (A) and (B) are expressed as mean ± SD, $n = 2$ (each experiment performed as quadruplicate).

Vero cells (Figure 6B). Confocal microscopy showed bright green foci and partial colocalization with early endosomes (Figure 6B), which is attested by the yellow staining in the merged channel. Control experiments were performed as described for biotin-labeled fluorescein and displayed no signal in the green channel (data not shown). In summary, our data clearly demonstrate the successful application of the novel transporter as delivery system for biotinylated molecules.

DISCUSSION

In the present study, we describe the successful generation of a novel molecular Trojan horse based on genetic engineering of the clostridial C2 toxin and a dimeric streptavidin, which is superior to biochemical conjugation with regard to homogeneity and its site-directed character. The novel fusion protein C2IN−streptavidin was overexpressed in *E. coli* and purified to homogeneity followed by removal of the GST tag. This native isolation procedure resulted in moderate yields, but led to soluble and functionally active protein. Alternative purification under denaturing conditions provides higher yields, but the protein precipitated on a biotin−agarose column, most likely due to improper refolding (data not shown). The purified fusion protein displayed a moderate affinity for biotinylated proteins as shown by an overlay blot technique and real-time SPR measurements. Compared to the dimeric streptavidin mutant ($K_D = 1.5 \times 10^{-7}$ M) (*24*), the affinity is slightly reduced probably due to steric constraints of the fusion protein affecting the biotin binding. This decreased affinity should allow for the reversible binding of internalized biotinylated molecules. In particular, endogenous free biotin generated by biotinidase (*32*) could displace biotinylated cargo by competition on the binding sites after internalization into the cytosol. On the other hand, this feature may be unfavorable with regard to the stability of the C2IN−streptavidin−biotin complex in vivo, which may be disrupted by serum proteins. Molecular Trojan horses employing wild-type avidin or streptavidin exhibit a very tight (strept) avidin−biotin binding, which is stable in the bloodstream in vivo (*33, 34*).

Moreover, we demonstrated the successful delivery of C2IN−streptavidin into the cytosol of diverse eukaryotic cell lines of human, rodent, and monkey origin. The observed slight variations in the internalization efficiency of the protein among the different cell types might be due to different expression levels of the C2 toxin receptor and/or for different velocities of endocytosis and intracellular protein translocation processes. Importantly, all hitherto tested vertebrate cell lines and primary cultured cells express the C2 toxin receptor on their cell surface, thus rendering these cells sensitive for C2 intoxication (*13*). Therefore, our novel delivery system comprising C2IN−streptavidin and C2IIa is suitable for a plethora of eukaryotic cell types. In contrast, conventional molecular Trojan horses encompassing receptor-specific antibodies are species-specific and limited to the expression pattern of the receptor. In addition, the novel C2-derived transporter did not affect cell viability over a time period of 48 h, nor did it induce any morphological changes, thus permitting its unrestricted application in cell cultures studies. Finally, we provided proof-of-principle for our novel delivery system using biotin−fluorescein as cargo, which was specifically internalized into Vero cells. Interestingly, biotin−fluorescein was detected in the cytosol of Vero cells and showed no colocalization with early endosomes. However, fluorescein exhibits no fluorogenic properties below pH 6, which may result in loss of signal during the acidification of endosomes. Therefore, biotin−fluorescein localized to early/late endosomes may not be detectable by confocal microscopy. To overcome this limitation, the fluorescent tracer biocytin−Alexa488 was applied. This conjugate is cell-impermeable due to its polarity and offers superior pH stability, allowing for the fluorescence detection even in acidic cellular compartments. Intriguingly, biocytin−Alexa488 was specifically delivered into Vero cells in a C2IN−streptavidin/C2IIa-dependent manner and showed partial colocalization with early endosomes.

The uptake mechanism of the binary C2 toxin of *C. botulinum* has been extensively characterized and is well-understood in most aspects, which also holds true for the novel fusion protein C2IN−streptavidin. Unlike the C2 toxin, the entry pathways of other delivery vectors such as cell penetrating peptides are still unclear and seem to involve different mechanisms (*35, 36*). With regard to the binary C2 system, C2IIa has two major functions. First, C2IIa mediates the binding of C2I via its N-terminal domain to the cell surface, and second, it facilitates

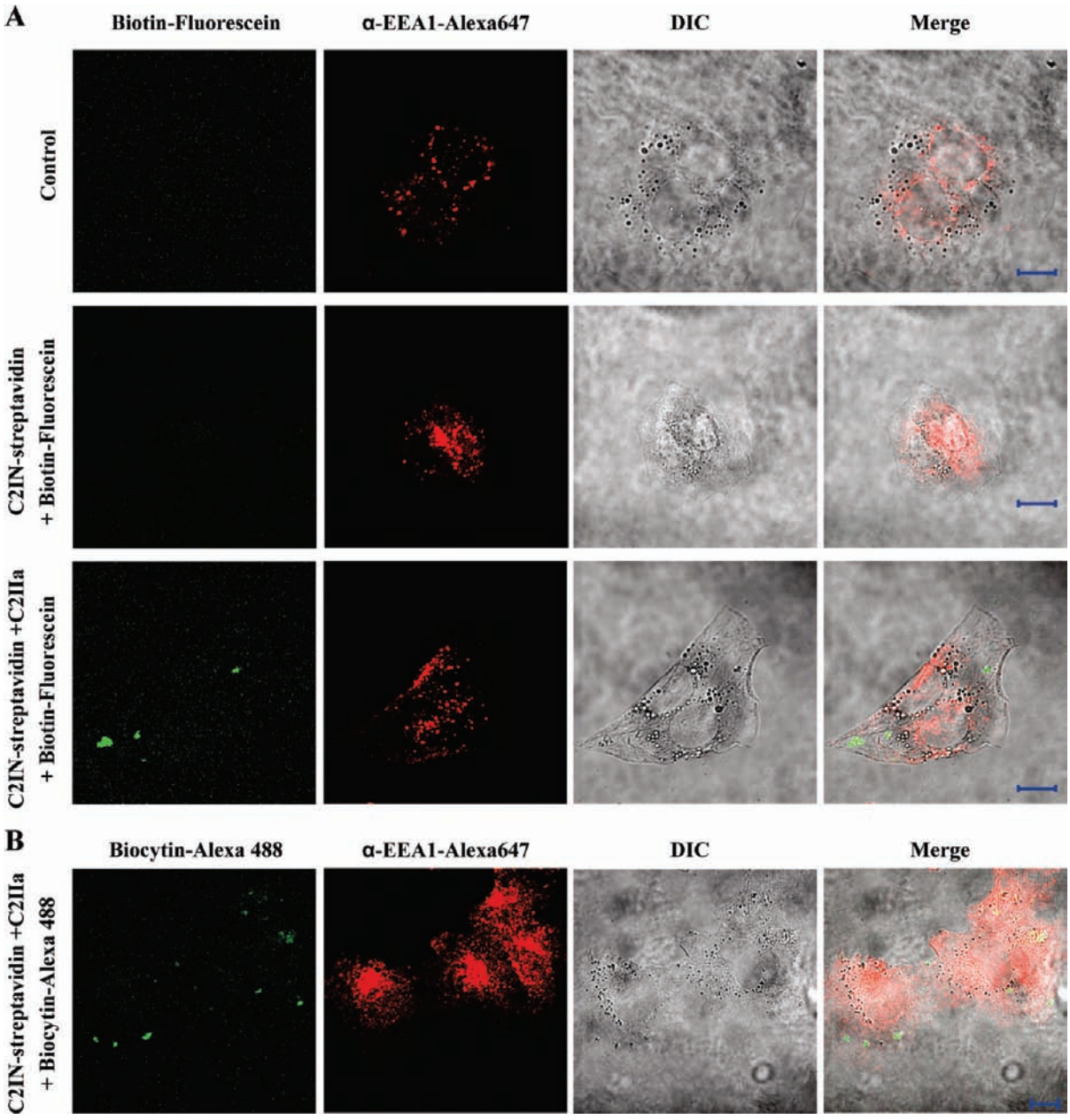


Figure 6. C2IN−streptavidin/C2IIa-mediated uptake of biotin-labeled fluorescent tracers into Vero cells. (A) Vero cells grown on coverslips were treated with a complex consisting of biotin−fluorescein in combination with the transporter C2IN−streptavidin/C2IIa. After 4 h, cells were fixed and permeabilized with Triton X-100. To visualize the endosomal marker protein EEA1, cells were stained with a polyclonal α-EEA1 antibody in conjunction with an Alexa647-coupled secondary antibody. Cells embedded in ProLong Gold antifade reagent were then analyzed by confocal microscopy and recorded thin layer *z*-stack images were processed and merged with *ImageJ*. Representative images thereof are displayed. Scale bars correspond to 10 μm. (B) Vero cells were treated and analyzed by confocal microscopy as describe above, except that biocytin−Alexa488 was used instead of biotin−fluorescein.

the membrane translocation of C2I from endosomes into the host cell cytosol by pore formation. The translocation channel formed by the C2IIa pore was shown to be 25−32 Å in width (*37*), which allows the passage of small molecules as attested by the transport of biotin−fluorescein into the cytosol of Vero cells in the present study. However, the narrow inner diameter of the translocation pore may limit the transport of larger molecules such as biotinylated proteins into the cytosol, thus trapping them in endosomes. To solve this problem, pH-responsive polymers such as poly(propylacrylic acid) (PPAA) could be used, which trigger endosomal membrane disruption upon luminal acidification (*38*). Biotinylated PPAA was reported to promote the internalization and endosomal release of an antibody complex containing streptavidin (*39*). It has also been successfully applied together with TAT−streptavidin to direct the uptake of a biotinylated protein to the cytosol, representing a useful tool for delivery systems (*21*).

With regard to immunogenicity, humans are only slightly responsive to the chicken homologue avidin, which may result from consumption of egg white causing oral tolerance (*40*). In contrast, streptavidin was shown to be immunogenic in humans, which might be a drawback for long-term or repetitive treatments, e.g., during cancer radioimmunotherapy (RIT) (*41*). Nevertheless, the use of streptavidin in cancer RIT led to promising clinical results, increasing the tumor/background ratio and the delivery of higher therapeutic doses (*15*). Lack of glycosylation is another advantage of streptavidin compared to chicken avidin, which shows unspecific binding due its carbohydrate modification, impairing its use in several applications (*42*).

The use of bacterial toxins as delivery systems is well-known and protein toxins such as diphtheria toxin (DT) have been employed as so-called immunotoxins to selectively kill cancer cells (*43*). For that purpose, the binding domain of DT has to be replaced by ligands that interact with surface antigens abundant on cancer cells, e.g., epidermal growth factor, allowing for a concentration of the toxin on the target cell. After translocation into the cytosol, DT catalyzes the ADP-ribosylation of elongation factor 2, thereby blocking protein synthesis, which results in cell death (*44*). As pointed out above, the binary C2 toxin represents a universal transport system due to the ubiquitous expression of its corresponding receptor on many eukaryotic cells. Previously, several chimeric fusion proteins based on the adaptor domain C2IN were created by genetic engineering (*10, 11*), allowing the cellular uptake and cell-biological characterization of proteins, which do not enter cells. However, the construction and expression of recombinant fusion proteins is time-consuming and cumbersome, whereas the use of the chimeric C2IN−streptavidin as versatile binding platform for a variety of biotinylated molecules is convenient and applicable to nearly all systems. Therefore, the novel cellular transporter C2IN−streptavidin/C2IIa should be a valuable tool for the uptake of biotinylated siRNA, peptides, and even proteins. A promising approach would be the targeted silencing of genes, e.g., involved in inflammation or carcinogenesis by siRNA. Very recently, Xia and co-workers reported the successful delivery of siRNA into the cytosol of human endothelial cells mediated by a molecular Trojan horse, showing efficient RNA interference similar to cationic polyplexes (*45*).

In summary, we have successfully established C2IN−streptavidin as a novel delivery system, which can be used as molecular Trojan horse in a variety of eukaryotic cells. Furthermore, we demonstrated C2IN−streptavidin/C2IIa-mediated internalization of fluorescent biotinylated tracers as cargo in Vero cells, providing proof-of-principle for this universal transporter.

ACKNOWLEDGMENT

We are grateful to Dr. Takeshi Sano, Boston, USA, for the generous gift of dimeric streptavidin cDNA and Bernd Betzler, University of Ulm, Germany, for the expression vector harboring streptavidin cDNA. We would like to thank Dr. Angelika Rück, ILM, University of Ulm, Germany, for kindly providing the confocal microscope facility and Dr. Alexander Bürkle, University of Konstanz, Germany, for critically reading the manuscript.

LITERATURE CITED

(1) Barth, H., Aktories, K., Popoff, M. R., and Stiles, B. G. (2004) Binary bacterial toxins: biochemistry, biology, and applications of common Clostridium and Bacillus proteins. *Microbiol. Mol. Biol. Rev. 68*, 373–402.

(2) Ohishi, I. (1987) Activation of botulinum C2 toxin by trypsin. *Infect. Immun. 55*, 1461–5.

(3) Eckhardt, M., Barth, H., Blocker, D., and Aktories, K. (2000) Binding of Clostridium botulinum C2 toxin to asparagine-linked complex and hybrid carbohydrates. *J. Biol. Chem. 275*, 2328–34.

(4) Barth, H., Blocker, D., Behlke, J., Bergsma-Schutter, W., Brisson, A., Benz, R., and Aktories, K. (2000) Cellular uptake of Clostridium botulinum C2 toxin requires oligomerization and acidification. *J. Biol. Chem. 275*, 18704–11.

(5) Ohishi, I. (1983) Response of mouse intestinal loop to botulinum C2 toxin: enterotoxic activity induced by cooperation of nonlinked protein components. *Infect. Immun. 40*, 691–5.

(6) Blocker, D., Pohlmann, K., Haug, G., Bachmeyer, C., Benz, R., Aktories, K., and Barth, H. (2003) Clostridium botulinum C2 toxin: low pH-induced pore formation is required for translocation of the enzyme component C2I into the cytosol of host cells. *J. Biol. Chem. 278*, 37360–7.

(7) Haug, G., Leemhuis, J., Tiemann, D., Meyer, D. K., Aktories, K., and Barth, H. (2003) The host cell chaperone Hsp90 is essential for translocation of the binary Clostridium botulinum C2 toxin into the cytosol. *J. Biol. Chem. 278*, 32266–74.

(8) Kaiser, E., Pust, S., Kroll, C., and Barth, H. (2009) Cyclophilin A facilitates translocation of the Clostridium botulinum C2 toxin across membranes of acidified endosomes into the cytosol of mammalian cells. *Cell Microbiol. 11*, 780–95.

(9) Aktories, K., Barmann, M., Ohishi, I., Tsuyama, S., Jakobs, K. H., and Habermann, E. (1986) Botulinum C2 toxin ADP-ribosylates actin. *Nature 322*, 390–2.

(10) Barth, H., Hofmann, F., Olenik, C., Just, I., and Aktories, K. (1998) The N-terminal part of the enzyme component (C2I) of the binary Clostridium botulinum C2 toxin interacts with the binding component C2II and functions as a carrier system for a Rho ADP-ribosylating C3-like fusion toxin. *Infect. Immun. 66*, 1364–9.

(11) Pust, S., Hochmann, H., Kaiser, E., von Figura, G., Heine, K., Aktories, K., and Barth, H. (2007) A cell-permeable fusion toxin as a tool to study the consequences of actin-ADP-ribosylation caused by the salmonella enterica virulence factor SpvB in intact cells. *J. Biol. Chem. 282*, 10272–82.

(12) Haug, G., Wilde, C., Leemhuis, J., Meyer, D. K., Aktories, K., and Barth, H. (2003) Cellular uptake of Clostridium botulinum C2 toxin: membrane translocation of a fusion toxin requires unfolding of its dihydrofolate reductase domain. *Biochemistry 42*, 15284–91.

(13) Barth, H., and Stiles, B. G. (2008) Binary actin-ADP-ribosylating toxins and their use as molecular Trojan horses for drug delivery into eukaryotic cells. *Curr. Med. Chem. 15*, 459–69.

(14) Laitinen, O. H., Hytonen, V. P., Nordlund, H. R., and Kulomaa, M. S. (2006) Genetically engineered avidins and streptavidins. *Cell. Mol. Life Sci. 63*, 2992–3017.

(15) Goldenberg, D. M., Sharkey, R. M., Paganelli, G., Barbet, J., and Chatal, J. F. (2006) Antibody pretargeting advances cancer radioimmunodetection and radioimmunotherapy. *J. Clin. Oncol. 24*, 823–34.

(16) Laitinen, O. H., Nordlund, H. R., Hytonen, V. P., and Kulomaa, M. S. (2007) Brave new (strept)avidins in biotechnology. *Trends Biotechnol. 25*, 269–77.

(17) Pardridge, W. M. (2007) shRNA and siRNA delivery to the brain. *Adv. Drug Delivery Rev. 59*, 141–52.

(18) Pardridge, W. M. (2006) Molecular Trojan horses for blood-brain barrier drug delivery. *Curr. Opin. Pharmacol. 6*, 494–500.

(19) Pardridge, W. M. (2002) Drug and gene targeting to the brain with molecular Trojan horses. *Nat. Rev. Drug Discovery 1*, 131–9.

(20) Wu, D., Yang, J., and Pardridge, W. M. (1997) Drug targeting of a peptide radiopharmaceutical through the primate blood-brain barrier in vivo with a monoclonal antibody to the human insulin receptor. *J. Clin. Invest. 100*, 1804–12.

(21) Albarran, B., To, R., and Stayton, P. S. (2005) A TAT-streptavidin fusion protein directs uptake of biotinylated cargo into mammalian cells. *Protein Eng. Des. Sel. 18*, 147–52.

(22) Rinne, J., Albarran, B., Jylhava, J., Ihalainen, T. O., Kankaanpaa, P., Hytonen, V. P., Stayton, P. S., Kulomaa, M. S., and Vihinen-Ranta, M. (2007) Internalization of novel non-viral vector TAT-streptavidin into human cells. *BMC Biotechnol. 7*, 1.

(23) Ng, P. P., Dela Cruz, J. S., Sorour, D. N., Stinebaugh, J. M., Shin, S. U., Shin, D. S., Morrison, S. L., and Penichet, M. L. (2002) An anti-transferrin receptor-avidin fusion protein exhibits both strong proapoptotic activity and the ability to deliver various molecules into cancer cells. *Proc. Natl. Acad. Sci. U.S.A. 99*, 10706–11.

(24) Sano, T., Vajda, S., Smith, C. L., and Cantor, C. R. (1997) Engineering subunit association of multisubunit proteins: a dimeric streptavidin. *Proc. Natl. Acad. Sci. U.S.A. 94*, 6153–8.

(25) Barth, H., Roebling, R., Fritz, M., and Aktories, K. (2002) The binary Clostridium botulinum C2 toxin as a protein delivery system: identification of the minimal protein region necessary for interaction of toxin components. *J. Biol. Chem. 277*, 5074–81.

(26) Laemmli, U. K. (1970) Cleavage of structural proteins during the assembly of the head of bacteriophage T4. *Nature 227*, 680–5.

(27) Sorensen, V., Zhen, Y., Zakrzewska, M., Haugsten, E. M., Walchli, S., Nilsen, T., Olsnes, S., and Wiedlocha, A. (2008) Phosphorylation of fibroblast growth factor (FGF) receptor 1 at Ser777 by p38 mitogen-activated protein kinase regulates translocation of exogenous FGF1 to the cytosol and nucleus. *Mol. Cell. Biol. 28*, 4129–41.

(28) Cooper, M. A. (2003) Label-free screening of bio-molecular interactions. *Anal. Bioanal. Chem. 377*, 834–42.

(29) Fahrer, J., Kranaster, R., Altmeyer, M., Marx, A., and Burkle, A. (2007) Quantitative analysis of the binding affinity of poly(ADP-ribose) to specific binding proteins as a function of chain length. *Nucleic Acids Res. 35*, e143.

(30) Wiedlocha, A., Nilsen, T., Wesche, J., Sorensen, V., Malecki, J., Marcinkowska, E., and Olsnes, S. (2005) Phosphorylation-regulated nucleocytoplasmic trafficking of internalized fibroblast growth factor-1. *Mol. Biol. Cell 16*, 794–810.

(31) Heine, K., Pust, S., Enzenmuller, S., and Barth, H. (2008) ADP-ribosylation of actin by the Clostridium botulinum C2 toxin in mammalian cells results in delayed caspase-dependent apoptotic cell death. *Infect. Immun. 76*, 4600–8.

(32) Wolf, B. (2005) Biotinidase: its role in biotinidase deficiency and biotin metabolism. *J. Nutr. Biochem. 16*, 441–5.

(33) Suzuki, T., Wu, D., Schlachetzki, F., Li, J. Y., Boado, R. J., and Pardridge, W. M. (2004) Imaging endogenous gene expression in brain cancer in vivo with 111In-peptide nucleic acid antisense radiopharmaceuticals and brain drug-targeting technology. *J. Nucl. Med. 45*, 1766–75.

(34) Wu, D., and Pardridge, W. M. (1996) Central nervous system pharmacologic effect in conscious rats after intravenous injection of a biotinylated vasoactive intestinal peptide analog coupled to a blood-brain barrier drug delivery system. *J. Pharmacol. Exp. Ther. 279*, 77–83.

(35) El-Andaloussi, S., Jarver, P., Johansson, H. J., and Langel, U. (2007) Cargo-dependent cytotoxicity and delivery efficacy of cell-penetrating peptides: a comparative study. *Biochem. J. 407*, 285–92.

(36) Wagstaff, K. M., and Jans, D. A. (2006) Protein transduction: cell penetrating peptides and their therapeutic applications. *Curr. Med. Chem. 13*, 1371–87.

(37) Schleberger, C., Hochmann, H., Barth, H., Aktories, K., and Schulz, G. E. (2006) Structure and action of the binary C2 toxin from Clostridium botulinum. *J. Mol. Biol. 364*, 705–15.

(38) Murthy, N., Robichaud, J. R., Tirrell, D. A., Stayton, P. S., and Hoffman, A. S. (1999) The design and synthesis of polymers for eukaryotic membrane disruption. *J. Controlled Release 61*, 137–43.

(39) Lackey, C. A., Press, O. W., Hoffman, A. S., and Stayton, P. S. (2002) A biomimetic pH-responsive polymer directs endosomal release and intracellular delivery of an endocytosed antibody complex. *Bioconjugate Chem. 13*, 996–1001.

(40) Weiner, H. L. (1994) Oral tolerance. *Proc. Natl. Acad. Sci. U.S.A. 91*, 10762–5.

(41) Breitz, H. B., Weiden, P. L., Beaumier, P. L., Axworthy, D. B., Seiler, C., Su, F. M., Graves, S., Bryan, K., and Reno, J. M. (2000) Clinical optimization of pretargeted radioimmunotherapy with antibody-streptavidin conjugate and ^{90}Y-DOTA-biotin. *J. Nucl. Med. 41*, 131–40.

(42) Hytonen, V. P., Laitinen, O. H., Airenne, T. T., Kidron, H., Meltola, N. J., Porkka, E. J., Horha, J., Paldanius, T., Maatta, J. A., Nordlund, H. R., Johnson, M. S., Salminen, T. A., Airenne, K. J., Yla-Herttuala, S., and Kulomaa, M. S. (2004) Efficient production of active chicken avidin using a bacterial signal peptide in Escherichia coli. *Biochem. J. 384*, 385–90.

(43) Frankel, A. E., Kreitman, R. J., and Sausville, E. A. (2000) Targeted toxins. *Clin. Cancer Res. 6*, 326–34.

(44) Pastan, I., Hassan, R., FitzGerald, D. J., and Kreitman, R. J. (2007) Immunotoxin treatment of cancer. *Annu. Rev. Med. 58*, 221–37.

(45) Xia, C. F., Boado, R. J., and Pardridge, W. M. (2009) Antibody-mediated targeting of siRNA via the human insulin receptor using avidin-biotin technology. *Mol. Pharm. 6*, 747–51.

BC900365B

Synthesis and Characterization of Biodegradable HPMA-Oligolysine Copolymers for Improved Gene Delivery

Rob S. Burke and Suzie H. Pun*

Department of Bioengineering, University of Washington, Seattle, Washington 98195. Received August 18, 2009; Revised Manuscript Received October 21, 2009

Bioactive peptides, including DNA-binding, endosomal release, and cell targeting peptides, have been integrated into synthetic gene carriers to improve delivery efficiency by enabling the vectors to overcome barriers to gene delivery. Our overall goal is to develop multifunctional, peptide-based polymers that incorporate motifs to condense DNA and facilitate sequential trafficking steps. One approach is to polymerize vinyl-terminated peptides by radical polymerization. In this work, cationic oligolysine peptides were designed to contain vinyl termini with internal reducible linkers. These peptides were copolymerized with HPMA to form biodegradable, DNA-condensing copolymers for gene delivery. The polymerization conditions were optimized by varying the initiator to monomer ratios, macromonomer to comonomer ratios, and reactant concentrations. The synthesized copolymers were shown to possess several important properties required for *in vivo* gene delivery applications, including (i) efficient DNA binding and condensation, (ii) the ability to stabilize particles against salt-induced aggregation, (iii) the ability to resist extracellular polyplex unpackaging, (iv) biocompatibility and the potential to be degraded into nontoxic components after cellular uptake, and (v) efficient delivery of plasmid to cultured cells.

INTRODUCTION

Polymeric gene delivery vectors have been widely studied over the past two decades as alternatives to viral vectors. Though there have been significant advances in the field of polymer-based delivery during this time, the limited efficiency of these vectors remains a weakness. Bioactive peptides can be incorporated into the delivery vehicles to aid in overcoming different barriers to delivery, and the functionalities of the peptides that have been used include DNA binding, targeting, and endosomal escape (*1*−*3*). Though many investigators have generated peptide-functionalized polymers by conjugating peptides to polymers, several groups have recently demonstrated polymerization of peptide monomers with an acrylamide comonomer (*4*−*8*). In this work, we apply this polymerization technique to synthesize peptide-based copolymers for use as gene delivery agents. These unique polymers possess integrated properties of DNA packaging, stability, and biodegradability in a single material without the need for further modification.

Cationic polymers used to deliver DNA can be highly toxic, so it is important to consider the interplay between the potential toxicity and transfection efficiency of the polymer when designing a new polycation. It has been shown that both the efficacy and toxicity of nonviral gene delivery vehicles are directly correlated to their molecular weight, leading to a situation where it is difficult to develop a system with both high delivery efficiency and low toxicity (*9*). To engineer a solution to this problem, investigators have cross-linked low-molecular-weight components using reducible cross-linkers to increase effective molecular weight for DNA condensation while ensuring that the cationic components can degrade into less toxic low molecular weight peptides or polymers (*9*−*15*). Reducible linkers are also attractive for gene delivery applications because such linkers enable the design of copolymers that maintain stability extracellularly, when a high molecular weight is needed to retain the DNA in a packaged state, and degrade intracellularly, when a low molecular weight is desired to facilitate unpackaging of the DNA for transcription.

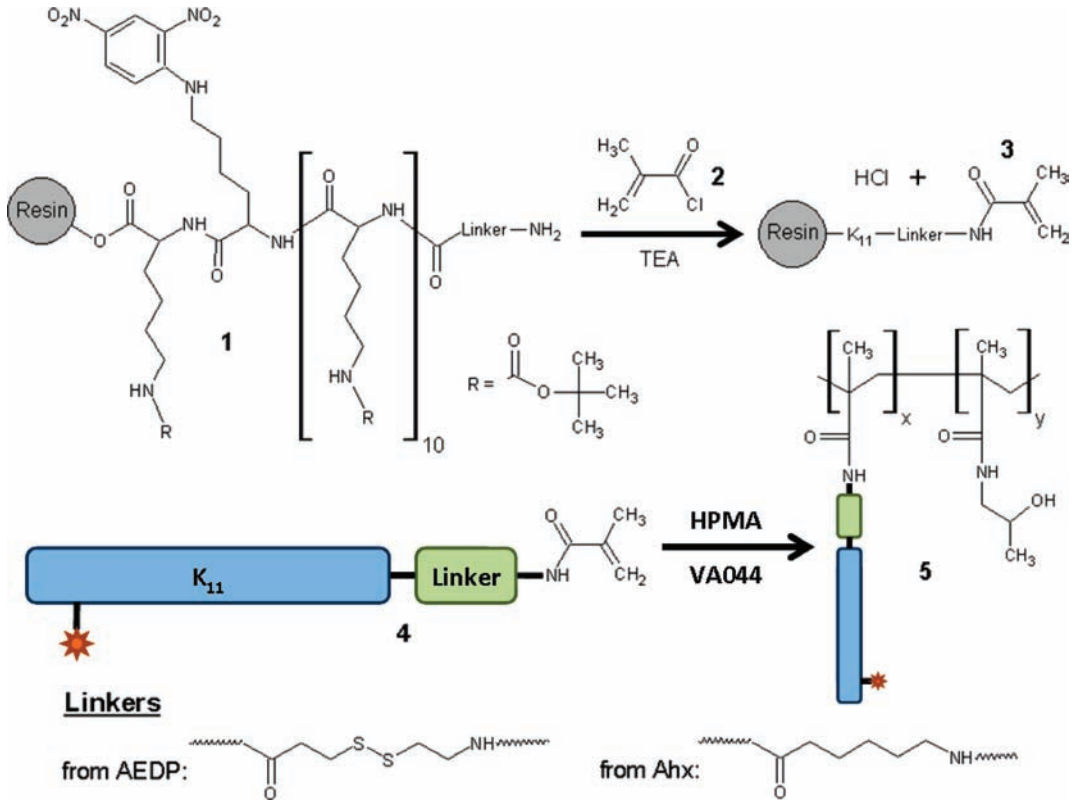
The peptide-based polymers presented here contain a linker between the polymerizable vinyl group and the peptide. A stable linker and a reducible linker were both used in order to evaluate the effect of polymer degradation on transfection efficiency and cell toxicity. A cationic oligolysine peptide was selected for polymerization due to its ability to package DNA through electrostatic interactions. Wadhwa et al. first studied the dependence of DNA condensation and transfection efficiency on the length of the oligolysine peptide used to condense the DNA (*16*). The authors found that peptides with 13 or more lysine residues bound tightly to DNA, condensed the DNA into small polyplexes around 100 nm in diameter, and mediated transfection. However, peptides possessing 8 lysine residues or fewer were drastically weakened in their ability to bind DNA and mediate effective transfection (*16*). The materials presented here contain oligolysines with 11 lysine residues. This length was selected so that the polymerized material could potentially mediate strong DNA binding, while the free peptides could easily be displaced after cleavage from the HPMA backbone, thus facilitating DNA unpackaging.

In summary, we report here the synthesis and evaluation of HPMA-peptide copolymers for gene delivery applications. First, a series of copolymers was synthesized in order to determine the effect of the polymerization conditions on the polymer properties. The copolymers were characterized for their molecular weight, composition, and ability to condense DNA. The most promising copolymers were studied further, and polyplexes of these copolymers and DNA were assessed for their size, ability to resist unpackaging, salt stability, transfection efficiency, and cellular toxicity in a series of *in vitro* experiments. Several copolymers were identified with transfection efficiencies similar to that of PLL but with much lower cellular toxicities. This copolymer system is modular, and this model system can be expanded to include other peptide monomers that further increase the gene delivery efficiency of the copolymers.

* E-mail: spun@u.washington.edu.

10.1021/bc9003662 © 2010 American Chemical Society
Published on Web 12/07/2009

Scheme 1. Methacryloylation of Linker-Conjugated Peptides (1) and Synthesis of Copolymers (5) by Radical Polymerization of Peptide Monomers (4) and HPMA



EXPERIMENTAL SECTION

Materials. gWiz-Luciferase plasmid (gWiz-Luc, Endotoxin-free) was purchased from Aldevron. All other materials were purchased from Sigma-Aldrich and used without further purification unless otherwise stated.

Synthesis of Fmoc-AEDP. *N*-(9-Fluorenylmethoxycarbonyl)-protected 3-[(2-aminoethyl)dithio] propionic acid (Fmoc-AEDP) was synthesized by a modified protocol based on published methods of Fields and co-workers (*17*). Briefly, 3 mmol of 9-fluorenylmethyl *N*-succinimidyl carbonate (Fmoc-OSu) was dissolved in 15 mL of dimethoxyethane (DME). Two millimoles of 3-[(2-aminoethyl)dithio] propionic acid (AEDP, from Pierce) and 4.4 mmol of sodium bicarbonate were dissolved in 5 mL of dH_2O and then added dropwise to the 15 mL of Fmoc-OSu in DME while stirring. The reaction was allowed to proceed overnight at RT with stirring in the dark. Reaction completion was checked by TLC using a running buffer of 97% chloroform/3% glacial acetic acid (v/v) with the following spots: AEDP ($R_f = 0$), Fmoc ($R_f = 1$), Fmoc-AEDP ($R_f = 0.95$). The reaction was filtered through a 0.2 μm pore size PVDF filter, and the DME was removed by rotary evaporation. Forty milliliters of 0.1 N HCl was added to the remaining solution and stirred for 1 h. Forty milliliters of chloroform was added and the solution was stirred for 4 h. The reaction mixture was extracted with two washes of 0.1 N HCl and two washes of dH_2O. The organic phase was isolated and filtered, the chloroform was removed by rotary evaporation, and a slightly yellow, oily substance was recovered.

Synthesis of DNP-Labeled K_{11} and Unlabeled K_{11} Peptides. One gram of Fmoc-Lys(Boc)-NovaSyn TGT resin (0.2 mmol lysine, from Novabiochem) was swelled in dimethylformamide (DMF), and the N-terminal amine groups of the Lys preloaded onto the resin were deprotected by two incubations for 10 min in 20% (v/v) piperidine in DMF. Four equivalents each of lysine-dinitrophenyl (Lys-DNP, from Novabiochem) and *O*-(7-azabenzotriazole-1-yl)-*N*,*N*,*N*′,*N*′-tetramethyluronium hexafluorophosphate (HATU, from GenScript Corp) were dissolved in 5 mL of 0.4 M *N*-methylmorpholine (NMM) in DMF. The activator and amino acid solution was then added to the resin, and the coupling reaction was allowed to proceed for 1 h at RT. The resin was washed with DMF, and the remainder of the peptide was synthesized using standard Fmoc-based solid-phase peptide synthesis (SPPS) conditions with 4 equiv of lysine amino acid (Fmoc-Lys(Boc), from Protein Technologies) and 4 equiv of HATU on a PS3 peptide synthesizer (Protein Technologies). Ten additional Lys residues were added for a total of eleven Lys residues with one Lys-DNP residue on the K_{11}-DNP peptide. The purity of the peptide was assessed by HPLC, and the mass was measured using an Esquire electrospray ion trap mass spectrometer (ESI-MS) from Bruker Daltonics (Supporting Information). The unlabeled K_{11} peptide was synthesized in exactly the same way, except without adding the Lys-DNP residue.

Synthesis of DNP-Labeled K_{11}-AEDP-MC and K_{11}-Ahx-MC Modified Peptides. Four equivalents each of Fmoc-AEDP and HATU dissolved in 5 mL of 0.4 M NMM in DMF were added to N-terminally deprotected K_{11}-DNP-resin containing 0.1 mmol peptide. The coupling reaction was allowed to proceed for 1 h at RT. The resin was washed with DMF and then deprotected by twice incubating the resin with 20% piperidine in DMF for 5 min at RT, yielding K_{11}-AEDP **1** (with the linker coming from AEDP). The peptide was then methacryloylated as shown in Scheme 1, following a protocol similar to that of O'Brien-Simpson et al. (*4*). The minimum amount of anhydrous DMF required to fluidize the resin was added and the resin was transferred to a reaction flask kept on ice under nitrogen. Triethylamine (TEA, 20 equiv) was injected into the flask, followed by dropwise addition of 10 equiv of methacryloyl chloride **2** (MC). The reaction was stirred for 1 h on ice and then 1 h at RT in O_2-free conditions, yielding compound **3**. The

Table 1. Reaction Conditions and Molecular Properties of the Copolymer Library

copolymer	initiator wt%[a]	peptide monomer mol % feed	total monomer conc (mg/mL)	M_w (kDa)	PDI	peptide mol % in copolymer	peptide wt % in copolymer	% yield[b]
A1	1	5	85.0	64.3	3.6	2.86	28.1	38
A2	3	5	85.0	55.7	4.2	2.95	28.7	76
A3	5	5	85.0	53.6	4.4	3.02	29.3	81
A4	7	5	85.0	47.9	4.8	3.12	30.0	79
B1	5	1	85.0	213.3	8.3	0.63	7.7	76
B2	5	1	56.7	94.0	7.0	0.40	5.1	91
C1	5	10	85.0	21.2	3.1	4.37	37.8	65
C2	5	10	42.5	13.2	2.2	3.94	35.3	54
D1	5	5	85.0	28.4	3.9	3.87	35.5	80

[a] The initiator wt % was calculated as a weight percent of HPMA monomer. [b] The percent yield is presented as the weight of polymer recovered divided by the total weight of the monomers added to the reaction.

resin was washed and the peptide cleaved by incubation with a cleavage cocktail of 95% trifluoroacetic acid (TFA), 2.5% triisopropylsilane (TIPS), and 2.5% dH_2O for 3 h at RT. The cleaved peptide K_{11}-AEDP-MC **4** was precipitated in diethyl ether three times, and the pellet was dried, yielding a chalky yellow solid, and stored at −20 °C. The synthesis of K_{11}-Ahx-MC **4** was performed in the same way, except that 4 equiv of Fmoc-6-aminohexanoic acid (Fmoc-Ahx, from Novabiochem) was used instead of Fmoc-AEDP to generate a peptide monomer that does not contain a cleavable disulfide linkage. The purity of the peptides was assessed by HPLC and found to be >90% (Supporting Information). Desired products were confirmed by mass spectrometry using an Esquire ESI-MS from Bruker Daltonics (Supporting Information).

Copolymerization of HPMA with Peptide Monomer. For each copolymer, 10 mg peptide monomer **4** was used in the feed at the mole percent shown in Table 1 with the required amount of HPMA monomer (Polysciences, Inc.). The weight of the initiator 2,2′-azobis[2-(2-imidazolin-2-yl)propane]dihydrochloride (VA044, from Wako Specialty Chemicals) used for each polymerization was calculated as a weight percent of HPMA monomer, as indicated in Table 1. For a given copolymerization, the appropriate amounts of peptide monomer, HPMA monomer, and VA044 initiator were dissolved in the amount of degassed reaction buffer (6 M guanidine hydrochloride, 2 mM EDTA, 0.5 M Tris base, buffered to pH 8.3 with HCl) to give the final total monomer concentration indicated in Table 1. The reaction solutions were transferred to glass reaction vials, bubbled with N_2 gas for 15 min, and then sealed and heated at 44 °C for 48 h to generate copolymers **5**. Four separate copolymer series were investigated, as shown in Table 1, where series A, B, and C used the noncleavable K_{11}-Ahx-MC **4** in the copolymers while series D used the disulfide-linked K_{11}-AEDP-MC **4**. Series A varied the weight percent of initiator, while series B and C varied the mole percent of peptide monomer and total monomer concentration.

Purification and Characterization of Copolymers. The copolymers were dialyzed against dH_2O using a 7 kDa MWCO membrane and purified by HPLC to remove any unreacted monomers. After organic solvent removal *in vacuo* and lyophilization to recover a fluffy yellow solid, the copolymers were dissolved at 5 mg/mL in running buffer (0.3 M sodium acetate buffered to pH 4.4 with acetic acid) for analysis by gel permeation chromatography (GPC) as described by Hennink and co-workers (*18*). A Viscotek GPCmax, which was controlled by Viscotek OmniSEC software, was used with an OHpak SB-G guard column (Shodex) in line with an OHpak SB-804 HQ column (Shodex) and a refractive index (RI) detector (Viscotek). The molecular weights of the copolymers were determined by using the OmniSEC software to compare the elution time of the copolymer to a standard curve generated from the elution times of narrow-polydispersity poly(ethylene oxide) TSK standards (Tosoh) of different molecular weights. The percent incorporation of peptide into the copolymer was determined by comparing to a standard curve of DNP absorbance at 360 nm (A_{360}).

Polymer Degradation Studies. Copolymers A4 and D1 were diluted to 5 mg/mL in HEPES buffered glucose (HBG; 20 mM HEPES and 5% glucose (w/v) buffered to pH 7.4 with NaOH) and analyzed by HPLC. HPLC was performed using a Jupiter 4 μm Proteo 90 Å (250 × 4.6 mm) reversed-phase analytical column (Phenomenex) and a gradient from 98% Buffer A (H_2O + 0.01% TFA) to 30% Buffer B (acetonitrile + 0.01% TFA) developed over 25 min. The same copolymers were then diluted to 5 mg/mL in HBG containing the reducing agent dithiothreitol (DTT, final concentration of 10 mM) and incubated for 5, 30, or 60 min before being analyzed by HPLC with detection at 215 nm.

Polyplex Formulation and Characterization. The gWiz-Luc plasmid was diluted in HBG to a concentration of 0.1 mg/mL and mixed with an equal volume of polymer (also diluted in HBG) at the desired lysine to DNA phosphate (N/P) ratio. For particle sizing measurements, all polyplexes were formed at N/P = 5. After mixing, the polyplexes were allowed to form for 5 min at room temperature. Twenty microliters of each polyplex sample (containing 1 μg DNA) was mixed with either 80 μL HBG or PBS and the 100 μL sample was assayed for particle size by dynamic light scattering (DLS) measured on a Brookhaven Instruments Corp ZetaPALS instrument. Particle sizing measurements were performed at a wavelength of 659.0 nm with a detection angle of 90° at RT.

DNA Condensation. The gWiz-Luc plasmid was mixed with the bis-intercalating dye YOYO-1 iodide (Invitrogen/Molecular Probes) at a dye/base pair (D/BP) ratio of 1:25 and incubated at 50 °C for 2 h to equilibrate the dye complexes with DNA (*19*). Polyplexes were formed at various N/P ratios from 0 to 5 by complexing YOYO-labeled DNA with the polymers or peptides in HBG as described above. Twenty microliters of the polyplex solution and 80 μL of HBG were added to each well of a 96-well plate, and the fluorescence from each well was measured on a Tecan Safire^2 plate reader with excitation at 491 nm and emission at 513 nm. Fluorescence signal from polyplexes with N/P > 0 was normalized to N/P = 0 (DNA only) signal.

Polyplex Unpackaging Studies. The gWiz-Luc plasmid was labeled with YOYO and poly(L-lysine) (PLL, 12−24 kDa, from Sigma), K_{11}-DNP peptide, and copolymers B1, C1, and D1 were used to form polyplexes at N/P = 5 in HBG as described above. Twenty microliters of polyplex solution were mixed with 80 μL of HBG, HBG containing 0.1 mg/mL heparan sulfate (HS, from Sigma), or HBG containing 0.5 mg/mL HS in each well of a 96-well plate. Additionally, 20 μL of polyplexes formed with copolymer B1 or D1 were mixed with 80 μL of HBG containing DTT and/or HS at specific concentrations in each well of a 96-well plate. The polyplexes mixed with 10 mM DTT were allowed to incubate for 30 min at RT, and the polyplexes

mixed with 25 mM DTT were allowed to incubate for 1 h at RT. The fluorescence from each well was measured on a Tecan Safire^2 plate reader with excitation at 491 nm and emission at 513 nm. Fluorescence signal from polyplexes with N/P > 0 was normalized to N/P = 0 (DNA only) signal.

***In Vitro* Transfection Efficiency.** Human cervix epithelial adenocarcinoma cells (HeLa, passage 25, ATCC # CCL-2) were seeded in complete cell culture medium (MEM + 10% FBS + 1% antibiotic/antimicrobial) at a density of 5×10^4 cells/well in each well of a 24-well plate. The 24-well plates were placed in a 37 °C incubator with 5% CO_2 for 24 h to allow the HeLa cells to attach. Polyplexes were formed at N/P = 5 using 1 μg of gWiz-Luc plasmid DNA in 20 μL total volume. Each sample was brought up to 200 μL with OptiMEM I (Invitrogen). The cells were washed twice with PBS, and the transfection solutions were added. The 24-well plates were returned to the incubator for 4 h, at which time the polyplex solution was replaced with complete cell culture media after washing the cells with PBS. The cells were returned to the incubator for a further 44 h. After a total incubation of 48 h, the luciferase expression was quantified with a luciferase assay kit (Promega Corp.) according to the manufacturer's instructions, except that a freeze−thaw cycle at −20 °C was included after the addition of the lysis buffer to ensure complete cell lysis. Luminescence intensity was measured on a Tecan Safire^2 plate reader with integration for 1 s. The total protein content in each well was measured by a BCA Protein Assay Kit (Pierce) according to the manufacturer's instructions so that the luciferase activity measured in each well could be normalized by the total protein content in each well. Each sample was tested in replicates with $n = 8$, but one outlier was identified in the copolymer D1 data set (using the interquartile method of identifying outliers). The statistical significance of differences in the samples was determined using Student's *t*-test, where a *p*-value of less than 0.05 was considered significant.

Cellular Toxicity. HeLa cells were seeded in complete cell culture medium at a density of 1×10^4 cells/well in each well of a 96-well plate. The 96-well plates were placed in a 37 °C incubator with 5% CO_2 for 24 h to allow the HeLa cells to attach. The cells were washed with PBS, the polymer and peptide samples were diluted to the indicated concentrations with OptiMEM, and 100 μL of polymer or peptide sample was added to the cells. The 96-well plates were returned to the incubator for 4 h, at which time the polymer or peptide solution was replaced with complete cell culture media after washing the cells with PBS. The cells were returned to the incubator for a further 40 h. Finally, 3-(4,5-dimethylthiazol-2-yl)-5-(3-carboxymethoxyphenyl)-2-(4-sulfophenyl)-2*H*-tetrazolium (MTS reagent, from Promega Corp.) was added to the cells, the cells were returned to the incubator for 4 h (for a total incubation of 48 h), and the number of viable cells in each well was quantified by measuring the absorbance at 490 nm on a Tecan Safire^2 plate reader.

RESULTS AND DISCUSSION

Synthesis of Fmoc-AEDP and Peptide Monomers. Oligolysine peptides containing 11 lysine residues and a lysine-DNP residue (K_{11}-DNP) were synthesized by SPPS. DNP was included as a label for the peptide; antibodies to DNP can be used in future studies to track the polymer. An Fmoc-protected, nonreducible or reducible linker (Ahx or AEDP, respectively) was then conjugated to the N-terminus of the peptides using the same SPPS chemistry. Finally, the deprotected N-termini of the linker-modified peptides **1** were reacted with MC **2** in order to introduce a reactive vinyl group for radical polymerization (Scheme 1). The masses of K_{11}-DNP, linker-modified, and MC-modified peptides agreed very well with the calculated masses, as shown in Table 2, and the purity of each peptide was found to be greater than 90% by HPLC (Supporting Information).

Table 2. Calculated Weights of the Various Peptide Monomers and Peptide Monomer Precursors Compared to the Weights Determined by ESI-MS

peptide	calculated (g/mol)	found (g/mol)[a]
K_{11}	1722.3	1722.6
K_{11}-Ahx	1835.3	1835.7
K_{11}-Ahx-MC	1903.3	1903.8
K_{11}-AEDP	1885.3	1885.7
K_{11}-AEDP-MC	1953.3	1953.7

[a] All weights found by mass spectrometry correlate within 0.03% of the actual mass.

Copolymerization of HPMA with Peptide Monomer. The vinyl-functionalized peptides **4** were copolymerized with HPMA by radical polymerization to generate copolymers **5** (Scheme 1). Poly(*N*-(2-hydroxypropyl)methacrylamide) (HPMA), originally synthesized by Kopeček and co-workers (*20, 21*), has been incorporated in polymer−drug conjugates that have entered phase I/II clinical trials (*22*−*26*). In a landmark clinical study, it was found that cumulative doses of HPMA copolymer in excess of 20 g/m^2 could be administered to patients without any polymer-related toxicity or immunogenicity (*22*). In addition, HPMA has been grafted onto quaternary amine-containing polymers and used to sterically stabilize polyplexes formed with these graft copolymers (*27*−*29*). HPMA was therefore chosen for copolymerization with peptide monomers due to its ease of incorporation into copolymers, ability to sterically stabilize colloids, and lack of toxicity when injected into human patients.

Three series of nonreducible poly(HPMA-*stat*-K_{11}) copolymers were synthesized in order to determine the effect of polymerization conditions on polymer properties and composition (Table 1). In series A, the amount of VA044 initiator used during polymerization was varied while keeping the total monomer concentration and ratios of comonomers (5 mol % peptide, 95 mol % HPMA) fixed. For uncontrolled radical polymerizations, increasing the radical to monomer ratio increases the number of chains initiated, thereby reducing the molecular weight of the resulting polymers. As expected, the copolymers synthesized in series A follow the trend of decreasing molecular weight with increasing amount of initiator (Table 1). HPLC analysis revealed that increasing the amount of initiator increased the incorporation of peptide into the copolymer but also increased the amount of HPMA homopolymer without any peptide. Thus, 5 wt % VA044 initiator was used for the subsequent polymerizations.

In series B and C, the amount of peptide monomer added in the feed was changed to 1 and 10 mol %, respectively. Among copolymers A3, B1, and C1, the weight percent initiator and total monomer concentration are constant, and the only difference is the mole percent of peptide monomer in the feed. A comparison of these copolymers shows that increasing the amount of peptide monomer in the feed leads to increased weight percent of peptide in the final copolymer, as well as a reduced overall molecular weight (Table 1). It is very likely that this reduction in overall molecular weight is caused by a lower reactivity of the peptide macromonomer, as it has been shown that macromonomers often have lower reactivities than smaller monomers (*30, 31*). Radke and Müller investigated copolymerization of macromonomers with methyl methacrylate and showed that increasing the macromonomer concentration leads to an increase in viscosity of the polymerization solution and a lower reactivity of the macromonomer due to decreased mobility of the larger macromonomer compared to the smaller comonomer (*30*). The authors also demonstrated that the average segment densities surrounding the propagating radical site

decrease with increasing distance between the reactive center and the nearest macromonomer (*30*). The macromonomer is therefore most reactive when it is at its lowest mole percent in the feed, resulting in long stretches of comonomer that extend the distance between macromonomers and reduce the steric hindrance of high segment densities that prevents the addition of the next macromonomer.

The incorporation efficiency of the peptide macromonomer decreases with increasing mole percent of peptide macromonomer in the feed (63% of feed for B1, 60% of feed for A3, and 44% of feed for C1), which is consistent with lower reactivity of the peptide monomer at higher mole percents in the feed. Furthermore, as the mole percent of peptide macromonomer is increased, the formation of long polymers becomes more dependent on the incorporation of the macromonomer to continue the polymerization. Thus, the decreased reactivity of the peptide macromonomer most likely plays a significant role in the reduction in total copolymer size seen with increasing mole percent of peptide monomer in the feed. Similar behavior was reported in another system where increasing the feed mole percent of a comonomer with lower reactivity decreased the overall molecular weight of the resulting copolymer (*32*). The decrease in molecular weight with increasing mole percent of peptide may also be attributed to the DNP label on the peptide, because it is known that DNP can act as a chain transfer agent during radical polymerization (*33, 34*). The ability of DNP to accept radicals retards the polymerization, extending the time required for polymerization in the presence of DNP compared to a polymerization in the same conditions except without DNP (*33*). Thus, the copolymers synthesized at the higher mole percent of peptide will be retarded the most due to the presence of the highest concentration of DNP, and 48 h may not be long enough to extend the chains fully, resulting in lower molecular weights.

Copolymers B2 and C2 were synthesized to determine the effect of changing the total monomer concentration in the polymerization solution. First, it should be noted that changing total monomer concentration had only a minor effect on the weight percent of peptide in the final copolymers. Also, the inverse relationship between peptide mole percent in the feed and resulting copolymer MW still held. Comparisons of B1 vs B2 and C1 vs C2 show that polymerizations at lower monomer concentrations led to copolymers with lower total molecular weights. It has been shown that the degree of polymerization (DP) of a polymer generated from macromonomers during uncontrolled radical polymerization increases with increasing macromonomer concentration, mainly due to the increase in viscosity at higher macromonomer concentrations (*35*). Higher viscosity reduces the rate of termination, thus extending the lifetime of the polymerization and increasing the DP, due to a diffusion-controlled limit on bimolecular termination (*35*). Thus, the viscosity of the reaction solution is an important factor for optimization: not only does a high viscosity decrease the reactivity of the macromonomers, which tends to lead to smaller copolymers, but a higher viscosity also decreases the rate of termination, which tends to allow for larger copolymers. Comparison within series B or series C in Table 1 shows that, for a given composition, increasing the monomer concentration leads to higher percent incorporation of the peptide in the final copolymer (44% for C1 compared to 39% for C2 and 63% for B1 compared to 40% for B2). Furthermore, when comparing between series, these studies demonstrate that the peptide monomer concentration has less of an effect on the percent peptide incorporation than does the mole percent of peptide monomer in the feed. Thus, the maximum concentration of 85 mg/mL (above which gelation of the reaction mixture would occur during polymerization) was employed for all further polymerizations.

Copolymer D1 was synthesized to investigate the effect of a reducible AEDP linker incorporated in the peptide monomer. The polymerization conditions for D1 were the same as for A3. Copolymer D1 has a lower MW and a slightly higher peptide mole percent incorporation in the final copolymer compared with A3. The difference in polymer properties might be due to the change in the hydrophobicity of the Ahx versus AEDP linkers in the peptide monomers, especially since the linker group is close to the propagating radical site. It is known that radical attack on an alkene can lead to radical transfer to a nearby sulfur atom and the opening of a ring during polymerization (*36*). However, the increased distance of the disulfide bond in the AEDP to the alkene group in the MC, compared to the single carbon spacer in the ring-opening polymerization (*36*), will greatly reduce the ability of the sulfur atom to accept radicals. Thus, only very minimal reversible chain transfer or chain extension through the sulfur atom is expected to occur in this system.

In summary, a library of p(HPMA-*stat*-K_{11}) copolymers was synthesized so that materials with a range of properties could be tested to determine the optimal formulation for gene delivery. The successful synthesis of copolymers with different amounts of peptide, different molecular weights, and reducible versus nonreducible linkages between the peptides and the copolymer backbone has been demonstrated.

Demonstration of Degradability of Copolymer D1. To test the degradation of copolymers synthesized with reducible (D1, with AEDP linker) and nonreducible (A4, with Ahx linker) peptides, D1 and A4 were incubated with the reducing agent DTT, and polymer degradation was monitored by HPLC (Figure 1). D1 copolymer elutes between 15 and 17 min. Treatment with 10 mM DTT results in free peptide release by 5 min (~14.7 min elution time). The resulting HPMA homopolymer elutes at 17.4 min. Taken together, these results show that, under reducing conditions, copolymer D1 is efficiently degraded into free peptide and the HPMA polymer backbone. Conversely, the DTT had no effect on the HPLC traces when incubated with nonreducible copolymer A4, indicating that the reducing agent was not able to cleave the peptide attached with a nonreducible linker (data not shown).

Polyplex Formulation and Characterization. Polyplexes were first formed by mixing copolymers with plasmid DNA in HBG. HBG was selected because it has previously been shown to be an ideal buffer for polyplex formulation with minimal aggregation (*37*). The cationic polymers poly(L-lysine) (PLL) and polyethylenimine (PEI) formed small polyplexes with sizes on the order of 200 nm when complexed with DNA at N/P = 5 in HBG (Figure 2). Similarly, all of the copolymers tested (A4, B1, C1, and D1) also formed small polyplexes with sizes around 200 nm when complexed with DNA at N/P = 5 in HBG. The size of polyplexes formed with unlabeled K_{11} peptide was very large (over 1 μm at N/P = 5 in HBG), consistent with the decreased ability of short cationic peptides to bind and condense DNA. Unexpectedly, the size of polyplexes formed with DNP-labeled K_{11} peptide at N/P = 5 in HBG was similar to the sizes of the polyplexes formed with the copolymers, PEI, and PLL. We hypothesize that the hydrophobic DNP label may increase the peptide's affinity for DNA, thus increasing its ability to condense DNA into small particles.

The salt stability of the polyplexes formed with the copolymers is an important characteristic, because polyplexes prepared for *in vivo* use will need to be salt stable when administered intravenously in order to avoid aggregation that can lead to embolism. The polyplexes are able to maintain small sizes in the low-salt HBG buffer because of intermolecular repulsion due to their positive surface charge at N/P = 5. However, when PBS is added, the higher amount of salt reduces the electrical

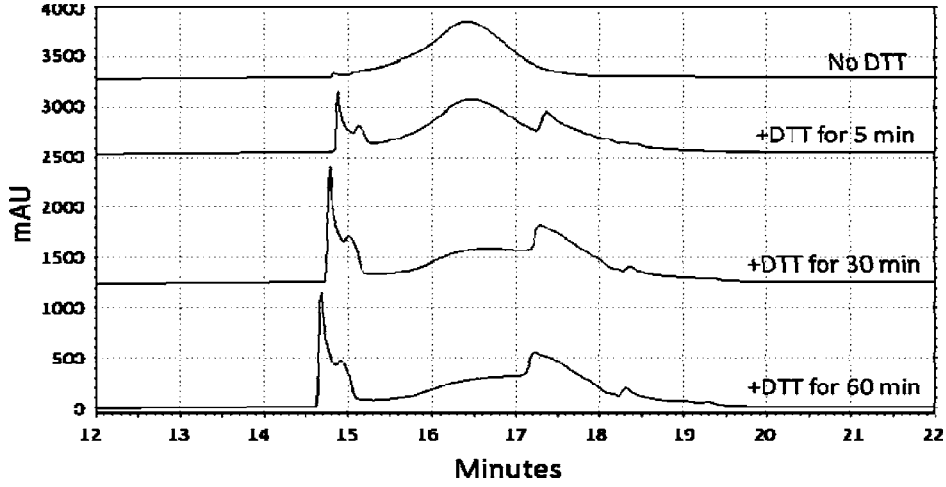


Figure 1. Evaluation of copolymer D1 degradation under reducing conditions. HPLC elution traces of copolymer D1 with no DTT and after being treated with DTT for various times. DTT treatment results in liberation of K_{11}-DNP peptide (14.7 min) and HPMA homopolymer (17.4 min).

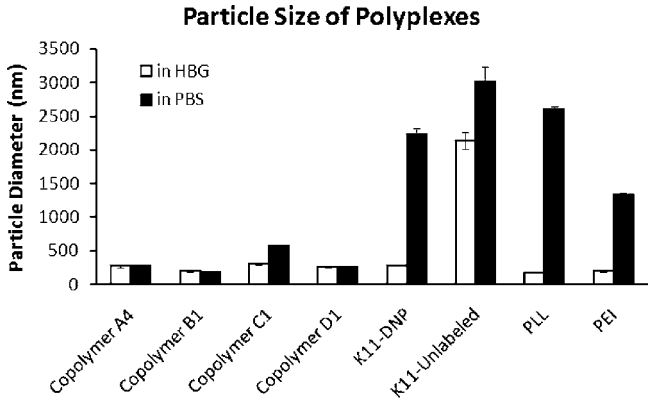


Figure 2. Polyplex size in HBG (20 mM salt) and 150 mM PBS. All peptides and polymers efficiently condensed plasmid in HBG to nanoparticles of <200 nm in diameter except unlabeled K_{11}. HPMA copolymers formed stabilized nanoparticles even in PBS.

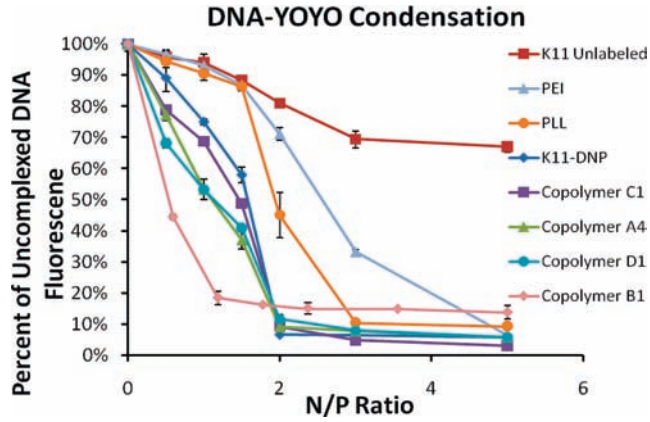


Figure 3. Extent of DNA condensation vs N/P ratio for HPMA copolymers, control polymers, and unpolymerized peptides. The fluorescence signal from DNA-YOYO was normalized to the fluorescence signal of DNA only (N/P = 0). Fluorescence signal decreases with increasing N/P ratio due to quenching of YOYO fluorescence resulting from DNA condensation.

double-layer thickness, rendering the particles susceptible to aggregation. As seen in Figure 2, PLL- and PEI-based polyplexes aggregate to sizes over 1 μm when diluted in PBS. Similar aggregation behavior is observed for the polyplexes formed with either unlabeled or DNP-labeled peptide. In contrast, polyplexes formed with all of the copolymers remain stable with a small size, even when diluted into PBS. It has been shown that cationic polymers modified with HPMA can be used to condense DNA and remain stable at high salt concentrations (*27*), where the HPMA is believed to take on a brush-like conformation on the surface and prevent aggregation by acting as a steric barrier. In a similar manner, a portion of the hydrophilic HPMA segments of the copolymer will be present on the surface of the polyplexes, and we hypothesize that they also adopt a brush-like conformation on the polyplex surface to resist aggregation. In support of this theory is the fact that copolymer C1, which has the lowest percentage of HPMA, almost doubles in size upon addition of PBS.

Determination of Plasmid Packaging Efficiency. The efficiency of plasmid condensation by polycations can be monitored by a YOYO-1 quenching assay (*19*). The fluorescence of the YOYO-1 DNA intercalator is quenched when YOYO-labeled plasmid is packaged into a condensed state. Addition of PLL or PEI to YOYO-labeled plasmid results in decreasing fluorescence with increasing N/P ratio, with full condensation occurring at N/P = 3 for PLL and N/P = 5 for PEI (Figure 3). The unlabeled K_{11} peptide is unable to efficiently condense plasmid at the N/P ratios investigated. These results are consistent with the particle sizing results, where at N/P = 5 the unlabeled peptide was not able to form small particles. In contrast, the DNP-labeled K_{11} peptide fully condensed DNA at N/P = 2. Again, these results are fully consistent with the particle sizing results, which indicated that the K_{11}-DNP peptide was able to condense DNA into small particles. The copolymers condensed DNA more efficiently than K_{11}-DNP likely due to the higher cationic valency of the copolymers. However, this effect is minor compared to the benefit derived from having HPMA in the copolymer. As can be seen in Figure 3, the copolymer able to most effectively condense DNA is B1, which has the lowest mole percent of peptide, and the copolymer to least effectively condense DNA is C1, which has the highest mole percent of peptide. Copolymers A4 and D1, which contain an intermediate amount of peptide between that of B1 and C1, possess an intermediate ability to condense DNA. These data suggest that the presence of HPMA drastically increases the affinity of the copolymer for the DNA. A YOYO condensation assay was performed with HPMA homopolymer, and YOYO fluorescence was partially quenched, lending support to the hypothesis that HPMA itself is able to interact with the DNA.

Determination of Plasmid Unpackaging. For systemic delivery applications, vector stability in the bloodstream and tissue is an important consideration. We and others have

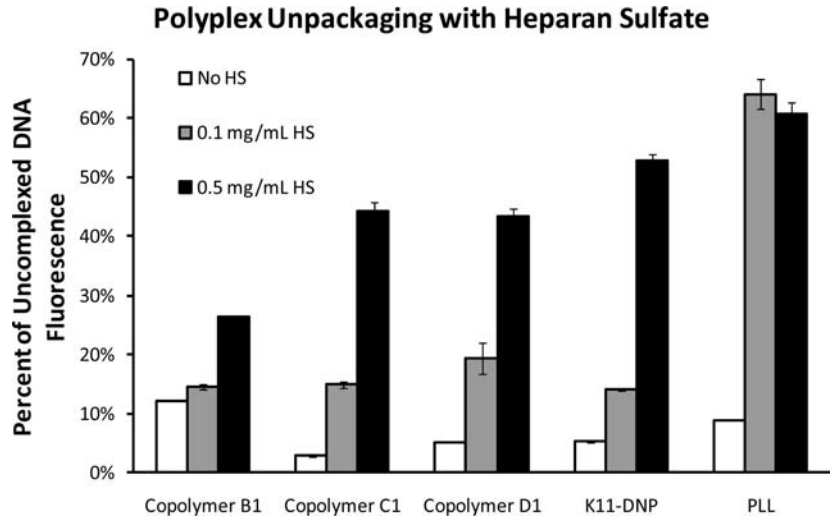


Figure 4. HS-mediated unpackaging of YOYO-labeled polyplexes. HS was diluted in HBG at various concentrations, and 80 μL of the indicated solution was added to 20 μL of polyplex (N/P = 5) containing 1 μg of DNA. Fluorescence signal increases after incubation with HS due to polyplex unpackaging and dequenching of YOYO fluorescence.

previously demonstrated that extracellular polyanions cause premature PEI polyplex unpackaging *in vivo* likely due to a polyelectrolyte exchange reaction (*19, 38, 39*). Polyplex stability in the presence of destabilizing agents can also be evaluated using a YOYO-based fluorescence assay. As can be seen in Figure 4, polyplexes formed at N/P = 5 and diluted with HBG containing no HS are fully packaged, indicated by low YOYO fluorescence. Polyplexes formed with PLL or PEI are fully unpackaged after dilution into HBG containing HS at a concentration of 0.1 mg/mL (PEI data not shown). In contrast, polyplexes formed with copolymer B1 maintained DNA in a fully condensed state after incubation with 0.1 mg/mL HS. Polyplexes formed with copolymer C1 or D1 and polyplexes formed with K_{11}-DNP were found to unpackage only slightly when incubated with 0.1 mg/mL HS. When the concentration of HS was increased to 0.5 mg/mL, polyplexes formed with K_{11}-DNP peptide fully unpackaged, while polyplexes formed with copolymers B1, C1, and D1 remained partially packaged. These results are consistent with the affinities of the copolymers for DNA determined in the DNA-YOYO condensation assay. We hypothesize that both the DNP label and the HPMA can interact with the DNA, thus increasing the affinity of the binding of the copolymers and peptides to DNA and decreasing the susceptibility of the polyplexes to unpackaging.

The optimal design of the polymeric *in vivo* gene delivery vehicle will need to allow for intracellular unpackaging, which is required for transcription (*40*). If the vectors are simply designed for maximum extracellular stability, they will be unable to unpackage intracellularly, and the delivered cargo will be rendered useless. To overcome this challenge, copolymers were synthesized containing the DNA-condensing peptides linked to the polymer backbone through a reducible disulfide linkage. When the peptides are cleaved from the copolymer backbone, the affinity for DNA should be decreased and unpackaging should be more likely. The extracellular milieu is known to be an oxidizing environment; in contrast, the cytosol is a highly reducing environment due to the excess of reduced glutathione (GSH), thioredoxin, glutaredoxin, peroxiredoxins, and nicotinamide adenine dinucleotides (NADH and NADPH) over the oxidized analogues of these molecules (*41*−*43*).

The extent of polyplex unpackaging due to competitive displacement of the polycation by HS was evaluated under reducing and nonreducing conditions for polyplexes formed with copolymer D1 (Figure 5). The polyplexes were first formed and then diluted in a buffer containing DTT, HS, or both. Reducing the linkage on copolymer D1 between peptide and polymer backbone without adding HS did not lead to any destabilization. Adding HS without DTT decreased the condensation state of the DNA-YOYO from 5% of uncomplexed DNA fluorescence to 19% of uncomplexed DNA fluorescence. Including 10 mM DTT or 25 mM DTT in the incubation with HS decreased the condensation state of the DNA-YOYO further, to 31% and 35% of uncomplexed DNA fluorescence, respectively. Reducing agents are present intracellularly at low millimolar concentrations (*41*), so these conditions were chosen to mimic the intracellular environment most closely. As can be seen from Figure 4, the maximum fluorescence recovery achieved with even 0.5 mg/mL HS was 60% of uncomplexed DNA fluorescence. There is a slight further increase in unpackaging when the DTT concentration and incubation time are increased. Thus, the polyplexes formed from copolymer D1 are more easily unpackaged under the reducing conditions of the cell cytosol. Polymers synthesized with peptides that do not contain the DNP label are expected to exhibit even more efficient DNA release under reducing conditions. In contrast, polyplexes formed from the nonreducible copolymer B1 were unaffected by any of the treatments.

***In Vitro* Transfection Efficiency.** gWiz-Luc plasmid was delivered to HeLa cells using various delivery vehicles, and the efficiency of delivery was determined by the quantitative luciferase reporter system (Figure 6). Unlabeled K_{11} peptide did not mediate increased gene delivery over plasmid DNA only (data not shown) most likely due to its inability to form stable polyplexes; however, the DNP-labeled K_{11} peptide, which was able to form stable polyplexes, did mediate an increased gene delivery efficiency compared to DNA only, though this difference was not statistically significant due to high variability. All of the copolymers were found to mediate statistically significant ($p < 0.01$) increases in transgene expression compared to plasmid only. In addition, copolymers A3, C1, and D1 mediated statistically significantly ($p < 0.01$) increased transfection efficiency compared to unpolymerized K_{11}-DNP peptide.

Since the delivery efficiency of oligolysine and PLL is known to depend on the molecular weight of the cationic delivery agent, it was expected that the copolymers that have more than one peptide incorporated and thus a higher effective molecular weight of lysine segments would have higher delivery efficiency than peptide alone. Due to the same effect, it was also expected that the copolymers based on the nonreducible Ahx linker would show increasing efficiency with increasing amounts of peptide

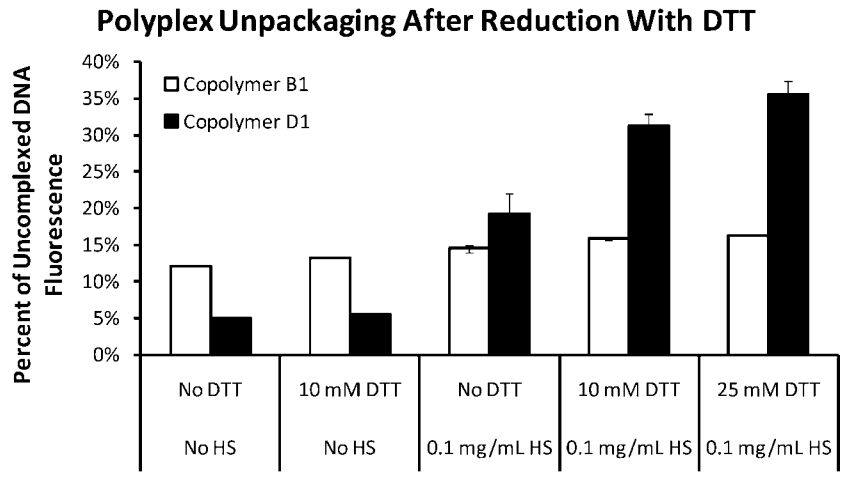


Figure 5. HS-mediated unpackaging of YOYO-labeled polyplexes formed with reducible (D1) and nonreducible (B1) copolymers before and after incubation with the reducing agent DTT. HS and DTT were diluted in HBG at various concentrations, and 80 μL of the indicated solution was added to 20 μL of polyplex (N/P = 5) containing 1 μg of DNA. The samples containing 10 mM DTT were incubated for 30 min and the samples containing 25 mM DTT were incubated for 1 h to ensure complete reduction of the disulfide linker.

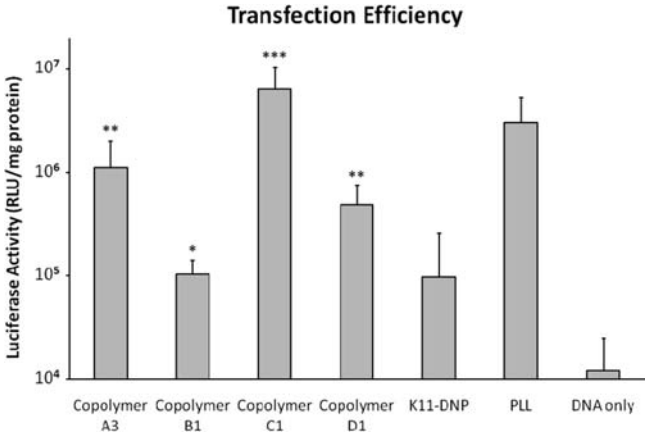


Figure 6. Gene delivery efficiency of selected carriers (formulated at N/P = 5) to HeLa cells as measured by luciferase activity 48 h after transfection. Results are reported as the mean RLU/mg protein ± SD for replicate samples, with all samples having $n > 7$. The asterisk (*) denotes that copolymer B1 was statistically significantly different from DNA only ($p < 0.01$). The double asterisk (**) denotes that copolymer A3 and copolymer D1 were both statistically significantly different from copolymer B1 ($p < 0.01$), K_{11}-DNP peptide ($p < 0.01$), and DNA only ($p < 0.01$). The triple asterisk (***) denotes that copolymer C1 was statistically significantly different from copolymer A3 ($p < 0.01$), copolymer B1 ($p < 0.01$), copolymer D1 ($p < 0.01$), K_{11}-DNP peptide ($p < 0.01$), PLL ($p < 0.05$), and DNA only ($p < 0.01$).

in the copolymer. This trend was observed, with C1 having 37.8 wt % peptide and the highest delivery efficiency, A3 having 30 wt % peptide and an intermediate delivery efficiency, and B1 having 7.7 wt % peptide and the lowest delivery efficiency. However, the average number of peptides per copolymer was inversely proportional to the copolymer transfection efficiency. These data indicate that the weight percent of peptide in the copolymer, not the absolute number of peptide monomers in the copolymer, is correlated with transfection efficiency.

One possible explanation is that the density of peptides in the copolymer could determine the cooperativity of the increase in effective polycation molecular weight. For example, copolymer B1 has an average of approximately 158 HPMA monomers per peptide monomer. In contrast, copolymer A3 has ~32 HPMA monomers per peptide monomer on average, and copolymer C1 has ~22 HPMA monomers per peptide monomer. Assuming even distribution of peptides in the polymer chain, copolymers with peptides that are more closely spaced could possess a higher effective polycation molecular weight and mediate more effective gene delivery, while the copolymers with peptides spaced further apart could have a lower effective polycation molecular weight and lower transfection efficiency.

Another possible explanation is that vector unpackaging affects transfection efficiency. Schaffer et al. have shown that the vectors with high intracellular stability mediated the lowest amounts of gene expression, while expression was greatly enhanced by using vehicles that easily dissociated from the DNA because the DNA could more easily be transcribed (*40*). From Figure 3, it can be seen that copolymer B1 condenses DNA most efficiently, while copolymer C1 condenses DNA least efficiently (among the Ahx-based copolymers). Analogously, from Figure 4, it can be seen that copolymer B1 is more resistant to unpackaging than copolymer C1.

A third possible explanation for the differences in transfection efficiencies is that polyplexes formed with the different copolymers may have unequal abilities to mediate cellular internalization. Polyplexes generated from covalently linked PLL-HPMA were found to have reduced cellular association and internalization compared to polyplexes formed with unmodified PLL (*29*). Conjugation of poly(ethylene glycol), another polar nonionic polymer, to PEI polyplexes causes a reduction in the amount of polyplex internalization that leads to a decreased transfection efficiency (*44, 45*). It has been noted that increasing the amount of shielding polymer PEG in PEI-based polyplexes reduces transfection efficiency (*45*), which is similar to the observed trends of decreasing transfection efficiency for poly(HPMA-*stat*-K_{11}) copolymers with increasing amounts of HPMA.

The AEDP-based, reducible copolymer D1 has a similar weight percent of peptide and resistance to unpackaging under nonreducing conditions when compared to copolymer C1 (Figure 4). However, from Figure 6, it can be seen that the transfection efficiency of copolymer D1 is statistically significantly lower ($p < 0.01$) than that of copolymer C1. If copolymer D1 degradation and plasmid release occurs much more rapidly than nuclear delivery of plasmid, the DNA may be degraded by nucleases before transcription can occur. Thus, the data suggest that there is an optimal intracellular stability of polyplexes for efficient gene expression.

It should be noted that copolymer C1 was found to mediate a higher transfection efficiency than PLL ($p < 0.05$). Copolymer C1 was able to more efficiently deliver DNA even though it only has about 8 kDa of mass from oligolysine in each copolymer. Copolymer C1 may have nearly optimal oligolysine

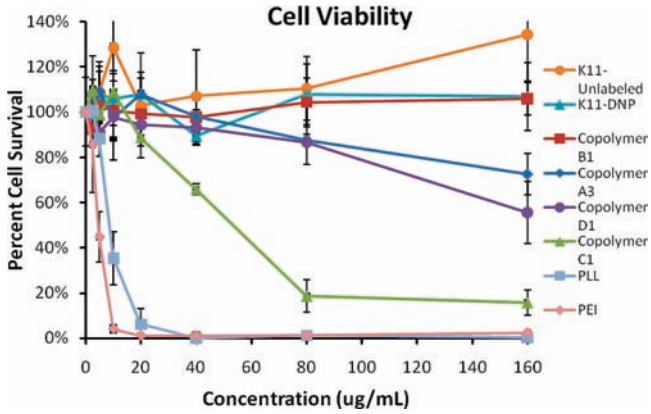


Figure 7. Cell viability of HeLa cells after incubation with free polymers, copolymers, and peptides at the indicated concentrations, as measured by an MTS assay.

content for DNA packaging without limiting intracellular DNA release. In this study, the copolymers were compared to PLL because, like PLL, they contain only primary amines on the lysine side chains to serve as cationic groups for DNA condensation. PEI, in contrast, has secondary and tertiary (in the case of branched PEI) amines that have lower pK_a values. It is currently believed that PEI mediates endosomal escape through a proton sponge effect due to this buffering capacity (*46*−*48*), which leads to typically higher transfection efficiencies than those achieved by PLL. This modular copolymer system has the ability to incorporate other peptides that may include endosomal escape functionality to further increase the transfection efficiency to rival that of PEI.

Cellular Toxicity. Both the efficacy and the toxicity of cationic polymer gene delivery vehicles are directly related to their molecular weight (*9*). The toxicity of the synthesized polymers, PLL, and PEI was tested in HeLa cells. Cheng et al. recently demonstrated that the toxicity profiles of polycations against HEK293, HeLa, and HepG2 are very similar (*49*); therefore, HeLa cell lines were used as a representative cell line. All of the synthesized copolymers were found to be much less toxic than PLL (Figure 7). One factor very likely contributing to the lower toxicity is that the copolymers contain HPMA, and HPMA has been shown to be nontoxic up to very high concentrations (*22*). Even still, copolymer A3 has, on average, 15.7 kDa of oligolysine for each polymer strand, which is comparable to the 12−24 kDa PLL that was used. Copolymer A3 is found to have good biocompatibility, with greater than 70% cell viability at the highest concentration tested. The lower toxicity may be due to the spacing of HPMA between peptides that reduces the toxicity associated with the cationic lysines. Copolymer C1 contains, on average, 8 kDa of oligolysine per polymer strand, but has a high peptide weight percent (and thus the fewest HPMA monomers spaced between its peptides) and was the most toxic of all the copolymers tested. It has been suggested that one mechanism for cationic polymer-induced cellular toxicity is for the polymers to form channels in the outer mitochondrial membrane, which allows the caspase-3 translocation and cytochrome *c* release that are hallmarks of apoptosis (*50*). We speculate that the HPMA between the peptides hinders the formation of these channels in the outer mitochondrial membrane, thus reducing the toxicity of the copolymers with large amounts of HPMA spaced between the peptides.

Several investigators have cross-linked low-molecular-weight polycations using reducible disulfide bonds to generate high-molecular-weight conjugates that efficiently condense and deliver DNA, but which become less cytotoxic fragments upon intracellular reduction (*9*−*15*). Copolymer D1 was synthesized to allow reduction of the peptide linkers and release of peptides from the polymer backbone. In composition, reducible copolymer D1 is very comparable to the nonreducible copolymer C1, with 10 kDa and 8 kDa from oligolysine in the copolymer, 35.5 and 37.8 wt % peptide, and 25 and 22 HPMA monomers between each peptide, respectively. Despite the similarities in composition, copolymer D1 is much less toxic than copolymer C1 (Figure 7).

CONCLUSIONS

We have demonstrated the synthesis of novel copolymers for gene delivery by radical copolymerization of a modified peptide monomer with an HPMA comonomer. These copolymers can condense DNA into small polyplexes that are stable at physiological salt concentrations and also resistant to unpackaging. The copolymers were also shown to deliver DNA into HeLa cells with an efficiency comparable to PLL while mediating much less cytotoxicity than PLL. This modular system has the capacity to incorporate other types of peptides into the polymer backbone, and these peptides may perform functions that increase transfection efficiency (such as endosomal escape) or specificity (such as targeting). Furthermore, the polymerization conditions could be further optimized to produce better copolymers. In contrast to traditional free radical polymerization that leads to suboptimal incorporation of macromonomers, it has been shown that controlled polymerization schemes greatly improve the incorporation of macromonomers into copolymers by reducing the disparity in reactivities between macromonomers and the smaller comonomers (*31*). Moving to a controlled radical polymerization technique also has the added benefit of producing more well-defined copolymers of more consistent composition and with lower PDIs. The development of nearly monodisperse, targeted copolymers that mediate high levels of gene delivery can be possible in the near future using this system as a basis for further improvements.

ACKNOWLEDGMENT

The authors would like to thank Dr. Anthony Convertine for helpful discussions regarding the polymerization strategy. Mass spectrometry was performed in the Department of Chemistry Mass Spectrometry Facility, with special thanks to Dr. Martin Sadilek for his training and support on the ESI-MS instrument. GPC was performed with equipment in the laboratory of Dr. Patrick Stayton and Dr. Allan Hoffman, with special thanks to Dr. Scott Henry for his assistance. This work was supported by an NSF CAREER Award (CBET-0448547) to S.H.P., and NIH/NINDS grants 5R21NS052030 and 1R01NS064404. R.S.B. is grateful to the National Science Foundation for a graduate research fellowship.

Supporting Information Available: Figure S1 shows the mass spectrum of K_{11} peptide. Figure S2 shows the mass spectrum of K_{11}-Ahx peptide. Figure S3 shows the mass spectrum of K_{11}-Ahx-MC peptide. Figure S4 shows HPLC chromatograms for K_{11}, K_{11}-AEDP, and K_{11}-AEDP-MC peptides. This material is available free of charge via the Internet at http://pubs.acs.org.

LITERATURE CITED

(1) Bergen, J., and Pun, S. (2005) Peptide-enhanced nucleic acid delivery. *MRS Bull. 30*, 663–667.
(2) Kwon, E., Bergen, J., Park, I., and Pun, S. (2008) Peptide-modified vectors for nucleic acid delivery to neurons. *J. Controlled Release 132*, 230–235.
(3) Martin, M. E., and Rice, K. G. (2007) Peptide-guided gene delivery. *AAPS J. 9*, E18−E29.

(4) O'Brien-Simpson, N. M., Ede, N. J., Brown, L. E., Swan, J., and Jackson, D. C. (1997) Polymerization of unprotected synthetic peptides: A view toward synthetic peptide vaccines. *J. Am. Chem. Soc. 119*, 1183–1188.
(5) Jackson, D. C., O'Brien-Simpson, N., Ede, N. J., and Brown, L. E. (1997) Free radical induced polymerization of synthetic peptides into polymeric immunogens. *Vaccine 15*, 1697–705.
(6) Graham, K. L., Zeng, W. G., Takada, Y., Jackson, D. C., and Coulson, B. S. (2004) Effects on rotavirus cell binding and infection of monomeric and polymeric peptides containing alpha 2 beta 1 and alpha × beta 2 integrin ligand sequences. *J. Virol. 78*, 11786–11797.
(7) Liu, Z. H., Li, M. Y., Cui, D. F., and Fei, J. (2005) Macro-branched cell-penetrating peptide design for gene delivery. *J. Controlled Release 102*, 699–710.
(8) Ding, H., Prodinger, W. M., and Kopecek, J. (2006) Identification of CD21-binding peptides with phage display and investigation of binding properties of HPMA copolymer-peptide conjugates. *Bioconjugate Chem. 17*, 514–523.
(9) Breunig, M., Lungwitz, U., Liebl, R., and Goepferich, A. (2007) Breaking up the correlation between efficacy and toxicity for nonviral gene delivery. *Proc. Natl. Acad. Sci. U.S.A. 104*, 14454–14459.
(10) McKenzie, D. L., Smiley, E., Kwok, K. Y., and Rice, K. G. (2000) Low molecular weight disulfide cross-linking peptides as nonviral gene delivery carriers. *Bioconjugate Chem. 11*, 901–909.
(11) Gosselin, M. A., Guo, W. J., and Lee, R. J. (2001) Efficient gene transfer using reversibly cross-linked low molecular weight polyethylenimine. *Bioconjugate Chem. 12*, 989–994.
(12) Siprashvili, Z., Scholl, F. A., Oliver, S. F., Adams, A., Contag, C. H., Wender, P. A., and Khavari, P. A. (2003) Gene transfer via reversible plasmid condensation with cysteine-flanked, internally spaced arginine-rich peptides. *Hum. Gene Ther. 14*, 1225–1233.
(13) Read, M. L., Singh, S., Ahmed, Z., Stevenson, M., Briggs, S. S., Oupicky, D., Barrett, L. B., Spice, R., Kendall, M., Berry, M., Preece, J. A., Logan, A., and Seymour, L. W. (2005) A versatile reducible polycation-based system for efficient delivery of a broad range of nucleic acids. *Nucleic Acids Res. 33*, e86.
(14) Kloeckner, J., Wagner, E., and Ogris, M. (2006) Degradable gene carriers based on oligomerized polyamines. *Eur. J. Pharm. Sci. 29*, 414–425.
(15) Peng, Q., Zhong, Z. L., and Zhuo, R. X. (2008) Disulfide cross-linked polyethylenimines (PEI) prepared via thiolation of low molecular weight PEI as highly efficient gene vectors. *Bioconjugate Chem. 19*, 499–506.
(16) Wadhwa, M. S., Collard, W. T., Adami, R. C., McKenzie, D. L., and Rice, K. G. (1997) Peptide-mediated gene delivery: influence of peptide structure on gene expression. *Bioconjugate Chem. 8*, 81–8.
(17) Fields, C. G., Fields, G. B., Noble, R. L., and Cross, T. A. (1989) Solid-phase peptide-synthesis of N-15-gramicidin-a, N-15-gramicidin-B, and N-15-gramicidin-C and high-performance liquid-chromatographic purification. *Int. J. Pept. Protein Res. 33*, 298–303.
(18) Jiang, X. L., van der Horst, A., van Steenbergen, M. J., Akeroyd, N., van Nostrum, C. F., Schoenmakers, P. J., and Hennink, W. E. (2006) Molar-mass characterization of cationic polymers for gene delivery by aqueous size-exclusion chromatography. *Pharm. Res. 23*, 595–603.
(19) Burke, R. S., and Pun, S. H. (2008) Extracellular barriers to in Vivo PEI and PEGylated PEI polyplex-mediated gene delivery to the liver. *Bioconjugate Chem. 19*, 693–704.
(20) Kopecek, J., and Bazilova, H. (1973) Poly[N-(2-hydroxypropyl)methacrylamide] 0.1. Radical polymerization and copolymerization. *Eur. Polym. J. 9*, 7–14.
(21) Strohalm, J., and Kopecek, J. (1978) Poly[N-(2-hydroxypropyl)methacrylamide] 0.4. Heterogeneous polymerization. *Angew. Makromol. Chem. 70*, 109–118.
(22) Vasey, P. A., Kaye, S. B., Morrison, R., Twelves, C., Wilson, P., Duncan, R., Thomson, A. H., Murray, L. S., Hilditch, T. E., Murray, T., Burtles, S., Fraier, D., Frigerio, E., and Cassidy, J. (1999) Phase I clinical and pharmacokinetic study of PK1 [N-(2-hydroxypropyl)methacrylamide copolymer doxorubicin]: first member of a new class of chemotherapeutic agents-drug-polymer conjugates. Cancer Research Campaign Phase I/II Committee. *Clin. Cancer Res. 5*, 83–94.
(23) Duncan, R., Gac-Breton, S., Keane, R., Musila, R., Sat, Y. N., Satchi, R., and Searle, F. (2001) Polymer-drug conjugates, PDEPT and PELT: basic principles for design and transfer from the laboratory to clinic. *J. Controlled Release 74*, 135–146.
(24) Duncan, R. (2003) The dawning era of polymer therapeutics. *Nat. Rev. Drug Discovery 2*, 347–360.
(25) Rihova, B., and Kubackova, K. (2003) Clinical implications of N-(2-hydroxypropyl)methacrylamide copolymers. *Curr. Pharm. Biotechnol. 4*, 311–22.
(26) Haag, R., and Kratz, F. (2006) Polymer therapeutics: concepts and applications. *Angew. Chem., Int. Ed. Engl. 45*, 1198–215.
(27) Oupicky, D., Konak, C., and Ulbrich, K. (1999) DNA complexes with block and graft copolymers of N-(2-hydroxypropyl)methacrylamide and 2-(trimethylammonio)ethyl methacrylate. *J. Biomater. Sci. Polym. Ed. 10*, 573–90.
(28) Oupicky, D., Konak, C., Dash, P. R., Seymour, L. W., and Ulbrich, K. (1999) Effect of albumin and polyanion on the structure of DNA complexes with polycation containing hydrophilic nonionic block. *Bioconjugate Chem. 10*, 764–72.
(29) Oupicky, D., Konak, C., Ulbrich, K., Wolfert, M. A., and Seymour, L. W. (2000) DNA delivery systems based on complexes of DNA with synthetic polycations and their copolymers. *J. Controlled Release 65*, 149–71.
(30) Radke, W., and Muller, A. H. E. (1992) Copolymerization of methacryloyl-terminated PMMA macromonomers with methylmethacrylate. *Makromol. Chem., Macromol. Symp. 545*, 583–594.
(31) Shinoda, H., Miller, P. J., and Matyjaszewski, K. (2001) Improving the structural control of graft copolymers by combining ATRP with the macromonomer method. *Macromolecules 34*, 3186–3194.
(32) Neugebauer, D., Zhang, Y., and Pakula, T. (2006) Gradient graft copolymers derived from PEO-based macromonomers. *J. Polym. Sci., Part A: Polym. Chem. 44*, 1347–1356.
(33) Lang, J. L. (1960) Retardation of polymerization in substituted styrenes by chelated nitrophenols. *J. Chem. Eng. Data 5*, 53–56.
(34) Motyakin, M. V., Wasserman, A. M., Stott, P. E., and Zaikov, G. E. (2004) Inhibitor radicals in styrene polymerization. *J. Appl. Polym. Sci. 91*, 1599–1603.
(35) Tsutsumi, K., Okamoto, Y., and Tsukahara, Y. (1994) Radical polymerization behavior of macromonomers 0.3. Effect of macromonomer concentration. *Polymer 35*, 2205–2209.
(36) Paulusse, J. M. J., Amir, R. J., Evans, R. A., and Hawker, C. J. (2009) Free radical polymers with tunable and selective bio- and chemical degradability. *J. Am. Chem. Soc. 131*, 9805–9812.
(37) Ogris, M., Steinlein, P., Kursa, M., Mechtler, K., Kircheis, R., and Wagner, E. (1998) The size of DNA/transferrin-PEI complexes is an important factor for gene expression in cultured cells. *Gene Ther. 5*, 1425–1433.
(38) Ruponen, M., Yla-Herttuala, S., and Urtti, A. (1999) Interactions of polymeric and liposomal gene delivery systems with extracellular glycosaminoglycans: physicochemical and transfection studies. *Biochim. Biophys. Acta Biomembr. 1415*, 331–341.
(39) Moret, I., Peris, J. E., Guillem, V. M., Benet, M., Revert, F., Dasi, F., Crespo, A., and Alino, S. F. (2001) Stability of PEI-DNA and DOTAP-DNA complexes: effect of alkaline pH, heparin and serum. *J. Controlled Release 76*, 169–181.
(40) Schaffer, D. V., Fidelman, N. A., Dan, N., and Lauffenburger, D. A. (2000) Vector unpacking as a potential barrier for receptor-mediated polyplex gene delivery. *Biotechnol. Bioeng. 67*, 598–606.
(41) Holmgren, A. (1989) Thioredoxin and glutaredoxin systems. *J. Biol. Chem. 264*, 13963–13966.

(42) Arunachalam, B., Phan, U. T., Geuze, H. J., and Cresswell, P. (2000) Enzymatic reduction of disulfide bonds in lysosomes: Characterization of a Gamma-interferon-inducible lysosomal thiol reductase (GILT). *Proc. Natl. Acad. Sci. U.S.A. 97*, 745–750.

(43) Yang, J., Chen, H., Vlahov, I. R., Cheng, J. X., and Low, P. S. (2006) Evaluation of disulfide reduction during receptor-mediated endocytosis by using FRET imaging. *Proc. Natl. Acad. Sci. U.S.A. 103*, 13872–13877.

(44) Mishra, S., Webster, P., and Davis, M. E. (2004) PEGylation significantly affects cellular uptake and intracellular trafficking of non-viral gene delivery particles. *Eur. J. Cell Biol. 83*, 97–111.

(45) Kursa, M., Walker, G. F., Roessler, V., Ogris, M., Roedl, W., Kircheis, R., and Wagner, E. (2003) Novel shielded transferrin-polyethylene glycol-polyethylenimine/DNA complexes for systemic tumor-targeted gene transfer. *Bioconjugate Chem. 14*, 222–231.

(46) Boussif, O., Lezoualch, F., Zanta, M. A., Mergny, M. D., Scherman, D., Demeneix, B., and Behr, J. P. (1995) A versatile vector for gene and oligonucleotide transfer into cells in culture and in-vivo - polyethylenimine. *Proc. Natl. Acad. Sci. U.S.A. 92*, 7297–7301.

(47) Sonawane, N. D., Szoka, F. C., and Verkman, A. S. (2003) Chloride accumulation and swelling in endosomes enhances DNA transfer by polyamine-DNA polyplexes. *J. Biol. Chem. 278*, 44826–44831.

(48) Akinc, A., Thomas, M., Klibanov, A. M., and Langer, R. (2005) Exploring polyethylenimine-mediated DNA transfection and the proton sponge hypothesis. *J. Gene Med. 7*, 657–663.

(49) Cheng, H., Zhu, J. L., Zeng, X., Jing, Y., Zhang, X. Z., and Zhuo, R. X. (2009) Targeted gene delivery mediated by folate-polyethylenimine-block-poly(ethylene glycol) with receptor selectivity. *Bioconjugate Chem. 20*, 481–487.

(50) Hunter, A. C. (2006) Molecular hurdles in polyfectin design and mechanistic background to polycation induced cytotoxicity. *Adv. Drug Delivery Rev. 58*, 1523–31.

BC9003662

Genetic Engineering of a Bifunctional IgG Fusion Protein with Iduronate-2-Sulfatase

Jeff Zhiqiang Lu,[†] Eric Ka-Wai Hui,[†] Ruben J. Boado,[†,‡] and William M. Pardridge*[,‡]

ArmaGen Technologies, Inc., Santa Monica, California 90401, and Department of Medicine, University of California Los Angeles, Los Angeles, California 90024. Received August 31, 2009; Revised Manuscript Received October 5, 2009

Iduronate-2-sulfatase (IDS) is a lysosomal sulfatase that prevents the accumulation within the brain of glycosoaminoglycans. However, IDS does not cross the blood−brain barrier (BBB). To enable BBB transport, human IDS, minus its signal peptide, was fused to the carboxyl terminus of the heavy chain of a chimeric monoclonal antibody (mAb) to the human insulin receptor (HIR). The HIRMAb crosses the BBB on the endogenous insulin receptor and acts as a molecular Trojan horse to ferry the IDS into brain. The HIRMAb-IDS fusion protein was expressed in COS cells and purified with protein A affinity chromatography. The size of the fusion heavy chain, as measured with Western blotting and antibodies to either human IDS or human IgG, was increased about 80 kDa, relative to the size of the heavy chain of the parent HIRMAb. The HIRMAb-IDS fusion protein retained high-affinity binding for the HIR. The IDS enzyme specific activity of the fusion protein was 51 ± 7 nmol/h per microgram of protein, which is comparable to the enzyme activity of recombinant IDS. The fusion protein was taken up by human fibroblasts, and the accumulation of glycosoaminoglycans in fibroblasts null for the sulfatase was decreased 84% by treatment with the fusion protein. The HIRMAb-IDS fusion protein is a bifunctional IgG-sulfatase fusion protein, which has been specifically engineered for targeted drug delivery across the human BBB.

INTRODUCTION

Mucopolysaccharidosis (MPS) type II (MPS-II), or Hunter's syndrome, is a lysosomal storage disorder caused by defects in the gene encoding the lysosomal enzyme, iduronate-2-sulfatase (IDS) (*1*). MPS-II is treated with recombinant human IDS in enzyme replacement therapy (*2*). However, many cases of MPS-II affect the central nervous system (*3, 4*), and enzyme replacement therapy is not effective for the brain, because the IDS does not cross the blood−brain barrier (BBB) (*4, 5*). In MPS-II cases that do affect the brain, the use of ERT is considered optional (*5*).

IDS, and other lysosomal enzymes, can be made to cross the human BBB following the re-engineering of the enzyme as a fusion protein with a BBB molecular Trojan horse (*6*). The latter is an endogenous peptide, or peptidomimetic monoclonal antibody (mAb), that crosses the BBB via an endogenous receptor-mediated transport system. The molecular Trojan horse with the highest BBB permeation rate is a mAb against the α-subunit of the human insulin receptor (HIR) (*7*). Genetically engineered forms of the chimeric or humanized HIRMAb have been produced (*8*), and these cross the BBB in the adult Rhesus monkey in vivo at rates comparable to small molecule penetration of the brain. Previously, the lysosomal enzyme, iduronidase (IDUA), the enzyme mutated in MPS-I (*9*), was re-engineered as a fusion protein with the HIRMAb (*10*). The HIRMAb-IDUA fusion protein retained high binding affinity for the HIR and high IDUA enzyme activity. The fusion protein normalized intracellular IDUA enzyme activity and glycosoaminoglycan (GAG) accumulation in MPS-I fibroblasts, and confocal microscopy demonstrated that the HIRMAb-IDUA fusion protein was targeted to the lysosomal compartment of MPS-I fibroblasts (*10*). The HIRMAb-IDUA fusion protein was rapidly transported across the Rhesus monkey BBB in vivo, at a level that would normalize the brain IDUA enzyme activity at a therapeutic dose of 0.6 mg/kg intravenously (*10*). The re-engineering of lysosomal enzymes as fusion proteins with BBB molecular Trojan horses represents a new approach to the treatment of the brain in lysosomal storage disorders.

The HIRMAb-IDUA described previously (*10*) is specific for MPS-I. Patients with MPS-II have mutations in IDS, which also adversely affects the brain. Therefore, the purpose of the present investigation was to engineer a new treatment of the brain in MPS-II, wherein the amino terminus of the mature human IDS is fused to the carboxyl terminus of the heavy chain of the HIRMAb. The structure of the HIRMAb-IDS fusion protein is shown in Figure 1. The HIRMAb-IDS fusion protein is a heterotetrameric protein comprising two heavy chains and two light chains. These studies examined the bifunctional properties of this IgG-enzyme fusion protein to determine if the new fusion protein both bound the HIR with high affinity and retained high IDS enzyme activity. The extent to which intracellular IDS enzyme activity and GAG accumulation were normalized in MPS-II fibroblasts was also investigated.

MATERIALS AND METHODS

Engineering of HIRMAb Heavy Chain-IDS Fusion Protein Expression Vector. The human IDS cDNA, encoding Ser^{26}-Pro^{550} (*1*), minus the 25 amino acid signal peptide (Genbank NP_000193), was produced by reverse transcription and PCR, starting with human liver polyA+ RNA (Clontech). Human liver cDNA was prepared using the SuperScript first-strand synthesis kit (Invitrogen, San Diego, CA) and oligodeoxythymidine priming. The IDS cDNA was cloned using 2 μL liver cDNA reverse transcription reaction, 0.2 μM IDS forward and reverse ODN primers, 0.2 mM deoxynucleotidetriphos-

* Corresponding author. Dr. William M. Pardridge, UCLA Warren Hall 13-164, 900 Veteran Ave., Los Angeles, CA 90024, Ph: +1 310 825 8858, Fax: +1 310 206 5163, Email address: wpardridge@mednet.ucla.edu.

[†] ArmaGen Technologies, Inc.

[‡] UCLA.

10.1021/bc900382q © 2010 American Chemical Society
Published on Web 12/14/2009

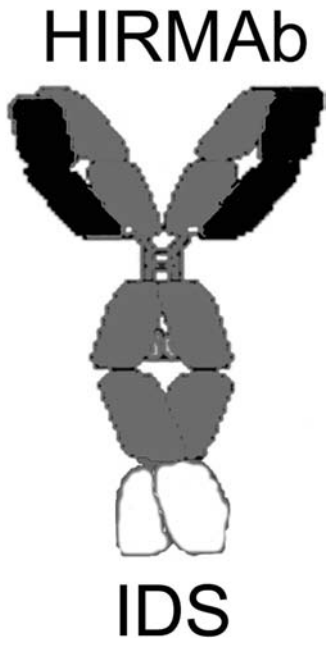


Figure 1. The HIRMAb-IDS fusion protein is formed by fusion of the amino terminus of the mature IDS to the carboxyl terminus of the CH_3 region of the heavy chain of the chimeric HIRMAb. The fusion protein is a bifunctional molecule: the fusion protein binds the HIR, at the BBB, to mediate transport into the brain, and expresses IDS enzyme activity, which is deficient in MPS type II (Hunter's syndrome).

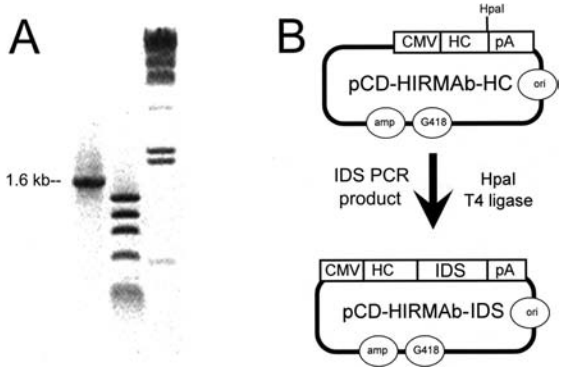


Figure 2. (A) Ethidium bromide stain of agarose gel of human IDS cDNA (lane 1), which was produced by PCR from human liver cDNA, and IDS-specific primers (Methods). Lanes 2 and 3: PhiX174 *Hae*III digested DNA standard, and Lambda *Hin*dIII digested DNA standard. (B) The heavy chain of the HIRMAb-IDS fusion protein is expressed by the pCD-HIRMAb-IDS plasmid, which is generated by subcloning the IDS cDNA into the *Hpa*I site of the pCD-HIRMAb-HC plasmid.

phates, and 2.5 U PfuUltra DNA polymerase (Stratagene, San Diego, CA) in a 50 μL Pfu buffer (Stratagene). The amplification was performed in a Mastercycler temperature cycler (Eppendorf, Hamburg, Germany) with an initial denaturing step of 95 °C for 2 min followed by 30 cycles of denaturing at 95 °C for 30 s, annealing at 55 °C for 30 s and amplification at 72 °C for 1 min. PCR products were resolved in 1% agarose gel electrophoresis, and the expected major single band of ~1.6 kb corresponding to the human IDS cDNA was isolated (Figure 2A). The cloned human IDS was inserted into the pCD-HIRMAb HC eukaryotic expression plasmid at the *Hpa*I site, and this expression plasmid was designated pCD-HIRMAb-IDS, as outlined in Figure 2B; the pCD-HIRMAb-HC expression plasmid encodes the heavy chain (HC) of the chimeric HIRMAb. The entire expression cassette of the plasmid was confirmed by bidirectional DNA sequencing. The IDS forward PCR primer was a 23-mer coding for the 7 amino acids at the beginning of the mature IDS protein. This primer introduces "CC" nucleotides to maintain the open reading frame and to introduce a Ser-Ser linker between the carboxyl terminus of the CH_3 region of the HIRMAb HC and the amino terminus of the IDS minus the 25 amino acid signal peptide of the enzyme. The IDS reverse PCR primer was a 27-mer complementary to the end of the IDS cDNA including the stop codon, "TGA", immediately after the terminal Pro of the mature human IDS protein. The fusion of the IDS monomer to the carboxyl terminus of each HC is depicted in Figure 1.

Transient Expression of HIRMAb-IDS Fusion Protein in COS Cells. COS cells were plated in 6-well cluster dishes and were dual-transfected with pHIRMAb-LC and pCD-HIRMAb-IDS plasmids using Lipofectamine 2000, with a ratio of 1:2.5 μg DNA:μL Lipofectamine, and conditioned serum free medium was collected at 3 and 7 days. The pHIRMAb-LC encodes for the light chain (LC) of the chimeric HIRMAb. Expression was confirmed by measurement of human IgG secreted to the medium by ELISA, as described previously (*10*). For production of larger amounts of fusion protein, COS cells were transfected in 10 × T500 flasks. The 3 day and 7 day media were pooled, and the 2 L of serum free conditioned medium was concentrated with tangential flow filtration (Millipore) followed by purification with protein A affinity chromatography.

SDS-PAGE and Western Blotting. The purity of protein A purified fusion protein produced by COS cells was evaluated with 12% sodium dodecyl sulfate polyacrylamide gel electrophoresis (SDS-PAGE) with 5% β-mercaptoethanol. Immunoreactivity was tested with a primary goat antibody to human IDS (R&D Systems, Minneapolis, MN) or a primary goat antiserum against human IgG heavy and light chains (Vector Laboratories, Burlingame, CA). Immunoreactivity of the HIRMAb-IDS fusion protein was compared to human recombinant IDS expressed in myeloma cells from R&D Systems.

HIR Receptor Assay. The affinity of the fusion protein for the HIR extracellular domain (ECD) was determined with ELISA. Chinese hamster ovary cells permanently transfected with the HIR ECD were grown in serum-free media, and the HIR ECD was purified with a wheat germ agglutinin affinity column, as previously described (*11*). The HIR ECD was plated on Nunc-Maxisorb 96 well dishes and the binding of the HIRMAb or the HIRMAb-IDS fusion protein to the HIR ECD was detected with a biotinylated goat antihuman IgG (H+L) secondary antibody, followed by avidin and biotinylated peroxidase (Vector Laboratories, Burlingame, CA). The concentration of either HIRMAb or HIRMAb-IDS fusion protein that gave 50% maximal binding was determined with a nonlinear regression analysis.

IDS Enzyme Assay. The IDS enzyme activity was determined with a fluorometric assay using 4-methylumbelliferyl α-L-iduronide-2-sulfate (4-MUS) (*12*), which was purchased from Moscerdam Substrates (Rotterdam, The Netherlands). This substrate is hydrolyzed by IDS to 4-methylumbelliferyl α-L-iduronide (MUBI), and the MUBI is hydrolyzed by iduronidase (IDUA, Aldurazyme, Genzyme, Boston, MA) to 4-methylumbelliferone (4-MU), which is detected fluorometrically with a Farrand filter fluorometer using an emission wavelength of 450 nm and an excitation wavelength of 365 nm. A standard curve was constructed with known amounts of 4-MU (Sigma-Aldrich, St. Louis, MO). The assay was performed by incubation at 37 °C at pH = 4.5 for 4 h in McIlvaine's buffer, followed by the addition of 12 ug of IDUA and an additional 24 incubation at 37 °C. The incubation was terminated by the addition of 0.2 mL of 0.5 M sodium carbonate (pH = 10.3). One unit = 1 nmol/h.

Fusion Protein Uptake and Biological Activity in MPS Type II Fibroblasts. Fibroblasts were chosen as a model system, since type II MPS Hunter fibroblasts (GM000298), as well as healthy human fibroblasts (GM000497), are available from the Coriell Institute for Medical Research (Camden, NJ). The cells were grown in 6-well cluster dishes to confluency. The medium was aspirated, wells washed with phosphate buffered saline (PBS), and incubated with 1 mL of Dulbecco's modified Eagle medium without serum, along with a range of concentrations of the HIRMAb-IDS fusion protein, for 2 h at 37 °C. The medium was aspirated, and the wells were washed extensively (1 mL/well, 5 washes) with PBS, and the monolayer was extracted in 0.3 mL/well of lysis buffer (5 mM sodium formate, 0.2% Triton X-100, pH = 4.0), followed by four freeze/thaw cycles, and microfuged 10 min 4 °C. The supernatant was removed for IDS enzyme activity and bicinchoninic acid protein (BCA) assay. The uptake of the fusion protein was expressed as nanomoles per hour of IDS enzyme activity per milligram of cell protein.

Sulfate incorporation into cellular glycosoaminoglycans (GAG) is increased in the absence of cellular IDS (*13*). Therefore, ^{35}S incorporation into the healthy and Hunter fibroblasts was measured with or without treatment of the cells with the HIRMAb-IDS fusion protein. Type II MPS or healthy human fibroblasts were plated in 6-well cluster dishes at 250 000 cells/well and grown for 4 days in DMEM with 10% fetal bovine serum. The medium was discarded, the wells were washed with PBS, and 1 mL/well of low-sulfate F12 medium with 10% dialyzed fetal bovine serum was added, along with 5 mM $CaCl_2$, the HIRMAb-IDS fusion protein (0.3 ug/mL), and 10 uCi/mL of ^{35}S-sodium sulfate (Perkin-Elmer, Boston, MA). Following a 24 h incubation at 37 °C, the medium was aspirated, the wells were washed with cold PBS (1 mL, 5 washes), and the cells were lysed with 0.4 mL/well of 1 N NaOH. The lysate was heated 60 °C for 60 min to solubilize protein, an aliquot was removed for BCA protein assay, and the sample was counted for radioactivity with a Perkin-Elmer Tri-Carb 2100 liquid scintillation counter. The data were expressed as ^{35}S counts per minute (CPM) per microgram of protein, as described previously (*10*). The percent normalization of GAG accumulation was computed from $[(A - B/(A - C)] \times 100$, where A = the ^{35}S radioactivity incorporated in untreated Hunter fibroblasts, B = the ^{35}S radioactivity incorporated in Hunter fibroblasts treated with the HIRMAb-IDS fusion protein, and C = the ^{35}S radioactivity incorporated in healthy human fibroblasts.

RESULTS

DNA sequencing of the expression cassette of the pCD-HIRMAb-IDS plasmid encompassed 4063 nucleotides (nt), including a 714 nt cytomegalovirus promoter, a 9 nt full Kozak site (GCCGCCACC), a 2970 nt HIRMAb HC-IDS fusion protein open reading frame, and a 370 nt bovine growth hormone polyA sequence. The plasmid encoded for a 989 amino acid protein, comprising a 19 amino acid IgG signal peptide, the 443 amino acid HIRMAb HC, a 2 amino acid linker (Ser-Ser), and the 525 amino acid human IDS minus the enzyme signal peptide. The predicted molecular weight of the heavy-chain fusion protein, minus glycosylation, is 108 029 Da, with a predicted isoelectric point (pI) of 6.03.

Dual transfection of COS cells with the pCD-HIRMAb-IDS and the pHIRMAb-LC produced 2.3 L of serum-free conditioned medium over a 7 day incubation. The HIRMAb-IDS fusion protein was purified by protein A affinity chromatography to homogeneity as demonstrated by SDS-PAGE (Figure 3). The size of the heavy chain of the HIRMAb-IDS fusion protein, 135 kDa, is about 80 kDa larger than the heavy chain of the HIRMAb, whereas both proteins have light chains of equal size

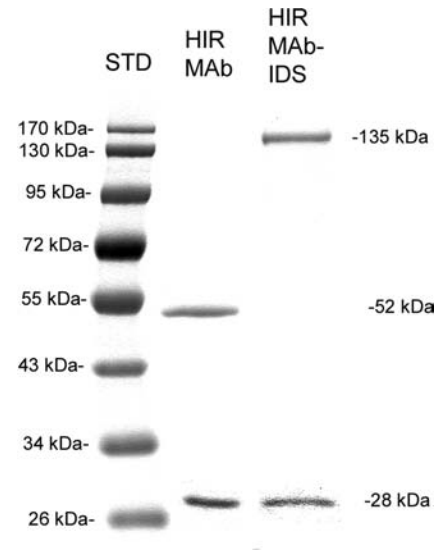


Figure 3. Reducing SDS-PAGE of molecular weight standards (STD), the purified HIRMAb, and the purified HIRMAb-IDS fusion protein.

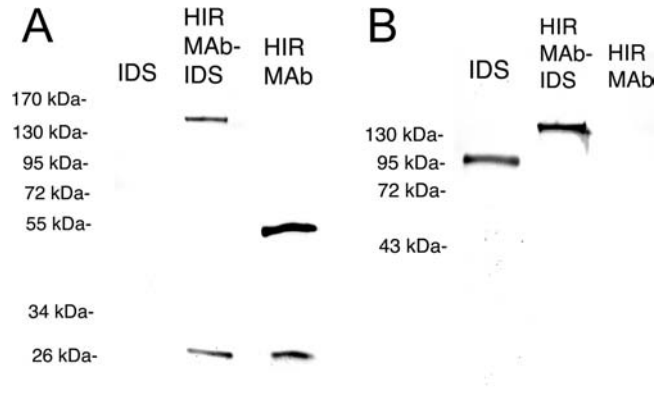


Figure 4. Western blot with either antihuman (h) IgG primary antibody (A) or antihuman IDS primary antiserum (B). The immunoreactivity of the HIRMAb-IDS fusion protein is compared to the chimeric HIRMAb and recombinant human IDS. Both the HIRMAb-IDS fusion protein and the HIRMAb have identical light chains on the anti-hIgG Western. The HIRMAb-IDS fusion heavy chain reacts with both the anti-hIgG and the antihuman IDS antibody, whereas the HIRMAb heavy chain only reacts with the anti-hIgG antibody. The size of the HIRMAb-IDS fusion heavy chain, 130 kDa, is about 80 kDa larger than the size of the heavy chain of the HIRMAb, owing to the fusion of the 80 kDa IDS to the 50 kDa HIRMAb heavy chain.

(Figure 3). On Western blotting of the purified HIRMAb and the HIRMAb-IDS fusion protein, the antihuman IgG antibody reacts with a 135 kDa heavy chain for the fusion protein, and a 52 kDa heavy chain for the HIRMAb, and the difference in size, 80 kDa, is due to the fusion of IDS (Figure 4A). The antihuman IgG antibody reacts equally with the light chain of either the HIRMAb-IDS fusion protein or the HIRMAb, since both proteins comprise the same light chain, but the antihuman IgG antibody does not react with recombinant human IDS (Figure 4A). The anti-IDS antibody reacts with the 135 kDa heavy chain of the fusion protein and with the recombinant IDS, but not with the heavy chain of the HIRMAb (Figure 4B).

The affinity of the fusion protein for the HIR extracellular domain (ECD) was determined with a ligand binding assay using lectin affinity purified HIR ECD (Materials and Methods section). There is comparable binding of either the chimeric HIRMAb or the HIRMAb-IDS fusion protein for the HIR ECD with ED_{50} of 0.32 ± 0.15 nM and 0.40 ± 0.04 nM, respectively (Figure 5). The IDS enzyme activity was determined with a

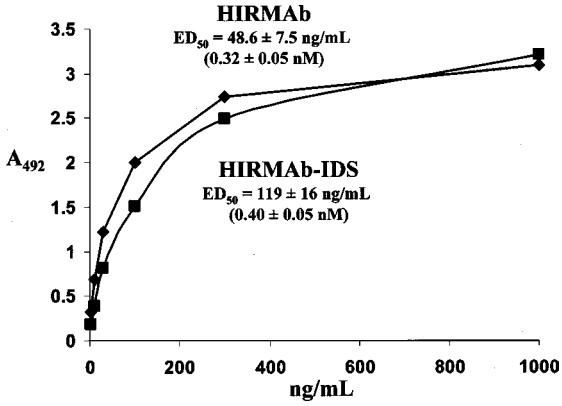


Figure 5. Binding of either the chimeric HIRMAb or the HIRMAb-IDS fusion protein to the HIR extracellular domain (ECD) is saturable. The ED_{50} of HIRMAb-IDS binding to the HIR ECD is comparable to the ED_{50} of the binding of the chimeric HIRMAb.

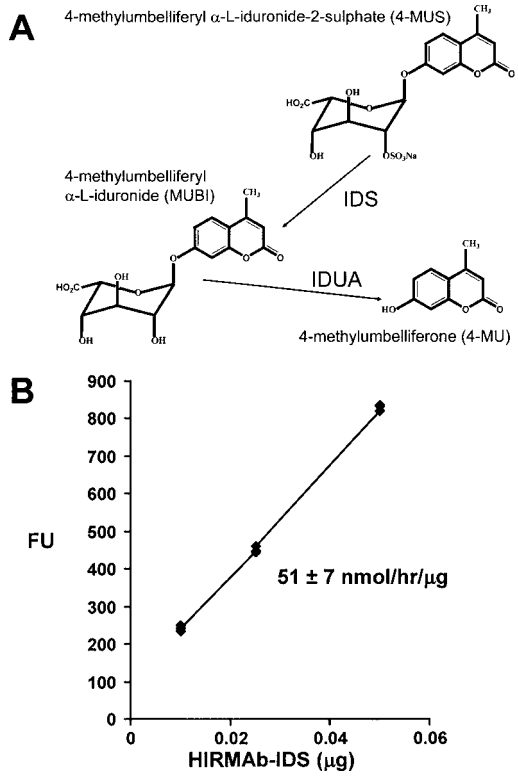


Figure 6. (A) Substrate (4-MUS), intermediate (MUBI), and product (4-MU) of the two-step enzymatic fluorometric assay of IDS enzyme activity. (B) The fluorometric units (FU) are proportional to the mass of purified HIRMAb-IDS fusion protein, and the average enzyme specific activity of the fusion protein is 51 ± 7 nmol/h/μg protein.

two-step enzymatic fluorometric assay outlined in Figure 6A. The fluorometric units were proportional to the mass of purified HIRMAb-IDS fusion protein, and the enzymatic activity of the fusion protein was 51 ± 7 nmol/h/μg protein (Figure 6B).

The HIRMAb-IDS fusion protein was taken up by MPS type II fibroblasts (Figure 7A). The basal IDS activity in these cells without treatment is very low, 10 ± 3 nmol/h/mg_p. The intracellular IDS enzyme activity increases in proportion to the concentration of medium HIRMAb-IDS (Figure 7). The normal IDS enzymatic activity in healthy human fibroblasts is shown by the horizontal bar in Figure 7. A medium concentration of the HIRMAb-IDS fusion protein of ~500 ng/mL causes a 100% normalization of intracellular IDS enzyme activity (Figure 7). The Hunter fibroblasts, with or without treatment with 0.3 ug/mL HIRMAb-IDS fusion protein in the medium, and the healthy

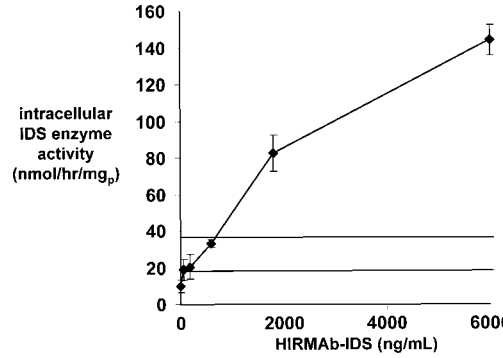


Figure 7. Intracellular IDS enzyme activity is increased in Hunter fibroblasts in proportion to the concentration of medium HIRMAb-IDS fusion protein. Data are means ± SE (n = 3 dishes/point). The horizontal bar is the IDS enzyme activity in healthy human fibroblasts (mean ± SD).

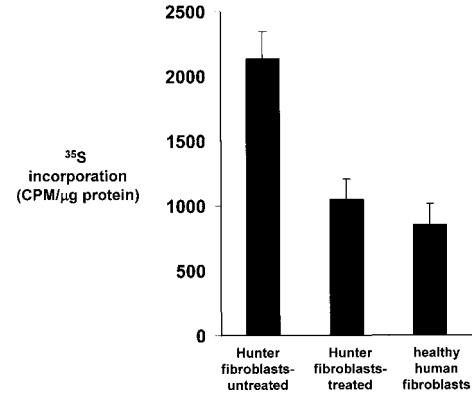


Figure 8. Reversal of glycosaminoglycan (GAG) accumulation in Hunter fibroblasts with a single treatment of 0.3 ug/mL of HIRMAb-IDS fusion protein in the medium. There is an 84% reduction in GAG accumulation, as compared to the ^{35}S incorporation in healthy human fibroblasts ($p < 0.0005$). Data are means ± SE (n = 4 dishes/point).

human fibroblasts, were incubated 24 h in the presence of ^{35}S-sodium sulfate, which is incorporated into intracellular GAGs. Treatment with the HIRMAb-IDS fusion protein reduces GAG accumulation in Hunter fibroblasts by 84% as compared to healthy fibroblasts ($p < 0.0005$) (Figure 8).

DISCUSSION

The results of this study are consistent with the following conclusions. First, a fusion gene has been genetically engineered that encodes the HIRMAb-IDS fusion protein depicted in Figure 1, and following expression in COS cells, the heavy chain of the fusion protein is about 80 kDa larger than the heavy chain of the chimeric HIRMAb (Figure 3), and the fusion protein heavy chain reacts with antibodies to both human IgG and human IDS (Figure 4). Second, the fusion protein is a bifunctional molecule and binds both the HIR ECD with comparable affinity to the chimeric HIRMAb (Figure 5) and has high IDS enzyme activity (Figure 6). Third, the HIRMAb-IDS fusion protein is taken up by Hunter fibroblasts (Figure 7) and causes an 84% decline in GAG accumulation with 24 h of treatment (Figure 8).

There are multiple approaches possible for the engineering of an IgG-enzyme fusion protein, as the enzyme could be fused to either the amino terminus or the carboxyl terminus of either the IgG heavy chain or light chain. If the enzyme is fused to the amino terminus of the IgG chain, then the enzyme is translated and folded before the IgG chain in the host cell, and this might ensure retention of enzyme activity in the fusion

protein. However, the antigen binding site of the IgG chain is near the amino terminus and fusion of the enzyme at the amino terminus could impair IgG binding to the target receptor. These considerations were confirmed in the engineering of a fusion protein of the HIRMAb and human β-glucuronidase (GUSB). Fusion of the GUSB to the amino terminus of the HIRMAb heavy chain resulted in a retention in GUSB enzyme activity, but greatly impaired binding of the fusion protein to the HIR (*14*). With regard to another lysosomal enzyme, IDUA, a HIRMAb-IDUA fusion protein retained high HIR binding and high IDUA enzyme activity following fusion of the IDUA to the carboxyl terminus of the CH_3 region of the HIRMAb heavy chain (*10*). A similar result is demonstrated in the present study on the engineering of the HIRMAb-IDS fusion protein shown in Figure 1. The fusion protein binds the HIR with the same high affinity as the HIRMAb (Figure 5). The IDS enzyme activity of the HIRMAb-IDS fusion protein is also retained, as the IDS enzyme specific activity, 51 $\pm$ 7 nmol/h/μg protein (Figure 6B), is comparable to the enzyme activity of human recombinant IDS (*15*). The engineering of the IgG-IDS fusion protein variant shown in Figure 1 places the IDS in a dimeric configuration. IDS is a member of a family of sulfatases, which includes arylsulfatase A (ASA) (*16*), and the natural configuration of ASA at neutral pH is a dimeric structure (*17*).

The retention of IDS enzyme activity in the HIRMAb-IDS fusion protein indicates this fusion protein is correctly processed in the host cell. The SDS-PAGE (Figure 3) and the IgG and IDS Western blotting (Figure 4) show that the fusion protein secreted to the medium is of the correct size. IDS is a member of a family of sulfatases (*16*), wherein the activity of the enzyme is activated following the conversion of Cys-59 to a formylglycine residue by a sulfatase modifying factor in the endoplasmic reticulum (*18*). The retention of IDS enzyme activity in the HIRMAb-IDS fusion protein indicates the IDS is activated within the host cell despite fusion to the HIRMAb heavy chain.

The HIRMAb-IDS heavy chain is triaged to the lysosome within the target cell following uptake via the cell membrane HIR, as evidenced by the 84% reduction in GAG accumulation within the Hunter fibroblast (Figure 8). Prior studies with the HIRMAb-IDUA fuson protein used confocal microscopy to confirm localization of the fusion protein within the lysosomal compartment of the human fibroblast (*10*). The reduction in GAG accumulation shown in Figure 8 was observed following exposure of the Hunter fibroblasts to a 0.3 ug/mL concentration of the HIRMAb-IDS fusion protein (Figure 8). A concentration of 0.3 ug/mL of the HIRMAb-IDS fusion protein is a subtherapeutic dose (Figure 7). This result corroborates prior studies, which suggest that partial restoration of intracellular lysosomal enzyme activity causes therapeutic effects within the cell (*19*).

The HIRMAb is specific for the human insulin receptor and cross-reacts with the Old World primate insulin receptor in Rhesus monkeys, but does not react with the insulin receptor in other species (*7*). Consequently, the HIRMAb-IDS fusion protein cannot be administered to mouse models of MPS-II, as the fusion protein would not be recognized by the murine insulin receptor. There is no known mAb against the mouse insulin receptor that can be used as a BBB Trojan horse. Furthur drug development of the HIRMAb-IDS fusion protein as a new therapy for treatment of the brain in MPS-II will require evaluations of the potential toxicity and immunogenicity of this fusion protein. With respect to immunogenicity of fusion proteins, recent studies report on the administration of high doses to Rhesus monkeys of a fusion protein of the HIRMAb and either glial derived neurotrophic factor (GDNF) (*20*) or IDUA (*21*). The administration of large doses of the HIRMAb fusion proteins, 10−20 mg/kg, caused no tissue toxicity and had no effect on glycemic control in plasma or cerebrospinal fluid (*20, 21*). A 20 mg/kg dose of fusion protein is large compared to the projected therapeutic dose of HIRMAb-enzyme fusion proteins, 0.6 mg/kg (*10*). There was minimal immune response to the HIRMAb fusion proteins (*20, 21*). The re-engineering of recombinant proteins as IgG fusion proteins may reduce the potential immunogenicity of the recombinant protein, which can be a side effect of enzyme replacement therapy (*22*). Recent work shows that the constant region of human IgG contains amino acid sequences, called Tregitopes, which induce immune tolerance (*23*). Therefore, the re-engineering of human IDS as the HIRMAb fusion protein shown in Figure 1 may reduce the immunogenicity of the lysosomal enzyme in MPS-II patients, as well as enable enzyme penetration of the BBB.

ACKNOWLEDGMENT

Winnie Tai and Phuong Tram provided expert technical assistance.

LITERATURE CITED

(1) Wilson, P. J., Morris, C. P., Anson, D. S., Occhiodoro, T., Bielicki, J., Clements, P. R., and Hopwood, J. J. (1990) Hunter syndrome: isolation of an iduronate-2-sulfatase cDNA clone and analysis of patient DNA. *Proc. Natl. Acad. Sci. U.S.A. 87*, 8531–8535.

(2) Muenzer, J., Wraith, J. E., Beck, M., Giugliani, R., Harmatz, P., Eng, C. M., Vellodi, Martin, A. R., Ramaswami, U., Gucsavas-Calikoglu, M., Vijayaraghavan, S., Wendt, S., Puga, A. C., Ulbrich, B., Shinawi, M., Cleary, M., Piper, D., Conway, A. M., and Kimura, A. (2006) A phase II/III clinical study of enzyme replacement therapy with idursulfase in mucopolysaccharidosis II (Hunter syndrome). *Genet. Med. 8*, 465–473.

(3) Vedolin, L., Schwartz, I. V., Komlos, M., Schuch, A., Puga, A. C., Pinto, L. L., Pires, A. P., and Giugliani, R. (2007) Correlation of MR imaging and MR spectroscopy findings with cognitive impairment in mucopolysaccharidosis II. *AJNR Am. J. Neuroradiol. 28*, 1029–1033.

(4) Al Sawaf, S., Mayatepek, E., and Hoffmann, B. (2008) Neurological findings in Hunter disease: pathology and possible therapeutic effects reviewed. *J. Inherit. Metab. Dis. 31*, 473–480.

(5) Wraith, J. E., Scarpa, M., Beck, M., Bodamer, O. A., De Meirleir, L., Guffon, L., Meldgaard Lund, A., Malm, G., Van der Ploeg, A. T., and Zeman, J. (2008) Mucopolysaccharidosis type II (Hunter syndrome): a clinical review and recommendations for treatment in the era of enzyme replacement therapy. *Eur. J. Pediatr. 167*, 267–77.

(6) Pardridge, W. M. (2008) Re-engineering biopharmaceuticals for delivery to brain with molecular Trojan horses. *Bioconjugate Chem. 19*, 1327–1338.

(7) Pardridge, W. M., Kang, Y. S., Buciak, J. L., and Yang, J. (1995) Human insulin receptor monoclonal antibody undergoes high affinity binding to human brain capillaries in vitro and rapid transcytosis through the blood-brain barrier in vivo in the primate. *Pharm. Res. 12*, 807–816.

(8) Boado, R. J., Zhang, Y., Zhang, Y., and Pardridge, W. M. (2007) Humanization of anti-human insulin receptor antibody for drug targeting across the human blood-brain barrier. *Biotechnol. Bioeng. 96*, 381–391.

(9) Scott, H. S., Anson, D. S., Orsborn, A. M., Nelson, P. V., Clements, P. R., Morris, C. P., and Hopwood, J. J. (1991) Human alpha-L-iduronidase: cDNA isolation and expression. *Proc. Natl. Acad. Sci. U.S.A. 88*, 9695–969.

(10) Boado, R. J., Zhang, Y., Zhang, Y., Xia, C. F., Wang, Y., and Pardridge, W. M. (2008) Genetic engineering of a lysosomal enzyme fusion protein for targeted delivery across the human blood-brain barrier. *Biotechnol. Bioeng. 99*, 475–484.

(11) Coloma, M. J., Lee, H. J., Kurihara, A., Landaw, E. M., Boado, R. J., Morrison, S. L., and Pardridge, W. M. (2000) Transport across the primate blood-brain barrier of a genetically engineered chimeric monoclonal antibody to the human insulin receptor. *Pharm. Res. 17*, 266–274.

(12) Voznyi, Y. V., Keulemans, J. L., and van Diggelen, O. P. (2001) A fluorimetric enzyme assay for the diagnosis of MPS II (Hunter disease. *J. Inherit. Metab. Dis. 24*, 675–680.

(13) Unger, E. G., Durrant, J., Anson, D. S., and Hopwood, J. J. (1994) Recombinant alpha-L-iduronidase: characterization of the purified enzyme and correction of mucopolysaccharidosis type I fibroblasts. *Biochem. J. 304*, 43–49.

(14) Boado, R. J., and Pardridge, W. M. (2009) Genetic engineering of IgG-glucuronidase fusion protein. *J. Drug Targeting*, in press.

(15) Zareba, G. (2007) Idursulfase in Hunter syndrome treatment. *Drugs Today (Barc) 43*, 759–767.

(16) Franco, B., Meroni, G., Parenti, G., Levilliers, J., Bernard, L., Gebbia, M., Cox, L., Maroteaux, P., Sheffield, L., Rappold, G. A., Andria, G., Petit, C., and Ballabio, A. (1995) A cluster of sulfatase genes on Xp22.3: mutations in chondrodysplasia punctata (CDPX) and implications for warfarin embryopathy. *Cell 81*, 15–25.

(17) Lukatela, G., Krauss, N., Theis, K., Selmer, T., Gieselmann, V., von Figura, K., and Saenger, W. (1998) Crystal structure of human arylsulfatase A: the aldehyde function and the metal ion at the active site suggest a novel mechanism for sulfate ester hydrolysis. *Biochemistry 37*, 3654–3664.

(18) Zito, E., Fraldi, A., Pepe, S., Annunziata, I., Kobinger, G., Di Natale, P. D., Ballabio, A., and Cosma, M. P. (2005) Sulphatase activities are regulated by the interaction of sulphatase-modifying factor 1 with SUMF2. *EMBO Rep. 6*, 655–660.

(19) Muenzer, J., and Fisher, A. (2004) Advances in the treatment of mucopolysaccharidosis type I. *N. Engl. J. Med. 350*, 1932–1934.

(20) Pardridge, W. M., and Boado, R. J. (2009) Pharmacokinetics and safety in Rhesus monkeys of a monoclonal antibody-GDNF fusion protein for targeted blood-brain barrier delivery. *Pharm. Res. 10*, 2227–2236.

(21) Boado, R. J., Hui, E. K.-W., Lu, J. Z., and Pardridge, W. M. (2009) AGT-181: Expression in CHO cells and pharmacokinetics, safety, and plasma iduronidase enzyme activity in Rhesus monkeys. *J. Biotechnol. 144*, 135–141.

(22) Hollak, C. E. M., and Linthorst, G. E. (2009) Immune response to enzyme replacement therapy in Fabry disease: Impact on clinical outcome. *Molec. Genet. Metab. 96*, 1–3.

(23) De Groot, A. S., Moise, L., McMurry, J. A., Wambre, E., Van Overtvelt, L., Moingeon, P., Scott, D. W., and Martin, W. (2008) Activation of natural regulatory T cells by IgG Fc-derived peptide "Tregitopes". *Blood 11*, 3303–3311.

BC900382Q

Transferrin Receptor-Targeted Liposomes Encapsulating anti-*BCR-ABL* siRNA or asODN for Chronic Myeloid Leukemia Treatment

Liliana S. Mendonça,[†,‡] Filipe Firmino,[§] João N. Moreira,[†,‡] Maria C. Pedroso de Lima,[‡,§] and Sérgio Simões*[,†,‡]

Laboratory of Pharmaceutical Technology, Faculty of Pharmacy, Center for Neuroscience and Cell Biology, and Department of Biochemistry, Faculty of Sciences and Technology, University of Coimbra, Coimbra, Portugal. Received October 7, 2009; Revised Manuscript Received November 4, 2009

The present work aimed at the development and application of transferrin receptor (TrfR)-targeted sterically stabilized liposomes encapsulating anti-*BCR-ABL* siRNA or asODN. Transferrin was coupled to the surface of liposomes encapsulating siRNA or asODN through the postinsertion method. Cell association and internalization were assessed by flow cytometry and confocal microscopy, respectively. *BCR-ABL* mRNA and Bcr-Abl protein levels were evaluated by qRT-PCR and Western blot, respectively. Cell viability was assessed using the resazurin reduction method. The amount of coupled transferrin and the size and stability over time of the liposomes were very satisfactory and reproducible. The siRNA encapsulation yield was dependent on the concentration of the encapsulation buffer used (20 or 300 mM), as opposed to asODN encapsulation yield which was high for both concentrations tested. Cell association and internalization studies were performed in leukemia cell lines treated with liposomes coupled to Trf (Trf-liposomes) or albumin (BSA-liposomes) or with nontargeted liposomes (NT-liposomes) encapsulating fluorescently labeled siRNA (Cy3-siRNA). These experiments clearly indicated that BSA- and NT-liposomes have no ability to promote the delivery of the encapsulated nucleic acids and that the Trf-liposomes deliver the nucleic acids by a Trf receptor-dependent mechanism. The Trf-liposomes encapsulating siRNA or asODN promote sequence-specific down-regulation of the *BCR-ABL* mRNA, although a certain extent of nonspecific sequence effects at the protein and cell viability level were observed. Overall, our results indicate that Trf-liposomes encapsulating gene silencing tools allow combining molecular and cellular targeting, which is a valuable approach for cancer treatment.

INTRODUCTION

Chronic myeloid leukemia (CML) is a hematopoietic stem cell disease caused by a t(9;22)(q34;q11) reciprocal translocation between chromosomes 9 and 22, leading to the *BCR-ABL* oncogene, that encodes a constitutively active tyrosine kinase, the Bcr-Abl protein, which is responsible for the malignant transformation in the disease (*1–3*).

Antisense oligonucleotides (asODN) are short, single-stranded molecules of DNA or RNA (typically 18−25 nucleotides in length) promoting targeted mRNA cleavage or blocking its translation (*4, 5*). Small interfering RNA (siRNA) are short, double-stranded RNA molecules normally with 21−23 nucleotides in each strand that promote the cleavage of complementary mRNA by activation of the RNA interference mechanism (*6–9*).

AsODN and siRNA are powerful gene silencing tools, although there are many obstacles to their *in vitro* and *in vivo* use, namely, enzymatic degradation mediated by nucleases present in the serum (*6, 10, 11*), low cellular uptake caused by the high molecular weight and the net negative charge (*10–12*), as well as renal excretion (*6, 10*). All these features contribute to poor *in vivo* pharmacokinetic properties of asODN and siRNA molecules. To overcome these limitations, different approaches have been tried in the past years, like chemical modifications of siRNA (*8, 10*) and asODN (*13, 14*), in an attempt to generate molecules more resistant to nuclease degradation and in some cases less prone to off-target effects (*8, 10*).

The use of liposomes to deliver siRNA or asODN allows protection of nucleic acids from nuclease degradation and can be engineered in order to confer sustained plasma concentration and targeted delivery, thus leading to more specific nucleic acid accumulation in tumor cells.

The transferrin receptor (TrfR) is a cell membrane-associated glycoprotein (*15–17*) that has been explored as a target to deliver liposomes into cancer cells (*18, 19*), due to its overexpression on tumor cells (*15, 16, 20*), accessibility on the cell surface, and constitutive endocytosis (*20*). Transferrin (Trf), an 80 kDa glycoprotein, is the natural ligand for TrfR and undergoes internalization mediated by this receptor (*17, 20*).

When considering intravenous administration, which is relevant for implementing a therapeutic approach against CML, it is important to confer long circulating times to the liposomes. This feature can be achieved by "insertion" of hydrophilic polymers in the liposome surface, with poly(ethylene glycol) (PEG) being one of the most extensively studied for this purpose. The main aim is to obtain an aqueous shield around the liposomes that prevents their aggregation during preparation and opsonization by serum components, which can further lead to blood elimination by macrophages of the mononuclear phagocytic system, thus improving biodistribution and consequently pharmacokinetics (*21–23*).

This work aimed at efficiently encapsulating asODN or siRNA (designed to specifically silence the *BCR-ABL* oncogene) in TrfR-targeted sterically stabilized liposomes. These liposomes were characterized in terms of their size, siRNA or asODN encapsulation yield, the amount of coupled Trf protein, and size stability over time. Our results clearly indicate that cellular

* Corresponding author. Sérgio Simões, Faculty of Pharmacy, University of Coimbra, Pólo das Ciências da Saúde, Azinhaga de Santa Comba, 3000-548 Coimbra, Portugal. Phone: +351 239859950; Fax: +351 239827126; e-mail address: ssimoes@ci.uc.pt.

[†] Faculty of Pharmacy.

[‡] Center for Neuroscience and Cell Biology.

[§] Faculty of Sciences and Technology.

10.1021/bc9004365 © 2010 American Chemical Society
Published on Web 12/11/2009

Table 1. Nucleic Acid Sequences

specific anti-*BCR-ABL* siRNA	5′AAGGGCUUUUGAACUCUGCdTdT3′
scrambled anti-*BCR-ABL* siRNA	5′GUCUCAAGUUUUCGGGAAGdTdT3′
specific anti-*BCR-ABL* asODN	5′G*A*A*G*G*G*C*T*T*T*T*G*A*A*C*T*C*T3′
scrambled anti-*BCR-ABL* asODN	5′G*G*T*A*T*G*T*G*A*T*G*T*A*T*C*A*C*C3′

* asODN exhibit phosphorothioate modifications. The siRNA sequences indicated are the antisense strands; the complementary sense strands exhibit dTdT overhangs.

internalization of the targeted liposomes occurs through TrfR-mediated endocytosis. In addition, it was demonstrated that the developed TrfR-targeted formulation allowed to achieve the desired gene silencing effect mediated by either siRNA or asODN. A correlation between the reduction of the levels of *BCR-ABL* mRNA and decrease of the corresponding Bcr-Abl protein and cytotoxicity was observed.

EXPERIMENTAL PROCEDURES

Chemicals. Cholesterol (Chol) was obtained from Sigma (St Louis, MO, USA); all the other lipids, *N*-palmitoyl-sphingosine-1-[succinyl(methoxypolyethylene glycol) 2000] (C16 mPEG 2000 Ceramide), 1,2-distearoyl-*sn*-glycero-3-phosphatidylcholine (DSPC), 1,2-dioleoyl-3-dimethylammonium-propane (DODAP); 1,2-distearoyl-*sn*-glycero-3-phosphatidylethanolamine-*N*-[maleimide (polyethylene glycol)2000] ammonium salt (DSPE-PEG-MAL), were obtained from Avanti Polar Lipids (Alabaster, AL, USA). Human holo-transferrin (Trf) and bovine serum albumin (BSA) were purchased from Sigma.

Small interfering RNA molecules were purchased from Dharmacon RNA Technologies (Lafayette, CO, USA). The Cy3-labeled anti-*BCR-ABL* siRNA (Cy3-siRNA) (custom synthesis) and asODN molecules were purchased from Ambion (Austin, TX, USA) and Microsynth AG (Switzerland), respectively. The sequences of the used nucleic acids are presented in Table 1. All the other chemicals were obtained from Sigma unless stated otherwise.

Preparation of Trf or BSA-Coupled PEG2000-DSPE Micelles. Trf and BSA proteins were modified with the addition of thiol groups through reaction with 2-iminothiolane hydrochloride (2-IT). For this purpose, Trf or BSA and 2-IT freshly dissolved in HEPES buffer (20 mM HEPES, 145 mM NaCl, pH 8) were mixed in a protein/2-IT molar ratio of 1:10 and gently stirred for 1 h, in the dark at room temperature.

A lipid film of DSPE-PEG-MAL was prepared by solvent evaporation under a mild stream of N_2 and further dried under vacuum for 2 h. This dried lipid film was then hydrated with MES buffer (20 mM HEPES, 20 mM MES, pH 6.5), at a concentration above 2.3 μM, the critical micellar concentration of the lipid (*24*). Micelles were formed by strong vortex followed by 15 s heating in a water bath at 38 °C and a second vortex shaking. Then, the freshly thiolated proteins were coupled to the freshly prepared DSPE-PEG-MAL micelles by a thioester linkage (protein to micelles molar ratio of 1:1). The coupling reaction was performed overnight, in the dark at room temperature with gentle stirring. Micelles without conjugated ligand were prepared, as controls for Trf-micelles, by adding HEPES buffer to the micelles.

The remaining free MAL groups in the micelles were quenched by the addition of β mercaptoethanol at a maleimide/β mercaptoethanol molar ratio of 1:5, under stirring for 30 min at room temperature.

Encapsulation of asODN or siRNA into Liposomes and Subsequent Postinsertion of Trf-conjugates. A solution containing 13 μmol of total lipid composed of Chol/DSPC/DODAP/C16 mPEG 2000 Ceramide (45:22:25:8, mol %) in 200 μL of absolute ethanol, and a solution of 0.041 μmol of siRNA or 0.096 μmol of asODN in 300 μL of 20 mM or 300 mM citrate buffer, pH 4, were heated at 60 °C. The lipids were then slowly added under strong vortex to the siRNA or asODN solution. Upon their formation, the liposomes were extruded, 21 times, in a LipoFast mini extruder (Lipofast, Avestin, Toronto, Canada) through 100-nm-diameter polycarbonate filters (Avestin, Toronto, Canada). Then, dialysis was performed in HBS, pH 7.4, through a regenerated cellulose tubular membrane with MWCO 6000−8000 (Cellu Sep T2, Membrane Filtration Products, Inc., Seguin, TX, USA) for 3 h at room temperature to remove ethanol and raise the external pH. Subsequently, the total lipid concentration was assessed by cholesterol quantification. For this purpose, samples were added to absolute ethanol (1:6, v:v) and Infinity Cholesterol Liquid Stable Reagent (Thermo Electron; Melbourne, Australia). Absorbance was measured at 500 nm in a spectrophotometer and the concentration assessed against a cholesterol standard curve. The cholesterol quantification allowed the determination of the total lipid that remained at this stage and consequently the determination of the amount of micelles to be added.

Finally, 2 or 4 mol % (relative to the total lipid concentration) of Trf/BSA-coupled PEG-DSPE micelles or PEG-DSPE micelles without ligand was added to the liposomes. The insertion of protein−conjugates onto the liposomes was performed upon incubation in a water bath at 38 °C for 17 or 24 h, in the dark.

Purification of Liposomes. After incubation with micelles, Trf/BSA-liposomes or NT-liposomes (nontargeted liposomes) were purified by size exclusion chromatography on a Sepharose CL-4B column, using HBS, pH 7.4, as running buffer to remove external siRNA or asODN, as well as nonconjugated micelles and chemical reagents used during the liposomal preparation.

Liposome Characterization. Particle size distribution was assessed by photon correlation spectroscopy (N5 submicrometer particle size analyzer, Beckman Coulter, Miami, FL, USA). For this purpose, liposomes were diluted in filtered HBS, pH 7.4, at room temperature, so that the required signal ($(1-10) \times 10^5$ counts/s) was achieved. Measurements were made at a 90° angle and at 20 °C. The quantification of Trf or BSA associated with the liposomes was made with the BCA Protein Assay Kit (Pierce, Rochford, IL, USA) against a BSA standard curve at 570 nm in a microplate reader, Multiskan Ex (Thermo Labsystems, Vantaa, Finland).

The amount of siRNA and asODN entrapped inside liposomes was assessed by the Quant-iT RiboGreen RNA assay (Molecular Probes, Invitrogen, Karlsruhe, Germany) against a siRNA/asODN standard curve. Liposomes were dissolved upon addition of 0.6 mM of octaethylene glycol monododecyl ether ($C_{12}E_8$) and the RiboGreen fluorescence (λ_{ex} 485 nm, λ_{em} 530 nm, cutoff 515 nm) was measured using a Spectra Max Gemini EM plate reader fluorimeter (Molecular Devices, Sunnyvale, CA).

Cell Lines. K562 and LAMA-84 cells purchased from DSMZ (Braunschweig, Germany) and BJ cells, human fibroblasts, kindly provided by Paulo J. Oliveira (Center for Neurocience and Cell Biology, University of Coimbra, Coimbra, Portugal) were maintained in culture at 37 °C, 5% CO_2, under humidified atmosphere, in RPMI-1640 medium supplemented with 10% (v/v) heat-inactivated fetal bovine serum (FBS) (Gibco, invitrogen, California, USA), penicillin (100 U/mL), and streptomycin (100 μg/mL) (Cambrex, NJ, USA).

Cell Transfection. K562 and LAMA-84 cells (20 000 cells/well) in RPMI-1640 culture medium supplemented with 10% FBS and antibiotics were seeded in 96 round well plates. BJ cells (8000 cells/well) also in RPMI-1640 culture medium supplemented with 10% FBS and antibiotics were seeded in 96 flat well plates. Cells were transfected with Trf- or BSA-

associated liposomes or with nontargeted liposomes at 37 °C for 4 h. After incubation with liposomes, the medium was replaced with fresh medium and cells further incubated for 44 h. Following this first transfection, cell culture medium was replaced with fresh medium, and a second transfection protocol was initiated (similar formulations and same concentrations of asODN or siRNA as used in the first transfection protocol). Concerning K562 and LAMA-84 cells, immediately after adding liposomes to cells, the resulting suspension was transferred to 48-well plates. After 4 h of incubation, 800 μL of culture medium were added to each well and cells were kept in culture.

Cell Viability. Cell viability was evaluated 48 h after the second transfection, by the resazurin reduction assay (*25*). The assay measures the chemical reduction of the resazurin dye resulting from cellular metabolic activity and allows the determination of viability over the culture period without harming the cells. Briefly, 200 μL of cell suspension, double transfected as described in the previous section, was transferred to 96-well plates, and the culture medium was replaced with 10% (v/v) resazurin dye in RPMI-1640 medium without serum and antibiotics. After 2.5 h of incubation at 37 °C, the absorbance at 540 nm (reduced form) and 630 nm (oxidized form) was measured in a microplate reader Multiskan Ex (Thermo Labsystems, Vantaa, Finland). Cell viability was calculated as percentage of control cells using the equation

$$[(A_{540} - A_{630})\text{treated cells} \times 100)/(A_{540} - A_{630})\text{control cells}]$$

Western Blot. Forty-eight hours after the second transfection, cells were collected, washed twice with cold PBS, and lysed with lysis buffer [25 mM HEPES, 1 mM EGTA, 1 mM EDTA·Na_2, 2 mM $MgCl_2$, 50 mM NaF, pH 7.5, containing freshly added 200 mM PMSF, 2 mM DTT, 1 mM $NaVO_4$, 0.1% (v/v) Triton X-100 and protease inhibitors (Chymostatin, Pepstatin A, Leupeptin L, Antipain Hydrochloride) (Sigma Chemical Co., St. Louis, MO, USA)]. Concentration of protein lysates was estimated through the Bradford method (Bio-Rad Protein Assay, Bio-Rad), and equal amounts (30 μg) of protein were loaded in a 4.5% stacking, 6% resolving SDS-polyacrylamide gel. Electrophoresis was carried out at 80 V for 15 min and 110 V for approximately 30 min. Proteins were transferred to polyvinylidene difluoride (PVDF) membranes (Amersham Biosciences, UK) and incubated under stirring for 1 h at room temperature in blocking solution (TBS containing 0.1% Tween 20 and 5% dry milk). Bcr-Abl protein and actin were detected with anti c-Abl monoclonal antibody (Santa Cruz, CA, USA) and mouse antiactin monoclonal antibody (Immuno, MP Biomedicals, Ohio, USA), respectively.

Proteins were detected by chemifluorescence using an alkaline phosphatase labeled secondary antibody, antimouse IgG + IgM alkaline phosphatase linked antibody (Amersham Biosciences, UK), and the enzyme substrate ECF (Amersham Biosciences, UK) to yield a highly fluorescent product detected in a VersaDoc imaging system (Bio-Rad). The analysis of band intensity was performed using the *Quantity One* software (Bio-Rad).

qRT-PCR. Cells (20 000 cells/well) were doubled-transfected as described above. Twenty-four hours after the second transfection (72 h after beginning the treatment), cells were collected and kept at −80 °C until RNA extraction.

Frozen cellular pellets were slightly thawed at room temperature and RNA extraction performed with RNeasy Mini Kit (Quiagen, Hilden, Germany), according to the manufacture's recommendations. RNA concentration was determined by the Quant-iT RiboGreen Assay Kit (Molecular Probes, Invitrogen, Karlsruhe, Germany) using a rRNA standard curve.

cDNA synthesis was performed with SuperScript III First-Strand Synthesis SuperMix Kit for qRT-PCR (Invitrogen, Karlsruhe, Germany). For each sample, cDNA was produced from 1 μg of total RNA and the reaction was performed according to the manufacturer's instructions and the following protocol: first step, 10 min at 25 °C; second step, 30 min at 50 °C; third step, 5 min at 85 °C. Then, samples were chilled on ice and incubated with RNase H at 37 °C for 20 min in order to remove any RNA contamination.

Table 2. Sequences of Primers Used in qRT-PCR

BCR-ABL	forward primer	5′TCCGCTGACCATCAATAAGGA3′
	reverse primer	5′CACTCAGACCCTGAGGCTCAA3′
B2M	forward primer	5′GAGTATGCCTGCCGTGTG3′
	reverse primer	5′AATCCAAATGCGGCATCT3′

Polymerase chain reaction was performed in real time (qPCR) with the iQ SYBR Green Supermix Kit (Bio-Rad). The endogenous gene (housekeeping gene, hk) β-2-microglobulin (*B2M*) was used as endogenous control. The housekeeping gene and respective primers used in this work were tested and selected by the Europe Against Cancer program (*26, 27*).The sequences are presented in Table 2, and the concentrations were optimized to 150 nM for *BCR-ABL* and *B2M*.

Briefly, 5 μL of the cDNA (2.5× diluted with DNase free deionized water) obtained in the reverse transcription reaction was used to evaluate *BCR-ABL* and housekeeping genes levels. Analysis was done in 96-well PCR plates (iCycler iQ, Bio-Rad), and qPCR was performed as follows: one single cycle at 95 °C for 1.30 min, followed by 40 cycles of two steps, first step of 15 s at 95 °C, second step of 30 s at 60 °C. A melting curve was always built to demonstrate a single amplification product reaction per well. The melting curve protocol started immediately after the qPCR and consisted of 10 s heating at 55 °C, followed by 80 steps of 10 s, with a 0.5 °C increase in temperature at each step. Nontemplate controls (cDNA was replaced with water to evaluate whether qPCR reagents were contaminated with the cDNA) were always evaluated. In addition, a negative control with a *BCR-ABL* negative cell line, HL-60, was performed. The threshold cycle (C_t) values were generated automatically by the iQ5 Optical System Software. To each gene, and in each experiment, a standard curve was performed. The reaction efficiencies of all genes were between 90% and 110%, and $r^2 > 0.99$, thus allowing the use of the comparative method for mRNA level quantification, according to the following formula: $2^{-\Delta\Delta Ct \times 100}$ (where *C*t is the threshold cycle and $\Delta\Delta C$t stands for ΔCt sample − ΔCt control ⇔ (*C*t *BCR-ABL* − *C*t hk) sample − (*C*t *BCR-ABL* − *C*t hk) control).

Flow Cytometry Studies. To evaluate the extent of cell association of Trf- or BSA-associated liposomes or NT-liposomes, cells were transfected with fluorescently labeled siRNA (Cy3-siRNA) encapsulated in each one of the mentioned liposomes. Cells were seeded in RPMI-1640 culture medium (200 000 cells/well) in 48-well plates. To demonstrate that the receptor-mediated internalization is temperature-dependent, cells were incubated 1 h at 4 °C or at 37 °C, prior to liposome addition. To demonstrate that the internalization of Trf-liposomes is mediated by TrfR, this receptor was saturated by incubating the cells for 30 min with 125 μM of free holo-transferrin (dissolved in HBS, pH 7.4), as performed by others (*19, 28*). After these pretreatments, cells were incubated with the formulations under study for 4 h at 37 or 4 °C. Subsequently, cells were collected in conic tubes (BD, Biosciences), washed twice with cold PBS, and resuspended in 500 μL of cold PBS. All samples were immediately analyzed in a FACS Calibur flow cytometer (BD, Biosciences). Cy3 fluorescence was evaluated in the FL-2 channel. The data were then analyzed by *Cell Quest* software (BD). Cell association was only assessed in viable cells, these being gated based on the morphological features and on Trypan Blue staining (FL-3 channel). The cell association efficiency of each formulation was assessed by comparing the relative fluorescence units (RFU)

increase relative to nontreated cells (RFU of cells treated with the formulation under study/RFU of nontreated cells).

Confocal Microscopy Studies. In order to assess the extent of cellular internalization of the developed liposomes, confocal microscopy studies on transfected cells were performed. Cells were transfected with the formulations under study as described in the previous section. Then, cells were collected in conic tubes (BD, Biosciences), washed with cold PBS, fixed with 4% paraformaldehyde for 20 min in the dark, at room temperature, washed with cold PBS, stained with the fluorescent DNA-binding dye Hoechst 33342 (Molecular Probes, Oregon, USA) (1 μg/mL) for 5 min, in the dark, washed with cold PBS, and mounted in Mowiol mounting medium (Fluka, Sigma). Confocal images were acquired in a point scanning confocal microscope Zeiss LSM 510 Meta (Zeiss, Germany), with a 40× EC Plan-Neofluar or with a 63× Plan-Apochromat oil immersion objectives, and argon (488 nm), DPSS (561 nm), diode (405 nm), and helium−neon (633 nm) lasers. Preparations were excited at 561 nm for the Cy3 (em: >560 nm) and at 405 nm for Hoechst 33342 (em: 420−480 nm). Differential interference contrast (DIC) images were obtained using the helium−neon (633 nm) laser. Digital images were acquired using the LSM 510 Meta software. All instrumental parameters pertaining to fluorescence detection and image analyses were held constant to allow sample comparison.

Statistical Analysis. All data are presented as mean ± standard deviation (SD), and are the result of at least three independent experiments. One-way ANOVA analysis of variance combined with Tukey post-test or regular two-way ANOVA analysis of variance combined with Bonferroni post-test were used for multiple comparisons. Statistical differences are presented at probability levels of $p > 0.05$, $p < 0.05$, $p < 0.01$, and $p < 0.001$.

RESULTS

Development of Trf-Liposomes Encapsulating siRNA or asODN. Stabilized nucleic acids lipid particles (SNALP) were prepared on the basis of previous work developed by Semple et al. (*29*). SNALP is the adopted designation for siRNA encapsulation mediated by electrostatic interaction with stabilized lipid particles, whereas the ODN-containing counterpart is designated by stabilized antisense lipid particles (SALP). However, in this paper the SNALP designation was adopted for liposomes encapsulating either siRNA or asODN.

In this study, liposomes composed of Chol/DSPC/DODAP/C16 mPEG 2000 Ceramide (45:22:25:8, mol %) were used. The inclusion of 25% of the ionizable aminolipid DODAP, which has a positive net charge at pH 4, and becomes neutral at physiological pH, allows to achieve high nucleic acid encapsulation efficiencies and simultaneous obtainment of liposomes with neutral net charge (*30*). Thus, the encapsulation step is performed at pH 4, under which conditions the majority of the DODAP lipid is positively charged, forming complexes with the negatively charged asODN or siRNA at a 2/1 (±) charge ratio, resulting in high encapsulation yields. The liposome external pH is then raised to 7.4, leading to neutralization of the DODAP and consequent release of the nucleic acids bound to the liposomal external membrane surface.

The encapsulation yields obtained for both asODN and siRNA were very high (Figure 1A). Remarkably, our results demonstrated that the buffer concentration is extremely important for siRNA encapsulation, since at 20 mM of citrate buffer a 92.17 ± 1.39% encapsulation yield was achieved, whereas at 300 mM a drastic reduction of the encapsulation yield to 7.72 ± 5.29% was observed. In contrast, asODN encapsulation was independent of the buffer concentration, reaching values of approximately 100% for both 20 and 300 mM citrate buffer.

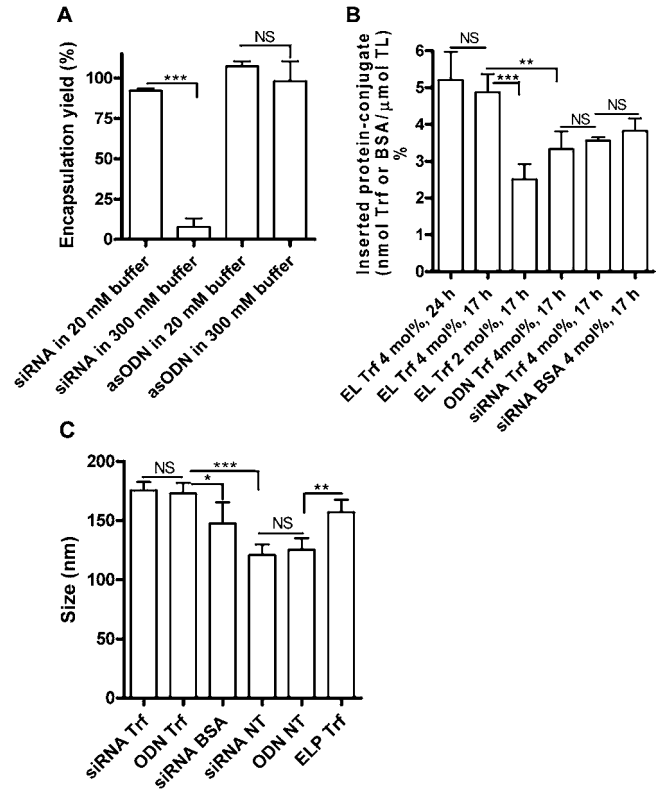


Figure 1. Physicochemical characterization of the developed liposomes. (A) Encapsulation yields: siRNA or asODN dissolved in 20 mM or 300 mM citrate buffer, pH 4, were encapsulated, as described in Experimental Procedures. The encapsulation yield was assessed by the RiboGreen assay. (B) Inserted protein−conjugate: the amount of protein−conjugate (Trf- or BSA-PEG-DSPE) inserted onto the liposomes was assessed by the BCA assay. The influence of using either 2 or 4 mol % of micelles and 17 or 24 h of incubation time, in the presence or absence of nucleic acids, on the extent of insertion of protein−conjugates onto preformed liposomes was evaluated. The tested conditions were as follows: empty liposomes incubated with 4 mol % Trf-micelles for 24 h (EL Trf 4 mol %, 24 h) or 17 h (EL Trf 4 mol %, 17 h); empty liposomes incubated with 2 mol % of Trf-micelles for 17 h (EL Trf 2 mol %, 17 h); liposomes encapsulating siRNA incubated for 17 h with 4 mol % BSA-micelles (siRNA BSA 4 mol %, 17 h) or with 4 mol % Trf-micelles (siRNA Trf 4 mol %, 17 h); and liposomes entrapping asODN incubated for 17 h with 4 mol % of Trf-micelles (ODN Trf 4 mol %, 17 h). (C) Liposome particle size: Particle size distribution of the Trf- or BSA-coupled liposomes encapsulating siRNA (siRNA Trf and siRNA BSA, respectively), Trf-coupled liposomes encapsulating asODN (ODN Trf), nontargeted liposomes encapsulating siRNA or asODN (siRNA NT and ODN NT, respectively), or Trf-coupled liposomes without nucleic acids (ELP Trf) were analyzed by photon correlation spectroscopy. One-way ANOVA analysis of variance combined with Tukey post-test was performed. NS $p > 0.05$, *$p < 0.05$, **$p < 0.01$, and *** $p < 0.001$.

The attachment of Trf or BSA to the liposomal surface was performed by postinsertion of Trf/BSA-coupled PEG_{2000}-DSPE conjugates (in a micellar form) into preformed liposomes, as described in Experimental Procedures. The influence of the incubation time and the percentage of micelles added to the liposomes on the amount of inserted protein−conjugate onto the liposomes was evaluated. As can be observed in Figure 1B, there is no advantage to prolonging the incubation time beyond 17 h, as no enhancement on the amount of inserted protein−conjugate is achieved (for 4 mol % of micelles). In contrast, the percentage of micelles incubated with the liposomes significantly affects the amount of inserted protein−conjugate. In fact, when preformed liposomes were incubated with 4 mol % of micelles, a value of 4.88 ± 0.49 nmol Trf/μmol total lipid (TL) was obtained, whereas incubation of preformed liposomes

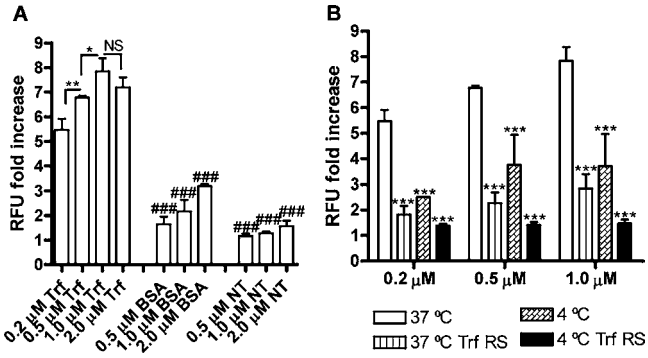


Figure 2. Extent of association of Trf-coupled liposomes loaded with Cy3-siRNA to LAMA-84 cells. (A) Cells were incubated at 37 °C for 4 h with different concentrations of Trf-coupled liposomes encapsulating 0.2−2.0 μM Cy3-siRNA (0.2−2.0 μM Trf), BSA-coupled liposomes encapsulating 0.5−2.0 μM Cy3-siRNA (0.5−2.0 μM BSA), or nontargeted liposomes encapsulating 0.5−2.0 μM Cy3-siRNA (0.5−2.0 μM NT). (B) Cells were incubated with different concentrations of Trf-liposomes loading Cy3-siRNA at 37 °C in the presence (37 °C Trf RS) or absence (37 °C) of an excess of free Trf or incubated at 4 °C in the presence (4 °C Trf RS) or absence (4 °C) of free Trf. The fluorescence of the Cy3-siRNA associated to LAMA-84 cells was assessed by flow cytometry. (A) One-way ANOVA analysis of variance combined with Tukey post-test and (B) regular two-way ANOVA analysis of variance combined with Bonferroni post-test for multiple comparisons were used. ***$p < 0.001$, **$p < 0.01$, *$p < 0.05$, and NS $p > 0.05$ when the comparison was established between the conditions indicated by the lines (A) or when comparison was established with cells treated at 37 °C in the absence of free Trf (B). ###$p < 0.001$ when the comparison was established with the corresponding concentration of siRNA encapsulated in Trf-liposomes (A).

with 2 mol % resulted only in 2.51 ± 0.41 nmol Trf/μmol TL. It was also observed that the postinsertion of Trf or BSA micelles is more efficient in empty liposomes (4.88 ± 0.49 nmol Trf/μmol TL) than in liposomes containing nucleic acids (3.55 ± 0.10 nmol Trf/μmol TL) and that Trf- and BSA-PEG-DSPE conjugates are transferred with the same efficiency by postinsertion.

Results obtained from photon correlation spectroscopy revealed that the size of all developed formulations is under 200 nm (Figure 1C) with a polydispersion index below 0.3 (data not shown), which indicates that liposomes exhibit a narrow particle size distribution. We also observed that, six months after liposome preparation, the size and polydispersion index did not change (data not shown), indicating a good stability of the formulations over time. As expected, the insertion of protein−conjugates onto the liposome surface slightly enhances liposomal size: Trf- (siRNA Trf) or BSA- (siRNA BSA) coupled liposomes encapsulating siRNA exhibit 175.5 ± 7.28 nm and 147.65 ± 17.81 nm, respectively, and NT-liposomes containing siRNA (siRNA NT) present 121.03 ± 8.83 nm. No differences in the particle size of liposome encapsulating siRNA or asODN were observed. The extent of protection conferred by the liposomal formulations to the encapsulated nucleic acids against the nuclease degradation was assessed. For this purpose, liposomes encapsulating siRNA or asODN were incubated with Quant-iT RiboGreen RNA reagent in the presence or absence of the surfactant $C_{12}E_8$. In the absence of the surfactant, the extent of the interaction between the probe and the nucleic acids is reduced to approximately 90%, indicating that these formulations confer a high degree of protection against nuclease degradation (data not shown).

Cell Association of Trf-Liposomes Is Specifically Mediated by Trf Receptor. The extent of association of liposomes bearing Trf or BSA attached at the end of PEG chains or of NT-liposomes, encapsulating Cy3-labeled siRNA, to LAMA-84 cells was assessed by flow cytometry. As can be observed in Figure 2A, the presence of Trf attached to the end of PEG-grafted lipids is the main thing responsible for the observed extent of liposome−cell association. Cells incubated with BSA-liposomes or NT-liposomes revealed no significant cell association, illustrated by the low increase of the fluorescence intensity of the transfected cells as compared to nontreated cells. As can be observed, the RFU fold increase for cells treated with 2.0 μM siRNA encapsulated in Trf-liposomes (2.0 μM siRNA Trf) was 7.20 ± 0.40, in contrast to 3.20 ± 0.07 and 1.57 ± 0.22 fold increase observed upon treatment of the cells with BSA-liposomes and NT-liposomes, respectively. Our results also indicate that the extent of cell association of Trf-coupled liposomes containing Cy3-siRNA is dependent on the lipid concentration incubated with the cells up to 0.34 mM of total lipid, which corresponds to 1.0 μM siRNA, since no significant difference on the RFU of cells treated with 1.0 μM or 2.0 μM siRNA encapsulated in Trf-liposomes was observed.

To clearly demonstrate that the ligand Trf coupled at the surface of the liposomes triggers their cell internalization through theTrfR, competitive inhibition studies were performed. Cells were incubated with 125 μM of free human holo-Trf to block the TrfR. As illustrated in Figure 2B, a drastic decrease of cell association of Trf-liposomes for all tested concentrations was observed. At 1.0 μM siRNA and incubation at 37 °C, the observed RFU was 7.84 ± 0.54, whereas with presaturation of the Trf receptor, the RFU decreased to 2.85 ± 0.54. The effect of the temperature on the extent of liposome−cell association was examined through the incubation of tumor cells with Trf-liposomes at 4 and 37 °C. As expected, incubation at 4 °C resulted in a significant reduction of the extent of liposome−cell association as compared to the incubation at 37 °C (at 1.0 μM siRNA, the RFU was reduced from 7.84 ± 0.54 to 3.72 ± 1.25). It was also observed that Trf receptor saturation performed at 4 °C resulted in the highest reduction observed for the extent of cellular association, with a RFU of 1.48 ± 0.15, indicating that binding of the liposomes to the cell surface is also affected by the saturation of TrfR.

The results of liposome−cell association obtained with Trf-, BSA-, or NT-liposomes encapsulating FAM-asODN were very similar to those obtained with correspondent counterparts containing Cy3-siRNA, suggesting that the association process is not dependent on the nature of the encapsulated nucleic acid (data not shown).

Cell Internalization of Trf-Liposomes Is Specifically Mediated by Trf Receptor. In order to gain further insights into the pathway of cell internalization of the developed formulations, confocal microscopy studies were performed (Figure 3). Upon incubation of the cells with liposomes, at 37 °C, cell internalization of Cy3-siRNA was only detected for the cells incubated with Trf-liposomes (Figure 3A,F). For BSA-(Figure 3B) or NT-liposomes (Figure 3C), no Cy3-siRNA inside the cells was observed. This same observation was registered upon saturation of the Trf receptor at 37 °C (Figure 3D) or upon treatment of the cells at 4 °C (Figure 3E).

The results obtained for cell internalization of liposomes encapsulating FAM-asODN were very similar to those obtained for Cy3-siRNA encapsulated into liposomes (data not shown). Therefore, altogether our results indicate that cell association and internalization of the developed formulations occur via temperature- and Trf receptor-dependent mechanisms.

Cytotoxicity Mediated by TrfR-Targeted Liposomes Encapsulating anti-*BCR-ABL* siRNA or asODN. In order to assess the biological activity of the developed formulations, toxicity in two leukemia cells lines, LAMA-84 and K562 cells, and in a nonmalignant cell line, BJ cells (human fibroblasts), was evaluated by the resazurin reduction method (Figure 4). As can be observed in Figure 4A, for LAMA-84 cells the nontargeted liposomes and the BSA-coupled liposomes do not

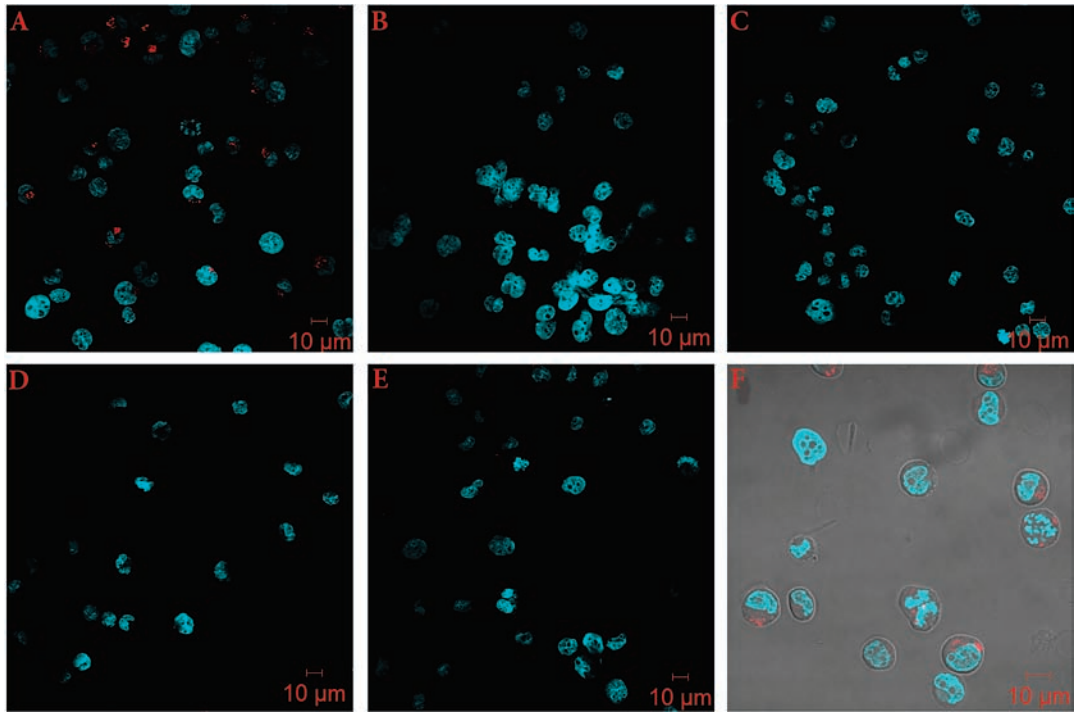


Figure 3. Confocal microscopy images from studies performed in LAMA-84 cells incubated with Trf-coupled liposomes loaded with Cy3-siRNA. Cells were incubated for 4 h, at 37 °C, with 1 μM of Cy3-siRNA encapsulated in (A,F) Trf-coupled liposomes, (B) BSA-coupled liposomes, (C) NT-liposomes, or (D) Trf-coupled liposomes in the presence of an excess of free Trf. (E) LAMA-84 cells incubated with Trf-coupled liposomes at 4 °C. Confocal images were acquired in a point scanning confocal microscope Zeiss LSM 510 Meta (Zeiss, Germany), (A−E) with a 40× EC Plan-Neofluar. (F) Differential interference contrast (DIC) images were taken with a 63× Plan-Apochromat oil immersion objectives.

cause significant effects on the cell viability. In contrast, Trf-liposomes encapsulating specific siRNA anti-*BCR-ABL* led to dose-dependent cytotoxicity, reaching, for example, a cell viability of 46.97 ± 2.73%, upon incubation with 2 μM siRNA. Sequence specificity was not proven for the entire range of concentrations tested, since the scrambled one also significantly decreased cell viability (57.93 ± 9.73% at 2 μM).

In order to validate the results obtained with LAMA-84 cells, Trf-liposomes and BSA-liposomes were tested in K562 cells, whose *BCR-ABL* mRNA levels are 1.72-fold higher than LAMA-84 cells, as assessed by qRT-PCR (data not shown). In addition, TrfR levels of LAMA-84 cells are 15.68-fold higher than K562 cells, as assessed by CD71 measurement using flow cytometry (data not shown). As observed for LAMA-84 cells, the BSA-liposomes promote much lower toxicity than Trf-liposomes on K562 cells (Figure 4B). Treatment of K562 cells with Trf-liposomes resulted in higher extent of cytotoxicity as compared to LAMA-84 cells. For K562 cells, the off-target effects, evaluated by the cytotoxicity promoted by the scrambled siRNA, are lower than those observed for LAMA-84 cells. Concerning the nonmalignant BJ cells, which have no *BCR-ABL* oncogene, Trf- or BSA-liposomes encapsulating anti-*BCR-ABL* siRNA at the tested concentrations led to very low cytotoxicity.

As illustrated in Figure 4C, the observed toxicity effect of liposomes loaded with asODN against LAMA-84 cells reinforced the results obtained with siRNA-loaded liposomes. As can be observed, the cytotoxicity promoted by Trf-liposomes is dependent on the asODN dose. However, off-target cytotoxic effects mediated by the scrambled asODN were observed at a certain extent (70.38 ± 3.077 of cell viability for 2.0 μM). In addition, nontargeted liposomes (2.0 μM specific NT) or empty TrfR-targeted liposomes (2.0 μM ELP Trf) at the same lipid concentration as the one used to treat cells with 2.0 μM asODN-containing Trf-liposomes do not induce cytotoxicity.

***BCR-ABL* mRNA Knockdown Mediated by TrfR-Targeted Liposomes Encapsulating anti-*BCR-ABL* siRNA or asODN.** To evaluate the *BCR-ABL* knockdown efficiency of the liposomes encapsulating anti-*BCR-ABL* siRNA or anti-*BCR-ABL* asODN, *BCR-ABL* mRNA levels were analyzed in LAMA-84 cells double-transfected with the formulations under study. It was observed that only the liposomes encapsulating asODN or siRNA targeted to the TrfR were able to reduce the *BCR-ABL* mRNA levels. Regarding the Trf-liposomes encapsulating siRNA (Figure 5A), the observed silencing effect is dependent on the siRNA concentration up to 1 μM (59.81 ± 2.90%) without significant differences between 1 and 2 μM. For the Trf-liposomes loading asODN (Figure 5B), a higher dose was required (double) to obtain the same *BCR-ABL* knockdown achieved by Trf-liposomes loading siRNA molecules, where a significant reduction on the *BCR-ABL* mRNA levels (64.32 ± 9.0%) was only observed at 2.0 μM asODN. The observed *BCR-ABL* mRNA knockdown can be considered sequence-specific for both gene silencing molecules, since no significant reduction in the mRNA levels was observed with the scrambled sequences at the tested concentrations.

Bcr-Abl Protein Levels upon Treatment with TrfR-Targeted Liposomes Encapsulating anti-*BCR-ABL* siRNA or asODN. To evaluate the impact of *BCR-ABL* mRNA knockdown mediated by anti-*BCR-ABL* siRNA and by anti-*BCR-ABL* asODN on the oncoprotein levels, Western blot of LAMA-84 cells double-transfected with liposomes encapsulating siRNA (Figure 6A) or asODN (Figure 6B,C) was performed. As expected, no effect on the oncoprotein levels was observed upon treatment of the cells with nontargeted liposomes. On the other hand, Trf-liposomes encapsulating specific siRNA promoted a reduction in the oncoprotein levels. This effect was dose-dependent up to 1 μM (60.54 ± 12.35), since no further reduction was observed when 2 μM siRNA encapsulated in Trf-liposomes was added to the cells (Figure 6A). Our results also indicate that the protein knockdown

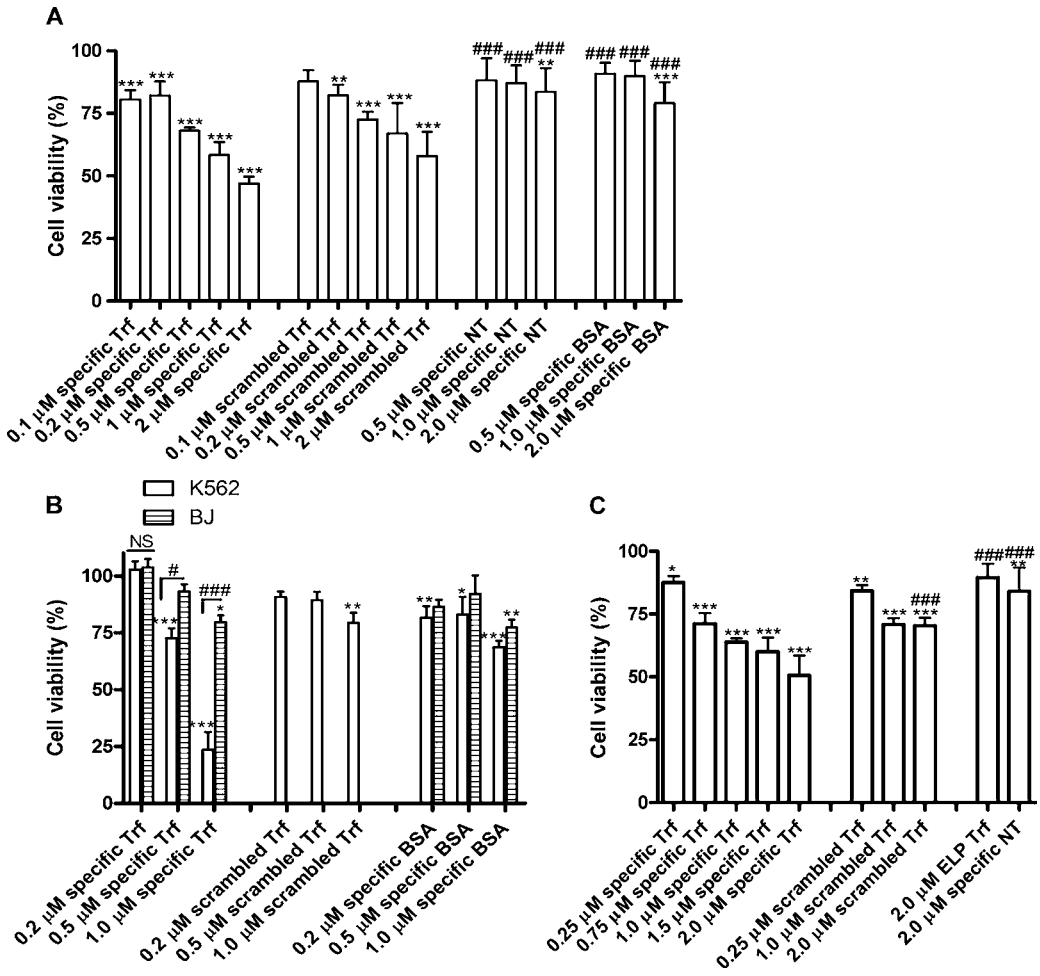


Figure 4. Cell viability upon two transfections with Trf-coupled liposomes loading anti-*BCR-ABL* siRNA or anti-*BCR-ABL* asODN. (A) LAMA-84, (B) K562, and BJ cells were incubated with different concentrations of specific or scrambled anti-*BCR-ABL* siRNA encapsulated in Trf-liposomes, BSA-liposomes, or NT-liposomes. (C) LAMA-84 cells were double-treated with specific or scrambled anti-*BCR-ABL* asODN encapsulated in Trf-liposomes or in NT-liposomes, as well as with empty Trf-liposomes (ELP Trf). Cell viability was assessed 48 h after the second transfection by the resazurin reduction method. (A,C) One-way ANOVA analysis of variance combined with Tukey post-test and (B) regular two-way ANOVA analysis of variance combined with Bonferroni post-test were used for multiple comparisons. ***$p < 0.001$; **$p < 0.01$; *$p < 0.05$, and no symbol $p > 0.05$ when comparison was established with nontreated cells; ###$p < 0.001$; #$p < 0.05$, and NS $p > 0.05$ comparison established with the corresponding concentration of specific siRNA/asODN encapsulated in Trf-liposomes (A,C) or comparison established between the conditions indicated by the lines (B).

is sequence-specific up to 1 μM, since the scrambled sequence did not promote any effect up to that concentration. However, for the highest concentration tested (2 μM), a significant reduction in the oncoprotein levels was observed (66.78 $\pm$ 13.13%) when cells were tested with scrambled sequence encapsulated in TrfR-targeted liposomes. Thus, at this concentration the protein knockdown cannot be considered sequence-specific. Concerning Trf-liposomes loaded with asODN (Figure 6B,C), the promoted effect by the specific asODN is dose-dependent for all tested concentrations. However, similarly to what was observed for siRNA, also off-target effects were observed upon treatment of the cells with 2 μM scrambled asODN loaded in TrfR-targeted liposomes.

Nevertheless, it should be emphasized that, independently of the sequence specificity of the siRNA/asODN molecules, reduction in the levels of Bcr-Abl protein is dependent on the cellular targeting specificity. As a matter of fact, in contrast to what was observed to the TrfR-targeted liposomes, no effect on the levels of protein was observed when cells were treated with 2 μM of specific siRNA or asODN encapsulated in BSA-coupled liposomes or nontargeted liposomes.

DISCUSSION

Gene silencing tools, such as siRNA and asODN, play an important role in therapeutic and fundamental research. However, these molecules have important limitations related to stability and pharmacokinetics. To circumvent these limitations, many approaches such as the use of delivery systems and chemical modifications of the nucleic acids have been tested. In fact, several strategies have been described referencing the design of chemically modified siRNA or asODN molecules less susceptible to nuclease degradation and less prone to immune system activation (*8, 10, 13, 31*). However, some of the major problems of these molecules are not overcome with these modifications, such as the poor pharmacokinetics, the unfavorable biodistribution throughout the body, and the inability to target specific diseased tissues or cells, like cancer cells. Therefore, the successful clinical application of gene silencing approaches is dependent on the development of effective delivery systems such as liposomes, capable of solving these issues by protecting the encapsulated molecules from nuclease degradation, conferring long circulation times in the bloodstream and with the ability to deliver the carried molecules to target cells through interaction with cell surface receptors.

The aim of this work was to encapsulate siRNA or asODN molecules, designed to specifically silence *BCR-ABL* mRNA, in liposomes targeted to the Trf receptor of leukemia cells. The encapsulation of anionic siRNA and asODN in the aqueous space of lipid vesicles by a passive encapsulation method leads

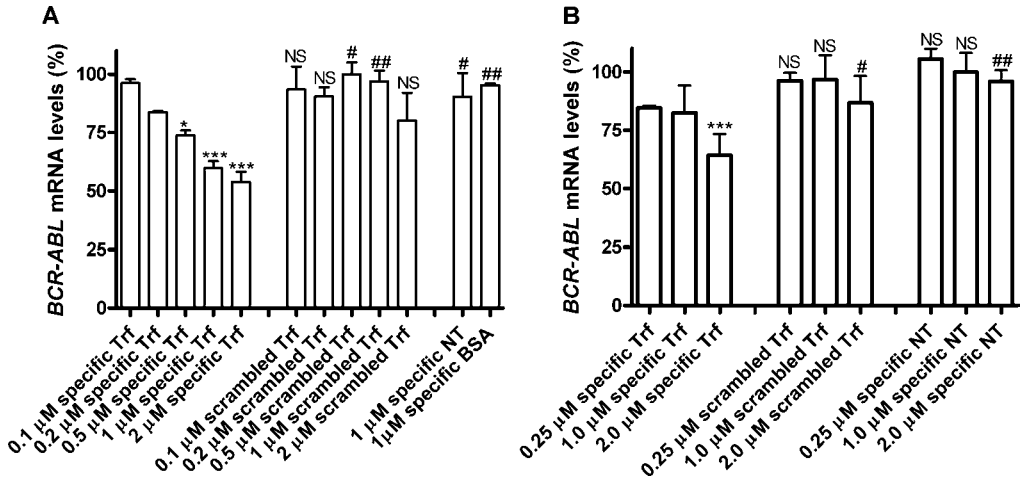


Figure 5. *BCR-ABL* mRNA levels in LAMA-84 cells upon treatment with anti-*BCR-ABL* siRNA or anti-*BCR-ABL* asODN. (A) LAMA-84 cells were double-transfected with different concentrations of specific or scrambled anti-*BCR-ABL* siRNA or (B) anti-*BCR-ABL* asODN, encapsulated in Trf-liposomes (Trf), BSA-liposomes (BSA), or NT-liposomes (NT). *BCR-ABL* mRNA levels of treated samples were evaluated as compared to those of nontreated cells, and were normalized against *B2M* housekeeping gene. Detection was performed by qRT-PCR, as described in Experimental Procedures. One-way ANOVA analysis of variance combined with Tukey post-test was used for multiple comparisons. ***$p < 0.001$, *$p < 0.05$, and no symbol $p > 0.05$ when comparison was established with nontreated cells; #$p < 0.05$, ##$p < 0.01$, and NS $p > 0.05$ when comparison was established with the corresponding concentration of specific siRNA/asODN encapsulated in Trf-liposomes.

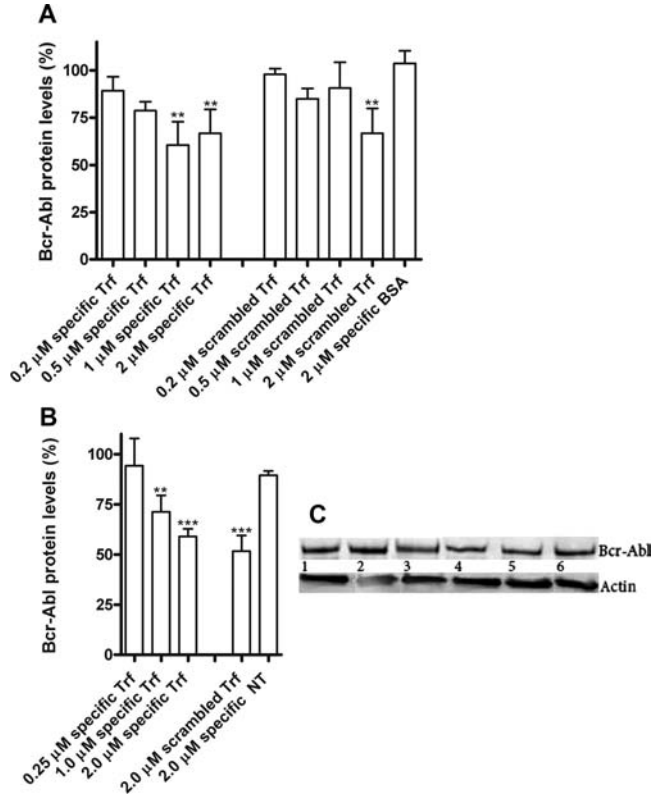


Figure 6. Bcr-Abl protein levels in LAMA-84 cells double-transfected with anti-*BCR-ABL* siRNA or anti-*BCR-ABL* asODN encapsulated in TrfR-targeted liposomes. (A) LAMA-84 cells were double-transfected with different concentrations of specific or scrambled anti-*BCR-ABL* siRNA or (B,C) different concentrations of specific or scrambled anti-*BCR-ABL* asODN encapsulated in Trf-liposomes, BSA-liposomes, or NT-liposomes. Cells were collected 48 h after the second transfection for evaluation of Bcr-Abl protein levels by Western blot. One-way ANOVA analysis of variance combined with Tukey post-test was used for multiple comparisons. ***$p < 0.001$, **$p < 0.01$, and no symbol $p > 0.05$ when comparison was established with nontreated cells. (C) is a representative Western blot result of LAMA-84 cells treated with anti-*BCR-ABL* asODN; lane 1, sample of nontreated cells; lane 2, cells treated with 2.0 μM of specific asODN encapsulated in NT-liposomes; lane 3, cells treated with 2.0 μM scrambled asODN encapsulated in Trf-liposomes; lanes 4, 5, and 6, cells treated with 2.0, 1.0, and 0.25 μM specifc asODN encapsulated in Trf-liposomes, respectively.

to very low encapsulation efficiencies and consequently to a tremendous waste of nucleic acids. Cationic liposomes, which form lipoplexes with the nucleic acids, can mediate reasonable levels of transfection *in vitro* without wasting nucleic acids during lipoplex preparation. However, their *in vivo* application is limited by their large size and net positive charge, which triggers rapid clearance from the blood circulation. In addition, lipoplexes are not tissue-specific, being mainly distributed into lung, liver, and spleen, and very often exhibit toxicity (*32–34*). Moreover, from the formulation point of view, lipoplexes are

thermodynamically unstable and display a tendency to form larger aggregates over time (*14, 35, 36*).

Semple et al. developed a new method to encapsulate asODN, leading to the so-called stabilized antisense lipid particles (SALP) (*29*). These authors demonstrated that the addition of lipids dissolved in ethanol to an aqueous solution of asODN resulted in the formation of small multilamellar liposomes encapsulating the asODN with a very good encapsulation yield. Thus, in this work we have explored this method to carry out asODN encapsulation and assessed whether by performing some modifications it could be applied as well to siRNA encapsulation. This nucleic acid entrapment process is based on the spontaneous electrostatic interaction with cationic liposomes together with the membrane destabilizing effect of ethanol and with the inclusion of PEG-derivatized lipids, which allows control of liposome size to avoid aggregation.

Thus, the high encapsulation yields achieved in this work, for both asODN and siRNA, are mainly attributed to the inclusion of the ionizable cationic lipid DODAP, which is positively charged at pH 4 and consequently able to complex anionic nucleic acids through electrostatic interactions. In our hands, yields of encapsulations of close to 100% were obtained. These high encapsulation yields were also reported by others using SALP for asODN encapsulation in a liposomal formulation similar to that used in this work (*29*) or for siRNA encapsulation in a different liposomal formulation (*37*).

Concerning the encapsulation process, our results clearly demonstrate that the major difference between siRNA and asODN encapsulation efficiency is in the significant impact of the citrate buffer concentration. As previously described, very low encapsulation yields of siRNA were observed when using 300 mM citrate buffer as opposed to 20 mM. In contrast, for asODN molecules both 300 mM and 20 mM allowed high encapsulation yields. These encapsulation yields can be explained by the different role of salt and buffer concentrations in the encapsulation of nucleic acid molecules, depending on their chemical characteristics. Indeed, as reported previously, concerning the phosphodiesters, as the siRNA molecules used in this work, the use of citrate buffers at 20 mM will be required to facilitate efficient charge interactions between DODAP and the nucleic acid, since at higher buffer concentration, these charge interactions are shielded, resulting in very low encapsulation yields (*38–40*). On the other hand, phosphorothioate nucleic acids, as the asODN molecules used in this work, bind strongly to cationic molecules, and therefore, the encapsulation efficiency is much less sensitive to the differences in the buffer and salt concentrations.

The covalent attachment of a protein to the liposome surface can be performed by active or passive coupling methods (*41*). However, as the maleimide group of derivatized lipids used for coupling the protein to the lipid is susceptible to hydrolysis, forming ring-opened maleamic acids which are unreactive (*41*), the implementation of coupling methods that allow a fast reaction of the maleimide function with the thiol functionalized protein is mandatory. Indeed, it has been demonstrated that the postinsertion method (passive coupling method) allows higher levels of protein coupling as compared to the active method (*41*). Thus, in this work, the postinsertion coupling method was selected. Trf and BSA coupled at the terminus of MAL-PEG-derivatized lipids, organized in a micellar form, were transferred into preformed liposomes encapsulating nucleic acids. It has been reported that postinsertion occurs in a temperature- and time-dependent manner (*24, 42, 43*) and frequently is performed close to the phase transition temperature (T_c) of the membrane-forming lipids. However, in this work, the postinsertion was performed for 17 or 24 h at 38 °C, which is below the T_c of the membrane forming lipid DSPC (55 °C), in an attempt to prevent transferrin denaturation observed at temperatures close to 55 °C. As a consequence of the low temperature used for the postinsertion, the obtained yields of protein−conjugate inserted onto the liposomal surface were very low (12.18 ± 1.23% for empty liposomes and 8.9 ± 0.24% for siRNA-encapsulating liposomes; data not shown). Another possible explanation for the low transfer yield is the high amount of PEG-Cer lipid existing in the preformed liposomes (8 mol %), which was reported to decrease the postinsertion efficacy (*41, 43*). Under these circumstances, prolonging the transfer time beyond 17 h did not improve the postinsertion yield. In addition, the incubation of 4 mol % instead of 2 mol % of protein-containing micelles led to a higher amount of protein coupled to liposomes, although the postinsertion yield was not enhanced. To the best of our knowledge, this is the first work establishing a correlation between the effect of transfer time (17 and 24 h) and content of Trf-micelles (2 and 4 mol %) added to the liposomes, and the amount of protein−conjugate transferred onto the liposome surface. Our results also indicate that the amount of protein transferred onto the liposomes is similar for both BSA and Trf, and therefore, BSA-liposomes are good control formulations for targeting specificity studies. The yield and the amount of protein−conjugate transferred are significantly higher for empty liposomes as compared to nucleic acid-loaded liposomes. A possible explanation is that loaded liposomes have more rigid lipid membranes and therefore are less prone to the insertion of protein−conjugates into the preformed liposomes, through replacement of pre-existing PEG-lipids (*41*).

Concerning the size of the liposomes, and similarly to what was previously reported (*19*), insertion of Trf or BSA protein−conjugates onto liposomes leads to a significant increase of particle size. A higher size enhancement was observed following Trf coupling as compared to BSA, which can be explained by the different molecular weight of these proteins (Trf ∼ 80 kDa and BSA ∼ 66 kDa). Nevertheless, it should be emphasized that all developed formulations exhibit sizes below 200 nm, with homogeneous particle size distribution (PI smaller than 0.3) and without aggregation during the six month period of observation upon storage at 4 °C. Thus, this liposome preparation method allowed the production of liposomes with reproducible protein/lipid ratio, high levels of nucleic acid encapsulation, and interesting shelf life properties. Therefore, it can be concluded that, from a production point of view, this technology allowed us to produce sophisticated formulations in a quite simple and reproducible way with a very good accuracy.

Results from targeting specificity and competitive inhibition studies clearly indicate that BSA- and NT-liposomes have no ability to promote the delivery of the encapsulated nucleic acids. Additionally, when TrfR was saturated and the temperature was decreased to 4 °C, the extent of cell association and internalization of Trf-liposomes was drastically reduced, clearly demonstrating that internalization of Trf-liposomes is mainly mediated by the TrfR at the cell surface.

The molecular and cellular effects promoted by the developed formulations on leukemia cells (LAMA-84 and K562) and on a nonmalignant cell line (BJ) were assessed. As expected, only Trf-liposomes encapsulating anti-*BCR-ABL* siRNA or asODN were able to promote modifications on *BCR-ABL* mRNA and oncoprotein Bcr-Abl levels, as well as on cell viability. Indeed, the advantage of targeted liposomes as compared to nontargeted liposomes concerning the intracellular delivery and consequently the biological activity of the delivered nucleic acids has been reported (*19, 44*). A dose-dependent cytotoxicity for both anti-*BCR-ABL* siRNA and asODN when delivered by Trf-liposomes was observed. Nevertheless, off-target effects mediated by scrambled sequences were also observed to a certain extent,

namely, for the highest concentration tested. The Trf-liposomes encapsulating anti-*BCR-ABL* siRNA or asODN were effective in decreasing viability in both leukemia cell lines tested, without significant effect on the nonmalignant cell line BJ that does not present the *BCR-ABL* translocation.

Our results from qRT-PCR indicated that the *BCR-ABL* mRNA downregulation was only possible when siRNA or asODN were delivered by Trf-liposomes. The anti-*BCR-ABL* siRNA led to more efficient reduction of mRNA levels as compared to the anti-*BCR-ABL* asODN, since siRNA promoted the same extent of gene silencing with lower concentrations. Both siRNA- and asODN-mediated *BCR-ABL* mRNA knockdown were sequence-specific at the tested concentrations.

At the protein level, Trf-liposomes encapsulating siRNA led to dose-dependent reduction of Bcr-Abl levels up to 1 μM, beyond which (at 2 μM siRNA) significant off-target effects were observed. Therefore, 2 μM of siRNA had no advantage since the slight enhancement in cytotoxicity, as compared to that observed for 1 μM concentration, is in part attributed to the enhancement of the off-target effects at the protein level. Thus, as previously reported by others (*45–47*), siRNA molecules mediate dose-dependent off-target effects. Therefore, it is possible that above a certain concentration (1 μM) siRNA molecules can knockdown proteins (including Bcr-Abl) by nonspecific mechanisms. This off-target effect observed at the 2 μM concentration was also observed for asODN molecules. Similarly to what was observed for *BCR-ABL* mRNA, at the Bcr-Abl protein level siRNA are more potent gene silencing tools than asODN, since 2 μM asODN was required to achieve the same extent of protein knockdown as 1 μM siRNA. This higher potency of siRNA as compared to asODN has been reported by other authors (*44, 48*) and is in agreement with our previous results (unpublished data). In contrast to the specificity observed at the mRNA level, off-target effects at 2 μM were observed for both siRNA and asODN molecules regarding protein knockdown. These findings suggest that the siRNA and asODN molecules are capable of interacting nonspecifically with the Bcr-Abl protein. In fact, it has been previously reported that both siRNA and asODN molecules can promote off-target effects even when the sequences are designed to have no physiological target (*49–51*). In addition, it was demonstrated that these molecules can act at the protein level without affecting the mRNA levels (*45, 51*), acting as aptamers (nucleic acids with the ability of interfering directly with protein, further leading to its degradation). Therefore, the cytotoxicity caused by off-target effects mediated by Trf-liposomes encapsulating scrambled siRNA or scrambled asODN, at the 2 μM concentration, is not caused by interference at the *BCR-ABL* mRNA level, but rather by unspecific interaction with Bcr-Abl protein and probably also with other proteins. Moreover, the possibility of siRNA scrambled sequences acting as a microRNA should not be excluded (*52*), and consequently, some of the off-target effects observed for the scrambled sequences at 2 μM concentration may result from off-target mRNA translation inhibition mediated by siRNA through mechanisms similar to those described for microRNA. Therefore, the assessment of the extent of off-target effects triggered by siRNA and asODN molecules is a very difficult task. In fact, it has been reported that some of the observed effects mediated by siRNA are siRNA sequence-specific rather than target-specific (*53*). Moreover, it has been demonstrated that some of the sequences most widely used as controls for siRNA off-target effects, such as the siRNA against GFP, deregulates endogenous genes (*49*). Therefore, it seems that off-target effects constitute a well-established limitation of this gene silencing approach, and consequently, caution should be employed in the interpretation of the results.

In conclusion, the developed liposomes exhibited excellent features in terms of asODN and siRNA encapsulating efficiency, particle size, stability over time, and reproducibility of manufacturing. Results from studies in LAMA-84 and K562 cells clearly demonstrated that cell association and internalization of Trf-liposomes are mediated by the TrfR and a notorious *BCR-ABL* mRNA and Bcr-Abl protein down-regulation leading to significant toxicity in leukemia cells. These results illustrate the importance of combining molecular and cellular targeting as a valuable approach for cancer treatment. Further *in vivo* studies are required to assess the clinical potential of the developed formulations for the treatment of CML.

ACKNOWLEDGMENT

Liliana S. Mendonça was recipient of a fellowship from the Portuguese Foundation for Science and Technology (SFRH/BD/18280/2004). The work was supported by the Portugal-Spain capacitation program in nanoscience and nanotechnology (ref.: NANO/NMed-AT/0042/2007).

LITERATURE CITED

(1) Pasternak, G., Hochhaus, A., Schultheis, B., and Hehlmann, R. (1998) Chronic myelogenous leukemia: molecular and cellular aspects. *J. Cancer Res. Clin. Oncol. 124*, 643–60.
(2) Goldman, J. M. (2004) Chronic myeloid leukemia-still a few questions. *Exp. Hematol. 32*, 2–10.
(3) Savona, M., and Talpaz, M. (2008) Getting to the stem of chronic myeloid leukaemia. *Nat. Rev. Cancer 8*, 341–50.
(4) Galderisi, U., Cascino, A., and Giordano, A. (1999) Antisense oligonucleotides as therapeutic agents. *J. Cell Physiol. 181*, 251–7.
(5) Tamm, I. (2006) Antisense therapy in malignant diseases: status quo and quo vadis? *Clin. Sci. (London) 110*, 427–42.
(6) Dykxhoorn, D. M., Palliser, D., and Lieberman, J. (2006) The silent treatment: siRNAs as small molecule drugs. *Gene Ther. 13*, 541–52.
(7) Dykxhoorn, D. M., Novina, C. D., and Sharp, P. A. (2003) Killing the messenger: short RNAs that silence gene expression. *Nat. Rev. Mol. Cell Biol. 4*, 457–67.
(8) Huang, C., Li, M., Chen, C., and Yao, Q. (2008) Small interfering RNA therapy in cancer: mechanism, potential targets, and clinical applications. *Expert Opin. Ther. Targets 12*, 637–45.
(9) Kumar, L. D., and Clarke, A. R. (2007) Gene manipulation through the use of small interfering RNA (siRNA): from in vitro to in vivo applications. *Adv. Drug Delivery Rev. 59*, 87–100.
(10) Kawakami, S., and Hashida, M. (2007) Targeted delivery systems of small interfering RNA by systemic administration. *Drug Metab. Pharmacokinet. 22*, 142–51.
(11) Zhang, C., Tang, N., Liu, X., Liang, W., Xu, W., and Torchilin, V. P. (2006) siRNA-containing liposomes modified with polyarginine effectively silence the targeted gene. *J. Controlled Release 112*, 229–39.
(12) Akhtar, S., and Benter, I. (2007) Toxicogenomics of non-viral drug delivery systems for RNAi: potential impact on siRNA-mediated gene silencing activity and specificity. *Adv. Drug Delivery Rev. 59*, 164–82.
(13) Mahato, R. I., Cheng, K., and Guntaka, R. V. (2005) Modulation of gene expression by antisense and antigene oligodeoxynucleotides and small interfering RNA. *Expert Opin. Drug Delivery 2*, 3–28.
(14) Patil, S. D., Rhodes, D. G., and Burgess, D. J. (2005) DNA-based therapeutics and DNA delivery systems: a comprehensive review. *AAPS J. 7*, E61–77.
(15) Daniels, T. R., Delgado, T., Rodriguez, J. A., Helguera, G., and Penichet, M. L. (2006) The transferrin receptor part I: Biology and targeting with cytotoxic antibodies for the treatment of cancer. *Clin. Immunol. 121*, 144–58.

(16) Li, H., and Qian, Z. M. (2002) Transferrin/transferrin receptor-mediated drug delivery. *Med. Res. Rev. 22*, 225–50.
(17) Ponka, P., and Lok, C. N. (1999) The transferrin receptor: role in health and disease. *Int. J. Biochem. Cell Biol. 31*, 1111–37.
(18) Visser, C. C., Stevanovic, S., Voorwinden, L. H., van Bloois, L., Gaillard, P. J., Danhof, M., Crommelin, D. J., and de Boer, A. G. (2005) Targeting liposomes with protein drugs to the blood-brain barrier in vitro. *Eur. J. Pharm. Sci. 25*, 299–305.
(19) Chiu, S. J., Liu, S., Perrotti, D., Marcucci, G., and Lee, R. J. (2006) Efficient delivery of a Bcl-2-specific antisense oligodeoxyribonucleotide (G3139) via transferrin receptor-targeted liposomes. *J. Controlled Release 112*, 199–207.
(20) Daniels, T. R., Delgado, T., Helguera, G., and Penichet, M. L. (2006) The transferrin receptor part II: targeted delivery of therapeutic agents into cancer cells. *Clin. Immunol. 121*, 159–76.
(21) Immordino, M. L., Dosio, F., and Cattel, L. (2006) Stealth liposomes: review of the basic science, rationale, and clinical applications, existing and potential. *Int. J. Nanomed. 1*, 297–315.
(22) Romberg, B., Hennink, W. E., and Storm, G. (2008) Sheddable coatings for long-circulating nanoparticles. *Pharm. Res. 25*, 55–71.
(23) Ryan, S. M., Mantovani, G., Wang, X., Haddleton, D. M., and Brayden, D. J. (2008) Advances in PEGylation of important biotech molecules: delivery aspects. *Expert Opin. Drug Delivery 5*, 371–83.
(24) Ishida, T., Iden, D. L., and Allen, T. M. (1999) A combinatorial approach to producing sterically stabilized (Stealth) immunoliposomal drugs. *FEBS Lett. 460*, 129–33.
(25) O'Brien, J., Wilson, I., Orton, T., and Pognan, F. (2000) Investigation of the Alamar Blue (resazurin) fluorescent dye for the assessment of mammalian cell cytotoxicity. *Eur. J. Biochem. 267*, 5421–6.
(26) Beillard, E., Pallisgaard, N., van der Velden, V. H., Bi, W., Dee, R., van der Schoot, E., Delabesse, E., Macintyre, E., Gottardi, E., Saglio, G., Watzinger, F., Lion, T., van Dongen, J. J., Hokland, P., and Gabert, J. (2003) Evaluation of candidate control genes for diagnosis and residual disease detection in leukemic patients using 'real-time' quantitative reverse-transcriptase polymerase chain reaction (RQ-PCR) - a Europe against cancer program. *Leukemia 17*, 2474–86.
(27) Gabert, J., Beillard, E., van der Velden, V. H., Bi, W., Grimwade, D., Pallisgaard, N., Barbany, G., Cazzaniga, G., Cayuela, J. M., Cave, H., Pane, F., Aerts, J. L., De Micheli, D., Thirion, X., Pradel, V., Gonzalez, M., Viehmann, S., Malec, M., Saglio, G., and van Dongen, J. J. (2003) Standardization and quality control studies of 'real-time' quantitative reverse transcriptase polymerase chain reaction of fusion gene transcripts for residual disease detection in leukemia - a Europe Against Cancer program. *Leukemia 17*, 2318–57.
(28) Cardoso, A. L., Simoes, S., de Almeida, L. P., Plesnila, N., Pedroso de Lima, M. C., Wagner, E., and Culmsee, C. (2008) Tf-lipoplexes for neuronal siRNA delivery: a promising system to mediate gene silencing in the CNS. *J. Controlled Release 132*, 113–23.
(29) Semple, S. C., Klimuk, S. K., Harasym, T. O., Dos Santos, N., Ansell, S. M., Wong, K. F., Maurer, N., Stark, H., Cullis, P. R., Hope, M. J., and Scherrer, P. (2001) Efficient encapsulation of antisense oligonucleotides in lipid vesicles using ionizable aminolipids: formation of novel small multilamellar vesicle structures. *Biochim. Biophys. Acta 1510*, 152–66.
(30) Maurer, N., Wong, K. F., Stark, H., Louie, L., McIntosh, D., Wong, T., Scherrer, P., Semple, S. C., and Cullis, P. R. (2001) Spontaneous entrapment of polynucleotides upon electrostatic interaction with ethanol-destabilized cationic liposomes. *Biophys. J. 80*, 2310–26.
(31) Kalota, A., Shetzline, S. E., and Gewirtz, A. M. (2004) Progress in the development of nucleic acid therapeutics for cancer. *Cancer Biol. Ther. 3*, 4–12.
(32) Pedroso de Lima, M. C., Simoes, S., Pires, P., Faneca, H., and Duzgunes, N. (2001) Cationic lipid-DNA complexes in gene delivery: from biophysics to biological applications. *Adv. Drug Delivery Rev. 47*, 277–94.
(33) Lv, H., Zhang, S., Wang, B., Cui, S., and Yan, J. (2006) Toxicity of cationic lipids and cationic polymers in gene delivery. *J. Controlled Release 114*, 100–9.
(34) Morille, M., Passirani, C., Vonarbourg, A., Clavreul, A., and Benoit, J. P. (2008) Progress in developing cationic vectors for non-viral systemic gene therapy against cancer. *Biomaterials 29*, 3477–96.
(35) Simoes, S., Filipe, A., Faneca, H., Mano, M., Penacho, N., Duzgunes, N., and de Lima, M. P. (2005) Cationic liposomes for gene delivery. *Expert Opin. Drug Delivery 2*, 237–54.
(36) Dass, C. R., and Choong, P. F. (2006) Selective gene delivery for cancer therapy using cationic liposomes: in vivo proof of applicability. *J. Controlled Release 113*, 155–63.
(37) Morrissey, D. V., Lockridge, J. A., Shaw, L., Blanchard, K., Jensen, K., Breen, W., Hartsough, K., Machemer, L., Radka, S., Jadhav, V., Vaish, N., Zinnen, S., Vargeese, C., Bowman, K., Shaffer, C. S., Jeffs, L. B., Judge, A., MacLachlan, I., and Polisky, B. (2005) Potent and persistent in vivo anti-HBV activity of chemically modified siRNAs. *Nat. Biotechnol. 23*, 1002–7.
(38) Semple, S. C., Harasym, T. O., Clow, K. A., Ansell, S. M., Klimuk, S. K., and Hope, M. J. (2005) Immunogenicity and rapid blood clearance of liposomes containing polyethylene glycol-lipid conjugates and nucleic Acid. *J. Pharmacol. Exp. Ther. 312*, 1020–6.
(39) Mui, B., Raney, S. G., Semple, S. C., and Hope, M. J. (2001) Immune stimulation by a CpG-containing oligodeoxynucleotide is enhanced when encapsulated and delivered in lipid particles. *J. Pharmacol. Exp. Ther. 298*, 1185–92.
(40) Stuart, D. D., Semple, S. C., and Allen, T. M. (2004) High efficiency entrapment of antisense oligonucleotides in liposomes. *Methods Enzymol. 387*, 171–88.
(41) Takasaki, J., Raney, S. G., Chikh, G., Sekirov, L., Brodsky, I., Tam, Y., and Ansell, S. M. (2006) Methods for the preparation of protein-oligonucleotide-lipid constructs. *Bioconjugate Chem. 17*, 451–8.
(42) Uster, P. S., Allen, T. M., Daniel, B. E., Mendez, C. J., Newman, M. S., and Zhu, G. Z. (1996) Insertion of poly(ethylene glycol) derivatized phospholipid into pre-formed liposomes results in prolonged in vivo circulation time. *FEBS Lett. 386*, 243–6.
(43) Allen, T. M., Sapra, P., and Moase, E. (2002) Use of the post-insertion method for the formation of ligand-coupled liposomes. *Cell. Mol. Biol. Lett. 7*, 889–94.
(44) Kim, S. H., Mok, H., Jeong, J. H., Kim, S. W., and Park, T. G. (2006) Comparative evaluation of target-specific GFP gene silencing efficiencies for antisense ODN, synthetic siRNA, and siRNA plasmid complexed with PEI-PEG-FOL conjugate. *Bioconjugate Chem. 17*, 241–4.
(45) Grimm, D., Streetz, K. L., Jopling, C. L., Storm, T. A., Pandey, K., Davis, C. R., Marion, P., Salazar, F., and Kay, M. A. (2006) Fatality in mice due to oversaturation of cellular microRNA/short hairpin RNA pathways. *Nature 441*, 537–41.
(46) Reynolds, A., Anderson, E. M., Vermeulen, A., Fedorov, Y., Robinson, K., Leake, D., Karpilow, J., Marshall, W. S., and Khvorova, A. (2006) Induction of the interferon response by siRNA is cell type- and duplex length-dependent. *RNA 12*, 988–93.
(47) Suggate, E. L., Ahmed, Z., Read, M. L., Eaton-Charnock, K., Douglas, M. R., Gonzalez, A. M., Berry, M., and Logan, A. (2009) Optimisation of siRNA-mediated RhoA silencing in neuronal cultures. *Mol. Cell. Neurosci. 40*, 451–62.
(48) Bertrand, J. R., Pottier, M., Vekris, A., Opolon, P., Maksimenko, A., and Malvy, C. (2002) Comparison of antisense oligonucleotides and siRNAs in cell culture and in vivo. *Biochem. Biophys. Res. Commun. 296*, 1000–4.
(49) Tschuch, C., Schulz, A., Pscherer, A., Werft, W., Benner, A., Hotz-Wagenblatt, A., Barrionuevo, L. S., Lichter, P., and Mertens, D. (2008) Off-target effects of siRNA specific for GFP. *BMC Mol. Biol. 9*, 60.
(50) Tschaharganeh, D., Ehemann, V., Nussbaum, T., Schirmacher, P., and Breuhahn, K. (2007) Non-specific effects of siRNAs on tumor cells with implications on therapeutic applicability using RNA interference. *Pathol. Oncol. Res. 13*, 84–90.

(51) Achenbach, T. V., Brunner, B., and Heermeier, K. (2003) Oligonucleotide-based knockdown technologies: antisense versus RNA interference. *ChemBioChem 4*, 928–35.
(52) Hannon, G. J., and Rossi, J. J. (2004) Unlocking the potential of the human genome with RNA interference. *Nature 431*, 371–8.
(53) Judge, A. D., Sood, V., Shaw, J. R., Fang, D., McClintock, K., and MacLachlan, I. (2005) Sequence-dependent stimulation of the mammalian innate immune response by synthetic siRNA. *Nat. Biotechnol. 23*, 457–62.

BC9004365

Modification of Thiol Functionalized Aptamers by Conjugation of Synthetic Polymers

Chiara Da Pieve,*,† Paul Williams,‡ David M. Haddleton,§ Richard M. J. Palmer,‡ and Sotiris Missailidis*,†

Department of Chemistry and Analytical Sciences, The Open University, Milton Keynes, United Kingdom MK6 7AA, Warwick Effect Polymers Limited, Coventry, United Kingdom CV4 7EZ, and Department of Chemistry, University of Warwick, Coventry, United Kingdom CV4 7AL. Received September 11, 2009; Revised Manuscript Received November 12, 2009

Aptamers are known for their short *in vivo* circulating half-life and rapid renal clearance. Their conjugation to poly(ethylene glycol) (PEG) is a way to improve their residence in the body. Two aptamers (AptD and AptF), having a disulfide protected thiol modification on the 3′ end, have been conjugated to maleimide activated PEGs of various molecular weights and structures (linear PEG20; branched PEG20 and 40; PolyPEG17, 40, and 60 kDa). The high yield coupling (70−80% in most of the cases) could be achieved using immobilized *tris*[2-carboxyethyl]phosphine hydrochloride (TCEP) as reducing agent at pH 4. The affinity of PEGylated AptD for its target was reduced by conjugation to linear PEG20 and branched PEG40, but not to branched PEG20 and PolyPEGs. This work demonstrates an alternative approach to PEGylation of aptamers, and that the effect of PEG on the affinity for the target varies according to the structure and conformation of the synthetic polymer.

INTRODUCTION

Aptamers are nucleic acid-based molecules (usually 8−15 kDa) that can selectively bind to almost any target such as extracellular proteins, peptides, enzymes, and small molecules. Aptamers can be selected using the systematic evolution of ligands by exponential enrichment (SELEX) method from libraries of oligonucleotides having random sequences. Moreover, they have shown low toxicity and immunogenicity. These characteristics make aptamers interesting and potentially powerful molecules for targeted therapy (*1*−*4*). Since aptamers are small and highly charged molecules, they are subject to rapid renal elimination, resulting in a short *in vivo* half-life. Conjugation to synthetic polymers such as poly(ethylene glycol) (PEG) is frequently used in order to improve the performance of biomolecules as therapeutics (*5*−*11*). The increase of the hydrodynamic volume/molecular weight of aptamers above the renal filtration cutoff, achievable by PEGylation, can overcome this potential limitation (*12, 13*). PEG shows low toxicity, nonimmunogenicity, and high solubility in water and is commercially available in various configurations (linear, branched, or comb-shaped) and molecular weights and with a large variety of terminal functional groups suitable for conjugation (*14*−*17*). A few examples of PEGylated aptamers can be found in the literature, and they have been prepared by coupling the activated polymer to amino-modified aptamers (*18*−*21*). In addition, comb polymers of PEG acrylate containing a pyridyl disulfide terminus have been reversibly conjugated to siRNA (*22*).

In this present work, a 3′-thiol-modified (disulfide protected) 25 base DNA aptamer, previously selected against the protein core of MUC1 glycoprotein (AptD) (*23*), has been successfully conjugated via a maleimide functional group to a range of PEG-based polymers of varying topology and molecular weight. This includes conventional linear PEG (LinPEG20 kDa) and branched PEGs (BrPEG20 and 40 kDa) and three novel PolyPEG structures (PolyPEG17, 40, and 60 kDa). PolyPEGs were selected as novel PEGylating agents due to their "comb-like" architecture based on a polymethacrylate backbone with PEG "teeth" attached to it by ester bonds. These α-functional polymers are prepared by transition-metal-mediated living radical polymerization (TMM-LRP) and have previously been shown to conjugate proteins and peptides via a range of functionalities (*24*−*26*). Recent studies have demonstrated that PolyPEG is particularly effective for conjugation to peptides such as salmon calcitonin, retaining bioactivity and conferring an increased half-life *in vivo* (*27*). The comb-shaped polymer has been shown to have interesting additional properties to linear PEGs such as reduced viscosity (*16*). Moreover, because the PEG "teeth" in PolyPEG are attached by ester bonds to the backbone, its structure could degrade to small units that are readily excreted over time from the body, avoiding the potential toxicological problems due to renal epithelial vacuolization on administration to animals shown by linear PEG (*28, 29*).

The affinity of the various PEGylated aptamer D for their target has been studied using a convenient fluorescent intercalator displacement (FID) assay to detect any influence of the polymers on the binding.

The optimized conjugation conditions were used to PEGylate a second 25 base thiol-modified DNA aptamer (AptF) previously selected for the tumor glycosylated MUC1 glycoprotein (*30*) in order to demonstrate that the high-yield conjugation reaction is not dependent on the aptamer sequence.

EXPERIMENTAL PROCEDURES

Materials and Methods. All polymerizations were carried out using standard Schlenk techniques under an inert atmosphere of nitrogen. Poly(ethylene glycol) methyl ether methacrylate (MeOPEGMA M_n = 1100 g·mol^{-1}) was purchased from Aldrich (Gillingham, UK). *N*-(Ethyl)-2-pyridylmethanimine and 2-bromo-2-methyl propionic acid 2-(3,5-dioxo-10-oxa-4-aza-tricyclo[5.2.1.02,6]dec-8-en-4-yl) (**1**) were synthesized as previously reported (*26, 31*). Copper(I) bromide (Aldrich, 98%) was

* To whom correspondences should be addressed at the Department of Chemistry and Analytical Sciences, The Open University, Walton Hall, Milton Keynes, UK MK6 7AA. Phone: +44 1908653366 (Chiara Da Pieve), +44 1908658382 (Sotiris Missailidis); Fax: +44 1908858327. E-mail: c.dapieve@open.ac.uk; s.missailidis@open.ac.uk.

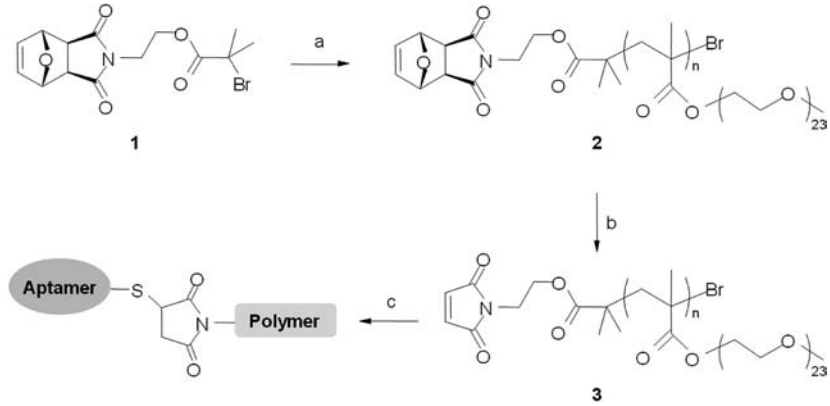
† The Open University.

‡ Warwick Effect Polymers Limited.

§ University of Warwick.

10.1021/bc900397s © 2010 American Chemical Society
Published on Web 12/10/2009

Scheme 1. Synthesis of α-Maleimide Functional PolyPEGs and Subsequent Conjugation to an Aptamer[a]



[a] Reagents and conditions: (a) $Cu^{I}Br$/*N*-(ethyl)-2-pyridylmethanimine/(methoxyPEG1100)methacrylate, toluene, 50°C; (b) toluene reflux, 6 h; (c) immobilized TCEP, ammonium formate buffer pH 4, 37 °C.

purified as described elsewhere (*32*). Hydrosart, stabilized cellulose, MWCO 10 kDa, filtration area 0.1 m^2, was purchased from Sartorius AG (Goettingen, Germany).

The sequences of AptD and AptF are, respectively, 5′-GCA GTT GAT CCT TTG GAT ACC CTG G-3′ and 5′-GGC GTA CGG TAG GCG GGG TCA ACT G-3′. Both aptamers have a 3′-thiol-modification protected as disulfide (−S-S-C_3H_6-OH) (IDT Integrated DNA Technologies, Leuven, Belgium). The control aptamer (AptX) is a 25 base oligo of random composition (12% A, 20% C, 32% G, and 36% T).

Linear PEG20 kDa and branched PEG20 and 40 kDa were acquired from Nektar Therapeutics (Huntsville, AL, USA). PolyPEG17, 40, and 60 kDa were provided by Warwick Effect Polymers Limited (Coventry, UK). Immobilized *tris*[2-carboxyethyl]phosphine hydrochloride (TCEP) disulfide reducing gel was purchased from Pierce (Illinois, USA). Agarose and PAGE gels were stained with ethidium bromide and imaged on Kodak Image Station 440.

$[Ru(phen)_2DPPZ](PF_6)_2$ was synthesized according to literature (*33*). The MUC1 core peptide (APDTRPAPG) was prepared by the Oligonucleotide and Peptide Synthesis Unit, University of Nottingham. The emission measurements were recorded in the range 450−700 nm on a FluoroMax-P Fluorometer (Jobin Yvon Horiba).

Synthesis of Maleimide Functional PolyPEGs (*3*). In a typical polymerization, a mixture of **1** (0.535 g, 1.49 mmol), poly(ethylene glycol) methyl ether methacrylate (50 g, 46.3 mmol), and copper(I) bromide (0.214 g, 1.49 mmol) in toluene (100 mL) was deoxygenated by a series of five freeze−pump−thaw cycles. Degassed *N*-(ethyl)-2-pyridylmethanimine (0.9 mL, 6.57 mmol) was added, and the resultant solution was stirred at 50 °C. Samples were removed periodically for molecular weight and conversion analysis. At the end of the polymerization, the solution was diluted with toluene (200 mL) and bubbled with air for 7 h. The solution was then filtered through a column containing basic alumina and the solvent removed under reduced pressure to yield an off-white solid, which was dissolved in water and purified by dialysis using Hydrosart membrane (MWCO 10 kDa). The solution was freeze−dried and the product **2** obtained as a white powder.

A solution of polymer **2** (3 g, 0.079 mmol) in toluene (30 mL) was warmed to reflux for 6 h. The solvent was then removed under reduced pressure and the off-white solid dissolved in water and purified by dialysis as above. The solution was freeze−dried and the product **3** obtained as a white powder.

Synthesis of the PEGylated Conjugates. In a typical PEGylation reaction, the 3′-disulfide protected aptamer (3 nmol) in 20 μL of 18 mM ammonium formate pH 4 was added to 30 nmol of each PEG (1:5 reduced aptamer to PEG molar ratio), followed by 3 μL of immobilized *tris*[2-carboxyethyl]phosphine hydrochloride (TCEP) disulfide reducing gel. The mixture was mixed for 1 h at 37 °C, centrifuged, and the supernatant lyophilized.

High-Performance Liquid Chromatography (HPLC) Analysis and Isolation of PEGylated Aptamer D. The HPLC analyses and isolation of the various PEGylated conjugates of AptD are described in the Supporting Information section and Figures S3 and S4. A 0.02 mM aqueous solution of AptD was used as the standard.

Fluorescent Intercalator Displacement (FID) Assay. A 50 nM solution of AptD, PEGylated AptD, or the control AptX in 5 mM $MgCl_2 \cdot 6H_2O$, 100 mM NaCl (pH 7.2), was titrated with a 0.1 mM solution of $[Ru(phen)_2DPPZ](PF6)_2$ in 5 mM $MgCl_2 \cdot 6H_2O$, 100 mM NaCl (pH 7.2), until saturation. The displacement of the aptamer-bound ruthenium complex was studied at the excitation wavelength of 434 nm by adding aliquots of a 20 mM solution of target peptide (MUC1 core peptide) in 5 mM $MgCl_2 \cdot 6H_2O$, 100 mM NaCl (pH 7.2).

RESULTS

Synthesis of Maleimide Functionalized PolyPEGs. The maleimide functionalized PolyPEGs used in this study were prepared via copper catalyzed living radical polymerization. The protected maleimide initiator (**1**) was used for the polymerization of (methoxyPEG_{1100}) methacrylate in the presence of $Cu^{I}Br$ and an iminopyridine ligand (*31*), followed by the reintroduction of the maleimide functionality by a retro-Diels−Alder reaction (*26*) (Scheme 1). Supporting Information Figures S1 and S2 show the ^1H NMR analyses of products **2** and **3**.

Separation of Unconjugated and PEGylated Aptamer D by Anion-Exchange HPLC. Conjugation reactions were monitored by anion-exchange chromatography and quantified from the peak areas using a 0.02 mM aqueous solution of AptD as standard. The unconjugated aptamer had a R_t of *ca.* 18.0 min, while the PEGylated products eluted earlier at *ca.* 12, 13, or 14 min, depending on the size and structure of the PEG (Supporting Information Figures S3 and S4). The conjugation yields were determined by absorbance at 260 nm, after confirming that the PEG moieties did not contribute to the absorption of the conjugates by comparing UV−vis calibration lines of the aptamer and the PEGs at this wavelength (data not shown). AptD-PolyPEG40 and AptD-PolyPEG60 did not elute consistently from the column under standard conditions, which was most probably due to their structure. Therefore, their conjugation yields were quantified by imaging of the agarose gel. Different

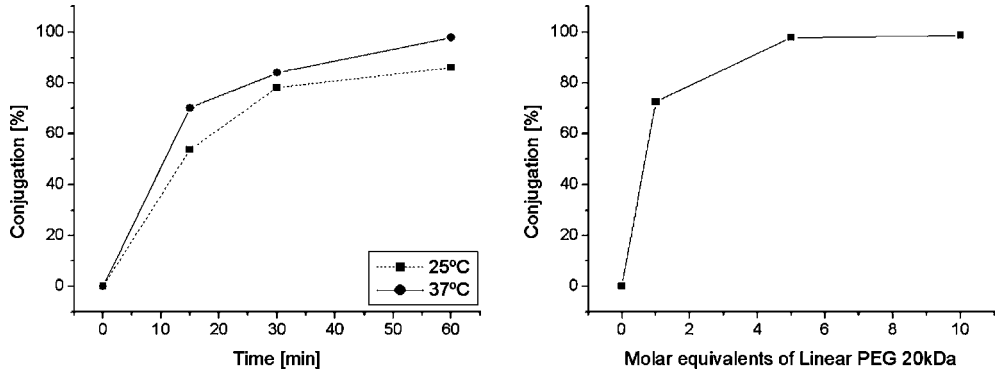


Figure 1. Conjugation yields of AptD with LinPEG20 kDa at different temperatures (left) and reduced aptamer-to-PEG molar ratios (right).

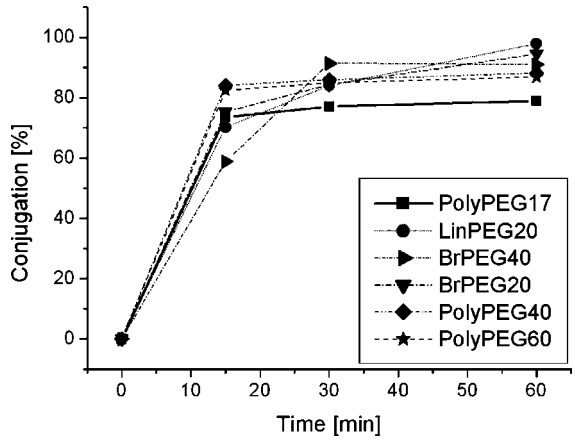


Figure 2. Kinetic study of the conjugation of AptD to various PEGs at 37 °C and 1:5 molar ratio (reduced aptamer/PEG).

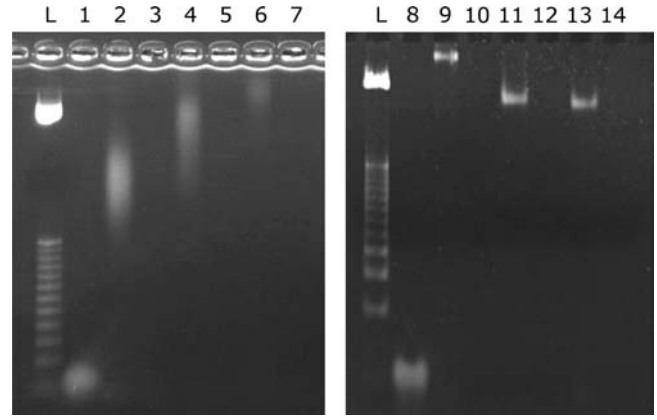


Figure 3. Agarose (2%) (left) and native PAGE (7%) gel (right) of the AptD−PEG conjugates. Lines: L, 25 base pair ladder; 1 and 8, AptD; 2, AptD-PolyPEG17; 3, free PolyPEG17; 4, AptD-PolyPEG40; 5, free PolyPEG40; 6, AptD-PolyPEG60; 7, free PolyPEG60; 9, AptD-BrPEG40; 10, free BrPEG40; 11, AptD-LinPEG20; 12, free LinPEG20; 13, AptD-BrPEG20; 14, free BrPEG20. The running buffer was 1 × TBE (Tris-Borate-EDTA).

HPLC conditions (eluents and gradient) for these conjugates need to be further investigated.

Optimizing the Reaction Conditions for High-Yield PEGylation. All PEGylations were performed using immobilized TCEP gel as reducing agent at pH 4. Very low conjugation was achieved using other reagents such as dithiotreitol (DTT) and non-immobilized TCEP. Preliminary aptamer−PEG conjugation reactions were performed at two different temperatures (25 and 37 °C). Anion-exchange HPLC analyses showed that an increase of the conjugation yield was achieved at 37 °C (Figure 1). Subsequently, the effect of the molar ratio of aptamer to PEG on conjugation was studied at 37 °C (Figure 1).

Optimal conjugation yields were achieved when the reaction was performed at 37 °C for 1 h using an aptamer/PEG molar ratio of 1:5 (reduced aptamer/PEG). A kinetic study of the conjugation of the thiol-modified aptamer to other polymers (branched PEG20 and 40 kDa; PolyPEG17, 40, and 60 kDa) using these optimized conditions also produced the highest yields of conjugate (>78%) after 1 h (Figure 2). The extension of the reaction time to 2 h did not improve the PEGylation yield further.

Identification of Conjugates by Gel Electrophoresis. The PEGylated aptamers (AptD-LinPEG20, AptD-PolyPEG17, AptD-BrPEG20, AptD-PolyPEG40, AptD-BrPEG40, and AptD-PolyPEG60) were isolated by preparative anionic-exchange HPLC and analyzed by agarose gel electrophoresis for the PolyPEG derivatives and native polyacrylamide gel electrophoresis (PAGE) for the linear and branched PEGs. The use of different gel matrices was due to the poor migration of the branched PEG 40 kDa conjugate in agarose gel. Unconjugated aptamer and PEGs were used as controls. The shift of the aptamer to higher molecular weights confirmed its successful conjugation (Figure 3).

Effect of Conjugation on AptD Affinity for Its Target Peptide. $[Ru(phen)_2DPPZ]^{2+}$ shows a strong photoluminescence only when in contact with DNA (double- or single-stranded) (*34, 35*). The FID assay studies the decrease in fluorescence due to the displacement of the ruthenium complex bound to the aptamer by adding the target peptide. The percent decrease in fluorescence and the extent of binding of the target to the aptamer are directly related. A control 25 base DNA aptamer (AptX), having unspecific binding affinity for the same peptide, and the unmodified aptamer D were used as controls. All compounds were dissolved in the same solution previously used for the selection of the aptamer (*23*). The data show that the displacement of the ruthenium complex from AptD, either unmodified or PEGylated, by the target peptide is cooperative (Figure 4). The midpoints and cooperativity values are summarized in Table 1. The data show that the various conjugates have different influences on binding, depending on the molecular weight and structure of the PEG component.

The midpoint values of AptD-LinPEG20 and AptD-BrPEG40 are higher compared to that of the unconjugated aptamer, whereas those for AptD-BrPEG20 and all of the AptD-PolyPEGs are similar to that of the unconjugated aptamer. In addition, the cooperativity of the PEG20 and BrPEG40 conjugated aptamer were increased, whereas those

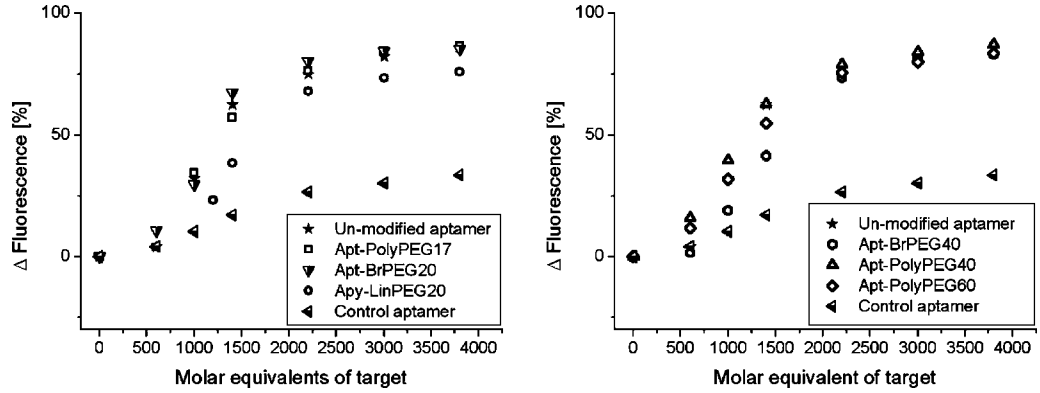


Figure 4. FID binding curves of the target peptide against AptD-PEG conjugates, AptD, and control aptamer (AptX). Displacement of the aptamer-bound ruthenium complex was studied at an excitation wavelength of 434 nm.

Table 1. Midpoints and Cooperativity Values of AptD and PEGylated AptD Obtained from the FID Studies[a]

conjugate	midpoint [mol equiv of target]	cooperativity [*n*]
Unmodified AptD	1140.50	3.92
AptD-LinPEG20	1420.07	4.80
AptD-BrPEG20	1100.80	4.62
AptD-BrPEG40	1375.76	4.22
AptD-PolyPEG17	1185.02	3.57
AptD-PolyPEG40	1051.30	3.01
AptD-PolyPEG60	1150.00	3.20

[a] The calculations were done using the Hill equation: $y = y_\infty + (y_0 - y_\infty)/[1 + (x/K)^n]$ (*42*), where y is the spectroscopic response, x is the concentration of the added reagent, y_0 is the response when $x = 0$, y_∞ is the maximal response when $x = \infty$, K is the concentration of x at the midpoint, and n is the degree of cooperativity.

for BrPEG20 and all PolyPEGs were similar to that for the unmodified aptamer.

DISCUSSION

The conjugation of high molecular weight polymers, such as PEG, to small biomolecules has been shown to prolong their circulating half-life *in vivo* by preventing rapid renal clearance. So far, the only examples of PEGylated aptamers in the literature have been prepared by coupling the activated polymer to an amino modification on the aptamer. Therefore, the aim of our work is to propose an alternative way to PEGylate aptamers *via* a maleimide−thiol reaction. Additionally, new comb-shaped PEGs (PolyPEGs) were synthesized and then conjugated to the aptamer as for the conventional and commercially available PEGs.

PolyPEG is a comb-shaped molecule with a polymethacrylate backbone and pendant PEG teeth formed by polymerization of commercially available PEG methacrylate monomers. This is prepared by living radical polymerization (*36*−*38*) which allows the incorporation of specific functionality on the chain end, which can be subsequently used for conjugation reactions (*26, 39, 40*). As expected for living polymerizations, the reaction exhibited linear kinetics with respect to monomer concentration and the polymers had narrow molecular weight distributions. Monomer conversions were calculated via ^{1}H NMR spectroscopy by monitoring the decrease of the integrals of the monomer vinyl signals (6.2 and 5.6 ppm) using the sharp peak at *ca*. 3.4 ppm (MeO end group) as the internal standard. The molecular weight of the polymer was calculated by comparing the relative integrals of the vinyl signal at 6.5 ppm and the MeO groups of the PEG branches (3.35 ppm) (Figure 5).

The optimized conjugation conditions (reduced aptamer/PEG ratio of 1:5, for 1 h at 37 °C) were used to PEGylate a second thiol-modified DNA aptamer (AptF). The resulting conjugates

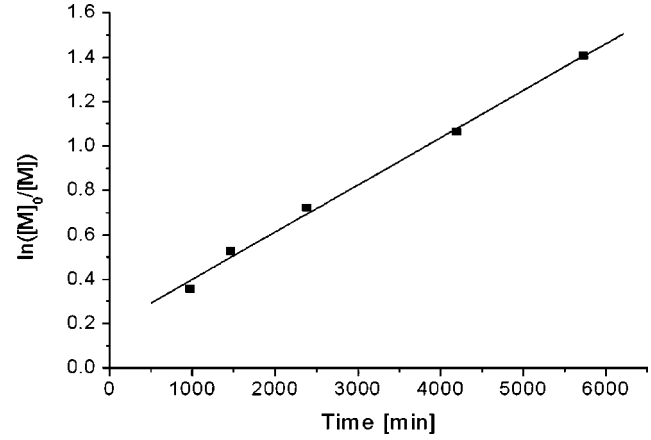


Figure 5. Typical first-order kinetics plot for the polymerization of a protected maleimide functional PolyPEG (PolyPEG40) (**2**).

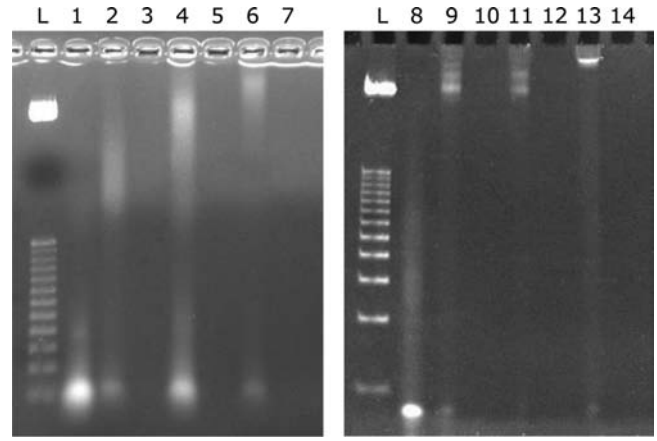


Figure 6. Agarose (left) and native PAGE (right) gels of the AptF-PEG conjugates. Lines: L, 25 base pair ladder; 1 and 8, AptF; 2, AptF-PolyPEG17; 3, free PolyPEG17; 4, AptF-PolyPEG40; 5, free PolyPEG40; 6, AptF-PolyPEG60; 7, free PolyPEG60; 9, AptF-LinPEG20; 10, free LinPEG20free; 11, AptF-BrPEG20; 12, free BrPEG20; 13, AptF-BrPEG40; 14, free BrPEG40.

were analyzed by gel electrophoresis (Figure 6). The conjugation yields, quantified by anion exchange HPLC using a 0.02 mM aqueous solution of AptF as standard and confirmed by band intensity on the gels, were >75%.

Post-selection modifications on an aptamer can alter its original structure and overall charge and thus its binding affinity for the target. A convenient fluorescent intercalator displacement (FID) assay using $[Ru(phen)_2DPPZ]^{2+}$ was performed to test

the retention of affinity for its target of the isolated AptD-PEG conjugates (*33*−*35, 41*).

Two parameters have been considered for the evaluation of the aptamer−peptide binding affinity: the concentration of peptide needed to displace 50% of the metal (midpoint), and the alteration in binding of a peptide molecule to the aptamer due to the prior binding of another peptide molecule to the same aptamer. The binding can be enhanced (positive cooperativity) or decreased (negative cooperativity). All FID plots in Figure 4 are sigmoid, showing a positive cooperative displacement of the Ru^{2+} moiety from the aptamer (either unmodified or PEGylated) by the addition of the target. Branched PEG40 kDa and linear PEG20 kDa clearly interfere with the binding of the aptamer to its target, decreasing the affinity. Compared to the unmodified aptamer, higher quantities of peptide are needed to displace 50% of the bound Ru^{2+} (higher midpoints) despite the greater effect on the displacement shown by the increase of the target concentration (higher cooperativities). The binding is, however, not completely compromised for the BrPEG40 conjugate, as the maximum effect is not reduced. In contrast, AptD-BrPEG20 shows a lower midpoint value, most possibly due to the higher cooperativity. The three aptamer−PolyPEG conjugates display similar binding affinities for the target, which were like that of the unmodified aptamer. In each case, although the PolyPEG products show a slight decrease in cooperativity, the midpoints are reached at very similar molar equivalents of target peptide to that required for the unmodified AptD used as a positive control. As expected, the 25 base aptamer having unspecific binding affinity (control AptX) showed only a 33.5% decrease in fluorescence after the addition of more than 3 times the molar equivalent of peptide necessary to reach the midpoint for the unmodified AptD.

In summary, we report an efficient, high-yielding method for the PEGylation of two thiol-modified aptamers using a range of PEG-based polymers of differing structures and molecular weights. This procedure can be considered as an alternative to the most common approach of using PEG active esters and amino modified aptamers. We have shown that PEGylation has a distinct influence (exemplified by a variation of midpoints and cooperativity values) upon the binding affinity of AptD for its target. Reduced binding affinity was only apparent for the AptD-LinPEG20 and AptD-BrPEG40 conjugates. This suggests that it is the physical size and conformation of the 20 kDa PEG (random coil) and 40 kDa (2 × 20 kDa) branched PEG that causes the reduction in affinity, since it is not observed with either branched 20 kDa (2 × 10 kDa) PEG and even larger molecular mass PolyPEG polymers, which are "brush-shaped". Further *in vivo* studies of the pharmacokinetic and biodistribution properties of the aptamer−PEG conjugates will be undertaken.

ACKNOWLEDGMENT

The work was supported by the Breast Cancer Campaign [2005May11]. The authors thank Warwick Effect Polymers Ltd, Graham Jeffs, Huma Kahn, Sergey Bylikin, and Dave Lambert for their help and assistance.

Supporting Information Available: ^{1}H NMR spectra of compounds **2** and **3**, and HPLC traces of AptD-LinPEG20, ApD-BrPEG20, ApD-BrPEG40, and ApD-PolyPEG17. This material is available free of charge via the Internet at http://pubs.acs.org.

LITERATURE CITED

(1) Hicke, B. J., and Stephens, A. W. (2000) Escort aptamers: a delivery service for diagnosis and therapy. *J. Clin. Invest. 106*, 923–928.

(2) Brody, E. N., and Gold, L. (2000) Aptamers as therapeutic and diagnostic agents. *Mol. Biotechnol. 74*, 5–13.

(3) Mayer, G., and Jenne, A. (2004) Aptamers in research and drug development. *Biodrugs 18*, 351–359.

(4) Khan, H., and Missailidis, S. (2008) Aptamers in oncology: a diagnostic perspective. *Gene Ther. Mol. Biol. 12*, 111–128.

(5) Bailon, P., and Berthold, W. (1998) Polyethylene glycol-conjugated pharmaceutical proteins. *Pharm. Sci. Technol. Today 1*, 352–356.

(6) Tsusumi, Y., Kihira, T., Tsunoda, S.-I., Okada, N., Kaneda, Y., Ohsugi, Y., Miyake, M., Nakagawa, S., and Mayumi, T. (1995) Polyethylene glycol modification of interleukin-6 enhances its thrombopoietic activity. *J. Controlled Release 33*, 447–451.

(7) Inada, Y., Furukawa, M., Sasaki, H., Kodera, Y., Hiroto, M., Nishimura, H., and Matsushima, A. (1995) Biomedical and biotechnological applications of PEG- and PM-modified proteins. *Trends Biotechnol. 13*, 86–91.

(8) Inoue, Y., Sugiyama, K.-I., Ueminami, H., Izawa, S., and Kimura, A. (1996) Modification of *Escherichia coli* B glutathione synthetase with polyethylene glycol for clinical application to enzyme replacement therapy for glutathione deficiency. *Clin. Diagn. Lab. Immunol. 3*, 663–668.

(9) Tan, Y., Sun, X., Xu, M., An, Z., Tan, X., Tan, X., Han, Q., Miljkovic, D. A., Yang, M., and Hoffman, R. M. (1998) Polyethylene glycol conjugation of recombinant methioninase for cancer therapy. *Protein Expr. Purif. 12*, 45–52.

(10) Duncan, R. (2003) The dawning era of polymer therapeutics. *Nat. Rev. Drug Discovery 2*, 347–360.

(11) Ng, E. W. M., Shima, D. T., Calias, P., Cunningham, E. T. J., Guyer, D. R., and Adamis, A. P. (2006) Pegaptanib, a targeted anti-VEGF aptamer for ocular vascular disease. *Nat. Rev. Drug Discovery 5*, 123–132.

(12) Adamis, A. P., Altaweel, M., Bressler, N. M., Cunningham, E. T. J., Davis, M. D., Goldbaum, M., Gonzales, C., Guyer, D. R., Barrett, K., and Patel, M. (2006) Changes in retinal neovascularization after pegaptanib (Macugen) therapy in diabetic individuals. *Ophthalmology 113*, 23–28.

(13) Zhou, B., and Wang, B. (2006) Pegaptanib for the treatment of age-related macular degeneration. *Exp. Eye Res. 83*, 615–619.

(14) Roberts, M. J., Bentley, M. D., and Harris, J. M. (2002) Chemistry for peptide and protein PEGylation. *Adv. Drug Delivery Rev. 54*, 459–476.

(15) Veronese, F. V., and Pasut, G. (2005) PEGylation, successful approach to drug delivery. *Drug Discovery Today 10*, 1451–1458.

(16) Ryan, S. M., Mantovani, G., Wang, X., Haddleton, D. M., and Brayden, D. J. (2008) Advances in PEGylation of important biothech molecules: delivery aspects. *Expert Opin. Drug Delivery 5*, 371–383.

(17) Harris, J. M., and Chess, R. B. (2003) Effect of pegylation on pharmaceuticals. *Nature 2*, 214–221.

(18) Ruckman, J., Green, L. S., Beeson, J., Waugh, S., Gillette, W. L., Henninger, D. D., Cleaesson-Welsh, L., and Janjić, N. (1998) 2′-Fluoropyrimidine RNA-based aptamers to the 165-amino acid form of vascular endothelial growth factor ($VEGF_{165}$). *J. Biol. Chem. 273*, 20556–20567.

(19) Floege, J., Ostendorf, T., Janssen, U., Burg, M., Radeke, H. H., Vargeese, C., Gill, S. C., LGreen, L. S., and Janjić, N. (1999) Novel approach to specific growth factor inhibition *in vivo*. *Am. J. Pathol. 154*, 169–179.

(20) Healy, J. M., Lewis, S. D., Kurz, M., Boomer, R. M., Thompson, K. M., Wilson, C., and McCauley, T. G. (2004) Pharmacokinetics and biodistribution of novel aptamer compositions. *Pharm. Res. 21*, 2234–2246.

(21) Hicke, B. J., Stephens, A. W., Gould, T., Chang, Y.-F., Lynott, K., Heil, J., Borkowski, S., Hilger, C.-S., Cook, G., Warren, S., and Schmidt, P. (2006) Tumor targeting by an aptamer. *J. Nucl. Med. 47*, 668–678.

(22) Heredia, K. L., Nguyen, T. H., Chang, C. W., Bulmus, V., Davis, T. P., and Maynard, H. D. (2008) Reversible siRNA-polymer conjugates by RAFT polymerization. *Chem. Commun. 28*, 3245–3247.

(23) Ferreira, C. S. M., Matthews, C. S., and Missailidis, S. (2006) DNA aptamers that bind to MUC1 tumour marker: design and characterisation of MUC1-binding single-stranded DNA aptamers. *Tumor Biol. 27*, 289–301.

(24) Lecolley, F., Tao, L., Mantovani, G., Durkin, I., Lautru, S., and Haddleton, D. M. (2004) A new approach to bioconjugates for proteins and peptides ("pegylation") utilising living radical polymerisation. *Chem. Commun. 18*, 2026–2027.

(25) Tao, L., Mantovani, G., Lecolley, F., and Haddleton, D. M. (2004) α-Aldehyde terminally functional methacrylic polymers from living radical polymerization: application in protein conjugation pegylation. *J. Am. Chem. Soc. 126*, 13220–13221.

(26) Mantovani, G., Lecolley, F., Tao, L., Haddleton, D. M., Clerx, J., Cornelissen, J. J. L. M., and Velonia, K. (2005) Design and synthesis of *N*-Maleimido-functionalised hydrophylic polimers via copper-mediated living radical polymerisation: a suitable alternative to PEGylation chemistry. *J. Am. Chem. Soc. 127*, 2966–2973.

(27) Ryan, S. M., Wang, X., Mantovani, G., Sayers, C. T., Haddleton, D. M., and Brayden, D. J. (2009) Conjugation of salmon calcitonin to a combed-shaped end functionalized poly-(poly(ethylene glycol) methyl ether methacrylate) yields a bioactive stable conjugate. *J. Controlled Release 135*, 51–59.

(28) Bendele, A., Seely, J., Richey, C., Sennello, G., and Shopp, G. (1998) Short Communication: Renal tubular vacuolation in animals treated with polyethylene-glycol-conjugated proteins. *Toxicol. Sci. 42*, 152–157.

(29) Conover, C. D., Linberg, R., Gilbert, C. W., Shum, K. L., and Shorr, R. G. L. (1997) Effect of polyethylene glycol conjugated bovine hemoglobin in both top-load and exchange transfusion rat models. *Artif. Organs 21*, 1066–1075.

(30) Gariepy, J., Ferreira, C. S. M., Missailidis, S. (2007) Aptamers directed to ricombinant MUC1. WIPO Patent WO2007129114.

(31) Haddleton, D. M., Crossman, M. C., Dana, B. H., Duncalf, D. J., Heming, A. M., Kukulj, D., and Shooter, A. J. (1999) Atom transfer polymerization of methyl methacrylate mediated by alkylpyridylmethanimine type ligands, copper(I) bromide, and alkyl halides in hydrocarbon solution. *Macromolecules 32*, 2110–2119.

(32) Keller, R. N., and Wycoff, H. D. (1946) Copper(I)chloride. *Inorg. Synth. 2*, 1–4.

(33) Hiort, C., Lincoln, P., and Norden, B. (1993) DNA binding of Δ- and Λ-$[Ru(phen)_2DPPZ]^{2+}$. *J. Am. Chem. Soc. 115*, 3448–3454.

(34) Friedman, A. E., Chambron, J.-C., Sauvage, J.-P., Turro, N. J., and Barton, J. K. (1990) Molecular "light switch" for DNA: $Ru(bpy)_2(dppz)^{2+}$. *J. Am. Chem. Soc. 112*, 4960.

(35) Moon, S. J., Kim, J. M., Choi, J. Y., Kim, S. K., Lee, J. S., and Jang, H. G. (2005) $[Ru(phen)_2DPPZ]^{2+}$ is in contact with DNA bases when it forms a luminescent complex with single-stranded oligonucleotides. *J. Inorg. Biochem. 99*, 994.

(36) Haddleton, D. M., Kukulj, D., Duncalf, D. J., Heming, A. M., and Shooter, A. J. (1998) Low-temperature living "radical" polymerization (atom transfer polymerization) of methyl methacrylate mediated by copper(I) *N*-alkyl-2-pyridylmethanimine complexes. *Macromolecules 31*, 5201–5205.

(37) Haddleton, D. M., Jasieczek, C. B., Hannon, M. J., and Shooter, A. J. (1997) Atom transfer radical polymerization of methyl methacrylate initiated by alkyl bromide and 2-pyridinecarbaldehyde imine copper(I) complexes. *Macromolecules 30*, 2190–2193.

(38) Kamigaito, M., Ando, T., and Sawamoto, M. (2001) Metal-catalyzed living radical polymerization. *Chem. Rev. 101*, 3689–3745.

(39) Nicolas, J., Mantovani, G., and Haddleton, D. M. (2007) Living radical polymerization as a tool for the synthesis of polymer-protein/peptide bioconjugates. *Macromol. Rapid Commun. 28*, 1083–1111.

(40) Lecolley, F., Tao, L., Mantovani, G., Durkin, I., Lautru, S., and Haddleton, D. M. (2005) A new approach to bioconjugates for proteins and peptides (pegylation) utilising living radical polymerization. *Chimica Oggi/Chemistry Today 23*, 45–48.

(41) Da Pieve, C., Perkins, A. C., and Missailidis, S. (2009) Anti-MUC1 aptamers: radiolabelling with ^{99m}Tc and biodistribution in MCF7 tumour bearing mice. *Nucl. Med. Biol. 36*, 703–710.

(42) De Lean, A., Munson, P. J., and Rodbard, D. (1978) Simultaneous analysis of families of sigmoidal curves: application to bioassay, radioligand assay, and physiological dose-response curves. *Am. J. Physiol. 235*, E97–E102.

BC900397S

γ-Glutamyl PAMAM Dendrimer as Versatile Precursor for Dendrimer-Based Targeting Devices

Tomoya Uehara,[†] Daisuke Ishii,[†] Tomoe Uemura,[†] Hiroyuki Suzuki,[†] Tomoko Kanei,[†] Kyoko Takagi,[†] Masashi Takama,[‡] Masahiro Murakami,[‡] Hiromichi Akizawa,[§] and Yasushi Arano*,[†]

Graduate School of Pharmaceutical Sciences, Chiba University, Chiba, Faculty of Pharmaceutical Sciences, Osaka Ohtani University, Osaka, and Health Sciences University of Hokkaido, Sapporo, Japan. Received September 16, 2009; Revised Manuscript Received November 24, 2009

Poly(amidoamine) (PAMAM) dendrimers are highly branched spherical polymers that have a unique surface of primary amine groups and provide a versatile design for targeted delivery of pharmaceuticals and imaging agents. Acetylation or succinylation of surface amine groups of PAMAM dendrimer derivatives is frequently performed to reduce nonspecific uptake. However, since targeting molecules, drugs/imaging agents, and acylating reagents react with the amine groups on dendrimer, such modification may limit the number of targeting molecules and/or drugs or may result in insufficient charge reduction. In this study, a γ-glutamyl PAMAM dendrimer was designed and synthesized as a new precursor for targeting device. The relationship between surface electrical properties of the PAMAM dendrimer derivatives and pharmacokinetics was also determined. A PAMAM dendrimer (generation 4.0) was modified with a small number of Bolton-Hunter reagent to prepare **Phe-P** (pI 9.2). The amine residues of **Phe-P** were γ-glutamylated to prepare **Glu-P** (pI 7.1). The α-amine residues of **Glu-P** were then acetylated or succinylated to prepare **Ac-Glu-P** (pI 5.3) or **Suc-Glu-P** (pI 3.6). For comparison, **Phe-P** was acetylated or succinylated to prepare **Ac-P** (pI 6.0) or **Suc-P** (pI 5.1). All the PAMAM dendrimer derivatives exhibited similar molecular size (7.2 to 7.8 nm) except for **Ac-P** (5.1 nm). The biodistribution studies were performed after radioiodination of each PAMAM dendrimer derivative with Na[^{125}I]I. When injected intravenously to mice, both **[^{125}I]Ac-P** and **[^{125}I]Suc-P** exhibited prolonged radioactivity levels in the blood and significantly lower hepatic and renal radioactivity levels than those of **[^{125}I]Phe-P**. Both **[^{125}I]Glu-P** and **[^{125}I]Ac-Glu-P** showed residence times in the blood similar to those of **[^{125}I]Ac-P** and **[^{125}I]Suc-P**. However, **[^{125}I]Glu-P** also registered higher radioactivity levels in the kidney. High hepatic and renal radioactivity levels were observed with highly anionic **[^{125}I]Suc-Glu-P**. These results indicate that, while the manipulation of pI between 5 to 6 would be appropriate to enhance blood retention and reduce renal and hepatic uptake, the amount of primary amine residues on dendrimer surface may also play a crucial role in their renal uptake. The findings in this study show that γ-glutamyl PAMAM dendrimers would constitute versatile precursors to prepare PAMAM dendrimer-based targeting devices due to their neutral molecular charge (pI 7.1) and the presence of a large number of α-amine residues available for conjugation of targeting molecules and drugs/imaging agents.

INTRODUCTION

Dendrimers are highly branched macromolecules with well-defined architecture. A large number of dendrimer derivatives of different constituent atoms and sizes have been synthesized so far (*1*). The unique characteristics of dendrimers such as uniform and controlled size, monodispersity, and modifiable surface group functionality make these molecules appealing for biomedical applications (*2*). The ability to functionalize their terminal groups with targeting molecules and drugs/imaging agents in a specific and controllable manner renders the molecules potential carriers for targeted drug delivery (*3*−*7*). In addition, their interior can encapsulate various molecules (*8*). Among the dendrimer derivatives, the starburst polyamidoamine (PAMAM) dendrimers, highly branched spherical polymers, are soluble in aqueous solution and have a unique surface of primary amine groups (*1*). PAMAM dendrimers have been investigated as carriers in gene transfection (*9*), MRI contrast agents, boron-neutron capture therapy (*10*) (*11*), and drug delivery applications (*8, 12, 13*).

When PAMAM dendrimers with surface amine groups were injected into mice, however, they were eliminated rapidly from circulation and accumulated in the liver, kidney, lung, and spleen (*14*−*16*). This would be attributable to the electrostatic interaction between positively charged dendrimer molecules and negative charged residues on cell surface at physiological pH (*17, 18*). Indeed, carboxylic acid-terminated dendrimers exhibit longer residence time in the blood and lower accumulations in the liver and kidney when compared with amine-terminated counterparts (*15, 19*). The acetylation or succinylation of free terminal amine groups of drug-conjugated PAMAM dendrimers also improved pharmacokinetics (*4, 20, 21*). However, since the acylation reagents, targeting molecules, and drugs/imaging agents react with amine groups on PAMAM dendrimer surface, such chemical modification may cause insufficient charge reduction and/or may limit the number of targeting molecules or drugs/imaging agents especially when the targeting molecules and/or drugs possess positive charges. The lack of knowledge concerning the relationship between molecular charges and pharmacokinetics of PAMAM dendrimer makes the modification cut-and-try, and further understanding of the relationship would provide insight for rationale design of PAMAM dendrimer-based targeting devices.

* Address correspondence to Yasushi Arano, Graduate School of Pharmaceutical Sciences, Chiba University, 1-8-1 Inohana, Chuo-ku, Chiba 260-8675, Japan. Phone: +81-43-226-2896, Fax: +81-43-226-2897, E-mail: arano@p.chiba-u.ac.jp.

[†] Chiba University.

[‡] Osaka Ohtani University.

[§] Health Sciences University of Hokkaido.

10.1021/bc900410q © 2010 American Chemical Society
Published on Web 12/15/2009

In the present study, γ-glutamylation of a PAMAM dendrimer was estimated as a new approach to manipulate the molecular charges of an amine-terminated PAMAM dendrimer (generation 4.0) without impairing the number of targeting molecules and drugs/imaging agents. The relationship between the molecular charges and pharmacokinetics a PAMAM dendrimer was also investigated.

EXPERIMENTAL PROCEDURES

Materials. Na[^{125}I]I was purchased from MP biomedicals Inc. (Irvine, CA). PAMAM dendrimer (polyamidoamine dendrimer, generation 4.0) was purchased from Aldrich (St. Louis, MO). TLC analyses were performed with silica plates (Silica gel 60 F_{254}, Merck, Tokyo) developed with 80% methanol. Proton nuclear magnetic resonance (^{1}H NMR) spectra were recorded on a JEOL JNM-ALPHA 400 spectrometer (JEOL Ltd., Tokyo) with tetramethylsilane as an internal standard. Fast atom bombardment mass spectra (FAB-MS) were taken on a JEOL JMS-HX-110A mass spectrometer (JEOL Ltd.). The diameter of PAMAM dendrimer derivatives was determined by dynamic light scattering using DLS-700 (Photal Otsuka Electronics, Osaka, Japan). Zeta potentials were measured using an electrophoretic light scattering spectrophotometer (ELS-6000, Photal Otsuka Electronics). *N*-Succimidyl-3-(4-hydroxyphenyl)propionate (compound **1**) was synthesized according to the procedure of Bolton et al. (*22*). Other reagents were of reagent grade and used as received.

Synthesis of *N*-α-*tert*-Butoxycarbonyl-L-glutamic Acid γ-*N*-Succinimidyl Ester α-*tert*-Butyl Ester (*2*). *N*-α-*tert*-Butoxycarbonyl-L-glutamic acid α-*tert*-butyl ester (Boc-Glu-OtBu; 3 g, 9.89 mmol) and *N*-hydroxysuccinimide (NHS; 1.25 g, 10.8 mmol) were dissolved in tetrahydrofuran (THF, 20 mL). The reaction mixture was cooled in an ice bath, and a solution of *N,N*′-dicyclohexylcarbodiimide (DCC, 2.2 g, 10.8 mmol) in THF (8 mL) was added dropwise while keeping the reaction temperature below 5 °C. The reaction mixture was then stirred at room temperature overnight. After removing precipitated DCC urea by filtration, the filtrate was purified by column chromatography on silica gel using a mixture of ethyl acetate/hexane (1:2) as an eluent to produce compound **2** (3.1 g, 79.3%) as a white solid. ^{1}H NMR ($CDCl_3$): δ 1.44−1.51 (18H, overlapped, Boc, *tert*-butyl), 2.02 (1H, m, CH), 2.26 (1H, m, CH), 2.70 (2H, m, CH_2), 2.83 (4H, s, CH_2), 4.25 (1H, s, CH), 5.14 (1H, d, CONH); FAB-MS $(M+H)^+$: *m*/*z* 401. Found: 401.

3-(4-Hydroxyphenyl)propionate-Conjugated PAMAM Dendrimer (Phe-P). Since the PAMAM dendrimer is supplied as a methanol solution, the solvent was replaced with a mixture of 8 mL *N*,*N*-dimethylformamide (DMF) and 1 mL water to prepare the PAMAM dendrimer at a concentration of 200 mg (1.4×10^{-5} mol)/9 mL. A solution of compound **1** (37.0 mg) in DMF (1 mL) was then added dropwise to the PAMAM solution, and the reaction mixture was stirred for 2 h at room temperature. The resulting **Phe-P** was purified by diafiltration using an Amicon Ultra-4 (NMWL 5 kDa, Millipore Japan, Tokyo). After removing the solvent in vacuo, **Phe-P** was obtained as a yellow oil (140 mg, 63.4%). ^{1}H NMR (D_2O): δ 2.26−2.54 (m, PAMAM methylene), 2.66 (s, PAMAM methylene), 2.75−3.00 (overlapped, PAMAM methylene, propionate methylene), 3.02−3.18 (overlapped, PAMAM methylene, propionate methylene), 3.18−3.38 (m, PAMAM methylene), 3.43 (t, PAMAM methylene), 6.73 (d, CH), 7.02 (d, CH).

Acetyl-PAMAM (Ac-P). To a solution of **Phe-P** (50 mg) in dimethyl sulfoxide (DMSO, 2 mL) was added a mixture of acetic anhydride (48.8 μL) and diisopropylethylamine (89.9 μL). After stirring for 2 days at room temperature, the solution was evaporated in vacuo. The residue was dissolved in 1 N NaOH solution (5 mL) and heated at 50 °C for 1 h. The resulting **Ac-P** was purified by diafiltration using the Amicon Ultra-4. After removing the solvent in vacuo, **Ac-P** was obtained as a yellow oil (33 mg, 55.8%).^{1}H NMR (D_2O): δ 1.95 (s, CH_3), 2.26−2.51 (m, PAMAM methylene), 2.62 (s, PAMAM methylene), 2.81 (overlapped, PAMAM methylene, propionate methylene), 3.04−3.38 (overlapped, PAMAM methylene, propionate methylene), 6.77 (d, CH), 7.06 (d, CH).

Succinyl-PAMAM (Suc-P). A solution of succinic anhydride (330 mg) in THF (5 mL) was added dropwise to a solution of **Phe-P** (150 mg) dissolved in a mixture of THF (3.3 mL) and 1 N NaOH (7.7 mL) while maintaining the reaction solution at pH 9 by an addition of 1 N NaOH. The reaction mixture was then stirred for 2 h at room temperature. The solvent was removed in vacuo, and the crude **Suc-P** dissolved in 0.5 M ammonium acetate buffer (pH 7.4) was purified by diafiltration using the Amicon Ultra-4. After removing the solvent in vacuo, **Suc-P** was obtained as a yellow oil (130 mg, 61.8%). ^{1}H NMR (D_2O): δ 2.38−2.58 (m, PAMAM methylene), 2.78 (s, PAMAM methylene), 2.95 (overlapped, PAMAM methylene, propionate methylene), 3.12−3.42 (overlapped, PAMAM methylene, propionate methylene), 6.77 (d, CH), 7.07 (d, CH).

γ-Glutamyl-PAMAM (Glu-P). To a solution of **Phe-P** (135 mg) in DMSO (1.5 mL) was added a mixed solution of compound **2** (380 mg) and diisopropylethylamine (248 μL) in DMSO (2 mL), and the reaction mixture was stirred for 2 h at room temperature. After removing the solvent in vacuo, the residue was purified by gel permeation chromatography (TOYOPEARL HW-40S, 1 cm × 25 cm) using methanol as an eluent to produce Boc-Glu(OtBu)-Phe-P. Boc-Glu(OtBu)-Phe-P was then dissolved in a mixture of trifluoroacetic acid (TFA, 4.5 mL) and anisole (0.5 mL), and the reaction mixture was stirred for 2 h at room temperature. The solution was neutralized with 1 N NaOH under cooling in an ice bath, and the conjugate (**Glu-P**) was purified by diafiltration using the Amicon Ultra-4. After removing the solvent in vacuo, **Glu-P** was obtained as a yellow oil (81 mg, 43.5%). ^{1}H NMR (D_2O): δ 2.08 (d, CH_2), 2.21−2.46 (m, PAMAM methylene, glutamic acid), 2.59 (s, PAMAM methylene), 2.78 (overlapped, PAMAM methylene, propionate methylene), 3.04−3.35 (m, PAMAM methylene), 6.73 (d, CH), 7.02 (d, CH).

Succinyl γ-Glutamyl PAMAM (Suc-Glu-P). To a solution of **Glu-P** (54 mg) in DMSO (2 mL) was added a mixed solution of diisopropylethylamine (123 μL) and succinic anhydride (42 mg) in DMSO (1 mL). The reaction mixture was stirred overnight at room temperature, and the resulting **Suc-Glu-P** was purified by diafiltration using the Amicon Ultra-4. After removing the solvent in vacuo, **Suc-Glu-P** was obtained as a yellow oil (26 mg, 39.3%). ^{1}H NMR (D_2O): δ 1.85 (d, CH_2), 2.10 (d, glutamic acid), 2.27 (d, glutamic acid), 2.32−2.57 (m, PAMAM methylene, glutamic acid), 2.65 (s, PAMAM methylene), 2.83 (m, PAMAM methylene), 2.95 (overlapped, PAMAM methylene, propionate methylene), 3.05−3.41 (m, PAMAM methylene), 3.48 (s, PAMAM methylene), 3.73 (t, glutamic acid), 4.11 (t, glutamic acid), 7.06 (d, CH), 7.64 (d, CH).

Acetyl γ-Glutamyl PAMAM (Ac-Glu-P). A mixed solution of diisopropylethylamine (190 μL) and acetic anhydride (51 μL) in DMSO (1 mL) was added to a solution of **Glu-P** (40 mg) in DMSO (1 mL). The reaction mixture was stirred overnight at room temperature. The resulting **Ac-Glu-P** was purified by diafiltration using the Amicon Ultra-4. After removing the solvent in vacuo, **Ac-Glu-P** was obtained as a yellow oil (32 mg, 72.7%). ^{1}H NMR (D_2O): δ 1.84 (d, CH_2), 1.97−2.15 (m, glutamic acid), 2.27 (t, glutamic acid), 2.35−2.66 (m, PAMAM methylene, glutamic acid), 2.69−3.19 (m, PAMAM methylene, propionate methylene), 3.23−3.53 (m, PAMAM methylene),

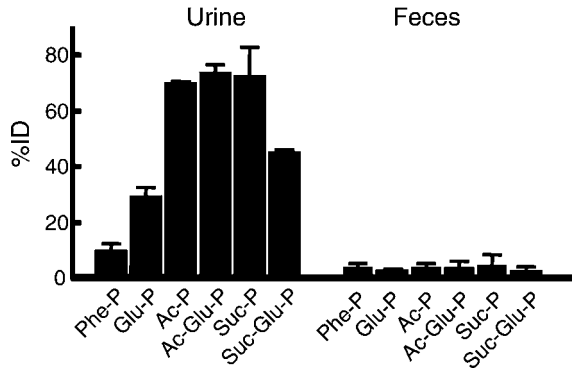


Figure 1. Cumulative radioactivity levels in urine and feces for 48 h postinjection of [^{125}I]PAMAM derivatives in normal mice.

3.61 (t, glutamic acid), 4.11 (t, glutamic acid), 6.78 (d, CH), 7.25 (2d, CH).

^{125}I-Labeled PAMAM Derivatives ([^{125}I]PAMAM Derivatives). A solution of 169 μg of freshly prepared chloramine-T in 10 μL of 0.1 M phosphate buffer (pH 7.4) was added to a mixture of Na[^{125}I]I (5 μL) in 0.01 M NaOH and a PAMAM derivative (0.22 mg/100 μL) in 0.1 M phosphate buffer (pH 7.4). The reaction mixture was incubated for 15 min before quenching the reaction with aqueous sodium bisulfite (73 μg, 10 μL). All the PAMAM derivatives were radioiodinated under similar conditions. [^{125}I]PAMAM derivatives were then purified by diafiltration using the Microcon YM-3 (NMWL 3 kDa, Millipore Japan). The radiochemical purity was determined by TLC.

Zeta Potential and Particle Size of PAMAM Derivatives. Each PAMAM derivatives were dissolved in 0.05 M phosphate buffer (pH 7.4) at a concentration of 5 mg/3−5 mL. The zeta potentials and the sizes of the PAMAM derivatives were determined by an electrophoretic light scattering spectrophotometer and by a dynamic light scattering.

Isoelectric Points (pIs) of [^{125}I]PAMAM Derivatives. Polyacrylamide isoelectric focusing (IEF) was performed to determine the pI values of each [^{125}I[PAMAM derivative. Aliquots of each [^{125}I]PAMAM derivative (3 μL) along with standard solution were applied onto the gel (TEFCO, Tokyo). IEF was performed at 100 V for 1 h, 200 V for 1 h, and 500 V for 30 min. The IEF gel was autoradiographed to reveal radioactive bands using a bioimaging analyzer, FUJIX BASS-2000 II (Fujifilm, Tokyo). The molecular markers were stained with Coomassie Brilliant.

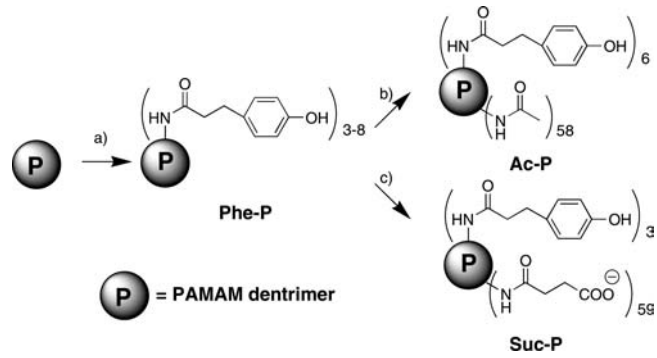
Biodistribution of [^{125}I]PAMAM Derivatives. Animal studies were conducted in accordance with our institutional guidelines and were approved by the Chiba University Animal Care Committee. The biodistribution of radioactivity after intravenous administration of [^{125}I]PAMAM derivatives (70.4 fmol, 100 μL) to 6-week-old mice was determined at 10 min, 1 h, 3 h, 24 h, and 48 h postinjection. Groups of 4−5 mice were used for the experiments. Organs of interest were removed and weighed, and the radioactivity counts were determined with an auto well gamma counter. Urine and feces were collected for 48 h postinjection, and the radioactivity counts were also determined (Figure 1).

Statistical Analysis. Data are expressed as the means ± SD where appropriate. Results were statistically analyzed using the unpaired Student's *t*-test. Differences were considered statistically significant when p was <0.05.

RESULTS

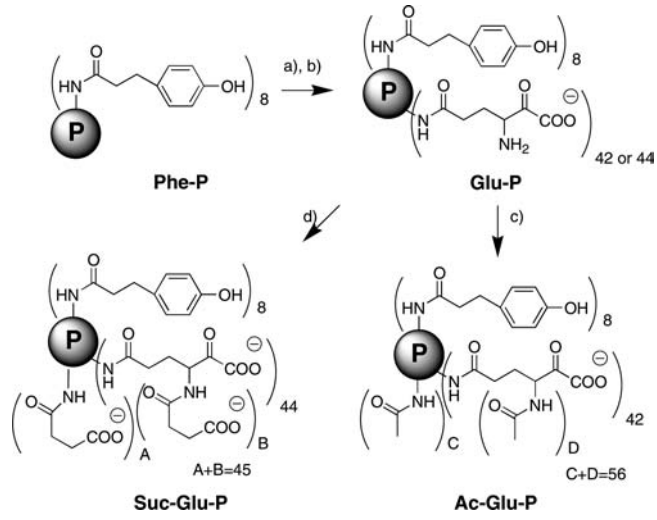
Preparation of [^{125}I]PAMAM Derivatives. PAMAM derivatives were synthesized according to the procedure outlined in Schemes 1 and 2. The reaction of the PAMAM dendrimer with *N*-succinimidyl-3-(4-hydroxyphenyl)propionate introduced 3 to 8 molecules of 3-(4-hydroxypenyl)propyl groups per molecule of the PAMAM dendrimer to prepare **Phe-P**. The treatment of **Phe-P** with acetic anhydride or succinic anhydride introduced 58 molecules of acetyl groups (**Ac-P**) or 59 molecules of succinyl groups (**Suc-P**). Similarly, the reaction of **Phe-P** with compound **2**, followed by deprotection of the Boc and *tert*-butyl groups provided **Glu-P** with 44 glutamyl groups per molecule of **Phe-P**. The acylation of **Glu-P** with acetic anhydride or succinic anhydride introduced 56 acetyl (**Ac-Glu-P**) or 45 succinyl groups (**Suc-Glu-P**) per molecule of **Glu-P**.

Scheme 1[a]



[a] (a) Compound **1**, (b) acetic anhydride, (c) succinic anhydride.

Scheme 2[a]



[a] (a) Compound **2**, diisopropylethylamine, (b) TFA, anisole, (c) acetic anhydride, (d) succinic anhydride.

Radioiodinatoin of each PAMAM derivative was performed by the chloramine-T method, and the [^{125}I]PAMAM derivatives were obtained with radiochemical yields and purities of over 35% and over 92.5%, respectively.

Zeta Potential, pI, and Size Measurements of the PAMAM Derivatives. Zeta potential, pI, and size of the PAMAM derivatives are summarized in Table 1. The mean particle sizes of the PAMAM derivatives were almost similar (7.2 to 7.8 nm) except for **Ac-P** (5.1 nm). **Phe-P** exhibited the highest pI of 9.2, while **Suc-Glu-P** reached the lowest pI of 3.6. The pIs for the PAMAM dendrimers ranged from 3.6 to 9.2, which correlated well with their zeta potentials ($R^2 = 0.85$), as shown in Figure 2.

Biodistribution of [^{125}I]PAMAM Derivatives in Mice. The biodistribution of radioactivity after injection of [^{125}I]PAMAM

Table 1. Properties of PAMAM Dendrimer Derivatives

Compound	pI	zeta potential (mV)	Diameter (nm)
Phe-P	9.2	3.0 ± 3.0	7.5
Glu-P	7.1	−12.4 ± 3.0	7.2
Ac-P	6.0	−11.3 ± 1.3	5.1
Ac-Glu-P	5.3	−23.2 ± 0.9	7.3
Suc-P	5.1	−27.6 ± 2.9	7.4
Suc-Glu-P	3.6	−25.0 ± 2.1	7.8

derivatives to mice is summarized in Tables 2 and 3. **[^{125}I]Phe-P** showed rapid elimination rate from the blood with high and persistent radioactivity levels in the liver, kidney, spleen, and lung. At 48 h postinjection, 10% and 3.7% injected dose was excreted in the urine and feces, respectively.

Both **[^{125}I]Ac-P** and **[^{125}I]Suc-P** showed similar biodistribution profiles. They showed longer residence time of the radioactivity in the blood and significantly lower radioactivity levels in the liver, lung, kidney, and spleen when compared with **[^{125}I]Phe-P**. At 48 h postinjection of **[^{125}I]Suc-P** and **[^{125}I]Ac−P**, over 70% of the injected radioactivity was excreted in the urine.

All the glutamyl-PAMAM derivatives exhibited prolonged residence time of the radioactivity in the blood. However, a large difference was observed in their tissue distribution profiles. **[^{125}I]Glu-P** showed low radioactivity levels in the liver, spleen, and lung but exhibited high and persistent radioactivity levels in the kidney. At 48 h postinjection, approximately 30% of the injected radioactivity was excreted in the urine. Contrary to **[^{125}I]Glu-P**, **[^{125}I]Ac-Glu-P** significantly reduced renal radioactivity levels with approximately 74% of the injected radioactivity excreted in the urine by 48 h. **[^{125}I]Suc-Glu-P**, on the other hand, exhibited moderate radioactivity levels in the kidney and the liver with 45% injected radioactivity being excreted by 48 h.

DISCUSSION

The pharmacokinetics of PAMAM dendrimer is predominantly determined by their molecular sizes and surface electrical properties (*14, 15*). The PAMAM dendrimer derivatives synthesized in this study possess similar molecular sizes at pH 7.4 except for **Ac-P** where all the amine residues were capped with acetyl or 3-(4-hydroxyphenyl)propyl groups (Table 1). The slightly smaller molecular size of **Ac-P** would be attributable to a lower amount of ionizable terminal groups on its surface, since ionization of terminal groups on dendrimers leads to a more expanded overall conformation (*23*−*25*). In addition, all the PAMAM derivatives possess molecular sizes much smaller than those recognized by the reticuloendothelial system of the body (*26*). In light of these findings, the pharmacokinetics of the PAMAM derivatives would predominantly be governed by their surface electrical properties. The good correlation between the zeta potentials and the pIs of the PAMAM derivatives shows that the surface electrical properties of the six PAMAM dendrimer derivatives can be characterized and expressed as their pIs.

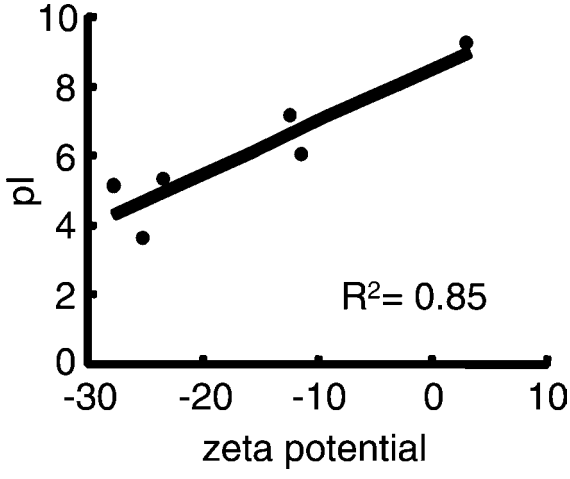


Figure 2. Correlation between pIs and zeta potentials of PAMAM denderimer derivatives.

Acetylation or succinylation of surface amine groups constitutes the most widely applied procedure to reduce surface charges of PAMAM dendrimers. The acetylation or succinylation of **Phe-P** (pI 9.2) decreased pIs of the resulting **Ac-P** (pI 6.0) or **Suc-P** (pI 5.1). The comparative biodistribution of **[^{125}I]Ac-P**, **[^{125}I]Suc-P**, and **[^{125}I]Phe-P** reinforced the previous finding that pI reduction is effective at prolonging the residence time in the blood and reducing accumulation in the liver, spleen, lung, and kidney. This is supported by higher amounts of radioactivity excreted in the urine for 48 h postinjection of **[^{125}I]Suc-P** and **[^{125}I]Ac-P**.

To further lower the pI of a PAMAM dendrimer, glutamylation of a PAMAM dendrimer was performed. Each modification converts an amine group to an amine and a carboxylic acid, and the resulting **Glu-P** showed pI 7.1. The acetylation or succinylation of the residual α-amine groups of **Glu-P** provided **Ac-Glu-P** or **Suc-Glu-P** with pI values of 5.3 and 3.6, respectively. In biodistribution studies, **[^{125}I]Glu-P** exhibited radioactivity levels in the blood significantly higher than and similar to those of **[^{125}I]Phe-P** and **[^{125}I]Ac-P**, respectively. However, **[^{125}I]Glu-P** registered high and persistent localization of radioactivity in the kidney. The renal accumulation of radioactivity observed with **[^{125}I]Glu-P** was significantly decreased by acetylation of the α-amine groups of **Glu-P**. These results suggest that, while blood clearance would predominantly be governed by their net charges, surface electrical properties (e.g., the amount of primary amine resides on the surface) would affect renal accumulation. This is supported by similar renal radioactivity levels and urinary excretion rates of the two acetylated PAMAM derivatives, **[^{125}I]Ac-P** and **[^{125}I]Ac-Glu-P**. The pI reduction is also found effective in reducing renal radioactivity levels of polypeptides and peptides (*27*−*31*). The findings in this study also suggest that the surface properties of polypeptides and peptides may be responsible for their renal reabsorption after glomerular filtration.

The extensive succinylation of **Glu-P** produced **Suc-Glu-P** with the lowest pI of 3.6. **[^{125}I]Suc-Glu-P** showed higher radioactivity levels in the kidney and the liver after injection when compared with **[^{125}I]Ac-P**, **[^{125}I]Suc-P**, and **[^{125}I]Ac-Glu-P**. Since scavenger receptors on Kupffer cells of liver can bind a variety of polyanionic ligands (*32, 33*), the hepatic accumulation of **[^{125}I]Suc-Glu-P** would be caused by the binding of the highly anionic PAMAM derivative to scavenger receptors. Similarly, renal accumulation of succinylated proteins (*32, 34*) (*35*) and ^{111}In-labeled minigastrin suggests that high carboxylate modification of PAMAM also facilitates renal accumulation.

In this study, Bolton-Hunter reagent was conjugated directly to the amine residues of PAMAM dendrimer (Scheme 1) for radioiodination. It is well-known that radioiodinated proteins using the reagent undergo rapid deiodination and the radioactivity levels decrease from tissues of accumulation. However, **[^{125}I]Phe-P**, **[^{125}I]Glu-P**, and **[^{125}I]Suc-Glu-P** showed persistent localization of radioactivity at tissues of accumulation (Tables 2 and 3). Similar results were reported by another group using a PAMAM derivative radioiodinated with *N*-succinimidyl 3-iodobenzoate (*21*). These results showed that the amide bond between the radioiodinated reagent and surface amine groups of PAMAM dendrimers is hardly cleaved in the lysosomes. These findings also reinforced the previous study that the

Table 2. Biodistribution of Radioactivity in Mice after Injection of Radioiodinated PAMAM Derivatives[a]

	time after injection				
	10 min	1 h	3 h	24 h	48 h
			Phe-P (pI = 9.2)		
blood	2.34 (0.36)	0.32 (0.05)	0.17 (0.03)	0.12 (0.03)	0.13 (0.02)
liver	17.79 (1.35)	26.64 (1.22)	29.85 (3.01)	27.19 (1.32)	31.06 (3.35)
intestine[b]	4.20 (0.48)	4.00 (0.61)	3.07 (0.25)	2.23 (0.50)	2.22 (0.34)
kidneys	17.60 (1.75)	20.88 (1.57)	14.26 (1.02)	13.96 (1.20)	12.10 (0.40)
spleen	32.08 (4.59)	42.30 (10.8)	38.36 (4.95)	34.65 (8.88)	56.35 (7.13)
lung	22.84 (4.23)	15.33 (3.01)	11.75 (1.74)	11.27 (4.24)	10.59 (1.46)
stomach[b]	1.13 (0.17)	1.35 (0.29)	0.72 (0.13)	0.59 (0.09)	0.67 (0.16)
			Ac-P (pI = 6.0)		
blood	4.96 (0.48)	1.80 (0.24)	0.64 (0.08)	0.13 (0.02)	0.05 (0.01)
liver	0.95 (0.13)	0.56 (0.08)	0.33 (0.05)	0.24 (0.01)	0.31 (0.02)
intestine[b]	2.03 (0.33)	1.29 (0.39)	0.91 (0.36)	2.27 (0.79)	0.25 (0.11)
kidneys	8.16 (2.24)	6.10 (1.90)	4.58 (1.73)	1.83 (0.51)	1.89 (0.31)
spleen	0.71 (0.06)	0.39 (0.07)	0.20 (0.03)	0.15 (0.03)	0.18 (0.06)
lung	2.88 (0.38)	1.07 (0.13)	0.45 (0.04)	0.15 (0.04)	0.10 (0.02)
stomach[b]	0.52 (0.04)	2.23 (0.96)	0.83 (0.40)	0.67 (0.28)	0.09 (0.04)
			Suc-P (pI = 5.1)		
blood	4.43 (0.67)	0.87 (0.11)	0.34 (0.06)	0.05 (0.00)	0.02 (0.00)
liver	0.85 (0.14)	0.35 (0.02)	0.31 (0.05)	0.28 (0.01)	0.23 (0.03)
intestine[b]	1.65 (0.15)	0.83 (0.15)	0.62 (0.13)	2.92 (0.69)	0.27 (0.08)
kidneys	10.21 (1.01)	4.35 (0.72)	3.22 (0.87)	1.95 (0.52)	2.23 (0.73)
spleen	0.77 (0.14)	0.44 (0.06)	0.28 (0.08)	0.22 (0.05)	0.18 (0.05)
lung	2.24 (0.22)	0.49 (0.09)	0.27 (0.06)	0.09 (0.01)	0.08 (0.01)
stomach[b]	0.71 (0.05)	4.48 (2.50)	1.02 (0.34)	0.90 (0.18)	0.14 (0.11)

[a] Tissue radioactivity is expressed as %ID/g [for each group, $n = 4-5$; results are reported as means (SD)]. [b] Expressed as %ID.

Table 3. Biodistribution of Radioactivity in Mice after Injection of Radioiodinated PAMAM Derivatives[a]

	time after injection				
	10 min	1 h	3 h	24 h	48 h
			Glu-P (pI = 7.1)		
blood	8.81 (1.23)	2.78 (0.09)	1.17 (0.12)	0.16 (0.02)	0.06 (0.02)
liver	1.57 (0.17)	0.65 (0.03)	0.45 (0.05)	0.36 (0.03)	0.35 (0.07)
intestine[b]	2.65 (0.27)	1.43 (0.08)	0.55 (0.35)	0.48 (0.13)	0.30 (0.08)
kidneys	95.16 (6.27)	132.61 (13.85)	132.45 (19.19)	118.92 (12.96)	106.84 (16.51)
spleen	1.21 (0.13)	0.50 (0.08)	0.34 (0.03)	0.23 (0.06)	0.28 (0.09)
lung	5.12 (0.36)	1.77 (0.17)	0.98 (0.31)	0.27 (0.03)	0.18 (0.07)
stomach[b]	0.80 (0.08)	0.92 (0.12)	0.72 (0.13)	0.21 (0.05)	0.11 (0.03)
			Glu-Ac-P (pI = 6.0)		
blood	6.10 (0.54)	2.95 (0.09)	1.24 (0.07)	0.24 (0.04)	0.11 (0.02)
liver	1.18 (0.36)	0.89 (0.18)	0.48 (0.08)	0.32 (0.03)	0.40 (0.07)
intestine[b]	1.86 (0.28)	2.02 (0.82)	1.11 (0.25)	3.49 (1.11)	0.37 (0.05)
kidneys	39.99 (5.10)	50.16 (5.29)	41.94 (9.78)	18.43 (3.74)	13.62 (2.90)
spleen	0.87 (0.22)	0.51 (0.03)	0.34 (0.07)	0.19 (0.02)	0.11 (0.03)
lungs	4.11 (0.04)	1.57 (0.18)	0.78 (0.12)	0.23 (0.09)	0.17 (0.06)
stomach[b]	0.48 (0.04)	4.28 (2.56)	0.85 (0.12)	1.65 (0.88)	0.11 (0.03)
			Ac-Glu-P (pI = 5.3)		
blood	7.64 (1.11)	2.36 (0.14)	1.25 (0.08)	0.11 (0.03)	0.05 (0.01)
liver	1.44 (0.20)	0.75 (0.10)	0.64 (0.04)	0.78 (0.07)	0.75 (0.21)
intestine[b]	2.52 (0.57)	1.27 (0.22)	1.44 (0.23)	1.96 (0.28)	0.31 (0.09)
kidneys	11.25 (1.86)	5.87 (0.44)	6.08 (0.96)	3.55 (0.40)	3.21 (0.39)
spleen	1.28 (0.09)	0.45 (0.07)	0.36 (0.02)	0.28 (0.09)	0.26 (0.03)
lung	3.61 (0.38)	1.24 (0.22)	0.69 (0.14)	0.14 (0.02)	0.09 (0.02)
stomach[b]	1.26 (0.11)	1.57 (0.29)	1.32 (0.28)	0.65 (0.13)	0.12 (0.05)
			Suc-Glu-P (pI = 3.6)		
blood	7.23 (0.60)	1.94 (0.13)	0.84 (0.06)	0.09 (0.01)	0.04 (0.01)
liver	2.95 (0.27)	3.12 (0.39)	3.31 (0.20)	2.38 (0.15)	2.31 (0.21)
intestine[b]	2.11 (0.18)	1.45 (0.12)	1.26 (0.07)	0.68 (0.11)	0.43 (0.08)
kidneys	49.75 (4.52)	47.17 (8.46)	52.95 (1.25)	32.69 (3.25)	28.92 (7.38)
spleen	1.31 (0.15)	0.81 (0.11)	0.80 (0.06)	0.63 (0.07)	0.77 (0.15)
lung	3.97 (0.70)	1.19 (0.16)	0.75 (0.10)	0.25 (0.03)	0.23 (0.05)
stomach[b]	0.98 (0.11)	1.45 (0.24)	1.71 (0.42)	0.29 (0.11)	0.17 (0.04)

[a] Tissue radioactivity is expressed as %ID/g [for each group, $n = 4-5$; results are reported as means (SD)]. [b] Expressed as %ID.

liberation of cytotoxic drugs was scarcely observed from dendrimers conjugated via amide bonds (*38*).

CONCLUSION

The findings in this study suggest that the reduction of pI to 5 to 6 would be appropriate to reduce nonspecific accumulation and prolong circulation time of PAMAM dendrimers. This study also indicates that γ-glutamyl PAMAM dendrimers would constitute versatile precursors to prepare PAMAM-based targeting devices even when targeting molecules and/or drugs of positive charges are used. This modification may also be useful to facilitate the release of drugs that are covalently conjugated with the primary amine residues of α-glutamic acids via amino acids (*39*) or a lysomotropic linkage (*36, 37*) (*40*−*42*) in lysosomal compartment of target tissues. In addition, γ-glutamyl PAMAM dendrimers may prevent toxicity by converting the primary amine groups to amphoteric ones (*4*).

ACKNOWLEDGMENT

The authors thank Mr. Takio Kobayashi for financial support. This study was also supported by Grants-in-Aid for Scientific Research (B) and for Exploratory Research, and Special Funds for Education and Research (Development of SPECT Probes for Pharmaceutical Innovation) from the Ministry of Education, Culture, Sports, Science and Technology, Japan.

LITERATURE CITED

(1) Tomalia, D. A., Naylor, A., and Goddard, A., W. (1990) Starburst dendrimers: Molecular-level control of size, shape, surface chemistry, topology, and flexibility from atoms to macroscopic matter. *Angew. Chem., Int. Ed. Engl. 29*, 138–175.

(2) Patri, A. K., Majoros, I. J., and Baker, J. R. (2002) Dendritic polymer macromolecular carriers for drug delivery. *Curr. Opin. Chem. Biol. 6*, 466–471.

(3) Shukla, R., Thomas, T. P., Peters, J. L., Desai, A. M., Kukowska-Latallo, J., Patri, A. K., Kotlyar, A., and Baker, J. R., Jr. (2006) HER2 specific tumor targeting with dendrimer conjugated anti-HER2 mAb. *Bioconjugate Chem. 17*, 1109–1115.

(4) Kukowska-Latallo, J. F., Candido, K. A., Cao, Z., Nigavekar, S. S., Majoros, I. J., Thomas, T. P., Balogh, L. P., Khan, M. K., and Baker, J. R., Jr. (2005) Nanoparticle targeting of anticancer drug improves therapeutic response in animal model of human epithelial cancer. *Cancer Res. 65*, 5317–5324.

(5) Padilla, D. J. O., Ihre, H. R., Gagne, L., Frechet, J. M., and Szoka, F. C. J. (2002) Polyester dendritic systems for drug delivery applications: in vitro and in vivo evaluation. *Bioconjugate Chem. 13*, 453–461.

(6) Quintana, A., Raczka, E., Piehler, L., Lee, I., Myc, A., Majoros, I., Patri, A. K., Thomas, T., Mule, J., and Baker, J. R., Jr. (2002) Design and function of a dendrimer-based therapeutic nanodevice targeted to tumor cells through the folate receptor. *Pharm. Res. 19*, 1310–1316.

(7) Kobayashi, H., Sato, N., Saga, T., Nakamoto, Y., Ishimori, T., Toyama, S., Togashi, K., Konishi, J., and Brechbiel, M. W. (2000) Monoclonal antibody-dendrimer conjugates enable radiolabeling of antibody with markedly high specific activity with minimal loss of immunoreactivity. *Eur. J. Nucl. Med. 27*, 1334–1339.

(8) Patri, A. K., Kukowska-Latallo, J. F., and Baker, J. R. J. (2005) Targeted drug delivery with dendrimers: comparison of the release kinetics of covalently conjugated drug and non-covalent drug inclusion complex. *Adv. Drug Delivery Rev. 57*, 2203–2214.

(9) Satija, J., Gupta, U., and Jain, N. K. (2007) Pharmaceutical and biomedical potential of surface engineered dendrimers. *Crit. Rev. Ther. Drug Carrier Syst. 24*, 257–306.

(10) Kobayashi, H., Sato, N., Hiraga, A., Saga, T., Nakamoto, Y., Ueda, H., Konishi, J., Togashi, K., and Brechbiel, M. W. (2001) 3D-micro-MR angiography of mice using macromolecular MR contrast agents with polyamidoamine dendrimer core with reference to their pharmacokinetic properties. *Magn. Reson. Med. 45*, 454–460.

(11) Shukla, S., Wu, G., Chatterjee, M., Yang, W., Sekido, M., Diop, L. A., Muller, R., Sudimack, J. J., Lee, R. J., Barth, R. F., and Tjarks, W. (2003) Synthesis and biological evaluation of folate receptor-targeted boronated PAMAM dendrimers as potential agents for neutron capture therapy. *Bioconjugate Chem. 14*, 158–167.

(12) Debbage, P. (2009) Targeted drugs and nanomedicine: present and future. *Curr. Pharm. Des. 15*, 153–72.

(13) Svenson, S. (2009) Dendrimers as versatile platform in drug delivery applications. *Eur. J. Pharm. Biopharm. 71*, 445–62.

(14) Nigavekar, S. S., Sung, L. Y., Llanes, M., El-Jawahri, A., Lawrence, T. S., Becker, C. W., Balogh, L., and Khan, M. K. (2004) ^{3}H dendrimer nanoparticle organ/tumor distribution. *Pharm. Res. 21*, 476–483.

(15) Malik, N., Wiwattanapatapee, R., Klopsch, R., Lorenz, K., Frey, H., Weener, J. W., Meijer, E. W., Paulus, W., and Duncan, R. (2000) Dendrimers: relationship between structure and biocompatibility in vitro, and preliminary studies on the biodistribution of ^{125}I-labelled polyamidoamine dendrimers in vivo. *J. Controlled Release 65*, 133–148.

(16) Roberts, J. C., Bhalgat, M. K., and Zera, R. T. (1996) Preliminary biological evaluation of polyamidoamine (PAMAM) Starburst dendrimers. *J. Biomed. Mater. Res. 30*, 53–65.

(17) Marquez, M., Nilsson, S., Lennartsson, L., Liu, Z., Tammela, T., Raitanen, M., and Holmberg, A. R. (2004) Charge-dependent targeting: results in six tumor cell lines. *Anticancer Res. 24*, 1347–1351.

(18) Varki, A. (1997) Sialic acids as ligands in recognition phenomena. *Faseb J. 11*, 248–255.

(19) Venuganti, V. V., and Perumal, O. P. (2009) Poly(amidoamine) dendrimers as skin penetration enhancers: Influence of charge, generation, and concentration. *J. Pharm. Sci. 98*, 2345–56.

(20) Zhu, W., Okollie, B., Bhujwalla, Z. M., and Artemov, D. (2008) PAMAM dendrimer-based contrast agents for MR imaging of Her-2/neu receptors by a three-step pretargeting approach. *Magn. Reson. Med. 59*, 679–685.

(21) Sato, N., Park, C. W., Kim, H. S., Han, E. S., Wong, K. J., Paik, R. S., Park, L. S., Yao, Z., Carrasquillo, J. A., and Paik, C. H. (2003) Synthesis of dendrimer-based biotin radiopharmaceuticals to enhance whole-body clearance. *Nucl. Med. Biol. 30*, 617–625.

(22) Bolton, A. E., and Hunter, W. M. (1973) The labelling of proteins to high specific radioactivities by conjugation to a ^{125}I-containing acylating agent. *Biochem. J. 133*, 529–539.

(23) Chen, W., Tomalia, D. A., and Thomas, J. L. (2000) Unusual pH-dependent polarity changes in PAMAM dendrimers: evidence for pH-responsive conformational changes. *Macromolecules 33*, 9169–9172.

(24) Welch, P., and Muthukumar, M. (1998) Tuning the density profile of dendritic polyelectrolytes. *Macromolecules 31*, 5892–5897.

(25) Rangarajan, B., Coons, L. S., and Scranton, A. B. (1996) Characterization of hydrogels using luminescence spectroscopy. *Biomaterials 17*, 649–61.

(26) Sahoo, S. K., and Labhasetwar, V. (2003) Nanotech approaches to drug delivery and imaging. *Drug Discovery Today 8*, 1112–1120.

(27) Akizawa, H., Uehara, T., and Arano, Y. (2008) Renal uptake and metabolism of radiopharmaceuticals derived from peptides and proteins. *Adv. Drug Delivery Rev. 60*, 1319–28.

(28) Onda, M., Nagata, S., Tsutsumi, Y., Vincent, J. J., Wang, Q., Kreitman, R. J., Lee, B., and Pastan, I. (2001) Lowering the isoelectric point of the Fv portion of recombinant immunotoxins leads to decreased nonspecific animal toxicity without affecting antitumor activity. *Cancer Res. 61*, 5070–7.

(29) Kim, I. S., Yoo, T. M., Kobayashi, H., Kim, M. K., Le, N., Wang, Q. C., Pastan, I., Carrasquillo, J. A., and Paik, C. H. (1999) Chemical modification to reduce renal uptake of disulfide-bonded variable region fragment of anti-Tac monoclonal antibody labeled with ^{99m}Tc. *Bioconjugate Chem. 10*, 447–53.

(30) Yao, Z., Zhang, M., Sakahara, H., Nakamoto, Y., Higashi, T., Zhao, S., Sato, N., Arano, Y., and Konishi, J. (1999) The relationship of glycosylation and isoelectric point with tumor accumulation of avidin. *J. Nucl. Med. 40*, 479–483.

(31) Khaw, B. A., Klibanov, A., O'Donnell, S. M., Saito, T., Nossiff, N., Slinkin, M. A., Newell, J. B., Strauss, H. W., and Torchilin, V. P. (1991) Gamma imaging with negatively charge-modified monoclonal antibody: modification with synthetic polymers. *J. Nucl. Med. 32*, 1742–51.

(32) Yamasaki, Y., Sumimoto, K., Nishikawa, M., Yamashita, F., Yamaoka, K., Hashida, M., and Takakura, Y. (2002) Pharmacokinetic analysis of in vivo disposition of succinylated proteins targeted to liver nonparenchymal cells via scavenger receptors: importance of molecular size and negative charge density for in vivo recognition by receptors. *J. Pharmacol. Exp. Ther. 301*, 467–477.

(33) Linehan, S. A., Martinez-Pomares, L., and Gordon, S. (2000) Mannose receptor and scavenger receptor: two macrophage pattern recognition receptors with diverse functions in tissue homeostasis and host defense. *Adv. Exp. Med. Biol. 479*, 1–14.

(34) Kuipers, M. E., Swart, P. J., Schutten, M., Smit, C., Proost, J. H., Osterhaus, A. D., and Meijer, D. K. (1997) Pharmacokinetics and anti-HIV-1 efficacy of negatively charged human serum albumins in mice. *Antiviral Res. 33*, 99–108.

(35) Behe, M., Kluge, G., Becker, W., Gotthardt, M., and Behr, T. M. (2005) Use of polyglutamic acids to reduce uptake of radiometal-labeled minigastrin in the kidneys. *J. Nucl. Med. 46*, 1012–5.

(36) Schiff, J. M., Fisher, M. M., and Underdown, B. J. (1984) Receptor-mediated biliary transport of immunoglobulin A and asialoglycoprotein: sorting and missorting of ligands revealed by two radiolabeling methods. *J. Cell. Biol. 98*, 7989.

(37) Vaidyanathan, G., and Zalutsky, M. R. (1990) Protein radiohalogenation: observations on the design of N-succinimidyl ester acylation agents. *Bioconjugate Chem. 1*, 269–273.

(38) Thomas, T. P., Patri, A. K., Myc, A., Myaing, M. T., Ye, J. Y., Norris, T. B., and Baker, J. R., Jr. (2004) In vitro targeting of synthesized antibody-conjugated dendrimer nanoparticles. *Biomacromolecules 5*, 2269–2274.

(39) Arano, Y., Mukai, T., Uezono, T., Wakisaka, K., Motonari, H., Akizawa, H., Taoka, Y., and Yokoyama, A. (1994) A biological method to evaluate bifunctional chelating agents to label antibodies with metallic radionuclides. *J. Nucl. Med. 35*, 890–8.

(40) Umemoto, N., Kato, Y., Endo, N., Takeda, Y., and Hara, T. (1989) Preparation and in vitro cytotoxicity of a methotrexate-anti-MM46 monoclonal antibody conjugate via an oligopeptide spacer. *Int. J. Cancer 43*, 677–84.

(41) Deshpande, S. V., Denardo, S. J., Meares, C. F., McCall, M. J., Adams, G. P., and Denardo, G. L. (1989) Effect of different linkages between chelates and monoclonal antibodies on levels of radioactivity in the liver. *Int. J. Rad. Appl. Instrum. B 16*, 587–97.

(42) Trouet, A., Masquelier, M., Baurain, R., and Deprez-De Campeneere, D. (1982) A covalent linkage between daunorubicin and proteins that is stable in serum and reversible by lysosomal hydrolases, as required for a lysosomotropic drug-carrier conjugate: in vitro and in vivo studies. *Proc. Natl. Acad. Sci. U.S.A. 79*, 626–9.

BC900410Q

TECHNICAL NOTES

Cleavable Linker for Photo-Cross-Linked Small-Molecule Affinity Matrix

Naoki Kanoh,*[,†,‡] Hiroshi Takayama,[†] Kaori Honda,[‡] Takashi Moriya,[†] Takayuki Teruya,[‡,§] Siro Simizu,[‡] Hiroyuki Osada,[‡] and Yoshiharu Iwabuchi[†]

Graduate School of Pharmaceutical Sciences, Tohoku University, and Antibiotics Laboratory, Advanced Science Institute, RIKEN, 2-1 Hirosawa, Wako, Saitama 351-0198, Japan. Received July 16, 2009; Revised Manuscript Received November 3, 2009

The introduction of a cleavable site in a photoactivatable linker, which is used to immobilize small molecules on an affinity matrix via a site-nonselective carbene addition/insertion reaction, makes it possible to verify the presence of the immobilized small molecule on the affinity matrix. It also permits the efficient detection of proteins covalently bound to the immobilized small molecule.

INTRODUCTION

The affinity purification of protein targets for biologically active small molecules (BASMs) has traditionally been used for forward chemical genetic studies (*1*). Such experiments have provided not only key information on the mode of action of BASMs, but also insights of relevance to other biological processes. The traditional target discovery/identification process consists of the following three steps: (1) the search for a position on a BASM of interest that does not significantly abrogate the intrinsic biological activity; (2) preparation of the BASM conjugate with a biotin or an affinity matrix that is covalently attached via a linker; and (3) biochemical pull-down experiments using the synthesized conjugate. Although this traditional approach has yielded many promising results in the past two decades, it remains both time-consuming and challenging in many cases.

In the course of our efforts to develop a rapid and widely applicable approach to enhance the target discovery/identification process, we recently reported a photo-cross-linked small-molecule affinity matrix in which the BASM of interest is immobilized on photoactivatable linker-coated (PALC) agarose beads **1a** via a site-nonselective carbene addition/insertion reaction when treated with UV irradiation (Figure 1) (*2*). This platform is very effective when the BASM of interest tolerates UV irradiation (365 nm), and has been used to pull down cellular targets for BASMs in our laboratory. Using this technology, we recently identified a detoxification enzyme, namely, glyoxalase I, as a molecular target of methyl gerfelin, a fungus-derived osteoclastogenesis inhibitor (*3*).

Despite these successes, we identified serious problems with the technology. First, there is a possible difference in the cross-linking efficiency between BASMs. We have already shown with LC/MS/MS that a variety of small molecules may be photo-cross-linked with the photoactivatable linker **1a** (*4, 5*). However, molecules having different functionalities and/or molecular sizes are thought to react differently with the photogenerated carbenes, resulting in different numbers of immobilized molecules. It was even difficult to verify the presence of the immobilized small molecule on the affinity matrix.

The second problem is the nature of covalent bond formation between the BASM and the PALC affinity matrix. A growing number of BASMs are known to bind covalently with their protein targets (*6*), but such ligand-reacting proteins are sometimes difficult to detach from the affinity matrix if the ligands are immobilized covalently on the affinity matrix.

These problems led us to consider the introduction of a cleavable site in the photoactivatable linker. Among the various

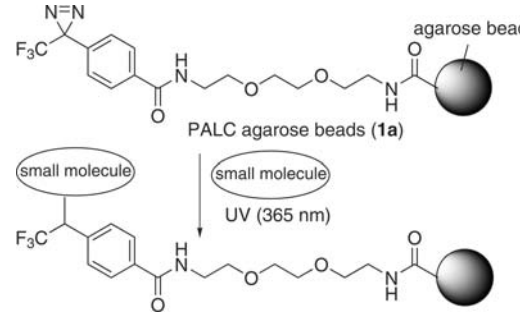


Figure 1. Photo-cross-linked small-molecule affinity matrix.

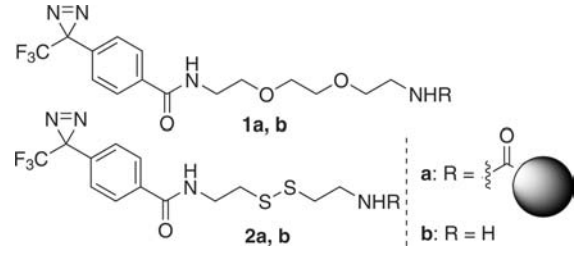


Figure 2. Chemical structure of photoactivatable linker-coated affinity matrix.

* To whom correspondence should be addressed. Naoki Kanoh, Graduate School of Pharmaceutical Sciences, Tohoku University, Aobayama, Sendai 980-8578, Japan. E-mail: kanoh@mail.pharm.tohoku.ac.jp; Fax: +81-22-795-6847; Tel: +81-22-795-6847.

[†] Tohoku University.

[‡] RIKEN.

[§] Present address: Okinawa Laboratory, Lequio Pharma Co., Ltd., Uruma, Okinawa 904-2234, Japan.

10.1021/bc900316q © 2010 American Chemical Society
Published on Web 12/22/2009

options, we selected a disulfide bond because it was reported to be stable in many biological applications and it can be cleaved selectively using mild reducing agents such as glutathione or dithiothreitol (DTT) (*7*). A cleavable photoactivatable heterobifunctional reagent utilizing disulfide linkage was reported as early as 1981 (*8*), but the utility in forward chemical genetic study has not yet been fully assessed.

We therefore designed and prepared the cleavable photoactivatable linker-coated (CPALC) affinity matrix **2a** (Figure 2) and compared it with **1a** in terms of its ability to immobilize BASM. We also demonstrate here that **2a** could be used for efficient detection of the BASM binding protein, especially in the context of the protein-reacting ligand.

EXPERIMENTAL PROCEDURES

Materials and Instrumentation. All chemical reactions were carried out under argon atmosphere with dehydrated solvents under anhydrous conditions, unless otherwise noted. Dehydrated THF and CH_2Cl_2 were purchased from Kanto Chemical Co., Inc. (Tokyo, Japan). Other solvents were dehydrated and/or distilled according to standard protocols. Reagents were obtained from commercial suppliers and used without further purification, unless otherwise noted. Reactions were monitored by thin-layer chromatography (TLC) carried out on Kieselgel 60 F_{254} silica gel plates (Merck KGaA) or NH-silica gel plates (Fuji Silysia Chemical Ltd., Aichi, Japan). Column chromatography was performed on silica gel 60N (spherical, neutral, 63-210 μm; Kanto Chemical Co., Inc., Osaka, Japan) or Chromatorex NHDM 1020 (amine-coated silica gel, 100−200 mesh; Fuji Silysia Chemical Ltd., Kasugai, Japan). IR spectra were recorded on a JASCO FT/IR-410 Fourier transform infrared spectrometer. ^{1}H NMR (400 MHz) and ^{13}C NMR (100 MHz) spectra were recorded on a JEOL JMN AL400 spectrometer. Mass spectra were recorded on JEOL JMS-DX303, JEOL JMS-700, and Waters Micromass ZQ2000 LC mass spectrometers.

Synthesis of Cleavable Photoactivatable Linker-Coated Agarose Beads

Disulfide 5. A solution of NHS ester **4** (72.2 mg, 0.221 mmol), *N*-(*tert*-butoxycarbonyl)cystamine (**3**) (87.5 mg, 0.347 mmol, 1.6 equiv), and Et_3N (310 μL, 2.21 mmol, 10 equiv) in CH_3CN (3 mL) was stirred at rt for 5.5 h. After an addition of water (10 mL), the mixture was extracted with ethyl acetate (2 × 70 mL). The combined organic layers were dried over $MgSO_4$, filtered, and concentrated in vacuo. The residue was purified via silica gel column chromatography (ethyl acetate/hexane = 1:2) to afford **5** (96.6 mg, 0.208 mmol, 94%) as a pale yellow oil. **5**: IR (neat) 3323, 2978, 2928, 1694, 1644, 940 cm^{-1}; ^{1}H NMR (400 MHz, $CDCl_3$) δ 7.90 (d, J = 8.2 Hz, 2H), 7.24 (d, J = 8.3 Hz, 2H), 4.95 (s, 1H), 3.78 (q, J = 6.1 Hz, 2H), 3.47 (q, J = 6.1 Hz, 2H), 2.99 (t, J = 5.5 Hz, 2H), 2.80 (t, J = 6.7 Hz, 2H), 1.41 (s, 9H); ^{13}C NMR (100 MHz, $CDCl_3$) δ 166.5, 156.0, 135.4, 132.2, 127.7, 126.5, 121.9 (q, $^1J_{CF}$ = 274.4 Hz), 79.8, 39.6, 39.0, 38.8, 37.7, 28.3, 28.3 (q, $^2J_{CF}$ = 40.9 Hz); HRMS (EI) m/z 464.1178 (M^+), calcd. for $C_{18}H_{23}O_3N_4F_3S_2$ 464.1164.

Cleavable Photoactivatable Linker 2b. To a solution of **5** (69.7 mg, 0.15 mmol) in CH_2Cl_2 (3 mL) was added trifluoroacetic acid (330 μL, 4.5 mmol, 30 equiv) at rt. After stirring for 3 h, the mixture was concentrated in vacuo, and the residue was purified via amine-coated silica gel column chromatography ($MeOH-CHCl_3$ 0:100 → 1:10 → 1:4) to afford **2b** (47.6 mg, 0.131 mmol, 87%) as a pale yellow oil. **2b** IR (neat) 3323, 1638, 1154 cm^{-1}; ^{1}H NMR (400 MHz, $CDCl_3$) δ 7.81 (d, J = 9.1 Hz, 2H), 7.25 (d, J = 8.4 Hz, 1H), 6.71 (1H, brs), 3.82 (t, J = 6.1 Hz, 2H), 3.03 (t, J = 6.1 Hz, 2H), 2.93 (d, J = 6.1 Hz, 2H), 2.80 (t, J = 6.1 Hz, 2H); ^{13}C NMR (400 MHz, $CDCl_3$) δ 166.3, 135.4, 132.4, 127.4, 126.6, 121.9 (q, $^1J_{CF}$ = 275.3 Hz), 42.3, 40.6, 38.8, 37.5, 28.3 (q, $^2J_{CF}$ = 40.1 Hz); HRMS (EI) m/z 364.0641 [$(M+H)^+$], calcd. for $C_{13}H_{15}ON_4F_3S_2$ 364.0639.

Cleavable Photoactivatable Linker-Coated (CPALC) Agarose Beads 2a. Commercially available NHS-activated Sepharose 4 fast flow beads (**6**) (GE Healthcare Bioscience, Uppsala, Sweden; 160−230 nmol NHS/10 μL of swelled beads, 150 μL) were washed successively with 1 mM aq HCl (5 × 1 mL) and coupling solution (1:1 dioxane−0.1 M aq $NaHCO_3$) (2 × 1 mL) at rt. To swelled beads (150 μL) was added a solution of **2b** (6.3 mg, 17.3 mmol) in coupling solution (100 μL) and methanol (50 μL) at rt. The mixture was shaken by using a CM-1000 mixer (EYELA, Tokyo, Japan) for 2 h. The resultant beads were washed with the coupling solution (5 × 1 mL). To the beads was added a 1 mM solution of ethanolamine in Tris−HCl buffer (0.1 M Tris−HCl, pH 8.0, 1 mL), and the mixture was shaken for an another 1 h. The beads were washed with Milli-Q (5 × 1 mL), then transferred into a spin column using 1 mL of Milli-Q. The beads were washed with methanol (3 × 400 μL), centrifuged, and dried in vacuo.

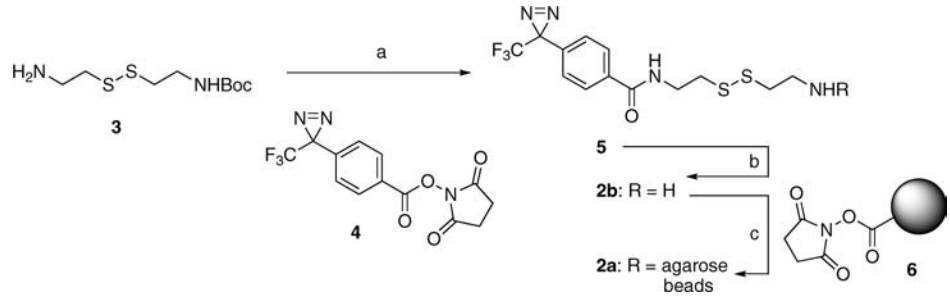
Immobilization of Small Molecules on the PALC- and CPALC-Agarose Beads. PALC- or CPALC-agarose beads (100 μL) were washed with Milli-Q (3 × 400 μL) using a spin column and transferred to a glass sample vial. Solution of a small molecule (10 mM in MeOH, 150 μL) was added to the vial, and the mixture was concentrated using a rotary evaporator and dried in vacuo. The beads were suspended in 2-propanol (200 μL), residual water absorbed on the beads was removed azeotropically using a rotary evaporator, and the beads were dried again in vacuo. The beads were irradiated at 365 nm (4 J/cm^2) by a CL-1000 L ultraviolet cross-linker (UVP Inc., San Gabriel, CA), then washed with 50% aq MeOH, MeOH, DMSO, and MeOH (3 × 400 μL each) to give small-molecule-immobilized beads. The beads were suspended in PBS (8 mM Na_2HPO_4, 1.5 mM KH_2PO_4, 137 mM NaCl, 3 mM KCl, pH 7.4) containing 1 mM sodium azide, and stored at 4 °C. The beads were washed with PBS before use.

Cleavage of Immobilized Small Molecules from the CPALC Small Molecule Beads and MS Analysis. CPALC small molecule beads (10 μL) were treated with a 100 mM DTT solution in ethanol (100 μL) at 50 °C for 10 min. The supernatant was analyzed by a Waters Micromass ZQ 2000 LC mass spectrometer.

Preparation of Phoslactomycin D-Immobilized Beads (PLM-D Beads). To NHS-activated Sepharose 4 fast flow beads (50 μL), which were washed and swelled as described for the synthesis of CPALC agarose beads (**2a**), was added phoslactomycin D (1.1 mg, 1.7 μmol) in coupling solution (100 μL) and MeOH (50 μL). The mixture was shaken for 2 h. The resultant beads were washed with Milli-Q (2 × 1 mL) and MeOH (5 × 1 mL). To the beads was added a 1 mM solution of ethanolamine in Tris−HCl buffer (0.1 M Tris−HCl, pH 8.0, 1 mL), and the mixture was shaken for 1 h. The beads were washed with Milli-Q (5 × 1 mL), then transferred into a spin column using 1 mL of Milli-Q. The beads were washed successively with 50% aq MeOH, MeOH, DMSO, and MeOH (3 × 400 μL each) to give PLM-D beads. The beads were suspended in PBS (8 mM Na_2HPO_4, 1.5 mM KH_2PO_4, 137 mM NaCl, 3 mM KCl, pH 7.4) containing 1 mM sodium azide, and stored at 4 °C. The beads were washed with PBS before use.

Detection of PP2A Subunits Using Phoslactomycin D-Immobilized Beads. HL-60 cells (RIKEN Cell Bank, Ibaraki, Japan) were washed twice with PBS, then suspended in binding buffer (50 mM Tris−HCl, 150 mM NaCl, 1 mM EDTA, and 2.5 mM EGTA, pH 7.5) containing 1 mM DTT, 0.1 mM $MgCl_2$, and Complete protease inhibitor cocktail (Roche Diagnostics GmbH). Suspended cells were lysed by sonication, and the resulting mixture was incubated at 4 °C

Scheme 1. Synthesis of Cleavable Photoactivatable Table Linker-Coated (CPALC) Agarose Beads[a]



[a] Reagents and conditions: (a) **4**, Et_3N, CH_3CN, 5.5 h, 94%; (b) trifluoroacetic acid, CH_2Cl_2, r.t., 3 h, 87%; (c) **6**, 0.1 M aq $NaHCO_3$−dioxane (1:1), r.t., 2 h, then ethanolamine, r.t., 1 h.

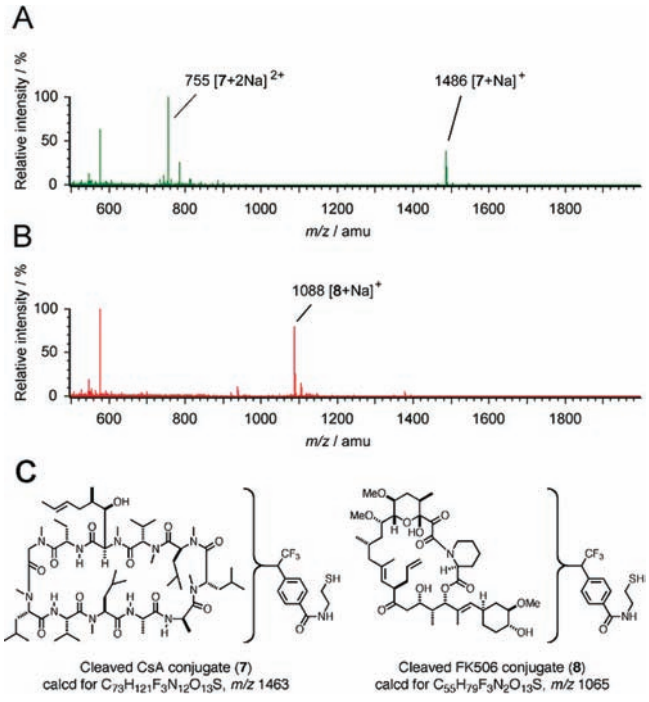


Figure 3. Electrospray ionization of photo-cross-linked products cleaved from the cleavable matrix by DTT reduction of disulfide bonds. (A) Cleaved product from the cyclosporin A-immobilized beads; (B) from the FK506-immobilized beads. (C) Structures and calculated masses for the cleaved products.

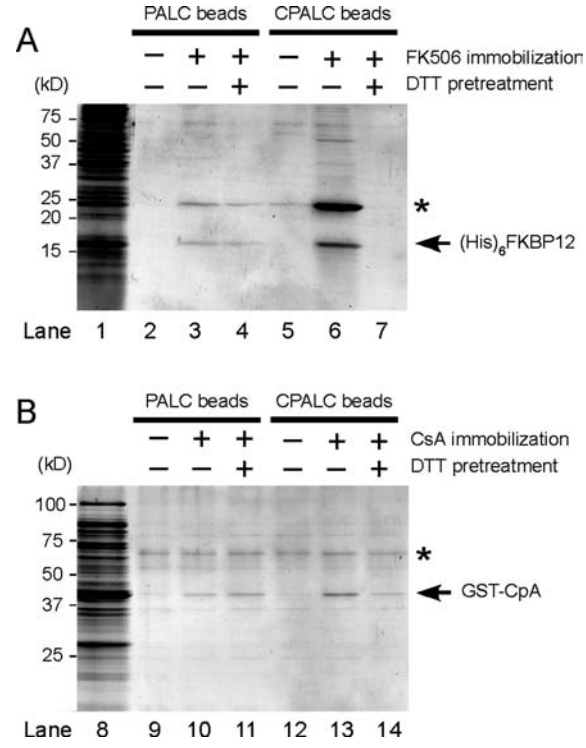


Figure 4. Detection of CsA- and FK506-binding proteins using PALC- and CPALC-agarose beads. (A) Detection of FKBP12 using FK506-immobilized beads: PALC- (lanes 2−4) or CPALC- (lanes 5−7) agarose beads were irradiated in the presence (lanes 3, 4, 6, and 7) or absence (lanes 2 and 5) of FK506. The beads were incubated with cell lysates of *E. coli* overexpressing $(His)_6$-FKBP12 overnight. Beads in lanes 4 and 7 were pretreated with DTT before being incubated with cell lysate. The beads were washed and analyzed by 15% SDS-PAGE followed by CBB staining. *protein unidentified. (B) Detection of cyclophilin A (CpA) using cyclosporin A (CsA)-immobilized beads.

for 2 h. After the insoluble material was removed by centrifugation (13 000 × *g*, 4 °C, 30 min), the supernatant was collected as cell lysate. The total protein concentration of the cell lysate was determined by the Bradford method to be 5.7 mg/mL. The lysate was diluted with binding buffer containing 0.1 mM DTT and 0.1 mM $MgCl_2$, and the diluted cell lysate (800 μL, 2 mg protein) was incubated with 10 μL of PLM-D beads or 20 μL of CPALC PLM-D beads at 4 °C for 1 h. The reacted beads were washed with binding buffer containing 0.2% NP-40 (5 × 700 μL). The bound proteins were eluted from the beads by boiling with 20 μL of SDS sample buffer (140 mM Tris−HCl, 22.4% glycerol, 6% SDS, 10% 2-mercaptoethanol, 0.02% bromophenol blue, pH 6.8) at 110 °C for 10 min. The total volume of sample eluted from CPALC PLM-D beads and 1/10 of the sample eluted from PLM-D beads were subjected to SDS-PAGE.

Western Blot Analysis. Eluted proteins from beads were separated on SDS−polyacrylamide gel (10%), and then transferred to PVDF membrane (Millipore, Bedford, MA). After blocking with TBS-T (10 mM Tris-HCl, 150 mM NaCl, 0.05% Tween 20, pH 8.0) containing 6% CS (#SH30072.03; Hyclone Laboratories Inc., Logan, UT) at rt for 1 h, the membrane was incubated with rabbit anti-PP2A/a antibody (#07−250; Millipore) in the same buffer at a dilution of 1:1000 at 4 °C overnight. After washing with TBS-T, the membrane was incubated with peroxidase-labeled antirabbit IgG antibody (#NA934 V; GE Healthcare) at a dilution of 1:1000 at rt for 1 h. PP2A/a protein was detected with SuperSignal West Pico chemiluminescent substrate (Pierce, Rockford, IL) according to the manufacturer's instructions. After the detection, the membrane was treated with stripping buffer (25 mM glycine−HCl, 1% SDS, pH 2) at rt for 45 min. The stripped membrane was incubated with anti-PP2A/cα antibody (#610555; BD Biosciences, San Jose, CA) in TBS-T containing 5% skim milk at a dilution of 1:1000 at 4

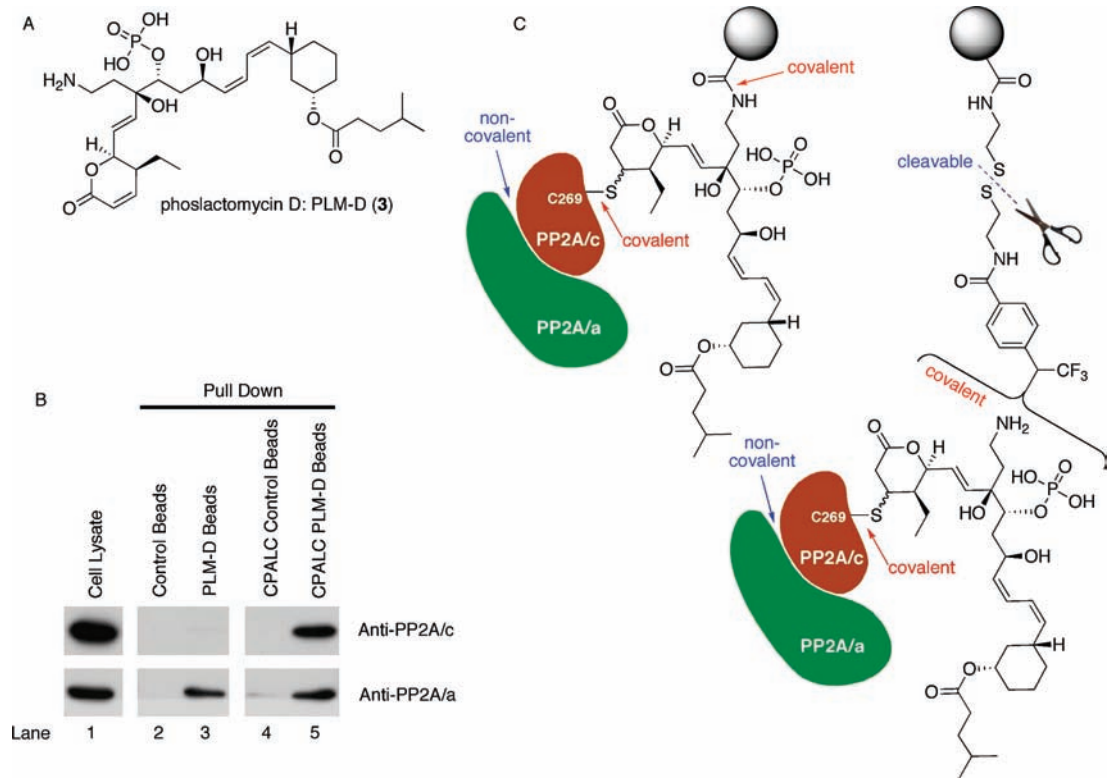


Figure 5. Detection of PP2A subunits using phoslactomycin D-immobilized beads. (A) Structure of phoslactomycin D (PLM-D). (B) Western blotting analysis of PP2A subunits coprecipitated with PLM-D beads and CPALC PLM-D beads. (C) Schematic presentation of PLM-D beads, CPALC PLM-D beads, and coprecipitated PP2A subunits.

°C overnight. PP2A/cα protein was detected with SuperSignal West Pico chemiluminescent substrate.

RESULTS AND DISCUSSION

The cleavable photoactivatable linker **2b** was synthesized in two steps using known *N*-(*tert*-butoxycarbonyl)cystamine and 4-[3-(trifluoromethyl)-3*H*-diazirin-3-yl]-benzoic acid *N*-hydroxysuccinimidyl ester (Scheme 1). Conjugation of **2b** on agarose beads was also quite straightforward, yielding the CPALC affinity matrix **2a**. The amount of the cleavable linker **2b** introduced on the matrix **2a** was estimated to be 269 ± 41 nmol in 1 mL of swollen beads using a spectroscopic method (*9*). This result is similar to the amount of **1a** introduced on the PALC agarose matrix (241 ± 5 nmol mL^{-1}).

First, we immobilized cyclosporin A (CsA) and FK506 onto **2a** by using the same procedure that was used for the immobilization of these compounds onto **1a** (*2*). Specifically, a solution of the respective small molecules was independently mixed with the CPALC beads **2a**, and the mixtures were concentrated and dried in vacuo. The dried beads covered with the respective small molecules were exposed to UV light (365 nm, 4 J/cm^2) and then washed thoroughly with methanol, DMSO, and PBS. Control beads were prepared by the photolysis of the CPALC beads **2a** in the absence of small molecules.

To verify the extent of compound immobilization, both the resulting CPALC CsA and FK506 beads were treated independently under the cleavage conditions (100 mM DTT in ethanol, 50 °C, 10 min). The MS analysis of the supernatant solution clearly confirmed the presence of cleaved photo-cross-linked products, as shown in Figure 3. No ion peaks from residual compounds (*m*/*z* 1202 and 803 for CsA and FK506, respectively) were observed. The MS analyses also confirmed that the above condition almost completely (>95%) cleaved the disulfide linkage, which was not affected in the absence of reducing agent (data not shown).

To validate the ability of the cleavable beads to capture and purify the binding protein in the context of the immobilized ligand, cleavable affinity beads were treated with a protein mixture containing their target proteins. The CsA molecule is known to bind to cyclophilin A (CpA) (*10*), a peptidyl prolyl cis−trans isomerase, with a K_D of 36.8 nM (*11*), whereas FK506 binds to another peptidyl cis−trans isomerase FKBP12 with a K_D of 0.4 nM (*12*). Cleavable CsA and FK506 beads were mixed with the cell lysates of an *E. coli* BL21(DE3)pLysS strain overexpressing GST-cyclophilin A conjugate (GST-CpA) and $(His)_6$-tagged FKBP12, respectively. Proteins that coprecipitated with the respective beads were then subjected to SDS gel electrophoresis.

As can be seen in Figure 4, CPALC CsA and FK506 beads can be used to purify their binding proteins (lanes 6 and 13 in Figure 4A and B, respectively), although we identified some difference between the cleavable and noncleavable versions, especially in the amount of nonspecific binding protein (denoted by the asterisks). However, when the cleavable beads were pretreated with DTT (100 mM in ethanol, 50 °C, 10 min) before being incubated with cell lysates, the beads largely lost their ability to isolate binding proteins because of the absence of the ligand.

This platform was then applied to detect a protein that forms a covalent bond with its ligand. We recently reported that the antifungal antibiotics known as phoslactomycins (*13*) inhibit protein phosphatase 2A (PP2A) through the covalent modification of cysteine-269 of the catalytic subunit of PP2A (PP2A/c) (*14*). However, when we prepared affinity beads on which phoslactomycin D (PLM-D: **3**, Figure 5A) was immobilized covalently through an amide linkage (Figure 5C, left) and used them for a pull-down experiment, only a very small amount of PP2A/c was detected by Western blot analysis (Figure 5B, lane 3, upper section) as compared to the amount of PP2Aa, a scaffolding subunit of PP2A that is known to bind to PP2A/c

through hydrogen bonding networks (*15, 16*) (lane 3, lower section). Although there are examples in which ligand-binding proteins were detected by using similar protocols (*17*), this was an obvious example in which the primary target molecule for a protein-reacting ligand was not detected sufficiently using an affinity matrix on which a small molecule was covalently immobilized. PALC PLM-D beads also gave similar results (data not shown). On the other hand, using the CPALC affinity matrix developed in the present study, the same analysis successfully detected both PP2A/c and PP2A/a (lane 5).

In summary, we have shown here that the cleavable small-molecule affinity matrix enables confirmation of small-molecule immobilization. We also confirmed its use in the detection of target proteins in the context of a protein-reacting ligand.

The combined use of this platform with LC/MS/MS may make it possible to quantitatively determine the amount of immobilized small molecule and/or small molecule−protein conjugate by comparison with an internal standard. Furthermore, it may be possible to determine what and how many conjugates are formed on the photo-cross-linked affinity matrix by combining this method with LC/MS/MS analysis. Efforts toward this goal are ongoing in our laboratory.

ACKNOWLEDGMENT

This work was supported by a Grant-in-Aid for Young Scientists (A) (No. 19681023; to NK) from the MEXT, Japan, and by the RIKEN Chemical Biology Project. We thank Dr. Takemichi Nakamura (RIKEN) for his helpful input. We also thank Prof. Takayuki Doi and Dr. Masahito Yoshida for assistance with the LC/MS analysis.

LITERATURE CITED

(1) Leslie, B. J., and Hergenrother, P. J. (2008) Identification of the cellular targets of bioactive small organic molecules using affinity reagents. *Chem. Soc. Rev. 37*, 1347–1360.

(2) Kanoh, N., Honda, K., Simizu, S., Muroi, M., and Osada, H. (2005) Photo-cross-linked small-molecule affinity matrix for facilitating forward and reverse chemical genetics. *Angew. Chem., Int. Ed. 44*, 3559–3562.

(3) Kawatani, M., Okumura, H., Honda, K., Kanoh, N., Muroi, M., Dohmae, N., Takami, M., Kitagawa, M., Futamura, Y., Imoto, M., and Osada, H. (2008) The identification of an osteoclastogenesis inhibitor through the inhibition of glyoxalase I. *Proc. Natl. Acad. Sci. U.S.A. 105*, 11691–11696.

(4) Kanoh, N., Asami, A., Kawatani, M., Honda, K., Kumashiro, S., Takayama, H., Simizu, S., Amemiya, T., Kondoh, Y., Hatakeyama, S., Tsuganezawa, K., Utata, R., Tanaka, A., Yokoyama, S., Tashiro, H., and Osada, H. (2006) Photo-cross-linked small-molecule microarrays as chemical genomic tools for dissecting protein-ligand interactions. *Chem. Asian J. 1*, 789–797.

(5) Kanoh, N., Nakamura, T., Honda, K., Yamakoshi, H., Iwabuchi, Y., and Osada, H. (2008) Distribution of photo-cross-linked products from 3-aryl-3-trifluoromethyldiazirines and alcohols. *Tetrahedron 64*, 5692–5698.

(6) Drahl, C., Cravatt, B. F., and Sorensen, E. J. (2005) Protein-reactive natural products. *Angew. Chem., Int. Ed. 44*, 5788–5809.

(7) Bryan, M. C., Fazio, F., Lee, H.-K., Huang, C.-Y., Chang, A., Best, M. D., Calarese, D. A., Blixt, O., Paulson, J. C., Burton, D., Wilson, I. A., and Wong, C.-H. (2004) Covalent display of oligosaccharide arrays in microtiter plates. *J. Am. Chem. Soc. 126*, 8640–8641.

(8) Vanin, E. F., and Ji, T. H. (1981) Synthesis and application of cleavable photoactivatable heterobifunctional reagent. *Biochemistry 20*, 6754–6760.

(9) Gaur, R. K., and Gupta, K. C. (1989) A spectrophotometric method for the estimation of amino groups on polymer supports. *Anal. Biochem. 180*, 253–258.

(10) Handschumacher, R. E., Harding, M. W., Rice, J., and Drugge, R. J. (1984) Cyclophilin - A specific cytosolic binding-protein for cyclosporin-A. *Science 226*, 544–546.

(11) Husi, H., and Zurini, M. G. M. (1994) Comparative binding studies of cyclophilins to cyclosporine A and derivatives by fluorescence measurements. *Anal. Biochem. 222*, 251–255.

(12) Harding, M. W., Galat, A., Uehling, D. E., and Schreiber, S. L. (1989) *Nature 341*, 758–760.

(13) Fushimi, S., Furihata, K., and Seto, H. (1989) Studies on new phosphate ester antifungal antibiotics phoslactomycins. 2. Structure elucidation of phoslactomycin-A to phoslactimycin-F. *J. Antibiot. 42*, 1026–1036.

(14) Teruya, T., Simizu, S., Kanoh, N., and Osada, H. (2005) Phoslactomycin targets cysteine-269 of protein phosphatase 2A catalytic subunit. *FEBS Lett. 579*, 2463–2468.

(15) Xing, Y., Xu, Y., Chen, Y., Jeffrey, P. D., Chao, Y., Lin, Z., Li, Z., Strack, S., Stock, J. B., and Shi, Y. (2006) Structure of protein phosphatase 2A core enzyme bound to tumor-inducing toxins. *Cell 127*, 341–353.

(16) Cho, U. S., and Xu, W. (2007) Crystal structure of a protein phosphatase 2A heterotrimeric holoenzyme. *Nature 445*, 53–57.

(17) von Rechenberg, M., Blake, B. K., Ho, Y.-S. J., Zhen, Y., Chepanoske, C. L., Richardson, B. E., Xu, N., and Kery, V. (2005) Ampicillin/penicillin-binding protein interactions as a model drug-target system to optimize affinity pull-down and mass spectrometric strategies for target and pathway identification. *Proteomics 5*, 1764–1773.

BC900316Q

Chemical Strategies for the Synthesis of Peptide−Oligonucleotide Conjugates

Kui Lu,*[,†,‡] Qun-Peng Duan,[†] Li Ma,[†] and Dong-Xin Zhao[†]

School of Chemistry and Chemical Engineering, Henan University of Technology, Zhengzhou 450001, China, and Henan Institute of Engineering, Zhengzhou 451191, China. Received April 8, 2009; Revised Manuscript Received September 16, 2009

The use of synthetic oligonucleotides and their mimics to inhibit gene expression by hybridizing with their target sequences has been hindered by their poor cellular uptake and inability to reach the nucleus. Covalent postsynthesis or solid-phase conjugation of peptides to oligonucleotides offers a possible solution to these problems. As feasible chemistry is a prerequisite for biological studies, development of efficient and reproducible approaches for convenient preparation of peptide−oligonucleotide conjugates has become a subject of considerable importance. The present review gives an account of the main synthetic methods available to prepare covalent conjugation of peptides to oligonucleotides.

INTRODUCTION

Synthetic oligonucleotides (ONs[1]) constitute a class of potential therapeutic agents for the treatment of viral infections and genetic diseases by therapeutic regulation of gene expression (*1*, *2*). However, their systemic therapeutic use is hindered by their poor cellular uptake and inability to reach the nucleus. In order to meet the requirements for therapeutic applications, chemically modified ONs have attracted great interest (*1*). Desired improvement of certain properties, such as cell-specific delivery, cellular uptake efficiency, intracellular distribution, and target specificity, can be achieved by covalent association to peptides (*3*). These covalently associated conjugates of peptides with antisense or siRNA ONs can bind to mRNA, double-stranded DNA, protein, or catalysts in antisense, triplex, aptamer, or ribozymes application, respectively. In addition, this covalent incorporation leads to a more consistent product in which the desired properties can be controlled and changed by structural variations. Thus, development of efficient and reproducible methods for convenient preparation of covalently linked peptide−oligonucleotide conjugates (POCs) has become a subject of considerable importance.

These covalently attached POCs can be synthesized either by postsynthetic coupling of prepurified peptides and ONs or by stepwise solid-phase synthesis without intermediate purification. The progress of this field has been reviewed every few years (*3*−*9*). This short review attempts to provide an overview of vast repertoire of chemical protocols developed so far for the chemical synthesis of POCs. In addition, the advantages and areas of concern associated with the use of postsynthetic and stepwise solid-phase approach are also discussed.

CHEMISTRY OF PEPTIDE−OLIGONUCLEOTIDE CONJUGATES

Conjugation of peptide to oligonucleotide (ON) mostly occurs at 5′- or 3′-ends of the ON. The 2′-position of ribose sugar and nucleobases has also been used for appending the peptides. The synthetic approaches employed for POCs synthesis fall into two general categories: the postsynthetic conjugation approach (or fragment coupling strategy) and the stepwise solid-phase synthesis (or online solid-phase synthesis) approach. On applying the postsynthetic conjugation approach, the ON and the peptide are built in a separate support utilizing standard protocols but are conveniently functionalized to be linked after synthesis. When using the stepwise solid-phase approach, the peptide−oligonucleotide conjugate is prepared in a single support using special protecting groups and modified protocols which minimize subreactions. These approaches are further categorized into two different categories depending on the type of covalent bond generated between the ON and the peptide. The different synthetic approaches are described in following sections.

Post-Synthetic Conjugation. One of the simplest solutions to the problem of chemical incompatibility between peptides and ONs is to avoid the issue by preparing both components separately utilizing peptide and ON standard synthetic methodologies followed by linking both compounds together. Prior to the conjugation, it is required to ensure a unique and specific linkage between peptides and ONs when attaching certain reactive functionalities to both molecules. There are a variety of chemical linkages that have been used to link the peptide and ON fragments. The following section reviews in detail the synthesis of POCs with these linkages.

Conjugation through Thioether or Disulfide Linkage. Several methods for preparation of POCs have been described, most of which are based on the specific reactivity of the thiol group. Thiols afford specific and rapid conjugation and react with a wide variety of substrates (*10*). In the past few years, there have been a couple of papers in which methods to synthesize the peptide conjugates of ONs or siRNA via thioether or disulfide linkage have been reviewed (*6*, *7*, *9*, *11*−*13*).

Thioether linkage is one of the most commonly used linkages for peptide conjugates of ONs due to its higher stability. There

* To whom correspondence should be addressed. Phone: +86-371-67756945. E-mail: luckyluke@haut.edu.cn.

[†] Henan University of Technology.

[‡] Henan Institute of Engineering

[1]ABBREVIATIONS: Aha, ε-aminohexanoic acid; AOQ, 4-(2-aminooxyethoxy)-2-(ethylureido) quinoline; Boc, *tert*-butyloxycarbonyl; Bpoc, 2-(biphenyl-4-yl)propan-2-yloxycarbonyl; CPG, controlled pore glass; Dde, 1-(4,4-dimethyl-2,6-dioxacyclohexylidene)ethyl; Ddz, 2-(3,5-dimethoxyphenyl)propan-2-yloxycarbonyl; DMF, *N*,*N*-dimethylformamide; Dnp, 2,4-dinitrophenyl; DTT, dithiothreitol; EDC, 1-ethyl-3-(3-dimethylaminopropyl)carbodiimide; Fm, 9-fluorenylmethyl; Fmoc, 9-fluorenylmethoxycarbonyl; HBTU, *O*-benzotriazole-*N*,*N*,*N*′,*N*′-tetramethyluronium hexafluorophosphate; HOBT, 1-hydroxybenzotriazole; Hse, homoserine; ON, oligonucleotide; T-FA, trifluoroacetic acid; Thr, threonine; Ser, serine; Tos, tosyl; Tyr, tyrosine.

10.1021/bc900158s © 2010 American Chemical Society
Published on Web 10/26/2009

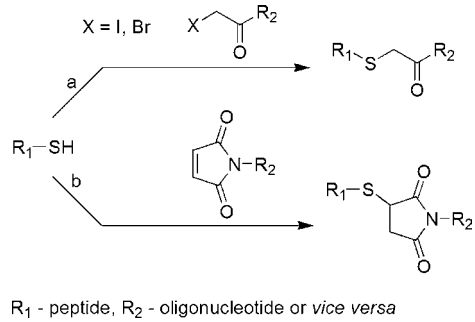


Figure 1. Formation of thioether-linked conjugates of peptides and oligonucleotides.

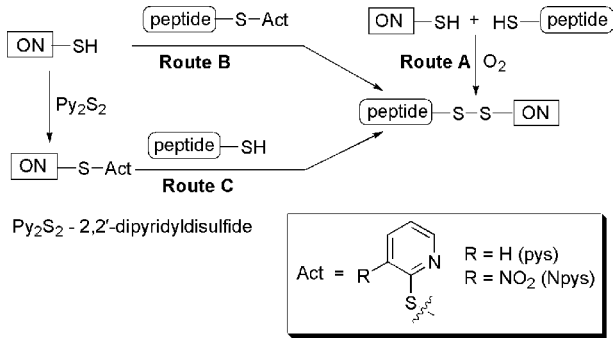


Figure 2. Formation of disulfide-linked conjugates of peptides and oligonucleotides.

are two main types of thioether linkage formation: nucleophilic substitution of haloacetamides (Figure 1a) and Michael-type addition of thiols to maleimides (Figure 1b). Halogenoacetyl group introduced into peptides using haloacetic anhydrides was reacted with 5′-deprotected thiol-containing oligonucleotide (*14*−*17*). Maleimide−thiol protocol provides the required selectivity in order to obtain unambiguous oligonucleotide−peptide conjugates from unprotected precursors in most cases (*18*). Coupling of thiolated ONs with maleimido-peptides has thus been used successfully for the synthesis of thioether-linked POCs (*10*, *14*, *19*). Furthermore, conjugation to maleimido-peptides gives rise to better results, as there are fewer side products (*19*). Tregear et al. have described that thiolated oligodeoxynucleotides can react selectively and efficiently with maleimide-derivatized 18mer TAT and 22mer C-terminal gp41 vector peptides (*10*). Alternatively, coupling of Cys-containing peptides (*20*−*23*) or thiolated peptides (*24*) obtained from SPPS using a disulfide bond-based linker (*25*) with 5′-maleimide-functionalized ONs has also been used successfully for the synthesis of thioether-linked POCs. Maeda et al. established a new, efficient method to synthesize the peptide conjugates of ONs via thioether linkage (*26*). In this method, ONs incorporating a vinyl purine in their sequences were synthesized and conjugated with glutathione or Cys-containing peptide through thioether bond formation.

The coupling of thiol-containing ON with thiol-containing peptide via a disulfide linkage has been used to prepare various ON 5′- or 3′-peptide conjugates. Three straightforward routes to generate disulfide cross-linked POCs are summarized in Figure 2. The disulfide linkage can be formed either by direct oxidation of two thiols (route A) (*27*) or by preliminary activation of one thiol with pyridylsulfenyl (Pys) or 3-nitropyridylsulfenyl (Npys) group followed by nucleophilic substitution (route B and C) (*24*, *28*−*34*). However, direct oxidation may produce mixtures of undesired homodimers as well as the desired asymmetric disulfide. By preactivation of one of the thiols, the possibility to produce undesired homodimers of ON or the peptide can be circumvented. Since Pys or Npys group protecting thiol acts as a very good leaving group in the presence of free thiol and thus leads to an efficient conjugation reaction. The yield of isolated conjugates depends on the route of coupling and the peptide's structure. A comparison of the yields revealed that route C appears to be the procedure of choice for preparation of the disulfide cross-linked POCs (*29*). An advantage of route C is that the preparation of ON in the smaller scale requires less manipulation prior to conjugation. In addition, these pyridyl groups are base-sensitive and hence cannot be used during the automated ON synthesis due to the harsh final basic treatment for nucleobase deprotection. Hence, ONs with free thiol are mostly used for conjugation, and the peptide is modified by thiol group masked with 2-thiopyridyl derivatives.

Gait et al. (*35*, *36*) and Corey (*37*) described full protocols for the conjugation of peptides to ONs or siRNA via a disulfide linkage. The reaction between two thiol-containing components, one of which is first activated with a Pys or Npys group before addition of the second thiol component, is very rapid and complete. However, in the case of hightly cationic peptide, there are severe problems in maintaining solubility of the components and the resultant conjugate in aqueous solution due to aggregation and precipitation. These factors reduce the yield considerably. This can be avoided by using a high concentration of denaturing agent in both conjugation and HPLC purification steps, which allows such disulfide conjugates to be readily isolated in the pure form (*29*, *31*, *35*, *37*). Another method to overcome the problem of precipitation is to load a preactivated thiol-containing ON on the anion exchange column and add the thiol-containing peptide, followed by thorough washing to remove the excess peptide, elution with a highly concentrated salt solution (*38*, *39*). Defrancq et al. developed a novel heterobifunctional linker molecule containing a thiol-reactive nitropyridyl disulfide group and an aldehyde-reactive aminooxy group (*40*). The disulfide linkage could be formed first, followed by the formation of the oxime linkage and vice versa. By utilizing the linker molecule, a peptide−oligonucleotide conjugate was prepared.

Conjugation through Amide Linkage. Conjugation of peptides to ONs through amide bond formation involves reaction of an amino group with an activated carboxylic group. There are considerable reports wherein the fragments of POCs are linked via amide linkages. The amide linkage formation between peptides and ONs is discussed below.

Bruick et al. have utilized an ON template to direct the ligation of unprotected peptides to ONs via a stable amide linkage in aqueous solution (*41*). In this template-directed ligation procedure, a C-terminal thioester peptide was converted to a thioester-linked oligonucleotide−peptide intermediate. The ON portion of the intermediate bound to a complementary oligonucleotide template, placing the peptide in close proximity to an adjacent template-bound ON that terminated in a 3′-amine. The ensuing reaction results in an amide-linked oligonucleotide−peptide conjugate. In this procedure, however, amino acid cyclization can be a problem; thus for certain small peptides that tend to adopt a cyclic conformation, the amine terminus of the peptide may compete with the amine-terminated ON, resulting in cyclization of the peptide rather than ligation of the peptide to the ON.

Similarly, the C-terminus of peptides was efficiently coupled to 3′-terminal alkyl-amines of protected ONs in a convergent manner to yield the corresponding POCs (*42*). This conjugation reaction requires extremely mild conditions and does not require a large excess of conjugate substrate. Furthermore, the conjugates were obtained in high isolated yields (83−99%).

Another method of chemoselective conjugation, which can form a stable amide linkage between the peptides and ONs, is called "native chemical ligation" (*43*). This native chemical ligation approach, originally devised for the coupling of

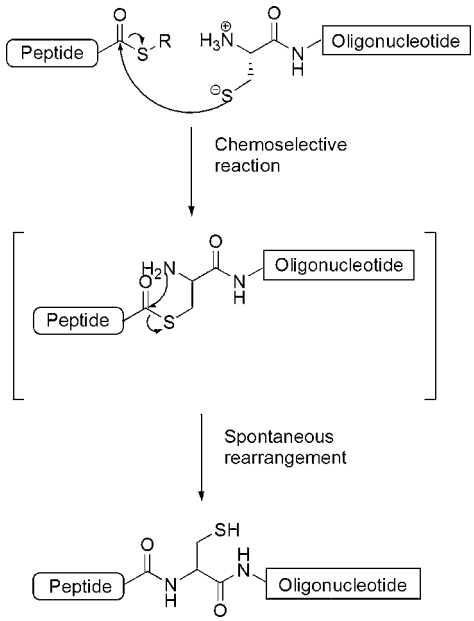


Figure 3. Chemical reaction involved in"native chemical ligation" conjugation of a peptide thioester and an oligonucleotide functionalized with a 5′-cysteine to form a stable amide linkage.

unprotected peptide segments in the chemical synthesis of proteins, has also been adapted to the conjugation of peptides to ONs. Stetsenko and co-workers have synthesized a range of POCs using this powerful approach (*44*−*46*). In this method, an N-terminal thioester peptide and a 5′-cysteinyl ON are first synthesized separately on solid supports. The unpurified, deprotected, functionalized peptide and ON can then be used in a native chemical ligation conjugation in aqueous solution (Figure 3). The advantage of this approach is that efficient coupling is achieved in the presence of denaturing agents and organic cosolvents. Thus, in principle, this method is suitable for both hydrophobic and hydrophilic peptides. Being similar to the template-directed ligation procedure, amino acid cyclization can also be a problem. Successful peptide−oligonucleotide conjugation occurred when amino acid cyclization side reactions could not take place, as was the case for peptides with an N-terminal proline, sarcosine, or alanine. In contrast, a peptide with an N-terminal glycine was prone to cyclization, and thus, no conjugation product was formed.

Gait and co-workers have reported several efficient methods for the synthesis of POCs by means of amide bond formation on a solid support (*47, 48*). They have successfully used substituted ON carrying a 5′-carboxylic acid function (**1**; Figure 4), while still attached to the solid support, to conjugate to a range of amines or to the N-termini of short peptides using normal peptide-coupling conditions to yield the highly pure conjugates (*47*). Similarly, they have also described an efficient method for the synthesis of ON 2′-peptide conjugates via amide bond formation on the solid phase. In this procedure, protected ONs bearing a 2′-*O*-carboxymethyl group were obtained by using a novel uridine 3′-phosphoramidite building block **2**, where the carboxylic acid moiety was introduced as its allyl ester. This protecting group is stable to the conditions used in solid-phase oligonucleotide assembly, but easily removed by treatment with palladium(0) and morpholine. The resulting ONs were then efficiently conjugated on a solid support under normal peptide coupling conditions to various amines or to the N-termini of small peptides to give pure products in good yield. Another procedure for the synthesis of POCs containing an amide linkage between the 2′-carboxy group of a modified ON and the amino terminus of a peptide has also been described by the same

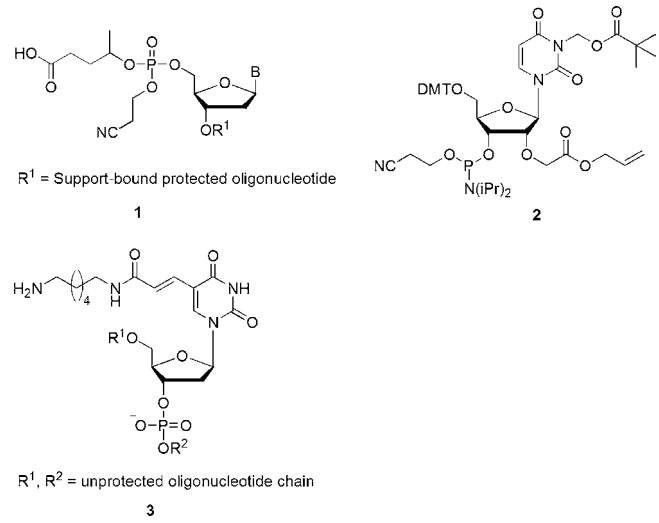


Figure 4. Building blocks for the synthesis of amide-linked POCs.

research group (*49*). In this procedure, fully deprotected ONs containing a carboxymethyl group at the 2′-position of the sugar residue were first obtained by a two-step oxidation of the 1,2-diol side chain of a 2′-modified ON by sodium periodate followed by sodium chlorite. The resulting 2′-*O*-carboxymethyl ONs were then reacted to a number of amino acid derivatives or short peptides containing N-terminal amine in the presence of a water-soluble carbodiimide to afford ON 2′-peptide conjugates in good yield (*49*). Thereby, using this method, ON 2′-peptide conjugates can be prepared via amide linkage.

In some POCs, the amino groups of the modified nucleobase have been linked to peptides through different functional groups. For example, Viladkar has used various amino acids and dipeptides to conjugate to ONs having the modified thymidine nucleoside **3**, which bears a reactive amino group on the C-5 position of pyrimidine (*50*). ONs containing the modified thymidine nucleotide were prepared, purified, and then coupled to fully or partially protected amino acids or dipeptides through their C-terminal carboxylic acids, in 50% DMF at pH 7.0. It may be noted that the ON and peptide fragments of the conjugates are separated by a spacer arm of 10 atoms. It is reported that the use of relatively highly concentrated EDC could improve the conjugation yield remarkably that depends on the presence of bulky amino acid chain, and complete conjugation can be achieved within a few hours.

Conjugation through Oxime, Thiazolidine, or Hydrazone Linkage. Covalent conjugates of ONs with peptides, which are linked by oxime, thiazolidine, or hydrazone groups, can be obtained by the reaction of carbonyl groups with aminooxy group, 1,2-aminothiol and hydrazino, or hydrazido group, respectively. There are numbers of review articles recently published in which conjugation of peptides to ONs through these founctional groups has been described (*7, 9, 51*). The present article therefore does not include an exhaustive account on the use of oxime, thiazolidine, and hydrazone reactions for oligonucleotide conjugation with peptides. Only some recent and representative examples are described below.

The aminooxy group reacts readily with a variety of electrophiles. The high nucleophilicity of this group is determined by an alpha-effect, or the presence of a lone electron pair on the adjacent heteroatom (*52*). The high reactivity of the aminooxy group toward aldehydes has been utilized for chemoselective ligation of aminooxy-modified peptides to aldehyde-modified ONs or vice versa, resulting in formation of a highly stable oxime linkage. Moreover, oxime bond formation has been successfully employed to prepare the POCs bearing

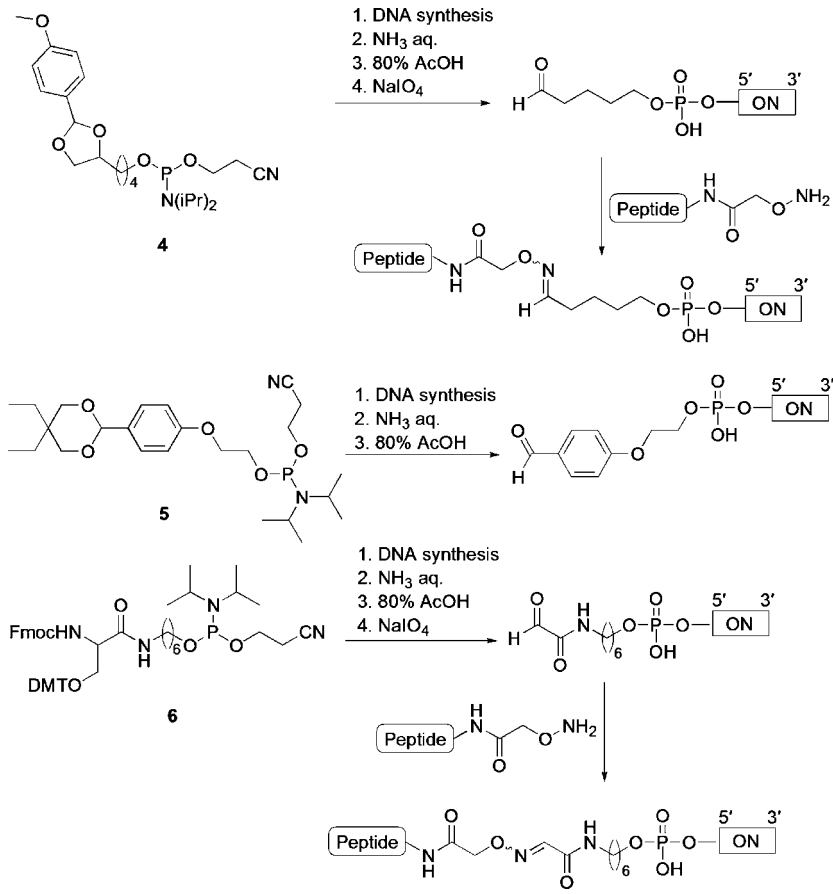


Figure 5. Synthesis of 5′-aldehyde and 5′-glyoxylyl oligonucleotides and conjugation with aminooxy peptides.

peptides at either 5′- or 3′-ends of the ON. Recently, two brief overviews of various synthetic approaches for the preparation of POCs through oxime bond formation have been described by Defrancq et al. (*53*, *54*).

There are three phosphoramidite derivatives (**4**−**6**; Figure 5) that are capable of introducing the aldehyde and glyoxylic aldehyde precursors at 5′-end of the ON (*55*−*57*). The phosphoramidite derivative **4** was prepared in two straight steps starting from 1,2,6-hexane triol and incorporated at the 5′-end of the ON during the solid-phase ON synthesis using the routine coupling procedure (*55*). Acetic acid treatment generated the ON carrying the 5′-diol moiety. The aldehyde-containing ON was prepared by periodate oxidation of 5′-diol. Subsequent conjugation with aminooxy modified peptide leads to the formation of 5′-conjugates with aldo-oxime bonds (Figure 5). The above phosphoramidite derivative was also employed to prepare glycopeptide−oligonucleotide conjugates bearing a glycocluster at the 5′-terminus of ONs (*58*). In this procedure, a cyclodecapeptide scaffold was used as a key intermediate to anchor the carbohydrate cluster and the ON through sequential oxime bond formation. Another phosphoramidite derivative **5** was also prepared in two straight steps starting from 4-(2-hydroxyethoxy)benzaldehyde and introduced at the 5′-end of the ON by the solid-phase ON synthesis (*56*). Acetic acid treatment generated the oligonucleotide carrying the 5′-benzaldehyde moiety (Figure 5). ON modified with this benzaldehyde moiety has been used for immobilization on semicarbazide-modified glass surfaces. The third phosphoramidite derivative **6** was prepared from serine (*57*). An O,N-blocked serine residue was introduced into ONs by use of this phosphoramidite during standard DNA synthesis, followed by ammonolysis and periodate oxidation to generate ONs with 5′-glyoxylic aldehyde. The resulting 5′-glyoxylic aldehyde ON is further reacted with aminooxy-containing peptide to obtain 5′-conjugates with glyoxylic oxime bond (Figure 5).

By using the above-mentioned strategies, conjugation of aldehyde or glyoxylic aldehyde modified ONs to RGD or NLS peptides was successfully achieved by Dumy′s research group (*55*, *57*). Similarly, conjugates of 5′-aminooxy modified ON with N-terminal glyoxylic aldehyde RGD and NLS peptide were also obtained by the same research group (*55*). However, the coupling of an aminooxy ON to an aldehyde peptide is less convenient to work up because free aminooxy ONs are very often prone to react with traces of carbonyl compounds, which are present in HPLC solvents or in the atmosphere. Therefore, this approach is not recommended for the synthesis of oxime conjugates. By comparing the relative stability of POCs linked by glyoxylic oxime linkage and aldo-oxime linkage, it was found that POCs linked by glyoxylic oxime linkage show higher stability at acidic to neutral pH but lower stability at alkaline pH (*55*, *57*).

Similar to the 5′-terminus, a postsynthetic oxidation strategy was used by Defrancq and co-workers for the production of aldehyde (*59*−*61*) and glyoxylic aldehyde (*62*) moiety at the 3′-position. The strategy utilized three commercially available modified long-chain alkyl amino-CPG (*7*−*9*) (Figure 6) supports to prepare aldehyde or glyoxylic aldehyde modified ONs. After the automated DNA synthesis, the ONs were cleaved from each support and deprotected by the conventional ammonia treatment to afford ONs **10**, **11**, and **12**. Subsequent periodate oxidation afford ONs with 3′-aldehyde or 3′-glyoxylic aldehyde. It must be mentioned that the solid support **8** gives irreproducible results, and the efficiency of the support for the introduction of 1,2-amino alcohol was found to decrease over a period of time even when stored at low temperature. Consequently, the other two commercially available solid supports were preferred for the

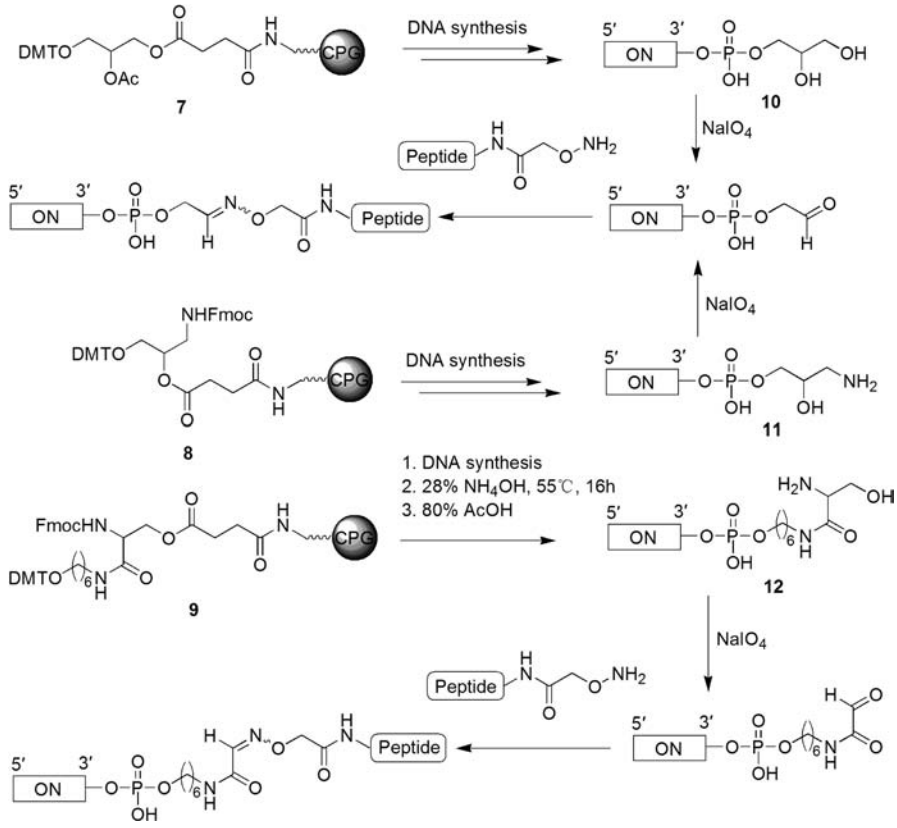


Figure 6. Synthesis of 3′-POCs through oxime bond formation.

introduction of the 3′-aldehyde or 3′-glyoxylic aldehyde into ONs. The 3′-aldehyde- or 3′-glyoxylic aldehyde-containing ON was used to prepare the ON conjugates with RGD or NLS peptides similar to the one discussed for 5′-conjugation (*59*−*62*) (Figure 6).

The aforementioned protocol described for the preparation of 3′- or 5′-conjugates can also be applied in sequential fashion for the preparation of 3′,5′-bis-conjugates. The preparation of ONs sustaining two aldehyde moieties at each terminus, followed by reaction with aminooxy-containing RGD or NLS peptides to afford 3′,5′-conjugates through oxime bond formation, has been reported by Defrancq and co-workers (*63*). This method employed bifunctionalised ONs in single step without the need of a protection strategy, under mildly acidic conditions. The conjugates were obtained in high yields. The major advantage of this ligation technique is that it requires neither a coupling reagent nor chemical manipulations. It just requires mixing the two fragments, namely, the aminooxy- and the aldehyde-containing oligomers. However, the above approach was limited to conjugation with similar peptides. Another method was later reported by the same research group in which bis-functionalized ON conjugates bearing different groups at the two extremities based on sequential formation of the oxime bonds were prepared (*64*). This strategy was utilized to prepare conjugates bearing two different peptides or a peptide and a fluorescent reporter group (*64*).

In addition to all of the above, the high reactivity of the aminooxy group toward ketones has also been utilized for chemoselective conjugation of peptides to ONs, resulting in formation of a highly stable oxime linkage (*65, 66*). Sheppard et al. have described the synthesis of DNA molecules bearing ketone functional groups (*ketone*-DNA) and the efficient postsynthetic modification of single-stranded *ketone*-DNA with an aminooxy RGD-peptide through oxime formation (Figure 7). In this approach, the methyl ketone-containing phosphoramidite derivative **13** (Figure 7) was first synthesized by modifying the C-5 position of uridine. Employing standard phosphoramidite coupling procedures, phosphoramidite **13** was used to synthesize *ketone*-DNAs. Reaction of single-stranded *ketone*-DNAs with the aminooxy RGD-peptide forms an oxime linkage (Figure 7) (*65*). Being in some ways analogous to this reported procedure, another alternative approach has been developed by Miller et al. in which the aminooxy group of AOQ-modified oligonucleotides can be conjugated to the ketone functionality introduced into the peptide via bromoacetone treatment forming a highly stable oxime linkage (Figure 8) (*32, 66*). This procedure was successfully used to prepare AOQ-modified 2′-*O*-methylribonucleoside conjugates of a tetrapeptide, RGDC, and a derivative of HIV tat peptide having a C-terminus cysteine.

Another useful fragment ligation approach in solution involves thiazolidine formation. In this approach, reaction of an aldehyde-containing ON with a cysteine-containing peptide forms a thiazolidine linkage (*55, 61, 67*) (Figure 9). For peptides containing free thiol groups, the reaction is sensitive to oxidizers so that the reaction must be carried out in the absence of oxygen.

Conjugation of aldehyde or glyoxylic aldehyde modified ONs to hydrazino peptides has been described by a number of publications. Melnyk et al. (*68*) used 5′-glyoxylyl ONs for conjugation with a hydrazino peptide (Figure 10). In this procedure, a 5′-amino ON was acylated via *O,O*′-diacetyl tartaric anhydride on a solid phase. At the end of the reaction, a glyoxylyl group was generated by a mild periodate oxidation after ON deprotection. It was found that almost 50% conjugation reaction occurs in a few seconds and the reaction was completed in 15 min (*68*). A new strategy to prepare ON modified by 5′-glyoxylic aldehyde group was also developed by the same research group (Figure 11) (*69*). This strategy utilized a novel phosphoramidite **14** derivatized by a bis[2-(*tert*-butyldisulfanyl)ethoxycarbonylamino]acetyl moiety for the synthesis of ONs modified at the 5′-end by an α-oxo aldehyde functionality. Incorporation of the phosphoramidite reagent onto the 5′-end

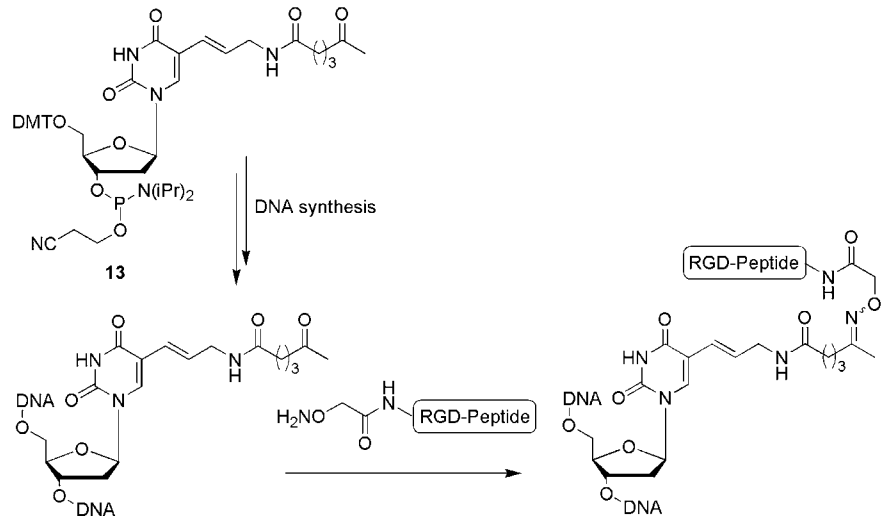


Figure 7. Synthesis of RGD-peptide−oligonucleotide conjugate using keto-oxime bond.

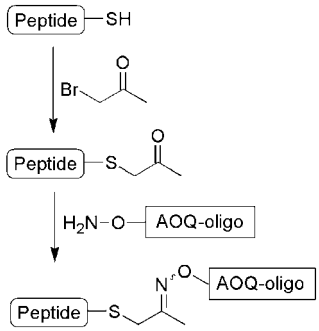


Figure 8. Synthesis of a keto-petide and conjugation to an AOQ-oligonucleotide.

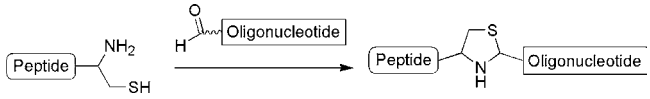


Figure 9. Conjugation of a cysteine-containing peptide to an aldehyde-containing oligonucleotide through thiazolidine linkage.

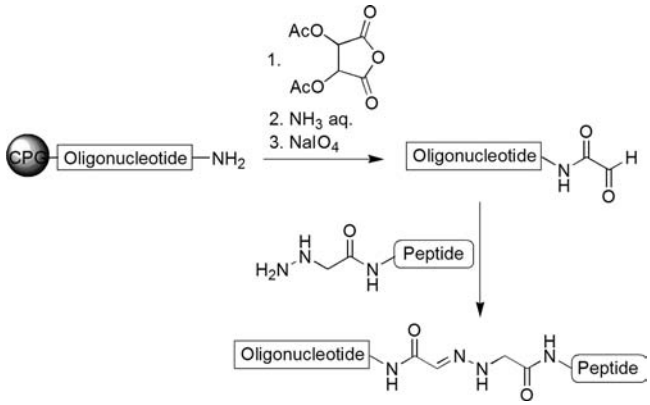


Figure 10. Synthesis of 5′-glyoxylyl oligonucleotides and conjugation with N-terminal hydrazino peptides through hydrazone linkage.

of ONs was performed after the automated solid-phase oligonucleotide synthesis. Simultaneous cleavage/deprotection of the ONs and unmasking of the α-oxo aldehyde group could be achieved using NaOH in aqueous methanol in the presence of excess dithiothreitol (100 equiv) (*69*).

Ligation of an aldehyde group onto the 5′- or 3′-end of an ON limits the number and position of conjugated moieties. There are a few papers describing the synthesis of POCs wherein a peptide is incorporated to the 2′-position via a 2′-aminonucleoside (*70*−*72*), but this scheme can suffer from low yield (*71*, *72*). In addition, the ligation of 2′-aminonucleosides and their acyl derivatives strongly decreases duplex stability (*73*). In contrast, synthesis of POCs with single and multiple peptides attached to 2′-aldehydes through thiazolidine, oxime, and hydrazone linkages has been shown by Zatsepin and co-workers (*74*). These POCs incorporating single or multiple peptides were obtained by synthesizing 2′-deoxyoligonucleotides and 2′-*O*-methyloligonucleotides carrying one or more 2′-aldehyde groups and then coupling it to peptides containing an N-terminal cysteine, aminooxy, or hydrazide group in good yield (Figure 12) (*74*). The same group also used a novel uridine phosphoramidite **15** (Figure 13) to generate aldehyde at the 2′-position and have successfully used it to prepare POCs through oxime or thiazolidine bond formation (*75*) (Figure 13). This facile conjugation approach allows specific coupling in aqueous solution of unprotected ONs containing aldehyde groups to unprotected N-terminally modified peptides. The advantages of this method were described as threefold: first, the reaction did not require use of a large excess of peptide (1.2−1.8 equiv); second, there is an ability to attach more than one peptide to ONs at defined sites and the freedom to attach additional moieties (i.e., fluorescent groups) at both the 3′- and 5′-ends of the ON; third, linkage by this process did not interfere with oligonucleotide-to-target hybridization. However, the hydrazones formed were liable to hydrolysis in the neutral and basic pH ranges. Thus, borohydride reduction was required (Figure 12). In addition, another method involving the conversion of the 2′-aldehyde group into a 2′-hydrazine and an efficient conjugation of the 2′-hydrazine ONs to *N*-glyoxylylpeptides has been reported by the same group (*76*). In this method, ONs containing a novel nucleoside, 2′-*O*-(2-hydrazinoethyl)uridine, were synthesized by reduction of hydrazones formed from 2′-*O*-(2-oxoethyl)oligonucleotides with 9-fluorenylmethyl carbazate with sodium cyanoborohydride, followed by concentrated aqueous ammonia deprotection. The resulting 2′-hydrazine ONs were used to synthesize POCs with *N*-glyoxylylpeptides via hydrazone formation (Figure 14).

Conjugation through the N-Acylphosphoramidate Linkage. The preparation of POCs with an N-acylphosphoramidate linkage has been described by Grandas and co-workers (*77*) wherein the N-acylphosphoramidate diesters can be obtained by either (i) phosphitylation of carbamoyl groups with chloroalkoxy(dialky1amino)phosphines and a tertiary base and

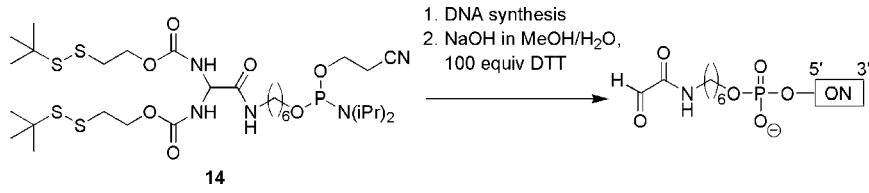


Figure 11. Synthesis of 5′-glyoxylyl oligonucleotides.

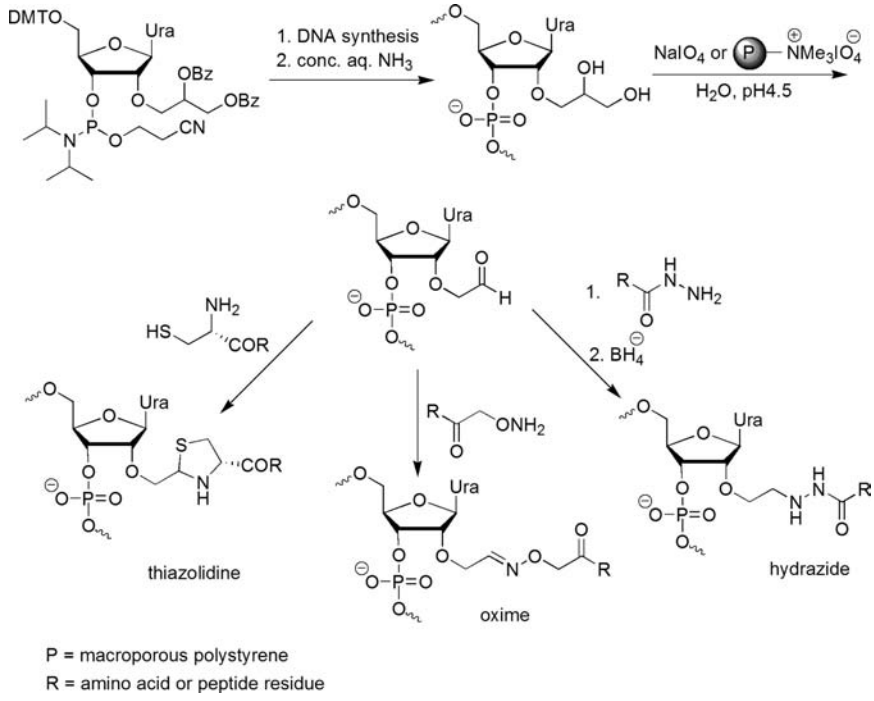


Figure 12. Preparation of 2′-O-carboxymethyl POCs through thiazolidine, oxime, and hydrazide linkages.

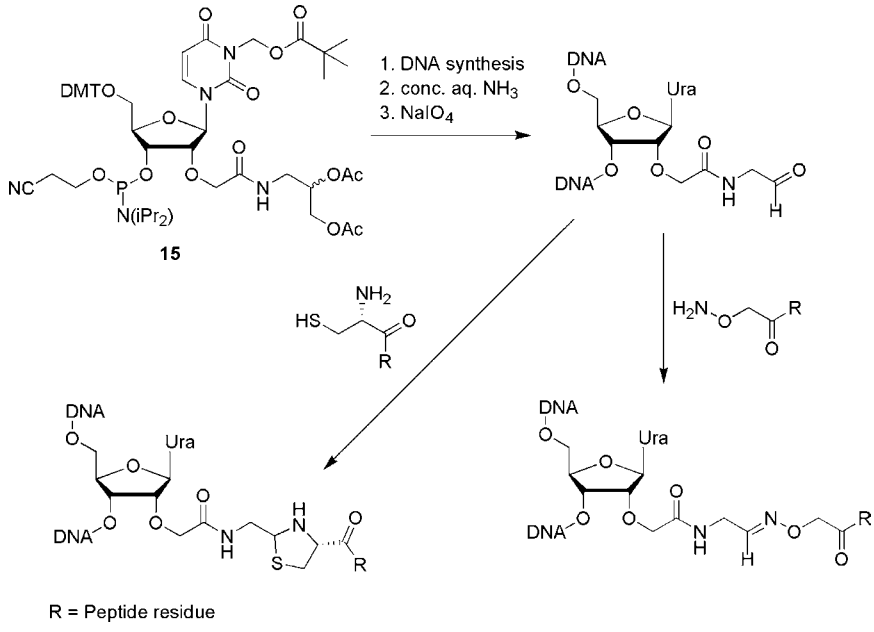


Figure 13. Preparation of 2′-aldehyde oligonucleotides and conjugation with N-terminal cysteinyl and aminooxy peptides.

reaction of the resulting phosphorodiamidite with an alcohol and tetrazole followed by oxidation, or (ii) tetrazole-mediated reaction of a phosphoramidite and a primary carboxamide and subsequent oxidation. Using the former, they have synthesized a POC with an N-acylphosphoramidate union for the first time. Furthermore, the resultant POC has been shown to be stable under a variety of basic conditions and labile to treatment with an acidic reagent, but the presence of the nitrogen-linked acyl group increases the acid stability compared with unmodified phosphoramidate groups (*77*).

Conjugation through Urea or Carbonyl Linkage. Fujii and co-workers have reported a universal method to prepare a series

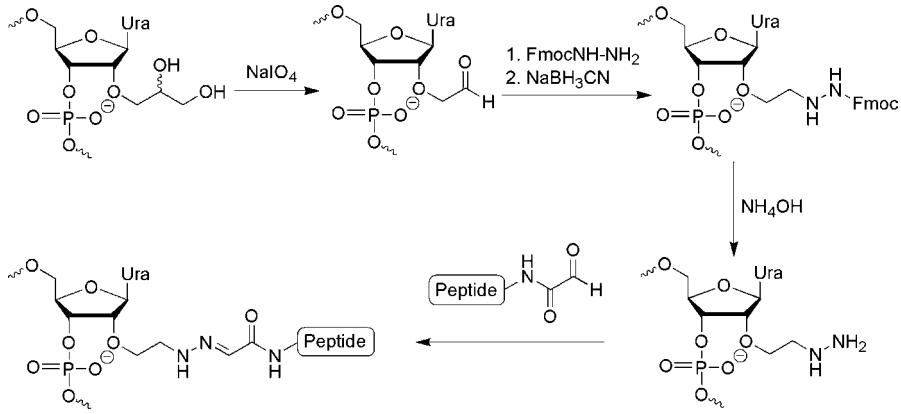


Figure 14. Synthesis of 2′-hydrazine oligonucleotides and conjugation with N-glyoxylylpeptides via hydrazone linkage.

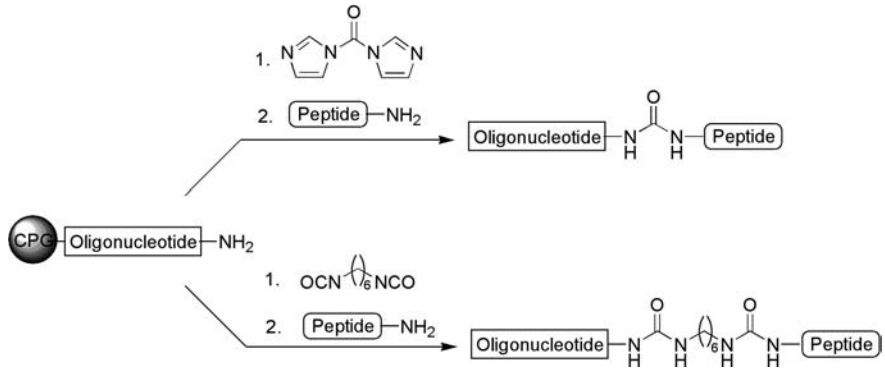


Figure 15. Postsynthetic conjugation of oligonucleotides to peptides through urea or carbonyl linkage.

types of POCs containing a urea (*78*, *79*) or a carbonyl (*80*) linkage as the linking functionality (Figure 15). The strategy of this protocol was that an ON fragment, carrying a free amino group prepared on a CPG support, was reacted with α,ω-diisocyanatoalkane or carbonyl diimidazole and then with a peptide fragment bearing a single reactive amino group. The resulting oligonucleotide−peptide conjugate covalently linked to a solid support was cleaved from the CPG and deprotected by treatment with ammonia (Figure 7). By this approach, a series of NLS peptides were covalently coupled to the 5′-end, to the 3′-end, and to the middle of the ON sequence. It is notable that all amino acids except for lysine and cysteine, whose ε-amino group and thiol group were protected by trifluoroacetyl group and acetyl group, respectively, could be used with their side chain unprotected during the coupling procedure. However, it is required that all the peptides, except peptides with a lysine at their C-termini, be coupled to β-alanine residue at their N-terminus as the reactive nucleophilic moiety for effective coupling in these methods. Conjugation of ONs to peptides with any component of amino acids can be obtained in good yield using this strategy.

Conjugation through Phosphate Linkage. Hayakawa et al. has reported a novel approach for the preparation of POCs with a base-labile phosphate linker between the peptide and ON via the allyl-protected phosphoramidite strategy (*81*). In this procedure, the phosphoramidite method was used with allyl protecting for the internucleosidic phosphate linkages and the C-terminal of the peptide and allyloxycarbonyl protecting for the nucleoside bases and the N-terminal of the peptide. The coupling proceeded between the terminal hydroxyl of an oligonucleotide still coupling to a solid phase and the phosphoramiditylated hydroxyl of a serine or threonine residue of a peptide followed by oxidized by *t*BuOOH to generate a phosphodiester bond. Finally, the removal of the allylic protecting groups and the detachment of the products were achieved under nonbasic or mild basic conditions. This method generally provides the target compounds in high yields and in good purity without conspicuous degradation of the base-labile phosphate linkage between the oligonucleotide and the peptide (*81*).

Conjugation through Diels−Alder Reaction. The Diels−Alder reaction is another strategy which offers the prospect of quickly and reliably linkage creating between a peptide and an oligonucleotide. This reaction is a cycloaddition between a conjugated diene and a dienophile to form a cyclohexene structure. Being fast and efficient in aqueous solution besides being chemoselective, the Diels−Alder reaction has been applied successfully to the bioconjugation of nucleic acids (*82*−*84*). Synthesis of POCs using the Diels−Alder reaction between a diene and a dienophile has been reported by Picken (*85*) and Grandas et al. (*86*). In this approach, the peptide was linked to a dienophile and the ON was linked to a diene. According to Picken's description, 2-furfuryl-NHCO$(CH_2)_4$CONH-oligonucleotide was reacted with a peptide−maleimide derivative to generate the Diels−Alder adduct (Figure 16a). Similarly, Grandas et al. obtained the POCs by the reaction between an acyclic diene linked to the ON chain and a maleimide-derivatized peptide (Figure 16b). Very recently, a nucleotide carrying a peptide via a Diels−Alder cyclohexene linkage was prepared and sequence-specifically incorporated into DNA (*87*). This cyclohexene-derivatized nucleotide carrying a peptide allows for the functional labeling of DNA strands under mild conditions without additional catalysts.

The cycloaddition reactions in water are clean, fast, and chemoselective, and they allow the straightforward synthesis of large peptide−oligonucleotide conjugates, containing any nucleoside or trifunctional amino acid, which are otherwise difficult to obtain (*86*). However, maleimide dienophile used in this reaction is susceptible for Michael addition reactions with other nucleophilic centers on peptides or oligonucleotides and may give rise to side reactions.

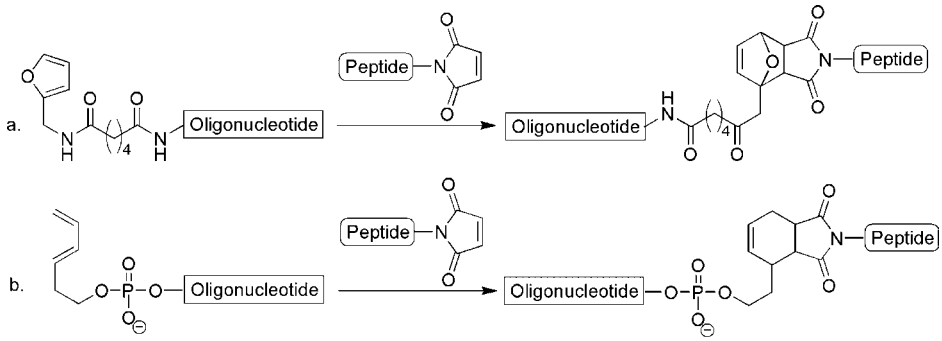


Figure 16. Schemes for the preparation of POCs by Diels−Alder reaction.

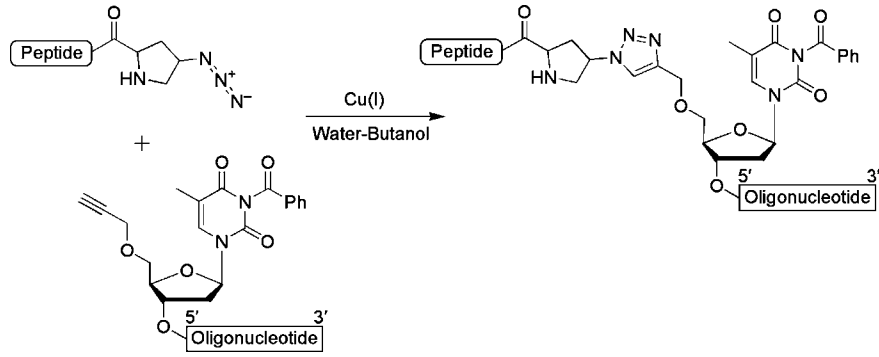


Figure 17. DNA-alkyne conjugation with 4-azidoprolyl-peptide using click reaction in solution.

Conjugation through Triazole Formation using 1,3-Dipolar Cycloaddition Reaction. The Huisgen 1,3-dipolar cycloaddition reaction involving reaction between alkyne and azide to form 1,2,3-triazoles, the so-called "click" reaction (*88, 89*), has been added to the repertoire of ONs modifying methods. The use of this click reaction for postsynthetic modification of ONs has been the subject of a recently published minireview article (*90*). Recently, this 1,3-dipolar cycloaddition reaction has been employed to synthesize POC using ligation of peptide-azide to DNA-alkyne through triazole formation (*91*). In this procedure, an ON labeled by an alkynyl group at the 5′-end and a peptide modified with an azido group at the N-terminus were synthesized. The corresponding 5′-alkynyl ON was used for "click-"conjugation with peptide-azide to produce a 1,2,3-triazole linkage between these two reactants in high purity and yield (Figure 17). This reaction can be carried out in either water or organic medium and be employed postsynthetically on purified units modified with alkynyl and azido functionalities, without additional functional group protecting strategies. This 1,3-dipolar cycloaddition chemistry is very chemoselective, only occurring between alkynyl and azido functional groups with high yield. In addition, the resulting 1,2,3-triazoles are stable under aqueous conditions and high temperature (*92*).

Total Stepwise Solid-Phase Synthesis Approach. The total stepwise solid-phase synthesis strategies suggested to date fall into two major categories: either a branched linker bearing an amino group for peptide synthesis and a hydroxyl function for subsequent assembly of the ON sequence is utilized, or a linker carrying a hydroxyl function is attached to the amino terminus of the support-bound peptide and used as a starting point for the ON chain assembly. Both approaches meet with the same difficulty, namely, incompatibility of the protecting group strategies usually applied to ON and peptide synthesis. The incompatibility of the protecting group strategies leads these approaches to be limited to incorporation of peptides with amino acids whose side chains are compatible with base-labile protecting groups or those amino acids that do not require protection. For this reason, special protecting groups that have been summarized by Kim et al. (*7*) and Grandas et al. (*93*) and modified deprotection protocols should be used. The chemistries used need to be mild enough to support the consecutive synthesis of ON and peptide, and the deprotection conditions must not affect the ON. Very recently, the methods described for the stepwise solid-phase synthesis of POCs have been reviewed as a part of a review article on the solid-supported synthesis of oligonucleotide conjugates (*94*).

Preparation of Oligonucleotide 3′-Peptide Conjugates. Most of the stepwise synthesis reported in the references generated POCs containing the peptide moiety at the 3′-end of ON (*38, 95−111, 117*). In this strategy, the peptide is first synthesized using two kinds of N-termini protected amino acids. One is the Boc-amino acids containing base labile protecting groups (Fmoc, Fm, Tfa, Tos, Dnp) for the protection of trifunctional amino acid side chains (*95, 97, 103, 106, 107, 117*). These base-labile protecting groups can be removed concomitantly with the nucleotide protecting groups. The other is the Fmoc-amino acids containing acid-labile (BOC) protecting groups for the protection of trifunctional amino acid side chains. These acid-labile protecting groups were removed by treatment with TFA-1,2-ethanedithiol (9:1) (*96, 98−102, 104, 105*). In the case of Boc-amino acids, the repetitive acid treatments used for the removal of the BOC group were performed without the presence of the oligonucleotide. Truffert et al. have reported a general automated procedure for the synthesis of oligonucleotide 3′-peptide conjugates (*104*). In order to avoid the use of strong acids, they used the Dde group for amino side-chain protection of lysine. Subsequent deprotection can be achieved by treatment with ethanolamine or hydrazine. Antopolsky and colleagues (*112*) have proposed a process using Fmoc-ornithine-methyltrityl (Mtt) as a precursor for arginine. Conversion of ornithine to arginine required additional steps, which involved treatment of the peptide containing Fmoc-Orn(Mtt) with TFA/dichloromethane, triethylamine/dichloromethane, and finally incubation in THF/triethylamine. Stromberg et al. have reported a uniform protection strategy (i.e., Bpoc group and Ddz group) for the N^{α} protection of the amino acids. Both groups could be

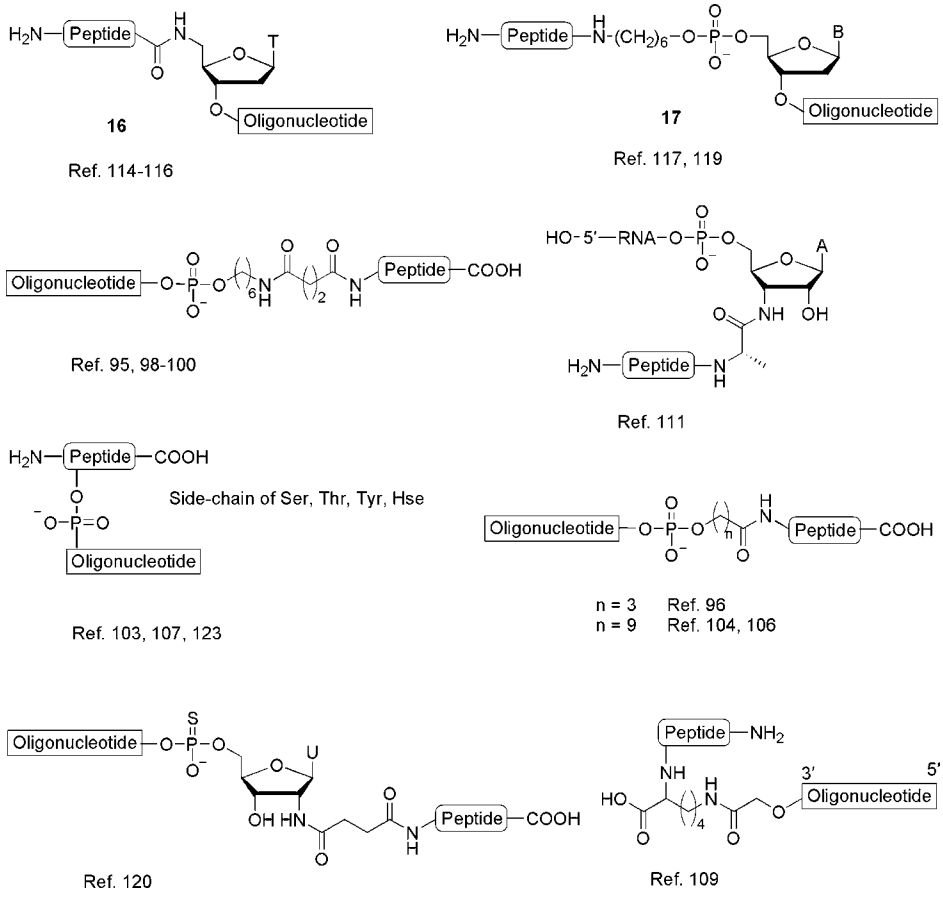


Figure 18. Linker molecules described for connecting the oligonucleotide and the peptide part in the stepwise solid-phase approach.

removed easily by treatment with TFA solution (0.2−3%) in a few minutes (*113*).

Preparation of Oligonucleotide 5′-Peptide Conjugates. In addition to oligonucleotide 3′-peptide conjugates, there are also some POCs which have been prepared carrying small peptides at the 5′-end of the ONs (*114*−*117*). For instance, 5′-amino-2′,5′-dideoxythymidine was coupled at the 5′-termini of the ON, generating an amino group from which peptide synthesis begins (*114*−*116*) (**16**; Figure 18). Further, Kool et al. have developed a simple and rapid one-pot approach to conversion of naturally substituted 5′-OH ONs (on the solid support) to 5′-amino-oligonucleotides (*118*). Compared to the typical multistep synthesis of modified phosphoramidites, this approach represents a great improvement in terms of cost and time. Thus, this approach to 5′-amine offers a substantial savings in time and effort for the total stepwise solid-phase synthesis of POCs. Recently, another straightforward approach for the synthesis of 5′-peptide oligonucleotide conjugates has been developed by Eritja and colleagues (*119*). In this approach, the ON was first assembled using standard phosphoramidite protocols. Subsequent introduction of *N*-6-MMT-aminohexyl phosphoramidite afforded 5′-amino-oligonucleotide. Then, the peptide was synthesized on support-bound oligonucleotide containing the free amino group by standard Fmoc chemistry. The POCs (**17**) were obtained after standard ammonia treatment. A similar approach has been attempted by Grandas et al. to synthesize methionine-containing peptide−oligonucleotide hybrids (*117*). However, great difficulties were encountered in coupling Fmoc-methionine to the H_2N-linker-oligonucleotide-resin. Only the use of the strongest carboxyl activating agents was found to allow quantitative coupling of the methionine derivatives.

Peptide−Oligonucleotide-Connected Linkers Used in Consecutive Synthesis of POCs. To connect via chemical bonds the peptide and ON fragment, different linker molecules have been described (Figure 18). These molecules carry a carboxyl group or an amino group for peptide synthesis and a hydroxyl function for assembly of the ON. The simplest case of the coupling linkers is the side chain of the amino acids containing hydroxyl functions. These amino acids include Ser, Thr, Tyr, and Hse.

Solid Support Used in Consecutive Synthesis of POCs. For the total stepwise solid-phase synthesis, it is necessary to choose a suitable solid support for conjugate synthesis and avoid unwanted side reactions. Polystyrene supports and CPG supports are used in peptide and ON synthesis, respectively. Most reports have described the successful use of CPG for the synthesis of POCs (*96*, *98*, *99*, *104*, *114*, *116*). However, CPG is not suitable in some cases. The yield can be improved when Teflon (*101*), polystyrene (PS) (*97*, *103*, *107*), poly(ethylene glycol) (PEG) (*121*), and poly(ethylene glycol)-polystyrene (PEG-PS) grafts (*95*, *122*) were used instead. Some of the low coupling yields reported on CPG are related to the method of activation for the amino acid or to an inherent property of a given CPG batch (*114*). Coupling reactions mediated by HBTU/HOBT are more efficient than coupling reactions with symmetrical anhydrides and some active esters (*114*). On the other hand, coupling reactions on Teflon, PS, and PEG-PS are less dependent on the activation manner during peptide synthesis but are less efficient in ON synthesis. The low coupling yields when using these supports for the synthesis of ON can be compensated by increasing the coupling time and changing the solvent to dissolve the phosphoramidites (*95*, *97*, *103*, *107*).

Solid-Phase-Anchored Linkers Used in Consecutive Synthesis of POCs. After choosing a suitable solid support, it is required to prepare an *ad hoc*-derivatized support linking a suitable spacer, which can be selectively cleaved at the end of the conjugate synthesis. The linkage between the peptide−oligonucleotide

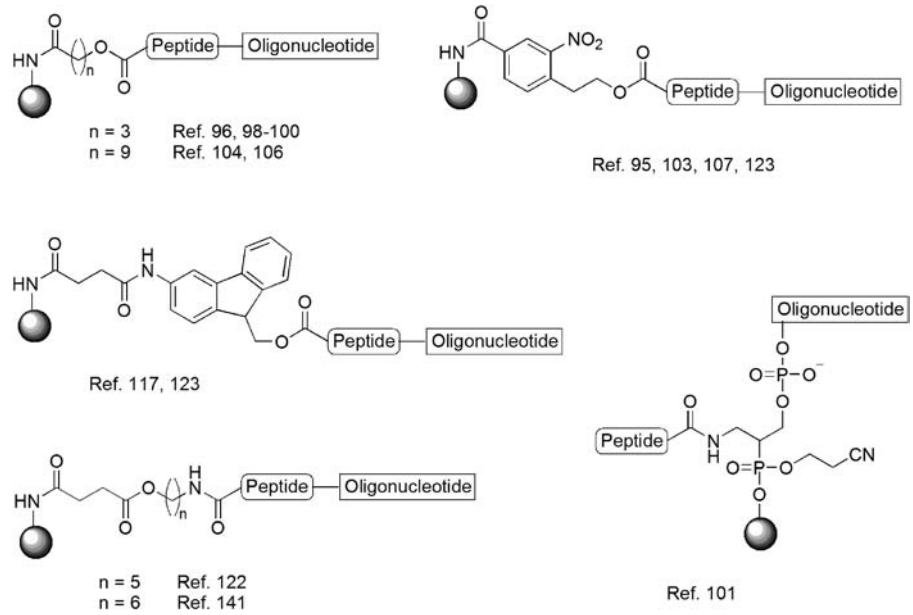


Figure 19. Linkers starting with the synthesis of the peptide between the POCs and the solid support.

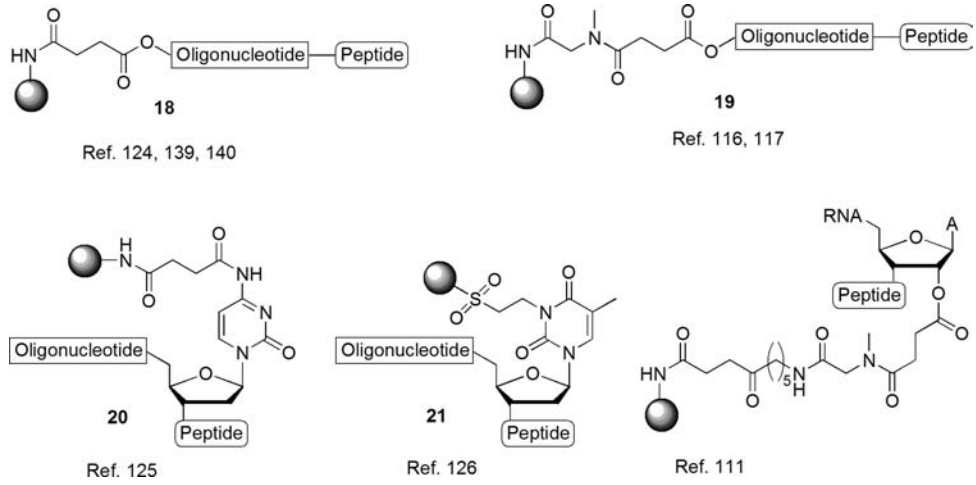


Figure 20. Linkers starting with the synthesis of the oligonucleotide between the POCs and the solid support.

conjugate and the solid support is usually a base-labile linker that starts with the synthesis of the peptide (Figure 19). Linkers from the peptide field are acid-labile and incompatible with the ON moiety. Thus, most of the linkers used to immobilize the peptide moiety have an ester function that can be cleaved with concentrated ammonia (*95, 100−104, 108*), ethylenediamine (*101*), ethanolamine (*104*), sodium hydroxide (*106*), or tetrabutylammonium fluoride (TBAF) (*103, 107, 123*). In most cases, treatment of traditional peptide handles with ammonia and primary amines generates a mixture of the C-terminal amide and carboxylate. The use of sodium hydroxide or TBAF gives the pure carboxylate peptides, but the complete deprotection of the nucleobases requires an additional ammonia treatment (*4*). Some linkages starting with the synthesis of the ON between the POCs and the solid support have also been reported (Figure 20). For instance, Grandas's research group (*124*) has used PS supports modified with a nucleotide building block to obtain nucleopeptide Boc-Ser(pTCT)-NHcHex (**18**; Figure 20). Bannwarth et al. (*116*) have used a sarcosine modified CPG support (**19**) to obtain the directly linked chimeric DNA-peptide-DNA conjugates wherein both the C- and N-termini of the peptides are conjugated to ONs. Piccialli and co-workers (*125, 126*) have designed and synthesized a cytidine-based support (**20**, **21**) for preparation of 3′- as well as 5′-peptide conjugates of ON. The conjugates were obtained in good isolated yields.

Other Methods. Besides the aforementioned chemical methods, the POCs have also been synthesized by enzymatic and mixed chemical and enzymatic methods. For example, Waldmann and colleagues have reported a method to prepare the small nucleopeptides by mixed chemical and enzymatic methods (*127, 128*). In this procedure, a combination of enzyme-labile and chemical protecting groups was used as C-terminal protecting groups. Advantages of this method are that the biocatalysts used are chemo- and stereoselective and the reaction can be carried out under mild conditions. Consequently, the peptide or phosphate bonds and other protecting groups are not cleaved under the reaction conditions. Silverman and co-workers have recently described the formation of nucleopeptide linkages catalyzed by deoxyribozymes (DNA enzymes) (*129*). They have demonstrated that deoxyribozymes have the ability to catalyze efficient formation of a Tyr-RNA nucleopeptide linkage between the side chain of tyrosine and a 5′-triphosphate-RNA. The reaction occurs when these functional groups are placed in an appropriate structural context, such as three-helix-junction architecture.

However, the analogous reactions of serine and lysine side chains are very inefficient and undetected, respectively.

CONCLUSIONS

During the past two decades, quite a number of POCs have been prepared and evaluated for various applications. It has been shown that linking peptides to oligonucleotides improves some of the desired properties of oligonucleotides such as cellular delivery (cell-penetrating properties) (*130*−*133*), increased stability to exonucleases (*97, 134*), improved binding to complementary sequences (*3, 4*), and greater rate of hybridization (*135*). Furthermore, peptide sequences have been used for the introduction of multiple nonradioactive labels in oligonucleotides (*98*−*100, 102, 105*), for the preparation of sequence-specific artificial nucleases (*104, 106, 107, 136, 137*), and as molecular bar codes in oligonucleotide combinatorial libraries (*114, 138, 139*).

In addition, several approaches for preparing POCs have been developed and evaluated over the past two decades. However, in the published procedures so far, both postsynthetic conjugation and stepwise approaches are methodologies that are far from routine. The reason for this is that there are advantages and defects for each route. For the postsynthetic approach, a major advantage is that peptides do not need to be stable under conditions of oligonucleotide assembly or vice versa. Thus, unlike the total stepwise approach, there is no issue of incompatibility of deprotection and assembly chemistries; all peptide side chains and nucleobases are deprotected before conjugation. However, the typically modest conjugation yield strongly depends on the varying solubilities of the peptides. In particular, highly basic peptides form nonspecific interactions with oligonucleotides, which may lead to poor coupling efficiency and low yield. Furthermore, this approach always requires several purification steps for both peptides and oligonucleotides, and finally the target conjugates as well. Conversely, the total stepwise method is typically characterized by a very high conjugation yield and a single purification step, and compatible with automation. Nevertheless, the stepwise solid-phase approach becomes tedious for synthesis of long conjugates. Moreover, there is still room for improvement in standard peptide synthesis technologies. For example, the limited choices of suitable protecting groups, which are compatible with peptide and oligonucleotide synthesis, is an important consideration.

Thereby, currently, the best choice for the preparation of small amounts of POCs wherein the peptide fragment is a protein or a large peptide is the postsynthetic conjugation approach, while the stepwise solid-phase protocol is suitable for the construction of large amounts of conjugates containing short peptide sequences. In addition, most of the studies on POCs focused only on synthesis, which may be related to the low yield. Therefore, the future development of a simple and straightforward procedure for generating highly pure POCs in high yield will be needed to inspire an increasing number of laboratories to prepare more conjugates, and thus enlarge their fields of application.

ACKNOWLEDGMENT

The authors would like to thank Xiu-Ling Cui for carefully revising the manuscript. This work was supported by National Natural Science Foundation of China (Grants 20572016 and 20772033) and Foundation of He'nan Educational Committee (G 2006KYCX017).

Note Added after ASAP Publication: The version of this paper published on October 26, 2009, contained errors in Figures 15 and 17. The corrected version was published on December 2, 2009.

LITERATURE CITED

(1) Crooke, S. T. (1992) Therapeutic applications of oligonucleotides. *Annu. Rev. Pharmacol. Toxicol. 32*, 329–376.
(2) Bennett, C. F. (1998) Antisense oligonucleotides: Is the glass half full or half empty? *Biochem. Pharmacol. 55*, 9–19.
(3) Tung, C. H., and Stein, S. (2000) Preparation and application of peptide-oligonucleotide conjugate. *Bioconjugate Chem. 11*, 605–618.
(4) Eritja, R. (2000) Synthesis of oligonucleotide-peptide conjugates and nucleopeptides, In *Solid-Phase Synthesis* (Kates, S. A., and Albericio, F., Eds.) pp 529−548, Marcel Dekker, New York.
(5) Zubin, E. M., Romanova, E. A., and Oretskaya, T. S. (2002) Modern methods for the synthesis of peptide-oligonucleotide conjugates. *Russ. Chem. Rev. 71*, 239–264.
(6) Zatsepin, T. S., Turner, J. J., Oretskaya, T. S., and Gait, M. J. (2005) Conjugates of oligonucle- otides and analogues with cell penetrating peptides as gene silencing agents. *Curr. Pharmaceut. Design 11*, 3639–3654.
(7) Venkatesan, N., and Kim, B. H. (2006) Peptide conjugates of oligonucleotides: synthesis and applications. *Chem. Rev. 106*, 3712–3761.
(8) Eritja, R. (2007) Solid-phase synthesis of modified oligonucleotides. *Int. J. Pept. Res. Therapeut. 13*, 53–68.
(9) Singh, Y., Spinelli, N., and Defrancq, E. (2008) Chemical strategies for oligonucleotide- conjugate synthesis. *Curr. Org. Chem. 12*, 263–290.
(10) Soukchareun, S., Haralambidis, J., and Tregear, G. (1998) Use of N_{α}-Fmoc-cysteine(S-thio-butyl) derivatized oligodeoxynucleotides for the preparation of oligodeoxynucleotide-peptide hybrid molecules. *Bioconjugate Chem. 9*, 466–475.
(11) Fischer, P. M., Krausz, E., and Lane, D. P. (2001) Cellular delivery of impermeable effector molecules in the form of conjugates with peptides capable of mediating membrane transloc- ation. *Bioconjugate Chem. 12*, 825–841.
(12) Mintzer, M. A., and Simanek, E. E. (2009) Nonviral vectors for gene delivery. *Chem. Rev. 109*, 259–302.
(13) Turner, J. J., Arzumanov, A. A., Ivanova, G., Fabani, M., and Gait, M. J. (2006) Peptide conjugates of oligonucleotide analogs and siRNA for gene expression modulation. In *Handbook of cell-penetrating peptides* (Langel, Ü., Ed.) pp 313−328, Chapter *18*, CRC Press, Boca Raton.
(14) Ede, N. J., Tregear, G. W., and Haralambidis, J. (1994) Routine preparation of thiol oligonucleotides: application to the synthesis of oligonucleotide-peptide hybrids. *Bioconjugate Chem. 5*, 373–378.
(15) Arar, K., Aubertin, A.-M., Roche, A.-C., Monsigny, M., and Mayer, R. (1995) Synthesis and antiviral activity of peptide-oligonucleotide conjugates prepared by using Nα-(Bromoacetyl)peptides. *Bioconjugate Chem. 6*, 573–577.
(16) Garcia de la Torre, B., Albericio, F., Saison Behmoaras, E., Bachi, A., and Eritja, R. (1999) Synthesis and binding properties of oligonucleotides carrying nuclear localization sequences. *Bioconjugate Chem. 10*, 1005–1012.
(17) Aubert, Y., Bourgerie, S., Meunier, L., Mayer, R., Roche, A. C., Monsigny, M., Thuong, N. T., and Asseline, U. (2000) Optimized synthesis of phosphorothioate oligonucleoxyribonucleotides substituted with a 5′-protected thiol function and a 3′-amino group. *Nucleic Acids Res. 28*, 818–825.
(18) Liu, F.-T., Zinnecker, M., Hamaoka, T., and Katz, D. H. (1979) New procedures for preparation and isolation of conjugates of proteins and a synthetic copolymer of D-amino acids and immunochemical characterization of such conjugates. *Biochemistry 18*, 690–697.
(19) Eritja, R., Pons, A., Escarceller, M., Giralt, E., and Albericio, F. (1991) Synthesis of defined peptide-oligonucleotide hybrids contining a nuclear transport signal sequence. *Tetrahedron 47*, 4113–4120.
(20) Tung, C.-H., Rudolph, M. J., and Stein, S. (1991) Preparation of oligonucleotide-peptide conjugates. *Bioconjugate Chem. 2*, 464–465.

(21) Harrison, J. G., and Balasubramanian, S. (1998) Synthesis and hybridization analysis of a small library of peptide-oligonucleotide conjugates. *Nucleic Acids Res. 26*, 3136–3145.
(22) Zanta, M. A., Belguise-Valladier, P., and Behr, J. P. (1999) Gene delivery: a single nuclear localization signal peptide is sufficient to carry DNA to the cell nucleus. *Proc. Natl. Acad. Sci. U.S.A. 96*, 91–96.
(23) Fraley, A. W., Pons, B., Dalkara, D., Nullans, G., Behr, J. P., and Zuber, G. (2006) Cationic oligonucleotide-peptide conjugates with aggregating properties enter efficiently into cells while maintaining hybridization properties and enzymatic recognition. *J. Am. Chem. Soc. 128*, 10763–10771.
(24) Bongartz, J.-P., Aubertin, A.-M., Milhaud, P. G., and Lebleu, B. (1994) Improved biological activity of antisense oligonucleotides conjugated to a fusogenic peptide. *Nucleic Acids Res. 22*, 4681–4688.
(25) Méry, J., Granier, C., Juin, M., and Brugidou, J. (1993) Disulfide linkage to polyacrylic resin for automated Fmoc peptide synthesis. Immunochemical applications of peptide resins and mercaptoamide peptides. *Int. J. Pept. Protein Res. 42*, 44–52.
(26) Ali, M. M., Nagatsugi, F., Sasaki, S., Nakahara, R., and Maeda, M. (2006) Application of 2-amino-6-vinylpurine as an efficient agent for conjugation of oligonucleotides. *Nucleosides, Nucleotides, Nucleic Acids 25*, 159–169.
(27) Chaloin, L., Vidal, P., Lory, P., Mery, J., Lautredou, N., Divita, G., and Heitz, F. (1998) Design of carrier peptide-oligonucleotide conjugates with rapid membrane translocation and nuclear localization properties. *Biochem. Biophys. Res. Commun. 243*, 601–608.
(28) Fisher, A. A., Sergueev, D. S., Fisher, M., Shaw, B. R., and Juliano, R. L. (2000) Antisense inhibition of P-glycoprotein expression using peptide-oligonucleotide conjugates. *Biochem. Pharmacol. 60*, 83–90.
(29) Antopolsky, M., Azhayeva, E., Tengvall, U., Auriola, S., Jääskeläinen, I., Rönkkö, S., Honkakoski, P., Urtti, A., Lönberg, H., and Azhayev, A. (1999) Peptide-oligonucleotide phosphorothioate conjugates with membrane translocation and nuclear localization properties. *Bioconjugate Chem. 10*, 598–606.
(30) Corey, D. R. (1995) 48000-fold acceleration of hybridisation by chemically modified oligonucleotides. *J. Am. Chem. Soc. 117*, 9373–9374.
(31) Vivès, E., and Lebleu, B. (1997) Selective coupling of a highly basic peptide to an oligonucleotide. *Tetrahedron Lett. 38*, 1183–1186.
(32) Prater, C. E., and Miller, P. S. (2004) 3′-Methylphosphonate-modified oligo-2′-*O*-methyl-ribonucleotides and their Tat peptide conjugates: uptake and stability in mouse fibroblasts in culture. *Bioconjugate Chem. 15*, 498–507.
(33) Medintz, I. L., Berti, L., Pons, T., Grimes, A. F., English, D. S., Alessandrini, A., Facci, P., and Mattoussi, H. (2007) A reactive peptidic linker for self-assembling hybrid quantum dot-DNA bioconjugates. *Nano Lett. 7*, 1741–1748.
(34) Tennilä, T., Antopolsky, M., Azhayev, A., and Azhayeva, E. (2008) Peptide-oligonucleotide conjugates form stable and selective complexes with antibody and DNA. *Bioconjugate Chem. 19*, 1361–1367.
(35) Turner, J. J., Williams, D., Owen, D., and Gait, M. J. (2006) Disulfide conjugation of peptides to oligonucleotides and their analogs. In *Current Protocols in Nucleic Acid Chemistry. Supplement 24: Synthesis of Modified Oligonucleotides and Conjugates* (Beaucage, S. L., Ed.) pp 1−21, Chapter 4, Unit 28, John Wiley and Sons, New York.
(36) Turner, J. J., Arzumanov, A. A., and Gait, M. J. (2005) Synthesis, cellular uptake and HIV-1 Tat-dependent trans-activation inhibition activity of oligonucleotide analogues disulphide-conjugated to cell-penetrating peptides. *Nucleic Acids Res. 33*, 27–42.
(37) Corey, D. R. (2004) Synthesis of oligonucleotide-peptide and oligonucleotide-protein conjugates. In *Methods of Molecular Biology. Volume 283: Bioconjugation Protocols: Strategies and Methods* (Niemeyer, C. M., Ed.) pp 197−206, Humana Press, Totowa, NJ.
(38) Chen, C. P., Zhang, L. R., Peng, Y. F., Wang, X. B., Wang, S. Q., and Zhang, L. H. (2003) A concise method for the preparation of peptide and arginine-rich peptide-conjugated antisense oligonucleotide. *Bioconjugate Chem. 14*, 532–538.
(39) Maurel, F., Debart, F., Cavelier, F., Thierry, A. R., Lebleu, B., Vasseur, J. J., and Vivès, E. (2005) Toward high yield synthesis of peptide-oligonucleotide chimera through a disulfide bridge: A simplified method for oligonucleotide activation. *Bioorg. Med. Chem. Lett. 15*, 5084–5087.
(40) Singh, Y., Spinelli, N., Defrancq, E., and Dumy, P. (2006) A novel heterobifunctional linker for facile access to bioconjugates. *Org. Biomol. Chem. 4*, 1413–1419.
(41) Bruick, R. K., Dawson, P. E., Kent, S. B., Usman, N., and Joyce, G. F. (1996) Template-directed ligation of peptides to oligonucleotides. *Chem. Biol. 3*, 49–56.
(42) McMinn, D. L., Matray, T. J., and Greenberg, M. M. (1997) Efficient solution phase synthesis of oligonucleotide conjugates using protected biopolymers containing 3′-terminal alkyl amines. *J. Org. Chem. 62*, 7074–7075.
(43) Dawson, P. E., Muir, T. W., Clark-Lewis, I., and Kent, S. B. H. (1994) Synthesis of proteins by native chemical ligation. *Science 266*, 776–779.
(44) Stetsenko, D. A., and Gait, M. J. (2000) Efficient conjugation of peptides to oligonucleotides by "native ligation. *J. Org. Chem. 65*, 4900–4908.
(45) Stetsenko, D. A., and Gait, M. J. (2000) New phosphoramidite reagents for the synthesis of oligonucleotides containing a cysteine residue useful in peptide conjugation. *Nucleosides, Nucleotides, Nucleic Acids 19*, 1751–1764.
(46) Stetsenko, D. A., and Gait, M. J. (2001) A new "native ligation" procedure for peptide- oligonucleotide conjugation. *Nucleosides, Nucleotides, Nucleic Acids 20*, 801–804.
(47) Kachalova, A. V., Stetsenko, D. A., Romanova, E. A., Tashlitsky, V. N., Gait, M. J., and Oretskaya, T. S. (2002) A new and efficient method for synthesis of 5′-conjugates of oligonucleotides through amide-bond formation on solid phase. *Helv. Chim. Acta 85*, 2409–2416.
(48) Kachalova, A., Zubin, E., Stetsenko, D., Gait, M., and Oretskaya, T. S. (2004) Oligonucleotides with 2′-*O*-carboxymethyl group: synthesis and 2′-conjugation *via* amide bond formation on solid phase. *Org. Biomol. Chem. 2*, 2793–2797.
(49) Kachalova, A. V., Stetsenko, D. A., Gait, M. J., and Oretskaya, T. S. (2004) Synthesis of oligonucleotide 2′-conjugates via amide bond formation in solution. *Bioorg. Med. Chem. Lett. 14*, 801–804.
(50) Viladkar, S. M. (2002) Guanine rich oligonucleotide-amino acid/peptide conjugates: preparation and characterization. *Tetrahedron 58*, 495–502.
(51) Zatsepin, T. S., Stetsenko, D. A., Gait, M. J., and Oretskaya, T. S. (2005) Use of carbonyl group addition-elimination reactions for synthesis of nucleic acid conjugates. *Bioconjugate Chem. 16*, 471–489.
(52) Um, I. H., and Buncel, E. (2000) The origin of the alpha-effect: dissection of ground-state and transition-state contributions. *J. Org. Chem. 65*, 577–582.
(53) Singh, Y., Edupuganti, O. P., Villien, M., Defrancq, E., and Dumy, P. (2005) The oxime bond formation as a useful tool for the preparation of oligonucleotide conjugates. *C. R. Chimie 8*, 789–796.
(54) Spinelli, N., Singh, Y., Defrancq, E., and Dumy, P. (2007) Aldehydic oligonucleotide: a key intermediate for the preparation of oligonucleotide conjugates through oxime bond formation. *Nucleosides, Nucleotides, Nucleic Acids 26*, 883–887.
(55) Forget, D., Boturyn, D., Defrancq, E., Lhomme, J., and Dumy, P. (2001) Highly efficient synthesis of peptide-oligonucleotide conjugates: chemoselective oxime and thiazolidine formation. *Chem.—Eur. J. 7*, 3976–3984.
(56) Podyminogin, M. A., Lukhtanov, E. A., and Reed, M. W. (2001) Attachment of benzaldehyde-modified oligodeoxynucleotide probes to semicarbazide-coated glass. *Nucleic Acids Res. 29*, 5090–5098.

(57) Singh, Y., Defrancq, E., and Dumy, P. (2004) New method to prepare peptide-oligonucleotide conjugates through glyoxylic oxime formation. *J. Org. Chem. 69*, 8544–8546.
(58) Singh, Y., Renaudet, O., Defrancq, E., and, and Dumy, P. (2005) Preparation of a multitopic glyco-peptide-oligonucleotide conjugate. *Org. Lett. 7*, 1359–1362.
(59) Forget, D., Renaudet, O., Boturyn, D., Defrancq, E., and Dumy, P. (2001) 3′-Oligonucleotides conjugation via chemoselective oxime bond formation. *Tetrahedron Lett. 42*, 9171–9174.
(60) Forget, D., Boturyn, D., Renaudet, O., Defrancq, E., and Dumy, P. (2003) Highly efficient synthesis of peptide- and carbohydrate-oligonucleotide conjugates using chemoselective oxime and thiazolidine formation. *Nucleosides, Nucleotides, Nucleic Acids 22*, 1427–1429.
(61) Villien, M., Defrancq, E., and Dumy, P. (2004) Chemoselective oxime and thiazolidine bond formation: a versatile and efficient route to the preparation of 3′-peptide-oligonucleotide conjugates. *Nucleosides, Nucleotides, Nucleic Acids 23*, 1657–1666.
(62) Spinelli, N., Edupuganti, O., Defrancq, E., and Dumy, P. (2007) New solid support for the synthesis of 3′-oligonucleotide conjugates through glyoxylic oxime bond formation. *Org. Lett. 9*, 219–222.
(63) Edupuganti, O. P., Renaudet, O., Defrancq, E., and Dumy, P. (2004) The oxime bond formation as an efficient chemical tool for the preparation of 3′,5′-bifunctionalised oligodeoxyribonucleotides. *Bioorg. Med. Chem. Lett. 14*, 2939–2842.
(64) Edupuganti, O. P., Singh, Y., Defrancq, E., and Dumy, P. (2004) New strategy for the synthesis of 3′,5′-bifunctionalized oligonucleotide conjugates through sequential formation of chemoselective oxime bonds. *Chem.—Eur. J. 10*, 5988–5995.
(65) Dey, S., and Sheppard, T. L. (2001) Ketone-DNA: a versatile postsynthetic DNA decoration platform. *Org. Lett. 3*, 3983–3986.
(66) Hamma, T., and Miller, P. S. (2003) 4-(2-Aminooxyethoxy)-2-(ethylureido)quinoline-oligonucleotide conjugates: synthesis, binding interactions, and derivatization with peptides. *Bioconjugate Chem. 14*, 320–330.
(67) Ghosh, S., Defrancq, E., Lhomme, J. H., Dumy, P., and Bhattacharya, S. (2004) Efficient conjugation and characterization of distamycin-based peptides with selected oligonucleotide stretches. *Bioconjugate Chem. 15*, 520–529.
(68) Ollivier, N., Olivier, C., Gouyette, C., Tam, H.-D., Gras-Masse, H., and Melnyk, O. (2002) Synthesis of oligonucleotide-peptide conjugates using hydrazone chemical ligation. *Tetrahedron Lett. 43*, 997–999.
(69) Far, S., Gouyette, C., and Melnyk, O. (2005) A novel phosphoramidite for the synthesis of α-oxo aldehyde-modified oligodeoxynucleotides. *Tetrahedron 61*, 6138–6142.
(70) Zubin, E. M., Romanova, E. A., Volkov, E. M., Tashlitsky, V. N., Korshunova, G. A., Shabarova, Z. A., and Oretskaya, T. S. (1999) Oligonucleotide-peptide conjugates as potential antisense agents. *FEBS Lett. 456*, 59–62.
(71) Hwang, J.-T., and Greenberg, M. M. (1999) Synthesis of modified oligodeoxyribonucleotides on a solid-phase support via derivatization of a selectively revealed 2′-amino-2′-deoxyuridine. *Org. Lett. 1*, 2021–2024.
(72) Hwang, J.-T., and Greenberg, M. M. (2001) Synthesis of 2′-modified oligodeoxynucleotides via on-column conjugation. *J. Org. Chem. 66*, 363–369.
(73) Hendrix, C., Devreese, B., Rozenski, J., van Aershot, A., De Bruyn, A., van Beeumen, J., and Herdewijn, P. (1995) Incorporation of 2′-amido-nucleosides in oligodeoxynucleotides and oligoribonucleotides as a model for 2′-linked conjugates. *Nucleic Acids Res. 23*, 51–57.
(74) Zatsepin, T. S., Stetsenko, D. A., Arzumanov, A. A., Romanova, E. A., Gait, M. J., and Oretskaya, T. S. (2002) Synthesis of peptide-oligonucleotide conjugates with single and multiple peptides attached to 2′-aldehydes through thiazolidine, oxime, and hydrazine linkages. *Bioconjugate Chem. 13*, 822–830.
(75) Zubin, E. M., Stetsenko, D. A., Zatsepin, T. S., Gait, M. J., and Oretskaya, T. S. (2005) Oligonucleotides containing 2′-*O*-[2-(2,3-dihydroxypropyl)amino-2-oxoethyl]uridine as suitable precursors of 2′-aldehyde oligonucleotides for chemoselective ligation. *Bioorg. Med. Chem. 13*, 4912–4920.
(76) Zatsepin, T. S., Gait, M. J., Oretskaya, T. S., and Stetsenko, D. A. (2006) Synthesis of 2′-hydrazine oligonucleotides and their eĉient conjugation with aldehydes and 1,3-diketones. *Tetrahedron lett. 47*, 5515–5518.
(77) Grandas, A., Robles, J., and Pedroso, E. (1995) Phosphitylation of primary carboxamides synthesis of peptide-oligonucleotide conjugates with acylphosphoramidate linkages. *Nucleosides, Nucleotides 14*, 825–828.
(78) Anno, Y., Kubo, T., Ueki, R., Yano, M., Sasaki, K., Ohba, H., and Fujii, M. (2003) Synthesis of DNA conjugates by solid phase fragment condensation. *Nucleosides, Nucleotides, Nucleic Acids 22*, 1451–1453.
(79) Kubo, T., Morikawa, M., Ohba, H., and Fujii, M. (2003) Synthesis of DNA-peptide conjugates by solid phase fragment condensation. *Org. Lett. 5*, 2623–2626.
(80) Kubo, T., Zhelev, Z., Rumiana, B., Ohba, H., Doi, K., and Fujii, M. (2005) Controlled intracellular localization and enhanced antisense effect of oligonucleotides by chemical conjugation. *Org. Biomol. Chem. 3*, 3257–3259.
(81) Sakakura, A., and Hayakawa, Y. (2000) A novel synthesis of oligonucleotide-peptide conjugates with a base-labile phosphate linker between the two components according to the allyl-protected phosphoramidite strategy. *Tetrahedron 56*, 4427–4435.
(82) Jaschke, A., and Seelig, B. (1997) Site-specific modification of enzymatically synthesized RNA: transcription initiation and Diels-Alder reaction. *Tetrahedron Lett. 38*, 7729–7732.
(83) Hill, K. W., Taunton-Rigby, J., Carter, J. D., Kropp, E., Vagle, K., Pieken, W., McGee, D. P. C., Husar, G. M., Leuck, M., Anziano, D. J., and Sebesta, D. P. (2001) Diels-Alder bioconjugation of diene-modified oligonucleotides. *J. Org. Chem. 66*, 5352–5358.
(84) Graham, D., Grondin, A., McHugh, C., Fruk, L., and Smith, W. E. (2002) Internal labeling of oligonucleotide probes by Diels-Alder cycloaddition. *Tetrahedron Lett. 43*, 4785–4788.
(85) Picken, D. J. (2000) Oligonucleotide conjugation. *PCT Int. Appl.* 38.
(86) Marchan, V., Ortega, S., Pulido, D., Pedroso, E., and Grandas, A. (2006) Diels-Alder cycloadditions in water for the straightforward preparation of peptide-oligonucleotide conjugates. *Nucleic Aids Res. 34*, e24.
(87) Borsenberger, V., and Howorka, S. (2009) Diene-modified nucleotides for the Diels-Alder-mediated functional tagging of DNA. *Nucleic Acids Res. 37*, 1477–1485.
(88) Kolb, H. C., Finn, M. G., and Sharpless, K. B. (2001) Click chemistry: diverse chemical function from a few good reactions. *Angew. Chem., Int. Ed. 40*, 2004–2021.
(89) Bock, V. D., Hiemstra, H., and Van Maarseveen, J. H. (2006) Cu(I)-catalyzed alkyne-azide "click" cycloadditions from a mechanistic and synthetic perspective. *Eur. J. Org. Chem. 1*, 51–68.
(90) Gramlich, P. M. E., Wirges, C. T., Manetto, A., and Carell, T. (2008) Postsynthetic DNA modification through the copper-catalyzed azide-alkyne cycloaddition reaction. *Angew. Chem., Int. Ed. 47*, 8350–8358.
(91) Gogoi, K., Mane, M. V., Kunte, S. S., and Kumar, V. A. (2007) A versatile method for the preparation of conjugates of peptides with DNA/PNA/analog by employing chemo-selective click reaction in water. *Nucleic Acids Res. 35*, e139.
(92) Seo, T. S., Li, Z., Ruparel, H., and Ju, J. (2003) Click chemistry to construct fluorescent oligonucleotides for DNA sequencing. *J. Org. Chem. 68*, 609–612.
(93) Grandas, A., Marchan, V., Debethune, L., Pedroso, E. (2007) Stepwise solid-phase synthesis of nucleopeptides. In *Current Protocols in Nucleic Acid Chemistry. Supplement 31: Synthesis of Modified Oligonucleotides and Conjugates* (Beaucage, S. L., Ed.) pp 1−54, Chapter *4*, Unite 22, John Wiley and Sons, New York.

(94) Lönnberg, H. (2009) Solid-phase synthesis of oligonucleotide conjugates useful for delivery and targeting of potential nucleic acid therapeutics. *Bioconjugate Chem. 20*, 1065–1094.
(95) Delatorre, B. G. , Avino, A., Tarrason, G., Piulats, J., Albericio, F., and, and Eritja, R. (1994) Stepwise solid-phase synthesis of oligonucleotide-peptide hybrids. *Tetrahedron Lett. 35*, 2733–2736.
(96) Soukchareun, S., Tregear, G. W., and Haralambidis, J. (1995) Preparation and characterization of antisense oligonucleotide-peptide hybrids containing viral fusion peptides. *Bioconjugate Chem. 6*, 43–53.
(97) Robles, J., Maseda, M., Beltran, M., Concernau, M., Pedroso, E., and Grandas, A. (1997) Synthesis and enzymatic stability of phosphodiester-linked peptide-oligonucleotide hybrids. *Bioconjugate Chem. 8*, 785–788.
(98) Haralambidis, J., Duncan, L., and Tregear, G. W. (1987) The solid phase synthesis of oligonucleotides containing a 3′-peptide moiety. *Tetrahedron Lett. 28*, 5199–5202.
(99) Haralambidis, J., Duncan, L., Angus, K., and Tregear, G. W. (1990) The synthesis of polyamide-oligonucleotide conjugate molecules. *Nucleic Acids Res. 18*, 493–499.
(100) Haralambidis, J., Angus, K., Pownall, S., Duncan, L., Chai, M., and GW, Tregear. (1990) The preparation of polyamide-oligonucleotide probes containing multiple non-radioactive labels. *Nucleic Acids Res. 18*, 501–505.
(101) Juby, C. D., Richardson, C. D., and Brousseau, R. (1991) Facile preparation of 3′ oligonucleotide-peptide conjugates. *Tetrahedron Lett. 32*, 879–882.
(102) Tong, G., Lawlor, J. M., Tregear, G. W., and Haralambidis, J. (1993) The synthesis of oligonucleotide-polyamide conjugate molecules suitable as PCR primers. *J. Org. Chem. 58*, 2223–2231.
(103) Robles, J., Pedroso, E., and Grandas, A. (1994) Stepwise solid-phase synthesis of the nucleopeptide Phac-Phe-Val-Ser(p3′ACT)-Gly-OH. *J. Org. Chem. 59*, 2482–2486.
(104) Truffert, J. C., Lorthioir, O., Asseline, U., Thuong, N. T., and Brack, A. (1994) On-line solid phase synthesis of oligonucleotide-peptide hybrids using silica supports. *Tetrahedron Lett. 35*, 2353–2356.
(105) Tong, G., Lawlor, J. M., Tregear, G. W., and Haralambidis, J. (1995) Oligonucleotide-polyamide hybrid molecules containing multiple pyrene residues exhibit significant excimer fluorescence. *J. Am. Chem. Soc. 117*, 12151–12158.
(106) Truffert, J. C., Asseline, U., Brack, A., and Thuong, N. T. (1996) Synthesis, purification and characterization of two peptide-oligonucleotide conjugates as potential artificial nucleases. *Tetrahedron 52*, 3005–3016.
(107) Beltran, M., Pedroso, E., and Grandas, A. (1998) A comparison of histidine protecting groups in the synthesis of peptide-oligonucleotide conjugates. *Tetrahedron Lett. 39*, 4115–4118.
(108) Antopolsky, M., and Azhayev, A. (1999) Stepwise solid-phase synthesis of peptide-oligonucleotide conjugates on new solid supports. *Helv. Chim. Acta 82*, 2130–2140.
(109) Antopolsky, M., Azhayeva, E., Tengvall, U., and Azhayev, A. (2002) Towards a general method for the stepwise solid-phase synthesis of peptide-oligonucleotide conjugates. *Tetrahedron Lett. 43*, 527–530.
(110) Chen, C.-P., Li, X.-X., Zhang, L.-R., Min, J.-M., Chan, J. Y.-W., Fung, K.-P., Wang, S.-Q., and Zhang, L.-H. (2002) Synthesis of antisense oligonucleotide-peptide conjugate targeting to GLUT-1 in HepG-2 and MCF-7 cells. *Bioconjugate Chem. 13*, 525–529.
(111) Terenzi, S., Biala, E., Nguyen-Trung, N. Q., and Strazewski, P. (2003) Amphiphilic 3′-peptidyl-RNA conjugates. *Angew. Chem., Int. Ed. 42*, 2909–2912.
(112) Antopolsky, M., and Azhayev, A. (2000) Stepwise solid-phase synthesis of peptide-oligonucleotide phosphorothioate conjugates employing Fmoc peptide chemistry. *Tetrahedron Lett. 41*, 9113–9117.
(113) Zaramella, S., Yeheskiely, E., and Stromberg, R. (2004) A method for solid-phase synthesis of oligonucleotide 5′-peptide-conjugates using acid-labile α-amino protections. *J. Am. Chem. Soc. 126*, 14029–14035.
(114) Tetzlaff, C. N., Schwope, I., Bleczinski, C. F., Steinberg, J. A., and Richert, C. (1998) A convenient synthesis of 5′-amino-5′-deoxythymidine and preparation of peptide-DNA hybrids. *Tetrahedron Lett. 39*, 4215–4218.
(115) Sarracino, D. A., Steinberg, J. A., Vergo, M. T., Woodworth, G. F., Tetzlaff, C. N., and Richert, C. (1998) 5′-Peptidyl substituents allow a tuning of the affinity of oligodeoxyribonucleotides for RNA. *Bioorg. Med. Chem. Lett. 8*, 2511–2516.
(116) Bergmann, F., and Bannwarth, W. (1995) Solid phase synthesis of directly linked peptide-oligodeoxynucleotide hybrids using standard synthesis protocols. *Tetrahedron Lett. 36*, 1839–1842.
(117) Marchan, V., Rodriguez-Tanty, C., Estrada, M., Pedroso, E., and Grandas, A. (2000) Alternative procedures for the synthesis of methionine-containing peptide-oligonucleotide hybrids. *Eur. J. Org. Chem. 13*, 2495–2500.
(118) Miller, G. P., and Kool, E. T. (2004) Versatile 5′-functionalization of oligonucleotides on solid support: amines, azides, thiols, and thioethers via phosphorus chemistry. *J. Org. Chem. 69*, 2404–2410.
(119) Ocampo, S. M., Albercio, F., Fernandez, I., Vilaseca, M., and Eritja, R. (2005) A straightforward synthesis of 5′-peptide oligonucleotide conjugates using N_α-Fmoc-protected amino acids. *Org. Lett. 7*, 4349–4352.
(120) Winkler, J., Urban, E., and Noe, C. R. (2005) Oligonucleotides conjugated to short lysine chains. *Bioconjugate Chem. 16*, 1038–1044.
(121) Adamo, I., Ballico, M., Campaner, P., Drioli, S., and Bonora, G. M. (2004) Interchangeable PEG-supported synthesis of peptide-oligonucleotide chimeras. *Eur. J. Org. Chem.* 2603–2609.
(122) Frieden, M., Avino, A., Tarrason, G., Escorihuela, M., Piulats, J., and Eritja, R. (2004) Synthesis of oligonucleotide-peptide conjugates carrying the c-*myc* peptide epitope as recognition system. *Chem. Biodiversity 1*, 930–938.
(123) Lin, Y., Padmapriya, A., Morden, K. M., and Jayasena, S. D. (1995) Peptide conjugation to an in vitro-selected DNA ligand improves enzyme inhibition. *Proc. Natl. Acad. Sci. U.S.A. 92*, 11044–11048.
(124) Robles, J., Pedroso, E., and Grandas, A. (1991) Solid phase synthesis of a model nucleopeptide with a phosphodiester bond between the 5′ end of a trinucleotide and a serine residue. *Tetrahedron Lett. 32*, 4389–4392.
(125) De Napoli, L., Messere, A., Montesarchio, D., Piccialli, G., Benedetti, E., Bucci, E., and Rossi, F. (1999) A new solid-phase synthesis of oligonucleotides 3′-conjugated with peptides. *Bioorg. Med. Chem. 7*, 395–400.
(126) De Champdore, M., De Napoli, L., Di Fabio, G., Messere, A., Montesarchio, D., and Piccialli, G. (2001) New nucleoside based solid supports. Synthesis of 5′ 3′ -derivatized thymidine analogues. *Chem. Commun.* 2598–2599.
(127) Waldmann, H. (1997) Chemoenzymatic synthesis of nucleopeptides. *Chem. Commun.* 1861–1862.
(128) Flohr, S., Jungmann, V., and Waldmann, H. (1999) Chemoenzymatic synthesis of nucleopeptides. *Chem.—Eur. J. 5*, 669–681.
(129) Pradeepkumar, P. I., Hobartner, C., Baum, D. A., and Silverman, S. K. (2008) DNA-catalyzed formation of nucleopeptide linkages. *Angew. Chem., Int. Ed. 47*, 1753–1757.
(130) Gait, M. J. (2003) Peptide-mediated cellular delivery of antisense oligonucleotides and their analogues. *Cell. Mol. Life Sci. 60*, 844–853.
(131) Lochmanna, D., Jaukb, E., and Zimmer, A. (2004) Drug delivery of oligonucleotides by peptides. *Eur. J. Pharm. Biopharm. 58*, 237–251.
(132) Veldhoen, S., Laufer, S. D., and Restle, T. (2008) Recent developments in peptide-based nucleic acid delivery. *Int. J. Mol. Sci. 9*, 1276–1320.
(133) Vivès, E., Schmidt, J., and Pèlegrin, A. (2008) Cell-penetrating and cell-targeting peptides in drug delivery. *Biochim. Biophys. Acta Rev. Cancer 1786*, 126–138.

(134) Leonetti, J.-P., Degols, G. , and Lebleu, B. (1990) Biological activity of oligonucleotide-poly(L-lysine) conjugates: mechanism of cell uptake. *Bioconjugate Chem. 1*, 149–153.
(135) Corey, D. R. (1995) 48000-fold acceleration of hybridization by chemically modified oligonucleotides. *J. Am. Chem. Soc. 117*, 9373–9374.
(136) Polushin, N. N., Chen, B. C., Anderson, L. W., and Cohen, J. S. (1993) Synthesis and characterization of imidazoyl-linked synthons and 3′-conjugated thymidine derivatives. *J. Org. Chem. 58*, 4606–4613.
(137) Bashkin, J. K., Gard, J. K., and Modak, A. S. (1990) Synthesis and characterization of nucleoside peptides: toward chemical ribonucleases. *J. Org. Chem. 55*, 5125–5132.
(138) Nielsen, J., Brenner, S., and Janda, K. D. (1993) Synthetic methods for the implementation of encoded combinatorial chemistry. *J. Am. Chem. Soc. 115*, 9812–9813.
(139) Brenner, S., and Lerner, R. A. (1992) Encoded combinatorial chemistry. *Proc. Natl. Acad. Sci. U.S.A. 89*, 5381–5383.
(140) Berlin, K., Jain, R. K., Tetzlaff, C., Steinberg, C., and Richert, C. (1997) Spectrometrically monitored selection experiments: quantitative laser desorption mass spectrometry of small chemical libraries. *Chem. Biol. 4*, 63–77.
(141) Stetsenko, D. A., Malakhov, A. D., and Gait, M. J. (2002) Total stepwise solid-phase synthesis of oligonucleotide-(3′→*N*)-peptide conjugates. *Org. Lett. 4*, 3259–3262.

BC900158S

Delivery of NADPH-Cytochrome P450 Reductase Antisense Oligos Using Avidin−Biotin Approach

Venkateswaran C. Pillai,[†] Rekha Yesudas,[‡] Imam H. Shaik,[†] Thomas J. Thekkumkara,[‡] Ulrich Bickel,[†] Kalkunte S. Srivenugopal,[‡] and Reza Mehvar*,[†]

Department of Pharmaceutical Sciences and Department of Biomedical Sciences, School of Pharmacy, Texas Tech University Health Sciences Center, 1300 Coulter, Amarillo, Texas 79106. Received October 14, 2009; Revised Manuscript Received December 21, 2009

Although avidin-mediated intracellular delivery of oligonucleotides or proteins has been shown before, the efficacy studies are lacking. Here, we tested the effectiveness of avidin for delivery of a cytochrome P450 reductase (CPR) antisense oligo in rat liver epithelial cells. A phosphorodiamidate morpholino oligo (PMO) against CPR was biotinylated using four reagents with short, cleavable, or long linkers, followed by conjugation with avidin. The dose-inhibitory response of the unmodified PMO in the presence of a transfection reagent (Endoporter, EP) and the effectiveness of the EP-assisted and avidin-assisted delivery of biotinylated PMOs were tested by Western blot analysis. Additionally, in a preliminary study, the avidin−biotin PMO with a long linker was also tested in vivo in rats. The biotinylated oligos were at least as effective as the unmodified oligo. Whereas the avidin conjugate of biotinylated PMO with the short linker was ineffective, those with the long linkers showed significant reductions in CPR protein expression. Finally, the in vivo study showed modest, but significant, reductions in CPR activity. In conclusion, these studies show for the first time that avidin-mediated intracellular delivery of biotinylated oligos can effectively knock down target genes in vitro, depending on the length of the linker. Additionally, the avidin−biotin approach may be of potential value for in vivo gene knockdown.

NADPH-cytochrome P450 reductase (CPR) is a flavoprotein first identified in the liver by Horecker in 1950 (*1*) as a cytochrome c reductase. The key function of CPR is to donate electrons mainly to cytochrome P450 enzymes. It has been reported (*2*−*5*) that CPR can generate reactive oxygen species (ROS) by direct and indirect mechanisms. The direct mechanisms include the generation of superoxide (*3*) and redox cycling of cellular Fe^{3+} (*2, 3*) and quinones/quinoid compounds (*5*) to generate hydroxyl radicals and free semiquinone radicals, respectively. Additionally, CPR contributes to generation of superoxide and hydrogen peroxide indirectly via uncoupling mechanism of the cytochrome P450 monoxygenases system (*6, 7*). Indeed, CPR has been suggested as a potential source of endogenous oxidative stress and DNA damage (*8*). Hence, CPR inhibition may reduce ROS generation and oxidative stress in different diseases of the liver.

In mammals, the expression of liver CPR is regulated by thyroid hormone (*9*−*11*). It has been reported that depletion of thyroid hormone by hypophysectomy (*9*) or treatment with the antithyroid drugs methimazole (*9*) or propylthiouracil (*11*) significantly reduces CPR activity and protein in the liver, an effect that is reversed by thyroxine therapy. However, manipulation of thyroid hormone levels is considered a nonspecific method of CPR inhibition because it affects a number of other physiological processes. Additionally, chemical inhibitors of CPR, such as diphenyleneiodonium (*12*) and α-lipoic acid (*13*), usually exert other nonspecific effects. On the other hand, inhibition of protein expression using antisense oligos or by RNA interference could potentially be relatively specific (*14*). Therefore, we chose to use the latter approach in our studies by applying a phosphorodiamidate morpholino oligo (PMO) (*15*) against CPR. PMOs are among the modified DNA analogues that block the translation initiation through an RNase-H independent process (*15, 16*). The modification of DNA in PMOs include replacement of deoxyribose sugars by morpholine and the charged phosphodiester linkages by nonionic phosphorodiamidate linkages (*15*). Consequently, PMOs are neutral and resistant to degradation by nucleases. Additionally, in contrast to phosphorothioates, which are known to bind nonspecifically to extracellular, cell surface, and intracellular proteins, PMOs exhibit little or no nonspecific protein binding (*15, 16*).

Because of their large size and physicochemical properties, unassisted delivery of antisense oligos into the cells is usually very limited after both in vitro and in vivo applications (*17*−*20*). Consequently, different methods, such as viral and nonviral vectors, have been used to improve their cellular delivery and effects. One of these methods is the use of avidin as a cationic carrier for delivery of biotinylated oligos (*21*−*24*). This method is based on the high-affinity binding of avidin to biotin (*25*) and entry of the avidin-bound cargo to the cell by endocytosis (*21*). Indeed, previous studies showed that the avidin−biotin approach can deliver antisense oligos or peptides to the isolated bovine capillaries in vitro (*21*) or antisense oligos to the liver of rodents in vivo (*23, 24*). However, we are not aware of any studies demonstrating that such an approach can indeed result in gene knockdown. Therefore, our main aim for the current study was to investigate the effectiveness of the avidin−biotin approach for delivery of a PMO antisense against CPR to a rat liver cell model. Because the binding of the avidin−biotinylated antisense to the target mRNA may be affected by the linker between biotin and antisense, we also tested the effects of linker length and cleavability on the effectiveness of the conjugates. Finally, the effectiveness of such an approach was tested in a

* Corresponding authors Reza Mehvar, Ph.D., School of Pharmacy, Texas Tech University Health Sciences Center, 1300 Coulter, Amarillo, TX 79106; Phone: (806) 356-4015 Ext. 337; FAX: (806) 356-4034; e-mail: reza.mehvar@ttuhsc.edu.

[†] Department of Pharmaceutical Sciences.

[‡] Department of Biomedical Sciences.

10.1021/bc900449b © 2010 American Chemical Society
Published on Web 01/11/2010

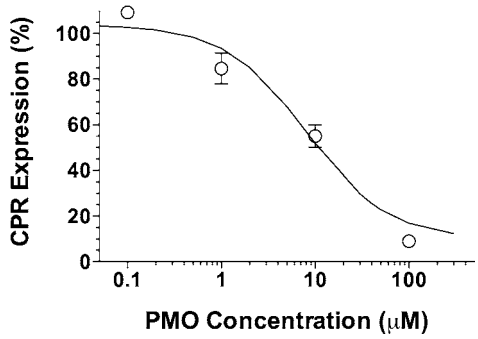


Figure 1. Relationship between the concentrations of unmodified PMO and CPR protein expression in rat liver epithelial cells. Cells were incubated with different concentrations of PMO in the presence of a 2 μM concentration of the transfection reagent Endoporter for 48 h. CPR expression was determined in the cell lysate by Western blot analysis. Symbols and bars represent experimental mean and SD (n = 3), respectively, and the line represents the model fitted relationship.

preliminary in vivo study in rats. Details of the experimental procedures are available in the Supporting Information.

Rat liver epithelial (WB-F344) cells (*26*, *27*) were incubated for 48 h in the presence of 0.0, 0.1, 1, 10, and 100 μM concentrations of a 25-mer phosphorodiamidate morpholino oligo (PMO) against CPR and 2 μM of an in vitro transfection reagent (Endoporter, EP). Afterward, cells were lysed, and the lysate was used for CPR protein analysis using Western blotting method. Unmodified PMO showed dose-dependent decreases in CPR protein expression (Figure 1). Whereas a 0.1 μM concentration of PMO showed no inhibition of CPR, a 100 μM concentration inhibited CPR protein expression by ~90%. The nonlinear regression fit to the data revealed an IC_{50} value of 8.05 μM and a maximum inhibition of 94.0% for the unmodified PMO in the presence of EP transfection reagent.

Next, four different linkers (L1, L2, L3, and L4; Figure 2) were used to biotinylate the PMO against CPR. The biotinylated PMOs were characterized before and after retention of the biotinylated moiety on an avidin affinity column. The pre- and post-avidin column samples were then subjected to size exclusion HPLC to quantitate the degree of biotinylation. Figure 3 shows the chromatograms of the biotinylated PMO with the L1 linker before (Figure 3A) and after (Figure 3B) passage through the avidin column. The difference between the post-column and precolumn peak areas reflects the biotinylated fraction retained on the avidin column. The percentages of biotinylation, estimated from the postcolumn and precolumn samples, analyzed in triplicate, were 80.8, 74.9, 86.6, and 87.9 for the samples with L1, L2, L3, and L4 linkers, respectively.

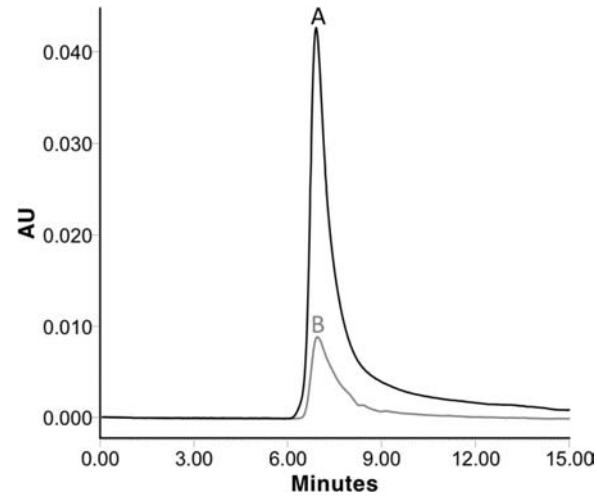


Figure 3. Representative chromatograms of a biotinylated PMO with linker 1 before (A) and after (B) passage through an avidin column that retains the biotinylated PMO. Chromatograms A and B represent the total (biotinylated plus free PMO) and free PMO, respectively.

These data indicate a relatively high degree of biotinylation with relatively small differences among biotinylation reagents with different linkers.

To determine the effect of biotinylation of PMO on its antisense effect, a 5 μM concentration of PMO biotinylated with L1 (PMO-L1-Biotin), L2 (PMO-L2-Biotin), L3 (PMO-L3-Biotin), or L4 (PMO-L4-Biotin) was incubated with WB cells for 48 h in the presence of EP. Additionally, unmodified PMO and invert PMO were used for comparison. As demonstrated in Figure 4, all four biotinylated PMOs inhibited CPR protein expression at least as effectively as the unmodified PMO (Figure 4). Interestingly, the biotinylated PMOs with the L1 (PMO-L1-Biotin) and L4 (PMO-L4-Biotin) linkers showed significantly (P <0.01 and <0.05, respectively) higher inhibition of CPR expression, compared with the unmodified PMO (Figure 4). As expected, the invert PMO did not significantly affect the CPR protein expression.

To determine the effectiveness of avidin for delivery of the biotinylated PMO, biotinylated PMOs were conjugated with avidin at a 1:1 molar ratio. The avidin conjugated biotinylated PMOs (5 μM) with L1 (PMO-L1-Biotin:Avidin), L2 (PMO-L2-Biotin:Avidin), L3 (PMO-L3-Biotin:Avidin), or L4 (PMO-L4-Biotin:Avidin) linkers were then incubated with WB cells for 48 h in the absence of the transfection reagent EP. Whereas avidin-conjugated biotinylated PMO with the short linker (L1) did not show any inhibitory effect, the two conjugates with the

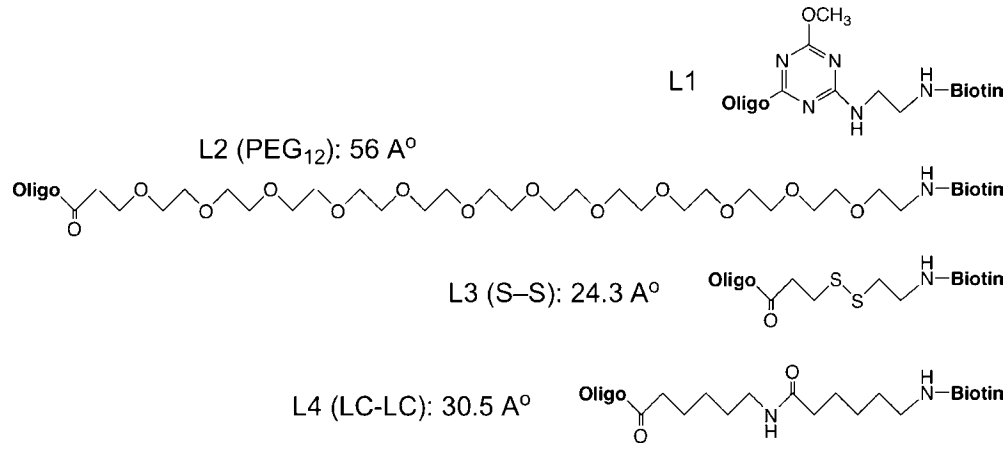


Figure 2. Chemical structures of various biotinylated linkers used in this study.

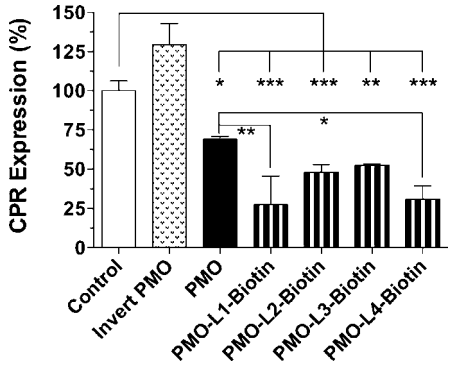


Figure 4. Effects of biotinylation with reagents containing linkers 1−4 on the inhibition of CPR protein expression by PMO in rat liver epithelial cells. Cells were incubated with a 5 μM concentration of PMO in the presence of a 2 μM concentration of the transfection reagent Endoporter for 48 h. CPR expression was determined in the cell lysate by Western blot analysis. Columns and bars represent mean and SD (n = 3), respectively. *P < 0.05, **P < 0.01, and ***P < 0.001 (one-way ANOVA, followed by Tukey's post hoc analysis).

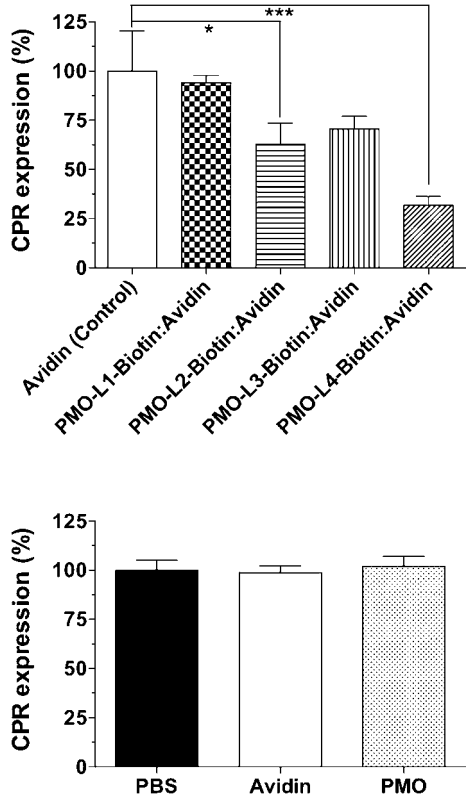


Figure 5. Effects of avidin-mediated delivery of PMO biotinylated with reagents containing linkers 1−4 on the inhibition of CPR protein expression in rat liver epithelial cells. Cells were incubated with a 5 μM concentration of avidin alone (control) or avidin−biotin PMOs (top) or with phosphate buffered saline (PBS) or a 5 μM concentration of avidin alone or PMO alone (bottom) in the absence of the transfection reagent Endoporter for 48 h. CPR expression was determined in the cell lysate by Western blot analysis. Columns and bars represent mean and SD (n = 3), respectively. *P < 0.05 and ***P < 0.001 (one-way ANOVA, followed by Tukey's post hoc analysis).

long linkers (L2 and L4) showed significant reductions in CPR protein expression (P < 0.05 and P < 0.001, respectively) (Figure 5, top). As for the conjugate with the cleavable linker (L3), the reduction in the CPR protein expression did not reach statistical significance. Overall, among all the tested conjugates, the avidin-conjugated biotinylated PMO with L4 showed the highest degree of CPR protein inhibition (∼70%). Control experiments with

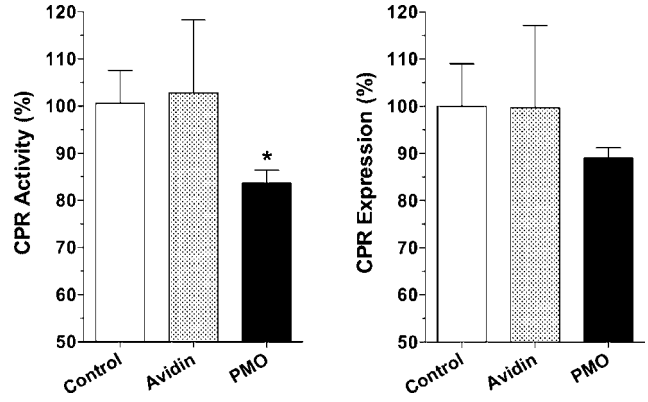


Figure 6. Microsomal CPR activity (left) and expression (right) in rat livers after intravenous administration of vehicle (control), 40 mg/kg/day of avidin (Avidin), or 5 mg/kg/day of PMO-L4-Biotin:Avidin (PMO) for 3 days. Microsomal CPR expression and activity were determined 24 h after the last dose. Columns and bars represent mean and S.D., respectively (n = 8 for the control group and 4 for the avidin and PMO groups). * Significant difference (P < 0.05, one-way ANOVA, followed by Tukey's post hoc analysis) between PMO and control and between PMO and avidin.

phosphate-buffered saline (PBS), avidin alone, and PMO alone demonstrated that neither PMO alone in the absence of any transfection reagent nor avidin alone had any suppressive effects on CPR expression (Figure 5, bottom).

Finally, in a preliminary study, male Sprague−Dawley rats (75−100 g) were treated intravenously with vehicle, avidin (40 mg/kg), or 5 mg/kg/day doses of PMO-L4-Biotin:Avidin for 3 days and the microsomal CPR activity (*28*) and protein expression were determined. The avidin-conjugated PMO showed (Figure 6) modest, but significant, reductions in the rat liver microsomal CPR activity, relative to the control (17% decline) and Avidin (19% decline) groups. As for the CPR protein contents, an 11% reduction in the PMO group, compared with the control or Avidin group, did not reach statistical significance using multiple comparisons.

One of the main hurdles in the CPR research is that there are no specific chemical inhibitors for this protein to be used for delineation of its role in oxidative injury. Hence, we sought to use the antisense approach in this study to specifically inhibit the translation of CPR at its mRNA level. Our dose−response data (Figure 1) using the PMO against CPR showed a dose-dependent inhibition of CPR in WB cells with an IC_{50} of 8 μM and 90% inhibition of CPR at a concentration of 100 μM (Figure 1). However, the reported (*29*) turnover half-life of CPR in rat liver microsomes is 29−35 h, which suggests that a complete inhibition of protein expression is expected to result in a maximum of 70% decline in the protein levels after 48 h of incubation. Therefore, a higher degree of inhibition observed after the PMO concentration of 100 μM (∼90%, Figure 1) suggests that the PMO antisense used in our study may exert some nonspecific effects at this high concentration.

To use avidin as a carrier, the antisense oligos are first biotinylated to take advantage of the high-affinity binding of avidin to biotin, which has a dissociation half-life of 89 days (*25*). Because biotinylation of antisense oligos may alter their physicochemical properties and binding to the target mRNA, we studied the effects of biotinylation with different linkers on the CPR inhibitory effect of our PMO antisense. Biotinylation of PMO not only did not adversely affect the inhibition of CPR expression, but also caused an improvement of their effects in the case of PMO-L1-Biotin and PMO-L4-Biotin (Figure 4). The reasons for this improvement are not clear from our studies. However, possible explanations could be an improvement in

the EP-mediated delivery of the PMO antisense to the cytosol and/or improved binding of the PMO to the target mRNA as a result of biotinylation. These results are in agreement with those reported by Boado and Pardridge (*22*) who showed that RNase H caused degradation of *tat* sense RNA in the presence of a biotinylated phosphodiester antisense oligo against *tat*. However, they did not compare the efficacy of the biotinylated oligo with that of nonbiotinylated oligo. Nevertheless, our studies appear to be the first examination of the effects of biotinylation on the inhibitory activity of PMO oligos.

An in vitro study using isolated bovine capillaries (*21*) showed that avidin acts as a carrier for cellular uptake of a biotinylated antisense oligonucleotide or a model peptide. It was suggested that the avidin-mediated uptake is associated with endocytosis and is based on the cationic nature of the avidin protein. Additionally, a more recent study (*24*) showed that a radiolabeled biotinylated oligo conjugated to avidin was internalized into the mouse hepatocytes without the assistance of transfection reagents. However, neither of these studies reported the effects of the antisense or peptide. When we first tested the inhibitory effects of an avidin conjugate of the commercially available biotinylated PMO against CPR (PMO-L1-Biotin:Avidin) in our WB cells, we were disappointed by the lack of inhibitory effect of this conjugate (Figure 5). Because the linker between biotin and PMO was short (L1, Figure 2), we hypothesized that this lack of effect is due to the steric hindrance of avidin, impeding the interaction of the oligo with its target mRNA. Therefore, in a subsequent study, we biotinylated our PMO with reagents that contained long (L2 and L4) or cleavable (−S−S−) linkers (Figure 2). In agreement with our hypothesis, all these linkers inhibited the CPR expression, although the reduction did not reach statistical significance with the cleavable linker (L3; Figure 5). Interestingly, CPR inhibition with the avidin-mediated delivery of PMO with L2 or L4 linkers (Figure 5) was as effective as or more effective than the inhibitory effect observed with the EP-mediated delivery of the unmodified PMO (Figure 4). These results suggest that avidin-mediated delivery using appropriate linkers may be an alternative approach to transfection reagents in the intracellular delivery of PMOs in vitro.

Although the in vivo distribution of avidin conjugates of biotinylated oligos has been reported previously in rodents (*23, 24*), we are not aware of any in vivo studies testing the inhibitory effects of these conjugates. The previously reported distribution studies (*23, 24*) suggested high accumulation of the conjugates in the liver. Therefore, we tested the efficacy of PMO-L4-Biotin:Avidin, which had shown the strongest in vitro effect (Figure 5), in a preliminary study in rats. The in vivo study (Figure 6) showed for the first time that an avidin-mediated in vivo gene knockdown is feasible. However, the relatively low level of inhibitory response suggests that such an approach may be limited by the potency of the gene knockdown agent. This is because, to deliver a 5 mg/kg dose of CPR PMO (M_w of 8476), we had to administer a 40 mg/kg dose of avidin (M_w of 68000) in a 1:1 molar ratio used in our studies. This is a relatively high dose for in vivo administration of avidin, limiting the dose of oligo that may be delivered by this approach. Thus, the avidin-mediated in vivo gene knockdown approach may be more suitable for delivery of more potent oligos or other gene knockdown agents, such as siRNAs, that inhibit CPR expression at nanomolar concentrations (*30*).

In conclusion, our studies show for the first time that avidin-mediated intracellular delivery of biotinylated oligos can effectively knock down target genes in vitro. Further, it was shown that the efficacy of an avidin-conjugate of biotinylated PMO antisense against rat liver epithelial cell CPR depends on the length of the linker between the biotin and PMO, with longer linkers being more effective than a short linker. Although preliminary studies indicated feasibility of in vivo gene knockdown by the avidin−biotin approach, the method may be limited by the requirement for relatively large amounts of avidin. Further studies are needed to test this approach for in vivo delivery of more potent agents, which require smaller amounts of avidin administration.

ACKNOWLEDGMENT

This study was supported in part by a Seed Grant from the Texas Tech University Health Sciences Center and by the Center for Vascular Drug Research at Texas Tech School of Pharmacy.

Supporting Information Available: Experimental procedures. This material is available free of charge via the Internet at http://pubs.acs.org.

LITERATURE CITED

(1) Horecker, B. L. (1950) Triphosphopyridine nucleotide-cytochrome c reductase in liver. *J. Biol. Chem. 183*, 593–605.
(2) Winston, G. W., Feierman, D. E., and Cederbaum, A. I. (1984) The role of iron chelates in hydroxyl radical production by rat liver microsomes, NADPH-cytochrome P-450 reductase and xanthine oxidase. *Arch. Biochem. Biophys. 232*, 378–90.
(3) Morehouse, L. A., Thomas, C. E., and Aust, S. D. (1984) Superoxide generation by NADPH-cytochrome P-450 reductase: the effect of iron chelators and the role of superoxide in microsomal lipid peroxidation. *Arch. Biochem. Biophys. 232*, 366–77.
(4) Bosterling, B., and Trudell, J. R. (1981) Spin trap evidence for production of superoxide radical anions by purified NADPH-cytochrome P-450 reductase. *Biochem. Biophys. Res. Commun. 98*, 569–75.
(5) Bachur, N. R., Gordon, S. L., Gee, M. V., and Kon, H. (1979) NADPH cytochrome P-450 reductase activation of quinone anticancer agents to free radicals. *Proc. Natl. Acad. Sci. U.S.A. 76*, 954–7.
(6) Zangar, R. C., Davydov, D. R., and Verma, S. (2004) Mechanisms that regulate production of reactive oxygen species by cytochrome P450. *Toxicol. Appl. Pharmacol. 199*, 316–31.
(7) Davydov, D. R. (2001) Microsomal monooxygenase in apoptosis: another target for cytochrome c signaling? *Trends Biochem. Sci. 26*, 155–60.
(8) Heine, T., Glatt, H., and Epe, B. (2006) Human cytochrome P450 reductase can act as a source of endogenous oxidative DNA damage and genetic instability. *Free Radic. Biol. Med. 40*, 801–7.
(9) Ram, P. A., and Waxman, D. J. (1992) Thyroid hormone stimulation of NADPH P450 reductase expression in liver and extrahepatic tissues. Regulation by multiple mechanisms. *J. Biol. Chem. 267*, 3294–301.
(10) Liu, D., and Waxman, D. J. (2002) Post-transcriptional regulation of hepatic NADPH-cytochrome P450 reductase by thyroid hormone: independent effects on poly(A) tail length and mRNA stability. *Mol. Pharmacol. 61*, 1089–96.
(11) Ross, A. D., Varghese, G., Oporto, B., Carmichael, F. J., and Israel, Y. (1995) Effect of propylthiouracil treatment on NADPH-cytochrome P450 reductase levels, oxygen consumption and hydroxyl radical formation in liver microsomes from rats fed ethanol or acetone chronically. *Biochem. Pharmacol. 49*, 979–89.
(12) Herrera, B., Murillo, M. M., Alvarez-Barrientos, A., Beltran, J., Fernandez, M., and Fabregat, I. (2004) Source of early reactive oxygen species in the apoptosis induced by transforming growth factor-beta in fetal rat hepatocytes. *Free Radic. Biol. Med. 36*, 16–26.
(13) Gan, L., Vonmoltke, L. L., Trepanier, L. A., Harmatz, J. S., Greenblatt, D. J., and Court, M. H. (2009) Role of NADPH

cytochrome P450 reductase and cytochrome b5/NADH b5 reductase in variability of CYP3A activity in human liver microsomes. *Drug Metab. Dispos. 37*, 90–96.
(14) Fattal, E., and Barratt, G. (2009) Nanotechnologies and controlled release systems for the delivery of antisense oligonucleotides and small interfering RNA. *Br. J. Pharmacol.* .
(15) Summerton, J., and Weller, D. (1997) Morpholino antisense oligomers: design, preparation, and properties. *Antisense Nucleic Acid Drug Dev. 7*, 187–95.
(16) Summerton, J. E. (2007) Morpholino, siRNA, and S-DNA compared: impact of structure and mechanism of action on off-target effects and sequence specificity. *Curr. Top. Med. Chem. 7*, 651–60.
(17) Fattal, E., and Bochot, A. (2008) State of the art and perspectives for the delivery of antisense oligonucleotides and siRNA by polymeric nanocarriers. *Int. J. Pharm. 364*, 237–48.
(18) Garcia-Chaumont, C., Seksek, O., Grzybowska, J., Borowski, E., and Bolard, J. (2000) Delivery systems for antisense oligonucleotides. *Pharmacol. Ther. 87*, 255–77.
(19) Rojanasakul, Y. Y. (1996) Antisense oligonucleotide therapeutics: Drug delivery and targeting. *Adv. Drug Delivery Rev. 18*, 115–131.
(20) White, P. J., Anastasopoulos, F., Pouton, C. W., and Boyd, B. J. (2009) Overcoming biological barriers to in vivo efficacy of antisense oligonucleotides. *Expert Rev. Mol. Med. 11*, e10.
(21) Pardridge, W. M., and Boado, R. J. (1991) Enhanced cellular uptake of biotinylated antisense oligonucleotide or peptide mediated by avidin, a cationic protein. *FEBS Lett. 288*, 30–2.
(22) Boado, R. J., and Pardridge, W. M. (1994) Complete inactivation of target mRNA by biotinylated antisense oligodeoxynucleotide-avidin conjugates. *Bioconjugate Chem. 5*, 406–10.
(23) Pardridge, W. M., Boado, R. J., and J. L., B. (1993) Drug delivery of antisense oligonucleotides or peptides to tissues in vivo using an avidin-biotin system. *Drug Delivery 1*, 43–50.
(24) Mamede, M., Saga, T., Ishimori, T., Higashi, T., Sato, N., Kobayashi, H., Brechbiel, M. W., and Konishi, J. (2004) Hepatocyte targeting of ^{111}In-labeled oligo-DNA with avidin or avidin-dendrimer complex. *J. Controlled Release 95*, 133–41.
(25) Green, N. M. (1990) Avidin and streptavidin. *Methods Enzymol. 184*, 51–67.
(26) Tsao, M. S., Smith, J. D., Nelson, K. G., and Grisham, J. W. (1984) A diploid epithelial cell line from normal adult rat liver with phenotypic properties of 'oval' cells. *Exp. Cell. Res. 154*, 38–52.
(27) Krishna, S. B., Alfonso, L. F., Thekkumkara, T. J., Abbruscato, T. J., and Bhat, G. J. (2007) Angiotensin II induces phosphorylation of glucose-regulated protein-75 in WB rat liver cells. *Arch. Biochem. Biophys. 457*, 16–28.
(28) Phillips, A. H., and Langdon, R. G. (1962) Hepatic triphosphopyridine nucleotide-cytochrome c reductase: isolation, characterisation, and kinetic studies. *J. Biol. Chem. 237*, 2652–2660.
(29) Shiraki, H., and Guengerich, F. P. (1984) Turnover of membrane proteins: kinetics of induction and degradation of seven forms of rat liver microsomal cytochrome P-450, NADPH-cytochrome P-450 reductase, and epoxide hydrolase. *Arch. Biochem. Biophys. 235*, 86–96.
(30) Han, J. F., Wang, S. L., He, X. Y., Liu, C. Y., and Hong, J. Y. (2006) Effect of genetic variation on human cytochrome p450 reductase-mediated paraquat cytotoxicity. *Toxicol. Sci. 91*, 42–8.

BC900449B

Tumor-Targeting Peptide Conjugated pH-Responsive Micelles as a Potential Drug Carrier for Cancer Therapy

Xiang Lan Wu,[†,‡] Jong Ho Kim,[†,||] Heebeom Koo,[§] Sang Mun Bae,[||] Hyeri Shin,[||] Min Sang Kim,[‡] Byung-Heon Lee,[||] Rang-Woon Park,[||] In-San Kim,[||] Kuiwon Choi,[§] Ick Chan Kwon,[§] Kwangmeyung Kim,*[,§] and Doo Sung Lee*[,‡]

Department of Polymer Science and Engineering, Sungkyunkwan University, Suwon, 440-746, Republic of Korea, Biomedical Research Center, Korea Institute of Science and Technology, Seongbuk-Gu, Seoul, 136-791, South Korea, and Advanced Medical Technology Cluster for Diagnosis & Prediction, Kyungpook National University, Daegu 700-422, South Korea.
Received December 2, 2009; Revised Manuscript Received January 4, 2010

Herein, we prepared tumor-targeting peptide (AP peptide; CRKRLDRN) conjugated pH-responsive polymeric micelles (pH-PMs) in cancer therapy by active and pH-responsive tumor targeting delivery systems, simultaneously. The active tumor targeting and tumoral pH-responsive polymeric micelles were prepared by mixing AP peptide conjugated PEG-poly(D,L-lactic acid) block copolymer (AP-PEG-PLA) into the pH-responsive micelles of methyl ether poly(ethylene glycol) (MPEG)-poly(β-amino ester) (PAE) block copolymer (MPEG-PAE). These mixed amphiphilic block copolymers were self-assembled to form stable AP peptide-conjugated and pH-responsive AP-PEG-PLA/MPEG-PAE micelles (AP-pH-PMs) with an average size of 150 nm. The AP-pH-PMs containing 10 wt % of AP-PEG-PLA showed a sharp pH-dependent micellization/demicellization transition at the tumoral acid pH. Also, they presented the pH-dependent drug release profile at the acidic pH of 6.4. The fluorescence dye, TRITC, encapsulated AP-pH-PMs (TRITC-AP-pH-PMs) presented the higher tumor-specific targeting ability in vitro cancer cell culture system and in vivo tumor-bearing mice, compared to control pH-responsive micelles of MPEG-PAE. For the cancer therapy, the anticancer drug, doxorubicin (DOX), was efficiently encapsulated into the AP-pH-PMs (DOX-AP-pH-PMs) with a higher loading efficiency. DOX-AP-pH-PMs efficiently deliver anticancer drugs in MDA-MB231 human breast tumor-bearing mice, resulted in excellent anticancer therapeutic efficacy, compared to free DOX and DOX encapsulated MEG-PAE micelles, indicating the excellent tumor targeting ability of AP-pH-PMs. Therefore, these tumor-targeting peptide-conjugated and pH-responsive polymeric micelles have great potential application in cancer therapy.

INTRODUCTION

Polymeric micelles formed by amphiphilic block copolymers in aqueous conditions have been investigated as a tumor-targeting drug delivery system in cancer therapy, because they can form a stable nanosized micellar structure, resulting in accumulation and extravasation into the target tumor tissue, which is called an enhanced permeation and retention effect (EPR effect) (*1, 2*). Importantly, pH-responsive polymeric micelles (pH-PMs) are more attractive for their sharp pH-dependent structural disruption in tumoral acidic pH, which results in rapid drug release at target tumor tissue (*3*−*5*). This is because tumor tissues have a more acidic environment, due to the lactic acid produced by acidic intracellular organelles and hypoxia. Due to the tumoral acidic pH microenvironments, various amphiphilic copolymers containing pH-responsive histidine and sulfonamide moieties have been designed to present a sharp pH-dependent micellization/demicellization transition, resulting in the demicellization leading to rapid drug release at target tumor tissues (*3, 6*). Therefore, pH-PMs not only successfully targeted at tumor tissue, but also enabled rapid drug release into the target tumor tissue (*7*−*9*).

We also developed pH-PMs composed of poly(ethylene glycol) methyl ether−poly(β-amino ester) (MPEG-PAE) (*10*), which presented a sharp pH-responsive micellization/demicellization transition at the tumoral acidic pH condition (pH 6.4−6.8), due to its tertiary amine with a pK_b of about 6.5 (*11, 12*). However, the pH-responsive MPEG-PAE micelles at the acidic pH buffer might take a few hours to present the sharp pH-dependent responsiveness at the tumoral weakly acidic pH microenvironment. It is also reported that most pH-responsive polymeric micelles at the acidic buffer condition required a prolonged reaction time to present a pH-responsiveness. On the basis of the time-delayed pH-responsiveness of polymeric micelles, the in vivo pH responsiveness of various polymeric micelles at the target tumor tissue might be less effective than that in the in vitro pH buffer condition, due to the very small tumor volume and the lower tumor targeting ability. Therefore, the pH-responsive polymeric micelles should be specifically targeted and remained for a long time at the target tumors, wherein the pH-responsive polymeric micelles might present a sharp pH-dependent micellization/demicellization transition.

Herein, to enhance the specificity and retention time of pH-PMs at the target tumor, we prepared tumor-specific peptide (AP peptide; CRKRLDRN)-conjugated pH-responsive MPEG-PAE micelles (AP-pH-PMs). It was reported that AP peptide had very specific binding affinity to IL-4 receptors of atherosclerotic plaques and breast tumor tissues (*13*−*15*). Therefore, we anticipated that AP-pH-PMs may increase the pH-responsiveness at the target tumors, due to the enhanced tumor

* To whom correspondence should be addressed.Tel: +82-2-958-5912; Fax: +82-2-958-5909; E-mail: kim@kist.re.kr (K. Kim). Tel: +82-31-290-7282; Fax: +82-31-292-8790; E-mail: dslee@skku.edu (D. S. Lee).
† Both authors contributed equally.
‡ Sungkyunkwan University.
§ Korea Institute of Science and Technology.
|| Kyungpook National University.

10.1021/bc9005283 © 2010 American Chemical Society
Published on Web 01/14/2010

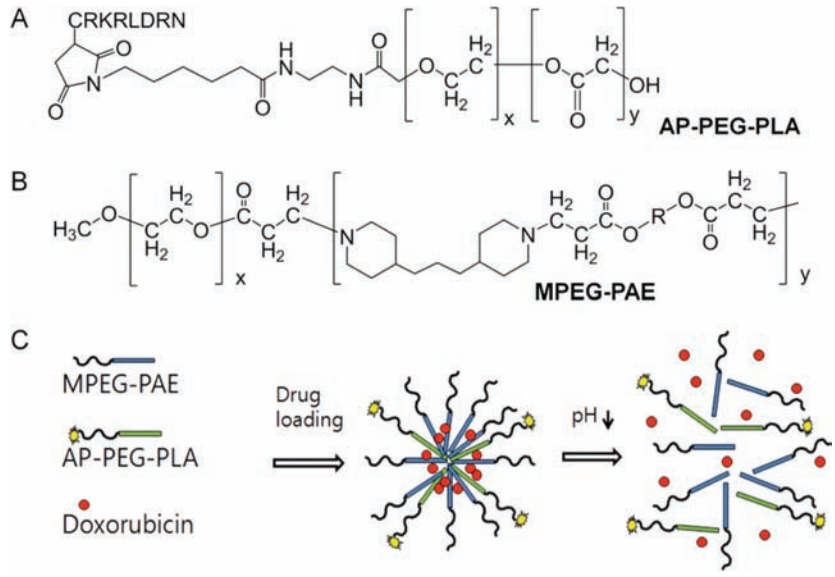


Figure 1. Design strategy of peptide-conjugated pH-responsive micelle: (A) Chemical structure of tumor-targeting AP peptide (CRKRLDRN) coupled PEG-PLA block copolymer (AP-PEG-PLA) and (B) pH-responsive MPEG-PAE block copolymer (MPEG-PAE). (C) Schematic diagram depicting tumor-targeting and pH-responsive polymeric micelles of AP-PEG-PLA/MPEG-PAE (AP-pH-PM), which triggered doxorubicin (DOX) release by the sharp pH-dependent micellization/demicellizaton transition at the tumoral acidic pH.

targeting ability in vivo. In order to prepare AP peptide-modified polymeric micelles, AP peptide grafted PEG-poly(D,L-lactic acid) block copolymer (AP-PEG-PLA) was prepared and mixed with pH-responsive MPEG-PAE block copolymer in aqueous condition. These mixed amphiphilic block copolymers were self-assembled to form stable AP-pH-PMs (Figure 1). The AP-pH-PMs containing 10 wt % of AP-PEG-PLA showed a sharp pH-dependent micellization/demicellization transition at the tumoral acid pH (pH 6.8−6.9). To assay the tumor targeting ability of AP-pH-PMs in MDA-MB231 human breast tumor-bearing mice, fluorescence dye, TRITC, encapsulated AP-pH-PMs were noninvasively monitored using optical fluorescence imaging technology. Finally, doxorubicin (DOX) was encapsulated into the AP-pH-PMs (DOX-AP-pH-PMs), and its enhanced therapeutic efficacy was studied in MDA-MB231 human breast tumor-bearing mice, compared to control free DOX and DOX encapsulated pH-responsive MEPG-PAE micelles (DOX-pH-PMs), respetively (*16*).

RESULTS AND DISCUSSION

In order to enhance the targeting specificity and retention time of pH-PMs at the target tumor, first, human breast tumor-specific AP peptide (CRKRLDRN) chemically conjugated to the PEG-PLA block copolymer (AP-PEG-PLA) was prepared by chemical coupling thiolated AP peptide to maleimide-terminated PEG-PLA block copolymer in acetonitrile/water (Figure 1A). After the reaction, the solution was lyophililized and reprecipitated in cold diethyl ether for twice the time, followed by drying in a vacuum oven for 12 h (yield: 85%), resulting in AP-PEG-PLA (M_w = 19.6 kDa). Second, pH-responsive block copolymer was prepared by a Michael-type step polymerization between hydrophilic methyl ether poly(ethylene glycol) (MPEG) and pH-responsive/biodegradable poly(β-amino ester) (PAE) (Figure 1B), wherein the MPEG-PAE (M_w = 17.4 kDa) has 2.6 mol equiv of PAE per 1 M of PEG (see the Supporting Information), as previously reported (*10*). The AP peptide-modified pH-responsive micelles (AP-pH-PMs) were simply prepared by a solvent evaporation method (Figure 1C). The polymer mixture containing 10 wt % of AP-PEG-PLA and 90 wt % of MPEG-PAE in organic solvent was evaporated to give the polymer thin film, and the film was incubated in distilled water or PBS at 37 °C for 30 min. After the incubation, the dried polymer film was dispersed by signification for 2 min. This amphiphilic AP-PEG-PLA/MPEG-PAE mixture was spontaneously self-assembled to form stable polymeric micelles with an average diameter of 156 nm at normal pH of 7.4. Also, the AP-pH-PMs showed a sharp micellization/demicellization transition at tumoral acidic pH values (pH 6.8−6.9). It is deduced that amphiphilic MEPEG-PAEs are ionized and completely dissolved at the weakly acidic condition.

For the assay, the tumor targeting ability and anticancer therapeutic efficacy of AP-pH-PMs, 10 wt % of fluorescence dye, TRITC, or 10 wt % of anticancer drug, doxorubicin (DOX), was encapsulated into the AP-pH-PMs by the solvent evaporation method, respectively (see Supporting Information) (*17*). Hydrophobic TRITC or DOX was well-encapsulated into the hydrophobic inner cores of the polymeric micelles with a higher loading efficiency of about 90%. The TRITC or DOX encapsulated polymeric micelles (TRITC-AP-pH-PMs or DOX-AP-pH-PMs) showed a slightly increased average size of about 180 nm, measured by dynamic light scattering (Figure 2A), wherein the polydisersity of each polymeric micelle was fairly low (0.021 mg/mL), indicating narrow size distribution of each polymeric micelle. The TEM images also showed the spherical particle morphologies of DOX-AP-pH-PMs. As control, TRITC or DOX was also encapsulated into the pH-PMs without AP peptide (TRITC-pH-PMs and DOX-pH-PMs) using the same solvent casting method. The overall characteristics of each polymeric micelle, including loading efficiency, average size, and pH transition, are summarized in Table 1.

As expected, DOX-AP-pH-PMs began to be rapidly demicellized with decreasing pH values because the tertiary amines of PEA polymer were completely ionized at the lower pH value (6.8−6.9) (Figure 2B). This pH-dependent micellization/demicellization transition of DOX-AP-pH-PMs was very similar to that of MPEG-PEA micelles at the pH of 6.4−6.8, which may specifically respond to the tumoral weakly acidic extracellular pH (*5*). DOX release profile from the AP-pH-PMs was examined using a dialysis method. It was obvious from Figure 2C that DOX release was highly influenced by pH value, indicating a pH-dependent drug release profile. At pH 7.4, the release rate of DOX was very low with less than 20% of the DOX released

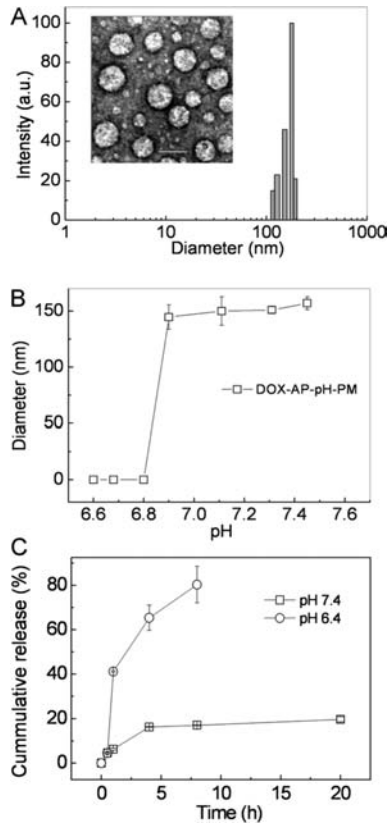


Figure 2. Characteristics of DOX-encapsulated AP-pH-PMs (DOX-AP-pH-PMs): (A) Size distribution of DOX-AP-pH-PMs (1 mg/mL in PBS at pH 7.4). The inset image presents TEM image of DOX-AP-pH-PMs (1 mg/mL in distilled water). (B) Average size change of DOX-AP-pH-PMs as a function of pH. (C) In vitro release profiles of DOX from DOX-AP-pH-PMs at different pH values (6.4 and 7.4) at 37 °C measured by UV−vis spectroscopy.

Table 1. Characterization of pH-Responsive Polymeric Micelles

sample	feed amount (wt %)	loading efficiency (%)	size (nm)[a]	μ^2/Γ^{2b}
pH-PM	−	−	62	0.014
AP-pH-PM	−	−	150	0.018
TRITC-pH-PM	10	86 ± 2.5	132	0.021
TRITC-AP-pH-PM	10	90 ± 2.8	182	0.019
DOX-pH-PM	10	82 ± 2.8	183	0.023
DOX-AP-pH-PM	10	86 ± 2.8	181	0.024

[a] The average size was measured with dynamic light scattering. [b] Polydispersity factor for polymeric micelles.

in 20 h, while a noticeably increased release rate of DOX was observed at pH 6.4 with more than 65% of the DOX released within 4 h. It is deduced that, at pH 7.4, most AP-pH-PMs maintained their micellar structure and kept DOX in the micellar core, while they were rapidly demicellized in a short time at pH 6.4, followed by releasing DOX. This drug release profile of AP-pH-PMs indicated that AP peptides on the micelle's surface did not have any effect on the pH-dependent drug release profile of pH-responsive MPEG-PEA micelles (*18*).

The tumor-specific targeting ability of fluorescence dye, TRITC, encapsulated polymeric micelles (TRITC-AP-pH-PMs) in the MDA-MB-231 human breast cancer cell culture system was evaluated using confocal laser microscopy, whereas, as control, TRITC-pH-PMs without AP peptide moieties at the micelle's surface were used. Figure 3 shows the enhancement of cellular uptake with AP-pH-PMs over pH-PMs, suggesting that AP peptide modified micelles were more rapidly taken into the cells by the specific binding affinity to IL-4 receptors of breast cancer cells (*15*). The TRITC's fluorescence intensity of

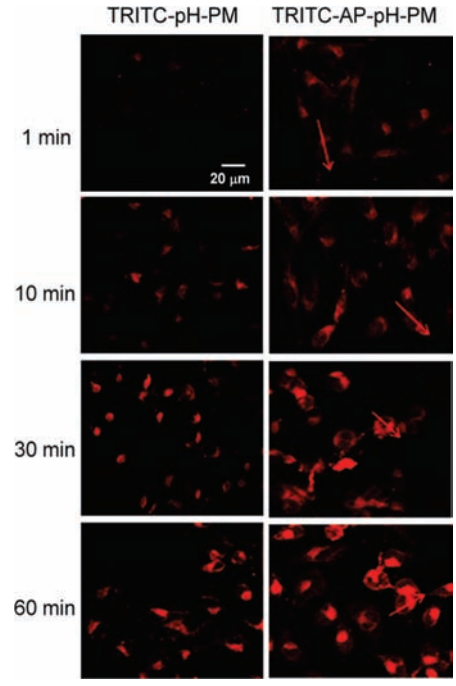


Figure 3. Confocal laser scanning microscopy of TRITC encapsulated pH-PMs (TRITC-pH-PMs) and AP-pH-PMs (TRITC-AP-pH-PMs) in MDA-MB-231 cancer cell culture system. The scale bar is 20 μm in the image.

the TRITC-AP-pH-PM treated cells was always higher than that of TRITC-pH-PM treated cells at any moment. In particular, only after 1 min postincubation, TRITC-AP-pH-PMs-treated cells presented substantial fluorescence intensity at the cytoplasm part, indicating rapid receptor-medicated endocytosis (red arrows; see NIR fluorescence histogram in Supporting Information Figure S1) (*19*). As incubation time increased, the fluorescence intensity increased up to 1 h and most cells presented strong fluorescence in the cytoplasm and perinuclear compartments. However, TRITC-pH-PMs did not present rapid cellular uptake in the cell culture system, due to the bioinert PEG surface of polymeric micelles. It suggested that the surface modification of pH-PMs with tumor-targeting AP peptides greatly enhanced the cellular uptake profile of pH-responsive polymeric micelles by rapid receptor-medicated cellular adherence and uptake.

The tumor targeting ability of the TRITC-AP-pH-PMs was also measured using noninvasive and live optical imaging system. When the tumor volume grew to 150−200 mm^3, TRITC-pH-PMs and TRITC-AP-pH-PMs containing 1 mg/kg of TRITC were administrated intravenously into the MDA-MB231 human breast tumor-bearing mice. After the scheduled time points, the fluorescence signals of TRITC-pH-PMs and TRITC-AP-pH-PMs were noninvasively quantified by measuring total photon counts at the target tumor tissues (Figure 4A) (*20*). At 1 h postinjection of TRITC-AP-pH-PMs, the inoculated tumor was clearly delineated from the body, indicating rapid tumor accumulation of TRITC-AP-pH-PMs. Moreover, the fluorescence signals gradually increased up to 24 h postinjection. However, TRITC-pH-PM-treated mice showed minimum fluorescence intensity at the target tumors up to 12 h. It means that pH-PMs without AP peptides might be less effective in targeting at the tumor tissues, due to the bioinert PEG surface of pH-PMs, compared to AP-pH-PMs. After 24 h postinjection, the delayed tumor targeting ability of pH-PMs was observed, indicating that the pH-responsiveness of MPEG-PAE micelles is not very effective in the real tumor model in vivo. The fluorescent total photon counts per gram of TRITC-AP-pH-PM-treated tumors were 2-fold higher than those of the TRITC-

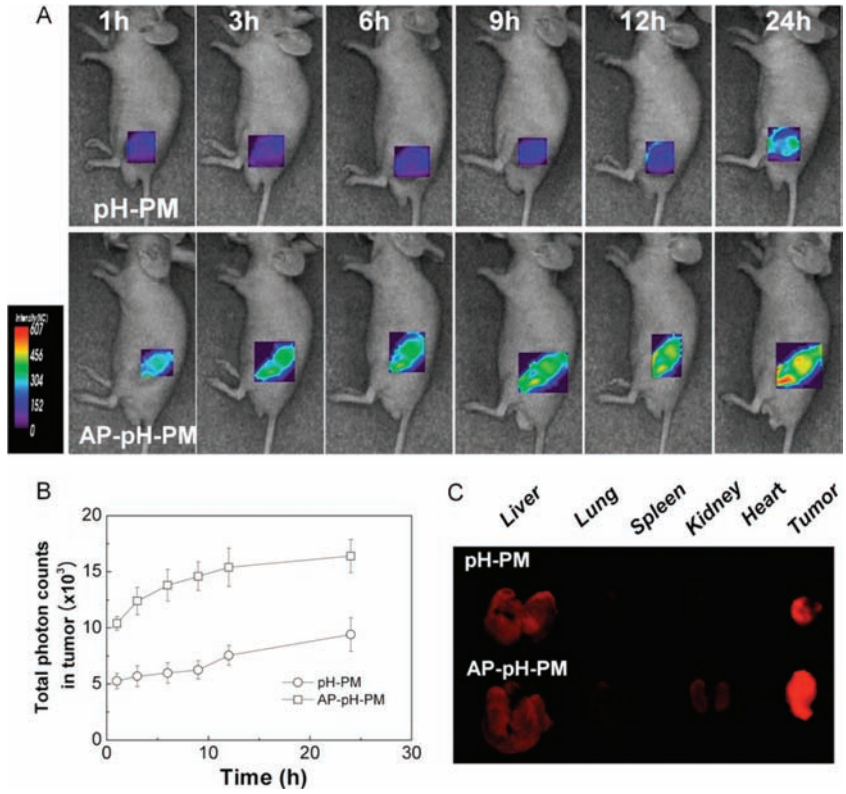


Figure 4. In vivo and ex vivo biodistribution of peptide conjugated pH-responsive micelles: (A) In vivo fluorescence images of MDA-MB-231 tumor xenografted athymic nude mice injected with TRITC-pH-PM and TRITC-AP-pH-PM, respectively. (B) Quantification of in vivo tumor targeting ability of TRITC-pH-PMs and TRITC-AP-pH-PMs were recorded as total photon counts per centimeter squared per steradian (p/s/cm^2/sr) per each tumor at 1 day postinjection ($n = 3$). The data represent mean ± s.e. (C) Ex vivo fluorescence image of dissected organs after 24 h postinjection of TRITC-pH-PMs and TRITC-AP-pH-PMs.

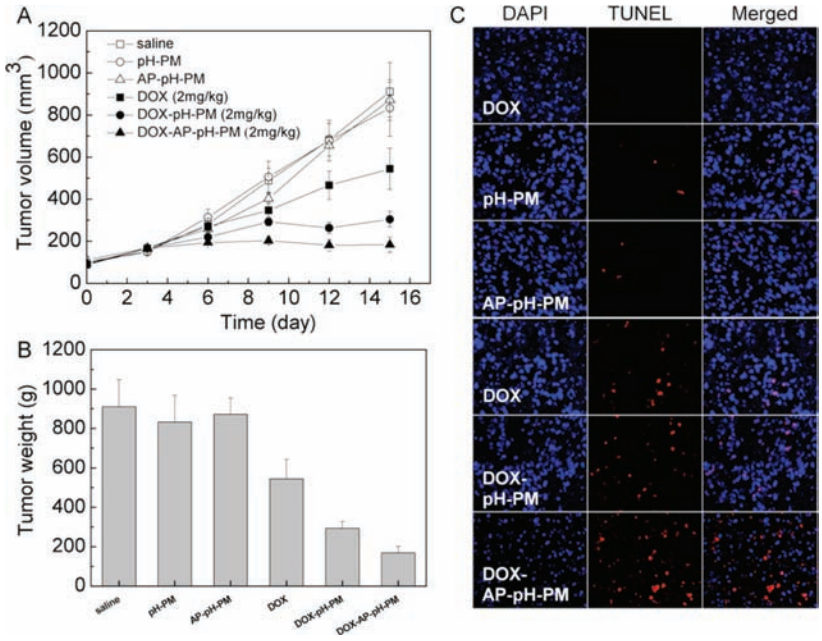


Figure 5. In vivo anti-tumor therapy of doxorubicin encapsulated micelles: (A) In vivo anti-tumor therapeutic efficacy of saline (□), pH-PM (○), AP-pH-PM (△), free DOX (2 mg/kg) (■), DOX- pH-PM with 2 mg/kg of DOX (•), and DOX-AP-pH-PM 2 mg/kg of DOX (Δ) ($n = 5$). Values represent the mean ± SD. (B) Tumor weights of MDA-MB-231 tumor-bearing mice 15 days post-treatment. (C) Immunohistological detection of apoptotic cells (TUNNEL assay) in MDA-MB-231 tumor-bearing mice 15 days post-treatment.

pH-PM-treated tumors over any time period (Figure 4B). These results indicated that the AP-pH-PMs could be specifically targeted in a short time period and localized for a long time at the target tumors. Interestingly, ex vivo fluorescence images of excised organs showed substantial evidence of the tumor-targeting ability of TRITC-AP-pH-PMs (Figure 4C). After 24 h postinjection, mice were sacrificed, and major organs such as liver, lung, spleen, kidney, and heart, as well as the tumors, were isolated to evaluate the in vivo biodistribution of TRITC-AP-pH-PMs and TRITC-pH-PMs. Strong fluorescence signals were observed in the tumor tissues, indicating the tumor targeting ability of both pH-PMs and AP-pH-PMs, while other

tissues showed negligible NIRF signals, except for the liver, in which biodegradable polymers were metabolized. Interestingly, TRITC-AP-pH-PMs presented the stronger fluorescence signal in the target tumor, compared to TRITC-pH-PM. The tumor targeting ability of AP peptide-modified polymeric micelles could increase the tumor targeting specificity and retention time at the target tumor.

The in vivo anti-tumor efficacy of the DOX-encapsulated AP-pH-PMs (DOX-AP-pH-PMs) was also evaluated in MDA-MB-231 human breast tumor-bearing mice (*21*). Figure 5A shows the growth curves of the tumors after intravenous injection of saline, polymeric micelles alone (pH-PMs, AP-pH-PMs), free DOX (2 mg/kg), or DOX-loaded polymeric micelles (DOX-pH-PMs, DOX-AP-pH-PMs) with 2 mg/kg of free DOX. The tumor growth rate of pH-PMs and AP-PMs-treated mice were similar to that of mice treated with saline, indicating that polymeric micelles had no therapeutic effect on the tumor growth. However, free DOX, DOX-pH-PMs, and DOX-AP-pH-PMs-treated mice showed significant anti-tumor therapeutic efficacy, respectively. At 15 day postinjection, the average tumor volume in free DOX-treated mice was suppressed and reached only 544 ± 98 mm^3, compared with 911 ± 137 mm^3 attained in saline-treated mice. DOX-pH-PM-treated mice also showed more efficient anti-tumor efficacy than free DOX, with the average tumor volume of 304 ± 37 mm^3. In particular, DOX-AP-pH-PM-treated mice decreased substantially the tumor volumes by 183 ± 37 mm^3, indicating that AP-pH-PMs could successfully deliver the encapsulated DOX at the target tumor. It suggested that AP peptide-modified polymeric micelles could specifically deliver encapsulated drugs to the target tumor by the tumor-targeting ability of AP peptides on their micelle's surface, as previously confirmed by in cell culture system and in vivo imaging data. At 15 day postinjection, DOX-AP-pH-PMs greatly suppressed the tumor weight to 18.6%, compared to the saline-treated mice, whereas free DOX and DOX-pH-PMs suppressed the tumor weight to 60% and 32%, respectively. The anti-tumor efficacy of pH-PM-DOX was also evaluated by the TUNEL assay, which detects apoptosis at the tumor tissues (Figure 4C) (*22*). No significant apoptotic cells were seen in tumors from saline and polymeric micelle-treated micelles. However, tumor tissues treated with DOX-AP-pH-PMs showed the highest TUNEL signals compared to tumors treated with free DOX and DOX-pH-PMs, indicating the excellent anticancer therapeutic efficacy of DOX-AP-pH-PMs.

Collective results from both in vitro and in vivo studies strongly supported the anticancer therapeutic efficacy of AP-pH-PMs as a new nanosized drug carrier with higher tumor-targeting ability. DOX molecules were efficiently loaded into the AP-pH-PMs and rapidly released under acidic conditions with higher tumor-targeting ability. The increased tumor-targeting characteristics of AP peptide-modified and pH-responsive polymeric micelles were evaluated in a cell culture system and tumor-bearing mice using a fluorescence imaging technique, which showed that AP-pH-PMs efficiently deliver anticancer drugs, resulting in excellent anticancer therapeutic efficacy. Taken together, the tumor-homing and pH-responsive AP-pH-PMs have great potential application in cancer therapy.

ACKNOWLEDGMENT

This work was financially supported by the Real-Time Molecular Imaging Project, 2009K 001594, and GRL Program of MEST and by grant to the Intramural Research Program (Theragnosis) of KIST, by a grant of by BK21 BNT Scientist Renovating for the Drug Development Coping with Aged Society, and Advanced Medical Technology Cluster for Diagnosis and Prediction at Kyungpook National University from MOCIE.

Supporting Information Available: Experimental procedures. This material is available free of charge via the Internet at http://pubs.acs.org.

LITERATURE CITED

(1) Yoshitomi, T., Suzuki, R., Mamiya, T., Matsui, H., Hirayama, A., and Nagasaki, Y. (2009) pH-sensitive radical-containing-nanoparticle (RNP) for the L-band-EPR imaging of low pH circumstances. *Bioconjugate Chem. 20*, 1792–1798.

(2) Maeda, H. (2001) The enhanced permeability and retention (EPR) effect in tumor vasculature: the key role of tumor-selective macromolecular drug targeting. *Adv. Enzyme Regul. 41*, 189–207.

(3) Lee, E. S., Na, K., and Bae, Y. H. (2005) Super pH-sensitive multifunctional polymeric micelle. *Nano Lett. 5*, 325–329.

(4) Gillies, E. R., and Frechet, J. M. J. (2005) pH-responsive copolymer assemblies for controlled release of doxorubicin. *Bioconjugate Chem. 16*, 361–368.

(5) Oishi, M., Kataoka, K., and Nagasaki, Y. (2006) pH-responsive three-layered PEGylated polyplex micelle based on a lactosylated ABC triblock copolymer as a targetable and endosome-disruptive nonviral gene vector. *Bioconjugate Chem. 17*, 677–688.

(6) Sethuraman, V. A., and Bae, Y. H. (2007) TAT peptide-based micelle system for potential active targeting of anti-cancer agents to acidic solid tumors. *J. Controlled Release 118*, 216–224.

(7) Tannock, I. F., and Rotin, D. (1989) Acid pH in tumors and its potential for therapeutic exploitation. *Cancer Res. 49*, 4373–4384.

(8) Engin, K., Leeper, D. B., Cater, J. R., Thistlethwaite, A. J., Tupchong, L., and McFarlane, J. D. (1995) Extracellular pH distribution in human tumours. *Int. J. Hyperthermia 11*, 211–216.

(9) Gerweck, L. E., and Seetharaman, K. (1996) Cellular pH gradient in tumor versus normal tissue: potential exploitation for the treatment of cancer. *Cancer Res. 56*, 1194–1198.

(10) Kim, M. S., Hwang, S. J., Han, J. K., Choi, E. K., Park, H. J., Kim, J. S., and Lee, D. S. (2006) pH-responsive PEG-poly(beta-amino ester) block copolymer micelles with a sharp transition. *Macromol. Rapid Commun. 27*, 447–451.

(11) Lynn, D. M., and Langer, R. (2000) Degradable poly(β-amino esters): synthesis, characterization, and self-assembly with plasmid DNA. *J. Am. Chem. Soc. 122*, 10761–10768.

(12) Lynn, D. M., Amiji, M. M., and Langer, R. (2001) pH-responsive polymer microspheres: rapid release of encapsulated material within the range of intracellular pH13. *Angew. Chem., Int. Ed. 40*, 1707–1710.

(13) Hong, H.-y., Lee, H. Y., Kwak, W., Yoo, J., Na, M.-H., So, I. S., Kwon, T.-H., Park, H.-S., Huh, S., Oh, G. T., Kwon, I.-C., Kim, I.-S., and Lee, B.-H. (2008) Phage display selection of peptides that home to atherosclerotic plaques: IL-4 receptor as a candidate target in atherosclerosis. *J. Cell. Mol. Med. 12*, 2003–2014.

(14) Park, K., Hong, H.-Y., Moon, H. J., Lee, B.-H., Kim, I.-S., Kwon, I. C., and Rhee, K. (2008) A new atherosclerotic lesion probe based on hydrophobically modified chitosan nanoparticles functionalized by the atherosclerotic plaque targeted peptides. *J. Controlled Release 128*, 217–223.

(15) Leland, P., Taguchi, J., Husain, S. R., Kreitman, R. J., Pastan, I., and Puri., R. K. (2000) Human breast carcinoma cells express type II IL-4 receptors and are sensitive to antitumor activity of a chimeric IL-4-Pseudomonas exotoxin fusion protein in vitro and in vivo. *Mol. Med. 6*, 165–178.

(16) Gillies, E. R., and Frechet, J. M. J. (2005) pH-Responsive copolymer assemblies for controlled release of doxorubicin. *Bioconjugate Chem. 16*, 361–368.

(17) Kim, J.-H., Kim, Y.-S., Park, K., Lee, S., Nam, H. Y., Min, K. H., Jo, H. G., Park, J. H., Choi, K., Jeong, S. Y., Park, R.-W., Kim, I.-S., Kim, K., and Kwon, I. C. (2008) Antitumor efficacy of cisplatin-loaded glycol chitosan nanoparticles in tumor-bearing mice. *J. Controlled Release 127*, 41–49.

(18) Ko, J., Park, K., Kim, Y.-S., Kim, M. S., Han, J. K., Kim, K., Park, R.-W., Kim, I.-S., Song, H. K., Lee, D. S., and Kwon, I. C. (2007) Tumoral acidic extracellular pH targeting of pH-responsive MPEG-poly(*β*-amino ester) block copolymer micelles for cancer therapy. *J. Controlled Release 123*, 109–115.

(19) Kim, K., Lee, M., Park, H., Kim, J.-H., Kim, S., Chung, H., Choi, K., Kim, I.-S., Seong, B. L., and Kwon, I. C. (2006) Cell-permeable and biocompatible polymeric nanoparticles for apoptosis imaging. *J. Am. Chem. Soc. 128*, 3490–3491.

(20) Min, K. H., Park, K., Kim, Y.-S., Bae, S. M., Lee, S., Jo, H. G., Park, R.-W., Kim, I.-S., Jeong, S. Y., Kim, K., and Kwon, I. C. (2008) Hydrophobically modified glycol chitosan nanoparticles-encapsulated camptothecin enhance the drug stability and tumor targeting in cancer therapy. *J. Controlled Release 127*, 208–218.

(21) Liu, D., Overbey, D., Watkinson, L., and Giblin, M. F. (2009) Synthesis and characterization of an ^{111}In-labeled peptide for the in vivo localization of human cancers expressing the urokinase-type plasminogen activator receptor (uPAR). *Bioconjugate Chem. 20*, 888–894.

(22) Doronina, S. O., Mendelsohn, B. A., Bovee, T. D., Cerveny, C. G., Alley, S. C., Meyer, D. L., Oflazoglu, E., Toki, B. E., Sanderson, R. J., Zabinski, R. F., Wahl, A. F., and Senter, P. D. (2005) Enhanced activity of monomethylauristatin F through monoclonal antibody delivery: effects of linker technology on efficacy and toxicity. *Bioconjugate Chem. 17*, 114–124.

BC9005283

Synthesis and Bioconjugation of 2 and 3 nm-Diameter Gold Nanoparticles

Christopher J. Ackerson,[†] Pablo D. Jadzinsky,[‡] Jonathan Z. Sexton,[§] David A. Bushnell, and Roger D. Kornberg*

Department of Structural Biology, Stanford School of Medicine, 299 Campus Drive West, Stanford, California 94305. Received March 28, 2009; Revised Manuscript Received November 9, 2009

By adjustment of solvent conditions for synthesis, virtually monodisperse 4-mercaptobenzoic acid (*p*-MBA) monolayer-protected gold nanoparticles, 2 and 3 nm in diameter, were obtained. Large single crystals of the 2 nm particles could be grown from the reaction mixture. Uniformity was also demonstrated by the formation of two-dimensional arrays and by quantitative high-angle annular dark-field scanning transmission electron microscopy. The 2 and 3 nm particles were spontaneously reactive for conjugation with proteins and DNA, and further reaction could be prevented by repassivation with glutathione. Conjugates with antibody Fc fragment could be used to identify TAP-tagged proteins of interest in electron micrographs, through the binding of a pair of particles to the pair of protein A domains in the TAP tag.

INTRODUCTION

Thiolate-monolayer protected gold nanoparticles (AuNPs) are stable, nanometer-scale metal nanoparticles, passivated by organothiolate monolayers. They have attracted attention for their ease of synthesis, and for their remarkable chemical and electronic properties (*1*). Synthesis by the method of Brust (*2*) results in polydisperse products (*3*), whose size range may be narrowed by purification (*4–8*), etching (*9*), annealing (*10*), or ripening (*11*). Homogenous thiolate AuNPs coupled to biomolecules, such as DNA or proteins (*12, 13*), hold great promise for electron microscopy (*14*), nanoscale construction (*15*), enzyme enhancement (*16*), and other applications.

We previously reported the formation of a linker-free bond between a thiolate AuNP and a protein (*17*). The method entailed a chemical oxidation step to activate the AuNP (*18*), followed by protein conjugation, and reduction to quench AuNP reactivity. As conjugation was incomplete, gel filtration was performed to remove unreacted protein and AuNP. The limitations of this work were a residual size heterogeneity of the purified AuNPs, the requirement for multiple steps of activation and deactivation, and incomplete conjugation.

We have now overcome these limitations, through the direct synthesis of essentially homogeneous thiolate AuNPs, a high intrinsic reactivity of the AuNPs, and efficient protein conjugation. The choice of thiolate and the conditions for AuNP synthesis were important for these advances. The implications extend beyond the particular examples and applications described for the formation and structure of thiolate AuNPs in general.

EXPERIMENTAL SECTION

Nanoparticle Synthesis. Screening of reaction conditions was performed in 96 well plates with 1 mL total volume per well. Following a reaction time of about 16 h, product was precipitated by the addition of 2 mL of methanol, product was collected by centrifugation, the supernatant was removed, and the product was redissolved in 50% aqueous glycerol. Product was analyzed by 15T/5C Tris-borate EDTA buffered polyacrylamide gel electrophoresis (TBE−PAGE), at no more than 150 V, until a satisfactory separation was observed in the gel. Reaction conditions explored in this manner included pH (2−13), *p*-MBA:Au(III) ratio (0.5:1−10:1), $NaBH_4$:Au(III) ratio (0.5:1−10:1), and concentration of aqueous methanol (5% to 95%). Synthesis of 3 nm AuNPs was identical to that of 2 nm AuNPs except that it was accomplished in 87% aqueous methanol. Further details of nanoparticle synthesis may be found in Section S1 of the Supporting Information.

Protein Conjugation. For analytical purposes, a mixture containing 0.8 μg of candidate protein, 300 μM Tris-carboxy ethyl phosphine (TCEP), and 200 μM Au_{144} AuNP was incubated in a total volume of 15 μL at 37 °C for 1 h. Control reactions contained water instead of Au_{144} AuNP. The reaction mixture was combined with an equal volume of 50% glycerol and fractionated by sodium dodecyl sulfate (SDS)−PAGE (12%/3.3C) for 1 h at 150 V.

Preparative Gel Electrophoresis. In order to drive the reaction to completion, a large excess of AuNP:scFv was used. Excess AuNP was removed by native gel electrophoresis. Up to 5 mL of sample may be loaded and separated in a 5T/5C TBE buffered acrylamide gel, in a Bio-Rad Mini-Protean III gel electrophoresis apparatus, with 1.5 mm plate spacing and a single well preparative comb, run at 80 V constant voltage. The bands are visible in the gel without enhancement by stain, because of the visible absorption of the AuNP. The bands may be excised with a razor blade, crushed by passing through a syringe, and eluted into a desired buffer.

Repassivation. In a typical repassivation experiment, a series of 15 2-fold dilutions of glutathione (GSH), varying from 650 mM to 20 μM, was prepared. Equal volumes (3 μL) of glutathione solution and gold/protein (500 μg/mL) or gold/DNA conjugate were mixed and incubated for 1 h at 37 °C, followed by analysis by 12T/3.3C or 10T/5C PAGE for gold/protein and gold/DNA conjugates, respectively.

Electron Microscopy. Particles shown in Figures 2, S1, S2, and S3 (Supporting Information) were drop cast on 400 mesh glow discharged carbon-coated copper electron microscope (EM) grids (EM Sciences) and examined in an FEI CM12 EM, operated at 100 kV accelerating voltage.

* To whom correspondence should be addressed. E-mail kornberg@stanford.edu.

[†] Present address: Department of Chemistry, Colorado State University, Fort Collins, CO.

[‡] Present address: Department of Neurobiology, Stanford University, Stanford, CA 94305.

[§] Present address: Biomanufacturing Research Institute and Technology Enterprise, North Carolina Central University, Durham, NC.

10.1021/bc900135d © 2010 American Chemical Society
Published on Web 01/25/2010

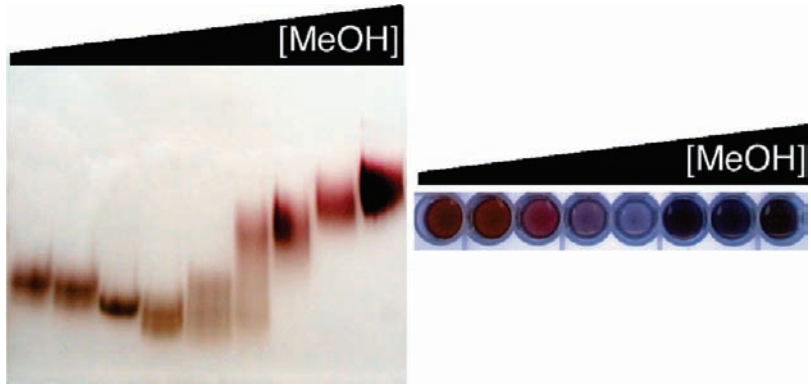


Figure 1. PAGE (15T/5C) revealing changes in product size and dispersity as a function of methanol concentration (from left to right, 7, 17, 27, 37, 47, 57, 67, 77, and 87% methanol) (left panel). The deep red color of the leftmost reactions indicates soluble product and the black color of the rightmost reactions indicates insoluble product. A reaction performed in 27% methanol, which produced 2 nm particles, is in the third well from the left.

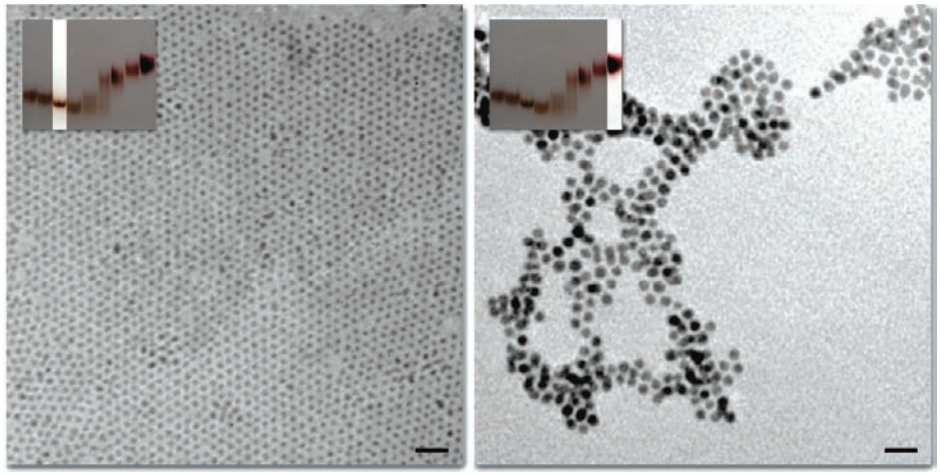


Figure 2. Transmission EM images of MPCs produced in 27% methanol (left panel) and 87% methanol (right panel). Scale bar represents 10 nm.

Cryo-EM. Samples (3 μL, approximately 0.2 mg protein/mL) were deposited on copper quantifoil grids (R2/4 spacing), blotted, and plunge-frozen in liquid ethane with an automated vitrification apparatus. Samples were imaged in a liquid-nitrogen cooled FEI Tecnai G2 Polara with an acceleration voltage of 300 kV. Images were recorded on a 2k X 2k Peltier-cooled CCD camera (Tietz TemCam-F224HD). Images were recorded at 2 μm underfocus to enhance the visibility of the nanoparticles. Contrast transfer function correction was not performed; therefore, protein density was not visible at this underfocus.

RESULTS

Nanoparticle Synthesis. Brust synthesis is accomplished in a two-step reaction, by mixing a 3-fold molar excess of organic thiol and a trivalent gold salt, with a phase transfer catalyst if necessary, to produce a gold-thiol polymer, which is then reduced with borohydride. The effects of varying the thiol:gold ratio and borohydride concentration have been widely reported. When a water-soluble product is synthesized, the reaction is typically performed in aqueous methanol. We undertook a systematic exploration of conditions for the synthesis of *p*-MBA-protected gold AuNPs (*19, 20*), varying the pH, reactant concentration, reduction time, and aqueous methanol concentration.

Reaction products were analyzed by polyacrylamide gel electrophoresis (PAGE) (*7*), and those with narrow size distributions were further analyzed by EM. Optimal yields of AuNPs were obtained with a pH of 13, a *p*-MBA: Au(III) mole ratio of 3.4:1, and an Au(III) concentration of 10 μM. Longer reduction (16−18 h) with less borohydride produced more uniform product than shorter reactions with more borohydride.

The percentage of methanol in the reaction affected both the size and uniformity of the product. Reactions performed in 27% and 87% aqueous methanol gave nearly uniform AuNPs, as shown by the sharp bands in PAGE (Figure 1) and the formation of two-dimensional ordered arrays on EM grids (Figure 2 and Supporting Information Figure S2). Approximate diameters of 2.0 and 3.0 nm were measured for the AuNPs. At other methanol concentrations, heterogeneous particles were obtained (Supporting Information, Figure S3).

The exceptional uniformity of the 2 nm AuNPs prompted an attempt at crystallization. In the presence of various salts, including sodium chloride and sodium borate (at least 0.15 M), and ammonium acetate (at least 0.2 M), single crystals were obtained. The largest crystals, approximately 300 μm in the longest dimension, were produced by slow evaporation from sodium chloride solution, and gave diffraction to 5.5 Å resolution (Supporting Information, Figure S4.) A similar synthesis, differing only in the pH prior to borohydride reduction, led to crystals of a 1.5 nm particle diffracting to 1.1 Å resolution (*21*).

The 2 nm AuNPs were further characterized by quantitative high-angle annular dark-field scanning transmission EM (HAADF-STM). A value of 144 ± 22 atoms for the gold core was obtained (Supporting Information, Figure S5.) For comparison, HAADF-STM gives a value of 13.6 ± 3.4 atoms for the gold core of an Au_{13} particle (*22*). The 15% standard deviation in the measurement of the 2 nm particles compares favorably with the 25% standard deviation in the measurement of the Au_{13} particle. Much of the measurement error may be attributed to unevenness in the carbon support film. The ^{1}H NMR spectrum of the 2 nm AuNP displayed a broad band centered on the

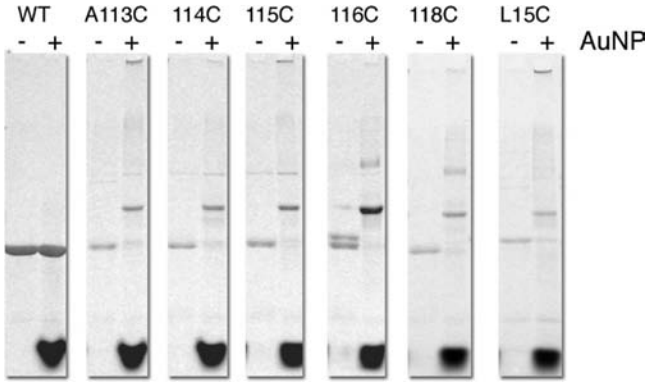


Figure 3. scFv reactivity. The leftmost gel shows the wild-type (WT) NC10 scFv in the presence (+) and absence (−) of gold. To the right is the A113C nested mutant in which a gel-shifted band appears in the presence of the 2 nm AuNP. The shifted band was observed in the presence of AuNP for all mutants of the NC10 scFv tested.

positions of the peaks from *p*-MBA, confirming the surface immobilization of the *p*-MBA and the absence of any chemical alteration by exposure to high pH or borohydride (Supporting Information, Figure S6). The UV/visible spectrum of the 2 nm AuNPs (Supporting Information, Figure S11) included peaks at ~300 and ~510 nm and was similar to the spectrum of the well studied 29 kDa compound (*23–26*). There are at least 4 previous reports of UV/vis spectra for the 29 kDa or Au_{144} compound, found in *refs* 23–25 and *26*. Each of these spectra differs in fine detail, but a hallmark of this compound is a very small surface-plasmon resonance-like inflection or peak at 510 nm or 2.4 eV. Differences between the three spectra and the spectrum accompanying our report may be accounted for by differences in the ligand comprising the monolayer and by differences in instrument sensitivity. This compound has recently been analyzed by high resolution mass spectroscopy and reported to have a core of Au_{144} (*25*, *26*).

Reaction of *p*-MBA AuNPs with Cysteine Mutant Proteins and Thiolated DNA. In our previous work, glutathione AuNPs were activated by oxidation with permanganate for conjugation with the NC10 scFv antibody fragment (*17*). Single cysteine residues were introduced at or near the C-terminus of NC10 for the purpose. Substitution mutants S112C and A113C contained cysteines in place of the last two structured residues of NC10 revealed by X-ray diffraction. C-terminal extension mutants 114C−118C contained cysteines one to five positions beyond the last structured residue. In addition, in mutants L15C, Q80C, G15C, and P14C, cysteines were substituted for surface residues elsewhere in the framework region of NC10. Glutathione AuNP conjugates were only obtained with C-terminal extension mutants 116C−118C, showing a requirement for exposure of the cysteine residue for reactivity (*17*). In contrast, the 2 nm *p*-MBA AuNP reacted with all NC10 mutants, resulting in a characteristic gel shift upon SDS−PAGE (Figure 3). Conjugate formation was essentially quantitative, except in the case of S112C, L15C, Q80C, and G15C mutants, whose reactivity was slightly diminished. A surface cysteine mutant of catalase, K560C, showed no reactivity at all (Supporting Information, Figure S7). The 2 nm *p*-MBA AuNP reacted rapidly and quantitatively with synthetic oligonucleotides bearing terminal thiol groups (*27*) (Supporting Information, Figure S8.)

Reaction of *p*-MBA AuNPs with native cysteine residues in proteins, and detection by EM. Reaction of *p*-MBA AuNPs was tested with two proteins bearing native cysteine residues, muscle actin and antibody Fc fragment. The 2 nm *p*-MBA AuNP formed conjugates with three of the seven cysteines in muscle actin, as shown by SDS−PAGE (Supporting Information, Figure S9). The antibody Fc fragment contains two polypeptide chains with a disulfide bond between them. Following the reduction of the disufide bond with TCEP, reaction with both 2 and 3 nm *p*-MBA AuNPs was observed. Detection in this case took advantage of the strong binding of Fc fragments to protein A, in particular to the two protein A domains in the widely used tandem affinity purification (TAP) tag (*28*). EM of AuNP-Fc bound to TAP-tagged protein showed pairs of closely apposed gold particles. These pairs of particles were clearly attributable to conjugates, and distinguishable from unreacted AuNP-Fc, scattered across the micrographs, on the basis of their characteristic spacing (Figure 4).

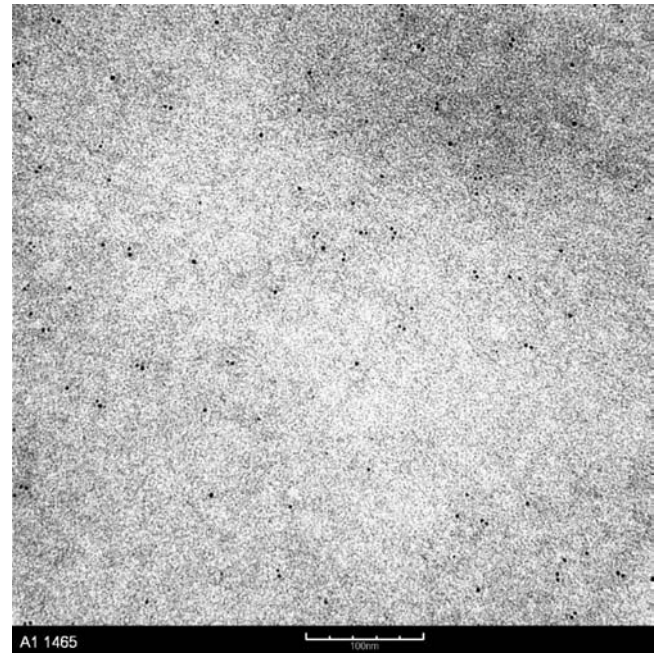


Figure 4. TAP-tagged RNA polymerase was incubated with Fc/2 nm particle conjugates and drop cast onto a carbon coated EM grid.

Quenching *p*-MBA AuNP Reactivity. In order to quench the reactivity of *p*-MBA AuNP−protein conjugates toward further protein sulfhydryls, we took advantage of the unreactivity of glutathione AuNPs noted previously. Treatment of the 2 nm *p*-MBA AuNP with 1 mM glutathione for 1 h at room temperature proved effective for the purpose. We presume that the product was repassivated (most or all *p*-MBA replaced by glutathione) because the AuNP remained intact (Supporting Information, Figure S10), while reactivity was lost. Following conjugation and repassivation, NC10 scFv retained affinity for its antigen, the tetrameric N9 neuraminidase, as shown by mixing with neuraminidase and cryo-EM. Characteristic sets of four gold particles were observed (Figure 5). The DNA in repassivated AuNP conjugates also remained capable of interaction, as shown by hybridization with the complementary strand and gel electrophoresis.

DISCUSSION

The notable results of this work include the following: the effect of solvent on the products of *p*-MBA AuNP synthesis; the formation of virtually monodisperse 2 and 3 nm particles; the growth of large single crystals of the 2 nm particle amenable to X-ray diffraction analysis; the spontaneous reactivity of *p*-MBA particles toward protein and DNA sulfhydryls; the quenching of reactivity by repassivation with glutathione; and a method for distinguishing particles bound to proteins of interest from free particles by EM.

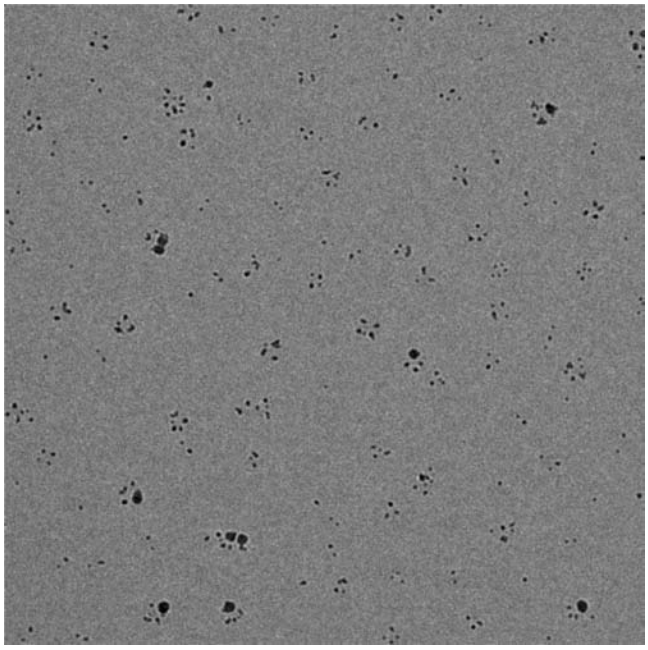


Figure 5. Cryo-EM of NC10/2 nm AuNP mixed with N9 neuraminidase. The tetrameric structure of N9 neuraminidase results in the binding of four scFv fragments. The larger particles observed are 10 nm AuNP, included as markers in this cryo-EM preparation.

On the basis of transmission EM, HAADF-STEM, and UV−vis spectroscopy, we identify the 2 nm particle as having an Au_{144} core, consistent with other recent assignments for an AuNP often referred to as a 29 kDa compound. An important contribution of our work is the direct synthesis, with no requirement for purification, annealing, ripening, or etching to obtain an essentially monodisperse product, as judged from the formation of single crystals, from an exceptionally narrow band in PAGE, from HAADF-STEM, and from TEM.

The 2 nm particles were insoluble at methanol concentrations above 27% (Figure 1, right panel). The uniformity of the particles may therefore be due, in part, from growth in solution to a critical size, at which precipitation occurs. The 3 nm particles appeared less uniform than the 2 nm particles and did not precipitate at the methanol concentration used. Their size distribution may be narrowed by a reduced reaction rate under the high pH conditions used. Others have suggested that reducing the rate of reduction may allow the creation of more uniform particles (*29*). We have observed that the color change indicative of particle formation requires hours for reactions performed at high pH, as opposed to seconds for reactions at low pH.

Metal nanoparticles are believed to be stabilized by electronic shell filling for smaller particles and geometric shell filling for larger particles. The concept of shell filling leads naturally to the idea of a magic number series. In the case of gold AuNPs, nominal inorganic masses of 5, 8, 15, 20, 29, 45, and 93 kDa have been derived (*6*, *30*, *31*). Recent X-ray structure determination of the 5 kDa (Au_{25}) (*32*) and 20 kDa (Au_{102}) (*21*) compounds led to the conclusion that even particles as large as Au_{102} are stabilized as electronic shell filling (*33*).

The structure and exact formulation of the 29 kDa compound, which we identify here as an Au_{144} 2 nm particle, remains a matter of conjecture. For 144 gold atoms, closure of a 90e- or 92e-electronic shell would require 52 or 54 ligands (on the assumption that each gold atom donates one electron and each *p*-MBA group withdraws one electron from the electronic shell) (*33*). This argument has been called into question, however, by recent mass spectroscopy, which led to a formulation of the 29 kDa compound as $Au_{144}(SR)_{59}$ (*24*), and a DFT calculation, which argued for an assignment of $Au_{144}(SR)_{60}$ (*34*).

Our previous work (*15*) established a method for the formation of rigid, specific, and discrete gold nanoparticle/protein conjugates. The method yields a direct bond between gold atoms of the gold nanoparticle core and the sulfhydryl moiety of a cysteine residue, whereas the commercial product, Nanogold (Nanoprobes, Yaphank, NY), relies on a flexible organic linker and a maleimide group to accomplish binding to cysteine residues. The elimination of the linker facilitates applications requiring rigid immobilization of AuNPs on proteins. Conjugates formed by electrostatic interaction with traditional colloidal gold may also be rigid, but will not necessarily have a precise number of AuNPs bound at the same location on every protein.

In contrast to our previous work with glutathione AuNPs, the formation of protein and DNA conjugates with *p*-MBA AuNPs was more facile and more promiscuous. Whereas the reaction of activated glutathione AuNPs with scFvs bearing reduced, exposed cysteine residues never surpassed 50%, the *p*-MBA AuNPs reacted quantitatively with exposed cysteine residues. Moreover, while glutathione AuNPs showed only slight reactivity toward the 116C extension mutant of the NC10 scFv and no reactivity toward the shorter 115C, 114C, A113C, and S112C extension mutants, *p*-MBA AuNPs reacts almost quantitatively with mutants 114C and longer.

The high reactivity of *p*-MBA AuNPs may in some cases capture nonnative conformations of the scFv or other protein target. While most conjugates formed with the NC10 scFv retained affinity for the N9 neuraminidase antigen, conjugates with the Q80C framework mutant of NC10 showed diminished affinity. The failure of conjugate formation with the K560C mutant of catalase is important in this regard. The cysteine residue in the K560C mutant is located in a depression on the protein surface, rendering it inaccessible to an AuNP of the diameter used (Supporting Information, Figure S7). The AuNP evidently did not induce protein denaturation sufficient for reactivity.

ACKNOWLEDGMENT

We thank Laurent Menard and Ralph Nuzzo for HAADF-STM analysis, Peter Loewen for catalase and catalase mutants, and Corey Liu and the SMRL for NMR. We also thank Pamela Bjorkman and Grant Jensen for their interest in large gold AuNPs, which stimulated our work. Portions of this research were carried out at the Stanford Synchrotron Radiation Laboratory, a national user facility operated by Stanford University on behalf of the U.S. Department of Energy, Office of Basic Energy Sciences. The SSRL Structural Molecular Biology Program is supported by the Department of Energy, Office of Biological and Environmental Research, and by the National Institutes of Health, National Center for Research Resources, Biomedical Technology Program, and the National Institute of General Medical Sciences. This research was supported by NSF grant CHE-0617050 and NIH grant AI21144.

Note Added in Proof: An additional mass spectrum of the extensively studied "29 kDa Compound," assigning a molecular formula of $Au_{144}(SR)_{60}$ was reported in December of 2009. The full reference is Qian, H. and Jin R. (2009) Controlling Nanoparticles with Atomic Precision: The case of $Au_{144}(SCH_2CH_2Ph)_{60}$. *Nano Lett. 9*, 4083–4087.

Supporting Information Available: Full details of the synthesis, supporting figures referenced in the text, and optical electronic spectra. This material is available free of charge via the Internet at http://pubs.acs.org.

LITERATURE CITED

(1) Daniel, M., and Astruc, D. (2004) Gold nanoparticles: assembly, supramolecular chemistry, quantum-size-related properties, and applications toward biology, catalysis, and nanotechnology. *Chem. Rev. 104*, 293–346.

(2) Brust, M., Fink, J., Bethell, D., Schiffrin, D. J., and Kiely, C. (1995) Synthesis and reactions of functionalized gold nanoparticles. *J. Chem. Soc., Chem. Commun.* 1655–1656.

(3) Alvarez, M. M., Khoury, J. T., Schaaff, T. G., Shafigullin, M. N., Vezmar, I., and Whetten, R. L. (1997) Critical sizes in the growth of Au clusters. *Chem. Phys. Lett. 266*, 91–98.

(4) Peterson, R. R., and Cliffel, D. E. (2005) Continuous free-flow electrophoresis of water-soluble monolayer-protected clusters. *Anal. Chem. 77*, 4348–4353.

(5) Schaaff, T. G., Knight, G., Shafigullin, M. N., Borkman, R. F., and Whetten, R. L. (1998) Isolation and selected properties of a 10.4 kDa gold:glutathione cluster compound. *J. Phys. Chem. B 102*, 10643–10646.

(6) Whetten, R. L., Khoury, J. T., Alvarez, M. M., Murthy, S., Vezmar, I., Wang, Z. L., Stephens, P. W., Cleveland, C. L., Luedtke, W. D., and Landman, U. (1996) Nanocrystal gold molecules. *Adv. Mater. 8*, 428–433.

(7) Schaaff, T. G., and Whetten, R. L. (1999) Controlled etching of Au:SR cluster compounds. *J. Phys. Chem. B 103*, 9394–9396.

(8) Whetten, R. L., Khoury, J. T., Alvarez, M. M., Murthy, S., Vezmar, I., Wang, Z. L., Stephens, P. W., Cleveland, C. L., Luedtke, W. D., and Landman, U. (1996) Nanocrystal gold molecules. *Adv. Mater. (Weinheim, Germany) 8*, 428–433.

(9) Schaaff, T. G., and Whetten, R. L. (1999) Isolation and selected properties of a 10.4 kDa gold:glutathione cluster compound. *J. of Phys. Chem. B 102*, 10643–10646.

(10) Hicks, J. F., Miles, D. T., and Murray, R. W. (2002) Quantized double-layer charging of highly monodisperse metal nanoparticles. *J. Am. Chem. Soc. 124*, 13322–13328.

(11) Prasad, B. L. V., Stoeva, S. I., Sorensen, C. M., and Klabunde, K. J. (2002) Digestive ripening of thiolated gold nanoparticles: the effect of alkyl chain length. *Langmuir 18*, 7515–7520.

(12) Aubin-Tam, M. E., Hwang, W., and Hamad-Schifferli, K. (2009) Site-directed nanoparticle labeling of cytochrome c. *Proc. Natl. Acad. Sci. U.S.A 106*, 4095–4100.

(13) Aubin-Tam, M. E., and Hamad-Schifferli, K. (2005) Gold nanoparticle-cytochrome C complexes: the effect of nanoparticle ligand charge on protein structure. *Langmuir 21*, 12080–12084.

(14) Jensen, G. J., and Kornberg, R. D. (1998) Single-particle selection and alignment with heavy atom cluster-antibody conjugates. *Proc. Natl. Acad. Sci. U.S.A 95*, 9262–9267.

(15) Zanchet, D., Micheel, C. M., Parak, W. J., Gerion, D., and Alivisatos, A. P. (2001) Electrophoretic isolation of discrete Au nanocrystal/DNA conjugates. *Nano Lett. 1*, 32–35.

(16) Xiao, Y., Patolsky, F., Katz, E., Hainfeld, J. F., and Willner, I. (2003) Plugging into Enzymes": nanowiring of redox enzymes by a gold nanoparticle. *Science 299* 1877–1881.

(17) Ackerson, C. J., Jadzinsky, P. D., Jensen, G. J., and Kornberg, R. D. (2006) Rigid, specific, and discrete gold nanoparticle/antibody conjugates. *J. Am. Chem. Soc. 128*, 2635–2640.

(18) Song, Y., and Murray, R. W. (2002) Dynamics and extent of ligand exchange depend on electronic charge of metal nanoparticles. *J. Am. Chem. Soc. 124*, 7096–7102.

(19) Johnson, S. R., Evans, S. D., and Brydson, R. (1998) Influence of a terminal functionality on the physical properties of surfactant-stabilized gold nanoparticles. *Langmuir 14*, 6639–6647.

(20) Ackerson, C. J., Jadzinsky, P. D., and Kornberg, R. D. (2005) Thiolate ligands for synthesis of water-soluble gold clusters. *J. Am. Chem. Soc. 127*, 6550–6551.

(21) Jadzinsky, P. D., Calero, G., Ackerson, C. J., Bushnell, D. A., and Kornberg, R. D. (2007) Structure of a thiol monolayer-protected gold nanoparticle at 1.1 A resolution. *Science 318*, 430–433.

(22) Menard, L. D., Gao, S. P., Xu, H., Twesten, R. D., Harper, A. S., Song, Y., Wang, G., Douglas, A. D., Yang, J. C., Frenkel, A. I., Nuzzo, R. G., and Murray, R. W. (2006) Sub-nanometer Au monolayer-protected clusters exhibiting molecule-like electronic behavior: Quantitative high-angle annular dark-field scanning transmission electron microscopy and electrochemical characterization of clusters with precise atomic stoichiometry. *J. Phys. Chem. B 110*, 12874–12883.

(23) Wyrwas, R. B., Alvarez, M. M., Khoury, J. T., Price, R. C., Schaaff, T. G., and Whetten, R. L. (2007) The colours of nanometric gold: optical response functions of selected gold-cluster thiolates. *Eur. Phys. J. D 43*, 91–95.

(24) Schaaff, T. G., Shafigullin, M., Khoury, J., Vezmar, I., and Whetten, R. L. (2001) Properties of a ubiquitous 29 kDa Au:SR cluster compound. *J. Phys. Chem. B 105*, 8785–8796.

(25) Huifeng, Q., and Jin, R. (2009) Controlling nanoparticles with atomic precision. *Nano Lett. 9*, 4083–4087.

(26) Chaki, N. K., Negishi, Y., Tsunoyama, H., Shichibu, Y., and Tsukuda, T. (2008) Ubiquitous 8 and 29 kDa gold:alkanethiolate cluster compounds: mass-spectrometric determination of molecular formulas and structural implications. *J. Am. Chem. Soc. 130*, 8608–8610.

(27) Ackerson, C. J., Sykes, M. T., and Kornberg, R. D. (2005) Defined DNA/nanoparticle conjugates. *Proc. Natl. Acad. Sci. U.S.A 102*, 13383–13385.

(28) Rigaut, G., Shevchenko, A., Rutz, B., Wilm, M., Mann, M., and Seraphin, B. (1999) A generic protein purification method for protein complex characterization and proteome exploration. *Nat. Biotechnol. 17*, 1030–1032.

(29) Zheng, N., Fan, J., and Stucky, G. D. (2006) One-step one-phase synthesis of monodisperse noble-metallic nanoparticles and their colloidal crystals. *J. Am. Chem. Soc. 128*, 6550–6551.

(30) Cleveland, C. L., Landman, U., Schaaff, T. G., Shafigullin, M. N., Stephens, P. W., and Whetten, R. L. (1997) Structural evolution of smaller gold nanocrystals: The truncated decahedral motif. *Phys. Rev. Lett. 79*, 1873–1876.

(31) Cleveland, C. L., Landman, U., Shafigullin, M. N., Stephens, P. W., and Whetten, R. L. (1997) Structural evolution of larger gold clusters. *Z. Phys. D 40*, 503–508.

(32) Heaven, M. W., Dass, A., White, P. S., Holt, K. M., and Murray, R. W. (2008) Crystal structure of the gold nanoparticle [N(C(8)H(17))(4)][Au(25)(SCH(2)CH(2)Ph)(18)]. *J. Am. Chem. Soc. 130*, 5940–5946.

(33) Walter, M., Akola, J., Lopez-Acevedo, O., Jadzinsky, P. D., Calero, G., Ackerson, C. J., Whetten, R. L., Gronbeck, H., and Hakkinen, H. (2008) A unified view of ligand-protected gold clusters as superatom complexes. *Proc. Natl. Acad. Sci. U.S.A 105*, 9157–9162.

(34) Lopez-Acevedo, O., Akola, J., Whetten, R. L., Gronbeck, H., and Hakkinen, H. (2009) Structure and bonding in the ubiquitous icosahedral metallic gold cluster Au-144(SR)(60). *J. Phys. Chem. C 113*, 5035–5038.

BC900135D

Synthesis of Peptide−Protein Conjugates Using *N*-Succinimidyl Carbamate Chemistry

Reda Mhidia,[†] Aurélie Vallin,[†] Nathalie Ollivier,[†] Annick Blanpain,[†] Getao Shi,[‡,§] Romain Christiano,[‡,§] Ludger Johannes,[‡] and Oleg Melnyk*[,†]

UMR CNRS 8161 Université de Lille Nord de France, Institut Pasteur de Lille, IFR 142, 1 rue du Pr Calmette 59021 Lille Cedex, France, Institut Curie − Centre de Recherche, Trafic, Signaling and Delivery Laboratory, 26 rue d'Ulm, 75248 Paris Cedex 05, France, and UMR CNRS 144, France. Received April 8, 2009; Revised Manuscript Received December 10, 2009

Peptide−protein conjugates are useful tools in different fields of research as, for instance, the development of vaccines and drugs or for studying biological mechanisms, to cite only few applications. *N*-Succinimidyl carbamate (NSC) chemistry has been scarcely used in this area. We show that unprotected peptides, featuring one lysine residue within their sequences, can be converted in good yield into NSC derivatives by reaction with disuccinimidylcarbonate (DSC). No hydrolysis of the NSC group was observed during RP-HPLC purification, lyophilization, or storage. NSC peptides reacted efficiently within minutes with lysozyme used as model protein. To illustrate usefulness of the method consisting of the synthesis of a peptide−protein conjugate of biological interest, a NSC peptide derived from a peptide substrate for tyrosylprotein sulfotransferase (TS) was synthesized and ligated to receptor-binding nontoxic B-subunit of Shiga toxin (STxB). Immunofluorescence studies showed the intracellular delivery of the TS-STxB conjugate and its ability to circulate to the Golgi as the native STxB protein. Moreover, we demonstrate that the TS label could be sulfated by tyrosylprotein sulfotransferases present in the Golgi. Thus, NSC chemistry permitted rapid synthesis of a peptide−protein conjugate worthwhile for studying the transport of proteins from the plasma membrane to the Golgi. The second part of this article describes a more general method for synthesizing peptide−protein conjugates without any limitation of the peptide sequence. The conjugates were assembled by combining NSC chemistry and α-oxo semicarbazone ligation. To this end, a glyoxylyl NSC peptide was synthesized and reacted with lysozyme. The glyoxylyl groups on the protein were then reacted with a semicarbazide peptide to produce the target peptide−protein conjugate. Both reactions, namely, urea bond formation and α-oxo semicarbazone ligation, were carried at pH 8.0 using a one-pot procedure.

INTRODUCTION

Nowadays, various methods are available for the synthesis of peptide−protein conjugates. Site-specific ligation methods, by exploiting a unique functional group present within the protein, lead to well-characterized conjugates. Reaction of a cysteine residue with haloacetyl (*1*) or maleimidyl (*2*) peptides is often used in this field. Alternatively, unnatural functional groups helpful for site-specific ligation such as keto or aldehyde groups can be introduced into protein-specific sites by using chemical methods (*3*, *4*), enzymatic techniques (*5*), or living organisms (*6*).

Random peptide−protein conjugates are also useful tools in different fields of research as, for example, the development of vaccines (*7*) or drugs (*8*, *9*) or for studying biological mechanisms (*1*). Their preparation is often carried out using *N*-succinimidyl carboxylic ester (NSCE)-based bifunctional reagents (*10*). Usually, the bifunctional reagent is reacted first with the protein leading to formation of amide bonds between surface-exposed ε-amino groups and NSCE moiety. Then, the second functional group is used to attach peptide molecules (*7*). The synthesis of peptide−protein conjugates by direct reaction of NSCE peptides with proteins is less common. For instance, Kida et al. have recently described the synthesis of a Tat-Cys-NSCE peptide by reacting Tat-Cys with 6-maleimidohexanoic acid *N*-succinimidyl ester (*11*). However, the sensitivity of Tat-Cys-NHSE peptide toward hydrolysis precluded its purification by RP-HPLC. Consequently, the crude Tat-Cys-NSCE peptide was stored at −80 °C and directly used in the conjugation experiments. A similar approach was reported by Inglese et al. for the attachment of a protein kinase A substrate to proteins (*12*).

N-Succinimidyl carbamate derivatives (NSC), whose chemistry is related to NSCE, have been scarcely used for the synthesis of conjugates. Morpurgo et al. reported the synthesis of an NSC derivative of biotin for protein labeling (*13*). Later on, Clavé et al. described the synthesis of a fully protected NSC dipeptide scaffold (*14*). This reagent was coupled to the N-terminal amino group of substance P. Pasut et al. described the synthesis of a PEG-β-alanine NSC derivative for protein pegylation (*15*). In these studies, besides the NSC group, no other functional moiety was present on the molecules. To the best of our knowledge, the synthesis of NSC peptides incorporating functional side chains, their purification, and coupling to proteins was not reported in the literature.

We describe here the synthesis of NSC peptides incorporating functional side chains (phenol group of tyrosine, hydroxyl group of serine, imidazole group of histidine, carboxylic acid group of glutamic acid, and/or indole group of tryptophan). These peptide derivatives were successfully purified by RP-HPLC and coupled to proteins. Lysozyme was used as a model protein to optimize preparation of conjugates. Obviously, the partial conversion of NSC group into an isocyanate group during the conjugation experiment is a fact. To illustrate the value of the method consisting of the synthesis of a peptide−protein

* Corresponding author. Phone: 333 20 87 12 14, Fax: 333 20 87 12 35, E-mail: oleg.melnyk@ibl.fr.

[†] UMR CNRS 8161.

[‡] Institut Curie − Centre de Recherche.

[§] UMR CNRS 144.

10.1021/bc900154r © 2010 American Chemical Society
Published on Web 01/07/2010

Table 1. Yields for Peptides 1−4a,b and MS Data

peptide	*m/z* calcd	*m/z* found	yield (%)
1a	1601.7[a]	1601.5[a]	73
2a	2183.1[a]	2182.8[a]	34
3a	2339.2[a]	2339.0[a]	42
4a	2495.3[a]	2495.2[a]	47
1b	871.9[b]	872.2[b]	59
2b	1162.6[b]	1163.1[b]	56
3b	1240.6[b]	1241.2[b]	56
4b	1318.7[b]	1319.5[b]	61

[a] $[M+H]^+$ MALDI-TOF analysis in a reflector mode using α-cyano-4-hydroxycinnamic acid as matrix. [b] $[M+2H]^{2+}$ LC-MS analysis (source temperature 120 °C, desolvation temperature 350 °C, cone 30 V, capillary 3000 V).

conjugate of biological interest, a NSC peptide derived from a peptide substrate for tyrosylprotein sulfotransferase (TS) (*10*) was synthesized and ligated to receptor-binding nontoxic B-subunit of Shiga toxin (STxB). STxB binds to glycosphingolipid Gb3 in the plasma membrane of target cells. After binding, STxB is transported to the endoplasmic reticulum, via endosomes and the Golgi. Due to this property, STxB can potentially be used for vectorization of drugs (*16*). The colocalization of TS-STxB conjugate with a Golgi marker was studied by confocal immunofluorescence microscopy. The ability of the TS label within the TS-STxB conjugate to be sulfated by Golgi tyrosylprotein sulfotransferase was also examined.

In the second part of this article, we describe a more general method for synthesizing peptide−protein conjugates, which is not limited by the peptide sequence. The conjugates are assembled using a one-pot procedure combining NSC chemistry and α-oxo semicarbazone ligation. To this end, a glyoxylyl NSC peptide was synthesized and reacted with lysozyme at pH 8.0 to produce glyoxylyl lysozyme. The crude reaction mixture was then reacted with a semicarbazide peptide. Ligation between the glyoxylyl groups on the protein and the semicarbazide group on the peptide resulted in one-pot formation of the target peptide−protein conjugate.

EXPERIMENTAL PROCEDURES

Solid-Phase Peptide Synthesis of Peptides 1−4a. Solid-phase synthesis was performed using the Fmoc/*tert*-butyl strategy on a Novasyn TGR resin (0.1 mmol scale) in a microwave peptide synthesizer (CEM μ WAVES, Saclay, France). Couplings were performed using 5-fold molar excess of each Fmoc L- or D-amino acid, 4.5-fold molar excess of HBTU, and 10-fold molar excess of DIEA. Final deprotection and cleavage from the resin was carried out with TFA/thioanisol/TIS/H_2O 92.5/2.5/2.5/2.5 by vol. The resin beads were filtered, and the filtrate was precipitated in diethyl ether/heptane 1/1 by vol, dissolved in water, and lyophilized. The crude peptide was purified by RP-HPLC on a 100 Å 5 μm C18 Nucleosil column using a linear water/acetonitrile gradient containing 0.05%TFA by vol (6 mL/min, detection 215 nm, 0−40% B in 60 min). Fractions were collected and lyophilized to produce **1−4a** (yields are indicated in Table 1). The purity of peptides **1−4a** was >95% as determined by analytical RP-HPLC and CZE. MS data are in accordance with the proposed structures (see Table 1 and Supporting Information).

Synthesis of NSC Peptides 1−4b. DSC (16.6 mg, 65 μmol) was dissolved in dry DMF (340 μL) at rt under N_2. Peptide **1−4a** (6.5 μmol) and triethylamine (0.45 μL, 3.2 μmol) were solubilized in dry DMF (85 μL) and then added in one portion to DSC solution. The mixture was stirred at rt for 1 h. The crude mixture was diluted with 20 mL of 1% by vol aqueous TFA and purified by RP-HPLC on a 100 Å 5 μm C18 Nucleosil column using a linear water/acetonitrile gradient containing 0.05% TFA by vol (6 mL/min, detection 215 nm, 0−40% B in 60 min). Fractions were collected and lyophilized to produce **1−4b** (yields are indicated in Table 1).

The purity of peptides **1−4b** was >95% as determined by analytical RP-HPLC and CZE. MS data are in accordance with the proposed structures (see Table 1 and Supporting Information).

Synthesis of NSCE Peptide 1c. A solution of suberic acid bis(*N*-succinimidyl ester) DSS (64 mg, 175 μmol) in dry DMF (700 μL) at rt under nitrogen was added to a stirred solution of peptide **1a** (30 mg, 17.5 μmol) and triethylamine (2.4 μL, 17.5 μmol) in dry DMF (340 μL). The mixture was stirred at rt for 1 h. The crude mixture was then diluted with 20 mL of 1% by vol aqueous TFA and purified by RP-HPLC on a 100 Å 5 μm C18 Nucleosil column using a linear water/acetonitrile gradient containing 0.05%TFA by vol (6 mL/min, detection 215 nm, 0−40% B in 60 min). Fractions were collected and lyophilized to produce 15 mg of pure peptide **1c** (46%). The purity of peptide **1c** was >95% as determined by analytical RP-HPLC. MS data are in accordance with the proposed structure (see Supporting Information).

Labeling of Lysozyme, General Procedure. Lysozyme (Appligene ref 130172, 0.41 mg, 0.028 μmol, 0.2 mM final concentration) in 10 mM pH = 7.4 PBS buffer (140 μL) was added to NSC peptide **1−4b** (0.2 μmol). The mixture was stirred at 4 °C for 1 h. Analysis of the reaction mixtures by RP-HPLC and CZE showed that ∼50% of lysozyme molecules were modified. MALDI-TOF analysis of the mixtures revealed the presence of up to 4 peptide chains on lysozyme.

Labeling of STxB. STxB was produced and purified as described elsewhere (*17*). STxB (1.11 mg, 0.14 μmol, 0.32 mM final concentration) in pH = 8.0 sodium phosphate buffer (450 μL) was added to NSC peptide **1b** (2.24 μmol). The mixture was stirred at rt for 1 h. The conversion was ∼70% as determined by LC-MS. MALDI-TOF analysis of the mixture revealed grafting of up to 3 peptide chains on STxB. The conjugate was purified by filtration to produce TS-STxB-a or purified by RP-HPLC to produce TS-STxB-b.

Purification by Filtration, TS-STxB-a. 300 μL of the above reaction mixture was filtered and washed with PBS (3 × 20 mL) on a 3 kD membrane (3000 MWCO PES Vivascience, UK). The total volume after this step was 750 μL. The solution concentration (0.92 μg/μL) was determined using the bicinchoninic BCA assay (*18*).

RP-HPLC Purification, TS-STxB-b. 100 μL of the above reaction mixture was purified by RP-HPLC on a 300 Å 5 μm C18 XBridge column (4.6 × 250 mm) using a linear water/acetonitrile gradient (1 mL/min, eluent A is 0.05% TFA in water, eluent B is 0.05% TFA in CH_3CN/water 4/1 by vol, 0−100% B in 30 min, detection at 215 nm). Fractions were collected and lyophilized to produce TS-STxB-b. The conjugate was dissolved in 100 μL of PBS. The solution concentration (0.5 μg/μL) was determined using the bicinchoninic BCA assay (*18*).

Synthesis of Peptide 5 and Glyoxylyl Peptide 6. Solid-phase synthesis of peptide **5** H-SAAFGGK-NH_2 was performed using the Fmoc/*tert*-butyl strategy on a Novasyn TGR resin (0.1 mmol scale) in a microwave peptide synthesizer (CEM μ WAVES, Saclay, France). Couplings were performed using 5-fold molar excess of each Fmoc L-amino acid, 4.5-fold molar excess of HBTU, and 10-fold molar excess of DIEA. Final deprotection and cleavage from the resin was carried out with TFA/TIS/H_2O 95/2.5/2.5 by vol. The resin beads were filtered and the filtrate was precipitated in diethylether/heptane 1/1 by vol, dissolved in water, and lyophilized to produce 71 mg of peptide **5** (82%). The purity of peptide **5** was >90% as determined by

analytical RP-HPLC and CZE. MS data are in accordance with the proposed structure (see Supporting Information).

A solution of peptide **5** (21.3 mg, 0.024 mmol) in 0.1 M pH 7.0 sodium phosphate buffer (6.4 mL) was reacted for 10 min with sodium periodate (10.5 mg, 0.049 mmol) at rt. The reaction mixture was quenched with ethanolamine (3.5 μL, 0.037 mmol) and purified immediately by RP-HPLC on a 100 Å 5 μm C18 Nucleosil column using a linear water/acetonitrile gradient containing 0.05% TFA by vol (6 mL/min, detection 215 nm, 0−40% B in 60 min). Fractions were collected and lyophilized to produce peptide **6** (11 mg, 64%).

The purity of peptide **6** was 90% by analytical RP-HPLC and 92% by CZE. MS data are in accordance with the proposed structure (see Supporting Information).

Synthesis of Glyoxylyl NSC Peptide 7. A solution of glyoxylyl peptide **6** (11 mg, 0.015 mmol) and triethylamine (1.07 μL, 0.007 mmol) in dry DMF (153 μL) was reacted with DSC (58.7 mg, 0.229 mmol). The mixture was stirred at rt for 1 h. The crude mixture was diluted with 10 mL of 0.3% by vol aqueous TFA and purified immediately by RP-HPLC on a 100 Å 5 μm C18 Nucleosil column using a linear water/acetonitrile gradient containing 0.05% TFA by vol (6 mL/min, detection 215 nm, 0−40% B in 60 min). Fractions were collected and lyophilized to produce glyoxylyl NSC peptide **7** (6 mg, 53%).

The purity of peptide was 87% by analytical RP-HPLC. MS data are in accordance with the proposed structure (see Supporting Information).

Preparation of Peptide−Protein Conjugates. Reaction of Lysozyme with Peptide 7 and then α-Oxo Semicarbazone Ligation with Peptide 8. The synthesis of semicarbazide peptide **8** was described in detail elsewhere (*19*). This peptide sequence is derived from HIV1 POL 476−484 protein.

Labeling with Peptide 7. A solution of lysozyme (0.85 mg, 0.06 μmol, 0.2 mM) in 0.1 M pH 8.0 sodium phosphate buffer (300 μL) was added to peptide **7** (0.30 mg, 0.42 μmol). The mixture was stirred at rt. The reaction was monitored by MALDI-TOF analysis. The reaction was complete after 1 h as visualized by MALDI-TOF mass spectrometry. The MS spectra showed grafting of up to three peptide **7** molecules to lysozyme.

Ligation between Glyoxylyl Lysozyme and Semicarbazide Peptide 8. The above mixture was then added to semicarbazide peptide **8** (1.00 mg, 0.84 μmol). The mixture was stirred at 37 °C for 2 h and then at rt for 72 h. MALDI-TOF analysis showed ligation of up to two semicarbazide peptide **8** molecules to lysozyme.

Retrograde Transport of TS-STxB-a,b Conjugates from the Plasma Membrane to the Trans Golgi Network. *Immunofluorescence Analysis.* 200 000 HeLa cells were placed on coverslip in 24-well test plate (TPP, Switzerland) and incubated with 2 μM TS-STxB-a,b conjugate or STxB for 40 min at 4 °C in PBS++ (PBS containing 0.9 mM $CaCl_2$, 0.52 mM $MgCl_2$ and 0.16 mM $MgSO_4$) and then shifted to 37 °C for 1 h (water-jacketed incubator, Forma Scientific). Cells were fixed with paraformaldehyde (300 μL of a 4% w/v solution in PBS), washed with PBS++, and then permeabilized with saponin solution (300 μL, 0.2% w/v saponin, 2% w/v BSA in PBS buffer). Each coverslip was incubated with 30 μL saponin solution containing 0.2% by vol of 13C4 murine anti-STxB antibody (hybridoma from ATCC #CRL 1794; see ref *20*) and 0.5% by vol of goat antibody against GM130 (C-19, Santa Cruz). Cells were washed with saponin solution and then incubated with 30 μL saponin solution containing 0.5% by vol antimurine Cy3-labeled secondary antibody (Beckman Coulter) and 0.5% by vol antigoat Alexa 488-labeled secondary antibody (Molecular Probes). Coverslips were mounted using 10% aqueous polyvinyl alcohol (Mowiol 4−88 from Fluka), 25% glycerol, and 59% Tris-HCl 0.2 M pH 8.5). Cells were analyzed by confocal microscopy (Leica Microsystems, Mannheim, Germany).

Sulfation Assay. Sulfation assay was performed as described elsewhere (*21*) using STxB, TS-STxB-a (conjugate purified by filtration), TS-STxB-b (conjugate purified by RP-HPLC), and TS-STxB-c. TS-STxB-c is a recombinant STxB protein modified at the C-terminus by two tandem sulfation sites. It is used as a positive control; see ref *22*. Proteins were incubated with 300 000 HeLa cells at 4 °C in sulfate-free Dulbecco's Modified Eagle Medium (DMEM, Invitrogen) for 30 min. Cells were washed with sulfate-free DMEM. 250 μL of radioactive sulfate ($^{35}SO_4^{2-}$, Perkin-Elmer) in sulfate-free DMEM (final activity 480 μCi/mL) were added to cells (120 μCi/300 000 cells). Cells were incubated for 2 h at 37 °C and then lysed in 900 μL of RIPA buffer (150 mM NaCl, 1% NP-40, 0.5% deoxycholic acid, 0.1% SDS, 50 mM Tris pH 8.0) and 9 μL of protease−inhibitor cocktail (1 mg/mL aprotinin, 1 mg/mL leupeptin, 1 mg/mL antipain, 1 mg/mL pepstatin, 1 M benzamidine, 40 mg/mL phenylmethanesulfonyl fluoride in DMSO). The cell lysate was precipitated with protein G-sepharose (GE Healthcare) loaded with anti-STxB antibody 13C4. Precipitated proteins were analyzed by tris-tricine gel (5 mL gel contains 1.7 mL 30% acrylamide,1.9% bis-acrylamide; 1.7 mL 3 M Tris-HCl with 0.3%SDS pH 8.45; 1.1 mL water; 0.7 mL glycerol; 50 μL 10% ammonium persulfate; 5 μL *N,N,N′,N′*-tetramethylethylenediamine) electrophoresis. Sulfated proteins were detected by autoradiography (STORM860, Molecular Dynamics).

RESULTS AND DISCUSSION

Molecules exposed at the plasma membrane can be circulated to early endosomes for recycling or targeted to lysosomes for degradation. Some molecules are directed to other cell compartments such as the Golgi apparatus or the endoplasmic reticulum (ER). This pathway, termed the retrograde route (*21*), plays a key role in important cellular functions such as antigen presentation (*16*) and cell signaling (*23*).

One strategy used to prove that a protein is transported from the plasma membrane to the Golgi is to modify it with a peptide sequence (TS) which can be enzymatically modified in the Golgi. Peptides presented in Table 1 are derived from the tyrosine sulfation site of rat chromogranin B (*24*). The tyrosine residue within the EEPEYGE motif is sulfated by tyrosylprotein sulfotransferase, an enzyme which is exclusively located in the trans Golgi network. Previous studies have shown TS−protein conjugates utility for studying the retrograde transport of proteins. Sulfation of the TS label was detected by incubating cells with radioactive sulfate followed by immunoprecipitation of the conjugate (*1*).

The work described in the first part of this article was motivated by the need to have an easy access to various TS−protein conjugates. TS peptides were modified at the C-terminus by a Lys(biotin) residue, thereby allowing capture of the TS−protein conjugates using streptavidin-coated beads. TS peptide sequence features four glutamic acid residues, with a negative charge at physiological pH. Thus, the labeling of proteins with TS peptide may significantly lower the isoelectric point (pI) of proteins. The solubility, binding, and biological properties of proteins heavily depend on their pI (*25*−*29*). The interactions of proteins with cell membranes (*28, 30*) are also often dictated by charge effects. Finally, pI control of labeled proteins by varying the label charge has been demonstrated to facilitate purification of labeled proteins by isoelectric focusing techniques (*31*). In this context, synthesis of a series of TS peptides with a range of pI was worth considering. To this end, 2 to 5 arg residues were incorporated at the N-terminus of peptides 1−4. D-Arg residues were chosen to minimize degradation of the peptide label in biological media.



Figure 1. TS-peptides **1**−**4** synthesized in this study. Two to five D-Arg residues were incorporated at the N-terminus of the TS substrate to modulate the pI of peptides.

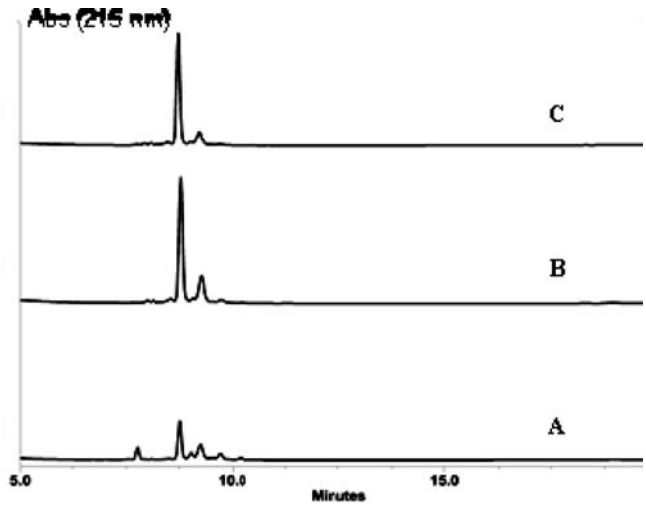


Figure 2. Effect of the DSC mode of addition and stoichiometry on the RP-HPLC yield. Peptide **1a** was reacted at rt in anhydrous DMF with DSC in the presence of triethylamine (2 equiv). (A) Peptide and base were mixed and added over 1 h period to DSC (2 equiv). (B) Peptide and base were mixed and added in one portion to DSC (2 equiv). (C) Same as B using 10 equiv of DSC.

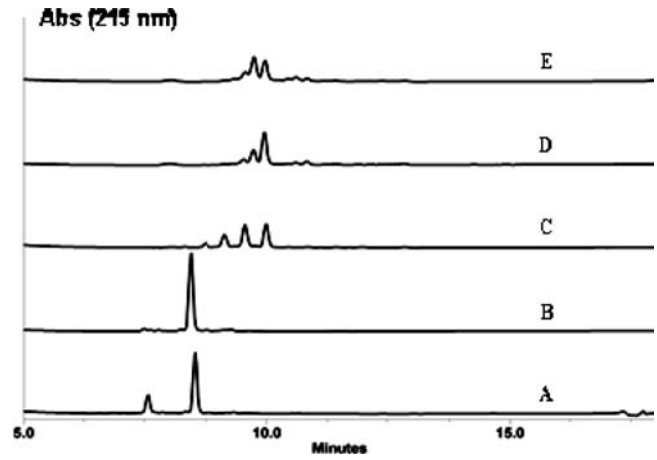


Figure 3. Effect of base stoichiometry on the RP-HPLC yield. Peptide **3a** was reacted at rt in anhydrous DMF with DSC (10 equiv) in the presence of triethylamine. Peptide and base were mixed and added in one portion to DSC. (A) TEA 0.5 equiv, 5 min; (B) TEA 0.5 equiv, 30 min; (C) TEA 10 equiv, 5 min; (D) TEA 10 equiv, 30 min; (E) TEA 10 equiv, 2 h.

NSC Peptide Synthesis and Stability. Peptides **1**−**4b** were obtained by reacting the corresponding precursors **1**−**4a** with DSC in anhydrous DMF. In a first approach, formation of the *N*-succimidylcarbamate moiety was examined using peptide **1a** and 2 equiv of both base and DSC. Slow addition of peptide **1a** to DSC led to a complex mixture (Figure 2A) in which target peptide **1b** represented only 37% of the total detected area. Alternately, addition of peptide **1a** in one portion (Figure 2B) led to a 67% RP-HPLC yield. The use of 10 equiv of DSC slightly improved the yield up to 73% (Figure 2C).

Next, the amount of DSC was fixed to 10 equiv, and we examined the influence of the base amount on the reaction yield using peptide **3a** (Figure 3). The use of an excess of base (Figure 3C−E) produced complex mixtures in which target peptide **3b** was not detected. Alternately, the use of 0.5 equiv of base (Figure 3A,B) permitted the clean conversion of peptide **3a** into NSC peptide **3b**. After 30 min, **3b** was formed nearly quantitatively (Figure 3B). The use of an excess of DSC minimized the formation of urea side-products by reaction of the formed NSC peptide **1**−**4b** with starting peptide **1**−**4a**. The critical role played by base stoichiometry can be explained by the potential conversion of NSC group into the highly reactive isocyanate moiety in basic conditions. Evidence for this degradation is introduced later on. Isocyanate groups react efficiently with amino groups as well as with the phenol group of tyrosine, and thus can be responsible for the multiple side-products observed when two or more equivalents of triethylamine were used. DSC high reactivity allows formation of NSC groups using substoichiometric amounts of base. In these experimental conditions, NSC group is stable and TS-peptides **1**−**4b** could be isolated

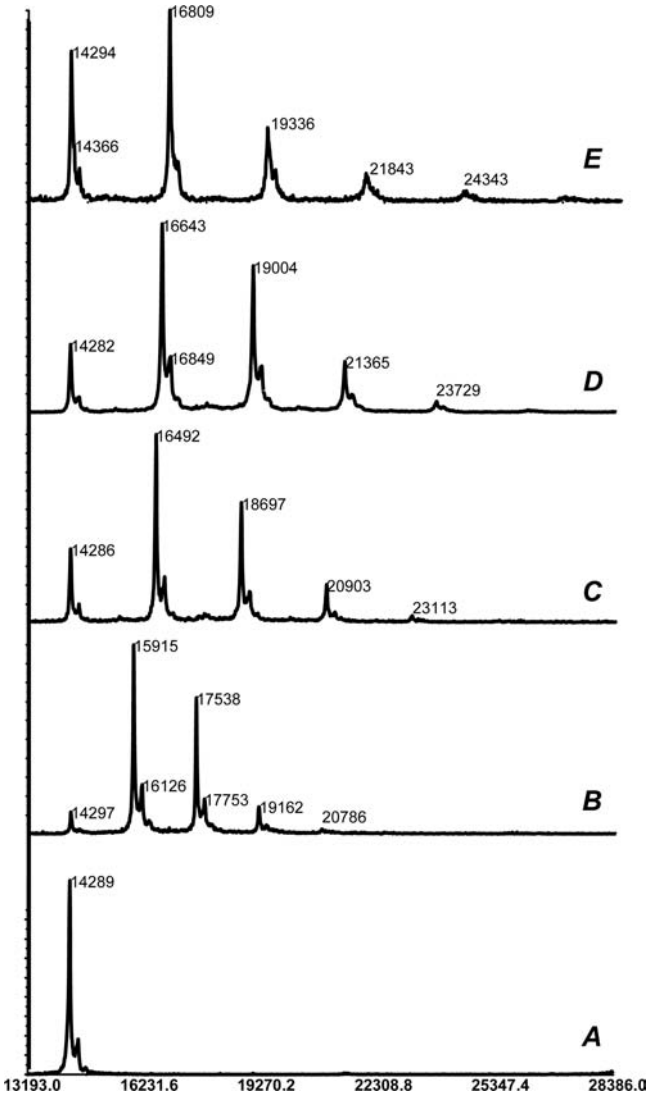


Figure 4. Reaction of lysozyme with peptides **1**−**4b**. MALDI-TOF analysis of the reaction mixtures after 1 h (pH 7.4, 4 °C). (A) without peptide, (B) peptide **1b**, (C) peptide **2b**, (D) peptide **3b**, (E) peptide **4b**.

successfully with a 59−61% yield after RP-HPLC purification. Lyophilized peptides **1**−**4b** were homogeneous by LC-MS and CZE; they displayed the expected molecular ions and were stable for months at −20 °C. ^{1}H and ^{13}C NMR analysis of peptide **1b** confirmed the NSC group presence on the ε-amino group of the C-terminal Lys residue. This procedure was successfully used for converting Ac-YLFSVHWPPLNKA-OH into corresponding NSC derivative Ac-YLFSVHWPPLNK(COOSu)A-OH, showing its compatibility with histidine, serine, tryptophan, and asparagine residues also (see Supporting Information).

For comparison, the same experimental conditions were used to convert peptide **1a** into **1c** in the presence of DSS (Figure 1). The RP-HPLC yield reached only 50% after 90 min of reaction. Peptide **1a** could efficiently be converted into peptide **1c** by using 1 equiv of base (46% isolated yield). Thus, synthesis of NSC peptides requires lower amounts of base compared to NSCE peptides, probably due to the higher reactivity of DSC compared to DSS.

Afterward, we examined the stability of peptides **1b**,**c** in water. Peptides **1b**,**c** were stable enough at room temperature in water containing TFA (pH 2) allowing their purification by RP-HPLC. Typically, hydrolysis of **1b** amounted to 3% after 3 h and only 19% after 18 h. The stability of peptides **1b**,**c** was also studied at pH 6.0. The half-life of NSCE peptide **1c** was 2 h. Peptide **1d** (Figure 1) was the sole species detected by RP-HPLC. The half-life of peptide **1b** was around 10 min. In this case, LC-MS analysis of the mixture revealed, besides peptide **1a**, formation of a novel compound corresponding to isocyanate **1e** (Figure 1). Reaction of this intermediate with benzylamine led to formation of urea **1f**, which displayed the expected fragment ions by matrix-assisted laser desorption ionization-time-of-flight postsource decay analysis.

In situ conversion of NSC peptide **1b** into isocyanate **1e** is probably at the origin of this peptide short half-life. Indeed, carbamates, which cannot be converted into isocyanates such as those derived from secondary amines, are known to be less reactive toward nucleophilic attack than parent carboxylic esters. For example, Gassman et al. have shown that a *p*-nitrophenyl-carbamate derived from a secondary amine is less reactive with nucleophiles than *p*-nitrophenyl acetate (*32*). As demonstrated later on, in situ formation of isocyanate moiety during the conjugation step might also explain the rapid formation of conjugates relative to NSCE derivatives.

Conjugation of Peptides 1−4b to Lysozyme. Lysozyme contains seven Lys residues within its sequence. Thus, 7 equiv of NSC peptide was used in the conjugation experiment. Lysozyme (0.2 mM final concentration) was reacted with NSC peptides **1**−**4b** at pH 7.4 in PBS buffer at 4 °C. A combination of RP-HPLC and CZE analyses showed a conversion of 50% for all tested NSC peptides. Lysozyme labeled with peptide **1b** coeluted by RP-HPLC with the native protein, whereas CZE permitted separation of the labeled protein from the native one due to the low pI of peptide **1b**. Alternately, lysozyme labeled with peptide **4b** could be separated from lysozyme by RP-HPLC, with the labeled material eluting earlier than the unlabeled one, whereas no separation was observed by CZE. The pI of peptide **4b** is close to the pI of lysozyme, explaining why the conjugate between peptide **4b** and lysozyme was not separated from the native protein by CZE. These experiments highlight the interest of varying the NSC peptide pI to match the physicochemical properties.

Figure 4 shows the MALDI-TOF spectra of the reaction mixtures. Up to four peptide chains were linked to lysozyme showing the efficiency of the conjugation reaction. Several studies have proven that NSCE derivatives react with ε-amino groups of proteins and sometimes with hydroxyl-containing amino acids too (*33*). Likewise, reaction of isocyanates with amino, thiol, hydroxyl, and/or imidazole groups within proteins is also possible (*34*). Thus, it cannot be excluded that such reactions might also occur with NSC peptides, which are at least partially converted in situ into isocyanate peptides.

RP-HPLC analysis of the crude reaction mixtures showed also, after 1 h, the absence of NSC peptides **1**−**4b** and two novel peaks in the TS peptide region. The latest eluting peak corresponded to peptides **1**−**4a**, formed by the NSC group hydrolysis. The other peak was attributed to cyclic peptide **1**−**4g** (Figure 5), resulting from the intramolecular reaction between the phenol group of tyrosine and the *N*-succinimidyl carbamate or isocyanate. Indeed, peptide **4g** showed a band at 263.5 nm, typical of an *O*-acetyl tyrosine, whereas the tyrosine residue within peptide **4a** displayed a band at 275.3 nm as expected. Peptide **4g** was isolated by RP-HPLC and treated with 0.1 M NaOH. These experimental conditions led to conversion of **4g** into a compound that coeluted with peptide **4a**. MALDI-TOF and UV spectra of **4a** and of the compound obtained from **4g** were also identical. Overall, these data support the structure proposed for cyclic peptides **1**−**4g**.

Finally, we have compared the reaction rate of peptides **1b**,**c** with lysozyme. LC-MS analysis of the reaction mixtures revealed that reaction of NSC peptide **1b** with lysozyme occurred in less than 5 min (50% conversion). Alternately, the

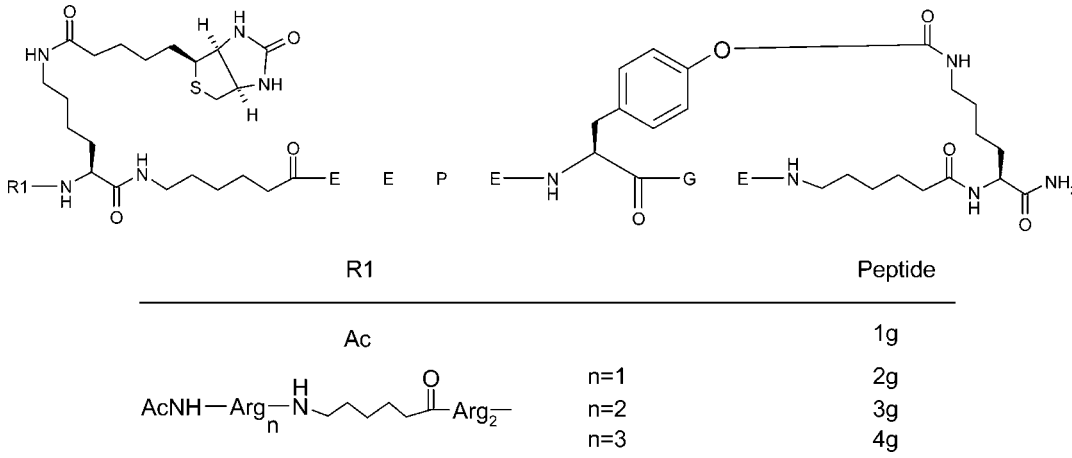


Figure 5. Cyclic peptides **1**−**4c** formed during the labeling reaction by reaction between the phenol group of tyrosine and the NSC group on C-terminal Lys residue.

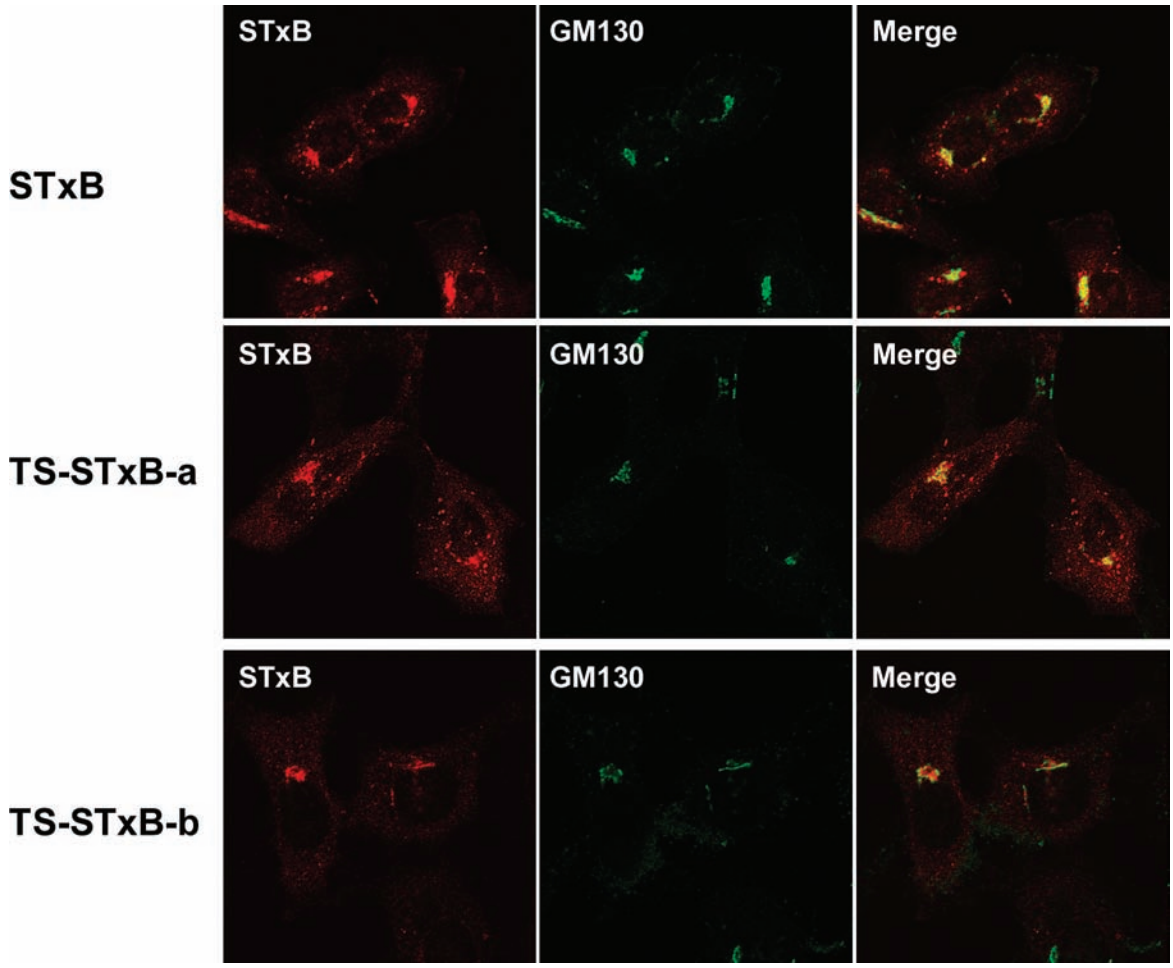


Figure 6. Immunofluorescence study of the retrograde transport of STxB and TS-STxB-a,b conjugates from the plasma membrane to the trans Golgi network. HeLa cells were incubated with 2 μM STxB or TS-STxB-a,b conjugates. Cells were fixed with paraformaldehyde, permeabilized with saponin, and then incubated with 13C4 murine anti-STxB antibody (hybridoma from ATCC #CRL 1794, see ref *20*) and C-19 goat antibody against GM130, a marker of the Golgi. Cells were washed with saponin solution and then incubated with secondary antibodies (Cy3-labeled antimurine, Alexa 488-labeled antigoat). Cells were analyzed by confocal microscopy (Leica Microsystems, Mannheim, Germany).

reaction of lysozyme with peptide **1c** led to only 20% conversion after 5 min and required about 1 h to go to completion (80% conversion). Thus, NSC peptides allow rapid conversion of proteins into peptide−protein conjugates, a property that can be an advantage for the labeling of unstable proteins.

Synthesis of TS-STxB Conjugates and Biological Studies. The retrograde route is used by Shiga toxin (*35*) to exert its toxic effects. This toxin has an AB5 structure. The A domain is responsible for the toxic effects of Shiga toxin. The B-subunit STxB (7.7 kD) forms a pentamer which preferentially binds the eukaryotic receptor globotriaosylceramide (Gb3). The B pentamer has the capacity of targeting the toxin to the retrograde route, allowing transfer of the A-subunit to the cytosol by retro-translocation from the endoplasmic reticulum. STxB is a

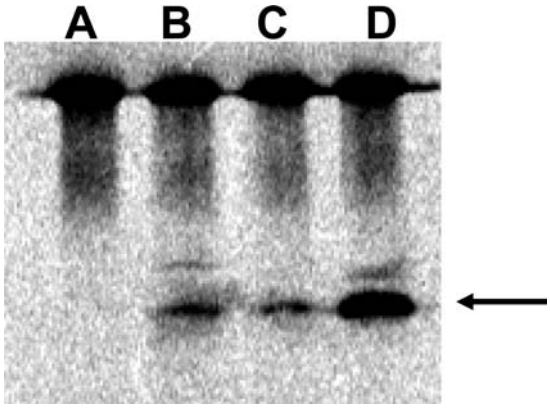


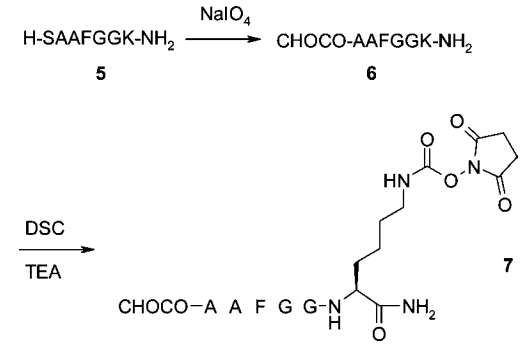
Figure 7. Sulfation assay using STxB (lane A), TS-STxB-a (lane B), TS-STxB-b (lane C), and TS-STxB-c (lane D). Proteins were incubated with HeLa cells at 4 °C in sulfate-free DMEM, and then incubated with $^{35}SO_4^{2-}$ in sulfate free DMEM at 37 °C for 2 h. Cells were lysed and STxB proteins were captured using protein G-sepharose loaded with anti-STxB antibody 13C4. Precipitated proteins were separated by tris-tricine gel electrophoresis, and gels were analyzed by autoradiography. The arrow points to the different STxB proteins.

valuable marker for the retrograde route and was used here to prove the usefulness of TS conjugates prepared using NSC chemistry.

STxB labeling was performed using peptide **1b** as described above. LC-MS analysis of the product revealed that 80% of STxB was modified. MALDI-TOF analysis of the product showed the presence of up to three TS peptides per STxB monomer. The conjugate was purified either by ultrafiltration on a 3 kD membrane (TS-STxB-a) or by RP-HPLC (TS-STxB-b). TS-STxB-a,b were identical by LC-MS. Both conjugates were tested to evaluate the impact of RP-HPLC and lyophilization steps on the TS-STxB-b biological activity.

The retrograde transport of STxB and of TS-STxB-a,b from the plasma membrane to the trans Golgi network was first studied by immunofluorescence confocal microscopy using HeLa cells (Figure 6). The three proteins colocalized with GM130, a protein which is bound to Golgi membranes (*36*). This experiment shows that modification of STxB by NSC

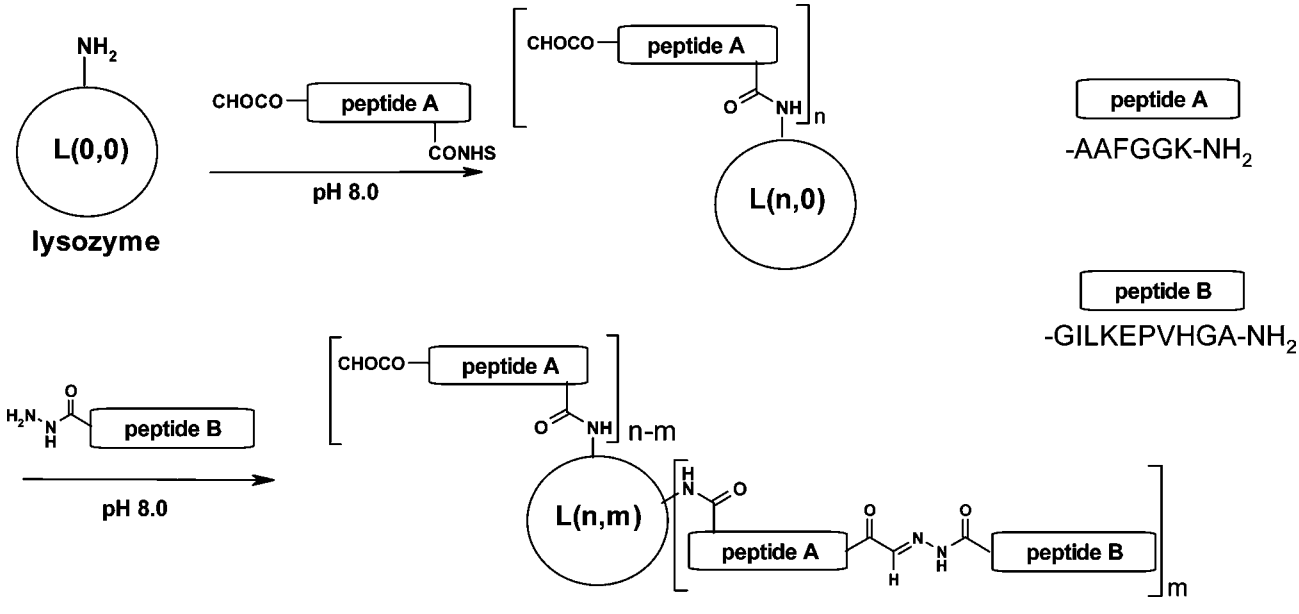
Scheme 2. Synthesis of Glyoxylyl NSC Peptide 7



peptide **1b** did not alter the capacity of the protein to target the retrograde route. We next studied the TS label capacity within the conjugates to be sulfated by tyrosylprotein sulfotransferase, an enzyme which is associated with the Golgi membrane (Figure 7) (*37*, *38*). STxB was used as a negative control (lane A, Figure 7), whereas TS-STxB-c, a recombinant STxB protein modified at the C-terminus by two tandem sulfation sites, was used as a positive control (*21*). Cells were first incubated with the different STxB proteins and then in the presence of $^{35}SO_4^{2-}$ in sulfate-free DMEM to allow incorporation of radioactive sulfate within the TS labels. Cells were lysed and STxB proteins were immunoprecipitated using anti-STxB monoclonal antibody. Radioactive bands were detected by autoradiography. The arrow in Figure 7 points to STxB proteins. This experiment shows a radioactive band for the positive control (TS-STxB-c, lane D) but not for the negative control (STxB, lane A). A band is also seen for TS-STxB a or b, showing that the TS label introduced using NSC chemistry is sulfated by tyrosylprotein sulfotransferase present in the Golgi. Overall, these data show that NSC chemistry allows the synthesis of conjugates that preserve the capacity of STxB protein to target the retrograde route and the ability of TS peptide to be sulfated in the cell.

One-Pot Synthesis of Peptide−Protein Conjugates. The method described above can only be used with peptides lacking Lys residues within their sequences such as the TS peptide described above. The two-step strategy depicted in Scheme 1 allows overcoming this limitation. The first step involves reaction of bifunctionnal peptide A with the protein using NSC

Scheme 1. One-Pot Synthesis of Peptide Protein Conjugates Can Be Performed by Combining NSC Chemistry and α-Oxo Semicarbazone Ligation



Scheme 3. Synthesis of Semicarbazide Peptide 8

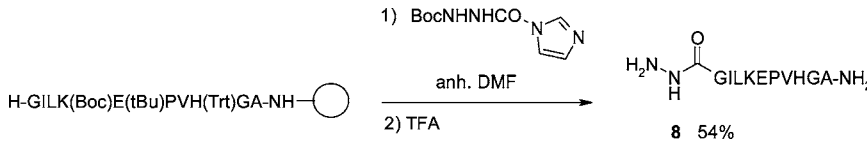


Table 2. MS Data for the One-Pot Reaction of Lysozyme with Glyoxylyl NSC Peptide 7 and Semicarbazide Peptide 8[a]

entries	lysozyme L(*n*,*m*)	calcd	found
1	0,0	14.306	14.306
2	1,0	14.936	14.937
3	2,0	15.567	15.571
4	3,0	16.198	16.198
5	1,1	15.996	15.995
6	2,1	16.626	16.626
7	2,2	17.684	17.684

[a] MALDI MS spectra were acquired in the linear mode by using a PerSeptive Biosystems Voyager DE-STR instrument fitted with a 337 nm nitrogen laser (25 kV, grid 92%, delay time 750 ns). Matrix: 3,5-Dimethoxy-4-hydroxycinnamic acid (20 mg/mL). Entry 1: lysozyme. Entries 2−4: reaction with peptide **7**. Entries 5−7: reaction with peptide **7** and peptide **8**.

chemistry. This allows introducing an α-oxo aldehyde group on the surface of the protein, which can be subsequently ligated chemoselectively with peptide B featuring a semicarbazide group at the N-terminus (Scheme 1). To date, semicarbazone chemistry has been mainly used for linking peptides to surfaces (*39*−*42*). To the best of our knowledge, however, ligation between semicarbazide and glyoxylyl peptides was not reported before. This may be due to the difficulty synthesizing peptides featuring a semicarbazide group at the N-terminus, because this moiety is rapidly hydrolyzed in the acid eluents (pH 2) often used for peptide RP-HPLC analysis or purification. A solution to this problem has recently been described by the use of a nearly neutral buffer instead for the purification step (*19*).

Peptide A synthesized in this work is used as spacer. A Phe residue was inserted into the sequence to facilitate UV detection. However, peptide A can potentially be used for introducing a bioactive sequence or a label depending on the final application.

The strategy described in Scheme 1 requires glyoxylyl NSC peptide **7** and semicarbazide peptide **8** synthesis. Peptide **7** was prepared starting from peptide **5** H-SAAFGGK-NH_2 (Scheme 2). Oxidation of peptide **5** into peptide **6** COCHO-AAFGG-NH_2 by sodium periodate was performed using standard experimental conditions (*4*). Glyoxylyl NSC peptide **7** was then synthesized by treating peptide **6** with 0.5 equiv of triethylamine and an excess of DSC, as described above for NSC TS peptides **1**−**4b**. Attempts to convert peptide **6** into the corresponding NSCE ester with DSS, as described above, failed probably due to imine formation between α-oxo aldehyde and ε-amino moieties in basic conditions.

Model peptide **8** synthesis was performed by coupling Boc-NHNHCO-imidazole to peptidyl resin assembled using Fmoc/*t*-Bu strategy (Scheme 3) (*19*). Semicarbazide peptide **8** was stable during TFA deprotection and cleavage and was purified by RP-HPLC in a pH 6.5 triethylamonium acetate buffer.

Lysozyme was used again as a model protein. Reaction between lysozyme and glyoxylyl NSC peptide **7** was performed in a pH 8.0 sodium phosphate buffer. MALDI-TOF analysis of the reaction mixture revealed grafting of up to three glyoxylyl NSC peptide **7** molecules (L1−3,0 see entries 2−4, Table 2; see also Figure 8). After 1 h, the reaction mixture was reacted with semicarbazide peptide **8** at same pH. Up to two semicarbazide peptide **8** molecules were linked to lysozyme (entries

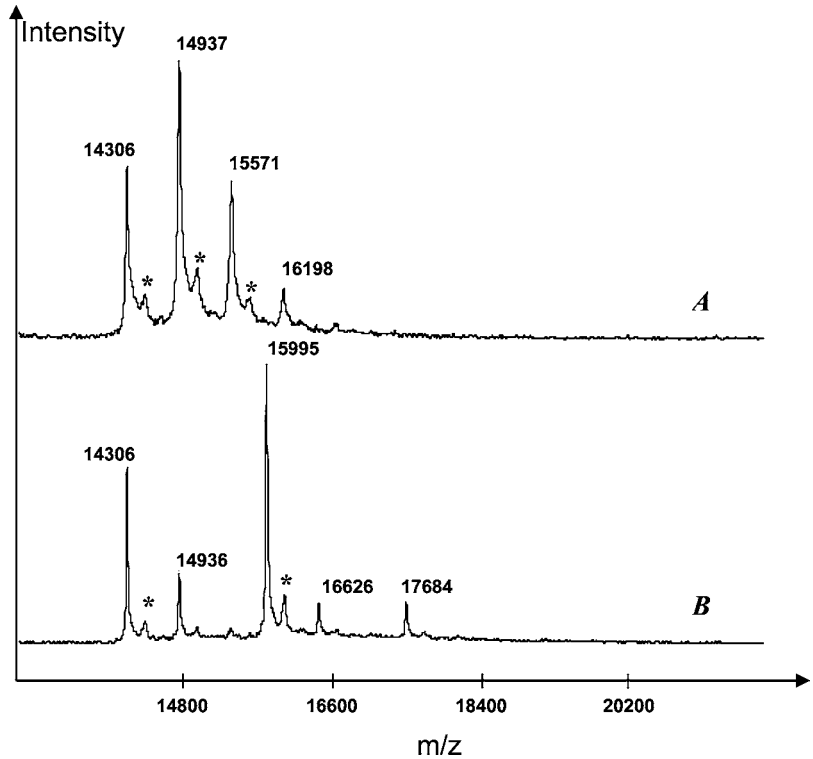


Figure 8. MALDI-TOF analysis of the one-pot conversion of lysozyme L into L(*n*,*m*) peptide-lysozyme conjugates. (A) after reaction with glyoxylyl NSC peptide **7**, (B) after reaction with peptide **7** and semicarbazide peptide **8**. See Table 2 for experimental conditions. The asterisk corresponds to protein−matrix adducts.

5−7, Table 2). Usually, Schiff-base formation between glyoxylyl peptides and peptide hydrazides is carried out at pH 5.5. In this study, successful formation of the α-oxo semicarbazone bond at pH 8.0 permitted the one-pot synthesis of peptide−protein conjugates in a straightforward manner.

In conclusion, we have shown that NSC peptides can easily be synthesized in high yield by reacting unprotected peptide precursors with DSC. The method requires the presence of only one reactive ε-amino group within the peptide sequence. Importantly, NSC peptides were stable during standard RP-HPLC purification at pH 2 and in the lyophilized form for months. Their reaction with ε-amino groups of proteins occurred efficiently and rapidly (<5 min), probably due to in situ partial conversion of NSC group into isocyanate moiety. The method was used for grafting a peptide substrate for tyrosylprotein sulfotransferase to lysozyme, a model protein, or STxB the receptor-binding nontoxic B-subunit of Shiga toxin, a valuable marker for the retrograde route. The biological activity of the STxB conjugate was verified by immunofluorescence confocal microscopy or using a sulfation assay. We have also described a novel method for synthesizing peptide−protein conjugates, which is compatible with all proteinogenic amino acids. The conjugates were assembled by combining NSC chemistry and α-oxo semicarbazone ligation. To this end, a glyoxylyl NSC peptide was synthesized and reacted with lysozyme to produce glyoxylyl lysozyme. The crude reaction mixture was then reacted with a semicarbazide peptide. Ligation between the glyoxylyl groups on the protein and the semicarbazide group on the peptide resulted in formation of the target peptide−protein conjugate. Both reactions were carried out at pH 8.0, thus allowing the one-pot synthesis of the conjugate without the need to adjust pH in between.

Overall, NSC chemistry described here is an interesting tool for preparation of conjugates of biological interest and complements the chemical toolbox of the peptide chemist.

ACKNOWLEDGMENT

We are grateful to the French Ministry of Research for its financial support, to the EEC, CNRS, Région Nord Pas-de-Calais and Cancéropôle Nord-Ouest for their grants. The work was performed in Chemistry Systems Biology platform facility of the Institute of Biology (Lille, France, http://csb.ibl.fr). GS was supported by a PhD fellowship from *Fondation pour la Recherche Médicale* (FRM).

Supporting Information Available: RP-HPLC, CZE and MS data for all compounds. ^{1}H NMR spectra for peptides **1a**,**b**. This material is available free of charge via the Internet at http://pubs.acs.org.

LITERATURE CITED

(1) Amessou, M., Popoff, V., Yelamos, B., Saint-Pol, A., Johannes, L. (2006) Measuring retrograde transport to the trans-Golgi network. In *Current Protocols in Cell Biology* (Bonifacino, J. S., Dasso, M., Harford, J. B., Lippincott-Schwartz, J., Yamada, K. M., Eds.) Chapter 15, Unit 15.10.1 15.10.21, John Wiley & Sons, Inc.

(2) Stoddart, C. A., Nault, G., Galkina, S. A., Thibaudeau, K., Bakis, P., Bousquet-Gagnon, N., Robitaille, M., Bellomo, M., Paradis, V., Liscourt, P., Lobach, A., Rivard, M. E., Ptak, R. G., Mankowski, M. K., Bridon, D., and Quraishi, O. (2008) Albumin-conjugated C34 peptide HIV-1 fusion inhibitor: equipotent to C34 and T-20 in vitro with sustained activity in SCID-hu Thy/Liv mice. *J. Biol. Chem. 283*, 34045–52.

(3) Dixon, H. B. (1964) Removal of the N-terminal residue of a peptide after transamination. *Biochem. J. 90*, 2C–3C.

(4) Geoghegan, K. F., and Stroh, J. G. (1992) Site-directed conjugation of nonpeptide groups to peptides and proteins via periodate oxidation of a 2-amino alcohol. Application to modification at N-terminal serine. *Bioconjugate Chem. 3*, 138–46.

(5) Werlen, R. C., Offord, R. E., Blakey, D. C., East, S. J., Melton, R. G., and Rose, K. (1995) In vitro and in vivo comparison of a randomly coupled antibody fragment-enzyme conjugate with a site-specific conjugate. *Biomed. Pept. Proteins Nucleic Acids 1*, 251–4.

(6) Wang, L., Zhang, Z., Brock, A., and Schultz, P. G. (2003) Addition of the keto functional group to the genetic code of Escherichia coli. *Proc. Natl. Acad. Sci. U.S.A. 100*, 56–61.

(7) Kafi, K., Betting, D. J., Yamada, R. E., Bacica, M., Steward, K. K., and Timmerman, J. M. (2009) Maleimide conjugation markedly enhances the immunogenicity of both human and murine idiotype-KLH vaccines. *Mol. Immunol. 46*, 448–56.

(8) Temming, K., Meyer, D. L., Zabinski, R., Senter, P. D., Poelstra, K., Molema, G., and Kok, R. J. (2007) Improved efficacy of alphavbeta3-targeted albumin conjugates by conjugation of a novel auristatin derivative. *Mol. Pharmacol. 4*, 686–94.

(9) Kumaresan, P. R., Luo, J., Song, A., Marik, J., and Lam, K. S. (2008) Evaluation of ketone-oxime method for developing therapeutic on-demand cleavable immunoconjugates. *Bioconjugate Chem. 19*, 1313–8.

(10) Kalkhof, S., and Sinz, A. (2008) Chances and pitfalls of chemical cross-linking with amine-reactive N-hydroxysuccinimide esters. *Anal. Bioanal. Chem. 392*, 305–12.

(11) Kida, S., Maeda, M., Hojo, K., Eto, Y., Gao, J. Q., Kurachi, S., Mizuguchi, H., Hayakawa, T., Mayumi, T., Nakagawa, S., and Kawasaki, K. (2006) Design and synthesis of a Tat-related gene transporter: a tool for carrying the adenovirus vector into cells. *Bioorg. Med. Chem. Lett. 16*, 743–5.

(12) Inglese, J., and Glickman, J. F. (1999) Radiolabeling of receptor ligands by chemical incorporation of phosphorylation sites. *Anal. Biochem. 274*, 104–9.

(13) Morpurgo, M., Bayer, E. A., and Wilchek, M. (1999) N-hydroxysuccinimide carbonates and carbamates are useful reactive reagents for coupling ligands to lysines on proteins. *J. Biochem. Biophys. Methods 38*, 17–28.

(14) Clave, G., Boutal, H., Hoang, A., Perraut, F., Volland, H., Renard, P. Y., and Romieu, A. (2008) A novel heterotrifunctional peptide-based cross-linking reagent for facile access to bioconjugates. Applications to peptide fluorescent labelling and immobilisation. *Org. Biomol. Chem. 6*, 3065–78.

(15) Pasut, G., Mero, A., Caboi, F., Scaramuzza, S., Sollai, L., and Veronese, F. M. (2008) A new PEG-beta-alanine active derivative for releasable protein conjugation. *Bioconjugate Chem. 19*, 2427–31.

(16) Pina, D. G., and Johannes, L. (2005) Cholera and Shiga toxin B-subunits: thermodynamic and structural considerations for function and biomedical applications. *Toxicon 45*, 389–93.

(17) Mallard, F., and Johannes, L. (2003) Shiga toxin B-subunit as a tool to study retrograde transport. *Methods Mol. Med. 73*, 209–20.

(18) Walker, J. M. (1994) The bicinchoninic acid (BCA) assay for protein quantitation. *Methods Mol. Biol. 32*, 5–8.

(19) Ollivier, N., Besret, S., Blanpain, A., and Melnyk, O. (2009) Silver-catalyzed azaGly ligation. Application to the synthesis of azapeptides and of lipid-peptide conjugates. *Bioconjugate Chem. 20*, 1397–403.

(20) Smith, M. J., Carvalho, H. M., Melton-Celsa, A. R., and O'Brien, A. D. (2006) The 13C4 monoclonal antibody that neutralizes Shiga toxin Type 1 (Stx1) recognizes three regions on the Stx1 B subunit and prevents Stx1 from binding to its eukaryotic receptor globotriaosylceramide. *Infect. Immunol. 74*, 6992–8.

(21) Mallard, F., Antony, C., Tenza, D., Salamero, J., Goud, B., and Johannes, L. (1998) Direct pathway from early/recycling endosomes to the Golgi apparatus revealed through the study of shiga toxin B-fragment transport. *J. Cell. Biol. 143*, 973–90.

(22) Johannes, L., Tenza, D., Antony, C., and Goud, B. (1997) Retrograde transport of KDEL-bearing B-fragment of Shiga toxin. *J. Biol. Chem. 272*, 19554–61.

(23) Liao, H. J., and Carpenter, G. (2007) Role of the Sec61 translocon in EGF receptor trafficking to the nucleus and gene expression. *Mol. Biol. Cell 18*, 1064–72.

(24) Niehrs, C., Huttner, W. B., and Ruther, U. (1992) In vivo expression and stoichiometric sulfation of the artificial protein sulfophilin, a polymer of tyrosine sulfation sites. *J. Biol. Chem. 267*, 15938–42.

(25) Hong, G., Chappey, O., Niel, E., and Scherrmann, J. M. (2000) Enhanced cellular uptake and transport of polyclonal immunoglobulin G and fab after their cationization. *J. Drug Targeting 8*, 67–77.

(26) Pardridge, W. M., Bickel, U., Buciak, J., Yang, J., Diagne, A., and Aepinus, C. (1994) Cationization of a monoclonal antibody to the human immunodeficiency virus REV protein enhances cellular uptake but does not impair antigen binding of the antibody. *Immunol. Lett. 42*, 191–5.

(27) Pardridge, W. M., Kang, Y. S., Yang, J., and Buciak, J. L. (1995) Enhanced cellular uptake and in vivo biodistribution of a monoclonal antibody following cationization. *J. Pharm. Sci. 84*, 943–8.

(28) Ryser, H. J., Drummond, I., and Shen, W. C. (1982) The cellular uptake of horseradish peroxidase and its poly(lysine) conjugate by cultured fibroblasts is qualitatively similar despite a 900-fold difference in rate. *J. Cell. Physiol. 113*, 167–78.

(29) Kohn, W. D., Micanovic, R., Myers, S. L., Vick, A. M., Kahl, S. D., Zhang, L., Strifler, B. A., Li, S., Shang, J., Beals, J. M., Mayer, J. P., and DiMarchi, R. D. (2007) pI-shifted insulin analogs with extended in vivo time action and favorable receptor selectivity. *Peptides 28*, 935–48.

(30) Monsigny, M., Sene, C., Obrenovitch, A., Roche, A. C., Delmotte, F., and Boschetti, E. (1979) Properties of succinylated wheat-germ agglutinin. *Eur. J. Biochem. 98*, 39–45.

(31) Nakashima, H., Hashimoto, M., Sadakane, Y., Tomohiro, T., and Hatanaka, Y. (2006) Simple and versatile method for tagging phenyldiazirine photophores. *J. Am. Chem. Soc. 128*, 15092–3.

(32) Gassman, J. M., and Magrath, J. (1996) An active-site titrant for chymotrypsin, and evidence that azapeptide esters are less susceptible to nucleophilic attack than ordinary esters. *Bioorg. Med. Chem. Lett. 6*, 1771–1774.

(33) Abello, N., Kerstjens, H. A., Postma, D. S., and Bischoff, R. (2007) Selective acylation of primary amines in peptides and proteins. *J. Proteome Res. 6*, 4770–6.

(34) Brown, W. E., Green, A. H., Cedel, T. E., and Cairns, J. (1987) Biochemistry of protein-isocyanate interactions: a comparison of the effects of aryl vs. alkyl isocyanates. *Environ. Health Perspect. 72*, 5–11.

(35) Sandvig, K., Dubinina, E., Garred, O., Prydz, K., Kozlov, J. V., Hansen, S. H., and van Deurs, B. (1992) Protein toxins: mode of action and cell entry. *Biochem. Soc. Trans. 20*, 724–7.

(36) Nakamura, N., Rabouille, C., Watson, R., Nilsson, T., Hui, N., Slusarewicz, P., Kreis, T. E., and Warren, G. (1995) Characterization of a cis-Golgi matrix protein, GM130. *J. Cell. Biol. 131*, 1715–26.

(37) Niehrs, C., Kraft, M., Lee, R. W., and Huttner, W. B. (1990) Analysis of the substrate specificity of tyrosylprotein sulfotransferase using synthetic peptides. *J. Biol. Chem. 265*, 8525–32.

(38) Niehrs, C., and Huttner, W. B. (1990) Purification and characterization of tyrosylprotein sulfotransferase. *Embo J. 9*, 35–42.

(39) Carion, O., Souplet, V., Olivier, C., Maillet, C., Medard, N., El-Mahdi, O., Durand, J. O., and Melnyk, O. (2007) Chemical micropatterning of polycarbonate for site-specific peptide immobilization and biomolecular interactions. *ChemBioChem 8*, 315–322.

(40) Duburcq, X., Olivier, C., Malingue, F., Desmet, R., Bouzidi, A., Zhou, F., Auriault, C., Gras-Masse, H., and Melnyk, O. (2004) Peptide-protein microarrays for the simultaneous detection of pathogen infections. *Bioconjugate Chem. 15*, 307–16.

(41) Duburcq, X., Olivier, C., Desmet, R., Halasa, M., Carion, O., Grandidier, B., Heim, T., Stievenard, D., Auriault, C., and Melnyk, O. (2004) Polypeptide semicarbazide glass slide microarrays: characterization and comparison with amine slides in serodetection studies. *Bioconjugate Chem. 15*, 317–25.

(42) Olivier, C., Hot, D., Huot, L., Ollivier, N., El-Mahdi, O., Gouyette, C., Huynh-Dinh, T., Gras-Masse, H., Lemoine, Y., and Melnyk, O. (2003) Alpha-oxo semicarbazone peptide or oligodeoxynucleotide microarrays. *Bioconjugate Chem. 14*, 430–9.

BC900154R

Synthesis of Specific SPECT-Radiopharmaceutical for Tumor Imaging Based on Methionine: ^{99m}Tc-DTPA-bis(methionine)

Puja Panwar Hazari, Gauri Shukla, Vijay Goel, Krishna Chuttani, Nitin Kumar, Rajnish Sharma, and Anil Kumar Mishra*

Division Cyclotron and Radiopharmaceutical Sciences, Institute of Nuclear Medicine and Allied Sciences, Brig SK Mazumdar Road, Delhi-110054, India. Received May 2, 2009; Revised Manuscript Received January 6, 2010

Methionine-diethylenetriaminepentaaceticacid-methionine [DTPA-bis(Met)] was synthesized by covalently conjugating two molecules of methionine (Met) to DTPA and was labeled with ^{99m}Tc in high radiochemical purity and specific activity (166−296 MBq/μmol). Kinetic analysis showed K_m of 12.95 ± 3.8 nM and a maximal transport rate velocity (V_{max}) of 80.35 ± 0.42 pmol μg protein^{-1} min^{-1} of ^{99m}Tc-DTPA-bis(Met) in U-87MG cells. DTPA-bis(Met) had dissociation constants (K_d) of 0.067 and 0.077 nM in U-87MG and BMG, respectively. ^{35}S-methionine efflux was trans-stimulated by ^{99m}Tc-labeled DTPA conjugate demonstrating concentrative transport. The blood kinetic studies showed fast clearance with $t_{1/2}$ (F) = 36 ± 0.5 min and $t_{1/2}$ (S) = 5 h 55 min ± 0.85 min. U-87MG and BMG tumors saturated at ∼2000 ± 280 nmol/kg of ^{99m}Tc-DTPA-bis(Met). Initial rate of transport of ^{99m}Tc-DTPA-bis(Met) in U-87MG tumor was found to be 4.68 × 10^{-4} μmol/kg/min. The tumor (BMG cell line, malignant glioma) grafted in athymic mice were readily identifiable in the gamma images. Semiquantitative analysis from region of interest (ROI) placed over areas counting average counts per pixel with maximum radiotracer uptake on the tumor was found to be 11.05 ± 3.99 and compared ROI with muscle (0.55 ± 0.13). The tumor-to-contralateral muscle tissue ratio of ^{99m}Tc-DTPA-bis(Met) was found to be 23 ± 3.3. Biodistribution revealed significant tumor uptake and good contrast in the U-87MG, BMG, and EAT tumor-bearing mice. In clinical trials, the sensitivity, specificity, and positive predictive values were found to be 87.8%, 92.8%, and 96.6%, respectively. ^{99m}Tc-DTPA-bis(Met) showed excellent tumor targeting and has promising utility as a SPECT-radiopharmaceutical for imaging methionine-dependent human tumors and to quantify the ratio of MET^+/HCY^-.

INTRODUCTION

Development of a highly specific and sensitive noninvasive imaging modality that can enhance the ability to closely correlate diagnosis with pathology, distinguish inflammation from tumors, differentiate tumor grades, accurately delineate tumor volume, monitor treatment responses, and identify residual tumor/recurrence remains a desirable goal to improve the current clinical management of cancers.

The natural amino acids are transported inside the cells by specific carrier-mediated transport systems and get incorporated into proteins and intermediary metabolites to different extents. Several transporters are based on system L such as LAT1, LAT2, LAT3, and LAT4, which have been identified at the molecular level (*1*−*5*). Among the identified transporters, LAT1 is consistently expressed at high levels in cancer cells as LAT1 transporter, and therefore is a candidate substrate for transport into cancer cells (*6*). Many synthetic derivatives, such as methyl-aminoisobutyric acid (MeAIB), and various halogenated derivatives of phenylalanine and tyrosine have also been shown to enter the cells using similar transport systems but are not metabolized. The role of overexpression of transporter systems of neutral amino acid has been reported in literature (*7*). Therefore, many natural amino acids (such as methionine, glycine, tyrosine, phenylalanine, and leucine) and their synthetic analogues have been labeled with radioactive isotopes and are being explored as tumor imaging agents for PET/SPECT (*8*−*13*).

The major metabolic functions of methionine are in protein synthesis and conversion to *S*-adenosylmethionine (Adomet), which is required in multiple metabolic pathways. Methionine (Met) dependence has been shown in vitro in a number of human cell lines of different cellular origin, and the dependence may reflect the overall imbalance in the transmethylation (*14*−*17*). Metabolic defects in cancer cells often manifest in the inability to grow in media where Met has been replaced by its precursor HCY (*18*, *19*). Increase in amino acid uptake is one of the earliest events associated with in vitro transformation (*20*) thus inducing upregulation of the amino acid transporter expression to enhance the facilitated transport (*21*). Because the uptake of amino acids (AA) in normal tissue is low and increases across glioma capillaries and tumors, the contrast between tumor and normal tissue is generally better with amino acid scanning as compared to FDG-PET or any other imaging modality (*22*−*25*). Currently, PET using L-[methyl-^{11}C]-methionine (MET) is the most popular AA-imaging modality for tumors, although its use is restricted to PET centers with an in-house cyclotron facility for successful use of isotope in amino acid labeling.

Polydentate ligands are of particular interest because of their capability to adopt an organized conformation in the complexed form. Entrapment of metal ion into a framework of multidentate poly(aminocarboxylates) such as DTPA covalently attached to mAbs with some metallic radionuclides, especially ^{111}In, and various other lanthanides has been proven to provide thermodynamically stable compounds suitable for clinical trials (*26*). The anhydride derivatives of DTPA are generally easier to synthesize because of the commercial availability of DTPA. In particular, complexation of DTPA moiety with ^{99m}Tc showed excellent results as a metallopharmaceutical for medical imaging.

* Corresponding author. Dr. Anil Kumar Mishra, Brig. S. K. Mazumdar Road, Delhi-110054, India, Phone: +91-11-2390-5118, Fax: +91-11-2391-9509, E-mail: akmishra@inmas.drdo.in.

10.1021/bc900197n © 2010 American Chemical Society
Published on Web 01/28/2010

The work reported in the literature has shown that the conjugated DTPA [DTPA-B-(SLex)A] forms stable complexes with lanthanides and transition metals (*27*). The main objective of our study was to design and synthesize a novel amino acid derivative based on DTPA, which forms stable complexes with most lanthanides and transition metals in the periodic table. Second, to introduce a chelating group without compromising the biological integrity of the amino acid for diagnosis of cancer using nuclear medicine and MR techniques.

As a part of our efforts to explore the application of targeted radiopharmaceuticals for site-directed diagnosis and cancer therapy, (*28*−*31*) we hereby report the synthesis, characterization, and radiochemistry of ^{99m}Tc labeled DTPA-bis(Met) conjugate and its evaluation in nude mice bearing human malignant glioma cell lines (U-87MG and BMG). Covalent attachment of a strong chelating agent, DTPA, with methionine provides binding sites to which reduced ^{99m}Tc is strongly bound. Radiolabeling of the purified methionine DTPA−conjugate with ^{99m}Tc, stability studies in human serum under physiological conditions, and blood kinetics in rabbits are reported. Cytotoxicity was determined by MTT and clonogenic assays. The efficiency of DTPA-bis(Met) in vitro was assessed by cell uptake assays in tumor cell lines (U-87MG and BMG) and human embryonic kidney cell line and in vivo by biodistribution studies with athymic mice bearing subcutaneous U-87MG and BMG cell line. Clinical studies in patients were carried out to establish the specificity and sensitivity of the new SPECT radiopharmaceutical in patients for better detection and delineation of metabolic tumors of different histological grades.

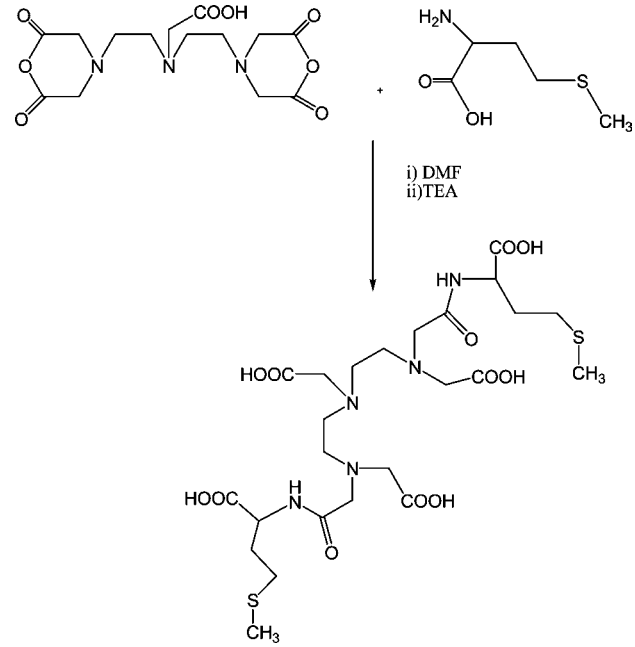
MATERIALS AND METHODS

Chemicals. Acetonitrile, methanol, and water (HPLC grade) were obtained from Merck Germany Ltd. L-Methionine, diethylenetriaminepentaacetic acid, DTPA bisanhydride, triethylamine, dimethylformamide, methanol, ethanol, stannous chloride dihydrated ($SnCl_2 \cdot 2H_2O$), trifluoroacetic acid, MTT, 2-methylaminoisobutyric acid (MeAIB), 2-amino-bicyclo-(2,2,1)-heptane-2-carboxylic acid (BCH), L-arginine, L-valine, L-alanine, L-leucine, and L-glutamine were purchased from Sigma-Aldrich Co. ^{99m}Tc and ^{35}S-L-methionine were procured from Regional Center for Radiopharmaceuticals (Northern Region), Board of Radiation and Isotope Technology (BRIT), Department of Atomic Energy, India.

Cell Culture. Monolayer cultures of human malignant glioma cells, U-87MG (obtained from NIMHANS, Bangalore), normal embryonic kidney cells, HEK, and BMG were maintained at 37 °C in a humidified CO_2 incubator (5% CO_2, 95% air) in DMEM (Sigma, USA) supplemented with 10% fetal bovine serum (GIBCO), 50 U/mL penicillin, 50 μg/mL streptomycin sulfate, and 2 μg/mL nystatin. Cells were routinely subcultured twice a week using 0.05% Trypsin (Sigma, USA) in 0.02% EDTA.

Instrumentation. ^{1}H NMR spectra were determined by using Bruker Avance II 400. Mass spectrum (ES^+MS) was recorded on a Aligent 6310 ion trap. HPLC analyses were performed on a Waters Chromatograph efficient with 600s coupled to a Waters 2487 photodiode array UV detector. The C-18 RP Beckman column (5 μ, 1 mm × 125 cm) column was used applying the elution system described in the text. C-18 Cartridges were purchased from Waters. Radioactive samples were counted using Capintech automated well-type counter. Beta scintillation counts were obtained by mixing samples in optiphase scintillation cocktail using Wallac Micro beta Trilux 1450 LSC, Perkin-Elmer (ACBR, Delhi University). Radioimaging and biodistribution studies were done using a planner gamma camera HAWKEYE. The clinical scintigraphs were obtained using a rectangular large field of view gamma camera (HAWKEYE dual head, GE medical systems, Milwaukee, Wisconsin, USA) with a low-energy all-purpose collimator.

Scheme 1. Synthesis of Diethylenetriaminepentaacetic Acid bis(methionine)[a]



[a] (i) DTPA-bis anhydride, (ii) L-methionine, (iii) DMF, (iv) triethylamine.

Animal Models. All animal experiments were performed in accordance with guidelines of INMAS animal ethics committee. New Zealand rabbits, athymic mice, and albino balb/c mice were used for blood clearance, imaging, and biodistribution. Mice and rabbits were housed under conditions of controlled temperature of 22 ± 2 °C and normal diet. Athymic mice were inoculated subcutaneous with 0.1 mL of cell suspension (5 × 10^6 BMG/U-87MG cells) just above the right hind leg under sterilized conditions. Balb/c mice were inoculated subcutaneously EAT (15 × 10^6 cells) in the right hind leg.

PATIENTS AND METHODS

Patients. Human protocols have been approved by Institutional human ethics committee.

Scintigraphy. Whole body images were obtained using dual head gamma camera. ^{99m}Tc-DTPA-bis(Met) imaging was performed after i.v. administration of 15 mCi (555 MBq) radiotracer. Whole body scan was done after 1 h, 3 h, 6 h, and 24 h injection of radiotracer as a standard protocol and 5 patients were also imaged at 5, 10, 30, 45, 60, and 180 min. Semiquantitative analysis was generated from region of interest (ROI) placed over areas counting average counts per pixels with maximum radiotracer uptake on the lesions and compared to symmetric counterparts with ROI in soft tissues. Thirty-three breast cancer patients underwent in-house FDG scan. Brain cancer patients also underwent MDP scan.

Statistical Methods. Data is reported as mean ± standard deviation (S.D.). Data were analyzed by the two-tailed Student's *t* test for comparison with the control. Value of $P < 0.05$ was considered statistically significant.

EXPERIMENTAL SECTION

Synthesis of Diethylenetriaminepentaacetic Acid Bis(methionine) Scheme 1. DTPA anhydride (500 mg; 1.4 mmol) and L-methionine (522 mg; 3.50 mmol) were dissolved in 5 mL of

DMF (anhyd.), and 15 mol equiv of triethylamine (2.35 mL) was then added. The reaction was allowed to proceed for 48 h at 55 °C.

Completion of the reaction was checked by running TLC plates in water (0.01% TFA) and methanol (7:3; v/v) [R_f for Met: 0.89; R_f for DTPA-bis(Met): 0.75]. Triethylamine and DMF were evaporated under reduced pressure using a rotaevaporator. The chemical purity of DTPA-bis(Met) conjugate was examined by analytical HPLC on Beckman C-18 reverse-phase column (4.6 mm × 250 mm). The mobile phase was 0.05% TFA in water (solvent A) and methanol (solvent B) with a flow rate of 0.5 mL/min. Gradient 0−14 min A/B 90/10−50/50, 14−23 min A/B 50/50−0/100, 23−28 min A/B 0/100−90/10.

Yield: 758 mg,1.16 mmol, 82.66%. IR (ν, cm^{-1}) 3437, 2817, 1610. ^{1}H NMR (400 MHz, D_2O): δ = 4.42−4.19 (m, NH−CH_2, 2H), 3.685 (br, s, CH_2, 4H), 3.7−2.37 (m, CH_2−CH_2, 22H), 2.026, 2.005 (br, s, 2H) ppm. ^{13}C NMR (400 MHz, D_2O): δ = 178.70, 178.35 (C═O), 173.18, 174.48 (COOH), 58.40, 58.09, 57.09, 56.16, 54.01, 53.89, 52.45, 49.77, 49.37 (CH_2−CH_2, 11C), 30.86, 29.87, 29.76, 28.79 (CH_2−S, 4C), 14.20, 13.87 (S-CH_3, 2C) ppm. Calculated mass $[M+H]^+$ 656.2 found *m/z* = 656.6 $[M+H]^+$, 678.2 $[M+Na]^+$ (see Supporting Information). Elemental analysis calcd for $C_{24}H_{41}N_5O_{12}S_2$: C, 43.96; H, 6.30; N, 10.68; O, 29.28; S, 9.78. Found C, 43.95; H, 6.31; N, 10.67; O, 29.29; S, 9.78.

Radiolabeling of DTPA-bis(Met) with ^{99m}Technetium. DTPA-bis(Met) (2 mg) was dissolved in a shielded vial and stannous chloride (300 μL; 1 mg dissolved in N_2 purged 1 mL of 10% acetic acid) was added followed by addition of freshly eluted (<1 h) ^{99m}Technetium pertechnetate (82 MBq; 200 μL). The pH of the reaction mixture was adjusted to 7 with 0.1 M Na_2CO_3 and purged with N_2, and shaken to mix. The vial was allowed to stand for 15 min at room temperature (25 °C).

Radiochemical Purity. The number of ligand molecules involved in complexation with ^{99m}Tc was determined by ascending thin layer chromatography on ITLC-SG (Paul Gelman, USA) strips using 100% acetone as developing solvent and simultaneously in pyridine/acetic acid/water (PAW) (3:5:1.5) and saline. Each TLC was cut in 0.5 cm segments and counts of each segment were taken. By using this method percentage of free $Na^{99m}TcO_4^-$, reduced/hydrolysed ^{99m}Tc, and the complex formed between ^{99m}Tc and DTPA-bis(Met) conjugate could be calculated. ^{99m}Tc-DTPA-bis(Met) conjugate remained at the origin, and free technetium traveled with the solvent front in acetone.

The radiolabeled conjugate was then purified using a C-18 reversed-phase extraction cartridge, which was preconditioned with 10 mL methanol and subsequently activated with 30% methanol. The cartridge was successively rinsed with 5 mL distilled water, and radiolabeled conjugate was eluted in 5 mL of 5% ethanol.

Human Serum Stability Evaluation. Human serum was prepared by allowing blood collected from healthy volunteers to clot for 1 h at 37 °C in a humidified incubator maintained at 5% carbon dioxide/95% air. Then, the samples were centrifuged at 400 *g*, and the serum was filtered through 0.22 μm syringe filter into sterile plastic culture tubes. The radiolabeled DTPA-bis(Met) was immediately placed in a CO_2 chamber incubated at 37 °C and then analyzed to check for any dissociation of the complex. Percentage of free pertechnetate at a particular time point that was estimated using acetone and pyridine, acetic acid, and water (PAW) (3:5:1.5) as mobile phase represented percentage dissociation of the complex at that particular time point in serum.

Cytotoxicity Studies of DTPA-bis(Met). Cytotoxicity was determined using the MTT [3-(4,5-dimethylthiazole-2-yl)-2,5-diphenyl-2*H*-tetrazolium bromide] assay. Exponentially growing cells were plated in a 96-well microtiter plate at a uniform cell density of 4000 cells/well, 24 h before treatment. Cells were treated with varying concentrations of drug (nM−mM range) for 2 h, and MTT assays were performed. At the end of treatment, negative control and treated cells were incubated with MTT at a final concentration of 0.05 mg/mL for 2 h at 37 °C, and the medium was removed. The cells were lysed, and the formazan crystals were dissolved using 150 μL of DMSO. Optical density is measured on 150 μL of extracts at 570 nm (reference filter: 690 nm). Mitochondrial activity was expressed as percentage of viability compared to negative control (mean ± SD of triplicate cultures). % of viability = [OD (570 nm − 630 nm) test product/OD (570 nm − 630 nm) negative control] × 100%.

Macrocolony Assay of DTPA-bis(Met). Monolayer cultures of U-87MG and BMG cell lines were trypsinized and 100 to1000 cells were plated depending upon the concentrations of the drug in 60 mm petridishes and incubated at 37 °C in 5% CO_2 humidified atmosphere for 8 days. Colonies were fixed in methanol and stained with 1% crystal violet. Colonies containing more than 50 cells were counted (Figure 2).

Cell Uptake and Efflux Studies of ^{99m}Tc-DTPA-bis(Met). *Measurement of ^{99m}Tc-DTPA-bis(Met) Transport.* U-87MG cells were plated at a density of 10^5 cells per well in a 96-well microtiter plates and allowed to adhere overnight prior to transport studies, which were carried out as described previously. Briefly, adherent cells were rinsed twice with a modified Hepes-buffered Krebs solution, and uptake was initiated by adding Hepes-buffered Krebs (50 μL per well; 37 °C) containing 10 μM of ^{99m}Tc-DTPA-bis(Met) to the monolayers. Incubations were terminated by placing the plates on melting ice and rinsing cells three times with 200 μL ice-cold Krebs buffer. 100 μL of the protein lysis buffer was then added to wells causing rapid lysis of cells. Bradfort protein reagent was added to the wells for total protein estimation. Absorbance values were determined at 595 nm on an ELISA plate reader after 20 min of incubation at room temperature. Values obtained were converted to total protein per well using a protein standard curve generated from bovine serum albumin. The amount of radioactivity (CPM) in cell lysates was determined by gamma scintillation counting. Uptake was then calculated and expressed in units of pmoles μg protein^{-1}·min^{-1}.

Time Course and Kinetics of Transport ^{99m}Tc-DTPA-bis-(Met) Transport. The time course of uptake of was monitored by incubating cells with (100 μM) in Hepes-buffered Krebs solution (50 μL; 37 °C) for varying time periods ranging from 30 s to 60 min. Transport was then terminated and total accumulated in cells determined as described above. In kinetic experiments, cells were incubated for 10 min in either normal Hepes-buffered Krebs solution (50 μL; 37 °C) or Na^+-free Krebs solution described above containing increasing concentrations (0.005−0.1 μM) of ^{99m}Tc-DTPA-bis(Met). The data obtained were fitted using the Michaelis−Menten equation.

Cell Binding Studies. The specificity of ^{99m}Tc-DTPA-bis(Met) to bind externally on tumor cells were examined by receptor binding assays on three human cell lines. U-87MG and BMG were grown in normal DMEM, 10% and 5% FBS, respectively. HEK was cultured in high-glucose DMEM with 10% FBS. Monolayer cultures of the cell lines were washed with HBSS and were then incubated for 2 h in HBSS at 37 °C prior to the experiment. Binding experiments was conducted at 37 °C. Cells were incubated for 30 min with increasing concentrations (0.01 nM−10 μM) of ^{99m}Tc-DTPA-bis(Met) in the absence and presence of the 100-fold excess unlabeled methionine to estimate the total binding and nonspecific binding respectively. Specific binding was obtained by subtracting nonspecific binding from total binding. At the end of each experiment, the cells were

washed with cold PBS four times. The cell-associated radioactivity was determined by gamma scintillation counting.

Selective and Na^+-Dependency of Transport. Inhibition of ^{99m}Tc-DTPA-bis(Met) transport by competitor amino acids was investigated by incubating cells with Krebs solution containing 10 μM ^{99m}Tc-DTPA-bis(Met) in the absence or presence of a 100-fold excess (1 mM) or increasing concentrations of a BCH inhibitor substrate. Parallel inhibition studies were carried out by replacing normal Krebs solution with Na^+-free Krebs. In sodium-free experiments, the buffer was modified by replacing NaCl, $NaHCO_3$, and NaH_2PO_4 with choline chloride, choline bicarbonate, and KH_2PO_4, respectively.

Cells were incubated with ^{99m}Tc-DTPA-bis(Met) for 30 min at 37 °C in standard Krebs buffer. After this period, cells were washed and incubated in fresh buffer containing 1 mM of either BCH, L-leucine, L-glutamine, or 2-methylaminoisobutyric acid (MeAIB), L-valine, and L-alanine. Radioactivity in the medium and in cell lysates was determined at 5, 10, and 15 min, and the efflux values expressed as percent of radioactivity released from the cells: radioactivity in medium/(radioactivity in medium + radioactivity in lysates) × 100%.

Trans-Stimulation of ^{35}S-L-Methionine Efflux in U-87MG Cells. To measure efflux of ^{35}S-methionine, U-87MG cells were preloaded with 10 μM (10 μCi) ^{35}S-methionine for 2 h at 25 °C. The loaded methionine was then allowed to efflux in HBSS solution in the presence and absence of 1 mM (10 mCi) of labeled DTPA-bis(Met). At end of the experiment, cells were washed with ice-cold buffer. The amount of methionine left was measured after the cells were digested. The accumulative amount effluxed plus the remaining ^{35}S-L-methionine in the cell monolayers were used to calculate the intracellular concentration of methionine at time zero. The efflux was calculated in micrograms per milliliter, and the efflux was compared with the control.

Blood Kinetics. In normal rabbit, 300 μL of the complex (11.1 MBq activity) was injected intravenously through the dorsal ear vein. Blood was withdrawn from the other ear vein at different time intervals starting from 5 min to 24 h. Persistence of activity in the circulation was calculated, assuming total blood volume as 7% of the body weight (Figure 3).

Dose Escalation and Biodistribution. Human malignant glioma U-87MG and BMG cells were injected subcutaneously just above the hind leg of nude mice. When the tumors were easily palpable and approximately 0.17 g, mice were used for dose escalation and biodistribution study. Dose escalation study was performed using increasing concentrations 10, 100, 1000, 1500, 2000, 2500, 3000, and 4000 nmol/kg of ^{99m}Tc-DTPA-bis(Met), which was injected into tumor-bearing nude mice and the mice were sacrificed after 4 h. In biodistribution study, intravenous injection of ^{99m}Tc-DTPA-bis(Met) conjugate in a volume of 100 μL (2.72 μmol/kg, 3.7 MBq activity) was injected through the tail vein of each mice. Mice were dissected at 1, 4, and 24 h post injection; different tissues were taken out, weighed, and counted in a gamma counter calibrated for ^{99m}Tc energy. A group of 5 mice were coinjected with a blocking dose of 618 μmol/kg of unlabeled methionine. Uptake of the radiotracer in each tissue was calculated and expressed as percentage injected dose per gram of the tissue (%ID/g) (Table 1). Animal protocols have been approved by Institutional Animal Ethics Committee.

In Vivo Tumor Pharmacokinetics and Scintigraphy in Tumor Bearing Nude Mice. The change in tumor concentration of ^{99m}Tc-DTPA-bis(Met) as a function of time was studied by administering 2.50 μmol/kg (2.96 MBq activity). Noninvasively dynamic study was performed at a time interval of 1 min up to 30 min and then at 60, 120, 150, 180, 210, 240, and 270 min. Semiquantitative analysis was carried out by generating ROI on tumor and soft tissue. Tumor imaging was performed in BMG cell line implanted tumor bearing nude mice administering 100 μL of the labeled conjugate (2.18 μmol/kg, 2.96 MBq activity). Images were taken using planar gamma camera. Images were obtained at different time intervals starting from 15 min to 24 h after post injection (Figure 4).

Table 1. Biodistribution of ^{99m}Tc-DTPA-bis(Met) in Athymic Mice Bearing U-87MG, BMG Tumors, and in Balb/c Mice Bearing EAT Tumors Following Intravenous (i.v.) Injection[a]

organ	time (h)	U-87MG	BMG	EAT
blood	1	0.081 ± 0.011	0.12 ± 0.041	1.2 ± 0.11
	4	0.030 ± 0.012	0.08 ± 0.021	0.99 ± 0.18
	24	0.015 ± 0.606	0.03 ± 0.006	0.03 ± 0.001
heart	1	0.361 ± 0.011	0.27 ± 0.06	0.68 ± 0.12
	4	0.182 ± 0.014	0.23 ± 0.013	0.39 ± 0.09
	24	0.120 ± 0.092	0.17 ± 0.002	0.13 ± 0.03
lungs	1	0.243 ± 0.012	0.14 ± 0.032	0.72 ± 0.18
	4	0.123 ± 0.023	0.11 ± 0.017	0.46 ± 0.13
	24	0.070 ± 0.011	0.09 ± 0.011	0.29 ± 0.12
liver	1	0.121 ± 0.031	0.11 ± 0.004	1.80 ± 0.119
	4	0.153 ± 0.060	0.17 ± 0.004	1.21 ± 0.101
	24	0.053 ± 0.068	0.009 ± 0.006	0.22 ± 0.06
kidneys	1	2.21 ± 0.080	3.24 ± 0.52	6.52 ± 1.20
	4	2.01 ± 0.631	2.04 ± 0.38	5.6 ± 1.41
	24	0.83 ± 0.020	1.78 ± 0.42	1.2 ± 0.36
stomach	1	0.21 ± 0.011	0.32 ± 0.032	0.6 ± 0.06
	4	0.14 ± 0.061	0.16 ± 0.05‘	0.4 ± 0.03
	24	0.14 ± 0.054	0.09 ± 0.019	0.12 ± 0.01
small intestine	1	0.003 ± 0.05	2.63 ± 0.22	0.6 ± 0.03
	4	0.022 ± 0.020	1.42 ± 0.11	0.4 ± 0.02
	24	0.141 ± 0.010	0.78 ± 0.15	0.2 ± 0.01
brain	1	0.101 ± 0.92	0.12 ± 0.05	0.08 ± 0.03
	4	0.812 ± 0.46	0.18 ± 0.07	0.12 ± 0.04
	24	0.481 ± 0.11	0.33 ± 0.12	0.09 ± 0.01
muscles	1	0.09 ± 0.021	0.08 ± 0.011	0.04 ± 0.032
	4	0.06 ± 0.012	0.06 ± 0.009	0.03 ± 0.010
	24	0.02 ± 0.054	0.03 ± 0.014	0.014 ± 0.001
tumor	1	2.14 ± 0.901	1.08 ± 0.11	1.50 ± 0.13
	4	3.15 ± 0.240	2.1 ± 0.23	2.8 ± 0.12
	24	0.99 ± 0.010	1.20 ± 0.11	0.91 ± 0.02

[a] Athymic mice and BALB/c mice, body weight = 22−30 g. Data from groups of five mice are expressed as mean %ID/g ± S.D. Based on estimates assuming blood volume = 7% of the body weight.

Clinical Studies. In the study, 55 patients were included to perform DTPA-bis(Met) SPECT imaging in tumors of different origin. Out of them, 47 female patients (median age 44 years, range 28−68 years) had palpable breast masses (*32*), and all of them underwent ultrasound, mammography, and fine needle aspiration cytology. Two patients having brain tumor, one with primary cancer, and another previously treated and now suspected as having recurrence were also included. Three patients had regional lymph node cancer and three had osteosarcoma. Twenty-four breast cancer and nine benign breast lump cases also underwent in-house FDG scan.

RESULTS

Synthesis of DTPA-bis(Met). The synthesis of DTPA-bis(Met) conjugate was performed by reacting DTPA bisanhydride with L-methionine (Scheme 1). The final product was obtained in 82.66% yield and purified using reversed-phase HPLC, and HPLC retention time was found to be 8.6 min for methionine and 5.8 min for DTPA-bis(Met). Mass spectroscopy confirmed the integrity of the product. MS, *m*/*z* calculated for $C_{24}H_{41}N_5O_{12}S_2$ $[M+H]^+$ 656.22, found $[M+H]^+$ and $[M+Na]^+$ at 656.3 and 678.2, respectively, in ESI positive mode (Figure 1).

Quality Control of Labeled DTPA-bis(Met) Conjugate. The labeled complex remained at the point of spotting and $^{99m}TcO_4^-$ moved toward the solvent front in acetone. The yield

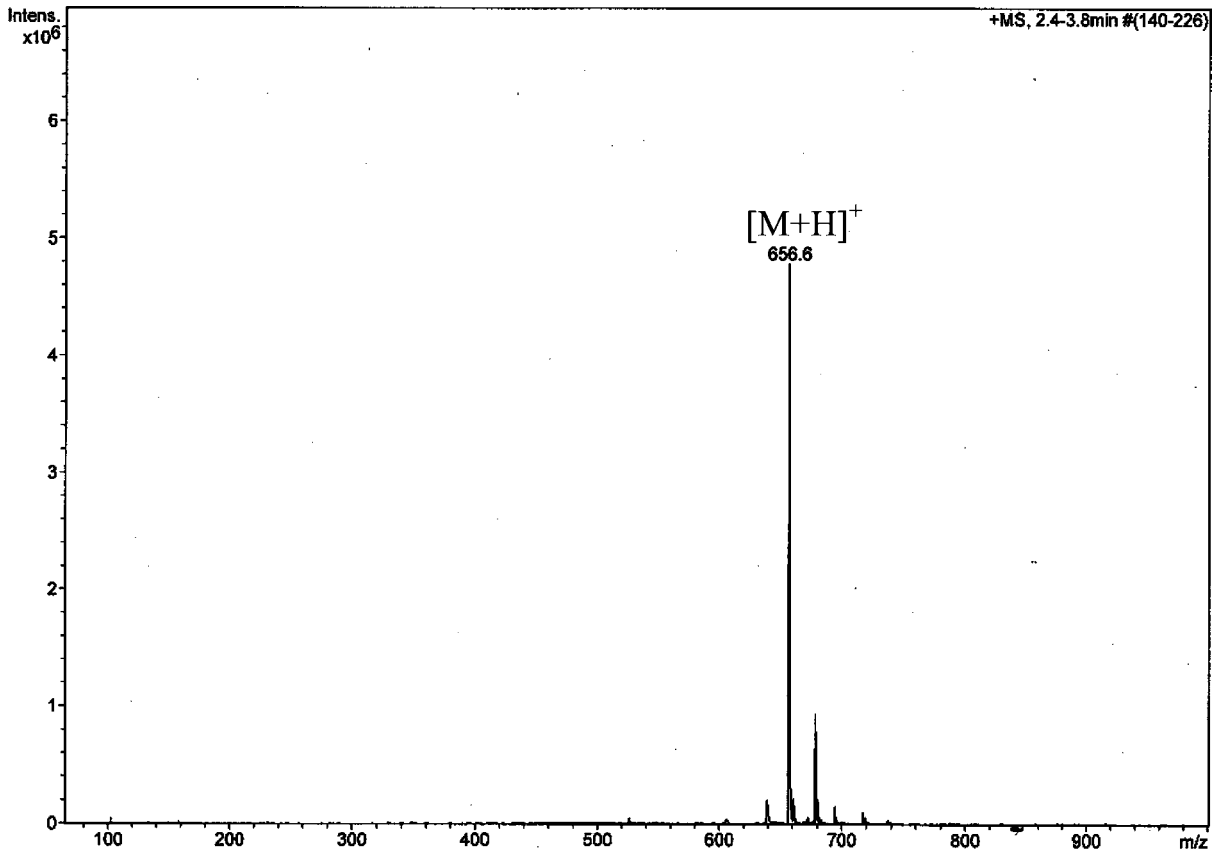


Figure 1. Mass spectrum of diethylenetriaminepentaacetic acid bis(methionine).

of free and complexed ligand, thus, could be estimated. The labeling yield was found to be greater than 96%, as determined by different solvent systems chromatographically. The reaction mixture was kept in saline for various time intervals carried out in in vitro stability studies. Percentage radiolabeling was calculated for 0, 2, 4, 6, and 24 h. Even up to 24 h, labeling efficiency was found to be 96.27%, implying that the labeled DTPA-bis(Met) conjugate was quite stable. The resulting solution was then eluted through a C-18 reverse-phase extraction cartridge. The metal binding assay confirmed the radiochemical purity to be >99%. Phosphor imaging showed a single spot indicating formation of only one species. Radiolabeled DTPA-bis(Met) conjugate was eluted in ≥99% radiochemical purity with specific activity of 4500−8000 μCi/μmol (166−296 MBq/μmol) through C-18 extraction cartridge. Radiochromatogram showed a single peak eluting at 6.4 min by C-18 reverse-phase column and came through flow using solvent system of 10 mM ammonium acetate and acetonitrile.

Human Serum Stability Evaluation. The purified ^{99m}Tc-DTPA-bis(Met) was incubated in freshly extracted human serum under physiological conditions. Radiolabeled conjugates were challenged with the proteins (albumin and transferrin) present in the serum to test the stability of the radiolabeled DTPA-bis(Met). Major transcomplexation of ^{99m}Tc was observed for unmodified Met to be 66% after 1 h. DTPA-bis(Met) showed 2.9% transcomplexation of ^{99m}Tc in serum. Approximately more than 94% of the radioactivity remains associated with the conjugate after 2 h challenge at 37 °C. It was sufficiently stable up to 24 h, as only 4% of the radiolabeled drug dissociated in serum at 24 h.

Cytotoxicity Studies of DTPA-bis(Met). By analysis of the MTT assay data at different concentrations (nM to mM range), it was found that, at a concentration of 1 mM, 2 h exposure resulted in lyses of 60% of U-87MG cells. It was observed that, when 10 μM of DTPA-bis(Met) was incubated with BMG cell line for 2 h, only 5% of the cells were killed. The two cell lines U-87MG and BMG showed concentration-dependent cytotoxicity. U-87MG showed survival value of 0.47 ± 0.028 at 1 mM for unlabeled DTPA-bis(Met). A surviving fraction of 0.54 ± 0.015 at 1 mM for the BMG cell line was observed in the clonogenic assay (Figure 2). The time-dependent curve showed a regain of the metabolic viability of the BMG cell line at 72 h post-treatment.

Cell Uptake Studies. *Time Course and Kinetics.* Time course experiments revealed that transport of ^{99m}Tc-DTPA-bis(Met) into cells was rapid and linear for up to 10 min, saturating thereafter, and reaching a plateau after 30 min of incubation. Kinetic analysis revealed that transport of ^{99m}Tc-DTPA-bis(Met) occurs via a saturable high-affinity carrier with a Michaelis constant (K_m) of 12.95 ± 3.8 nM and a maximal transport rate velocity (V_{max}) of 80.35 ± 0.42 pmol. μg protein^{-1} min^{-1} (Figure 3). A single linear regression line was obtained in the Eadie-Hofstee transformation (inset Figure 3B) indicative of the function of a saturable system or systems with comparable functional characteristics. When repeated in the absence of Na^+, transport of ^{99m}Tc-DTPA-bis(Met) was indistinguishable from that observed in normal Krebs buffer, since rates measured in Na^+-free Krebs solution were only marginally lower than those determined in the presence of Na^+.

Cell Binding Studies. The ability of DTPA-bis(Met) conjugate to bind LAT1 transporters on the surface of tumor cell lines U-87MG, BMG, and HEK was examined by binding assay using ^{99m}Tc- DTPA-bis(Met) as the labeled ligand. Nonspecific binding was determined using 100-fold excess of unlabeled methionine. Examination of binding curves showed significant external binding of the labeled DTPA-bis(Met) conjugate. Scatchard plot analysis revealed affinity of the labeled DTPA-bis(Met) on tumor cell lines. K_d was

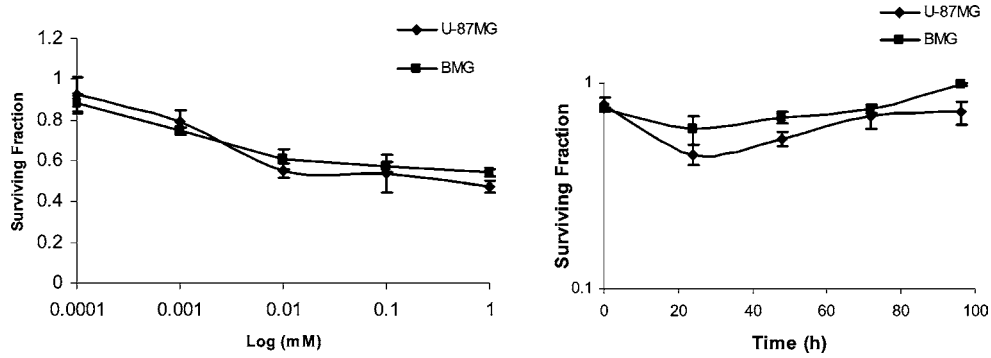


Figure 2. Cytotoxicity of DTPA-bis(Met) conjugate in U-87MG and BMG cell line: (a) concentration-dependent and (b) time-dependent curve as determined by clonogenic survival assay.

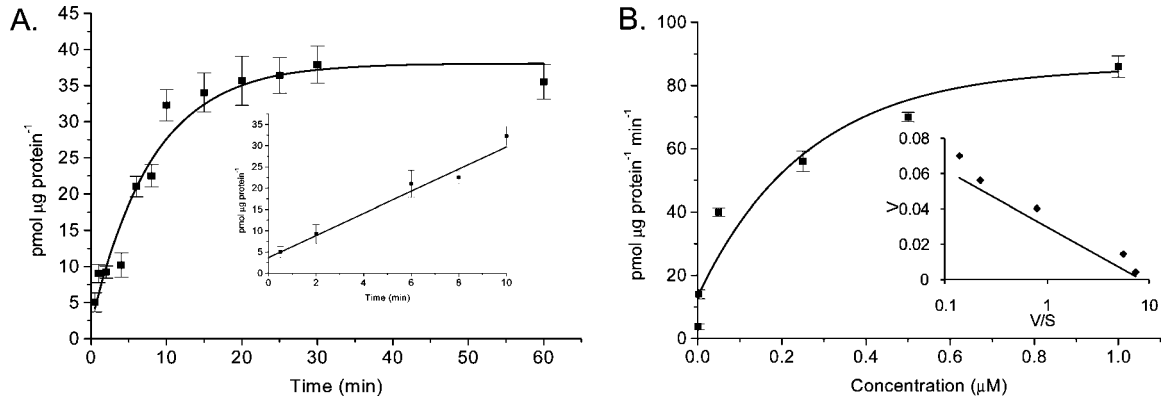


Figure 3. Time course and kinetics of ^{99m}Tc-DTPA-bis(Met). (A) Uptake was monitored from 30 s to 60 min. (B) Transport of ^{99m}Tc-DTPA-bis(Met) was monitored over 10 min period in U-87MG Cells. The inset shows an Eadie-Hofstee plot of saturable transport. Values are the mean ± SD of 3 replicate measurements in 3 separate experiments.

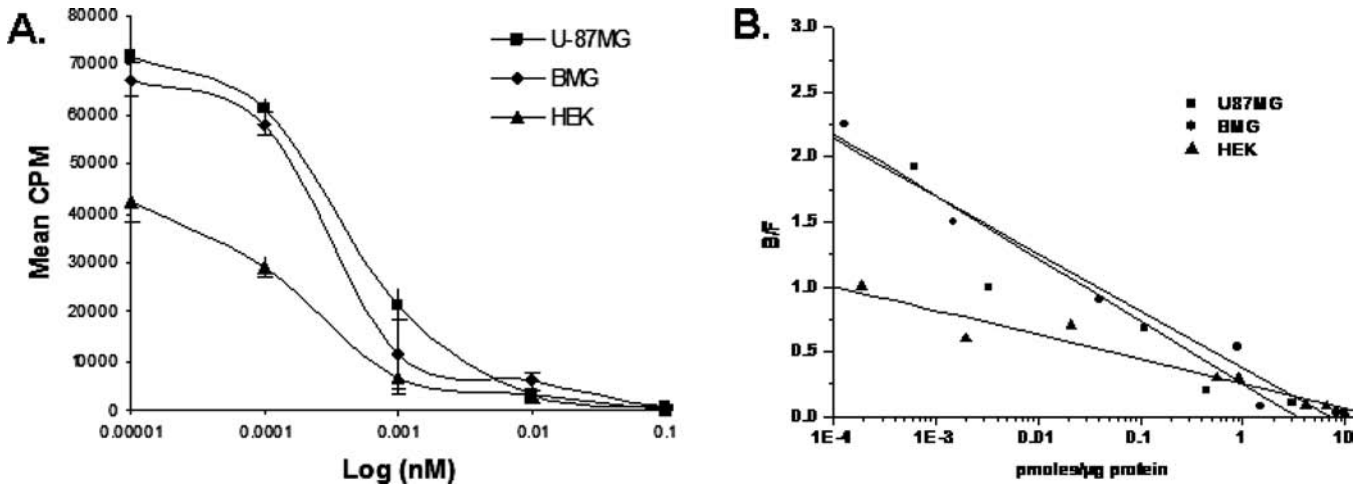


Figure 4. (A) Displacement using increasing concentrations of unlabeled methionine and labeled ^{99m}Tc-DTPA-bis(Met) was conducted in binding buffer The plot is representative of three independent experiments. (B) Scatchard plot of the specific binding data to the ratio of hound to free (B/F) for U-87MG, BMG, and HEK cell lines.

found to be 0.067 and 0.077 nM in U-87MG and BMG, respectively. In human embryonic kidney cell line, K_d was found to be 0.10 nM (Figure 4B).

Selectivity of ^{99m}Tc-DTPA-bis(Met) Transport. Cross inhibition studies were carried out in the presence and absence of Na^+ to evaluate the substrate specificity of the transporter associated with ^{99m}Tc-DTPA-bis(Met) uptake by U-87MG cells. Under these conditions, transport of ^{99m}Tc-DTPA-bis(Met) was not affected by a 100-fold excess of either 2-methylaminoisobutyric acid (MeAIB), a model substrate for system A, or L-valine and L-alanine, which are known substrates for the ASC system but was inhibited by 68 ± 1.9%, 52 ± 1.2%, and 36 ± 2.1% in the presence of 2-amino-bicyclo-(2,2,1)-heptane-2-carboxylic acid (BCH), L-phenylalanine, and L-leucine, respectively.

Trans-Stimulation of ^{35}S-L-methionine Efflux in U-87MG Cells. The efflux of ^{35}S-methionine was measured in the presence and absence of 1 mM (10 mCi) of ^{99m}Tc-labeled DTPA-bis(methionine). The amount of ^{35}S-L-methionine incorporated during the loading and subsequent washing protocol was less than 10 μM. It was evident from the experiment that ^{35}S-L-methionine efflux was trans-stimulated by extracellular 1 mM of DTPA-bis(Met). The magnitude of effect was observed to be higher at 30 min (0.32 ± 0.04 μg/mL). It was evident from the experiment that the presence of ^{99m}Tc-labeled DTPA-

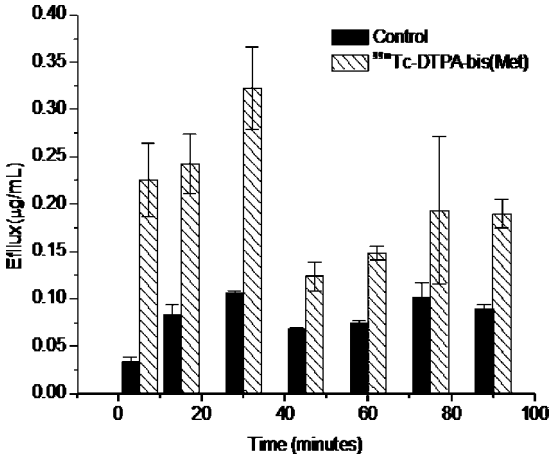


Figure 5. Trans-stimulation of ^{35}S-methionine efflux by extracellular ^{99m}Tc-labeled DTPA-bis(methionine). Efflux was measured for 90 min at 25 °C. Values mean ± SD, $n = 3$, each performed in duplicate $P < 0.05(0.0016)$ compared with control.

bis(Met) in the culture medium significantly ($P < 0.05$) trans-stimulated efflux of ^{35}S-methionine (Figure 5).

Blood Kinetics. In vivo clearance in rabbits revealed that there was a rapid clearance of DTPA-bis(Met) from the circulation, as only 17.6% of injected activity remained in the circulation at 30 min. After 30 min, the clearance followed a slow pattern, and at 24 h, approximately 0.76% activity persisted in the blood (Figure 6). The biological half-life was found to be $t_{1/2}$ (F) = 36 ± 0.5 min and $t_{1/2}$ (S) = 5 h 55 min ± 0.85 min.

Biodistribution. Dose escalation studies were performed to determine the concentration of ^{99m}Tc-DTPA-bis(Met) that would saturate U-87MG and BMG tumors. U-87MG tumor grafted nude mice were injected with increasing concentrations in the range 10−4000 nmol/kg, and after allowing 4 h for clearance of unbound conjugates from the tissues, tumor and normal tissue were dissected. U-87MG and BMG tumors were saturated at ∼2000 ± 280 nmol/kg of ^{99m}Tc-DTPA-bis(Met). In contrast, soft tissue (muscles) accumulated negligible quantities of the conjugate. Biodistribution studies in mice conducted to quantify localization of the radiolabeled DTPA conjugate on U-87MG, BMG, and EAT tumors are shown in Table 1. Athymic mice implanted with U-87MG and BMG cell line exhibited accumulation in kidneys (2.21 ± 0.08% ID/g) and 3.24 ± 0.52% ID/g, respectively, at 1 h showing that the complex is excreted by renal routes. Biodistribution revealed high tumor uptake in the U-87MG tumor bearing nude mice; tumor to muscle ratio reached 52.5 at 4 h postinjection. Biodistribution studies in nude mice xenographed with U-87MG and BMG human malignant glioma cell lines have shown that tumor uptake of ^{99m}Tc was found to be 2.14 ± 0.9% ID/ g and 1.08 ± 0.11% ID/ g at 1 h.

Comparative biodistribution was carried out for ^{99m}Tc-labeled methionine and ^{99m}Tc-DTPA-bis(Met) in EAT tumor. It was evident from the study that directly labeled methionine accumulated in liver and a major part of the radiolabeled methionine cleared through the hepatobiliary route (Figure 7). Localization of the radioactivity in the liver, stomach, and small intestine was low, less than 2% ID/g at 1 h for ^{99m}Tc-DTPA-bis(Met). Good clearance of the radiolabeled conjugate was also observed from these organs. EAT tumor uptake at 1 h was 2.8 ± 0.12% ID/g for ^{99m}Tc-DTPA-bis(Met) at 4 h.

^{99m}Tc-DTPA-bis(Met) was administered through the ear vein in U-87MG grafted athymic mice with and without coadministration of a 250 μg blocking dose of methionine, which showed significant blocking of the receptors at the tumor site with uptake of 0.36 ± 0.06% ID/g as compared to 2.14 ± 0.9% ID/ g for ^{99m}Tc-DTPA-bis(Met) at 1 h (Figure 8).

In Vivo Tumor Kinetics and Scintigraphy. In vivo tumor kinetics was studied in U-87MG cells over a time period ranging from 1 to 270 min. Initial rate of transport of ^{99m}Tc-DTPA-bis(Met) was found to be 4.68×10^{-4} μmol/kg/min (Figure 9).

Further, the rate was decreased to 6.77×10^{-5} μmol/kg/min over 30 min and found to saturate at 1.02×10^{-5} μmol/kg/min. However, the initial rate of soft tissue uptake was 3.23×10^{-5} μmol/kg/min. After 30 min, the rate of transport further increases 100-fold as compared to the accumulation in the soft tissue.

Imaging of animals was carried out at different time intervals after administering labeled compound intravenously. The mice depicted the beginning of accumulation of activity in tumor at 30 min, which reached a maximum at 4 h and remained almost stable for 6 h. The tumors (BMG cell line) grafted in athymic mice were readily identifiable in the γ images (Figure 10).

Semiquantitative analysis generated from region of interest (ROI) placed over areas counting average counts per pixel with maximum radiotracer uptake on the tumor was found to be 11.05 ± 3.99 and compared to ROI with muscle (0.55 ± 0.13). The tumor-to-contralateral muscle tissue ratio of ^{99m}Tc-DTPA-bis(Met) was found to be 23 ± 3.3. In the mice that received coadministration of 250 μg blocking dose of

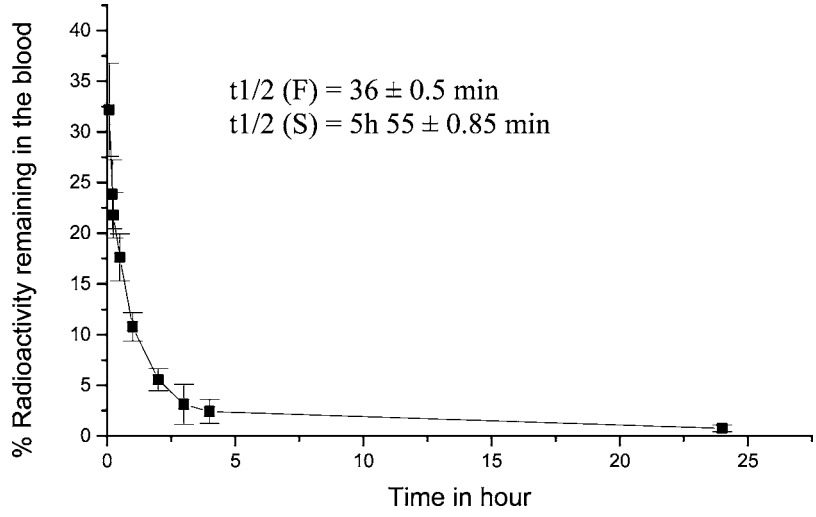


Figure 6. Blood clearance of ^{99m}Tc-DTPA-bis(Met) (11.1 MBq activity) administered through ear vein in normal rabbit.

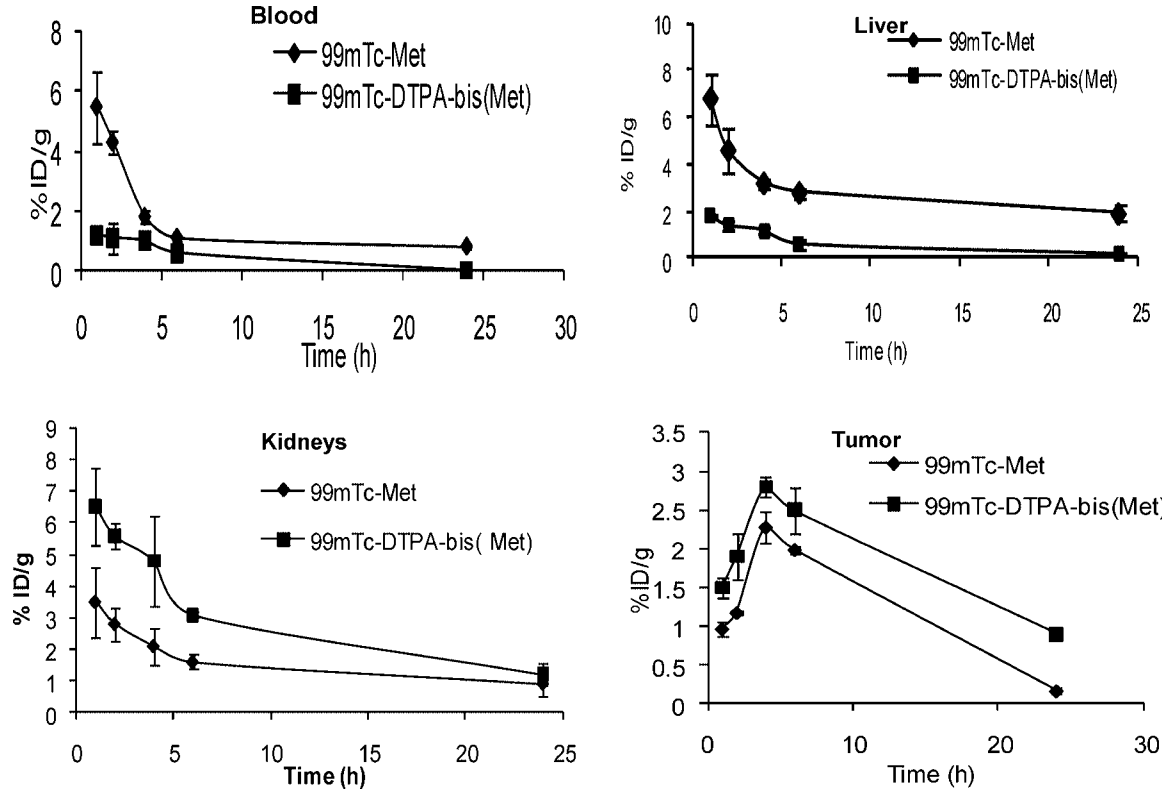


Figure 7. Comparative biodistribution of ^{99m}Tc-Met and ^{99m}Tc-DTPA-bis(Met) (11.1 MBq activity) administered through ear vein in EAT tumor-grafted Balb/c mice.

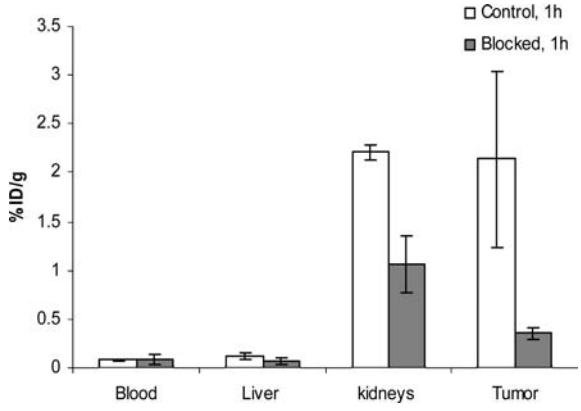


Figure 8. Tumor, blood, liver, and kidney activity of ^{99m}Tc-DTPA-bis(Met) administered through the ear vein in U-87MG grafted athymic mice with and without a coadministration of a blocking dose.

methionine, the uptake in the tumor was 0.46 ± 0.06% ID/g, significantly lower at 1 h postinjection (Figure 9). Comparative evaluation of biodistribution of ^{99m}Tc-labeled methionine and ^{99m}Tc-DTPA-bis(Met) in normal rabbits was also conducted (see Supporting Information). It was found that directly labeled methionine accumulated in the liver, whereas negligible uptake was seen for ^{99m}Tc-DTPA-bis-(Met).

Clinical Studies. Clinical studies in normal volunteers showed fast renal clearance in patients. Two hours after administration of ^{99m}Tc-DTPA-bis(Met), a good percentage of the injected activity was cleared through the kidneys. Insignificant tracer accumulation was observed in the hepatic region. Semiquantitative analysis was generated from region of interest (ROI) placed over areas counting average counts per pixel with maximum radiotracer uptake at the tumor site and compared to symmetric counterparts with ROI in soft tissues (target to nontarget ratios are shown in Table 2).

DISCUSSION

The polyaminopolycarboxylate ligand having two reactive sites (bisanhydride of DTPA) for the conjugation of amino acid favors the formation of complex with only one ligand per metal atom, which is required for in vivo stability and biological activity. The conjugate was labeled with ^{99m}Tc and evaluated in vitro and in vivo for its competence in clinical diagnosis of metabolic tumors. Radiochemical analysis showed that the drug is specifically coordinated with ^{99m}Tc radionuclide. In vitro human serum stability studies under physiological conditions suggested that there was least transcomplexation of the labeled drug.

This targeted agent was tested for the ability to induce cytotoxicity in the cancer cell lines using both an assay of mitochondrial activity (in a MTT assay) and a clonogenic assay. The unlabeled conjugate showed concentration-dependent cytotoxicity. A direct correlation was observed between MTT assay and clonogenic assay. Receptor binding experiments were performed to verify the biological integrity upon modification of methionine. Scatchard analysis confirmed good binding affinity to its target, as K_d values on malignant cancer cell lines were found to be in sub-picomolar range.

The expression and function of L-type amino acid transporter 1 (LAT1), a major catalytic subunit of system L, in human glioma cells have been reported in the literature (*33*). Several of the amino acid transport systems can be distinguished by their dependence on Na^+, response to other competitive AA, and response to specific nonmetabolizable AA analogues. System A, for example, is inhibited by α-(methylamino)isobutyric acid (MeAIB), whereas system L is inhibited by BCH. A combination of treatments was applied to incubated skin strips to define the AA transport systems operating for L-Ala, L-Leu,

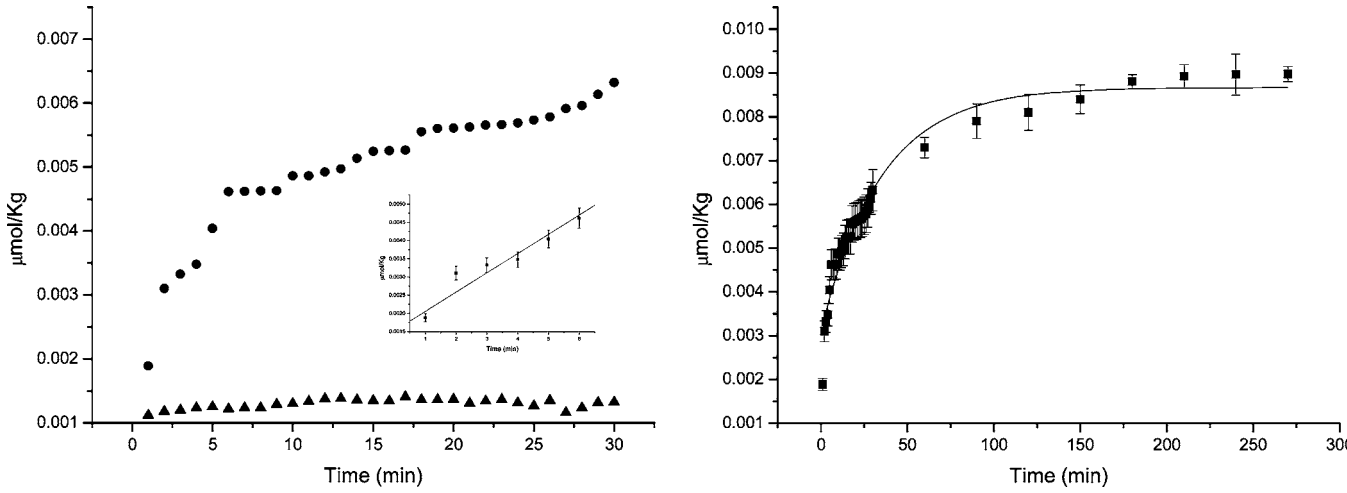


Figure 9. In vivo U-87MG tumor kinetics of ^{99m}Tc-DTPA-bis(Met) as a function of time after i.v. administration of a saturating dose of 2500 nmol/kg in tumor-bearing nude mice. (A) Rate of transport at an interval of 1 min over 30 min time period (inset: initial rate up to 5 min). (B) Rate of transport over 270 min time period.

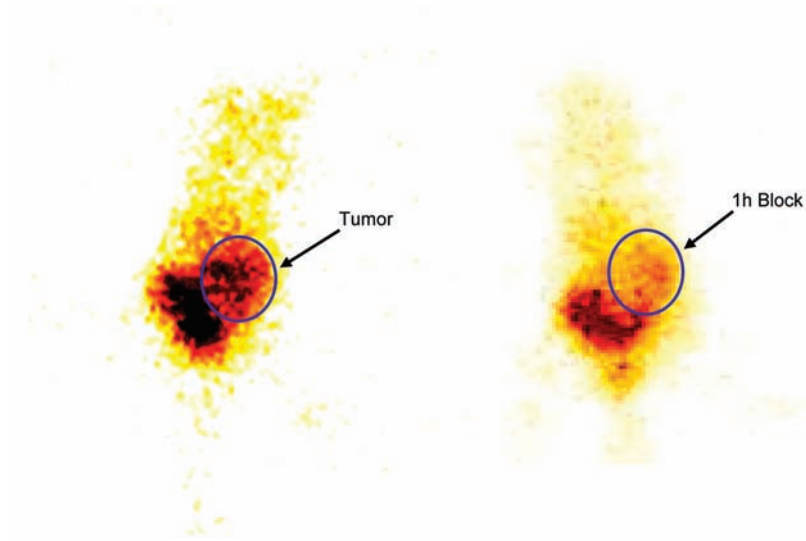


Figure 10. Whole-body γ image of female athymic mice with subcutaneous BMG tumor above the right hind leg at 1 h with and without coadministration of blocking dose.

Table 2. Semiquantative ROI Analysis Showing Lesion Target to Nontarget Ratios (T/NT) in Patients Expressed as Mean ± S.D.

no. of patients	patients	ROI (T/NT)	results
47	palpable breast masses, median age 44 (range 28−68 years), 33 breast carcinoma, 14 benign masses	3.7 ± 0.29 (range 2.73−6.06)	true positive DTPA-bis(Met) uptake in 29/33 patients, negative in 4 patients. 13 benign masses came out to be negative and 1 positive. Sensitivity = 87.8%; Specificity = 92.8%
3	brain cancer, median age 65 (range 45−82) 2 brain malignancy, 1 suspected recurrence	4.72 ± 0.48 (range 4.38−5.06)	positive in brain malignancies, recurrence not observed for 1 patient in both DTPA-bis(Met) and FDG scan
2	regional lymph node cancer	3.47 ± 2.05 (range 2.01−4.92)	DTPA-bis(Met) scan positive in all cases
3	osteosarcoma	5.31 ± 0.93 (range 4.64−6.38)	DTPA-bis(Met) scan positive in all cases

L-Cys, and L-Lys. The L system for which there is strong evidence of its involvement in the uptake process of ^{99m}Tc-DTPA-bis(Met) is the Na^+-insensitive system L, which shows high specificity for branched-chain and aromatic amino acids and utilizes the nonmetabolizable bicyclic BCH analogue as a system-specific substrate. Thus, since BCH was found to block the transport of ^{99m}Tc-DTPA-bis(Met) in competitive binding studies, it is reasonable to conclude that this pathway does contribute to the uptake of ^{99m}Tc-DTPA-bis(Met) to a significant extent. Moreover, the system L substrates such as L-leucine and L-phenylalanine caused marked inhibition of ^{99m}Tc-DTPA-bis(Met) transport. The inhibition was found to be independent of the presence of Na^+, which is a characteristic of the L transporter. Thus, the marked inhibition caused by L-leucine and BCH strongly supports the idea that system L is being utilized by ^{99m}Tc-DTPA-bis(Met) for entry into cells. Moreover, ^{99m}Tc-DTPA-bis(Met) demonstrated trans-stimulation of ^{35}S-L-methionine indicated for an exchange mechanism of transport. The data provide direct evidence for transport against a concentration gradient and not just via passive diffusion only.

The pharmacokinetic profile of ^{99m}Tc-DTPA-bis(Met) showed its high target uptake with the diagnostically useful target-to-nontarget ratio over a short period of time. The labeled drug

showed fast clearance that resulted in a decrease in the background activity.

The high specificity of results in selective uptake and distribution of the radiolabeled receptor ligand at the tissues, which are known to contain a substantial concentration of the target receptor that can be visualized in the high-quality images, obtained 1 h after administration of ^{99m}Tc-DTPA-bis(Met) in animal models with and without coadministration of blocking dose, which allows the advantage of comparing in vitro receptor binding studies and tumor-bearing animal studies. Dynamic study as a function of time revealed the rate of transport of ^{99m}Tc-DTPA-bis(Met) at the tumor site and soft tissue. The biodistribution studies showed that ^{99m}Tc-labeled methionine persisted in the liver up to 4 h, which indicates its hepatobiliary clearance, and the radiolabeled DTPA-conjugate cleared through renal routes.

Accurate interpretation of SPECT scans in suspected tumors relies on comparison of the amount of methionine taken up by the lesion with the normal value for that region of soft tissue. A normal value is typically determined by measuring uptake in the corresponding region of the contralateral tissue.^{99m}Tc-DTPA-bis(Met) accumulated in nearly all cancers with varying histology and histological grades. ^{99m}Tc-DTPA-bis(Met) imaging with SPECT is an effective method for evaluating head and neck cancer and, apparently, other types of human cancer. Furthermore, SPECT images of the tumors appeared to correlate well with the extent of cancers determined by other methods. It can provide useful information with reasonably high sensitivity and specificity in prognostic value for determining tumor masses. Normal tissues such as the salivary glands, however, accumulate ^{99m}Tc-DTPA-bis(Met), which may impair the detection of small tumors with a low uptake.

In summary, we have synthesized a new imaging agent ^{99m}Tc-DTPA-bis(Met) showing substantial promise for tumor scintigraphy, as significant accumulation is observed in athymic mice bearing the subcutaneous BMG cell line (malignant glioma). Breast, head, and neck cancers of varying histology can be imaged with ^{99m}Tc-DTPA-bis(Met). Although accumulation of the tracer in the salivary and lachrymal glands may occasionally interfere with image interpretation, ^{99m}Tc-DTPA-bis(Met) SPECT is a cost-effective method for imaging breast, head, and neck cancer. It can detect malignancy with reasonably high sensitivity and specificity. It may also be useful in the assessment of tumor extent when management of cancer is planned. This system has an added advantage over ^{11}C-methionine, as there are logistical hindrances in its use at centers that do not have an on-site cyclotron. Therefore, considering the apparent usefulness of new SPECT radiopharmaceutical ^{99m}Tc DTPA-bis(Met), future clinical study is warranted with attractive radionuclides and metal ions used in diagnosis and therapy.

ACKNOWLEDGMENT

We thank Dr. R. P. Tripathi, Director INMAS, for providing necessary facilities. The work was supported by Defence Research and Development Organization, Ministry of Defence, under R&D project INM −311.

Supporting Information Available: ^{1}H, ^{13}C NMR, and mass spectra of DTPA-bis(Met). Comparative evaluation of biodistribution of ^{99m}Tc-labeled methionine and ^{99m}Tc-DTPA-bis(Met) in normal rabbit. Clinical scintigraphs of ^{99m}Tc-DTPA-bis(Met) depicting breast carcinoma, regional lymph node cancer, and osteosarcoma. This material is available free of charge via the Internet at http://pubs.acs.org.

LITERATURE CITED

(1) Torrents, D., Estevez, R., Pineda, M., Fernandez, E., Lloberas, J., Shi, Y. B., Zorzano, A., and Palacin, M. (1998) Identification and characterization of a membrane protein (y1L amino acid transporter-1) that associates with 4F2hc to encode the amino acid transport activity y1L: a candidate gene for lysinuric protein intolerance. *J. Biol. Chem. 273*, 32437–32445.

(2) Verrey, F. (2003) System L: heteromeric exchangers of large, neutral amino acids involved in directional transport. *Pflugers Arch. 445*, 529–533.

(3) Lahoutte, T., Caveliers, V., Camargo, S. M., Franca, R., Ramadan, T., Veljkovic, E., Mertens, J., Bossuyt, A., and Verrey, F. (2004) SPECT and PET amino acid tracer influx via system L (h4F2hc-hLAT1) and its transstimulation. *J. Nucl. Med. 45*, 1591–1596.

(4) Campbell, W. A., and Thompson, N. L. (2001) Overexpression of LAT1/CD98 light chain is sufficient to increase system L-amino acid transport activity in mouse hepatocytes but not fibroblasts. *J. Biol. Chem. 276*, 16877–16884.

(5) Bodoy, S., Martín, L., Zorzano, A., Palacín, M., Estévez, R., and Bertran, J. (2005) Identification of LAT4, a novel amino acid transporter with system L activity. *J. Biol. Chem. 280*, 12002–12011.

(6) Kim, D. K., Kim, I.J., Hwang, S., Kook, J. H., Lee, M. C., Shin, B. A., Bae, C. S., Yoon, J. H., Ahn, S. G., Kim, S. A., Kanai, Y., Endou, H., and Kim, J. K. (2004) System L-amino acid transporters are differently expressed in rat astrocyte and C6 glioma cells. *Neurosci. Res. 50*, 437–446.

(7) Fuchs, B. C., and Bode, B. P. (2005) Amino acid transporters ASCT2 and LAT1in cancer: partners in crime. *Semin. Cancer. Biol. 15*, 254–266.

(8) Ogawa, T., Miura, S., Murakami, M., Tida, H., Hatazawa, J., Inugami, A., Kanno, I., Yasui, N., Sasajima, T., and Uemura, K. (1996) Quantitative evaluation of neutral amino acid transport in cerebral gliomas using positron emission tomography and fluorine-18 fluorophenylalanine. *Eur. J. Nucl. Med. 23*, 889–895.

(9) Wienhard, K., Herholz, K., Coenen, H. H., Rudolf, J., Kling, P., Stöcklin, G., and Heiss, W. D. (1991) Increased amino acid transport into brain tumors measured by PET of L-(2Y18F)fluorotyrosine. *J. Nucl. Med. 32*, 1338–1346.

(10) Wester, H. J., Herz, M., Weber, W., Heiss, P., Senekowitsch-Schmidtke, R., Schwaiger, M., and Stöcklin, G. (1999) Synthesis and radiopharmacology of O-(2-[18F]fluoroethyl)-L-tyrosine for tumor imaging. *J. Nucl. Med. 40*, 205–212.

(11) Weber, W. A., Wester, H. J., Grosu, A. L., Herz, M., Dzewas, B., Feldmann, H. J., Molls, M., Stöcklin, G., and Schwaiger, M. (2000) O-(2-[18F]fluoroethyl)-L-tyrosine and L-[methyl-11C]methionine uptake in brain tumours: initial results of a comparative study. *Eur. J. Nucl. Med. 27*, 542–549.

(12) Dirk, P., Gabriele, S., Winfried, S., Kurt, H., Dagmar, B., Lutz, T., Hans, H., Stefan, B., Heinz, H. C., and Karl, J. L. (2005) PET with O-(2−18FFluoroethyl)-L-tyrosine in peripheral tumors: first clinical results. *J. Nucl. Med. 46*, 411–416.

(13) Pieter, L. J., Willem, V., Jan, P., Elisabeth, G. E., de Vries, K. J., Langen, and Albertus, P. (2001) Radiolabeled amino acids: basic aspects and clinical applications in oncology. *J. Nucl. Med. 42*, 432–445.

(14) Stern, P. H., Wallace, C. D., and Hoffman, R. M. (1984) Altered methionine metabolism occurs in all members of a set of diverse human tumor cell lines. *J. Cell Physiol. 119*, 29–34.

(15) Tisdale, M. (1980) Effect of methionine deprivation on methylation and synthesis of macromolecules. *Br. J. Cancer 42*, 121–128.

(16) Kreis, W., and Goodenow, M. (1978) Methionine requirement and replacement by homocysteine in tissue cultures of selected rodent and human malignant and normal cells. *Cancer Res. 38*, 2259–2262.

(17) Mecham, J., Rowitch, D., Wallace, C. D., Stern, P. H., and Hoffman, R. M. (1983) The metabolic defect of methionine dependence occurs frequently in human tumor cell lines. *Biochem. Biophys. Res. Commun. 117*, 429–434.

(18) Hoffman, R. M. (1985) Altered methionine metabolism and transmethylation in cancer. *Anticancer Res. 5*, 1–30.

(19) Judde, J. G., Ellis, M., and Frost, P. (1989) Biochemical analysis of the role of transmethylation in the methionine dependence of tumor cells. *Cancer Res. 49*, 4859–4865.
(20) Isselbacher, K. J. (1972) Increased uptake of amino acids and 2-deoxy-2-glucose by virus-transformed cells in culture. *Proc. Natl. Acad. Sci. U.S.A. 69*, 585–589.
(21) Miyagawa, T., Oku, T., and Uehara, H. (1998) Facilitated amino acid transport is upregulated in brain tumors. *J. Cereb. Blood Flow Metab. 18*, 500–509.
(22) Chung, J. K., Kim, K., Kim, S. K., Lee, Y. J., Paek, S., Yeo, J. S., Jeong, J. M., Lee, D. S., Jung, H. W., and Lee, M. C. (2002) Usefulness of ^{11}C-methionine PET in the evaluation of brain lesions that are hypo- or isometabolic on ^{18}F-FDG PET. *Eur. J. Nucl. Med. Mol. Imaging 29*, 176–18.
(23) Singhal, T., Narayanan, T. K., Jain, V., Mukherjee, J., and Mantil, J. (2008) ^{11}C-L-Methionine positron emission tomography in the clinical management of cerebral gliomas. *Mol. Imaging Biol. 10*, 1–18.
(24) Kracht, L. W., Friese, M., Herholz, K., Schroeder, R., Bauer, B., Jacobs, A., and Heiss, W. D. (2003) Methyl-[^{11}C]- l-methionine uptake as measured by positron emission tomography correlates to microvessel density in patients with glioma. *Eur. J. Nucl. Med. Mol. Imaging 30*, 868–873.
(25) Herholz, K., Holzer, T., Bauer, B., Herholz, K., Hölzer, T., Bauer, B., Schröder, R., Voges, J., Ernestus, R. I., Mendoza, G., Weber-Luxenburger, G., Löttgen, J., Thiel, A., Wienhard, K., and Heiss, W. D. (1998) ^{11}C-Methionine PET for differential diagnosis of low-grade gliomas. *Neurology 50*, 1316–1322.
(26) Ali, M. S., and Quadri, S. M. (1996) Maleimido derivatives of diethylenetriaminepentaacetic acid and triethylenetetraamine-hexaacetic acid: their synthesis and potential for specific conjugation with biomolecules. *Bioconjugate Chem. 7* (5), 576–83.
(27) Fu, Y., Laurent, S., and Muller, R. N. (2002) Synthesis of a silyl lewis mimetic conjugated with DTPA, potential ligand of new contrast agents for medical. *Imaging Eur. J. Org. Chem. 23*, 3966–3973.
(28) Panwar, P., Iznaga, E. N., Mishra, P., Shrivastava, V., Sharma, R. K., Chandra, R., and Mishra, A. K. (2005) Radiolabeling and biological evaluation of DOTA-Ph-Al derivative conjugated to anti-EGFR antibody ior egf/r3 for targeted tumor imaging and therapy. *Cancer Biol. Ther. 4* (8), 854–860.
(29) Panwar, P., Shrivastava. V, Tandon, V., Mishra, P., Chuttani, K., Sharma, R. K., Chandra, R., and Mishra, A. K. (2004) ^{99m}Tc-Tetraethylenepentamine-folate—a new ^{99m}Tc-based folatederivative for the detection of folate receptor positive tumors: synthesis and biological evaluation. *Cancer Biol. Ther. 3* (10), 995–1001.
(30) Mishra, A. K., Panwar, P., Hosono, M., Chuttani, K., Mishra, P., Sharma, R. K., and Chatal, J. F. (2004) A new bifunctional chelating agent conjugated with monoclonal antibody and labelled with technetium-99m for targeted scintigraphy: 6-(4-isothiocyanatobenzyl)-5,7-dioxo-1,11-(carboxymethyl)-1,4,8,11-tetraazacyclotridecane. *J. Drug Targeting 12* (9−10), 556–559.
(31) Mishra, A. K., Panwar, P., Chopra, M., Sharma, R. K., and Chatal, J. F. (2003) Synthesis of novel bifunctional schiff based ligands derived from condensation of 1-(p-nitrobenzyl) ethylenediamine and 2-(-nitrobenzyl)-3-monooxo-1, 4,7-triazaheptane with salicylaldehyde. *New J. Chem. 27*, 1054–1058.
(32) Sharma, R., Tripathi, M., Panwar, P., Chuttani, K., Jaimini, A., Maitra, S., Chopra, M. K., Sawroop, K., Shukla, G., Mondal, A., and Mishra, A. K. (2009) ^{99m}Tc-methionine scintimammography in the evaluation of breast cancer. *Nuc. Med. Commun. 12* (1), 22–25.
(33) Keiichi, K., Ohnishi, P. A., Shimizu, J., Kanai, S., Shiokawa, Yoshiaki, Y., and Motoo, N. (2008) Enhanced tumor growth elicited by L-type amino acid transporter 1 in human malignant glioma cells. *Neurosurgery 62* (2), 493–504.

BC900197N

Effect of Cross-Linking Reagents for Hyaluronic Acid Hydrogel Dermal Fillers on Tissue Augmentation and Regeneration

Junseok Yeom,[†] Suk Ho Bhang,[‡] Byung-Soo Kim,[‡] Moo Seok Seo,[§] Eui Jin Hwang,[§] Il Hwan Cho,[§] Jung Kyu Park,[†] and Sei Kwang Hahn*[,†]

Department of Materials Science and Engineering, Pohang University of Science and Technology (POSTECH), San 31, Hyoja-dong, Nam-gu, Pohang, Kyungbuk 790-784, Korea, School of Chemical and Biological Engineering, Seoul National University, San 56-1, Sillim-dong, Gwanak-gu, Seoul 151-744, Korea, and Biotechnology Department, Central Research Institute of Shinpoong Pharmaceutical Company, 434-4 Moknae-dong, Danwon-gu, Ansan, Kyunggi 425-100, Korea. Received June 15, 2009; Revised Manuscript Received December 6, 2009

A novel, biocompatible, and nontoxic dermal filler using hyaluronic acid (HA) hydrogels was successfully developed for tissue augmentation applications. Instead of using highly reactive cross-linkers such as divinyl sulfone (DVS) for Hylaform, 1,4-butanediol diglycidyl ether (BDDE) for Restylane, and 1,2,7,8-diepoxyoctane (DEO) for Puragen, HA hydrogels were prepared by direct amide bond formation between the carboxyl groups of HA and hexamethylenediamine (HMDA) with an optimized carboxyl group modification for effective tissue augmentation. The HA-HMDA hydrogels could be prepared within 5 min by the addition of HMDA to HA solution activated with 1-ethyl-3-[3-(dimethylamino)propyl]carbodiimide (EDC) and 1-hydroxybenzotriazole monohydrate (HOBt). Five kinds of samples, a normal control, a negative control, a positive control of Restylane, adipic acid dihydrazide grafted HA (HA-ADH) hydrogels, and HA-HMDA hydrogels, were subcutaneously injected to wrinkled model mice. According to the image analysis on dorsal skin augmentation, the HA-HMDA hydrogels exhibited the best tissue augmentation effect being stable longer than 3 months. Furthermore, histological analyses after hematoxylin-eosin (H&E) and Masson's trichrome staining revealed the excellent biocompatibility and safety of HA-HMDA hydrogels. The dermal thickness and the dermal collagen density in wrinkled mice after treatment with HA-HMDA hydrogels for 12 weeks were comparable to those of normal mice. Compared with HA-DVS hydrogels and Restylane, the excellent tissue augmentation by HA-HMDA hydrogels might be ascribed to the biocompatible residues of amine groups in the cross-linker of HMDA. The HA-HMDA hydrogels will be investigated further as a novel dermal filler for clinical applications.

INTRODUCTION

Recently, tissue augmentation has been studied extensively for cosmetic applications such as antiaging treatment and plastic surgery (*1, 2*). Various dermal fillers were developed for long-lasting soft tissue augmentation with reduced allergic reaction in clinical applications. Bovine collagen, which is an FDA approved dermal filler, has been used for longer than 20 years (*3, 4*). However, the bovine collagen has been reported to cause an allergic reaction by nonhuman origin materials such as scarring, urticaria, redness, and so forth (*5*). Accordingly, human-origin collagen was developed to reduce the side effects with a duration of less than 6 months in the body. In order to reduce side effects and prolong the tissue augmentation effect, hyaluronic acid (HA) hydrogels were developed as a novel dermal filler (*6*). Hylaform was synthesized with divinyl sulfone (DVS), Restylane and Juvederm with 1,4-butanediol diglycidyl ether (BDDE) (*6*), and Puragen with 1,2,7,8-diepoxyoctane (DEO). The softness and tissue augmentation effect of dermal fillers were controlled by changing the cross-linking density with various cross-linkers. The tissue augmentation by Restylane, which is widely used all over the world, lasts for 6 months with significantly reduced side effects. All dermal fillers were prepared by the cross-linking of hydroxyl groups of HA with various cross-linkers. However, we have previously reported a protocol to control the molecular degradation of HA hydrogels for tissue augmentation by the cross-linking of carboxyl groups of HA with bis(sulfosuccinimidyl)suberate (BS^3) (*7*). Adipic acid dihydrazide modified HA (HA-ADH) hydrogels with ADH content higher than 70 mol % degraded slowly, being stable longer than 6 months, whereas HA-DVS hydrogels degraded almost completely within 6 months after subcutaneous injections to ICR mice (*7, 8*).

HA is a biodegradable, biocompatible, nonimmunogenic, and natural linear polysaccharide. HA is the only nonsulfated glycosaminoglycan (GAG) that is abundant in synovial fluid and extracellular matrix (ECM) (*9*). The molecular weight (MW) of HA ranges from several thousands to more than millions. High MW HA in the tissues degrades by HA receptor mediated degradation in the lymph node, liver, and kidney (*10*). In particular, when HA degrades to specific sizes of 3−10 repeating units, the resulting oligomeric HA promotes differentiation, vascularization, and migration of stem cells (*11, 12*). Due to the excellent biological and physicochemical properties, HA and chemically modified HA have been widely used for various medical applications such as arthritis treatment, ocular surgery, drug delivery, and tissue engineering (*13–17*). However, HA is known to have a very short half-life of several hours in the body, which should be overcome for tissue augmentation applications. The residence time of HA can be prolonged by the chemical modification of carboxyl groups of HA (*7, 18*) on the basis of the fact that carboxyl groups are the recognition site of hyaluronidase (*11*) and HA receptors (*19–22*).

* Corresponding author. S. K. Hahn, Ph.D. Tel.: +82-54-279-2159; Fax: +82-54-279-2399. Email: skhanb@postech.ac.kr.
[†] POSTECH.
[‡] Seoul National University.
[§] Central Research Institute of Shinpoong Pharmaceutical Company.

10.1021/bc9002647 © 2010 American Chemical Society
Published on Web 01/15/2010

In this work, we developed a novel, biocompatible, and nontoxic dermal filler using HA hydrogels for tissue augmentation applications. Instead of using highly reactive cross-linkers such as DVS, BDDE, and DEO, HA hydrogels were prepared by direct amide bond formation between the carboxyl groups of HA and hexamethylenediamine (HMDA) with an optimized carboxyl group modification for effective tissue augmentation. HMDA used as a cross-linker for the preparation of collagen hydrogels was reported to be nontoxic and promote the attachment and proliferation of keratinocytes and fibroblasts (*23*). Wrinkled model mice were prepared for tissue augmentation tests by daily treatment of the dorsal skins with 0.2 μg of 1α-25-dihydroxyvitamin D_3 in ethanol for 4 weeks (*24*). Five different samples of a normal control, a negative control, a positive control of Restylane, HA-ADH hydrogels, and HA-HMDA hydrogels were injected into the dorsal subcutaneous tissues of wrinkled model mice. The tissue augmentation effect was assessed using a surface image analyzer with histological analyses after hematoxylin−eosin (H&E) and Masson's trichrome staining. The novel HA-HMDA hydrogels were discussed for further clinical applications.

MATERIALS AND METHODS

Materials. Sodium hyaluronate, sodium salt of hyaluronic acid (HA), with a molecular weight (MW) of 234 kDa was purchased from Lifecore Co. (Chaska, MN) and HA with a MW of 1.0 MDa was kindly provided by Shinpoong Pharmaceutical Co. (Ansan, Korea). Bis(sulfosuccinimidyl) suberate (BS^3) was purchased from Pierce Chemical Co. (Rockford, IL). 1-Ethyl-3-[3-(dimethyl amino)propyl]carbodiimide (EDC), phosphate buffered saline (PBS) tablet, hexamethylenediamine (HMDA), potassium cyanide, hematoxylin−eosin (H&E), Masson's trichrome, and hyaluronidase from *Streptomyces hyalurolyticus* were purchased from Sigma-Aldrich (St. Louis, MO). Adipic acid dihydrazide (ADH) and divinyl sulfone (DVS) were purchased from Tokyo Chemical Industry Co. (Tokyo, Japan) and 3-(4-carboxybenzoyl)quinoline-2-carboxaldehyde (CBQCA) from Invitrogen Co. (Carlsbad, CA). Hydrochloric acid (HCl), sodium hydroxide (NaOH), methanol, and 1-hydroxybenzotriazole monohydrate (HOBt) were obtained from Wako Pure Chemical Industries (Osaka, Japan). Restylane was purchased from Q-Med AB (Uppsala, Sweden). All reagents were used without further purification.

Synthesis of HA-ADH Hydrogels. HA-ADH (MW = 234 kDa) with ca. 70 mol % ADH content was prepared as described elsewhere (*7*, *8*). Then, HA-ADH was dissolved in PBS (0.01 M, pH 7.4) for 2 h. As a specific cross-linker to hydrazide, BS^3 was also dissolved in PBS, which was added to the HA-ADH solution. The amount of BS^3 was 20 mol % of hydrazide groups in HA-ADH. The final precursor solution was mixed and incubated at 37 °C for 1 h to complete the cross-linking reaction for HA-ADH hydrogel preparation.

Synthesis of HA-DVS Hydrogels. HA (MW = 234 kDa) was dissolved at a concentration of 4.0 wt % in 0.2 N NaOH (pH = 13). After complete dissolution, DVS was added to the HA solution for the cross-linking reaction with hydroxyl groups of HA (*7*, *8*). The molar ratio of DVS to HA repeating units was 1:1. The final precursor solution was mixed and incubated at 37 °C for 1 h to complete the cross-linking reaction for HA-DVS hydrogel preparation. Then, the hydrogels were sealed within a prewashed dialysis membrane tube (MWCO of 7 kDa) and dialyzed against PBS for 24 h. The ions (Na^+ and OH^-) diffused out though the dialysis membrane neutralizing the pH inside the HA-DVS hydrogels.

Synthesis of HA-HMDA Hydrogels. HA (MW = 234 kDa) was dissolved at a concentration of 4.0 wt % in double distilled water. After complete dissolution, HMDA was added to the HA solution for cross-linking reaction with carboxyl groups of HA. The molar ratio of HMDA to the carboxyl group of HA was 1:1. EDC and HOBt, activating the carboxyl groups of HA, were dissolved in water and added to the mixed solution of HA and HMDA for HA-HMDA hydrogel preparation. The final precursor solution was incubated at 37 °C for 1 h to complete the cross-linking reaction. Then, prepared HA-HMDA hydrogels were sealed within prewashed dialysis membrane tube (MWCO of 7 kDa) and dialyzed against PBS for 3 days to remove the remaining EDC, HOBt, and HMDA completely. HPLC analysis of HA-HMDA hydrogels degraded by the treatment with hyaluronidase (100 U/mL) was carried out to confirm that there was no remaining reactant within the HA-HMDA hydrogels. In order for in vivo tissue augmentation tests, HA-HMDA hydrogels were prepared by the cross-linking of HA (MW = 1.0 MDa) solution at a concentration of 1.0 wt % with 25 mol % HMDA of HA repeating units.

Characterization of HA Hydrogels. After preparation of three kinds of HA hydrogels, the resulting characteristics of HA hydrogels were investigated by ^{1}H NMR analysis of degraded HA hydrogels after treatment with hyaluronidase (100 U/mL). The residual contents of BS^3, DVS, and HMDA were quantified in comparison with the methyl resonance (δ = 1.85−1.95 ppm) of acetamido moiety of the *N*-acetyl-D-glucosamine. In addition, the amine content of pendant HMDA in HA-HMDA hydrogels was quantified by CBQCA analysis (*25*, *26*).

In Vitro Degradation Tests of HA Hydrogels. Each HA hydrogel for in vitro degradation tests was prepared in a syringe as described in our previous work (*7*, *8*). Three kinds of HA hydrogel samples, HA-ADH hydrogels, HA-DVS hydrogels, and HA-HMDA hydrogels, were put into vials, respectively. PBS (0.2 M, pH 6.2) containing 50 U of hyaluronate lyase was added to each vial, which was incubated at 37 °C for predetermined time intervals (0−48 h). After that, the supernatant was completely removed and the remaining weight of HA hydrogels was measured with a balance. The degree of HA hydrogel degradation was represented by a weight ratio (%) of the remaining HA hydrogel to the original HA hydrogel.

In Vivo Tissue Augmentation Tests of HA Hydrogels. Wrinkled model mice were prepared by daily treatment of dorsal skins of female ICR hairless mice at an age of 6 weeks with 0.2 μg of 1α-25-dihydroxyvitamin D_3 in ethanol for 4 weeks as described elsewhere (*24*). In order to measure the wrinkled surface area, a square (1.5 × 1.5 cm^2) was tattooed on the dorsal skin of ICR mouse (n = 5 for each sample). Two HA hydrogels of HA-ADH hydrogels and HA-HMDA hydrogels were mixed with equal volume of PBS and completely micronized with a homogenizer (T-18 basic, IKA, Tokyo, Japan) at 8000 rpm for 5 min, respectively. Each 400 μL of the prepared HA microhydrogels was injected to fill evenly the wrinkled area within the dorsal tattooed rectangle. For comparison, three kinds of control groups were also tested, normal mice as a normal control, wrinkled mice without tissue augmentation as a negative control, and those treated with Restylane as a positive control. Tissue augmentation was assessed by measuring the area of square on the dorsal skin with an image analyzer once a week for 11 weeks. The mice were sacrificed in 12 weeks for histological analyses (n = 3 for each sample). The dissected tissue around the tattooed square was fixed in 10% (v/v) buffered formaldehyde, dehydrated with a graded ethanol series, and embedded in paraffin. The specimen was sliced into 4-μm-thickness sections and stained with hematoxylin and eosin (H&E) to investigate the inflammation and soft tissue regeneration. The sliced specimens were also stained with Masson's trichrome to investigate a collagen density in the dermis. More than 50 random sites of Masson's trichrome-positive area in blue color in the dermis were analyzed for quantification with *Adobe*

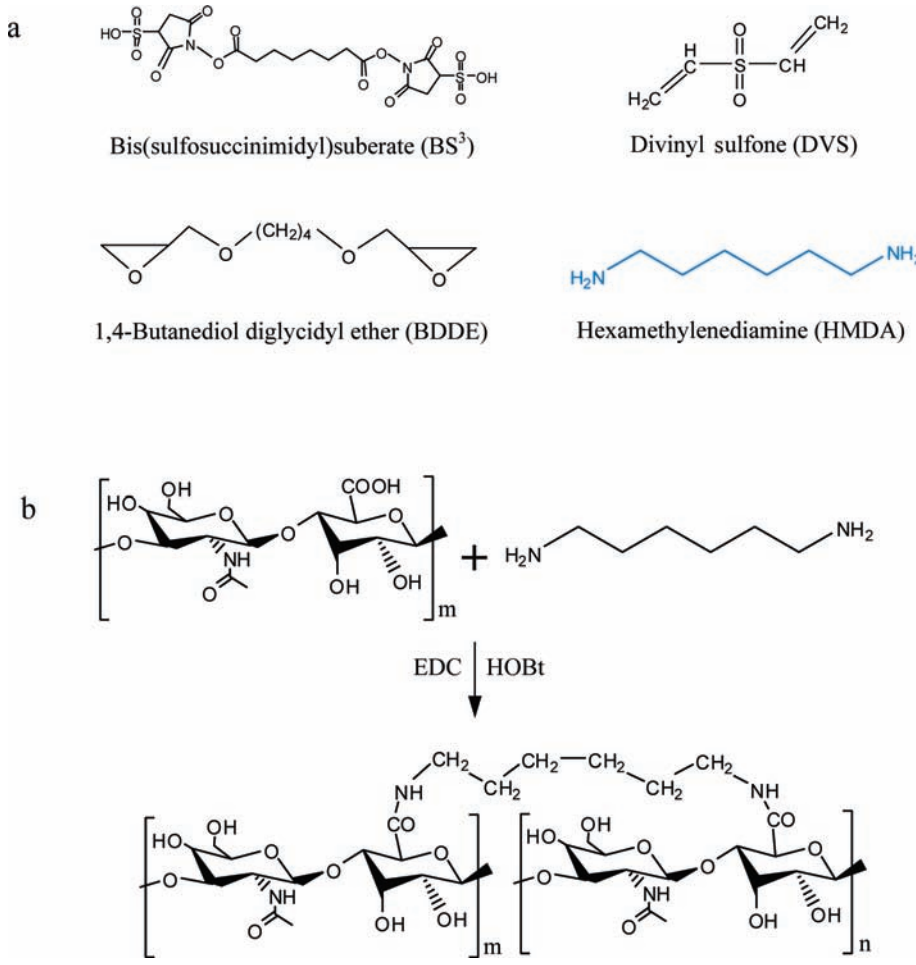


Figure 1. Schematic representations of (a) the cross-linkers for the preparation of hyaluronic acid (HA) hydrogel dermal fillers and (b) the preparation of HA hydrogels cross-linked with hexamethylenediamine (HMDA) after activation with 1-ethyl-3-[3-(dimethylamino)propyl] carbodiimide and 1-hydroxybenzotriazole monohydrate (HOBt).

Photoshop CS2 (Adobe System Inc., San Jose, CA) and *Image-Pro Plus* (Media Cybernetics, Silver Spring) software packages.

Statistical Analysis. The data are expressed as means ± SD from several separate experiments. Statistical analysis was performed by *t*-test using *SigmaPlot 9.0* software. Statistical significance was assigned for P values of < 0.05 (95% confidence level).

RESULTS AND DISCUSSION

Preparation, Characterization, and in Vitro Degradation Tests of HA Hydrogels. Many kinds of dermal fillers using HA hydrogels were commercialized under the trade names of Hylaform, Restylane, Juvederm, Puragen, and so on. All dermal fillers were prepared by the cross-linking of hydroxyl groups of HA with various cross-linkers such as DVS, BDDE, and DEO. We have previously reported the sustained degradation of HA-ADH hydrogels with carboxyl group modifications in comparison with HA-DVS hydrogels cross-linked by Michael addition between DVS and hydroxyl groups of HA. HA-ADH hydrogels with ADH content higher than 70 mol % appeared to be stable longer than 6 months, whereas HA-DVS hydrogels degraded almost completely within 6 months after subcutaneous injections to ICR mice (*7*). The results could be explained by the fact that the carboxyl group of HA is known to be the recognition site of hyaluronidase and HA receptors (*19–22*).

However, with increasing chemical modification of carboxyl groups, HA-ADH hydrogel became brittle and its swelling ratio decreased drastically. HA is hygroscopic due to carboxyl groups on the backbone. The swelling property is influenced by negative charge repulsion of HA-COOH, which may have a significant effect on tissue augmentation (*9, 27*). In addition, considering that all functional groups in the reactive cross-linkers (Figure 1a) are not reacted for the preparation of HA hydrogels, we tried to synthesize HA hydrogels with a relatively nonreactive HMDA after direct activation of HA-COOH with EDC and HOBt. Figure 1b shows a schematic representation for the preparation of HA-HMDA hydrogels with sustained degradation and good swelling characteristics in the body. HA hydrogels were prepared by the amide bond formation between carboxyl groups of HA and HMDA with an optimized amount of intact carboxyl groups for effective tissue augmentation. After exhaustive dialysis, the HPLC analysis of HA-HMDA hydrogels degraded by the treatment with hyaluronidase confirmed that there was no remaining EDC, HOBt, and HMDA within the HA-HMDA hydrogels. According to ^{1}H NMR analysis of degraded HA hydrogels, the amount of cross-linkers within the HA-HMDA hydrogels was ca. 8 mol % of HA repeating units. In addition, CBQCA analysis revealed that the pendant amine content in HA-HMDA hydrogels was ca. 3.7 mol % of HA repeating units, reflecting the incomplete reaction of both amine groups in HMDA.

In vitro degradation tests of HA hydrogels were carried out to investigate their degradation and swelling characteristics by measuring the remaining weight of HA hydrogels after treatment with hyaluronidase. As shown in Figure 2, HA-DVS hydrogels degraded completely in 26 h, whereas HA-ADH hydrogels

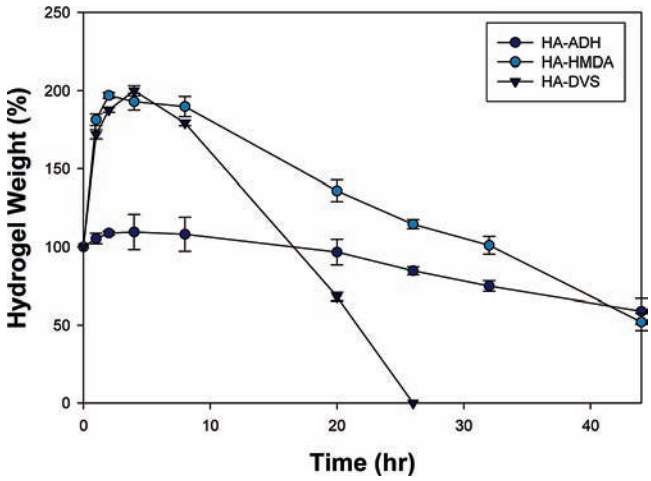


Figure 2. In vitro degradation of adipic acid dihydrazide modified hyaluronic acid (HA-ADH, black ●) hydrogels, HA hydrogels cross-linked with hexamethylenediamine (HA-HMDA, blue ●) after activation with 1-ethyl-3-[3-(dimethylamino)propyl]carbodiimide and 1-hydroxybenzotriazole monohydrate (HOBt), and HA hydrogels cross-linked with divinyl sulfone (HA-DVS, ▼) by the treatment with hyaluronidase from *Streptomyces hyalurolyticus*.

degraded only partially in 44 h. Interestingly, the degradation rate of HA-HMDA hydrogels was in the middle with comparable swelling characteristics to HA-DVS hydrogels. The swelling ratio of HA-HMDA hydrogels and HA-DVS hydrogels was twice that of HA-ADH hydrogels. The more rapid degradation of HA-HMDA hydrogels with 8 mol % HMDA of HA repeating units than HA-ADH hydrogels with 70 mol % ADH and ca. 10 mol % BS[3] might be ascribed to the lower degree of carboxyl group modification. From the results, we supposed that the novel HA-HMDA hydrogels would be successfully applied for tissue augmentation.

In Vivo Tissue Augmentation Tests of HA Hydrogels. The newly developed HA-HMDA hydrogels were assessed in wrinkled model mice for tissue augmentation applications in comparison with Restylane. HA-HMDA hydrogels were synthesized and completely micronized with a homogenizer for the preparation of injectable microhydrogels. ^{1}H NMR analysis of Restylane after treatment with hyaluronidase revealed that the amount of cross-linkers within the hydrogel network was ca. 3−5 mol %. Wrinkled model mice were prepared by daily treatment of the dorsal skins with 0.2 μg of 1α-25-dihydroxyvitamin D_3 in ethanol for 4 weeks as described elsewhere (*24*). Five different samples of a normal control, a negative control, a positive control of Restylane, HA-ADH hydrogels, and HA-HMDA hydrogels were subcutaneously injected to eight tattooed sites on the back of wrinkled model mice. Due to the soft and viscoelastic properties, HA-HMDA microhydrogels could be injected through 30-gauge needle, whereas HA-ADH hydrogels were done through 24-gauge needle. The HA-ADH hydrogels with highly modified carboxyl groups appeared to be brittle and were not easily distributed evenly in the wrinkled tissue.

Figure 3 shows the tissue augmentation effect of HA hydrogels in 7 weeks. The wrinkled dorsal skin in the negative control group remained without tissue augmentation. As shown in Figure 3c, HA-ADH hydrogels appeared to have a tendency to conglomerate in the wrinkled tissue with increasing postin-

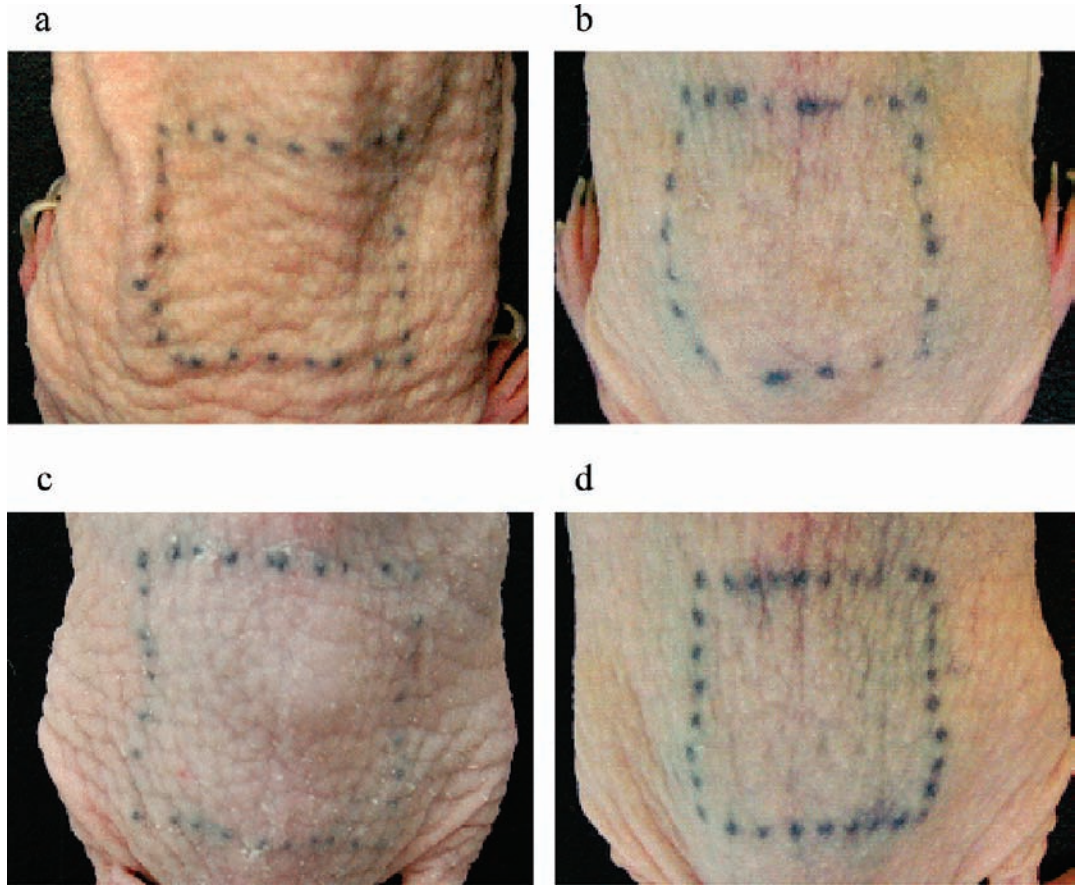


Figure 3. In vivo tissue augmentation by hyaluronic acid (HA) hydrogels in ICR hairless mice in 7 weeks: (a) wrinkled mice without tissue augmentation as a negative control, those treated with (b) Restylane as a positive control, (c) adipic acid dihydrazide (ADH) modified HA-ADH hydrogels, and (d) HA hydrogels cross-linked with hexamethylenediamine after activation with 1-ethyl-3-[3-(dimethylamino)propyl]carbodiimide and 1-hydroxybenzotriazole monohydrate (HOBt).

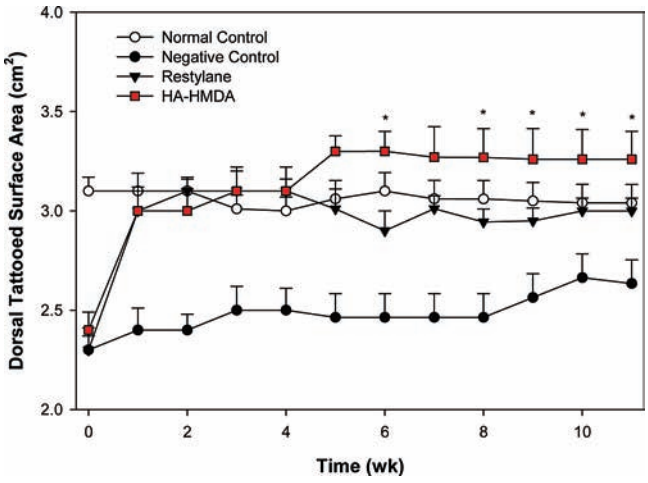


Figure 4. Effect of hyaluronic acid (HA) hydrogels on tissue augmentation determined by measuring the dorsal tattooed surface area in ICR hairless mouse once per a week for 11 weeks: (○) normal mice without treatment as a normal control, (●) wrinkled mice without tissue augmentation as a negative control, those treated with (▼) Restylane as a positive control, and (■) HA hydrogels cross-linked with hexamethylenediamine (HMDA) after activation with 1-ethyl-3-[3-(dimethylamino)propyl] carbodiimide and 1-hydroxybenzotriazole monohydrate (HOBt). Statistical analyses using *t*-test clearly revealed the difference in tissue augmentation effect between Restylane and HA-HMDA hydrogels (* $P < 0.05$).

jection time. We could recover the conglomerated HA hydrogels from the subcutaneous of wrinkled mice. Accordingly, HA-ADH hydrogels prepared with a reactive cross-linker of BS^3 were not considered for further development. However, HA-HMDA hydrogels resulted in comparable tissue augmentation to Restylane on the photoimages in 7 weeks (Figure 3b,d). The results might be ascribed to the good swelling characteristics of HA-HMDA hydrogels as well as sustained degradation. There was no outward inflammation or adverse effects during in vivo tests. Figure 4 shows the change of tattooed surface area on the back of an ICR mouse after injection of various dermal filler samples. The tattooed surface areas of the normal control group and the negative control group without tissue augmentation were not changed significantly until the end of in vivo tests (Figure 4). The tissue augmentation effect of HA-HMDA hydrogels was maintained continuously up to 11 weeks, which was statistically better than that of Restylane ($P < 0.05$ in Figure 4). The results were thought to reflect the higher stability of HA-HMDA hydrogels with carboxyl group modifications than Restylane with hydroxyl group modifications in the subcutaneous tissue of ICR mouse.

Histological Analysis after Tissue Augmentation Tests. Histological analysis was carried out with H&E staining at 12 weeks after treatments with HA hydrogels. The daily treatment of dorsal skins of mice with 0.2 μg of 1α-25-dihydroxyvitamin D_3 in ethanol caused the induction of wrinkling in the mice. In comparison to normal mice (Figure 5a), epidermis was flattened and dermis became coarse, reflecting the skin damage in wrinkled mice (Figure 5b). Treatments with Restylane and HA-HMDA hydrogels (Figure 5c,d) caused significant changes in the epidermis, dermis, and hypodermis of wrinkle-induced mice. The epidermis was meandered and became similar to that of normal mice. Moreover, the subcutaneous injection of Restylane and HA-HMDA hydrogels (Figure 5c,d) induced significant dermis regeneration compared to the negative control (Figure 5b). In particular, the thickness of regenerated dermis by HA-HMDA hydrogel was comparable to that of normal mouse (Figure 5a,d). Compared to other groups, the most distinguished advantage of HA-HMDA hydrogels was found in the regenerated hypodermis. The treatment with HA-HMDA hydrogels (Figure 5d) resulted in a mild infiltration with comparable numbers of macrophages and lymphocytes to those of normal mice (Figure 5a), whereas infiltration numbers significantly increased in other groups (Figure 5b,c). Figure 5e−g shows the representative images of macrophage and lymphocyte infiltration in the negative control, positive control of Resylane, and HA-HMDA hydrogels. The relatively high biocompatibility of HA-HMDA hydrogels might be ascribed to the nontoxic amine residues in contrast to the possible toxic remaining groups of BDDE in Restylane and DVS in HA-DVS hydrogels (Hylaform). The amine pendant groups within HA-HMDA hydrogels might be advantageous for cellular attachment and proliferation (*23*). Figure 6 shows a quantification of the thickness of regenerated dermis after treatment with various HA hydrogel samples. The regeneration of dermis by HA-HMDA hydrogel was the most effective contributing to tissue augmentation. According to a statistical analysis using *t*-test, the thickness of regenerated dermis by HA-HMDA hydrogel was significantly thicker than those of the positive control (* $P < 0.05$) and the negative control (** $P < 0.01$), but not so much different from that of the normal control (*** $P = 0.41$).

Histological sections of skin samples were also subjected to Masson's trichrome staining to visualize the extracellular matrix (ECM) components, especially the collagen in dermis. The collagenous component of dermal extracellular matrix is responsible for the strength and resiliency of skin (*28*). The blue color region in dermis corresponds to the collagen layer (Figure 7). Compared to the negative control, a remarkable increase of collagen bundles was observed after treatment with Restylane and HA-HMDA hydrogels. In particular, the regenerated collagen density by HA-HMDA hydrogel was comparable to that of normal mice (Figure 7d). The induction of wrinkling in the dorsal skin resulted in significantly reduced collagen density (Figure 7b), which might be ascribed to the reduced collagen biosynthesis by 1α-25-dihydroxyvitamin D_3 treatment and the following damage in the dermis. Figure 8 shows a quantification of the collagen density of regenerated dermis after treatment with various HA hydrogel samples. HA-HMDA hydrogel showed the most effective regeneration of collagen bundles. According to a statistical analysis using *t*-test, the regenerated collagen density by HA-HMDA hydrogel was significantly higher than those of the positive control (* $P < 0.05$) and the negative control (** $P < 0.01$), but not much different from that of the normal control (*** $P = 0.27$). Considering all these results, HA-HMDA hydrogels were thought to be a novel dermal filler with excellent biocompatibility as well as statistically significant tissue augmentation.

CONCLUSIONS

HA-HMDA hydrogels were successfully developed as a novel dermal filler with excellent biocompatibility and tissue augmentation effect. Instead of using reactive cross-linkers such as DVS, BDDE, and DEO, HA-HMDA hydrogels were prepared by direct amide bond formation between HMDA and the carboxyl groups of HA activated with EDC and HOBt. According to in vitro degradation tests with hyaluronidase, the degradation rate of HA-HMDA hydrogels with an optimized carboxyl group modification for effective tissue augmentation could be controlled between those of HA-ADH hydrogels and HA-DVS hydrogels. The image analysis on dorsal skin augmentation in wrinkled model mice showed that HA-HMDA hydrogels resulted in the best tissue augmentation being stable longer than 3 months. Furthermore, histological analyses with H&E and Masson's trichrome staining revealed the excellent biocompatibility of HA-HMDA hydrogels possibly due to the nontoxic residues of amine groups in the cross-linker of HMDA. The thickness of regenerated dermis and the regenerated

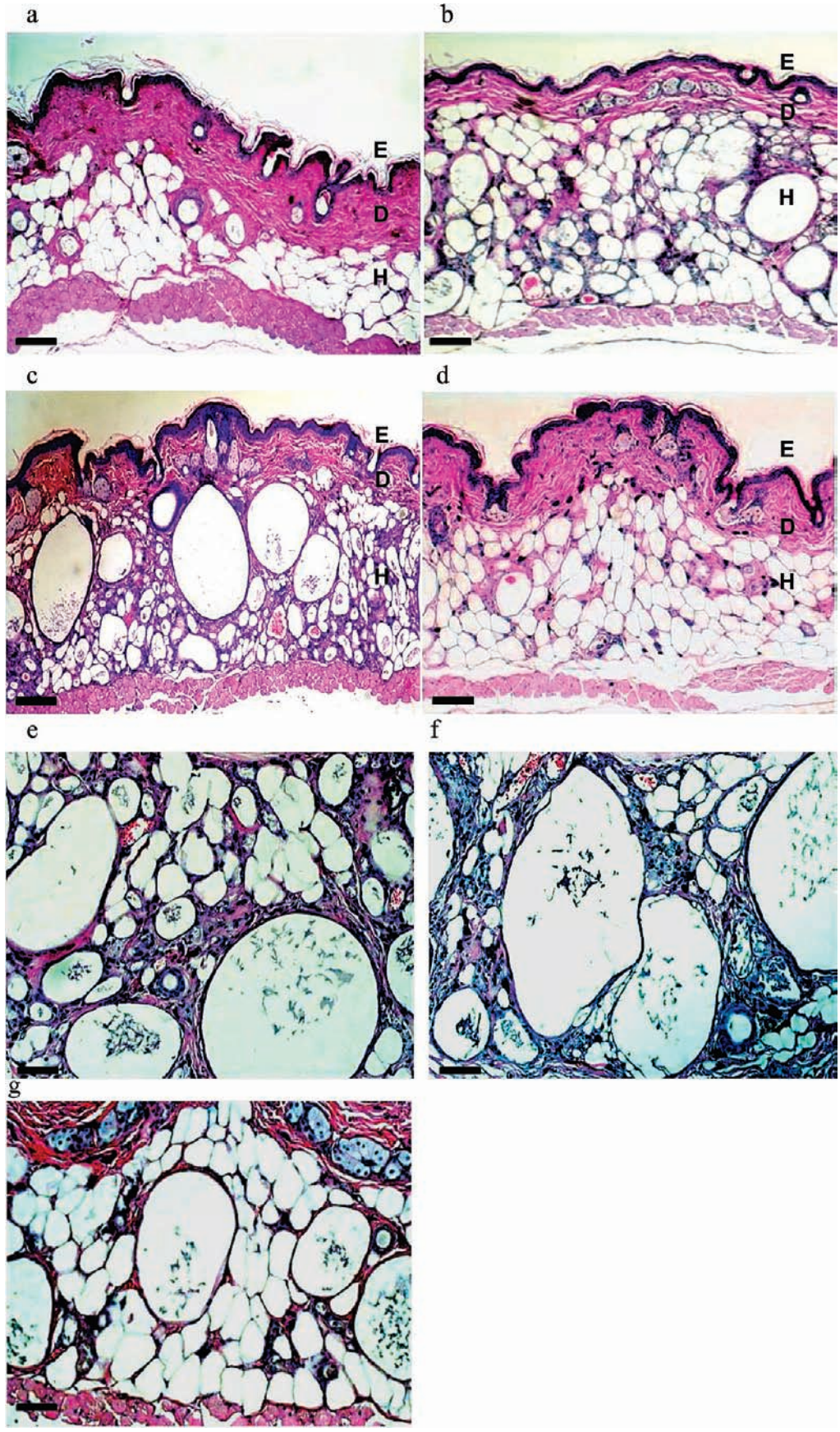


Figure 5. Histological analysis of ICR hairless mouse skin treated with hyaluronic acid (HA) hydrogel samples after hematoxylin and eosin (H&E) staining in 12 weeks: (a) normal mice without treatment as a normal control, (b) wrinkled mice without tissue augmentation as a negative control, those treated with (c) Restylane as a positive control, and (d) HA hydrogels cross-linked with hexamethylenediamine (HMDA) after activation with 1-ethyl-3-[3-(dimethylamino)propyl] carbodiimide and 1-hydroxybenzotriazole monohydrate (HOBt) (E: epidermis, D: dermis, and H: hypodermis). Representative images of macrophage and lymphocyte infiltration in (e) negative control, (f) positive control, and (g) those treated with HA-HMDA hydrogels (scale bar: 100 μm).

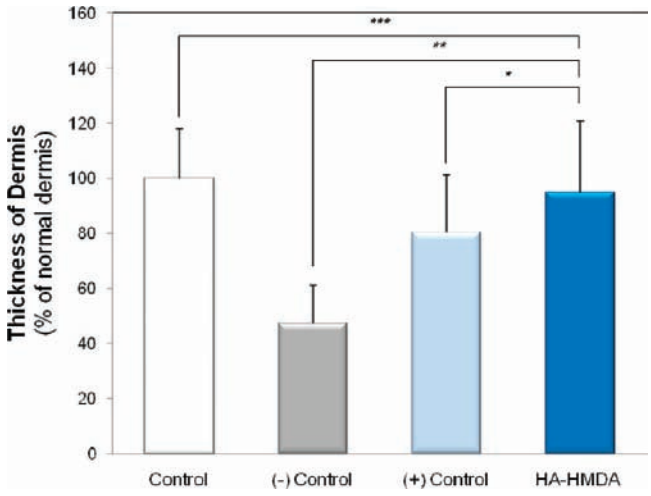


Figure 6. Dermal thickness analysis of ICR hairless mouse skin treated with hyaluronic acid (HA) hydrogel samples after hematoxylin and eosin (H&E) staining in 12 weeks: Normal mice without treatment as a normal control, wrinkled mice without tissue augmentation as a negative control, those treated with Restylane as a positive control, and HA hydrogels cross-linked with hexamethylenediamine (HMDA) after activation with 1-ethyl-3-[3-(dimethylamino)propyl] carbodiimide and 1-hydroxybenzotriazole monohydrate (HOBt). Statistical analysis was carried out using *t*-test (* $P < 0.05$, ** $P < 0.01$, * $P = 0.41$).

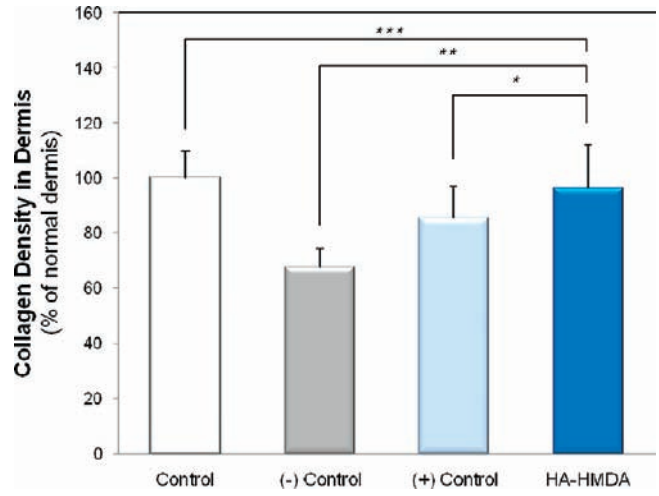


Figure 8. Collagen density analysis in the dermis of ICR hairless mouse skin treated with hyaluronic acid (HA) hydrogel samples after Masson's trichrome staining in 12 weeks: normal mice without treatment as a normal control, wrinkled mice without tissue augmentation as a negative control, those treated with Restylane as a positive control and HA hydrogels cross-linked with hexamethylenediamine (HMDA) after activation with 1-ethyl-3-[3-(dimethylamino)propyl] carbodiimide and 1-hydroxybenzotriazole monohydrate (HOBt). Statistical analysis was carried out using *t*-test (* $P < 0.05$, ** $P < 0.01$, *** $P = 0.27$).

collagen density by HA-HMDA hydrogels were comparable to those of normal tissues in 12 weeks. The HA-HMDA hydrogels with excellent biocompatibility as well as tissue augmentation effect will be investigated further for clinical applications.

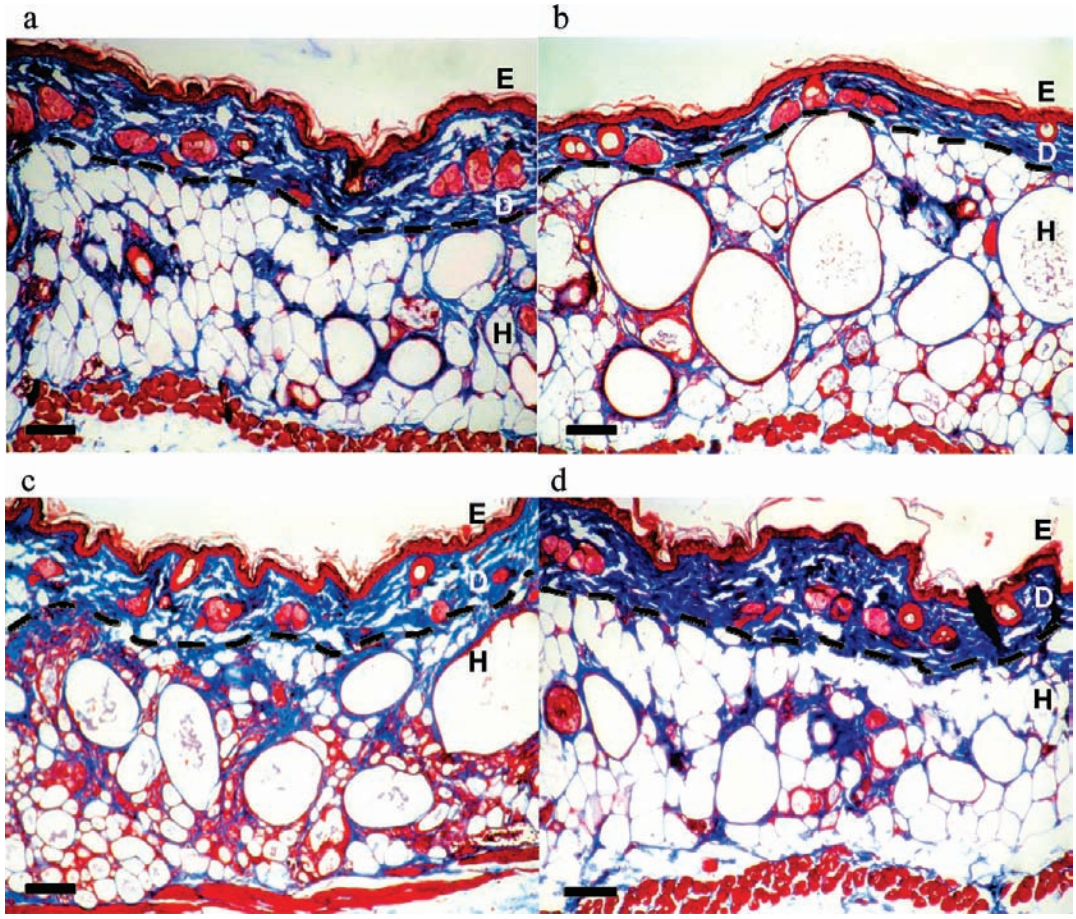


Figure 7. Histological analysis of ICR hairless mouse skin treated with hyaluronic acid (HA) hydrogel samples after Masson's trichrome staining in 12 weeks: (a) normal mice without treatment as a normal control, (b) wrinkled mice without tissue augmentation as a negative control, those treated with (c) Restylane as a positive control, and (d) HA hydrogels cross-linked with hexamethylenediamine (HMDA) after activation with 1-ethyl-3-[3-(dimethylamino)propyl] carbodiimide and 1-hydroxybenzotriazole monohydrate (HOBt). Scale bars indicate 100 μm (E: epidermis, D: dermis, and H: hypodermis).

ACKNOWLEDGMENT

This study was supported by a grant of the Korea Health 21 R&D Project, Ministry of Health & Welfare, Republic of Korea (A084132). This research was also supported by the Converging Research Center Program through the National Research Foundation of Korea (NRF) funded by the Ministry of Education, Science and Technology (2009-0081871).

LITERATURE CITED

(1) Von Buelow, S. M., Von Heimburg, D. M., and Pallua, N. M. (2005) Efficacy and safety of polyacrylamide hydrogel for facial soft-tissue augmentation. *Plast. Reconstr. Surg. 116*, 1137–1146.

(2) Hemmrich, K., Van de Sijpe, K., Rhodes, N. P., Hunt, J. A., Di Bartolo, C., Pallua, N., Blondeel, P., and von Heimburg, D. (2008) Autologous in vivo adipose tissue engineering in hyaluronan-based gels - a pilot study. *J. Surg. Res. 144*, 82–88.

(3) Clark, D., Hanke, C., and Swanson, N. (1989) Dermal implants: safety of products injected for soft tissue augmentation. *J. Am. Acad. Dermatol. 21*, 992–998.

(4) Klein, A. (1989) In favor of double testing. *J. Dermatol. Surg. Oncol. 15*, 263–263.

(5) Cheng, J., Perkins, S., and Hamilton, M. (2002) Collagen and injectable fillers. *Otolaryngol. Clin. North Am. 35*, 73–85.

(6) Tezel, A., and Fredrickson, G. (2008) The science of hyaluronic acid dermal fillers. *J. Cosmet. Laser Ther. 10*, 35–42.

(7) Oh, E. J., Kang, S. W., Kim, B. S., Jiang, G., Cho, I. H., and Hahn, S. K. (2008) Control of the molecular degradation of hyaluronic acid hydrogels for tissue augmentation. *J. Biomed. Mater. Res., Part A 86*, 685–693.

(8) Hahn, S. K., Park, J. K., Tomimatsu, T., and Shimoboji, T. (2007) Synthesis and degradation test of hyaluronic acid hydrogels. *Int. J. Biol. Macromol. 40*, 374–380.

(9) Denlinger, J. L. (1998) Hyaluronan and its derivatives as viscoelastics in medicine, in *Chemistry, biology and medical applications of hyaluronan and its derivatives* (Laurent, T. C., and Balazs, E. A., Eds.), Potland Press, London.

(10) Carreira, C., Nasser, S., di Tomaso, E., Padera, T., Boucher, Y., Tomarev, S., and Jain, R. (2001) LYVE-1 is not restricted to the lymph vessels expression in normal liver blood sinusoids and down-regulation in human liver cancer and cirrhosis 1. *Cancer Res. 61*, 8079–8084.

(11) Chao, K. L., Muthukumar, L., and Herzberg, O. (2007) Structure of human hyaluronidase-1, a hyaluronan hydrolyzing enzyme involved in tumor growth and angiogenesis. *Biochemistry 46*, 6911–6920.

(12) Slevin, M., Kumar, S., and Gaffney, J. (2002) Angiogenic oligosaccharides of hyaluronan induce multiple signaling pathways affecting vascular endothelial cell mitogenic and wound healing responses. *J. Biol. Chem. 277*, 41046–41059.

(13) Balazs, E. A., and Denlinger, J. L. (1993) Viscosupplementation: a new concept in the treatment of osteoarthritis. *J. Rheumatol. Suppl. 39*, 3–9.

(14) Balazs, E. A. (1983) *Sodium hyaluronate and viscosurgery*, Wiley, New York.

(15) Hahn, S. K., Kim, S. J., Kim, M. J., and Kim, D. H. (2004) Characterization and in vivo study of sustained-release formulation of human growth hormone using sodium hyaluronate. *Pharm. Res. 21*, 1374–1381.

(16) Kim, S. J., Hahn, S. K., Kim, M. J., Kim, D. H., and Lee, Y. P. (2005) Development of a novel sustained release formulation of recombinant human growth hormone using sodium hyaluronate microparticles. *J. Controlled Release 104*, 323–335.

(17) Ohri, R., Hahn, S. K., Hoffman, A. S., Stayton, P. S., and Giachelli, C. M. (2004) Hyaluronic acid grafting mitigates calcification of glutaraldehyde-fixed bovine pericardium. *J. Biomed. Mater. Res., Part A 70*, 328–334.

(18) Kuo, J. W., Swann, D. A., and Prestwich, G. D. (1991) Chemical modification of hyaluronic acid by carbodiimides. *Bioconjugate Chem. 2*, 232–241.

(19) Entwistle, J., Hall, C. L., and Turley, E. A. (1996) HA receptors: regulators of signalling to the cytoskeleton. *J. Cell. Biochem. 61*, 569–577.

(20) Kim, J., Kim, K. S., Jiang, G., Kang, H., Kim, S., Kim, B. S., Park, M. H., and Hahn, S. K. (2008) In vivo real-time bioimaging of hyaluronic acid derivatives using quantum dots. *Biopolymers 89*, 1144–1153.

(21) Lee, H., Mok, H., Lee, S., Oh, Y. K., and Park, T. G. (2007) Target-specific intracellular delivery of siRNA using degradable hyaluronic acid nanogels. *J. Controlled Release 119*, 245–252.

(22) Schledzewski, K., Falkowski, M., Moldenhauer, G., Metharom, P., Kzhyshkowska, J., Ganss, R., Demory, A., Falkowska-Hansen, B., Kurzen, H., Ugurel, S., Geginat, G., Arnold, B., and Goerdt, S. (2006) Lymphatic endothelium-specific hyaluronan receptor LYVE-1 is expressed by stabilin-1+, F4/80+, CD11b+ macrophages in malignant tumours and wound healing tissue in vivo and in bone marrow cultures in vitro: implications for the assessment of lymphangiogenesis. *J. Pathol. 209*, 67–77.

(23) Mckegney, M., Taggart, I., and Grant, M. (2001) The influence of crosslinking agents and diamines on the pore size, morphology and the biological stability of collagen sponges and their effect on cell penetration through the sponge matrix. *J. Mater Sci. Mater. Med. 12*, 833–844.

(24) Fujimura, T., Moriwaki, S., Takema, Y., and Imokawa, G. (2000) Epidermal change can alter mechanical properties of hairless mouse skin topically treated with 1alpha, 25-dihydroxyvitamin D_3. *J. Dermatol. Sci. 24*, 105–111.

(25) Liu, J., Jsieh, Y., Wiesler, D., and Novotny, M. (1991) Design of 3-(4-carboxybenzoyl)-2-quinolinecarboxaldehyde as a reagent for ultrasensitive determination of primary amines by capillary electrophoresis using laser fluorescence detection. *Anal. Chem. 63*, 408–412.

(26) You, W. W., Haugland, R. P., Ryan, D. K., and Haugland, R. P. (1997) 3-(4-Carboxybenzoyl)quinoline-2-carboxaldehyde, a reagent with broad dynamic range for the assay of proteins and lipoproteins in solution. *Anal. Biochem. 244*, 277–282.

(27) Dulong, V., Cerf, D. L., Picton, L., and Muller, G. (2006) Carboxymethylpullulan hydrogels with an ionic and/or amphiphilic behavior: Swelling properties and entrapment of cationic and/or hydrophobic molecules. *Colloids Surf. A 274*, 163–169.

(28) Tsukahara, K., Nakagawa, H., Moriwaki, S., Takema, Y., Fujimura, T., and Imokawa, G. (2006) Inhibition of ultraviolet-B-induced wrinkle formation by an elastase-inhibiting herbal extract: implication for the mechanism underlying elastase-associated wrinkles. *Int. J. Dermatol. 45*, 460–468.

BC9002647

Versatile and Selective Synthesis of "Click Chemistry" Compatible Heterobifunctional Poly(ethylene glycol)s Possessing Azide and Alkyne Functionalities

Shigehiro Hiki[†] and Kazunori Kataoka*[,†,‡,§]

Department of Materials Engineering, Graduate School of Engineering, and Center for NanoBio Integration, The University of Tokyo, 7-3-1 Hongo, Bunkyo-ku, Tokyo 113-8656, Japan, Core Research Program for Evolutional Science and Technology (CREST), Japan Science and Technology Agency (JST), Tokyo, Japan, and Center for Disease Biology and Integrative Medicine, Graduate School of Medicine, The University of Tokyo, 7-3-1 Hongo, Bunkyo-ku, Tokyo 113-0033, Japan.
Received June 16, 2009; Revised Manuscript Received December 9, 2009

Versatile route for "click chemistry" compatible heterobifunctional PEGs was established through preparation of α-tetrahydropyranyloxy-ω-hydroxyl poly(ethylene glycol) (THP-PEG-OH) via ring-opening polymerization of ethylene oxide using 2-(tetrahydro-2*H*-pyran-2-yloxy)ethanol as an initiator, followed by the functionalization of ω-OH group to either the azido or alkyne group. Quantitative azidation of THP-PEG-OH was confirmed from the analysis of molecular functionality of the derivatives. While the conversion efficiency of ω-alkynation was appropriately 70%, the unreacted THP-PEG-OH fraction was successfully removed by ion-exchange chromatography after the carboxylation of the hydroxyl group with succinic anhydride. Then, the protecting group of the α-end, THP, was removed in mild acidic media, followed by two- or three-step modification of the resulting α-hydroxyl group to primary amino or thiol groups. Consequently, "click chemistry" compatible heterobifunctional PEG derivatives (X-PEG-Y; X = NH_2 and SH, Y =Azide and Alkyne) were synthesized with high efficiency and controlled molecular weight.

INTRODUCTION

Conjugation and immobilization of biomolecules (e.g., proteins, peptides, and carbohydrates) with functional small molecules and synthetic polymers have widely been used as a useful research tool in chemical, biological, and pharmaceutical fields. The former group mainly consists of fluorescence reagents such as organic dyes, which were exploited for target detection and quantification (*1, 2*). The latter has been aimed at alteration or improvement of the physicochemical properties of biomacromolecules. The most successful strategy employs poly(ethylene glycol) (PEG) as the conjugating polymer, termed "PEGylation" (*3*−*5*). In general, PEGylation improves water solubility, reduces toxicity, and increases the tolerance against enzymatic degradation and the in vivo half-lives of bioactive macromolecules (*3*−*6*). Indeed, several PEGylated therapeutic proteins have clinically been investigated (*7, 8*).

The Cu(I)-catalyzed 1,3-dipolar cycloaddition of azides and terminal alkynes to form a triazole ring, "click chemistry" coined by Sharpless, has recently received considerable attention (*9*−*11*) and been utilized as a versatile ligation reaction in the field of bioconjugation including PEGylation (*12, 13*). This "click" reaction is highly chemoselective and can be performed under mild conditions in aqueous buffers with a wide range of pH, indicating high applicability for site-specific conjugation. Therefore, the PEGylation technique integrated with "click chemistry" is a promising approach for site-specific modification of bioactive macromolecules (*14, 15*). Indeed, there are several reports including the "click"-based PEGylation procedure for the preparation of well-defined polymers and functional nanostructures, demonstrating the efficient reaction with high conversion in aqueous condition as well as in organic solvents (*16*−*18*). Additionally, to construct PEGylated biopharmaceutics with multifunctionality, development of α,ω-heterobifunctional PEGs with both well-controlled molecular weight and high derivatizability is inevitable. Although preparation of heterobifunctional PEG having an azido or alkyne group at one end may be feasible using of homobifunctional PEGs as the starting materials, the synthetic methods contain some drawbacks such as repeated column purification in each reaction step and, consequently, low yield. Thus, exploiting of versatile synthetic design of α,ω-heterobifunctional PEGs with high productivity and compatibility to "click"-based conjugation is essential.

In a previous paper, we reported the preparation of azido-terminated heterobifunctional PEGs using a radical addition of thiol compounds to the allyl terminus of PEG derivative (*19*). This radical addition method, however, is inadaptable to the utilization of the alkyne moiety. Herein, we wish to communicate the facile synthetic route applicable to heterobifunctional PEGs possessing azido or alkyne function at one chain end with controlled molecular weight via the ring-opening polymerization of ethylene oxide. Monoprotected ethylene glycol derivative, which was obtained by tetrahydropyranylation of one hydroxyl group, was prepared and applied to an initiator of polymerization as the first step. The tetrahydropyranyl (THP) group is one of the useful protecting species of hydroxyl group, and shows both easy installation and general stability under nonacidic condition (*20*). Moreover, after the acid-catalyzed hydrolysis of THP, the deprotected hydroxyl group can then be devoted to further derivatization (Scheme 1).

* To whom correspondence should be addressed. Professor Kazunori Kataoka, Tel: +81-3-5841-7138. Fax: +81-3-5841-7139, e-mail: kataoka@bmw.t.u-tokyo.ac.jp.

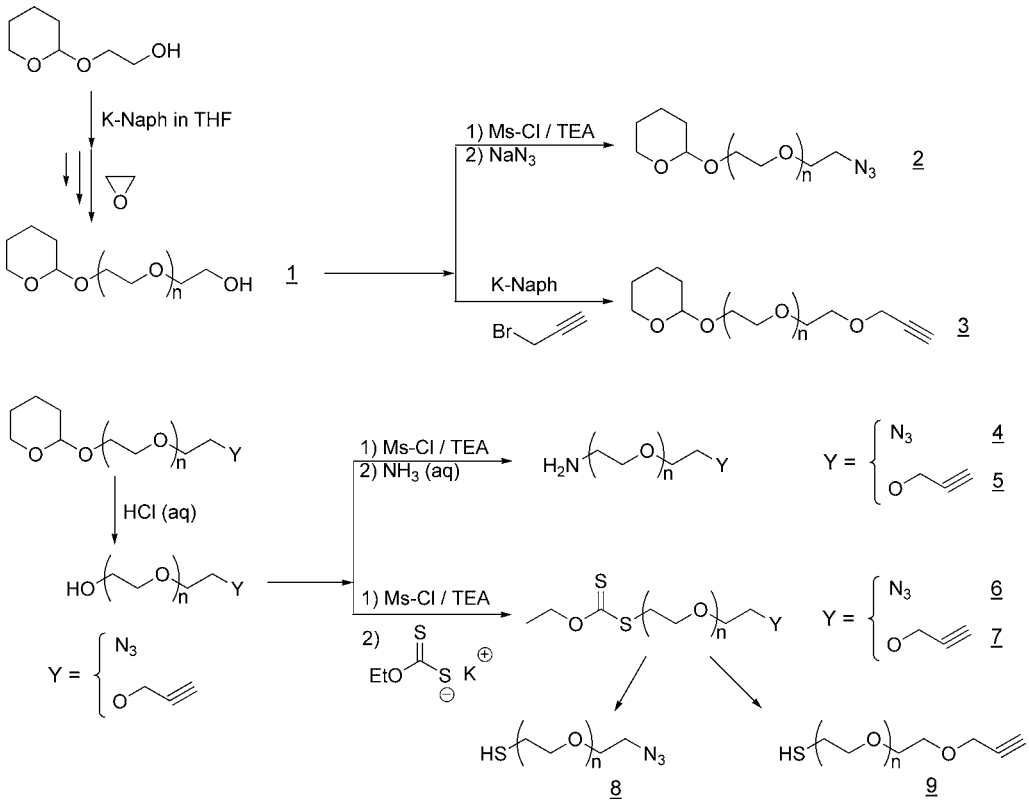
[†] Graduate School of Engineering, The University of Tokyo, and CREST, JST.

[‡] Center for NanoBio Integration, The University of Tokyo.

[§] Graduate School of Medicine, The University of Tokyo.

10.1021/bc900253p © 2010 American Chemical Society
Published on Web 01/15/2010

Scheme 1. Synthetic Route to Heterobifunctional PEG Derivatives Possessing Azido and Alkyne Functional Groups



EXPERIMENTAL PROCEDURES

Materials. 2-(Tetrahydro-2*H*-pyran-2-yloxy)ethanol (Fluka, US) and ethylene oxide (EO; Sumitomo Seika Chemical, Japan) were dried over calcium hydride and distilled under an argon atmosphere. Potassium naphthalene was prepared as a tetrahydrofuran (THF) solution according to a previous paper (*21*), whose concentration was determined by titration. *N*,*N*-Dimethylformamide (DMF), THF, triethylamine (TEA), and methanesulfonyl chloride (Ms-Cl) were purchased from Wako Pure Chemical Industries, Ltd., (Osaka, Japan) and purified by conventional methods. Ammonia solution (ca. 25% (NH_3)), propargyl bromide in toluene solution (80 wt %), sodium azide, potassium ethyl xanthogenate, and other reagents were used as received.

Synthesis of THP-PEG-OH (1). General procedure: monoprotected ethylene glycol, 2-(tetrahydro-2*H*-pyran-2-yloxy)ethanol (1.43 mmol, 195 μL), and potassium naphthalene (1.23 mmol) in 4.1 mL of THF were added to dry THF (90 mL) in a 200 mL flask equipped with a three-way stopcock under argon atmosphere to form potassium alcoholate as an initiator. After stirring for 10−15 min, liquid EO (381 mmol, 16.8 g) was added to the solution via a cooled syringe. The mixture was allowed to react for 48 h at 25 °C and followed by a pouring into diethyl ether to precipitate the polymer. The recovered polymeric sample was dried in vacuo and then freeze−dried from benzene. The yield of obtained polymer was 97% (16.2 g). GPC: number-average molecular weight (M_n) = 11 500, M_w/M_n = 1.03. ^{1}H NMR (500 MHz, $CDCl_3$, δ in ppm): 1.46−1.83 (m, CH-(C$\underline{H}_2$)$_3$-CH_2 of THP), 3.85 (t, CH-$(CH_2)_3$-C$\underline{H}_2$-O of THP), 4.59 (t, O−C$\underline{H}$-O of THP).

Synthesis of THP-PEG-Azide (2). The azide end group was introduced by the mesylation of the hydroxyl terminus and subsequent substitution with sodium azide, according to the previous method (*19*).

Freeze−dried polymer **1** (THP-PEG-OH) (1.13 g, 0.20 mmol) from benzene (30 mL) was dissolved in anhydrous THF (15 mL) followed by the addition of TEA (102 mg, 1.01 mmol). The mixture was then added to a solution of Ms-Cl (102 mg, 0.89 mmol) in THF (3 mL) under Ar stream, and stirred overnight at room temperature. After the reaction, the polymer was recovered by precipitation into ether and dried in vacuo, yielding a white solid.

This mesylated polymer (1.00 g, 0.15 mmol) was dissolved in DMF (12 mL), followed by sodium azide (400 mg, 6.15 mmol) addition, and was stirred at 45 °C for 3 days. After the reaction, DMF was partially evaporated and diluted with water (40 mL), then extracted by dichloromethane (6 × 120 mL). The combined organic layer was dried over $MgSO_4$, filtered, concentrated, and then reprecipitated into ether. The recovered polymer was freeze−dried from benzene. (0.83 g, 83%). ^{1}H NMR (500 MHz, $CDCl_3$, δ in ppm): 1.46−1.85 (m, CH-(C$\underline{H}_2$)$_3$-CH_2 of THP), 3.46 (t, CH_2-C$\underline{H}_2$-N_3), 3.85 (t, CH-$(CH_2)_3$-C$\underline{H}_2$-O of THP), 4.59 (t, O-C$\underline{H}$-O of THP).

Synthesis of THP-PEG-Alkyne (3). To prepare THP-PEG-Alkyne (**3**), modification of hydroxyl group of polymer **1** and the removal of unalkynated PEG was performed. Polymer **1** (THP-PEG-OH, 1.50 g, 0.25 mmol) was freeze−dried from benzene and dissolved in anhydrous THF (15 mL). Subsequently, potassium naphthalene solution was added until the solution turned pale green to reactivate the chain end and stirred for 15 min. To the solution was added propargyl bromide (299 mg, 2.51 mmol) as toluene solution, and the reaction mixture was stirred at room temperature for 48 h. Then, the polymer was recovered by precipitation into ether twice and dried by freeze−drying with benzene. 1.35 g (0.23 mmol) of the resulting polymer was dissolved in dichloromethane (3 mL), followed by the addition of pyridine (1 mL). After the stirring for 1.5 h, 2 mL of solution of succinic anhydride (40 mg, 0.40 mmol) in dichloromethane was introduced and reacted at 30 °C for 24 h. To quench the remaining succinic anhydride, ethanol (about 1 mL) was added and stirred for another 24 h. The resulting polymer was recovered by precipitation into ether and dried in

vacuo. To isolate THP-PEG-Alkyne (**3**), this polymer mixture was dissolved in the mixed-solvent (H_2O/acetonitrile = 4/1 v/v) and separated through an ion exchange column (DEAE-Sephadex). Further purification was carried out by dialyzing against distilled, deionized water using a Spectrapro dialysis membrane (MW cutoff 3500) and then freeze−drying to obtain THP-PEG-Alkyne (**3**) (535 mg, 40%). ^{1}H NMR (300 MHz, $CDCl_3$, δ in ppm): 1.46−1.85 (m, CH-(C$\underline{H}_2$)$_3$-CH_2 of THP), 2.43 (t, C$\underline{H}$ of Alkyne), 4.20 (s, O-C$\underline{H}_2$-C of Alkyne), 4.59 (t, O-C$\underline{H}$-O of THP).

Deprotection of THP Group. A 1.0 g sample of the THP-ended PEG (**2** or **3**) was dissolved into methanol (ca. 15 mL), and 4−5 drops of 1 mol/L hydrochloric acid (HCl) aqueous solution was added. After stirring around 4 h at ambient temperature, the reaction mixture was poured into ether to precipitate the PEG sample. The recovered polymer was washed with ether carefully and dried in vacuo. The removal of the THP group was confirmed by ^{1}H NMR spectroscopy.

Amination Reaction of HO-PEG-Y (Y = N_3 and OCH_2−C≡CH). To prepare amino-terminated heterobifunctional PEG, NH_2-PEG-Azide, or NH_2-PEG-Alkyne, two-step modification was performed: activation of hydroxyl group by methanesulfonyl ester formation and substitution with ammonia. In the first step, the mesylation reaction of the resultant polymer, HO-PEG-Y (Y = N_3 and OCH_2−C≡CH), was carried out according to the same procedure as described above. After precipitation into ether, filtration, and freeze−drying from benzene, the mesylated polymer was mixed with 25 wt % ammonia aqueous solution and stirred at room temperature for about 4 days. After the reaction, to remove excess ammonia, the mixture was partially evaporated and dialyzed first against diluted ammonia solution (ca. 0.125 N in H_2O) and then against distilled water using a Spectrapro dialysis membrane (MW cutoff 3500). Lyophilization of the dialyzed solution gave the amine-functionalized polymer, NH_2-PEG-Y (Y = N_3 (**4**) and OCH_2−C≡CH (**5**)).

Synthesis of Dithiocarbonate Introduced HO-PEG-Y (Y = N_3 (6) and OCH_2−C≡CH (7)). To derivatize HO-PEG-Y (Y = N_3 and OCH_2−C≡CH) with dithiocarbonate moiety, preparation of the methanesulfonyl ester of the polymer and subsequent substitution with potassium ethyl xanthogenate was carried out according to a previous report (*22*). The mesylation reaction of the resultant polymer, HO-PEG-Y (Y = N_3 and OCH_2−C≡CH), was carried out according to the same procedure as described above. After the precipitation into ether, filtration, and freeze−drying from benzene, the mesylated HO-PEG-OCH_2-C≡CH (207 mg) was dissolved in THF (20 mL). After the stirring for 20 min, 4 mL of cosolvent (THF/DMF = 5/5 vol %) containing potassium xanthogenate (111 mg, 0.69 mmol) was added and stirred at room temperature for 10 h. The reaction mixture was then mixed with dichloromethane (100 mL) and washed with a saturated NaCl aqueous solution several times. The organic layer was dried over $MgSO_4$, filtered, concentrated, and then reprecipitated into ether. The recovered polymer, CH_3CH_2-O-(C═S)-S-PEG-OCH_2-C≡CH was freeze−dried from benzene (176 mg, 85%). To introduce the *O*-ethyldithiocarbonate group at the hydroxyl terminus of HO-PEG-N_3, the same procedure was performed. After freeze−drying, the yield of the recovered sample was determined to be 83%.

Synthesis of HS-PEG-Y (Y = N_3 (8) and OCH_2-C≡CH (9)). To prepare the thiol-terminated PEG derivatives, HS-PEG-Y (Y = N_3 and OCH_2−C≡CH), simple reaction with propylamine (*22*) or sodium hydroxide solution was conducted. The azido-terminated PEG containing dithiocarbonate moiety (polymer **6**) (100 mg) was dissolved in methanol (2 mL), and sodium hydroxide (66 mg) aqueous solution (500 μL) was slowly added. The mixture was stirred for 12 h at room temperature and then dialyzed against distilled water. After the lyophilization of the dialyzed solution, the thiolated sample, HS-PEG-N_3 (**8**) was obtained as white powder (86 mg, yield = 86%). ^{1}H NMR (500 MHz, $CDC1_3$, δ in ppm): 2.88 (t, CH_2-C$\underline{H}_2$-SH and C$\underline{H}_2$-SS-C$\underline{H}_2$), 3.49 (t, CH_2-C$\underline{H}_2$-N_3).

Thiolation reaction of alkyne-terminated sample (polymer **7**) was performed by reference to the previous method (*22*). Polymer **7** (40 mg) was dissolved in THF (1 mL) and reacted with propylamine (100 μL) at room temperature. After the reaction for 3 h, the polymer solution was dialyzed against MeOH followed by the complete evaporation of the solvent under vacuum. The polymer was purified by reprecipitation into cold ether and dried in vacuo (33 mg, yield = 80%). ^{1}H NMR (500 MHz, $CDCl_3$, δ in ppm): 2.44 (t, C$\underline{H}$ of Alkyne), 2.88 (t, CH_2-C$\underline{H}_2$-SH and C$\underline{H}_2$-SS-C$\underline{H}_2$), 4.20 (s, O-C$\underline{H}_2$-C of Alkyne).

Table 1. Results of Ring-Opening Polymerization of EO[a]

			$10^{-3} \times M_n$			
run	[M]/[I]	yield[b] (%)	calcd	GPC[c]	MS[d]	M_w/M_n[c]
1	100	96	4.4	4.2	4.5	1.04
2	136	97	6.0	5.9	6.1	1.03
3	264	97	11.7	11.5	11.7	1.03

[a] Polymerization was conducted in THF at 25 °C for 48 h. [b] After reprecipitation into ether. [c] Determined by GPC (DMF eluent) calibrated with commercial PEO standards. [d] Determined by MALDI-TOF MS spectra.

Polymer Analysis. ^{1}H NMR spectra were recorded on JEOL JNM-AL (300 MHz) or JEOL Alpha series (500 MHz) spectrometer (JEOL, Tokyo, Japan). ^{13}C NMR spectra were recorded on JNM-AL model at 75.45 MHz. Chemical shifts are reported in parts per million (ppm) downfield from tetramethylsilane. Number-average molecular weight (M_n) and molecular weight distribution (M_w/M_n) were determined using a GPC (TOSOH HLC-8220) system equipped with two TSK gel columns (G4000HHR and G3000HHR) and an internal refractive index (RI) detector. Columns were eluted with DMF containing lithium chloride (10 mM) with a flow rate of 0.8 mL/min and at a temperature of 40 °C. Molecular weights were calibrated with poly(ethylene glycol) standards (Polymer Laboratories, Ltd., UK). MALDI-TOF-MS spectra were recorded using Bruker REFLEX III. α-Cyano-4-hydroxycinnamic acid was used as the matrix for the ionization operated in the reflection mode.

RESULTS AND DISCUSSION

Although the hydroxyl group does not show high reactivity in itself comparing with other functional groups, the hydroxyl group can be converted to useful reactive groups through the activation and subsequent nucleophilic substitution. Hence, the availability of the hydroxyl group is potentially high. If homotelechelic HO-PEG-OH is used as a starting material for the preparation of heterobifunctional PEG derivatives, however, undesired yield of homobifunctional product and multiple column purification process are inevitable. Here, we designed a simple synthetic procedure containing preparation of hydroxyl-terminated PEG as the intermediate, of which one hydroxyl group is protected quantitatively, and alternating functionalization of both terminal ends.

Preparation of Monoprotected PEG via Polymerization of EO. In this study, monotetrahydropyranylated ethylene glycol derivative, 2-(tetrahydro-2*H*-pyran-2-yloxy)ethanol, was selected as an initiator for anionic polymerization of EO, because the tetrahydropyranyl (THP) group is one of the useful protecting species of hydroxyl group (*20*), and shows both easy installation and general stability under nonacidic conditions. In other words, it is expected that the THP protecting group is stable under

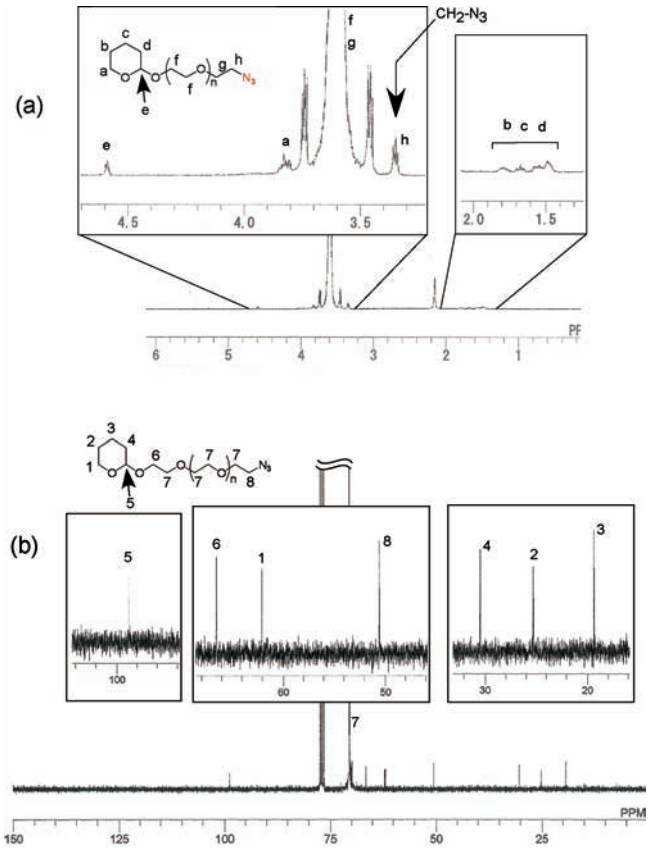


Figure 1. (a) 500 MHz ^{1}H NMR spectrum of THP-PEG-Azide (in $CDCl_3$ at 20 °C). (b) ^{13}C NMR spectrum of THP-PEG-Azide (in $CDCl_3$).

polymerization condition of EO and subsequent functionalization step with azide/alkyne. Table 1 shows the results of the polymerization of EO in the presence of monotetrahydropyranylated ethylene glycol as an initiator. All polymerization proceeded with excellent isolated yields of the polymeric samples (>96%), and the M_n values determined by GPC and MALDI-TOF MS showed good agreement with calculated values, indicating the controlled molecular weight of THP-PEG-OH (**1**) without any side reaction.

Azidation Reaction of THP-PEG-OH. To demonstrate the versatility of THP-PEG-OH (**1**), selective and quantitative modification of the ω-hydroxyl end was examined. First, the azidation reaction was conducted through the two-step modification, the mesylation and the substitution by sodium azide, of hydroxyl function as described in the Experimental Section.

In the ^{1}H NMR spectrum of the product after azidation (run 2 in Table 1), the proton signals of THP group are detected at δ 4.63 ppm (e), 3.86 ppm (a), and 1.46−1.85 ppm (b, c, d), respectively. In addition to these signals, the methylene unit adjacent to the azido group ($CH_2\underline{CH_2}N_3$ (h)) was observed at 3.39 ppm (Figure 1a). With comparison of the integral ratio of proton signals at α- (δ 4.63 ppm (e)) and ω-ends (δ 3.39 ppm (h)), the quantitative conversion from the hydroxyl to the azido group was indicated. Additionally, the ^{13}C NMR spectrum shows that the methylene and methyne signals of the THP structure are detected around δ 99.4 ppm (C5), 65.3, ppm (C6), 62.0 ppm (C1), 30.3 ppm (C4), 25.4 ppm (C2), and 19.7 ppm (C3), respectively (Figure 1b). Moreover, no signal of the methylene carbon adjacent to the hydroxyl terminus ($CH_2\underline{C}H_2OH$: δ = 61.5 ppm) (*23*) was detected. These results strongly support the quantitative introduction of azido functionality at the ω-end of THP-PEG-OH.

Preparation of THP-PEG-Alkyne (3). To represent the selective derivatization of THP-PEG-OH (**1**) applicable to "click chemistry", the introduction of alkyne moiety, the counterpart of azide/alkyne cycloaddition reaction, was studied. For alkynation of the hydroxyl group of THP-PEG-OH, Williamson's ether synthetic method with propargyl bromide was performed after the formation of alcolate by the addition of potassium naphthalene. From ^{1}H NMR analysis of the resulting product, the proton signals of the

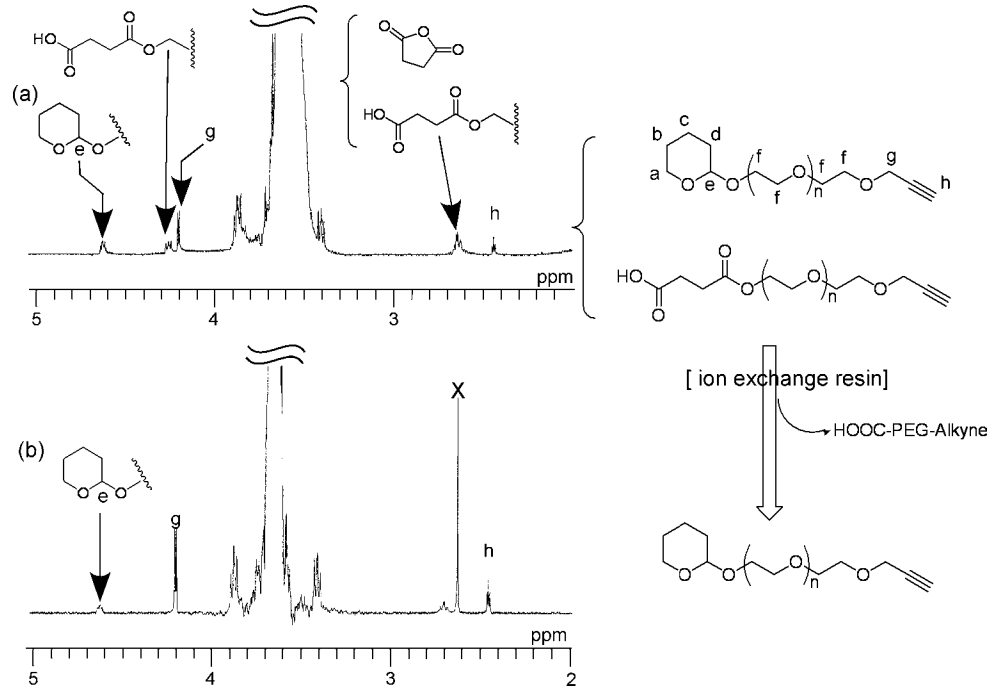


Figure 2. ^{1}H NMR spectra of alkyne-terminated PEGs; sample after the carboxylation reaction (a) and sample through DEAE-Sephadex resin column (b) (300 MHz in $CDCl_3$).

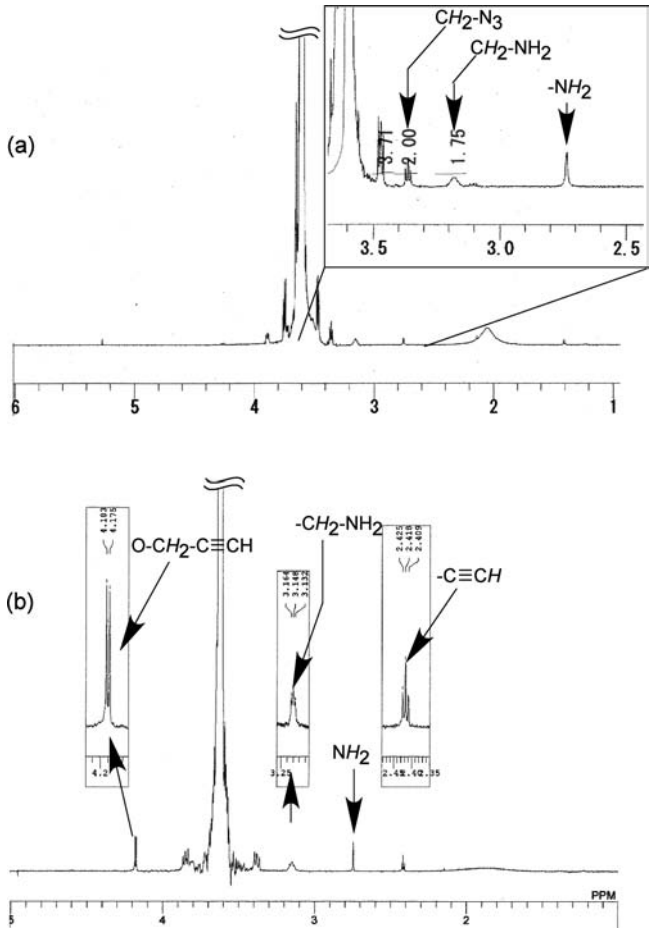


Figure 3. (a) 500 MHz ^{1}H NMR spectrum of NH_2-PEG-Azide (in $CDCl_3$). (b) ^{1}H NMR spectrum of NH_2-PEG-Alkyne (in $CDCl_3$).

alkyne moiety are detected at δ 2.43 ppm (h) and 4.20 ppm (g), respectively, with the signals assigned to the THP group, indicating the efficient alkynation (Figure 2a). However, the conversion rate of alkynation estimated by ^{1}H NMR analysis was relatively low (around 70%). The polymer sample with remaining THP-PEG-OH will yield the undesired byproduct, homobifunctional HO-PEG-OH, after the deprotection of the THP group. Then, separation of the unalkynated THP-PEG-OH from the sample was examined with simple column purification. After the carboxylation of the remaining hydroxyl group with succinic anhydride in dichloromethane, the polymer mixture was passed through the ion exchange column. The carboxylated PEG was separated from the mixture by ionic absorption with DEAE-Sephadex resin in a column, whereas the alkynated sample, THP-PEG-Alkyne, was eluted without retention. In the ^{1}H NMR spectrum of the sample after the dialysis and lyophilization, no signal based on the carboxylated PEG was observed, suggesting the effective removal of unalkynated fraction and isolation of the quantitative alkyne-functionalized THP-PEG.

Preparation of NH_2-PEG-Y (Y = N_3 (4) and OCH_2−C≡CH (5)). Removal of protective group, THP, will allow further derivatization of the α-terminal end of azido- or alkyne-terminated PEG. Deprotection of THP was carried out under acidic condition with diluted HCl, and ^{1}H NMR spectrum of the resulting sample indicated absence of the proton signals corresponding to the THP group (data not shown). To convert a hydroxyl group of the deprotected samples, HO-PEG-Azide and HO-PEG-Alkyne, to primary amino group, mesylation and subsequent nucleophilic substitution by ammonia was performed. In the ^{1}H NMR spectrum of aminated sample (Figure 3a), the characteristic methylene signals adjacent to both the azido group (-$C\underline{H}_2N_3$: δ = 3.36 ppm) and the primary amino group (-$C\underline{H}_2NH_2$: δ = 3.18 ppm) were clearly observed. Additionally, the amination degree estimated from the integral ratio of these proton signals was 85% and above, indicating successful preparation of NH_2-PEG-N_3. Likewise, the ^{1}H NMR spectrum of aminated HO-PEG-Alkyne exhibits the distinguishing signals assigned to both the alkyne moiety (C$\underline{H}$ of Alkyne: δ = 2.41 ppm and O-C$\underline{H}_2$-C of Alkyne: 4.18 ppm) and the primary amino group (-C$\underline{H}_2NH_2$: δ = 3.14 ppm) in Figure 3b. Moreover, to confirm the quantitative terminal functionalization of this alkyne-terminated PEG sample, the analysis by MALDI-TOF MS spectroscopy was also conducted. Figure 4 shows the MS spectrum of NH_2-PEG-Alkyne (**5**). The major series of the molecular masses of the product is expressed in the following equation

$$MW_{MS} = 44.053n(EO) + 39.05(\text{Alkyne moiety; } CH_2C \equiv CH) + 16.02(NH_2) + 22.99(\text{sodium})$$

In this analysis, only parent ions of each polymer molecule as expected are observed, without the signal assigned to the byproduct NH_2-PEG-NH_2. These data strongly support the successful preparation of NH_2-PEG-Alkyne (**5**).

Preparation of HS-PEG-Y (Y = N_3 (8) and OCH_2−C≡CH (9)). To demonstrate the versatility of this synthetic route based on THP-PEG-Y (Y = Azide and

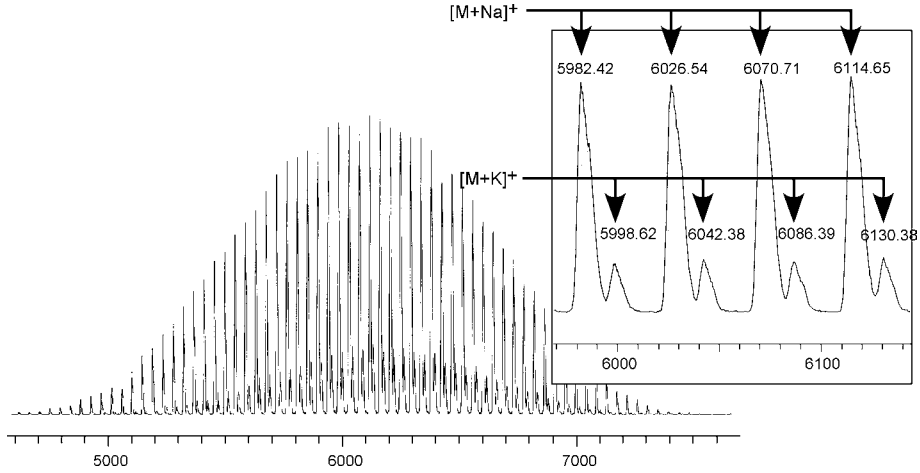


Figure 4. MALDI-TOF MS spectrum of NH_2-PEG-Alkyne.

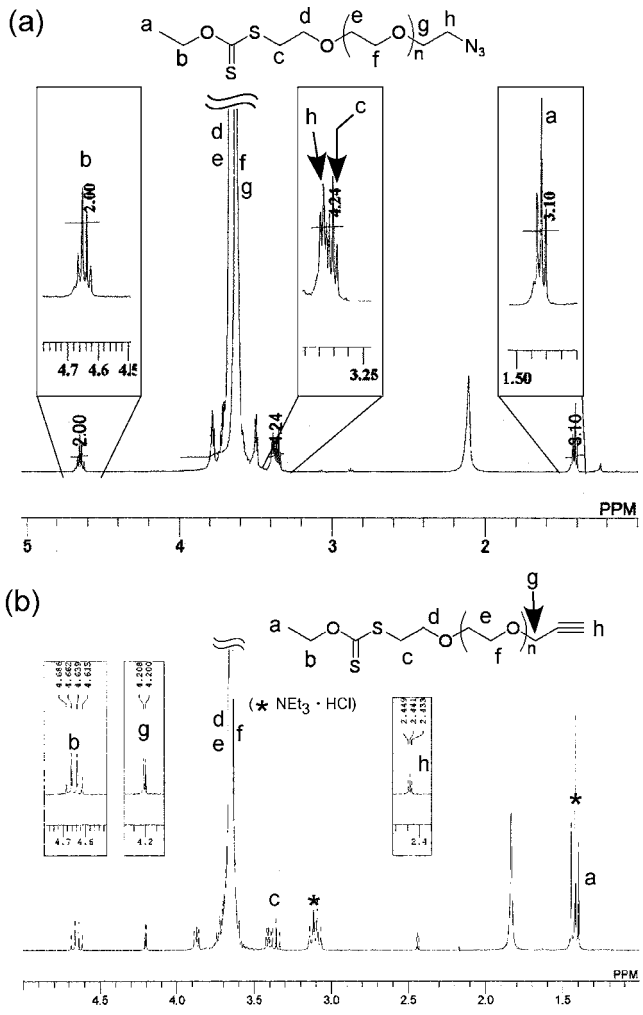


Figure 5. ^{1}H NMR spectra of derivatized samples with dithiocarbonate moiety: Azide-PEG (a) (500 MHz in $CDCl_3$) and Alkyne-PEG (b) (300 MHz in $CDCl_3$).

Alkyne), the derivatization of the α-terminal end to the thiol functional group was examined after the removal of the THP protective group. PEG derivatives introduced with the dithiocarbonate moiety at the α-position were prepared as the first step to HS-PEG-Y (Y = Azide and Alkyne) through the two-step modification, the mesylation and the substitution by potassium xanthogenate, of hydroxyl function as described in the Experimental Section. In the ^{1}H NMR spectrum (Figure 5a), the characteristic methyl and methylene signals of the dithiocarbonate unit were clearly observed at 1.85 ($S(C{=}S)-OCH_2C\underline{H}_3$), and 4.65 ppm ($S(C{=}S)O-C\underline{H}_2CH_3$), respectively, and the proton signal assigned to the azido group ($-C\underline{H}_2N_3$: δ = 3.37 ppm) was also detected. In addition, comparison between the integral ratios of these signals indicated the quantitative conversion of the hydroxyl group to the dithiocarbonate structure without any damage on the azido functionality. For derivatization of HO-PEG-Alkyne, the reaction similar to the azido-terminated PEG sample was conducted. From the ^{1}H NMR analysis of the resultant polymer, both signals assigned to the alkyne moiety (C$\underline{H}$ of Alkyne: δ = 2.41 ppm and O-C$\underline{H}_2$-C of Alkyne: 4.18 ppm) and the dithiocarbobnate structure ($S(C{=}S)-OCH_2C\underline{H}_3$): δ = 1.85 and $S(C{=}S)O-C\underline{H}_2CH_3$): δ = 4.65 ppm) were clearly detected (Figure 5b). These results indicate the successful derivatization of heterobifunctional THP-PEG-Y (Y = Azide and Alkyne) with dithiocarbonate moiety under the mild reaction condition. Figure 6 shows the ^{1}H NMR spectrum of the obtained HS-PEG-Azide. The proton signals corresponding to the ethyldithiocarbonate moiety completely disappeared, while the characteristic signals of both azide and methylene proton adjacent to thiol group were detected ($CH_2C\underline{H}_2N_3$: δ 3.39, and $CH_2C\underline{H}_2S$: δ 2.89 ppm, respectively). In addition, no decomposition of the azido group during the alkali reaction was detected in the ^{1}H NMR spectrum, suggesting the end-functionalization with the high reaction conversion. After the thiolation reaction of alkyne-terminated PEG, the characteristic signals were observed without any side reaction (see the Experimental Section). These investigations indicated that the thiolation reaction of PEGs possessing azido or alkyne function proceeded under the mild conditions.

In conclusion, the facile synthesis of the azido- or alkyne-possessing heterobifunctional PEGs via EO polymerization was demonstrated in this study. Controlling the MW and the selective functionalization of the α- and ω-termini of heterobifunctional PEGs was successfully presented. These functional PEG derivatives can be used in Cu(I)-catalyzed 1,3-dipolar cycloaddition reaction (click chemistry) to introduce versatile biofunctional moieties into the azido or alkyne terminus, and are thus relevant to a wide range of applications in the field of bioconjugate chemistry.

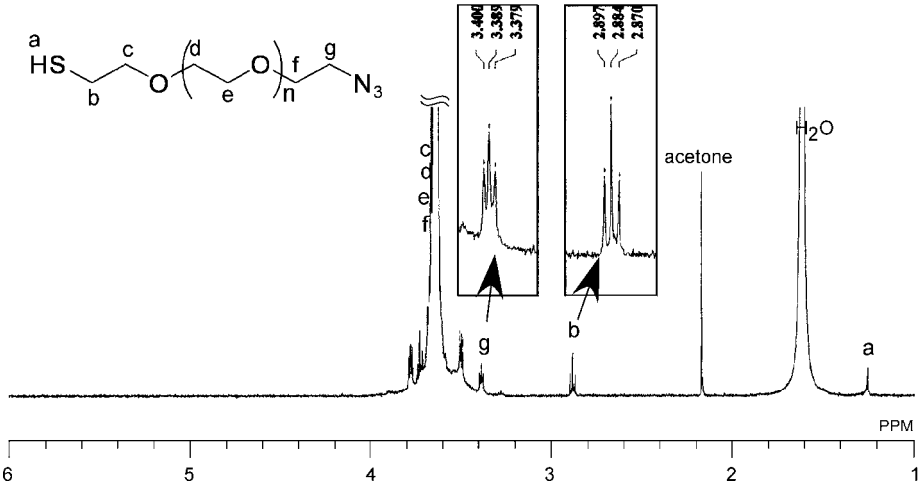


Figure 6. 500 MHz ^{1}H NMR spectrum of HS-PEG-Azide (in $CDCl_3$).

ACKNOWLEDGMENT

This work was supported by the Core Research for Evolutional Science and Technology (CREST) from the Japan Science and Technology Agency (JST).

Supporting Information Available: MALDI-TOF MS spectra of THP-PEG-OH and THP-PEG-N_3. This material is available free of charge via the Internet at http://pubs.acs.org.

LITERATURE CITED

(1) Beddard, G. S., and West, M. A., Eds. (1981) *Fluorescent Probes*, Academic Press, London.

(2) Kraayenhof, R., Visser, A. J. W. G.; and Gerritsen, H. C. (2002) *Fluorescence Spectroscopy, Imaging and Probes: New Tools in Chemical, Physical and Life Sciences (Springer Series on Fluorescence, 2)*, Springer-Verlag, Berlin.

(3) Abuchowski, A., McCoy, J. R., Palczuk, N. C., Van Es, T., and Davis, F. F. (1977) Effect of covalent attachment of polyethylene glycol on immunogenicity and circulating life of bovine liver catalase. *J. Biol. Chem. 252*, 3582–3586.

(4) Harris, J. M., Ed. (1992) *Poly(ethylene glycol) Chemistry: Biotechnical and Biomedical Applications*, Plenum Press, New York.

(5) Roberts, M. J., Bentley, M. D., and Harris, J. M. (2002) Chemistry for peptide and protein PEGylation. *Adv. Drug Delivery Rev. 54*, 459–476.

(6) Katre, N. V. (1993) The conjugation of proteins with polyethylene glycol and other polymers. Altering properties of proteins to enhance their therapeutic potential. *Adv. Drug Delivery Rev. 10*, 91–114.

(7) Graham, L. M. (2003) Pegaspargase: a review of clinical studies. *Adv. Drug Delivery Rev. 55*, 1293–1302.

(8) Duncan, R. (2003) The drawing era of polymer therapeutics. *Nat. Rev. Drug Discovery 2*, 347–360.

(9) Rostovtsev, V. V., Green, L. G., Fokin, V. V., and Sharpless, K. B. (2002) A stepwise Huisgen cycloaddition process: copper(I)-catalyzed regioselective "ligation" of azides and terminal alkynes. *Angew. Chem., Int. Ed. 41*, 2596–2599.

(10) Wang, Q., Chan, T. R., Hilgraf, R., Fokin, V. V., Sharpless, K. B., and Finn, M. G. (2003) Bioconjugation by copper(I)-catalyzed azide-alkyne [3 + 2] cycloaddition. *J. Am. Chem. Soc. 125*, 3192–3193.

(11) Lutz, J. F. (2007) 1,3-Dipolar cycloadditions of azides and alkynes: A universal ligation tool in polymer and materials science. *Angew. Chem., Int. Ed. 46*, 1018–1025.

(12) Link, A. J., and Tirrell, D. A. (2003) Cell surface labeling of *Escherichia coli* via copper(I)-catalyzed [3 + 2] cycloaddition. *J. Am. Chem. Soc. 125*, 11164–11165.

(13) Deiters, A., Cropp, T. A., Mukherji, M., Chin, J. W., Anderson, J. C., and Schultz, P. G. (2003) Adding amino acids with novel reactivity to the genetic code of *Saccharomyces cerevisiae*. *J. Am. Chem. Soc. 125*, 11782–11783.

(14) Lin, P. C., Ueng, S. H., Tseng, M. C., Ko, J., Huang, K. T., Yu, S. C., Adoak, A. K., Chen, Y. J., and Lin., C. C. (2006) Site-specific protein modification through Cu-catalyzed 1,2,3-triazole formation and its implementation in protein microarray fabrication. *Angew. Chem., Int. Ed. 45*, 4286–4290.

(15) Natarajan, A. (2007) Construction of di-scFv through a trivalent alkyne-aizde 1,3-dipolar cycloaddition. *Chem. Commun.* 695–697.

(16) Opsteen, J. A., and van Hest, J. C. M. (2005) Modular synthesis of block copolymers via cycloaddition of terminal azide and alkyne functionalized polymers. *Chem. Commun.* 57–59.

(17) Peng, S.-M., Chen, Y., Hua, C., and Dong, C.-M. (2009) Dendron-like polypeptide/linear poly(ethylene oxide) biohybrids with both asymmetrical and symmetrical topologies synthesized via the combination of click chemistry and ring-opening polymerization. *Macromolecules 42*, 104–113.

(18) Lee, S.-M., Chen, H., O'Halloran, T. V., and Nguyen, S. T. (2009) "Clickable" polymer-caged nanobins as a modular drug delivery platform. *J. Am. Chem. Soc. 131*, 9311–9320.

(19) Hiki, S., and Kataoka, K. (2007) A facile synthesis of azido-terminated heterobifunctional poly(ethylene glycol)s for "click" conjugation. *Bioconjugate Chem. 18*, 2191–2196.

(20) Wuts, P. G. M., and Greene, T. W. (2006) *Greene's Protective Groups in Organic Synthesis*, 4th ed.; John Wiley & Sons Inc.

(21) Szwarc, M., Levy, M., and Milkovich, R. (1956) Polymerization initiated by electron transfer to monomer. A new method of formation of block polymers. *J. Am. Chem. Soc. 78*, 2656.

(22) Akiyama, Y., Nagasaki, Y., and Kataoka, K. (2004) Synthesis of heterotelechelic poly(ethylene glycol) derivatives having α-benzaldehyde and ω-pyridyl disulfide groups by ring opening polymerization of ethylene oxide using 4-(diethoxymethyl)benzyl alkoxide as a novel initiator. *Bioconjugate Chem. 15*, 424–427.

(23) Zalipsky, S. (1995) Functionalized poly(ethylene glycol) for preparation of biologically relevant conjugates. *Bioconjugate Chem. 6*, 150–165.

BC900253P

Site-Specific Incorporation of *p*-Propargyloxyphenylalanine in a Cell-Free Environment for Direct Protein−Protein Click Conjugation

Bradley C. Bundy[†,§] and James R. Swartz*[,†,‡]

Department of Chemical Engineering, Stanford University, Stanford, California 94305-5025, and Department of Bioengineering, Stanford University, Stanford, California, 94305-5444. Received June 30, 2009; Revised Manuscript Received November 20, 2009

The tyrosine analog *p*-propargyloxyphenylalanine (pPa), like tyrosine, has limited water solubility. It has been postulated that this limited solubility has contributed to reduced cellular uptake of pPa and thus reduced *in vivo* incorporation of pPa into proteins. Using a cell-free protein synthesis system (CFPS) to circumvent cellular uptake, pPa has been incorporated site-specifically into proteins with high specificity at yields up to 27 times greater than the highest previously reported yield. The alkyne group present on proteins incorporated with pPa provides a reactive residue for site-specific bioconjugation with the copper(I)-catalyzed azide−alkyne [3 + 2] cycloaddition (CuAAC). Previously, incorporation of another CuAAC-compatible unnatural amino acid *p*-azido-L-phenylalanine (pAz) was demonstrated with CFPS. However, incorporation of pPa may be preferred over pAz due to the instability of the pAz's aryl-azido moiety upon UV or near-UV light exposure. Also, the ability to incorporate site-specifically both reactants of the CuAAC (the alkyne group of pPa and the azido group of pAz) into proteins enables direct site-specific conjugation of heterologous proteins. We have demonstrated (for the first time to our knowledge) a one-step, linker-less, site-specific, direct protein-to-protein conjugation using CuAAC and unnatural amino acids.

INTRODUCTION

With the advent of recombinant protein production and an ever increasing tool kit for protein optimization, proteins have become some of the most valuable molecules on earth (estimated $90+ billion U.S. market share in 2009) (*1*). A powerful tool for both optimizing protein function and creating new protein-based materials is the covalent modification of proteins. This is especially important to improve pharmaceutical protein pharmacokinetics, study protein function and trafficking, perform artificial post-translational modification, and construct new biomolecule-based materials (*2*, *3*). Although a number of methods have been developed for post-translational protein modification, only a few methods enable site-specific protein conjugation. By employing a cell-free approach, we seek to improve the yields of a particularly attractive method for site-specific conjugation. We also seek to demonstrate for the first time to our knowledge a direct, one-step, linker-less, site-specific protein-to-protein conjugation using the well-accepted copper(I)-catalyzed azide−alkyne [3 + 2] cycloaddition (CuAAC)[1] reaction.

A wide variety of methods targeting natural amino acid residues have been developed to facilitate covalent conjugation to proteins. However, only a few are widely used, and these typically target nucleophilic moieties present on lysine, cysteine, aspartic acid, and glutamic acid residues. In fact, over 70% of the protein conjugating reagents available from Molecular Probes and Pierce Biotechnology target lysine and cysteine (*4*). Unfortunately, these methods do not conjugate site-specifically when more than one residue of the targeted amino acid is surface-accessible. To obtain site-specific attachment, the protein must be mutated to remove the conjugation-targeted amino acid from undesirable attachment locations, and additional mutagenesis is often required to present the conjugation-targeted amino acid at the desired site. However, protein modification of this scale often negatively affects protein folding, function and/or stability.

Targeting the C- and N-terminus of proteins for post-translational conjugation has also been considered (*5*). However, this is complicated by similar chemical functionality found on the side chains of lysine and arginine or aspartic and glutamic acid (*5*). Although some progress has been made toward specifically conjugating at the protein termini, there are many cases when the terminus is inaccessible for attachment or, more importantly, when attachment to a different location is necessary for the desired function (*6*).

A particularly attractive method of circumventing issues related to natural amino acid mediated protein bioconjugation is the use of unnatural amino acids. Tirrell and co-workers have demonstrated the ability to substitute methionine with unnatural amino acids that display uniquely reactive residues (such as azido homoalanine) using methionine auxotrophic strains. Although protein can be produced at reasonable yields of around 20−50 μg/mL (*7*), this technique only offers a global replacement of methionine and would require the same protein modifications discussed previously if multiple methionines in the wild-type protein are surface-accessible. Further, global replacement of methionine could significantly alter the protein structure and compromise protein function.

* Corresponding author. James R. Swartz, Department of Chemical Engineering, Stanford University, Stanford, California 94305-5025. Telephone: 650-723-5398. Fax: 650-725-0555. E-mail: jswartz@stanford.edu.

[†] Department of Chemical Engineering.

[‡] Department of Bioengineering.

[§] Current affiliation: Department of Chemical Engineering, Brigham Young University, Provo, Utah 84602. Telephone: 801-422-2807. E-mail: bundy@byu.edu.

[1] Abbreviations: CFPS, cell-free protein synthesis; CuAAC, copper(I)-catalyzed azide−alkyne [3 + 2] cycloaddition; DHFR, *E. coli* dihydrofolate reductase; *Mj*tRNA$^{Tyr}_{CUA}$, *Methanococcus jannaschii* tyrosyl-tRNA with amber stop anticodon; *Mj*TyrRS, *Methanococcus jannaschii* tyrosyl-aminoacyl-tRNA synthase; *Mj*TyrRS^{pAz}, *Mj*TyrRS specific for **2**; *Mj*TyrRS^{pPa}, *Mj*TyrRS specific for **1**; pAz, *p*-azido-L-phenylalanine; pAzDHFR, DHFR with **2** incorporated; pAzGFP, sfGFP with **2** incorporated; pPa, *p*-propargyloxyphenylalanine; pPaDHFR, DHFR with **1** incorporated; pPaGFP, sfGFP with **1** incorporated; sfGFP, superfolder green fluorescent protein.

10.1021/bc9002844 © 2010 American Chemical Society
Published on Web 01/25/2010

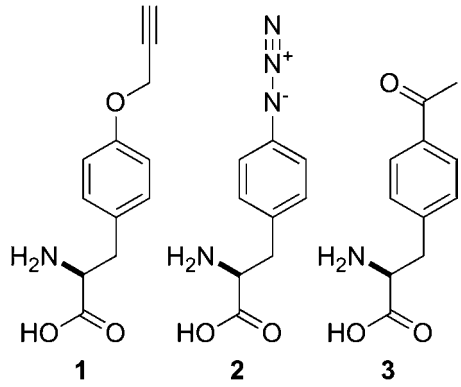


Figure 1. Structure of *p*-propargyloxyphenylalanine (**1**), *p*-azido-L-phenylalanine (**2**), and *p*-acetyl-L-phenylalanine (**3**).

Schultz and co-workers have developed a technology for truly site-specific incorporation of functionally unique unnatural amino acids by expressing othogonal tRNAs and aminoacyl-tRNA synthetases (*8*). Their *Escherichia coli*-based system uses (1) a *Methanococcus jannaschii* tyrosyl-aminoacyl-tRNA synthase (*Mj*TyrRS) evolved to exclusively charge a given unnatural amino acid and (2) a *Methanococcus jannaschii* tyrosyl-tRNA with an amber stop anticodon (MjtRNA$^{Tyr}_{CUA}$). By expressing the above pair and including the unnatural amino acid in the *E. coli* fermentation media, the unnatural amino acid is incorporated into proteins only in the location encoded by the amber stop codon UAG on the corresponding mRNA (*8, 9*). Similar technology has also been transferred to yeast and mammalian cells (*10, 11*). Site-specific conjugation using proteins expressed with this system requires minimal protein modification, as the unnatural amino acid is only incorporated at the desired location. The gene needs only to be modified by installing the amber stop codon at the desired location. Over 30 unnatural amino acid have been incorporated in this way with, for the most part, high selectivity for the unnatural amino acid, although at typically lower product yields (1 to 20 μg/mL) (*12, 13*). Further optimization work with one unnatural amino acid (*p*-benzoyl-L-phenylalanine) did increase protein yields to 40 μg/mL (*14*). Although the yield and incorporation efficiency varies depending on the unnatural amino acid, one unnatural amino acid in particular, *p*-propargyloxyphenylalanine, **1** (Figure 1), was found to be expressed only at lower yields (0.05 μg/mL and 2.0 μg/mL in *E. coli*) and at lower incorporation efficiencies (80% to 91% versus >93%) relative to other unnatural amino acids (*15*−*17*). It has been postulated that the cause was limited transport of **1** into the cell which could be due to the low aqueous solubility of **1** (*11*). **1** is an analogue of tyrosine, the least soluble of the natural amino acids (*18*), and like tyrosine, has poor solubility. The incorporation of **1** is of particular interest, as it contains a stable alkyne group that can be used for bioconjugation.

To overcome the putative transport limitation to incorporation of **1**, we expanded a cell-free protein synthesis (CFPS) approach. Recently, our *E. coli* based cell-free system was modified to include the *Mj*TyrRS/MjtRNA$^{Tyr}_{CUA}$ pair for the site-specific incorporation of *p*-azido-L-phenylalanine, **2**, and *p*-acetyl-L-phenylalanine, **3** (Figure 1). Protein yields up to 660 μg/mL and 110 μg/mL, respectively, were reported (*12*); however, both **2** and **3** have reasonably good water solubility, as they are analogues of phenylalanine, which is 60 times more water-soluble than tyrosine. Additionally, both **2** and **3** have been incorporated *in vivo* with high selectivity (>95%) and at relatively high yields suggesting that cellular uptake of these unnatural amino acids is not limiting (*17, 19, 20*).

Although the cell-free incorporation of both **2** and **3** is attractive, the open translation environment of the cell-free protein synthesis system (CFPS) is potentially even better suited for incorporation of unnatural amino acids with poor cellular uptake and with low water solubility. We seek to further demonstrate the utility of CFPS by site-specifically incorporating the potentially cell-transport-limited and poorly water soluble **1** into the model proteins dihydrofolate reductase (DHFR) and superfolder green fluorescent protein (sfGFP) (Figure 2). The unnatural amino acid **1** is of particular importance, as it contains an alkyne group that can be conjugated to azido containing entities with the highly selective copper(I)-catalyzed azide−alkyne [3 + 2] cycloaddition (CuAAC). Unlike **2**, which can also be used with CuAAC, **1** is not UV sensitive. Also, as will be described, efficient production of pairs of proteins, one with **1** and the other with **2**, enable the site-specific conjugation of two proteins in a one-step reaction without requiring an additional chemical linker (Scheme 1).

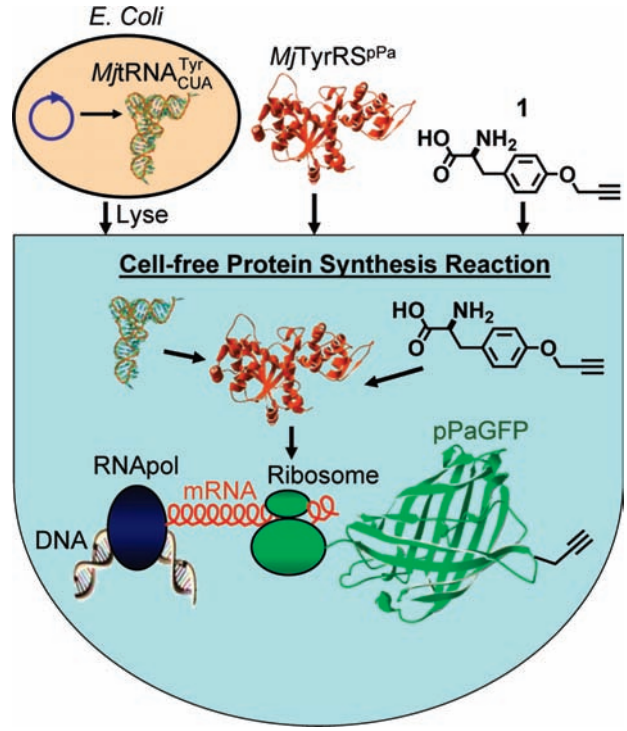
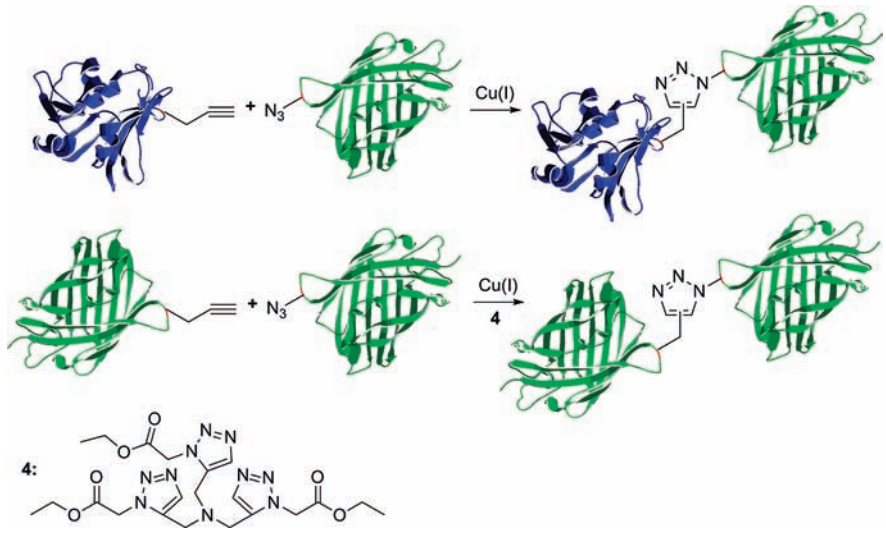


Figure 2. Cell-free protein synthesis reaction incorporating *p*-propargyloxyphenylalanine. The transcription and translation machinery and the MjtRNA$^{Tyr}_{CUA}$ were added as part of the *E. coli* lysate. *Mj*TyrRS^{pPa}, **1**, T7 RNA polymerase (RNApol), DNA plasmid template encoding pPaGFP, and other necessary cofactors were added directly to the CFPS environment.

EXPERIMENTAL PROCEDURES

Plasmid Construction. The sequence encoding the streptag (WSHPQFEK) was added directly before the stop codon on the 3′ end of the DHFR10 gene by PCR using the plasmid pK7eDHFR10−6H (*12*) as the DHFR10 gene source. The resulting gene was ligated into plasmid pY71 at the *Nde*I and *Sal*I restriction sites generating plasmid pY71eDHFR-V10unAA. The pY71 plasmid is a simplified version of the pK7 plasmid previously reported for use in CFPS (Supporting Information) (*21*). The plasmid pET15bsfGFP was a kind gift from Kevin P. Kent and Steven G. Boxer and contains a superfolder GFP variant with the sequence codon optimized for expression in *E. coli* (Supporting Information) (*22*). The codon encoding threonine 216 was replaced by the amber stop codon, and the streptag encoding sequence was added to the 3′ end by PCR. The resulting gene was ligated into pY71 at the *Nde*I and *Sal*I restriction sites creating plasmid pY71sfGFP-T216unAA. A

Scheme 1. Copper(I)-Catalyzed Azide−Alkyne [3 + 2] Cycloadditions (CuAAC) of pPaDHFR + pAzGFP (top) and pPaGFP + pAzGFP (bottom)



plasmid expressing *Mj*TyrRS^{pPa} (*Mj*TyrRS specific for *p*-propargyloxyphenylalanine, **1**) was generated to contain the *Mj*TyrRS^{pPa} sequence previously reported on plasmid pPR-MjRS-1 (*16*). The *Mj*TyrRS^{pPa} gene with a 3′-hexahistidine tag sequence was constructed using plasmid pK7pAzRS-6H (*12*) as a template and making the necessary mutations by overlap PCR. The resulting gene was ligated into pY71 at the *Nde*I and *Sal*I restriction sites resulting in the plasmid pY71pPaRS-6H.

***p*-Propargyloxyphenylalanine Synthesis and Solubility Analysis.** *p*-Propargyloxyphenylalanine, **1**, was synthesized as reported previously (*23*), and the product was characterized by electrospray mass spectrometry (Supporting Information Figure S1). The solubility of **1** at 25 °C was determined by first incubating 5 mM of **1** in Milli-Q water for three days with continuous end-over-end agitation. The solution was subjected to 21 000 × *g* for 1 h, and the soluble **1** solution was aspirated, after which the precipitated **1** was dried overnight under vacuum. The solubility of **1** was calculated on the basis of the weight of the dried insoluble **1** compared to the initial quantity of **1** added.

Cell-Free Protein Synthesis. *Extract and MjTyrRS Preparation. E. coli* extract used for CFPS was prepared from an *E. coli* KC6 strain harboring the pDule-tRNA plasmid with the *Mj*TyrRS^{pAz} (*Mj*TyrRS specific for **2**) gene removed (*12*). The strain was fermented in 1 L of defined media (*24*) using a 2.5 L Tunair fully baffled shake flask (Shelton Scientific, Shelton, CT, USA) at 37 °C and constant shaking at 280 rpm. The culture was harvested at OD 4.0 (3.5 h after inoculation), and the cells were pelleted and washed 3 times with S30 buffer (*24*). After the final wash, the cells were resuspended in 1 mL S30 buffer per gram cells and lysed by single pass homogenization (700 Rotary Homogenizer, Fisher Scientific, Pittsburgh, PA) at pressures of 17 000 to 25 000 psi. The homogenate was clarified by discarding the pellet after each of two rounds of centrifugation for 30 min at 30 000 × *g*. The clarified extract was activated by incubating at 37 °C for 80 min while shaking at 280 rpm; after which, the extract was flash-frozen and stored at −80 °C until use. *Mj*TyrRS^{pPa} and *Mj*TyrRS^{pAz} were affinity purified from BL21pLys cells harboring the plasmid pY71pPaRS-6H or pK7pAzRS-6H using a previously described protocol (*12*).

Cell-Free Protein Synthesis Reaction. Cell-free protein synthesis (CFPS) reactions for incorporating **1** or **2** were performed with a few modifications to the standard PANOxSP system (*25*). The reactions were preformed in 1.5 mL Eppendorf tubes or 6-well plates (Fisher Scientific, Waltham, MA) at 15 μL to 1 mL volumes and incubated for 8 h at 30 °C unless noted otherwise. The reactions contain the following components obtained from Sigma-Aldrich (St. Louis, MO) unless otherwise specified: 1.2 mM ATP, 0.85 mM GTP, 0.85 mM UTP, 0.85 mM CTP, 34 μg/mL folinic acid, 0.33 mM nicotinamide adenine dinucleotide (NAD), 0.27 mM coenzyme A (CoA), 1.5 mM spermidine, 1 mM putrescine, 175 mM potassium glutamate, 10 mM ammonium glutamate, 13 mM magnesium glutamate, 2.7 mM sodium oxalate, 2 mM each of the 20 standard proteinogenic amino acids, 2 mM of **1** (synthesized) or **2** (Chem-Impex Int., Wood Dale, IL), 30 mM phosphoenolpyruvate (Roche Molecular Biochemicals, Indianapolis, IN), 85 μg/mL *E. coli* tRNA mixture (Roche Molecular Biochemicals), 100 μg/mL T7 RNA polymerase (prepared as described previously (*21*), 5 to 25 μM l-[U-14C] Leucine (GE Healthcare, Piscataway, NJ), 0.8 to 5 mg/mL *Mj*TyRS^{pPa} or *Mj*TyrRS^{pAz} prepared as described above, 28% v/v of extract prepared from *E. coli* lysate as described above, and 12 nM plasmid (either pY71eDHFR-V10unAA or pY71sfGFP-T216unAA purified with Qiagen Plasmid Maxi Kit, Valencia, CA).

Cell-Free Protein Synthesis Yield Analysis. Total synthesized protein yields were determined from the percent of radioactive ^{14}C-leucine incorporated into protein. Radioactivity measurements were made using Beckman ReadySafe Scintillation Cocktail and a Beckman LS3801 Liquid Scintillation Counter (Beckman Coulter, Fullerton, CA). ^{14}C-leucine labeled proteins were precipitated and washed three times with 0.5% trichloroacetic acid, TCA, before measuring radioactivity levels. Soluble yields were determined by centrifuging the CFPS reaction product at 4 °C and 21 000 *g* for 15 min before TCA-precipitation and scintillation counting of the supernatant. The detailed procedure has been described previously (*21*). Soluble full-length yields were determined by subjecting the supernatant after the above-mentioned centrifugation to SDS-PAGE gel electrophoresis followed by autoradiography and densitometry. Specfically, NuPAGE 10% Bis-Tris and 4−12% Bis-Tris Gels (Invitrogen, Carlsbad, CA), Mark12 Unstained Standard MW Marker (Invitrogen), SimplyBlue SafeStain (Invitrogen), and Kodak BioMax MR Autoradiography Films (Rochester, NY) were used following manufacture's instructions. *ImageJ* 1.36b software (National Institutes of Health, USA) was used to estimate the relative intensity of the protein bands for densitometry (*26*).

Activity Assays. *DHFR.* The specific activity of DHFR (and DHFR variants containing unnatural amino acids) was measured with the Dihydrofolate Reductase Assay Kit (Sigma-Aldrich)

by following the conversion of NADPH to $NADP^+$ as determined by absorbance at 340 nm. Prior to the activity assay, DHFR was purified using the C-terminal streptag and 0.2 mL gravity-flow *Strep*-Tactin Sepharose mini-columns per manufacture's instructions (IBA GmbH, Gottingen, Germany).

sfGFP. An *in vivo* produced and affinity purified sfGFP (courtesy of Kevin P. Kent and Steven G. Boxer, Stanford University) was used as a reference for sfGFP activity (*22*); with 100% activity being equivalent to the specific activity of *in vivo* produced sfGFP. The specific activity of sfGFP (and variants containing unnatural amino acids) was measured using either (1) a NanoDrop 3300 Fluorimeter (Thermo Scientific, Waltham, MA) with blue excitation source setting and emission measurement at 511 nm or (2) a Mithras Multimode Microplate Reader LB 940 (Berthold Technologies, Wildbad, Germany) with a F485 excitation filter and a F535 emission filter.

***p*-Propargyloxyphenylalanine Incorporation Selectivity Analysis.** To verify the previously reported high selectivity of *Mj*TyrRS^{pPa} for **1** (*16*), CFPS reactions were performed with and without **1**. The product was subjected to electrophoresis using NuPAGE 10% Bis-Tris SDS-PAGE gels. Autoradiography of the dried SDS-PAGE gel was performed to determine the amount (if detectable) of full-length product produced in the absence of **1** compared to the amount of full-length product produced in the presence of **1**.

Extraction and Characterization of tRNA from CFPS Extract. The tRNA from 100 μL of cell extract (prepared from KC6 with *Mj*tRNA$^{Tyr}_{CUA}$ expression) was extracted with an equivalent volume of phenol/chloroform/isoamyl alcohol 25:24:1 followed by vortexing, phase separation by a 2 min spin at 21 000 $\times$ *g*, and aspiration of the aqueous phase. Both a 0.1 equiv of 3 M sodium acetate, pH 5, and a 2.5 equiv of 200 proof ethanol were added to the aspirated aqueous phase. After an overnight incubation at 4 °C, the solution was subjected to centrifugation at 21 000 $\times$ *g* for 20 min. The resulting pellet was washed with 70% ethanol and repelleted by centrifugation at 21 000 $\times$ *g* for 20 min. After air-drying, the pellet was resuspended in 25 μL of 10 mM phosphate buffer pH 8.0. The Nanodrop 2000 Spectrophotometer and the Qubit-iT 5−100 ng RNA Assay (Invitrogen) were used to determine the relative amount of DNA and RNA purified. The concentration of ethanol-extracted tRNA was compared to the concentration of tRNA in the CFPS extract using 15% TBE-urea SDS-PAGE gel electrophoresis with ethidium bromide staining and densitometry with *ImageJ* 1.36b software (*26*).

CuAAC Reactions. CuAAC reactions were performed anaerobically with equimolar concentrations of the **1**-containing and **2**-containing proteins. The Cu(I) complex tetrakis(acetonitrile)copper(I) hexafluorophosphate ($[(CH_3CN)_4Cu]PF_6$) (Sigma-Aldrich) was used as a catalyst at final concentrations ranging from 0.1 to 1 mM. In GFP dimerization CuAAC reactions, a tris-triazole ligand **4** (Scheme 1), which helps facilitate the CuAAC reaction (*27*), was added at 2 equiv of the Cu(I) complex concentration. The reaction was buffered with 10 mM potassium phosphate, pH 8.0. The final concentration of each reactant was 1.6 μM in the pPaDHFR and AzGFP CuAAC reaction. The pPaGFP and pAzGFP CuAAC conjugation reactions contained 4.7 to 5.8 μM of each reactant. All reactions were performed anaerobically for 8 h or overnight. Post-CuAAC activity assays were performed as described above. The extent of completion of the CuAAC reactions was evaluated by NuPAGE 10% or 4−12% Bis-Tris SDS-PAGE gel electrophoresis followed by autoradiography and densitometry (*ImageJ* software). Desalting of CuAAC reaction product to remove Cu(I) was performed using Illustra Microspin G-25 Columns (GE Healthcare) per the manufacture's specifications.

Size-Exclusion Separation of the Click Reaction Product. A 2.5 mm $\times$ 250 mm column was fabricated from a 1 mL Serological polystyrene pipet (Fisher Scientific, Waltham, MA) and the membrane from a Pharmacia Biotech XK 16 column. The column was packed with Superdex75 resin (GE Healthcare) at a 0.3 mL/min flow rate using 10 mM potassium phosphate buffer at pH 8.0 and a peristaltic pump. Prior to size exclusion separation, the column was transported to an anaerobic environment and flushed with deoxygenated 10 mM phosphate buffer at pH 8.0. The click reaction product (20 μL) was added directly to the column followed by deoxygenated phosphate buffer pH 8.0 at 0.3 mL/min. Fractions of 0.1 mL were collected, and the specific activity of sfGFP in each fraction was determined by (1) scintillation counting to determine sfGFP concentration and (2) measuring fluorescence with the Mithras Multimode Microplate Reader. The distribution of dimerized sfGFP and monomeric sfGFP in each fraction was visualized by NuPAGE 10% Bis-Tris SDS-PAGE electrophoresis with Novex Sharp Prestained Standard (Invitrogen) and SimplyBlue SafeStain.

RESULTS AND DISCUSSION

Cell-Free Incorporation of *p*-Propargyloxyphenylalanine. Although *p*-propargyloxyphenylalanine, **1**, (Figure 1) has been reported to have lower solubility than other unnatural amino acids (*11*), the solubility limit of this amino acid has not been previously reported. After synthesis of **1** using methods described previously (*23*) and characterization by mass spectroscopy (Supporting Information Figure S1), we found the equilibrium solubility of **1** in water at 25 °C to be 1.9 mM (standard deviation = $\pm$0.9 mM, $n = 3$). The limited solubility of **1** is not surprising, as it is a hydrophobic analogue of tyrosine, the least water-soluble natural amino acid (2.5 mM water solubility at 25 °C) (*18*). Incorporation of **1** into proteins provides a unique terminal alkyne residue which can be exploited for protein conjugation using the copper(I)-catalyzed azide−alkyne [3 + 2] cycloaddition (CuAAC) "click" reaction. However, the incorporation of **1** into proteins using *in vivo* techniques has resulted in lower yields (0.05 to 2.0 μg/mL in *E. coli*) and low incorporation efficiencies (*15*−*17*). It has been postulated that limited cellular uptake of **1**, potentially due to low solubility of **1**, is the cause (*11*). To overcome the potential cellular uptake barrier to producing proteins containing **1** at higher yields, we evaluated the open transcription/translation environment of cell-free protein synthesis (CFPS).

Previously, by incorporating the *Mj*TyrRS/*Mj*tRNA$^{Tyr}_{CUA}$ pair developed by the Schultz lab into our *E. coli* based CFPS reactions, the unnatural amino acids *p*-azido-L-phenylalalnine, **2**, and *p*-acetyl-L-phenylalanine, **3**, were site-specifically incorporated into proteins (Figure 1) (*12*). **2** contains a terminal azide moiety which, like terminal-alkyne moiety of **1**, can be used with the CuAAC reaction for protein modification. However, unlike **1**, care must be taken to prevent UV and near-UV exposure to **2** before and after incorporation, as the terminal azide is destabilized by its neighboring aromatic ring and rapidly degrades upon exposure to UV or near-UV light (*28*). In cases where UV and near-UV light exposure is difficult to avoid, incorporation of the UV-insensitive **1** may be a better choice as it also facilitates site-specific bioconjugation by CuAAC. Also, the ability to incorporate site-specifically both the alkyne moiety by **1** and the azide moiety by **2** at significant yields provides a way to site-specifically conjugate two different proteins to each other in a one-step, linker-less manner as will be described in detail later.

In demonstrating site-specific incorporation of **1** with our CFPS reaction, superfolder green fluorescent protein (sfGFP) and *E. coli* dihydrofolate reductase (DHFR) were chosen as model proteins. Incorporation of **1** at surface-accessible locations

Table 1. CFPS Reaction Yields of Total Protein, Soluble Protein, Soluble Full-Length Protein, and Active Soluble Full-Length Protein

protein	total protein (μg/mL)[a]	soluble protein (μg/mL)[a]	full-length soluble protein (μg/mL)[b]	percent active full-length soluble protein (%)[c]
pPaGFP	1188 ± 50	978 ± 71	175 ± 16	109 ± 4.1
pPaDHFR	111 ± 9.4	86 ± 0.6	86 ± 0.6	116 ± 25
pAzGFP	1047 ± 71	801 ± 29	141 ± 5.3	99 ± 3.2
pAzDHFR	155 ± 10	129 ± 1.9	129 ± 1.9	90 ± 15

[a] The total and soluble protein yields were determined based on scintillation counting of TCA precipitated ^{14}C-labeled proteins as detailed in the Experimental Procedures. [b] The yield of full-length soluble protein was determined by densitometry using the autoradiogram of the SDS-PAGE gel loaded with the soluble fraction of the CFPS product. [c] The percent of active full-length soluble protein was determined from specific activity of soluble affinity purified protein compared to the reported specific activity of 45 units/mg for *E. coli* DHFR (*12*) and the specific activity of *in vivo* produced sfGFP. The number following ± symbol represents 1 standard deviation and $n \geq 3$ except for the soluble protein yield where $n = 2$.

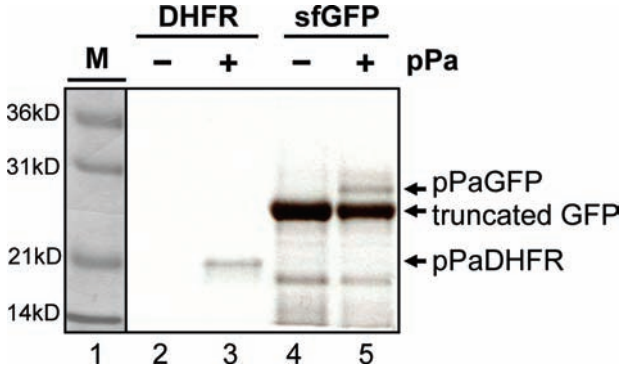


Figure 3. Verifying selectivity of *Mj*TyrRS^{pPa} for *p*-propargyloxyphenylalanine. Autoradiogram of SDS-PAGE gel of CFPS products when attempting to express pPaDHFR without **1** (lane 2), pPaDHFR with **1** (lane 3), pPaGFP without **1** (lane 4), and pPaGFP with **1** (lane 5). Lane 1 is the Coomassie stained SDS-PAGE image of the Mark 12 protein standard (Invitrogen) aligned with the autoradiogram. The molecular weight (MW) is 19kD for pPaDHFR, 27kD for pPaGFP, and 24kD for GFP truncated at the incorporation site of **1**.

(T216 for sfGFP and V10 for DHFR) was encoded by substituting in the amber stop codon. To facilitate incorporation of **1**, *Mj*TyrRS^{pPa} (*Mj*TyrRS specific for **1**), **1**, *E. coli*-extract containing *Mj*tRNA$^{Tyr}_{CUA}$ and other cofactors were combined in a cell-free protein synthesis reaction as detailed in the Experimental Procedures (Figure 2). Using this modified CFPS reaction, both pPaGFP (sfGFP with **1** incorporated at the T216 site) and pPaDHFR (DHFR with **1** incorporated at the V10 site) were produced. As shown in Table 1, the volumetric yield of full-length, soluble pPaGFP and pPaDHFR was over 8 times the highest reported yield for *in vivo* produced protein containing **1** (2 μg/mL in *E. coli* and 10 μg/mL in *S. cerevisiae*) (*16, 17*). The full-length soluble pPaGFP and pPaDHFR produced with CFPS were affinity purified and assayed for activity. The emission spectra of pPaGFP was identical to *in vivo* produced and affinity purified sfGFP (courtesy Boxer Lab, Stanford University), and both pPaGFP and pPaDHFR were found to be completely active (Table 1, Supporting Information Figure S2). The selectivity of the CFPS reaction for incorporation of **1** over other natural amino acids at the amber stop codon was also evaluated by excluding **1** from the CFPS reaction. High selectivity for **1** was verified, as full-length product of both pPaGFP and pPaDHFR was undetectable when **1** was excluded from the CFPS reactions; however, significant product was observed after **1** was added (Figure 3). Tryptic digestion of pPaDHFR and LC-MS further confirmed the incorporation of **1** at the location encoded by the amber stop codon (Supporting Information Figure S3). The volumetric yields listed in Table 1 were obtained from 0.5 mL reactions (43 μg pPaDHFR and 87.5 μg pPaGFP per 0.5 mL reaction), and similar yields were observed with 30 μL and 0.75 mL CFPS reactions. Also, the scalability of our base *E. coli* based CFPS reactions from 15 μL to 1 L without a decrease in protein production yield has previously been demonstrated (*29*).

As a comparison and to enable the direct protein-to-protein attachment that will be discussed later, **2** was also incorporated into sfGFP (pAzGFP) and DHFR (pAzDHFR) at the same location as **1** using CFPS. The same reagents were used to incorporate **2** as used with **1** with the exception of replacing *Mj*TyrRS^{pPa} with a *Mj*TyrRS specific for **2** (*Mj*TyrRS^{pAz}) and replacing **1** with **2**. Similar yields and activities of pAzGFP and pAzDHFR were obtained compared to pPaGFP and pPaDHFR (Table 1, Supporting Information Figure S2).

Optimization for Incorporation of *p*-Propargyloxyphenylalanine. As shown in Table 1, only 15% of the 1.2 mg/mL of protein produced in the pPaGFP cell-free reaction is full-length pPaGFP, 27 kD. The majority of protein (~1 mg/mL) produced is a truncated product that matches the molecular weight of sfGFP truncated at the amber stop codon (24 kD) (Figure 3). This suggests that the CFPS reaction has the potential to produce ~1 mg/mL of active pPaGFP; however, the ability to incorporate **1** at the amber stop codon is limiting. pAzGFP gave similar results with only 13% of the 1.0 mg/mL of protein produced corresponding to full-length soluble protein (Table 1). The production of pPaDHFR and pAzDHFR is also likely limited by the incorporation of the unnatural amino acid, as active DHFR production has been reported at yields of 930 μg/mL using a similar CFPS system (*12*). In the case of pPaDHFR and pAzDHFR, the relatively small difference in total and full-length yields is likely due to the short, truncated DHFR (9 amino acids long) being rapidly degraded by peptidases in the cell extract.

To optimize for incorporation of **1**, we first assessed temperature effects. The CFPS reactions are typically performed at the optimal *E. coli* fermentation growth temperature of 37 °C (*30*). Since translation is slower at lower temperatures, this might provide more time for the *Mj*tRNA$^{Tyr}_{CUA}$ to be charged or for the charged *Mj*tRNA$^{Tyr}_{CUA}$ to be accepted by the ribosome. Although *Mj*tRNA$^{Tyr}_{CUA}$ has been shown to be accepted by the *E. coli* ribosome, the *Methanococcus jannaschii* tRNA has a smaller variable loop (5 nucleotides) compared to the *E. coli* tRNA's larger variable loop (13 nucleotides), and this could decrease the affinity of the *E. coli* translational complex for *Mj*tRNA$^{Tyr}_{CUA}$ (*31*). Also, previous work incorporating **2** using a similar CFPS system demonstrated that reactions conducted at 30 °C provided higher yields by prolonging the duration of protein synthesis (*12*). The expression of pPaGFP responded similarly with double the amount of active pPaGFP produced at 30 °C (156 μg/mL, SD = 20 μg/mL) compared to 37 °C (75 μg/mL, SD = 17 μg/mL) (Figure 4AB). While the production rate of total protein and incorporation of **1** drops off rapidly after the first hour at 37 °C, the prolonged translation between hours 1 and 8 at 30 °C appears to be responsible for higher incorporation yields at 30 °C (over 80% of the active pPaGFP was produced during this period). Dropping the temperature further to 25 °C decreased total protein production by 68%, but did not significantly reduce the rate of **1** incorporation or reduce the total amount of protein containing **1** produced. At

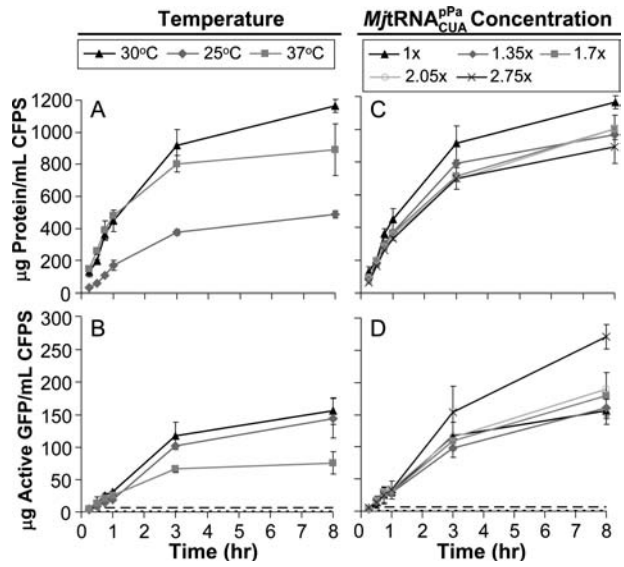


Figure 4. Effect of temperature and *Mj*tRNA$^{Tyr}_{CUA}$ concentration on cell-free protein synthesis yields of pPaGFP. The total protein production yields (full-length and truncated pPaGFP) (A,C) and active pPaGFP production yields (B,D) are shown over the course of an 8 h CFPS reaction at temperatures 25 to 37 °C (A,B) and tRNA concentrations 1 to 2.75 times the tRNA concentration in a standard 30 °C CFPS reaction incorporating **1** (C, D). Background fluorescence from the CFPS reaction (without expressing sfGFP) was insignificant (black, dotted line). Fluorescence due to 1 mg/mL of GFP truncated at the **1** incorporation site (black, dashed line) is also shown.

25 °C, incorporation of **1** is still limiting, as only 30% of the protein is produced as full-length active pPaGFP (Figure 4AB).

Another potential factor limiting **1** incorporation is the concentration of charged-*Mj*tRNA$^{Tyr}_{CUA}$ available to the ribosome. As *Methanococcus jannaschii* is a hyperthermophile that optimally grows at 85 °C (*32*), the activity of the *Mj*TyrRS^{pPa} may be significantly lower at the optimal CFPS temperature of 30−37 °C. Increasing the concentration of the enzyme *Mj*-TyrRS^{pPa} and/or the reactants *Mj*tRNA$^{Tyr}_{CUA}$ and **1** should increase the overall concentration of charged-*Mj*tRNA$^{Tyr}_{CUA}$, assuming the concentration of ATP is not limiting. We first assessed increasing the concentration of *Mj*TyrRS^{pPa} above the typical concentration of 1.6 mg/mL used in this study and found that 2- and 3-fold increases in *Mj*TyrRS^{pPa} concentration did not increase incorporation of **1** (results not shown). This result is not surprising, as the concentration of *Mj*TyrRS^{pPa} used in this study was five times greater than the concentration of TyrRS previously reported for incorporation of unnatural amino acids in a CFPS reaction (*12*).

We did not assess increasing the concentration of **1** in the CFPS reaction, as (1) the current 2 mM concentration of **1** in CFPS is close to its water solubility limit at 25 °C (1.9 mM) and (2) increasing **2** concentrations above 2 mM did not increase the yield of protein containing **2** (*12*). However, with an increase in the concentration of *Mj*tRNA$^{Tyr}_{CUA}$, the other reactant involved in charging *Mj*tRNA$^{Tyr}_{CUA}$ with **1** was assessed. The concentration of *Mj*tRNA$^{Tyr}_{CUA}$ is likely limiting, as (1) the CFPS environment is 20 times more dilute than the *E. coli* cytoplasm (*33*), and thus the concentration of *Mj*tRNA$^{Tyr}_{CUA}$ is also diluted 20 times relative to the *in vivo* system, and (2) in the *in vivo* system, the concentration of *Mj*tRNA$^{Tyr}_{CUA}$ was found to be limiting, as 30−40% higher yields of proteins containing unnatural amino acids were recently reported when the *Mj*tRNA$^{Tyr}_{CUA}$ was expressed at higher concentrations (*14*). To increase the *Mj*tRNA$^{Tyr}_{CUA}$ concentration in the CFPS reaction, the nucleic acid (including the *Mj*tRNA$^{Tyr}_{CUA}$) was extracted by ethanol precipitation from our *E. coli* lysate and added directly to the CFPS reaction. The amount of extra *Mj*tRNA$^{Tyr}_{CUA}$ added to the CFPS reaction was estimated on the basis of the relative concentrations of extracted tRNA compared to tRNA in the *E. coli* lysate (Supporting Information Figure S4). The addition of the extracted RNA increased the yield of active product containing **1**, although a modest drop in total protein production of ∼20% was observed (Figure 4CD). The most significant increase in **1** incorporation occurred at the highest *Mj*tRNA$^{Tyr}_{CUA}$ concentration estimated to be 2.75 times the original concentration. At this *Mj*tRNA$^{Tyr}_{CUA}$ concentration, the yield of active pPaGFP increased 75% to 271 μg/mL (SD = 19 μg/mL), which is 27 times greater than the highest published yield for protein containing **1** (Figure 4D) (*17*).

Although a substantial gain in the yield of pPaGFP was observed by increasing the *Mj*tRNA$^{Tyr}_{CUA}$ concentration, room for improvement remains, as only 30% of the total protein produced was active full-length pPaGFP. As the CFPS provides a unique environment with direct access to biochemical reactions (including translation and tRNA-charging), the CFPS is well-suited for continued work to study and increase the efficiency of unnatural amino acid incorporation. For example, the impact of the competition for the amber stop codon between **1**-charged-*Mj*tRNA$^{Tyr}_{CUA}$ and release factor 1 (an essential protein) could be assessed by removing the release factor 1 from the CFPS extract before the CFPS reaction. Also, CFPS provides the opportunity to simplify the system to assess different steps along a biochemical pathway. As an example, the *Mj*tRNA$^{Tyr}_{CUA}$ could potentially be charged with **1** at a higher temperature before being added to the CFPS reaction to directly assess the effect of **1**-charged-*Mj*tRNA$^{Tyr}_{CUA}$ concentration on the incorporation of pPa into proteins. Improvements made to the CFPS system could also be applied in further optimizing the incorporation of unnatural amino acids.

Direct Site-Specific Protein−Protein Conjugation. Proteins with **1** incorporated have a unique terminal alkyne moiety, which can be covalently conjugated to azido moieties with the copper(I)-catalyzed azide−alkyne [3 + 2] cycloaddition (CuAAC). The CuAAC reaction is considered the "cream of the crop" of click chemistries and has been widely used since its discovery (*34, 35*). The ability to perform the CuAAC at biologically friendly conditions (physiological temperature and pH) and achieve high conjugation efficiencies with relatively low reactant concentrations is particularly attractive for protein conjugation applications (*36*). The CuAAC reaction has been successfully used to bioconjugate proteins, enzymes, viruses, oligonucleotides, and cell surfaces for a number of applications including drug and gene delivery, bioseparation, and cell-surface display (*37, 38*).

With the ability to site-specifically incorporate either an alkyne (**1**) or azido (**2**) moiety, the CuAAC reaction could also be used to site-specifically conjugate proteins in a one-step reaction without using a chemical linker. Potential applications include (1) creating fusion proteins when a single polypeptide of the fusion partners does not express and/or fold correctly, (2) linking protein complexes together to form protein-based materials, and (3) decorating protein complexes such as virus-like particles for vaccine and drug delivery applications.

As proof of concept, pPaDHFR and pAzGFP were directly bioconjugated using the CuAAC reaction (Scheme 1). Both pPaDHFR and pAzGFP were anaerobically incubated overnight at room temperature with 1 mM of the Cu(I) complex tetrakis(acetonitrile)copper(I) hexafluorophosphate ([$(CH_3CN)_4$Cu]-PF_6) resulting in a conjugation yield of about 43% based on densitometry (Figure 5). However, after the CuAAC reaction, the activity of pPaDHFR was undetectable and the activity of pAzGFP dropped to only 8.7% (SD = 0.5%, n = 3) of the original activity. The control reactions mimicking the CuAAC

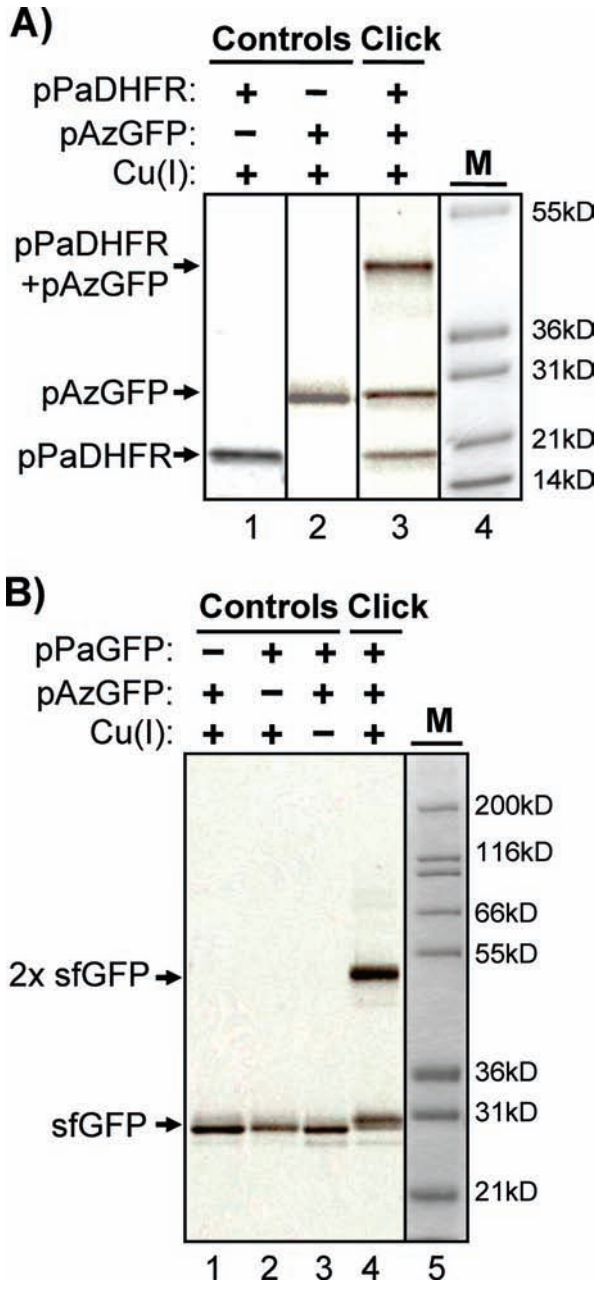


Figure 5. Copper(I)-catalyzed azide−alkyne [3 + 2] cycloaddition results. (A) Autoradiogram of the SDS-PAGE gel containing the CuAAC reaction product of pPaDHFR and pAzGFP (lane 3) and controls of pPaDHFR alone (lane 1) and pAzGFP alone (lane 2). In all cases, the Cu(I) complex concentration was 1 mM and the samples were incubated overnight anarobically. (B) Autoradogram of the SDS-PAGE gel containing the pPaGFP and pAzGFP CuAAC reaction product (lane 4). Controls were the combined pPaGFP and pAzGFP but without the Cu(I) complex (lane 1) and the pAzGFP (lane 2) or pPaGFP (lane 3) separately exposed to the Cu(I) complex. The concentration of the Cu(I) complex was 0.25 mM in all cases where the Cu(I) complex was added and samples were incubated for 8 h anaerobically. Lane 4 of A and lane 5 of B represent the Coomassie-stained Mark 12 protein standard aligned to the autoradiogram. The light band below sfGFP is likely truncated sfGFP (Figure 3).

reaction conditions but with pPaDHFR and pAzGFP in separate tubes also resulted in undetectable pPaDHFR activity and a drop in pAzGFP activity to only 14% (SD = 4%, $n = 3$) of the original activity. When pPaDHFR and pAzGFP were incubated anaerobically overnight without the Cu(I) complex, no loss in activity was observed, suggesting that the Cu(I) complex is the cause of the loss in protein activity. The inhibition of activity due to copper is not completely unexpected, as the addition of a few millimoles of copper ion has been reported to completely quench GFP fluorescence (*39*). In addition, the presence of the Cu(I) has been reported as a problem in a few other cases causing disassembly of some viruses, degradation of oligonucleotides, and cellular toxicity (*36, 37, 40*).

As sfGFP appears more resistant to the Cu(I) complex exposure than DHFR, direct pPaGFP-pAzGFP bioconjugation was used to evalutate the impact of lowering Cu(I) concentration on activity (Scheme 1). In addition to lowering the Cu(I) concentration, a tris-triazole ligand **4** (*27*) (Scheme 1) was added at 2 equiv of the Cu(I) concentration to increase the CuAAC reaction rate. The reaction time was also decreased to 8 h. A 75% reduction in the Cu(I) compound concentration to 0.25 mM increased post-Cu(I) compound exposure activity from 9% to 57% of the original activity, and pPaGFP-pAzGFP was directly conjugated at 62% reaction efficiency as determined by densitomitry (Figure 5).

As the CuAAC has been reported as less efficient at lower Cu(I) concentrations (*38*), we next sought to assess the impact of removing the Cu(I) compound before measuring activity to determine the reversibility of the inhibition. Similar to the results above, the pPaGFP and pAzGFP specific activity dropped by 30% after a CuAAC reaction with 0.25 mM Cu(I) complex and the tris-triazole ligand **4** when compared to a control where the Cu(I) complex was not added. However, post CuAAC reaction removal of the Cu(I) complex using a G-25 desalting column restored the specific activity of the sfGFP mixture (conjugated pPaGFP-pAzGFP, unreacted pPaGFP, and unreacted pAzGFP) to pre-Cu(I) complex exposure levels (Figure 6CD).

To further confirm that direct conjugation of pPaGFP to pAzGFP without a chemical spacer did not inhibit activity, conjugated pPaGFP-pAzGFP was separated from the unconjugated monomers using a 2.5 mm × 250 mm Superdex75 size exclusion column (Figure 6B,D). The specific activity of covalently conjugated pPaGFP-pAzGFP (lane 5 of Figure 6D) was similar to the specific activity of monomeric pPaGFP and pAzGFP (Figure 6C and lane 8 of Figure 6D), with the measurements within 1 standard deviation of each other. A similar specific activity was also measured from size exclusion fractions 6 and 7 which contained a mixture of conjugated and unconjugated pPaGFP and pAzGFP. On the basis of these results, it appears that the effect of the Cu(I) complex on the activity of pPaGFP and pAzGFP is reversible upon removal of the Cu(I) complex after the CuAAC reaction. In addition, direct protein−protein conjugation without a chemical linker as a spacer did not inhibit sfGFP specific activity. This is the first time to our knowledge that proteins have been site-specifically conjugated without a chemical linker using a single CuAAC reaction.

Although the CuAAC worked effectively in the above protein−protein conjugation and for the majority of applications previously attempted, there are a few cases where the Cu(I) catalyst has been reported to be problematic in causing disassembly of some macromolecular structures, degradation of oligonucleotides, and cellular toxicity (*34, 36−38, 40*). To minimize or eliminate the negative effect of Cu(I) in these instances, our laboratory and others are working to increase the reaction efficiency while reducing the reaction time and the concentration of Cu(I) catalyst needed. It has recently been demonstrated that, by applying an electrochemical potential, a CuAAC reaction was performed with 98% conjugation efficiency in 15 min with 0.1 mM Cu(I) (*36*). Also, chemical additives, such as the tris-triazole ligand **4** used in this work, can stabilize the less stable Cu(I) from oxidizing to the Cu(II) oxidation state. Another alternative being developed is the use of a copper-free CuAAC reaction that uses a strained cycloalkyne which conjugates with high chemoselectivly to azido

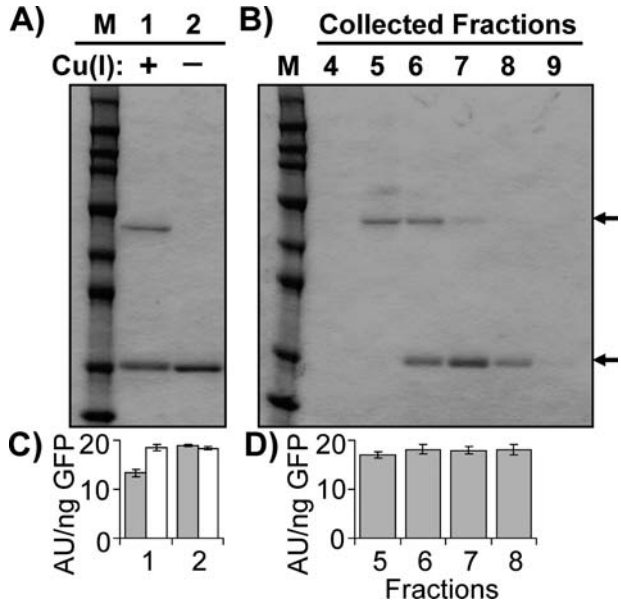


Figure 6. Restoration of the specific activity of sfGFP. (A) Coomassie-stained SDS-PAGE gel containing the pPaGFP and pAzGFP CuAAC reaction product with 0.25 mM Cu(I) complex (lane 1) and a control reaction product performed identically to the CuAAC but without the Cu(I) complex (lane 2). Lane M was loaded with Novex Sharp Prestained Standard (Invitrogen, bottom to top band kDs: 20, 30, 40, 50, 60, 80, 110, 160, 260). (B) Coomassie-stained SDS-PAGE gel containing the 0.1 mL fractions collected off the 2.5 mm × 250 mm Superdex75 size exclusion column. Lanes 4−9 represent fractions 4−9, as the radiolabeled protein was detected predominantly in only fractions 5−8, although fractions 1−28 were collected and tested for the presence of sfGFP. Lane M was loaded with the same protein standard and has the same band distribution as A. Arrows represent the expected location of sfGFP (lower) and covalently dimerized sfGFP (upper). (C) Specific activity of sfGFP in emission AU (arbitrary units) per nanogram of sfGFP following the CuAAC reaction (1, same as lane 1 of A) and the reactants without the Cu(I) complex (2, same as lane 2 of A). Gray bars represent specific activity after CuAAC reaction, and white bars represent specific activity after CuAAC and G-25 desalting (GE Healthcare) to remove the Cu(I) complex. (D) sfGFP specific activity of the 0.1 mL fractions 5−8 collected from the Superdex75 size exclusion column. Note that the size exclusion column should separate the sfGFP from the Cu(I) complex. The error bars in C and D represent 1 standard deviation of $n \geq 3$ measurements. Note: the lower conjugation efficiency of 37% (measured by densitometry) is attributed to a longer exposure time to UV light experienced by this pAzGFP reactant compared to the pAzGFP used in the previous reactions (Figure 5).

moieties in the absence of Cu(I) (*41*). By synthesizing an unnatural amino acid containing the strained cycloalkyne group and evolving a *Mj*TyrRS specific for this unnatural amino acid, the copper-free CuAAC could also be employed for site-specific, linker-less protein−protein conjugation.

CONCLUSIONS

We have demonstrated for the first time to our knowledge a linker-less one-step protein−protein bioconjugation that is site-specific and requires minimal protein mutagenesis (only an insertion or substitution of *p*-propargyloxyphenylalanine, **1**, and *p*-azido-L-phenylalanine, **2**). The conjugation uses the copper(I)-catalyzed azide−alkyne [3 + 2] cycloaddition (CuAAC), which is considered biocompatible, as it is performed at physiological conditions with high conjugation efficiencies at low reactant concentrations (*36, 37*). Initial work verified that pPaDHFR and pAzGFP were conjugated at 43% efficiency and the addition of a tris-triazole ligand **4** resulted in a 62% conjugation efficiency for pPaGFP+pAzGFP. Although a reduction in protein activity due to exposure to Cu(I) did occur, post-CuAAC removal of Cu(I) restored protein activity. Also, the direct protein−protein conjugation without a chemical spacer did not appear to inhibit protein activity. Current work to increase conjugation efficiency while seeking to minimize the duration and concentration of Cu(I) exposure during CuAAC for Cu(I) sensitive applications is underway. A copper-less CuAAC could provide an effective solution for Cu(I) sensitive applications. By increasing the conjugation efficiency and expanding the technology to copper sensitive applications, the one-step linker-less conjugation provides an attractive technology to overcome the current conjugation limitations requiring (1) significant mutagensis to enable site-specific conjugation, (2) a chemical linker, and/or (3) multiple reactions with intermediate purifications.

The **1**- and **2**-incorporated proteins used for direct conjugation were produced using cell-free protein synthesis (CFPS) reactions. The CFPS environment was shown to be particularly useful when cellular uptake of an unnatural amino acid such as **1** might limit incorporation. This has led to a 27-fold improvement of protein incorporated with **1** compared to the highest reported yields for *in vivo* incorporation of **1** (*17*). Also, as demonstrated, direct access to the tRNA-charging and translation environment in the CFPS reaction allows the researcher to rapidly evaluate potential limitations to unnatural amino acid incorporation for optimization of product synthesis. Finally, insights gained from the CFPS system could potentially be used in developing a better *in vivo* system for incorporating unnatural amino acids.

ACKNOWLEDGMENT

We would like to thank the Zhenan Bao Lab at Stanford University, specifically Ying Jiang, for help with the synthesis of *p*-propargyloxyphenylalanine. The Christopher E. D. Chidsey Lab of Stanford University kindly supplied the tris-triazole ligand used to accelerate the CuAAC reaction. Kevin P. Kent and Steven G. Boxer of Stanford University kindly provided the gene encoding for sfGFP and *in vivo* produced sfGFP. Chris Adams and Theresa McLaughlin of the Vincent Coates Foundation Mass Spectrometry Laboratory, Stanford University (http://mass-spec.stanford.edu) performed the mass spectroscopy assays and analysis in this work.

Supporting Information Available: Plasmid and sfGFP sequences. Emission profile of sfGFP, pPaGFP, and pAzGFP. Mass spectra of **1** and digested pPaDHFR. *Mj*tRNA$^{Tyr}_{CUA}$ concentration estimate. This material is available free of charge via the Internet at http://pubs.acs.org.

LITERATURE CITED

(1) Hess, G. (2008) Generic biologics. *Chem. Eng. News 86*, 34–35.
(2) Hermanson, G. T. (2008) *Bioconjugate techniques*, 2nd ed., pp 745−1045, Academic Press, Boston.
(3) Esser-Kahn, A. P., and Francis, M. B. (2008) Protein-cross-linked polymeric materials through site-selective bioconjugation. *Angew. Chem., Int. Ed. Engl. 47*, 3751–3754.
(4) Antos, J. M., and Francis, M. B. (2006) Transition metal catalyzed methods for site-selective protein modification. *Curr. Opin. Chem. Biol. 10*, 253–262.
(5) Hermanson, G. T. (1996) *Bioconjugate Techniques*, 1st ed., pp 6−8, Academic Press, San Diego.
(6) Gilmore, J. M., Scheck, R. A., Esser-Kahn, A. P., Joshi, N. S., and Francis, M. B. (2006) N-terminal protein modification through a biomimetic transamination reaction. *Angew. Chem., Int. Ed. Engl. 45*, 5307–5311.
(7) Strable, E., Prasuhn, D. E., Jr., Udit, A. K., Brown, S., Link, A. J., Ngo, J. T., Lander, G., Quispe, J., Potter, C. S., Carragher, B., Tirrell, D. A., and Finn, M. G. (2008) Unnatural amino acid

incorporation into virus-like particles. *Bioconjugate Chem. 19*, 866–875.
(8) Wang, L., Brock, A., Herberich, B., and Schultz, P. G. (2001) Expanding the genetic code of *Escherichia coli*. *Science 292*, 498–500.
(9) Xie, J., and Schultz, P. G. (2006) A chemical toolkit for proteins--an expanded genetic code. *Nat. Rev. Mol. Cell. Biol. 7*, 775–782.
(10) Chin, J. W., Cropp, T. A., Anderson, J. C., Mukherji, M., Zhang, Z., and Schultz, P. G. (2003) An expanded eukaryotic genetic code. *Science 301*, 964–967.
(11) Liu, W., Brock, A., Chen, S., and Schultz, P. G. (2007) Genetic incorporation of unnatural amino acids into proteins in mammalian cells. *Nat. Methods 4*, 239–244.
(12) Goerke, A. R., and Swartz, J. R. (2009) High-level cell-free synthesis yields of proteins containing site-specific non-natural amino acids. *Biotechnol. Bioeng. 102*, 400–416.
(13) Wang, L., Xie, J., Deniz, A. A., and Schultz, P. G. (2003) Unnatural amino acid mutagenesis of green fluorescent protein. *J. Org. Chem. 68*, 174–176.
(14) Ryu, Y., and Schultz, P. G. (2006) Efficient incorporation of unnatural amino acids into proteins in *Escherichia coli*. *Nat. Methods 3*, 263–265.
(15) Iida, S., Asakura, N., Tabata, K., Okura, I., and Kamachi, T. (2006) Incorporation of unnatural amino acids into cytochrome c3 and specific viologen binding to the unnatural amino acid. *ChemBioChem 7*, 1853–1855.
(16) Deiters, A., and Schultz, P. G. (2005) In vivo incorporation of an alkyne into proteins in *Escherichia coli*. *Bioorg. Med. Chem. Lett. 15*, 1521–1524.
(17) Chen, S., Schultz, P. G., and Brock, A. (2007) An improved system for the generation and analysis of mutant proteins containing unnatural amino acids in *Saccharomyces cerevisiae*. *J. Mol. Biol. 371*, 112–122.
(18) O'Neil, M. J., Heckelman, P. E., Koch, C. B., and Roman, K. J., Eds. (2006) *The Merck Index: An Encyclopedia of Chemicals, Drugs, and Biologicals*, 14th ed., Merck & Co., Inc., Whitehouse Station, N.J.
(19) Wang, L., Zhang, Z., Brock, A., and Schultz, P. G. (2003) Addition of the keto functional group to the genetic code of *Escherichia coli*. *Proc. Natl. Acad. Sci. U.S.A. 100*, 56–61.
(20) Chin, J. W., Santoro, S. W., Martin, A. B., King, D. S., Wang, L., and Schultz, P. G. (2002) Addition of p-azido-L-phenylalanine to the genetic code of *Escherichia coli*. *J. Am. Chem. Soc. 124*, 9026–9027.
(21) Swartz, J. R., Jewett, M. C., and Woodrow, K. M. (2004) Cell-free protein synthesis with prokaryotic combined transcription-translation, in *Recombinant gene expression: reviews and protocols* (Balbas, P., and Lorence, A., Eds.) pp 169−182, Humana Press, Totowa, NJ.
(22) Kent, K. P., Childs, W., and Boxer, S. G. (2008) Deconstructing green fluorescent protein. *J. Am. Chem. Soc. 130*, 9664–9665.
(23) Deiters, A., Cropp, T. A., Mukherji, M., Chin, J. W., Anderson, J. C., and Schultz, P. G. (2003) Adding amino acids with novel reactivity to the genetic code of *Saccharomyces cerevisiae*. *J. Am. Chem. Soc. 125*, 11782–11783.
(24) Zawada, J., and Swartz, J. (2005) Maintaining rapid growth in moderate-density *Escherichia coli* fermentations. *Biotechnol. Bioeng. 89*, 407–415.
(25) Jewett, M. C., and Swartz, J. R. (2004) Mimicking the *Escherichia coli* cytoplasmic environment activates long-lived and efficient cell-free protein synthesis. *Biotechnol. Bioeng. 86*, 19–26.
(26) Abramoff, M. D., Magelhaes, P. J., and Ram, S. J. (2004) Image processing with ImageJ. *Biophoton. Int. 11*, 36–42.
(27) van Kasteren, S. I., Kramer, H. B., Jensen, H. H., Campbell, S. J., Kirkpatrick, J., Oldham, N. J., Anthony, D. C., and Davis, B. G. (2007) Expanding the diversity of chemical protein modification allows post-translational mimicry. *Nature 446*, 1105–1109.
(28) Scriven, E. F. V. (1984) *Azides and nitrenes: reactivity and utility*, Academic Press, Orlando, FL.
(29) Voloshin, A. M., and Swartz, J. R. (2008) Large Scale Batch Reactions for Cell-free Protein Synthesis, in *Cell-free Protein Synthesis: Methods and Protocols* (Spirin, A. S., and Swartz, J. R., Eds.) pp 207−236, Wiley-VCH Verlag GmbH & Co., Weinheim.
(30) Bundy, B. C., Franciszkowicz, M. J., and Swartz, J. R. (2008) Escherichia coli-based cell-free synthesis of virus-like particles. *Biotechnol. Bioeng. 100*, 28–37.
(31) Bonnefond, L., Giege, R., and Rudinger-Thirion, J. (2005) Evolution of the tRNA(Tyr)/TyrRS aminoacylation systems. *Biochimie 87*, 873–883.
(32) Boonyaratanakornkit, B. B., Simpson, A. J., Whitehead, T. A., Fraser, C. M., El-Sayed, N. M., and Clark, D. S. (2005) Transcriptional profiling of the hyperthermophilic methanarchaeon *Methanococcus jannaschii* in response to lethal heat and non-lethal cold shock. *Environ. Microbiol. 7*, 789–797.
(33) Underwood, K. A., Swartz, J. R., and Puglisi, J. D. (2005) Quantitative polysome analysis identifies limitations in bacterial cell-free protein synthesis. *Biotechnol. Bioeng. 91*, 425–435.
(34) Kolb, H. C., Finn, M. G., and Sharpless, K. B. (2001) Click chemistry: diverse chemical function from a few good reactions. *Angew. Chem. Int. Ed. Engl. 40*, 2004–2021.
(35) Tornoe, C. W., Christensen, C., and Meldal, M. (2002) Peptidotriazoles on solid phase: [1,2,3]-triazoles by regiospecific copper(i)-catalyzed 1,3-dipolar cycloadditions of terminal alkynes to azides. *J. Org. Chem. 67*, 3057–64.
(36) Hong, V., Udit, A. K., Evans, R. A., and Finn, M. G. (2008) Electrochemically protected copper(I)-catalyzed azide-alkyne cycloaddition. *ChemBioChem 9*, 1481–1486.
(37) Lutz, J. F. (2008) Copper-free azide-alkyne cycloadditions: new insights and perspectives. *Angew. Chem., Int. Ed. Engl. 47*, 2182–2184.
(38) Link, A. J., and Tirrell, D. A. (2003) Cell surface labeling of Escherichia coli via copper(I)-catalyzed [3 + 2] cycloaddition. *J. Am. Chem. Soc. 125*, 11164–11165.
(39) Jung, K., Park, J., Maeng, P. J., and Kim, H. (2005) Fluorescence quenching of green fluorescent protein. *Bull. Korean Chem. Soc. 26*, 413–417.
(40) Prescher, J. A., and Bertozzi, C. R. (2005) Chemistry in living systems. *Nat. Chem. Biol. 1*, 13–21.
(41) Baskin, J. M., Prescher, J. A., Laughlin, S. T., Agard, N. J., Chang, P. V., Miller, I. A., Lo, A., Codelli, J. A., and Bertozzi, C. R. (2007) Copper-free click chemistry for dynamic in vivo imaging. *Proc. Natl. Acad. Sci. U.S.A. 104*, 16793–16797.

BC9002844

Modification of Porous Protein Crystals in Development of Biohybrid Materials

Tomomi Koshiyama,[†] Naomi Kawaba,[§] Tatsuo Hikage,[‡] Masanobu Shirai,[†] Yuki Miura,[§] Cheng-Yuan Huang,[||] Koichiro Tanaka,[†] Yoshihito Watanabe,[||] and Takafumi Ueno*[,†,⊥]

Institute for Integrated Cell-Material Sciences (iCeMS), Funai Center, Kyoto University Katsura, Nishikyo-ku, Kyoto 615-8510, Japan, Department of Chemistry, Graduate School of Science, High Intensity X-ray Diffraction Laboratory, and Research Center for Materials Science, Nagoya University, Furo-cho, Chikusa-ku, Nagoya 464-8602, Japan, PRESTO, Japan Science and Technology Agency (JST), Honcho Kawaguchi, Saitama 332-0012, Japan. Received July 11, 2009; Revised Manuscript Received December 22, 2009

Protein assemblies have attracted increasing attention for construction of biohybrid materials. Protein crystals can also be regarded as solid protein assemblies. The present work demonstrates that protein crystals can be employed as porous biomaterials by site-specific modifications of the crystals of recombinant sperm whale myoglobin mutants. The myoglobin crystals of space group *P*6 provide hexagonal pores consisting of the building blocks of six Mb molecules, which form a pore with a diameter of 40 Å. On the basis of the lattice structure of the Mb crystals, we have selected appropriate residues located on the surface of the pores for replacement with cysteine. This enables modification of the pore surface via coupling with maleimide derivatives. We have succeeded in crystallizing the modified Mb mutants, retaining the *P*6 lattice, and consistently aligning nanosized functional molecules such as fluorescein, eosin, and $Ru(bpy)_3$ into the hexagonal pores of the Mb crystals. Our strategy for site-specific modification of protein crystal pores is applicable to various protein crystals with porous structures. We believe that modified porous protein crystals will provide attractive candidates for novel solid materials in nanotechnology applications.

INTRODUCTION

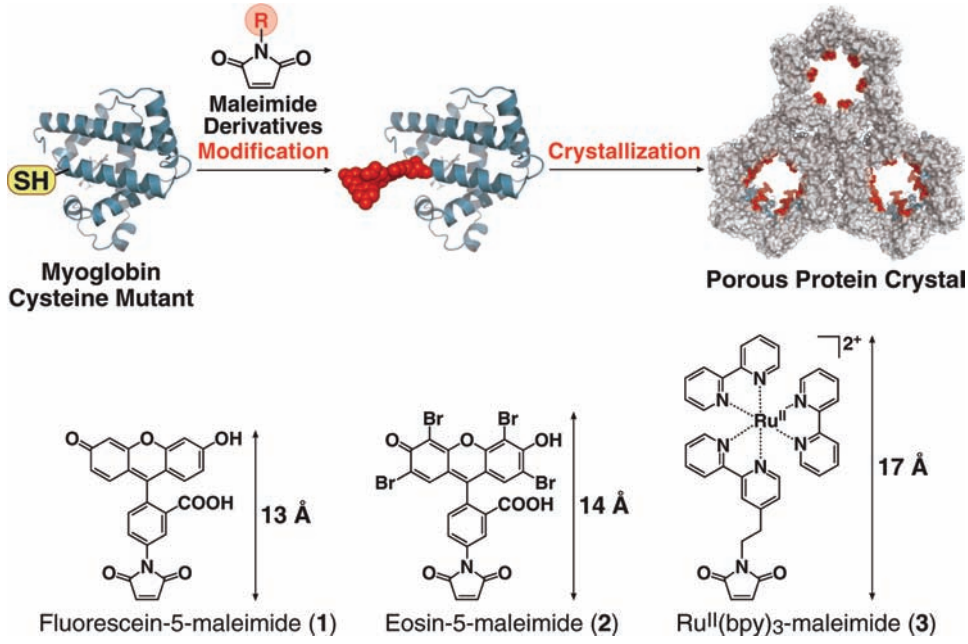
It has been recently recognized that the design of protein assemblies holds promise for construction of biohybrid materials which have the potential to play crucial roles in the field of biotechnology (*1–8*). Efforts to modify nanosized space of caged, tubular, and two-dimensional protein assemblies have recently attracted increasing attention because nanospaces are expected to provide sufficient space to accommodate large and complex functional molecules for biotechnological applications (*3, 6, 8–13*). Protein crystals can also be regarded as solid protein assemblies. Malgolin et al. have indicated that protein crystals consist of highly ordered protein assemblies with unique nanosized porous structures (*14, 15*). The protein crystals comprise solvent-filled pores ranging from 30% to 65% of the total crystal volume with the advantageous properties of high porosity (0.5−0.8), large surface area (800−2000 m^2/g), and a wide range of pore sizes (20−100 Å). These properties comparable to typical porous materials suggest that pores of protein crystals are able to provide enough spaces to promote various reactions (*15–17*).

Protein crystals are able to serve as heterogeneous catalysts even under extreme conditions including high temperature, organic solvents, and extreme acidity or basicity when stabilized by cross-linkages (*14*). A recent report has described that soaking of cross-linked virus crystals in a buffer solution containing metal ions causes the metal ions to be deposited within the porous spaces of the crystals and converted into metallic materials in the presence of reducing reagents (*18*). It has been recognized that transport of water, ions, and organic molecules in protein channels are crucial processes in various biological reactions. Experimental and theoretical studies of diffusion and absorption of small molecules in porous protein crystals have been reported (*19, 20*). These reports suggest that porous protein crystals may be useful as biohybrid materials if the pore surfaces could be selectively modified by a combination of site-directed mutagenesis and bioconjugation techniques. However, there have been no reports of modification of the pore surfaces of porous protein crystals because the consensus has been that even small a amount of modified proteins (<10 mol %) would have serious effects on the nucleation process and the quality of the crystals (*21*). In order to overcome these problems, we demonstrate site-specific modifications of the porous protein crystals of recombinant sperm whale myoglobin (Mb) mutants by a cysteine−maleimide coupling reaction as shown in Scheme 1 (*22, 23*). The Mb crystals belong to space group *P*6 and provide hexagonal pores consisting of six Mb molecules, which provide a pore with a diameter of 40 Å (Figure 1) (*22*). On the basis of the lattice structure of the Mb crystal, we selected appropriate residues on the surface of the pores for replacement with cysteine to modify the pore surface by the coupling reaction with maleimide derivatives. This is necessary because Mb does not have any natural cysteine residues (*22*). We have succeeded in crystallizing the modified Mb mutants which retain the *P*6 lattice and have reproducibly aligned functional molecules into the hexagonal channels of the Mb crystals. We have characterized the structures and the properties

* Institute for Integrated Cell-Material Sciences (iCeMS), Funai Center, Kyoto University, Katsura, Nishikyo-ku, Kyoto 615-8510, Japan. Tel/Fax: +81-75-383-2812. E-mail: taka@icems.kyoto-u.ac.jp.
[†] iCeMS, Kyoto University.
[§] Department of Chemistry, Graduate School of Science, Nagoya University.
[‡] High Intensity X-ray Diffraction Laboratory, Nagoya University.
[||] Research Center for Materials Science, Nagoya University.
[⊥] PRESTO, Japan Science and Technology Agency (JST).

10.1021/bc9003052 © 2010 American Chemical Society
Published on Web 01/25/2010

Scheme 1. Schematic Representations of the Arrangement of Functional Molecules in the Hexagonal Pores of the Mb Crystal and the Molecular Structures of the Maleimide Derivatives



of functional molecules aligned in the channels of the Mb crystals by X-ray structural analysis and microscopic spectroscopy.

EXPERIMENTAL PROCEDURES

Materials. Reagents were purchased from Molecular Probes, Nacalai Tesque, Wako, TCI, Sigma-Aldrich, and Hampton Research and used without further purification. Synthesis of Ru^{II}(bpy)$_3$-maleimide (**3**) is described in Supporting Information.

Modification of Mb Cysteine Mutants with Maleimide Derivatives. Myoglobin cysteine mutant genes were prepared using a Stratagene Quikchange Multi Site kit. The expression and purification of proteins were performed as reported previously (*24*). DMF solution of 5 equiv maleimide derivative was added to a solution of Mb cysteine mutant in 10 mM Tris−HCl pH 7.0. The reaction mixture was stirred at 18 °C for 2 h in the dark. The mixture was centrifuged and passed through Sephadex G-25 equilibrated with 15 mM potassium phosphate pH 6.0. The resulting solution was loaded onto a CM52 column on an ÄKTA explorer 10S FPLC system (GE Healthcare). The protein was eluted with a linear gradient of 15 mM potassium phosphate buffer (pH 6.0) and 30 mM potassium phosphate buffer (pH 9.0). The protein concentration of samples was determined by the pyridine hemochromogen method (*25*). The concentration of **1** was estimated by measuring the absorbance at 493 nm (extinction coefficient 83 000 cm^{-1} M^{-1}) (Supporting Information Figure S1).

Crystallization of Mbs Modified with Maleimide Derivatives. Crystallization of Mbs modified with maleimide derivatives was carried out as described previously (*22*). The purified protein in 10 mM potassium phosphate buffer (pH 7.5) was concentrated to 30 mg/mL. Crystals were obtained using the sitting-drop vapor diffusion method. A 2 μL protein solution was added to a 4 μL reservoir solution (2.5−2.7 M ammonium sulfate in 20 mM Tris/HCl pH 9.0) and equilibrated against a 1000 μL reservoir solution. The hexagonal crystals grew within one week (0.15 × 0.15 × 0.05 mm^3). The X-ray data collection and crystallographic refinement are described in the Supporting Information. The coordinate of **1**·K102CMb has been deposited in the Protein Data Bank under accession codes of 3A2G.

Soaking of WTMb Crystals in the Mother Liquid Buffer Containing Uranine and Eosin Y. WTMb crystals were placed in mother liquor of crystallization (2.5 M ammonium sulfate in 20 mM Tris/HCl pH 9.0) containing dye molecules for 16 h at 4 °C. Then, the crystals were soaked in solution of 2.5 M

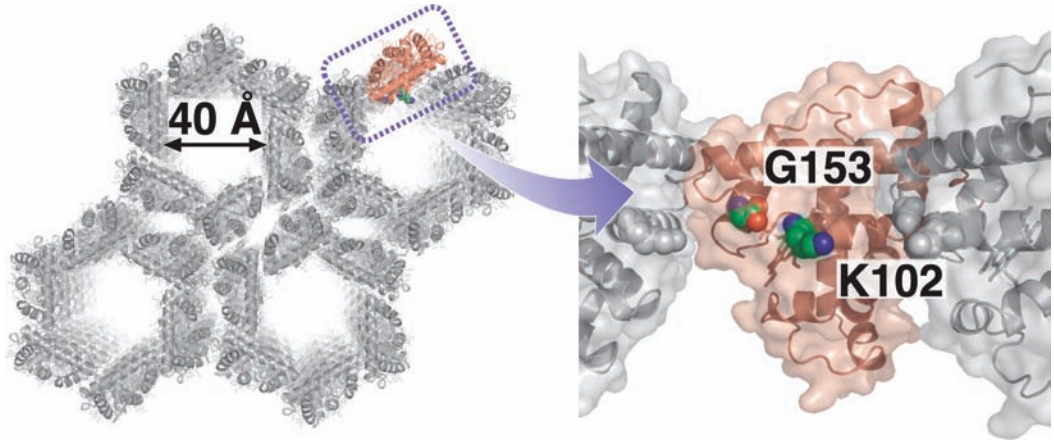


Figure 1. Positions of K102 and G153 replaced with cysteine residues (CPK model) viewed from the 6-fold axis (PDB: 2MBW).

Table 1. Summary of X-ray Data Collection and Refinement Statistic for 1•K102CMb, 2•K102CMb, 3•K102CMb, and 1•G153CMb

	1•K102CMb	**2**•K102CMb	**3**•K102CMb	**1**•G153CMb
Space group	*P*6	*P*6	*P*6	*P*6
Unit cell, Å				
a (Å)	90.4	90.5	90.4	90.4
b (Å)	90.4	90.5	90.4	90.4
c (Å)	45.3	45.3	45.2	45.3
resolution range[a]	30−1.75 (1.81−1.75)	30−1.79 (1.85−1.79)	30−1.35 (1.40−1.35)	30−1.40 (1.45−1.40)
X-ray wavelength, Å	1	1	1	1
completeness (%)[a]	100 (99.9)	100 (100)	99.9 (99.3)	99.9 (99.4)
R_{merge} (%)[a,b]	9.2 (30.4)	7.5 (30.1)	5.1 (30.1)	5.3 (30.8)
I/σ (*I*)[a]	30.0 (5.4)	22.4 (4.3)	32.1 (3.0)	30.7 (3.7)
R-factor (%)[c]	17.8	18.1	18.0	18.4
R_{free} (%)[d]	19.7	21.6	19.3	19.4
rms diviation from ideality				
bonds (Å)	0.011	0.012	0.006	0.007
angle (°)	1.3	1.1	1	1.1

[a] Values in parentheses are for the highest-resolution shell. [b] $R_{merge} = \Sigma|I - \langle I\rangle|/\Sigma I$, where I is the integrated intensity of a given reflection. [c] $R = \Sigma||F_o| - |F_c||/\Sigma|F_o|$, where F_o and F_c are the observed and calculated structure factor amplitudes, respectively. [d] R_{free}: an *R* factor calculated on a partial set that is not used in the refinement of the structure.

ammonium sulfate in 20 mM Tris/HCl pH 9.0 for 3 days at 4 °C. The soaking solution was changed two times during this process.

Time-Resolved Luminescence Spectroscopy in Single Protein Crystal of 3•K102CMb. A specialized microspectrophotometer was constructed to measure time-resolved spectra in single protein crystals. A crystal was briefly immersed in a cryoprotectant solution that consisted of 20% (v/v) glycerol and 2.6 M ammonium sulfate in 20 mM Tris/HCl pH 9.0. Then, the crystal was mounted to a Mounted CryoLoop and set in a helium chamber at 100 K. The crystal was excited with 355 nm (0.15 mJ/cm^2, 4 ns laser pulse) generated from a Q-switched Nd:YAG laser (Quantel Brilliant). The emission decay of excited state of **3** in **3**•K102CMb crystals was monitored at 580 nm.

Physical Measurements. UV−vis spectra were recorded on a Shimadzu UV-3101PC UV/vis spectrophotometer. ESI-TOF mass spectra were measured on a LCT-Premier XE (Waters, UK) and CsI (1 mg/mL) in 50% H_2O/CH_3CN was used for mass scale calibration. All samples were dialyzed against 5 mM ammonium acetate buffer at 4 °C. Fluorescence measurements were obtained on a F-7000 fluorescence spectrophotometer (Hitachi) at 12 °C in 20 mM Tris-HCl pH 9.0. A specialized microspectrophotometer was constructed to measure UV−vis and fluorescence spectra in single crystals (Bunkoh-keiki Co., LTD). Thin protein crystals (0.15 × 0.15 × 0.01 mm^3) were used for the measurements.

RESULTS AND DISCUSSION

We replaced Lys102 and Gly153 with cysteine residues because these residues (i) do not participate in intermolecular interactions in the crystal and (ii) are exposed to the internal surface of the hexagonal pores in spite of size and hydrophobicity of the residues (Figure 1). Thus, two cysteine mutants, K102CMb and G153CMb, were prepared for conjugation with functional molecules on the interior surface of the hexagonal pores in the Mb crystal lattice. To elucidate the effects of hydrophobicity, charge, and size of functional molecules on the crystal formation of the Mb mutants, fluorescein-5-maleimide (**1**) and eosin-5-maleimide (**2**) were selected (Scheme 1). These compounds have different hydrophobicity. Since fluorescent molecules are known to be very sensitive to the surrounding environment, marked changes in their absorption and fluorescence spectra would be expected if the molecules interact with each other (*26*). Furthermore, $Ru^{II}(bpy)_3$-maleimide (**3**), which has a positive charge, was chosen to estimate the effects of charge and larger size (17 Å) on the modification of the pores (Scheme 1).

In order to modify K102CMb with **1**, a DMF solution of **1** was added to a buffer solution of K102CMb at pH 7.0 as previously reported (*23*). After stirring for 2 h at 18 °C, the mixture was purified by column chromatography (G-25 and CM-52). **1**•K102CMb was obtained with an isolated yield of 33%. The UV/vis spectrum of **1**•K102CMb has two peaks at 409 and 493 nm, which originate from the Soret band of Fe(III)-heme and the fluorescein molecule, respectively, in a 1:1 ratio, as estimated from their extinction coefficients (see Supporting Information Figure S1). The ESI-TOF mass spectrum of purified **1**•K102CMb has a peak assignable to **1**•K102CMb (measured: 18 348 Da, calcd: 18 348 Da) (see Supporting Information Figure S2). The modification site of **1**•K102CMb was confirmed by the MALDI-TOF-MS spectra of the **1**•K102CMb fragments digested with Lys-C *Achromobacter* and chymotrypsin after purification with a reverse-phase HPLC (see Supporting Information). These results indicate that K102CMb is conjugated with **1**. The other conjugates, **2**• and **3**•K102CMb and **1**•G153CMb, were prepared under the same conditions. The ESI-TOF mass spectra of **2**•K102CMb, **3**•K102CMb, and **1**•G153CMb indicate molecular weights of 18 664 Da (calcd: 18 663 Da), 18 612 Da (calcd: 18 613 Da), and 18 419 Da (calcd: 18 419 Da), respectively.

Crystallization of the purified **1**•, **2**•, and **3**•K102CMbs and **1**•G153CMb was carried out according to a previously reported method for recombinant sperm-whale myoglobin (*22*). The crystal structures of **1**•, **2**•, and **3**•K102CMb and **1**•G153CMb were refined to resolutions of 1.75, 1.79, 1.35, and 1.40 Å, respectively, with the space group *P*6 (Table 1). The root-mean-square deviations (rmsds) for C_αs from WTMb were 0.34, 0.26, 0.34, and 0.52 for **1**, **2**, and **3**•K102CMb and **1**•G153CMb, respectively (*22*). The results indicate that perfect modification of the pore surfaces of the *P*6 lattice Mb crystals has been achieved by crystallization of the modified Mb mutants.

The electron density map of **1**•K102CMb indicates a clear $2|F_o| - |F_c|$ electron density at the K102C residue. This is consistent with the presence of two conformations of the maleimide moiety of **1** (Figure 2a). The electron density maps of **2**• and **3**•K102CMb showed that $2|F_o| - |F_c|$ electron densities appear immediately above the sulfur atoms of the cysteine residues at position 102 as observed in **1**•K102CMb, while these densities were too low to fit the models of **2** and **3** (Figure 2b,c). We could not determine the exact location of the G153C residue modified with **1** because the electron density of residues 151−153 is disordered as shown in Figure 2d. In addition, relative to WTMb, conformational changes of the residues surrounding the fluorescent moieties were not observed. These results suggest that the functional moieties can be oriented in

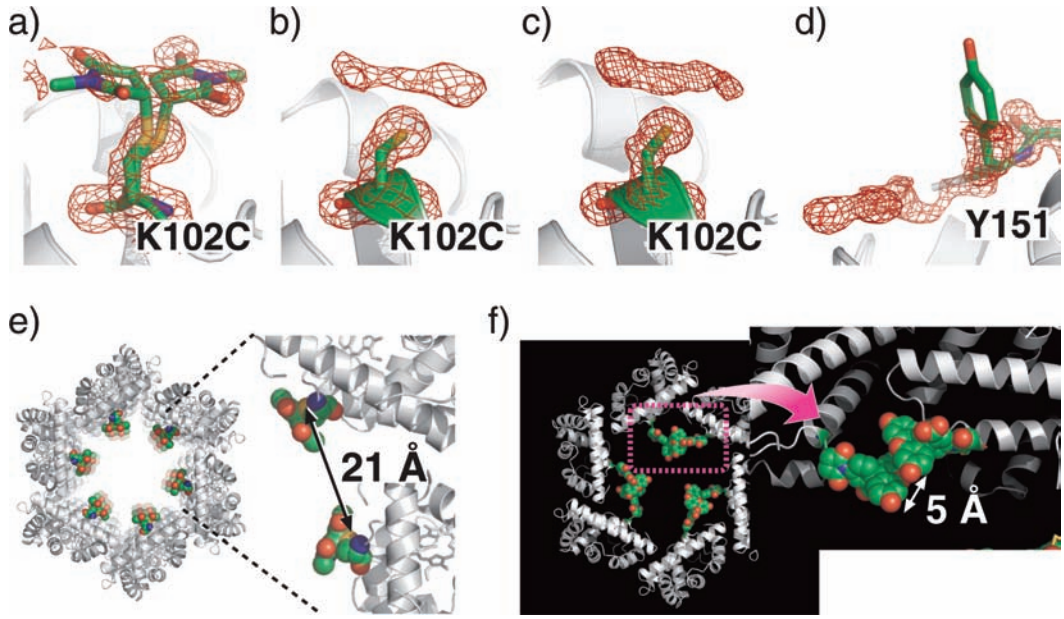


Figure 2. Crystal structures of (a) **1**•K102CMb, (b) **2**•K102CMb, (c) **3**•K102CMb, and (d) **1**•G153CMb. Close-up views of the K102C and the G153C residues with the $2|F_o| - |F_c|$ electron density at the modified cysteine residues at the 1 σ level are shown in red. (e) Crystal packing diagram of **1**•K102CMb. The distance between two cysteinyl sulfur atoms at position 102 of two adjacent Mb molecules is indicated by the arrow. (f) Proposed structure of fluorescein dimers fixed in the hexagonal pores of **1**•K102CMb.

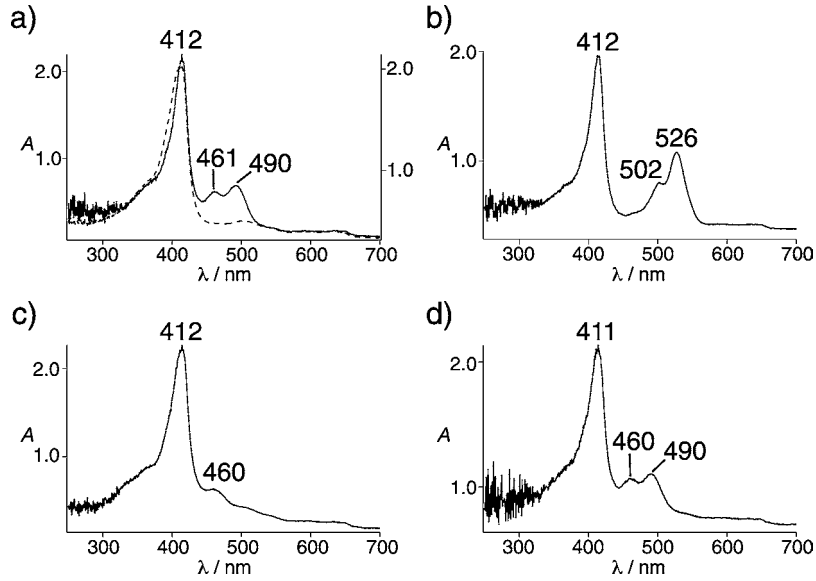


Figure 3. UV/vis spectra of the crystals of (a) **1**•K102CMb (solid line) and WTMb (dashed line), (b) **2**•K102CMb, (c) **3**•K102CMb, and (d) **1**•G153CMb.

several directions at the conjugation sites, regardless of their hydrophobicity, charge, and size, because they are not involved in any specific interactions with nearby residues.

In order to evaluate the environment in the proximity of **1**, the absorption spectra of **1**•K102CMb and **1**•G153CMb were measured in the crystal state (Figure 3). The absorption spectrum of the crystal of **1**•K102CMb has three absorption maxima at 412, 461, and 490 nm (Figure 3a), while **1**•K102CMb in solution has two absorption maxima at 409 and 493 nm derived from heme and the **1** moiety, respectively (Supporting Information Figure S1). The Soret bands at 412 nm in the crystal state and 409 nm in solution indicate that the coordination structure of the five-coordinate high-spin Fe(III)-heme in solution is retained in the crystals (*27*). The new peaks at ca. 460 nm of **1**•K102CMb and **1**•G153CMb were exclusively observed in the crystal state due to the formation of a ground-state complex (H-type dimer) of the fluorescein moieties (Figure 3a,d) (*28*). In the **1**•K102CMb crystal pore, the fluorescein moieties, which are conjugated to cysteine residues, appear to form an H-type dimer in parallel planes placed at a distance of ca. 5 Å as shown in Figure 2f (*28*), even though the distance between the two sulfur atoms of cysteine 102 residues on adjacent Mb molecules is 21 Å (Figure 2e). This is a somewhat unexpected result in light of a previous report of an undecapeptide with two fluorescein molecules conjugated to two amines whose nitrogen atoms are separated by a distance of 13.6 Å (*29, 30*). In this molecule, the fluorescein moieties are unable to form a dimer in solution due to the small dimerization constant of fluorescein and the relative flexibility of the undecapeptide (*29, 30*). Our observations of **1**•K102CMb indicate that even the small dimerization constant of fluorescein is enough to facilitate the formation of the dimer within the Mb crystal pore. Moreover, upon soaking the K102CMb crystals in the mother liquid buffer containing 10 mM fluorescein sodium salt for 16 h, only 0.01 free-fluorescein molecule/Mb was

observed to remain inside the pore space without dimer formation after several instances of equilibration with the mother liquid buffer without the fluorescein salt. These results indicate that the covalent conjugation of **1** into the Mb crystal pores restricts the orientation of the fluorescein moieties. Thus, the double conformation of **1** in **1**•K102CMb (Figure 2a) appears to be caused by the dimer formation with the **1** moiety of the other Mb molecule, which is in parallel orientation in the Mb crystal pores as shown in Figure 2f (*28*, *31*). The dimer formation of **1** in **1**•G153CMb crystals appears to be due to the restricted mobility of the peptide fragment (151−153) conjugated with the **1** moiety in the pore space despite the disorder of the fragment (Figure 2d).

It is also concluded that the eosin moiety (**2**) in the **2**•K102CMb crystal forms the H-type dimer structure which is similar to **1** in the **1**•K102CMb crystal (Figure 2f). Evidence for this assignment is provided by the characteristic absorption peaks at 502 and 526 nm (Figure 3b) (*30*). These results suggest that, when the fluorescent moieties are conjugated at the appropriate positions of the Mb crystal pores, they are able to accumulate and form dimers regardless of the hydrophobicity of the fluorescent molecules. The absorption peak at 460 nm of **3**•K102Mb shows that the coordination structure of $Ru^{II}(bpy)_3$ is retained within the pore (Figure 3c) (*26*). The $Ru^{II}(bpy)_3$ complex in the **3**•K102CMb crystal exhibits an emission peak at 580 nm with excitation at 355 nm. The emission decay of the excited state of **3** (^{3}MLCT) in the **3**•K102CMb crystal exhibits two components with short (1.6 μs, 66%) and long (10.4 μs, 33%) emission lifetimes at 100 K. These components are assignable to the bimolecular (triplet−triplet annihilation) and monomolecular reactions of ^{3}MLCT of **3**, respectively, as observed in the $[Ru^{II}(bpy)_3]^{2+}$ in micelles or the crystal state (*32*, *33*). The predominant bimolecular reaction suggests that $[Ru^{II}(bpy)_3]^{2+}$ complexes are closely packed with each other in the **3**•K102CMb crystal, although we expect that **3** cannot form a dimer structure in the pores of the Mb crystals because the dimer of $[Ru(bpy)_3]^{2+}$ molecules is not observed even if they are densely packed in the crystal state of $[Ru(bpy)_3](PF_6)_2$ (*34*).

In conclusion, we have succeeded in accumulating nanosized functional molecules into the hexagonal pores of Mb crystals with high efficiency by crystallization of Mb mutants covalently conjugated to extrinsic functional molecules. The results demonstrate that the process of crystallization of the modified Mb mutants is not affected by hydrophobicity or charge state of the functional molecules when conjugated to the specifically designed Mb sites. Moreover, this method provides for fixation of molecules which cannot be absorbed by soaking techniques, into the Mb crystal pores. Our strategy for site-specific modification of protein crystal pores is applicable to various protein crystals with porous structures. We believe that modified porous protein crystals will provide attractive candidates for novel solid materials in nanotechnology applications.

ACKNOWLEDGMENT

We thank the members of BL38B1 of SPring-8 for assistance during the diffraction data collection. Grant-in-Aid for Scientific Research (grant no. 1865504 for T.U.) from the Ministry of Education, Culture, Sports, Science and Technology, Japan, and PRESTO, JST. Synchrotron radiation experiments were conducted under the approval of 2008A1124, 2008B1301, and 2009A1185 at SPring-8.

Supporting Information Available: Synthesis of $Ru^{II}(bpy)_3$-maleimide, digestion analysis, and X-ray data collection and crystallographic refinement. This material is available free of charge via the Internet at http://pubs.acs.org.

LITERATURE CITED

(1) Mirkin, C. A., and Niemeyer, M. (2007) Nanobiotechnology II: More Concepts and Applications, Wiley-VCH, Weinheim.
(2) Niemeyer, C. M. (2001) Nanoparticles, proteins, and nucleic acids: Biotechnology meets materials science. *Angew. Chem., Int. Ed. 40*, 4128–4158.
(3) Uchida, M., Klem, M. T., Allen, M., Suci, P., Flenniken, M., Gillitzer, E., Varpness, Z., Liepold, L. O., Young, M., and Douglas, T. (2007) Biological containers: Protein cages as multifunctional nanoplatforms. *Adv. Mater. 19*, 1025–1042.
(4) Yeates, T. O., and Padilla, J. E. (2002) Designing supramolecular protein assemblies. *Curr. Opin. Struct. Biol. 12*, 464–470.
(5) Channon, K., Bromley, E. H. C., and Woolfson, D. N. (2008) Synthetic biology through biomolecular design and engineering. *Curr. Opin. Struct. Biol. 18*, 491–498.
(6) Ringler, P., and Schulz, G. E. (2003) Self-assembly of proteins into designed networks. *Science 302*, 106–109.
(7) Carlson, J. C. T., Jena, S. S., Flenniken, M., Chou, T. F., Siegel, R. A., and Wagner, C. R. (2006) Chemically controlled self-assembly of protein nanorings. *J. Am. Chem. Soc. 128*, 7630–7638.
(8) Carette, N., Engelkamp, H., Akpa, E., Pierre, S. J., Cameron, N. R., Christianen, P. C. M., Maan, J. C., Thies, J. C., Weberskirch, R., Rowan, A. E., Nolte, R. J. M., Michon, T., and Van Hest, J. C. M. (2007) A virus-based biocatalyst. *Nat. Nanotechnol. 2*, 226–229.
(9) Wang, Q., Lin, T. W., Tang, L., Johnson, J. E., and Finn, M. G. (2002) Icosahedral virus particles as addressable nanoscale building blocks. *Angew. Chem., Int. Ed. 41*, 459–462.
(10) Hooker, J. M., Kovacs, E. W., and Francis, M. B. (2004) Interior surface modification of bacteriophage MS2. *J. Am. Chem. Soc. 126*, 3718–3719.
(11) Abedin, M. J., Liepold, L., Suci, P., Young, M., and Douglas, T. (2009) Synthesis of a cross-linked branched polymer network in the interior of a protein cage. *J. Am. Chem. Soc. 131*, 4346–4354.
(12) Howorka, S., Cheley, S., and Bayley, H. (2001) Sequence-specific detection of individual DNA strands using engineered nanopores. *Nat. Biotechnol. 19*, 636–639.
(13) Ueno, T. (2008) Functionalization of viral protein assemblies by self-assembly reactions. *J. Mater. Chem. 18*, 3741–3745.
(14) Margolin, A. L., and Navia, M. A. (2001) Protein crystals as novel catalytic materials. *Angew. Chem., Int. Ed. 40*, 2205–2222.
(15) Vilenchik, L. Z., Griffith, J. P., St Clair, N., Navia, M. A., and Margolin, A. L. (1998) Protein crystals as novel microporous materials. *J. Am. Chem. Soc. 120*, 4290–4294.
(16) Matthews, B. W. (1968) Solvent content of protein crystals. *J. Mol. Biol. 33*, 491–497.
(17) Kitagawa, S., Kitaura, R., and Noro, S. (2004) Functional porous coordination polymers. *Angew. Chem., Int. Ed. 43*, 2334–2375.
(18) Falkner, J. C., Turner, M. E., Bosworth, J. K., Trentler, T. J., Johnson, J. E., Lin, T. W., and Colvin, V. L. (2005) Virus crystals as nanocomposite scaffolds. *J. Am. Chem. Soc. 127*, 5274–5275.
(19) Cvetkovic, A., Straathof, A. J. J., Krishna, R., and van der Wielen, L. A. M. (2005) Adsorption of xanthene dyes by lysozyme crystals. *Langmuir 21*, 1475–1480.
(20) Hu, Z. Q., and Jiang, J. W. (2008) Molecular dynamics simulations for water and ions in protein crystals. *Langmuir 24*, 4215–4223.
(21) Takahashi, D., Nishimoto, E., Murase, T., and Yamashita, S. (2008) Protein-protein interaction on lysozyme crystallization revealed by rotational diffusion analysis. *Biophys. J. 94*, 4484–4492.
(22) Phillips, G. N., Arduini, R. M., Springer, B. A., and Sligar, S. G. (1990) Crystal-structure of myoglobin from a synthetic gene. *Proteins Struct. Funct. Genet. 7*, 358–365.
(23) Hermanson, G. T. (1996) *Bioconjugate Techniques*, Academic Press, San Diego.

(24) Springer, B. A., Egeberg, K. D., Sligar, S. G., Rohlfs, R. J., Mathews, A. J., and Olson, J. S. (1989) Discrimination between oxygen and carbon-monoxide and inhibition of autooxidation by myoglobin - site-directed mutagenesis of the distal histidine. *J. Biol. Chem. 264*, 3057–3060.

(25) Paul, K. G., Theorell, H., and Akeson, A. (1953) The molar light absorption of pyridine ferroprotoporphyrin (pyridine haemochromogen). *Acta Chem. Scand. 7*, 1284–1287.

(26) Lakowicz, J. R. (2006) *Principles of Fluorescence Spectroscopy*, 3rd ed. pp 277–330 and pp 683–687, Springer, Berlin.

(27) Springer, B. A., and Sligar, S. G. (1987) High-level expression of sperm whale myoglobin in escherichia-coli. *Proc. Natl. Acad. Sci. U.S.A. 84*, 8961–8965.

(28) Arbeloa, I. L. (1981) Dimeric and trimeric states of the fluorescein dianion 0.1. molecular-structures. *J. Chem. Soc., Faraday Trans. II 77*, 1725–1733.

(29) Packard, B. Z., Komoriya, A., Nanda, V., and Brand, L. (1998) Intramolecular excitonic dimers in protease substrates: Modification of the backbone moiety to probe the H-dimer structure. *J. Phys. Chem. B 102*, 1820–1827.

(30) Packard, B. Z., Komoriya, A., Toptygin, D. D., and Brand, L. (1997) Structural characteristics of fluorophores that form intramolecular H-type dimers in a protease substrate. *J. Phys. Chem. B 101*, 5070–5074.

(31) Rohatggi, K. K., and Mukhopadhyay, A. K. (1972) Hypochromism and exciton interaction in halofluorescein dyes. *J. Phys. Chem. 76*, 3970–3973.

(32) Lachish, U., Ottolenghi, M., and Rabani, J. (1977) Triplet-triplet annihilation of $Ru(bpy)_3^{2+}$ in micelle solutions. *J. Am. Chem. Soc. 99*, 8062–8063.

(33) Ikeda, N., Yoshimura, A., Tsushima, M., and Ohno, T. (2000) Hopping and annihilation of 3MLCT in the crystalline solid of $[Ru(bpy)_3]X_2$ ($X = Cl^-$, ClO_4^- and PF_6^-). *J. Phys. Chem. A 104*, 6158–6164.

(34) Biner, M., Bürgi, H. B., Ludi, A., and Röhr, C. (1992) Crystal and molecular structures of $[Ru(bpy)_3](PF_6)_3$ and $[Ru(bpy)_3](PF_6)_2$ at 105 K. *J. Am. Chem. Soc. 114*, 5197–5203.

BC9003052

Synthesis and Evaluation of a Near-Infrared Fluorescent Non-Peptidic Bivalent Integrin $\alpha_v\beta_3$ Antagonist for Cancer Imaging

Feng Li,[†] Jiacheng Liu,[†] Gouri S. Jas,[‡] Jiawei Zhang,[†] Guoting Qin,[†] Jiong Xing,[†] Claudia Cotes,[†] Hong Zhao,[†] Xukui Wang,[†] Laura A. Diaz,[†] Zheng-Zheng Shi,[†] Daniel Y. Lee,[†] King C. P. Li,[†] and Zheng Li*[,†]

Department of Radiology, The Methodist Hospital Research Institute, 6565 Fannin Street, B5-022, Houston, Texas 77030, and Department of Chemistry, Biochemistry, and Institute of Biomedical Studies, Baylor University Sciences Building, Room C322, Baylor University, 101 Bagby Avenue, Waco, Texas 76706. Received July 14, 2009; Revised Manuscript Received December 22, 2009

Computer modeling approaches to identify new inhibitors are essentially a very sophisticated and efficient way to design drugs. In this study, a bivalent nonpeptide intergrin $\alpha_v\beta_3$ antagonist (bivalent IA) has been synthesized on the basis of an in silico rational design approach. A near-infrared (NIR) fluorescent imaging probe has been developed from this bivalent compound. *In vitro* binding assays have shown that the bivalent IA ($IC_{50} = 0.40 \pm 0.11$ nM) exhibited improved integrin $\alpha_v\beta_3$ affinity in comparison with the monovalent IA ($IC_{50} = 22.33 \pm 4.51$ nM), resulting in an over 50-fold improvement in receptor affinity. NIR imaging probe, bivalent-IA-Cy5.5 conjugate, also demonstrated significantly increased binding affinity ($IC_{50} = 0.13 \pm 0.02$ nM). Fluorescence microscopy studies showed integrin-mediated endocytosis of bivalent-IA-Cy5.5 in U87 cells which was effectively blocked by nonfluorescent bivalent IA. We also demonstrated tumor accumulation of this NIR imaging probe in U87 mouse xenografts.

INTRODUCTION

Integrins, a family of cell adhesion molecules, are involved in a wide range of cell−extracellular matrix (ECM) and cell−cell interactions (*1*, *2*). Up to now, 18 α and 8 β subunits have been described, which assemble into 24 different receptors (*3*). Among them, integrin $\alpha_v\beta_3$ has been intensively studied due to its important role in tumor angiogenesis and tumor metastasis. It is highly expressed on activated tumor endothelial cells and fast-growing tumor cells but not resting endothelial cells and normal organs; the receptor is therefore suggested as a molecular target for tumor therapy and imaging. Targeting $\alpha_v\beta_3$ by directly inhibiting its function is potentially an effective strategy for cancer treatment. Cyclic arginine-glycine-aspartic acid (RGD) peptide, Vitaxin (MedImmune), and cilengitide (EMD Serono) are currently undergoing clinical trials with melanoma and glioblastoma multiforme patients (*4*, *5*). Although a series of monomeric and multivalent RGD peptides have been reported as an anchor for targeting $\alpha_v\beta_3$ in molecular imaging, nonpeptide antagonists were rarely used and few of them have used rational design to construct the optimal multivalent integrin $\alpha_v\beta_3$ ligands (*6*, *7*). In this report, we describe the synthesis and evaluation of a bivalent nonpeptide small molecule intergrin $\alpha_v\beta_3$ antagonist based on an in silico rational design approach. A near-infrared (NIR) fluorescent imaging probe has been developed for tumor angiogenesis imaging from this bivalent compound. We demonstrated the improved receptor binding affinity, receptor binding specificity of the bivalent IA, and a promising tumor accumulation of the NIR bivalent IA imaging probe in mouse xenografts.

Previously, we have developed an integrin $\alpha_v\beta_3$ targeting small molecular fluorescent probe derived from a small molecule $\alpha_v\beta_3$ antagonist, 4-[2-(3,4,5,6-tetrahydropyrimidine-2-lamino)-ethyloxy]benzoyl-2-(*S*)-aminoethylsulfonyl-amino-*h*-alanine (Figure 1, IA) (*8*). We have also developed a polymerized liposome-based vascular targeted nanoparticle delivery system using IA as tumor targeting ligand while carrying a payload for simultaneous imaging and therapy (*9*). In this study, we used IA as parent compound and constructed a bivalent ligand with a computer modeling designed linker to enable multivalent ligands to mimic, compete with, or inhibit natural interactions. Linker length and rigidity can affect the multivalent ligand−receptor interaction. In addition, the linkers used should have good physicochemical properties such as high stability and low toxicity. Hence, we chose carbon chain as the backbone of linkers and studied linkers with different lengths by computer simulation to predict the optimal structure for bivalent ligands followed by chemical synthesis and *in vitro* and *in vivo* validation (Figure 1).

Considering more avid binding could improve the tumor targeting properties, we further developed a NIR optical imaging probe based on the bivalent IA for tumor $\alpha_v\beta_3$ integrin imaging. The utilization of NIR probes in cancer imaging strategies has attracted wide attention, because light scattering in tissue decreases with the reciprocal of the fourth power of wavelength and hemoglobin has minimal absorbance and autofluorescence in the NIR window (*10*, *11*). NIR imaging technology is relatively inexpensive and absent the biological effects of radioactive probes. In this investigation, our plan was to develop a cyanine dye (Cy5.5) conjugated NIR fluorescent $\alpha_v\beta_3$ bivalent imaging probe (bivalent-IA-Cy5.5) with strong and specific binding. If successful, this imaging probe has great potential for early detection of tumors and micrometastatic lesions.

EXPERIMENTAL PROCEDURES

General. All solvents and reagents were purchased from commercial sources and used without further purification. ^{1}H NMR and ^{13}C NMR were obtained on a Bruker Ultrashield at 300 and 75 MHz, respectively. Chemical shifts were reported in ppm (δ) downfield of tetramethylsilane and coupling constants were given in hertz. The purification of the crude product was carried out on a semipreparative reversed-phase high-perfor-

* Corresponding author. Tel.: +1 713 441 7962. Fax: +1 713 790 3018. E-mail address: zli@tmhs.org.
[†] The Methodist Hospital Research Institute.
[‡] Baylor University.

10.1021/bc900313d © 2010 American Chemical Society
Published on Web 01/26/2010

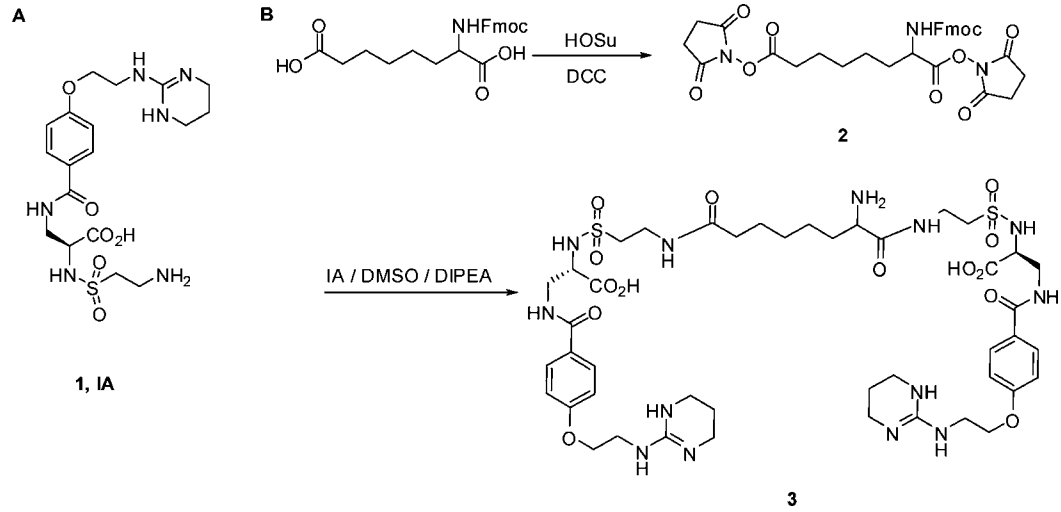


Figure 1. Schematic structure of IA **1** (A); synthetic scheme of bivalent IA **3** (B).

mance liquid chromatography (HPLC) system equipped with a diode array UV−vis absorbance detector (Agilent 1200 HPLC system). Mass spectral data were recorded on a ThermoFinnigan LCQ Fleet using electrospray as the ionization method. U-87 glioblastoma cells were obtained from American Type Culture Collection and were grown in Dulbecco's Modified Eagle's Medium DMEM (DMEM) supplemented with 10% fetal bovine serum (FBS) at 37 °C in humidified atmosphere.

Computer Modeling. The *AutoDock* program (version 3.0.5) was used for docking calculations (*12*). The graphical program *SYBYL* (version 16.91, Tripos, Inc.) was used for model building of the ligand structures, to generate missing hydrogen atoms and assign partial charges for protein targets used in AutoDock runs, and for energy minimization of initial ligand structures. Structural figures were generated using *WebLab Pro*.

Protein Coordinates. The structure of extracellular segment of integrin $\alpha_v\beta_3$ (PDB entry 1jv2) was used for the docking simulations of integrin $\alpha_v\beta_3$. The extracellular segment of the human integrin structure contains two subunits α (957 residues) and β (692 residues). The $\alpha_v\beta_3$ when complexed with Arg-Gly-Asp (RGD) reveals that the pentagonal peptide inserts into a crevice between the propeller and βA domains on the integrin head (*4*). The RGD sequence makes the main contact area with the integrin, and each residue participates extensively in the interaction, which is completely buried in the protein interior. For our simulations, we selected subunit β, and used Glu^{220}, Asn^{215}, Asp^{217}, and Pro^{219} as the target coordinate for binding, as they are in close contact with RGD. No water molecules were included. Sybyl was used to add essential hydrogens and assign partial charges from the Kollman united-atom force field to the target protein.

Ligand Coordinates. The structures of bivalent-IA-Cy5.5 were built in SYBYL Biopolymer package and energy minimized with MMFF94 force field by 100 steps. The orientations of ligands were overlaid on the integrin $\alpha_v\beta_3$ in the crystal structure to allow similar starting coordinates to be used. Prior to docking runs, all ligand structures were translated arbitrarily 30 Å from the surface of the $\alpha_v\beta_3$. Because the ligands are highly flexible, with multiple rotatable dihedrals present even in the monvalent system, we adopted a two-stage strategy for protein/ligand complex structure modeling, involving simulated annealing (SA) and rigid docking, that partially takes into account ligand flexibility. In the SA step, a 1 ns MD trajectory was generated for each ligand at a temperature of 1500 K. Structures saved every 1 ps underwent energy minimization, and the optimized structures were sorted by energy. Our long-term goal is to use 5−10 lowest-energy structures of the ligand, thus identified, in rigid docking to the integrin. In our preliminary studies, we only employed a single conformer for each ligand—the lowest-energy structure from the SA run. At this stage, the conformational analysis was approximate, as a crude solvation model was employed, with interactions with solvent described by introducing a distance-dependent dielectric constant.

Simulation of Substrate Binding Using AutoDock. The auxiliary program AutoGrid was used for generation of affinity grid fields. The program assigned the center of the grids automatically. The dimensions of the grid were 60.0 Å × 60.0 Å × 60.0 Å with grid points separated by 0.375 Å. The ligands were then docked using the Lamarckian Genetic Algorithm (LGA). The parameters for the LGA configurational search were identical for all docking jobs. Ligand flexibility was taken into account by including rotations around bivalent-IA-Cy5.5 single bonds in the conformational search. The maximum translation step was kept constant at 0.2 Å for every cycle, but the maximum quaternion rotation step and dihedral rotation step had a reduction factor of 0.99 per cycle starting from a maximum rotation of 5.0°. For the search to be extensive, the program uses a multiple starting approach in combination with a time-dependent random number generator. The number of runs was set to 10. For each run, a population of 50 individuals was used, with at most 250 000 function evaluations used and run for at most 27 000 generations. The first top individual was preserved each generation. The mutation rate was 0.02 and the crossover rate 0.80. The GA's selection window was 10 generations; the α parameter was set to 0. After docking simulations had been carried out, the 10 solutions produced were grouped into clusters such that the ligand rms deviations within each cluster were below 0.5 Å. The clusters were also ranked by the value of the lowest-energy solution within each cluster. The lowest-energy solution and the solutions with energies within 5 kcal/mol of this value were considered as possible binding models.

Bivalent Ligands Synthesis. Bivalent ligand 3 was synthesized in three steps (Figure 1). To a solution of the 2-(((9*H*-fluoren-9-yl)methoxy) carbonylamino) octanedioic acid (100 mg, 0.24 mmol) in EtOAc (20 mL), dicyclohexylcarbodiimide (110 mg, 0.53 mmol), and *N*-hydroxysuccinimide (60 mg, 0.52 mmol) were added at 0 °C. The mixture was stirred at 0 °C for 8 h (detected by TLC). Solvent was evaporated under reduced pressure to get the crude intermediate **2**. Compound **2** was dissolved in DMSO (9 mL) for next step reaction without further purification. To this DMSO solution, IA (250 mg, 0.50 mmol) and diisopropylethylamine (0.2 mL, 1 mmol) were added and the mixture was stirred at ambient temperature for 24 h. After

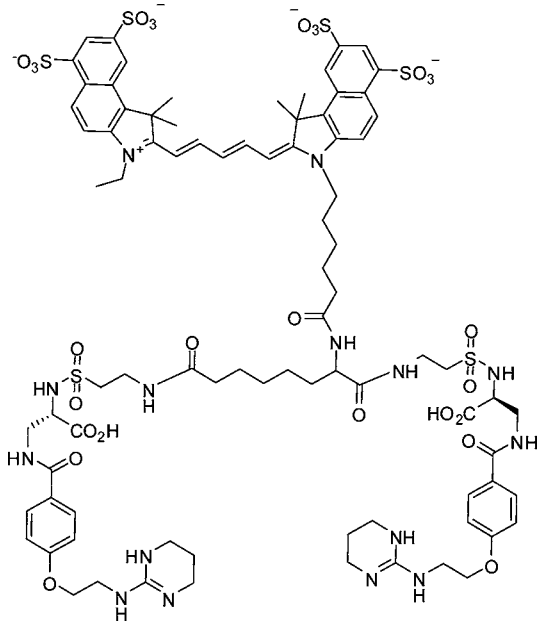


Figure 2. Schematic structure of bivalent-IA-Cy5.5 conjugate.

removing solvent at reduced pressure, 10 mL of water was added, and the white solid was removed by filtration. The aq solution was lyophilized, and the residue was recrystallized in methanol and acetone (1:3) to give pure bivalent IA **3** with 50% yield as white solid. ^{1}H NMR (300 MHz, D_2O): 7.65 (m, 4H), 6.93 (m, 4H), 4.16 (m, 7H), 3.84 (m, 4H), 3.30 (m, 10H), 3.21 (m, 10H), 2.05 (t, 2H, J = 7.0 Hz), 1.80 (m, 6H), 1.43 (m, 2H), 1.18 (m, 4H). MS (electrospray): *m*/*z* 1066.3 (100, $[M+H]^+$, calculated 1065.4); 533.8 ($[M+2H]^{2+}$. calculated 533.7).

Bivalent-IA-Cy5.5 Conjugate Synthesis. (Figure 2) Bivalent IA **3** (1.5 mg, 1.4 μmol) and 1.2 equiv of Cy5.5-NHS (2.0 mg, 1.7 μmol) were dissolved in 1 mL DMSO, and then 0.1 mL triethylamine was added. The reaction mixture was stirred in the dark at ambient temperature overnight and then quenched by adding 200 μL of 5% acetic acid (HOAc). The crude product was purified by a semipreparative reversed-phase HPLC employing a PhenomenexLuna C-18 column (250 mm × 10 mm) with the mobile phase starting from 95% solvent A (0.05% ammonia acetate in water) and 5% solvent B (acetonitrile) to 40% solvent A and 60% solvent B at 30 min, and the flow rate is 4 mL/min. Fractions containing bivalent-IA-Cy5.5 conjugates were collected, lyophilized, redissolved in saline at a concentration of 1 mg/mL, and stored in the dark at −20 °C until use. The analytical HPLC method was performed with the same gradient system, but with a Phenomenex C-18 column (250 mm × 4.6 mm) and flow rate of 1 mL/min. The purity of Cy5.5-labeled bivalent IA was over 98% from analytical HPLC analysis. The yield of bivalent-IA-Cy5.5 conjugate was over 70%. The purified bivalent-IA-Cy5.5 conjugate was characterized by mass spectroscopy (MS). MS (electrospray): *m*/*z* 1965.7 ($[M+H]^+$, calculated 1965.2); 983.1 (100, $[M+2H]^{2+}$, calculated 983.6). The absorption and fluorescence emission characteristics of bivalent IA-Cy5.5 conjugates were identical to those of free Cy5.5, as apparent from the spectra measured in H_2O (data not shown).

U-87 MG Xenograft Model. Animal procedures were performed according to a protocol approved by The Methodist Hospital Research Institute Animal Care and Use Committee (IACUC). Female athymic nude mice (nu/nu), obtained from Charles River Laboratories, Inc. (Cambridge, MA) at 4−6 weeks of age, were injected subcutaneously in the right rear thigh with 1×10^7 U-87 MG cells (see general procedures) suspended in 100 μL of phosphate-buffered saline (PBS). The cancer cells were harvested from subconfluent cultures with 0.25% trypsin. Trypsinization was stopped with DMEM containing 10% FBS, after which the cells were washed once in serum-free medium and resuspended in PBS. Trypan blue exclusion was performed to ensure >90% cell viability. The tumor bearing mice were subjected to *in vivo* imaging studies when the tumors reached 0.4−0.6 cm in diameter.

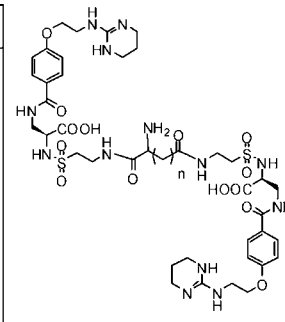
***In Vitro* Binding Assay.** To determine the receptor-binding ability, the bivalent ligands were tested for their ability to competitively inhibit the attachment of the natural ligand vitronectin to purified human $\alpha_v\beta_3$ by enzyme-linked immunosorbent assay (ELISA). Purified integrin $\alpha_v\beta_3$ protein (Chemicon International, Temecula, CA) was applied to 96-well polystyrene microtiter plates at 0.1 μg/well. After overnight incubation at 4 °C, the plates were washed and then blocked with milk solution (KPL, Inc., Gaithersburg, MD) at room temperature for 2 h. The blocking buffer was removed, and the plates were inoculated in quadruplicate with bivalent IAs with a typical starting concentration of 125 nM. Serial dilutions were prepared in the 96-well plates using multichannel pipettes. Biotinylated vitronectin solution (0.1 μg/well) was added to each well as a standard competitor. The plates were incubated at room temperature for 3 h, washed, and the bound vitronectin detected using NeutrAvidin-HRP conjugate at 0.01 μg/well (Pierce, Rockford, IL) and LumiGlo chemiluminescent substrate system (KPL, Inc., Gaithersburg, MD). The luminescence was read using a FLUOstar OPTIMA Microplate Reader (Durham, NC). The concentration of inhibitor producing 50% inhibition (IC_{50}) of vitronectin binding to $\alpha_v\beta_3$ was calculated on the basis of a curve fitting model using *KaleidaGraph 3.5* (Synergy Software, Reading, PA). c-[RGDfV] (Peptides International, Inc.) was also tested using the same method described above.

Fluorescence Microscopic Studies. To demonstrate that the bivalent-IA-Cy5.5 imaging probe can act as a specific ligand for $\alpha_v\beta_3$ integrin receptor in living cells, and to demonstrate the binding and subcellular localization of the bivalent probe, U-87 MG (ATCC HTB-14), a human glioblastoma cell line known to overexpress integrin $\alpha_v\beta_3$, was used in a probe binding assay (*4*). For fluorescence microscopy studies, 1×10^4 U87 cells were cultured on 35 mm MatTek glass-bottomed culture dishes. After 24 h, cells were washed with PBS and then incubated with bivalent-IA-Cy5.5 (200 nM) at 37 °C for 45 min. Integrin specificity of the probe binding was verified by incubating U87 cells with and without a blocking dose of the nonfluorescent bivalent IA (20 μmol/L). After the incubation period, the cells were washed three times with ice-cold PBS. The fluorescence signal of the cells was recorded using FluoView 1000 laser scanning confocal microscope (Olympus) under a 40× oil immersion objective, with laser excition at 675 nm (Cy5.5). A differential interference contrast image was also taken so that the origin of fluorescent signals could be confirmed.

***In Vivo* Fluorescence Imaging of Tumors.** ~3×10^6 U-87 cells were implanted bilaterally in the posterior flanks of immunocompromised (nu/nu) mice and grown to ~4−6 mm in diameter. Imaging was carried out with a group of 5 mice. After palpable masses were detected, animals were manually restrained and imaging probes were intravenously administered (lateral tail vein) using a 30 G needle via aseptic technique. Free Cy5.5 was prepared by dissolving the same Cy5.5NHS ester used for labeling the bivalent IA (GE Healthcare) in phosphate buffered saline (PBS), pH 7.4, overnight at 4 °C. Stock concentration of free Cy5.5 was measured optically using the molar exctinction coefficient of 250 000 M^{-1} cm^{-1} using a UV−visible spectrophotometer using the maximum absorbance wavelength (675 nm) as recommended by the supplier (GE Healthcare). The bivalent-IA-Cy5.5 was weighed and confirmed

Table 1. Conformational Energy of Bivalent IA and NIR Imaging Probe

Form of IA	Linker composition	Linker Length	Conformational Energy (kcal/mol)
Monomer	N/A	N/A	-17.0 ± 2.0
Dimer (IA-X-IA)	$(-C-)_n$	n = 1	-37.0 ± 2.0
		n = 2	-50.0 ± 2.0
X = linkers		n = 3	-53.0 ± 2.0
		n = 4	-49.0 ± 2.0
		n = 5	-60.0 ± 2.0
Near Infrared (NIR) (IA-X-P-IA) X = linker; P =probe molecule	(-C-)n	n =5	-53.0 ± 2.0



IA dimer

by spectrophotometer measurements. Appropriate dilutions of each probe were made in PBS, pH 7.4, and filter sterilized (0.2 μm) immediately prior to use. All animals weighing between 18 and 20 g received 10 nmol of imaging probe (total volume of 100 uL). Fluorescence imaging was performed with a small animal dedicated optical imaging system (Xenogen/Caliper IVIS-200, Mountain View, CA) under continuous 1.5−2.0% isoflurane delivered through the integrated anesthesia system. At 2, 4, 7, 24, and 48 h postinjection, images were acquired with the surface of the tissue of interest (tumor) approximating a perpendicular viewing angle relative to the camera line of sight; this viewing angle was also used for normal tissue selection. For determining tumor contrast, mean fluorescence intensities of the tumor area (*T*) defined as radiance (photons/s/cm^2/sr) at the right rear leg of the animal and of the area (*N*) at the right flank (normal tissue) were calculated by region-of-interest (ROI) analysis using the corresponding photograph of each image acquisition data set to identify the tumor region. Preinjection imaging was also performed to determine baseline autofluorescence. For competitive inhibition studies, mice (n = 3) were coinjected with 500 nmol bivalent IA and 10 nmol of imaging probe (bivalent-IA-Cy5.5) following the same procedure described above. Free Cy5.5 studies were performed in the same manner following the intravenous injection of 10 nmol. For ex vivo biodistribution imaging, two tumor-bearing mice were imaged 24 h post injection of bivalent-IA-Cy5.5 and thereafter euthanized per IACUC protocol (CO_2 and cervical dislocation). Tumor and major internal organs (heart, lung, liver, spleen, gastrointestinal tract, and kidneys) were harvested, weighed, and imaged against a black paper background. All image acquisition parameters were as follows: epi-illumination; Cy5.5 Em/Ex; Bin: (HR)4, FOV: 12.9; f2; 0.2 s.

Data Processing and Statistics. All data are given as means ± SD of n independent measurements. Statistical significance was assigned for P values less than the boundaries of tumors. Quantitative data were acquired with the software provided from the instrument's manufacturer (*Living Image*, v 3.1). Statistics software from R Development Core Team (2009). (R: A language and environment for statistical computing. R Foundation for Statistical Computing, Vienna, Austria. ISBN 3-900051-07-0, URL http://www.R-project.org).

RESULTS

Computer Modeling. From calculations of binding energies and ligand spatial distributions, the prediction of favored protein−ligand binding modes, interaction strengths, and binding specificity can be obtained with AutoDock simulations. Ten (10) LGA (Lamarckian genetic algorithm) docking runs were performed for each protein−ligand pair, with each run producing one possible binding mode or solution. The solutions were first sorted in terms of the binding mode, i.e., the position and orientation of the ligand relative to the protein target. The solutions were clustered on the basis of rms (root-mean-square) deviations in ligand atomic positions, with structures with rmsd of less than 0.5 Å grouped into a cluster. The total number of generated low-energy clusters measures the specificity of binding (*12–15*). A small number of clusters indicates that the ligand has only a few possible binding modes and interacts with a specific site (or sites) on the target protein. On the other hand, a large number of clusters implies existence of a wide range of binding modes and lack of specific ligand−target interactions. The second step in sorting solutions involves identification of the solution of lowest binding energy within each cluster and ranking the different clusters according to this energy value. The solution with the lowest energy in the top-ranked cluster and all solutions with energies higher by up to 5.0 kcal/mol were considered as possible binding modes for ligand to target.

Docking of Bivalent-IA-Cy5.5 to the Integrin $\alpha_v\beta_3$. A summary of the AutoDock results is presented in Table 1; the docked structures of the first and second clusters are shown in Figure 3. The docking of bivalent-IA-Cy5.5 to the integrin $\alpha_v\beta_3$ produced 3 clusters out of 10 runs. There were 5 solutions in the first cluster with an average docking energy of −34.04 kcal/mol. The binding site defined by this cluster is in the cleft between the RGD binding domain in integrin $\alpha_v\beta_3$. It is observed that bivalent-IA-Cy5.5 stays at that site in the presence of the whole protein. This cluster presents the best model for a possible bivalent-IA-Cy5.5 interaction to the integrin $\alpha_v\beta_3$. A comparison of the AutoDock results suggests that this binding conformation corresponding to the linker length of the bivalent-IA-Cy5.5 is a better substrate of integrin $\alpha_v\beta_3$. The binding of bivalent-IA-

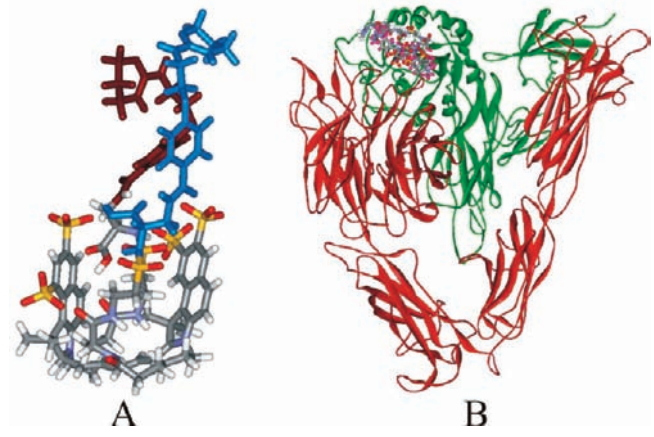


Figure 3. The lowest-energy conformation of bivalent-IA-Cy5.5 conjugate (A). Interaction of bivalent-IA-Cy5.5 with the Integrin (B). The lowest energy conformation is obtained from the analysis of molecular dynamics trajectories. Integrin structure is obtained from the open form of integrin crystal structure (1JV2).

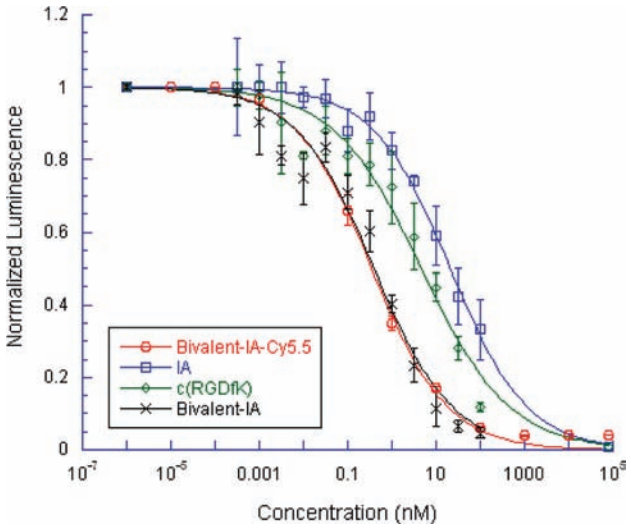


Figure 4. Enzyme-linked immunosorbent assay (ELISA) of IA (IC_{50}: 22.33 ± 4.51 nM), bivalent IA (IC_{50}: 0.40 ± 0.11 nM), bivalent-IA-Cy5.5 conjugate (IC_{50}: 0.13 ± 0.02 nM), and c-[RGDfV] (IC_{50}: 4.80 ± 3.01 nM). All of the points were done in triplicate.

Cy5.5 to the protein is stronger (lower energy) and more specific (small number of clusters) compared to other conformations with different linker length. The microscopic reason for these effects appears to be a lack of fit between different Cy5.5 conformation and the inhibitor/substrate binding site. The docking results are approximate. The scoring is based on an empirical energy function, solvation effects treated with a highly simplified model, and only ligand flexibility taken into account, with the protein structure kept fixed (*12–15*). Thus, the AutoDock results should only be considered as qualitative. The calculated binding energy results are in qualitative agreement with the observed inhibitory effects. Additionally, the simulations suggest that bivalent-IA-Cy5.5 with this conformation has a higher specificity and better fit into the known active site than other conformations.

***In Vitro* Binding Affinity.** Enzyme-linked immunosorbent assay (ELISA) was used to measure the competitive binding of antagonists and biotinylated human vitronectin for the immobilized integrin $\alpha_v\beta_3$. The IC_{50} value for parent compound IA, bivalent IA, bivalent-IA-Cy5.5 conjugate, and c-[RGDfV] were 22.33 ± 4.51, 0.40 ± 0.11, 0.13 ± 0.02, and 4.80 ± 3.01 nM, respectively (Figure 4). Cy5.5 conjugation did not decrease the receptor binding affinity of the resulting NIR fluorescent bivalent IA.

Fluorescence Microscopy. Bivalent-IA-Cy5.5 conjugate was incubated with U87 cells known to overexpress integrin $\alpha_v\beta_3$. Images were taken with a confocal fluorescent microscope. Receptor-mediated endocytosis was observed in the cells. The binding of bivalent-IA-Cy5.5 to U87 cells was effectively blocked by coincubation with nonfluorescent bivalent IA (Figure 5).

***In Vivo* Imaging of Integrin Overexpression in Xenograft U-87 Tumors.** Whole animal fluorescence imaging of subcutaneously implanted U-87 xenograft tumors demonstrated increased signal in tumor sites at 7, 24, and 48 h postconstrast injection (Figure 6). Imaging at earlier time points (2 and 4 h) showed intense systemic fluorescence signal due to relatively slow clearance of the compound. However, at 7 h, there is sufficiently high tumor-to-normal tissue (*T*/*N*) contrast to clearly discern the lesion; and by 24 and 48 h, the most intense signal is evident at the tumor site. Region of interest (ROI) analysis was performed by determining the boundaries of superficial tumors based on photographic images; this region was then measured for fluorescence signal (radiance units, photons/s/cm^2/steradian). Normal tissue was selected by copying the ROI of each sample to a site in the anterior flank. As plotted in Figure 7, *T*/*N* ratios reach a plateau at 24 h with an average maximum of ∼1.84. For the 7, 24, and 48 h time points, the fluorescence signals of the tumor and normal tissues were statistically significantly different (two sample, one side *t* test, *p*-value 0.006, 0.015, and 0.007, respectively, $n = 5$).

To ascertain the specificity of this tumor tissue signal localization, competitive inhibition studies were carried out using the nonfluorescent (without Cy5.5) bivalent IA. Using the same tumor model, a 10-fold excess of bivalent IA was coadministered with 10 nmol of bivalent-IA-Cy5.5 and were imaged at

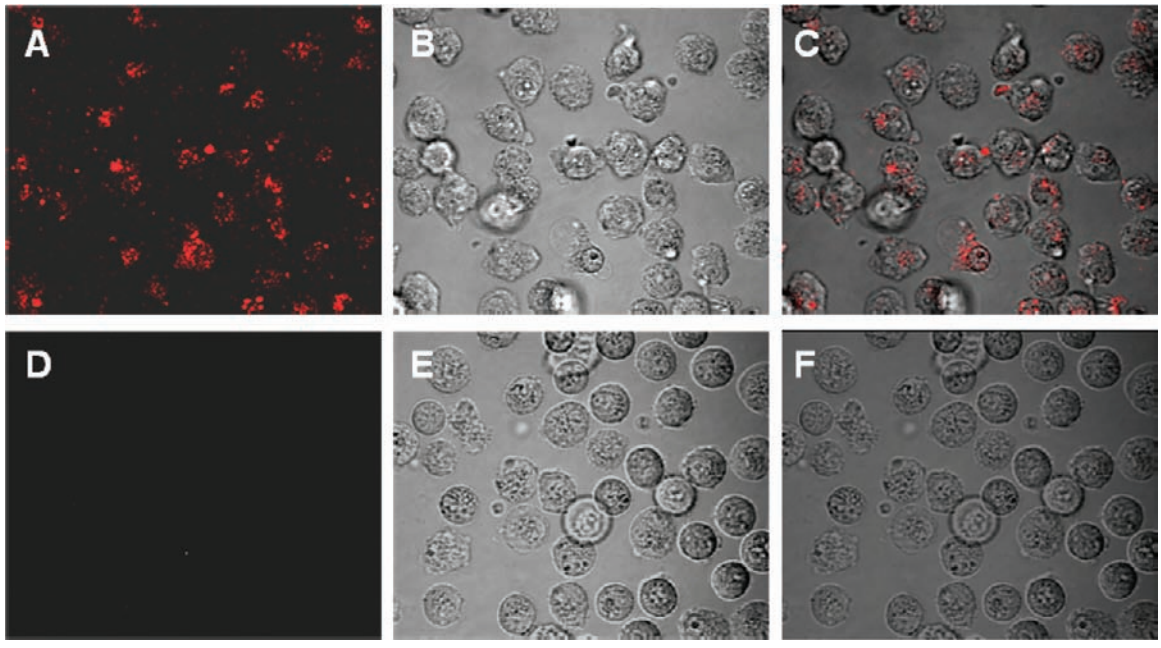


Figure 5. Specific binding of the bivalent-IA-Cy5.5 with U-87 cells. The left (A,D), middle (B,E), and right panels (C,F) represent fluorescence, brighten, and fusion images, respectively, taken from the same field of view. Confocal laser-scanning microscopy images of U-87 glioblastoma incubated with bivalent-IA-Cy5.5 demonstrated endocytosis of the imaging probes (A−C). U-87 cells blocking experiment with nonfluorescent bivalent IA demonstrated a complete blockage of endocytosis of the imaging probes (D−F).

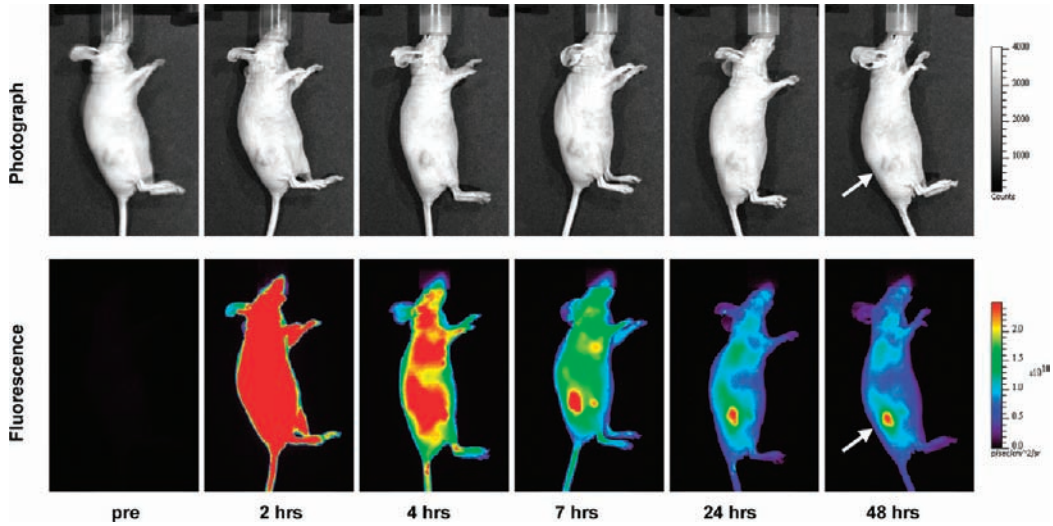


Figure 6. In vivo fluorescence imaging of live U-87 xenograft tumor-bearing mice. Photograph images (top panel) of representative mouse subject at selected time points. Photon scale is shown in the right; corresponding near-infrared fluorescence imaging (bottom panel). Radiance scale is shown in the color bar to the right (p/s/cm^2/sr). Subject was anesthetized with 1.5−2.0% isoflurane through a nose-cone. Arrow indicates tumor.

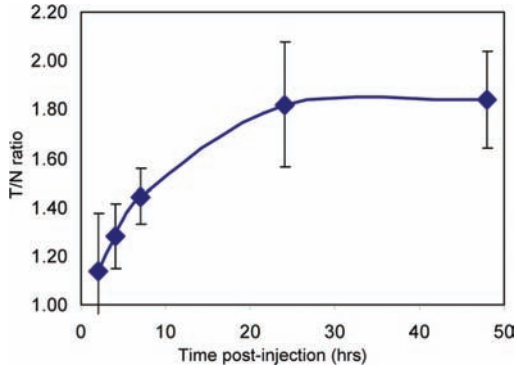


Figure 7. Region of interest (ROI) analysis of fluorescence signal (radiance) from tumor relative to normal tissue (*T*/*N*) vs time course following bivalent-IA-Cy5.5 administration (in hours). Error bars at each time point represents standard deviation from $n = 5$ subjects.

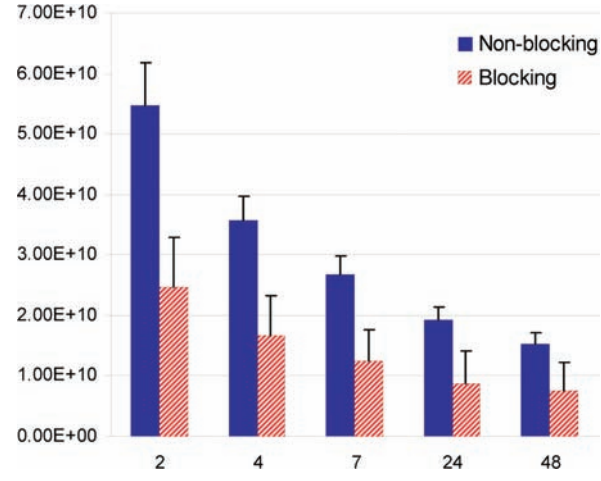


Figure 8. Competitive inhibition of bivalent-IA-Cy5.5 conjugate with nonfluorescent bivalent IA. Significant blocking of tumor fluorescence signal (*y*-axis) was observed at all time points (*x*-axis). Units of radiance (p/s/cm^2/sr). Error bars indicate SD from SD ($n = 6$ blocked, $n = 4$ nonblocked).

2, 4, 7, 24, and 48 h. ROI analysis was again performed as described above. When compared between blocking and nonblocking controls, fluorescence signals within tumors were reduced at all time points measured but were most pronounced in the earlier time points (2, 4, and 7 h), perhaps due to differing clearance rates of the two compounds (Figure 8). Nonetheless, the observed blocking effect was significant at all time points (two samples, one side *t* test, $p = 0.001$ (2 h); 0.002 (4 h); 0.003 (7 h); 0.012 (24 h); and 0.019 (48 h); $n = 6$ (blocking); $n = 4$ (nonblocking control). As a negative control, two tumor-bearing animals were intravenously injected with 10 nmol of the free Cy5.5 and imaged at 24 h post-injection. As shown in Figure 9, there is an overall reduction in systemic fluorescence signal from the entire animal. The relative amount of fluorescence signal from the tumor appears to be slightly higher than the background but is lower than that achieved with the bivalent-IA-Cy5.5 (Figure 9, compare left and right panels). This result is best explained by a higher clearance rate of the free fluorophore and a certain degree of nonspecific binding to tumors as observed by other investigators (*16*). Collectively, these data support the specificity of the bivalent-IA-Cy5.5 for integrin $\alpha_v\beta_3$ associated with U-87 tumors.

Given the intrinsic limitation in tissue penetration of excitation and emission photons from fluorophores, ex vivo imaging was performed to assess the fluorescence signal of the tumor relative to internal organs. Following the intravenous administration of the bivalent-IA-Cy5.5, two tumor-bearing animals were imaged as described above, imaged at 24 h postinjection and immediately thereafter euthanized for harvest of internal organs. Tumors and the major organs—heart/lung (en bloc), liver, spleen, gastrointestinal tract, and bilateral kidneys—were resected and placed on a black background and imaged under the same imaging acquisition protocol (Figure 10). Quantitative analysis was performed by measuring the total photon flux of each selected tissue and divided by the mass (Figure 11). The highest signal per mass of tissue was observed for the tumor, followed next by the heart and lung (en bloc), and kidneys. These data indicate that the bivalent-IA-Cy5.5 is specific for the tumor tissue, likely through binding to its cognate integrin receptor. Given the moderate level of fluorescence signal in the heart and lung, this compound is likely to have a relatively slow blood pool clearance rate. Fluorescence signal from the kidneys suggests mainly renal clearance of the agent, and minimal liver signal suggest low hepatic metabolism. Detailed bio-

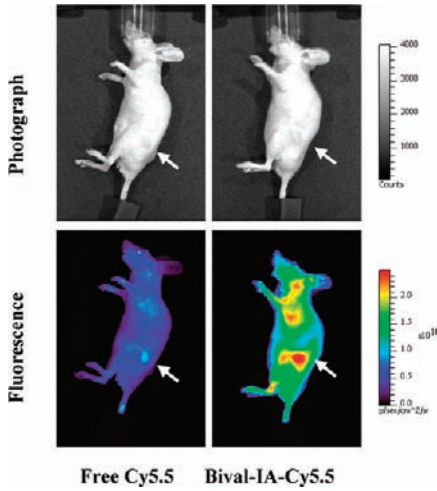


Figure 9. *In vivo* fluorescence imaging of live U-87 xenograft tumor-bearing mice at 24 h postintravenously administered unconjugated Cy5.5 (left panel) vs bivalent IA-Cy5.5 (right panel). Photograph images (top panel) of representative mouse subject. Photon scale is shown in the right; corresponding near-infrared fluorescence imaging (bottom panel). Radiance scale is shown in the color bar to the right (p/s/cm^2/sr). Mice were anesthetized with 1.5−2.0% isoflurane through a nose-cone. Black paper was used to cover the injection sites in the lateral tail veins. Arrows indicates tumors.

distribution, pharmacokinetic, and toxicity studies will be reported separately.

DISCUSSION

Glioblastoma multiforme (GBM) is the most common primary brain tumor, as well as the deadliest (*17*). Malignant gliomas present some of the greatest challenges in the management of cancer patients worldwide, despite notable recent achievements in oncology. Even with aggressive surgical resections using state-of-the-art preoperative and intraoperative neuroimaging, along with recent advances in radiotherapy and chemotherapy, the prognosis for GBM patients remains dismal. Mean survival after diagnosis is about 1 year (*18*). Preclinical data indicate that angiogenesis is essential for the proliferation and survival of malignant glioma cells, which suggests that inhibition of angiogenesis might be an effective therapeutic strategy.

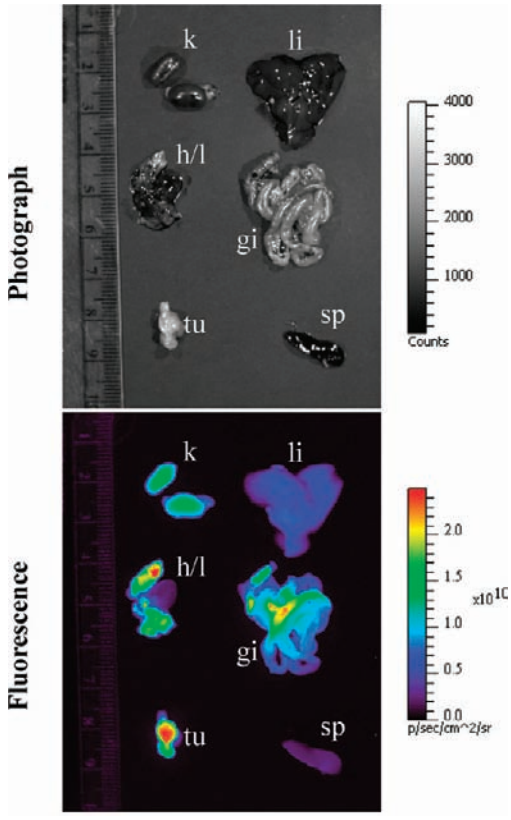


Figure 10. Representative *ex vivo* NIR imaging of major internal organs harvested from a xenograft tumor-bearing mice at 24 h post i.v. injection of bivalent IA-Cy5.5. Top panel: photograph (photon scale is shown to the right). Bottom: fluorescence image (p/s/cm^2/sr). Harvested organs are as follows: (k) kidneys; (li) liver; (h/l) heart and lungs; (gi) small and large intestines; (t) U-87 tumor; (sp) spleen.

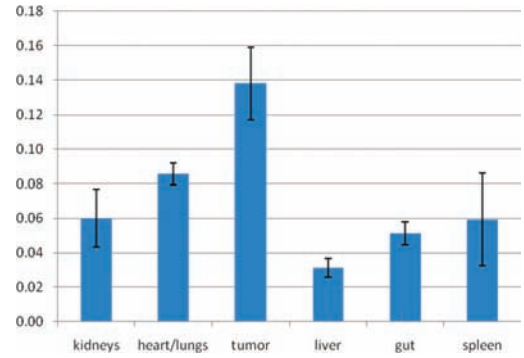


Figure 11. Biodistribution of bivalent IA-Cy5.5 at 24 h post-injection averaged from 2 subjects. *Y*-axis is total photon flux per gram of tissue.

NIRF imaging has been proven to be a very powerful tool for noninvasive imaging of various diseases in preclinical models especially in rodents (*10*). In an effort to leverage this robust modality, we sought to apply NIRF imaging techniques for studying an important molecular target, integrin $\alpha_v\beta_3$, expressed by glioblastoma cells. Our ultimate goal was to develop imaging and therapeutic agents targeted to integrin $\alpha_v\beta_3$ for early detection, treatment, and monitoring of glioblastoma as well as other malignancies. To achieve this goal, we set out to design and develop a highly specific and sensitive NIRF agent for this clinically important target.

Computer-assisted approaches to identify new inhibitors via pharmacophore, molecular modeling, docking, and structural interaction fingerprints is rapidly becoming an integral part of rational approaches to drug design. In silico assessment of the free energy and the binding affinity of receptor-inhibitors prior to synthesis permits sophisticated and efficient methods to design drugs. Hood et al. demonstrated that the integrin antagonist, 4-[2-(3,4,5,6-tetrahydropyrimidine-2-lamino)ethyloxy]benzoyl-2-(*S*)-aminoethylsulfonyl-amino-*h*-alanine (IA) can be used as a targeting agent for gene delivery to tumor neovasculature (*2*). A rationally designed bivalent IA by computer modeling could theoretically have better binding affinity and thus greater avidly to target cells expressing this receptor. In an effort to develop the bivalent IA probe for tumor angiogenesis imaging, an extensive simulation with varying linker lengths and composition was carried out. Our results (shown in Table 1) demonstrated that bivalent IAs with linkers containing 5 to 8 carbons (n = 2−5) exhibited descending conformational energy, while the linker shorter than 5 carbons (n < 2) had a significantly higher energy. On the basis of these simulation results, we chose the 8-carbon linker (n = 5), which has the lowest conformational energy to construct the first bivalent IA. Among various commercially available linkers, 2-aminododecanedioic acid, which carries two carboxylic acid groups at each end with a total of eight carbons (n = 5), was chosen as the best linker for the prototype construct. This analysis predicted that the bivalent IA with an 8-carbon linker (n = 5) containing the NIR fluorophore, Cy5.5 dye, would not sterically impact the binding to the integrin protein.

In vitro binding assays have shown that the bivalent IA ($IC_{50} = 0.40 \pm 0.11$ nM) exhibited significantly improved integrin $\alpha_v\beta_3$ affinity when compared to the parent compound IA ($IC_{50} = 22.33 \pm 4.51$ nM), resulting in a 50-fold improvement in receptor affinity (IC_{50}) over that of the parent compound IA and a 10-fold improvement over c-[RGDfV] ($IC_{50} = 4.80 \pm 3.01$ nM). NIR imaging probe, bivalent-IA-Cy5.5 conjugate, also demonstrated significantly increased binding affinity ($IC_{50} = 0.13 \pm 0.02$ nM). Fluorescence microscopy studies demonstrated integrin-mediated endocytosis of the bivalent-IA-Cy5.5 conjugate in U-87 cells, which was effectively blocked by nonfluorescent bivalent IA. This result provides strong supporting evidence that bivalent-IA-Cy5.5 binds specifically to the $\alpha_v\beta_3$ integrin receptor expressed on the tumor cell surface.

Systemically administered bivalent-IA-Cy5.5 in tumor-bearing mice resulted in modest accumulation at the tumor site with improved tumor/normal tissue signal over time (up to 48 h). This effect is best explained by the relatively slow clearance of the probe from the circulation as evident from the high fluorescence observed throughout the test animals at earlier time points (up to 24 h). Consistent with prior studies using a monomeric integrin peptidomimetic conjugated to a chelate for radioisotope imaging, tumor accumulation was time-dependent and required washout from normal tissue for optimal contrast (*8*). Although the tissue penetration of excitation and emission photons of near-infrared light is superior to wavelengths of the visible spectrum, a substantial percentage of light is attenuated as a function of tissue depth. Hence, fluorescence measurements likely underestimate the true accumulation of integrin-specific probes at the target tissue.

The experimental results presented here demonstrate the ability to noninvasively image integrin $\alpha_v\beta_3$ overexpression in live whole animals using a bivalent small molecule with improved receptor binding properties generated by in silico design. A major impetus for our experimental design was to demonstrate proof of concept in generating a new class of targeted imaging agents by leveraging known structure activity relationships and in silico modeling to further improve receptor binding properties of existing molecules. Prior multivalency studies have clearly shown the utility of expanding the repertoire of drugs by reconfiguring molecules as multimers (*19*, *20*). We propose that such approaches will have significant impact in the drug discovery process by providing a mechanism to alter the pharmacologic properties of existing as well as novel drugs.

CONCLUSION

We have successfully synthesized and evaluated a novel near-infrared fluorescent nonpeptidic bivalent integrin $\alpha_v\beta_3$ antagonist for tumor imaging with improved binding avidity relative to the monovalent ligand. The design of this bivalent compound was facilitated by in silico modeling which guided synthetic strategy in a practical application of optimizing a biologically relevant imaging probe. We suggest that this approach represents a general paradigm to improve receptor binding affinities of extant compounds through rationally designed multivalent configurations. More research will be carried out to rationally design bivalent ligands with different types of linkers using computer modeling followed by *in vitro* and *in vivo* evaluation.

ACKNOWLEDGMENT

This work was supported by The Methodist Hospital Research Institute, the M.D. Anderson Foundation, and the Vivian L. Smith Foundation. GSJ would like to acknowledge support from Baylor Supercomputing Center and internal funding. We appreciate Dr. Shi Ke for discussion and advice on biological study.

LITERATURE CITED

(1) Brooks, P. C., Clark, R. A., and Cheresh, D. A. (1994) Requirement of vascular integrin alpha v beta 3 for angiogenesis. *Science 264*, 569–71.

(2) Hood, J. D., Bednarski, M., Frausto, R., Guccione, S., Reisfeld, R. A., Xiang, R., and Cheresh, D. A. (2002) Tumor regression by targeted gene delivery to the neovasculature. *Science 296*, 2404–7.

(3) Takagi, J., and Springer, T. A. (2002) Integrin activation and structural rearrangement. *Immunol. Rev. 186*, 141–63.

(4) Delbaldo, C., Raymond, E., Vera, K., Hammershaimb, L., Kaucic, K., Lozahic, S., Marty, M., and Faivre, S. (2008) Phase I and pharmacokinetic study of etaracizumab (Abegrin), a humanized monoclonal antibody against alphavbeta3 integrin receptor, in patients with advanced solid tumors. *Invest. New Drugs 26*, 35–43.

(5) Schottelius, M., Laufer, B., Kessler, H., and Wester, H. J. (2009) Ligands for mapping $\alpha_v\beta_3$-integrin expression in vivo. *Acc Chem Res 42*, 969–80.

(6) Chen, X., Conti, P. S., and Moats, R. A. (2004) In vivo near-infrared fluorescence imaging of integrin alphavbeta3 in brain tumor xenografts. *Cancer Res. 64*, 8009–14.

(7) Cheng, Z., Wu, Y., Xiong, Z., Gambhir, S. S., and Chen, X. (2005) Near-infrared fluorescent RGD peptides for optical imaging of integrin alphavbeta3 expression in living mice. *Bioconjugate Chem. 16*, 1433–41.

(8) Burnett, C. A., Xie, J., Quijano, J., Shen, Z., Hunter, F., Bur, M., Li, K. C., and Danthi, S. N. (2005) Synthesis, in vitro, and in vivo characterization of an integrin alpha(v)beta(3)-targeted molecular probe for optical imaging of tumor. *Bioorg. Med. Chem. 13*, 3763–71.

(9) Xie, J., Shen, Z., Li, K. C., and Danthi, N. (2007) Tumor angiogenic endothelial cell targeting by a novel integrin-targeted nanoparticle. *Int. J. Nanomed. 2*, 479–85.

(10) Ntziachristos, V., Bremer, C., and Weissleder, R. (2003) Fluorescence imaging with near-infrared light: new technological advances that enable in vivo molecular imaging. *Eur. Radiol. 13*, 195–208.

(11) Sevick-Muraca, E. M., Houston, J. P., and Gurfinkel, M. (2002) Fluorescence-enhanced, near infrared diagnostic imaging with contrast agents. *Curr. Opin. Chem. Biol. 6*, 642–50.

(12) Morris, G. M., Goodsell, D. S., Halliday, R. S., Huey, R., Hart, W. E., Belew, R. K., and Olson, A. J. (1998) Automated docking using a Lamarckian genetic algorithm and empirical binding free energy function. *J. Comput. Chem. 19*, 1639–1662.

(13) Goodsell, D. S., and Olson, A. J. (1990) Automated docking of substrates to proteins by simulated annealing. *Proteins 8*, 195–202.

(14) Morris, G. M., Goodsell, D. S., Huey, R., and Olson, A. J. (1996) Distributed automated docking of flexible ligands to proteins: parallel applications of AutoDock 2.4. *J. Comput. Aided Mol. Des. 10*, 293–304.

(15) Xiong, J. P., Stehle, T., Zhang, R., Joachimiak, A., Frech, M., Goodman, S. L., and Arnaout, M. A. (2002) Crystal structure of the extracellular segment of integrin alpha Vbeta3 in complex with an Arg-Gly-Asp ligand. *Science 296*, 151–5.

(16) Cheng, Z., Levi, J., Xiong, Z., Gheysens, O., Keren, S., Chen, X., and Gambhir, S. S. (2006) Near-infrared fluorescent deoxyglucose analogue for tumor optical imaging in cell culture and living mice. *Bioconjugate Chem. 17*, 662–9.

(17) Parsons, D. W., Jones, S., Zhang, X., Lin, J. C., Leary, R. J., Angenendt, P., Mankoo, P., Carter, H., Siu, I. M., Gallia, G. L., Olivi, A., McLendon, R., Rasheed, B. A., Keir, S., Nikolskaya, T., Nikolsky, Y., Busam, D. A., Tekleab, H., Diaz, L. A., Jr., Hartigan, J., Smith, D. R., Strausberg, R. L., Marie, S. K., Shinjo,

S. M., Yan, H., Riggins, G. J., Bigner, D. D., Karchin, R., Papadopoulos, N., Parmigiani, G., Vogelstein, B., Velculescu, V. E., and Kinzler, K. W. (2008) An integrated genomic analysis of human glioblastoma multiforme. *Science 321*, 1807–12.

(18) Kanu, O. O., Mehta, A., Di, C., Lin, N., Bortoff, K., Bigner, D. D., Yan, H., and Adamson, D. C. (2009) Glioblastoma multiforme: a review of therapeutic targets. *Expert Opin. Ther. Targets 13*, 701–18.

(19) Rao, J., Lahiri, J., Isaacs, L., Weis, R. M., and Whitesides, G. M. (1998) A trivalent system from vancomycin.D-ala-D-Ala with higher affinity than avidin.biotin. *Science 280*, 708–11.

(20) Mulder, A., Huskens, J., and Reinhoudt, D. N. (2004) Multivalency in supramolecular chemistry and nanofabrication. *Org. Biomol. Chem. 2*, 3409–24.

BC900313D

Synthesis of Conjugates of 6-Aminophenanthridine and Guanabenz, Two Structurally Unrelated Prion Inhibitors, for the Determination of Their Cellular Targets by Affinity Chromatography

Fabienne Gug,[†] Nassima Oumata,[†] Déborah Tribouillard-Tanvier,[‡,||] Cécile Voisset,[‡] Nathalie Desban,[§] Stéphane Bach,[§] Marc Blondel,[‡] and Hervé Galons*[,†]

Laboratoire de Chimie Organique 2, INSERM U648, Université Paris-Descartes, 4 avenue de l'Observatoire, 75270 Paris cedex 06, France, INSERM U613, Faculté de Médecine et des Sciences de la Santé, CHU Morvan, Université de Bretagne Occidentale, Brest, F-29200, France, and CNRS USR3151, Station Biologique, Protein Phosphorylation and Disease Laboratory, place Georges Teissier, 29680 Roscoff, France. Received July 15, 2009; Revised Manuscript Received December 7, 2009

The synthesis of affinity matrices for 6-aminophenanthridine (6AP) and 2,6-dichlorobenzylidenaminoguanidine (Guanabenz, GA), two unrelated prion inhibitors, is described. In both cases, the same simple spacer, ε-aminocaproylaminopentanol, was introduced by a Mitsunobu reaction and the choice of the anchoring position of the linker was determined by the study of the residual antiprion activity of the corresponding 6AP or GA conjugates. Very recently, these two affinity matrices were used for chromatography assays leading to the identification of ribosome (via the rRNA) as a common target of these two antiprion drugs. Here, we show, using competition experiments with Quinacrine (QC) and Chlorpromazine (CPZ), two other antiprion drugs, that QC, but not CPZ, may also directly target the rRNA.

INTRODUCTION

Prion-based diseases are transmissible and yet incurable fatal neurodegenerative disorders (*1*). Among these diseases are Creutzfeldt-Jakob disease (CJD) in humans, bovine spongiform encephalopathies in cattle, and Scrapie in sheep and goats. These diseases are associated with neuronal cell death, which leads to characteristic "spongiform" vacuolation of the brain, and are therefore termed spongiform encephalopathies. According to the "protein-only" hypothesis, prions are mostly if not solely composed of an abnormally folded form (PrP^{Sc}) of the PrP protein (PrP^{C}), a glycosyl-phosphatidyl inositol (GPI) anchored protein normally expressed at the surface of a number of cell types including in particular neurons. Transmissibility necessitates the conversion of host PrP^{C} by exogenous PrP^{Sc}. PrP^{Sc} isoform displays a pronounced protease resistance, shows an increase in β-sheet structures, and forms amyloid fibers. Despite intensive works devoted to the study of prions and their mechanisms of propagation, many fundamental questions related to the mechanism of the infection and subsequently to the mechanisms of action of known antiprion compounds remain unanswered. On the basis of the assumption that PrP^{Sc} corresponds to (or at least is part of) the pathogenic entity, various approaches aimed at reducing PrP^{Sc} or PrP^{C} levels for the development of prion disease therapies are currently being explored (comprehensively reviewed in ref *2*). A proof of concept for these approaches has been made recently by showing that depleting PrP^{C} from neurons of prion-infected mice in which the *Prnp* gene can be turned off, not only prevented progression of disease, but also reversed spongiosis and early cognitive and neurophysiological dysfunctions (*3, 4*). Therefore, approaches leading to reduction of endogenous PrP^{C} and/or PrP^{Sc} levels may well be effective after the appearance of the neurological symptoms. Among these approaches are identifications of pharmacological compounds promoting PrP^{Sc} clearance. Some of these identifications are based on the use of cell-free systems (*5–8*), whereas others are based on the use of mammalian cells chronically infected with prions (*9–12*) and reviewed in ref *13*. All these assays are time- and money-consuming, in particular, because experiments have to be carried out in highly secured laboratories. For these reasons, we recently developed a rapid and economical budding yeast (*Saccharomyces cerevisiae*) based two-step assay to screen for antiprion molecules (*14, 15*). This assay allows easy detection of compounds active against two yeast prions and has led, among others, to the isolation of 6-aminophenanthridine (6AP) **1a** and 2,6-dichlorobenzylidenaminoguanidine (Guanabenz, GA) **1b** (Figure 1). This yeast-based assay was validated for the isolation of drugs active against mammalian prions, since most of the active compounds isolated, including 6AP and GA, turned out to also be active against mammalian prions in mammalian cell-based assays mentioned above (*16*). In addition, both 6AP and GA exhibited significant activity in a mouse model for scrapie (*17*).

Although direct interaction with the prion protein PrP^{C} has been established by NMR spectroscopy (*18*) or by surface plasmon resonance (*19*) for some drugs, this has not been evaluated with most of the known antiprion agents. Recently, using immobilized 9-aminoacridine, Prusiner's group was able to discriminate PrP^{C} and PrP^{Sc} in an affinity chromatography assay (*20*). Moreover, even if some of the compounds are known to bind PrP, it is not established whether their antiprion activities exclusively rely on this binding ability. Therefore, the mechanism of action of most antiprions remains unclear, and at least two different mechanisms can be envisioned: drugs can either act in *cis* directly on prion aggregates or in *trans* on cellular elements required for prion propagation. In addition, identification of these unknown biological mechanisms may provide new

* Corresponding author. E-mail: herve.galons@parisdescartes.fr, Phone +33(0)153739684, Fax +33(0)143290598.

[†] INSERM U648.

[‡] INSERM U613.

[§] CNRS USR3151.

[||] Present address: Laboratory of Persistent Viral Diseases, Rocky Mountain Laboratories, National Institute of Health, Hamilton, Montana 59840, USA.

10.1021/bc900314n © 2010 American Chemical Society
Published on Web 01/21/2010

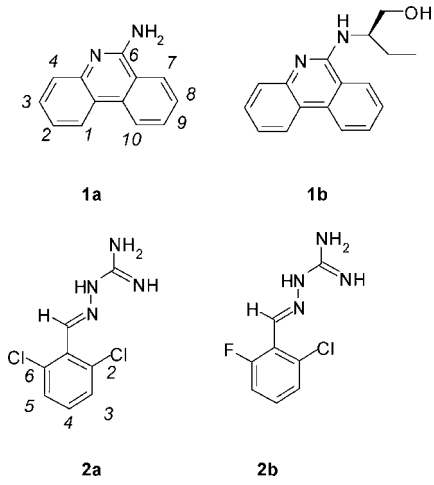


Figure 1. 1a, 6-aminophenanthridine (6AP) and **2a**, 2,6-dichlorobenzylidenaminoguanidine: Guanabenz (GA), two antiprion drugs active against both yeast and mammalian prions and their respective inactive controls, **1b** (6APi) and **2b** (GAi).

insights for other neurodegenerative disorders characterized by the occurrence of protein misfolding as observed in prion diseases (*21*).

For these reasons, identification of these mechanisms using reverse screening approaches is of particular interest. Several comprehensive methods exist to decipher cellular mechanisms targeted by small chemical compounds, including affinity chromatography on immobilized drugs.

Affinity chromatography has been used in the determination of the molecular targets of several compounds. Most of them are kinase inhibitors such as flavopiridol (*22*), purvalanol (*23*), (*R*)-roscovitine (*24*), gefitinib (*25*), and SU6668 (*26*). Affinity chromatography has also been performed with the immunosuppressor FK506 (*27*) and geldanamycin, which was therefore shown to be a specific inhibitor of HSP 90 (*28*).

As a typical example, the determination of the molecular targets of (*R*)-roscovitine led, apart from the expected cyclin-dependent kinases, to the identification of pyridoxal kinase, an unexpected target. This was confirmed by X-ray crystallography, and surprisingly, roscovitine appeared to bind the pyridoxal pocket rather than the ATP binding site (*29*).

In affinity chromatography experiments, a spacer arm is introduced between the compound of interest and the solid supports with the aim of avoiding steric hindrance. The structure of the spacer arm matters considerably. Polyoxyethylenic linkages are generally used. A carboxylic acid group is often introduced on the active molecules. Therefore, the introduction of the spacer on the bioactive compound is frequently achieved by a multiple-step procedure. The position of the linkage is critical, as the conjugate should, at least partially, retain biological activity. Linkage should be introduced at several positions of the molecule under study and the biological activity of the resulting conjugates tested. If available, structure−activity relationships provide useful information on the positions of linkage which are more likely to allow molecular recognition by the biological targets (for a review, see ref *30*).

In this paper, we report the synthesis of affinity matrices for the two unrelated antiprion drugs cited above: 6-aminophenanthridine (6AP) and 2,6-dichlorobenzylidenaminoguanidine (guanabenz, GA) by immobilization of the conjugates on preactivated Sepharose beads. The 6AP and GA affinity beads were very recently used and allowed to determine that protein folding activity of the rRNA (Ribosome-borne Protein Folding Activity, RPFA) is a selective target of both 6AP and GA (*31*). Here, using competition experiments on 6AP and GA affinity matrices with free quinacrine (QC) and chlorpromazine (CPZ), two other active antiprion compounds, we found that QC, but not CPZ, may also target the ribosome directly.

EXPERIMENTAL PROCEDURES

Chemical Methods. Reactions were monitored by TLC using Merk silica gel 60F-254 thin layer plates. Column chromatography experiments were carried out on SDS Chromagel 60 ACC, 40−63 μm. Column chromatography (CC) was performed using silica gel (70−200 μm). Melting points were determined on a Kofler hot-stage (Reichert) and are uncorrected. NMR spectra were recorded on Bruker Avance 400 MHz. Chemical shifts are given in parts per million (ppm) downfield of tetramethylsilane (TMS) used as an internal standard. Infrared spectra were recorded on a FTIR Schimadzu 8300. The HPLC analyses were carried out on a system consisting of a Waters 600 system controller, a Jones chromatography heater−chiller oven, and a Waters 994 photodiode array detector. Mass spectra (electrospray ionization (ESI) were measured on a TSQ Quantum (Thermo Electron Corporation) instrument. Elemental analyses for C, H, and N were performed on a Thermoquest EA-110 apparatus. 6AP was prepared as described previously (*32, 33*). Commercially available GA was used or obtained upon condensation of aminoguanidine with 2,6-dichlorobenzaldehyde.

(*R*)-6-(1-Hydroxybut-2-ylamino)phenanthridine, 6APi (1b). A mixture of 6-chlorophenanthridine (2.14 g, 10 mmol), (*R*)-2-aminobutanol (3 mL, 35 mmol), and NEt_3 (3 mL, 40 mmol) was heated at 110 °C for 2 h. After cooling to rt, 30 mL H_2O was added, and the mixture was extracted with CH_2Cl_2 (2 × 10 mL). The solvent was evaporated and **1b** crystallized from EtOAc. Mp 176−178 °C. Anal. ($C_{17}H_{18}N_2O$) C, H, N. ^{1}H NMR ($CDCl_3$) δ 1.19 (t, J = 7 Hz, 3H, C*H*$_3$); 1.78 (p, 2H, C*H*$_2$CH$_3$); 3.76 (t, 1H, J = 9 Hz, 1H, C*H*$_2$OH); 3.98 (d, J = 10.9 Hz, 1H, C*H*$_2$OH); 4.26 (m, 1H, C*H*CH$_2$OH); 5.57 (br s, 1H, O*H*); 6.75 (br s, 1H, N*H*); 7.34 (t, $J_{1-2} = J_{2-3}$ = 7.5 Hz, 1H, 2-H); 7.54 (t, $J_{7-8} = J_{8-9}$ = 7.5 Hz, 1H, 8-H); 7.59 (t, 1H, 3-H); 7.70 (d, J_{3-4} = 8 Hz, 1H, 4-H); 7.77 (t, 1H, J_{9-10} = 7.5 Hz, 9-H); 7.86 (d, 1H, 7-H); 8.31 (d, 1H, 1-H); 8.51 (d, 1H, 10-H). ^{13}C NMR ($CDCl_3$) δ 10.8; 24.7; 56.8; 68.2; 118.5; 120.3; 121.5; 121.8; 122.5; 122.6; 125.7; 126.7; 128.7; 130.2; 133.6; 142.9; 153.7.

2-Chloro-6-fluoro-benzylideneaminoguanidine, GAi (2b). Aminoguanidine hydrochloride (2.20 g, 20 mmol) was added to a solution of 2-chloro-2-fluorobenzaldehyde (3.16 g, 20 mmol) in 50 mL EtOH followed by the addition of AcONa, 5H_2O (2.72 g, 20 mmol). After 2 h reflux, the hot mixture was filtered, and **2b** precipitated upon cooling to rt. Yield 87%. Mp 164−167 °C. Anal. ($C_8H_8ClFN_4$) C, H, N. ^{1}H NMR (DMSO) δ 5.50 (br s, 4H, 2 N*H* + N*H*$_2$); 7.15 (t, $J_{3-4} = J_{4-5}$ = 8 Hz, 1H, 4-H); 7.50 (d, 1H, 3-H); 7.65 (dd, J_{F-5} = 10 Hz, 1H, 5-H); 8.20 (s, 1H, NC*H*).

Benzyloxy-6-aminophenanthridines 1c−e (reaction in liquid ammonia). Ammonia (200 mL) was introduced into a flask connected with an efficient condenser followed by $Fe(NO_3)_3$ (0.02 g) and piece by piece Na (0.23 g, 10 mmol) additions. The solution was stirred for 0.5 h during this period; the initial blue color of the solution of Na gradually turned to gray indicating the complete conversion into $NaNH_2$. To this suspension, benzyloxyanilines (1.99, 10 mmol) dissolved in the minimum amount of anhydrous Et_2O were added. The mixture was stirred for 0.5 h followed by the addition of 2-chlorobenzonitrile (1.37 g, 10 mmol) in anhydrous Et_2O. The mixture was stirred for 2 h, and lithium (0.14 g, 20 mmol) was then added. After 2 h stirring, NH_4Cl (10 g) was gradually introduced under vigorous stirring. Ammonia was evaporated overnight. After addition of H_2O (50 mL), the mixture was extracted with CH_2Cl_2 (3 × 30 mL), and the organic layer was first washed with brine (40 mL), then dried with Na_2SO_4 and evaporated.

The residue was applied to a silica gel column and eluted first with CH_2Cl_2 and then with CH_2Cl_2−MeOH (99:1 to 95:5).

1-Benzyloxy-6-aminophenanthridine (1c) and 3-benzyloxy-6-aminophenanthridine (1e). 3-Benzyloxyaniline led to a mixture of compounds **1c** and **1e**. The two isomers could not be separated by column chromatography. They were isolated in 23% yield as a (1:1) mixture.

2-Benzyloxy-6-aminophenanthridine (1d). Prepared from 4-benzyloxyaniline. Yield 45%. Mp 138−141 °C. Anal. ($C_{20}H_{16}N_2O$) C, H, N. ^{1}H NMR ($CDCl_3$) δ 5.22 (s, 2H, CH_2); 5.47 (brs, 2H, NH_2); 7.31 (dd, $J_{3-4} = 9$ Hz, $J_{1-3} = 2.4$ Hz, 1H, 3-H); 7.32 (t, $J = 7.2$ Hz, 1H, C_6H_5); 7.37 (t, 2H, $J = 7.2$ Hz, C_6H_5); 7.41 (m, 3H, C_6H_5 + 8-H); 7.52 (d, $J_{3-4} = 8$ Hz, 1H, 4-H); 7.69 (t, 1H, 9-H); 7.86 (s, 1H, 1-H); 8.09 (d, $J_{7-8} = J_{8-9} = 8$ Hz, 1H, 7-H); 8.42 (d, $J_{9-10} = 8.2$ Hz, 10-H).

3-Benzyloxy-6-aminophenanthridine (1e) (by Suzuki-Miyaura cross coupling). A solution of 5-benzyloxy-2-bromoaniline (1 g, 3.6 mmol) in 20 mL dioxane and 6 mL 1 M Na_2CO_3 was stirred under N_2 for 5 min. Pd[P(C_6H_5)$_3$]$_4$ (0.2 g, 0.17 mmol) was then introduced followed by 2-(4,4,5,5-tetramethyl-[1,3,2]-dioxaborolan-2-yl)-benzonitrile (3.6 mmol, 0.825 g). The mixture was refluxed for 12 h and then concentrated. The residue was extracted with CH_2Cl_2 (3 × 10 mL). The organic solution was washed with H_2O and dried with Na_2SO_4 and evaporated. The final compound was purified by column chromatography (CH_2Cl_2−EtOH, 98:2) and crystallized from EtOAc. Yield: 63%. Mp 121−123 °C. Anal. ($C_{20}H_{16}N_2O$) C, H, N. ^{1}H NMR ($CDCl_3$) δ 5.20 (s, 2H, CH_2); 5.32 (br s, 2H, NH_2); 7.11 (dd, $J_{1-2} = 9.2$ Hz, $J_{2-4} = 2.4$ Hz, 1H, 2-H); 7.26 (d, 1H, 4-H); 7.34 (t, $J_{3'-4'} = J_{4'-5'} = 7.2$ Hz, 1H, 4′-H); 7.41 (t, 2H, $J_{2'-3'} = J_{5'-6'} = 7.2$ Hz, 3′-H and 5′-H); 7.50 (d, 2H, 2′-H, and 6′-H); 7.55 (td, $J_{8-10} = 1$ Hz, $J_{8-9} = 8$ Hz, 1H, 8-H); 7.76 (td, $J_{9-10} = 0.8$ Hz, 1H, 9-H); 7.86 (d, $J_{7-8} = 8$ Hz, 1H, 7-H); 8.34 (d, 1H, 1-H); 8.44 (d, $J_{9-10} = 8.4$ Hz, 1H, 10-H). ^{13}C NMR ($CDCl_3$) δ 70.5; 108.7; 114.6; 115.9; 117.9; 122.7; 123.4; 123.7; 126.4; 128.0; 128.4; 129.0; 131.2; 134.8; 137.3; 146.2; 155.5; 160.1. IR (KBr) γ 517; 621; 681; 718; 757; 811; 856; 890; 994; 1020; 1085; 1135; 1178; 1220; 1253; 1300; 1357; 1402; 1460; 1514; 1547; 1600; 1657; 1755; 1824; 1958; 2368; 2848; 2851; 3114; 3314; 3742.

Phthalylation of Benzyloxy-6-Aminophenanthridines. The amines **1c**−**e** (0.7 g, 2.3 mmol) were dissolved in THF (30 mL) containing 1 mL NEt_3. Phthalic anhydride (0.34 g, 2.3 mmol) was then added, and the mixture was refluxed for 6 h. THF was removed under reduced pressure. Water (20 mL) was added and the mixture extracted with CH_2Cl_2 (3 × 10 mL). The organic layer was dried (Na_2SO_4) and evaporated. The residue was subjected to chromatography (CH_2Cl_2 100%) and crystallization from *i*-PrOH.

2-(1-Benzyloxyphenanthridin-6-yl)-isoindole-1,3-dione (3c). Yield: 80%. Mp 189−193 °C. Anal. ($C_{28}H_{18}N_2O_3$) C, H, N. ^{1}H NMR ($CDCl_3$) δ 5.45 (s, 2H, CH_2); 7.33 (d, $J_{2-3} = 8$ Hz, 1H, 2-H); 7.42 (t, $J_{3'-4'} = J_{4'-5'} = 7.2$ Hz, 1H, 4′-H); 7.47 (t, $J_{2'-3'} = J_{5'-6'} = 7.2$ Hz, 2H, 3′-H and 5′-H); 7.60 (d, 2H, 2′-H and 6′-H); 7.65 (t, $J_{7-8} = J_{8-9} = 8$ Hz, 1H, 8-H); 7.70 (t, $J_{3-4} = 8$ Hz, 1H, 3-H); 7.80 (t, 1H, 9-H); 7.88 (m, 3H, phthalyl and 4-H); 7.93 (d, 1H, 7-H); 8.05 (dd, $J = 5.6$ Hz, $J = 3.2$ Hz, 2H, phthalyl); 9.72 (d, $J_{9-10} = 8.8$ Hz, 1H, 10-H). MS (E^+) *m*/*z*: 431 $[M + H]^+$; 453 $[M + Na]^+$.

2-(2-Benzyloxy-phenanthridin-6-yl)-isoindole-1,3-dione (3d). Yield: 81%. Mp 138−141 °C. Anal. ($C_{28}H_{18}N_2O_3$) C, H, N. ^{1}H NMR ($CDCl_3$) δ 5.30 (s, 2H, CH_2); 7.40 (t, $J_{3'-4'} = J_{4'-5'} = 7.2$ Hz, 1H, 4′-H); 7.45 (t, $J_{2'-3'} = J_{5'-6'} = 7.2$ Hz, 2H, 3′-H + 5′-H); 7.50 (dd, $J_{3-4} = 9.4$ Hz, $J_{1-3} = 2.4$ Hz, 1H, 3-H); 7.57 (d, 2H, 2′-H and 6′-H); 7.69 (t, $J_{7-8} = J_{8-9} = 8$ Hz, 1H, 8-H); 7.90 (m, 4H, phthalyl, 9-H and 4-H); 8.05 (m, 3H, phthalyl and 1-H); 8.15 (d, 1H, 7-H); 8.62 (d, $J_{9-10} = 8.8$ Hz, 1H, 10-H).

2-(3-Benzyloxyphenanthridin-6-yl)-isoindole-1,3-dione (3e). Yield: 83%. Mp 121−123 °C. Anal. ($C_{28}H_{18}N_2O_3$) C, H, N. ^{1}H NMR ($CDCl_3$) δ 5.24 (s, 2H, CH_2); 7.35 (t, $J_{3'-4'} = J_{4'-5'} = 7.2$ Hz, 1H, 4′-H); 7.41 (t, $J_{2'-3'} = J_{5'-6'} = 7.2$ Hz, 2-H, 3′-H + 5′-H); 7.48 (dd, $J_{1-2} = 9.4$ Hz, $J_{2-4} = 2.4$ Hz; 1H, 2-H); 7.50 (d, 2H, 2′-H and 6′-H); 7.61 (t, $J_{7-8} = J_{8-9} = 8$ Hz, 1H, 8-H); 7.70 (d, 1H, 4-H); 7.87 (dd, $J = 3.2$ Hz, $J = 5.6$ Hz, 2H, phthalyl); 7.88 (m, 2H, 7-H and 9-H); 8.04 (dd, 2H, phthalyl); 8.55 (d, 1H, 1-H); 8.61 (d, $J_{9-10} = 8.8$ Hz, 10-H). ^{13}C NMR ($CDCl_3$) δ 70.7; 111.4; 119.6; 120.4; 122.5; 123.3; 123.9; 124.5; 126.1; 127.4; 128.1; 128.6; 129.1; 132.1; 132.6; 135.1; 135.5; 136.7; 145.3; 146.4; 159.9; 167.7. IR (KBr) γ 537; 575; 631; 681; 700; 721; 755; 785; 814; 842; 884; 947; 1027; 1072; 1102; 1138; 1181; 1214; 1257; 1302; 1370; 1404; 1452; 1472; 1574; 1600; 1715; 1792; 2991; 3031; 3044; 3434; 3600; 3708; 3831; 3894 cm^{-1}. MS (E+) *m*/*z*: 431 $[M + H]^+$; 453 $[M + Na]^+$.

Debenzylation of 2-(Benzyloxyphenanthridin-6-yl)-isoindole-1,3-diones. Preparation of Phenols 4c−e. 0.1 g of 10% Pd/C and 0.5 mL of AcOH were added to a solution of 2-(benzyloxyphenanthridin-6-yl)-isoindole-1,3-dione (1.9 mmol, 0.65 g) in 50 mL EtOH and 50 mL CH_2Cl_2. The mixture was stirred under H_2 atmosphere (AP) for 12 h. The catalyst was removed by filtration through a Whatman filter. The filter was washed once with 5 mL EtOH. The phenols crystallized upon concentration of the ethanolic solution.

2-(1-Hydroxyphenanthridin-6-yl)-isoindole-1,3-dione (4c). Yield: 97%. Mp 189−193 °C. Anal. ($C_{21}H_{12}N_2O_3$) C, H, N.^{1}H NMR ($CDCl_3$) δ 7.23 (d, $J_{2-3} = J_{3-4} = 8$ Hz, 1H, 2-H); 7.52 (t, 1H, 3-H); 7.59 (t, $J_{7-8} = J_{8-9} = 8$ Hz, 1H, 8-H); 7.68 (d, 1H, 4-H); 7.82 (m, 4H, phthalyl and 7-H and 9-H); 7.97 (dd, $J = 3.2$ Hz, $J = 5.6$ Hz, phthalyl); 9.80 (d, $J_{9-10} = 8.4$ Hz, 1H, 10-H); 10.9 (br s, 1H, OH).

2-(2-Hydroxyphenanthridin-6-yl)-isoindole-1,3-dione (4d). Yield: 82%, Mp 201−203 °C. Anal. ($C_{21}H_{12}N_2O_3$) C, H, N. ^{1}H NMR ($CDCl_3$) δ 7.35 (t, 1H); 7.63 (dd, 1H, $J_{3-4} = 8.5$ Hz, $J_{1-3} = 3$ Hz, 3-H); 7.71 (t, 1H); 7.95 (m, 5H, phthalyl + 1H); 8.10 (m, 4H, phthalyl); 8.18 (d, 1H, 7-H); 8.60 (d, 1H, 10-H); 8.75 (brs, OH).

2-(3-Hydroxyphenanthridin-6-yl)-isoindole-1,3-dione (4e). Yield: 98%. Mp 169−172 °C. Anal. ($C_{21}H_{12}N_2O_3$) C, H, N.^{1}H NMR ($CDCl_3$) δ 7.30 (dd, $J_{1-2} = 8.8$ Hz, $J_{2-4} = 2.4$ Hz, 1H, 2-H); 7.49 (t, $J_{7-8} = J_{8-9} = 8$ Hz, 1H, 8-H); 7.52 (d, 1H, 4-H); 7.80 (m, 4H, phthalyl + 7-H + 9-H); 7.97 (dd, $J = 5.6$ Hz, $J = 3.2$ Hz, phthalyl); 8.41 (d, 1H, 1-H); 8.52 (d, $J_{9-10} = 8.2$ Hz, 1H, 10-H); 9.50 (brs, 1H, OH).

Preparation of Spacers (5a,b). *N*-Hydroxybenzotriazole (2.83 g, 21 mmol) and dicyclohexylcarbodiimide (4.14 g, 20 mmol) were added to a cooled (5 °C) solution of *ε*-*Z*-aminocaproic acid (6.62 g, 25 mmol) in 50 mL EtOAc. The mixture was left under stirring for 2 h at rt. The precipitated dicyclohexylurea was filtrated and washed once with 10 mL EtOAc. 5-Aminopentan-1-ol (2.16 g, 21 mmol) and NEt_3 (5 mL) were added to the combined filtrates. After 3 h stirring, the mixture was diluted in 150 mL EtOAc and washed with 20 mL 1 N HCl followed by 50 mL saturated $NaHCO_3$ and then with 20 mL H_2O. Derivatives **5** crystallized upon concentration of the solvent. Further purification could be achieved by crystallization from EtOAc.

5-(6-Benzyloxycarbonylaminohexanoylamino)pentan-1-ol (5a). Yield: 85%. Mp: 108−110 °C. Anal. ($C_{19}H_{30}N_2O_4$) C, H, N. ^{1}H NMR ($CDCl_3$) δ 1.25−1.85 (m, 12H, 6 × CH_2); 2.15 (t, $J = 7.4$ Hz, 2H, CH_2CO); 3.19 (q, $J = 6.4$ Hz, 2H, CH_2NH); 3.26 (q, $J = 6.4$ Hz, 2H, CH_2NH); 3.64 (t, $J = 6.4$ Hz, CH_2OH); 4.88 (br s, 1H, NH); 5.08 (s, 2H, CH_2C$_6$H$_5$); 5.56 (br s, 1H, N*H*); 7.28−7.38 (m, 5H, C_6H_5). ^{13}C NMR ($CDCl_3$) δ 23.4; 25.3; 25.6; 25.9; 29.7; 30.0; 32.5; 36.9; 39.6; 41.2; 62.9; 67.0; 128.5; 128.9; 137.0; 156.9; 173.3. IR (KBr) γ 528; 586; 700; 636;

779; 950; 986; 1042; 1200; 1236; 1214; 1235; 1258; 1329; 1434; 1474; 1528; 1621; 1679; 2857; 2871; 3015; 3331; 3365; 3378; 3600; 3729 cm^{-1}. MS (E^+) *m/z*: 351 $[M + H]^+$; 373 $[M + Na]^+$.

5-(6-*tert*-Butyloxycarbonylaminohexanoylamino)pentan-1-ol (5b). Yield 67%. Mp 67−72 °C. Anal. ($C_{15}H_{30}N_2O_4$) C, H, N. ^1H NMR ($CDCl_3$) δ 1.3 (m, 12 H, 6 × CH_2); 1.5 (s, 9H, $(CH_3)_3$); 2.1 (t, 2H, CH_2CO); 3.03 (q, $J = 6.4$ Hz, 2H, CH_2NH); 3.20 (q, 2H, CH_2NH); 3.55 (t, 2H, CH_2OH); 4.55 (s, 1H, NHCOO); 5.5 (s, 1H, CH_2NHCO). MS (E^+) *m/z*: 303$[M + H]^+$; 325 $[M + Na]^+$.

General Procedure for the Mitsunobu Reaction. Synthesis of Conjugates (6c−e). *Z*-Aminocaproylaminopentanol (**5a**) (1.8 mmol, 0.63 g) and triphenylphosphine (1.8 mmol, 0.47 g) were added to a solution of 2-(hydroxyphenanthridin-6-yl)-isoindole-1,3-dione (**4c−e**) (1.8 mmol, 0.61 g) in THF (30 mL). The mixture was cooled to 0 °C, and *iso*-propyl diazodicarboxylate (1.8 mol, 0.378 g) was introduced under vigorous stirring. After 2 h at rt, the reaction mixture was concentrated and H_2O (20 mL) was added. The aqueous suspension was extracted with CH_2Cl_2 (3 × 15 mL), the organic layer was dried with Na_2SO_4, and the solvent was evaporated. The final compound was obtained after column chromatography (EtOAc−CH_2Cl_2−toluene: 50−25−25).

(5-{5-[6-(1,3-Dioxo-1,3-dihydroisoindol-2-yl)-phenanthridin-1-yloxy]-pentylcarbamoyl}-pentyl)-carbamic Acid Benzyl Ester 6c. Yield 92%. Mp 134−137 °C. Anal. (C_{40} $H_{40}N_4O_6$) C, H, N. ^1H NMR ($CDCl_3$) δ 1.58 to 1.68 (m, 12H, (6 × CH_2); 2.09 (t, $J = 7.4$ Hz, 2H, CH_2CO); 3.14 (q, $J = 6.4$ Hz, 2H, CH_2NH); 3.32 (q, $J = 6.4$ Hz, 2H, CH_2NH); 4.32 (t, $J = 6.4$ Hz, 2H, CH_2O); 4.83 (br s, 1H, NH); 5.07 (s, 2H, $CH_2C_6H_5$); 5.46 (br s, 1H, NH); 7.24 (d, $J_{2-3} = J_{3-4} = 8$ Hz, 1H, 2-H); 7.34 (m, 5H, C_6H_5); 7.68 (m, 2H, 3-H + 8-H); 7.82 (m, 4H, phthalyl + 9-H + 4-H); 7.89 (d, $J_{7-8} = 8$ Hz, 1H, 7-H); 8.02 (dd, $J = 5.6$ Hz, $J = 3.2$ Hz, phthalyl); 9.71 (d, $J_{9-10} = 8.4$ Hz, 1H, 10-H). ^{13}C NMR ($CDCl_3$) δ 24.0; 25.4; 26.5; 29.2; 29.7; 29.8; 36.8; 39.6; 41.0; 66.8; 69.3; 110.4; 115.9; 123.3; 124.3; 124.4; 125.4; 127.6; 128.3; 128.5; 128.8; 129.0; 131.7; 132.4; 134.9; 135.3; 136.9; 145.4; 146.4; 156.7; 157.7; 167.6; 173.1. IR (KBr) cm^{-1} 478; 532; 671; 717; 771; 887; 964; 1033; 1080; 1157; 1273; 1373; 1458; 1535; 1635; 1689; 1728; 1913; 2314; 2862; 2931; 3063; 3302; 3749; 3865. MS (E^+) *m/z*: 673 $[M + H]^+$; 695 $[M + Na]^+$.

(5-{5-[6-(1,3-Dioxo-1,3-dihydroisoindol-2-yl)-phenanthridin-2-yloxy]-pentylcarbamoyl}-pentyl)-carbamic Acid Benzyl Ester (6d). Yield 65%. Mp 131−132 °C. Anal. (C_{40} $H_{40}N_4O_6$) C, H, N. ^1H NMR ($CDCl_3$) δ 1.50 to 1.52 (m, 12H, 6 × CH_2); 2.18 (t, $J = 7.4$ Hz, 2H, CH_2CO); 3.20 (q, $J = 6.4$ Hz, 2H, CH_2NH); 3.25 (q, $J = 6.4$ Hz, 2H, CH_2NH); 4.22 (t, $J = 6.4$ Hz, 2H, CH_2O); 4.80 (brs, 1H, NH); 5.10 (s, 2H, $CH_2C_6H_5$); 5.50 (brs, 1H, NH); 7.37 to 7.48 (m, 5H, C_6H_5); 7.54 (d, $J_{3-4} = 8$ Hz, 1H, 3-H); 7.68 (m, 2H, 4-H and 8-H); 7.89 (m, 3H, phthalyl and 9-H); 7.95 (s, 1H, 1-H); 8.45 (dd, $J = 3.2$ Hz, $J = 5.6$ Hz, phthalyl); 8.12 (d, $J_{7-8} = 8$ Hz, 1H, 7-H); 8.64 (d, $J_{9-10} = 8.2$ Hz, 1H, 10-H). MS (E^+) *m/z*: 673 $[M + H]^+$; 695 $[M + Na]^+$.

(5-{5-[6-(1,3-Dioxo-1,3-dihydroisoindol-2-yl)-phenanthridin-3-yloxy]-pentylcarbamoyl}-pentyl)-carbamic Acid Benzyl Ester (6e). Yield 97%. Mp 155−157 °C. Anal. (C_{40} $H_{40}N_4O_6$) C, H, N. ^1H NMR ($CDCl_3$) δ 1.41−1.67 (m, 12H, 6 CH_2); 2.12 (t, $J = 7.4$ Hz, 2H, CH_2CO); 3.11 (q, $J = 6.4$ Hz, 2H, CH_2NH); 3.19 (q, $J = 6.4$ Hz, 2H, CH_2NH); 3.24 (t, $J = 6.4$ Hz, 2H, CH_2OAr); 4.81 (br s, 1H, NH); 5.01 (s, 2H, $CH_2C_6H_5$); 5.71 (brs, 1H, NH); 7.24 (m, 5H, C_6H_5); 7.32 (dd, $J_{1-2} = 8$ Hz, $J_{2-3} = 2.4$ Hz, 2-H); 7.55 (m, 2H, 4-H and 8-H); 7.81 (m, 4H, phthalyl and 7-H and 9-H); 7.98 (dd, $J = 3.2$ Hz, $J = 5.6$ Hz, phthalyl); 8.48 (d, 1H, 1-H); 8.55 (d, $J_{9-10} = 8.4$ Hz, 10-H). MS (E^+) *m/z*: 673 $[M + H]^+$; 695 $[M + Na]^+$.

Removal of the Phthalyl Protecting Group: Preparation of 7c−e. Hydrazine hydrate (0.2 mL) was added to a solution of **6c−e** (0.336 g, 0.5 mmoL) in DMF (1 mL). The mixture was heated at 70 °C for 15 min and then cooled to rt. After evaporation under vacuum, the solid residue was taken up with CH_2Cl_2 (30 mL). The solution was washed with H_2O (2 × 5 mL), dried, and concentrated. Compounds **7c−e** were purified by column chromatography (CH_2Cl_2−EtOH−NEt_3, 95:5:0.1).

6-Amino-1-(benzyloxycarbonylaminohexanoylaminopentyloxy)phenanthridine (7c). Yield 65%. Mp 147−151 °C. Anal. ($C_{32}H_{38}N_4O_4$) C, H, N. ^1H NMR ($CDCl_3$) δ 1.51 to 1.72 (m, 12H, (6 × CH_2); 2.05 (t, $J = 7.0$ Hz, 2H, CH_2CO); 3.20 (q, $J = 6.5$ Hz, 2H, CH_2NH); 3.38 (q, $J = 6.5$ Hz, 2H, CH_2NH); 4.23 (t, $J = 6.5$ Hz, 2H, CH_2O); 5.12 (s, 2H, $CH_2C_6H_5$); 5.55 (br s, 3H, NH); 7.25 (d, $J_{2-3} = J_{3-4} = 8$ Hz, 1H, 2-H); 7.24 (m, 5H, C_6H_5); 7.73 (m, 2H, 3-H and 8-H); 7.82 (m, 2H, 9-H and 4-H); 7.85 (d, $J_{7-8} = 8$ Hz, 1H, 7-H); 9.45 (d, $J_{9-10} = 8.4$ Hz, 1H, 10-H). MS (E+) *m/z*: 543 $[M + H]^+$; 565 $[M + Na]^+$.

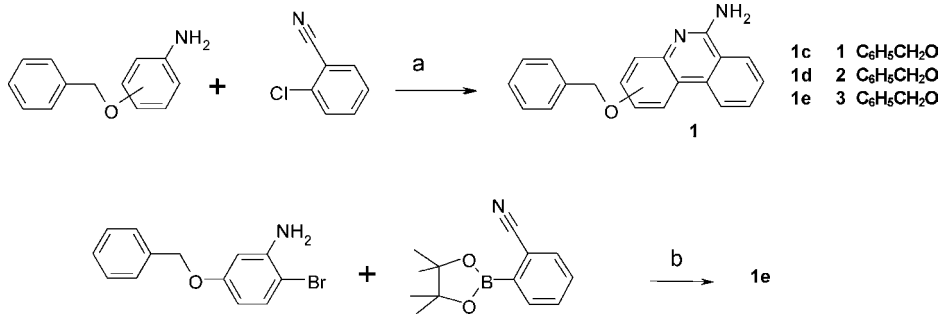
6-Amino-2-(benzyloxycarbonylaminohexanoylaminopentyloxy)phenanthridine (7d). Yield 62%, Mp 118−122 °C. Anal. ($C_{32}H_{38}N_4O_4$) C, H, N. ^1H NMR ($CDCl_3$) δ 1.47 to 1.62 (m, 12H, 6 × CH_2); 2.23 (t, $J = 6.5$ Hz, 2H, CH_2CO); 3.20 (q, $J = 6.5$ Hz, 2H, CH_2NH); 3.35 (q, $J = 6.5$ Hz, 2H, CH_2NH); 4.22 (t, $J = 6.4$ Hz, 2H, CH_2O); 4.85 (brs, 1H, NH); 5.12 (s, 2H, $CH_2C_6H_5$); 5.85 (br s, 2H, NH_2); 7.32 (m, 5H, C_6H_5); 7.52 (d, $J_{3-4} = 7.5$ Hz, 1H, 3-H); 7.65 (m, 2H, 4-H + 8-H); 7.85 (m, 1H, 9-H); 7.96 (s, 1H, 1-H); 8.10 (d, $J_{7-8} = 8$ Hz, 1H, 7-H); 8.54 (d, $J_{9-10} = 8.2$ Hz, 1H, 10-H).

6-Amino-3-(benzyloxycarbonylaminohexanoylaminopentyloxy)phenanthridine (7e). Yield 48%. Mp: 123−125 °C. Anal. ($C_{32}H_{38}N_4O_4$) C, H, N. ^1H NMR ($CDCl_3$) δ 1.42−1.69 (m, 12H, 6 CH_2); 2.15 (t, $J = 7.3$ Hz, 2H, CH_2CO); 3.13 (q, $J = 6.4$ Hz, 2H, CH_2NH); 3.22 (q, $J = 6.4$ Hz, 2H, CH_2NH); 4.06 (t, $J = 6.6$ Hz, 2H, CH_2OAr); 5.01 (s, 2H, $CH_2C_6H_5$); 5.71 (br s, 2H, NH_2); 7.24 (m, 5H, C_6H_5); 7.39 (dd, $J_{1-2} = 8$ Hz, $J_{2-3} = 2.4$ Hz, 2-H); 7.52 (m, 2H, 4-H and 8-H); 7.81 (m, 2H, 7-H + 9-H); 8.38 (d, 1H, 1-H); 8.50 (d, $J_{9-10} = 8.2$ Hz, 10-H). MS (E^+) *m/z*: 543 $[M + H]^+$; 565 $[M + Na]^+$.

Removal of the Z-group. Preparation of 3-(6-Aminocaproylaminopentyloxy)-6-phtalimidophenanthridine (8e). Pd/C 10% (0.1 g) and 35% hydrochloric acid (0.2 mL) were added to a solution of **6e** (0.336 g, 0.5 mmoL) in 10 mL EtOH and 10 mL CH_2Cl_2. The mixture was stirred under H_2 atmosphere (AP) for 12 h. The catalyst was removed by filtration through a Whatman filter. The filter was rinsed once with 1 mL EtOH. The hydrochloride was isolated upon concentration under vacuum and used in the immobilization step without further purification.

{5-[5-(3,5-Dichloro-4-formylphenyloxy)-pentylcarbamoyl]-pentyl}-carbamic Acid *tert*-Butyl Ester (11). Boc-aminocaproylaminopentanol (3 mmol, 0.906 g) and triphenylphosphine (3 mmol, 0.786 g) were added to a solution of 2,6-dichloro-4-hydroxybenzaldehyde **10** (*35*) (3 mmol, 0.525 g) dissolved in 30 mL of THF. The mixture was cooled to 0 °C, and *iso*-propyl diazodicarboxylate (3 mmol, 0.590 g) was introduced under vigorous stirring. After 2 h at rt, the reaction mixture was concentrated and H_2O (20 mL) was added. The aqueous suspension was extracted with CH_2Cl_2 (3 × 10 mL), and the organic layer was dried with Na_2SO_4 and the solvent evaporated. The final compound was obtained after column chromatography (EtOAc−toluene: 50−50). Yield: 83%. Mp: 68−70 °C. Anal. ($C_{23}H_{34}Cl_2N_2O_5$) C, H, N. ^1H NMR ($CDCl_3$) δ 1.52 (s, 9H, $C(CH_3)_3$); 1.36−1.71 (m, 10H, CH_2); 1.86 (q, 2H, CH_2); 2.20 (t, 2H, $J = 7.5$ Hz, CH_2CO); 3.12 (dd, 2H, $J = 6.3$ Hz, CH_2NH); 3.29 (dd, 2H, $J = 6.3$ Hz, CH_2NH); 4.04 (t, 2H, $J = 6.1$ Hz,

Scheme 1. Preparation of Benzyloxy-6-aminophenanthridines 1c−e[a]



[a] (a) $NaNH_2$, $LiNH_2$, NH_3; (b) Na_2CO_3, $Pd[P(C_6H_5)_3]$, dioxane, H_2O.

CH_2O); 4.56 (br s, 1H, NH); 5.54 (br s, 1H, NH); 6.92 (s, 2H, H-3 + H-5); 10.44 (s, 1H, C*H*O).

{5-[5-(3,5-Dichloro-4-benzylidenaminoguanidine)-pentylcarbamoyl]-pentyl}-carbamic Acid *tert*-Butyl Ester (12). Aminoguanidine hydrochloride (0.22 g, 2 mmol) was added to a solution of conjugate **11** (0.98 g, 2 mmol) in 10 mL EtOH followed by the addition of AcONa, $5H_2O$ (0.27 g, 2 mmol). After 2 h refluxing, the hot mixture was filtered, and **12** precipitated upon cooling to rt. Yield: 54%. Anal. ($C_{24}H_{38}Cl_2N_6O_4$) C, H, N. ^{1}H NMR ($CDCl_3$) δ 1.24−1.63 (m, 10H, 5 × CH_2); 1.43 (s, 9H, $C(CH_3)_3$); 1.74 (q, 2H, CH_2); 2.17 (t, J = 7 Hz, 2H, CH_2CO); 3.08 (q, J = 6.03 Hz, 2H, CH_2NH); 3.25 (q, 2H, CH_2NH); 3.95 (t, J = 6 Hz, 2H, CH_2−O); 5.79 (br s, 2H, NH_2); 6.35 (br s, 1H, NH); 6.88 (s, 2H, 3-H and 5-H); 8.36 (s, 1H, NCH). ^{13}C NMR ($CDCl_3$) δ 23.0; 25.1; 26.1; 28.2; 28.3; 29.0; 29.4; 36.1; 39.0; 68.0; 78.6; 115.2; 123.9; 134.8; 141.4; 155.9; 157.9; 160.6; 172.9.

2,6-Dichloro-4-(ε-aminocaproylaminopentyloxy)-benzylidenaminoguanidine) Trifluoroacetate (13). CF_3COOH (1 mL) was added to a solution of **12** (0.27 g, 0.5 mmol) in CH_2Cl_2 (10 mL). The solution was stirred for 2 h at rt and then concentrated until dryness. The viscous oil crystallized upon trituration with 2 mL cyclohexane followed by trituration with 2 mL Et_2O. Yield 76%, mp 75−78 °C. ^{1}H NMR (DMSO-d_6) δ 1.21−1.88 (m, 12 H, 6 × CH_2); 2.21 (t, J = 7 Hz, 2H, CH_2CO); 3.03 (m, 4H, 2CH_2NH); 4.02 (t, J = 6 Hz, 2H, CH_2−O); 6.23 (m, 4H, NH); 6.84 (s, 2H, 3-H and 5-H); 8.25 (s, 1H, NCH).

Immobilization of Ligands on Activated Sepharose Beads. Ligands were attached to CNBr-activated Sepharose 4 fast flow from Amersham Pharmacia according to the manufacturer's directions. A solution of 0.1 mmol ligands **8e** or **13** in 2 mL DMSO was added to 38 mL pH 8.3 solution (0.02 M $NaHCO_3$ + 0.1 M NaCl). This solution (0, 1, 2, 5 mL) was added to approximately 1 mL of beads suspended in pH 8.3 solution (final volume in each cartridge 10 mL). The cartridges were allowed to shake for 12 h at rt. The solutions were then drained from the beads, and 10 mL ethanolamine buffered solution (pH 8.5) was added to each cartridge, which was allowed to shake for 3 h at rt. This quenching step was repeated once. The phthalyl protecting group of 6AP-beads was then removed. A 3 mL solution of H_2O, DMF, and hydrazine hydrate (1:1:1) was added to the cartridges. After 15 min shaking, the solution was drained and the beads washed 3 times with 10 mL buffer. Finally, 10 mL buffer containing 1 g·L^{-1} NaN_3 was added to each cartridge, which was stored at 4 °C.

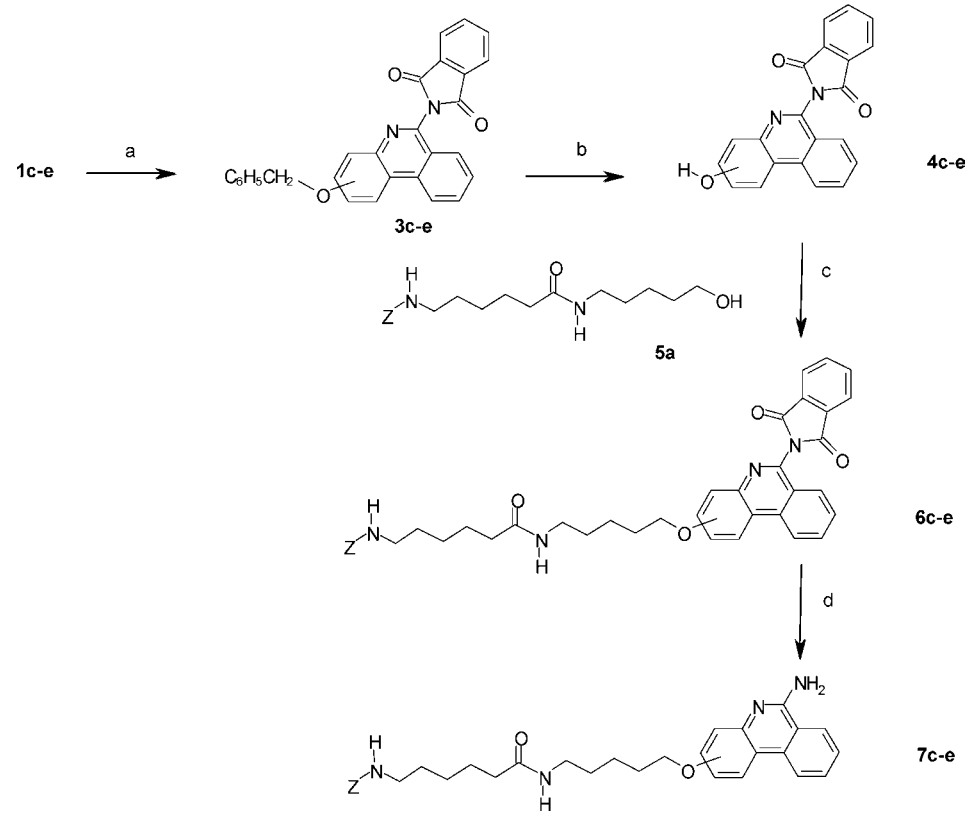
Affinity Chromatography Experiments on Immobilized 6AP and GA. These experiments were performed as previously described (*31*). Briefly, yeast (*Saccharomyces cerevisiae*) cell extracts were prepared using homogenization buffer (25 mM Tris-HCl (pH 7.4), 100 mM NaCl, 0.2% Triton X-100, and 1 mM PMSF). Yeast protein extracts were obtained from a culture growing at 30 °C ($OD_{600\ nm}$ = 0.8). Cell pellets were resuspended in homogenization buffer (300 μL/100 mL of culture) and lysed using acid-washed glass beads (purchased from Sigma, 300 μL/100 mL of culture). Homogenates were vortexed for 30 s followed by 30 s ice-cooling (six times) and then centrifuged for 3 min at 3000 rpm at 4 °C. Supernatants were recovered, assayed for protein content (using Bio-Rad protein assay), and immediately loaded batchwise on the affinity matrices. Just before use, 6AP and GA beads were washed with 1 mL of bead buffer (50 mM Tris−HCl (pH 7.4), 5 mM NaF, 250 mM NaCl, 5 mM EDTA, 5 mM EGTA, 0.1% Nonidet P-40, 10 μg/mL of leupeptin, aprotinin, and soybean trypsin inhibitor, and 100 μM benzamidine) and diluted 4 times in this buffer. 200 μg of yeast protein extract were added to 40 μL of diluted beads (10 μL of packed beads). The volume was adjusted to 600 μL by adding bead buffer, and the tubes were rotated at 4 °C for 30 min. Competitions with active or inactive drugs were performed with free compounds (or the corresponding volume of DMSO) at a final concentration of 1 mM incubated with cell extracts for 3 min before the mixture was added to the affinity matrix. Then, bead buffer containing the same quantity (1 mM) of the corresponding free compound was added immediately (as described previously) to reach a final volume of 600 μL. After incubation, a brief spin at 10 000 *g* at 4 °C, and removal of the supernatant, the beads were washed 4 times with bead buffer before addition of 35 μL of 2× Laemmli sample buffer. Following heat denaturation for 3 min at 95 °C, bound proteins were analyzed by 10% SDS-PAGE as described below.

Electrophoresis and Silver Staining. The proteins bound to 6AP or GA matrices were separated by 10% SDS-PAGE (precast NuPAGE−InVitrogen−1 mm thick gel) followed by silver staining using a GE Healthcare Life Sciences SDS-PAGE silver staining kit.

RESULTS

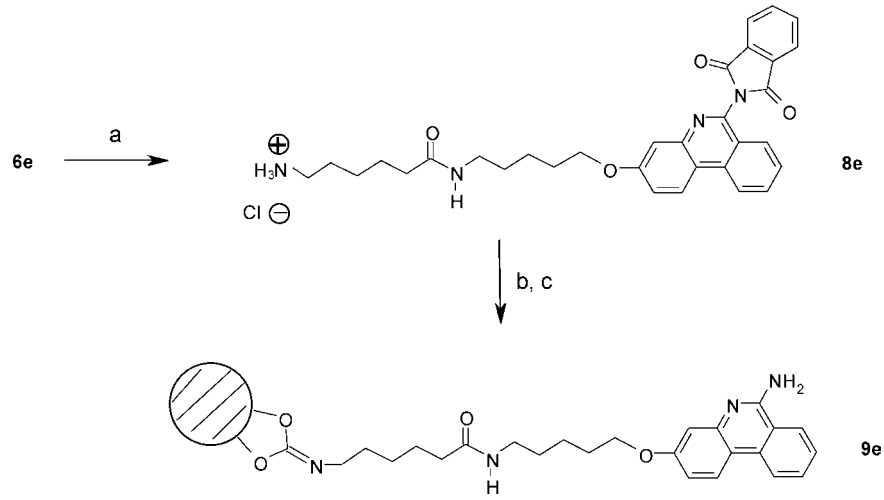
Preparation of 6-Aminophenanthridine Beads. The synthesis of the conjugates of 6AP is depicted in Schemes 1 and 2. Condensation of 2- or 3-benzyloxyaniline with 2-chlorobenzonitrile in liquid ammonia using metal amides (*32*) led to benzyloxy-6-aminophenanthridine **1c−e**. The mixture of **1c** and **1e** could not be separated on column chromatography. Alternatively, 3-benzyloxy-6-aminophenanthridine **1e** was obtained in a Suzuki−Myaura coupling procedure (*33*). Phthalylation of 6-aminophenanthridines **1c−e** afforded derivatives **3c−e**. The benzyl group was removed by catalytic hydrogenation to afford phenols **4c−e**. The spacer arms **5** were obtained by acylation of 5-aminopentanol with Boc or *Z*-ε-aminocaproic acid. Condensation of phenols **4c−e** with spacer **5a** under Mitsunobu reaction conditions led to conjugates **6c−e**. Finally, the phtalimido protecting group was eliminated to afford **8c−e**. Following the evaluation of **8c−e** in the antiprion test, the removal of

Scheme 2. Synthesis of 6AP Conjugates[a]



[a] (a) Phthalic anhydride, NEt_3, THF; (b) H_2, Pd/C; (c) $(C_6H_5)_3P$, di-*iso*-propyl diazodicarboxylate, THF; (d) hydrazine hydrate, H_2O, DMF.

Scheme 3. Synthesis of 6AP Beads[a]



[a] (a) H_2 Pd/C, HCl, EtOH; (b) Sepharose preactivated beads; (c) hydrazine hydrate, H_2O, DMF.

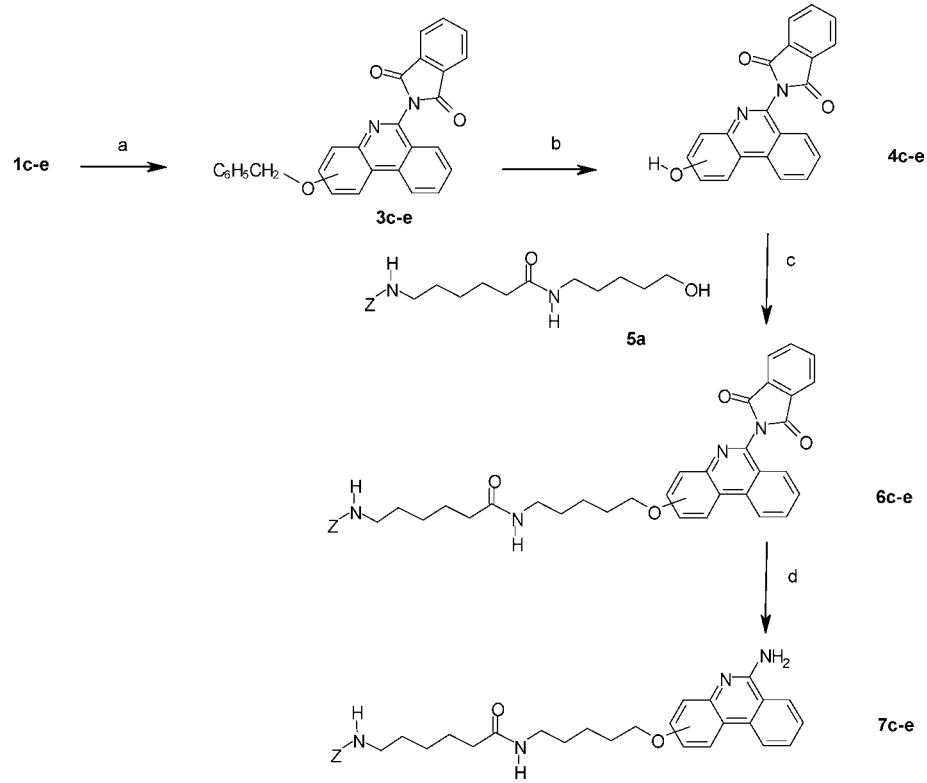
the Z-group was performed only on **6e**, which bears the spacer arm in position 3.

Elimination of the Z protecting group of **6e** led to the conjugate **8e**. The immobilization of conjugate **8e** was performed on commercially available preactivated beads (CNBr). Several ratios of ligand conjugated to the Sepharose beads were tested. In the following affinity chromatography experiments, optimal results were obtained with the matrices made using the bigger volume of ligand solution (5 mL). Residual activated groups were quenched by aminoethanol. Finally, the phthalyl protective group was removed by hydrazinolysis. Optimization of reaction conditions led to the selection of a DMF, H_2O, hydrazine hydrate (1:1:1) mixture (Scheme 3).

Preparation of Guanabenz Beads. The conjugate was easily obtained from 2,6-dichloro-4-hydroxybenzaldehyde **10** (*35*). Coupling of the Boc-protected spacer arm **5b** was achieved under Mitsunobu conditions leading to conjugate **11**. This aldehyde gave the protected GA conjugate **12** upon refluxing with aminoguanidine in EtOH. Acidic cleavage of the Boc protecting group led to the trifluoroacetate **13**, which was eventually coupled to Sepharose preactivated beads to obtain GA-beads **14** (Scheme 4).

Affinity Chromatography Assays. The ability of CPZ and QC to compete for ribosomal components binding on 6AP and GA beads is depicted in Figure 2. As can be seen, QC (lanes

Scheme 4. Preparation of GA Beads[a]



[a] (a) $(C_6H_5)_3P$, di-*iso*-propyl diazodicarboxylate, THF; (b) aminoguanidine, EtOH; (c) CF_3COOH, CH_2Cl_2; (d) Sepharose preactivated beads.

6), but not CPZ (lanes 5), was able to compete for the binding of ribosomal components to both 6AP and GA beads.

DISCUSSION

We have previously described two single-step routes for the synthesis of 6APs (*32, 33*). In the present work, these two approaches were used. In preliminary structure−activity studies, we noticed that derivatives substituted on the amino group were devoid of any antiprion activity. Therefore, **1b** was selected as an inactive control useful for the affinity chromatography assays. This also indicates that the spacer arm should not be linked to the 6-amino group. Further, this amino group of 6AP appeared to be rather nucleophilic and then, if unprotected, would likely react in the coupling procedure on the activated Sepharose beads. In order to circumvent this major problem, a protective group which could be eliminated after grafting the conjugate to the beads was required. It implies that the deprotection of the 6-amino group of 6AP derivatives should be achieved under mild conditions. The phthalyl protective group fulfilled this requirement. The antiprion activity of conjugates **7c**−**e** has been evaluated in the yeast prion-based assay. Only the **7e** derivative substituted in position 3 retained some antiprion activity of **1a**, whereas conjugates **7c** and **7d**, substituted in position 1 or 2 respectively, were totally inactive (*31*). Therefore, **8e** was selected for the affinity chromatography study. Concerning GA beads, we noticed that arginine-containing peptides have been previously grafted on Sepharose beads. In these assays, the unprotected amidine group did not interfere in the coupling process (*34*). Therefore, in contrast to the preparation of 6AP beads, it was estimated that the amidine group of Guanabenz conjugate did not need to be protected.

Affinity chromatography experiments were performed with both 6AP and GA beads. Interestingly, although the two compounds are chemically unrelated, they were both found to interact with the ribosome in an RNA-dependent manner (*31*). First, both 6AP and GA showed specific interactions with ribosomal components: most of the proteins specifically bound to 6AP or GA beads turned out to be ribosomal proteins. The binding of these ribosomal proteins was specific, as they were absent from control beads (Figure 2, panel B, lane 1 in both gels), present on 6AP or GA beads (lane 2) and respectively competed away by free 6AP (left gel, lane 3) or by free GA (right gel, lane 3) but not by free 6APi (left gel, lane 4) or by free GAi (right gel, lane 4). The interaction of both 6AP and GA with ribosomal components was then shown to be RNA-dependent, as a treatment of the cellular extracts with RNase A before affinity chromatography purification completely abolished the binding of all ribosomal proteins. 6AP and GA were further shown to selectively interact with the domain V of the large rRNA (rRNA) of the large subunit of the ribosome. Therefore, the binding of ribosomal components to 6AP or GA beads is best explained by postulating that, in affinity chromatography experiments, immobilized 6AP or GA retains the entire ribosome due to the ability to specifically interact with domain V of the large rRNA. Interestingly, in parallel to their ability to specifically interact with domain V of the large rRNA, both 6AP and GA were shown to specifically inhibit its protein folding activity. Indeed, in addition, to bear the peptidyl transferase activity involved in translation, domain V of the large rRNA of the large subunit of the ribosome has also been shown to be able to assist protein folding, at least *in vitro* (*36*). We thus found that both 6AP and GA inhibit this ribosome-borne protein folding activity (RPFA) without any effect on the peptidyl transferase activity of the ribosome. Both 6APi (**1b**) and GAi (**2b**), which are inactive as antiprion chemical derivatives of, respectively, 6AP and GA, were unable to compete for the binding of ribosomal components to both 6AP and GA beads and also to inhibit RPFA (*30*). We thus proposed that the antiprion effect of both 6AP and GA could be due to their ability to inhibit the RPFA, and thus, RPFA could be involved in prion propagation. Therefore,

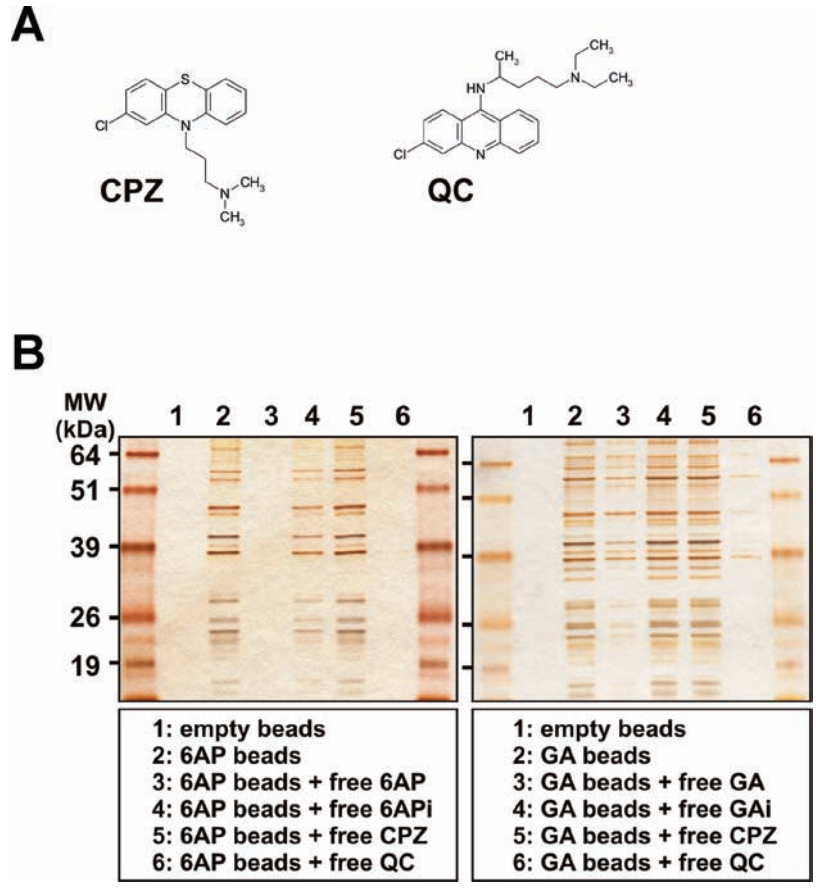


Figure 2. Competition experiments with Chlorpromazine (CPZ) and Quinacrine (QC). A. Molecular structures of CPZ and QC were depicted. B. Extracts from yeast were incubated with 6AP beads (left panel) or GA beads (right panel). The beads were then washed extensively and the bound proteins analyzed by SDS-PAGE. Proteins were then silver-stained. Most of the bands were previously identified as ribosomal proteins from both the small and large subunits of the ribosome. In both gels, lane 1 corresponds to chromatography using control beads without 6AP (left gel) or GA (right gel), and lane 2 to chromatography using 6AP (left gel) or GA (right gel) beads. Note that, in both cases, the patterns of eluted ribosomal proteins were rather similar. In both gels, lanes 3 to 6 correspond to competition experiments with the indicated free compounds. Note that QC, but not CPZ, was able to compete for the binding of ribosomal components to both 6AP and GA beads.

we were interested in determining if other known antiprion drugs could compete for the binding of ribosomal components on 6AP and GA beads when added to a mix of 6AP or GA beads and cellular extracts. This possibility is particularly appealing, as free 6AP was shown to efficiently compete for the binding of ribosomal components to GA beads, and vice versa (*31*), clearly indicating that they share overlapping binding sites on rRNA, which was indeed recently shown to be the case (*37*). Therefore, the ability of other unrelated antiprion drugs to compete for the binding of the ribosome to 6AP and GA beads would be an indication that these compounds share at least some common binding sites on domain V of the large rRNA of the large ribosomal subunit with 6AP or GA. Hence, all these molecules could share the same biological target accounting for their antiprion effect. Quinacrine (QC) and Chlorpromazine (CPZ) are two drugs already in use in humans for the treatment of malaria and psychosis, respectively. They were recently isolated as active *ex vivo* against mammalian prion in a N2a cell-based model (*8*) and the latter against yeast prions (*13*). The ability of CPZ and QC to compete for ribosomal components binding on 6AP and GA beads was determined (Figure 2). Interestingly, whereas QC was clearly able to efficiently compete for the binding of ribosomal components to both 6AP and GA beads (at least as efficiently as 6AP and GA themselves), CPZ was not, as observed for 6APi and GAi, derivatives of 6AP and GA that are inactive as antiprion drugs. These results suggest that QC, but not CPZ, could share at least some binding sites with 6AP and GA on the large rRNA. The fact that CPZ was unable to compete for the binding of rRNA on 6AP and GA beads suggests that either it has other biological target(s) or it also targets the ribosome and possibly also the large rRNA but on different and nonoverlapping binding sites than 6AP and GA.

CONCLUSION

In the present study, we have used a simple chemical spacer arm easy to introduce by Mitsunobu reaction. Therefore, the introduction of the linker requires the synthesis of phenols obtained from their benzyl ether precursors compatible themselves with the various reaction conditions used in the synthesis of the tricyclic phenanthridine moitie. This spacer arm can be considered less hydrophilic than classical polyoxyethylenic linkers, thus greatly facilitating the purification of the conjugates by column chromatography. The two hydrophobic parts of the spacer should not be able to establish interactions either with the bioactive molecule or with the hydrophilic Sepharose beads. The amide bond in the middle of the linker reduces the flexibility of the spacer. To the best of our knowledge, the deprotection of functional groups after grafting on the beads has not been previously reported. Using this procedure, we synthesized affinity chromatography matrices for both 6AP and GA, two antiprion drugs active from yeast to mammals. The identification of the protein folding activity of the ribosome as a common target of both compounds suggests the intriguing possibility that this largely unknown function borne by the large rRNA could be involved in prion propagation. Finally, it has been recently found that PrP^C is an amyloid-β oligomers receptor (*38*).

Because amyloids β-fibers are found in the brains of people suffering from Alzheimer's disease, this finding enhances the interest of studies aiming at deciphering the cellular mechanisms involved in the appearance and/or propagation of prion-based diseases.

ACKNOWLEDGMENT

We thank Sophie Mairesse-Lebrun for the microanalyses determinations of compounds and the ANR "blanche" from the French Ministère de la Recherche for financial support. DTT was supported by a PhD program from the French "Ministère de la Recherche" and CV by a Junior Contract from INSERM.

LITERATURE CITED

(1) Aguzzi, A., and Heikenwalder, M. (2006) Pathogenesis of prion diseases: current status and future outlook. *Nat. Rev. Microbiol. 4*, 765–775.

(2) Trevitt, C. R., and Collinge, J. (2006) A systematic review of prion therapeutics in experimental models. *Brain 129*, 2241–2265.

(3) Mallucci, G., Dickinson, A., Linehan, J., Klöhn, P. C., Brandner, S., and Collinge, J. (2003) Depleting neuronal PrP in prion infection prevents disease and reverses spongiosis. *Science 302*, 871–874.

(4) Mallucci, G. R., White, M. D., Farmer, M., Dickinson, A., Khatun, H., Powell, A. D., Brandner, S., Jefferys, J. G., and Collinge, J. (2007) Targeting cellular prion protein reverses early cognitive deficits and neurophysiological dysfunction in prion-infected mice. *Neuron 53*, 325–335.

(5) Soto, C., Kascsak, R. J., Saborio, G. P., Aucouturier, P., Wisniewski, T., Prelli, F., Kascsak, R., Mendez, E., Harris, D. A., Ironside, J., Tagliavini, F., Carp, R. I., and Frangione, B. (2000) Reversion of prion protein conformational changes by synthetic beta-sheet breaker peptides. *Lancet 355*, 192–197.

(6) Cordeiro, Y., Lima, L. M., Gomes, M. P., Foguel, D., and Silva, J. L. (2004) Modulation of prion protein oligomerization, aggregation, and beta-sheet conversion by 4,4′-dianilino-1,1′-binaphthyl-5,5′-sulfonate (bis-ANS). *J. Biol. Chem. 279*, 5346–5352.

(7) Bertsch, U., Winklhofer, K. F., Hirschberger, T., Bieschke, J., Weber, P., Hartl, F. U., Tavan, P., Tatzelt, J., Kretzschmar, H. A., and Giese, A. (2005) Systematic identification of antiprion drugs by high-throughput screening based on scanning for intensely fluorescent targets. *J. Virol. 79*, 7785–7791.

(8) Supattapone, S., Nguyen, H. O., Cohen, F. E., Prusiner, S. B., and Scott, M. R. (1999) Elimination of prions by branched polyamines and implications for therapeutics. *Proc. Natl. Acad. Sci. U.S.A. 96*, 14529–14534.

(9) Korth, C., May, B. C., Cohen, F. E., and Prusiner, S. B. (2001) Acridine and phenothiazine derivatives as pharmacotherapeutics for prion disease. *Proc. Natl. Acad. Sci. U.S.A. 98*, 9836–9841.

(10) Vilette, D., Andreoletti, O., Archer, F., Madelaine, M. F., Vilotte, J. L., Lehmann, S., and Laude, H. (2001) Ex vivo propagation of infectious sheep scrapie agent in heterologous epithelial cells expressing ovine prion protein. *Proc. Natl. Acad. Sci. U.S.A. 98*, 4055–4059.

(11) Archer, F., Bachelin, C., Andreoletti, O., Besnard, N., Perrot, G., Langevin, C., Le Dur, A., Vilette, D., Baron-Van Evercooren, A., Vilotte, J. L., and Laude, H. (2004) Cultured peripheral neuroglial cells are highly permissive to sheep prion infection. *J. Virol. 78*, 482–490.

(12) Doh-Ura, K., Iwaki, T., and Caughey, B. (2000) Lysosomotropic agents and cysteine protease inhibitors inhibit scrapie-associated prion protein accumulation. *J. Virol. 74*, 4894–4997.

(13) Vilette, D. (2008) Cell models of prion infection. *Vet. Res. 39*, 10.

(14) Bach, S., Talarek, N., Andrieu, T., Vierfond, J. M., Mettey, Y., Galons, H., Dormont, D., Meijer, L., Cullin, C., and Blondel, M. (2003) Isolation of drugs active against mammalian prions using a yeast-based screening assay. *Nat. Biotechnol. 21*, 1075–1081.

(15) Bach, S., Tribouillard, D., Talarek, N., Desban, N., Gug, F., Galons, H., and Blondel, M. (2006) A yeast-based assay to isolate drugs active against mammalian prions. *Methods 39*, 72–77.

(16) Tribouillard, D., Bach, S., Gug, F., Desban, N., Beringue, V., Andrieu, T., Dormont, D., Galons, H., Laude, H., Vilette, D., and Blondel, M. (2006) Using budding yeast to screen for anti-prion drugs. *Biotechnol. J. 1*, 58–67.

(17) Tribouillard-Tanvier, D., Beringue, V., Desban, N., Gug, F., Bach, S., Voisset, C., Galons, H., Laude, H., Vilette, D., and Blondel, M. (2008) Antihypertensive drug guanabenz is active in vivo against both yeast and mammalian prions. *PLoS ONE 3*, e1981.

(18) Vogtherr, M., Grimme, S., Elshorst, B., Jacobs, D. M., Fiebig, K., Griesinger, C., and Zahn, R. (2003) Antimalarial drug quinacrine binds to C-terminal helix of cellular prion protein. *J. Med. Chem. 46*, 3563–3564.

(19) Touil, F., Pratt, S., Mutter, R., and Chen, B. (2006) Screening a library of potential prion therapeutics against cellular prion proteins and insights into their mode of biological activities by surface plasmon resonance. *J. Pharm. Biomed. Anal. 40*, 822–832.

(20) Phuan, P. W., Zorn, J. A., Safar, J., Giles, K., Prusiner, S. B., Cohen, F. E., and May, B. C. (2007) Discriminating between cellular and misfolded prion protein by using affinity to 9-aminoacridine compounds. *J. Gen. Virol. 88*, 1392–401.

(21) Chaudhuri, T. K., and Paul, S. (2006) Protein-misfolding diseases and chaperone-based therapeutic approaches. *FEBS J. 273*, 1331–1349.

(22) Schnier, J. B., Kaur, G., Kaiser, A., Stinson, S. F., Sausville, E. A., Gardner, J., Nishi, K., Bradbury, E. M., and Senderowicz, A. M. (1999) Identification of cytosolic aldehyde dehydrogenase 1 from non-small cell lung carcinomas as a flavopiridol-binding protein. *FEBS Lett. 454*, 100–104.

(23) Knockaert, M., Lenormand, P., Gray, N., Schultz, P., Pouyssegur, J., and Meijer, L. (2002) p42/p44 MAPKs are intracellular targets of the CDK inhibitor purvalanol. *Oncogene 21*, 6413–6424.

(24) Bach, S., Knockaert, M., Reinhardt, J., Lozach, O., Schmitt, S., Baratte, B., Koken, M., Coburn, S. P., Tang, L., Jiang, T., Liang, D. C., Galons, H., Dierick, J. F., Pinna, L. A., Meggio, F., Totzke, F., Schachtele, C., Lerman, A. S., Carnero, A., Wan, Y., Gray, N., and Meijer, L. (2005) Roscovitine targets, protein kinases and pyridoxal kinase. *J. Biol. Chem. 280*, 31208–31219.

(25) Brehmer, D., Greff, Z., Godl, K., Blencke, S., Kurtenbach, A., Weber, M., Muller, S., Klebl, B., Cotten, M., Keri, G., Wissing, J., and Daub, H. (2005) Cellular targets of gefitinib. *Cancer Res. 65*, 379–382.

(26) Godl, K., Wissing, J., Kurtenbach, A., Habenberger, P., Blencke, S., Gutbrod, H., Salassidis, K., Stein-Gerlach, M., Missio, A., Cotten, M., and Daub, H. (2003) An efficient proteomics method to identify the cellular targets of protein kinase inhibitors. *Proc. Natl. Acad. Sci. U.S.A. 100*, 15434–15439.

(27) Shiyama, T., Furuya, M., Yamazaki, A., Terada, T., and Tanaka, A. (2004) Design and synthesis of novel hydrophilic spacers for the reduction of nonspecific binding proteins on affinity resins. *Bioorg. Med. Chem. 12*, 2831–2841.

(28) Whitesell, L., Mimnaugh, E. G., De Costa, B., Myers, C. E., and Neckers, L. M. (1994) Inhibition of heat shock protein HSP90-pp60v-src heteroprotein complex formation by benzoquinone ansamycins: essential role for stress proteins in oncogenic transformation. *Proc. Natl. Acad. Sci. U.S.A. 91*, 8324–8328.

(29) Tang, L., Li, M. H., Cao, P., Wang, F., Chang, W. R., Bach, S., Reinhardt, J., Ferandin, Y., Galons, H., Wan, Y., Gray, N., Meijer, L., Jiang, T., and Liang, D. C. (2005) Crystal structure of pyridoxal kinase in complex with roscovitine and derivatives. *J. Biol. Chem. 280*, 31220–31229.

(30) Guiffant, D., Tribouillard, D., Gug, F., Galons, H., Meijer, L., Blondel, M., and Bach, S. (2007) Identification of intracellular targets of small molecular weight chemical compounds using affinity chromatography. *Biotechnol. J. 2*, 68–75.

(31) Tribouillard-Tanvier, D., Dos Reis, S., Gug, F., Voisset, C., Beringue, V., Sabate, R., Kikovska, E., Talarek, N., Bach, S., Huang, C., Desban, N., Saupe, S. J., Supattapone, S., Thuret, J. Y., Chedin, S., Vilette, D., Galons, H., Sanyal, S., and Blondel, M. (2008) Protein folding activity of ribosomal RNA is a selective target of two unrelated antiprion drugs. *PLoS ONE 3*, e2174.

(32) Gug, F., Bach, S., Blondel, M., Vierfond, J.-M., Martin, A.-S., and Galons, H. (2004) A single step synthesis of 6-aminophenanthridines from anilines and 2-chlorobenzonitriles. *Tetrahedron 60*, 4705–4708.

(33) Gug, F., Blondel, M., Desban, N., Bouaziz, S., Vierfond, J.-M., and Galons, H. (2005) An expeditious synthesis of 6-aminophenanthridines. *Tetrahedron Lett. 46*, 3725–3727.

(34) Vidal, M., Liu, W. Q., Lenoir, C., Salzmann, J., Gresh, N., and Garbay, C. (2004) Design of peptoid analogue dimers and measure of their affinity for Grb2 SH3 domains. *Biochemistry 43*, 7336–7344.

(35) Bringmann, G., Menche, D., Muhlbacher, J., Reichert, M., Saito, N., Pfeiffer, S. S., and Lipshutz, B. H. (2002) On the verge of axial chirality: atroposelective synthesis of the AB-biaryl fragment of vancomycin. *Org. Lett. 4*, 2833–2836.

(36) Voisset, C., Thuret, J. Y., Tribouillard-Tanvier, D., Saupe, S. J., and Blondel, M. (2008) Tools for the study of ribosome-borne protein folding activity. *Biotechnol J. 3*, 1033–1040.

(37) Samanta, D., Voisset, C., Blondel, M., and DasGupta, C. Personnal communication.

(38) Laurén, J., Gimbel, D. A., Nygaard, H. B., Gilbert, J. W., and Strittmatter, S. M. (2009) Cellular prion protein mediates impairment of synaptic plasticity by amyloid-β oligomers. *Nature 457*, 1128–1132.

BC900314N

Intracellular Trafficking and Unpacking of siRNA/Quantum Dot-PEI Complexes Modified with and without Cell Penetrating Peptide: Confocal and Flow Cytometric FRET Analysis

Hyukjin Lee, In-Kyoung Kim, and Tae Gwan Park*

Department of Biological Sciences and Graduate School of Nanoscience and Technology, Korea Advanced Institute of Science and Technology, Daejeon 305-701, Korea. Received August 3, 2009; Revised Manuscript Received November 16, 2009

Cationic quantum dots (QDs) were utilized to complex small interfering RNA (siRNA) for studying intracellular trafficking, unpacking, and gene silencing. Positively charged polyethylenimine (PEI) was covalently conjugated on the surface of QDs to complex with cyanine dye labeled vascular endothelial growth factor siRNA (cy5-VEGF siRNA) for the formation of nanosized polyelectrolyte complexes (PEC). Fluorescence resonance energy transfer (FRET) was achieved between cy5-VEGF siRNA and PEI conjugated QDs (QD625) in the complex. From confocal microscopic analysis, intracellular uptake and release of siRNA from the PEC were visualized as a function of incubation time. The extent of cy5-siRNA release from the PEC was quantitatively evaluated by flow cytometric analysis. In addition, PEI conjugated QDs were further modified with a protein transduction domain (PTD) from human transcriptional factor, Hph-1. The two siRNA/QD-PEI complexes with and without Hph-1 have shown markedly different intracellular uptake behaviors and unpacking kinetics of cy5-siRNA. However, they exhibited similar extent of VEGF gene knockout regardless of Hph-1, but showed much higher gene silencing efficiency than siRNA/PEI complexes. The present study demonstrates that PEI conjugated QDs can be utilized as a useful siRNA carrier to analyze intracellular trafficking and unpacking pathway as well as to effectively silence a target gene.

INTRODUCTION

In recent years, small interfering RNA (siRNA) attracted much attention as a potent therapeutic nucleic acid drug for treatment of various diseases (*1–3*). Intracellularly delivered siRNA triggers RNA interference (RNAi), resulting in the specific down-regulation of target gene expression (*4–7*). Contrary to antisense oligonucleotides (ODN), siRNA requires a much lower dosage to achieve a sequence-specific gene inhibition effect. Although siRNA is a powerful gene regulation agent, therapeutic applications are limited mainly due to poor cellular uptake and accelerated degradation in biological fluids (*8, 9*). To overcome various intra- and extracellular delivery problems, cationic polymers and lipids have been popularly utilized as gene condensing agents to form positively charged, nanosized polyelectrolyte complexes (PEC) (*10, 11*). Among the cationic polymers, polyethylenimine (PEI) has been widely used for its superior buffering capacity, which allows excellent cargo translocation from endosomes to the cytoplasm by the "proton sponge" effect (*12, 13*). It was also previously reported that chemically modified PEI derivatives such as poly(ethylenimine)-*g*-poly(ethylene glycol) (PEI-g-PEG) and PEI-g-PEG-folate exhibited prolonged circulation in bloodstream and allowed target-specific cellular uptake via receptor-mediated endocytosis (*14–16*).

However, cellular uptake, cytosol specific release, and subcellular trafficking events of siRNA using cationic gene carriers are still unclear (*17*). Many studies have been pursued to discover different cellular uptake mechanisms and complicated intracellular fates (*18–20*). In particular, initial uptake and subcellular trafficking pathways of nucleic acid drugs need to be addressed in detail, when specific cellular uptake mechanisms, such as receptor-mediated endocytosis and cell membrane penetrating transcytosis, are employed. Fluorescently labeled nucleic acids and/or cationic carriers were widely used to investigate intracellular trafficking of PEC (*21, 22*). While these studies provide some valuable information about the localization of therapeutic nucleic acids and carriers within the cell, they mostly fail to show the decomplexation kinetics of the intracellular PEC. Recently, fluorescence resonance energy transfer (FRET) employing a pair of donor/acceptor organic fluorescent dyes has been utilized for dynamic monitoring of intracellular PEC fates (*23*). However, due to inherent instability of organic fluorescent dyes, semiconductor quantum dots (QDs) have emerged as an alternative FRET donor for proximal organic acceptor dyes (*24*). Since QDs have unique properties that surpass the conventional organic fluorescence dyes, such as tunable fluorescence emission, narrow photoemission, broad absorption spectrum, high extinction coefficients, and photostability, a wide range of surface-engineered QDs are extensively used as versatile molecular and cellular imaging agents (*25–27*). More recently, it was shown that QDs can be utilized to monitor the intracellular delivery and decomplexation of plasmid DNA (pDNA) (*28*). However, this approach required complex image analysis and data collection procedures from a particle-specific voxel-based method to evaluate the intracellular release of pDNA from QD-labeled polyplexes.

In this study, we report an alternative method for rapid analysis of intracellular siRNA uptake as well as the quantitative evaluation of siRNA unpacking from the cationic QD carriers. Instead of using a particle-specific voxel-based imaging analysis, we have used flow cytometric analysis to study the FRET interactions between cyanine dye labeled siRNA (cy5-siRNA) and cationic QD carriers. To prepare cationic QD carriers, PEI conjugated QD625 (QD-PEI) was synthesized for nanocomplexing with cy5-siRNA. The siRNA/QD-PEI complexes were utilized to investigate the time course for endocytic cellular uptake, subcellular trafficking, and unpacking of cy5-siRNA.

* Corresponding author. E-mail: tgpark@kaist.ac.kr.

10.1021/bc900342p © 2010 American Chemical Society
Published on Web 01/15/2010

Protein transduction domain (Hph-1) peptide conjugated QD-PEI was also prepared to monitor nonendocytic cellular uptake and to study its effect on the trafficking and unpacking behavior of cy5-siRNA. Hph-1 was chosen as a cell penetrating domain to test its ability to cross the cell membrane and deliver the complexes without the assistance of the ATP-dependent endocytic pathway (*29, 30*). The analysis was performed at various time points to support the results obtained from confocal image analysis. Gene-silencing efficiencies of QD-based cationic carriers were comparatively evaluated in the serum containing condition.

EXPERIMENTAL PROCEDURES

Materials. Carboxylic acid modified quantum dots (Qdot625 ITK) were purchased from Invitrogen (Eugene, OR). 1-Ethyl-3-(3-dimethylaminopropyl)-carbodiimide hydrochloride (EDC) and succinimidyl 4-(*p*-maleimidophenyl) butyrate (SMPB) were obtained from TCI (Tokyo, Japan) and Pierce (Rockford, IL), respectively. Branched polyethylenimine (PEI, M_w 25 000) was provided from Sigma-Aldrich (St. Louis, MO). Vascular endothelial growth factor (VEGF) siRNA and cyanine 5 conjugated VEGF siRNA (sense, 5′-GGAGUACCCUGAUGAGAUCdTdT-3′; antisense, 5′-GAUCUCAUCAGGGUACUCCdTdT-3′) were purchased from Dharmacon (Lafayette, CO). Protein transduction domain (PTD) peptide from human transcriptional factor, Hph-1 (YARVRRRGPRRGGC), was obtained from Forhuman Tech (Seoul, Korea). Penicillin/streptomycin, fetal bovine serum (FBS), and Rosewell Park Memorial Institute 1640 medium (RPMI 1640) were supplied from Gibco BRL (Grand Island, NY). All other chemicals and reagents were of analytical grade.

Synthesis of PEI-Modified QDs (QD-PEI). To prepare PEI-conjugated QDs, EDC was used as a coupling agent to form an amide bond between primary amine group of PEI and carboxylic acid group of QD625. One hundred microliters of EDC (50 mg/mL) diluted in 400 μL of pH 7.4 phosphate buffered saline (PBS) solution was added into 200 μL of PEI solution (10 mg/mL in PBS) in a vial. Ten microliters of QD625 stock solution (8 μM) was added in 290 μL of PBS solution. The QD solution was slowly added into the activated PEI solution and stirred for 2 h in dark condition at room temperature. The unconjugated PEI fraction was removed by centrifugation at 10 000 rpm for 10 min using an ultrafiltration filter tube (Vivaspin, MWCO: 50 000 Da). The remaining solution was washed 2 times with PBS solution. The resultant PEI conjugated QD625 was referred to as QD-PEI. The volume of QD-PEI solution was adjust to 100 μL with PBS solution and stocked at 4 °C for further use.

Synthesis of QD-PEI-Hph-1 Conjugate. QD-PEI conjugated with Hph-1 was produced using a bifunctional cross-linker, SMPB. One milligram of SMPB was dissolved in 500 μL of DMSO before adding 400 μL of PBS solution. The solution was added into 500 μL of Hph-1 (2 mg/mL) and stirred for 1 h to activate a sulfhydryl group of Hph-1. The resultant solution was dialyzed (MWCO: 1000) for 2 h to remove unreacted SMPB. After dialysis, the solution in a dialysis membrane was collected and transferred into a vial to react with QD-PEI. Two microliters of QD-PEI was added to the vial, stirred for 1 h, and dialyzed (MWCO: 25 000) overnight at 4 °C. The QD-PEI conjugated Hph-1 was referred to as QD-PEI-Hph-1. The prepared QD-PEI-Hph-1 conjugate was stored at 4 °C.

Preparation and Characterization of QD-PEI/cy-siRNA Complexes. VEGF siRNA modified with a cyanine-5 dye at the 5′ end of its sense strand was utilized. QD-PEI was incubated with cy5-siRNA at 100, 200, 400, 800, 1000, 1600, and 3200 molar ratio of siRNA to QD-PEI at room temperature for 15 min in deionized water. The formation of siRNA/QD-PEI complexes were characterized by gel retardation and decomplexation assay, transmission electron microscopy (TEM) image analysis, and FRET-based assay. The morphology of QD-PEI was obtained using TEM. Twenty microliters of cy5-siRNA/QD-PEI complex solution at a molar ratio of 400:1 was deposited onto a 300 mesh copper grid. The grid was air-dried at room temperature and analyzed by Zeiss Omega 912 TEM (Carl Zeiss, Oberkochen, Germany). For decomplexation of cy5-siRNA/QD-PEI, 1 μg of heparin solution (100 mg/mL) was added to the complex solution prepared with a 3200:1 molar ratio of cy5-siRNA to QD-PEI and incubated for 15 min at room temperature. Decomplexation was analyzed by gel electrophoresis (2% agarose gel). FRET between QD and cyanine dye conjugated to siRNA was examined for various complexes prepared at different molar ratios of QD-PEI to cy5-siRNA (1:100, 1:200, 1:400, 1:800, and 1:1000). The emission spectra of the QD-PEI/cy5-siRNA complexes were measured by spectrofluorophotometer (SLM-AMINCO 8100, SLM Instrunments Inc., Rochester, NY) at an excitation of 350 nm.

Cell Cultures. Human prostate carcinoma cell line (PC-3) expressing VEGF was provided from the Korean Cell Line Bank (Seoul, Korea). The cells were maintained in RPMI1640 with 10% FBS, 100 IU/mL penicillin, and 100 μL streptomycin at 37 °C in a 5% CO_2 humidified atmosphere.

Confocal Image Analysis. For conical images, PC-3 cells were seeded in a 35 mm Petri dish (Ibidi, Germany) at a density of 5×10^4 and maintained for 48 h. Two kinds of complexes, QD-PEI/cy5-siRNA and QD-PEI-Hph-1/cy5-siRNA, at 1:400 molar ratio were prepared in serum-free media and incubated for 15 min at room temperature. After serum-containing media were added into the solution, cells were transfected with the complexes and incubated for 30 min, 2 h, and 6 h. After the transfection, the media were discarded and the cells were washed 3 times with PBS solution. After the cells were fixed with 3.7% paraformaldehyde solution, confocal images were obtained at each time point using LSM510 confocal laser scanning microscope (Carl Zeiss Inc., USA). To acquire a fluorescence signal of QD-PEI (emission: 625 nm), each sample was excited at 488 nm. A fluorescence signal of cy5-siRNA was detected at 670 nm with an excitation at 643 nm. A FRET signal was obtained at 670 nm with an excitation at 488 nm.

Fluorescence Activated Cell Sorter (FACS) Analysis. To quantitatively examine intracellular uptake and unpacking of QD-PEI/cy5-siRNA and QD-PEI-Hph-1/cy5-siRNA complexes, flow cytometric analysis was conducted. PC-3 cells were seeded into a 6-well-plate at a density of 3×10^5 and maintained for 24 h. One microgram of cy5-siRNA was complexed with QD-PEI, and then cells were transfected for 1 h at 37 °C. After the transfection, the cells were washed three times with PBS solution and incubated with fresh media for 0 to 5 h. For flow cytometry analysis, the resultant cells were trypsinized and collected in an Eppendorf tube. The cells were sieved with a cell strainer (BD Bioscience, USA), and the volume of samples was adjusted to 2 mL with cold PBS solution. Fifteen thousand cells were monitored and evaluated by FACSAria (BD Bioscience, USA) to determine the cellular uptake and unpacking of cy5-siRNA/QD-PEI complexes. To calculate overall uptake and unpacking of PEC in the cells, fluorescence intensity of cy5-siRNA was first obtained (F_{cy5}). Fluorescence intensity of QD-PEI and FRET mediated cy5 emission was abbreviated as F_Q and $F_{f,cy5}$, respectively. The percent release of cy5-siRNA from PEC (F_r) at each time point was calculated from eq 1.

$$F_r = (1 - F_{f,cy5}/F_{cy5}) \times 100 \quad (1)$$

Gene Silencing Efficiency. PC-3 cells were seeded on a 12-well plate at a density of 1×10^5 and maintained for 24 h. Five micrograms of siRNA was used to formulate PEC with QD-PEI, QD-PEI-Hph-1, LipofectAmine, and PEI. After 15 min

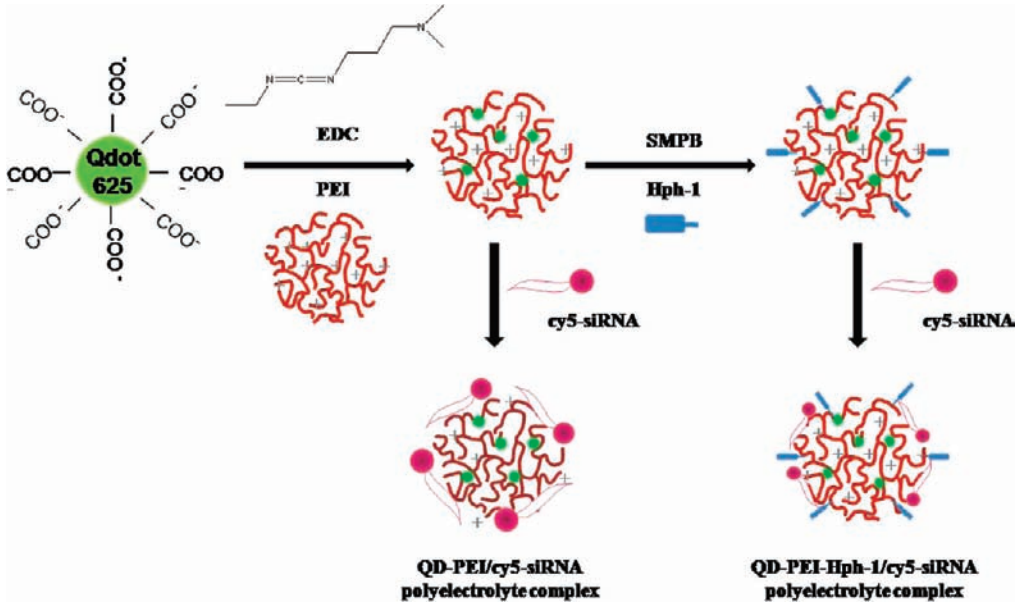


Figure 1. Schematic illustration of QD-PEI and QD-PEI-Hph-1 conjugates.

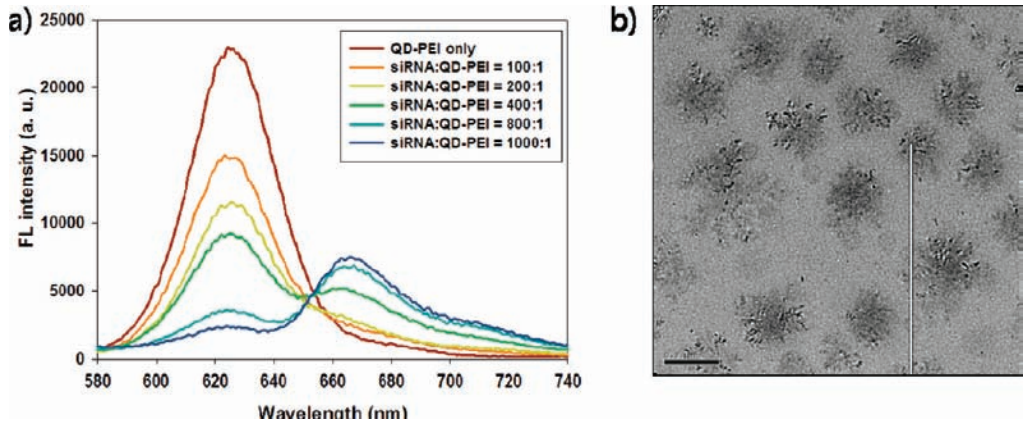


Figure 2. (a) Fluorescence spectra of QD-PEI/cy5-siRNA complexes excited at 350 nm with increasing molar ratio of cy5-siRNA. (b) TEM image of QD-PEI/cy5-siRNA complexes (scale bar is 200 nm).

incubation with different gene carriers, PC-3 cells were transfected for 2 h. After the transfection, the media were replaced with fresh serum-containing media and incubated for 6 h. The media were discarded in order to remove endogenously secreted VEGF, and fresh media were added to the cells. After 16 h, the incubating media were collected to measure the amount of released VEGF by using Quantikine human VEGF immunoassay kit (R&D System, Minneapolis, MN).

RESULTS AND DISCUSSION

Figure 1 shows the schematic illustration of QD-PEI and QD-PEI-Hph-1 conjugates. Carboxylic acid groups of QDs were activated using EDC to generate *O*-acylisourea active intermediates, and reacted with primary amine groups of PEI. A thiol group of Hph-1 peptide was additionally conjugated on the QD-PEI using a heterobifunctional coupling reagent (SMPB). By forming nanosized polyelectrolyte complexes (PEC) by electrostatic interactions between cationic QD carriers and anionic cy5-siRNA, it was expected that FRET occurred by emitting a fluorescence signal at 670 nm when QDs were excited at 350 nm. On the contrary, upon unpacking and releasing of cy5-siRNA from the PEC, emission fluorescence signals of free QD-PEI and cy5-siRNAs would be separately observed along with the gradual decrease of the FRET emission signal over time. To test our hypothesis, intensity of QD fluorescence signal emitting at 625 nm was monitored with increasing amount of cy5-siRNA for PEC formation (Figure 2a). Since QD had a broad excitation wavelength range, QD-PEI was excited at a wavelength of 350 nm to avoid the excitation of cy5-siRNA. From the fluorescence spectra, it was observed that emission spectra of QD were well-overlapped with absorption spectra of cy5-siRNA to allow sufficient energy transfer to generate FRET signal. It was also noticeable that the formation of PEC between QD-PEI and cy5-siRNA induced reduced fluorescence intensity of QD signal at 625 nm. At a molar ratio over 400:1 (siRNA/QD), the emission fluorescence signal of cy5-siRNA via energy transfer was clearly identified. The particle size and morphology of QD-PEI/cy5-siRNA complexes were studied by TEM (Figure 2b). About 200 nm sized spherical PEC were observed in a well-dispersed state, and several dark objects were identified within the complex structure due to the presence of electron-dense QDs. The QD-PEI/cy5-siRNA complexes were further characterized by gel electrophoresis. Surface charge of complexes and the number of cy5-siRNA loaded onto QD-PEI were estimated by gel retardation assay. Negatively charged carboxylic acid group modified QDs migrated downward, while QD-PEI disappeared from the gel due to the highly positive surface charge (see Supporting Information Figure S1). To mimic the intracellular unpacking of cy5-siRNA from QD-PEI, negatively charged heparin was incubated with QD-PEI/cy5-siRNA com-

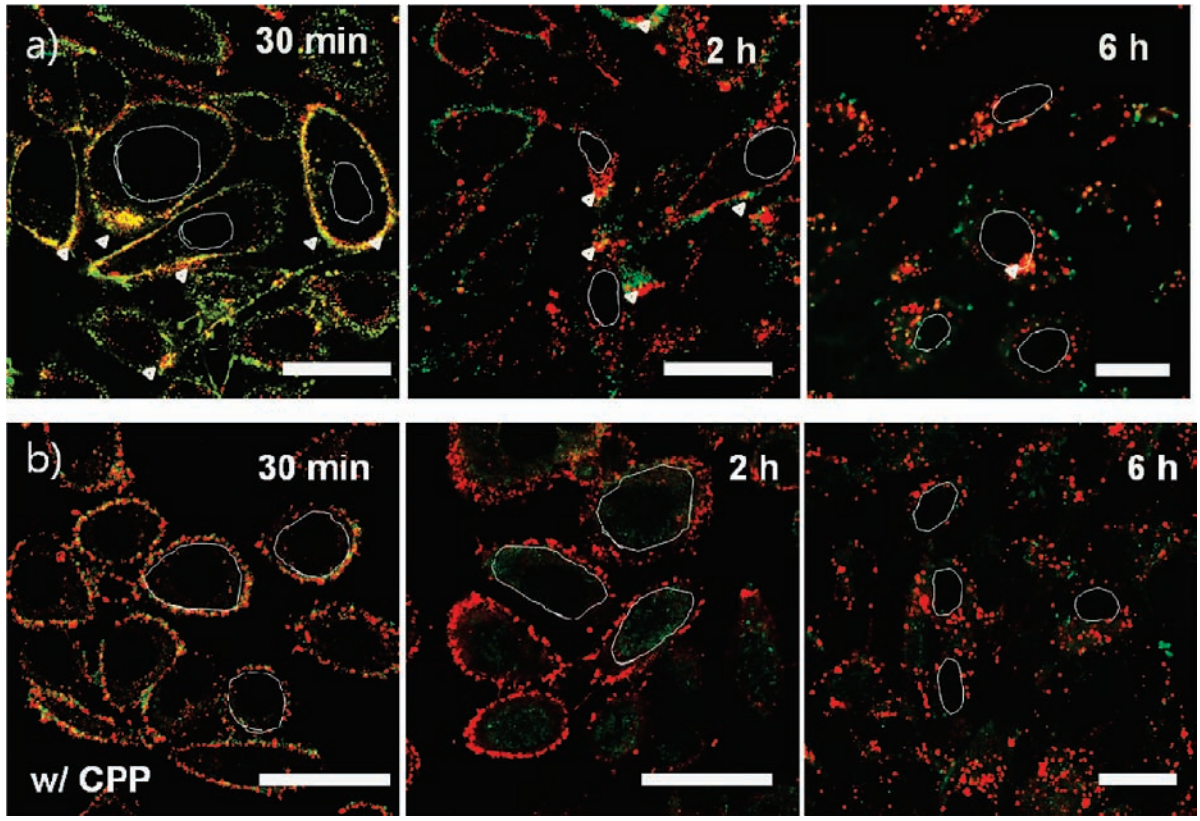


Figure 3. Intracellular uptake of cationic QD-PEI/cy5-siRNA complexes: (a) QD-PEI/cy5-siRNA and (b) QD-PEI-Hph-1/cy5-siRNA after 30 min, 2 h, and 6 h. Nucleus membranes are marked in white (scale bar is 10 μm).

plexes. It was observed that QD-PEI/cy5-siRNA complexes were fully decomplexed by releasing cy5-siRNA from the PEC (see Supporting Information Figure S1).

To investigate two different intracellular delivery mechanisms of QD-PEI and QD-PEI-Hph-1 complexed with cy5-siRNA, confocal images after transfection were obtained in a time-dependent manner. Ten picomoles of cy5-siRNA was utilized to prepare PEC with QD-PEI and QD-PEI-Hph-1 at the molar ratio of 400:1. QD-PEI and cy5-siRNA could be visualized in green and red color, respectively. As shown in Figure 3a, most QD-PEI/cy5-siRNA complexes were bound onto the cell membrane at 30 min and appeared in yellow color (merged image of green and red color). The cell surface bound complexes were probably due to the initial electrostatic interactions between positively charged PEC and negatively charged cell membrane (*21*). The yellow color in the image indicated that QD-PEI and cy5-siRNA were colocalized as a result of intact nanocomplex structure. After 2 h incubation, the subcellular uptake of QD-PEI/cy5-siRNA complexes could be seen along with the partial dissociation of cy5-siRNA from the PEC. Unpacked QD-PEI and cy5-siRNA could be visualized predominantly in the endosomal compartment near the inner cell membrane. In addition, unpacked cy5-siRNA in red color could be visualized as scattered dots in the cytoplasmic region. At 6 h incubation, it could be observed that siRNA was fully unpacked and released from the PEC and mostly sequestered in the cytoplasm, possibly interacting with some subcellular organelles. When an endosomal marker was used to label early endosomes, it was clearly visualized that most QD-PEI/cy5-siRNA complexes were located within endosomes until 2 h incubation (see Supporting Information Figure 2S). The time-dependent trafficking observation also suggested that QD-PEI/cy5-siRNA complexes started to escape from the early endosomes and cy5-siRNA was released from the PEC as early as 2 h incubation, in accordance with a typical endocytic and subsequent subcellular trafficking process (*28*).

On the other hand, the intracellular uptake manner of Hph-1 modified PEC was substantially different from that of QD-PEI/cy5-siRNA. After 30 min incubation, the QD-PEI-Hph-1/cy5-siRNA complexes were already located within the cells, and they were accumulated in the perinuclear region (Figure 3b). In addition, the intensity of the yellow image near the nuclear membrane was greatly reduced compared to that of QD-PEI/cy5-siRNA, indicating that the unpacking process of cy5-siRNA from the PEC was initiated within the cells as early as 30 min incubation. This reveals that the surface-conjugated cell-penetrating Hph-1 could facilitate intracellular uptake of QD gene carrier directly via a transcytosis process, and the PEC near the nucleus in the cytoplasm was readily decomplexed to release unpacked siRNA. At 2 h incubation, more cy5-siRNA was unpacked and released from the PEC, but still bound onto the nuclear membrane, while some part of the QD-PEI-Hph-1 entered into the nucleus. Endosome staining results revealed that cy5-siRNA was not located within endosomes, supporting direct transcytosis of Hph-1 conjugated QD complexes (see Supporting Information Figure 2S). After 6 h incubation, free cy5-siRNA was clearly visualized throughout the cytoplasm as punctuated dots. It is likely that Hph-1 originally derived from a human transcription factor played a key role not only in transporting the PEC within cells via a nonendocytic pathway, but also in targeting to the nucleus (*29, 30*). In fact, the nuclear migration behavior of Hph-1 has been previously identified, and many cell-penetrating peptides exhibit a strong tendency to migrate into the nucleus and accumulate in the perinuclear region (*31*).

Intracellular unpacking kinetics of siRNA from each complex was quantitatively evaluated by flow cytometry analysis. Compared to the conventional pixel-counting method using the

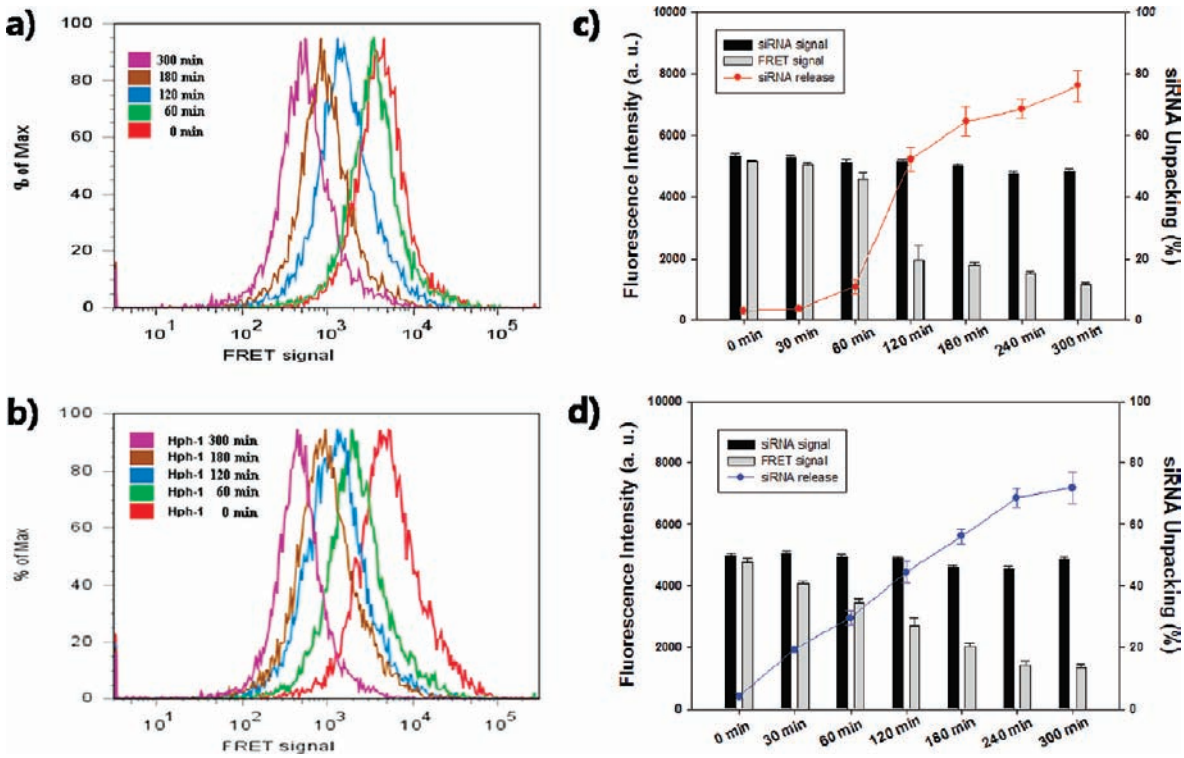


Figure 4. Intensity change of FRET-mediated signals during the incubation time. (a) QD-PEI and (b) QD-PEI-Hph-1. The comparison of cy5-siRNA signals versus FRET-mediated signals and the release of cy5-siRNAs during the incubation time ($n = 5$). (c) QD-PEI and (d) QD-PEI-Hph-1.

confocal images, the flow cytometry based FRET analysis offers more precise data for quantitative evaluation of time-dependent siRNA unpacking within live cells (*32–34*). For cytometry analysis, two different laser sources and detectors were utilized to measure the separate fluorescence signals from cy5-siRNA and QD-PEI, simultaneously. As shown in Figure 4, the intensity of cy5-siRNA signals within the cells was monitored as a function of time as compared to that of FRET-induced fluorescence signals. Since the transfection time was fixed to 1 h for all samples, the total amount of siRNA within the cells remained similar in all time points. Unlike the cy5-siRNA signal, FRET-induced fluorescence signal emitted from the PEC was decreased dramatically with the incubation period. It was assumed that, at zero incubation time, most of the cy5-siRNA within the cells formed compact PEC. The intensity changes in FRET-induced fluorescence signal at each time point are shown in Figure 4a,b. The higher FRET intensity value indicates the compact structure of QD-PEI/cy5-siRNA complexes within the cells. On the other hand, decreasing FRET-induced fluorescence signal indicates the unpacking of cy5-siRNA from the PEC. In Figure 4a, it is shown that FRET-induced fluorescence signals minimally decreased until 1 h postincubation using QD-PEI as a gene carrier. The FRET intensity value only decreased about $5.4 \pm 0.3\%$ at 1 h, but started to reduce dramatically thereafter resulting in $53.7 \pm 3.2\%$ reduction of FRET intensity value at 2 h. Further decrease in FRET intensity value was observed in a time-dependent manner until 5 h postincubation. In the case of QD-PEI-Hph-1, the initial uptake amount of cy5-siRNA was similar to that of QD-PEI (Figure 4b). However, unpacking the kinetic rate of cy5-siRNA from QD-PEI-Hph-1 was much faster than that of QD-PEI, showing $29.7 \pm 2.6\%$ reduction of FRET-induced fluorescence signal at 1 h. Furthermore, QD-PEI-Hph-1 complexes exhibited an almost constant release of cy5-siRNA for an entire 5 h incubation period. It was likely that the delayed release of cy5-siRNA from the QD-PEI complexes was due to their ATP-dependent endocytic cellular uptake, followed by endosomal escape of cy5-siRNA into the cytoplasm (*35*). From the comparative unpacking kinetics of siRNA, it was clear that Hph-1 conjugated QD complexes were directly taken up by cells in a non-endocytic manner with accelerating decomplexation of cy5-siRNA in the cytosol, which was also supported by facile intracellular uptake of Hph-1 conjugated QD complexes in ATP-deficient conditions (see Supporting Information Figure 3S). The flow cytometry results of siRNA unpacking were well-correlated with the confocal images shown in Figure 3.

To evaluate the gene silencing efficiency of QD-PEI/siRNA and QD-PEI-Hph-1/siRNA, VEGF overexpressing PC-3 cells were used. Cationic QD-based gene carriers were applied to the cells in 10% serum-containing media as well as conventional cationic carriers such as PEI and LipofectAmine to compare the relative gene inhibition efficiency of each carrier. As shown in Figure 5, QD-PEI/siRNA and QD525-PEI-Hph-1/siRNA exhibited VEGF expression of 228.0 ± 20.0 pg/mL and 193.2 ± 16.4 pg/mL, respectively. These gene inhibition efficiencies were comparable to that of LipofectAmine (209.3 ± 46.6 pg/mL). On the other hand, PEI exhibited much lower gene inhibition efficiency of 548.8 ± 91.9 pg/mL. It is known that, in the presence of serum proteins, cationic polymers such as PEI often show reduced gene silencing effects due to nonspecific protein adsorption on the positively charged surface of the complexes (*35*). From our results, it is still not clear why the PEI conjugated QDs show superior gene silencing efficiency compared to PEI. It seems that PEI with embedded multiple QDs could facilitate the endocytic cellular uptake of the complexes more than naked PEI. This was based on the assumption that QD-PEI/siRNA complexes were hard nanospheres, whereas PEI/siRNA complexes were soft and elastic ones. It is likely that not only the size, but also the morphology and hardness of QD-PEI/siRNA complexes may affect intracellular uptake of siRNA (*36*). As a result, enhanced cellular uptake of QD-based PEC along with maintaining the "proton sponge" effect might lead to the observed superior gene silencing effect. It is also interesting to observe similar gene silencing extents between QD-PEI and QD-PEI-Hph-1, although QD-PEI-

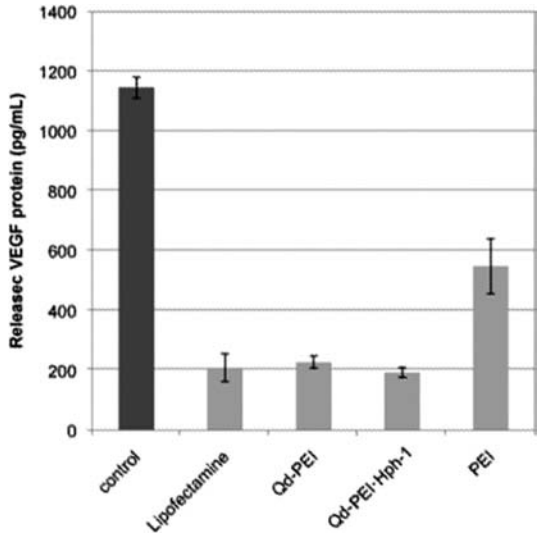


Figure 5. Inhibition of VEGF gene expression by QD-PEI/siRNA and QD-PEI-Hph-1/siRNA complexes compared to that of Lipofectamine and PEI ($n = 5$).

Hph-1 showed much faster cytosolic delivery of PEC than that of QD-PEI. This discrepancy was likely due to the fact that the amount of VEGF in the transfected cells was analyzed after 24 h post-transfection, which was sufficiently long for QD-PEI/siRNA complexes to completely release free siRNA in the cytosol (*37*). This could result in no difference in apparent gene silencing efficiency. Lastly, it should be noted that PEI-modified QD carriers showed markedly reduced cytotoxicity as compared to PEI (see Supporting Information Figure 4S), which makes them an ideal carrier for siRNA delivery as well as for intracellular FRET analysis.

CONCLUSION

We have synthesized two different QD based gene carriers, QD-PEI and QD-PEI-Hph-1, which could form PEC with cy5-siRNA by electrostatic interactions. Using the QD-based nanocarriers, intracellular trafficking of cy5-siRNA was successfully monitored by confocal analysis as a function of incubation time. Furthermore, flow cytometry analysis enabled the quantitative evaluation of cy5-siRNA unpacking from the QD-PEI and QD-PEI-Hph-1 complexes. To the best of our knowledge, this is the first report on the quantitative flow cytometry analysis of siRNA release from the gene carrier within live cells. This study also demonstrates that QD-PEI and QD-PEI-Hph-1 carriers could be employed as excellent siRNA delivery carriers.

ACKNOWLEDGMENT

This work was supported by the grants of WCU, A3 program, and National Research Laboratory from the Ministry of Education, Science, and Technology, Korea.

Supporting Information Available: Gel electrophoresis results, confocal images with colocalization with endosomal marker, non-ATP dependent cellular uptake of cy5-siRNA/QD-PEI-Hph-1 complexes, and cellular cytotoxicity of QD-based gene carrier. This material is available free of charge via the Internet at http://pubs.acs.org.

LITERATURE CITED

(1) Michael, T. M., and Philip, A. S. (2002) Gene silencing in mammals by small interfering RNAs. *Nat. Rev. Genet. 3*, 737–747.

(2) Reynolds, A., Leake, D., Boese, Q., Scaringe, S., Marshall, W. S., and Khvorova, A. (2004) Rational siRNA design for RNA interference. *Nat. Biotechnol. 22*, 326–330.

(3) Tebes, S. J., and Kruk, P. A. (2005) The genesis of RNA interference, its potential clinical applications, and implications in gynecologic cancer. *Gynecol. Oncol. 99*, 735–741.

(4) Zamore, P. D., Tuschl, T., Sharp, P. A., and Bartel, D. P. (2000) RNAi: double-stranded RNA directs the ATP-dependent cleavage of mRNA at 21 to 23 nucleotide intervals. *Cell 101*, 25–33.

(5) Berstein, E., Caudy, A. A., Hammond, S. M., and Hannon, G. J. (2001) Role for a bidentateribonuclease in the initiation step of RNA interference. *Nature 409*, 363–366.

(6) Song, E., Lee, S. K., Wang, J., Ince, N., Ouyang, N., Min, J., Chen, J., Shankar, P., and Lieberman, J. (2003) RNA interference targeting Fas protects mice from fulminant hepatitis. *Nat. Med. 9*, 347–351.

(7) Gartel, A. L., and Kandel, E. S. (2006) RNA interference in cancer. *Biomol. Eng. 23*, 17–34.

(8) Jones, L., Hamilton, A. J., Voinnet, O., Thomas, C. L., Maule, A. J., and Baulcombe, D. D. (1999) RNA-DNA interactions and DNA methylation in post-transcriptional gene silencing. *Plant Cell 11*, 2291–2301.

(9) Novina, C. D., and Sharp, P. A. (2004) The RNAi revolution. *Nature 430*, 161–164.

(10) Gary, D. J., Puri, N., and Won, Y. Y. (2007) Polymer-based siRNA delivery: Perspectives on the fundamental and phenomenological distinctions from polymer-based DNA delivery. *J. Controlled Release 121*, 64–73.

(11) Jeong, J. H., Mok, H., Oh, Y. K., and Park, T. G. (2009) siRNA conjugate delivery systems. *Bioconjugate Chem. 20*, 5–14.

(12) Thomas, M., Lu, J. J., Ge, Q., Zhang, C., Chen, J., and Klibanov, A. M. (2005) Full deacylation of polyethylenimine dramatically boots its gene delivery efficiency and specificity to mouse lung. *Proc. Natl. Acad. Sci. U.S.A. 102*, 5679–5684.

(13) Urban-Klein, B., Werth, S., Abuharbeid, S., Czubayko, F., and Aigner, A. (2005) RNAi-mediated gene targeting through systemic application of polyethylenimine(PEI)-complexed siRNA in vivo. *Gene Ther. 12*, 461–466.

(14) Lee, H., Jeong, J. H., and Park, T. G. (2001) A new gene delivery formulation of polyethylenimine/DNA complexes coated with PEG conjugated fusogenic peptide. *J. Controlled Release 76*, 183–192.

(15) Kichler, A. (2004) Gene transfer with modified polyethylenimines. *J. Gene Med. 6*, S3–10.

(16) Kim, S. H., Jeong, J. H., Cho, K. C., Kim, S. W., and Park, T. G. (2005) Target-specific gene silencing by siRNA plasmid DNA complexed with folate-modified poly(ethylenimine). *J. Controlled Release 104*, 223–232.

(17) Godbey, W. T., Wu, K. K., and Mikos, A. G. (1999) Tracking the intracellular path of poly(ethylenimine)/DNA complexes for gene delivery. *Proc. Natl. Acad. Sci. U.S.A. 96*, 5177–5181.

(18) Walsh, M., Tangney, M., O'Neill, M. J., Larkin, J. O., Soden, D. M., McKenna, S. L., Darcy, R., O'Sullivan, G. C., and O'Discoll, C. M. (2006) Evaluation of cellular uptake and gene transfer efficiency of pegylated poly-L-lysine compacted DNA: implications for cancer gene therapy. *Mol. Pharmaceutics 3*, 644–653.

(19) Feng, M., Lee, D., and Li, P. (2006) Intracellular uptake and release of poly(ethyleneimine)-co-poly(methyl methacrylate) nanoparticle/pDNA complexes for gene delivery. *Int. J. Pharm. 311*, 209–214.

(20) Luhmann, T., Rimann, M., Bittermann, A. G., and Hall, H. (2008) Cellular uptake and intracellular pathways of PLL-g-PEG-DNA nanoparticles. *Bioconjugate Chem. 19*, 1907–1916.

(21) Lee, S. H., Bae, K. H., Kim, S. H., Lee, K., and Park, T. G. (2008) Amine-functionalized gold nanoparticles as non-cytotoxic and efficient intracellular siRNA delivery carriers. *Int. J. Pharm. 364*, 94–101.

(22) Shim, M. S., and Kwon, Y. J. (2008) Controlled delivery of plasmid DNA and siRNA to intracellular targets using ketalized polyethylenimine. *Biomacromolecules 9*, 444–455.
(23) Itaka, K., Harada, A., Yamasaki, Y., Nakamura, K., Kawaguchi, H., and Kataoka, K. (2004) In situ single cell obervation by fluorescence resonance energy transfer reveals fat intracytoplasmic delivery and easy release of plasmid DNA complexed with linear polyethylenimine. *J. Gene. Med. 6*, 76–84.
(24) Howarth, M., Takao, K., Hayashi, Y., and Ting, A. Y. (2005) Targeting quantum dots to surface proteins in living cells with biotin ligase. *Proc. Natl. Acad. Sci. U.S.A. 102*, 7583–7588.
(25) Alivisatos, A. P. (1996) Semiconductor clusters, nanocrystals, and quantum dots. *Science 271*, 933–937.
(26) Clapp, A. R., Medintz, I. L., Mauro, J. M., Fisher, B. R., Bawendi, M. G., and Mattoussi, H. (2004) Fluorescence resonance energy transfer between quantum dot donors and dye-labeled protein acceptors. *J. Am. Chem. Soc. 126*, 301–310.
(27) Gao, X., Cui, Y., Levenson, R. M., Chung, L. W. K., and Nie, S. (2004) In vivo cancer targeting and imaging with semiconductor quantum dots. *Nat. Biotechnol. 22*, 969–976.
(28) Chen, H. H., Ho, Y. P., Jiang, X., Mao, H., Wang, T., and Leong, K. W. (2008) Quantitative comparison of intracellular unpacking kinetics of polyplexes by a model constructed from quantum dot-FRET. *Mol. Ther. 16*, 324–332.
(29) Choi, J. M., Ahn, M. H., Chae, W. J., Jung, Y. G., Park, J. C., Song, H. M., Kim, Y. E., Shin, J. A., Park, C. S., Park, J. W., Park, T. K., Lee, J. H., Seo, B. F., Kim, K. D., Kim, E. S., Lee, D. H., Lee, S. K., and Lee, S. K. (2006) Intranasal delivery of the cytoplasmic domain of CTLA-4 using a novel protein transduction domain prevents allergic inflammation. *Nat. Med. 12*, 574–579.
(30) Green, I., Christison, R., Voyce, C. J., Bundell, K. R., and Lindsay, M. A. (2003) Protein transduction domains: are they delivering? *Trends Pharmacol. Sci. 24*, 213–215.
(31) Vives, E., Brodin, P., and Lebleu, B. (1997) A truncated HIV-1 Tat protein basic domain rapidly translocateds through the plasma membrane and accumulates in the cell nucleus. *J. Biol. Chem. 272*, 16010–16017.
(32) Breunig, M., Lungwitz, U., Liebl, R., and Goepferich, A. (2006) Fluorescence resonance energy transfer: Evaluation of the intracellular stability of polyplexes. *Eur. J. Pharm. Biopharm. 63*, 156–165.
(33) Johansson, D. X., Brismar, H., and Persson, M. A. A. (2007) Fluorescent protein pair emit intracellular FRET signal suitable for FACS screening. *Biochem. Biophys. Res. Commun. 352*, 449–455.
(34) Adachi, T., and Tsubata, T. (2008) FRET-based Ca^{2+} measurement in B lymphocyte by flow cytometry and confocal microscopy. *Biochem. Biophys. Res. Commun. 367*, 377–382.
(35) Lee, H., Mok, H. J., Lee, S., Oh, Y. K., and Park, T. G. (2007) Target-specific intracellular delivery of siRNA using degradable hyaluronic acid nanogels. *J. Controlled Release 119*, 245.
(36) Mitragotri, S., and Lahann, J. (2009) Physical approaches to biomaterial design. *Nat. Mater. 8*, 15–23.
(37) Kim, S. H., Jeong, J. H., Lee, S. H., Kim, S. W., and Park, T. G. (2006) PEG conjugated VEGF siRNA for anti-angiogenic gene therapy. *J. Controlled Release 116*, 123–129.

BC900342P

Reducible Poly(amido ethylenimine)-Based Gene Delivery System for Improved Nucleus Trafficking of Plasmid DNA

Ji Hoon Jeong,*[,†,‡] Sun Hwa Kim,[§] Lane V. Christensen,[‡] Jan Feijen,[||] and Sung Wan Kim[‡]

College of Pharmacy, Sungkyunkwan University, Suwon 440-746, Republic of Korea, Department of Pharmaceutics and Pharmaceutical Chemistry, University of Utah, Salt Lake City, Utah 84112, Yonsei Integrative Research Institute for Cerebral and Cardiovascular Diseases, Yonsei University Health System, Seoul 120-752, Republic of Korea, and Department of Polymer Chemistry and Biomaterials, and Institute for Biomedical Technology (BMTI), Faculty of Science and Technology, University of Twente, P.O. Box 217, 7500 AE Enschede, The Netherlands. Received August 10, 2009; Revised Manuscript Received December 13, 2009

In a nonviral gene delivery system, localization of a plasmid DNA in the nucleus is a prerequisite for expression of a desired therapeutic protein encoded in the plasmid DNA. In this study, a reducible polymer-based gene delivery system for improved intracellular trafficking and nuclear translocation of plasmid DNA is introduced. The system is consisted of two components, a plasmid DNA having repeated binding sequence for a karyophilic protein, NFκB, and a reducible polymer. A reducible poly(amido ethylenimine), poly(TETA-CBA), was synthesized by a Michael-type addition polymerization between cystamine bisacrylamide and triethyl tetramine. The polymer forming tight complexes with plasmid DNA could be degraded in the reductive cytosol to release the plasmid DNA. The triggered release mechanism in the cytosol could facilitate the interaction between cytosolic NFκB and the plasmid DNA having repeated NFκB biding motif. Upon activation of NFκB by interleukin-1β (IL-1β), most of the plasmid distributed in the cytoplasm was localized within the nucleus, resulting in significantly higher gene transfection efficiency than controls with nondegradable PEI. The current study suggests an alternative way of improving transfection efficiency by taking advantage of endogenous transport machinery for intracellular trafficking and nuclear translocation of a plasmid DNA.

INTRODUCTION

Over the last decades, a lot of nonviral gene delivery systems based on synthetic materials have been developed to replace virus-originated gene carriers that are often questioned for safety issues (*1, 2*). However, there is still room to improve transfection efficiency of nonviral methods. Synthetic carriers should overcome a number of extracellular and intracellular barriers to deliver plasmid DNA to the cell nucleus where gene transcription occurs. Among the challenging barriers, the dissociation of plasmid DNA from a carrier complex, the transport of plasmid DNA to the peri-nuclear space in the cytoplasm, and the passage of plasmid DNA across the nuclear membrane are considered rate-limiting steps in a polymer-based gene delivery carrier (*3, 4*). Although efficient intracellular trafficking and nuclear translocation of plasmid DNA is essential to achieve desirable transfection efficiency, the delivery mechanism by a nonviral gene carrier has not been clearly understood. One possible mechanism is the nucleus localization of plasmid DNA by disruption of the nuclear envelope during mitotic cell division (*5*). Active nuclear transport of plasmid DNA by employing a nuclear localization signal (NLS) was previously suggested (*6*), but the effectiveness of NLS in transfection still seems to be controversial (*7*). Recent studies showed that plasmids containing a specific sequence recognized by a nuclear protein (nuclear factor κB, NFκB) could improve transfection possibly due to nuclear-protein guided intracellular trafficking and active nuclear translocation of the plasmid DNA (*8*−*10*). However, in this case, the release of plasmid DNA from carrier/DNA complexes is a prerequisite for the interaction of the nuclear protein to plasmid DNA that may lead to the guided trafficking and nuclear transport of plasmid DNA.

We previously demonstrated that reducible poly(amido ethylenimine)s successfully carry out unpacking of complexes owing to a reductive degradation of the polymer backbone in the cytoplasm, leading to enhanced transfection efficiency (*11, 12*). In this study, we used a plasmid DNA containing repeated NFκB binding sites in conjunction with the reducible poly(amido ethylenimine) to improve cytosolic release of plasmid DNA. It was hypothesized that the triggered release of the plasmid DNA with the NFκB binding sites in the reductive cytoplasm would facilitate the access of NFκB to the plasmid DNA to improve nuclear translocation, which may consequently lead to enhancement of transfection efficiency.

MATERIALS AND METHODS

Materials. For polymer synthesis, triethylenetetramine (TETA) and cystamine bisacrylamide (CBA) were purchased from Sigma-Aldrich (St. Louis, MO) and Polysciences (Warrington, PA), respectively, and were used without further purification. Branched polyethylenimine (bPEI, M_w 25 000), ethidium bromide, buthionine sulfoxamine (BSO), dithiothreitol (DTT), and (3-(4,5-dimethylthyazolyl-2)-2,5-diphenyl tetrazolium bromide) (MTT) was obtained from Sigma-Aldrich (St. Louis, MO). All cell culture products including fetal bovine serum (FBS) and Dulbecco's Modified Eagle's Medium (DMEM) were purchased from Invitrogen (Carlsbad, CA). Mouse interleukin-1β (IL-1β) and a protease inhibitor cocktail containing aprotinin, bestatin, leupeptin, E-64, and pepstatin A were obtained from Sigma-Aldrich (St. Louis, MO).

* Corresponding author. Tel: 82-21-290-7783, Fax: 82-31-292-8800, E-mail: jhjeong@skku.edu.
† Sungkyunkwan University.
‡ University of Utah.
§ Yonsei University Health System.
|| University of Twente.

10.1021/bc9003525 © 2010 American Chemical Society
Published on Web 01/15/2010

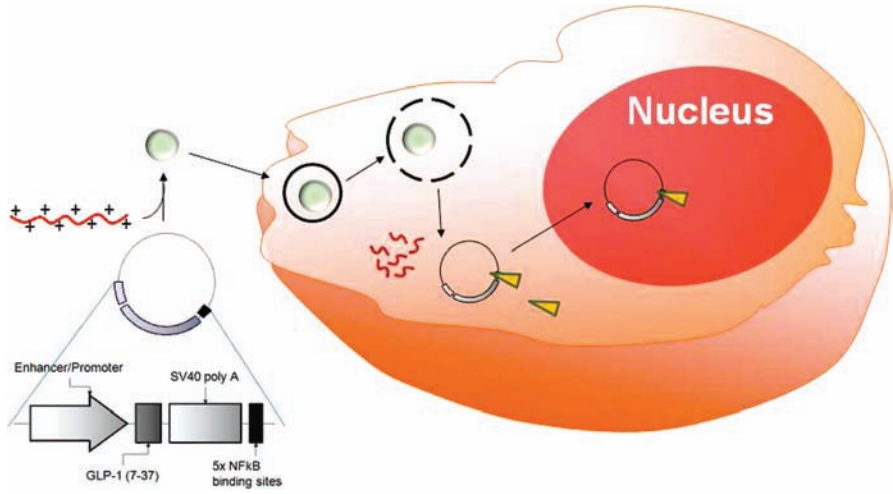


Figure 1. Schematic illustration of a gene delivery system based on a reducible polymer and a plasmid that can interact with cytosolic karyophilic protein, NFκB.

Synthesis of a Reducible TETA-CBA Copolymer. Reducible TETA-CBA copolymer was synthesized by Michael-type addition polymerization as described previously (*11*). Briefly, addition polymerization between TETA (449 mg, 3.1 mmol) and CBA (800 mg, 3.1 mmol) was performed in 10% aqueous methanol at 50 °C for 16 h. The reaction was terminated by adding an excess amount of the amine donor (TETA). The product was purified by ultrafiltration (MWCO 1000) and lyophilized. The chemical composition of the synthesized polymer was estimated by using ^{1}H NMR. The polymer molecular weight (M_w) was 3350, as determined by gel permeation chromatography (GPC).

Plasmid DNA. A plasmid DNA (pSIGLP1NFκB) containing an expression cassette of GLP-1 and five direct repeats of NFκB binding motif (5′-GGGGACTTTCC-3′) was constructed as described in a previous report (*9*). The repeated NFκB binding sites was inserted after SV40 polyadenylation site (Figure 1). Plasmid DNA was purified from *E. coli* by an alkaline lysis method using a silica-based anion exchange column (Qiagen, Valencia, CA).

Electrophoretic Mobility Shift Assays. Varying amounts of poly(TETA/CBA) and a fixed amount of plasmid DNA (300 ng) were separately diluted in PBS. The diluted polymer and DNA solutions were combined at varying weight ratios and mixed with gentle vortexing to form complexes. Dithiothreitol (DTT, 2.5 mM) was added to one of the test groups to observe the release of plasmid DNA by a reductive degradation of the polymer. The complexes were allowed to be stabilized for 30 min at ambient temperature and loaded onto 0.8% agarose gel. Electrophoresis was performed with a current of 120 V for 20 min in TAE buffer solution (40 mM Tris/HCl, 1% (v/v) acetic acid, 1 mM EDTA). Retardation of the complexes was visualized by using an image analyzer equipped with UV transilluminator (GelDoc, BioRad, Hercules, CA) after ethidium bromide staining.

Cell Culture and Transfection. Mouse fibroblast cells (NIH3T3) was cultured in DMEM supplemented with 10% FBS and maintained at 37 °C in a humidified 5% CO_2 atmosphere. Before transfection, the cells were trypsinized and 10^5 cells per well were plated in a six-well plate (35 mm diameter). The cells were then incubated at 37 °C in a humidified 5% CO_2 atmosphere for 24 h.

Before transfection, the plasmid DNA (2 μg) and the desired amount of either TETA-CBA (DNA/polymer = 10:1 w/w) or bPEI 25 kDa (DNA/polymer = 0.75:1 w/w) were separately diluted in PBS and mixed. The mixture was incubated to form complexes for 15 min at room temperature and added to the cells. The cell culture medium was replaced with serum-free medium prior to the addition of the complexes. After 3 h incubation at 37 °C, the medium was removed and supplemented with a fresh cell culture medium containing 10% FBS and a protease inhibitor cocktail. For the activation and nuclear translocation of cytoplasmic NFκB, IL-1β (20 ng/mL) was added to the medium. The concentration of GLP-1 was determined by ELISA (Linco Research, St. Charles, MO), as previously described (*13*).

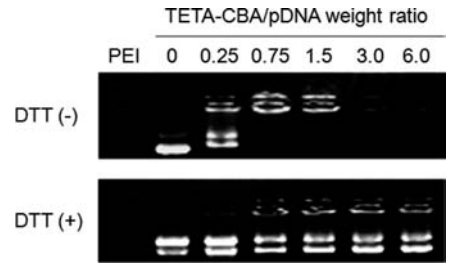


Figure 2. Electrophoretic mobility shift assays of poly(TETA/CBA)/plasmid DNA complexes at various polymer/siRNA weight ratios. Dithiothreitol (DTT, 2.5 mM) was added to generate a reductive environment to trigger the release of plasmid DNA from the complexes.

Flow Cytometry. To determine cellular association of the transfection complexes formed from a desired polymer (either TETA-CBA or PEI), the transfected cells were trypsinized and washed three times with cold PBS, and fixed by 1% paraformaldehyde at 4 °C before flow cytometric analysis (FACS Caliber, Becton-Dickinson, Mount View, CA). At least 1×10^4 events were analyzed to generate each diagram.

Confocal Microscopy. The cells were grown in glass-bottomed dishes (Glass Bottom Microwells; MatTek Corp., Ashland, MA). The plasmid DNA was fluorescently labeled with Cy3 by using Label-IT kit (Mirus Bio, Madison, WI). The transfection and NFκB activation were carried out as described above. The transfected cells were incubated for additional 2 h in the absence and presence of 20 ng/mL of IL-1β, prior to the observation. The cells were then washed five times with cold PBS, fixed by submerging the cells in 1% paraformaldehyde at 4 °C for 30 min, and washed three times with cold PBS. The subcellular localization of the complexes was visualized by a laser scanning confocal fluorescence microscopy using Olympus Fluoview FV300 microscope (Melville, NY). An oil immersion objective lens was used for the epidetection configuration.

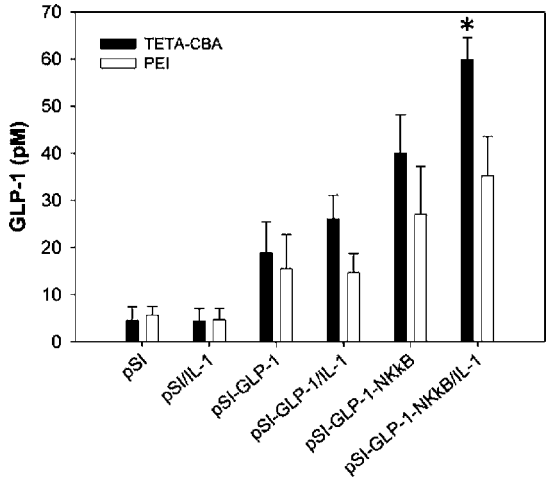


Figure 3. Transfection efficiencies of various formulations based on either TETA-CBA or PEI. IL-1β was added to activate nuclear translocation of NFκB. The expression level of secreted GLP-1 was determined by ELISA and given as the mean $\pm$ SD ($n = 3$). *$p < 0.01$ compared to the PEI-based control.

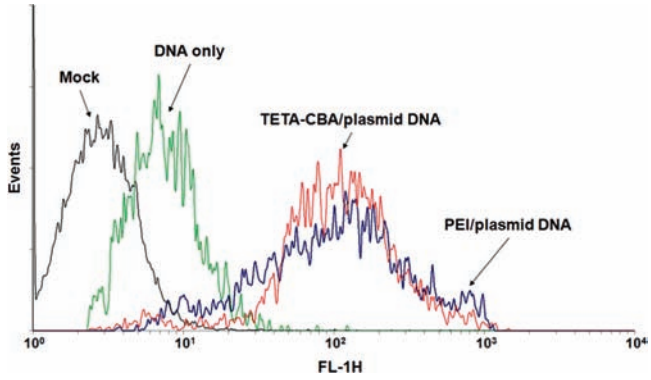


Figure 4. Cellular association of pSIGLP1NFκB/TETA-CBA and pSIGLP1NFκB/PEI complexes, analyzed by flow cytometry.

Nuclear localization of plasmid DNA was quantified by relating fluorescence intensities from two arbitrarily defined regions of interest (ROIs): the whole cell (FL_{cell}) and the nucleus ($FL_{nucleus}$). Fluorescence intensity from each ROI was separately analyzed by using *ImageJ* v 1.42 software (http://rsb.info.nih.gov/ij). Percent fluorescence in the selected nucleus region ($FL_{nucleus}/FL_{cell} \times 100$) was calculated and presented as mean percent nuclear localization $\pm$ SEM ($n = 50$).

RESULTS AND DISCUSSION

Viruses have evolved to transfer their genetic information to host cells for the production of progeny. For the efficient delivery of its genome to the host nucleus, a virus contains multiple functional components that facilitate cellular entry, endosomal escape, the dissociation of genetic material from capsid protein complex, and nuclear transfer by the aid of host nuclear localization mechanism. It has long been a challenging problem to develop a synthetic carrier that mimics the viral infection machinery (*14*). Gene therapy based on a plasmid DNA encoding a desired therapeutic gene depends largely on successful entry of plasmid DNA into the nucleus, independent of the type of gene delivery method. After cellular entry and endosomal escape, a carrier/plasmid DNA complex or a plasmid DNA released from the complex should move toward the perinuclear space where nuclear translocation of a plasmid DNA occurs. However, the nanoparticular complex or plasmid DNA with several millions of molecular weight can hardly pass through a highly viscous medium of the cytoplasm filled with an extensive network of cytoskeletons, proteins, mRNAs, and various subcellular organelles (*15, 16*). In addition, the passage of macromolecules through the nuclear envelope is also restricted. The nuclear pore complex only allows passage of biological macromolecules with molecular weight of less than 60 kDa unless they have a signal peptide for nuclear localization (NLS), which can be recognized by nuclear importins, carrier proteins for nuclear localization of various karyophilic proteins. Therefore, we designed a virus-mimicking gene delivery system that can use an endogenous nuclear transport mechanism by using a reducible polymer that is degradable in the cytoplasm and a plasmid DNA containing a repeated binding motif for NFκB, an endogenous transcription factor. The plasmid DNA was designed to use the transcription factor as an intracellular carrier for active nuclear translocation of a plasmid DNA. A ubiquitously expressed transcription factor, NFκB, mainly exists as an inactive heterodimer with IκB protein in the cytoplasm (*17*). When the cell is stimulated by a specific signal, IκB is phosphorylated and rapidly degraded. This results in the exposure of NLS motif, leading to rapid nuclear translocation of NFκB (*18*). It was previously reported that a plasmid containing NFκB binding sequence demonstrated enhanced cytoplasmic mobility and nuclear translocation of the plasmid DNA (*8*), leading to enhanced transfection efficiency (*9, 19*). Since the interaction between the plasmid DNA and NFκB is a prerequisite to achieve efficient karyophilic protein-guided cytosolic trafficking and nuclear translocation, unpackaging of the plasmid DNA/polymer complexes should be occurring soon after the endosomal escape of the complexes. An endosomal escape and the cytosolic unpacking of the complexes could be facilitated by using a reducible polymer, TETA-CBA.

A reducible TETA-CBA copolymer was synthesized by Michael addition polymerization between amine donor (TETA) and bisacrylate (CBA), as described previously (*11*). The disulfide linkages in TETA-CBA are expected to be cleaved into amidoamine monomers in the reductive cytoplasm. The proton buffering and reductive degradation properties of the copolymer were studied in a previously published result (*11, 12*). The cationic copolymer interacts with plasmid DNA to form tight complexes for efficient gene delivery to cells (*11, 20*). Once localized inside the cells, the backbone of TETA-CBA may be degraded by the action of intracellular reduced glutathione, resulting in the cytosolic release of the plasmid DNA. The released plasmid DNA containing the repeated NFκB motif could then bind to the DNA binding domain of cytosolic NFκB without interference of the cationic carrier. The NFκB bound to the plasmid could act as an intracellular vehicle for the plasmid DNA. Stimulation of the cells with a cytokine such as IL-1β causes the degradation of the IκB unit and the exposure of an NLS moiety of NFκB, leading to intracellular trafficking of the NFκB-plasmid DNA to the perinuclear space and concurrent transfer of the NFκB-plasmid DNA into the nucleus. The hypothetical intracellular delivery mechanism based on a reducible polycation and a plasmid DNA with a karyophilic protein binding site is illustrated in Figure 1.

A plasmid DNA (pSIGLP1NFκB) encoding glucagon-like peptide-1 (GLP-1) was previously constructed (*9*) and used to evaluate gene transfection efficiency. The electrostatic interaction between the plasmid DNA and TETA-CBA polymer could form tight complexes, which could be readily degraded to release the plasmid DNA in the presence of a reducing force (Figure 2). The degradation of the polymer in a reductive environment agrees well with previous results (*11*). The pSIGLP1NFκB/TETA-CBA formulation demonstrated only a slightly higher production of GLP-1 in mouse fibroblast cells (NIH3T3) than a formulation with a nondegradable control polymer, PEI 25

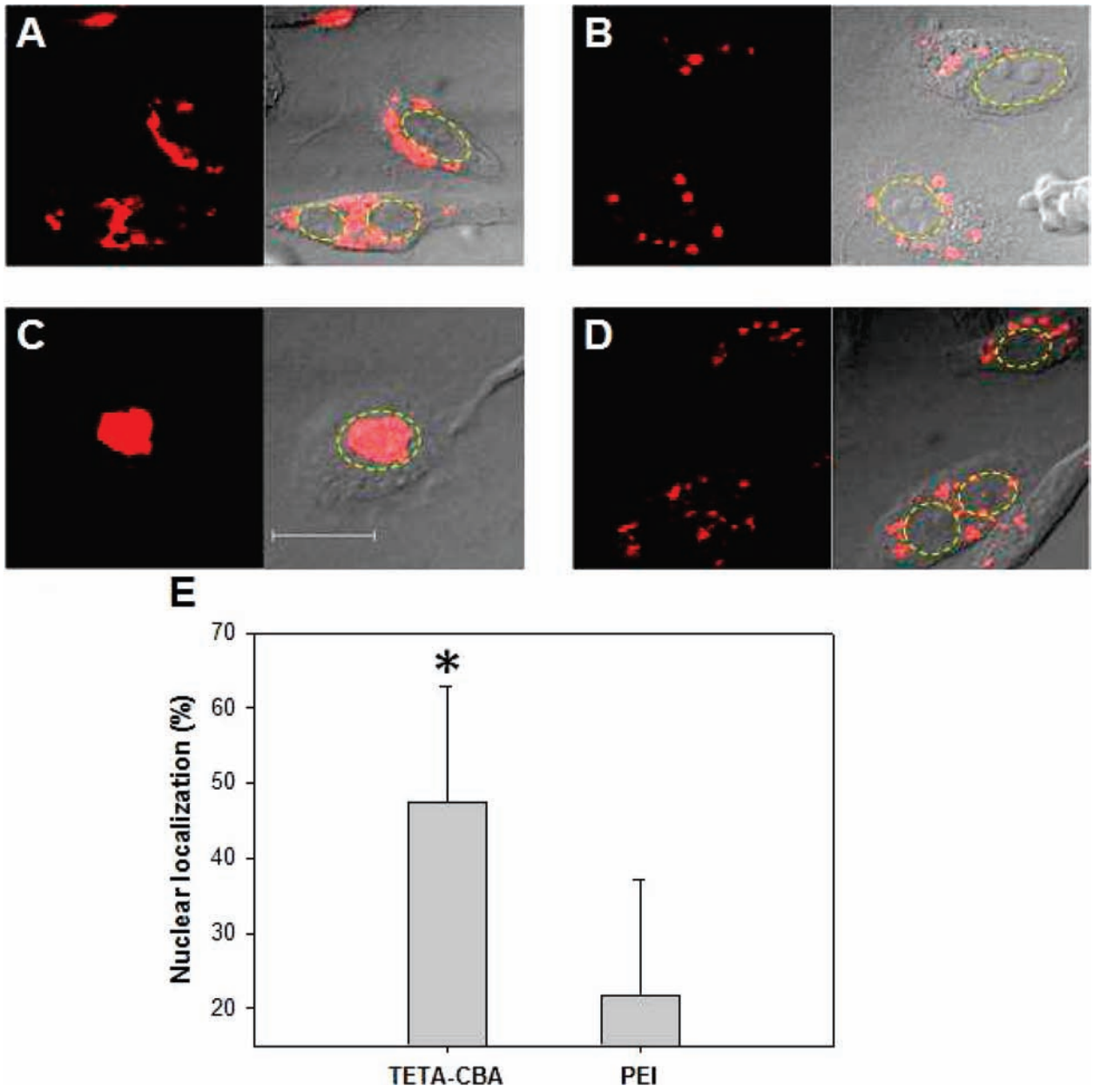


Figure 5. Subcellular localization of Cy3-labeled pSIGLP1NFκB formulated with either TETA-CBA (A,C) or PEI (B,D) after transfection in NIH3T3 cells. Prior to observation, the cells were incubated for additional 2 h in the absence (A,B) and presence (C,D) of IL-1β stimulation. Dashed line indicates the nucleus. (E) Nuclear association of plasmid DNA after IL-1β stimulation was determined by relating two arbitrarily defined regions of interest (ROIs: ROI_1 = the whole cell, ROI_2 = the nucleus) and given as percent nuclear localization ± SD ($n = 50$). *$p < 0.05$ compared to the PEI-based control.

kDa (Figure 3). The addition of IL-1β, which can initiate the dissociation of IκB from NFκB heterodimer and the nuclear translocation of NFκB (*18*), to the cells treated with the pSIGLP1NFκB/TETA-CBA formulation resulted in a significant increase in GLP-1 expression. However, the control formulation (pSIGLP1NFκB/PEI) failed to show a significant increase in GLP-1 expression after the IL-1β stimulation. A cellular association profile of the transfection complexes from either TETA-CBA or PEI-based formulation was not significantly different from that of the other (Figure 4). The results suggest that the improved transfection efficiency may be due to the NFκB-guided intracellular trafficking and active nuclear translocation of the plasmid DNA. To test the hypothetical suggestion, the subcellular localization of plasmid DNA after transfection was observed using confocal laser scanning microscopy. The Cy-3 labeled plasmid DNA formulated with TETA-CBA was distributed over the cytoplasm 5 h after transfection (Figure 5A). However, most of the fluorescently labeled plasmid DNA was localized in the cytoplasmic space, rather than in the nucleus, suggesting that the DNA dissociated from the polymer/DNA complex could not penetrate the nuclear membrane via passive diffusion. The uneven distribution of the plasmid DNA in the cytoplasm may be due to restricted movement of high molecular weight plasmid DNA in the highly viscous mesh-like network of the cytoplasm. The cytosolic reductive release of genetic materials such as plasmid DNA and siRNA could also be observed in previous observations with reducible polymeric carriers (*21*, *22*). In contrast to the TETA-CBA formulation, PEI formulations seemed to exist as complexes or larger aggregates in a specific location, suggesting that complexes formed from PEI and plasmid DNA may not be readily dissociated in the cytoplasm (Figure 5B). When stimulated by IL-1β, nuclear accumulation of the fluorescently labeled plasmid DNA (pSIGLP1NFκB) could be observed in the cells treated

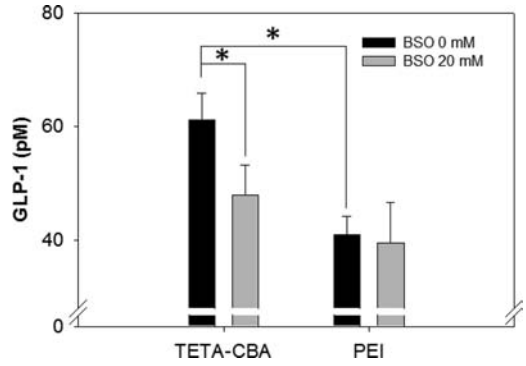


Figure 6. Effect of DL-buthionine sulfoxamine (BSO) on transfection efficiencies of formulations based on either TETA-CBA or PEI. Activation and nuclear translocation of NFκB was initiated by the addition of IL-1β. The expression level of secreted GLP-1 was determined by ELISA and given as the mean $\pm$ SD ($n = 3$). *$p < 0.01$ compared to the PEI-based control.

with the pSIGLP1NFκB/TETA-CBA formulation (Figure 5C). However, no significant movement of the plasmid DNA to the nuclear region was detected in the cells transfected with the pSIGLP1NFκB/PEI formulation, even after IL-1β treatment (Figure 5D). The improved nuclear localization was quantitatively measured by using image analysis software (*ImageJ*). Nuclear localization of the fluorescently labeled plasmid DNA was obtained by relating fluorescence intensities from two arbitrarily defined regions of interest (ROIs): the whole cell (FL_{cell}) and the nucleus ($FL_{nucleus}$). After stimulation with IL-1β, the pSIGLP1NFκB/TETA-CBA formulation showed a significantly higher accumulation of the plasmid DNA in the nuclear region compared to PEI formulation. In conjunction with the qualitative observation with confocal microscopy, the data suggest that the reductive degradation of the reducible polymer and release of the plasmid DNA in the cytoplasm would play an important role in the NFκB-mediated cytosolic trafficking and the nuclear import of the plasmid DNA by facilitating the interaction between NFκB and the binding motif in the plasmid DNA.

The role of cytosolic reductive degradation of the TETA-CBA in NFκB-mediated nuclear translocation of pSIGLP1NFκB was further studied by using DL-buthionine sulfoxamine (BSO), which effectively reduces the level of intracellular reduced glutathione (*23*). Pretreatment of the cells with BSO caused a reduction in transfection efficiency of TETA-CBA. In addition, the extent of reduction in GLP-1 expression was much higher in the cells treated with the TETA-CBA formulation when IL-1β stimulation was given (Figure 6). However, PEI-mediated transfections were not affected by the BSO treatment. This result strongly supports our initial hypothesis in which the triggered release of the plasmid DNA in the cytoplasm could promote the chance of interaction between NFκB and the plasmid DNA. The interaction would lead to the improved nuclear translocation, resulting in enhanced expression of GLP-1.

Mimicking the viral infection mechanism for improved transfection requires the elaborate integration of functional elements, including targeting moieties, endosomal escape, intracellular trafficking, and nuclear translocation functionalities into a nanoscale container, i.e., a nanoparticle. In this study, we introduced a gene delivery system that can take advantage of endogenous nuclear transport mechanisms by combining a reducible polymeric gene carrier and a plasmid DNA containing repeated binding motif for a karyophilic protein, NFκB. The delivery system could successfully achieve enhanced transfection by efficient coordination of cytosolic triggered release and NFκB-mediated nuclear translocation mechanisms. This demonstrates an alternative strategy for integrating several functionalities in a polyelectrolyte-based nanoparticular container. Besides the intracellular delivery, additional functionalities, including improved extracellular stability and tissue specificity, are to be incorporated to produce a gene delivery system that eventually mimics virus infection machinery.

ACKNOWLEDGMENT

This work is supported by the grant from the National Research Foundation of Korea (NRF) funded by the Ministry of Education, Science and Technology (331-2008-1-D00756, 2009-0093632, 2009-0059223, 2009-0088722) and U.S. NIH (NIDDK-DK77703).

LITERATURE CITED

(1) Park, T. G., Jeong, J. H., and Kim, S. W. (2006) Current status of polymeric gene delivery systems. *Adv. Drug Delivery Rev. 58*, 467–86.
(2) Glover, D. J., Lipps, H. J., and Jans, D. A. (2005) Towards safe, non-viral therapeutic gene expression in humans. *Nat. Rev. Genet. 6*, 299–310.
(3) Schaffer, D. V., Fidelman, N. A., Dan, N., and Lauffenburger, D. A. (2000) Vector unpacking as a potential barrier for receptor-mediated polyplex gene delivery. *Biotechnol. Bioeng. 67*, 598–606.
(4) Varga, C. M., Tedford, N. C., Thomas, M., Klibanov, A. M., Griffith, L. G., and Lauffenburger, D. A. (2005) Quantitative comparison of polyethylenimine formulations and adenoviral vectors in terms of intracellular gene delivery processes. *Gene Ther. 12*, 1023–32.
(5) Tseng, W. C., Haselton, F. R., and Giorgio, T. D. (1999) Mitosis enhances transgene expression of plasmid delivered by cationic liposomes. *Biochim. Biophys. Acta 1445*, 53–64.
(6) Branden, L. J., Mohamed, A. J., and Smith, C. I. (1999) A peptide nucleic acid-nuclear localization signal fusion that mediates nuclear transport of DNA. *Nat. Biotechnol. 17*, 784–7.
(7) Tanimoto, M., Kamiya, H., Minakawa, N., Matsuda, A., and Harashima, H. (2003) No enhancement of nuclear entry by direct conjugation of a nuclear localization signal peptide to linearized DNA. *Bioconjugate Chem. 14*, 1197–202.
(8) Mesika, A., Kiss, V., Brumfeld, V., Ghosh, G., and Reich, Z. (2005) Enhanced intracellular mobility and nuclear accumulation of DNA plasmids associated with a karyophilic protein. *Hum. Gene Ther. 16*, 200–8.
(9) Choi, S., Oh, S., Lee, M., and Kim, S. W. (2005) Glucagon-like peptide-1 plasmid construction and delivery for the treatment of type 2 diabetes. *Mol. Ther. 12*, 885–91.
(10) Goncalves, C., Ardourel, M. Y., Decoville, M., Breuzard, G., Midoux, P., Hartmann, B., and Pichon, C. (2009) An optimized extended DNA kappa B site that enhances plasmid DNA nuclear import and gene expression. *J. Gene Med. 11*, 401–11.
(11) Christensen, L. V., Chang, C. W., Kim, W. J., Kim, S. W., Zhong, Z., Lin, C., Engbersen, J. F., and Feijen, J. (2006) Reducible poly(amido ethylenimine)s designed for triggered intracellular gene delivery. *Bioconjugate Chem. 17*, 1233–40.
(12) Jeong, J. H., Christensen, L. V., Yockman, J. W., Zhong, Z., Engbersen, J. F. J., Kim, W. J., Feijen, J., and Kim, S. W. (2007) Reducible poly(amido ethylenimine) directed to enhance RNA interference. *Biomaterials 28*, 1912–1917.
(13) Oh, S., Lee, M., Ko, K. S., Choi, S., and Kim, S. W. (2003) GLP-1 gene delivery for the treatment of type 2 diabetes. *Mol. Ther. 7*, 478–83.
(14) Jeong, J. H., Kim, S. W., and Park, T. G. (2007) Molecular design of functional polymers for gene therapy. *Prog. Polym. Sci. 32*, 1239–1274.
(15) Luby-Phelps, K., Castle, P. E., Taylor, D. L., and Lanni, F. (1987) Hindered diffusion of inert tracer particles in the cytoplasm of mouse 3T3 cells. *Proc. Natl. Acad. Sci. U.S.A. 84*, 4910–3.

(16) Dowty, M. E., Williams, P., Zhang, G., Hagstrom, J. E., and Wolff, J. A. (1995) Plasmid DNA entry into postmitotic nuclei of primary rat myotubes. *Proc. Natl. Acad. Sci. U.S.A. 92*, 4572–6.

(17) Carlotti, F., Chapman, R., Dower, S. K., and Qwarnstrom, E. E. (1999) Activation of nuclear factor kappaB in single living cells. Dependence of nuclear translocation and anti-apoptotic function on EGFPRELA concentration. *J. Biol. Chem. 274*, 37941–9.

(18) Ding, G. J., Fischer, P. A., Boltz, R. C., Schmidt, J. A., Colaianne, J. J., Gough, A., Rubin, R. A., and Miller, D. K. (1998) Characterization and quantitation of NF-kappaB nuclear translocation induced by interleukin-1 and tumor necrosis factor-alpha. Development and use of a high capacity fluorescence cytometric system. *J. Biol. Chem. 273*, 28897–905.

(19) Mesika, A., Grigoreva, I., Zohar, M., and Reich, Z. (2001) A regulated, NFkappaB-assisted import of plasmid DNA into mammalian cell nuclei. *Mol. Ther. 3*, 653–7.

(20) Christensen, L. V., Chang, C. W., Yockman, J. W., Conners, R., Jackson, H., Zhong, Z., Feijen, J., Bull, D. A., and Kim, S. W. (2007) Reducible poly(amido ethylenediamine) for hypoxia-inducible VEGF delivery. *J. Controlled Release 118*, 254–61.

(21) Lee, Y., Mo, H., Koo, H., Park, J. Y., Cho, M. Y., Jin, G. W., and Park, J. S. (2007) Visualization of the degradation of a disulfide polymer, linear poly(ethylenimine sulfide), for gene delivery. *Bioconjugate Chem. 18*, 13–8.

(22) Kim, S. H., Jeong, J. H., Kim, T. I., Kim, S. W., and Bull, D. A. (2009) VEGF siRNA delivery system using arginine-grafted bioreducible poly(disulfide amine). *Mol. Pharmaceutics 6*, 718–26.

(23) Read, M. L., Singh, S., Ahmed, Z., Stevenson, M., Briggs, S. S., Oupicky, D., Barrett, L. B., Spice, R., Kendall, M., Berry, M., Preece, J. A., Logan, A., and Seymour, L. W. (2005) A versatile reducible polycation-based system for efficient delivery of a broad range of nucleic acids. *Nucleic Acids Res. 33*, e86.

BC9003525

Site-Specific and Stoichiometric Conjugation of Cationic Porphyrins to Antiangiogenic Monoclonal Antibodies

Cristina M. A. Alonso,[†,‡] Alessandro Palumbo,[†,§] Aaron J. Bullous,[‡] Francesca Pretto,[§] Dario Neri,*[,§] and Ross W. Boyle*[,‡]

Department of Chemistry, University of Hull, Cottingham Road, HU6 7RX, Kingston-upon-Hull, United Kingdom, and Institute of Pharmaceutical Sciences, Swiss Federal Institute of Technology Zurich, Wolfgang-Pauli-Str. 10, HCI G396, 8093 Zurich, Switzerland. Received August 11, 2009; Revised Manuscript Received December 1, 2009

Synthesis of three new cationic thiol-reactive maleimide−porphyrin derivatives and their use in site-specific conjugation to monoclonal antibodies is reported. The selective reactivity toward thiols is demonstrated using competition experiments, where both thiols and amines are present. This selectivity was used to successfully achieve specific conjugation of two porphyrins to cysteine residues present in the antiangiogenic antibody L19, expressed in small immunoprotein (SIP) format. The effect of length and hydrophilicity of the linkage between porphyrin and maleimide was also investigated, and maximum photocytotoxicity was achieved with the longest and most hydrophilic chain. Immunoreactivity and in vitro photocytotoxicity for these well-characterized porphyrin−antibody conjugates are described.

INTRODUCTION

Photodynamic therapy (PDT) is now an established clinical cancer treatment (*1*). PDT combines a photosensitizing compound, light, and oxygen to promote the destruction of localized neoplastic lesions (*2, 3*). Although PDT is employed in most of the developed countries of the world with good effect, the selectivity of commercial PDT agents for tumor tissue remains an area where there is considerable room for improvement. Typically, tumor to peritumoral tissue ratios are significantly below 10:1 at the time of treatment (*4*). Lack of selectivity requires the administration of increased doses of photosensitizer to achieve the desired clinical effect, which in turn causes generalized photosensitivity for the patient and leads to small safety margins when treating tumors in sensitive areas, such as the brain.

In order to improve targeting of photodynamic sensitizers to tumor tissue, a number of strategies have been devised (*5*−*8*). One of the most promising of these targeting methods is the use of antibodies or antibody fragments, often termed photoimmunotherapy (PIT). PIT combines the photosensitizing properties of a photosensitizer and the targeting capabilities of an antibody, usually by conjugating one to the other in such a way that neither photophysical nor immunogenic properties are compromised (*9*).

Many different monoclonal antibodies (mAb) (*9*−*21, 33*) and antibody fragments of different formats, including scFv (single chain Fv antibody fragment) (*21*−*24*), F(ab′)$_2$ (*13, 25*−*28*), and SIP (small immunoprotein, or mini-antibody) (*21*), have been used to obtain photoimunoconjugates for targeted photodynamic therapy. From all the different available formats, small immunoproteins (SIP) appear to offer the best compromise among stability, blood clearance, and tumor accumulation (*29*−*31*).

The majority of these antibodies and antibody fragments are specific to antigens overexpressed on tumor cells; however, normal cells can also express these antigens, leading to nonspecific uptake (*9, 32*). Several research groups have avoided this problem by using immunoconjugates that target markers in the tumor vasculature (*18, 19, 21, 23, 24, 33, 34*).

The most common method used for conjugation of photosensitizers to antibodies involves coupling the terminal amino group of lysine residues on the antibody to a reactive group on the porphyrinic photosensitizer. These reactive groups are often some form of active ester, generated from carboxy-bearing photosensitizers, or isothiocyanates. Only a few reports describe the conjugation of photosensitizers to the thiol groups of cysteine residues (*14, 15, 25*−*28, 40*). Cysteine residues represent an attractive bioconjugation target because, unlike lysine residues, cysteines on antibodies are remote from the binding site.

Clearly, in order to effectively target cysteine residues, reactive groups which are selective for thiols must be incorporated into the photosensitizer structure. Recently, several porphyrins bearing thiol-reactive functionalities have been reported in the literature (*12, 35*−*41*); however, to our knowledge, none of these molecules has been used to generate a functional photoimmunotherapy conjugate.

In the present work, we report the synthesis and utility of novel water-soluble porphyrin derivatives bearing maleimide moieties for the site-specific and stoichiometrically controlled labeling of a reduced small immunoprotein of the antiangiogenic L19 antibody [SIP(L19)]. The full water solubility promoted by the presence of three quaternized pyridyl groups avoids the noncovalent binding often found with more hydrophobic photosensitizers. Contamination with noncovalently bound photosensitizers is a significant problem in the developed photoimmunoconjugates, as this material can transfer to other serum components upon systemic administration. The combination of full water solubility with the highly thiol selective maleimide moiety renders the conjugation procedure simple, reproducible, and fast, generating well-characterized functional photoimmunoconjugates.

Finally, the effect of length and hydrophilicity of the linker between porphyrin and maleimide was examined, due to the

* Corresponding author. Ross W. Boyle, E-mail: r.w.boyle@hull.ac.uk, Phone: (+44)1482466353. Fax: (+44)1482466410. Dario Neri, E-mail: neri@pharma.ethz.ch, Phone: (+41)446337401, Fax: (+41)446331358.
† Authors contributed equally.
‡ University of Hull.
§ Swiss Federal Institute of Technology Zurich.

10.1021/bc9003537 © 2010 American Chemical Society
Published on Web 01/14/2010

close proximity of the two available cysteines on SIP(L19) and the possibility that this may lead to self-quenching of photosensitizer excited states and consequent lowering of photodynamic activity.

EXPERIMENTAL PROCEDURES

General. ^{1}H and ^{13}C NMR spectra were recorded on JEOL Eclipse 400 and JEOL lambda 400 spectrometers (operating at 400 MHz for ^{1}H and 100 MHz for ^{13}C). $CDCl_3$ was used as solvent and TMS as internal reference for all the non-water-soluble porphyrin derivatives, DMSO-d_6 was used as solvent and as internal reference for all the water-soluble porphyrin derivatives (in this case, chemical shifts are reported in δ (ppm) from the central reference peak of the solvent: DMSO-d_6 2.50 ppm and 39.5 ppm for ^{1}H and ^{13}C NMR, respectively). All the chemical shifts are expressed in δ (ppm) and the coupling constants (J) in Hertz (Hz). Unequivocal ^{1}H assignments were made using 2D COSY; ^{13}C assignments were made on the basis of 2D HSQC and HMBC experiments (delay for long-range J C/H couplings were optimized for 7 Hz). Mass spectra (low and high resolution) were performed by the EPSRC Mass Spectrometry Service, Swansea. UV−vis spectra were recorded on an Agilent 8453 spectrophotometer using dichloromethane, dichloromethane/methanol mixtures, or water as solvent. Preparative thin-layer chromatography was carried out on 20 × 20 cm^2 glass plates precoated with silica gel 60 (0.5 mm thick, Uniplate, Analthech). Flash chromatography was carried in silica gel 60 (MP Biomedicals, 32−63 μm). Analytical TLC was carried out on precoated sheets with silica gel 60 (Fluka, 0.2 mm thick). Commercial solvents and reagents were used without further purification unless stated otherwise. The starting porphyrins 5-(4-aminophenyl)-10,15,20-tri-(4-pyridyl)porphyrin **1** (*45*) and 5-(4-carboxyphenyl)-10,15,20-tri-(4-pyridyl)porphyrin **5** (*46*) were prepared according to literature procedures.

Synthesis. *5-[4-(N-Phenylmaleamic acid)]-10,15,20-tri-(4-pyridyl)porphyrin,* ***2.*** To a stirred solution of 5-(4-aminophenyl)-10,15,20-tri-(4-pyridyl)porphyrin (100.0 mg, 0.159 mmol) **1** in nitrobenzene (15 mL) was added maleic anhydride (37.0 mg, 0.381 mmol, 2.4 equiv). The reaction mixture was protected from moisture and kept under constant stirring at 100 °C for 22 h. After allowing the reaction to cool to room temperature, *n*-hexane was added in order to promote the precipitation of the product and to remove the nitrobenzene. Upon filtration, the obtained solid was taken up in dichloromethane and purified by flash chromatography using as first eluent a mixture of dichloromethane/methanol (85:15) and as second eluent dichloromethane/methanol (70:30). After precipitation with *n*-hexane, the product was obtained as a brown solid in 96% yield (112.6 mg). ^{1}H NMR ($CDCl_3$, 400 MHz), δ: −2.99 (br s, 2H, N*H*), 6.12 (d, J = 13.2 Hz, 1H, -NHCOCHC*H*CO$_2$H), 6.40 (d, J = 13.2 Hz, 1H, -NHCOC*H*CHCO$_2$H), 8.02 and 8.07 (AB, J = 8.2 Hz, 4H, 5-Ar-*o*,*m*-H), 8.11 and 8.14 (2d, J = 4.9 Hz, 4 + 2H, 10,15,20-Ar-*o*-H), 8.56−8.86 (m, 8H, H-β), 8.88 and 8.91 (2d, J = 4.9 Hz, 4 + 2H, 10,15,20-Ar-*m*-H), 13.2 (s, 1H,-CO$_2$*H*). ^{13}C NMR ($CDCl_3$, 100 MHz), δ: 116.4, 116.9, 118.2 (5-Ar-*m*-C), 121.6, 129.4, and 129.5 (10,15,20-Ar-*o*-C), 130.1 (−COCH=*C*HCO$_2$H), 134.9 (5-Ar-*o*-C), 136.3 (−CO*C*H=CHCO$_2$H), 136.7, 138.6, 147.5, and 147.6 (10,15,20-Ar-*o*-C), 150.52, 150.54, 164.6 (−NH*C*O−), 172.4 (-*C*O$_2$H). UV/vis (CH_2Cl_2/MeOH- 25%), λ_{max} (log ε): 419 (5.44), 515 (4.24), 549 (3.89), 589 (3.78), 645 (3.45). HRMS (ESI) m/z calcd for $C_{45}H_{31}N_8O_3$ $(M + H)^+$ 713.2514, found: 713.2520.

5-(4-Maleimidophenyl)-10,15,20-tri-(4-pyridyl)porphyrin, ***3.*** To a stirred solution of 5-[4-(*N*-phenylmaleamic acid)]-10,15,20-tri-(4-pyridyl)porphyrin **2** (107.2 mg, 0.147 mmol) in acetic anhydride (15 mL) was added sodium acetate (15.7 mg, 0.191 mmol, 1.3 equiv). The resulting reaction mixture was kept at 80 °C, under constant stirring, and protected from moisture for 3.5 h. After this period, the reaction was allowed to cool to room temperature and the solvent was removed under reduced pressure. The residue was taken up in dichloromethane, washed with distilled water, and the organic layer dried over anhydrous sodium sulfate. After purification by flash column chromatography, using a mixture of dichloromethane/methanol (95:5) as eluent, the product was precipitated from dichloromethane by addition of methanol to obtain the title compound as a purple solid in 84% yield (88.0 mg). ^{1}H NMR ($CDCl_3$, 400 MHz), δ: −2.89 (br s, 2H, N*H*), 7.02 (s, 2H, −COC*H*=C*H*CO−), 7.80 (AA′XX′, 2H, 5-Ar-*m*-H), 8.17 (dd, J = 1.5 Hz, J = 4.2 Hz, 6H, 10,15,20-Ar-*o*-H), 8.30 (AA′XX′, 2H, 5-Ar-*o*-H), 8.85 (d, J = 4.9 Hz, 2H, H-β), 8.86−8.91 (m, 4H, H-β), 8.97 (d, J = 4.9 Hz, 2H, H-β), 9.05 (dd, J = 1.5 Hz, J = 4.2 Hz, 6H, 10,15,20-Ar-*m*-H). ^{13}C NMR ($CDCl_3$, 100 MHz), δ: 117.2, 117.5, 120.3, 124.1 (5-Ar-*m*-C), 129.4 (10,15,20-Ar-*o*-C), 131.4, 134.5 (−CO*C*H=*C*HCO−), 135.0 (5-Ar-*o*-C), 140.9, 148.3 (10,15,20-Ar-*m*-C), 150.0, 169.6, (−*C*OCH=CH*C*O−). UV/vis (CH_2Cl_2/MeOH- 3%), λ_{max} (log ε): 417 (5.31), 513 (4.12), 547 (3.64), 588 (3.63), 643 (3.31). HRMS (ESI) calcd for $C_{45}H_{29}N_8O_2$ $(M + H)^+$ 713.2408, found: 713.2400.

5-(4-Maleimidophenyl)-10,15,20-tri-(4-N-methyl-pyridiniumyl)porphyrin Triiodide, ***4.*** To a stirred solution of 5-(4-maleimidophenyl)-10,15,20-tri-(4-pyridyl)porphyrin **3** (35.8 mg, 0.050 mmol) in dry DMF (2.5 mL) in a two-necked flask equipped with a condenser and a rubber septum was added a large excess of iodomethane (0.50 mL, 8.03 mmol, 160 equiv) via syringe. The reaction mixture was stirred at 40 °C for 4 h; after allowing it to cool to room temperature, the porphyrinic material was precipitated with dry dichloromethane and diethyl ether (1:1) and washed thoroughly with the same mixture to remove any vestigial amounts of iodomethane. The methylated porphyrin was obtained as a brown solid in 95% yield (54.2 mg). ^{1}H NMR (DMSO-d_6, 400 MHz), δ: −3.01 (br s, 2H, N*H*), 4.73 (s, 9H, 3 × C*H*$_3$), 7.40 (s, 2H, −COC*H*=C*H*CO−), 7.90 (d, J = 8.1 Hz, 2H, 5-Ar-*m*-H), 8.37 (d, J = 8.1 Hz, 2H, 5-Ar-*o*-H), 8.95−9.05 (m, 2H, H-β), 9.02 (d, J = 6.2 Hz, 6H, 10,15,20-Ar-*o*-H), 9.06−9.13 and 9.14−9.24 (2 m, 6H, H-β), 9.45 (d, J = 6.2 Hz, 6H, 10,15,20-Ar-*m*-H). ^{13}C NMR (DMSO-d_6, 100 MHz), δ: 47.9 (3 × *C*H$_3$), 114.7, 115.4, 121.9, 125.0 (5-Ar-*m*-C), 132.1 (10,15,20-Ar-*o*-C), 134.6 (5-Ar-*o*-C), 135.0 (−CO*C*H=*C*HCO−), 139.3, 144.2 (10,15,20-Ar-*m*-C), 156.4, 156.5, 170.1(−*C*OCH=CH*C*O−). UV/vis (H_2O), λ_{max} (log ε): 422 (5.35), 520 (3.95), 558 (3.58), 584 (3.61), 641 (2.92). HRMS (ESI) calcd for $C_{48}H_{37}N_8O_2$ (M^{3+}) 252.4341, found: 252.4344.

5-[4-(Succinimide-N-oxycarbonyl)phenyl]-10,15,20-tri-(4-pyridyl)porphyrin, ***6.*** To a stirred solution of 5-(4-carboxyphenyl)-10,15,20-tri-(4-pyridyl)porphyrin **5** (51.1 mg, 0.077 mmol) in dry pyridine (5 mL) was slowly added thionyl chloride (0.10 mL, 1.37 mmol, 18 equiv). The reaction was then stirred at 50 °C, protected from light and atmospheric moisture, for 30 min. After this period, *N*-hydroxysuccinimide (200 mg, 1.74 mmol, 23 equiv) was added and the mixture maintained under the previous conditions for 3 h. The pyridine was then removed under vacuum, and the residue taken up in dichloromethane and washed with an aqueous saturated solution of sodium carbonate. The organic layer was dried over anhydrous sodium sulfate and concentrated under reduced pressure. Precipitation of the residue in *n*-hexane over chloroform afforded pure 5-[4-(succinimide-*N*-oxycarbonyl)phenyl]-10,15,20-tri-(4-pyridyl)porphyrin **6** in 90% yield (52.3 mg). ^{1}H NMR ($CDCl_3$, 400 MHz), δ: −2.90 (br s, 2H, N*H*), 3.03 (br s, 4H, 2 × C*H*$_2$), 8.17 (dd, J = 1.6 Hz, J = 4.3 Hz, 6H, 10,15,20-Ar-*o*-H), 8.37 (d, J = 6.5 Hz, 2H, 5-Ar-*m*-H), 8.57 (d, J = 6.5 Hz, 2H, 5-Ar-*o*-H), 8.85 (d, J = 4.8 Hz, 2H, H-β), 8.86−8.90 (m, 6H, H-β), 9.06 (dd, J = 1.6

Hz, $J = 4.3$ Hz, 6H, 10,15,20-Ar-*m*-H). ^{13}C NMR ($CDCl_3$, 100 MHz), δ: 25.8 ($2 \times \underline{C}H_2$), 117.7, 117.8, 119.2, 124.9, 129.1, 129.3, 131.5, 134.8, 148.5, 149.8, 162.0, 169.3 ($2 \times \underline{C}O$). UV/vis (CH_2Cl_2), λ_{max} (log ε): 418 (5.66), 513 (4.43), 547 (3.93), 588 (3.91), 644 (3.50). HRMS (ESI) calcd for $C_{53}H_{50}N_90_3$ (M + H)$^+$ 759.2463, found: 759.2446.

5-[4-(N-Boc-1,6-diaminohexyl-N-oxycarbonyl)phenyl]-10,15,20-tri-(4-pyridyl)porphyrin, ***7.*** To a stirred solution of 5-[4-(succinimide-*N*-oxycarbonyl)phenyl]-10,15,20-tri-(4-pyridyl)porphyrin **6** (51.3 mg, 0.067 mmol) in dry DMSO (6 mL) was added *N*-Boc-1,6-diaminohexane (42.8 mg, 0.169 mmol, 2.5 equiv) and potassium carbonate (58.4 mg, 0.422 mmol, 2.5 equiv relative to the amine). The reaction mixture was kept under constant stirring at 40 °C and protected from atmospheric moisture and light. After 40 min, full consumption of the starting porphyrin was achieved (confirmed by TLC) and the reaction mixture was diluted with dichloromethane and extracted with water. The organic layer was dried over anhydrous sodium sulfate and the solvent removed under reduced pressure. The product was obtained in 82% yield (47.5 mg) after purification by flash chromatography (eluent: dichloromethane/methanol, 94:6) and precipitation in *n*-hexane over dichloromethane. ^{1}H NMR ($CDCl_3$, 400 MHz), δ: −2.90 (br s, 2H, N$\underline{H}$), 1.44 (s, 9H, $-CO_2C(C\underline{H}_3)_3$), 1.53−1.62 (m, 4H, $2 \times C\underline{H}_2$), 1.79 (quintet, $J = 7.0$ Hz, 2H, C$\underline{H}_2$), 3.01−3.14 (m, 2H, CH_2), 3.15−3.25 (m, 2H, C$\underline{H}_2$), 3.64 (q, $J = 6.6$ Hz, 2H, -NHC$\underline{H}_2$(CH_2)$_5$NHCO$_2$^{t}Bu), 4.64 (br s, 1H, -NH(CH_2)$_6$N$\underline{H}$CO$_2$^{t}Bu), 4.89 (br s, 1H, -N$\underline{H}$(CH_2)$_6$NHCO$_2$^{t}Bu), 8.10−8.18 (m, 6H, 10,15,20-Ar-*o*-H), 8.23 (d, $J = 8.1$ Hz, 2H, 5-Ar-*m*-H), 8.28 (d, $J = 8.1$ Hz, 2H, 5-Ar-*o*-H), 8.82 (d, $J = 4.8$ Hz, 2H, H-β), 8.84−8.87 (m, 4H, H-β), 8.88 (d, $J = 4.8$ Hz, 2H, H-β), 8.90−8.09 (m, 6H, 10,15,20-Ar-*m*-H). ^{13}C NMR ($CDCl_3$, 100 MHz), δ: 25.9, 26.1, 28.2 ($3 \times \underline{C}H_3$), 29.1, 29.5, 29.7, 39.7, 39.8, 116.6, 117.0, 120.1, 120.7, 125.5, 129.7 (10,15,20-Ar-*o*-C), 134.2, 134.4, 142.2, 146.9 (10,15,20-Ar-*m*-C), 151.2, 151.3, 156.5 (−NH$\underline{C}$O$_2$^{t}Bu), 167.9 (−$\underline{C}$ONH(CH_2)$_6$NHCO$_2$^{t}Bu). UV/vis (CH_2Cl_2), λ_{max} (log ε): 417 (5.66), 513 (4.38), 547 (3.89), 589 (3.87), 644 (3.51). HRMS (ESI) calcd for $C_{53}H_{50}N_90_3$ (M + H)$^+$ 860.4031, found: 860.4029.

5-[4-{O-(2-Aminoethyl)-O′-[2-(Boc-amino)ethyl]hexaethylene glycol}-N-oxycarbonyl}phenyl]-10,15,20-tri-(4-pyridyl)porphyrin, ***8.*** 5-[4-(Succinimide-*N*-oxycarbonyl)phenyl]-10,15,20-tri-(4-pyridyl)porphyrin **6** (68.4 mg,0.090 mmol), *O*-(2-aminoethyl)-*O′*-[2-(Boc-amino)ethyl]-hexaethylene glycol (110.0 mg, 0.23 mmol, 2.6 equiv) and anhydrous potassium carbonate (50.6 mg, 0.366 mmol, 1.6 equiv relatively to the amine) were dissolved in dry DMSO (7 mL). The reaction mixture was protected from light and atmospheric moisture and kept under stirring at 40 °C for 5 days. After this period, the reaction was allowed to cool to room temperature, diluted with dichloromethane, and the organic layer washed with water and dried over anhydrous sodium sulfate. The solvent was then removed under reduced pressure, and the mixture was purified by flash chromatography using as eluent a mixture of dichloromethane/methanol (92:8). Porphyrin **8** was obtained as a purple solid in 53% (54.4 mg) after precipitation from *n*-hexane over dichloromethane. ^{1}H NMR ($CDCl_3$, 400 MHz), δ: −2.89 (br s, 2H, N$\underline{H}$), 1.40 (s, 9H, $-CO_2C(C\underline{H}_3)_3$), 3.24 (q, $J = 5.0$ Hz, 2H, -OCH$_2$C$\underline{H}_2$-NHCO$_2$^{t}Bu), 3.44 (t, $J = 5.0$ Hz, 2H, -OC$\underline{H}_2$CH$_2$NHCO$_2$^{t}Bu); 3.47−5.51, 3.52−3.58, 3.59−3.66, 3.67−3.73 and 3.74−3.80 (5 m, 24H, -(OC$\underline{H}_2$C$\underline{H}_2$)$_6$-); 3.81−3.90 (m, 4H, -CONHC$\underline{H}_2$-C$\underline{H}_2$O-), 5.10 (br s, 1H, -OCH$_2$CH$_2$N$\underline{H}$CO$_2$^{t}Bu), 7.55 (br s, 1H, -CON$\underline{H}$CH$_2$CH$_2$O-), 8.17 (d, $J = 5.9$ Hz, 6H, 10,15,20-Ar-*o*-H), 8.27−8.29 (m, 4H, 5-Ar-*o*,*m*-H), 8.84 (d, $J = 4.7$ Hz, 2H, H-β), 8.86−8.88 (m, 4H, H-β), 8.89 (d, $J = 4.7$ Hz, 2H, H-β), 9.06 (d, $J = 5.9$ Hz, 6H, 10,15,20-Ar-*m*-H). ^{13}C NMR ($CDCl_3$, 100 MHz), δ: 28.4 ($3 \times \underline{C}H_3$), 40.1 (-CONH$\underline{C}H_2$$\underline{C}H_2$O-), 40.3 (-OCH$_2$$\underline{C}H_2$NHCO$_2$^{t}Bu); 70.11, 70.13, 70.2, 70.3, 70.4, 70.47, 70.50, 70.53, 70.59, and 70.61 (-O$\underline{C}$H$_2$CH$_2$NHCO$_2$^{t}Bu); 117.4, 117.6, 120.4, 125.8 (5-Ar-*m*-C), 129.4 (10,15,20-Ar-*o*-C), 131.3 (C-β), 134.4, 134.5 (5-Ar-*o*-C), 144.6, 148.4 (10,15,20-Ar-*m*-C), 149.9, 156.0 (-NH$\underline{C}$O$_2$^{t}Bu), 167.4 (-$\underline{C}$ONHCH$_2$CH$_2$O-). UV/vis (CH_2Cl_2), λ_{max} (log ε): 417 (5.90), 513 (4.52), 548 (3.98), 588 (3.95), 644 (3.56). HRMS (ESI) calcd for $C_{63}H_{70}N_90_{10}$ (M + H)$^+$ 1112.5240, found: 1112.5228.

5-[4-(1,6-Diaminohexyl)SMCC]-10,15,20-tri-(4-pyridyl)porphyrin, ***9.*** Trifluoroacetic acid (6 mL) was added to a stirred solution of porphyrin **7** (35.2 mg, 0.0409 mmol) in dry dichloromethane (6 mL). The mixture was then kept under stirring at room temperature, protected from light and moisture, for 50 min. The mixture was then poured into an aqueous solution of sodium carbonate and ice and the organic layer washed with water and dried over anhydrous sodium sulfate. The solvent was then removed under reduced pressure and the resulting mixture promptly dissolved in anhydrous DMF (4 mL). To the resulting solution was added succinimidyl-4-(*N*-maleimidomethyl)cyclohexane-1-carboxylate (SMCC) (16.5 mg, 0.0494 mmol, 1.2 equiv) and *N*,*N*-diisopropylethylamine (35 μL, 0.204 mmol, 4.1 equiv relative to the SMCC). The reaction mixture was protected from light and moisture and allowed to stir for 1 h at room temperature. After this period, the porphyrinic material was precipitated with diethyl ether (50 mL) and *n*-hexane (5 mL) to remove all the DMF used as solvent. The obtained precipitate was then dissolved in dichloromethane and purified by flash chromatography using as eluent a mixture of chloroform/methanol (95:5). After precipitation from *n*-hexane over dichloromethane porphyrin, **9** was obtained pure in 85% yield (34.0 mg). ^{1}H NMR ($CDCl_3$, 400 MHz), δ: −2.90 (s, 2H, N$\underline{H}$), 0.94−1.09 (m, 1H of **b**-C$\underline{H}_2$ and 1H of **f**-C$\underline{H}_2$); 1.40−1.51, 1.52−1.63, and 1.64−1.88 (3 m, 11H, $5 \times$ C$\underline{H}_2$ + **d**-C$\underline{H}$); 1.89−1.99 (m, 2H, C$\underline{H}_2$), 2.00−2.11 (m, 1H, **a**-C$\underline{H}$), 3.28−3.42 (m, 4H, -(CH_2)$_5$C$\underline{H}_2$NHCO- and -C$\underline{H}_2$-maleimide), 5.62 (t, $J =$ 5.9 Hz, 1H, -CH$_2$CH$_2$N$\underline{H}$CO-), 6.62 (s, 2H, -COC$\underline{H}$=C$\underline{H}$CO-), 6.89 (t, $J = 5.9$ Hz, 1H, -N$\underline{H}$COCH$_2$CH$_2$-), 8.10−8.21 (m, 6H, 10,15,20-Ar-*o*-H), 8.23 and 8.29 (AB, $J = 8.1$ Hz, 4H, 5-Ar-*o*,*m*-H), 8.84 (d, $J = 4.6$ Hz, 2H, H-β), 8.85−8.87 (m, 4H, H-β), 8.88 (d, $J = 4.6$ Hz, 2H, H-β), 8.98−9.16 (m, 6H, 10,15,20-Ar-*m*-H). ^{13}C NMR ($CDCl_3$, 100 MHz), δ: 25.6 ($\underline{C}H_2$), 25.8 ($\underline{C}H_2$), 29.0 (**c**-$\underline{C}$H$_2$ and **e**-$\underline{C}$H$_2$), 29.5, 29.6, 29.7, 29.9, 36.4, 38.5 ($\underline{C}H_2$), 39.5 (-$\underline{C}$H$_2$-maleimide), 43.6, 45.4, 117.4, 117.6, 120.3, 125.5 (5-Ar-*m*-C), 129.4 (10,15,20-Ar-*o*-C), 131.3 (C-β), 133.9 (-CO$\underline{C}$H=$\underline{C}$HCO-), 134.5, 134.6 (5-Ar-*o*-C), 144.6, 148.4 (10,15,20-Ar-*m*-C), 149.9, 167.5 (-NH$\underline{C}$OCH$_2$CH$_2$-), 171.0 (-$\underline{C}$OCH=CH$\underline{C}$O-), 175.8(-CH$_2$CH$_2$NH$\underline{C}$O-). UV/vis (CH_2Cl_2), λ_{max} (log ε): 417 (5.51), 513 (4.23), 547 (3.83), 588 (3.81), 644 (3.43). HRMS (ESI) calcd for $C_{60}H_{55}N_{10}0_4$ (M + H)$^+$ 979.4402, found: 979.4398.

5-[4-(PEG-SMCC)phenyl]-10,15,20-tri-(4-pyridyl)porphyrin, ***10.*** The synthesis of porphyrin **10** followed the same procedure adopted to prepare porphyrin **9**. After dissolving porphyrin **8** (99.5 mg, 0.0895 mmol) in dichloromethane (9 mL), trifluoroacetic acid (9 mL) was added and the reaction was allowed to stir at room temperature, protected from light and moisture, for 50 min. Once the reaction was complete, the same workup procedure was carried out as for **9**, the solvent removed, and the mixture promptly used in the reaction next step. After dissolving the residue in anhydrous DMF (10 mL), succinimidyl-4-(*N*-maleimidomethyl)cyclohexane-1-carboxylate (36.1 mg, 0.108 mmol, 1.2 equiv) and *N*,*N*-diisopropylethylamine (0.10 mL,0.584 mmol, 5.4 equiv relative to the SMCC) were added and the reaction was allowed to stir overnight. After removing the DMF by promoting precipitation of the porphyrinic material with diethyl ether (50 mL) and *n*-hexane (5 mL), the obtained solid was then dissolved in dichloromethane and purified by

flash chromatography using as eluent a mixture of chloroform/methanol (92:8). After precipitation from *n*-hexane over dichloromethane, porphyrin **10** was obtained pure in 55% yield (60.3 mg). ^{1}H NMR ($CDCl_3$, 400 MHz), δ: inner N*H* not observed, 0.83−0.94 (m, 2H, 1H of **c**-C*H*$_2$ and 1H of **e**-C*H*$_2$), 1.25−1.38 (m, 2H, 1H of **b**-C*H*$_2$ and 1H of **f**-C*H*$_2$), 1.49−1.66 (m, 3H, **d**-C*H*, 1H of **c**-C*H*$_2$, and 1H of **e**-C*H*$_2$), 1.67−1.80 (m, 2H, 1H of **b**-C*H*$_2$ and 1H of **f**-C*H*$_2$), 1.88−1.95 (m, 1H, **a**-C*H*), 3.19 (d, J = 7.0 Hz, 2H, -C*H*$_2$-maleimide), 3.24 (t, J = 5.0 Hz, 2H, C*H*$_2$), 3.38 (t, J = 5.0 Hz, 2H, C*H*$_2$), 3.42−3.53 (m, 20H, 10 × C*H*$_2$), 3.53−3.59 (m, 4H, 2 × C*H*$_2$), 3.60−3.66 (m, 4H, 2 × C*H*$_2$), 6.56 (s, 2H, -COC*H*═C*H*CO-), 8.15−8.25 (m, 10H, 5-Ar-*o*,*p*-H and 10,15,20-Ar-*m*-H), 8.62−8.91 (m, 8H, H-β), 8.97 (d, J = 5.5 Hz, 6H, 10,15,20-Ar-*o*-H). ^{13}C NMR ($CDCl_3$, 100 MHz), δ: 28.5 (**b**-C H$_2$ and **f**-C H$_2$), 29.6 (**c**-C H$_2$ and **e**-C H$_2$), 38.8 (**d**-C H), 43.4 (-C H$_2$-maleimide), 44.7 (**a**-C H); 69.6, 69.8, 69.9, 70.0, 70.16, 70.22, 70.25, 70.29 and 70.30 (C H$_2$); 116.7, 117.0, 120.7, 125.7 (5-Ar-*m*-C), 129.7(10,15,20-Ar-*o*-C), 133.8 (-COC H═C HCO-), 134.1, 134.4 (5-Ar-*o*-C), 144.3, 146.9 (10,15,20-Ar-*m*-C), 151.3, 167.98 (-NHC OCH$_2$CH$_2$O-), 171.0 (-C OCH═CHC O-), 176.5 (-OCH$_2$CH$_2$NHC O-). UV/vis (CH_2Cl_2), λ_{max} (log ε): 417 (5.75), 513 (4.40), 548 (3.94), 588 (3.91), 644 (3.61). HRMS (ESI) calcd for $C_{70}H_{75}N_{10}0_{11}$ (M + H)$^+$ 1231.5611, found: 1231.5575.

5-[4-(1,6-Diaminohexyl)SMCC]-10,15,20-tri-(4-N-methylpyridiniumyl)porphyrin Triiodide, ***11.*** Preparation of this porphyin derivative followed the same procedure adopted for maleimide−porphyrin **4**. In this case, to the stirred solution of porphyrin **9** (21.2 mg, 0.0216 mmol) in dry DMF (2.6 mL) was added a large excess of methyl iodide (0.20 mL, 3.21 mmol, 160 equiv) and the mixture was left to react at 40 °C for 4 h. The methylated porphyrin **11** was obtained as a brown solid in 80% yield (24.3 mg). ^{1}H NMR (DMSO-d_6, 400 MHz), δ: −3.03 (s, 2H, N*H*), 0.83−0.97 (m, 2H, 1H of **c**-C*H*$_2$ and 1H of **e**-C*H*$_2$), 1.20−1.36 (m, 2H, 1H of **b**-C*H*$_2$ and 1H of **f**-C*H*$_2$), 1.37−1.54 (m, 7H, 3 × C*H*$_2$ and **d**-C*H*), 1.59−1.78 (m, 6H, 1 × C*H*$_2$, 1H of **b**-C*H*$_2$, 1H of **f**-C*H*$_2$, 1H of **c**-C*H*$_2$, and 1H of **e**-C*H*$_2$), 1.98−2.10 (m, 1H, **a**-C*H*), 3.02−3.10 (m, 2H, -CH$_2$C*H*$_2$NHCO-), 3.23 (d, 2H, -C*H*$_2$-maleimide, J = 6.9 Hz), 3.41−3.47 (m, 2H, -NHCOC*H*$_2$-CH$_2$-), 4.72 and 4.73 (2s, 6H+3H, 3 × C*H*$_3$), 6.97 (s, 2H,-COC*H*═C*H*CO-), 7.72 (t, J = 5.5 Hz, 1H, -CH$_2$CH$_2$N*H*CO-), 8.32 and 8.35 (AB, J = 8.4 Hz, 4H, 5-Ar-*o*,*m*-H), 8.87 (t, J = 5.6 Hz, 1H, -N*H*COCH$_2$CH$_2$-), 8.95−9.06 (m, 8H, 2 × H-β and 10,15,20-Ar-*o*-H), 9.06−9−08 (m, 2H, H-β), 9.19−9.24 (m, 4H, H-β), 9.48 (d, J = 6.9 Hz, 6H, 10,15,20-Ar-*m*-H). ^{13}C NMR (DMSO-d_6, 100 MHz), δ: 26.1(**b**-C H$_2$ and **f**-C H$_2$), 26.2 (**d**-C H$_2$), 28.6 (C H$_2$), 29.2, 29.4 (**c**-C H$_2$ and **e**-C H$_2$), 36.1 (**d**-C H), 43.1 (-(CH$_2$)$_5$C H$_2$NHCO-), 43.8 (-C H$_2$-maleimide), 47.9 (3 × C H$_3$), 48.5, 114.7, 115.3 (10,15,20-C), 126.0 (5-Ar-*m*-C), 132.1 (10,15,20-Ar-*o*-C), 134.1 (5-Ar-*o*-C), 134.3 (-COC H═C HCO-), 134.6 (-NHCOC H$_2$CH$_2$-), 142.9, 144.2 (10,15,20-Ar-*m*-C), 156.5, 165.8 (-NHC OCH$_2$CH$_2$-), 171.2 (-C OCH═CHC O-), 174.8 (-CH$_2$CH$_2$NHC O-). UV/vis (H_2O), λ_{max} (log ε): 424 (5.32), 519 (4.18), 555 (3.81), 588 (3.78), 643 (3.31). HRMS (ESI) calcd for $C_{63}H_{63}N_{10}0_4$ (M $^{3+}$) 341.1672, found: 341.1675.

5-[4-(PEG-SMCC)phenyl]-10,15,20-tri-(4-N-methylpyridiniumyl)porphyrin Triiodide, ***12.*** Preparation of this porphyin derivative followed the same procedure adopted for maleimide−porphyrin **4** and **11**. In this case, to the stirred solution of porphyrin **10** (30.5 mg, 0.0248 mmol) in dry DMF (3 mL) was added a large excess of methyl iodide (0.30 mL, 4.82 mmol, 200 equiv) and the mixture was left to react at 40 °C for 4 h. The methylated porphyrin **12** was obtained as a brown solid in 75% yield (30.9 mg). ^{1}H NMR (DMSO-d_6, 400 MHz), δ: −3.02 (s, 2H, N*H*), 0.76−0.92 (m, 2H, 1H of **c**-C*H*$_2$ and 1H of **e**-C*H*$_2$), 1.15−1.24 (m, 2H, 1H of **b**-C*H*$_2$ and 1H of **f**-C*H*$_2$), 1.40−1.52 (m, 1H, **d**-C*H*), 1.52−1.60 (m, 2H, **b**-C*H*$_2$ and 1H of **f**-C*H*$_2$), 1.61−1.70 (m, 2H, 1H of **b**-C*H*$_2$ and 1H of **f**-C*H*$_2$), 1.94−2.06 (m, 1H, **a**-C*H*), 3.07−3.13 (m, 2H, -NHC*H*$_2$CH$_2$O-), 3.15 (d, 2H, -C*H*$_2$-maleimide, J = 7.3 Hz), 3.29−3.33 (m, 2H, -NHCH$_2$-C*H*$_2$O-), 3.41−3.75 (m, 32H, 16 × C*H*$_2$), 4.73 and 4.74 (2s, 6H+3H, 3 × C*H*$_3$), 6.80 (s, 2H,-COC*H*═C*H*CO-), 7.72 (t, J = 5.6 Hz, 1H, -CH$_2$CH$_2$N*H*CO-), 8.35 and 8.38 (AB, J = 8.4 Hz, 4H, 5-Ar-*o*,*m*-H), 8.98 (t, J = 5.6 Hz, 1H, -N*H*COCH$_2$CH$_2$-), 9.00−9.06 (m, 8H, 2H-β and 10,15,20-Ar-*o*-H), 9.07−9.12 (m, 2H, H-β), 9.14−9.25 (m, 4H, H-β), 9.50 (d, J = 6.6 Hz, 6H, 10,15,20-Ar-*m*-H). ^{13}C NMR (DMSO-d_6, 100 MHz), δ: 28.5, 29.4, 34.4 (**d**-C H), 38.3 (-C H$_2$-maleimide), 43.0 (-NHC H$_2$CH$_2$O-), 47.8 (3 × C H$_3$); 69.0, 69.5, 69.6, 69.70, 69.72, 69.74, 69.75, 69.80, and 69.82 (C H$_2$); 114.7, 115.4, 121.9, 126.1 (5-Ar-*m*-C), 132.1 (10,15,20-Ar-*o*-C), 134.2, 134.3 (-COC H═C HCO-), 143.0 (5-Ar-*o*-C), 144.2 (10,15,20-Ar-*m*-C), 156.5, 166.0 (-NHC OCH$_2$-CH$_2$-), 171.2 (-C OCH═CHC O-), 175.0 (-OCH$_2$CH$_2$NHC O-). UV/vis (H_2O), λ_{max} (log ε): 425 (5.28), 519 (4.16), 556 (3.77), 589 (3.74), 645 (3.29). MALDI-MS *m/z* for $C_{73}H_{83}N_{10}0_{11}I_3$ (M − I)$^+$ 1529.2.

Reaction of 5-(4-Maleimidophenyl)-10,15,20-tri-(4-pyridyl)porphyrin with 1-Propylamine, ***13.*** To a stirred solution of 5-(4-maleimidophenyl)-10,15,20-tri-(4-pyridyl)porphyrin **3** (13.5 mg, 0.019 mmol) in dry DMF (2 mL) was added 1-propylamine (0.10 mL, 1.22 mmol, 64 equiv). The reaction was kept under constant stirring and protected from moisture until all the starting porphyrin was consumed (10 min, according to TLC). After this period, the product was precipitated with diethyl ether (50 mL) and *n*-hexane (5 mL), filtered, and redissolved in dichloromethane. After purification by preparative TLC, using a mixture of dichloromethane/methanol (95:5) as eluent, and precipitation with methanol over dichloromethane, the pure product was obtained as a purple solid in 84% yield (14.6 mg). ^{1}H NMR ($CDCl_3$, 400 MHz), δ: −2.90 (s, 2H, N*H*), 1.06 (t, J = 7.3 Hz, 3H, -CH$_3$), 1.67 (sextet, J = 7.3 Hz, 2H, -CH$_2$C*H*$_2$CH$_3$), 2.72−2.81 and 2.82−2.88 (2 m, 2H, -C*H*$_2$CH$_2$CH$_3$), 2.92 (dd, J = 5.1 Hz, J = 17.9 Hz, 1H, H″), 3.29 (dd, J = 8.4 Hz, J = 17.9 Hz, 1H, H‴), 4.13 (dd, J = 5.1 Hz, J = 8.4 Hz, 1H, H′), 7.77 (d, J = 8.5 Hz, 2H, 5-Ar-*m*-H), 8.16 (d, J = 5.9 Hz, 6H, 10,15,20-Ar-*o*-H), 8.32 (d, J = 8.5 Hz, 2H, 5-Ar-*o*-H), 8.84 (d, J = 5.0 Hz, 1H, H-β), 8.85−8.90 (m, 4H, H-β), 8.96 (d, J = 5.0 Hz, 1H, H-β), 9.06 (d, J = 5.9 Hz, 6H, 10,15,20-Ar-*m*-H). ^{13}C NMR ($CDCl_3$, 100 MHz), δ: 11.8 (-C H$_3$), 23.4 (-CH$_2$C H$_2$CH$_3$), 36.8 (-C H$_2$CH$_2$CH$_3$), 49.8 (-COC H$_2$CH(NC$_3$H$_7$)CO-), 56.7 (-COCH$_2$C H(NHC$_3$H$_7$)CO-), 117.4, 117.7 (10,15,20-C), 120.2, 123.3, 124.7 (5-Ar-*m*-C), 129.5 (10,15,20-Ar-*o*-C), 131.8 (C-β), 135.1 (5-Ar-*o*-C), 135.3 (C-β), 136.8, 141.9, 148.5 (10,15,20-Ar-*m*-C), 150.0 (10,15,20-Ar-*p*-C), 174.5 (-CHC O-), 177.3 (-CH$_2$C O-). UV/vis (CH_2Cl_2/MeOH- 3%), λ_{max} (log ε): 417 (6.25), 513 (4.99), 547 (4.36), 588 (4.35), 643 (4.03). HRMS (ESI) calcd for $C_{48}H_{38}N_9O_2$ (M + H)$^+$ 772.3143, found: 772.3140.

Reaction of 5-(4-Maleimidophenyl)-10,15,20-tri-(4-pyridyl)porphyrin with 1-Propanethiol, ***14.*** To a stirred solution of 5-(4-maleimidophenyl)-10,15,20-tri-(4-pyridyl)porphyrin **3** (15.2 mg, 0.0213 mmol) in dry DMF (2 mL) was added 1-propanethiol (0.10 mL, 1.10 mmol, 52 equiv). The reaction was kept under constant stirring and protected from moisture until all the starting porphyrin was consumed (10 min, according to TLC). After this period, the product was precipitated with diethyl ether (50 mL) and *n*-hexane (5 mL), filtered, and dissolved in dichloromethane. After purification by preparative TLC, using a mixture of dichloromethane/methanol (97: 3) as eluent, and precipitation with methanol over dichloromethane, the pure product was isolated in 82% yield (13.7 mg) as a purple solid. ^{1}H NMR ($CDCl_3$, 400 MHz), δ: −2.90 (s, 2H, N*H*), 1.03 (t, J = 7.3 Hz, 3H, -C*H*$_3$), 1.63−1.83 (m, 2H, -CH$_2$C*H*$_2$CH$_3$), 2.78 (dd, J = 3.5 Hz, J = 18.6 Hz, 1H, H″), 2.79−2.87 and

2.98−3.06 (2 m, 2H, -C$\underline{H}_2$CH$_2$CH$_3$), 3.40 (dd, J = 9.2 Hz, J = 18.6 Hz, 1H, H‴), 3.94 (dd, J = 3.5 Hz, J = 9.2 Hz, 1H, H′), 7.68 (d, J = 8.2 Hz, 2H, 5-Ar-*m*-H), 8.08 (d, J = 5.2 Hz, 6H, 10,15,20-Ar-*o*-H), 8.23 (d, J = 8.1 Hz, 2H, 5-Ar-*o*-H), 8.76 (d, J = 4.7 Hz, 1H, H-β), 8.76−8.81 (m, 4H, H-β), 8.88 (d, J = 4.7 Hz, 1H, H-β), 8.97 (d, J = 5.2 Hz, 6H, 10,15,20-Ar-*m*-H). ^{13}C NMR ($CDCl_3$, 100 MHz), δ: 13.6 (-$\underline{C}$H$_3$), 22.6 (-CH$_2$-$\underline{C}$H$_2$CH$_3$), 34.2 (-$\underline{C}$H$_2$CH$_2$CH$_3$), 36.4 (-CO$\underline{C}$H$_2$CH(SC$_3$H$_7$)-CO-), 39.3 (-COCH$_2$$\underline{C}$H(SC$_3H_7$)CO-), 117.4, 117.7 (10,15,20-C), 120.2, 124.8 (5-Ar-*m*-C), 129.4 (10,15,20-Ar-*o*-C), 131.9 (5-Ar-*p*-C), 135.1 (5-Ar-*o*-C), 141.9, 148.5 (10,15,20-Ar-*m*-C), 150.0 (10,15,20-Ar-*p*-C), 174.0 (-CH$\underline{C}$O-), 175.9 (-CH$_2$$\underline{C}$O-).

UV/vis (CH_2Cl_2/MeOH- 3%), λ_{max} (log ε): 417 (6.14), 513 (4.92), 547 (4.37), 588 (4.35), 643 (3.93). HRMS (ESI) calcd for $C_{48}H_{36}N_8O_2S$ $(M + H)^+$ 789.2755, found: 789.2768.

Reaction of 5-(4-Maleimidophenyl)-10,15,20-tri-(4-pyridyl)porphyrin with and N_α-Acetyl-L-lysine Methyl Ester Hydrochloride, ***15.*** A solution of N_α-acetyl-L-lysine methyl ester hydrochloride (15.0 mg, 0.0525 mmol, 2.5 equiv) and anhydrous potassium carbonate (8.7 mg, 0.0638 mmol, 1.2 equiv relatively to lysine) in dry DMF (2 mL) was allowed to stir at room temperature for 10 min. Then, 5-(4-maleimidophenyl)-10,15,20-tri-(4-pyridyl)porphyrin **3** (15.0 mg, 0.0210 mmol) was added and the reaction mixture kept under constant stirring and protected from moisture until all the starting porphyrin was consumed (6 min, according to TLC). After this period, the product was precipitated with diethyl ether (50 mL) and *n*-hexane (5 mL), filtered, and redissolved in a mixture of dichloromethane/methanol. After purification by preparative TLC, using a mixture of dichloromethane/methanol (94:6) as eluent, and precipitation with methanol over dichloromethane, the pure product was obtained as a purple solid in 75% yield (14.8 mg). ^{1}H NMR ($CDCl_3$, 400 MHz), δ: inner N$\underline{H}$ not observed, 1.45−1.58 (m, 2H, -NH(CH$_2$)$_2$C$\underline{H}_2$CH$_2$CH(NHCOCH$_3$)CO$_2$CH$_3$), 1.61−1.72 (m, 2H, -NHCH$_2$C$\underline{H}_2$(CH$_2$)$_2$CH(NHCOCH$_3$)CO$_2$CH$_3$), 1.73−1.82 and 1.89−1.96 (2 m, 2H, -NH(CH$_2$)$_3$C$\underline{H}_2$CH(NHCOCH$_3$)-CO$_2$CH$_3$), 2.08 (s, 3H, -NHCOC$\underline{H}_3$), 2.74−2.83 and 2.85−2.95 (2 m, 2H, -NHC$\underline{H}_2$(CH$_2$)$_3$CH(NHCOCH$_3$)CO$_2$CH$_3$), 2.90 (dd, J = 5.2 Hz, J = 17.7 Hz, 1H, H″), 3.29 (dd, J = 8.5 Hz, J = 17.7 Hz, 1H, H‴), 3.80 (s, 3H, -CO$_2$C$\underline{H}_3$), 4.12 (dd, J = 5.2 Hz, J = 8.5 Hz, 1H, H′), 4.66−4.73 (m, 1H, -NH(CH$_2$)$_4$-C$\underline{H}$(NHCOCH$_3$)CO$_2$CH$_3$), 6.13 (d, J = 8.2 Hz, 1H, -N$\underline{H}$-COCH$_3$), 7.76 (d, J = 8.5 Hz, 2H, 5-Ar-*m*-H), 8.16 (d, J = 5.5 Hz, 6H, 10,15,20-Ar-*o*-H), 8.31 (d, J = 8.5 Hz, 2H, 5-Ar-*o*-H), 8.84 (d, J = 4.9 Hz, 2H, H-β), 8.85−8.89 (m, 4H, H-β), 8.96 (d, J = 4.9 Hz, 2H, H-β), 9.05 (d, J = 5.5 Hz, 6H, 10,15,20-Ar-*m*-H). ^{13}C NMR ($CDCl_3$, 100 MHz), δ: 23.0 (-NH-(CH$_2$)$_2$$\underline{C}H_2CH_2CH_2$CH), 23.4 (-NHCO$\underline{C}H_3$), 29.6 (-NHCH$_2$$\underline{C}H_2$(CH$_2$)$_2$-CH-), 32.6 (-NH(CH$_2$)$_3$$\underline{C}H_2$CH-), 36.7 (-CO$\underline{C}H_2$CHNH(CH$_2$)$_4$-CH-), 47.6 (-NH$\underline{C}H_2CH_2$(CH$_2$)$_2$CH-), 52.1 (-NHCH$_2CH_2$(CH$_2$)$_2$-$\underline{C}$H-), 52.6 (-CO$_2$$\underline{C}H_3$), 56.7 (-COCH$_2$$\underline{C}$HNH(CH$_2$)$_4$CH-), 117.4, 117.7, 120.2, 124.7 (5-Ar-*m*-C), 129.5 (10,15,20-Ar-*o*-C), 131.8 (C-β), 135.1 (5-Ar-*o*-C), 141.9, 148.5 (10,15,20-Ar-*m*-C), 150.0, 170.0 (-NH$\underline{C}$OCH$_3$), 173.2 (-$\underline{C}$O$_2$CH$_3$), 174.5 (-CH$\underline{C}$O), 177.2 (-$\underline{C}$OCH$_2$). UV/vis (CH_2Cl_2/MeOH- 3%), λ_{max} (log ε): 417 (5.60), 513 (4.06), 548 (3.58), 588 (3.57), 644 (3.18). HRMS (ESI) calcd for $C_{54}H_{47}N_5O_{10}$ $(M + H)^+$ 915.3725, found: 915.3721.

Reaction of 5-(4-Maleimidophenyl)-10,15,20-tri-(4-pyridyl)porphyrin with N-Acetyl-L-cysteine Methyl Ester, ***16.*** To a stirred solution of 5-(4-maleimidophenyl)-10,15,20-tri-(4-pyridyl)porphyrin **3** (15.0 mg, 0.0210 mmol) in dry DMF (2 mL) was added *N*-acetyl-L-cysteine methyl ester (9.3 mg, 0.0526 mmol, 2.5 equiv). The reaction was kept under constant stirring and protected from moisture until all the starting porphyrin was consumed (6 min, according to TLC). After this period, the product was precipitated with diethyl ether (50 mL) and hexane (5 mL), filtered, and redissolved in a mixture of dichloromethane/methanol. After purification by preparative TLC, using a mixture of dichloromethane/methanol (95:5) as eluent, and precipitation with methanol over dichloromethane, the product (isolated as a mixture of two diasteriomers not separable by TLC, designated as **D1** and **D2**) was obtained as a purple solid in 94% yield (17.8 mg). ^{1}H NMR ($CDCl_3$, 400 MHz), δ: −2.90 (s, 2H, N$\underline{H}$), 2.15 and 2.16 (2s, 6H, **D1**+**D2**-NHCOC$\underline{H}_3$), 2.81 (dd, J = 3.9 Hz, J = 18.8 Hz, 1H, **D1**-H″), 2.88 (dd, J = 3.9 Hz, J = 18.8 Hz, 1H, **D2**-H″), 3.12 (dd, J = 7.8 Hz, J = 14.1 Hz, 1H, **D1**-SC$\underline{H}_2$CH(NHCOCH$_3$)CO$_2$CH$_3$), 3.37 (dd, J = 5.0 Hz, J = 14.4 Hz, 1H, **D2**-SC$\underline{H}_2$CH(NHCOCH$_3$)CO$_2$CH$_3$), 3.51 (dd, J = 9.2 Hz, J = 18.8 Hz, 1H, **D1**-H‴), 3.53 (dd, J = 9.2 Hz, J = 18.8 Hz, 1H, **D2**-H‴), 3.66 (dd, J = 5.0 Hz, J = 14.4 Hz, 1H, **D2**-SC$\underline{H}_2$CH(NHCOCH$_3$)CO$_2$CH$_3$), 3.77 (dd, J = 4.0 Hz, J = 14.1 Hz, 1H, **D1**-SC$\underline{H}_2$CH(NHCOCH$_3$)CO$_2$CH$_3$), 3.86 and 3.87 (2s, 6H, **D1**+**D2**-CO$_2$C$\underline{H}_3$), 4.14 (dd, J = 3.9 Hz, J = 9.2 Hz, 1H, **D2**-H′), 4.34 (dd, J = 3.9 Hz, J = 9.2 Hz, 1H, **D1**-H′), 5.02−5.08 (m, 1H, **D2**-SCH$_2$C$\underline{H}$(NHCOCH$_3$)-CO$_2$CH$_3$), 5.07−5.14 (m, 1H, **D1**-SCH$_2$C$\underline{H}$(NHCOCH$_3$)-CO$_2$CH$_3$), 6.53 (d, J = 8.1 Hz, 1H, **D1**-SCH$_2$CH(N$\underline{H}$COCH$_3$)-CO$_2$CH$_3$), 6.92 (d, J = 7.8 Hz, 1H, **D2**-SCH$_2$CH-(N$\underline{H}$COCH$_3$)CO$_2$CH$_3$), 7.77 (dd, J = 1.9 Hz, J = 8.4 Hz, 4H, **D1**+**D2** 5-Ar-*m*-H), 8.16 (d, J = 5.8 Hz, 12H, **D1**+**D2** 10,15,20-Ar-*o*-H), 8.33 (dd, J = 1.9 Hz, J = 8.4 Hz, 4H, **D1**+**D2** 5-Ar-*o*-H), 8.84 (d, J = 4.7 Hz, 4H, **D1**+**D2** H-β), 8.86−8.89 (m, 8H, **D1**+**D2** H-β), 8.95 (d, J = 4.7 Hz, 4H, **D1**+**D2** H-β), 9.06 (d, J = 5.8 Hz, 12H, **D1**+**D2** 10,15,20-Ar-*m*-H). ^{13}C NMR ($CDCl_3$, 100 MHz), δ: 23.3 (**D1**+**D2**-NHCO$\underline{C}$H$_3$), 34.7 (**D1**-S$\underline{C}$H$_2$CH(NHCOCH$_3$)CO$_2$CH$_3$), 35.0 (**D2**-S$\underline{C}$H$_2$CH(NHCOCH$_3$)-CO$_2$CH$_3$), 36.0 and 36.6 (**D1**+**D2**-CO$\underline{C}$H$_2$CHSCH$_2$CH-(NHCOCH$_3$)CO$_2$CH$_3$), 38.8 (**D1**-COCH$_2$$\underline{C}$HSCH$_2$CH(NHCOCH$_3$)-CO$_2CH_3$), 40.2 (**D2**-COCH$_2$$\underline{C}$HSCH$_2$CH(NHCOCH$_3$)CO$_2CH_3$), 51.3 (**D1**-COCH$_2$CHSCH$_2$$\underline{C}$H(NHCOCH$_3$)CO$_2CH_3$), 52.4 (**D2**-COCH$_2$CHSCH$_2$$\underline{C}$H(NHCOCH$_3$)CO$_2CH_3$), 53.1 and 53.2 (**D1**+**D2**-CO$_2$$\underline{C}H_3$); 117.4, 117.7, 120.07, 120.10, 124.76, and 124.79 (**D1**+**D2** 5-Ar-*m*-C); 129.5 (10,15,20-Ar-*o*-C), 131.6 and 131.7 (C-β), 135.2 (5-Ar-*o*-C), 142.08, 142.14, 148.4 (10,15,20-Ar-*m*-C), 150.0, 170.2 (**D1**-NH$\underline{C}$OCH$_3$), 170.4 (**D2**-NH$\underline{C}$OCH$_3$), 171.2 (**D2**-$\underline{C}$O$_2$CH$_3$), 171.3 (**D1**-$\underline{C}$O$_2$CH$_3$); 173.4 and 173.6 (**D1**+**D2**-CH$\underline{C}$O), 176.0 and 176.1 (**D1**+**D2**-$\underline{C}$OCH$_2$). UV/vis (CH_2Cl_2/MeOH- 3%), λ_{max} (log ε): 417 (6.04), 513 (4.67), 547 (4.16), 588 (4.16), 643 (3.71). HRMS (ESI) calcd for $C_{52}H_{39}N_9O_5S$ $(M + H)^+$ 890.2868, found: 890.2862.

Competition Experiments. *Reaction of 5-(4-Maleimidophenyl)-10,15,20-tri-(4-pyridyl)porphyrin* ***3*** *with 1-Propylamine and 1-Propanethiol.* To a stirred solution of 5-(4-maleimidophenyl)-10,15,20-tri-(4-pyridyl)porphyrin **3** (13.2 mg, 0.0185 mmol) in dry DMF (2 mL) was added a mixture of 1-propylamine (76 μL, 0.924 mmol, 50 equiv) and 1-propanethiol (84 μL, 0.928 mmol, 50 equiv). The reaction was kept under constant stirring and protected from moisture for 10 min. After this period, the product was precipitated with diethyl ether (50 mL) and *n*-hexane (5 mL), filtered, and redissolved in dichloromethane.

Reaction of 5-(4-Maleimidophenyl)-10,15,20-tri-(4-pyridyl)porphyrin ***3*** *with N-Acetyl-L-cysteine Methyl Ester and N_α-Acetyl-L-lysine Methyl Ester Hydrochloride.* To a stirred solution of N_α-acetyl-L-lysine methyl ester hydrochloride (16.3 mg, 0.070 mmol, 2.6 equiv) in dry DMF (3 mL) was added anhydrous potassium carbonate (11.6 mg, 0.084 mmol, 1.2 equiv relative to lysine). After allowing the mixture to stir at room temperature for 10 min, in order to promote the amino acid neutralization, *N*-acetyl-L-cysteine methyl ester (12.4 mg, 0.070 mmol, 2.6 equiv) was added. Once the amino acid was completely dissolved, 5-(4-maleimidophenyl)-10,15,20-tri-(4-pyridyl)porphyrin **3** (18.9 mg, 0.0265 mmol) was added and the reaction mixture was allowed to stir at room temperature and protected

from moisture. After 10 min, diethyl ether (50 mL) and *n*-hexane (5 mL) were added to the reaction mixture to promote precipitation of the porphyrinic material.

BIOLOGICAL DATA

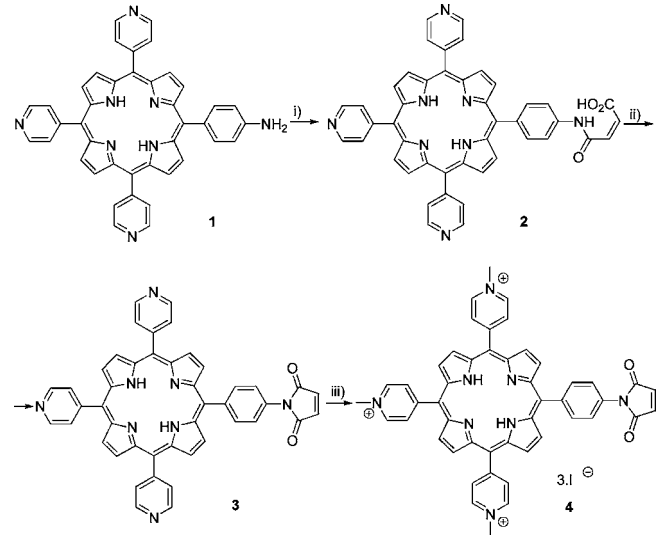
Preparation of SIP(L19). The cloning, expression, and purification of SIP(L19) antibody have been described elsewhere (*29, 42*). Briefly, SIP(L19) cDNA had been cloned into the pCDNA3.1 vector (Invitrogen). The derived construct was transfected in CHO-S cells (Gibco - Invitrogen), and selected stable clones were grown in PowerCHO-CD 2 media (Lonza) and used to express the protein, which was purified from the supernatant by protein A affinity chromatography.

Preparation of Photoimmunoconjugates. SIP(L19)-PS conjugates were prepared as follows: ~30-fold molar excess of TCEP (tris-(2-carboxyethyl)phosphine hydrochloride, Pierce) was added to purified SIP antibody (0.5 mg/mL, PBS pH 7.4) and incubated for 12 h at 4 °C. Then, a 40-fold excess of maleimide-porphyrin (**4**, **11**, or **12**) (1 mg/mL in DMSO) was added to the mixture and incubated for 3 h at room temperature, gently shaking. The antibody−photosensitizer conjugates were then purified from free photosensitizer over a PD-10 column (GE Healthcare) and dialyzed overnight against PBS pH 7.4 at 4 °C.

Quality of the Photoimmunoconjugates. SIP−photosensitizer (SIP-PS) conjugates were analyzed by SDS-PAGE under non-reducing conditions using the Invitrogen PAGE system following manufacturer instructions. The gels were first analyzed under Cy5 filter lamp and then stained with Coomassie blue. The labeling ratio was estimated spectroscopically by measuring the absorbance at 280 nm for the SIP (assuming that a 1 mg/mL of SIP solution gives absorption of 1.4 units at 280 nm) and at 422 nm for porphyrin **4** ($\varepsilon = 255\,390\ M^{-1}\ cm^{-1}$), 424 nm for porphyrin **11** ($\varepsilon = 248\,208\ M^{-1}\ cm^{-1}$), and 425 nm for porphyrin **12** ($\varepsilon = 188\,489\ M^{-1}\ cm^{-1}$). Furthermore, mass spectrometric analysis was also used to assess the labeling ratio. For MALDI-TOF analysis, the SIP(L19) and the conjugates were mixed with a sinapinic matrix (10 mg/mL in 50% CAN and 0.05% TFA) at a 1:4 dilution and spotted onto the MALDI target plate. The analysis of samples was performed on a freshly tuned AB4800 MALDI-TOF/TOF mass spectrometer. For data analysis, the *Data Explorer* software (version 4.8) from Applied Biosystem was used. The immunoreactivity of the SIP-PS conjugates was measured by BIAcore (*43*) and by ELISA assay over 7B89 (*44*), an EDB-containing protein (data not shown).

Photocytotoxicity Assay. L-M fibroblasts (ATCC number: CCL-1.2, L-M) were grown in DMEM (Gigbo-Invitrogen) media supplemented with 10% FCS and antibiotics and maintained at 37 °C in 5% CO_2. For the in vitro phototoxicity assay, 30 000 cells/well in a 96 well plate were seeded and incubated overnight at 37 °C in 5% CO_2. The next day, media were removed and cells were incubated with 50 μL of SIP or SIP−porphyrin conjugate in the appropriate dilutions (in PBS) for 1 h at 37 °C. Cells were subsequently washed with PBS twice in order to remove unbounded antibodies, and cells were then covered with 50 μL of PBS. The cells were then irradiated using as light source the KL 1500 electronic (Zeiss) tungsten halogen lamp equipped with a 620/60 filter (Chroma) for a total light dose of 60 J/cm^2 (*21*). After light treatment, PBS was removed and 100 μL of fresh medium were added. The cells were then incubated at 37 °C, 5% CO_2 atmosphere overnight. Controls include SIP−porphyrin conjugate without light, PBS only plus light, unconjugated SIP plus light, and no PBS or medium only without light. The following day, cell viability was measured using the Cell Titer 96Aqueous One Solution Cell Proliferation Assay (Promega), performed according to the manufacturer's instruction. The percentage of cell growth inhibition was calculated as a ratio of the counts between treated cell over the relative control (cells treated with SIP−porphyrin conjugate without light exposure).

Scheme 1. Synthesis of Maleimide−Porphyrin 4



Reagents and conditions: (i) maleic anhydride, nitrobenzene, 100°C, 22 h, 96%; (ii) sodium acetate, acetic anhydride, 80 °C, 4 h, 84%; (iii) methyl iodide, DMF, 40 °C, 4 h, 95%.

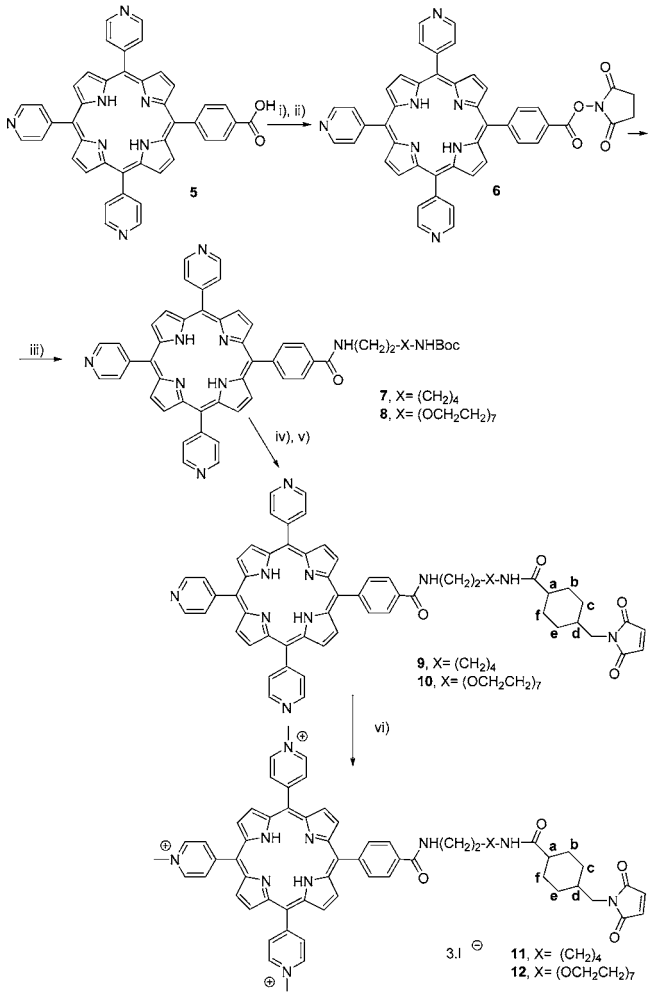
RESULTS AND DISCUSSION

Chemistry. *Synthesis of the Water-Soluble Porphyrin Photosensitizers.* Three different synthetic strategies were used in order to obtain maleimide−porphyrin derivatives **4**, **11**, and **12**. In the first one, the maleimide moiety is directly connected to the *para* position of a phenyl ring present on the macrocycle (Scheme 1); in the second, a hydrocarbon spacer was built-in and the maleimide moiety was introduced using the heterofunctional linker SMCC (succinimidyl-4-(*N*-maleimidomethyl) cyclohexane-1-carboxylate) (Scheme 2). The final synthetic procedure involved the simultaneous extension of the linker between porphyrin and maleimide, and introduction of increased hydrophilicity by using a poly(ethylene glycol) chain (Scheme 2), as opposed to the hydrocarbon linker used in the synthesis of **11**. The three maleimide−porphyrins were synthesized in order to first allow site-specific conjugation to cysteine residues on the antibody, but also to probe the effect of enforced proximity of the porphyrins, caused by the close location of cysteine residues used for conjugation on the SIP. SIP(L19) exists as a homodimer in aqueous solution (*21*), even after reduction of the disulfide bridge, due to hydrophobic interactions of the two monomers; thus, the two thiols used for conjugation are always found in close proximity.

The starting porphyrins (**1** and **5**) required for these syntheses were obtained by established methods using, respectively, Adler (*45*) and modified Rothemund (*46*) conditions.

5-(4-Aminophenyl)-10,15,20-tri-(4-pyridyl)porphyrin **1** was used as starting material for the preparation of the water-soluble maleimide−porphyrin **4**. The pyridyl groups provide the water-solubilizing units, upon quaternization, and the amino group represents the chemical moiety needed for the introduction of the maleimide (Scheme 1). Upon reaction of porphyrin **1** with maleic anhydride in nitrobenzene, derivative **2** was obtained in 96% yield after purification by flash chromatography and precipitation from methanol over dichloromethane. Subsequent treatment with sodium acetate and acetic anhydride afforded the required maleimide−porphyrin **3** in 84% yield. The last step of this synthetic procedure involved quaternization of the pyridyl

Scheme 2. Synthesis of Maleimide−Porphyrins 11 and 12[a]



[a] Reaction conditions: (i) $SOCl_2$, pyridine, 50 °C, 30 min; (ii) *N*-hydroxysuccinimide, 50 °C, 3 h, 90%; (iii) $NH_2(CH_2)_6NHBoc$, K_2CO_3, DMSO, 40 °C, 40 min, 82% or $NH_2(CH_2)_2(OCH_2CH_2)_7NHBoc$, K_2CO_3, DMSO, 40 °C, 5 d, 53%; (iv) TFA/CH_2Cl_2 (1:1), rt, 50 min; (v) SMCC, DIEA, DMF, rt, 1 h, 85% for **9** or SMCC, DIEA, DMF, rt, overnight, 55% for **10**; (vi) CH_3I, DMF, 40 °C, 4 h, 80% for **11** or CH_3I, DMF, 40 °C, 4 h, 75% for **12**.

nitrogens with methyl iodide; the reaction was carried out at 40 °C for 4 h and afforded the water-soluble maleimide−porphyrin **4** in 95% yield after precipitation with diethyl ether/dichloromethane.

During the implementation of our synthetic procedure, two reports appear in the literature with similar strategies for preparing maleimide−porphyrin derivatives (*35, 36*). The differences in these procedures rely mainly in the starting porphyrin derivatives, solvents, and temperatures used. In both cases, non-water-soluble tetraphenylporphyrin (*35*) or the corresponding water-soluble anionic trisulfonated derivatives were obtained (*35, 36*). As mentioned before, hydrophobic porphyrins cannot be used for bioconjugation to proteins due to unacceptable amounts of noncovalently bound material (*45*). Sulfonated maleimide−porphyrins may be of use for bioconjugation; however, cationic water-soluble porphyrins resist aggregation to much higher concentrations, thus facilitating conjugation procedures.

The synthesis of maleimide−porphyrins **11** and **12** (Scheme 2) involved the use of 5-(4-carboxyphenyl)-10,15,20-tri-(4-pyridyl)porphyrin **5** as starting material and 1,6-diaminohexane or *O,O′*-di-(2-aminoethyl)hexaethylene glycol as spacers between the porphyrin macrocycle and the maleimide group.

After converting the carboxylic acid into the respective *N*-hydroxysuccinimidyl ester **6** via the acyl chloride, *N*-Boc-1,6-diaminohexane was coupled in dry DMSO using potassium carbonate as base. Derivative **7** was obtained in 82% after purification by flash chromatography and precipitation in *n*-hexane over dichloromethane.

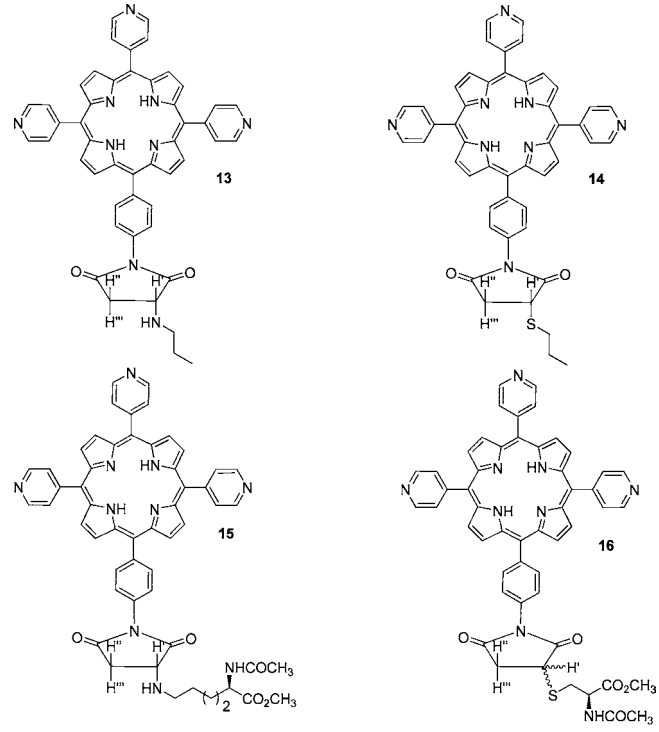


Figure 1. Conjugates obtained from the reaction of maleimide-porphyrin **3** with 1-propylamine (*13*), 1-propanethiol (*14*), N_α-acetyl-L-lysine methyl ester hydrochloride (*15*), and *N*-acetyl-L-cysteine methyl ester (*16*).

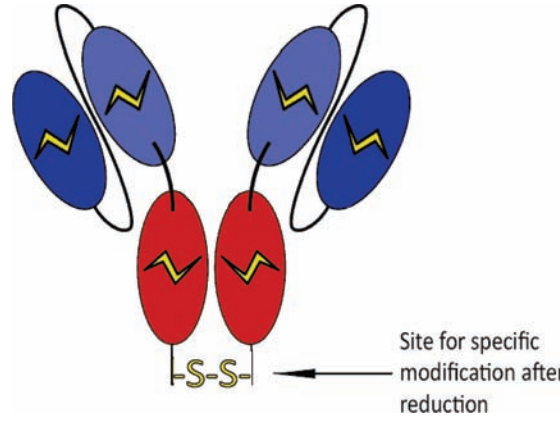


Figure 2. Schematic representation of SIP(L19) showing the conjugation site.

The maleimide−porphyrin **9** was obtained in 85% yield after removal of the Boc-protecting group in TFA/CH_2Cl_2 and subsequent coupling with SMCC in dry DMF in the presence of DIEA. The free amine turned out to be very unstable and hence was not isolated or characterized. The crude mixture obtained after TFA treatment was neutralized with aqueous sodium carbonate, extracted with dichloromethane, dried over sodium sulfate, concentrated under reduced pressure, and promptly used in the reaction with SMCC.

For the PEG-linked derivative **10**, a similar strategy was used, but the 1,6-diaminohexane was replaced by or *O,O′*-di-(2-aminoethyl)hexaethylene glycol. In this instance, the PEG-porphyrin **10** was obtained in 55% yield.

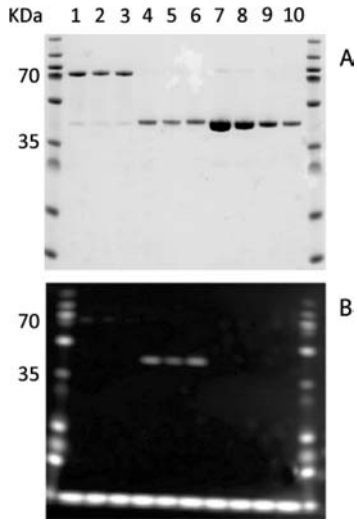


Figure 3. SDS-PAGE of SIP(L19) and SIP(L19) conjugates (Lanes 1−3: control reaction of SIP(L19) conjugated with porphyrins **4**, **11**, and **12** without reducing procedure. Lanes 4−6: SIP(L19) conjugated with porphyrins **4**, **11**, and **12**. Lanes 7−10: SIP(L19) reference standards (0.8 mg/mL, 0.4 mg/mL, 0.2 mg/mL, and 0.1 mg/mL). A: Coomassie blue staining. B: Cy5 fluorescence imaging. The signal at the bottom of the gel is due to the bromophenol blue contained in the SDS sample loading buffer.

Finally, in both cases water solubility was introduced, similarly to derivative **4**, by quaternization of the pyridine rings with methyl iodide affording porphyrins **11** and **12** in 80% and 75% yields, respectively.

Reactivity of the Maleimide Moiety toward Thiols Vs Amines. Porphyrin derivative **3** was chosen to probe the reactivity of the maleimide moiety toward thiols and amines. In order to achieve this, a set of experiments were planned using as amines 1-propylamine and N_α-acetyl-L-lysine methyl ester hydrochloride and as thiols 1-propanethiol and *N*-acetyl-L-cysteine methyl ester.

Under the test conditions (dry DMF at room temperature), both 1-propylamine and 1-propanethiol were found to react with the maleimide−porphyrin **3** over 10 min (Figure 1, compounds **13** and **14**).

The reactions carried out with N_α-acetyl-L-lysine methyl ester hydrochloride and *N*-acetyl-L-cysteine methyl ester also afforded the expected conjugates with both amino acid derivatives (Figure 1, compounds **15** and **16**). Since the N_α-acetyl-L-lysine methyl ester was in its hydrochloride form, the experimental procedure had to be adjusted and carried out in the presence of potassium carbonate. The resulting conjugates **15** and **16** were obtained, after purification by TLC, in respective yields of 75% and 94%. Concerned that the addition of potassium carbonate was responsible for the lower yield obtained with conjugate **15**, we tested the stability of maleimide−porphyrin **3** in DMF and in the presence of the inorganic base. It was found that potassium carbonate provoked some decomposition of the starting material, with ∼50% decomposition after 60 min. Notwithstanding this fact, the coupling reaction, under the tested conditions, is extremely fast (6 min according to TLC), so the decomposition rate promoted by potassium carbonate is believed not to interfere significantly with the coupling reaction.

These experiments demonstrate that there is no inherent specificity of the maleimide moiety when challenged with amines and thiols separately, both behaving as nucleophiles in an identical manner. Although as the next experiments would show, the scenario changes when both amines and thiols are present in the reaction mixture.

Two independent experiments were set up: one using the aliphatic thiol and amine and the other one the amino acid derivatives. In both cases, the same number of equivalents of amine and thiol were used, and the reactions were protected from atmospheric moisture and allowed to stir for 10 min. After this period, diethyl ether and hexane were added to the mixture in order to precipitate all the porphyrinic material. After dissolution and reprecipitation from methanol over dichloromethane, the ^{1}H NMR spectra from the obtained products revealed that in both cases, i.e., 1-propylamine/1-propanethiol and N_α-acetyl-L-lysine/*N*-acetyl-L-cysteine methyl esters, only the thioethers were obtained.

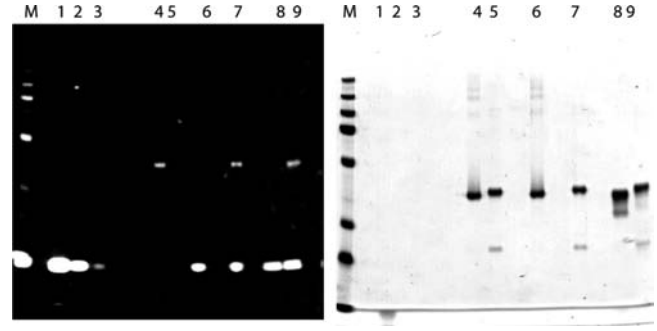


Figure 4. SDS-PAGE analysis (left panel, Cy5 fluorescence imaging; right panel, blue Coomassie staining). Lanes 1−3: Dilution series of porphyrin **4** (250 μg/mL; 25 μg/mL; 0.25 μg/mL). Lanes 4 and 5: SIP(L19) and SIP(L19)-PS**4** using transparent loading buffer. Lanes 6 and 7: SIP(L19) and SIP(L19)-PS**4** using transparent loading buffer spiked in with ∼25 ng of porphyrin **4**. Lanes 8 and 9: SIP(L19) and SIP(L19)-PS**4** using standard (containing bromophenol blue) loading buffer.

These results confirm that, despite the fact that the maleimide moiety is able to react with both amines and thiols separately, when both are present in the reaction mixture and compete for reaction with the maleimide, the thioether conjugate is isolated exclusively, probably due to significant differences in kinetics of nucleophilic attack. These results are supported by the data collected from the bioconjugation experiments with the reduced SIP(L19) as we will demonstrate later.

Biology. *Preparation and Characterization of Photoimmunoconjugates.* SIP(L19) is a third-generation (*47*), clinical-stage, recombinant antibody specific against the tumor neoangiongenesis marker EDB of fibronectin (*48*). The antibody consists of a homodimer covalently linked through a c-terminal disulfide bridge with a molecular weight of ∼80 kDa (Figure 2) and was expressed in mammalian cells and purified to homogeneity on a protein A sepharose column.

In order to achieve site-specific labeling of the cysteine residues at the protein c-term, without affecting the intradomain disulfide bridges, optimal reducing conditions for the SIP were achieved using TCEP (tris-(2-carboxyethyl)phosphine hydrochloride) and a longer time exposure to the reducing agent, compared to standard reducing conditions using DTT. TCEP has the advantage, compared to other common reducing agents (i.e., DTT), to be stable over time at physiological pH and does not need to be removed from the reaction mixture prior to coupling with maleimide derivatives (*49*, *50*).

The quality of the SIP−photosensitizer (SIP-PS) conjugates was assessed after the reaction cleanup steps (gel filtration and dialysis) by SDS-PAGE (Figure 3 and Figure 4).

Imaging of the gel by fluorescence revealed no free, noncovalently bound photosensitizer (*24*) in the conjugate solution (Figure 3B, lower panel). As expected, the antibody bands of the control reactions (SIP plus maleimide−porphyrin without reduction) did not show a significant fluorescence signal. The gel was then stained with Coomassie blue to confirm the purity and concentration of the conjugates (Figure 3A, upper panel).

Reduction and coupling does not affect the dimeric nature of the SIP in aqueous solution (Figure 5) or its immunoreactivity

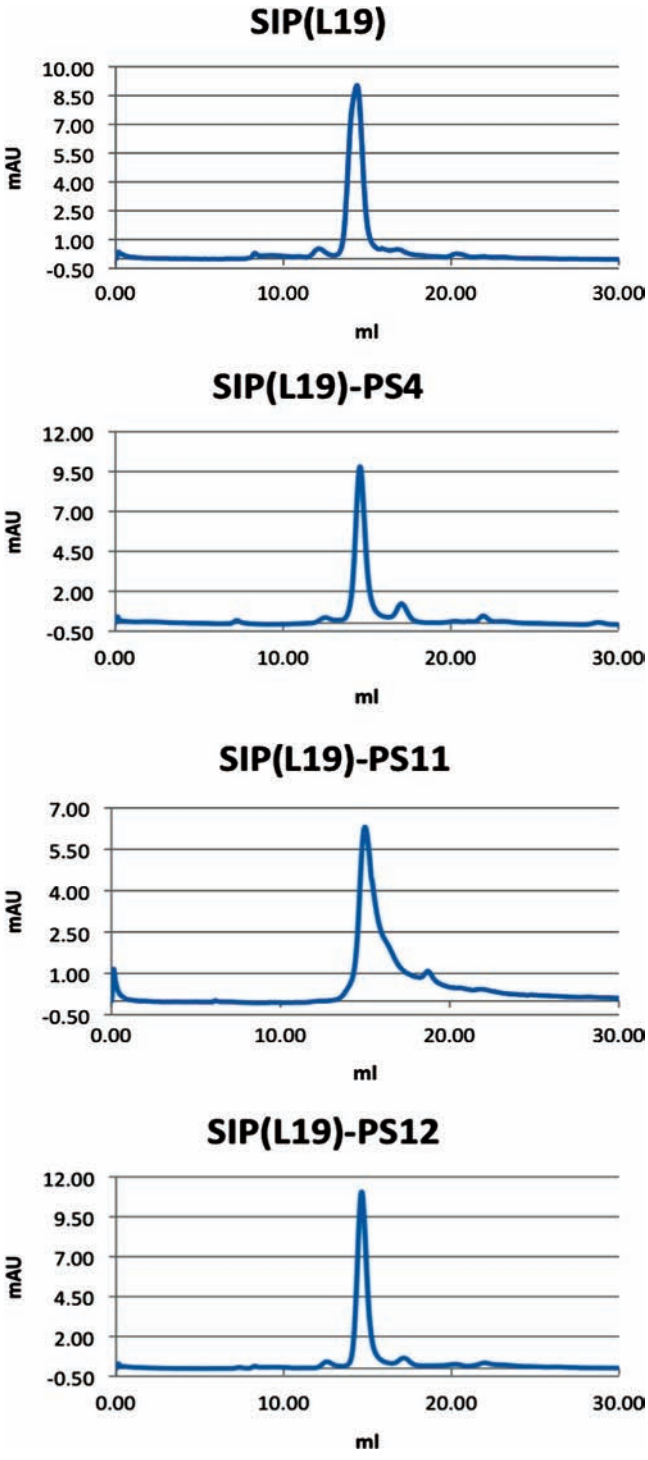


Figure 5. Size-exclusion chromatography profile of SIP(L19) and SIP(L19)−PS conjugates.

(*21*). Furthermore, no precipitation of the conjugates was observed, even after freeze/thawing procedure. The immunoreactivity, analyzed by ELISA and BIAcore, was above 90% when compared to the unmodified SIP(L19) (data not shown).

The theoretical photosensitizer (PS) loading ratio of the SIP is two photosensitizers per antibody molecule, based on available cysteine residues, and this is in perfect agreement with mass spectrometry data (Figure 6 and Figure 7), showing that after reduction and labeling reactions one PS moiety is covalently coupled per antibody monomer (as with SDS-PAGE, the conditions used for MALDI-MS lead to detection of the SIP in its monomeric form), without detection of the unmodified SIP.

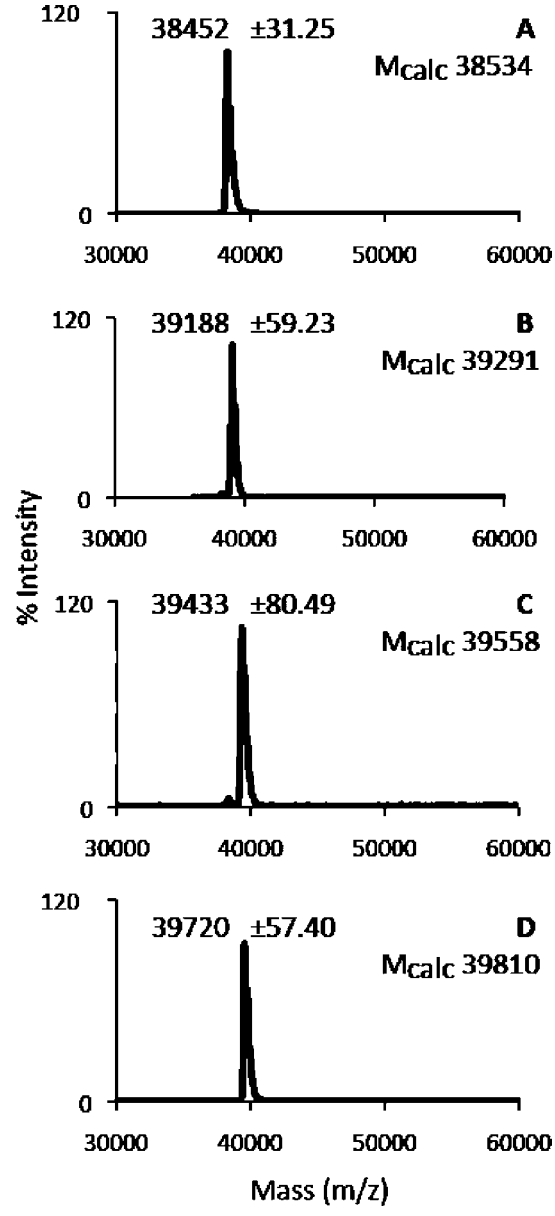


Figure 6. MALDI TOF/TOF spectra for (A) SIP(L19), (B) SIP(L19)-PS**4**, (C) SIP(L19)-PS**11**, and (D) SIP(L19)-PS**12**.

Although the chemical competition experiments described above indicated that the maleimide−porphyrin **3** was capable of reacting with the amino groups of lysine residues, these experiments were performed in a nonaqueous environment without pH control. The fact that using a large excess of maleimide−porphyrin results in two porphyrins per antibody, and the negligible reactivity with nonreduced antibody, strongly suggests that these have conjugated preferentially to the two available cysteine residues generated by reduction. The selectivity of conjugation is in agreement with the reported specificity of maleimides for thiols in the pH range 6.5−7.5 (*51*−*53*).

The number of porphyrins per antibody was also determined spectrophotometrically and gave estimated loading ratios (Porphyrin/SIP) of 0.76 for derivative **4**, 0.9 for **11**, and 1.75 for **12**. The fact that the apparent ratio of porphyrin/SIP determined by UV−visible spectroscopy increases as the length of spacer chain between porphyrin and maleimide increases suggests again that both porphyrins are attached to positions in close proximity on the antibody.

LM-fibroblasts were chosen to evaluate photocytotoxicity of the conjugates (Figure 8) because they naturally produce the

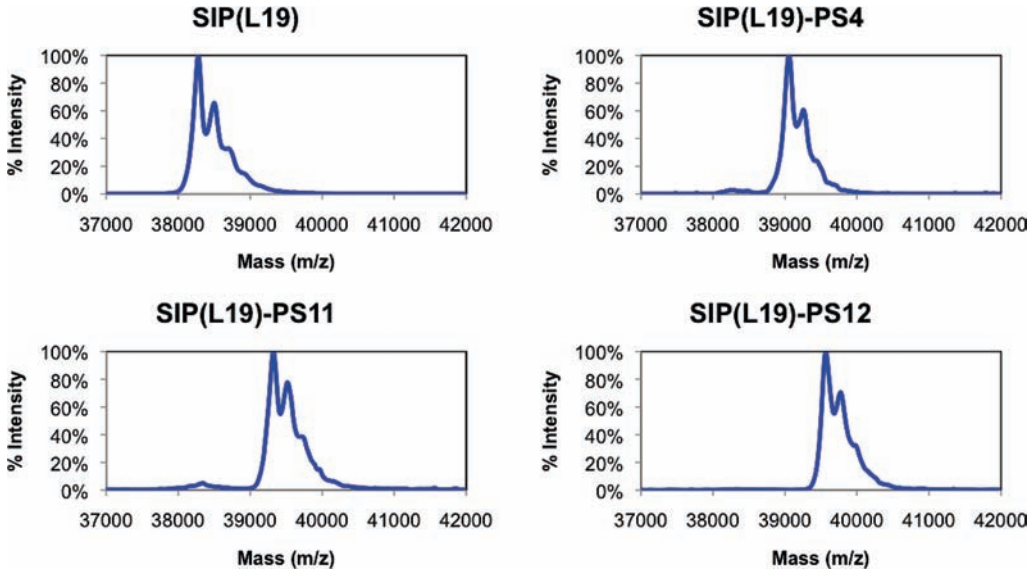


Figure 7. Magnified mass spectra, from Figure 4, of SIP(L19) and SIP(L19)-PS conjugates.

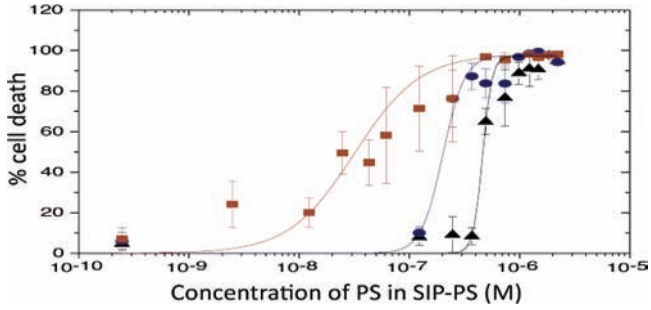


Figure 8. Photocytotoxicity for SIP(L19)-PS**4** (black ▲), SIP(L19)-PS**11** (blue •), SIP(L19)-PS**12** (red ■) carried out in L-M fibroblasts using the MTS assay (the obtained values are the means of at least three independent experiments ± SD). The solid line represents the fit of the data using the Hill equation.

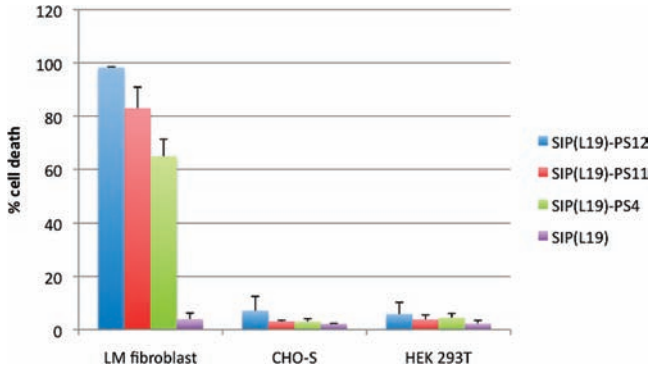


Figure 9. Activity of SIP(L19) and SIP(L19)-PS conjugates (5×10^{-7} M with respect to PS for conjugates and 20 mg/mL protein in all cases) on antigen-positive (LM fibroblast) and antigen-negative (CHO-S, HEK 293T) cells.

antigen for the L19 antibody (EDB + Fibronectin), thus avoiding either chemical coupling of the antigen or genetic manipulation on cells. Furthermore, LM-fibroblasts are stable over multiple passages, thus representing a good model system for the in vitro testing of L19 photoimmunoconjugates. This experiment showed the crucial importance of the length and nature of the linker between the SIP and the photosensitizer, as porphyrin **12** proved to be approximately 1 log more effective when compared to the conjugate **4**. As the porphyrin macrocycle is the same in each case, this could be caused by excited-state quenching between photosensitizers when coupled to the SIP, again suggesting the possibility of two porphyrin moieties in close proximity with each other. The increasing trend in activity observed in going from **4** to **11** and then **12** is consistent with increased freedom of movement associated with longer linkers.

Importantly, immuno-photocytotoxicity is antigen-specific, as evidenced by the lack of L19-photosensitizer killing in cells (CHO-S, HEK 293T) which do not express EDB(+)-fibronectin (Figure 9).

CONCLUSIONS

The data presented here clearly show that it is possible to perform site-specific conjugation of porphyrin-based photosensitizers to cysteine residues present on a monoclonal antibody with relevance to the photodynamic therapy of cancer. The well-characterized conjugates retain both the immunoreactivity of the antibody and the photodynamic activity of the photosensitizer. Enhancement of approximately 1 order of magnitude in photocytotoxicity using antigen-positive cells is possible by optimization of the linkage between porphyrin and the maleimide group used for conjugation with the cysteines. We believe the ability to generate well-characterized and photodynamically active antibody-photosensitizer conjugates with a clinically relevant antibody is a significant step toward the translation of this technology into a realistic treatment for solid tumors.

ACKNOWLEDGMENT

The authors thank the European commission for a FP6 grant to fund the Immuno-PDT consortium (FP6 LSHC-CT-2006-037489-ImmunoPDT). Financial contributions from the Swiss National Science Foundation, the ETH Zürich, the European Union (ADAMANT project), the Swiss Cancer League, the SwissBridge Foundation and the Stammbach Foundation are also gratefully acknowledged. We thank the EPSRC mass spectrometry centre, Swansea, for analyses.

LITERATURE CITED

(1) Brown, S. B., Brown, E. A., and Walker, I. (2004) The present and future role of photodynamic therapy in cancer treatment. *The Lancet 5*, 497–508.

(2) Pandey, R. K., and Zengh, G. (2000) Porphyrins as photosensitizers in photodynamic therapy, *The Porphyrin Handbook. Volume 6: Applications: Past, Present and Future* (Kadish, K. M., Smith, K. M., and Guilard, R., Eds.) pp 157−225, Chapter 43, Academic Press, New York.

(3) Josefsen, L. V., and Boyle, R. W. (2008) Photodynamic therapy and the development ofmetal-based photosensitisers. *Met. Based Drugs 2008*, 1–24.

(4) Boyle, R., and Dolphin, D. (1996) Structure and biodistribution relationships of photodynamic sensitizers. *Photochem. Photobiol. 64*, 469–485.

(5) Hamblin, M. R., and Mroz, P., Eds. (2008) *Advances in Photodynamic Therapy: Basic, Translational and Clinical*, Artech House, Boston, pp 179−234.

(6) Sharman, W. M., van Lier, J. E., and Allen, C. M. (2004) Targeted photodynamic therapy via receptor mediated delivery systems. *Adv. Drug. Delivery Rev. 56*, 53–76.

(7) Solban, N., Rizvi, I., and Hasan, T. (2006) Targeted photodynamic therapy. *Lasers Surg. Med. 38*, 522–531.

(8) Hudson, R., and Boyle, R. W. (2004) Strategies for selective delivery of photodynamic sensitisers to biological targets. *J. Porphyrins Phthalocyanines 8*, 954–975.

(9) van Dongen, G. A. M. S., Visser, G. W. M., and Vrouenraets, M. B. (2004) Photosensitizer-antibody conjugates for detection and therapy of cancer. *Adv. Drug Delivery Rev. 56*, 31–52.

(10) Bedel-Cloutour, C. H., Maneta-Peyret, L., Pereyre, M., and Bezian, J. H. (1991) Synthesis of a monoclonal antibody-indium-111-porphyrin conjugate. *J. Immunol. Methods 144*, 35–41.

(11) Jiang, F. N., Richter, A. M., Jain, A. K., Levy, J. G., and Smits, C. (1993) Biodistribution of a benzoporphyrin derivative-monoclonal antibody conjugate in A549-tumor-bearing nude mice. *Biotechnol Ther. 4*, 43–61.

(12) Milgrow, L. R., and O'Neill, F. (1995) Towards synthetic-porphyrin/monoclonal antibody conjugates. *Tetrahedron 51*, 2137–2144.

(13) Goff, B. A., Blake, J., Bamberg, M. P., and Hasan, T. (1996) Treatment of ovarian cancer with photodynamic therapy and immunoconjugates in a murine ovarian cancer model. *Br. J. Cancer 74*, 1194–1198.

(14) Del Governatore, M., Hamblin, M. R., Picinnini, E. E., Ugolini, G., and Hasan, T. (2000) Targeted photodestruction of human colon cancer cells using charged 17.1A chlorin$_{e6}$ immunoconjugates. *Br. J. Cancer 82*, 56–64.

(15) Hamblin, M. R., Del Governatore, M., Rizvi, I., and Hasan, T. (2000) Biodistribution of charged 17.1A photoimmunoconjugates in a murine model of hepatic metastasis of colorectal cancer. *Br. J. Cancer 83*, 1544–1551.

(16) Vrouenraets, M. B., Visser, G. W. M., Loup, C., Meunier, B., Stigter, M., Oppelaar, H., Stewart, F. A., Snow, G. B., and van Dongen, G. A. M. S. (2000) Targeting of a hydrophilic photosensitizer by use of internalizing monoclonal antibodies: A new possibility for use in photodynamic therapy. *Int. J. Cancer 88*, 108–114.

(17) Hudson, R., Carcenac, M., Smith, K., Madden, L., Clarke, O. J., Pèlegrin, A., Greenman, J., and Boyle, R. W. (2005) The development and characterisation of porphyrin isothiocyanate-monoclonal antibody conjugates for photoimmunotherapy. *Br. J. Cancer 92*, 1442–1449.

(18) Savellano, M. D., and Hasan, T. (2005) Photochemical targeting of epidermal growth factor receptor: a mechanistic study. *Clin. Cancer Res. 11*, 1658–1668.

(19) Savellano, M. D., Pogue, B. W., Hoopes, P. J., Vitetta, E. S., and Paulsen, D. K. (2005) Multiepitope HER2 targeting enhances photoimmunotherapy of HER2-Overexpressing cancer cells with pyropheophorbide-a immunoconjugates. *Cancer Res. 65*, 6371–6379.

(20) Borbas, K. E., Mroz, P., Hamblin, M. R., and Lindsey, J. S. (2006) Bioconjugatable porphyrins bearing a compact swallowtail motif for water solubility. *Bioconjugate Chem. 17*, 638–653.

(21) Fabbrini, M., Trachsel, E., Soldani, P., Bindi, S., Alessi, P., Bracci, L., Kosmehl, H., Zardi, L., Neri, D., and Neri, P. (2006) Selective occlusion of tumor blood vessels by targeted delivery of an antibody-photosensitizer conjugate. *Int. J. Cancer 118*, 1085–1813.

(22) Staneloudi, C., Smith, K. A., Hudson, R., Malatesti, N., Savoie, H., Boyle, R. W., and Greenman, J. (2007) Development and characterization of novel photosensitizer: scFv conjugates for use in photodynamic therapy of cancer. *Immunology 120*, 512–517.

(23) Kuimova, M. K., Bhatti, M., Deonarain, M., Yahioglu, G., Levitt, J. A., Stamati, I., Suhling, K., and Phillips, D. (2007) Fluorescence characterisation of multiply-loaded anti-HER2 single chain Fv-photosensitizer conjugates suitable for photodynamic therapy. *Photochem. Photobiol. Sci. 6*, 933–939.

(24) Bhatti, M., Yahioglu, G., Milgrom, L. R., Garcia-Maya, M., Chester, K. A., and Deonarain, M. P. (2008) Targeted photodynamic therapy with multiply-based recombinant antibody fragments. *Int. J. Cancer 122*, 1155–1163.

(25) Hamblin, M. R., Miller, J. L., and Hasan, T. (1996) effect of charge on the interaction of site-specific photoimmunoconjugates with human ovarian cancer cells. *Cancer Res. 56*, 5205–5210.

(26) Duska, L. R., Hamblin, M. R., Bamberg, M. P., and Hasan, T. (1997) Biodistribution of charged F(ab′)$_2$ photoimmunoconjugates in a xenograft model of ovarian cancer. *Br. J. Cancer 75*, 837–844.

(27) Hamblin, M. R., Bamberg, M. P., Miller, J. L., and Hasan, T. (1998) Cationic photoimmunoconjugates between monoclonal antibodies and hematoporphyrin: selective photodestruction of ovarian cancer cells. *Appl. Opt. 37*, 7184–7192.

(28) Molpus, K. L., Hamblin, M. R., Rizvi, I., and Hasan, T. (2000) Intraperitoneal photoimmunotherapy of ovarian carcinoma xenografts in nude mice using charged photoimmunoconjugates. *Gynecol. Oncol. 76*, 397–404.

(29) Borsi, L., Balza, E., Bestagno, M., Castellani, P., Carnemolla, B., Biro, A., Leprini, A., Sepulveda, J., Burrone, O., Neri, D., and Zardi, L. (2002) Selective targeting of tumoral vasculature: comparison of different formats of an antibody (L19) to the ED-B domain of fibronectin. *Int. J. Cancer 102*, 75–85.

(30) Smith, K. A., Nelson, P. N., Warren, P., Astley, S. J., Murray, P. G., and Greenman, J. (2004) Demystified. recombinant antibodies. *J. Clin. Pathol. 57*, 912–917.

(31) Schliemann, C., and Neri, D. (2007) Antibody-based targeting of the tumor vasculature. *Biochim. Biophys. Acta 1776*, 175–192.

(32) Wojtyk, J. T. C., Goyan, R., Gudgin-Dickson, E., and Pottier, R. (2006) Exploiting tumour biology to develop novel drug delivery strategies for PDT. *Med. Laser Appl. 21*, 225–238.

(33) Savellano, M. D., and Hasan, T. (2003) Targeting Cells that overexpress the epidermal growth factor receptor with polyethylene glycolated BPD verteporfin photosensitizer immunoconjugates. *Photochem. Photobiol. 77*, 431–439.

(34) Soukos, N. S., Hamblin, M. R., Richard, S. K., Fabian, L., Deutsch, T. F., and Hasan, T. (2001) Epidermal growth factor receptor-targeted immunophotodiagnosis and photoimmunotherapy of oral precancer *in vivo*. *Cancer Res. 61*, 4490–4496.

(35) Chen, Y., Parr, T., Holmes, A. E., and Nakanishi, K. (2008) Porphyrinmaleimides: towards thiol probes for cysteine residues in proteins. *Bioconjugate Chem. 19*, 5–9.

(36) Endo, M., Fujitsuka, M., and Majima, T. (2008) Programmable conformational regulation of porphyrin dimers on geometric scaffold of duplex DNA. *Tetrahedron 64*, 1839–1846.

(37) Borbas, K. E., Kee, H. L., Holten, D., and Lindsey, J. S. (2008) A compact water-soluble porphyrin bearing an iodoacetamido bioconjugatable site. *Org. Biomol. Chem. 6*, 187–194.

(38) Choma, C. T., Kaestle, K., Åkerfeldt, K., Kimb, R. M., Groves, J. T., and DeGrado, W. F. (1994) A general method for coupling unprotected peptides to bromoacetamido porphyrin templates. *Tetrahedron Lett. 35*, 6191–6194.

(39) Chaloin, L., Bigey, P., Loup, C., Marin, M., Galeotti, N., Piechaczyk, M., Heitz, F., and Meunier, B. (2001) Improvement of porphyrin cellular delivery and activity by conjugation to a carrier peptide. *Bioconjugate Chem. 12*, 691–700.

(40) Halime, Z., Michaudet, L., Lachkar, M., Brossier, P., and Boitrel, B. (2004) Influence of pendant arms bearing ligating groups on the structure of bismuth porphyrins: implications for labeling immunoglobulins used in medical applications. *Bioconjugate Chem. 15*, 1193–1200.

(41) Barragán, F., Gordillo, B., Vargas, G., Cortez, Ma. T., Jaramillo, B. E., Villa-Treviño, S., Fattel-Fazenda, S., Ortega, J., and Velazcoe, L. (2005) DNA replication inhibition and fluorescence microscopy of non-cationic porphyrins in malignant cells. *Arkivoc vi* 436–448.

(42) Zuberbühler, K., Palumbo, Bacci, A. C., Giovannoni, L., Sommavilla, R., Kaspar, M., Trachsel, E., and Neri, D. (2009) A general method for the selection of high-level scFv and IgG antibody expression by stably transfected mammalian cells. *Protein. Eng. Des. Sel. 22*, 169–174.

(43) Huber, A., Demartis, S., and Neri, D. (1999) The use of biosensor technology for the engineering of antibodies and enzymes. *J. Mol. Recognit. 12*, 198–216.

(44) Carnemolla, B., Neri, D., Castellani, P., Leprini, A., Neri, G., Pini, A., Winter, G., and Zardi, L. (1996) Phage antibodies with pan-species recognition of the oncofoetal angiogenesis marker fibronectin ED-B domain. *Int. J. Cancer 68*, 397–405.

(45) Sutton, J. M., Clarke, O. J., Fernandez, N., and Boyle, R. W. (2002) Porphyrin, chlorin, and bacteriochlorin isothiocyanates: useful reagents for the synthesis of photoactive bioconjugates. *Bioconjugate Chem. 13*, 249–263.

(46) Tomé, J. P. C., Neves, M. G. P. M. S., Tomé, A. C., Cavaleiro, J. A. S., Soncin, M., Magaraggia, M., Ferro, S., and Jori, G. (2004) Synthesis and Antibacterial activity of new poly-*s*-lysine-porphyrin conjugates. *J. Med. Chem. 47*, 6649–6652.

(47) Nelson, A. L., and Reichert, J. M. (2009) Development trends for therapeutic antibody fragments. *Nat. Biotechnol. 27*, 331–337.

(48) Sauer, S., Erba, P. A., Petrini, M., Menrad, A., Giovannoni, L., Grana, C., Hirsch, B., Zardi, L., Paganelli, G., Mariani, G., Neri, D., Dürkop, H., and Menssen, H. D. (2009) Expression of the oncofetal ED-B-containing fibronectin isoform in hematologic tumors enables ED-B-targeted 131I-L19SIP radioimmunotherapy in Hodgkin lymphoma patients. *Blood 113*, 2265–2274.

(49) Albrecht, H., Burke, P. A., Natarajan, A., Xiong, C.-Y., Kalicinsky, M., DeNardo, G. L., and DeNardo, S. J. (2004) Production of soluble ScFvs with C-terminal-free thiol for site-specific conjugation or stable dimeric ScFvs on demand. *Bioconjugate Chem. 15*, 16–26.

(50) Natarajan, A., Xiong, C.-Y., Albrecht, H., DeNardo, G. L., and DeNardo, S. J. (2005) Characterization of site-specific ScFv PEGylation for tumor-targeting pharmaceuticals. *Bioconjugate Chem. 16*, 113–121.

(51) Partis, M. D., Griffiths, D. G., Robersts, G. C., and Beechley, R. B. (1983) Cross-linking of proteins by w-maleimido alkanoyl *N*-hydroxysuccinimido esters. *J. Protein Chem. 2*, 263–277.

(52) Gorin, G., Martin, P. A., and Doughty, G. (1966) Kinetics of the reaction of *N*-ethylmaleimide with cysteine and some congeners. *Arch. Biochem. Biophys. 115*, 593–507.

(53) Smyth, D. G., Blumenfeld, O. O., and Konigsberg, W. (1964) Reaction of *N*-ethylmaleimide with peptides and amino acids. *Biochem. J. 91*, 589–595.

BC9003537

Radioimmunotherapy of Human Colon Cancer Xenografts with ^{131}I-Labeled Anti-CEA Monoclonal Antibody

Zhaofei Liu,[#] Cunjing Jin,[#] Zilin Yu, Jing Zhang, Yan Liu, Huiyun Zhao, Bing Jia,* and Fan Wang*

Medical Isotopes Research Center, Peking University, Beijing 100191, China. Received August 12, 2009; Revised Manuscript Received December 15, 2009

Radioimmunotherapy (RIT) is a promising approach for the treatment of a wide variety of malignancies. The aim of this study was to investigate the therapeutic efficacy of ^{131}I-labeled anticarcinoembryonic antigen (CEA) monoclonal antibody CL58 in a human colon cancer mouse model. In vitro and in vivo characteristics of ^{125}I-CL58 were evaluated in LS180 human colon cancer cells and the nude mouse model. ^{131}I-CL58 was prepared and its in vivo therapeutic efficacy was tested. ^{125}I-CL58 showed high affinity to LS180 cells, as well as high tumor uptake and long tumor retention in LS180 tumor xenografts. ^{131}I-CL58 exhibited dose-dependent inhibition of LS180 tumor growth. With the excellent in vitro and in vivo characteristics, and the effective therapy for colon cancer in animal model, ^{131}I-CL58 is a promising agent for RIT of CEA-positive tumors including colon cancer.

INTRODUCTION

Colorectal cancer, accounting for higher morbidity and mortality, is the second most lethal and third most common malignancy in western developed countries (*1*) and the third common gastrointestinal tumor in China (*2, 3*). Although multiple kinds of managements in prevention, screening, treatment, and surveillance of this disease have been developed systematically in the last decades, the major cause of cancer mortality is most likely due to dissemination and distant metastasis.

In the exploration of methods to manage colorectal cancer, chemotherapy is the principal adjuvant therapy, and the addition of radiotherapy to chemotherapy has not been shown to improve outcomes (*4*). To reduce the systemic toxicity elicited from the chemotherapy, tactics involving biomarkers on cancer cells recognized by exogenous targeted molecules (e.g., peptides, oligonucleotides, aptamers, and antibodies) were conducted. Among these investigations, radioimmunitherapy (RIT), which typically consists of radionuclide and antibody, has been investigated extensively as a useful strategy for the treatment of a variety of neoplasms (*5*−*7*). For the agents of RIT, the antibody acts as a vehicle for selective delivery of cytotoxic radionuclides to destroy the tumor while sparing the normal organs and tissues. FDA approval of two radiolabeled antibody-based products for the treatment of non-Hodgkin's lymphoma (NHL) was an initial success of hardworking investigation of the subject of RIT in the past decades (*8, 9*). Although the efficacy of RIT for solid tumors was less encouraging than that of hematologic tumors (*10*), it indeed gives hope for this subject; moreover, some lessons and experiences have already been acquired for further investigation.

Many colorectal cancer markers, such as carcinoembryonic antigen (CEA), TAG-72, A33, Ep-CAM (17−1A), and CSA-p, have been studied as the therapeutic targets in preclinical or clinical settings (*11*). Among all the colon cancer markers, CEA was first described as a gastrointestinal onco-fetal antigen, although it is now well-known to be overexpressed in a majority of carcinomas, including gastrointestinal cancers, respiratory and genitourinary cancers, and also breast cancers (*12, 13*). ^{131}I-labeled anti-CEA antibodies for RIT of colon cancer have shown encouraging results in preclinical and clinical trials (*14, 15*). Moreover, an adjuvant regimen of RIT showed exciting results in patients with colorectal cancer and liver metastases (*16*).

CL58 is a murine anti-CEA monoclonal antibody (IgG1 subtype). Previous studies have shown the successful application of radiolabeled CL58 for CEA-positive tumor imaging and radioimmunoguided surgery (*17, 18*). In this study, in vitro and in vivo characteristics of iodinated CL58 were evaluated, and the RIT efficacy of ^{131}I-labeled CL58 in nude mice bearing human colon cancer xenografts was investigated.

EXPERIMENTAL PROCEDURES

Radiolabeling of mAb. The murine anti-CEA monoclonal antibody CL58 was generated as previously reported (*17, 18*). An isotype-matched control murine IgG1 (mIgG) was purchased from Sigma. Iodination of mAb CL58 or mIgG was performed using Iodogen method as previously described (*19, 20*). Briefly, 2 mCi (74 MBq) of ^{125}I or ^{131}I (Beijing Atom High Tech, Beijing, China), 50 μg of mAb CL58 or mIgG, and 100 μL of 0.2 M phosphate buffer (pH 7.4) were added in the vial coated with 50 μg Iodogen (Sigma-Aldrich, St. Loius, MO). After reacting for 7−10 min at room temperature, the mixture was purified with PD-10 column (Amersham, Piscataway, NJ). Labeling yield and radiochemical purity of the products were measured by ITLC (85% methanol as the mobile phase) on a radio-thin layer scanner (Bioscan AR2000, Washington, DC).

Cell Culture and Animal Model. The human colon carcinoma cell line LS180, with a cell surface CEA expression rate of 81% (*17*), was maintained in Dulbecco's modified Eagle medium (DMEM) supplemented with 10% fetal bovine serum (FBS) at 37 °C under a humidified atmosphere containing 5% CO_2. All animal experiments were performed in accordance with Guidelines of Peking University Health Science Center Animal Care and Use Committee. Five-week-old female BALB/c nude mice were purchased from the Department of Experimental

* To whom correspondence should be addressed. Dr. Fan Wang, Medical Isotopes Research Center, Peking University, 38 Xueyuan Road, Beijing 100191, China. Phone and Fax: 86-10-82801145, E-mail: wangfan@bjmu.edu.cn; or Dr. Bing Jia, Phone: 86-10-82802871, Fax: 86-10-82801145, E-mail: jiabing@bjmu.edu.cn.

[#] These authors contributed equally to this work.

10.1021/bc9003603 © 2010 American Chemical Society
Published on Web 01/15/2010

Animal, Peking University Health Science Center (Beijing, China). The LS180 tumor model was generated by subcutaneous injection of 1×10^7 LS180 cells into the left flanks of the nude mice.

Affinity of ^{125}I-CL58. The equilibrium dissociation constant (K_d) of ^{125}I-CL58 was determined by saturation binding study using the previously described method with some modifications (*20*). Briefly, LS180 cells seeded in 48-well plates were incubated in triplicate with increasing concentration of ^{125}I-CL58 (from 20 ng/mL to 1.2 μg/mL, in 1% BSA binding buffer). The total volume of each well was adjusted to 200 μL. Nonspecific binding at each concentration was determined by adding an excess dose of unlabeled CL58 (~100-fold). After 2 h of incubation at 4 °C, the reaction medium was removed and cells were washed with ice-cold PBS. The cells were lysed with 2 M NaOH, and the cell-associated radioactivity was measured in a gamma counter (Wallac 1470-002, Perkin-Elmer, Finland). Results were analyzed by nonlinear regression (one-site binding) using GraphPad *Prism 4.0* (GraphPad Software, San Diego, CA) to obtain the best-fit K_d and B_{max} values, and a Scatchard transformation was subsequently performed. Data were expressed as the average of triplicate samples.

Biodistribution. LS180 tumor-bearing nude mice were randomly divided into groups ($n = 4$/group) when the tumor size reached 0.5−0.8 cm in diameter (~10 days after inoculation). Each mouse was injected intravenously with 100 μL of ^{125}I-CL58 (5 μCi, 5 μg). At selected time points (4 h; 1, 3, 5, and 7 d), mice were euthanized, and samples or organs of interest were removed, weighed, and counted in a gamma counter. The results were calculated as a percentage of the injected dose per gram tissue (%ID/g). To determine the specific accumulation of ^{125}I-CL58 in LS180 tumors, ^{125}I-mIgG (5 μCi, 5 μg) was injected intravenously into a group of 4 tumor-bearing mice, and the biodistribution (3 d postinjection) was determined as depicted above.

γ-Imaging. For planar gamma imaging studies, two LS180 tumor-bearing mice were injected intravenously with 200 μCi of ^{125}I-CL58 via tail vein after anesthetization. Mice were placed prone on a two-head γ-camera (Siemens, E.Cam) equipped with a parallel-hole, low-energy, and high-resolution collimator. Imaging was performed at 1, 2, and 6 d postinjection. After completion of imaging, mice were euthanized.

Radioimmunotherapy of ^{131}I-CL58. Therapy studies of ^{131}I-CL58 were investigated in LS180 tumor-bearing mice (the original tumor volume was 135 ± 58 mm^3). Animals were randomly divided into six groups, each of which had 6 mice. The tumor-bearing mice in therapeutic groups were administrated intravenously with escalating doses (150 μCi, 300 μCi, and 450 μCi) of ^{131}I-CL58 via tail vein. The mice in the control groups were administrated with normal saline, cold mAb CL58, and 150 μCi of ^{131}I-mIgG via tail vein, respectively. The tumor volume was estimated, assuming the tumors were ellipsoid, using the formula/volume = $4\pi/3$ (1/2 length × 1/2 width × 1/2 height). Tumor size and animal weight were measured every 2−3 days, and the mouse was culled and euthanatized once the tumor volume reached >1500 mm^3 or the body weight lost >20% of its original weight. Normal tissues including liver and kidney were isolated, fixed in 5% buffered formalin, embedded in paraffin, and sections were stained with hematoxylin and eosin (H&E) for histopathological analyses.

Statistical Analysis. Quantitative data were expressed as mean ± SD. Statistical analysis was done using a one-way ANOVA for multiple groups and an unpaired Student's *t* test.

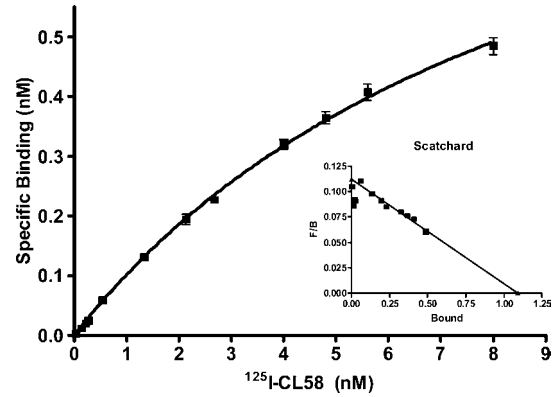


Figure 1. Saturation binding of ^{125}I-CL58 to EGFR on LS180 human colon cancer cells. Results were analyzed by nonlinear regression using GraphPad *Prism 4.0* software, and a Scatchard transformation was subsequently performed. Data are expressed as the means ± standard deviation (SD) ($n = 3$).

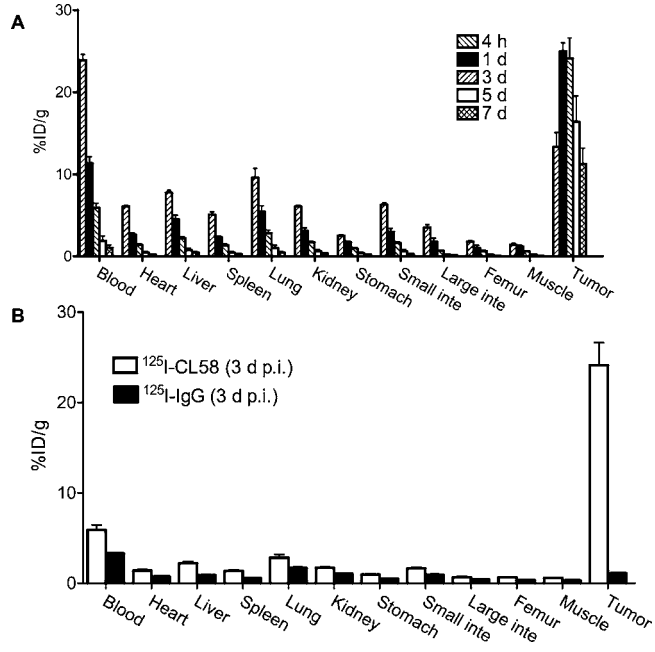


Figure 2. (A) Biodistribution of ^{125}I-CL58 (5 μCi per mouse) in LS180 tumor-bearing nude mice at 4 h, and 1, 3, 5, and 7 d postinjection. (B) Biodistribution comparison of ^{125}I-CL58 and ^{125}I-mIgG (isotype-matched control) (5 μCi per mouse) in LS180 tumor-bearing nude mice on 3 d postinjection. Data are expressed as %ID/g ± SD ($n = 4$ per group).

P values of <0.05 were considered statistically significant (GraphPad *Prism 4.0*).

RESULTS

Saturation Binding Assay. Anti-CEA monoclonal antibody CL58 was labeled with ^{125}I or ^{131}I using the Iodogen method. The labeling yield was >70% and the radiochemistry purity was >99% after purification with PD-10 column. The binding affinity of ^{125}I-CL58 to LS180 cells was determined by a saturation binding assay. As shown in Figure 1, the equilibrium dissociation constant (K_d) was determined to be 9.73 ± 0.84 nM, and B_{max} was calculated to be approximate 8.20×10^6 sites/cell. (means ± SD, $n = 3$).

Biodistribution Studies of ^{125}I-CL58. Biodistribution studies of ^{125}I-CL58 were performed in BALB/c nude mice bearing LS180 human colon carcinoma xenografts. As shown in Figure 2A, the tumor uptake of ^{125}I-CL58 at 4 h, and 1, 3, 5, and 7 d

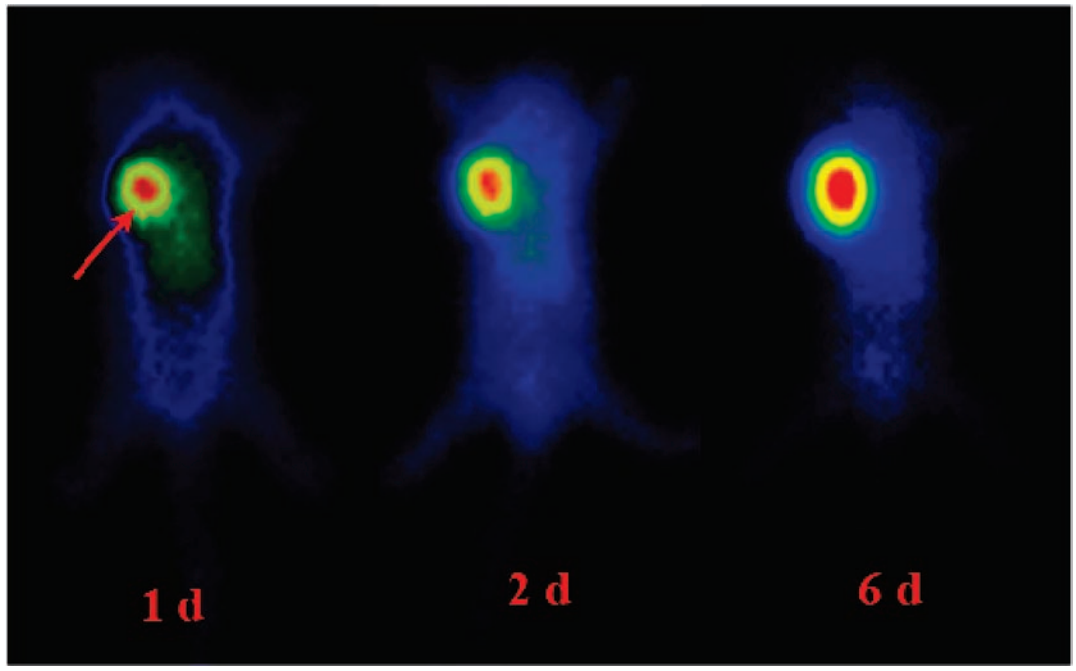


Figure 3. Representative planar γ images of ^{125}I-CL58 (200 μCi per mouse) in LS180 tumor-bearing nude mice on 1, 2, and 6 d postinjection. Arrow indicates the location of tumor.

postinjection were 13.34 ± 3.43%ID/g, 24.99 ± 2.00%ID/g, 24.11 ± 4.99%ID/g, 16.41 ± 5.40%ID/g, and 11.25 ± 3.82%ID/g, respectively, which were significantly higher than that of other organs after 1 d postinjection ($p < 0.001$). The blood radioactivity eliminated from 23.91 ± 1.35%ID/g to 1.05 ± 0.66%ID/g from 4 h to 7 d postinjection. For most normal organs, there was a progressive washout of radioactivity with the time, which was concomitant with the clearance of radioactivity from blood. The uptake of ^{125}I-CL58 in all normal organs was <0.5%ID/g on 7 d postinjection. The tumor-to-nontumor (T/NT) ratio of ^{125}I-CL58 showed an increasing trend for all organs during the entire period of this study, indicating the pretty good tumor targeting property of ^{125}I-CL58 in CEA-positive tumor model.

The in vivo CEA binding specificity of ^{125}I-CL58 was confirmed by performing the biodistribution of ^{125}I-mIgG in LS180 tumor-bearing nude mice. As shown in Figure 2B, the tumor uptake of ^{125}I-CL58 was significantly higher than that of mIgG (24.11 ± 4.99 vs 1.13 ± 0.04%ID/g, $P < 0.0001$) on 3 d postinjection, indicating the tumor targeting specificity of ^{125}I-CL58.

Gamma Imaging of ^{125}I-CL58. The representative planar gamma images of LS180 tumor-bearing mice acquired at different time points are shown in Figure 3. The tumors were clearly visualized on 1 d postinjection, and a small amount of radioactivity was also found in blood-rich organs, such as lung and heart, as well as liver. The background activity decreased with time, which was consistent with the ex vivo biodistribution data at the same time points. The images with higher contrast were obtained on 6 d postinjection.

Radioimmunotherapy of ^{131}I-CL58. The RIT efficacy of ^{131}I-CL58 was investigated in BALB/c nude mice bearing CEA-positive LS180 tumors. In all three control groups (saline, mAb CL58, and 150 μCi mIgG), the tumors grew rapidly, and the average tumor size reached >1500 mm^3 on day 12 post-treatment. Lower or moderate dose (150 μCi or 300 μCi) of ^{131}I-CL58 delayed tumor progression significantly compared with the control groups. The tumor size of mice receiving 150 μCi ^{131}I-CL58 was significantly different to that in unlabeled mAb CL58 group on day 12 ($P < 0.001$). Mice receiving 300 μCi ^{131}I-CL58 exhibited significant tumor growth inhibition until day 19 before exponential growth of tumors resumed. For the group treated with the highest dose of 450 μCi, the tumor growth was significantly suppressed, and the average tumor size maintained in a similar level up to day 55 post-treatment. The tumor size in 450 μCi group was smaller than that in other groups from day 9 post-treatment. On day 30, the tumor volume of 450 μCi group was significantly smaller than that in 150 μCi and 300 μCi groups ($p < 0.01$). A dose-dependent effect was observed in this study as the tumor therapeutic efficacy of ^{131}I-CL58 followed the order of 450 μCi > 300 μCi > 150 μCi (Figure 4A).

The CEA-targeted radioimmunotherapy with ^{131}I-CL58 significantly prolonged the survival time of mice. As shown in Figure 4B, all mice in the control groups (saline, mAb CL58, and 150 μCi mIgG) died before day 23, whereas the median survival time for 150 μCi and 300 μCi therapeutic groups was prolonged to be 41 days and 48 days, respectively. All mice in the 450 μCi ^{131}I-CL58 treatment group were still alive on day 55 post-treatment, and the median survival time was 84 days. All mice injected with ^{131}I-CL58 did not show obvious signs of body weight loss (less than 20%), and histopathologic staining results revealed that no renal and hepatic toxicity was observed (Supporting Information Figure S1−S2), indicating the limited toxicity of ^{131}I-CL58 in this therapeutic study.

DISCUSSION

In this study, we evaluated the in vitro and in vivo characteristics of radioiodinated anti-CEA monoclonal antibody CL58 and investigated whether ^{131}I-labeled CL58 could be used for radioimmunotherapy of colon cancers.

RIT can specifically deliver radiation to tumors with minimal toxicity to normal organs. The radiation energy given off by the radionuclides would also kill the adjacent tumor cells, which do not express the target antigen (so-called crossfire). Herein, we have chosen carcinoembryonic antigen (CEA) as the target for RIT of colon cancer xenografts because CEA is expressed at high levels in approximately 95% of colorectal carcinomas but is restrictedly expressed in normal tissues. CEA is located

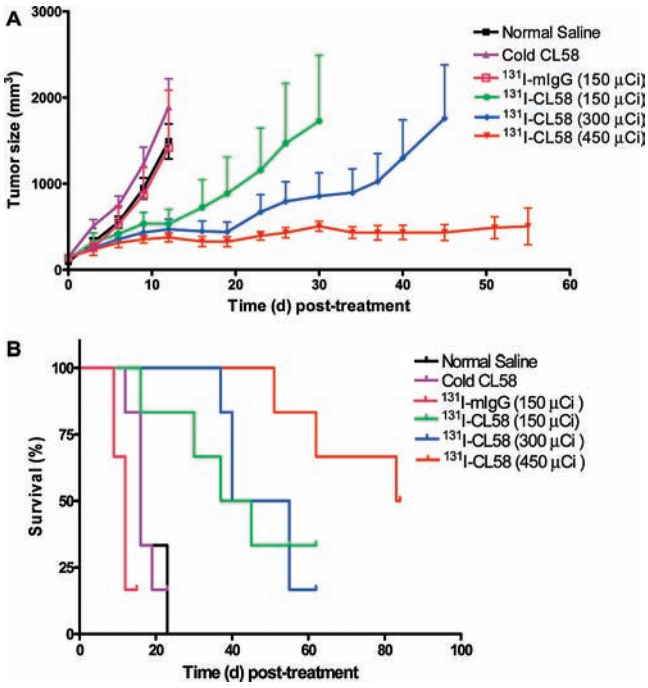


Figure 4. (A) Radioimmunotherapy of established LS180 tumors in nude mice with saline, unlabeled mAb CL58, ^{131}I-mIgG (150 μCi), or different doses (150, 300, and 450 μCi) of ^{131}I-CL58. Volumes of tumors in each treatment group were measured and expressed as a function of time (means ± SD, $n = 6$ per group). (B) Kaplan−Meier plots of individual treatment groups receiving saline, unlabeled CL58, ^{131}I-mIgG (150 μCi), or different doses (150, 300, and 450 μCi) of ^{131}I-CL58.

on the cell surface of tumor cells, and it has been one of the first tumor-associated antigens (TAA) used for RIT. A series of anti-CEA antibodies have been investigated for colon cancer targeted RIT, some of which have been used for clinical trials (see review, ref *21*). In this study, we used a murine anti-CEA monoclonal antibody CL58 as the vehicle for radiation delivery. The mAb CL58, which has been successfully used in clinical trials for tumor imaging and radioimmunoguided surgery (*17, 18*), exhibited a moderate affinity ($K_d = 9.73 \pm 0.84$ nM) to CEA-positive LS180 cells (Figure 1). The low antigen binding affinity of an antibody will certainly affect the in vivo radionuclide delivery in RIT trials; however, it has also been hypothesized that very high affinity interactions between antibodies and tumor antigens may impair efficient tumor penetration of the antibodies and thus diminish effective in vivo targeting (*22*). Consequently, antibodies with moderate affinity may be advantageous, as they can effectively penetrate into tumors and exhibit longer retention on tumor cells (*23*). LS180 cells had an extremely high CEA expression level (Figure 1). In the clinical situation, the CEA expression of other types of colon cancers may not reach such a high level as LS180 tumors, but the highly restrictive expression of CEA in colon cancers as compared with normal organs would still allow the specific delivery of radiation by the anti-CEA mAb CL58.

The in vivo behavior of ^{125}I-CL58 was tested in nude mice bearing CL180 colon cancer xenografts by both biodistribution and gamma imaging studies. ^{125}I-CL58 showed efficient tumor targeting properties, with rapid normal organ clearance and high tumor-to-nontumor ratios (Figures 2 and 3). The longer tumor retention of radioactivity was also found by the biodistribution study, and the tumor uptake of ^{125}I-CL58 was still as high as 11.25 ± 3.82%ID/g on 7 d postinjection. We tested the internalization property of ^{125}I-CL58 by the method reported previously (*20*), and the result demonstrated that ^{125}I-CL58 exhibited an undetectable internalization after binding to CL180 cells (data not shown). The negligible internalization property of ^{125}I-CL58 would effectively avoid the rapid diffusion of iodotyrosine in the target cells after internalization and catabolism of the radioiodinated mAb, leading to the high tumor uptake and long tumor retention of ^{125}I-CL58 in LS180 tumor xenografts. Importantly, the liver and spleen uptake of ^{125}I-CL58 was relatively low compared with that of metal isotope (e.g., ^{64}Cu, ^{111}In) labeled antibodies (*24, 25*), which possibly makes radioiodinated CL58 less toxic. The significantly higher tumor uptake of ^{125}I-CL58 as compared with ^{125}I-mIgG clearly demonstrated the in vivo CEA-targeting specificity of mAb CL58 (Figure 2B).

^{131}I and ^{90}Y are the most commonly used isotopes for radioimmunotherapy. Compared with the pure β emitter ^{90}Y, ^{131}I is much easier for radiolabeling, lower cost, and can also be used for imaging, which makes it possible for monitoring the therapeutic efficacy during the period of RIT. The experimental RIT study using ^{131}I-CL58 showed promising results on the therapy of colon cancer xenografts. In the 450 μCi ^{131}I-CL58 group, the tumor growth was efficaciously inhibited up to the end of therapy study (Figure 4A). The overall body weight loss of mice was <20% (Supporting Information Figure S1), and no signs of liver and kidney damage were found, revealing the limited toxicity of ^{131}I-CL58 at the dose of 450 μCi. In the lower dose groups (150 μCi and 300 μCi), ^{131}I-CL58 could partially inhibit the growth of CL180 tumors with prolonged survival time (Figure 3). The tumor growth inhibition efficacy of ^{131}I-CL58 was obviously superior to that of unlabeled mAb CL58 at the same dose due to the radiation effect of ^{131}I. Compared with ^{131}I-IgG, the same radioactive dose of ^{131}I-CL58 was more effective in slowing tumor growth, demonstrating that mAb CL58 can specifically deliver the radiation to the CEA-positive tumors. Several investigators have reported that dose fractionation could be less toxic and more efficacious than a single dose (*26, 27*). Therefore, further investigation of the direct comparison of a single dose with the fractionated administration of ^{131}I-CL58 may be helpful to optimize the therapeutic dose and select the better regimen for RIT of CEA-positive tumors.

In summary, this study has demonstrated the in vitro and in vivo tumor targeting properties of radioiodinated anti-CEA monoclonal antibody CL58 in CEA-positive colon cancer. ^{131}I-CL58 exhibited obvious therapeutic efficacy of tumor xenografts in the nude mouse model, which guaranteed its further investigation as a promising agent for radioimmunotherapy of CEA-positive tumors.

ACKNOWLEDGMENT

We thank Dr. Zhi Yang for his enthusiastic help with the γ imaging of animals, and also thank Ms. Hong Zhang for preparing mAb CL58. This work is supported, in part, by NSFC projects (30640067, 30870728, 30930030, 30900373, and 20820102035), an 863 project (2007AA02Z467) and grants from the Ministry of Science and Technology of China (2009ZX09103-733, 2009ZX09103-746 and 2009ZX09301-010).

Supporting Information Available: Body weight changes of nude mice receiving saline, unlabeled CL58, ^{131}I-mIgG (150 μCi) or different doses (150 μCi, 300 μCi and 450 μCi) of ^{131}I-CL58. Liver and kidney histological examinations of nude mice receiving 150 μCi, 300 μCi or 450 μCi of ^{131}I-CL58. This material is available free of charge via the Internet at http://pubs.acs.org.

LITERATURE CITED

(1) Lynch, B. M., Youlden, D., Fritschi, L., Newman, B., Pakenham, K. I., Leggett, B., Owen, N., and Aitken, J. F. (2008) Self-reported information on the diagnosis of colorectal cancer was

reliable but not necessarily valid. *J. Clin. Epidemiol. 61*, 498–504.

(2) Wang, X. L., Yuan, Y., Zhang, S. Z., Cai, S. R., Huang, Y. Q., Jiang, Q., and Zheng, S. (2006) Clinical and genetic characteristics of Chinese hereditary nonpolyposis colorectal cancer families. *World J. Gastroenterol. 12*, 4074–7.

(3) Lv, W., Zhang, C., and Hao, J. (2006) RNAi technology: a revolutionary tool for the colorectal cancer therapeutics. *World J. Gastroenterol. 12*, 4636–9.

(4) Martenson, J. A., Jr., Willett, C. G., Sargent, D. J., Mailliard, J. A., Donohue, J. H., Gunderson, L. L., Thomas, C. R., Jr., Fisher, B., Benson, A. B., 3rd, Myerson, R., and Goldberg, R. M. (2004) Phase III study of adjuvant chemotherapy and radiation therapy compared with chemotherapy alone in the surgical adjuvant treatment of colon cancer: results of intergroup protocol 0130. *J. Clin. Oncol. 22*, 3277–83.

(5) DeNardo, S. J., and Denardo, G. L. (2006) Targeted radionuclide therapy for solid tumors: an overview. *Int. J. Radiat. Oncol. Biol. Phys. 66*, S89–95.

(6) Sharkey, R. M., and Goldenberg, D. M. (2005) Perspectives on cancer therapy with radiolabeled monoclonal antibodies. *J. Nucl. Med. 46* (1), 115S–27S.

(7) Jhanwar, Y. S., and Divgi, C. (2005) Current status of therapy of solid tumors. *J. Nucl. Med. 46* (1), 141S–50S.

(8) Vose, J. M. (2004) Bexxar: novel radioimmunotherapy for the treatment of low-grade and transformed low-grade non-Hodgkin's lymphoma. *Oncologist 9*, 160–72.

(9) Gordon, L. I., Witzig, T., Molina, A., Czuczman, M., Emmanouilides, C., Joyce, R., Vo, K., Theuer, C., Pohlman, B., Bartlett, N., Wiseman, G., Darif, M., and White, C. (2004) Yttrium 90-labeled ibritumomab tiuxetan radioimmunotherapy produces high response rates and durable remissions in patients with previously treated B-cell lymphoma. *Clin. Lymphoma 5*, 98–101.

(10) Boswell, C. A., and Brechbiel, M. W. (2007) Development of radioimmunotherapeutic and diagnostic antibodies: an inside-out view. *Nucl. Med. Biol. 34*, 757–78.

(11) Sharkey, R. M., and Goldenberg, D. M. (2008) Use of antibodies and immunoconjugates for the therapy of more accessible cancers. *Adv. Drug Delivery Rev. 60*, 1407–20.

(12) Hammarstrom, S. (1999) The carcinoembryonic antigen (CEA) family: structures, suggested functions and expression in normal and malignant tissues. *Semin. Cancer Biol. 9*, 67–81.

(13) Goldenberg, D. M., Preston, D. F., Primus, F. J., and Hansen, H. J. (1974) Photoscan localization of GW-39 tumors in hamsters using radiolabeled anticarcinoembryonic antigen immunoglobulin G. *Cancer Res. 34*, 1–9.

(14) Behr, T. M., Liersch, T., Greiner-Bechert, L., Griesinger, F., Behe, M., Markus, P. M., Gratz, S., Angerstein, C., Brittinger, G., Becker, H., Goldenberg, D. M., and Becker, W. (2002) Radioimmunotherapy of small-volume disease of metastatic colorectal cancer. *Cancer 94*, 1373–81.

(15) Behr, T. M., Blumenthal, R. D., Memtsoudis, S., Sharkey, R. M., Gratz, S., Becker, W., and Goldenberg, D. M. (2000) Cure of metastatic human colonic cancer in mice with radiolabeled monoclonal antibody fragments. *Clin. Cancer Res. 6*, 4900–7.

(16) Liersch, T., Meller, J., Bittrich, M., Kulle, B., Becker, H., and Goldenberg, D. M. (2007) Update of carcinoembryonic antigen radioimmunotherapy with ^{131}I-labetuzumab after salvage resection of colorectal liver metastases: comparison of outcome to a contemporaneous control group. *Ann. Surg. Oncol. 14*, 2577–90.

(17) Yao, Y. F., Yang, Z., Li, Z. F., and Gu, J. (2007) Immunoscintigraphy of local recurrent rectal cancer with 99mTc-labeled anti-CEA monoclonal antibody CL58. *World J. Gastroenterol. 13*, 1841–6.

(18) Gu, J., Zhao, J., Li, Z., Yang, Z., Zhang, J., Gao, Z., Wang, Y., and Xu, G. (2003) Clinical application of radioimmunoguided surgery in colorectal cancer using ^{125}I-labeled carcinoembryonic antigen-specific monoclonal antibody submucosally. *Dis. Colon Rectum 46*, 1659–66.

(19) Shao, W., Zhao, S., Liu, Z., Zhang, J., Ma, S., Sato, J. D., Zhang, P., Tong, M., Han, J., Wang, Y., Bai, D., Wang, F., and Sun, L. (2006) Inhibition of human tumor xenograft growth in nude mice by a conjugate of monoclonal antibody LA22 to epidermal growth factor receptor with anti-tumor antibiotics mitomycin C. *Biochem. Biophys. Res. Commun. 349*, 816–24.

(20) Liu, Z., Yu, Z., He, W., Ma, S., Sun, L., and Wang, F. (2009) In-vitro internalization and in-vivo tumor uptake of anti-EGFR monoclonal antibody LA22 in A549 lung cancer cells and animal model. *Cancer Biother. Radiopharm. 24*, 15–24.

(21) Bertagnolli, M. M. (2005) Radioimmunotherapy for colorectal cancer. *Clin. Cancer Res. 11*, 4637–8.

(22) Fujimori, K., Covell, D. G., Fletcher, J. E., and Weinstein, J. N. (1990) A modeling analysis of monoclonal antibody percolation through tumors: a binding-site barrier. *J. Nucl. Med. 31*, 1191–8.

(23) Adams, G. P., Schier, R., McCall, A. M., Simmons, H. H., Horak, E. M., Alpaugh, R. K., Marks, J. D., and Weiner, L. M. (2001) High affinity restricts the localization and tumor penetration of single-chain fv antibody molecules. *Cancer Res. 61*, 4750–5.

(24) Cai, W., Wu, Y., Chen, K., Cao, Q., Tice, D. A., and Chen, X. (2006) In vitro and in vivo characterization of ^{64}Cu-labeled Abegrin, a humanized monoclonal antibody against integrin $\alpha_v\beta_3$. *Cancer Res. 66*, 9673–81.

(25) Veeravagu, A., Liu, Z., Niu, G., Chen, K., Jia, B., Cai, W., Jin, C., Hsu, A. R., Connolly, A. J., Tse, V., Wang, F., and Chen, X. (2008) Integrin $\alpha_v\beta_3$-targeted radioimmunotherapy of glioblastoma multiforme. *Clin. Cancer Res. 14*, 7330–9.

(26) Schlom, J., Molinolo, A., Simpson, J. F., Siler, K., Roselli, M., Hinkle, G., Houchens, D. P., and Colcher, D. (1990) Advantage of dose fractionation in monoclonal antibody-targeted radioimmunotherapy. *J. Natl. Cancer Inst. 82*, 763–71.

(27) Violet, J. A., Dearling, J. L., Green, A. J., Begent, R. H., and Pedley, R. B. (2008) Fractionated ^{131}I anti-CEA radioimmunotherapy: effects on xenograft tumour growth and haematological toxicity in mice. *Br. J. Cancer 99*, 632–8.

BC9003603

Luminescent Probes for Ultrasensitive Detection of Nucleic Acids

Lev N. Krasnoperov,[†] Salvatore A. E. Marras,*[,‡] Maxim Kozlov,[‡] Laura Wirpsza,[†,‡] and Arkady Mustaev[‡]

Department of Chemistry and Environmental Sciences, New Jersey Institute of Technology, 151 Tiernan Hall, University Heights, Newark, New Jersey 07102, and PHRI Center, New Jersey Medical School, Department of Microbiology and Molecular Genetics, University of Medicine and Dentistry of New Jersey, 225 Warren Street, Newark, New Jersey 07103.
Received September 14, 2009; Revised Manuscript Received November 11, 2009

Novel amino-reactive derivatives of lanthanide-based luminescent labels of enhanced brightness and metal retention were synthesized and used for the detection of cDNA oligonucleotides by molecular beacons. Time-resolved acquisition of the luminescent signal that occurs upon hybridization of the probe to the target enabled the avoidance of short-lived background fluorescence, markedly enhancing the sensitivity of detection, which was less than 1 pM. This value is about 50 to 100 times more sensitive than the level achieved with conventional fluorescence-based molecular beacons, and is 10 to 60 times more sensitive than previously reported for other lanthanide-based hybridization probes. These novel luminescent labels should significantly enhance the sensitivity of all type of nucleic acid hybridization probes, and could dramatically improve the detection limit of other biopolymers and small compounds that are used in a variety of biological applications.

INTRODUCTION

Some lanthanide chelates possess the unique spectral property known as luminescence (*1*−*9*). The principle features of luminescence are long-lived excited states (in the microsecond to millisecond range) and narrow emission spectra. Temporal and spectral gating enables unusually sensitive detection of lanthanide emission, even in samples that exhibit significant, short-lived autofluorescence (e.g., biological specimens or tissues). These compounds are therefore potentially useful in a wide variety of technical and biological tasks, such as tracing analysis, immunoanalysis, tissue-specific imaging, and detection of single molecules in living cells. Despite the benefits offered by this technique, its widespread use is impeded by the limited choice of instrumentation and the extremely high price of commercial probes. Yet, existing lanthanide-based probes could be improved to meet the requirements of new challenging applications.

Due to their very low absorbance ($\varepsilon < 1$ M^{-1} cm^{-1}), lanthanide ions have to be "pumped", which is achieved by tethering the lanthanide ion (through chelation) to an appropriate organic fluorophore (antenna). In such constructs, the energy absorbed by the antenna is transferred radiationlessly to the lanthanide, which finally emits the light. The chelating group also shields the lanthanide ion from the quenching effects of the medium, increasing the quantum yield of the probe. Development of new luminescent probes is challenging, since the transfer of energy from the antenna to the lanthanide is complex (a process not yet well understood) and very sensitive to subtle structural variations in the fluorophore. Another challenge is the necessity of combining three functional units within the same reporting probe: an antenna, a chelated lanthanide, and a cross-linking group (for attachment to the biomolecule of interest). This requires a complex synthetic strategy, eventually leading to compounds whose size often exceeds 1000 Da.

Two commonly used classes of lanthanide chelates are diethylenetriaminepentaacetic acid (DTPA) and tetraethylene-tetraminohexaacetic acid (TTHA). These chelates attached to 7-animo quinolones (*10*−*17*) are known as DTPA and/or TTHA-cs124 derivatives. The advantage of these classes of compounds is their high quantum yield, high solubility in water, and the possibility of introducing chemical modifications in the fluorophore to spectrally optimize the transfer of energy to the lanthanide and to enable the attachment of a cross-linking group. A number of methods for the conjugation of these chelates to biomolecules have been suggested. One of them is to use the dianhydride form of DTPA, in which one of the anhydrides modifies the amino group of the chromophore, while the other anhydride reacts with amino group of the biomolecule (*17*). Even though this approach is technically simple, it raises concerns about the side reactions (modification of other nucleophilic groups) due to the high reactivity of anhydrides. The second approach takes advantage of the conjugation of one of the DTPA anhydride groups with the cs124 moiety, followed by reaction of the remaining anhydride with the diamine. The unmodified amino group of the resulted adduct can then be converted to an amino-reactive isothiocyano or thiol-reactive groups (*12*). This mode of attachment of the cross-linking group weakens the retention of the lanthanide within the chelate by eliminating one ligating carboxylate, and it also reduces the brightness of the lanthanide (*14*) (30% to 1000%) due to the quenching effect of the additional coordinated water molecule. These factors restrict *in vivo* applications where high concentration of metal scavengers is an issue (e.g., intracellular imaging). Analogous derivatives of the fluorophore coumarine have been suggested and used in biophysical studies (*18*). However, compared to their quinolone counterparts, they are less bright and do not support terbium (Tb) luminescence.

To further perfect lanthanide probes, we now report the development of two novel approaches for the introduction of cross-linking groups into DTPA and/or TTHA-cs124 chelates by modification of the chromophore moiety. We demonstrate that the synthesized luminescent probes (Chart 1) are more resistant to EDTA challenge than previously described DTPA-cs124-based probes, and we demonstrate that these new probes are highly luminescent. These compounds were validated as

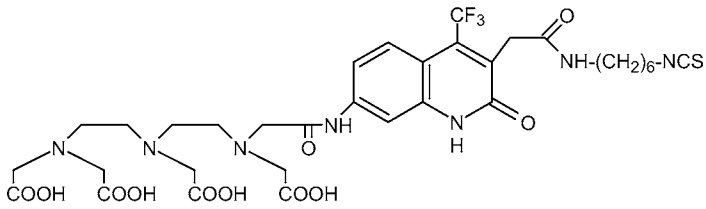
* To whom correspondence should be addressed: marrassa@umdnj.edu.

[†] New Jersey Institute of Technology.

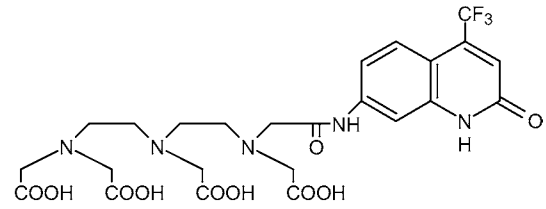
[‡] University of Medicine and Dentistry of New Jersey.

10.1021/bc900403n © 2010 American Chemical Society
Published on Web 01/19/2010

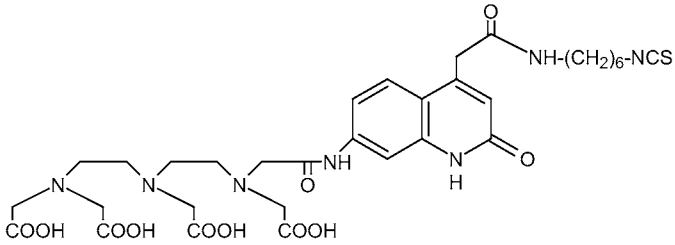
Chart 1. Structure of Reactive Luminescent Probes and Reference Compounds Used in This Study



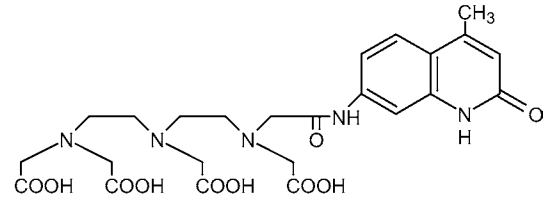
DTPA-cs124-CF_3-NCS (Probe 1)



DTPA-cs124-CF_3



DTPA-cs124-NCS (Probe 2)



DTPA-cs124

luminescent labels by including them in molecular beacon probes, which are widely used for DNA and RNA detection (*19*). The resulting sensitivity of these molecular beacons was between 0.5 and 1 pM, which is the most sensitive level of detection ever reported for nonamplified DNA detection systems.

EXPERIMENTAL PROCEDURES

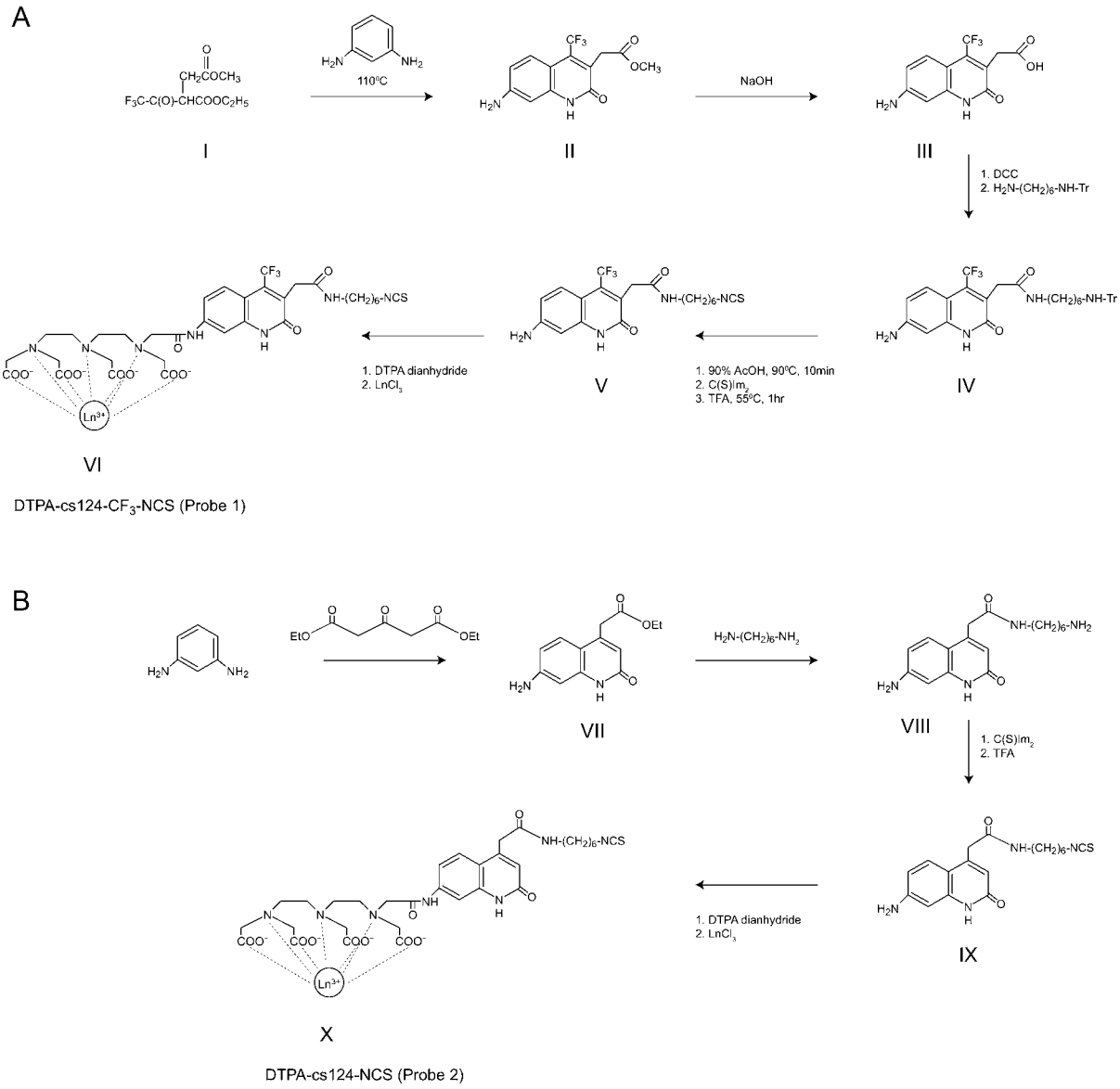
Synthesis. The following reagents were purchased from Aldrich: diethylenetriaminepentaacetic acid dianhydride (DTPA), triethylamine, 1,3-phenylenediamine, ethyl 4,4,4-trifluoroacetoacetate, ethylacetoacetate, 1,3-dicyclohexylcarbodiimide (DCC), ethylenedianime, *N*-trityl-1,6-diaminohexane, methylbromacetate, anhydrous dimethylformamide and dimethylsulfoxide, 1-butanol, ethylacetate, chloroform, acetonitrile, ethanol, sodium and potassium hydroxide, $ZnCl_2$, Na_2SO_4, Na_2CO_3, acetic acid, citric acid, thiocarbonyldiimadazole, $TbCl_3$, $EuCl_3$, $SmCl_3$ and $DyCl_3$, silica gel TLC plates on aluminum foil (200 μm layer thick with a fluorescent indicator). Only distilled and deionized water (18 MΩ cm^{-1}) was used. All experiments, including the preparation and use of lanthanide complexes, were performed either in glassware washed with mixed acid solution and rinsed with metal-free water or in metal-free plasticware purchased from Bio-Rad. All chemicals were the purest grade available.

Probe 1 (Scheme 1A). *1. 7-Amino-4-trifluoromethyl-3-carbomethoxymethyl-2(1H) quinolone (**II**) (cs124CF_3−CH_2-$COOCH_3$).* 4,4,4-Trifluoroacetoacetate (2.2 mL, 15 mmol) and KOH (0.86 g, 15 mmol) were mixed in 7 mL of dimethylformamide and stirred at 40 °C until dissolved. To this mixture, 1.5 mL of methylbromoacetate was added and the solution was incubated overnight at room temperature. Three hundred milligrams (5.2 mmol) of KOH was then added, and incubation continued at 60 °C for 1 h. This mixture was diluted by the addition of 20 mL of water and was then extracted with chloroform. The organic layer was collected, dried over anhydrous sodium sulfate, and then evaporated in vacuo, first at 30 °C, and then at 70 °C for 30 min. The residue (1.9 g, product **I**) was dissolved in 3.5 mL of DMSO, and then 0.76 g (7 mmol) of 1,3-phenylenediamine was added, followed by incubation at 110 °C for 6 h. Under these conditions, four fluorescent products were detected by thin layer chromatography in ethyl acetate as developing solvent: $R_f = 0.90$ (green−blue fluorescence); $R_f = 0.45$ (blue fluorescence); $R_f = 0.30$ (blue fluorescence); and $R_f = 0.03$ (green−blue fluorescence). This mixture was diluted with 30 mL of 0.05 M aqueous NaOH and extracted with ether (2 × 40 mL). The aqueous layer was separated and treated as described below (section 2). The organic layer was extracted with 1 vol 0.1 M citric acid, and then collected, dried over anhydrous sodium sulfate, and evaporated in vacuo. The residue was subjected to silica gel chromatography on a 40 mL column, using a hexane/acetone mixture (3:1) as eluent. Fractions corresponding to the products migrating with $R_f = 0.45$ (product **II**) were collected and evaporated to dryness. The residue was then washed with chloroform and dried. Yield ∼ 130 mg. UV: $\lambda_{max} = 365$ nm ($\varepsilon = 14\,300$ M^{-1} cm^{-1}), $\lambda_{min} = 295$ nm ($\varepsilon = 2800$ M^{-1} cm^{-1}). ^{1}H NMR chemical shifts (d) in DMF were as follows: 3.65 (3H, methyl), 3.94 (q, 2H, 3-methylene, $J = 3.6$), 6.24 (broad, 7 amine), 6.72 (m, 1H, 6H), 6.72 (m, 1H, 8H), 7.48 (1H, 5H), and 11.9 (broad, amide).

*2. 7-Amino-4-trifluoromethyl-3-carboxy-2(1H) quinolone (**III**) (cs124CF_3-CH_2COOH).* One milliliter of 1 M aqueous NaOH was added to 100 mg of product **II** dissolved in 2 mL dioxane. After 4 h incubation at 50 °C, the mixture was diluted by the addition of 15 mL water and extracted with ether. The product (**III**) was precipitated from the aqueous phase by the addition of citric acid to pH 3−3.5, collected by centrifugation, washed a few times with water until neutral reaction, and dried in vacuo. Yield ∼ 70 mg.

The aqueous phase obtained after ether extraction (see previous section), containing product **III**, was acidified by the addition of citric acid to pH 3−3.5; the precipitate was collected, washed a few times with water, dried, and then combined with the above. Recrystallization from ethyl acetate resulted in the isolation of pure product **III** (total yield ∼ 200 mg). ^{1}H NMR chemical shifts (*d*) in DMF were as follows: 3.93 (2H, 4

Scheme 1. Schemes for the Synthesis of Probe 1 (A) and Probe 2 (B)



methylene), 6.19 (2H broad, 7 amine), 6.71 (1H, 6H), 6.71 (1H, 8H), 7.48 (1H, 5H), 11.85 (broad, amide), and 12.75 (broad, carboxyl).

3. cs124CF$_3$-CH$_2$C(O)-NH(CH$_2$)$_6$NH-Tr (***IV***). 100 mg (∼0.3 mmol) of product **III** were dissolved in 8 mL of THF and supplemented with 210 mg (1 mmol) of DCC. After 1 h incubation, thin layer chromatographic analysis in ethyl acetate/ethanol (10:1) revealed a single product ($R_f = 0.80$) with intense blue fluorescence. 450 μmol of *N*-trityl-1,6-diaminohexane were added and incubation continued for another 30 min at 20 °C. Thin layer chromatography in ethylacetate/ethanol (10:1) revealed the main reaction product ($R_f = 0.70$). This mixture was diluted with 20 mL of 0.1 M aqueous Na_2CO_3 and extracted with an equal volume of chloroform. The organic phase was then collected and rinsed with 1 volume 0.2 M citric acid, dried over anhydrous sodium sulfate, and the solvent removed by evaporation under reduced pressure. The product was purified by silica gel chromatography, using ethylacetate/ethanol (10:1) mixture as eluent. Yield ∼ 160 mg. ^{1}H NMR chemical shifts (*d*) in DMF were as follows: 1.45 (m, 8H), 1.65 (m, 2H), 1.78 (m, 2H), 2.03 (q, 2H, $J = 7.25$), 2.41 (t, 1H, $J = 7.2$), 3.08 (q, 2H, $J = 7.2$), 3.82 (q, 2H, 4CH$_2$-, $J = 4.0$), 6.14 (s, 2H, broad, 7 amine), 6.7 (1H, 8H), 6.7 (1H, 6H), 7.18 (t, 3H, p-ArH, $J =$ 7.2), 7.30 (t, 6H, m-ArH, $J = 7.4$), 7.48 (d, 6H, o-ArH, $J =$ 7.4), 7.48 (1H, 5H), and 11.75 (1H, broad, amide).

4. cs124CF$_3$-CH$_2$C(O)-NH(CH$_2$)$_6$N═C═S (***V***). 140 mg of compound **IV** were dissolved in 2 mL of 90% acetic acid and incubated at 90 °C for 15 min. After evaporation in vacuo, the resulting residue was suspended in water and extracted with ether to remove triphenylcarbinol. The aqueous phase was then evaporated to dryness. The resulting residue was dissolved in 2 mL of methanol, and 80 mg of thiocarbonyldiimadazole was then slowly added to this solution under rigorous agitation. After 10 min incubation at room temperature, the mixture was supplemented with 100 μL trifluoroacetic acid and kept at 50 °C. Thin layer chromatographic analysis in ethylacetate/ethanol (12:1) revealed nearly quantitative conversion of the original compound ($R_f = 0.05$) to an isothiocyanate ($R_f = 0.40$). This product was purified by column chromatography using the same eluent. Yield ∼ 60 mg. ^{1}H NMR chemical shifts (*d*) in DMF were as follows: 1.35 (m, 4H), 1.46 (m, 2H), 1.65 (m, 2H), 3.13 (m, 2H, $J = 7.25$), 3.69 (t, 1H, $J = 7.2$), 3.08 (q, 2H, $J =$ 7.2), 3.82 (q, 2H, 3CH$_2$-, $J = 3.7$), 6.14 (s, 2H, broad, 7 amine), 6.7 (1H, 8H), 6.7 (1H, 6H), 7.48 (m, 1H, 5H), 7.76 (t, 1H, $J =$ 5.5), and 11.77 (1H, broad, amide).

5. Lanthanide Complexes of DTPA-cs124-CF_3-NCS (probe 1). Thirty milligrams (0.1 mmol) of compound **V** were added to a solution of 80 mg (0.3 mmol) of DTPA dianhydride in 0.8 mL of DMSO. After incubation (45 min at 50 °C), the mixture was supplemented with 10 mL of ether, and the resulting precipitate was spun down, washed with ether, air-dried, dissolved in 1 mL of DMF, and mixed with 0.3 mL of water. After incubation for 10 min at 45 °C, the mixture was diluted with 5 mL of water and extracted with 40 mL of butanol. The organic phase was separated and divided into four equal parts. Each portion was mixed with 0.3 mL of a 0.1 M solution of a lanthanide trichloride (Tb^{3+}, europium (Eu^{3+}), dysprosium (Dy^{3+}), and samarium (Sm^{3+})). After vigorous agitation, the organic phase was collected and concentrated by co-evaporation with water in vacuo at 30 °C. Analytical thin layer chromatography, using an acetonitrile/water system (3:1) as the developing solvent, revealed two main Ln^{3+} products ($R_f = 0.25$ and 0.50). The products with $R_f = 0.50$ (desired compound) were purified using preparative thin layer chromatography under the same conditions. The fluorescent material was eluted with 50% aqueous ethanol and was recovered as a colorless powder after evaporation in vacuo. UV: $\lambda_{max} = 347$ nm ($\varepsilon = 14\,800$ M^{-1} cm^{-1}), $\lambda_{min} = 270$ nm ($\varepsilon = 4700$ M^{-1} cm^{-1}). MS: Eu^{3+}DTPA-cs124-CF_3-CH_2C (O)-NH$(CH_2)_6$N═C═S (-H^+) 950.1 (found), 950.0 (calculated). Ln^{3+} complexes of DTPA-cs124-CF_3 were obtained using the same protocol.

Probe 2 (Scheme 1B). *1. 7-Amino-4-carboethoxymethyl-2(1H) quinolone (**VII**).* A suspension of 1.36 g (10 mmol) of $ZnCl_2$ in 5 mL of DMSO was supplemented with 1.08 g (10 mmol) of 1,3-phelylenediamine and 2.02 g (10 mmol) of diethyl-1,3-acetonedicarboxylate. The mixture was kept at 95 to 100 °C for 24 h. Thin layer chromatography in chloroform/ethanol (10:1) detected one main fluorescent product ($R_f = 0.35$). This mixture was diluted with 8 mL of ethanol, poured into 150 mL of ice-cold 0.1 M citric acid, and left for 3 h at 4 °C. The residue was filtered and successively washed with water (2 × 10 mL), and with hot acetonitrile (2 × 5 mL), and then dried in vacuo. Yield ~ 1.4 g (60%). ^{1}H NMR chemical shifts (*d*) in DMSO were as follows: 1.17 (t, 3H, -OCH_2CH_3, $J = 7.2$), 3.76 (s, 2H, 3-methylene), 4.06 (q, 2H, -OCH_2CH_3, $J = 7.2$), 5.81 (2H, broad, 7 amino), 6.01 (s, 1H, 3H), 6.37 (d, 1H, 8H, $J = 2.4$), 6.43 (dd, 1H, 6H, $J_1 = 7.2$, $J_2 = 2.4$), 7.25 (d, 1H, 5H, $J = 7.2$), and 11.28 (1H, broad, amide).

*2. 7-Amino-4-carboxamido(6-aminohexyl)methyl-2(1H) quinolone (**VIII**).* Premelted 1,6-diaminohexane (2 g, 17 mmol) was mixed with 7-amino-4-carboethoxymethyl-2(1*H*) quinolone (0.5 g, 2 mmol). After incubation (15 h, 90 °C), the mixture was poured into 30 mL of water. The precipitate was washed with water (3 × 30 mL) and ethyl acetate (3 × 20 mL), and then stirred with hot methanol (50 mL), filtered, and the filtrate evaporated to dryness in vacuo. The product appeared as light-brown crystals. Yield ~ 0.5 g. ^{1}H NMR chemical shifts (*d*) in DMSO were as follows: 1.2−1.4 (m, 10H), 3.04 (q, 2H, α-CH_2, $J = 7.2$), 3.49 (s, 2H, 4-methylene), 5.75 (2H, broad, 7 amino), 5.98 (s, 1H, 3H), 6.36 (d, 1H, 8H, $J = 2.4$), 6.43 (dd, 1H, 6H, $J_1 = 7.2$, $J_2 = 2.4$), 7.38 (d, 1H, 5H, $J = 7.2$), 8.07 (t, 1H, amide, $J = 7.2$), and 11.3 (1H, broad, amide quinolone).

*3. 7-Amino-4-carboxamido (6-isothiocyanohexyl) methyl-2 (1H) quinolone (**IX**).* 44 mg (0.22 mmol) of 1,1′-thiocarbonyldiimidazole was added to a solution of 63 mg (0.2 mmol) of product **VIII** dissolved in 4 mL methanol. After 5 min, this mixture was supplemented with 10 μL of TFA and incubated for 40 min at 50 °C. The solvent was removed by evaporation in vacuo, and the product was then washed with water and purified by column chromatography on silica gel using a chloroform/ethanol mixture (4:1) as eluent. Yield ~ 40 mg. ^{1}H NMR chemical shifts (*d*) in DMSO were as follows: 1.2−1.5 (m, 6H), 1.60 (m, 2H, e-CH_2, $J = 7.2$), 3.04 (m, 2H, α-CH_2, $J = 7.2$), 3.49 (s, 2H, 4-methylene), 3.64 (t, 2H, ζ-CH_2, $J = 7.2$), 5.75 (s, 2H, broad, 7 amine), 5.98 (s, 1H, 3H), 6.36 (d, 1H, 8H, $J = 2.4$), 6.43 (dd, 1H, 6H, $J_1 = 7.2$, $J_2 = 2.4$), 7.38 (d, 1H, 5H, $J = 7.2$), 8.07 (t, 1H, amide, $J = 7.2$), and 11.20 (1H, broad, amide quinolone).

4. Lanthanide Complexes of DTPA-cs124 and DTPA-cs124-NCS (probe 2). These products were obtained and purified essentially as described for the synthesis of analogous probe 1 compounds in section 5 above; however, the incubation time of the corresponding isothiocyano compound (**IX**) with DTPA dianhydride was 15 min at 20 °C. UV: $\lambda_{max} = 341$ nm ($\varepsilon = 18\,900$ M^{-1} cm^{-1}), $\lambda_{min} = 308$ nm ($\varepsilon = 10\,000$ M^{-1} cm^{-1}). MS: Tb-DTPA-cs124-NCS (−1) 888.3 (found), 888.0 (calcd); and Eu-DTPA-cs124-NCS (−1) 882.3 (found), 882.0 (calcd).

Synthesis of Luminescent Hybridization Probes. A 10 μL water solution containing 3 to 7 nmol of an oligonucleotide (5′ amino - CTTCGTCCACAAACACAACTCCTGAAG - 3′ Black-hole Quencher 2), prepared according to protocols described previously (*20*), was supplemented with 5 μL of $Na_2B_4O_7$ (pH 10.0), and 15 μL of a 10 to 20 mM aqueous solution of luminescent probe 1 or probe 2. After incubation for 3.5 h at 56 °C, the probe conjugated oligonucleotide was precipitated by the addition of 200 μL of ethanol, and then collected by centrifugation after cooling at −80 °C for 15 min. This procedure was repeated 3 to 4 times. Finally, the residue was dissolved in water and purified by HPLC chromatography, as described in Supporting Information. Yield 40−80%.

Physical Methods. Excitation and emission fluorescence spectra in a steady-state mode were recorded using a QuantaMaster 1 (Photon Technology International) digital fluorometer at ambient temperature. Time-resolved and gated luminescence measurements were performed using a home-built experimental setup (Supporting Information Figure S1). A Suprasil fluorescence cell filled with sample solutions was irradiated by pulsed (ca. 15 ns) UV light from an excimer laser (351 nm, XeF). Before passing through the cell, the laser beam was formed by a rectangular aperture 0.5 cm × 1.0 cm (width × height). Fluorescence from the cell collected at an angle of 90 degrees was focused onto the entrance slit of a grating spectrograph (SpectraPro-300i, Acton Research Corporation, diffraction grating 150 grooves/mm blazed at 500 nm) using a fused silica lens with a focal distance of 2.5 cm. The spectrograph was equipped with a gated intensified CCD Camera (ICCD-MAX, Princeton Instruments) to record transient spectra. A slit width of 0.5 mm was used for time-resolved luminescence measurements, which corresponds to a spectral resolution of 5 nm. Time-gated spectra were recorded with a spectral resolution of 0.3 nm (a slit width of 0.01 mm in combination with a pixel size on the ICCD camera of 0.026 mm). ICCD gating, with a delay after the laser pulse, was used to determine the temporal behavior of the transient fluorescence. For measurements of luminescence lifetimes, the light was diverted to a photomultiplier tube mounted on the exit slit of the spectrograph. The PMT signal was preamplified and averaged, using a digital storage oscilloscope (LeCroy 9310A). High-resolution spectra were recorded with a time delay of 1 μs and a gate width of 1 ms for probe 1 chelated with Eu and Sm and for probe 2 chelated with Tb and Dy.

Steady-State Fluorescence Measurements. Hybridization experiments of the lanthanide-based molecular beacon with its complementary target DNA (5′ TTAGGAGTTGTGTTTGTG-GACTT 3′) were performed in a measuring cell (150 μL) in a hybridization buffer containing 50 mM KCl, 3 mM $MgCl_2$, and 10 mM Tris-HCl (pH 8.0). The concentrations of the molecular beacon and the cDNA oligonucleotide (target) were 300 nM

and 1000 nM, respectively. Water-based or deuterium oxide-based solutions were used.

Time-Resolved Luminescence Measurements. *Protocol A.* Ten microliters of various concentrations (0−100 nM) of target DNA (see previous section) was added to 3 mL of a 1 nM solution of molecular beacons in hybridization buffer (see previous section), and was then transferred to a measuring cell. The luminescence of the sample was measured at different time intervals.

Protocol B. Different concentrations (0−3 nM) of DNA target were added to 3 mL of 10 pM molecular beacon hybridization buffer in a glass tube, and this solution was left for 3 days at room temperature. The solution was then transferred to the measuring cell. The glass tube was washed with 1 mL of the same hybridization buffer containing 30% ethanol, and this solution was also transferred to the measuring cell. The resulting luminescent signal was then measured as described above.

RESULTS

Synthesis and Properties of Cross-Linkable Lanthanide Chelates. The structure of the synthesized luminescent lanthanide probes is shown schematically in Chart 1. These probes are derivatives of previously described cs124 and cs124-CF_3 fluorophores (*10*−*17*). For the synthesis of these compounds, we used an approach based on the condensation of 1,3-phenylenediamine with an ester of an acetoacetic acid derivative. Scheme 1A presents the synthetic strategy developed for probe 1. Alkylation of trifluoroacetoacetate by methylbromoacetate in the presence of a proton acceptor produced trifluoroacetylmethylethylsuccinate (compound **I**). Reaction of the latter with 1,3-phenylenediamine resulted in fluorescent quinolone derivative **II**, which was converted to the corresponding carboxyl derivative **III** by saponification. We intended to introduce the amino function in this compound by treatment with DCC in the presence of 4-nitrophenol and subsequent reaction of nitrophenyl ester with aliphatic diamine. Surprisingly, incubation with DCC and 4-nitrophenol yielded a product that did not contain 4-nitrophenol. The ultraviolet spectrum of this product differed significantly from that of compound **III**. In aqueous medium, this product converted into **III** with a half-time of about 30 min at 20 °C. Incubation of this product with aliphatic amines resulted in acylation of the amino groups. Most likely, this reactive intermediate emerged as a result of intramolecular acylation of the amide oxygen of **III** by activated carboxylate. Incubation of this compound with monotritylated 1,6-diaminohexane yielded the desired compound **IV**. After deprotection, the resulting aminoalkyl derivative was converted to isothiocyanate (compound **V**) by treatment with thiocarbonyldiimidazole and trifluoroacetic acid. Under these conditions, the aromatic amino group of the compound remains intact. Acylation of compound **V** by DTPA anhydride in anhydrous medium, followed by hydrolysis of the second anhydride group, resulted in compound **VI** (probe 1), which was separated from the excess of DTPA by partitioning in butanol/water. Further addition of aqueous lanthanide trichloride to the butanol extract led to complexes between the lanthanides and the probes. The lanthanide complexes were analyzed and purified by thin layer chromatography in acetonitrile:water mixtures that proved to be highly efficient (see Figure 1).

For the synthesis of probe 2, we developed the strategy shown in Scheme 1B. The first step of this synthesis was based on a published protocol (*13*) that includes incubation of *m*-phenylenediamine with diethyl 1,3-acetonedicarboxylate at high temperature to yield quinolone derivative **VII**. Compared to published protocols, a dramatic improvement in the yield of the final product (from <1% to ca. 60%) was achieved by using a mild Lewis acid ($ZnCl_2$) as a catalyst, which allowed lowering

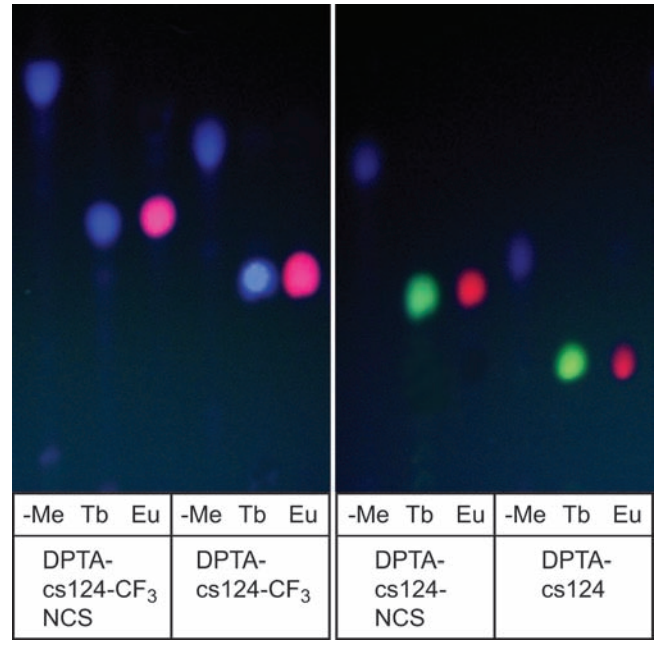


Figure 1. Image recorded by ultraviolet excitation of ligand antenna compounds (−Me) and their lanthanide complexes (Tb and Eu), after separation by thin layer chromatography.

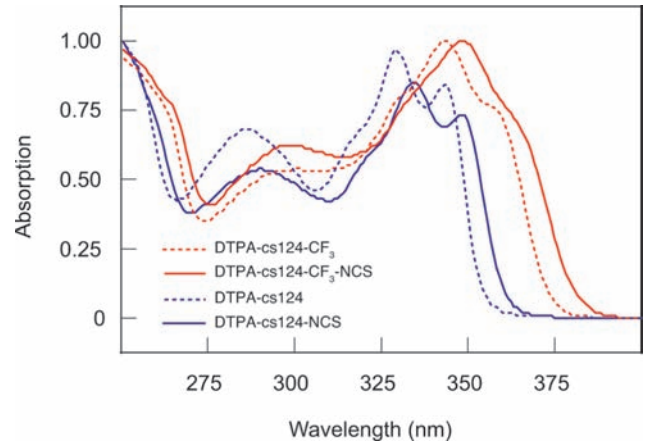


Figure 2. UV absorption spectra of synthesized reactive luminescent probes and reference compounds used in this study.

of the reaction temperature. Reaction of this product with a diamine (added in a few-fold excess to avoid cross-linked products) at high temperature resulted in the formation of aminoalkyl derivative **VIII**, with nearly quantitative yield. Cross-linkable DTPA derivative (**X**, probe 2) was obtained in the same manner as probe 1.

Absorption Spectra. Absorption spectra of the synthesized cs124 and cs124-CF_3 derivatives are shown in Figure 2. They were nearly identical to published spectra for analogous compounds (*10*−*17*). A small red shift of 6 nm was observed for probe 1 (comparing to the reference compound cs124-CF_3) and probe 2 (comparing to the reference compound cs124). The molar extinction coefficients for DTPA-cs124 and DTPA-cs124-CF_3 were determined by direct comparison of the absorption spectra of the original compounds (ε_{max} = 18 900 M^{-1} cm^{-1} at 341 nm for cs124 and ε_{max} = 14 500 M^{-1} cm^{-1} at 360 nm for cs124-CF_3) to their acylated derivatives, which was achieved by monitoring spectral changes in the reaction mixture during the course of the reaction (see Supporting Information Figures S2A and S2B). The presence of isosbestic points in both cases was indicative of the conversion of the original compounds to

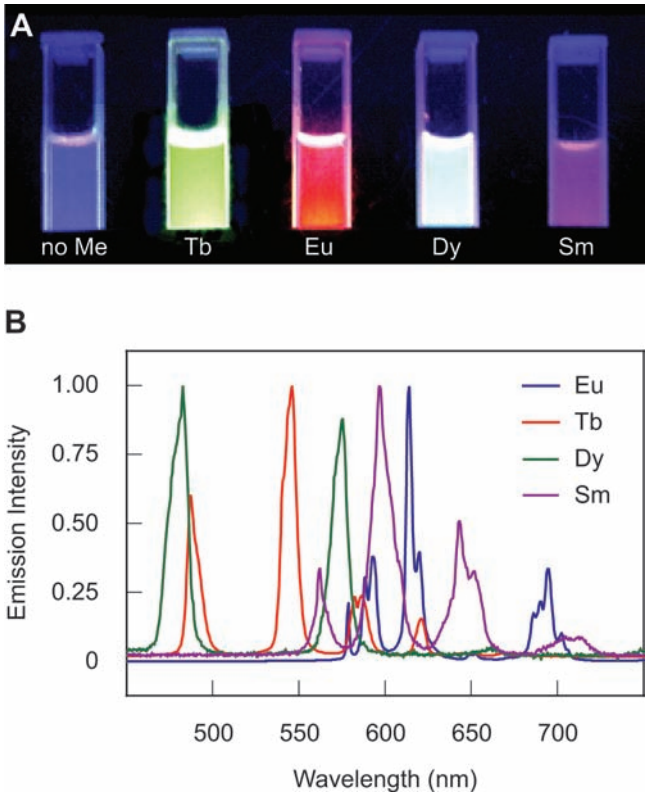


Figure 3. (A) Luminescence of 50 μM solutions of probe 2 (no Me) and its lanthanide complexes: terbium (Tb), europium (Eu), dysprosium (Dy), samarium (Sm); in heavy water, excited at 308 nm. (B) Normalized time-resolved emission of probe 1 Eu and Sm chelates and of probe 2 Tb and Dy chelates.

a single reaction product. Indeed, chromatographic analysis confirmed the formation of single acylation products in both cases. Thus, values of $\varepsilon_{max} = 18\ 200\ M^{-1}\ cm^{-1}$ at 328 nm and $\varepsilon_{max} = 14\ 800\ M^{-1}\ cm^{-1}$ at 341 nm were obtained for DTPA-acylated derivatives of cs124 and cs124-CF_3, respectively. Essentially the same values were obtained for probes 1 and 2 (data not shown). A significant difference in the absorption spectra of probes 1 and 2 (18 nm) allows selective excitation by common sources (at 351 nm by excimer XeF laser for probe 2, and at 365 nm by mercury UV lamp for probe 2). Such selective excitation is important for applications relying on simultaneous monitoring of two independent processes in the same sample.

Emission Spectroscopy of Lanthanide Complexes. The ease of observing the luminescence of these lanthanide complexes is illustrated in Figure 3A for probe 2. All complexes displayed the narrow emission spectrum typical of luminescent lanthanide chelates (Figure 3B). Table 1 shows the luminescence intensities of the synthesized reactive lanthanide chelates, as well as for the intensities obtained for the reference compounds, cs124 and cs124-CF_3 described earlier (*11*, *17*). The process of antenna-mediated lanthanide emission includes the transfer of energy from the antenna fluorophore to the coordinated metal and the subsequent emission of photons by the excited lanthanide. The first step is the most crucial part of the process, because even slight modifications of chromophore-antenna structure dramatically affect lanthanide luminescence (*13*). In this work, we explored a synthetic approach that allows the introduction of a cross-linking group in position 3 (probe 1) or position 4 (probe 2) of quinolone-based antenna fluorophores. Comparison with reference fluorophores (with a non-substituted quinolone at position 3 or a methyl-substituted quinolone at position 4) demonstrates that the structural modification affected the brightness of the lanthanide chelates in different ways. For cs124-CF_3-based antennae, a significant decrease in brightness was observed for Tb^{3+} chelates (ca. 20-fold) and for Dy^{3+} chelates (>30-fold), while the emission of Eu^{3+} and Sm^{3+} chelates was not significantly affected. A similar effect of substitution was previously observed for the analogous Tb-cs124 chelates (*13*). In the case of probe 2, the substitution of a cross-linking group for a methyl group in position 4 did not significantly alter the brightness of all lanthanide complexes. Moreover, a detectable increase in the brightness for Eu (1.5-fold), Dy (1.7-fold), and Sm (1.6-fold) complexes was observed. This is consistent with the results (*13*) previously obtained for the analogous Tb and Eu derivatives of cs124 containing a carboxymethyl group at position 4. Surprisingly, significant luminescence was detected for Tb^{3+}-DTPA-cs124-CF_3 chelates, which were previously reported to be nonluminescent. We do not know the reason for this discrepancy. As seen in Table 1, comparing the emission of probe 1 and probe 2, probe 1 gives brighter complexes with Eu and Sm, while probe 2 is optimal for Tb and Dy. Time-resolved measurements indicated that there is a single-exponential decay mode for the luminescent signal from probe 1 chelates and from probe 2 chelates (not shown), which is indicative of the homogeneity of the complexes.

Effect of Heavy Water on Lanthanide Chelate Emission. The quantum yield of the excited lanthanide ion (defined as the probability of the excited state emitting a photon) in the antenna−chelate complex depends strongly on the number of coordinated water molecules (*21*), due to nonradiative dissipation of the energy of the excited state through the vibration of O−H bonds. This process does not occur with heavy water due to the different frequency of O−D bond vibration. This effect accounts for the enhanced brightness of lanthanide luminescence in heavy water. Indeed, as seen from Table 1 for DTPA ligands in D_2O, the brightness of the Tb^{3+} chelates was 1.3- to 1.5-fold higher than in H_2O-based solutions. As expected, the effect was more pronounced for DTPA-Eu^{3+} chelates (~3- to 3.8-fold), as well as for Dy^{3+} and Sm^{3+} complexes (~ 4- to 6-fold). The number of coordinated water molecules in Tb^{3+} and Eu^{3+} complexes can be calculated from the luminescence lifetime in water and in deuterium oxide-based solutions (*22*). For our probes, the number of coordinated water molecules was close to unity (see Table 1), which is in agreement with the results reported for similar compounds. The same is expected for Dy^{3+} and Sm^{3+} chelates, since they have analogous coordination chemistry.

Effect of EDTA on the Rate of Lanthanide Chelate Decay. The ability to retain the chelated metal ion is an important characteristic of lanthanide probes. This property is especially crucial for intracellular applications, due to the abundance of metal scavengers in living cells (such as free amino acids, amino acid residues in proteins, nucleoside triphosphates, nucleic acids, etc.). To this end, we investigated the decay rates of the lanthanide chelates used in our probes and in those probes described previously (*15*). Reaction of cs124 with excess of DTPA dianhydride yields a primary adduct possessing a preserved acylation function. In previous studies, this function was used to attach the cross-linking group to the chelate construct by subsequent treatment with diamine, which yielded aminoalkylamide derivatives whose amino group was converted to amine reactive isothiocyanates. This modification of the chelating group is likely to weaken the retention of metal. To this end, as a model, we synthesized analogous, but nonreactive, compounds containing a butylamide group. In accordance with expectations, the lanthanide complexes were about 10 times less stable (comparing to those possessing nonmodified chelating groups) when challenged with EDTA (see Supporting Information Figure S3).

Table 1. Emission and Relative Brightness of Lanthanide Chelates under Various Conditions

compound	emission in H_2O, counts	emission in D_2O, counts	relative brightness D_2O/H_2O	relative brightness in H_2O (%)	life time in H_2O (ms)	life time in D_2O (ms)	number of coordinated H_2O molecules
			Dysprosium (Dy^{3+}) Complexes (emission at 482 nm)				
DTPA-cs124-CF_3[b]	555	917	1.75	20	0.0023	0.0045	
DTPA-cs124-CF_3-NCS (probe 1)	-	-	-	-	-	-	
DTPA-cs124[b]	2720	10522	3.87	100	0.011	0.033	-
DTPA-cs124-NCS (probe 2)	4550	13000	2.86	167	0.009	0.027	-
			Terbium (Tb^{3+}) Complexes (emission at 545 nm)				
DTPA-cs124-CF_3[b]	12,200	14170	1.16	7.2	0.2	0.2	-
DTPA-cs124-CF_3-NCS (probe 1)	833	790	0.95	0.5	-	-	-
DTPA-cs124[b]	169000	260000	1.53	100	1.5 (1.55[a])	2.3 (2.63[a])	0.97 (1.1[a])
DTPA-cs124-NCS (probe 2)	137000	190000	1.40	81	1.2	1.7	1.03
			Samarium (Sm^{3+}) Complexes (emission at 598 nm)				
DTPA-cs124-CF_3[b]	192	764	3.98	168	0.0080	0.036	
DTPA-cs124-CF_3-NCS (probe 1)	230	900	3.91	200	0.0092	0.042	
DTPA-cs124[b]	114	513	4.50	100	0.0082	0.023	-
DTPA-cs124-NCS (probe 2)	180	1010	6.60	158	0.0082	0.034	-
			Europium (Eu^{3+}) Complexes (emission at 615 nm)				
DTPA-cs124-CF_3[b]	10350	41000	3.96	205	0.5	1.9	1.54
DTPA-cs124-CF_3-NCS (probe 1)	9450	35000	3.70	187	0.5	1.7	1.47
DTPA-cs124[b]	5050	22000	4.36	100	0.6 (0.62[a])	1.6 (2.42[a])	1.1 (1.26[a])
DTPA-cs124-NCS (probe 2)	7300	25000	3.42	145	0.6	2.0	1.19

[a] Determined in ref *13*. [b] Model compounds.

Chemical Reactivity of Synthesized Luminescent Probes. The chemical reactivity of the synthesized probes was evaluated first in reactions with aliphatic diamines and with cysteine, because the resulting reaction products (corresponding thioureas and thiocarbamates) can easily be identified by thin layer chromatography, due to the strong retardation effect. Under the incubation conditions that were used, a nearly quantitative conversion of the probes to the corresponding reaction products was observed, either immediately upon mixing (with 0.1 M cysteine) or after 2 to 3 h at 56 °C (with 10 mM diamine), suggesting that the isothiocyanate groups in the probes survived purification. At the same time, nonreactive control chelates (Ln^{3+}-DTPA-cs124 and Ln^{3+}-DTPA-cs124-CF_3) did not change their mobility after incubation under the same conditions (see Supporting Information).

Synthesis of Luminescent-Based Molecular Beacon Probes. With conventional strategies, the nucleic acids are first coupled with metal-free probe derivatives, followed by the addition of a lanthanide to the probe conjugated products, which is not convenient. To this end, we obtained metal-chelated, ready-to-use luminescent tags. This was especially important for probe 1, since a metal-free compound is not stable.

For the attachment of the luminescent tags to the oligonucleotides, we obtained aliphatic isothiocyanate-reactive probes, as opposed to their more reactive aromatic counterparts that are typically used for modification of biopolymers. Partially, this choice was due to a synthetic strategy that required survival of the reactive cross-linking group during acylation by DTPA dianhydride (see Scheme 1) and during subsequent purification. Also, a closely positioned aromatic moiety of isothiocyanate could affect the energy transferred to the lanthanide by the occurrence of stacking interactions with antenna fluorophores. Under optimized reaction conditions, we were able to achieve a 70% coupling efficiency with amine-containing oligonucleotide constructs. The resulting hybridization probes were purified by ethanol precipitation, followed by size-exclusion chromatography and HPLC. Comparison of the absorption spectra of 3′ BHQ-2 labeled oligonucleotides, with and without probe 2 attached to their 5′ terminal (Figure 4B), revealed additional absorption in the range 300−350 nm due to the presence of the luminescent label. The survival of the lanthanide chelates during all of these operations is indicative of the extraordinarily high chemical stability of these probes.

Steady-State Fluorescence Measurements of Molecular Beacon Probes. Molecular beacon probes are nucleic acid hybridization probes that fluoresce when they bind to a target DNA or RNA sequence (*19*). When they are free in solution and not hybridized to a target nucleic acid, they remain nonfluorescent. Figure 4A illustrates the principle of molecular beacon probes. The probes are single-stranded oligonucleotides that form a stem-and-loop structure. The loop portion of the oligonucleotide is a probe sequence that is complementary to a target sequence in a nucleic acid. The probe sequence is embedded between two "arm" sequences, which are complementary to each other. Under assay conditions, the arms bind to each other to form a double-helical stem hybrid that encloses the probe sequence, forming a hairpin structure. A reporter fluorophore is attached to one end of the oligonucleotide and a nonfluorescent quencher is attached to the other end of the oligonucleotide. The stem hybrid brings the fluorophore and quencher in close proximity, allowing energy from the fluorophore to be transferred directly to the quencher through contact quenching. At assay temperatures, when the probe encounters a target nucleic acid, it forms a relatively rigid probe−target hybrid that is longer and more stable than the stem hybrid. Consequently, the molecular beacon probe undergoes a conformational reorganization that forces the stem hybrid to dissociate, and results in the separation of the fluorophore and the quencher, restoring fluorescence.

Currently, most molecular beacon probes are labeled with organic fluorophore labels (*23*). To increase the sensitivity of detection, we explored the performance of lanthanide-based molecular beacons by using the novel luminescent probes described in this study, instead of probes possessing conventional fluorophores. An example is shown in Figure 4C. In this case, we used a europium complex of probe 1 as the luminophore for molecular beacon. As expected, the addition of a cDNA target resulted in the development of a signal that is distinguished by the narrow emission peaks that occur in lanthanide luminescence. Remarkably, the ratio of the intensity of the luminescence signal to the intensity of the background fluorescence of the molecular beacon (which is due to the fluorescence of the molecular beacon after subtraction of the background fluorescence of the medium) was >400, which is significantly higher than the signal-to-background ratio typically obtained for fluorophore-based hybridization probes, including molecular beacons (*23*). This higher signal-to-background ratio

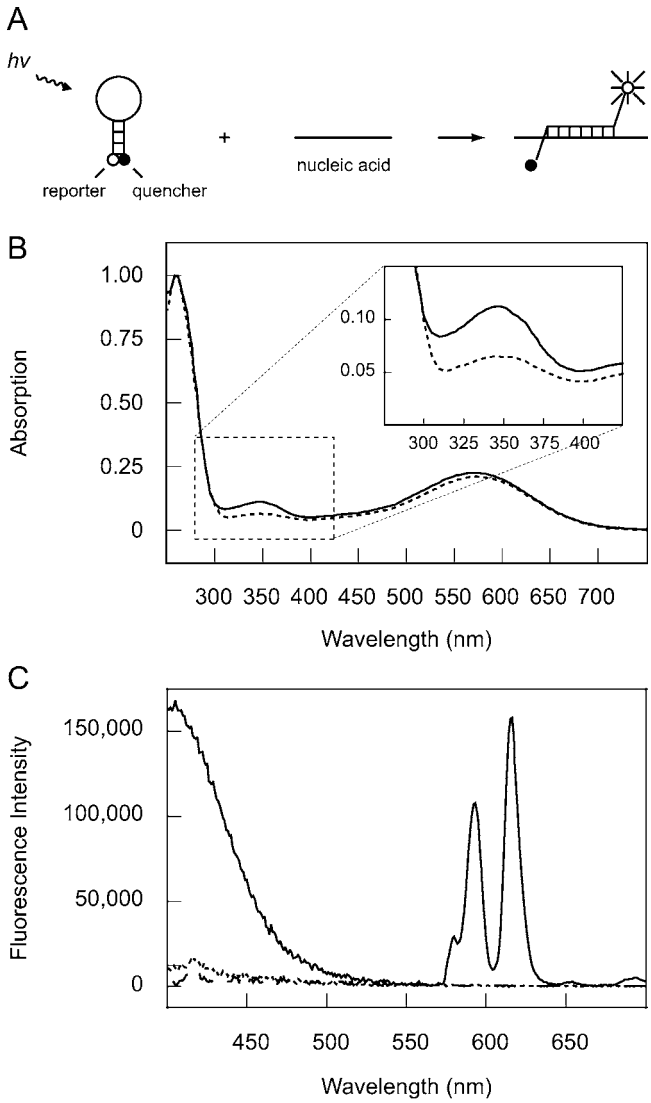


Figure 4. Detection of cDNA oligonucleotide targets using luminescence-based molecular beacons labeled by probe 1 Eu chelate in a steady-state mode. (A) Principle of detection. (B) Normalized absorption spectra of 3′ BHQ-2 labeled oligonucleotides, with (solid line) and without (dotted line) probe 2 conjugated to their 5′ terminal. (C) Luminescence emission spectra of the hybridization buffer (dashed line), the molecular beacon alone (dotted line), and the molecular beacon after hybridization to a complementary oligonucleotide (solid line).

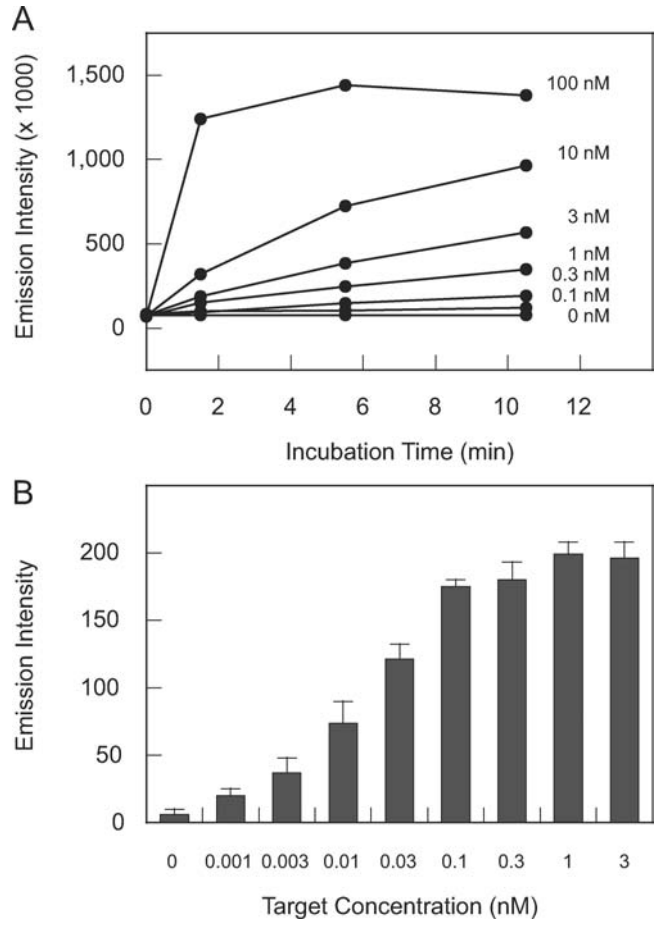


Figure 5. Time-resolved detection of a cDNA oligonucleotide target using a Eu-probe 1-based luminescent molecular beacon. (A) Emission intensity of a molecular beacon (1 nM) in the presence of different concentrations of target. (B) End-point emission detection of an oligonucleotide target at different concentrations in the presence of a 10 pM molecular beacon.

is due to both the suppression of the fluorescence of the antenna and the luminescence of the lanthanide in the "closed" form of the molecular beacon by the quencher. As expected, the signal that occurs upon hybridization of the probe to its target is significantly brighter in heavy water-based solutions.

Time-Resolved Luminescence Measurement of Molecular Beacons Probes. Figure 5A shows the time-course for the development of the luminescence signal that is detected in the time-resolved mode from hybridization mixtures that contain probe 1-based molecular beacons and various concentrations of complementary target DNA. The results demonstrate that, when 1 nM hybridization probe is present, subnanomolar concentrations of the target can be detected after only 10 min of incubation at ambient temperature. As seen from the time-course curves at low concentrations of the target, the hybridization rate decreases significantly, suggesting that the sensitivity of the detection can be improved by increasing the incubation time. Indeed, by lowering the concentration of the hybridization probe to 10 pM (to reduce background emission), and by prolonging the incubation time, we were able to achieve detection limits as low as 0.5−1 pM (Figure 5B), which is about 50- to 100-fold more sensitive than the results that are obtained in the same system using conventional fluorescein-based molecular beacons. Moreover, these detection limits are better than those reported previously for other lanthanide-based hybridization probes.

DISCUSSION

The unique photon emission properties of lanthanide-based probes render them suitable for a wide variety of applications that require ultrasensitive detection of biomolecules. Progress in this field depends on the availability of efficient probes. The mechanism of energy pathways in luminescent lanthanide chelates is not fully understood, leaving much room for improvements in their applications as labels for probes. Even though the first probes of this class were synthesized more than three decades ago and are not very efficient, many of them continue to be used for commercial applications. The development of more efficient probes is highly desirable, because new, more challenging applications have arisen (e.g., for the detection of rare pathogens in environmental samples, and for the detection of single molecules in cells).

In the present studies, we have taken advantage of new synthetic strategies that enable the preparation of highly luminescent probes with high yield. The resulting probes are ready-to-use, since they contain prebound lanthanides, unlike the lanthanide-labeled probes utilized in earlier applications, in

which the biomolecule of interest was first modified with metal-free chelates, followed by the addition of a lanthanide (*10*, *15*). The new compounds that we describe were tested in the form of molecular beacons, which are widely utilized nucleic acid hybridization probes. Our experiments revealed a higher sensitivity of detection than can be achieved with conventional fluorescence-based molecular beacons. Moreover, the detection sensitivity was 10 to 60 times better than previously reported for other lanthanide-based hybridization probes (*24*, *25*). Also, the brightness of the probes is significantly increased in heavy water, suggesting the use of this medium to increase the sensitivity of detection. Because of the superior properties, these new compounds could also be used as luminescent labels in other biopolymers, such as proteins and polysaccharides, as well as labels for small compounds, such as drugs and cellular metabolites.

ACKNOWLEDGMENT

Authors are grateful to Fred Russell Kramer and Sanjay Tyagi for helpful discussion and comments. This program was supported by NIH grant R01 GM-30717-21 for AM and by NIH grant RO1 MH-079197 for SM.

Supporting Information Available: Detailed protocols, including protocols for determining the luminescent and optical properties of the synthesized compounds, studies of their chemical reactivity and stability, as well as a description for purification of the molecular beacon hybridization probes.This material is available free of charge via the Internet at http://pubs.acs.org.

LITERATURE CITED

(1) Bunzli, J. C. (2006) Benefiting from the unique properties of lanthanide ions. *Acc. Chem. Res. 39*, 53–61.

(2) Dickson, E. F., Pollak, A., and Diamandis, E. P. (1995) Time-resolved detection of lanthanide luminescence for ultrasensitive bioanalytical assays. *J. Photochem. Photobiol. B 27*, 3–19.

(3) Dickson, E. F., Pollak, A., and Diamandis, E. P. (1995) Ultrasensitive bioanalytical assays using time-resolved fluorescence detection. *Pharmacol. Ther. 66*, 207–35.

(4) Hemmila, I., and Laitala, V. (2005) Progress in lanthanides as luminescent probes. *J. Fluoresc. 15*, 529–42.

(5) Heyduk, T. (2001) Luminescence Resonance Energy Transfer analysis of RNA polymerase complexes. *Methods 25*, 44–53.

(6) Johansson, M. K., Cook, R. M., Xu, J., and Raymond, K. N. (2004) Time gating improves sensitivity in energy transfer assays with terbium chelate/dark quencher oligonucleotide probes. *J. Am. Chem. Soc. 126*, 16451–5.

(7) Parker, D. (2004) Excitement in f block: structure, dynamics and function of nine-coordinate chiral lanthanide complexes in aqueous media. *Chem. Soc. Rev. 33*, 156–65.

(8) Petoud, S., Muller, G., Moore, E. G., Xu, J., Sokolnicki, J., Riehl, J. P., Le, U. N., Cohen, S. M., and Raymond, K. N. (2007) Brilliant Sm, Eu, Tb, and Dy chiral lanthanide complexes with strong circularly polarized luminescence. *J. Am. Chem. Soc. 129*, 77–83.

(9) Selvin, P. R. (2002) Principles and biophysical applications of lanthanide-based probes. *Annu. Rev. Biophys. Biomol. Struct. 31*, 275–302.

(10) Chen, J., and Selvin, P. R. (1999) Thiol-reactive luminescent chelates of terbium and europium. *Bioconjugate Chem. 10*, 311–5.

(11) Chen, J., and Selvin, P. R. (2000) Synthesis of 7-amino-4-trifluoromethyl-2-(1H)-quinolinone and its use as an antenna molecule for luminescent europium polyaminocarboxylates chelates. *J. Photochem. Photobiol. A 135*, 27–32.

(12) Ge, P., and Selvin, P. R. (2003) Thiol-reactive luminescent lanthanide chelates: part 2. *Bioconjugate Chem. 14*, 870–6.

(13) Ge, P., and Selvin, P. R. (2004) Carbostyril derivatives as antenna molecules for luminescent lanthanide chelates. *Bioconjugate Chem. 15*, 1088–94.

(14) Ge, P., and Selvin, P. R. (2008) New 9- or 10-dentate luminescent lanthanide chelates. *Bioconjugate Chem. 19*, 1105–11.

(15) Li, M., and Selvin, P. R. (1997) Amine-reactive forms of a luminescent diethylenetriaminepentaacetic acid chelate of terbium and europium: attachment to DNA and energy transfer measurements. *Bioconjugate Chem. 8*, 127–32.

(16) Selvin, P. R., and Hearst, J. E. (1994) Luminescence energy transfer using a terbium chelate: improvements on fluorescence energy transfer. *Proc. Natl. Acad. Sci. U.S.A. 91*, 10024–8.

(17) Selvin, P. R., Rana, T. M., and Hearst, J. E. (1994) Luminescence Resonance Energy Transfer. *J. Am. Chem. Soc. 116*, 6029–6030.

(18) Heyduk, E., and Heyduk, T. (1997) Thiol-reactive, luminescent Europium chelates: luminescence probes for resonance energy transfer distance measurements in biomolecules. *Anal. Biochem. 248*, 216–27.

(19) Tyagi, S., and Kramer, F. R. (1996) Molecular beacons: probes that fluoresce upon hybridization. *Nat. Biotechnol. 14*, 303–8.

(20) Tyagi, S., Marras, S. A. E., Vet, J. A. M., and Kramer, F. R. (2000) Molecular beacons: hybridization probes for detection of nucleic acids in homogeneous solutions, in *Nonradioactive Analysis of Biomolecules*, 2nd ed. (Kessler, C., Ed.) pp 606−16, Springer Verlag, Berlin, Germany.

(21) Li, M., and Selvin, P. R. (1995) Luminescent polyaminocarboxylate chelates of terbium and europium: The effect of chelate structure. *J. Am. Chem. Soc. 117*, 8132–8138.

(22) Xiao, M., and Selvin, P. R. (2001) Quantum yields of luminescent lanthanide chelates and far-red dyes measured by resonance energy transfer. *J. Am. Chem. Soc. 123*, 7067–73.

(23) Marras, S. A., Kramer, F. R., and Tyagi, S. (2002) Efficiencies of fluorescence resonance energy transfer and contact-mediated quenching in oligonucleotide probes. *Nucleic Acids Res. 30*, e122.

(24) Sueda, S., Yuan, J., and Matsumoto, K. (2000) Homogeneous DNA hybridization assay by using europium luminescence energy transfer. *Bioconjugate Chem. 11*, 827–31.

(25) Wang, G., Yuan, J., Matsumoto, K., and Hu, Z. (2001) Homogeneous time-resolved fluorescence DNA hybridization assay by DNA-mediated formation of an EDTA-Eu(III)-beta-diketonate ternary complex. *Anal. Biochem. 299*, 169–72.

BC900403N

Platinum(II)−Dendrimer Conjugates: Synthesis and Investigations on Cytotoxicity, Cellular Distribution, Platinum Release, DNA, and Protein Binding

Timo Kapp, Anja Dullin, and Ronald Gust*

Institute of Pharmacy, Freie Universität Berlin, Königin Luise Strasse 2 + 4, 14195 Berlin, Germany. Received September 24, 2009; Revised Manuscript Received November 10, 2009

A set of polyamidoamine dendrimers were modified in such a way that they are able to act as carrier and drug delivery systems for cytostatics. The terminal binding of the non-proteinogenic D,L-2,3-diaminopropionic acid allowed the attachment of the cytotoxic PtX_2 moiety (X = Cl, I: **A(PtI$_2$)$_2$**, **A(PtCl$_2$)$_2$**, **B(PtI$_2$)$_2$**, **B(PtCl$_2$)$_2$**), while the 2-carboxypentanedioic acid acted as leaving group for [*meso*-1,2-bis(4-fluorophenyl)ethylenediamine]-platinum(II) (**(m-4F-Pt)$_3$C**, **(m-4F-Pt)$_3$D**). Poly(ethylene glycol) chains at **C(PtI$_2$)$_3$** and **C(PtCl$_2$)$_3$** as well as **(m-4F-Pt)$_3$C** and **(m-4F-Pt)$_3$D** mediated sufficient water solubility. Additional dansyl residues (**B(PtI$_2$)$_2$** and **(m-4F-Pt)$_3$D**) made a simultaneous determination of platinum (graphite furnace atomic absorption spectroscopy (GF-AAS)) and dendrimer (fluorimetry) possible. The ethylenediamine-terminated dendrimers were typically accumulated into MCF-7 cells in clathrin-dependent pathways and targeted the platinum moieties to the nuclear compartment. The highest intracellular platinum concentration and DNA binding caused the dendrimers **A(PtX$_2$)$_2$** and **B(PtX$_2$)$_2$**. A coordinative DNA binding, however, is very unlikely because of low cytotoxic effects. **(m-4F-Pt)$_3$C** and **(m-4F-Pt)$_3$D** are labile conjugates and liberated the **m-4F-Pt** moiety in biological systems. The effects of these dendrimers were similar to that of the reference compounds **m-4F-PtCl$_2$** and **m-4F-Pt(H$_2$O)$_2$**.

INTRODUCTION

Natural and synthetic macromolecules are attractive and promising drug delivery systems for cytostatics. The advantage of synthetic polymers is the possibility to design them in such a way that they combine drugs, fluorescence markers, and solubilizing groups at their surface (*1*). Furthermore, the renal excretion is reduced if the polymer exceeded a molecular mass of 40 kD and allows a preferred accumulation of the polymers in the tumor tissue by the EPR (enhanced permeability and retention) effect, the property by which macromolecules build up in the tumor due to the special properties of the tissue (for example, poor lymphatic drainage). This tumor selectivity reduced the side effects of the conventional used cytostatics in nontarget tissues (*2*−*5*).

Platinum complexes represent important drugs, which are used in the first-line therapy of several kinds of tumoral diseases (*6*). However, the therapy is not without obstacles. Intolerable side effects such as nephrotoxicity, neurotoxicity, and myelosuppression and development of resistance during the therapy limited the therapeutic use (*7*−*9*).

First attempts to optimize the pharmacological properties of platinum complexes due to the binding to macromolecular carriers started about 10 years ago (*10*−*15*). Despite the pharmacological benefits, there are still problems resulting from their architecture. Linear polymers adopt in solution a coiled structure, which partly buried the bound drugs in the core of the molecule. Further problems result from the heterogeneous and polydisperse structure of the molecules. It is difficult to maintain reproducible polymer properties, drug delivery ability, and therapeutic efficacy (*16*). Thus, dendrimers represent an ideal drug delivery system, because they are characterized by a low polydispersity and a globular structure with good accessible terminal groups as demonstrated by Duncan et al. (*17*).

In a previous study, we synthesized amino-functionalized dendrimers (*18*, *19*) and derived them with the non-proteinogenic D,L-2,3-diaminopropionic acid to yield ethylenediamine-terminated dendrimers of type **A** (see Scheme 1). These dendrimers coordinate the cytotoxic PtX_2 moiety in a very stable five-membered chelate ring (see **A(PtX$_2$)** in Scheme 1) (*11*).

The dendrimers of type **B** combine three fluorescent dansyl moieties with three terminal amide-bound 2,3-diaminopropionic acids and made pharmacological studies in MCF-7 cells possible using fluorescence spectroscopy and graphite furnace atomic absorption spectroscopy (GF-AAS) after coordination of PtX_2.

Poly(ethylene glycol) (PEG) chains of dendrimers **C** and **D** mediate water solubility, and the terminal amino groups were derived with either 2,3-diaminopropionic acid to coordinate PtX_2 (**C**) or with 2-carboxypentanedioic acid to bind [*meso*-1,2-bis(4-fluorophenyl)ethylenediamine]platinum(II) (**C** and **D**) (*20, 21*). The G2 generation dendrimer **D** additionally bears a dansyl marker.

Diiodoplatinum(II) complexes **A(PtI$_2$)$_2$**, **B(PtI$_2$)$_2$**, and **C-(PtI$_2$)$_2$** represent hydrolytically stable derivatives of related $PtCl_2$ compounds (**A(PtCl$_2$)$_2$**, **B(PtCl$_2$)$_2$**, **C(PtCl$_2$)$_2$**). In the case of **m-4F-Pt)$_3$C** and **(m-4F-Pt)$_3$D**, the dendrimers act as leaving groups for the cytotoxic m-4F-Pt moiety. While the [2-carboxyethylenediamine]platinum(II) complexes are relatively stably bonded to the dendrimer via an amide bond, aquation and substitution reactions might cleave m-4F-Pt from the dendrimer.

In this study, we investigated the suitability of dendrimers **A**−**D** to carry cytotoxic moieties into the tumor cells and act as drug delivery systems. Platinum (GF-AAS) and dansyl moieties (fluorescence analysis) were used as analytic probe.

EXPERIMENTAL PROCEDURES

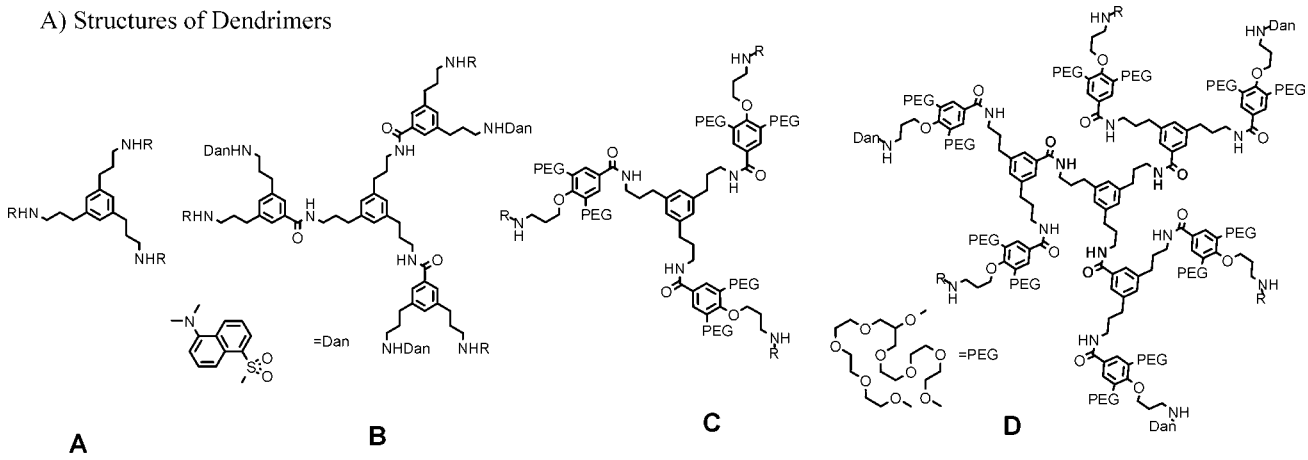
Synthesis. All reagents and solvents were purchased from Acros Organics, Fluka Chemie, Lancaster, Merck, or Sigma-

* Institut für Pharmazie der FU Berlin, Königin Luise Str. 2 + 4, D-14195 Berlin, Germany. Phone: (030) 838 53272, Telefax: (030) 838 56906, E-mail: rgust@zedat.fu-berlin.de.

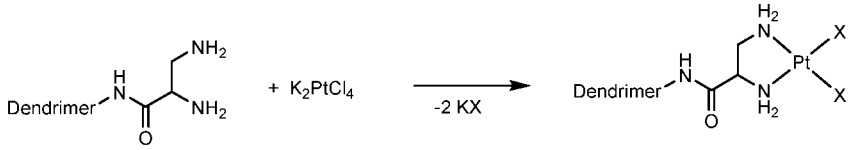
10.1021/bc900406m © 2010 American Chemical Society
Published on Web 01/27/2010

Scheme 1. Synthesis and Structures of the Platinum(II) Dendrimer Complexes

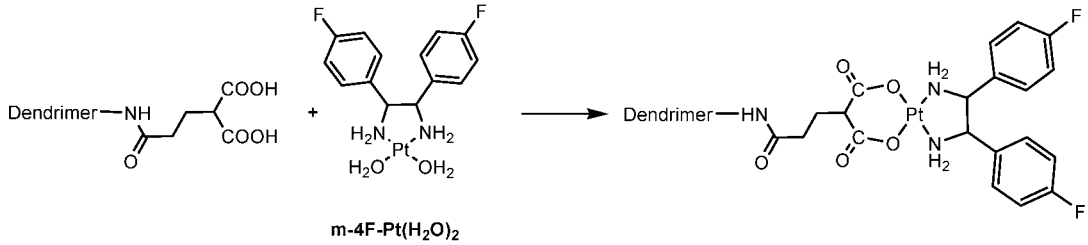
A) Structures of Dendrimers



B) Binding of Platinum to Dendrimer-NH-R



compound	type of dendrimer	leaving group X	platinum atoms per molecule
A(PtCl$_2$)$_2$	**A**	Cl^-	2
A(PtI$_2$)$_2$	**A**	I^-	2
B(PtCl$_2$)$_2$	**B**	Cl^-	2
B(PtI$_2$)$_2$	**B**	I^-	2
C(PtCl$_2$)$_3$	**C**	Cl^-	3
C(PtI$_2$)$_3$	**C**	I^-	3



compound	type of dendrimer	platinum atoms per molecule
(m-4F-Pt)$_3$C	**C**	3
(m-4F-Pt)$_3$D	**D**	3

Aldrich. ^{1}H NMR: Advance DPX-400 spectrometer (Bruker, Karlsruhe/Germany) at 400 MHz (internal standard: TMS). Elemental analyses: Microlaboratory of the Freie Universität Berlin. Diaqua[*meso*-1,2-bis(4-fluorophenyl)ethylenediamine]-platinum(II) sulfate (**m-4F-Pt(H$_2$O)$_2$**) and dendrimers **A** to **D** were prepared as already described (*18*−*20*).

General Procedure for Preparation of the Platinum−Dendrimer Complexes. The respective dendrimer (0.01 mmol) was dissolved in water and treated with K_2PtCl_2, K_2PtI_2, or **m-4F-Pt(H$_2$O)$_2$** (0.03 mmol, respectively). Precipitated conjugates were sucked off and dried over P_2O_5. Otherwise, the water-soluble conjugates were extracted at least three times with CH_2Cl_2. The solvent was evaporated and the product was obtained in suitable purity. The purity was determined using capillary electrophoresis. All electropherograms documented the presence of only one species (see Supporting Information).

Platinum Conjugates of Dendrimer Type A. A(PtI$_2$)$_2$. Yield: 9.33 mg (0.006 mmol); 66% brown powder. ^{1}H NMR ([D7]-DMF): δ = 1.88 (m, 6H, CH_2), 2.58 (t, 6H, CH_2Ar), 3.27 (m, 3H, CH_2N), 3.38 (m, 3H, $CHCH_2$), 3.45 (m, 3H, CH_2N), 3.47 (dd, 3H, $CHCH_2$), 4.19 (t, 3H, CH), 4.92 (br, 3H, NH), 5.43 (br, 6H, NH_2), 5.85 (br, 3H, NH), 6.90 (s, 3H, ArH), 8.42 (br, 3H, NH).

A(PtCl$_2$)$_2$. Yield: 8.65 mg (0.008 mmol); 83% yellow powder. ^{1}H NMR ([D7]-DMF): δ = 1.86 (m, 6H, CH_2), 2.55 (t, 6H, CH_2Ar), 3.30 (m, 3H, CH_2N), 3.38 (m, 3H, $CHCH_2$), 3.44 (m, 3H, CH_2N), 3.47 (dd, 3H, $CHCH_2$), 4.19 (t, 3H, CH), 4.92 (br,

3H, NH), 5.44 (br, 6H, NH_2), 5.87 (br, 3H, NH), 6.88 (s, 3H, ArH), 8.45 (br, 3H, NH).

Platinum Conjugates of Dendrimer Type B. $B(PtI_2)_2$. Yield: 14.72 mg (0.006 mmol); 53% brown powder. ^{1}H NMR ([D7]-DMF): δ = 1.28 (m, 6H, H−CH_2), 1.63−1.81 (m, 6H, CH_2), 1.85−1.95 (m, 6H, CH_2), 2.53 (t, 6H, CH_2), 2.66 (m, 12H, CH_2+CH_2), 2.84 (t, 6H, NH−CH_2), 2.96 (s, 18H, CH_3), 3.21 (m, 3H, NH−CH_2), 3.39 (m, 6H, NH−CH_2), 3.41 (m, 3H, NH−CH_2), 3.46 (dd, 3H, NH_2−CH_2), 3.53 (dd, 3H, NH_2−CH_2), 3.80 (t, 3H, CO−CH_2), 4.95 (br, 3H, NH), 5.47 (br, 6H, NH_2), 5.90 (br, 3H, NH), 6.96 (s, 3H, Ar−H), 7.07 (s, 3H, Ar−H), 7.28 (s, 3H, Ar−H), 7.40 (d, 3H, Ar−H), 7.58 (s, 3H, Ar−H), 7.53 (t, 3H, Ar−H), 7.68 (d, 3H, 2 × Ar−H), 8.19 (d, 3H, 2 × Ar−H), 8.21 (d, 3H, 2 × NH_2−CH_2), 8.43 (t, 3H, Ar−H).

$B(PtCl_2)_2$. Yield: 14.90 mg (0.005 mmol); 50% white powder. ^{1}H NMR ([D7]-DMF): δ = 1.28 (m, 6H, CH_2), 1.63−1.81 (m, 6H, CH_2), 1.85−1.95 (m, 6H, CH_2), 2.53 (t, 6H, CH_2), 2.66 (m, 12H, 2 × CH_2), 2.84 (t, 6H, NH−CH_2), 2.96 (s, 18H, CH_3), 3.21 (m, 3H, NH−CH_2), 3.39 (m, 6H, NH−CH_2), 3.41 (m, 3H, NH−CH_2), 3.46 (dd, 3H, NH_2−CH_2), 3.53 (dd, 3H, NH_2−CH_2), 3.80 (t, 3H, CO−CH_2), 4.95 (br, 3H, NH), 5.47 (br, 6H, NH_2), 5.90 (br, 3H, NH), 6.96 (s, 3H, Ar−H), 7.07 (s, 3H, Ar−H), 7.28 (s, 3H, Ar−H), 7.40 (d, 3H, Ar−H), 7.58 (s, 3H, Ar−H), 7.53 (t, 3H, Ar−H), 7.68 (d, 3H, 2 × Ar−H), 8.19 (d, 3H, 2 × Ar−H), 8.21 (d, 3H, 2 × NH_2−CH_2), 8.43 (t, 3H, Ar−H).

Platinum Conjugates of Dendrimer Type C. $C(PtI_2)_2$. Yield: 19.88 mg (0.0042 mmol); 42% colorless oil. ^{1}H NMR ([D7]-DMF): δ = 1.82 (m, 6H, CH_2), 1.84 (m, 6H, CH_2), 2.50 (t, 6H, Ar−CH_2), 3.18 (s, 36H, -OCH_3), 3.25 (t, 6H, NH−CH_2), 3.31−3.54 (2 m, 144H, -OCH_2CH_2O), 3.48 + 3.59 (2 m, 12H, O−CH_2+NH−CH_2), 3.63 (m, 24H, -$OCH(CH_2)_2$), 3.98 + 4.33 + 4.36 (3 m, 9H, −$CHNH_2$ + −CH_2NH_2), 4.58 (quint, 6H, -$OCH(CH_2)_2$), 5.40 (br, 8H, NH_2), 5.78 (br, 4H, NH_2), 6.82 (s, 3H, Ar−H:Core), 7.16 (s, 6H, Ar−H:Gallate).

$C(PtCl_2)_2$. Yield: 17.65 mg (0.004 mmol); 42% colorless oil. ^{1}H NMR ([D7]-DMF): δ = 1.82 (m, 6H, CH_2), 1.84 (m, 6H, CH_2), 2.50 (t, 6H, Ar−CH_2), 3.18 (s, 36H, -OCH_3), 3.25 (t, 6H, γ-CH_2), 3.31−3.54 (2 m, 144H, -OCH_2CH_2O), 3.48 + 3.59 (2 m, 12H, O−CH_2+NH−CH_2), 3.63 (m, 24H, -$OCH(CH_2)_2$), 3.98 + 4.33 + 4.36 (3 m, 9H, −$CHNH_2$ + −CH_2NH_2), 4.58 (quint, 6H, -$OCH(CH_2)_2$), 5.40 (br, 8H, NH_2), 5.78 (br, 4H, NH_2), 6.82 (s, 3H, Ar−H:Core), 7.16 (s, 6H, Ar−H:Gallate).

$(m\text{-}4F\text{-}Pt)_3C$. Yield: 16.52 mg (0.0037 mmol); 37% colorless powder. ^{1}H NMR ([D6]-DMSO): δ = 1.88 (m, 12H, CH_2), 2.10 (t, 6H, CH_2), 2.26 (t, 6H, CO−CH_2), 2.61 (t, 6H, Ar−CH_2), 3.28 (brs, 39H, -OCH_3+COOH−CH), 3.35 (t, 6H, NH−CH_2), 3.41 (t, 6H, NH−CH_2), 3.42−3.64 (2 m, 144H, -OCH_2CH_2O), 3.72 (m, 24H, -$OCH(CH_2)_2$), 4.05 (t, 6H, O−CH_2), 4.60 (quint, 6H, -$OCH(CH_2)_2$), 6.06 (br, 2H, NH), 6.25 (br, 4H, NH), 6.51 (br, 2H, NH), 6.69 (br, 4H, NH), 6.89 (s, 3H, Ar−H:Core), 7.02−7.15 (m, 24H, Ar−H), 7.16−7.28 (m, 12H, Ar−H), 7.23 (s, 6H, Ar−H:Gallate).

Platinum Conjugates of Dendrimer Type D. $(m\text{-}4F\text{-}Pt)_3D$. Yield: 21.22 mg (0.0023 mmol); 23% colorless powder. ^{1}H NMR ([D6]-DMSO): δ = 1.61 (m, 6H, CH_2), 1.74 (m, 24H, CH_2+CH_2), 1.96 (m, 6H, CH_2), 2.13 (m, 6H, CO−CH_2), 2.45 (t, 6H, Ar−CH_2), 2.52 (m, 12H, Ar−CH_2), 3.03 (t, 6H, NH−CH_2), 3.11 (s, 18H, -$N(CH_3)_2$), 3.12 (2s, 72H, -OCH_3), 3.21 (m, 21H, COOH−CH+NH−CH_2), 3.26 (m, 6H, NH−CH_2), 3.27−3.42 (2 m, 288H, -OCH_2CH_2O), 3.45 + 3.56 (2 m, 48H, -$OCH(CH_2)_2$), 3.80 (t, 6H, O−CH_2), 3.92 (t, 6H, O−CH_2), 4.37 (q, 6H, -$OCH(CH_2)_2$), 4.45 (q, 6H, -$OCH(CH_2)_2$), 6.62 (br, 4H, NH), 6.74 (s, 3H, Ar−H:Core), 6.93 (br, 8H, NH), 7.05 (s, 6H, Ar−H:Gallate), 7.09 (s, 3H, Ar−H:Dendron), 7.11 (s, 6H, Ar−H:Gallate), 7.18−7.24 (m, 18H, Ar−H), 7.26−7.32 (m, 18H, Ar−H), 7.33 (m, 6H, Ar−H:Dendron), 7.55 (m, 3H, Ar−H:Dansyl), 7.63 (m, 6H, Ar−H:Dansyl), 8.18 (d, 3H, Ar−H:Dansyl), 8.32 (d, 6H, Ar−H:Dansyl), 8.87 (d, 6H, Ar−H:Dansyl).

Characterization of Fluorophoric Characteristics. Compounds were dissolved in ethanol as stock solutions. If characterization in other solutions was required, the stock solution was diluted with those solutions in such a way that the concentration of ethanol never exceeded 1%. Measurements were done at room temperature with a spectrofluorimeter (F-4500, Hitachi) equipped with a 450 W xenon arc lamp. Because in earlier experiments the excitation wavelength did not alter under the chosen conditions, this was set to 340 nm (bandwidth 5 nm).

BIOLOGICAL METHODS

General. Chemicals were purchased from Sigma and Fluka. Drugs were freshly prepared as stock solutions in dimethylformamide (DMF) or H_2O and diluted with cell culture media or buffer when used for the biochemical experiments (final DMF concentration: 0.1% (v/v)). Platinum amounts were determined by graphite furnace atomic absorption spectroscopy (GF-AAS) with deuterium background correction (AAS vario 6; AnalytikJena AG) using a detection wavelength of 265.9 nm. The program consisted of drying at 105 °C for 30 s (ramp rate = 10 °C/s) and at 120 °C for 20 s (ramp rate = 15 °C/s), ashing at 50 °C for 30 s (ramp rate = 45 °C/s), at 1000 °C for 10 s (ramp rate = 100 °C/s) and at 1700 °C for 10 s (ramp rate = 300 °C/s) as well as atomizing at 2400 °C for 4 s (ramp rate = 1500 °C/s). Purge gas flow rate was 2 L argon/min except at the atomization where it was stopped. Limit of detection was approximately 0.005 mg/L (injection volume: 20 μL).

Binding Behavior to Human Serum Albumine (HSA). Three micromolar quantities of each compound were incubated with HSA (40 mg/mL) in Delbecco's buffer (137.0 mM NaCl, 2.7 mM KCl, 0.9 mM $CaCl_2$, 0.5 mM $MgCl_2$, 1.5 mM KH_2PO_4, 8.0 mM Na_2HPO_4, pH 7.4). Aliquots were taken after appropriate incubation periods and were 2-fold diluted with ice-cold ethanol. The probe was stored after vigorous stirring at −18 °C for at least 4 h. Then, the protein solution was centrifuged (4000 *g*, 4 °C, 10 min), and 300 μL of the supernatant was diluted with 100 μL twice-distilled water and stabilized for GF-AAS determination by addition of 100 μL hydrochloric acid (18% w/v). The recovery rate was calculated from three independent experiments as the ratio of platinum found in the supernatant and the total amount of platinum. Pseudo-first-order kinetic fitting was done using *Origin 7.0* after calculating the platinum found as the percentage of the amount recovered at the beginning of the experiment (n = 2).

Aliquots of 200 μL were transferred immediately after addition of the compounds into centrifugal filter devices (Microcon YM-30 Millipore) to determine the recovery by ultrafiltration. After centrifugation (6000 *g*, 4 °C, 10 min), 50 μL of the ultrafiltrate was stabilized by addition of 350 μL Triton X-100 (1% (w/w)) and 100 μL hydrochloric acid (18% w/v) for GF-AAS determination. The experiments were performed in triplicate. Calculations were done analogously to the ethanol precipitation experiments.

Cell Culture. The human MCF-7 breast cancer cell line was obtained from the American Culture Collection (ATCC, Rockville, Md.). The cells were maintained in Eagle's minimal essential medium (EMEM) containing L-glutamine, supplemented with $NaHCO_3$ (2.2 g/L), sodium pyrovate (110 mg/L), gentamycin (50 mg/L), and 10% fetal calf serum (FCS; Gibco Eggenheim, Germany) using 75 cm^2 culture flasks (Nunc) in a water-saturated atmosphere (5% CO_2) at 37 °C. The cells were serially passaged weekly following trypsinization using 0.05% trypsin/0.02% ethylenediaminetetraacetic acid (EDTA). Myco-

plasma contamination was routinely monitored, and only mycoplasma-free cultures were used.

In Vitro Chemosensitivity Assay. The in vitro testing of the compounds for cytotoxic activity was carried out on exponentially dividing cancer cells according to a previously published microtiter assay (*22*). Briefly, in 96-well microtiter assay plates (Nunc), 100 μL of a cell suspension at 7000 cells/mL culture medium was plated into each well and incubated at 37 °C for 3 days in a water-saturated atmosphere (5% CO_2). By addition of an adequate volume of a stock solution of the respective compound to the medium, the desired test concentration was obtained. For each test concentration and for the control, which contained the corresponding amount of DMF or H_2O (0.1% v/v), respectively, 16 wells were used. The medium was removed after appropriate incubation periods, and the cells were fixed with a glutaraldehyde solution and stored at 4 °C. Cell biomass was determined by a crystal violet staining technique. The influence of the complexes on cell growth is expressed as corrected *T*/*C* value according to the following equations:

$$\text{cytostatic effect:} \quad T/C_{\text{corr}}[\%] = [(T - C_0)/(C - C_0)] \times 100$$

where *T* (test) and *C* (control) are the optical densities at 590 nm of the crystal violet extract of the cell lawn in the wells (i.e., the chromatin-bound crystal violet extracted with ethanol 70%), C_0 is the density of the cell extract immediately before treatment, and

$$\text{cytocidal effect:} \quad \tau[\%] = [(T - C_0)/C_0] \times 100$$

For automatic determination of the optical density of the crystal violet extract in the wells, a microplatereader (Flashscan S19 AnalytikJena AG) was used.

Cellular Uptake Studies. MCF-7 cells were seeded in 6-well plates (Nunc). When the cells had reached 50−60% confluence (approximately after 5 days of incubation) the medium was exchanged by serum-free EMEM containing the drugs. The medium was removed after appropriate incubation periods, and the cells were washed with ice-cold PBS. After trypsination, the cells were harvested, washed two times with ice-cold PBS and centrifuged (2000 *g*, 4 °C, 5 min) for storage at −18 °C until analysis.

For determination of platinum content, the cell pellet was homogenized by sonification in a Triton X-100 solution (1% (w/w)) and was adequately diluted for protein determination (*23*) and for the platinum analysis (GF-AAS). Calibrations were done under identical conditions with K_2PtCl_4 standard solutions. The results were calculated as the average of three experiments. The cellular concentration of the compounds in the MCF-7 cells was determined as previously published (*24*). The accumulation grade was the ratio of cell-associated platinum and compound concentration in the medium.

For the endocytosis inhibitor studies, the medium was exchanged with serum-free EMEM containing the inhibitors (chlorpromazine 10 μg/mL, amiloride 1 mM, nystatin 25 μg/L, genistein 0.4 mM) and preincubated for 15 min. Then, the medium was removed and medium containing platinum compound and inhibitor was added. The control groups were not preincubated, and only platinum compound was added to them. The medium was removed after 2 h, and the cells were washed with ice-cold PBS.

For determination of the content of dansyl fluorophor, the cells were homogenized in TET buffer (0.5% w/v Triton X-100, 0.5% w/v EDTA, 10 mM Tris−Buffer adjusted to pH 8). The protein content was determined as described above. For fluorescence measurement, the samples were diluted with 0.5 aliquot ethanol and 0.5 aliquot TET buffer. Calibrations were done with the respective compound dissolved in ethanol added to blank pellets worked up by the described procedure. Fluorescence was measured using a microtiterplate reader (Victor^2 1420 multilabel counter Perkin-Elmer; filters: Exc. 360 nm; Em. 500 nm).

Platinum Content in the Nuclei. MCF-7 cells were seeded in 175 cm^2 flasks and incubated until 60−70% confluency was reached. Then, the cells were incubated for 24 h with serum-free medium containing the respective drug. The cells were harvested by trypsination, washed with ice-cold PBS, resuspended in ice-cold RSB buffer (0.01 M Tris−HCl, 0.01 M NaCl, 1.5 mM $MgCl_2$, pH 7.4) and incubated on ice for 5 min. Nonidet-P40 was added to the swollen cells to a concentration of 0.25%, and the cells were lysed by vigorous stirring. After 5 min incubation on ice, the raw nuclei were stirred once more and sedimented by centrifugation (1000 *g*) at 4 °C for 5 min. The nuclei pellet was resuspended in 0.25 M sucrose containing 3 mM $CaCl_2$ and layered on a 0.88 M sucrose solution. Nuclei were purified by centrifugation for 10 min at 2500 *g*. The supernatant was removed, and the nuclei were stored at −18 °C until analysis.

For analysis, the nuclei were homogenized in 300 μL Triton X-100 solution (1% (w/w)) by ultrasonification. The homogenate was adequately diluted for protein assay by the method of Bradford (*23*) and for platinum determination by means of GF-AAS. The results were expressed as means of three independent experiments as nanograms of platinum per milligram of nuclear protein.

Platinum Content of Nuclear DNA. MCF-7 cells were treated as described above to yield a raw nuclei pellet, which was incubated with proteinase K and RNase A in a 0.5% (w/v) sodium dodecylsulfonate containing TE-buffer (10 mmol Tris, 1 mmol EDTA, pH 7.8) for 4 h at 55 °C. Purification was performed by using the chloroform phenol extraction method. DNA pellets were obtained by adding 0.1 aliquots of 3 M sodium acetate solution and two aliquots of ice-cold ethanol. For GF-AAS analysis, this pellet was dissolved in 100 μL of water and 50 μL of DNA solution was diluted with 50 μL of 0.01 N HCl containing 0.05% (w/w) Triton X-100. For calibration, equal amounts of salmon sperm DNA were added to the K_2PtCl_4 standards.

DNA content was measured according to Vytasek in a miniaturized assay (*25*). Briefly, the DNA was hydrolyzed by 1 M $HClO_4$. The liberated ribose reacted with 3,5-diaminobenzoic acid under alkaline conditions to a fluorescent chinoline derivative. Reaction was stopped by addition of ice-cold hydrochloric acid. Fluorescence was measured using a microtiterplate reader (Victor^2 1420 multilabel counter Perkin-Elmer; filters: Exc. 405 nm; Em. 500 nm). Calibration was done in the range 0−2.5 μg using salmon sperm DNA.

The purity of the DNA was determined by UV spectroscopy. Each workup showed the ratio E_{260}/E_{280} higher than 1.8 and the ratio E_{260}/E_{230} higher than 2.2. The absorption minimum was always lower than 232 nm (*26*). Results are expressed as means of three independent experiments as picograms of platinum per microgram of nuclear DNA.

RESULTS AND DISCUSSION

Synthesis and Spectroscopic Characterization. The diaminopropionic derived dendrimers of types **A** and **B** should retain at least one free ethylenediamine group to guarantee solubility under physiological conditions. Therefore, K_2PtCl_4 or K_2PtI_4 was reacted with the respective dendrimer (Scheme 1) in a small amount of water (up to 5 mL). Coordination of PtX_2 moieties at two of the three ethylenediamine binding sites reduced the

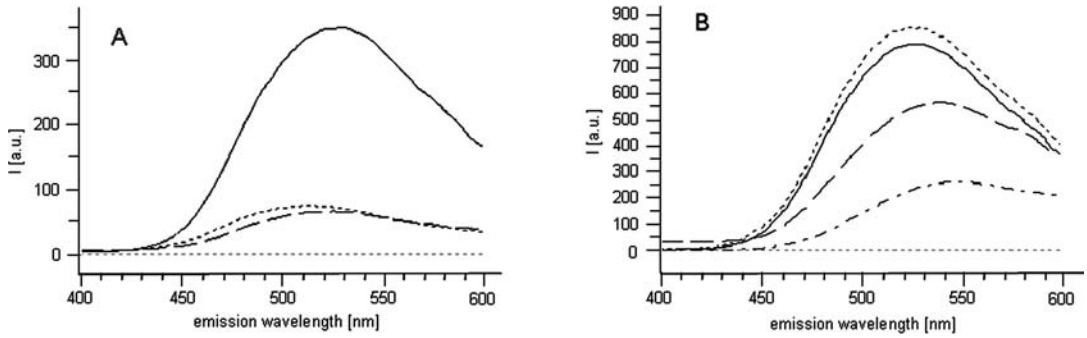


Figure 1. (A) Fluorescence of dendrimer **B** — (0.5 μM), **B(PtI$_2$)$_2$** – – – (2 μM), and **B(PtCl$_2$)$_2$** ------ (2 μM) in ethanol. (B) Fluorescence of dendrimer **D** ------ and compound **(m-4F-Pt)$_3$D** in ethanol —, in TET buffer – – –, and in water – •– (all 0.5 μM).

water solubility of the dendrimers and the conjugates **A(PtI$_2$)$_2$**, **A(PtCl$_2$)$_2$**, **B(PtI$_2$)$_2$**, and **B(PtCl$_2$)$_2$** precipitated, respectively.

The PEG chains of the ethylenediamine-terminated dendrimer **C** mediated a sufficient water solubility so that the molecule can be completely platinated with K_2PtCl_4 or K_2PtI_4 (three [ethylenediamine]platinum moieties per molecules: **C(PtCl$_2$)$_3$** and **C(PtI$_2$)$_3$**.). Repeated extraction with CH_2Cl_2 yielded the analytically pure conjugates.

The carboxyl-terminated polymers were treated with the diaqua[*meso*-1,2-bis(4-fluorophenyl)ethylenediamine-]platinum(II) sulfate (**m-4F-Pt(H$_2$O)$_2$**). The resulting conjugates **(m-4F-Pt)$_3$C** and **(m-4F-Pt)$_3$D** were soluble in water and were isolated by extraction with CH_2Cl_2.

All dendrimers were characterized by their fully assigned ^{1}H NMR spectra. The diastereomeric splitting of the NH_2 protons resulting in characteristic signals in the region of $\delta = 4.9$ to 5.9 (see Experimental Procedures section) comparable to that of the free [2-carboxyethylenediamine]platinum(II) complexes confirmed the coordination of platinum to the ethylenediamine.

The purity of the dendrimers was verified by capillary electrophoresis (see Supporting Information). Free platinum derivatives were not found. The amount of platinum per molecule was determined by GF-AAS using K_2PtCl_4 as the standard and corresponds to the proposed occupation of the dendrimers (Scheme 1 and Supporting Information).

The dansyl labeled dendrimers B and D showed in their fluorescence spectra emission maxima at 530 nm (Figure 1). Coordination of PtX_2 to the terminal ethylenediamine at dendrimer **B** drastically reduced the fluorescent properties (*19, 27*) as is well-known for other metal ions bound to dansyl-labeled macromolecules (*27, 28*). The fluorescence intensity of the conjugates **B(PtI$_2$)$_2$** and **B(PtCl$_2$)$_2$** is reduced independent of the leaving group to about 5% of **B** accompanied by a hypsochromic shift of the emission maximum from 530 to 514 nm (solvent: ethanol).

The PEG-bearing dendrimer **D** showed in ethanol a higher fluorescence than **B**, which is maintained upon binding of three molecules m-4F-Pt (**(m-4F-Pt)$_3$D**). The use of water, however, reduced the intensity by 70%, and the emission maximum is bathochromically shifted from 530 to 550 nm. This quenching effect is not as pronounced by the addition of TET buffer (*27*) designed for uptake studies. Nevertheless, these compounds confirmed the limitation for the fluorescence microscopic detection in intact cells as already reported for dendrimers **B** and **D** before (*27*).

Biological Properties. The biological properties, e.g., the accumulation in cells and nuclei, the binding to DNA, and the cytotoxicity, were evaluated at the MCF-7 cell line. Furthermore, possible inactivation reactions with human serum albumin (HSA) were of interest.

Cisplatin was used as reference for PtX_2 conjugates, diaqua-[*meso*-1,2-bis(4-fluorophenyl)ethylenediamine]platinum(II) sulfate (**m-4F-Pt(H$_2$O)$_2$**) or [*meso*-1,2-bis(4-fluorophenyl)ethylenediamine]dichloroplatinum(II) (**m-4F-PtCl$_2$**) for the dendrimers **(m-4F-Pt)$_3$D** and **(m-4F-Pt)$_3$D**.

Cellular Uptake Studies. MCF-7 cells were incubated for 24 h with the respective derivative. The intracellular platinum content was quantified using GF-AAS and correlated with the extracellular platinum concentration (5 μM) giving the accumulation grade (Figure 2).

The accumulation grade of cisplatin amounted to 3.7-fold compared to extracellular medium at the end of the experiment (24 h; see Figure 2A) and correlated very well with the results of earlier studies (*21, 32*).

The 2,3-diamino-*N*-(3-{3,5-bis[3-(2,3-diaminopropionylamino)-propyl]phenyl}propyl)propionamide represents an excellent carrier for PtX_2 moieties. In contrast to cisplatin, which showed a nearly linear graph, **A(PtI$_2$)$_2$** and **A(PtCl$_2$)$_2$** accumulated very fast and reached their maximum after 8 h (891- and 213-fold, respectively, in relation to the extracellular platinum as well as 445- and 106-fold in relation to the dendrimer-bound Pt atoms; see Figure 2A).

3,5-Bis(3-aminopropyl)-*N*-(3-{3,5-bis[3-{3,5-bis(3-aminopropyl)-benzoylamino}propyl]phenyl}propyl)benzamide bearing three dansyl and two PtX_2 moieties showed a reduced accumulation grade (**B(PtI$_2$)$_2$**, 14.8-fold after 24 h; **B(PtCl$_2$)$_2$**, 18.0-fold after 24 h) and an accumulation kinetic without saturation after 24 h (Figure 2A).

The reduced uptake into the tumor cells might be the consequence of the higher dendrimer generation or the lower numbers of amino groups in relation to the molecular mass. Protonable NH_2 groups might be necessary to attach the dendrimer at the cell surface, the first step of endocytotic transport through the membrane.

The water-soluble **C(PtCl$_2$)$_3$** bearing PEG chains at the 3,5-positions of the terminal aromatic rings showed an accumulation comparable to **B(PtX$_2$)**, while the intracellular platinum concentration obtained with **C(PtI$_2$)$_3$** was as low as determined for cisplatin, however, with a clear indication of saturation after 8 h (Figure 2A).

The carboxyl-terminated dendrimers **C** and **D** bound three [*meso*-1,2-bis(4-fluorophenyl)ethylenediamine]platinum(II) moieties (**(m-4F-Pt)$_3$C** and **(m-4F-Pt)$_3$D)**), respectively. The platinum content in cells treated with **(m-4F-Pt)$_3$D** increased with a slightly faster linear kinetic compared to **(m-4F-Pt)$_3$C**. Both did not reach an intracellular saturation after 20−24 h. The accumulation against the media was nearly half of that obtained with the reference compound **m-4F-Pt(H$_2$O)$_2$**. The reason seems to be the long PEG chains, which hinder the transport through the cell membrane.

Therefore, uptake of the dendrimers was quantified in a second experiment by fluorescence measurement. The dansyl label is inert against hydrolytic cleavage as determined by

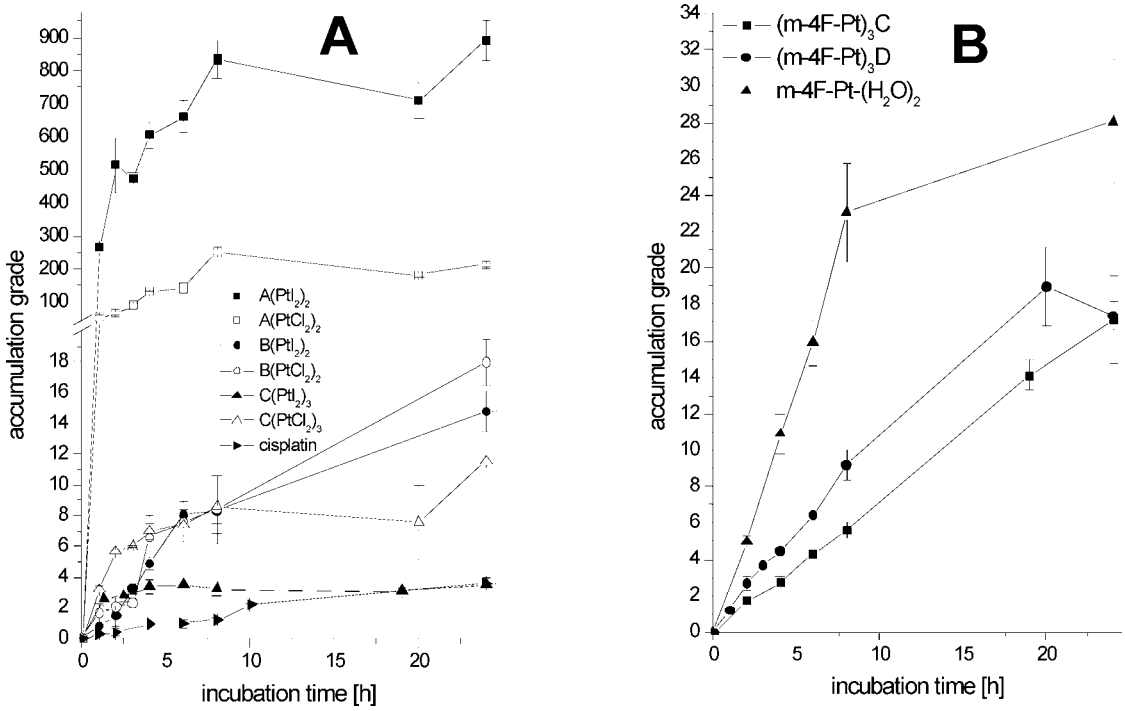


Figure 2. Accumulation of PtX_2−dendrimer conjugates (X = Cl, I) (A) and dendrimer-bound [*meso*-1,2-bis(4-fluorophenyl)ethylenediamine]-platinum(II) (B) in MCF-7 cells ($n = 3$).

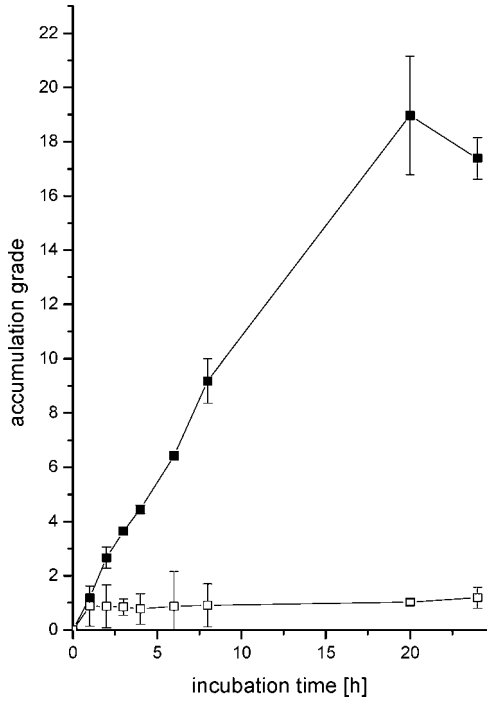


Figure 3. Cellular uptake of **(m-4F-Pt)D** by MCF-7 cells determined by GF-AAS (■) and fluorimetry (□) ($n = 3$).

capillary electrophoretic assays (*29*) so that the cellular content of fluorophor correlates with the cellular content of the dendrimer.

The fluorimetric measurement indicated an accumulation grade of 1 for the platinum-free dendrimer **D** (*27*) and **(m-4F-Pt)$_3$D** (Figure 3). Therefore, the increased platinum content in the tumor cells as depicted in Figures 2 and 3 determined by GF-AAS resulted from a platinum release in cell medium and a transfer into the cells independent of the dendrimer. The graphs of **(m-4F-Pt)$_3$C** and **(m-4F-Pt)$_3$D** depicted in Figure 2B indicate a slow release (not a burst) of the platinum complexes.

As the **m-4F-Pt** molecules are bound by carboxylic groups to the dendrimer, it is possible to release **m-4F-Pt(H$_2$O)$_2$** complexes in hydrolytic processes or substitution reactions. From studies with carboplatin and related m-4F-Pt derivatives (*30*−*32*), it is well-known that hydrolysis is very slow, but nucleophiles, e.g., chlorine, liberate platinum complexes in a faster kinetic. Therefore, it is very likely that the platinum(II) complexes were taken up as neutral dichloro rather than cationic aqua or diaqua species (*33*). This assumption was confirmed by the results of the same experiment done with the very stable **B(PtI$_2$)$_2$**. The intracellular platinum concentration correlated with the fluorophor content (data not shown) and demonstrated an incorporation of the platinum bound dendrimer into the cells without degradation.

Studies on the Uptake Mechanism. The uptake of polymeric compounds in tumor cells can be achieved in various pathways (*39*). In order to get information about possible pathways for cellular uptake, we selectively block those using specific inhibitors.

In an initial study, the cells were treated with the compounds at 4 and 37 °C. The reduced uptake at 4 °C determined for **A(PtI$_2$)$_2$**, **A(PtCl$_2$)$_2$**, and **C(PtI$_2$)$_3$** (40−50%) and for **(m-4F-Pt)$_3$D** and **m-4F-Pt(H$_2$O)$_2$** (more than 90%) indicated energy-depending pathways including the endosomal routes (e.g., macropinocytosis) and caveolin/clathrin-dependent uptake.

In the next step, the cells were coincubated with inhibitors of endocytosis (Figure 4). Chlorpromazine suppressed the accumulation of **A(PtI$_2$)$_2$**, **A(PtCl$_2$)$_2$**, and **C(PtI$_2$)$_3$** comparable to the temperature lowering experiment (about 40−50%), while other inhibitors such as amiloride and nystatin caused no effect. Therefore, we concluded that these conjugates cross the membrane by clathrin-dependent endocytosis after adsorption to the cell surface.

No inhibitor coincubated with **(m-4F-Pt)$_3$D** or **m-4F-Pt(H$_2$O)$_2$** showed effects as strong as the reduction of the temperature to 4 °C. Chlorpromazine (about 20% for **(m-4F-Pt)$_3$D** and **m-4F-Pt(H$_2$O)$_2$**) and genistein (about 20% for **(m-4F-Pt)$_3$D** and 40% for **m-4F-Pt(H$_2$O)$_2$**) reduced the cellular uptake. Nystatin and amiloride only inhibited the uptake of

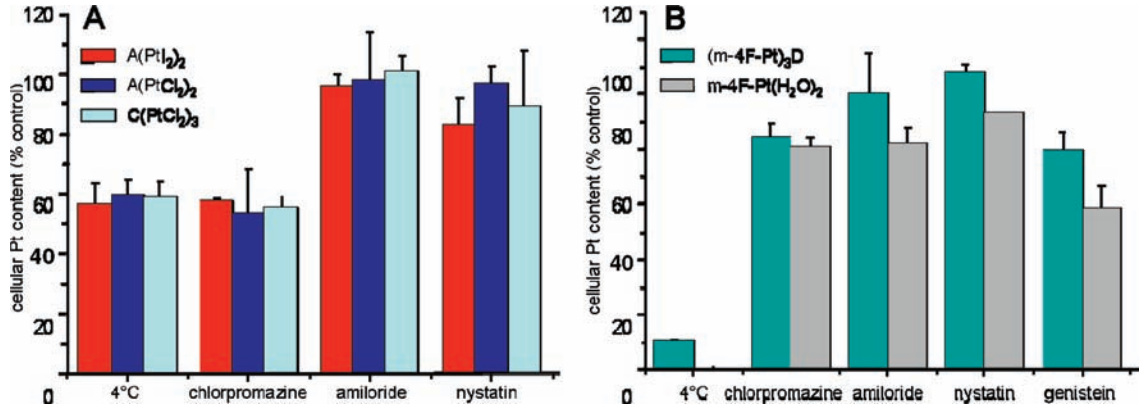


Figure 4. Effect of different endocytosis inhibitors on the cellular uptake of **A(PtI$_2$)$_2$**, **A(PtCl$_2$)$_2$**, and **C(PtCl$_2$)$_3$** (A) and **(m-4F-Pt)$_3$D** and **m-4F-Pt(H$_2$O)$_2$** (B).

Table 1. Quantification of Platinum in the Nuclei and DNA of MCF-7 Cells ($n = 3$)

compound	total amount of platinum in the nuclei [ng Pt/mg protein]	DNA-bound fraction [pg Pt/μg DNA]
cisplatin	10.00 ± 1.12	17.6 ± 1.0
A(PtCl$_2$)$_2$	2107 ± 267	325 ± 34
A(PtI$_2$)$_2$	10594 ± 346	1081 ± 258
B(PtCl$_2$)$_2$	1866 ± 298	122 ± 25
B(PtI$_2$)$_2$	7647 ± 676	44 ± 6
C(PtCl$_2$)$_3$	157 ± 5	19 ± 3
C(PtI$_2$)$_3$	216 ± 25	12.5 ± 2.2
m-4F-PtCl$_2$	165 ± 8	35.0 ± 7.2
(m-4F-Pt)$_3$C	147 ± 7	49 ± 2
(m-4F-Pt)$_3$D	43.7 ± 0.7	14.5 ± 0.4

Table 2. Protein Binding Characteristics with Human Serum Albumin (HSA) ($n = 3$ for the recovery experiments)

compound	free amount of Pt after ultrafiltration [%]	free amount of Pt after ethanol precipitation [%]	reaction rate for the irreversible binding to HAS $k \times 10^3$[min^{-1}]
cisplatin	76 ± 4	100 ± 6	5.35
m-4F-PtCl$_2$	51 ± 6	92 ± 5	6.81
m-4F-Pt(H$_2$O)$_2$	19 ± 1	37 ± 1	6.40
carboplatin	77 ± 1	101 ± 5	0.22
A(PtCl$_2$)$_2$	20 ± 1	62 ± 1	10.5
A(PtI$_2$)$_2$	1.6 ± 0.9	0.6 ± 0.3	n.d.
B(PtCl$_2$)$_2$	1.4 ± 0.8	4 ± 0.1	n.d.
B(PtI$_2$)$_2$	1.5 ± 0.3	1.5 ± 0.2	n.d.
C(PtCl$_2$)$_3$	32 ± 4	95 ± 1	16.7
C(PtI$_2$)$_3$	6 ± 1	49 ± 1	n.d.
(m-4F-Pt)$_3$C	23 ± 1	49 ± 1	3.40
(m-4F-Pt)$_3$D	20 ± 2	47 ± 2	1.88

n.d.: not determinable.

m-4F-Pt(H$_2$O)$_2$ by about 10% and 20%, respectively. Due to the low effects, a clear statement about the accumulation pathway of these compounds is impossible.

Platinum Content in Nuclei and Binding to DNA. After transfer through the membrane, the conjugates can reach various cell compartments. As the DNA represents the main target of platinum complexes in tumor cells, it is of interest to know the platinum content in the nuclei. For this purpose, MCF-7 cells were incubated for 24 h with the respective platinum−dendrimer conjugate (concentration: 5 μM). The nuclei and DNA were isolated, and the platinum content was measured by GF-AAS (Table 1).

The reference cisplatin caused a nuclear platinum content of 10.0 ng Pt/mg protein, efficiently bound to DNA. The recovered platinum amounted to 17.6 pg Pt/μg DNA and correlated with data from the literature (*34*).

The platinum contents in the nuclei of cells treated with **A(PtCl$_2$)$_2$** and **A(PtI$_2$)$_2$** were 210-fold (2107.0 ng Pt/mg protein) and 1060-fold (10 594.0 ng Pt/mg protein), respectively, higher compared to cisplatin, while at the DNA, only 18.5- and 61.5-fold higher platinum contents were determined.

Higher dendrimer generation and dansyl residues did not substantially change the platinum amount in the nuclei (**B(PtCl$_2$)$_2$**, 1866.0 ng Pt/mg protein; **B(PtI$_2$)$_2$**, 7647.0 ng Pt/mg protein) but reduced the DNA-bound fraction to 122.0 pg Pt/μg DNA (**B(PtCl$_2$)$_2$**, 6.9-fold compared to cisplatin) and 44.0 pg Pt/μg DNA (**B(PtI$_2$)$_2$**, 2.5-fold compared to cisplatin). An explanation of these findings might be the precipitation of the dendrimers at the surface of the nuclei as microscopically demonstrated for these dendrimers carrying 6 dansyl labels (*18*). They also showed a nearly linear accumulation kinetic without saturation comparable to **B(PtI$_2$)$_2$** and **B(PtCl$_2$)$_2$** (*27*).

This assumption was supported by the results of the water-soluble derivatives **C(PtI$_2$)$_2$** and **C(PtCl$_2$)$_2$**, which showed lowered nuclear platinum contents (**C(PtI$_2$)$_2$**, 216.0 ng Pt/mg protein; **C(PtCl$_2$)$_2$**, 157.0 ng Pt/mg protein) and DNA binding (**C(PtCl$_2$)$_2$**, 19.0 pg Pt/μg DNA: **C(PtI$_2$)$_2$**, 12.5 pg Pt/μg DNA). An effect of the PEG chain cannot be excluded because **(m-4F-Pt)$_3$C** and **(m-4F-Pt)$_3$D** showed results in the same range.

The results of **(m-4F-Pt)$_3$C** and **(m-4F-Pt)$_3$D**, however, have to be interpreted with caution because of their instability and release of **m-4F-Pt** moieties. Therefore, **m-4F-PtCl$_2$** was used as a reference. This selection is suitable since **m-4F-Pt(H$_2$O)$_2$** if released is quickly converted (less than 1 h) in the presence of chlorine into **m-4F-PtCl$_2$** (*20*).

The nuclei of cells treated with **m-4F-PtCl$_2$** showed a 16.5-fold higher platinum content (165.0 ng Pt/mg protein) than cisplatin, very similar to that obtained with **(m-4F-Pt)$_3$C** (147.0 ng Pt/mg protein). Interestingly, **(m-4F-Pt)$_3$D** (43.7 ng Pt/mg protein) caused only a third of the nuclear platinum content of **m-4F-PtCl$_2$** and **(m-4F-Pt)$_3$C**.

Cells treated with **m-4F-PtCl$_2$** showed a two times higher DNA platination (35.0 pg Pt/μg DNA) than cisplatin despite a 16.5-fold higher nuclear content. For the PEG-bearing conjugates, a clear trend could not be derived. **(m-4F-Pt)$_3$C** caused higher (49.0 pg Pt/μg DNA) and **(m-4F-Pt)$_3$D** lower (14.5 pg Pt/μg DNA) platinum content at the DNA than **m-4F-PtCl$_2$**.

In conclusion, the DNA platination achieved with the conjugates was higher than that obtained with cisplatin. An exception represented **(m-4F-Pt)$_3$D** with a DNA-Pt adduct content comparable to cisplatin.

Binding to Human Serum Albumin. Finally, it is necessary to estimate the binding to human serum albumin (HSA), because it is well-known that the binding to HSA alters the biological activity of platinum complexes. The reactivity of bound complexes is lowered, and they only marginally contribute to the antitumor activity as already reported for a set of polynuclear

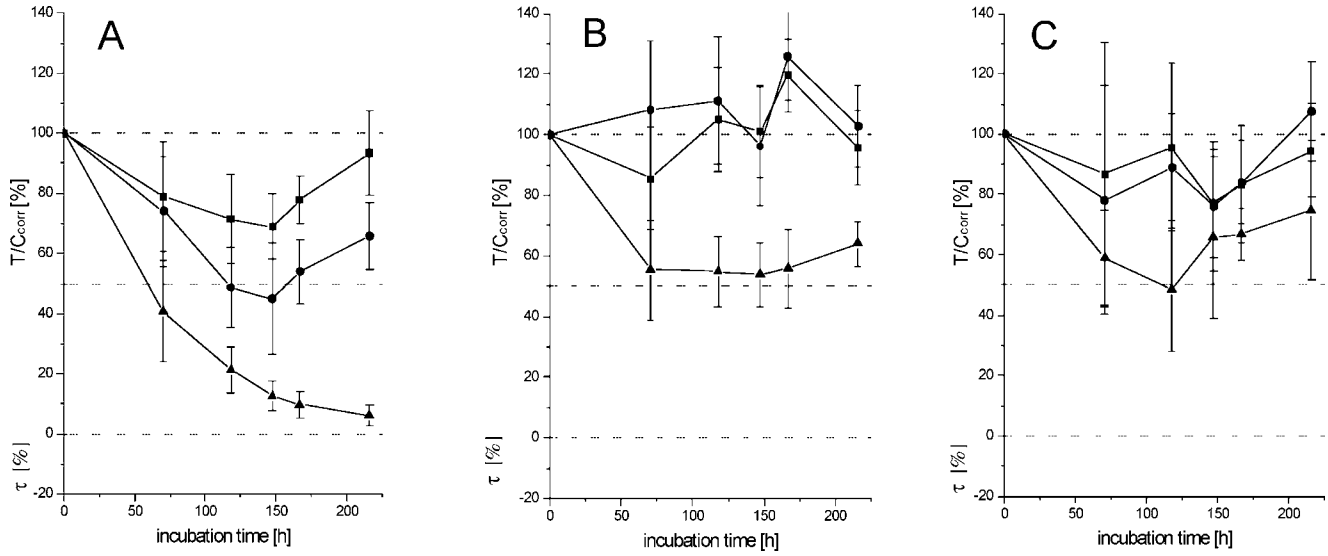


Figure 5. Cytotoxicity of cisplatin (A), **A(PtCl$_2$)$_2$** (B), and **C(PtCl$_2$)$_3$** (C) against MCF-7-cells (■ 0.5 μM, ● 1.0 μM, ▲ 5.0 μM) (n = 16).

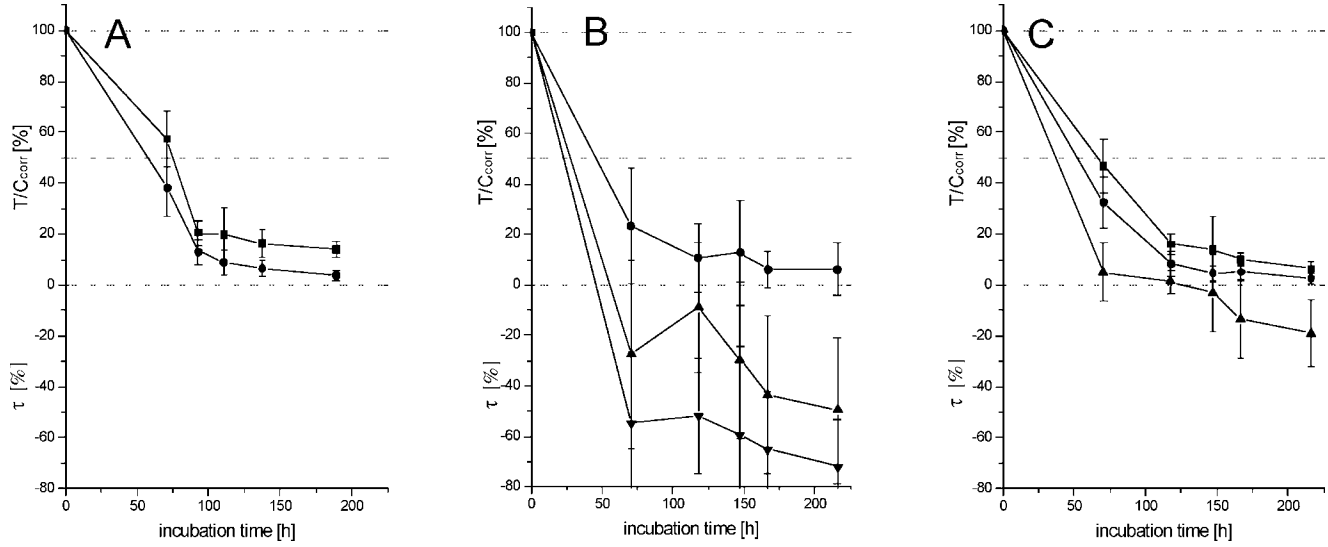


Figure 6. Cytotoxicity of **m-4F-Pt(H$_2$O)$_2$** (A), (**m-4F-Pt)$_3$C** (B), and **(m-4F-Pt)$_3$D** (C) against MCF-7 cells (■ 2.5 μM, ● 5.0 μM, ▲ 10.0 μM, ▼ 20 μM) (n = 16).

drugs (*39*). Therefore, the platinum−dendrimer conjugates were incubated with HSA and the protein-unbound fraction was quantified after ultrafiltration (quantification of unbound drug) and ethanolic precipitation (quantification of reversible lipophilic bound drug) by GF-AAS (Table 2).

Cisplatin, carboplatin, **m-4F-Pt(H$_2$O)$_2$**, and **m-4F-PtCl$_2$** were used as references. After ultrafiltration, they showed recovery rates of 76%, 77%, 19%, and 51%, respectively. The free proportion of platinum increased, except for **m-4F-Pt(H$_2$O)$_2$**, in all cases to 90−100% after ethanol precipitation. This means that **m-4F-Pt(H$_2$O)$_2$** is much more strongly bound to the proteins than the other complexes, very likely by coordination.

All platinum−dendrimer conjugates strongly interact with HSA. For **A(PtI$_2$)$_2$**, **B(PtI$_2$)$_2$**, **B(PtCl$_2$)$_2$**, and **C(PtI$_2$)$_3$**, a very low recovery rate (below 6%) was determined, which increased only for **C(PtI$_2$)$_3$** after ethanol precipitation (49%). **A(PtCl$_2$)$_2$** and **C(PtCl$_2$)$_3$** were much more weakly bound (recovery in the ultrafiltrate, 20% and 32%; after ethanol precipitation, 62% and 95%, respectively). The m-4F derivatives **(m-4F-Pt)$_3$C** and **(m-4F-Pt)$_3$D** (recovery in the ultrafiltrate of about 22%; after ethanol precipitation about 48%) showed a binding characteristic to HSA similar to that of **m-4F-Pt(H$_2$O)$_2$**. A complete displacement from the protein comparable to **m-4F-PtCl$_2$** was not achieved. This confirmed the release of the [*meso*-1,2-bis(4-fluorophenyl)ethylenediamine]platinum(II) from the polymer.

In order to gain insight into the mode of action, we calculated the reaction rate of irreversible protein binding. The reference compounds **m-4F-PtCl$_2$** and **m-4F-Pt(H$_2$O)$_2$** had a slightly higher reactivity toward HSA (6.81 and 6.4 $\times$ 10^{-3} min^{-1}, respectively) than cisplatin (5.35 $\times$ 10^{-3} min^{-1}).

The dichloroplatinum(II) derivatives **A(PtCl$_2$)$_2$** and **C(PtCl$_2$)$_3$** are somewhat more reactive (10.5 and 16.7 $\times$ 10^{-3} min^{-1}, respectively) than cisplatin or the other reference compounds. Because these compounds possess two (**A(PtCl$_2$)$_2$**) or three (**C(PtCl$_2$)$_3$**) platinum moieties, the optimal orientation to the binding sites seems to be possible, resulting in faster HSA binding.

Carboxyl groups lower the reactivity of platinum(II) complexes. For instance, carboplatin did not hydrolyze in aqueous solution (*30*) but underwent direct substitution reactions with bionucleophils, resulting in a low reaction rate of 0.22 $\times$ 10^{-3} min^{-1} for the irreversible HSA binding.

The Pt−O bond of the dendrimers **(m-4F-Pt)$_3$C** and **(m-4F-Pt)$_3$D** is not as stable as in carboplatin and is cleaved with a

higher reaction rate (**(m-4F-Pt)$_3$C**, 3.4 × 10^{-3} min^{-1}; **(m-4F−Pt)$_3$D**, 1.88 × 10^{-3} min^{-1}).

For carboplatin and its derivatives, it is suggested that activation by S-containing nucleophils such as methionine (*35*) occurs. A total of five specific binding sites were identified for cisplatin at HSA, including the cysteine residue C34, two methionine sites (M329, M548), and the tyrosine and aspartate O-donor sites Y150 (or Y148) and D375 (or E376) (*36*). So, we assume that the methionine residues were able to replace the dicarboxylate acid in carboplatin (*37*), **(m-4F-Pt)$_3$C**, and **(m-4F-Pt)$_3$D**.

Cytotoxicity against MCF-7 Cells. The platinum−dendrimer conjugates were tested for cytotoxicity against MCF-7 breast cancer cells. Because of the lower water solubility, the concentration of **A(PtX$_2$)$_2$** and **B(PtX$_2$)$_2$** was limited to 5 μM, while the PEG conjugates **(m-4F-Pt)$_3$C** and **(m-4F-Pt)$_3$D** were tested up to 20 μM.

The obtained results confirmed our assumption of weak interactions between platinum−dendrimer conjugates and the DNA. Although all conjugates caused higher platinum content in the nuclei and at the DNA than cisplatin, the cytotoxic effects are quite low. It is well-known that inactivity of PtI_2 complexes results from the low hydrolysis rate of the Pt−I bond, while the $PtCl_2$ moieties can bind after aquation to nucleobases. If the $PtCl_2$ group is attached at macromolecules, steric effects hinder the binding to nucleobases. This might be the reason for the inactivity of **A(PtI$_2$)$_2$**, **B(PtI$_2$)$_2$**, **B(PtCl$_2$)$_2$**, and **C(PtI$_2$)$_3$**. **A(PtCl$_2$)$_2$** and **C(PtCl$_2$)$_3$** showed at a concentration of 5 μM about 50% inhibition of cell proliferation after 72−96 h (Figure 5B,C).

A(PtCl$_2$)$_2$ seems to be small enough to be coordinated to DNA. It can be interpreted as dinuclear platinum compounds, which were preferentially accumulated in tumor cells by endocytosis (*38*) taken up to a high extent in the nucleus and bound to DNA (*39*). For compounds of similar molecular weights, an inhibitory effect on cell proliferation was observed (*39*−*42*). **C(PtCl$_2$)$_3$** caused a significantly lower platinum concentration in the tumor cells/nuclei compared to **A(PtCl$_2$)$_2$** but showed comparable cytotoxicity. Therefore, another mode of action of action is very likely.

The dendrimers act in **(m-4F-Pt)$_3$C** and **(m-4F-Pt)$_3$D** as leaving groups. Such dicarboxylic platinum(II) compounds were activated in the tumor cells by hydrolysis reactions or nucleophilic attack. The released m-4F-Pt complex interacted then with the DNA building intrastrand cross-links (*43*, *44*). However, this reaction can occur prior to the transfer into the tumor cells.

m-4F-Pt(H$_2$O)$_2$, **(m-4F-Pt)$_3$C**, and **(m-4F-Pt)$_3$D** reduced at 5 μM the proliferation of MCF-7 cells comparable to cisplatin (compare Figures 5 and 6). Higher concentrations (10 and 20 μM) of **(m-4F-Pt)$_3$D** did not increase the cytotoxicity (Figure 6C), while in the case of **(m-4F-Pt)$_3$C**, strong cytocidal effects were detected (Figure 6B). Like cisplatin, all three compounds showed their maximum effect after 200 h, without recovery of cell proliferation.

In contrast to dendrimer **B**, which reduced the proliferation of MCF-7 cells by 80% (*18*), dendrimers **C** and **D** did not influence the cell growth. The observed cytotoxicity must be the consequence of the release of m-4F-Pt species from the macromolecule. A contamination of nonbound platinum complex resulting from the synthesis can be excluded because of the high purity determined in CE analyses (see Supporting Information).

CONCLUSION

In this structure−activity study, we investigated the pharmacological characteristics of platinum−dendrimer conjugates. The antiproliferative activity, the cellular uptake, the platinum content in cell nuclei, and the binding to DNA and HSA were determined. Conjugates were taken up by adsorptive endocytosis and reached the nuclei. The data pointed to weak binding to DNA not able to cause antiproliferative effects. Only **A(PtCl$_2$)$_2$** and **C(PtCl$_2$)$_2$** were active against MCF-7 cells. M-4F-Pt conjugates were at least as cytotoxic as cisplatin. It is very likely that **(m-4F-Pt)$_3$C** and **(m-4F-Pt)$_3$D** liberate **m-4F-Pt(H$_2$O)$_2$** or **m-4F-PtCl$_2$** as the real antitumor agent unfortunately before entering the cells. Dendrimer **A**, however, was identified as an excellent carrier molecule and caused very high intracellular platinum content (up to 445-fold in relation to dendrimer (**A(PtCl$_2$)$_2$**)-bound Pt molecules). In the next step, we will modify the conjugates (e.g., **A(PtCl$_2$)$_2$**) in such a way that cytostatics are selectively released in tumor cells.

ACKNOWLEDGMENT

The technical assistance of M. Wenzel is acknowledged. The presented study was supported by grants Gu285/4-1, Gu285/5-1 and Gu285/5-2 from the Deutsche Forschungsgemeinschaft.

Supporting Information Available: Electropherograms of the target compounds. This material is available free of charge via the Internet at http://pubs.acs.org.

LITERATURE CITED

(1) De Jesus, O. L. P., Ihre, H. R., Gagne, L., Frechet, J. M. J., and Szoka, F. C. (2002) Polyester dendritic systems for drug delivery applications: In vitro and in vivo evaluation. *Bioconjugate Chem. 13*, 453–461.

(2) Noguchi, Y., Wu, J., Duncan, R., Strohalm, J., Ulbrich, K., Akaike, T., and Maeda, H. (1998) Early phase tumor accumulation of macromolecules: A great difference in clearance rate between tumor and normal tissues. *Cancer Res. 89*, 307–314.

(3) Gillies, E. R., Dy, E., Frechet, J. M. J., and Szoka, F. C. (2005) Biological evaluation of polyester dendrimer: Poly(ethylene oxide) "bow-tie" hybrids with tunable molecular weight and architecture. *Mol. Pharmacol. 2*, 129–138.

(4) Maeda, H. (1991) SMANCS and polymer-conjugated macromolecular drugs: Advantages in cancer chemotherapy. *Adv. Drug Delivery Rev. 6*, 181–202.

(5) Tarakura, Y., Mahato, R. I., and Hashida, M. (1998) Extravasation of macromolecules. *Adv. Drug Delivery Rev. 34*, 93–108.

(6) Barnes , K. R., and Lippard, S. J. (2004) Cisplatin and related anticancer drugs: Recent advances and insights, In *Metal Ions in Biological Systems* (Sigel, A., Sigel, H., and Sigel, R., Eds.) Vol. 42, Metal Complexes in Tumor Diagnosis and as Anticancer Agents, pp 143−177, Marcel Dekker.

(7) Fuertes, M. A., Castilla, J., Alonso, C., and Perez, J. M. (2002) Novel concepts in the developement of platinum antitumor drugs. *Curr. Med. Chem. Anti-Cancer Agents 2*, 539–551.

(8) Ishida, S., Lee, J., Thiele, D. J., and Hershkowitz, I. (2002) Uptake of the anticancer drug cisplatin mediated by the copper transporter Ctr1 in yeast and mammals. *Proc. Natl. Acad. Sci. U.S.A. 99*, 14298–14302.

(9) Katano, K., Kondo, A., Safaei, R., Holzer, A., Samimi, G., Mishima, M., Kuo, Y. M., Rochdi, M., and Howell, S. B. (2002) Acquisition of resistance to cisplatin is accompanied by changes in the cellular pharmacology of copper. *Cancer Res. 62*, 6559–6565.

(10) Gianasi, E., Buckley, R. G., Latigo, J., Wasil, M., and Duncan, R. (2002) HPMA-copolymers platinates containing dicarboxylato ligands. Preparation, characterisation and in vitro and in vivo evaluation. *J. Drug Targeting 10*, 549–556.

(11) Gianasi, E., Wasil, M., Evagorou, E. G., Keddle, A., Wilson, G., and Duncan, R. (1999) HPMA-copolymer platinates as novel antitumor agents: In-vitro properties, pharmacokinetics and antitumor activity in vivo. *Eur. J. Cancer 35*, 994–1002.

(12) Neuse, E. W., Caldwell, G., and Perlwitz, A. G. (1995) Cis-diaminedichloroplatinum(II) complexes reversibly bound to water-soluble polyaspartamide carriers for chemotherapeutic applications. II: Platinum coordination to ethylenediamine ligands attached to poly(ethylene oxide)-grafted carrier polymers. *J. Inorg. Organomet. Polym. 5*, 195–207.

(13) Schechter, B., Pauzner, R., Wilchek, M., and Arnon, R. (1986) Cis-platinum(II) complexes of carboxy-dextran as potential antitumor agents II. In vitro and in vivo activity. *Cancer Biochem. Biophys. 8*, 289–298.

(14) Ohya, Y., Masunaga, T., Baba, T., and Ouchi, T. (1996) Synthesis and cytotoxic activity of dextran-immobilizing platinum(II) complex through chelate-type coordination bond. *J.M.S. Pure Appl. Chem A33*, 1005–1016.

(15) Imai, T., Fujii, K., Shiraishi, S., and Otagiri, M. (1997) Alteration of pharmacokinetics and nephrotoxicity of cisplatin by alginates. *J. Pharm. Sci. 86*, 244–247.

(16) Malik, N., Duncan, R., Tomalia, D., and Esfand, E. (2003) Dendritic-antineoplastic drug delivery system, U.S. Patent 2003 0064050.

(17) Malik, N., Evagorou, E. G., and Duncan, R. (1999) Dendrimer-platinate: A novel approach to cancer chemotherapy. *Anti-Cancer Drugs 10*, 767–776.

(18) Fuchs, S., Kapp, T., Otto, H., Schöneberg, T., Franke, P., Gust, R., and Schlüter, A. D. (2004) A surface-modified dendrimer set for potential application as drug delivery vehicles: Synthesis, in vitro toxicity, and intracellular localization. *Chem.—Eur. J. 10*, 1167–1192.

(19) Müller, S., and Schlüter, A. D. (2005) Synthesis of water-soluble, multiple functionalizable denrons for the conversion of large dendrimers or other molecular objects into potential drug carriers. *Chem.—Eur. J. 11*, 5589–5610.

(20) Müller, R., Gust, R., Jennerwein, M., Reile, H., Laske, R., Krischke, W., Bernhardt, G., Spru*β*, T., Engel, J., and Schönenberger, H. (1989) Tumor inhibiting [1,2-bis(4-fluorophenyl)ethylenediamine]platinum(II) complexes. Part I: Synthesis. *Eur. J. Med. Chem. 24*, 341–348.

(21) Bernhardt, G., Reile, H., Spru*β*, T., Koch, M., Gust, R., Schönenberger, H., Hollstein, M., Lux, F., and Engel, J. (1991) (±)-(D,L)-[1,2-Bis(4-fluorophenyl)ethylenediamine]dichloroplatinum-(II). *Drugs Fut. 16*, 899–903.

(22) Reile, H., Birnböck, H., Bernhardt, G., Spru*β*, T., and Schönenberger, H. (1990) Computerized determination of growth kinetic curves and doubling times from cells in microculture. *Anal. Biochem. 187*, 262–267.

(23) Bradford, M. M. (1976) A rapid and sensitive method for the quantitation of microgram quantities of protein utilizing the principle of protein-dye binding. *Anal. Biochem. 72*, 248–254.

(24) Gust, R., Schnurr, B., Krauser, R., Bernhardt, G., Koch, M., Schmid, B., Hummel, E., and Schönenberger, H. (1998) Stability and cellular studies of [rac-1,2-bis(4-fluorophenyl)ethylenediamine][cyclobutane-1,1-dicarboxylato]platinum(II), a novel, highly active carboplatin derivative. *J. Cancer Res. Clin. Oncol. 124*, 585–597.

(25) Vytasek, R. (1982) A sensitive fluorometric assay for the determination of DNA. *Anal. Biochem. 120*, 243–248.

(26) Laws, G. M., and Adams, S. P. (1996) Measurement of 8-OHdG in DNA by HPLC/ ECD: The importance of DNA purity. *Biotechniques 20*, 36–38.

(27) Kapp, T., Schäfer, M., and Gust, R. Cellular uptake of dansyl labeled dendrimers. in preparation

(28) Balzani, V., Ceroni, P., Gestermann, S., Gorka, M., Kauffmann, C., and Vögtle, F. (2000) Effect of proton and metal ions on the fluorescence properties of a polylysine dendrimer containing twenty four dansyl units. *J. Chem. Soc., Dalton Trans.* 3765–3771.

(29) Kapp, T., Francke, P., and Gust, R. (2008) Investigations on surface modified dendrimers: enzymatic hydrolysis and uptake into MCF-7 breast cancer cells. *ChemMedChem 3*, 635–641.

(30) Schnurr, B., and Gust, R. (1999) Investigations on the stability of carboplatin infusion solutions. *Monatsh. Chem. 130*, 637–644.

(31) Gust, R., Krauser, R., Schmid, B., and Schönenberger, H. (1998) Synthesis and antitumor activity of [1,2-bis(4-fluorophenyl)ethylenediamine][dicarboxylato]platinum(II) complexes. *Arch. Pharm.- Pharm. Med. Chem. 331*, 27–35.

(32) Schäfer, S., Ott, I., Gust, R., and Sheldrick, W. S. (2007) Influence of the polypyridyl (pp) ligand size on the DNA binding properties, cytotoxicity and cellular uptake of organoruthenium(II) complexes of the type $[(\eta^6\text{-}C_6Me_6)Ru(L)(pp)]^{n+}$ [L = Cl, $n = 1$; L = $(NH_2)_2CS$, $n = 2$]. *Eur. J. Inorg. Chem. 19*, 3034–3046.

(33) Reile, H., Bernhardt, G., Koch, M., Schönenberger, H., Hollstein, M., and Lux, F. (1992) Chemosensivity of human MCF-7 breast cancer cells to diastereomeric diaqua(1,2-diphenylethylenediamine)platinum(II) sulfates and specific platinum accumulation. *Cancer Chemother. Pharmacol. 30*, 113–122.

(34) Amtmann, E., Zöller, M., Wesch, H., and Schilling, G. (2001) Antitumoral activity of a sulphur-containing platinum complex with an acidic pH optimum. *Cancer Chemother. Pharmacol. 41*, 461–466.

(35) Natarajan, G., Malathi, R., and Holler, E. (1999) Increased DNA-binding activity of cis-1,1-cyclobutanedicarboxylatodiammineplatinum(II) (carboplatin) in the presence of nucleophiles and human breast cancer MCF-7 cell cytoplasmic extracts: Activation theory revisted. *Biochem. Pharmacol. 58*, 1625−1629.

(36) Will, J., Wolters, D. A., and Sheldrick, W. S. (2008) Characterisation of cisplatin binding sites in human serum proteins using hyphenated multidimensional liquid chromatography and ESI tandem mass spectrometry. *ChemMedChem 3*, 1696–1707.

(37) Guo, Z., Hambley, T. W., Socorro, P., Sadler, P. J., and Frey, U. (1997) Chelate-ring-opened adducts of [Pt(en)(Me-Mal-O, O')] (en=ethane-1,2-diamine, Me-Mal=2-methylmalonate) with methionine derivatives: Relevance to the biological activity of platinum anticancer agents. *J. Chem. Soc., Dalton Trans.* 469–478.

(38) Kapp, T., Müller, S., and Gust, R. (2006) Dinuclear alkylamine platinum(II) complexes of [1,2-bis(4-fluorophenyl)ethylenediamine]platinum(II): Influence of endocytosis and copper and organic cation transport systems on cellular uptake. *ChemMedChem 1*, 560–564.

(39) Kapp, T., Dullin, A., and Gust, R. (2006) Mono- and polynuclear [alkylamine]platinum(II) complexes of [1,2-bis(4-fluorophenyl)ethylendiamine]platinum(II): Synthesis and investigations on cytotoxicity, cellular distribution and DNA and protein binding. *J. Med. Chem. 49*, 1182–1190.

(40) Cesar, E. T., de Almeida, M. V., Fontes, A. P. S., Maia, E. C. P., Garnier-Suillerot, A., Couri, M. R. C., and Felicio, E. C. A. (2003) Synthesis, characterization, cytotoxic activity, and cellular accumulation of dinuclear platinum complexes derived from N, N'-di-(2-aminoethyl)-1,3-diamino-2-propanol, aryl substituted N-benzyl-1,4-butanediamines, and N-benzyl-1,6-hexanediamines. *J. Inorg. Biochem. 95*, 297–305.

(41) Messori, L., Shaw, J., Camalli, M., Mura, P., and Marcon, G. (2003) Structural features of a new dinuclear platinum(II) complex with significant antiproliferative activity. *Inorg. Chem. 42*, 6166–6168.

(42) Teixeira, L. J., Seabra, M., Reis, E., da Cruz, M. T. G., de Lima, M. C. P., Pereira, E., Miranda, M. A., and Marques, M. P. M. (2004) Cytotoxic activity of metal complexes of biogenic polyamines: Polynuclear platinum(II) chelates. *J. Med. Chem. 47*, 2917–2925.

(43) Vom Orde, H.-D., Reile, H., Müller, R., Gust, R., Bernhardt, G., Spru*β*, T., Schönenberger, H., Burgemeister, T., and Mannschreck, A. (1990) Tumor-inhibiting [1,2-bis(fluorophenyl)ethylenediamine]platinum(II) complexes. *J. Cancer Res. Clin. Oncol. 116*, 434–438.

(44) Lindauer, E., and Holler, E. (1996) Cellular distribution and cellular reactivity of platinum (II) complexes. *Biochem. Pharmacol. 52*, 7–14.

BC900406M

Asymmetric Secondary and Tertiary Streptavidin/DNA Complexes Selectively Formed in a Nanometer-Scale DNA Well

Kentaro Numajiri, Akinori Kuzuya,* and Makoto Komiyama*

Research Center for Advanced Science and Technology, The University of Tokyo, 4-6-1 Komaba, Meguro, Tokyo 153-8904, Japan. Received September 26, 2009; Revised Manuscript Received January 7, 2010

Rectangular DNA motifs, which each have a built-in cavity in the middle, were prepared by bundling nine DNA helices into a U-shaped tile first and then assembling two of them together. The cavity was modified with two or three biotin molecules and was used as a nanometer-sized well to capture a single streptavidin (SA) tetramer size-selectively. Selective, one-step formation of asymmetric secondary or tertiary SA/DNA complexes via bidentate or tridentate capture have been shown by analyses of the complexes with denaturing polyacrylamide gel electrophoresis. When biotinylated DNA was simply added to the solution of SA, only symmetric SA/DNA complexes were formed as a mixture of primary to quaternary complexes, depending on the amount of DNA. However, when the DNA motif was preformed prior to SA addition, the asymmetric secondary complex was preferentially formed. The yield of the asymmetric secondary complex was ca. 50% when biotins were tethered to the two-turn well (6.8 nm wide) via 2.3 nm linkers, whereas the yield of the mixture of symmetric and asymmetric secondary complexes was only 7% for the reaction in bulk solution under the corresponding conditions. The larger the size of the well, the lower the yield became. Selective formation of asymmetric tertiary complex was also successful. Treatment of a SA tetramer captured in a well with a biotinylated, long dsDNA has shown that the captured SA still preserves its binding ability to additional biotinylated target.

INTRODUCTION

Protein nanoarrays of regularly ordered and orientated individual molecules should have important roles in future proteome studies. DNA nanotechnology (*1, 2*), which is based on programmed assembly of branched DNA helices, has been attracting great interest as a key technology in preparing scaffolds for nanopatterning of proteins. To date, various DNA nanostructures have been used as a scaffold for protein nanoarrays (*3*−*18*). Recently, we proposed a new strategy for fixation of proteins to a DNA scaffold that leads to robust and regulated protein nanoarrays; this strategy entails making nanometer-scale wells embedded in a DNA sheet and selectively capturing the target protein in these wells in a single-molecule manner, by "anchoring" it with two linkers (bidentate capture strategy, Scheme 1a.) We prepared either a tape-like DNA scaffold, by assembling U-shaped DNA tiles made of nine DNA helices (*19*), or a stick-like DNA origami (*20*), and put regularly arranged nanometer-scale wells in it. By attaching two biotins to the ends of DNA components at the two edges of each well, we have successfully and size-selectively captured just one streptavidin (SA) tetramer in a well and formed regular SA nanoarrays. The SA tetramers captured in a well are quite stable against repetitive AFM-tip scanning, providing a consistently clear image of the individual molecules. Although a significant difference in the stability of SA in a well was observed between the bidentate capture system and the monodentate system (*20*), there has been no direct evidence of the formation of an asymmetric secondary SA/DNA complex, in which two different biotinylated DNA strands are bound to SA. In addition to elucidating the size-selective SA capture, selective formation of such an asymmetric complex should be useful as a key component for nanofabrication of protein−DNA hybrids in other research fields related to protein engineering.

* (+81) 3 5452 5200; FAX: (+81) 3 5452 5209; E-mail: kuzu@mkomi.rcast.u-tokyo.ac.jp, komiyama@mkomi.rcast.u-tokyo.ac.jp.

SA is a tetrameric protein (molecular weight ≈ 58 kDa) and is one of the most popular tools in biochemical research along with its related proteins, such as avidin, owing to its enormously high affinity to biotin ($K_a \approx 10^{14}$ M^{-1} for free biotin, or 10^8 M^{-1} for avidin/PEGylated biotin interaction) (*21, 22*). Multiple studies on the formation of SA/DNA complexes and their applications in nanotechnology have been reported by several groups to date (*23*−*26*). However, the DNA portion employed in these studies is rather long (80 bp to 2 kbp) double-stranded (ds) DNA, and the properties of complexes between short single-stranded (ss) DNA and SA have not been well-studied. In addition, previously reported SA/DNA complexes are mostly symmetric complexes, in which the same DNA portion is multiply bound to SA, and as far as we know, there are no reports of simultaneous modification of SA with different strands as expected in the bidentate capture.

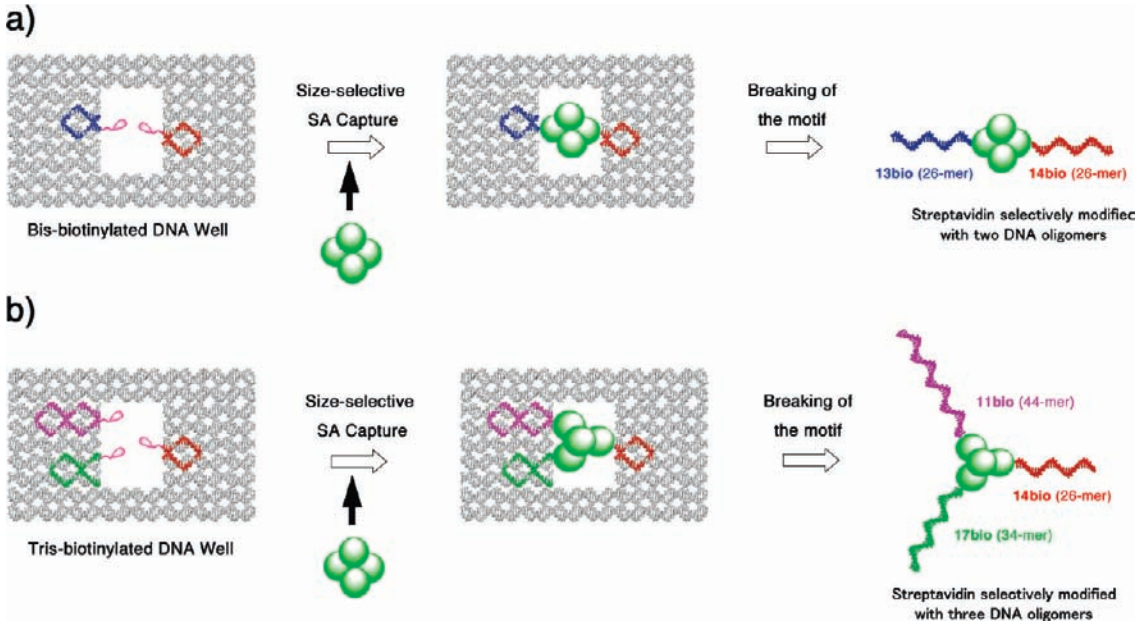
In this study, we have prepared new DNA motifs, each of which has a single well of varying size and biotinylated patterns, by assembling two U-shaped DNA bundles. After size-selectively capturing one SA molecule in a well, the motifs were broken down into the ssDNA components again under mild denaturing conditions, and the SA/DNA complexes formed in the well were analyzed in detail by polyacrylamide gel electrophoresis (PAGE).

EXPERIMENTAL PROCEDURES

Materials. Unmodified DNA strands were purchased from Sigma-Genosys (Japan) and used without further purification. Biotin-triethylene glycol (TEG)-modified strands for SA capture were chemically synthesized on an automated DNA synthesizer using biotin-TEG phosphoramidite monomer (Glen Research, VA) for the 5′-end and purified by denaturing PAGE and reverse-phase HPLC. SA was purchased from Sigma, GelStar was from Lonza Rockland (ME), and Quick-CBB was from Wako Pure Chemicals (Japan).

10.1021/bc900426p © 2010 American Chemical Society
Published on Web 01/21/2010

Scheme 1. Schematic Diagram of the Bidentate (a) and Tridentate (b) Capture of SA in a Well



Formation of DNA Tiles. The motifs were first formed as a U-shaped nine-helix bundle with 1 μM DNA (for each strand) in a solution containing 40 mM Tris, 20 mM acetic acid, 2 mM ethylenediaminetetraacetic acid, and 12.5 mM magnesium acetate (1× TAE/Mg buffer, total volume 100 μL). This mixture was cooled from 95 to 25 °C at a rate of −1.0 °C/min using a PCR thermal cycler. Separately annealed solutions of the two U-shaped bundles that correspond to the right and the left portions of the motif were then mixed together to form the desired dimer motif. After being kept at room temperature for 5 min, the mixture was treated with a gel-filtration microspin column (Microspin S-400HR, GE Healthcare, UK), which was equilibrated to 1× TAE/Mg buffer in advance, to remove incomplete fragments that are not precisely annealed. The concentration of the motifs after this process was estimated by measuring the UV absorbance at $\lambda = 260$ nm. Then, excess SA (final concentration, 1 μM) was added to the solution for size-selective capture.

AFM Imaging. AFM imaging of DNA tiles was performed on a SPA-300HV system (SII, Japan). After addition of SA, the DNA tile solution (3 μL) was deposited on a freshly cleaved mica substrate, additional 1× TAE/Mg buffer (200 μL) was added, and imaging was done using the fluid DFM scanning mode with a BL-AC40TS tip (Olympus, Japan).

Denaturing PAGE and Ferguson Analyses. Denaturing PAGE analyses were performed in gels containing 8−14% acrylamide (37.5:1, acrylamide/bisacrylamide), 4 M urea, 45 mM Tris, 45 mM boric acid, and 0.5 mM EDTA (0.5× TBE). Each sample solution was mixed with an equivalent amount of loading buffer containing 0.5× TBE, 7 M urea, 0.03% bromophenol blue, and 0.03% xylene cyanol FF and then loaded onto each gel without heating. For the size markers, a 100 bp DNA duplex ladder was used. It was carefully confirmed that the loading and running conditions without heating did not denature these long DNA duplexes (data not shown). After a 90 min run (37.5 V/cm, constant voltage) at room temperature, the gel was stained with GelStar, and each band was quantified with a FujiFilm FLA-3000G fluorescent imaging analyzer. To calculate the yield of the complexes, the band intensity of GelStar fluorescence was normalized by the expected number of nucleotides in the complex. The migration distances for Ferguson analysis were measured on the digital images. The gel stained by Quick-CBB for staining of SA was scanned on a Canon scanner.

Nondenaturing PAGE. A DNA tile-containing solution was mixed with the appropriate amount of 6× Blue/Orange Loading Dye (Promega) and then loaded onto gels containing 4% acrylamide (37.5:1, acrylamide/bisacrylamide) and 1× TAE/Mg buffer. After a 180 min run (18.6 V/cm, constant voltage) at room temperature, the gel was stained with GelStar and analyzed as above. To test for secondary target binding, a fragment of pBR322 plasmid (nucleotides 1786−3057) was amplified by PCR using a combination of native forward primer and biotinylated reverse primer, and 2 equiv of the resulting 1272 bp dsDNA was added to the solution of SA/**2b** complex, kept at room temperature for 5 min, and analyzed by nondenaturing PAGE as described above.

RESULTS AND DISCUSSION

Design and Construction of the DNA Motifs Bearing a Nanometer-Scale Cavity in the Middle. The structure of the DNA motifs used in this study is shown in Figure 1 (see Supporting Information Figure S1 for the detailed sequence). To assess the effect of the size of the well on size-selective SA capture, three kinds of motifs were prepared by assembling a U-shaped nine-helix bundle (**1**) and its derivatives. The nine-helix bundle **1** consists of four helices that are eight turns long (84 bp) and five helices that are six turns long (63 bp). These helices are connected to the adjacent helices via immobile four-way junctions at two positions, which are two or four helical turns apart. Consequently, a flat, raft-like, nine-helix DNA bundle is formed. The longer helices are placed two by two at the edges of the motif, so **1** has a rectangular concavity that is two turns wide and five helices long at one side. The 5′ ends of the longer helices are sticky ends 5 bases long, and **1** can be further assembled into a dimer motif, which bears a nanometer-scale well with a theoretical dimension of $6.8 \times 10 \times 2.0$ nm^3 in the middle (**2a** and **2b**), by assigning the appropriate sequence to these sticky ends. For the size-selective capture of SA in the well, some of the DNA strands composing the motif were modified with a biotin-TEG residue either at the 5′ end (**13bio**, blue strand; **11bio**, pink strand; **17bio**, green strand) or at the 3′ end (**14bio**, red strand). When **13bio** is used in combination with **14bio**, two biotin molecules are placed in a well via a

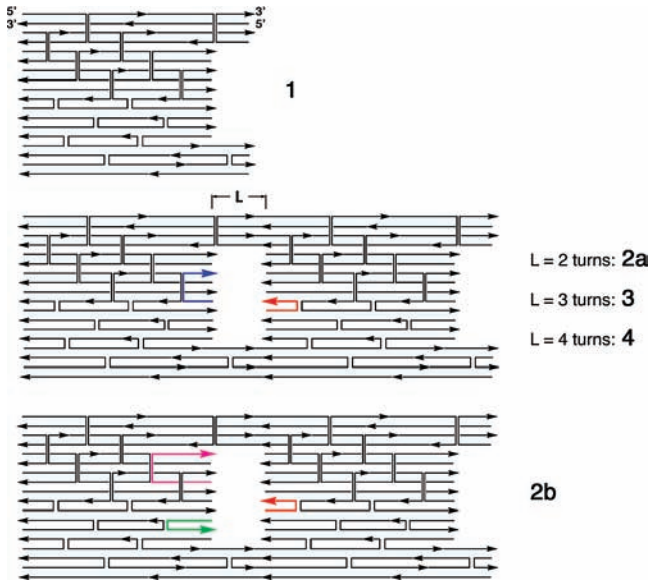


Figure 1. Structures of the DNA motifs used in this study. A U-shaped nine-helix DNA bundle (**1**) and its derivatives were separately annealed and then assembled into rectangular motifs (*2*−*4*) via sticky ends attached to the edges of each bundle (see Supporting Information Figure S1 for the full sequence). By changing the length of the arms of one of the bundles (two helical turns or 6.8 nm for **2**, three turns or 10.2 nm for **3**, and four turns or 13.6 nm for **4**), the width of the well was precisely controlled. For SA capture, biotin-TEG residues were attached to the ends of the strands depicted in colors. Two biotinylated strands (**13bio**, blue; **14bio**, red) were used for bidentate capture (**2a**), and three biotinylated strands (**14bio**, red; **11bio**, pink; **17bio**, green) were used for tridentate capture (**2b**) of SA.

2.3-nm-long linker (*27*), from the opposite two edges 6.8 nm apart (**2a**). Similarly, the combination of three biotinylated strands (**11bio**, **17bio**, and **14bio)** produces a tris-biotinylated well (**2b**). The size of the cavity can also be precisely controlled by changing the length of the arms in **1**. Two additional bis-biotinylated motifs, with a cavity that is three turns wide (10.2 × 10 × 2.0 nm^3, **3**) and one that is four turns wide (13.6 × 10 × 2.0 nm^3, **4**), respectively, were prepared by using the appropriate arm length. Successful formation of the motifs was fully confirmed by analyzing the annealed mixture of the motifs by nondenaturing PAGE and observing a single sharp band for each motif (data not shown).

Size-Selective Capture of a Single SA Molecule in a Well. Size-selective capture of SA in bis-biotinylated wells was first done by adding excess SA to a solution of bis-biotinylated motif **2a** (Scheme 1a). Figure 2a shows an AFM image of SA/**2a** complexes formed in 1× TAE/Mg buffer solution. As clearly seen in the image, exactly one SA tetramer is selectively trapped in a well. This observation is in complete agreement with the findings of previous studies (*19, 20*). In addition to a tape-like DNA scaffold and DNA origami, size-selective capture of SA is also possible with a simple dimer motif. Some SA complexes with incompletely annealed DNA fragments were observed in AFM images at the same time (indicated by the arrow in Figure 2a). The yield of complete SA/**2a** complexes estimated from AFM imaging is ∼70% (Supporting Information Figure S2). Note that such incomplete fragments do not migrate as a band in nondenaturing PAGE analysis, but are visualized only as a smear (vide infra).

Individual SA/DNA complexes formed in a well were then analyzed by denaturing PAGE after breaking down the motif with urea (Figure 2b). An equivalent volume (10 μL) of loading dye containing 1× TBE and 7 M urea was added to the SA/**2a** complex solution (16 nM and 1.25 μM for lanes 2 and 3, respectively), and the resulting mixture was directly loaded onto

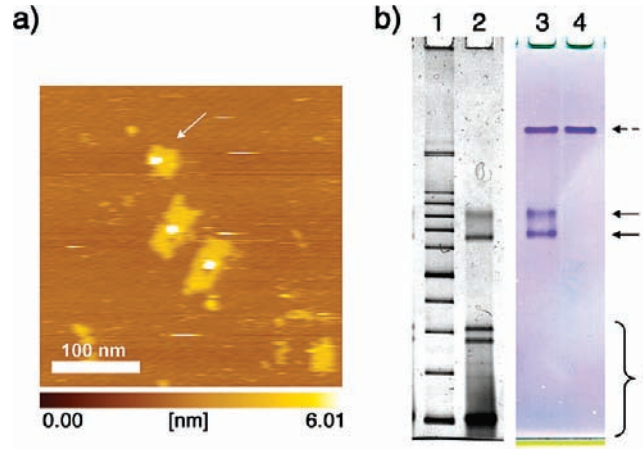


Figure 2. (a) A typical AFM image of **2a** with one SA tetramer in the well. The bright spots are SA. An SA complex with an incomplete fragment (indicated by the arrow) and small flakes of DNA were also observed. (b) A 12% denaturing PAGE analysis of the SA/**2a** complex. The gel was stained with GelStar (stains DNA, lane 2) or Quick-CBB (stains proteins, lanes 3 and 4). Lane 1, 100 bp dsDNA ladder; lanes 2 and 3, the SA/**2a** complex; lane 4, SA only. All sample solutions were mixed with an equivalent volume of loading buffer containing 7 M urea and loaded onto the gel without heating. The bands indicated with an asterisk (*) are unmodified DNA oligomers making up the DNA tile.

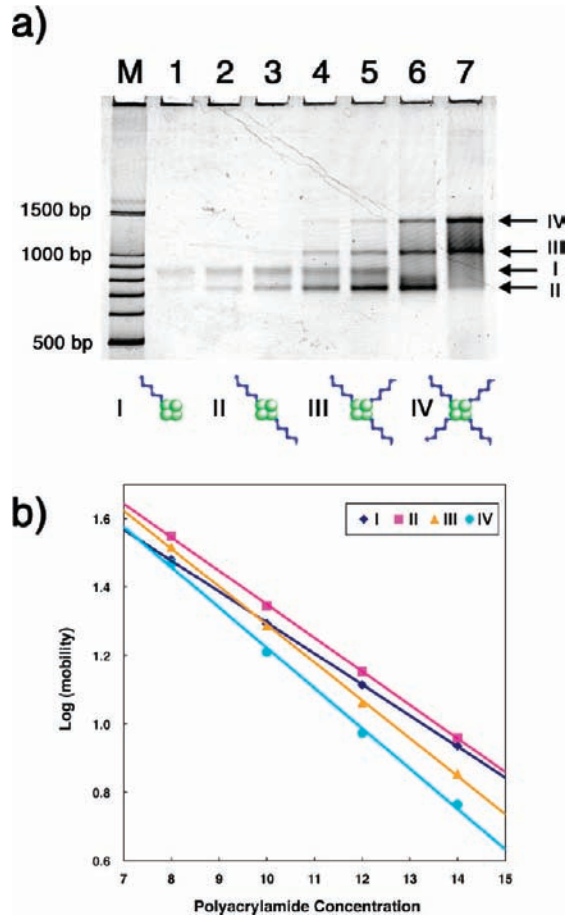


Figure 3. Formation of symmetric SA/DNA complexes in bulk solution. (a) 12% denaturing PAGE analysis of SA/DNA complexes prepared in bulk solution. The gel was stained with GelStar. SA was mixed with various amounts of biotinylated DNA 26-mers (**13bio**). Conditions: [SA] = 1 μM, [**13bio**] = 0.063, 0.13, 0.25, 0.50, 1.0, 2.0, and 4.0 μM (from lanes 1 to 7, respectively). The gel was stained with GelStar. (b) Ferguson plots of the four species observed in (a). The slopes are (I) −0.091, (II) −0.098, (III) −0.111, and (IV) −0.118, and the intercepts are (I) 2.20, (II) 2.32, (III) 2.40, and (IV) 2.40.

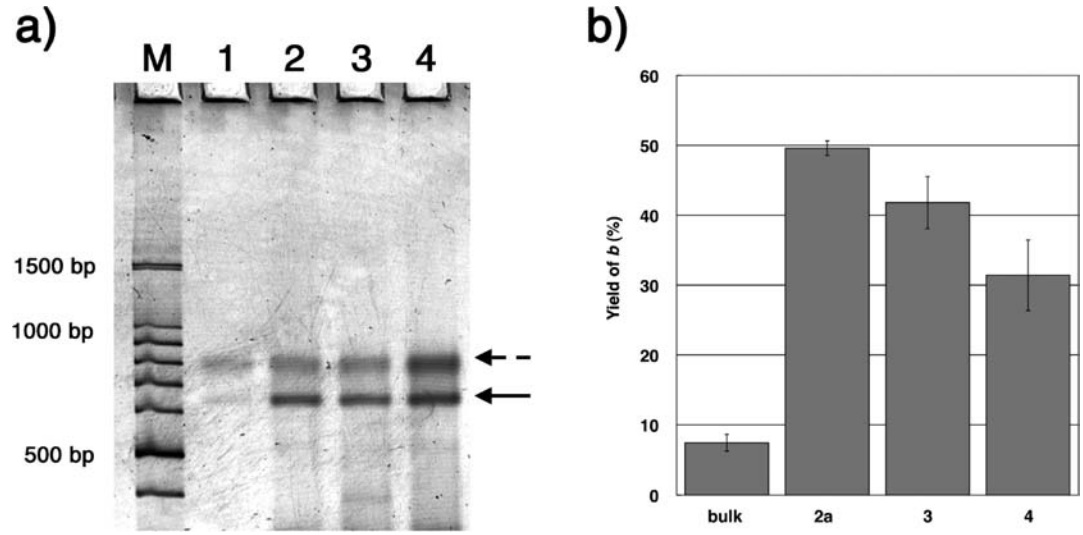


Figure 4. Analyses of SA tetramers captured in motifs with differently sized wells (**2a**, **3**, and **4**). (a) A 12% denaturing PAGE analysis of SA captured in **2a**, **3**, and **4**. The gel was stained with GelStar. Lane 1, SA/DNA complexes prepared in bulk solution; lane 2, SA captured in **2a**; lane 3, SA in **3**; lane 4, SA in **4**. The lower bands indicated by the solid arrow are the asymmetric secondary SA/DNA complex, and the upper bands indicated by the dashed arrow are due to either of the primary SA/DNA complexes (SA/**13bio** or SA/**14bio)**. Conditions: [SA] = 1.1 μM, [**13bio**] = [**14bio**] = 14 nM (lane 1), [DNA motifs] = 14 nM (lanes 2−4). (b) The yield of the secondary complex in (a). Quantified intensities of GelStar fluorescence were normalized by the expected number of nucleotides in the complex.

the gel without heating. The gel was then run at room temperature. When the gel was stained with GelStar, which stains both dsDNA and ssDNA, two significant bands (indicated by the solid arrows) with mobility similar to an 800 bp duplex were observed, along with many other bands with higher mobility (lane 2). These two bands were also stained by Quick-CBB, which stains only proteins (lane 3). Other lower bands in lane 2 were not stained by Quick-CBB. The mobility of the two bands was much greater than that of unmodified SA, which is indicated by the dashed arrow (lane 4). These results suggest that the two bands indicated by the solid arrows are SA/DNA complexes and that two main species are formed when SA is captured in a bis-biotinylated two-turn well. The greater mobility of the SA/DNA complexes than unmodified SA is probably due both to increased total negative charge in the complexes and to conformational changes of SA caused by biotin binding (*28*).

Formation of Symmetric SA/DNA Complexes in Bulk Solution. To characterize the bands in PAGE analyses, SA/DNA conjugates were separately prepared in a bulk solution without forming any DNA motifs. A biotinylated strand (**13bio**, 26-mer) was added to the solution of SA in a variety of ratios to SA (Figure 3a). When the amount of DNA was small enough (0.06 equiv to SA), a faint but reproducible single band (indicated as I) was observed near the 900-bp marker (lane 1). Another sharp band II appeared below I, when the amount of DNA was increased to 0.13 equiv (lane 2). When 0.5 equiv of DNA was added to the solution, the third band (III) appeared above I (lane 4), and finally, the fourth band (IV) above III became obvious after the DNA ratio reached 1 equiv (lane 5). Bands I and II disappeared when SA was treated with excess DNA (lane 7). This order of appearance strongly indicates that bands I, II, III, and IV are the primary, secondary, tertiary, and quaternary SA/DNA complexes, respectively, and that the mobility of the secondary SA/DNA complex is greater than that of the primary complex. Gel electrophoresis depends on both the particle size and surface net charge density. Figure 3b shows the Ferguson plots of the four bands observed in Figure 3a (*29*). The slopes for the primary (I), secondary (II), tertiary (III), and quaternary (IV) complexes are −0.091, −0.098, −0.111, and −0.118, respectively. These plots indicate that the reversed mobility between the primary complex and the secondary complex is observed only when the concentration of polyacrylamide is below ∼16%. The order of the slope is fairly reasonable since it reflects the order of the particle sizes. The intercepts of the plots, which represent the surface net charge densities of the particles, are (I) 2.20, (II) 2.32, (III) 2.40, and (IV) 2.40. Again, these numbers are reasonably ordered.

Biotin binding to SA has been known to drastically enhance the stability of the SA tetramer (*28*). However, the form of SA under denaturing conditions has been a matter of controversy. Sano and Cantor suggested in 1990 that SA saturated with biotin in the presence of 6 M urea dissociates into its dimeric form, based on gel filtration chromatography observations (*28*), and later, González et al. reported partial (60%) dissociation of SA tetramer into its dimeric form in the presence of 8 M urea, based on fast protein liquid chromatography (FPLC) (*30*). By contrast, Kurzban et al. claimed that SA saturated with biotin is intact in its tetrameric form even in the presence of 6 M urea, based on gel filtration chromatography (*31*). At least under the conditions employed in our study (4 M urea), SA seems to stay in its tetrameric form, since sequential formation of all four possible complexes was observed on a gel, and reproducible and fairly proportional plots in the Ferguson analyses were accomplished, although we also observed significant dissociation of the complex if the complex/loading dye mixture was heated at 90 °C for 1 min prior to gel electrophoresis. The binding constant of urea to SA is known to be $K_a \approx 1.3\ M^{-1}$ (*31*), and thus, ligand exchange between biotin and urea during electrophoresis is almost negligible.

Characterization of SA/DNA Complexes Formed in the Well. The complexes formed in the well of **2a** were compared with the products formed in bulk solution (Figure 4). Here, SA (final concentration, 1.1 μM) was added either to a solution of **2a** (lane 2; final concentration, 14 nM) or to a simple mixture of biotinylated strands (lane 1; final concentration, 14 nM). In bulk solution, the primary complex (upper band) is dominantly formed since the number of biotinylated strands is so low compared with that of SA (lane 1). When SA was added to **2a**, a sharp lower band was clearly observed. This band was further analyzed by a Ferguson plot (Supporting Information Figure S3). The slope and the intercept were −0.097 and 2.32, respectively, which are almost the same as those of the secondary complex in Figure 3b. Thus, this lower band can be identified as the desired secondary complex. The yield of this

secondary complex estimated from the quantification of the bands was 50 ± 1%. The yield was also estimated by using a FAM-labeled biotinylated strand, and a similar number was obtained (Supporting Information Figure S4). The rather low yield of the secondary SA/DNA complex in **2a** may be due to the existence of incompletely formed DNA fragments as observed in Figure 2a. Other motifs with a wider three-turn well (**3**) or four-turn well (**4**) were also treated with SA and analyzed by PAGE (lanes 3 and 4). Both of the motifs produced significant amounts of secondary complexes, but more monodentate complexes were formed. The yield of the secondary complex decreased as the size of the well was increased. The yields of the secondary complex were 42 ± 4% in **3** and 31 ± 5% in **4**. Formation of secondary complexes even in wider wells may be attributable to the flexible nature of DNA and DNA nanostructures. A similar pattern but with lower yields of secondary complexes was obtained when the linkers connecting the biotin and DNA were shortened relative to the TEG linker (Supporting Information Figure S5). In any case, the yield of secondary complexes was far higher than that obtained in the bulk system (lane 1, the yield of secondary complexes is 7 ± 1%), showing the importance of the nanometer-scale prepositioning of the strands in the motifs.

Formation of an Asymmetric Tertiary SA/DNA Complex in a Well. Although the aforementioned bidentate capture strategy may be enough to obtain uniformly orientated SA molecules in the future, the possibility of forming a tertiary SA complex in a well was also examined (Scheme 1b). For this purpose, another motif with a tris-biotinylated two-turn well was prepared by using three biotinylated DNA strands (**2b** in Figure 1). Here, the three biotin-TEG residues were attached to the ends of the strands roughly 7 nm apart from each other. Due to the difference in the length of each strand (26-mer for **14bio**, 34-mer for **17bio**, and 44-mer for **11bio**; 104 nucleotides (nt) in total), simple identification of the band corresponding to the tertiary complex using Ferguson analysis is impossible. We thus prepared fluorescently labeled strands corresponding to each of the biotinylated strands. In these three modified strands, a 6-fluorescein amide (6-FAM) residue was inserted between the biotin-TEG residue and the DNA. Figure 5 shows the denaturing PAGE analysis of the FAM-labeled SA/DNA complexes formed in **2b**. Here, excess SA (final concentration, 1 μM) was added to the solution of **2b** (final concentration, 50 nM), in which each of the three biotinylated strands was individually exchanged, one at a time, with the FAM-labeled counterpart (lane 2, **14bio**; lane 3, **17bio**; lane 4, **11bio**). As indicated by the arrow, a common sharp band with the lowest mobility was observed for lanes 2−4. The slope of the Ferguson plot of this common band was −0.117 (Supporting Information Figure S6), which is a fairly reasonable number compared to those for symmetric tertiary SA/DNA complexes separately prepared in bulk solution (−0.111 for SA/**14bio**$_3$ bearing 78 nt, −0.117 for SA/**17bio**$_3$ bearing 102 nt, and −0.149 for SA/**11bio**$_3$ bearing 132 nt). This band was never formed in the mixture of the three FAM-labeled strands and SA in bulk solution (lane 1). Preformation of DNA motif is essential for the efficient formation of these asymmetric tertiary complexes.

We tried to isolate this asymmetric tertiary complex by cutting out the band and eluting the contents into a buffered solution. However, we were unsuccessful since the complex easily equilibrated into a mixture of various complexes with various combinations of strands on SA within a few days at room temperature (reported half-life for the exchange rate of SA/biotin binding is 2.9 days at pH 7.0) (*21*, *32*). This fact conversely emphasizes the stability of the asymmetric tertiary complex in a well, which produced virtually the same PAGE pattern as in Figure 5 even after the solution of SA/**2b** was kept at room temperature for several days. Both cooperativity and the proximity effect, the two essential factors in biomolecular systems, may have key roles in achieving this tremendously high stability. We also attempted MALDI-TOF/MS analysis of SA/DNA complexes before and after purification. However, we could only observe dissociated SA dimer and monomer.

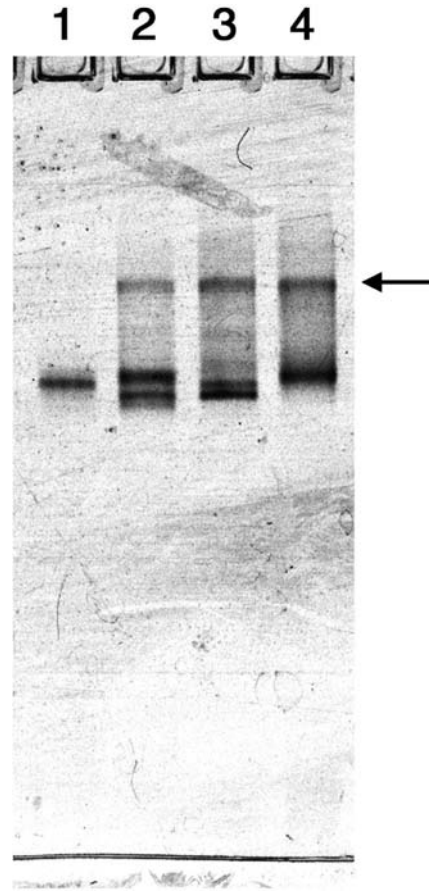


Figure 5. 12% denaturing PAGE analysis of SA captured in the wells of **2b**. The fluorescence of FAM was imaged. In lanes 2−4, one of the three biotinylated strands was exchanged with a FAM-labeled counterpart one by one. Thus, the common band indicated by the arrow contains all three biotinylated strands. Lane 1, SA and the three biotinylated strands (**14bio**, 26-mer; **17bio**, 34-mer; **11bio**, 44-mer) labeled with FAM were mixed in bulk solution; lane 2, SA captured in **2b** containing FAM-labeled **14bio**; lane 3, SA in **2b** containing FAM-labeled **17bio**; lane 4, SA in **2b** containing FAM-labeled **11bio**. Conditions: [SA] = 1 μM, [FAM-labeled **14bio**] = [FAM-labeled **17bio**] = [FAM-labeled **11bio**] = 50 nM (lane 1), [DNA motifs] = 50 nM (lanes 2−4).

Further Modification of SA Captured in a Well with a Long dsDNA. One of the latest topics in DNA nanotechnology is whether proteins attached to DNA scaffolds still preserve their intrinsic structures and functions (*33*, *34*). Although the possibility of tridentate capture of one SA tetramer in a well has been confirmed, it is still unclear whether the empty binding sites in an SA embedded in a well are accessible to the external solvent and retain strong biotin binding activity. To assess the possibility of additional modification of SA embedded in a well with a biotinylated molecule, a 1272 bp biotinylated linear dsDNA was added to a solution of SA/**2b** complexes. In nondenaturing PAGE analysis, the band corresponding to the SA/**2b** complex completely disappeared after the addition of 2 equiv of the biotinylated dsDNA, and a new band with much lower mobility was observed (indicated by the arrow in Figure 6). Similarly, addition of the preformed complex of SA and the 1272 bp biotinylated dsDNA to the solution of **2b** resulted in the disappearance of the band corresponding to **2b** and



Figure 6. Further modification of SA captured in a well. A biotinylated dsDNA (1272 bp) was added to the solution containing SA/**2b** complexes, the mixture was subjected to 4% nondenaturing PAGE, and the fluorescence of FAM was imaged. SA/**2b**/dsDNA ternary complexes were observed as indicated by the arrow. Lane 1, **1** containing FAM-labeled **11bio** and **17bio**; lane 2, **2b** containing FAM-labeled **11bio** and **17bio**; lane 3, **2b** containing FAM-labeled **11bio** and **17bio** mixed with SA; lanes 4 and 5, biotinylated dsDNA added to **2b** containing FAM-labeled **11bio** and **17bio** mixed with SA. Conditions: [DNA motifs] = 33 nM, [SA] = 67 nM (lanes 3−5), [biotinylated dsDNA] = 67 nM (lane 4), or 133 nM (lane 5).

appearance of a similar new band with lower mobility (Supporting Information Figure S7). These results show that the SA captured in a well still preserved its binding ability toward additional targets and that selective preparation of asymmetric quaternary complexes may be also possible in the future.

CONCLUSIONS

Here, we have shown selective formation of asymmetrically modified secondary or tertiary SA/DNA complexes via bidentate or tridentate size-selective capture of SA in a nanometer-sized well formed in DNA motifs. The yield of the secondary complex was ca. 50% for the two-turn well that is 6.8 nm wide when 2.3 nm linkers were used to tether two biotin molecules in a well and capture SA with a diameter of 5 nm. The larger the size of the well, the lower the yield became. The SA captured in a well still preserved its ability to bind additional biotinylated target; thus, it is possible to make protein nanoarrays by additionally conjugating biotinylated proteins to SA captured in wells embedded in various DNA nanostructures such as DNA origami assemblies. Cooperative capture may be feasible also for protein/ligand interactions other than SA/biotin binding such as His-tag/Ni-NTA binding, especially when the protein of interest is a dimer or a multimer (*18, 35*).

Isolation of the asymmetric complex with simple extraction from gels was unsuccessful because SA/biotin binding is still a noncovalent, reversible interaction. A similar process may be possible, however, by using covalent-bond formation for the capture of target proteins in the motif. For example, amide-bond formation between carboxyl or amino groups on the surface of the protein and their activated counterpart on DNA, disulfide-bond formation between thiol groups, or a click reaction between a functionalized protein surface and DNA can be used to capture proteins on the motif and possibly to develop a "molecular operation table", which functionalizes a single protein molecule with multiple DNA strands in the desired geometry, in one pot and one step.

ACKNOWLEDGMENT

This work was supported in part by a Grant-in-Aid for Specially Promoted Scientific Research (18001001) and a Grant-in-Aid for Young Scientists (B) (20750126) from the Ministry of Education, Science, Sports, Culture, and Technology, Japan. Support from the Global COE Program for Chemistry Innovation and from the Association for the Progress of New Chemistry is also acknowledged.

Supporting Information Available: Detailed sequence of the strands making up the DNA motifs, AFM images of SA/**2a** complexes and SA/**2b** complexes, Ferguson plots, quantification of the complexes with FAM-labeling, bidentate capture of SA using shorter linkers between biotins and DNA, and further modification of SA in a well by biotinylated long dsDNA. This material is available free of charge via the Internet at http://pubs.acs.org.

LITERATURE CITED

(1) Seeman, N. C. (1982) Nucleic-acid junctions and lattices. *J. Theor. Biol. 99*, 237–247.
(2) LaBean, T. H., and Li, H. (2007) Constructing novel materials with DNA. *Nano Today 2*, 26–35.
(3) Winfree, E., Liu, F. R., Wenzler, L. A., and Seeman, N. C. (1998) Design and self-assembly of two-dimensional DNA crystals. *Nature 394*, 539–544.
(4) Yan, H., Park, S. H., Finkelstein, G., Reif, J. H., and LaBean, T. H. (2003) DNA-templated self-assembly of protein arrays and highly conductive nanowires. *Science 301*, 1882–1884.
(5) Li, H. Y., Park, S. H., Reif, J. H., LaBean, T. H., and Yan, H. (2004) DNA-templated self-assembly of protein and nanoparticle linear arrays. *J. Am. Chem. Soc. 126*, 418–419.
(6) Malo, J., Mitchell, J. C., Venien-Bryan, C., Harris, J. R., Wille, H., Sherratt, D. J., and Turberfield, A. J. (2005) Engineering a 2D protein-DNA crystal. *Angew. Chem., Int. Ed. 44*, 3057–3061.
(7) Liu, Y., Lin, C. X., Li, H. Y., and Yan, H. (2005) Protein nanoarrays - Aptamer-directed self-assembly of protein arrays on a DNA nanostructure. *Angew. Chem., Int. Ed. 44*, 4333–4338.
(8) Lund, K., Liu, Y., Lindsay, S., and Yan, H. (2005) Self-assembling a molecular pegboard. *J. Am. Chem. Soc. 127*, 17606–17607.
(9) Park, S. H., Yin, P., Liu, Y., Reif, J. H., LaBean, T. H., and Yan, H. (2005) Programmable DNA self-assemblies for nanoscale organization of ligands and proteins. *Nano Lett. 5*, 729–733.
(10) Park, S. H., Pistol, C., Ahn, S. J., Reif, J. H., Lebeck, A. R., Dwyer, C., and LaBean, T. H. (2006) Finite-size, fully addressable DNA tile lattices formed by hierarchical assembly procedures. *Angew. Chem., Int. Ed. 45*, 735–739.
(11) He, Y., Tian, Y., Ribbe, A. E., and Mao, C. D. (2006) Antibody nanoarrays with a pitch of similar to 20 nanometers. *J. Am. Chem. Soc. 128*, 12664–12665.
(12) Li, H. Y., LaBean, T. H., and Kenan, D. J. (2006) Single-chain antibodies against DNA aptamers for use as adapter molecules on DNA tile arrays in nanoscale materials organization. *Org. Biomol. Chem. 4*, 3420–3426.
(13) Chhabra, R., Sharma, J., Ke, Y. G., Liu, Y., Rinker, S., Lindsay, S., and Yan, H. (2007) Spatially addressable multiprotein nanoarrays templated by aptamer-tagged DNA nanoarchitectures. *J. Am. Chem. Soc. 129*, 10304–10305.

(14) Williams, B. A. R., Lund, K., Liu, Y., Yan, H., and Chaput, J. C. (2007) Self-assembled peptide nanoarrays: An approach to studying protein-protein interactions. *Angew. Chem., Int. Ed. 46*, 3051–3054.

(15) Cohen, J. D., Sadowski, J. P., and Dervan, P. B. (2007) Addressing single molecules on DNA nanostructures. *Angew. Chem., Int. Ed. 46*, 7956–7959.

(16) Cohen, J. D., Sadowski, J. P., and Dervan, P. B. (2008) Programming multiple protein patterns on a single DNA nanostructure. *J. Am. Chem. Soc. 130*, 402–403.

(17) Rinker, S., Ke, Y., Liu, Y., Chhabra, R., and Yan, H. (2008) Self-assembled DNA nanostructures for distance-dependent multivalent ligand-protein binding. *Nat. Nanotechnol. 3*, 418–422.

(18) Shen, W., Zhong, H., Neff, D., and Norton, M. L. (2009) NTA directed protein nanopatterning on DNA origami nanoconstructs. *J. Am. Chem. Soc. 131*, 6660–6661.

(19) Kuzuya, A., Numajiri, K., and Komiyama, M. (2008) Accommodation of a single protein guest in nanometer-scale wells embedded in a "DNA Nanotape". *Angew. Chem., Int. Ed. 47*, 3400–3402.

(20) Kuzuya, A., Kimura, M., Numajiri, K., Koshi, N., Ohnishi, T., Okada, F., and Komiyama, M. (2009) Precisely programmed and robust 2D streptavidin nanoarrays by using periodical nanometer-scale wells embedded in DNA origami assembly. *ChemBioChem 10*, 1811–1815.

(21) Michael Green, N., Meir, W., and Edward, A. B. (1990) Avidin and streptavidin. In *Methods in Enzymology*, Vol. 184, pp 51−67, Academic Press, London.

(22) Ke, S., Wright, J. C., and Kwon, G. S. (2007) Intermolecular interaction of avidin and PEGylated biotin. *Bioconjugate Chem. 18*, 2109–2114.

(23) Niemeyer, C. M., Adler, M., Gao, S., and Chi, L. F. (2000) Supramolecular nanocircles consisting of streptavidin and DNA. *Angew. Chem., Int. Ed. 39*, 3055–3059.

(24) Niemeyer, C. M., Adler, M., Lenhert, S., Gao, S., Fuchs, H., and Chi, L. F. (2001) Nucleic acid supercoiling as a means for ionic switching of DNA-nanoparticle networks. *ChemBioChem 2*, 260–264.

(25) Tian, Y., He, Y., Ribbe, A. E., and Mao, C. D. (2006) Preparation of branched structures with long DNA duplex arms. *Org. Biomol. Chem. 4*, 3404–3405.

(26) Wilkinson, S., Diechtierow, M., Estabrook, R. A., Schmidt, F., Hüben, M., Weinhold, E., and Reich, N. O. (2007) Molecular scale architecture: Engineered three- and four-way junctions. *Bioconjugate Chem. 19*, 470–475.

(27) Palma, E., Klapper, D. G., and Cho, M. J. (2005) Antibodies as drug carriers III: Design of oligonucleotides with enhanced binding affinity for immunoglobulin G. *Pharm. Res. 22*, 122–127.

(28) Sano, T., and Cantor, C. (1990) Cooperative biotin binding by streptavidin. Electrophoretic behavior and subunit association of streptavidin in the presence of 6 M urea. *J. Biol. Chem. 265*, 3369–3373.

(29) Rodbard, D., and Chrambach, A. (1971) Estimation of molecular radius, free mobility, and valence using polyacrylamide gel electrophoresis. *Anal. Biochem. 40*, 95–134.

(30) González, M., ArgaraÒa, C. E., and Fidelio, G. D. (1999) Extremely high thermal stability of streptavidin and avidin upon biotin binding. *Biomol. Eng 16*, 67–72.

(31) Kurzban, G. P., Bayer, E. A., Wilchek, M., and Horowitz, P. M. (1991) The quaternary structure of streptavidin in urea. *J. Biol. Chem. 266*, 14470–14477.

(32) Holmberg, A., Blomstergren, A., Nord, O., Lukacs, M., Lundeberg, J., and Uhlén, M. (2005) The biotin-streptavidin interaction can be reversibly broken using water at elevated temperatures. *Electrophoresis 26*, 501–510.

(33) Lin, C., and Yan, H. (2009) DNA nanotechnology: A cascade of activity. *Nat. Nanotechnol. 4*, 211–212.

(34) Wilner, O. I., Weizmann, Y., Gill, R., Lioubashevski, O., Freeman, R., and Willner, I. (2009) Enzyme cascades activated on topologically programmed DNA scaffolds. *Nat. Nanotechnol. 4*, 249–254.

(35) Goodman, R. P., Erben, C. M., Malo, J., Ho, W. M., McKee, M. L., Kapanidis, A. N., and Turberfield, A. J. (2009) A facile method for reversibly linking a recombinant protein to DNA. *ChemBioChem 10*, 1551–1557.

BC900426P

Preparation of Targeting Proteoliposome by Postinsertion of a Linker Molecule Conjugated with Recombinant Human Epidermal Growth Factor

Sang Youn Hwang,[†] Do Youn Cho,[†,⊥] Hak Kyoung Kim,[†] Seung Hun Cho,[⊥,‡] Jaebum Choo,[‡,§] Won Joong Yoon,[||] and E. K. Lee*[,||]

Department of Chemical Engineering, Department of Bionanotechnology, and Department of Applied Chemistry, Hanyang University, Ansan, 425-791 Korea, and College of Bionanotechnology, Kyungwon University, Seongnam, Korea 461-701.
Received October 7, 2009; Revised Manuscript Received November 10, 2009

To develop a sterically stable, targeting proteoliposome, a postinsertion method was employed to biofunctionalize the liposome surface with a biocompatible anchor molecule (BAM) linker conjugated with epidermal growth factor (EGF) as a homing molecule. In this method, EGF was first conjugated with BAM that consisted of a hydrophilic reactive group at one end and oleic acid chains at the other end. The EGF-BAM complex was then inserted into the liposomal phospholipid bilayer through lipophilic interaction. When compared with the traditional surface modification method by amine coupling, the modification efficiency with BAM at 25 °C was about 2.5-fold higher, and the 24 h stability of the inserted BAM at 25 °C was also about 2.5-fold higher. The insertion affinity and stability of the BAM to the liposomal bilayer was not influenced by an increase in cholesterol concentration, a component in liposome preparation. Confocal microscopy studies showed that the proteoliposomes biofunctionalized with the BAM-EGF complex encapsulating Cy5 fluorescent dye were selectively bound to the surface of MDA-MB-231 cells overexpressing EGFR (epidermal growth factor receptor), but not to MCF-7 cells, which did not express EGFR. The same proteolipome encapsulating doxorubicin was selectively targeted to MDA-MB-231 cells and killed them. In sum, BAM could be used as a suitable postinsertion linker for biofunctionalization of liposome surface with high modification efficiency and stability. Furthermore, the protein used as a homing molecule maintained its bioactivity after the biofunctionalization.

INTRODUCTION

Among various nanoparticles used as drug delivery systems, liposomes are the most well studied materials because of their amphiphilic and biocompatible characteristics (*1, 2*). A liposome is composed of a vesicular lipid bilayer surrounding a large inner aqueous phase. Their therapeutic advantages include the targeting ability to deliver a large amount of encapsulated drug to specific sites, resulting in improved drug pharmacokinetics and efficacy and reduced drug toxicity (*3*−*5*). One of the drawbacks of a liposomal system is that it can be easily cleared by the reticular endothelial system (RES) resulting in a reduced targeting yield (*6*−*8*). This can be overcome by modifying the liposome surface with flexible hydrophilic polymers such as poly(ethylene glycol) (PEG) to produce so-called "stealth" liposomes (*9*−*13*). This PEGylated liposome was usually prepared by using phosphatidylethanolamine (PE) or PEG-cholesterol derivatives (*12*), and the common method to prepare it (i.e., simple mixing with other phospholipid components) reduced the inner space resulting in lower drug loading capacity (*14*).

Active targeting usually uses guidance ligand molecules called "homing molecules" that have high affinity for cell surface receptors or epitopes (*15*−*17*). Thus, conjugation of a proteineous homing molecule to liposome surface, i.e., targeting proteoliposome, would be interesting for targeted delivery. *N*-Glutaryl phosphatidylethanolamine (NGPE) is a commonly used phospholipid for surface modification, since its carboxyl groups can react with amine groups on proteins (*18*). However, interliposomal aggregation can be problematic especially at high concentrations of both lipids and proteins. Another method of protein conjugation uses thiol-reactive surface of liposome that could couple with sulfhydryl groups of proteins (*19*−*21*). For this type of liposome, 4-(*p*-maleimidophenyl)butyryl phosphatidylethanolamine (MPB-PE) is frequently used as a phospholipid component. However, this sulfhydryl binding method can also cause liposome aggregation at high concentrations of liposome and protein (*22, 23*). One method to avoid or reduce interliposomal aggregation would be to use a relatively inert phospholipid component, e.g., phosphatidylcholine (PC), in liposome formulation. Furthermore, PC is the predominant phospholipid found in natural cell membranes, a lamella-forming lipid, and the most readily available, all of which would render it the ideal phospholipid for liposome formulation.

To prepare targeting liposome composed of relatively inert phospholipid such as PC, a "postinsertion" method for liposome surface modification was employed. It could attach the homing molecule only on the outer surface, maintaining the liposome inner space (*24*−*26*). However, a relatively high temperature (up to 60 °C) was required for postinsertion, which could reduce the activity of the ligand biomolecules, although a thermostable molecule such as affibody was postinserted at 55 °C and still maintained the antigen-binding activity (*26*). Recently, a postinsertion method operating at ambient temperature was reported for stable insertion into various liposomal surfaces (*27*); however, it characterized only the postinsertion linker and did not present surface modification efficiency or liposomal targeting efficiency.

* Corresponding author. E-mail: eklee@kyungwon.ac.kr, Tel. +82-31-750-8982, Fax+82-31-750-8769.

[†] Department of Chemical Engineering, Hanyang University.

[‡] Department of Bionanotechnology, Hanyang University.

[§] Department of Applied Chemistry, Hanyang University.

[||] Kyungwon University.

[⊥] Present address: Center for Bionanotechnology Research, Korean Research Institute of Biosciences and Biotechnology, Daejeon, Korea.

10.1021/bc9004409 © 2010 American Chemical Society
Published on Web 01/15/2010

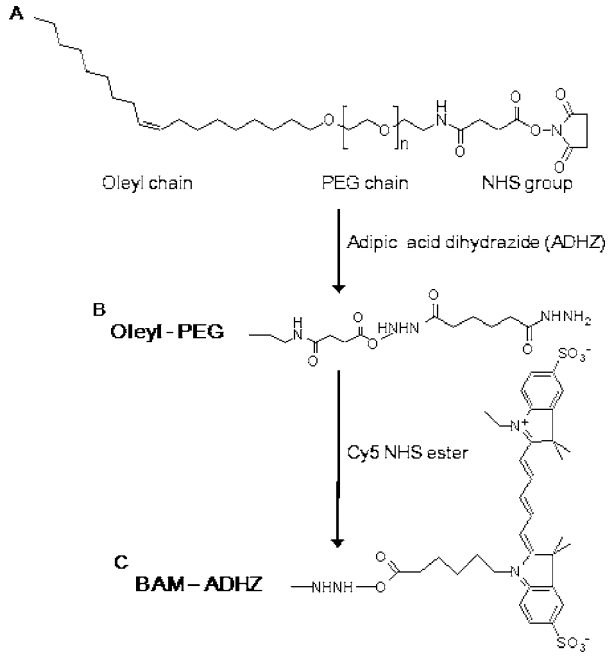


Figure 1. Molecular schematics of (A) BAM, (B) BAM aminated by apidic dihydrazide, and (C) a complex of aminated BAM and Cy5-NHS ester.

In this study, we report the preparation of proteoliposome of which the surface was biofunctionalized by using a commercially available linker, biocompatible anchor molecule (BAM). First, the insertion efficiency and stability of the BAM-protein complex in a relatively inert liposomal bilayer (100% DPPC) was compared with those of the more reactive liposome (90% DPPC with 10% DPPE). Second, the effect of cholesterol content in the phospholipid bilayer on the insertion stability of BAM was investigated. Last, *in vitro* targeting and delivery performance of the proteoliposome to a breast cancer cell line was experimentally demonstrated.

EXPERIMENTAL PROCEDURES

Materials and Liposome Preparation. Both dipalmitoylphosphatidylcholine (DPPC) and dipalmitoylphosphatidylethanolamine (DPPE) was purchased from Avanti Polar Lipid, Inc., USA, and cholesterol (Chol) and dicetylphosphate (DCP) were from Sigma Aldrich, USA. All other chemicals used such as chloroform were of reagent grade. For liposome preparation, DPPC, cholesterol, and DCP were dissolved in a 64:30:6 molar ratio in 5 mL of chloroform and mixed in a 50 mL round-bottom flask. The mixture was evaporated under vacuum in a rotary evaporator to produce a thin lipid film. To thoroughly remove the residual chloroform, the lipid film was stored under vacuum overnight. Six milliliters of 10 mM PBS (pH 7.4) were added to the lipid film, which was then warmed at 45 °C for 10 min and finally peeled off the flask. The mixture was then subjected to 5 cycles of freezing (−70 °C) and thawing (45 °C). Finally, the liposome solution was extruded 15 times through a 200 nm polycarbonate membrane using a mini-extruder (Avanti Polar Lipids, USA).

BAM (Sunbright OE-080CS, NOF, Japan) was used as a postinsertion linker. BAM is commonly used to immobilize floating cells on a solid surface (*28*). Figure 1A shows its molecular schematics: It consists of an oleyl group as a hydrophobic membrane anchor at one end, an *N*-hydroxysuccinimide (NHS) group for protein conjugation at the other end, and they are connected by a linear PEG chain (molecular weight of ca. 3350 Da) for increased solubility and stealth effect. Because of its lipophilic interaction ability, the oleyl chain of BAM is expected to interact with the hydrophobic domains inside the phospholipid bilayers so as to be inserted into the liposomal bilayer.

To quantitatively determine the affinity between liposomal surface and BAM, a surface plasmon resonance system (BIACORE 3000, Biacore AB, Sweden) equipped with lipophilic L1 chip was used. Kinetic values such as the dissociation constant (k_d), association constant (k_a), and affinity constant (K_D) were evaluated.

Temperature Effect on BAM Insertion Efficiency and Stability of Inserted BAM. The BAM insertion efficiency into 100% DPPC liposome was compared with that of a more conventional liposome, i.e., 90% DPPC/10% DPPE. PE was traditionally used as a phospholipid component for the liposomes to be surface-modified by the amine coupling method (*29*). To determine the efficiency of surface modification and the stability of the inserted BAM, a fluorescent dye, Cy5 (Cy5-NHS ester, GE Healthcare, USA), was conjugated to BAM and the conjugate's fluorescence intensity was monitored by a confocal laser scanning microscopy (TCS SL, Leica, Germany). Since Cy5-NHS ester is known to readily react with amine group, the NHS group of the BAM (1 mg/mL) was converted into an amine group by 1.25 mM adipic acid dihydrazide (ADHZ) for 2 h at room temperature as described in Figure 1B. Unreacted ADHZ was removed by centrifugal membrane filtration (MWCO 3 kD, Microgon, USA) at 13 000 rpm for 15 min. Then, the aminated BAM was reacted with Cy5-NHS ester for 1 h at 25 °C in the dark (see Figure 1C). Unreacted Cy5-NHS ester was removed by the same centrifugal membrane filtration.

To identify the temperature effect on the surface modification and to confirm the positive effect of BAM as a postinsertion linker, the BAM-Cy5 conjugate was incubated with 100% DPPC liposome at 22, 32, or 42 °C, and Cy5-NHS ester itself was reacted with 90% DPPC/10% DPPE liposome at the same temperatures. The incubation time was 2 h in both cases. Unassociated BAM-Cy5 conjugate or unreacted Cy5-NHS ester was removed by the centrifugal membrane filtration (MWCO 10 kDa). Two microliters each of the BAM-Cy5 inserted DPPC and Cy5-reacted DPPC/DPPE were spotted on a glass slide and allowed to dry at room temperature. After 0 and 24 h incubation, Cy5 fluorescence intensity was measured by a fluorescence scanner (Genepix, Axon Instrument, Ontario, Canada). The wavelengths for the emission filter and excitation filter was 650 and 668 nm, respectively. The fluorescence intensity was analyzed and quantified by using the *ImageJ* program downloaded from the U.S. National Institutes of Health Web site (http://rsb.info.nih.gov/ij/disclaimer.html). The spot area was designated by determining the spot boundary (or edge), and the average fluorescence intensity was calculated by scanning the spot area by the *ImageJ* program.

Effect of Cholesterol Concentration on Stability of Inserted BAM. To monitor the effect of cholesterol concentration on stability of BAM insertion into the liposomal bilayer, the SPR sensor was used. Liposomes containing various cholesterol concentrations (0%, 10%, 20%, or 30%) were immobilized on L1 chips. The L1 chip contained lipophilic groups on its surface, in which intact liposomes were reported to be stably retained (*30*). PBS (10 mM, pH 7.4) was used as a running buffer. Each liposome solution was injected onto an L1 chip for 5 min at 10 μL/min flow rate. The chip was then washed with 50 mM NaOH for 1 min at 10 μL/min to remove free or weakly bound liposomes. BAM solution (1 mg/mL) in 10 mM PBS (pH 7.4) was injected to the liposome-immobilized chip for 1 min at 5 μL/min. From the sensorgrams, the association and dissociation constants between BAM and

liposome were evaluated by BIA evaluation software, assuming a 1:1 Langmuir binding model. All experiments were performed at 25 °C.

Encapsulation of Cy5 and Biofunctionalization with EGF-BAM Conjugate. To image and trace the liposomal targeting, Cy5-NHS ester was encapsulated inside the liposome. When rehydrating the lipid film, Cy5-NHS ester (2 mg) was added to 6 mL of 10 mM PBS (pH 7.4). The Cy5-encapsulated liposomes were separated from free or unreacted Cy5-NHS ester by gel permeation chromatography (Sephadex G-25, GE Healthcare, USA) using 10 mM PBS (pH 7.4) as an elution buffer.

Preparation of Proteoliposome. For the proteoliposome, epidermal growth factor (EGF) was used as a homing molecule to target the liposome to breast cancer cells since 20−30% of breast cancer cell lines overexpress human epidermal growth factor receptor (EGFR) on their surfaces (*31, 32*). Recombinant human EGF, a stable protein known to undergo receptor-mediated endocytosis (*33, 34*), was gifted from DaeWoong Pharmaceutical Co Ltd., Seoul, Korea. To biofunctionalize the liposome surface with EGF, three sequential steps were performed as follows: (1) BAM was first dissolved in 10 mM PBS (pH 7.4) to yield 1 mg/mL; (2) to form a BAM-EGF complex, 1 mg/mL of EGF solution was incubated with 1 mg/mL of BAM solution for 3 h at room temperature; and (3) for the postinsertion to the liposome surface, the BAM-EGF complex was incubated with the liposome for 2 h at room temperature.

In Vitro Active Targeting of Biofunctionalized Proteoliposomes. MDA-MB-231 mammary gland breast cancer cell line (Korean Cell Line Bank #30026) that overexpresses EGFR on its surface was used as the target cell line. MCF-7 mammary gland breast cancer cell line (Korean Cell Line Bank #30022), which does not express EGFR on its surface, was used as the negative control cell line. Both cell lines were propagated in DMEM supplemented with 10% FBS (fetal bovine serum), 100 IU/mL penicillin, and 100 IU/mL streptomycin (GIBCO, Belgium). The cells were incubated at 37 °C in humidified air containing 5% CO_2. Ca. 5×10^4 of MCF-7 and MDA-MB-231 cells were prepared on a coverslip in a 24 well plate 1 day beforehand. The medium was suctioned, and the cells were washed twice with 2 mL of 10 mM cold PBS for 5 min. Cy5-encapsulated liposomes of which the surface was modified with BAM-EGF complex (100 μg/mL) were incubated with MCF-7 and MDA-MB-231 cells for 1 h at 37 °C. Two milliliters of 3.7% paraformaldehyde were added for fixation and allowed to react for 15 min. The coverslip was washed 5 times with 10 mM PBS (pH 7.4) for 5 min. The interaction between Cy5-encapsulated liposome and the cell was monitored by the confocal laser scanning microscopy. The excitation wavelength was 488 nm, and the emission wavelength was 580−620 nm.

Preparation of Doxorubicin-Encapsulated Liposome. After confirming the targeting performance of the EGF-BAM inserted proteoliposome, its subsequent intracellular delivery performance was investigated by encapsulating doxorubicin inside the proteoliposome. Doxorubicin-HCl (6.5 mg) (Fluka, USA) was dissolved in methanol (11 mL) in a round-bottom flask, and the methanol was evaporated. Then, 21 mg of DPPC and 7.5 mg cholesterol in 5 mL chloroform were added to the dried doxorubicin, and the mixture was stirred to achieve a homogeneous solution, followed by chloroform evaporation. This doxorubicin-HCl concentration was reported to be sufficiently lethal to the cells (*35*). The flask was then placed into a vacuum desiccator for at least 12 h to ensure complete solvent removal. The dried lipid film was resuspended with 6 mL of 10 mM PBS (pH 7.4). The mixture was subjected to 5 freeze−thaw cycles and extruded 15 times through the 200 nm polycarbonate filter using the mini-extruder. The BAM-EGF complex was inserted into a doxorubicin-encapsulated liposome as described above. The free or unencapsulated doxorubicin was removed by the gel permeation chromatography (Sephadex G-25, GE Healthcare, USA) with 10 mM PBS (pH 7.4).

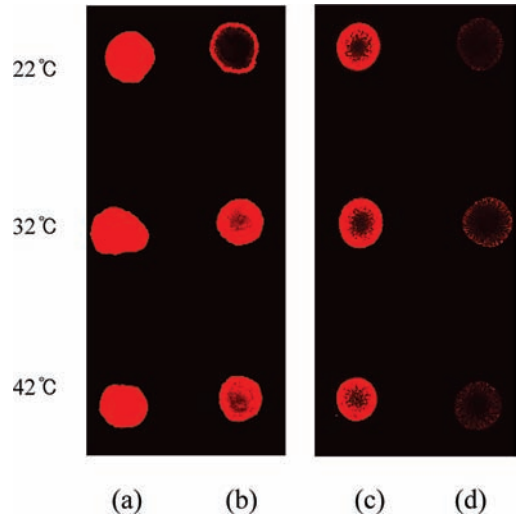


Figure 2. Temperature effect on efficiency and stability of the BAM-mediated liposome surface modification: (a) Cy5 conjugated to the 100% DPPC by the BAM-mediated modification immediately after the modification, (b) Cy5 conjugated to the 90% DPPC/10% DPPE by the conventional amine coupling immediately after the modification at 24 h after the modification, (c) Cy5 conjugated to the 100% DPPC by the BAM-mediated modification at 24 h after the modification, and (d) Cy5 conjugated to the 90% DPPC/10% DPPE by the conventional amine coupling at 24 h after the modification.

SYTOX Green (Invitrogen, USA) was used as a dye to visualize the cytotoxicity. The mixture of 0.1 μg/mL doxorubicin-encapsulated liposomes and 2.5 μM of SYTOX Green were incubated with MCF-7 and MDA-MB-231 cells for 1 h at 37 °C. Two milliliters of 3.7% paraformaldehyde were added and allowed to react for 15 min. The coverslip was washed 5 times with 10 mM PBS (pH 7.4) for 5 min. CLSM was used to check the toxicity of doxorubicin-encapsulated liposomes toward EGFR overexpressing breast cancer cells. The excitation wavelength was 488 nm for both SYTOX green and doxorubicin, and the emission wavelengths were 515−525 nm and 580−600 nm, respectively.

RESULTS

Effects of Temperature and Phospholipid on Efficiency and Stability of BAM Insertion. The effect of incubation temperature on the efficiency of the surface modification was evaluated at various temperatures (22, 32, and 42 °C). As shown in Figure 2a, the fluorescence densities of the Cy5-labeled BAM inserted into 100% DPPC liposomes were nearly the same with respect to the incubation temperature (82.8. 82.9, and 83.0 AU (arbitrary unit)/mm^2 for 22, 32, and 42 °C, respectively). However, the fluorescence intensity of the conventional amine coupling to 10% DPPE/90% DPPC varied with temperatures (27.8, 73.8, and 68.9/mm^2 at 22, 32, and 42 °C, respectively) (see Figure 2b). The result would suggest the superiority of the BAM-mediated surface modification over the amine coupling method.

The stability of the inserted BAM was evaluated by calculating the fluorescence intensity of the conjugated Cy5 at 24 h after the incubation by using the *ImageJ* program. As shown in Figure 2d, the fluorescence intensity by the conventional amine coupling method to 90% DPPC/10% DPPE decreased significantly from the initial intensity (by about 49%, 75%, and 76%

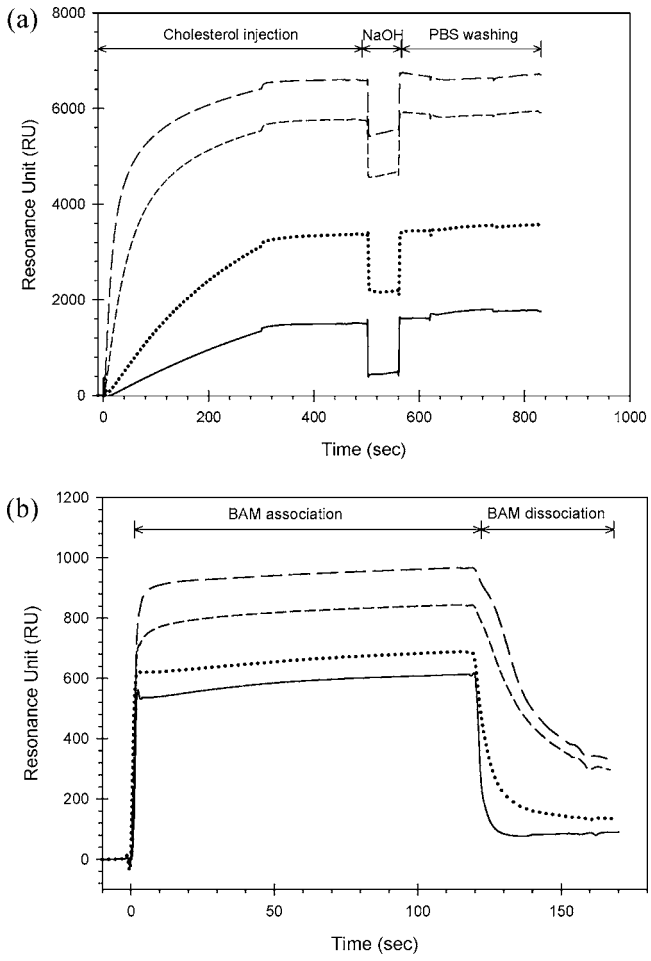


Figure 3. SPR sensorgrams to evaluate the affinity of BAM to liposome. (a) Immobilization of liposome at various cholesterol concentrations on L1 chip, and (b) association and dissociation curves of BAM to liposome containing various cholesterol concentrations. Solid line, 0%; dotted line, 10%; short dashed line, 20%; and long dashed line, 30% cholesterol concentration.

for 22, 32, and 42 °C, respectively). However, as can be seen in Figure 2c, the fluorescence intensity of the BAM-Cy5 conjugate inserted into 100% DPPC decreased much less from the initial density at 24 h after the immobilization (by about 23%, 23%, and 20% for 22, 32, and 42 °C, respectively). These results indicated that the BAM-mediated postinsertion could provide more stable attachment than the conventional amine coupling.

Effect of Cholesterol Concentration on BAM Insertion Stability. The kinetics as well as the amount of BAM insertion into the DPPC liposomes containing various cholesterol concentrations (0%, 10%, 20%, and 30%) was evaluated by using SPR. As shown in Figure 3a, as the cholesterol composition was increased, more liposomes were bound to the lipophilic L1 chip. Figure 3b shows the amount of inserted BAM also increased as the cholesterol concentration was increased. The amount of inserted BAM in liposomes was normalized by dividing the amount of inserted BAM by the amount of immobilized liposome (Table 1). The amount of inserted BAM per unit mass of liposome was similar regardless of the cholesterol concentration. Table 2 shows the kinetic values: K_a, K_d, and K_D. As the cholesterol concentration was increased, the association constant (K_a) increased while the dissociation constant (K_d) decreased. It indicated that at 30% cholesterol composition the BAM was readily inserted with high affinity and stability at even below the T_m of DPPC (41 °C).

Table 1. Effect of Cholesterol Composition in Liposome on BAM Insertion Efficiency

% cholesterol in DPPC	immobilized liposome [RU]	inserted BAM into liposome [RU]	normalized amount of inserted BAM per unit mass of liposome [−]
0	1612	109	0.068
10	3441	155	0.045
20	5910	307	0.052
30	6681	332	0.050

Table 2. Effect of Cholesterol Content in Liposome on BAM Association and Dissociation

% cholesterol in DPPC	K_a (M^{-1} s^{-1})	K_d (s^{-1})	K_D (mM)
0%	8.3	0.050	6.02
10%	490	0.079	1.63
20%	1270	0.036	0.03
30%	1650	0.033	0.02

Targeting Efficiency of Proteoliposome Biofunctionalized with BAM-EGF Complex. Figure 4 shows the schematics of a proteoliposome of which the surface is modified with BAM-EGF complex for targeting and the core is encapsulated with Cy5 dye for fluorescence tracing. For the proteoliposome to have targeting ability, the conjugated EGF should maintain its binding activity toward EGFR after the postinsertion step. To demonstrate the active targeting to EGFR expressed on the cell surface, the proteoliposomes biofunctionalized with BAM-EGF complex were incubated with MDA-MB-231 (EGFR-positive cell) or MCF-7 cells (EGFR-negative cell). As shown in Figure 5, the BAM-EGF inserted liposome was selectively targeted to the MDA-MB-231 cells, but not to the MCF-7 cells. After 1 h incubation, most liposomes were bound to the MDA-MB-231 cell surface on which EGFR was expressed.

To further demonstrate that the proteoliposome could be actually delivered into a cell, cytotoxic doxorubicin was encapsulated inside the same biofunctionalized liposome. Doxorubicin is a DNA interacting drug widely used in cancer chemotherapy. As a cell viability probe, SYTOX Green, a nucleic acid dye, was used. It was used to image only dead cells, since it could easily penetrate plasma membranes of weak or damaged integrity yet could not cross the membranes of healthy live cells. As shown in Figure 6b,e, doxorubicin was taken up and distributed only in the MDA-MB-231 cells and not in MCF-7 cells. The SYTOX green fluorescence was detected also only in the MDA-MB-231 cells, which indicated that most of the MDA-MB-231 cells were not viable (Figure 6f). In contrast, Figure 6c shows no intracellular green fluo-

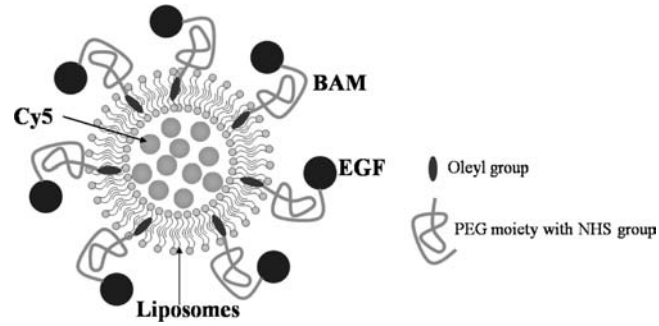


Figure 4. Schematic diagram of proteoliposome biofunctionalized with BAM-EGF complex. Cy5 was encapsulated inside the liposome for fluorescence tracing. EGF was conjugated at the end of the BAM by reacting with NHS group. The PEG moiety connects the EGF and oleyl groups. BAM-EGF conjugate was inserted only into the outside of the liposome by lipophilic interaction between oleyl group and phospholipids.

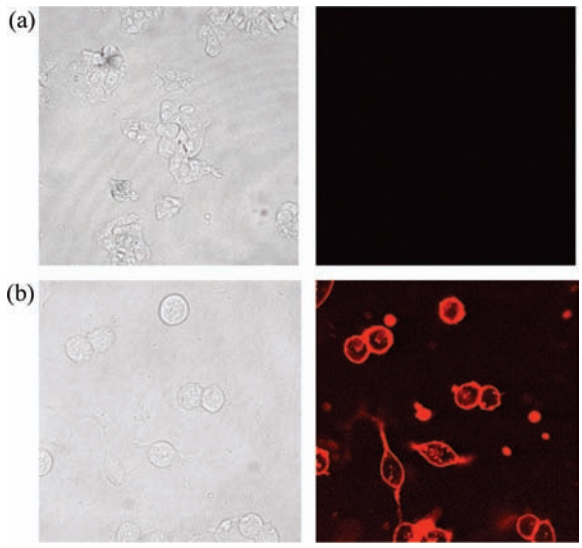


Figure 5. Microscopic images of active cell targeting by the BAM-EGF inserted proteoliposome to breast cancer cells: (a) MCF-7 cells (EGFR-negative), (b) MDA-MB-231 cells (EGFR-positive). Transmitted images are on the left side, and fluorescent images are on the right side. Cy5 was encapsulated inside the liposome. Liposome was incubated with each cell line for 1 h at 37 °C, and a fluorescent image was taken by confocal laser scanning microscopy (λ_{ex} = 488 nm, λ_{em} = 580−620 nm).

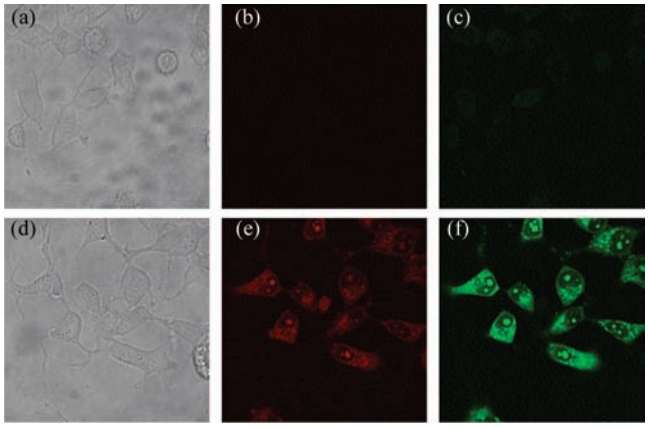


Figure 6. Cytotoxicity evaluation of doxorubicin-loaded, BAM-EGF inserted liposomes by confocal microscopy (λ_{ex} = 488 nm, λ_{em} for doxorubicin = 580−600 nm, λ_{em} for SYTOX green = 515−525 nm). Doxorubicin-loaded proteoliposome was incubated with (a−c) MCF-7 cells, (d−f) MDA-MB-231 cells. (a,d) transmitted image, (b,e) doxorubicin fluorescent image, (c,f) SYTOX green fluorescent image.

rescence, meaning that the EGF-BAM complex liposome was not targeted to MCF-7 cells.

DISCUSSION

The surface modification efficiency and stability of BAM inserted into 100% DPPC liposome were compared with those of a more conventional liposome surface, i.e., 90% DPPC/10% DPPE. PE that contains a primary amine as a reactive group in the amine coupling method was traditionally used as a phospholipid component of liposomes to be surface-modified by the amine coupling method (*29*). In addition, it was reported that the PE composition of 10% was commonly used to prepare the liposomes for surface activation (*27, 36*). Our experimental data clearly indicated that the BAM-mediated modification was superior to the traditional amine coupling to PE. Also, incubation temperature did not influence the BAM insertion into the 100% DPPC. Considering that the T_m (melting point) of DPPC is 41 °C, the result suggested that the BAM's oleyl group was inserted well even below the T_m, which in turn suggested that the insertion was little affected by the fluidity or rigidity of the liposomal bilayer. Dioleylphosphatidylethanolamine (DOPE) with unsaturated chains would have increased the fluidity over DPPE. However, in this study, we used DPPE with saturated chains for the following reasons: First, we intended to focus on the direct comparison between the relatively less reactive choline in DPPC and more reactive ethanolamine in DPPE. Second, DPPE at 10% composition is frequently used to prepare liposomes for surface modification. Furthermore, the T_m of DOPE is 10 °C, so it was not suited as a phospholipid for targeting liposome at the physiological temperature.

The 24 h stability of the inserted BAM was much higher than amine coupling modification. Since the bilayer of 90% DPPC/10% DPPE liposome was supposedly more rigid than 100% DPPC liposome, this result can be compared with a previous report, in which the insertion stability of the tresylated PEG-sterol anchor was dependent on the liposome fluidity (*27*); rigid liposome showed about 40% stability of that of flexible liposome. In addition, while the previous postinsertion methods required incubation at 55−60 °C (*14, 24, 26*), the BAM-mediated postinsertion can be accomplished at room temperature with good stability. Thus, it can serve as a more effective method to biofunctionalize the liposome surface with temperature-sensitive proteins.

Cholesterol has a pronounced effect on the physical properties of membranes, particularly on the structure, fluidity, and permeability of the phospholipid bilayer. Cholesterol has several beneficial effects on liposome rigidity, resulting in increased retention of water-soluble drugs, prevention of lipid phase transitions, and increased resistance against *in vivo* liposomal degradation (*16, 37*). Our data strongly indicated that the higher the cholesterol concentration in the liposomal bilayer, the higher the BAM insertion efficiency and stability. It suggested that the presence of cholesterol would intensify the packing of phospholipids so as to enhance the stability of the inserted BAM. However, the "specific" BAM insertion, i.e.., the amount of BAM inserted into the unit mass of liposome, was little affected by the cholesterol concentration among 0%, 10%, 20%, and 30%.

For the proteoliposome to be targeting, the conjugated homing protein molecule should maintain its binding activity after the postinsertion step. We demonstrated it by monitoring the targeting ability of the postinserted EGF toward the EGFR on the cell surfaces. The fluorescence tracing clearly showed that the proteoliposome biofunctionalized with BAM-EGF complex could be selectively targeted to the EGFR-expressing cells. However, it took a longer time (about 1 h) for the BAM-EGF biofunctionalized liposomes to bind to the MDA-MB-231 cell surface than the liposomes modified with anti-EGFR antibody (about 30 min) (*38*). This is probably because the PEG moiety of the BAM not only induced the protective stealth effect but also decreased the targeting yield.

Since intracellular delivery is another important function of a proteoliposome, we encapsulated DNA interacting doxorubicin inside the proteoliposome and monitored its cytotoxic effect by using a nucleic acid dye, SYTOX Green. The result indicated that the proteoliposome was successfully endocytosed into a cell and released the encapsulated doxorubicin. This result of selective targeting followed by endocytosis is in agreement with the reported observation that the immunoliposomes biofunctionalized with anti-EGFR antibody via maleimide group showed ca. 27-fold higher cytotoxicity toward EGFR expressing cells than those lacking EGFR expression (*38*). We did not determine the degree of cytotoxicity; however, our data clearly

demonstrated the effectiveness of the postinsertion proteoliposome as an intracellular delivery vehicle.

CONCLUSION

Sterically stable, ligand-targeted liposomes were prepared by postinsertion modification using BAM as a linker. By measuring the fluorescence density of Cy5 bound to the liposome surface, we showed that the modification efficiency of BAM-mediated biofunctionalization as well as the stability of the inserted BAM was clearly higher than those of the conventional amine coupling method. The amount of BAM insertion increased with an increase in the cholesterol composition in the liposomal bilayer; however, the "specific" binding affinity of BAM was little affected by the cholesterol composition. By using a fluorescence marker, we confirmed the selective and active targeting of the BAM-EGF-modified liposome to the EGFR overexpressing MDA-MB-231 cells. Furthermore, the doxorubicin-loaded proteoliposome biofunctionalized with EGF showed distinct cytotoxicity only to the MDA-MB-231 cells. It clearly indicated that the EGF maintained its binding bioactivity after the postinsertion. To our knowledge, this is the first report of employing the postinsertion method to obtain a proteoliposome of which the surface was biofunctionalized with both PEG moiety and a protein homing molecule.

ACKNOWLEDGMENT

This work was supported by the Korea Science and Engineering Foundation (KOSEF) grant funded by Korea government (MEST) (R11-2008-044-01001-0). It was partially supported by the Ministry of Knowledge Economy (MKE) and Korea Industrial Technology Foundation (KOTEF) through the Human Resource Training Project for Strategic Technology.

LITERATURE CITED

(1) Koo, O. M., Rubinstein, I., and Onyuksel, H. (2005) Role of nanotechnology in targeted drug delivery and imaging: a concise review. *Nanomedicine 1*, 193–212.

(2) Bohl Kullberg, E., Bergstrand, N., Carlsson, J., Edwards, K., Johnsson, M., Sjoberg, S., and Gedda, L. (2002) Development of EGF-conjugated liposomes for targeted delivery of boronated DNA-binding agents. *Bioconjugate Chem. 13*, 737–43.

(3) Bally, M. B., Lim, H., Cullis, P. R., and Mayer, L. D. (1998) Controlling the drug delivery attributes of lipid-based drug formulations. *J. Liposome Res. 8*, 299–335.

(4) Lundberg, B. (1994) The solubilization of lipophilic derivatives of podophyllotoxins in submicron sized lipid emulsions and their cytotoxic activity against cancer-cells in culture. *Int. J. Pharmaceut. 109*, 73–81.

(5) Lundberg, B. B., Griffiths, G., and Hansen, H. J. (2004) Cellular association and cytotoxicity of anti-CD74-targeted lipid drug-carriers in B lymphorna cells. *J. Controlled Release 94*, 155–161.

(6) Torchilin, V. P. (1996) Liposomes as delivery agents for medical imaging. *Mol. Med. Today 2*, 242–249.

(7) Allen, T. M. (1997) Liposomes - Opportunities in drug delivery. *Drugs 54*, 8–14.

(8) Torchilin, V. P. (1998) Polymer-coated long-circulating microparticulate pharmaceuticals. *J. Microencapsul. 15*, 1–19.

(9) Gabizon, A., Catane, R., Uziely, B., Kaufman, B., Safra, T., Cohen, R., Martin, F., Huang, A., and Barenholz, Y. (1994) Prolonged circulation time and enhanced accumulation in malignant exudates of doxorubicin encapsulated in polyethyleneglycol coated liposomes. *Cancer Res. 54*, 987–992.

(10) Maruyama, K., Yuda, T., Okamoto, A., Kojima, S., Suginaka, A., and Iwatsuru, M. (1992) Prolonged circulation time in vivo of large unilamellar liposomes composed of distearoyl phosphatidylcholine and cholesterol containing amphipathic poly(ethylene glycol). *Biochim. Biophys. Acta 1128*, 44–9.

(11) Klibanov, A. L., Maruyama, K., Torchilin, V. P., and Huang, L. (1990) Amphipathic polyethyleneglycols effectively prolong the circulation time of liposomes. *FEBS Lett. 268*, 235–237.

(12) Allen, T. M., Hansen, C., Martin, F., Redemann, C., and Yauyoung, A. (1991) Liposomes containing synthetic lipid derivatives of poly(ethylene glycol) show prolonged circulation half-lives in vivo. *Biochim. Biophys. Acta 1066*, 29–36.

(13) Fenske, D. B., Palmer, L. R., Chen, T., Wong, K. F., and Cullis, P. R. (2001) Cationic poly(ethyleneglycol) lipids incorporated into pre-formed vesicles enhance binding and uptake to BHK cells. *Biochim. Biophys. Acta 1512*, 259–272.

(14) Nicholas, A. R., Scott, M. J., Kennedy, N. I., and Jones, M. N. (2000) Effect of grafted polyethylene glycol (PEG) on the size, encapsulation efficiency and permeability of vesicles. *Biochim. Biophys. Acta 1463*, 167–178.

(15) Suzuki, S., Watanabe, S., Masuko, T., and Hashimoto, Y. (1995) Preparation of long-circulating immunoliposomes containing adriamycin by a novel method to coat immunoliposomes with poly(ethylene glycol). *Biochim. Biophys. Acta 1245*, 9–16.

(16) Nam, S. M., Kim, H. S., Ahn, W. S., and Park, Y. S. (1999) Sterically stabilized anti-G(M3), anti-Le(x) immunoliposomes: Targeting to B16BL6, HRT-18 cancer cells. *Oncol. Res. 11*, 9–16.

(17) Pagnan, G., Montaldo, P. C., Pastorino, F., Raffaghello, L., Kirchmeier, M., Allen, T. M., and Ponzoni, M. (1999) GD2-mediated melanoma cell targeting and cytotoxicity of liposome-entrapped fenretinide. *Int. J. Cancer 81*, 268–274.

(18) Weissig, V., and Gregoriadis, G. (1992) *Liposome technology*, 2nd ed.; CRC press Inc., Boca Raton.

(19) Torchilin, V. P. (2005) Recent advances with liposomes as pharmaceutical carriers. *Nat. Rev. Drug Discovery 4*, 145–160.

(20) Hwang, S. Y., Kumada, Y., Seong, G. H., Choo, J., Katoh, S., and Lee, E. K. (2007) Characteristics of a liposome immunoassay on a poly(methyl methacrylate) surface. *Anal. Bioanal. Chem. 389*, 2251–2257.

(21) Messerschmidt, S. K. E., Kolbe, A., Mueller, D., Knoll, M., Pleiss, J., and Kontermann, R. E. (2008) Novel single-chain Fv' formats for the generation of immunoliposomes by site-directed coupling. *Bioconjugate Chem. 19*, 362–369.

(22) Torchilin, V. P., and Weissig, V. (2003) *Liposomes: a practical approach*, 2nd ed.; Oxford University Press, Oxford.

(23) Torchilin, V. P., Trubetskoy, V. S., Milshteyn, A. M., Canillo, J., Wolf, G. L., Papisov, M. I., Bogdanov, A. A., Narula, J., Khaw, B. A., and Omelyanenko, V. G. (1994) Targeted delivery of diagnostic agents by surface-modified liposomes. *J. Controlled Release 28*, 45–58.

(24) Ishida, T., Iden, D. L., and Allen, T. M. (1999) A combinatorial approach to producing sterically stabilized (Stealth) immunoliposomal drugs. *FEBS Lett. 460*, 129–133.

(25) Iden, D. L., and Allen, T. M. (2001) In vitro and in vivo comparison of immunoliposomes made by conventional coupling techniques with those made by a new post-insertion approach. *Biochim. Biophys. Acta 1513*, 207–216.

(26) Beuttler, J., Rothdiener, M., Mueller, D., Frejd, F. Y., and Kontermann, R. E. (2009) Targeting of epidermal growth factor receptor (EGFR)-expressing tumor cells with sterically stabilized affibody liposomes (SAL). *Bioconjugate Chem. 20*, 1201–1208.

(27) Steenpass, T., Lung, A., and Schubert, R. (2006) Tresylated PEG-sterols for coupling of proteins to preformed plain or PEGylated liposomes. *Biochim. Biophys. Acta 1758*, 20–28.

(28) Chung, H. A., Kato, K., Itoh, C., Ohhashi, S., and Nagamune, T. (2004) Casual cell surface remodeling using biocompatible lipid-poly(ethylene glycol)(n): Development of stealth cells and monitoring of cell membrane behavior in serum-supplemented conditions. *J. Biomed. Mater. Res., Part A 70A*, 179–185.

(29) Kirby, C., Clarke, J., and Gregoriadis, G. (1980) Effect of the cholesterol content of small unilamellar liposomes on their stability in vivo and in vitro. *Biochem. J. 186*, 591–8.

(30) Baird, C. L., Courtenay, E. S., and Myszka, D. G. (2002) Surface plasmon resonance characterization of drug/liposome interactions. *Anal. Biochem. 310*, 93–99.

(31) Hynes, N. E., and Stern, D. F. (1994) The biology of Erbb-2 Neu Her-2 and its role in cancer. *Biochim. Biophys. Acta 1198*, 165–184.
(32) Collins, V. P. (1993) Amplified genes in human gliomas. *Semin. Cancer Biol. 4*, 27–32.
(33) Kikuchi, A., Sugaya, S., Ueda, H., Tanaka, K., Aramaki, Y., Hara, T., Arima, H., Tsuchiya, S., and Fuwa, T. (1996) Efficient gene transfer to EGF receptor overexpressing cancer cells by means of EGF-labeled cationic liposomes. *Biochem. Biophys. Res. Commun. 227*, 666–671.
(34) Wiley, H. S., Shvartsman, S. Y., and Lauffenburger, D. A. (2003) Computational modeling of the EGF-receptor system: a paradigm for systems biology. *Trends Cell Biol. 13*, 43−50.
(35) Cheung, R. Y., Rauth, A. M., Ronaldson, P. T., Bendayan, R., and Wu, X. Y. (2006) In vitro toxicity to breast cancer cells of microsphere-delivered mitomycin C and its combination with doxorubicin. *Eur. J. Pharm. Biopharm. 62*, 321–331.
(36) Park, J. W., Kirpotin, D. B., Hong, K., Shalaby, R., Shao, Y., Nielsen, U. B., Marks, J. D., Papahadjopoulos, D., and Benz, C. C. (2001) Tumor targeting using anti-her2 immunoliposomes. *J. Controlled Release 74*, 95–113.
(37) Senior, J., and Gregoriadis, G. (1982) Stability of small unilamellar liposomes in serum and clearance from the circulation - the effect of the phospholipid and cholesterol components. *Life Sci. 30*, 2123–2136.
(38) Mamot, C., Drummond, D. C., Greiser, U., Hong, K., Kirpotin, D. B., Marks, J. D., and Park, J. W. (2003) Epidermal growth factor receptor (EGFR)-targeted immunoliposomes mediate specific and efficient drug delivery to EGFR- and EGFRvIII-overexpressing tumor cells. *Cancer Res. 63*, 3154–61.

BC9004409

Comparing Lipid Photo-Cross-linking Efficacy of Penetratin Analogues Bearing Three Different Photoprobes: Dithienyl Ketone, Benzophenone, and Trifluoromethylaryldiazirine

Chen-Yu Jiao, Isabel D. Alves, Vanessa Point, Solange Lavielle, Sandrine Sagan, and Gérard Chassaing*

UPMC Paris 06 - ENS - CNRS, UMR 7203, Laboratoire des BioMolécules, FR 2769 Chimie Moléculaire, Université Pierre et Marie Curie, Case courier 182, 4, Place Jussieu, 75252 Paris Cedex 05, France. Received October 26, 2009; Revised Manuscript Received January 4, 2010

Photoactivatable penetratin analogues bearing three different photoprobes, which do not disturb the membranotropic properties of the peptides, have been tested for their photo-cross-linking efficacy in glycerol and lipid media. In the case of glycerol, photo-cross-linking was observed, whereas in the case of SDS (used as a membrane model system), the dynamics of the SDS/penetratin assemblies and the photosensitizer properties of the probes prevented the cross-linking between the peptide and SDS. Bilayers of DMPG were partially photo-cross-linked by the penetratin analogues containing either a benzophenone or a trifluoromethylaryl-diazirine, whereas dithienyl ketone acted exclusively as a photosensitizer. The characterization by MALDI-TOF mass spectrometry of the photoadducts formed after irradiation required basic hydrolysis of DMPG for an efficient capture of the biotinylated peptide analogues with streptavidin-coated magnetic beads. MALDI-TOF analysis of the photoadducts between the photoactivatable penetratin and DMPG allowed an unambiguous identification of the covalent bond formed with the lipids. Altogether, we show herein that the efficacy of the lipid photo-cross-linking depends on the environment, the dynamics of the supramolecular assembly, and the physicochemical properties of the photoprobe.

INTRODUCTION

The formation of a covalent bond, after irradiation of a photoactivatable molecule, is a commonly used strategy for linking ligands to both hard and soft surfaces (*1*−*3*). For that purpose, four types of photoactivatable aryl reagents are mainly used: aryldiazonium salts, diazoaryl, trifluoromethylaryldiazirines, and phenylketone (*4*). To study by photolabeling the interaction topography between a ligand and its protein partner, the specifications are more stringent, since the photoactivatable probe should be located in the immediate vicinity of the binding domain and, upon irradiation, should form promptly a covalent bond with the protein (*5*). The bioconjugated construct possesses different "moieties". A peptide ligand usually includes an adequately positioned photoprobe in its sequence, together with a recognition moiety (e.g., biotin) used to purify the covalent complex from the incubation mixture (*6*). The tricky step is often the correct rational design of a ligand that retains a high and specific affinity for the protein partner.

Upon irradiation, the photoactivatable probe is transformed into a highly reactive radical species that can abstract a hydrogen atom present in its close environment within the protein binding site. Thus, an important aspect to consider is the reactivity of the chosen photoreactive probe, which must lead to molecular species reactive enough within the time scale of the ligand−protein complex half-life time. Generally, the binding affinity of peptide ligands for their receptor is high (in the nanomolar range), corresponding to formation of complexes with a half-life time in the minutes range. This corresponds to a much longer time than what is mostly observed for reactive species ($t_{1/2}$ values around microseconds or shorter). Even in "host−guest" complexes such as benzophenone/cyclodextrin or transmembrane peptide/phospholipids in which the affinity is low ($t_{1/2}$ value around milliseconds), the irradiation-assisted cross-linking was not inhibited (*7*, *8*). The confinement of the reactive species and the "freezing" of internal movements of both the ligand and the receptor (or guest molecule) within these complexes restrain the intrinsic mobility of both molecules. Thus, it is believed that the covalent bond formation likely represents a snapshot of the interaction.

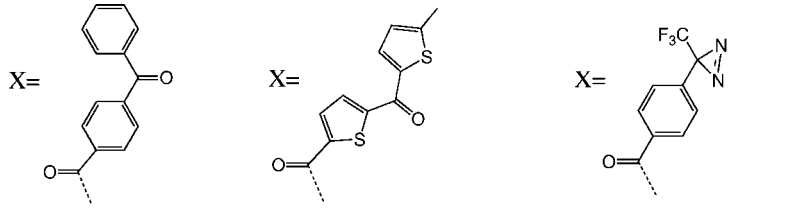
The goal of the present study was to test the feasibility and the limitations of photochemistry in the analysis of the interaction(s) of a cationic peptide with a highly dynamic system, such as plasma membranes constituted of a large range of molecular components and supramolecular assemblies. Plasma membranes are considered a mosaic of coexisting domains: the fluid lipid matrix in disordered phase, lipid ordered domains (rafts), nanodomains associated with different types of proteins (caveolins, clathrin, actin, receptors, protein channels, etc.) and some transient confinement zones (*9*, *10*). The overall dynamic of this mosaic is considered to occur in the nano- to milliseconds time scale (*11*). However, if one considers the rotation around a C−C bond or along the membrane axis and the aliphatic chain wobbling in the disordered phase, the correlation times of phospholipids greatly vary from 10^{-12} to 10^{-7} s. The correlation time for the lateral diffusion is greater than 10^{-5} s and supramolecular assemblages occur starting from very small rafts (diameter <10 nm) to larger ones (from 30 to 230 nm) in time scales of 10^{-3} s (*12*, *13*). Photoactivatable lipids have been used to probe the interaction within lipids (*14*). Modifications of lipids by highly reactive radicals, such as oxygen-derived species, have also been reported (*15*). Herein, we address the question of the photochemistry strategy as a reliable method to study peptide/lipid interaction.

Penetratin, (corresponding to helix-3 of Antennapedia homeodomain: Arg-Gln-Ile-Lys-Ile-Lys-Phe-Gln-Asn-Arg-Arg-Met-Lys-Trp-Lys-Lys), is a cationic membranotropic peptide,

* Corresponding author. Dr. Gérard Chassaing, UMR 7203, Laboratoire des BioMolécules, Case courier 182, 4, Place Jussieu, 75252 Paris Cedex 05, France. Fax: +33 1 44 27 71 50. Tel: +33 1 44 27 32 61. E-mail: gerard.chassaing@upmc.fr.

10.1021/bc900466q © 2010 American Chemical Society
Published on Web 01/20/2010

Scheme 1. Structures of the Three Photoactivatable Probes (X = Bz, DTK, or TMD) Attached to Lys48 within the Sequence of Penetratin[a]



Benzophenone (Bz) Dithienylketone (DTK) Trifluoromethylaryldiazirines (TMD)

Biotin-(Gly)$_4$-Arg^{43}-Gln-Ile-Lys-Ile-Lys^{48}-Phe-Gln-Asn-Arg-Arg-Met(O)-Lys-Trp-Lys-Lys^{58}-CONH$_2$

NH-X with X = Bz Pen(Lys48Bz): MW = 2864

Biotin(O$_2$)-(Gly)$_4$-Arg^{43}-Gln-Ile-Lys-Ile-Lys^{48}-Phe-Gln-Asn-Arg-Arg-Met-Lys-Trp-Lys-Lys^{58}-CONH$_2$

NH-X with X = DTK or TMD Pen(Lys48DTK): MW = 2906; Pen(Lys48TMD): MW = 2886

[a] The three penetratin analogues are modified at the N-terminus by Biotinylated-(Gly)$_4$ and are abbreviated herein as Pen(Lys48Bz), Pen(Lys48DTK), and Pen(Lys48TMD).

a prototype of cell-penetrating peptide, which is able to enter eukaryotic cells without cytotoxity, and which presents antimicrobial activities in some prokaryotic cells (*16, 17*). Even if parallel orientations of penetratin to bilayer were clearly established by various biophysical methods, a direct translocation has been shown as one of the entry mechanism of penetratin in eukaryotic cells (*18*). As Trp48 was found located in the hydrophobic area of phospholipids (*19, 20*), we have substituted this residue by an acylated lysine on the side-chain with three different photoprobes: phenylketone, dithienylketone, or trifluoromethylaryldiazirine (Scheme 1). As we have already described for other studies (*18, 21*−*23*), these photoactivatable penetratin analogues were also functionalized with biotin, separated from the penetratin sequence by a spacer of four glycines, which allows an easy purification through streptavidin-grafted magnetic beads before MALDI-TOF mass spectrometry analysis. The influence of the different photoprobes on the membranotropic properties of penetratin has been analyzed by monitoring their effect on lipid phase transition using differential scanning calorimetric (DSC). Since electrostatic interactions have been shown to play an important role in lipid interaction with penetratin (*24, 25*) large multilamellar vesicles (MLVs) made of dimyristoylphosphatidylglycerol (DMPG) were used as models of the highly dynamic cell membrane. The photochemical behavior of the different peptide analogues has been analyzed in water, glycerol, and sodium dodecyl sulfate (SDS) as models of aqueous, polar headgroups and lipophilic environment of the membrane, respectively. DMPG MLVs were irradiated with the photoactivatable analogues (above the phase transition temperature) and the resulting photoadducts analyzed by mass spectrometry to compare their cross-linking efficacy.

EXPERIMENTAL PROCEDURES

DMPG was purchased from Genzyme (Switzerland) and was used without further purification. 4-Carboxybenzophenone and 4-(trifluoroacetyl)benzoic acid were purchased from Aldrich and Apollo Scientific Limited, respectively. The 5-carboxy-5′-methyl-2,2′-dithienylketone was a generous gift, from the "Laboratoire d'Ingénierie Moléculaire et Biochimie Pharmacologique", Université Paul Verlaine, Metz, France.

Syntheses of Photoactivatable Probes. *4-[1-(trifluoromethyl)-3H-diazirinin-3-yl]benzoic Acid.* The synthesis of 4-[1-(trifluoromethyl)-3*H*-diazirinin-3-yl]benzoic acid was based on a series of reactions already used for this type of photoprobes (*26, 27*).

4-(trifluoroacetyl)benzoic tert-Butyl Ester **1.** 4-(Trifluoroacetyl) benzoic *tert*-butyl ester **1** was prepared from *tert*-butyl alcohol and 4-(trifluoroacetyl)benzoic acid using anhydrous magnesium sulfate and sulfuric acid. To a suspension of $MgSO_4$ (92 mmol) in CH_2Cl_2 (100 mL), H_2SO_4 (23 mmol) was added dropwise After 15 min of stirring, *tert*-butyl alcohol and 4-(trifluoroacetyl)benzoic acid were added. The mixture was stirred for two days and the reaction was quenched by addition of saturated $NaHCO_3$ (170 mL). The extraction with CH_2Cl_2 led to 10 mmol of pure 4-(trifluoroacetyl)benzoic *tert*-butyl ester. R_F (cyclohexane/ethyl actetate, 8/2) = 0.3. ^{1}H NMR ($CDCl_3$), δ: 1.62 (s, 9H), 8.13 (s, 4H). The unreacted starting material was recovered after acidification of the aqueous phase and extraction with CH_2Cl_2.

4-(2-Trifluoroethanoneoxime)benzoic tert-Butyl Ester **2.** To a stirred mixture of hydroxylamine hydrochloride (8 mmol) and NaOH (8 mmol) in 33 mL of boiling ethanol, compound **1** (8 mmol in EtOH, 4 mL) was added dropwise. After refluxing for 3 days, ether was added, and the organic layers were washed with 0.01 N HCl (3×) and with water (3×). R_F ($CHCl_3$) = 0.25. ^{1}H NMR ($CDCl_3$), δ: 1.6 (s, 9H), 7.59 (d, 2H), 8.10 (q, 2H), 8.38 (s, broad 1H).

4-(2-Trifluoroethanone-O-(p-tolylsulfonyl)oxime)benzoic tert-Butyl Ester **3.** A mixture of compound **2** (19 mmol) and of *p*-sulfonyl chloride (38 mmol) in dry pyridine (30 mL) was refluxed for 3 days. After solvent evaporation, the pure product (yield 73%) was obtained after flash chromatography, (cyclohexane/ethyl acetate, 95/5). R_F ($CHCl_3$) = 0.66. ^{1}H NMR ($CDCl_3$), δ: 1.6 (s, 9H), 2.48 (s, 3H), 7.41 (t, 4H), 7.86 (d, 2H), 8.06 (d, 2H).

4-(Trifluoromethyldiaziridine)benzoic tert-Butyl Ester **4.** Compound **3** (2 mmol) was introduced in a Parr Instrument of 0.3 L capacity, then liquid ammonia (20 g) was condensed after cooling the autoclave in liquid nitrogen for 15 min. The mixture was stirred for two days. After evaporation, the pure product (yield 88%) was obtained after flash chromatography using CH_2Cl_2. R_F ($CHCl_3$) = 0.5. ^{1}H NMR ($CDCl_3$), δ: 1.6 (s, 9H), 2.25 (d, 1H), 2.80 (d, 1H), 7.58 (d, 2H), 8.05 (d, 2H).

4-[1-(Trifluoromethyl)-3H-diazirinin-3-yl]benzoic tert-Butyl Ester **5.** Compound **4** (1 mmol) was mixed with freshly prepared Ag_2O (5 mmol). After stirring for 3 h in the dark, the mixture was filtered on Celite and purified by flash chromatography using cyclohexane. R_F ($CHCl_3$) = 0.75. ^{1}H NMR ($CDCl_3$), δ: 1.59 (s, 9H), 7.24 (d, 2H), 8.01 (d, 2H).

4-[1-(Trifluoromethyl)-3H-diazirinin-3-yl]benzoic Acid **6.** Compound **5** (10 mmol) was stirred with TFA (50 mmol) in CH_2Cl_2 (10 mL). The reaction was completed after two hours stirring, leading after usual workup to compound **6**. R_F ($CHCl_3$) = 0.2. ^{1}H NMR (DMSO), δ: 7.40 (d, 2H), 8.06 (d, 2H), 13.34 (s, 1H).

Synthesis of Penetratin Analogues. The penetratin analogues [Lys^{48}(Bz)]Penetratin, [Lys^{48}(DTK)]Penetratin, and [Lys^{48}(TMD)]-Penetratin abbreviated as Pen(Lys48Bz), Pen(Lys48DTK), and Pen(Lys48TMD), respectively, and modified on Lys48 (number 48 corresponding to the Trp position in the sequence of the *Antennapedia* homeodomain (*28*) were synthesized by solid-phase methodology on a ABI 431 Synthesizer, using either a Rink amide resin or Rink amide MBHA resin by Fmoc or Boc strategies, respectively. Lys48 side chain was protected either by Fmoc or Dde protecting groups for the Boc and Fmoc strategies, respectively. After selective removal of the protecting group, the free amine of Lys48 was acylated either by 4-carboxybenzophenone, 5-carboxy-5′-methyl-2,2′-dithienylketone or 4-[3-(trifluoromethyl)-3*H*-diazirinin-3-yl]benzoic acid, using DCC/HOBt for the activation. The subsequent Ile45 was then introduced manually. The other amino acids were coupled on the synthesizer using standard protocols of Boc and Fmoc chemistries and amino acid activation with DCC/HOBt in NMP. After removal of the last protecting group from the N-terminal glycine, the peptides were biotinylated in NMP, as already described (*18*, *21*−*23*). The resins were washed with NMP, CH_2Cl_2, and MeOH and dried under vacuum. The peptides were cleaved from the resin with TFA/H_2O/TIS (Fmoc strategy) (95/2.5/2.5) or HF/anisole (Boc strategy). The crude peptides were lyophilized and purified by RP-HPLC. The peptides were characterized by MALDI-TOF mass spectrometry leading to *m*/*z* 2864 for Pen(Lys48Bz), 2908 for Pen(Lys48DTK), and 2886 for Pen(Lys48TMD).

Differential Scanning Calorimetry. The calorimetry was performed on a high-sensitivity differential scanning calorimeter (Calorimetry Sciences Corporation). A scan rate of 1 °C/min was used, and there was a delay of 10 min between sequential scans in a series that allow for thermal equilibration. Data analysis was performed with the fitting program *Cpcalc* provided by CSC and plotted with *Igor*. DMPG (1 mg/mL) was used at peptide/lipid ratio of 1/25. Samples containing the peptide alone, dissolved in buffer at similar peptide concentrations, exhibited no thermal events over the temperature range 0−100 °C. This indicates that the peptides do not denature over this temperature range and that the endothermic events observed in this study arise solely from phase transitions of the phospholipid vesicles. A minimum of at least three to four heating and cooling scans were performed for each analysis depending on whether or not the spectra was reproducible.

Photolabeling. The sample of Pen(Lys48Bz), Pen(Lys48DTK), or Pen(Lys48TMD) dissolved at micromolar concentration in water or glycerol (500 μL) was irradiated on ice for 1 h at 365 nm with an UV light (HPR 125-W) located between 6 to 10 cm from the Eppendorf tube corresponding to a surface area of 0.39 cm^2. Then, 1 μL of the irradiated sample was deposited on the sample holder for direct MALDI-TOF mass spectrometry analysis.

DMPG (1 μM in 20 mM ammonium acetate buffer at pH 7.5) was mixed with Pen(Lys48Bz), Pen(Lys48DTK), or Pen(Lys48TMD) at 1/10 peptide/lipid ratio. Theses samples were irradiated on ice for 1 h, under the conditions described above, followed by a basic hydrolysis in MeOH/H_2O (50/50) using NaOH (0.1 M) at 37 °C overnight. After neutralization with acetic acid, the methanol was evaporated before affinity purification.

Purification with Streptavidin-Coated Magnetic Beads. The hydrolyzed sample containing 0.1% of Triton was incubated with streptavidin-coated magnetic beads (100 μg, Dynabeads M280, Dynal) for 30 to 60 min under gentle agitation. The washing steps (5× each) were performed with (1) buffer (Tris pH 7, 50 mM) containing 0.1% SDS, (2) 50 mM Tris pH 7, (3) NaCl 1 M, and (4) H_2O/ACN 50/50. The same procedure was used for the experiments performed in SDS, excepted that no Triton was added during the incubation step.

MALDI-TOF Mass Spectrometry Analysis. The photoadducts were eluted from the magnetic beads with the 2,5-dihydroxybenzoic acid (DHB) matrix, in 1:1 (v/v) CH_3CN/H_2O (1% phosphoric acid) used for MALDI analysis. After 10 min incubation, 1 μL of bead-free supernatant was deposited on the sample holder.

Quantification by MALDI-TOF Mass Spectrometry. After irradiation in glycerol of deuterated Pen(Lys48Bz) (penetratin analogue with four deuterated glycines), a known amount (2 nmol) of hydrogenated Pen(Lys48Bz) (with four 1*H*-glycines) was added to the medium. The photoadduct was then purified by incubating the mixture with streptavidin-coated magnetic beads for 30 to 60 min under gentle agitation. After elution of all biotinylated peptides (photoadduct or free peptide) with the matrix as described above, 1 μL of bead-free supernatant was deposited on the sample holder. The ratio of the ^{1}H/^{2}H MH+ *m*/*z* signals allowed the quantitative determination of the starting peptide that remained intact after irradiation.

RESULTS

Hydrophobic Character of Penetratin Analogues. The modification of the hydrophobic/hydrophilic balance induced by the photoprobes on the behavior of these penetratin analogues can be related to the concentration of acetonitrile required to elute the corresponding peptides by HPLC (in mixture of acetonitrile water 0.1% of TFA). The concentrations required correspond to 32.4% CH_3CN for Pen(Lys48Bz), 21.5% CH_3CN for Pen(Lys48DTK), and 32% CH_3CN for Pen(Lys48TMD), leading to the following hydrophobic scale: Pen(Lys48DTK) > Pen(Lys48Bz) ≈ (Lys48TMD).

Effect of the Medium on the Photochemical Properties of the Different Photoprobes. Ammonium acetate buffer, glycerol, and sodium dodecyl sulfate (SDS) were used as models of the membrane interface. The crude products obtained after irradiation (1 h) at 365 nm of these photoactivatable penetratin analogues within one of the media were analyzed by MALDI-TOF mass spectrometry. As already observed for peptides containing benzophenone, the Pen(Lys48Bz) analogue was mainly unaffected by irradiation in ammonium acetate buffer. Pen(Lys48DTK) was strongly oxidized as a consequence of the irradiation, MALDI-TOF spectra showing the incorporation of one to four oxygen atoms. Pen(Lys48TMD) was nearly totally oxidized but with the incorporation of a single oxygen atom (+16).

The polar heads of phospholipids represent a borderline between two media, with a high dielectric constant (ε = 80, i.e., the aqueous phase) and a low dielectric constant (ε = 3, i.e., the lipid phase). This interface can be mimicked by glycerol (ε = 40). Glycerol adducts were efficiently formed with Pen(Lys48Bz), since a signal with a mass increase of 92 was observed. The signal intensity of the photoadduct was shown to increase as a function of the irradiation time (Figure 2). The disappearance as a function of time of the starting peptide Pen(Lys48Bz) (bearing four deuterated glycines) was quantified by addition after the irradiation of an internal standard (2 pmol) of Pen(Lys48Bz) (bearing four hydrogenated glycines) (*21*). The intact peptide remaining after irradiation was measured by integrating the ^{1}H and ^{2}H *m*/*z* signals (2864.3 and 2872.4, respectively), revealing an almost linear decrease of the starting material (Figure 2) as a function of the irradiation time. In the case of Pen(Lys48TMD), a mass increase of only 90, instead of 92, was observed, which probably resulted from the alcohol oxidation of the glycerol adduct. For Pen(Lys48TMD), the starting peptide and the photoadduct coexisted with the mono- and dioxidized forms. Weak signals were detected for Pen(Lys48DTK)

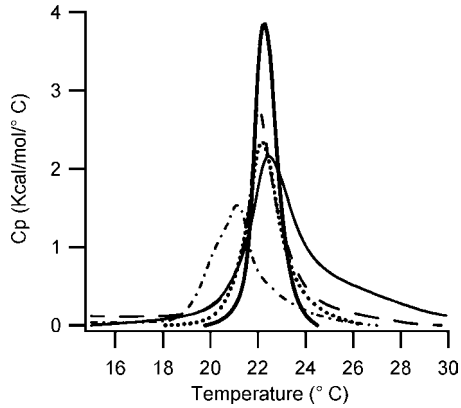


Figure 1. High-sensitivity DSC heating scans. The spectra illustrate the effect of adding penetratin (-•-) and penetratin photoactivatable analogues: Pen(LysBz) (••••), Pen(LysDTK) (- -), and Pen(LysTMD) (—) on the thermotropic phase behavior of DMPG multilamellar vesicles (— bold) at P/L of 1/25. Thermodynamic parameters are given in Table 1.

with a limited number of oxidized states compared to those observed in aqueous solution.

Finally, the reactivity of the photoactivatable penetratin analogues in a lipophilic medium was mimicked by photoirradiation of the peptides in SDS solution. In that environment, very low levels of cross-linking were detected, regardless of the photoprobe used. A small photoadduct signal was only observed for Pen(Lys48TMD). However, a high percentage of peptide oxidation was observed after irradiation under these conditions.

Analysis of the Photoadducts Obtained after Irradiation of Peptides with Phospholipid Bilayers. No photoadduct was observed by mass spectrometry after irradiation of DMPG vesicles in the presence of photoactivatable penetratin analogues, both using a crude preparation and after the purification step with streptavidin-coated magnetic beads. In order to observe photoadducts, the lipid moiety (hydrophobic character) of the adducts had to be removed by basic hydrolysis, which was performed overnight with NaOH (0.1 mol/L) in MeOH/H_2O (50/50) at 37 °C, followed by neutralization with acetic acid. MALDI-TOF mass spectrometry analysis was performed after a subsequent capture with streptavidin-coated magnetic beads in the presence of Triton X-100 (0.1%), followed by the described washing procedure and elution using the 2,5-dihydroxybenzoic acid matrix (*21*).

Photolabeling experiments with Pen(Lys48Bz) (2864.1) and DMPG vesicles led to three pairs of signals: one pair (3092.3 and +16) corresponding to photoadduct with the myristoyl and its oxidized form (+ 228 and + 244, respectively); another pair (2922.1 and +16) that was assigned to the dehydrated form of glycerol adducts formed during the basic treatment, and the third pair corresponding to the starting peptide and its oxidized form. Similar behavior and photoadducts were observed with Pen(Lys48TMD). Besides the oxidized form of Pen(Lys48TMD), previously observed in ammonium acetate buffer, two pairs of signals were detected, corresponding to mass increases of 228 and 72, which were assigned to photoadducts of myristoyl and oxidized/dehydrated glycerol, respectively. Finally, only degraded (low-molecular weights) forms of Pen(Lys48DTK) were detected after irradiation with DMPG vesicles (Figure 3).

Effect on the Organization of the Phospholipid Bilayer. DSC is used to study peptide/lipid interaction by monitoring the ability of peptides to interact and perturb the lipid acyl chain packing (Figure 1). A lipid bilayer composed of a single phospholipid, in the presence of water excess, can undergo two phase transitions upon heating: pretransition and main phase transition occurring at phase transition temperatures T_p and T_m (*29*). The peak area corresponds to the enthalpy of the phase transitions and the $\Delta H/T_m$ ratio to the entropy change. The main phase transition is related to the chain melting during the gel-to-liquid-crystalline phase change, whereas the pretransition reflects changes in headgroup tilting and organization.

In agreement with previous studies, the addition of the cationic peptide, penetratin, to anionic DMPG phospholipids suppressed the pretransition temperature and decreased both the enthalpy and the phase transition temperature (T_m) of the main lipid transition (*30*). One would expect that the introduction of hydrophobic probes in penetratin might promote the insertion of the peptide into the lipid fatty acid chains and so lead to an increased perturbation in the lipid phase transition. This was not the case; indeed, the photoactivatable probes did not significantly change the T_m and overall led to a smaller perturbation in the main phase transition compared to the original penetratin peptide. When comparing the three photoactivatable analogues, Pen(Lys48DTK) perturbed least the pretransition (that was not completly abolished) and main phase transition, leading to a very small reduction in the enthalpy of transition (Table 1). Altogether, the results demonstrate that the introduction of the photoactivatable probes in penetratin did not perturb the overall membranotropic properties of the peptide.

DISCUSSION

All experiments were performed in air-saturated water, in order to mimic the cellular environment. It has to be noted that, in the experiments described herein, 10 nmol of peptide was irradiated in the presence of about 90 nmol of oxygen (air-saturated water). Oxygen or water must be the first source(s), which might prevent the bimolecular photo-cross-linking of the photoactivated probes. The lifetime of the benzophenone triplet is 1.5 μs in air-saturated water, and much longer (20 μs) in degassed water (*31*). Oxygen efficiently quenches the benzophenone triplet by energy transfer, leading to the reactive singlet oxygen species with a short lifetime 4.2 μs in water (*32*), and its deactivation occurs by light emission and electronic-to-vibrational energy transfer and by intermolecular interaction with specific amino acids such as Phe or Trp, which are both present in penetratin (*33*). The benzophenone triplet can also be quenched by intra- or intermolecular interactions, by charge transfer, hydrogen abstraction, or light emission. However, all these reactions are fast and reversible, with the exception of the hydrogen abstraction step. The concentrations of the two active forms, i.e., the ketone triplet and the singlet oxygen, must be low under the irradiation conditions used herein, since the consumption of the starting peptide is slow (total disappearance occurs in over 2 h under permanent irradiation). For the dithienyl ketone triplet in air-saturated water, a large proportion of oxidized forms was observed showing that the singlet oxygen concentration must be much higher than for the benzophenone triplet. The carbene generated from trifluoromethylaryldiazirines has a very short lifetime ($t_{1/2} \approx$ ns) (*34*) because it reacts rapidly and irreversibly with oxygen. However, this competitive reaction with oxygen does not totally prevent the hydrogen abstraction, which can either occur intra- or intermolecularly.

With the benzophenone-substituted penetratin analogue, we have shown that the gradual decrease as a function of time up to the total disappearance of the starting peptide is slow. The intermolecular self-reaction is unlikely since no dimer was observed by MALDI-TOF MS (data not shown). The intramolecular reactions (hydrogen abstraction and radical combination) leading to cyclic peptides cannot be excluded with the techniques used. Photo-cross-linking with other species has already been reported for hydrophobic molecules (peptides, fatty acids,

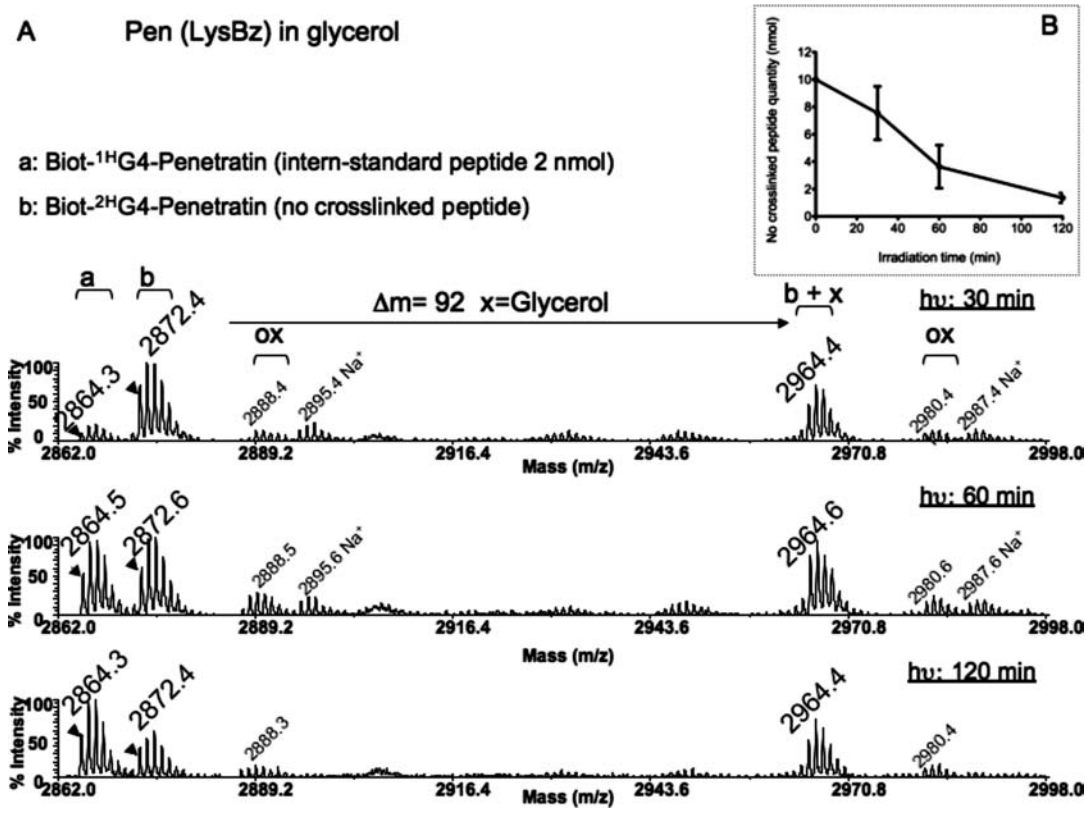


Figure 2. Quantification of remaining Pen(Lys48Bz) by MALDI-TOF mass spectrometry, after different irradiation times (30, 60, and 120 min irradiation) in glycerol. Insert top right, quantification of the areas of B vs A. A corresponds to 2 pmol of the peptide with four hydrogenated glycines added after the irradiation as an internal standard, the irradiation being performed with the same peptide bearing four deuterated glycines; *m*/*z* correspond to peaks B. For the capture by streptavidin-coated magnetic beads and the detection by MALFDI-TOF mass spectrometry as described in the experimental section.

Table 1. Thermodynamic Parameters Obtained by DSC for the Interaction of Penetratin and Its Photoactivatable Analogues with DMPG MLVs at P/L of 1/25

	pretransition		main transition	
	ΔH (kcal/mol)	T_p (° C)	ΔH (kcal/mol)	T_m (° C)
lipid alone	0.4	9.6	6.2	22.3
penetratin	−[a]	−	3.8	22.1
Pen(LysBz)	−	−	4.6	22.3
Pen(LysDTK)	0.2	8.8	6	22.1
Pen(LysTMD)	−	−	8	22.5

[a] − the transition was abolished.

phospholipids, glycolipids) soluble/inserted into a lipophilic phase, such as micelles or vesicles (*8*, *14*, *35*−*38*). A pioneer work has been reported on the labeling of "lipid mimics", i.e., sodium dodecylsulfate (SDS) micelles, with 10 mM benzophenone, using a 1/1 molar ratio (*35*). The very high peptide concentration and peptide/lipid ratio used in this study allowed the observation of the radical combination step, even though SDS exchange between micelles and free components and molecular motion (τ_c between 10^{-10} and 10^{-12} s) is a fast process ($t_{1/2} = 10^{-7}$ s) (*39*). Because the biological effects of membrane active peptides are generally observed at micromolar concentration and P/L ratios of ∼1/50, cross-linking experiments presented here have been performed at micromolar concentrations.

No efficient cross-linking was observed between the three tested photoactivatable peptides, at micromolar concentration in the presence of SDS micelles. These results suggest that a high concentration of photoreactive species is required to compensate the fast dynamics of supramolecular assemblage of SDS in micelles.

However, using DMPG vesicles and also micromolar concentrations of photoactivatable Pen(Lys48Bz) or Pen(Lys48TMD), phospholipid photoadducts were detected, even if the lateral diffusion in the disordered lamellar phase is around $10^{-7} > T_D < 5.10^{-9}$ cm^2.s^{-1} (*40*) with fast phospholipid motion (10^{-12} to 10^{-7} s) and fast exchange between free and bound peptide (with a dissociation constant in the micromolar range). The combination reaction occurs at time scales (10^{-6} s) slower than most phospholipid motion. Thus, the detection of photo-cross-linking with DMPG vesicles indicates the following: (i) cooperative diffusion of the penetratin photoactivatable analogues and the surrounding anionic phospholipids and (ii) restricted motion of the anionic phospholipids.

In a polar microenvironment such as glycerol, the triplet radical state can react by energy transfer like a photosensitizer, which, in the presence of oxygen, leads to the formation of singlet state oxygen. Finally, in a lipophilic medium the triplet radical might react with compounds possessing carbon-bound removable hydrogen atoms, which function as a quencher, as long as the intrinsic movements of the two molecules are slow enough to allow radical combination (DMPG). The cross-linking yield with trifluoromethylaryldiazirines, Pen(Lys48TMD), was also relatively low due to a competitive reaction, the carbene leading to a fast irreversible reaction with oxygen. The oxidation and β-elimination of the polar headgroups by basic hydrolysis prevent the assignment of the exact structures of the photoadducts. Finally, the triplet radical of dithienylketone, Pen(Lys48DTK), must act as a photosensitizer, regardless of the medium, since only oxidized and degraded species (lower molecular mass species) were found.

Thus, among the three photoprobes tested herein, only benzophenone (Bz) and trifluoromethylaryldiazirine (TMD) led to covalent bond formation with lipids, which were identifiable

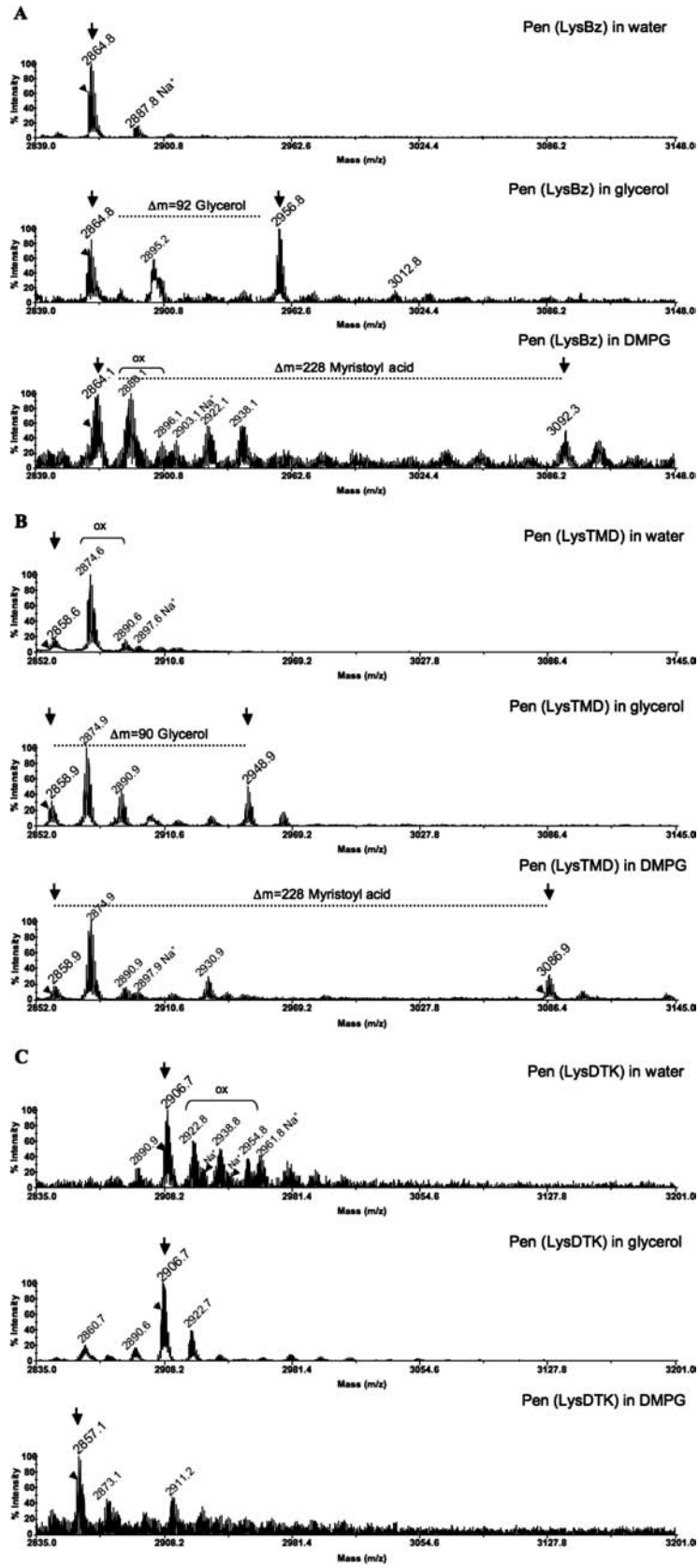


Figure 3. MALDI-TOF mass spectra of Pen(Lys48Bz) (A), Pen(Lys48DTK) (B), and Pen(Lys48TMD) (C) obtained after irradiation in water, glycerol, and DMPG vesicles. Pen(Lys48Bz), Pen(Lys48DTK), or Pen(Lys48TMD) dissolved at micromolar concentration in water or glycerol (500 μL) was irradiated on ice for 1 h at 365 nm. Then, 1 μL of the irradiated sample was deposited on the sample holder for MALDI-TOF mass spectrometry analysis. DMPG (1 mg/mL) was mixed with Pen(Lys48Bz), Pen(Lys48DTK), or Pen(Lys48TMD) at 1/25 peptide/lipid ratio. Theses samples were irradiated on ice for 1 h, at the same conditions as above, followed by an overnight basic hydrolysis. The hydrolyzed sample containing 0.1% of Triton was incubated with streptavidin-coated magnetic beads (100 μg, Dynabeads M280, Dynal). The same procedure was used for the experiments performed in SDS, except that no Triton was added during the incubation step. After different steps of washings, the photoadducts were eluted from the magnetic beads with the 2,5-dihydroxybenzoic acid (DHB) matrix. After 10 min incubation, 1 μL of bead-free supernatant was deposited on the sample holder for MALDI-TOF mass spectrometry analysis.

by MALDI-TOF mass spectrometry. Benzophenone (Bz) appeared to be the most appropriated photoprobe compared to TMD, since Bz leads to similar phase transition effects to those of penetratin, while TMD leads to great changes in the cooperativity of the transition, suggesting that TMD probably inserts deeper into the fatty acid chain region.

CONCLUSION

Herein, the photo-cross-linking of three photoactivatable penetratin peptides in glycerol, SDS, and lipid (DMPG) was evaluated. The dynamics of both SDS and the SDS/penetratin assemblies and the micromolar concentration of photoactivatable penetratin analogues used (in the range of biologically active concentrations) prevented peptide cross-linking to SDS. Regarding glycerol and lipids, even though photo-cross-linking occurred in both cases, the direct MS analysis of the photoadducts formed upon irradiation of the three different photoactivatable penetratin analogues was only achieved in the first one. The characterization of the photoadducts formed after lipid irradiation required basic hydrolysis of the lipid before extraction; otherwise, the capture with streptavidin-coated magnetic beads was ineffective. Bilayers of DMPG were photo-cross-linked with penetratin analogues, containing either benzophenone or trifluoromethylaryl diazirines but not phenylketone. With both photoactivatable penetratin analogues, MALDI-TOF analysis of the photoadducts formed after irradiation of the peptides with DMPG allowed unambiguous identification of the covalent bond formed with this lipid. Therefore, these analogues can be used to analyze the specific lipid(s) recruitment by penetratin, which represents an essential step in the understanding of the translocation mechanism of this cationic cell-penetrating peptide.

ACKNOWLEDGMENT

This work was supported by the Association Nationale pour la Recherche (ANR-Prob DOM). We thank the Pr. Gilbert Kirsch and his co-workers from the "Laboratoire d'Ingénierie Moléculaire et Biochimie Pharmacologique" Metz, France, for the generous gift of 5-carboxy-5′-methyl-2,2′-dithienylketone.

LITERATURE CITED

(1) Park, E. J., Carroll, G. T., Turro, N. J., and Koberstein, J. T. (2009) Shedding light on surfaces using photons to transform and pattern material surfaces. *Soft Matter 5*, 36–50.

(2) Dormán, G., and Prestwich, G. D. (2000) Using photolabile ligands in drug discovery and development. *TIBTECH 18*, 64–76.

(3) Brunner, J. (1996) Use of photocrosslinkers in cell biology. *Trends Cell Biol. 6*, 154–157.

(4) Kotzyba-Hibert, F., Kapfer, I., and Goeldner, M. (1995) Recent trends in photoaffinity labeling. *Angew. Chem., Int. Ed. 34*, 1296–1312.

(5) Fillion, D., Deraët, M., Holleran, B. J., and Escher, E. (2005) Stereospecific synthesis of a carbene-generating angiotensin ii analogue for comparative photoaffinity labeling: improved incorporation and absence of methionine selectivity. *J. Med. Chem. 48*, 3980–3990.

(6) Lequin, O., Bolbach, G., Fabrice, F., Convert, O., Girault-Lagrange, S., Chassaing, G., Lavielle, S., and Sagan, S. (2002) Involvement of the second extracellular loop (E2) of the neurokinin-1 receptor in the binding of substance P: Photoaffinity labeling and modeling studies. *J. Biol. Chem. 277*, 22386–22394.

(7) Jullian, V., Courtois, F., Bolbach, G., and Chassaing, G. (2003) Carbon-carbon bond ligation between cyclodextrin and peptide by photo-irradiation. *Tetrahedron Lett. 44*, 6437–6440.

(8) Ridder, A. N. J. A., Spelbrink, R. E. J., Demmers, J. A. A., Rijkers, D. T. S., Liskamp, R. M., Brunner, J., Heck, A. J. R., de Kruijff, B., and Killian, J. A. (2004) Photo-crosslinking analysis of preferential interactions between a transmembrane peptide and matching lipids. *Biochemistry 43*, 4482–4489.

(9) Maxfield, F. R. (2002) Plasma membrane microdomains. *Curr. Opin. Cell Biol. 14*, 483–487.

(10) Engelman, D. M. (2005) Membranes are more mosaic than fluid. *Nature 438*, 578–580.

(11) Lenne1, P.-F., Wawrezinieck, L., Fabien Conchonaud, F., Wurtz, O., Boned, A., Guo, X.-J., Rigneault, H., He, H.-T., and Marguet, D. (2006) Dynamic molecular confinement in the plasma membrane by microdomains and the cytoskeleton meshwork. *EMBO J. 25*, 3245–3256.

(12) Lagerholm, B. C., Weinreb, G. E., Jacobson, K., and Thompson, N. L. (2005) Detecting microdomains in intact cell membranes. *Ann. Rev. Phys. Chem. 56*, 309–333.

(13) Chachaty, C., Rainteau, D., Tessier, C., Quinn, P. J., and Wolf, C. (2005) Building up of the liquid-ordered phase formed by sphingomyelin and cholesterol. *Biophys. J. 88*, 4032–4044.

(14) Bino, J. B., Kumar, E. R., and Lala, A. K. (2000) Depth-dependent analysis of membranes using benzophenone-based phospholipids. *Biophys. Chem. 87*, 37–42.

(15) Coates Barclay, L. R., Baskin, K. A., Locke, S. J., and Schaefer, T. D. (1987) Benzophenone-photosensitized autoxidation of linoleate in solution and sodium dodecyl sulfate micelles. *Can. J. Chem. 65*, 2529–2540.

(16) Zhu, W. L., and Shin, S. Y. (2009) Antimicrobial and cytolytic activities and plausible mode of bactericidal action of the cell penetrating peptide penetratin and its Lys-linked two-stranded peptide. *Chem. Biol. Drug Des. 73*, 209–15.

(17) Palm, C., Netzereab, S., and Hällbrink, M. (2006) Quantitatively determined uptake of cell-penetrating peptides in non-mammalian cells with an evaluation of degradation and antimicrobial effects. *Peptides 27*, 1710–6.

(18) Balayssac, S., Burlina, F., Convert, O., Bolbach, G., Chassaing, G., and Lequin, O. (2006) Comparison of penetratin and other homeodomain-derived cell-penetrating peptides: interaction in a membrane-mimicking environment and cellular uptake efficiency. *Biochemistry 45*, 1408–1420.

(19) Christiaens, B., Symoens, S., Vanderheyden, S., Engelborghs, Y., Joliot, A., Prochiantz, A., Vandekerckhove, J., Rosseneu, M., and Vanloo, B. (2002) Tryptophan fluorescence study of the interaction of penetratin peptides with model membranes. *Eur. J. Biochem. 269*, 2918–2926.

(20) Christiaens, B., Grooten, J., Reusens, M., Joliot, A., Goethals, M., Vandekerckhove, J., Prochiantz, A., and Rosseneu, M. (2004) Membrane interaction and cellular internalization of penetratin peptides. *Eur. J. Biochem. 271*, 1187–1197.

(21) Burlina, F., Sagan, S., Bolbach, G., and Chassaing, G. (2005) Quantification of the cellular uptake of cell-penetrating peptides by MALDI-TOF mass spectrometry. *Angew. Chem., Int. Ed. 44*, 4244–4247.

(22) Aussedat, B., Sagan, S., Chassaing, G., Bolbach, G., and Burlina, F. (2006) Quantification of the efficiency of cargo delivery by peptidic and pseudo-peptidic trojan carriers using MALDI-TOF mass spectrometry. *Biochem. Biophys. Acta 1758*, 375–383.

(23) Delaroche, D., Aussedat, B., Aubry, S., Chassaing, G., Burlina, F., Clodic, G., Bolbach, G., Lavielle, S., and Sagan, S. (2007) Tracking a new cell-penetrating peptide, (RW)9, through an enzyme-stable mass spectrometry reporter. TAG. *Anal. Chem. 79*, 1932–1938.

(24) Magzoub, M., Eriksson, L. E., and Gräslund, A. (2002) Conformational states of the cell-penetrating peptide penetratin when interacting with phospholipid vesicles: effects of surface charge and peptide concentration. *Biochim. Biophys. Acta 1563*, 53–63.

(25) Binder, H., and Lindblom, G. (2003) Charge-dependent translocation of the Trojan peptide penetratin across lipid membranes. *Biophys. J. 85*, 982–95.

(26) Brunner, J., Senn, H., and Richards, F. M. (1980) 3-Trifluoromethyl-3-phenyldiazirine a new carbene generating group for photolabeling reagents. *J. Biol. Chem. 255*, 3313–3318.

(27) Nassal, M. (1983) 4-(1-Azi- 2,2,2-trifluoroethyl)benzoic acid a highly photolabile carbene generating label readly fixable to biochemical agents. *Liebigs Ann. Chem.* 1510–1523.
(28) Derossi, D., Joliot, A. J., Chassaing, G., and Prochiantz, A. (1994) The third helix of the Antennapedia homeodomain translocates through biological membranes. *J. Biol. Chem. 269*, 10444–10450.
(29) McElhaney, R. N. (1986) Differential scanning calorimetric studies of lipid-protein interactions in model membrane systems. *Biochim. Biophys. Acta 864*, 361–421.
(30) Alves, I. D., Goasdoué, N., Correia, I., Aubry, S., Galanth, C., Sagan, S., Lavielle, S., and Chassaing, G. (2008) Membrane interaction and perturbation mechanisms induced by two cationic cell penetrating peptides with distinct charge distribution. *Biochim. Biophys. Acta 1780*, 948–959.
(31) Canonica, S., Hellrung, B., and Wirz, J. (2000) Oxidation of Phenols by Triplet Aromatic Ketones in Aqueous Solution. *J. Phys. Chem. A 104*, 1226–1232.
(32) Rodgers, M. A. J. (1983) Solvent-induced deactivation of singlet oxygen: additivity relationships in nonaromatic solvents. *J. Am. Chem. Soc. 105*, 6201–6205.
(33) Harada, Y., Suzuki, K., Hashimoto, M., Tsukagoshi, K. and H., and Kimoto, H. (2009) Chemiluminescence from singlet oxygen that was detected at two wavelengths and effects of biomolecules on it. *Talanta 77*, 1223–1227.
(34) Gaudin, Y., Ruigrok, R. W. H., and Brunner, J. (1995) Low-pH induced conformational changes in viral fusion proteins: implications for the fusion mechanism. *J. Gen. Virol. 76*, 1541–1556.
(35) Breslow, R., Kitabatake, S., and Rothbard, J. (1978) Photoreactions of charged benzophenone with amphiphiles in micelles and multicomponent aggregates as conformational probes. *J. Am. Chem. Soc. 100*, 8156–8160.
(36) Delfino, J. M., Schreiber, S. L., and Richards, F. M. (1993) Design, synthesis, and properties of a photoactivatable membrane-spanning phospholipidic probe. *J. Am. Chem. Soc. 115*, 3458–3474.
(37) Lala, A. K., and Kumar, E. R. (1993) Orientation of the benzophenone group at various depths in bilayers. *J. Am. Chem. Soc. 115*, 3982–3988.
(38) Wendeler, M., Hoernschemeyer1, J., Hoffmann, D., Kolter, T., Schwarzmann, G., and Sandhoff, K. (2004) Photoaffinity labeling of the human GM2-activator protein mechanistic insight into ganglioside GM2 degradation. *Eur. J. Biochem. 271*, 614–627.
(39) Barker, C., Saul, D., Tiddy, G., Wheeler, B., and Willis, E. (1974) Phase structure, nuclear magnetic resonance and. rheological properties of viscoelastic sodium. dodecyl sulphate and trimethylammonium bromide mixtures. *J. Chem. Soc., Faraday Trans 1 70*, 154–162.
(40) Jain, M. K., and White, H. B. (1977) Long-range order in biomembranes. *Adv. Lipid Res. 15*, 1–60.

BC900466Q

"HFP" Fluorinated Cationic Lipids for Enhanced Lipoplex Stability and Gene Delivery

Emmanuel Klein,[†] Miahala Ciobanu,[†] Jérôme Klein,[†] Valérie Machi,[†] Christian Leborgne,[‡] Thierry Vandamme,[†] Benoît Frisch,[†] Françoise Pons,[†] Antoine Kichler,[‡] Guy Zuber,[†] and Luc Lebeau*[,†]

Laboratoire de Conception et Application de Molécules Bioactives, CNRS—Université de Strasbourg, 74 route du Rhin, BP 60024, 67401 Illkirch Cedex, France, and Généthon-FRE 3087 CNRS, 1 rue de l'Internationale, BP 60, 91002 Évry, France.
Received October 28, 2009; Revised Manuscript Received January 5, 2010

Although a great number of cationic lipids have been designed and evaluated as gene delivery systems, there is still a need for improvement of nonviral vectors. Recently, cationic lipids incorporating terminal fluoroalkyl segments ("FHP" lipids) have been described to display remarkable transfection potency. Here, we describe the synthesis of a new family of fluorinated triblock cationic lipids in which a fluorous segment lays between the cationic and the lipophilic parts of the molecule ("HFP" lipids). The compounds were designed so their self-assembly would offer enhanced resistance toward the host's degradation mechanisms mediated by lipophilic insertion. Self-assembly properties of these cationic lipids were evaluated at the air−water interface where they collapse in a highly ordered liquid phase. The HFP lipids efficiently condense DNA, and the resulting lipoplexes display enhanced resistance to amphiphilic agents when compared to nonfluorinated or FHP cationic lipids. Transfection properties of the fluorinated vectors, alone or as mixtures with different helper lipids (DOPE and a fluorinated analogue of DOPE), were then investigated on different cell lines (BHK-21, HepG2, and HeLa) and compared to those of the reference cationic lipid DOTAP. Data show that impermeabilization of the lipidic phase by fluorous segments alter significantly the gene transfection activities. Remarkably, incorporation of DOPE within the lipoplexes provides the particles with high gene transfection activity without reducing their resistance to amphiphilic agents.

INTRODUCTION

The delivery of a "medicine" gene in somatic cells involves the use of vectors, the function of which is to help the therapeutic gene cross the biological barriers and reach the nucleus of the target cells where it will be processed into mRNA and, later on, translated into proteins. Due to their high transfection efficiency, viral vectors such as adenoviruses, adeno-associated viruses (AAVs), or retroviruses are the most widespread vectors used in the laboratory or in clinical trials (*1*). However, their performance cannot overcome several major side effects, which include adverse immunogenic reactions, insertional mutagenesis, and sometimes fatal toxicity (*2, 3*). An additional limitation of these vectors lies in the restricted size of the DNA fragments they can introduce into a cell (less than 5 Kbp). The nonviral vectors, including cationic lipids, present interesting activity in vitro, but always appeared rather disappointing when evaluated in vivo. However, these vectors are devoid of some of the limitations of viruses (size restriction of the nucleic acid to be transfected, difficulty of production and purification, immunogenicity, etc.) and allow for specialized delivery options such as time-enhanced circulation, time-dependent release, and targeted delivery (*4*).

Since the first studies were conducted, hundreds of cationic lipids have been synthesized as candidates for nonviral gene delivery (*5*−*7*). Cationic lipids interact with negatively charged DNA through electrostatic interactions leading to condensed nucleic acid particles (lipoplexes). Optimum transfection efficacy invariably requires excess of cationic lipid for full DNA condensation and protection from serum nuclease. On the other hand, the cationic residual charge induces a poor circulation time of lipoplexes in blood, mostly due to their interaction with serum components. Many strategies have been developed to improve gene transfer mediated by cationic lipids. Those aiming at improving lipoplex circulation time are essentially based on the use of a poly(ethylene glycol) (PEG) coating of the cationic particles. However, introduction of PEG at the lipoplex surface unexpectedly does not highly increase the residential time of particles in the blood, which may be related to the drastic increase of the critical micelle concentration (cmc) of a lipid provoked by PEGylation (by a ca. 10^6-fold factor) (*8*). In addition, it may have rather adverse effects by inhibiting gene transfer in some cases (*9, 10*). A related strategy proposed by Mignet and Scherman results from the combination of cationic lipoplexes and PEGylated anionic liposomes (*11*). These pH-sensitive PEGylated anionic particles display interesting DNA delivery properties and are supposed to reverse to non-PEGylated cationic ones in the acidic endosome compartment. Behr and Vierling developed an alternative strategy to improve lipoplex circulation time by introducing a highly hydrophobic fluoroalkyl short segment at the extremity of the fatty acid chains of the cationic lipids (*12*−*17*). Owing to their increased hydrophobic character, these lipids (further named "FHP" fluorinated lipids to indicate that the fluoroalkyl moiety, F, is separated by an alkyl segment, H, from to the polar head, P) condense DNA into lipoplexes with higher stability than conventional cationic lipids. FHP lipid assemblies, however, are not expected to efficiently prevent anchoring/insertion of amphiphilic or lipophilic compounds to/within the bilayer structure, with such an event most often being a prelude to lipoplex destruction (i.e., lipid solubilization, recruitment of amphiphilic proteins triggering particle elimination by the reticuloendothelial system, activation of the complement system and opsonization, etc.). Importantly, FHP helper lipids have been

* Corresponding author. Tel.: +33(0)3 6885 4303, Fax: +33(0)3 6885 4306. E-mail address: llebeau@unistra.fr.
[†] CNRS—Université de Strasbourg.
[‡] Généthon-FRE 3087 CNRS.

10.1021/bc900469z © 2010 American Chemical Society
Published on Web 01/25/2010

described to enhance in vitro and in vivo gene delivery by cationic lipids (*18, 19*).

Recently, some of us showed that phospholipids that are fluorinated close to their polar head spread at the air−water interface into monolayers which are stable for several hours in the presence of high concentrations of detergents (*20, 21*). In the same conditions, conventional phospholipid monolayers hardly resist a few seconds. This remarkable property only partly results from the high hydrophobicity of fluorinated species as is the case with FHP lipids. Indeed, displaying the fluoroalkyl segment close to the lipid polar head likely induces a stabilization of higher magnitude, which may be explained by the interactions between adjacent fluorine atoms in the same perfluorinated chain that cause the chain to twist into a rigid, helical conformation (*22*). Consequently, close packing of the rigid fluoroalkyl segments does substantiate a kind of fluorous repelling shield that is highly impermeable to nonfluorinated hydrophilic, lipophilic, as well as amphiphilic compounds (*23*). Thus, by preventing or reducing insertion of surface active compounds within the lipid layer it is possible to efficiently prevent the destruction of the lipid assembly. We made the hypothesis that cationic lipids displaying such characteristics would condense DNA into fluorinated lipoplexes with original capabilities in gene transfer experiments. By resisting serum component adsorption (and subsequent destruction triggered by insertion of hydrophobic anchors of recruited proteins or other destruction mechanisms) (*24*), such lipoplexes are expected to present an extended half-life time, and possibly a higher transfection efficiency, however keeping in mind that intracellular trafficking of the delivery system requires at some points disassembly of the lipid−DNA complexes. Therefore, the immediate goal of this study was to prepare cationic lipids fluorinated close to their polar head (further named "HFP" fluorinated lipids, a terminal alkyl chain, H, being separated by a fluoroalkyl segment, F, from the polar head, P) and to evaluate (i) their capability to form complexes with DNA, (ii) the stability of the resulting lipoplexes, and (iii) the gene delivery efficacy of the latter in vitro. In the following, we describe the design, synthesis, characterization, and evaluation of a series of unprecedented HFP fluorinated triblock cationic lipids.

EXPERIMENTAL PROCEDURES

Chemicals and Materials. Unless otherwise stated, all chemical reagents were purchased from Alfa Aesar (Bischeim, France) and used without purification. α,ω-Diiodoperfluoroalkanes were from Apollo Scientific Ltd. (Bredbury, Cheshire, UK). When required, solvents were dried by standard procedures just before use (*25*). Products were purified by chromatography over silica gel (Silica Gel 60, 40−63 μm, Merck, Darmstadt, Germany). Reverse-phase filtration was carried out with Sep-Pack classic short-body C-18 cartridges (Waters, Division of Millipore, Milford, MA, USA).

N-[1-(2,3-Dioleoyloxy)propyl]-*N,N,N*-trimethylammonium chloride (DOTAP chloride), 1,2-dioleoyl-*sn*-glycero-3-phosphoethanolamine (DOPE), sodium *n*-dodecyl sulfate (SDS), 3-[(3-cholamidopropyl)dimethylammonio]-1-propanesulfonate (CHAPS), sodium cholate (NaCh), cetyltrimethylammonium bromide (CTAB), Tween 80, 3-(4,5-dimethylthiazol-2-yl)-2,5-diphenyl tetrazolium bromide (MTT), penicillin, streptomycin, L-glutamine, D-glucose, and tryptose phosphate broth were from Sigma-Aldrich (Saint-Quentin Fallavier, France). Culture media Dulbecco's Modified Eagle Medium Glutamax (DMEM) and Minimum Essential Eagle Medium (MEM) were from GIBCO-BRL (Cergy-Pontoise, France). Fetal calf serum (FCS) was from Perbio (Brebières, France). Lysis and luciferin solutions for monitoring luciferase activity were purchased from Promega (Charbonnières, France). Human hepatocarcinoma cells (HepG2), Syrian hamster kidney cells (BHK-21), and immortalized human epithelial cells (HeLa) were from ATCC-LGC (Molsheim, France). pSMD2-LucΔITR (7.6 kpb) or pEGFP-Luc (6.4 kpb) expression plasmids (BD Biosciences Clontech, Franklin Lakes, NJ, USA) were used as reporter genes to monitor transfection activity. Both plasmids encoded the firefly luciferase gene under the control of a strong promoter. HepG2 cells were transfected with the pSMD2-Luc and the other cell lines with the pEGFP-Luc.

Preparation of Cationic Lipids. *2,3-Bis(3,3,4,4,5,5,6,6,7,7,8,8-dodecafluorotetradecanoyloxy)-propyl-1-trimethylammonium Chloride (**1a**).* The acid **7a** (209 mg, 0.47 mmol) in anhydrous CH_2Cl_2 (2 mL) was stirred at room temperature with oxalyl chloride (0.2 mL, 2.29 mmol) and a catalytic amount of DMF (5 μL) for 4 h. Volatiles were removed under reduced pressure, and the residue was coevaporated twice with anhydrous toluene. The crude acid chloride was dissolved in anhydrous CH_2Cl_2 (2 mL), and the resulting solution was added dropwise to a mixture of anhydrous diol **8** (32 mg, 0.19 mmol) and pyridine (38 μL, 0.47 mmol) in THF/CH_2Cl_2 (2:1 v/v, 3 mL). The resulting suspension was sonicated for 2 h and stirred overnight at room temperature. Solvent was removed under reduced pressure at room temperature, and the residue was purified by flash chromatography over silica gel ($CHCl_3$/MeOH 100:0 to 60:40) to yield compound **1a** (51 mg, 26%; containing 37% of elimination byproduct) as a white wax.

*2,3-Bis(3,3,4,4,5,5,6,6-octafluorohexadecanoyloxy)-propyl-1-trimethylammonium Chloride (**1b**).* Compound **1b** (79 mg, 24%; containing 18% of elimination byproduct) was obtained as a white wax starting from compound **7b** following the same procedure as described for the preparation of **1a**.

*2,3-Bis(3,3,4,4,5,5,6,6,7,7,8,8-dodecafluorooctadecanoyloxy)-propyl-1-trimethylammonium Chloride (**1c**).* Compound **1c** (54 mg, 28%; containing 11% of elimination byproduct) was obtained as a white wax starting from compound **7c** following the same procedure as described for the preparation of **1a**.

*2,3-Bis(3,4,4,5,5,6,6,7,7,8,8-undecafluorotetradecen-2-oyloxy)-propyl-1-trimethylammonium Chloride (**2a**).* Compound **1a** (25 mg, 24.5 μmol) in CH_3CN/CH_2Cl_2 (2:1 v/v, 3 mL) was stirred for 2 h with 2 M triethylamine in THF (36 μL, 62.0 μmol) at room temperature. The reaction mixture was filtered over a pad of finely powdered $NaHCO_3$, and the filtrate was reduced under vacuum to yield **2a** (20 mg, 84%) as a white wax.

*2,3-Bis(3,4,4,5,5,6,6-heptafluorohexadecen-2-oyloxy)-propyl-1-trimethylammonium Chloride (**2b**).* Compound **2b** (6 mg, 88%) was prepared from **1b** following the same procedure as described for **1a**.

*2,3-Bis(3,4,4,5,5,6,6,7,7,8,8-undecafluorooctadecen-2-oyloxy)-propyl-1-trimethylammonium Chloride (**2c**).* Compound **2c** (10 mg, 86%) was prepared from **1c** following the same procedure as described for **1a**.

*1,2-Di[(Z)-3,3,4,4,5,5,6,6,7,7,8,8-dodecafluorohexadec-9-enoyl]-sn-glycero-3-phosphatidylethanolamine (**3**).* Triphenyl phosphine (4.1 mg, 15.7 μmol) and azido compound **15** (6.0 mg, 5.2 μmol) in THF/CH_2Cl_2/CF_3CH_2OH/HCl 2% (3:1:1:0.1 v/v, 3 mL) were stirred for 48 h at room temperature. Volatiles were removed under reduced pressure, and the residue was purified by silica gel chromatography ($CHCl_3$/MeOH/H_2O 10:0:0 to 10:6:1). The fluorinated analogue of DOPE was obtained as a colorless oil (3.0 mg, 51%; mixture of isomers, Z/E = 85:15).

*3,3,4,4,5,5,6,6,7,7,8,8-Dodecafluoro-1,10-diiodotetradecyl Benzoate (**4a**).* Sodium dithionite (3.14 g, 17.8 mmol) was slowly added to a mixture of 1,6-diiodoperfluorohexane (5.00 g, 9.0 mmol), vinyl benzoate (1.25 mL, 9.0 mmol), 1-hexene (1.12 mL, 9.0 mmol), and $NaHCO_3$ (1.91 g, 18.0 mmol) in CH_3CN/H_2O (8:7 v/v, 18.4 mL) at 0 °C. The resulting solution was stirred for 50 min at 0 °C, brought to pH 5−7 with HCl 3N,

and stirred for an additional 20 min period at room temperature. Water was added, and the solution was extracted with CH_2Cl_2. The organic layer was dried over $MgSO_4$, filtered, and reduced under vacuum. The residue was purified by silica gel chromatography (C_6H_{14}/CH_2Cl_2 95:5) to yield benzoate **4a** (2.03 g, 28%) as a slightly yellow waxy solid.

*3,3,4,4,5,5,6,6-Octafluoro-1,8-diiodohexadecyl Benzoate (**4b**).* Compound **4b** (2.46 g, 29%) was prepared from 1,4-diiodoperfluorobutane, vinyl benzoate, and 1-decene following the same procedure as described for **4a**.

*3,3,4,4,5,5,6,6,7,7,8,8-Dodecafluoro-1,10-diiodooctadecyl Benzoate (**4c**).* Compound **4c** (1.53 g, 33%) was prepared from 1,6-diiodoperfluorohexane, vinyl benzoate, and 1-decene following the same procedure as described for **4a**.

*3,3,4,4,5,5,6,6,7,7,8,8-Dodecafluorotetradecyl Benzoate (**5a**).* Tributyltin hydride (173 μL, 0.64 mmol) was added to compound **4a** (100 mg, 0.13 mmol) and AIBN (2 mg, 0.01 mmol) in Et_2O (3 mL). The reaction mixture was refluxed under the light of a domestic halogen lamp (I.CEM Züblin AG, type 0201, 500 W) for 15 h. Solvent was removed under reduced pressure and the residue was purified by flash chromatography over silica gel (n-C_6H_{14}/CH_2Cl_2 9:1) to yield benzoate **5a** (61 mg, 90%) as a white waxy solid.

*3,3,4,4,5,5,6,6-Octafluorohexadecyl Benzoate (**5b**).* Compound **5b** (1.38 g, 96%) was prepared from **4b** following the same procedure as described for **5a**.

*3,3,4,4,5,5,6,6,7,7,8,8-Dodecafluorooctadecyl Benzoate (**5c**).* Compound **5c** (1.49 g, 90%) was prepared from **4c** following the same procedure as described for **5a**.

*3,3,4,4,5,5,6,6,7,7,8,8-Dodecafluorotetradecanol (**6a**).* Compound **5a** (3.0 g, 5.61 mmol) was stirred in methanolic 1 M LiOH (20 mL) for 3 h at room temperature. Solvent was removed under vacuum, and the residue was dissolved in CH_2Cl_2, then washed with water and brine. The organic layer was dried over $MgSO_4$ and evaporated, and compound **6a** (2.21 g, 91%) was obtained as a white waxy solid after purification over silica gel (n-C_6H_{13}/CH_2Cl_2 1:1).

*3,3,4,4,5,5,6,6-Octafluorohexadecanol (**6b**).* Compound **6b** (0.60 g, 86%) was prepared from **5b** following the same procedure as described for **6a**.

*3,3,4,4,5,5,6,6,7,7,8,8-Dodecafluorooctadecanol (**6c**).* Compound **6c** (0.47 g, 77%) was prepared from **5c** following the same procedure as described for **6a**.

*3,3,4,4,5,5,6,6,7,7,8,8-Dodecafluorotetradecanoic Acid (**7a**).* Alcohol **6a** (1.0 g, 2.32 mmol) was dissolved in acetone (40 mL) and water (0.5 mL). Jones' reagent was added dropwise at room temperature until a persistent red−brown solution was obtained. The reaction mixture was stirred for 1 h, added with *i*-PrOH (2 mL), and stirred for an additional 15 min period. Solvent was then removed under reduced pressure, water (5 mL) was added, and the resulting mixture was extracted with Et_2O. The organic layer was washed with H_2O, brine, dried over $MgSO_4$, filtered, and reduced under vacuum to yield acid **7a** (0.93 g, 90%) as a white waxy solid.

*3,3,4,4,5,5,6,6-Octafluorohexadecanoic Acid (**7b**).* Compound **7b** (0.37 g, 92%) was prepared from **6b** following the same procedure as described for **7a**.

*3,3,4,4,5,5,6,6,7,7,8,8-Dodecafluorooctadecanoic Acid (**7c**).* Compound **7c** (1.64 g, 89%) was prepared from **6c** following the same procedure as described for **7a**.

*N-[1-(2,3-Dihydroxy)propyl]-N,N,N-trimethylammonium Chloride (**8**).* (±)-Glycidol (2 mL, 30.1 mmol), trimethylamine hydrochloride (2.88 g, 30.1 mmol), and *N,N*-diisopropylethylamine (5.25 mL, 30.1 mmol) in methanol (20 mL) were stirred for 12 h at room temperature. Solvent was removed under reduced pressure, and compound **8** (3.65 g, 71%) was purified by recrystallization in EtOH/acetone (1:1 v/v).

*Benzyl 2-Bromoethyl Phosphite (**9**).* *N,N*-Diisopropylethylamine (1.0 mL, 5.73 mmol) was added dropwise to phosphorus trichloride (0.5 mL, 5.73 mmol) in anhydrous THF (10 mL). The reaction mixture was cooled down to −78 °C, and benzyl alcohol (0.6 mL, 5.73 mmol) in THF (20 mL) was added with a syringe driver under vigorous stirring over a 3 h period. The resulting suspension was stirred for 30 min, and a second portion of *N,N*-diisopropylethylamine (1.0 mL, 5.73 mmol) was added. Then, freshly distilled 2-bromoethanol (0.4 mL, 5.73 mmol) in THF (20 mL) was added dropwise over a 3 h period. Stirring was prolonged for 90 min at −78 °C before water (7 mL) was added. The reaction mixture was warmed to room temperature, THF was removed under vacuum, and the residue was washed twice with AcOEt. The organic layer was dried over MgSO4, reduced under vacuum, and purified over silica gel (n-C_6H_{14}/AcOEt 5:5) to yield compounds **9** (1.08 g, 67%) as a slightly yellow oil.

*Benzyl 2-Bromoethyl (2,2-Dimethyl-1,3-dioxolan-4-yl)methyl Phosphate (**10**).* Sulfuryl chloride (4.3 mL, 53.5 mmol) was added dropwise at 0 °C to phosphite **9** (5.0 g, 17.9 mmol) in dry CCl_4 (50 mL). Stirring was prolonged 30 min at 0 °C and 10 min at room temperature. Volatile was removed under vacuum, and the residue was coevaporated twice with anhydrous toluene. Benzyl 2-bromoethyl chlorophosphate was obtained as a colorless oil and was used without purification. (*R*)-(-)-2,2-Dimethyl-1,3-dioxolane-4-methanol (2.37 g, 17.9 mmol) in anhydrous THF (200 mL) was treated with sodium hydride (60% oil suspension, 0.86 g, 21.5 mmol) at 0 °C for 30 min. Then, previously prepared chlorophosphate was added, and the reaction mixture was stirred for 3 h at room temperature. THF was removed under vacuum, saturated aqueous NH_4Cl (100 mL) was added, and the resulting solution was extracted with AcOEt. The organic layer was washed with H_2O, brine, dried over $MgSO_4$, and reduced under vacuum. The residue was purified over silica gel (n-C_6H_{14}/Et_2O 5:5 to 8:2) to yield **10** (4.6 g, 63%, mixture of diastereomers) as a yellow oil.

*2-Azidoethyl Benzyl (2,2-Dimethyl-1,3-dioxolan-4-yl)methyl Phosphate (**11**).* Compound **10** (0.50 g, 1.22 mmol) and sodium azide (0.10 g, 1.54 mmol) were stirred in anhydrous DMF (6 mL) for 2 h at 50 °C. Water (15 mL) was added, and the resulting solution was extracted with Et_2O. The organic layer was dried over $MgSO_4$, reduced under vacuum, and purified by flash chromatography (n-C_6H_{14}/AcOEt 5:5 to 8:2) to yield **11** (0.34 g, 75%, mixture of diastereomers) as a yellow oil.

*2-Azidoethyl Benzyl 2,3-dihydroxypropyl Phosphate (**12**).* Compound **11** (118 mg, 0.32 mmol) was stirred in EtOH (8 mL) with strongly acidic cation exchange resin Dowex 50 × 8 (H^+ form) for 12 h at room temperature. The resin was filtered off, solvent was removed under vacuum, and the residue was purified by flash chromatography (AcOEt/EtOH 10:0 to 8:2) to yield **12** (69 mg, 64%) as a yellow oil.

*(Z)-3,3,4,4,5,5,6,6,7,7,8,8-Dodecafluorohexadec-9-enoic Acid (**13**).* Unsaturated acid **13** (0.14 g, 99%, Z/E = 85:15) was obtained as a colorless oil starting from alcohol **17** and following the same procedure as described for **7a**.

*2-Azidoethyl Benzyl 3-{1,2-di[(Z)-3,3,4,4,5,5,6,6,7,7,8,8-dodecafluorohexadec-9-enoyl]-sn-glycero} Phosphate (**14**).* Unsaturated acid **13** (250 mg, 0.53 mmol) in anhydrous CH_2Cl_2 (2 mL) was stirred at room temperature for 4 h with oxalyl chloride (0.25 mL, 2.86 mmol) and DMF in catalytic amount. Volatiles were removed under reduced pressure, and the residue was coevaporated twice with anhydrous toluene and dissolved in CH_2Cl_2 (2 mL). Then, diol **12** (68 mg, 0.21 mmol) and pyridine (45 μL, 0.56 mmol) in anhydrous THF (3 mL) were added, and the reaction mixture was stirred at room temperature for 8 h. Saturated aqueous NH_4Cl was added, and the mixture was extracted with Et_2O. The organic layer was dried over $MgSO_4$,

filtered, and reduced under vacuum. The residue was purified by flash chromatography (*n*-C_6H_{14}/CH_2Cl_2/AcOEt 6:2:2 to 0:0:10) to yield **15** (172 mg, 68%; mixture of isomers, *Z*/*E* = 85:15) as a colorless oil.

*2-Azidoethyl 3-{1,2-di[(Z)-3,3,4,4,5,5,6,6,7,7,8,8-dodecafluorohexadec-9-enoyl]-sn-glycero} Hydrogen Phosphate (**15**).* Bromotrimethylsilane (35 μL, 265 μmol) was added to compound **14** (84 mg, 68 μmol) in anhydrous CH_2Cl_2 (5 mL). The reaction mixture was stirred for 3 h at room temperature and moist THF is added. Solvent was removed under vacuum, and the residue was purified over silica gel ($CHCl_3$/MeOH 10:0 to 6:4) to yield compound **15** (74 mg, 95%; mixture of isomers, *Z*/*E* = 85:15) as a colorless oil.

*3,3,4,4,5,5,6,6,7,7,8,8-Dodecafluoro-1,10-diiodotetradec-9-enyl Benzoate (**16**).* A degassed mixture of 1,6-diiodoperfluorohexane (200 mg, 0.36 mmol), 1-octyne (80 μL, 0.54 mmol), vinyl benzoate (75 μL, 0.54 mmol), and AIBN (12 mg, 0.07 mmol) was stirred for 15 h at 80 °C in a sealed tube. The resulting mixture was cooled down to room temperature, volatiles were removed under reduced pressure, and the residue was purified by silica gel chromatography (*n*-C_6H_{14}/CH_2Cl_2 9:1 to 0:10) to yield compound **16** (105 mg, 36%, *Z*/*E* = 15:85) as a yellow waxy solid.

*(Z)-3,3,4,4,5,5,6,6,7,7,8,8-Dodecafluorohexadec-9-enyl Alcohol (**17**).* Diiodoester **16** (354 mg, 0.44 mmol) in anhydrous THF (4 mL) was added dropwise to a suspension of $LiAlH_4$ (100 mg, 2.63 mmol) in refluxing THF (8 mL). The resulting mixture was stirred at 66 °C for 30 min and cooled down at room temperature, and excess reagent was slowly decomposed by addition of solid NH_4Cl. Ether (15 mL) was then added, and the organic layer was washed with water and brine, dried over $MgSO_4$, filtered, and reduced under vacuum. The crude residue was purified over silica gel (*n*-C_6H_{14}/CH_2Cl_2 5:5 to 0:10) to yield alcohol **17** (135 mg, 68%, *Z*/*E* = 88:12) as a colorless oil.

Film Formation and Surface Pressure Measurements. Monolayer experiments were performed on a computer-controlled Langmuir film balance KSV 3000 (KSV, Helsinki, Finland). Surface pressure isotherms were recorded on a Teflon trough (570 × 150 mm) with a Wilhelmy plate coupled to a linear transducer. Monolayers were spread from 0.5 mM lipid solutions in hexane/chloroform (1/1: v/v). Volumes ranging from 100 to 300 μL were delivered at several locations across the water surface with a Hamilton microsyringe. At least 15 min were allowed for the spreading solvent to evaporate before monolayer compression. The subphase consisted of purified water (pH 5.35, Millipore filtration system, Barnstead, NANO pure 11) with a resistivity of $18.2 \cdot 10^6$ Ω cm. Compressions were realized using a hydrophilic Delrin barrier (polyacetal). Surface pressure vs molecular area curves were recorded at 21.0 ± 0.5 °C with a compression speed of 2−5 Å^2 per lipid molecule per minute. All measurements were carried out in triplicate. Specific areas A_s, lift-off areas A_{lo}, and collapse pressures π_c were determined as previously described (*26*).

Cell Culture. Human hepatocarcinoma cells (HepG2) were cultured in DMEM supplemented with 100 units/mL penicillin, 100 μg/mL streptomycin, 292 mg/L L-glutamine, 4.5 g/L D-glucose, and 10% heat-inactivated FCS. The syrian hamster kidney fibroblast cell line (BHK-21) was cultured in MEM supplemented with 100 units/mL penicillin, 100 μg/mL streptomycin, 10 mg/mL L-glutamine, 50 mg/mL tryptose, and 10% FCS. The HeLa cell line was cultured in MEM supplemented with 100 units/mL penicillin, 100 μg/mL streptomycin, 292 mg/L L-glutamine, and 10% FCS.

Lipoplex Preparation. For transfection experiments, cationic lipid (30 μL of a 1.8 mM solution in ethanol) and DOPE (6 μL of a 18 mM solution in ethanol) were mixed and added to 10 mM Hepes pH 7.5, 150 mM NaCl (150 μL). After stirring by vortex, the solution was added to the plasmid DNA (6 μg) in 10 mM Hepes pH 7.5, 150 mM NaCl (150 μL). The solution was vortexed again and incubated for 20 min at room temperature before addition to the cells. For gel retardation analysis, the same concentration and procedure were used except that the amount of DNA per sample was 1 μg.

Dynamic Light Scattering Measurements. The average particle size and the polydispersity of the lipoplexes were measured by using photon correlation spectroscopy (Malvern Zetasizer nanoZS, Malvern Instruments Inc., UK) using the multimodal analysis and the automatic mode. Lipoplex solutions (100 μL, vide supra) were diluted 10 times, in DMEM medium unless stated otherwise.

DNA Retardation Assays. After 15 min incubation, complexes were analyzed by electrophoresis through a 1% agarose gel. The gel was run in a 40 mM Tris-acetate-EDTA buffer pH 8.0 (TAE). DNA was then visualized with ethidium bromide solution at 0.5 μg/mL.

Transfection Procedure. Cells were plated in 24-well plates one day before transfection in order to obtain 60−80% confluent cultures at the time of the experiment. Transfection mixture (110 μL containing 2 μg of DNA plasmid, vide supra) was deposited in each well of the triplicate. After a 24 h incubation period, cells were harvested in lysis buffer (250 μL: 8 mM $MgCl_2$, 1 mM DTT, 1 mM EDTA, 1% Triton X-100, 15% glycerol, in 25 mM Tris-phosphate buffer pH 7.8). The cell lysate was centrifuged for 5 min at 10 000 *g* to pellet cell debris. Luciferase light units were measured in a 96-well plate format with a PhL luminometer (Mediators Diagnostika) from an aliquot of the supernatant (50 μL) with 10 s integration after automatic injection of assay buffer (100 μL: lysis buffer without Triton X-100 but supplemented with 2 mM ATP) and 167 μM luciferin (100 μL). The protein content of each cell lysate was measured using the BioRad protein assay. The transfection efficiency was expressed as relative light units/10 s/mg protein (RLU/mg protein) after subtraction of background luciferase value from each sample value. Values of each sample are the means of triplicate determinations.

Lipoplex Cytotoxicity Assessment. Lipoplex cytotoxicity was assessed using a tetrazolium-based assay. Cells were seeded in 24-well culture plates at a density of 5.0×10^4 cells per well and cultured at 37 °C for 24 h. On the next day, culture medium was changed to fresh DMEM medium supplemented with 10% FCS before addition of lipoplexes (100 μL) prepared as previously described. After a 24 h incubation period at 37 °C, culture supernatant was removed, cells were carefully washed with PBS, and 0.5 mg/mL MTT (1 mL) in complete culture medium was added. After a 2 h incubation period at 37 °C, MTT solution was removed and DMSO (1 mL) was added to lyse cells and dissolve reduced MTT. Intensity of MTT reduction was then evaluated by measuring absorbance at 570 nm. Viability of cells treated with lipoplexes was expressed as a percentage of the absorbance measured in untreated cells. Each treatment was assessed in triplicate, and data are presented as means ± sem of $n = 3$ values.

RESULTS AND DISCUSSION

Molecular Design and Chemistry. To investigate the influence of fluoroalkyl moieties located in the vicinity of the headgroup of a cationic lipid on its transfection efficiency, we first need a reference compound and selected the widely used DOTAP (Figure 1). The introduction of fluoroalkyl segments in its structure must fulfill some preliminary requirements in terms of chemical stability. Considering the high reactivity of α,α′-difluoroesters toward water with half-life time for hydrolysis in the range 0.1−5 min (*27*), we decided on structures in which one methylene group lies in between the fluoroalkyl chain

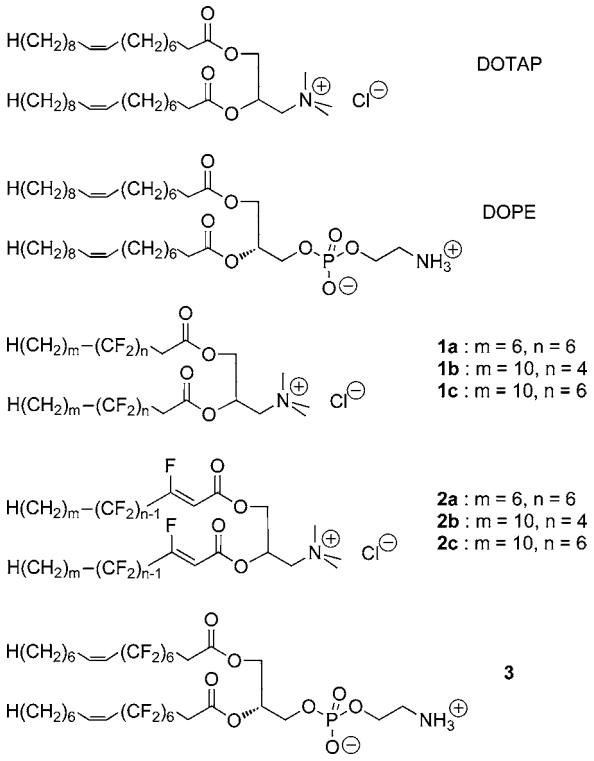
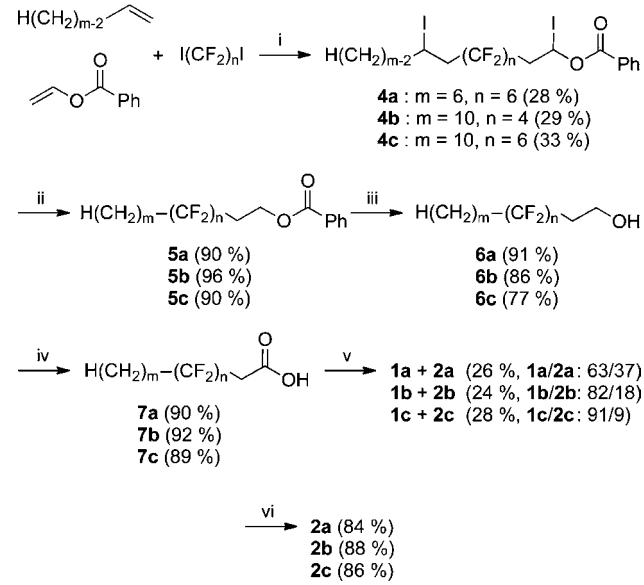


Figure 1. Structures of DOTAP, DOPE, and fluorinated cationic lipids developed.

and the carboxyl group. We thus designed compounds **1a**−**c** with modulated lengths for fluoroalkyl and terminal alkyl moieties. In order to target compounds with hydrophobicity tentatively comparable with that of DOTAP, we varied the number of methylene (*m*) and difluoromethylene (*n*) groups in the chains, considering the "1 CF_2 = 1.5 CH_2" rule (*28, 29*) and its variations (1.5 $CH_2 \leq 1$ $CF_2 \leq 4$ CH_2) (*30*). Under mild basic conditions, β,β'-difluoroesters easily eliminate HF, and compounds **2a**−**c** result from a double elimination in **1a**−**c** (vide infra).

A number of transfection protocols with cationic lipids use dioleoylphosphatidylethanolamine (DOPE) as a helper lipid (Figure 1). The role of DOPE in transfection assays has been extensively studied (*31, 32*). The mechanism of action of that lipid has been attributed to its capacity to induce transition of a lipid bilayer from the liquid-crystalline lamellar phase into the inverted hexagonal H_{II} phase. Vierling et al. examined the use of terminal fluorinated glycerophosphoethanolamines analogues of DOPE as helper lipids in nonfluorinated cationic lipid-mediated gene transfer (*18, 19*). A fluorinated segment was introduced at the extremity of the ester at C^1 (or C^1 and C^2) on the glycerol backbone, and the resulting increase in transfection efficiency by cationic lipids was attributed to the pronounced cone-shaped geometry of the molecule, displaying a greater tendency to promote a transition from the lamellar phase into the inverted hexagonal H_{II} phase. Considering the results obtained with lipoplexes prepared from mixtures of **1a**−**c** and DOPE (vide infra), we were especially interested in evaluating a fluorinated analogue of DOPE displaying two fluorous segments close to the lipid polar head. Consequently, we designed HFP compound **3** that displays all structural features of DOPE and displays a fluorous segment in between the double bond and the carboxyl group of the two fatty acid chains. Chain length is less than C_{18} to compensate for enhanced hydrophobicity due to fluorine. Stereochemistry of the double bond is *Z* in order to tentatively preserve the original chain conformation of oleoyl chains. Last, C^2 stereochemistry on glycerol backbone was imposed to fit with that in natural phospholipids.

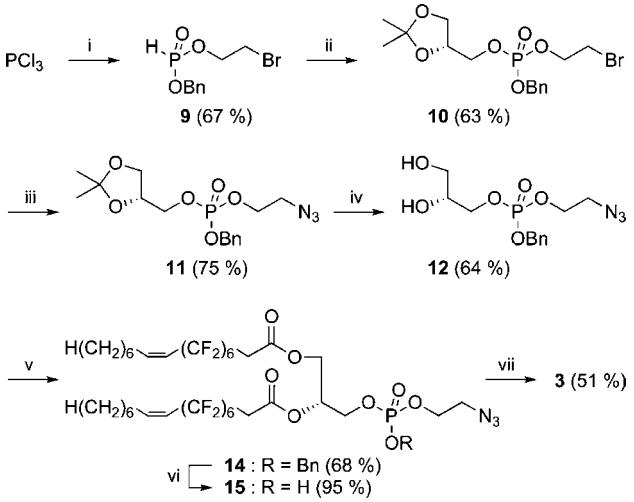
Scheme 1. Synthesis of Compounds 1a−c and 2a−c[a]



[a] Conditions: (i) $NaHCO_3$, $Na_2S_2O_4$; (ii) Bu_3SnH, AIBN; (iii) LiOH; (iv) CrO_3, H_2SO_4; (v) $(COCl)_2$, *N*-[1-(2,3-dihydroxy)propyl]-*N*,*N*,*N*-trimethylammonium chloride (**8**), py; (vi) Et_3N.

The synthesis of compounds **1a**−**c** was realized starting from α,ω-diiodoperfluoroalkanes according to Scheme 1. Hemifluorinated fatty acids **7a**−**c** were key intermediates. Their preparation involved the well-described radical addition of a iodoperfluoroalkane to an alkenyl compound (*33*). However, the homobifunctional fluorinated starting material introduced some difficulty, as heterofunctionalization was required. The reaction of a large excess of diiodoperfluoroalkane with 1 equiv of alkene allows high yield but low conversion and is not acceptable due to high cost of the fluorinated reagents. When the reaction was carried out with diiodo and alkenyl compounds in stoichiometric amounts, the proportion of monoalkylated product obtained was close to 50%, which is in agreement with statistics. Nevertheless, the process of the radical reaction remained difficult to monitor and reduction compounds R_F-H rapidly appeared as alkene concentration decreased in the reaction mixture. Consequently, the heterobifunctionalization of the diiodo starting material was carried out using a one-step procedure involving stoichiometric amounts of both alkenyl reagents. Perfluoroalkyl iodide addition to alkene can be promoted in many ways (by photolysis, pyrolysis, electrolysis, free radical initiator, enzymes, metals, and transition metal complexes). In that work, radicals were generated under the conditions described by Rong and Keese, and using sodium dithionite and sodium carbonate in CH_3CN/H_2O (*34*). The yield of the double transformation was close to 30% and was higher than that by any multistep procedure we have experienced. Efforts to run the reaction under anhydrous conditions with triethylborane (*35*) did not give better results either. Radical reduction of compounds **4a**−**c** using Bu_3SnH and AIBN (*36*) proved efficient and **5a**−**c** were obtained in high yield. Benzoate hydrolysis and Jones oxidation of the resulting alcohols **6a**−**c** afforded hemifluorinated fatty acids **7a**−**c** (*37, 38*). Further conversion into acyl chlorides allowed direct coupling with *N*-[1-(2,3-dihydroxy)propyl]-*N*,*N*,*N*-trimethylammonium chloride **8** straightforwardly prepared from glycidol. Fluorinated cationic lipids **1a**−**c** were obtained in 26−28% yield. Important to note is the high sensitivity of compounds **1a**−**c** that very easily eliminate HF even at room temperature. As a consequence, they were obtained as a mixture with eliminated byproducts that were very difficult to separate (**1a**, 37% elimination byproduct; **1b**, 18% elimination byproduct; **1c**, 11% elimination byproduct).

Scheme 2. Synthesis of the Fluorinated Analogue of DOPE 3[a]



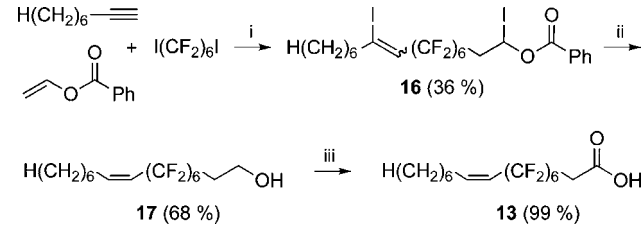
[a] Conditions: (i) Et_3N, BrC_2H_4OH, H_2O; (ii) SO_2Cl_2, (*S*)-2,2-dimethyl-1,3-dioxolane-4-methanol, NaH; (iii) NaN_3; (iv) Dowex 50 × 8 (H^+ form); (v) **13**, $(COCl)_2$, py; (vi) TMSBr, H_2O; (vii) PPh_3, H_2O.

In order to tentatively assume better control of the composition and properties of later lipoplexes, compounds **1a**−**c** were quantitatively transformed into the corresponding unsaturated cationic lipids **2a**−**c** upon treatment with Et_3N. The unsaturated double bonds are in the *Z* configuration as was determined from the coupling constant $^3J_{H-F} \approx 29$ Hz, a value which is characteristic of the trans position between fluorine and hydrogen on ethylenic double bonds (*39*, *40*). Lipid **1c**, however, was considered for further biophysical and biological investigations (vide infra), as it was obtained at the lower contamination rate.

Synthesis of the fluorinated analogue of DOPE **3** was achieved according to Scheme 2. Benzyl 2-bromoethyl phosphite **9** was prepared in one step from phosphorus trichloride. Transformation of **9** into corresponding chlorophosphate allowed condensation with (*S*)-2,2-dimethyl-1,3-dioxolane-4-methanol. Resulting phosphotriester **10** was obtained in 53% yield. Bromide nucleophilic displacement with sodium azide provided compound **11**, and the isopropylidene protecting group was removed upon treatment with a strongly acidic cation exchange resin. Resulting diol **12** was then acylated with unsaturated hemifluorinated fatty acid **13** to give **14** in 68% yield. Interestingly, elimination byproducts were not obtained or could not be detected. In the preparation of compounds **2a**−**c**, due to the amphiphilicity of the compounds, the crude reaction mixture was not submitted for aqueous work up but reduced in vacuo and directly purified by silica gel chromatography. This could possibly indicate that HF elimination occurs during concentration of the crude reaction mixture and may be avoided by aqueous workup prior to solvent evaporation. Debenzylation of **14** was achieved with bromotrimethylsilane (*41*, *42*). The final step was reduction of the azide group in **15** via a Staudinger reaction affording **3** in 51% yield.

Unsaturated fluorinated fatty acid **13** was a key compound for the preparation of the fluorinated DOPE analogue. It was prepared in three steps (Scheme 3). The first one involved the reaction of R_FI with an alkynyl compound (*43*−*45*). It was similar to the preparation of **4a**−**c** except that 1-alkene was replaced with 1-octyne. The double radical oxidative addition of 1,6-diiodoperfluorohexane on a stoichiometric mixture of vinylbenzoate and alkyne furnished vinyl iodide **16** as *E*/*Z* mixture (*E*:*Z* = 85:15). Reduction of compound **16** under the conditions employed by Takagi (*n*BuLi, Et_2O, −78 °C) for the synthesis of fluorinated analogues of oleic acid displaying

Scheme 3. Synthesis of Unsaturated Hemifluorinated Fatty Acid 13[a]



[a] Conditions: (i) Na_2CO_3, $Na_2S_2O_4$, AIBN. (ii) $LiAlH_4$. (iii) CrO_3, H_2SO_4.

the fluorous part opposite the carboxyl group proved inadequate (*44*, *45*). Reduction using nBu$_3$SnH-AIBN (*46*) gave a mixture of cis and trans alkenes (*Z*:*E* = 60:40) revealing extended isomerization of the intermediate vinyl radical. More satisfactorily, treatment with lithium aluminum hydride allowed extensive reduction of compound **16** into **17** in better favor of the cis isomer (*47*). Under these conditions, reduction proceeded with full retention of the configuration (*Z*:*E* = 88:12), and concomitant reduction of the benzoate moiety occurred with release of the free primary hydroxyl group. The last step consisted of oxidation of alcohol **17** that was quantitatively transformed into unsaturated hemifluorinated fatty acid **13** upon treatment with CrO_3−H_2SO_4.

Self-Assembly Properties of the Fluorinated Cationic Lipids. Self-assembly properties of fluorinated cationic lipids were investigated at the air/water interface (due to their high content in elimination byproduct, samples **1a** and **1b** were not subjected to monolayer study). Compounds were spread from a hexane/chloroform solution, and the surface pressure π vs area A was recorded. All the compounds analyzed exhibited similar behavior (see Supporting Information). The pressure regularly increased up to collapse pressure at 28−34 mN/m. No surface pressure decrease was recorded at high lateral pressure ($\pi < 30$ mN/m) when the compression barrier was stopped, indicating that the monolayers formed at the air/water interface were stable. The values for specific area A_s, lift-off area A_{lo}, and collapse pressure π_c for compounds **1c** and **2a**−**c** are presented in Supporting Information.

Monolayer spread from saturated lipid **1c** (containing 11% of elimination products) collapsed in a more condensed state than those from unsaturated compounds **2a**−**c**. This indicates that unsaturation to some extent opposes close packing of the compounds. That is further supported by the lower value for the lift-off area recorded for **1c** when compared to those of **2a**−**c**. However, the *Z* configuration of the double bonds in **2a**−**c** seems to be contradictory to these results. Indeed, it is expected that **1c** and the *Z* conformer of **2c** display comparable monolayer properties and more particularly similar specific areas (mean molecular area in the more condensed state of the monolayer). The large difference in specific area between the two compounds could then reflect some unusual conformation of the glycerol backbone in **2c**, and computational modeling would be necessary to get a deeper insight in the packing properties of the compounds. The measured value for specific area of lipid **1c** at the air/water interface was close to twice that of a section of crystalline fluoroalkyl chain (2 × 24.9 Å^2) (*48*). That indicates that compound **1c** collapsed in a highly ordered liquid phase, as no phase transition could be detected through isothermal monolayer compression. The same held for compounds **2a**−**c** though slightly higher A_s values were recorded. For comparison, the A_s value for DOTAP is 50 Å^2, which is larger than twice the section of alkyl chain (16 Å^2) and accounts for a higher free volume within the lipidic phase. That may be correlated to susceptibility to detergents (vide infra).

Table 1. Semiquantitative Evaluation of Lipoplex Stability in the Presence of Surface Active Compounds

	detergent resistance (mM)[b]				
cationic lipid[a]	SDS	NaCh	Tween 80	CHAPS	CTAB
DOTAP	(1)[c]	10	<1	50	1
1c	1 (10)[c]	100	150	150	150
2a	1	10	<1	10 (50)[c]	150
2b	1	10	<1	10	1 (150)[c]
2c	1	50 (150)[c]	1	50	10 (150)[c]
DOTAP/DOPE[d]	1	10	<1	10	1
1c/DOPE[d]	(1)[c]	100	<1	150	1 (150)[c]
2a/DOPE[d]	1	10	<1	50	1 (150)[c]
2b/DOPE[d]	1	10	<1	10	1
2c/DOPE[d]	1	150	<1	50	150

[a] Lipoplexes were prepared as indicated in the experimental section, with N/P = 3. [b] Detergent was added to reach 1, 10, 50, 100, and 150 mM final concentration (concentration of cationic lipid: 0.18 mM). Concentration reported corresponds to the higher one tested at which lipoplexes were 100% preserved. [c] At that detergent concentration, only partial release of plasmid DNA (±10%) is observed. [d] Cationic lipid/DOPE was in the ratio 1/2.

Characterization of Lipid−DNA Complexes. The ability of the fluorinated cationic lipids to interact electrostatically with DNA was studied by conventional electrophoretic DNA retardation assays in which a full retard of plasmid DNA is observed at a lipid/DNA phosphate ratio (N/P) corresponding to electroneutrality. As expected, all the fluorinated lipids led to a full complexation of the plasmid at N/P 1, indicating that the fluorous block does not impact on the ability of the cationic headgroup to interact with the DNA phosphate groups (data not shown).

Cationic lipoplexes destruction may occur essentially through ionic competition or detergence of the lipidic phase (*49*−*52*). Both cause DNA to dissociate from the complex and release nucleic acids then being vulnerable to nuclease attack. We therefore evaluated the resistance of fluorinated lipoplexes in the presence of various surfactants: anionic, cationic, or neutral ones (Table 1). Plasmid DNA was first condensed with fluorinated lipids **1c** and **2a**−**c** at N/P 3 to form overall cationic complexes with putative transfection activity. Complexes were then treated with increasing amounts of surfactant. The resulting mixtures were homogenized and analyzed by gel electrophoresis to allow semiquantitative evaluation of lipoplex destruction by monitoring DNA release. Results indicate that, regardless of the cationic lipid, lipoplexes hardly resisted to anionic surfactant SDS. This is consistent with an effect mediated by electrostatic competition between sulfate and phosphate for the cationic lipid headgroup, coupled to high lipid detergence by the alkyl chain. Sodium cholate (NaCh), the other anionic detergent tested, is a poorer competitor of phosphate for ammonium complexation (due to a higher pk_a value) and lipoplexes resisted better. Integrity of DOTAP, **2a**, and **2b** lipoplexes was respected to up to 10 mM cholate. Remarkably, the higher fluorinated homologues **1c** and **2c** were revealed to form highly stable complexes with DNA that resisted 150 mM sodium cholate, suggesting that these lipids may be impermeable to the hydrophobic cholyl moiety. A similar but less pronounced effect was reported by Vierling's group with FHP lipospermine−DNA complexes that resist a taurocholate concentration twice as high as the corresponding nonfluorinated lipoplex (17.5 mM vs. 10 mM) (*13*, *16*). Next, and to minimize destabilization by anionic contribution, we evaluated the stability of DNA lipoplexes in the presence of neutral (Tween 80), zwitterionic (CHAPS), and cationic (CTAB) detergents. A little surprisingly, neutral surfactant Tween 80 showed drastic effects on lipoplex stability. DOTAP-DNA complexes did not resist much and were fully destroyed even at the lowest detergent concentration investigated (1 mM). The same held for **2a**−DNA and **2b**−DNA complexes. As already observed with SDS and sodium cholate, cationic lipids **1c** and **2c** were revealed to be more potent, likely due to their greater hydrophobic character (longer fatty acid chains, higher fluorine content). The zwitterionic detergent CHAPS, though neutral, exhibited very different behavior and destabilized lipoplexes poorly. Most of them survived to 10−50 mM, and once again, **1c**−DNA and **2c**−DNA were characterized by higher stability. Lastly, cationic CTAB proved highly detrimental to DOTAP-DNA complexes but affected fluorinated lipoplexes only weakly. Thus, even if a superficial positive charge of the lipoplexes may shield the particles from other cations, 1 mM CTAB revealed enough to fully destabilize DOTAP-DNA complexes, whereas fluorinated lipoplexes mostly resisted up to 150 mM. It is interesting to note that the stability of **1c**−DNA complexes was invariably higher than for **2c**−DNA, especially in the presence of Tween 80. The difference in lipoplex stability between **1c**−DNA and **2c**−DNA probably cannot be explained just considering fluorine content (24 vs 22 F atoms). More likely, chain conformation imposed by unsaturation in **2c** thwarts close packing of helical fluorinated chains (vide supra), resulting in higher free volume in the external lipid layer of the lipoplex and consequently higher permeability. Such a permeability increase facilitates access of detergent molecules to the condensed DNA core and favors lipoplex destruction.

As DOPE was used as the lipid helper (vide infra), we characterized the mixed lipoplexes (lipid/DOPE/DNA) and looked at their stability. Considering DOTAP and DOTAP/DOPE lipoplexes, no significant difference was observed in detergent resistance. As DOTAP and DOPE are more likely similarly solubilized by detergents, behavior of a mixed lipoplex was indeed expected to be the same as for the pure DOTAP lipoplex. For mixed fluorinated lipid/DOPE lipoplexes, we could possibly anticipate some differences. Actually, no such deviation was observed, and DNA condensed particles resisted detergents in the same concentration range as with pure fluorinated cationic lipids. Whether DOPE remained associated to the lipoplexes or was depleted via micelle formation was not checked.

From that series of experiments, we conclude that the fluorous segments within the lipid structure indeed increase the stability of the lipoplexes in the presence of surfactants, and the longer the fatty acid chains and the higher the fluorine content, the more stable the lipoplexes are.

It is well-known that the size of transfecting complexes is an important parameter that impacts the cell entry mechanism of the particles. Most cationic particles establish electrostatic interaction with proteoglycans and enter adherent cells entrapped into endosomal vesicles. Escape from these recycling compartments occurs only for complexes incorporating molecules with endosomolytic activity and is the result of the specific activity of such endosomolytic element(s) (*53*, *54*). Efficiency of current and multipurpose lipid or polymeric nucleic acid delivery agents seems to rely on the preparation of "large" complexes with diameter in the 100−1000 nm range for optimal cell anchorage and subsequent intracellular routing activity. Such complexes offer excellent transfection efficiency for adherent cell lines for which multitissular organization does not impede accessibility of large particles to cell surface receptors (*55*−*60*). Even if particles smaller than 100 nm might be more suited for in vivo administration, their efficiency seems to rely on the use of endosomolytic agents with high activity (*61*), and large delivery systems have shown some effectiveness upon regional administration (*62*, *63*).

Classically, optimal gene transfection efficacies are obtained when DNA lipoplexes are prepared in 150 mM NaCl at N/P charge ratio of 3 and above. In these conditions, DNA plasmids assemble with cationic lipids to form cationic aggregates of optimal size. We therefore carried out dynamic light scattering

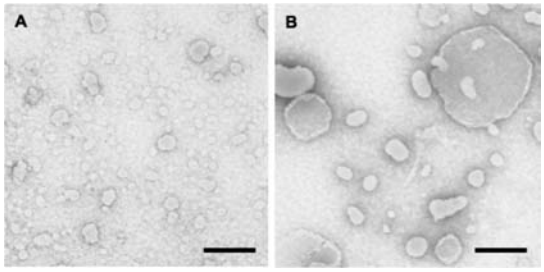


Figure 2. TEM images of **1c**/DOPE (A) and **1c**/DOPE-DNA (B). Figure shows negatively stained samples (uranyle acetate) obtained with fluorinated lipid/DOPE molar ratio 1/2 and total lipid concentration of 1.16 mM (A) and 0.42 mM (B, see Experimental Procedures). Charge ratio N/P is 3. Scale bars correspond to 200 nm.

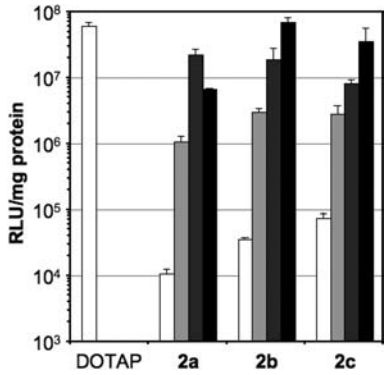


Figure 3. Expression of luciferase in HepG2 cells treated with DNA complexes with DOTAP and fluorinated **2a**−**c** with various compositions. Lipids were mixed with DOPE in different molar ratios (lipid/DOPE molar ratio: white, 1/0; light gray, 1/1; deep gray, 1/2; black, 1/3). Lipoplexes were prepared in 150 mM NaCl, 10 mM Hepes, pH 7.5, at charge ratio N/P 4.

measurements for evaluating the size of lipoplexes DOTAP/DOPE-DNA, **1c**/DOPE-DNA, and **2c**/DOPE-DNA, assembled in 150 mM NaCl (cationic lipid/DOPE 1/2, N/P 3). In these conditions, DOTAP-based lipoplexes show a mean particle size of 140 nm. Lipoplexes prepared from **1c** and **2c** appear as larger particles with mean diameter of 250 and 400 nm, respectively. Lipoplexes were analyzed as well by electron microscopy. No significant difference was observed between DOTAP and fluorinated particles, which presented similar globular morphology, except that negative staining of the latter was more difficult and provided lower contrast (Figure 2). That last point is consistent with some exacerbation of the peripheral hydrophobicity of the particles due to the presence of fluorous segments very close to the surface exposed to the hydrophilic staining material (UO_2^{2+}).

Transfection Biology. The transfection activity of fluorinated lipoplexes was first evaluated on HepG2 cells. The activity of different formulations of lipids **2a**−**c** is shown in Figure 3. Experiments were carried out at a charge ratio commonly used with cationic lipids (N/P 4), and DOTAP was used as a control. Lipoplexes were classically incubated with cells in serum-free conditions for a 4 h period before addition of serum-complemented culture medium. The expression level of luciferase was low for **2a**−**c**/DNA complexes. Transfection efficiency was, however, drastically increased upon addition of the helper lipid DOPE. With **2**/DOPE molar ratio between 1/2 and 1/3, transfection efficacy of most fluorinated lipoplexes was comparable to that of DOTAP. Further optimization of the charge ratio (in the N/P range 1−6) indicated that the transfection efficacy reached a plateau for N/P 3−4, a behavior that was already noticed for classical cationic lipids (*64*).

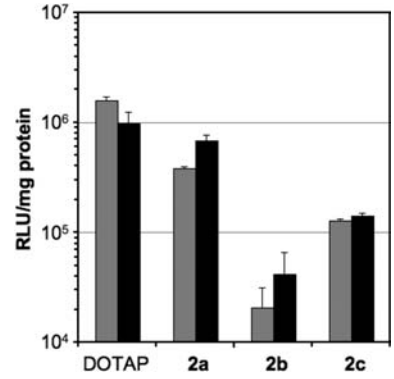


Figure 4. Expression of luciferase in HepG2 cells treated with DNA complexes with cationic lipids DOTAP (N/P 4) and **2a**−**c**/DOPE (1/1 molar ratio, N/P 3) in serum-free conditions (gray) or in the presence of 25% FCS (black).

One serious shortcoming of gene delivery mediated by cationic lipids is that the transfection mostly requires serum-free conditions to be effective. Serum proteins are negatively charged and interact with cationic liposomes, thereby competing with DNA for cationic lipids (*50*). Untimely DNA decomplexation even to a low extent usually results in transfection inhibition. To investigate the effect of serum, we then tested transfection activity of our fluorinated lipoplexes by direct addition of DNA complexes to cells in serum-free conditions and in the presence of 25% fetal calf serum (Figure 4). Lipoplexes were incubated with cells for a 4 h period before the cell culture medium, which contained either too much or too little FCS for optimal cell growth, was replaced with DMEM containing 10% serum. Luciferase expression was monitored 24 h later. Whereas DOTAP transfection efficiency was invariably reduced by 30−40% in the presence of serum, that of fluorinated lipoplexes was preserved or even increased. This might be tentatively interpreted considering that lower adsorption of plasma elements onto fluorinated particles would not significantly provoke their degradation (as is the case with DOTAP particles) but rather would induce or amplify sedimentation, which would result in improved cellular internalization.

Having shown that the transfection activity of fluorinated lipoplexes is not impaired by a high concentration of FCS, we simplified the gene transfection procedure. The following experiments were conducted on the BHK-21 cell line, which is more convenient to culture and to handle than HepG2. DNA lipoplexes were directly added to cells in culture medium containing 10% serum, and transfection/toxicity activities were measured 24 h later without any medium change. The effect of chain unsaturation in fluorinated cationic lipids is presented in Figure 5. At optimal charge ratio N/P 3, DOTAP/DOPE, **1c**/DOPE, and **2c**/DOPE (in a 1/2 molar ratio) roughly displayed similar transfection efficiency in BHK-21 cells. An increase of charge ratio provoked a rapid loss of transfection activity with saturated lipid **1c**, whereas activity remained much better preserved with unsaturated compound **2c** or DOTAP.

The efficiency of DOPE as a helper lipid in fluorinated lipoplexes was somehow uncertain, as DOPE and fluorinated cationic lipids are supposed to segregate. In fact, DOPE was revealed to be even more potent when mixed with compound **1c** than when mixed with DOTAP (Figure 6). DOPE increased DOTAP transfection efficiency by a 40-fold factor, whereas that of **1c** gained up to 4 orders of magnitude. From there, the evaluation of a HFP fluorinated analogue of DOPE appeared inevitable to us. We assumed that the mixture of **1c** and fluorinated DOPE analogue **3** would exhibit different aggregation properties than **1c** and DOPE. Properties of the resulting lipoplexes should thus differ from and, possibly, outdo those

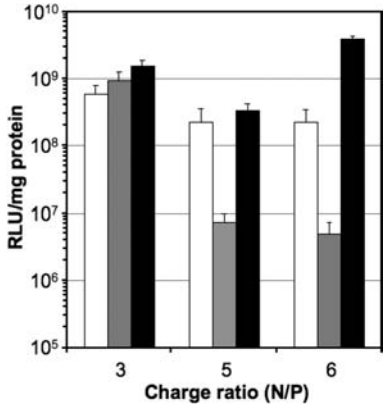


Figure 5. Expression of luciferase in BHK-21 cells treated with DNA complexes with DOTAP (white) and saturated and unsaturated fluorinated lipids **1c** and **2c** (gray and black, respectively). Cationic lipids were mixed in a 1/2 molar ratio with DOPE. Lipoplexes were prepared in 150 mM NaCl, 10 mM Hepes, pH 7.5. Transfection was performed in cell culture medium containing 10% FCS.

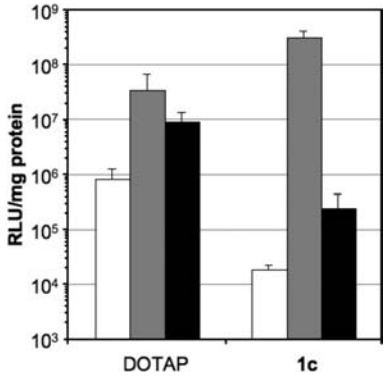


Figure 6. Transfection efficiency of DOTAP and fluorinated cationic lipid **1c**, pure (white) and mixed with DOPE (gray) and its fluorinated analogue **3** (black) in a 1/2 molar ratio. Lipoplexes were prepared at charge ratio N/P 3, in 150 mM NaCl, 10 mM Hepes, pH 7.5. BHK-21 cells were transfected in the presence of 10% FCS.

of **1c**/DOPE-DNA particles. Results did not completely meet our expectations, as **3** only improved transfection efficiency of **1c** by 1 order of magnitude. However, the same quantitative effect was observed with DOTAP and a similar effect was observed with FHP DOPE analogues (*18*, *19*). Although they are surprising at first sight, these results may be rationalized and attributed to the introduction of some lipid heterogeneity in membranes upon fusion/internalization of liposomes/lipoplexes and possibly modifying the internalization pathway and intracellular trafficking. On one hand, mixed lipoplexes, i.e., those containing both fluorinated and nonfluorinated lipids (DOTAP/**3**-DNA and **1c**/DOPE-DNA), most likely exhibit a heterogeneous lipid distribution resulting from partial segregation of the fluorinated and nonfluorinated components. Lipoplexes may thus display discrete nonfluorinated lipid domains at their periphery. These domains are brought into close contact with the negatively charged membrane of cells through electrostatic interactions and may trigger the fusion/internalization process. Incorporation of some fluorinated lipid components into the cell membrane is supposed to introduce additional heterogeneity in the lipid bilayer, possibly resulting in endosome destabilization. On the other hand, fusion of homogeneous fully fluorinated lipoplexes (**1c**/**3**−DNA) with cell membrane is made difficult due to the low miscibility of fluorocarbon−hydrocarbon mixture. Though contact between the fluorinated cationic surface of lipoplexes and the negatively charged cell membrane may be tight, most probably it does not suffice to provoke efficient

Table 2. Mean Size of Lipoplexes in Different Media as Determined by Light Scattering Experiments[a]

	DOTAP/DOPE-DNA (nm)[b]		**1c**/DOPE-DNA (nm)[b]	
incubation medium	− FCS	+ FCS	− FCS	+ FCS
water[c]	100 (0.1)	180 (0.22)	731 (0.25)	1635 (1.00)
150 mM NaCl[c]	140 (0.08)	225 (0.24)	255 (0.38)	400 (0.68)
5% glucose[c]	95 (0.11)	175 (0.22)	1200 (0.55)	1015 (0.47)
MEM	1400 (0.2)	2080 (0.93)	675 (0.35)	680 (0.93)

[a] Complexes were prepared as described for gene transfection assays (cationic lipid/DOPE 1/2, charge ratio N/P 3) and incubated in the absence or presence of 10% FCS. [b] Polydispersity index is indicated into brackets. [c] Solution contains 10 mM Hepes, pH 7.5.

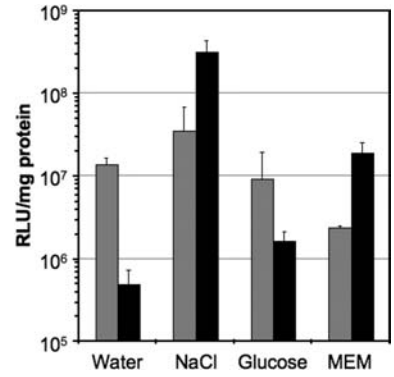


Figure 7. Transfection efficiency of DOTAP/DOPE (gray) and **1c**/DOPE (black) in a 1/2 molar ratio as a function of medium used for lipoplex preparation (for composition, see text). Lipoplexes were prepared at charge ratio N/P 3, and BHK-21 cells were transfected in the presence of 10% FCS.

lipid exchange from lipoplexes to lipid bilayer of the endosomes. Consequent rupture of the endosome and DNA escape are therefore reduced.

Transfection with cationic lipids is known to be significantly affected by the procedure and medium used for the preparation of lipoplexes. Differences probably may be interpreted by considering the size of the resulting complexes, but not exclusively. Therefore, we investigated the influence of the lipoplex preparation medium on the size of the particles (Table 2) and on the level of luciferase expression in BHK-21 cells (Figure 7). Dried lipid mixtures (DOTAP/DOPE and **1c**/DOPE in 1/2 molar ratio) were hydrated in different solutions ((i) 10 mM Hepes buffer, pH 7.5; (ii) 150 mM NaCl, 10 mM Hepes, pH 7.5; (iii) 5% glucose, 10 mM Hepes, pH 7.5; (iv) MEM) before DNA condensation at N/P 3. The size and gene delivery efficacy of these complexes were then evaluated. With the DOTAP-based lipoplex, the mean particle size was in the 100−255 nm range except in MEM (>1 μm). In the presence of 10% FCS, size of the lipoplexes was increased by ca. 50−80%, and the larger particles (obtained in MEM) showed poor transfection efficacy, likely because micrometric size impairs particle endocytosis. The same was observed with fluorinated lipoplexes unless smaller particles were produced in 150 mM NaCl and larger in water or glucose 5%. The fluorinated segment, however, has a significant effect on the assembly process, and **1c**/DOPE-DNA complexes formed in 150 mM NaCl were roughly twice as large as DOTAP/DOPE-DNA complexes. Obtainment of these larger complexes resulted in enhanced transfection activity for reasons discussed earlier. It is important to note, in identical conditions, that the size of **2c**/DOPE-DNA complexes was 690 and 400 nm with and without FCS, respectively, indicating that unsaturation does not significantly alter the assembly process. The larger size of lipoplexes and associated transfection efficacies measured when they were prepared in the medium with higher ionic strength (150 mM NaCl, 10 mM Hepes, pH 7.5) may be explained by considering

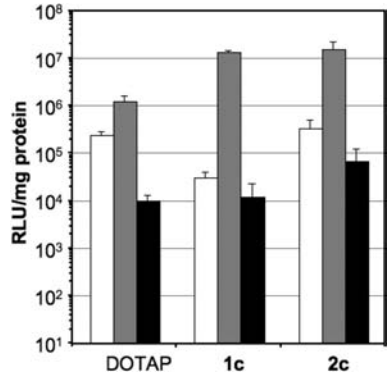


Figure 8. Expression of luciferase in cells treated with pEGFP-Luc complexed by DOTAP/DOPE, **1c**/DOPE, and **2c**/DOPE (1/2 molar ratio) at N/P 3. Three cell lines were investigated: HepG2 (white), BHK-21 (gray), and HeLa (black). Transfection experiments were carried out in the presence of 10% FCS.

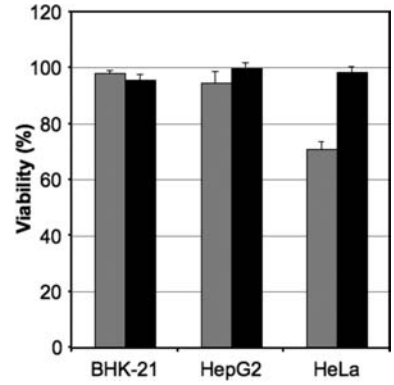


Figure 9. Cytotoxicity of DOTAP/DOPE-DNA (gray) and **1c**/DOPE-DNA (black) on different cell lines. Experiments were conducted at N/P 3 in culture medium supplemented with 10% FCS.

that increasing ionic strength exacerbates hydrophobic interactions and shields electrostatic repulsions. Such conditions allowed kinetically formed and thermodynamically unstable cationic lipoplexes to equilibrate toward lower-energy systems (aggregation). As two fluoroalkyl segments increase hydrophobicity in **1c**, exacerbation of cohesive interactions by ionic strength is stronger than with DOTAP-based particles, provoking a stabilizing effect on the lipid phase and micellar aggregation of higher magnitude. The behavior of **1c**/DOPE-DNA in low ionic strength media is interesting. The absence of salts is supposed to stabilize the colloidal solution to small sizes by favoring electrostatic repulsions (*56*) and large sizes were observed. One possible explanation is that hydration of the fluorinated lipid is much more sensitive to the medium composition than that of classical lipids. When NaCl was substituted for glucose, transfection efficiency was close to that observed when lipoplexes were prepared in 10 mM Hepes buffer pH 7.5, which is consistent with the previous results. The negative influence of MEM on transfection efficiency might be interpreted in terms of both equilibration between phosphate (DNA) and carboxylate (MEM amino acids, 5−6 mM) for ammonium complexation and possible insertion of the side chain of the more hydrophobic amino acids into the lipid phase of the particles. That could account for both destabilization of the DOTAP-based particles and stabilization of **1c**-based ones, the latter being more resistant to both phenomena (vide supra) and taking advantage of ionic strength increase to a greater extent.

Transfection efficiency mediated by nonviral vectors is strongly affected by the cell type. We investigated three different cell lines: HepG2, BHK-21, and HeLa (respectively hepatoma, kidney, and epithelial cells). These cells were treated with mixed **1c**/DOPE, **2c**/DOPE, or DOTAP/DOPE lipoplexes in the presence of FCS. Results are shown in Figure 8. In the BHK-21 cell line, fluorinated lipoplexes appeared more potent than DOTAP-based lipoplex by 1 to 2 orders of magnitude. In HeLa cells, **2c**/DOPE proved superior by almost an order of magnitude to the other formulations. Formulations **2c**/DOPE and DOTAP/DOPE displayed same transfection efficiency in hepatoma cells HepG2, whereas **1c**/DOPE appeared less effective.

To complete our evaluation of fluorinated lipoplexes, we assessed their cytotoxicity as a function of charge ratio and cell type. In a first set of experiments, BHK-21 cells were treated with **1c**/DOPE-DNA or **2c**/DOPE-DNA complexes at various charge ratios (cationic lipid/DOPE 1/2, molar ratio) and using the same amount of DNA plasmid (2 μg) when compared to gene transfection assays (see Supporting Information). Cell viability generally tends to decrease with increasing N/P ratio. That may be explained by considering that positively charged lipoplexes strongly interact with negatively charged cell membranes through electrostatic forces, with potent negative impact on cell membrane integrity and therefore cell homeostasis. In the case of DOTAP lipoplexes, 36% cytotoxicity was observed at N/P 6, and a similar tendency was observed with fluorinated lipoplexes, although these complexes exhibited a limited effect, with cytotoxicity not exceeding 10−20% at N/P 6. In another set of experiments, cytotoxicity of **1c**/DOPE-DNA was evaluated at N/P 3 on three different cell lines, BHK-21, HepG2, and HeLa (Figure 9). No real difference was observed between DOTAP and fluorinated lipoplexes, except for the HeLa cell line. In this cell line, whereas DOTAP lipoplexes provoked 30% cytotoxicity, viability was fully maintained in the presence of **1c**/DOPE-DNA complexes.

CONCLUSIONS

Although a great number of cationic lipids have been designed and evaluated as gene delivery systems, there is still a need for improvement in the design of synthetic lipids for gene transfer. Novel cationic lipids with triblock structure were designed with the purpose of achieving optimal condensation of DNA and enhancing transfection performances. Cationic lipids displaying a fluorous moiety close to their ammonium headgroup were prepared. Self-assembly properties of these cationic lipids were evaluated. They revealed efficient DNA condensing agents, and the resulting lipoplexes displayed enhanced resistance to amphiphilic agents. Transfection data obtained from the fluorinated vectors, alone or as a mixture with different helper lipids, on different cell lines and at various charge ratio revealed in vitro activities that are comparable to that of parent DOTAP, with similar or lower associated toxicity. Due to the fluorous segments within the lipid structure, lipoplexes displayed improved stability, and gene delivery appeared to be regardless of the presence of serum. On the other hand, in vitro transfection efficiency appeared to be very sensitive to the preparation protocol when compared to DOTAP-based lipoplexes. This work highlights the very atypical properties of these fluorinated triblock cationic lipids. Although their in vitro use did not lead to a significant improvement of transfection efficiency, this result does not prejudge their behavior in vivo, as many additional variables, and especially resilience of delivery systems, may induce changes in the behavior of lipoplexes in vivo. Effective impermeabilization of the lipid phase, combined with a preserved ability to deliver genes across endosomal membrane, make these molecules potent building blocks for the preparation of novel gene delivery systems with improved stability and resilience in an in vivo context. In vivo evaluation is currently underway to establish the utility of these new vectors in gene therapy.

ACKNOWLEDGMENT

This work was supported by Association Française contre les Myopathies (AFM, France) and Agence Nationale de la Recherche (ANR, France). We wish to thank Centre National de la Recherche Scientifique (CNRS, France) and Région Alsace for a grant to J.K.

Supporting Information Available: Characterization of compounds; isothermal pressure−area curves, values for specific area A_s, lift-off area A_{lo}, and collapse pressure π_c for compounds **1c** and **2a**−**c**; additional cytotoxicity data for compounds **1c** and **2c**. This material is available free of charge via the Internet at http://pubs.acs.org.

LITERATURE CITED

(1) Schaffer, D. V., Koerber, J. T., and Lim, K. I. (2008) Molecular engineering of viral gene delivery vehicles. *Annu. Rev. Biomed. Eng. 10*, 169–194.

(2) Baum, C., Dullmann, J., Li, Z. X., Fehse, B., Meyer, J., Williams, D. A., and von Kalle, C. (2003) Side effects of retroviral gene transfer into hematopoietic stem cells. *Blood 101*, 2099–2114.

(3) Sakurai, H., Kawabata, K., Sakurai, F., Nakagawa, S., and Mizuguchi, H. (2008) Innate immune response induced by gene delivery vectors. *Int. J. Pharm. 354*, 9–15.

(4) Morille, M., Passirani, C., Vonarbourg, A., Clavreul, A., and Benoit, J.-P. (2008) Progress in developing cationic vectors for non-viral systemic gene therapy against cancer. *Biomaterials 29*, 3477–3496.

(5) Nicolazzi, C., Garinot, M., Mignet, N., Scherman, D., and Bessodes, M. (2003) Cationic lipids for transfection. *Curr. Med. Chem. 10*, 1263–1277.

(6) Bhattacharya, S., and Bajaj, A. (2009) Advances in gene delivery through molecular design of cationic lipids. *Chem. Commun.* 4632–4656.

(7) Mintzer, M. A., and Simanek, E. E. (2009) Nonviral Vectors for Gene Delivery. *Chem. Rev. 109*, 259–302.

(8) Sou, K., Endo, T., Takeoka, S., and Tsuchida, E. (2000) Poly(ethylene glycol)-modification of the phospholipid vesicles by using the spontaneous incorporation of poly(ethylene glycol)-lipid into the vesicles. *Bioconjugate Chem. 11*, 372–379.

(9) Mishra, S., Webster, P., and Davis, M. E. (2004) PEGylation significantly affects cellular uptake and intracellular trafficking of non-viral gene delivery particles. *Eur. J. Cell Biol. 83*, 97–111.

(10) Li, W., Huang, Z., MacKay, J. A., Grube, S., and Szoka, F. C. (2005) Low-pH-sensitive poly(ethylene glycol) (PEG)-stabilized plasmid nanolipoparticles: effects of PEG chain length, lipid composition and assembly conditions on gene delivery. *J. Gene Med. 7*, 67–79.

(11) Mignet, N., Richard, C., Seguin, J., Largeau, C., Bessodes, M., and Scherman, D. (2008) Anionic pH-sensitive pegylated lipoplexes to deliver DNA to tumors. *Int. J. Pharm. 361*, 194–201.

(12) Remy, J.-S., Sirlin, C., Vierling, P., and Behr, J.-P. (1994) Gene-transfer with a series of lipophilic DNA-binding molecules. *Bioconjugate Chem. 5*, 647–654.

(13) Gaucheron, J., Santaella, C., and Vierling, P. (2001) Improved in vitro gene transfer mediated by fluorinated lipoplexes in the presence of a bile salt surfactant. *J. Gene Med. 3*, 338–344.

(14) Gaucheron, J., Santaella, C., and Vierling, P. (2001) Highly fluorinated lipospermines for gene transfer: Synthesis and evaluation of their in vitro transfection efficiency. *Bioconjugate Chem. 12*, 114–128.

(15) Gaucheron, J., Santaella, C., and Vierling, P. (2002) Transfection with fluorinated lipoplexes based on fluorinated analogues of DOTMA, DMRIE and DPPES. *Biochim. Biophys. Acta 1564*, 349–358.

(16) Boulanger, C., Di Giorgio, C., Gaucheron, J., and Vierling, P. (2004) Transfection with fluorinated lipoplexes based on new fluorinated cationic lipids and in the presence of a bile salt surfactant. *Bioconjugate Chem. 15*, 901–908.

(17) Fabio, K., Di Giorgio, C., and Vierling, P. (2005) New perfluorinated polycationic dimerizable detergents for the formulation of monomolecular DNA nanoparticles and their in vitro transfection efficiency. *Biochim. Biophys. Acta 1724*, 203–214.

(18) Gaucheron, J., Boulanger, C., Santaella, C., Sbirrazzuoli, N., Boussif, O., and Vierling, P. (2001) In vitro cationic lipid-mediated gene delivery with fluorinated glycerophosphoethanolamine helper lipids. *Bioconjugate Chem. 12*, 949–963.

(19) Boussif, O., Gaucheron, J., Boulanger, C., Santaella, C., Kolbe, H. V. J., and Vierling, P. (2001) Enhanced in vitro and in vivo cationic lipid-mediated gene delivery with a fluorinated glycerophosphoethanolamine helper lipid. *J. Gene Med. 3*, 109–114.

(20) Held, P., Lach, F., Lebeau, L., and Mioskowski, C. (1997) Synthesis and preliminary evaluation of a new class of fluorinated amphiphiles designed for in-plane immobilization of biological macromolecules. *Tetrahedron Lett. 38*, 1937–1940.

(21) Lebeau, L., Lach, F., Venien-Bryan, C., Renault, A., Dietrich, J., Jahn, T., Palmgren, M. G., Kuhlbrandt, W., and Mioskowski, C. (2001) Two-dimensional crystallization of a membrane protein on a detergent-resistant lipid monolayer. *J. Mol. Biol. 308*, 639–647.

(22) Tsao, M. W., Hoffmann, C. L., Rabolt, J. F., Johnson, H. E., Castner, D. G., Erdelen, C., and Ringsdorf, H. (1997) Studies of molecular orientation and order in self-assembled semifluorinated n-alkanethiols: single and dual component mixtures. *Langmuir 13*, 4317–4322.

(23) Klein, E., Kerth, P., and Lebeau, L. (2008) Enhanced selective immobilization of biomolecules onto solid supports coated with semifluorinated self-assembled monolayers. *Biomaterials 29*, 204–214.

(24) Johnstone, S. A., Masin, D., Mayer, L., and Bally, M. B. (2001) Surface-associated serum proteins inhibit the uptake of phosphatidylserine and poly(ethylene glycol) liposomes by mouse macrophages. *Biochim. Biophys. Acta 1513*, 25–37.

(25) Lebeau, L., Olland, S., Mioskowski, C., and Oudet, P. (1992) Rational design and synthesis of phospholipids for the two-dimensional crystallization of DNA gyrase, a key element in chromosome organization. *Chem. Phys. Lipids 62*, 93–103.

(26) Lebeau, L., Mioskowski, C., and Oudet, P. (1988) Systematic study of phospholipids linked to a steroid derivative, spread into a monolayer at the air/water interface. *Biochim. Biophys. Acta 939*, 417–429.

(27) Faurote, P. D., Henderson, C. M., Murphy, C. M., O'Rear, J. G., and Ravner, H. (1956) Partially fluorinated esters and ethers as temperature-stable liquids. *Ind. Eng. Chem. 48*, 445–454.

(28) Shinoda, K., Hato, M., and Hayashi, T. (1972) The physicochemical properties of aqueous solutions of fluorinated surfactants. *J. Phys. Chem. 76*, 909–14.

(29) Mukerjee, P., and Handa, T. (1981) Adsorption of fluorocarbon and hydrocarbon surfactants to air-water, hexane-water, and perfluorohexane-water interfaces. Relative affinities and fluorocarbon-hydrocarbon nonideality effects. *J. Phys. Chem. 85*, 2298–303.

(30) Sadtler, V. M., Giulieri, F., Krafft, M.-P., and Riess, J. G. (1998) Micellization and adsorption of fluorinated amphiphiles: Questioning the $1CF_2$ approximate to $1.5CH_2$ rule. *Chem.—Eur. J. 4*, 1952–1956.

(31) Hui, S. W., Langner, M., Zhao, Y. L., Ross, P., Hurley, E., and Chan, K. (1996) The role of helper lipids in cationic liposome-mediated gene transfer. *Biophys. J. 71*, 590–599.

(32) Koltover, I., Salditt, T., Radler, J. O., and Safinya, C. R. (1998) An inverted hexagonal phase of cationic liposome-DNA complexes related to DNA release and delivery. *Science 281*, 78–81.

(33) Brace, N. O. (1999) Synthesis with perfluoroalkyl radicals from perfluoroalkyl iodides. A rapid survey of synthetic possibilities with emphasis on practical applications. Part one:

alkenes, alkynes and allylic compounds. *J. Fluorine Chem. 93*, 1–25.
(34) Rong, G. B., and Keese, R. (1990) The addition of perfluorobutyl iodide to carbon-carbon multiple bonds and the preparation of perfluorobutylalkenes. *Tetrahedron Lett. 31*, 5615–5616.
(35) Roper, T. D., Friedrich, P. E., Gees, T., Lackey, W. J., Mader, C., Vierling, P., and Santaella, C. (1999) An efficient and scalable synthesis of perfluorinated phosphatidylcholines. *Org. Proc. Res. Dev. 3*, 67–70.
(36) Metzger, J. O., and Linker, U. (1992) Synthesis of linear and branched perfluoroalkylated carboxylic-acids by radical-addition of perfluoroalkyl iodides to unsaturated fatty-acids. *Liebigs Ann. Chem.* 209–216.
(37) Takakura, T., Yamabe, M., and Kato, M. (1988) Synthesis of fluorinated difunctional monomers. *J. Fluorine Chem. 41*, 173–183.
(38) Achilefu, S., Mansuy, L., Selve, C., and Thiebaut, S. (1995) Synthesis of 2H,2H-perfluoroalkyl and 2H-perfluoroalkenyl carboxylic acids and amides. *J. Fluorine Chem. 70*, 19–26.
(39) Bégué, J.-P., Bonnet-Delpont, D., Mesureur, D., and Ourévitch, M. (1991) Determination of *Z* and *E* configurations in trifluoromethylated vinyl compounds: $^3J_{CF}$ coupling constants as a criterion for configurational assignments. *Magn. Reson. Chem. 29*, 675–678.
(40) Hudlicky, M. In *Chemistry of Organic Fluorine Compounds*, 2nd ed., p 592, Ellis Horwood, Chichester, 1992.
(41) McKenna, C. E., Higa, M. T., Cheung, N. H., and McKenna, M. C. (1977) The facile dealkylation of phosphonic acid dialkyl esters by bromotrimethylsilane. *Tetrahedron Lett. 18*, 155–158.
(42) Brossette, T., LeFaou, A., Goujon, L., Valleix, A., Créminon, C., Grassi, J., Mioskowski, C., and Lebeau, L. (1999) Synthesis of polyphosphorylated AZT derivatives for the development of specific enzyme immunoassays. *J. Org. Chem. 64*, 5083–5090.
(43) Amato, C., Naud, C., Calas, P., and Commeyras, A. (2002) Unexpected selective monoadduct formation from 2-methyl-3-butyn-2-ol and alpha,omega-diiodoperfluorobutane. *J. Fluorine Chem. 113*, 55–63.
(44) Takai, K., Takagi, T., Baba, T., and Kanamori, T. (2004) Highly fluorinated C_{18} fatty acids: synthesis and interfacial properties. *J. Fluorine Chem. 125*, 1959–1964.
(45) Takagi, T., Takai, K., Baba, T., and Kanamori, T. (2007) Synthesis of phospholipids containing perfluorooctyl group and their interfacial properties. *J. Fluorine Chem. 128*, 133–138.
(46) Kuivila, H. G., and Menapace, L. W. (1963) Reduction of alkyl halides by organotin hydrides. *J. Org. Chem. 28*, 2165–2167.
(47) Chung, S. K. (1980) Stereochemistry in the reduction of vinyl bromides with lithium aluminum hydride. *J. Org. Chem. 45*, 3513–3514.
(48) Wunderlich, B. In *Macromolecular Physics*, p 97, Academic Press, New York, 1973.
(49) Xu, Y. H., and Szoka, F. C. (1996) Mechanism of DNA release from cationic liposome/DNA complexes used in cell transfection. *Biochemistry 35*, 5616–5623.
(50) Zelphati, O., Uyechi, L. S., Barron, L. G., and Szoka, F. C. (1998) Effect of serum components on the physico-chemical properties of cationic lipid/oligonucleotide complexes and on their interactions with cells. *Biochim. Biophys. Acta 1390*, 119–133.
(51) Kim, T. W., Chung, H., Kwon, I. C., Sung, H. C., and Jeong, S. Y. (2000) In vivo gene transfer to the mouse nasal cavity mucosa using a stable cationic lipid emulsion. *Mol. Cells 10*, 142–147.
(52) Kim, T. W., Chung, H. S., Kwon, I. C., Sung, H. C., Shin, B. C., and Jeong, S. Y. (2005) Airway gene transfer using cationic emulsion as a mucosal gene carrier. *J. Gene Med. 7*, 749–758.
(53) Remy, J.-S., Abdallah, B., Zanta, M. A., Boussif, O., Behr, J.-P., and Demeneix, B. (1998) Gene transfer with lipospermines and polyethylenimines. *Adv. Drug Delivery Rev. 30*, 85–95.
(54) Fraley, A. W., Pons, B., Dalkara, D., Nullans, G., Behr, J.-P., and Zuber, G. (2006) Cationic oligonucleotide-peptide conjugates with aggregating properties enter efficiently into cells while maintaining hybridization properties and enzymatic recognition. *J. Am. Chem. Soc. 128*, 10763–10771.
(55) Labat-Moleur, F., Steffan, A. M., Brisson, C., Perron, H., Furstenberger, P., Oberling, F., Brambilla, E., and Behr, J.-P. (1996) An electron microscopy study into the mechanism of gene transfer with lipopolyamines. *Gene Ther. 3*, 1010–1017.
(56) Radler, J. O., Koltover, I., Salditt, T., and Safinya, C. R. (1997) Structure of DNA-cationic liposome complexes: DNA intercalation in multilamellar membranes in distinct interhelical packing regimes. *Science 275*, 810–814.
(57) Ogris, M., Steinlein, P., Kursa, M., Mechtler, K., Kircheis, R., and Wagner, E. (1998) The size of DNA/transferrin-PEI complexes is an important factor for gene expression in cultured cells. *Gene Ther. 5*, 1425–1433.
(58) Brissault, B., Leborgne, C., Guis, C., Danos, O., Cherdame, H., and Kichler, A. (2006) Linear topology confers in vivo gene transfer activity to polyethylenimines. *Bioconjugate Chem. 17*, 759–765.
(59) Lleres, D., Weibel, J.-M., Heissler, D., Zuber, G., Duportail, G., and Mely, Y. (2004) Dependence of the cellular internalization and transfection efficiency on the structure and physicochemical properties of cationic detergent/DNA/liposomes. *J. Gene Med. 6*, 415–428.
(60) Creusat, G., and Zuber, G. (2008) Self-assembling polyethylenimine derivatives mediate efficient siRNA delivery in mammalian cells. *ChemBioChem 24*, 2787–2789.
(61) Zuber, G., Dontenwill, M., and Behr, J.-P. (2009) Synthetic viruslike particles for targeted gene delivery to alpha(v)beta(3) integrin-presenting endothelial cells. *Mol. Pharmacol. 6*, 1544–1552.
(62) Williams, J. H., Sirsi, S. R., Latta, D. R., and Lutz, G. J. (2006) Induction of dystrophin expression by exon skipping in mdx mice following intramuscular injection of antisense oligonucleotides complexed with PEG-PEI copolymers. *Mol. Ther. 14*, 88–96.
(63) Hobbs, S. K., Monsky, W. L., Yuan, F., Roberts, W. G., Griffith, L., Torchilin, V. P., and Jain, B. K. (1998) Regulation of transport pathways in tumor vessels: role of tumor type and microenvironment. *Proc. Natl. Acad. Sci. U.S.A. 95*, 4607–4612.
(64) Behr, J.-P., Demeneix, B., Loeffler, J.-P., and Perez-Mutul, J. Efficient gene-transfer into mammalian primary endocrine-cells with lipopolyamine-coated DNA. *Proc. Natl. Acad. Sci. U.S.A. 86*, 6982−6986.

BC900469Z

Polyamidoamine (PAMAM) Dendrimer Conjugates of "Clickable" Agonists of the A_3 Adenosine Receptor and Coactivation of the $P2Y_{14}$ Receptor by a Tethered Nucleotide

Dilip K. Tosh,[†] Lena S. Yoo,[†] Moshe Chinn,[†] Kunlun Hong,[‡] S. Michael Kilbey II,[‡] Matthew O. Barrett,[§] Ingrid P. Fricks,[§] T. Kendall Harden,[§] Zhan-Guo Gao,[†] and Kenneth A. Jacobson*[,†]

Molecular Recognition Section, Laboratory of Bioorganic Chemistry, National Institute of Diabetes and Digestive and Kidney Diseases, National Institutes of Health, Bethesda, Maryland 20892, Center for Nanophase Materials Sciences, Oak Ridge National Laboratory, Oak Ridge, Tennessee 37831, and Department of Pharmacology, University of North Carolina School of Medicine, Chapel Hill, North Carolina 27599. Received October 29, 2009; Revised Manuscript Received December 9, 2009

We previously synthesized a series of potent and selective A_3 adenosine receptor (AR) agonists (North-methanocarba nucleoside 5′-uronamides) containing dialkyne groups on extended adenine C2 substituents. We coupled the distal alkyne of a 2-octadiynyl nucleoside by Cu(I)-catalyzed "click" chemistry to azide-derivatized G4 (fourth-generation) PAMAM dendrimers to form triazoles. A_3AR activation was preserved in these multivalent conjugates, which bound with apparent K_i of 0.1−0.3 nM. They were substituted with nucleoside moieties, solely or in combination with water-solubilizing carboxylic acid groups derived from hexynoic acid. A comparison with various amide-linked dendrimers showed that triazole-linked conjugates displayed selectivity and enhanced A_3AR affinity. We prepared a PAMAM dendrimer containing equiproportioned peripheral azido and amino groups for conjugation of multiple ligands. A bifunctional conjugate activated both A_3 and $P2Y_{14}$ receptors (via amide-linked uridine-5′-diphosphoglucuronic acid), with selectivity in comparison to other ARs and P2Y receptors. This is the first example of targeting two different GPCRs with the same dendrimer conjugate, which is intended for activation of heteromeric GPCR aggregates. Synergistic effects of activating multiple GPCRs with a single dendrimer conjugate might be useful in disease treatment.

INTRODUCTION

Poly(amidoamine) (PAMAM)[1] dendrimers are treelike polymers that have wide application in drug delivery in vivo (*1, 2*). We recently reported the first example of using a PAMAM dendrimeric scaffold for the polyvalent, nanoscale presentation of nucleosides and nucleotides to selectively activate adenosine receptors (ARs) and P2Y receptors to induce intracellular signal transduction (*3*−*5*). Both of these receptor families are cell-surface G protein-coupled receptors (GPCRs). The dendrimer carriers greatly multiply the size of the monomer agonist derivatives, and these multivalent conjugates are intended to bridge multiple binding sites present in GPCR dimers and other higher-order receptor aggregates. In general, we might expect the stability of the ligand in biological systems and its pharmacokinetic and pharmacodynamic properties to be enhanced in the conjugates in comparison to the monomeric ligands.

The A_3AR is found at various levels of expression in neutrophils, eosinophils, cardiac myocytes, skeletal muscle, astrocytes, neurons, and other cell types (*6*) and has distinct effects on cell survival and response to stress. The A_3AR agonist N^6-(3-iodobenzyl)-5′-*N*-methylcarboxamidoadenosine (IB-MECA, CF101) **1** (Chart 1) and its 2-chloro derivative deregulate the NFκB pathway and are currently in clinical trials for the treatment of autoimmune inflammatory diseases and cancer, respectively (*7*−*11*). Anti-ischemic effects of A_3AR agonists also suggest their use in protection of the heart, lung, nervous system, and skeletal muscle (*6, 12, 13*).

We previously synthesized a series of North (N)-methanocarba nucleoside 5′-uronamides as A_3AR agonists of high affinity and selectivity (*14*). These selective agonists, including the anti-ischemic nucleoside MRS3558 **2**, contained a rigid bicyclo[3.1.0]hexane (methanocarba) ring system of the (N) conformation in place of the freely twisting ribose moiety (*9, 11, 12*). These agonists also contained an optimized N^6-(3-chlorobenzyl) group, which enhanced A_3AR selectivity in humans, mice, rats, and other species (*14*). Recently, we extended this series to include dialkyne groups on an extended adenine C2 substituent, e.g., **3a** (*21*). We expected the proximal alkyne to promote receptor recognition and the distal alkyne to serve as a site for coupling to reporter groups while maintaining receptor recognition. Thus, we have selected a region on the nucleoside for attachment that is

* Corresponding author. kajacobs@helix.nih.gov, Bldg. 8A, Rm. B1A-19, NIH, National Institute of Diabetes and Digestive and Kidney Diseases, Bethesda, MD 20892-0810, Tel. 301-496-9024, Fax 301-480-8422.

[†] National Institutes of Health.

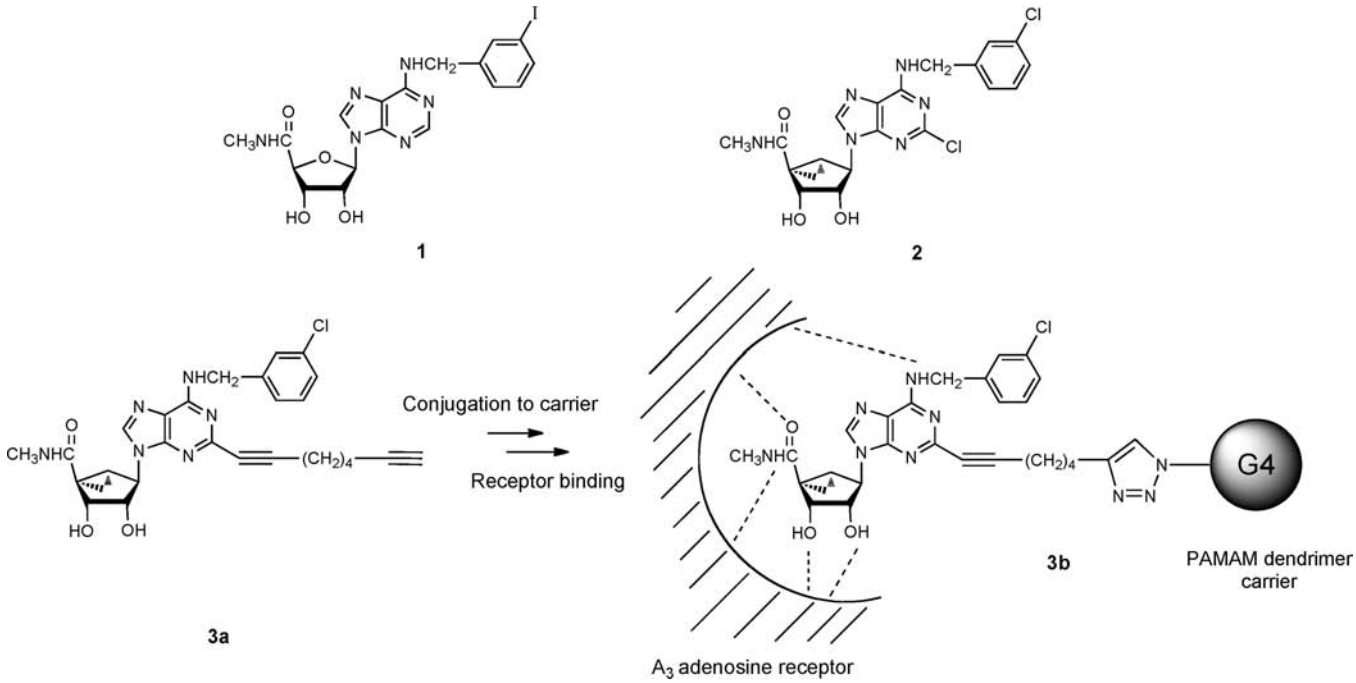
[‡] Oak Ridge National Laboratory.

[§] University of North Carolina School of Medicine.

[1] Abbreviations: AR, adenosine receptor; DMSO, dimethylsulfoxide; EDC, *N*-ethyl-*N*′-dimethylaminopropylcarbodiimide; GPCR, G protein-coupled receptor; IBMX, 3-isobutyl-1-methylxanthine; AR, adenosine receptor; cAMP, adenosine 3′,5′-cyclic phosphate; CHO, Chinese hamster ovary; IB-MECA, N^6-(3-iodobenzyl)-5′-*N*-methylcarboxamidoadenosine; DMEM, Dulbecco's modified Eagle's medium; EDTA, ethylenediaminetetraacetic acid; GPCR, G protein-coupled receptor; HATU, 2-(1*H*-7-azabenzotriazol-1-yl)-1,1,3,3-tetramethyl uronium hexafluorophosphate methanaminium; HEK, human embryonic kidney; I-AB-MECA, 2-[*p*-(2-carboxyethyl)phenyl-ethylamino]-5′-*N*-ethylcarboxamidoadenosine; MS, mass spectrometry; NECA, 5′-*N*-ethylcarboxamidoadenosine; NMR, nuclear magnetic resonance; DIPEA, diisopropylethylamine; DMF, *N*,*N*-dimethylformamide; HEPES, 4-(2-hydroxyethyl)-1-piperazineethanesulfonic acid; PAMAM, polyamidoamine; PLC, phospholipase C; UDPG, uridine-5′-diphosphoglucose; UDPGA, uridine-5′-diphosphoglucuronic acid.

10.1021/bc900473v © 2010 American Chemical Society
Published on Web 02/01/2010

Chart 1. Structures of Adenosine A_3AR Agonist Monomers (1−3a) and the Design of Multivalent Dendrimer Conjugates in the (N)-Methanocarba Series, Represented by the Triazole Derivative of General Formula 3b[a]



[a] Compound **3a** was reported in ref *21*.

distal from the pharmacophore and is predicted by modeling to extend into the extracellular region of the A_3AR (*15*).

Here, we coupled the distal alkyne of an A_3AR agonist containing a 2-octadiyne group to azido-derivatized G4 (fourth-generation) PAMAM dendrimer carriers with Cu(I)-catalyzed alkyne-azide cycloaddition, a type of click chemistry (*16*−*18*), to form triazole derivatives, as in conjugate **3b**, and determined the receptor-binding affinity and selectivity. This variation of click chemistry was used previously for coupling biologically active molecules to polymers (*19*). In our previous studies of dendrimer-bound ligands for GPCRs, the small molecular ligands were amide-linked to the carrier (*3*−*5*). For this study, we compared the amide linkages to PAMAM dendrimers with the use of azido groups for conjugation of alkyne derivatives.

We also included PAMAM dendrimers with mixed peripheral azido and amino groups in this study. The incorporation of azides for click chemistry along with the conventional terminal amino/carboxylic groups of the PAMAM dendrimers for amide coupling allowed the facile conjugation of ligands for two different GPCRs (Figure 1). We present the first example of coactivation of two GPCRs by a hybrid PAMAM dendrimer conjugate. The anti-inflammatory A_3AR and the $P2Y_{14}$ receptor, which is activated by endogenous uridine-5′-diphosphoglucose (UDPG) in the neuroimmune system (*20*), serve to illustrate this approach.

EXPERIMENTAL PROCEDURES

Chemical Synthesis. *Materials and Methods.* All reactions were carried out under a nitrogen atmosphere. We purchased *N*-ethyl-*N*′-dimethylaminopropylcarbodiimide hydrochloride (EDC.HCl), UDPG acid trisodium salt (UDPGA), UDPG, G2.5 PAMAM (10 wt % solution in methanol), G3 PAMAM (20 wt % solution in methanol), PAMAM dendrimers (G4, G5.5, and G6, 5 wt % solution in methanol) with an ethylenediamine core from Sigma-Aldrich (St. Louis, MO). All other reagents and solvents, except those indicated, came from Sigma-Aldrich. We purchased dialysis membranes (Spectra/Pore Membrane, MWCO 3500, flat width 18 mm) from Spectrum Laboratories (Rancho Dominguez, CA). Synthesis of compound **3a** is described elsewhere (*21*).

Nuclear magnetic resonance (NMR) spectra were recorded on a Bruker DRX-600 spectrometer with D_2O as a solvent. The chemical shifts are expressed as relative ppm from HOD (4.80). We performed electrospray ionization mass spectrometry (MS) and matrix-assisted laser desorption ionization (MALDI) time-of-flight MS experiments on a Waters LCT Premier mass spectrometer at the Mass Spectrometry Facility, National Institute of Diabetes and Digestive and Kidney Diseases (NIDDK), NIH. We analyzed the azido dendrimer precursors on a Varian 500 MHz NMR and on a Bruker Vertex 70 FT-IR. Galbraith Laboratories (Knoxville, TN) performed the elemental analysis.

*G4 PAMAM, Conjugated with 6-Heptynoic acid (**15**).* We added freshly prepared aqueous sodium ascorbate (1 M, 42 μL, 42.1 μmol) to a mixture of G4 PAMAM dendrimer **13** (6.74 mg, 0.42 μmol) and 6-heptynoic acid (1.33 mg, 10.5 μmol) in a mixture of *t*-butanol (0.3 mL) and water (0.3 mL), then added 7.5% aqueous cupric sulfate (70 μL, 20.8 μmol). The reaction mixture was stirred at room temperature overnight, and the product was purified by dialysis in water. The mixture was lyophilized to yield compound **15** (5.45 mg, 68%) as a white, foamy solid. MALDI-MS: calcd 19 029; found 18 928.

*G4 PAMAM, Conjugated with A_3AR Agonist **3a** and 6-Heptynoic Acid (**7**).* We added freshly prepared aqueous sodium ascorbate (1 M, 31 μL, 31 μmol) to a mixture of compound **15** (5.45 mg, 0.28 μmol) and compound **3a** (4.13 mg, 7.74 μmol) in a mixture of *t*-butanol (0.3 mL) and water (0.3 mL), then added 7.5% aqueous cupric sulfate (51 μL, 14.3 μmol). The reaction mixture was stirred at room temperature overnight, and the product was purified by dialysis in water. The mixture was lyophilized to yield compound **7** (5.8 mg, 60%) as a white, foamy solid. ^{1}H NMR (DMSO-d_6, 600 MHz) δ 8.51 (s), 8.14 (s), 7.61 (s), 7.31−7.41 (m), 5.46 (s), 5.68−5.95 (m),

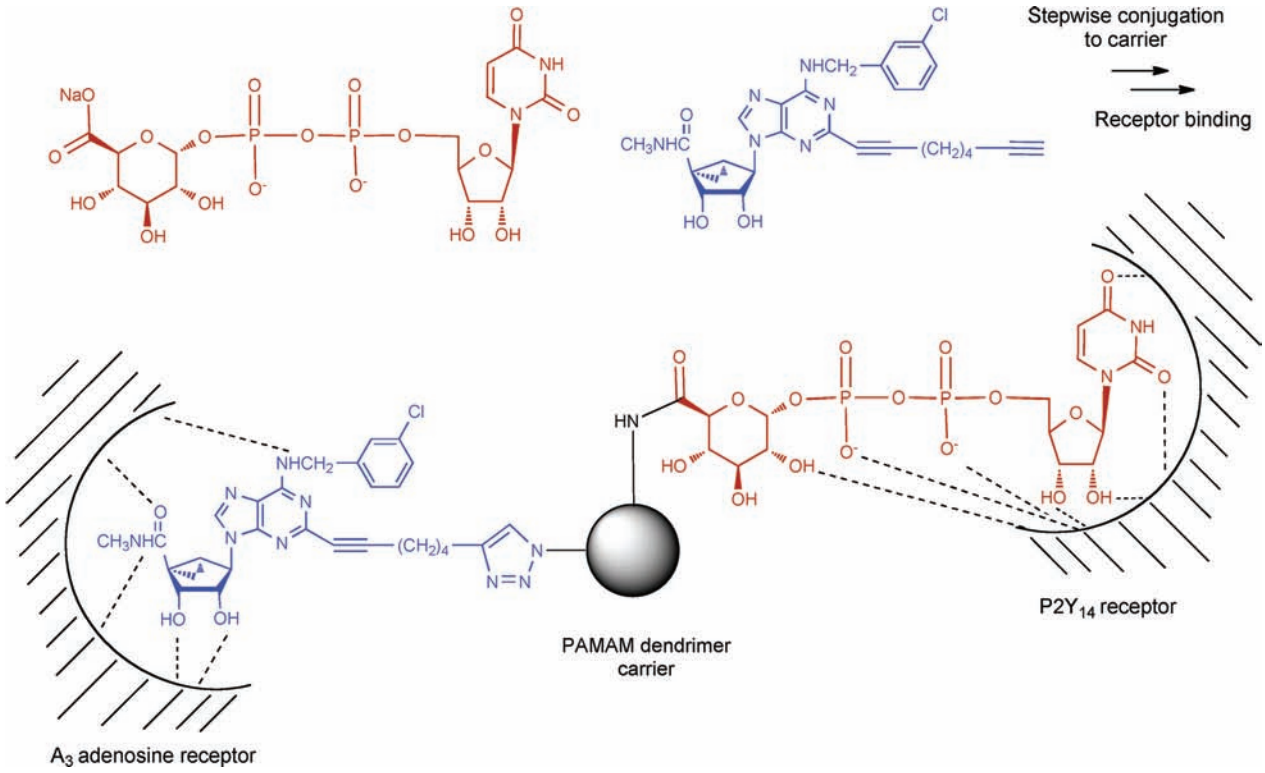


Figure 1. Design of a bifunctional PAMAM dendrimer conjugate for the coactivation of two different GPCRs; shown here are agonists of the A_3AR and the $P2Y_{14}$ receptor. Both receptors are distributed in the immune system and may occur on the same cell (*27*). The stoichiometry of substitution of the dendrimer is not indicated.

3.86 (s), 2.66 (s), 2.21 (s), 1.8 (s), 1.61 (bs), 1.11−1.29 (m). MALDI-MS: calcd 33 852; found 34 088.

*G4 PAMAM, Conjugated with A_3AR Agonist **3a** (**6**).* We followed the procedure used for compound **7** to synthesize compound **6** (69%) from **3a**.^{1}H NMR (DMSO-d_6, 400 MHz) δ 8.50 (bs), 8.15 (bs), 7.60 (s), 7.29−7.59 (m), 5.44 (s), 4.67−5.05 (m), 4.16 (s), 3.86 (s), 2.78 (s), 2.67 (s), 2.08−2.23 (m), 1.82 (s), 1.61 (s), 0.98−1.30 (m). MALDI-MS: calcd 49 991; found 50 844.

*G4 PAMAM, Conjugated with UDPGA (**17**).* We added EDC.HCl (12.5 mg, 65.2 μmol) to a solution of compound **5** (15.3 mg, 1.01 μmol) and UDPGA trisodium salt **16** (22.9 mg, 35.43 μmol) in dimethylsulfoxide (DMSO), then added 0.1 M 2-(*N*-morpholino)ethanesulfonic acid buffer (140 μL). We used 0.1 M HCl to adjust the pH of the reaction mixture to 4.5−5.0. The reaction mixture was stirred at room temperature overnight, and the product was purified by extensive dialysis followed by lyophilization to yield compound **17** (22 mg, 64%). ^{1}H NMR (DMSO-d_6, 400 MHz) δ 8.19 (s), 7.86−8.14 (m), 6.55 (m), 5.80 (s), 5.67 (s), 5.38−5.47 (m), 4.07 (s), 3.97 (s), 3.63 (br s), 3.25 (s), 3.12 (s), 2.91 (s), 2.69 (s), 2.24 (s). MALDI-MS: calcd 33 060; found 33 036.

*G4 PAMAM, Conjugated with UDPGA and A_3AR Agonist **3a** (**8**).* We followed the procedure used for compound **7** to synthesize compound **8** (66%) from compound **17**. MALDI-MS: calcd 50 092; found 50 610.

*G2.5 PAMAM, Conjugated with A_3AR Agonist **19** (**9**).* We followed the procedure used for compound **17** to synthesize compound **9** (54%) from dendrimer **18** and compound **19**.^{1}H NMR (D_2O, 600 MHz) δ 7.98 (br s), 6.88 (br s), 4.56 (br s), 3.85 (br s), 3.55 (br s), 3.45 (br s), 3.16−3.36 (m), 3.16 (br s), 3.08 (br s), 2.56−2.98 (m), 2.54 (s), 2.24−2.48 (m), 1.92 (br s), 1.68 (br s). MALDI-MS: calcd. 10 598; found 10 783.

*G2.5 PAMAM, Conjugated with A_3AR Agonist **20** (**10**).* We followed the procedure used for compound **17** to synthesize compound **10** (67%) from dendrimer **18** and compound **20**.^{1}H NMR (DMSO-d_6, 600 MHz) δ 8.11 (s), 7.85−8.01 (m), 7.58 (s), 7.36 (s), 7.18−7.32 (m), 5.06−5.21 (m), 4.88−4.93 (m), 4.65 (s), 4.59 (s), 3.86−3.91 (m), 3.07 (s), 2.65 (s), 2.39 (s), 2.21 (s), 1.85 (s), 1.74 (br s), 1.59 (br s), 1.21−1.33 (m), 1.03 (br s). MALDI-MS: calcd 8370; found 8369.

*G3 PAMAM, Conjugated with A_3AR Agonist **22** (**11**).* We followed the procedure used for compound **17** to synthesize compound **11** (71%) from dendrimer **21** and compound **22**.^{1}H NMR (DMSO-d_6, 600 MHz) δ 8.88 (s), 8.11 (s), 7.73−8.05 (m), 7.58 (s), 7.32 (s), 7.13−7.28 (m), 5.43 (s), 5.03−5.21 (br s), 4.87−4.96 (s), 4.85 (br s), 4.67 (s), 4.61 (s), 3.89 (s), 3.06 (s), 2.82 (s), 2.65 (s), 2.34−2.46 (m), 2.19 (s), 1.83 (s), 1.69−1.78 (m), 1.61 (s), 1.29 (s). MALDI-MS: calcd 13 694; found 13 304.

*G4 PAMAM, Conjugated with A_3AR Agonist **24** (**12**).* We added HATU (4.67 mg, 12.28 μmol) to a mixture of compound **24** (6.72 mg, 12.35 μmol) and dendrimer **23** (2.73 mg, 12.28 μmol) in dry DMF (0.5 mL), then added DIPEA (2.15 μL, 12.22 μmol). The reaction mixture was stirred at room temperature overnight, extensively dialyzed with water, then lyophilized to yield compound **12** (5.5 mg, 61%).^{1}H NMR (DMSO-d_6, 400 MHz) δ 8.46 (br s), 8.10 (s), 7.79−7.93 (m), 7.60 (s), 7.27−7.36 (m), 5.45 (s), 4.67−4.93 (m), 3.87 (s), 3.08 (s), 2.86 (s), 2.66 (s), 2.41 (s), 2.19 (s), 1.78 (s), 1.61 (s), 1.23 (t, J = 24 Hz), 0.80−0.89 (m). MALDI-MS: calcd 47 495; found 47 985.

*Imidazole-1-Sulfonyl Azide Hydrochloride (**26**).* A modification of a published procedure was used (*22*). A suspension of 6.53 g NaN_3 (**25**, 100 mmol, Aldrich, >99.5%) and 100 mL acetonitrile (Aldrich, 99.8% anhydrous) in a 500 mL round-bottom flask was cooled in an ice water bath under a flow of nitrogen. We then added 8.15 mL sulfuryl chloride (100 mmol, TCI American, >98.0%) in 20 mL anhydrous acetonitrile dropwise to the ice-cooled suspension. The mixture was stirred overnight at room temperature, after which we cooled the white suspension to ~0 °C with ice water and added 13.03 g imidazole (191 mmol, TCI America, >98.0%). We warmed the resulting

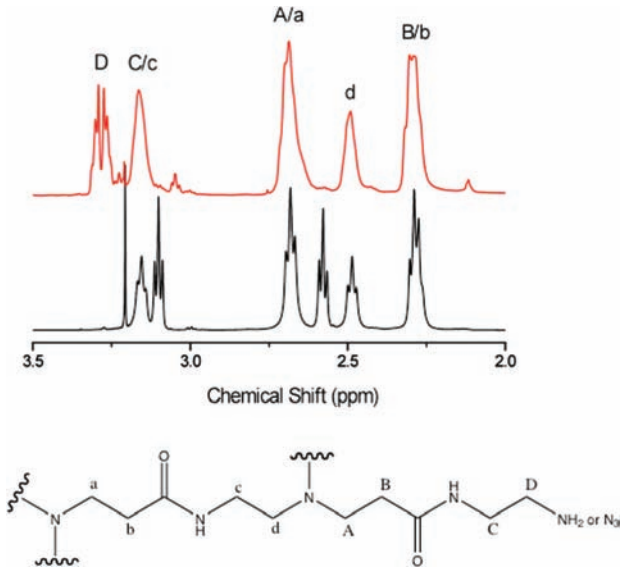


Figure 2. ^{1}H NMR spectra of G4-N_3 (**5**, top), G4-NH_2 from D_2O (**23**, middle). Schematic indication of assignments of the methylene groups (bottom).

white slurry to room temperature, then stirred it for 3 h. We then diluted it with ethyl acetate (200 mL) and separated and discarded the aqueous layer. We washed the organic layer twice with deionized water (2 × 100 mL), then twice with saturated aqueous $NaHCO_3$ (2 × 100 mL). We then dried it over anhydrous $MgSO_4$ overnight and filtered it. We added an ethanolic HCl solution (196 mmol) dropwise to the filtrate while stirring at ice−water temperature. After we added ∼3 mL, a large amount of white solid appeared. We kept the mixture in an ice bath for 15 min, then at room temperature for 30 min, after which we filtered it. We washed the filter cake with ethyl acetate (3 × 100 mL) to give **26** as a colorless solid (8.65 g, 49.9%), mp 99−101 °C. IR (KBr) 2173, 1383, and 1160 cm^{-1}. ^{1}H NMR (D_2O, 500 MHz) δ 7.61 (dd), 8.02 (dd), 9.39 (dd); ^{13}C NMR (D_2O, 125 MHz) δ = 120.0, 123.5, 137.6. Element Analysis: calcd C, 17.19; H, 1.92; N, 33.41. Found: C, 17.38; H, 1.98; N, 32.97.

*Synthesis of Fully Azido-Derivatized PAMAM (G4) (**13**).* We added anhydrous methanol (10 mL, Aldrich, >99.8%) and 18.15 g G4 PAMAM dendrimer (**23**, Dendritech, Midland, MI, 14.93 w/w % in methanol, [NH_2] = 12.2 mmol) to a 250 mL round-bottom flask. We then added 3.12 g K_2CO_3 (Aldrich, >99.0%, 22.6 mmol) and 31.4 mg $CuSO_4 \cdot 5H_2O$ (Aldrich, 98.0%, 0.126 mmol), causing the solution to take on a pale bluish color. We next added 2.73 g imidazole-1-sulfonyl azide hydrochloride (**26**, 13.1 mmol) to the reaction mixture, and it was stirred at room temperature overnight. The mixture was then dialyzed against deionized water for 7 d, during which we changed the water every 2 h for the first 2 d and thereafter every 4 h. After lyophilization, we collected 2.51 g azide-derivatized G4 dendrimer. The proton NMR is shown in Figure 2. Element analysis: PAMAM-G4: calcd C, 52.81; H, 8.48; N, 24.70, O, 14.01. Fully azide-derivatized G4 PAMAM: calcd C, 47.03; H, 7.15; N, 33.31, O, 12.49; found C, 49.91; H, 7.55; N, 28.07; O, 13.12. The element analyses indicated that 98.0% of primary amines were replaced with azides.

*Synthesis of Partially Azido-Derivatized PAMAM (G4) (**5**).* We added anhydrous methanol (5 mL, Aldrich, >99.8%) and 5.13 g G4 PAMAM dendrimer (**23**, Dendritech, 14.93 w/w % in methanol, [NH_2] = 3.45 mmol) to a 100 mL round-bottom flask. We then added 0.803 g K_2CO_3 (Aldrich, >99.0%, 5.81 mmol) and 17.2 mg $CuSO_4 \cdot 5H_2O$ (Aldrich, 98.0%, 0.069 mmol); the solution took on a pale bluish color. Next, we added 0.43 g imidazole-1-sulfonyl azide hydrochloride (**26**, 2.05 mmol) to the reaction mixture, which was stirred at room temperature overnight. We then dialyzed the mixture against deionized water for 7 d, changing the water every 2 h during the first 2 d and every 4 h thereafter. After lyophilization, we collected 0.45 g partially azide-derivatized G4 dendrimer. Elemental analysis of the partially azide-derivatized G4 PAMAM found C, 49.91; H, 7.55; N, 28.07; O, 13.12. We compared results of the element analysis with the composition of the G4 PAMAM dendrimer and found that 47.2% of the primary amines were replaced with azides, corresponding to ∼31 amines per dendrimer in 64 terminal positions.

Biological Methods: $P2Y_{14}$ Receptor. *Materials.* We purchased 3-isobutyl-1-methyl-xanthine from Sigma-Aldrich and [^{3}H]adenine from American Radiolabeled Chemicals (St. Louis, MO). We obtained all cell culture medium and serum from Gibco (Invitrogen, Carlsbad, CA).

Cell Culture. We generated C6 glioma cells stably expressing the human $P2Y_{14}$-R ($P2Y_{14}$-C6 cells) as previously described by Fricks et al. (*23*). We cultured $P2Y_{14}$-C6 cells in Dulbecco's modified Eagle's medium (DMEM) supplemented with 5% fetal bovine serum, 1% Geneticin (Gibco), and 1% antibiotic−antimocotic (Gibco) at 37 °C in a 5% CO_2 environment.

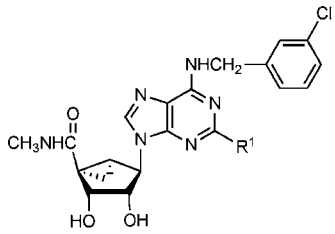
Accumulation of Adenosine 3′,5′-Cyclic Phosphate (cAMP). We grew $P2Y_{14}$-C6 cells in 24-well plates and incubated them with 1 μCi [^{3}H]adenine/well in serum-free DMEM for at least 2 h prior to assay. We initiated the assays by adding HEPES-buffered, serum-free DMEM containing 200 μM 3-isobutyl-1-methyl-xanthine and 30 μM forskolin, with or without drugs, and incubation continued for 15 min at 37 °C. We terminated incubations by aspirating the medium and adding 450 μL ice-cold 5% trichloroacetic acid. We isolated [^{3}H]cAMP by sequential Dowex and alumina chromatography and quantified it by liquid scintillation counting as previously described by Harden et al. (*24*).

Data Analysis. We measured the concentrations of the dendrimer−ligand complexes by the concentration of the dendrimer, not the attached ligand. We determined EC_{50} and apparent K_i values with *Prism* software (GraphPad, San Diego, CA); they are presented as mean ± SE. The number of nucleoside moieties on a given dendrimer that are accessible to receptors is uncertain; the data are therefore shown as apparent K_i values. We repeated all experiments at least three times.

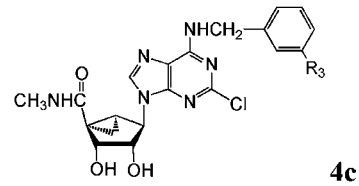
Biological Methods: ARs. *Receptor-Binding and Functional Assays.* We obtained [^{3}H]adenosine-5′-*N*-methyluronamide ([^{3}H]-NECA, 42.6 Ci/mmol) from PerkinElmer Life and Analytical Science (Boston, MA). We purchased [^{3}H](2-[*p*-(2-carboxyethyl)phenyl-ethylamino]-5′-*N*-ethylcarboxamido-adenosine) ([^{3}H]-CGS21680, 40.5 Ci/mmol) and [^{125}I]*N*^{6}-(4-amino-3-iodobenzyl)-adenosine-5′-*N*-methyluronamide ([^{125}I]I-AB-MECA, 2200 Ci/mmol) from PerkinElmer. We prepared test compounds as 5 mM stock solutions in DMSO and stored them frozen at −20 °C.

Cell Culture and Membrane Preparation. We cultured Chinese hamster ovary (CHO) cells stably expressing the recombinant hA_1 and hA_3 and human embryonic kidney (HEK) 293 cells stably expressing the $hA_{2A}AR$ in DMEM and F12 (1:1) supplemented with 10% fetal bovine serum, 100 units/mL penicillin, 100 μg/mL streptomycin, and 2 μmol/mL glutamine. In addition, we added 800 μg/mL Geneticin to the A_{2A} media and 500 μg/mL hygromycin to the A_1 and A_3 media. After harvesting the cells, we homogenized them with an electric homogenizer for 10 s, pipetted them into 1 mL vials, and then stored them at −80 °C until we conducted the binding experiments. We measured the protein concentration with a BCA Protein Assay Kit from Pierce Biotechnology (Rockford, IL) (*25*).

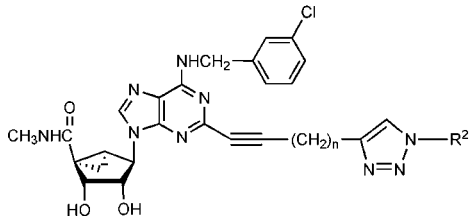
Table 1. Potency of a Series of Nucleoside-Dendrimer Conjugates at Three Subtypes of Human ARs



2, 3a, 4b



4c



4a, 5 – 12

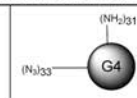
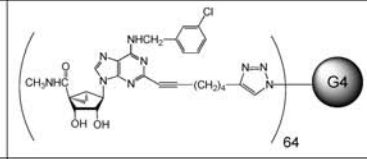
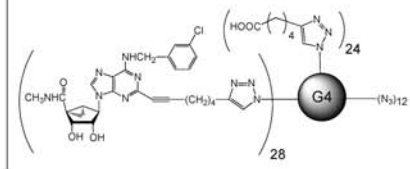
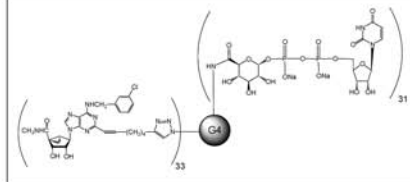
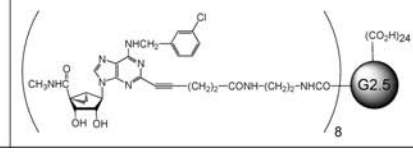
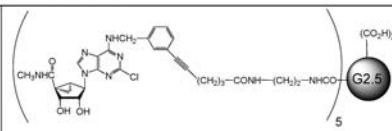
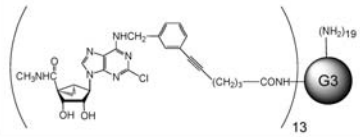
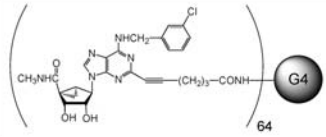
Compd	Structure, R^1, R^2, or R^3	Affinity (K_i, nM) or *% inhibition*[a]		
		A_1	A_{2A}	A_3
Model compounds				
1[b] ***IB-MECA***		51	2900	1.8
2[b,c]	R^1 = Cl	260±60[b]	2300±100	0.29±0.04
3a[b,c]	R^1 = C≡C$(CH_2)_4$C≡CH	*(31±2%)* at 10 μM	7040±1430	29.4±9.8
4a[b,c]	R^2 = $(CH_2)_2$NHCOCH$_3$	*(12±4%)* at 10 μM	2440±320	22.3±1.6
4b[b]	R^1 = C≡C$(CH_2)_2$CH$_3$	1040±80	*(80%)* at 10 μM	0.82±0.20
4c[b]	R^3 = C≡C$(CH_2)_4$CONH$(CH_2)_2$NHCOCH$_3$	181±22	*(80%)* at 10 μM	2.88±0.54
Dendrimer derivatives				
5[d]		NA	NA	NA
6[c]		22.6±6.9	32.2±6.4	0.14±0.09
7[c]		35.1±7.5	34.4±1.8	0.32±0.03
8[c]		78±31	584±48	39.5±11.8
9		ND	*(27±7%)* at 10 μM	31.4±2.8

Table 1. Continued

Compd	Structure, R^1, R^2, or R^3	Affinity (K_i, nM) or *% inhibition*[a]		
		A_1	A_{2A}	A_3
Dendrimer derivatives				
10		77	*(3±2%)* at 1 μM	41.7±6.4
11[c]		7.1	5750± 1600	17.6±2.8
12		1.92±1.25	727±168	11.8±2.2

[a] NA: not active in inhibition of radioligand binding (<10%) at 1 μM. All experiments were done on CHO or HEK293 (A_{2A} only) cells stably expressing one of four subtypes of human ARs. The binding affinity for A_1, A_{2A}, and A_3ARs was expressed as K_i values ($n = 3-5$) and was determined by using agonist radioligands ([^{3}H]NECA, [^{3}H]CGS21680, or [^{125}I]I-AB-MECA, respectively), unless noted. A percentage in parentheses refers to inhibition of radioligand binding at the indicated concentration. The concentrations of the dendrimer-ligand complexes were measured by the concentration of the dendrimer, not the ligand. Therefore, all binding K_i values of dendrimers are expressed as apparent K_i values. [b] Affinity values from Tosh et al. (*15, 21*) and Melman et al. (*14*). [c] **2**, MRS3558; **3a**, MRS5221; **4a**, MRS5233; **6**, MRS5246; **7**, MRS5247; **8**, MRS5259; **11**, MRS5216. [d] Coumpound **5** is the dendrimer precursor of **8** and is similar to the dendrimer precursor of **6** and **7**.

Binding Assays. Each tube in the binding assay contained 50 μL of increasing concentrations of the test ligand in Tris-HCl buffer (50 mM, pH 7.5) containing 10 mM $MgCl_2$, 50 μL of the appropriate agonist radioligand, and 100 μL membrane suspension, added sequentially. For the A_1AR (20 μg protein/tube), we used the radioligand [^{3}H]NECA (~3.5 nM, precise final concentration is calculated for each experiment). For the A_{2A}AR (20 μg/tube), we used the radioligand [^{3}H]CGS21680 (~10 nM). For the A_3AR (21 μg/tube), we used the radioligand [^{125}I]I-AB-MECA (~0.3 nM). We determined nonspecific binding with a final concentration of 10 μM unlabeled NECA diluted with the buffer. We incubated the mixtures at 25 °C for 60 min in a shaking water bath. We terminated binding reactions by filtration through Brandel GF/B filters under a reduced pressure with a M-24 cell harvester (Brandel, Gaithersburg, MD). We washed filters three times with 3 mL of 50 mM ice-cold Tris−HCl buffer (pH 7.5). We then placed filters for A_1 and A_{2A}AR binding in scintillation vials containing 5 mL Hydrofluor scintillation buffer and counted with a PerkinElmer Liquid Scintillation Analyzer (Tri-Carb 2810TR). We counted filters for A_3AR binding with a Packard Cobra II γ-counter (PerkinElmer). We determined the K_i values with GraphPad *Prism* for all assays.

Accumulation of cAMP. To determine cAMP production (*26*), we incubated protein kinase A with [^{3}H]cAMP (2 nM) in K_2HPO_4/EDTA buffer (K_2HPO_4, 150 mM; EDTA, 10 mM), 20 μL cell lysate, and 30 μL 0.1 M HCl or 50 μL cAMP solution (0−16 pmol/200 μL for standard curve). We separated bound radioactivity by rapid filtration through Whatman GF/C filters and washed the filters once with cold buffer. We measured bound radioactivity with liquid scintillation spectrometry.

RESULTS

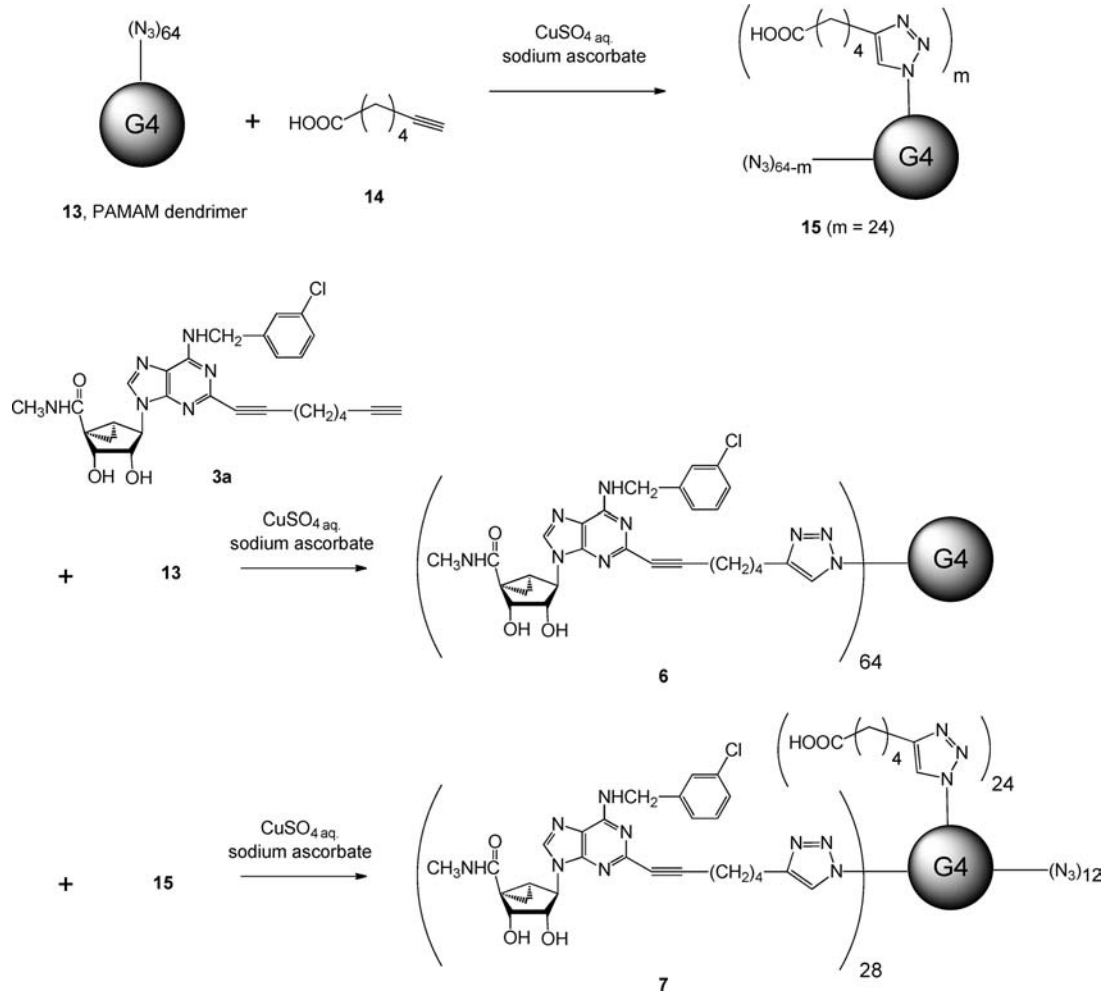
Chemical Synthesis. We prepared various PAMAM dendrimer derivatives of nucleosides and nucleotides (Table 1, **6**−**12**) to act as multivalent ligands of GPCRs. The peripheral groups of the precursor dendrimers contained either all azido groups (Scheme 1), mixtures of azido and amino groups (Scheme 2), or the conventional all amino/carboxylate groups (Scheme 3). The synthetic methods used to partially or fully substitute terminal amino groups of a G4 PAMAM dendrimer with azides are shown in Scheme 4 (*22*). Schemes 1−4 and Table 1 indicate the approximate, average number of attached moieties on each dendrimer, which is actually a statistical distribution of substitution.

We recently introduced terminal alkynyl groups at the C2 position of (N)-methanocarba nucleoside derivatives to serve as sites on the A_3AR agonists for cross-linking by click chemistry (*21*). Thus, a dialkyne was introduced at the C2 position in **2**, and further reaction with azides generally occurred exclusively at the distal alkyne. Prior to coupling the nucleosides to dendrimer carriers, we explored in detail the structure−activity relationship at the distal region of an alkyne-functionalized chain at the 2 position and the resultant click products (*21*).

The synthetic route to the multivalent dendrimer conjugates of nucleosides for activation of the A_3AR that contain 5′-*N*-methyluronamide (N)-methanocarba 2-alkynyl triazoles **6** and **7** is shown in Scheme 1. Click chemistry efficiently coupled the A_3AR agonist **3a** to a PAMAM dendrimer fully substituted with peripheral azido groups. We used two versions of this azido-functionalized dendrimeric scaffold: **15**, containing extra appended carboxylic acid groups for increasing water solubility, and **13**, lacking these groups. We added the carboxylic acid moieties to the azido dendrimer **13** by partial reaction of the peripheral azido groups with hexynoic acid **14**. Thus, we prepared two nucleoside-containing dendrimer derivatives **6** and **7**. Derivative **6** was fully substituted with the adenosine analogue, with 64 nucleoside moieties per dendrimer molecule. Derivative **7** was partially (28 out of 64) substituted with the adenosine analogue and contained 24 carboxylic acid moieties. Twelve azido groups per molecule of **7** remained unreacted.

In the next phase of our study, we combined different GPCR ligands, i.e., the A_3AR and another receptor, on the same dendrimer carrier. We selected the $P2Y_{14}$ receptor, which is activated by naturally occurring uridine-5′-diphosphoglucose (UDPG), for this purpose, because, like the A_3AR, it occurs on

Scheme 1. Use of Click Chemisry to Synthesize PAMAM Dendrimer Derivatives 6 and 7, Containing a Functionalized 2-Alkynyl A_3AR Agonist[a]



[a] An optional water-solubilizing group was added in **7**, in the form of an aliphatic carboxylic acid.

immune cells and because we recently introduced high-potency dendrimer conjugates for this subtype (*5*, *27*). Each ligand would provide selectivity for a particular GPCR subtype, and the overall selectivity of the conjugate would be a function of the union of the sets of selectivity of the attached nucleosides. We sequentially coupled alkyne and carboxylic acid derivatized ligands for the two receptors to a novel multifunctional PAMAM dendrimer. Thus, alkynes reacted exclusively with azido terminal groups and carboxylic acids with terminal amino groups on the same dendrimer to randomly (but in a defined ratio) produce a multivalent, binary conjugate.

We proceeded to synthesize a multivalent, binary conjugate of a mixed azido/amino dendrimer **5**, as shown in Scheme 2. In the dendrimer precursor **5**, we determined, through NMR (*28*) (Figure 2) and elemental analysis, that the ratio of amines to azides was ~31:33. Therefore, of the 64 terminal groups on each G4 dendrimer, ~33 would be available for cycloaddition, and the remaining terminal groups would be available for amide formation. We first coupled the amino groups of **5** to the functionalized, $P2Y_{14}$-selective nucleotide UDPGA **16**, which we previously showed to be a suitable functionalized congener for chain attachment without loss of receptor activation (*5*). We then coupled the azido groups of **17** to the functionalized nucleoside **3a**, which is a suitable functionalized congener for chain attachment without loss of binding affinity at the A_3AR (*21*). The product of this second coupling reaction was the mixed dendrimer **8**, in which the average ratio of UDGPA and nucleoside moieties was ~31:33 per G4 dendrimer. Thus, conjugate **8** would be expected to potently activate both A_3 and $P2Y_{14}$ receptors and perhaps maintain selectivity over other ARs and P2Y receptors.

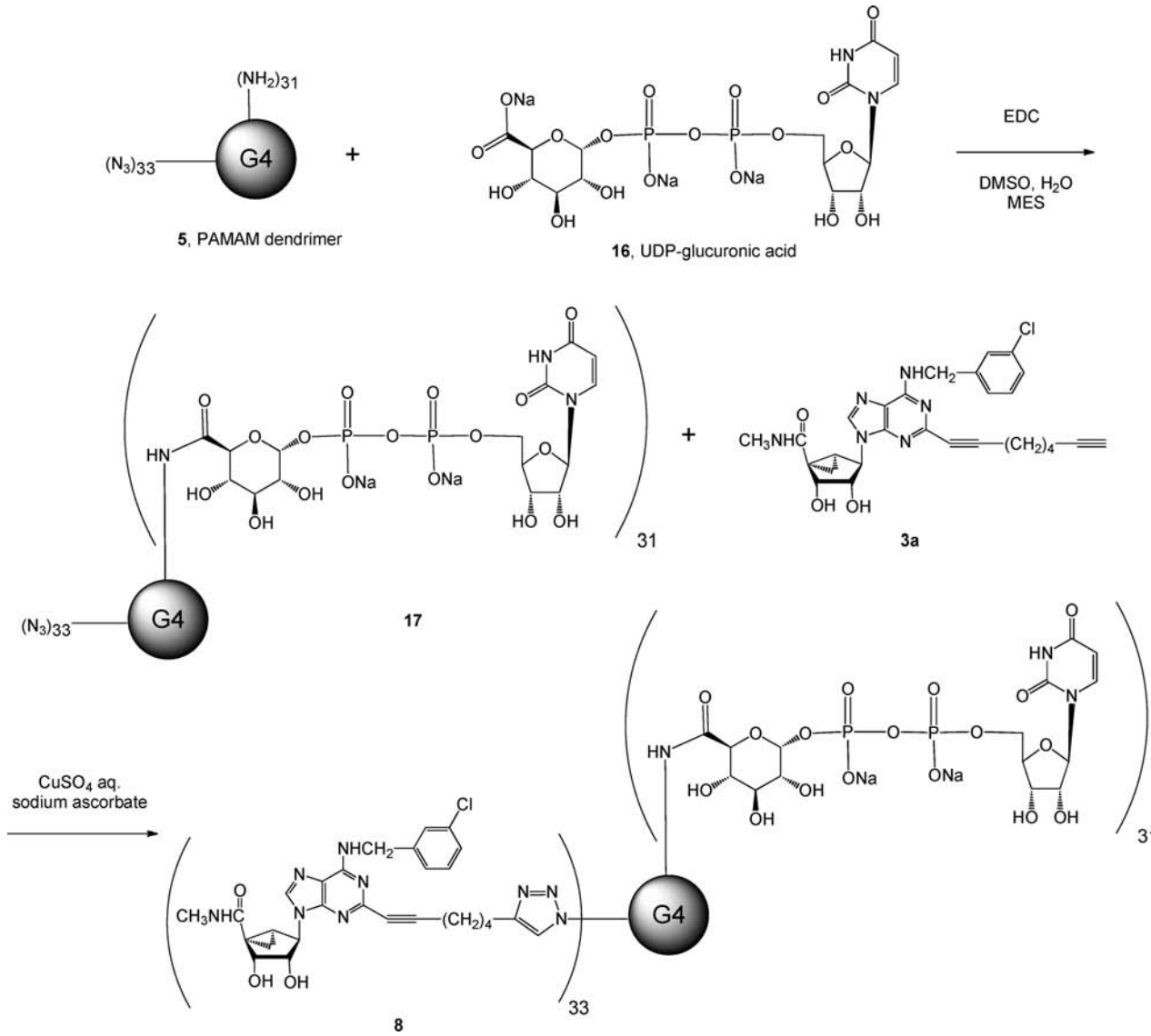
To compare alkyne-azide click chemistry with the more standard amide formation as a means of linking A_3AR-selective agonists to PAMAM dendrimers, we prepared various dendrimer derivatives starting with our previously reported amino and carboxylic-functionalized congeners **19**, **20**, **22**, and **24** (*14*, *15*). The reaction sequences are shown in Scheme 3. We included a variety of dendrimer sizes and sites of conjugation on the nucleoside.

The synthesis of the PAMAM dendrimer intermediate **5** containing equiproportioned peripheral azido and amino groups for conjugation of multiple ligands is shown in Scheme 4. We used the reagent imidazole-1-sulfonyl azide hydrochloride **26** for the conversion of peripheral amino groups to azido groups (*22*). We prepared a fully azido-derivatized G4 dendrimer **13** similarly and used it to synthesize conjugates **6** and **7**.

Quantification of Pharmacological Activity. We tested the dendrimer nucleoside conjugates similarly in binding assays at three hAR subtypes; we used standard radioligands (*29*−*31*) and membrane preparations from CHO cells (A_1 and A_3) or HEK293 cells (A_{2A}) stably expressing a hAR subtype (Table 1) (*32*, *33*). We used the previously reported agonist molecular probes of the A_3AR (**1**, **2**, **3a**, and **4**) for comparison in the biological assays (*15*, *21*).

We included the parent dendrimer **5**, which contained both amino and azido groups, as a control; it was inactive in AR

Scheme 2. Synthesis of Two PAMAM Dendrimer Derivatives Containing a Functionalized Agonist of the $P2Y_{14}$ Receptor Derived by Amide Linkage of UDPGA 16[a]



[a] Conjugate **17** contains only the $P2Y_{14}$ receptor agonist; conjugate **8** contains an A_3AR agonist linked through a click reaction of its 2-alkynyl functionalized chain. The dendrimer precursor **5** contained a random distribution of peripheral amino and azido groups in a ratio of ~33:31.

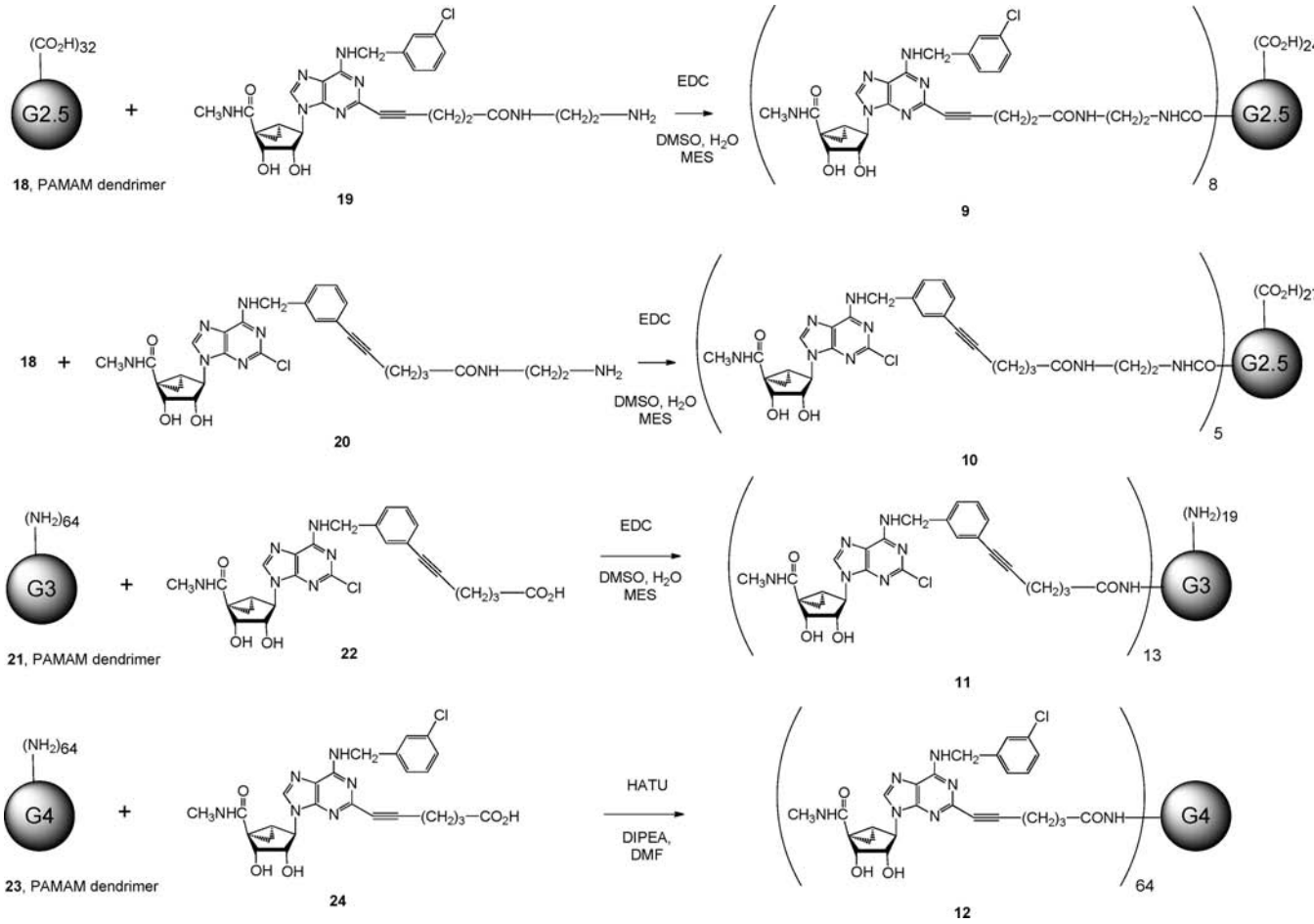
binding at 1 μM. We considered compound **4a** to be a model compound for the attachment of the 2-octadiyne derivative **3a** to azido-bearing PAMAM dendrimers by click chemistry. As reported previously, the triazole-containing monomer **4a** maintained both high potency and selectivity (at least 100-fold) for the A_3AR (*21*).

The multivalent dendrimer derivatives **6** and **7** obtained from **3a** through click conjugation were considerably more potent than **4a** in binding assays at the A_1, A_{2A}, and A_3 ARs. The affinity of **6** and **7** in binding to the A_3AR was particularly high, with K_i values of 0.1−0.3 nM (Figure 3). The fully substituted dendrimer **6** was only 2.3-fold more potent at the A_3AR than the less heavily loaded **7**, which was substituted with nucleosides at 44% of the theoretically available terminal positions. The selectivity of these dendrimer conjugates for the A_3AR in comparison to the A_1AR was still present (161- and 110-fold for **6** and **7**, respectively) but diminished in comparison to the monomer **4a** (>500-fold). However, the A_3AR selectivity of **6** (230-fold) and **7** (180-fold) in comparison to the $A_{2A}AR$ was similar to that of **4a**. Thus, the presence of the carboxylic acid chain in **7** had only minor effects on the observed AR affinity and selectivity, but it increased the observed aqueous solubility. Both **6** and **7** were readily soluble in DMSO at a concentration of 1 mM, but when we diluted the DMSO stock solutions with phosphate-buffered saline for a final calculated concentration of 30 μM, we observed some cloudiness in **6** but not in **7**.

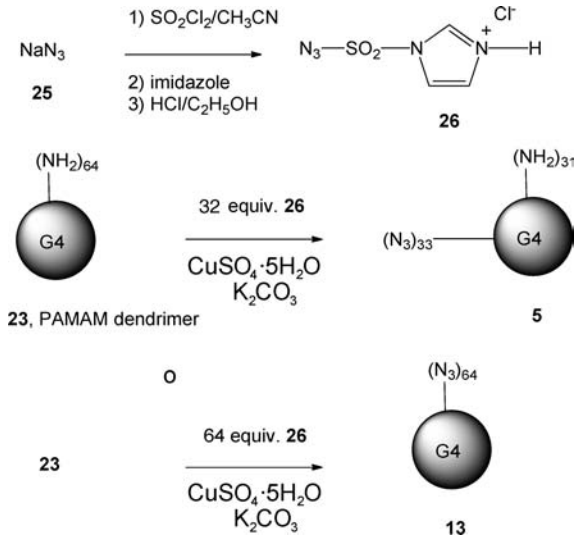
Dendrimer derivative **8** contained an additional covalently bound GPCR ligand, a nucleotide designed to activate the $P2Y_{14}$ receptor. We found that combining strategically functionalized nucleosides and nucleotides on the same dendrimer carrier—for example, to activate both adenosine and P2Y receptors—provided high-affinity recognition at both GPCRs. However, the K_i value of **8** in binding to the A_3AR (39.5 nM) indicated that it was considerably less potent than conjugates **6** and **7**, which contained only the A_3AR agonist ligand. The A_3AR selectivity of **8** was only 2-fold in comparison to the A_1AR and 15-fold in comparison to the $A_{2A}AR$. Thus, it was much less A_3AR selective than were **6** and **7**.

A functional assay of adenylate cyclase inhibition carried out in C6 cells expressing the human $P2Y_{14}$ receptor demonstrated that potency at this receptor was enhanced in the dendrimer conjugate **8** over that of the monomer, with an EC_{50} value of 2.24 ± 0.80 nM (Figure 4). Both UDPG and UDPGA displayed potencies in the same assay of 200−300 nM (*5*). This degree

Scheme 3. Preparation of Amide-Linked Nucleoside Conjugates of PAMAM Dendrimers



Scheme 4. Synthesis of Azido-Derivatized PAMAM Dendrimers, Which Served As Precursors for the GPCR Ligand Conjugates by Reacting with Imidazole-1-Sulfonyl Azide Hydrochloride 26



of potency enhancement at the $P2Y_{14}$ receptor was consistent with previous results of conjugation of UDPGA derivatives to PAMAM carriers (*5*). Dendrimer **17**, which contained only the ligand of the $P2Y_{14}$ receptor (i.e., 31 nucleotides bound per G4 dendrimer) and not the A_3AR-activating moiety, displayed an EC_{50} value at the $P2Y_{14}$ receptor of 2.41 ± 0.77 nM. Curiously, nucleotide-containing dendrimers **8** and **17** also interacted with at least one other subtype of P2Y receptor, but nevertheless with selectivity for the $P2Y_{14}$ receptor. Dendrimers **8** and **17** displayed EC_{50} values in activation of phospholipase C (PLC) by the human $P2Y_2$ receptor of 1.39 ± 0.54 μM and 733 ± 223 nM ($n = 3$), respectively, assayed as described in stably transfected 1321N1 astrocytoma cells (*34*). The native agonist of the $P2Y_{14}$ receptor, UDPG, also activated the human $P2Y_2$ receptor, with an EC_{50} value of 10 μM (*34*).

PAMAM dendrimer conjugates (**9**−**12**) of carboxylic- and amino-functionalized congeners of A_3AR-selective agonists consistently displayed lower affinity in A_3AR binding than did the click-linked dendrimers **6** and **7**. The amide-linked conjugates included derivatives of both terminal carboxylic acid-functionalized dendrimers **9** and **10** and terminal amine-functionalized dendrimers **11** and **12**, ranging from generation 2.5 to 4. The affinities of these dendrimers at the hA_3AR were in the range 12−42 nM, and the nature of the residual terminal groups of the dendrimer carrier had little effect. We did not observe the subnanomolar affinity seen in click-linked nucleoside−dendrimer conjugates. Thus, the high affinity is partially the result of the linkers and the coupling chemistry used, which in **6** and **7** produce a triazole rather than an amide linkage.

The selectivity of the amide-linked dendrimers in comparison to the $A_{2A}AR$ was high (*x*-fold, for compound): >300, **9**; ≫24, **10**; 327, **11**; 62, **12**. However, there was a substantial gain in affinity at the A_1AR over the corresponding monomeric nucleosides. Thus, **10** and **11** lost selectivity for the A_3AR in comparison to the A_1AR. Compound **12** was reversed in its selectivity (6-fold more potent at the A_1AR than at the A_3AR). Conversely, we considered compound **4b** to be a model nucleoside derivative for the amide-linked dendrimer derivatives

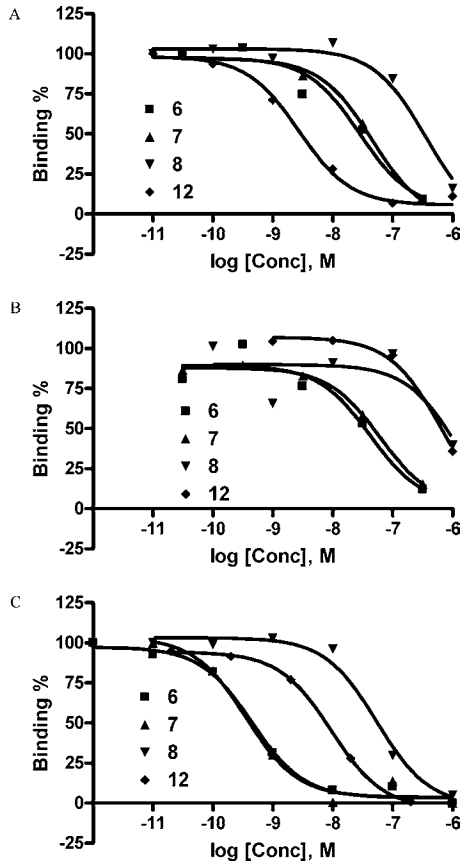


Figure 3. Inhibition of radioligand binding by dendrimer nucleoside conjugates in membranes of CHO cells expressing the human A_1 (A) and A_3 (C) ARs and HEK-293 cells expressing the human A_{2A}AR (B). Inhibition curves at three ARs are shown for the dendrimer−nucleoside conjugates **6** and **7**, in which the linkage to an azide-derivatized dendrimer was formed by click cycloaddition, for the mixed nucleoside/nucleotide conjugate **8** and for the amide-linked nucleoside conjugate **12**. Both **6** and **7** were highly selective for the hA_3AR in comparison to the hA_1 and hA_{2A}ARs.

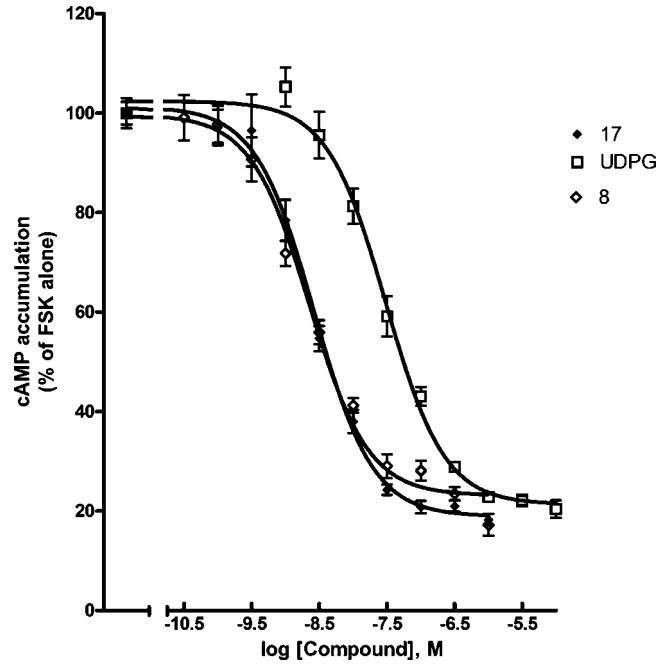


Figure 4. Activation of the G_i-coupled $P2Y_{14}$ receptor stably expressed in C6 cells by the mixed nucleoside/nucleotide G4 dendrimer conjugate **8** (MRS5259) and the nucleotide G4 dendrimer conjugate **17** (MRS2949). Inhibition of forskolin (FSK)-stimulated cAMP is shown in comparison to the effects of UDPG ($n = 3$).

Table 2. Maximal Efficacy of (N)-Methanocarba Adenosine Derivatives in a Functional Assay at the A_3AR

compound	concentration (μM)	% inhibition of cAMP accumulation[a] at the hA_3AR
IB-MECA	1.0	99 ± 6
Cl-IB-MECA	1.0	97
NECA	1.0	100
3a	10	60.2 ± 17.0
4a[b]	10	93.6 ± 17.7
5	1.0	1.7 ± 1.4
6	0.1	98.7 ± 14.3
7	0.1	91.4 ± 20.2
8	0.1	111 ± 20
9[c]	1.0	88.2 ± 15.1
10	1.0	91.3 ± 12.3
11	1.0	101 ± 10
12	0.1	92.1 ± 21.2

[a] The efficacy at the human A_3AR was determined by inhibition of forskolin-stimulated cyclic AMP production in AR-transfected CHO cells, as described in the text. Percent inhibition is shown at the indicated concentration, in comparison to the maximal effect of a full agonist NECA at 1 μM. Data are expressed as mean ± standard error ($n = 3-5$). ND, not determined. [b] Values from Tosh et al. (*21*). [c] EC_{50} values were determined with full curves for compounds **7** (0.12 ± 0.03 nM), **8** (1.36 nM), and **11** (2.93 ± 0.37 nM).

9 and **12**, and it was clearly A_3AR selective. Compound **4c** (63-fold selective for the A_3AR versus the A_1AR) was a model for N^6-functionalized dendrimer conjugates **10** and **11**, although it was a higher homologue with 4 methylenes. Thus, both model compounds **4b** and **4c** were more potent and selective in binding to the A_3AR than were the corresponding amide-linked dendrimers.

We determined binding at the rat A_3AR expressed in CHO cells for selected compounds. The K_i values of the N^6-chain derivatized, amide-linked dendrimers **10** and **11** were 62.0 ± 36.5 and 4.94 ± 1.96 nM ($n = 3$), respectively. The triazole-linked adenosine conjugate **7** with water-solubilizing groups displayed a K_i value of 0.08 ± 0.02 nM in binding to the rat A_3AR. Thus, there was a relatively low degree of species-dependent variation in the observed A_3AR affinity (4-fold greater in rat than human).

We tested the nucleoside conjugates in a functional assay at the A_3AR (inhibition of forskolin-stimulated cAMP production in A_3AR-expressing CHO cells) as shown in Table 2. These multivalent derivatives displayed A_3AR agonist properties with varying degrees of maximal inhibition of forskolin-stimulated cAMP production at 0.1−10 μM (concentration selected to be in >100-fold excess of the K_i value for each). In general, the relative efficacy was similar to that of NECA (1 μM), taken as a reference standard. The dendrimer control was inactive. The EC_{50} value of the amide-linked adenosine conjugate **11** was 2.93 ± 0.37 nM, determined with a full curve in CHO cells stably expressing the human A_3AR (Figure 5). Conjugate **11** was a full agonist in the A_3AR-mediated inhibition of cAMP production. We also determined EC_{50} values for cAMP inhibition with full curves for the triazole-linked adenosine conjugate with water-solubilizing groups **7** (0.12 nM) and **8** (1.36 nM).

DISCUSSION

We used the Cu(I)-catalyzed alkyne-azide click reaction for linking functionalized congeners of AR ligands (*21*, *35*) to other moieties, specifically PAMAM dendrimer derivatives. In this study, we compared different chemical strategies for tethering GPCR ligands to macromolecular carriers. Dendrimer derivatives prepared by click chemistry were particu-

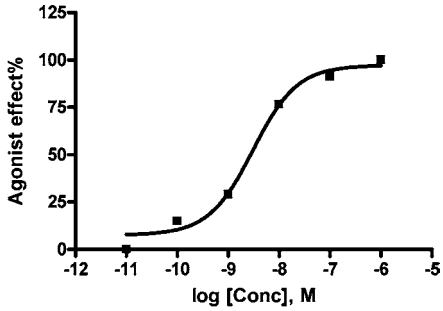


Figure 5. Activation of the G_i-coupled A_3AR stably expressed in CHO cells by **11**. The agonist effect measured is inhibition of forskolin-stimulated cAMP production, in comparison to the maximal effect of a full agonist NECA at 1 μM. Curve is representative of three determinations.

larly potent and selective in binding to the A_3AR. Multivalent nucleoside−dendrimer conjugates **6** and **7** showed much greater A_3AR affinity than the corresponding monomer, the model nucleoside **4a**. Furthermore, amide-linked nucleoside conjugates were considerably weaker than click-linked conjugates in binding to the A_3AR. This illustrates the dramatic effect that both the multivalency and the intermediate structures contained within the functionalized chain can have on interaction with the target receptor (*35*). A comparison with various amide-linked dendrimers showed that the triazole linkage had a general A_3AR affinity−enhancing effect. Click chemistry was previously used to link small molecules to dendrimeric structures, but ours is the first application for studying PAMAM dendrimer derivatives of small-molecular GPCR ligands. Recently, peptide ligands were conjugated to dendrimers by click chemistry for activation of a GPCR (*18*).

Other studies have focused on PAMAM dendrimers as reversible drug carriers, for example, to deliver anticancer drugs that dissociated at the site of action (*36*). Our approach derivatizes a small molecule but allows it to remain active while covalently attached to the carrier (*35*). The binding sites of the receptors are accessible from the extracellular medium. Thus, activation of the desired receptor would not benefit from either drug release or cellular internalization of the dendrimer. The flexible dendrimer conjugate is available to spread over the cell surface and to adopt a conformation that can bridge multiple binding sites (*37*).

The efficiency of the click reaction readily allowed complete substitution in the case of one of the dendrimer derivatives, i.e., **6**. In previous experiences with amide coupling of functionalized nucleosides, we encountered difficulty in the complete substitution of amine-terminated dendrimers (*3, 4*). Click chemistry proved to be a more efficient coupling technique and allowed orthogonal reaction control over the coupling chemistry when two distinct receptor ligands were bound to the same dendrimer carrier (as in **8**). This conjugate was most readily synthesized by amide coupling of the carboxy-functionalized nucleotide followed by click coupling of the alkyne-functionalized adenosine derivative.

This study presents the first example of targeting two different GPCRs with the same dendrimer conjugate, intended for activation of heteromeric aggregates of GPCRs. Each ligand provided selectivity for a particular GPCR subtype, and the overall selectivity of the conjugate was a function of the union of the sets of selectivity of the attached nucleosides. Specifically, the dendrimer conjugate **8** contained ligands for both the A_3AR and the $P2Y_{14}$ receptor. The principle of attachment of UDPG derivatives to PAMAM dendrimers to enhance potency was introduced previously (*5*). This bifunctional dendrimer potently activated both A_3 and $P2Y_{14}$ receptors, although not to the exclusion of other ARs.

The bifunctional dendrimer **8** and its nucleotide−dendrimer precursor **17** both activated one other P2Y receptor examined, the $hP2Y_2$ receptor, with intermediate potency. UDPG itself activates the $hP2Y_2$ receptor with an EC_{50} of 10 μM for stimulation of PLC in stably transfected 1321N1 cells (*34*). Therefore, the potency at both subtypes of P2Y receptors was much greater in the dendrimer conjugates than in the monomer, but the desired selectivity for the $P2Y_{14}$ receptor was maintained. Thus, both covalently tethered GPCR ligands, which were previously shown to be suitable functionalized congeners for coupling to carriers, retained their activity as the mixed dendrimer conjugate **8**. This conjugate had reduced A_3AR affinity in the presence of tethered nucleotide moieties but not reduced $P2Y_{14}$ potency due to the tethered nucleoside moieties. This is the first example of targeting two different GPCRs with the same dendrimer conjugate, which is intended for activation of heteromeric aggregates of GPCRs.

Many examples exist of two small molecules linked with a spacer group to make binary conjugates for activation of two different GPCRs (*35, 38, 39*). Some researchers have systematically varied the length of the spacer to achieve the correct fit to the two adjacent binding sites. This multivalent approach was taken in part because of uncertainty about the geometric orientation of protomer binding sites in a GPCR dimer. Flexible dendritic carriers facilitate empirical testing of a variety of spatial orientations of the same conjugate. This obviates the need to probe the optimal geometry a priori of a single spacer chain to achieve simultaneous binding to two sites.

Both A_3 and $P2Y_{14}$ receptors are distributed in the immune system and appear to occur on the same cell, as was shown for RBL-2H3 mast cells (*27*). Further experiments will be needed to determine whether heteromers composed of A_3 and $P2Y_{14}$ receptors exist and whether this conjugate is capable of bridging the binding sites on both protomers. This approach of mixing receptor ligands on the same dendrimer carrier can be extended to many other combinations of GPCRs.

We know that GPCRs tend not to be evenly or randomly distributed over the surface of a given cell; we demonstrated this for the A_3AR expressed heterologously in CHO cells (*4*). In general, GPCRs may exist as complexes with other receptors and associated proteins. The receptors to which a given GPCR pairs or forms a higher-order aggregate can dramatically affect its pharmacology, and the binding of agonist to both protomers does not have equivalent pharmacological effects (*40*). We lack effective ligand tools for separating the effects of one receptor dimeric combination from another. This approach of mixing ligands for two different receptors (*35, 38, 39, 41*) promises to be a means of achieving selectivity for receptors in a given tissue, based on association or aggregation of GPCRs, in comparison to another tissue in which the same receptor may be alternatively paired. At this early stage, we do not know the topological requirements for selectively targeting these combinations of receptors, because we are just beginning to detect their existence. The multivalent binding to other types of cell surface receptors has been explored through structural modification of the carrier polymer (*42*).

Multivalent conjugates of GPCR ligands provide quantitatively and qualitatively different pharmacological properties than do monomers. Prosthetic groups for targeting or therapeutic purposes or reporter groups for diagnostic purposes might be introduced. Specific combinations of receptor ligands on the same dendrimer carrier might achieve synergistic effects and prove useful for disease treatment, such as inflammatory conditions, to which the current example of adenosine and P2Y receptor ligands apply. Various combinations may be proposed

for targeted therapeutic applications, but the linking strategy to achieve the desired potency and selectivity still requires development. We are working on prototypical examples that could be applied to other combinations of dendrimer-bound GPCR ligands.

ACKNOWLEDGMENT

We thank Dr. John Lloyd and Dr. Noel Whittaker (NIDDK) for the mass spectral determinations. We thank Dr. Bruce Liang (Univ. of Connecticut) for helpful discussion. This research was supported by the Intramural Research Program of the NIH, NIDDK. Research conducted at the Center for Nanophase Materials Sciences at Oak Ridge National Laboratory is sponsored by the Scientific User Facilities Division, Office of Basic Energy Sciences, U.S. Department of Energy.

Supporting Information Available: ^{1}H NMR and mass spectra of representative compounds **6** and **11**. This material is available free of charge via the Internet at http://pubs.acs.org.

LITERATURE CITED

(1) Nwe, K., and Brechbiel, M. W. (2009) Growing applications of "click chemistry" for bioconjugation in contemporary biomedical research. *Cancer Biother. Radiopharm. 24*, 289–302.

(2) Tomalia, D. A., Reyna, L. A., and Svenson, S. (2007) Dendrimers as multi-purpose nanodevices for oncology drug delivery and diagnostic imaging. *Biochem. Soc. Trans. 35*, 61–67.

(3) Kim, Y., Hechler, B., Klutz, A., Gachet, C., and Jacobson, K. A. (2008) Toward multivalent signaling across G protein-coupled receptors from poly(amidoamine) dendrimers. *Bioconjugate Chem. 19*, 406–411.

(4) Klutz, A. M., Gao, Z. G., Lloyd, J., Shainberg, A., and Jacobson, K. A. (2008) Enhanced A_3 adenosine receptor selectivity of multivalent nucleoside-dendrimer conjugates. *J. Nanobiotechnol. 6*, 12.

(5) Das, A., Zhou, Y., Ivanov, A. A., Carter, R. L., Harden, T. K., and Jacobson, K. A. (2009) Enhanced potency of nucleotide-dendrimer conjugates as agonists of the $P2Y_{14}$ receptor: Multivalent effect in G protein-coupled receptor recognition. *Bioconjugate Chem. 20*, 1650–1659.

(6) Jacobson, K. A., and Gao, Z. G. (2006) Adenosine receptors as therapeutic targets. *Nat. Rev. Drug Discovery 5*, 247–264.

(7) Gessi, S., Merighi, S., Varani, K., Cattabriga, E., Benini, A., Mirandola, P., Leung, E., Mac Lennan, S., Feo, C., Baraldi, S., and Borea, P. A. (2007) Adenosine receptors in colon carcinoma tissues and colon tumoral cell lines: focus on the A_3 adenosine subtype. *J. Cell. Physiol. 211*, 826–836.

(8) Yang, H., Avila, M. Y., Peterson-Yantorno, K., Coca-Prados, M., Stone, R. A., Jacobson, K. A., and Civan, M. M. (2005) The cross-species A_3 adenosine-receptor antagonist MRS 1292 inhibits adenosine-triggered human nonpigmented ciliary epithelial cell fluid release and reduces mouse intraocular pressure. *Curr. Eye Res. 30*, 747–754.

(9) Hua, X., Chason, K. D., Fredholm, B. B., Deshpande, D. A., Penn, R. B., and Tilley, S. L. (2008) Adenosine induces airway hyperresponsiveness through activation of A_3 receptors on mast cells. *J. Allergy Clin. Immunol. 122*, 107–113.

(10) Fishman, P., Jacobson, K. A., Ochaion, A., Cohen, S., and Bar-Yehuda, S. (2007) The anti-cancer effect of A_3 adenosine receptor agonists: A novel, targeted therapy. *Immun. Endoc. Metab. Agents Med. Chem. 7*, 298–303.

(11) Silverman, M. H., Strand, V., Markovits, D., Nahir, M., Reitblat, T., sMolad, Y., Rosner, I., Rozenbaum, M., Mader, R., Adawi, M., Caspi, D., Tishler, M., Langevitz, P., Rubinow, A., Friedman, J., Green, L., Tanay, A., Ochaion, A., Cohen, S., Kerns, W. D., Cohn, I., Fishman-Furman, S., Farbstein, M., Yehuda, S. B., and Fishman, P. (2008) Clinical evidence for utilization of the A_3 adenosine receptor as a target to treat rheumatoid arthritis: Data from a phase II clinical trial. *J. Rheumatol. 35*, 41–48.

(12) Zheng, J., Wang, R., Zambraski, E., Wu, D., Jacobson, K. A., and Liang, B. T. (2007) A novel protective action of adenosine A_3 receptors: Attenuation of skeletal muscle ischemia and reperfusion injury. *Am. J. Physiol.; Heart Circ. Physiol. 293*, 3685–3691.

(13) Zhang, M., Hu, H., Zhang, X., Lu, W., Lim, J., Eysteinsson, T., Jacobson, K. A., Laties, A. M., and Mitchell, C. H. (2010) The A_3 adenosine receptor attenuates the calcium rise triggered by NMDA receptors in retinal ganglion cells, *Neurochem. Int. 56*, 35−41.

(14) Melman, A., Gao, Z. G., Kumar, D., Wan, T. C., Gizewski, E., Auchampach, J. A., and Jacobson, K. A. (2008) Design of (N)-methanocarba adenosine 5′-uronamides as species-independent A_3 receptor-selective agonists. *Bioorg. Med. Chem. Lett. 18*, 2813–2819.

(15) Tosh, D. K., Chinn, M., Ivanov, A. A., Klutz, A. M., Gao, Z. G., and Jacobson, K. A. (2009) Functionalized congeners of A_3 adenosine receptor-selective nucleosides containing a bicyclo[3.1.0]hexane ring system. *J. Med. Chem. 52*, 7580–7592.

(16) Agard, N. J., Baskin, J. M., Prescher, J. A., Lo, A., and Bertozzi, C. R. (2006) A comparative study of bioorthogonal reactions with azides. *ACS Chem. Biol. 1*, 644–648.

(17) Camponovo, J., Hadad, C.; Ruiz, J., Cloutet, E., Gatard, S., Muzart, J., Bouquillon, S., and Astruc, D. "Click" glycodendrimers containing 27, 81, and 243 modified xylopyranoside termini. *J. Org. Chem. 74*, 5071−5074.

(18) Yim, C.-B., Boerman, O. C., de Visser, M., de Jong, M., Dechesne, A. C., Rijkers, D. T. S., and Liskamp, R. M. J. (2009) Versatile conjugation of octreotide to dendrimers by cycloaddition ("Click") chemistry to yield high-affinity multivalent cyclic peptide dendrimers. *Bioconjugate Chem. 20*, 1323–1331.

(19) van Dijk, M., Rijkers, D. T. S., Liskamp, R. M. J., van Nostrum, C. F., and Hennink, W. E. (2009) Synthesis and applications of biomedical and pharmaceutical polymers via click chemistry methodologies. *Bioconjugate Chem. 20*, 2001–2016.

(20) Abbracchio, M. P., Burnstock, G., Boeynaems, J. M., Barnard, E. A., Boyer, J. L., Kennedy, C., Fumagalli, M., King, B. F., Gachet, C., Jacobson, K. A., and Weisman, G. A. (2006) International Union of Pharmacology. Update of the P2Y G protein-coupled nucleotide receptors: from molecular mechanisms and pathophysiology to therapy. *Pharmacol. Rev. 58*, 281–341.

(21) Tosh, D. K., Chinn, M., Yoo, L., Kang, D. W., Luecke, H., Gao, Z. G., and Jacobson, K. A. (2010) 2-Dialkynyl derivatives of (N)-methanocarba nucleosides: "Clickable" A_3 adenosine receptor-selective agonists. *Bioorg. Med. Chem. 18*, 508−517.

(22) Goddard-Borger, E. D., and Stick, R. V. (2007) An efficient, inexpensive, and shelf-stable diazotransfer reagent: Imidazole-1-sulfonyl azide hydrochloride. *Org. Lett. 9*, 3797–3800.

(23) Fricks, I., Maddiletti, S., Carter, R., Lazarowski, E. R., Nicholas, R. A., Jacobson, K. A., and Harden, T. K. (2008) UDP is a competitive antagonist at the human $P2Y_{14}$ receptor and a full agonist at the rat $P2Y_{14}$ receptor. *J. Pharm. Exp. Ther. 325*, 588–594.

(24) Harden, T. K., Scheer, A. G., and Smith, M. M. (1982) Differential modification of the interaction of cardiac muscarinic cholinergic and beta-adrenergic receptors with a guanine nucleotide binding component(s). *Mol. Pharmacol. 21*, 570–580.

(25) Bradford, M. M. (1976) A rapid and sensitive method for the quantitation of microgram quantities of protein utilizing the principle of protein-dye binding. *Anal. Biochem. 72*, 248–254.

(26) Nordstedt, C., and Fredholm, B. B. (1990) A modification of a protein binding method for rapid quantification of cAMP in cell-culture supernatants and body fluid. *Anal. Biochem. 189*, 231–234.

(27) Gao, Z. G., Ding, Y., and Jacobson, K. A. (2010) UDP-glucose acting at $P2Y_{14}$ receptors is a mediator of mast cell degranulation. *Biochem. Pharmacol. 79*, 873−879.

(28) Gomez, M. V., Guerra, J., Velders, A. H., and Crooks, R. M. (2009) NMR Characterization of fourth-generation PAMAM dendrimers in the presence and absence of palladium dendrimer-encapsulated nanoparticles. *J. Am. Chem. Soc. 131*, 341–350.

(29) Klotz, K. N., Lohse, M. J., Schwabe, U., Cristalli, G., Vittori, S., and Grifantini, M. (1989) 2-Chloro-*N*6-[^{3}H]cyclopentyladenosine ([^{3}H]CCPA)-a high affinity agonist radioligand for A_1 adenosine receptors. *Naunyn Schmiedebergs Arch. Pharmacol. 340*, 679–683.

(30) Jarvis, M. F., Schutz, R., Hutchison, A. J., Do, E., Sills, M. A., and Williams, M. (1989) [^{3}H]CGS 21680, an A_2 selective adenosine receptor agonist directly labels A_2 receptors in rat brain tissue. *J. Pharmacol. Exp. Ther. 251*, 888–893.

(31) Olah, M. E., Gallo-Rodriguez, C., Jacobson, K. A., and Stiles, G. L. (1994) 125I-4-Aminobenzyl-5′-N-methylcarboxamidoadenosine, a high affinity radioligand for the rat A_3 adenosine receptor. *Mol. Pharmacol. 45*, 978–982.

(32) Englert, M., Quitterer, U., and Klotz, K. N. (2002) Effector coupling of stably transfected human A_3 adenosine receptors in CHO cells. *Biochem. Pharmacol. 64*, 61–65.

(33) Jacobson, K. A., Park, K. S., Jiang, J.-l., Kim, Y. C., Olah, M. E., Stiles, G. L., and Ji, X. d. (1997) Pharmacological characterization of novel A_3 adenosine receptor-selective antagonists. *Neuropharmacology 36*, 1157–1165.

(34) Ko, H., Das, A., Carter, R. L., Fricks, I. P., Zhou, Y., Ivanov, A. A., Melman, A., Joshi, B. V., Kováč, P., Hajduch, J., Kirk, K. L., Harden, T. K., and Jacobson, K. A. (2009) Molecular recognition in the $P2Y_{14}$ receptor: Probing the structurally permissive terminal sugar moiety of uridine-5′-diphosphoglucose. *Bioorg. Med. Chem. 17*, 5298–5311.

(35) Jacobson, K. A. (2009) Functionalized congener approach to the design of ligands for G protein-coupled receptors (GPCRs). *Bioconjugate Chem. 20*, 1816–1835.

(36) Kojima, C., Kono, K., Maruyama, K., and Takagishi, T. (2000) Synthesis of polyamidoamine dendrimers having poly(ethyleneglycol) grafts and their ability to encapsulate anticancer drugs. *Bioconjugate Chem. 11*, 910–917.

(37) Ivanov, A. A., and Jacobson, K. A. (2008) Molecular modeling of a PAMAM-CGS21680 dendrimer bound to an A_{2A} adenosine receptor homodimer. *Bioorg. Med. Chem. Lett. 18*, 4312–4315.

(38) Portoghese, P. S., Ronsisvalle, G., Larson, D. L., Yim, C. B., Sayre, L. M., and Takemori, A. E. (1982) Opioid agonist and antagonist bivalent ligands as receptor probes. *Life Sci. 31*, 1283–1286.

(39) Morphy, R., and Rankovic, Z. (2005) Designed multiple ligands. An emerging drug discovery paradigm. *J. Med. Chem. 48*, 6523–6565.

(40) Han, Y., Moreira, I. S., Urizar, E., Weinstein, H., and Javitch, J. A. (2009) Allosteric communication between protomers of dopamine class A GPCR dimers modulates activation. *Nat. Chem. Biol. 5*, 688–695.

(41) Soriano, A., Ventura, R., Molero, A., Hoen, R., Casadó, V., Cortés, A., Fanelli, F., Albericio, F., Lluís, C., Franco, R., and Royo, M. (2009) Adenosine A_{2A} receptor-antagonist/dopamine D_2 receptor-agonist bivalent ligands as pharmacological tools to detect A_{2A}-D2 receptor heteromers. *J. Med. Chem. 52*, 5590–5602.

(42) Cairo, C. W., Jason, E., Gestwicki, J. E., Kanai, M., and Kiessling, L. L. (2002) Control of multivalent interactions by binding epitope density. *J. Am. Chem. Soc. 124*, 1615–1619.

BC900473V

Design and Application of Antibody Cysteine Variants

Vladimir Voynov,[†] Naresh Chennamsetty,[†] Veysel Kayser,[†] Hans-Joachim Wallny,[‡] Bernhard Helk,[‡] and Bernhardt L. Trout*,[†]

Massachusetts Institute of Technology, Chemical Engineering, Cambridge, Massachusetts, and Novartis Pharma AG, CH-4057, Basel, Switzerland. Received November 19, 2009; Revised Manuscript Received December 30, 2009

Antibodies are multidomain proteins that are extensively used as a research tool in molecular biology and as therapeutics in medicine. In many cases, antibodies are engineered to contain surface cysteines for the site-specific conjugation of payloads. These antibodies can serve as payload vehicles in targeting a diseased cell to which the conjugated molecules exercise their activity. Here, we design and analyze a set of fourteen new IgG1 cysteine variants, with at least one variant per immunoglobulin fold domain. The cross-linking propensity of these mutants correlates very well with a tool we have developed for measuring aggregation propensity in silico, called spatial aggregation propensity (SAP). Our results indicate the utility of the SAP technology in selecting antibody cysteine variants with desired properties. Moreover, the different oligomerization propensity of the variants suggests a variety of applications in molecular biology and medicine, such as payload delivery, structural analysis, electrophoresis, and chromatography.

INTRODUCTION

Monoclonal antibodies are of significant laboratory and therapeutic use. Antibody derivatives with engineered site-specific fluorescence or binding properties have been developed and used for many years. Antibodies have also been developed as therapeutic agents, currently the fastest growing class of pharmaceuticals (*1*). Antibodies are multidomain proteins of two light and two heavy chains held together by disulfide bonds. The variable regions specify binding to a particular antigen, and part of the constant region is responsible for effector functions via binding to Fc receptors on the surface of immune cells.

Engineering of antibody conjugates has further increased the versatility of antibody applications. In many laboratory techniques, enzymes or fluorescent probes are conjugated to antibodies to carry out an assay function, for example, quantification of antigen abundance. In targeted therapy, conjugation is used to generate new therapeutics with highly specific functions (*2*). For example, toxic small molecules are attached to antibodies that specifically bind biomarkers on diseased cells, and the targeted cells are destroyed by the toxic molecules (*3–6*). Various approaches to antibody conjugation have been pursued, for example, attachment to surface lysines (*7*), to Fc carbohydrates (*8*), or to partially reduced interchain disulfides (*9*).

Antibody conjugation to engineered surface cysteines remains a very attractive option because most antibodies do not have cysteines other than the ones involved in intra- and interchain disulfide bonds. Small molecules can be attached at the specific site of cysteine substitution via thiol-reactive chemistry with molecules such as maleimides (*10–16*). Engineering the C_H1 and C_H3 domains has been favored to avoid interference with antigen binding of the variable regions and effector function of C_H2. Different criteria for successful antibody conjugation via engineered cysteines have been considered. For example, the antibody domain in which to carry out mutations, the exposure of the mutated site, and the amino acid to be substituted are several of the aspects to take into account. A high-throughput screening approach to identifying sites suitable for cysteine engineering and conjugation has been developed (*17*). Yet, there is no universal tool for predicting whether an antibody cysteine variant will be stable and efficiently conjugated, and cysteine variants currently exist only for the C_L, C_H1, and C_H3 domains (*10, 11, 13, 14, 17*).

In this report, we present a new approach to design cysteine variants and the application of that approach to develop a new set of 14 human IgG1 cysteine variants, chosen so that there is at least 1 variant per immunoglobulin fold domain. Most of the variants are stable and efficiently conjugated. In several cases, we observe antibody oligomerization due to intermolecular disulfide bonding and cross-linking of the engineered cysteines. The extent of oligomerization is qualitatively and quantitatively expressed as cross-linking propensity (CLP). We also compare CLP of the variants to a recently developed spatial-aggregation propensity (SAP) parameter (*18–20*). SAP is a measure of the dynamic exposure of hydrophobic patches (see Experimental Procedures). SAP identifies protein aggregation prone regions, which were validated earlier by designing antibodies that were experimentally shown to be significantly more stable than the wild type (*19*). The analysis presented here demonstrates the utility of the SAP technology in designing antibody cysteine variants as well as the various applications of some of the new variants.

EXPERIMENTAL PROCEDURES

Design of Cysteine Variants. Variants 1−13 were designed based on the X-ray structure of antibody-1. Variant 15 was selected from the structure of another IgG1, antibody-2, built by homology modeling based on the structure of antibody-1 (*19*). Variant 14 has the same engineered cysteine as variant 15 but in a modified antibody-2 with mutations W100K and F101K in the heavy chain (*19*). All engineered cysteine sites were exposed on the antibody surface. Polar residues, such as serine, threonine, and asparagine, or charged residues, such as lysine, were substituted with cysteine.

Production of Cysteine Variants. DNA vectors encoding the light and heavy chains of proprietary human IgG1 antibodies

* To whom correspondence should be addressed. E-mail: trout@mit.edu.

[†] Massachusetts Institute of Technology.

[‡] Novartis Pharma AG.

10.1021/bc900509s © 2010 American Chemical Society
Published on Web 01/21/2010

1 and 2 were kindly provided by Dr. Burkhard Wilms from Novartis. The two antibodies have κ-variable light chains and H3 variable heavy chains and are indicated for the treatment of inflammatory and respiratory diseases. The light and heavy chain genes of each antibody were subcloned in vector gWIZ (Genlantis), engineered for protein expression by transient transfection of mammalian cells. Antibody variants were either de novo synthesized (GeneArt) or generated by in-house site-directed mutagenic PCR and confirmed by sequencing. Antibody wild types and variants were expressed by transient transfection of Freestyle HEK 293 cells (Invitrogen) and purified as previously described (*19*) and further specified here. Cell cultures were transfected with filter-sterilized DNA, purified on DNA Maxi Prep columns (Invitrogen) and with linear polyethyleneimine MW 25 000 (PEI) (Polysciences) as the transfection reagent. For each liter of culture, 1 mg of total DNA was incubated with 20 mL of OptiPro (Invitrogen), while 2 mL of 1 mg/mL solution of PEI was incubated with 20 mL of OptiPro. After 15 min incubation at room temperature, the PEI solution was added to the DNA solution, and after another 15 min incubation, the PEI-DNA-OptiPro mix was added to the cell culture. The transfected cell cultures were incubated at 37 °C and 5% carbon dioxide atmosphere. Supernatants were collected 7−10 days post-transfection by centrifugation and filtering through 0.2 μm filters. If transfections were at higher than 1 L volume, the filtered supernatants was concentrated by diafiltration with a 30 kDa molecular weight cutoff membrane before purification. Antibodies were purified on a protein A column (GE Healthcare), eluted with 50 mM citrate buffer, pH 3.5, buffer-exchanged in 50 mM Tris pH 7.0 buffer, and concentrated to 15−50 mg/mL with 30 kDa molecular weight cutoff filters. Typically, antibody-1 wild type was expressed with yield of 25 mg/L and antibody-2 wild type at 24 mg/L. In most cases, the cysteine variants were expressed at comparable levels, with a few exceptions where the mutation affects expression levels.

Thiol Reduction and Labeling. Different methods were attempted for the specific reduction of the engineered surface thiols before labeling. Tris, 2-carboxyethyl, phosphine hydrochloride (TCEP), and a stronger reducing agent, dithiothreitol (DTT), were two of the reagents used, and levels of free thiol were quantified using Ellman's reagent (Invitrogen). We found L-cysteine to work best in our site-specific labeling experiments, so the following two-step protocol was used. First, the variants were incubated with 100−200-fold excess of L-cysteine for 4 h at 37 °C, followed by buffer exchange into TE buffer, pH 7.2. Second, the samples were incubated with 5−10-fold molar excess of Alexa488 maleimide dye (Invitrogen) for 1 h at room temperature or with 10-fold excess of pyrene maleimide dye (Invitrogen) for 12 h at room temperature.

In certain cases, labeling conditions such as time of reaction and dye to protein ratio had to be optimized on an individual basis because not all engineered cysteines were equally amenable to conjugation. Free dye was removed by centrifuging the samples through Sephadex G25 (GE Healthcare) 2−3 times. Then, the labeled protein samples were buffer-exchanged in 50 mM phosphate buffer pH 7.0 and concentrated to 20−50 mg/mL on 30 kDa molecular weight cutoff spin filters. The efficiency of protein labeling was calculated as mole of dye per mole of protein according to manufacturer's protocols (Invitrogen). For carbohydrate labeling, the antibody variant sample was first treated with 10 mM sodium meta-periodate in 100 mM sodium acetate, pH 5.5, (Pierce) to oxidize the carbohydrates. Then, the antibody conjugation was carried out with Alexa350-hydrazide (Invitrogen) at 5−10-fold molar excess of dye at room temperature for 2 h. During labeling, exposure of the fluorophores to light was avoided as much as possible.

Protein Characterization. Antibody samples were analyzed by SDS-PAGE. Gels of 7.5%, 10%, and 12% were used for nonreducing analysis. Gels of 12% were used for reducing analysis of heated samples with DTT. We used a molecular weight marker "Precision Plus Protein Standards" from BioRad, containing proteins of 250, 150, 100, 75, 50, 37, 25, 20, 15, and 10 kDa. Usually, samples of 5−10 μg were loaded per lane. Fluorescent images were taken under UV light before staining with Coomassie Blue. Antibody digestion was carried out by GluC (1:20 wt enzyme per wt antibody, at 25 °C for 12−24 h) and Pronase (1:20 wt enzyme per wt antibody, at 37 °C for 1 h).

We also used size-exclusion high-performance liquid chromatography (SEC-HPLC) to determine monomer levels of labeled antibody variants. Samples were resolved on a TSKgel Super SW3000 column (TOSOH Bioscience), and percent monomer was calculated as the area of the monomeric peak divided by the total area of all peaks.

Reporter Gene Assay. The biological activity of antibody-1 wild type and variants 1−6 was measured in a reporter gene assay, using a genetically modified cell line. This cell line was derived from human embryonic kidney cell and was stably transfected with a reporter construct of a promoter (responsive to signaling via the soluble target that antibody-1 binds) fused upstream of the luciferase gene. In this cell line, exposure to the target stimulated the expression of luciferase in a dose-dependent manner. Addition of graded amounts of antibody-1 to a fixed, submaximal dose of target caused a decrease in the expression of luciferase during an incubation period of 5.5 up to 18 h. At the end of the incubation period, the amount of luciferase was quantified based on its enzymatic activity in the cell lysate. Luciferase catalyzed the conversion of the substrate luciferin to oxyluciferin, a chemiluminescent product. The resultant glow-type chemiluminescence was then determined with an appropriate luminometer. The biological potency of a test sample was determined by comparing its ability to inhibit the target-dependent induction of luciferase activity to that of antibody-1 wild type. The samples were normalized on the basis of protein content. Relative biological activity of the antibody-1 variants was then calculated using a parallel line assay according to European Pharmacopoeia.

SAP Values. Spatial aggregation propensity (SAP) of amino acids in a protein is a tool that was recently developed in our lab based on amino acid surface-accessible area (SAA) and hydrophobicity (*19*), and we already applied to the identification of aggregation prone motifs in IgG antibodies (*18*). The SAP values for radius $R = 5$ Å are calculated from the equation

$$(\mathrm{SAP})_{\mathrm{atom}i} = \sum_{\substack{\text{Simulation}\\ \text{Average}}} \left\{ \sum_{\substack{\text{Residues with at least}\\ \text{one side chain atom}\\ \text{within } R \text{ from atom } i}} \left(\frac{\substack{\text{SAA of side chain atoms}\\ \text{within radius } R}}{\substack{\text{SAA of side chain atoms}\\ \text{of fully exposed residue}}} \times \text{residue hydrophobicity} \right) \right\}$$

RESULTS

Design of a Set of 14 Antibody Variants for Site-Specific Conjugation. We designed a set of 14 IgG1 cysteine variants for site-specific conjugation. Mutations 1−13 were generated in antibody-1. Mutation 14 was generated in wild-type antibody-2 (resulting in variant 15), as well as a modified antibody-2 (resulting in variant 14), leading to a total of 15 variants

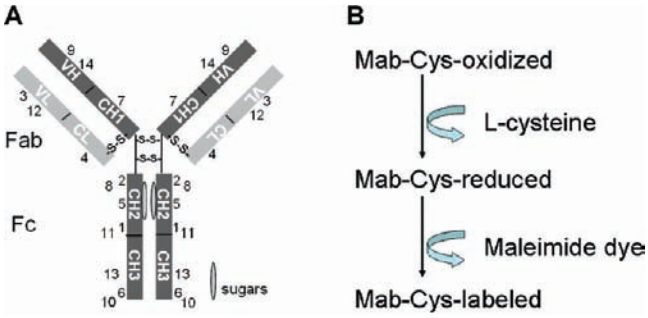


Figure 1. A set of human IgG1 cysteine variants. (A) Relative location of the amino acids substituted with cysteines in the antibody. (B) Outline of a two-step conjugation protocol of antibody cysteine variants.

presented in this report. The idea was to have a distribution of the variants along the antibody surface, with at least one variant per immunoglobulin fold domain (Figure 1A). We substituted polar (ser, thr, asn) or charged (lys) amino acids that are exposed on the antibody surface, so that substitution with the polar amino acid cysteine does not cause a significant change in surface charge distribution and structure of the protein. Different methods for conjugating the engineered surface cysteines were applied, and the one using free cysteine in the first, reducing step worked best for us (Figure 1B).

Certain Cysteine Variants Are More Amenable to Conjugation than Others. Following expression and purification of antibody variants, the engineered surface cysteines are mostly oxidized. For example, both variants 4 and 6 have less than 0.3 free thiol per antibody molecule as opposed to the anticipated 2.0 (1.0 per half antibody) for the antibodies with engineered surface cysteines. We compared the effect of a mild reducing agent, TCEP (Tris, 2-carboxyethyl, phosphine hydrochloride), and a stronger reducing agent, DTT (dithiothreitol), on two of the variants, variant 4 and variant 6. Initially, the non-oligomerizing variant 4 shows 0.13 free thiols per antibody, and the highly oligomerizing variant 6 has 0.25 free thiols per antibody. Aliquots of wild type, variant 4, and variant 6 were treated in four different conditions, 10- and 20-fold molar excess of TCEP, and 5- or 10-fold excess of DTT. After removal of the reducing agent, the samples were resolved on nonreducing PAGE (Supporting Information Figure 1A), and were quantified for free thiol (Supporting Information Figure 1B). A comparison of the results for wild type and variants indicates that the TCEP treatment is sufficient to reduce cysteines in nonoligomerized form (variant 4) with little effect on WT. However, cysteines from oligomers (variant 6) are reduced only after a harsher treatment. Treatment with DTT even at low levels leads to antibody fragmentation. Most non-oligomerizing variants like variant 4 were consequently labeled with ideal efficiency of 2.0; however, oligomerizing variants like variant 6 were underlabeled with efficiencies of 1.0−1.5. Thus, the sites where the surface cysteines are introduced have a profound effect on the ability to decap and conjugate the engineered cysteines.

Distinction of Five Classes of Antibody Cysteine Variants Based on CLP. All variants were expressed by transient transfection and were labeled with Alexa-488 maleimide and Alexa-532 maleimide. Labeled and unlabeled samples were resolved on nonreducing SDS-PAGE for quality control (Figure 2 and Supporting Information Figure 2). Nonreducing gels show monomers as well as the presence of dimers, trimers, and in some cases even higher oligomers. We distinguish five classes of variants. Class I comprises variants that are monomeric and remain stable after labeling (variants 3, 4, 7, 10, 12, 14). Variants of class II contain a small percent of dimers before and after labeling (variants 1, 2, 13). Class III variants have a more pronounced propensity to oligomerize including formation of some trimers (variants 5, 9). Class IV variants have an even higher propensity to oligomerize as evidenced by the presence of aggregates larger than trimer, especially after labeling (variant 6). Class V includes variants of high oligomerization propensity similar to variants of class III and IV with additional structural abnormalities such as fragmentation (variant 8), coloration of purified concentrated sample (variant 11), or extremely poor expression yield (variant 15).

The oligomerization propensity of variants 1−6 was compared on nonreducing SDS-PAGE for unlabeled (Figure 2A) as well as labeled (Figure 2C) samples. The CLP of variants 7−14 was analyzed in a similar fashion (Supporting Information Figure 2A). At least three molecular weight species of unlabeled variants 8 and 11 are resolved by gel filtration and electrophoresis (Figure 2E). The observed coloration in variant 11 most likely occurs because of binding of phenol red from the tissue culture media to erroneously exposed sites of the molecule, indicative of structural abnormalities of this variant. We also note that variant 14 is expressed at a level more than 100 times higher than that of variant 15 (Supporting Information Figure 2B, and Figure 4A). The mutation S7C on the heavy chain is very poorly tolerated in an antibody with a high-SAP patch in the V_H domain (variant 15) resulting in very low expression levels. In contrast, a variant with the same S7C mutation is expressed well when two amino acids in the high-SAP patch, W100 and F101, are substituted with lysines (variant 14). In addition to nonreducing SDS-PAGE, labeled variants were also analyzed by size-exclusion high-performance liquid chromatography (SEC-HPLC). Variants of class I and II are usually more than 95% but at least 80% monomeric, while variants of other classes are less than 70% monomeric, with the rest of the samples forming aggregates of various sizes (Supporting Information Figure 2C).

Engineered Variants Retain Antigen-Binding Activity and Are Specifically Labeled. Labeled and unlabeled variants 1−6 were analyzed for biological activity in a reporter gene bioassay. The variants retain activity within 80% and 130% of wild type, with loss of activity in the range 1−27% of the labeled variants in comparison to their unlabeled counterparts (Figure 2B). Variants 1−14 are labeled exclusively at the light or heavy chain that carries the engineered cysteine, as shown on reducing SDS-PAGE (Figure 2D, Supporting Information Figure 2A). The specificity of labeling is also demonstrated on the differential fluorescence band patterns of variants digested with Pronase and resolved on reducing SDS-PAGE (Supporting Information Figure 2D). Proteolytic treatment of the variants with Pronase yields different fluorescence patterns for most variants but similar patterns for variants with neighboring substitutions, such as variant 3 and 12. Thus, the analyzed engineered variants retain biological activity similar to wild type and are site-specifically labeled.

Correlation between CLP and SAP of the Engineered Variants Suggests a Rational Approach to the Design of Antibody Variants for Site-Specific Conjugation. To determine the correlation between the positions of the cysteine-substituted amino acids and their SAP values, we map the substituted amino acids on the SAP plots for the Fab and Fc parts of antibody-1 (Figure 3A and B). These plots were obtained as shown before (*19*). All substituted residues have neutral or negative SAP. Furthermore, we map the substituted amino acids on the three-dimensional structure of the antibody with SAP (Figure 3c). The overlaid CLP and SAP three-dimensional representation yields another level of information—proximity of the selected sites to hydrophobic patches (high SAP regions) indicated in red. Variants of class I CLP have SAP values between 0 and −0.07 and are not close to hydrophobic patches. Variants of class II are not close to

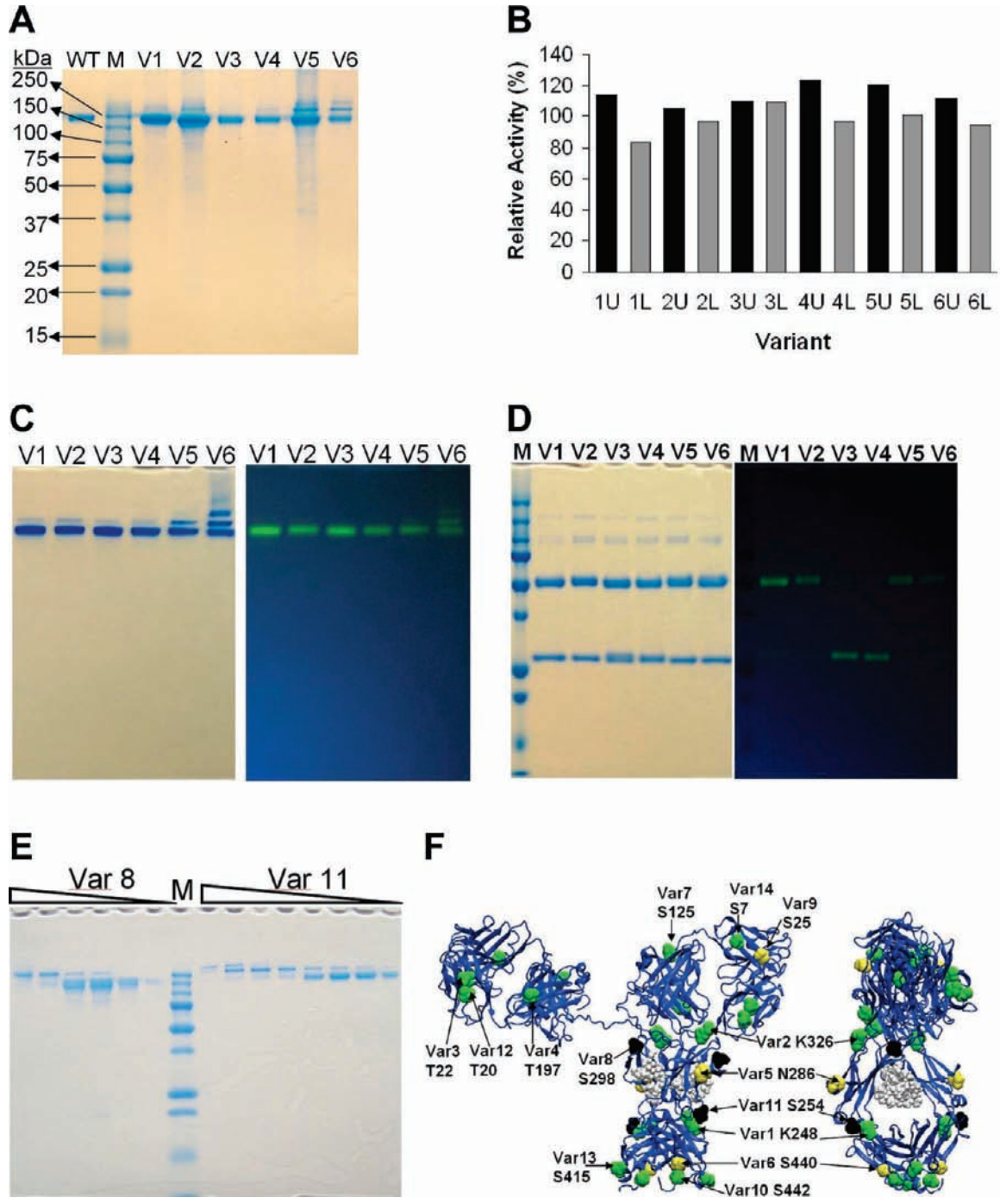


Figure 2. Quality control assessment of the engineered variants. (A) Nonreducing SDS-PAGE protein gel for variants 1−6 before labeling. M is the molecular weight marker (BioRad) used in this, as well as in all other protein gels shown. The molecular weight of each individual band in the ladder is shown in kDa. (B) Biological activity of unlabeled (U) and labeled (L) antibody variants, relative to antibody-1 wild type. (C) Nonreducing SDS-PAGE protein gel for variants 1−6 after labeling: image of the Coomassie stained gel and a fluorescence image of the same gel before staining. (D) Reducing SDS-PAGE protein gel for variants 1−6 after labeling: image of the Coomassie stained gel and a fluorescence image of the same gel before staining. For each antibody variant, the protein band at about 50 kDa corresponds to the antibody heavy chain, and the protein band at about 25 kDa corresponds to the antibody light chain. (E) Gel filtration fractions of variants 9 and 11. (F) Location of each engineered variant on the antibody three-dimensional structure. Green is CLP I and II, yellow is CLP III and IV, and black is CLP V. Variants 1−13 were generated in antibody-1. Variants 14 and 15 were generated in another antibody-2.

hydrophobic patches but have a more negative SAP value, from −0.12 to −0.23. Variants of class III have SAP like those of class I and II but are close (although not immediately adjacent) to hydrophobic sites. Variant 6 of class IV has an SAP value of −0.09 and is not adjacent to high-SAP patches. Yet, this variant is highly oligomerizing, presenting an exception to the SAP/CLP pattern. Variants of class V (variants 8 and 11) have cysteines engineered in immediate proximity to hydrophobic regions with high SAP. These variants show high CLP as well as additional structural abnormalities, regardless of the SAP value of the substituted amino acid. Thus, the comparison of CLP, SAP of the substituted amino acid, and presence or absence of nearby high SAP site (Figure 4A) yield several straightforward and useful criteria for selecting sites for introducing surface cysteines (Figure 4B).

In brief, the correlation between CLP and SAP values of the set of engineered IgG1 variants can be summarized as follows. Cysteine substitution of amino acids of partial exposure (SAP

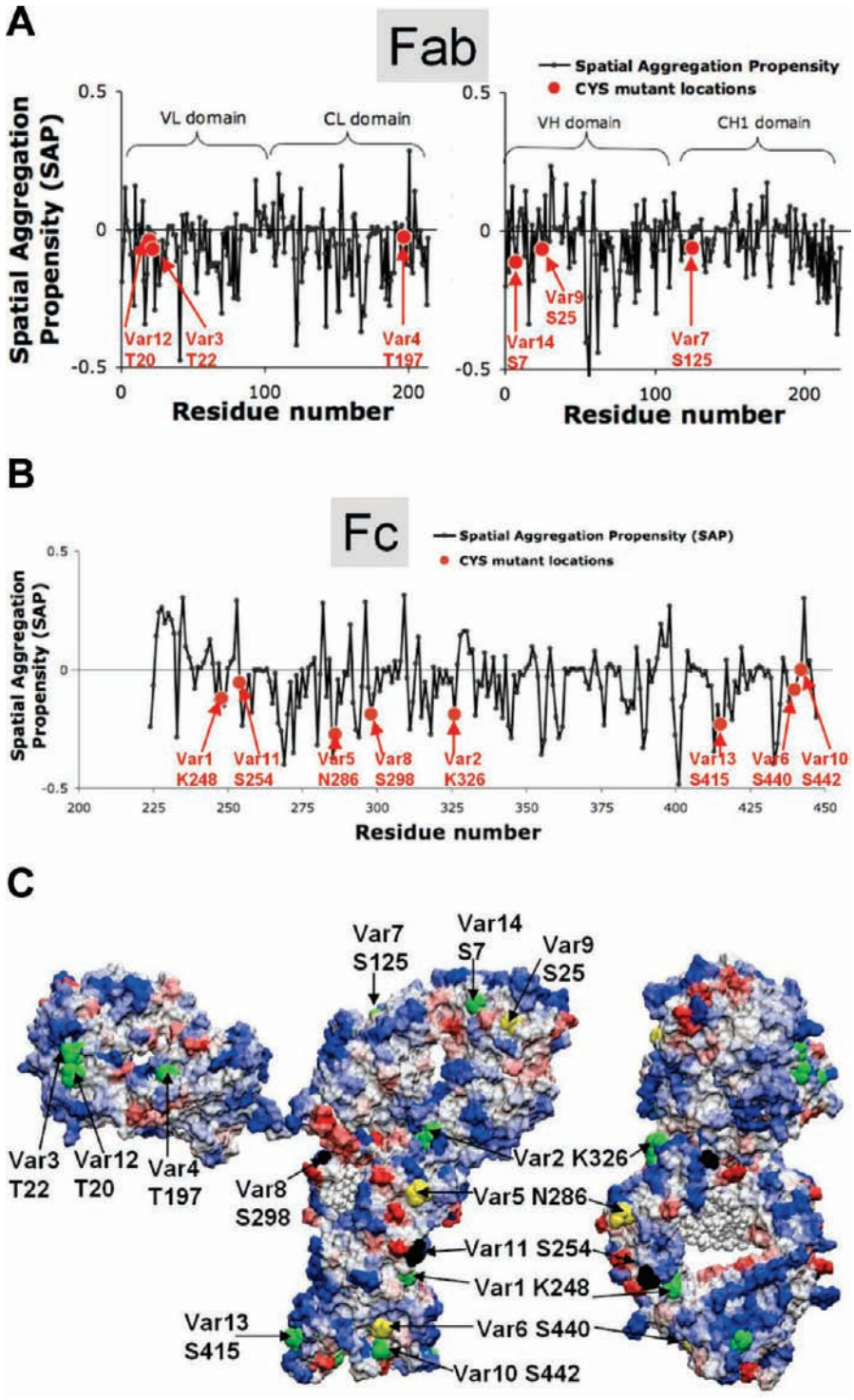


Figure 3. SAP values for the substituted amino acids in variants 1−14 in (A) Fab and (B) Fc. (C) Mutated amino acids on the antibody-1 structure in the SAP context. For comparison, S7 of variant 14 is shown in antibody-1, although it was produced and analyzed in antibody-2. Both front and side views of the antibody molecule are shown. Red is high-SAP, and blue is low-SAP. Green is CLP I and II, yellow is CLP III and IV, and black is CLP V.

from 0.00 to −0.11), and away from high-SAP patches, show low CLP. Cysteine substitutions of amino acids of higher exposure (SAP from −0.12 to −0.23) show some CLP even in the absence of nearby high-SAP patches. The presence of adjacent high-SAP patches leads to high CLP and other structural abnormalities regardless of the SAP value of the particular substituted amino acid.

Most variants were produced by transient transfection with yield between 11 and 37 mg/L with several exceptions (Figure 4A). Variants 9, 12, and 15 were expressed at lower levels. At the same time, variants even with high CLP, such as variants 6, 8, and 11, maintained high levels of expression. For comparison, antibody-1 wild type had an average yield of 25 mg/L, and antibody-2 of 24 mg/L, with our expression methods.

Site-Specifically Labeled Antibody Variants Are Used to Monitor Structural Dynamics of Antibody Domains. We were also interested in applications of the antibody cysteine variants presented here. Successful labeling already indicates potentially efficient conjugation of most variants. In search of additional applications, we noticed a specific emission pattern of one of the variants conjugated with the fluorophore pyrene maleimide. When two pyrene molecules are close together there

A

Var	Domain	Residue	Yield (mg/L)	CLP	SAP	Nearby High SAP
1	CH2	K 248	35	II	-0.12	N
2	CH2	K 326	20	II	-0.19	N
3	VL	T 22	14	I	-0.07	N
4	CL	T 197	19	I	-0.03	N
5	CH2	N 286	11	III	-0.27	~Y
6	CH3	S 440	15	IV	-0.09	N
7	CH1	S 125	26	I	-0.06	N
8	CH2	S 298	33	V	-0.19	Y
9	VH	S 25	8	III	-0.07	~Y
10	CH3	S 442	23	I	0.00	N
11	CH2	S 254	37	V	-0.06	Y
12	VL	T 20	6	I	-0.04	N
13	CH3	S 415	19	II	-0.23	N
14	VH	S 7	35	I	s.c.	N
15	VH	S 7	0.34	V	s.c.	Y

B

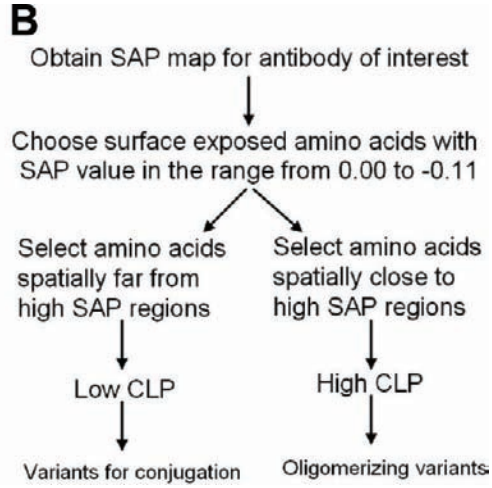


Figure 4. A rational approach to design antibody variants for site-specific conjugation. (A) Correlation between CLP and SAP for the 15 engineered cysteine variants. The domain that contains the mutation, the mutated amino acid, and the expression levels for each variant are shown. For comparison, antibody-1 and antibody-2 wild type were expressed at an average of 25 and 24 mg/L, respectively. Full green cell is CLP I, partial green cell is CLP II, yellow is CLP III and IV, and black is CLP V. Variants 1−13 are generated in antibody-1. Variants 14 and 15 are generated in another antibody-2, and thus, s.c. indicates separate case. Variant 14 is different from variant 15 by two surface amino acid substitutions, W100K and F101K, that is, W and F in variant 15 are replaced with lysines in variant 14. In the column "nearby high SAP", "N" denotes absence, "Y" indicates presence, and "~Y" denotes presence of a less pronounced high-SAP patch. (B) Application of the SAP technology to select surface amino acids for substitution to cysteines that would result in variants with low or high cross-linking propensity.

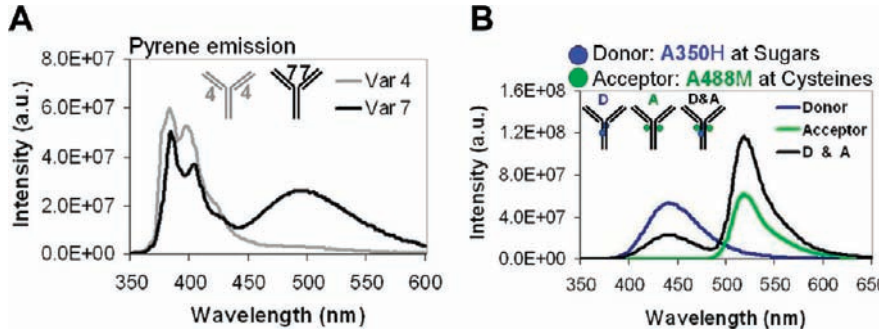


Figure 5. Use of labeled cysteine variants in montoring domain structural dynamics. (A) Fluorescence emission spectra of pyrene-labeled antibody variants 4 and 7. (B) Emission spectra of variant 2 labeled at the carbohydrates, at the engineered cysteines, or at both the carbohydrates and the cysteines.

is a characteristic increase of emission at 465 nm known as excimer fluorescence. We labeled variants 4 and 7 with pyrene maleimide and monitored emission spectra. While variant 4 shows no emission at 465 nm, variant 7 shows strong excimer fluorescence (Figure 5A). Considering the position of the engineered cysteine in C_H1 for variant 7, on the inner side of the Fab domains, the observed result correlates with the known scissoring effect of the Fab's with respect to Fc. Thus, the variant can be used in the analysis of antibody domain dynamics, for example, in examining antibody pluripotence with respect to antigen targets.

As another example of applications to structural dynamics, cysteine variants can be double-labeled, once at the engineered cysteines via maleimide chemistry and once at the carbohydrates via hydrazide chemistry. The engineered cysteines of variant 2 are in Fc and are proximal to the carbohydrate moiety. We observe a significant fluorescence energy transfer between donor and acceptor of double-labeled variant 2 (Figure 5B). Similar fluorescence analysis among different variants and at different conditions permits analysis of protein−carbohydrate interactions (*21*).

An Antibody Variant with High CLP Is a Useful Molecular Weight Control. The strong oligomerization propensity of variant 6 suggested another utility of IgG1 cysteine variants and was explored in greater detail. Labeled variant 6 was subjected to gel filtration chromatography in order to separate monomer from oligomers, and protein-containing fractions were resolved on a 7.5% nonreducing SDS-PAGE, shown after (Figure 6A) and before (Figure 6B) staining with Coomassie Blue. The gel filtration analysis on variant 6 indicates a competition between utilization of the engineered surface cysteines in labeling and in cross-linking: the higher the MW of the species (more cysteines consumed in cross-linking), the lower the labeling efficiency (fewer cysteines available for labeling) (Figure 6B). The highest MW species (five asterisks) has a labeling efficiency of 0.5, while the monomeric species (one asterisk) has a labeling efficiency of 1.0, with the original labeled sample of labeling efficiency 0.8. An antibody variant with multiple oligomers, variant 6, thus presents a suitable standard for high molecular weight proteins, with the additional functionality that it can be site-specifically labeled. Unlike commercially available markers of mixture of proteins, this standard consists of only one protein that can be expressed at very high yield and can be efficiently purified. Moreover, the currently available high molecular weight markers for denaturing gels do not exceed 250 kDa, while variant 6 covers the broad range from 150 kDa (monomer) up to 750 kDa (pentamer).

DISCUSSION

Although the cysteine engineering of proteins and more specifically antibodies has been practiced for many years (*10, 11, 14, 16*), it is still difficult to predict whether an antibody cysteine variant

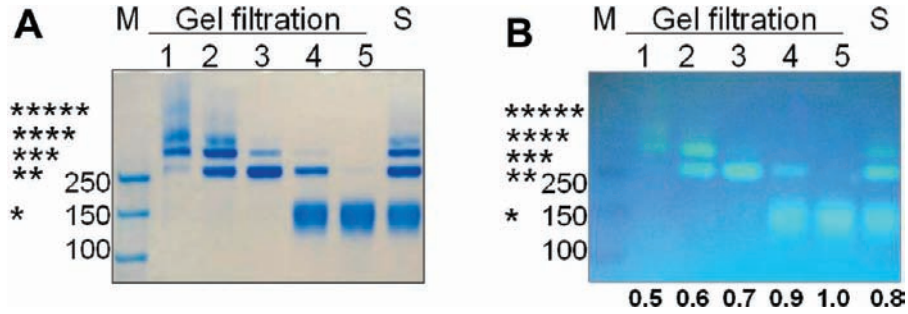


Figure 6. Variant 6 contains at least five species. (A) Gel filtration of Alexa-488 labeled variant 6 species performed on Superdex 200. Aliquots of each protein-containing fraction were analyzed on a 7.5% PAGE under nonreducing conditions. M is molecular weight markers, in kDa, and S is the original labeled sample. The gel is shown after Coomassie staining. Antibody variant 6 monomer (one asterisk) and at least four higher molecular weight species (two, three, four, and five asterisks) are resolved. (B) Fluorescence image of the same protein gel before Coomassie staining. The numbers below the fluorescent image indicate labeling efficiency for each fraction.

will have the desired properties and serve the intended purposes. Two of the most common problems associated with antibody cysteine variants are oligomerization and specificity of labeling. To date, antibody cysteine variants in C_L, C_H1, and C_H3 have been designed (*10, 11, 13, 14, 17*).

We have designed a set of human IgG1 cysteine variants that are broadly distributed on the antibody molecule with at least one variant per immunoglobulin fold domain. Most of these variants are stable and can be conjugated efficiently and specifically without significant loss of biological activity. Thus, the stable antibody variants (for example, variants 1, 3, 4, and 7) add to the repertoire of variants for site-specific conjugation of payload molecules. Engineered surface cysteines on antibodies provide functionality for conjugation of small molecules, for example, cytotoxins. The therapeutic benefit of such immunoconjugates is that, when an antibody to a cell surface antigen binds its target, the toxin or other small molecule is specifically delivered to diseased cells that express that antigen. As another application, if fluorophores are attached to the engineered cysteines, the dynamics of particular domains can be analyzed. Here, we used antibody-1 and antibody-2 as model antibodies. While the mutations in the variable regions of these two antibodies may not apply to antibodies of other allotypes, we expect that our observations on variants with mutations in the constant regions apply to most human IgG1 antibodies.

The observed deviations in biological activity in variants 1−6 compared to wild type may result from variations in post-translational modifications during expression or other minor structural changes. The consistent loss of some activity upon labeling probably reflects structural changes such as partial unfolding or oligomerization in the multiple steps of chemical and mechanical stress during labeling.

Variants 6, 8, and 11 show good expression levels in comparison to wild type even though these variants have high CLP. This suggests that the observed aggregation is a result of specific cross-linking via the surface cysteines and not of a general misfolding and aggregation problem. In contrast, the lower expression levels of variants 9, 12, and 15 in comparison to the corresponding wild-type antibodies suggests that the introduced mutations lead to some folding or secretion problem.

In summary, comparison of the cross-linking propensity of the variants with the SAP values of the substituted sites and the spatial regions around those sites yields a straightforward approach for selecting sites for cysteine substitution and site-specific conjugation. First, less exposed residues (SAP from 0.00 to −0.11) are less likely to lead to oligomerization than more exposed residues (SAP from −0.12 and lower). Second, our results suggest that nearby or immediately adjacent hydrophobic sites exacerbate the cross-linking propensity even of sites with ideal SAP values. Hydrophobic patches are likely to interact and bring adjacent molecules together, thus facilitating intermolecular cross-linking via disulfide bonding of nearby surface cysteines.

The boundaries of the suggested optimal range of 0.00 to −0.11 arise from several criteria developed on the basis of our results. In this report, we considered substitution of polar or charged amino acids with cysteines as opposed to hydrophobic amino acids to avoid significant changes in surface charge; thus, the negative half of the SAP spectrum is represented. The −0.11 limit for variants with low CLP is based on the result for K248 of variant 1. That site has an SAP of −0.12. An exception to the SAP criteria and CLP observations is variant 6, possibly because of fluctuations and exposure at the tip of the C_H3 domain. Our SAP results indicate a higher exposure for S440 (variant 6, SAP = −0.09) than for S442 (variant 10, SAP = 0.00) consistent with the observed lower CLP of variant 10.

CONCLUSION

We propose the implementation of the SAP technology in designing antibody, and by extension any protein, variants for site-specific conjugation. In order to select variants, the following steps should be made: (1) an SAP map for a protein of interest is obtained as previously described (*19*); (2) sites with SAP values between 0.00 and −0.11 are selected; (3) the vicinity of the selected sites are inspected for the presence of high-SAP regions; (4) if such regions are absent, the selected sites are chosen for modification to cysteines. These variants are expected to have low CLP and no structural abnormalities, and thus be suitable for efficient site-specific conjugation. The results presented here demonstrate the better utility of the SAP technology to existing methods in the rational design of protein variants for site-specific conjugation, as well as possible applications of the new variants.

ACKNOWLEDGMENT

We thank a number of colleagues at Novartis: Dr. Burkhard Wilms provided the DNA vectors encoding for the wild-type antibodies, Dr. Holger Heine provided training and advice on transient transfection and antibody purification, Dr. Michael Vetsch suggested using L-cysteine to reduce protein surface cysteines before labeling. We thank Prof. Wittrup from MIT and his students for discussions and for sharing lab equipment. We also thank Dr. Rajaraman Krishnan from MIT/Whitehead Institute for a discussion and suggestions on pyrene labeling, and Anna Levina for technical assistance. This work was supported by Novartis Pharma AG.

Supporting Information Available: Two supplementary figures on cysteine variant reduction with TCEP and DTT,

specificity of labeling by SDS-PAGE, and determination of monomer levels by SEC-HPLC. This material is available free of charge via the Internet at http://pubs.acs.org/.

LITERATURE CITED

(1) Carter, P. J. (2006) Potent antibody therapeutics by design. *Nat. Rev. 6*, 343–57.

(2) Meares, C. F. (2008) The chemistry of irreversible capture. *Adv. Drug. Delivery Rev. 60*, 1383–8.

(3) Wu, A. M., and Senter, P. D. (2005) Arming antibodies: prospects and challenges for immunoconjugates. *Nat. Biotechnol. 23*, 1137–46.

(4) Polakis, P. (2005) Arming antibodies for cancer therapy. *Curr. Opin. Pharmacol. 5*, 382–7.

(5) Kaminski, M. S., Zasadny, K. R., Francis, I. R., Milik, A. W., Ross, C. W., Moon, S. D., Crawford, S. M., Burgess, J. M., Petry, N. A., Butchko, G. M., Glenn, S. D., and Wahl, R. L. (1993) Radioimmunotherapy of B-cell lymphoma with [131I]anti-B1 (anti-CD20) antibody. *N. Engl. J. Med. 329*, 459–65.

(6) King, D. J., Antoniw, P., Owens, R. J., Adair, J. R., Haines, A. M., Farnsworth, A. P., Finney, H., Lawson, A. D., Lyons, A., Baker, T. S., Baldock, D., Mackintosh, J., Gofton, C., Yarranton, G. T., McWilliams, W., Shochat, D., Leichner, P. K., Welt, S., Old, L. J., and Mountain, A. (1995) Preparation and preclinical evaluation of humanised A33 immunoconjugates for radioimmunotherapy. *Br. J. Cancer 72*, 1364–72.

(7) Khaw, B. A., Fallon, F. T., Strauss, H. W., and Haber, E. (1980) Myocardial infarct imaging of antibodies to canine cardiac myosin with indium-111-diethylenetriamine pentaacetic acid. *Science 209*, 295–7.

(8) Rodwell, J. D., Alvarez, V. L., Lee, C., Lopes, A. D., Goers, J. W., King, H. D., Powsner, H. J., and McKearn, T. J. (1986) Site-specific covalent modification of monoclonal antibodies: in vitro and in vivo evaluations. *Proc. Natl. Acad. Sci. U.S.A. 83*, 2632–6.

(9) Sun, M. M., Beam, K. S., Cerveny, C. G., Hamblett, K. J., Blackmore, R. S., Torgov, M. Y., Handley, F. G., Ihle, N. C., Senter, P. D., and Alley, S. C. (2005) Reduction-alkylation strategies for the modification of specific monoclonal antibody disulfides. *Bioconjugate Chem. 16*, 1282–90.

(10) Junutula, J. R., Raab, H., Clark, S., Bhakta, S., Leipold, D. D., Weir, S., Chen, Y., Simpson, M., Tsai, S. P., Dennis, M. S., Lu, Y., Meng, Y. G., Ng, C., Yang, J., Lee, C. C., Duenas, E., Gorrell, J., Katta, V., Kim, A., McDorman, K., Flagella, K., Venook, R., Ross, S., Spencer, S. D., Lee Wong, W., Lowman, H. B., Vandlen, R., Sliwkowski, M. X., Scheller, R. H., Polakis, P., and Mallet, W. (2008) Site-specific conjugation of a cytotoxic drug to an antibody improves the therapeutic index. *Nat. Biotechnol. 26*, 925–32.

(11) Lyons, A., King, D. J., Owens, R. J., Yarranton, G. T., Millican, A., Whittle, N. R., and Adair, J. R. (1990) Site-specific attachment to recombinant antibodies via introduced surface cysteine residues. *Protein Eng. 3*, 703–8.

(12) Shopes, B. (1992) A genetically engineered human IgG mutant with enhanced cytolytic activity. *J. Immunol. 148*, 2918–22.

(13) Shopes, B. (1993) A genetically engineered human IgG with limited flexibility fully initiates cytolysis via complement. *Mol. Immunol. 30*, 603–9.

(14) Stimmel, J. B., Merrill, B. M., Kuyper, L. F., Moxham, C. P., Hutchins, J. T., Fling, M. E., and Kull, F. C., Jr. (2000) Site-specific conjugation on serine right-arrow cysteine variant monoclonal antibodies. *J. Biol. Chem. 275*, 30445–50.

(15) Zheng, Y., Shopes, B., Holowka, D., and Baird, B. (1991) Conformations of IgE bound to its receptor Fc epsilon RI and in solution. *Biochemistry 30*, 9125–32.

(16) Zheng, Y., Shopes, B., Holowka, D., and Baird, B. (1992) Dynamic conformations compared for IgE and IgG1 in solution and bound to receptors. *Biochemistry 31*, 7446–56.

(17) Junutula, J. R., Bhakta, S., Raab, H., Ervin, K. E., Eigenbrot, C., Vandlen, R., Scheller, R. H., and Lowman, H. B. (2008) Rapid identification of reactive cysteine residues for site-specific labeling of antibody-Fabs. *J. Immunol. Methods 332*, 41–52.

(18) Chennamsetty, N., Helk, B., Voynov, V., Kayser, V., and Trout, B. L. (2009) Aggregation prone motifs in IgG antibodies. *J. Mol. Biol. 391*, 404–13.

(19) Chennamsetty, N., Voynov, V., Kayser, V., Helk, B., and Trout, B. L. (2009) Design of therapeutic proteins with enhanced stability. *Proc. Natl. Acad. Sci. U.S.A. 106*, 11937–42.

(20) Chennamsetty, N., Voynov, V., Kayser, V., Helk, B., and Trout, B. L. (2010) The Prediction of Aggregation Prone Regions of Therapeutic Proteins. Submitted.

(21) Voynov, V., Chennamsetty, N., Kayser, V., Helk, B., Forrer, K., Zhang, H., Fritsch, C., Heine, H., and Trout, B. L. (2009) Dynamic fluctuations of protein-carbohydrate interactions promote protein aggregation. *PLoS One 4*, e8425.

BC900509S

Detection of HIV-1 Specific Monoclonal Antibodies Using Enhancement of Dye-Labeled Antigenic Peptides

Kim E. Sapsford,[†] Juan B. Blanco-Canosa,[‡] Philip E. Dawson,[‡] and Igor L. Medintz*[,§]

Division of Biology, Office of Science and Engineering Laboratories, FDA, Silver Spring, Maryland 20993, Departments of Cell Biology and Chemistry and the Skaggs Institute for Chemical Biology, The Scripps Research Institute, La Jolla, California 92037, and Center for Bio/Molecular Science and Engineering, Code 6900, U.S. Naval Research Laboratory, Washington, DC 20375. Received August 19, 2009; Revised Manuscript Received December 3, 2009

A simple bifunctional colorimetric/fluorescent sensing assay is demonstrated for the detection of HIV-1 specific antibodies. This assay makes use of a short peptide sequence coupled to an environmentally sensitive dye that absorbs and emits in the visible portion of the spectrum. The core peptide sequence is derived from the highly antigenic six-residue epitope of the HIV-1 p17 protein and is situated adjacent to a terminal cysteine residue which enables site-specific fluorescent labeling with Cy3 cyanine dye. Interaction of the Cy3-labeled p17 peptide with monoclonal anti-p17 antibody resulted in an up to 4-fold increase in dye absorption and greater than 5-fold increase in fluorescent emission, yielding a limit of detection as low as 73 pM for the target antibody. This initial study demonstrates both proof-of-concept for this approach and suggests that the resulting sensor could potentially be used as a rapid screening method for HIV-1 infection while requiring minimal equipment and reagents. The potential for utilizing this assay in simple field-portable point-of-care and diagnostic devices is discussed.

INTRODUCTION

Halting the spread of human immunodeficiency virus or HIV (along with many other virulent diseases) is a continuing international health priority. In developing countries where healthcare funding, facilities, and treatment are limited, this is of particular concern as infection rates continue to grow. Reducing infection and providing adequate treatment in the third world will be predicated on the development of rapid diagnostics for HIV screening that are sensitive, cheap, robust, and simple to use, have long-term stability, and require minimal equipment and limited-to-no sample preparation. In the most simplistic terms, these diagnostics must be suitable for use in extreme resource-limited environments (UAIDS/WHO report (2007) AIDS epidemic update http://data.unaids.org/pub/EPISlides/2007/2007_epiupdate_en.pdf). Simultaneous developments in two related technologies will help achieve this goal, namely, simple point-of-care (POC) devices combined with robust diagnostic assays. The last two decades have seen tremendous progress in microfabricated POC devices to the point where transition to the field and deployment around the world is now a growing reality (WHO report (2004) Performance evaluations of HIV test kits http://www.who.int/diagnostics_laboratory/publications/evaluations/en/index.html) (*1*−*4*). Although PCR-based detection of conserved HIV-1 DNA sequences has been proposed (*1, 5*), testing for the presence of serological antibodies against HIV is still among the most common initial screening techniques (*1*). These tests often target the viral envelope glycoprotein antigens from HIV type 1 or type 2 (HIV-1, HIV-2), while others screen for the presence of core viral antigen proteins (*1*). Among the latter, the HIV-1 p17 protein has been found to play an active role in viral infection, and antibodies reactivity to a number of the gag-proteins including p17 have also been shown to significantly decrease at the later stages of infection (*6*−*9*). According to a recent UNAIDS/WHO report, 33 million people (∼0.5% of the world population) are living with HIV with the majority of cases being directly attributable to infection with the HIV-1 strain. This establishes the p17 protein as a prime target antigen for HIV detection that can also be more specifically reflective of the initial stages of HIV-1 infection (*5*).

Immunoassay-based techniques such as Western blotting and enzyme-linked immunosorbent assays (ELISAs) are considered the gold standard for the detection of p17 exposure. Various other methods have also been developed that utilize surface-immobilized p17 protein as a capture reagent for detection of HIV-1 p17 specific antibodies (*10, 11*). However, all techniques including PCR commonly require the use of dedicated laboratory equipment for analysis as compared to control samples and standards. Furthermore, the use of the full p17 protein as a capture reagent can be problematic from a field-portable perspective in that functionalized surfaces need to be prepared and will require storage in a buffered environment and/or refrigeration. Clearly, simple and robust immunoassays for HIV detection that can function in complement with POC devices are still needed.

Plaxco's group have been developing peptide-based beacons, which function in a manner somewhat analogous to DNA molecular beacons, and initial attempts to utilize them for detecting HIV-1 specific p17 antibodies have yielded rather promising results (*12, 13*). In their approach, a short peptide sequence comprising a highly antigenic six-residue epitope of the HIV-1 p17 protein was labeled with both a long-lived ruthenium(II) bisbipyridine−phenanthroline fluorophore exhibiting a ∼800 ns lifetime at one terminus and the electron-accepting contact-quencher methyl viologen at the other terminus. Significant quenching of the fluorophore was observed in the unstructured polypeptide while in solution until addition and subsequent binding of the target, anti-p17 antibody forced the peptide into a rigid extended conformation, separating the fluorophore and quencher and generating a 6-fold increase in fluorophore emission (*13*). The resulting optical biosensor

* Corresponding author. Igor.Medintz@nrl.navy.mil.
[†] FDA.
[‡] The Scripps Research Institute.
[§] U.S. Naval Research Laboratory.

10.1021/bc9003712 © 2010 American Chemical Society
Published on Web 01/08/2010

demonstrated a limit of detection (LOD) for p17 HIV-1 antibody of 250 pM and was functional in both serum and saliva samples. Although a sensing configuration utilizing this particular fluorophore combination may not yet be directly transferrable to the simplest field-portable devices, it does highlight several inherent advantages. The use of an extremely short peptidyl sequence as opposed to the full p17-protein is preferred, as it can be readily dried down and stored lyophilized for long periods of time prior to reconstitution in an assay. Additionally, monitoring of antibody binding to labeled peptide simplifies the overall assay procedure significantly. Here, we combine a p17 HIV-1 antibody-specific short peptide sequence with a fluorescent Cy3 dye to create a simplified sensor specific for anti-p17 antibodies that is equally functional in both colorimetric and fluorescent assays. This proof-of-concept study demonstrates a significantly lower LOD than previously described sensors and highlights the simplicity of this approach for generalized screening purposes.

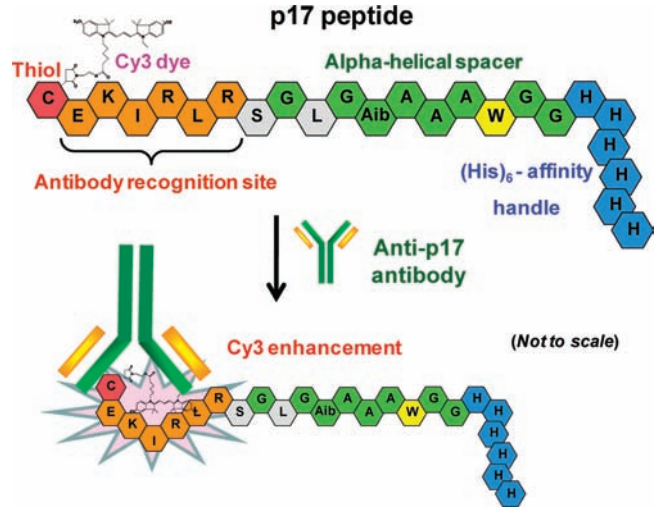
EXPERIMENTAL SECTION

Materials. All chemicals were reagent grade and used as received from the manufacturer. Phosphate buffered saline (10 mM phosphate, 137 mM NaCl, 2.7 mM KCl, pH 7.4, PBS), *N*-[2-hydroxyethyl]piperazine-*N*′[2-ethane sulfonic acid] (HEPES), bovine serum albumin (BSA), imidazole, dimethyl sulfoxide (DMSO), HPLC-grade acetonitrile and Corning 96-well white polystyrene nonbinding surface (NBS) microtiter plates were obtained from Sigma-Aldrich. Chicken immunoglobulin G protein (IgG) was obtained from Jackson ImmunoResearch Laboratories Inc. (West Grove, PA). Murine monoclonal antibody specific for HIV-1 p17 protein (α-p17, Clone 32/1.24.89 IgG1 isotype that reacts to p17 residues 17−22 EKIRLR) was purchased from Zeptometrix Corporation (Buffalo, NY). Cy3-maleimide monoreactive dye (λ_{max} absorption 550 nm, λ_{max} emission 570 nm,) was purchased from GE Healthcare (Piscataway, NJ). Nickel-nitroloacetic acid (Ni-NTA) agarose media was purchased from Qiagen (Valencia, CA). Oligonucleotide purification cartridges (OPC) and triethylamine acetate buffer (TEAA) were obtained from Applied Biosystems (Foster City, CA).

Peptide Synthesis. The antigenic peptide recognized by the monoclonal α-p17 antibody (p17-peptide) was prepared using standard *in situ* neutralization cycles for Boc-solid-phase-peptide synthesis (Boc-SPPS) as described (*14, 15*) and consisted of the sequence CEKIRLRSGLGAibAAAWGGHHHHHH-NH_2 (M_w of 2652, Aib is the non-natural amino acid α-aminoisobutyric acid, and NH_2 is an amide group blocking the C-terminal carboxyl in this sequence). Following synthesis and deprotection, the peptide was purified and isolated by HPLC and both the purity (>99%) and the sequence confirmed by mass-spectral analysis (see Supporting Information for data). The modular design of this peptide (*16*), as highlighted by the different colors in Scheme 1, includes a unique N-terminal cysteine allowing site-specific dye-labeling, the six-residue EKIRLR antigenic epitope recognized by the α-p17, an AibAAA α-helical spacer which is disrupted by flanking G residues, W allowing UV absorption monitoring if needed, and a C-terminal hexahistidine sequence $(His)_6$ which provides an affinity handle for purification via metal-affinity chromatography.

Fluorescent Dye Labeling of p17-Peptide. The peptide was labeled and purified in a manner similar to the method described in detail in ref *17*. Briefly, ∼1 mg of the purified p17-peptide was dissolved in 1 mL 10× PBS pH 7.4 and combined with a large excess of Cy3-maleimide monoreactive dye to ensure complete labeling. The reaction mixture was incubated overnight at 4 °C, and unreacted Cy3 dye was removed using three consecutive 0.5 mL Ni-NTA-agarose columns. The reaction mixture was loaded onto Ni-NTA-agarose media as the C-terminal $(His)_6$ sequence provides a specific affinity handle for this type of purification. Bound peptide was then washed with 10 mL 1× PBS to remove unreacted free dye, and the Cy3-labeled p17-peptide (abbreviated as Cy3-p17-peptide) was eluted using 300 mM imidazole in 1× PBS. A reverse-phase media containing OPC was then used to remove the imidazole and desalt the Cy3-p17-peptide. The OPC cartridge was first equilibrated with 3 mL acetonitrile followed by 3 mL 2 M TEAA before the Cy3-p17-peptide was loaded in. The cartridge was then washed with 50 mL 0.02 M TEAA before the Cy3-p17-peptide was eluted with ∼1 mL 70% acetonitrile in H_2O. The OPC media were regenerated for further rounds of Cy3-p17-peptide purification, as needed, by washing with 3 mL acetonitrile followed by 3 mL 2 M TEAA until the original Ni-NTA-imidazole elutant became clear. Desalted Cy3-p17-peptide was quantitated using UV−vis spectroscopy by measuring the Cy3 absorption (150,000 M^{-1} cm^{-1} at 550 nm) before being aliquoted, dried down, and stored at −20 °C in a desiccator until required.

Scheme 1. Cy3-p17-Peptide Interactions with Monoclonal α-p17 Antibody[a]



[a] (Not to scale). The peptide contains several functional modules including a $(His)_6$ affinity sequence for purification over Ni-NTA media (blue), an Aib-alanine containing helical spacer sequence that is disrupted by flanking glycine residues (green), the antibody recognition element (orange), and a unique terminal cysteine (red) for site-specific fluorophore labeling. α-p17 antibody binding to the Cy3-p17-peptide alters the peptide structure and/or dye environment significantly enhancing both dye absorption and emission and thus transducing signal.

Assays Monitoring Binding of Anti-p17 Antibody to Cy3-p17-Peptide. Interactions of Cy3-p17-peptide with murine α-p17 antibody were monitored by exposing increasing concentrations of antibody to dye-labeled peptide dissolved in buffer. Cy3-p17-peptide was resuspended by first dissolving in DMSO (∼5% of the final volume) followed by 20 mM HEPES buffer pH 8.0. Samples consisted of either 300 or 600 nM (30 or 60 pmol/well in 100 uL final volume) Cy3-p17-peptide exposed to increasing concentrations of the α-p17, control chicken IgG, or BSA ranging from 0 to 10 nM in HEPES buffer. These concentrations were chosen by initially testing the peptide against the antibody for optimal concentrations that allowed sensitive fluorescent and absorption detection prior to the assay (data not shown). The solutions were incubated for 1 h at room temperature before being transferred to 96-well microtiter plates and fluorescence measurements (spectra and intensities) were measured using 530 nm excitation on a Tecan Safire Dual Monochromator Multifunctional Plate Reader (Tecan, Research Triangle Park, NC). Intensities were an average of 9 readings

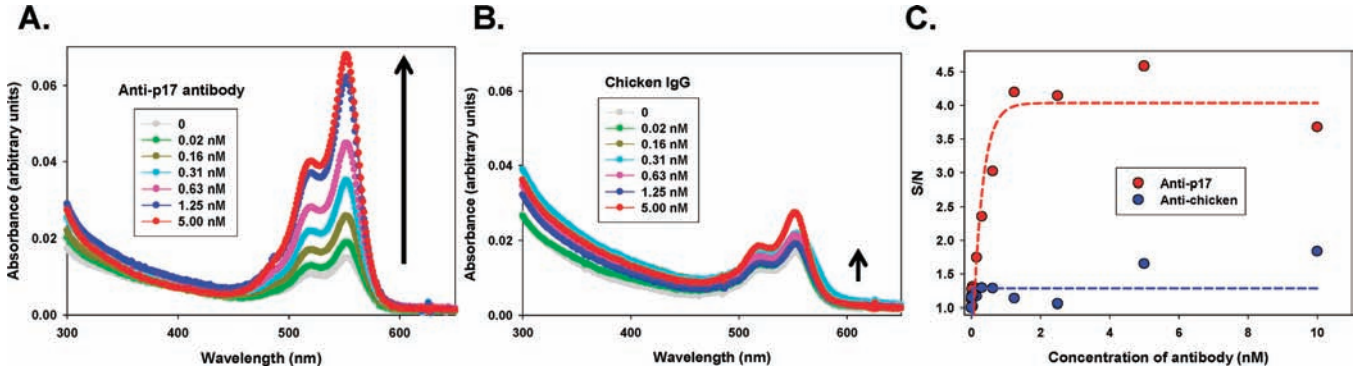


Figure 1. UV−vis absorbance data. Data from a representative experiment that monitored changes in the absorbance spectra of Cy3-p17-peptide (600 nM) exposed to (A) the indicated increasing concentrations of α-p17 antibody or (B) nonspecific control chicken IgG protein. (C) Summary of the corresponding signal-over-noise (S/N) ratio monitored at the Cy3 absorbance maxima (555 nm) versus antibody concentration for both the α-p17 antibody and control chicken IgG.

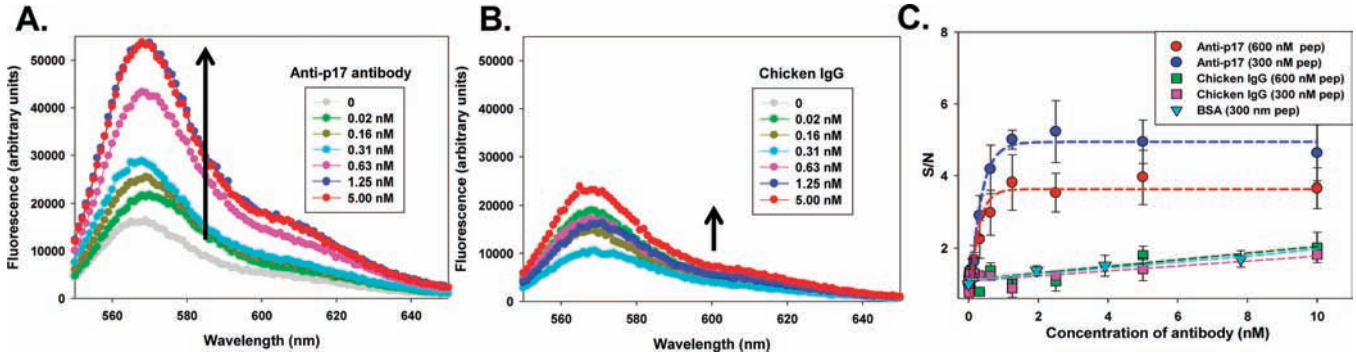


Figure 2. Fluorescence data. Representative changes in the fluorescence spectra of Cy3-p17-peptide (600 nM) exposed to (A) the indicated increasing concentrations of α-p17 antibody or (B) the control chicken IgG protein. (C) Summary of the fluorescent S/N ratio monitored at the Cy3 emission maxima (570 nm) with samples consisting of either 300 nM or 600 nM Cy3-p17-peptide versus increasing α-p17 antibody, chicken IgG, and BSA protein concentrations. (n = 4 or 6, duplicate or triplicate wells measured twice for the data shown).

per well. UV−vis spectra of the solutions were recorded using an Agilent Technologies 8453 UV−vis spectrophotometer (Santa Clara, CA). Data from the assays were analyzed and plotted using Microsoft *Excel* (Microsoft, Redmond, WA) and *SigmaPlot* (Systat Software Inc., San Jose, CA), respectively.

RESULTS AND DISCUSSION

A schematic overview of the α-p17 sensing assay discussed here is shown in Scheme 1. The freely diffusing Cy3-p17-peptide in solution has a nominal Cy3-fluorescent emission. Addition of α-p17 to the sensing solution results in specific antibody recognition and binding to the antigenic EKIRLR epitope which is proximal to the dye attachment site. This binding event alters the peptide structure and/or dye environment resulting in a significant enhancement of the Cy3 fluorescent dye photophysical properties which serves as the overall mechanism of signal transduction. We evaluated the α-p17 induced changes in both Cy3 absorbance and emission properties following binding to the labeled peptide.

Figure 1A,B shows representative UV−vis spectra collected from samples consisting of 600 nM Cy3-p17-peptide samples consecutively exposed to increasing concentrations of either α-p17 antibody or a nonspecific chicken IgG control, respectively. The data from this UV−vis analysis is summarized and directly compared in Figure 1C, which plots the signal-over-noise (S/N) ratio at 550 nm (Cy3 absorbance maximum) versus the α-p17 and IgG concentrations. The data clearly show a significant increase in the intensity of the Cy3 absorbance spectra as a function of the α-p17 antibody concentration added. For α-p17 antibody binding, the effect appears to reach an asymptotic plateau at around a 4-fold increase, and this plateau is observed starting at a minimal concentration of ∼1.25 nM. Importantly, almost no significant changes in Cy3 absorption were noted when the Cy3-p17-peptide was exposed to the same concentrations of control chicken IgG; a protein with a similar size and conserved structure as the IgG class of antibody proteins. Using just these changes in Cy3 absorption, an overall LOD (defined as a S/N ratio that is greater than 1 plus 3 times the standard deviation of the blank) of ∼0.156 nM could be derived for α-p17 binding to the Cy3-p17-peptide.

The corresponding fluorescent emission spectra for the same samples prepared in the same manner were also recorded, and representative data are shown in Figure 2. As with the UV−vis data, the fluorescence intensity of 600 nM Cy3-p17-peptide increased as a direct function of the α-p17 antibody concentration added (Figure 2A). The fluorescent enhancement appears to also reach a maximum effect beginning at around 1.25 nM of α-p17 which corresponds to the same concentration noted for the plateau in the absorption data (*vide supra*). Although the data from Cy3-p17-peptide exposed to equivalent concentrations of chicken IgG do show some changes in Cy3 emission, these appear to consist of both increases and decreases in the emission and do not seem to become significant (S/N of 1.1 ± 0.1 for 2.5 nM chicken IgG) until a concentration of 5 nM, which is five times the minimal amount of α-p17 antibody needed for the maximal enhancement effect (Figure 2B). The data from the fluorescence analysis are summarized and compared in Figure 2C, which plots the S/N ratio at 570 nm (Cy3 emission maximum) versus the IgG/α-p17 concentration for sample sets consisting of either 300 nM or 600 nM Cy3-p17-peptide substrate. Exposure of α-p17 antibody to the lower concentration Cy3-p17-peptide was found to generate an up to

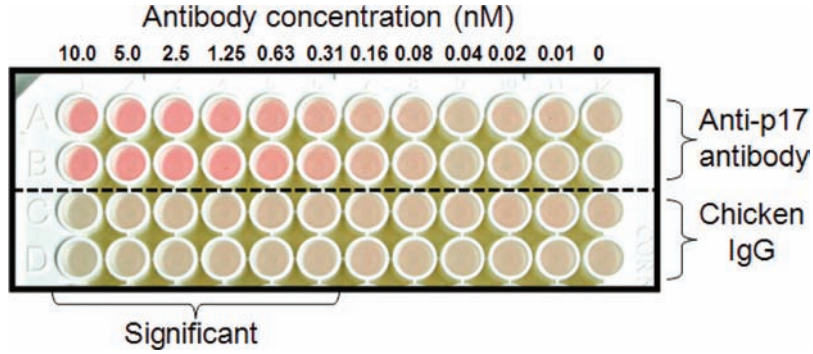


Figure 3. Photographic image of a typical assay performed in a 96-well white microtiter plate where each well contains 600 nM Cy3-p17-peptide. The concentration of the α-p17 antibody in the top two rows (A,B) and the chicken IgG control in the bottom two rows (C,D) is steadily increased (0−10 nM) from right to left.

5-fold increase in the fluorescence emission at 570 nm, with a corresponding LOD of 0.073 nM α-p17 antibody. Overall α-p17 LOD's, determined across multiple studies ($n = 5$), were 0.098 ± 0.012 and 0.073 ± 0.060 nM for the 600 and 300 nM Cy3-p17-peptide samples, respectively. The 73 pM LOD represents a 3.4-fold improvement over that determined by Oh and co-workers using their contact-quenching peptide beacon design (*13*).

We did not note any dye enhancement when α-p17 antibody was exposed to a similarly labeled generic control peptide lacking the antigenic epitope (see Supporting Information Figure 3). Beyond chicken IgG, we also tested 600 nM Cy3-p17-peptide interactions with BSA at a similar concentration range. In this case, BSA represents a nonspecific protein commonly found in serum samples and also often utilized as a blocking agent. The BSA elicits an almost identical response to the nonspecific chicken IgG at the same concentration ranges; see Figure 2C. We also noted that concentrations of BSA ≥ 1000 nM, which is ≥100 times that of the highest α-p17 antibody concentration used, approached a S/N of ∼3 with some sensor configurations (different amounts of Cy3-p17-peptide were tested, data not shown) which is still below the upper S/N limit detected with α-p17 antibody.

The enhancement of Cy3 absorbance and fluorescence properties observed upon α-p17 binding to the labeled-peptide sequence is likely a result of several putative changes in the dye's localized environment. These may include a decrease in polarity or solvation around the dye in the presence of the antibody as well as a reduction in the conformational/rotational mobility of the dye, as suggested by Gruber and co-workers who investigated anomalous fluorescence enhancement of Cy3 upon covalent attachment to IgG and noncovalent binding to avidin (*18*). Similar changes in Cy3 properties have been previously exploited in conjunction with the conformationally coupled bacterial periplasmic maltose binding protein (MBP) to prototype a number of maltose sensing modalities. For these, reduction of Cy3-labeled MBP emission upon maltose addition was either monitored directly (*19*) or in conjunction with semiconductor quantum dot donors in steady-state, excited-state lifetime, single-molecule, and multiphoton fluorescence resonance energy transfer sensing configurations (*20*−*22*). The overall concept based on pairing of fluorogenic dyes with myriad cognate protein or nucleic acid partners such that each has limited fluorescence independently but a strong emission upon binding to each other during biosensing has recently been termed "fluoromodules" (*23*). Indeed, several cyanine dyes structurally analogous to Cy3 have been tested against various single-chain antibodies (scFV) for this type of activity and suggested the exciting possibility of a range of such fluoromodules that can span most of the visible to near-IR spectrum (*23*).

As our overall goal was to evaluate this biosensing approach for the most basic screening purposes, we focused last on demonstrating assay utility with minimal to no electronic instrumentation. Figure 3 shows a digital color image taken of duplicate samples consisting of Cy3-p17-peptide in buffer exposed to increasing concentrations of either α-p17 antibody and the chicken IgG control, top and bottom two rows, respectively. The enhancement in Cy3 dye color intensity upon α-p17 binding, as compared to the IgG control, is most significant for the six antibody concentrations starting at 0.31 nM and higher. This colorimetric approach alone suggests that a rapid assessment of positive binding can easily be made by visual comparison of the samples versus controls against a white background in a microtiter well plate or even a test tube. Should observation of fluorescence also be desired, samples prepared in a similar fashion could be investigated using some form of LED or equivalent light source combined with CCD detection, both powered by batteries in the simplest configuration (*24*, *25*). The enhancement of Cy3 absorption or emission is far more desirable for signal transduction and assay monitoring than observing losses in these properties as the latter can also be caused by a variety of nonspecific or ancillary processes, for example, pH changes, ion presence, or chemical denaturation. We have also found that the Cy3-p17-peptide can be stored lyophilized for long periods of time (6 months to 1 year) and still remain fully functional. This is another desirable property, as it can allow reagents to be prepared beforehand, dried, shipped, and stored until use on an as-needed basis.

CONCLUSIONS

We have shown here a proof-of-concept design for a simple colorimetric and/or fluorescent sensing platform that uses a highly specific peptide coupled with a cyanine dye for the sensitive detection of α-p17 antibodies with a demonstrated LOD of 73 pM. This represents both a first use of a monoclonal antibody with such a fluorescent peptide in this type of sensing strategy and the detection of a clinically relevant and important target with both absorption and fluorescent emission signal transduction modalities. Although encouraging, these initial results also suggest that much research and engineering remains before transitioning to field studies. The overall enhancement mechanism is not yet been fully elucidated, and a greater understanding of the process is still warranted to answer a variety of complex mechanistic questions. For example, the extremely low concentration of antibody utilized to elicit a maximal enhancement effect (1 antibody per ∼4000 Cy3-p17-peptides for the 300 nM peptide sample in Figure 2) strongly suggests that only a very small fraction of the dyes are appropriately responsive perhaps reflecting the antibodies bind-

ing affinity/constant for the epitope in this context. The influence of Cy3 dye spacing/position relative to the epitope sequence on the peptide is clearly important and may be amenable to improvement to allow even more signal enhancement, while placement too far from the epitope may disrupt productive sensing. Iterative testing of such placement along with fluorescent polarization and anisotropy studies may help address this aspect. Testing a variety of other environmentally sensitive dyes in the sensor, including both cyanine-based and other structures, may provide better LODs, larger observed enhancements, and wider sensing ranges with the caveat that signal transduction in the visible portion of the spectrum is preferred for simplicity. Optimization of the dye attachment site in the peptide structure may also contribute similar benefits.

Although similar concentrations of nonspecific antibody or dye-labeled generic peptide lacking the epitope did not trigger any significant sensor changes, we did note that excess concentrations of BSA (>100 times that of the antibody) were able to elicit a sensor response. Therefore, while this platform has demonstrated potential for the sensitive detection of α-p17 antibodies, it is likely that some sample dilution and/or purification may be required before analysis where complex matrices such as blood are used. Significant dilution of serum samples or utilizing an integrated sample cleanup and concentration module are generally accepted sample-pretreatment strategies commonly utilized prior to POC device analysis and can readily help accomplish this (*1*, *2*, *4*, *26*, *27*). Testing of relevant spiked controls and clinical samples will help answer and optimize the LOD and sample dilution/pretreatment issues (using approved BSL III facilities).

These results in combination with other studies (*12*, *13*, *23*) strongly suggest the possibility of developing similar fluoromodule-based assays that are specifically targeted to sensing a variety of other antibodies or antigens. In principle, the method should be applicable to most antibody−epitope interactions regardless of peptide substrate length, as dye-positioning is the determinant. The various fluoromodules could be arrived at by screening combinatorially synthesized peptide libraries against targets of choice in parallel formats. Following on this, it is not hard to envision assays where several different dye-labeled peptides, each expressing different specific epitopes, are utilized in parallel-simultaneous formats to detect the presence of many different antibodies. This could allow the detection of other antibodies associated with different HIV infection stages, secondary infections, or even different strains of HIV. In conclusion, this report adds to the growing body of work which suggests that simplified bioassay formats, such as those exemplified by the fluoromodule-based assays described here, may have much to offer for challenging global health and biosecurity concerns especially in resource-poor environments (*28*).

ACKNOWLEDGMENT

The authors thank Dr. J. Golden (NRL/CBMSE) for the digital photograph shown in Figure 3. This work was supported in part by CDRH/OSEL/Division of Biology funds. The mention of commercial products, their sources, or their use in connection with material reported herein is not to be construed as either an actual or implied endorsement of such products by the Department of Health and Human Services. IM acknowledges the CB Directorate/Physical S&T Division DTRA/ARO, ONR, NRL, and the NRL-NSI for financial support. J.B.B−C. gratefully acknowledges the Marie Curie Foundation for a postdoctoral fellowship.

Supporting Information Available: The peptide purification protocol, along with HPLC and mass spectroscopy characterization, and a control study involving exposure of a generic Cy3 peptide to the p17 antibody. This material is available free of charge via the Internet at http://pubs.acs.org.

LITERATURE CITED

(1) Branson, B. M. (2003) Point-of-care rapid tests for HIV antibodies. *J. Lab. Med. 27*, 288–295.

(2) Soper, S. A., Brown, K., Ellington, A., Frazier, B., Garcia-Manero, G., Gau, V., Gutman, S. I., Hayes, D. F., Korte, B., Landers, J. L., Larson, D., Ligler, F., Majumdar, A., Mascini, M., Nolte, D., Rosenzweig, Z., Wang, J., and Wilson, D. (2006) Point-of-care biosensor systems for cancer diagnostics/prognostics. *Biosens. Bioelectron. 21*, 1932–1942.

(3) Pai, N. P., Tulsky, J. P., Cohan, D., Colford, J. M., and Reingold, A. L. (2007) Rapid point-of-care HIV testing in pregnant women: a systematic review and meta-analysis. *Trop. Med. Intern. Health 12*, 162–173.

(4) Warsinke, A. (2009) Point-of-care testing of proteins. *Anal. Bioanal. Chem. 393*, 1393–1405.

(5) Brooks Jackson, J., Parsons, J. S., Nichols, L. S., Knoble, N., Kennedy, S., and Piwowar, E. M. (1997) Detection of human immunodeficiency virus type 1 (HIV-1) antibody by Western blotting and HIV-1 DNA by PCR in patients with AIDS. *J. Clin. Microbiol. 35*, 1118–1121.

(6) Papsidero, L. D., Sheu, M., and Ruscetti, F. W. (1989) Human immunodeficiency virus type 1-neutralizing monoclonal antibodies which react with p17 core protein: Characterization and epitope mapping. *J. Virol. 63*, 267–272.

(7) Massiah, M. A., Starich, M. R., Paschall, C., Summers, M. F., Christensen, A. M., and Sundquist, W. I. (1994) Three-dimensional structure of the human immunodeficiency virus type 1 matrix protein. *J. Mol. Biol. 244*, 198–223.

(8) De Francesco, M. A., Baronio, M., Fiorentini, S., Signorini, C., Bonfanti, C., Poiesi, C., Popovic, M., Grassi, M., Garrafa, E., Bozzo, L., Lewis, G. K., Licenziati, S., Gallo, R. C., and Caruso, A. (2002) HIV-1 matrix protein p17 increases the production of proinflammatory cytokines and counteracts IL-4 activity by binding to a cellular receptor. *Proc. Natl. Acad. Sci. U.S.A. 99*, 9972–9977.

(9) Fiorentini, S., Marini, E., Bozzo, L., Trainini, L., Saadoune, L., Avolio, M., Pontillo, A., Bonfanti, C., Sarmientos, P., and Caruso, A. (2004) Preclinical studies on immunogenicity of the HIV-1 p17-based synthetic peptide AT20-KLH. *Biopolymers 76*, 334–343.

(10) Hashida, S., Hashinaka, K., Nishikata, I., Oka, S., Shimada, K., Saito, A., Takamizawa, A., Shinagawa, H., and Ishikawa, E. (1996) Shortening of the window period in diagnosis of HIV-1 infection by simultaneous detection of p24 antigen and antibody IgG to p17 and reverse transcriptase in serum with ultrasensitive enzyme immunoassay. *J. Virol. Meth. 62*, 43–53.

(11) Ishikawa, S., Hashinaka, K., Hashida, S., Oka, S., and Ishikawa, E. (1999) Use of indirectly immobilized recombinant p17 antigen for detection of antibodies to HIV-1 by enzyme immunoassay. *J. Clin. Lab. Anal. 13*, 9–18.

(12) Oh, K. J., Cash, K. J., Lubin, A. A., and Plaxco, K. W. (2007) Chimeric peptide beacons: A direct polypeptide analog of DNA molecular beacons. *Chem. Commun. 46*, 4869–4871.

(13) Oh, K. J., Cash, K. J., Hugenberg, V., and Plaxco, K. W. (2007) Peptide beacons: A new design for polypeptide-based optical biosensors. *Bioconjugate Chem. 18*, 607–609.

(14) Schnolzer, M., Alewood, P., Jones, A., Alewood, D., and Kent, S. B. H. (1992) In situ neutralization in Boc chemistry solid phase peptide synthesis. Rapid, high yield assembly of difficult sequences. *Int. J. Pept. Protein Res. 40*, 180–193.

(15) Delehanty, J. B., Medintz, I. L., Pons, T., Brunel, F. M., Dawson, P. E., and Mattoussi, H. (2006) Self-assembled quantum dot-peptide bioconjugates for selective intracellular delivery. *Bioconjugate Chem. 17*, 920–927.

(16) Medintz, I. L., Clapp, A. R., Brunel, F. M., Tiefenbrunn, T., Uyeda, H. T., Chang, E. L., Deschamps, J. R., Dawson, P. E.,

and Mattoussi, H. (2006) Proteolytic activity monitoring by fluorescence resonance energy transfer through quantum-dot-peptide conjugates. *Nat. Mater. 5*, 581–589.

(17) Sapsford, K. E., Farrell, D., Sun, S., Rasooly, A., Mattoussi, H., and Medintz, I. L. (2009) Monitoring of enzymatic proteolysis on an electroluminescent-CCD microchip platform using quantum dot-peptide substrates. *Sens. Actuators, B 139*, 13–21.

(18) Gruber, H. J., Hahn, C. D., Kada, G., Riener, C. K., Harms, G. S., Ahrer, W., Dax, T. G., and Knaus, H.-G. (2000) Anomalous fluorescence enhancement of Cy3 and Cy3.5 versus anomalous fluorescence loss of Cy5 and Cy7 upon covalent linking to IgG and noncolvalent binding to avidin. *Bioconjugate Chem. 11*, 696–704.

(19) Medintz, I. L., and Mauro, J. M. (2004) Use of a cyanine dye as a reporter probe in reagentless maltose sensors based on E. Coli maltose binding protein. *Anal. Lett. 37*, 191–202.

(20) Medintz, I. L., Clapp, A. R., Melinger, J. S., Deschamps, J. R., and Mattoussi, H. (2005) A reagentless biosensing assembly based on quantum dot-donor Forster resonance energy transfer. *Adv. Mater. 17*, 2450–2455.

(21) Pons, T., Medintz, I. L., Wang, X., English, D. S., and Mattoussi, H. (2006) Solution-phase single quantum dot fluorescence resonance energy transfer. *J. Am. Chem. Soc. 128*, 15324–15331.

(22) Clapp, A. R., Pons, T., Medintz, I. L., Delehanty, J. B., Melinger, J. S., Tiefenbrunn, T., Dawson, P. E., Fisher, B. R., O'Rourke, B., and Mattoussi, H. (2007) Two-photon excitation of quantum-dot-based fluorescence energy transfer and its applications. *Adv. Mater. 19*, 1921–1926.

(23) özhalici-Unal, H., Pow, C. L., Marks, S. A., Jesper, L. D., Silva, G. L., Shank, N. I., Jones, E. W., Burnette III, J. M., Berget, P. B., and Armitage, B. A. (2008) A rainbow of fluoromodules: a promiscuous scFv protein binds to and activates a diverse set of fluorogenic cyanine dyes. *J. Am. Chem. Soc. 130*, 12620–12621.

(24) Sapsford, K. E., Sun, S., Francis, J., Sharma, S., Kostov, Y., and Rasooly, A. (2008) A fluorescence detection platform using spatial electroluminescence excitation for measuring botulinum neurotoxin A activity. *Biosens. Bioelectron. 24*, 618–625.

(25) Breslauer, D. N., Maamari, R. N., Switz, N. A., Lam, W. A., Fletcher, D. A. (2009) Mobile phone based clinical microscopy for global health applications. *PLoS ONE 4*, article # e6320.

(26) Moreno-Bondi, M. C., Taitt, C. R., Shriver-Lake, L. C., and Ligler, F. S. (2006) Multiplexed measurement of serum antibodies using an array biosensor. *Biosens. Bioelectron. 21*, 1880–1886.

(27) Yeung, S. H., Liu, P., Del Bueno, N., Greenspoon, S. A., and Mathies, R. A. (2009) Integrated sample cleanup-capillary electrophoresis microchip for high-performance short tandem repeat genetic analysis. *Anal. Chem. 81*, 210–217.

(28) Sapsford, K. E., Bradburne, C., Delehanty, J. B., and Medintz, I. L. (2008) Sensors for detecting biological agents. *Mater. Today 11*, 38–49.

BC9003712

Metal- and Metallocycle-Binding Sites Engineered into Polyvalent Virus-Like Scaffolds

Andrew K. Udit,* William Hollingsworth, and Kang Choi

Department of Chemistry, Occidental College, 1600 Campus Road, Los Angeles, California 90041. Received September 14, 2009; Revised Manuscript Received December 16, 2009

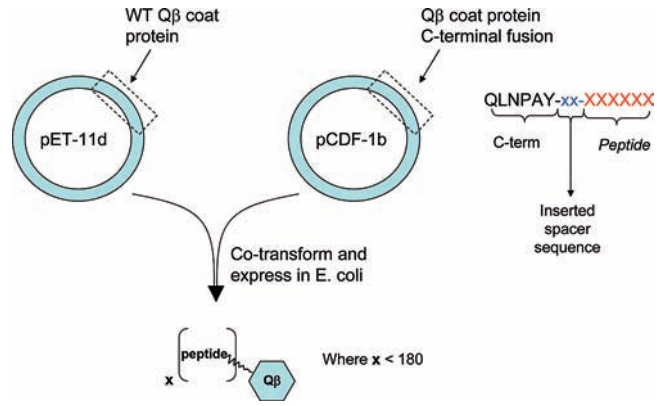
Metal-binding motifs appear on protein scaffolds throughout nature and are critical for a vast array of functions that span structure, electron transfer, and catalysis. In an effort to reproduce and exploit this activity in vitro, described herein are versatile bacteriophage Qβ particles bearing metal-binding motifs polyvalently. The three motifs, His_6, His_6-His_6, and Cys-His_6, were incorporated into the capsid via a coexpression methodology at ratios of 1.1:1, 1.1:1, and 2.3:1 for wild-type to modified coat protein. Size-exclusion chromatography yielded elution profiles identical to wild-type particles, while Ni-NTA affinity chromatography resulted in retention times that increase according to Qβ-His_6 < Qβ-Cys-His_6 < Qβ-His_6-His_6. In addition to interacting with metal-derivatized surfaces, Qβ-Cys-His_6 and Qβ-His_6-His_6 bind heme as evidenced by the appearance of new absorbances at 416 and 418 nm, respectively, upon addition of hemin-Cl. The heme-bearing particles were also found to be electrochemically active as a surface-confined system. While both constructs yield similar $E_{1/2}$ values anaerobically and with carbon monoxide present, and both display similar pH dependences, a standard rate constant $k°$ could only be measured for Qβ-Cys-His_6 (83 s^{-1}), as electron transfer for Qβ-His_6-His_6 was too rapid to estimate. Experiments with rotated-disk electrodes yielded significant activity of the constructs toward dioxygen reduction. The versatility of the particles is further underscored by their multivalent nature, permitting simultaneously a range of activities for applications demanding polyfunctionality.

INTRODUCTION

The critical physiological functions performed by endogenous metal-binding proteins has resulted in decades of research aimed at attempting to recapitulate this activity in vitro in order to both understand and exploit native functions (*1–4*). Harnessing such activity can prove difficult, with key challenges that include design/preservation of catalytically competent centers, activation of these centers (photochemically, electrochemically), immobilization (facilitating stability, separation, etc.), longevity, and optimization of activity (*5*). Hence, there remains great interest in developing alternative (semi)artificial systems that can perform the desired functions (*6–11*). In view of this goal, exploiting reliably self-assembling biological structures is especially attractive; specifically, virus capsids provide convenient polyvalent nanoparticle platforms for building a variety of materials (*12–14*). A handful of groups have demonstrated the potential of these scaffolds with reports that include virus-based batteries (*15*), charge transfer mediators (*16*), catalysts (*17*), and metal nanopatterning (*18*).

The versatile polyhistidine motif has seen primary use in protein purification (*19, 20*), but has also demonstrated utility in areas that include immobilizing redox-active proteins for biosensors (*21*) and cell uptake of antibody−marker conjugates (*22*). More recently, two specific studies describe attempts to engineer metal-binding sites into virus-like particles utilizing this motif. The first appended hexahistidine tags to the hepatitis B virus (HBV[1]) capsid protein (*23*). The added motif was well-tolerated as evidenced by the ability of the particle to assemble while possessing the hexahistidine tag on each of the 80 coat protein subunits. The construct was capable of binding heme moieties via bis-histidine ligation and displayed spectroscopic and electrochemical behavior analogous to that of c-type cytochromes. Interestingly, the chelating tags were apparently not sufficiently accessible to interact with metal-derivatized surfaces, as demonstrated by the inability of the particles to be retained on Ni-NTA substrates. Alternatively, the second notable study incorporated hexahistidine motifs into the capsid of bacteriophage Qβ (Qβ) (*24*). Unlike HBV, displaying hexahistidine tags on Qβ was only achievable using a coexpression methodology (Scheme 1). This yielded particles with variable ratios of wild-type to modified coat proteins where the final ratio is governed by the spontaneous capsid self-assembly process. In contrast to HBV, this clearly indicates that having hexahistidine tags at each of the 180 coat proteins that make up the Qβ capsid is far too disruptive to particle assembly. Similarly divergent and intriguing were the recorded observations: while capable of interacting with a series of metal-derivatized surfaces, the engineered Qβ virions displayed no

Scheme 1. Coexpression Methodology Used to Incorporate Metal-Binding Motifs into the Qβ Capsid



* Corresponding author. ph 323-259-1471, fax 323-341-4912, udit@oxy.edu.

[1]Abbreviations: Qβ, bacteriophage Qβ; HBV, hepatitis B virus; FPLC, fast-protein liquid chromatography; KP_i, potassium phosphate.

10.1021/bc900399e © 2010 American Chemical Society
Published on Web 01/21/2010

Table 1. Summary of Parameters for the Virus Constructs

construct	C-terminal amino acid sequence	molecular weight (kDa)[a]	coat protein ratio (WT:fusion)	Ni-NTA retention time (min)
Qβ-(His_6-His_6)	SGHHHHHHGSGSGHHHHHH	16.3	1.1:1	24.5
Qβ-(Cys-His_6)	GSGSGCGSGSGHHHHHH	15.7	2.3:1	22.2
Qβ-(His_6)	GSGSGHHHHHH	15.3	1.1:1	18.6

[a] The wild-type coat protein is 14.1 kDa.

propensity to bind metallocycles in solution. As such, in an effort to generate truly versatile platforms, described herein are engineered Qβ capsids that combine all of the aforementioned activities.

EXPERIMENTAL PROCEDURES

Mutagenesis, Protein Expression, Virus Purification, and Characterization. Mutagenesis and cloning protocols proceeded as previously described, using the same forward primer (*24*). Reverse primers were ATA *CTC GAG* TTA GTG GTG GTG GTG GTG GTG GCC ACT GCC ACT GCC ATG ATG ATG ATG ATG ATG TCC TGA and ATA *CTC GAG* TTA GTG GTG GTG GTG GTG GTG GCC ACT GCC ACT GCC ACA TCC TGA TCC TGA TCC ATA CG for Qβ-(His_6-His_6) and Qβ-(Cys-His_6), respectively (restriction sites italicized, priming regions underlined). For Qβ-(His_6-His_6), the previously constructed Qβ-(His_6) was used as the template for PCR.

Protein expression and purification proceeded as previously described (*25*), except instead of ultracentrifugation the particles were purified from sucrose gradients via a second ammonium sulfate precipitation. For expression experiments with Qβ-(Cys-His_6) in the presence of added metals, growth media were supplemented with 0.5 mM of either Hg_2Cl_2, $CoCl_2$, or δ-aminolevulinic acid. Protein was quantified using the Modified Lowry Assay (Pierce).

MALDI-TOF MS. 60 μL of 10 M urea and 10 μL of 1 M DTT were added to 40 μL of ~10 mg of virus. The solution was incubated at 37 °C for 1 h, and then dried down in a vacuum microcentrifuge. The samples were resuspended in 0.2% TFA in H_2O (50 μL) and purified with ZipTips (Millipore) by using the following solutions in the manufacturer-specified protocol: wetting solution 50% MeCN in H_2O, equilibration solution 0.2% TFA in H_2O, wash solution 0.1% TFA/5% MeOH in H_2O, elution solution 5 mL of 0.1% TFA/65% MeCN in H_2O. The resulting solutions of purified peptides (1 μL) were spotted onto the MALDI-MS plate with a saturated solution of α-cyano-4-hydroxycinnamic acid (1 μL, in 1:1 MeCN/H_2O).

Chromatography. FPLC was performed using a Bio-Rad BioLogic Workstation. 400 μL of virus at 1 mg/mL in 100 mM KP_i pH 7 buffer was analyzed per FPLC run. Size-exclusion chromatography (Superose 6) was performed at 0.3 mL/min with isocratic elution using 100 mM KPi buffer pH 7. Affinity chromatography was conducted using prepacked 1 mL Ni-NTA columns (GE Healthcare) with elution using a linear gradient of 0 to 0.5 M imidazole in 100 mM KPi buffer pH 7 at 1 mL/min.

Electronic Absorption Spectroscopy. Samples for spectroscopy consisted of 5 μM hemin-Cl (1/1000 dilution from a 5 mM aqueous stock in 25 mM K_2CO_3) and 0.2 mg/mL virus in 100 mM KP_i pH 7. The resulting spectra were corrected for absorption from free heme in solution. Samples were reduced by adding sodium dithionite to a final concentration of 5 mM.

Cyclic Voltammetry. Voltammograms were recorded using a CH Instruments Electrochemical Workstation and a three-compartment cell with AgCl/Ag reference and platinum wire counter electrodes. Voltammetry was conducted in 100 mM KP_i pH 7 argon-degassed buffer unless otherwise stated. Virus-coated glassy carbon working electrodes (5 mm diameter) were prepared by polishing with a 0.3 μm alumina slurry followed by sonication and then drying in air. An aqueous stock solution of 2 mM hemin-Cl with 5% DMSO was diluted to a final concentration of 100 μM into 100 μL of 10 mg/mL virus solution in 100 mM KP_i pH 7. The polished electrode was submerged into the virus-heme solution and incubated overnight at 12 °C. Before conducting voltammetry, the electrodes were gently washed by repeated dipping in buffer.

Electrolyses and Amplex Red Peroxide Assay. Glassy carbon rotated-disk electrodes were polished exactly as electrodes for voltammetry. Heme-virus solutions were also prepared exactly as for voltammetry, except the final solution was then diluted further to 300 μL with 100 mM KP_i pH 7 buffer. Electrodes were incubated in the heme-virus solution overnight at 12 °C. Experiments were conducted at room temperature (20 °C) in a three-compartment cell using silver and platinum wires as pseudoreference and counter electrodes, respectively. The working chamber was filled with 2 mL of air-saturated 100 mM KP_i buffer pH 7 ($[O_2] = 290$ μM at 20 °C), and electrolyses were conducted for 20 min at −0.5 V at various rotation rates under the control of a Pine Instruments rotator. Electrolyses for assaying the amount of hydrogen peroxide produced were performed at 200 rpm. Cyclic voltammograms were recorded before and after rotation. Hydrogen peroxide content after electrolysis was assessed using the manufacturer-specified protocol for the Amplex Red fluorescence assay (Molecular Probes).

RESULTS AND DISCUSSION

The powerful co-expression technique permitted production of Qβ particles possessing the coat protein sequences listed in Table 1, which include the hexahistidine construct previously described (Qβ-(His_6)) (*24*) and particles bearing either C-terminal double hexahistidine (Qβ-(His_6-His_6)) or cysteine-hexahistidine appendages (Qβ-(Cys-His_6)). Expression and purification using established protocols regularly produced ~20 mg of virus per liter of culture, a good yield, although approximately 3-fold less compared to production of wild-type particles. Denaturing SDS-PAGE showed both wild-type and modified coat proteins with the expected sizes and indicated relatively pure preparations (Figure 1). MALDI-TOF analysis of the coat proteins revealed well-defined peaks at the expected molecular masses; relative coat protein ratios were estimated by integration of the peaks (Table 1). Intact particles were

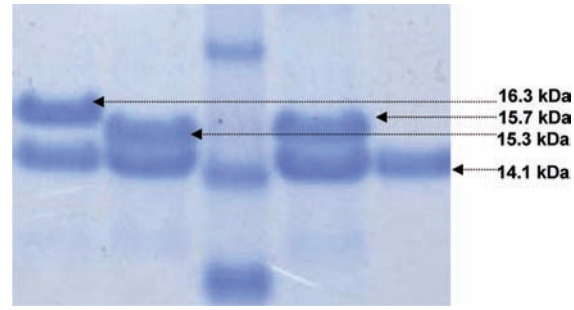


Figure 1. Protein gel (SDS-PAGE) of the purified virus particles showing the coexpressed coat proteins. From left to right: Qβ-(His_6-His_6); Qβ-(His_6); size marker; Qβ-(Cys-His_6); WT.

confirmed by size-exclusion fast-protein liquid chromatography (FPLC), with elution profiles for the mixed particles identical to wild-type (Supporting Information Figure S1). Notably, the ratio of wild-type to fusion coat proteins was not markedly affected by the presence of sucrose, which for some constructs has been shown to alter coat protein ratios (see Udit, Brown, et al. for further discussion).

Virions were found to be stable at 4 °C for months. However, prolonged storage of Qβ-(Cys-His_6) at high concentration (>∼15 mg/mL) resulted in significant aggregation and precipitation, likely via formation of disulfide bonds from the incorporated Cys residues. This is consistent with previous observations for Qβ particles possessing the K16C mutation (most surface-accessible residue (*25*)) in the analogous co-expressed particles, where significant aggregation and precipitation resulted during attempts to purify the virions (data not shown). Indeed, this also suggests a reason for the observed coat protein ratio, as only those particles possessing fewer Cys residues are isolable. To explore the possible stabilizing effects of metals, the Qβ-(Cys-His_6) construct was expressed in the presence of either $CoCl_2$ or Hg_2Cl_2, as well as under conditions typically used for the expression of P450 cytochromes (see Experimental Procedures section for details). No benefits were observed using these protocols, as the purified particles possessed similar coat protein ratios to those expressed under regular conditions (Supporting Information Figure S2). Furthermore, while dilute virus samples were soluble, the addition of 50 μM heme to samples of virus at greater than 2 mg/mL (∼0.8 μM particles) in 0.1 M KP_i pH 7 resulted in aggregation of the particles. The virus-heme aggregates could be partially redispersed by adding DMSO to 20%.

Qβ-(His_6) particles were previously found to interact strongly with metal-derivatized surfaces (*24*). Similar behavior was anticipated and confirmed for the new viruses generated here. The observed retention times during chromatography using Ni-NTA resins are listed in Table 1. Qβ-(His_6-His_6) displayed the longest retention time, consistent with it possessing the greatest number of hexahistidine motifs. Interestingly, Qβ-(Cys-His_6) exhibited the second longest retention time despite it possessing fewer hexahistidine tags compared to Qβ-(His_6). This may indicate that the thiol also participates in binding to the Ni-NTA resin, analogous to prior studies on proteins that display Ni(II)-thiol ligation (*26*). By extension, one can draw comparisons to well-known metal-binding structural motifs in nature (e.g., zinc fingers (*27*)).

As mentioned above, a key motivation for this work was to generate particles that could coordinate heme. While the wild-type and Qβ-(His_6) particles showed no evidence of heme binding (*24*), adding heme to samples of Qβ-(His_6-His_6) and Qβ-(Cys-His_6) immediately gave rise to distinct color changes: the broad absorption maximum at ∼390 nm for free hemin-Cl was replaced by well-defined peaks at 418 and 416 nm for Qβ-(His_6-His_6) and Qβ-(Cys-His_6) (Figure 2), reminiscent of the ferric state of typical heme proteins (e.g., P450, cytochrome c) (note: attempts to resolve the Q-band region were unsuccessful). Consistent with this were the approximate 10 nm red shifts of the absorption maxima upon addition of sodium dithionite, indicative of reduction to ferrous heme (data not shown). Notably, the concentrations used (5 μM hemein-Cl and 0.2 mg/mL virus, 14.2 μM total subunit) did not lead to noticeable aggregation. Although the precise extinction coefficients are not available, values for the analogous cytochrome c and P450 proteins are known to be similar (∼100 mM^{-1} cm^{-1}) (*28–30*). Given this, the relative magnitudes of the absorption maxima are also consistent with the differences in coat protein ratios, as Qβ-(His_6-His_6) displays 1.7 times the absorption intensity

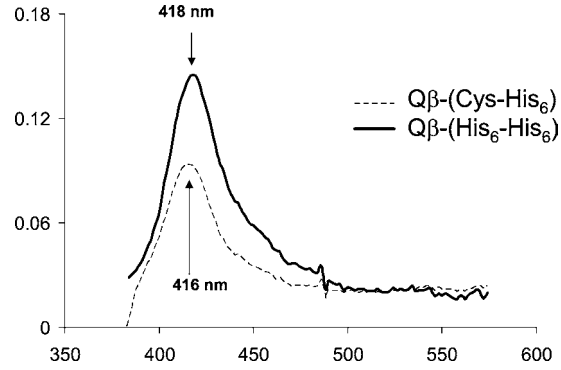


Figure 2. UV−visible absorption spectra of 0.2 mg/mL Qβ particles with 5 μM hemin-Cl recorded in 100 mM KP_i pH 7 buffer with 25 μM K_2CO_3. Spectra are corrected for background absorption from free hemin-Cl.

and possesses 1.3 times as many coat protein fusions compared to Qβ-(Cys-His_6) (note: preparing samples for ICP-MS analysis in order to determine the number of hemes per particle proved intractable due to difficulties in separating free heme from heme-saturated protein solutions via dialysis and size-exclusion chromatography).

Significantly, the Qβ-(His_6-His_6) and Qβ-(Cys-His_6) particles accomplish what the previously reported Qβ-(His_6) and HBV-(His_6) particles could only do uniquely; that is, while Qβ-(His_6) could only interact with metal-derivatized surfaces and HBV-(His_6) could only coordinate heme, the two new particles generated here can perform both functions. Presumably, this is a consequence of placing metal-coordinating ligands (bis-His or Cys-His) in good proximity to each other by having them appear at adequately spaced positions along the same peptide sequence.

The ability to chemically reduce the heme suggested that electrochemical activity may be possible if the heme groups were sufficiently exposed. Thus, samples of 100 μM heme and ∼10 mg/mL virus (700 μM total subunit) were incubated with glassy carbon electrodes at 4 °C overnight. Subsequent voltammetry yielded strong responses for both virus-heme samples: representative voltammograms are shown in Figure 3 and a summary of the electrochemical data is presented in Table 2. Notably, the well-defined voltammogram in Figure 3a is distinct from that of electrodes incubated with only hemin-Cl which yielded a quasi-reversible response (Supporting Information Figure S3). The redox active virus-heme complexes appeared to be surface-confined, as plots of peak current versus scan rate were linear. Given the diameters of the electrode (5 mm) and virus (approximately 30 nm), monolayer coverage would result in 4.6×10^{-14} mol of particles on the surface (9.5×10^{-12} mol of subunits), assuming a close-packed arrangement. By integrating the voltammograms to ascertain the amount of charge passed during each sweep and dividing this number by the value for theoretical monolayer coverage, one obtains average values of 361 and 326 mol of electrons per mole of particle for Qβ-(His_6-His_6) and Qβ-(Cys-His_6). As each particle contains 180 subunits and only a fraction of these per particle have heme binding sites, and since substoichiometric quantities of heme were used to avoid direct cofactor adsorption, this indicates that greater than monolayer coverage has been achieved.

Interestingly, the two constructs display similar electrochemical behavior, as both have comparable half-wave potentials under degassed and CO-saturated conditions (note: while potential shifts were observed in the presence of CO, no changes in the absorption spectra were noted; this may indicate that the virus-heme complexes can more readily participate in ligand exchange when confined to the electrode surface). Also, both

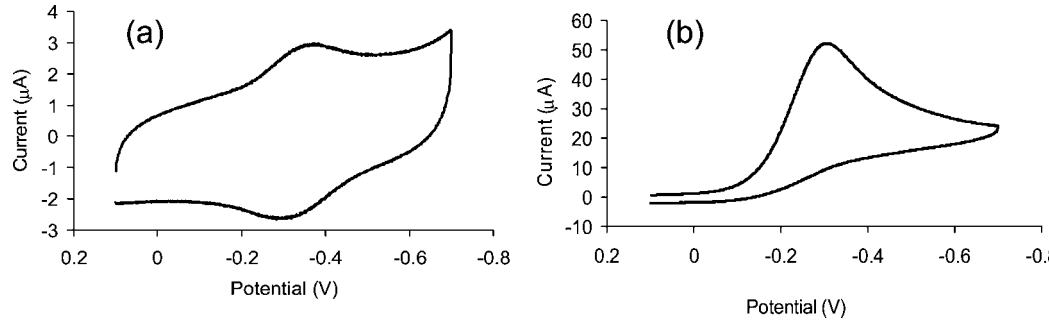


Figure 3. Representative cyclic voltammograms recorded at 100 mV/s in 0.1 M KPi buffer pH 7: (a) Qβ-(Cys-His_6), anaerobic; (b) Qβ-(Cys-His_6) in air saturated buffer.

Table 2. Cyclic Voltammetry Data for the Heme-Virus Complexes

particle	$E_{1/2}$ (mV)[a]	$E_{1/2}$ with CO (mV)[a]	$k°$ (s^{-1})	electroactive centers (coulombs)[c]	mV/pH[d]
Qβ-(His_6-His_6)	−365	−303	n.d.[b]	361	−40
Qβ-(Cys-His_6)	−364	−302	83	326	−37

[a] Potentials vs AgCl/Ag. [b] Not determined, insufficient peak separation up to 30 V/s. [c] Determined at 100 mV/s. [d] pH range 4−9.

catalytically reduce dioxygen at similar potentials (Figure 3b), although qualitatively, Qβ-(His_6-His_6) displayed greater catalytic currents, consistent with it possessing more heme sites per particle. The comparable behavior observed is not entirely unexpected, as surface effects are known to strongly influence the electrochemical behavior of heme proteins on electrodes (*31–34*); the effect is likely to be magnified in this case, as the heme sites should be displayed on the surface of the viruses and are thus largely influenced by the immediate microenvironment of the solvent and electrode. Conversely, significant differences were observed in the standard rate constants ($k°$). Laviron's theory (*35*) was used to evaluate $k°$, which provides an estimate of this value for surface confined systems when the peak separation exceeds 200 mV. At 30 V/s (note: interpretable voltammograms were not obtained above this scan rate), $k°$ for Qβ-(Cys-His_6) was found to be 84 s^{-1}, while a value was not estimated for Qβ-(His_6-His_6), as the peak separation was only 160 mV. Thus, heme−electrode electron transfer appears to be faster for hemes bound to Qβ-(His_6-His_6) compared to Qβ-(Cys-His_6). This is reminiscent of analogous biological systems where bis-His coordinated heme groups are often associated with rapid electron transfer reactions (e.g., cycotchrome c) while cysteine-ligated hemes serve other purposes, such as catalysis (e.g., P450 cytochromes) (note: Raman spectroscopy was attempted in an effort to further distinguish bis-His vs Cys-His ligation; however, data acquisition proved difficult given the inability to achieve high concentrations and the propensity of the samples to aggregate over time). The ability to mimic such behavior in the virus-heme system alludes to the potential for fine-tuning the observed activity by, for example, mutation to alter the heme electronic environment.

The strong catalytic response of the virus-heme complexes to dioxygen was further explored using rotated-disk electrodes. While prolonged rotation at 400 rpm lead to a gradual decrease in catalytic activity, within the measurable window the catalytic currents for both virus-heme complexes were strong and well above background (Supporting Information Figure S4). Qβ-(His_6-His_6) was found to draw the greater current during electrolysis in air-saturated buffer, consistent with it possessing more heme binding sites per particle compared to Qβ-(Cys-His_6) and in agreement with the qualitative interpretation of the aerobic cyclic voltammograms (discussed above).

Given the different standard rate constants observed, the mechanisms and products of dioxygen reduction for each construct could be markedly different (*36*); indeed, of specific interest is the possibility of dioxygen activation for substrate oxidation (note: heme-mediated dioxygen reduction presents the possibility of dioxygen activation followed by substrate oxidation; preliminary electrolyses using styrene and thioanisole as substrates did not yield any oxidized products). The nature of the dioxygen reduction reaction was examined via electrolysis and the Amplex Red fluorescence assay for peroxide. Electrolyses were conducted with films on rotated-disk electrodes at 200 rpm and −0.5 V (vs AgCl/Ag) for 20 min followed by Amplex Red analysis of an aliquot from the reaction. Using the coulometric data acquired, the total charge passed was used to calculate the moles of peroxide that should have been formed presuming that all of the electrons were used for this purpose; this value was then divided by the moles of peroxide found via Amplex Red. The calculations yield ratios of theoretical peroxide (via coulometry) to measured peroxide (via Amplex Red) for the virus-heme complexes of 0.6 ± 0.2, 12 ± 5, and 11 ± 3 for the negative control (bare electrode), Qβ-(His_6-His_6), and Qβ-(Cys-His_6), respectively. The data therefore indicate that the virus-heme complexes are consuming far more charge than what can be accounted for by the peroxide present in solution. One possible explanation is that the unaccounted charge does indeed yield peroxide, which is then consumed via oxidative damage to the protein; alternatively, the electrons may be used to generate water, analogous to prior studies (*37–39*) (note: ideally, one would use rotated ring-disk electrodes to characterize the dioxygen reduction reaction; however, the instability of the films to prolonged rotation makes this unfeasible). It is presently unclear how this reaction proceeds. Reduction at either the heme periphery or the iron center are possible, although the latter mechanism would require ligand exchange, presuming a coordinatively saturated heme.

In summary, by exploiting a coexpression methodology it was possible to polyvalently display versatile metal-binding motifs on bacteriophage Qβ. The capsid self-assembly process and the resulting stability of the particle resulted in twice as many His_6-His_6 peptides tolerated compared to Cys-His_6, which leads to longer retention on Ni-NTA resins for Qβ-(His_6-His_6). Following heme-binding, it was possible to characterize the particles electrochemically, with both virus-heme complexes exhibiting good catalytic activity toward dioxygen reduction. Although the two particles did not display markedly divergent properties, it is likely possible to fine-tune/alter this activity by selectively mutating the coat protein; for example, incorporating hydrogen bonding residues adjacent to the heme-binding moieties may modulate catalytic activity (*36, 40*). Indeed, this further extends the potential applications: that the particles interact with both metallocycles and immobilized metals, one can easily look toward applications such as immobilizing the particles onto a surface while simultaneously binding a cofactor for catalysis. The potential benefit is further magnified given the polyvalent nature of the scaffold employed.

ACKNOWLEDGMENT

This work was funded by the American Chemical Society Petroleum Research Fund (ACS PRF UNI to AKU), the Dreyfus Foundation (startup grant to AKU), and the HHMI (undergraduate education grant). We are grateful to Mike Hill, Chris Craney, and Aram Nersissian (Occidental College) for use of their facilities; Weidong Wang (Occidental College) for technical support; Mona Shagholi (Caltech) for assistance with MALDI-TOF MS; Don Walker (Caltech), and Hannah Shafaat and Judy Kim (UCSD) for preliminary Raman experiments.

Supporting Information Available: Size-exclusion FPLC data, protein gel of virus grown in the presence of metals, negative control cyclic voltammograms, and rotated-disk voltammetry and coulometry. This material is available free of charge via the Internet at http://pubs.acs.org.

LITERATURE CITED

(1) Sala, X., Romero, I., Rodriguez, M., Escriche, L., and Antoni, L. (2009) Molecular catalysts that oxidize water to dioxygen. *Angew. Chem., Int. Ed. 48*, 2842–2852.

(2) Meyer, D., Buehler, B., and Schmid, A. (2006) In *Process and catalyst design objectives for specific redox biocatalysis*, Vol *59*, Elsevier Academic Press.

(3) Baniulis, D., Yamashita, E., Zhang, H., Hasan, S. S., and Cramer, W. A. (2008) Structure-function of the cytochrome b_6f complex. *Photochem. Photobiol. 84*, 1349–1358.

(4) Gillam, E. M. (2008) Engineering cytochrome P450 enzymes. *Chem. Res. Toxicol. 21*, 220–231.

(5) Hatti-Kaul, R., Tornvall, U., Gustaffson, L., and Borjesseon, P. (2007) Industrial biotechnology for the production of bio-based chemicals - a cradle-to-grave perspective. *Trends Biotechnol. 25*, 119–124.

(6) Rojas, N. R. L., Kamtekar, S., Simons, C. T., Mclean, J. E., Vogel, K. M., Spiro, T. G., Farid, R. S., and Hecht, M. H. (1997) De novo heme proteins from designed combinatorial libraries. *Protein Sci. 6*, 2512–2524.

(7) Albrecht, T., Li, W., Ulstrup, J., Haehnel, W., and Hildebrandt, P. (2005) Electrochemical and spectroscopic investigations of immobilized de novo designed heme proteins on metal electrodes. *ChemPhysChem 6*, 961–970.

(8) Matthews, J. M., Loughlin, F. E., and Mackay, J. P. (2008) Designed metal-binding sites in biomolecular and bioinorganic interactions. *Curr. Opin. Struct. Biol. 18*, 484–490.

(9) Koder, R. L., Anderson, J. L. R., Solomon, L. A., Reddy, K. S., Moser, C. C., and Dutton, P. L. (2009) Design and engineering of an O-2 transport protein. *Nature 458*, 305–309.

(10) Lu, Y. (2006) Biosynthetic inorganic chemistry. *Angew. Chem., Int. Ed. 45*, 5588–5601.

(11) Monien, B. H. (2007) Detection of heme oxygenase activity in a library of four-helix bundle proteins: towards the de novo synthesis of functional heme proteins. *J. Mol. Biol. 371*, 739–753.

(12) Steinmetz, N. F., Lin, T., Lomonossoff, G., and Johnson, J. E. (2009) In *Structure-based engineering of an icosahedral virus for nanomedicine and nanotechnology*, Vol *327*, Springer-Verlag, Berlin.

(13) Young, M., Willits, D., Uchida, M., and Douglas, T. (2008) Plant viruses as biotemplates for materials and their use in nanotechnology. *Ann. Rev. Phytopathol. 46*, 361–384.

(14) Destito, G., Schneemann, A., and Manchester, M. (2009) In *Biomedical nanotechnology using virus-based nanoparticles*, Vol *327*, Springer-Verlag, Berlin.

(15) Nam, K. T., Kim, D.-W., Yoo, P. J., Chiang, C.-Y., Meethong, N., Hammond, P. T., Chiang, Y.-M., and Belcher, A. M. (2006) Virus-enabled synthesis and assembly of nanowires for lithium ion battery electrodes. *Science 312*, 885–888.

(16) Steinmetz, N. F., Lomonossoff, G., and Evans, D. J. (2006) Decoration of cowpea mosaic virus with multiple, redox-active organometallic complexes. *Small 2*, 530–533.

(17) Avery, K. N., Schaak, J. E., and Schaak, R. E. (2009) M13 bacteriophage as a biological scaffold for magnetically-recoverable metal nanowire catalysts: combining specific and nonspecific interactions to design multifunctional nanocomposites. *Chem. Mater. 21*, 2176–2178.

(18) Klem, M. T., Young, M., and Douglas, T. (2008) Biomimetic synthesis of beta-TiO2 inside a viral capsid. *J. Mater. Chem. 18*, 3821–3823.

(19) Porath, J., Carlsson, J., Olsson, I., and Belfrage, G. (1975) Metal chelate affinity chromatography, a new approach to protein fractionation. *Nature 258*, 598–599.

(20) Hochuli, E., Dobeli, H., and Schacher, A. (1987) New metal chelate adsorbent selective for proteins and peptides coontaining neighbouring histidine residues. *J. Chromatogr. 411*, 177–184.

(21) Benson, D. E., Conrad, D. W., de Lorimer, R. M., Trammell, S. A., and Hellinga, H. W. (2001) Design of bioelectronic interfaces by exploiting hinge-bending motions in proteins. *Science 293*, 1641–1644.

(22) Nielsen, U. B., Kirpotin, D. B., Pickering, E. M., Drummond, D. C., and Marks, J. D. (2006) A novel assay for monitoring internalization of nanocarrier coupled antibodies. BMC Immunol. *7*

(23) Prasuhn, D. E., Jr., Kuzelka, J., Strable, E., Udit, A. K., Cho, S.-H., Lander, G. C., Quispe, J. D., Diers, J. R., Bocian, D. F., Potter, C., Carragher, B., and Finn, M. G. (2008) Polyvalent display of heme on hepatitis B virus capsid protein through coordination to hexahistidine tags. *Chem. Biol. 15*, 513–519.

(24) Udit, A. K., Brown, S., Baksh, M. M., and Finn, M. G. (2008) Immobilization of bacteriophage Qb on metal-derivatized surfaces via polyvalent display of hexahistidine tags. *J. Inorg. Biochem. 102*, 2142–2146.

(25) Strable, E., Jr., Udit, A. K., Brown, S. D., Link, A. J., Ngo, J. T., Lander, G., Quispe, J., Potter, C. S., Carragher, B., Tirrell, D. A., and Finn, M. G. (2008) Unnatural amino acid incorporaton into virus-like particles. *Bioconjugate Chem. 19*, 866–875.

(26) Iwig, J. S., Leitch, S., Herbst, R. W., Maroney, M. J., and Chivers, P. T. (2008) Ni(II) and Co(II) sensing by *Escherchia coli* RcnR. *J. Am. Chem. Soc. 130*, 7592–7606.

(27) Lippard, S. J., and Berg, J. M. (1994) *Principles of Bioinorganic Chemistry*, University Science Books, Mill Valley.

(28) Nakani, S., Viriyakul, T., Mitchell, R., Vitello, L. B., and Erman, J. E. (2006) Characterization of a covalently linked yeast cytochrome c - cytochrome c peroxidase complex: evidence for a single catalytically active cytochrome c binding site on cytochrome c peroxidase. *Biochemistry 45*, 9887–9893.

(29) Omura, T., and Sato, R. (1964) The carbon monoxide pigment of liver microsomes. *J. Biol. Chem. 239*, 2370–2378.

(30) Butt, W. D., and Keilin, D. (1962) Absorption spectra and some other properties of cytochrome c and of its compounds with ligands. *Proc. R. Soc. London, Ser. B 156*, 429–458.

(31) Clark, R. A., and Bowden, E. F. (1997) Voltammetric peak broadening for cytochrome c/alkanethiolate monolayer structures: dispersion of formal potentials. *Langmuir 13*, 559–565.

(32) Zhang, Z., Nassar, A.-E., Lu, Z., Schenkman, J. B., and Rusling, J. F. (1997) Direct electron injection from electrodes to cytochrome P450CAM in biomembrane-like films. *J. Chem. Soc., Faraday Trans. 93*, 1769–1774.

(33) Tanimura, R., Hill, M. G., Margoliash, E., Niki, K., Ohno, H., and Gray, H. B. (2002) Active carboxylic acid-terminated alkanethiol self-assembled monolayers on gold bead electrodes for immobilization of cytochromes c. *Electrochem. Solid State Lett. 5*, E67–E70.

(34) Tezcan, F. A., Winkler, J. R., and Gray, H. B. (1998) Effects of ligation and folding on reduction potentials of heme proteins. *J. Am. Chem. Soc. 120*, 13383–13388.
(35) Laviron, E. (1979) General expression of the linear potential sweep voltammogram in the case of diffusionless electrochemical systems. *J. Electroanal. Chem. 101*, 19–28.
(36) Udit, A. K., Hindoyan, N., Hill, M. G., Arnold, F. H., and Gray, H. B. (2005) Protein-surfactant film voltammetry of wild type and mutant cytochrome P450 BM3. *Inorg. Chem. 44*, 4109–4111.
(37) Udit, A. K., Hill, M. G., Bittner, V. G., Arnold, F. H., and Gray, H. B. (2004) Reduction of dioxygen catalyzed by pyrene-wired heme domain cytochrome P450 BM3 electrodes. *J. Am. Chem. Soc. 126*, 10218–10219.
(38) Anson, F. C., Shi, C., and Steiger, B. (1997) Novel multinuclear catalysts for the electroreduction of dioxygen directly to water. *Acc. Chem. Res. 30*, 437–444.
(39) Chang, C. J., Loh, Z.-H., Shi, C., Anson, F. C., and Nocera, D. G. (2004) Targeted proton delivery in the catalyzed reduction of oxygen to water by bimetallic pacman porphyrins. *J. Am. Chem. Soc. 126*, 10013–10020.
(40) Udit, A. K., Hagen, K. D., Gillan, J. M., Goldman, P. J., Star, A., Gray, H. B., and Hill, M. G. (2006) Spectroscopy and electrochemistry of cytochrome P450 BM3-surfactant films assemblies. *J. Am. Chem. Soc. 128*, 10320–10325.

BC900399E

Dendrimers for Vaccine and Immunostimulatory Uses. A Review

Peter M. H. Heegaard,*,† Ulrik Boas,†,‡ and Nanna Skall Sorensen†

Innate Immunology Group, National Veterinary Institute, Technical University of Denmark, Copenhagen, Denmark, and Chemical Institute, University of Copenhagen, Copenhagen, Denmark. Received July 3, 2009; Revised Manuscript Received September 14, 2009

Dendrimers are well-defined (monodisperse) synthetic globular polymers with a range of interesting chemical and biological properties. Chemical properties include the presence of multiple accessible surface functional groups that can be used for coupling biologically relevant molecules and methods that allow for precise heterofunctionalization of surface groups. Biologically, dendrimers are highly biocompatible and have predictable biodistribution and cell membrane interacting characteristics determined by their size and surface charge. Dendrimers have optimal characteristics to fill the need for efficient immunostimulating compounds (adjuvants) that can increase the efficiency of vaccines, as dendrimers can provide molecularly defined multivalent scaffolds to produce highly defined conjugates with small molecule immunostimulators and/or antigens. The review gives an overview on the use of dendrimers as molecularly defined carriers/presenters of small antigens, including constructs that have built-in immunostimulatory (adjuvant) properties, and as stand-alone adjuvants that can be mixed with antigens to provide efficient vaccine formulations. These approaches allow the preparation of molecularly defined vaccines with highly predictable and specific properties and enable knowledge-based vaccine design substituting the traditional empirically based approaches for vaccine development and production.

VACCINES: SOME CHALLENGES AND PROMISES

Infectious diseases continue to pose problems to human and animal populations, although they have been known for a long time, with the associated phenomenon of inflammation being among the earliest described medical symptoms, and although the universal principle of preventive action, vaccination, has been around for more than 300 years. Then known as variolation (*1*), this covers the rather delicate practice of preventing infectious disease by injecting infectious material into an individual. A vaccine traditionally contains pathogens (microbial agents that can cause disease) modified in a way that makes the pathogen lose its disease inducing capacity while at the same time maintaining a sufficient similarity with the unmodified pathogen to provoke the vaccinated host to become immune to disease through the actions of the immune system of the host.

Vaccination has proven to be a very cost-effective way of controlling infectious diseases caused by microbial pathogens and has been known in its modern form since the pioneering work in the late 18th century when Jenner introduced vaccinia (cowpox virus) as the first reliable vaccine (*1*). Subsequently, a range of other successful vaccines have been developed, empirically, on the basis of attenuated or killed microorganisms or their toxins. Nevertheless, efficient vaccines are still lacking against HIV[1] , tuberculosis, malaria, and a range of respiratory and intestinal infectious diseases.

Vaccination has had great successes, for example, resulting in the eradication of smallpox (officially declared extinct in 1980) and the dramatic decrease in formerly widespread diseases like polio, measles, and rinderpest (cattle disease). Even so, a wide range of infectious diseases are still abundantly present around the globe (malaria, tuberculosis, and bacterial and viral diarrhea being the most widespread). Such diseases are generally caused by complex pathogens where a more rational approach in vaccine design is needed (*2*). Some of these "difficult" pathogens attack the immune system itself or are able to change rapidly to avoid the immune system.

There is therefore a growing need for new-generation vaccines to target these infectious diseases. With an increased knowledge of the molecular actions of the immune system, there is now a unique possibility to exploit well-defined chemical methods to create such new vaccines with optimal qualities.

INTERACTIONS BETWEEN THE INNATE AND THE ADAPTIVE IMMUNE SYSTEM

The immune system is a complex of organs, cells, and molecules involved in the difficult task of controlling host defenses against infection. On one hand, it has to react promptly toward different groups of pathogens by mounting different types of protective effector responses. On the other hand, it has to ignore self-antigens and innocuous environmental antigens and microorganisms from food and environment. The decision of whether to react or not is governed by the innate immune system (*3*). This is composed of cellular actors like macrophages and granulocytes, which have the ability to take up and kill ("phagocytose") microbes, and of soluble mediators, such as the complement system and antimicrobial peptides, which function by flagging microbes for phagocytosis or by directly killing them (*4*). The innate immune system, in collaboration with tissue cells, acts as the first line of defense against pathogens (*3*).

* Corresponding author. National Veterinary Institute, Technical University of Denmark, Bülowsvej 27, DK 1790 Copenhagen V, Denmark, +45 35886241 (ph.), +45 35886001 (fax), pmhh@vet.dtu.dk (email).

† Technical University of Denmark.

‡ University of Copenhagen.

[1]ABBREVIATIONS: Aib, α-amino isobutyric acid; APC, antigen presenting cell; DNA, DNA; DC, dendritic cell; Th, helper T cell; HIV, human immunodeficiency virus; HPLC, high pressure liquid chromatography; Ig, immunoglobulin; LCP, lipid core peptide; MAP, multiple antigen peptide; MHC, major histocompatibility complex; MS, mass spectrometry; PAMAM, poly(amido amine); PAMP, pathogen associated molecular pattern; PBS, phosphate buffered saline; PEG, poly(ethylene glycol); PPI, poly(propylene imine); PRR, pattern recognition receptor; SOC, sequential oligopeptide carrier; TLR, Toll-like receptor.

10.1021/bc900290d © 2010 American Chemical Society
Published on Web 11/04/2009

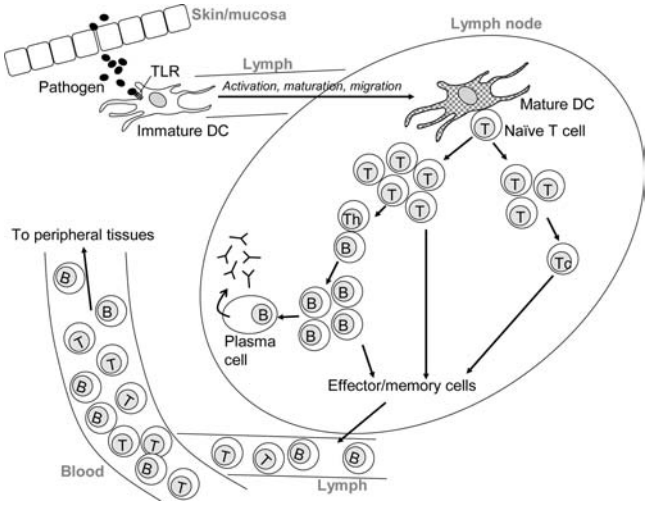


Figure 1. The general "physiology" of an immune response, including the innate response of dendritic cells (DC) at the site of infection through interaction of the pathogen with Toll-like receptors (TLR) and the following adaptive responses located in the lymph nodes resulting in the production of antigen-specific effector cells and molecules transported through the lymphatics and the blood vessels to the infection site.

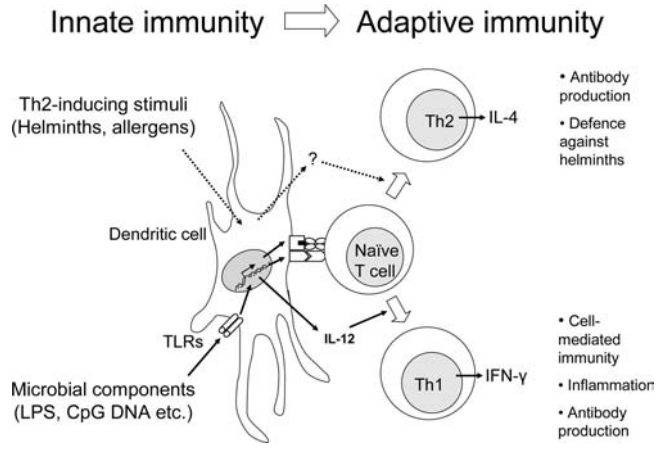


Figure 2. The concept of the polarization or biasing of the adaptive immune responses characterized by the proliferation of different T cell subsets secreting distinct patterns of soluble immune mediators (cytokines) as a result of differences in the nature of the initial microbial stimulus.

Throughout evolution, the innate immune system has developed the ability to become activated by recognizing highly conserved molecular structures specific to microbes (so-called pathogen-associated molecular patterns, or PAMPs) (*5*) by corresponding pattern recognition receptors including the Toll-like receptors (TLR). Binding of PAMPs triggers a fast innate immune response, producing molecular signals that report on the nature of the threat and control the ensuing early defense mechanisms as well as the balance of the subsequent adaptive immune responses (*3*). The adaptive immune system consists of T cells and B cells, which both use receptors with a wide range of specificities. T cell receptors recognize the complex of short peptides (= T cell epitopes) bound to MHC (major histocompatibility complex)-molecules on the surface of APCs (antigen presenting cells). B cell receptors are also secreted as antibodies which are the soluble version of the specific receptor from a given B cell. Antibodies as a protein class are known as the immunoglobulins, and they constitute the active component of humoral (soluble) immunity. In contrast to the T cell receptors, binding of antigens to B cell receptors (and antibodies) is not dependent on their prior binding to MHC molecules, i.e., their binding is not MHC-restricted. A B cell epitope is the site of an antigen molecule that is directly involved in the binding by a particular antibody. An antigen is, however, only an immunogen if it is able to induce an immune response. Functionally, an adaptive immune response comprises the production of antibodies by antigen-specific B cells generally aided by T helper cells in the following way: Upon binding of a protein antigen by the B cell receptor, the B cell will degrade it into peptides and load these onto MHC molecules on its surface, and only if an antigen-experienced (also known as a primed) T helper cell recognizes the peptide-MHC-complex will the B cell be licensed to produce its antibodies (see Figure 1). Such antibody responses are T cell dependent. Thus, although any structure can be recognized as an antigen, only protein-based antigens elicit efficient, full-fledged adaptive immune responses, because only proteins and peptides can engage the T cells required. Therefore, in order for non-protein structures to induce an adaptive immune response and immunological memory, such structures have to be attached to a protein (or peptide) carrier. The priming process is governed by dendritic cells (DCs) (reviewed in ref *6*) and DCs are the only cells that can serve as efficient antigen-presenting cells for this process (*6, 7*). As an example and as shall be seen below, this has formed the basis for a number of carbohydrate−peptide constructs rendering otherwise nonimmunogenic oligosaccharide antigens immunogenic. This is of considerable interest, as carbohydrate antigens are found on, e.g., tumor cells and viruses and have great biological and medical significance.

As a part of the innate immune system, the DCs form networks throughout the body along the skin and mucosal surfaces where they continuously take up antigens from their surroundings serving as sentinels and initiators of the adaptive immune response. Detection of microbes by TLRs on the DCs up-regulates surface expression of MHC molecules presenting pathogen-derived peptides and of co-stimulatory molecules (*3*). During an infection, large numbers of DCs activated in this way will migrate to the nearest draining lymph node, where they interact with and prime only the T cells that are specific for the presented peptides. The general "physiology" of this process is depicted in Figure 1. In addition, the binding of PAMPs to TLRs on DCs induce their release of various soluble mediators (cytokines and chemokines), which will influence the nature of the developing response (*3, 6, 8*). As a result, different effector T helper (Th) cell subsets will develop to promote different types of adaptive responses. A range of pathogens induce DCs to produce IL-12 and other inflammatory cytokines promoting the development of a Th cell subset called Th1 cells. Th1 cells are characterized by their production of interferon- (IFN-) γ. IFN-γ promotes cell-mediated immunity by activating macrophages and by inducing specific subsets of antibodies that enhance macrophage uptake and clearance of pathogens, and by helping to induce cytotoxic T cells. Other types of stimuli (*9*) will not result in the production of inflammatory mediators and will induce Th2 cells producing IL-4, IL-5, and IL-13 promoting another type of immunity characterized by antibody subtypes that can neutralize extracellular pathogens and toxins (*8, 10*) (see Figure 2).

The ability of DCs to take up and present soluble protein antigen in vivo is facilitated by the physical association between the TLR ligand and the protein in question (*11*). In addition, the efficiency of processing and presenting antigens from phagocytosed cargo appears to depend on the presence of TLR ligands within the same cargo (*12*). This means that antigen and TLR ligand have to be associated within the same molecular complex in order for the TLR ligand to efficiently enhance the immunogenicity of the antigen.

Table 1. Different Types of Conventional Adjuvants Classified after Dominant Mode of Action

delivery systems (aggregated/particular)	membrane active adjuvants
Freund's incomplete adjuvant water-in-oil susension aluminum salts liposomes ISCOMs[a] Polymers (PLG[b,c]), etc.)	saponins (quil A, tomatine a.o.) monophosphoryl lipid A[a] DDA[b]
immunomodulatory adjuvants	**mixed mode**
muramyl dipeptide cytokines nonmethylated CpG nucleotides	Freund's complete adjuvant oil-in-water suspensions RIBI, SAF, Titermax, Emulsigen, and others)

[a] Also immunomodulatory. [b] DDA: dimethyldioctadecylammonium bromide. [c] PLG: poly (lactide-*co*-glycolide).

Effector T cells, in contrast to naive T cells, will not enter lymph nodes and instead migrate to relevant nonlymphoid tissues to execute their effector functions (*8, 10*). Importantly, after a microbe has been cleared a subset of effector T cells survives and differentiates into long-lasting memory T cells that are able to respond rapidly to low doses of antigen even in the absence of co-stimulation (*8, 10*). Likewise, memory B cell responses are faster and result in higher-affinity antibodies of subclasses efficiently linking up with cellular immunity (*8*). Thus, immunological memory is a state characterized by enhanced numbers of long-lived and optimally reactive antigen-specific T and B cells and long-lived plasma cells producing high-affinity antibodies (*2, 13*).

VACCINES AND ADJUVANTS

Vaccines are nonpathogenic imitations of pathogens, which, when administered to a host (vaccination), induce immediate as well as long-lasting immunity (host resistance) against the pathogen. This is based on the ability of the immune system of the host to adapt to and thereby *remember* infectious challenges. Modern vaccine design relies on the careful selection of one or a few subunits of the pathogen (antigens). As subunits are often weak immunogens, they normally have to be formulated using adjuvants (latin, adjuvare = to help), i.e., substances enhancing immune responses to antigens mixed with them. Adjuvants can either be delivery systems or immune potentiators (*14*). Delivery systems in general function by aggregating and/or polymerizing antigens, minimizing their spreading from the injection site, increasing their half-life and enhancing their uptake and processing by local antigen-presenting cells (APCs, see below) (*14*−*16*). Immune potentiators may be microbial products or their synthetic versions, or endogenous immunoactive compounds, such as cytokines, chemokines, or costimulatory molecules (*14*). The development of adjuvants has, like that of vaccines, generally been empirically based, and to a large extent, the most efficient adjuvants are complex and somewhat undefined mixtures of surface-active compounds, microbial components, and/or various polymers and lipids (see Table 1), most of which cannot be approved for human use.

An exception is adjuvants based on aluminum salts, broadly referred to as alum, which have good safety profiles with relatively mild side effects and therefore can be applied for human use (*14*). Alum functions as an aggregate delivery system promoting increased uptake by APCs and a Th2 biased antibody production (see below). Next to alum, emulsions of water-in-oil or vice versa stabilized by surfactants are most frequently used (*16*). With a range of important infections, a Th1 response (see below) is needed to obtain protection against disease, but safe and efficient Th1 inducing adjuvants are generally lacking or unsuitable for human use, an example being Freund's complete adjuvant (*16, 17*). Well-known delivery systems include liposomes and microparticles, which are inert carriers of antigen unless immune potentiators have been added to them (*16*). Examples of promising immune potentiators are microbe-derived structures like monophosphoryl lipid A and unmethylated CpG oligonucleotides (*16*). Immune potentiators also may be employed as targeting devices leading the immunogen to optimal antigen presenting cells, e.g., at mucosal surfaces.

Whether a relevant immune response and an ensuing immunological memory directed against the desired antigens will actually provide protection against pathogen-induced disease is dependent on many factors. Early and topically precise responses at the initial site of infection are highly efficient, as the race between the kinetics of a memory-based immune reactivation and pathogen-driven disease development is decisive in the outcome of the infection (*13*). If pre-existing antibodies are present to neutralize a pathogen or its toxins early in the establishment of the infection, vaccine induced immunity boosted at the same time by the infection will cooperate with the pre-existing antibodies to eradicate the pathogen (sterilizing immunity) (*2*). Systemic and mucosal immunity can play together in this, the most efficient immunity achievable to completely prevent establishment of infection.

In order to improve vaccines for the future, there is a need for development of efficient and safe adjuvants for induction of Th1-biased responses, and for inducing immunity at mucosal surfaces. Furthermore, such new adjuvant systems should preferably be molecularly defined. Delivery systems may be combined with immune potentiators to induce Th1-biased immune responses. However, the challenge is to develop adjuvants that are as simple, definable, stable, safe, and generally usable as possible and at the same time in a very efficient way induce the complex responses needed for the creation of optimal immunity. On the basis of relevant scientific and patent literature, the use of highly branched, synthetic polymers known as dendrimers for this purpose is described here.

DENDRIMERS: HISTORY AND STRUCTURES

Dendrimers are a relatively new class of well-defined (i.e., monodisperse) hyperbranched polymers first developed under the name cascade polymers by the group of Vögtle in 1978 (*18*). These initially small hyperbranched molecules constitute the foundation for the later design of polypropylene imine (PPI) dendrimers, developed by the Meijer and Mühlhaupt groups in the early 1990s (*19, 20*). In 1983, Tomalia et al. reported on a new class of dendrimers based on a mixture of amines and amides, the so-called polyamido amine dendrimers, commonly known as PAMAM dendrimers (*21*). A number of other dendrimer designs were reported by various research groups during the 1980s and 1990s, and the development of new dendrimer designs is still ongoing (for an early alternative to PPI and PAMAM dendrimers, see ref *22*).

The dendritic theme was, early in dendrimer history, already taken up by chemists working in the biosciences. In 1988, Tam and co-workers developed the multiple antigen peptide (MAP) system; a dendrimer (or dendron) based on lysine as the monomer (*23a*) and several peptide-based dendrimer designs emerged later (*23b*).

The general structure of dendrimers comprises a well-defined branching pattern from the core and out toward the periphery. The branching defines the dendrimer "generation", with generation 1 being the dendrimer containing only one layer of branching points. The branching principle means that addition of one new branching shell, i.e., an increase in dendrimer generation, will also lead to a doubling of the number of functional groups on the surface of the dendrimer. A fifth-generation PAMAM dendrimer or, more briefly, a G5-PAMAM

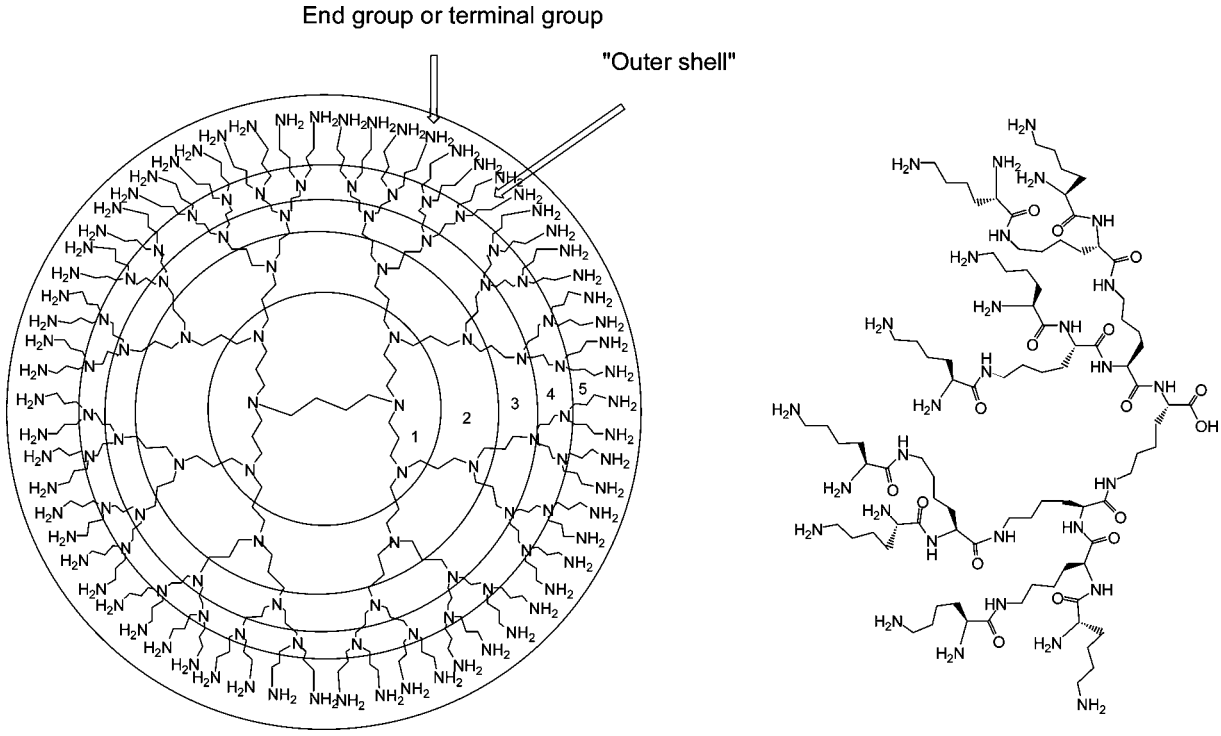


Figure 3. Two examples of dendrimer designs. Left: A G5-PPI (generation 5 poly(propyleneimine)) dendrimer; generations ("shells") are indicated. Right: multiple antigen peptide (MAP) dendron.

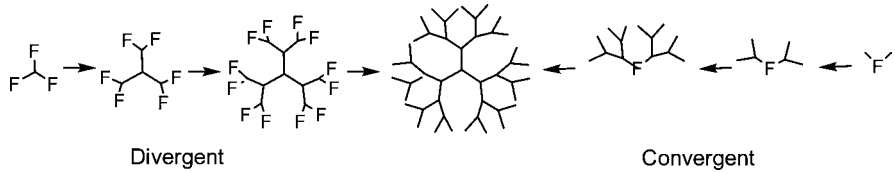


Figure 4. Divergent versus convergent strategy for synthesis of dendrimers. F: "focal points", i.e., starting or branching points where a new shell may be formed either by attaching new "branches" (divergent synthesis) or by coupling entities together to form a bigger dendron (convergent synthesis).

thus contains five branching shells. The inner structure of globular dendrimers is organized into so-called dendrons, which are "tree-shaped" molecular "subgroups" of the dendrimer (see Figure 3). The PAMAM and PPI dendrimer design has a symmetric spherical structure, but other designs as, e.g., the MAP dendrimer are more dendron-like (i.e., tree-shaped) in their design. As a consequence of the intense branching in the dendrimer structure, the higher-generation dendrimers become increasingly globular in structure, with a high number of functional (i.e., terminal) groups displayed at the surface. In the higher-generation dendrimers (G > G3), the dendrimer structure becomes progressively more compartmentalized, with a core region increasingly shielded off from the surrounding solution by the outer shell (the molecular area just beneath the surface), which becomes much more molecularly dense with higher generations.

Dendrimers exhibit a highly multivalent surface conferring a strong potential for interactions with the surroundings. In biology, this property can be rationally exploited, e.g., using dendrimers carrying multiple surface ligand molecules leading to stronger binding per ligand unit compared to the corresponding monomeric ligand. This synergistic increase in binding affinity is due to the preorganization of the ligands at the dendrimer surface, which reduces the loss in entropy upon binding to the dendrimer. This phenomenon is called "the dendritic effect" (also known as the "chelate effect" or "cluster effect"). Dendrimers are flexible molecules varying in hydrodynamic volume depending of solvent type (polarity), salt concentration, and pH, i.e., the dendrimer can show environmentally sensitive extended or contracted conformations. This behavior is intimately connected with the chemical buildup of the dendrimer, with some dendrimers contracting at physiological conditions and others increasing their volume.

Synthesis of Dendrimers. Generally, dendrimers can be synthesized by two approaches. The approach initially applied in the synthesis of PPI and PAMAM dendrimers is called the divergent strategy (Figure 4, left part) in which the dendrimer is synthesized starting from the core and functionalized out toward the periphery. This method has the drawback that the strongly increasing number of reaction points (i.e., surface functionalitites) as a result of the hyperbranching strongly increases the risk of introducing deletions in the structure. Such defective dendrimers are difficult to remove from the final product mixture because of the great molecular similarity with the product. To circumvent this problem, an alternative approach was developed by Hawker and Fréchet relying on the synthesis of the dendrimer from the surface and inward, i.e., the synthetic sequence ends up by joining two or more large dendron segments together at the core to synthesize the final dendrimer (Figure 4, right part). This approach was named the convergent approach (*24*) and has the advantage that intermediate purification is facilitated because of the larger molecular difference (large difference in molecular size and polarity) between the product and the reactants.

Biocompatibility of Dendrimers. For application of dendrimers for biological or biomedical purposes, including therapy,

diagnostic purposes and vaccination, their biocompatibility, i.e., cytotoxicity, immunogenicity, and ability to penetrate various physiological and cellular barriers (including cell membranes), their biodistribution and biological fate (half-life in circulation, excretability, etc.) is of obvious interest.

As a rule, the dendrimer interior structure is to a large extent shielded from the surroundings by the outer shell and the surface, meaning that the biological properties of a dendrimer to a large extent are governed by the characteristics of the surface groups and of the size of the dendrimer. Amino surface groups interact strongly with biological membranes as a result of their highly positive charge and the negative charge of most cell membranes resulting in a high cellular uptake of these molecules by endocytosis. However, with higher-generation (G > G3) amino terminated dendrimers their membrane affinity leads to a more destructive interaction with the membrane resulting in cellular lysis and high cytotoxicity both in vitro and in vivo. The opposite behavior is observed with dendrimers having negatively charged surfaces, e.g., carboxylic acid surfaces. These dendrimers do not interact with most cellular surfaces and hence do not show significant generation dependent cytotoxicity. Noncharged groups may be divided into polar and nonpolar groups, polar membrane noninvasive groups like poly(ethylene glycol) (PEG) chains resulting in a nontoxic behavior of the dendrimer, whereas nonpolar groups as, e.g., lipids interact with the cellular membrane by hydrophobic interactions, in some cases rendering the dendrimer cytotoxic. However, lipids, being an important part of, e.g., bacterial surfaces and molecular targets of the immune system can endow dendrimers with immunostimulating properties (see below). Generally, dendrimers with higher molecular size show a lower biopermeability, regardless of the nature of their surface groups, and in vivo, high-generation dendrimers have high clearance rates from the body via renal excretion, as their size and lack of flexibility result in limited permeability of these dendrimers into the tissues (for a more thorough discussion on this matter, see ref *25*). This results in high levels of dendrimer being deposited in the organs (e.g., liver and kidneys) before excretion. High-generation dendrimers having noncharged PEG chains or negatively charged carboxylate groups on their surfaces show no toxicity. Carboxylate surfaced dendrimers are cleared more rapidly from the bloodstream and deposited into the organs compared to PEG modified dendrimers. The longer blood circulation times of the PEG covered dendrimers are presumably due to the noninvasive character of PEG, which reduces interaction with the vascular walls. High-generation cationic dendrimers (G > G6) may cause problems of toxicity in vivo (*26*). In addition to the tissue toxicity, high-generation amino surfaced dendrimers also result in inflammation and activation of the complement system. As with the membrane interacting, lipid-bearing dendrimers there is a fine balance between cytotoxicity and stimulation of cellular components of the immune system (see below).

DENDRIMER CARRIERS FOR COVALENT ATTACHMENT AND MULTIVALENT DISPLAY OF ANTIGENS

To increase the specificity of vaccines, they should employ highly defined, small parts (subunits) of the pathogen, for example, a peptide representing a part of a microbial protein. There is also a specific need for antibodies directed against small molecules for a wide range of other applications such as diagnostic assays, detection of small molecules (pesticides, peptides, a variety of inorganic molecules) and for research purposes (medical, life sciences, etc.) where exquisite specificity (sub-biomacromolecule) is needed.

Small molecules, however, as a rule, are not immunogenic (*27*). The traditional solution to this has been to couple the antigen of interest to a carrier protein or, in the case of peptides, to polymerize it (*28*−*30*), as increasing the size of the molecule has been empirically known to increase immunogenicity, possibly aided by the presence of multiple copies of the antigen in the molecule and the presence in the carrier protein of T cell epitopes (*30*). Traditional carrier proteins include albumin, ovalbumin, keyhole limpet hemocyanin, and others (*30*). Dendrimers as well-defined, multivalent, derivatizable, and stable molecules are ideal carriers of small antigens, making it possible to prepare multimeric antigenic conjugates with well-defined molecular properties (vide infra) also for human uses. As described above, dendrimers are prepared by highly efficient reactions and therefore, at least for low- and mid-generation dendrimers, are definable at a level normally achievable with much smaller molecules only, leading to molecularly defined antigen-carrier conjugates. To this can be added flexibility in design, ease of handling, and a relatively low price.

It is implicitly assumed for the long list of proposed in vivo uses of dendrimers (imaging, targeting, stabilization (*25*)) that dendrimers do not induce adverse host responses, including immune and/or inflammatory reactions upon administration. With a few exceptions, this generalization seems to hold true for "naked" (i.e., nonderivatized) dendrimers of most types; however, there are very few studies reporting on systematic investigations of this aspect of dendrimer biology. Plank et al. (*31*) reported on complement activation by DNA−dendrimer complexes, and as will be presented below, some dendrimers do seem to exhibit stand-alone adjuvanticity (*32*−*34*). As carriers, dendrimers can be considered immunologically inert scaffolds, and this is the most widespread use of dendrimers for promoting immunogenicity.

Multiple Antigenic Peptide (MAP) System. Interest has focused on one specific class of dendrimers, namely, the peptide dendrons of Tam et al. first described in 1988 (*23a*) (see Figure 3). Historically, these structures were rooted in the peptide world rather than the dendrimer world, peptides being the subject of intense interest as antigens in the 1980s due to the advances in peptide solid-phase synthesis occurring at that time (*35, 36*) and due to the realization that high-affinity immune reactivity demanded efficient methods for presenting peptides to the immune system to be developed and implemented.

Further peptidic dendron designs were described in a number of patents and scientific papers in the 1990s (*23a, 37*−*43*) with some developments described later (*44*), and the MAP carrier is by far the most investigated dendrimer for immunization and vaccination purposes to date (*45*). An excellent review on the structure and synthesis of peptide-based dendrimers in general has been published by Crespo et al. (*23b*).

The basic structure described by Tam (*23a, 37*) is a dendron constructed solely from lysine, taking advantage of the two amino groups (α and ε) being present in each lysine molecule thus constituting branching points for logarithmic growth. A two-layer dendron thus has four free amino groups and a three-layer has eight, equally divided between α- and ε-amino groups (see Figure 5 and Table 2). Tam coined the name "major antigenic peptide" (MAP) for such a structure derivatized with molecules of interest, not limited to peptides but any small molecule that could bind covalently to the terminal amino groups of the MAP "core" dendron.

MAP "cores" are presently available commercially most often bound by a specifically cleavable bond to a solid phase for easy access to stepwise solid-phase peptide synthesis.

The characteristic high-density multimers obtained by this method are claimed to have a favorable immunogenicity, stabilized attached peptide structures, a shielded MAP core not interfering with immune reactions, and an adequate molecular weight (>10 kD) for stimulating immune responses (see

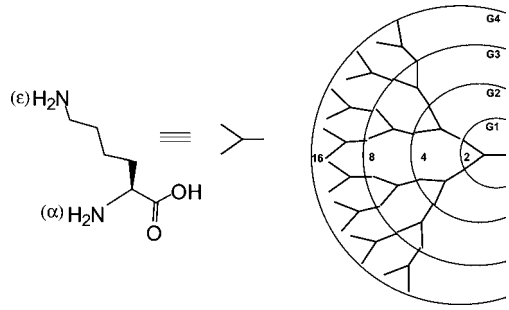


Figure 5. The basic MAP core, based on lysine (left) as the only monomer, indicating core structure and generation dependent increase of amino group numbers, leading to increasing crowding of amino groups in shells of higher generation.

Table 2. PAMAMs and MAPs: Physicochemical Characteristics

type	generation[a]	molecular weight	no. of surface primary amines
PAMAM[b]	1	517	4
	2	1430	8
	3	3256	16
	4	6909	32
	5	14 215	64
	6	28 826	128
MAP	1	147	2
	2	405	4
	3	921	8
	4	1953	16
	5	4017	32

[a] Generation as defined for PPI dendrimers; see text. [b] Data obtained from www.dendritech.com.

reviews (*46*−*50*) and Sadler and Tam (*45*)). Tetra- and octameric MAP cores are preferred, as higher generations are associated with synthesis problems because of increased steric hindrance (incomplete acylations) and increased insolubility due to intra- and intermolecular aggregation phenomena (see discussion below), and increasing the MAP generation often does not improve immunogenicity (*48, 49*).

Molecularly defined immunogen constructs based on the MAP system (*23a, 40, 41, 45*) have been reported to produce peptide-specific antibodies (*45*) and have been applied for vaccine use, for example, a MAP-based malaria vaccine (*42, 51, 52*) which has been tested in phase I clinical trials. This approach seems, however, to have been abandoned for more simple (linear) constructs that seemingly work just as well, provided that a universal T cell epitope was included and mixing with adjuvant was done (*53*). The paper states that "the technical challenges of synthesizing large quantities of homogenous, physical-chemically characterized branched peptides prevented scale-up for production of peptides".

There is also a demand for carriers for efficient presentation of other antigenic moieties than peptides, especially carbohydrates which are found as viral and bacterial surface constituents. When present in their natural membrane environment, these substances are often immunogenic due to noncarbohydrate membrane constituents (lipids and proteins), but on their own, carbohydrates as a rule show low immunogenicity (*27*). Another group of carbohydrate antigens of significant clinical interest is the cancer-specific antigens found on the surface of transformed cells. Such antigens are of diagnostic interest and are evidently also of interest as therapeutic targets or as "address labels" for targeting cytotoxic compounds to transformed cells (*25*). While some types of carbohydrates presented on glycodendrimers (Gal (β1−3) GalNac on G1-G4 PAMAM) are explicitly nonimmunogenic despite their surface-localized, multimeric presentation (*54*), MAPs have been used for presentation of the cancer-specific carbohydrate Tn-antigen (*55*) (αGal-Ser/Thr). In that study, a tetrameric MAP core structure was coupled with the Tn-antigen and with a T cell epitope and was shown to react with monoclonal antibodies against Tn. The same MAP core containing the T cell epitope coupled with trimeric Tn-antigens, i.e., $(\alpha$Gal-Ser/Thr$)_3$ coupled to each of the four "branches" of the MAP was shown to be immunogenic in mice using alum as an adjuvant (*56*). The construct could be used for active immunization against colon carcinomas in BALB/c mice. As both the MAP analogue carrying mono-Tn epitopes and a linear analogue containing two tri-Tn moieties were much less efficient immunogens, it was concluded that the precise spatial arrangement and clustering of the Tn-epitope was very important for the immunogenicity.

Importantly, the MAP core by itself does not seem to be immunogenic and does not confer adjuvanticity to a MAP complex, and accordingly, an adjuvant is needed to boost immune responses against its coupled antigens. Almost all immunizations with MAP constructs reported in the literature have been performed with traditional adjuvants, including aluminum hydroxide, Freund's adjuvant, and saponin adjuvants (*57*). Moreno et al. (*42*) compared the efficiency of a number of such adjuvants with a MAP containing malarial T- and B-epitope peptides in monkeys and mice using subcutaneous administration. A satisfactory response was obtained in both species using the saponin adjuvant QS21 (see Table 3).

As with conventional immunogens, the success of MAPs in vaccination is heavily dependent on choice of adjuvant, dose, and administration route. For example, an octameric FIV (feline immunodeficiency virus) MAP administered with Freund's adjuvant gave rise to high levels of FIV-neutralizing antibodies, while administration with the saponin QS21, although leading to antibodies and cytotoxic cellular responses against the immunizing peptide, did not induce neutralizing activity (*58*). The inclusion of immunopotentiating moieties in MAP structures to ensure adjuvanticity has been demonstrated and is discussed below.

In addition to the lack of adjuvanticity of the MAP core, this structure evidently does not contain T cell epitopes that are needed to achieve a complete adaptive immune response, in contrast to conventional high molecular weight carrier proteins where such epitopes are normally present (*30*). It is thus advantageous to be able to include both B- and T-cell epitopes in a MAP.

The MAP "core" is simple to synthesize by conventional solid-phase peptide synthesis, allowing branching to occur by deprotecting both amino groups in each amino acid residue at the same time (see Figure 6) achieving maximum branching and multimericity in minimal space. Moreover, with peptide antigens, these may be synthesized by solid-phase synthesis, in one synthesis series, on the free amino ends of a solid-phase-coupled MAP core, completing synthesis of the whole immunogen in one peptide synthesis setup accomplishable by automated solid-phase peptide synthesis (*23a*) (Figure 6).

Convergent synthesis strategies have also been reported. Here, coupling of peptides or other molecules is performed in one step to the free amino groups of the MAP core. By using orthogonal protection strategies and/or chemoselective coupling methods, the controlled coupling of different peptides to the same MAP core can be achieved (*48, 59*). Convergent synthesis strategies can be used to overcome problems with stepwise synthesis as, e.g., incomplete acylation steps due to aggregation of the growing peptide chain during synthesis, which is quite often observed, in a sequence-specific manner at high peptide densities during solid phase peptide synthesis (*36*). Also, unprotected peptide segments to be coupled can be purified to homogeneity before coupling, increasing the raw product purity of the MAP, facilitating purification of the MAP. Spacer

Table 3. Peptide Dendrimer Vaccination Results (Serum Titers[b]) with and without Additional Adjuvant (Selected Examples)[a]

	titer, no adjuvant	titer, with adjuvant/type of adjuvant[c]
MAP Carriers		
T cell receptor peptide (*37*)	ND[d]	10^3-10^5/CFA+IFA 10^3-10^4/Alum
malarial peptides (*42*)	ND	10^4/Alum 2×10^5/Alum+QS21
carbohydrate antigen (Tn) (*56*)	ND	5×10^5/Alum
MAP Carriers with Built-in Adjuvanticity		
T cell epitope inclusion: malarial peptides (*76*)	low	6.5×10^4/Titermax 5.3×10^4/CFA+IFA 2.4×10^4/P1004-MPL
lipid core peptide		
streptococcal peptides (i and ii)	1.0×10^5 (i), 6.9×10^3 (ii)	2.2×10^6 (i), 2.6×10^6 (ii)/CFA
peptide alone (*77*)	ND (i), none (ii)	2.0×10^6 (i), 9.0×10^4 (ii)/CFA
chlamydial peptide (chimeric)	ND	5.1×10^5/CFA, 2.6×10^5/NAGO
peptide alone (*39*)	ND	160/CFA
tripalmitate peptide: HIV gp120 peptide, intragastric route (*82*)	1020	ND
Other Peptide Carriers with Built-In Adjuvanticity		
SOC with palmitate tail: lupus autoantigen (*69*)	2.5×10^4	2.5×10^4/CFA+IFA

[a] All immunizations in mice. For complete immunization protocols, consult references. [b] Serum titer against peptide antigen defined as highest dilution giving an OD significantly over the background OD (normal mouse serum), as tested against immunizing peptide. Titers are not comparable between different experiments and antigens. [c] CFA, complete Freund's adjuvant; IFA, incomplete Freund's adjuvant; NAGO, neuraminidase/galactose oxidase; MPL, monophosphoryl lipid A; P1004 and Titermax, nonionic block copolymers; QS21, purified saponin. [d] ND: not determined.

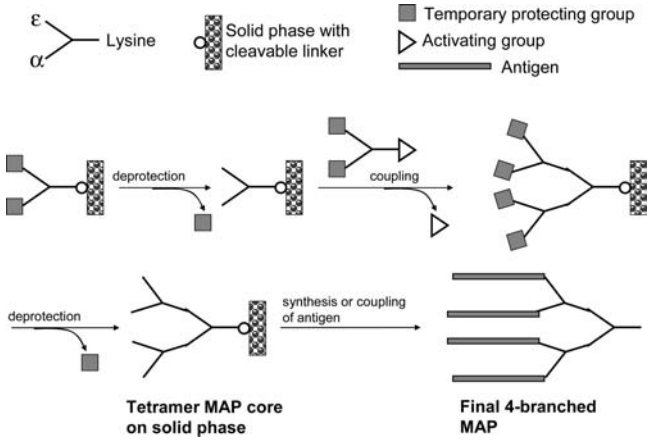


Figure 6. Steps in the solid-phase synthesis of a MAP structure (core and antigens).

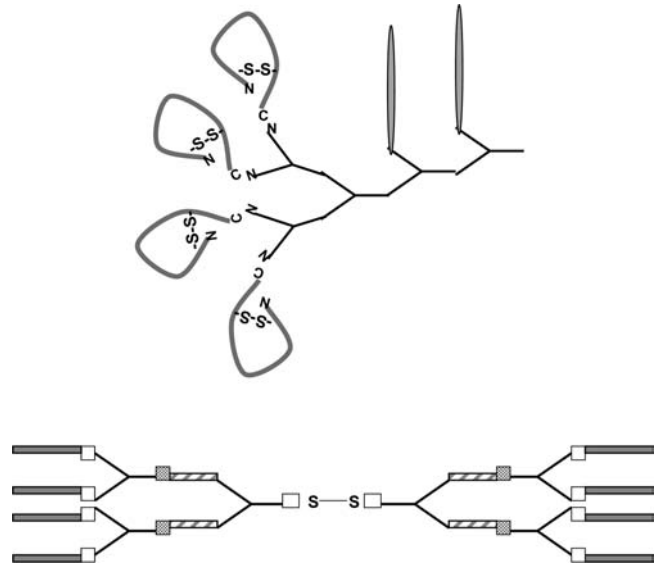


Figure 7. Examples of incorporation of spacers, lipids, and cyclic molecules in MAP structures. Top: Tetrabranched MAP with a dilipidated core and four copies of a cyclic foot-and-mouth disease peptide (*61*). Bottom: Two-dendron 8-branched MAP with two different antigenic peptides (elongated squares) and two different types of peptide spacers (small squares), one type (gray) being cathepsin cleavable (*84*).

segments can be introduced to increase flexibility and accessibility (*46*), and highly structure-stabilized cyclic peptides can also be accommodated in the MAP (*60*), increasing chances of building accurate antigenic peptide mimics for loops and turns in proteins; an example of this is the tetravalent MAP containing cyclic foot-and-mouth disease virus peptides described by Oliveira et al. (*61*) (see Figure 7).

Efficient chemoselective methods for coupling unprotected peptides to MAP cores include creating nonpeptidic bonds between the MAP core and the peptide, e.g., by reacting a thiol nucleophile, which could be the thiol group in the side chain of a cysteine residue, a thiol group introduced by 2-iminothiolane (Traut's reagent), or a thiocarboxylic acid, with a haloacetylated amine, readily obtained by reacting a primary amine with haloacetic anhydride, typically bromoacetic anhydride. In this way, an α,ε-bromoacetylated MAP core can be reacted with thiol-containing peptides forming stable thioether bonds or less stable thioester bonds. Thioester bonds are unstable at pH 7 and above. Chemoselectivity introducing nonpeptidic bonds is also obtained by reacting aldehydes with weak bases, for example, hydroxylamine or substituted hydrazine, forming oxime and substituted hydrazone, respectively (*59*) (see Figure 8). This can be done under acidic conditions inhibiting the competing reaction of nucleophilic groups, which are commonly found in peptide side chains, with the weak base. Aldehydes are not normally present in peptides but can be introduced by mild oxidation of serine, threonine, or cysteine. In this way, an aldehyde containing MAP core can be reacted with aminooxyacetylated peptides forming oxime linkages that are stable at pH 2−7 or with peptide acylhydrazine forming hydrazone-linkages that may be reduced to the more stable hydrazine (Tam (*49*) and Tam and Spetzler (*59*) review these chemistries). Amino-oxyacetic acid is commercially available and can be attached to an amino group of choice, and peptide acylhydrazine can be obtained by reacting a peptide ester with hydrazine.

By using selectively cleavable (orthogonal) protection groups on the α- and ε-amino groups of the MAP core, respectively, the activation, e.g., by bromoacetylation can be confined to one

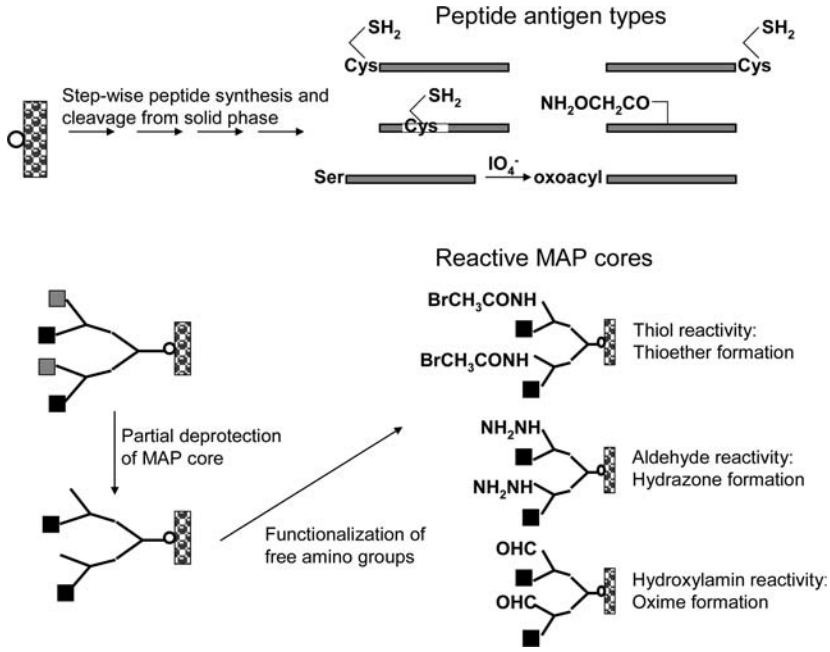


Figure 8. Examples of chemoselective schemes for convergent synthesis of heterofunctionalized MAPs with examples of different types of natural and unnatural peptide functional groups that can be coupled to MAP cores with different reactive groups (after Tam and Spetzler (*59*)). Note that chemistries can be "turned around", i.e., a functional group may be added to either the peptide antigen or the MAP core as desired (as both molecules are peptides).

of these types of amino groups, leaving the other one free for another type of coupling. This allows two different moieties, e.g., T cell peptide epitopes and B cell peptide epitopes, to be coupled to the MAP core in a controlled way. The orientation of the peptide to be coupled can be controlled by the position of the cysteine residue in the peptide (*49, 59*). If the peptide contains a cysteine residue in its natural sequence, this of course limits the possibilities.

Even when using convergent synthesis strategies and low-generation MAPs, which are much less crowded than higher generations, steric hindrance can be present as, for example, described for the preparation of a foot-and-mouth disease virus tetramer MAP by segment coupling: here, a significant proportion of trimer MAP was obtained in the raw product in addition to the desired tetramer (*61*). It has also been reported that even small, commercially available MAP cores may not always show the expected valency (*62*).

The toxicity of MAP structures is generally proportional to the number of free amino groups present. This was investigated for the lipid core peptides (LCP) constructs of Toth (*39*) (see below), and it was demonstrated that cytotoxicity was closely related to the number of cationic groups (amines) on the dendrimer and that toxicity was counteracted by lipid moieties; i.e., molecules with high lipid/amino group ratios were less toxic than molecules with low ratios even at the same number of amino groups (*44*). If amines were substituted, the lipidated dendrimers showed no toxicity. The correlation between cation character and cytotoxicity is a recurring theme with dendrimers (*25*) and can be hypothesized to be caused by the positive charge favouring cell surface interactions facilitating cell membrane perturbation.

Although native peptide structure has been directly shown to be stabilized in a MAP structure (*63*), this is apparently not always the case (*46*). This can be a problem when attempting to raise antibodies that are not only able to react with the immunizing peptide but also with the cognate protein. Limited aqueous solubility has been reported for some MAP constructs (*46*), most probably due to the formation of intermolecular aggregates and/or by intramolecular collapse of peptide conformations in the "branches" of the MAP molecule. In addition to the loss of native peptide structure and the resulting problem with achieving cognate protein immunoreactivity, this leads to problems of handling and dosing such immunogens and, importantly, dramatically decreases the possibility of analyzing the molecule by high-resolution high-precision methods such as mass spectrometry (MS) and HPLC-MS, compromising the possibility of documenting these structures (*42*) or demanding extensive purification to be carried out (*64*), making large-scale production of such vaccine constructs challenging (*53*).

In reality, the propensity of MAP structures to aggregate into difficult-to-analyze complexes may be an important factor in ensuring high immunogenicity of MAP constructs, providing supramolecular structures (aggregates) with very high molecular weights being highly "visible" to the immune system and with high biological stability. This may be promoted by the dense packing of fully substituted lysine residues in the MAP core, which therefore is very hydrophobic and highly amenable to aggregation in aqueous solvents.

Other Peptide-Based Branched Carrier Systems. The concept of using branched peptides for a conformationally controlled display of peptide antigens was also addressed in two different systems of Heegaard et al. (*65*) and Tsikaris et al. (*66*), respectively. Although not strictly dendrimeric in the narrow definition of the term, the main idea here is that the attachment with an optimized spacing to a conformationally stabilized peptide carrier of peptide antigens will restrict the conformational freedom of the peptide antigens, presenting them with better spatial definition than the free peptides, thereby allowing a higher chance of cross-reactivity of the ensuing antibody response with the conformationally defined peptides in their protein of origin. The sequential oligopeptide carriers (SOCs) of Tsikaris et al. (*66, 67*) are thus constrained peptide scaffolds, made up of α-amino isobutyric acids (Aib), e.g., repetition of Lys-Aib-Gly or Aib-Lys-Aib-Gly, in which the ε-amino group of Lys forms attachment points for peptides (Figure 9). Aib was chosen for its pronounced ability to promote α-helix conformation (*68*). Depending on the spacing of the derivatizable lysine residues, antigenic peptides are displayed

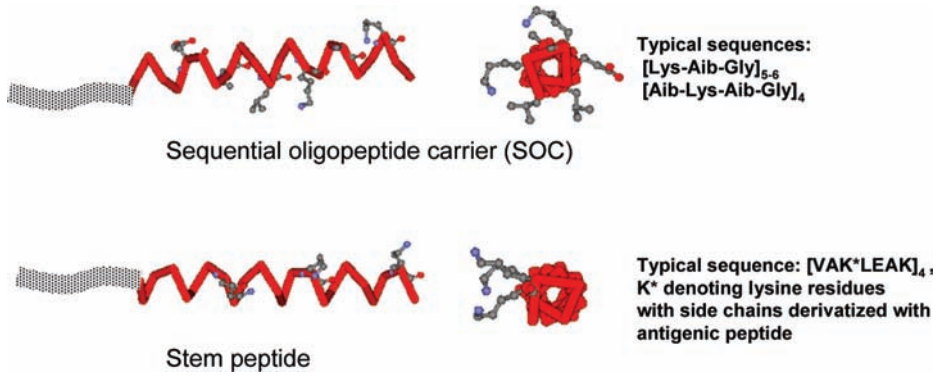


Figure 9. α-Helical model peptide structure (derived from PDB file 1cos.pdb) indicating distribution of attachment points for the sequential oligopeptide carriers of Tsikaris et al. (*66*) and the stem peptide carriers of Heegaard et al. (*65*) as viewed from the side (left) and from the end (right) of the helix. A lipophilic moiety has been included in these structures at the positions indicated (fat dotted line).

at different directions from the carrier helix axis, presumably affecting both antigenic and immunogenic properties (see, e.g., Kargakis et al. (*69*)). The presence of the unnatural amino acid Aib is claimed to cause increased biological stability and hence a prolonged presence of the immunogen, helping to increase efficiency of the immunogen.

These carriers are designed to support the structure (conformation) of the attached peptides, i.e., the peptides will show a more "native" conformation when coupled to the carrier, since peptides coupled to a carrier and being in close contact with the carrier and with each other will experience an environment resembling the crowded peptide-filled space in a folded protein.

The phenomenon of stabilization of inherent conformational structure in small peptides by organizing them on a template has been demonstrated by Tuchscherer et al. in so-called template assisted synthetic peptides (TASP) structures (*70*) in which four identical peptides are coupled to a cyclic template. The increased conformational definition of the coupled peptides compared to the free peptides was shown for a number of different peptides in the TASP system (*70, 71*). None of these systems have reached the popularity of the MAP carriers, maybe due to the simplicity of the MAP carriers.

Non-Peptide-Based Dendrimer Carrier Systems. G5-PAMAM (Starburst) dendrimers have also been used as carriers of the carbohydrate Tn-antigen (see above). These Tn-antigen−dendrimer conjugates were not immunogenic, whereas a Tn-antigen carrying protein (asialo submaxillary mucin) and a dimeric Tn-antigen-conjugated to tripalmitoyl-*S*-glycerylcysteinyl serine lipopeptide gave rise to antibody responses (*72*). In contrast, an octavalent G2-PAMAM with the cancer-related monosaccharide GlcNAc coupled on its surface was immunogenic and resulted in increased cellular immunity leading to reduced tumor growth of previously inoculated melanoma cells in mice, and thus holds promise as a therapeutic agent against this type of cancer (*73*).

Carbohydrate-based (*74*) and polyphenylene-based (*75*) dendrimers have also been reported to be useful as carriers of peptides for immunization purposes; however, no evidence has been presented regarding the immunogenicity obtained with these molecules.

Dendrimer Carriers with Built-In Adjuvanticity. Ideally, a molecularly defined carrier system should not need traditional, molecularly undefined adjuvants to attain sufficient immunogenicity, and should also be able to induce T cell immunity and T cell help.

In the MAP system, different variants of the basic MAP construct containing defined mixtures of B- and T-cell epitopes have been reported (*45, 76*) as have lipid-containing MAPs ("lipid core peptides" (*43, 77*), tripalmitate structures (*78*)), with the lipid serving as a built-in adjuvant (some examples of lipidated constructs are shown in Figure 10, and Table 3 summarizes the immunological properties of some of these carriers).

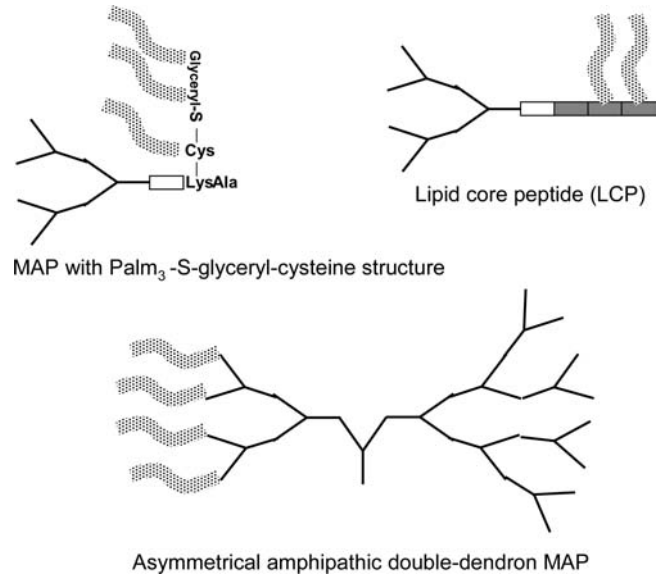


Figure 10. Examples of published self-contained adjuvant MAP structures. Fat dotted lines indicate fatty acid moieties.

Early examples of derivatizable MAP carriers with built-in adjuvanticity (*38*) contained a core region comprising a covalently coupled synthetic adjuvant moiety, viz., the immunostimulating tripalmitoyl-glyceryl structure (see below) coupled via a spacer to the core lysine residue of a MAP structure. This enabled immunization without added adjuvant and represents a molecularly defined complete immunogen that show a reasonable ability to induce antibodies and cellular immunity against HIV-derived peptides in mice. The same idea lies behind the design of the so-called lipid core peptide (LCP) carriers developed and patented by Toth (*39*) wherein MAP structures are attached to a core comprising a number of lipoaminoacids, i.e., amino acids with fatty acid (typically C12−C14) lipophilic side groups. LCP carriers have been used to construct a tetrameric MAP with 2 × 2 peptides corresponding to different regions of a streptococcal membrane protein (*77*). The core of this LCP contained three octyl side chains, and upon subcutaneous immunization without added adjuvant, the construct gave rise to antibody responses and protection levels indistinguishable from those obtained after immunization in the presence of Freund's complete adjuvant (the most powerful adjuvant known). LCPs were also shown to induce cytotoxic T cells using an ovalbumin model peptide and also slowed the development

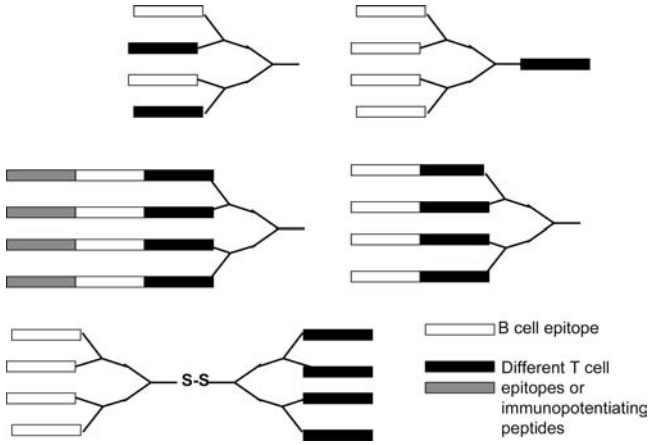


Figure 11. Examples of arrangements of T and B cell epitope peptides in MAP molecules. All of these arrangements have been published.

of tumors in a mouse model, provided an additional alum-type adjuvant was used (*79*). Lipids and MAP structured dendrons are also combined in the carriers described by Florence et al. (*44*); however, in this case the lipid is introduced as fatty acid amides in one-half on the dendron, while the other half is derivatized with relevant antigenic molecules.

The inclusion of lipid PAMPs such as the highly active TLR2-binding tripalmitate-*S*-glyceryl cysteine structure, which is a minimal synthetic analogue of an *E. coli* lipoprotein (*78, 80*) and simple linear saturated fatty acids (e.g., palmitic or myristic acids) (*39, 41, 43*) leads to dramatic increases in immunogenicity of MAPs. This is most probably accomplished by the lipidic moieties promoting contacts with the cell surface membranes of APCs, thereby optimizing exposure of the peptide antigens to these cells and, at the same time, by acting as a TLR agonist activating the cells to secrete immune activating substances (cytokines). In addition to these effects, lipids may enhance the uptake into APCs through pathways leading to MHC I-presentation, which is a prerequisite for induction of cytotoxic T cells that are crucial for the combat of intracellular infections, including viral infections (*81*).

Lipidated MAPs may also have certain advantages as mucosal immunogens, as they are supposed to be able to penetrate mucosal membranes. Thus, a tripalmitate tetravalent MAP containing HIV-peptides was able to induce secretory mucosal immunoglobulin (IgA) as well as serum immunoglobulin (IgG) by oral delivery and also induced cytotoxic, MHC class I dependent T cell responses by intragastric delivery in mice (*82*).

MHC-restriction of T cell activation can be circumvented by using broadly reactive ("universal" or "promiscuous") T cell peptide epitopes, which can be introduced in a MAP structure alongside any antigen of interest, as long as orthogonal chemical strategies (protection groups) can be established that allow the control over this kind of heterofunctionalization (see above and, e.g., ref *49.*). Quite a number of methods and arrangements have been reported for this purpose, some of which are illustrated in Figure 11, and a wide range of orthogonally protected lysine derivatives are commercially available for this purpose. T and B cell epitopic peptides may also be combined by dimerizing two MAPs (see Figure 11), each containing its own type of peptide (the T cell epitope was a promiscuous peptide from tetanus toxoid, B cell epitope was from HIV-1 gp120) (*83*). Dimerization was done by reacting two thiol groups from C-terminal cysteines to form a disulfide bond between the two dendrimer moieties. In this study, it was also investigated whether coupling of such dendrimers to carrier proteins (bovine serum albumin and Hepatitis B surface antigen) affected immunogenicity upon immunization of mice using Freund's adjuvant. The MAP-protein constructs led to broader antigen specificities than the MAP dimer as analyzed by ELISA using peptide antigens corresponding to different HIV gp120 V3 variants, confirming an earlier study (*84*), while the same antibody titers were obtained by the two methods.

MAPs have been shown to be able to directly enhance T cell stimulation as measured by the immune response to fluorescein included as a hapten in a MAP construct also containing a T cell epitope to a level comparable to that obtained after immunization with fluorescein coupled to a carrier protein containing the same T cell stimulatory sequence (*62*). The antibody response was increased several hundredfold to that obtained by immunization with either a monomer fluorescein T cell peptide conjugate or a fluorescein dendrimer not containing the T cell binding peptide. This is direct evidence of the amplifying effect obtained by the MAP-dependent multimerization of the T cell peptide (*62*).

These structures maintain the feature of synthetic simplicity inherent in the MAP concept, and documentation of purity (another important step forward) was possible by mass spectrometry at least in a few cases. Just as with the MAP constructs, SOC constructs with built-in adjuvants (e.g., an interleukin-1 nonapeptide) and also including a promiscuous Th epitope (*85*) and, most recently, constructs containing palmitate have been reported (*69*). These constructs induced antibodies with specificity for the antigenic peptide coupled to the carrier by immunization of rabbits and mice without the addition of adjuvant. Antibody titers were indicated to reach the same level as seen upon immunization in the presence of Freund's incomplete adjuvant (after six immunizations).

A specific subclass of "immunoactive" dendrimers are constituted by dendrimers with targeting moieties in addition to TLR ligands and antigenic moieties, as, e.g., described by Kantchev et al. (*64*) in which a MAP structure is endowed with mannosyl residues in addition to viral peptidic antigens. The rationale behind mannose displaying constructs is to target the MAP to dendritic cells carrying a mannose binding receptor on their surface. Although no vaccination/immunogenicity data are provided, the molecules were obtained by a relatively simple solid-phase strategy and were analyzable by HPLC and mass spectrometry.

Dendrimers as Stand-Alone Adjuvants for Mixing with Antigens. It is clear from the above examples that dendrimers, especially MAP structures, can be endowed with intrinsic adjuvanticity by coupling with various immunopotentiating and/or targeting structures and using them as carriers for delivery of antigens. However, basic MAP structures and other dendrimers may also exhibit stand-alone adjuvanticity in the classical way for mixing with an antigen to increase its immunogenicity.

Contrary to the assumption that dendrimers are immunologically inert structures, which is in some ways a precondition for their use as carriers as described above, a number of examples exist showing that certain underivatised dendrimers may exhibit adjuvant like properties. Thus, there is some evidence that MAP constructs may have an intrinsic ability to overcome MHC-restriction (*49*) and even sometimes can activate T cells without the presence of T cell epitope peptides in the construct (*86*), i.e., a non-lipidated MAP structure in effect working as a stand-alone adjuvant. Olszewska et al. (*86*) found that the immunogenicity obtained was comparable to that of a linear construct containing two copies of a universal T-helper cell epitope from measles virus F protein and a B cell peptide epitope from the same protein. However, the MAP construct achieved this without including T cell epitopes in the construct, implying that T cell help was provided by the MAP construct itself, in some way stimulating APCs to provide the signals necessary to

Table 4. Effects of PAMAM Dendrimers on the Immunogenicity of Influenza Antigens in Mice (Adapted from ref *32*)[a]

antigen/dendrimer (μg)/(mg)	H1N1 IFA titer[b] (1 imm.)	(2 imm.)	toxicity, dead/challenged
0.21/G1 n.a.	134	n.a	n.a.
0.021/G1 n.a.	15	n.a	n.a.
0.21/G4 n.a.	448	n.a	n.a.
0.021/G4 n.a.	154	n.a.	n.a.
0.21/G7 0.29	2586	4096	0/10
0.021/G7 0.029	109	448	0/10
1.7/0	n.a.	240	0/10
0.17/0	36	176	0/8
0.017/0	0.6	20	0/7
1.7/G7 2.9 s	−		10/10
0/G7 2.9	−		10/10
0/G7 0.29	−		0/10
0/G7 0.029	−		0/10

[a] n.a.: not available. Antigen: H1N1 subvirion Pasteur Merieux in PBS. Injection volume: 100 μL. IFA: indirect immunofluorescence assay. [b] Reciprocal of the highest dilution of antiserum detected as positive.

activate the T cells. In another study (*81*), it was shown that MAPs were processed in APCs by the intracellular antigen processing route, providing a powerful MHC I-restricted cytotoxic T cell response. Again, this was achieved with a nonlipidated MAP. Poupot et al. (*87*) studied a range of phosphorylated dendrimers and found them to activate isolated human monocytes in culture. This process depended on the multimericity of the dendrimer and the surface localization of phosphonic acid and involved TLR2.

While the use of MAP structures as stand-alone adjuvants has not been reported to any great extent, some data are available concerning the potential of other types of dendrimers to act as stand-alone adjuvants, including G3, G5, and other midgeneration PAMAM dendrimers (*32, 33*). A G7 PAMAM administered with influenza antigens was compared to immunization with the antigen in PBS (*32*) in mice, and while the highest concentration of dendrimer was toxic to the mice (the dose corresponded to 290 μg/mouse), 1/10 and 1/100 doses were nontoxic and showed considerable adjuvant activity, increasing antibody titers up to more than 100 times after two immunizations (see Table 4). G1, G4, and G7 PAMAM were tested; G1 did not stimulate antibody production, whereas the other dendrimers showed adjuvant activity linearly correlated with the number of amines. The mechanism is speculated to be through electrostatic adsorption of the virus antigens on the surface of the dendrimer, as the influenza virus hemagglutinin surface antigens have low isoelectric points, i.e., being anionic at neutral pH and binding to the cationic surface groups of PAMAM dendrimers. This classifies the PAMAM dendrimers in these experiments as delivery system type adjuvants.

In another study, Rajananthanan et al. (*33, 34*) looked at G6 PAMAM in comparison with a tomatine ISCOM (*88*)-like adjuvant formulation, tomatine being a saponin glycoalkaloid (quil A-like), and a formulation consisting of glycolipid aggregates. Also, Freund's incomplete adjuvant, Alum, and Provax were used as reference adjuvants for coinjection or 3 h later injection (at a different injection site). Using ovalbumin as a model antigen, mice were immunized s.c. using 50 μg antigen, and the resulting serum antibody reactivity against ovalbumin was analyzed by ELISA. While the tomatine system was shown to induce the highest antibody titers, the simple mixing of antigen and PAMAM also induced "good" antibody responses against ovalbumin, and some effect was also seen when administering PAMAM separately and later than the antigen, suggesting a systemic effect. The dose of PAMAM was 50 μg, and no toxicity (inflammation) was observed. There was no preferential induction of either IgG_1 or IgG_{2a} antibodies indicative of a mixed Th1/Th2 response. Analyzing for cytokine production and proliferation of antigen-restimulated spleen cells from immunized mice, the dendrimer was seen to lead to significant recall proliferation responses compared to antigen alone but lower than the tomatine response, and primarily, Th2-like cytokines (IL-4 and IL-5) were induced by the restimulation. No hypothesis on the method of action of the dendrimer was presented, but systemic effects in addition to antigen adsorption (delivery) effects were indicated to be at play.

DNA vaccination holds great promise for induction of Th1 biased immunity both systemically and at mucosal surfaces (*89*). However, despite initial success in rodents the application of DNA vaccination in humans and in large animals has often proven problematic, as the efficacy is often very low (*90*). The delivery of DNA to host cells upon injection has been identified as one of the main hurdles of DNA immunization in nonrodents (*90, 91*), but although cationic polymers have been investigated for ameliorating this problem (*91*) and although cationic fractured PAMAM-type dendrimers are used on a routine basis for nonviral gene delivery (*92*), there are surprisingly few reports on the use of dendrimers to increase DNA immunization efficacy. Audonnet et al. (*93*) described the use of a number of cationic lipids, lipoamines, and polymers including SuperFect (Qiagen), which is a heat-fractured PAMAM dendrimer, all known as efficient DNA transfection reagents (gene delivery) for their ability to enhance immune responses after immunization with DNA in the form of naked DNA plasmids. An increase in serum titer was demonstrated after two immunizations with plasmid DNA mixed with cationic lipid/neutral lipid from bovine herpes virus-1 in cattle compared to immunization with the plasmid alone. Also, the weight gain of pigs challenged by porcine respiratory virus was increased when pigs were vaccinated with PRV plasmid plus lipids compared to pigs vaccinated with the plasmid only. However, no experimental data using dendrimers were presented in this work (*93*).

CONCLUDING REMARKS

Despite the molecular characteristics of dendrimers (multimericity, definability, derivatizability, and molecular weights above 2 kD), they have at present only to a limited extent been used as carrier molecules to enhance immunogenicity of antigens for vaccine purposes, with the exception being the lysine-based MAP carrier dendrons emerging from the peptide field. Although developed specifically for presenting small peptide antigens to the immune system, the accommodation of nonpeptidic haptens (e.g., carbohydrates (*72*)) and of several different types of peptides simultaneously (B and T cell epitopes) have also been demonstrated. Also, convergent strategies for MAP synthesis have been developed (*49*) as has the synthesis of self-adjuvating (lipid containing) MAPs (*43*). After the first descriptions, further developments/improvements have, however, been few, and in at least one case, the MAP dendrimer approach has been left for the benefit of a linear combination of T and B cell stimulatory peptides (*53*). The use of dendrimers as stand-alone adjuvants is even less well described and investigated.

It is obvious that the application of dendrimers as molecular adjuvants should be further explored and developed especially in the case of DNA vaccination where one of several critical steps is the delivery of DNA to the target cell—a step which is known to be facilitated by administration of certain dendrimer types, at least in vitro. DNA−dendrimer complex formation could even be imagined to help overcome two other pivotal steps in the DNA vaccination method, viz., protecting the DNA against breakdown and targeting the DNA to specific host cells, e.g., in the mucosa (by exploiting the heterofunctionalization potential of the dendrimer to include targeting ligands in the

construct). It is also clear that the potential of dendrimers for other vaccine purposes, both as antigen carriers and as adjuvants, and as combinations of these, is far from fully explored. Being monodisperse polymers, dendrimers offer the possibility of producing molecularly defined adjuvants combining very specific immunomodulating activities with targeting to relevant tissues, e.g., mucosal surfaces, and antigen transportation. The resulting macromolecular constructs are expected to behave as highly immunoactive and specific adjuvant/carrier compounds. Thus, dendrimers are useful generic platforms for developing defined and safe vaccines with new properties and application potentials and will also be useful for basic investigations of the mechanisms behind the induction and control of immunity.

ACKNOWLEDGMENT

This work was supported by the EU Network of Excellence, EPIZONE (Contract No. FOOD-CT-2006-016236).

Note Added after ASAP Publication: The version of this paper published on November 4, 2009, had errors in the reference 23 callouts. The corrected version was published November 6, 2009.

LITERATURE CITED

(1) Mullin, D. (2003) Prometheus in Gloucestershire: Edward Jenner, 1749−1823. *J. Allergy Clin. Immunol. 112*, 810–14.
(2) Kaufmann, S. H. (2007) The contribution of immunology to the rational design of novel antibacterial vaccines. *Nat. Rev. Microbiol. 5*, 491–04.
(3) Pasare, C., and Medzhitov, R. (2004) Toll-like receptors: linking innate and adaptive immunity. *Microbes. Infect. 6*, 1382–87.
(4) Dempsey, P. W., Vaidya, S. A., and Cheng, G. (2003) The art of war: Innate and adaptive immune responses. *Cell. Mol. Life Sci. 60*, 2604–21.
(5) Janeway, C. A., Jr. (1989) Approaching the asymptote? Evolution and revolution in immunology. *Cold Spring Harb. Symp. Quant. Biol. 54* (Pt 1), 1–13.
(6) Steinman, R. M., and Hemmi, H. (2006) Dendritic cells: translating innate to adaptive immunity. *Curr. Top. Microbiol. Immunol. 311*, 17–58.
(7) McHeyzer-Williams, L. J., Malherbe, L. P., and Heyzer-Williams, M. G. (2006) Helper T cell-regulated B cell immunity. *Curr. Top. Microbiol. Immunol. 311*, 59–83.
(8) Pulendran, B., and Ahmed, R. (2006) Translating innate immunity into immunological memory: implications for vaccine development. *Cell 124*, 849–63.
(9) Wills-Karp, M. (2007) Complement activation pathways: a bridge between innate and adaptive immune responses in asthma. *Proc. Am. Thorac. Soc. 4*, 247–51.
(10) Lanzavecchia, A., and Sallusto, F. (2001) Regulation of T cell immunity by dendritic cells. *Cell 106*, 263–66.
(11) Yarovinsky, F., Kanzler, H., Hieny, S., Coffman, R. L., and Sher, A. (2006) Toll-like receptor recognition regulates immunodominance in an antimicrobial CD4+ T cell response. *Immunity 25*, 655–64.
(12) Blander, J. M., and Medzhitov, R. (2006) On regulation of phagosome maturation and antigen presentation. *Nat. Immunol. 7*, 1029–35.
(13) Campos, M., and Godson, D. L. (2003) The effectiveness and limitations of immune memory: understanding protective immune responses. *Int. J. Parasitol. 33*, 655–61.
(14) Fraser, C. K., Diener, K. R., Brown, M. P., and Hayball, J D. (2007) Improving vaccines by incorporating immunological coadjuvants. *Expert Rev. Vaccines 6*, 559–78.
(15) Xiang, S. D., Scholzen, A., Minigo, G., David, C., Apostolopoulos, V., Mottram, P. L., and Plebanski, M. (2006) Pathogen recognition and development of particulate vaccines: does size matter? *Methods 40*, 1–9.
(16) Guy, B. (2007) The perfect mix: recent progress in adjuvant research. *Nat. Rev. Microbiol. 5*, 505–17.
(17) Aguilar, J. C., and Rodriguez, E. G. (2007) Vaccine adjuvants revisited. *Vaccine 25*, 3752–62.
(18) Buhleier, E., Wehner, E., and Vögtle, F. (1978) Cascade-chain like and nonskid-chain-like syntheses of molecular cavity topologies. *Synthesis* 155–58.
(19) Wörner, C., and Mühlhaupt, R. (1993) Polynitrile-functional and polyamine-functional poly(trimethylene imine) dendrimers. *Angew. Chem., Int. Ed. Engl. 32*, 1306–8.
(20) Brabander van den Berg, E. M. M., and Meijer, E. W. (1993) Poly(propylene imine) dendrimers- large scale synthesis by heterogeneously catalysed hydrogenations. *Angew. Chem., Int. Ed. Engl. 32*, 1308–11.
(21) Tomalia, D. A., Baker, H., Dewald, J., Hall, M., Kallos, G., Martin, S., Roeck, J., Ryder, J., and Smith, P. (1985) A new class of polymers: Starburst-dendritic macromolecules. *Polym. J. 17*, 117–32.
(22) Newkome, G. R., Yao, Z. Q., Baker, G. R., and Gupta, V. K. (1985) Micelles. 1. Cascade molecules- A new approach to micelles- a (27)-arborol. *J. Org. Chem. 50*, 2003–04.
(23) (a) Tam, J. P. (1988) Synthetic peptide vaccine design-synthesis and properties of a high-density multiple antigenic peptide system. *Proc. Natl. Acad. Sci. U.S.A. 85*, 5409–13. (b) Crespo, L., Sanclimens, G., Pons, M., Giralt, E., Royo, M., and Albericio, F. (2005) Peptide and amide-bond containing dendrimers. *Chem. Rev. 105*, 1663–1681.
(24) Hawker, C., and Fréchet, J. M. J. (1990) A new convergent approach to monodisperse dendritic macromolecules. *J. Chem. Soc. Chem. Commun.* 1010–13.
(25) Boas, U., Christensen, J. B., and Heegaard, P. M. H. (2006) *Dendrimers in Medicine and Biotechnology*, RSC Publishers, Cambridge.
(26) Malik, N., Wiwattanapatapee, R., Klopsch, R., Lorentz, K., Frey, H., Weener, J. W., Meijer, E. W., Paulus, W., and Duncan, R. (2000) Relationship between structure and biocompatibility in vitro, and preliminary studies on the biodistribution of 125-I labelled dendrimers in vivo. *J. Controlled Release 65*, 133–48.
(27) Janeway, C. A., Travers, P., Walport, M., and Shlomchik, M., Eds. (2001) *Immunobiology*, 5th ed., Garland Publishing.
(28) Patterson, L. J., Robey, F., Muck, A., van Remoortere, K., Aldrich, K., Richardson, E., Alvord, W. G., Markham, P. D., Cranage, M., and Robert-Guroff, M. (2001) A conformational C4 peptide polymer vaccine coupled with live recombinant vector priming is immunogenic but does not protect against rectal SIV challenge. *AIDS Res. Hum. Retroviruses 17*, 837–49.
(29) Jackson, D. C., O'Brien-Simpson, N., Ede, N. J., and Brown, L. E. (1997) Free radical induced polymerization of synthetic peptides into polymeric immunogens. *Vaccine 15*, 1697–705.
(30) van Regenmortel, M. H., Briand, J. P., Muller, S., and Plaue, S. (1988) *Synthetic Polypeptides as Antigens*, Elsevier, Amsterdam.
(31) Plank, C., Mechtler, K., Szoka, F C., and Wagner, E. (1996) Activation of the complement system by synthetic DNA complexes: a potential barrier for intravenous gene delivery. *Hum. Gene Ther. 7*, 1437–47.
(32) Wright, D. C. (to Novavax, Inc.) Adjuvant properties of poly(amidoamine) dendrimers, U.S. Patent 5,795,582, 1998.
(33) Rajananthanan, P., Attard, G. S., Sheikh, N. A., and Morrow, W. J. (1999) Evaluation of novel aggregate structures as adjuvants: composition, toxicity studies and humoral responses. *Vaccine 17*, 715–30.
(34) Rajananthanan, P., Attard, G. S., Sheikh, N. A., and Morrow, W. J. (2000) Novel aggregate structure adjuvants modulate lymphocyte proliferation and Th1 and Th2 cytokine profiles in ovalbumin immunized mice. *Vaccine 18*, 140–52.
(35) Fields, G. B., and Noble, R. L. (1990) Solid phase peptide synthesis utilizing 9-fluorenylmethoxycarbonyl amino acids. *Int. J. Pept. Protein Res. 35*, 161–214.
(36) Chan, W. C., and White, P. D. (2000) *Fmoc Solid Phase Peptide Synthesis*, Oxford University Press, New York,

(37) Tam, J. P. (to The Rockefeller University), Multiple antigen peptide system, U.S. Patent 5,229,490, 1993.
(38) Tam, J. P. Multiple antigen peptide system having adjuvant properties, vaccines prepared there from and methods of use thereof, U.S. Patent 5,580,563, 1996.
(39) Toth, I., and Gibbons, W. A. (to The School of Pharmacy, University of London), Peptide compounds, U.S. Patent 5,882,645, 1999.
(40) Posnett, D. N., McGrath, H., and Tam, J. P. (1988) A novel method for producing anti-peptide antibodies. Production of site-specific antibodies to the T cell antigen receptor beta-chain. *J. Biol. Chem. 263*, 1719–25.
(41) Defoort, J. P., Nardelli, B., Huang, W., and Tam, J. P. (1992) A rational design of synthetic peptide vaccine with a built-in adjuvant. A modular approach for unambiguity. *Int. J. Pept. Protein Res. 40*, 214–21.
(42) Moreno, C. A., Rodriguez, R., Oliveira, G. A., Ferreira, V., Nussenzweig, R. S., Rosa Moya Castro, R., Mauricio Calvo-Calle, J., and Nardin, E. (2000) Preclinical evaluation of a synthetic *Plasmodium falciparum* MAP malaria vaccine in Aotus monkeys and mice. *Vaccine 116*, 89–99.
(43) Toth, I., Danton, M., Flinn, N., and Gibbons, W. A. (1993) A combined adjuvant and carrier system for enhancing synthetic peptides immunogenicity utilizing lipidic amino-acids. *Tetrahedron Lett. 34*, 3925–28.
(44) Florence, A. T., Sakthivel, T., Wilderspin, A. F., and Toth, I. (to The School of Pharmacy University of London), Dendritic polypeptides, U.S. Patent 6,194,543, 2001.
(45) Sadler, K., and Tam, J. P. (2002) Peptide dendrimers: applications and synthesis. *J. Biotechnol. 90*, 195–229.
(46) Briand, J. P., Barin, C., van Regenmortel, M. H., and Muller, S. (1992) Application and limitations of the multiple antigen peptide (MAP) system in the production and evaluation of anti-peptide and anti-protein antibodies. *J. Immunol. Methods 156*, 255–65.
(47) Haro, I., and Gomara, M. J. (2004) Design of synthetic peptidic constructs for the vaccine development against viral infections. *Curr. Protein Pept. Sci. 5*, 425–33.
(48) Veprek, P., and Jezek, J. (1999) Peptide and glycopeptide dendrimers. Part II. *J. Pept. Sci. 5*, 203–20.
(49) Tam, J. P. (1996) Recent advances in multiple antigen peptides. *J. Immunol. Methods 196*, 17–32.
(50) Nardin, E. H., Oliveira, G. A., Calvo-Calle, J. M., and Nussenzweig, R. S. (1995) The use of multiple antigen peptides in the analysis and induction of protective immune responses against infectious diseases. *Adv. Immunol. 60*, 105–49.
(51) Nardin, E. H., Calvo-Calle, J. M., Oliveira, G. A., Nussenzweig, R. S., Schneider, M., Tiercy, J. M., Loutan, L., Hochstrasser, D., and Rose, K. (2001) A totally synthetic polyoxime malaria vaccine containing *Plasmodium falciparum* B cell and universal T cell epitopes elicits immune responses in volunteers of diverse HLA types. *J. Immunol. 166*, 481–89.
(52) Nardin, E. H., Oliveira, G. A., Calvo-Calle, J. M., Castro, Z. R., Nussenzweig, R. S., Schmeckpeper, B., Hall, B. F., Diggs, C., Bodison, S., and Edelman, R. (2000) Synthetic malaria peptide vaccine elicits high levels of antibodies in vaccinees of defined HLA genotypes. *J. Infect. Disease 182*, 1486–96.
(53) Calvo-Calle, J. M., Oliveira, G. A., Watta, C. O., Soverow, J., Parra-Lopez, C., and Nardin, E. H. (2006) A linear peptide containing minimal T- and B-cell epitopes of *Plasmodium falciparum* circumsporozoite protein elicits protection against transgenic sporozoite challenge. *Infect. Immunol. 74*, 6929–39.
(54) Baek, M. G., and Roy, R. (2002) Synthesis and protein binding properties of T-antigen containing GlycoPAMAM dendrimers. *Bioorg. Med. Chem. 10*, 11–17.
(55) Bay, S., Lo-Man, R., Osinaga, E., Nakada, H., Leclerc, C., and Cantacuzene, D. (1997) Preparation of a multiple antigen glycopeptide (MAG) carrying the Tn antigen. A possible approach to a synthetic carbohydrate vaccine. *J. Pept. Res. 49*, 620–25.
(56) Lo-Man, R., Vichier-Guerre, S., Bay, S., Deriaud, E., Cantacuzene, D., and Leclerc, C. (2001) Anti-tumor immunity provided by a synthetic multiple antigenic glycopeptide displaying a tri-Tn glycotope. *J. Immunol. 166*, 2849–54.
(57) Stills, H F. (2005) Adjuvants and antibody production: Dispelling myths associated with Freund's complete and other adjuvants. *ILAR J. 46*, 280–93.
(58) Rigby, M. A., Mackay, N., Reid, G., Osborne, R., Neil, J. C., and Jarrett, O. (1996) Immunogenicity of a peptide from a major neutralising determinant of the feline immunodeficiency virus surface glycoprotein. *Vaccine 14*, 1095–102.
(59) Tam, J. P., and Spetzler, J. C. (1995) Chemoselective approaches to the preparation of peptide dendrimers and branched artificial proteins using unprotected peptides as building blocks. *Biomed. Pept. Proteins Nucleic Acids 1*, 123–32.
(60) Spetzler, J. C., and Tam, J. P. (1996) Self-assembly of cyclic peptides on a dendrimer: multiple cyclic antigen peptides. *Peptide Res. 9*, 290–96.
(61) de Oliveira, E., Villen, J., Giralt, E., and Andreu, D. (2003) Synthetic approaches to multivalent lipopeptide dendrimers containing cyclic disulfide epitopes of foot-and-mouth disease virus. *Bioconjugate Chem. 14*, 144–52.
(62) Cavenaugh, J. S., Wang, H.-K., Hansen, C., Smith, R. S., and Herron, J. N. (2003) How well can a T-cell epitope replace its parent carrier protein? A dose-response study. *Pharm. Res. 4*, 591–96.
(63) Esposito, G., Fogolari, F., Viglino, P., Cattarinussi, S., de Magistris, M. T., Chiappinelli, L., and Pessi, A. (1993) Conformational study of a short Pertussis toxin T cell epitope incorporated in a multiple antigen peptide template by CD and two-dimensional NMR. Analysis of the structural effects on the activity of synthetic immunogens. *Eur. J. Biochem. 217*, 171–87.
(64) Kantchev, E. A., Chang, C.-C., and Chang, D.-K. (2005) Direct Fmoc/tert-Bu solid phase synthesis of octamannosyl polylysine dendrimer-peptide conjugates. *Biopolymers (Peptide Science) 84*, 232–40.
(65) Heegaard, P. M. H., Bøg, Y. S., Jakobsen, P. H., Holm, A. (1998) A stem peptide carrier for the immunogenic presentation of peptides. *Innovation and Perspectives in Solid Phase Synthesis* (Epton R., Ed.) pp 143−147, Mayflower Scientific Ltd, Birmingham.
(66) Tsikaris, V., Sakarellos, C., Sakarellos-Daitsiotis, M., Cung, M. T., Marraud, M., Konidou, G., Tzinia, A., and Soteriadou, K. P. (1996) Use of sequential oligopeptide carriers (SOCn) in the design of potent Leishmania gp63 immunogenic peptides. *Pept. Res. 9*, 240–47.
(67) Sakarellos-Daitsiotis, M., Krikorian, D., Panou-Pomonis, E., and Sakarellos, C. (2006) Artificial carriers: a strategy for constructing antigenic/immunogenic conjugates. *Curr. Top. Med. Chem. 6*, 1715–35.
(68) Mahalakshmi, R., and Balaram, P. (2006) Non-protein amino acids in the design of secondary structure scaffolds. *Methods Mol. Biol. 340*, 71–94.
(69) Kargakis, M., Zevgiti, S., Krikorian, D., Sakarellos-Daitsiotis, M., Sakarellos, C., and Panou-Pomonis, E. (2007) A palmitoyl-tailed sequential oligopeptide carrier for engineering immunogenic conjugates. *Vaccine 25*, 6708–12.
(70) Tuchscherer, G., Dömer, B., Sila, U., Kamber, B., and Mutter, M. (1993) The TASP concept: Mimetics of peptide ligands, protein surfaces and folding units. *Tetrahedron 49*, 3559–75.
(71) Zhou, M., and Ghosh, I. (2004) Noncovalent multivalent assembly of jun peptides on a leucine zipper dendrimer displaying fos peptides. *Org. Lett. 6*, 3561–64.
(72) Toyokuni, T., Hakomori, S., and Singhal, A. K. (1994) Synthetic carbohydrate vaccines: synthesis and immunogenicity of Tn antigen conjugates. *Bioorg. Med. Chem. 2*, 1119–32.
(73) Vannucci, L., Fiseriva, A., Sadalapure, K., Lindhorst, T. K., Kuldova, M., Rossmann, P., Horvath, O., Kren, V., Krist, P.,

Bezouska, K., Luptovcova, M., Mosca, F., and Popisil, M. (2003) Effects of N-acetyl-glucosamine-coated glycodendrimers as biological modulators in the B16F10 melanoma model in vivo. *Int. J. Oncol. 23*, 285–96.

(74) McGeary, R. P., Jablonkai, I., and Toth, I. (2001) Carbohydrate-based templates for synthetic vaccines and drug delivery. *Tetrahedron 57*, 8733–42.

(75) Mihov, G., Grebel-Koehler, D., Lubbert, A., van der Meulen, G. W., Herrmann, A., Klok, H. A., and Mullen, K. T. (2005) Polyphenylene dendrimers as scaffolds for shape-persistent multiple peptide conjugates. *Bioconjugate Chem. 16*, 283–93.

(76) Wang, R., Charoenvit, Y., Corradin, G., Porrozzi, R., Hunter, R. L., Glenn, G., Alving, C. R., Church, P., and Hoffman, S. L. (1995) Induction of protective polyclonal antibodies by immunization with a *Plasmodium yoelii* circumsporozoite protein multiple antigen peptide vaccine. *J. Immunol. 154*, 2784–93.

(77) Olive, C., Batzloff, M., Horvath, A., Clair, T., Yarwood, P., Toth, I., and Good, M. F. (2003) Potential of lipid core peptide technology as a novel self-adjuvanting vaccine delivery system for multiple different synthetic peptide immunogens. *Infect. Immunol. 71*, 2373–83.

(78) Deres, K., Schild, H., Wiesmüller, K. H., Jung, G., and Rammensee, H. G. (1989) In vivo priming of virus-specific cytotoxic T lymphocytes with synthetic lipopeptide vaccine. *Nature 342*, 561–64.

(79) White, K., Kearns, P., Toth, I., and Hook, S. (2004) Increased adjuvant activity of minimal CD8 T cell peptides incorporated into lipid-core-peptides. *Immunol. Cell Biol. 82*, 517–22.

(80) Spohn, R., Buwitt-Beckmann, U., Brock, R., Jung, G., Ulmer, A. J., and Wiesmüller, K. H. (2004) Synthetic lipopetide adjuvants and Toll-like receptor 2 structure-activity relationships. *Vaccine 22*, 2494–99.

(81) Ota, S., Ono, T., Morita, A., Uenaka, A., Harada, M., and Nakayama, E. (2002) Cellular processing of a multibranched lysine core with tumor antigen peptides and presentation of peptide epitopes recognized by cytotoxic T lymphocytes on antigen-presenting cells. *Cancer Res. 62*, 1471–76.

(82) Nardelli, B., Haser, P. B., and Tam, J. P. (1994) Oral administration of an antigenic synthetic lipopeptide (MAP-P3C) evokes salivary antibodies and systemic humoral and cellular responses. *Vaccine 14*, 1335–39.

(83) Iglesias, E., Aguilar, J. C., Cruz, L. J., and Reyes, O. (2005) Broader cross-reactivity after conjugation of V3 based multiple antigen peptides to HBsAg. *Mol. Immunol. 42*, 99–104.

(84) Cruz, L. J., Iglesias, E., Aguilar, J. C., Cabrales, A., Reyes, O., and Andreu, D. (2004) A comparative study of different presentation strategies for an HIV peptide immunogen. *Bioconjugate Chem. 15*, 112–20.

(85) Krikorian, D., Panou-Pomonis, E., Voitharou, C., Sakarellos, C., and Sakarellos-Daitsiotis, M. (2005) A peptide carrier with a built-in vaccine adjuvant: construction of immunogenic conjugates. *Bioconjugate Chem. 16*, 812–19.

(86) Olszewska, W., Obeid, O. E., and Steward, M. W. (2000) Protection against measles virus-induced encephalitis by anti-mimotope antibodies: the role of antibody affinity. *Virology 272*, 98–105.

(87) Poupot, M., Griffe, L., Marchand, P., Maraval, A., Rolland, O., Martinet, L., L'Faqihi-Olive, F. E., Turrin, C. O., Caminade, A. M., Fournié, J. J., Majoral, J. P., and Poupot, R. (2006) Design of phosphorylated dendritic architectures to promote human monocyte activation. *FASEB J. 20*, 2339–51.

(88) Morein, B., Villacres-Eriksson, M., and Lovgren-Bengtsson, K. (1998) Iscom, a delivery system for parenteral and mucosal vaccination. *Dev. Biol. Stand. 92*, 33–39.

(89) Tang, D. C., DeVit, M., and Johnson, S. A. (1992) Genetic immunization is a simple method for eliciting an immune response. *Nature 356*, 152–54.

(90) Babiuk, L. A., Pontarello, R., Babiuk, S., Loehr, B., and van Drunen Littel-van den Hurk, S. (2003) Induction of immune responses by DNA vaccines in large animals. *Vaccine 21*, 649–58.

(91) Greenland, J. R., and Letvin, N. L. (2007) Chemical adjuvants for plasmid DNA vaccines. *Vaccine 25*, 3731–41.

(92) Ruponen, M., Honkakoski, P., Rönkkö, S., Pelkonen, J., Tammi, M., and Urtti, A. (2003) Extracellular and intracellular barriers in non-viral gene delivery. *J. Controlled Release 93*, 213–17.

(93) Audonnet, J.-C. F., Fischer, L. B., and Barzu-Le-Roux, S. (to Merial) DNA vaccines for farm animals in particular bovines and porcines, U.S. Patent 6,852,705, 2005.

BC900290D

Urocanic Acid Improves Transfection Efficiency of Polyphosphazene with Primary Amino Groups for Gene Delivery

Yongxin Yang, Zhiwen Zhang, Lingli Chen, Wangwen Gu, and Yaping Li*

Shanghai Institute of Materia Medica, Chinese Academy of Sciences, Shanghai 201203, China. Received June 17, 2009; Revised Manuscript Received November 17, 2009

The biodegradable cationic poly(2-(2-aminoethoxy)ethoxy)phosphazene (PAEP) bearing primary amino groups and a new PAEP derivative, urocanic acid (UA) modified PAEP (UA-PAEP), were synthesized and investigated for gene delivery. The results indicated that PAEP was able to condense DNA into complex nanoparticles with the size around 120 nm at the polymer/DNA ratio (N/P) of 35, at which PAEP/DNA complex nanoparticles (PACNs) showed efficient transfection activity in complete medium. After conjugating with UA at the substitution degree of 7% (UA-PAEP7), UA-PAEP7/DNA complex nanoparticles (UP7CNs) exhibited higher transfection efficiency than PACNs and UA-PAEP25/DNA complex nanoparticles (UP25CNs) and much lower cytotoxicity compared with PEI/DNA complex nanoparticles (PEICNs). The transfection experiment using a proton pump inhibitor suggested that the gene expression of PACNs and UP-PAEP/DNA complex nanoparticles (UPCNs) was dependent on the endosomal acidification process. The acetate solution (20 mM, pH5.7) improved the transfection activity of UP7CNs in HeLa and COS 7 cell lines, which was almost comparable to PEICNs at the N/P ratio of 35. Therefore, the results suggested that UP7CNs could be a promising carrier for gene delivery.

INTRODUCTION

A number of cationic polymers such as polyethylenimine (PEI) (*1*), chitosan (*2*), poly(L-lysine) (PLL) (*3*), and polyamidoamine dentrimers (*4*), have been widely investigated for gene delivery due to their obvious advantages over viral gene vectors such as low safety risks, preparation in large quantities easily, and low costs. Among these cationic polymers, PEI has become a golden standard of nonviral gene delivery systems (*5*), but the high cytotoxicity and nonbiodegradability limit its usage. So far, great efforts have been made to design and develop novel biodegradable polymers with high transfection activity and low cytotoxicity for gene delivery (*6, 7*). Unfortunately, the ideal cationic polymer has not been found yet.

Polyphosphazenes have been investigated for biomedical and pharmaceutical applications such as drug delivery systems (*8*) and protein matrices (*9*) because of their synthetic flexibility, excellent hydrolytic degradability, and nontoxic degradable products. For gene delivery, the cationic polyphosphazenes have shown good activity in gene transfection recently (*10*−*12*). However, more efforts have to be made before polyphosphazene derivatives with the optimal gene transfer efficiency are found. In our previous work (*13*), poly(imidazole/DMAEA)phosphazene (PIDP) bearing ternary amino groups showed the ability to condense DNA into complex nanoparticles with a size around 100 nm, which could mediate more efficient transfection than PEI/DNA complex nanoparticles (PEICNs) and poly(di-DMAEA)phosphazene/DNA complex nanoparticles at the same polymer/DNA ratio (w/w) in serum-free medium. However, PIDP/DNA complex nanoparticles exhibited much lower gene expression level in medium containing 10% FBS. In order to meet the requisites of in vivo gene delivery, we are looking for a novel cationic polyphosphazene derivative that could achieve efficient transfection in the presence of serum.

On the cellular level, the complex nanoparticles must overcome many obstacles before they release nucleic acid at the target site of action. The first obstacle is traversing the cellular membrane. Complex nanoparticles are able to pass the cellular membrane via endocytosis as long as they have the suitable surface properties such as the appropriate size range and the positive charges (*14, 15*). However, endocytotic uptake may not only expose complex nanoparticles to enzymatic degradation in the lysosome, but also entrap and never release them.

To circumvent above difficulties, we synthesized biodegradable poly(2-(2-aminoethyoxy)ethoxy)phosphazene (PAEP) bearing primary amino groups for efficient gene delivery first. Considering urocanic acid (UA) with an imidazole ring for enhanced endosomal escape, a new PAEP derivative, UA modified PAEP (UA-PAEP), was synthesized in an attempt to improve the transfection activity. In this work, the buffering capacity of polymers, the transfection activity of complex nanoparticles in the presence of serum, and the influence of UA substitution degree on the transfection efficiency were investigated. In addition, the physicochemical property and the cell uptake of the polymer/DNA complex nanoparticles were characterized for further exploration of the mechanism of in vitro gene transfection.

EXPERIMENTAL PROCEDURES

All the reagents (analytical grade) were purchased from Sinopharm Chemical Reagent Co., Ltd. (China), unless otherwise noted. NH_4Cl was dried in a desiccator over P_2O_5 (Panreac). Tetrahydrofuran (THF) was treated with KOH and distilled twice from Na in the presence of benzophenone. Petroleum ether refers to that fraction with a boiling point in the range 60−90 °C. PCl_5 was purified by sublimation. Sulfamic acid (HSO_3NH_2), $CaSO_4 \cdot 2H_2O$, 2-(2-aminoethyoxy)ethanol (Aldrich), sodium hydride (Fluka), and 1,2,4-trichlorobenzene were used as purchased. Trifluoroacetic acid (TFA), *N*,*N*′-dicyclohexylcarbodiimide (DCC), and *N*-hydroxysuccinimide (NHS) were purchased from GL Biochem (Shanghai) Ltd.

* Corresponding author. Address: 555 Zuchongzhi Road, Shanghai 201203 China. Tel.: +86-21-5080-6820. Fax: +86-21-5080-6820. E-mail address: ypli@mail.shcnc.ac.cn.

10.1021/bc900267g © 2010 American Chemical Society
Published on Web 02/02/2010

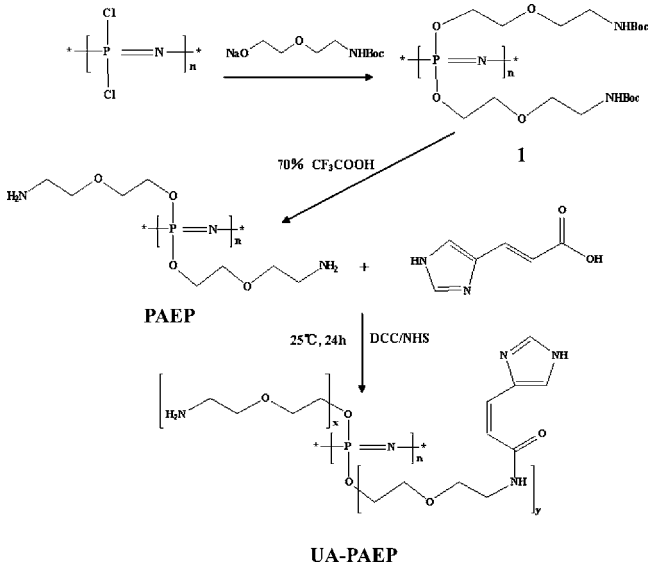


Figure 1. Synthetic scheme of poly(2-(2-aminoethyoxy)ethoxy) phosphazene(PAEP) and UA-PAEP.

Polyethylenimine (PEI 25K), poly(L-lysine) (PLL), and UA were obtained from Aldrich. YOYO-1 was obtained from Invitrogen and Trypan Blue from TianGen. Bafilomycin A1 was purchased from Sigma. pEGFP-N1 (4.7 kb) encoding green fluorescent protein driven by immediate early promoter of CMV was purchased from Clontech Laboratories (Palo Alto, CA, USA). pGL-2Luc was purchased from Promega Corp. (Madison, WI, USA). The plasmid DNA (pDNA) was amplified in DH5α strain of *E. coli* and purified by EndFree Plasmid Mega Kit (Qiagen GmbH, Hilden, Germany).

Cell Lines. Hela cells and COS 7 cells were obtained from the American Type Culture Collection (ATCC, Manassas, VA, USA) and were grown in DMEM containing 10% fetal bovine serum (FBS), streptomycin at 40 μg/mL, and ampicillin at 40 U/mL. Cells were maintained at 37 °C in a humidified and 5% CO_2 incubator.

Synthesis of PAEP and UA-PAEP. Poly(dichloro)phosphazene was prepared directly from PCl_5 and NH_4Cl as described in our previous work (*13*). The synthesis of PAEP (Figure 1) was carried out according to the Allcock's procedure (*16*). To synthesize UA-PAEP, the carboxyl group of UA was activated by the NHS/DCC dissolved in dimethylformamide (5 mL). DCC was 1.2-fold molar excess over UA and NHS/DCC molar ratio was 1:1. The activated UA solution was added to PAEP solution and triethylamine in methanol (10 mL), and the resultant solution was stirred for one day at room temperature. The reaction mixture was dialyzed using cellulose membrane (MW cutoff 6000−8000) against distilled water for 3 days. The resulting solution was lyophilized, and the composition of UA-PAEP was determined by NMR spectra. ^1H NMR and ^{31}P NMR spectra of polymer were obtained from Varian Mercury Plus-400 NMR spectrometer (Varian, USA). The chemical shifts were given relative to tetramethsilane or 85% H_3PO_4 as an external standard. The molecular weight and distribution were determined by gel permeation chromatography (GPC, Waters 600) with acetonitrile/water/trifluoro acetic acid (10/90/0.05, v/v) as the eluent with flow rate (0.5 mL/min). The calibrations were peptide standards.

Buffering Capacity. The buffering capacity of PAEP, UA-PAEP, PLL, and PEI were measured by titration according to the method described by Tseng (*17*). The polymers were diluted to a final concentration of 0.3 mg/mL with 0.1 N NaCl. The solution was adjusted to pH 7.5 before titration proceeded. An aliquot of 0.1 N HCl was successively added into 30 mL of polymer solution (0.3 mg/mL), and the change in pH was monitored by a pH meter (Sartorius, Germany).

Preparation and Characteristics of Polymer/DNA Complex Nanoparticles. The polymer/DNA complex nanoparticles were prepared by adding 100 μL polymer solution with various amounts of polymer to 100 μL of pEGFP (20 μg) in distilled water or 20 mM acetate (pH 5.7) and vortexed for 10 s. The resulting complex nanoparticles were allowed to sit at room temperature for 30 min, then confirmed by electrophoresis on a 1% agarose gel with Tris-acetate-EDTA buffer system (pH 8.0) at 110 V/cm for 45 min. DNA was visualized using ethidium bromide staining. The polymer/DNA charge ratio (N/P) was defined as the ratio between the moles of the amine groups of PAEP or UA-PAEP to those of the phosphate ones of DNA. For plasmid DNA, 330 g/mol corresponds with the average mass of a repeating unit bearing one negative phosphate group.

Size and ζ-potential of complex nanoparticles were measured by laser light scattering following their dilution with water or 20 mM acetate (pH 5.7) using a Nicomp 380/ZLS zeta potential analyzer (Santa California, USA) at 25 °C. For size measurement, scattered light was detected at a 90° angle and the instrument was calibrated with an aqueous poly(styrene) dispersion of particles of 100 nm. ζ-potential measurements of the complexes were carried out in the standard capillary electrophoresis cell at 25 °C.

In Vitro Transfection Experiment. In vitro transfection efficiency was evaluated on Hela and COS 7 cell lines using a plasmid containing a reporter gene encoding enhanced green fluorescence protein (EGFP). Cells were seeded into a 24-well plates at a density of 1×10^5 cells per well in 500 μL of complete medium 24 h prior to transfection. After the polymer/DNA complex nanoparticles containing 2.5 μg of DNA were incubated with cells at 37 °C for 4 h, the medium was replaced with fresh complete medium. After 48 h, the cells were washed twice with PBS and collected. The fluorescence intensity of positive cells was measured with a flow cytofluorometer (Becton Dickinson, USA) equipped with an argon ion laser. PEICNs were used as positive control. The transfection experiment involving bafilomycin A1 was performed as described above except that the cells were preincubated with 200 nM bafilomycin A1 at 37 °C for 30 min.

Cell Viability Assays. The cytotoxicity of complex nanoparticles was determined by MTT assay. The cells were plated on a 96-well culture dish at a density of 2×10^4 cells/well and cultivated in complete medium. After 24 h, the culture medium was replaced with fresh complete medium containing complex nanoparticles at different polymer/DNA (N/P) ratio. After 4 h, the incubation medium was replaced again with fresh medium and incubation for an additional 42 h. The medium was removed and MTT solution (5 mg/mL) was added. Cells were incubated for 4 h at 37 °C in 5% CO_2. Then, the medium containing MTT was removed, and 150 μL of DMSO was added to dissolve the crystals formed by living cells. The absorbance was measured at test wavelengths of 490 nm (Bio-Rad model 550, Hercules, CA, USA).

Cell Uptake of Polymer/DNA Complex Nanoparticles. To evaluate cellular uptake efficiency and subsequent intracellular routing of complex nanoparticles, pGL-2Luc encoding luciferase was used and labeled with YOYO-1. Briefly, 200 μL of pGL-2Luc (0.2 μg/mL) was mixed with 10 μL of 50 μM YOYO-1 and incubated at room temperature for 1 h in the dark. At 24 h prior to uptake experiment, the cells were seeded at a density of 1×10^5 cells/well in 24-well microtiter plates. Then, the complex nanoparticles containing 2.5 μg of YOYO-1-labeled plasmid DNA were added to the cells in fresh complete DMEM medium. After incubation for 1 h at 37 °C, the cells were washed

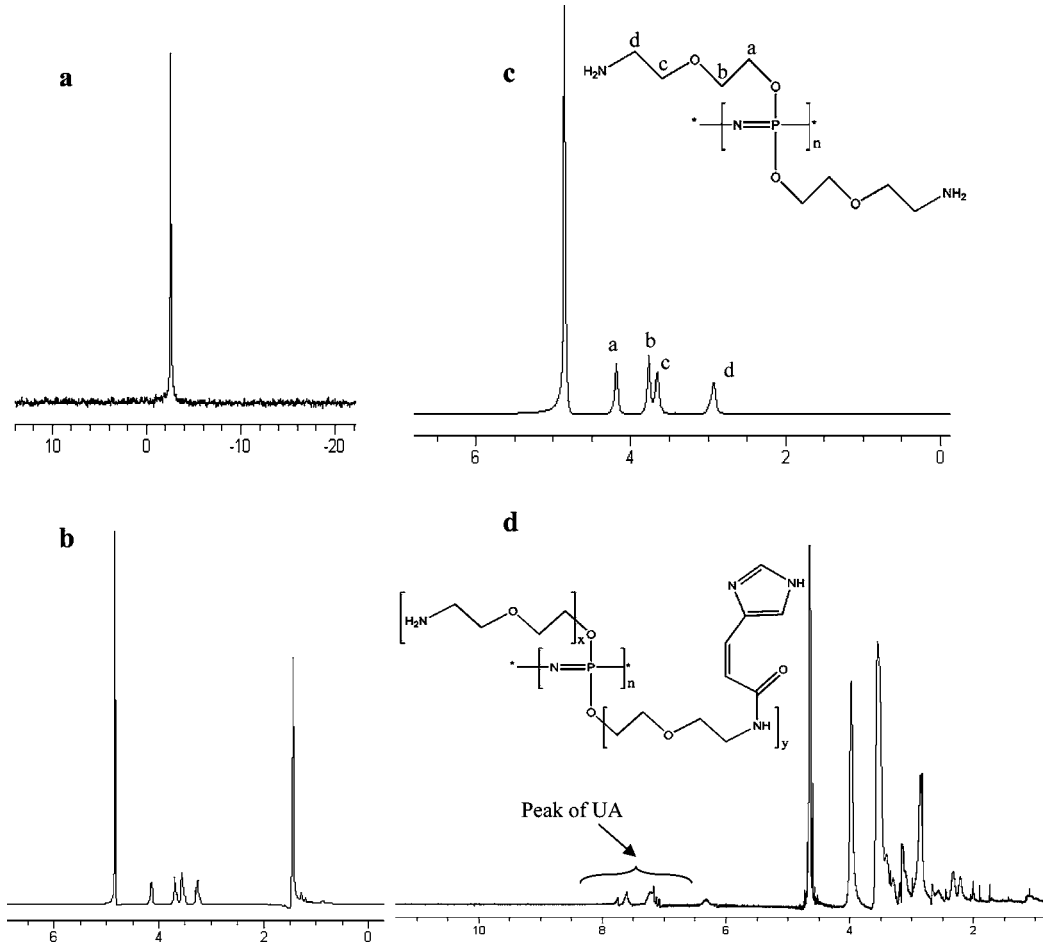


Figure 2. ^{31}P NMR spectra of PAEP (a); ^{1}H NMR spectra of polymer 1 (b), PAEP (c), and UA-PAEP (d).

with cold PBS twice. Fluorescent microscope images of cells were taken simultaneously using an Oliympus Inverted microscope (Japan). Finally, the cells were harvested by trypsinization. To quench the extracellular fluorescence, the cell suspension was mixed with 25 μL of a 0.4% trypan blue (TB) solution in PBS. The mean fluorescence intensity (MFI) of the cells was measured with a flow cytofluorometer. MFI of PEICNs was normalized to 100.

The uptake mechanism of PACNs and UPCNs in Hela cells was examined by means of specific inhibitors of the different endocytic pathways. For inhibition experiments, the cells were first incubated with one of the following inhibitors: 56 μM chlorpromazine (to inhibit clathrin-mediated endocytosis), 10 μM nystatin (to inhibit microtubule-mediated endocytosis), 3 μM cytochalasin D (to inhibit macropinocytosis), or 200 μM genistein (an inhibitor of caveolae-mediated endocytosis) for 30 min in completed medium prior to addition of complex nanoparticles to the cells. Inhibitors were used at concentrations in which they were shown to be active but not cytotoxic in COS 7 cells (*18*).

Statistical Analysis. Statistical analysis was performed using a Student's *t*-test. The differences were considered significant for $p < 0.05$ and $p < 0.01$ indicative of a very significant difference.

RESULTS AND DISCUSSION

Synthesis of PAEP And UA-PAEP. Prior to the substitution reaction, one of the two nucleophilic groups in 2-(aminoethoxy)ethanol had to be protected lest cross-linking of the polymer occurred. In this work, the *tert*-butoxycarbonyl (Boc) group, which decomposes readily by treatment with acid and remains intact under basic conditions, was used to protect amine groups of 2-(aminoethoxy)ethanol. Once polymer 1 was obtained, the deprotection of *tert*-butoxycarbonyl group was carried out by trifluoroacetic acid. Since the deprotection reaction was carried out under acidic condition, chain cleavage was considered to be a possible side reaction. However, no signal that could be attributed to decomposition was observed in ^{31}P NMR of PAEP (Figure 2a). A strong single peak of ^{1}H NMR for Boc group, as shown at 1.36 ppm (Figure 2b), disappeared in ^{1}H NMR spectra of PAEP (Figure 2c). The molecular weight of PAEP was 1.47×10^4 Da. To facilitate the endosome escape, PAEP was coupled with UA using an active ester method to obtain UA-PAEP. PAEP was first dissolved in methanol because it was not soluble in aprotic solvents and diluted with dimethylformamide to react with activated UA. ^{1}H NMR of UA-PAEP in D_2O was shown in Figure 2d. The substitution degrees of UA were 7% (UA-PAEP7) and 25% (UA-PAEP25) of the total amine functions, respectively.

Buffering Capacity of Polymers. The buffering capacity of polymer was tested via titration with 0.1 N HCl. Figure 3 showed that the buffering capacities of UA-PAEP7 and UA-PAEP25 were higher than that of PAEP in the range of pH 4−6.6, which indicated that the involvement of UA improved the buffering capacity of PAEP. The buffering capacity of UA-PAEP slightly increased when the substitution value of UA increased from 7% to 25%. As positive control, PEI showed excellent buffering capacity. PLL exhibited much lower buffering capacity than other polymers as a negative control. It is believed that the correlation of the pH range to the transfection process is between pH 5 and pH 7. In this work, the range of pH 4−6.6 was chosen to compare the buffering capacities of

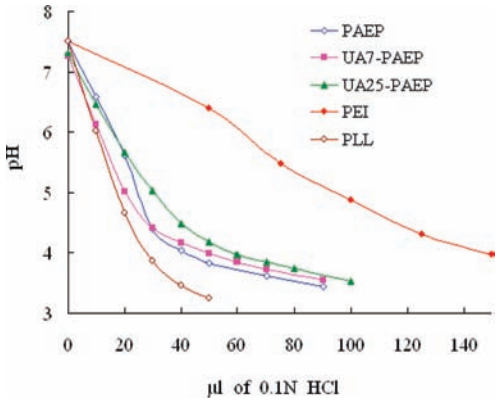


Figure 3. Titration curve of PAEP, UA-PAEP7, UA-PAEP25, and PEI solution (0.3 mg/mL). The polymer solution was titrated with 0.1 N HCl.

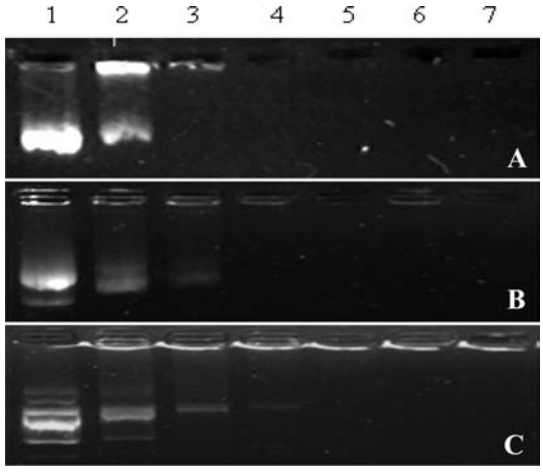


Figure 4. DNA retardation assay by agarose gel electrophoresis using 1% agarose in Tris-acetate running buffer (pH 8.0). (A) Lane 1, DNA control; lanes 2−7, PAEP/DNA (N/P) = 1.2, 2.5, 5, 7.5, 25, and 37, respectively. (B) Lane 1, DNA control; lanes 2−7, UA-PAEP7/DNA (N/P) = 1.2, 2.5, 5, 7.5, 25, and 37, respectively. (C) Lane 1, DNA control; lanes 2−7, UA-PAEP25/DNA (N/P) = 1.2, 2.5, 5, 6.7, 7.5, and 25, respectively.

the polymers according to ref *19*. On the other hands, UP7CNs showed obvious difference in their buffering effects compared with PAEP in the pH range 4−6.6 rather than in the pH range 5−7.

Characterization of Polymer/DNAComplex Nanoparticles. The formation of polymer/DNA complex nanoparticles was confirmed by gel retardation assay. The ratio of polymer/DNA (N/P) at which the electrophoretic mobility of DNA was completely retarded was 2.5:1 for PAEP, 5:1 for UA-PAEP7, and 6.7:1 for UA-PAEP25, respectively (Figure 4). The results indicated that the ability of UA-PAEP condensing DNA was less efficient than PAEP due to the decreased positive charges. It has been reported that the suitable surface property and size range enable the cationic polymer/DNA complex nanoparticles to pass the cellular membrane via endocytosis (*14*). PAEP could condense DNA into nanoparticles with an average diameter around 120 nm at the polymer/DNA (N/P) ratio from 2.5 to 35 in distilled water. According to transfection experiment (see following section), the polymer/DNA complex nanoparticles prepared either in water or in 20 mM acetate (pH 5.7) at the N/P ratio of 35 were used for following experiments. Table 1 showed that the particle sizes of all complex nanoparticles prepared in water were about 120 nm, which were much smaller than those prepared in 20 mM acetate (pH 5.7). Meanwhile, the surface charges of the above complex nanoparticles prepared

Table 1. Average Particle Size and ζ Potential of Polymer/DNA Nanoparticles Prepared in Different Media at the Polymer/DNA Ratio (N/P) of 35

	distilled water		20 mM acetate (pH 5.7)
polymer	particle size (nm)	ζ-potential (mV)	particle size (nm)
PAEP	119.4 ± 5.5	30.5 ± 6.1	161.4 ± 5.2
UA-PAEP7	1230.6 ± 6.2	23.9 ± 4.8	168.8 ± 6.6
UA-PAEP25	115.9 ± 4.3	6.7 ± 3.3	145.7 ± 5.9

in distilled water decreased with increasing degree of UA substitution. The ζ potential of PACNs was the highest (30.5 mV), and that of UA-PAEP25/DNA complex nanoparticles (UP25CNs) was only 6.7 mV. Apparently, the conjugation of UA with the amino groups in PAEP decreased the DNA binding ability of polymer, as well as the charge density of complex nanoparticles.

In VitroTransfection Efficiency. In order to know the transfection activity of PACNs, the experiment was first performed in Hela cells using pEGFP in serum-free medium. As shown in Figure 5A, PACNs yielded the highest transfection efficiency at the N/P ratio of 7.5, which was almost the same order of magnitude as PEICNs at the optimal ratio (N/P = 35). This behavior of PAEP was so different from that of another structurally similar polyphosphazene derivative, poly(di-DMAE-A)phosphazene (*11*), which showed much lower transfection efficiency compared with the PEI polyplexes. PAEP and poly(di-DMAEA)phosphazene are two cationic polyphosphazenes with an identical backbone containing different side chains, which are primary and tertiary amino groups, respectively. It has been reported that the type of charge group is one of the most important parameters for efficient gene transfer (*20*−*22*). Among all carriers with various types of charge groups, polymers with primary amino groups were found to be most efficient in transfecting cell lines (*23, 24*). So, the different types of charge groups might bring about the variance of transfection level between PAPE and poly(di-DMAEA)phosphazene. Then, in vitro transfection efficiency of PACNs prepared in distilled water was evaluated in Hela and COS 7 cell lines to look for the optimal condition of transfection in complete medium. Figure 5B showed that PACNs mediated the highest level of gene expression at the N/P ratio of 35 in both Hela and COS 7 cell lines. The increase of the optimal transfection ratio (N/P) of PACNs from 7.5 in serum-free medium to 35 in complete medium might result from the decreased positive charges of complex nanoparticles after interaction with the components of serum. It was reported that 20 mM acetate (pH 5.7) could ensure a higher positive charge density (*11*). So, the transfection efficiencies of PACNs, UPCNs, and PEICNs prepared either in distilled water or in 20 mM acetate (pH 5.7) at the N/P ratio of 35 were investigated to understand the relationship between preparation medium and transfection activity. The results showed that UP7CNs exhibited higher transfection activity compared with PACNs or UP25CNs in both media (Figure 5C) and the transfection level of UP7CNs was almost comparable to that of PEICNs. Despite the slightly lower buffering effect compared to that of UA-PAEP25, UP7CNs showed higher transfection efficiency than UP25CNs. The superior transfection activity of UP7CNs could result from its suitable positive charges, which are helpful for endocytosis, stability in cytoplasm, and dissociation of pDNA from UP7CNs. Besides, improved buffering capacity of UA-PAEP7 could be another reason accounting for the higher level of gene expression of UP7CNs than that of PACNs. With higher buffering capacity than UA-PAEP7, UP25CNs showed a much lower level of gene expression than UP7CNs. Possibly, fewer positive charges of UP25CNs resulted in weaker electrostatic attractions between pDNA and UA-PAEP25 after UP25CNs escaped from endo-

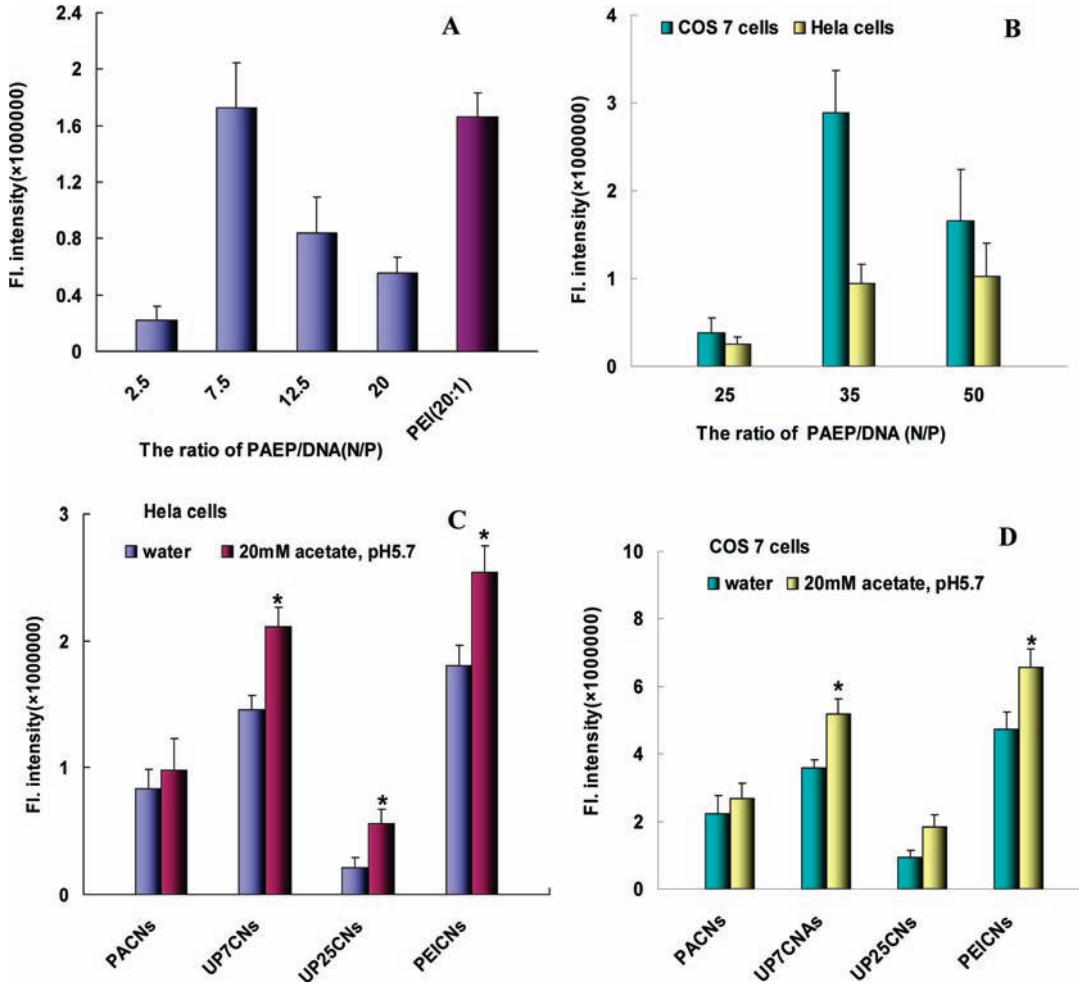


Figure 5. Transfection efficiency of Hela cells mediated by PACNs at various polymer/DNA ratios (N/P) in serum-free DMEM, PEICNs at the N/P ratio of 20 as control group (A). The transfection efficiency of PACNs prepared in water for Hela and COS 7 cells (B). Transfection efficiency of PACNs, UPCNs, and PEICNs prepared in water or acetate pH 5.7 at N/P ratio of 35 for Hela (C) and COS 7 cells (D) ($n = 3$, error bars represent standard deviation). The transfection efficiency was expressed as total fluorescence intensity of 1×10^4 cells. $^*p < 0.05$ compared with the transfection of complex nanoparticles prepared in water.

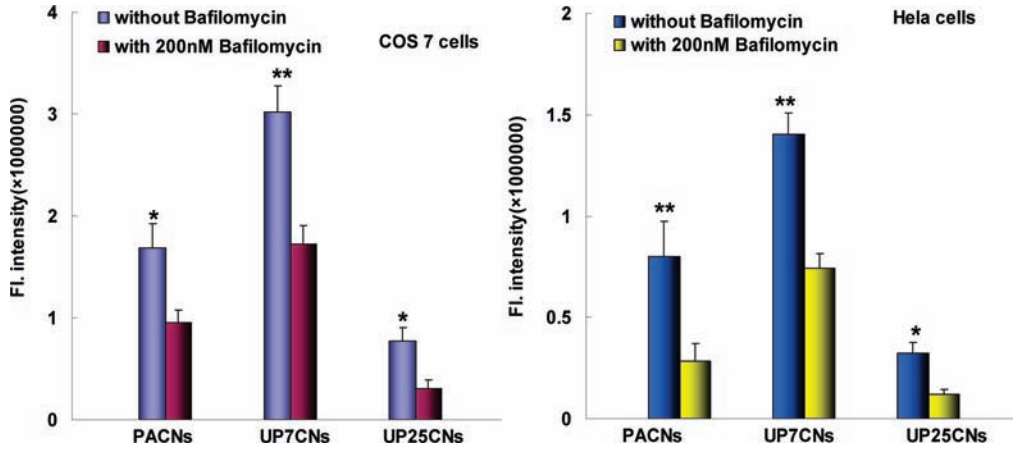


Figure 6. Effect of proton pump inhibitor bafilomycin A1 on transfection mediated by polymer/DNA complex nanoparticles at the polymer/DNA ratio (N/P) of 35. COS 7 cells and Hela cells were transfected in the presence of 200 nM or without Bafilomycin A1, respectively. The transfection efficiency was expressed as total fluorescence intensity of 1×10^4 cells ($n = 3$). $^{**}p < 0.01$ or $^*p < 0.05$ compared with the transfection of complex nanoparticles in the presence of bafilomycin A1.

some into cytosol with higher pH, thus inducing DNA to dissociate with complex nanoparticles and to be hydrolyzed by lysosomal enzyme. Therefore, the poor transfection efficiency of UP25CNs might be attributed to instability resulting from low zeta potential rather than buffering capacity. However, the absence of endosomal escape could be one of reasons accounting for unsatisfactory transfection activity of UP25CNs compared with UP7CNs as well. As for PACNs with the highest zeta potential, inferior buffering capacity might be one of the factors leading to a lower level of gene transfection than UP7CNs.

The acetate solution (20 mM, pH 5.7) improved the transfection activity of UPCNs (especially UP25CNs) in Hela cells

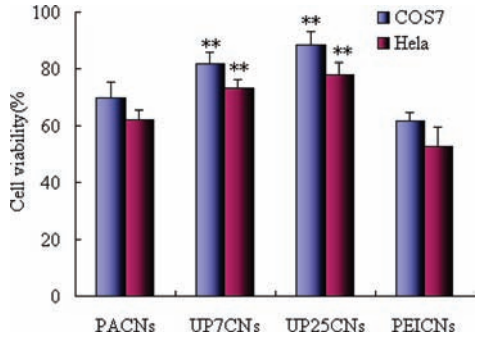


Figure 7. Cytotoxicity of PACNs and UPCNs at polymer/DNA ratio (N/P) on COS 7 cells and HeLa cells measured by MTT assay. PEICNs as control ($n = 3$, error bars represent standard deviation). $^{**}p < 0.01$ compared with the cytotoxicity of PEICNs.

(Figure 9) and COS 7 cells, while this effect was not observed in the case of PACNs. The results suggested that the increased transfection efficiency of UPCNs in 20 mM acetate (pH5.7) could be due to increased positive charges and the enhancement of the protonation from imidazole moieties, especially for UP25CNs with higher UA denstity. However, for PACNs, a permanent positive charge from basic amino groups induced the little alteration of the stability in cytosol as well as the transfection activity without regard to pH of preparation medium. Bafilomycin A1, a proton pump inhibitor, is used to testify whether the buffering-based endosomolytic activity plays an important role on the transfection efficiency. Bafilomycin A1 is an antibiotic that selectively inhibits vacuolar type of H^+-ATPases (*25*). Figure 6 showed that the involvement of Bafilomycin A1 resulted in a significant decrease in the gene expression levels of PACNs and UPCNs in Hela and COS 7 cell lines, which suggested that the transfection efficiencies of all the above complex nanoparticles were dependent on the endosomal acidification process. Because of this, it is very meaningful to conjugate the UA moiety with PAEP to increase the buffering capacity, which benefits the endosomal escape of complex nanoparticles to improve the transfection efficiency. Even if, in the presence of a proton pump inhibitor, the transfection activity of UP7CNs was still higher than that of other complex nanoparticles, which also meant that the marginally increased buffering capacity of UA-PAEP7 was not enough to explain its higher transfection efficiency.

Cytotoxicity of Polymer/DNA Complex Nanoparticles. The cytotoxicity of complex nanoparticles at polymer/DNA ratio (N/P) of 35 in COS 7 and Hela cells was shown in Figure 7. In COS 7 cells, the cell viability of PACNs was 69%, which was slightly higher than that of PEICNs. When PAEP was modified by UA, the cell viability of complexed nanoparticles increased from 81% to 88% with the substitute degree of UA from 7% to 25%. The descending cytotoxicity of polymer modified by UA could be due to the decreased positive charges. The similar results of cytotoxicity also occurred in Hela cells. So, it was obvious that the cytotoxicity of UPCNs was much lower than that of PEICNs in both cell lines.

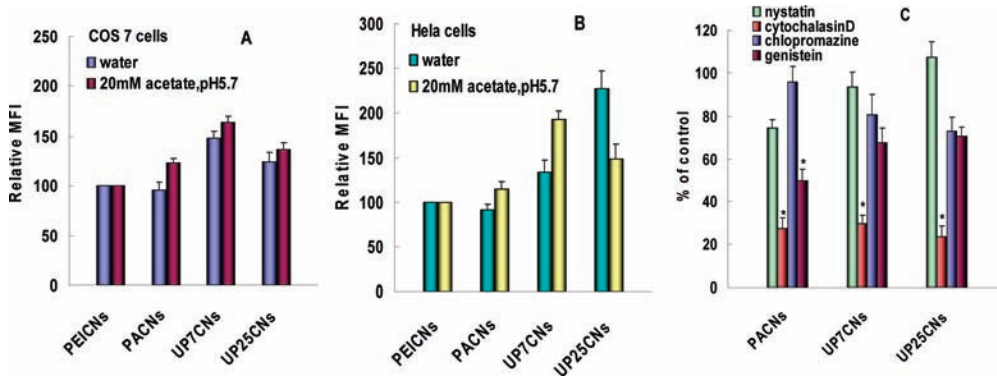


Figure 8. Cellular uptake of nanoparticles prepared in water or acetate (pH 5.7) on COS 7 cells (A) and Hela cells (B). The cells were incubated for 1 h with YOYO-1-labeled nanoparticles. After a subsequent washing and trypsinization, the mean fluorescence intensity (MFI) was analyzed with a flow cytoflurometer. MFI of PEICNs was normalized to 100. Nanoparticles were prepared at the N/P ratio of 35. Cellular uptake of PACNs, UP7CNs, or UP25CNs by Hela cells after incubation with various inhibitors (C). Percentages of cellular uptake expressed as % of control were means ± SD from three independent experiments. *Values significantly different from control ($p < 0.05$).

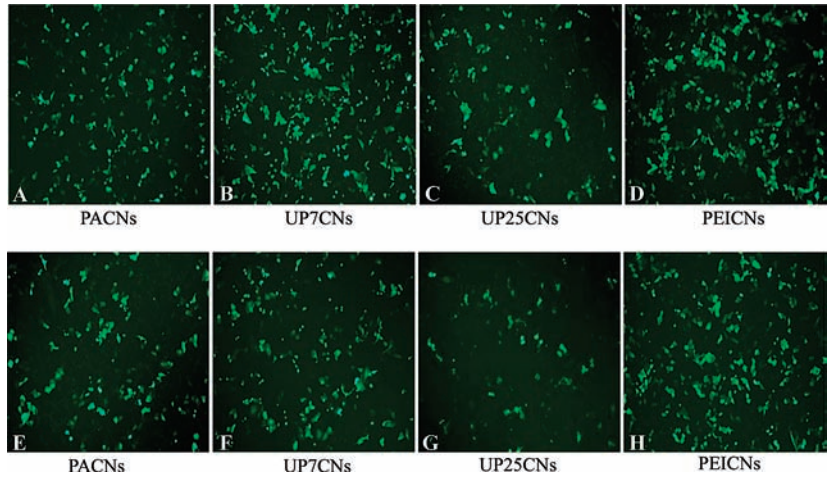


Figure 9. Images of Hela cells transfected with PACNs, UP7CNs, UP25CNs, and PEICNs prepared either in 20 mM acetate (pH 5.7) (A,B,C,D) or in distilled water (E,F,G,H) observed under fluorescent microscope (20× magnification) at the N/P ratio of 35.

Cell Uptake of Polymer/DNA Complex Nanoparticles. Uptake of polymer/DNA complex nanoparticles through endocytosis into the cells is the first step during intracellular gene delivery. It is essential to investigate the cellular uptake of complex nanoparticles for more insight into the diversity of transfection activity among three complex nanoparticles. The amount of pDNA internalized by Hela or COS 7 cells was estimated after quenching the fluorescence of the complex nanoparticles adsorbed on the cell surface by adding trypan blue to the cell suspension in PBS. The PACNs, UPCNs, and PEICNs were prepared at the polymer/DNA ratio (N/P) of 35. As shown in Figure 8A, the DNA uptake efficiency mediated by UP7CNs prepared in either distilled water or 20 mM acetate (pH 5.7) was much higher than that of other complex nanoparticles under same condition in COS 7 cell lines. So, the higher cell uptake level of UP7CNs could be one of the reasons for their superior transfection activity. Although the uptake level of PEICNs was lower than UP7CNs, the strong buffering capacity of PEI 25K, which would benefit intracellular trafficking of nanoparticles, could result in its higher transfection efficiency than UP7CNs. Although UPCNs prepared in 20 mM acetate (pH 5.7) showed enhancement of transfection activities than that prepared in water, no significant difference in terms of DNA uptake of complex nanoparticles between different preparation systems was observed. The results indicated that a weak acid preparation system could improve the compaction of UPCNs rather than their cellular uptake. In Hela cell lines, the uptake of complex nanoparticles prepared in 20 mM acetate (pH 5.7) was similar to that in COS 7 cells, while the DNA uptake level mediated by UP25CNs prepared in distilled water surprisingly was the highest among the three complex nanoparticles.

Current evidence suggests that the positively charged polymer/DNA complex nanoparticles are taken up by means of endocytosis (*26, 27*). Since different endocytic pathways exist, it is important to have a more detailed knowledge of the cellular uptake and routing mechanism of polymer/DNA complex nanoparticles. To know whether the type of endocytosis would bring about the above phenomenon of UP25CNs, quantitative measurement of the uptake of complex nanoparticles in the presence of endocytosis inhibitors was investigated in Hela cell lines. In our experiments, disruption of macropinocytosis by means of cytochalasin D decreased all of PACN, UP7CN, and UP25CN uptake to less than 30%, as a percentage of control (i.e., without preincubation with inhibitor) (Figure 8C). Inhibition of caveolae-mediated uptake by genistein, an inhibitor of tyrosine kinases involved in caveolae-mediated endocytosis, inhibited uptake of UP7CNs and UP25CNs by 67% and 70%, respectively, while the internalization of PACNs was significantly reduced by almost 50%. Inhibition of clathrin-mediated uptake by chlorpromazine and microtubule-mediated by nystatin did not significantly reduce the uptake of PACNs, UP7CNs, and UP25CNs. These results demonstrated that macropinocytosis dominated the uptake routes of three complex nanoparticles. Caveolae-mediated endocytosis was also involved in the uptake of PACNs, while clathrin-mediated and microtubule-mediated pathways were not involved in the uptake of three complex nanoparticles. There was no significant difference in endocytic pathway between UP7CNs and UP25CNs.

It seemed likely that the improvement of transfection mediated by UP7CNs was related to the following parameters including ζ-poptential, pH buffering capacity, and cellular DNA uptake. However, the intracellular trafficking and nuclear uptake are two crucial processes involved in enhanced gene expression of UP7CNs.

CONCLUSION

A biodegradable cationic polyphosphazene with (2-(2-aminoethoxy)ethoxy) as side chains bearing primary amino groups was synthesized and first used for gene delivery. PACNs could mediate efficient transfection in complete medium at the polymer/DNA ratio (N/P) of 35. UP7CNs could enhance the transfection efficiency compared with PACNs and decrease cytotoxicity compared with PEICNs in HeLa and COS 7 cell lines. The transfection experiment using a proton pump inhibitor suggested that the gene expression of PACNs, UPCNs were dependent on the endosomal acidification process. The acetate solution (20 mM, pH 5.7) could further improve the transfection activity of UPCNs, which was almost comparable to PEICNs in HeLa and COS 7 cell lines. So, UP7CNs could be a more potential carrier for gene delivery. Further studies would focus on evaluating in vivo transfection efficiency of UP7CNs.

ACKNOWLEDGMENT

The National Basic Research Program of China (nos 2007CB935800 and 2009CB930300), the National Natural Science Foundation of China (30873169), the Important Direction Program of CAS (KJCX2.YW.M02, KSCX1-YW-R-21, KSCX2-YW-R-09), and Shanghai Nanomedicine Program (0852 nm05700) are gratefully acknowledged for financial support.

LITERATURE CITED

(1) Wightman, L., Kircheis, R., Rö ssler, V., Carotta, S., Ruzicka, R., Kursa, M., and Wagner, E. (2001) Different behavior of branched and linear polyethylenimine for gene delivery in vitro and in vivo. *J. Gene. Med. 3*, 362–372.

(2) Koping-Hoggard, M., Mel'nikovas, Y. S., Varum, K. M., Lindman, B., and Artursson, P. (2003) Relationship between the physical shape and the efficiency of oligomeric chitosan as a gene delivery system in vitro and in vivo. *J. Gene. Med. 5*, 130–141.

(3) Ahn, C. H., Chae, S. Y., Bae, Y. H., and Kim, S. W. (2004) Synthesis of biodegradable multi-block copolymers of poly(L-lysine) and poly(ethylene glycol) as a non-viral gene carrier. *J. Controlled Release 97*, 567–574.

(4) Vincent, L., Varet, J., Pille, J. Y., Bompais, H., Opolon, P., Maksimenko, A., Malvy, C., Mirshahi, M., Lu, H., Vannier, J. P., Soria, C., and Li, H. (2003) Efficacy of dendrimer-mediated Angiostatin andTIMP-2 gene delivery on inhibition of tumor growth and angiogenesis:in vitro and in vivo studies. *Int. J. Cancer 105*, 419–429.

(5) Ahn, H. H., Lee, J. H., Kim, K., Lee, J. Y., Kim, M. S., Khang, G., Lee, I. W., and Lee, H. B. (2008) Polyethyleneimine-mediated gene delivery into human adipose derived stem cells. *Biomaterials 29*, 2415–2422.

(6) Lavertu, M., Méthot, S., Tran-Khanh, N., and Buschmann, M. D. (2006) High efficiency gene transfer using chitosan/DNA nanoparticles with specific combinations of molecular weight and degree of deacetylation. *Biomaterials 27*, 4815–4824.

(7) Nimesh, S., Kumar, R., and Chandra, R. (2006) Novel polyallylamine-dextran sulfate-DNA nanoplexes:Highly efficient non-viral vector for gene delivery. *Int. J. Pharm. 320*, 143–149.

(8) Zhang, J. X., Li, X. J., Qiu, L. Y., Li, X. H., Yan, M. Q., Jin, Y., and Zhu, K. J. (2006) Indomethacin-loaded polymeric nanocarriers based on amphiphilic polyphosphazenes with poly (N-isopropylacrylamide) and ethyl tryptophan as side groups: Preparation, in vitro and in vivo evaluation. *J. Controlled Release 116*, 322–329.

(9) Caliceti, P., Veronese, F. M., and Lora, S. (2000) Polyphosphazene microspheres for insulin delivery. *Int. J. Pharm. 211*, 57–65.
(10) Luten, J., van Steenis, J. H., van Someren, R., Kemmink, J., Schuurmans-Nieuwenbroek, N. M. E., Koning, G. A., Crommelin, D. J. A., van Nostrum, C. F., and Hennink, W. E. (2003) Water-soluble biodegradable cationic polyphosphazenes for gene delivery. *J. Controlled Release 89*, 483–497.
(11) de Wolf, H. K., Luten, J., Snel, C. J., Oussoren, C., Hennink, W. E., and Storm, G. (2005) *J. Controlled Release 109*, 275–287.
(12) Luten, J., van Steenbergen, M. J., Lok, M. C., de Graaff, A. M., van Nostrum, C. F., Talsma, H., and Hennink, W. E. (2008) In vivo tumor transfection mediated by polyplexes based on biodegradable poly(DMAEA)-phosphazene. *Eur. J. Pharm. Sci. 33*, 241–251.
(13) Yang, Y. X., Xu, Z. H., Jiang, J. G., Gao, Y., Gu, W. W., Chen, L. L., Tang, X. Z., and Li, Y. P. (2008) Poly(imidazole/DMAEA)phosphazene/DNA self-assembled nanoparticles for gene delivery: Synthesis and in vitro transfection. *J. Controlled Release 127*, 273–279.
(14) Remy-Kristensen, A., Clamme, J. P., Vuilleumier, C., Kuhry, J. G., and Mely, Y. (2001) Role of endocytosis in the transfection of L929 fibroblasts by polyethylenimine/DNA complexes. *Biochim. Biophys. Acta 1514*, 21–32.
(15) Merdan, T., Kunath, K., Fischer, D., Kopeček, J., and Kissel, T. (2002) Intracellular processing of poly(ethylene imine)/ribozyme complexes can be observed in living cells by using confocal laser scanning microscopy and inhibitor experiments. *Pharm. Res. 19*, 140–146.
(16) Allcock, H. R., and Chang, J. Y. (1991) Poly(organophosphazenes) with oligopeptides as side groups:prospective biomaterials. *Macromolecules 24*, 993–999.
(17) Tseng, W. C., Fang, T. Y., Su, L. Y., and Tang, C. H. (2005) Dependence of transgene expression and the relative buffering capacity of dextran-grafted polyethylenimine. *Mol. Pharmaceutics 2*, 224–232.
(18) Huth, U., Schubert, R., and Peschka-Suss, R. (2006) Investigating the uptake and intracellular fate of pH-sensitive liposomes by flow cytometry and spectral bio-imaging. *J. Controlled Release 110*, 490–504.
(19) Zhang, P. C., Wang, J., Leong, K. W., and Mao, H. Q. (2005) Ternary complexes comprising polyphosphoramidate gene carriers with different types of charge groups improve transfection efficiency. *Biomacromolecules 6*, 54–60.
(20) van de Wetering, P., Moret, E. E., Schuurmans-Nieuwenbroek, N. M., van Steenbergen, M. J., and Hennink, W. E. (1999) Structure-Activity relationships of water-soluble cationic methacrylate/methacrylamide polymers for nonviral gene delivery. *Bioconjugate Chem. 10*, 589–597.
(21) Thomas, M., and Klibanov, A. M. (2002) Enhancing polyethylenimine's delivery of plasmid DNA into mammalian cells. *Proc. Natl. Acad. Sci. U.S.A. 99*, 14640–14645.
(22) Reschel, T., Konak, C., Oupicky, D., Seymour, L. W., and Ulbrich, K. (2002) Physical properties and in vitro transfection efficiency of gene delivery vectors based on complexes of DNA with synthetic polycations. *J. Controlled Release 81*, 201–217.
(23) Wang, J., Zhang, P. C., Lu, H. F., Ma, N., Wang, S., Mao, H. Q., and Leong, K. W. (2002) New polyphosphoramidate with a spermidine side chain as a gene carrier. *J. Controlled Release 83*, 157–168.
(24) Wolfert, M. A., Dash, P. R., Nazarova, O., Oupicky, D., Seymour, L. W., Smart, S., Strohalm, J., and Ulbrich, K. (1999) Polyelectrolyte vectors for gene delivery: influence of cationic polymer on biophysical properties of complexes formed with DNA. *Bioconjugate Chem. 10*, 993–1004.
(25) Singh, R. S., Gonçalves, C., Sandrin, P., Pichon, C., Midoux, P., and Chaudhuri, A. (2004) On the gene delivery efficacies of pH-sensitive cationic lipids via endosomal protonation: A chemical biology investigation. *Chem. Biol. 11*, 713–723.
(26) Cho, Y. W., Kim, J. D., and Park, K. (2003) Polycation gene delivery systems: escape from endosomes to cytosol. *J. Pharm. Pharmacol. 55*, 721–734.
(27) Lechardeur, D., Verkman, A. S., and Lukacs, G. L. (2005) Intracellular routing of plasmid DNA during non-viral gene transfer. *Adv. Drug Delivery Rev. 57*, 755–767.

BC900267G

Increased Sensitivity in Antigen Detection with Fluorescent Latex Nanosphere−IgG Antibody Conjugates

Tao Ji,* M. Catherine Muenker, Rao V. L. Papineni, John W. Harder, Douglas L. Vizard, and William E. Mclaughlin

Carestream Molecular Imaging, Carestream Health, Inc., New Haven, Connecticut 06511. Received July 6, 2009; Revised Manuscript Received January 4, 2010

IgG antibodies were conjugated to Kodak X-Sight nanospheres to develop fluorescent-labeled antibodies using two different synthetic routes: one involving the DTT reduction method, and the other involving Traut's Reagent modification method. These two methods result in different conjugation efficiencies and different performances in antigen detection. Western blotting shows that the nanosphere−IgG antibody conjugates synthesized using the DTT reduction method are more immunospecific than the conjugates synthesized using Traut's Reagent modification method. In addition, the conjugates synthesized using DTT reduction also show higher antigen detection sensitivity than other commercially available fluorescent-IgG antibody conjugates, including Alexa Fluor, Qdot, and CyDye conjugates.

INTRODUCTION

Fluorescent antibodies have been widely used in immunodetection both in life-science research and in clinical applications (*1*−*10*). Most of the fluorescent labels used for the labeling of antibodies are organic molecules that suffer from photobleaching and relatively low fluorescence intensity. Efforts to improve the sensitivity of immunodetection by exploring highly fluorescent and photostable labels have gained considerable momentum over the past decade (*11*−*16*).[1]

We have introduced a class of highly fluorescent organic nanospheres, Kodak X-Sight nanospheres (*17*), for fluorescent labeling of biomolecules. Our nanospheres are approximately 20 nm in diameter and are composed of a cross-linked polymer core coated with a poly(ethylene glycol) derivative that confers over 200 primary amines to the particle periphery. Each nanosphere encapsulates multiple dye molecules in the core, producing bright fluorescence and improved photostability. The primary amine-functionalized poly(ethylene glycol) layer on the surface provides water solubility and allows a variety of biomolecules, such as antibodies, streptavidins, DNA, or enzymes, to be covalently attached through different linking chemistries.

Here, we present the conjugation of IgG antibodies to Kodak X-Sight nanospheres and demonstrate the performance of the conjugates in antigen detection. We also address the challenge of quantitative determination of the number of biomolecules attached to the nanospheres—a problem typical of any nanoparticle-based conjugate system—by the development of a simple and sensitive method based on UV spectroscopy. To the best of our knowledge, this is the first report on utilizing this method to quantify the number of antibodies attached per nanosphere.

A variety of species-specific and highly cross-adsorbed IgG antibodies were successfully conjugated to the nanospheres in four excitation and emission wavelengths ranging from visible to near-infrared (Figure 1). These nanosphere conjugates exhibited increased brightness, high sensitivity, and enhanced signal-to-background ratio in Western blotting assays. We demonstrated up to a 10× improvement in antigen detection over other commercially available, spectrally similar, fluorescent−IgG antibody conjugates. The multiple colors of these nanosphere−antibody conjugates also enable multiplex detection, such as multiplex Western blotting assays, which allows for the detection of several proteins simultaneously on a single blot.

EXPERIMENTAL PROCEDURES

Materials. Kodak X-Sight 549 nanosphere, Kodak X-Sight 650 nanosphere, Kodak X-Sight 691 nanosphere, and Kodak X-Sight 761 nanosphere were manufactured by Carestream Health, Inc. All the reagents used for the X-Sight nanosphere synthesis are reagent grade or better unless otherwise specified. Goat anti-mouse, goat anti-rabbit, and goat anti-rat IgG antibodies were purchased from Jackson Immuno Research Laboratories. *N*-[β-Maleimidopropyloxy]succinimide ester, Traut's Reagent, BupH phosphate buffer saline (0.1 M sodium phosphate, 0.15 M NaCl, pH 7.2), PBS (0.137 M sodium chloride, 0.0027 M potassium chloride, and 0.0119 M phosphates, pH 7.4), Ellman's Reagent, β-mercaptoethanol, diethyl ether, methanol, and nonfat dry milk were obtained from Thermo Fisher Scientific. Dithiothreitol, dimethyl sulfoxide, sodium phosphate monobasic, sodium phosphate dibasic, sodium chloride aqueous solution (5 M), ethylenediaminetetraacetic acid disodium salt solution (0.5 M), conalbumin, trypsin, poly(ethylene glycol) dimethacrylate (Mn, 875), hydrochloric acid (37%), sodium hydroxide, ethyl acetate, hydrogen chloride, ethylene glycol methyl ether methacrylate, divinylbenzene (technical grade), cetylpyridinium chloride, sodium bicarbonate, tetrahydrofuran, and Dowex 50WX4−200 ion-exchange resin were purchased from Sigma-Aldrich. 10× PBS (0.1 M sodium phosphate, 1.5 M NaCl, pH 7.2) was purchased from Bio-Rad Laboratories. NuPAGE 4−12% BT gel, MOPS SDS running buffer (20×),

* To whom correspondence should be addressed. Carestream Molecular Imaging, Carestream Health, Inc., New Haven, CT 06511, USA. Phone: (203) 786-5686. Fax: (203) 624-3143. E-mail: tao.ji@carestreamhealth.com.

[1] Abbreviations: AMAS, *N*-[α-Maleimidoacetoxy]succinimide ester; BME, β-mercaptoethanol; BMPS, *N*-[β-maleimidopropyloxy]succinimide ester; DMSO, dimethylsulfoxide; DTT, dithiothreitol; EDTA, ethylenediaminetetraacetic acid disodium salt; NHS, *N*-hydroxysuccinimide; PVDF, polyvinylidene difluoride; SATA, *N*-succinimidyl-*S*-acetylthioacetate; Sulfo-SMCC, sulfosuccinimidyl 4-[*N*-maleimidomethyl]cyclohexane-1-carboxylate; THF, tetrahydrofuran.

10.1021/bc900295v © 2010 American Chemical Society
Published on Web 02/17/2010

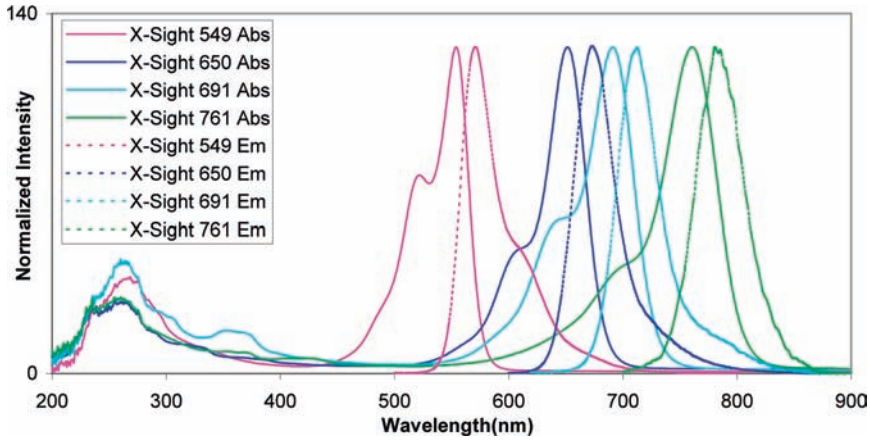


Figure 1. UV absorption and emission spectra of X-Sight nanospheres. Absorption/emission maxima: X-Sight 549, 549 nm/569 nm; X-Sight 650, 650 nm/573 nm; X-Sight 691, 691 nm/715 nm; X-Sight 761, 761 nm/789 nm.

NuPAGE sample reducing agent (10×), NuPAGE antioxidant, NuPAGE transfer buffer (20×), NuPAGE LDS sample buffer (4×), 4−20% tris-glycine gel, Novex native tris-glycine sample buffer (2×), NativeMark protein standard, tris-glycine native running buffer, Alexa Fluor IgG antibody conjugates, and Qdot IgG antibody conjugates were purchased from Invitrogen. ECL Plex Fluorescent Rainbow Marker, illustra NAP-5 columns, Superdex 200 gel media, and Cy3 goat anti-mouse were purchased from GE Healthcare. Cy5 goat anti-mouse, Cy5.5 goat anti-mouse, and NIH/3T3 whole cell lysate were purchased from Rockland Immunochemicals. Immobilon-FL PVDF membrane, Microcon YM-30, and Microcon YM-100 were purchased from Millipore. Primary IgG antibodies (rabbit antibeta tubulin, mouse anti-beta actin, rat anti-HSC 70) were purchased from Abcam. Magnesium sulfate was purchased from Alfa Aesar. Cysteamine was purchased from TCI America. 2,2-Azobis(*N*,*N*-dimethyleneisobutyramidine) dihydrochloride was purchased from Wako Pure Chemical Industries. Spectra/Por dialysis membrane (MWCO 3500) was purchased from VWR.

Instrumentation. SDS PAGE gel was imaged on a KODAK Gel Logic 212 imaging system. Western blot images were taken on a KODAK Image Station 4000MM digital imaging system or on a KODAK In-Vivo Multispectral Imaging System FX. UV spectra were measured on a PerkinElmer Lambda 25 UV/vis spectrometer. Fluorescence spectra were measured on a PerkinElmer luminescence spectrometer LS 50B. Centrifugation was performed on an Eppendorf microcentrifuge 5415R. Chromatography of the conjugates, IgG antibody, and proteins was carried out on a Waters HPLC 2796 equipped with a Superdex 200 column.

Buffer Preparation. PBS (0.1 M sodium phosphate, 0.15 M NaCl, pH 7.5), PBS/5 mM EDTA (0.1 M sodium phosphate, 0.15 M NaCl, 5 mM EDTA, pH 8.0), and phosphate buffer/1 mM EDTA (0.1 M sodium phosphate, 1 mM EDTA, pH 8.0) were prepared from sodium phosphate monobasic, sodium phosphate dibasic, NaCl and EDTA. BupH PBS/10 mM EDTA (0.1 M sodium phosphate, 0.15 M NaCl, 10 mM EDTA, pH 7.2) was constructed from BupH phosphate buffer saline and EDTA. 1× PBS (0.01 M sodium phosphate, 0.15 M NaCl, pH 7.2) was diluted from 10× PBS.

Preparation of Fluorescent Nanospheres. The preparation is described briefly here. For a detailed description of the preparation, see U.S. patent application (*17*)

Preparation of Amine-Terminated Poly(ethylene glycol) Macromonomer. PEG dimethacrylate (335 g) in 100 mL of methanol was treated with cysteamine (5.8 g) and diisopropylethylamine (0.08 g). The mixture was stirred at room temperature for 2 days and then concentrated using a rotary evaporator. The residue was taken up in 1 L of ethyl acetate and extracted with aqueous HCl solution (10%). The aqueous layer was collected, made basic by adding 50% aqueous sodium hydroxide solution, and then extracted with ethyl acetate. The organic layer was dried over magnesium sulfate, filtered, and concentrated. The residue was taken up in anhydrous diethyl ether and treated with gaseous HCl and allowed to stand. The ether was decanted, and the residual dark blue oil was washed with fresh diethyl ether, which was then decanted. The dark blue oil was dried on a rotary evaporator to yield 37 g of the desired product in the form of the hydrochloride salt. ^{1}H NMR (300 MHz, $CDCl_3$): 1.18 (doublet, 3H), 1.93 (broad singlet, 3H), 2.04 (broad singlet, 2H), 2.43−2.77 (broad multiplet, 7H), 3.6−3.7 (broad singlet, $-CH_2CH_2O-$), 3.73 (broad triplet, 2H), 3.29 (broad triplet, 2H), 5.56 (broad singlet, 1H), 6.12 (broad singlet, 1H).

Synthesis of Nanospheres. Typical example: A 500 mL 3-neck round-bottomed flask was modified with Ace #15 glass threads at the bottom and a series of adapters allowing connection of 1/16 in i.d. Teflon tubing. The flask (hereafter referred to as the header flask) was outfitted with a mechanical stirrer and rubber septum with syringe needle nitrogen inlet. The header was charged with methoxyethyl methacrylate (5.63 g), divinylbenzene (0.63 g, mixture of isomers, 80% pure with remainder being ethylstyrene isomers), amine-terminated poly(ethylene glycol) macromonomer (6.25 g), 2,2-azobis(*N*,*N*-dimethyleneisobutyramidine) dihydrochloride (0.06 g), cetylpyridinium chloride (0.31 g), and distilled water (78.38 g). The header contents were brought to pH 5 with 1 N NaOH. A 1 L 3-neck round-bottomed flask outfitted with a mechanical stirrer, reflux condenser, nitrogen inlet, and rubber septum (hereafter referred to as the reactor) was charged with distilled water (159.13 g), 2,2-azobis(*N*,*N*-dimethyleneisobutyramidine) dihydrochloride (0.06 g), sodium bicarbonate (0.06 g), and cetylpyridinium chloride (0.94 g). Both the header and the reactor contents were stirred until homogeneous and were bubble degassed with nitrogen for 20 min. The reactor flask was placed in a thermostatted water bath at 60 °C, and the header contents were added to the reactor over 2 h using a model QG6 lab pump. The reaction was allowed to stir at 60 °C for 16 h. The latex was then dialyzed against distilled water for 48 h using a Spectra/Por dialysis membrane (MWCO 3500) and was stirred over 27.5 g Dowex 50WX4−200 ion-exchange resin (sodium form) overnight to afford 312 g of clear latex of 3.26% solids. The volume average diameter of the nanosphere was found to be 20.89 nm with a coefficient of variation of 0.24 by quasi-elastic light scattering.

Loading the Nanospheres with Dyes. For the synthesis of the dyes loaded inside the nanospheres, see patent application (*17*).

Typical dye loading example: Under dim lighting, 1.4365 g of a dye stock solution of 0.2784% (w/w) in THF was added to a tinted glass vial and was diluted with THF to a final weight of 10.0 g. The amine-functionalized nanosphere (9.996 g) was added to the vial, and the solution was mixed and concentrated to approximately 40−50% volume on a rotary evaporator. Residual THF was further removed by twice adding 3−5 mL of distilled water and stripping ∼1/4−1/3 of the volatiles. 9.4 g of dye-loaded nanospheres of 4.27% (w/w) solids containing 3.94×10^{-3} mol dye per gram of solid nanospheres was obtained.

Fuctionalization of Nanospheres with BMPS. X-Sight 549, 650, 691, and 761 nanospheres, modified with maleimide functional groups, were prepared. In a typical procedure, 549 (40 μL, 32 μM) was added to 60 μL of PBS (0.1 M, 0.15 M NaCl, pH 7.5) and was then added with 6.4 μL (192.2 nmol) of 30 mM BMPS dissolved in anhydrous DMSO. The mixture was stirred at room temperature for 1 h. The maleimide-modified nanospheres were purified on an Illustra NAP-5 column eluted with BupH PBS/10 mM EDTA. ∼500 μL of the purified nanospheres was collected and stored on ice. The concentration of the purified nanospheres, as determined by UV absorbance, was 2.28 μM. The number of maleimide groups attached per nanosphere was quantified by Ellman's Reagent and is ∼80 maleimide groups per nanosphere.

Preparation of SH Groups Containing IgG Antibodies. *DTT Reduction Method.* Typical example: IgG antibody (0.5 mg) was dissolved in BupH PBS/10 mM EDTA (500 μL) at 1 mg/mL. Five microliters of 1 M DTT dissolved in BupH PBS/10 mM EDTA was added to the IgG solution. The mixture was incubated at RT for 1 h on a rotator and transferred to a Microcon YM-30 filter unit. The solution in the Microcon filter unit was concentrated to ∼50 μL by spinning at 13 400 *g* in an Eppendorf microcentrifuge for 11 min. The filtrate was discarded, and the remaining solution in the filter unit was brought up to 500 μL by BupH PBS/10 mM EDTA and spun again at 13 400 *g* for 11 min. This concentration−dilution cycle was repeated three more times. Roughly 50 μL of the modified IgG solution was collected.

Traut's Reagent Modification Method. Typical example: IgG antibody (0.5 mg) was dissolved in PBS (0.1 M, 0.15 M NaCl, pH 8.0)/5 mM EDTA buffer (500 μL) at 1 mg/mL. 4.76 μL of 7 mM Traut's Reagent dissolved in PBS (0.1 M, 0.15 M NaCl, pH 8.0)/5 mM EDTA buffer was added to the above IgG solution. The mixture was incubated at RT for 1 h on a rotator and transferred to a Microcon YM-30 filter unit. The solution in the Microcon filter unit was concentrated to ∼50 μL by spinning at 13 400 *g* in an Eppendorf microcentrifuge for 11 min. The filtrate was discarded, and the remaining solution in the filter unit was brought up to 500 μL by BupH PBS/10 mM EDTA and spun again at 13 400 *g* for 11 min. This concentration−dilution cycle was repeated one more time. Roughly 50 μL of the modified IgG solution was collected.

Conjugation of IgG Antibodies to Nanospheres. *DTT Reduction Method.* Maleimide-functionalized nanospheres (2.28 μM, 255.7 μL) and BupH PBS/10 mM EDTA (70 μL) were added to the above SH group-containing IgG (50 μL) synthesized by DTT reduction method. The mixture was incubated at RT for 2 h on a rotator. The mixture was then transferred to a Microcon YM-100 filter unit, and the volume was reduced to ∼50 μL on an Eppendorf microcentrifuge. The concentrated solution was fractionated on a self-packed Superdex 200 column eluted with 1× PBS (10 mM sodium phosphate, 0.15 M NaCl, pH 7.2). ∼500 μL of the conjugates was collected. The concentration of the purified nanosphere−IgG antibody conjugates was determined by UV absorbance at λ_{max} to be ∼0.6 μM. The number of IgG antibodies incorporated per nanosphere was quantified by UV absorbance to be 4.4 IgG antibodies per nanosphere.

Traut's Reagent Modification Method. Maleimide-functionalized nanospheres (2.28 μM, 128 μL) and BupH PBS/10 mM EDTA (120 μL) were added to the above SH group-containing IgG (50 μL) synthesized by Traut's Reagent modification method. The mixture was incubated at RT for 2 h on a rotator. The mixture was then transferred to a Microcon YM-100 filter unit, and the volume was reduced to ∼50 μL on an Eppendorf microcentrifuge. The concentrated solution was fractionated on a self-packed Superdex 200 column eluted with 1× PBS (10 mM sodium phosphate, 0.15 M NaCl, pH 7.2). ∼500 μL of the conjugates was collected. The concentration of the purified nanosphere−IgG antibody conjugates was determined by UV absorbance at λ_{max} to be ∼0.4 μM. The number of IgG antibodies incorporated per nanosphere was quantified by UV absorbance to be 3.6 IgG antibodies per nanosphere.

Determination of the Number of Maleimide Groups Attached per Nanosphere. The quantification was done by taking advantage of the high reactivity of BME with the maleimide group. BME reacts with maleimide group in a 1:1 stoichiometry; thus, the number of maleimide groups was determined by the decrease in bulk BME concentration using Ellman's Reagent, which reacts with sulfhydryl group to form a colored compound (molar extinction coefficient of 14 150 cm^{-1} M^{-1} at 412 nm). Briefly, 200 μL of the maleimide functionalized nanosphere (∼0.5 nmol) was incubated with 10 μL of 10 mM BME in BupH PBS/10 mM EDTA for 1 h at RT. Then, 100 μL of the reaction mixture was taken out and mixed with 850 μL of phosphate buffer/1 mM EDTA (0.1 M sodium phosphate, 1 mM EDTA, pH 8.0) and 50 μL of 10 mM Ellman's Reagent predissolved in phosphate buffer/1 mM EDTA. The mixture was incubated for 15 min at RT, and the absorbance at 412 nm was recorded. In the control experiment, 10 μL of 10 mM BME in BupH PBS/10 mM EDTA was incubated with 200 μL of BupH PBS/10 mM EDTA without maleimide functionalized nanospheres for 1 h at RT and was analyzed similarly to estimate the total amount of BME added to the reaction mixture. For the maleimide-modified nanospheres synthesized using the method described in this paper, there are generally about 70−80 maleimide groups attached per nanosphere.

Determination of the Number of Sulfhydryl Groups Generated on the IgG Antibody. The quantification of the sulfhydryl groups on the IgG after DTT reduction and Traut's Reagent modification was done using Ellman's Reagent following the manufacturer's protocol. Briefly, 1 mg of DTT reduced or Traut's Reagent modified goat anti mouse IgG was diluted to 950 μL with phosphate buffer/1 mM EDTA (0.1 M sodium phosphate, 1 mM EDTA, pH 8.0) and was incubated

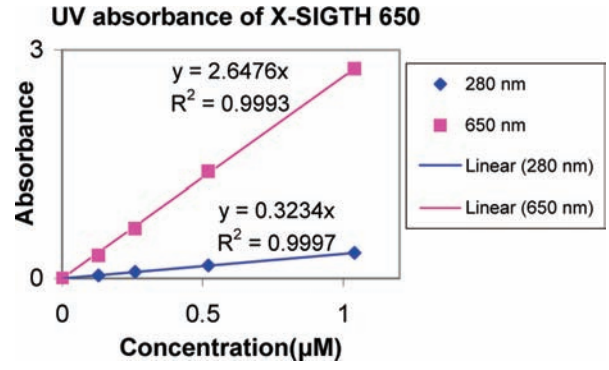
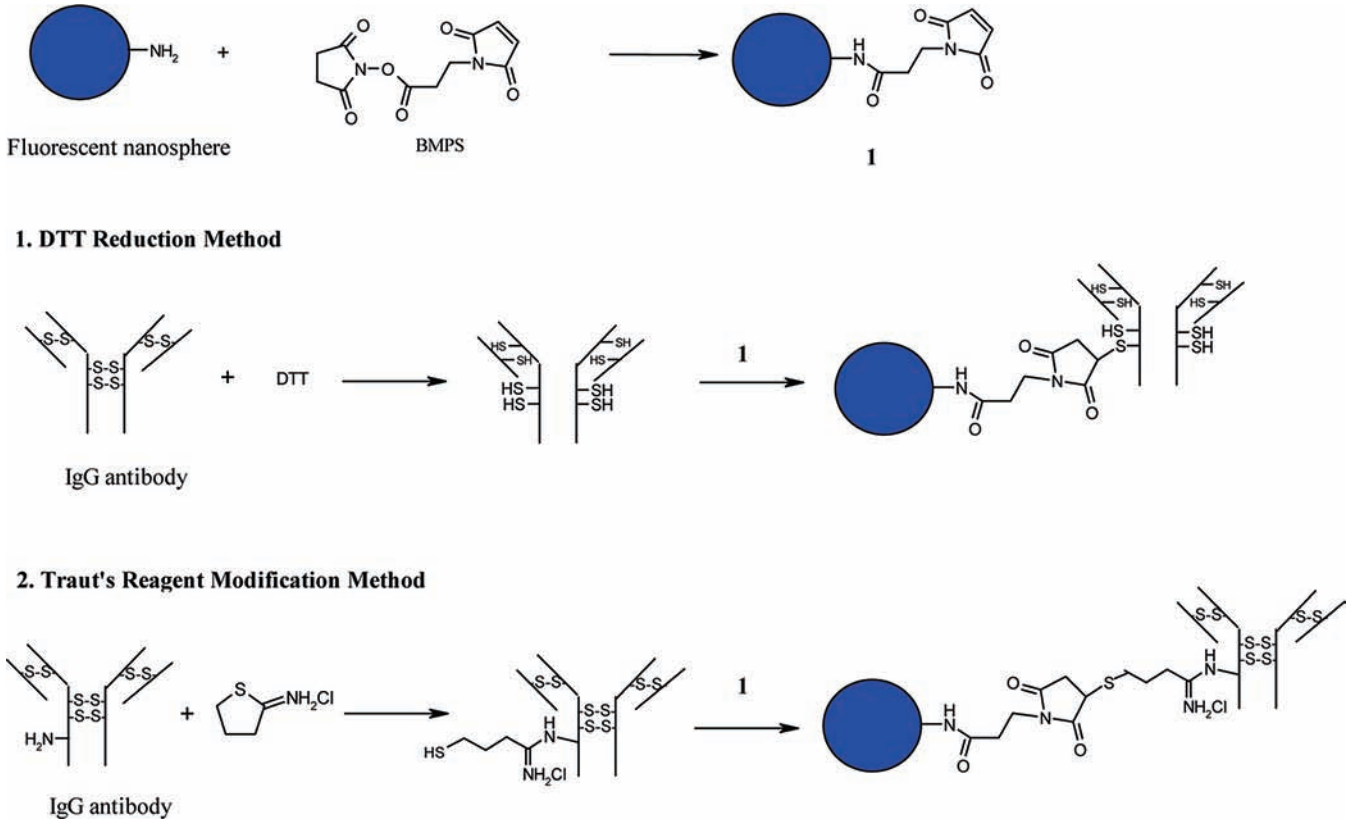


Figure 2. Determination of the ratio (r_f) of the absorbance of nanospheres at 280 nm to the absorbance at 650 nm, $r_f = A_{280}/A_{650} = 0.32/2.65 = 0.12$.

Scheme 1. Synthesis of Nanosphere−IgG Antibody Conjugates



with 50 μL of 10 mM Ellman's Reagent predissolved in phosphate buffer/1 mM EDTA for 15 min at RT. The absorbance of the mixture at 412 nm was recorded. As a blank, 50 μL of 10 mM Ellman's Reagent predissolved in phosphate buffer/1 mM EDTA was incubated with 950 μL of phosphate buffer/1 mM EDTA for 15 min at RT, and the absorbance at 412 nm was recorded. According to the Beer−Lambert law and the extinction coefficient of 14 150 cm^{-1} M^{-1} at 412 nm, the number of sulfhydryl groups per IgG was calculated. Generally, there are about 16 sulfhydryl groups per DTT reduced goat anti mouse IgG and 3−4 sulfhydryl groups per goat anti mouse IgG modified by Traut's Reagent.

Quantification of the Number of IgG Antibodies Attached per Nanosphere. Quantification was done according to eq 1. N is the number of IgG antibodies per nanosphere. C_{ab} is the concentration of IgG attached to the nanospheres. C_p is the concentration of the nanospheres in the conjugates. A_{280} is the absorbance of the conjugates at 280 nm. A_{max} is the absorbance of the conjugates at λ_{max}. 210 000 is the molar extinction coefficient of the IgG antibody at 280 nm in cm^{-1} M^{-1}. r_f is the ratio of the absorbance of the nanospheres at 280 nm to the absorbance at λ_{max}, e.g., the r_f of the 650 nanosphere is 0.12, as shown in Figure 2. k is the slope in M^{-1} of the standard curve of the nanospheres themselves, generated in a series of known concentrations. The light path in the UV absorbance measurement is 1 cm.

The IgG antibody has a typical UV absorbance at 280 nm. According to the Beer−Lambert law, the concentration of IgG antibodies attached to nanospheres could be calculated as $C = A_{280}/\varepsilon$, where the light path is 1 cm. However, the nanospheres also have some absorbance and scattering at 280 nm (Figure 1). In order to get the net absorbance of the IgG antibodies at 280 nm, the contribution of nanospheres at 280 nm is deducted. In the conjugates, the absorbance of the nanospheres at 280 nm was calculated by $A_{max} \times r_f$; A_{max} multiplied by r_f. The concentration of nanospheres in the conjugates was obtained by A_{max}/k. Thus, the number of IgG antibodies attached per nanosphere was determined by the ratio of the concentration of IgG to the concentration of nanospheres in the conjugates.

$$N = \frac{C_{ab}}{C_p} = \frac{(A_{280} - A_{max} \times r_f)/_{210000}}{A_{max}/_k} = \frac{(A_{280} - A_{max} \times r_f) \times k}{210000 \times A_{max}} \quad (1)$$

SDS PAGE. Different amounts of goat anti-mouse IgG antibody with and without DTT treatment were mixed with NuPAGE LDS sample buffer (4×) and loaded into the wells of a 10-well, 4−12% NuPAGE gel. Five microliters of the ECL Plex Rainbow Marker was loaded as a protein ladder. The gel was run at 150 V in MOPS SDS running buffer for about 1.5 h.

Native PAGE. Different amounts of goat anti-mouse IgG antibody with and without DTT treatment were mixed with Novex native tris-glycine sample buffer (2×) and loaded into the wells of a 10-well, 4−20% tris-glycine gel. Five microliters of NativeMark protein standard was loaded as a protein ladder. The gel was run at 150 V in tris-glycine native running buffer for about 5 h.

Western Blotting. *Protein Electrophoresis for Western Blotting.* 3T3 cell lysate was added with a sample reducing agent(10×), boiled at 95 °C for 5 min, and placed immediately on ice. Ten micrograms of the 3T3 cell lysate was loaded per well into a 12-well, 4−12% NuPAGE gel. Five microliters of ECL Plex Rainbow Marker was loaded into the well next to the protein. The gel was run at 100−125 V in MOPS SDS running buffer for about 2 h.

Membrane Transfer. The gel was transferred to an Immobilon-FL PVDF membrane at 30 V at 4 °C on a stirrer overnight.

Blocking and Detection. The membrane was blocked in PBS with 5% nonfat milk for 1 h. Then, it was incubated in primary antibody diluted in PBS with 5% nonfat milk for 1 h at RT

with gentle shaking. The membrane was washed with PBS 3 times for 5 min each at RT. Then, it was incubated in fluorescent IgG antibody diluted in PBS with 5% nonfat milk for 1 h at RT with gentle shaking. The membrane was washed with PBS 3 times for 5 min each at RT. Then, it was imaged on the Image Station 4000MM or the In-Vivo Multispectral Imaging System FX.

Data Analysis of Western Blotting Images. The data were analyzed using KODAK MI Software. The protein band region was selected as a region of interest (ROI). Net intensity is defined as the sum of background-subtracted pixel intensities within the ROI. Background intensity is defined as the median intensity of the perimeter of each ROI. Signal/background is the ratio of net intensity to background intensity.

RESULTS AND DISCUSSION

Synthesis of Fluorescent Nanosphere−IgG Antibody Conjugates. The nanosphere−IgG antibody conjugates were synthesized through three steps: modification of nanospheres by a heterobifunctional linker, such as Sulfo-SMCC, BMPS, AMAS, and so forth; introduction of sulfhydryl groups to the IgG antibodies; and the coupling of the IgG antibodies to the nanospheres. The synthetic routes are shown in Scheme 1. The heterobifunctional linker contains an NHS ester moiety that is reactive toward the amino group and a maleimide group that is reactive toward the sulfhydryl group (*18*). Different starting ratios of linker to nanospheres vs the conjugation efficiency were evaluated. The results show that, if the ratio is too low, the conjugation of the IgG to the nanospheres is not efficient. If the ratio is too high, the solubility of the maleimide-modified nanospheres in aqueous solution decreases tremendously, and some of the nanospheres precipitate out of the solution. It was found that a ratio of linker to nanosphere in the range of ∼100:1 to 150:1 resulted in high conjugation efficiency, little aggregation, and excellent performance of nanosphere−IgG antibody conjugates in Western blotting assays. When the ratio is 150:1, there are generally about 80 maleimide groups attached per nanosphere, and the remaining primary amines on the nanosphere are over 120.

There are several different methods to incorporate sulfhydryl groups into antibodies, such as SATA modification (*19*), Traut's Reagent modification (*20*), and DTT reduction. Here, we report the conjugation using two different methods: DTT reduction and Traut's Reagent modification. DTT was reported to partially reduce the disulfide bonds in the hinge region of the IgG antibody, and the yielded sulfhydryl groups were successfully used as the attachment sites for dyes and other molecules. The advantage of this method is that the attachment sites were in the hinge region—away from the antigen-binding sites—and therefore, the attached molecules did not affect the activity of the IgG antibody (*21*−*25*). However, a recent report indicates that DTT completely dissociates the IgG antibody into heavy and light chains, causing the antibody to lose biological activity (*28*). In the case of SATA and Traut's Reagent modification, the bifunctional linkers randomly react with the primary amino groups on the antibody; therefore, the antigen-binding regions are also subject to modification. Extensive modification of the antigen-binding regions will cause the antibody to lose activity. Therefore, the ratio of the linker to the antibody needs to be carefully controlled.

In this paper, we evaluated both the DTT reduction and Traut's Reagent modification methods and the biological activity of the yielded conjugates. The goat anti-mouse, goat anti-rabbit, and goat anti-rat IgG antibodies used in the experiments are affinity purified and highly cross-adsorbed polyclononal antibodies that are composed of a mixture of IgG1 and IgG2 subclasses. There are quite a few reports in the literature of using DTT to partially reduce the disulfide bonds in the IgG. The experimental conditions varied from mild (10−100-fold molar excess of DTT to IgG, 30 min reaction at RT or at 37 °C) to more harsh conditions (300−7500-fold molar excess of DTT to IgG, 30 min reaction at RT) (*21*−*25*). It was also reported that all the interchain disulfides in IgG were cleaved when 150−1000-fold molar excess of DTT to IgG was used and the reaction was 1−3 h at 37 °C (*26, 27*). Our experimental conditions reported here show that DTT not only reduced the disulfide bonds in the hinge region, but it also reduced the interchain disulfide bonds between the heavy and light chains, which was indicated by the SDS PAGE results in Figure 3a. This finding is consistent with the some of the reports (*26*−*28*). IgG antibodies treated with DTT using the same protocol used in the DTT reduction conjugation were loaded on the gel (Figure 3a, lanes 1−4). Five bands in each lane were detected, of which two major bands were in the lower molecular weight region. These five bands corresponded to a light chain (25 kDa), a heavy chain (50 kDa), a small amount of a half IgG antibody (75 kDa), a whole IgG antibody losing one light chain (125 kDa), and a whole IgG antibody (150 kDa), respectively, while the IgG antibody without DTT treatment showed one main band at 150 kDa (Figure 3a, lanes 5−8). However, SDS PAGE could not deduce whether the antibodies dissociate in the nondenatured condition, because SDS denatures the protein and could dis-

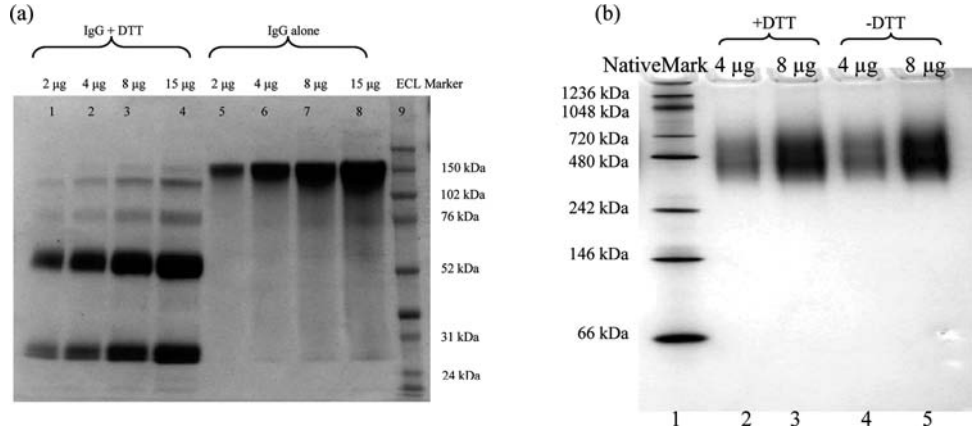


Figure 3. (a) 4−12% SDS PAGE of goat anti-mouse IgG. Lanes 1−4: IgG was treated with 10 mM DTT for 1 h at RT, and then a different amount was loaded on the gel. Lanes 5−8 were loaded with a different amount of IgG without DTT treatment. The gel was run at 150 V for ∼1.5 h. (b) Goat anti-mouse IgG on a 4−20% native PAGE. Lane 1: NativeMark protein standard. Lanes 2−3: IgG was treated with 10 mM DTT for 1 h at RT, and then a different amount was loaded on the gel. Lanes 4−5 were loaded with a different amount of IgG without DTT treatment. The gel was run at 150 V for ∼5 h.

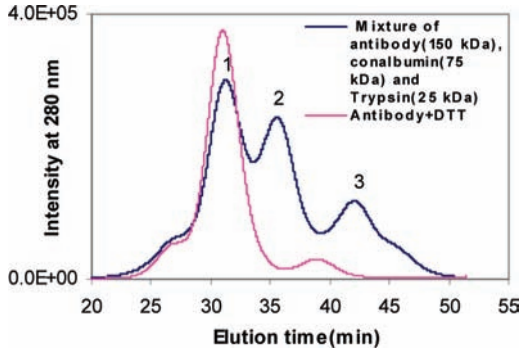


Figure 4. Chromatograms of proteins on HPLC detected at 280 nm. Elution rate: 2 mL/min. Blue curve is the mixture of goat anti-mouse IgG, conalbumin, and trypsin. Pink curve is the goat anti-mouse IgG treated with DTT. 1:1.7 mg/mL of goat anti-mouse IgG, M_w 150 kDa. 2:1.7 mg/mL of conalbumin, M_w 75 kDa. 3:3.0 mg/mL of trypsin, M_w 21 kDa. Mobile phase of blue curve: PBS, pH 7.4. Mobile phase of pink curve: PBS, pH 7.4/10 mM DTT.

sociate heavy and light chains of the antibody treated with DTT. As such, a native PAGE that separates the protein according to the charge, size, and conformation was run, and the result show that DTT reduced antibodies and unreduced antibodies show a similar pattern (Figure 3b), which indicates that the antibody fragments were still held together by noncovalent forces, even though the disulfide linkages were broken. Two bands were detected in both DTT-reduced and unreduced IgG antibodies (Figure 3b), for which the reason is not clear. A similar electrophoresis pattern was observed from more than one IgG antibody preparation. The integrity of the IgG antibodies was also checked by size-exclusion chromatography. In order to establish a running condition that could separate the IgG, half IgG, and the IgG light chain, a mixture of IgG, conalbumin, and Trypsin was used to simulate the mixture of IgG, half IgG, and IgG light chain. Conalbumin is a 75 kDa protein whose size is similar to that of a half IgG, and the molecular weight of trypsin is 21 kDa, similar to an IgG light chain. Three peaks corresponding to IgG, conalbumin, and trypsin, respectively, were detected (Figure 4, blue curve), which indicated that the running condition should be able to separate the IgG antibody, half IgG antibody, and light chain, with the half IgG antibody being eluted out at the similar elution time with that of the conalbumin and the light chain being eluted out at the similar elution time with that of trypsin. In the size-exclusion chromatography of the DTT-reduced IgG antibody, 10 mM DTT was incorporated into the mobile phase to prevent the reformation of the disulfide bridges. One single peak at the same elution time with that of the unreduced antibody corresponding to a molecular weight of 150 kDa was detected (Figure 4, pink curve), indicating that the antibody fragments were still held together by noncovalent interactions under native conditions, even though the interchain disulfide bonds were cleaved. Therefore, with the DTT reduction method, the IgG antibodies attached to the nanospheres were still whole antibodies (Scheme 1).

In the DTT reduction conjugation approach, the feed ratio of IgG antibody to nanosphere was 5.7 to 1, assuming there was no loss of the antibody after DTT reduction and purification. The corresponding conjugation efficiency and yield were determined by UV absorbance measurement according to eq 1. The results showed that the number of IgG antibodies attached was ~4.4 whole antibodies. The conjugation efficiency was also checked on an HPLC equipped with a Superdex 200 column. The chromatogram showed that the peak corresponding to the unconjugated antibody was very small; integration of the peak showed that ~90% of the antibodies were conjugated to the nanospheres (Figure 5a).

Traut's Reagent is very stable in neutral buffers. The hydrolysis is slow compared with the amine reaction rate. Therefore, thiolation with Traut's Reagent does not require a large excess of reagent like SATA. It was reported that, for IgG molecules, a 10-fold molar excess of Traut's Reagent would yield the antibody molecules modified with at least three sulfhydryl groups. Different stoichiometries of Traut's Reagent to IgG antibody (5:1 and 10:1) and IgG antibody to nanosphere (5.7:1 and 11:1) vs the conjugation efficiency and the performance of the conjugates in Western blotting assays was investigated. We found that the overall conjugation efficiency was low relative to the DTT reduction conjugation approach. When 10:1 ratio of Traut's Reagent to IgG antibody was used, a 5.7:1 of antibody-to-nanosphere ratio yielded 2 antibodies attached per nanosphere, and a 11:1 of antibody-to-nanosphere ratio yielded 3.6 antibodies attached per nanosphere, as calculated from eq 1. The low conjugation efficiency was also confirmed by HPLC analysis (Figure 5b). Western blotting results also showed that the 10:1 ratio of Traut's Reagent to antibody did not adversely affect the antibody function compared with 5:1 ratio of Traut's Reagent to antibody.

Western Blotting of the Nanosphere−IgG Antibody Conjugates. The performance of the conjugates synthesized through both the DTT reduction and Traut's Reagent modification method and other commercially available fluorescent−IgG antibody conjugates was investigated by Western blotting assays (Figures 6−9). In order to obtain an accurate comparison, all the Western blotting experimental conditions were kept identical. For example, the blots used for the comparison were transferred from the same gel to avoid the variation in the amount of protein transferred from different gels. The blots were blocked in the same blocker and incubated in the same primary antibody solution, and so forth. After being probed with the fluorescent antibodies, the blots in comparison were placed side by side on

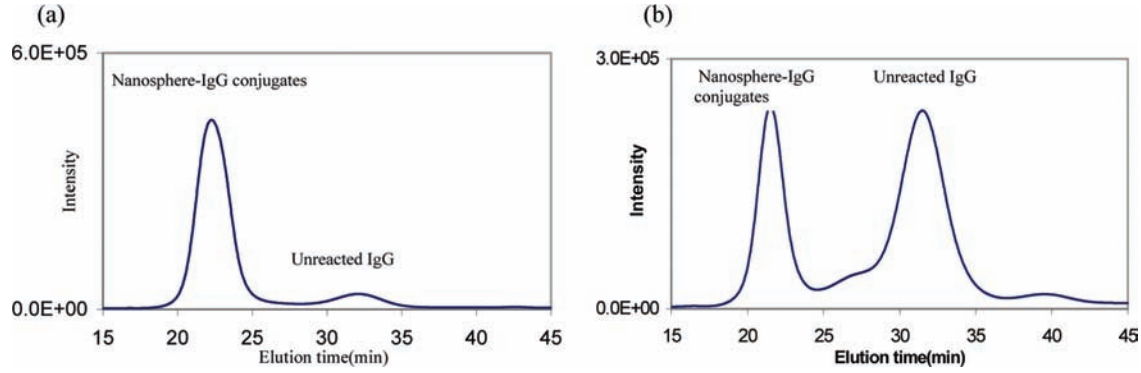


Figure 5. Chromatograms of the X-Sight 650 nanosphere−goat anti-mouse IgG conjugate mixture on HPLC detected at 280 nm. Mobile phase: PBS, pH 7.4. (a) DTT reduction method. (b) Traut's Reagent modification method, Ab: nanosphere = 11:1.

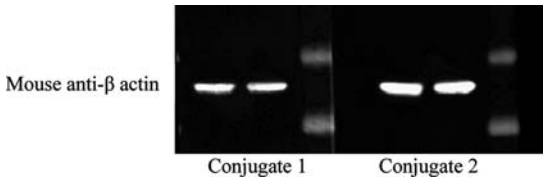


Figure 6. Western blot image of the X-Sight 650 nanosphere−goat anti-mouse IgG conjugates. Each blot contains two duplicated protein bands and a protein ladder on the right-hand side. The concentration of the conjugates in Western blotting assay was 3 nM. Conjugate **1** was synthesized using the Traut's Reagent modification method and has 3.6 antibodies attached per nanosphere. Conjugate **2** was synthesized using DTT reduction method and has 4.4 antibodies attached per nanosphere. Image was scanned for 4 min using excitation/emission filter set 630 nm/700 nm. Data analysis was done using KODAK MI software. The net intensity, background intensity, and signal/background of conjugate **2** was 2.2-fold, 0.8-fold, and 2.8 fold, respectively, of that of conjugate **1**.

the imaging system, and the images were acquired using the optimal excitation/emission filter sets for each fluorescent antibody. In addition, each of the blots was made to contain two duplicate protein bands, and the detected intensity was averaged in the data analysis to minimize the error. The results show that the conjugate synthesized through the DTT reduction method has much better performance than that synthesized through Traut's Reagent modification method, even though they both have about four antibodies attached per nanosphere, and the concentration of both conjugates in the Western blotting assay was the same (Figure 6). The image analysis shows that the net intensity and background intensity of the conjugates synthesized through the DTT reduction method is about 2× and 0.8×, respectively, of the net intensity and background intensity of the conjugates synthesized through Traut's Reagent modification method, and hence the signal-to-background ratio is about 2.8×. It has been demonstrated that nonspecific binding of the nanospheres to the PVDF membrane has contributed substantially to the background intensity in the Western blotting (data not shown). We speculate that the IgG antibody attached to the nanospheres helps to suppress the nanosphere/membrane interaction. The more antibodies that are attached per nanosphere, the lower the background intensity. A smaller difference in the background intensity between conjugates **1** and **2** further indicates that both conjugates have similar amounts of antibody attached per nanosphere. The conjugates synthesized through the DTT reduction method shows higher net intensity, which suggests that the antibodies in the conjugates are more active. The higher activity might be due to the nanospheres' attachment to the hinge region of the antibody, i.e., remote from the antigen binding sites and having less effect on the antibody activity. In the DTT reduction method, the thiol groups in the hinge region cleaved by DTT are more accessible to nanospheres than those in the other regions because the hinge region of the antibody is more flexible, which allows the lateral and rotational movement of the Fab fragments (*29*). With the Traut's Reagent modification method, the nanospheres' attachment sites on the antibodies are not controlled. The nanospheres could be attached to the antigen binding sites, which results in the antibodies losing activity.

The comparison of the performance of the conjugates synthesized through the DTT reduction method with Alexa Fluor IgG antibody conjugates shows that the performance is related to the concentration of the conjugates. Both the signal-to-background ratio and the net intensity increase with increasing concentration from 1.5 nM to 6 nM (Figure 7). For lower wavelength conjugates (Figure 7a,b), the nanosphere conjugates at a concentration of 1.5 nM have comparable

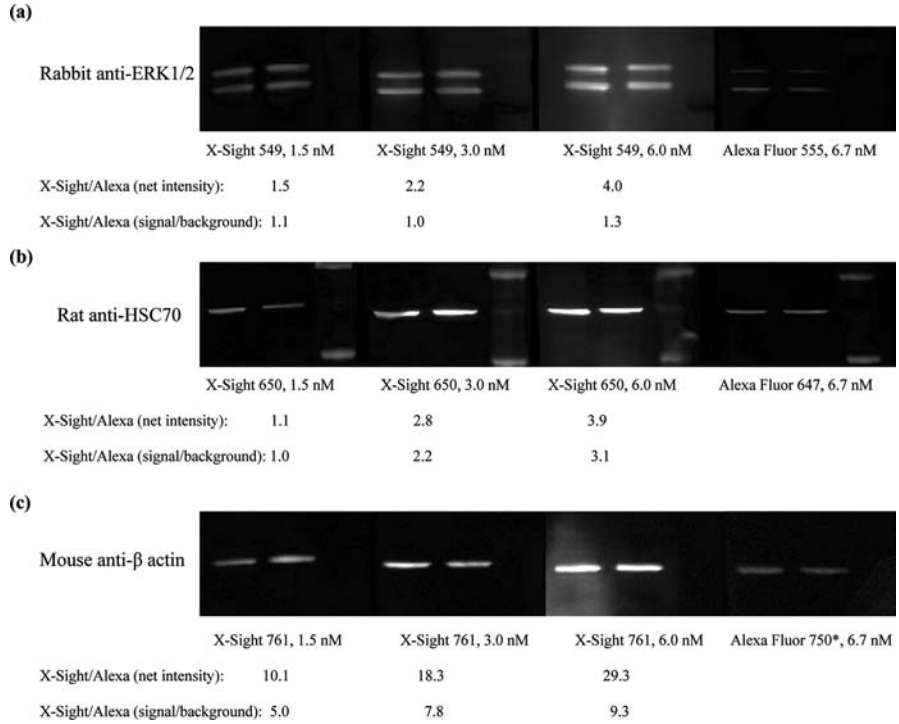


Figure 7. Western blot images of Alexa Fluor IgG antibody conjugates vs the X-Sight nanosphere−IgG antibody conjugates at different concentrations. The images were taken on an Image Station 4000MM. (a) The image was scanned for 25 s using an excitation/emission filter set 515 nm/570 nm. (b) The image was scanned for 30 s using an excitation/emission filter set 610 nm/670 nm. (c) The image was scanned for 3 min using an excitation/emission filter set 730 nm/790 nm. Each blot contains two duplicated protein bands and a protein ladder on the right-hand side. The concentration of the conjugates in the Western blotting assay ranged from 1.5 nM to 6.7 nM. The net intensity and signal/background of X-sight conjugates and Alexa Fluor conjugates were analyzed using MI software. X-Sight/Alexa (net intensity): the ratio of the net intensity of X-Sight nanosphere conjugates to that of Alexa Fluor conjugates. X-Sight/Alexa (signal/background): the ratio of the signal to background of X-Sight nanosphere conjugates to that of Alexa Fluor conjugates.

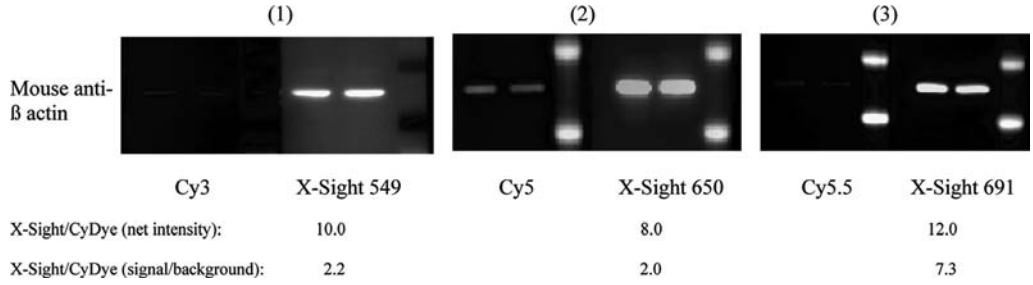


Figure 8. Western blot images of the X-Sight nanosphere−goat anti-mouse IgG conjugates vs CyDye-goat anti-mouse IgG conjugates. The images were taken on an Image Station 4000MM. (1) The image was scanned for 1 min using excitation/emission filter set 515 nm/570 nm. (2) The image was scanned for 1 min using an excitation/emission filter set 635 nm/700 nm. (3) The image was scanned for 1 min using an excitation/emission filter set 635 nm/700 nm. Each blot contains two duplicated protein bands and a protein ladder on the right-hand side. The concentration of the conjugates in Western blotting assay was 3 nM. The net intensity and signal/background of X-sight conjugates and CyDye conjugates were analyzed using MI software. X-Sight/CyDye (net intensity): the ratio of the net intensity of X-Sight nanosphere conjugates to that of CyDye conjugates. X-Sight/CyDye (signal/background): the ratio of the signal to background of X-Sight nanosphere conjugates to that of CyDye conjugates.

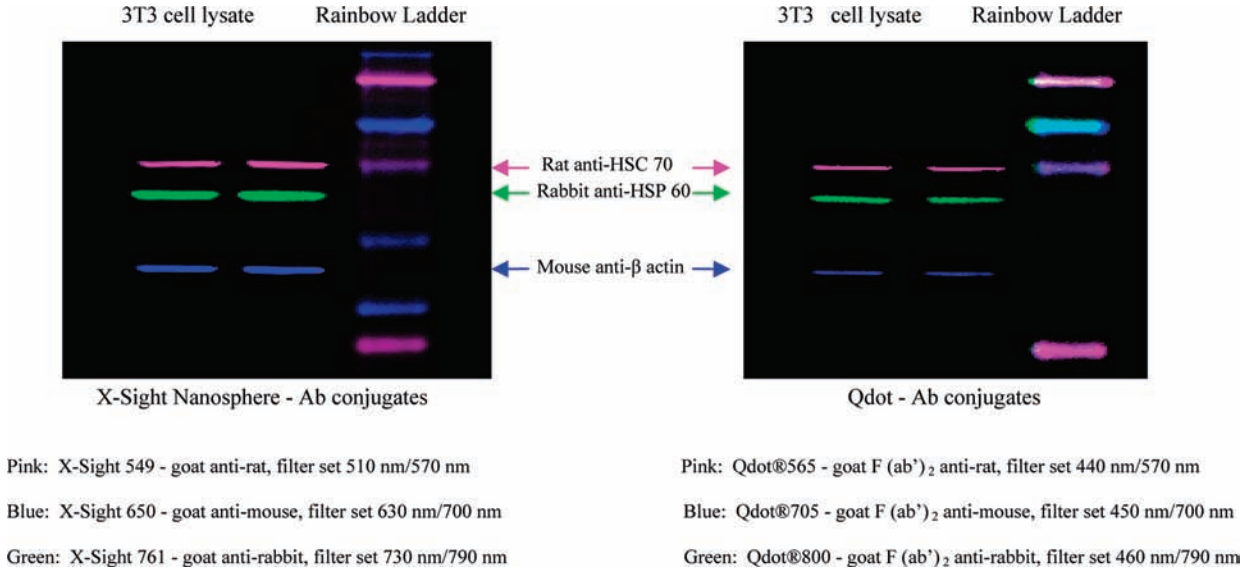


Figure 9. Multiplex Western blot of the X-Sight nanosphere−IgG antibody conjugates vs Qdot IgG antibody conjugates. Blots were probed with the mixture of rabbit anti-HSP60, mouse anti beta actin, and rat anti-HSC 70 primary antibodies followed by the mixture of X-Sight nanosphere-IgG antibody conjugates or the mixture of Qdot−IgG antibody conjugates. Each blot contains two duplicated protein bands and a protein ladder on the right-hand side. Images were captured for 30 s using an optimal excitation/emission filter set for each of the antibody conjugates on the In-Vivo Multispectral Imaging System FX and then overlaid in Photoshop. The concentration of the conjugates in the Western blotting assay was 2 nM. The net intensity and signal/background of X-sight conjugates and Qdot conjugates were analyzed using MI software. X-sight 549/Qdot 565: net intensity, 4.2; signal/background, 4.0. X-sight 650/Qdot 705: net intensity, 2.9; signal/background, 2.1. X-sight 761/Qdot 800: net intensity, 6.3; signal/background, 1.4.

performance with Alexa Fluor conjugates at a concentration of 6.7 nM. At similar concentration of the conjugates, the nanosphere conjugates (6 nM) have much higher signal-to-background ratio and net intensity than Alexa Fluor conjugates (6.7 nM). The X-Sight 761 nanosphere conjugates show higher brighteness and sensitivity than Alexa Fluor 750 conjugates, even at a much lower concentration (1.5 nM) (Figure 7c). Figure 8 shows that our nanosphere conjugates also have higher sensitivity than CyDye conjugates at all comparable wavelengths at matched concentration (3 nM) of the conjugates. It is noteworthy that our nanosphere conjugates not only exhibit higher signal-to-background ratio but also a much higher net intensity. In other words, our nanosphere conjugates were much brighter than Alexa Fluor and CyDye conjugates. Figure 7 shows that the X-Sight 549 and 650 nanosphere conjugates are ~4 times brighter than Alexa Fluor conjugates, and the X-Sight 761 nanosphere conjugates are up to 29 times brighter than Alexa Fluor conjugates. The advantage of relative higher brightness is that the acquisition time for the detection of a certain amount of signal is relatively shortened.

Quantum dots have been widely used in biological applications because of their superior brightness and photostability. The performance of our nanosphere-IgG antibody conjugates and spectrally similar Qdot IgG antibody conjugates in Western blotting assays was also evaluated (Figure 9). Multiplex Western blotting of the X-Sight nanospheres and Qdot conjugates is shown in Figure 9. The images were taken using the optimal filter sets for the X-Sight nanospheres and Qdots conjugates, respectively. The optimal excitation/emission filter sets were evaluated based on the signal-to-background ratio. Figure 9 shows that all of the X-Sight nanosphere conjugates have better performance than the counterparts of Qdot conjugates; they show not only higher signal-to-background ratio, but also much higher net intensity.

CONCLUSIONS

Two different coupling chemistries, BMPS-DTT and BMPS-Traut's Reagent, were evaluated for the synthesis of fluorescent nanosphere−IgG antibody conjugates. Native PAGE and size exclusion chromatography indicate that the DTT reduction

conditions (used herein) minimally disturb the antibody conformation, minimizing the effect upon biological activity of the antibody, even though the disulfide bridges in the antibody were cleaved. Moreover, BMPS-DTT chemistry gives higher conjugation efficiency, and the yielded conjugates show better performance in antigen detection. Side-by-side comparisons with other commercially available fluorescent IgG antibodies, like Alexa Fluor, Qdot, and CyDye antibody conjugates, show that the X-Sight nanosphere conjugates synthesized through BMPS-DTT chemistry provide increased brightness and higher signal-to-background in the detection of antigens.

ACKNOWLEDGMENT

This article would not have materialized without the support of the Molecular Imaging Division at Carestream Health, Inc.

LITERATURE CITED

(1) Donoghue, P. M., McManus, C. A., O'Donoghue, N. M., Pennington, S. R., and Dunn, M. J. (2006) CyDye immunoblotting for proteomics: co-detection of specific immunoreactive and total protein profiles. *Proteomics 6*, 6400–6404.

(2) Osorio, M., Espinoza, J. C., and Kuznar, J. (2005) Visualization of infectious pancreatic necrosis virus (IPNV) particles labeled with fluorescent probes. *J. Virol. Methods 130*, 140–144.

(3) Zarozinski, C. C., Pawlak, D. W., Stillman, B. A., Harvey, M. A., Parker, B. O., and Frisse, A. (2005) A new system for determining serum protein profiles. *BIOspektrum 11*, 468–469.

(4) Wallberg, F., Sundstroem, H., Ledung, E., Hewitt, C. J., and Enfors, S. O. (2005) Monitoring and quantification of inclusion body formation in Escherichia coli by multi-parameter flow cytometry. *Biotechnol. Lett. 27*, 919–926.

(5) Kirkeby, S., and Thomsen, C. E. (2005) Quantitative immunohistochemistry of fluorescence labelled probes using low-cost software. *J. Immunol. Methods 301*, 102–113.

(6) Yang, X., Li, X., Prow, T. W., Reece, L. M., Bassett, S. E., Luxon, B. A., Herzog, N. K., Aronson, J., Shope, R. E., Leary, J. F., and Gorenstein, D. G. (2003) Immunofluorescence assay and flow-cytometry selection of bead-bound aptamers. *Nucleic Acids Res. 31*, e54/1−8.

(7) Lamvik, J., Hella, H., Liabakk, N. B, and Halaas, O. (2001) Nonlabeled secondary antibodies augment/maintain the binding of primary, specific antibodies to cell membrane antigens. *Cytometry 45*, 187–193.

(8) Wang, Y., Su, P., Zhang, X., and Chang, W. (2001) Enhancement of the sensitivity of a capillary electrophoresis immunoassay for estradiol with laser-induced fluorescence based on a fluorescein-labeled secondary antibody. *Anal. Chem. 73*, 5616–5619.

(9) Carter, R. M., Blake, R. C. II, Mayer, H. P., Echevarria, A. A., Nguyen, T. D., and Bostanian, L. A. (2000) A fluorescent biosensor for detection of zearalenone. *Anal. Lett. 33*, 405–412.

(10) Cunningham, R. E. (1999) Indirect immunofluorescent labeling of viable cells. *Method Mol. Biol. 115*, 261–263.

(11) Chan, W. C. W., and Nie, S. (1998) Quantum dot bioconjugates for ultrasensitive nonisotopic detection. *Science 281*, 2016–2018.

(12) Chan, W. C. W., Maxwell, D. J., Gao, X., Bailey, R. E., Han, M., and Nie, S. (2002) Luminescent quantum dots for multiplexed biological detection and imaging. *Curr. Opin. Biotechnol. 13*, 40–46.

(13) Fu, A., Gu, W., Boussert, B., Koski, K., Gerion, D., Manna, L., Le Gros, M., Larabell, C. A., and Alivisatos, A. P. (2007) Semiconductor quantum rods as single molecule fluorescent biological labels. *Nano Lett. 7*, 179–182.

(14) Ohnson, I. (2002) New fluorescent labeling technologies for ultrasensitive cytochemical and histochemical imaging. *Microscopy Today 10*, 12–14.

(15) Ow, H., Larson, D., Srivastava, M., Baird, B., Webb, W., and Wiesner, U. (2005) Bright and stable core-shell fluorescent silica nanospheres. *Nano Lett. 5*, 113–117.

(16) Yang, W., Zhang, C. G., Qu, H. Y., Yang, H. H., and Xu, J. G. (2004) Novel fluorescent silica nanosphere probe for ultrasensitive immunoassays. *Anal. Chim. Acta 503*, 163–169.

(17) Leon, J. W., Harrison, W. J., Kelley, B. J., Bennett, J. R., Stegman, D. A., Wang, R., Harder J. W. Loaded latex optical molecular imaging probes. U.S. Patent Application Publication No. 20080181965.

(18) Instruction book of BMPS from Pierce Chemical Co. and the references cited therein

(19) Duncan, R. J. S., Weston, P. D., and Wigglesworth, R. (1983) A new reagent which may be used to introduce sulfhydryl groups into proteins, and its use in the preparation of conjugates for immunoassay. *Anal. Biochem. 132*, 68–73.

(20) Instruction book of Traut's Reagent from Pierce Chemical Co. and the references cited therein

(21) Youle, R. J., and Neville, D. M. (1980) Anti-Thy 1.2 monoclonal antibody linked to ricin is a potent cell-type specific toxin. *Proc. Natl. Acad. Sci. U.S.A. 77* (9), 5483–5486.

(22) Kortylewicz, J. B., and Kassis, A. I. (1993) Labeling of immunoglobulins with bifunctional, sulfhydryl-selective, and photoreactive coumarins. *Bioconjugate Chem. 4*, 300–304.

(23) Hermentin, P., Doenges, R., Gronski, P., Bosslet, K., Kraemer, H. P., Hoffmann, D., Zilg, H., Steinstraesser, A., Schwarz, A., Kuhlmann, L., Luben, G., and Seiler, F. R. (1990) Attachment of rhodosaminylanthracyclinone-type anthracyclines to the hinge region of monoclonal antibodies. *Bioconjugate Chem. 1*, 100–107.

(24) Packard, B., and Edidin, M. (1986) Site-directed labeling of a monoclonal antibody: targeting to a disulfide bond. *Biochemistry 25*, 3548–3552.

(25) Hermentin, P., Doenges, R., Franssen, U., Bieva, C., Vander Brugghen, F. J., Stryckmans, P., Friesen, H. -J., Optaczy, B., Schneider, S., Ax, W., Enssle, K. H., Kurrle, R., and Seiler, F. R. (1990) Hinge-thiol coupling of monoclonal antibody to silanized iron oxide particles and evaluation of magnetic cell depletion. *Bioconjugate Chem. 1*, 411–418.

(26) del Rosario, R. B., Wahl, R. L., Brocchini, S. J., Lawton, R. G., and Smith, R. H. (1990) Sulfhydryl site-specific cross-linking and labeling of monoclonal antibodies by a fluorescent equilibrium transfer alkylation cross-link reagent. *Bioconjugate Chem. 1*, 51–59.

(27) Goldberg, M., Knudsen, K. L., Platt, D., Kohen, F., Bayer, E. A., and Wilchek, M. (1991) Specific interchain cross-linking of antibodies using bismaleimides. Repression of ligand leakage in immunoaffinity chromatography. *Bioconjugate Chem. 2*, 275–280.

(28) Pathak, S., Davidson, M. C., and Silva, G. A. (2007) Characterization of the functional binding properties of antibody conjugated quantum dots. *Nano Lett. 7*, 1839–1845.

(29) Harlow, E. D., and Lane, D. (1988) *Antibodies: A laboratory Manual*; pp 8−9, Cold Spring Harbor Laboratory, New York.

BC900295V

A Dual-Labeled Knottin Peptide for PET and Near-Infrared Fluorescence Imaging of Integrin Expression in Living Subjects

Richard H. Kimura,[†] Zheng Miao,[†] Zhen Cheng,[†] Sanjiv S. Gambhir,[†,‡] and Jennifer R. Cochran*[,‡]

Department of Radiology, Molecular Imaging Program, and Department of Bioengineering, Cancer Center, Bio-X Program, Stanford University, Stanford, California 94305. Received July 13, 2009; Revised Manuscript Received October 19, 2009

Previously, we used directed evolution to engineer mutants of the *Ecballium elaterium* trypsin inhibitor (EETI-II) knottin that bind to $\alpha_v\beta_3$ and $\alpha_v\beta_5$ integrin receptors with low nanomolar affinity, and showed that Cy5.5- or ^{64}Cu-DOTA-labeled knottin peptides could be used to image integrin expression in mouse tumor models using near-infrared fluorescence (NIRF) imaging or positron emission tomography (PET). Here, we report the development of a dual-labeled knottin peptide conjugated to both NIRF and PET imaging agents for multimodality imaging in living subjects. We created an orthogonally protected peptide-based linker for stoichiometric coupling of ^{64}Cu-DOTA and Cy5.5 onto the knottin N-terminus and confirmed that conjugation did not affect binding to $\alpha_v\beta_3$ and $\alpha_v\beta_5$ integrins. NIRF and PET imaging studies in tumor xenograft models showed that Cy5.5 conjugation significantly increased kidney uptake and retention compared to the knottin peptide labeled with ^{64}Cu-DOTA alone. In the tumor, the dual-labeled ^{64}Cu-DOTA/Cy5.5 knottin peptide showed decreased wash-out leading to significantly better retention ($p < 0.05$) compared to the ^{64}Cu-DOTA-labeled knottin peptide. Tumor uptake was significantly reduced ($p < 0.05$) when the dual-labeled knottin peptide was coinjected with an excess of unlabeled competitor and when tested in a tumor model with lower levels of integrin expression. Finally, plots of tumor-to-background tissue ratios for Cy5.5 versus ^{64}Cu uptake were well-correlated over several time points post injection, demonstrating pharmacokinetic cross validation of imaging labels. This dual-modality NIRF/PET imaging agent is promising for further development in clinical applications where high sensitivity and high resolution are desired, such as detection of tumors located deep within the body and image-guided surgical resection.

INTRODUCTION

The formation of new blood vessels that enable tumor growth is mediated in part by the differential expression or overexpression of various proteins. Among these are the integrin receptors, a family of heterodimeric cell surface receptors that bind extracellular matrix proteins to mediate cell attachment and signaling (*1*). There are currently over twenty different integrin subtypes known. In particular, $\alpha_v\beta_3$ and $\alpha_v\beta_5$ integrins have been shown to be overexpressed on many different types of tumors and the tumor neovasculature (*2, 3*). These integrins have been proposed to play a role in mediating tumor growth, angiogenesis, and metastasis, making them attractive targets for cancer therapy (*4*−*6*). In addition, diagnostic agents are critically needed to monitor disease progression and to help identify patients who will best respond to integrin-targeted treatments (*7*−*9*).

Multimodal molecular imaging has emerged as a powerful tool in cancer diagnosis, treatment, and management, as well as in drug development (*10, 11*). Many clinical and preclinical imaging applications are based on positron emission tomography (PET), single-photon emission computed tomography (SPECT),[1] near-infrared fluorescence imaging (NIRF), bioluminescence, magnetic resonance imaging (MRI), and ultrasound. Each imaging modality has its own unique strengths and weaknesses; thus, combinations of different imaging modalities are now being used to overcome inherent limitations (*10, 12*). Dual-modality NIRF/PET tracers may find important clinical applications where high-resolution optical imaging is coupled with the sensitivity of nuclear imaging. For example, in tumor detection coupled with surgical procedures, the radionuclide component could initially be used to accurately map lesions that have grown deep within the body. When the radionuclide has sufficiently decayed, the optical mode could aid in image-guided surgery to precisely verify tumor margins during and following resection, using a minimally invasive laparoscopic instrument equipped with a NIRF detection system.

In this study, we developed a dual-modality NIRF/PET imaging agent based on the engineered integrin-binding knottin peptide 2.5D, which binds to $\alpha_v\beta_3$ and $\alpha_v\beta_5$ integrin receptors with high affinity (*13*). Cy5.5 and ^{64}Cu-1,4,7,10-tetra-azacyclododecane-*N*,*N*′,*N*″,*N*‴-tetraacetic acid (^{64}Cu-DOTA), were both chemically conjugated to the knottin N-terminus using a peptide-based linker that contained orthogonal protecting groups for sequential and precise coupling. We measured the integrin binding affinity and specificity of the DOTA/Cy5.5-conjugated knottin peptide compared to unlabeled knottin peptide and peptides conjugated only to DOTA or Cy5.5. Next, we used NIRF and PET imaging to evaluate tumor uptake, pharmaco-

* To whom correspondence should be addressed. 318 Campus Drive, The James H. Clark Center, Stanford, CA 94305-5439; Phone (650)724-7808, E-mail: jennifer.cochran@stanford.edu.

[†] Department of Radiology, Molecular Imaging Program.

[‡] Department of Bioengineering, Cancer Center, Bio-X Program.

[1] Abbreviations: EETI-II, *Ecballium elaterium* trypsin inhibitor; DOTA, 1,4,7,10-tetra-azacyclododecane-*N*,*N*′,*N*″,*N*‴-tetraacetic acid; NIRF, near-infrared fluorescence; PET, positron emission tomography; RGD, arginine-glycine-aspartic acid; SPECT, single-photon emission computed tomography; MRI, magnetic resonance imaging; CT, computed tomography; Fmoc, 9-fluorenylmethyloxycarbonyl; PBS, phosphate buffered saline; IBB, integrin binding buffer; BSA, bovine serum albumin; DMF, *N*,*N*-dimethylformamide; TFA, trifluoroacetic acid; HPLC, high pressure liquid chromatography; MALDI-TOF MS, matrix-assisted laser desorption/ionization time-of-flight mass spectrometry; DCC, *N*,*N*′-dicyclohexylcarbodiimide; NHS, *N*-hydroxysuccinimide; DIEA, *N*,*N*-diisopropylethylamine; ROI, region of interest.

10.1021/bc9003102 © 2010 American Chemical Society
Published on Web 02/04/2010

kinetics, and biodistribution of the dual-labeled ^{64}Cu-DOTA/Cy5.5 knottin peptide in human tumor xenograft models and compared these results to imaging studies performed with knottin peptides conjugated only to ^{64}Cu-DOTA or Cy5.5. Compared to ^{64}Cu-DOTA, the hydrophobic Cy5.5 dye had a dramatic effect on probe pharmacokinetics and tissue biodistribution, with robust imaging signals lasting well beyond 24 h. In addition to generating a dual-modality NIRF/PET imaging agent, the cross-linking strategy presented here could be useful in creating other multimodal imaging agents, as well as in creating molecules for theranostic applications that combine imaging diagnostics with therapy.

EXPERIMENTAL PROCEDURES

Materials, Cell Lines, and Reagents. All 9-fluorenylmethyloxycarbonyl (Fmoc) protected amino acids were purchased from Novabiochem/EMD Chemicals Inc. (La Jolla, CA) with the exception of Fmoc-*N*-ε-1-(4,4-dimethyl-2,6-dioxocyclohex-1-ylidene)-3-methylbutyl-L-lysine (Fmoc-Lys(ivDde)-OH) which was purchased from Bachem (Torrance, CA) and Fmoc-L-Tyr(tBu)-Wang Resin which was purchased from CS Bio Company (Menlo Park, CA). The U87MG human glioblastoma cell line was obtained from American Type Culture Collection (Manassas, VA). Detergent-solubilized $\alpha_v\beta_3$, $\alpha_v\beta_5$ integrin receptors (both octyl-β-D-glucopyranoside formulations) and $\alpha_5\beta_1$ integrin (Triton X-100 formulation) were purchased from Millipore (Billerica, MA), and $\alpha_{iib}\beta_3$ (Triton X-100 formulation) was purchased from Enzyme Research Laboratories (South Bend, IN). ^{125}I-labeled echistatin and the backbone cyclized pentapeptide c(RGDyK) were purchased from Amersham/GE Healthcare (Piscataway, NJ) and Peptides International (Louisville, KY), respectively. Phosphate buffered saline (PBS) was from Gibco/Invitrogen (Carlsbad, CA). All other chemicals were purchased from Thermo Fisher Scientific (Pittsburgh, PA) unless otherwise specified. Integrin binding buffer (IBB) was composed of 25 mM Tris pH 7.4, 150 mM NaCl, 2 mM $CaCl_2$, 1 mM $MgCl_2$, 1 mM $MnCl_2$, and 0.1% bovine serum albumin (BSA).

Knottin Peptide Synthesis and Folding. Knottin peptides were synthesized on a CS Bio CS336 instrument using Fmoc-based solid-phase peptide synthesis with Rink amide resin (CS Bio Company). Fmoc groups were removed with 20% piperidine in *N,N*-dimethylformamide (DMF). Amino acid coupling was performed using HOBt/diisopropylcarbodiimide chemistry in DMF. After synthesis, side-chain deprotection and resin cleavage was achieved by addition of a 94:2.5:2.5:1 (v/v) mixture of trifluoroacetic acid (TFA)/triisopropylsilane/ethanedithiol/water for 2 h at room temperature. The crude product was precipitated with cold anhydrous diethyl ether and purified by reversed-phase HPLC using a Varian Prostar instrument and Vydac C_{18} columns. Linear gradients of 90% acetonitrile in water containing 0.1% (v/v) TFA were used for all peptide purifications, which were monitored at an absorbance of 220 nm. Peptide purity was analyzed by analytical-scale reversed-phase HPLC using a Vydac C_{18} column. Molecular masses were determined by matrix-assisted laser desorption/ionization time-of-flight mass spectrometry (MALDI-TOF MS) on a Perseptive Voyager-DE-RP Biospectrometry instrument (Stanford Protein and Nucleic Acid facility). Folding reactions were performed by incubating peptides with 2.5 mM reduced glutathione and 20% dimethlysulfoxide (v/v) in 0.1 M ammonium bicarbonate, pH 9, with gentle rocking overnight. The final oxidized product was purified by reversed-phase HPLC as described above and lyophilized. Purified peptides were dissolved in water, and concentrations were determined by amino acid analysis (AAA Service Laboratory, Damascus, OR). Peptide purity and molecular masses were determined by analytical-scale reversed-phase HPLC and MALDI-TOF MS.

Synthesis of the Chemical Linker, Fmoc-Lys(ivDde)-Gly-Gly-Tyr-N-Hydroxysuccinimide Ester. Fmoc-Lys(ivDde)-Gly-Gly-Tyr was synthesized as described above using a preloaded Fmoc-L-Tyr(tBu)-Wang resin and Fmoc-Lys(ivDde)-OH. This peptide was cleaved from the resin and was purified as described above, leaving the Fmoc and ivDde protecting groups attached. The C-terminal carboxyl group of the peptide was activated as an NHS ester by reaction with *N,N′*-dicyclohexylcarbodiimide (DCC; Pierce Chemical Company, Rockford, IL) and *N*-hydroxysuccinimide (NHS) in DMF and was purified by reversed-phase HPLC to yield Fmoc-Lys(ivDde)-Gly-Gly-Tyr-NHS ester.

Chemical Conjugation of Cy5.5 and DOTA. Knottin peptide 2.5D was reacted with Fmoc-Lys(ivDde)-Gly-Gly-Tyr-NHS ester in DMF containing 2% *N,N*-diisopropylethylamine (DIEA) to yield Fmoc-Lys(ivDde)-Gly-Gly-Tyr-2.5D. The Fmoc group was then removed by incubating this intermediate in DMF with 10% piperidine for 0.5 h to yield NH_2-Lys(ivDde)-Gly-Gly-Tyr-2.5D. This intermediate was reacted with a 5-fold molar excess of an NHS ester-activated DOTA group (DOTA-NHS ester; Macrocyclics, Dallas, TX) in DMF containing 2% DIEA for 0.5 h to yield DOTA-Lys(ivDde)-Gly-Gly-Tyr-2.5D. Next, the ivDde group was removed by incubation in DMF containing 2% hydrazine (Alfa Aesar, Ward Hill, MA) for 0.5 h at room temperature. Finally, DOTA-Lys(NH_2)-Gly-Gly-Tyr-2.5D was reacted with an excess of Cy5.5-NHS ester (Amersham) in DMF containing 2% DIEA for 0.5 h at room temperature to yield DOTA-Lys(Cy5.5)-Gly-Gly-Tyr-2.5D. Following each step, the intermediates were purified by reversed-phase HPLC. Molecular masses were determined by MALDI-TOF MS, and peptide products were analyzed by analytical-scale reversed-phase HPLC as described above (Supporting Information Figure S1).

^{64}Cu Radiolabeling. For each radiolabeling reaction, approximately 10−25 μg DOTA-Lys(Cy5.5)-Gly-Gly-Tyr-2.5D was incubated with 1−2 mCi $^{64}CuCl_2$ (University of Wisconsin−Madison, Madison, WI) in 0.1 N sodium acetate (pH 6.3) for 1 h at 42 °C. The reaction was terminated with the addition of EDTA. ^{64}Cu-DOTA-Lys(Cy5.5)-Gly-Gly-Tyr-2.5D was purified using a PD-10 column (Amersham Biosciences/GE Healthcare) and eluted with PBS (pH 7.4) and passed through a 0.22 μm filter for animal experiments. The radiochemical purity, determined as the ratio of the main product peak to other peaks, was determined by HPLC to be >95%. The radiochemical yield, determined as the ratio of final activity of the product over the starting activity used for the reaction, was usually over 80%. The specific activity of the probe was ∼500 Ci/mmol.

Cell Surface Integrin Receptor Binding and Uptake Assays. Cell surface competition binding assays were performed as previously described (*14, 15*). Briefly, 2×10^5 U87MG cells were incubated with 0.06 nM ^{125}I-labeled echistatin (Amersham) and varying concentrations of peptides in IBB at room temperature for 3 h. The cell-bound radioactivity remaining after washing was measured by scintillation counting. Half-maximal inhibitory competition (IC_{50}) values were determined by nonlinear regression analysis using *Kaleidagraph* (Synergy Software), and are presented as the average of experiments performed on three separate days.

For cell uptake studies, 5×10^5 U87MG or MDA-MB-435 cells were suspended in 50 μL IBB and incubated with ^{64}Cu-DOTA-Lys(Cy5.5)-Gly-Gly-Tyr-2.5D (1.5 μCi/tube in 100 μL IBB) with or without 1 μg of c(RGDyK) at 37 °C for 30, 60, and 120 min. Cells were then washed three times with chilled PBS and pelleted by centrifugation. The radioactivity of the cell pellet was measured using a gamma counter (PerkinElmer 1470, Waltham, MA). Cell binding and uptake of the dual-labeled

^{64}Cu-DOTA/Cy5.5 knottin peptide was expressed as the percentage of added radioactivity. Experiments were performed in triplicate.

Solid-Phase Integrin Receptor Competition Binding Assay. Integrin receptor competition binding assays were performed as previously described (*15, 16*). Briefly, detergent-solubilized $\alpha_v\beta_3$, $\alpha_v\beta_5$, $\alpha_5\beta_1$, or $\alpha_{iib}\beta_3$ integrin receptors were diluted to a final concentration of 1 μg/mL in IBB, and 100 μL aliquots were used to coat wells of Maxisorb plates (NalgeNunc, Thermo Fisher Scientific), overnight at 4 °C. The wells were washed and blocked with IBB containing 1% BSA for 2 h at room temperature. ^{125}I-labeled echistatin (0.06 nM) and varying concentrations of unlabeled peptides were incubated in the wells for 3 h at room temperature with gentle rocking and washed 3 times in IBB. Plate-bound radioactivity was solubilized with 200 μL of boiling 2 N NaOH followed by gamma counting. Each data point represents the average value of triplicate wells, and error bars represent the standard deviation.

Tumor Xenograft Models. U87MG glioblastoma cells and MDA-MB-435 melanoma cells were maintained at 37 °C in a humidified atmosphere containing 5% CO_2 in Dulbecco's Modified Eagle Medium or Leibovitz L-15 Medium, respectively, containing 10% heat-inactivated fetal bovine serum and penicillin−streptomycin (all from Invitrogen). Animal procedures were carried out according to a protocol approved by Stanford University Administrative Panels on Laboratory Animal Care. Female athymic nude mice (nu/nu), obtained at 4−6 weeks of age (Charles River Laboratories, Inc., Wilmington, MA), were injected subcutaneously in the right or left shoulder with $\sim 10^7$ U87MG or 5×10^6 MDA-MB-435 cells suspended in 100 μL of PBS. Mice were used for in vivo imaging studies when their tumors reached approximately 8−10 mm in diameter.

Near-Infrared Fluorescence and MicroPET Imaging of Tumor Xenografts. NIRF imaging was performed with an IVIS 200 (Xenogen, Hopkinton, MA) as previously described (*14*). Briefly, a Cy5.5 filter set was used, and fluorescence emission was normalized to photons per second per centimeter squared per steradian (p/s/cm^2/sr). Images were acquired and analyzed using *Living Image 2.50.1* (Xenogen). For all experiments, U87MG tumor-bearing mice ($n = 3$ for each probe) were injected via tail vein with ~1.5 nmol of probe in 100 μL PBS and imaged at various times post injection. Tumor contrast was quantified by drawing identically sized regions of interest (ROI) around the tumor and background tissue located in the mouse's flank (average radiance, p/s/cm^2/sr). Data points represent the average tumor/tissue ratio for a group of three animals.

U87MG or MDA-MB-435 tumor-bearing mice ($n = 3$ or more for each probe) were injected with ~100 μCi (~0.5 nmol) of probe via the tail vein and imaged with a microPET R4 rodent model scanner (Siemens Medical, Knoxville, TN) using 3 or 5 min static scans. Images were reconstructed by a two-dimensional ordered expectation maximum subset algorithm and calibrated as previously described (*17*). ROIs were drawn over the tumor on decay-corrected whole body images using *ASIPro VM* software (Siemens Medical). The mean counts per pixel per minute were obtained from the ROI and converted to counts per milliliter per minute with a calibration constant. ROIs were converted to counts/g/min, and %ID/g values were determined assuming a tissue density of 1 g/mL. No attenuation correction was performed. In NIRF and PET blocking experiments, mice were coinjected with 330 μg (~0.5 μmol) of unlabeled c(RGDyK). For whole animal NIRF/PET correlation plots, the average tumor-to-background tissue ratios were determined using an ROI over tumor tissue and dividing by an ROI over the thigh area for three mice per time point post injection. Linear regression analysis in Microsoft *Excel* was used to determine the R^2 value, and error bars represent the standard deviation.

In Vivo Biodistribution Studies. Anesthetized nude (nu/nu) mice bearing U87MG tumor xenografts were injected with ~100 μCi (~0.5 nmol) of ^{64}Cu-DOTA-Lys(Cy5.5)-Gly-Gly-Tyr-2.5D via the tail vein, and were euthanized at 1, 4, and 24 h post injection. Blood, bone, brain, heart, kidney, liver, lung, muscle, pancreas, skin, spleen, and tumor tissue were removed and weighed. The fluorescence flux (photons per second) or gamma emissions (counts per minute) of the tissue were measured by fluorescence imaging or by gamma counting, respectively. For the fluorescence component, the results are expressed as flux/gram of tissue and represent the mean and standard deviation of experiments performed on three mice. Total flux was determined for dissected tissue by drawing a ROI around the entire tissue and subtracting the total background flux from an adjacent equally sized ROI. For studies involving radioactivity, the results were expressed as the percent injected dose per gram (%ID/g) of tissue and represent the mean and standard deviation of experiments performed on three mice. For each mouse, the activity of tissue samples was calibrated against a premeasured aliquot of the radiotracer and normalized to the whole body-weight and to the residual radioactivity present in the tail. For correlation analysis of biodistribution data from three mice, average Cy5.5 tumor-to-tissue ratios were plotted versus average ^{64}Cu tumor-to-tissue ratios for 1, 4, and 24 h time points. Linear regression analysis in Microsoft *Excel* was used to determine the R^2 value, and error bars represent the standard deviation.

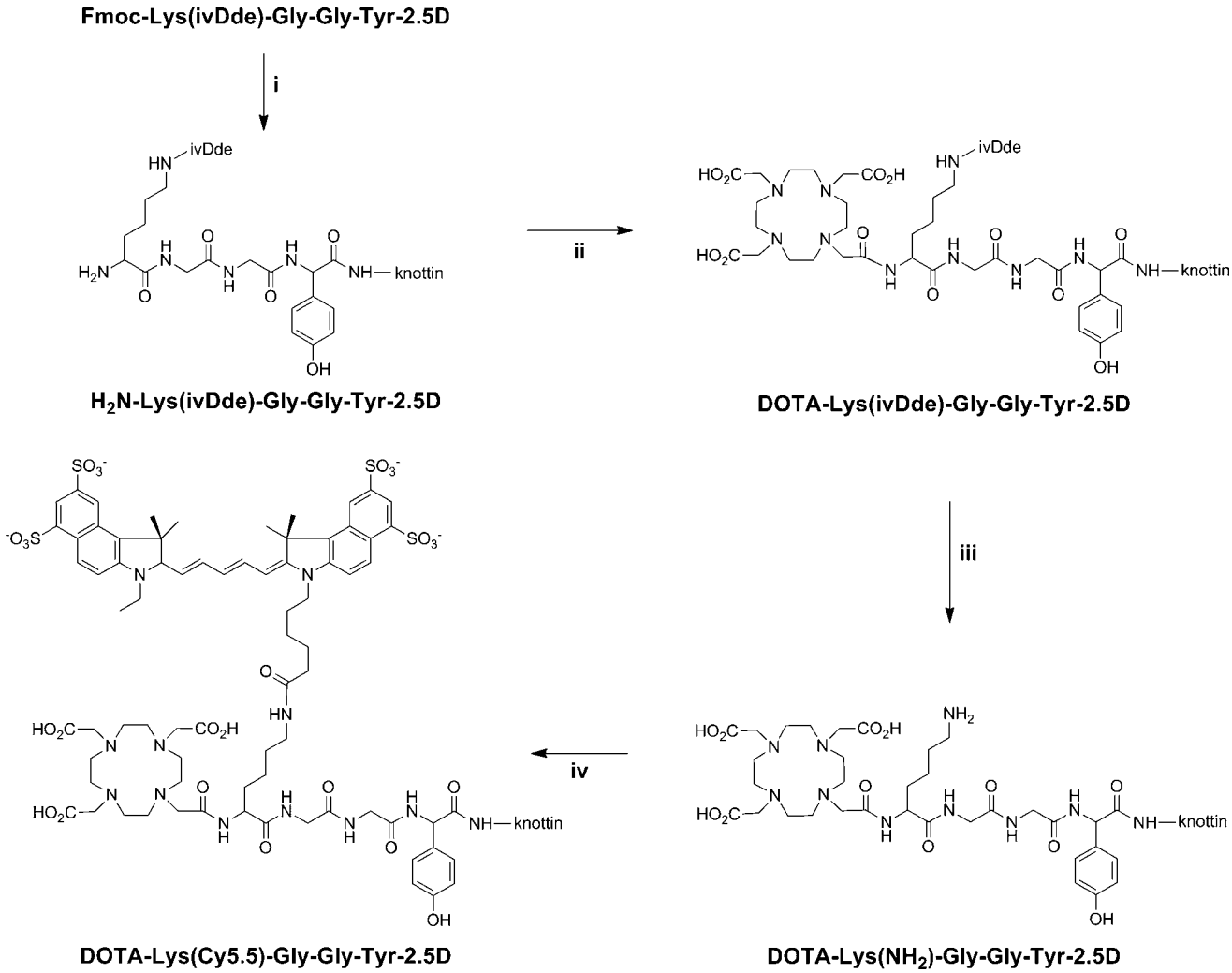
In Vivo Metabolite Analysis. For metabolite analysis, anesthetized nude (nu/nu) mice bearing U87MG tumor xenografts were injected with 200−400 μCi of ^{64}Cu-DOTA-Lys(Cy5.5)-Gly-Gly-Tyr-2.5D via the tail vein and were euthanized at 1, 4, or 24 h post injection. Blood, liver, kidney, and tumor tissue were removed and suspended in ~500 μL PBS. An additional 500−1000 μL DMF was added, and the tissues were homogenized with a mortar and pestle. The homogenate was filtered using a Costar Spin-X (Corning, Lowell, MA) 0.2 μm nylon microcentrifuge filter to isolate soluble metabolites. The filtrates were analyzed by reversed-phase HPLC. Eluted fractions were collected in 30 s intervals, and a gamma counter was used to determine counts per minute (cpm).

Statistical Analysis. All data are presented as the average value ± SD of n independent measurements. Statistical analysis for animal studies and binding studies were performed by two-factor ANOVA without replication analysis using Microsoft *Excel*. Significance was assigned for p values of <0.05.

RESULTS

Synthesis and Characterization of a Knottin Peptide Conjugated to Both DOTA and Cy5.5. To create a dual-modality NIRF/PET imaging agent, we developed a chemical strategy to couple both ^{64}Cu-DOTA and Cy5.5 to an engineered knottin peptide (knottin 2.5D), which binds to $\alpha_v\beta_3$ and $\alpha_v\beta_5$ integrin receptors with low nanomolar affinity (*13*). A peptide-based linker (Fmoc-Lys(ivDde)-Gly-Gly-Tyr-NHS ester) enabled stochiometric chemical coupling of these two different imaging labels specifically to the knottin N-terminus. The conjugation chemistry is shown in Scheme 1. Fmoc-Lys(ivDde)-Gly-Gly-Tyr was first treated with DCC/NHS to activate the C-terminal carboxylate and generate a reactive succinimide ester group. The tyrosine residue appeared to stabilize the succinimide ester intermediate and afforded a convenient handle for peptide detection and quantification by absorbance at 280 nm. This linker was coupled to the N-terminus of knottin 2.5D through formation of a peptide bond. The Fmoc and the ivDde groups were then selectively and sequentially removed to allow precise coupling of DOTA to the N-terminal amine and Cy5.5 to the ε-amino group of the lysine residue. Each reaction intermediate was purified by reversed-phase HPLC, and the correct mass was

Scheme 1. Chemical Conjugation of DOTA and Cy5.5 to Knottin Peptide 2.5D[a]



[a] The peptide-based cross-linker Fmoc-Lys(ivDde)-Gly-Gly-Tyr was first synthesized and coupled to the N-terminus of the folded knottin peptide 2.5D using succinimide ester activation chemistry. Next, the Fmoc group was removed from the N-terminus of the cross-linker (i: 10% piperidine/DMF, 0.5 h, RT), and the resulting compound was reacted with a 5-fold molar excess of an NHS ester-activated DOTA group (ii: DMF/2% DIEA, 0.5 h, RT) to generate DOTA-Lys(ivDde)-Gly-Gly-Tyr-2.5D. Finally, the ivDde group was removed from the ε-amino group of Lys (iii: 2% hydrazine/DMF, 0.5 h, RT), and the resulting compound was reacted with Cy5.5 NHS ester (iv: DMF/2% DIEA, 0.5 h, RT) to give the final product DOTA-Lys(Cy5.5)-Gly-Gly-Tyr-2.5D, which was used for NIRF imaging experiments, or radiolabeled with ^{64}Cu and used for PET imaging experiments.

verified by MALDI-TOF MS (Supporting Information Figure S1). To reduce sample loss associated with purification, we subsequently found that the ivDde deprotection step could be performed in the same reaction vessel used to couple the DOTA group. Next, the resulting integrin-binding knottin bioconjugate DOTA-Lys(Cy5.5)-Gly-Gly-Tyr-2.5D (abbreviated DOTA/Cy5.5-2.5D) was radiolabeled with ^{64}Cu through chelation with the DOTA group. We measured the stability of ^{64}Cu-DOTA-Lys(Cy5.5)-Gly-Gly-Tyr-2.5D (abbreviated ^{64}Cu-DOTA/Cy5.5-2.5D) upon exposure to mouse serum. Radio-HPLC analysis indicated minimal probe degradation after incubation in a solution of 50% mouse serum for 1 h at 37 °C (Supporting Information Figure S2). Degradation levels increased over time and intact probe was unrecoverable after incubation in serum for 24 h.

Binding of the DOTA/Cy5.5-Conjugated Knottin Peptide to Integrin-Expressing Tumor Cells. To test whether conjugation of Cy5.5 and DOTA to the knottin N-terminus affected binding to integrin receptors, we measured the ability of DOTA/Cy5.5-2.5D to compete with ^{125}I-labeled echistatin for binding to U87MG glioblastoma cells. Echistatin, a polypeptide from snake venom, has a K_D of approximately 0.4 nM for $\alpha_v\beta_3$ integrin (*18*). For comparison, we also measured the relative binding affinities of knottin peptide 2.5D with DOTA or Cy5.5 groups conjugated directly to the N-terminus. All knottin peptides were shown to bind in a dose-dependent matter to U87MG cells. The half-maximal inhibitory concentration (IC_{50}) values of DOTA/Cy5.5-2.5D and unlabeled knottin 2.5D were 30 ± 7 nM and 19 ± 6 nM (*15*), respectively, which were not statistically different ($p < 0.23$) (Table 1). In contrast, the relative binding affinities of DOTA-conjugated knottin 2.5D (IC_{50} = 9 ± 3 nM), and Cy5.5-lableled knottin 2.5D (IC_{50} = 5 ± 1 nM) were statistically significant compared to DOTA/Cy5.5-2.5D ($p < 0.05$). These results indicate that integrin binding affinity is

Table 1. U87MG Cell Binding Data, Reported as IC_{50} Values

ligand	IC_{50}
Echistatin	4 ± 1 nM[a]
Knottin 2.5D	19 ± 6 nM
Cy5.5−2.5D	5 ± 1 nM[a]
DOTA-2.5D	9 ± 3 nM[a]
DOTA/Cy5.5−2.5D	30 ± 7 nM

[a] Difference compared to DOTA/Cy5.5−2.5D is statistically significant ($p < 0.05$).

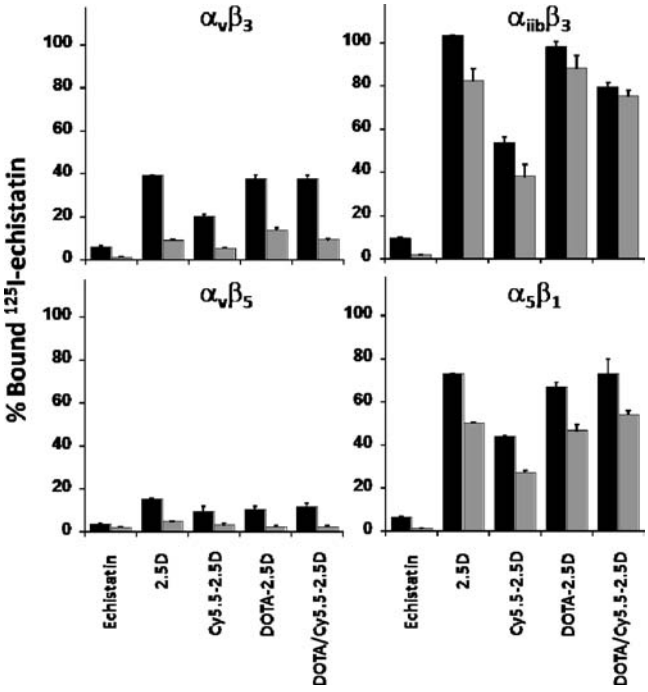


Figure 1. Competition binding of peptides to surface-immobilized integrins. ^{125}I-labeled echistatin was allowed to compete for binding with 5 nM (black bars) or 50 nM (gray bars) unlabeled peptides to detergent-solubilized integrin receptor subtypes $\alpha_v\beta_3$, $\alpha_v\beta_5$, $\alpha_5\beta_1$, and $\alpha_{iib}\beta_3$. Unlabeled echistatin, which binds to all four integrins with high affinity, was used as a positive control. Error bars represent the standard deviation of measurements performed in triplicate.

relatively unaffected by the addition of both Cy5.5 and DOTA through a flexible peptide linker. The binding isotherms of all of these compounds are shown in Supporting Information Figure S3 to facilitate direct comparison.

Integrin Binding Specificity of the DOTA/Cy5.5-Conjugated Knottin Peptide. We next tested whether conjugation of both Cy5.5 and DOTA to the N-terminus of knottin 2.5D affected its integrin binding specificity. Since U87MG cells have been shown to express $\alpha_v\beta_5$ and $\alpha_5\beta_1$ integrins in addition to $\alpha_v\beta_3$ integrin (*19*), we measured integrin binding specificity by competition of ^{125}I-echistatin to detergent-solubilized $\alpha_v\beta_3$, $\alpha_v\beta_5$, $\alpha_5\beta_1$, or $\alpha_{iib}\beta_3$ integrin receptors coated onto microtiter plates. Unlabeled echistatin was used as a positive control since it has been previously shown to bind to all four receptors with high affinity (*13, 20*). DOTA/Cy5.5-2.5D exhibited strong binding to $\alpha_v\beta_3$ and $\alpha_v\beta_5$ integrins, modest binding to $\alpha_5\beta_1$ integrin, and weak binding to $\alpha_{iib}\beta_3$ integrin (Figure 1). In comparison, similar results were observed with unlabeled knottin 2.5D and DOTA-conjugated knottin 2.5D (*15*). However, knottin peptide 2.5D labeled directly at its N-terminus with Cy5.5 showed increased binding to integrin receptors compared to the other knottin peptides we tested (Table 1 and Figure 1). This increase in binding was statistically significant for all data points compared to unlabeled knottin 2.5D ($p < 0.05$) and could be due to the close proximity of the hydrophobic Cy5.5 dye molecule to the integrin binding epitope. Interestingly, this effect was not observed with the dual-labeled knottin, which has its Cy5.5 and DOTA groups conjugated through the peptide-based linker and not directly at the knottin N-terminus (Figure 1). Cy5.5-labeled peptides, such as the backbone-cyclized pentapeptide c(RGDyK), have also shown increased integrin-binding affinities compared to unmodified compounds (*14*).

In Vivo Near-Infrared Fluorescence Imaging with the DOTA/Cy5.5-Conjugated Knottin Peptide. We tested the ability of the DOTA/Cy5.5-conjugated knottin peptide to target tumors in living subjects to evaluate its potential as an in vivo molecular imaging agent. Figure 2A shows typical NIRF images of athymic nude mice bearing subcutaneous U87MG glioblastoma tumors after tail vein injection of 1.5 nmol of probe. DOTA/Cy5.5-2.5D generated increasing tumor-to-background tissue ratios of 2.96 ± 0.42, 3.11 ± 0.66, 3.60 ± 0.84, and 4.04 ± 0.34 at 1, 2, 4, and 24 h post injection, respectively (Figure 2C). In comparison, knottin peptide 2.5D labeled directly at its N-terminus with Cy5.5 generated similar signals 1, 2, and 4 h post injection (2.09 ± 0.61, 2.57 ± 0.79, and 3.99 ± 0.55, respectively), which persisted at the 24 h time point (4.47 ± 0.39) (*15*). Co-injection of a molar excess of unlabeled c(RGDyK) significantly decreased uptake of DOTA/Cy5.5-2.5D, particularly at later time points ($p < 0.05$) (Figure 2B). At 1 h post injection, the tumor-to-background tissue ratio generated by this mixture was 2.16 ± 0.15 and did not increase to any significant extent at later time points (2.47 ± 0.34 at 24 h) (Figure 2C). This background signal is similar to that observed in other studies with Cy5.5-labeled peptides, including a negative control Cy5.5-labeled knottin peptide we previously tested (*14, 15*).

MicroPET Imaging of U87MG Xenografts with the ^{64}Cu-DOTA/Cy5.5-Conjugated Knottin Peptide. We tested the potential of the ^{64}Cu-DOTA/Cy5.5-conjugated knottin peptide for use as a PET imaging probe in mice bearing U87MG human tumor xenografts. ^{64}Cu-DOTA/Cy5.5-2.5D rapidly accumulated at the tumor site and persisted there throughout the course of the experiment (Figure 2D). We observed tumor uptake values of 4.27 ± 0.46, 4.19 ± 0.36, 4.52 ± 0.31, and 5.02 ± 0.05%ID/g at 1, 2, 4, and 24 h post injection, respectively (Figure 2F). In contrast, knottin peptide 2.5D labeled directly at its N-terminus with ^{64}Cu-DOTA generated similar tumor uptake values at the 1 h time point (4.47 ± 1.21%ID/g) but exhibited significantly faster wash-out (1.48 ± 0.51%ID/g at 24 h). Tumor uptake of ^{64}Cu-DOTA/Cy5.5-2.5D was significantly decreased ($p < 0.05$) by coinjection of ~0.5 μmol of unlabeled c(RGDyK) (Figure 2E), resulting in values of approximately 1−1.5%ID/g from 1 to 24 h post injection (Figure 2F).

A plot of tumor-to-background tissue ratios for NIRF versus PET imaging showed good linear correlation ($R^2 = 0.85$) over 1−24 h, indicating that the two labels are effectively delivered to the tumor, and can be detected by both imaging modalities over the time course of the experiment (Figure 2G). A direct 1:1 correlation is not observed due to inherent differences in the background tissue measured with each noninvasive in vivo imaging technique. More specifically, although the depth of fluorescence light penetration is several millimeters into the muscle, the background signal quantified by NIRF imaging results mainly from high autofluorescence of the skin. In contrast, the background signal obtained in microPET imaging is quantified on the muscle tissue.

Comparative Cell Uptake and MicroPET Imaging in MDA-MB-435 Xenografts. To further confirm integrin specificity, we tested binding and uptake of ^{64}Cu-DOTA/Cy5.5-2.5D in two cell lines: U87MG and MDA-MB-435, a melanoma cell line which expresses 2×10^4 integrin receptors, compared to approximately 1×10^5 integrin receptors expressed on U87MG cells (*21*). As expected, lower levels of probe uptake were observed over time in MDA-MB-435 versus U87MG cells, correlating with their lower levels of integrin receptor expression (Figure 3A). In both cell lines, binding and uptake were blocked by addition of an excess of c(RGDyK). Consistent with these results, tumor uptake of ^{64}Cu-DOTA/Cy5.5-2.5D in MDA-MB-435 xenograft models was much lower compared to uptake in U87MG tumors, exhibiting values of 1.33 ± 0.02%ID/g and 1.01 ± 0.10%ID/g at 1 and 24 h post injection (Figure 3B). Furthermore, MDA-MB-435 tumor uptake was significantly

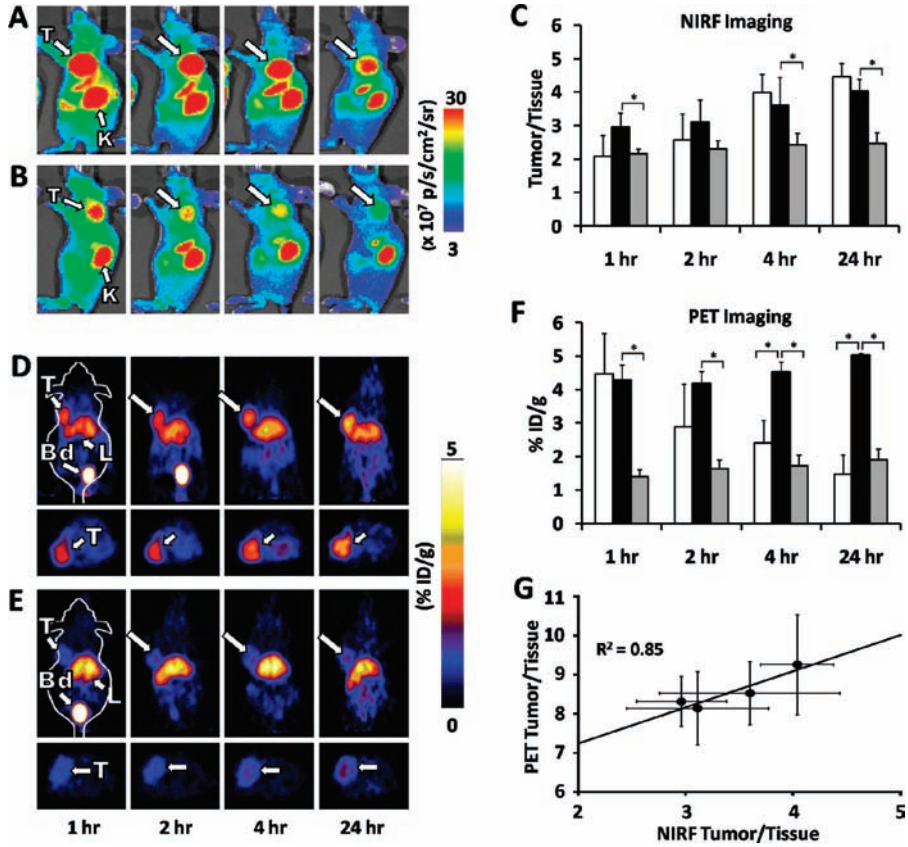


Figure 2. NIRF and microPET imaging of knottin probes in murine human tumor xenograft models. Mice bearing U87MG tumors were injected via tail vein with either (A) 1.5 nmol of DOTA/Cy5.5−2.5D or (D) ∼100 μCi of ^{64}Cu-DOTA/Cy5.5−2.5D. For blocking experiments (B,E), mice were coinjected with an excess (0.5 μmol) of unlabeled c(RGDyK) in addition to labeled knottin peptides. Representative images are shown at 1, 2, 4, and 24 h post injection. T = tumor; K = kidney; Bd = bladder; L = liver. (C) NIRF imaging, represented as the tumor-to-background tissue (tumor/tissue) ratio for Cy5.5−2.5D (white bars), DOTA/Cy5.5−2.5D (black bars), and DOTA/Cy5.5−2.5D plus excess unlabeled c(RGDyK) blocking peptide (gray bars). (F) MicroPET imaging, quantified as the % ID/g of ^{64}Cu-DOTA-2.5D (white bars), ^{64}Cu-DOTA/Cy5.5−2.5D (black bars), and ^{64}Cu-DOTA/Cy5.5−2.5D plus an excess of unlabeled c(RGDyK) blocking peptide (gray bars). (G) Correlation analysis of average tumor-to-background tissue ratios for NIRF and microPET images acquired at 1, 2, 4, and 24 h post injection. Error bars represent the SD of measurements performed on at least three mice. (* $p < 0.05$).

decreased to 0.82 ± 0.05%ID/g and 0.60 ± 0.09%ID/g at 1 and 24 h post injection ($p < 0.05$) upon co-injection of a molar excess of unlabeled c(RGDyK).

Biodistribution Studies of ^{64}Cu-DOTA/Cy5.5- and DOTA/Cy5.5-Conjugated Knottin Peptides. We determined the tissue biodistribution of DOTA/Cy5.5- and ^{64}Cu-DOTA/Cy5.5-conjugated knottin peptides in U87MG tumor-bearing mice using fluorescence and radioactivity measurements. Mice were injected with DOTA/Cy5.5-2.5D and fluorescent images of individual organs were obtained at various time points. In these studies, probe accumulated rapidly at the tumor site at early time points and decreased over time with fluorescence flux/gram values of 373.1 ± 111.3 and 146.1 ± 26.5 for 1 and 24 h post injection, respectively (Figure 4A). Next, mice were injected with ^{64}Cu-DOTA/Cy5.5-2.5D and individual organs were analyzed by gamma counting. For tumor tissue, we observed biodistribution values of 3.24 ± 0.87, 5.64 ± 0.83, and 4.57 ± 0.70%ID/g at 1, 4, and 24 h post injection, respectively (Figure 4B). Higher liver uptake (∼4−7% ID/g at 1 and 4 h) and kidney uptake (∼80%ID/g for 1−4 h) were observed compared to other organs (Figures 4B and 5B). Kidney uptake was reduced at 24 h (∼30%ID/g) in both Cy5.5 and ^{64}Cu biodistribution studies (Figure 5).

To further compare the DOTA/Cy5.5- and ^{64}Cu-DOTA/Cy5.5-knottin biodistribution data, tumor-to-tissue ratios were calculated (Figure 4C−D). In general, the tumor-to-blood and tumor-to-muscle ratios were slightly higher for fluorescence imaging (Cy5.5 uptake) compared to radioactivity measurements (^{64}Cu uptake). This trend was also observed for the tumor-to-tissue ratios for the liver, lung, and spleen. Plots of tumor-to-background tissue ratios for Cy5.5 versus ^{64}Cu uptake in various organs showed good correlation, with an intercept of zero and R^2 values of 0.75, 0.83, and 0.82 for 1, 4, and 24 h post injection, respectively, demonstrating relatively uniform distribution of imaging labels in tumors and off-target tissues (Supporting Information Figure S4). The high tumor-to-blood ratios and high tumor-to-muscle-ratios observed at 1, 4, and 24 h post injection suggest that ^{64}Cu-DOTA/Cy5.5-2.5D may be useful for whole body radiographic imaging where the tumor signal is not obscured by a strongly emitting background signal from nontargeted organs.

Metabolic Stability. Finally, we tested the in vivo stability of ^{64}Cu-DOTA/Cy5.5-2.5D. The metabolic breakdown of probe was examined after recovery from whole mouse blood, tumor, liver, and kidney 1 h post injection. The radioactivity recovered in the soluble tissue extract ranged 50−80% compared to the insoluble cellular debris or pellet fraction. This soluble extract was filtered and separated by reversed-phase HPLC, and fractions were analyzed by gamma counting. The dual-labeled ^{64}Cu-DOTA/Cy5.5 knottin peptide appeared to have similar stability in serum and blood after 1 h incubation (Figure 6 and Supporting Information Figure S2). In contrast, significant breakdown of probe was seen in the tumor, and intact probe was not able to be recovered from the liver and kidney. In these

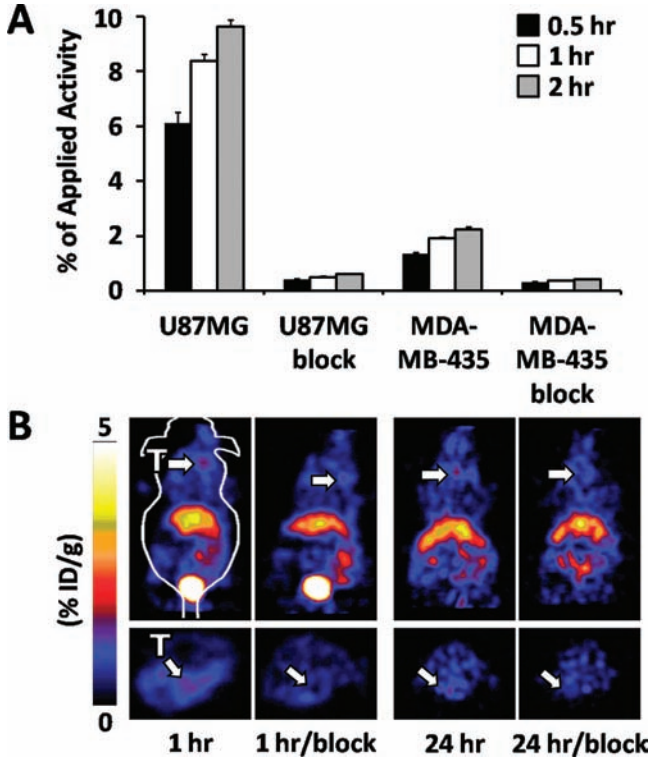


Figure 3. Uptake and imaging in MDA-MB-435 cells and xenograft tumors. (A) Uptake of ^{64}Cu-DOTA/Cy5.5−2.5D in U87MG or MDA-MB-435 cells at 0.5, 1, and 2 h. Blocking studies, indicated by "block", were performed in parallel using a large molar excess of c(RGDyK). (B) MicroPET images of mice bearing subcutaneous MDA-MB-435 tumors at 1 and 24 h post injection. Blocking experiments with unlabeled c(RGDyK) were performed to further demonstrate probe specificity.

samples, metabolites with retention times between 3 and 6 min were present at high levels.

DISCUSSION

A chemical cross-linking strategy was developed to couple two complementary molecular imaging agents onto a disulfide-rich knottin peptide that has been engineered to bind to $\alpha_v\beta_3$ and $\alpha_v\beta_5$ integrins with high affinity. The folding of cystine knot peptides is highly dependent on primary structure (*22*). We observed that simple N-terminal acetylation or biotinylation of EETI-II severely affected its ability to properly fold, consistent with another study on permutants of the cyclotide kalata B1 (*23*). These stringent folding requirements dictated that all conjugation chemistry be performed in solution after the knottin was folded, instead of using on-bead labeling of side-chain protected linear peptides immediately following synthesis. Therefore, we used a cross-linking strategy that selectively and sequentially exposed reactive groups for precise, stoichiometric coupling of both an optical imaging dye and a radiochelator to the knottin N-terminus. The method we developed is flexible and can be used to accommodate a variety of imaging labels, therapeutics, or pharmacokinetic modulators for diverse biomedical applications. Importantly, we demonstrated that attachment of several chemical groups to the N-terminus of the engineered EETI-II knottin peptide did not interfere with its ability to bind to integrin receptors with high affinity.

Stability studies showed that the ^{64}Cu-DOTA-Lys(Cy5.5)-Gly-Gly-Tyr-2.5D probe is relatively labile, both in high concentrations of serum and after injection into the body. This breakdown is most likely due to proteolysis of the cross-linking moiety, as we previously showed that knottin peptide ^{64}Cu-DOTA-2.5D exhibited only minimal fragmentation after incubation in serum for 24 h and was recovered intact from the blood, tumor, and kidneys 1 h after injection into mice (*15*). Given that similar maximal tumor uptake levels were observed from ^{64}Cu-DOTA-2.5D and ^{64}Cu-DOTA-Lys(Cy5.5)-Gly-Gly-Tyr-2.5D, this proteolysis did not appear to affect its rapid tumor accumulation. However, degradation could have influenced kidney uptake and retention of dye molecules or metals. Cross-linkers composed of non-natural amino acids or peptoids may facilitate a more stable linkage (*24*). In addition, the use of D-amino acids has been shown to stabilize a variety of imaging peptides such as somatostatin (*25*). We are currently using these strategies to create more stable cross-linkers for the development of theranostic agents that will apply molecular imaging to quantify the delivery of cytotoxic drugs to tumors.

The use of a dual-labeled agent has distinct advantages as opposed to coadministering separate single-labeled agents. Having both labels on the same affinity ligand allows pharmacokinetic quantification of a single compound. This is beneficial because, as our study showed, the hydrophobic Cy5.5 dye strongly influenced the pharmacokinetics and tissue biodistribution of the radionuclide imaging agent. In addition, dual labeling allows quantitative cross validation and direct comparison between nuclear and optical imaging using an affinity ligand (*26*). Several groups have developed dual-labeled NIRF/SPECT probes using near-infrared dyes and ^{111}In or ^{99m}Tc radiolabels (*26*−*31*); these probes are specific to a variety of disease targets and have been recently reviewed (*32*). Studies describing chemically defined, dual-labeled NIRF/PET probes have been more limited. NIRF/PET probes have been developed by decorating quantum dots with tumor targeting moieties and radiolabeling the resulting nanoparticles with ^{64}Cu (*33, 34*). Compared to our knottin peptides, these nanoparticles exhibited extremely high uptake in the liver, spleen, lymph nodes, and bone marrow.

Addition of Cy5.5 had both a positive and negative effect on the pharmacokinetics and biodistribution of the probe. In comparison to ^{64}Cu-DOTA-2.5D, which rapidly washed out of the tumor, ^{64}Cu-DOTA-Lys(Cy5.5)-Gly-Gly-Tyr-2.5D was significantly retained by the tumor at later time points (Figure 2D). This tumor uptake was specific and mediated by integrin receptors as demonstrated by blocking experiments with c(RGDyK), which interacts with the same integrin binding site as the engineered knottin peptides (Figure 2), as well as the lower levels of tumor uptake in MDA-MB-435 tumors, which express lower levels of integrin receptors compared to U87MG tumors (Figure 3). Moreover, in previous studies we used knottin peptides containing a scrambled sequence to validate the integrin binding specificity of ^{64}Cu-DOTA- and Cy5.5-labeled knottin probes (*13, 15*).

Cy5.5 rapidly accumulated in the kidneys over the course of the imaging experiments (Figures 2A and 5A), consistent with the high levels of kidney uptake and retention we observed with knottin peptide 2.5D labeled only with Cy5.5 (*15*). In our previous studies, the kidney uptake for ^{64}Cu-DOTA-2.5D was 8.08 ± 0.67, 2.69 ± 0.48, and 1.25 ± 0.11%ID/g at 1, 4, and 24 h post injection, respectively (*15*). In contrast, kidney uptake for ^{64}Cu-DOTA-Lys(Cy5.5)-Gly-Gly-Tyr-2.5D was 78.4 ± 13.9 and 80.9 ± 14.9%ID/g for 1 and 4 h post injection; however, after 24 h the radioactivity in the kidneys decreased to 32.2 ± 2.2%ID/g, suggesting that ^{64}Cu metabolites are cleared by the kidneys at later time points. This decrease in kidney signal is not due to the short half-life of ^{64}Cu (12.7 h), as the data have been normalized to account for radioactive decay. Liver uptake (∼4−7%ID/g at 1−24 h post injection) was also higher than previously observed for ^{64}Cu-DOTA-2.5D, in which values of ∼1−2%ID/g were observed 1 to 4 h post injection. Increased liver and kidney uptake may preclude the use of this probe to

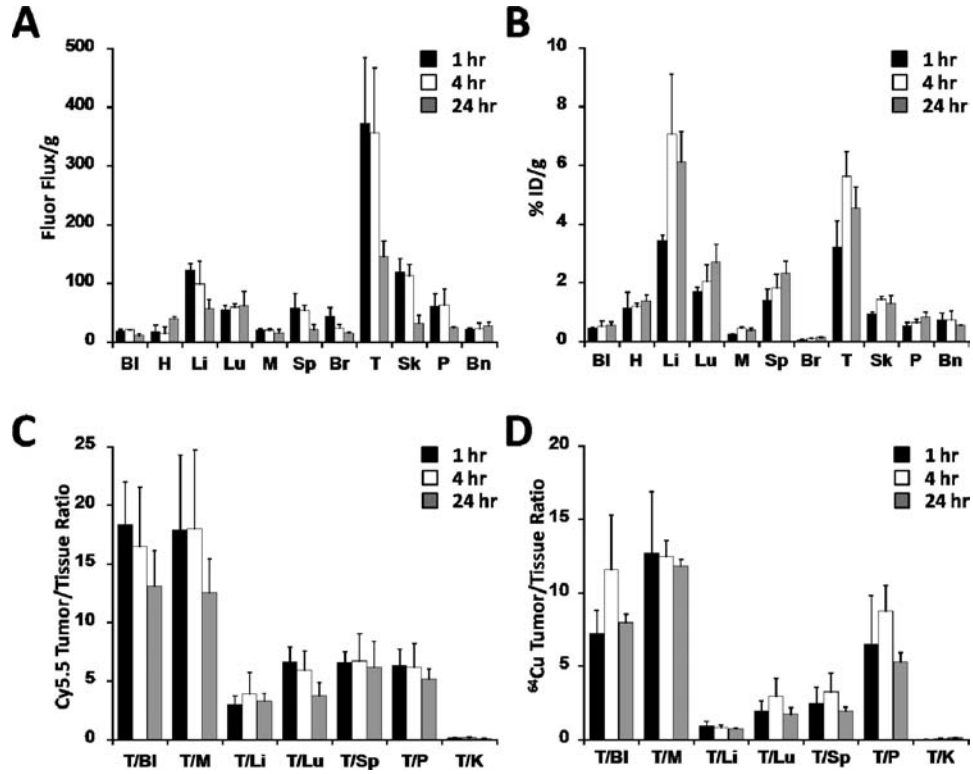


Figure 4. Comparison of Cy5.5 and ^{64}Cu tissue biodistribution. The amount of (A) DOTA/Cy5.5−2.5D or (B) ^{64}Cu-DOTA/Cy5.5−2.5D accumulation was measured in the blood (Bl), heart (H), liver (Li), lung (Lu), muscle (M), spleen (Sp), brain (Br), tumor (T), skin (Sk), pancreas (P), and bone (Bn). (A) Cy5.5 uptake, measured as the fluorescence flux (photons per second) per gram of tissue. (B) ^{64}Cu uptake, quantified as the %ID/g. Comparison of tumor/tissue ratios observed at 1, 4, and 24 h post injection for (C) DOTA/Cy5.5−2.5D or (D) ^{64}Cu-DOTA/Cy5.5−2.5D.

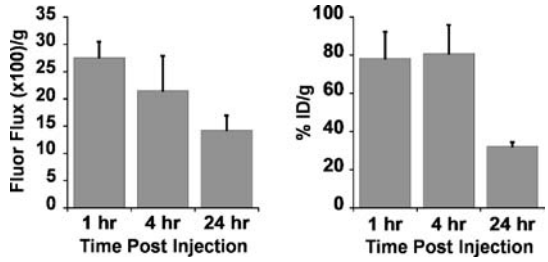


Figure 5. Comparison of Cy5.5 and ^{64}Cu accumulation in the kidney. Uptake of Cy5.5 resulting from injection of DOTA/Cy5.5−2.5D (left panel) was measured as the fluorescence flux (photons per second) per gram of tissue. Uptake of ^{64}Cu-DOTA/Cy5.5−2.5D (right panel) was quantified as the %ID/g.

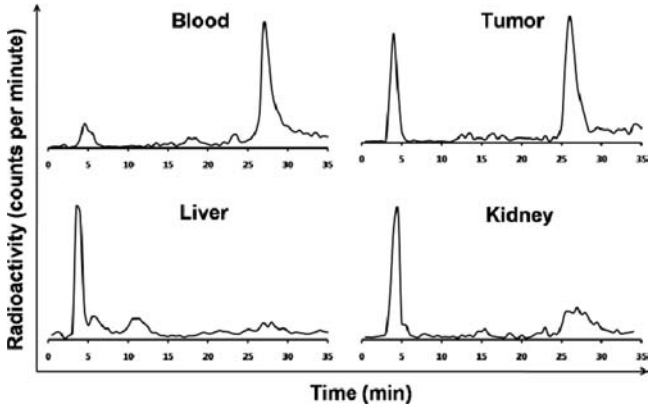


Figure 6. In vivo metabolic stability of ^{64}Cu-DOTA/Cy5.5−2.5D. Homogenized tissues were analyzed by radio-HPLC and gamma counting 1 h post injection. The intact radiotracer elutes at around 27 min.

identify lesions located in the abdomen; however, the spatial resolution of PET imaging, which is in the millimeter range, may allow identification of small lesions in close proximity to these organs. In addition, while kidney uptake and retention were high from Cy5.5-labeled probes, in future studies the use of alternate fluorescent dyes with more favorable biodistribution properties may help address this issue. Small amounts of probe are used for imaging applications; thus, we do not expect this probe to be immunogenic. However, as with any new compound intended for clinical use, this will have to be determined empirically.

In summary, the cross-linking strategy we describe here has broad applicability for site-specific coupling of two different imaging labels, or an imaging label and a therapeutic moiety, to knottin peptides for cancer diagnosis or therapy, or both. Conjugation of a tumor-specific knottin peptide to both a PET imaging agent and a chemotherapeutic agent could allow simultaneous and quantitative measurement of biodistribution and pharmacokinetics, drug delivery to tumors, and tumor response during the course of treatment. Moreover, different combinations of imaging labels may yield additional or unique information during a multimodal scan. The molecular tools developed here will allow research in these areas to be explored.

ACKNOWLEDGMENT

We thank Adam Silverman, Bryan Smith, and Douglas Jones for helpful discussions and critical feedback, Fred Chin and David Dick in the Stanford Cyclotron Facility, and Tim Doyle, Laura Pisani, and Frezghi Habte in the Stanford Small Animal Imaging Facility. We also thank Edwin Chang for providing the MDA-MB-435 mouse xenograft models. This work was funded by the NIH National Cancer Institute (NCI) Howard Temin Award 5K01 CA104706 and the Mallinckrodt Faculty Scholar Award (to J.R.C.), NIH ICMIC P50 CA114747, NCI 5R25 CA118681, and the Canary Foundation (to S.S.G.), and a Stanford Molecular Imaging Scholars postdoctoral fellowship R25 CA118681 (to R.H.K.).

Supporting Information Available: Characterization of compounds by reversed-phase HPLC and MALDI-TOF MS, serum stability of ^{64}Cu-DOTA/Cy5.5-2.5D, competition binding of knottin peptides to integrins expressed on tumor cells, and correlation analysis of Cy5.5 and ^{64}Cu biodistribution data. This material is available free of charge via the Internet at http://pubs.acs.org.

LITERATURE CITED

(1) Hynes, R. O. (1992) Integrins: versatility, modulation, and signaling in cell adhesion. *Cell 69*, 11–25.

(2) Brooks, P. C., Clark, R. A., and Cheresh, D. A. (1994) Requirement of vascular integrin alphav beta3 for angiogenesis. *Science 264*, 569–571.

(3) Friedlander, M., Brooks, P. C., Shaffer, R. W., Kincaid, C. M., Varner, J. A., and Cheresh, D. A. (1995) Definition of two angiogenic pathways by distinct alphav integrins. *Science 270*, 1500–1502.

(4) Alghisi, G. C., and Ruegg, C. (2006) Vascular integrins in tumor angiogenesis: mediators and therapeutic targets. *Endothelium 13*, 113–135.

(5) Mizejewski, G. J. (1999) Role of integrins in cancer: survey of expression patterns. *Proc. Soc. Exp. Biol. Med. 222*, 124–138.

(6) Stupack, D. G., and Cheresh, D. A. (2004) Integrins and angiogenesis. *Curr. Top. Dev. Biol. 64*, 207–238.

(7) Cai, W., Gambhir, S. S., and Chen, X. (2005) Multimodality tumor imaging targeting integrin alphav beta3. *Biotechniques 39*, S6–S17.

(8) Cai, W., Rao, J., Gambhir, S. S., and Chen, X. (2006) How molecular imaging is speeding up antiangiogenic drug development. *Mol. Cancer Ther. 5*, 2624–2633.

(9) Haubner, R. (2006) Alphav beta3-integrin imaging: a new approach to characterise angiogenesis? *Eur. J. Nucl. Med. Mol. Imaging 33* (Suppl 1), 54–63.

(10) Massoud, T. F., and Gambhir, S. S. (2003) Molecular imaging in living subjects: seeing fundamental biological processes in a new light. *Genes Dev. 17*, 545–580.

(11) Rudin, M., and Weissleder, R. (2003) Molecular imaging in drug discovery and development. *Nat. Rev. Drug Discovery 2*, 123–131.

(12) Willmann, J. K., van Bruggen, N., Dinkelborg, L. M., and Gambhir, S. S. (2008) Molecular imaging in drug development. *Nat. Rev. Drug Discovery 7*, 591–607.

(13) Kimura, R. H., Levin, A. M., Cochran, F. V., and Cochran, J. R. (2009) Engineered cystine knot peptides that bind alphav beta3, alphav beta5, and alpha5 beta1 integrins with low nanomolar affinity. *Proteins: Struct., Funct., Bioinf. 77*, 359–369.

(14) Cheng, Z., Wu, Y., Xiong, Z., Gambhir, S. S., and Chen, X. (2005) Near-infrared fluorescent RGD peptides for optical imaging of integrin alphav beta3 expression in living mice. *Bioconjugate Chem. 16*, 1433–1441.

(15) Kimura, R. H., Cheng, Z., Gambhir, S. S., and Cochran, J. R. (2009) Engineered knottin peptides: A new class of agents for imaging integrin expression in living subjects. *Cancer Res. 69*, 2435–2442.

(16) Orlando, R. A., and Cheresh, D. A. (1991) Arginine-glycine-aspartic acid binding leading to molecular stabilization between integrin alphav beta3 and its ligand. *J. Biol. Chem. 266*, 19543–19550.

(17) Wu, Y., Zhang, X., Xiong, Z., Cheng, Z., Fisher, D. R., Liu, S., Gambhir, S. S., and Chen, X. (2005) microPET imaging of glioma integrin alphav beta3 expression using ^{64}Cu-labeled tetrameric RGD peptide. *J. Nucl. Med. 46*, 1707–1718.

(18) Kumar, C. C., Nie, H., Rogers, C. P., Malkowski, M., Maxwell, E., Catino, J. J., and Armstrong, L. (1997) Biochemical characterization of the binding of echistatin to integrin alphav beta3 receptor. *J. Pharmacol. Exp. Ther. 283*, 843–853.

(19) Bruning, A., and Runnebaum, I. B. (2003) CAR is a cell-cell adhesion protein in human cancer cells and is expressionally modulated by dexamethasone, TNFalpha, and TGFbeta. *Gene Ther. 10*, 198–205.

(20) Pfaff, M., McLane, M. A., Beviglia, L., Niewiarowski, S., and Timpl, R. (1994) Comparison of disintegrins with limited variation in the RGD loop in their binding to purified integrins alphaIIb beta3, alphav beta3 and alpha5 beta1 and in cell adhesion inhibition. *Cell Adhes. Commun. 2*, 491–501.

(21) Zhang, X., Xiong, Z., Wu, Y., Cai, W., Tseng, J. R., Gambhir, S. S., and Chen, X. (2006) Quantitative PET imaging of tumor integrin alphav beta3 expression with ^{18}F-FRGD2. *J. Nucl. Med. 47*, 113–121.

(22) Wentzel, A., Christmann, A., Kratzner, R., and Kolmar, H. (1999) Sequence requirements of the GPNG beta-turn of the Ecballium elaterium trypsin inhibitor II explored by combinatorial library screening. *J. Biol. Chem. 274*, 21037–21043.

(23) Simonsen, S. M., Daly, N. L., and Craik, D. J. (2004) Capped acyclic permutants of the circular protein kalata B1. *FEBS Lett. 577*, 399–402.

(24) de Visser, M., Janssen, P. J., Srinivasan, A., Reubi, J. C., Waser, B., Erion, J. L., Schmidt, M. A., Krenning, E. P., and de Jong, M. (2003) Stabilised ^{111}In-labelled DTPA- and DOTA-conjugated neurotensin analogues for imaging and therapy of exocrine pancreatic cancer. *Eur. J. Nucl. Med. Mol. Imaging 30*, 1134–1139.

(25) Pless, J., Bauer, W., Briner, U., Doepfner, W., Marbach, P., Maurer, R., Petcher, T. J., Reubi, J. C., and Vonderscher, J. (1986) Chemistry and pharmacology of SMS 201−995, a long-acting octapeptide analogue of somatostatin. *Scand. J. Gastroenterol. Suppl. 119*, 54–64.

(26) Bhushan, K. R., Misra, P., Liu, F., Mathur, S., Lenkinski, R. E., and Frangioni, J. V. (2008) Detection of breast cancer microcalcifications using a dual-modality SPECT/NIR fluorescent probe. *J. Am. Chem. Soc. 130*, 17648–17649.

(27) Houston, J. P., Ke, S., Wang, W., Li, C., and Sevick-Muraca, E. M. (2005) Quality analysis of in vivo near-infrared fluorescence and conventional gamma images acquired using a dual-labeled tumor-targeting probe. *J. Biomed. Opt. 10*, 054010.

(28) Li, C., Wang, W., Wu, Q., Ke, S., Houston, J., Sevick-Muraca, E., Dong, L., Chow, D., Charnsangavej, C., and Gelovani, J. G. (2006) Dual optical and nuclear imaging in human melanoma xenografts using a single targeted imaging probe. *Nucl. Med. Biol. 33*, 349–358.

(29) Sampath, L., Kwon, S., Ke, S., Wang, W., Schiff, R., Mawad, M. E., and Sevick-Muraca, E. M. (2007) Dual-labeled trastuzumab-based imaging agent for the detection of human epidermal growth factor receptor 2 overexpression in breast cancer. *J. Nucl. Med. 48*, 1501–1510.

(30) Wang, W., Ke, S., Kwon, S., Yallampalli, S., Cameron, A. G., Adams, K. E., Mawad, M. E., and Sevick-Muraca, E. M. (2007) A new optical and nuclear dual-labeled imaging agent targeting interleukin 11 receptor alpha-chain. *Bioconjugate Chem. 18*, 397–402.

(31) Zhang, Z., Liang, K., Bloch, S., Berezin, M., and Achilefu, S. (2005) Monomolecular multimodal fluorescence-radioisotope imaging agents. *Bioconjugate Chem. 16*, 1232–1239.

(32) Lee, S., and Chen, X. (2009) Dual-modality probes for in vivo molecular imaging. *Mol. Imaging 8*, 87–100.

(33) Cai, W., Chen, K., Li, Z. B., Gambhir, S. S., and Chen, X. (2007) Dual-function probe for PET and near-infrared fluorescence imaging of tumor vasculature. *J. Nucl. Med. 48*, 1862–1870.

(34) Chen, K., Li, Z. B., Wang, H., Cai, W., and Chen, X. (2008) Dual-modality optical and positron emission tomography imaging of vascular endothelial growth factor receptor on tumor vasculature using quantum dots. *Eur. J. Nucl. Med. Mol. Imaging 35*, 2235–2244.

BC9003102

Formulation of a Peptide Nucleic Acid Based Nucleic Acid Delivery Construct

Peter G. Millili,[†,||] Daniel H. Yin,[⊥] Haihong Fan,[⊥] Ulhas P. Naik,[†,‡,§,||] and Millicent O. Sullivan*[,†,||]

Department of Chemical Engineering, Department of Biological Sciences, Department of Chemistry and Biochemistry, and Delaware Biotechnology Institute, University of Delaware, Newark, Delaware 19716, and Department of Pharmaceutical Research, Development, Merck Research Laboratories, West Point, Pennsylvania 19486. Received July 27, 2009; Revised Manuscript Received November 25, 2009

Gene delivery biomaterials need to be designed to efficiently achieve nuclear delivery of plasmid DNA. Polycations have been used to package DNA and other nucleic acids within submicrometer-sized particles, offering protection from shear-induced or enzymatic degradation. However, cytotoxicity issues coupled with limited in vivo transfection efficiencies minimize the effectiveness of this approach. In an effort to improve upon existing technologies aimed at delivering nucleic acids, an alternative approach to DNA packaging was explored. Peptide nucleic acids (PNAs) were used to directly functionalize DNA with poly(ethylene glycol) (PEG) chains that provide a steric layer and inhibit multimolecular aggregation during complexation. DNA prePEGylation by this strategy was predicted to enable the formation of more homogeneous and efficiently packaged polyplexes. In this work, DNA-PNA-peptide-PEG (DP3) conjugates were synthesized and self-assembled with 25 kDa poly(ethylenimine) (PEI). Complexes with small standard deviations and average diameters ranging 30−50 nm were created, with minimal dependence of complex size on N/P ratio (PEI amines to DNA phosphates). Furthermore, PEI−DNA interactions were altered by the derivatization strategy, resulting in tighter compaction of the PEI−DP3 complexes in comparison to PEI−DNA complexes. Transfection experiments in Chinese hamster ovary (CHO) cells revealed comparable transfection efficiencies but reduced cytotoxicities of the PEI−DP3 complexes relative to PEI−DNA complexes. The enhanced cellular activities of the PEI−DP3 complexes were maintained following the removal of free PEI from the PEI−DP3 formulations, whereas the cellular activity of the conventional PEI−DNA formulations was reduced by free PEI removal. These findings suggest that DNA prePEGylation by the PNA-based strategy might provide a way to circumvent cytotoxicity and formulation issues related to the use of PEI for in vivo gene delivery.

INTRODUCTION

Nonviral, biomimetic nucleic acid delivery systems have been developed with the aim of designing modular, targeted, and safe constructs for gene therapy. Such an approach has the potential to bring about practical pharmaceutical products with great improvement in combating disease. While viral vectors have achieved efficient delivery of exogenous DNA, their innate immunogenicity and toxicity have raised significant concerns over their clinical development. Despite these limitations, the multiple functionalities and responsiveness of these viral systems provide key insight into how biomimetic vehicles can be more effectively designed.

One widely explored method of nonviral vehicle formulation involves the use of polycations to condense DNA into nano- to submicrometer-scale particles (*1*−*5*). For example, poly(ethylenimine) (PEI) is a cationic polymer that contains a high density of primary, secondary, and tertiary amine groups, and has been used to package DNA and RNA within nanosized complexes (*2, 5*−*7*). Polyplexes made from PEI constitute a highly effective delivery system in vitro, an effect which has been attributed to the capacity of PEI to promote endosomal escape via pH-buffering (*8*−*10*). Unfortunately, concerns about the toxicity of PEI (*11*) and challenges in formulating PEI-based vehicles have limited its applicability in vivo. Cationic polyplexes tend to aggregate and interact with serum proteins after systemic administration, leading to their rapid phagocytic elimination (*12, 13*). They are also nonspecifically internalized by liver cells (*14*−*16*).

One way to overcome the serum instability and nonspecificity of polyplexes is through the steric stabilization of polyplexes with hydrophilic, uncharged polymers. Poly(ethylene glycol) (PEG) has been conjugated to PEI and other DNA-condensing polymers via reaction with primary amine groups along the backbone of the polycation, resulting in enhanced polyplex stability (*6, 17*−*20*). To enhance cell-specific uptake, cell-targeting and other functional peptides have been added directly to the polycation or to the conjugated PEG (*2, 6, 21*−*24*). PEGylation and functionalization of polycationic gene delivery carriers have been explored both pre- and postcomplexation with DNA. Precomplexation PEGylation, involving the complexation of DNA with PEGylated complexation agents, was developed with the intention of minimizing polyplex aggregation during formulation. Polyplexes are inherently heterogeneous due to uncontrolled self-aggregation during the formulation process. Consequently, PEGylated complexation agents have the potential to produce more monodisperse particles (*22, 25, 26*). However, the charge density of the polycation is reduced by PEGylation, making precomplexation PEGylation ineffective for low molecular weight polycations (*3, 27*), and in general, lowering the condensation efficiency (*4, 25, 26, 28*−*30*).

* Corresponding author. Millicent O. Sullivan, 213 Colburn Laboratory, Department of Chemical Engineering, University of Delaware, Newark, DE 19716, 302-831-8072, 302-831-3009 (fax), msulliva@udel.edu.

[†] Department of Chemical Engineering, University of Delaware.

[‡] Department of Biological Sciences, University of Delaware.

[§] Department of Chemistry and Biochemistry, University of Delaware.

[||] Delaware Biotechnology Institute, University of Delaware.

[⊥] Merck Research Laboratories.

10.1021/bc900328j © 2010 American Chemical Society
Published on Web 02/04/2010

The addition of PEG postcomplexation can be accomplished by PEG grafting onto surface-exposed amine groups on the polyplex and has been shown to effectively stabilize PEI-based polyplexes containing high molecular weight PEI (*6*); in contrast, polyplexes formed from lower molecular weight polycations can be destabilized by this process (*31*). Surface PEGylation has also been shown to alter the intracellular trafficking of particles and to reduce their gene transfer capability (*20*). In an effort to circumvent these limitations, nondisruptive PEGylation strategies have been pursued. For example, cyclodextrin-based polycations have been developed that allow DNA complexation and PEGylation in a single-step reaction. PEGylation occurs by inclusion complex formation between adamantine-PEGs and cyclodextrins, and has no adverse effects on DNA−cation interactions (*22, 31, 32*).

To enable the formulation of polyplexes appropriate for systemic administration and efficient cellular utilization, we have explored a novel formulation strategy that employs peptide nucleic acid (PNA)−peptide conjugates as linkers for the direct and reversible PEGylation of DNA. PNAs are nucleic acid analogues that contain a peptide backbone and can hydrogen bond to cDNA (or RNA) via either conventional Watson−Crick base pairing in the antiparallel direction or Hoogsteen base pairing in the parallel direction. Because PNAs contain a neutral backbone, the PNA−DNA duplex is more stable than the corresponding DNA−DNA duplex, and PNAs can interact with one strand of double-stranded DNA by strand invasion (*33*−*35*). Symmetric PNA oligomers linked by a flexible spacer (PNA "clamps"; Figure 1) form stable PNA−DNA−PNA triplexes (*35*−*38*). PNA clamp binding to plasmid DNA outside of the coding region does not interfere with transcriptional activity and has been previously used to label plasmids with fluorophores and other tags that enable DNA tracking or targeting during gene delivery (*39, 40*).

Our formulation design scheme (Figure 1) employs PNA clamps as linkage points for the direct functionalization of plasmid DNA with protease-sensitive peptides and PEG. The peptide linker serves as a cleavable bridge that will allow cell-triggered dePEGylation (by protease secretion), which we expect should promote improved DNA internalization. Furthermore, because PEG prevents polyplex aggregation, we expect that prePEGylation of the DNA followed by polyplex formation should enable the creation of homogeneous single plasmid complexes, without compromising the efficiency of polycation−DNA compaction. Precise particle size control during formulation can be beneficial in overcoming a variety of physiological barriers such as vascular extravasation (*41*−*45*), interstitial transport (*46, 47*), and cellular internalization (*48*−*53*). For example, studies on the design requirements for effective transcapillary flux of antibody therapies have demonstrated that smaller, positively charged molecules are more efficient at vascular extravasation (*54*−*56*). With respect to interstitial transport, smaller adenoviral particles (∼25 nm) move more efficiently than larger particles (∼100 nm) through multicellular extracellular matrix spheroids (*47*). Furthermore, previous studies have suggested that particles 50 nm or less are optimal for receptor-mediated endocytosis (*57, 58*). Coincidentally, DNA polyplexes containing a single plasmid are believed to be approximately 30 nm in diameter (*59*). Hence, methods to form homogeneous, small particles have clear advantages with respect to in vivo efficacy, as well as from a manufacturing/patient-dosing perspective.

In this work, we demonstrate the development of DNA-PNA-peptide-PEG (DP3) conjugates and observe the corresponding effect of DNA prePEGylation on polyplex formation and in vitro bioactivity. The starting components for these polyplexes (DP3 conjugates and PEI) represent stable compounds, and the methods for polyplex formation are amenable to bedside formulation. Furthermore, with the first demonstration of direct DNA PEGylation for gene therapy, we show that we can form 30−50 nm particles of a homogeneous size distribution that have improved nucleic acid packaging efficiency, low cytotoxicity, and activity that is independent of free PEI in solution. Proof-of-principle of our PNA-based design will lay the foundation for its exploration in vivo.

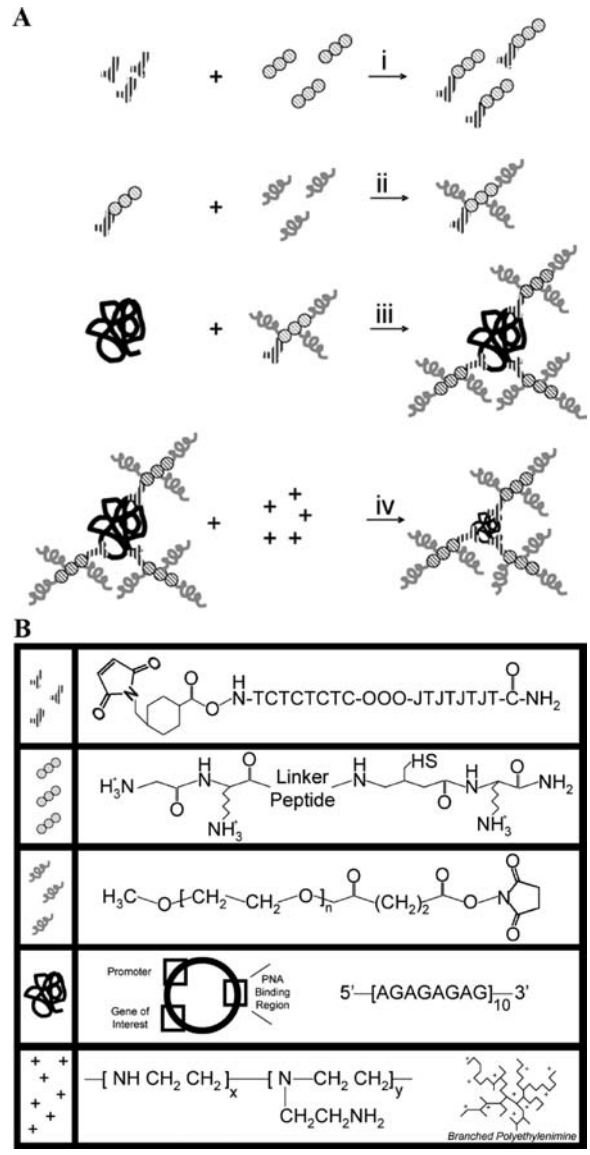


Figure 1. PNA-based vehicle formulation design. (A) The linker peptide (circles; see detailed expansion in [B]) was bound to the PNA ("Y"s) by the reaction of the cysteine thiol with the terminal PNA maleimide (i). Then, succinimidyl-PEG chains (gray squiggles) were bound to the amines on the peptide N-terminus and lysine residues (ii). The PNA-peptide-PEG conjugates were purified and then bound to GWiz plasmid DNA (black scribble) via sequence-specific hydrogen bonding interactions (iii). The final DNA-PNA-peptide-PEG (DP3) conjugate was purified, and 25 kDa branched PEI (+) was added to complex the DNA (iv). (B) Detailed structures of the components of the DP3 conjugates. Figure not to scale.

MATERIALS AND METHODS

Reagents and Materials. PNA clamps (AlexaFluor488/AlexaFluor555/maleimide-TCTCTCTC-OOO-JTJTJTJT-$CONH_2$ (*34*), where O = 8-amino-3,6-dioxaoctanoic acid and J = pseudoisocytosine) with either an AlexaFluor488, AlexaFluor555, or maleimide terminus were synthesized by solid-

phase synthesis and HPLC-purified to >95% purity by Panagene (Daejeon, Korea). The GWiz green fluorescent protein (GFP)-expressing plasmid containing 10 sequential copies of the repeated PNA binding sequence 5′-AGAGAGAG-3′ was purchased from Genlantis (San Diego, CA) (see Supporting Information Figure 1D for the sequence of the PNA binding region), and the non-PNA binding plasmid (SV40-Renilla) was purchased from Promega (Madison, WI). Both plasmids were amplified in *E. coli* and purified with a Qiagen MegaPrep kit. Briefly, competent DH-5α cells were transformed with the appropriate plasmid and cultured overnight in Lysogeny Broth. Cells were lysed and the amplified plasmid was purified and recovered in accordance with the manufacturer's protocols. A 22 amino acid linker peptide (NH_2-*GKG**GPQG/IWGQ**GRGD-SPGDRCK*-$CONH_2$) was synthesized by solid-phase synthesis and HPLC-purified to >95% by Global Peptide Services (Huntsville, AL). This peptide contains an MMP-1-sensitive region (boldfaced with the exact cleavage site indicated by a backslash) (*60*). α-Methoxy, ω-succinimide poly(ethylene glycol) (MW = 5000 g/mol) was synthesized, purified, and analyzed by gel permeation chromatography (GPC) and Fourier transform infrared spectroscopy (FTIR) by Polymer Source, Inc. (Montreal, Canada). 25 kDa branched poly(ethylenimine) (PEI) was purchased from Sigma (St. Louis, MO). Polymer molecular weight was validated by light scattering and GPC by the manufacturer.

Conjugate Development and Particle Formation. *PNA-Peptide-PEG Conjugate Formation.* To form PNA−peptide conjugates, 2 μM of the maleimide-terminated PNA and 0.2 μM of peptide were incubated in 100 μL of 20 mM 4-(2-hydroxyethyl)-1-piperazineethanesulfonic acid (HEPES) buffer (pH 7.4) overnight at 37 °C. A 10-fold excess of PNA was used in this reaction to minimize the presence of unreacted peptide at the end of the reaction. To derivatize the PNA−peptides with succinimide-terminated PEG, 1.25 μL of 4 mM PEG in 20 mM HEPES buffer (pH 7.4) was added to the PNA−peptide reaction mixture (corresponding to a 250-fold molar excess), and the resulting solution was incubated overnight at 37 °C. Following this reaction, unreacted components were removed via centrifugal filtration with a YM-10 centrifugal filtration column (10 000 Da molecular weight cutoff [MWCO], Millipore, Billerica, MA). For this process, the membrane was first primed with a 500 μL distilled water rinse at 12 000 *g* for 30 min in a table-top centrifuge. Following this rinse, sample was added to the column and centrifuged for 30 min at 12 000 *g*. Three separate wash steps followed; in each wash, 500 μL of distilled water was added to the column and subsequently centrifuged for 30 min at 12 000 *g*. To collect the retentate at the end of the washes, the membrane was inverted into a clean tube, and 20 μL of distilled water was added to the membrane. The column was then centrifuged for 2 min at 12 000 *g*. The final recovered volumes were raised to 100 μL by the addition of 20 mM HEPES buffer (pH 7.4).

Estimation of PNA−DNA Hybridization Efficiency. 0.6 pM of the GWiz PNA-binding plasmid or of the SV40-Renilla non-PNA-binding plasmid was incubated with 0−200 pM of AF-PNA in a 10 mM HEPES/50 mM NaCl buffer (pH 7.4) overnight at 37 °C. After incubation, the samples were analyzed by gel electrophoresis on a 1% agarose gel, and the gel was stained with a 1% ethidium bromide solution and visualized on a Bio-Rad Gel Doc XR (Hercules, CA).

DP3 Formation by Hybridization of DNA with PNA-Peptide-PEG Conjugates. 6 pM of DNA was added to the purified PNA-peptide-PEG conjugates in a total volume of 100 μL of 20 mM HEPES buffer (pH 7.4), and the mixture was allowed to incubate overnight at 37 °C (*39*). Unbound PNA-peptide-PEG was removed via centrifugal filtration by a similar procedure as that described for the PNA-peptide-PEG conjugates; a YM-100 column was used (100 000 MWCO, Millipore), and spin times were reduced to 10 min per spin to prevent membrane clogging.

Assessment of DP3 Conjugate Stoichiometry. Tryptophan fluorescence analyses were performed on a Jasco FP-6500 spectrofluorimeter (excitation $\lambda = 280$ nm; emission $\lambda = 350$ nm). An ETC-273T temperature controller and a Julabo AWC-100 water chiller enabled sample analysis to be done at 25 °C. For analysis of peptide standards, peptide was dissolved in a 20 mM HEPES buffer (pH 7.4) at the indicated concentrations and assessed fluorimetrically.

UV/vis spectroscopy measurements were performed on a Nanodrop ND 1000 spectrophotometer (ND-1000) (Thermo Scientific - Nanodrop Products, Wilmington, DE). DNA concentrations were determined as per the manufacturer's protocol. Briefly, 2 μL of sample were placed onto the sample platform. The absorbances at 230 nm, 260 nm, and 280 nm were analyzed, and a corresponding concentration and measure of DNA purity were assessed.

Attenuated total reflectance FTIR (ATR-FTIR) analyses were performed on a Spectrum One FTIR Spectrometer (Perkin-Elmer, Waltham, MA). Ten μL of each sample were dried with air onto a diamond ATR crystal, and 200 runs per sample were subsequently conducted under ambient conditions. Spectra were acquired between 4000 cm^{-1} and 1000 cm^{-1}.

DNA Complexation. 25 kDa PEI solutions were added to DP3 conjugate solutions or free plasmid solutions at varying N/P (PEI nitrogen/DNA phosphate) ratios, following existing protocols (*5*). Briefly, a 500 μL PEI solution was added to a 500 μL DP3 (or free plasmid) solution containing 20 μg of plasmid. The PEI solution was added to the DNA solution in a dropwise fashion while vortexing, and the combined solutions were allowed to form complexes at room temperature for 10 min prior to sample analysis.

DNA Complex Purification. Free PEI was removed from the suspensions of PEI complexes by centrifugal filtration of the complex suspensions with a YM-100 filter. First, the filters were primed with 500 μL of double-distilled water (ddH_2O) for 5 min at 12 000 *g*. Then, 500 μL of complex suspension was added and centrifuged at 100 *g* for 30 min. One 500 μL wash was performed with ddH20. Complex sizes were assessed via dynamic light scattering (DLS) prior to and following purification.

Polyplex Characterization. *Dynamic Light Scattering (DLS) and Zeta Potential Analyses.* DLS and zeta potential analyses were performed at a 90° angle with a Brookhaven (Holtsville, NY) BI9000AT correlator and a Lexel (Fremont, CA) model 95 argon ion laser operating at 488 nm. All measurements were performed at 20 ± 0.2 °C, with sample temperature controlled by an external circulating bath. For DLS, the CONTIN algorithm was used to analyze the autocorrelation functions and estimate the mean diameters and size distributions of the complexes formed. The measured effective hydrodynamic diameters for each sample run were the average values from a total of 5 runs of 2 min each, while the measured zeta potentials for each sample run were the average of 10 runs of 2 min each.

Atomic Force Microscopy. Atomic force microscopy (AFM) was performed on a Nanoscope IIIa atomic force microscope (Digital Instruments, Santa Barbara, CA) used in conjunction with an MLCT cantilever tip (60 nm backside gold coating, 3 μm tip, Veeco, Santa Barbara, CA). Contact-mode AFM images were collected under ambient conditions at approximately 25 °C. Samples were prepared by the complex formulation procedure described above. 50 μL of complex suspension containing 1 μg of DNA was dried for 24 h onto a 77 mm^2 mica substrate. Height and deflection error modes were used for imaging, with scan rates of ∼1 Hz. Image processing was performed using the Nanoscope IIIa software package.

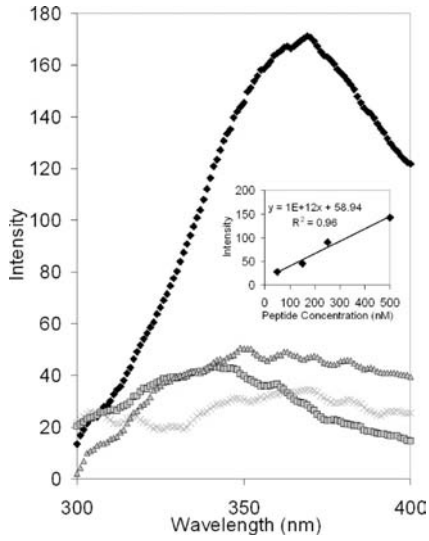


Figure 2. Intrinsic fluorescence of the DNA-PNA-peptide-PEG conjugate. The purified DP3 conjugates and conjugates prepared identically but in the absence of one component were analyzed via intrinsic fluorescence spectroscopy to detect tryptophan residues present in the linker peptide (excitation 280 nm; emission 350 nm). The DP3 conjugate (black diamonds) exhibited significant fluorescence at 350 nm, indicative of the presence of the linker peptide. In contrast, samples prepared in the absence of DNA (gray squares), PNA (gray "X"s), or peptide (gray triangles) had minimal fluorescence at the same wavelength. Inset: the fluorescence emission peak intensities of various linker peptide solutions were analyzed (excitation 280 nm; emission 350 nm).

Scanning Electron Microscopy. Scanning electron microscopy (SEM) was performed on a Hitachi S-4700 field emission scanning electron microscope (Pleasanton, CA). Fifty μL of complex suspension containing 1 μg of DNA was prepared as described and dried overnight onto a 127 mm^2 glass coverslip, fixed with glutaraldehyde, and treated with osmium tetroxide via standard protocols. The complexes were then sputtered with gold, and the sputtered samples were fixed in the sample holder and placed in the vacuum chamber of the microscope under low vacuum (10^{-3} Torr) for imaging.

Ethidium Bromide Exclusion Assays and Nuclease Protection Assays. Ethidium bromide exclusion assays were performed by agarose gel electrophoresis. Complexes were formed as described, over a range of N/P ratios from 0 to 10. Ten μL aliquots of each sample were analyzed on 1% agarose gels formed in the presence of 1% ethidium bromide, and the resulting gels were imaged as described.

Nuclease protection assays were conducted by a modification of existing protocols (*22*). Briefly, 10 μL of 100% mouse serum (Sigma) was added to 10 μL of complex suspension (200 ng of DNA), and the mixture was incubated for 4 h at 37 °C. Subsequently, termination buffer (labeled STOP) containing 38 mM EDTA, 154 mM NaOH, and 38 mM NaCl was added to stop the serum degradation process, and the resulting mixture was incubated for 15 min at 4 °C. DNA was then displaced from the complexes by incubation with 1 mg/mL heparin (stock solution of 10 mg/mL) (Sigma). Samples were then analyzed by agarose gel electrophoresis as described.

In Vitro Transfection and Viability Assays. *Cell Culture.* Chinese hamster ovary (CHO) cells (ATCC, Manassas, VA) were maintained in a humidified, 37 °C atmosphere in Dulbecco's modified eagle medium (DMEM) containing 10% fetal bovine serum (FBS), 100 μg/mL penicillin, and 100 μg/mL streptomycin (Invitrogen).

Transfection. For transfection, 200 000 cells were seeded into each well of a 6 well dish and the cells were grown overnight. Immediately prior to transfection, the growth medium was removed and replaced with 2 mL of serum-free Opti-Mem medium (Invitrogen). 500 μL of complex suspension (containing 10 μg DNA) was formed and added to the cells in a dropwise manner. The complexes were then allowed to incubate with the cells in serum-free medium for 3 h. At that time, the serum-free medium was removed, the cells were washed in PBS, and growth medium was added. The cells were analyzed by flow cytometry and fluorescence microscopy 24 h after transfection. For flow cytometry, the cells were trypsinized, washed in 0.1% BSA, and reconstituted in PBS for analysis with a BD Biosciences FACSCalibur cytometer (San Jose, CA). For fluorescence microscopy, live cells were imaged with a Leica microscope according to established protocols.

Viability. For cell viability assays, an ethidium homodimer dye (Invitrogen) was used to stain for dead cell nuclei. Four microliterse of a 2 mM dye solution was added to the transfected cell cultures, and the cells and dye were incubated for 10 min at room temperature. The cells were subsequently imaged by fluorescence microscopy.

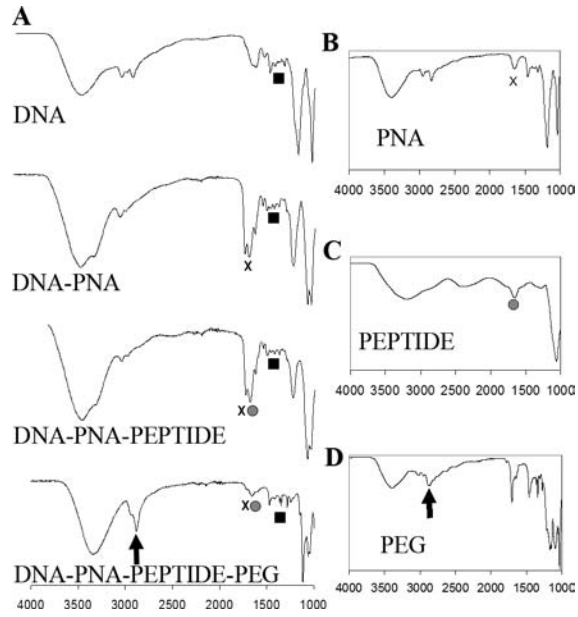


Figure 3. ATR-FTIR characterization of the DP3 conjugates. (A) ATR-FTIR spectra of the GWiz plasmid (top), the DP3 conjugate (bottom), and conjugates lacking one or more conjugate components (middle). The main absorption bands of DNA (black squares) are as follows: 1063 cm^{-1} (symmetric stretching vibration of the phosphate groups), 1222 cm^{-1} (antisymmetric stretching vibration of the phosphate group), 1017 cm^{-1} (vibration of C═N of ribose), and 1693 cm^{-1} (vibrations of C6═O of guanine and C4═O of thymine). Amide bonds, found in both PNA (B) and peptide (C), have an expected peak at approximately 1630 cm^{-1} (black "*x*"s in [A] and [B] and gray circles in [A] and [C]). Peaks attributable to PEG (D) are observed at 2890 cm^{-1} (black arrows in [A] and [D]), indicative of the $-CH_2$-stretching vibrations.

RESULTS

DP3 Conjugate Formation. *PNA-Peptide-PEG Conjugate Formation.* The PNA-peptide-PEG conjugates were formed by the stepwise reaction of the individual components, as summarized in Figure 1. In the first step, PNA−peptide conjugates were formed by the reaction of the N-terminal PNA maleimide groups on the maleimide-terminated PNAs with the cysteine thiol residues near the C-terminus of the peptides. Next, the N-terminus and the two lysine side-chain amine groups on the peptides were reacted with succinimide-terminated PEG. The PNA-peptide-PEG conjugates were purified by centrifugal microconcentration, and the stoichiometry of these conjugates was assessed by fluorescence spectroscopy and ATR-FTIR, as discussed below.

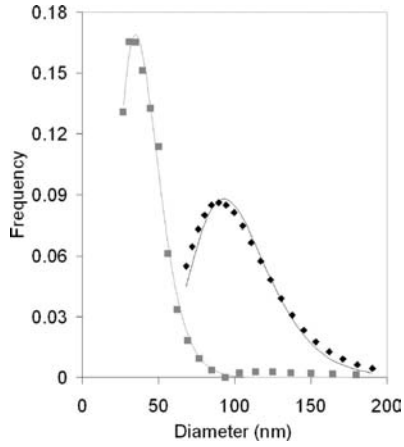


Figure 4. PEI−DP3 and PEI−DNA polyplex size distributions. PEI−DP3 (gray squares) and PEI−DNA (black diamonds) polyplexes were formed at an N/P of 10 and analyzed via DLS. The resulting autocorrelation functions were transformed into the relevant size distributions by the CONTIN algorithm.

PNA-Peptide-PEG Hybridization with Plasmid DNA. To estimate the PNA-peptide-PEG:DNA incubation ratio that would enable saturation of the DNA, the GWiz PNA-binding plasmid and the SV40-Renilla non-PNA-binding plasmid were incubated with AlexaFluor488-labeled PNA (AF-PNA) over a range of ratios to enable PNA strand invasion and PNA−DNA hydrogen bonding. The resulting mixtures were analyzed by gel electrophoresis (Supporting Information Figure 1). An approximate 3-fold molar site excess of AF-PNA:PNA binding sites (equal to a 30-fold molar excess of AF-PNA:GWiz) was effective at achieving saturation of GWiz DNA with PNA, consistent with previous work (*39*), whereas no binding of AF-PNA to the SV40-Renilla DNA was observed.

To form the hybridized DP3 conjugates, the GWiz PNA-binding plasmid was incubated with the PNA-peptide-PEG conjugates, and the DP3 conjugates were purified by centrifugal microconcentration. Intrinsic fluorescence spectroscopy and ATR-FTIR spectroscopy were used to analyze the stoichiometry of the DP3 conjugates. The peptide incorporated into the conjugates included a tryptophan residue whose fluorescence enabled analysis of peptide concentration. Figure 2 illustrates the fluorescence emission spectrum of the DP3 conjugate, as well as the spectra for various control samples that were prepared identically but in the absence of one of the conjugate components. The observed fluorescence of the DP3 conjugate corresponded to a peptide concentration that was a 7-fold molar excess over the concentration of the plasmid (assessed by UV/vis spectroscopy; data not shown), suggesting that PNA-peptide-PEG conjugates were bound to approximately 70% of the available PNA binding sites on the plasmid. Samples prepared identically, but in the absence of peptide, exhibited minimal fluorescence, as expected; samples prepared in the absence of PNA also exhibited minimal fluorescence, suggesting that PNA-peptide-PEG hybridization to the plasmid was mediated by PNA−DNA interactions. Samples prepared in the absence of DNA exhibited minimal fluorescence and provided validation of the efficiency of the purification process.

ATR-FTIR spectroscopy was used as a secondary means of conjugate validation (Figure 3). The DP3 sample spectrum exhibited characteristic peaks indicative of DNA, PNA, peptide, and PEG (Figure 3A, bottom). The DNA spectrum (Figure 3A,

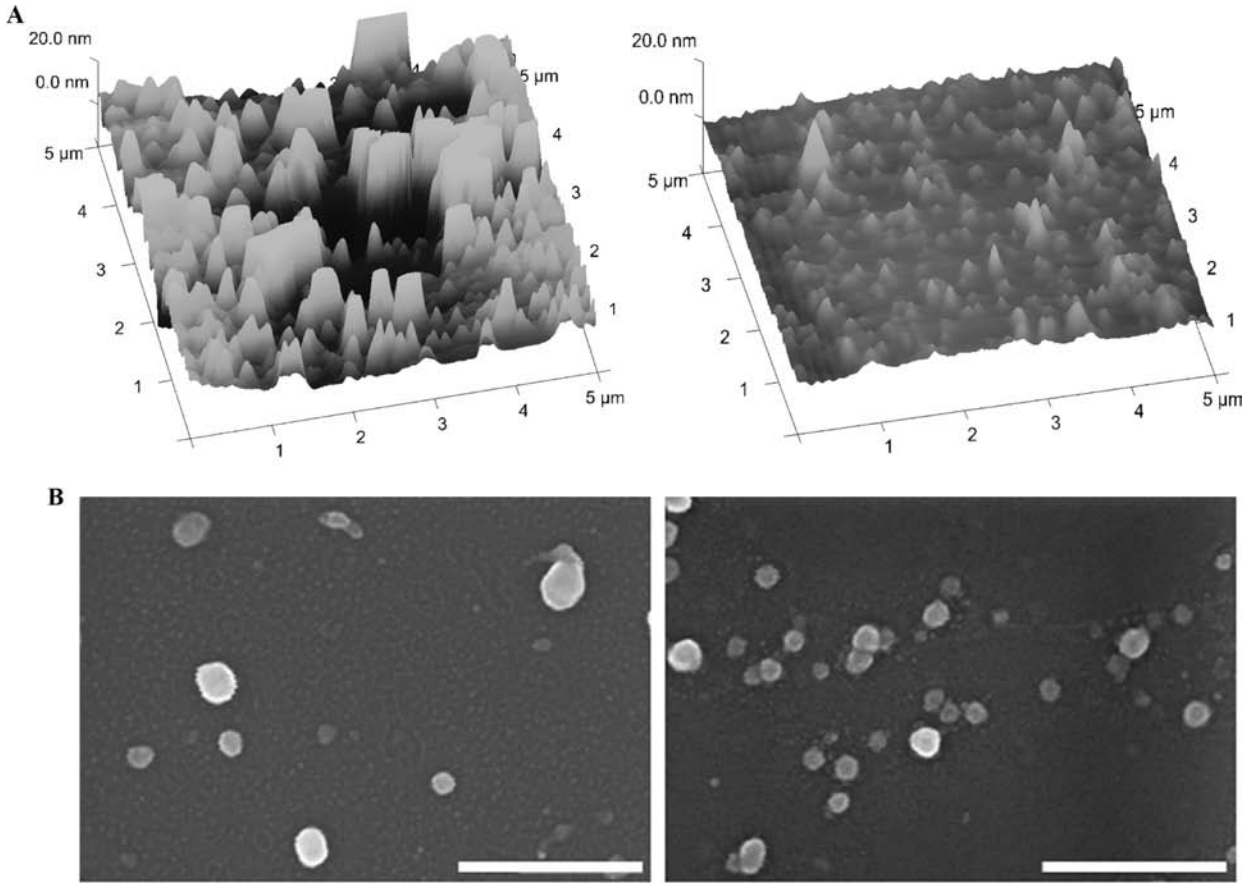


Figure 5. PEI−DP3 and PEI−DNA polyplex shape and size. (A) AFM images of PEI−DNA (left) and PEI−DP3 (right) complexes dried on a mica strip and imaged in contact mode (N/P = 10). (B) SEM images of PEI−DNA (left) and PEI−DP3 (right) complexes dried onto glass substrates (N/P = 10). Scale bar = 500 nm.

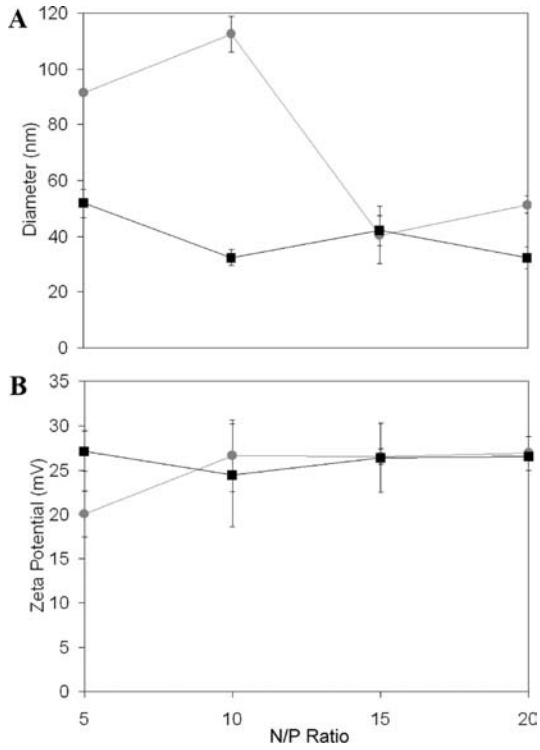


Figure 6. PEI−DP3 and PEI−DNA polyplex characterization by light scattering. (A) DLS was used to assess PEI−DP3 (black squares) and PEI−DNA (open circles) polyplex diameters at N/P = 5−20. Number averaged distributions obtained with the CONTIN algorithm were used to calculate average polyplex diameters. Statistically significant differences are noted at N/P ratios of 5 ($p = 0.006$) and 10 ($p = 0.021$). (B) Phase analysis light scattering was employed to determine the zeta potentials of polyplexes prepared at the same N/P ratios. All data represent the mean values obtained from three separately prepared and analyzed samples per data point. Error bars represent one standard deviation from the mean.

top) had characteristic vibrational signals in the 1000−1500 cm^{-1} region. The PNA and the peptide spectra both exhibited characteristic amide bond signals (1630 cm^{-1}), as expected (Figure 3B and C), whereas the PEG spectrum had a signal at around 2800 cm^{-1}, indicative of the carbon−carbon vibrational stretching along the backbone of the polymer (Figure 3D). In contrast, conjugate samples that were missing one or more of the conjugate components exhibited spectra missing the corresponding signals (Figure 3A, top and middle). Notably, the presence of the characteristic PEG signal only in the DP3 conjugate sample suggested direct DNA prePEGylation.

Physical Characterization of DNA Complexes. *Complex Size and Charge.* The DP3 conjugates and unmodified plasmids were self-assembled with 25 kDa PEI, and the resulting complexes were analyzed by DLS. As shown in Figure 4, the PEI−DP3 complexes were smaller and less heterogeneous than the PEI−DNA complexes at an N/P ratio of 10. By a log-normal statistical fit, the mean of the PEI−DP3 size distribution was reduced in comparison with that of the PEI−DNA size distribution from approximately 100 to 40 nm; the standard deviation of the PEI−DP3 size distribution was reduced by half (from 28 to 14 nm) in comparison with that of the PEI−DNA size distribution. As previously mentioned, the wide standard deviation of PEI−DNA complex diameters is typical for these systems, and is a direct consequence of the multimolecular aggregation that occurs during the formulation process. To further examine this observation, AFM and SEM were utilized to characterize the PEI−DP3 and PEI−DNA complexes (Figure 5A and B). Complex suspensions were dried onto AFM and SEM substrates and the substrates were subsequently analyzed.

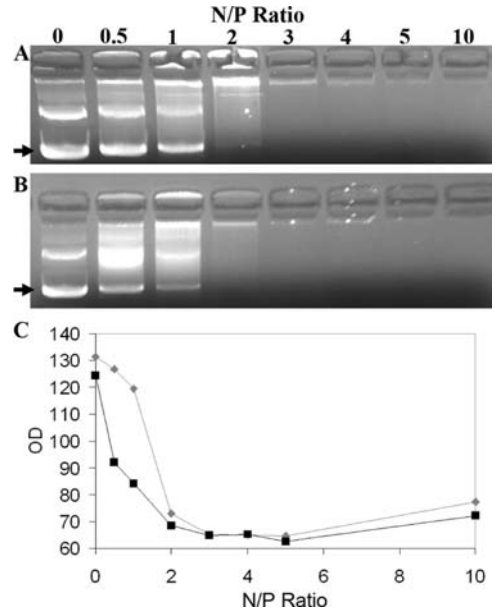


Figure 7. Assessment of complexation efficiency by ethidium bromide exclusion assays. PEI−DNA (A) and PEI−DP3 (B) polyplexes were prepared and analyzed by agarose gel electrophoresis at N/P ratios ranging from 0 to 10. The bands corresponding to supercoiled plasmid DNA are indicated (arrows). (C) Optical density measurements of the supercoiled DNA band for PEI−DP3 (black boxes) and PEI−DNA (white diamonds) polyplexes for the gel shown in A. The trends in optical density were consistent in replicates of the same experiment. Other bands on the gel include open circular and nicked plasmid DNA, as well as DNA aggregates found in the wells of the gel.

AFM and SEM images of the complexes supported the finding that smaller and less heterogeneous complexes formed when the DNA was directly PEGylated prior to complexation.

The size of PEI−DNA complexes depends upon the N/P ratio at which they are formed because of the dependence of colloidal stability on surface charge (*61*). In contrast, it was expected that DNA prePEGylation would reduce this N/P dependence by steric stabilization of the PEI−DP3 complexes. DLS and zeta potential analyses were therefore used to assess the mean complex size and zeta potential as a function of the N/P ratio (Figure 6). As predicted, the PEI−DP3 complexes had similar average diameters, regardless of the amount of polycation introduced, whereas the PEI−DNA complexes were larger at lower N/P ratios (Figure 6A). Zeta potential analyses (Figure 6B) revealed no significant differences between the trends for the PEI−DP3 and PEI−DNA samples.

Complexation Efficiency and Nuclease Protection. Because polymer PEGylation has been shown to destabilize polyplexes (*4, 25, 26, 28−30*), the complexation efficiency and nuclease protection of the PEI−DP3 complexes were explored. Ethidium bromide exclusion assays revealed that complexation efficiency increased as a consequence of the DNA prePEGylation strategy employed with the DP3 conjugate (Figure 7). In this assay, any reduction in DNA band intensity is a consequence of the complexation process excluding ethidium bromide from the nucleic acid, inhibiting its ability to intercalate and fluoresce. At low N/P ratios, the band intensity (as quantified via optical density measurements) for supercoiled DP3 was lower than that for DNA (Figure 7A and B), suggesting that PEI was able to more effectively condense the PEGylated nucleic acid.

Nuclease protection assays were used to examine the resistance of DNA within the PEI−DP3 complexes to serum nucleases. Consistent with the finding that the PEI−DP3 complexes were packaged efficiently at N/P ratios greater than 3, these complexes were also able to protect DNA from

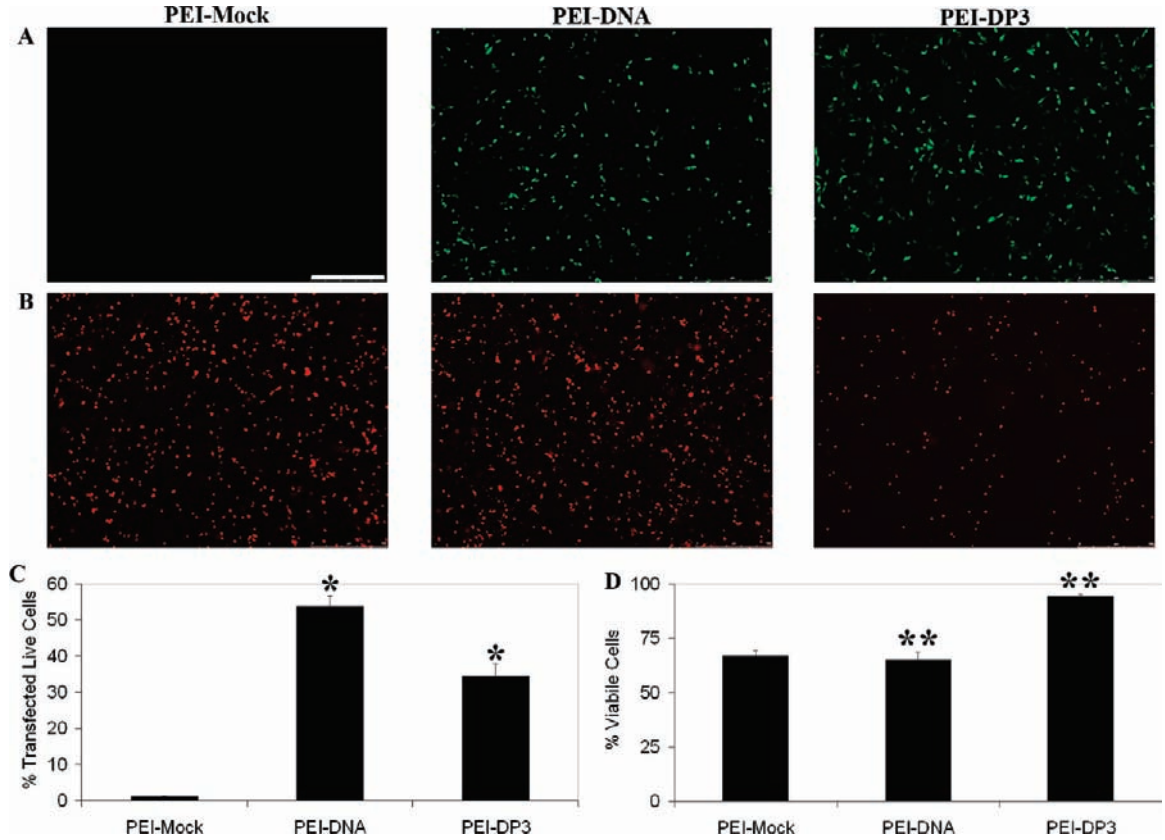


Figure 8. Transfection efficiency and cytotoxicity assays. The transfection efficiencies of PEI-Mock (complexes made with PEI and a non-GFP-expressing plasmid), PEI−DNA, and PEI−DP3 complexes formulated at N/P = 10 were assessed in CHO cells 24 h post-transfection by fluorescence microscopy (A) and flow cytometry (C) to detect GFP fluorescence. The scale bar (shown in [A]) = 500 μm. The data in (C) represent the mean values obtained from three separate transfection experiments, and the error bars represent one standard deviation from the mean. Statistically significant differences were observed between the indicated samples (p [*] = 0.038). (B) The cytotoxicities of the same complexes were evaluated with a ethidium homodimer stain and fluorescence microscopy (B). Quantification was performed by image analysis (D), and [**] indicate a statistically significant difference between the indicated samples (p [**] = 0.0001).

enzymatic degradation (Supporting Information Figure 2). Previous studies have shown the effectiveness of PEI at achieving this goal (*62, 63*).

Complex Bioactivity. *Transfection Efficiency and Cell Viability.* To determine whether DNA prePEGylation and the resulting alterations in complex size influenced cellular transfection, the PEI−DP3 and PEI−DNA complexes were used to transfect CHO cells. After 24 h, a reduction in the transfection efficiency was observed when the PEI−DP3 complexes were used for transfection in comparison with when the PEI−DNA complexes were used (PEI-Mock complexes containing a non-GFP-expressing plasmid were also examined to account for any nonspecific autofluorescence associated with PEI) (Figure 8A and C). Similar trends were observed when transfection was assessed by flow cytometry and image analysis. However, while the transfection efficiency was somewhat lower with PEI−DP3 than with PEI−DNA, the cytotoxicity of the PEI−DP3 complexes was significantly reduced relative to those of both the PEI-Mock and the PEI−DNA complexes (Figure 8B and D).

Complex Purification Effects. Previous work has shown that the in vitro cytotoxicity of PEI−DNA formulations depends largely upon the excess PEI that remains in solution following complexation, and thus can be reduced through complex purification via size exclusion chromatography (*64*). To examine the effects on PEI−DP3 transfection efficiency and cytotoxicity following free PEI removal, centrifugal filtration was used to purify the complexes. As expected, a reduction in cytotoxicity was observed for the PEI-Mock and PEI−DNA complexes following purification (Figure 9). However, the PEI−DP3 complexes retained their low level of cytotoxicity following purification, suggesting that the amount of free PEI in solution following complexation was significantly reduced in these formulations in comparison with conventional PEI−DNA formulations.

While purification of PEI−DNA complexes lowers their cytotoxicity, previous work has shown that the removal of the excess PEI in solution reduces transfection efficiency (*64*). This observation was previously attributed to the role of free PEI in solution in assisting endosomal buffering following cellular internalization (*64*). This particular point is of concern when considering the potential in vivo applicability of PEI−DNA complexes, since the in vitro concentration of free PEI is not an appropriate reflection of the physiological situation. Figure 10 illustrates that the transfection efficiency of the PEI−DP3 complexes increased following purification, whereas that of the PEI−DNA complexes decreased. These changes resulted in transfection levels that were approximately 12% higher when PEI−DP3 was used for transfection as opposed to PEI−DNA (as confirmed by both image analysis [data not shown] and flow cytometry).

DISCUSSION

PEI-based formulations are highly efficient in vitro gene delivery vehicles, in large part because of their capacity to induce endosomal release by pH-buffering (*8*). Unfortunately, the in vivo applicability of these formulations is questionable, given the inherent cytotoxicity of PEI (*64*) and challenges in formulation. In particular, the process of multimolecular aggregation during polyplex formation is a significant issue that results in highly heterogeneous complexes at sizes larger than the optimum for either receptor-mediated internalization or for effective in vivo

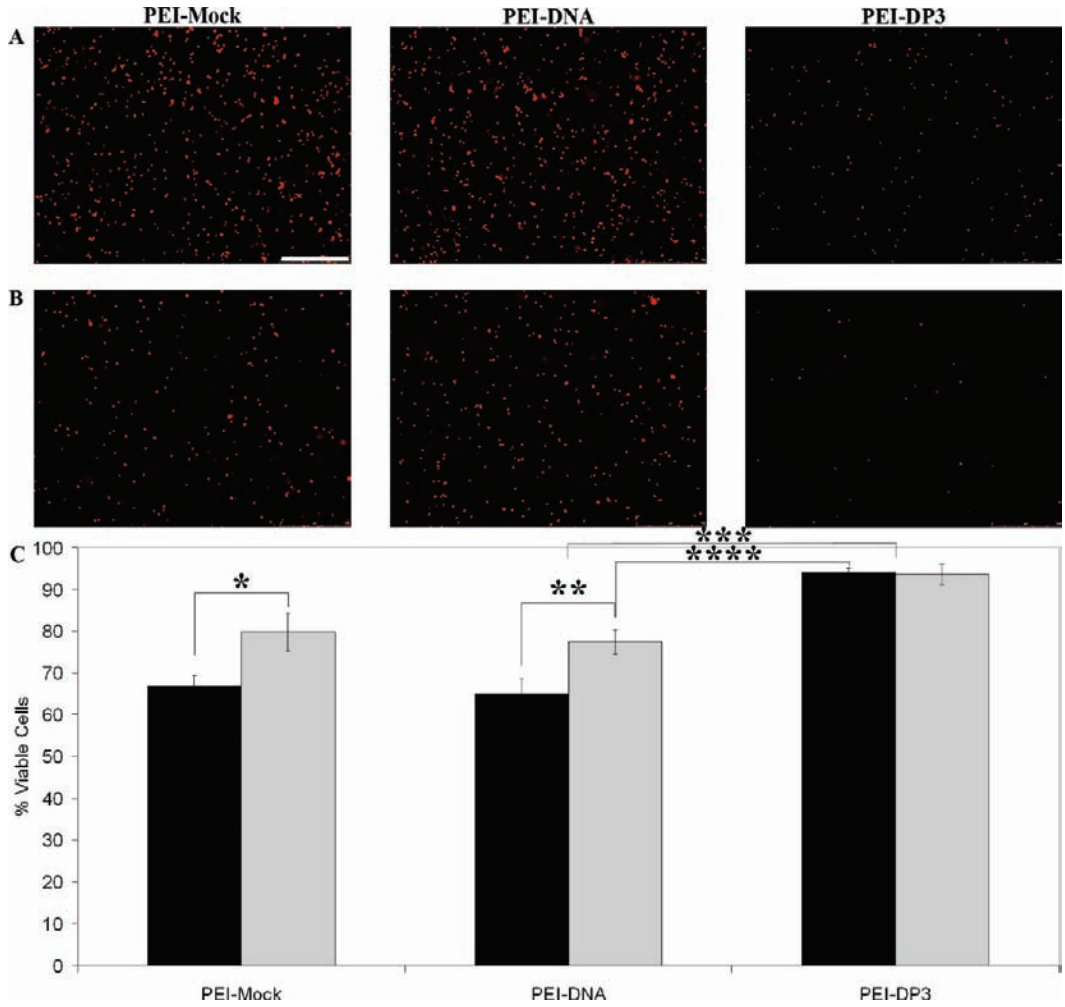


Figure 9. Effect of complex purification on cytotoxicity. unpurified (A) and purified (B) PEI-Mock, PEI−DNA, and PEI−DP3 complexes were used at N/P = 10 to transfect CHO cells, and the cytotoxicity of each formulation was analyzed by ethidium homodimer staining and fluorescence microscopy. Quantification for the unpurified (black bars) and purified (gray bars) formulations was performed by image analysis (C) and indicated statistically significant differences between the indicated samples (p [*] = 0.002; p [**] = 0.02; p [***] = 0.00005; p [****] = 0.00005). All data represent the mean values obtained from three separate transfection experiments, and the error bars represent one standard deviation from the mean. The scale bar (shown in [A] = 500 μm).

administration. Furthermore, the in vitro activity of PEI-based formulations depends upon the presence of free PEI at levels higher than would be feasible in vivo (*64*). To address these issues in PEI polyplex formulation, a novel strategy for DNA prePEGylation has been explored in this work with the goals of reducing aggregation during formulation and producing less heterogeneous and more efficiently packaged polyplexes.

With this aim in mind, PNA-peptide-PEG conjugates were synthesized as the basis for a new class of gene delivery materials. When these PNA-peptide-PEGs were hybridized with DNA, the resulting DP3 conjugates behaved differently than unmodified DNA when they were self-assembled with PEI. The PEI−DP3 complexes were smaller and less heterogeneous than PEI−DNA complexes formulated at the same N/P ratio (Figures 4−6). This observation was confirmed via DLS analysis of particle scattering, as well as by AFM and SEM imaging, which enabled visualization of individual particles. Furthermore, when the N/P ratio was varied, the size of the PEI−DP3 complexes remained constant at ∼30−50 nm, whereas the size of the PEI−DNA complexes was larger at low N/P ratios. Given that DNA polyplexes containing a single plasmid are believed to be approximately 30 nm in diameter (*59*), this result suggested that single plasmid-containing complexes were formed with the DP3 conjugate. This effect was attributed to steric stabilization of the PEI−DP3 complexes by DNA prePEGylation. However, unlike typical surface PEGylation strategies which introduce a brush layer of PEG, the observed shifts in the complex size distribution were the result of a small number of PEG molecules bound to each plasmid through the PNA−peptide linker (∼10−20 PEG molecules, assuming the PNA−peptides were saturated with PEG). As a result, PNA-based DNA prePEGylation did not produce measurable effects on polyplex zeta potential (Figure 6B). Furthermore, the PEI−DP3 complexes did not exhibit significant improvements in salt stability in comparison with PEI−DNA complexes, presumably because a large amount of their surface area was not covered by PEG (data not shown).

Although polymer PEGylation has been shown to destabilize polyplexes (*4, 25, 26, 28−30*), the complexation efficiency and nuclease protection of the PEI−DP3 complexes were not adversely affected by DNA prePEGylation (Figure 7 and Supporting Information Figure 2). To the contrary, ethidium bromide exclusion assays suggested that PEI formed tighter complexes at low charge ratios with the DP3 conjugates than with DNA, suggesting that more polycation was able to bind per DP3-contained plasmid. With more polycation per plasmid, less free PEI would remain in solution. This result would be highly desirable from a cytotoxicity perspective, since the presence of free polycation in solution has been shown to contribute to cell death (*64*). Furthermore, it was consistent with our findings on the cellular activity of the PEI−DP3 complexes (discussed subsequently).

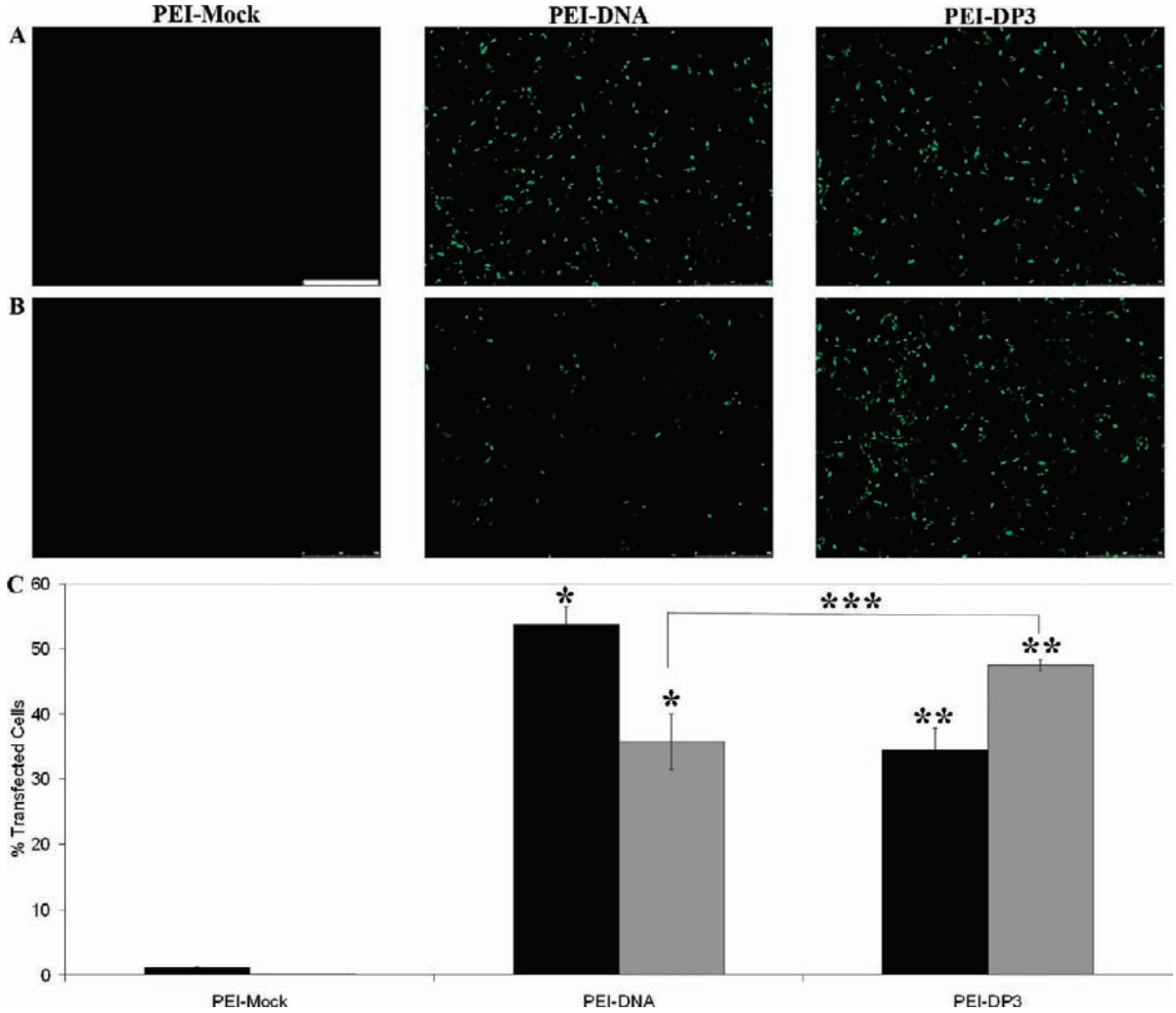


Figure 10. Effect of complex purification on transfection efficiency. Unpurified (A) and purified (B) PEI-Mock, PEI−DNA, and PEI−DP3 complexes were used at N/P = 10 to transfect CHO cells, and the transfection efficiency obtained by each formulation was analyzed by ethidium homodimer staining and fluorescence microscopy. Quantification was performed by flow cytometry for both the unpurified (black bars) and purified (gray bars) formulations (C). All data represent the mean values obtained from three separate transfection experiments, and the error bars represent one standard deviation from the mean. Statistically significant differences were observed between the indicated samples (p [*] = 0.045; p [**] = 0.045; p [***] = 0.046). The scale bar (shown in [A] = 500 μm).

Recognizing the physical differences associated with this proposed formulation, PEI−DP3 complex bioactivity was explored in CHO cells. When transfections were performed with unpurified PEI−DP3 and PEI−DNA complexes (i.e., formulations containing free PEI, as are typically used *7*−*9, 21*), the transfection efficiencies of the PEI−DP3 complexes were slightly lower than those of the PEI−DNA complexes (Figure 8A and C). However, a 30% reduction in cytotoxicity was observed for the PEI−DP3 complexes, most likely as a consequence of the improved complexation brought on by DNA prePEGylation (and the resulting reductions in the levels of free PEI in solution) (Figure 8B and D) (Note: We do not believe that the differences in bioactivity between the two formulations were related to the MMP-1-cleavable peptide incorporated into the PEI-DP3 complexes, given that CHO cells do not express high levels of MMP-1 under the conditions studied.) In an effort to further investigate this effect, free PEI was removed from the formulations and cellular transfections were performed with the purified complexes. The cytotoxicity of the purified PEI−DP3 complexes remained significantly lower than that for the conventional PEI formulations, whereas the transfection efficiency of these complexes increased following purification (Figures 9 and 10). In contrast, the cytotoxicity of the purified PEI−DNA complexes was lower after purification, as expected, and the transfection efficiency of these complexes decreased.

The effects of free PEI removal on the transfection efficiencies achieved by both the PEI−DP3 and PEI−DNA complexes were attributed in part to the known in vitro activity of PEI. The findings with the PEI−DNA complexes were consistent with previous work suggesting that free PEI in solution significantly adds to the activity of PEI formulations by enhancing endosomal buffering (*64*). Thus, the removal of free PEI would be expected to adversely affect transfection efficiency, as was observed. Clearly, a dependence on free polycation to promote efficient gene delivery is not desirable for in vivo applications. The PEI−DP3 complexes appeared to overcome this issue through the inclusion of more PEI per plasmid within the complex, which would enhance the innate endosomal buffering capacity of the complexes. The reasons for the increase in transfection efficiency following the removal of free PEI from the PEI−DP3 formulations were less clear. One possibility is that, with the unpurified PEI−DP3 formulations, the residual PEI in solution blocks polyplex internalization by saturating the available binding sites on the cells.

With a subtle modification of plasmid DNA (the conjugation of ∼10−20 PEG molecules), the complexation and delivery efficiency of a well-known polymer in the gene delivery field has been significantly altered. The effects of DNA prePEGylation on the size distribution, cytotoxicity, and gene delivery efficiency of PEI-based polyplexes are expected to have important impacts

on in vivo activity. As discussed, particles of ~10−100 nm are capable of both avoiding renal clearance (*65*), efficiently exiting the bloodstream, and traveling through interstitial tissues (*46, 47*). Furthermore, the low cytotoxicity and innate activity of the PEI−DP3 complexes in the absence of free PEI should significantly improve in vivo effectiveness. Future work will explore both the dose response of the PEI−DP3 complexes at various N/P ratios in multiple cell lines and the potential benefits of this modified nucleic acid formulation in vivo. The described studies suggest the importance of future efforts focused not only on developing new biomaterials, but also on improving existing systems in the field.

ACKNOWLEDGMENT

M.O.S. thanks the NSF (CBET-0707583), the University of Delaware Research Foundation, the USARO (W911NF-08-1-0241), and the NIH/NCRR INBRE (2 P20 RR016472-07) for financial support for this project. P.G.M. acknowledges fellowship funding from the NSF IGERT Program (DGE-0221651) and from Merck Research Laboratories.

Supporting Information Available: Validation of DNA−PNA conjugation. Nuclease stability of modified and unmodified complexes. This material is available free of charge via the Internet at http://pubs.acs.org.

LITERATURE CITED

(1) Demeneix, B., Behr, J., Boussif, O., Zanta, M. A., Abdallah, B., and Remy, J. (1998) Gene transfer with lipospermines and polyethylenimines. *Adv. Drug Delivery Rev. 30*, 85–95.

(2) Ogris, M., Steinlein, P., Carotta, S., Brunner, S., and Wagner, E. (2001) DNA/polyethylenimine transfection particles: influence of ligands, polymer size, and PEGylation on internalization and gene expression. *AAPS PharmSci 3*, E21.

(3) Garrett, S. W., Davies, O. R., Milroy, D. A., Wood, P. J., Pouton, C. W., and Threadgill, M. D. (2000) Synthesis and characterisation of polyamine-poly(ethylene glycol) constructs for DNA binding and gene delivery. *Bioorg. Med. Chem. 8*, 1779–1797.

(4) Wolfert, M. A. S. L. W. (1996) Atomic force microscopic analysis of the influence of the molecular weight of poly(L)lysine on the size of polyelectrolyte complexes formed with DNA. *Gene Ther. 3*, 269–273.

(5) Boussif, O., Lezoualc'h, F., Zanta, M. A., Mergny, M. D., Scherman, D., Demeneix, B., and Behr, J. P. (1995) A versatile vector for gene and oligonucleotide transfer into cells in culture and in vivo: polyethylenimine. *Proc. Natl. Acad. Sci. U.S.A. 92*, 7297–301.

(6) Ogris, M., Brunner, S., Schuller, S., Kircheis, R., and Wagner, E. (1999) PEGylated DNA/transferrin-PEI complexes: reduced interaction with blood components, extended circulation in blood and potential for systemic gene delivery. *Gene Ther. 6*, 595–605.

(7) Godbey WT, W. K., and Mikos, A. G. (1999) Poly(ethylenimine) and its role in gene delivery. *J. Controlled Release 60*, 149–60.

(8) Boussif, O., Lezoualc'h, F., Zanta, M. A., Mergny, M. D., Scherman, D., Demeneix, B., and Behr, J.-P. (1995) A versatile vector for gene and oligonucleotide transfer into cells in culture and in vivo: polyethylenimine. *Proc. Natl. Acad. Sci. U.S.A. 92*, 7297–7301.

(9) Akinc, A., Thomas, M., Klibanov, A. M., and Langer, R. (2005) Exploring polyethylenimine-mediated DNA transfection and the proton sponge hypothesis. *J. Gene Med. 7*, 657–663.

(10) Brunner, S., Sauer, T., Carotta, S., Cotten, M., Saltik, M., and Wagner, E. (2000) Cell cycle dependence of gene transfer by lipoplex, polyplex and recombinant adenovirus. *Gene Ther. 7*, 401–407.

(11) Chollet, P., Favrot, M., Hurbin, A., and Coll, J.-L. (2001) Side-effects of a systemic injection of linear polyethylenimine-DNA complexes. *J. Gene Med. 4*, 84–91.

(12) Dash, P., Read, M., Barrett, L., Wolfert, M., and Seymour, L. (1999) Factors affecting blood clearance and in vivo distribution of polyelectrolyte complexes for gene delivery. *Gene Ther. 6*, 643–650.

(13) Nishikawa, M., Takemura, S., Takakura, Y., and Hashida, M. (1998) Targeted delivery of plasmid DNA to hepatocytes in vivo: optimization of the pharmacokinetics of plasmid DNA/galactosylated poly(L-lysine) complexes by controlling their physicochemical properties. *J. Pharm. Exp. Ther. 287*, 408–415.

(14) Burke RS, P. S. (2008) Extracellular barriers to in Vivo PEI and PEGylated PEI polyplex-mediated gene delivery to the liver. *Bioconjugate Chem. 19*, 693–704.

(15) Collard, W. T., Yang, Y., Kwok, K. Y., Park, Y., and Rice, K. G. (2000) Biodistribution, metabolism, and in vivo gene expression of low molecular weight glycopeptide polyethylene glycol peptide DNA co-condensates. *J. Pharm. Sci. 89*, 499–512.

(16) Ward, C. M., Read, M. L., and Seymour, L. W. (2001) Systemic circulation of poly(L-lysine)/DNA vectors is influenced by polycation molecular weight and type of DNA: differential circulation in mice and rats and the implications for human gene therapy. *Blood 97*, 2221–2229.

(17) Kircheis, R., Blessing, T., Brunner, S., Wightman, L., and Wagner, E. (2001) Tumor targeting with surface-shielded ligand--polycation DNA complexes. *J. Controlled Release 72*, 165–70.

(18) Brus, C. P. H., Aigner, A., Czubayko, F., and Kissel, T. (2004) Physicochemical and biological characterization of polyethylenimine-graft-poly(ethylene glycol) block copolymers as a delivery system for oligonucleotides and ribozymes. *Bioconjugate Chem. 15*, 677–84.

(19) Merdan, T., K, K., Petersen, H., Bakowsky, U., Voigt, K. H., Kopecek, J., and Kissel, T. (2005) PEGylation of poly(ethylene imine) affects stability of complexes with plasmid DNA under in vivo conditions in a dose-dependent manner after intravenous injection into mice. *Bioconjugate Chem. 16*, 785–92.

(20) Mishra, S., Webster, P., and Davis, M. E. (2004) PEGylation significantly affects cellular uptake and intracellular trafficking of non-viral gene delivery particles. *Eur. J. Cell Biol. 83*, 97–111.

(21) Blessing, T., Kursa, M., Holzhauser, R., Kircheis, R., and Wagner, E. (2001) Different strategies for formation of pegylated EGF-conjugated PEI/DNA complexes for targeted gene delivery. *Bioconjugate Chem. 12*, 529–37.

(22) Bartlett DW, D. M. (2007) Physicochemical and biological characterization of targeted, nucleic acid-containing nanoparticles. *Bioconjugate Chem. 18*, 456–468.

(23) Wagner, E., Zenke, M., Cotten, M., Beug, H., and Birnstiel, M. L. (1990) Transferrin-polycation conjugates as carriers for DNA uptake into cells. *Proc. Natl. Acad. Sci. U.S.A. 87*, 3410–4.

(24) Varga, C. M., Wickham, T. J., and Lauffenburger, D. A. (2000) Receptor-mediated targeting of gene delivery vectors: insights from molecular mechanisms for improved vehicle design. *Biotechnol. Bioeng. 70*, 593–605.

(25) Rimann, M., Luhmann, T., Textor, M., Guerino, B., Ogier, J., and Hall, H. (2008) Characterization of PLL-*g*-PEG-DNA nanoparticles for the delivery of therapeutic DNA. *Bioconjugate Chem. 19*, 548–57.

(26) Choi, Y. H., Liu, F., Kim, J. S., Choi, Y. K., Park, J. S., and Kim, S. W. (1998) Polyethylene glycol-grafted poly-L-lysine as polymeric gene carrier. *J. Controlled Release 54*, 39–48.

(27) Nguyen, H. K., Lemieux, P., Vinogradov, S. V., Gebhart, C. L., Guerin, N., Paradis, G., Bronich, T. K., Alakhov, V. Y., and Kabanov, A. V. (2000) Evaluation of polyether-polyethylenimine graft copolymers as gene transfer agents. *Gene Ther. 7*, 126–138.

(28) Kaminskas LM, B. B., Karellas, P., Krippner, G. Y., Lessene, R., Kelly, B., and Porter, C. J. (2008) The impact of molecular weight and PEG chain length on the systemic pharmacokinetics

of PEGylated poly l-lysine dendrimers. *Mol. Pharm. 5*, 449–463.
(29) Walsh, M., Tangney, M., O'Neill, M. J., Larkin, J. O., Soden, D. M., McKenna, S. L., Darcy, R., O'Sullivan, G. C., and O'Driscoll, C. M. (2006) Evaluation of cellular uptake and gene transfer efficiency of pegylated poly-L-lysine compacted DNA: implications for cancer gene therapy. *Mol. Pharm. 3*, 644–653.
(30) Pun, S. H., and Davis, M. E. (2002) Development of a nonviral gene delivery vehicle for systemic application. *Bioconjugate Chem. 13*, 630–9.
(31) Pun, S. H., and Davis, M. E. (2002) Development of a nonviral gene delivery vehicle for systemic application. *Bioconjugate Chem. 13*, 630–639.
(32) Pun SH, B. N., Liu, A., Jensen, G., Machemer, T., Quijano, E., Schluep, T., Wen, S., Engler, H., Heidel, J., and Davis, M. E. (2004) Cyclodextrin-modified polyethylenimine polymers for gene delivery. *Bioconjugate Chem. 15*, 831–840.
(33) Egholm, M., Christensen, L., Dueholm, K. L., Buchardt, O., Coull, J., and Nielsen, P. E. (1995) Efficient pH-independent sequence-specific DNA binding by pseudoisocytosine-containing bis-PNA. *Nucleic Acids Res. 23*, 217–22.
(34) Zelphati, O., Liang, X., Hobart, P., and Felgner, P. L. (1999) Gene chemistry: functionally and conformationally intact fluorescent plasmid DNA. *Hum. Gene Ther. 10*, 15–24.
(35) Egholm, M., Buchardt, O., Christensen, L., Behrens, C., Freier, S. M., Driver, D. A., Berg, R. H., Kim, S. K., Norden, B., and Nielsen, P. E. (1993) PNA hybridizes to complementary oligonucleotides obeying the Watson-Crick hydrogen-bonding rules. *Nature 365*, 566–8.
(36) Demidov, V. V., Potaman, V. N., Frank-Kamenetskii, M. D., Egholm, M., Buchard, O., Sonnichsen, S. H., and Nielsen, P. E. (1994) Stability of peptide nucleic acids in human serum and cellular extracts. *Biochem. Pharmacol. 48*, 1310–3.
(37) Zelphati, O., Liang, X., Nguyen, C., Barlow, S., Sheng, S., Shao, Z., and Felgner, P. L. (2000) PNA-dependent gene chemistry: stable coupling of peptides and oligonucleotides to plasmid DNA. *Biotechniques 28*, 304–10, 312−4, 316.
(38) Dean, D. A. (2000) Peptide nucleic acids: versatile tools for gene therapy strategies. *Adv. Drug Delivery Rev. 44*, 81–95.
(39) Liang, K. W., Hoffman, E. P., and Huang, L. (2000) Targeted delivery of plasmid DNA to myogenic cells via transferrin-conjugated peptide nucleic acid. *Mol. Ther. 1*, 236–43.
(40) Koppelhus, U., and Nielsen, P. E. (2003) Cellular delivery of peptide nucleic acid (PNA). *Adv. Drug Delivery Rev. 55*, 267–80.
(41) Yuan, F., Dellian, M., Fukumura, D., Leunig, M., Berk, D. A., Torchilin, V. P., and Jain, R. K. (1995) Vascular permeability in a human tumor xenograft: molecular size dependence and cutoff size. *Cancer Res. 55*, 3752–6.
(42) Dvorak, H. F., Brown, L. F., Detmar, M., and Dvorak, A. M. (1995) Vascular permeability factor/vascular endothelial growth factor, microvascular hyperpermeability, and angiogenesis. *Am. J. Pathol. 146*, 1029–39.
(43) Gerlowski, L. E., and Jain, R. K. (1986) Microvascular permeability of normal and neoplastic tissues. *Microvasc. Res. 31*, 288–305.
(44) Sevick, E. M., and Jain, R. K. (1991) Measurement of capillary filtration coefficient in a solid tumor. *Cancer Res. 51*, 1352–5.
(45) Maeda, H. (2001) The enhanced permeability and retention (EPR) effect in tumor vasculature: the key role of tumor-selective macromolecular drug targeting. *Adv. Enzyme Regul. 41*, 189–207.
(46) Goodman, T. T., Ng, C. P., and Pun, S. H. (2008) 3-D tissue culture systems for the evaluation and optimization of nanoparticle-based drug carriers. *Bioconjugate Chem. 19*, 1951–9.
(47) Enger, P. O., Thorsen, F., Lonning, P. E., Bjerkvig, R., and Hoover, F. (2002) Adeno-associated viral vectors penetrate human solid tumor tissue in vivo more effectively than adenoviral vectors. *Hum. Gene Ther. 13*, 1115–25.
(48) Aoyama, Y., Kanamori, T., Nakai, T., Sasaki, T., Horiuchi, S., Sando, S., and Niidome, T. (2003) Artificial viruses and their application to gene delivery. Size-controlled gene coating with glycocluster nanoparticles. *J. Am. Chem. Soc. 125*, 3455–7.
(49) Nakai, T., Kanamori, T., Sando, S., and Aoyama, Y. (2003) Remarkably size-regulated cell invasion by artificial viruses. Saccharide-dependent self-aggregation of glycoviruses and its consequences in glycoviral gene delivery. *J. Am. Chem. Soc. 125*, 8465–75.
(50) Osaki, F., Kanamori, T., Sando, S., Sera, T., and Aoyama, Y. (2004) A quantum dot conjugated sugar ball and its cellular uptake. On the size effects of endocytosis in the subviral region. *J. Am. Chem. Soc. 126*, 6520–1.
(51) Chithrani, B. D., Ghazani, A. A., and Chan, W. C. (2006) Determining the size and shape dependence of gold nanoparticle uptake into mammalian cells. *Nano Lett. 6*, 662–8.
(52) Wagner, E., Cotten, M., Foisner, R., and Birnstiel, M. L. (1991) Transferrin-polycation-DNA complexes: the effect of polycations on the structure of the complex and DNA delivery to cells. *Proc. Natl. Acad. Sci. U.S.A. 88*, 4255–9.
(53) Perales, J. C., Ferkol, T., Beegen, H., Ratnoff, O. D., and Hanson, R. W. (1994) Gene transfer in vivo: sustained expression and regulation of genes introduced into the liver by receptor-targeted uptake. *Proc. Natl. Acad. Sci. U.S.A. 91*, 4086–90.
(54) Rippe, B., and Haraldsson, B. (1987) Fluid and protein fluxes across small and large pores in the microvasculature. Application of two-pore equations. *Acta Physiol. Scand. 131*, 411–28.
(55) Melkko, S., Halin, C., Borsi, L., Zardi, L., and Neri, D. (2002) An antibody-calmodulin fusion protein reveals a functional dependence between macromolecular isoelectric point and tumor targeting performance. *Int. J. Radiat. Oncol. Biol. Phys. 54*, 1485–90.
(56) Dellian, M., Yuan, F., Trubetskoy, V. S., Torchilin, V. P., and Jain, R. K. (2000) Vascular permeability in a human tumour xenograft: molecular charge dependence. *Br. J. Cancer 82*, 1513–8.
(57) Gao, H., Shi, W., and Freund, L. B. (2005) Mechanics of receptor-mediated endocytosis. *Proc. Natl. Acad. Sci. U.S.A. 102*, 9469–74.
(58) Prabha, S., Zhou, W. Z., Panyam, J., and Labhasetwar, V. (2002) Size-dependency of nanoparticle-mediated gene transfection: studies with fractionated nanoparticles. *Int. J. Pharm. 244*, 105–15.
(59) Dauty, E., Remy, J. S., Zuber, G., and Behr, J. P. (2002) Intracellular delivery of nanometric DNA particles via the folate receptor. *Bioconjugate Chem. 13*, 831–9.
(60) Lutolf MP, L.-F. J., Schmoekel, H. G., Metters, A. T., Weber, F. E., Fields, G. B., and Hubbell, J. A. (2003) Synthetic matrix metalloproteinase-sensitive hydrogels for the conduction of tissue regeneration: engineering cell-invasion characteristics. *Proc. Natl. Acad. Sci. U.S.A. 100*, 5413–5418.
(61) Hiemenez, P., and Rajagopalan, R. (1997) *Principles of Colloid and Surface Chemistry*, 3rd ed., CRC Press, Boca Raton, FL.
(62) Vinogradov, S. V., Bronich, T. K., and Kabanov, A. V. (1998) Self-assembly of polyamine-poly(ethylene glycol) copolymers with phosphorothioate oligonucleotides. *Bioconjugate Chem. 9*, 805–12.
(63) Ferrari, S., Pettenazzo, A., Garbati, N., Zacchello, F., Behr, J. P., and Scarpa, M. (1999) Polyethylenimine shows properties of interest for cystic fibrosis gene therapy. *Biochim. Biophys. Acta 1447*, 219–25.
(64) Boeckle, S., von Gersdorff, K., van der Piepen, S., Culmsee, C., Wagner, E., and Ogris, M. (2004) Purification of polyethylenimine polyplexes highlights the role of free polycations in gene transfer. *J. Gene Med. 6*, 1102–11.
(65) Choi, H. S., Liu, W., Misra, P., Tanaka, E., Zimmer, J. P., Itty Ipe, B., Bawendi, M. G., and Frangioni, J. V. (2007) Renal clearance of quantum dots. *Nat. Biotechnol. 25*, 1165–70.

BC900328J

Comb-Shaped Conjugates Comprising Hydroxypropyl Cellulose Backbones and Low-Molecular-Weight Poly(*N*-isopropylacryamide) Side Chains for Smart Hydrogels: Synthesis, Characterization, and Biomedical Applications

F. J. Xu,*,† Y. Zhu,† F. S. Liu,‡ J. Nie,† J. Ma,§ and W. T. Yang*,†

State Key Laboratory of Chemical Resource Engineering, Key Laboratory of Carbon Fiber and Functional Polymers, Ministry of Education, College of Materials Science & Engineering, Beijing University of Chemical Technology, Beijing, China 100029, Brain Tumor Research Center, Beijing Neurosurgical Institute, Capital University of Medical Science, Beijing, China 100050, and State Key Laboratory of Molecular Oncology, Cancer Institute & Hospital, Chinese Academy of Medical Sciences, Beijing, China 100021. Received July 30, 2009; Revised Manuscript Received February 11, 2010

Hydroxypropyl cellulose (HPC) possesses a lower critical solution temperature (LCST) above 40 °C, while the poly(*N*-isopropylacrylamide) (P(NIPAAm)) exhibits a LCST of about 32 °C. Herein, comb-shaped copolymer conjugates of HPC backbones and low-molecular-weight P(NIPAAm) side chains (HPC-*g*-P(NIPAAm) or HPN) were prepared via atom transfer radical polymerization (ATRP) from the bromoisobutyryl-functionalized HPC biopolymers. By changing the composition ratio of HPC and P(NIPAAm), the LCSTs of HPNs can be adjusted to be lower than the body temperature. The MTT assay from the HEK293 cell line indicated that HPNs possess reduced cytotoxicity. Some of the hydroxyl groups of HPNs were used as cross-linking sites for the preparation of stable HPN hydrogels. In comparison with the HPC hydrogels, the cross-linked HPN hydrogels possess interconnected pore structures and higher swelling ratios. The *in vitro* release kinetics of fluorescein isothiocyanate-labeled dextran and BSA (or dextran-FITC and BSA-FITC) as model drugs from the hydrogels showed that the HPN hydrogels are suitable for long-term sustained release of macromolecular drugs at body temperature.

INTRODUCTION

Cross-linked hydrogels are of interest in biomedical applications, because of their tunable chemical and three-dimensional physical network structures, high water content in an aqueous medium without dissolution, and good mechanical properties (*1*−*3*). Intelligent or smart hydrogels, which can undergo volume changes in response to changes in temperature, pH, and antigen, are of great interest in drug delivery, cell encapsulation, and tissue engineering (*4*−*6*). Among the temperature-sensitive hydrogels, poly(*N*-isopropylacrylamide) (P(NIPAAm))-based hydrogels are the most widely studied. P(NIPAAm) is a well-known thermoresponsive polymer and exhibits a lower critical solution temperature (LCST) of about 32 °C in an aqueous medium. P(NIPAAm)-based hydrogels absorb water and exist in swollen states below the LCST. On the other hand, they undergo an abrupt and drastic shrinkage in volume as the medium temperature is raised above the LCST. These characteristics make P(NIPAAm)-based hydrogels specially useful in biomedical applications, such as in controlled release of drugs and in tissue engineering (*7*−*12*).

Natural polysaccharides are very suitable candidates for the design of novel biomaterials, because they are renewable and nontoxic materials. It has been reported that P(NIPAAm) can be grafted to polysaccharide biopolymers, including chitosan (*13, 14*), dextran (*3, 15*), and methylcellulose (*16*), for the preparation of thermosensitive biomaterials. Hydroxypropyl cellulose (HPC) is a derivative of natural polysaccharide cellulose, where some of the hydroxyl groups of cellulose have been hydroxypropylated to form hydrophobic propylene oxide groups (*1, 17*). HPC materials have been approved by the USFDA and widely used in food and drug formulations (*1*). The hydrohphobic and hydrophilic groups impart HPC with a LCST of >40 °C (*1, 17, 18*). However, such LCST is far higher than the body temperature of 37 °C.

In the present work, the body temperature-responsive comb-shaped copolymer conjugates (HPC-*g*-P(NIPAAm) or HPN) composed of HPC backbones and low-molecular-weight P(NIPAAm) side chains are prepared via atom transfer radical polymerization (ATRP) (*19*−*21*) from the bromoisobutyryl-functionalized HPC (HPC-Br) backbones (Scheme 1). Some of the unreacted hydroxyl groups of HPNs are used as cross-linking sites for the preparation of stable HPN hydrogels. The resultant cross-linked HPN hydrogels with controllable LCSTs possess interconnected pore structures. In this work, the in vitro controlled release properties of the smart hydrogels were studied by using fluorescein isothiocyanate-labeled dextran and BSA (or dextran-FITC and BSA-FITC) as model macromolecular hydrophilic drugs. Dextran and BSA labeled or not labeled with FITC have been widely used as models for macromolecular drugs, such as proteins and peptides, in the studies of in vitro release kinetics of drug delivery systems (*22*−*25*). In comparison with HPC hydrogels, the HPN hydrogels can provide the long-term sustained release of macromolecular drugs at body temperature. Such porous HPN hydrogels with body-temperature responsive properties will have potential applications as biomedical materials.

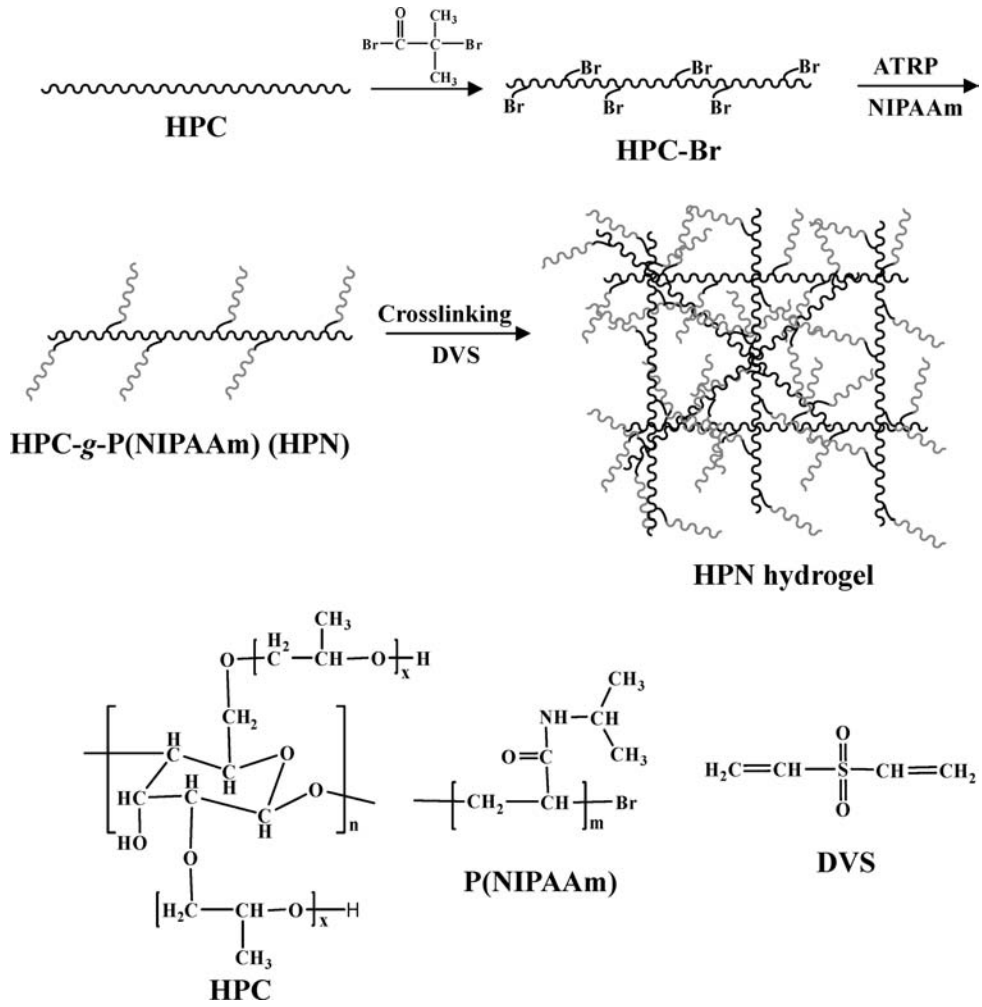
EXPERIMENTAL PROCEDURES

Materials. Hydroxypropyl cellulose powder (HPC, Sigma-Aldrich cat #435007: M_n = 10 000 g/mol and M_w = 80 000 g/mol; from gel permeation chromatography (GPC) with THF as mobile phase: M_n = 28 015 g/mol and M_w = 64 655 g/mol;

* To whom all correspondence should be addressed. E-mail: xufj@mail.buct.edu.cn, yangwt@mail.buct.edu.cn.
† Beijing University of Chemical Technology.
‡ Capital University of Medical Science.
§ Chinese Academy of Medical Sciences.

10.1021/bc900337p © 2010 American Chemical Society
Published on Web 02/23/2010

Scheme 1. Schematic Diagram Illustrating the Processes for the Preparation of the HPC-*g*-P(NIPAAm) (HPN) Copolymers via ATRP of NIPAAm from the Alkyl Bromide-Functionalized HPC Macroinitiator and the Formation of Stimuli-Responsive HPN Hydrogel via Cross-Linking



molar substitution of propylene oxide groups (MS) of about 3 per glucose unit (*19*), 2-bromoisobutyryl bromide (BIBB, 98%), *N*-isopropylacrylamide (NIPAAm, >99%), poly(*N*-isopropylacrylamide) (P(NIPAAm), $M_n = 20\,000-25\,000$), 1,1,4,7,10,10-hexamethyltriethyenetetramine (HMTETA, 99%), copper(I) bromide (CuBr, 99%), and divinyl sulfone (DVS, >98%), 3-(4,5-dimethylthiazol-2-yl)-2,5-diphenyl tetrazolium bromide (MTT), penicillin, streptomycin, fluorescein isothiocynate (FITC)-conjugated BSA (BSA-FITC), and FITC-conjugated dextran (dextran-FITC, $M_w \sim 40\,000$) were obtained from Sigma-Aldrich Chemical Co., St. Louis, MO. The HEK293 cell lines were purchased from the American Type Culture Collection (ATCC, Rockville, MD). Dulbecco's phosphate buffered saline (PBS, pH 7.4), used for the drug delivery experiments, was prepared freshly according to the recipes.

Synthesis of HPC-*g*-P(NIPAAm) Comb-Shaped Copolymers (HPNs) via Atom Transfer Radical Polymerization (ATRP). The starting bromoisobutyryl-functionalized HPC (HPC-Br) was synthesized according to the following procedures. About 2.0 g of HPC was dissolved completely in 100 mL of anhydrous methylene chloride with stirring and then kept in an ice bath. About 0.3 mL of BIBB in 5 mL of methylene chloride was added dropwise into the flask through an equalizing funnel over a period of 10 min at 0 °C. After this addition, the flask was sealed. The reaction was allowed to proceed at room temperature for another 5 h to produce the HPC-Br macroinitiator. The final reaction mixture was precipitated with 1000 mL of diethyl ether. The crude polymer was purified by reprecipitation thrice in diethyl ether. Finally, the HPC-Br macroinitiator for the subsequent ATRP was dried under reduced pressure.

The HPC-*g*-P(NIPAAm) comb-like copolymers (HPNs, Scheme 1) were synthesized using a [monomer (2.0 g)]:[CuBr (25.4 mg)]:[HMTETA (77.6 μL)] molar feed ratio of 100:1:1.5 in 15 mL of dioxane containing 0.4 g of HPC-Br at 60 °C. The reaction was performed in a 25 mL flask equipped with a magnetic stirrer and under the typical conditions for ATRP (*20*). NIPAAm, HPC-Br, and HMTETA were introduced into the flask containing 10 mL of dioxane. After HPC-Br and NIPAAm had dissolved completely, the reaction mixture was degassed by bubbling argon for 30 min. Then, CuBr was added into the mixture under an argon atmosphere. The reaction mixture was purged with argon for another 10 min. The flask was then sealed with a rubber stopper under an argon atmosphere. The polymerization was allowed to proceed under continuous stirring at room temperature for 8 to 24 h. The reaction was stopped by exposing to air. The reaction mixture was diluted with about 150 mL of THF. The catalyst complex was removed by passing the blue dilute polymer solution through a short aluminum oxide column where neutral aluminum oxide 90 (Activity I, 0.063−0.200 mm, pH 7.3, Merck & Co., Inc.) was used. A colorless solution was obtained. After removal of THF in a rotary evaporator, the HPNs were precipitated in excess *n*-hexane. The crude polymer was purified by reprecipitation cycles to remove the reactant residues (*21*), prior to being dried under reduced pressure.

Preparation of HPN Hydrogels. The temperature-responsive hydrogels were prepared from the HPN comb-shaped copolymers. Some of the unreacted hydroxyl groups of HPNs were cross-linked using the similar procedures reported earlier (*1, 17*). A homogeneous polymer solution was obtained by adding 1.0 g of the HPN to 10 mL of deionized water. The solution was stirred slowly overnight to ensure uniform mixing while avoiding bubble formation. Then, 40 wt % NaOH was used to adjust the pH of solution to about 13. Subsequently, about 0.1 mL of divinylsulfone (DVS) was added to the copolymer solution. The mixture was stirred for 2 min at room temperature. The mixture was then centrifuged to remove the air bubbles trapped during the stirring process. The air bubble-free sticky solution was kept at 30 °C for 12 h. After the cross-linking reaction, the sample was removed and immersed into distilled water (about 500 mL) at room temperature for 72 h to remove the reactant residues. The water was changed at a 6 h interval. The cross-linked HPN hydrogel was finally freeze−dried.

Polymer Characterization and Cytotoxicity Assay. The temperature-responsive polymers were characterized by gel permeation chromatography (GPC), X-ray photoelectron spectroscopy (XPS), Fourier transform infrared (FTIR) spectroscopy, nuclear magnetic resonance (NMR) spectroscopy, and differential scanning calorimetry (DSC). GPC measurements were performed on a Waters GPC system equipped with Waters Styragel columns, a Waters-2487 dual wavelength (λ) UV detector, and a Waters-2414 refractive index detector. THF with 2 vol % triethylamine was used as the eluent at a low flow rate of 1.0 mL/min. Monodispersed polystyrene standards were used to generate the calibration curve. The XPS measurements were performed on a Kratos AXIS HSi spectrometer equipped with a monochromatized Al K_α X-ray source (1486.6 eV photons), using the same procedures as those described earlier (*20*). After the samples were pressed into KBr pellets, the FTIR spectra were measured on a Bio-Rad FTS 135 FT-IR spectrophotometer. Each spectrum was collected by cumulating 64 scans. ^{1}H NMR spectra were measured on a Bruker ARX 300 MHz spectrometer, using *d*-chloroform (CCl_3D) as the solvent with 1000 scans at a relaxation time of 2 s. The LCST of the HPN samples was determined by DSC (TA 2920 modulated DSC, TA Instruments). All samples were immersed in deionized water at room temperature for 24 h to reach the equilibrium state. These wetted samples were placed in individual hermetic sample pans and then sealed. The thermal analysis of the swollen samples was performed at a heating rate of 3 °C/min in the temperature range 10−60 °C under a nitrogen flow rate of 40 mL/min, using deionized water as the reference.

The cytotoxicity of the HPNs was evaluated using the MTT assay in HEK293 cell lines. Before cell culture, the control commercial P(NIPAAm) was purified by reprecipitation cycles in excess *n*-hexane to remove the potential reactant residues (*21*). The cell lines were cultured in Dulbecco's modified eagle medium (DMEM), supplemented with 10% heat-inactivated fetal bovine serum (FBS), 100 units/mL of penicillin and 100 μg/mL of streptomycin at 37 °C, under 5% CO_2, and 95% relative humidity atmosphere. The cells were seeded in a 96-well microtiter plate (Nunc Co., Wiesbaden, Germany) at a density of 10^4 cells/well and incubated in 100 μL of DMEM/well for 24 h. The culture media were replaced with fresh culture media containing serial dilutions of polymers, and the cells were incubated for 24 h. The culture media were replaced with fresh media. Then, 10 μL of sterile-filtered MTT stock solution in PBS (5 mg/mL) was added to each well, reaching a final MTT concentration of 0.5 mg/mL. After 5 h, the unreacted dye was removed by aspiration. The produced formazan crystals were dissolved in DMSO (100 μL/well). The absorbance was measured using a microplate reader (Spectra Plus, Tecan, Zurich, Switzerland) at a wavelength of 570 nm. The cell viability (%) relative to control cells cultured in media without polymers was calculated from $[A]_{test}/[A]_{control} \times 100\%$, where $[A]_{test}$ and $[A]_{control}$ are the absorbance values of the wells (with the polymers) and control wells (without the polymers), respectively. For each sample, the final absorbance was the average value measured from six wells in parallel.

Hydrogel Characterization. The morphology of the HPN hydrogels was imaged using a JEOL scanning electron microscope (SEM, model 5600LV). Prior to the SEM measurements, specimens of the hydrogels were fixed on the metal holders and sputtered with a thin Pt layer. The dry weight (W_d) of each sample was determined after drying the gel to a constant weight under reduced pressure overnight. For the study of temperature-dependent equilibrium swelling ratios, the dry hydrogel samples were equilibrated in deionized water for at least 48 h at a predetermined temperature between 25 and 60 °C. The swelling ratios of the samples were measured gravimetrically. After the excess water on the sample surfaces was wiped off with moist filter papers, the samples were weighed (W_w) (*20*). The weights from three measurements were averaged, and the swelling ratio was calculated from the following formula:

$$\text{swelling ratio} = W_s/W_d$$

where W_s ($= W_w - W_d$) is the weight of water in the swollen sample at a specific temperature.

Drug Loading and in Vitro Release. Dextran-FITC and BSA-FITC were selected as model hydrophilic macromolecular drugs to study the release behaviors of the HPN hydrogels. Drug loadings were achieved by immersing about 60 mg of the freeze−dried hydrogels in about 3 mL of 30 mg/mL PBS solution of dextran-FITC or BSA-FITC at 4 °C for 3 days. The total drug uptake was calculated from weight differences between the freeze−dried hydrogels with and without the drug loading. In vitro protein release analyses of the drug-loaded hydrogels were carried out in 5 mL of PBS buffer at 37 or 20 °C. At a specified sample collection time, 5 mL of the solution was removed and the medium in the test tube was replenished with 5 mL of fresh PBS buffer. The concentrations of the released dextran-FITC and BSA-FITC were determined using a Shimadzu RF 5301PC luminescence spectrophotometer (excitation at 495 nm, emission at 515 nm) with reference to the standard calibration curve. In addition, the circular dichroism (CD) spectra of the released BSA proteins were measured using a CD spectrometer (J-810, JASCO Co., Japan) in the wavelength range 200−250 nm. A JASCO cell of path length of 0.1 cm was used. The α-helix content corresponds to the ellipticity at 208 nm.

Statistical Analysis. All experimental data used for the statistical analysis were obtained from at least three repeated runs. The data were collected in triplicate and expressed as mean ± standard deviations. Error bars represent the standard deviation. The statistical assay was performed using the Student's *t*-test and the differences were considered statistically significant with $p < 0.05$.

RESULTS AND DISCUSSION

Synthesis of Comb-Shaped Copolymers (HPC-*g*-P(NIPAAm) or HPN) Composed of HPC Backbones and P(NIPAAm) Side Chains via ATRP. The preparation of functional polymers is usually carried out in organic solvent. Because of its unique characteristics of both water and organic solubility, HPC is an ideal substrate for developing novel polysaccharide-based biomaterials. The molecular weight (M_n) of the HPC used in this work, as determined from gel permeation chromatography (GPC), is about 2.80×10^4 g/mol, with the

Table 1. Characterization of HPC-*g*-P(NIPAAm) (HPN) Copolymers

	polymers						
samples	reaction time (h)	[N]/[C][b]	M_n (g/mol)[c]	PDI[c]	P(NIPAAm) content (wt/wt %)		LCST[e] (°C)
HPC	--	--	2.80×10^4	2.3	--	--	47.7
HPC-*g*-P(NIPAAm)1, or HPN1[a]	8	0.062	4.06×10^4	2.1	31[c]	35[d]	33.3−40.5
HPC-*g*-P(NIPAAm)1, or HPN2[a]	16	0.101	5.57×10^4	1.9	50[c]	56[d]	34.1
HPC-*g*-P(NIPAAm)1, or HPN3[a]	24	0.113	7.18×10^4	1.8	61[c]	64[d]	33.7

[a] Synthesized using a [monomer (2.0 g)]:[CuBr (25.4 mg)]:[HMTETA (77.6 μL)] molar feed ratio of 100:1:1.5 in 15 mL of dioxane containing 0.4 g of HPC-Br at 60 °C. [b] Determined from XPS N 1s and C 1s core-level spectral area ratios. [c] Determined from the GPC results. PDI = Weight average molecular weight/Number average molecular weight, or M_w/M_n. [d] Determined from the XPS [N]/[C] ratios and the molecular weights of NIPAAm ($M_{[NIPAAm]}$ = 113 g/mol) and HPC unit ($C_{15}H_{27}O_8$; $M_{[HPC]}$ = 335 g/mol), where $[N]/[C] \approx n_{[NIPAAm]}/(6n_{[NIPAAm]} + 15\ m_{[HPC]})$. [e] The temperatures at the minimum points of the endotherms are referred to as the lower critical solution temperatures (LCSTs).

corresponding polydispersity index (PDI) of about 2.3. In order to prepare comb-like copolymers using HPC as a backbone via ATRP, it is essential to introduce alkyl halide initiators onto HPC. In this work, the bromoisobutyryl-functionalized HPC (HPC-Br) (*19*) was prepared via the reaction of hydroxyl groups of HPC with 2-bromoisobutyryl bromide (BIBB) (Scheme 1). Well-defined comb-shaped copolymer conjugates of HPC and P(NIPAAm) (HPC-*g*-P(NIPAAm) or HPN) were subsequently synthesized via ATRP of NIPAAm from HPC-Br. The HPNs with different contents of P(NIPAAm) can be synthesized by varying the ATRP time. Table 1 summarizes the GPC results of HPN1 (from 8 h of ATRP), HPN2 (from 16 h of ATRP), and HPN3 (from 24 h of ATRP). With the increase in reaction time from 8 to 24 h, the M_n of HPN increases from 4.06×10^4 to 7.18×10^4 g/mol, and the P(NIPAAm) content in HPN increases accordingly from 31 to 61 wt %. In addition, the PDIs of HPNs are slightly lower than that of the pristine HPC (Table 1), indicating that the ATRP of NIPAAm is well-controlled.

XPS Analysis. The chemical compositions of the polymers were first determined by XPS. The C 1s core-level spectra of the pristine HPC and HPC-Br samples are shown in Figure 1a,b, respectively. The C 1s core-level spectrum of the pristine HPC can be curve-fitted into three peak components with binding energies (BE's) at about 284.6, 286.2, and 287.6 eV, attributable to the C−H/C−C, C−O, and O−C−O species, respectively (*19*). From the [C−O]/[O−C−O] ratio of 11, the average number of propylene oxide groups ($-OCH_2CH(OH)CH_3$) per anhydroglucose unit of HPC is determined to be about 3, as reported earlier (*19*). When ATRP is carried out from a multifunctional backbone with a high local concentration of initiation sites, the radical−radical coupling of the propagating chains will occur and result in a gel. In order to avoid potential gelation, the starting HPC-Br with moderate concentration of initiation sites was prepared (*19*). The XPS C 1s core-level spectrum of HPC-Br can be curve-fitted into four peak components with BE's at about 284.6, 286.2, 287.6, and 288.4 eV, attributable to the C−H/C−C, C−O/C−Br, O−C−O, and O=C−O species, respectively (*19, 20*). The new O−C=O peak component is associated with the bromide-capped ester groups of HPC-Br. The corresponding Br 3d core-level spectrum is shown in Figure 1b′. From the [Br]/[C] ratio of 0.011 (determined from the sensitivity factor-corrected Br 3d and C 1s core-level spectral area ratio), it can be deduced that about 6 glucose units of HPC-Br possess one ATRP initiation site, or every HPC chain contains about 13 ATRP initiation sites on the average. No gelation was found during subsequent ATRP from such HPC-Br multifunctional initiators.

Figure 1 also shows the C 1s core-level spectra of (c) HPN1 (from 8 h of ATRP), (e) HPN2 (from 16 h of ATRP), and (g) (from 24 h of ATRP). The C 1s core-level spectra of HPNs can be curve-fitted into four peak components with BE's at about 284.6, 285.5, 286.2, and 287.6 eV, attributable to the C−H/C−C, C−N, C−O and O−C−O/O=C−N species, respectively (*22*). The C−N and O=C−N peak components are associated with the P(NIPAAm) side chains. The increase (and decrease)

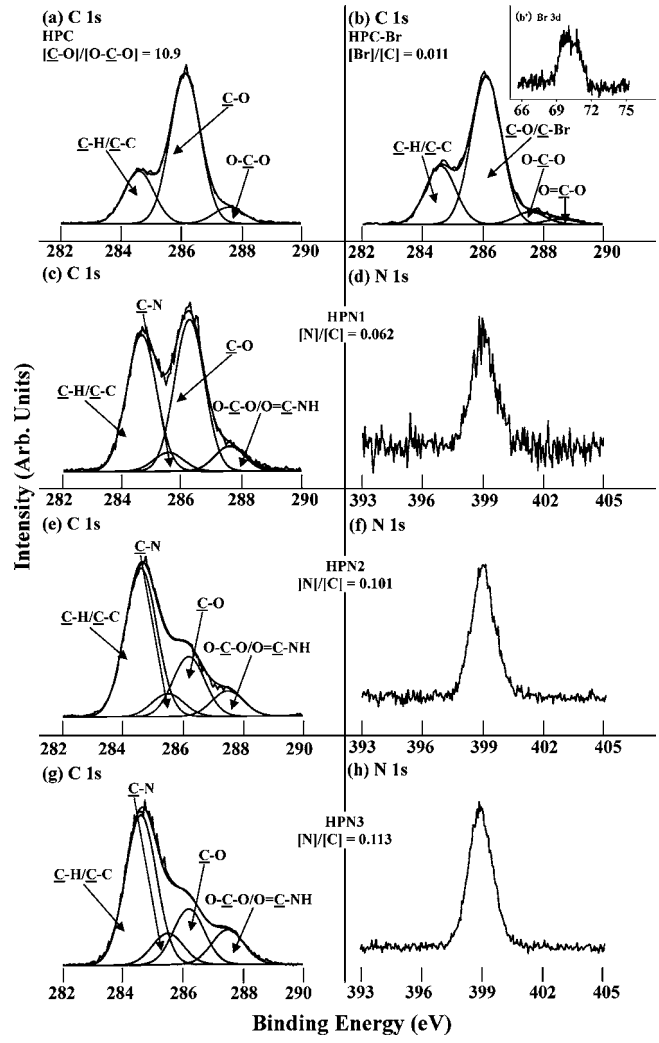


Figure 1. C 1s core-level spectrum of (a) HPC, C 1s, and Br 3d core-level spectra of (b,b′) HPC-Br, and C 1s and N 1s core-level spectra of (c,d) HPN1, (e,f) HPN2, and (g,h) HPN3.

in intensities of the C−N and O=C−N (and C−O) species with ATRP time is consistent with the increase in P(NIPAAm) contents. The corresponding N 1s core-level spectra of HPN1, HPN2, and HPN3 are shown in Figure 1d,f, and h, respectively. From the [N]/[C] ratios determined by XPS, the P(NIPAAm) contents of HPNs can be calculated and are summarized in Table 1. The results are in fairly good agreement with those obtained from the GPC measurements.

FTIR and ^{1}H NMR Studies. Figure 2 shows the FTIR spectra of the (a) pristine HPC, (b) HPC-Br, (c) HPN1, (d) HPN2, and (e) HPN3 polymers. In comparison with that of HPC, the new characteristic band at about 1736 cm^{-1} (peak 1, $\upsilon_{O=C-O}$) is associated with the bromide-capped ester groups of HPC-Br. In all the IR spectra of HPNs, the two strong amide

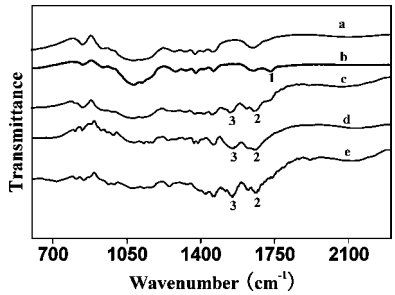


Figure 2. FTIR spectra of (a) HPC, (b) HPC-Br, (c) HPN1, (d) HPN2, and (e) HPN3. (peak 1, 1736 cm^{-1} ($\upsilon_{O=C-O}$); peak 2, 1650 cm^{-1} ($\upsilon_{O=C-NH}$); and peak 3, 1540 cm^{-1} (υ_{N-H}).)

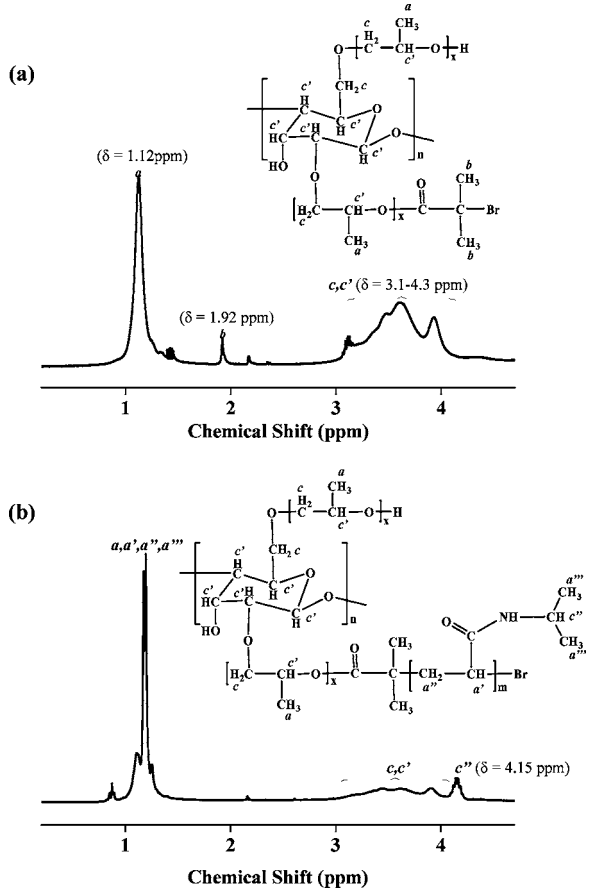


Figure 3. 300 MHz ^{1}H NMR spectra of (a) HPC-Br and (b) HPN3 in CCl_3D.

absorption bands at about 1650 ($\upsilon_{O=C-NH,}$ peak 2) and 1540 cm^{-1} ($\upsilon_{N-H,}$ peak 3) are associated with the P(NIPAAm) side chains (*20*). The relative intensity of peaks 2 and 3 increase significantly with the increases in P(NIPAAm) content. The FTIR results are thus consistent with the XPS results of Figure 1.

The chemical structures of HPC-Br and HPN are also characterized by ^{1}H NMR spectroscopy. Figure 3a shows the ^{1}H NMR spectrum of the HPC-Br macroinitiator. The chemical shift at $\delta = 1.12$ ppm is attributable to the methyl protons of propylene oxide groups (***a***, C−$\underline{CH_3}$). The chemical shift at $\delta = 1.92$ ppm is associated with the methyl protons (***b***, C(Br)−$\underline{CH_3}$) of 2-bromoisobutyryl. The broad chemical shifts in the region 2.9−4.3 ppm are mainly associated with the inner methylidyne and methylene protons (***c***, ***c′***, O−$\underline{CH}$ and O−$\underline{CH_2}$) on the glucose units and propylene oxide groups. From the area ratio of peak ***a*** and peak ***b***, the initiator density of HPC-Br corresponds to one initiator site for every 6.8 glucose units (*19*),

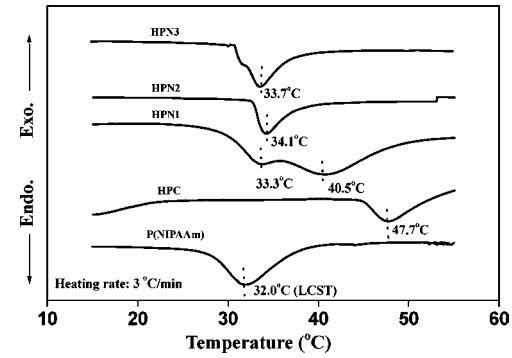


Figure 4. Typical DSC thermograms of HPC, P(NIPAAm), HPN1, HPN2, and HPN3 (the temperatures at the minimum points of the endotherms are referred as LCSTs).

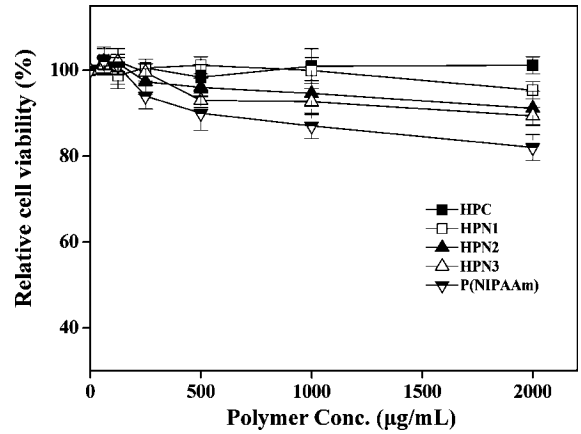


Figure 5. Cell viability assay in HEK293 cell lines with various concentrations of HPC, P(NIPAAm), HPN1, HPN2, and HPN3. Cell viability was determined by the MTT assay and expressed as a percentage of the control cell culture.

fairly consistent with that determined by XPS. Figure 3b shows the ^{1}H NMR spectrum of HPN3. The chemical shifts (***a′***, C−$\underline{CH}$; ***a″***, C−$\underline{CH_2}$; ***a‴***, C−$\underline{CH_3}$) associated with the P(NIPAAm) side chains overlapped completely with the methyl protons of propylene oxide groups (***a***, C−$\underline{CH_3}$) of the HPC backbone. The new chemical shift at $\delta = 4.15$ ppm corresponds to the (***c″***) N−$\underline{CH}Me_2$ methylidyne protons of P(NIPAAm) (*24*). The signal intensities associated with the HPC backbone (***c***, ***c″***) have decreased substantially. Due to the serious overlaps in the characteristic shifts of the components, it is difficult to quantify the P(NIPAAm) segments by ^{1}H NMR.

Lower Critical Solution Temperature (LCST). The LCSTs of HPNs were determined by differential scanning calorimetry (DSC). Figure 4 shows the typical DSC thermograms of the HPC, commercial P(NIPAAm), HPN1, HPN2, and HPN3 polymers. The temperature at the minimum point of the endotherm is referred to as the LCST of the sample. The pristine HPC used in this work exhibits a LCST of about 47.7 °C, similar to that reported earlier (*18*). The LCST of HPC is the consequence of hydrophobic (associated with propylene oxide groups) and hydrophilic (associated with hydroxyl groups) interaction (*17, 18*). HPCs from different batches may have obviously different LCSTs, due to their difference in substituent distribution along the polymer chains (*20*). Nevertheless, their general LCST is significantly higher than body temperature (37 °C). The control commercial P(NIPAAm) with average M_n of 20 000−25 000 has a LCST of about 32 °C, due to the hydrophobic (associated with isopropyl groups) and hydrophilic (associated with amide moiety in the pendant groups) interaction (*20*). As shown in Figure 4, the LCST of HPN decreases with

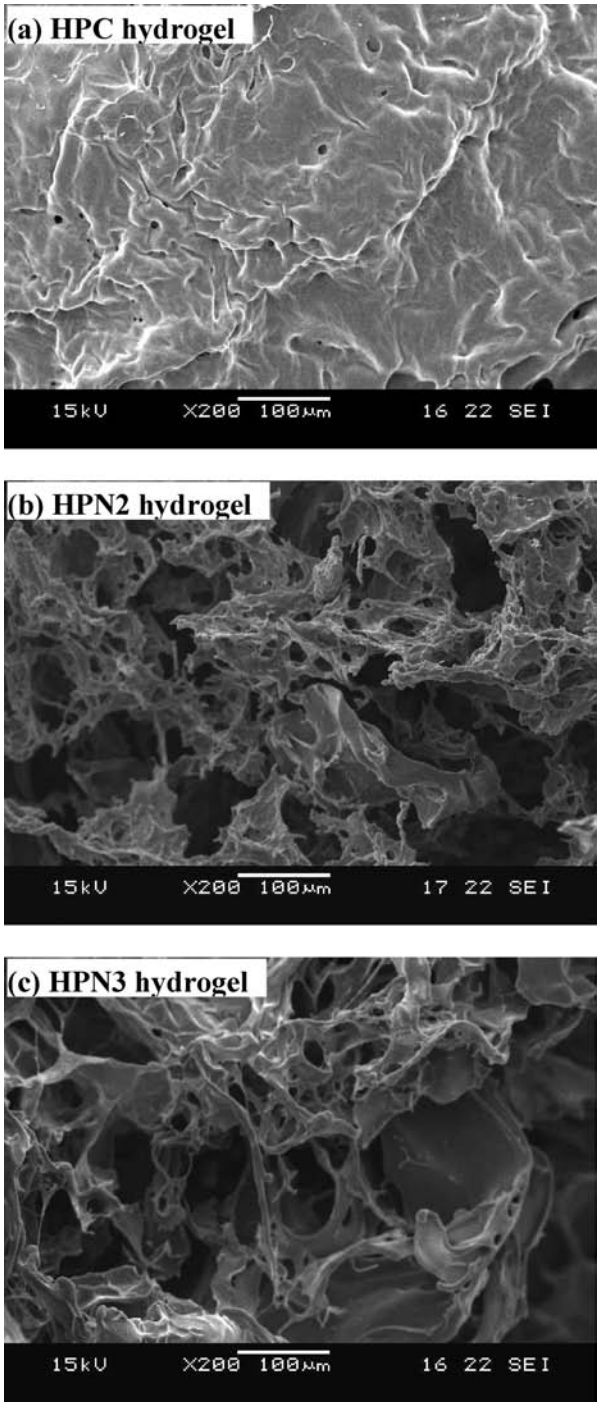


Figure 6. SEM images of (a) HPC, (b) HPN2, and (c) HPN3 hydrogels.

the increase in P(NIPAAm) content (Table 1). The HPN1 with average P(NIPAAm) content of about 33 wt % exhibits a very broad LCST range of 33 to 41 °C. When average the P(NIPAAm) content in HPN2 or HPN3 reaches above 53 wt %, only one minimum point in the DSC endotherm is observed and the corresponding LCST becomes lower than body temperature of 37 °C. The LCST of HPN in this work is the consequence of synergistic hydrophobic and hydrophilic interactions arising from HPC and P(NIPAAm) individual components.

Cytotoxicity Assay. Cytotoxicity is one of the most important factors to be considered in selecting biomaterials. Figure 5 shows the in vitro MTT assay results of cytotoxicity of HPC, commercial P(NIPAAm), HPN1, HPN2, and HPN3 at various concentrations in HEK293 cell lines. HPC does not show any

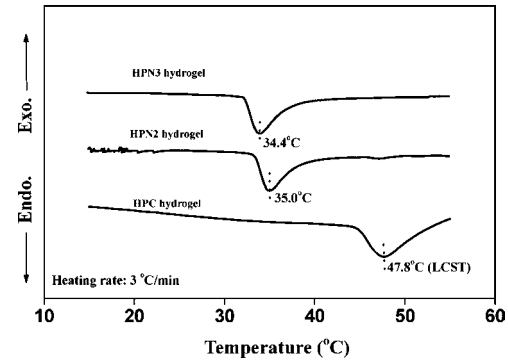


Figure 7. Typical DSC thermograms of HPC, HPN2, and HPN3 hydrogels.

cytotoxicity at polymer concentrations up to 2.0 mg/mL. No acute cytotoxicity associated with the commercial P(NIPAAm) was found, consistent with that reported earlier (*6*). However, the MTT assay suggested that the HPNs at higher polymer concentrations are better tolerated by the cell lines than those of the P(NIPAAm) homopolymer, probably because of the introduction of HPC biopolymer.

Stimuli-Responsive HPN Hydrogels. Because of their lower LCSTs than the body temperature (Figure 4), HPN2 and HPN3 were selected for the preparation of the temperature-responsive HPN hydrogels. Some of the remaining hydroxyl groups of HPN2 and HPN3 can be cross-linked by divinylsulfone (DVS) to produce the corresponding stable HPN2 and HPN3 hydrogels. DVS introduces cross-linking by an addition reaction with the hydroxyl groups on either the HPC backbone or the substituent groups, saturating the DVS carbon−carbon double bond in alkaline solution (*1, 17*). Figure 6 shows the SEM images of the freeze−dried (a) HPC, (b) HPN2, and (c) HPN3 hydrogels. The HPN2 and HPN3 hydrogels possess interconnected pore structures, while no obvious pore structures were observed on the HPC hydrogel under similar conditions. The P(NIPAAm) components may possess some different physical properties (such as solubility) from the HPC counterparts in aqueous medium. The resultant poor incompatibility or phase separation during the hydrogel preparation probably has led the formation of pore structures.

In comparison with those in Figure 4, the DSC thermographs of the hydrogels in Figure 7 suggest that the presence of DVS in the cross-linked matrix do not have a serious effect on the LCSTs (Table 1 and Table 2). The temperature dependence of the swelling ratios of HPC, HPN2, and HPN3 hydrogels was also investigated. Figure 8 shows the typical temperature-dependent swelling ratio of the three hydrogels over the temperature range of 25 to 60 °C in deionized water. The equilibrium swelling ratios of three hydrogels exhibit a similar trend of temperature dependence. As the temperature was increased, the swelling ratio decreases, with the most drastic decrease being observed at around the respective LCSTs of HPC, HPN2, and HPN3 hydrogels (Figure 7). Generally, the main reason for this distinctive characteristic of the hydrogels can be attributed to the unique and rapid transformation between the hydrophilic and hydrophobic states (*20*). At temperatures below the LCST, the hydrophilic groups of the hydrogels form hydrogen bonds with water molecules. These bonds act cooperatively to form a stable shell of hydration around the hydrophobic groups, resulting in greater water uptake and producing a larger swelling ratio. As the external temperature increases, the associative interactions among the hydrophobic groups release the entrapped water molecules from the hydrogel networks. In addition, HPN2 and HPN3 hydrogels possess higher initial swelling ratios than HPC hydrogels at starting

Table 2. Characterization of HPC-*g*-P(NIPAAm) (HPN) Hydrogels

	hydrogels[b]						
				cumulative drug released[d] (%)			
		drug loading[c] (mg/mg dry gel)		dextran		BSA	
samples	LCST[a] (°C)	dextran	BSA	20 °C	37 °C	20 °C	37 °C
HPC	47.8	0.25	0.34	80.3	82.1	75.2	76.4
HPC-*g*-P(NIPAAm)1, or HPN1[a]	--	--	--	--	--	--	--
HPC-*g*-P(NIPAAm)1, or HPN2[a]	35.0	0.47	--	89.4	83.8	--	--
HPC-*g*-P(NIPAAm)1, or HPN3[a]	34.4	--	0.59	--	--	85.6	79.5

[a] The temperatures at the minimum points of the endotherms are referred to as the lower critical solution temperatures (LCSTs). [b] Prepared in about 10 mL of pH 13 water containing 1.0 g of polymers and 0.1 mL of DVS at 30 °C. [c] Obtained by immersing 60 mg of dry gels in 3 mL of the drug-loaded solution of 30 mg/mL at 4 °C for 3 days. [d] After 10-day in vitro release.

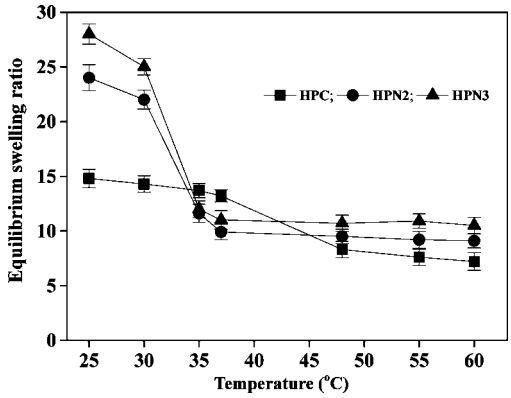


Figure 8. Temperature-dependent equilibrium swelling ratio of HPC, HPN2, and HPN3 hydrogels.

temperature of 25 °C (far lower than their LCSTs), arising probably from the interconnected pore structures of HPN2 and HPN3 hydrogels (Figure 6).

In Vitro Controlled Drug Release. In this work, the in vitro controlled release properties of the smart hydrogels were studied by using fluorescein isothiocyanate-labeled dextran and BSA (or dextran-FITC and BSA-FITC) as model macromolecular hydrophilic drugs. The drug loadings were achieved by immersing the dry HPC, HPN2, and HPN3 gels in 30 mg/mL solution of dextran-FITC (or BSA-FITC) at 4 °C for 3 days. From the data in Table 2, the amount of loaded drug per unit mass of HPN2 and HPN3 gels is higher than that in the corresponding HPC gels, probably due to the interconnected pore structures of HPN2 and HPN3 hydrogels (Figure 6). The release behavior of the loaded drugs was studied at 37 and 20 °C.

Figure 9 shows the release profiles of (a) dextran from the HPC and HPN2 hydrogels and (b) BSA from the HPC and HPN3 hydrogels. The release profile was characterized by an initial burst, followed by a slower and sustained release. This release behavior is a typical biphasic release pattern, similar to those reported (*26, 27*). The initial burst may have been caused by the release of drug molecules located on the outer surfaces, while the sustained release was probably due to the slow macromolecular diffusion from the interior of the hydrogels. There is no obvious difference between the release profiles of HPC hydrogels at 20 and 37 °C (lower than the LCST of HPC of about 48 °C). However, the sustained drug release from the HPN2 and HPN3 hydrogels was slower at 37 °C than at 20 °C. At 37 °C above the LCST of HPN2 and HPN3 (Figure 7), their hydrogel mesh size has decreased upon hydrogel collapse, which in turn decreases the diffusivity of the macromolecules through the hydrogel network and leads to the slower drug release.

The slow and sustained release could provide a continuous drug delivery, prevent the problems of cyclic variations in the

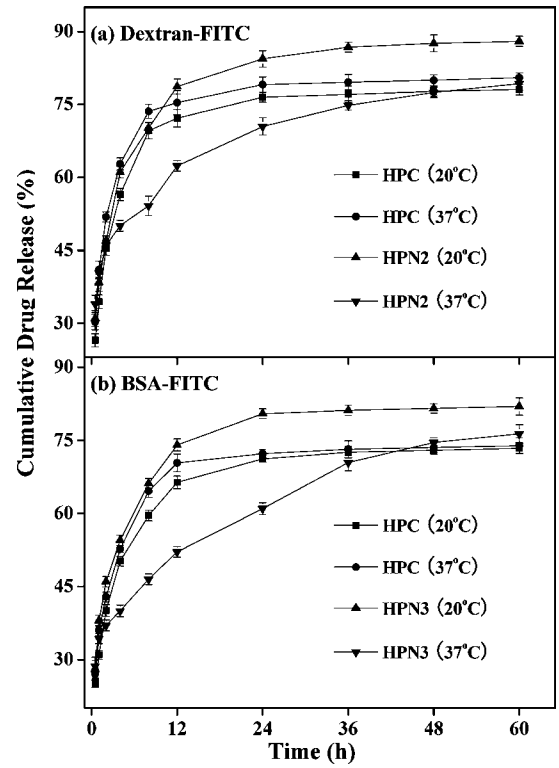


Figure 9. Release profiles of (a) dextran-FITC from HPC and HPN2 hydrogels and (b) BSA-FITC from HPC and HPN3 hydrogels at 20 and 37 °C.

drug concentrations in blood, and produce the maximum pharmacological efficiency (*27, 28*). In addition, the drug release at 20 °C for the HPN2 and HPN3 hydrogels was slightly faster than that of the corresponding HPC hydrogel. The pore structures of the HPN2 and HPN3 hydrogels probably have facilitated the diffusion of drug molecules into the in vitro medium. After 10-day in vitro release (Table 2), the loaded drugs were still not released completely. This phenomenon is very common in drug delivery systems. The presence of physical interactions between the drug and hydrogels probably has hindered the drug diffusion (*28, 29*).

The functions and structures of proteins are inherently correlated. Here, UV-circular dichroism (CD) was used to examine whether the released BSA has retained its native secondary structures. In general, proteins possess three common secondary structures of α-helix, β-sheets, and random coil. The quantitative structural changes of proteins can be evaluated by analyzing the preserved content of α-helix. The α-helix content of proteins can be estimated from the following formula (*29, 30*):

$$\%\ \alpha\text{-helix} = (\theta_{mrd} - 4000)/(33\,000 - 4000)$$

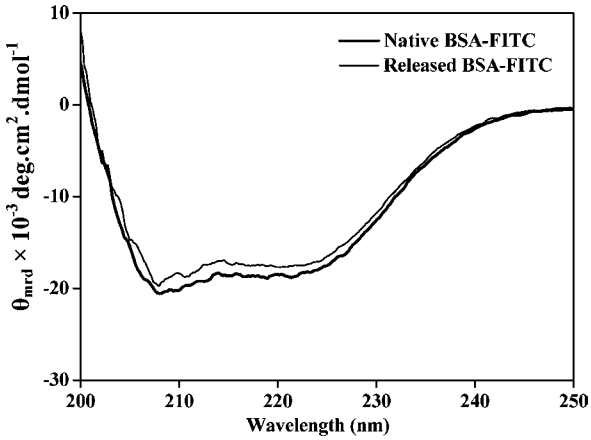


Figure 10. Circular dichroism (CD) spectra of the native BSA-FITC and released BSA-FITC from HPN3 hydrogel.

where θ_{mrd} is the mean molar ellipticity per amino acid residue at 208 nm (deg.cm^2. dmol^{-1}). θ_{mrd} can be calculated using the following formula

$$\theta_{mrd} = (\theta_d M_0)/(10CL)$$

where, θ_d is the measured ellipticity in the unit of mdeg from the CD spectrometer, M_0 is the average molecular weight (Da) per amino acid residue, C is the BSA concentration (mg.mL^{-1}), and L is the sample cell path length (cm). BSA is an ellipsoidal protein with the dimensions of $14 \times 4 \times 4$ nm^3. Its average molecular weight (Da) per amino acid residue is about 118 Da (*31*). Figure 10 shows the typical CD spectra of BSA-FITC released from the HPN3 hydrogel and native BSA-FITC. The CD spectrum of the released BSA is similar to that of the native BSA. The calculated α-helix contents in the released and native BSA are 53% and 57%, respectively, indicating that the conformation of BSA has not been severely or irreversibly altered by adsorption in the hydrogels.

CONCLUSIONS

The comb-shaped copolymer conjugates composed of HPC backbones and short P(NIPAAm) side chains (HPC-*g*-P(NIPAAm) or HPN) have been successfully prepared via ATRP from the bromoisobutyryl-functionalized HPC backbones. The HPN with average P(NIPAAm) content of above 53 wt % exhibited a LCST below the body temperature of 37 °C. The MTT assay from the HEK293 cell line indicated that HPNs possess reduced cytotoxicity. Some of the remaining unreacted hydroxyl groups of HPNs were used as cross-linking sites for the preparation of stable HPN hydrogels. In comparison with the HPC hydrogels, the resultant cross-linked HPN hydrogels possess interconnected pore structures and higher swelling ratios. The HPN hydrogels can also provide the long-term sustained release of macromolecular drugs at body temperature. Such porous smart hydrogels of HPN with controllable LCSTs are potentially useful for biomedical applications. However, it should be noted that such hydrogels may be not suitable as implanted or injected devices due to their poor degradability.

ACKNOWLEDGMENT

This work was supported by Research Fund for the Doctoral Program of Higher Education of China (project no. 20090010120007), National Natural Science Foundation of China (grant no. 50903007), Chinese Universities Scientific Fund (project no. ZZ0904), and Program for New Century Excellent Talents in University.

LITERATURE CITED

(1) Harsh, D. C., and Gehrke, S. H. (1991) Controlling the swelling characteristics of temperature sensitive cellulose ether hydrogels. *J. Controlled Release 17*, 175–186.

(2) Debord, J. D., and Lyon, L. A. (2007) On the unusual stability of succinimidyl esters in pNIPAm-AAc microgels. *Bioconjugate Chem. 18*, 601–604.

(3) Zhang, J. T., Bhat, R., and Janda, K. D. (2009) Temperature-sensitive PVA/PNIPAAm semi-IPN hydrogels with enhanced responsive properties. *Acta Biomater. 5*, 488–497.

(4) Cohen, J. A., Beaudette, T. T., Tseng, W. W., Bachelder, E. M., Mende, I., Engleman, E. G., and Fréchet, J. M. J. (2009) T-Cell activation by antigen-loaded pH-sensitive hydrogel particles *in vivo*: the effect of particle size. *Bioconjugate Chem. 20*, 111–119.

(5) Vazquez-Duhalt, R., Tinoco, R., D'Antonio, P., Topoleski, L. D. T., and Payne, G. F. (2001) Enzyme conjugation to the polysaccharide chitosan: smart biocatalysts and biocatalytic hydrogels. *Bioconjugate Chem. 12*, 301–306.

(6) Comolli, N., Neuhuber, B., Fischer, I., and Lowman, A. (2009) In vitro analysis of PNIPAAm-PEG, a novel, injectable scaffold for spinal cord repair. *Acta Biomater. 5*, 1046–1055.

(7) Hsiue, G. H., Hsu, S. H., Yang, C. C., Lee, S. H., and Yang, I. K. (2002) Preparation of controlled release ophthalmic drops for glaucoma therapy using thermosensitive poly-*N*-isopropyl-acrylamide. *Biomaterials 23*, 457–462.

(8) Vihola1, H., Laukkanen, A., Valtola, L., Tenhu, H., and Hirvonen, J. (2005) Cytotoxicity of thermosensitive polymers poly(*N*-isopropylacrylamide), poly(N-vinylcaprolactam) and amphiphilically modified poly(*N*-vinylcaprolactam). *Biomaterials 26*, 3055–3064.

(9) Okajima, S., Sakai, Y., and Yamaguchi, T. (2005) Development of a regenerable cell Culture system that senses and releases dead cells. *Langmuir 21*, 4043–4049.

(10) Zhang, X., Wu, D., and Chu, C. C. (2004) Synthesis and characterization of partially biodegradable, temperature and pH sensitive Dex-MA/PNIPAAm hydrogels. *Biomaterials 25*, 4719–4730.

(11) Chen, J. P., and Cheng, T. H. (2006) Thermo-responsive chitosan-*graft*-poly(*N*-isopropylacrylamide) injectable hydrogel for cultivation of chondrocytes and meniscus cells. *Macromol. Biosci. 6*, 1026–1039.

(12) von Recum, H., Okano, T. S., and Kim, W. (1998) Growth factor release from thermally reversible tissue culture substrates. *J. Controlled Release 55*, 121–130.

(13) Don, T. M., and Chen, H. R. (2005) Synthesis and characterization of AB-crosslinked graft copolymers based on maleilated chitosan and *N*-isopropylacrylamide. *Carbohydr. Polym. 61*, 334–347.

(14) Alvarez-Lorenzo, C., Concheiro, A., Dubovik, A. S., Grinberg, N. V., Burova, T. V., and Grinberg, V. Y. (2006) Temperature-sensitive chitosan-poly(*N*-isopropyl acrylamide) interpenetrated networks with enhanced loading capacity and controlled release properties. *J. Controlled Release 102*, 629–641.

(15) Lu, D., Liu, Z., Zhang, M., Wang, X., and Liu, Z. (2006) Dextran-grafted-PNIPAAm as an artificial chaperone for protein refolding. *Biochem. Engin. J. 27*, 336–343.

(16) Liu, W., Zhang, B., Lu, W. W., Li, X., Zhu, D., Yao, K. D., Wang, Q., Zhao, C., and Wang, C. (2004) A rapid temperature-responsive sol-gel reversible poly(*N*-isopropylacrylamide)-*g*-methylcellulose copolymer hydrogel. *Biomaterials 25*, 3005–3012.

(17) Anbergen, U., and Oppermannt, W. (1990) Elasticity and swelling behaviour of chemically crosslinked cellulose ethers in aqueous systems. *Polymer 31*, 1854–1858.

(18) Schagerlöf, H., Richardson, S., Momcilovic, D., Brinkmalm, G., Wittgren, B., and Tierneld, F. (2006) Characterization of chemical substitute of hydroxypropyl cellulose using enzymatic degradation. *Biomacromolecules 7*, 80–85.

(19) Xu, F. J., Ping, Y., Ma, J., Yang, W. T., Kang, E. T., and Neoh, K. G. (2009) Comb-shaped copolymers composed of hydroxypropyl cellulose backbones and cationic poly((2-dimethyl amino)ethyl methacrylate) side chains for gene delivery. *Bioconjugate Chem. 20*, 1449–1458.

(20) Xu, F. J., Kang, E. T., and Neoh, K. G. (2006) pH- and temperature-responsive hydrogels from crosslinked triblock copolymers prepared via consecutive atom transfer radical polymerizations. *Biomaterials 27*, 2787–2796.

(21) Bontempo, D., Li, R. C., Ly, T., Brubaker, C. E., and Maynard, H. D. (2005) One-step synthesis of low polydispersity, biotinylated poly(*N-isopropylacrylamide*) by ATRP. *Chem. Commun.* 4702–4704.

(22) Liu, S. Q., Yang, Y. Y., Liu, X. M., and Tong, Y. W. (2003) Preparation and characterization of temperature-sensitive poly(*N*-isopropylacrylamide)-*b*-poly(D, L-lactide) microspheres for protein delivery. *Biomacromolecules 4*, 1784–1793.

(23) Kelner, A., and Schacht, E. H. (2005) Tailor-made polymers for local drug delivery: release of macromolecular model drugs from biodegradable hydrogels based on poly(ethylene oxide). *J. Controlled Release 101*, 13–20.

(24) Martin, L., Wilson, C. G., Koosha, F., Tetley, L., Gray, A. I., Senel, S., and Uchegbu, I. F. (2002) The release of model macromolecules may be controlled by the hydrophobicity of palmitoyl glycol chitosan hydrogels. *J. Controlled Release 80*, 87–100.

(25) Remuñán-López, C., Lorenzo-Lamosa, M. L., Vila-Jato, J. L., and Alonso, M. J. (1998) Development of new chitosan-cellulose multicore microparticles for controlled drug delivery. *Eur. J. Pharm. Biopharm. 45*, 49–56.

(26) Wu, J. Y., Liu, S. Q., Heng, P. W. S., and Yang, Y. Y. (2005) Evaluating proteins release from and their interactions with thermosensitive poly(*N*-isopropyia-crylamide) hydrogels. *J. Controlled Release 102*, 361–72.

(27) Zhang, X. Z., Lewis, P. J., and Chu, C. C. (2005) Fabrication and characterization of a smart drug delivery system: microsphere in hydrogel. *Biomaterials 26*, 3299–3309.

(28) Rafati, H., Coombes, A. G. A., Adler, J., Holland, J., and Davis, S. S. (1997) Protein-loaded poly(lactide-*co*-glycolide) microparticles for oral administration: formulation, structural and release characteristics. *J. Controlled Release 43*, 89–102.

(29) Greenfield, N., and Fasman, G. D. (1969) Computed circular dichroism spectra for the evaluation of protein conformation. *Biochemistry 8*, 4108–4116.

(30) Peng, Z. G., Hidajat, K., and Uddin, M. S. (2004) Conformational change of adsorbed and desorbed bovine serum albumin on nano-sized magnetic particles. *Colloids Surf., B: Biointerfaces 33*, 15–21.

(31) Nakanishi, E., Sato, H., and Nakajima, A. (1984) Conformation study on the interactions of plasma proteins with anionic lipids and heparin. *Polym. Bull. 11*, 305–312.

BC900337P

Linker Chemistry Determines Secondary Structure of $p53_{14-29}$ in Peptide Amphiphile Micelles

Dimitris Missirlis,*[,†,‡] Marc Farine,[†] Mark Kastantin,[†] Badriprasad Ananthanarayanan,[†] Thorsten Neumann,[†,‡] and Matthew Tirrell[†,‡]

Department of Chemical Engineering and Materials and Materials Research Laboratory, University of California, Santa Barbara, California 93106, and Department of Bioengineering, University of California, Berkeley, California, 94720. Received September 1, 2009; Revised Manuscript Received February 9, 2010

Biofunctional micelles formed via self-assembly of synthetic peptide-lipid conjugates are a class of promising biomaterials with applications in drug delivery and tissue engineering. The micelle building block, termed peptide amphiphile, consists of a lipid-like chain covalently linked through a spacer to a peptide headgroup. Self-assembly results in formation of a hydrophobic core surrounded by a dense shell with multiple, functional peptides. We report here on the effect that different linkers between a palmitic tail and a bioactive peptide ($p53_{14-29}$) have on headgroup secondary structure. Peptide $p53_{14-29}$ may act as an inhibitor of the interaction between tumor suppressor p53 and human double minute-2 (hDM2) proteins by binding hDM2 in a partially helical form, leading to the release of p53 and the induction of apoptosis in certain tumors. Circular dichroism and fluorescence spectroscopy data revealed that the extent and type of secondary structure of $p53_{14-29}$ are controlled through size and hydrogen bond potential of the linker. In addition, the structure of the self-assembled micelles was influenced through linker-dependent altered headgroup interactions. This study provides insight into the mechanisms through which headgroup structuring occurs on peptide amphiphile micelles, with implications on the bioactivity, stability, and morphology of the self-assembled entities.

INTRODUCTION

Self-assembly of peptide amphiphiles (PAs) represents a versatile methodology for preparation of nanostructures with defined shapes and functionalities (*1, 2*). PAs are composed of a hydrophobic segment, generally a single- or double-alkyl tail, linked to a hydrophilic peptide "headgroup". An appealing way to view the supramolecular aggregates formed by PAs in aqueous solutions is as protein analogous micelles held together by hydrophobic interactions in their interior and presenting a high density of functional peptides on their surface. Through appropriate PA design, self-assembly can lead to formation of fibrous scaffolds similar to extracellular matrix proteins for cell attachment and growth (*3, 4*); with different PA molecular architectures, colloidal structures can be prepared to mimic soluble globular protein function (*5*−*7*).

In order to harness the full potential of PAs as building blocks, appropriate functional peptide presentation is required, which can be achieved via control of monomer interactions. The hydrophobic effect is the predominant driving force responsible for self-assembly; however, in contrast to traditional, low molecular weight detergents, the more complex peptide headgroup may provide additional stabilizing interactions such as reversible disulfide formation (*8, 9*), hydrogen bonding (*10*−*12*), and electrostatic bridging between neighboring peptide chains (*3, 13*). A direct consequence and particularly attractive feature of these interactions in the tethered, close-packed surface of the self-assembled structure is their ability to induce peptide folding in distinct secondary structure motifs, thus displaying peptides in a more native manner (*14*).

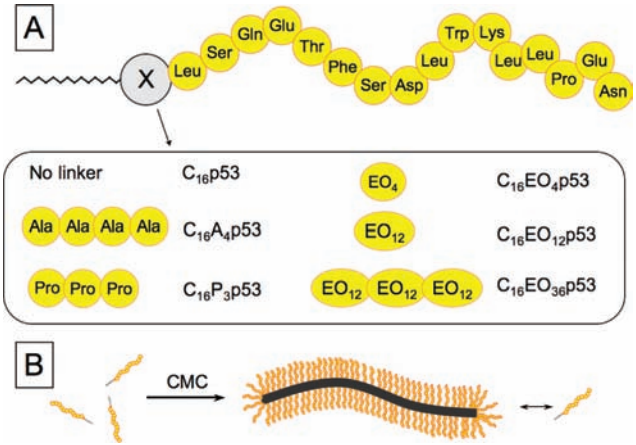
Conformational sensitivity is key in achieving specificity in biomolecular interactions. The spatial arrangement of amino acids resulting from folding of the polypeptide chain determines the activity of the protein or enzyme. The same sequence folded in a different manner usually has reduced or even altered activity as is most strikingly evidenced in the activity of misfolded proteins. Thus, the ability to mimic naturally occurring secondary structure motifs and present them on supramolecular constructs could lead to development of more potent peptide ligands/inhibitors. A very common protein-folding pattern is the α helix, which possesses diverse functionalities ranging from protein−protein interactions (*15*) and protein−DNA interactions (*16*) to cell membrane pore formation (*17*). Formation of α-helical domains normally occurs upon protein folding into the native protein conformation. Their typical size is 7−14 residues long corresponding to 2−3 helical turns. However, when the same peptide sequence is isolated from the protein it loses its folding ability. The reasons for this loss of secondary structure are primarily the increase in entropy associated with peptide freedom to probe a larger conformational space and the lack of stabilizing forces from neighboring parts of the protein.

To counterbalance the entropic cost of folding, several approaches have been explored (*18*). Adsorption of the peptide on a surface (*19*) or inside a host template (*20*) have both shown to help in helical stabilization. Chemical modification of the peptide with unnatural amino acids and subsequent cross-linking of the side chains has also proven to provide enough stabilizing energy for helix formation (*21*−*26*). Alternatively, the side chains of appropriately inserted natural amino acids (e.g., histidines) can be used for helix stabilization through metal complexation (*21, 27*). Our group as well as others have shown that secondary structure can be induced in a number of different peptides also as a result of their hydrophobic modification with a lipid tail and subsequent self-assembly into micelles (*6, 14, 28, 29*). Crowding effects and conformational

* Corresponding author. Dimitris Missirlis Materials Research Laboratory, University of California, Santa Barbara, CA 93106, Tel. 805 452 6319, Fax. 805 893 8124, E-mail dimis@engineering.ucsb.edu.
† University of California, Santa Barbara.
‡ University of California, Berkeley.

10.1021/bc900383m © 2010 American Chemical Society
Published on Web 02/18/2010

Scheme 1. Schematic Representation of the Peptide Amphiphiles Used in This Study (A) and Proposed Self-Assembly Scheme (B)



constraints due to dense surface "tethering" of peptide chains on the surface of the micelles are presumed to be the driving forces for assembly (*30, 31*). The type of secondary structure adopted is not solely dictated by the amino acid sequence of the peptide, as has been seen by the folding of the same peptide on a surface into different motifs (*32*). Such observations are reminiscent of peptide misfolding associated with a number of important diseases, e.g., amyloid-β fiber formation (*33*).

Here, we have studied secondary structure conformation of a bioactive peptide in peptide amphiphile micelles and how it is affected by incorporation of different linkers between the peptide and the hydrophobic palmitoyl tail. The peptide we used is derived from the hDM2 binding region of tumor suppressor p53 and has shown potential as an inhibitor of the p53-hDM2 interaction with concomitant reactivation of apoptotic pathways in appropriate cancer cells (*34*). Moreover, peptide activity is linked to its propensity to fold into a short α helix (*23, 35*), and enhanced hDM2 binding of the peptide was reported when helicity was induced through a stapling mechanism (*23*), revealing the importance that secondary structure plays in this protein−protein interaction. Our main goal was to gain understanding of the factors that control peptide folding and supramolecular structure and how these can be manipulated through chemical design of the micelle building block.

EXPERIMENTAL PROCEDURES

Peptide Amphiphile Synthesis. Peptide $p53_{14-29}$ (sequence: LSQETFSDLWKLLPEN) on a Rink amide resin was purchased from Anaspec. Peptide amphiphiles were synthesized from resin-bound peptides using manual Fmoc solid-phase synthesis as previously described (*36*). Following cleavage from the resin, peptide amphiphiles were purified using high-performance liquid chromatography (HPLC; Shimadzu Corporation) on a reverse-phase C_4 column (Vydac), with gradients of acetonitrile in water, containing 0.1% trifluoracetic acid (TFA). A list of the peptide amphiphiles synthesized is presented in Scheme 1 and the chemical structures are shown in Supporting Information Figure S1. Identity of the peptide amphiphiles was verified by electrospray ionization mass spectrometry (Supporting Information Table S1) and purity was determined using analytical HPLC on a reverse-phase C_4 column (Vydac). Peptide amphiphiles with purity greater than 95% were used.

Micelle Preparation. Peptide amphiphiles were dissolved in a 1:1 mixture of chloroform and methanol. The organic solvents were then evaporated under N_2 flow eventually forming a film on a glass vial wall. The film was then dried in vacuum and hydrated in water or buffer at 60 °C for 1 h. Mixed micelles were prepared by hydrating PA films with solutions of Tween 40 (Sigma) at different Tween/PA ratios at 60 °C for 1 h. Following cooling to room temperature, the aqueous micelle solutions were filtered through a 0.45 μm polycarbonate syringe filter (Millipore). All samples were stored at 4 °C and used within 1 week of preparation unless otherwise noted. Fluorescence, circular dichroism, and light scattering measurements were not significantly changed within this time period.

Fluorescence Spectroscopy. Fluorescence was recorded using a Varian Cary Eclipse fluorescence spectrophotometer, equipped with a cuvette holder thermostatted at 25 °C, unless otherwise noted. In steady-state fluorescence emission measurements, tryptophan (Trp) was excited at 280 nm and emission was recorded between 300 and 400 nm. Steady-state anisotropy was measured using manual polarization lenses and calculated using the following equation (*37*):

$$r = \frac{I_{VV} - I_{VH}I_{HV}/I_{HH}}{I_{VV} + 2I_{VH}I_{HV}/I_{HH}} \quad (1)$$

I_{VV}, I_{HH}, I_{VH}, and I_{HV} are fluorescence intensities; the subscripts V and H stand for vertical and horizontal orientations of polarizers, respectively, with the first subscript corresponding to the excitation light and the second to the emitted light. Values of anisotropy presented here are averaged over a range of wavelengths (340−370 nm) after excitation at 290 nm.

Fluorescence quenching measurements were performed after addition of aliquots of a freshly prepared 5 M KI to a solution of p53 or C_{16}p53 (100 uM). Dynamic (collisional) quenching is described by the Stern−Volmer equation (*38*)

$$\frac{I_0}{I} = 1 + K_{SV}[Q] \quad (2)$$

where $[Q]$ is the quencher (KI) concentration, I_0 and I are the fluorescence intensities in the absence and presence of quencher respectively, and K_{SV} is the Stern−Volmer constant. The slope of the plot I_0/I against [KI] gives K_{SV}.

Pyrene Fluorescence Measurements. Dried peptide amphiphile films were dissolved in aqueous pyrene stock solution (6×10^{-7} M) containing traces of tetrahydrofuran (THF) and left to equilibrate at 37 °C for 1 h. Fluorescence emission spectra were recorded at different PA concentrations and the intensity ratio of the third (I_3) to the first (I_1) vibrational band of pyrene was determined. The critical micellar concentration (cmc) was determined as the concentration at the onset of I_3/I_1 ratio increase. The equilibrium constant K_v for partitioning of pyrene between the micellar and aqueous phase was estimated using the equation

$$\frac{F - F_{min}}{F_{max} - F} = \frac{K_v x_{core}(C - \text{cmc})}{\rho_{core}} \quad (3)$$

F_{min}, F_{max}, and F are the minimum, maximum, and intermediate intensity ratio (I_1/I_3), respectively, x_{core} is the micellar core weight fraction and ρ_{core} the density of that core.

Circular Dichroism. CD spectra of PA solutions were acquired using an Olis RSM spectrophotometer in the far UV region (190−250 nm) using quartz cuvettes of 0.5 mm path length. Baseline spectra were subtracted from sample spectra and smoothed using the software supplied by the manufacturer. Mean residual ellipticity, θ, as a function of wavelength, is presented. Temperature scans were performed from 10 to 80 °C to monitor peptide folding stability. It is important to note that using our experimental setup there was a cutoff at approximately 200 nm when PBS 10 mM was used due to buffer component absorption.

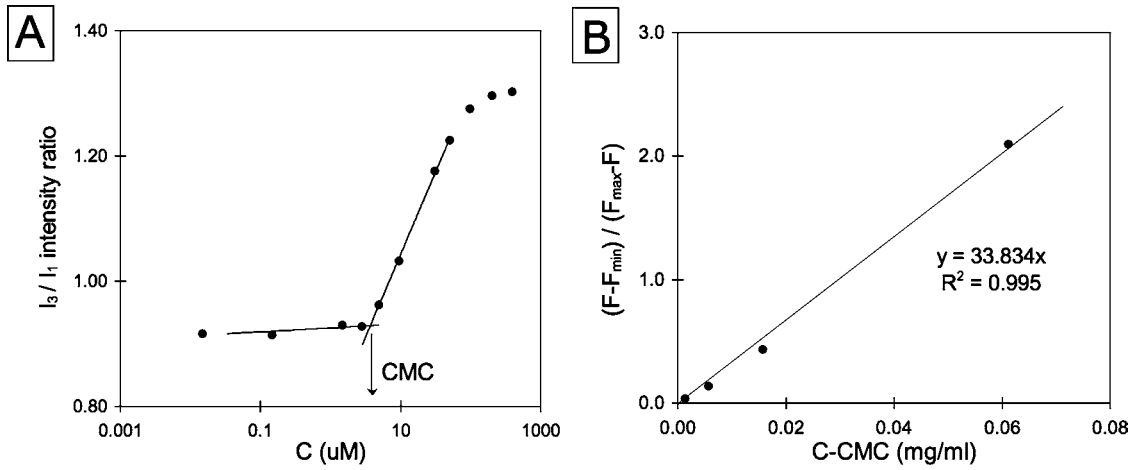


Figure 1. Critical micelle concentration (cmc) determination of C_{16}p53 in PBS 10 mM using the pyrene solubilization method. The onset of increase of the I_3/I_1 intensity ratio of pyrene emission peaks corresponds to the cmc (A). The partition coefficient of pyrene between the hydrophobic core and the aqueous phase is derived from the slope of (B) using eq 3.

Dynamic Light Scattering (DLS). Micelle size was assessed using a DLS system (Brookhaven Instruments) that consisted of an avalanche photodiode detector to measure scattering intensity from a 632.8 nm HeNe laser (Melles Griot) as a function of delay time. Temperature was maintained at 25.0 ± 0.1 °C using a circulating water bath unless otherwise noted. The first-order autocorrelation function was measured at different angles between 40° and 120° to cover a range of scattering wave vector, q, of 0.0090 to 0.0229 nm^{-1}. The autocorrelation function was then fit using a second-order cumulant to extract the average decay rate, Γ_1. The quantity Γ_1/q^2 was then taken as the apparent diffusion coefficient, D_{app}. D_{app} at $q = 0.0132$ nm^{-1} (60°) was used to estimate the translational diffusion coefficient, and the Stokes−Einstein relationship was used to calculate the size of an equivalent hydrodynamic sphere for this particle. This analysis provided a means to compare the relative hydrodynamic size of each micelle but was not taken as an accurate measure of the true hydrodynamic diameter. No extrapolation was performed to $q = 0$ because of the uncertainty in this process for a nonspherical particle.

In order to extract properties of a worm-like micelle from these data, D_{app} was plotted as a function of q. Given the theoretical results of Winkler et al. (*39*), D_{app} will be independent of q for $q < 1/r_g$. As q increases, two regimes may appear: an intermediate scattering vector regime ($1/r_g < q < p$) in which D_{app} increases linearly with q and a large scattering vector regime ($q > p$) in which internal bending modes become important causing D_{app} to increase as $q^{2/3}$. Here, $1/2p$ is the persistence length of the micelle. Thus, the scaling behavior of D_{app} can provide an estimate of the radius of gyration and persistence length.

Atomic Force Microscopy (AFM). AFM analysis was performed using an MFP-3D AFM from Asylum research. The images were recorded in tapping mode using moderate force ratio under ambient conditions equipped with commercial silicon tips (Olympus AC240TS) with resonance frequency $f = 70$ kHz and spring constant of $k = 2$ $^{N}/_{m}$. A typical scan range of 5 μm with a resolution of 512 × 512 pixels was used for each image. Each sample was analyzed in multiple regions. Raw data were leveled by a first and second order of plane fit correction in order to remove the sample tilt.

RESULTS

A series of peptide amphiphiles was synthesized differing only in the linkage between the palmitic tail and the N-terminus of $p53_{14-29}$ peptide in order to investigate the effect of linker length, rigidity, and hydrogen bonding potential on peptide folding and self-assembly (Scheme 1). Linkers and palmitic tail were coupled directly on the resin-bound peptide, providing a simple and efficient methodology of preparing the hybrid molecules (*40*). The A_4 linker was selected since alanines are commonly used to promote the creation of PA fibers through β-sheet formation of peptide headgroups (*3, 11*). Prolines on the other hand have been shown to disrupt H-bonding close to the micelle core and promote assembly into spherical geometries (*41*). Oligo-ethylene oxides of varying lengths were used as flexible spacers between the peptide and the hydrophobic core to investigate the effect of headgroup size without introducing additional chemical interactions between monomers. The chemical structure, along with the measured molecular mass for each peptide amphiphile, is given in the Supporting Information section (Figure S1 and Table S1).

Critical Micellar Concentration. Our hypothesis is that peptide folding occurs as a result of crowding in the micelle corona of peptide amphiphile micelles, and thus, we first aimed at determining the cmc's of the different PA analogues. The cmc's were calculated using the pyrene solubilization method (*42*): the onset of an increase in intensity ratio of the third to the first highest energy emission peaks (I_3/I_1) of pyrene emission spectrum denotes its partitioning into a more hydrophobic microenvironment. For C_{16}p53, this shift corresponds to a cmc of 2.2 μM or 4.7 μg/mL (Figure 1). We estimated the pyrene partition equilibrium constant K_v using eq 3, assuming the density of the micellar core to be that of hexadecane (0.775 g/mL) (*43*). The estimated value of 2.5×10^5 may be compared to a value of 2.0×10^5 extracted from the data of Almgren et al. for sodium hexadecanesulfonate (*43*), suggesting that the hydrophobicity of the core in the two systems is similar and is that of phase-segregated alkane chains.

The cmc values for the other PAs were calculated in the same manner and are given in Table 1. The A_4 linker had no appreciable effect on cmc, whereas an increase was recorded with increasing length of ethylene oxide linker, because of the hydrophilic nature of ethylene oxide oligomers. The unmodified peptide did not cause any appreciable change in pyrene fluorescence emission up to the highest concentration studied (5 mg/mL).

Tryptophan Fluorescence Studies. Tryptophan fluorescence spectroscopy was used to gain insight in peptide folding through steady state, quenching, and anisotropy measurements. Steady-state fluorescence of Trp is sensitive to the polarity of the microenvironment, which is expected to change upon folding

Table 1. Critical Micellar Concentration, Trp_{23} Fluorescence Emission Maximum (λ_{max}), and Trp Anisotropy Values for Unmodified $p53_{14-29}$ and $p53_{14-29}$ Peptide Amphiphiles

	cmc (μM)	λ_{max} (nm)	system anisotropy, r
p53	-	355	0.030 ± 0.004
C_{16}p53	2.2	347	0.056 ± 0.003
$C_{16}EO_4$p53	5.7	347	0.050 ± 0.004
$C_{16}EO_{12}$p53	9.6	344	0.047 ± 0.003
$C_{16}EO_{36}$p53	17.1	344	0.044 ± 0.004
$C_{16}P_3$p53	n.d.*	353	0.060 ± 0.003
$C_{16}A_4$p53	1.9	355	0.065 ± 0.004

* n.d.: not determined.

into an amphipathic helix. A maximum emission wavelength (λ_{max}) at 355 nm for Trp on the unmodified peptide revealed that the fluorophore is fully hydrated (*38*) (Figure 2A). A blue shift of λ_{max} to 347 nm for C_{16}p53 above its cmc indicated a more hydrophobic environment; reduced aqueous solvation of Trp upon self-assembly could result from Trp association (e.g., via stacking (*44*)) with other hydrophobic amino acid side chains in the same or neighboring peptides. The maximum emission wavelength varied among the peptide amphiphiles studied, suggesting different polarity for the tryptophan side chain (Table 1). Compared to C_{16}p53, λ_{max} red-shifted when A_4 or P_3 linkers were incorporated and blue-shifted for the longer EO linkers (EO_{12} and EO_{36}). It is important to note here that λ_{max} for Trp on p53 peptide dissolved in tetraethylene glycol was found to be 339 nm, reflecting the lower polarity of ethylene glycol compared to water.

We used dynamic quenching of tryptophan fluorescence by iodine ions to further probe the polarity of the microenvironment surrounding the chromophores and their accessibility from the aqueous phase. Stern−Volmer plots yielded straight lines confirming dynamic quenching of Trp by I^- (Figure 2B). A decrease of K_{SV} for C_{16}p53 in comparison to the peptide reflects decreased accessibility of the quencher and a more shielded environment of Trp (*44*).

The presence of tryptophan on the self-assembled structure also affected its rotational diffusion as monitored by fluorescence anisotropy (Table 1). In the absence of resonance energy transfer, as is the case for tryptophan, anisotropy provides a measure of the fluorophore's rotational diffusion (*38*), which is related to its microenvironment and is also coupled to the size of the structure onto which it is attached (*37, 45*). The value of Trp anisotropy in $p53_{14-29}$ ($r = 0.030 \pm 0.004$) was the same as that measured for L-tryptophan ($r = 0.031 \pm 0.004$) indicating unhindered rotation of the fluorophore within its excited-state lifetime and a hydrated environment. In contrast, Trp in self-assembled C_{16}p53 exhibited markedly higher anisotropy (Table 1). This increase could arise from Trp confinement due to steric constraints in the molecular level or from its presence on larger structures that have slower rotational diffusion. In order to discern between these two alternatives, we examined peptide anisotropy in a solution of 2,2,2-trifluoroethanol (TFE) at 29 °C. TFE at this temperature has the same viscosity as the aqueous solution used to obtain the values in Table 1 (*46*) and the peptide is in α-helical conformation (see below) but not aggregated. The obtained value of 0.057 ± 0.005 in TFE indicated that anisotropy increases primarily from the reduction in rotational freedom of Trp as a result of peptide folding and the ensuing interactions with the other hydrophobic side chains. Accordingly, disassembly of C_{16}p53 micelles and concomitant loss of peptide folding in a solution of 80% acetonitrile resulted in a decrease of anisotropy to 0.021 ± 0.004. In this case, the lower anisotropy value relative to the peptide arises from the markedly lower viscosity of the solvent.

Anisotropy values for the different PA analogs were higher than that of the unmodified peptide and varied depending on the linker (Table 1). A decrease in anisotropy was observed with increasing length of ethylene oxide linker suggesting higher rotational freedom of Trp and decreased folding. A higher anisotropy of $C_{16}A_4$p53 on the other hand indicated a more constrained microenvironment for Trp in this PA compared to C_{16}p53. Considering the high λ_{max} for $C_{16}A_4$p53, the reason for the higher anisotropy seems to differ qualitatively from the other PAs; a different type of secondary structure that induces tighter peptide packing is responsible for the observed anisotropy, as will be discussed in the following section.

Circular Dichroism Studies. Peptide folding into secondary structure elements was investigated by CD spectroscopy at concentrations of PAs exceeding their cmc. The unmodified peptide exhibited a predominantly random coil conformation with minimal helical content in aqueous solutions at 25 °C as previously reported (*23*) and shown here in Figure 3A. On the contrary, the CD spectrum of C_{16}p53 in water revealed significant folding with a maximum at 195 nm, a deep minimum at 207 nm, a shoulder at 222 nm, and low ellipticity at 230 nm. The spectrum does not resemble that of a typical α-helix, which shows minima at both 207 and 222 nm distinctly, at an intensity ratio close to 1. We suspected that Trp absorption contributes to the unusual CD spectral characteristics (*47−49*). A shift in the ratio between the two minima due to stacking with other aromatic side chains (*50*) and introduction of an additional peak around 230 nm (*48*), which may be positive or negative depending on the orientation of tryptophan relative to the peptide backbone, have both been reported. Oxidation of the tryptophan to an oxindole derivative by NBS resulted in a typical helical CD spectrum exhibiting both minima at 207 and 222 nm at approximately 1:1 ratio (Figure 3C) in accordance with a previous report (*50*). We argue that the absence of the second minimum for C_{16}p53 is indeed related to Trp interference and not the absence of α-helical structure. Oxidation of unmodified peptide did not in itself induce folding as evidenced by the minimal effects on its CD spectrum (Supporting Information Figure S2). However, we cannot exclude the possibility that the polarity change resulting from NBS oxidation did not induce changes in the type of folding. Nevertheless, fitting the NBS-oxidized C_{16}p53 spectrum using a linear combination of basis spectra based on poly(L-lysine) and poly(L-glutamic acid) (*6*) yielded an α-helical content of 63% with the remaining 37% being in random coil conformation (Supporting Information Figure S3).

The similarity of C_{16}p53 spectra in water and 10 mM PBS suggests that there is no effect of ionic strength on folding up to physiological values, and therefore, electrostatic interactions are not the main driving force for folding (Figure 3A). In the presence of 50% TFE, a solvent known to enhance peptide folding (*51*), the amount of α-helicity increased for both peptide and C_{16}p53 as expected (Figure 3B).

Folding stability was studied by monitoring ellipticity of the NBS-oxidized sample at 222 nm with increasing temperature (Figure 3D). A gradual loss of peptide secondary structure was observed; however, even at the highest temperature studied (80 °C), a substantial amount of peptide was folded, indicating a high thermal stability in the aggregate state.

We next analyzed EO-containing PAs in PBS (10 mM; pH 7.4) at 25 °C (Figure 4A). Short ethylene oxide spacers ($C_{16}EO_4$p53 and $C_{16}EO_{12}$p53) resulted in a small shift of the first minimum to 205 nm, which also became deeper, a higher molar ellipticity at 222 nm, and the clear appearance of a negative peak at 230 nm when compared to C_{16}p53. The longer linker ($C_{16}EO_{36}$p53) exhibited a similar spectrum but with higher ellipticity at 205 nm. The spectra indicated a decreasing degree of folding with increasing ethylene oxide length, which becomes more obvious when the NBS-oxidized spectra are compared

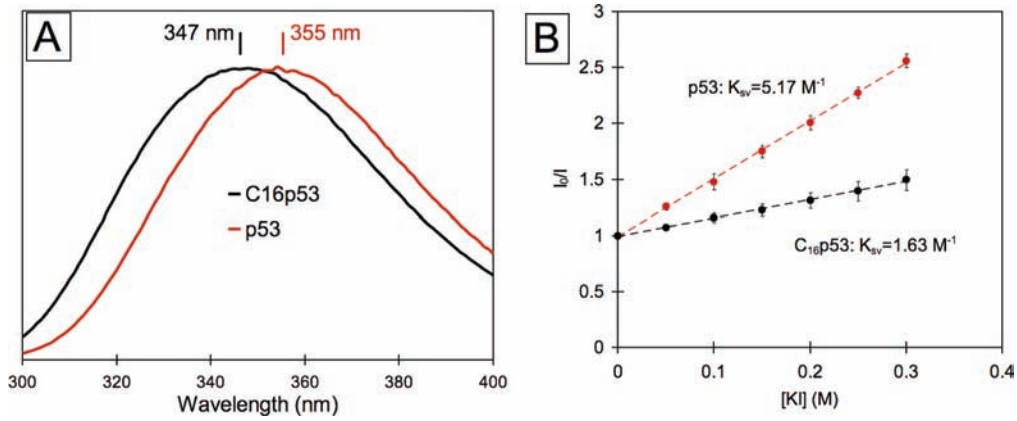


Figure 2. Comparison of Trp fluorescencence spectra of $p53_{14-29}$ and $C_{16}p53$ (A) and Stern−Volmer plots from iodine ion quenching experiments (B).

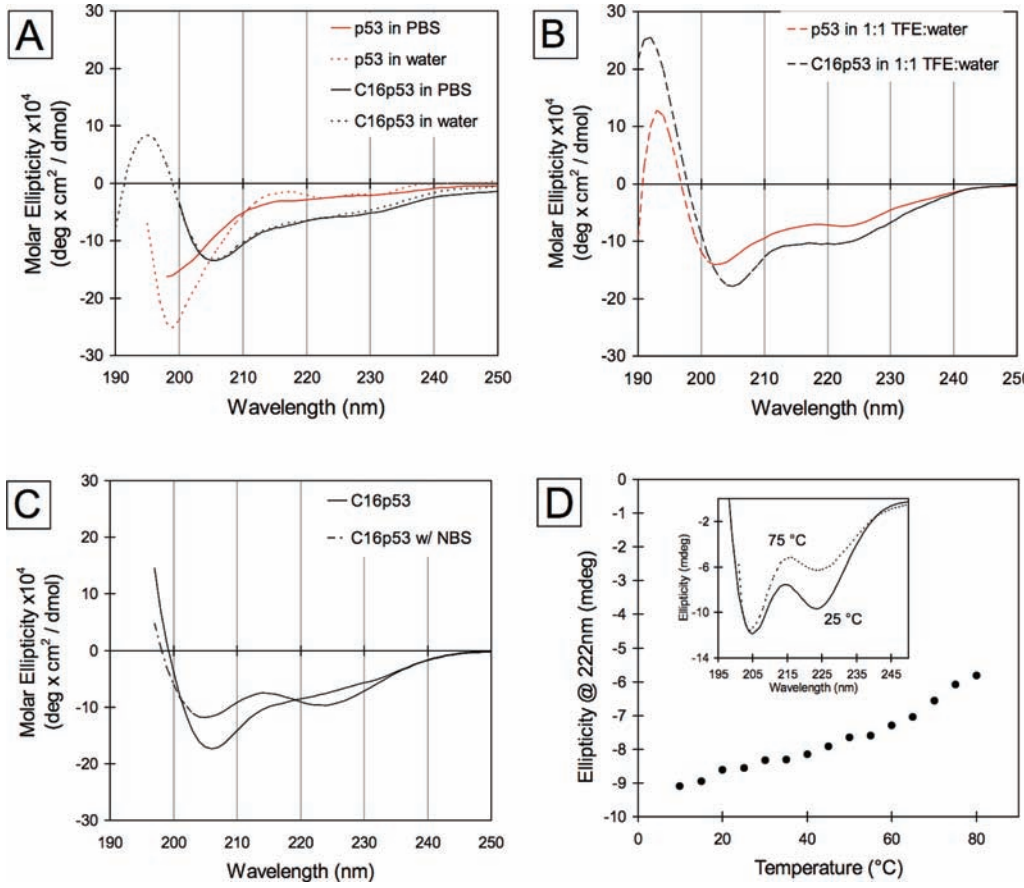


Figure 3. Circular dichroism spectra of $p53_{14-29}$ and $C_{16}p53$ in water and PBS 10 mM (A) and 2,2,2-trifluoroethanol (B). Oxidation of $C_{16}p53$ with 2 equiv. NBS resulted in a 1:1 ratio between ellipticities at 207 and 222 nm consistent with α-helix formation (C). Ellipticity at 222 nm as a function of temperature for NBS-oxidized $C_{16}p53$ (D) and corresponding spectra at 25 °C and 75°(D inset).

(Figure 5A−C). In these oxidized spectra, it is also apparent that the peak at 230 nm is due to tryptophan interference as has previously been predicted (*47*) and experimentally shown (*48, 49, 52−54*) and that the oxidized PAs clearly adopt an α-helical conformation. The peak at 230 nm is not visible in $C_{16}p53$, but this is most likely due to the lower ellipticity for this PA in the vicinity of 222 nm. We calculated α-helical contents of 54%, 45%, and 31% for oxidized $C_{16}EO_4p53$, $C_{16}EO_{12}p53$, and $C_{16}EO_{36}p53$, respectively.

In the PA with the proline linker ($C_{16}P_3p53$), changes were subtle; a slight blue shift of the negative peak at 207 nm and higher ellipticity at 222 nm suggest a slightly lower helical content compared to $C_{16}p53$ (Figure 4B). On the contrary, a dramatic change in the spectrum of $C_{16}A_4p53$ was evidenced (Figure 4B): a negative peak at 214 nm characteristic of β-sheet formation was recorded, in contrast to all previous samples. Oxidation with NBS in this case did not alter the CD spectrum (Figure 5D), which fitted to 91% β-sheet conformation.

Shape and Size of Micelles. The observed differences in peptide folding for the different PA analogues raise the question of how these affect and are in turn affected by micelle geometry. To this end, we performed multiangle dynamic light scattering measurements of PAs above their cmc's. All autocorrelation curves were satisfactorily fit using a cumulant fit to obtain a single average decay rate Γ_1 with moderate values (0.2−0.3) of the parameter Γ_2/Γ_1^2, which defines the width of the

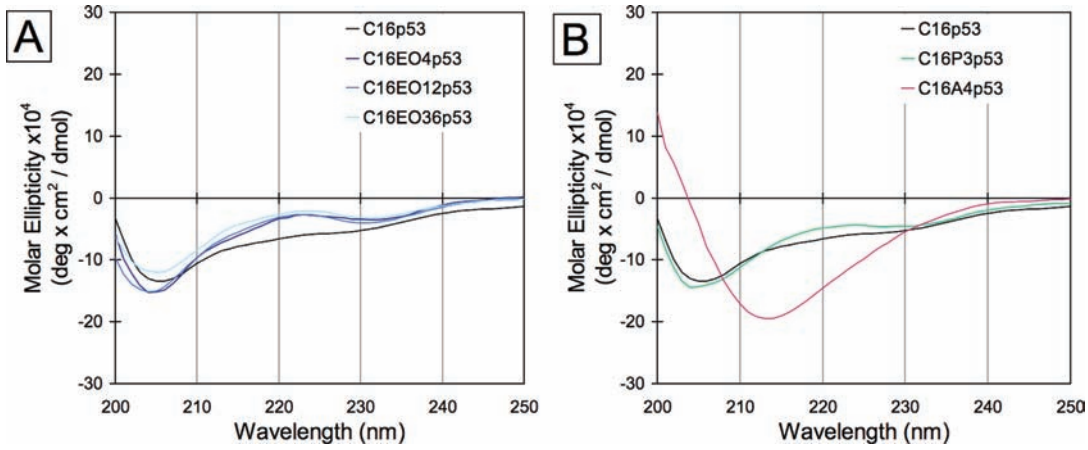


Figure 4. Circular dichroism spectra of ethylene oxide containing analogues (A) and $C_{16}A_4p53$ and $C_{16}P_3p53$ (B) in PBS 10 mM. CD spectrum of $C_{16}p53$ has been added for comparison purposes.

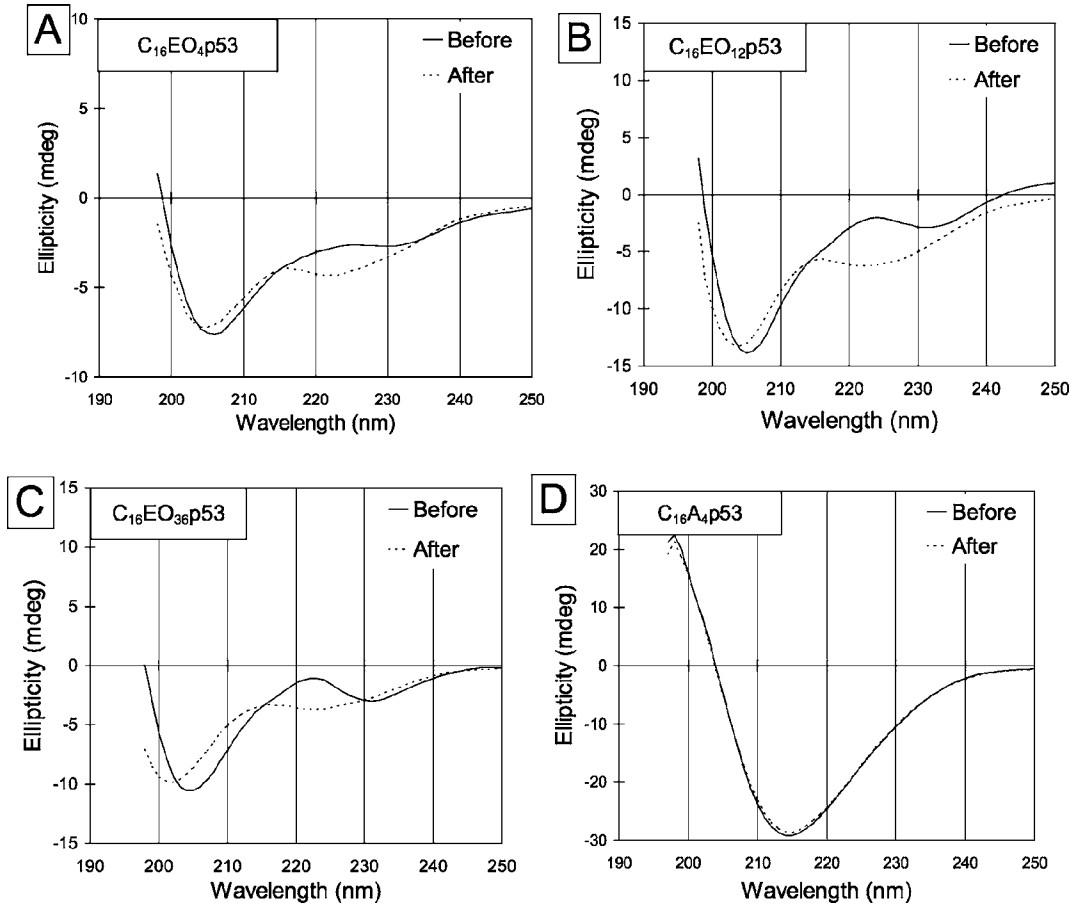


Figure 5. Comparison of CD spectra of peptide amphiphiles before and after oxidation with 2 mol equiv of *N*-bromosuccinimide (NBS). Spectra were acquired in PBS 10 mM, at 25 °C.

distribution. As an example of the pronounced q-dependence of the apparent diffusion coefficient $D_{app} = \Gamma_1/q^2$, results for $C_{16}p53$ aqueous solutions are presented (Figure 6). The apparent translational diffusion coefficient for the self-assembled structures was estimated at a scattering angle of 60°. Values of 1.91×10^{-8} cm²/s and 1.73×10^{-8} cm²/s were obtained for PBS 10 mM and water, respectively, which correspond to apparent spherical hydrodynamic diameters of 257 and 284 nm. These values exclude the formation of small spherical micelles and along with the observation of angular dependence point to formation of larger anisotropic structures. The insensitivity to ionic strength up to physiological salt concentration (0.15 M) further shows that electrostatic interactions are not the main determining factor in $C_{16}p53$ self-assembly (Figure 6). Hydrodynamic diameters of $C_{16}p53$ at a fixed angle of 90° did not seem to depend largely on concentration showing a small decrease from 0.5 to 2.5 mg/mL (Supporting Information Figure S4). Instead, an influence of temperature on size was noted: larger apparent hydrodynamic diameters were calculated when temperature increased from 5 to 55 °C (Supporting Information Figure S5).

We calculated the apparent hydrodynamic diameters for different batches of the PAs, at a scattering angle of 60° in PBS 10 mM (Figure 7). Interestingly, no major differences between analogues were noted with the exception of $C_{16}EO_{12}p53$. Even though the protocol developed for micelle formation gave far

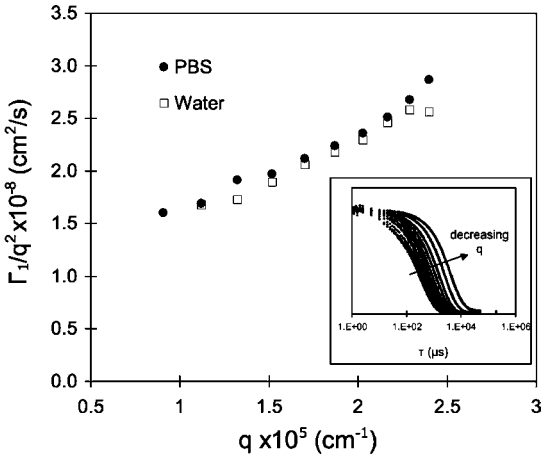


Figure 6. Angular dependence of apparent diffusion coefficient ($D_{app} = \Gamma_1/q^2$) of C_{16}p53 micelles in water and PBS 10 mM, at 25 °C. Normalized autocorrelation curves are shown in the inset for sample in PBS.

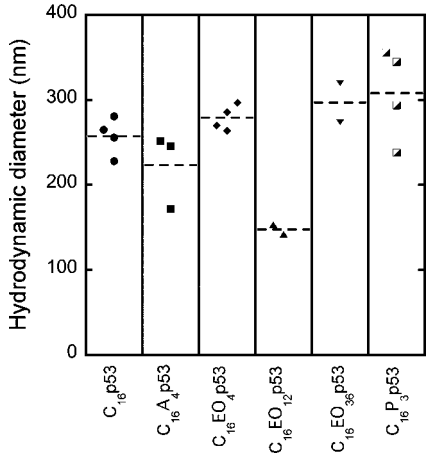


Figure 7. Hydrodynamic diameters of peptide amphiphile micelles in PBS 10 mM at 25 °C. Hydrodynamic diameters were calculated from apparent diffusion coefficients at 60° ($q = 0.0132$ nm^{-1}) and do not represent physical dimensions; they provide values for comparison between the different PA analogues. Each point represents a different batch.

more reproducible DLS results than direct dissolution of the lyophilized PAs and PAs were of high purity, we still observed some batch-to-batch variability indicating that micelle formation was sensitive to sample history and possible impurities. One of our initial hypotheses was that increasing length of the ethylene oxide linker would induce a high degree of curvature on the micelles due to larger headgroups and steric hindrances and thus a decrease in size (*7*). Although sample $C_{16}EO_{12}$p53 showed significantly faster diffusion (smaller size) than C_{16}p53, $C_{16}EO_{36}$p53 did not follow the trend.

The apparent hydrodynamic diameter provides values that are convenient for comparisons but do not correspond to actual physical dimensions. We sought shape information of the supramolecular structures by the use of atomic force microscopy. C_{16}p53 aqueous solutions deposited on freshly cleaved mica and imaged after water evaporation revealed the presence of elongated micelles (Figure 8). These images complement previously reported cryogenic transmission electron micrographs, where elongated structures were observed (*55*). We avoided extracting quantitative values for the size of the self-assembled structures based on AFM, since surface adsorption and the drying process could result in changes of the actual dimensions of the micelles in solution.

Analysis of the scaling behavior of the DLS data revealed no region in which D_{app} was independent of q (Figure 9 and

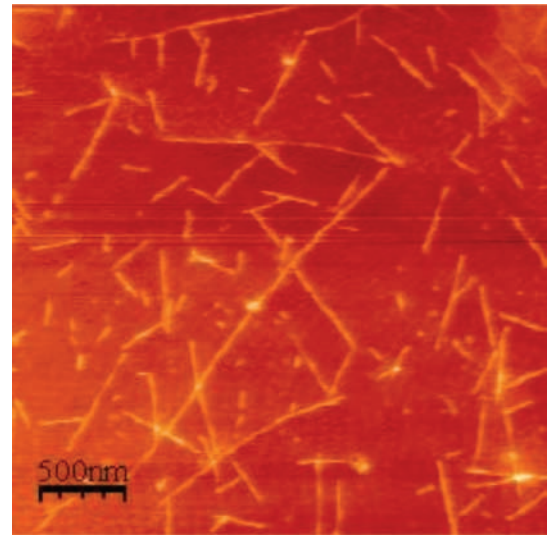


Figure 8. Atomic force micrograph showing formation of elongated micelles of C_{16}p53 deposited on mica following water evaporation.

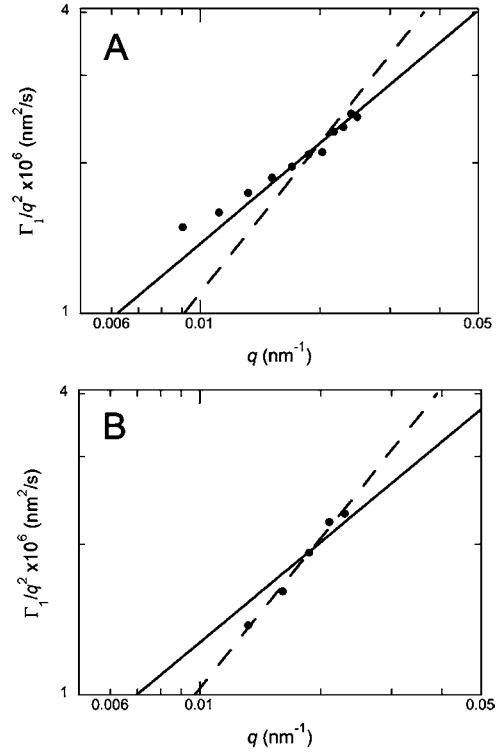


Figure 9. Angular dependence of calculated diffusion coefficient ($D_{app} = \Gamma_1/q^2$) of C_{16}p53 (A) and $C_{16}P_3$p53 (B) micelles in PBS 10 mM, at 25 °C. Solid lines correspond to the relation $D_{app}(q) \sim q^{2/3}$, while dashed lines represent $D_{app}(q) \sim q$.

Supporting Information Figure S6). Thus, the radius of gyration for all micelles is larger than ~100 nm. One exception to this statement is $C_{16}A_4$p53 micelles, for which the low scattering vector regime was found to extend to $q \approx 0.0135$ nm^{-1} corresponding to $r_g \approx 74$ nm (Supporting Information Figure S6). Scaling behavior for C_{16}p53 and $C_{16}EO_x$p53 micelles showed that $D_{app} \sim q^{2/3}$ and had no intermediate scaling region (Supporting Information Figure S6). This observation indicates that the micelles are fairly stiff, as their persistence length may approach $r_g/2$, exceeding 50 nm. In contrast, $C_{16}A_4$p53 and $C_{16}P_3$p53 micelles exhibited only the intermediate scaling region where $D_{app} \sim q$. From this, it can be concluded that $p > 0.022$ nm^{-1} and that the persistence length is less than 20 nm for these

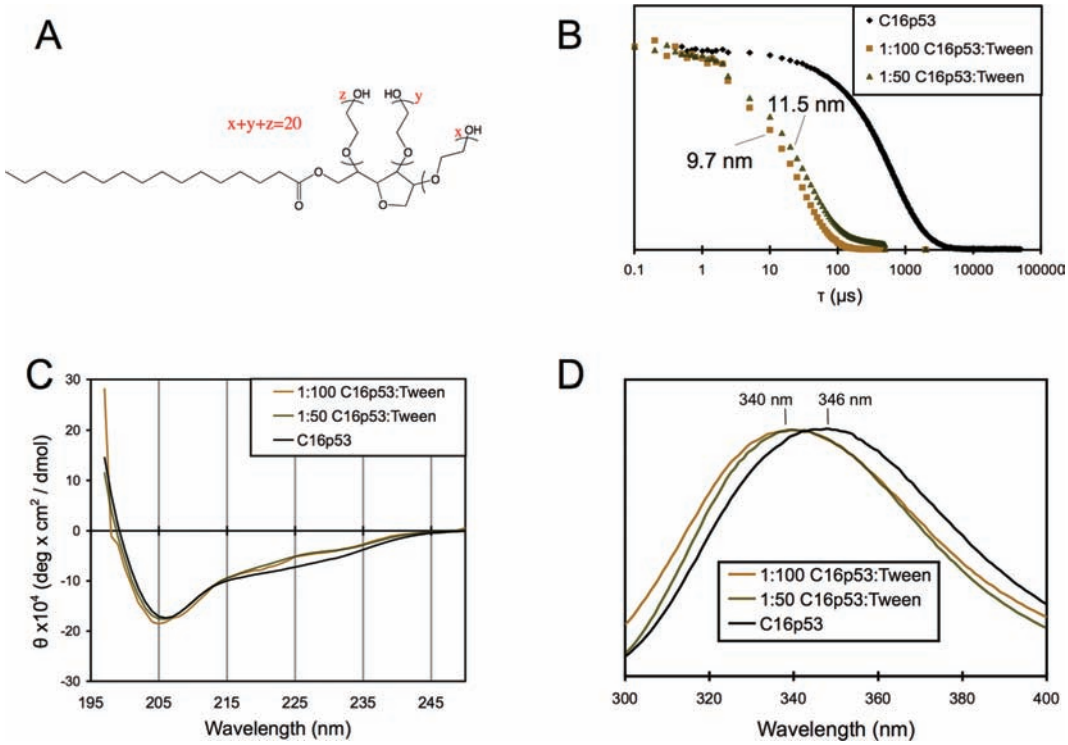


Figure 10. Mixing of C_{16}p53 with Tween 40 (A) at two different molar ratios resulted in formation of small spherical micelles. (B) Normalized autocorrelation curves of mixed micelles compared to single component C_{16}p53 micelles and calculated hydrodynamic diameters. (C) Circular dichroism spectra in PBS 10 mM at 25 °C and (D) Trp fluorescence spectra in PBS 10 mM in mixed micelles.

micelles. Thus, the A_4 and P_3 spacers result in more flexible micelles, although their overall hydrodynamic size is not significantly smaller than that of their C_{16}p53 and $C_{16}EO_x$p53 counterparts.

Formation of Small Spherical Micelles. We hypothesized that peptide folding and headgroup interactions are responsible for the elongated morphology of the self-assembled micelles instead of the highly curved micelles expected from the presence of large peptide headgroups. Indeed, in the absence of these interactions between PAs, formation of small spherical micelles occurred, consistent with monomer geometry. Mixing C_{16}p53 with Tween 40 (Figure 10A) resulted in the formation of small spherical micelles, similar in size to those formed by the surfactant alone (*56*) (Figure 10B). The two different molar ratios examined corresponded to an average of approximately one and two PAs per micelle, based on the reported aggregation number of 95 for pure Tween 40 micelles (*56*). Interestingly, circular dichroism revealed that peptides were folded, albeit to a lesser extent than single component C_{16}p53 micelles (Figure 10C). Examination of Trp fluorescence spectra showed its emission maximum at 340 nm (Figure 10D). The blue shift compared to C_{16}p53-only micelles is most likely a reflection of the ethylene glycol-rich corona formed by the Tween 40.

In contrast to C_{16}p53, the enhanced interactions between monomers of $C_{16}A_4$p53 did not allow the formation of mixed micelles. Mixing of this PA with Tween 40 at a molar ratio of 1:50 was not sufficient to disrupt H-bonding between peptide headgroups and resulted in two micelle populations as evidenced by DLS and β-sheet formation as measured by CD spectroscopy, respectively (Supporting Information Figures S6−S7).

DISCUSSION

Our present findings support conclusions from previous studies to the effect that attachment of a hydrophobic tail to an unfolded peptide and subsequent peptide amphiphile self-assembly induce secondary structure. This study further provides insight on the effect of different incorporated linkers between the palmitic tail and peptide $p53_{14-29}$ on peptide folding and supramolecular structure, demonstrating that secondary structure type and extent can be controlled by appropriate linker selection.

The main driving force for peptide amphiphile self-assembly is the hydrophobic effect of the attached hydrocarbon tails. In their absence, the unmodified peptide does not self-associate at concentrations up to 5 mg/mL, as evidenced by lack of scattering from objects larger than 2 nm or change in pyrene fluorescence spectra. The peptide remains unfolded, present mostly as a random coil, and as a consequence, tryptophan is fully hydrated and easily accessible to quenching ions. Peptide palmitoylation, micelle formation, and minimization of the interfacial area between the oily core and water results in close packing of the peptide headgroups. Loss of conformational freedom due to tethering and confinement leads to folding into defined secondary structure motifs and concomitant Trp fluorescence changes. Such behavior has been predicted using mechanistic models and lattice simulations and has been shown for a number of peptides with differing secondary structure motifs, including α-helices, triple helices, and β-sheets (*6, 14, 28, 29, 57, 58*). Peptide−peptide interactions are not necessary for folding: crowding with oligomeric ethylene oxide headgroups in Tween 40 mixed micelles also induced peptide folding.

However, our results demonstrate the importance of peptide−peptide interactions in determining the peptide secondary structure motifs of different PA analogues. These interactions were altered through the choice of linker and indicate that peptide folding is controlled by a subtle interplay of stabilizing forces. Similar conclusions were recently obtained by a study showing how secondary structure of a leucine-rich peptide was determined from the curvature of the gold particles it was attached onto (*32*). In contrast to that report, curvature in our system is not set a priori but is determined through the self-assembly process. In order to better understand our results, it is important to consider the structure of $p53_{14-29}$ in its physiological

state. There is no crystal structure available for the N-terminus of soluble p53; however, in a complex with hDM2, $p53_{18-26}$ forms an amphipathic α-helix, which inserts into a groove on the surface of hDM2 (*59*). The hydrophobic face of the helix displays the side chains of Phe_{19}, Trp_{23}, and Leu_{26}, which are critical for strong binding, with the aromatic rings of Phe and Trp stacked in close proximity to each other (*59*).

In the simplest PA where palmitic acid is directly attached to the N-terminus of the peptide via an amide bond (C_{16}p53), evidence points to a similar helical structure being formed. The unusual α-helical CD spectrum arises from Trp stacking, consistent with the blue shift that is observed in Trp fluorescence spectroscopy, a reduced accessibility to quenching iodide ions (*44*) and higher fluorescence anisotropy. The CD spectrum could be mistaken for that of a 3−10 helix (*60, 61*), but the demonstration that NBS-oxidized PAs exhibit an α-helical signature, as well as the fact that ellipticity at 195 nm is significantly higher than 0, point to an α-helical conformation. Trp_{23} seems to stack with Phe_{19}, as was found for the hDM2-bound peptide, rather than with another aromatic side chain of a neighboring peptide, since the spectra of C_{16}p53 "diluted" in Tween 40 mixed micelles were identical to those of C_{16}p53 micelles and anisotropy values of isolated peptides folded in the presence of TFE exhibited the same Trp anisotropy as that of folded C_{16}p53. We would like to note that it is not possible to exclude the scenario that NBS oxidation causes a structural change in the folded state of the peptide. Future infrared and/or NMR measurements should be pursued to clarify this point.

When hydrophilic ethylene oxide spacers of increasing length were interposed between peptide and tail, the extent of folding was lower. Again, significant changes in CD spectra upon NBS oxidation helped correlate the negative peak at 230 nm with Trp interference and quantify the decrease of folding in EO-containing analogues. A concomitant decrease in anisotropy was a result of partial unfolding, which increased rotational freedom of the fluorophor, while the blue shift in λ_{max} compared to C_{16}p53 is most likely linked to the presence of ethylene oxide in the micelle corona, which alters the local polarity of Trp. By comparison of the structures of C_{16}p53 and $C_{16}EO_x$p53, it is logical to assume that the observed changes arise from the more flexible nature of the oligo(ethylene oxide) backbone, which positions the peptide further from the core−corona interface, alleviating the molecular frustrations of the peptides, in that region. Moreover, control of α-helical content via ethylene oxide linker length could provide a powerful tool in examining its effect in situations where secondary structure is believed to be important in function.

Inclusion of four alanines linking the peptide with the palmitic tail resulted in formation of β-sheets between peptides. Consequently, Trp is no longer stacked with other side chains and its λ_{max} shows full hydration. The high anisotropy observed is presumably a consequence of the rigidity of the peptide due to the β-sheet structure along the micelle axis. The size of the A_4 linker is comparable to the shortest EO linker (EO_4); the noted difference in secondary structure is therefore a consequence of altered chemistry rather than different positioning of the peptide. Alanine is generally considered an α-helix promoter that favors a condensed state and helix formation is relatively uninhibited due to its small hydrophobic side chain (*62*); here, instead, the alanine side chain from neighboring peptides adjacent to the micelle core come in close proximity with each other, forming the condensed state with hydrogen bonds between them. This allows a tight packing and more parallel orientation of the alkane chains resulting in beneficially smaller interfacial area between the oily core and the aqueous phase. Inclusion of alanines has been shown to promote fiber formation of PAs through β-sheet formation along the fiber axis in a number of previous studies (*4, 10, 11, 13*). It appears that the stabilizing H-bonds from 4 alanines provide enough energy to overcome the tendency of the peptide to fold into an α-helix (*63*). The resulting micelles are stable such that mixing with a nonionic detergent (Tween 40) is not sufficient to disrupt the interactions between monomers, in contrast to what was observed for C_{16}p53 micelles.

Prolines are not able to form H-bonds due to their unique structure (*64*) and therefore disrupt the common secondary structure motifs α-helix and β-sheets. It has also been suggested that Pro may serve as a helix initiator when found at the N-termini of a helix, providing an initial twist and N-capping H-bonds (*65*). In our study, insertion of a rigid short proline linker did not seem to enhance helicity, but on the contrary, a decrease was noted, presumably in an analogous manner as for the EO-containing PAs.

The above findings confirm the importance of amino acid composition and H-bonding availability near the micellar core−corona interface on the folded structure of peptides in the corona. Peptide headgroup structuring and interactions are expected to additionally control the architecture of the self-assembled structure. Indeed, if we assume the peptide as a random coil and calculate the packing parameter (P) (*66*) for C_{16}p53 we obtain $p = 0.10$, predicting the formation of spherical micelles ($P \ll 1/3$): $P = (v)/(Al)$, where $l = 2.2$ nm is the length of the hydrophobic tail, $v = 0.46$ nm^3 its volume, and $A = 2.1$ nm^2 the surface area of the peptide headgroup that we can estimate from a headgroup volume of 2.32 nm^3 (using 0.73 cm^3/g as protein partial specific volume) and its 2-D projection of a peptide "sphere". The observation that elongated structures are formed is therefore consistent with peptide folding and concomitant headgroup area decrease with the peptide extending from the hydrocarbon−peptide interface. Recently, our group described the kinetic process of a simultaneous transition in secondary structure and micelle size to the above effect confirming this link (*67*). Here, no transitions were observed in the period of a week and equilibrium was reached within minutes, presumably due to differences in peptide headgroup as well as in the preparation protocol.

We did not observe major differences in the overall dimensions of the different analogues that we tested. We anticipated that increasing ethylene oxide length would promote spherical micelle formation due to steric effects of the larger headgroup. Nonionic surfactants composed of a 16-carbon tail and oligo(ethylene oxide) (also known as Brij surfactants) have been shown to transform from rod-like micelles (*68*) ($C_{16}EO_6$) to small spherical micelles having a diameter of approximately 11 nm (*69*) ($C_{16}EO_{20}$) with increasing number of ethylene oxide units. Attachment of the peptide at the end of an even longer EO linker did not have the anticipated effect on size presumably due to peptide−peptide interactions that persist even as the peptides are positioned further away from the hydrophobic core. This is consistent with the retention of a degree of peptide folding. Our understanding at this point is that the ethylene oxide segments extend away from the interface more so than would be expected if they adopted a random coil conformation. In contrast, when C_{16}p53 was mixed with an excess of Tween 40, small spherical mixed micelles were formed. This finding implies that peptide−peptide interactions are controlling micelle structure, even though they are not necessary for peptide folding as discussed previously.

Unlike overall size, we observed differences in micelle flexibility. Compared to C_{16}p53, flexibility was not affected by the addition of an EO spacer of any length but rather, by the incorporation of peptide spacers A_4 and P_3. It is possible that the P_3 spacer becomes more disruptive to packing within the micelle corona, causing correlations to decay faster along the micelle length than an extended EO layer. In the case of the A_4

spacer, we believe that β-sheet peptide structure plays a role in micelle flexibility. The coiling of β-sheet tapes may be responsible for cylindrical micelle structure and permit flexibility, as the hydrogen bonding pattern in these coiled tapes runs quasi-radially rather than axially down the micelle. Regardless of the precise mechanism, it is clear that variations in the linker between functional peptide and hydrophobic tail can affect micelle flexibility in addition to peptide secondary structure.

In conclusion, our study demonstrates that we can control the type and extent of peptide folding on self-assembled structures composed of peptide amphiphiles through inclusion of appropriate linkers in the region between the peptide of interest and the hydrophobic domain. Subtle modifications brought about strong effects, which are essential to design efficient PA assemblies. This understanding and control is required in cases where secondary structure is important for function, as in peptide−protein interactions or antibody production (*70*). In particular, the peptide we selected ($p53_{14-29}$) has been shown to exhibit enhanced binding to hDM2 when its α-helical content was increased through chemical modifications (*23*); our next steps are to examine binding of peptide amphiphile micelles to hDM2 and additionally correlate it with peptide folding.

ACKNOWLEDGMENT

This work was supported by National Heart, Lung and Blood Institute grant 5 U54 CA119335-04 and the MRSEC Program of the National Science Foundation under award DMR05-20415.

Supporting Information Available: Chemical structure (Supplementary figure S1) and molecular masses (Table S1) of peptide amphiphiles used are presented. Additional circular dichroism data (Supplementary figures S2 and S7) and dynamic light scattering results (Supplementary figures S3−S6) are also shown. This material is available free of charge via the Internet at http://pubs.acs.org.

LITERATURE CITED

(1) Jun, H. W., Paramonov, S. E., and Hartgerink, J. D. (2006) Biomimetic self-assembled nanofibers. *Soft Matter 2*, 177–181.
(2) Kokkoli, E., Mardilovich, A., Wedekind, A., Rexeisen, E. L., Garg, A., and Craig, J. A. (2006) Self-assembly and applications of biomimetic and bioactive peptide-amphiphiles. *Soft Matter 2*, 1015–1024.
(3) Beniash, E., Hartgerink, J. D., Storrie, H., Stendahl, J. C., and Stupp, S. I. (2005) Self-assembling peptide amphiphile nanofiber matrices for cell entrapment. *Acta Biomater. 1*, 387–97.
(4) Silva, G. A., Czeisler, C., Niece, K. L., Beniash, E., Harrington, D. A., Kessler, J. A., and Stupp, S. I. (2004) Selective differentiation of neural progenitor cells by high-epitope density nanofibers. *Science 303*, 1352–5.
(5) Karmali, P. P., Kotamraju, V. R., Kastantin, M., Black, M., Missirlis, D., Tirrell, M., and Ruoslahti, E. (2009) Targeting of albumin-embedded paclitaxel nanoparticles to tumors. *Nanomedicine 5*, 73–82.
(6) Bitton, R., Schmidt, J., Biesalski, M., Tu, R., Tirrell, M., and Bianco-Peled, H. (2005) Self-assembly of model DNA-binding peptide amphiphiles. *Langmuir 21*, 11888–95.
(7) Kastantin, M., Ananthanarayanan, B., Karmali, P., Ruoslahti, E., and Tirrell, M. (2009) Effect of the lipid chain melting transition on the stability of DSPE-PEG(2000) micelles. *Langmuir 25*, 7279–86.
(8) Hartgerink, J. D., Beniash, E., and Stupp, S. I. (2001) Self-assembly and mineralization of peptide-amphiphile nanofibers. *Science 294*, 1684–8.
(9) Hartgerink, J. D., Beniash, E., and Stupp, S. I. (2002) Peptide-amphiphile nanofibers: a versatile scaffold for the preparation of self-assembling materials. *Proc. Natl. Acad. Sci. U.S.A. 99*, 5133–8.
(10) Behanna, H. A., Donners, J. J., Gordon, A. C., and Stupp, S. I. (2005) Coassembly of amphiphiles with opposite peptide polarities into nanofibers. *J. Am. Chem. Soc. 127*, 1193–200.
(11) Paramonov, S. E., Jun, H. W., and Hartgerink, J. D. (2006) Self-assembly of peptide-amphiphile nanofibers: the roles of hydrogen bonding and amphiphilic packing. *J. Am. Chem. Soc. 128*, 7291–8.
(12) Cui, H., Muraoka, T., Cheetham, A. G., and Stupp, S. I. (2009) Self-assembly of giant peptide nanobelts. *Nano Lett.*
(13) Stendahl, J. C., Rao, M. S., Guler, M. O., and Stupp, S. I. (2006) Intermolecular forces in the self-assembly of peptide amphiphile nanofibers. *Adv. Funct. Mater. 16*, 499–508.
(14) Yu, Y. C., Berndt, P., Tirrell, M., and Fields, G. B. (1996) Self-assembling amphiphiles for construction of protein molecular architecture. *J. Am. Chem. Soc. 118*, 12515–12520.
(15) Murray, J. K., and Gellman, S. H. (2007) Targeting protein-protein interactions: Lessons from p53/MDM2. *Biopolymers 88*, 657–686.
(16) Landschulz, W. H., Johnson, P. F., and McKnight, S. L. (1988) The leucine zipper: a hypothetical structure common to a new class of DNA binding proteins. *Science 240*, 1759–64.
(17) Zelezetsky, I., and Tossi, A. (2006) Alpha-helical antimicrobial peptides--using a sequence template to guide structure-activity relationship studies. *Biochim. Biophys. Acta 1758*, 1436–49.
(18) Henchey, L. K., Jochim, A. L., and Arora, P. S. (2008) Contemporary strategies for the stabilization of peptides in the alpha-helical conformation. *Curr. Opin. Chem. Biol. 12*, 692–7.
(19) Ghosh, P. S., Verma, A., and Rotello, V. M. (2007) Binding and templation of nanoparticle receptors to peptide alpha-helices through surface recognition. *Chem. Commun. (Camb.)* 2796–8.
(20) Tashiro, S., Tominaga, M., Yamaguchi, Y., Kato, K., and Fujita, M. (2005) Folding a de novo designed peptide into an alpha-helix through hydrophobic binding by a bowl-shaped host. *Angew. Chem., Int. Ed. Engl. 45*, 241–4.
(21) Torres, O., Yuksel, D., Bernardina, M., Kumar, K., and Bong, D. (2008) Peptide tertiary structure nucleation by side-chain crosslinking with metal complexation and double "click" cycloaddition. *ChemBioChem 9*, 1701–5.
(22) Walensky, L. D., Kung, A. L., Escher, I., Malia, T. J., Barbuto, S., Wright, R. D., Wagner, G., Verdine, G. L., and Korsmeyer, S. J. (2004) Activation of apoptosis in vivo by a hydrocarbon-stapled BH3 helix. *Science 305*, 1466–70.
(23) Bernal, F., Tyler, A. F., Korsmeyer, S. J., Walensky, L. D., and Verdine, G. L. (2007) Reactivation of the p53 tumor suppressor pathway by a stapled p53 peptide. *J. Am. Chem. Soc. 129*, 2456–2457.
(24) Zhang, F., Sadovski, O., Xin, S. J., and Woolley, G. A. (2007) Stabilization of folded peptide and protein structures via distance matching with a long, rigid cross-linker. *J. Am. Chem. Soc. 129*, 14154–5.
(25) Kutchukian, P. S., Yang, J. S., Verdine, G. L., and Shakhnovich, E. I. (2009) All-atom model for stabilization of alpha-helical structure in peptides by hydrocarbon staples. *J. Am. Chem. Soc. 131*, 4622–4627.
(26) Chapman, R. N., Dimartino, G., and Arora, P. S. (2004) A highly stable short alpha-helix constrained by a main-chain hydrogen-bond surrogate. *J. Am. Chem. Soc. 126*, 12252–3.
(27) Ghadiri, M. R., and Choi, C. (1990) Secondary structure nucleation in peptides - transition-metal ion stabilized alpha-helices. *J. Am. Chem. Soc. 112*, 1630–1632.
(28) Forns, P., Lauer-Fields, J. L., Gao, S., and Fields, G. B. (2000) Induction of protein-like molecular architecture by monoalkyl hydrocarbon chains. *Biopolymers 54*, 531–46.
(29) Laczko, I., Hollosi, M., Vass, E., and Toth, G. K. (1998) Liposome-induced conformational changes of an epitopic peptide and its palmitoylated derivative of influenza virus hemagglutinin. *Biochem. Biophys. Res. Commun. 249*, 213–7.
(30) Wattenbarger, M. R., Chan, H. S., Evans, D. F., Bloomfield, V. A., and Dill, K. A. (1990) Surface-induced enhancement of internal structure in polymers and proteins. *J. Chem. Phys. 93*, 8343–8351.

(31) Chan, H. S., Wattenbarger, M. R., Evans, D. F., Bloomfield, V. A., and Dill, K. A. (1991) Enhanced structure in polymers at interfaces. *J. Chem. Phys. 94*, 8542–8557.
(32) Mandal, H. S., and Kraatz, H. B. (2007) Effect of the surface curvature on the secondary structure of peptides adsorbed on nanoparticles. *J. Am. Chem. Soc. 129*, 6356–7.
(33) Roberson, E. D., and Mucke, L. (2006) 100 years and counting: prospects for defeating Alzheimer's disease. *Science 314*, 781–4.
(34) Chene, P. (2003) Inhibiting the p53-MDM2 interaction: an important target for cancer therapy. *Nat. Rev. Cancer 3*, 102–9.
(35) Li, C., Liu, M., Monbo, J., Zou, G., Li, C., Yuan, W., Zella, D., Lu, W. Y., and Lu, W. (2008) Turning a scorpion toxin into an antitumor miniprotein. *J. Am. Chem. Soc. 130*, 13546–8.
(36) Berndt, P., Fields, G. B., and Tirrell, M. (1995) Synthetic lipidation of peptides and amino-acids - monolayer structure and properties. *J. Am. Chem. Soc. 117*, 9515–9522.
(37) Kastantin, M., Ananthanarayanan, B., Lin, B., Ressl, J., Black, M., and Tirrell, M. (2007) Increase of fluorescence anisotropy upon self-assembly in headgroup-labeled surfactants. *Macromol. Biosci. 7*, 189–94.
(38) Lakowicz, J. R. (1999) *Principles of fluorescence spectroscopy*, 2nd ed., Kluwer Academic/Plenum, New York.
(39) Winkler, R., Harnau, L., and Reineker, P. (1997) Distribution functions and dynamical properties of stiff macromolecules. *Macromol. Theory Simul. 6*, 1007–1035.
(40) Tu, R. S., and Tirrell, M. (2004) Bottom-up design of biomimetic assemblies. *Adv. Drug Delivery Rev. 56*, 1537–63.
(41) Guler, M. O., Claussen, R. C., and Stupp, S. I. (2005) Encapsulation of pyrene within self-assembled peptide amphiphile nanofibers. *J. Mater. Chem. 15*, 4507–4512.
(42) Astafieva, I., Zhong, X. F., and Eisenberg, A. (1993) Critical micellization phenomena in block polyelectrolyte solutions. *Macromolecules 26*, 7339–7352.
(43) Almgren, M., Grieser, F., and Thomas, J. K. (1979) Dynamic and static aspects of solubilization of neutral arenes in ionic micellar solutions. *J. Am. Chem. Soc. 101*, 279–291.
(44) Vazquez-Ibar, J. L., Guan, L., Svrakic, M., and Kaback, H. R. (2003) Exploiting luminescence spectroscopy to elucidate the interaction between sugar and a tryptophan residue in the lactose permease of Escherichia coli. *Proc. Natl. Acad. Sci. U.S.A. 100*, 12706–11.
(45) Ross, J. B., Rousslang, K. W., and Brand, L. (1981) Time-resolved fluorescence and anisotropy decay of the tryptophan in adrenocorticotropin-(1−24). *Biochemistry 20*, 4361–9.
(46) Kobayashi, K., and Nagashima, A. (1985) Measurement of the viscosity of trifluoroethanol and its aqueous-solutions under high-pressure. *Bull. JSME 28*, 1453–1458.
(47) Woody, R. W. (1994) Contributions of tryptophan side chains to the far-ultraviolet circular dichroism of proteins. *Eur. Biophys. J. 23*, 253–62.
(48) Ladokhin, A. S., Selsted, M. E., and White, S. H. (1999) CD spectra of indolicidin antimicrobial peptides suggest turns, not polyproline helix. *Biochemistry 38*, 12313–9.
(49) Mahalakshmi, R., Shanmugam, G., Polavarapu, P. L., and Balaram, P. (2005) Circular dichroism of designed peptide helices and beta-hairpins: Analysis of Trp- and Tyr-rich peptides. *ChemBioChem 6*, 2152–2158.
(50) Arnold, G. E., Day, L. A., and Dunker, A. K. (1992) Tryptophan contributions to the unusual circular dichroism of fd bacteriophage. *Biochemistry 31*, 7948–56.
(51) Roccatano, D., Colombo, G., Fioroni, M., and Mark, A. E. (2002) Mechanism by which 2,2,2-trifluoroethanol/water mixtures stabilize secondary-structure formation in peptides: a molecular dynamics study. *Proc. Natl. Acad. Sci. U.S.A. 99*, 12179–84.
(52) Friedrich, C. L., Rozek, A., Patrzykat, A., and Hancock, R. E. (2001) Structure and mechanism of action of an indolicidin peptide derivative with improved activity against gram-positive bacteria. *J. Biol. Chem. 276*, 24015–22.
(53) Vuilleumier, S., Sancho, J., Loewenthal, R., and Fersht, A. R. (1993) Circular dichroism studies of barnase and its mutants: characterization of the contribution of aromatic side chains. *Biochemistry 32*, 10303–13.
(54) Ohmae, E., Sasaki, Y., and Gekko, K. (2001) Effects of five-tryptophan mutations on structure, stability and function of Escherichia coli dihydrofolate reductase. *J. Biochem. 130*, 439–47.
(55) Missirlis, D., Khant, H., and Tirrell, M. (2009) Mechanisms of peptide amphiphile internalization by SJSA-1 cells in vitro. *Biochemistry 48*, 3304–14.
(56) Bester-Rogac, M. (2007) Micellar properties of nonionic surfactant Tween 40 (R) in water: Small-angle X-ray scattering study. *Acta Chim. Slov. 54*, 452–459.
(57) Boato, F., Thomas, R. M., Ghasparian, A., Freund-Renard, A., Moehle, K., and Robinson, J. A. (2007) Synthetic virus-like particles from self-assembling coiled-coil lipopeptides and their use in antigen display to the immune system. *Angew. Chem., Int. Ed. Engl. 46*, 9015–8.
(58) Meijer, J. T., Roeters, M., Viola, V., Lowik, D. W. P. M., Vriend, G., and van Hest, J. C. M. (2007) Stabilization of peptide fibrils by hydrophobic interaction. *Langmuir 23*, 2058–2063.
(59) Kussie, P. H., Gorina, S., Marechal, V., Elenbaas, B., Moreau, J., Levine, A. J., and Pavletich, N. P. (1996) Structure of the MDM2 oncoprotein bound to the p53 tumor suppressor transactivation domain. *Science 274*, 948–53.
(60) Silva, R. A. G. D., Yasui, S. C., Kubelka, J., Formaggio, F., Crisma, M., Toniolo, C., and Keiderling, T. A. (2002) Discriminating 3(10)- from alpha helices: Vibrational and electronic CD and IR absorption study of related Aib-containing oligopeptides. *Biopolymers 65*, 229–243.
(61) Toniolo, C., Polese, A., Formaggio, F., Crisma, M., and Kamphuis, J. (1996) Circular dichroism spectrum of a peptide 3(10)-helix. *J. Am. Chem. Soc. 118*, 2744–2745.
(62) Blaber, M., Zhang, X. J., and Matthews, B. W. (1993) Structural basis of amino-acid alpha-helix propensity. *Science 260*, 1637–1640.
(63) Velichko, Y. S., Stupp, S. I., and de la Cruz, M. O. (2008) Molecular simulation study of peptide amphiphile self-assembly. *J. Phys. Chem. B 112*, 2326–2334.
(64) Li, S. C., Goto, N. K., Williams, K. A., and Deber, C. M. (1996) Alpha-helical, but not beta-sheet, propensity of proline is determined by peptide environment. *Proc. Natl. Acad. Sci. U.S.A. 93*, 6676–81.
(65) Richardson, J. S., and Richardson, D. C. (1988) Amino acid preferences for specific locations at the ends of alpha helices. *Science 240*, 1648–52.
(66) Israelachvili, J. N. (1992) *Intermolecular and surface forces*, 2nd ed., Academic Press, San Diego.
(67) Shimada, T., Lee, S., Bates, F. S., Hotta, A., and Tirrell, M. (2009) Wormlike micelle formation in peptide-lipid conjugates driven by secondary structure transformation of the headgroups (dagger). *J. Phys. Chem. B*
(68) Cummins, P. G., Staples, E., Penfold, J., and Heenan, R. K. (1989) Geometry of micelles of the poly(oxyethylene) nonionic surfactants C16e6 and C16e8 in the presence of electrolyte. *Langmuir 5*, 1195–1199.
(69) D'Errico, G., Ciccarelli, D., and Ortona, O. (2005) Effect of glycerol on micelle formation by ionic and nonionic surfactants at 25 degrees C. *J. Colloid Interface Sci. 286*, 747–54.
(70) Muhs, A., Hickman, D. T., Pihlgren, M., Chuard, N., Giriens, V., Meerschman, C., van der Auwera, I., van Leuven, F., Sugawara, M., Weingertner, M. C., Bechinger, B., Greferath, R., Kolonko, N., Nagel-Steger, L., Riesner, D., Brady, R. O., Pfeifer, A., and Nicolau, C. (2007) Liposomal vaccines with conformation-specific amyloid peptide antigens define immune response and efficacy in APP transgenic mice. *Proc. Natl. Acad. Sci. U.S.A. 104*, 9810–5.

BC900383M

Binding of Europium(III) to a Non-Nucleosidic Phenanthroline Linker in DNA

Ching-Hui Huang,[†] Austin Parish,[†] Florent Samain,[‡] Florian Garo,[‡] Robert Häner,[‡] and Janet R. Morrow*[,†]

Department of Chemistry, 526 Natural Sciences Complex, University at Buffalo, State University of New York, Amherst, New York 14260-3000, and Department of Chemistry and Biochemistry, University of Bern, Freiestrasse 3, 3012 Bern, Switzerland.
Received September 1, 2009; Revised Manuscript Received January 9, 2010

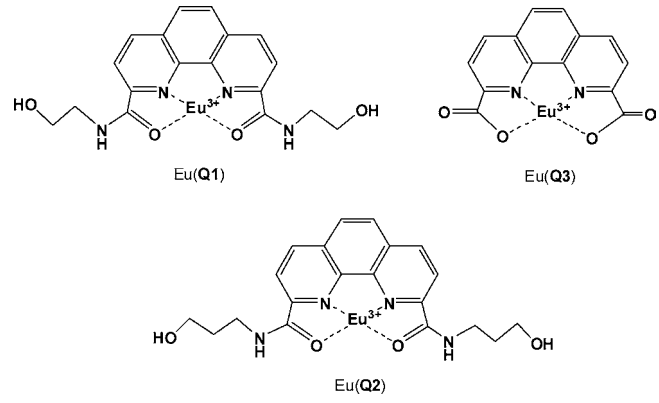
Eu(III) complexes of DNA containing a non-nucleosidic linker, a derivative of 1,10-phenanthroline-2,6-dicarboxamide (**Q**), are studied with the goal of forming novel lanthanide ion binding sites that are incorporated in the backbone of DNA. One oligonucleotide is short and unstructured (TTTQTTT (**QT6**)) and the other (5′-AGCTCGGTCAQCGAGAGTGCA-3′ (**SQ**)) is studied both in single-stranded form and in the presence of a partially complementary DNA strand. Luminescence spectroscopy studies show that Eu(III) binds to **SQ**, **QT6**, **AQB**, or **QB** 1100-, 56-, 23-, or 27-fold more tightly, respectively, than to a simple 1,10-phenanthroline-2,6-dicarboxamide ligand (**Q1**). Direct excitation and phenanthroline sensitized luminescence spectroscopy supports binding of Eu(III) to the phenanthroline linker in **QT6** and in double-stranded DNA formed from **SQ** and partially complementary sequences that place **Q** in a bulge-like position. Eu(III) hydration numbers range from 3 to 5 when bound to the phenanthroline moiety in modified DNA, consistent with binding to the tetradentate linker and, in some cases, coordination to other groups in the DNA. Thermal melting experiments show that **Q** in a bulge-like structure stabilizes double-stranded DNA and that Eu(III) binding does not markedly affect the stability of the duplex.

INTRODUCTION

There is much interest in the study of DNA that has been functionalized to bind metal ions with useful magnetic, optical, or redox properties. These hybrid materials rely on the self-assembly properties of DNA or DNA analogues to build large organized structures with unique characteristics (*1*−*4*). The incorporation of unnatural ligating groups for metal ions into DNA facilitates the formation of these nucleic acid/metal ion hybrid materials. Such ligands may be incorporated as base modified nucleotides (*2*−*6*) or as non-nucleosidic ligands (*1, 7*−*10*). Ligands may be appended to either the 5′ or 3′-termini of DNA (*11*−*14*) or, alternately, incorporated in midsequence of the DNA (*1, 7, 15, 16*). Ligands appended to the termini of DNA allow for the formation of large supramolecular structures through interaction of metal ions with ligands on distinct DNA strands (*17*). However, ligands incorporated in midsequence sites ultimately are more versatile for control of the metal ion environment within the nucleic acid (*18*). Our interest lies in the formation of metal ion complexes that are incorporated internally within the DNA, but retain open coordination sites at the metal ion center. Such complexes may be useful for the construction of agents for optical and magnetic resonance imaging (*18, 19*).

To date, most reports of ligands incorporated into DNA bind transition metal ions or Zn(II) (*1*−*6*). There are few examples of f-element coordination, despite interest in the rich luminescence, magnetic, and catalytic properties of the lanthanide ions (*12, 20*−*22*). Here, we report, to the best of our knowledge, the first example of a lanthanide(III) complex of a heterocyclic aromatic ligand which is incorporated as a linker into the DNA phosphate diester backbone. The present study incorporates a non-nucleoside building block based on a 1,10-phenanthroline-2,6-dicarboxamide derivative (*23, 24*) into single- and double-stranded DNA. Oligonucleotides are prepared that contain the phenanthroline-containing linker in a sequence containing only thymidines, as an example of a relatively unstructured DNA sequence and in two duplexes in a bulge-like position that lack an opposing nitrogenous base on the complementary strand. The linker was chosen on the basis of the favorable binding and luminescent properties of Ln(III) complexes of analogous 1,10-phenanthroline derivatives that contain either carboxylates (*25, 26*) or alcohols as additional donor groups (Scheme 1) (*27, 28*).

Scheme 1



EXPERIMENTAL PROCEDURES

Materials. $Eu(CF_3SO_3)_3$ was purchased from Aldrich. Unmodified DNAs were purchased from Integrated DNA Technologies (IDT) in desalted form. Oligonucleotides were annealed by heating solutions containing 100 mM NaCl, 20 mM buffer, and oligonucleotide to 90 °C for 10 min and allowed to cool to room temperature overnight. Phenanthroline modified DNA was prepared as reported previously (*18, 19, 26*).

Synthesis. 2,9-Bis(2-hydroxyethylamide)-1,10-phenanthroline (Q1). A mixture of 2,9-bis(methoxycarbonyl)-1,10-phenanthroline (0.094 g, 0.32 mmol) (*29, 30*) and aminoethanol (0.04

* Janet R. Morrow, jmorrow@buffalo.edu, phone: 716-645-4187, fax: 716-645-6963.
[†] State University of New York.
[‡] University of Bern.

10.1021/bc900386w © 2010 American Chemical Society
Published on Web 02/10/2010

mL, 0.66 mmol) was placed under reflux in ethanol (2 mL) for 4 h. The mixture was dried and the resulting solid was added to ethanol with a few drops of chloroform added to promote dissolution. Ether was added until the solution turned cloudy and the solution was placed in the freezer overnight. Yellow needle-shaped crystals were obtained as pure product. Yield: 50%. ESI-MS *m/e*: {**Q1** + H^+}, 355; {**Q1** + Na^+}, 377. ^{1}H NMR (400 MHz, DMSO) δ 9.3 (t, 2H, −NH), 8.8, 8.5 (d, 4H, ring), 8.2 (s, 2H, ring), 4.9 (t, 2H, −OH), 3.7 (t, 4H, $-CH_2OH$), 3.6 (t, 4H, $-CH_2$). ^{13}C NMR (300 MHz, DMSO) δ 164.4, 150.2, 144.2, 138.9, 130.9, 128.5, 121.6, 60.4, 42.4.

2,9-Bis(3-hydroxypropylamide)-1,10-phenanthroline (Q2). A solution containing 2,9-bis(methoxycarbonyl)-1,10-phenanthroline (0.202 g, 0.68 mmol) and 3-amino-1-propanol (0.105 mL, 1.38 mmol) was placed under reflux in ethanol (2 mL) for 4 h. The mixture was dried and the resulting solid was added to ethanol with a few drops of chloroform added to promote dissolution. Ether was added until the solution turned cloudy and the solution was placed in the freezer overnight. Small white crystals were obtained as product. Yield: 50%. ESI-MS *m/e*: {**Q2** + H^+}, 383; {**Q2** + Na^+}, 405. ^{1}H NMR (500 MHz, DMSO) δ 9.5 (t, 2H, −NH), 8.7, 8.4 (d, 4H, ring), 8.2 (s, 2H, ring), 4.8 (t, 2H, −OH), 3.7 (t, 4H, $-CH_2OH$), 3.6 (t, 4H, $-CH_2$), 1.8 (t, 4H, $-CH_2$). ^{13}C NMR (300 MHz, DMSO) δ 164.3, 150.3, 144.3, 138.9, 130.9, 128.5, 121.6, 60.4, 37.9, 32.7.

Instrumentation. An Orion research digital ionalyzer, model 510, equipped with a temperature compensation probe was used for all pH measurements. All ^{1}H and ^{13}C NMR were recorded on a Varian Gemini-300, Varian Inova-400 or Inova-500 spectrometer. Modified DNA was synthesized as reported previously (*23*). DNA thermal melting experiments were carried out on a Beckman Coulter DU 800 spectrophotometer equipped with a high performance temperature controller Peltier. The T_m values were calculated by using the MeltWin program and are given in Table 1 (*31*).

Luminescence Spectroscopy (Direct Excitation). Eu(III) excitation spectra and excited-state lifetimes were obtained using a Spectra-Physics Quanta Ray PRO-270−10 Q-switched Nd:YAG pump laser (10 Hz, 60 mJ/pulse) and a MOPO SL for all luminescence measurements (*27*). The $^7F_0 \rightarrow {}^5D_0$ transition of the Eu(III) ion was scanned between 578 and 581 nm while the $^5D_0 \rightarrow {}^7F_2$ emission band was monitored at 628 ± 27 nm using a band-pass filter. Excitation spectra were fit by using the program *Peak Fit 4.12* (Jandel). Time resolved luminescence measurements were collected by using a digital Tektronix TDS 3034B oscilloscope. Five data sets per wavelength were fit to a single exponential decay by using *Graphpad Prism 4* (Graphpad Prism Software, Inc.) and averaged (*28, 29*).

Isotherms from Eu(III) binding to DNA and to phenanthroline modified DNA were fit to eq 1 by using *Sigmaplot 10* (systat). Here, C is the Eu(III) aquo complex, CA is Eu(III) complex bound to DNA, A is the DNA concentration, *X* is mole fraction, and *I* is luminescence intensity at a chosen wavelength. K_d is the dissociation constant. The solution includes 20 μM complex, 20 mM HEPES buffer, 100 mM NaCl.

$$\begin{aligned} F &= [C]_{tot} + [A]_{tot} + K_d \\ [CA] &= \left(F - \sqrt{(F^2 - 4[C]_{tot}[A]_{tot})}\right)/2 \\ X_{CA} &= \frac{[CA]}{[C]_{tot}} \\ X_C &= 1 - X_{CA} \\ I_{obsd} &= X_C I_C + X_{CA} I_{CA} \end{aligned} \quad (1)$$

Luminescence Spectroscopy (Ligand Sensitized). Excitation and emission spectra were obtained using a Cary Eclipse fluorimeter. Excitation spectra were recorded with 0.2 ms delay time and 5 ms gate time in the excitation range 270−320 nm. Emission spectra were recorded for Eu(III) complex in the range 565−720 nm with selective irradiation at 295 nm (λ_{ex} = 295 nm) and for excitation spectra, the wavelength 615 nm (λ_{em} = 615 nm) was monitored.

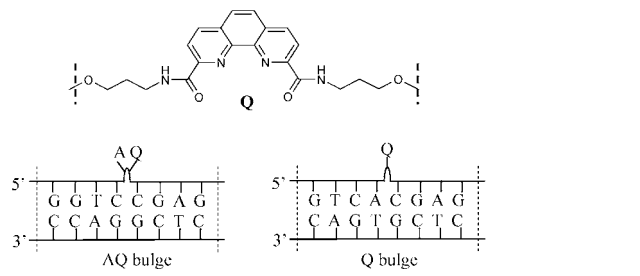
RESULTS

DNA Sequences. Two different DNA sequences were prepared with a 1,10-phenanthroline-2,9-dicarboxamide incorporated midsequence. The first sequence, 5′-TTTQTTT-3′, was prepared as an example of a simple single-stranded DNA which lacks significant secondary structure (Q represents the 1,10-phenanthroline-2,9-dicarboxamide linker in Table 1). The second sequence, 5′-AGCTCGGTCAQCGAGAGTGCA-3′, was used in combination with partially complementary strands to form two different DNA duplexes that have either Q or an AQ lacking an opposing base on the unmodified DNA strand to give a bulge-like structure (**QB** and **AQB**, see Table 1). For comparison, three DNA duplexes, one fully complementary, one containing a single T-bulge and one containing an AT bulge were studied (Table 1). In addition, the ligands **Q1** and **Q2** were prepared for comparison with the modified DNA sequences (Scheme 1).

The stability of the five DNA duplexes was studied by using optical thermal melting experiments. These experiments showed that **AQB** and **QB** DNA have higher stability in comparison to the natural AT or T bulged DNA (Table 1) with T_m values that increase by 20 °C for the modified duplexes at equal concentrations. This suggests that the phenanthroline linker stabilizes the duplex through stacking interactions with bases in the helix. A more modest increase in stability was previously observed for DNA duplexes that contain Q opposite an abasic site (*23*). The T_m values of all duplexes here were only slightly affected (1−4 °C) by the addition of 1 equiv of Eu(III) (Table 1) at 3, 19, or 25 μM DNA. In addition, Eu(III) has little effect on either the

Table 1. DNA Used in This Study and Data from Optical Thermal Melting Studies[b]

DNA	Duplex	T_m(°C)	ΔT_m(°C)[a]
AQB	(5′) AGCTCGGTCAQCGAGAGTGCA (3′) TCGAGCCAG --- GCTCTCACGT	66.0	-2.2
QB	(5′) AGCTCGGTCAQCGAGAGTGCA (3′) TCGAGCCAGT-- GCTCTCACGT	69.8	-3.9
AT bulge	(5′) AGCTCGGTCATCGAGAGTGCA (3′) TCGAGCCAG --- GCTCTCACGT	45.1	-1.5
T bulge	(5′) AGCTCGGTCATCGAGAGTGCA (3′) TCGAGCCAGT--GCTCTCACGT	50.0	-1.7
Stem	(5′) AGCTCGGTCATCGAGAGTGCA (3′) TCGAGCCAGTAGCTCTCACGT	71.2	-1.5
SQ	(5′) AGCTCGGTCAQCGAGAGTGCA	---	---
QT6	(5′)TTTQTTT	---	---



[a] ΔT_m = Change in T_m upon addition of 3.00 uM $EuCl_3$. ΔT_m of solutions containing 25 uM AQB and 25 μM $EuCl_3$ is −1.0 °C, ΔT_m of 19 uM QB and 19 μM $EuCl_3$ is −1.0 °C. [b] All solutions contain 3.00 uM DNA, 20.0 mM MES buffer, and 100 mM NaCl at pH 6.5.

hyperchromicity or cooperativity of the transition as shown from the similarity of the optimal thermal melting curves in the absence or presence of Eu(III) ion (Supporting Information Figure S1). This shows that binding of Eu(III) under these conditions does not markedly destabilize the DNA duplex.

Luminescence Spectroscopy. Both direct excitation luminescence spectroscopy and phenanthroline linker-sensitized luminescence spectroscopy of Eu(III) bound to modified DNA and **Q1** were used for characterization. For direct excitation luminescence spectroscopy, the Eu(III) $^7F_o \rightarrow {}^5D_o$ transition was excited and the intense luminescence emission band ($^5D_o \rightarrow {}^7F_2$) was monitored. The $^7F_o \rightarrow {}^5D_o$ transition occurs between two electronic states that are nondegenerate and thus not split by ligand fields. This gives rise to a single excitation peak for each Eu(III) complex species, barring overlap of peaks (*32, 33*). In addition, time-resolved luminescence studies give information on the hydration state of the Eu(III) ion by taking into account quenching of the excited state through vibronic coupling with OH and NH groups. The number of bound waters, q, is estimated by using eq 2 (*33, 34*) where A is a constant specific to Eu(III) (1.1 ms), and k_{H2O} and k_{D2O} are the rate constants for luminescence decay in H_2O and D_2O, respectively. The $k_{HNC=O}$ term is to account for quenching by amides (0.075 ms^{-1} for each NH) and α is the total outersphere quenching (0.25 ms^{-1}). Alternately, a simplified form that gives an estimate of q without luminescence lifetime data in D_2O or assumptions about additional ligand quenching contributions, eq 3 (*35*), was used with $A' = 1.05$ ms and $\alpha' = 0.44$. Use of this simplified form is warranted in systems that do not have well-characterized quenching contributions from first and second sphere ligands such as the systems studied here. Amide and second sphere quenching parameters are well-established for macrocyclic complexes (*34*), but not for phenanthroline ligands conjugated to DNA.

$$q = A(k_{H2O} - k_{D2O} - \delta k_{NHC=O} - \alpha) \quad (2)$$

$$q' = A'(k_{H2O} - \alpha') \quad (3)$$

The $^7F_o \rightarrow {}^5D_o$ excitation spectrum of the Eu(III) complex of a simple ligand that is structurally similar to the DNA linker (**Q1** in Scheme 1) has a single peak at 579.32 nm, supportive of a single Eu(III) species in solution (Supporting Information Figure S2). The effective dissociation constant for Eu(**Q1**), determined at pH 6.5, 100 mM NaCl in 20 mM MES buffer, from a plot of the UV−vis absorbance spectrum of **Q1** as a function of Eu(III) (Supporting Information Figure S3) is 46 μM. The complex was further characterized by using time-resolved luminescence spectroscopy. Recovered luminescence lifetimes collected in H_2O and D_2O were used to calculate q values by using either eq 2 or 3 (Table 2). The q values are consistent with tetradentate coordination of the ligand **Q1** to form a Eu(III) complex with five water ligands and an overall coordination number of nine. Nonintegral values of q arise from the inherent uncertainty in the determination of luminescence lifetimes (*32*) as well as the lack of well-established inner- or outer-sphere ligand quenching parameters for Eu(III) phenanthroline derivatives. Nonetheless, a q number of five for Eu(**Q1**) is consistent with tetradentate coordination of **Q1**. This shows that the alcohol groups do not coordinate to Eu(III). Consistent with this postulate that the alcohols are not donor groups, we determined that a related ligand with a longer hydroxyalkyl chain (**Q2**) binds Eu(III) similarly. The effective dissociation constant for Eu(**Q2**), determined at pH 6.5, 100 mM NaCl in 20 mM MES buffer, from a plot of the UV−vis absorbance spectrum of **Q2** as a function of Eu(III) is 41 μM, close to that of Eu(**Q1**) (data not shown). Eu(**Q2**) has a q number of five, also consistent with no coordination of the alcohol groups (Scheme 1, Table 2). Further direct Eu(III) excitation studies were carried out in the presence of up to a 14- or 16-fold excess of **Q1** or **Q2** ligand, respectively (Supporting Information Figure S4). The retention of a single excitation peak and the constancy of the luminescence lifetimes show that the 1:1 complex predominates in solution even under conditions of excess ligand.

Table 2. Luminescence Lifetime Data and the Number of Metal Bound Water Ligands (q) for Eu(III) Complexes of Q1, Q2, and Q-DNA[a]

ligand	λ (nm)[c]	τ_{H2O} (ms)	k_{H2O} (ms^{-1})	τ_{D2O} (ms)	k_{D2O} (ms^{-1})	q[d]	q'[e]
Q1	579.40	0.183	5.46	2.074	0.482	5.0	5.3
Q2	579.40	0.188	5.32	2.424	0.413	4.9	5.1
SQ[b]	578.80	0.174	5.75	–	–	–	5.6
	579.46	0.182	5.49	–	–	–	5.3
	579.92	0.188	5.32	–	–	–	5.1
AQB[b]	578.88	0.153	6.54	1.390	0.719	6.0	6.4
	579.50	0.181	5.52	1.377	0.726	4.8	5.4
	580.00	0.204	4.90	1.399	0.715	4.1	4.7
QB[b]	579.10	0.167	5.99	1.489	0.672	5.4	5.8
	579.36	0.190	5.26	1.489	0.672	4.6	5.1
	579.90	0.204	4.90	1.514	0.661	4.2	4.7
QT6[b]	579.48	0.316	3.16	–	–	–	2.9
	579.90	0.318	3.14	–	–	–	2.9

[a] Standard deviations in lifetime values are typically ≤7% in H_2O and ≤3% in D_2O (*28*). [b] 25.0 uM DNA, 20.0 mM MES buffer, and 100 mM NaCl with 25.0 uM $EuCl_3$ at pH 6.5. [c] Excitation wavelength is chosen to collect separate lifetime decays for each species. [d] q is the number of bound waters as calculated from eq 2. [e] q' is the number of bound waters as calculated from eq 3.

It is notable that the analogous carboxylate ligand **Q3** (*26*) binds strongly to lanthanide ions and coordinates to the similarly sized Ca(II) ion as a tetradentate ligand through the phenanthroline nitrogens and carbonyl oxygens. However, **Q3** binds Ln(III) many orders of magnitude more strongly than does **Q1** or **Q2** (log $K = 16$ for Gd(**Q3**)), consistent with amides being weaker donor groups than carboxylates (*26, 27*).

The $^7F_o \rightarrow {}^5D_o$ excitation spectrum of Eu(III) in the presence of **QT6** shows two major peaks (579.89 nm, 579.44 nm) and a minor peak (579.05 nm) as shown in Figure 1a. The two major excitation peaks are substantially red-shifted in comparison to Eu(III) aqua ion (*36*) or Eu(III) bound to unmodified DNA (see below). The wavelength of the middle excitation peak is similar to that of the simple ligands **Q1** or **Q2**. Luminescence lifetimes for both major excitation peaks are consistent with a q value of three and are identical within experimental error. This suggests that the two peaks arise from two different species with distinct conformations that both have three bound water molecules. The unexpectedly low q value supports interaction of Eu(III) to DNA groups in addition to the phenanthroline moiety. The identity of the species that gives rise to the minor peak at 579.05 nm is uncertain. One assignment, based on excitation peak wavelength, is Eu(III) bound to unmodified DNA (see below). However, the peak is very small and buried underneath the excitation peaks of the major species, so that it is not possible to obtain luminescence lifetime data to enable making a definitive assignment of the Eu(III) species.

The dissociation binding constant for Eu(III) with **QT6** DNA was determined from a plot of the luminescence intensity of the complex at 579.89 nm as a function of **QT6** DNA and fit to eq 1 to give a K_d of 0.82 μM, 56-fold tighter than for the simple ligand **Q1** (Supporting Information Figures S5, S6). The stronger binding of Eu(III) to **QT6** compared to **Q1** suggests that either the environment of the DNA or other ligating groups on the DNA such as phosphate esters or nucleobases influence the strength of Eu(III) complex formation. However, it is clear that Eu(III) binds primarily to the phenanthroline linker in Q-containing DNA and not solely to the unmodified DNA as shown by comparison to excitation spectra and q numbers of Eu(III) titrated with unmodified DNA (see below). In addition,

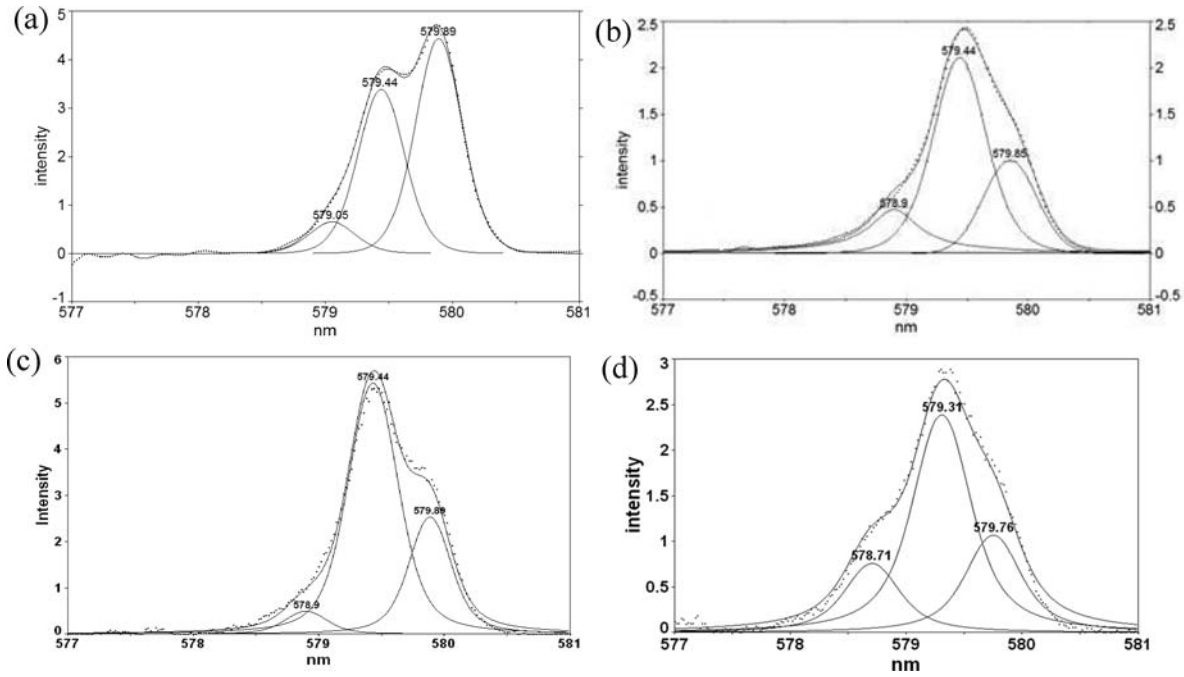


Figure 1. Deconvolution of peaks for the $^7F_0 \rightarrow {}^5D_0$ excitation spectrum with emission monitored at 628 ± 27 nm ($^5D_0 \rightarrow {}^7F_2$) for four phenanthroline DNA Eu(III) complexes. (a) **QT6**, (b) **AQB** (c) **SQ**, (d) **QB**. All samples contain 25.0 uM $EuCl_3$, 25.0 uM DNA, 20.0 mM MES buffer, and 100 mM NaCl at pH 6.5.

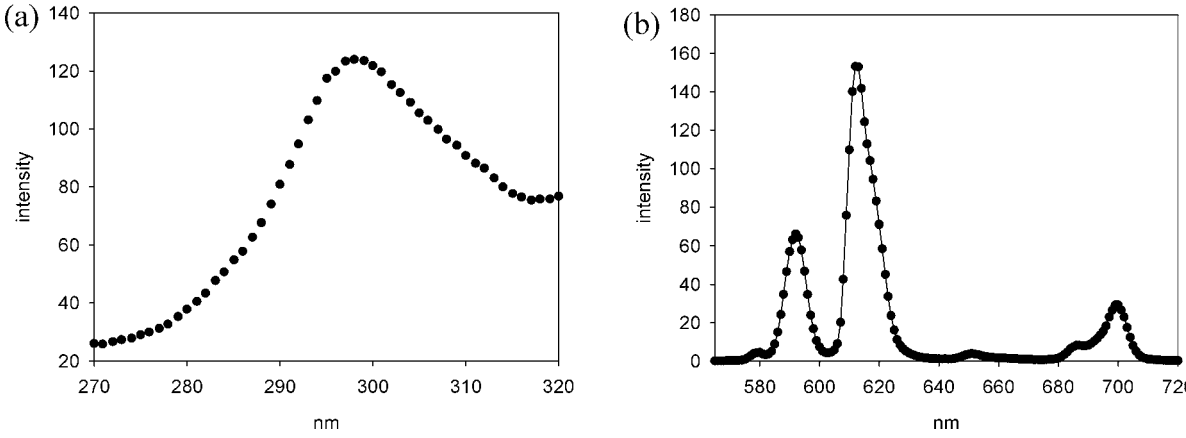


Figure 2. Sensitized luminescence of 50 μM **QT6** and 20 μM $EuCl_3$ at pH 6.5, 100 mM NaCl and 20 mM MES buffer, pH 6.5. (a) Excitation spectrum monitored with luminescence emission at 615 nm. (b) Emission spectrum upon excitation at 296 nm.

studies show that excitation of the phenanthroline linker sensitizes luminescence of Eu(III), supportive of coordination of the Eu(III) to the linker.

Excitation of Eu(**Q1**) at 296 nm gives rise to a typical luminescence emission spectrum of Eu(III) (Supporting Information Figure S7) with the hypersensitive $^5D_o \rightarrow {}^7F_2$ emission at 615 nm as the most intense band. Irradiation of **QT6** in the presence of an equivalent of Eu(III) at 296 nm gives a similar emission spectrum (Figure 2). The excitation spectrum, obtained by monitoring emission at 615 nm for the Eu(**Q1**) or Eu(**QT6**), shows a broad featureless excitation peak that resembles the UV−visible spectrum of the Eu(**Q1**) complex (Figure 2 and Supporting Information Figure S7). This shows that the phenanthroline linker both alone and incorporated into DNA sensitizes luminescence of Eu(III). Under similar conditions, excitation of Eu-bound to unmodified DNA at 296 nm lacks any of the luminescence emission bands of Eu(III) (Supporting Information Figure S8).

Direct Eu(III) excitation spectroscopy of the two double-stranded DNA sequences containing the phenanthroline linker in either bulges **AQB** or **QB** or the single-stranded sequence (**SQ**) is used to monitor binding of Eu(III) to the modified DNA (Table 2 and Figure 1). The dissociation binding constants for Eu(III) with these DNA oligonucleotides were determined from a plot of the excitation luminescence intensity of the complexes at 579.3 nm as a function of DNA and fit to eq 1 to give K_d values of 43 nM, 2.0 μM, and 1.7 μM, for **SQ**, **ABQ**, and **QB**, respectively (Supporting Information Figure S9). For the Eu(III) complex of **SQ**, the concentration of Eu(III) was lowered to 500 nM to attempt to obtain a binding isotherm that was sufficiently gradual to obtain an accurate dissociation constant by fitting to eq 1. However, even at 500 nM Eu(III), our lower limit for obtaining excitation data for binding curves of this complex, our data is indicative of tight binding and can only be used to obtain an upper limit on the dissociation constant ($K_d \leq 43$ nM). Binding of Eu(III) to **SQ**, **AQB**, and **QB** is 1100-, 23-, and 27-fold tighter, respectively, than for the simple ligand **Q1.**

Deconvolution of the steady-state excitation spectra of Eu(III) bound to **AQB**, **QB**, and **SQ** shows three excitation peaks for

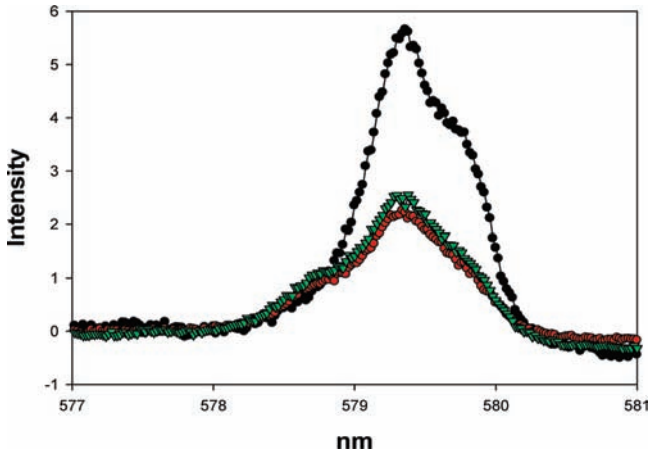


Figure 3. Overlay of the $^7F_0 \rightarrow {}^5D_0$ excitation spectrum with emission monitored at 628 ± 27 nm ($^5D_0 \rightarrow {}^7F_2$) for three phenanthroline DNA Eu(III) complexes. **SQ** (black), **QB** (green), **AQB** (red). All samples contain 2.0 uM $EuCl_3$, 4.0 uM DNA, 20.0 mM MES buffer, and 100 mM NaCl at pH 6.5.

each modified DNA. The middle excitation peaks (579.44, 579.31, and 579.44 nm, respectively) have wavelengths and associated luminescence lifetimes that give *q* numbers of approximately five, similar to that of Eu(**Q1**). The farthest red-shifted peak at 579.89 nm for **SQ** arises from a species with a *q* number that is similar to the middle peak. In contrast, the red-shifted peaks (579.76 and 579.85 nm) for **QB** and **AQB** have associated *q* numbers that are slightly less than their corresponding middle peaks, consistent with additional donor group interactions from DNA and/or fewer quenching contributions from second-sphere interactions. Assignment of the middle and red-shifted excitation peaks in **QB**, **SQ**,and **AQB** to Eu(III) bound to the phenanthroline linker is supported by the fact that the excitation peak wavelengths are too far red-shifted to originate from Eu(III) bound to unmodified DNA and the associated species have *q* numbers which are much lower than those of Eu(III) bound to unmodified DNA (see below). In addition, excitation of the phenanthroline linker leads to Eu(III) luminescence (Supporting Information Figure S8 for Eu(III) bound to **QB**).

The most blue-shifted peaks, which are the lowest intensity in all sequences, are more difficult to assign because they are small and overlap substantially with the middle peak. Interference from luminescence of the other species makes it difficult to obtain accurate *q* numbers to enable making an assignment. The excitation peak wavelengths of the small blue-shifted peaks (578.90, 578.90, and 578.71 nm for **AQB**, **SQ**, and **QB**, respectively) are close to that of Eu(III) bound to unmodified DNA, one possible assignment for this species. The higher *q* number and lower excitation peak wavelength suggests that this site has Eu(III) bound to DNA groups, and not to the phenanthroline linker in **QB** DNA.

In order to compare the luminescence properties of the Eu(III) complex of single-stranded **SQ** to those of bulged duplexes, **QB** and **AQB**, Eu(III) excitation spectra were taken of samples with identical concentrations and laser/MOPO system power (Figure 3). These data show that the major excitation peaks of the Eu(III) complexes of **AQB** and **QB** are less intense in comparison to the Eu(III) complex of the single-stranded **SQ** and that the blue-shifted peak is more prominent in the bulged duplexes.

In comparison, the $^7F_o \rightarrow {}^5D_o$ excitation luminescence spectra of Eu(III) titrated with the unmodified DNAs including stem, AT bulged, and T bulged DNA show a slight red-shift of the excitation peak of the Eu(III) aqua complex from 578.80 to 578.83 nm with a concomitant increase in luminescence intensity (Supporting Information Figure S10). The luminescence lifetimes of solutions containing 20 μM $EuCl_3$ and 4-fold excess DNA at 578.8 nm for stem, AT-, and T-bulged DNA are 105, 120, and 130 μs, respectively, close to the value of 115 μs for fully hydrated Eu(III). These luminescence lifetimes give *q* numbers of 9.6, 8.3, and 7.6, respectively, from eq 2. The moderately increased lifetimes for Eu(III) bound to bulged DNA suggests a displacement of a single water molecule from Eu(III) aqua complex. In contrast, addition of 5 equiv of a pentanucleotide containing thymidine (TTTTT) to $EuCl_3$ under similar conditions shows no apparent change in either the Eu(III) excitation spectrum or luminescence lifetime (*37*).

DISCUSSION

Characterization of lanthanide ion binding sites in DNA and modified DNA is challenging. There are many potential ligand donor groups such as nitrogenous bases and phosphate esters that form binding sites within different DNA secondary structures (*37*−*40*). Direct excitation luminescence spectroscopy facilitates characterization of the Eu(III) environment through comparison of the wavelength and number of the $^7F_o \rightarrow {}^5D_o$ excitation peaks and by determination of hydration (*q*) numbers, yet there are few direct excitation luminescence studies that probe lanthanide ion binding to well-defined DNA (*38, 39*) or RNA (*41*−*43*) structures reported to date. We show here that Eu(III) does not readily lose water molecules upon binding to unmodified double-stranded DNA or bulged DNA. Eu(III) binds with replacement of approximately one water ligand ($q = 7.6$) for T-bulge and binds without losing water ligands to the stem sequence. A hallmark of Eu(III) bound to DNA is that the $^7F_o \rightarrow {}^5D_o$ excitation peak wavelength is very similar to that of the Eu(III) aqua ion with either a small red-shift (<0.1 nm) or no measurable shift at all as shown here and elsewhere (*37*).

Luminescence spectroscopy data support binding of Eu(III) to the phenanthroline linker in modified DNA. This is shown both by the low *q* numbers observed for the two major species (3−5) and by the shift of the excitation peak toward wavelengths that are similar to that observed for phenanthroline derived ligands, such as **Q1**. In addition, sensitized luminescence through excitation of the phenanthroline linker is observed, consistent with binding of Eu(III) to the phenanthroline moiety.

DNA sequence and structure modulates the metal ion environment in the Eu(III)-bound to the phenanthroline linker. **QT6** binds Eu(III) quite strongly with an increased binding strength of 56-fold in comparison to **Q1**. The thymidine sequence produces additional ligating groups around the Eu(III) center that lead to replacement of an additional two water molecules and this may contribute to the tighter binding constant. At this juncture, it is not clear whether the flexibility of the DNA or the type of available nucleobase groups as donors contributes to the reduced *q* value. In contrast, the longer sequence **SQ** binds Eu(III) to give major species with *q* numbers that are close to those in the simple ligand **Q1**. Similarly, the major Eu(III) species of **QB** and **AQB** have *q* numbers that are consistent with a tetradentate phenanthroline ligand. Interestingly, **SQ** binds extremely tightly to Eu(III) with $K_d \leq 43$ nM, or at least 1100-fold tighter-binding than to **Q1**. In comparison, the bulged duplexes **QB** and **AQB** bind Eu(III) with micromolar dissociation constants. Incorporation of Q into the mixed-sequence single-stranded DNA thus increases the strength of Eu(III) binding, most likely through more favorable electrostatic interactions between Eu(III) cation and polyanionic DNA. These Eu(III) interactions are not as favorable if the phenanthroline linker is constrained within a bulged DNA.

There are two major phenanthroline linker-bound Eu(III) complex species for all modified DNA sequences as shown by

direct excitation Eu(III) luminescence spectroscopy. The similarity of the hydration numbers along with the difference in excitation peak frequencies is most consistent with two species that have slightly different Eu(III) coordination environments. In comparison, Eu(**Q1**) has only a single excitation peak. This suggests that DNA gives rise to the two different species in Q-containing DNA strands. The red-shift in the major excitation peak is consistent with coordination of the Eu(III) phenanthroline to an anionic ligand such as a phosphate diester group (*44*).

The third blue-shifted excitation peak is of low intensity in all sequences. This species is associated with a higher than expected *q*-value for a phenanthroline-bound Eu(III) and has an excitation peak maximum that is close to that of Eu(III) bound to unmodified DNA. Thus, it is feasible that this species is Eu(III) bound primarily to DNA and not to the phenanthroline linker moiety. The prominence of this peak in **QB** and **AQB** compared to the single-stranded **SQ** (Figure 3) suggests that there is an additional Eu(III) binding pocket in the bulged region of the DNA.

Further comparison of the luminescence properties of Eu(III) bound to single-stranded **SQ** and bulged duplexes **QB** and **AQB** shows that the Eu(III) complex is quenched in the bulged duplexes in comparison to the single-stranded analogue. These differences are not attributed to water ligand quenching, because the luminescence lifetimes of the two major species in the three Eu(III) bound oligonucleotides are the same within experimental error. Luminescence intensity differences may arise from slight changes in symmetry at the Eu(III) ion or from a different distribution of Eu(III) ion bound to phenanthroline linker versus unmodified DNA. It is noteworthy that previous studies have shown quenching of the Eu(III) excited state by readily oxidized bases such as guanine upon intercalation of Eu(III) complexes with appended aromatic groups into a DNA duplex (*45*). However, this should lead to a decreased Eu(III) luminescence lifetime, which is not observed here.

An important criterion for the construction of metal ion binding sites in defined DNA structures is that metal ion binding should not disrupt DNA structure. Previous studies that had terpyridine linkers incorporated in hairpin loop structures showed that metal ion binding substantially destabilized these structures (*8*). Thermal melting experiments here support stacking of the phenanthroline linker on bases in the DNA helix and show that binding of Eu(III) does not markedly disrupt these structures. The relatively high thermal melting temperatures observed for Eu(III) complexes of bulges **AQB** and **QB** supports stabilization of the bulge-like structure through base stacking or perhaps electrostatic interactions. This bodes well for the preparation of structurally well-defined DNA containing Eu(III) phenanthroline units for sensing and imaging applications.

CONCLUSIONS

This work shows that Eu(III) binds to DNA containing a non-nucleosidic phenanthroline linker, which is incorporated either in single-stranded DNA or in a duplex as part of a bulged loop. Binding of Eu(III) to the modified DNA is 20−1100-fold stronger than to the simple **Q1** or **Q2** ligands, suggesting that other groups on the DNA interact with Eu(III) phenanthroline and/or that electrostatic interactions with the DNA strand increases binding strength. The non-nucleosidic phenanthroline linker has the advantage that it is a planar aromatic group that can stack on the nitrogenous bases of DNA for stabilization of nucleic acid structures as well as act as a luminescence sensitizer for Eu(III) (*25*). As shown here, incorporation of the phenanthroline linker into a site lacking an opposing base gives rise to DNA structures that bind Eu(III) without a marked change in stability. This study shows that it is feasible to incorporate a lanthanide(III) ion complex that retains a large number of water ligands into a site in DNA that contains secondary structure.

ACKNOWLEDGMENT

J.R.M. gratefully acknowledges the National Science Foundation (CHE0911375) for support of this work and for a major instrumentation award (CHE-0321058) to build the MOPO laser system. A.P. was a participant in a National Science Foundation Research Experiences for Undergraduates site at the University at Buffalo (CHE-0851700). R.H. gratefully acknowledges financial support by the Swiss National Foundation (grant 200020-117617). We thank David Watson for use of his fluorimeter.

Supporting Information Available: Optical thermal melting curves for DNA, europium(III) excitation spectra, binding isotherms of europium(III) bound to modified or natural DNA. This material is available free of charge via the Internet at http://pubs.acs.org.

LITERATURE CITED

(1) Franzini, R. M., Watson, R. M., Patra, G. K., Breece, R. M., Tierney, D. L., Hendrich, M. P., and Achim, C. (2006) Metal binding to bipyridine-modified PNA. *Inorg. Chem. 45*, 9798–9811.

(2) Shionoya, M., and Tanaka, K. (2004) Artificial metallo-DNA: a bio-inspired approach to metal array programming. *Curr. Opin. Chem. Biol. 8*, 592–597.

(3) Tanaka, K., and Shionoya, M. (2007) Programmable metal assembly on bio-inspired templates. *Coord. Chem. Rev. 251*, 2732–2742.

(4) Guido, H., Clever, C. K., and Carell, T. (2007) DNA-metal base pairs. *Angew. Chem., Int. Ed. 46*, 6226–6236.

(5) Zimmermann, N., Meggers, E., and Schultz, P. G. (2004) A second-generation copper(II)-mediated metallo-DNA-base pair. *Bioorg. Chem. 32*, 13–25.

(6) Meggers, E., Holland, P. L., Tolman, W. B., Romesberg, F. E., and Schultz, P. G. (2000) A novel copper-mediated DNA base pair. *J. Am. Chem. Soc. 122*, 10714–10715.

(7) Rohr, K., and Vogel, S. (2006) Poly-aza crown ethers as non-nucleosidic building block in DNA conjugates: synthesis and remarkable stabilization of dsDNA. *ChemBioChem 7*, 463–470.

(8) Bianké, G., and Häner, R. (2004) A metal-coordinating DNA hairpin mimic. *ChemBioChem 5*, 1063–1068.

(9) Brotschi, C., and Leumann, C. J. (2003) Transition metal ligands as novel DNA-base substitutes. *Nucleosides Nucleotides Nucl. Acids 22*, 1195–1197.

(10) Knagge, M. M., and Wilker, J. J. (2007) Ligand-based backbone modifications for metal-chelating nucleic acids. *Chem. Commun.* 3356–3358.

(11) Coates, J., Sammes, P. G., Yahioglu, G., Westa, R. M., and Garmanb, A. J. (1994) A new homogeneous identification method for DNA. *J. Chem. Soc., Chem. Commun.* 2311–2312.

(12) Loennberg, T., Suzuki, Y., and Komiyama, M. (2008) Prompt site-selective DNA hydrolysis by Ce(IV)-EDTA using oligonucleotide multiphosphonate conjugates. *Org. Biomol. Chem. 6*, 3580–3587.

(13) Bianké, G., Chaurin, V., Egorov, M., Lebreton, J., Constable, E. C., Housecroft, C. E., and Häner, R. (2006) Copper complex-assisted DNA hybridization. *Bioconjugate Chem. 17*, 1441−1446.

(14) Bianké, G., and Häner, R. (2007) Hairpin mimics with phenanthroline- and bipyridine-derived linkers. *Nucleosides Nucleotides Nucl. Acids 26*, 949–952.

(15) Schlegel, M. K., Zhang, L., Pagano, N., and Meggers, E. (2009) Metal-mediated base pairing within the simplified nucleic acid GNA. *Org. Biomol. Chem. 7*, 476–482.

(16) Kitamura, Y., Ihara, T., Tsujimura, Y., Osawa, Y., Sasahara, D., Yamamoto, M., Okada, K., Tazaki, M., and Jyo, A. (2008)

Template-directed formation of luminescent lanthanide complexes: Versatile tools for colorimetric identification of single nucleotide polymorphism. *J. Inorg. Biochem. 102*, 1921–1931.

(17) Czlapinski, J. L., and Sheppard, T. L. (2005) Template-directed assembly and characterization of metallosalen-DNA conjugates. *Bioconjugate Chem. 16*, 169–177.

(18) Escudier, J.-M., Dupouy, C., Fountain, M. A., del Mundo, I. M. A., Jacklin, E. M., and Morrow, J. R. (2009) Synthesis and luminescence properties of a trinucleotide-europium(III) complex conjugate. *Org. Biomol. Chem. 7*, 3251–3257.

(19) Nwe, K., Andolina, C. M., Huang, C.-H., and Morrow, J. R. (2009) PARACEST properties of a dinuclear neodymium(III) complex bound to DNA or carbonate. *Bioconjugate Chem. 20*, 1375–1382.

(20) Baker, B. F., Lot, S. S., Kringel, J., Cheng-Flournoy, S., Villiet, P., Sasmor, H. M., Siwkowski, A. M., Chappell, L. L., and Morrow, J. R. (1999) Oligonucleotide-europium complex conjugate designed to cleave the 5′ cap structure of the ICAM-1 transcript potentiates antisense activity in cells. *Nucleic Acids Res. 27*, 1547–1551.

(21) Magda, D., Wright, M., Crofts, S., Lin, A., and Sessler, J. L. (1997) Metal complex conjugate of antisense DNA which displays ribozyme-like activity. *J. Am. Chem. Soc. 119*, 6947–6948.

(22) Canaple, L., Hüsken, D., Hall, J., and Häner, R. (2002) Artificial ribonucleases: Efficient and specific in vitro cleavage of human c-raf-1 RNA. *Bioconjugate Chem. 13*, 945–951.

(23) Langenegger, S. M., and Häner, R. (2005) Remarkable stabilization of duplex DNA containing an abasic site by non-nucleosidic phenanthroline and pyrene building blocks. *ChemBioChem 6*, 848–851.

(24) Langenegger, S. M., and Häner, R. (2004) DNA containing phenanthroline- and phenanthrene-derived, non-nucleosidic base surrogates. *Tetrahedron Lett. 45*, 9273–9276.

(25) Templeton, E. F. G., and Pollak, A. (1989) Spectroscopic characterization of 1,10-phenanthroline-2,9-dicarboxylic acid and its complexes with europium(III): luminescent europium chelates useful for analytical applications in aqueous solution. *J. Lumin. 43*, 195–205.

(26) Melton, D. L., VanDerveer, D. G., and Hancock, R. D. (2006) Complexes of greatly enhanced thermodynamic stability and metal ion size-based selectivity, formed by the highly preorganized non-macrocyclic ligand 1,10-phenanthroline-2,9-dicarboxylic acid. A thermodynamic and crystallographic study. *Inorg. Chem. 45*, 9306–9314.

(27) Gephart, R. T., Williams, N. J., Reibenspies, J. H., De Sousa, A. S., and Hancock, R. D. (2008) Metal ion complexing properties of the highly preorganized ligand 2,9-bis(hydroxymethyl)-1,10-phenanthroline: A crystallographic and thermodynamic study. *Inorg. Chem. 47*, 10342–10348.

(28) Hancock, R. D., Melton, D. L., Harrington, J. M., McDonald, F. C., Gephart, R. T., Boone, L. L., Jones, S. B., Dean, N. E., Whitehead, J. R., and Cockrell, G. M. (2007) Metal ion recognition in aqueous solution by highly preorganized non-macrocyclic ligands. *Coord. Chem. Rev. 251*, 1678–1689.

(29) Newkome, G. R., Kiefer, G. E., Puckett, W. E., and Vreeland, T. (1983) Chemistry of heterocyclic compounds. Part 83. α-Methyl functionalization of electron-poor heterocycles: 2,9-bis(chloromethyl)-1,10-phenanthroline. Synthesis of a [3.3]cyclophane containing the 1,10-phenanthrolino moiety. *J. Org. Chem. 48*, 5112–5114.

(30) Makela, M., Zhang, L., Zetterberg, K., and Hansson, S. (1992) A new route to synthesize 2,9-dicarbonitrile-1,10-phenanthroline. *Synth. Commun. 22*, 2811–2814.

(31) McDowell, J. A., and Turner, D. H. (1996) Investigation of the structural basis for thermodynamic stabilities of tandem gu mismatches: solution structure of $(rgaggucuc)_2$ by Two-Dimensional NMR and simulated annealing. *Biochemistry 35*, 14077–14089.

(32) Andolina, C. M., Holthoff, W. G., Page, P. M., Mathews, R. A., Morrow, J. R., and Bright, F. V. (2009) Spectroscopic system for direct lanthanide photoluminescence spectroscopy with nanomolar detection limits. *Appl. Spectrosc. 63*, 483–493.

(33) Supkowski, R. M., and Horrocks, W. D., Jr. (2002) On the determination of the number of water molecules, q, coordinated to europium(III) ions in solution from luminescence decay lifetimes. *Inorg. Chim. Acta 340*, 44–48.

(34) Beeby, A., Clarkson, I. M., Dickins, R. S., Faulkner, S., Parker, D., Royle, L., Sousa, A. S. d., Williams, J. A. G., and Woods, M. (1999) Non-radiative deactivation of the excited states of europium, terbium and ytterbium complexes by proximate energy-matched OH, NH and CH oscillators: an improved luminescence method for establishing solution hydration states. *J. Chem. Soc., Perkin Trans. 2*, 493–504.

(35) Kimura, T., and Kato, Y. (1998) Luminescence study on hydration states of lanthanide(III)-polyaminopolycarboxylate complexes in aqueous solution. *J. Alloys Compd. 275−277*, 806–810.

(36) Andolina, C. M., Mathews, R. A., and Morrow, J. R. (2009) Solution chemistry of europium(III) aqua ion at micromolar concentrations as probed by direct excitation luminescence spectroscopy. *Helv. Chim. Acta 92*, 2330–2348.

(37) Mathews, R. A. (2008) Ph. D. Thesis, University at Buffalo.

(38) Klakamp, S. L., and Horrocks, W. D., Jr. (1992) Lanthanide ion luminescence as a probe of DNA structure. 1. Guanine-containing oligomers and nucleotides. *J. Inorg. Biochem. 46*, 175–192.

(39) Klakamp, S. L., and Horrocks, W. D., Jr. (1990) The europium (III)-induced conformational transitions of poly(dG-dC) • poly(dG-dC) as studied by europium(III) luminescence, UV, and CD spectroscopy. *Biopolymers 30*, 33–43.

(40) Fu, P. K. L., and Turro, C. (1999) Energy transfer from nucleic acids to Tb(III): selective emission enhancement by single DNA mismatches. *J. Am. Chem. Soc. 121*, 1–7.

(41) Feig, A. L., Panek, M., Horrocks, W. D., Jr., and Uhlenbeck, O. C. (1999) Probing the binding of Tb(III) and Eu(III) to the hammerhead ribozyme using luminescence spectroscopy. *Chem. Biol. 6*, 801–810.

(42) Greenbaum, N. L., Mundoma, C., and Peterman, D. R. (2001) Probing of metal-binding domains of RNA hairpin loops by laser-induced lanthanide(III) luminescence. *Biochemistry 40*, 1124–1134.

(43) Mundoma, C., and Greenbaum, N. L. (2002) Sequestering of Eu(III) by a GAAA RNA tetraloop. *J. Am. Chem. Soc. 124*, 3525–3532.

(44) Frey, S. T., and Horrocks, W. D., Jr. (1995) On correlating the frequency of the $^7F_0 \rightarrow {}^5D_0$ transition in Eu^{3+} complexes with the sum of 'nephelauxetic parameters' for all of the coordinating atoms. *Inorg. Chim. Acta 229*, 383–390.

(45) Bobba, G., Frias, J. D., and Parker, D. (2002) Highly emissive, nine-coordinate enantiopure lanthanide complexes incorporating tetraazatriphenylenes as probes for DNA. *Chem Commun.* 890–891.

BC900386W

Single Molecule Sensitive Multivalent Polyethylene Glycol Probes for RNA Imaging

Aaron W. Lifland, Chiara Zurla, and Philip J. Santangelo*

Georgia Institute of Technology and Emory University, Atlanta, Georgia. Received September 2, 2009; Revised Manuscript Received December 14, 2009

The imaging of RNA in live cells presents a methodological challenge both in the mechanism by which the probes are delivered to the cell and in the sensitivity of the probe. Probes must be delivered to the correct cellular compartment and, once inside the cell, should bind to the target RNA rapidly and with enough sensitivity to detect small numbers of RNA molecules. Here, we report the characterization of a single-molecule sensitive, multivalent RNA imaging probe that utilizes an eight-armed poly(ethylene glycol) core. This probe allowed for the accurate imaging of the human respiratory syncytial virus (hRSV) genomic RNA when delivered into live cells using either reversible membrane permeabilization or TAT-peptide mediated membrane transduction. Neither reversible membrane permeabilization nor TAT mediated delivery proceeded through the endosomal pathway, and both delivery methods demonstrated fast binding kinetics of less than 10 min. Subcellular distributions of RNA were visualized in live cells, as well as RNA-protein colocalization, after fixation and immunostaining of the hRSV RNA binding protein N.

INTRODUCTION

In recent years, the imaging of RNAs in live cells has garnered growing attention with a variety of interesting methods developed for this purpose. This research has been driven by the increased appreciation for the role of post-transcriptional regulation on the function of RNA molecules (*1*), for the role of genomic RNA in viral assembly, and for the stress response of cells in pathogenesis (*2*). From previous research on RNA imaging methods, several design criteria have emerged. Imaging methods must be sensitive enough to detect RNA molecules, which are generally present in low copy numbers, and to enable the tracking of single RNA granules over time in live cells. For probe-based methods, delivery into the correct cellular compartment is critical in order for the probes to bind rapidly to their target. Delivery methods that result in accumulation of probe in the nucleus of cells or utilize endocytic vesicles can lead to nonspecific signal and degradation of the probe.

Single molecule imaging of native and nonengineered RNAs in live cells has recently been achieved by the use of multiply labeled tetravalent RNA imaging probes (MTRIPs) (*3*). These probes consist of four fluorescently labeled linear oligonucleotides bound together by a biotin−streptavidin linkage and recognize their intracellular target RNA through Watson−Crick base pairing. Signal is raised above background by the binding of 2−3 probes per target RNA and through the natural localization of the target RNA. Prior to the introduction of MTRIPs, single molecule studies of specific RNA localization and transport in live cells were limited to plasmid derived RNAs either containing binding site repeats for the MS2-GFP fusion protein (*4*) or containing binding site repeats for a molecular beacon (*5*). Plasmid derived RNAs offer tremendous methodological flexibility, but they preclude the study of native RNA or nonengineered viral RNA and do not allow for imaging native RNAs in vivo.

* Correspondence and requests for materials should be addressed to Philip J. Santangelo (philip.santangelo@bme.gatech.edu), PH: 404-385-2116, FAX: 404-894-4243.

While MTRIPs have proven to be capable of targeting a number of RNAs in various cell types with single RNA sensitivity, the use of a streptavidin core imparts some limitations. Probes with a streptavidin core have a maximum of four noncovalently bound ligands, which limits the number of fluorophores that can be added to a single probe. Streptavidin also contributes significantly to the molecular weight of the probe (∼53 kDa) and might affect the delivery pathway during cell penetrating peptide-mediated delivery (*6*).

Here, we report the synthesis and application of a multivalent RNA imaging probe that utilizes an eight-armed poly(ethylene glycol) (PEG) core. These probes overcome the main limitations imposed by streptavidin by increasing the number of bound ligands while reducing the molecular weight of the core (20 kDa). Moreover, the probes are stabilized by employing a covalent bond between the ligand and the core. PEG was chosen, since it has been shown to reduce toxicity, reduce nonspecific binding, and improve internalization when conjugated to macromolecules and utilized in vivo (*7*−*9*).

In order to demonstrate the efficiency of probe delivery and targeting, we utilized the genomic viral RNA (vRNA) of human respiratory syncytial virus (hRSV) as a model system. The localization of the vRNA of hRSV has been previously characterized by both molecular beacons and MTRIPs and showed high concentrations of viral RNA in cytoplasmic foci termed inclusion bodies (*3, 10, 11*). Delivery of probe into live cells was achieved using reversible membrane permeabilization with streptolysin O (SLO), which has been shown to allow for efficient and homogeneous delivery of macromolecules into the cytoplasm (*3*).The use of SLO results in ∼100% probe delivery efficiency and results in minimal cytotoxicity (*3*). Alternatively, as a delivery strategy, we also used the cell penetrating peptide (CCP) TAT, which, when conjugated to macromolecules, has been shown to transduce them across the plasma membrane (*12*). Indeed, the use of the PEG core permits an increase in the number of bound ligands and allows for the conjugation of delivery and targeting peptides along with RNA targeting oligonucleotides, while maintaining single molecule sensitivity. CPP-conjugated probes are currently of great interest in mo-

10.1021/bc9003876 © 2010 American Chemical Society
Published on Web 02/08/2010

lecular imaging, since they have the advantage of being suitable for use in vivo when labeled with near-infrared fluorophores. As with SLO, CPP based delivery allows for ~100% delivery efficiency and low cytotoxicity at low concentrations and eliminates the need for permeabilization of the membrane, reducing the complexity of the experimental procedure (*13*).

EXPERIMENTAL PROCEDURES

Multivalent PEG Probes. 2′-O-Me RNA/DNA chimeric oligonucleotides were synthesized by Biosearch Technologies, Inc. (Novato, CA) with the following sequence, 5′-**U**XTXT-TX**AAAAAXGGGGCAAAXAA**-3′, where the boldface type is 2′-*O*-Methyl RNA, the X is a dT-C6-NH2 (Supporting Information Figure S3), the 5′-**U** contains a free thiol group (Supporting Information Figure S4), and all others are DNA. The binding region is underlined. Probes were synthesized by first labeling the individual ligands with amine reactive NHS-ester fluorophores Atto 488 (ATTO-TEC GmbH), Cy3B (GE Healthcare), or Atto 647N (ATTO-TEC GmbH) using the manufacturer's protocols. Ligands were subsequently linked to 20 kDa eight-armed maleimide poly(ethylene glycol) (8-Arm PEG) cores (Supporting Information Figure S5) (NOF America) by incubation in a 64:1 molar ratio in PBS (Ambion) and 1 mM EDTA (Ambion) for 12 h at room temperature. 8-Armed PEG probes with TAT were synthesized by adding ligand, Cys-TAT (Anaspec, Cys-TAT 47−57), and 8-Arm-PEG cores in a 64:8:1 molar ratio in 10× PBS, and 1 mM EDTA for 12 h at room temperature. All probes were filtered to remove free ligand and reaction buffer using 30 kDa molecular weight cutoff Nanosep centrifugal devices (Pall Corp.). Purified probes were resuspended in nuclease free PBS and stored at 4 °C.

Cells and Virus. A549 human lung carcinoma cells (ATCC CCL-185) were cultured in DMEM (Lonza) with 10% FBS (Hyclone), 100 U/mL penicillin, and 100 U/mL streptomycin (Invitrogen). Cells were plated on glass coverslips one day prior to experiments. The A2 strain of human respiratory syncytial virus (hRSV) (Crowe laboratory, Vanderbilt University) was used at a MOI = 1 and a titer of 1×10^6 $TCID_{50}$ mL^{-1}.

Probe Delivery. Probes were delivered into A549 cells using reversible membrane permeabilization and peptide mediated delivery. For reversible membrane permeabilization, 2 U/mL Streptolysin O (SLO) (Sigma) were first reduced using 7.5 mM Tris(2-carboxyethyl)phosphine (TCEP) (Peirce) for 1 h at 37 °C. Infected and noninfected cells were rinsed using PBS (-Ca^{2+} -Mg^{2+}) (Thermo) and then incubated with delivery medium containing 0.2 U/mL SLO and 5 nM probe in PBS (-Ca^{2+} -Mg^{2+}) for 10 min at 37 °C. The delivery medium was then removed and replaced with complete growth media for 15 min. For TAT mediated delivery of probes, infected and noninfected cells were incubated in complete medium containing 5 nM TAT conjugated probe for 10 min at 37 °C, after which it was replaced with complete medium for 15 min. For live cell imaging experiments, growth media was replaced with Leibovitz's L15 medium (Invitrogen) immediately prior to image acquisition.

Immunostaining. After probe delivery, cells were rinsed in PBS (Ambion), fixed with 4% paraformaldehyde (Electron Microscopy Science) in PBS, permeabilized using 0.2% Triton-X 100 (Sigma), and blocked with 5% bovine serum albumin (Ambion). Cells were then incubated with a mouse monoclonal primary antibody against the hRSV N Viral Protein (Abcam), CD63 (Developmental Studies Hybridoma Bank), or LAMP-1 (Developmental Studies Hybridoma Bank) for 30 min at 37 °C and with a goat antimouse secondary antibody labeled with Alexa 488 (Invitrogen) for 30 min at 37 °C. After DAPI staining (Invitrogen), cells were mounted on slides using PVA with DABCO (Sigma).

Fluorescence Imaging. Samples were imaged using a Zeiss Axiovert 200 M epifluorescent microscope with a 63×/1.4 NA Plan-Apochromat objective, using Chroma 49002 ET-GFP (FITC/Cy2), 49004 ET Cy3, 49006 ET Cy5 filter sets, an EXFO excite 120 for fluorescence excitation, a Polytek PI objective piezo for taking stacks of images, and a Hamamatsu ORCA-ER AG for capturing digital images. Image *z*-stacks were acquired in 200 nm steps using Volocity (Improvision). Exposure times for probes on glass (Figure 2) were approximately 500 ms. Exposure times for probes in endosomal and lysosomal marker colocalization studies were 400 ms for noninfected cells (Figure 3c,d) and 30 ms for infected cells (Figure 3e,f). Exposure times for RSV vRNA in infected cells and controls, both fixed and live, were approximately 100 ms (Figures 4−5). Identical exposure times in Figures 4 and 5 were used for comparison of intensities.

Image Analysis. All images were deconvolved using the iterative restoration algorithm in *Volocity*. Histograms of mean fluorescence intensity were generated by identifying objects with minimum and maximum intensities set to 4 SD and 100 SD, respectively. Objects smaller than 1 point spread function were removed. Intensity Profiles were generated using *ImageJ* (NIH) Color Profiler plug-in and data tables were imported into *Sigma Plot 11* (Systat Software Inc.) for plotting. Manders overlap coefficient was calculated using *Volocity* software.

RESULTS AND DISCUSSION

hRSV specific ligands were composed of 2′-O-Methyl-RNA and DNA chimeric oligonucleotides with five amine-modified thymidines and a 5′ thiol modification (Supporting Information Figures S3 and S4). The oligonucleotide sequence was designed to be complementary to a gene-end-intergenic-gene-start sequence of hRSV which has three exact repeats in the hRSV genome and is not present in the human genome. The sequence used has previously been shown to be accessible by antisense knockdown experiments, molecular beacon imaging, and MTRIP imaging (*3, 11, 14*). The targeting of three repeats per RNA raises signal significantly above background for even a single RNA per point spread function.

The amine-modified thymidines of the ligands were used to conjugate NHS-ester fluorophores, and the thiol group was used to link the individual ligands to the PEG cores, which were functionalized with eight maleimide active groups (Figure 1a Supporting Information Figure S5). Absorption spectroscopy showed that, on average, 3 dyes were conjugated to each ligand and 6.5 ligands were conjugated to each PEG core (Supporting Information). Probes utilizing the TAT CPP contained an average of 4 oligonucleotides ligands and 1 TAT peptide (Supporting Information). By increasing the brightness of the probes through the use of multiple ligands, rather than increasing the number of fluorophores per ligand, self-quenching was minimized and ligand size was kept to approximately 20 bases. The fluorophores (Atto 488, Cy3B, and Atto 647N) were chosen for their strong absorption in visible wavelengths commonly used for imaging, high quantum efficiency, and low triplet state excitation. The use of ligands with a 2′-O-Methyl backbone conferred increased affinity for the target mRNA, increased signal-to-noise ratio, and nuclease resistance (*15−18*).

In order to test the ligands for nonspecific aggregation, the probes were labeled with Atto 488, Cy3B, or Atto 647N fluorophores and were adsorbed onto a cover glass at 1 nM concentration. Using wide-field fluorescence microscopy, the probes were visible as distinct spots on the glass without apparent aggregation (Figure 2a). Lack of aggregation was confirmed both by fluorescence intensity histograms (Figure 2b−d) and by the lack of colocalization of probes labeled with different fluorophores. When the probes were delivered at 5 nM

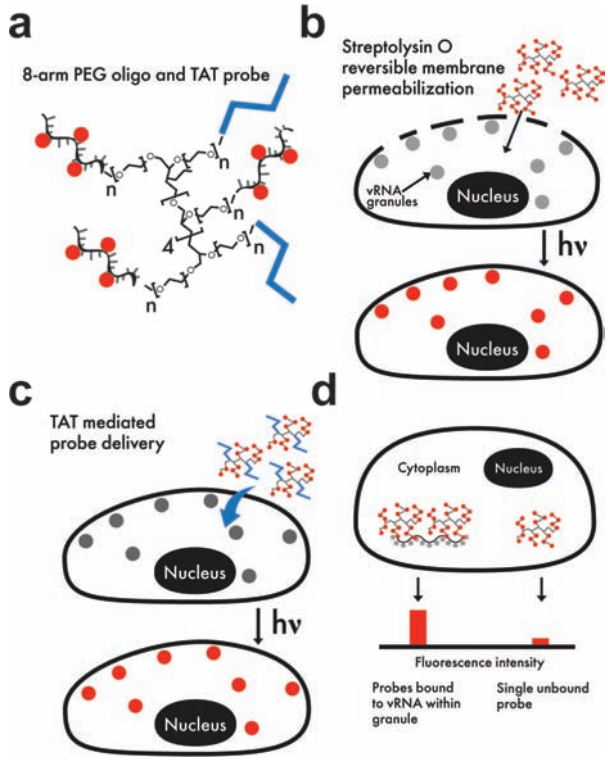


Figure 1. Design, delivery, and imaging of probes. (a) Schematic of the 8-arm PEG conjugated to fluorescently labeled oligonucleotides and TAT peptide (blue). (b) Cells, reversibly permeabilized with streptolysin O, allow for diffusion of probes into the cytoplasm. Probes bound to target RNA are visualized under a fluorescence microscope. (c) Transduction of TAT-PEG probe without streptolysin O permeabilization. (d) Detection of RNA is achieved through the increased signal intensity when multiple probes are bound to a single RNA.

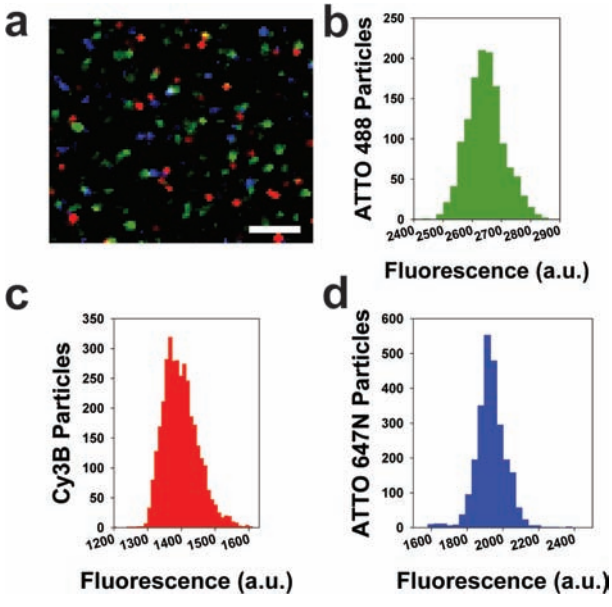


Figure 2. Characterization of single probes on glass. (a) Atto 488 (green), Cy3B (red), and Atto 647N (blue) labeled probes were adsorbed onto glass and analyzed for the colocalization and aggregation. Corresponding intensity histograms (b, c, and d) show a unimodal distribution consistent with single probes. Scale bar is 2 μm.

concentration in A549 cells either by SLO permeabilization (Figure 3a) or by TAT conjugation (Figure 3b), similar spots were visible as seen in the extended focus images. Extended focus images are a projection of all the *z*-planes into a two-dimensional image. The images were presented in this format

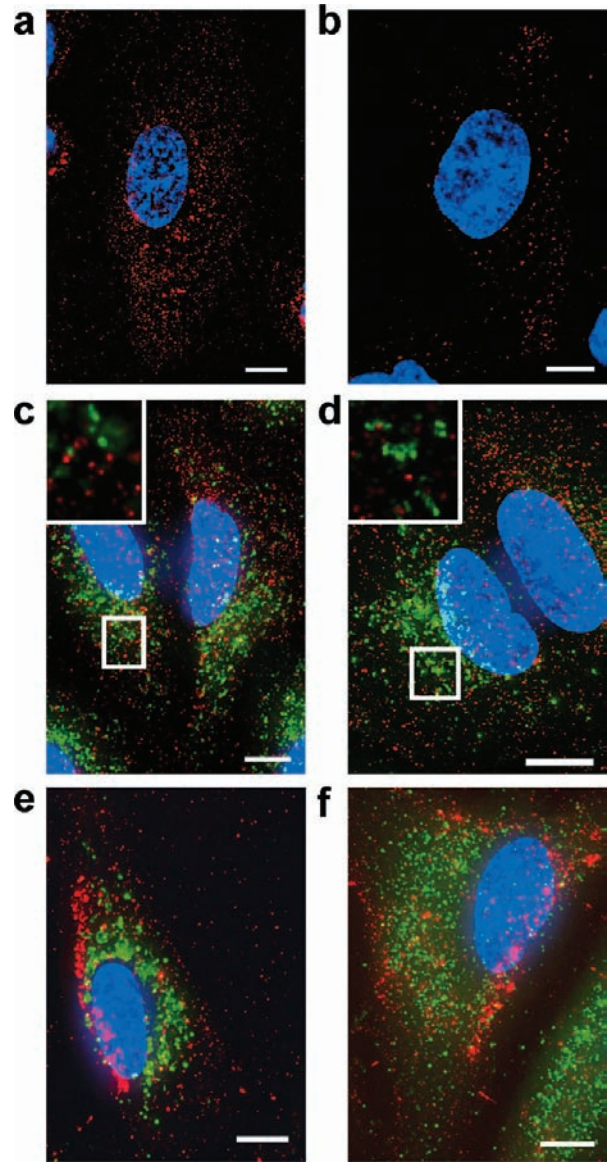


Figure 3. Distribution of PEG probes targeted against hRSV in A549 cells and colocalization with endosomal marker CD63 and lysosomal marker LAMP1. Extended focus of noninfected cells with probe (red) delivered (a) by SLO permeabilization and (b) by TAT conjugation. Extended focus of noninfected cells with probe (red) delivered by TAT conjugation and (c) stained for CD63 (green) and (d) LAMP1 (green). Insets in c and d show single plane from boxed region. Extended focus of hRSV infected cells with probe (red) delivered by TAT conjugation and stained for (e) CD63 (green) and (f) LAMP1 (green). Scale bars are 10 μm.

to include all the relevant signal within the three-dimensional cell. The uniformity of the signal within the cytoplasm indicated that probe was not aggregating due to nonspecific interaction with cellular components.

Recent reports have shown that macromolecule uptake by TAT can proceed through an endocytic pathway, even if this has been suggested to be dependent upon the conjugated macromolecule (*19, 20*). Nonendosomal transduction of the probes is recommended, since it reduces the exposure of the probe to nucleases and eliminates the need for endosomal releasing agents such as poly(propylacrylic acid) to be added to the delivery medium. In order to determine whether or not TAT conjugated probes entered cells through the endosomal pathway, TAT-probes were delivered at 5 nM into uninfected and hRSV infected cells that were subsequently fixed and immunostained for endosomal and lysosomal markers. Cells

were immunostained for cluster of differentiation 63 (CD63) (Figure 3c,e) and lysosomal associated membrane protein 1 (LAMP1) (Figure 3d,f). Multicolor images were obtained by wide-field fluorescence microscopy and deconvolution, and revealed little colocalized signal between the TAT-conjugated probe and protein markers. In these figures, extended views were shown to illustrate the signal within the cell. Some apparent colocalization may be perceived using this presentation due to the merging of signal from different *z*-planes. Inset images from one *z*-plane were included to show the lack of colocalization qualitatively. This was confirmed quantitatively by low Manders overlap coefficients ($R < 0.1$) for the colocalization of the probe with CD63 and with LAMP1 using three-dimensional reconstructions of the images.

In order to demonstrate the applicability of these probes for live cell imaging, the viral genomic RNA of hRSV was imaged in A549 cells both live and after fixation and immunostaining of the hRSV N protein. The hRSV N protein has been shown to reside within inclusion bodies, to colocalize with the hRSV genome in imaging experiments, and to bind to hRSV vRNA (*3, 21*). Co-localization with the N protein served to demonstrate the accurate targeting of the probe to the vRNA. A549 cells were infected with the A2 strain of hRSV and incubated for 24 h. Probes were then delivered at 5 nM via SLO membrane permeabilization and allowed to recover. Subsequently, cells were either fixed with 4% paraformaldehyde for immunostaining or stained with Hoechst 33342 for live cell imaging. Cells fixed and immunostained for the hRSV N protein showed vRNA localization near the plasma membrane and exhibited colocalization with hRSV N protein similar to previously reported data (Figure 4a) (*3*). In order to quantify the degree of colocalization between the vRNA and N protein, Manders overlap coefficients were generated using voxel intensities. Overlap coefficients were generally high, typically $R > 0.8$. Figure 4a shows a representative cell with an overlap coefficient of 0.843. In addition to whole cell automatic colocalization, intensity profiles showed correlation between the hRSV genomic and N protein signal (Figure 4c,d). In the live cell images, similar localization of the vRNA was observed with vRNA predominantly residing in inclusion bodies close to the cell membrane (Figure 4e). Delivery of probe into noninfected cells served as a negative control and resulted in little to no signal when imaged under the same conditions as the infected cells (Figure 4b,f). Interestingly, probes delivered into noninfected cells demonstrated no significant nuclear background.

We subsequently delivered the TAT conjugated probes at 5 nM concentration into hRSV infected and noninfected A549 cells. These probes revealed a similar pattern of RNA localization as the SLO-delivered ones in infected cells both live and upon fixation. In the latter case, colocalization with the viral N protein at the plasma membrane confirmed efficient vRNA targeting (Figure 5a,c,d). In noninfected cells, TAT-conjugated probes exhibited little to no signal (Figure 5b) and appeared to be homogeneously distributed in the cytoplasm (Figure 3b). While the mechanism for TAT-mediated probe delivery is not yet fully understood, our data strongly suggest that it does not involve an endosomal pathway and are consistent with previous reports (*20, 22*). In particular, Vives et al. (*22*) reported that fluorescently labeled TAT peptides were efficiently taken up by cells within 5 min at concentrations as low as 100nM, and the internalization process was shown not to involve an endocytic pathway. The sensitivity of the fluorescein reporter precluded measurements using TAT concentrations below 100nM (*22*). In our case, uptake of probes occurred in less than 10 min at a concentration of 5 nM. Moreover, our probes showed no colocalization with endosomal and lysosomal markers, and colocalized well with the N protein, yielding a

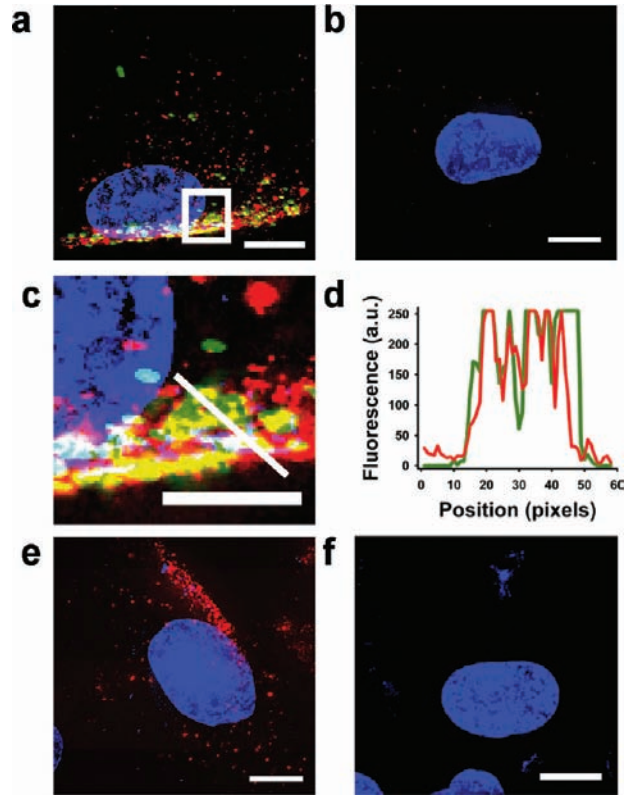


Figure 4. SLO-mediated delivery of PEG probes targeted against hRSV and colocalization with the viral protein N. Distribution of probes (red) into fixed hRSV (a) infected and (b) noninfected cells and staining for the viral protein N (green) and DAPI (blue). (c) Magnification of boxed region in Figure 4a. (d) Intensity profile along line in Figure 4c. Distribution of probes (red) into live hRSV (e) infected and (f) noninfected cells. Nuclei were stained using Hoechst 33342. Scale bars in a,b,e,f are 10 μm. Scale bar in c is 5 μm.

distribution similar to the one observed in SLO membrane permeabilization-based delivery. Additionally, live cell imaging experiments confirmed the results and indicated that cell fixation does not alter probe localization (Figure 5e,f).

CONCLUSION

The importance of trans-acting factors, such as RNA binding proteins and noncoding RNAs, in the regulation of mRNA and viral RNAs has recently garnered increased attention (*23*). These factors are responsible for the post-translational regulation of mRNAs and for the late stages of the viral life cycle such as replication and packaging of viral genomic RNA (*24*). The RNA molecule, along with trans-acting factors, ultimately determines the function of the RNA. In vitro methods for studying these ribonucleoprotein complexes (RNPs) give only an averaged view of the function of these complexes. However, within the cellular context, these RNPs are often heterogeneous, and as such, methods are needed that enable the study of the spatial and temporal dynamics of RNA and interaction with RNA binding proteins within the cell (*25*). These methods must be sensitive because of the low concentration of specific RNAs inside the cell, and must be able to provide accurate subcellular localization of RNA.

Using an eight-arm activated PEG core as a multifunctional platform, we have developed a single molecule sensitive RNA imaging probe. Fluorescently labeled oligonucleotides bound to the PEG core were delivered into live cells using two delivery methods, reversible membrane permeabilization and TAT-mediated transduction. Individual probes were visible both on glass and inside the cells using widefield fluorescence micros-

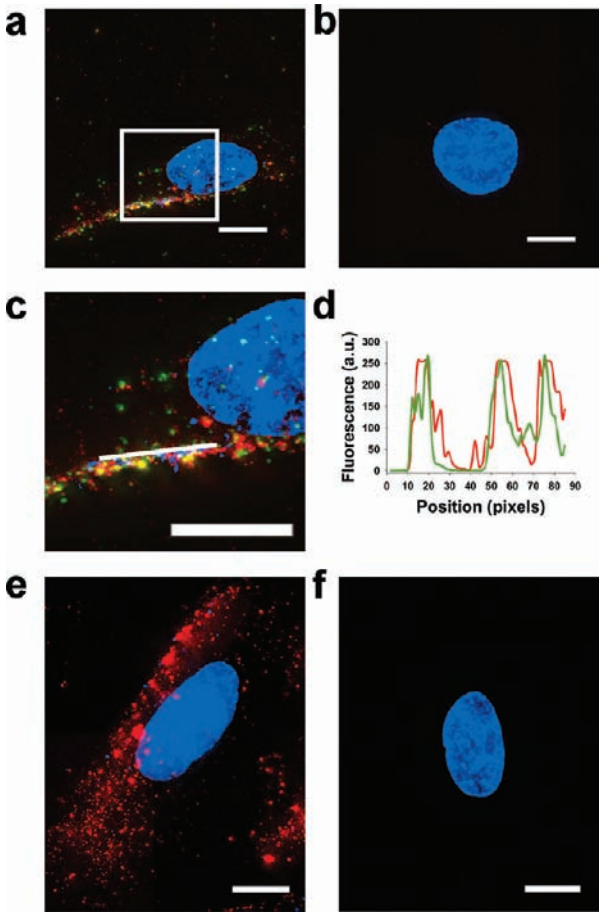


Figure 5. TAT-mediated delivery of PEG probes targeted against hRSV and colocalization with the viral protein N. Distribution of probes (red) into fixed hRSV (a) infected and (b) noninfected cells and staining for the viral protein N (green) and DAPI (blue). (c) Magnification of boxed region in Figure 5a. (d) Intensity profile along line in Figure 5c. Distribution of probes (red) into live hRSV (e) infected and (f) noninfected cells. Nuclei were stained using Hoechst 33342. Scale bars in a,b,e,f are 10 μm. Scale bar in c is 5 μm.

copy. TAT-mediated delivery did not result in accumulation of probes in endosomes, nor did it result in the nonspecific aggregation of probes inside the cell. To demonstrate the accurate targeting of RNA in the cell, probes targeted against RSV vRNA were delivered into infected cells and demonstrated subcellular localization at the plasma membrane, colocalization with known vRNA binding proteins, and signal substantially higher than in mock infected controls. Signal was observed in less than 10 min regardless of the delivery method and in the presence of probe concentrations of 5 nM. The rapid binding of the probes to their target is an essential feature for the study of RNA dynamics, because it allows for the observation of phenomena that occur on short time scales. In addition to this, the low concentration of the probes contributes to reduce nonspecific binding. Our results suggest that TAT (or other CPPs) conjugated PEG probes may allow for the imaging of specific RNAs in vivo when combined with fluorophores that absorb in the near-infrared wavelengths (*26*).

ACKNOWLEDGMENT

This study was supported by the Georgia Institute of Technology administration (P.J.S.). Strain A2 of hRSV was a kind gift from James E. Crowe Jr. The monoclonal antibodes for CD63 and LAMP1 developed by J. Thomas August and James E. K. Hildreth were obtained from the Developmental Studies Hybridoma Bank developed under the auspices of the NICHD and maintained by The University of Iowa, Department of Biology, Iowa City, IA 52242.

Supporting Information Available: Further characterization of the conjugates, structure of the 5′-thiol, structure of amine-modified thymidines, and structure of the 8-Arm PEG. This material is available free of charge via the Internet at http://pubs.acs.org.

LITERATURE CITED

(1) Anderson, P., and Kedersha, N. (2009) RNA granules: post-transcriptional and epigenetic modulators of gene expression. *Nat. Rev. Mol. Cell Biol. 10*, 430–6.
(2) Beckham, C. J., and Parker, R. (2008) P bodies, stress granules, and viral life cycles. *Cell Host Microbe 3*, 206–12.
(3) Santangelo, P. J., Lifland, A. W., Curt, P., Sasaki, Y., Bassell, G. J., Lindquist, M. E., and Crowe, J. E., Jr. (2009) Single molecule-sensitive probes for imaging RNA in live cells. *Nat. Methods 6*, 347–9.
(4) Fusco, D., Accornero, N., Lavoie, B., Shenoy, S. M., Blanchard, J. M., Singer, R. H., and Bertrand, E. (2003) Single mRNA molecules demonstrate probabilistic movement in living mammalian cells. *Curr. Biol. 13*, 161–7.
(5) Vargas, D. Y., Raj, A., Marras, S. A., Kramer, F. R., and Tyagi, S. (2005) Mechanism of mRNA transport in the nucleus. *Proc. Natl. Acad. Sci. U.S.A. 102*, 17008–13.
(6) Rinne, J., Albarran, B., Jylhava, J., Ihalainen, T. O., Kankaanpaa, P., Hytonen, V. P., Stayton, P. S., Kulomaa, M. S., and Vihinen-Ranta, M. (2007) Internalization of novel non-viral vector TAT-streptavidin into human cells. *BMC Biotechnol. 7*, 1.
(7) Rapozzi, V., Cogoi, S., Spessotto, P., Risso, A., Bonora, G. M., Quadrifoglio, F., and Xodo, L. E. (2002) Antigene effect in K562 cells of a PEG-conjugated triplex-forming oligonucleotide targeted to the bcr/abl oncogene. *Biochemistry 41*, 502–10.
(8) Healy, J. M., Lewis, S. D., Kurz, M., Boomer, R. M., Thompson, K. M., Wilson, C., and McCauley, T. G. (2004) Pharmacokinetics and biodistribution of novel aptamer compositions. *Pharm. Res. 21*, 2234–46.
(9) Suzuki, T., Kanbara, N., Tomono, T., Hayashi, N., and Shinohara, I. (1984) Physicochemical and biological properties of poly(ethylene glycol)-coupled immunoglobulin G. *Biochim. Biophys. Acta 788*, 248–55.
(10) Santangelo, P., Nitin, N., LaConte, L., Woolums, A., and Bao, G. (2006) Live-cell characterization and analysis of a clinical isolate of bovine respiratory syncytial virus, using molecular beacons. *J. Virol. 80*, 682–8.
(11) Santangelo, P. J., and Bao, G. (2007) Dynamics of filamentous viral RNPs prior to egress. *Nucleic Acids Res. 35*, 3602–11.
(12) Nitin, N., Santangelo, P. J., Kim, G., Nie, S., and Bao, G. (2004) Peptide-linked molecular beacons for efficient delivery and rapid mRNA detection in living cells. *Nucleic Acids Res. 32*, e58.
(13) Tunnemann, G., Ter-Avetisyan, G., Martin, R. M., Stockl, M., Herrmann, A., and Cardoso, M. C. (2008) Live-cell analysis of cell penetration ability and toxicity of oligo-arginines. *J. Pept. Sci. 14*, 469–76.
(14) Player, M. R., Barnard, D. L., and Torrence, P. F. (1998) Potent inhibition of respiratory syncytial virus replication using a 2−5A-antisense chimera targeted to signals within the virus genomic RNA. *Proc. Natl. Acad. Sci. U.S.A. 95*, 8874–9.
(15) Molenaar, C., Marras, S. A., Slats, J. C., Truffert, J. C., Lemaitre, M., Raap, A. K., Dirks, R. W., and Tanke, H. J. (2001) Linear 2′ O-Methyl RNA probes for the visualization of RNA in living cells. *Nucleic Acids Res. 29*, E89–9.
(16) Majlessi, M., Nelson, N. C., and Becker, M. M. (1998) Advantages of 2′-O-methyl oligoribonucleotide probes for detecting RNA targets. *Nucleic Acids Res. 26*, 2224–9.
(17) Sproat, B. S., Lamond, A. I., Beijer, B., Neuner, P., and Ryder, U. (1989) Highly efficient chemical synthesis of 2′-O-methylo-

ligoribonucleotides and tetrabiotinylated derivatives; novel probes that are resistant to degradation by RNA or DNA specific nucleases. *Nucleic Acids Res. 17*, 3373–86.

(18) Kubota, T., Ikeda, S., Yanagisawa, H., Yuki, M., and Okamoto, A. (2009) Hybridization-sensitive fluorescent probe for long-term monitoring of intracellular RNA. *Bioconjugate Chem. 20*, 1256–61.

(19) Fischer, R., Waizenegger, T., Kohler, K., and Brock, R. (2002) A quantitative validation of fluorophore-labelled cell-permeable peptide conjugates: fluorophore and cargo dependence of import. *Biochim. Biophys. Acta 1564*, 365–74.

(20) Ter-Avetisyan, G., Tunnemann, G., Nowak, D., Nitschke, M., Herrmann, A., Drab, M., and Cardoso, M. C. (2009) Cell entry of arginine-rich peptides is independent of endocytosis. *J. Biol. Chem. 284*, 3370–8.

(21) Murphy, L. B., Loney, C., Murray, J., Bhella, D., Ashton, P., and Yeo, R. P. (2003) Investigations into the amino-terminal domain of the respiratory syncytial virus nucleocapsid protein reveal elements important for nucleocapsid formation and interaction with the phosphoprotein. *Virology 307*, 143–53.

(22) Vives, E., Brodin, P., and Lebleu, B. (1997) A truncated HIV-1 Tat protein basic domain rapidly translocates through the plasma membrane and accumulates in the cell nucleus. *J. Biol. Chem. 272*, 16010–7.

(23) Keene, J. D. (2007) RNA regulons: coordination of post-transcriptional events. *Nat. Rev. Genet. 8*, 533–43.

(24) Emara, M. M., and Brinton, M. A. (2007) Interaction of TIA-1/TIAR with West Nile and dengue virus products in infected cells interferes with stress granule formation and processing body assembly. *Proc. Natl. Acad. Sci. U.S.A. 104*, 9041–6.

(25) Martin, K. C., and Ephrussi, A. (2009) mRNA localization: gene expression in the spatial dimension. *Cell 136*, 719–30.

(26) Mahmood, U., Tung, C. H., Bogdanov, A., Jr., and Weissleder, R. (1999) Near-infrared optical imaging of protease activity for tumor detection. *Radiology 213*, 866–70.

BC9003876

Targeted Dendrimeric Anticancer Prodrug: A Methotrexate-Folic Acid-Poly(amidoamine) Conjugate and a Novel, Rapid, "One Pot" Synthetic Approach

Yuehua Zhang, Thommey P. Thomas, Ankur Desai, Hong Zong, Pascale R. Leroueil, Istvan J. Majoros, and James R. Baker, Jr.*

Michigan Nanotechnology Institute for Medicine and Biological Sciences, Department of Internal Medicine, University of Michigan, Ann Arbor, Michigan 48109. Received September 8, 2009; Revised Manuscript Received December 3, 2009

A targeted dendrimeric anticancer prodrug, a conjugate of generation 5 (G5) polyamidoamine (PAMAM) dendrimer, folic acid (FA), and methotrexate (MTX), has been successfully synthesized by using a novel "one pot" approach which is simple, reproducible, and feasible for large-scale synthesis. All dendrimer products have been characterized by ^{1}H NMR, MALDI-TOF, GPC, and HPLC. With this new method, the ratio of FA versus MTX attached to the dendrimer can be easily tuned to achieve the desired therapeutic effect. A new analytical approach for calculating the numbers of FA and MTX attached to the dendrimer has been established. In vitro studies performed on FA receptor-expressing KB cells show that the new conjugate has a similar affinity and cytotoxic potency to G5-FA-MTX synthesized using the traditional multiple-step approach.

INTRODUCTION

PAMAM dendrimers are highly branched, narrowly dispersed synthetic macromolecules with well-defined chemical structures. PAMAM dendrimers can be easily modified and conjugated with multiple functionalities such as targeting molecules, imaging agents, and drugs (*1*). They are water-soluble, biocompatible, and cleared from the blood through the kidneys (*2*), which eliminates the need for biodegradability. Because of these desirable properties, PAMAM dendrimers have been widely investigated for drug delivery (*3*−*7*), gene therapy (*8*−*10*), and imaging applications (*11*).

Folic acid belongs to the vitamin B family. It is important in cell division because it participates in the biosynthesis of nucleotide bases. There are two membrane-bound folic acid receptors (FR), FR-α and FR-*β*. Both of the 38 kDa FR isoforms bind folic acid with a high affinity (KD < 1 nM) (*12*). The expression of FR in normal tissues is low and restricted to various epithelial cells, such as those of the placenta, choroid plexus, lungs, thyroid, and kidneys (*13, 14*). However, the folate receptors are overexpressed in many epithelial cancer cells, including breast, ovary, endometrium, kidney, lung, head and neck, brain, and myeloid cancers (*14*−*17*), and is internalized into cells after ligand binding (*18*). Although FR is expressed in some normal tissues, as the normal epithelial cells but not the tumor cells are highly polarized and as the FR has been shown to be exclusively localized in the apical side of the cells (e.g., the urine side in kidney), an FR-targeted drug delivery has been shown to cause only minimum nonspecific cytotoxicity when administered systemically (*19, 20*). Tumor-selective targeting has been achieved by an FA-targeted PEG-gemcitabine prodrug (*21*), FA-conjugated multiarm-block copolymer-doxorubicin (*22*), FA-conjugated liposomes encapsulating an antineoplastic drug (*23*) or antisense oligonucleotides (*24*), FA-conjugated protein toxin (*25*), and FA-derivatized antibodies or their Fab/scFv fragments binding to the T-cell receptor (*26*). In vivo studies from our own group showed that the administration of multivalent, folate-targeted dendrimer-methotrexate conjugates resulted in significantly lower toxicity and a 10-fold enhancement in efficacy compared to free methotrexate at an equal cumulative dose (*5, 27*).

* jbakerjr@umich.edu.

In our previous studies, FA and MTX were conjugated to PAMAM dendrimers through amide and ester linkages, respectively, using a multiple-step synthetic route (*5, 6, 28*). The synthetic steps involved partial acetylation of the dendrimer, conjugation of FA using EDC chemistry through amide bonds, glycidation of the remaining amino groups, and finally conjugation of MTX through ester linkage through some of the glycidol moieties. The variability in efficiency of each of these synthetic steps resulted in batch-to-batch reproducibility problems, which limited the application of this technology. In order to address this issue, we have developed a simplified approach for synthesizing multifunctional dendrimers that is amenable to large-scale synthesis. In this approach, the dendrimer is initially fully glycidated and the FA and MTX are simultaneously conjugated to the dendrimer through ester linkages in a "one pot" reaction.

EXPERIMENTAL PROCEDURES

Materials. Amine-terminated G5-PAMAM dendrimer (G5-NH_2) was purchased from Dendritech, Inc. (Midland, MI, USA) and characterized at the Michigan Nanotechnology Institute for Medicine and Biological Sciences, University of Michigan. All chemicals were purchased from Sigma-Aldrich and used as received, unless otherwise specified. Water used in all experiments was purified by a Milli-Q Plus 185 water purification system (Millipore, Bedford, MA) with resistivity higher than 18 MΩ cm. The Spectra/Por dialysis membranes (MWCO 1000 and MWCO 10 000) and phosphate buffer saline were acquired from Fisher.

Nuclear Magnetic Resonance Spectrometry (NMR). ^{1}H NMR spectra were recorded on a 400 MHz Varian Inova 400 nuclear magnetic spectrometer in dimethyl sulfoxide (DMSO-d_6).

Matrix-Assisted Laser Desorption Ionization-Time of Flight (MALDI-TOF) Mass Spectrometry. MALDI-TOF mass spectra were recorded on a Waters TofSpec-2E spectrometer (Beverly, MA, USA), running in linear mode with the high-mass PAD detector, and 2,5-dihydroxybenzoic acid (DHB) in acetonitrile/water (50:50, v/v) was used as the matrix. The instrument was calibrated with bovine serum albumin (BSA, $M_w = 66.43 \times 10^3$) in sinapic acid. The data were acquired and processed by *MassLynx 3.5* software.

10.1021/bc9003958 © 2010 American Chemical Society
Published on Web 02/03/2010

High-Performance Liquid Chromatography (HPLC). A reverse-phase HPLC instrument consisting of a System GOLD 126 solvent module, a model 507 auto sampler equipped with a 100 μL loop and a model 166 UV detector (Beckman Coulter, Fullerton, CA USA), and a Phenomenex (Torrance, CA, USA) Jupiter C5 silica-based HPLC column (250 × 4.6 mm, 300 Å) were used for analysis of the products in this work. Two Phenomenex safety guards were installed upstream of the HPLC column. The mobile phase for elution of the PAMAM dendrimer products was a linear gradient beginning with 100:0 water/acetonitrile (ACN) (both containing 0.14 wt % TFA) at a flow rate of 1 mL/min., reaching 20:80 (or 50:50) within 35 min. Trifluoroacetic acid (TFA) (0.14 wt % in both water and ACN) was used as a counterion to make the dendrimer-conjugate surface hydrophobic. All samples were dissolved in the aqueous mobile phase (water containing 0.14% TFA). The injection volume in each case was 35 μL with a sample concentration of 1 mg/mL, and the detection wavelength was 210 or 280 nm. The analysis was performed using Beckman's System GOLD Nouveau software.

Gel Permeation Chromatography (GPC). GPC was used to evaluate the molecular weights and molecular weight distribution of the G5-PAMAM dendrimer, dendrimer derivatives, and conjugates. GPC experiments were performed on an Alliance Waters 2690 separation module (Waters Corp., Milford, MA) equipped with a Waters 2487 dual wavelength UV absorbance detector (Waters Corp.), a Wyatt Dawn HELEOS light scattering detector (Wyatt Technology Corp., Santa Barbara, CA), an Optilab rEX differential refractometer (Wyatt Technology Corp.), and TosoHaas TSK-Gel Guard PHW 06762 (75 × 7.5 mm, 12 μm), G 2000 PW 05761 (300 × 7.5 mm, 10 μm), G 3000 PW 05762 (300 × 7.5 mm, 10 μm), and G 4000 PW (300 × 7.5 mm, 17 μm) columns. Column temperature was maintained at 25 ± 0.2 °C with a Waters temperature control module. Citric acid buffer (0.1 M) with 0.025% sodium azide in water, pH 2.74, was used as a mobile phase at a flow rate of 1 mL/min. The sample concentration was 2 mg/mL, with an injection volume of 100 μL. The number average molecular weight M_n, weight average molecular weight M_w and polydispersity index (PDI) were calculated using *ASTRA 5.34.14* software (Wyatt Technology Corp.)

Synthesis of Hydroxyl-Terminated G5 PAMAM Dendrimer (G5-Gly-OH 2). G5-GLY−OH was synthesized using methods similar to that which has been previously reported (*28*−*30*). G5-NH_2 (500 mg, 0.0174 mmol) was dissolved in methanol (10 mL) in a 50 mL flask. To the solution was added glycidol (442 mg, 4.77 mmol). The mixture was stirred at room temperature under nitrogen overnight. The mixture was dialyzed against water (4 × 4 L) with a cellulose dialysis membrane (MWCO = 1000) for 48 h and was dried by lyophilization (3 days) to yield G5-Gly-OH as a white solid (677 mg, 85%).

Synthesis of a Conjugate of G5 PAMAM Dendrimer, Folic Acid, and Methotrexate (G5-FA-MTX) 3. A solution of G5-Gly-OH **2** (200 mg, 5.06×10^{-3} mmol), MTX (34.1 mg, 0.075 mmol), and FA (17.7 mg, 0.040 mmol) in dimethyl sulfoxide (15 mL) was stirred at room temperature under nitrogen. To the solution was added 2-chloro-1-methylpyridinium iodide (35.3 mg, 0.138 mmol) and 4-(dimethylamino)pyridine (33.7 mg, 0.276 mmol). The mixture was further stirred overnight at room temperature and then poured into water (75 mL). The product was purified by dialysis against isotonic phosphate buffered saline (PBS) buffer (3 × 4 L) and then water (3 × 4 L) with a cellulose dialysis membrane (MWCO = 10 000) over 48 h. The final product was dried by lyophilization (3 days) to yield G5-FA-MTX as a yellow solid (231 mg, 98%).

Measurement of Cellular Binding and Cytotoxicity. KB cells, a subline of the cervical carcinoma HeLa cells (ATCC, Manassas, VA, USA), were grown as a monolayer cell culture at 37 °C and 5% CO_2 in FA-deficient RPMI 1640 medium supplemented with 10% fetal bovine serum (FBS). The 10% FBS provided an FA concentration equivalent to that present in the human serum (~20 nM).

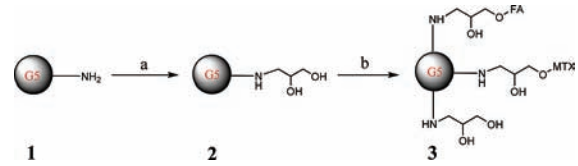


Figure 1. Synthesis of a G5-FA-MTX conjugate using folic acid (FA), methotrexate (MTX), and G5 polyamidoamine (PAMAM) dendrimer. Reagents and conditions: (a) glycidol, methanol, room temperature, 24 h; (b) FA, MTX, 2-chloro-1-methylpyridinium iodide, 4-(dimethylamino)pyridine, dimethyl sulfoxide, room temperature, 24 h.

For assessment of the cellular binding of the synthesized conjugate, we have utilized the competition of the conjugate with another previously synthesized dendrimer conjugate ("G5-FI-FA-MTX") that contained 4 molecules of the fluorescent dye fluorescein isothiocyanate (FI), 5 molecules of FA, and 7 molecules of MTX (*7*). The KB cells, plated in 24-well plates, were treated with a mixture of 100 nM of the G5-FI-FA-MTX and varying concentrations of the newly synthesized G5-FA-MTX, added as a mixture at the same time. The cells were incubated at 37 °C for 1 h, and the FL1 fluorescence of 10 000 cells was determined by flow cytometry, as described previously (*7*).

For the cytotoxicity experiments, the cells were seeded in 96-well microtiter plates (3000 cells/well) in medium containing dialyzed serum. Two days after plating, the cells were treated with the dendrimer conjugates in tissue culture medium under the indicated conditions. A colorimetric "XTT" (sodium 3-[1-(phenylaminocarbonyl)-3,4-tetrazolium]-bis(4-methoxy-6-nitro) benzene sulfonic acid hydrate) assay (Roche Molecular Biochemicals, Indianapolis, IN) was performed, following the vendor's protocol. After incubation with the XTT labeling mixture, the microtiter plates were read on an ELISA reader (Synergy HT, BioTek) at 492 nm with the reference wavelength at 690 nm (*7*).

RESULTS AND DISCUSSION

Synthesis. In this study, G5-NH_2 **1** was used as the starting material to synthesize the targeted dendrimeric anticancer drug G5-FA-MTX **3** (Figure 1). The number of available primary amino groups on the surface of G5-NH_2 is 110 (*31*). Starting with G5-NH_2 **1**, the amino groups of G5-NH_2 react with glycidol to yield G5-Gly-OH **2**. In this reaction, excess glycidol was used (glycidol/NH_2 = 3:1) to fully cap the free amino groups on the surface of **1**. Each amino group can theoretically react with two molecules of glycidol to form a tertiary amine. However, calculations based upon the MALDI indicated that the hydroxylation reaction was incomplete, as previous reported by us (*30*). It is hypothesized that steric hindrance prevents some of the terminal amines residing inside the dendrimer from being available for hydroxylation, resulting in an incomplete reaction (*32*). The G5-Gly-OH **2** was purified by dialysis with a cellulose dialysis membrane against water. MTX and FA were attached to the hydroxyl groups of the G5-Gly-OH **2** through ester bonds in a one-pot reaction, using 2-chloro-1-methylpyridinium iodide and 4-(dimethylamino)pyridine as the coupling reagents (Mukaiyama reagent), which is efficient for preparation of esters from equimolar amounts of free carboxylic acid and alcohol. The reaction was conducted in DMSO under nitrogen at room temperature for 24 h. The final product, conjugate **3**, was purified by dialysis with a cellulose dialysis membrane against PBS buffer and then water. The G5-FA-MTX is highly water-soluble, even with 5 FAs and 15 MTXs attached. It was also observed that the numbers of FA and MTX attached on the surface of the PAMAM dendrimer can be easily and reproducibly

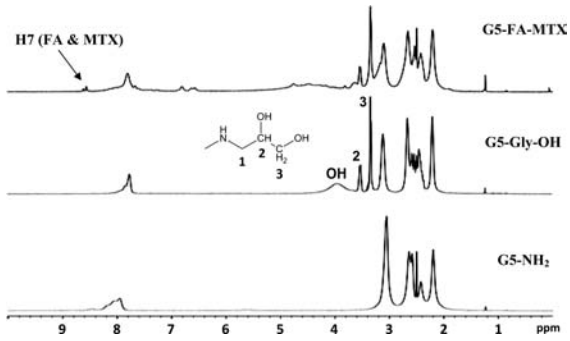
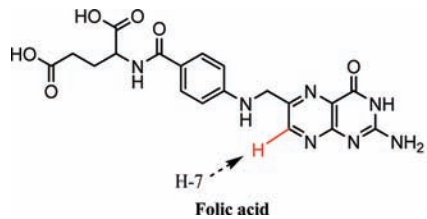


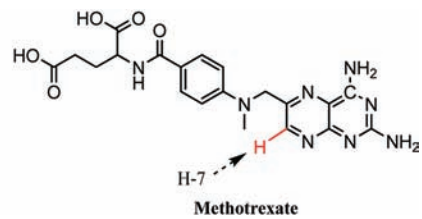
Figure 2. Comparison of the ^{1}HNMR spectra of the G5 PAMAM dendrimer, the hydroxyl-terminated G5 PAMAM dendrimer, and the conjugate of G5 PAMAM dendrimer, FA, and MTX.

adjusted by changing the feeding ratio of FA and MTX in the feed. The numbers of FA and MTX attached on the PAMAM dendrimer were calculated using results from MALDI-TOF, GPC, and ^{1}H NMR. Despite the fact that we have used dialysis as a purification step in these procedures, the application of ultrafiltration would make the synthetic procedure feasible for scale-up synthesis.

^{1}H NMR Spectroscopy. ^{1}H NMR was used to confirm the surface capping of the terminal amines of the dendrimer with glycidol and the attachment of the FA and MTX to the hydroxyl group of the G5-Gly-OH (Figure 2). The ^{1}H NMR of the G5 PAMAM dendrimer shows 6 broad peaks, which correspond to the protons of the amide bond (CONH) at 7.95 ppm, the amino groups (NH_2), the internal methylene groups (CH_2), and those CH_2 next to the amino groups at 3.05, 2.64, 2.58, 2.42, and 2.20 ppm. The ^{1}H NMR spectrum of the G5-Gly-OH clearly shows three new peaks, compared with that of the G5-NH_2. The peak at 3.348 ppm (peak 3) is the resonance of protons of the CH_2 at position 3 of the 2,3-dihydroxylpropyl group. The peak at 3.542 ppm (peak 2) belongs to the CH at position 2 of the 2,3-dihydroxylpropyl group. The broad peak at 3.961 ppm is attributed to two hydroxyl groups of the 2,3-dihydroxylpropyl group. The peak at about 2.47 ppm (*30*) belongs to the protons of the CH_2 at position 1 of the 2,3-dihydroxylpropyl group, which overlaps with peaks associated with the internal protons of the G5-NH_2. Compared with the spectrum of the G5-Gly-OH, the spectrum of the G5-FA-MTX shows additional peaks. Some of the peaks overlap with the peaks of the G5-Gly-OH. The H-7 peaks of the conjugated FA and MTX are present at 8.617 ppm and 8.561 ppm, respectively. They are sharp and well-separated single peaks. The integration ratio of these two peaks represents the molar ratio of MTX and FA, because both MTX and FA contain only one H-7 (Figure 3). Significantly, it is also found that the integration ratio of these two protons is proportional to the feed ratio of MTX and FA in the "one-pot" reaction (Table 1). Therefore, the actual numbers of FA and MTX conjugated to the surface of the dendrimer can be calculated using this integration ratio and molecular weight gain from G5-Gly-OH **2** to G5-FA-MTX **3**, as measured by MALDI-TOF and GPC.



Folic acid



Methotrexate

MALDI-TOF Mass Spectrometry. MALDI-TOF mass spectrometry has been proven to be an important technique for characterization of dendrimers and dendrimer derivatives. It not only provides the average molecular weight, but also gives information about the success of each conjugation reaction and the number of molecules that have been conjugated. Figure 4 shows the MALDI-TOF mass spectra of the G5-NH_2, G5-Gly-OH, and G5-FA-MTX. The molecular weight increase for each species along the synthetic pathway is clearly seen and demonstrates that the hydroxylation (first step) and conjugation (second step: the "one pot" reaction) have occurred. The molecular weight gain of the G5-Gly-OH from the G5-NH_2 is due to the attachment of the 2,3-dihydroxylpropyl group. The average number of 2,3-dihydroxylpropyl groups attached to each amino group may be calculated by the difference divided by the molecular mass of the 2,3-dihydroxylpropyl group and the number of the amino groups on the surface of the dendrimer. The molecular weight increase from the G5-Gly-OH to the G5-FA-MTX is due to the addition of both FA and MTX. The numbers of FAs and MTXs attached to the dendrimer can be calculated using eqs 1 and 2, which are based on the molecular weight gain from the G5-Gly-OH to the G5-FA-MTX, as measured by MALDI-TOF or GPC, and the integration ratio of H-7 of the conjugated FA and MTX. Calculation results have been listed in Table 1.

$$N_{FA} = \frac{\Delta MW \times F_{FA/(MTX+FA)}}{MW_{FA} - 18} \quad (1)$$

$$N_{MTX} = \frac{\Delta MW \times F_{MTX/(FA+MTX)}}{MW_{MTX} - 18} \quad (2)$$

where N_{FA} = molecules of folic acid attached to each PAMAM dendrimer molecule; N_{MTX} = molecules of MTX attached to each PAMAM dendrimer molecule; ΔMW = molecular weight gain of the conjugate from hydroxyl-terminated PAMAM dendrimer; F_{FA} = ^{1}H NMR integration fraction of H-7 (FA over FA and MTX); F_{MTX} = ^{1}H NMR integration fraction of H-7 (MTX over FA and MTX); MW_{FA} = molecular weight of FA; MW_{MTX} = molecular weight of MTX.

High-Performance Liquid Chromatography (HPLC). High-performance liquid chromatography (HPLC) is a widely accepted method for separation and purification of small molecules and macromolecules and is commonly used in chemical, pharmaceutical, and biotechnology laboratories. Recently, HPLC has been used as a vital tool to analyze PAMAM dendrimers of various generations and terminal groups, as well as their conjugates (*33*−*35*). In this study, we used HPLC to evaluate the purity and molecular weight distributions of the conjugates. Small molecule impurities such as unreacted FA, MTX, coupling reagent, and byproduct are very easily differentiated from the dendrimers (G5-NH_2, G5-Gly-OH, and G5-FA-MTX) by HPLC due to the significant difference in retention time. Figure 5 is a representative chromatogram of the conjugate (G5-FA-MTX) under UV 280 nm, which shows a single symmetric peak of the conjugate and a few small impurity peaks attributed to the presence of less than 0.1% free FA, MTX, and other impurities. The result also indicates that the FA and MTX have been successfully attached to the G5-Gly-OH, resulting in a very narrow molecular weight distribution, which is in agreement with the GPC results shown below.

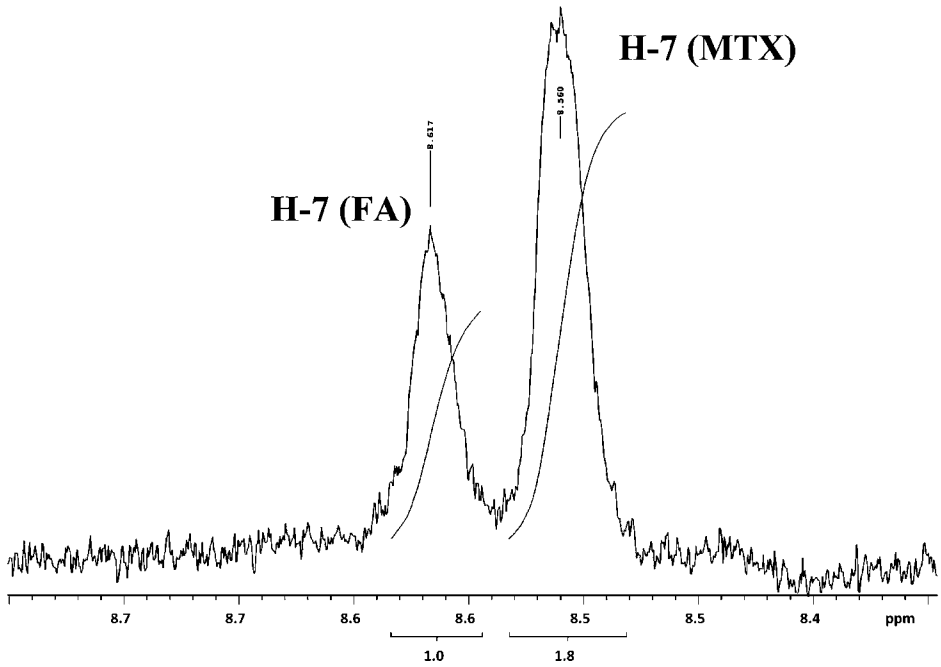


Figure 3. Enlarged scale of the ^{1}H NMR spectrum of proton-7 of conjugated FA and MTX.

Table 1. Reaction Feed Molar Ratio of MTX/FA/G5-Gly-OH, ^{1}H NMR Integration Ratio of H-7 of MTX/FA, and Numbers of MTX and FA on the Conjugate (G5-FA-MTX)

reaction feed molar ratio of MTX/ FA/ G5-Gly-OH	^{1}H NMR integration ratio of H-7s (MTX/FA)	average number of MTX and FA attached on PAMAM
10:7:1	1.38:1.00	6.79 and 5.20
15:8:1	1.86:1.00	9.44 and 5.22
23:8:1	2.83:1.00	14.90 and 5.42
15:10:1[a]	1.33:1.00	9.26 (±0.28[b]) and 7.18 (±0.1[c])

[a] Three batches of parallel synthesis under the same condition: G5-Gly-OH (50 mg), MTX (8.54 mg), FA (5.52 mg), 2-chloro-1-methylpyridinium iodide (8.00 mg), 4-(dimethylamino)pyridine (7.65 mg), DMSO (2.5 mL), N_2, 24 h, cellulose membrane dialysis (6 times 4 L over 48 h), and lyophilization (72 h). [b] Standard deviation of average number of MTX. [c] Standard deviation of average number of FA.

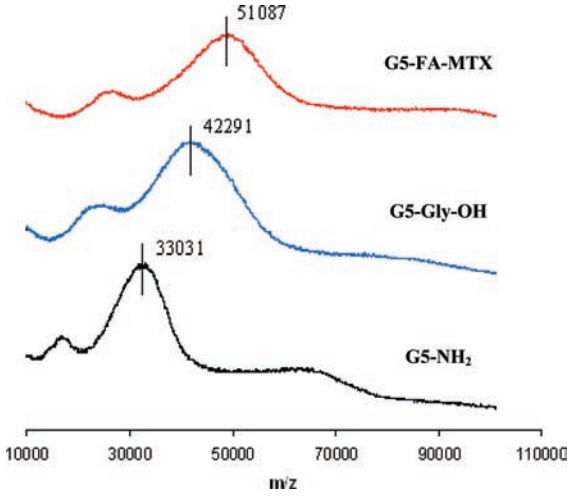


Figure 4. MALDI-TOF mass spectra of the G5 PAMAM dendrimer, the hydroxyl-terminated G5 PAMAM dendrimer, and the conjugate of G5 PAMAM dendrimer, folic acid, and methotrexate.

Gel Permeation Chromatography (GPC). A gel permeation chromatography (GPC) instrument equipped with two detectors, a multiangle laser light scattering (MALLS) and a differential refractive index, was used to evaluate the molar mass of the starting PAMAM dendrimer, the hydroxyl-terminated PAMAM dendrimer, and the conjugates. Figure 6 shows the differential mass fraction profile of the G5-NH_2, G5-Gly-OH, and G5-FA-MTX, respectively. All dendrimer samples exhibit a single peak. The number average molecular weights M_n and polydispersity indexes (PDI: M_w/M_n) of the G5-NH_2, G5-Gly-OH, and G5-FA-MTX are 26 060 (1.025), 39 110 (1.042), and 52 800 (1.044), respectively. The ratios of weight- to number-average molecular weights of the G5-NH_2, G5-Gly-OH, and G5-FA-MTX are very close to 1. This indicates that the distribution mass of the individual components is narrow and that the conjugation process at each step is nearly uniform.

The GPC results are somewhat different from those measured by MALDI-TOF, as shown by Figures 4 and 6. This difference is due to the broadening of the MALDI-TOF spectra, as compared to the GPC spectra. Generally, however, GPC is thought to reflect the real average molar mass.

In Vitro Studies. The binding of the newly synthesized G5-FA-MTX onto FA receptor-expressing KB cells was examined. For this, we utilized a previously synthesized G5-FI-FA-MTX conjugate in which the FA and MTX were conjugated to the dendrimer through the classic synthetic pathway (*28*). In addition, a fluorescent dye FITC (FI) was conjugated to the surface of the dendrimer. As shown in Figure 7, at a fixed concentration of G5-FI-FA-MTX (100 nM; concentrations shown are for the intact conjugates), the G5-FA-MTX competed with the former for binding, with a 50% inhibition of binding occurring at ~60 nM. This shows that the G5-FA-MTX binds through the FA receptor with an affinity similar to or slightly better than the G5-FA-MTX synthesized through the classic synthetic pathway (*28*).

The cytotoxicity of the newly synthesized conjugate was determined by the XTT assay, as described in Methods. We have compared the cytotoxicity with another batch of G5-FA-MTX synthesized by Cambrex Inc., using the classic synthetic pathway in which the FA and MTX were conjugated through amide and ester linkages, respectively. Our previous studies have shown that this batch of Cambrex conjugates was cytotoxic in

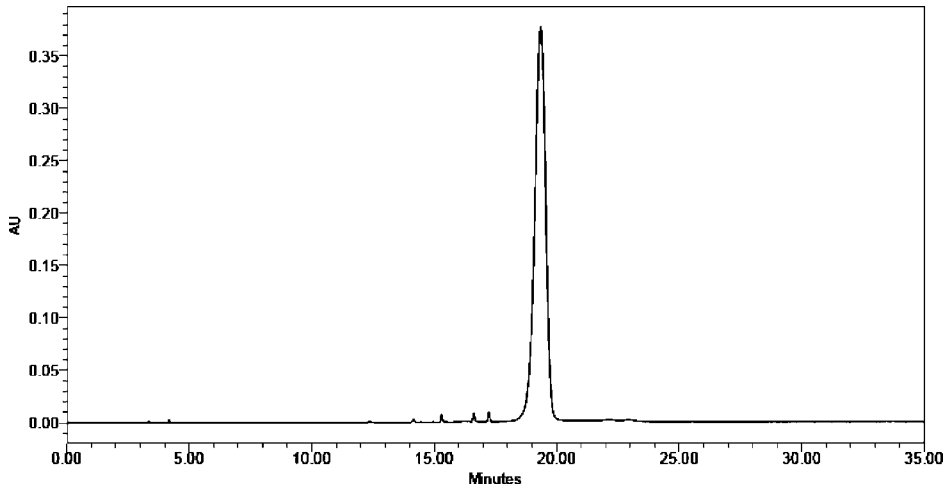


Figure 5. HPLC chromatogram of the conjugate (G5-FA-MTX) under 280 nm.

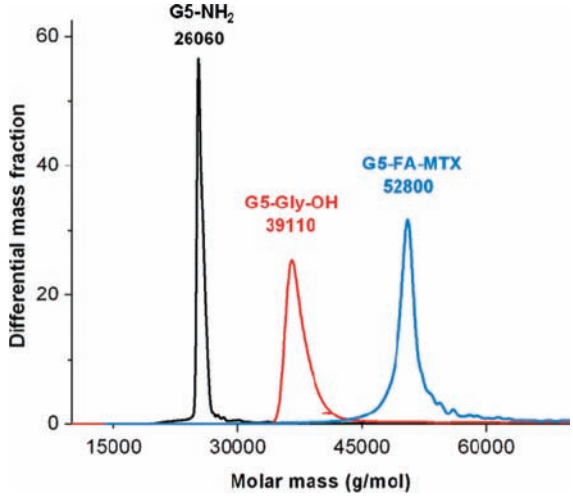


Figure 6. Graph showing the differential molar mass fractions for the G5 PAMAM dendrimer, the hydroxyl-terminated G5 PAMAM dendrimer, and the conjugate of G5 PAMAM dendrimer, FA, and MTX.

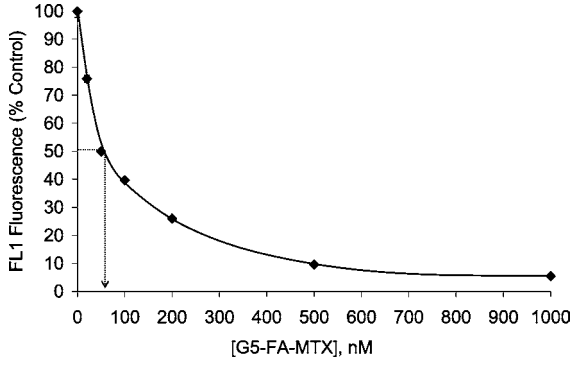


Figure 7. Competition of G5-FA-MTX synthesized using the "one-pot" approach with G5-FI-FA-MTX. The KB cells were treated with the two conjugates simultaneously, as described in Methods, and the mean FL1 fluorescence of 10 000 cells was determined by flow cytometry. The data are expressed as the percent fluorescence obtained for the binding of 100 nM G5-FI-FA-MTX in the absence of G5-FA-MTX. As indicated by the arrow, the concentration of G5-FA-MTX that is required for 50% reduction in binding of the G5-FI-FA-MTX is ~60 nM.

vitro and tumoricidal in vivo, with a potency similar to that of our previously published compound (*5*). As shown in Figure 8,

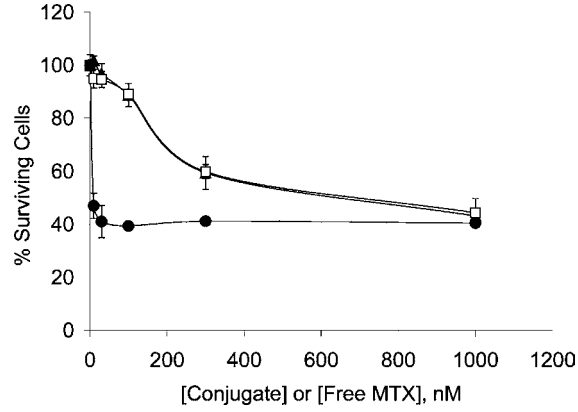


Figure 8. In vitro cytotoxicity of the newly synthesized G5-FA-MTX. The KB cells were treated with different concentrations of the newly synthesized G5-FA-MTX (▲) and free MTX (•). The data also show the cytotoxicity of G5-FA-MTX synthesized through the classic synthetic pathway in which the FA and MTX were conjugated through amide and ester linkages, respectively (□). The cells were treated with the drugs for 5 days, with one change of fresh medium/drug after 3 days, and the live cells were quantified by the XTT assay as described in Methods. The data represent the mean ± SE of 5 replicate cell samples in a representative experiment, with identical data obtained in 3 independent experiments.

the newly synthesized conjugate was as cytotoxic as the Cambrex batch.

CONCLUSION

A targeted dendrimeric anticancer prodrug, a conjugate of PAMAM dendrimer, FA, and MTX, has been successfully synthesized using an improved and simple "one pot" approach. Using this method, FA and MTX can be attached to the dendrimer in any desired ratios in a simple one-step reaction. A new analytical approach for calculating the molecules of FA and MTX attached to each dendrimer molecule has been established. The in vitro studies performed on FA receptor-expressing KB cells show that the new conjugates have similar affinity and cytotoxic potency as the G5-FA-MTX synthesized using the traditional multiple step approach. The results of parallel syntheses have demonstrated that this method is reproducible. The new method will allow easy conjugation of multiple functionalities such as a targeting agent, a drug, and even an imaging agent by utilizing the simple "one-pot" synthetic approach.

ACKNOWLEDGMENT

This project has been funded in whole or in part with Federal funds from the National Cancer Institute, National Institutes of Health, under award 1 R01 CA119409.

Supporting Information Available: ^{1}H NMR spectrum of folic acid (FA), methotrexate (MTX), G5 PAMAM dendrimer (G5-NH_2), hydroxyl-terminated G5 dendrimer (G5-Gly-OH), and conjugates (G5-FA-MTX) in DMSO-d_6; MALDI-TOF mass spectrum and GPC chromatogram of G5-NH_2, G5-Gly-OH), and G5-FA-MTX; HPLC chromatograms of G5-FA-MTX under UV 210 and 280 nm; and three batches of parallel synthesis of G5-FA-MTX and characterization. This material is available free of charge via the Internet at http://pubs.acs.org.

LITERATURE CITED

(1) Thomas, T. P., Shukla, R., Majoros, I. J., Myc, A., and Baker, J. R., Jr. (2007) Poly (amidoamine) dendrimer-based multifunctional nanoparticles. In *Nanobiotechnology: Concepts, Methods and Perspectives* (Mirkin, Ed.) Wiley-VCH.

(2) Peer, D., Karp, J. M., Hong, S., FarokHzad, O. C., Margalit, R., and Langer, R. (2007) Nanocarriers as an emerging platform for cancer therapy. *Nat. Nanotechnol. 2*, 751–760.

(3) Esfand, R., and Tomalia, D. A. (2001) Poly(amidoamine) (PAMAM) dendrimers: from biomimicry to drug delivery and biomedical applications. *Drug Discovery Today 6*, 427–436.

(4) Patri, A. K., Majoros, I. J., and Baker, J. R. (2002) Dendritic polymer macromolecular carriers for drug delivery. *Curr. Opin. Chem. Biol. 6*, 466–471.

(5) Kukowska-Latallo, J. F., Candido, K. A., Cao, Z. Y., Nigavekar, S. S., Majoros, I. J., Thomas, T. P., Balogh, L. P., Khan, M. K., and Baker, J. R. (2005) Nanoparticle targeting of anticancer drug improves therapeutic response in animal model of human epithelial cancer. *Cancer Res. 65*, 5317–5324.

(6) Quintana, A., Raczka, E., Piehler, L., Lee, I., Myc, A., Majoros, I., Patri, A. K., Thomas, T., Mule, J., and Baker, J. R. (2002) Design and function of a dendrimer-based therapeutic nanodevice targeted to tumor cells through the folate receptor. *Pharm. Res. 19*, 1310–1316.

(7) Thomas, T. P., Majoros, I. J., Kotlyar, A., Kukowska-Latallo, J. F., Bielinska, A., Myc, A., and Baker, J. R., Jr. (2005) Targeting and inhibition of cell growth by an engineered dendritic nanodevice. *J. Med. Chem. 48*, 3729–35.

(8) KukowskaLatallo, J. F., Bielinska, A. U., Johnson, J., Spindler, R., Tomalia, D. A., and Baker, J. R. (1996) Efficient transfer of genetic material into mammalian cells using Starburst polyamidoamine dendrimers. *Proc. Natl. Acad. Sci. U.S.A. 93*, 4897–4902.

(9) Eichman, J. D., Bielinska, A. U., Kukowska-Latallo, J. F., and Baker, J. R., Jr. (2000) The use of PAMAM dendrimers in the efficient transfer of genetic material into cells. *Pharm. Sci. Technol. Today 3*, 232–245.

(10) Luo, D., Haverstick, K., Belcheva, N., Han, E., and Saltzman, W. M. (2002) Poly(ethylene glycol)-conjugated PAMAM dendrimer for biocompatible, high-efficiency DNA delivery. *Macromolecules 35*, 3456–3462.

(11) Kobayashi, H., Kawamoto, S., Jo, S. K., Bryant, H. L., Brechbiel, M. W., and Star, R. A. (2003) Macromolecular MRI contrast agents with small dendrimers: Pharmacokinetic differences between sizes and cores. *Bioconjugate Chem. 14*, 388–394.

(12) Elnakat, H., and Ratnam, M. (2004) Distribution, functionality and gene regulation of folate receptor isoforms: implications in targeted therapy. *Adv. Drug Delivery Rev. 56*, 1067–84.

(13) Sudimack, J., and Lee, R. J. (2000) Targeted drug delivery via the folate receptor. *Adv. Drug Delivery Rev. 41*, 147–162.

(14) Weitman, S. D., Lark, R. H., Coney, L. R., Fort, D. W., Frasca, V., Zurawski, V. R., and Kamen, B. A. (1992) Distribution of the folate receptor Gp38 in normal and malignant-cell lines and tissues. *Cancer Res. 52*, 3396–3401.

(15) Weitman, S. D., Weinberg, A. G., Coney, L. R., Zurawski, V. R., Jennings, D. S., and Kamen, B. A. (1992) Cellular-localization of the folate receptor - potential role in drug toxicity and folate homeostasis. *Cancer Res. 52*, 6708–6711.

(16) Campbell, I. G., Jones, T. A., Foulkes, W. D., and Trowsdale, J. (1991) Folate-binding protein is a marker for ovarian-cancer. *Cancer Res. 51*, 5329–5338.

(17) Ross, J. F., Chaudhuri, P. K., and Ratnam, M. (1994) Differential regulation of folate receptor isoforms in normal and malignant-tissues in-vivo and in established cell-lines - physiological and clinical implications. *Cancer 73*, 2432–2443.

(18) Antony, A. C., Kane, M. A., Portillo, R. M., Elwood, P. C., and Kolhouse, J. F. (1985) Studies of the role of a particulate folate-binding protein in the uptake of 5-methyltetrahydrofolate by cultured human Kb cells. *J. Biol. Chem. 260*, 4911–4917.

(19) Hilgenbrink, A. R., and Low, P. S. (2005) Folate receptor-mediated drug targeting: From therapeutics to diagnostics. *J. Pharm. Sci. 94*, 2135–2146.

(20) Low, P. S., Henne, W. A., and Doorneweerd, D. D. (2008) Discovery and development of folic-acid-based receptor targeting for Imaging and therapy of cancer and inflammatory diseases. *Acc. Chem. Res. 41*, 120–129.

(21) Pasut, G., Canal, F., Dalla Via, L., Arpicco, S., Veronese, F. M., and Schiavon, O. (2008) Antitumoral activity of PEG-gemcitabine prodrugs targeted by folic acid. *J. Controlled Release 127*, 239–48.

(22) Prabaharan, M., Grailer, J. J., Pilla, S., Steeber, D. A., and Gong, S. Q. (2009) Amphiphilic multi-arm-block copolymer conjugated with doxorubicin via pH-sensitive hydrazone bond for tumor-targeted drug delivery. *Biomaterials 30*, 5757–5766.

(23) Lee, R. J., and Low, P. S. (1995) Folate-mediated tumor-cell targeting of liposome-entrapped doxorubicin in-vitro. *Biochim. Biophys. Acta Biomembr. 1233*, 134–144.

(24) Wang, S., Lee, R. J., Cauchon, G., Gorenstein, D. G., and Low, P. S. (1995) Delivery of antisense oligodeoxyribonucleotides against the human epidermal growth-factor receptor into cultured Kb cells with liposomes conjugated to folate via polyethylene-glycol. *Proc. Natl. Acad. Sci. U.S.A. 92*, 3318–3322.

(25) Leamon, C. P., and Low, P. S. (1994) Selective targeting of malignant-cells with cytotoxin-folate conjugates. *J. Drug Targeting 2*, 101–112.

(26) Rund, L. A., Cho, B. K., Manning, T. C., Holler, P. D., Roy, E. J., and Kranz, D. M. (1999) Bispecific agents target endogenous murine T cells against human tumor xenografts. *Int. J. Cancer 83*, 141–149.

(27) Hong, S., Leroueil, P. R., Majoros, I. J., Orr, B. G., Baker, J. R., and Holl, M. M. B. (2007) The binding avidity of a nanoparticle-based multivalent targeted drug delivery platform. *Chem. Biol. 14*, 107–115.

(28) Majoros, I. J., Thomas, T. P., Mehta, C. B., and Baker, J. R. (2005) Poly(amidoamine) dendrimer-based multifunctional engineered nanodevice for cancer therapy. *J. Med. Chem. 48*, 5892–5899.

(29) Kramer, M., Perignon, N., Haag, R., Marty, J. D., Thomann, R., Lauth-de Viguerie, N., and Mingotaud, C. (2005) Water-soluble dendritic architectures with carbohydrate shells for the templation and stabilization of catalytically active metal nanoparticles. *Macromolecules 38*, 8308–8315.

(30) Shi, X. Y., Lesniak, W., Islam, M. T., Muniz, M. C., Balogh, L. P., and Baker, J. R. (2006) Comprehensive characterization of surface-functionalized poly (amidoamine) dendrimers with acetamide, hydroxyl, and carboxyl groups. *Colloids Surf., A 272*, 139–150.

(31) Majoros, I. J., Myc, A., Thomas, T., Mehta, C. B., and Baker, J. R. (2006) PAMAM dendrimer-based multifunctional conjugate for cancer therapy: Synthesis, characterization, and functionality. *Biomacromolecules 7*, 572–579.

(32) Maiti, P. K., Cagin, T., Wang, G. F., and Goddard, W. A. (2004) Structure of PAMAM dendrimers: Generations 1 through 11. *Macromolecules 37*, 6236–6254.

(33) Islam, M. T., Shi, X. Y., Balogh, L., and Baker, J. R. (2005) HPLC separation of different generations of poly(amidoamine) dendrimers modified with various terminal groups. *Anal. Chem. 77*, 2063–2070.

(34) Islam, M. T., Majoros, I. J., and Baker, J. R. (2005) HPLC analysis of PAMAM dendrimer based multifunctional devices. *J. Chromatogr., B: Anal. Technol. Biomed. Life Sci. 822*, 21–26.

(35) Shi, X. Y., Bi, X. D., Ganser, T. R., Hong, S. P., Myc, L. A., Desai, A., Holl, M. M. B., and Baker, J. R. (2006) HPLC analysis of functionalized poly(amidoamine) dendrimers and the interaction between a folate-dendrimer conjugate and folate binding protein. *Analyst 131*, 842–848.

BC9003958

Tumor-Targeting, pH-Responsive, and Stable Unimolecular Micelles as Drug Nanocarriers for Targeted Cancer Therapy

Xiaoqiang Yang,[†] Jamison J. Grailer,[‡] Srikanth Pilla,[†] Douglas A. Steeber,[‡] and Shaoqin Gong*[,†,§,||]

Department of Mechanical Engineering, Department of Biological Sciences, and Department of Materials, University of Wisconsin-Milwaukee, Milwaukee, Wisconsin 53211, and Department of Biomedical Engineering and Wisconsin Institute for Discovery, University of Wisconsin-Madison, Madison, Wisconsin 53706. Received September 23, 2009; Revised Manuscript Received January 31, 2010

A new type of multifunctional unimolecular micelle drug nanocarrier based on amphiphilic hyperbranched block copolymer for targeted cancer therapy was developed. The core of the unimolecular micelle was a hyperbranched aliphatic polyester, Boltorn H40. The inner hydrophobic layer was composed of random copolymer of poly(ε-caprolactone) and poly(malic acid) (PMA-*co*-PCL) segments, while the outer hydrophilic shell was composed of poly(ethylene glycol) (PEG) segments. Active tumor-targeting ligands, i.e., folate (FA), were selectively conjugated to the distal ends of the PEG segments. An anticancer drug, i.e., doxorubicin (DOX) molecules, was conjugated onto the PMA segments with pH-sensitive drug binding linkers for pH-triggered drug release. Transmission electron microscopy (TEM) and dynamic light scattering (DLS) analysis showed that the unimolecular micelles were uniform with a mean hydrodynamic diameter around 25 nm. The drug loading content was determined to be 14.2%. The drug release profile, cell uptake and distribution, and cytotoxicity of the unimolecular micelles were evaluated *in vitro*. The folate-conjugated micelles can be internalized by the cancer cells *via* folate-receptor-mediated endocytosis; thus, they exhibited enhanced cell uptake and cytotoxicity. At pH 7.4, the physiological condition of bloodstream, DOX conjugated onto the unimolecular micelles exhibited excellent stability; however, once the micelles were internalized by the cancer cells, the pH-sensitive hydrazone linkages were cleavable by the intracellular acidic environment, which initially caused a rapid release of DOX. These findings indicate that these unique unimolecular micelles may offer a very promising approach for targeted cancer therapy.

INTRODUCTION

Micelles formed by self-assembly of amphiphilic block copolymers have attracted significant attention in various biomedical fields, including drug and gene delivery (*1–4*). Micelle drug delivery systems can improve the solubility of hydrophobic drugs, stabilize and protect drugs that are sensitive to the surrounding environment, reduce the nonspecific uptake by the reticuloendothelial system (RES), and facilitate targeted drug delivery; however, conventional multimolecuclar micelle drug delivery systems based on the linear amphiphilic block copolymers suffer from instability *in vivo*. Multimolecular micelles are only thermodynamically stable above the critical micelle concentration (cmc) of the amphiphilic copolymers. Above the cmc, micelles are in dynamic equilibrium with the free copolymer molecules in solution, continuously breaking and reforming (*5*). When the concentration of the copolymer is below the cmc, micelles disassemble, thereby releasing the drug prematurely before reaching the tumor target. Furthermore, there are a number of other factors that may affect the *in vivo* stability of the multimolecular micelles including flow stress, interactions between the micelles and the serum components, and variations in temperature, pH, and ionic strength.

The *in vivo* instability problem associated with multimolecular micelles can be overcome by developing unimolecular micelles based on amphiphilic copolymers with a dendritic or hyperbranched structure (*6, 7*). Unimolecular micelles do not disassemble upon dilution and are stable to environmental changes due to their covalent nature, thereby providing excellent *in vivo* stability. Unimolecular micelles also offer other advantages, including high drug loading capacity and narrow nanoparticle size distribution. Furthermore, the highly branched structure of the copolymers can provide many end groups for further functionalization (*8, 9*).

To improve the efficacy of cancer therapy using drug nanocarriers such as unimolecular micelles, the unimolecular micelles must exhibit a number of desirable properties, including *in vivo* stability, high drug loading capacity, and well-controlled nanoparticle sizes, as described previously. In addition, the ability to actively target the tumor cells *via* specific targeting ligands and the ability for controlled drug release *via* stimulus-responsive drug−copolymer linkers are essential.

Drug nanocarriers are desirable for cancer therapy because they can target the tumor tissue through the enhanced permeability and retention (EPR) effect (i.e., passive targeting) (*10*). To further improve the delivery efficiency and cancer specificity, active tumor-targeting ability is also required. Active targeting can be achieved by functionalizing the nanocarriers with targeting ligands such as small molecules (e.g., folate (FA)), peptides (e.g., cRGD) and antibodies, which can recognize and bind to specific receptors/integrins that are unique to or positively expressed on cancer cells (*11*). In terms of controlled drug release, ideally, anticancer drug should not be released during circulation in the bloodstream; however, once the drug nanocarriers are internalized by the cancer cells, a sufficient

* To whom correspondence should be addressed. University of Wisconsin-Madison, Madison, WI 53706, USA; Tel: +1-(608) 890-3463, E-mail: sgong@engr.wisc.edu.

[†] Department of Mechanical Engineering, University of Wisconsin-Milwaukee.

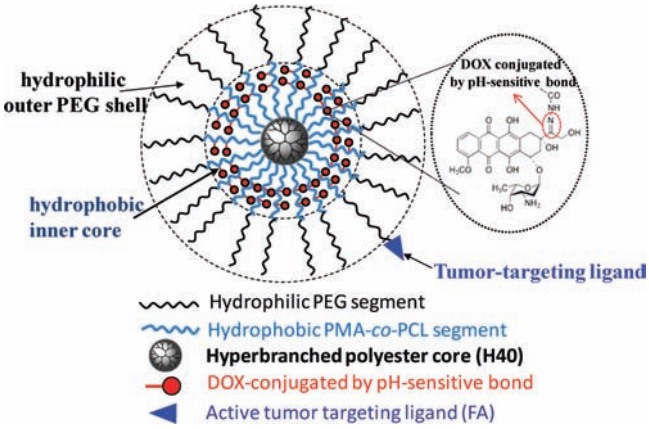
[‡] Department of Biological Sciences, University of Wisconsin-Milwaukee.

[§] Department of Materials, University of Wisconsin-Milwaukee.

[||] University of Wisconsin-Madison.

10.1021/bc900422j © 2010 American Chemical Society
Published on Web 02/17/2010

Scheme 1. Schematic Structure of Unimolecular Micelle Based on H40-(poly(β-malic acid)-hydrazone-doxorubicin-*co*-poly(ε-caprolactone))-methoxy-poly(ethylene glycol)-poly(ethylene glycol)-folate (H40-(PMA-Hyd-DOX-*co*-PCL)-MPEG/PEG-FA) Polymer

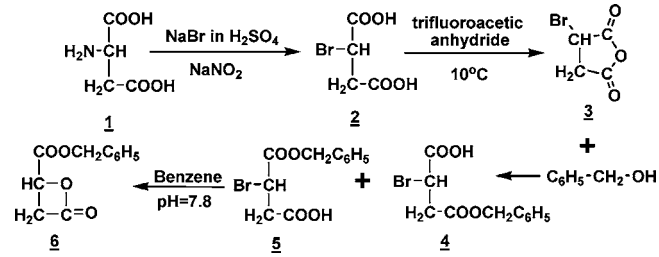


amount of anticancer drug should be released relatively quickly initially in order to effectively kill the cancer cells. The pH value of the bloodstream is approximately 7.4, while that of the endocytic compartments of the cells generally ranges from 4.5 to 6.5. This difference in pH value makes pH-triggered drug release possible (*12*).

Boltorn H40 has received much attention in the design of amphiphilic hyperbranched block copolymers for drug delivery application because of its biodegradability, biocompatibility, globular architecture, and high number of chain end functionalities (*13, 14*). Several excellent reports on drug nanocarriers using the hyperbranched aliphatic polyester, Boltorn H40 as the core are available in the literature. For instance, Prabaharan et al. reported a unimolecular micelle system made of a hyperbranched amphiphilic block copolymer based on Bolton H40 and copolymer of polylactide (PLA) and poly(ethylene glycol) (PEG) using FA as the active tumor-targeting ligands (*15*). Chen et al. reported a drug nanocarrier based on Bolton H40 and copolymer of polycaprolactone (PCL) and PEG, also using FA as the tumor-targeting ligand (*16*); however, in these systems, the anticancer drug, doxrubincin (DOX), was physically encapsulated only in the drug nanocarriers *via* hydrophobic interaction. As such, a significant amount of DOX may be released in the bloodstream during circulation, leading to poor targeting and reduced therapeutic effect.

In this paper, we developed a new type of multifunctional unimolecular micelle based on Boltron H40 as drug nanocarrier for targeted cancer therapy, which exhibited a pH-triggered drug release profile (Scheme 1). These unimolecular micelles were formed by amphiphilic hyperbranched copolymer, H40-((poly(β-malic acid)-hydrazone-doxorubicin)-*co*-poly(ε-caprolactone))-methoxy-poly(ethylene glycol)/poly(ethylene glycol)-folate (H40-(PMA-Hyd-DOX-*co*-PCL)-MPEG/PEG-FA) in aqueous solution. As shown in Scheme 1, Bolton H40 was used as the core of the amphiphilic hyperbranched copolymer. The hydrophobic segments of the amphiphilic copolymer arms were formed by random copolymerization of poly(β-malic acid) (PMA) and poly(ε-caprolactone) (PCL). The hydrophilic segments of the amphiphilic copolymer arms were formed by methoxy poly(ethylene glycol) (MPEG) or FA conjugated PEG (MPEG/PEG-FA). FA was used as the active tumor-targeting agent. FA is a vitamin with low molecular weight (M_w = 441.4) and behaves as a ligand because it has high affinity for its receptor, folate-binding protein, which is selectively overexpressed on the surface of many types of human cancer cells (*17, 18*). The PMA and PCL are important biodegradable aliphatic polyesters and of interest for biomedical applications owing to their good

Scheme 2. Synthesis Procedure of Benzyl Malolactonate Monomer



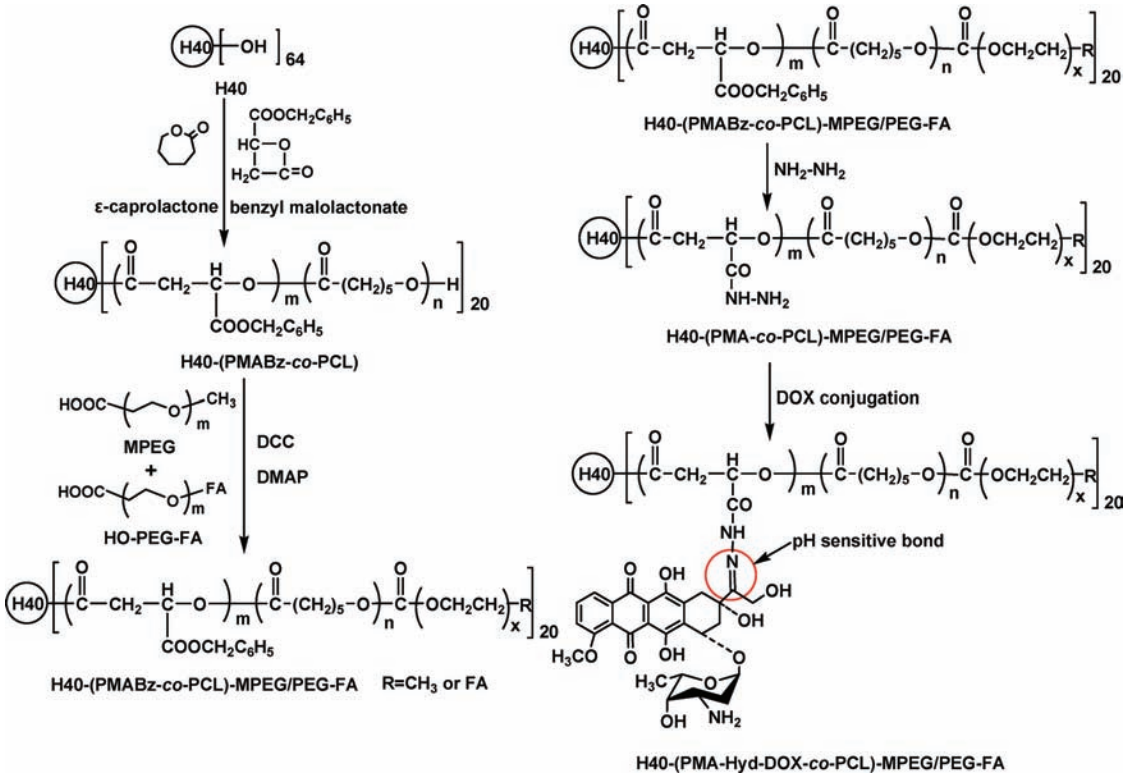
biocompatibility and low immunogenicity (*19*). The anticancer drug, doxorubicin (DOX), is widely used as an antitumor therapeutic agent and was conjugated onto the PMA-*co*-PCL segments through an acid-sensitive hydrazone bond. The random copolymer of PMA and PCL allows the DOX molecules to effectively conjugate onto the PMA segments due to the much reduced steric hindrance from the neighboring MA unit in the random copolymer. The acid-cleavable hydrazone linkages reduce the unwanted DOX release during blood circulation, yet provide quick DOX release initially once inside the tumor cells. This tumor-targeting unimolecular micelle nanosystem with a pH-triggered drug release profile and potentially excellent *in vivo* stability will open many exciting opportunities for targeted cancer therapy.

EXPERIMENTAL PROCEDURES

Materials. L-Aspartic acid, sodium bromide, sodium nitrite, trifluoroacetic anhydride, benzyl alcohol, and stannous octanoate ($Sn(Oct)_2$) were purchased from Fisher Scientific Inc., USA. Boltron H40 (64 hydroxyl groups per molecule theoretically and M_n of 2830 Da) was provided by Perstorp Polyols Inc., USA, and purified with tetrahydrofuran (THF). ε-Caprolactone (ε-CL, from Sigma-Aldrich) was purified by vacuum distillation over calcium hydride (CaH_2). Folic acid, dicyclohexylcarbodiimide (DCC), 4-dimethylamino pyridine (DMAP), and anhydrous hydrazine were purchased from Sigma-Aldrich, USA. MPEG was obtained from Fluka. α-Hydroxy-ω-amino poly(ethylene glycol) (HO-PEG-NH_2) with a M_w of 2000 was purchased from Iris Biotech GmbH and methoxy poly(ethylene glycol) (MPEG, M_w: 2000) was purchased from Fisher Scientific Inc., USA. Doxorubicin hydrochloride (DOX·HCl) was supplied by Tecoland Corporation, USA, and used as supplied. All other chemicals used were of analytical reagent grade. Phosphate and acetate buffered solutions were prepared in our laboratory. RPMI-1640 was purchased from Gibco BRL, USA. The mouse mammary carcinoma, 4T1 (ATCC), was cultured in RPMI medium supplemented with 10% fetal calf serum.

Synthesis of Benzyl Malolactonate Monomer (Scheme 2). Benzyl malolactonate monomer was prepared by a reported simple and reproducible method following Scheme 2 (*20*). First, to an ice-cold clear solution of L-aspartic acid (**1**, 50 g) and NaBr (200 g) in 2 N H_2SO_4 (300 mL), $NaNO_2$ was added progressively over a period of 2 h. The whole mixture was further stirred for 1.5 h at room temperature. After the excess reagents were decomposed by adding urea, the bromosuccinic acid was extracted with ethyl acetate twice. The extracts were combined and washed with slightly acidic water and dried over anhydrous sodium sulfate. The product **2** was recovered after evaporation of ethyl acetate. Second, the product **2** (20 g) was dissolved in anhydrous tetrahydrofuran (THF) (100 mL) containing trifluoroactetic anhydride (23.5 g) in a three-neck flask at 10 °C. The mixture was allowed to stir for 1.5 h at 10 °C and 2 h at room temperature. The THF and trifluoroacetic acid were then distillated under vacuum to yield bromosuccinic anhydride (**3**), a white crystalline compound. Then, benzyl alcohol (13 g) was immediately added to the flask containing **3**.

Scheme 3. Synthesis Procedure of H40-(PMA-Hyd-DOX-*co*-PCL)-MPEG/PEG-FA Polymer



The mixture was allowed to react for 4 h at room temperature and 1 h at 60 °C yielding a mixture of bromosuccinic acid monobenzyl ester isomers (**4** and **5**). Finally, the resulting mixture was dissolved in sodium hydroxide water with a pH value of 7.8. Subsequently, 200 mL of benzene was added into the mixture, which was stirred overnight at 50 °C. After cooling, the organic layer was separated from the aqueous phase and crude benzyl malolactonate was recovered after evaporation of the solvent. The product **6** was purified using column chromatography and further vacuum distilled.

Random Copolymerization of Benzyl Malolactonate and ε-Caprolactone Using H40 as Macroinitiator (H40-(PMABz-*co*-PCL)-OH). H40-(PMABz-*co*-PCL)-OH was prepared by the ring-opening polymerization of benzyl malolactonate and ε-caprolactone using H40 as a macroinitiator and $Sn(Oct)_2$ as a catalyst (Scheme 3). H40 (200 mg, 4.5 mmol of hydroxyl groups), benzyl malolactonate (0.5 g 2.43 mmol), ε-caprolactone (3.0 g 26.3 mmol), and catalyst ([catalyst]/[ε-caprolactone] = 1:1000) were added into a 250 mL flame-dried flask under N_2. The reaction was carried out under stirring at 110 °C for 24 h. After the reaction was complete, the mixture was diluted with THF, precipitated into diethyl ether, and washed with diethyl ether to produce a white H40-(PMABz-*co*-PCL)-OH powder.

Synthesis of α-Carboxyl-ω-FA Poly(ethylene glycol) (FA-PEG-COOH). FA-PEG-HO was prepared according to our previous work with a slight modification (*15*). The γ-NHS-FA was dissolved into 5 mL of a mixture of anhydrous DMSO and triethylamine (TEA) with a volume ratio of 10:1. An equimolar amount of HO-PEG-NH_2 was added to the mixture and the reaction was carried out under an anhydrous condition overnight. The product, FA-PEG-HO, was freeze−dried after dialysis against deionized water using cellulose tubing (M_w cutoff: 2000 Da). FA-PEG-COOH was prepared by reacting FA-PEG-OH (2 g, 0.57 mmol) with succinic anhydride (170 mg, 1.7 mmol) in the presence of pyridine. The reaction was carried out in anhydrous toluene under N_2 atmosphere at 70 °C for 24 h. Crude polymer obtained by precipitation into cold diethyl ether was redissolved in dichloromethane (DCM). The resulting DCM solution was washed three times with aqueous hydrochloric acid (10% in v/v) and then four times with a saturated NaCl solution. Then, the organic phase was isolated, dried over magnesium sulfate, and filtered. The final product, FA-PEG-COOH, was recovered by precipitation into cold diethyl ether and dried under vacuum.

MPEG-COOH was prepared from MPEG-OH using a procedure similar to the one described above.

Synthesis of H40-(PMABz-*co*-PCL)-MPEG/PEG-FA. H40-(PMABz-*co*-PCL)-MPEG/PEG-FA copolymer was synthesized by reacting the terminal hydroxyl groups of H40-(PMABz-*co*-PCL)-OH with the terminal carboxyl groups of anhydrous MPEG-COOH and FA-PEG-COOH. The molar ratio of MPEG-COOH and FA-PEG-COOH was 19:1 (the number of PMABz-*co*-PCL arms was 20, which was calculated according to the GPC analysis). For example, H40-(PMABz-*co*-PCL)-OH (5.52 g, 0.044 mmol) was dissolved in 30 mL anhydrous chloroform. Then, a mixture of MPEG-COOH (2.51 g, 1.26 mmol) and FA-PEG-COOH (152 mg, 0.06 mmol), DCC (272 mg, 1.32 mmol) and DMAP (161 mg, 1.32 mmol) in 20 mL anhydrous chloroform was added into the chloroform solution of H40-(PMABz-*co*-PCL)-OH. The reaction was carried out at room temperature for 24 h under stirring. The resulting solution was precipitated with cold diethyl ether twice. The precipitate was dried under vacuum. The impurities and unreacted materials of the product were removed by dialysis against deionized water using cellulose tube (M_w cutoff: 12 000 Da) for 48 h. After dialysis, the H40-(PMABz-*co*-PCL)-MPEG/PEG-FA copolymer was obtained by freeze−drying.

Synthesis of H40-(PMA-Hyd-DOX-*co*-PCL)-MPEG/PEG-FA. The benzyl groups of H40-(PMABz-*co*-PCL)-MPEG/PEG-FA were substituted with hydrazide groups for DOX binding by an ester-amide exchange aminolysis reaction (Scheme 3). H40-(PMABz-*co*-PCL)-MPEG/PEG-FA (2 g, 0.012 mmol) was dissolved in 100 mL of anhydrous DMF. Then, anhydrous hydrazine (5 mg, 0.156 mmol) was added to this solution. The reaction was allowed to proceed at 40 °C for 24 h, followed by dialysis against 0.25% ammonia solution using cellulose tube

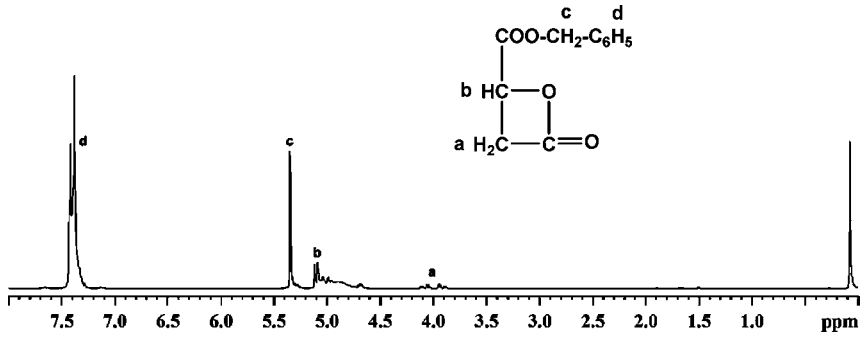


Figure 1. [1]H NMR spectrum of benzyl malolactonate monomer.

(M_w cutoff: 2000 Da) and freeze−drying. To conjugate DOX onto the amphiphilic hyperbranched copolymer, H40-(PMA-Hyd-*co*-PCL)-MPEG/PEG-FA (1.5 g, 0.009 mmol) was dissolved in 50 mL of DMF, and excess amount of DOX·HCl (150 mg, 0.26 mmol) was added. The mixture solution was stirred at room temperature for 24 h while being protected from light. The reaction solution was concentrated to a volume of 10 mL under reduced pressure and dialyzed against deionized water using cellulose tube (M_w cutoff: 2000 Da) for 48 h, followed by gel purification using Sephadex LH-20 to completely remove unbound DOX. For comparison, the H40-(PMA-Hyd-DOX-*co*-PCL)-MPEG copolymer without FA targeting ligands was synthesized following the same procedure as described above.

Preparation of H40-(PMA-Hyd-DOX-*co*-PCL)-MPEG/PEG-FA Micelles. H40-(PMA-Hyd-DOX-*co*-PCL)-MPEG/PEG-FA micelles were prepared using the dialysis method. Briefly, 10 mg of H40-(PMA-Hyd-DOX-*co*-PCL)-MPEG/PEG-FA polymer was dissolved in 3 mL of DMF under stirring. Then, 5 mL of deionized water was added dropwise into the above solution. Thereafter, the mixture was dialyzed against deionized water using a dialysis tube (M_w cutoff: 2000 Da) for three days followed by freeze−drying.

Characterization. [1]H NMR spectrum was recorded on a Bruker DPX 300 spectrometer. Gel permeation chromatography (GPC) analysis was carried out at ambient temperature using the 270max Viscotek (Viscotek, USA) GPC system equipped with triple detectors, including a refractive index detector, a viscometer detector, and a light-scattering detector. THF was used as an eluent with a flow rate of 1 mL/min and polystyrene (PS) standards were used for column calibration. The amphiphilic hyperbranched block copolymer solutions in THF (5 mg/mL) were prepared. Absorbance measurements were carried out using a Varian Cary 100 Bio UV−visible spectrophotometer. The size and size distribution of the unimolecular micelles were determined by dynamic light scattering (DLS) (Beckman Coulter PCS submicrometer particle size analyzer, USA) with an angle detection at 90°. Samples for transmission electron microscopy (TEM, Hitachi H-600) analysis were prepared by drying a dispersion of the unimolecular micelles on a copper grid coated with amorphous carbon. Subsequently, a small drop of phosphotungstic acid (PTA) solution (2 wt % in water) was added to the copper grid; after 30 s the grid was blotted with filter paper for TEM observation. The DOX-loading content (DLC), defined as the weight percentage of DOX in unimolecular micelles, was quantified by UV−vis analysis using a Varian Cary model 100 Bio UV−vis spectrophotometer. The DOX was released from the unimolecular micelles in 0.1 N HCl solution to cleave the hydrazone bonds. To determine the drug content in the solution, the absorbance of DOX at 485 nm was measured using a previously established calibration. The DLC measurements were performed in triplicate for each of the samples.

Evaluation of pH Sensitivity. The unimolecular micelle's pH-responsive DOX release behavior was studied using an UV spectrophotometer. First, 50 mg freeze−dried micelle samples were dispersed in 5 mL of medium, placed in a dialysis bag with a molecular weight cutoff of 2000 Da, and then placed into various pH conditions from 7.4 to 4.0 (10 mM phosphate buffer (pH 7.4−6.0), 10 mM acetate buffer (pH 5.8−4.0)). The dialysis bag was then immersed in 100 mL of the release medium and kept in a horizontal laboratory shaker maintaining a constant temperature and stirring. At selected time intervals, the buffered solution (5 mL) outside the dialysis bag was removed for UV−vis analysis and replaced by fresh buffered solution with same volume. The amount of released DOX was analyzed with UV spectrophotometer at 485 nm. Each sample was measured three times.

Cellular Uptake and Cytotoxicity. The cellular uptake and distribution of micelles were performed using flow cytometry and confocal laser scanning microscopy (CLSM). For CLSM studies, 4T1 cells (1×10^6) were seeded onto 22 mm round glass coverslips placed in 6-well plates and grown overnight. Cells were treated with free DOX, DOX-conjugated H40-(PMA-Hyd-DOX-*co*-PCL)-MPEG/PEG-FA (i.e., FA-targeted), or H40-(PMA-Hyd-DOX-*co*-PCL)-MPEG (i.e., nontargeted) micelles for 2 h (DOX concentration 20 μg/mL). Then the cells were washed and fixed with 1.5% formaldehyde. Coverslips were placed onto glass microscope slides and DOX uptake was analyzed using a Leica TCS SP2 Confocal System installed on an upright compound microscope (Leica, Wetzler, Germany). Digital monochromatic images were acquired using Leica Confocal Software (v 2.61).

To determine the DOX distribution in the nucleus and cytoplasm of the 4T1 cells, the DOX mean fluorescence intensity (MFI) in the CLSM images was measured in a 4 μm^2 area located in the nucleus or cytoplasm ($n = 10$ cells) for each sample using *ImageJ* software (http://rsb.info.nih.gov/ij). For flow cytometry, 4T1 cells (1×10^6) were seeded in 6-well culture plates and grown overnight. The cells were then treated with free DOX, DOX-conjugated H40-(PMA-Hyd-DOX-*co*-PCL)-MPEG/PEG-FA, or H40-(PMA-Hyd-DOX-*co*-PCL)-MPEG micelles for 2 h (DOX concentration 20 μg/mL). Thereafter, the cells were lifted using a cell stripper (Media Tech, Inc.) and washed. The DOX uptake was analyzed using an FACSCalibur flow cytometer (BD bioscience). A minimum of 2×10^4 cells were analyzed from each sample with the fluorescence intensity shown on a four-decade log scale.

The cytotoxicity of the unimolecular micelles against 4T1 cells was studied using the MTT assay. First, 4T1 cells (1×10^4) were seeded in 96-well plates and incubated for 24 h. The media were replaced with fresh media containing free DOX, H40-(PMA-Hyd-DOX-*co*-PCL)-MPEG/PEG-FA, H40-(PMA-Hyd-DOX-*co*-PCL)-MPEG micelles with different DOX concentrations or control media and incubated for 48 h. Thereafter, the wells were washed three times with warm phosphate buffer

solution and incubated again for another 3 h with RPMI containing 250 μg/mL of MTT. After discarding the culture medium, 200 μL of DMSO was added to dissolve the precipitates, and the resulting solution was measured for absorbance at 570 nm with a reference wavelength of 690 nm using a microplate reader (Molecular Devices).

RESULTS AND DISCUSSION

Synthesis and Characterization of Benzyl Malolactonate Monomer and H40-(PMA-Hyd-DOX-*co*-PCL)-MPEG/PEG-FA. Benzyl malolactonate is a β-substituted β-lactone monomer and was prepared by a reported simple and reproducible method according to Scheme 2 (*20*). This monomer was purified by reverse-phase silica (octadecylsilyl silica (ODS)) and then vacuum-distilled twice (bp = 90 °C, 10^{-3} mm Hg). Figure 1 shows the ^{1}H NMR spectrum of the monomer, confirming the monomer was successfully synthesized (a, 4.0 (d); b, 5.12 (t); c, 5.34 (s); d, 7.35 (s) in $CDCl_3$).

The synthesis of the H40-(PMA-Hyd-DOX-*co*-PCL)-MPEG/PEG-FA copolymer was carried out according to Scheme 3. First, H40-(PMABz-*co*-PCL)-OH was prepared by the random copolymerization of benzyl malolactonate and ε-caprolactone using H40 as a macroinitiator in the presence of $Sn(Oct)_2$ catalyst. This copolymer was purified by twice precipitating into diethyl ether from chloroform solution followed by filtering and was then dried under vacuum. The structure of the H40-(PMABz-*co*-PCL)-OH copolymer was confirmed by ^{1}H NMR (Figure 2a). The molar ratio of the PMABz and PCL repeat unit was approximately 1:15, which was calculated from the integral ratio of the characteristic peaks at 5.1 (MABz) and 3.9 (CL) ppm). On the basis of the absolute M_w determined by GPC (Table 1), it was estimated that each PMABz-*co*-PCL-OH arm on the hyperbranched H40-(PMABz-*co*-PCL)-OH copolymer had 2 MABz repeat units and 29 CL repeat units. To prepare the nontargeted unimolecular micelles, which can serve as a control for the study of cellular uptake and cytotoxicity of FA-targeted unimolecular micelles, the H40-(PMABz-*co*-PCL)-MPEG amphiphilic copolymer was synthesized by reacting H40-(PMABz-*co*-PCL)-OH with MPEG-COOH in the presence of DCC and DMAP. The number of arms in H40-(PMABz-*co*-PCL)-MPEG was calculated using the following equation: Number of arms = [(M_w of H40-(PMABz-*co*-PCL)-MPEG − M_w of H40-(PMABz-*co*-PCL)-OH)]/M_w of MPEG = [164 540−125 460/2000] ≈ 20. This result is consistent with our previous finding (*15*).

To achieve active tumor-targeting property, the H40-(PMA-Hyd-DOX-*co*-PCL)-MPEG/PEG-FA copolymer was prepared by reacting H40-(PMABz-*co*-PCL)-OH with a mixture of MPEG-COOH and FA conjugated PEG, i.e., FA-PEG-COOH, in the presence of DCC and DMAP. It is known that folate moieties with pterin heterocycles can self-assemble in an aqueous solution by hydrogen bonds and stacking interactions (*21*). As a result, introducing too many FA moieties to the amphiphilic copolymer decreases the stability of the micelles formed by the amphiphilic copolymer. In addition, the possible formation of dimers, trimers, or self-assembled tubular quarters (*21*) at a higher FA concentration is highly unfavorable for tumor cell targeting because the folate receptor can bind only one FA molecule; thus, the self-assembled FA multimers are incapable of binding to the folate receptors.

During this study, the molar ratio of the FA targeting ligand was controlled through the molar ratio between MPEG-COOH and FA-PEG-COOH, which was kept at 19:1. Thus, the estimated FA molar ratio in H40-(PMABz-*co*-PCL)-MPEG/PEG-FA was 1/20, i.e., 5%. Figure 2b shows the ^{1}H NMR spectrum of the H40-(PMABz-*co*-PCL)-MPEG/PEG-FA copolymer. The typical NMR peaks from the FA moiety appeared

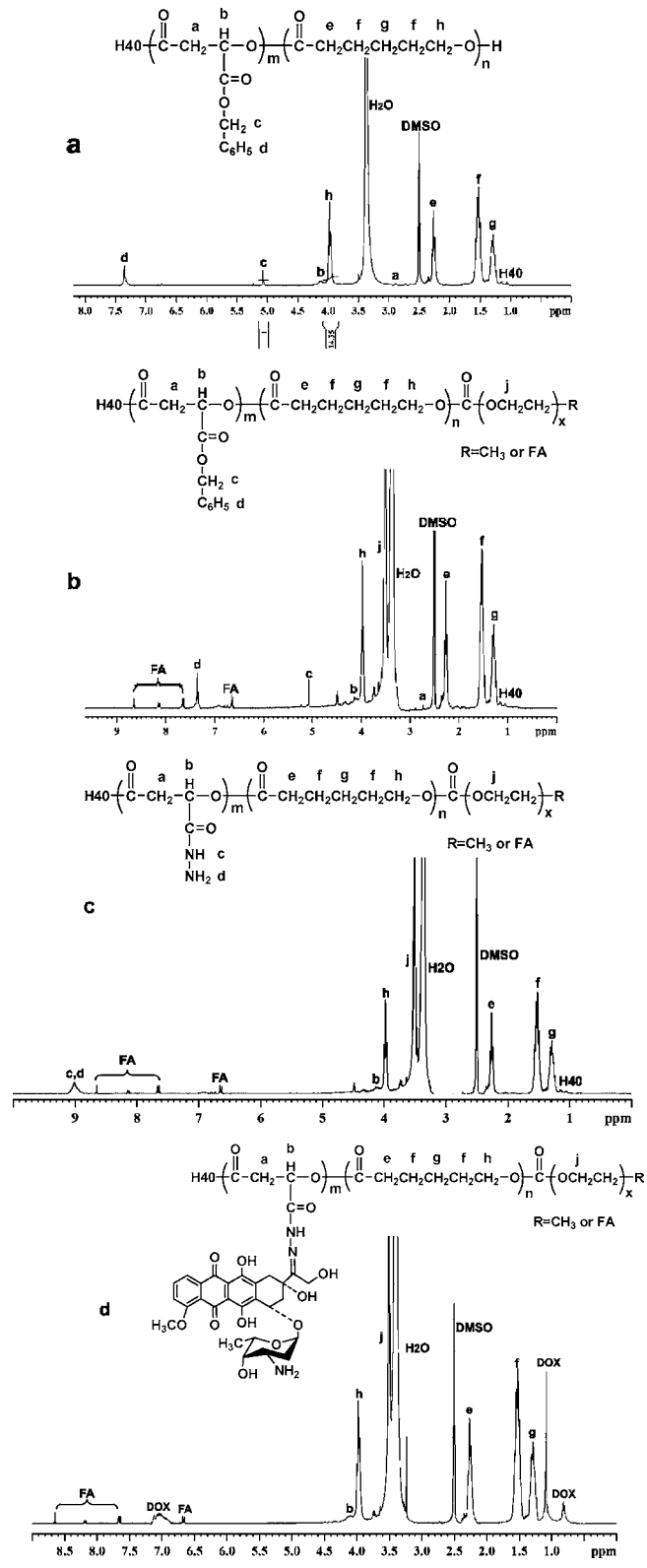


Figure 2. ^{1}H NMR spectra of (a) H40-[(poly(benzyl β-malate)-*co*-poly(ε-caprolactone)] (H40-(PMABz-*co*-PCL)-OH; (b) H40-[(poly-(benzyl β-malate)-*co*-poly(ε-caprolactone)]-methoxy-poly(ethylene glycol)-poly(ethylene glycol)-folate (H40-(PMABz-*co*-PCL)-MPEG/PEG-FA); and (c) H40-[(poly(β-malic acid-hydrazide)-*co*-poly(ε-caprolactone)]-methoxy-poly(ethylene glycol)-poly(ethylene glycol)-folate (H40-(PMA-Hyd-*co*-PCL)-MPEG/PEG-FA); (d) H40-[(poly(β-malic acid-hydrazone-DOX)-*co*-poly(ε-caprolactone)]-methoxy-poly(ethylene glycol)-poly(ethylene glycol)-folate (H40-(PMA-Hyd-DOX-*co*-PCL)-MPEG/PEG-FA).

Table 1. GPC Results of H40, H40-(PMABz-*co*-PCL)-OH, and H40-(PMABz-*co*-PCL)-MPEG

samples	M_n	M_w	M_w/M_n
H40	2 830	5 100	1.80
H40-(PMABz-*co*-PCL−OH)	76 500	125 460	1.64
H40-(PMABz-*co*-PCL)-MPEG	115 506	164 540	1.42

at 8.68, 8.17, 7.68, 6.98, and 6.67 ppm. The appearance of these peaks confirms the successful conjugation of FA to the hyperbranched copolymer.

The benzyl groups of the H40-(PMABz-*co*-PCL)-MPEG/PEG-FA copolymer were substituted with hydrazide groups for DOX binding through the ester-amide exchange (EAE) aminolysis reaction (*22*). The reaction was allowed to proceed at 40 °C for 24 h. The structure was confirmed by ^{1}H NMR spectrum as shown in Figure 2c. The NMR peaks originated from the benzyl ester groups (5.1 and 7.4 ppm) presented at the PMABz segments disappeared; meanwhile, the characteristic NMR peak corresponding to the hydrazine groups (9.0 ppm broadening peak) was observed. After the H40-(PMA-Hyd-*co*-PCL)-MPEG/PEG-FA copolymer was purified, it was reacted with an excess amount of DOX to form the H40-(PMA-Hyd-DOX-*co*-PCL)-MPEG/PEG-FA copolymer. After the reaction was complete, the polymer solution was dialyzed and further purified using Sephadex LH-20 to completely remove any unbound DOX. The structure of the H40-(PMA-Hyd-DOX-*co*-PCL)-MPEG/PEG-FA copolymer was confirmed by ^{1}H NMR. As shown in Figure 2d, the corresponding peaks of DOX appeared at 0.8, 1.1, and 7.0 ppm, indicating the DOX molecules were successfully conjugated onto the PMA segments by hydrazone bonds. The drug loading content determined by the UV measurement was 14.2 ± 0.3%. Theoretically, if all the hydrazide groups attached on the PMA segments are conjugated with the DOX molecules during the DOX conjugation reaction step, the DOX loading content is close to 15%. Thus, based on the DOX loading content measured by UV (14. 2%) and the theoretical maximum DOX loading content (∼15%), it can be deduced that both PMA repeat units in each arm of the 20-arm hyperbranched copolymer were conjugated with DOX molecules. Namely, there were approximately 40 DOX molecules per H40-(PMA-Hyd-DOX-*co*-PCL)-MPEG/PEG-FA molecule.

Micelle Properties of the H40-(PMA-Hyd-DOX-*co*-PCL)-MPEG/PEG-FA Copolymer. Figure 3A shows the morphology of the H40-(PMA-Hyd-DOX-*co*-PCL)-MPEG/PEG-FA unimolecular micelles observed by TEM. It can be seen the unimolecular micelles were spherical and most of them had a relatively uniform size, which was about 20 nm. The size and size distribution of the unimolecular micelles were further determined by DLS. The hydrodynamic size of the H40-(PMA-Hyd-DOX-*co*-PCL)-MPEG/PEG-FA unimolecular micelles was about 25 ± 2 nm, which was somewhat higher than the particle size determined by TEM (i.e., ∼20 nm), as expected. The size distribution, expressed by polydispersity index, was 0.145 ± 0.002. It should be noted that the resulting H40-(PMA-Hyd-DOX-*co*-PCL)-MPEG/PEG-FA copolymer micelles were stable over several weeks and displayed no changes in size or size distribution within experimental accuracy during this period.

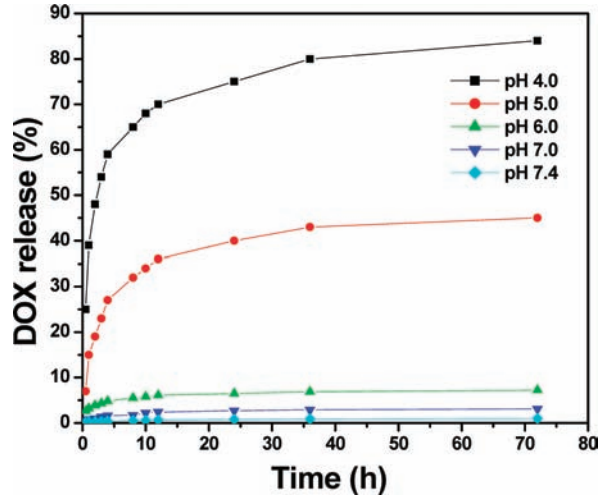


Figure 4. Release profile of DOX from the H40-(PMA-Hyd-DOX-*co*-PCL)-MPEG/PEG-FA micelles at different pH values.

Effect of pH on the *in Vitro* DOX Release Rate. The pH-sensitive DOX release behavior of the unimolecular micelles was evaluated at a series of pH values. As shown in Figure 4, the DOX release rate from the unimolecular micelles increased consistently with lower pH values within the pH range of 4.0 to 7.4. A negligible amount of drug release was observed at pH 7.4, the physiological condition of the bloodstream; thus, almost no DOX will be released from the unimolecular micelles during blood circulation, which is a desirable drug delivery characteristic for drug nanocarriers. The pH values of the endocytic compartments in which the FA-conjugated unimolecular micelles are located once internalized by the tumor cells *via* FA-receptor mediated endocytosis generally ranges from 4.5 to 6.5. As shown in Figure 4, the DOX released rate increased significantly within this pH range. In acidic conditions, the acid-sensitive hydrazone bonds are cleaved releasing unmodified DOX from the unimolecular micelles, which are subsequently diffused into the cytoplasm and eventually to the nucleus. At pH 5.0, about 48% DOX was released after 72 h. Thus, once the unimolecular micelles are internalized into the tumor cells, the conjugated DOX can be released effectively to improve the therapeutic outcome of the chemotherapy.

Cellular Uptake of the Unimolecular Micelles. The behaviors of cellular uptake of the FA-conjugated H40-(PMA-Hyd-

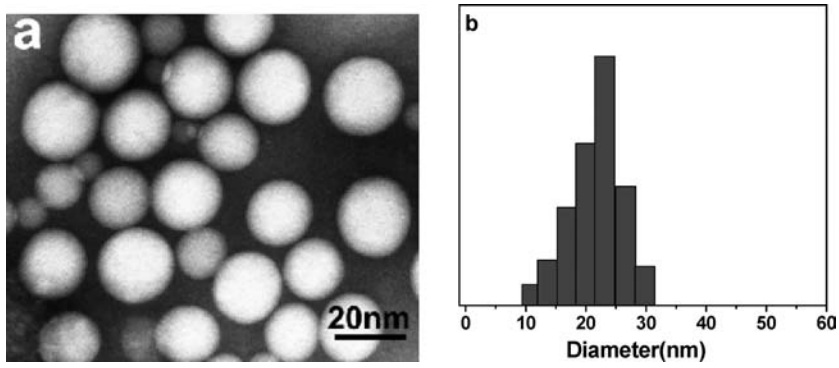


Figure 3. (a) TEM micrograph and (b) DLS histogram of unimolecular micelles based on H40-(PMA-Hyd-DOX-*co*-PCL)-MPEG/PEG-FA polymer.

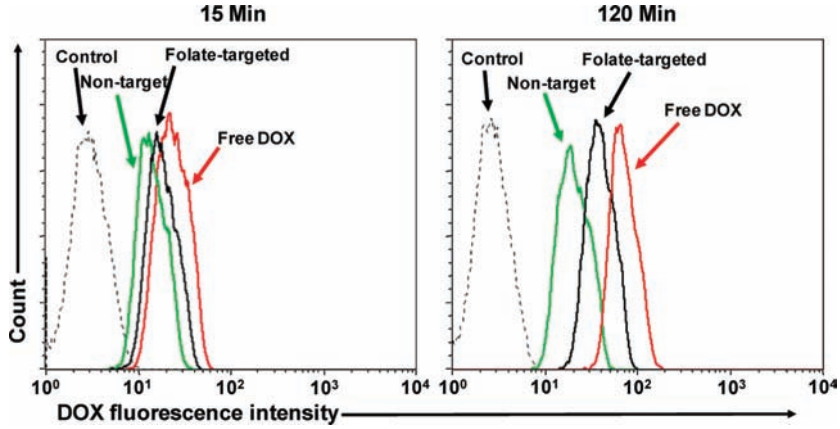


Figure 5. Flow cytometry results of 4T1 cells treated with free DOX, H40-(PMA-Hyd-DOX-*co*-PCL)-MPEG micelles and H40-(PMA-Hyd-DOX-*co*-PCL)-MPEG/PEG-FA micelles at 37 °C for 15 and 120 min (DOX concentration 20 μg/mL).

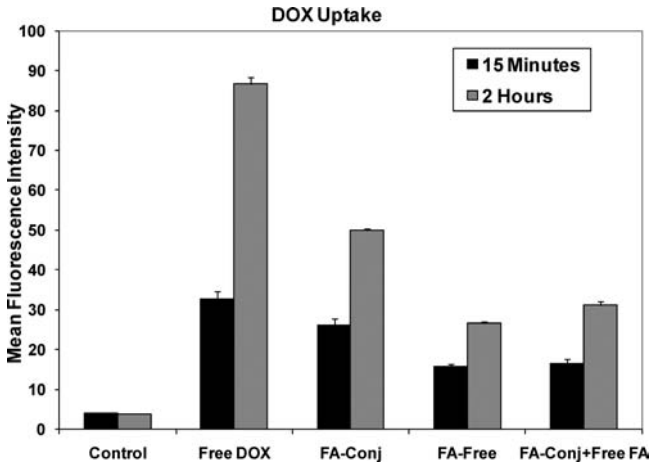


Figure 6. DOX mean fluorescence intensity (MFI) located in the 4T1 cells incubated with free DOX, nontargeted, and FA-conjugated unimolecular micelles for 15 and 120 min.

co-PCL)-MPEG/PEG-FA unimolecular micelles and nontargeted H40-(PMA-Hyd-*co*-PCL)-MPEG unimolecular micelles against folate receptor (FR) positive 4T1 cells were studied using both flow cytometry and CLSM. Figure 5 shows the flow cytometry histograms of the 4T1 cells incubated with free DOX, FA-conjugated micelles, or nontargeted micelles for 15 min and 2 h. As the figure shows, 4T1 cells without any DOX treatment were used as a negative control and showed only the autofluorescence of the cells. The DOX fluorescence intensity (Figure 6) clearly indicated that the cellular uptake of DOX was the highest in 4T1 cells incubated with free DOX, followed by FA-conjugated micelles and then nontargeted micelles. After 15 and 120 min incubation, FA-conjugated micelles showed an increase in cellular uptake, which was approximately 1.7 and 1.9 times (Student's t test; $p < 0.005$ and $p < 0.0001$, respectively) of the cellular uptake of nontargeted micelles, respectively, while the cellular uptake of free DOX was approximately 1.3 and 1.7 times ($p < 0.05$ and $p < 0.00005$, respectively) the cellular uptake of FA-conjugated micelles, respectively. The higher cellular uptake of free DOX compared with DOX conjugated onto unimolecular micelles can be attributed to the different cellular uptake mechanism. Free DOX was transported into cells *via* diffusion (*4*), while unimolecular micelles were taken up *via* an endocytosis process (*23*). However, the higher cellular uptake by the 4T1 cells incubated with FA-conjugated micelles compared with those incubated with nontargeted micelles clearly demonstrated that FA was an effective tumor-targeting ligand for tumor cells with positive FR. Moreover, the FA competition experiment also showed that the cellular uptake level of FA-conjugated micelles in the presence of free FA was dramatically reduced and became essentially equivalent to that of nontargeted micelles indicating the cell uptake of FA-conjugated micelles was FR mediated endocytosis process (Figure 6). These findings were further confirmed by the CLSM images as shown in Figure 7. 4T1 cells incubated with free DOX (Figure 7a) showed the highest DOX fluorescence intensity in both cytoplasm and nuclear after 2 h incubation. This is because free DOX can quickly diffuse into the cytoplasm through the cell membrane and transport into the nucleus, where it can interrupt the DNA replication process (*24*). Consistent with the flow cytometry finding, 4T1 cells incubated with FA-conjugated micelles showed a much higher DOX fluorescence intensity than those incubated with nontargeted micelles due to the FA-receptor mediated endocytosis process.

Cytotoxicity of the Unimolecular Micelles. The cytotoxic effects of free DOX, H40-(PMA-Hyd-DOX-*co*-PCL)-MPEG,

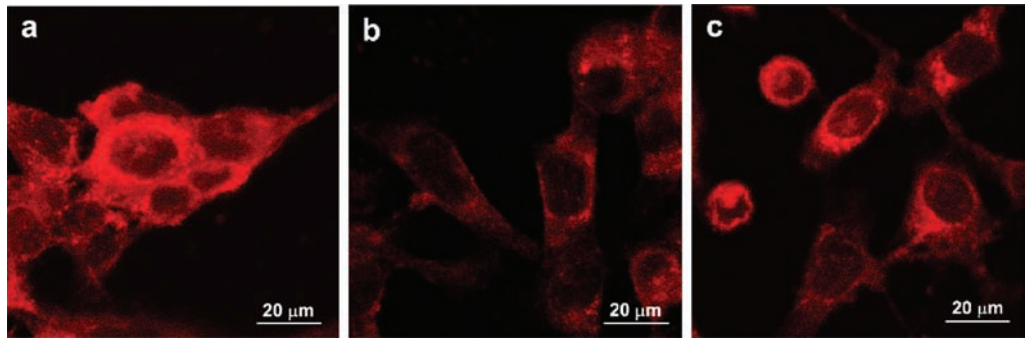


Figure 7. CLSM images of 4T1 cells treated with (a) free DOX; (b) H40-(PMA-Hyd-DOX-*co*-PCL)-MPEG micelles; (c) H40-(PMA-Hyd-DOX-*co*-PCL)-MPEG/PEG-FA micelles at 37 °C for 2 h (DOX concentration 20 μg/mL).

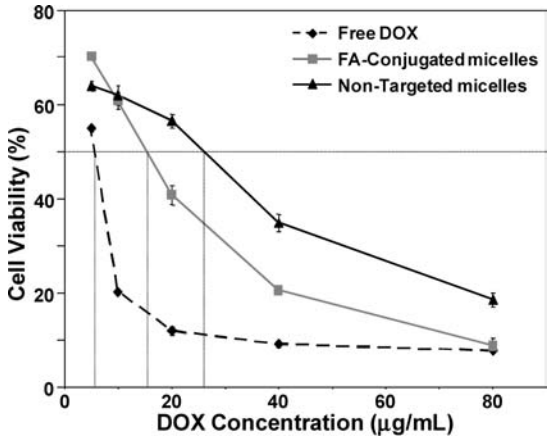


Figure 8. Cytotoxicity of free DOX, H40-(PMA-Hyd-DOX-*co*-PCL)-MPEG micelles, and H40-(PMA-Hyd-DOX-*co*-PCL)-MPEG/PEG-FA micelles with different DOX concentrations against 4T1 cells (incubation time 48 h).

and H40-(PMA-Hyd-DOX-*co*-PCL)-MPEG/PEG-FA micelles with different DOX concentrations against 4T1 cells after 48 h incubation were studied using the MTT assay. As shown in Figure 8, at the same DOX concentration, free DOX showed the highest cytotoxicity, which is consistent with the fact that 4T1 cells incubated with free DOX had the highest cellular uptake according to the CLSM and flow cytometry analysis. In addition, free DOX can rapidly diffuse into the cell nuclei once inside the 4T1 cells and effectively inhibit the DNA replication in the cancer cells. FA-targeted micelles demonstrated a higher cytotoxicity compared with nontargeted micelles, which is also consistent with its higher cellular uptake observed by CLSM and flow cytometry. Moreover, the concentration yielding half-inhibition to cell growth (IC_{50}) was detected at 5.7, 15.5, and 26.2 μg/mL for free DOX and FA-conjugated and nontargeted micelles, respectively. The enhanced cytotoxicity exhibited by the FA-conjugated micelles again indicates that FA tumor-targeting ligands were effective in enhancing the cellular uptake of the unimolecular micelles.

CONCLUSIONS

Tumor-targeting multifunctional unimolecular micelles that exhibit a pH-triggered drug release profile and potentially excellent *in vivo* stability were developed for targeted cancer chemotherapy. The unimolecular micelles were formed by 20-arm hyperbranched amphiphilic H40-(PMA-Hyd-DOX-*co*-PCL)-MPEG/PEG-FA copolymers. Hyperbranched polyester Boltorn H40 was used as the macroinitiator for the random ring-opening copolymerization of PMABz and PCL, serving as the hydrophobic segments of the amphiphilic copolymers. The anticancer drug DOX was conjugated onto the PMA segments by acid-sensitive hydrazone bonds. Folate, the tumor-targeting ligand, was conjugated selectively (5% molar ratio) to the distal ends of the hydrophilic PEG segments. The hydrodynamic diameter of the unimolecular micelles was 25 $\pm$ 2 nm, determined by DLS. The DOX loading content was found to be 14.2%. There was very little DOX release at pH 7.4 indicating the DOX-conjugated unimolecular micelles will be very stable during blood circulation. On the other hand, DOX was released relatively quickly at lower pH values, indicating a sufficient amount of DOX may be released in the acid endocytic compartments once internalized by the tumor cells. The cellular uptake of the FA-conjugated unimolecular micelles was much higher than that of the nontargeted unimolecular micelles resulting from the FA-receptor mediated endocytosis, thereby leading to a much higher cytotoxicity. Thus, these novel tumor-targeting, pH-responsive, and potentially *in vivo* stable unimolecular micelles may provide a very promising approach for targeted cancer therapy and greatly improve the quality of cancer patient care.

ACKNOWLEDGMENT

The authors acknowledge the financial support from the National Science Foundation (DMR 0906641) for this project.

LITERATURE CITED

(1) Kataoka, K., Harada, A., and Nagasaki, Y. (2001) Block copolymer micelles for drug delivery: design, characterization and biological significance. *Adv. Drug Delivery Rev. 47*, 113–131.

(2) Wang, F., Bronich, T. K., Kabanov, A. V., Rauh, R. D., and Roovers, J. (2005) Synthesis and evaluation of a star amphiphilic block copolymer from poly(ε-caprolactone) and poly(ethylene glycol) as a potential drug delivery carrier. *Bioconjugate Chem. 16*, 397–405.

(3) Criscione, J. M., Le, B. L., Stern, E., Brennan, M., Rahner, C., Papademetris, X., and Fahmy, T. M. (2009) Self-assembly of pH-response fluorinated dendrimer-based particulates for drug delivery and noninvasive imaging. *Biomaterials 30*, 3946–3955.

(4) Shuai, X. T., Ai, H., Nasongkla, N., Kim, S. J., and Gao, J. M. (2004) Micellar carrier based on block copolymers of poly(ε-caprolactone) and poly(ethylene glycol) for doxorubicin delivery. *J. Controlled Release 98*, 415–426.

(5) Hall, D. G., and Pethica, B. A. (1967) Thermodynamics of micelle formation. *Nonionic surfactants* (Schick, M., Ed.) pp 516−557, Marcel Dekker, New York.

(6) Kikuchi, A., and Nose, T. (1996) Unimolecular micelle formation of poly(methyl methacrylate)-graft-polystyrene in mixed selective solvents of acetonitrile/acetoacetic acid ethyl ether. *Macromolecules 29*, 6770–6777.

(7) Aryal, S., Prabaharan, M., Pilla, S., and Gong, S. Q. (2009) Biodegradable and biocompatible multi-arm star amphiphilic block copolymer as a carrier for hydrophobic drug delivery. *Int. J. Biol. Macromol. 44*, 346–352.

(8) Kreutzer, G., Ternat, C., Nguyen, T. Q., Plummer, C. J. G., Manson, J. E., Castelletto, V., Hamley, I. W., Sun, F., Sheiko, S. S., Herrmann, A., Ouali, L., Sommer, H., Fieber, W., Velazco, M. I., and Klok, H. A. (2006) Water-soluble, unimolecular containers based on amphiphilic multiarm star block copolymers. *Macromolecules 39*, 4507–4516.

(9) Zou, J. H., Zhao, Y. B., and Shi, W. F. (2006) Encapsulation mechanism of molecular nanocarriers based on unimolecular micelle forming dendritic core-shell structure polymers. *J. Phys. Chem. B 110*, 2638–2642.

(10) Maeda, H., and Matsumura, Y. (1989) Tumoritropic and lymphotropic principles of macromolecular drugs. *Crit. Rev. Ther. Drug Carrier Syst. 6*, 193–210.

(11) Langer, R. (1998) Drug delivery and targeting. *Nature 392*, 5–10.

(12) Duncan, R. (1992) Drug-polymer conjugates: potential for improved chemotherapy. *Anti-Cancer Drugs 3*, 175–210.

(13) Luo, S., Xu, J., Zhu, Z., Wu, C., and Liu, S. (2006) Phase transition behavior of unimolecular micelles with thermoresponsive poly(N-isopropylacrylamide) coronas. *J. Phys. Chem. B 110*, 9132–9139.

(14) Kitajyo, Y., Nawa, Y., Tamaki, M., Tani, H., Takahashi, K., Kaga, H., Satoh, T., and Kakuchi, T. (2007) A unimolecular nanocapsule: encapsulation property of amphiphilic polymer based on hyperbranched polythreitol. *Polymer 48*, 4683–4690.

(15) Prabaharan, M., Grailer, J. J., Pilla, S., Steeber, D. A., and Gong, S. Q. (2009) Folate-conjugated amphiphilic hyperbranched block copolymers based on Boltorn ® H40, poly(L-lactide) and poly(ethylene glycol) for tumor targeted drug delivery. *Biomaterials 30*, 3009–3019.

(16) Chen, S., Zhang, X. Z., Cheng, S. X., Zhuo, R. X., and Gu, Z. W. (2008) Functionalized amphiphilic hyperbranched polymers for targeted drug delivery. *Biomacromolecules 9*, 2578–2585.
(17) Weitman, S. D., Lark, R. H., Coney, L. R., Fort, D. W., Frasca, V., Zurawski, V. R., and Kamen, B. A. (1992) Distribution of the folate receptor GP38 in normal and malignant cells lines and tissues. *Cancer Res. 52*, 3396–3401.
(18) Campbell, I. G., Jones, T. A., Foulkes, W. D., and Trowsdale, J. (1991) Folate-binding protein is a marker for ovarian cancer. *Cancer Res. 51*, 5329–5338.
(19) Ramakrishna, S., Mayer, J., Wintermantel, E., and Leong, K. W. (2001) Biomedical applications of polymer-composite materials: a review. *Compos. Sci. Technol. 61*, 1189–1224.
(20) Guerin, P., Vert, M., Braud, C., and Lenz, R. W. (1985) Optically active poly(β-malic acid). *Polym. Bull. 14*, 187–192.
(21) Ciuchi, F., Nicola, G. D., Franz, H., Gottarelli, G., Mariani, P., Grazia, M., Bossi, P., and Spada, G. P. (1994) Self-recognition and self-assembly of folic acid salts: columnar liquid crystalline polymorphism and the column growth process. *J. Am. Chem. Soc. 116*, 7064–7071.
(22) Bae, Y., Jang, W. D., Nishiyama, N., Fukushima, S., and Kataoka, K. (2005) Multifunctional polymeric micelles with folate-mediated cancer cell targeting and pH-triggered drug releasing properties for active intracellular drug delivery. *Mol. BioSyst. 1*, 242–250.
(23) Prabaharan, M., Grailer, J. J., Pilla, S., Steeber, D. A., and Gong, S. Q. (2009) Gold nanoparticles with a monolayer of doxorubicin-conjugated amphiphilic block copolymer for tumor-targeted drug delivery. *Biomaterials 30*, 6065–6075.
(24) Lee, Y., Park, S. Y., Mok, H., and Park, T. G. (2008) Synthesis, characterization, antitumor activity of pluronic mimicking copolymer micelles conjugated with doxorubicin *via* acid-cleavable linkage. *Bioconjugate Chem. 19*, 525–531.

BC900422J

Bioinspired Synthesis and Characterization of Gadolinium-Labeled Magnetite Nanoparticles for Dual Contrast T_1- and T_2-Weighted Magnetic Resonance Imaging

Ki Hyun Bae,[†] Young Beom Kim,[‡] Yuhan Lee,[†] JinYoung Hwang,[‡] HyunWook Park,[‡] and Tae Gwan Park*[,†]

Department of Biological Sciences and Graduate School of Nanoscience and Technology, and Department of Electrical Engineering, Korea Advanced Institute of Science and Technology, Daejeon 305-701, South Korea. Received September 23, 2009; Revised Manuscript Received November 24, 2009

Gadolinium-labeled magnetite nanoparticles (GMNPs) were synthesized via a bioinspired manner to use as dual contrast agents for T_1- and T_2-weighted magnetic resonance imaging. A mussel-derived adhesive moiety, 3,4-dihydroxy-L-phenylalanine (DOPA), was utilized as a robust anchor to form a mixed layer of poly(ethylene glycol) (PEG) chains and dopamine molecules on the surface of iron oxide nanoparticles. Gadolinium ions were subsequently complexed at the distal end of the dopamine molecules that were prefunctionalized with a chelating ligand for gadolinium. The resultant GMNPs exhibited high dispersion stability in aqueous solution. Crystal structure and superparamagnetic properties of magnetite nanocrystals were also maintained after the complexation of gadolinium. The potential of GMNPs as dual contrast agents for T_1 and T_2-weighted magnetic resonance imaging was demonstrated by conducting in vitro and in vivo imaging and relaxivity measurements.

INTRODUCTION

Over the past decade, a variety of inorganic nanomaterials, such as gold nanoparticles, iron oxide nanocrystals, and quantum dots, have drawn significant attention because of their unique and controllable optical, magnetic, and electronic properties (*1*−*3*). Among them, superparamagnetic magnetite nanocrystals have been utilized as useful platform materials for diverse biomedical applications including magnetic drug targeting, biomolecule separation, and hyperthermal cancer therapy (*3*−*5*). Although uniform and highly crystalline magnetite nanoparticles have been recently developed by thermal decomposition processes, they are poorly dispersed in aqueous solution due to their hydrophobic surface coatings (*6, 7*). For biomedical applications, the surface of the magnetite nanoparticles needs to be suitably engineered to acquire improved colloidal stability in physiological media, biocompatibility, drug encapsulation ability, and specific targetability to ensure desirable interactions with cells or tissues. To this end, magnetite nanocrystals have been coated with hydrophilic polymers (e.g., dextran and polyvinylpyrrolidone) or inorganic shells (e.g., gold and silica) (*8, 9*) and encapsulated into polymeric micelles or nanoparticles (*10, 11*).

Magnetic resonance imaging (MRI) has been recognized as a powerful noninvasive diagnostic technique to visualize the fine structure of a human body in a high spatial resolution (*12*). The use of MR contrast agents enables achievement of clear images for accurate diagnosis, by exerting an influence on the longitudinal (T_1) or transverse (T_2) relaxation time of the surrounding tissue. For example, paramagnetic complexes containing gadolinium (Gd^{3+}) or manganese (Mn^{2+}) ions induce the local relaxation change of the nearby water protons and mainly reduce T_1, providing positive contrast (bright signal) on T_1-weighted MR image (*13*). On the other hand, superparamagnetic magnetite nanoparticles have been widely utilized as ultrasensitive negative contrast agents for stem cell tracking and early detection of cancers due to their strong T_2 shortening effect (*14*−*16*). Nevertheless, their clinical applications are quite limited because of the negative contrast effect and magnetic susceptibility artifacts. Since the magnetite nanoparticles represent dark areas in MR images, their negative contrast is often confused with a low-level MR signal arising from adjacent tissues such as bone or vasculature (*17, 18*). Furthermore, susceptibility artifacts can occur as a result of the steep change of local magnetic field around iron oxide nanoparticles, leading to the locally distorted anatomy of surrounding tissue in MR image (*19*).

In the present study, we synthesize and characterize gadolinium-labeled magnetite nanoparticles (GMNPs) using 3,4-dihydroxy-L-phenylalanine (DOPA) as a bioinspired adhesive, and demonstrate their utility as dual contrast agents for T_1- and T_2-weighted MRI. DOPA is a modified amino acid abundantly found within adhesive proteins, which are secreted by marine mussels (*Mytilus edulis*) (*20*). DOPA is known to play an important role in the strong attachment of marine mussels on a wide range of organic and inorganic substrates (*21, 22*). Recently, it was discovered that DOPA and its analogue dopamine can be effectively utilized for anchoring small organic molecules or polymers onto the surface of metal oxides such as TiO_2, Al_2O_3, and Fe_3O_4 (*23*−*25*). Taking advantage of its strong and versatile binding ability, magnetite nanoparticles were surface-coated by a mixed layer of DOPA-terminated poly(ethylene glycol) chains and dopamine molecules, resulting in high water dispersibility and good biocompatibility. The surface of magnetite nanoparticles was further modified with multiple chelating ligands for complexing gadolinium ions. The resultant GMNPs are expected to induce a simultaneous positive and negative contrast enhancement according to the MR imaging protocols employed, making them useful as dual-functional MRI contrast agents (*26*). Depending on the tissue site of interest, GMNPs can be selectively visualized by T_1- or T_2-weighted MRI in order to achieve complementary information that cannot be obtained by the use of only one type of contrast agent, thereby

* Corresponding author. Tel: +82-42-350-2621; Fax: +82-42-350-2610; E-mail address: tgpark@kaist.ac.kr (T.G. Park).

[†] Department of Biological Sciences and Graduate School of Nanoscience and Technology.

[‡] Department of Electrical Engineering.

10.1021/bc900424u © 2010 American Chemical Society
Published on Web 02/18/2010

leading to more precise diagnosis. We examined the stability, morphology, and crystalline structures of GMNPs by using transmission electron microscopy (TEM) and X-ray diffraction (XRD) analysis. The capability of GMNPs to generate dual contrast for T_1- and T_2-weighted MRI was also validated by performing in vitro and in vivo imaging and relaxivity measurements.

EXPERIMENTAL PROCEDURES

Materials. Methoxy-poly(ethylene glycol)-succinic acid (mPEG-SA, M_w = 2000) was obtained from Sunbio Co. (Anyang, Korea). Dopamine hydrochloride (3-hydroxytyramine hydrochloride), 3,4-dihydroxy-L-phenylalanine (DOPA), *N*,*N*′-dicyclohexylcarbodiimide (DCC), *N*-hydroxysuccinimide (NHS), and gadolinium(III) chloride hexahydrate ($GdCl_3 \cdot 6H_2O$) were purchased from Sigma Chemical Co. (St. Louis, MO). 2-(*p*-Isothiocyanatobenzyl)diethylene triamine pentaacetic acid (*p*-SCN-benzyl-DTPA) was purchased from Macrocyclics (Dallas, TX). Ferumoxides suspension (Feridex) and gadopentetate dimeglumine (Magnevist, Gd-DTPA) were supplied by Berlex Laboratories (Wayne, NJ). Extracel hydrogel kit obtained from Glycosan BioSystems, Inc. (Salt Lake City, UT) was used according to the manufacturer's instruction. All other chemicals were of analytical grade.

Synthesis of DOPA-Conjugated Poly(ethylene glycol) (mPEG-DOPA). mPEG-DOPA was synthesized by conjugating an amino group of DOPA with a carboxylic acid group of mPEG-SA using DCC/NHS succinimidyl carbonate chemistry (*23*). Briefly, mPEG-SA (2116 mg) and DCC (654 mg) were first dissolved in 20 mL of distilled dichloromethane. Then, NHS (183 mg) dissolved in 5 mL of acetone was slowly added to the above solution. After 12 h of reaction under nitrogen atmosphere, the solution was precipitated into excess of cold ethyl ether and then evaporated under vacuum for 2 day. The activated PEG (1120 mg) dissolved in 10 mL of methanol was added to 30 mL of 0.1 M $Na_2B_4O_7$ solution (pH = 9.32) containing 313.5 mg of DOPA. After reaction for 12 h, the solution was dialyzed against acidified deionized water (pH 4) by a Spectra/Por dialysis membrane with a MW cutoff of 1 kDa and then lyophilized. The chemical structure of the product was confirmed by a Bruker DRX 400 ^{1}H NMR spectrometer operating at 400 MHz. The degree of substitution was estimated to be ca. 80% by comparing the relative peak area ratio between two methylene protons from an ethylene oxide group (3.6 ppm) and three protons on a DOPA phenyl ring (6.5−6.9 ppm).

Synthesis of mPEG-DOPA/Dopamine Stabilized Magnetite Nanoparticles. Oleic acid-coated magnetite nanoparticles with an average diameter of 17 nm were produced by thermal decomposition of Fe-oleate complex (*6, 11*). Oleic acid-coated magnetite nanoparticles (5 mg) dispersed in 3 mL of dichloromethane were mixed with 0.5 mL of dimethylformamide containing mPEG-DOPA (13.2 mg) and dopamine hydrochloride (3.3 mg). The solution was added to 10 mL of deionized water, and then sonicated for 2 min by using a Branson sonifier 450 (20 kHz, output control 3, duty cycle 40%). The oil-in-water emulsion was subjected to rotary evaporation at 40 °C for 10 min to remove residual solvent under reduced pressure. The product was purified by dialysis against deionized water for 1 day (MW cutoff of 12 kDa) and then lyophilized.

Synthesis of Gadolinium-Labeled Magnetite Nanoparticles (GMNPs). Five milligrams of the dried mPEG-DOPA/dopamine stabilized magnetite nanoparticles were dispersed in 5 mL of dimethylformamide, and then added in a dropwise manner to a stirred solution of dimethylformamide containing 22.6 mg of *p*-SCN-benzyl-DTPA. After reaction for 16 h, the excess of unreacted DTPA was removed by dialysis against deionized water for 1 day (MW cutoff of 12 kDa). To the colloidal solution of DTPA-grafted magnetite nanoparticles, 25.8 mg of $GdCl_3 \cdot 6H_2O$ was added. After incubation for 24 h, the resultant GMNPs were purified by extensive dialysis against deionized water for 2 days (MW cutoff of 12 kDa), and then stored at 4 °C until use.

Particle Characterization. The core size and dispersion stability of magnetite nanoparticles were investigated by transmission electron microscopy (TEM). The solution of nanoparticles was air-dried on a 300 mesh Formvar/carbon-coated copper grid, and then observed by a Philips F20 transmission electron microscope. The average particle size was determined by measuring the diameters of more than 50 particles in the TEM image. The hydrodynamic diameter of the magnetite nanoparticles was analyzed by using a dynamic light scattering instrument (Zeta-Plus, Brookhaven, NY) equipped with a He−Ne laser at a wavelength of 632 nm. The ζ potential values of the particles dispersed in 0.1 M phosphate-buffered saline solution (PBS, pH 7.4) were also measured in triplicate at a concentration of 0.5 mg/mL at 37 °C. Fourier transform infrared (FT-IR) spectra were recorded in the 500−4000 cm^{-1} region using an EQUINOX55 spectrometer (Bruker, Germany). Lyophilized samples were mixed with dried potassium bromide (KBr) and then compressed to prepare a pellet. For thermogravimetric analysis, dried samples were placed in aluminum sample cells, and a thermogram for each sample was obtained using a TG 209 F3 Tarsus thermo-microbalance (NETZSCH Instruments, Inc., Burlington, MA). Samples were heated at a rate of 10 °C/min up to 700 °C under a flow of nitrogen gas. Elemental analysis data were obtained using a FlashEA 1112 element analyzer (Thermo Finnigan, Italia). The metal concentration of the nanoparticles was quantified using inductively coupled plasma absorption emission spectroscopy (ICP-AES). X-ray powder diffraction profiles were measured using Rigaku D/max-IIIC diffractometer with CuKα radiation (40 kV, 80 mA). The field-dependent magnetization curves of samples were measured at room temperature with a vibrating sample magnetometer (VSM). All the characterizations were performed within 3 months after sample preparation.

***T_1*- and *T_2*-Weighted MRI Experiments.** To verify contrast characteristics of the nanoparticles as MRI contrast agents, longitudinal ($1/T_1$) and transverse ($1/T_2$) relaxation rates were calculated from the magnetic resonance images. The synthesized GMNPs were compared with aqueous $GdCl_3$ solution and Magnevist (Gd-DTPA) at various gadolinium concentration (50, 100, 150, 200, and 250 μM), as well as with mPEG-DOPA/dopamine stabilized magnetite nanoparticles and Feridex at equivalent iron concentration. All samples were diluted in deionized water and compared to pure water as a control. In addition, normal saline (0.9% w/v NaCl, pH 7.4) solution was also used to simulate the relaxation properties of the samples in the physiological environment. All MRI measurements were performed on a whole body scanner (ISOL Technology, South Korea) with a human head coil at a clinically relevant field strength of 3.0 T. Conventional spin−echo pulse sequence was used for both T_1 and T_2 measurements with a single slice of 4 mm thickness, a flip angle of 90°, the number of signal averages of 2, 128 × 128 mm field of view, and 128 × 128 matrices. T_1 relaxation measurements were acquired with repetition time (TR) of 100, 300, 600, 1000, 2000, and 3000 ms with an echo time (TE) of 12 ms, and T_2 relaxation measurements with TE of 12, 30, 60, 100, 200, and 300 ms with a TR of 3000 ms. The longitudinal (T_1) and transverse (T_2) relaxation time were obtained by calculating the mean signal intensity of each sample individually in the respective region of interest of MR images. The specific relaxivities (r_1 and r_1) of the samples were determined by measuring the relaxation rates based on the metal concentration (Supporting Information).

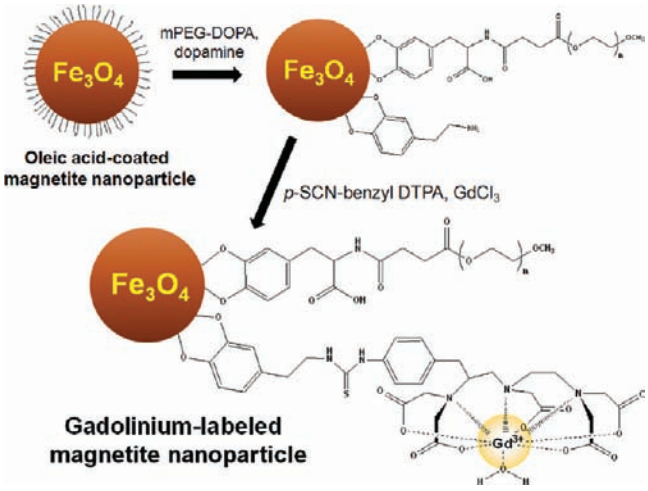


Figure 1. Schematic illustration for the synthesis of gadolinium-labeled magnetite nanoparticles (GMNPs) as dual contrast agents for T_1- and T_2-weighted magnetic resonance imaging.

To evaluate the dual contrast ability of GMNPs in a live animal model, in vivo MRI experiments were performed using BALB/c nude mice. All animal experiments were conducted based on the guidelines provided by Korea Advanced Institute of Science and Technology. GMNPs were suspended in Extracel hydrogel solution with a gadolinium concentration of 0.379 mM in order to prevent leakage from the injection site. A 200 μL aliquot of the suspension was injected subcutaneously into dorsal flanks of nude mice. For comparison, mice were also injected with Magnevist or Feridex at equivalent gadolinium or iron concentration. As a control, only the hydrogel solution was applied for injection. Two mice were included in each group. In vivo MRI was obtained from the same scanner, which was used in in vitro imaging, using a customized quadrature radio frequency (RF) coil with a diameter of 9 cm. T_1-weighted MR images were acquired using a conventional spin−echo sequence using the following parameters: TR/TE = 600/17 ms, 256 × 256 matrices, 100 × 100 mm field of view, a slice thickness of 3 mm, and the number of signal averages of 1. For T_2-weighted MR images, a fast spin−echo sequence was used to reduce acquisition time with the same parameters of T_1-weighted MRI, except for TR/TE = 3500/114 ms and the number of signal averages of 2. Each in vivo scan was completed within an hour.

RESULTS AND DISCUSSION

Figure 1 illustrates a synthetic scheme of gadolinium-labeled magnetite nanoparticles (GMNPs). Oleic acid-coated magnetite nanoparticles with a uniform and highly crystalline structure were first synthesized by the thermal decomposition of iron oleate complexes, as previously reported (*6, 11*). These nanoparticles can only be dispersed in an organic solvent because an oleic acid layer ionically adsorbed on the surface acts as a hydrophobic shell around the iron oxide core (*7*). However, for biomedical applications, it is necessary to make them hydrophilic and well-dispersed in aqueous solution. To prepare water-dispersible magnetite nanoparticles, we utilized DOPA as a bioinspired adhesive to immobilize hydrophilic polymers on the surface of ion oxide structures. Previously, we surface-coated iron oxide nanoparticles with hyaluronic acid (HA) by using dopamine-grafted HA. They showed an excellent water dispersibility while maintaining a superparamagnetic property, useful for HA receptor-specific MRI of cancer cells (*27*). The surface modification process was accomplished by simply incubating oleic acid-coated magnetite nanoparticles with a mixture of DOPA-conjugated poly(ethylene glycol) (mPEG-DOPA) and dopamine in an organic solvent. Since the ortho-

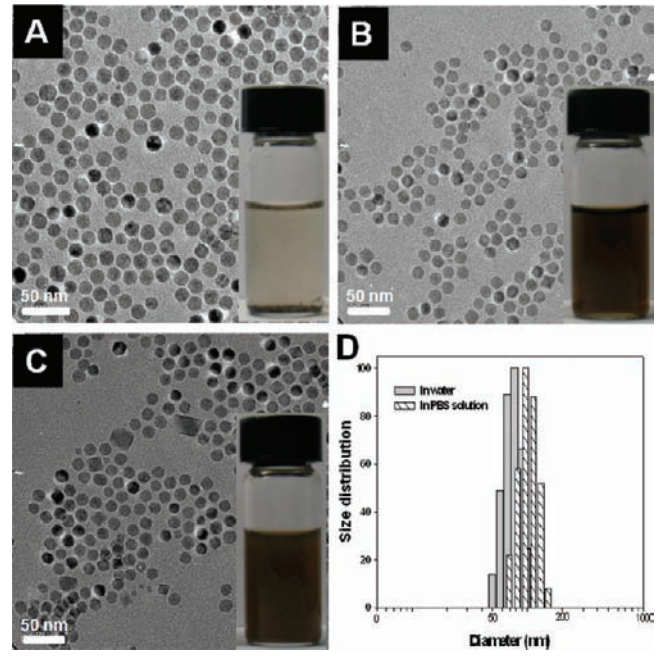


Figure 2. TEM images of (A) oleic acid-coated magnetite nanoparticles, (B) mPEG-DOPA/dopamine stabilized magnetite nanoparticles, and (C) GMNPs. The inset photographs show the dispersion of the magnetite nanoparticles in deionized water. (D) Hydrodynamic diameters of GMNPs dispersed in deionized water and in PBS solution.

dihydroxylphenyl (catechol) group of DOPA and its analogue dopamine forms strong coordination bonds with the surface of iron oxides (e.g., γ-Fe_2O_3, Fe_3O_4) (*25, 28*), it was anticipated that the magnetite nanoparticles was decorated with a mixed layer of mPEG chains and dopamine molecules. The resulting magnetite nanoparticles dispersed in an organic phase could be readily dispersed into an aqueous phase after solvent evaporation. For synthesis of GMNPs, these magnetite nanoparticles were further derivatized with diethylene triamine pentaacetic acid (DTPA), a chelating ligand for binding a paramagnetic gadolinium (Gd^{3+}) ion (*29*). The conjugation reaction of DTPA was carried out through the formation of an isothiourea bond between an isothiocyanate derivative of DTPA (*p*-SCN-benzyl DTPA) and a primary amine group in the dopamine molecule bound on the nanoparticles. Thereafter, DTPA-grafted magnetite nanoparticles were reacted with excess amount of $GdCl_3 \cdot 6H_2O$, resulting in the direct complexation of Gd^{3+} into the particles by chelation. Once nonchelated Gd^{3+} was removed by extensive dialysis against deionized water, GMNPs comprising magnetite nanoparticles carrying numerous gadolinium chelates were successfully produced.

We investigated the size distribution and dispersion stability of GMNPs in aqueous solution by using transmission electron microscopy (TEM) and dynamic light scattering (DLS) analysis. As shown in Figure 2A, oleic acid-coated magnetite nanoparticles were produced with a spherical morphology and an average diameter of 17.2 ± 1.3 nm. The TEM images obviously showed that the core size and shape of magnetite nanoparticles did not significantly change after surface modification with mPEG-DOPA and dopamine, even after the incorporation of paramagnetic gadolinium chelates. It should be noted that the dispersion stability of the oleic acid-coated magnetite nanoparticles was greatly changed after the ligand exchange reaction on the surface from oleic acid to mPEG-DOPA and dopamine (inset photographs). While the oleic acid-coated magnetite nanoparticles were not dispersible in deionized water and finally precipitated out of solution, mPEG-DOPA/dopamine stabilized magnetite nanoparticles and GMNPs exhibited excellent stability

in deionized water, forming a transparent brown solution. This dramatic difference was probably attributed to the hydrophilic nature of PEG chains anchored on the surface of the magnetite nanoparticles. It has been shown previously that the immobilization of PEG on various polymeric and inorganic nanoparticles improves their colloidal stability in aqueous physiological environment due to the steric stabilization effect of surface-exposed PEG chains (*16, 23*). Additionally, it was likely that the surface coating of dopamine molecules might partially contribute to the improved dispersion stability through the charge stabilization of magnetite nanoparticles (*27, 30*). As shown in Figure 2B and C, the magnetite nanoparticles were well-separated from each other without observable aggregation, suggesting that they were effectively stabilized in aqueous solution by the hydrophilic protective shell layer comprising hydrophilic PEG chains and dopamine molecules. Figure 2D presents the hydrodynamic diameters of GMNPs dispersed in deionized water and in PBS solution. The size of GMNPs (73.8 ± 7.6 nm) measured by DLS analysis was larger than the value obtained from TEM, probably due to the swelling of the PEG shell layer on the magnetite nanoparticles in water (*28*). It was also noteworthy that the hydrodynamic diameters and dispersion stability of GMNPs were not greatly changed after the incubation in PBS solution, suggesting that the adhesive properties of DOPA and dopamine molecules bound on the magnetite nanoparticles were significantly maintained in aqueous physiological environment.

Fourier transform infrared (FT-IR) spectroscopy was performed in order to examine the ligand exchange on the surface of magnetite nanoparticles (Figure 3A). The FT-IR spectrum of oleic acid-coated magnetite nanoparticles showed strong absorption bands at 2852 and 2923 cm^{-1}, arising from symmetric and asymmetric C−H stretch in the oleyl chains, respectively. The characteristic bands of oleic acid remarkably decreased after the ligand exchange, whereas new absorption bands centered at 1110 and 1635 cm^{-1} appeared. Since these absorption bands can be assigned to the C−O−C ether stretch of PEG and C═C vibration of catechol rings, respectively, it was evident that the oleic acid on the surface of magnetite nanoparticles was efficiently replaced by PEG chains and dopamine molecules. In the FT-IR spectrum of DTPA-grafted magnetite nanoparticles, an absorption band associated with the O−H stretch in carboxylic acid groups appeared at 3447 cm^{-1}, accounting for the conjugation of DTPA to the dopamine molecule bound on the nanoparticles. The differential thermograms of oleic acid-coated magnetite nanoparticles indicated that the thermal decomposition of oleic acid took place mainly at 282 and 453 °C (Figure 3B). After the ligand exchange, however, the magnetite nanoparticles exhibited a strong mass loss at 405 °C without any signs of the decomposition of oleic acid. This result revealed that the organic layer was completely removed from the particle surface, and mPEG-DOPA chains were anchored onto them concomitantly. It was also found that the weight loss of DTPA-grafted magnetite nanoparticles occurred over a broad range of temperature around 375 °C, presumably due to the desorption of DTPA molecules from the particles. Taken together, these results demonstrated that PEG chains and DTPA molecules were stably immobilized onto the surface of the magnetite nanoparticles via a catechol−metal coordination interaction.

The surface modification processes were further investigated by examining surface charge properties of magnetite nanoparticles. As shown in Figure 4, magnetite nanoparticles coated with only mPEG-DOPA showed a slightly negative ζ potential of −2.9 ± 2.2 mV, which was in agreement with the previous finding (*30*). In contrast, mPEG-DOPA/dopamine stabilized magnetite nanoparticles had a positively charged surface (10.5

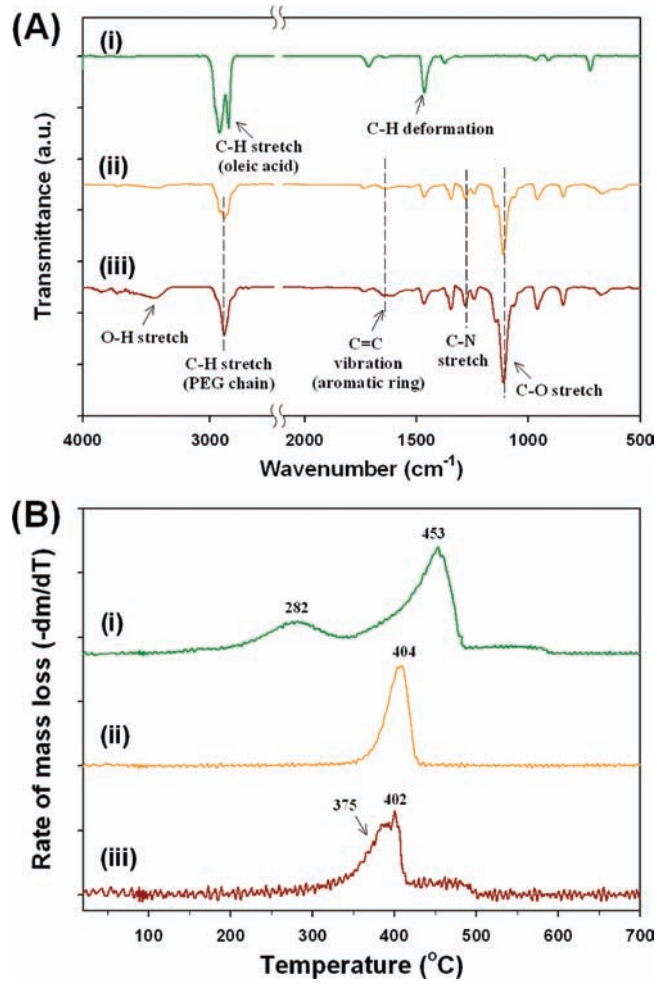


Figure 3. (A) FT-IR spectra and (B) differential thermograms of (i) oleic acid-coated magnetite nanoparticles, (ii) mPEG-DOPA/dopamine stabilized magnetite nanoparticles, and (iii) DTPA-grafted magnetite nanoparticles.

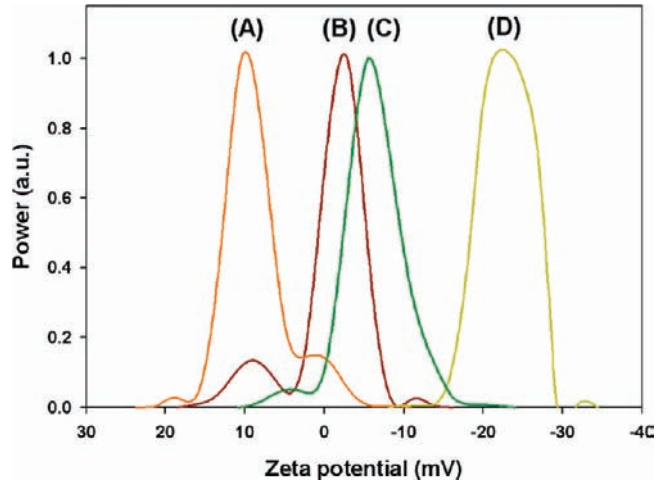


Figure 4. The ζ potential values of (A) mPEG-DOPA/dopamine stabilized magnetite nanoparticles, (B) magnetite nanoparticles coated with mPEG-DOPA, (C) GMNPs, and (D) DTPA-grafted magnetite nanoparticles.

± 2.8 mV) owing to the presence of dopamine molecules bearing free amine groups. It was also found that DTPA-grafted magnetite nanoparticles displayed a negative ζ potential of −21.3 ± 4.9 mV, which can be explained by the surface coverage of the particles with negatively charged DTPA

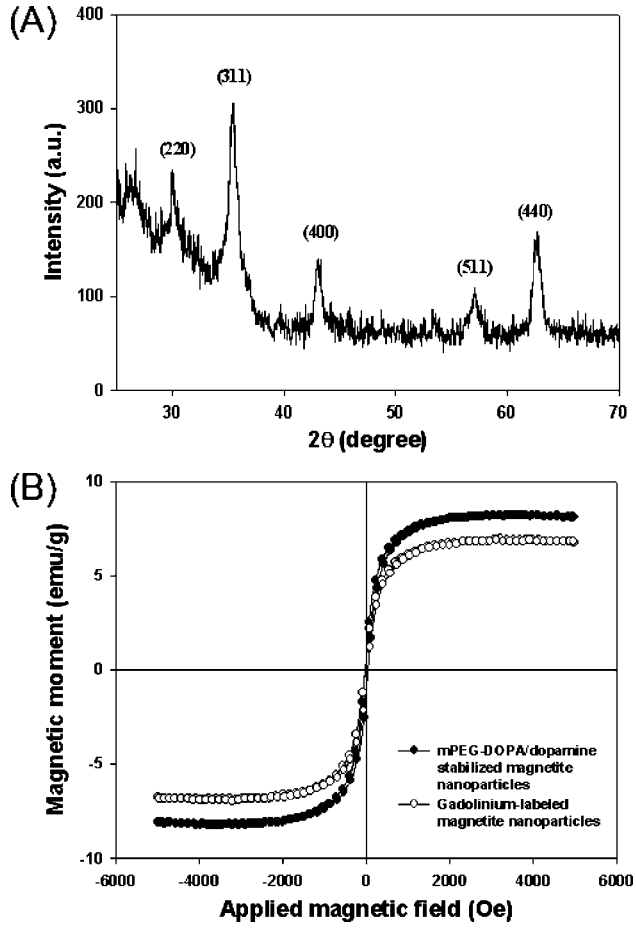


Figure 5. (A) X-ray diffraction pattern of GMNPs. (B) Field-dependent magnetization curve of mPEG-DOPA/dopamine stabilized magnetite nanoparticles (black dots) and GMNPs (hollow dots) at room temperature.

molecules. However, their ζ potential value was dramatically changed to -5.5 ± 3.1 mV upon incubating with an aqueous $GdCl_3$ solution, presumably because cationic Gd^{3+} ions were coordinated to anionic carboxylate groups in DTPA molecules, resulting in the neutralization of the negative surface charge (*31*). ICP-AES analysis of GMNPs indicated that each particle contained 11.5 wt % of Gd atoms, indicating that a single magnetite nanoparticle was covered with ca. 7010 gadolinium chelates. Taking into account the number of the conjugated dopamine molecules determined by elemental analysis, almost 68% of the dopamine molecules immobilized on the surface were estimated to participate in the incorporation of the gadolinium chelates (Supporting Information). It was previously reported that the surface density of Gd^{3+} paramagnetic species might have a profound impact on the positive contrast enhancement of Gd^{3+}-labeled nanoparticles (*32*). In the present study, the surface density of the gadolinium chelates could be controlled by simply changing the ratio of mPEG-DOPA and dopamine, resulting in the formation of GMNPs with tunable compositions and contrast properties. The above results revealed that GMNPs could hold a large number of Gd^{3+} ions within the DTPA-functionalized shell layer around the iron oxide core, and hence they were advantageous for generating gadolinium-enhanced contrast in MRI images.

X-ray diffraction (XRD) pattern was examined to confirm the crystal structure of magnetite nanoparticles (Figure 5A). The XRD pattern of GMNPs displayed characteristic diffraction peaks corresponding to a face-centered cubic (fcc) lattice of magnetite crystals (*9*). This was consistent with the XRD pattern of oleic acid-coated magnetite nanoparticles, suggesting that the surface modification with mPEG-DOPA and gadolinium chelates did not induce any change on the crystallinity of the iron oxide core. Figure 5B shows the field-dependent magnetization curve of the magnetite nanoparticles before and after the functionalization with gadolinium chelates. GMNPs had a lower saturation magnetization value (6.85 emu/g) as compared with that of mPEG-DOPA/dopamine stabilized magnetite nanoparticles (8.12 emu/g), which was probably attributed to the decrease in iron oxide content of the particles (*30, 33*). It was noteworthy that GMNPs exhibited no hysteresis in the magnetization curve, suggesting that the magnetite nanoparticles maintained their superparamagnetic behavior after paramagnetic Gd^{3+} ions were coordinated onto the surface.

To validate the potential of GMNPs as a dual contrast agent, we acquired the T_1- and T_2-weighted MR images and measured the relaxation rates as a function of metal concentration using a 3.0 T MRI scanner. As shown in Figure 6A, GMNPs induced a bright signal enhancement in a concentration-dependent manner on the T_1-weighted images. It should be noted that they exhibited better T_1 positive contrast compared to a clinically available Gd-DTPA-based contrast agent (Magnevist), while there was very little signal enhancement from the magnetite nanoparticles without Gd^{3+} ions. Moreover, the specific relaxivity (r_1) of GMNPs (11.17 mM^{-1} s^{-1}) was markedly higher than r_1 of Magnevist (5.39 mM^{-1} s^{-1}), suggesting that they were much more efficient in enhancing T_1 positive contrast than Magnevist (Figure 6B). It was reported previously that the r_1 values of Gd-based contrast agents were strengthened when bound to large molecules such as proteins and polymers due to the limited molecular motion of Gd^{3+} ions (*29, 34*). Hence, it was conceivable that the remarkably high r_1 value of GMNPs resulted from the reduced mobility of Gd^{3+} ions tightly incorporated into nanometer-scale particles. Despite the high r_1 value (10.15 mM^{-1} s^{-1}), aqueous $GdCl_3$ solution is not approved for clinical use due to toxicity of free Gd^{3+} ions (*13*). Since the covalently immobilized DTPA shell on GMNPs allowed for the strong coordination of Gd^{3+} ions onto the particles, GMNPs were considered to be safer than aqueous $GdCl_3$ solution.

As shown in the T_2-weighted images (Figure 6C), GMNPs also displayed a significant signal reduction with increasing the particle concentration. It was found that the r_2 value of magnetite nanoparticles decreased from 225.81 to 30.32 mM^{-1} s^{-1} after the labeling with Gd^{3+} ions (Figure 6D), suggesting that the paramagnetic gadolinium chelates interfered with the T_2 relaxation processes of the neighboring magnetite nanoparticles (*35, 36*). The observed decrease in the r_2 value was partially attributed to the reduced magnetization of the particles (*7, 37*). Although GMNPs had a lower r_2 compared to that of commercially available Feridex (148.95 mM^{-1} s^{-1}), their T_2 contrast effect was sufficiently strong to generate negative contrast enhancement on the MR images. Since the relaxivities of GMNPs were not diminished in normal saline ($r_1 = 14.45$ mM^{-1} s^{-1}, $r_2 = 36.68$ mM^{-1} s^{-1}), it was anticipated that their relaxation properties were maintained in physiological environment.

We performed in vivo MRI experiments to demonstrate the dual contrast ability of GMNPs in a live animal model. In order to prevent leakage from the injection site, GMNPs suspended in Extracel hydrogel solution were injected subcutaneously into dorsal flanks of nude mice, and then, the hydrogel formed at the injection site was examined by using a 3.0 T MRI scanner. Figure 7A shows that the hydrogel containing Magnevist appears as a bright area in the T_1-weighted MRI. In contrast, a dark signal void can be observed at the injection site of Feridex, indicative of its strong T_2 negative contrast (Figure 7B). As shown in Figure 7C and D, GMNPs displayed a bright signal enhancement

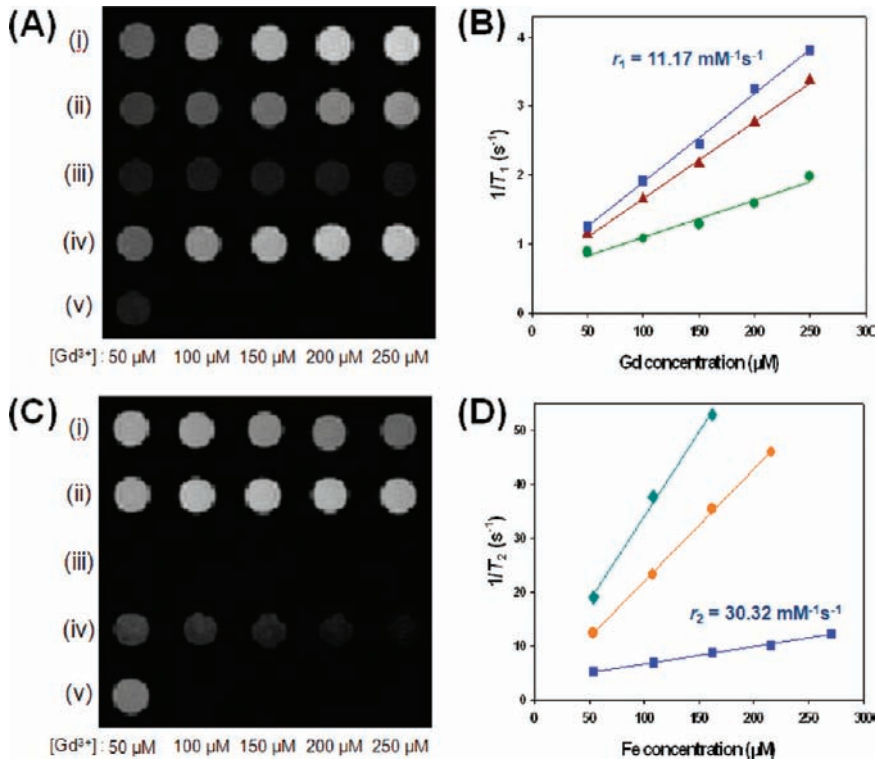


Figure 6. (A) T_1-weighted and (C) T_2-weighted magnetic resonance images of (i) aqueous $GdCl_3$ solution, (ii) Magnevist (Gd-DTPA), (iii) mPEG-DOPA/dopamine stabilized magnetite nanoparticles, (iv) GMNPs, and (v) pure deionized water. The mPEG-DOPA/dopamine-stabilized magnetite nanoparticles were compared to GMNPs at equivalent Fe concentration. The magnetic resonance images of Feridex are not shown here for a clear presentation. (T_1-weighted images: repetition time = 600 ms, echo time = 12 ms; T_2-weighted images: repetition time = 3000 ms, echo time = 200 ms). (B) Longitudinal relaxation rates of aqueous solutions of GMNPs (squares), $GdCl_3$ (triangles), and Magnevist (circles). (D) Transverse relaxation rates of mPEG-DOPA/dopamine stabilized magnetite nanoparticles (diamonds), Feridex (circles), and GMNPs (squares).

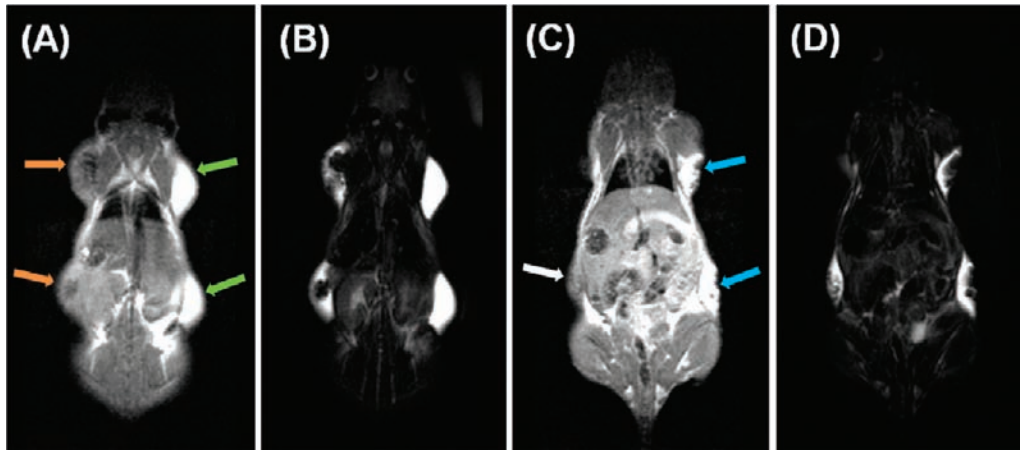


Figure 7. (A) T_1-weighted and (B) T_2-weighted magnetic resonance images of a mouse injected with Feridex and Magnevist (the orange arrows indicate the injection sites of Feridex, and the green arrows indicate the injection sites of Magnevist). (C) T_1-weighted and (D) T_2-weighted magnetic resonance images of a mouse injected with GMNPs and the hydrogel solution as a control (the white arrow indicates the injection site of the hydrogel solution, and the blue arrows indicate the injection sites of GMNPs).

and a marked signal drop at the injection site on the T_1- and T_2-weighted MR image, respectively, while no apparent contrast was detected from the control site containing only the gel matrix. Consequently, the above results demonstrated that GMNPs having high r_1 and r_2 relaxivities exhibited both positive and negative contrast enhancement on the MR images. Due to their dual contrast effect, GMNPs can be utilized to achieve both T_1- and T_2-weighted MR images of the tissue site of interest, and hence increase the accuracy of diagnosis. Furthermore, this dual contrast approach may help to overcome the limitations of traditional iron oxide-based and gadolinium-based contrast agents, thereby expanding opportunities of MRI for diverse therapeutic and diagnostic applications.

CONCLUSIONS

Gadolinium-labeled magnetite nanoparticles were developed as dual contrast agents for T_1- and T_2-weighted magnetic resonance imaging. These nanoparticles were produced through the formation of a mixed layer of poly(ethylene glycol) chains and dopamine molecules via strong coordination bonds of DOPA to iron oxides, and subsequent immobilization of gadolinium chelates onto the nanoparticle surface. The surface modification process did not disturb the crystal structure and

superparamagnetic properties of the magnetite nanoparticles, suggesting that the current strategy would afford stabilization and functionalization of various inorganic nanomaterials, which are poorly soluble and processable in aqueous solution. Moreover, we demonstrated that GMNPs not only had the ability to improve surrounding water proton signals on the T_1-weighted image, but also could induce significant signal reduction on the T_2-weighted image. These novel nanomaterials having both positive and negative contrast could be potentially utilized as molecular imaging probes for a wide range of diagnostic and therapeutic applications.

ACKNOWLEDGMENT

This research was partly supported by the Ministry for Health, Welfare and Family Affairs, the Ministry of Knowledge Economy, and the World Class University project and the National Research Laboratory program from the Ministry of Education, Science and Technology, Republic of Korea. We would like to thank Jaewon Lee and Prof. Jung Hee Lee in Samsung Medical Center for helpful discussion and synthesis of iron oxide nanocrystals, and Myung Wook Song for VSM measurements.

Supporting Information Available: ^{1}H NMR spectrum of DOPA-conjugated poly(ethylene glycol) (mPEG-DOPA), the elemental analysis results of mPEG-DOPA coated magnetite nanoparticles, and the method for the calculation of the Gd chelation efficiency and the relaxation time (T_1 and T_2). This material is available free of charge via the Internet at http://pubs.acs.org.

LITERATURE CITED

(1) Alivisatos, A. P. (2004) The use of nanocrystals in biological detection. *Nat. Biotechnol. 22*, 47–52.

(2) Nie, S., Xing, Y., Kim, G. J., and Simons, J. W. (2007) Nanotechnology applications in cancer. *Annu. Rev. Biomed. Eng. 9*, 257–88.

(3) Rosi, N. L., and Mirkin, C. A. (2005) Nanostructures in biodiagnostics. *Chem. Rev. 105*, 1547–62.

(4) Sonvico, F., Mornet, S., Vasseur, S., Dubernet, C., Jaillard, D., Degrouard, J., Hoebeke, J., Duguet, E., Colombo, P., and Couvreur, P. (2005) Folate-conjugated iron oxide nanoparticles for solid tumor targeting as potential specific magnetic hyperthermia mediators: synthesis, physicochemical characterization, and in vitro experiments. *Bioconjugate Chem. 16*, 1181–8.

(5) Sun, C., Lee, J. S. H., and Zhang, M. (2008) Magnetic nanoparticles in MR imaging and drug delivery. *Adv. Drug Delivery Rev. 60*, 1252–65.

(6) Park, J., An, K., Hwang, Y., Park, J.-G., Noh, H.-J., Kim, J.-Y., Park, J.-H., Hwang, N.-M., and Hyeon, T. (2004) Ultra-large-scale syntheses of monodisperse nanocrystals. *Nat. Mater. 3*, 891–5.

(7) Jun, Y.-W., Lee, J.-H., and Cheon, J. (2008) Chemical design of nanoparticle probes for high-performance magnetic resonance imaging. *Angew. Chem., Int. Ed. 47*, 5122–35.

(8) Gupta, A. K., and Gupta, M. (2005) Synthesis and surface engineering of iron oxide nanoparticles for biomedical applications. *Biomaterials 26*, 3995–4021.

(9) Lee, J., Yang, J., Ko, H., Oh, S. J., Kang, J., Son, J.-H., Lee, K., Lee, S.-W., Yoon, H.-G., Suh, J.-S., Huh, Y.-M., and Haam, S. (2008) Multifunctional magnetic gold nanocomposites: human epithelial cancer detection via magnetic resonance imaging and localized synchronous therapy. *Adv. Funct. Mater. 18*, 258–64.

(10) Herdt, A. R., Kim, B.-S., and Taton, T. A. (2007) Encapsulated magnetic nanoparticles as supports for proteins and recyclable biocatalysts. *Bioconjugate Chem. 18*, 183–9.

(11) Kim, J., Lee, J. E., Lee, S. H., Yu, J. H., Lee, J. H., Park, T. G., and Hyeon, T. (2008) Designed fabrication of a multifunctional polymer nanomedical platform for simultaneous cancer-targeted imaging and magnetically guided drug delivery. *Adv. Mater. 20*, 478–83.

(12) Rudin, M., and Weissleder, R. (2003) Molecular imaging in drug discovery and development. *Nat. Rev. Drug Discovery 2*, 123–31.

(13) Meade, T. J., Taylor, A. K., and Bull, S. R. (2003) New magnetic resonance contrast agents as biochemical reporters. *Curr. Opin. Neurobiol. 13*, 597–602.

(14) Bulte, J. W. M., Zhang, S.-C., Van Gelderen, P., Herynek, V., Jordan, E. K., Duncan, I. D., and Frank, J. A. (1999) Neurotransplantation of magnetically labeled oligodendrocyte progenitors: Magnetic resonance tracking of cell migration and myelination. *Proc. Natl. Acad. Sci. U.S.A. 96*, 15256–61.

(15) Josephson, L., Tung, C. H., Moore, A., and Weissleder, R. (1999) High-efficiency intracellular magnetic labeling with novel superparamagnetic-Tat peptide conjugates. *Bioconjugate Chem. 10*, 186–91.

(16) Lee, H., Lee, E., Kim, D. K., Jang, N. K., Jeong, Y. Y., and Jon, S. (2006) Antibiofouling polymer-coated superparamagnetic iron oxide nanoparticles as potential magnetic resonance contrast agents for in vivo cancer imaging. *J. Am. Chem. Soc. 128*, 7383–9.

(17) Bulte, J. W. M., and Kraitchman, D. L. (2004) Iron oxide MR contrast agents for molecular and cellular imaging. *NMR Biomed. 17*, 484–99.

(18) Kim, Y. B., Bae, K. H., Yoo, S.-S., Park, T. G., and Park, H. W. (2009) Positive contrast visualization for cellular magnetic resonance imaging using susceptibility-weighted echo-time encoding. *Magn. Reson. Imaging 27*, 601–10.

(19) Zhuo, J., and Gullapalli, R. P. (2006) MR artifacts, safety, and quality control. *RadioGraphics 26*, 275–97.

(20) Deming, T. J. (1999) Mussel byssus and biomolecular materials. *Curr. Opin. Chem. Biol. 3*, 100–5.

(21) Lee, H., Scherer, N. F., and Messersmith, P. B. (2006) Single-molecule mechanics of mussel adhesion. *Proc. Natl. Acad. Sci. U.S.A. 103*, 12999–13003.

(22) Holten-Andersen, N., Mates, T. E., Toprak, M. S., Stucky, G. D., Zok, F. W., and Waite, J. H. (2009) Metals and the integrity of a biological coating: The cuticle of mussel byssus. *Langmuir 25*, 3323–6.

(23) Dalsin, J. L., Lin, L., Tosatti, S., Vörös, J., Textor, M., and Messersmith, P. B. (2005) Protein resistance of titanium oxide surfaces modified by biologically inspired mPEG-DOPA. *Langmuir 21*, 640–6.

(24) Lee, H., Dellatore, S. M., Miller, W. M., and Messersmith, P. B. (2007) Mussel-inspired surface chemistry for multifunctional coatings. *Science 318*, 426–30.

(25) Xu, C., Xu, K., Gu, H., Zheng, R., Liu, H., Zhang, X., Guo, Z., and Xu, B. (2004) Dopamine as a robust anchor to immobilize functional molecules on the iron oxide shell of magnetic nanoparticles. *J. Am. Chem. Soc. 126*, 9938–9.

(26) Choi, D., Han, A., Park, J. P., Kim, J. K., Lee, J. H., Kim, T. H., and Kim, S. W. (2009) Fabrication of $Mn_xFe_{1-x}O$ colloidal solid solution as a dual magnetic-resonance-contrast agent. *Small 5*, 571–3.

(27) Lee, Y., Lee, H., Kim, Y. B., Kim, J., Hyeon, T., Park, H. W., Messersmith, P. B., and Park, T. G. (2008) Bioinspired surface immobilization of hyaluronic acid on monodisperse magnetite nanocrystals for targeted cancer imaging. *Adv. Mater. 20*, 4154–7.

(28) Xie, J., Xu, C., Kohler, N., Hou, Y., and Sun, S. (2007) Controlled PEGylation of monodisperse Fe_3O_4 nanoparticles for reduced non-specific uptake by macrophage cells. *Adv. Mater. 19*, 3163–6.

(29) Turner, J. L., Pan, D., Plummer, R., Chen, Z., Whittaker, A. K., and Wooley, K. L. (2005) Synthesis of gadolinium-labeled shell-crosslinked nanoparticles for magnetic resonance imaging applications. *Adv. Funct. Mater. 15*, 1248–54.

(30) Yuan, J.-J., Armes, S. P., Takabayashi, Y., Prassides, K., Leite, C. A. P., Galembeck, F., and Lewis, A. L. (2006) Synthesis of biocompatible poly[2-(methacryloyloxy)ethyl phosphorylcholine]-coated magnetite nanoparticles. *Langmuir 22*, 10989–93.

(31) Debouttière, P.-J., Roux, S., Vocanson, F., Billotey, C., Beuf, O., Favre-Réguillon, A., Lin, Y., Pellet-Rostaing, S., Lamartine, R., Perriat, P., and Tillement, O. (2006) Design of gold nanoparticles for magnetic resonance imaging. *Adv. Funct. Mater. 16*, 2330–9.

(32) Voisin, P., Ribot, E. J., Miraux, S., Bouzier-Sore, A.-K., Lahitte, J.-F., Bouchaud, V., Mornet, S., Thiaudie're, E., Franconi, J.-M., Raison, L., Labruge're, C., and Delville, M.-H. (2007) Use of lanthanide-grafted inorganic nanoparticles as effective contrast agents for cellular uptake imaging. *Bioconjugate Chem. 18*, 1053–63.

(33) Fan, Q.-L., Neoh, K.-G., Kang, E.-T., Shuter, B., and Wang, S.-C. (2007) Solvent-free atom transfer radical polymerization for the preparation of poly(poly(ethyleneglycol) monomethacrylate)-grafted Fe_3O_4 nanoparticles: synthesis, characterization and cellular uptake. *Biomaterials 28*, 5426–36.

(34) Nakamura, E., Makino, K., Okano, T., Yamamoto, T., and Yokoyama, M. (2006) A polymeric micelle MRI contrast agent with changeable relaxivity. *J. Controlled Release 114*, 325–33.

(35) Vilringer, A., Rosen, B. R., Belliveau, J. W., Ackerman, J. L., Lauffer, R. B., Buxton, R. B., Chao, Y.-S., Wedeenand, V. J., and Brady, T. J. (1988) Dynamic imaging with lanthanide chelates in normal brain: Contrast due to magnetic susceptibility effects. *Magn. Reson. Med. 6*, 164–74.

(36) Loubeyre, P., De Jaegere, T., Bosmans, H., Miao, Y., Ni, Y., Landuyt, W., and Marchal, G. (1999) Comparison of iron oxide particles (AMI 227) with a gadolinium complex (Gd-DOTA) in dynamic susceptibility contrast MR imagings (FLASH and EPI) for both phantom and rat brain at 1.5 T. *J. Magn. Reson. Imaging 9*, 447–53.

(37) Seo, S.-B., Yang, J., Lee, T.-I., Chung, C.-H., Song, Y. J., Suh, J.-S., Yoon, H.-G., Huh, Y.-M., and Haam, S. (2008) Enhancement of magnetic resonance contrast effect using ionic magnetic clusters. *J. Colloid Interface Sci. 319*, 429–34.

BC900424U

Synthesis and Biophysical Studies of Coronene Functionalized 2′-Amino-LNA: A Novel Class of Fluorescent Nucleic Acids

Pankaj Gupta, Niels Langkjær, and Jesper Wengel*

Nucleic Acid Center, Department of Physics and Chemistry, University of Southern Denmark, 5230 Odense M, Denmark.
Received September 23, 2009; Revised Manuscript Received December 27, 2009

Incorporation of 2′-*N*-(coronen-1-yl)methyl-2′-amino-LNA monomer **X** or 2′-*N*-4-(coronen-1-yl)-4-oxobutanoyl-2′-amino-LNA monomer **Y** into short DNA strands induces high binding affinity toward DNA or RNA and a marked red-shift in steady-state fluorescence emission upon hybridization to cDNA or RNA.

INTRODUCTION

Fluorescent labeling of nucleosides and oligonucleotides is explored for structural studies, nucleic acid sequencing, molecular diagnostics, and other applications relating to genomics (*1*). "Molecular beacons" (*2*−*4*), fluorophore−quencher combination probes (*5*), "scorpion" (*6*), "Pacman" (*7*) or "sunrise primers," (*8*) specific pyrene-conjugated DNA or RNA probes (*9*−*24*), and fluorescence resonance energy transfer (FRET) probes (*5, 25, 26*) are typical example of such probes. Other fluorescent probes have been designed by labeling of oligonucleotides with a single hybridization sensitive moiety (*17, 27*−*37*). These methods have several potential advantages such as sensitivity, flexibility, safety, and relative inexpensiveness compared to the classical radiolabeling method.

The high-affinity hybridization of LNA (locked nucleic acid) (*37*−*42*), 2′-amino-LNA (*43*−*45*), and α-L-LNA (*46*) and the properties of LNA modified oligonucleotides as diagnostic tools and therapeutic agents (*47, 48*) encouraged us to appraise N-functionalized derivatives of 2′-amino-LNA. Recently, LNAs have been functionalized by fluorescent groups such as pyrene (*15, 18, 49, 50*), perylene (*51, 52*), and (phenylethynyl)pyrene (*53*). These pyrene-functionalized LNAs exhibit appealing properties and can be used to sense full complementarity of DNA or RNA counterparts.

Recently, Hrdlicka et al. (*18*) investigated multilabeled pyrene-functionalized 2′-amino-LNA probes which exhibited high-affinity hybridization to DNA/RNA complements, quenched fluorescence of single-stranded probe, and large increase of the quantum yield and fluorescence brightness upon hybridization. More recently, Astakhova et al. (*52, 53*) reported multilabeled perylene- and (phenylethynyl)pyrenecarbonyl-functionalized 2′-amino-LNA probes which exhibited high-affinity hybridization toward cDNA/RNA, considerably quenched fluorescence of single-stranded multilabeled probes, increased fluorescence brightness upon hybridization, high fluorescence quantum yields, and red-shifted emission compared to pyrene-functionalized 2′-amino-LNA probes. However, there is still a need to find optimal fluorochromes which, e.g., display a long-wave emission spectrum relative to pyrene, perylene, and (phenylethynyl)pyrenecarbonyl.

Coronene is a fluorochrome which resembles pyrene in its chemical behavior but differentiates from pyrene with respect to photochemical properties (*54*). Coronene is very stable, showing the properties of a fully benzenoid hydrocarbon. The extra stability of coronene imparted by the sextet ring current has been called "superaromaticity". Unlike pyrene, coronene is not a common fluorescent dye for modification of oligonucleotides, whereas it has been used in the field of lipids (*55*). Nagata et al. (*56*) described coronene as an external binder of DNA, but later, Zinger et al. (*57*) described that the planner coronene molecules partially insert between adjacent DNA bases. Herein, we report the synthesis of monomer **X** (with a methylcoronene moiety attached to 2′-amino-LNA) and monomer **Y** (with a oxobutanoylcoronene moiety attached to 2′-amino-LNA) and oligonucleotides involving them, together with their hybridization and fluorescence properties.

EXPERIMENTAL PROCEDURES

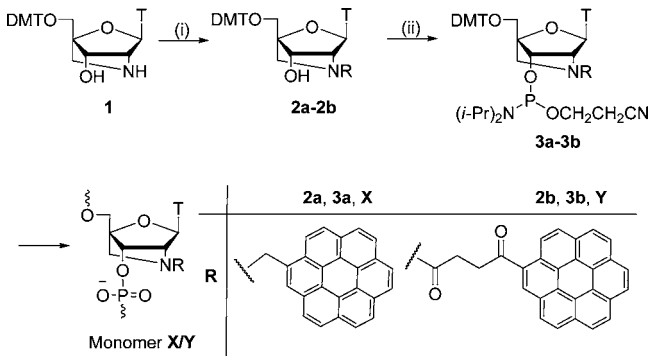
General. Anhydrous reactions were carried out under an atmosphere of nitrogen. Solvents used were of HPLC grade. Acetonitrile and dichloromethane were made anhydrous by storage over molecular sieves (4 Å). TLC was run with Merck silica 60 F_{254} aluminum sheets. ^{1}H NMR spectra were recorded at 300 MHz, ^{13}C NMR spectra at 75.5 MHz, and ^{31}P NMR spectra at 121.5 MHz (δH: $CDCl_3$ 7.26 ppm, DMSO-d_6 2.50; δC: $CDCl_3$ 77.0 ppm, DMSO-d_6 39.4). Chemical shifts are reported in ppm relative to either tetramethylsilane or the deuterated solvent as an internal standard for ^{1}H NMR and ^{13}C NMR, and relative to 85% H_3PO_4 as external standard for ^{31}P NMR. Assignments of NMR spectra, when given, are based on 2D NMR experiments. Coupling constants (*J* values) are given in Hertz. ESI-HRMS were recorded in positive ion mode on an API QSTAR mass spectrometer.

Synthesis of ON2−**ON10.** Nucleoside phosphoramidites **3a** and **3b** were used as building blocks for incorporation of 2′-*N*-(coronen-1-yl)methyl-2′-amino-LNA monomer **X** and 2′-*N*-(coronen-1-yl)-4-oxo-butanoyl-2′-amino-LNA monomer **Y**, respectively, into DNA oligonucleotides (Scheme 1, Table 1) in 0.2 μmol scale synthesis using an automated DNA synthesizer. Standard procedures were used for unmodified monomers (i.e, 3% trichloroacetic acid in CH_2Cl_2 as detritylation reagent; 0.25 M 4,5-dicyanoimidazole (DCI) in CH_3CN as activator; acetic anhydride in THF as cap A solution; *N*-methylimidazole in THF as cap B solution; and 0.02 M iodine in H_2O/pyridine/THF as the oxidizing solution). The stepwise coupling yields were >99% for unmodified phosphoramidites (2 min coupling time) and for **3a** and **3b** 95% and 99% (10 min coupling time, 1*H*-tetrazole as activator), respectively, based on the absorbance of the dimethoxytriyl cation released after each coupling step. After deprotection and cleavage from solid support (32% aq ammonia, 55 °C, 12 h), the modified ONs were precipitated and repeatedly washed with ethanol, and their composition and purity (>80%) verified by MALDI-MS analysis and ion-exchange HPLC, respectively.

* E-mail jwe@ifk.sdu.dk.

10.1021/bc900421r © 2010 American Chemical Society
Published on Web 01/25/2010

Scheme 1[a]



[a] Reagents and conditions: (i) (**2a**) Coronene-1-carbaldehyde, $NaBH(OAc)_3$, $ClCH_2CH_2Cl$, rt, 60%; (**2b**) 4-(coronen-1yl)-4-oxobutanoic acid, 1-ethyl-3-(3-dimethylaminopropyl)carbodiimide hydrochloride (EDC·HCl), CH_2Cl_2, 59%; (ii) bis(*N*,*N*-diisopropylamino)-2-cyanoethoxyphosphine, *N*,*N*-diisopropylammonium tetrazolide, MeCN/CH_2Cl_2 (5:2), 2 h for **3a**/35 °C, 3 h for **3b**/rt; **3a**, 80%; **3b**, 75%. T = thymin-1-yl. DMT = 4,4′-dimethoxytrityl.

Table 1. Thermal Denaturation Studies Towards DNA/RNA[a]

	DNA		RNA	
oligonucleotides	T_m/°C	ΔT_m/°C	T_m/°C	ΔT_m/°C
ON1 5′-d(GTG ATA TGC)[b]	28.5	ref.	26.5	ref.
ON2 5′-d(GCA TAT CAC)	28.5	ref.	24.5 ref.	
ON3 5′-d(GTG A**X**A TGC)[c,d]	31.5	+3.0	28.0	+1.5
ON4 5′-d(GCA TA**X** CAC)	27.0	−1.5	24.0	−0.5
ON5 5′-d(GCA **X**AT CAC)	30.5	+2.0	27.5	+3.0
ON6 5′-d(GCA **X**A**X** CAC)	17.5/36.5		18.0/37.0	
ON7 5′-d(GTG A**Y**A TGC)[c,d]	43.0	+14.5	36.0	+9.5
ON8 5′-d(GCA TA**Y** CAC)	37.5	+9.0	36.5	+12.0
ON9 5′-d(GCA **Y**AT CAC)	43.5	+15.0	35.0	+10.5
ON105′-d(GCA **Y**A**Y** CAC)	31.5	+1.5	19.0	−2.7

[a] Thermal denaturation temperatures [T_m values (°C) (ΔT_m = change in T_m value calculated relative to DNA/DNA or DNA/RNA reference duplex)] measured as the maximum of the first derivative of the melting curve (A_{260} vs temperature) recorded in 10 mM phosphate buffer ([Na^+] = 110 mM, [Cl^-] = 100 mM, [EDTA] = 0.1 mM, pH 7.0) using 1.0 μM concentrations of the two complementary strands. T_m values are averages within ±1 °C of at least two measurements. See Scheme 1 for structure of monomer **X** and monomer **Y**. MALDI-MS *m*/*z* ([M-H]$^-$; found/calc.): **ON3**, 3092/3093; **ON4**, 3020/3022; **ON5**, 3021/3022; **ON6**, 3360/3361; **ON7**, 3161/3163; **ON8**, 3088/3092; **ON9**, 3090/3092; **ON10**, 3500/3501. [b] **ON1** is the cDNA strand to **ON2/ON4/ON5/ON6/ON8/ON9/ON10**; **ON2** is the cDNA strand to **ON3/ON7**. [c] T_m values (°C) toward DNA strands containing a single mismatch in the central position, monomer **X**: G/C/T: 24.0/31.5/28.0; monomer **Y**: G/C/T: 36.5/30.0/35.5. [d] T_m values (°C) toward RNA strands containing a single mismatch in the central position, monomer **X**: G/C/U: 21.0/21.0/18.5; monomer **Y**: G/C/U: 30.0/17.0/22.0.

Thermal Denaturation Studies. Concentrations of oligonucleotides were calculated using the following extinction coefficients (OD/μmol): G, 10.5; A, 13.9; T/U, 7.9; C, 6.6; coronene units, 36.0. The two complementary strands (~1.0 μM) were thoroughly mixed, and the duplex denatured by heating to 80 °C followed by cooling to the starting temperature (5 °C) of the experiment. Quartz optical cells with a path length of 1.0 cm were used. Thermal denaturation curves were obtained on a Perkin-Elmer Lambda 35 UV/vis spectrometer equipped with a PTP-6 peltier temperature programmer. Melting temperatures (T_m values/°C) determined as the maximum of the first derivative of the thermal denaturation curve (A_{260} vs temperature) recorded in 10 mM phosphate buffer ([Na^+] = 110 mM, [Cl^-] = 100 mM, [EDTA] = 0.1 mM, pH 7.0). A temperature range from 5 to 75 °C with a ramp of 1.0 °C/min was used.

UV Absorption Measurements. UV absorption measurements (200−500 nm) were performed on a Shimadzu UV-160A spectrophotometer using quartz optical cells with a path length of 1.0 cm. Measurements were conducted using 1.0 μM of strands in 10 mM phosphate buffer ([Na^+] = 110 mM, [Cl^-] = 100 mM, [EDTA] = 0.1 mM, pH 7.0).

(1*R*,3*R*,4*R*,7*S*)-5-[4-Coronen-1-ylmethyl]-1-(4,4′-dimethoxytrityloxymethyl)-7-hydroxy-3-(thymin-1-yl)-2-oxa-5-azabicyclo[2.2.1]heptane (2a). Nucleoside **1** (*58*) (0.23 g, 0.40 mmol) was dissolved in anhydrous 1,2-dichloroethane (5 mL). To this stirred solution at rt were added coronene-1-carbaldehyde (0.14 g, 0.42 mmol) and sodium triacetoxyborohydride (0.12 g, 0.60 mmol). After stirring at rt for 6 h, saturated aq $NaHCO_3$ (2 mL) was added and the mixture diluted with ethylacetate (20 mL). The organic phase was washed with saturated aq $NaHCO_3$ (10 mL) and the aq phase was extracted with ethylacetate (2 × 20 mL). The combined organic phase was dried over Na_2SO_4, filtered, and evaporated to dryness under reduced pressure, and the resulting residue was purified by silica gel column chromatography (20−70% EtOAc in petroleum ether, v/v) to afford nucleoside **2a** as a yellowish solid material (210 mg; 60%). R_f = 0.35 (7% MeOH in CH_2Cl_2, v/v); ESI-HRMS *m*/*z* 906.3127 ([M+Na]$^+$, $C_{57}H_{45}N_3O_7$·Na^+ calc. 906.3149); ^{1}H NMR (DMSO-d_6) δ (selected signals) 11.39 (s, NH), 9.16−8.91 (m, Ar), 7.70 (s, H6), 7.48−6.88 (m, Ar), 5.94 (s, 3′−OH), 5.74 (d, J = 6.0 Hz, H1′), 5.21 (d, J = 14.4 Hz, CH_2Ar), 5.03 (d, J = 14.7 Hz, CH_2Ar), 4.35 (d, J = 4.5 Hz, H2′), 3.78−3.72 (m, H3′ and 2 × OCH_3), 3.48 (d, J = 10.8 Hz, H5′a/b), 3.38−3.35 (m, H5′a/b overlapping with H_2O), 3.18 (d, J = 9.6 Hz, H5″a), 2.97 (d, J = 6.0 Hz, H5″b), 1.55 (s, CH_3); ^{13}C NMR (DMSO-d_6) δ 163.8, 158.1, 150.0, 144.7, 135.4, 135.2, 134.7, 134.0, 129.8, 129.7, 128.1, 128.0, 127.9, 127.8, 127.6, 126.9, 126.8, 126.3, 126.1, 126.0, 125.8, 122.6, 121.8, 121.6, 121.5, 121.3, 121.2, 120.8, 113.2, 108.2, 88.5, 86.2, 85.6, 70.7, 66.5, 59.7, 58.1, 56.8, 55.0, 12.4.

(1*R*,3*R*,4*R*,7*S*)-5-[4-Coronen-1-ylmethyl]-7-[2-cyanoethoxy-(diisopropylamino)-phosphinoxy]-1-(4,4′-dimethoxytrityloxymethyl)-3-(thymin-1-yl)-2-oxa-5-azabicyclo [2.2.1]heptane (3a). Nucleoside **2a** (0.13 g, 0.14 mmol) was dissolved in anhydrous acetonitrile (5 mL) under stirring at rt. *N*,*N*-Diisopropylammonium tetrazolide (0.037 g, 0.22 mmol) and bis(*N*,*N*-diisopropylamino)-2-cyanoethoxyphosphine (0.14 mL, 0.44 mmol) were added under nitrogen. The reaction mixture was stirred for 3 h at 35 °C and then diluted with EtOAc (40 mL), washed with H_2O (30 mL), 5% aq $NaHCO_3$ (30 mL) and H_2O (30 mL), dried over Na_2SO_4, filtered, and evaporated to dryness under reduced pressure. The residue was purified by silica gel column chromatography (20−60% EtOAc in petroleum ether, v/v) to afford nucleoside **3a** as a yellowish solid material (118 mg; 74%). R_f = 0.60 (60% EtOAc in petroleum ether, v/v); ESI-HRMS *m*/*z* 1106.4259 ([M+Na]$^+$, $C_{66}H_{62}N_5O_8P$·Na^+ calc. 1106.4227); ^{31}P NMR ($CDCl_3$) δ 149.1.

(1*R*,3*R*,4*R*,7*S*)-5-[4-(Coronen-1-yl)-4-oxo-butanoyl]-1-(4,4′-dimethoxytrityloxy methyl)-7-hydroxy-3-(thymin-1-yl)-2-oxa-5-azabicyclo[2.2.1]heptane (2b). Nucleoside **1** (*58*) (0.40 g, 0.69 mmol) was dissolved in anhydrous dichloromethane (20 mL). To this stirred solution were added *N*-(3-dimethylaminopropyl-*N*′-ethylcarbodiimide hydrochloride (EDC·HCl, 0.14 g, 0.76 mmol) and 3-coronenyl propionic acid (0.30 g, 0.76 mmol) at 0 °C. After warming to rt, the reaction mixture was stirred for 18 h, whereupon it was diluted with dichloromethane (50 mL) and successively washed with brine (40 mL) and H_2O (40 mL). The organic phase was evaporated to dryness under reduced pressure, and the resulting residue was purified by silica gel column chromatography (0−2% MeOH in CH_2Cl_2, v/v) to afford a rotameric mixture (~1:0.43 by ^{1}H NMR) of **2b** as a yellowish solid material (380 mg; 58%). R_f = 0.32 (7% MeOH in CH_2Cl_2, v/v); ESI-HRMS *m*/*z* 976.3291 ([M+Na]$^+$, $C_{60}H_{47}N_3O_9$·Na^+ calc. 976.3210); ^{1}H NMR (DMSO-d_6) δ

(selected signals) 11.50 (br s, NHA), 11.35 (br s, NHB), 9.53−8.92 (m, Ar), 7.79 (s, H6), 7.63−6.82 (m, Ar), 5.68 (s, H-1′A), 5.52 (br s, H-1′B), 4.77 (br s, H-2′B), 4.63 (br s, H-2′A), 4.14 (br s, H-3′A and H-3′B), 1.83 (br s, CH_3-A), 1.16 (br s, CH_3−B); ^{13}C NMR (DMSO-d_6) δ 203.6, 202.1, 170.7, 170.5, 164.0, 157.8, 150.1, 148.3, 140.2, 134.9, 134.9, 133.9, 132.1, 132.0, 129.2, 129.1, 128.9, 128.4, 128.3, 128.0, 127.9, 127.6, 127.4, 127.1, 126.9, 126.8, 126.6, 126.5, 126.4, 126.2, 126.0, 124.8, 124.0, 122.5, 121.9, 121.2, 121.1, 120.9, 120.7, 113.9, 112.7, 109.9, 108.3, 108.2, 89.4, 88.8, 86.4, 79.9, 68.4, 63.3, 56.6, 55.0, 54.9, 50.8, 45.6, 42.0, 36.9, 28.5, 12.4, 10.9.

(1*R*,3*R*,4*R*,7*S*)-5-[4-(Coronen-1-yl)-4-oxo-butanoyl]-7-[2-cyanoethoxy(diisopropylamino)phosphinoxy]-1-(4,4′-dimethoxytrityloxymethyl)-3-(thymin-1-yl)-2-oxa-5-azabicyclo[2.2.1]-heptane (3b). Nucleoside **2b** (0. 32 g, 0.33 mmol) was dissolved in a mixture of anhydrous acetonitrile (7.0 mL) and dichloromethane (2.0 mL) under stirring at rt. *N*,*N*-Diisopropylammonium tetrazolide (0.057 g, 0.50 mmol) and bis(*N*,*N*-diisopropylamino)-2-cyanoethoxyphosphine (0.31 mL, 1.00 mmol) were added under nitrogen. The reaction mixture was stirred for 2 h and then diluted with EtOAc (60 mL), washed successively with H_2O (40 mL), 5% aq $NaHCO_3$ (40 mL) and H_2O (40 mL), dried over Na_2SO_4, filtered, and evaporated to dryness under reduced pressure. The residue was purified by silica gel column chromatography (30−90% EtOAc in petroleum ether, v/v) to afford nucleoside **3b** as a yellowish solid material (300 mg; 79%). R_f = 0.60 (80% EtOAc in petroleum ether, v/v); ESI-HRMS *m*/*z* 1176.4282 ([M+Na]$^+$, $C_{69}H_{64}N_5O_{10}P\cdot Na^+$ calc. 1176.4333); ^{31}P NMR ($CDCl_3$) δ 149.0, 150.2.

RESULTS

The bicyclic nucleoside **1** was synthesized according to a published procedure (*58*) and was selectively N-alkylated by reductive amination using coronene-1-carbaldehyde producing *N*-(coronen-1-yl)methyl derivative **2a**. Furthermore, **1** was N-acylated by 4-(coronen-1yl)-4-oxobutanoic acid giving the corresponding nucleoside **2b**. The phosphoramidite building blocks **3a** and **3b** were obtained by standard phoshphitylation of nucleosides **2a** and **2b**, respectively, using bis(*N*,*N*-diisopropylamino)-2-cyanoethoxyphosphine as phosphitylating agent (Scheme 1).

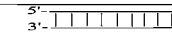
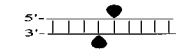
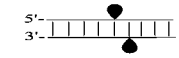
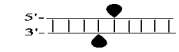
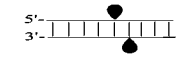
Synthesis of oligonucleotides (ONs) containing 2′-amino-LNA monomers **X** and **Y** was performed in 0.2 μmol scale using an automated DNA synthesizer. 1*H*-Tetrazole was used as coupling agent for monomers **X** and **Y** resulting in 95% and 99% stepwise coupling yields, respectively, based on the absorbance of the dimethoxytrityl cation released after each coupling step (see Experimental Procedures section for details). All synthesized ONs were purified by RP-HPLC, and their identity was confirmed by MALDI-TOF mass spectroscopy and ion-exchange HPLC, respectively.

The influence of the functionalized 2′-amino-LNA monomers **X** and **Y** on duplex thermal stabilities was studied toward DNA and RNA complements (Table 1) by UV thermal denaturation experiments using a 10 mM phosphate buffer ([Na^+] = 110 mM, [Cl^-] = 100 mM, [EDTA] = 0.1 mM, pH 7.0). In all cases, the denaturation curves displayed monophasic transitions.

Earlier, it was reported that conjugates containing functionalized 2′-amino-LNA monomers form stable duplexes toward both DNA and RNA complements, and that N2′-acylated 2′-amino-LNA derivatives exhibit higher thermal stabilities than the corresponding N2′-alkylated derivatives (*18, 49*). Our results are in good agreement with these earlier results. Incorporation of a single monomer **X** in mixed 9-mer **ON3** and **ON5** induced an increase in duplex stability toward cDNA (ΔT_m = +2.0 and +3.0 °C compared to the unmodified reference duplex **ON1**:**ON2**) (Table 1). A similar effect was observed for **ON3** and **ON5** with complementary RNA. Surprisingly, **ON4** showed minor destabilization toward cDNA (ΔT_m = −1.5 °C) and complementary RNA (ΔT_m = −0.5 °C). In contrast to the melting temperature results of monomer **X**, a single incorporation of monomer **Y** in mixed DNA 9-mer ONs (**ON7**−**ON9**) induced high-affinity hybridization toward DNA (ΔT_m = +9.0 to +15.0 °C) and RNA (ΔT_m = +9.5 to +12.0 °C). When comparing thermal stabilities of duplexes involving ONs singly functionalized with monomer **Y**, (**ON7**−**ON9**) were higher than those of the corresponding unmodified duplexes and of duplexes involving a perylenemethyl-2′-amino-LNA monomer (*51*), (phenylethynyl)pyrene-functionalized-2′-amino-LNAs (*53*) and N2′-pyrenecarbonyl-functionalized 2′-amino-LNAs (*18*). This indicates that attachment of coronene moieties to 2′-amino-LNA monomers is compatible with duplex formation. To evaluate this further, we performed CD experiments on duplexes formed between **ON8** or **ON9**, each containing one **Y** monomer, and cDNA or RNA (S7, ESI). These spectra indicate similar duplex structures of the modified duplexes and the unmodified reference (**ON2**:DNA and **ON2**:RNA) duplexes, which support that one **Y** modification can be accommodated without significantly disturbing overall duplex structure.

Incorporation of two modifications may, however, have a more profound effect on duplex structure. N2′-Substituents of 2′-amino-LNAs are known to point toward the minor groove (*15, 49*) and may therefore be affected by the narrow minor grooves in A-type duplexes (*59*). Incorporation of two **X** monomers separated by one nucleotide in a 9-mer DNA strand (**ON6**)

Table 2. Thermal Denaturation Studies in Zipper Arrangements[a]

Duplexes	T_m/°C	ΔT_m/°C	Schematic illustration	Constitution
ON1:5′-d(GTG ATA TGC) **ON2**:3′-d(CAC TAT ACG)	28.5	Ref.		
ON3:5′-d(GTG A**X**A TGC) **ON4**:3′-d(CAC **X**AT ACG)	49.0	+20.5		-1 Zipper
ON3:5′-d(GTG A**X**A TGC) **ON5**:3′-d(CAC TA**X** ACG)	33.5	+5.0		+1 Zipper
ON7:5′-d(GTG A**Y**A TGC) **ON8**:3′-d(CAC **Y**AT ACG)	57.0	+28.5		-1 Zipper
ON7:5′-d(GTG A**Y**A TGC) **ON9**:3′-d(CAC TA**Y** ACG)	47.0	+18.5		+1 Zipper

[a] Thermal denaturation temperatures were recorded under the same conditions as described in Table 1. See Scheme 1 for structures of monomer **X** and monomer **Y**. The black droplets illustrate the coronene moieties of **X** and **Y** monomers.

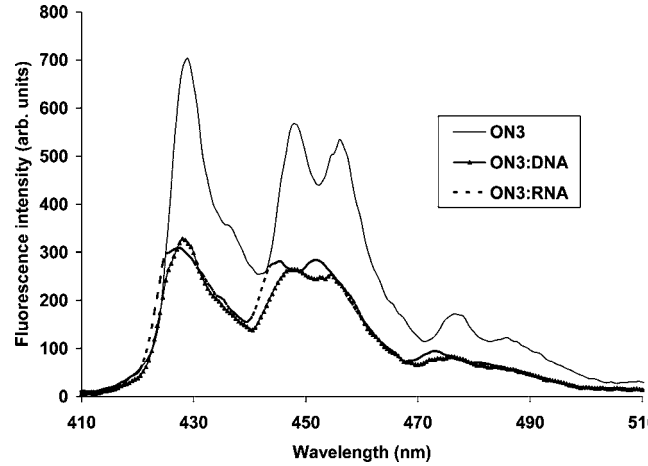


Figure 1. Steady-state fluorescence emission spectra of single-stranded probe **ON3** (with monomer **X**) and of duplexes formed between **ON3** and cDNA (**ON3:DNA**) or RNA (**ON3:RNA**).

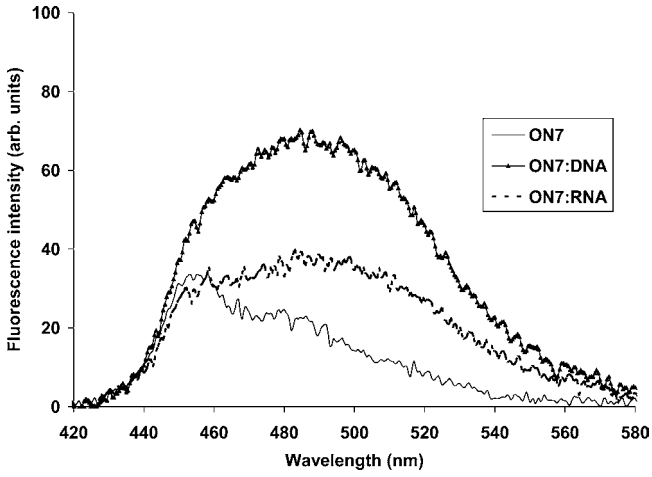


Figure 2. Steady-state fluorescence emission spectra of single-stranded probe **ON7** (with monomer **Y**) and of duplexes formed between **ON7** and cDNA (**ON7:DNA**) and RNA (**ON7:RNA**).

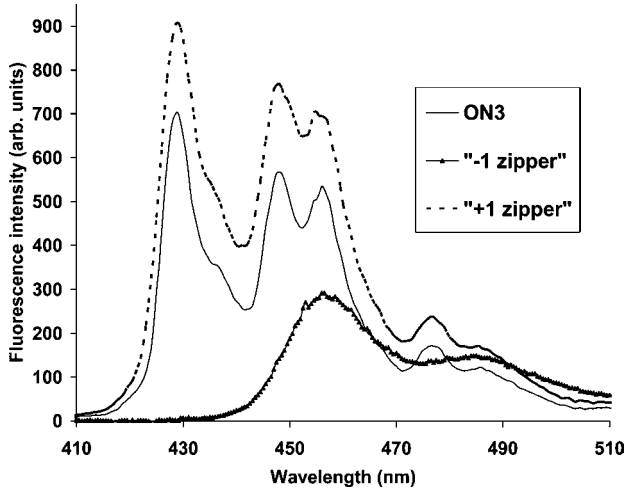


Figure 3. Steady-state fluorescence emission spectra of single-stranded probe **ON3** (with monomer **X**) and of duplexes formed between **ON3** and **ON4** ("−1 zipper" constitution) and **ON3** and **ON5** ("+1 zipper" constitution).

resulted in two melting transitions, which we at present are unable to explain; no transition was observed for **ON6** without a complementary strand. On the contrary, single transitions upon incorporation of two **Y** monomers separated by one nucleotide (**ON10**) were obtained with enhanced thermal stability of the duplex with cDNA (ΔT_m = +1.5 °C per modification) but decreased thermal stability of the duplex with complementary RNA (ΔT_m = −2.7 °C per modification). Relative destabilization toward DNA/RNA complements upon sequential incorporation of two monomers **Y** (relative to incorporation of one **Y** monomer) suggests that the minor groove is too narrow to accommodate the two coronene moieties.

The Watson−Crick base pair selectivity of monomers **X** and **Y** was evaluated by observing thermal denaturation temperatures of duplexes formed between **ON3/ON7** and DNA or RNA strands containing a single mismatched nucleotide opposite monomer **X** or **Y** (see Table 1; footnotes c and d). The base pair selectivity of monomer **X** was satisfactory in the case of T:G DNA and T:U RNA mismatches (−7.5 °C/−9.5 °C, respectively). A relatively weak decrease in thermal stability was observed for the T:T DNA mismatch (−3.5 °C), whereas no mismatch discrimination was observed for the T:C DNA mismatch. Against RNA, **ON3** showed appreciable mismatch discrimination. The base pairing selectivity of monomer **Y** was

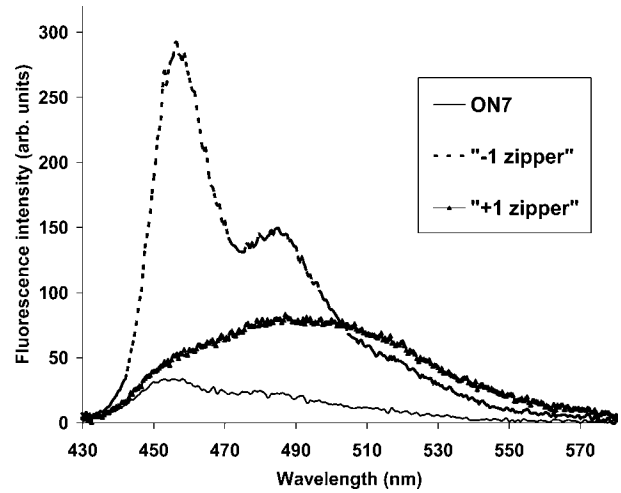


Figure 4. Steady-state fluorescence emission spectra of single-stranded probe **ON7** (with monomer **X**) and of duplexes formed between **ON7** and **ON8** ("−1 zipper" constitution) and **ON7** and **ON9** ("+1 zipper" constitution).

satisfactory in both DNA and RNA contexts: T:T/U (−7.5 °C/−14.0 °C, respectively), T:G (−6.5 °C/−6.0 °C, respectively), and T:C (−13.0 °C/−19.0 °C, respectively).

Studies with **X/Y** monomers positioned in both strands of a duplex were performed in −1 and +1 interstrand zipper (*15*) arrangements of monomer **X** or **Y** (Table 2). Insertion of two **X** monomers in a "−1 zipper" constitution induced extensively increased thermal stability (Table 2, ΔT_m = +20.5 °C), as did insertion of two **Y** monomers (+28.5 °C). On the other hand, insertion of two **X** monomers in a "+1 zipper" constitution induced a limited increase in thermal stability (+5.0 °C), whereas insertion of two **Y** monomers in a "+1 zipper" constitution again induced a significant increase in thermal stability (+18.5 °C). The thermal denaturation temperatures of duplexes involving two modified strands are thus remarkably higher than those of duplexes containing monomers **X** or **Y** in only one strand, indicating that interstrand communication between coronene moieties in the studied "zipper" pattern contributes to overall duplex stability.

The steady-state fluorescence emission spectra of **ON3**−**ON6** containing monomer **X** when excited at its UV absorption maximum λ_{max} 310 nm (10 °C, ±1 °C) showed three emission bands. Insertion of a single **X** monomer in ONs (**ON3**−**ON5**) in general results in quenching of fluorescence intensities (up to half of the intensity of single-stranded ONs) upon hybridization to cDNA or RNA, though a minor increase of fluorescence intensity in the case of **ON4** was observed upon hybridization to cDNA. (Figure 1, and ESI S4.1 to S4.4). However, **ON6** with two **X** monomers separated by one nucleotide upon hybridization with cDNA displayed increased fluorescence intensity (∼2-fold) with unchanged emission wavelength and upon hybridization with complementary RNA slightly increased fluorescence intensity at nearly the same emission wavelength (see ESI S4.5). Incorporation of monomer **X** in ONs (**ON3**−**ON6**) results in fluorescence emission maxima at ∼429 nm, which is 25 nm red-shifted relative to the corresponding pyrenecarbonyl-2′-amino-LNA ONs (*18*), 61 nm blue-shifted relative to the corresponding perylene-3-carbonyl-2′-amino-LNA ONs (*52*) and 1−26 nm blue-shifted relative to the corresponding (phenylethynyl)pyrenecarbonyl-2′-amino-LNA ONs (*53*).

In contrast, insertion of a single **Y** monomer into ONs (**ON7**−**ON9**) in general results in a marked red shift with similar or increased fluorescence intensities upon hybridization to cDNA or RNA (Figure 2 and ESI, S4.6 to S4.9). Surprisingly, **ON10** containing two **Y** monomers upon duplex formation with DNA/

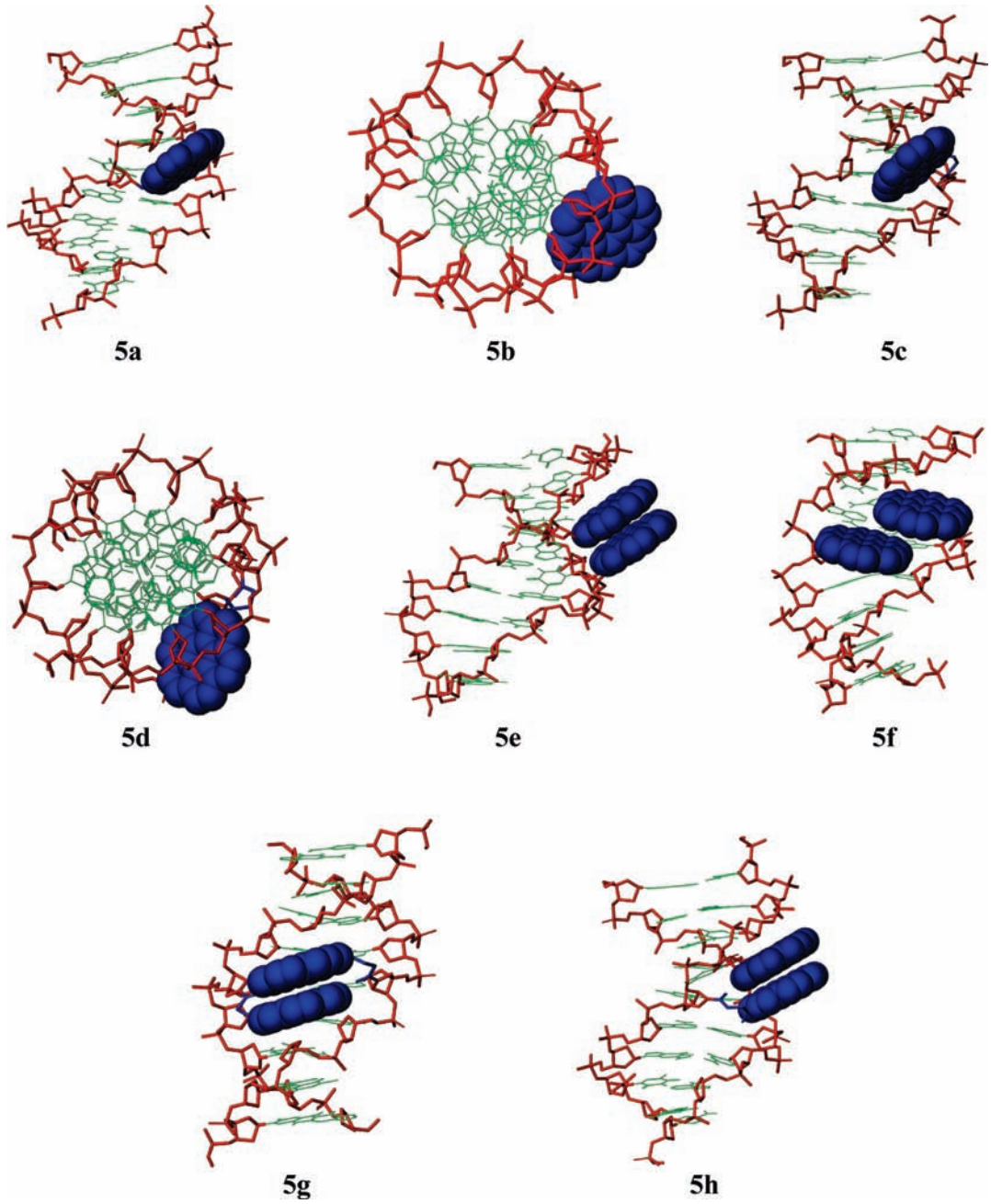


Figure 5. Energy-minimized structures of duplexes. (5a) **ON3**:**DNA** (monomer **X** in side view); (5b) **ON3**:**DNA** (monomer **X** in top view); (5c) **ON7**:**DNA** (monomer **Y** in side view); (5d) **ON7**:**DNA** (monomer **Y** in top view); (5e) **ON3**:**ON4** (monomer **X**, "−1 zipper" arrangement); (5f) **ON3**:**ON5** (monomer **X**, "+1 zipper" arrangement); (5g) **ON7**:**ON8** (monomer **Y**, "−1 zipper" arrangement); and (5h) **ON7**:**ON9** (monomer **Y**, "+1 zipper" arrangement) in side view. Color code: Sugar phosphate backbone (red); coronene (blue); nucleobases (green).

RNA complements showed a slight shift in emission maxima (∼4 nm) to shorter wavelengths with a weakly increased fluorescence intensity (∼1.5-fold) (see ESI S4.10).

Incorporation of a single **Y** monomer in ONs (**ON7**−**ON10**) thus results in a broad, unstructured band with fluorescence emission maxima at ∼453 nm, which is 51 nm red-shifted relative to pyrenecarbonyl-2′-amino-LNA ONs (*18*), 37 nm blue-shifted relative to perylene-3-carbonyl-2′-amino-LNA ONs (*52*), and 7−23 nm blue-shifted relative to (phenylethynyl)pyrene-carbonyl-2′-amino-LNA ONs (*53*). No characteristic changes in the shape of the spectral curves were observed.

Next, fluorescence properties of duplexes formed by **ON3**/**ON7** and singly mismatched DNA/RNA targets were investigated. Noteworthy, as mentioned earlier, the mismatched duplexes display T_m values of more than 19 and 30 °C for **ON3** and **ON7**, respectively. The resulting fluorescence spectra (recorded at 10 °C) are shown in the electronic Supporting Information (Figures S4.1, S4.2, S4.6, and S4.7). Probe **ON3** was seen to be equally sensitive to the presence of mismatched nucleosides in DNA and RNA targets with a ∼2-fold increase in fluorescence intensity for all singly mismatched complexes (Supporting Information Figures S4.1−S4.2). For probe **ON7** containing a single monomer **Y**, the fluorescence effect of mismatches relative to the single-stranded **ON7** and fully matched duplexes did not allow straightforward detection of mismatches (Supporting Information Figures S4.6−S4.7).

All duplexes having monomers **X** in both complementary strands displayed an unstructured emission band at $\lambda_{em} \sim 430$ nm. The fluorescence intensity of the "zippers" was lower in "−1 zipper" constitution and slightly higher in "+1 zipper" constitution than of the previously described duplexes having coronene monomer **X** in only one strand (Figure 3). Duplexes

having monomer **Y** in both complementary strands displayed an unstructured emission band at $\lambda_{em} \sim 484$ nm. In contrast, the fluorescence intensity of the "zippers" was higher in "−1 zipper" constitution and lower in "+1 zipper" constitution than of the previously described duplexes having coronene monomer **Y** in only one strand (Figure 4). Excimer emission was observed neither in single-stranded ONs (**ON3**−**ON10**) nor in their duplexes with DNA/RNA complements, whereas microcrystals of coronene showed both monomer and excimer emission bands (*60*). In contrast, insertion of pyrene-functionalized LNAs in "−1 zipper" motif resulted in strong excimer formation combined with increased thermal stability (*15, 53*).

Molecular modeling of duplexes formed between **ON3** (containing monomer **X**) or **ON7** (containing monomer **Y**) and cDNA (**ON2**) was performed using the AMBER force field (*61, 62*) as implemented in *MacroModel v 8.5* (*63*). Interstrand zipper arrangement modeling were also performed using the same method. All 9-mer duplexes were constructed with the coronene moiety of monomers **X** and **Y** in an extrahelical position. The observed low-energy structures were used for molecular dynamics simulations.

The model structure of the **ON3**:**ON2** hybrid suggests that the attachment of the methylcoronene moiety at the 2′-nitrogen atom of 2′-amino-LNA does not induce significant changes in the duplex geometry and that coronene binds in the minor groove without stacking with the nucleobases (Figure 5a,b). On the other hand, the model structure of hybrid **ON7**:**ON2** revealed many low-energy conformations during dynamics. This can be explained by the more flexible nature of the 4-oxobutanoyl linker of monomer **Y** though the coronene moiety shown still to be positioned in the minor groove (Figure 5c,d). Modeling results of zipper hybrid **ON3**:**ON4** showed the two coronene moieties to be stacking while being positioned in the minor groove (Figure 5e), which could explain the high T_m value measured for this "−1 zipper" duplex. This is substantiated for the **ON3**:**ON5** hybrid in which the two coronene moieties only partially stack (Figure 5f), thus offering an explanation of the lower T_m value observed in this case. The model structure of hybrid **ON7**:**ON8** showed the closest arrangement of the two coronene moieties stacking with each other and with nucleobases (Figure 5g), which correlates with the very high T_m value measured. Hybrid **ON7**:**ON9** showed the two coronene moieties to nicely stack in the minor groove (Figure 5h), but without stacking with the nucleobases.

CONCLUSION

We have studied hybridization and fluorescence properties of coronene moieties attached to the N2-nitrogen atom of 2′-amino-LNA. Incorporation of a single **X** monomer containing a methylcoronene moiety attached to 2′-amino-LNA induced increased T_m values (up to 3 °C) together with quenching of fluorescence intensity when bound to cDNA/RNA. Interestingly, upon incorporation of two **X** monomers separated by one nucleotide in a short **ON**, a 2-fold increase in fluorescence intensity of the resulting duplex with cDNA was observed. Additionally, significant mismatch discrimination was observed by fluorescence changes when a single monomer **X** was incorporated into an ON. Incorporation of monomer **Y** containing an oxobutanoylcoronene moiety attached to 2′-amino-LNA led to remarkably increased thermal affinity toward DNA/RNA complements (up to 15 °C per modification) together with a bathochromic shift in UV absorption upon hybridization with cDNA/RNA. No specific difference in fluorescence intensity was observed by hybridization upon incorporation of two **Y** monomers into a short ON. Interestingly, incorporation of a single monomer **Y** into a short ON allowed better mismatch discrimination toward RNA compared to DNA. The fluorescence properties of the coronene-modified ONs introduced herein, such as fluorescence induced mismatch discrimination and a bathochromic shift in UV absorption upon hybridization with cDNA/RNA, testify to a significant potential for applications in nucleic acid based diagnostics.

ACKNOWLEDGMENT

The Nucleic Acid Center is a research center of excellence funded by the Danish National Research Foundation. We thank the Danish National Research Foundation for financial support.

Note Added after ASAP Publication: Due to a production error, an uncorrected version of this paper was inadvertently published on Jan 25, 2010. The corrected version was reposted on Feb 3, 2010.

Supporting Information Available: Steady-state fluorescence studies of ONs; protocol for molecular modeling studies; absorption and emission maxima of ONs; steady-state fluorescence emission spectras; An illustrative example of thermal denaturation curve and ^{1}H NMR spectra of **2a** and **2b**. This material is available free of charge via the Internet at http://pubs.acs.org.

LITERATURE CITED

(1) Ranasinghe, R. T., and Brown, T. (2005) Fluorescence based strategies for genetic analysis. *Chem. Commun.* 5487–5502.
(2) Tyagi, S., and Kramer, F. R. (1996) Molecular beacons: Probes that fluoresce upon hybridization. *Nat. Biotechnol. 14*, 303–308.
(3) Seo, Y. J., Ryu, J. H., and Kim, B. H. (2005) Quencher-free, end-stacking oligonucleotides for probing single-base mismatches in DNA. *Org. Lett. 7*, 4931–4933.
(4) Marx, A., and Seitz, O. (2008) Methods in Molecular Biology Vol. 429, *Molecular Beacons: Signalling Nucleic Acid Probes*, Humana Press, Totowa, NJ.
(5) Kodama, S., Asano, S., Moriguchi, T., Sawai, H., and Shinozuka, K. (2006) Novel fluorescent oligo DNA probe bearing a multi-conjugated nucleoside with a fluorophore and a non-fluorescent intercalator as a quencher. *Bioorg. Med. Chem. Lett. 16*, 2685–2688.
(6) Whitcombe, D., Theaker, J., Guy, S. P., Brown, T., and Little, S. (1999) Detection of PCR products using self-probing amplicons and fluorescence. *Nat. Biotechnol. 17*, 804–807.
(7) Holland, P. M., Abramson, R. D., Watson, R., and Galfand, D. H. (1991) Detection of specific polymerase chain reaction product by utilizing the 5′−3′ exonuclease activity of Thermus aquaticus DNA polymerase. *Proc. Natl. Acad. Sci. U.S.A. 88*, 7276–7280.
(8) Nazarenko, I. A., Bhatnagar, S. K., and Hohman, R. J. (1997) A closed tube format for amplification and detection of DNA based on energy transfer. *Nucleic Acids Res. 25*, 2516–2521.
(9) Yamana, K., Gokota, T., Ozaki, H., Nakono, H., Sangen, O., and Shimidzu, T. (1992) Enhanced fluorescence in the binding of oligonucleotides with a pyrene group in the sugar fragment to complementary polynucleotides. *Nucleosides Nucleotides 11*, 383–390.
(10) Lewis, F. D., Zhang, Y., and Letsinger, R. L. (1997) Bispyrenyl excimer fluorescence: A sensitive oligonucleotide probe. *J. Am. Chem. Soc. 119*, 5451–5452.
(11) Kostenko, E., Dobrikov, M., Pyshnyi, D., Petyuk, V., Komarova, N., Vlassov, V., and Zenkova, M. (2001) 5′-Bis-pyrenylated oligonucleotides displaying excimer fluorescence provide sensitive probes of RNA sequence and structure. *Nucleic Acids Res. 29*, 3611–3620.
(12) Yamana, K., Ohtani, Y., Nakano, H., and Saito, I. (2003) Bispyrene labeled DNA aptamer as an intelligent fluorescent biosensor. *Bioorg. Med. Chem. Lett. 13*, 3429–3431.
(13) Dioubankova, N. N., Malakhov, A. D., Stetsenko, D. A., Gait, M. J., Volynsky, P. E., Efremov, R. G., and Korshun, V. A. (2003) Pyrenemethyl *ara*-uridine-2′-carbamate: a strong inter-

strand excimer in the major groove of a DNA duplex. *ChemBioChem 4*, 841–847.
(14) Okamoto, A., Ichiba, T., and Saito, I. (2004) Pyrene-labeled oligodeoxynucleotide probe for detecting base insertion by excimer fluorescence emission. *J. Am. Chem. Soc. 126*, 8364–8365.
(15) Hrdlicka, P. J., Babu, B. R., Sørensen, M. D., and Wengel, J. (2004) Interstrand communication between 2′-*N*-(pyren-1-yl)-methyl-2′-amino-LNA monomers in nucleic acid duplexes: directional control and signalling of full complementarity. *Chem. Commun.* 1478–1479.
(16) Kawai, K., Yoshida, H., Takada, T., Tojo, S., and Majima, T. (2004) Formation of pyrene dimer radical cation at the internal site of oligodeoxynucleotides. *J. Phys. Chem. B 108*, 13547–13550.
(17) Okamoto, A., Kanatani, K., and Saito, I. (2004) Pyrene-labeled base-discriminating fluorescent DNA probes for homogeneous SNP typing. *J. Am. Chem. Soc. 126*, 4820–4827.
(18) Hrdlicka, P. J., Babu, B. R., Sørensen, M. D., Harrit, N., and Wengel, J. (2005) Multilabeled pyrene-functionalized 2′-amino-LNA probes for nucleic acid detection in homogeneous fluorescence assays. *J. Am. Chem. Soc. 127*, 13293–13299.
(19) Nakamura, M., Fukunaga, Y., Sasa, K., Ohtoshi, Y., Kanaori, K., Hayashi, H., Nakano, H., and Yamana, K. (2005) Pyrene is highly emissive when attached to the RNA duplex but not to the DNA duplex: the structural basis of this difference. *Nucleic Acids Res. 33*, 5887–5895.
(20) Novopashina, D. S., Stetsenko, D. A., Totskaya, O. S., Repkova, M. N., and Venyaminova, A. G. (2005) 2′-Bis-pyrene modified oligonucleotides: sensitive fluorescent probes of nucleic acids structure. *Nucleosides Nucleotides Nucleic Acids 24*, 729–734.
(21) Yamana, K., Fukunaga, Y., Ohtani, Y., Sato, S., Nakamura, M., Kim, W. J., Akaike, T., and Maruyama, A. (2005) DNA mismatch detection using a pyrene-excimer-forming probe. *Chem. Commun.* 2509–2511.
(22) Hrdlicka, P. J., Kumar, T. S., and Wengel, J. (2005) Targeting of mixed sequence double-stranded DNA using pyrene-functionalized 2′-amino-α-L-LNA. *Chem. Commun.* 4279–4281.
(23) Dohno, C., and Saito, I. (2005) Discrimination of single nucleotide alterations by G-specific fluorescence quenching. *ChemBioChem 6*, 1075–1081.
(24) Honcharenko, D., Zhou, C., and Chattopadhyaya, J. (2008) Modulation of pyrene fluorescence in DNA probes depends upon the nature of the conformationally restricted nucleotide. *J. Org. Chem. 73*, 2829–2842.
(25) Didenko, V. V. (2006) Methods in Molecular Biology Vol. 335, *Fluorescent Energy Transfer Nucleic Acid Probes*, Humana Press, Totowa, NJ.
(26) Marras, S. A. E., Tyagi, S., and Kramer, F. R. (2006) Real-time assays with molecular beacons and other fluorescent nucleic acid hybridization probes. *Clin. Chim. Acta 363*, 48–60.
(27) French, D. J., Archard, C. L., Brown, T., and McDowell, D. G. (2001) HyBeacon™ probes: a new tool for DNA sequence detection and allele discrimination. *Mol. Cell. Probes 15*, 363–374.
(28) Crockett, A. O., and Wittwer, C. T. (2001) Fluorescein-labeled oligonucleotides for real-time PCR: using the inherent quenching of deoxyguanosine nucleotides. *Anal. Biochem. 290*, 89–97.
(29) Yamana, K., Zako, H., Asazuma, K., Iwase, R., Nakano, H., and Murakami, A. (2001) Fluorescence detection of specific RNA sequences using 2′-pyrene-modified oligoribonucleotides. *Angew. Chem., Int. Ed. Engl. 40*, 1104–1106.
(30) French, D. J., Archard, C. L., Andersen, M. T., and McDowell, D. G. (2002) Ultra-rapid DNA analysis using HyBeacon™ probes and direct PCR amplification from saliva. *Mol. Cell. Probes 16*, 319–326.
(31) Yamana, K., Iwai, T., Ohtani, Y., Sato, S., Nakamura, M., and Nakano, H. (2002) Bis-pyrene-labeled oligonucleotides: sequence specificity of excimer and monomer fluorescence changes upon hybridization with DNA. *Bioconjugate Chem. 13*, 1266–1273.
(32) Korshun, V. A., Stetsenko, D. A., and Gait, M. J. (2002) Novel uridin-2′-yl carbamates: synthesis, incorporation into oligodeoxyribonucleotides, and remarkable fluorescence properties of 2′-pyren-1-ylmethylcarbamate. *J. Chem. Soc., Perkin Trans. 1*, 1092–1104.
(33) Mahara, A., Iwase, R., Sakamoto, T., Yamana, K., Yamaoka, T., and Murakami, A. (2002) Bispyrene-conjugated 2′-*O*-methyloligonucleotide as a highly specific RNA-recognition probe. *Angew. Chem., Int. Ed. 41*, 3648–3650.
(34) Dobson, N., McDowell, D. G., French, D. J., Brown, L. J., Mellor, J. M., and Brown, T. (2003) Synthesis of HyBeacons and dual-labelled probes containing 2′-fluorescent groups for use in genetic analysis. *Chem. Commun.* 1234–1235.
(35) Vaughn, C. P., and Elenitoba-Johnson, K. S. J. (2003) Hybridization-induced dequenching of fluorescein-labeled oligonucleotides: a novel strategy for PCR detection and genotyping. *Am. J. Pathol. 163*, 29–35.
(36) Leijon, M., Mousavi-Jazi, M., and Kubista, M. (2006) LightUp probes in clinical diagnostics. *Mol. Asp. Med. 27*, 160–175.
(37) Singh, S. K., Nielsen, P., Koshkin, A. A., and Wengel, J. (1998) LNA (locked nucleic acids): synthesis and high-affinity nucleic acid recognition. *Chem. Commun.* 455–456.
(38) Obika, S., Nanbu, D., Hari, Y., Andoh, J., Morio, K., Doi, T., and Imanishi, T. (1998) Stability and structural features of the duplexes containing nucleoside analogues with a fixed N-type conformation, 2′-O,4′-*C*-methyleneribonucleosides. *Tetrahedron Lett. 39*, 5401–5404.
(39) Koshkin, A. A., Singh, S. K., Nielsen, P., Rajwanshi, V. K., Kumar, R., Meldgaard, M., Olsen, C. E., and Wengel, J. (1998) LNA (Locked Nucleic Acids): Synthesis of the adenine, cytosine, guanine, 5-methylcytosine, thymine and uracil bicyclonucleoside monomers, oligomerisation, and unprecedented nucleic acid recognition. *Tetrahedron 54*, 3607–3630.
(40) Koshkin, A. A., Nielsen, P., Meldgaard, M., Rajwanshi, V. K., Singh, S. K., and Wengel, J. (1998) LNA (Locked Nucleic Acid): An RNA mimic forming exceedingly stable LNA:LNA duplexes. *J. Am. Chem. Soc. 120*, 13252–13253.
(41) Wengel, J. (1999) Synthesis of 3′-*C*- and 4′-*C*-branched oligodeoxynucleotides and the development of Locked Nucleic Acid (LNA). *Acc. Chem. Res. 32*, 301–310.
(42) Bondensgaard, K., Petersen, M., Singh, S. K., Rajwanshi, V. K., Kumar, R., Wengel, J., and Jacobsen, J. P. (2000) Structural studies of LNA:RNA duplexes by NMR: conformations and implications for RNase H activity. *Chem.—Eur. J. 6*, 2687–2695.
(43) Singh, S. K., Kumar, R., and Wengel, J. (1998) Synthesis of 2′-amino-LNA: A novel conformationally restricted high-affinity oligonucleotide analogue with a handle. *J. Org. Chem. 63*, 10035–10039.
(44) Babu, B. R., Hrdlicka, P. J., McKenzie, C. J., and Wengel, J. (2005) Optimized DNA targeting using *N*,N-bis(2-pyridylmethyl)-*β*-alanyl-2′-amino-LNA. *Chem. Commun.* 1705–1707.
(45) Højland, T., Kumar, S., Babu, B. R., Umemoto, T., Albæk, N., Sharma, P. K., Nielsen, P., and Wengel, J. (2007) LNA (locked nucleic acid) and analogs as triplex-forming oligonucleotides. *Org. Biomol. Chem. 5*, 2375–2379.
(46) Sørensen, M. D., Kværnø, L., Bryld, T., Hakansson, A. E., Verbeure, B., Gaubert, G., Herdewijn, P., and Wengel, J. (2002) α-L-ribo-configured Locked Nucleic Acid (r-L-LNA): Synthesis and properties. *J. Am. Chem. Soc. 124*, 2164–2176.
(47) Petersen, M., and Wengel, J. (2003) LNA: a versatile tool for therapeutics and genomics. *Trends Biotechnol. 21*, 74–81.
(48) Elmén, J., Lindow, M., Schütz, S., Lawrence, M., Petri, A., Obad, S., Lindholm, M., Hedtjärn, M., Hansen, H. F., Berger, U., Gullans, S., Kearney, P., Sarnow, P., Straarup, E. M., and Kauppinen, S. (2008) LNA-mediated microRNA silencing in non-human primates. *Nature 452*, 896–899.
(49) Sørensen, M. D., Petersen, M., and Wengel, J. (2003) Functionalized LNA (locked nucleic acid): high-affinity hybridization of oligonucleotides containing N-acylated and N-alkylated 2′-amino-LNA monomers. *Chem. Commun.* 2130–2131.

(50) Kumar, T. S., Wengel, J., and Hrdlicka, P. J. (2007) 2′-N-(Pyren-1-yl)acetyl-2′-Amino-α-L-LNA: Synthesis and detection of single nucleotide mismatches in DNA and RNA targets. *ChemBioChem 8*, 1122–1125.

(51) Lindegaard, D., Madsen, A. S., Astakhova, I. V., Malakhov, A. D., Babu, B. R., Korshun, V. A., and Wengel, J. (2008) Pyrene-perylene as a FRET pair coupled to the N2′-functionality of 2′-amino-LNA. *Bioorg. Med. Chem. 16*, 94–99.

(52) Astakhova, I. V., Korshun, V. A., Jahn, K., Kjems, J., and Wengel, J. (2008) Perylene attached to 2′-amino-LNA: synthesis, incorporation into oligonucleotides, and remarkable fluorescence properties *in vitro* and in cell culture. *Bioconjugate Chem. 19*, 1995–2007.

(53) Astakhova, I. V., Korshun, V. A., and Wengel, J. (2008) Highly fluorescent conjugated pyrenes in nucleic acid probes: (phenylethynyl)pyrenecarbonyl-functionalized Locked Nucleic Acids. *Chem.—Eur. J. 14*, 11010–11026.

(54) Nijegorodov, N., Mabbs, R., and Downey, W. S. (2001) Evolution of absorption, fluorescence, laser and chemical properties in the series of compounds perylene, benzo(ghi) perylene and coronene. *Spectrochim. Acta, Part A 57*, 2673–2685.

(55) Davenport, L., Shen, B., Joseph, T. W., and Straher, M. P. (2001) A novel fluorescent coronenyl-phospholipid analogue for investigations of submicrosecond lipid fluctuations. *Chem. Phys. Lipids 109*, 145–156.

(56) Nagata, C., Kodama, M., Tagashira, Y., and Imamura, A. (1966) Interaction of polynuclear aromatic hydrocarbons, 4-nitroquinoline 1-oxides, and various dyes with DNA. *Biopolymers 4*, 409–427.

(57) Zinger, D., and Geacintov, N. E. (1988) Acrylamide and molecular oxygen fluorescence queching as a probe of solvent-accessibility of aromatic fluorophores complexed with DNA in relation to their cofnormations:coronene-DNA and other complexes. *Photochem. Photobiol. 47*, 181–188.

(58) Rosenbohm, C., Christensen, S. M., Sørensen, M. D., Pedersen, D. S., Larsen, L.-E., Wengel, J., and Koch, T. (2003) Synthesis of 2′-amino-LNA: a new strategy. *Org. Biomol. Chem. 1*, 655–663.

(59) Woods, K. K., Maehigashi, T., Howerton, S. B., Sines, S. B., Sines, C. C., Tannenbaum, S., and Williams, L. D. (2004) High-resolution structure of an extended A-tract: $[d(CGCAAATTTGCG)]_2$. *J. Am. Chem. Soc. 126*, 15330–15331.

(60) Seko, T., Ogura, K., Kawakami, Y Y., Sugino, H., Toyotama, H., and Tanaka, J. (1998) Excimer emission of anthracene, perylene, coronene and pyrene microcrystals dispersed in water. *Chem. Phys. Lett. 291*, 438–444.

(61) Weiner, S. J., Kollman, P. A., Case, D. A., Singh, U. C., Ghio, C., Alagona, G., Profeta, S., and Weiner, P. (1984) A new force field for molecular mechanical simulation of nucleic acids and proteins. *J. Am. Chem. Soc. 106*, 765–784.

(62) Weiner, S. J., Kollman, P. A., Nguyen, D. T., and Case, D. A. (1986) An all atom force field for simulations of proteins and nucleic acids. *J. Comput. Chem. 7*, 230–252.

(63) *MacroModel v 8.5*, Schrödinger, LLC, New York, 2007.

BC900421R

Synthesis of Biotinylated α-D-Mannoside or *N*-Acetyl *β*-D-Glucosaminoside Decorated Gold Nanoparticles: Study of Their Biomolecular Recognition with Con A and WGA Lectins

Xiaoze Jiang,[†,‡] Abdelghani Housni,[†,‡] Guillaume Gody,[§,||] Paul Boullanger,[||] Marie-Thérèse Charreyre,*[,§,⊥] Thierry Delair,[§] and Ravin Narain*[,†,‡]

Department of Chemical and Materials Engineering, University of Alberta, ECERF, Edmonton, Alberta T6G2G6, Canada, Department of Chemistry and Biochemistry, Laurentian University, 935, Ramsey Lake Road, P3E 2C6, ON, Canada, Unité Mixte CNRS-bioMérieux, Ecole Normale Supérieure de Lyon, IFR 128, 46 allée d'Italie, 69364 Lyon Cedex 07, France, and Laboratoire de Chimie Organique II, UMR 5622 CNRS/UCBL, 69616 Villeurbanne Cedex, France. Received September 30, 2009; Revised Manuscript Received January 6, 2010

Gold nanoparticles (NPs) functionalized with a mixed shell of well-defined biotinylated glycopolymers and polyethylene glycol (PEG) provide an effective platform for the biomolecular recognition of proteins both in solution and on surfaces. Well-defined biotinylated glycopolymers were first synthesized by the reversible addition−fragmentation chain transfer (RAFT) process. They contain two types of carbohydrate residues either *N*-acetyl *β*-D-glucosaminopyranoside (**GlcNAc**) or α-D-mannopyranoside (**Man**) as pendent groups. The biotinylated glycopolymers and polyethylene glycol were subsequently used in the *in situ* formation of gold glyconanoparticles via an easy photochemical process. The obtained biotinylated glyconanoparticles were characterized by dynamic light scattering (DLS) and transmission electron microscopy (TEM). The bioavailability of the biotin and specific carbohydrate residues at the periphery of the NPs were assessed using the diffraction optic technology (DOT) system. The studies showed the accessibility of the biotin ligands for conjugation to immobilized avidin on the DOTLab biosensor. Furthermore, these avidin conjugated glyconanoparticles were found to selectively immobilize lectins. The specificity of lectin binding was dependent on the type of carbohydrate residues. As such, *N*-acetyl *β*-D-glucosaminoside decorated gold nanoparticles were found to specifically interact with wheat germ agglutinin (WGA) lectin, whereas α-D-mannoside ones were found to specifically interact with Concanavalin A (Con A) lectin.

INTRODUCTION

Gold nanoparticles are receiving enormous attention as they are very promising for biomolecular applications such as labeling, detection, and transfer of genetic materials (*1*).To improve the water stability of synthesized gold cores, different methods were used to prepare water-dispersible and size-tunable gold nanoparticles via the reduction of gold salts in the presence of appropriate stabilizing agents that prevent particle aggregation (*2–6*). Among the preparation methods of gold nanoparticles, the gold salts, chloroaurate ($AuCl_4^-$), were usually reduced with a reducing agent such as sodium tetrahydroborate ($NaBH_4$) in the presence of the desired capping ligands.

Recently, a new photochemical method, reported by Scaiano et al. (*7*), was used to prepare unprotected water-soluble gold nanoparticles via the reduction of $HAuCl_4$ by photochemical decomposition of Irgacure-2959, a water-soluble benzoin, under mild conditions in one step. The preparation process of gold nanoparticles is fast from seconds to minutes, and their sizes could be easily controlled by the intensity of illumination (UV). Following this principle, ligand functionalized water-soluble gold nanoparticles such as biotinylated glyconanoparticles (*8*) and BSA protein-stabilized gold nanoparticles (*9*) have been prepared by our groups via a photochemical process. This method would be a versatile approach for the preparation of surface-coated gold nanoparticles with RAFT prepared polymers.

Focusing on their actual applications in biomedicine and biotechnology, we believe that it is important to consider the surface chemistry for the long-term stability of gold nanoparticles and their biocompatibility. It has been reported that a variety of biocompatible molecules such as proteins (*10, 11*), polyethylene glycol (PEG) (*12*), DNA (*13, 14*), and carbohydrate moieties (*8, 15*) have been utilized to stabilize gold nanoparticles. Following the development of living radical polymerization, various water-soluble polymers with versatile composition and functionality prepared by RAFT polymerization (*16*) were exploited to modify the surface of gold nanoparticles as stabilizers via thiol chemistry after the reduction of the thiocarbonylthio chain-end.

The incorporation of these water-soluble polymers into the shell of gold nanoparticles not only provides a protective shield to prevent their aggregation but also introduces new functions at their periphery. Another important aspect of the surface immobilized polymers bearing reactive functional groups is to provide an opportunity for further surface functionalization. It has been shown that the polymers can tailor the properties of nanoparticles and that the gold cores can also modify the physical properties of polymers (*17–21*).

* To whom correspondence should be addressed. (M.-T.C.) Phone: (+33) (0)4 72728938. Fax: (+33) (0)4 72728787. E-mail: marie-therese.charreyre@ens-lyon.fr. (R.N.) Phone: (780) 492-1736or (705) 675-1151ext. 2186. Fax: (780) 492 1736 or (705) 675-4844. E-mail: narain@ualberta.ca or rnarain@laurentian.ca.

† University of Alberta.

‡ Laurentian University.

§ Unité Mixte CNRS-bioMérieux.

|| UMR 5622 CNRS/UCBL.

⊥ Current address: Laboratoire Joliot-Curie et Laboratoire Ingenierie des Materiaux Polymeres, Ecole Normale Supérieure de Lyon, IFR128, 46 Allee d'Italie 69364 Lyon Cedex 07, France.

10.1021/bc900431p © 2010 American Chemical Society
Published on Web 02/03/2010

Carbohydrate modified gold nanoparticles have recently attracted much attention since lectin−carbohydrate interactions play crucial roles in a variety of biological processes, including fertilization, cell migration, cancer, and host−pathogen interactions (*22, 23*). Using the gold nanoparticles as a carrier, the outer carbohydrate moieties located on the surface as many antennae increase the ability of carbohydrate−protein interaction as a result of the cluster glycoside effect (*24, 25*). Russell et al. reported the study of gold nanoparticles stabilized with a self-assembled monolayer of a mannose derivative, 2-mercaptoethyl α-D-mannopyranoside, and exploited the α-D-mannoside decorated nanoparticles to examine the binding specificity of the well-known lectin, Concanavalin A (Con A), using UV−visible spectrophotometry (*15*). Lactose-conjugated gold nanoparticles reported by Kataoka et al. (*26*) were prepared from PEG-stabilized gold nanoparticles bearing acetal groups on the outer shell, by reaction with *p*-aminophenyl-*a*-lactosyl. These *a*-lactosyl decorated nanoparticles exhibit specific recognition of *Recinus communis* agglutinin (RCA_{120}) and could be applied in bioassays and biorecognition. Although these nanoparticles were successfully used to study the carbohydrate−lectin interactions, this study was limited to only one kind of lectins and one type of carbohydrate.

In order to investigate the lectin−carbohydrate interaction mechanism, many systems bearing different carbohydrate (or lectin) moieties were developed to study the specific interaction with different lectins (or carbohydrates) by different approaches such as the surface plasmon resonance (SPR), quartz crystal microbalance (QCM), isothermal titration calorimetry (ITC), fluorescence techniques, atomic force microscopy (AFM), and electrochemical impedance spectroscopy (EIS) (*25, 27–32*). Although existing approaches have been partially successful, these reported methods usually require extensive instrumental setup and synthetic complication for the fixation of the targeted group (carbohydrate or lectin) onto the surface of the sensor, which obviously limited the investigation of their interactions. Accordingly, a sensitive, rapid, simple, reliable, and cost-effective method should be found to study these interactions.

Herein, we describe the synthesis of well-defined biotinylated glycopolymers via the RAFT polymerization process. The obtained glycopolymers containing two types of carbohydrate residues, either *N*-acetyl β-D-glucosaminoside (**GlcNAc**) or α-D-mannoside (**Man**) as pendent groups, were subsequently used with PEG for the *in situ* formation of glyconanoparticles via a photochemical process. Combining the photochemical method and RAFT process, different surface-functionalized gold nanoparticles were prepared with or without the biotin and/or the carbohydrate moieties. The obtained nanoparticles were characterized by dynamic light scattering (DLS) and transmission electron microscopy (TEM). To access the availability of the biotin and specific carbohydrate residues located on the nanoparticle surface, a simple instrument, diffraction optics technology (DOT) system, was used to probe the attachment of biotinylated nanoparticles on the surface of the avidin sensor chip, which further provided the possibility of studying specific lectin−carbohydrate interactions between the carbohydrates (GlcNAc or Man) and the lectins (WGA or Con A).

EXPERIMENTAL SECTION

Materials. *N*-Acryloylmorpholine (NAM) (Aldrich, 97%) was distilled under reduced pressure (120 °C, 10 mmHg). 2,2′-Azobis(isobutyronitrile) (AIBN) (Fluka, 98%) was purified by recrystallization from ethanol. 1,4-Dioxane (Acros, 99%) was distilled over $LiAlH_4$ (110 °C). Trioxane (Acros, 99%), EZ-Link Biotin PEO-Amine ((+)-biotinyl-3, 6-dioxaoctanediamine, Pierce), and other materials were used without further purification. Syntheses of *tert*-butyl dithiobenzoate (*t*BDB) (*21*) and *N*-[8-((+)-biotinamido)-3,6-dixoaoctyl]-2-[[2-phenyl-1-thioxoethyl]thio]-propanamide (BEDBA) (*33*) have been described previously. Syntheses of the mannose derivative, 8-acrylamido-3,6-dioxaoctyl 2,3,4,6-tetra-*O*-acetyl-α-D-mannopyranoside (ManAm), and of the *N*-acetyl-glucosamine derivative, 8-acrylamido-3,6-dioxaoctyl 2-acetamido-3,4,6-tri-*O*-acetyl-2-deoxy-β-D-glucopyranoside (GlcNAcAm), have been described elsewhere (*34*). Synthesis of the biotinylated PNAM homopolymers has been described previously (*33*). Biotin-CTA, *N*-[8-((+)-biotinamido)-3,6-dioxaoctyl]-2-[[2-phenyl-1-thioxo]thio]-4-cyanopentanoate (BCBDBA), was synthesized from succinimido-4-[[2-phenyl-1-thioxo]thio]-4-cyanopentanoate and (+)-biotinyl-3,6-dioxaoctanediamine as shown in Figure S1 in Supporting Information. The photoinitiator, Irgacure-2959, was given by CIBA Specialty Chemicals.

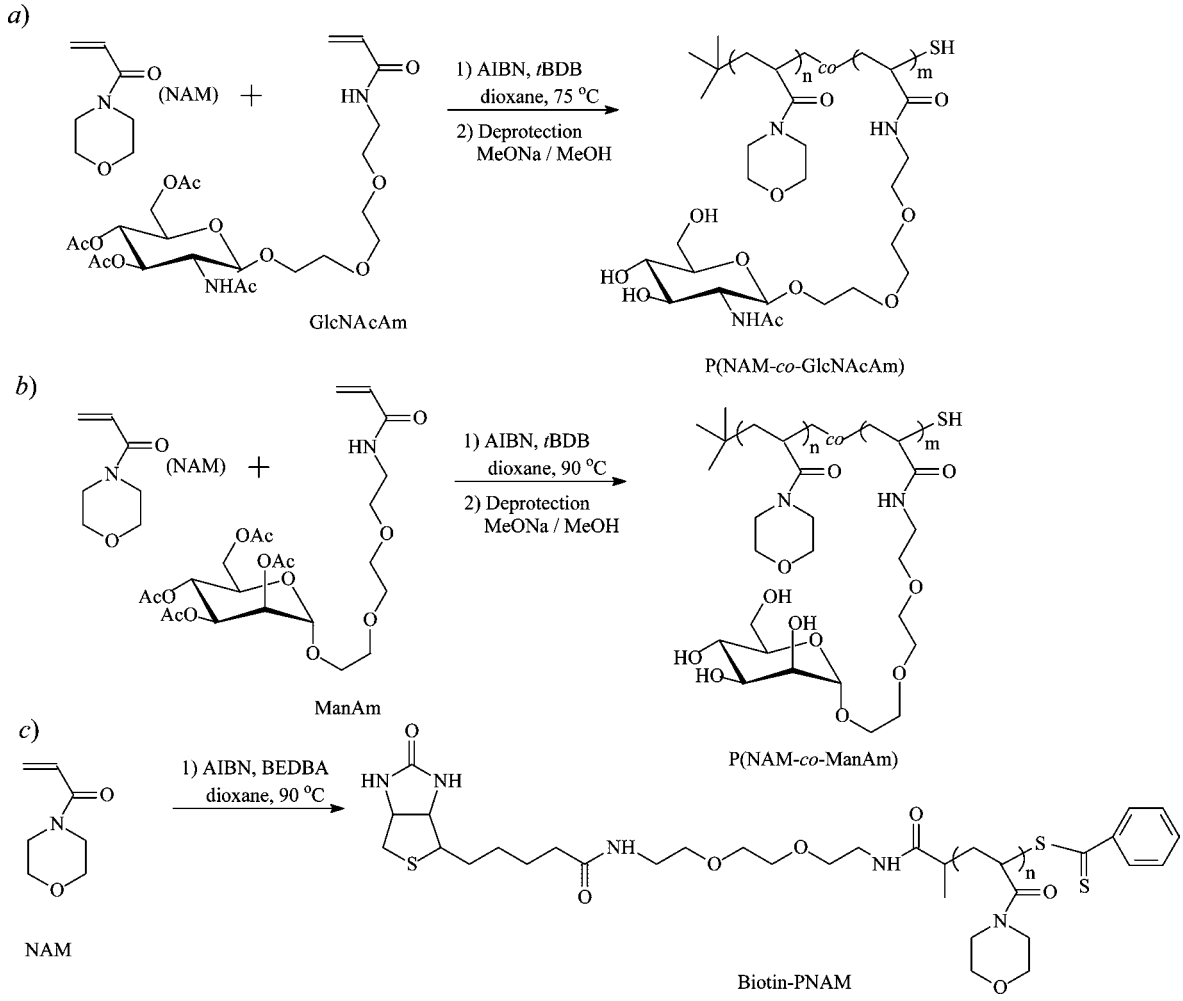
RAFT Polymerization of the Mannose and *N*-Acetylglucosamine Derivatives (ManAm and GlcNAcAm) with Biotin-CTA. RAFT copolymerization of ManAm or GlcNAcAm with *N*-acryloylmorpholine in the presence of biotin-CTA (BCBDBA) has been performed (shown in Schemes 1 and 2) using a procedure similar to that recently reported for a Galactose derivative (*35*) except that the reaction was performed directly inside the NMR spectrometer.

Typical runs for ManAm and for GlcNAcAm are described below. NAM (91 mg, 0.65 mmol), ManAm (85 mg, 0.16 mmol), biotin-CTA (BCBDBA, 7.3 mg, 0.011 mmol), AIBN (0.31 mg, 1.9×10^{-3} mmol), 1,4-d_8-dioxane (423 μL), and trioxane (2.3 mg, internal reference for ^{1}H NMR determination of monomer consumption) (*36*) were introduced in a NMR tube fitted with a Young's valve. The mixture was degassed by five freeze−evacuate−thaw cycles. A first NMR acquisition was carried out at 27 °C. Then, the tube was removed, and the temperature was set at 75 °C. The tube was then reintroduced (time t_0), and acquisitions were regularly performed. The progress of the reaction was monitored by the disappearance of the vinyl proton signals, by comparison of the vinyl protons of NAM (5.7 ppm) and of ManAm (5.6 ppm) with trioxane (5.08 ppm).

NAM (108 mg, 0.765 mmol), GlcNAcAm (102 mg, 0.192 mmol), biotin-CTA (BCBDBA, 1.74 mg, 2.74×10^{-3} mmol), AIBN (0.045 mg, 2.74×10^{-4} mmol), and 1,4-d_8-dioxane (504 μL) were introduced in a NMR tube fitted with a Young's valve. The mixture was degassed by five freeze−evacuate−thaw cycles. A first NMR acquisition was carried out at 27 °C. Then, the tube was removed, and the temperature was set at 90 °C. The tube was then reintroduced (time t_0), and acquisitions were regularly performed. The progress of the reaction was monitored by the disappearance of the vinyl proton signals, by comparison of the vinyl protons of NAM and of GlcNAcAm with nonvinyl protons of GlcNAcAm (3H: H_1, H_3, H_4, 4.76−5.35 ppm) used as the internal reference. Similar experimental conditions were used with *t*BDB instead of biotin-CTA (BCBDBA). Polymer samples were precipitated in a large volume of diethyl ether, recovered by centrifugation, and finally dried under vacuum before SEC analysis.

Deprotection of the Glycopolymer Samples. Typically, for polymer sample biotin-P(NAM-*co*-ManAm), (47 mg, 4.7×10^{-6} mol) was dissolved in a CH_2Cl_2/methanol (1/2 v/v) anhydrous mixture (1.5 mL). A catalytic amount of sodium methylate (sodium methoxide, 25% (w/w) solution in methanol, 0.04 equiv) was added. The mixture was left under stirring at room temperature for 24 h. After evaporation, water was added, and the samples were mixed with some Amberlite IR120PLUS resin (Aldrich), filtrated, neutralized with sodium hydrogenocarbonate ($NaHCO_3$) solution, and purified by dialysis using Slide-A-Lyzer Dialysis Cassettes (Pierce) with a 3,500 molecular weight cutoff (MWCO) for samples with expected molecular weights lower

Scheme 1. Synthetic Route to the Preparation of P(NAM-*co*-GlcNAcAm) and P(NAM-*co*-ManAm) Glycopolymers, and Biotin-PNAM Homopolymer



than 10,000 g·mol^{-1} and a 10,000 MWCO for all other polymers as shown in Table 1.

Formation of Gold Glyconanoparticles (AuNPs). The following protocol is carried out for the synthesis of gold glyconanoparticles, and detailed results are shown in Table 2. Polyethylene glycol having terminal thiol groups (PEG-SH) and the (non) biotinylated glycopolymer were mixed together in an aqueous solution containing $HAuCl_4$ and Irgacure-2959 at a fixed molar ratio of $HAuCl_4 \cdot 3H_2O$, Irgacure-2959, PEG-SH, and glycopolymer of 1:3:0.8:0.2, respectively. This mixture was stirred at room temperature for 10 min. The clear solution was then irradiated for 5 min in a Rayonet photoreactor (Southern N.E. Ultraviolet Co.) using 16 75W UV lamps having a 350 nm wavelength. The color of the final solution changes to purple or pink, indicating the formation of gold nanoparticles. These gold nanoparticle solutions showed very good colloidal stability over several weeks.

Characterization. *NMR.* ^{1}H NMR spectra were recorded on a 200 MHz Bruker AC 200 spectrometer or on a 500 MHz Varian Unity Plus 500 spectrometer, at 25 °C in *d*-chloroform ($CDCl_3$).

Glycopolymer SEC Analysis. Molecular weight distributions of the protected glycopolymers were determined by SEC in THF (SDS, 99%), using a Waters column (Styragel HR4E). The flow rate was maintained at 1 mL·min^{-1} using a Waters 1515 isocratic HPLC pump. Analyses were performed by injection of 20 μL of polymer solution (10 mg·mL^{-1}) in THF. Detection was performed using a Waters 2410 differential refractometer. The molecular weight and polydispersity data were determined using the Waters Breeze software package, according to a PNAM calibration.

Nanoparticle Size Analysis. A model 802 Viscotek DLS instrument operating at a laser wavelength of 825−832 nm was used for particle size measurements in highly dilute aqueous gold dispersions. TEM analyses were also performed to determine the sizes of gold nanoparticles on a Hitachi 800 transmission electron microscope at an acceleration voltage of 200 kV. The samples for TEM were prepared by placing a drop of the nanoparticle solution on carbon coated copper grids.

Diffractive Optics Technology (DOT) Measurements. DotLab data were measured on a Diffractive Optics Technology (DOT) system from Axela Biosensors Inc.; the sensor chip was composed of polystyrene as the substrate and avidin groups have been attached on the surface. PBS buffer was used as the eluent. The nanoparticle samples were loaded into the sensor according to the designed program, the binding events were taking place on the surface of the sensor chip by avidin−biotin interactions, and the height of the diffractive pattern was increased (Scheme 3). The increase in signals was detected synchronously using a laser-based optical system, and the real-time data generated are presented in dotLab software.

RESULTS AND DISCUSSION

Syntheses of Homopolymer and Statistical Copolymers Using RAFT Polymerization. *N*-Acryloylmorpholine (NAM), an acrylamide derivative, has received enormous attention for

Scheme 2. Synthetic Route to the Preparation of Biotinylated Thiol-Terminated Glycopolymers, Biotin-P(NAM-*co*-GlcNAcAm) and Biotin-P(NAM-*co*-ManAm)

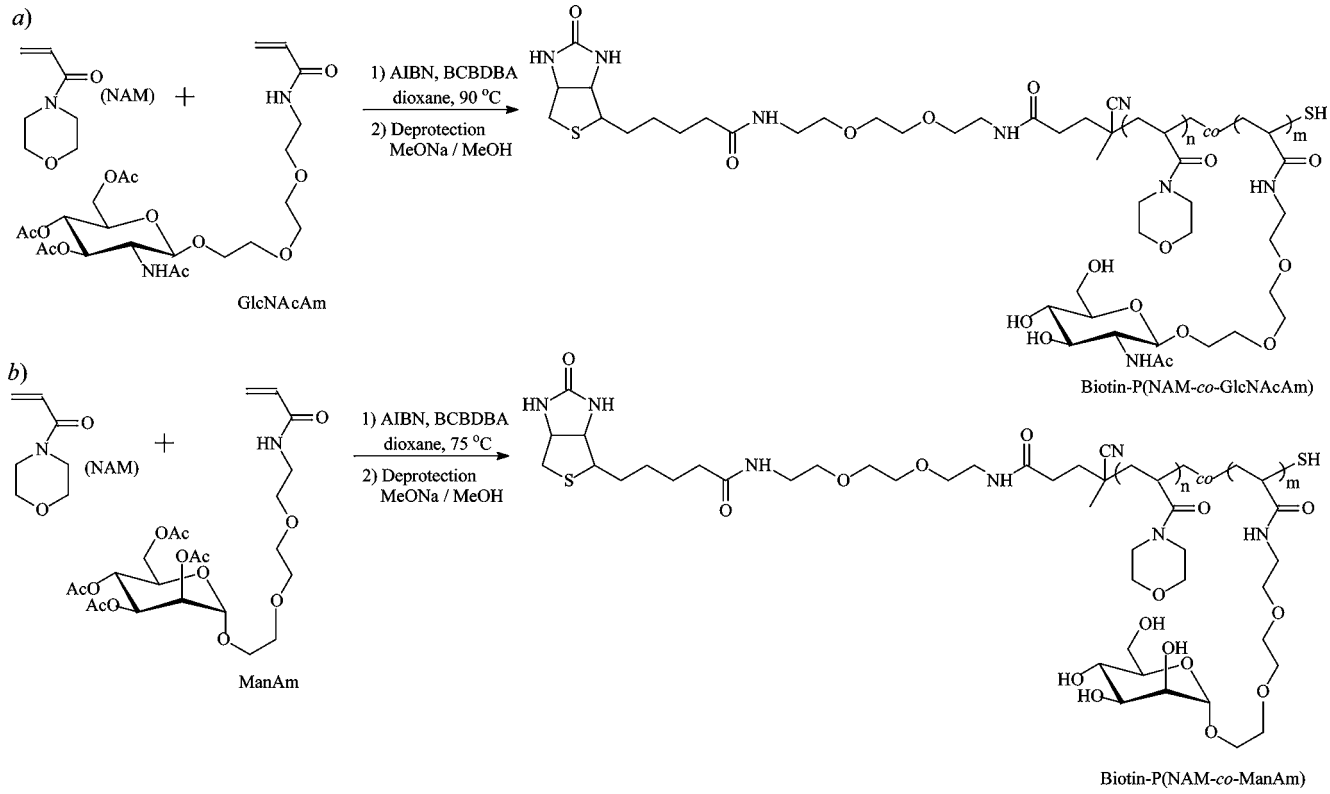


Table 1. Summary of Molecular Parameters of Synthesized Biotinylated and Nonbiotinylated Polymers

sample name	global conv. (%)	$M_{n\ calc.}$ (g·mol^{-1})	$M_{n\ calc.}$ (g·mol^{-1})	$M_{n\ exp.}$ (g·mol^{-1})	M_w/M_n (PDI)	NAM (DP)	sugar (DP)	dead chains[g]	biotin labeled[g]
biotin-PNAM$_{21}$	69	3,400[a]	/	3,500[d]	1.08[d]	21	0	9%	91%
biotin-PNAM$_{287}$	74	37,700[a]	/	41,200[e]	1.06[e]	287	0	9%	91%
P(NAM$_{234}$-*co*-GlcNAcAm$_{52}$)	93	61,200[b]	54,600[c]	62,300[f]	1.46[f]	234	52	12%	/
P(NAM$_{40}$-*co*-ManAm$_4$)	83	8,000[b]	7,300[c]	9,700[f]	1.14[f]	40	4	8%	/
biotin-P(NAM$_{225}$-*co*-GlcNAcAm$_{51}$)	85	59,300[b]	52,900[c]	53,700[f]	1.60[f]	225	51	7%	93%
biotin-P(NAM$_{40}$-*co*-ManAm$_7$)	73	10,100[b]	8,900[c]	12,700[f]	1.20[f]	40	7	6%	94%

[a] Calculated M_n (PNAM): $M_n = ([NAM]_0 \times M_{NAM} \times C_{NAM}/[CTA]_0) + M_{CTA}$. [b] Calculated M_n (protected form of the sugar): $M_n = (([NAM]_0 \times M_{NAM} \times C_{NAM} + [sugar]_0 \times M_{sugar\ protected} \times C_{sugar})/[CTA]_0) + M_{CTA}$. [c] Calculated M_n (deprotected form of the sugar): $M_n = (([NAM]_0 \times M_{NAM} \times C_{NAM} + [sugar]_0 \times M_{sugar\ deprotected} \times C_{sugar})/[CTA]_0) + M_{CTA}$. [d] Experimental M_n and PDI, determined by MALDI-TOF MS. [e] Experimental M_n and PDI, determined by SEC/RI/LS in aqueous phase (borate buffer). [f] Experimental M_n (protected form of the sugar) and PDI, determined by SEC/THF with a PNAM calibration. [g] Calculated value.

Table 2. DLS Results for the Synthesized Biotinylated and Nonbiotinylated Gold Nanoparticles via a Photochemical Process, Where the Molar Ratios of $HAuCl_4 \cdot 3H_2O$, Irgacure-2959, PEG-SH, and Synthetic Polymers Were Fixed at 1:3:0.8:0.2, Respectively

ref (AuNPs)	AuNPs prepared from relative polymers	DLS mass distribution		
		$\langle R_h \rangle$/nm	% area	% RSD
611ab	biotin-PNAM$_{21}$	6.2	99.4	8.8
612ab	biotin-PNAM$_{287}$	5.1	100	16.6
613ab	P(NAM$_{234}$-*co*-GlcNAcAm$_{52}$)	5.6	100	13.0
614ab	P(NAM$_{40}$-*co*-ManAm$_4$)	4.0	100	43.0
615ab	biotin-P(NAM$_{225}$-*co*-GlcNAcAm$_{51}$)	6.7	99.3	17.3
616ab	biotin-P(NAM$_{40}$-*co*-ManAm$_7$)	5.2	100	25.4

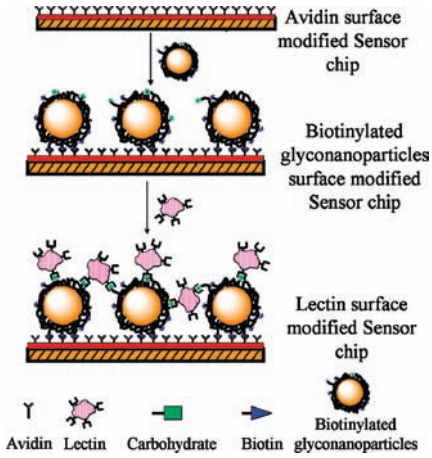
its special outstanding features such as the good solubility of PNAM in a wide range of solvents and its virtual lack of toxicity. The synthesized polymers were also used for various biological applications (*37–39*).

With the development of living radical polymerization, reversible addition−fragmentation chain transfer (RAFT) polymerization has proved to be a robust technique for the polymerization of the NAM monomer (*21, 33–35*). Among the studied dithiobenzoates reported by Favier et al. (*21*), *tert*-butyl dithiobenzoate (*t*BDB) has been shown to be a very efficient RAFT agent for NAM polymerization. Well-defined PNAM homopolymers with controlled dimension could be obtained in the presence of *t*BDB using AIBN as the initiator in 1,4-dioxane.

In order to study the specific carbohydrate−lectin interactions, two monomers containing carbohydrate moieties, a mannose derivative, the 8-acrylamido-3,6-dioxaoctyl 2,3,4,6-tetra-*O*-acetyl-α-D-mannopyranoside (ManAm), and a *N*-Acetyl-glucosamine derivative, the 8-acrylamido-3,6-dioxaoctyl 2-acetamido-3,4,6-tri-*O*-acetyl-2-deoxy-β-D-glucopyranoside (GlcNAcAm), were synthesized and copolymerized with NAM to get the targeted P(NAM-*co*-ManAm) and P(NAM-*co*-GlcNAcAm) copolymers. The conversions of monomers were high (above 80%), and well-controlled polymer chains were obtained as shown in Scheme 1 and Table 1. Their polymerization degrees were calculated to be P(NAM$_{40}$-*co*-ManAm$_4$) and P(NAM$_{234}$-*co*-GlcNAcAm$_{52}$) from the ^{1}H NMR and SEC results.

The RAFT technique is a versatile polymerization process that can be applied to the polymerization of many different monomers both in aqueous and organic solvents. Moreover, it is rather easy to introduce a ligand at the α-chain-end using an appropriate functional RAFT agent. A small biomolecule, biotin, was chosen to be introduced at the terminus of the RAFT agent.

Scheme 3. Schematic Illustration of Surface Bimolecular Recognitions of Biotinylated Surface-Functionalized Gold Glyco-Nanoparticles Interacting with Avidin and Lectin in Sequence on the dotLab Sensor Surface



Using this kind of method, the terminal α-end of each polymer chain contains, in theory, one biotin group. On the basis of this principle, two biotin CTAs, *N*-[8-((+)-biotinamido)-3,6-dioxaoctyl]-2-[[2-phenyl-1-thioxoethyl] thiopropanamide (BEDBA) and *N*-[8-((+)-biotinamido)-3,6-dioxaoctyl]-2-[[2-phenyl-1-thioxo]thio]-4-cyano-pentanoate (BCBDBA), possessing stable bonds between the biotin and the dithioester moieties (amide and ether bonds) were synthesized to perform the homopolymerization of the NAM monomer and statistical copolymerization of NAM with ManAm or GlcNAcAm, respectively.

The synthesis of BEDBA has already been reported in the literature (*33*). BCBDBA, a new biotinylated RAFT agent, was synthesized using an approach similar to that for BEDBA (detailed synthesis and characterization are shown in Supporting Information). After activation of the carboxyl groups using *N*-hydroxysuccinimide (NHS) to form a succinimide-terminated RAFT agent, the biotin moiety (EZ-Link Biotin PEO-Amine) was introduced. These biotin-CTAs proved to be very efficient for the synthesis of the homopolymers of NAM and for the copolymerization of NAM with a protected galactose derivative (*33, 35*). The biotin-PNAM, biotin-P(NAM-*co*-ManAm), and biotin-P(NAM-*co*-GlcNAcAm) copolymers bearing the biotin moiety were synthesized as shown in Scheme 2, and detailed information is collected and presented in Table 1 and Figure 1. After polymerization for 30 min to 2 h, the targeted statistical glycopolymers in protected form were obtained. The global monomer conversion is about 85% and 73% for biotin-P(NAM-*co*-GlcNAcAm) and biotin-P(NAM-*co*-ManAm) copolymers, respectively. From the conversion values, the calculation of the DP was determined and gave biotin-P(NAM_{40}-*co*-$ManAm_7$) and biotin-P(NAM_{225}-*co*-$GlcNAcAm_{51}$). SEC traces show a monomodal peak with a low polydispersity index for biotin-P(NAM_{40}-*co*-$ManAm_7$) and a monomodal peak with a little broad polydispersity index for biotin-P(NAM_{225}-*co*-$GlcNAcAm_{51}$) as shown in Figure 1c. The experimental M_n and M_w/M_n values of biotin-P(NAM_{40}-*co*-$ManAm_7$) and biotin-P(NAM_{225}-*co*-$GlcNAcAm_{51}$) were determined as 12,700 $g \cdot mol^{-1}$ and 1.20 and 53,700 $g \cdot mol^{-1}$ and 1.60, respectively, which is consistent with the theoretical molecular weight calculated from the conversion values using ^1H NMR monitoring of the copolymerization. The end-label biotin functionalization was also calculated to be above 90%, which means that almost each polymer chain has a biotin group at the α terminus.

Using *t*BDB and biotin-CTAs as the RAFT agents, six different kinds of polymer chains were obtained via the RAFT process, and then six telechelic water-soluble glycopolymers (bearing a thiol group at the chain-end), named as biotin-$PNAM_{21}$, biotin-$PNAM_{287}$, P(NAM_{234}-*co*-$GlcNAcAm_{52}$), P(NAM_{40}-*co*-$ManAm_4$), biotin-P(NAM_{225}-*co*-$GlcNAcAm_{51}$), and biotin-P(NAM_{40}-*co*-$ManAm_7$), were generated after deprotection of the sugar rings by the addition of sodium methylate in methanol. The ^1H NMR spectra before and after deprotection are shown in Figure S2 in Supporting Information. It should be noted that two special samples, the biotin-P(NAM_{225}-*co*-$GlcNAcAm_{51}$) and biotin-P(NAM_{40}-*co*-$ManAm_7$), are our focused products because they possess both biotin groups and carbohydrate moieties and could be used to investigate biomolecular recognition, especially for the specific (or nonspecific) binding of different lectins. The other samples are used as control samples to evaluate nonspecific binding.

Fabrication of Gold Glyconanoparticles via a Photochemical Process. Gold nanoparticles have received enormous attention because of their unique optical and electronic properties (*1*). To improve their biocompatibility and colloidal stability, the gold nanoparticles were usually surface modified by thiol terminated water-soluble polymers such as PEG chains. Recently, biocompatible gold glyconanoparticles have become the focus of intense interest in biology because surface-functionalized nanoparticles containing bioactive groups such as biotin and carbohydrates could be used as model systems to investigate the biological recognition phenomena involving carbohydrates and proteins.

Gold nanoparticles were usually synthesized by two well-known methods, the Burst and Turkevish methods. Recently, a novel photochemical method reported by Scaiano et al. (*7*) has been used to prepare gold nanoparticles using UV-irradiation. This new method has attracted much attention as the sizes and shapes of gold nanoparticles could be justly controlled by the intensity of UV radiation. They have reported the preparation of highly disperse and stable gold nanoparticles via a photochemical reduction of $HAuCl_4$ with a water-soluble photoinitiator, Irgacure-2959, which decomposes quantitatively in the presence of UV light at a wavelength of 350 nm. Protein-stabilized gold nanoparticles and biotinylated glyconanoparticles have also been reported by our group using this photochemical method (*8, 9*). This new method has proved to be an easy strategy in generating surface-functionalized gold nanoparticles using RAFT-synthesized polymers. However, in the case of those glyconanoparticles, the carbohydrate moieties were introduced to bring hydrophilicity and biocompatibility but were not appropriate to recognize lectins since the sugar ring (galactose) was linked by the C-6 position. Hence, another synthetic strategy was chosen here for the carbohydrate derivatives so that the resulting glycopolymers were bearing the carbohydrate in the C-1 position, then were presenting a structure especially favorable for specific lectin recognition.

In order to study the biomolecular recognition of different proteins and carbohydrates, the functionalized monodisperse gold colloids bearing carbohydrate and biotin moieties on the surface were prepared using photochemical reduction. A mixture of Irgacure-2959, $HAuCl_4$, copolymer, and PEG-SH, at a molar ratio of 3:1:0.2:0.8, was first dissolved in filtered distilled deionized water. The resulting pale yellow solution was then placed in a photochemical reactor for a period of approximately 5−10 min. The clear solution changes from pale yellow to pink, indicating the formation of gold nanoparticles. For purification, the gold colloid solution was then dialyzed against water. It should be noted that the *in situ* reduction minimizes the formation of disulfide bridges between the thiol-terminated polymers.

Particle size measurements of the formed gold nanoparticles were obtained by dynamic light scattering (DLS), and the data were collected after purification. The results are tabulated in

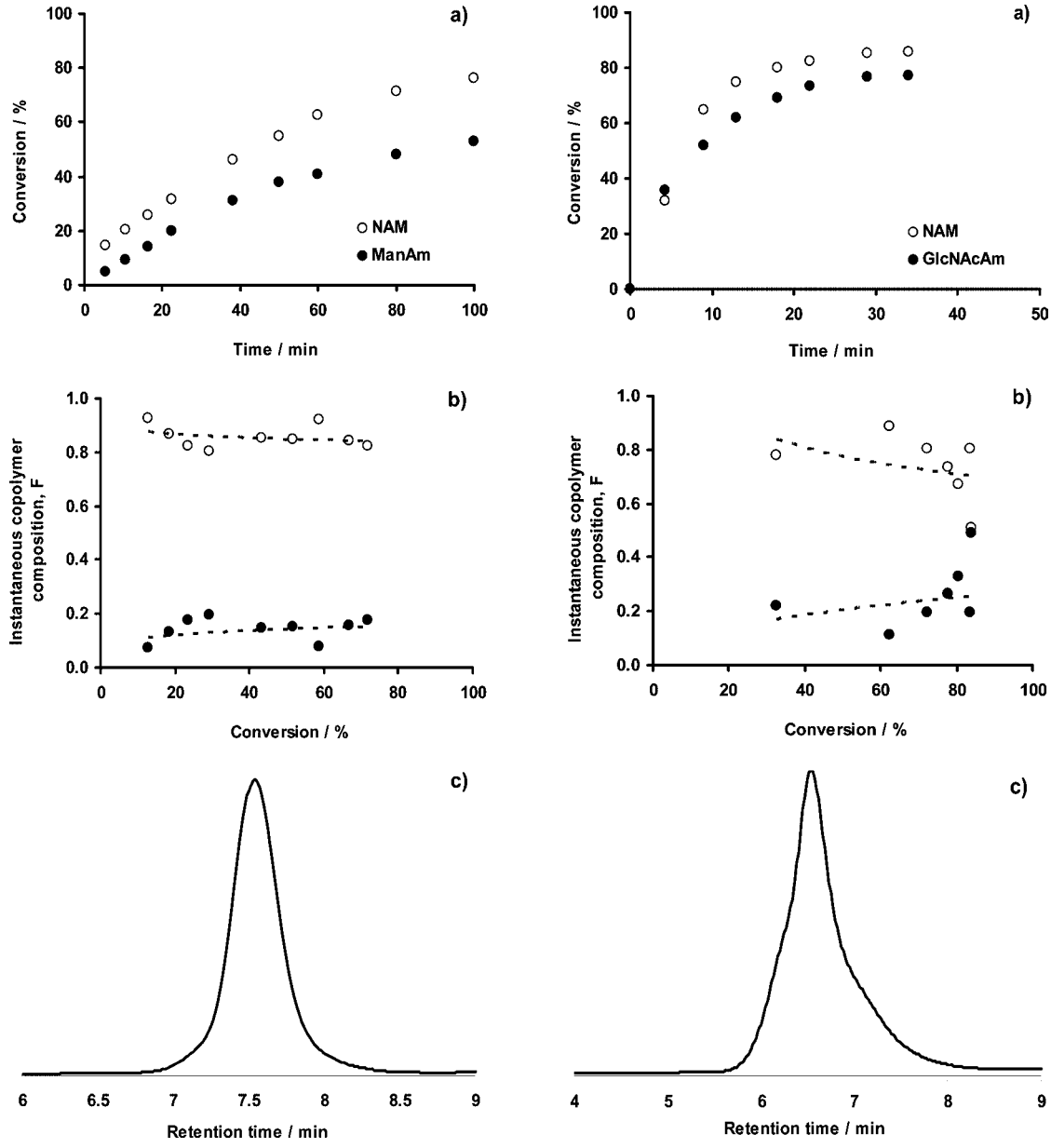


Figure 1. Monomer conversions (a), copolymer compositions (b), and SEC analysis (c) for NAM/ManAm copolymerization (left) and for NAM/GlcNAcAm copolymerization (right) using BCBDBA as the RAFT agent.

Table 2. The sizes of nanoparticles were about 4−6 nm in radius, and the polydispersities were below 0.2. This clearly shows that the mixture of the glycopolymer and -PEG-SH resulted in the formation of relatively monodisperse gold nanoparticles. The obtained gold nanoparticles were very stable, and the sizes of the glyconanoparticles did not change over weeks, which is indicative of the very high stability similar to that of PEGylated gold colloids (*12*). To further characterize the nanoparticles, the P(NAM_{234}-*co*-$GlcNAcAm_{52}$)-functionalized nanoparticles (613ab) were chosen to measure their sizes and shapes using transmission electron microscopy (TEM). Figure 2 shows the spherical and uniform morphology of these gold glyconanoparticles with a size of 4−6 nm in diameter. It should be noted that the smaller size from the TEM image may reveal only the visible gold core compared with that from DLS results. Concerning the stability, the interaction gold-thiol group is generally considered as a strong interaction. A constant diameter (and diameter distribution) was observed over weeks, which indicates a good stability of the gold nanoparticles produced. Glycopolymers, PNAM and PEG, are all biocompatible polymers used in the surface functionalization of the nanoparticles.

Diffraction Optics Technology (DOT). With the development of optical biosensors, a novel diffractive optics technology (DOT) has emerged for the potential applications in the immunoassays fields (*40*). It takes advantage of the inherent properties of diffractive optics to offer label-free real-time measurements and delivers a cost-effective, robust, optical biosensor that detects biomolecular binding even at low concentrations.

The dotLab system used includes precision fluidic control of reagents, buffers, and samples, a proprietary integrated optical assembly designed to function with the dotLab sensor, and software for acquisition, control, and user-interface. The used plastic consumable sensors consist of the polystyrene substrates and avidin-modified surfaces, and the modified surfaces possess nonrandom patterns, which were exposed to coherent light, and then well-defined diffractive images were produced. As the samples bearing biotin groups are loaded in the sensor, the

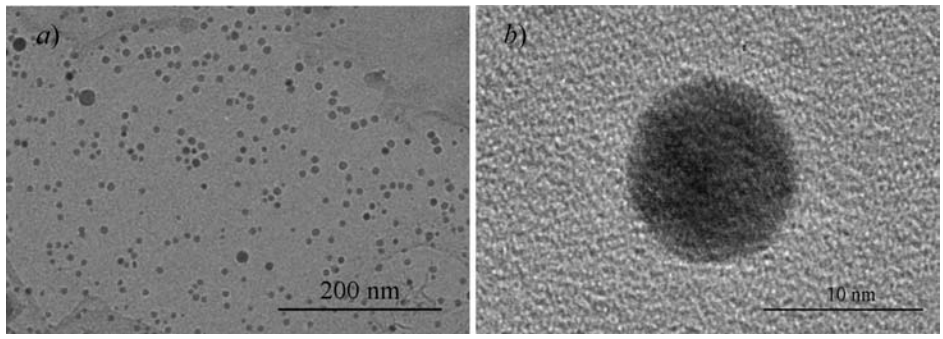


Figure 2. Typical TEM images of glyconanoparticles (613ab) prepared from the P(NAM_{234}-*co*-$GlcNAcAm_{52}$) glycopolymer.

samples are immobilized onto the surface of the sensor via the well-known biotin−avidin interactions that lead to an increase in the height of the diffractive pattern. This in turn increases the diffractive efficiency and diffractive order intensity monitored by a photodiode, and an increased signal of diffractive intensity is shown simultaneously by the software. Owing to the special design of the dotLab sensor with an integrated prism situated below the flow channel, we could monitored biomolecular binding in real time and in complex media because the light source interrogates the diffractive grating without passing through the bulk solution.

Biomolecular Recognition Involving the Carbohydrates and Lectins Detected via DOT. The surface-functionalized gold glyconanoparticles, prepared via the photochemical method, were used to study the availability of the carbohydrates and biotin toward biomolecular recognition processes. Several reference samples were used. The biotinylated nanoparticles (611ab and 612ab) without carbohydrate moieties were prepared from biotin-$PNAM_{21}$ and biotin-$PNAM_{287}$, respectively. The glyconanoparticles (613ab and 614ab) without biotin groups were prepared from P(NAM_{234}-*co*-$GlcNAcAm_{52}$) and P(NAM_{40}-*co*-$ManAm_4$), respectively. It should be noted that the biotinylated glyconanoparticles (615ab and 616ab) elaborated from biotin-P(NAM_{225}-*co*-$GlcNAcAm_{51}$) and biotin-P(NAM_{40}-*co*-$ManAm_7$) possess both biotin and carbohydrate moieties. However, the carbohydrate moieties are different (α-D-mannoside and *N*-acetyl *β*-D-glucosaminoside) and can be used as models to study the biomolecular specific recognition involving carbohydrates and lectin proteins.

Lectins are carbohydrate-binding proteins which possess a high degree of specificity toward carbohydrates. They play an important role in biological recognition phenomena involving cells and proteins, and some lectins have been widely used as a model system to understand the molecular basis of how the proteins recognize carbohydrates. It has been shown that some lectins were found on the surface of mammalian liver cells which specifically recognize galactose residues. The recognition of lectins and carbohydrates essentially occurs via multiple weak interactions (*25*). In order to further study the specific binding of carbohydrates and lectins, the lectins Concanavalin A (Con A) and wheat germ agglutinin (WGA), were chosen since they are known to specifically interact with α-D-mannoside and *N*-acetyl *β*-D-glucosaminoside moieties, respectively, that are the carbohydrates present on the prepared gold glyconanoparticles to study biomolecular recognition via dotLab measurements.

We first investigated the availability of the biotins incorporated on the surface of the nanoparticles to specifically interact with avidin located on the surface of the sensor using four control samples. The glyconanoparticles (613ab and 614ab) prepared from P(NAM_{234}-*co*-$GlcNAcAm_{52}$) and P(NAM_{40}-*co*-$ManAm_4$) (negative control samples), and two biotinylated nanoparticles (611ab and 612ab) prepared from biotin-$PNAM_{21}$ and Biotin-$PNAM_{287}$ (positive control samples), respectively, were loaded in the dotLab biosensor, and the results are shown in Figure 3. Because of the absence of biotin groups on the surface, the gold nanoparticles (613ab and 614ab) could not be immobilized on the avidin coated sensor chip. The recovery of the initial signal after wash is indicative of the fact that the gold nanoparticles were not attached on the surface of the sensor chip. However, after the biotinylated nanoparticles (611ab and 612ab) were injected into the dotLab instrument containing a preloaded avidin coated sensor chip, a signal could be observed and remained even after the wash with buffer (see Figure 3a and b), which is indicative of the specific interaction of the biotinylated nanoparticles with the avidin-coated sensor chip. These results are consistent with the work of Borisenko and co-workers regarding the aggregation of biotinylated mouse monoclonal antiNT-proBNP onto the streptavidin coated dotLab sensor (*40*) and our groups' recently reported work (*41*).

When the biotinylated glyconanoparticles (615ab and 616ab) elaborated from biotin-P(NAM_{225}-*co*-$GlcNAcAm_{51}$) and biotin-P(NAM_{40}-*co*-$ManAm_7$) were loaded into the dotLab sensor, higher responses were observed as shown in Figures 4 and 5. Because of the presence of biotin on the surface of glyconanoparticles, the nanoparticles remained immobilized on the surface of the avidin-sensor chip even after the wash with buffer.

Two different lectin solutions, Con A and WGA, were loaded following the immobilization of the biotinylated glyconanoparticles on the sensor chip. For *N*-acetyl glucosamine based carbohydrates, after the WGA lectin loading, a high response was observed while, when the same lectin solution was introduced onto PNAM-coated nanoparticles (611ab and 612ab), no increase of signal was observed because of the lack of carbohydrate groups on the surface of the nanoparticles. This indicates that there is no influence of PNAM itself on the carbohydrate/lectin interactions. The fact that the response was still present after the wash clearly showed the specific biomolecular interaction of *N*-Acetyl *β*-D-glucosaminoside residues of (615ab) with WGA. On the contrary, in the cross-experiment, almost no response was observed after the injection of Con A solution, which indicated a low nonspecific interaction and was consistent with the QCM and SPR results reported by Zhang et al. (*28*).

In addition, a strong signal was obtained after the injection of Con A solution to the immobilized glyconanoparticles (616ab) on the sensor chip, showing the specific and expected interactions of Con A with α-D-mannoside, and almost no response was observed when WGA was injected. In both cases, the cross-experiment indicated a low (<10%) nonspecific interaction between lectins and carbohydrates. This clearly demonstrates that the specific interaction of different carbohydrates and lectins such as α-D-mannoside (**Man**) with Con A and *N*-acetyl *β*-D-glucosaminoside (**GlcNAc**) with WGA could be investigated using this biosensing instrument. It further confirmed that the gold nanoparticles are carriers, and the outer carbohydrate moieties seem like many antennae increasing the specific

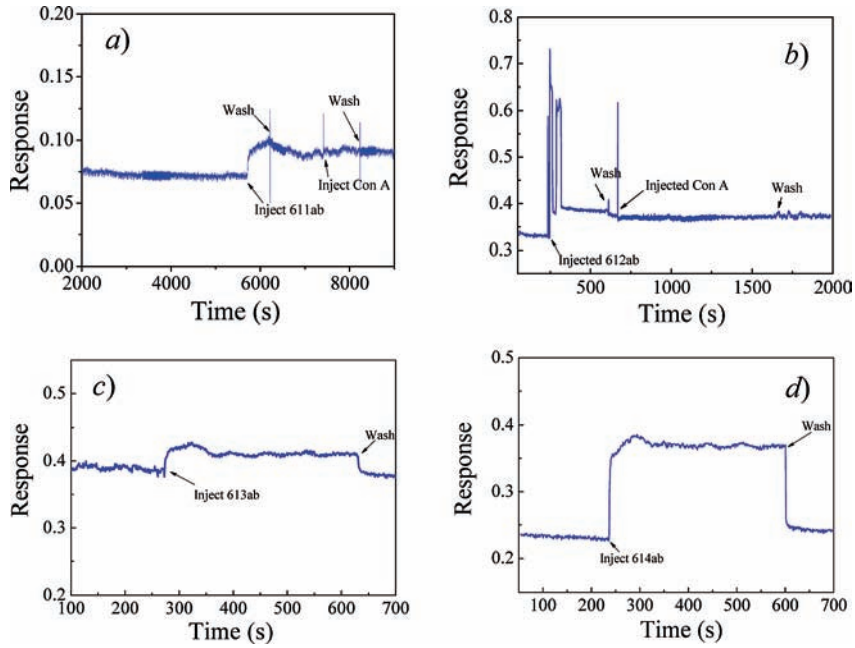


Figure 3. DotLab responses of gold nanoparticles prepared from biotin-$PNAM_{21}$ (611ab), biotin-$PNAM_{287}$ (612ab), P(NAM_{234}-*co*-$GlcNAcAm_{52}$) (613ab), and P(NAM_{40}-*co*-$ManAm_4$) (614ab) polymers.

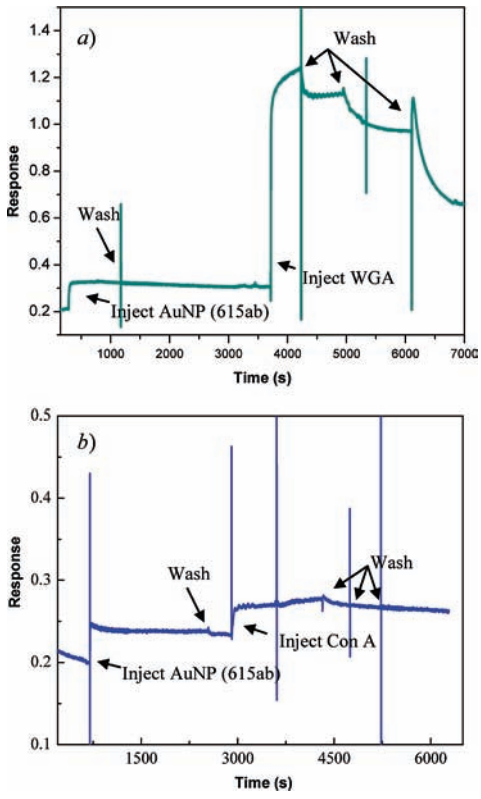


Figure 4. DotLab responses of biotinylated gold glyconanoparticles (615ab) prepared from the biotin-P(NAM_{225}-*co*-$GlcNAcAm_{51}$) glycopolymer with WGA (a) and Con A (b) lectins.

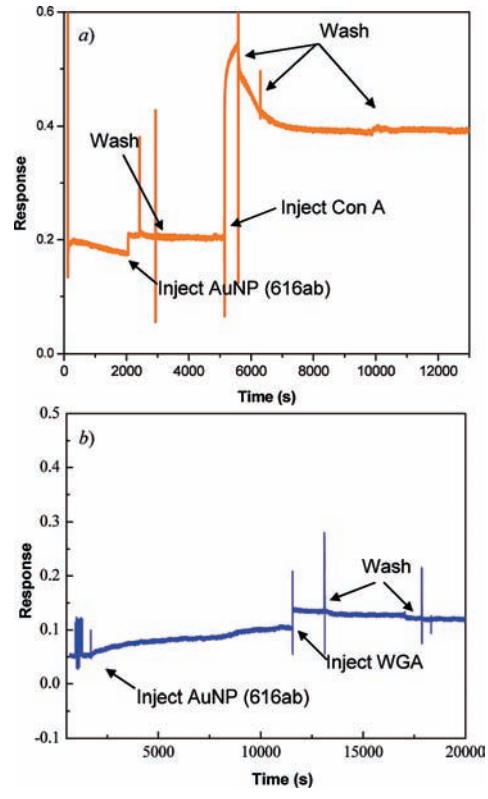


Figure 5. DotLab responses of biotinylated gold glyconanoparticles (616ab) prepared from the biotin-P(NAM_{40}-*co*-$ManAm_7$) glycopolymer with Con A (a) and WGA (b) lectins.

interaction of lectins and carbohydrates for the cluster glycoside effect. It should be noted that the number of carbohydrate moieties present on the surface of the nanoparticle and how many of those interact with the lectin are important parameters for this study. While this could potentially be calculated, we did not have all the parameters to exactly determine the number of chains per particle and hence the number of carbohydrate groups per particle. For this study, we just wanted to explore the specific recognition of given carbohydrate groups toward specific lectin. Besides, as the carbohydrate−lectin interactions are generally weak, it would be difficult for us to accurately measure the number of carbohydrates that are involved in those interactions.

Conclusions. Carbohydrate-based copolymers containing *N*-acetyl β-D-glucosaminopyranoside (**GlcNAc**) or α-D-mannopyranoside (**Man**) residues were prepared via RAFT polym-

erization using a biotin-CTA or *tert*-butyl dithiobenzoate as the RAFT agents. The obtained copolymers were then conjugated to the surface of gold nanoparticles by thiol chemistry that led to the formation of biotinylated or nonbiotinylated gold glyconanoparticles via a facile photochemical process. The prepared nanoparticles have uniform sizes and narrow polydispersities and are stable in water for weeks. Furthermore, the biotinylated glyconanoparticles were immobilized on the avidin-coated dotLab sensor chip because of the strong affinity between biotin and avidin, and subsequently used as the model to study the specific biomolecular recognition between lectins and carbohydrates. The specific recognitions for different carbohydrates and lectins such as α-D-mannoside with Con A and *N*-acetyl β-D-glucosaminoside with WGA were confirmed by the dotLab biosensing device. Because of the presence of PEG, biotin, and carbohydrate-based copolymer chains on the surface, these gold glyconanoparticles could be applied in biology as highly stable and biocompatible materials.

ACKNOWLEDGMENT

This work is supported jointly by Natural Sciences and Engineering Research Council of Canada and Ontario Centres of Excellence, Emerging Materials and Knowledge (OCE-EMK). We thank Axela Biosensors Inc. (Dr. Jean F. Houle) for providing the DOTLab instrument and sensor chips for this study. We thank Dr Maël Bathfield for the biotin-PNAM samples as well as Professor Stéphane Parola and Dr. Fernand Chassagneux (LMI, University of Lyon) for the TEM micrographs. We thank BioMerieux S.A. company for a Ph.D. grant for Guillaume Gody.

Supporting Information Available: Detailed synthesis and characterization of the biotinylated chain transfer agent and ^{1}H NMR data of the copolymer P(NAM-*co*-ManAm) before and after deprotection. This material is available free of charge via the Internet at http://pubs.acs.org.

LITERATURE CITED

(1) Daniel, M.-C., and Astruc, D. (2004) Gold nanoparticles: assembly, supramolecular chemistry, quantum-size-related properties, and applications toward biology, catalysis, and nanotechnology. *Chem. Rev. 104*, 293–346.

(2) Rosi, N. L., and Mirkin, C. A. (2005) Nanostructures in biodiagnostics. *Chem. Rev. 105*, 1547–1562.

(3) Brust, M., Walker, M., Bethell, D., Schiffrin, D. J., and Whyman, R. (1994) Synthesis of thiol-derivatised gold nanoparticles in a two-phase liquid-liquid system. *J. Chem. Soc. Chem. commun.* 801–802.

(4) Templeton, A. C., Wuelfing, W. P., and Murray, R. W. (2000) Monolayer-protected cluster molecules. *Acc. Chem. Res. 33*, 27–36.

(5) Grabar, K. C., Freeman, R. G., Hommer, M. B., and Natan, M. J. (1995) Preparation and characterization of Au colloid monolayers. *Anal. Chem. 67*, 735–743.

(6) Frens, G. (1973) Controlled nucleation for the regulation of the particle size in monodisperse gold solution. *Nature Phys. Sci. 241*, 20–22.

(7) McGilvray, K. L., Decan, M. R., Wang, D., and Scaiano, J. C. (2006) Facile photochemical synthesis of unprotected aqueous gold nanoparticles. *J. Am. Chem. Soc. 128*, 15980–15981.

(8) Narain, R., Housni, A., Gody, G., Boullanger, P., Charreyre, M.-T., and Delair, T. (2007) Preparation of biotinylated glyconanoparticles via a photochemical process and study of their bioconjugation to streptavidin. *Langmuir 23*, 12835–12841.

(9) Housni, A., Ahmed, M., Liu, S., and Narain, R. (2008) Monodisperse protein stabilized gold nanoparticles via a simple photochemical process. *J. Phys. Chem. C 112*, 12282–12290.

(10) Ryan, J. A., Overton, K. W., Speight, M. E., Oldenburg, C. N., Loo, L., Robarge, W., Franzen, S., and Feldheim, D. L. (2007) Cellular uptake of gold nanoparticles passivated with BSA-SV40 large T antigen conjugates. *Anal. Chem. 79*, 9150–9159.

(11) Shang, L., Wang, Y., Jiang, J., and Dong, S. (2007) pH-dependent protein conformational changes in albumin: gold nanoparticle bioconjugates: a spectroscopic study. *Langmuir 23*, 2714–2721.

(12) Liu, Y., Shipton, M. K., Ryan, J., Kaufman, E. D., Franzen, S., and Feldheim, D. L. (2007) Synthesis, stability, and cellular internalization of gold nanoparticles containing mixed peptide-poly(ethylene glycol) monolayers. *Anal. Chem. 79*, 2221–2229.

(13) Alivisatos, A. P., Johnsson, K. P., Peng, X., Wislon, T. E., Loweth, C. J., Bruchez, M. P., Jr., and Schultz, P. G. (1996) Organization of 'nanocrystal molecules' using DNA. *Nature 382*, 609–611.

(14) Mirkin, C. A., Letsinger, R. L., Mucic, R. C., and Storhoff, J. J. (1996) A DNA-based method for rationally assembling nanoparticles into macroscopic materials. *Nature 382*, 607–609.

(15) Schofield, C. L., Haines, A. H., Field, R. A., and Russell, D. A. (2006) Silver and gold glyconanoparticles for colorimetric bioassays. *Langmuir 22*, 6707–6711.

(16) Chiefari, J., Chong, Y. K., Ercole, F., Krstina, J., Jeffery, J., Le, T. P. T., Mayadunne, R. T. A., Meijs, G. F., Moad, C. L., Moad, G., Rizzardo, E., and Thang, S. H. (1998) Living free-radical polymerization by reversible addition fragmentation chain transfer: the RAFT process. *Macromolecules 31*, 5559–5562.

(17) Lowe, A. B., Sumerlin, B. S., Donovan, M. S., and McCormick, C. L. (2002) Facile preparation of transition metal nanoparticles stabilized by well-defined (co)polymers synthesized via aqueous reversible addition-fragmentation chain transfer polymerization. *J. Am. Chem. Soc. 124*, 11562–11563.

(18) Shan, J., and Tenhu, H. (2007) Recent advances in polymer protected gold nanoparticles: synthesis, properties and applications. *Chem. Commun.* 4580–4598.

(19) Corbierre, M. K., Cameron, N. S., Sutton, M., Mochrie, S. G. J., Lurio, L. B., Ruhm, A., and Lennox, R. B. (2001) Polymer-stabilized gold nanoparticles and their incorporation into polymer matrices. *J. Am. Chem. Soc. 123*, 10411–10412.

(20) Yurekli, K., Karim, A., Amis, E. J., and Krishnamoorti, R. (2003) Influence of layered silicates on the phase-separated morphology of PS-PVME blends. *Macromolecules 36*, 7256–7267.

(21) Favier, A., Charreyre, M.-T., Chaumont, P., and Pichot, C. (2002) Study of the RAFT polymerization of a water-soluble bisubstituted acrylamide derivative. 1. Influence of the dithioester structure. *Macromolecules 35*, 8271–8280.

(22) Goldstein, I. J., Iyer, R. N., Smith, E. E., and So, L. L. (1967) Protein- carbohydrate interaction. XX. The interaction of concanavalin A with sophorose and some of its derivatives. *Biochemistry 6*, 2373–2377.

(23) Hong, C.-H. (2003) *Carbohydrate-Based Drug Discovery*, Wiley-VCH, Weinheim, Germany.

(24) Lee, Y. C., and Lee, R. T. (1995) Carbohydrate-protein interactions: basis of glycobiology. *Acc. Chem. Res. 28*, 321–327.

(25) Lundquist, J. J., and Toone, E. J. (2002) The cluster glycoside effect. *Chem. Rev. 102*, 555–578.

(26) Otsuka, H., Akiyama, Y., Nagasaki, Y., and Kataoka, K. (2001) Quantitative and reversible lectin-induced association of gold nanoparticles modified with α-lactosyl-ω-mercapto-poly(ethylene glycol). *J. Am. Chem. Soc. 123*, 8226–8230.

(27) Touhami, A., Hoffmann, B., Vasella, A., Denis, F. A., and Dufrene, Y. F. (2003) Probing specific lectin-carbohydrate interactions using atomic force microscopy imaging and force measurements. *Langmuir 19*, 1745–1751.

(28) Zhang, Y., Luo, S., Tang, Y., Yu, L., Hou, K.-Y., Cheng, J.-P., Zeng, X., and Wang, P. G. (2006) Carbohydrate-protein interactions by "clicked" carbohydrate self-assembled monolayers. *Anal. Chem. 78*, 2001–2008.

(29) Hone, D. C., Haines, A. H., and Russell, D. A. (2003) Rapid, quantitative colorimetric detection of a lectin using mannose-stabilized gold nanoparticles. *Langmuir 19*, 7141–7144.

(30) La Belle, J. T., Gerlach, J. Q., Svarovesky, S., and Joshi, L. (2007) Label-free impedimetric detection of glycan-lectin interactions. *Anal. Chem. 79*, 6959–6964.
(31) Dai, Z., Kawde, A.-N., Xiang, Y., La Belle, J. T., Gerlach, J., Bhavanandan, V. P., Joshi, L., and Wang, J. (2006) Nanoparticle-based sensing of glycan-lectin interactions. *J. Am. Chem. Soc. 128*, 10018–10019.
(32) Gestwicki, J. E., Cairo, C. W., Strong, L. E., Oetjen, K. A., and Kiessling, L. L. (2002) Influencing receptor-ligand binding mechanisms with multivalent ligand architecture. *J. Am. Chem. Soc. 124*, 14922–14933.
(33) Bathfield, M., D'Agosto, F., Spitz, R., Charreyre, M.-T., and Delair, T. (2006) Versatile precursors of functional RAFT agents. Application to the synthesis of bio-related end-functionalized polymers. *J. Am. Chem. Soc. 128*, 2546–2547.
(34) Gody, G. (2008) Synthesis of saccharide monomers for preparation of gradient, alpha-functionalized and block glycopolymers by the RAFT process. Application in immobilization of biomolecules by specific recognition or covalent link, Ph.D. Thesis, University Claude Bernard, Lyon, France.
(35) Gody, G., Boullanger, P., Ladavière, C., Charreyre, M.-T., and Delair, T. (2008) Biotin α-end-functionalized gradient glycopolymers synthesized by RAFT copolymerization. *Macromol. Rapid Commun. 29*, 511–519.
(36) D'Agosto, F., Charreyre, M. T., Veron, L., Llauro, M. F., and Pichot, C. (2001) Kinetic study of free-radical solution copolymerization of *N*-acryloylmorpholine with an activated ester-type monomer, *N*-acryloxysuccinimide. *Macromol. Chem. Phys. 202*, 1689–1699.
(37) Torchilin, V. P., Trubetskoy, V. S., Whiteman, K. R., Caliceti, P., Ferruti, P., and Veronese, F. M. (1995) New synthetic amphiphilic polymers for steric protection of liposomes in vivo. *J. Pharm. Sci. 84*, 1049–1053.
(38) Ranucci, E., Spagnoli, G., Sartore, L., Ferruti, P., Caliceti, P., Schiavon, O., and Veronese, F. M. (1994) Synthesis and molecular weight characterization of low molecular weight end-functionalized poly(4-acryloylmorpholine). *Macromol. Chem. Phys. 195*, 3469–3479.
(39) Ushakova, V., Panarin, E., Ranucci, E., Bignotti, F., and Ferruti, P. (1995) Synthesis of low molecular weight poly(*N*-acryloylmorpholine) end-functionalized with primary amino groups, and its use as macromonomer for the preparation of poly(amidoamines). *Macromol. Chem. Phys. 196*, 2927−2939.
(40) Borisenko, V., Hu, W., Tam, P., Chen, I., Houle, J.-F., and Ausserer, W. (2006) Diffractive optics technology: a novel detection technology for immunoassays. *Clin. Chem. 52*, 2168–2170.
(41) Deng, Z. C., Li, S. Q., Jiang, X. Z., and Narain, R. (2009) Well-defined galactose- containing multi-functional copolymers and glyco-nanoparticles for biomolecular recognition processes. *Macromolecules 42*, 6393–6405.

BC900431P

Evaluation of Bifunctional Chelates for the Development of Gallium-Based Radiopharmaceuticals

Cara L. Ferreira,*[,†] Eric Lamsa,[†] Michael Woods,[†] Yin Duan,[‡] Pasan Fernando,[‡] Corinne Bensimon,[‡] Myra Kordos,[‡] Katharina Guenther,[§] Paul Jurek,[||] and Garry E. Kiefer[||]

MDS Nordion, 4004 Wesbrook Mall, Vancouver, British Columbia, Canada V6T 2A3, Ottawa Heart Institute, Ottawa, Ontario, Canada, MDS Nordion, Kanata, Ontario, Canada, and Macrocyclics, Dallas, Texas. Received October 9, 2009; Revised Manuscript Received January 4, 2010

Ga radioisotopes, including the generator-produced positron-emitting isotope ^{68}Ga ($t_{1/2}$ = 68 min), are of increasing interest for the development of new radiopharmaceuticals. Bifunctional chelates (BFCs) that can be efficiently radiolabeled with Ga to yield complexes with good *in vivo* stability are needed. To this end, we undertook a systematic comparison of four BFCs containing different chelating moieties: two novel BFCs, *p*-NO_2-Bn-Oxo (1-oxa-4,7,10-triazacyclododecane-4,7,10-triacetic acid) and *p*-NO_2-Bn-PCTA (3,6,9,15-tetraazabicyclo [9.3.1]pentadeca-1(15),11,13-triene-3,6,9-triacetic acid), and two more commonly used BFCs, *p*-NO_2-Bn-DOTA (1,4,7,10-tetraazacyclododecane-1,4,7,10-tetraacetic acid) and *p*-NO_2-Bn-NOTA (1,4,7-triazacyclononane-1,4,7-triacetic acid). Each BFC was compared with respect to radiolabeling conditions, radiochemical yield, stability, and in vivo clearance properties. *p*-NO_2-Bn-PCTA, *p*-NO_2-Bn-Oxo, and *p*-NO_2-Bn-NOTA were all more efficiently radiolabeled with Ga compared to *p*-NO_2-Bn-DOTA. *p*-NO_2-Bn-DOTA required longer reaction time, higher concentrations of BFC, or heating to obtain equivalent radiochemical yields. Better stability was observed for *p*-NO_2-Bn-NOTA and *p*-NO_2-Bn-PCTA compared to *p*-NO_2-Bn-DOTA and *p*-NO_2-Bn-Oxo, especially with respect to transmetalation to transferrin. Ga-radiolabled *p*-NO_2-Bn-Oxo was found to be kinetically labile and therefore unstable in vivo. Ga-radiolabeled *p*-NO_2-Bn-NOTA and *p*-NO_2-Bn-PCTA were relatively inert, while Ga-radiolabeled *p*-NO_2-Bn-DOTA had intermediate stability, losing >20% of Ga in less than one hour when incubated with apo-transferrin. Similar stability differences were seen when incubating at pH 2. In vivo PET imaging and biodistribution studies in mice showed that ^{68}Ga-radiolabeled *p*-NO_2-Bn-PCTA, *p*-NO_2-Bn-NOTA, and *p*-NO_2-Bn-DOTA all cleared through the kidneys. While there was no statistical difference in the biodistribution results of ^{68}Ga-radiolabeled *p*-NO_2-Bn-PCTA and *p*-NO_2-Bn-DOTA, ^{68}Ga-radiolabeled *p*-NO_2-Bn-NOTA cleared more rapidly from blood and muscle tissue but retained at up to 5 times higher activity in the kidneys.

INTRODUCTION

Gallium radioisotopes have long been of interest in nuclear medicine. ^{67}Ga is currently used for infection and tumor imaging (*1, 2*). Another gallium isotope gaining the attention of the nuclear imaging community is ^{68}Ga (*3*−*5*). ^{68}Ga is a generator-produced positron-emitter with a 68 min half-life. There are only a few generator-produced isotopes applicable to positron emission tomography (PET) imaging, and most have short half-lives limiting their applications due to the time requirements for both radiolabeling and target uptake in vivo. The wide use of single photon emission computed tomography (SPECT) imaging can be partially attributed to the convenience of the Tc-99 m generator and the simplicity of the kit chemistry. Despite having higher resolution, PET has had slower adoption because of the need for a nearby cyclotron to produce F-18 and the more complex chemistry needed to incorporate F-18 into the radiopharmaceutical. The availability of a ^{68}Ga generator and kit chemistry to produce ^{68}Ga-based molecular imaging agents could have a significant impact on PET (*4*).

For ^{68}Ga to be effectively used in molecular imaging, agents must be developed with applicable radiochemistry and appropriate biological properties. Due to the short half-life, the radiolabel incorporation needs to be efficient, preferably under mild conditions, and not require subsequent purification. Radiolabeling that yields an injectable radiopharmaceutical with high specific activity after simply adding the ^{68}Ga generator eluant directly to a reagent containing vial would be ideal. The agent also needs to be stable *in vivo* and clear background tissues quickly to allow imaging within the first few hours after injection.

A factor that influences the radiochemistry as well as the biological properties of the agent is the chemical method of incorporating ^{68}Ga. Typically, a bifunctional chelate (BFC) is used to stably chelate the metal and link the metal to a target vector, such as a peptide (*6*). Choosing the right BFC can greatly affect the radiolabeling kinetics and conditions, increase the resulting compound's stability, and influence, to some degree, the pharmacokinetics. The most commonly used BFC for ^{68}Ga is DOTA (1,4,7,10-tetraazacyclododecane-1,4,7,10-tetraacetic acid), but the radiochemistry typically requires conventional or microwave heating to obtain adequate yields and specific activities quickly (*7*−*11*). More recently, NOTA (1,4,7-triazacyclononane-1,4,7-triacetic acid) and derivatives have been radiolabeled efficiently with ^{68}Ga at lower temperatures (*12, 13*) and even at ambient temperature (*14, 15*).

Previously, we have examined two novel bifunctional chelates, *p*-NO_2-Bn-PCTA and *p*-NO_2-Bn-Oxo, for the development of Cu-64 based radiopharmaceuticals (*16*). In this work, we examined the same two BFCs for their potential use in

* Cara L. Ferreira; cara.ferreira@mdsinc.com, phone 1-604-228-8952, fax 1-604-228-5990.
[†] MDS Nordion, British Columbia.
[‡] Ottawa Heart Institute.
[§] MDS Nordion, Ontario.
[||] Macrocyclics.

10.1021/bc900443a © 2010 American Chemical Society
Published on Web 02/22/2010

developing gallium-radiolabeled nuclear imaging agents. These BFCs each contain a 12-membered macrocyclic chelate, *p*-NO_2-Bn-Oxo (1-oxa-4,7,10-triazacyclododecane-4,7,10-triacetic acid), *p*-NO_2-Bn-PCTA (3,6,9,15-tetraazabicyclo [9.3.1]pentadeca-1(15),11,13-triene-3,6,9-triacetic acid), and a *p*-nitrobenzyl substituent, which can be modified for attachment of a targeting vector. To determine whether *p*-NO_2-Bn-PCTA and *p*-NO_2-Bn-Oxo offered an advantage over the currently used BFCs for Ga-based radiopharmaceutical development, direct comparison of the novel BFCs was made to the analogous BFCs containing the DOTA and NOTA chelating moieties. The BFCs were examined with respect to radiochemistry and stability with both ^{67}Ga and ^{68}Ga. The pharmacokinetics of the Ga-radiolabeled BFCs was also compared through biodistribution and imaging studies in mice.

EXPERIMENTAL SECTION

Materials and Methods. All solvents and reagents were used as received unless otherwise noted. The BFCs, *p*-NO_2-Bn-DOTA, *p*-NO_2-Bn-NOTA, *p*-NO_2-Bn-Oxo, and *p*-NO_2-Bn-PCTA, were acquired from Macrocyclics Inc. (Texas). ^{67}Ga and ^{68}Ga were obtained as 0.1 N HCl solutions (MDS Nordion Inc.). Water was deionized using a Milli-Q biocel A-10 water purification system. Reaction vials were acid-washed to remove impurities and trace metals.

The HPLC system used for analysis consists of a Waters Alliance HT 2795 separation module equipped with a Raytest Gabbistar NaI detector and a Waters 996 photodiode array (PDA) detector. Analysis of radiolabeled complexes was done on a Phenomenex Hydrosynergy RP C18 4.6 × 150 mm analytical column using a binary solvent system: solvent A = acetonitrile, solvent B = 0.05% trifluoroacetic acid in water. Method 1 was used for *p*-NO_2-Bn-DOTA, *p*-NO_2-Bn-Oxo, and *p*-NO_2-Bn-PCTA: gradient elution 5% A/95% B to 30% A/70% B over 20 min at 1.5 mL/min. Method 2 was used for *p*-NO_2-Bn-NOTA: gradient elution 5% A/95% B to 50% A/50% B over 30 min at 1.5 mL/min. Positive identification of the ^{67}Ga and ^{68}Ga radiolabeled BFCs was made by comparison of the retention time of the radiodetector peak and the UV detector peak associated with macroscopic scale Ga complex of the respective BFC, whose identity was verified by mass spectroscopy using positive-ion mode electrospray ionization with a Micromass Q-TOF Ultima API time-of-flight mass spectrometer by Mr. Andras Szeitz (University of British Columbia, Department of Pharmaceutical Sciences). Analysis of the stability samples was done by HPLC using the method described above or using a size-exclusion column, Phenomenex BIOSEP SEC2000 7.8 × 300 mm, eluting with 10 mM sodium bicarbonate buffer pH 6.9 at 1.0 mL/min.

^{67}Ga Radiolabeling Study of Reaction Kinetics. The ^{67}Ga solution (50−100 μL, 25 mCi/mL) was added to a reaction vial containing one of the chelates, *p*-NO_2-Bn-DOTA, *p*-NO_2-Bn-NOTA, *p*-NO_2-Bn-Oxo, or *p*-NO_2-Bn-PCTA, in a 10 mM sodium acetate buffer at pH 4−5. The final concentration of chelate ranged 6−300 μM, and the final concentration of Ga^{3+} ranged 3−6 μM. The reactions were done in triplicate and were analyzed by HPLC for radiochemical yield after 5, 10, 30, and 60 min.

^{67}Ga Radiolabeling at Different pH Values. ^{67}Ga (50 μL, 20 mCi/mL) was added to a solution containing one of the BFCs, *p*-NO_2-Bn-DOTA, *p*-NO_2-Bn-NOTA, *p*-NO_2-Bn-Oxo, or *p*-NO_2-Bn-PCTA (50 μL, 60 μM) diluted in 1 mL of buffer (10 mM) at different pH values ranging from 2 to 6. All reactions were done in triplicate. Radiochemical yield was determined by HPLC analysis after 5 and 60 min.

^{68}Ga Radiolabeling Comparison and Optimization. Carrier-free ^{68}Ga (50−400 μL, 1 mCi) was added to BFC (2−2000 nmol) in 1 mL of 200 mM sodium acetate buffer (pH 4). Reactions proceeded at room temperature, 40, or 80 °C and were monitored by HPLC at different time points.

Stability Assessment. Stability assessments were done with both ^{67}Ga and ^{68}Ga radiolabeled BFCs. For ^{67}Ga, carrier-free ^{67}Ga (3−4 mCi) was added to one of the four BFCs (30 μM in 1.0 mL 10 mM sodium acetate buffer pH 4). After 10 min, the radiochemical yield was determined by HPLC. For ^{68}Ga, carrier-free ^{68}Ga (1−2 mCi) was added to one of the four BFCs (20 μM in 1.0 mL 400 mM sodium acetate buffer pH 4), and the resulting solution was heated at 80 °C for 15 min to ensure reaction completion. The radiochemical yield was confirmed by HPLC.

Aliquots of the radiolabeling reactions (200 μL) were added to 800 μL of either a pH 2 buffer (0.1 mM glycine) or an apotransferrin solution (3 mg/mL, pH 6.9 10 mM sodium bicarbonate buffer). The stability solutions were incubated at 37 °C and analyzed by HPLC at different time points to determine the amount of radiolabeled BFC that remained intact.

Biodistribution and Imaging in Mice. A total of 48 male CD1 (25−30 g) mice (Charles River, Canada) were used for the animal study. Each of the four different ^{68}Ga radiolabeled BFCs prepared as described above (10−20 Ci/mmol of BFC) was injected via the lateral tail vein into 12 mice. Animals were injected under light anesthesia with isoflurane; isoflurane levels were maintained at 1.5−2%. Ten of the mice were injected with ∼10 μCi, while two of the mice were injected with ∼50 μCi and used for both imaging and the 4 h biodistribution data. The mice were sacrificed by cervical dislocation while under anesthesia. Tissues were harvested at 15 min, 1 h, and 4 h after injection, with $n = 4$ for each time point and included heart, liver, kidneys, spleen, intestines, skeletal muscle (quadriceps), bone (femur), brain, blood, and urine. Tissues were weighed, and their activity was counted on a gamma counter. The tissue activity was decay-corrected and converted to %ID/g. Student *t* tests were used for analysis, with a $p < 0.05$ considered statistically significant.

PET imaging was carried out on a Siemens Inveon small animal PET scanner (Siemens, Knoxville, Tennessee). The scanner was started 10 s prior to radiotracer injection in order to capture the entire input function. A bolus injection of approximately 50 μCi in 0.15 mL of the ^{68}Ga-radiolabeled BFC was injected intravenously over a 10 s period. List-mode data were acquired for 90 min using a 350−650 keV energy window and a coincidence timing window of 3.4 ns. List-mode PET data were histogrammed two different ways (32 frames of 12 × 10 s, 3 × 60 s, and 17 × 300 s and 2 frames of 1 × 300 s and 1 × 5100 s). The data were reconstructed on a 256 × 256 image matrix with 0.29 × 0.29 × 0.80 mm^3 pixel size using OSEM3D/MAP ($\beta = 0$, OSEM3D iterations = 2, MAP iterations = 18) with corrections for dead-time, isotope decay, detector efficiencies, and randoms.

RESULTS

Radiochemistry. Standards were prepared by adding naturally abundant gallium to each of the BFCs (Figure 1). The parent-ion weight and isotopic distribution observed in the mass spectra confirm the coordination of Ga to the BFCs; Ga-*p*-NO_2-Bn-PCTA $m/z = 581.4, 583.1$; Ga-*p*-NO_2-Bn-Oxo $m/z = 549.2, 551.2$; Ga-*p*-NO_2-Bn-DOTA $m/z = 606.1, 608.1$, Ga-*p*-NO_2-Bn-NOTA $m/z = 505.1, 507.2$. The natural Ga complexes were used as UV/visible detectable standards for HPLC identification of the radiolabeled compounds. Representative HPLC traces for the *p*-NO_2-Bn-PCTA BFC with natural Ga, ^{67}Ga, and ^{68}Ga are shown in Figure 2.

The radiolabeling yield was measured after a fixed reaction time at room temperature at several different pH values. *p*-NO_2-

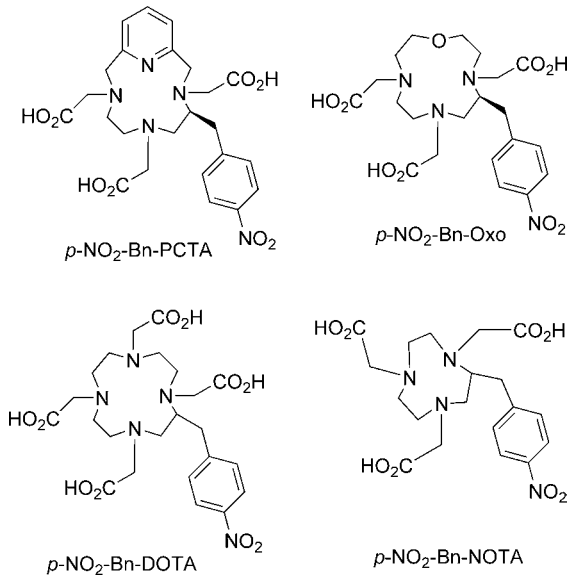


Figure 1. Bifunctional chelates evaluated for gallium radiolabeling.

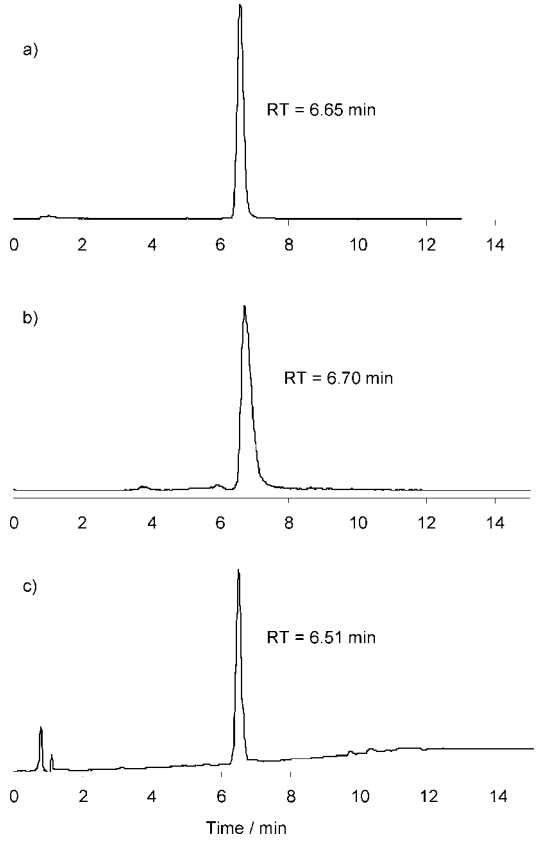


Figure 2. HPLC traces for (a) ^{67}Ga-*p*-NO_2-Bn-PCTA (radiation detector), (b) ^{68}Ga-*p*-NO_2-Bn-PCTA (radiation detector), (c) Ga-*p*-NO_2-Bn-PCTA (UV/visible detector, $\lambda = 280$ nm).

Bn-DOTA was most sensitive to variation in pH, with optimal radiochemical yields at pH 4, 99% after 60 min, and yields dropping to less than 80% at pH 3 and 5. *p*-NO_2-Bn-PCTA, *p*-NO_2-Bn-Oxo, and *p*-NO_2-Bn-NOTA were radiolabeled efficiently with yields >95% between pH 3 and pH 5. All BFCs showed inferior radiolabeling yields at pH 2 and at pH >6.

The radiolabeling kinetics of each of the BFCs was examined with ^{67}Ga and ^{68}Ga. Table 1 summarizes the optimal reaction conditions, with respect to radiochemical yield and specific activity, determined for each BFC. The BFC concentration had

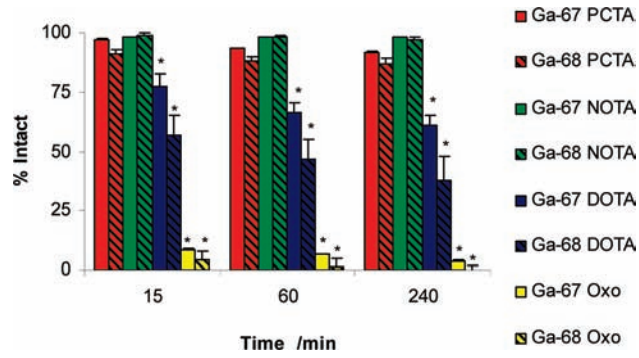


Figure 3. % Ga-BFC intact after incubation in 3 mg/mL apo-transferrin at 37 °C over 4 h. *Values significantly different compared to other Ga-BFC species at the same time point ($p < 0.005$).

the largest impact on reaction time and radiochemical yield. At higher concentrations (>30 μM), all the BFCs achieve >95% radiochemical yield after only 5 min at room temperature. At lower concentrations, slightly longer reaction times (10 min) are required to obtain >95% radiochemical yield for ^{67}Ga-*p*-NO_2-Bn-PCTA and *p*-NO_2-Bn-Oxo, but *p*-NO_2-Bn-DOTA required significantly longer reaction times (60 min). A similar trend was observed for ^{68}Ga radiolabeling. *p*-NO_2-Bn-PCTA, *p*-NO_2-Bn-Oxo, and *p*-NO_2-Bn-NOTA were efficiently labeled at room temperature, even when using low concentrations of BFC, while *p*-NO_2-Bn-DOTA had slower reaction kinetics. Heating the reaction at 80 °C was necessary to obtain ^{68}Ga-*p*-NO_2-Bn-DOTA in radiochemical yields and specific activities comparable to those obtained for the other BFCs at room temperature.

Stability. The stability of the Ga-radiolabeled BFCs was assessed in different buffer solutions and in the presence of excess apo-transferrin. No degradation or loss of Ga was observed in the buffered solutions at pH 4 and higher. After 1 h incubating at pH 2, the ^{67}Ga radiolabled BFCs showed negligible degradation or loss of ^{67}Ga, but after 24 h, ^{67}Ga radiolabeled *p*-NO_2-Bn-Oxo and *p*-NO_2-Bn-DOTA showed a 20% and 36% loss, respectively, of ^{67}Ga from the BFC. The kinetic stability in the presence of apo-transferrin for each of the BFCs followed the same trend, whether radiolabeled with ^{67}Ga or ^{68}Ga. *p*-NO_2-Bn-NOTA allowed negligible transfer of the radioisotope to the protein. *p*-NO_2-Bn-DOTA, and to a lesser extent *p*-NO_2-Bn-PCTA, allowed some loss of radioisotope to apo-transferrin over the 4 h time period, while *p*-NO_2-Bn-Oxo was kinetically labile, with almost all of the radioisotope transferred to the protein in less than 15 min.

Biodistribution. The %ID/g for select tissues was determined for each of the ^{68}Ga radiolabeled BFCs in mice at 15 min, 1 h, and 4 h post injection; the results are summarized in Figures 4−8. The majority of activity was found in the kidneys and urine, indicating renal clearance. ^{68}Ga-radiolabeled *p*-NO_2-Bn-NOTA had significantly more activity in the kidney at all time points, 4−14 times greater than the kidney %ID/g of ^{68}Ga-radiolabeled *p*-NO_2-Bn-PCTA or *p*-NO_2-Bn-DOTA. The %ID/g of all tissues for ^{68}Ga-radiolabeled *p*-NO_2-Bn-PCTA and *p*-NO_2-Bn-DOTA were not statistically different. For the liver, intestine, and brain tissue, ^{68}Ga-radiolabeled *p*-NO_2-Bn-NOTA, *p*-NO_2-Bn-PCTA, and *p*-NO_2-Bn-DOTA were similar, but for blood, heart, muscle, bone, and spleen tissue ^{68}Ga *p*-NO_2-Bn-NOTA cleared more rapidly with statistically ($p < 0.05$) lower activity after 1 h; 80−90% of the activity at 15 min was cleared by 1 h for ^{68}Ga-radiolabeled *p*-NO_2-Bn-NOTA compared to 45−75% of the activity for ^{68}Ga-radiolableled *p*-NO_2-Bn-PCTA and *p*-NO_2-Bn-DOTA in these tissues. In contrast to the other BFCs, ^{68}Ga-radiolabeled *p*-NO_2-Bn-Oxo did not appreciably clear from

Table 1. Optimized Reaction Conditions for ^{67}Ga and ^{68}Ga Radiolabeling of BFCs[a]

bifunctional chelate	isotope	reaction conditions ([BFC], temperature, time)	radiochemical yield	specific activity (mCi/μmol)
p-NO_2-Bn-PCTA	^{67}Ga	3 μM, RT, 10 min	96.9%	166
	^{67}Ga	15 μM, RT, 5 min	98.4%	35
p-NO_2-Bn-Oxo	^{67}Ga	3 μM, RT, 10 min	98.4%	163
p-NO_2-Bn-NOTA	^{67}Ga	3 μM, RT, 5 min	99.9%	167
p-NO_2-Bn-DOTA	^{67}Ga	3 μM, RT, 60 min	97.4%	162
	^{67}Ga	20 μM, RT, 30 min	96.4%	25
p-NO_2-Bn-PCTA	^{68}Ga	1 μM, RT, 5 min	98.9%	499
p-NO_2-Bn-Oxo	^{68}Ga	1 μM, RT, 5 min	98.5%	496
p-NO_2-Bn-NOTA	^{68}Ga	1 μM, RT, 5 min	98.6%	488
p-NO_2-Bn-DOTA	^{68}Ga	1 μM, 80 °C, 10 min	92.5%	472
	^{68}Ga	10 μM, RT, 30 min	87.5%	45
	^{68}Ga	10 μM, 80 °C, 5 min	95.2%	48

[a] All reactions done in sodium acetate buffer pH 4−5, RT = room temperature, specific activity without purification reported as mCi of isotope incorporated/μmol of BFC.

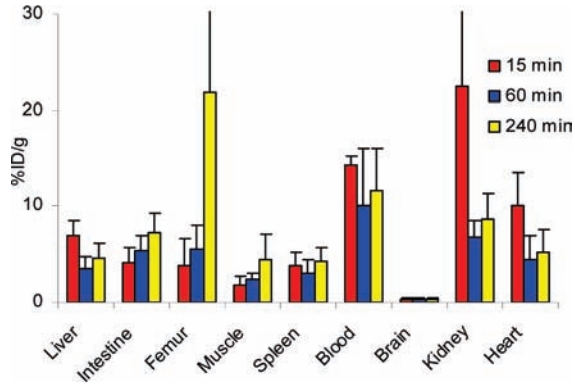


Figure 4. ^{68}Ga-*p*-NO_2-Bn-Oxo biodistribution in CD1 mice over 4 h.

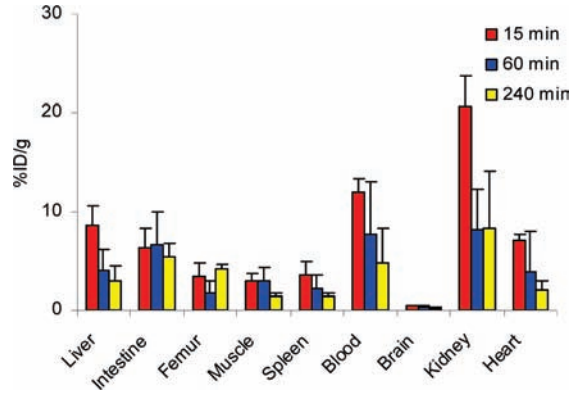


Figure 5. ^{68}Ga-*p*-NO_2-Bn-PCTA biodistribution in male CD1 mice (n = 4) over 4 h.

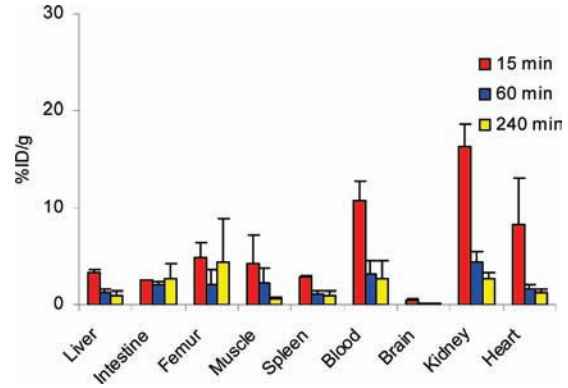


Figure 6. ^{68}Ga-*p*-NO_2-Bn-DOTA biodistribution in male CD1 mice (n = 4) over 4 h.

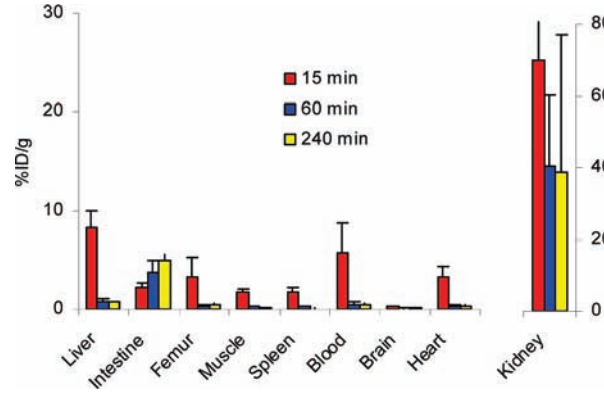


Figure 7. ^{68}Ga-*p*-NO_2-Bn-NOTA biodistribution in male CD1 mice (n = 4) over 4 h.

tissue, other than the kidneys, and in some tissues, such as bone, muscle, and intestines, the %ID/g increased over time.

PET imaging experiments were in agreement with the biodistribution studies. The kidney and bladder were clearly visible and contained the highest activity for all of the ^{68}Ga-radiolabeled BFCs. The activity per unit volume measured in the kidney was on average 4.5 times higher for the ^{68}Ga-radiolabeled *p*-NO_2-Bn-NOTA compared to the other ^{68}Ga-radiolabeled BFCs. While no other tissues could be delineated for ^{68}Ga-radiolabeled *p*-NO_2-Bn-NOTA, heart and intestine were visible for the other three ^{68}Ga-radiolabeled BFCs at early time points and were most notable in the images of mice injected with ^{68}Ga-radiolabeled *p*-NO_2-Bn-Oxo.

DISCUSSION

To determine if the novel BFCs, *p*-NO_2-Bn-PCTA and *p*-NO_2-Bn-Oxo, offered any advantage for Ga-based radiopharmaceutical development, they were directly compared to the currently used BFCs, *p*-NO_2-Bn-PCTA DOTA and *p*-NO_2-Bn-NOTA. Numerous other reports of radiolabeling and animal studies with DOTA and NOTA containing compounds typically focus on targeted conjugates and not the BFC alone. As well, different isotope suppliers, methods, and reagents can all impact experimental results. So, a direct comparison of the novel BFCs to the analogous DOTA and NOTA containing BFCs was warranted to best evaluate *p*-NO_2-Bn-PCTA and *p*-NO_2-Bn-Oxo for use with Ga radioisotopes.

Efficient incorporation of the radioisotope in high yields and high specific activity is particularly important for ^{68}Ga, due to the short half-life of radioisotope. If the radiolabeling reaction were to yield product with high radiochemical purity and specific activity, post-radiolabeling purification could be obviated. The need for purification of ^{68}Ga-radiolabeled peptides (*9, 11*−*13, 15*),

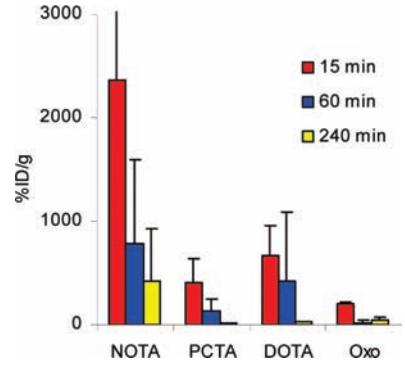


Figure 8. ^{68}Ga-BFC %ID/g in urine in male CD1 mice ($n = 4$) over 4 h.

typically done by HPLC, is not optimal, as it is time-consuming and not necessarily accessible in clinical settings. As some targeting vectors may be sensitive to heat, organic solvents, or extreme pH, radiolabeling reactions that can be done under mild conditions, such as in near neutral aqueous buffers and at room temperature, are preferred.

Comparison of the four BFCs suggested that for labeling with gallium radioisotopes the two novel BFCs, *p*-NO_2-Bn-PCTA and *p*-NO_2-Bn-Oxo, as well as *p*-NO_2-Bn-NOTA, were all superior to *p*-NO_2-Bn-DOTA. The radiolabeling efficiency of *p*-NO_2-Bn-DOTA was greatly impacted by pH, required longer reaction times or heating, and gave lower yields and lower specific activities. Radiolabeling of DOTA conjugates has typically been done at elevated temperatures (*7, 9, 10*), and the slow radioisotope incorporation at room temperature has also been reported (*8*). In contrast, NOTA and NOTA conjugates have recently been reported to radiolabel efficiently under ambient conditions (*14*). The two novel BFCs, *p*-NO_2-Bn-PCTA and *p*-NO_2-Bn-Oxo, also shared this property. Using either ^{67}Ga or ^{68}Ga radiolabeling at room temperature, *p*-NO_2-Bn-PCTA, *p*-NO_2-Bn-Oxo, and *p*-NO_2-Bn-NOTA were all efficiently radiolabeled with ^{67}Ga or ^{68}Ga in minutes without the need for heating or purification.

Similar trends were observed whether the radiochemistry was done with ^{67}Ga or ^{68}Ga, as would be expected, but the results were not identical. Differences observed in radiolabeling may be due to differences in the level of trace metal impurities found in the isotope. *p*-NO_2-Bn-DOTA was found to have slower reaction kinetics for ^{68}Ga labeling compared to ^{67}Ga labeling. Trace metals that are coeluted from the ^{68}Ge generator can compete with ^{68}Ga for the BFC (*7, 17*). It has been suggested that heating may improve the selectivity of the BFCs for ^{68}Ga over other trace metals (*17*), which is supported by the high radiochemical yields and specific activities obtained when the ^{68}Ga radiolabeling of *p*-NO_2-Bn-DOTA was performed at 80 °C. The ^{68}Ga radiolabeling efficiency of *p*-NO_2-Bn-NOTA was not impacted by the increased level of metal impurities, possibly due to the smaller macrocycle having a greater preference for the small Ga^{3+} ion.

The greater stability of *p*-NO_2-Bn-PCTA and *p*-NO_2-Bn-NOTA was illustrated in the transferrin challenge study. Transferrin is an iron transfer protein found in blood. Due to the similar ionic radius and charge of Fe^{3+} (0.645 Å) and Ga^{3+} (0.620 Å) (*18*), ^{67}Ga or ^{68}Ga are known to bind to transferrin (*1*). In the transferrin challenge experiment, each of the Ga-radiolabeled BFCs was incubated in the presence of excess apo-transferrin, and the amount of Ga lost from the BFC and bound to transferrin was monitored over time. Both Ga-radiolabeled *p*-NO_2-Bn-NOTA and *p*-NO_2-Bn-PCTA proved to be relatively inert over 4 h, which is an appropriate period for imaging with ^{68}Ga. Ga-radiolabeled *p*-NO_2-Bn-DOTA showed some loss of Ga to apo-transferrin over time. The instability of Ga-radiolabeled *p*-NO_2-Bn-DOTA in the presence of serum proteins, such as transferrin, has been previously reported (*8, 9*). Ga-radiolabeled *p*-NO_2-Bn-Oxo was determined to be kinetically labile and was predicted to be unstable in vivo, despite having a thermodynamic stability constant similar to *p*-NO_2-Bn-DOTA (Ga-*p*-NO_2-Bn-Oxo pK = 21.3 (*19*), Ga-*p*-NO_2-Bn-DOTA pK = 21.33 (*20*)). The biodistribution results for Ga-radiolabeled *p*-NO_2-Bn-Oxo supported the *in vivo* instability of this species, as negligible clearance from the blood and other tissues was observed, as well as ^{68}Ga accumulation in bone and muscle tissue.

Mouse biodistribution and imaging studies with the three stable ^{68}Ga-radiolabeled BFCs, *p*-NO_2-Bn-PCTA, *p*-NO_2-Bn-NOTA, and *p*-NO_2-Bn-DOTA, provided information on the effect the BFC has on background uptake and clearance. Because of the short half-life of ^{68}Ga, imaging is done soon after injection leaving minimal time for the radiopharmaceutical to clear from blood and other tissue. All three of the BFCs cleared over time, mainly through the kidneys. For all tissues, the %ID/g values for ^{68}Ga-radiolabeled *p*-NO_2-Bn-PCTA compared to ^{68}Ga-radiolabeled *p*-NO_2-Bn-DOTA were not statistically different. The biodistributions of these two BFCs were similar despite the structural differences, the slight differences noted in stability, and the difference in charge (at physiological pH, Ga-*p*-NO_2-Bn-PCTA is expected to be neutral, while Ga-*p*-NO_2-Bn-DOTA would be monoanionic) (*21, 22*). While the biodistribution of ^{68}Ga-radiolabeld *p*-NO_2-Bn-NOTA was statistically similar to those of ^{68}Ga-radiolabled *p*-NO_2-Bn-PCTA and *p*-NO_2-Bn-DOTA with respect to uptake and clearance in the intestine, liver, and bone, large differences were observed for all other tissues. ^{68}Ga-radiolabeled *p*-NO_2-Bn-NOTA cleared much more rapidly from the blood, heart, muscle, and spleen, but had 5 to 20 times more activity retained in the kidney and bladder (urine). The fast clearance from ubiquitous background tissue, such as blood and muscle, appears advantageous for obtaining superior target to background ratios, as long as the imaging target is not in proximity of the kidneys or bladder. Contrastingly, the fast blood clearance may limit the accumulation of the Ga-radiolabeled agent by limiting the circulation time of the agent. By 15 min, ^{68}Ga-radiolabeled *p*-NO_2-Bn-NOTA in the blood (%ID/g) is already half that of ^{68}Ga-radiolabeled *p*-NO_2-Bn-PCTA and *p*-NO_2-Bn-DOTA, and by 1 h, ^{68}Ga-radiolabeled *p*-NO_2-Bn-NOTA has almost completely cleared from the blood. ^{68}Ga-radiolabeled *p*-NO_2-Bn-PCTA and *p*-NO_2-Bn-DOTA also clear from the blood and related tissues, but at a slower rate. The need for relatively fast blood clearance may need to be balanced with adequate circulation time to ensure target accumulation. The addition of a targeting vector such as a peptide is expected to impact the nontargeted tissue distribution. Dependent on the nature and size of the targeting vector, the blood circulation time of the agent may increase and more activity may be retained in the kidney and/or liver due to metabolic processes. Further studies comparing targeted-peptide-conjugated BFCs for molecular imaging are planned to determine how differences in the clearance rates of blood and other tissues affect target uptake and target to background ratios.

CONCLUSIONS

In this study, we evaluated two novel BFCs, *p*-NO_2-Bn-PCTA and *p*-NO_2-Bn-Oxo, for Ga-based radiopharmaceutical development by direct comparison to the commonly used BFCs, *p*-NO_2-Bn-DOTA and *p*-NO_2-Bn-NOTA. Of the four BFCs, *p*-NO_2-Bn-NOTA and *p*-NO_2-Bn-PCTA were found to be more efficiently radiolabeled under milder conditions and to yield kinetically inert complexes that have appropriate clearance properties in vivo. The biodistribution of ^{68}Ga-radiolabeled

p-NO_2-Bn-PCTA was not statistically different than that of ^{68}Ga-radiolabeled *p*-NO_2-Bn-DOTA. However, *p*-NO_2-Bn-PCTA could be radiolabeled with Ga more efficiently under mild conditions compared to *p*-NO_2-Bn-DOTA. Due to superior Ga-radiolabeling efficiency, *p*-NO_2-Bn-PCTA may be an improved alternative to *p*-NO_2-Bn-DOTA in Ga isotope based radiopharmaceutical development. Radiolabeling with *p*-NO_2-Bn-NOTA gave high radiochemical yields in short reactions times and could be done at room temperature. Fast clearance from most tissue was observed for ^{68}Ga-*p*-NO_2-Bn-NOTA, but considerably higher retention in the kidneys was also noted. While the fast background clearance is advantageous, the fast blood clearance of ^{68}Ga-*p*-NO_2-Bn-NOTA could potentially limit target accumulation and requires further investigation.

LITERATURE CITED

(1) Weiner, R. E. (1996) The mechanism of ^{67}Ga localization in malignant disease. *Nucl. Med. Biol. 23*, 745–752.

(2) Weiner, R. E., and Thakur, M. L. (2003) Chemistry of galllium and indium radiopharmaceuticals, in *Handbook of Radiopharmaceuticas Radiochemistry and Applications* (Welch, M., and Redvanly, C. S., Eds.), John Wiley and Sons Ltd., West Sussex, England.

(3) Khan, M. U., Khan, S., El-Refaie, S., Win, Z., Rubello, D., and Al-Nahhas, A. (2009) Clinical indication for Gallium-68 positron emission tomography imaging. *EJSO 35*, 561–567.

(4) Fani, M., Andre, J. P., and Maecke, H. (2008) ^{68}Ga-PET: a powerful generator-based alternative to cyclotron-based PET radiopharmacueticals. *Contr. Med. Mol. Imaging 3*, 53–62.

(5) Maecke, H., Hofmann, M., and Haberkorn, U. (2005) ^{68}Ga-labeled peptides in tumor imaging. *J. Nucl. Med. 46*, 172S–178S.

(6) Fichna, J., and Janecka, A. (2003) Synthesis of target-specific radiolabeled peptides in diagnostic imaging. *Bioconjugate Chem. 14*, 3–17.

(7) Velikyan, I., Beyer, G. J., and Langstrom, B. (2004) Microwave-supported preparation of ^{68}Ga bioconjugates with high sepcific radioactivity. *Bioconjugate Chem. 15*, 554–560.

(8) Blom, E., Langstrom, B., and Velikyan, I. (2009) ^{68}Ga-Labeling of biotin analogues and their characterization. *Bioconjugate Chem. 20*, 1146–1151.

(9) Decristoforo, C., Gonzalez, I. H., Carlsen, J., Rupprich, M., Huisman, M., Virgolini, I., Wester, H.-J., and Haubner, R. (2008) ^{68}Ga- and ^{111}In-labelled DOTA-RGD peptides for imaging $\alpha_v\beta_3$ integrin expression. *Eur. J. Nucl. Med. Mol. Imaging 35*, 1507–1515.

(10) Griffiths, G. L., Chang, C.-H., McBride, W. J., Rossi, E. A., Sheerin, A., Tejada, G. R., Karacay, H., Sharkey, R. M., Horak, I. D., Hansen, H. J., and Goldenberg, D. M. (2004) Reagents and methods for PET using bispecific antibody pretargeting and ^{68}Ga-radiolabeled bivalent hapten-peptide-chelate conjugates. *J. Nucl. Med. 45*, 30–39.

(11) Ren, G., Zhang, R., Liu, Z., Webster, J. M., Miao, Z., Gambhir, S. S., Syud, F. A., and Cheng, Z. (2009) A 2-helix small protein labeled with ^{68}Ga for PET imaging of HER2 expression. *J. Nucl. Med. 50*, 1492–1499.

(12) Liu, Z., Yan, Y., Liu, S., Wang, F., and Chen, X. (2009) ^{18}F, ^{64}Cu, and ^{68}Ga labeled RGD-bombesin heterodimeric peptides for PET imaging of breast cancer. *Bioconjugate Chem. 20*, 1016–1025.

(13) Li, Z.-B., Chen, K., and Chen, X. (2008) ^{68}Ga-labeled multimeric RGD peptides for microPET imaging of integrin $\alpha_v\beta_3$ expression. *Eur. J. Nucl. Med. Mol. Imaging 35*, 1100–1108.

(14) Velikyan, I., Maecke, H., and Langstrom, B. (2008) Convenient preparation of Ga-68 based PET-radiopharmaceuticals at room temperature. *Bioconjugate Chem. 19*, 569–573.

(15) Jeong, J. M., Hong, M. K., Chang, Y. S., Lee, Y.-S., Kim, Y.-J., Cheon, G. J., Lee, D. S., Chung, J.-K., and Lee, M. C. (2008) Preparation of a promising angiogenesis PET imaging agent: ^{68}Ga-Labeled c(RGDyK)-Isothiocyanatobenzyl-1,4,7-triazacyclononane-1,4,7-triacetic acid and feasibility studies in mice. *J. Nucl. Med. 49*, 830–836.

(16) Ferreira, C. L., Yapp, D. T., Lamsa, E., Gleave, M., Bensimon, C., Jurek, P., and Kiefer, G. E. (2008) Evaluation of novel bifunctional chelates for development of Cu-64 based radiopharmaceuticals. *Nucl. Med. Biol. 35*, 875–882.

(17) Velikyan, I., Beyer, G. J., Bergstrom-Pettermann, E., Johansen, P., Bergstrom, M., and Langstrom, B. (2008) The importance of high specific radioactivity in the performance of ^{68}Ga-labeled peptide. *Nucl. Med. Biol. 35*, 529–536.

(18) Shannon, R. D. (1976) Revised effective radii and systematic studies of interatomic distances in halide and chalcogenides. *Acta Crystallogr. A32*, 751–767.

(19) Delgado, R., Quintino, S., Teixeira, M., and Zhang, A. (1996) Metal complexes of a 12-membered tetraaza macrocycle containing pyridine and N-carboxymethyl groups. *J. Chem. Soc., Dalton Trans.* 55–63.

(20) Clarke, E. T., and Martell, A. E. (1991) Stabilities of trivalent metal ion complexes of the tetraacetate derivatives of 12-, 13- and 14-membered tetraazamacrocycles. *Inorg. Chim. Acta 190*, 37–46.

(21) Tircso, G., Benyo, E. T., Suh, E. H., Jurek, P., Kiefer, G. E., Sherry, A. D., and Kovacs, Z. (2009) (S)-5-(*p*-Nitrobenzyl)-PCTA, a promising bifunctional ligand with advantageous metal ion complexation kinetics. *Bioconjugate Chem. 20*, 565–575.

(22) Woods, M., Kovacs, Z., Kiraly, R., Brucher, E., Zhanng, S. R., and Sherry, A. D. (2004) Solution dynamics and stability of lanthanide(III) (S)-2-(*p*-nitrobenzyl)DOTA complexes. *Inorg. Chem. 43*, 2845–2851.

BC900443A

Novel Fusogenic Liposomes for Fluorescent Cell Labeling and Membrane Modification

Agnes Csiszár,*,† Nils Hersch,† Sabine Dieluweit,† Ralf Biehl,‡ Rudolf Merkel,† and Bernd Hoffmann†

Institute of Bio- and Nanosystems, IBN-4, Biomechanics, and Institute of Solid State Research, IFF-5, Neutron Scattering, Forschungszentrum Jülich GmbH, 52425 Jülich, Germany. Received October 28, 2009; Revised Manuscript Received January 20, 2010

Efficient delivery of biomolecules into membranes of living cells as well as cell surface modifications are major biotechnological challenges. Here, novel liposome systems based on neutral and cationic lipids in combination with lipids modified by aromatic groups are introduced for such applications. The fusion efficiency of these liposome systems was tested on single cells in culture like HEK293, myofibroblasts, cortical neurons, human macrophages, smooth muscle cells, and even on tissue. Fusogenic liposomes enabled highly efficient incorporation of molecules into mammalian cell membranes within 1 to 30 min at fully unchanged cell growth conditions and did not affect cell behavior. We hypothesize that membrane fusions were induced in all cases by the interaction of the positively charged lipids and the delocalized electron system of the aromatic group generating local dipoles and membrane instabilities. Selected applications ranging from basic research to biotechnology are envisaged here.

INTRODUCTION

Phospholipid vesicles (liposomes) are widely used, e.g., for cell tracking (*1, 2*), for nonviral gene transfer (transfection) (*3–5*), or for drug delivery (*6, 7*). On the basis of their compositions, liposomes are more bioavailable than synthetic polymer capsules (*8*) or quantum dots (QD). Their cellular uptake has been intensely investigated and shows a strong preference of endocytotic cellular uptake over fusion or lipid mediated poration (*9*). Unfortunately, endocytotic pathways go along with limited efficiencies, often below 1%. Increasing efficiencies is therefore of major interest and approached by enhancing the uptake probability of whole liposomes by techniques as, e.g., electroporation (*10*) or microinjection (*11*). The drawback of these techniques is extreme cell stress, and most of them result in high cell death rates. Furthermore, electroporation can hardly be performed on tissues or adherent cells, and protocols as well as reagents still need to be optimized for every cell type.

The more promising alternative for efficiency enhancement is the induction of membrane fusion between liposomes and the plasma membrane of the mammalian cell. Unfortunately, changes in the chemical composition of liposomes like addition of free fatty acids or alcohols (*12*) or increasing of the chain unsaturations in the hydrophobic region of lipids alone seemed not to be sufficient to develop a universally deployable incorporation system for molecules, just to slightly increase fusion efficiency. At the current state, the most effective factors promoting fusion have biological origins. For example, generation of membrane connecting tubuli (*13*) and integration of fusion proteins (*14–17*), as well as viral membrane components (*18, 19*) in the particle surfaces, are effective biochemical techniques to yield high fusion efficiencies. Although effective, these methods are expensive and time-consuming.

Here, a new, simple, and almost universal fusogenic liposome system containing neutral and positively charged lipid molecules, as well as an additional lipid component with an extended conjugated π electron system, variable in the head or chain region of lipid molecules, has been introduced. The fusion efficacy and toxicity of these liposomes was tested on numerous cell types in culture and even on cell tissue. We furthermore present a possible mechanism underlying this constantly high fusion efficiency.

MATERIALS AND METHODS

Materials. 1,2-Dioleoyl-*sn*-glycero-3-phosphoethanolamine (DOPE), 1,2-dioleoyl-3-trimethylammonium-propane, chloride salt (DOTAP), 1,2-dioleoyl-*sn*-glycero-3-phosphoethanolamine-*N*-(lissamine rhodamine B sulfonyl) (ammonium salt) (LR-DOPE), 1,2-dioleoyl-*sn*-glycero-3-phosphoethanolamine-*N*-(1-pyrenesulfonyl) (ammonium salt) (Pyrene-DOPE), and 1,2-dioleoyl-*sn*-glycero-3-phosphoethanolamine-*N*-(7-nitro-2-1,3-benzoxadiazol-4-yl) (ammonium salt) (NBD-DOPE), 1,2-dioleoyl-*sn*-glycero-3-phosphoethanolamine-*N*-(cap biotinyl) (sodium salt) (capBio-DOPE), and L-α-lysophosphatidylinositol (sodium salt) (PI) were purchased from Avanti Polar Lipids, Inc. (Alabaster, AL). All other modified lipids like 1-hexadecanoyl-2-(1-pyrenedecanoyl)-*sn*-glycero-3-phosphocholine (*β*-Pyrene-C10-HPC), DiOC18(3)3,3′-dioctadecyloxacarbocyanine perchlorate (DiO), 2-(4,4-difluoro-5-methyl-4-bora-3*a*,4*a*-diaza-*s*-indacene-3-dodecanoyl)-1-hexadecanoyl-*sn*-glycero-3-phosphocholine (*β*-BODIPY-C_{12}HPC), *N*-(4,4-difluoro-5,7-dimethyl-4-bora-3*a*,4*a*-diaza-*s*-indacene-3-propionyl)-1,2-dihexadecanoyl-*sn*-glycero-3-phosphoethanolamine (triethylammonium salt) (BODIPY FL-DHPE), 1,2-dioleoyl-*sn*-glycero-3-phosphoethanolamine-*N*-(carboxyfluorescein) (ammonium salt) (Fluorescein-DHPE), *N*-(6-tetramethylrhodaminethiocarbamoyl)-1,2-dihexadecanoyl-*sn*-glycero-3-phosphoethanolamine (triethylammonium salt) (TMR-DHPE), 2-(4,4-difluoro-5,7-diphenyl-4-bora-3*a*,4*a*-diaza-s-indacene-3-pentanoyl)-1-hexadecanoyl-*sn*-glycero-3-phosphocholine (*β*-BODIPY-C_5-HPC), and Texas Red 1,2-dihexadecanoyl-*sn*-glycero-3-phosphoethanolamine (triethylammonium salt) (TR-DHPE) were ordered from Invitrogen (Eugene, OR).

Liposome Preparation. Lipid components like DOPE, DOTAP, and lipids bonded to aromatic groups were mixed in

* Corresponding author. Forschungszentrum Jülich GmbH, 52425 Jülich, Germany, Tel.: ++49 (0)2461 61 1415, Fax: + +49 (0)2461 61 3907, e-mail: a.csiszar@fz-juelich.de.

† Institute of Bio- and Nanosystems, IBN-4, Biomechanics.

‡ Institute of Solid State Research, IFF-5, Neutron Scattering.

10.1021/bc900470y © 2010 American Chemical Society
Published on Web 02/25/2010

chloroform in a weight ratio of DOPE/DOTAP/aromatic lipid of 1/1/0.1. Chloroform was evaporated under vacuum for 0.5−1 h. Then, lipids were dispersed in 20 mM 2-(4-(2-hydroxyethyl)-1-piperazinyl)-ethansulfonic acid (HEPES) buffer (VWR, Darmstadt, Germany) in a total lipid concentration of 2 mg/mL. The solution was vortexed for approximately 1−2 min to produce multilamellar liposomes. After homogenization in an ultrasonic bath for 10−20 min, mainly unilamellar vesicles or liposomes were formed.

Dynamic Light Scattering (DLS). Liposomes made from DOPE/DOTAP (1/1 w/w), DOPE/DOTAP/TR-DHPE (1/1/0.1), and DOPE/DOTAP/β-BODIPY-C_{12}HPC (1/1/0.1) mixtures were studied by dynamic light scattering (*20*) (DLS) in a concentration of 0.02 mg/mL. DLS measurements were performed on a DLS standard setup with an argon ion laser (514 nm) and an Avalanche Photo Diode (APD, ALV, Germany) mounted on an ALV-125 compact goniometer together with an ALV5000E digital correlator (both ALV, Germany). The temperature of the sample was fixed to 20 and 37 °C by a temperature-controlled environment. To account for polydispersity, we evaluated the data according to the CONTIN algorithm (*21*) provided by the ALV-correlator software. The resulting relaxation rate distribution was converted to a hydrodynamic radius distribution according to the Stokes−Einstein relation. A weighting of the relaxation distribution function according to a Rayleigh-Debye theory is not appropriate here because the micelle size is far above the limits of the Rayleigh-Debye theory.

Freeze−Fracture/Transmission Electron Microscopy (TEM). Liposomes made from DOPE/DOTAP (1/1 w/w), DOPE/DOTAP/LR-DOPE (1/1/0.1), and DOPE/DOTAP/β-BODIPY-C_{12}HPC (1/1/0.1) mixtures were studied by freeze−fracture in a concentration of 1 mg/mL. Samples were incubated at 20 °C or at 37 °C for at least 10 min. After incubation, samples were rapidly frozen by plunging into liquid propane cooled by liquid nitrogen. Fracturing was performed at −150 °C in a freeze−fracture apparatus (BAF 400 D, Bal-Tec, Liechtenstein). Etching was achieved by warming the samples to −110 °C for 1 min followed by shadowing with platinum in an electron beam at an angle of 45° and subsequently with carbon at an angle of 90°. The replicas were cleaned with a methanol (VWR, Darmstadt, Germany)/water mixture (9/1 v/v). Replica were captured with copper grids and examined in an EM902 (Carl Zeiss SMT, Oberkochen, Germany) microscope.

Light Microscopy. Samples were imaged at 37 °C using a laser scanning microscope LSM 710 (Carl Zeiss MicroImaging GmbH, Jena, Germany) equipped with an argon ion laser (488 nm) and a helium−neon laser (543 nm). To detect the fluorescent signal of TMR, LR, and TR (excitation 543 nm), a long pass filter LP 650 nm, for BODIPY, DiO, NBD, and fluorescein (excitation 488 nm), a band-pass filter BP 500−520 nm was used. The microscope was equipped with an oil immersion objective EC Plan-Neofluar 40×/1.30 Ph3 (Carl Zeiss). The images were analyzed with the LSM 710 ZEN software (Carl Zeiss).

Fluorescent recovery after photobleaching (FRAP) was used to determine the diffusion constant of lipid components in living cell membranes. For these measurements, an intense, focused laser beam of appropriate wavelength (488 nm for BODIPY FL and 543 nm for LR-DOPE) bleached a small circular spot (ca. 0.5−1 μm^2) on the cell membrane for 50−100 ms. Subsequently, the same beam with a strongly reduced intensity of approximately 3% monitored the reappearance of fluorescence within the circle due to the diffusion of unbleached molecules. The fluorescence recovery curve, $I(t)$ (fluorescence intensity vs time after bleaching) was first corrected as described by Möhl et al. (*22*). Diffusion constants (D) of fluorescent labeled lipids were calculated as follows (*23*):

$$D = 0.224r^2/t_{1/2} \quad (1)$$

where r is radius of the bleached spot and $t_{1/2}$ is half time of fluorescent recovery.

Cell Culture. *Isolation of Rat Embryonic Myofibroblasts.* Fibroblasts were isolated from 18-day old Wistar rat embryos as described earlier (*24*). Cells were seeded on fibronectin coated glass surfaces (2.5 $\mu g/cm^2$ human plasma fibronectin (BD Biosciences, San Jose, CA)). Cells were maintained in F10 Ham's medium (Sigma Aldrich, St. Louis, MO, USA) supplemented with 10% fetal bovine serum and a 1/100 dilution of antibiotics (10 000 units penicillin and 10 mg/mL streptomycin in 0.9% NaCl, (Sigma)). For additional isolation of pericardial tissue, the pericardium was carefully detached from embryonic heart, washed in cold Hanks Balanced Salt Solution (HBSS) (Sigma), and maintained as described above for myofibroblasts.

Isolation of Rat Embryonic Cortical Neurons. Rat embryos were recovered from pregnant rats at day 18 of gestation as described in refs *25* and *26*. Isolated cortical neurons were resuspended in 1 mL Neurobasal Medium (Invitrogen), 1% B27 supplement (Invitrogen), 0.5 mM L-glutamine per hemisphere isolated, and seeded on poly-D-lysine (Sigma) coated glass surfaces (1 $\mu g/cm^2$).

Additional cell types investigated in this study were purchased from different providers and cultivated in the recommended media (Table 1). All cell types listed in Table 1 were cultivated in a humidified incubator at 37 °C and 5% CO_2.

Isolation of Macrophages. Human monocytes were isolated according to the protocol from Noble and Cutts (*27*) using the Leucosep-System (Greiner bio-one, Kremsmünster, Austria). Isolated leucocytes were resuspended in RPMI medium (Sigma) supplemented with 10% fetal bovine serum and a 1/100 dilution of an antibiotic solution (10,000 units penicillin and 10 mg streptomycin in 0.9% NaCl, (Sigma)) and seeded on fibronectin (BD Bioscience, San Jose, CA USA) coated glass surfaces. Nonadherent cells were washed away after four hours. Since monocytes attach to culture surfaces more rapidly than other lymphocytes, this step resulted in an enriched culture. After two days, medium was completely replaced by fresh RPMI containing 0.1 ng/mL granulocyte macrophage colony stimulating factor (G-MCF) (Sigma). After further 3−4 days, monocytes were differentiated to macrophages.

Membrane-Fusion Experiments. For fusion experiments, 5 μL of liposome stock solution was diluted 1/100 with appropriate cell culture medium (Table 1) and gently shaken for 1−2 min at room temperature. Cells in a Petri dish (∅ = 3.5 cm) (20 000−30 000 per dish) were incubated in 500 μL of fusogenic liposomes solution (pH 7.4) for 10−30 min at 37 °C. Subsequently, the fusion mixture was replaced by fresh medium, and cells were imaged by light microscopy.

RESULTS

As lipid base, we used a 1:1 (w/w) ratio of a neutral phospholipid, 1,2-dioleoyl-*sn*-glycero-3-phosphatidylethanolamine (DOPE), and a cationic lipid, 1,2-dioleoyl-3-trimethylammonium-propane (DOTAP). Figure 1 shows the molecular structures of these lipids. This lipid mixture was not able to fuse with cell membranes resulting in low uptake efficiencies (data not shown). The addition of a third lipid component containing large delocalized π electron systems coupled to either the hydrophobic or the hydrophilic lipid parts completely changed the cellular uptake processes. Table 2 summarizes some of the tested aromatic lipid molecules. However, all of them are widely used for fluorescent membrane labeling and none of these molecules can be transferred spontaneously into membranes (*28*) (exception here are lipids of the Di- series, e.g., DiO). Only the synergetic interaction of the three components,

Table 1. Summary of All Cell Types Investigated in This Study

cell name	cell type	organism	provider	medium
myofibroblast	primary cell	embryonic rat	isolated (*24*)	F10 Ham's medium, 10% FBS, 1× penicillin−streptomycin
keratinocyte	primary cell	human	purchased at Lonza	keratinocyte basal medium
cortical neuron	primary cell	embryonic rat	isolated (*25, 26*)	neurobasal medium, 1% B27 supplement
macrophage	primary cell	human	isolated (*27*)	RPMI-1640 medium, 10% FBS, 1× penicillin−streptomycin
HEK293 cell	cell-line	human	purchased at DSMZ	DMEM medium, 10% FBS, 1× penicillin−streptomycin
bronchial smooth muscle cell	primary cell	human	purchased at Lonza	BSMC, 10% FBS, 1× penicillin−streptomycin
pericardial tissue	primary tissue	embryonic rat	isolated	F10 Ham's medium, 10% FBS, 1× penicillin−streptomycin

neutral lipid, cationic lipid, and aromatic lipid resulted in an effective fusogenic mixture.

Characterization of the Fusogenic Liposomes. Although DOPE/DOTAP (1/1 w/w) liposomes did not fuse measurably with cell membranes, they were chosen as reference sample to compare their physicochemical behavior with that of the fusogenic liposomes. After preparation, the average radius of the DOPE/DOTAP liposomes was 0.72 ± 0.09 μm (Figure 2a) according to dynamic light scattering analyses. Freeze−fracture and subsequent electron microscopy further specified them as unilamellar vesicles with smooth surfaces at room temperature as well as at 37 °C (Figure 2b).

The addition of aromatic lipid components to a DOPE/DOTAP mixture, e.g., lissamine rhodamine B fluorescent dye coupled to DOPE (Table 2) or β-BODIPY coupled to C_{12}-HPC (Figure 1 and Table 2), just slightly affected the size distributions of liposomes with an average radius of 0.78 ± 0.07 μm and 0.94 ± 0.10 μm, respectively. Smaller vesicles or larger aggregates of vesicles were not observed in the dynamic light scattering analyses (Figure 2a). Vesicles were observed as unilamellar, spherical structures with smooth, nonstructured surfaces at both temperatures similar to the reference sample (Figure 2b).

Administration of Fusogenic Liposomes to Single Cells. In order to prove fusion, HEK293 cells were imaged during incubation with fusogenic liposomes made from DOPE/DOTAP/BODIPY FL-DHPE (1/1/0.1 w/w) lipid mixture (Figure 1a). Immediately after vesicle addition (Figure 3a: 0 s), small green dots, i.e., vesicles, were observed in the BODIPY FL channel. After 100 s, the first fluorescently labeled cell membranes appeared, and 200 s later, most of the plasma membranes could

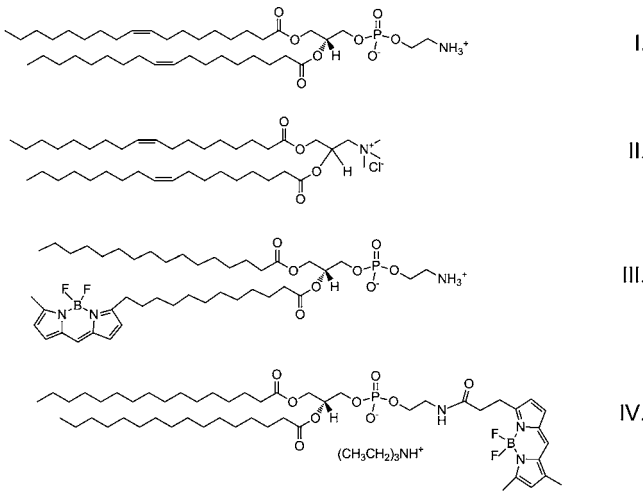


Figure 1. Molecular structure of (I) 1,2-dioleoyl-*sn*-glycero-3-phosphatidylethanolamine (DOPE) as a neutral lipid component, (II) 1,2-dioleoyl-trimethylammonium-propane (DOTAP) as a cationic lipid component, (III) 2-(4,4-difluoro-5-methyl-4-bora-3*a*,4*a*-diaza-*s*-indacene-3-dodecanoyl)-1-hexadecanoyl-*sn*-glycero-3-phosphocholine (β-BODIPY C_{12}-HPC) as a chain modified lipid, and (IV) *N*-(4,4-difluoro-5,7-dimethyl-4-bora-3*a*,4*a*-diaza-*s*-indacene-3-propionyl)-1,2-dihexadecanoyl-*sn*-glycero-3-phosphoethanolamine, triethylammonium salt (BODIPY FL-DHPE) as a head modified lipid.

Table 2. Summary of Aromatic Lipids Used in This Study to Induce Membrane Fusion with Living Cells[a]

Aromatic Group	Ex/Em (nm)	Structure of Aromatic Group	Aromatic Group Covalently Bound to	Efficiency
Pyrene (UV)	340/346		DOPE head	*
Pyrene (UV)	340/346		C_{10}HPC chain	*
DiO, $DiOC_{18}$(3)	484/501		-	***
β-BODIPY	500/510		C_{12}HPC chain	***
BODIPY FL	505/511		DHPE head	***
Fluorescein	496/519		DOPE head	**
NBD	463/536		DOPE head	**
Tetrametyl-rhodamine	540/566		DHPE head	***
Lissamine Rhodamine B	560/581		DOPE head	***
β-BODIPY	581/591		C_6HPC chain	**
Texas Red	583/601		DHPE head	***

[a] Rainbow scale (left) describes their corresponding emission spectra. Fusion efficiency is indicated by asterisks ranging from poor (*) to very good (***).

be imaged in the green fluorescence channel (Figure 3a). Cellular plasma membranes were homogenously labeled by BODIPY FL without liposome clumps on the surface. Unchanged cell behavior and cell growth were detected in the phase contrast channel simultaneously with the appearance of the fluorescent signal in the cell membranes. After successful membrane fusion, excess liposomes were replaced by cell medium, and cell survival and clearance of fluorescent lipids from the plasma membrane were determined. Cell growth of HEK293 was not influenced by liposome fusion, and a healthy cell layer completely covered the glass surface 24 h after fusion. Most dye lipid disappeared from the cell membrane during this time period as shown in Figure 3b.

Several aromatic phospholipid molecules were tested for fusion capacity. Although they all induced membrane fusion with living cells, clear differences were seen in fusion time,

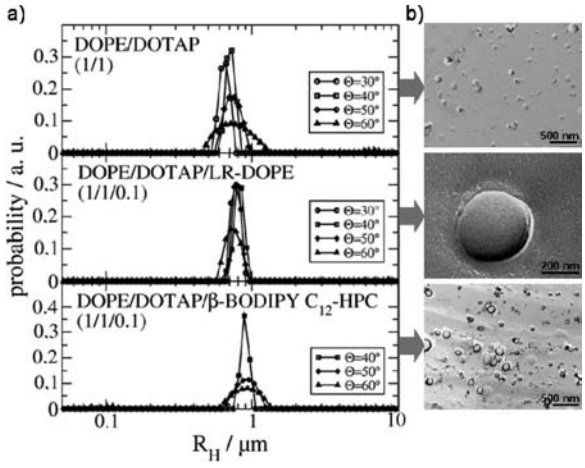


Figure 2. Physico-chemical characterization of fusogenic liposomes. (a) Hydrodynamic radius distribution from dynamic light scattering after CONTIN analysis of DOPE/DOTAP (1/1 w/w), DOPE/DOTAP/LR-DOPE (1/1/0.1 w/w), and DOPE/DOTAP/β-BODIPY-C_{12}HPC (1/1/0.1 w/w) mixtures at 20 μg/mL concentration in 20 mM HEPES buffer. Measurements were carried out at the indicated scattering angles. (b) The same fusogenic vesicles at 2 mg/mL concentration were freeze−fractured and subsequently analyzed by transmission electron microscopy. Note their unilamellar composition and smooth surface.

fusion efficiency, and signal homogeneity in the plasma membrane. These parameters together entered an admittedly subjective efficiency scale (Table 2). The most effective and fast fusion processes with homogeneously distributed fluorescence signals in the cell membrane were induced by large aromatic groups containing hetero atoms with a significantly higher electronegativity, e.g., oxygen, nitrogen, or boron coupled to fluorine (Table 2: ***). Dye molecules as pyrene with a homogenously distributed π electron system without hetero atoms correspondingly were found to be less effective fusion promoters (Table 2: *). Cyclic groups coupled to lipid molecules that were not in compliance with Hückel's rule were also investigated (e.g., capbiotin-DOPE or phosphatidylinositol), and no fusion with cell membranes was detected. Furthermore, the efficiency of pH-sensitive dyes like fluorescein depended on their ionic form. At low pH values where the dye group was deprotonated, they were less effective than at higher pH in the protonated form (Table 2: **).

Table 3. Lateral Diffusion Constant (*D*) and Fluorescence Recovery of Head and Chain-Labeled Lipids Measured in HEK293 Cell Membranes after Liposome Fusion (mean ± sd for *n* measurements)

dye lipid	D (μm^2/s)	recovery (%)	n
LR-DOPE	0.21 ± 0.14	84 ± 5	8
BODIPY FL-DHPE	0.16 ± 0.08	76 ± 6	9
β-BODIPY C_{12}HPC	0.15 ± 0.05	75 ± 7	9

The successful incorporation of aromatic lipid molecules was furthermore controlled by detecting their lateral diffusion constants using fluorescence recovery after photobleaching technique (FRAP) (*29, 30*). Liposome fusion events were induced in HEK293 cells by LR-DOPE and BODIPY FL-DHPE as headgroup-modified lipids and β-BODIPY C_{12}HPC as chain-labeled lipid. Plasma membranes were first localized by confocal imaging. Subsequently, diffusion constants (D) and fluorescence recovery of the dye lipids in the plasma membrane were determined. A typical recovery curve is shown in Figure 3b, and all results are summarized in Table 3. The resulting diffusion constants of all investigated dye lipids were found to be relatively similar with values around 0.18 μm^2/s. Even the location of the aromatic group in the polar head or apolar chain region did not significantly influence the diffusion behavior. Fluorescence recovery, frequently called mobile fraction, was also determined, and the values also appeared statistically similar

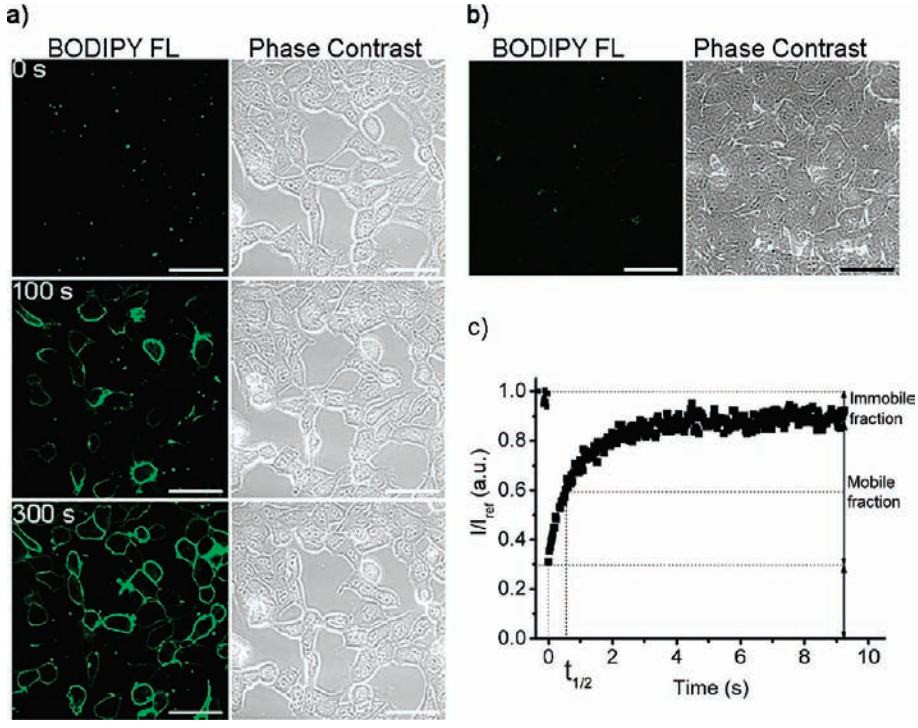


Figure 3. Vesicle fusion with plasma membranes. (a) HEK293 cells were incubated with vesicles made from DOPE/DOTAP/BODIPY FL-DHPE (1/1/0.1 w/w) and analyzed over 300 s in fluorescence (left) and phase contrast (right). Within this time period, efficient membrane fusion was detected with unchanged cell behavior. Scale bars = 50 μm. (b) Uninfluenced cell growth (phase contrast channel) and completely degraded liposomes (BODIPY FL channel) were observed 24 h after membrane fusion. Scale bars = 80 μm (c). Fluorescence recovery curve of LR-DOPE in HEK293 plasma membrane after membrane fusion. The diffusion parameters of LR-DOPE calculated from the FRAP curve confirm the incorporation of fluorescently labeled lipid into the cell membrane.

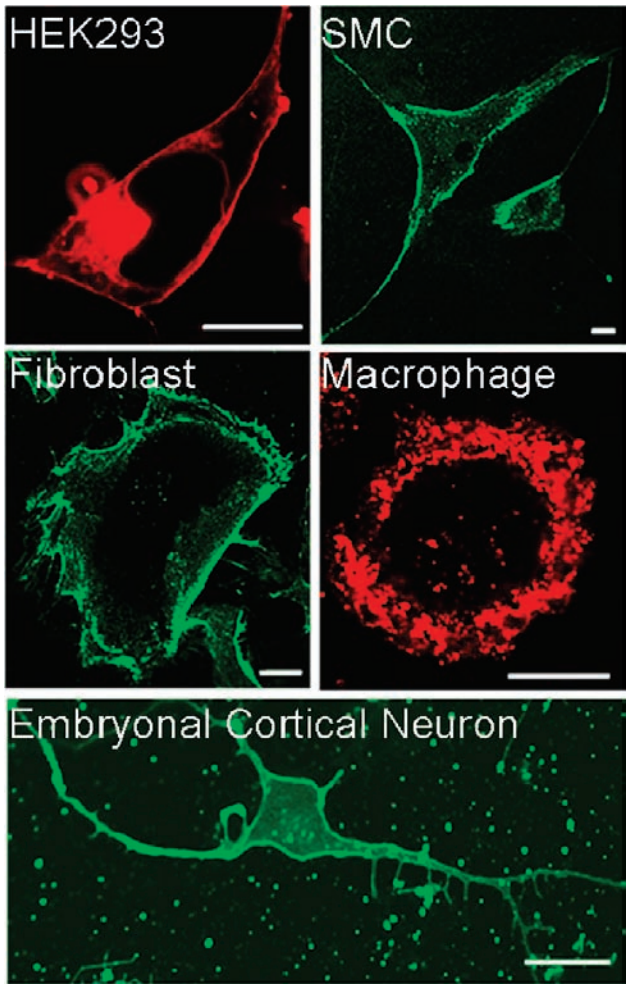


Figure 4. Cell membranes of HEK293, smooth muscle cells (SMC), rat myofibroblasts, human macrophages, and embryonal cortical neurons were fluorescently labeled by vesicle fusion. As aromatic lipids, either LR-DOPE (red) or BODIPY FL-DHPE (green) was used. Scale bars = 10 μm.

to each other (around 78 ± 6%) independent from the dye and its location in the lipid molecule. The measured values were in good agreement with other values given for fluorescent tracer lipid diffusion in cell membranes (*23, 31*).

The ubiquitous ability of our system to induce fusion was successfully proven by labeling many other cell types as human keratinocytes, human macrophages, rat embryonic cortical neurons, bronchial smooth muscle cells, and rat myofibroblasts. For all of these cell types, cell labeling efficiency reached an almost complete labeling of all cells. Only in the case of myocytes was an increased resistance against fusogenic liposomes observed (data not shown). Some labeled cells are presented in Figure 4.

Administration of Fusogenic Liposomes on Cellular Tissue. As an exemplary tissue sample, rat embryonic pericardium, a multicelled layer of defined thickness around the contractile heart apparatus was chosen and incubated with fusogenic liposomes made from DOPE/DOTAP/BODIPY FL-DHPE (1/1/0.1 w/w) lipid mixture for one hour. This prolonged incubation period was necessary due to the increased cell number and the cell stacks on top of each other. Confocal imaging revealed an almost complete staining of all pericardial surface cells. Additionally, almost all cell layers (three to four)

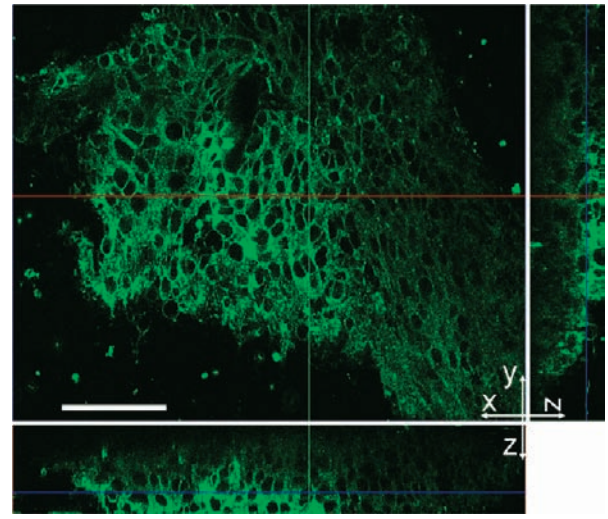


Figure 5. Isolated pericardial tissues were incubated for 1 h using DOPE/DOTAP/BODIPY FL-DHPE (1/1/0.1 w/w) mixture as fusogenic liposomes and subsequently imaged by confocal microscopy. Small micrographs below and on the right of the main image indicate the cross sections parallel to *xz*- and *yz*-planes respectively. Cross section images revealed several fluorescently labeled cell layers below the top layer. Scale bar = 100 μm.

below the top layer were labeled with similar efficiency in spite of the relatively large liposomal size (Figure 5).

DISCUSSION

Classical liposomes used for DNA delivery are based on a composition of neutral and positively charged lipid molecules. The cellular uptake processes of these vesicles have been investigated earlier and have shown a strong preference of endocytotic pathways with a limited efficiency (*32*). Here, the addition of a third lipid component converted these liposomes to a nearly universal fusogenic system. The third lipid component needed to meet the criteria of (a) amphiphilic molecular character to be easily incorporated into biological or biomimetic membranes and (b) a delocalized conjugated π-electron system located in the polar or apolar molecular range. Interestingly, these criteria were fulfilled by almost all fluorescent labels when coupled to phospholipids. Table 2 summarized all successfully tested molecules. Other molecules meeting these criteria should work as well but have not been explicitly tested here since fluorescently labeled lipids had the strong advantage of direct visualization of fusion to unravel the functional mechanism.

The synergistic interaction of the three components, neutral lipid, positively charged lipid, and lipids with an aromatic group resulted in an effective fusogenic mixture. Although the mechanism of action has not yet been elucidated, it is to assume that the neutral molecule DOPE has a cone-like effective shape and supports fusion intermediate states (*33*). The positive charge of DOTAP in the polar headgroup region interacts with the negatively charged glycocalyx of the cell membrane decreasing the distance between liposome and cell membrane and increasing the probability of fusion, respectively (*3*). Additionally, the strong positive charges in the headgroup of liposomes polarize the delocalized π electrons inducing local dipoles. These dipoles presumably yield local instabilities and disorders of molecular arrangements in the bilayer. Cevc and Richardsen reported that such effects could positively influence membrane fusion processes (*12*). Moreover, the presence of an additional heteroatom with high electronegativity, e.g., fluorine (χ = 4 on the Pauling scale) in BODIPY dyes (Figure 1a) or oxygen (χ = 3.5) and nitrogen (χ = 3.0) increased the dipole character in the aromatic group resulting in a higher fusion

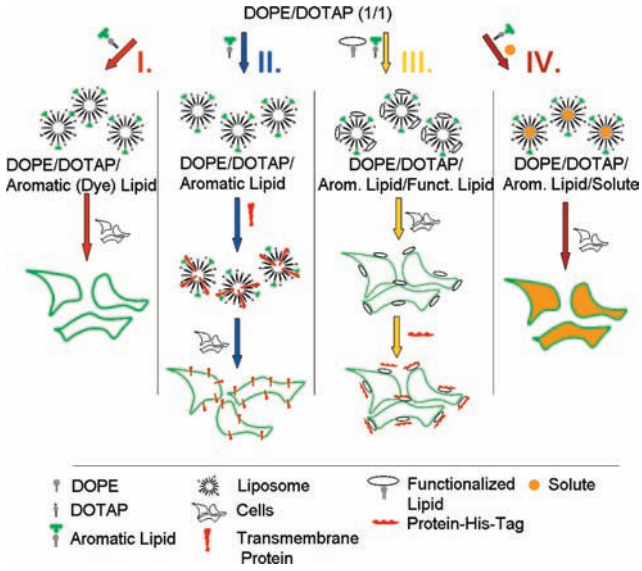


Figure 6. Overview of the potential fields of application for fusogenic liposomes: (I), plasma membrane visualization (II), transmembrane protein incorporation into plasma membranes, (III) cell surface functionalization, and (IV) content delivery.

potential, while molecules with a large but homogenously distributed π electron system like pyrene (Table 2) revealed reduced fusion behavior. Cyclic groups without aromaticity and coupled to phospholipids did not induce fusion processes with membranes of living cells.

Delocalized electron systems could be bound to the head as well as the chain regions of lipids (Table 2, e.g., pyrene or BODIPY) without any influence on the fusion efficiency. The most effective composition ratio between the three components was found from 1/1/0.05 to 1/1/0.2 (w/w) of DOPE/DOTAP/aromatic lipid. A lower amount of aromatic lipids is often not sufficient to promote fusion, while higher concentrations can be toxic to cells. In general, an approximate weight ratio of 1/1/0.1 could be successfully used for the first experimental approaches. The digestion of lipids used in fusogenic liposomes in a weight ratio of 1/1/0.1 of DOPE/DOTAP/aromatic lipid by HEK293 was investigated, and their full degradation was observed in a time period of 24 h accompanied by completely unchanged cell growth. On the basis of these observations, we propose that administration of these novel liposomes yielded highly efficient cell membrane modifications without noticeable toxic side effects.

Liposome fusion events were successfully observed in several cell types like HEK293 cells, human macrophages, rat embryonic cortical neurons, smooth muscle cells, and rat myofibroblasts (Figure 4). After membrane fusion, diffusion constants (D) of aromatic lipids were determined with 0.18 $\pm$ 0.14 $\mu m^2/s$ (Table 3) corresponding to other values given for lipid diffusion in cell membranes (*23, 31*). This value is approximately one magnitude lower in comparison to lipid diffusion in model membranes without hindering proteins where the diffusion constant of NBD-DOPE was found to be 2.5 $\pm$ 0.2 $\mu m^2/s$ (*34, 35*). This fact supports the hypothesis of membrane fusion against liposomal adhesion on cell membrane surfaces. Additionally, the selective fluorescent signal of the cell membrane as well as the short uptake time and the high efficiency suggested a membrane fusion against endocytosis as main uptake mechanism.

These results open a large number of possible pharmaceutical and biotechnological application fields as schematically summarized in Figure 6. Fluorescent membrane labeling is only one of the numerous cell membrane modifications (Figure 6 I). With addition of other functionalized molecules like chelator lipids or biotinylated or antigenic lipids at an optional low concentration, surface functionalization of living cells can be achieved (Figure 6 III). This membrane modification can be completed in an additional step by protein coupling to the cell surface. Furthermore, it is assumed that membrane proteins in addition to functionalized lipids can also be incorporated into fusogenic liposomes and, corresponding to this, into cell membranes as well (Figure 6 II). Nevertheless, if the membrane mixing is accompanied by content mixing, highly efficient delivery of soluble molecules to living cells can be performed (Figure 6 IV). Fusogenic liposomes could easily be modified by tumor specific targeting and used for medical purposes.

In conclusion, we have designed a new, simple and almost universal fusogenic liposome system containing neutral and positively charged lipid molecules as well as additional lipid components with aromatic molecular groups. The liposomes mediate highly effective fusion processes with living cell membranes without toxic side effects. As fusion mechanism, we hypothesize a synergistic interaction of the positively charged lipids and the delocalized electron system of the aromatic group inducing local dipoles and membrane instabilities. However, the exact mechanism has to be investigated in the future. This new type of fusogenic liposomes opens a large number of biotechnological application fields.

ACKNOWLEDGMENT

We thank R. Fricke and K. Michael for isolation of rat cortical neurons. We are also grateful to J. Fleischhauer for technical support.

LITERATURE CITED

(1) Gopalakrishnan, G., Delon, C., and Vogel, H. (2006) Multifunctional lipid/quantum dot hybrid nanocontainers for controlled targeting of live cells. *Angew. Chem., Int. Ed. Engl. 45*, 5478–5483.

(2) Seo, J. W., Zhang, H., Kukis, D. L., Meares, C. F., and Ferrara, K. W. (2008) Novel method to label preformed liposomes with ^{64}Cu for positron emission tomography (PET) imaging. *Bioconjugate Chem. 19*, 2577–2584.

(3) Chesnoy, S., and Huang, L. (2000) Structure and function of lipid-DNA complexes for gene delivery. *Annu. Rev. Biophys. Biomol. Struct. 29*, 27–47.

(4) Kawakami, S., Yamasgita, F., and Hashida, M. (2005). Liposomal in vivo gene delivery. In *Modern Biopharmaceuticals* (Jörg Knäblein, Ed.) pp 1507−1519, Chapter 7, WILEY-VCH Verlag GmbH & Co. KGaA, Weinheim.

(5) Narang, A. S., Thoma, L., Miller, D. D., and Mahato, R. I. (2005) Cationic lipids with increased DNA binding affinity for nonviral gene transfer in dividing and nondividing cells. *Bioconjugate Chem. 16*, 156–168.

(6) Gregoriadis, G. (2007) *Liposome Technology*; Informa Healthcare, New York.

(7) Sawant, R. M., Hurley, J. P., Salmaso, S., Kale, A., Tolcheva, E., Levchenko, T. S., and Torchilin, V. P. (2006) SMART" drug delivery systems: double-targeted pH-responsive pharmaceutical nanocarriers. *Bioconjugate Chem. 17*, 943–949.

(8) Pack, D. W., Hoffman, A. S., Pun, S., and Stayton, P. (2005) Design and development of polymers for gene delivery. *Nat. Rev. Drug Discovery 4*, 581–593.

(9) Li, W., and Szoka, F. C., Jr. (2007) Lipid-based nanoparticles for nucleic acid delivery. *Pharm. Res. 24*, 438–449.

(10) Gresch, O., Engel, F. B., Nesic, D., Tran, T. T., England, H. M., Hickman, E. S., Körner, I., Gan, L., Chen, S., Castro-Obregon, S., Hammermann, R., Wolf, J., Müller-Hartman, H., Nix, M., Siebenkotten, G., Kraus, G., and Lun, K. (2004) New non-viral method for gene transfer into primary cells. *Methods 33*, 151–163.

(11) Johnston, S. A., and Tang, D. C. (1994) Gene gun transfection of animal cells and genetic immunization. *Methods Cell Biol. 43*353–365.

(12) Cevc, G., and Richardsen, H. (1999) Lipid vesicles and membrane fusion. *Adv. Drug Delivery Rev. 38*, 207–232.

(13) Tareste, D., Shen, J., Melia, T. J., and Rothman, J. E. (2008) SNAREpin/Munc18 promotes adhesion and fusion of large vesicles to giant membranes. *Proc. Natl. Acad. Sci. U.S.A. 105*, 2380–2385.

(14) Sakaguchi, N., Kojima, C., Harada, A., Koiwai, K., and Kono, K. (2008) The correlation between fusion capability and transfection activity in hybrid complexes of lipoplexes and pH-sensitive liposomes. *Biomaterials 29*, 4029–4036.

(15) Sakaguchi, N., Kojima, C., Harada, A., Koiwai, K., Emi, N., and Kono, K. (2008) Effect of transferrin as a ligand of pH-sensitive fusogenic liposome-lipoplex hybrid complexes. *Bioconjugate Chem. 19*, 1588–1595.

(16) Kobayashi, S., Nakase, I., Kawabata, N., Yu, H. H., Pujals, S., Imanishi, M., Giralt, E., and Futaki, S. (2009) Cytosolic targeting of macromolecules using a pH-dependent fusogenic peptide in combination with cationic liposomes. *Bioconjugate Chem. 20*, 953–959.

(17) Bánóczi, Z., Tantos, A., Farkas, A., Tompa, P., Friedrich, P., and Hudecz, F. (2007) Synthesis of cell-penetrating conjugates of calpain activator peptides. *Bioconjugate Chem. 18*, 130–137.

(18) Hatefi, A., and Canine, B. F. (2009) Perspectives in vector development for systemic cancer gene therapy. *Gene Ther. Mol. Biol. 13* (A), 15–19.

(19) Roemer, W., Berland, L., Bassereau, P., and Johannes, L. (2007) Shiga toxin induced tubular membrane invaginations for its uptake into cells. *Nature 450*, 670–675.

(20) Berne, B. J., and Pecora, R. (1975) *Dynamic Light Scattering*, John Wiley, San Francisco.

(21) Provencher, S. W. (1982) A constrained regularization method for inverting data represented by linear algebraic or integral equations. *Comput. Phys. Commun. 27*, 213–227.

(22) Möhl, C., Kirchgessner, N., Schäfer, C., Küpper, K., Born, S., Diez, G., Goldmann, W. H., Merkel, R., and Hoffmann, B. (2009) Becoming stable and strong: the interplay between vinculin exchange dynamics and adhesion strength during adhesion site maturation. *Cell Motil. Cytoskeleton 66*, 350–364.

(23) Greenberg, M. L., and Axelrod, D. (1993) Anomalously slow mobility of fluorescent lipid probes in the plasma membrane of the yeast *Saccharomyces cerevisiae*. *J. Membr. Biol. 131*, 115–127.

(24) Cesa, M. C., Kirchgessner, N., Mayer, D., Schwarz, U. S., Hoffmann, B., and Merkel, R. (2007) Micropatterned silicone elastomer substrates for high resolution analysis of cellular force patterns. *Rev. Sci. Instrum. 78*, 0343011034301−10.

(25) Brewer, G. J., Torricelli, J. L., Evege, E. K., and Price, P. J. (1993) Optimized survival of hippocampal neurons in B27-supplemented Neurobasal, a new serum-free medium combination. *J. Neorosci. Res. 35*, 567–576.

(26) Vogt, A. K., Wrobel, G., Meyer, W., Knoll, W., and Offenhäusser, A. (2005) Synaptic plasticity in micropatterned neuronal networks. *Biomaterials 26*, 2549–2557.

(27) Noble, P. B., and Cutts, J. H. (1967) Separation of blood leukocytes by Ficoll gradient. *Can. Vet. J. 8*, 110–111.

(28) Malinin, V. S., Haque, M. E., and Lentz, B. R. (2001) The rate of lipid transfer during fusion depends on the structure of fluorescent lipid probes: a new chain-lableled lipid transfer probe pair. *Biochemistry 40*, 8292–8299.

(29) Chen, Y., Lagerholm, C., Yang, B., and Jacobson, K. (2006) Methods to measure the lateral diffusion of membrane lipids and proteins. *Methods 39*, 147–153.

(30) Soumpasis, D. M. (1983) Theoretical analysis of fluorescence photobleaching recovery experiments. *Biophys. J. 41*, 95–97.

(31) de Monvel, J. B., Brownell, W. E., and Ulfendahl, M. (2006) Lateral diffusion anisotropy and membrane lipid/skeleton interaction in outer hair cells. *Biophys. J. 91*, 364–381.

(32) Simberg, D., Weisman, S., Talmon, Y., and Barenholz, Y. (2004) DOTAP (and other cationic lipids): chemistry, biophysics, and transfection. *Crit. Rev. Ther. Drug Carrier Syst. 21*, 257–317.

(33) Chernomordik, L. V., and Kozlov, M. M. (2008) Mechanics of membrane fusion. *Nat. Struct. Mol. Biol. 15*, 675–683.

(34) Fenz, S., Merkel, R., and Sengupta, K. (2009) Diffusion and intermembrane distance: case study of avidin and E-cadherin mediated adhesion. *Langmuir 25*, 1074–1085.

(35) Horton, M. R., Reich, C., Gast, A. P., Raedler, J. O., and Nickel, B. (2007) Structure and dynamics of crystalline protein layers bound to supported lipid bilayers. *Langmuir 11*, 6263–6269.

BC900470Y

Synthesis and AFM Characterization of Poly(dG)-poly(dC)-gold Nanoparticle Conjugates

Dragoslav Zikich, Natalia Borovok, Tatiana Molotsky, and Alexander Kotlyar*

Department of Biochemistry, George S. Wise Faculty of Life Sciences, Tel Aviv University, The Center for Nanoscience and Nanotechnology, Tel Aviv University, Ramat Aviv, 69978. Received December 1, 2009; Revised Manuscript Received January 29, 2010

In the present work, we have synthesized conjugates between the 5 nm gold nanoparticles (Au-NP) and 5′ thiol-functionalized, 700 bp poly(dG)-poly(dC). We have completely separated and purified to homogeneity conjugates bearing different number of poly(dG)-poly(dC) molecules per Au-NP by electrophoresis and HPLC. The conjugates were directly visualized by atomic force microscopy. We have demonstrated that Au NP-bound poly(dG)-poly(dC) can be considerably extended by Klenow exo$^-$ polymerase in the presence of dCTP and dGTP.

INTRODUCTION

Since the pioneering works by Alivisatos and Mirkin (*1, 2*), interaction of Au-NP with thiol-modified single-stranded (ss) DNA has become a subject of extensive investigation by chemists, biologists, and physicists. Because of their small size, Au-NP-DNA conjugates exhibit unique physical, chemical, and optical properties and have been used as bases for development of applications in various aspects of nanoassembly (*3, 4*), biodiagnostics (*5*−*7*), and nanoelectronics (*8, 9*). The ability of DNA to form well-defined secondary and tertiary structures offers a variety of possibilities for nanostructure design in a bottom-up approach (*10*). The vast majority of studies in this field were focused on the interaction of ssDNA with metal nanoparticles; much less emphasis has been placed on formation of conjugates between long, functionalized dsDNA and the particles. It has been shown that DNA molecules connected to a particle retain their functional activity and can be processed by restriction enzymes (*10*−*12*), polymerases (*13*), and ligases (*14*). Tsai and co-workers have successfully used a ligase-based approach for the formation of complexes between long (1714 base pairs) random-sequence thiolated dsDNA and gold nanoparticles (*15*). The conjugates bearing a different number of DNA molecules per particle have been efficiently separated from each other by electrophoresis and seen by AFM (*15*). To the best of our knowledge, no nanoparticle conjugates with homogeneous dsDNA polymers have been reported so far. The results of theoretical calculations show that poly(dG)-poly(dC) exhibits better conductance than other homopolymeric DNA form, poly(dA)-poly(dT) (*16*). Therefore, poly(dG)-poly(dC) homopolymer seems to be a promising new candidate for use in DNA-based nanodevices.

We have recently invented a new enzymatic method for the synthesis of homogeneous dsDNA polymers (*17*). This method enables us to synthesize poly(dG)-poly(dC) molecules, ranging from tens to tens of thousands base pairs that are characterized by a narrow length distribution. In addition, these molecules can be functionalized at one or at both 5′-ends with SH-groups or other residues. The ability to introduce SH-groups into the synthesized molecules provides a tool for their covalent attachment to gold surfaces. Attachment of metal particles might provide good electric communication between the electrode and the DNA-NP conjugate via metal/metal contact interactions, thus promoting charge migration though the DNA.

Here, we describe an efficient method for production of poly(dG)-poly(dC) Au-NPs conjugates bearing a different number of DNA molecules per Au-NP. The conjugates were efficiently separated by agarose gel electrophoresis and visualized by AFM. We demonstrate that poly(dG)-poly(dC) molecules connected to a Au-NP can be extended by Klenow exo$^-$ fragment of DNA polymerase.

EXPERIMENTAL PROCEDURES

Synthesis of Au Nanoparticles. Au-NPs of 5 nm in diameter were prepared by the modified citrate reduction method (*18, 19*). 5.9 mg of $HAuCl_4$ was dissolved in 1 mL of double distilled water and added into 47 mL of H_2O to the final concentration of 0.3 mM. The solution was incubated with constant stirring at 25 °C for 10 min. 0.5 mL of 50 mM sodium citrate solution was added to the reaction mixture to a final concentration of 0.5 mM, and the solution was incubated under constant stirring for another 10 min. 0.67 mL of cooled 0.1 M $NaBH_4$ was added into the stirred mixture; the solution developed an orange−red color. The resulting nanoparticles were screened for their size and uniformity by TEM, revealing an average diameter of 5 ± 1.5 nm. The UV−vis spectra showed a characteristic absorption peak at 520 nm. The particles were stabilized with BSPP (bis sulfonatophenylphosphine dehydrate dipotassium salt, Strem Chemicals, USA) as follows. The Au-NPs above were incubated with 0.1 mM BSPP in the dark for 20 h at RT and concentrated using Microcon device YM-50 (Millipore, USA). The excess of BSPP was removed by passing the particles though G-25 Sephadex column (15 × 50 mm, Healthcare, USA) in 20 mM Tris-acetate buffer, pH 7.5. The Au-NPs eluted in the void volume of the column were concentrated using YM-50 Microcon device (Millipore, USA). Concentration of the particles was calculated using an extinction coefficient (ε) of 9.3×10^6 M^{-1} cm^{-1} at 517 nm.

DNA Samples. The $(dC)_{12}$ and SH-$(dG)_{12}$ oligonucleotides were purchased from Alpha DNA (Montreal, Canada). The SH-group in SH-$(dG)_{12}$ was linked to the terminal base at the 5′ end of G-12mer $(dG)_{12}$ oligonucleotides via a six-carbon linker. The oligonucleotides were purified to homogeneity essentially as described (*20*). Purified SH-$(dG)_{12}$ and $(dC)_{12}$ oligomers were incubated in 0.1 M NaOH at an equimolar ratio for 15 min at room temperature and further dialyzed against 20 mM Tris-acetate buffer, pH 7.5, containing 2 mM DTT for 1 h. The

* To whom correspondence should be addressed. Phone: 972 3 6407138; Fax: 972 3 6406834; E-mail: s2shak@post.tau.ac.il.

10.1021/bc900527a © 2010 American Chemical Society
Published on Web 02/18/2010

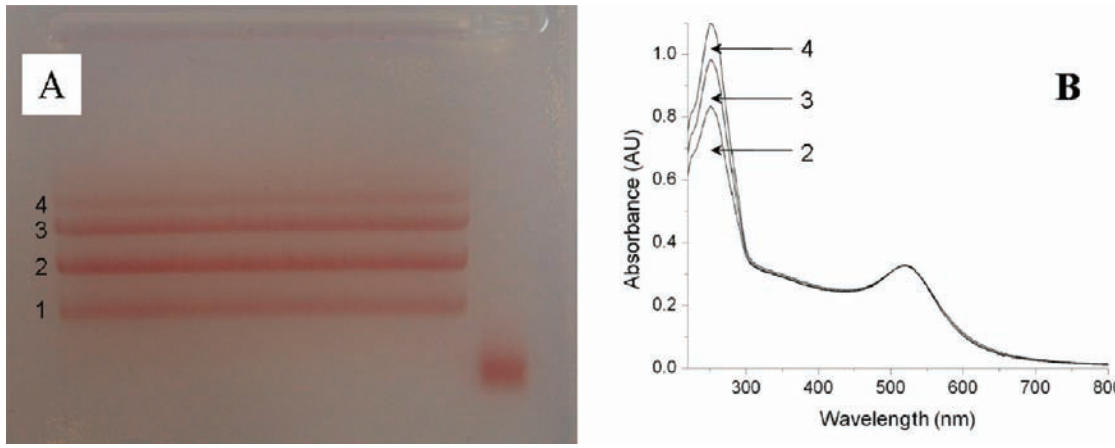


Figure 1. Electrophoretic separation of Au-NP poly(dG)-poly(dC) conjugates.700 bp 5′-SH-poly(dG)-poly(dC) molecules were incubated with 5 nm Au-NPs at a 4 to 1 molar ratio for 2 h at 60 °C in 20 mM Tris-acetate pH 7.5, containing 0.1 M NaCl. (A) Separation of the sample was conducted on 1.2% agarose gel (7 × 7 cm) at 130 V for 25 min at RT in TEA buffer. The wine-colored bands marked with the numbers correspond to the conjugates bearing one, two, three, and four poly(dG)-poly(dC) molecules, correspondingly. The band in the lower right corner of the gel corresponds to 5 nm Au-NPs. (B) Normalized absorption spectra of samples extracted from gel slices corresponding to bands 2, 3, and 4 (see left panel). Two distinct absorption maxima at 260 and 520 nm correspond to DNA and Au nanoparticle, respectively. The amount of individual conjugates extracted from the gel was quantified by measuring absorption at 520 nm. The relative yield of conjugates was calculated by multiplying the volume by absorption at 520 nm for each individual fraction and dividing the resulting value with that obtained for the initial mixture of conjugates (before electrophoresis). The calculated yields are correspondingly equal to 0.15, 0.37, 0.31, and 0.09 for conjugates bearing one, two, three, and four poly(dG)-poly(dC) molecules.

dialysis was continued against the same buffer not containing DTT for one more hour. Concentrations of G- and C-oligonucleotides were calculated using extinction coefficients at 260 nm of 11.7 and 7.5 mM^{-1} cm^{-1} for G and C bases (*21*), respectively.

DNA Synthesis Reactions. Synthesis of 5′SH-poly(dG)-poly(dC) was performed as described previously (*20*) in a standard reaction assay containing: 60 mM KPi, pH 7.4, 5 mM $MgCl_2$, 5 mM DTT, 1.5 mM dCTP, 1.5 mM dGTP, 0.2 μM Klenow exo$^-$, and 1 μM HPLC purified (see above) template-primer, 5′-SH-$(dG)_{12}$-$(dC)_{12}$. The synthesis was conducted for 2 h at 37 °C. The reaction was terminated by the addition of EDTA to a final concentration of 10 mM.

HPLC Purifications. The separation of synthesized DNA molecules from nucleotides, template-primer, and other reaction components was achieved with a TSK-gel G-DNA-PW HPLC column (7.8 × 300 mm) from TosoHaas (Japan) by isocratic elution with 20 mM Tris-acetate, pH 7.0, for 30 min at a flow rate of 0.5 mL/min. HPLC purification of the oligonucleotides and the synthesized DNA was conducted on an Agilent 1100 HPLC system with a photodiode array detector. Peaks were identified from their retention times obtained from the absorbance at 260 nm for DNA.

Electrophoresis. The poly(dG)-poly(dC) and Au NP-poly(dG)-poly(dC) conjugates were loaded onto 1.2% agarose gel 7 × 7 cm, and then electrophoresed at room temperature at 130 V for 25 min. TAE buffer, in addition to being used to prepare the agarose, also served as the running buffer.

Atomic Force Microscopy. Atomic force microscopy was performed on the molecules adsorbed onto muscovite mica surfaces. A 20 μL aliquot of 1.0−2.0 nM Au NP-DNA sample in 2.0 mM $MgCl_2$ or 2.0 mM $NiCl_2$ was deposited on freshly cleaved mica plates for 2 min, then washed with distilled water and dried by nitrogen blow. AFM imaging was performed on a Solver PRO AFM system (NT-MDT, Russia), in a semicontact (tapping) mode, using 130-μm-long Si-gold-coated cantilevers (NT-MDT, Russia) with resonance frequency of 119−180 kHz. The images were "flattened" (each line of the image was fitted to a second-order polynomial, and the polynomial was then subtracted from the image line) by the Nova image processing software (NT-MDT, Russia). The images were analyzed and visualized using a Nanotec Electronica S.L (Madrid) *WSxM* imaging software (*22*).

RESULTS

To produce the Au-NP-DNA conjugates, 700 bp 5′-thiolated poly(dG)-poly(dC) was mixed with Au-NPs at 4 to 1 molar ratio in 20 mM Tris buffer, pH 7.5, in the presence of 0.1 M NaCl, for 2 h at 60 °C. The incubation resulted in the formation of Au-NP-DNA conjugates bearing a different number of DNA molecules per nanoparticle. The conjugates were separated by electrophoresis in a 1.2% agarose gel, as shown in the Figure 1. The wine-colored bands in the gel (see Figure 1A) correspond to the conjugate products containing distinct number of poly(dG)-poly(dC) molecules per Au-NP. Each band was cut out of the gel with a razor blade. Colored gel slices were placed in dialysis bags containing TAE buffer; each sample was then electroeluted into the bag and collected. Absorption spectra of the eluted Au-NP-DNA conjugates are shown in Figure 1B. The spectra are characterized by absorption maxima at 260 and 520 nm. The absorption at 260 nm is mainly due to DNA, while absorption at 520 nm is due to Au-NPs. Thus, the 260 to 520 nm absorption ratio in the spectrum reflects a relative amount of the DNA molecule per particle (see Figure 1B).

Fractions extracted from the gel slices were further purified and characterized by size-exclusion HPLC. Figure 2A displays the superimposed size-exclusion chromatograms of Au-NP DNA conjugates extracted from the four individual bands in the gel (see Figure 1A). As seen in Figure 2, the conjugates are eluted from the column as single and symmetrical peaks, indicating their high-purity complexes. The HPLC, in addition to confirming their purity, completely separates the conjugates from relatively low molecular weight agarose oligomers, extracted from the gel slices together with the conjugates.

The molecular morphology of HPLC purified Au-NP-poly(dG)-poly(dC) conjugates was elucidated by AFM. The molecules eluted from the HPLC column were deposited onto freshly cleaved, 1 × 1 cm mica and imaged by AFM in a tapping mode. The images of gel-extracted fraction are shown in Figure 3. The vast majority of conjugates seen on A, B, C, and D panels of Figure 3 are composed of 1, 2, 3, or 4 poly(dG)-poly(dC) molecules bound to a single nanoparticle (seen as bright spots

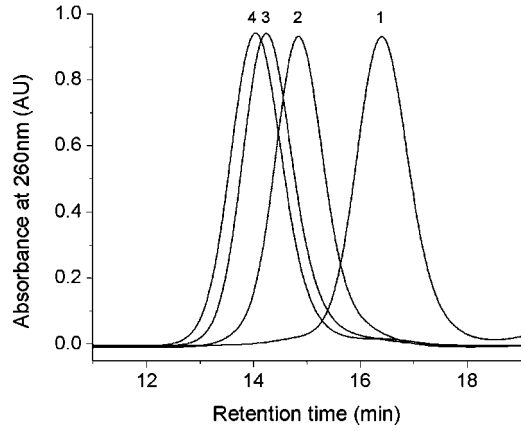


Figure 2. Size-dependent HPLC separation of Au-NP poly(dG)-poly(dC) conjugates. The individual conjugates extracted from the gel (see Figure 1) were loaded onto the size-exclusion column equilibrated with 20 mM Tris-acetate, pH 7.5. Elution profiles of conjugates corresponding to bands 1, 2, 3, and 4 in Figure 1 are indicated with numbers 1 through 4, respectively. The elution was followed at 260 nm.

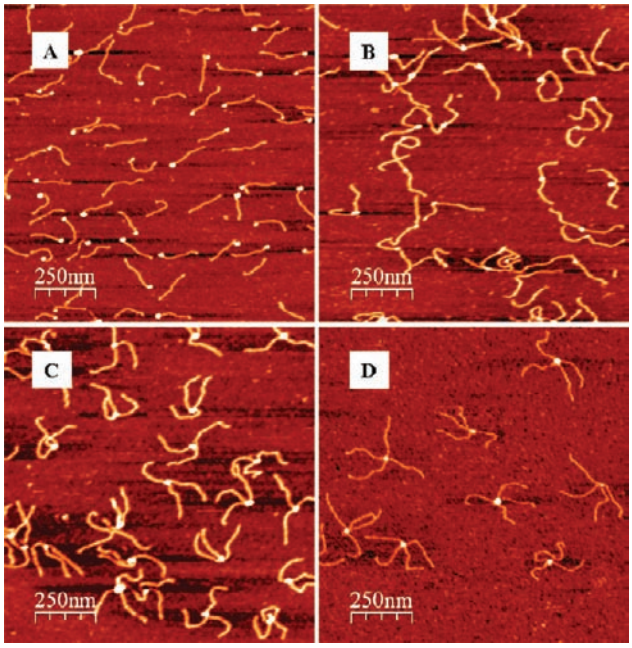


Figure 3. AFM images of Au-NP poly(dG)-poly(dC) conjugates. The conjugates were extracted from the gel (see Figure 1) and purified by size-exclusion HPLC as shown in Figure 2. All conjugates were deposited on a mica surface in 2 mM $NiCl_2$ and scanned in a tapping mode as described in Experimental Procedures. Panels A, B, C, and D present images of conjugates extracted from bands 1, 2, 3, and 4 (see Figure 1) correspondingly.

on the images), respectively. The average estimated contour length of bound DNA molecules is equal to 170 ± 22 nm. This value corresponds well with the contour length of 700 bp poly(dG)-poly(dC) molecules deposited on mica (*23*).

We have investigated the ability of DNA polymerase to extend poly(dG)-poly(dC) molecules attached to a gold nanoparticle. The conjugates comprising two or three poly(dG)-poly(dC) molecules per Au-NP (see Figure 4A,B, respectively) were subjected to the enzymatic reaction with Klenow exo$^-$ DNA polymerase, in the presence of dGTP, dCTP nucleotides, for 20 h at 37 °C. The products of the synthesis were subsequently purified by size-exclusion HPLC and analyzed using AFM. Figure 4 shows that incubation with the enzyme causes considerable increase of the DNA length; the average

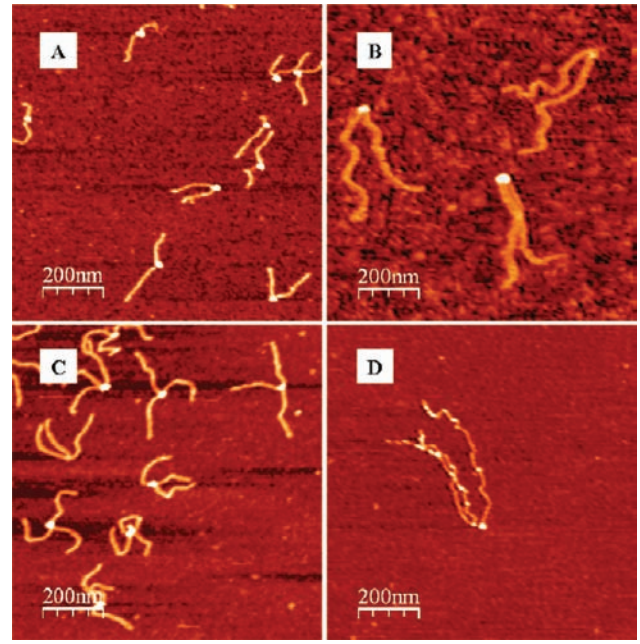


Figure 4. Enzymatic extension of poly(dG)-poly(dC) molecules bound to a Au-NP. The conjugates comprising two (A and B) and three (C and D) poly(dG)-poly(dC) molecules per Au-NP before (A and C) and after (B and D) enzymatic extension. The conjugates were extracted from the gel (Figure 1) and purified by HPLC as shown in Figure 2. The conjugates were incubated in an assay mixture containing 60 mM KPi buffer, pH 7.4, 5 mM $MgCl_2$, 5 mM DTT, 1.5 mM dCTP, 1.5 mM dGTP, and 0.2 μM Klenow exo$^-$, for 20 h at 37 °C, and deposited on a mica surface in 2 mM $NiCl_2$, as described in Experimental Procedures.

contour length of DNA molecules attached to the particle is increased from 170 nm to approximately 450 nm (compare DNA lengths in right and left panels of Figure 4). This clearly demonstrates that Klenow exo$^-$ DNA polymerase is capable of elongating poly(dG)-poly(dC) molecules connected to the Au-NP. The rate of particle-bound poly(dG)-poly(dC) extension is, however, two orders in magnitude lower than that of nonbound DNA (data not shown).

DISCUSSION

The ability to control the number and the length of DNA molecules attached to a single nanoparticle is essential for assembly of DNA-NP conjugates into new functional nanomaterials. Incubation of functionalized oligonucleotides and DNA species with NPs, however, results in a mixture of DNA-NP conjugates bearing different numbers of DNA molecules. Alivisatos and colleagues demonstrated that binding of single-stranded oligonucleotides produces a significant effect on the particle mobility in the electrical field and succeeded to separate conjugates bearing different numbers of oligonucleotides per particle by electrophoresis (*24, 25*). The efficiency of the DNA-NP conjugate separation in gels decreases as the particle size increase and increases as the DNA length increases. Indeed, an excellent separation of the NP conjugates with long random sequence dsDNA was demonstrated by Tsai and co-workers (*15*). In the latter study, random sequence dsDNA molecules were attached to Au-NPs through the SH-group introduced into the DNA, using a ligase-dependent reaction. Here, we employed a polymerase-based method (*17*) to produce the Au-NP conjugates with a homogeneous dsDNA polymer, poly(dG)-poly(dC). This method enables us to synthesize uniform double-stranded poly(dG)-poly(dC) or poly(dA)-poly(dT) wires of desired length (varied from several nanometers to several micrometers), as well as the DNA functionalized with SH groups or/and random oligonucleotide sequences. We have shown that incubation of the

synthesized 700 bp SH-poly(dG)-poly(dC) with Au-NPs yielded a mixture of Au-NP-DNA conjugates bearing different number of DNA molecules per particle that can be easily and completely separated from each other using electrophoresis. The AFM visualization of these products (see Figure 2) confirms that the conjugates extracted from the discrete bands in the gel contain the exact number of poly(dG)-poly(dC) molecules per nanoparticle.

We have demonstrated that Klenow exo$^-$ catalyzes extension of poly(dG)-poly(dC) molecules connected to a Ag-NP, in the presence of dGTP and dCTP. This result corresponds nicely with earlier observations showing that Au-NP-bound DNA molecules can be manipulated with various enzymes, such as ligases (*14, 15, 26*), polymerases (*13*), and restriction enzymes (*10*−*12*).

The formation of conjugates between long (hundreds of base pairs) homogeneous dsDNA polymers and metal NPs has never been shown before. Due to its regular structure, a double-stranded poly(dG)-poly(dC) composed of G- and C-homopolymers provides better conditions for π overlap compared to random sequence DNA. In addition, guanines, which have the lowest ionization potential among DNA bases, promote charge migration through the DNA. This property is especially useful for application of the conjugates in nanoelectronics. Moreover, the polymerase-based method for synthesis used in this work can be effectively employed with the range of functionalities attached to the DNA terminals. In addition to the SH group used for attaching Au-NP, one can functionalize the DNA, for instance, with a random oligonucleotide sequence. The NP-DNA conjugates containing random single-stranded overhang sequences will be recognized by the complementary ones attached to different DNA-NP conjugates, thus connecting DNA wires to one another. These functionalized conjugates may serve a basis for the design and construction of two- and three-dimensional DNA-NP structures. Such NP-DNA structures might possess interesting electrical and plasmonic properties and can be used in the fields of nanoelectronics and nano-optics.

ACKNOWLEDGMENT

This work was supported by European Commission FP6 Information Society Technologies program, grant "DNABased Nanodevices", and by the ISF Converging Technologies program, grant 1714/07.

LITERATURE CITED

(1) Alivisatos, A. P., Johnsson, K. P., Peng, X., Wilson, T. E., Loweth, C. J., Bruchez, M. P., Jr., and Schultz, P. G. (1996) Organization of 'nanocrystal molecules' using DNA. *Nature 382*, 609–11.

(2) Mirkin, C. A., Letsinger, R. L., Mucic, R. C., and Storhoff, J. J. (1996) A DNA-based method for rationally assembling nanoparticles into macroscopic materials. *Nature 382*, 607–9.

(3) Mitchell, G. P., Mirkin, C. A., and Letsinger, R. L. (1999) Programmed assembly of DNA functionalized quantum dots. *J. Am. Chem. Soc. 121*, 8122–8123.

(4) Fu, A., Micheel, C. M., Cha, J., Chang, H., Yang, H., and Alivisatos, A. P. (2004) Discrete nanostructures of quantum dots/Au with DNA. *J. Am. Chem. Soc. 126*, 10832–10833.

(5) Goluch, E. D., Nam, J. M., Georganopoulou, D. G., Chiesl, T. N., Shaikh, K. A., Ryu, K. S., Barron, A. E., Mirkin, C. A., and Liu, C. (2006) A bio-barcode assay for on-chip attomolar-sensitivity protein detection. *Lab Chip 6*, 1293–9.

(6) Nam, J. M., Stoeva, S. I., and Mirkin, C. A. (2004) Bio-bar-code-based DNA detection with PCR-like sensitivity. *J. Am. Chem. Soc. 126*, 5932–3.

(7) Nam, J. M., Thaxton, C. S., and Mirkin, C. A. (2003) Nanoparticle-based bio-bar codes for the ultrasensitive detection of proteins. *Science 301*, 1884–6.

(8) Braun, E., Eichen, Y., Sivan, U., and Ben-Yoseph, G. (1998) DNA-templated assembly and electrode attachment of a conducting silver wire. *Nature 391*, 775–8.

(9) Park, S.-J., Lazarides, A. A., Mirkin, C. A., Brazis, P. W., Kannewurf, C. R., and Letsinger, R. L. (2000) The electrical properties of gold nanoparticle assemblies linked by DNA13. *Angew. Chem. 39*, 3845–3848.

(10) Kanaras, A. G., Wang, Z., Bates, A. D., Cosstick, R., and Brust, M. (2003) Towards multistep nanostructure synthesis: programmed enzymatic self-assembly of DNA/gold systems. *Angew. Chem., Int. Ed. Engl. 42*, 191–4.

(11) Kanaras, A. G., Wang, Z., Brust, M., Cosstick, R., and Bates, A. D. (2007) Enzymatic disassembly of DNA-gold nanostructures. *Small 3*, 590–4.

(12) Qin, W. J., and Yung, L. Y. (2005) Nanoparticle-DNA conjugates bearing a specific number of short DNA strands by enzymatic manipulation of nanoparticle-bound DNA. *Langmuir 21*, 11330–4.

(13) Nicewarner Pena, S. R., Raina, S., Goodrich, G. P., Fedoroff, N. V., and Keating, C. D. (2002) Hybridization and enzymatic extension of au nanoparticle-bound oligonucleotides. *J. Am. Chem. Soc. 124*, 7314–23.

(14) Xu, X., Rosi, N. L., Wang, Y., Huo, F., and Mirkin, C. A. (2006) Asymmetric functionalization of gold nanoparticles with oligonucleotides. *J. Am. Chem. Soc. 128*, 9286–7.

(15) Tsai, C.-Y., Shiau, A.-L., Cheng, P.-C., Shieh, D.-B., Chen, D.-H., Chou, C.-H., Yeh, C.-S., and Wu, C.-L. (2004) A biological strategy for fabrication of Au/EGFP nanoparticle conjugates retaining bioactivity. *Nano Lett. 4*, 1209–1212.

(16) Hennig, D., Starikov, E. B., Archilla, J. F. R., and Palmero, F. (2004) Charge transport in poly(dG)-poly(dC) and poly(dA)-poly(dT) DNA polymers. *J. Biol. Phys. 30*, 227–238.

(17) Kotlyar, A. B., Borovok, N., Molotsky, T., Fadeev, L., and Gozin, M. (2005) In vitro synthesis of uniform poly(dG)-poly(dC) by Klenow exo- fragment of polymerase I. *Nucleic Acids Res. 33*, 525–35.

(18) Frens, G. (1973) Controlled nucleation for the regulation of the particle size in monodisperse gold suspensions. *Nat. Phys. Sci. 241*, 20–22.

(19) Turkevich, J., Stevenson, P. C., and Hillier, J. (1951) A study of the nucleation and growth processes in the synthesis of colloidal gold. *Discuss. Faraday Soc. 11*, 55–75.

(20) Kotlyar, A., Borovok, N., Molotsky, T., Klinov, D., Dwir, B., and Kapon, E. (2005) Synthesis of novel poly(dG)-poly(dG)-poly(dC) triplex structure by Klenow exo- fragment of DNA polymerase I. *Nucleic Acids Res. 33*, 6515–21.

(21) Cantor, C. R., Warshaw, M. M., and Shapiro, H. (1970) Oligonucleotide interactions. 3. Circular dichroism studies of the conformation of deoxyoligonucleotides. *Biopolymers 9*, 1059–77.

(22) Horcas, I., Fernandez, R., Gomez-Rodriguez, J. M., Colchero, J., Gomez-Herrero, J., and Baro, A. M. (2007) WSXM: a software for scanning probe microscopy and a tool for nanotechnology. *Rev. Sci. Instrum. 78*, 013705.

(23) Borovok, N., Molotsky, T., Ghabboun, J., Cohen, H., Porath, D., and Kotlyar, A. (2007) Poly(dG)-poly(dC) DNA appears shorter than poly(dA)-poly(dT) and possibly adopts an A-related conformation on a mica surface under ambient conditions. *FEBS Lett. 581*, 5843–6.

(24) Zanchet, D., Micheel, C. M., Parak, W. J., Gerion, D., and Alivisatos, A. P. (2001) Electrophoretic isolation of discrete Au nanocrystal/DNA conjugates. *Nano Lett. 1*, 32–35.

(25) Zanchet, D., Micheel, C. M., Parak, W. J., Gerion, D., Williams, S. C., and Alivisatos, A. P. (2002) Electrophoretic and structural studies of DNA-directed Au nanoparticle groupings. *J. Phys. Chem. B 106*, 11758–11763.

(26) Claridge, S. A., Mastroianni, A. J., Au, Y. B., Liang, H. W., Micheel, C. M., Frechet, J. M., and Alivisatos, A. P. (2008) Enzymatic ligation creates discrete multinanoparticle building blocks for self-assembly. *J. Am. Chem. Soc. 130*, 9598–605.

BC900527A

Tumor Uptake of the RGD Dimeric Probe ^{99m}Tc-G_3-$2P_4$-RGD2 is Correlated with Integrin $\alpha_v\beta_3$ Expressed on both Tumor Cells and Neovasculature

Zhaofei Liu,[†] Bing Jia,*[,†] Jiyun Shi,[†] Xiaona Jin,[‡] Huiyun Zhao,[†] Fang Li,[‡] Shuang Liu,[§] and Fan Wang*[,†]

Medical Isotopes Research Center, Peking University, Beijing 100191, China, Department of Nuclear Medicine, Peking Union Medical College Hospital, Beijing 100730, China, and School of Health Sciences, Purdue University, West Lafayette, Indiana 47907. Received December 10, 2009; Revised Manuscript Received February 6, 2010

Integrin $\alpha_v\beta_3$ has been well-documented as one of the key players in the process of tumor angiogenesis. Radiolabeled RGD (Arg-Gly-Asp) peptides that specifically target integrin $\alpha_v\beta_3$ have great potential for tumor early detection and noninvasively monitoring the status of tumor angiogenesis. We developed a cyclic RGD dimeric probe ^{99m}Tc-HYNIC-Gly_3-E[PEG_4-c(RGDfK)]$_2$ (^{99m}Tc-G_3-$2P_4$-RGD2) (using tricine and TPPTS as the coligands, TPPTS = trisodium triphenylphosphine-3,3′,3″-trisulfonate), and investigated whether it could be used to noninvasively visualize and quantify integrin $\alpha_v\beta_3$ expression in vivo. HYNIC-Gly_3-E[PEG_4-c(RGDfK)]$_2$ was synthesized and labeled with ^{99m}Tc. The biodistribution and planar γ-imaging studies of ^{99m}Tc-G_3-$2P_4$-RGD2 were performed in both U87MG (human integrin $\alpha_v\beta_3$ positive/murine integrin $\alpha_v\beta_3$ positive) and HT-29 (human integrin $\alpha_v\beta_3$ negligible /murine integrin $\alpha_v\beta_3$ positive) tumor-bearing nude mouse models. The correlation of ^{99m}Tc-G_3-$2P_4$-RGD2 tumor uptake values (measured by ex vivo biodistribution) with expression levels of human integrin $\alpha_v\beta_3$ or murine integrin $\alpha_v\beta_3$ (measured by Western blot) were determined in U87MG and HT-29 tumor models, respectively. ^{99m}Tc-G_3-$2P_4$-RGD2 exhibited increased receptor binding affinity and in vivo tumor uptake as compared with previously reported RGD dimeric tracer ^{99m}Tc-RGD2 (without Gly_3 and PEG_4 spacers). The tumor uptake of ^{99m}Tc-G_3-$2P_4$-RGD2 was related to the expression levels of both human integrin $\alpha_v\beta_3$ (expressed on tumor cells) and murine integrin $\alpha_v\beta_3$ (expressed on newborn tumor vasculature). Our results demonstrate that ^{99m}Tc-G_3-$2P_4$-RGD2 is a useful agent for integrin $\alpha_v\beta_3$ imaging. The relationship between ^{99m}Tc-G_3-$2P_4$-RGD2 uptake and integrin $\alpha_v\beta_3$ expression level as determined by this study would provide useful information for clinical translation of RGD probes.

INTRODUCTION

Tumor angiogenesis, the formation of new blood vessels from pre-existing vasculature, is one of the key steps for tumor malignancy, invasion, and metastasis (*1*). Angiogenesis depends on specific molecular interactions between vascular cells and components of the extracellular matrix (ECM). Integrins, a family of cell adhesion molecules composed of noncovalently associated α and β subunits, are involved in a wide range of cell−ECM and cell−cell interactions (*2, 3*). Among the integrin family members, integrin $\alpha_v\beta_3$ is highly expressed on activated endothelial cells, but not resting vessels during angiogenesis, and plays an important role in the regulation of tumor growth, local invasiveness, and metastatic potential (*3*). The important role of integrin $\alpha_v\beta_3$ during tumor angiogenesis has stimulated intensive investigation of integrin $\alpha_v\beta_3$-targeted antiangiogenic strategies for cancer treatment and the prevention of cancer recurrence or metastasis (*4, 5*). Noninvasive imaging of integrin $\alpha_v\beta_3$ expression by molecular imaging techniques would also be of great help for early detection of malignancy, evaluation of tumor progress, and monitoring treatment efficacy of anti-angiogenic drugs.

In recent years, a series of Arg-Gly-Asp (RGD) peptide-based multimodality probes were developed for noninvasive imaging of integrin $\alpha_v\beta_3$ expression (*6*−*9*), and several PET (positron emission tomography) probes have been used in clinical investigations (*10*−*14*). To improve the capacity of tumor targeting and in vivo imaging quality, we and others recently designed and synthesized several new RGD dimeric peptides with Gly_3 or PEG_4 (Gly_3 = glycine−glycine−glycine; PEG_4 = 15-amino-4,7,10,13-tetraoxapentadecanoic acid) spacers between the two RGD motifs in homodimeric peptides. The insertion of the spacers significantly increased the tumor uptake and improved the in vivo pharmacokinetics in mouse models (*15*−*18*).

Besides specific expression on the activated tumor vasculature, integrin $\alpha_v\beta_3$ also highly expressed on some tumor cells, such as late-stage glioblastoma, breast and prostate cancers, malignant melanoma, and ovarian carcinoma (*19, 20*). Therefore, in the mouse models bearing human integrin $\alpha_v\beta_3$-positive tumors, RGD peptides would bind to both the murine integrin $\alpha_v\beta_3$ expressed on the activated endothelial cells and the human integrin $\alpha_v\beta_3$ expressed on tumor cells (*21*). However, the relationship between the tumor uptake values of RGD probes and the expression levels of human integrin $\alpha_v\beta_3$ as well as murine integrin $\alpha_v\beta_3$ has not yet been sufficiently illuminated by the literature.

In this study, a new RGD dimeric peptide with two PEG_4 spacers between the two RGD motifs and one Gly_3 spacer on the glutamate α-amino group of the RGD dimer, Gly_3-E[PEG_4-c(RGDfK)]$_2$, was prepared and labeled with ^{99m}Tc by using HYNIC (6-hydrazinonicotinyl) as a chelator (Figure 1). The in vitro and in vivo characteristics of ^{99m}Tc-HYNIC-Gly_3-E[PEG_4-c(RGDfK)]$_2$ (^{99m}Tc-G_3-$2P_4$-RGD2) was compared with the ^{99m}Tc-labeled RGD dimer without Gly_3 and PEG_4 spacers ^{99m}Tc-

* To whom correspondence should be addressed. Fan Wang, Medical Isotopes Research Center, Peking University, 38 Xueyuan Road, Beijing 100191, China. Tel. and Fax: 86-10-82801145. E-mail: wangfan@bjmu.edu.cn. Bing Jia, Tel.: 86-10-82802871, Fax: 86-10-82801145. E-mail: jiabing@bjmu.edu.cn.

[†] Peking University.

[‡] Peking Union Medical College Hospital.

[§] Purdue University.

10.1021/bc900547d © 2010 American Chemical Society
Published on Web 02/25/2010

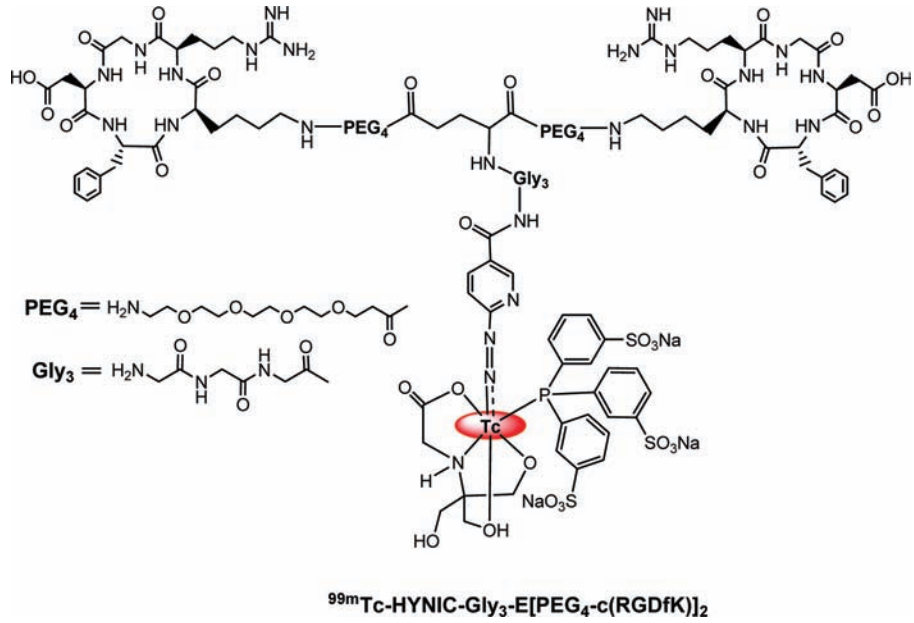


Figure 1. Chemical structure of ^{99m}Tc-HYNIC-Gly$_3$-E[PEG$_4$-c(RGDfK)]$_2$ (^{99m}Tc-G$_3$-2P$_4$-RGD2).

HYNIC-E[-c(RGDfK)]$_2$ (^{99m}Tc-RGD2). The biodistribution properties of ^{99m}Tc-G$_3$-2P$_4$-RGD2 were tested in both human integrin $\alpha_v\beta_3$-positive U87MG human glioma mouse model and human integrin $\alpha_v\beta_3$-negative HT-29 human colon cancer mouse model. The correlation of ^{99m}Tc-G$_3$-2P$_4$-RGD2 tumor uptake values vs the human integrin $\alpha_v\beta_3$ and murine integrin $\alpha_v\beta_3$ expression levels was also investigated.

EXPERIMENTAL PROCEDURES

All chemicals obtained commercially were of analytical grade and used without further purification. Cyclic RGD peptides, c(RGDyK), E[c(RGDfK)]$_2$ (RGD2), and Gly$_3$-E[PEG$_4$-c(RGDfK)]$_2$ (G$_3$-2P$_4$-RGD2) were custom-made by Peptides International (Louisville, KY). Sodium succinimidyl 6-(2-(2-sulfonatobenzaldehyde)hydrazono)nicotinate (HYNIC-NHS) was prepared according to the literature method (*22*). Synthesis of HYNIC-E[c(RGDfK)]$_2$ (HYNIC-RGD2) was described in our previous communication (*23*). Na^{99m}TcO$_4$ was obtained from a commercial ^{99}Mo/^{99m}Tc generator (Beijing Atom High Tech Co., Ltd.). Reversed-phase extraction Sep-Pak C$_{18}$ cartridges were obtained from Waters and were pretreated with ethanol and water immediately prior to use. The syringe filter and poly(ether sulfone) membranes (pore size 0.22 μm; diameter 13 mm) were obtained from Nalge Nuc International. The reversed-phase high-performance liquid chromatography (HPLC) system was the same as that previously reported (*17, 18*). For HYNIC-peptide purification, a Zorbax C$_{18}$ semiprep column (9.4 mm $\times$ 250 mm, 100 Å pore size) was used with a flow rate of 3 mL/min. The gradient mobile phase started with 95% solvent A (0.1% TFA in H$_2$O) and 5% solvent B (0.1% TFA in CH$_3$CN) to 60% solvent A and 40% solvent B at 25 min to 40% solvent A and 60% solvent B at 30 min. The radio-HPLC method used a HP Hewlett-Packard Series 1100 HPLC system equipped with Radioflow Detector LB509 and Agilent Zorbax SB-C$_{18}$ column (4.6 mm $\times$ 250 mm, 5 μm). The flow rate was 1.0 mL/min. The mobile phase was isocratic with 90% solvent A (25 mM NaOAc buffer, pH = 5.0) and 10% solvent B (acetonitrile) at 0−2 min, followed by a gradient mobile phase going from 10% solvent B at 2 min to 15% solvent B at 5 min and to 20% solvent B at 20 min, then to 10% solvent B at 25 min.

Synthesis of HYNIC-Conjugated G$_3$-2P$_4$-RGD2. HYNIC-G$_3$-2P$_4$-RGD2 conjugate was prepared as previously described (*17, 18*). In brief, a solution of 2 μmol of G$_3$-2P$_4$-RGD2 was mixed with 6 μmol of HYNIC-NHS in 1 mL of a mixture containing DMF and water (1:1 = v:v). The pH was adjusted to 8.5−9.0 using 0.1 N NaOH. After stirring overnight at room temperature, HYNIC-G$_3$-2P$_4$-RGD2 was isolated by semi-preparative HPLC. The collected fractions (Rt = 19.3 min) were combined and lyophilized to yield the final product as a white powder. HYNIC-G$_3$-2P$_4$-RGD2 was obtained in 56% yield with >95% HPLC purity. Matrix-assisted laser desorption/ionization (MALDI) time-of-light (TOF) mass spectrometry (MS): *m*/*z* 2305.92 for [M+NH$_4$]$^+$ (C$_{100}$H$_{147}$N$_{27}$O$_{33}$S, calculated molecular weight 2287.46). HYNIC-RGD2 was prepared as we previously described (*23*).

^{99m}Tc Radiolabeleing. HYNIC-G$_3$-2P$_4$-RGD2 and HYNIC-RGD2 were labeled with ^{99m}Tc using tricine and TPPTS (trisodium triphenylphosphine-3,3′,3″-trisulfonate) as the coligands, and then purified with Sep-Pak C$_{18}$ cartridges as previously described (*23*). After purification, the radiochemical purity of the products ^{99m}Tc-G$_3$-2P$_4$-RGD2 and ^{99m}Tc-RGD2 was both higher than 98% as analyzed by radio-HPLC.

Cell Culture and Animal Models. The U87MG human glioma cell line and HT-29 human colon cancer cell line were purchased from American Type Culture Collection (Manassas, VA). U87MG cells were cultured in low glucose Dulbecco's Modified Eagle's Medium (DMEM) culture medium and HT-29 cells were cultured in high glucose DMEM culture medium. Both cell lines were cultured in medium supplemented with 10% (v/v) fetal bovine serum (FBS) at 37 °C in a humidified atmosphere with 5% CO$_2$. Female BALB/c nude mice (4−5 weeks of age) were purchased from Department of Experimental Animal, Peking University Health Science Center. All animal experiments were performed in accordance with guidelines of Institutional Animal Care and Use Committee (IACUC) at Peking University. U87MG tumor model and HT-29 tumor model were established by subcutaneous injection of 2 $\times$ 10^6 U87MG tumor cells and 2 $\times$ 10^6 HT-29 tumor cells into the right upper flanks of nude mice, respectively. The mice were subjected to γ-imaging and biodistribution studies when the tumor volume reached 200−300 mm^3 (3−4 weeks after inoculation for U87MG tumors, and 2−3 weeks for HT-29 tumors).

Cell Binding Assay. In vitro integrin $\alpha_v\beta_3$-binding affinities and specificities of c(RGDyK), HYNIC-RGD2, and HYNIC-

G_3-$2P_4$-RGD2 were compared via displacement cell-binding assays using ^{125}I-c[RGDyK] as the radioligand. ^{125}I-c(RGDyK) was prepared by labeling c(RGDyK) with Na^{125}I at a high specific activity (~44.4 TBq/mmol) according to the method described in the literature (*24*). Experiments were performed on U87MG cells (human integrin $\alpha_v\beta_3$-positive) as we have previously described (*15, 16, 25*). The best-fit 50% inhibitory concentration (IC_{50}) values were calculated by fitting the data with nonlinear regression using *GraphPad Prism 4.0* (GraphPad Software). Experiments were performed twice with triplicate samples.

Integrin $\alpha_v\beta_3$ Expression on Tumor Cells. The integrin $\alpha_v\beta_3$ expression levels of U87MG and HT-29 cells were determined by saturation binding assay (*26, 27*). Briefly, the antihuman integrin $\alpha_v\beta_3$ antibody Abegrin (*27*−*29*) was labeled with ^{125}I, and then, ^{125}I-Abegrin was used as the integrin $\alpha_v\beta_3$-specific radioligand. U87MG or HT-29 tumor cells were incubated with increasing concentrations of ^{125}I-Abegrin. Nonspecific binding was determined with a 100-fold excess dose of Abegrin. Scatchard plots were derived by plotting bound/free ligand versus bound ligand, and the maximum numbers of binding sites (B_{max}) were calculated by GraphPad Prism software.

Immunofluorescence Staining. The integrin $\alpha_v\beta_3$ expression patterns of U87MG and HT-29 tumor tissues were analyzed by fluorescence staining as previously described (*27, 30*). Frozen tumor tissue sections were incubated with hamster antimouse integrin β_3 antibody (1:100; BD Biosciences, San Jose, CA) and Abegrin (10 μg/mL), and then visualized by Cy3-conjugated donkey antihamster secondary antibody (1:200; Jackson ImmunoResearch Laboratories) and FITC-conjugated donkey antihuman secondary antibody (1:200) under the microscope (Carl Zeiss Axiovert 200M, Carl Zeiss, Thornwood, NY).

Western Blot. The frozen U87MG or HT-29 tumor tissues were homogenized and extracted using T-PER tissue protein extraction buffer. Protein concentration was determined using a microBCA protein assay kit (Pierce Biotechnology, Inc., Rockford, IL, USA) and adjusted to equivalent values using lysis buffer. After SDS-PAGE and transfer, the polyvinylidene fluoride (PVDF) membrane (Invitrogen Corp.; Carlsbad, CA, USA) was blocked with 5% nonfat milk blocking buffer, and then incubated overnight at 4 °C with hamster antimouse CD61 (integrin β_3) primary antibody (BD Biosciences, San Jose, CA) or mouse antihuman CD61 (BD Biosciences, San Jose, CA) primary antibody followed by incubation at room temperature for 1 h with horseradish peroxidase-conjugated secondary antibodies (GE Healthcare). β-actin was used as the loading control, and the bands were detected using enhanced chemiluminescent Western blotting detection system (GE Healthcare). After development, the films were scanned using grayscale mode, and the images were opened in *ImageJ* (http://rsb.info.nih.gov/ij/). A ROI was drawn on the first lane, and the same size/shape ROI was applied to the other lanes and the background to obtain quantitative data of each band intensity. The background signal was subtracted before correlating with the biodistribution data.

Biodistribution and Blocking Studies. Female nude mice bearing U87MG xenografts were injected with 0.37 MBq (10 μCi) of ^{99m}Tc-G_3-$2P_4$-RGD2 or ^{99m}Tc-RGD2 via tail vein to evaluate the biodistribution of the probes in the major organs of mice. At 0.5 and 2 h postinjection (p.i), mice were sacrificed. Blood, tumor, major organs, and tissues were collected, wet-weighed, and measured using a γ counter. The results were presented as percentage of injected dose per gram of tissue (%ID/g). Values are expressed as means ± SD for a group of four animals (n = 4 per group). A blocking study was also performed in a group of four mice bearing U87MG tumors by coinjecting ^{99m}Tc-G_3-$2P_4$-RGD2 with 300 μg unlabeled E[c(RGDfK)]$_2$. At 0.5 h p.i., all four animals were sacrificed for determination of organ biodistribution as described above. As a control study, two groups of HT-29 tumor-bearing nude mice (4 animals per group) were coinjected 0.37 MBq (10 μCi) of ^{99m}Tc-G_3-$2P_4$-RGD2 via tail vein with or without a blocking dose of 300 μg unlabeled E[c(RGDfK)]$_2$. At 0.5 h p.i., all animals were sacrificed for determination of organ biodistribution as described above.

Planar γ Imaging. Each nude mouse bearing U87MG or HT-29 tumor xenografts was injected with ~18.5 MBq (500 μCi) of ^{99m}Tc-G_3-$2P_4$-RGD2 via tail vein (n = 3 per group). Animals were anesthetized with intraperitoneal injection of sodium pentobarbital at a dose of 45.0 mg/kg, then were placed supine on a two-head-camera (GE Infinia Hawkeye) equipped with a parallel-hole, low-energy, and high-resolution collimator. Anterior images were acquired at 0.5 and 2 h p.i. and stored digitally in a 128 × 128 matrix. The acquisition count limits were set at 200 K.

Correlation of ^{99m}Tc-G_3-$2P_4$-RGD2 Tumor Uptake with Integrin $\alpha_v\beta_3$ Expression. To establish tumor models with different integrin $\alpha_v\beta_3$ expression levels, 36 nude mice were randomly divided into 12 groups (3 mice per group), 7 groups of which were used for U87MG (2×10^6 cells/mouse) tumor inoculation and 5 groups of which were used for HT-29 (2×10^6 cells/mouse) tumor inoculation. Groups of nude mice were subcutaneously inoculated with U87MG or HT-29 tumor cells every 3 days to obtain tumors with different sizes. At 5 weeks after initial inoculation of tumor cells, each tumor-bearing nude mouse was injected with 0.37 MBq (10 μCi) of ^{99m}Tc-G_3-$2P_4$-RGD2 via tail vein. At 1 h p.i., all mice were sacrificed, and the tumors were harvested. Half of each tumor tissue was wet-weighed and measured using a γ counter to calculate the tumor uptake (%ID/g), while the other half was used for Western blotting to determine the integrin β_3 level. The relative integrin β_3 expression levels of tumor tissue lysates was correlated with ^{99m}Tc-G_3-$2P_4$-RGD2 tumor uptake using GraphPad software. The %ID/tumor organ value of each tumor (the tumor tissues with obvious necrosis were discarded) was plotted against the quantitative Western blot data. Applying a linear fit, the correlation coefficient (r^2) was calculated to measure the strength of association between the tumor uptake (measured by ex vivo biodistribution) and the integrin β_3 expression level (measured by Western blot). P values less than 0.05 were considered to indicate a statistically significant linear correlation between the two results.

RESULTS

Chemistry and Radiochemistry. HYNIC-G_3-$2P_4$-RGD2 was prepared by direct conjugation of G_3-$2P_4$-RGD2 with HYNIC-NHS in the yield of 56%. The products were purified by HPLC and characterized by MALDI-TOF MS. The HPLC purity of HYNIC-G_3-$2P_4$-RGD2 was >95% before being used for the receptor binding assay and ^{99m}Tc radiolabeling. The labeling procedure was done within 30 min with a yield ranging from 93% to 96%. The radiochemical purity was >98%, and the specific activity of ^{99m}Tc-G_3-$2P_4$-RGD2 was >296 GBq/μmol.

Cell Binding Assay. The receptor-binding affinity of HYNIC-G_3-$2P_4$-RGD2 was determined by performing competitive displacement studies using ^{125}I-c(RGDyK) (integrin $\alpha_v\beta_3$-specific) as the radioligand. For comparison purpose, we also evaluated c(RGDyK) and HYNIC-RGD2 using the same in vitro assay. As shown in Figure 2, all the peptides inhibited the binding of ^{125}I-c(RGDyK) to U87MG cells in a concentration-dependent manner. The IC_{50} values for c(RGDyK), HYNIC-RGD2, and HYNIC-G_3-$2P_4$-RGD2 were 39.41 ± 0.87, 8.13 ± 0.61, and 3.37 ± 0.84 nM, respectively (n = 3, repeated twice). The comparable IC_{50} values of compounds suggest that the

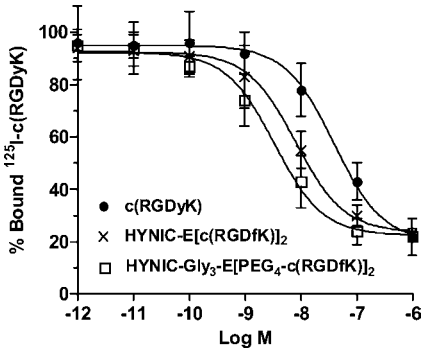


Figure 2. Inhibition of ^{125}I-c(RGDyK) binding to integrin $\alpha_v\beta_3$ on U87MG cells by c(RGDyK) (•, $IC_{50} = 39.41 \pm 0.87$ nM), HYNIC-E[c(RGDfK)]$_2$ (×, $IC_{50} = 8.13 \pm 0.61$ nM), and HYNIC-Gly$_3$-E[PEG$_4$-c(RGDfK)]$_2$ (□, $IC_{50} = 3.37 \pm 0.84$ nM) ($n = 3$, mean ± SD).

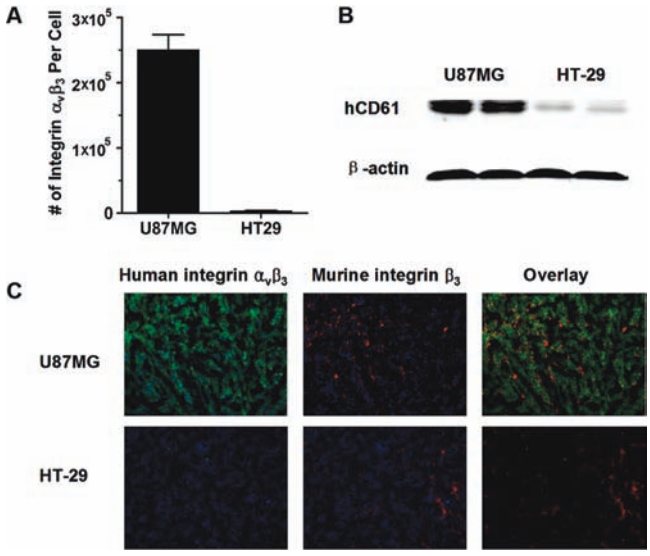


Figure 3. (A) Number of integrin $\alpha_v\beta_3$ per cell for U87MG and HT-29 cells ($n = 3$, mean ± SD). (B) Western blot of human integrin β_3 (hCD61) expression on U87MG and HT-29 cells ($n = 2$). (C) Human integrin $\alpha_v\beta_3$ and mouse integrin β_3 staining of U87MG and HT-29 tumor sections. The antihuman integrin $\alpha_v\beta_3$ and antimurine β_3 antibodies were used as the primary antibodies, respectively.

insertion of the Gly$_3$ and PEG$_4$ linkers increased the receptor-binding affinity of the RGD dimer peptide.

Integrin $\alpha_v\beta_3$ Expression Patterns of U87MG and HT-29 Tumors. We quantified the $\alpha_v\beta_3$ integrin expression levels of U87MG and HT-29 cells through saturation binding assay using ^{125}I-Abegrin as a radioligand. As shown in Figure 3A, U87MG cells expressed a high level of integrin $\alpha_v\beta_3$ ($(2.5 \pm 0.2) \times 10^5$ receptors/cell), while there was a very low integrin $\alpha_v\beta_3$ density on HT-29 cell surface ($<3 \times 10^3$ receptors/cell). After inoculating tumor cells into the nude mice, the human integrin β_3 expression level on U87MG tumor tissues was also significantly higher than that on HT-29 tumor tissues as determined by Western blot (Figure 3B). From fluorescence staining of tumor tissues (Figure 3C), we can clearly see that U87MG tumor expressed a high level of human integrin $\alpha_v\beta_3$, whereas HT-29 tumor did not express human integrin $\alpha_v\beta_3$. Both tumor tissues expressed a moderate level of murine integrin $\alpha_v\beta_3$, which is supposed to be derived from the newly formed tumor vasculature.

Biodistribution. The biodistribution of ^{99m}Tc-G$_3$-2P$_4$-RGD2 was determined in nude mice bearing U87MG tumors. The results are depicted in Figure 4A. The uptake of ^{99m}Tc-G$_3$-2P$_4$-RGD2 in U87MG tumors was 7.94 ± 1.74%ID/g at 0.5 h p.i., which was slightly decreased to 6.01 ± 1.30%ID/g at 2 h p.i. (n = 4/group). ^{99m}Tc-G$_3$-2P$_4$-RGD2 cleared predominantly through the renal pathway as evidenced by higher kidney uptake (15.04 ± 0.72%ID/g and 10.55 ± 1.44%ID/g at 0.5 and 2 h p.i., respectively). The other organs such as heart, liver, spleen, lung, muscle, and brain showed very low uptake. The high intestine uptake of the radioprobe was observed, with 18.37 ± 1.54%ID/g and 11.64 ± 1.91%ID/g at 0.5 and 2 h p.i., respectively.

Integrin $\alpha_v\beta_3$ receptor specificity of ^{99m}Tc-G$_3$-2P$_4$-RGD2 was demonstrated by a blocking experiment with coinjection of E[c(RGDfK)]$_2$. The tumor uptake at 0.5 h p.i. was reduced from 7.94 ± 1.74%ID/g to 2.01 ± 1.30%ID/g (Figure 4B), indicating the receptor-mediated targeting of ^{99m}Tc-G$_3$-2P$_4$-RGD2 in U87MG tumors. At 0.5 h p.i., the uptake values of ^{99m}Tc-G$_3$-2P$_4$-RGD2 in U87MG and HT-29 tumors were compared (Figure 4B). The U87MG (high human integrin $\alpha_v\beta_3$ expression, Figure 3) tumor uptake of ^{99m}Tc-G$_3$-2P$_4$-RGD2 was also significantly higher than the HT-29 (none or low human integrin $\alpha_v\beta_3$ expression, Figure 3) tumor uptake ($n = 4$, $P < 0.01$), which also confirmed the integrin $\alpha_v\beta_3$-specific tumor accumulation of ^{99m}Tc-G$_3$-2P$_4$-RGD2. The HT-29 tumor uptake was also reduced after blocking with an excess dose of unlabeled E[c(RGDfK)]$_2$ (Figure 4B), revealing the specific binding of ^{99m}Tc-G$_3$-2P$_4$-RGD2 to the murine integrin $\alpha_v\beta_3$ receptors that expressed on the tumor vasculature.

The U87MG tumor uptake of ^{99m}Tc-G$_3$-2P$_4$-RGD2 was compared with that of ^{99m}Tc-RGD2. As shown in Figure 4C, the uptake of ^{99m}Tc-G$_3$-2P$_4$-RGD2 in U87MG tumors was more than twice that of ^{99m}Tc-RGD2 at any time tested (7.94 ± 1.74 vs 2.50 ± 1.20%ID/g and 6.01 ± 1.30 vs 1.70 ± 0.80%ID/g at 0.5 and 2 h p.i., respectively).

Planar γ Imaging. Representative planar γ-images of U87MG or HT-29 tumor-bearing mice at 0.5 and 2 h p.i. after intravenous injection of ~18.5 MBq (500 μCi) of ^{99m}Tc-G$_3$-2P$_4$-RGD2 are shown in Figure 5. In the U87MG tumor model, the tumors were clearly visible with high contrast to the contralateral background at 0.5 h p.i. With the clearance of the probe, the tumor radioactivity decreased from 0.5 to 2 h. Prominent renal uptake and bladder accumulation of the probe was also observed. The uptake of the probe in other organs such as liver was very low. In the HT-29 tumor model (human integrin $\alpha_v\beta_3$-negligible/murine $\alpha_v\beta_3$-positive), the tumors could also be visualized with moderate tumor-to-background contrast at 0.5 h p.i., which was most likely due to the recognition of the probe to murine $\alpha_v\beta_3$ expressed on the newly formed tumor vasculature; the tumor uptake of ^{99m}Tc-G$_3$-2P$_4$-RGD2, however, was significantly lower than that in the U87MG tumors. ^{99m}Tc-G$_3$-2P$_4$-RGD2 also showed high renal uptake and bladder accumulation in the HT-29 tumor-bearing mice, suggesting the renal clearance of the probe. In both tumor models, high activity accumulation in the abdomen, resulting from high kidney and intestine uptake of the probe (Figure 4A), was observed, which may limit the application of ^{99m}Tc-G$_3$-2P$_4$-RGD2 in the detection of abdominal metastases of integrin $\alpha_v\beta_3$-positive tumors.

Correlation of ^{99m}Tc-G$_3$-2P$_4$-RGD2 Tumor Uptake with Integrin $\alpha_v\beta_3$ Expression. Because integrin α_v and β_3 subunites cannot be kept as one entity after protein extraction, we assessed both human and murine integrin β_3 expression in the U87MG and HT-29 tumor tissues using Western blotting. Figure 6A depicts representative Western blots of the murine integrin β_3 in different sizes of HT-29 tumors. Due to the limited expression of human integrin $\alpha_v\beta_3$ on the HT-29 tumor cells, the Western blot of human integrin β_3 was not obtained. U87MG tumors expressed a detectable level of both human and murine integrin β_3. There was a certain variation in the β-actin band intensity

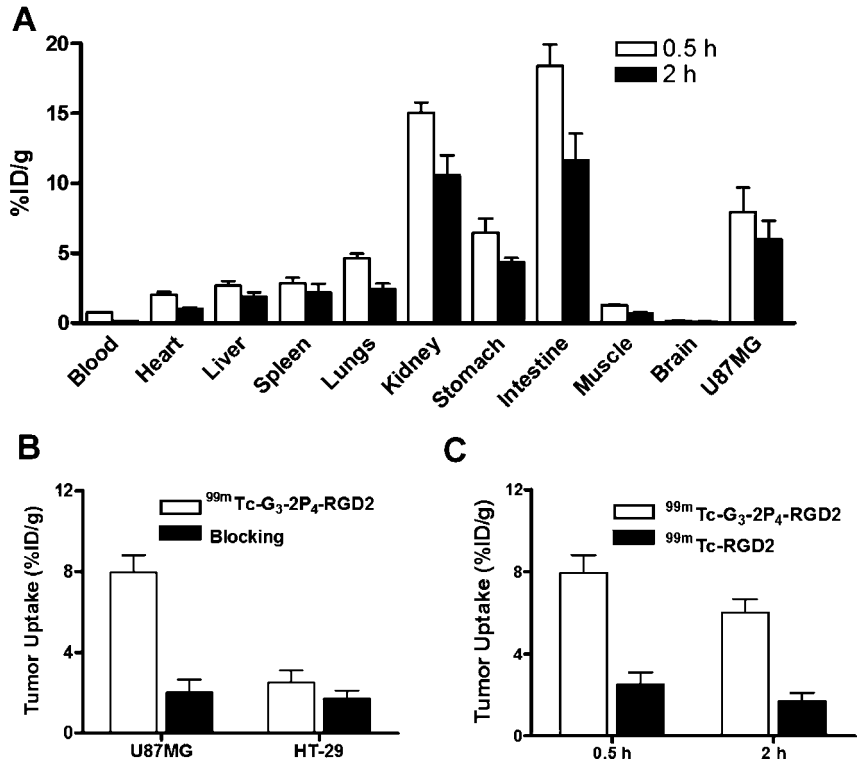


Figure 4. (A) Biodistribution of ^{99m}Tc-G$_3$-2P$_4$-RGD2 in U87MG tumor-bearing nude mice at 0.5 and 2 h postinjection. (B) Tumor uptake values of ^{99m}Tc-G$_3$-2P$_4$-RGD2 in U87MG and HT-29 tumor-bearing nude mice with and without coinjection of 300 μg unlabeled E[c(RGDfK)]$_2$ as the blocking agent at 0.5 h postinjection. (C) Comparison of tumor uptake of ^{99m}Tc-G$_3$-2P$_4$-RGD2 and ^{99m}Tc-RGD2 in U87MG tumor-bearing nude mice at 0.5 and 2 h postinjection. Data are expressed as %ID/g ± SD (n = 4 per group).

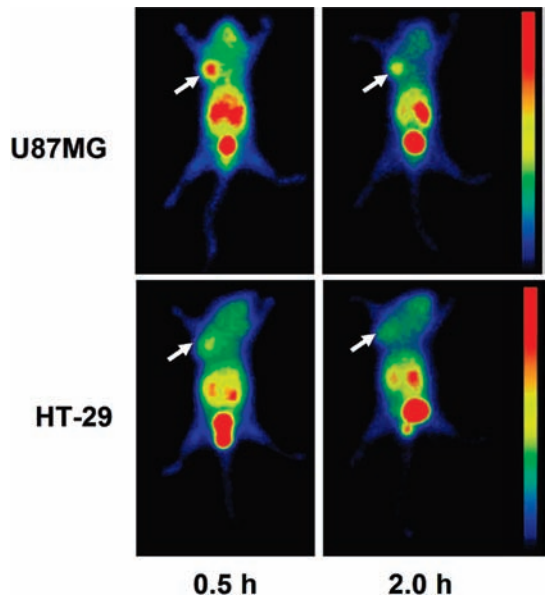


Figure 5. Representative planar γ images of U87MG or HT-29 nude mouse models at 0.5 and 2 h after intravenous injection of ~18.5 MBq (500 μCi) of ^{99m}Tc-G$_3$-2P$_4$-RGD2 (n = 3 per tumor group). Tumors are indicated by white arrows.

among the tumors with different sizes. The Western blot of tumor tissue lysates was analyzed using *ImageJ* to obtain the quantitative data. Relative integrin β_3 expression was calculated for each tumor to correlate with the ^{99m}Tc-G$_3$-2P$_4$-RGD2 tumor uptake measured by the ex vivo biodistribution study. RGD peptide can recognize integrin $\alpha_v\beta_3$ of different origins, therefore, ^{99m}Tc-G$_3$-2P$_4$-RGD2 can bind to both human and murine integrin $\alpha_v\beta_3$ in vivo. In the U87MG tumors, the human integrin $\alpha_v\beta_3$ was expressed in a much higher level than murine integrin $\alpha_v\beta_3$, so it is supposed that most of ^{99m}Tc-G$_3$-2P$_4$-RGD2 was accumulated to the human integrin $\alpha_v\beta_3$ on the U87MG tumor cell surface, leading to a linear correlation between the ^{99m}Tc-G$_3$-2P$_4$-RGD2 tumor uptake and the human integrin β_3 expression (r^2 = 0.51, P = 0.0004, Figure 6B). There is no linear correlation between the ^{99m}Tc-G$_3$-2P$_4$-RGD2 tumor uptake (1 h p.i.) and the relative murine integrin β_3 expression, probably due to the much lower expression of the murine integrin $\alpha_v\beta_3$ compared with human integrin $\alpha_v\beta_3$ in U87MG tumor tissues (Figure 6B). In the HT-29 tumors, the human integin $\alpha_v\beta_3$ was not detectable (Figure 3), so most of ^{99m}Tc-G$_3$-2P$_4$-RGD2 recognized the murine integrin $\alpha_v\beta_3$ that expressed on the tumor newborn vasculature, which resulted in a better linear correlation of the tumor uptake values vs the murine integrin $\alpha_v\beta_3$ expression levels (r^2 = 0.84, P < 0.0001, Figure 6C) in HT-29 tumors.

DISCUSSION

In this study, we have prepared a new RGD dimeric probe ^{99m}Tc-G$_3$-2P$_4$-RGD2 for integin $\alpha_v\beta_3$ targeting. The insertion of two PEG$_4$ spacers between the two RGD motifs and one Gly$_3$ on the glutamate α-amino group of E[c(RGDfK)]$_2$ increased the in vitro integrin $\alpha_v\beta_3$ binding affinity, and the tumor uptake of ^{99m}Tc-G$_3$-2P$_4$-RGD2 was also significantly higher than that of ^{99m}Tc-RGD2 in integrin $\alpha_v\beta_3$-positive U87MG tumor model. The feasibility of ^{99m}Tc-G$_3$-2P$_4$-RGD2 for the noninvasive detection of integrin $\alpha_v\beta_3$ expression was evaluated in both U87MG and HT-29 tumor models.

We and others recently demonstrated that the insertion of spacers (e.g., Gly$_3$, PEG$_4$) between the two RGD motifs in the RGD dimeric molecule will significantly increase the integrin $\alpha_v\beta_3$ binding affinity, enhance the tumor uptake, and improve the in vivo pharmacokinetics of the new RGD dimeric probes (*31*). In this study, besides the insertion of two PEG$_4$ spacers between the two monomeric RGD motifs, we also inserted a

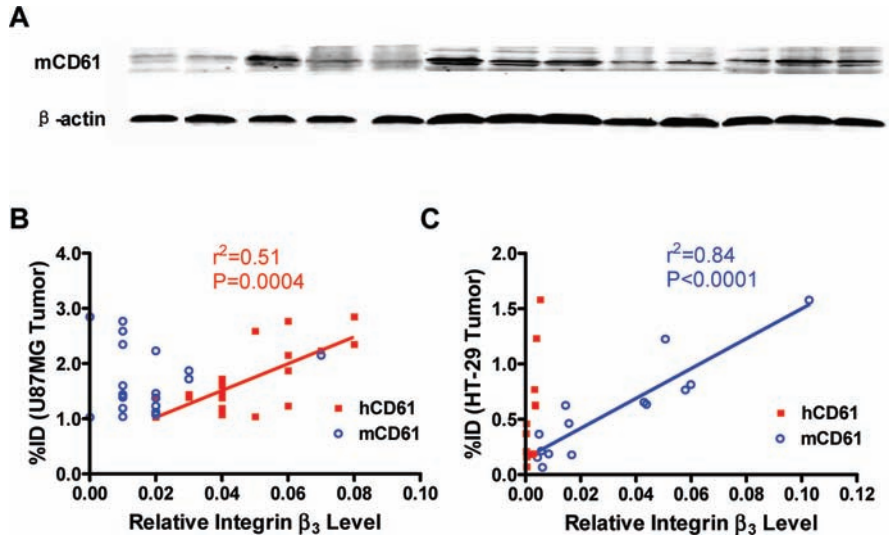


Figure 6. (A) Western blot of murine integrin β_3 (mCD61) expression in HT-29 tumor tissues with different tumor sizes. (B) Correlation of human or murine integrin β_3 (hCD61 and mCD61) expression levels (measured by Western blot) and U87MG tumor uptake values (%ID) at 1 h after intravenous injection of 0.37 MBq (10 μCi) of ^{99m}Tc-G$_3$-2P$_4$-RGD2. (C) Correlation of human or murine integrin β_3 (hCD61 and mCD61) expression levels (measured by Western blot) and HT-29 tumor uptake values (%ID) at 1 h after intravenous injection of 0.37 MBq (10 μCi) of ^{99m}Tc-G$_3$-2P$_4$-RGD2.

Gly$_3$ linker onto the glutamate α-amino group of the RGD dimer, which was suggested to increase the overall hydrophilicity and to alleviate the steric hindrance, thereby increasing the HYNIC conjugation efficiency and ^{99m}Tc labeling yield (*15*). The HYNIC-G$_3$-2P$_4$-RGD2 conjugate showed increased integrin $\alpha_v\beta_3$ binding affinity compared with HYNIC-RGD2 as determined by cell binding assay (Figure 2). Because the Gly$_3$ linker on the glutamate α-amino group of the RGD dimer would not contribute to the enhancement of the receptor-binding affinity, the increased affinity of HYNIC-G$_3$-2P$_4$-RGD2 was therefore most likely due to the insertion of two PEG$_4$ linkers between two RGD motifs. The affinity of HYNIC-G$_3$-2P$_4$-RGD2 was about 2-fold higher than that of the HYNIC-RGD2 (3.37 ± 0.84 nM vs 8.13 ± 0.61 nM) (Figure 2), which is similar to the results of other RGD dimers with Gly$_3$ and PEG$_4$ linkers as we previously reported (*31*). Therefore, although without direct comparison, we can speculate that HYNIC-G$_3$-2P$_4$-RGD2 possesses comparable integrin $\alpha_v\beta_3$ binding affinity with the previously reported new types of RGD dimers. Note that caution should be taken when directly comparing the IC$_{50}$ values of RGD peptides with those reported in the literatures due to the different radioligands (^{125}I-c(RGDyK) or ^{125}I-echistatin) and tumor cells (U87MG or MDA-MB-435) used in different laboratories. The enhanced integrin $\alpha_v\beta_3$ binding affinity of HYNIC-G$_3$-2P$_4$-RGD2 over HYNIC-RGD2 was well evidenced by the significantly increased U87MG tumor uptake of ^{99m}Tc-G$_3$-2P$_4$-RGD2 compared to that of ^{99m}Tc-RGD2 at any time points examined in the nude mouse model (Figure 4C).

U87MG tumor cells express a very high level of human integrin $\alpha_v\beta_3$, while HT-29 tumor cells express negligible human integrin $\alpha_v\beta_3$ (Figure 3A,B). After inoculating tumor cells into the nude mice, in addition to expressing human integrin $\alpha_v\beta_3$, U87MG tumor tissues also expressed murine integrin $\alpha_v\beta_3$ due to the incorporation of murine endothelial cells during tumor angiogenesis. On the other hand, HT-29 tumor tissues expressed only murine integrin $\alpha_v\beta_3$ due to the negligible expression of human integrin $\alpha_v\beta_3$ on the tumor cells. We tested the in vivo behaviors of the new RGD dimeric probe ^{99m}Tc-G$_3$-2P$_4$-RGD2 in both U87MG and HT-29 tumor models. The tumor uptake of ^{99m}Tc-G$_3$-2P$_4$-RGD2 in U87MG tumors was significantly higher than that in HT-29 tumors, most likely due to the fact that the total integrin $\alpha_v\beta_3$ (both human and murine origins) in U87MG tumors was much higher than that in HT-29 tumors. It should be noted that we have not considered the difference of nonspecific uptake values of ^{99m}Tc-G$_3$-2P$_4$-RGD2 in the two different tumor models here, because the relatively low molecular weight of ^{99m}Tc-G$_3$-2P$_4$-RGD2 would not lead to a high nonspecific tumor accumulation, as evidenced by effective inhibition of tumor uptake in the presence of excess amounts of cold RGD peptide (Figure 4B).

There has been growing interest in the use of noninvasive imaging technology to the drug discovery process and cancer patient management over the past decade (*32, 33*). The ability to noninvasively visualize and quantify integrin $\alpha_v\beta_3$ expression in vivo will certainly provide new opportunities to document tumor angiogenesis, to select patients for antiangiogenic treatment, and to monitor the therapeutic efficacy of antiangiogenic drugs in cancer patients. Although numerous RGD probes have been developed for integrin $\alpha_v\beta_3$ imaging in the past decade, the reports about quantitative correlation between the integrin $\alpha_v\beta_3$ expression levels in vivo and the noninvasive imaging data is rare (*34*−*37*). Haubner et al. (*35*) investigated the relationship between the tumor uptake of RGD probe and the integrin $\alpha_v\beta_3$ expression level for the first time. Several subcutaneous tumor models were produced by inoculating different mixtures of M21 (integrin $\alpha_v\beta_3$ positive) and M21-L (integrin $\alpha_v\beta_3$ negative) cells. The tumor-to-background ratios and the tumor-to-muscle ratios of [^{18}F]Galacto-RGD obtained from PET imaging and direct tissue sampling were compared with relative integrin α_v expression measured by Western blot analysis, and a good correlation was found. In a following clinical study (*36*), a significant correlation of the SUVs of [^{18}F]Galacto-RGD with the integrin $\alpha_v\beta_3$ intensity of immunohisochemical staining as well as with the microvessel density were confirmed. To increase the tumor uptake, Zhang X et al. (*34*) developed a ^{18}F-labeled dimeric RGD probe with enhanced receptor binding affinity and increased tumor uptake compared with monomeric RGD probes, and investigated the relationship of tumor uptake vs the integrin expression level in multiple tumor models. A good correlation was found between the tumor tissue receptor density (number of receptors/milligrams protein measured from SDS-PAGE/autoradiography using ^{125}I-echistatin as radioligand) and the binding potential (BP, calculated from Logan plot transformation of dynamic microPET data). Although the good correlations between the tumor uptake of RGD probes and the integrin $\alpha_v\beta_3$ expression levels were determined in previous reports, the

integrin $\alpha_v\beta_3$ expressed on tumor cells or tumor newborn vasculature has not been well distinguished. In addition, the sensitivity using previously reported RGD probes may be limited due to their relative low tumor uptake and tumor-to-nontumor ratios. For our interests in developing a more sensitive RGD probe that can be used for noninvasively determining the in vivo integrin $\alpha_v\beta_3$ expression, we investigated the integrin $\alpha_v\beta_3$ correlation properties of ^{99m}Tc-G_3-$2P_4$-RGD, which had much higher binding affinity and tumor uptake values compared with ^{99m}Tc-labeled RGD dimer. We determined the correlation between the ^{99m}Tc-G_3-$2P_4$-RGD2 tumor uptake and either murine integrin $\alpha_v\beta_3$ or human integrin $\alpha_v\beta_3$ in both high integrin $\alpha_v\beta_3$ expressing U87MG and low integrin $\alpha_v\beta_3$ expressing HT-29 tumor xenografts.

The significant correlation between the tumor uptake of ^{99m}Tc-labeled RGD probe and integrin $\alpha_v\beta_3$ expression at a fixed time point postinjection is very important for clinical applications, since it would determine the integrin $\alpha_v\beta_3$ expression level by a simple, noninvasive, whole-body SPECT scaning. The U87MG tumor uptake of ^{99m}Tc-G_3-$2P_4$-RGD2 showed linear correlation with human integrin $\alpha_v\beta_3$, yet the r^2 value was relatively low ($r^2 = 0.51$, Figure 6B) because the RGD probe also bound to the murine integrin $\alpha_v\beta_3$ in the U87MG tumors. Note that the total integrin $\alpha_v\beta_3$ expression level (both human and murine origins) cannot be simply obtained by the sum of murine and human integrin $\alpha_v\beta_3$ densities determined by Western blot, due to the difference of the secondary antibodies used in the separated studies. HT-29 tumor tissues expressed negligible human integrin $\alpha_v\beta_3$, so almost all ^{99m}Tc-G_3-$2P_4$-RGD2 would bind to the murine integrin $\alpha_v\beta_3$, which leads to a much better correlation ($r^2 = 0.84$) between the HT-29 tumor uptake and murine integrin $\alpha_v\beta_3$ expression (Figure 6C).

Our results showed that this study cannot be simply translated to clinical situations, because integrin $\alpha_v\beta_3$ expressed on some tumor cells and tumor newborn vasculature in patients are both of human origin. However, our data can validate that, in clinical situations, the RGD probes would target both the integrin $\alpha_v\beta_3$-positive tumor cells and the newborn tumor vasculature. Therefore, caution should be taken when using RGD probes for the noninvasive imaging of tumor angiogenesis in patients, whose tumor itself is integrin $\alpha_v\beta_3$-positive. Biopsy or immunohistochemistry may be needed to confirm the integrin $\alpha_v\beta_3$ expression in tumors after RGD imaging. For patients with integrin $\alpha_v\beta_3$-negative tumors, ^{99m}Tc-G_3-$2P_4$-RGD2 would be a promising probe for characterizing tumor angiogenesis due to the good correlation between the probe uptake and the integrin $\alpha_v\beta_3$ expression on newborn blood vessels.

CONCLUSION

In this study, we prepared a new ^{99m}Tc-labeled RGD dimeric probe ^{99m}Tc-G_3-$2P_4$-RGD2 with increased in vitro receptor binding affinity and in vivo tumor uptake as compared with our previously reported ^{99m}Tc-labeled RGD dimer. The easy availability with high yield and high integrin $\alpha_v\beta_3$ affinity/specificity makes ^{99m}Tc-G_3-$2P_4$-RGD2 promising for noninvasive SPECT imaging of integrin $\alpha_v\beta_3$ expression and allows kit formulation and routine clinical preparation. The tumor uptake of ^{99m}Tc-G_3-$2P_4$-RGD2 was related to both the human integrin $\alpha_v\beta_3$ (expressed on integrin $\alpha_v\beta_3$-positive tumor cells) and murine integrin $\alpha_v\beta_3$ (expressed on newborn tumor vasculature) expression. The data presented in this study would also provide useful information for clinical translation of ^{99m}Tc-labeled RGD probes for tumor imaging, evaluating tumor angiogenesis, and monitoring treatment efficacy of antiangiogenic drugs. Indeed, the preliminary clinical application of the ^{99m}Tc-labeled new RGD dimer for cancer screening is currently in progress.

ACKNOWLEDGMENT

This work was supported, in part, by NSFC projects (30870728, 20820102035, and 30930030 to F.W.; 30900373 to B.J.), an "863" project (2007AA02Z467 to F.W.) and grants from the Ministry of Science and Technology of China (2009ZX09103-733 and 2009ZX09301-010 to F.W.; 2009ZX09103-746 to B.J.).

LITERATURE CITED

(1) Bergers, G., and Benjamin, L. E. (2003) Tumorigenesis and the angiogenic switch. *Nat. Rev. Cancer 3*, 401–410.

(2) Brooks, P. C., Clark, R. A., and Cheresh, D. A. (1994) Requirement of vascular integrin $\alpha_v\beta_3$ for angiogenesis. *Science 264*, 569–571.

(3) Hood, J. D., and Cheresh, D. A. (2002) Role of integrins in cell invasion and migration. *Nat. Rev. Cancer 2*, 91–100.

(4) Cai, W., and Chen, X. (2006) Anti-angiogenic cancer therapy based on integrin $\alpha_v\beta_3$ antagonism. *Anticancer Agents Med. Chem. 6*, 407–428.

(5) Liu, Z., Wang, F., and Chen, X. (2008) Integrin $\alpha_v\beta_3$-targeted cancer therapy. *Drug Dev. Res. 69*, 329–339.

(6) Dijkgraaf, I., Beer, A. J., and Wester, H. J. (2009) Application of RGD-containing peptides as imaging probes for $\alpha_v\beta_3$ expression. *Front. Biosci. 14*, 887–899.

(7) Beer, A. J., and Schwaiger, M. (2008) Imaging of integrin $\alpha_v\beta_3$ expression. *Cancer Metastasis Rev. 27*, 631–644.

(8) Liu, S. (2006) Radiolabeled multimeric cyclic RGD peptides as integrin $\alpha_v\beta_3$ targeted radiotracers for tumor imaging. *Mol. Pharm. 3*, 472–487.

(9) Chen, X. (2006) Multimodality imaging of tumor integrin $\alpha_v\beta_3$ expression. *Mini Rev. Med. Chem. 6*, 227–234.

(10) Schnell, O., Krebs, B., Carlsen, J., Miederer, I., Goetz, C., Goldbrunner, R. H., Wester, H. J., Haubner, R., Popperl, G., Holtmannspotter, M., Kretzschmar, H. A., Kessler, H., Tonn, J. C., Schwaiger, M., and Beer, A. J. (2009) Imaging of integrin $\alpha_v\beta_3$ expression in patients with malignant glioma by [^{18}F]galacto-RGD positron emission tomography. *Neuro Oncol. 11*, 861–870.

(11) Kenny, L. M., Coombes, R. C., Oulie, I., Contractor, K. B., Miller, M., Spinks, T. J., McParland, B., Cohen, P. S., Hui, A. M., Palmieri, C., Osman, S., Glaser, M., Turton, D., Al-Nahhas, A., and Aboagye, E. O. (2008) Phase I trial of the positron-emitting Arg-Gly-Asp (RGD) peptide radioligand 18F-AH111585 in breast cancer patients. *J. Nucl. Med. 49*, 879–886.

(12) Beer, A. J., Niemeyer, M., Carlsen, J., Sarbia, M., Nahrig, J., Watzlowik, P., Wester, H. J., Harbeck, N., and Schwaiger, M. (2008) Patterns of $\alpha_v\beta_3$ expression in primary and metastatic human breast cancer as shown by ^{18}F-Galacto-RGD PET. *J. Nucl. Med. 49*, 255–259.

(13) Beer, A. J., Grosu, A. L., Carlsen, J., Kolk, A., Sarbia, M., Stangier, I., Watzlowik, P., Wester, H. J., Haubner, R., and Schwaiger, M. (2007) [^{18}F]galacto-RGD positron emission tomography for imaging of $\alpha_v\beta_3$ expression on the neovasculature in patients with squamous cell carcinoma of the head and neck. *Clin. Cancer Res. 13*, 6610–6616.

(14) Beer, A. J., Lorenzen, S., Metz, S., Herrmann, K., Watzlowik, P., Wester, H. J., Peschel, C., Lordick, F., and Schwaiger, M. (2008) Comparison of integrin $\alpha_v\beta_3$ expression and glucose metabolism in primary and metastatic lesions in cancer patients: a PET study using ^{18}F-galacto-RGD and 18F-FDG. *J. Nucl. Med. 49*, 22–29.

(15) Liu, Z., Liu, S., Wang, F., Liu, S., and Chen, X. (2009) Noninvasive imaging of tumor integrin expression using ^{18}F-labeled RGD dimer peptide with PEG_4 linkers. *Eur. J. Nucl. Med. Mol. Imaging 36*, 1296–1307.

(16) Liu, Z., Niu, G., Shi, J., Liu, S., Wang, F., Liu, S., and Chen, X. (2009) 68Ga-labeled cyclic RGD dimers with Gly_3 and PEG_4 linkers: promising agents for tumor integrin $\alpha_v\beta_3$ PET imaging. *Eur. J. Nucl. Med. Mol. Imaging 36*, 947–957.

(17) Shi, J., Wang, L., Kim, Y. S., Zhai, S., Liu, Z., Chen, X., and Liu, S. (2008) Improving tumor uptake and excretion kinetics of 99mTc-labeled cyclic arginine-glycine-aspartic (RGD) dimers with triglycine linkers. *J. Med. Chem. 51*, 7980–7990.

(18) Wang, L., Shi, J., Kim, Y. S., Zhai, S., Jia, B., Zhao, H., Liu, Z., Wang, F., Chen, X., and Liu, S. (2009) Improving tumor-targeting capability and pharmacokinetics of 99mTc-labeled cyclic RGD dimers with PEG$_4$ linkers. *Mol. Pharm. 6*, 231–245.

(19) Hynes, R. O. (1992) Integrins: versatility, modulation, and signaling in cell adhesion. *Cell 69*, 11–25.

(20) Seftor, R. E., Seftor, E. A., Gehlsen, K. R., Stetler-Stevenson, W. G., Brown, P. D., Ruoslahti, E., and Hendrix, M. J. (1992) Role of the $\alpha_v\beta_3$ integrin in human melanoma cell invasion. *Proc. Natl. Acad. Sci. U.S.A. 89*, 1557–1561.

(21) Liu, Z., Liu, S., Niu, G., Wang, F., Liu, S., and Chen, X. (2010) Optical imaging of integrin $\alpha_v\beta_3$ expression with near-infrared fluorescent RGD dimer with tetra(ethylene glycol) linkers. *Mol. Imaging 9*, 21–29.

(22) Harris, T. D., Sworin, M., Williams, N., Rajopadhye, M., Damphousse, P. R., Glowacka, D., Poirier, M. J., and Yu, K. (1999) Synthesis of stable hydrazones of a hydrazinonicotinyl-modified peptide for the preparation of 99mTc-labeled radiopharmaceuticals. *Bioconjugate Chem. 10*, 808–814.

(23) Jia, B., Shi, J., Yang, Z., Xu, B., Liu, Z., Zhao, H., Liu, S., and Wang, F. (2006) 99mTc-labeled cyclic RGDfK dimer: initial evaluation for SPECT imaging of glioma integrin $\alpha_v\beta_3$ expression. *Bioconjugate Chem. 17*, 1069–1076.

(24) Liu, Z., Yan, Y., Chin, F. T., Wang, F., and Chen, X. (2009) Dual integrin and gastrin-releasing peptide receptor targeted tumor imaging using 18F-labeled PEGylated RGD-bombesin heterodimer 18F-FB-PEG3-Glu-RGD-BBN. *J. Med. Chem. 52*, 425–432.

(25) Liu, Z., Li, Z., Cao, Q., Liu, S., Wang, F., and Chen, X. (2009) Small-Animal PET of Tumors with ^{64}Cu-Labeled RGD-Bombesin Heterodimer. *J. Nucl. Med. 50*, 1168–1177.

(26) Liu, Z., Yu, Z., He, W., Ma, S., Sun, L., and Wang, F. (2009) In-vitro internalization and in-vivo tumor uptake of anti-EGFR monoclonal antibody LA22 in A549 lung cancer cells and animal model. *Cancer Biother. Radiopharm. 24*, 15–24.

(27) Liu, Z., Jia, B., Zhao, H., Chen, X., and Wang, F. Specific targeting of human integrin $\alpha_v\beta_3$ with 111In-labeled Abegrin™ in nude mouse models. *Mol. Imaging Biol.* in press.

(28) Veeravagu, A., Liu, Z., Niu, G., Chen, K., Jia, B., Cai, W., Jin, C., Hsu, A. R., Connolly, A. J., Tse, V., Wang, F., and Chen, X. (2008) Integrin $\alpha_v\beta_3$-targeted radioimmunotherapy of glioblastoma multiforme. *Clin. Cancer Res. 14*, 7330–7339.

(29) Cai, W., Wu, Y., Chen, K., Cao, Q., Tice, D. A., and Chen, X. (2006) In vitro and in vivo characterization of ^{64}Cu-labeled Abegrin, a humanized monoclonal antibody against integrin $\alpha_v\beta_3$. *Cancer Res. 66*, 9673–9681.

(30) Liu, Z., Niu, G., Wang, F., and Chen, X. (2009) 68Ga-labeled NOTA-RGD-BBN peptide for dual integrin and GRPR-targeted tumor imaging. *Eur. J. Nucl. Med. Mol. Imaging 36*, 1483–1494.

(31) Liu, S. (2009) Radiolabeled cyclic RGD peptides as integrin $\alpha_v\beta_3$-targeted radiotracers: maximizing binding affinity via bivalency. *Bioconjugate Chem. 20*, 2199–2213.

(32) Cai, W., Rao, J., Gambhir, S. S., and Chen, X. (2006) How molecular imaging is speeding up antiangiogenic drug development. *Mol. Cancer Ther. 5*, 2624–2633.

(33) Willmann, J. K., van Bruggen, N., Dinkelborg, L. M., and Gambhir, S. S. (2008) Molecular imaging in drug development. *Nat. Rev. Drug Discovery 7*, 591–607.

(34) Zhang, X., Xiong, Z., Wu, Y., Cai, W., Tseng, J. R., Gambhir, S. S., and Chen, X. (2006) Quantitative PET imaging of tumor integrin $\alpha_v\beta_3$ expression with 18F-FRGD2. *J. Nucl. Med. 47*, 113–121.

(35) Haubner, R., Weber, W. A., Beer, A. J., Vabuliene, E., Reim, D., Sarbia, M., Becker, K. F., Goebel, M., Hein, R., Wester, H. J., Kessler, H., and Schwaiger, M. (2005) Noninvasive visualization of the activated $\alpha_v\beta_3$ integrin in cancer patients by positron emission tomography and [^{18}F]Galacto-RGD. *PLoS Med. 2*, e70.

(36) Beer, A. J., Haubner, R., Sarbia, M., Goebel, M., Luderschmidt, S., Grosu, A. L., Schnell, O., Niemeyer, M., Kessler, H., Wester, H. J., Weber, W. A., and Schwaiger, M. (2006) Positron emission tomography using [^{18}F]Galacto-RGD identifies the level of integrin $\alpha_v\beta_3$ expression in man. *Clin. Cancer Res. 12*, 3942–3949.

(37) Jung, K. H., Lee, K. H., Paik, J. Y., Ko, B. H., Bae, J. S., Lee, B. C., Sung, H. J., Kim, D. H., Choe, Y. S., and Chi, D. Y. (2006) Favorable biokinetic and tumor-targeting properties of 99mTc-labeled glucosamino RGD and effect of paclitaxel therapy. *J. Nucl. Med. 47*, 2000–2007.

BC900547D

A Phospholipid−PEG2000 Conjugate of a Vascular Endothelial Growth Factor Receptor 2 (VEGFR2)-Targeting Heterodimer Peptide for Contrast-Enhanced Ultrasound Imaging of Angiogenesis

R. Pillai,[†] E. R. Marinelli,[†] H. Fan,[†] P. Nanjappan,[†] B. Song,[†] M. A. von Wronski,[†] S. Cherkaoui,[‡] I. Tardy,[‡] S. Pochon,[‡] M. Schneider,[‡] A. D. Nunn,[†] and R. E. Swenson*,[†]

The Ernst Felder Laboratories, Bracco Research USA, 305 College Road East, Princeton, New Jersey 08540, and Bracco Research SA, Route de la Galaise, 31, CH-1228 Plan-les-Ouates, Geneva, Switzerland. Received December 21, 2009; Revised Manuscript Received January 26, 2010

The transition of a targeted ultrasound contrast agent from animal imaging to testing in clinical studies requires considerable chemical development. The nature of the construct changes from an agent that is chemically attached to microbubbles to one where the targeting group is coupled to a phospholipid, for direct incorporation to the bubble surface. We provide an efficient method to attach a heterodimeric peptide to a pegylated phospholipid and show that the resulting construct retains nanomolar affinity for its target, vascular endothelial growth factor receptor 2 (VEGFR2), for both the human (kinase insert domain-containing receptor - KDR) and the mouse (fetal liver kinase 1 - Flk-1) receptors. The purified phospholipid-PEG-peptide isolated from TFA-based eluents is not stable with respect to hydrolysis of the fatty ester moieties. This leads to the time-dependent formation of the lysophospholipid and the phosphoglycerylamide derived from the degradation of the product. Purification of the product using neutral eluent systems provides a stable product. Methods to prepare the lysophospholipid (hydrolysis product) are also included. Biacore binding data demonstrated the retention of binding of the lipopeptide to the KDR receptor. The phospholipid-PEG2000-peptide is smoothly incorporated into gas-filled microbubbles and provides imaging of angiogenesis in a rat tumor model.

INTRODUCTION

Molecular imaging is unprecedented in its ability to noninvasively provide in vivo information for diagnosis, prognosis, and monitoring of disease. Of the common modalities, ultrasound imaging is noteworthy for its cost effectiveness, portability, and ease of use. The injection of small (2−5 μm diameter) echogenic gas-filled unilamellar vesicles, commonly referred to as microbubbles, allows improved image definition due to the administered microbubble contrast agent. Recently, the use of targeting groups on the surface of these microbubbles has allowed the monitoring of biochemical processes in the body in real time with sensitivity comparable to that of nuclear medicine (*1*).

One of the important biological processes for imaging is angiogenesis. Tumor growth requires the development of new blood vessels, which is correlated with aggressiveness (*2*). Microbubbles targeted to $\alpha_v\beta_3$ (*3*) or via the targeting tripeptide RRL (*4*) have been used to image angiogenesis. However, the receptor tyrosine kinase VEGFR2, or KDR, has been shown to be one of the major mediators of angiogenesis (*5*). Ultrasound bubbles bearing antibodies to VEGFR2 have also shown good imaging of angiogenesis (*6*). For this reason, we focused on developing a peptide-based targeting agent for imaging the KDR receptor with ultrasound bubbles.

We previously described the use of phage display to generate two families of KDR-binding peptides. Each family of peptides was found to bind to a distinct, noncompeting epitope on KDR as evidenced by the finding that members of each family could not displace the KDR-binding of members of the other family. This was exploited by preparation of heterodimer peptides containing one member of each family of peptides. In binding and functional assays, these constructs were superior to individual peptides and homodimer constructs based on each family of peptides. Chemical optimization of a peptide selected from each family and their linkage provided a potent heterodimer peptide ligand for KDR (*7*). A versatile chemical approach for preparation of a range of heterodimeric peptides using disuccinimidyl glutarate (DSG) was also developed (*8*).

Targeted microbubbles for research applications are routinely prepared by the conjugation of biotinylated antibodies, peptides, or small molecules to preformed streptavidin-bound biotinylated bubbles (*9*). Commercial availability of streptavidin-coated bubbles (Target-Ready MicroMarker bubbles, VisualSonics, Toronto, Ontario, Canada) has facilitated adoption of this technique for research studies. The use of streptavidin-coated microbubbles bearing biotinylated targeting vectors in humans is undesirable due to the antigenicity of streptavidin (*10*). Hence, for clinical product applications, covalent attachment of the targeting group to the phospholipid of the bubble surface is optimal. A number of approaches for preparation of targeting microbubbles in this manner have been offered in the literature, including attachment of thiolated targeting groups to maleimide or bromoacetylated bubbles (*11*), carbamate formation by reaction of amines of targeting groups with mixed alkoxy-nitrophenyl carbonates (*12*), amide coupling reactions (*13*), chemical ligation approaches (*14*), and preparation of artificial lipids (*15*).

Success with these strategies has been limited by inconsistent yields, undesired side reactions, deactivation of coupling partners, or concerns about toxicity of unnatural

* Author to who correspondence should be addressed. Dr. Rolf E. Swenson, Discovery Chemistry,The Ernst Felder Laboratories, Bracco Research USA, 305 College Road East, Princeton, NJ 08540; Tel. 609-514-2526; Fax: 609-514-2446; e-mail: rswenson@bru.bracco.com.

[†] Bracco Research USA.

[‡] Bracco Research SA.

10.1021/bc9005688 © 2010 American Chemical Society
Published on Web 02/19/2010

lipid conjugates. Therefore, the preparation of targeted bubbles still provides challenges. Additional complexity results from the need to incorporate an appropriate spacer group to separate the targeting group from the lipid surface of the bubble. The most commonly used spacers are PEGs (poly(ethylene glycols)) of different chain lengths. Other issues include the incompatibility of the phospholipid ester groups with the conditions of peptide synthesis, particularly the TFA-mediated cleavage/deprotection step. This paper provides a method for the preparation of a viable product for targeted ultrasound clinical imaging.

EXPERIMENTAL PROCEDURES

Materials. All common reagents were commercially available and used as received. Disuccinimidyl glutarate (DSG) and 1,2-distearoyl-*sn*-glycero-3-phospho-ethanolamine-*N*-[amino (poly(ethylene glycol))2000] ammonium salt, [DSPE-PEG2000-NH_2] were obtained from Pierce Chemical Co. (Rockford, IL) and Avanti Polar Lipids (Alabaster, AL), respectively. Fmoc-Gly-Gly-Gly-OH was prepared in-house from triglycine by reaction with *N*-hydroxysuccinimidyl-9-fluorenylmethyl carbonate (Fmoc-OSu). AG MP-50 ion-exchange resin was obtained from Bio-Rad (Hercules, CA).

Analytical HPLC. For routine work, analytical HPLC data were obtained using a Shimadzu LC-10AT VP dual-pump gradient system employing a Waters XTerra MS-C18 50 mm × 4.6 mm column, (5 μm particle, 120 Å pore) and gradient or isocratic elution systems using H_2O (0.1% TFA) as eluent A and CH_3CN (0.1% TFA) or CH_3CN-CH_3OH 1:1 (v/v) (0.1% TFA) as eluent B. Detection of compounds was accomplished using a UV detector at 220 and 254 nm. Analytical and purity studies of the phospholipid-PEG2000-peptide derivatives were conducted employing a YMC C4 (250 mm × 4.6 mm, 5 μm particle, 300 Å pore) column or on a Zorbax 300 SB-C3 (150 mm × 3 mm, 3.5 μm particle, 300 Å pore) column and gradient elution using H_2O (10 mM NH_4OAc) as eluent A and CH_3CN-H_2O 9:1 (v/v) (10 mM NH_4OAc) as eluent B. Detection of compounds was accomplished with a SEDEX 55 evaporative light scattering detector (ELSD) and a UV detector.

Preparative HPLC. Preparative HPLC was conducted on a Shimadzu LC-8A dual-pump gradient system equipped with a SPD-10AV UV detector fitted with a preparative flow cell. The solution containing the crude peptide was loaded onto a reversed-phase C18, C4, or C3 column, depending on the compound characteristics, using a third pump attached to the preparative Shimadzu LC-8A dual-pump gradient system. After the solution of the crude product mixture was applied to the preparative HPLC column, the reaction solvents and solvents employed as diluents, such as DMF or DMSO, were eluted from the column at low percentage organic phase composition. Then, the desired product was eluted using a gradient elution of eluent B into eluent A. Product-containing fractions were combined on the basis of their purity, as determined by analytical HPLC and mass spectral analysis. The combined fractions were lyophilized to provide the desired product.

Mass Spectroscopy. Mass spectral data were obtained from MScan Inc. (West Chester, PA) or in-house on an Agilent LC-MSD 1100 mass spectrometer.

Indirect CE-UV for the Simultaneous Analysis of Trifluoroacetate and Acetate Ions. The simultaneous determination of trifluoroacetate and acetate was carried out by capillary electrophoresis (CE) with indirect UV detection at 232 nm. CE data were generated using a PA800 Beckman Coulter system (Fullerton, CA, USA) equipped with an on-column diode-array detector, an autosampler, and a power supply able to deliver up to 30 kV. The separations were performed on a 75 μm (i.d.) × 60 cm (total length)/50 cm (length to the detector) fused silica capillary. A Beckman 32 Karat software package was used for instrument control, data acquisition, and data handling.

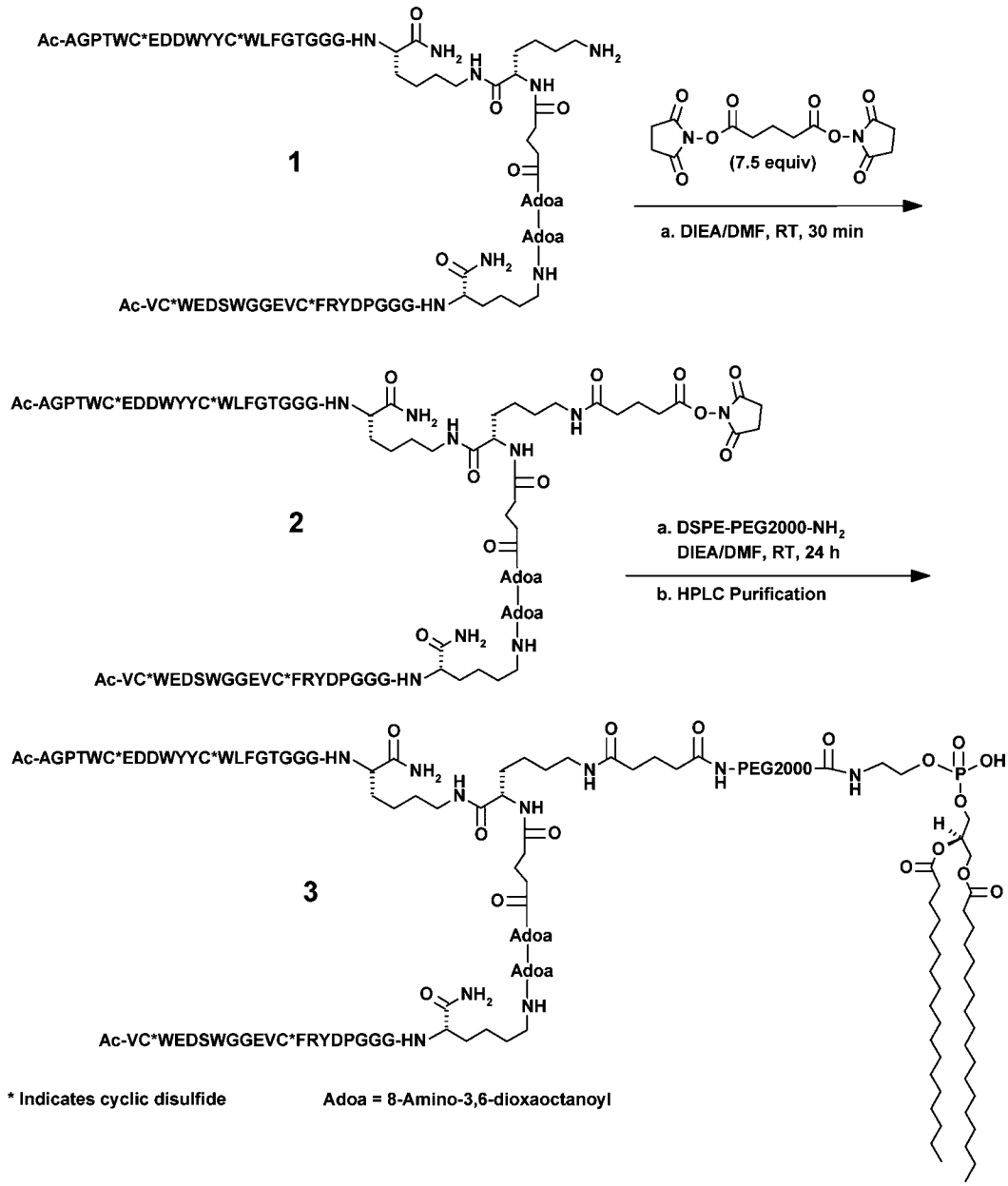
CeofixAnions5 kit (Analis, Namur, Belgium), including a pyridine-dicarboxylic acid buffer at pH 5.6, was used for the quantification of trifluoroacetate and acetate. First, the capillary was rinsed with the initiator buffer, which contains a polycation, to form a positive dynamic coating and invert the electroosmotic flow. Second, the capillary was filled with the accelerator background electrolyte containing a chromophore which absorbs at 232 nm. For quantitative purposes, propionic acid was used as an internal standard. After sample injection by pressure, separation was carried out by applying a high voltage. All experiments were carried out in anionic mode (cathode at the inlet and anode at the outlet). The capillary was thermostatted at 25 °C and a constant voltage of 30 kV (−50 μA) for 6 min, with an initial ramping of 1 min, was applied during analysis. Samples were kept at ambient temperature in the autosampler and injection (~20 nL injection volume) was achieved by low-pressure mode for 15 s at 0.5 psi. Both standard and test solutions were prepared in DMSO−50 mM aqueous NaOH 1:4 (v/v).

Before its first use, the capillary was flushed with 0.1 M NaOH for 1 min, paused for 4 min, then rinsed 0.5 min with 0.1 M NaOH followed by H_2O for 1 min. This initialization procedure was also employed after prolonged storage. Between analyses, the capillary was flushed with 0.1 M NaOH and H_2O (20 psi, 0.5 min each). Before each run, the capillary was pressure-rinsed and filled with the initiator and the accelerator solutions. To achieve reproducible and accurate results, the CEofix buffer solutions were replaced every 20 runs and the first runs of a day were systematically discarded. When not in use, the capillary was washed with 0.1 M NaOH, then H_2O, and stored dry.

Preparation of Heterodimer Peptide Conjugate 1 Having Low TFA Levels. Heterodimer peptide **1** (Scheme 1) was synthesized as a TFA salt following procedures described previously (*8*). Compound **1** as the TFA salt, [120 mg in 80 mL of CH_3CN-H_2O 3:7 (v/v)] was loaded onto an AG MP-50 column and the column was washed with the same eluent until the conductivity was stable at 1 μS/cm. A step gradient elution of the column with NH_4OAc in CH_3CN-H_2O 3:7 (v/v) was conducted using 100 mL aliquots of 200 mM and 400 mM salt followed by 200 mL aliquots of 600 mM and 800 mM salt. The compound eluted at ca. 600 mM salt. The pure product-containing fractions were pooled and lyophilized. The resulting isolate was dissolved in CH_3CN-H_2O 3:7 (v/v) and lyophilized several times to constant weight. This gave 104 mg (86.7% yield) of the pure material **1** as the acetate salt. HPLC: t_R = 5.2 min; assay >99% (area %); column, Waters XTerra MS-C18, 50 mm × 4.6 mm, 5 μm particle, 120 Å pore; eluents: A, H_2O (0.1% TFA); B, CH_3CN (0.1%TFA); elution, initial condition 20% B, linear gradient 20−60% B over 8 min; flow rate, 3 mL/min; detection, UV at 220 nm; MS, API-ES neg. ion; m/z = 1816.3 [M−3H]/3, 1362.0 [M−4H]/4, 1089.2 [M−5H]/5; CE analysis (counter-ion % wt/wt) TFA 0.2%; acetate 0.15%.

Preparation and Purification of the Phospholipid-PEG2000-Peptide Conjugate 3 as Its Acetate Salt from Heterodimer Peptide 1 Acetate Salt (Scheme 1). A solution of the heterodimer peptide (**1**, acetate salt) (0.108 g, 0.02 mmol) in anhydrous DMF (1.0 mL) was added to a solution of disuccinimidyl glutarate (DSG) (50.0 mg, 0.15 mmol) in anhydrous DMF (0.5 mL) containing diisopropylethylamine (DIEA) (0.07 mL, 0.4 mmol, 20 equiv) with vigorous stirring over a period of 2 min and the reaction mixture was stirred for 30 min. HPLC analysis on a Waters XTerra C-18 column and MS showed the disappearance of the starting material

Scheme 1. Preparation of DSPE-PEG2000-Heterodimer Peptide Conjugate 3

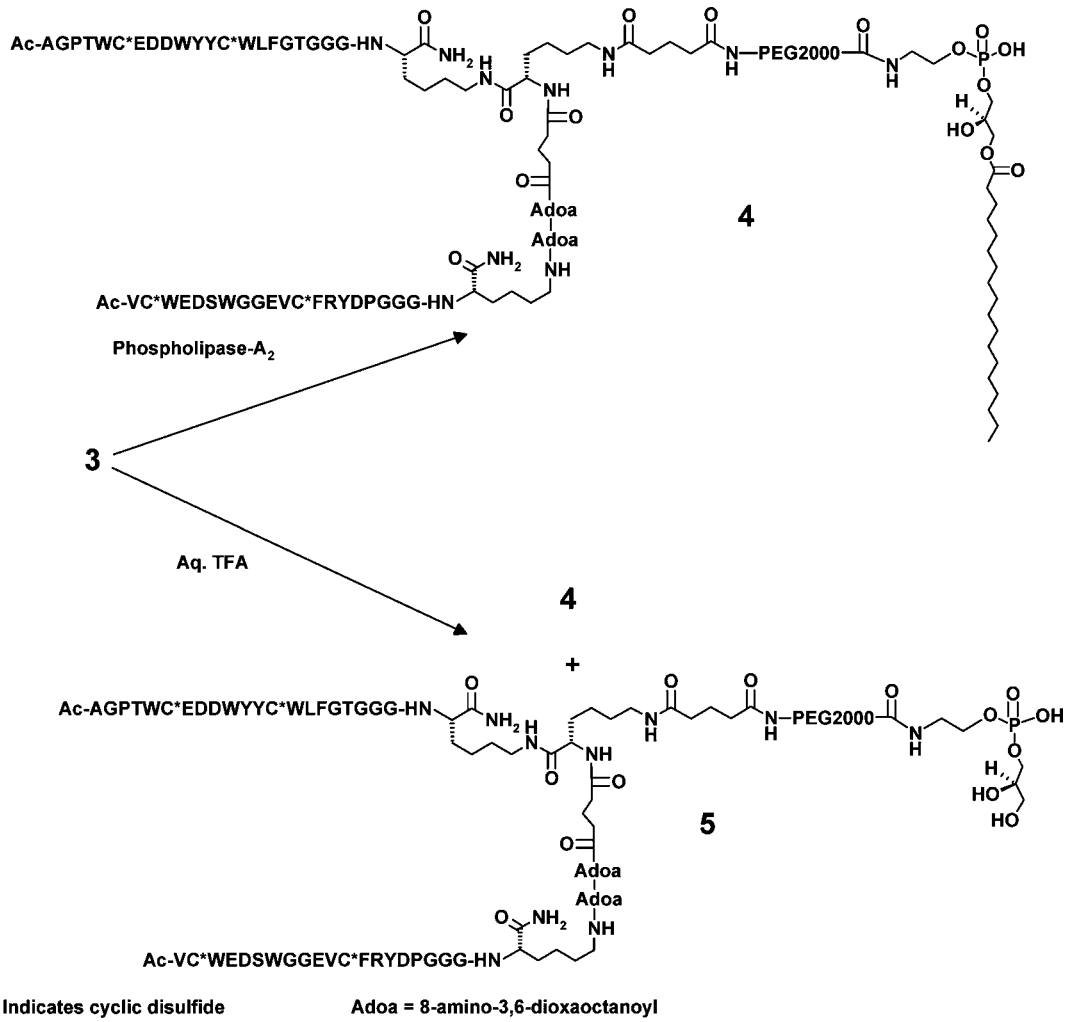


and formation of a new product. The solution was concentrated at reduced pressure. The viscous material was stirred with 10 mL of ethyl acetate for 10 min. The precipitated solid, the glutaric acid monoamide mono-NHS ester **2** of the heterodimer peptide **1**, was centrifuged to a pellet. The ethyl acetate was decanted, and this process was repeated three more times and the solid was finally washed with hexane (10 mL) and dried under vacuum (20 mmHg) for 20 min.

A solution of DSPE-PEG2000-NH_2-ammonium salt (0.055 g, 0.02 mmol, 1 equiv) in anhydrous DMF (0.5 mL) was added to a solution of heterodimer intermediate **2** in anhydrous DMF (1.0 mL) containing DIEA (0.07 mL, 0.4 mmol, 20 equiv), and the mixture was stirred at ambient temperature. The reaction was monitored by analytical HPLC and was complete in 24 h. The reaction mixture was then diluted with H_2O (15 mL), and the resulting solution was loaded onto a reversed-phase C4 preparative column (Kromasil Prep C4, 250 × 20 mm, 10 μm particle, 300 Å pore), which had been pre-equilibrated with a buffer containing 20% of CH_3CN-H_2O 9:1 (v/v) containing 10 mM ammonium acetate (NH_4OAc) (eluent B) in 10 mM aqueous NH_4OAc (eluent A) at a flow rate of 25 mL/min. During the application of the sample solution to the column, the flow of the equilibrating eluent from the preparative HPLC system was stopped. After the sample solution was loaded, the flow of the equilibrating eluent was reinitiated and the column was eluted with the equilibrating buffer until the DMF used in the reaction was removed. The column was then eluted with a gradient of 30−100% B over a period of 40 min. Fractions (15 mL) were collected using UV (220 nm) as an indicator of product elution.

Fractions were checked for purity on an analytical HPLC system (YMC C3, 150 mm × 4.6 mm, 5 μm particle, 300 Å pore) using UV at 220 nm and an ELS detector (temp 50 °C, pressure 3.2 psi, sensitivity 10). The latter detector was employed to detect any trace amount of unreacted DSPE-PEG2000-NH_2 which is nearly UV silent at 220 nm. The fractions containing the pure product were pooled and lyophilized. The product was redissolved in H_2O-CH_3CN 4:1 (v/v) and freeze−dried to afford 94 mg (62% yield) of the required compound **3**. HPLC: t_R 9.32 min; assay >99% (area %); column, YMC C4, 50 mm × 4.6 mm, 5 μm particle, 300 Å pore; eluents:

Scheme 2. Hydrolysis of Compound 3 to Compounds 4 and 5



A, H_2O (0.1% TFA); B, $CH_3CN-MeOH$ 1/1 (v/v) (0.1% TFA); elution, initial condition 70% B, linear gradient 70−100% B over 20 min; flow rate, 3.0 mL/min; detection, UV at 220 nm and ELS (temp 50 °C, pressure 3.2 psi, sensitivity 10); CE analysis (counterion % wt/wt): % wt TFA, 0.3%; % wt acetate, 0.4%. MALDI-TOF MS: *m/z* (%) = 8367.7 (100), $[M+NH_4^+ + CH_3CN]^+_{calc} = 8367.6$.

Preparation of Lysophospholipid 4 and Phosphoglyceryl Ester 5 from Phospholipid-PEG2000-Peptide Conjugate 3 by Acid Hydrolysis (Scheme 2). TFA (300 μL) was added to a solution of compound **3** (50 mg) in 30 mL of CH_3CN-H_2O 1:2 (v/v), and the mixture was stirred at room temperature for 7 days. The mixture was purified by preparative HPLC on a YMC C4 (250 mm × 10 mm) column using 10 mm NH_4OAc in H_2O as eluent A and 9:1 CH_3CN-H_2O containing 10 mM NH_4OAc as eluent B. A gradient 10−100% B over a period of 40 min at a flow rate of 10.0 mL/min with UV detection at 220 nm was employed. Fractions were analyzed by HPLC, and those containing pure compound were combined and lyophilized to afford pure products. Compounds **4** (9.8 mg) and **5** (3.2 mg) were isolated. HPLC: t_R Compound **4**, 11.3 min; t_R Compound **5**, 4.09 min; column, Agilent C3, 150 mm × 3 mm, 3.5 μm particle, 300 Å pore; eluents: A, H_2O (10 mM NH_4OAc); B, CH_3CN-H_2O 9:1 (v/v) (10 mM NH_4OAc); elution, linear gradient, 50−100% B over 30 min; flow rate, 1.0 mL/min; detection, ELSD, temp 50 °C, pressure 3.2 psi, sensitivity 10. Under these conditions, t_R of compound **3** was 19.0 min. MALDI-TOF MS: Compound **4**, *m/z* (%) = 8069.0 (100), $[M+Na]^+_{calc} = 8065.1$; Compound **5**, *m/z* (%) = 7801.5 (100), $[M+Na]^+_{calc} = 7798.6$.

Preparation of Lysophospholipid 4 by Enzymatic Hydrolysis of Phospholipid-PEG2000-Peptide Conjugate 3 with Phospholipase-A_2. A solution of compound **3** (40 mg) in 20 mL of $CH_3CN-1.0$ M aqueous HEPES buffer (pH 8.5) 1:2 (v/v) was stirred with a solution of Phospholipase-A_2 (*16*) from honey bee venom (Sigma, 40 units in 25 μL HEPES buffer) at room temperature for 1 h. HPLC analysis indicated the complete conversion of the starting material to the lysophospholipid compound **4**. The crude reaction mixture was treated with 20 mg of hydroxylamine in 2.0 mL of ethanol for 30 min. The resulting solution was purified by preparative HPLC as described above. Fractions were analyzed by HPLC, and those containing the pure product were combined and lyophilized to afford 28 mg (76% yield) of compound **4**, which, in HPLC analysis, coeluted with the material obtained by acid hydrolysis. MALDI-TOF MS: Compound **4**, *m/z* (%) = 8062.0 (100), $[M+Na]^+_{calc} = 8065.1$.

Surface Plasmon Resonance (SPR) Measurements of Binding of Compounds 1 and 3 to Human and Mouse VEGFR2. SPR measurements of the binding kinetics of compound **1** and compound **3** to human and mouse VEGFR2/Fc (R&D Systems, Minneapolis, MN) were carried out on a Biacore X100 instrument (General Electric, Piscataway, NJ). Protein A (Zymed, South San Francisco, CA) was covalently coupled to a CM5 sensor chip (General Electric) using an amine coupling kit (General Electric). For compound **1**, the sample

and running buffer was PBS with 0.005% P20 (General Electric). For compound **3**, the buffer was PBS with the amount of P20 increased to 0.1% to block nonspecific interactions with the sensor chip. For each measurement cycle, human or mouse VEGFR2/Fc was immobilized on the Protein A-conjugated sensor chip at 5 μL/min, then varying concentrations of the compound solution were injected for 3 min at 30 μL/min. Dissociation of the compound from its binding target was measured for 10 min after the end of each injection. The chip was regenerated between cycles with serial injections of 10 mM glycine (pH 2) and 0.025% SDS in H_2O. The sensorgrams obtained for each compound were fit globally to a bivalent binding model using Biacore X100 Evaluation Software v 1.0.

Preparation of VEGFR2-Targeted Microbubbles for Ultrasound Imaging. Compound **3** was incorporated in the phospholipid membrane of microbubbles as previously described (*17*). A 2 mL aliquot of a 5% glucose solution (B. Braun Medical, Sempach, Switzerland) was added to the resulting lyophilized product (BR55). After dissolution of the cake, a suspension of VEGFR2-targeted microbubbles was obtained.

In Vivo Ultrasound Imaging. Ultrasound imaging of VEGFR2-targeted microbubbles (BR55) was performed in an orthotopic breast tumor model in rats as previously described (*17*). Briefly, tumor was induced by injection of 13762 MAT B III rat mammary adenocarcinoma cells (5×10^5 in 100 μL of culture medium) (American Tissue Culture Collection, Manassas, VA) in the mammary fat pad of female Fischer 344 rats (Charles River Laboratories, France). Ultrasound imaging was performed after eight days of tumor growth using a Sequoia 512 scanner (Siemens Medical Systems, Issaquah, WA) equipped with a 15L8 linear transducer (transmit frequency, 7 MHz). BR55 (2.4×10^7 microbubbles) was injected intravenously, and intermittent tumor imaging ($T = 0$ s, $T = 20$ s, $T = 10$ min) was performed using contrast pulse sequencing (CPS) mode at low acoustic power (MI = 0.25) to follow the accumulation of the targeted microbubbles in the tumor. After the 10 min imaging time point, microbubbles present in the tumor were destroyed by increasing the acoustic power (MI = 1.9) and the tumor was imaged immediately thereafter ($T = 11$ min).

RESULTS

Synthesis, Purification, Characterization, and Stability Studies of Phospholipid-PEG2000-Peptide Conjugate 3. We have shown that the affinity of a heterodimer obtained by linking of two phage-derived noncompetitive VEGFR2 (KDR) binding peptides is significantly enhanced vs that of the constituent monomer peptides (*8*). The heterodimer peptide **1** was reacted with DSG (disuccinimidyl glutarate) to provide **2**, the glutaric acid mono-NHS ester monoamide of the heterodimer peptide **1**. The remaining DSG was removed by trituration of compound **2** with ethyl acetate, pelleting and decanting the DSG-rich supernatant. Then, the heterodimer peptide glutaric acid monoamide mono-NHS ester **2** was reacted with DSPE-PEG2000-NH_2 to provide the DSPE-PEG2000-NH-glutaryl heterodimer peptide **3** (Scheme 1).

The crude product was purified by preparative HPLC on a C3 column using an eluent system containing 0.1% TFA. It was observed that the isolated product, bearing TFA, was not stable and, upon standing in solution or as a lyophilizate, undergoes a time-dependent degradation to a lysophospholipid **4** via hydrolysis of one of the stearoyl groups. The formation of compound **4** could be demonstrated by accelerated hydrolysis in the presence of higher concentrations of TFA than that obtained by dissolution of the isolated product **3**. Lysophospholipid **4** was also obtained by enzymatic hydrolysis of compound **3** using Phospholipase A_2 (Scheme 2). Both methods

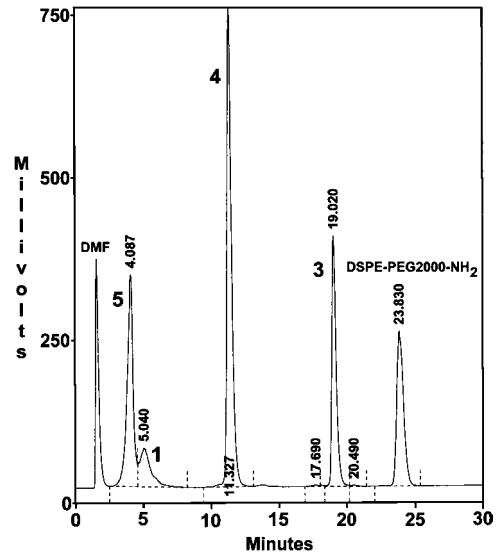


Figure 1. HPLC chromatogram of a mixture containing heterodimer peptide **1**, its DSPE-PEG2000 conjugate **3**, degradation products **4** and **5** and DSPE-PEG2000-NH_2. Conditions: column, Agilent C3, 150 mm $\times$ 3 mm, 3.5 μm particle, 300 Å pore; eluents; A H_2O (10 mM NH_4OAc), B CH_3CN-H_2O 9:1 (v/v) (10 mM NH_4OAc); gradient 50−100% B over 30 min, flow rate 1.0 mL/min; detection, ELSD, temp 50 °C, pressure 3.2 psi, sensitivity 10. **5** = peptide phosphoglyceryl ester, **1** = heterodimer peptide, **3** = DSPE-PEG2000-Glut-heterodimer peptide **1** conjugate, **4** = lysophospholipid.

provided a product which displayed the same HPLC retention time and mass spectrum as the initially detected lysophospholipid **4**.

Lysophospholipid formation could be eliminated by conversion of the trifluoroacetate salt of heterodimer peptide **1** to the stable acetate salt by ion exchange chromatography on AG MP-50 ion-exchange resin and use of this material for the conjugation reaction that provides compound **3**. The decrease in TFA content could be quantified with capillary electrophoresis. The DSPE-PEG2000-NH-glutaryl-heterodimer peptide acetate salt was prepared using DSG followed by preparative HPLC purification using an eluent system buffered with ammonium acetate (Scheme 1) instead of TFA. The HPLC analysis conditions for the separation of the desired product, as well as intermediates and side products, are shown in Figure 1. Studies showed that the material isolated using this procedure is very stable in the solid state and in solution. As an example, aqueous solutions of the isolated material were stable for 21 days at ambient temperature.

After isolation of the acetate salt of **3**, we were surprised to find that this material has a very high affinity for TFA, perhaps due to the PEG linker. Increases in TFA content were obtained from lyophilization with other TFA-containing peptides or during preparative HPLC with ammonium acetate buffer on a column that had previously been used with TFA-containing eluent systems.

Binding Studies of Heterodimer Peptide 1 and Phospholipid-PEG2000-Peptide Conjugate 3. SPR analysis of compound **1** binding to human VEGR-2/Fc indicated that the peptide bound tightly with a K_D of 0.22 nM (Table 1). This is somewhat lower than the K_D of 0.5 nM reported for this compound earlier (*7*), most likely due to the present method of immobilizing VEGFR2/Fc with Protein A, which may better orient the target for binding than did direct amine coupling to the sensor chip. The binding of compound **1** to mouse VEGFR2/Fc was almost 8-fold weaker, with a K_D of 1.6 nM indicating a partial binding preference for the human protein. The phospholipid-PEG2000 conjugate **3** bound human VEGFR2/Fc with a K_D of 4.8 nM (Table 1). The

Table 1. Surface Plasmon Resonance Analysis of Heterodimeric Peptides Binding to Human and Mouse VEGFR2/Fc

	Human VEGFR2/Fc				Mouse VEGFR2/Fc			
	k_{on} (M^{-1} s^{-1}) × 10^6	k_{off} (s^{-1}) × 10^{-4}	K_D (pM)	n^a	k_{on} (M^{-1} s^{-1}) × 10^6	k_{off} (s^{-1}) × 10^{-4}	K_D (pM)	n^a
cmpd **1**	1.2 ± 0.2	2.6 ± 0.3	220 ± 20	3	0.36 ± 0.07	5.5 ± 1.1	1600 ± 570	2
cmpd **3**	0.024 ± 0.007	1.1 ± 0.01	4800 ± 1,500	2	nd[b]	nd[b]	nd[b]	–

[a] *n*, number of determinations. [b] nd, not determined.

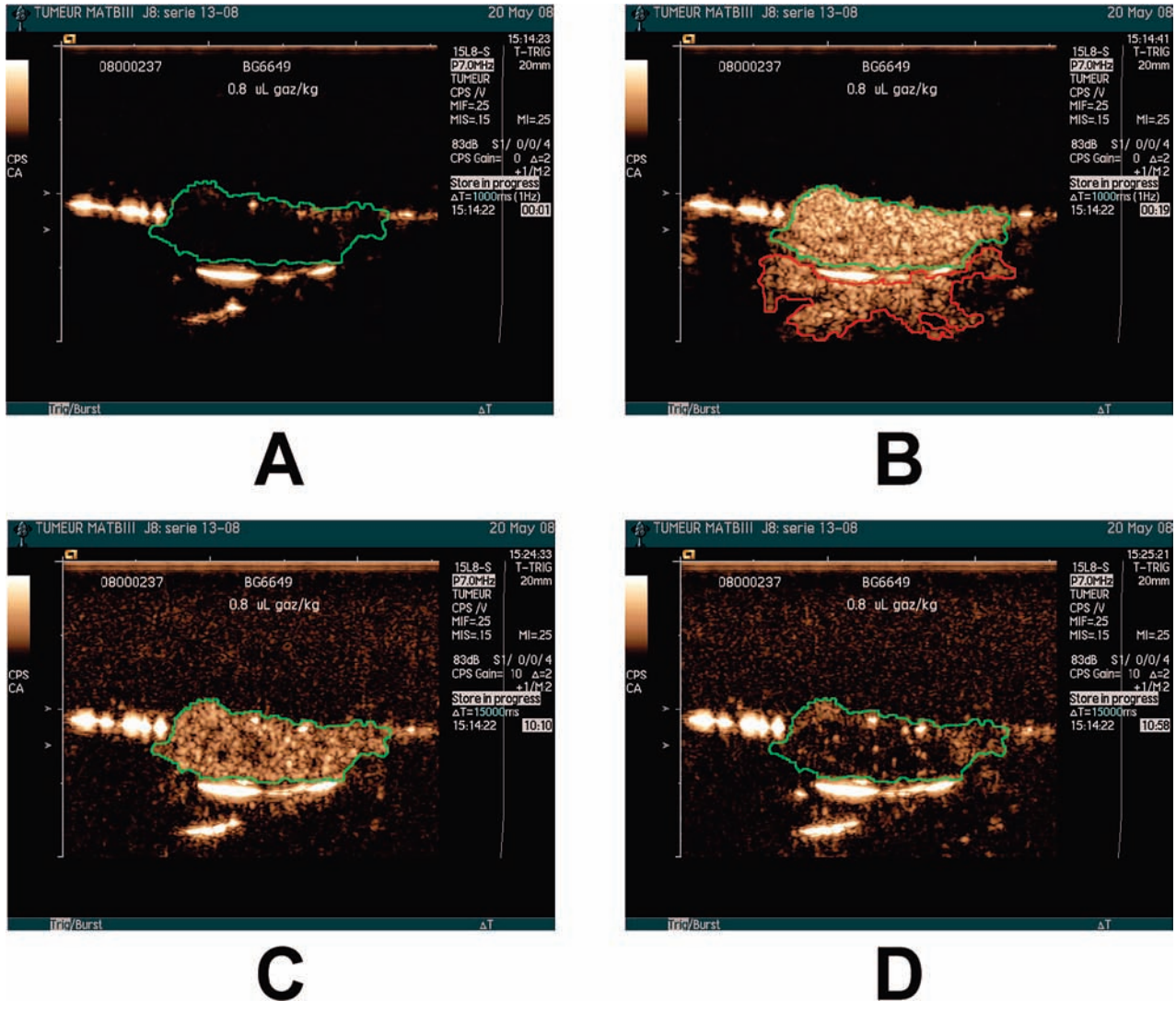


Figure 2. Ultrasound images of MAT B III tumors in CPS mode. Tumor, green outline; nontumoral vasculature, red outline. A: Baseline image before injection of BR55 - the white areas are high intensity reflections of hyperechoic structures. B: At 20 s after injection of BR55 (peak intensity), the circulating microbubbles delineate the vasculature feeding the tumor and the tumor vasculature. C: At 10 min after injection of BR55, freely circulating microbubbles are cleared from the circulation, while the VEGFR2-targeted microbubbles are adherent to the tumor vasculature. D: At 11 min, imaging after destruction of bubbles in the tumor with high acoustic pressure followed by a waiting period for refilling of the tumor with residual circulating bubbles, demonstrated that >95% of the intensity of the image in panel C was due to tumor-bound microbubbles. Depth = 20 mm.

difference in K_D relative to compound **1** was entirely due to a much slower on-rate. Since a higher concentration of P20 detergent had to be used when testing compound **3** to prevent excessive nonspecific binding, it is possible that the kinetic values obtained underestimate the binding to human VEGFR2/Fc. Regardless, it is clear that compound **3** retained potent human VEGFR2 binding capability.

Ultrasound Imaging Results with VEGFR2-Targeted Microbubbles (BR55). BR55 was evaluated in a group of five rats bearing MAT B III mammary tumors of approximately 5−8 mm in diameter (Figure 2). Prior to injection of BR55, ultrasound imaging of the tumor and surrounding area displayed a dark field with small areas of high intensity (panel A); these are artifacts due to highly echogenic anatomical structures (*18*). Following injection of BR55, the strong signal enhancement, due to circulating microbubbles both in the vasculature feeding the tumor and in the intratumoral vasculature, indicated good perfusion of the lesion (panel B). Ten minutes after injection, when microbubbles are largely cleared from the circulation, the signal from the tumor was still enhanced (panel C), indicating that microbubbles were bound to the tumoral endothelium (*19*). Contrast enhancement in the tumor was reduced to background values following the application of a burst of high acoustic pressure and a 1 min waiting period to allow residual circulating

microbubbles to perfuse the tumor (panel D). This confirmed that >95% of the tumoral signal intensity obtained in panel C was due to targeted microbubbles.

DISCUSSION

The preparation of targeted ultrasound bubbles extends the value of contrast enhanced ultrasound. Targeted bubbles are routinely formed in a lab environment by conjugating biotinylated antibodies, peptides or small molecules to streptavidin-coated bubbles (e.g., Target Ready MicroMarker bubbles, VisualSonics). This approach is ideal for a lab environment but not acceptable for human clinical trials, due to the antigenicity of streptavidin (*10*) and the need to conjugate the targeting group to the bubble at the time of use.

For clinical use, there are obvious advantages to direct incorporation of the peptide into the lipid shell of the bubbles. Although a number of different methods for covalent attachment of peptides to lipids have been published, we have found that the coupling of peptides to DSPE-PEG2000 amine with disuccinimidyl glutarate is a mild high-yield process. Although other lengths of PEG spacers were evaluated, the PEG2000 linker was optimal and provided a phospholipid−peptide conjugate with good binding as indicated by surface plasmon resonance studies.

In order to minimize TFA in the product, it proved advantageous to use the acetate salt of the heterodimer peptide **1** in the synthesis of the phospholipid−peptide **3**. Preparative-HPLC employing a dedicated TFA-free system, ammonium acetate buffered eluents, and analysis of collected fractions using an ELS detector was ideal for obtaining a pure and stable product. Adventitious contamination of the isolated fractions with TFA was further prevented by lyophilization of the pooled product-containing fractions on a TFA-free lyophilization unit.

This resulting pure DSPE-PEG2000-heterodimer peptide conjugate **3** could then be incorporated into microbubbles which provided images of active angiogenesis in a rat tumor model. Compound **3** is suitable for further advanced animal studies, as well as clinical studies. The methods for synthesis, purification, and analysis described herein should prove applicable to other phospholipid-PEG linked peptides or antibodies for targeted ultrasound clinical studies.

Supporting Information Available: HPLC chromatogram of purified compound **3**, MALDI-TOF mass spectra of compounds **3** and **4**. This material is available free of charge via the Internet at http://pubs.acs.org.

LITERATURE CITED

(1) Klibanov, A. L. (2005) Ligand-carrying gas-filled microbubbles: ultrasound contrast agents for targeted molecular imaging. *Bioconjugate Chem. 16*, 9–17.

(2) Carmeliet, P. (2005) Angiogenesis in life, disease and medicine. *Nature 438*, 932–936.

(3) Ellegala, D. B., Leong-Poi, H., Carpenter, J. E., Klibanov, A. L., Kaul, S., Shaffrey, M. E., Sklenar, J., and Lindner, J. R. (2003) Imaging tumor angiogenesis with contrast ultrasound and microbubbles targeted to $\alpha_v\beta_3$. *Circulation 108*, 336–341.

(4) Weller, G. E. R., Wong., M. K. K., Modzelewski, R. A., Lu, E., Klibanov, A. L., Wagner, W. R., and Villanueva, F. S. (2005) Ultrasonic imaging of tumor angiogenesis using contrast microbubbles targeted via the tumor-binding peptide Arginine-Arginine-Leucine. *Cancer Res. 65*, 533–539.

(5) Ferrara, N., Gerber, H. P., and LeCouter, J. (2003) The biology of VEGF and its receptors. *Nat. Med. 9*, 669–676.

(6) Willmann, J. K., Cheng, Z., Davis, C., Lutz, A. M., Schipper, M. L., Nielsen, C. H., and Gambhir, S. S. (2008) Targeted microbubbles for imaging tumor angiogenesis: assessment of whole-body biodistribution with dynamic micro-PET in mice. *Radiology (Oak Brook, IL, U. S.) 249*, 212–219.

(7) Shrivastava, A., von Wronski, M. A., Sato, A. K., Dransfield, D. T., Sexton, D., Bogdan, N., Pillai, R., Nanjappan, P., Song, B., Marinelli, E., DeOliveira, D., Luneau, C., Devlin, M., Muruganandam, A., Abujoub, A., Connelly, G., Wu, Q. L., Conley, G., Chang, Q., Tweedle, M. T., Ladner, R. C., Swenson, R. E., and Nunn, A. D. (2005) A distinct strategy to generate high-affinity peptide binders to receptor tyrosine kinases. *Prot. Eng. Des. Sel. 18*, 417–424.

(8) Pillai, R., Marinelli, E. R., and Swenson, R. E. (2006) A flexible method for preparation of peptide homo- and heterodimers functionalized with affinity probes, chelating ligands, and latent conjugating groups. *Biopolymers 84*, 576–585.

(9) Lindner, J. R., Song, J., Christiansen, J., Klibanov, A. L., Xu, F., and Ley, K. (2001) Ultrasound assessment of inflammation and renal tissue injury with microbubbles targeted to P-selectin. *Circulation 104*, 2107–2112.

(10) Meyer, D. L., Schultz, J., Lin, Y., Henry, A., Sanderson, J., Jackson, J., Goshorn, S., Rees, A. R., and Graves, S. S. (2001) Reduced antibody response to streptavidin through site-directed mutagenesis. *Protein Sci. 10*, 491–503.

(11) Kirpotin, D., Park, J. W., Hong, K., Zalipsky, S., Li, W. L., Carter, P., Benz, C. C., and Papahadjpoulos, D. (1997) Sterically stabilized anti-HER2 immunoliposomes: design and targeting to human breast cancer cells in vitro. *Biochemistry 36*, 66–75.

(12) Torchilin, V. P., Levchenko, T. S., Lukyanov, A. N., Khaw, B. A., Klibanov, A. L., Rammohan, R., Samokhin, G. P., and Whiteman, K. R. (2001) p-Nitrophenylcarbonyl-PEG-PE-liposomes: fast and simple attachment of specific ligands, including monoclonal antibodies, to distal ends of PEG chains via p-nitrophenylcarbonyl groups. *Biochim. Biophys. Acta, Biomembr. 1511*, 397–411.

(13) Maeda, N., Takeuchi, Y., Takada, M., Namba, Y., and Oku, N. (2003) Synthesis of angiogenesis-targeted peptide and hydrophobized polyethylene glycol conjugate. *Bioorg. Med. Chem. Lett. 14*, 1015–1017.

(14) Grogan, M. J., Kaizuka, Y., Conrad, R. M., Groves, J. T., and Bertozzi, C. R. (2005) Synthesis of lipidated green fluorescent protein and its incorporation in supported lipid bilayers. *J. Am. Chem. Soc. 127*, 14383–14387.

(15) Schumann, P. A., Christiansen, J. P., Quigley, R. M., McCreery, T. P., Sweitzer, R. H., Unger, E. C., Lindner, J. R., and Matsunaga, T. O. (2002) Targeted-microbubble binding selectively to GPIIb IIIa receptors of platelet thrombi. *Invest. Radiol. 37*, 587–593.

(16) Dennis, E. A. (1987) The Regulation of Eicosanoid Production: Role of Phospholipases and Inhibitors. *Bio/Technology 5*, 1294–1300.

(17) Pochon, S., Tardy, I., Bussat, P., Bettinger, T., Brochot, J., Von Wronski, M., Passantino, L., and Schneider, M. (2010) BR55: A lipopeptide-based VEGFR2-targeted ultrasound contrast agent for molecular imaging of angiogenesis. *Invest. Radiol. 45*, 89–95.

(18) Farrow, C. S. (1996) How ultrasound works. *Small Animal Imaging* (Green, R. W. , Ed.) pp 19−27, Chapter 2, Lippincott, Williams and Williams, Philadelphia, PA.

(19) Lindner, J. R., Song, J., Xu, F., Klibanov, A. L., Singbartl, K., Ley, K., and Kaul, S. (2000) Noninvasive ultrasound imaging of inflammation using microbubbles targeted to activated leukocytes. *Circulation 102*, 2745–2750.

BC9005688

Transfection Efficiency of Cationic Lipids with Different Hydrophobic Domains in Gene Delivery

DeFu Zhi,[†,‡] ShuBiao Zhang,*[,†] Bing Wang,[†] YiNan Zhao,[†] BaoLing Yang,[†] and ShiJun Yu[‡]

Key Laboratory of Biotechnology and Bioresources Utilization, The State Ethnic Affairs Commission-Ministry of Education, College of Life Science, Dalian Nationalities University, Dalian, Liaoning, China 116600, and School of Chemistry and Chemical Engineering, Liaoning Normal University, Dalian, Liaoning, China 116029. Received September 7, 2009; Revised Manuscript Received January 4, 2010

The structure of cationic lipids is a major factor for their transfection activity. A cationic lipid generally contains four functional domains: a hydrophilic headgroup, a linker, a backbone domain, and a hydrophobic domain. The structure of the hydrophobic domain determines the phase transition temperature and the fluidity of the bilayer and influences the stability of liposomes, the DNA protection from nucleases, the endosomal escape, the DNA release from complex, and the nuclear penetration. Also, toxicity of the lipids is influenced by the hydrophobic domain. The compounds used for gene delivery are classified according to the structure of the hydrophobic domain as follows: aliphatic chains, steroid domain, and fluorinated domain. In this review, we summarized recent research results concerning the structures of the hydrophobic domain, in order to find the effect of the hydrophobic domain on transfection efficiency. Understanding these would be very important for scientists to prepare novel cationic lipids and design novel formulations with high transfection efficiency.

INTRODUCTION

Over the past decades, gene therapy was expected to lead to new, powerful approaches for curing many diseases, which were currently being explored in worldwide clinical trials. Gene therapy offers extraordinary long-term potential for the treatment of human diseases, including inherited and acquired disorders, such as cancer, cystic fibrosis, and AIDS (*1*−*3*). This approach of traditional gene therapy is based on the delivery of genes by transfection vectors and subsequent expression of exogenous DNA into the host genome for long-term expression (*4*−*7*). Broadly speaking, transfection vectors commonly used in gene therapy are mainly classified into two categories: viral and nonviral (*6, 8*). In early clinical trials, although viral vectors such as adenovirus and retrovirus have achieved some success particularly in cancer gene therapy (*9*), they bring about a number of disadvantages, inducing adverse immunogenic responses, high cost, and so forth. Because of these reasons, people try to find a more efficient and flexible security system in the category of nonviral vectors (*6*). Nonviral vectors can be grouped into three main categories—cationic lipids, cationic polymers, and peptides. Compared to their viral counterparts, these vectors are currently considerably less efficient, but their well-defined physical and chemical composition as well as their reduced immunogenicity and toxicity make them promising candidates for gene delivery (*1, 10*−*14*). Cationic lipids have been favored for many potential advantages compared with other nonviral vectors, including significant simplicity and ease of production, good repeatability and biodegradability, potential commercial value, and wide range of clinical application and safety (*15*).

Felgner et al. (*16*) synthesized a glycerol backbone-based cationic transfection lipid−DOTMA[1] (see Figure 1), which was used for introduction of plasmids into cells in 1987. The first in vivo experiments using cationic lipids were conducted in mice

* Correspondence should be sent to ShuBiao Zhang, Key Laboratory of Biotechnology and Bioresources Utilization, The State Ethnic Affairs Commission-Ministry of Education, College of Life Science, Dalian Nationalities University, No. 18, Liaohe West Road, Economic & Technical Development Zone, Dalian, Liaoning, China 116600. +86-411-87656141 (ph.), +86-411-87656141 (fax), zsb@dlnu.edu.cn (email).

† Dalian Nationalities University.

‡ Liaoning Normal University.

[1] Abbreviations: DOTMA, *N*-[1-(2,3-dioleyloxy)-propyl])-*N,N,N*-trimethylammonium chloride; GL-67, N4-spermine cholesterylcarbamate; DOTAP, *N*-[1-(2,3-dioleoyloxy)propyl]-*N,N,N*-trimethylammonium methyl sulfate; DMRIE, *N*-(2-hydroxyethyl)-*N,N*-dimethyl-2,3-bis(tetradecyloxy)-1-propanaminium bromide; EDMPC, dimyristoylglyceroethylphosphocholine; DOTIM, octadecenoylloxy (ethyl-2-heptadecenyl-3-hydroxyethyl) imidazolinium chloride; DOSPER, 3-dioleoyloxy-2-(6-carboxyspermyl)-propylamid; CFTR, cystic fibrosis transmembrane conductance regulator; IL, interleukin; HLA, Helen langridge associates; DOSPA, 2,3-dioleyloxy-*N*-[2-(sperminecarboxyamido)ethyl]-*N,N*-dimethyl-1-propaniminium bromide; CTAB, cetyl trimethylammonium bromide; LHON, 6-lauroxyhexyl ornithinate; OLON, oleoyl ornithinate; BGDA, pentacosa-10,12-diynoic-acid-{2[bis-(2-guanidinoethyl)-amino]-ethyl}-amide; BGTC, bis-guanidiniumtren-cholesterol; DOPE, dioleoyl phosphatidylethanolamine; DODAC, *N,N*-dioleyl-*N,N*-dimethylammonium chloride; TODMAC3, *N,N,N′,N′*-tetraoelyl-*N,N′*-dimethyl-1,3-propanediammonium chloride; TODMAC6, *N,N,N′,N′*-tetraoelyl-*N,N′*-dimethyl-1,6-hexanediammonium chloride; SAINT-2, *N*-methyl-4-(dioleyl)methylpyridinium-chloride; SAINT-5, *N*-methyl-4-(distearyl)methylpyridiniumchloride; DLPE, dilauroylphosphatidylethanolamine; DMPE, dimiristoylphosphatidylethanolamine; DPPE, dipalmitoyl phosphatidylethanoiamine; DPyPE, 1,2-diphytanoyl-*sn*-glycero-3-phosphoethanolamine; DSPE, distearoylphosphatidylethanolamine; GAP-DLRIE, *N*-(3-aminopropyl)-*N,N*-dimethyl-2,3-(bis-dodecyloxy)-1-propanaminium bromide; GAP-DMORIE, *N*-(3-aminopropyl)-*N,N*-dimethyl-2,3-bis(cis-9-tetradecenyloxy)-1-propanaminium bromide; NADPH, nicotinamide adenine dinucleotide phosphate; GSH, glutathione; DC-Chol, 3β-[*N*-(*N′,N′*-dimethylaminoethane)-carbamoyl]cholesterol hydrochloride; GL-67, N5-cholesteryloxycarbonyl-5,10-diazatetradecane-1,14-diamine; F-DMAEA, *N*-[1-(2,3-di-11-(F-butyl)undecyloxy)-propyl]-*N,N*-dimethyl-*N*-(2-aminoethyl) ammonium hydroxide; F-DOSPA, *N*-[1-(2,3-di-11-(F-butyl)undecyloxy)-propyl]-*N*-[2-(sperminecarboxamido)ethyl]-*N,N*-dimethylammonium; DOGS, *N,N*-dioctadecylamidoglycylspermine; GalSper, α-galacto-ω-spermine bolaamphiphile; PEI, polyethyleneimine; PE, polyethylene.

10.1021/bc900393r © 2010 American Chemical Society
Published on Web 02/01/2010

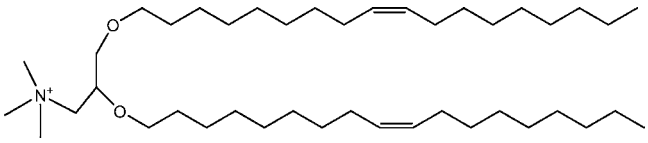


Figure 1. Chemical structure of DOTMA.

in 1989 (*17, 18*). Since then, a series of efficient cationic transfection lipids have been synthesized (*19*−*23*) and used for delivery of nucleic acids into cells in culture and reported high transgene expression properties (both in vitro and in vivo). Many of these efficient cationic transfection lipids became commercially available as transfection reagents in the late 20th century, and a few liposome formulations have been used in gene therapy clinical trials for treatment of cancer and other genetic disorders (see Table 1).

The basic structure of most of the cationic lipids employed for gene delivery is made up of four chemical functional domains: (i) a hydrophilic headgroup, which is positively charged and allow interactions with negatively charged DNA, usually via the protonation of one (monovalent lipid) or several (multivalent lipid) amino groups; (ii) a hydrophobic domain composed of a steroid or of alkyl chains (saturated or unsaturated); (iii) a linker bond which is between the hydrophobic domain and the backbone, between the cationic headgroup and the backbone or directly and between the hydrophobic domain and the cationic headgroup (often one or more amino acid, or ether, or ester bond); and (iv) a backbone domain which separates the headgroup from the hydrophobic domain, and acts as a scaffold on which the cationic lipid is built (the most common backbone is glycerol-based) (see Figure 2) (*24*). Cationic lipids have become a major research tool for transferring DNA into cells in vitro and are being investigated in a variety of in vivo gene therapy trials on human. As a vector, the geometry of the cationic lipid is an important property regarding its application. The hydrophobic domains represent the nonpolar hydrocarbon moieties of cationic lipids and can be grouped into three categories: aliphatic chains, steroid domain, and fluorinated domain.

Before any discussion of cationic lipids, it should be noted that the separate analysis of each domain is somewhat artificial (*24*−*28*). Transfection efficiency can be affected by structural variations in the hydrophobic domain such as length, the specific type of chemical bonds, and the relative position of the hydrocarbon chains, which can also affect toxicity of cationic lipids. We shall not comment on the relationship of toxicity and structure of cationic lipids in gene delivery here, because we have already published a review about this (*3*). This review is chiefly concerned with the effect of the different hydrophobic domains of cationic lipids on transfection efficiency. The majority of the work studying cationic lipids structure/activity relationship has involved the in vitro delivery of genes.

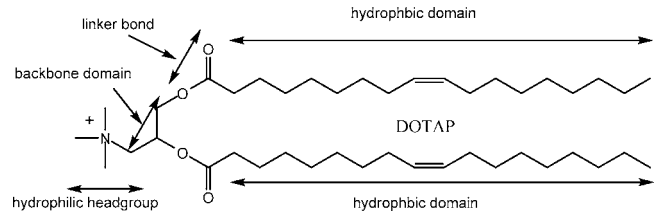


Figure 2. Schematic representation of DOTAP, a commonly used cationic lipid for gene delivery.

ALIPHATIC CHAINS

Cationic lipids with aliphatic chains have been thoroughly researched. The chains are either linear and saturated or linear and monounsaturated and used in liposomal vectors ranging from C_5 to C_{25}, but oleyl, lauryl, myristyl, palmityl, and stearyl have been the most researched ones (*24*). A common variation is the use of branched (*29*), acetylenic (*30, 31*) chains, and *cis*-monounsaturated alkyl chains (*32*) have also been reported.

Number of Aliphatic Chains. It is commonly believed that cationic lipids have one to four hydrocarbon chains. Several studies have also shown that incorporating aliphatic chains with different numbers can improve transfection efficiency potentially by promoting endosomal escape (*16*−*21, 33*−*46*).

Since the pioneering work of Felgner et al. (*16*−*18*) who used the cationic lipid DOTMA with two aliphatic chains, several other related compounds (commercially available transfection reagents with two aliphatic chains, e.g., DOSPA, DOTAP, and DOSPER) have proved moderately successful for gene therapy of pulmonary diseases in animal models (*28*). DOTAP and DOSPER differ from the ether bond-containing reagents DOTMA and DOSPA because DOTAP and DOSPER contain ester bonds, which are endogenous to natural lipids. DOTAP and DOSPER offer higher transfection efficiency and lower cytotoxicity as compared with DOTMA, which may result from the fact that cellular lipases or esterases easily degrade the artificial lipid (*19, 28*).

Most cationic lipids with linear hydrocarbons have two chains in the hydrophobic domain, but cationic lipids with one, three, or four chains are sometimes researched. For aliphatic chains, single-tailed cationic lipids were originally reported to have low transfection efficiency and high toxicity in plasmid delivery (*33, 34*). However, some examples showed that single-tailed cationic lipids may also function in plasmid transfection. Cameron et al. (*34*) described a new class of cationic lipids which offered various numbers of palmitoyl groups in the

Table 1. Clinical Trials Using Cationic Lipid

cationic lipid	commercial name	gene (s)	supplier	phase
DC-Chol		Ad5 E1A/HLA-B7/CFTR/ HLA-A2/HLA-B13/H-2K	Xing et al., 1998; Nabel et al., 1994; Gill et al., 1997; Hui et al., 1997	I/II
GL-67/DOPE		CFTR	Zabner et al., 1997	I
GL-67		CFTR	Ruiz et al., 2001	I
DMRIE/Cholesterol 1:1 (M/M)	DMRIE-C Reagent	CFTR/HLA-B7	Invitrogen (Life Technologies Gibco BRL)	I/II
DMRIE/DOPE		IL-2/HLA-B7	Hersh et al., 1995	I
EDMPC		CFTR	Noone et al., 2000	I/II
DOTIM-cholesterol		EV-CLDC	McHutchinson et al., 2008	I
DOTAP	DOTAP	CFTR	Roche Molecular	II
DOTAP/Cholesterol		Fus 1	Charles et al., 2002	I
DOTAP/DOPE 1:1 (w/w)	Escort	CFTR	Sigma-Aldrich	I/II
DOTMA/Cholesterol		IL-2	Zarrabi et al., 1999	II
DOTMA/DOTAP	LIPOFECTIN	α1-Antitrypsin	Invitrogen(Life Technologies Gibco BRL)	II
DOSPER	DOSPER	p53	Roche Molecular	I
DOSPA/DOPE 3:1 (w/w)	LIPOFECTAMINE	IFN-γ	Invitrogen (Life Technologies Gibco BRL)	I

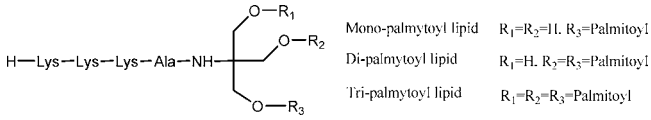


Figure 3. Cationic lipids with one, two, or three palmitoyl chains.

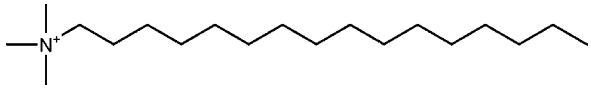


Figure 4. Chemical structure of CTAB.

hydrophobic domain to prove that the transfection efficiency of the lipid with one chain was inferior to the di- or tri-substituted counterparts (see Figure 3).

In a few examples, single-tailed cationic lipids were successful as transfection reagents. Huang et al. (*33*) compared the transfection properties of several quaternary ammonium detergents on fibroblasts and found that CTAB was most efficient (see Figure 4), but somewhat less than its double-tailed counterparts, such as DOTMA.

Tang et al. (*35*) studied the transfection of liposomes produced from double-tailed 1′,2′-dioleyl-*sn*-glycero-3′-succinyl-1,6-hexanediol ornithine conjugate (DOGSHDO) with an ornithine headgroup, single-tailed OLON with an ornithine headgroup, single-tailed LHON with an ornithine headgroup, double-tailed DOTAP with a quaternary amine group, and single-tailed CTAB with a quaternary amine group. They found that OLON had more transfection activity than its double-tailed analogue, DOGSHDO, whereas double-tailed DOTAP had higher transfection activity than its single-tailed analogue, CTAB. This result shows that neither the headgroup nor the tail group by its own can be the determinant of transfection activity of cationic lipids (*36, 37*). The toxicity of cationic lipid was decreased by introducing a biodegradable ester linkage (LHON) (see Figure 5) and taking the place of the double bond in the middle of the chain without sacrificing the transfection activity.

Then, Patel et al. (*30*) synthesized a cationic lipid, BGDA (see Figure 6), characterized by a bisguanidinium headgroup (actually identical to that in BGTC) and a chain with a diacetylene unit and 25 carbon atoms. It was efficient for in vitro transfection when used in formulations with a similar neutral diacetylene colipid or with DOPE. In the report that inclusion of DOPE may increase the stability of the lipoplexes, BGDA/DOPE liposomes containing high proportions of DOPE were able to completely condense the DNA at lower charge ratios than liposomes with low proportions of DOPE. Within the formulations, cationic lipids can adopt various structural phases, including the micellar, lamellar, cubic, and inverted

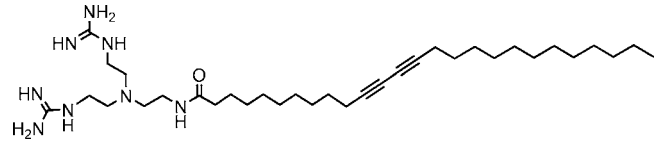


Figure 6. Chemical structures of BGDA.

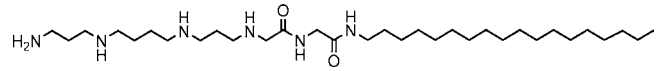


Figure 7. Chemical structures of RPR 228091.

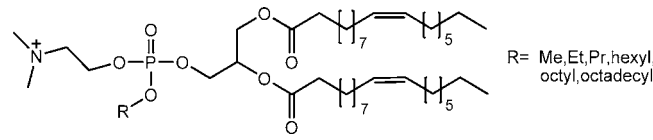


Figure 8. Chemical structures of *O*-alkyl dioleoylphosphatidylcholinium cationic analogues.

hexagonal phase, and arrange back-to-back in bilayers. High transfection activity will be acquired for inverted hexagonal structure when membrane fusion is dominant, but when serum is present, the lamellar structure lipoplexes show great superiority for their inhibition dissociation by serum during lipoplexes transporting. The mechanism by which DOPE exerts its catalytic activity is still poorly defined, but prevailing evidence suggests that its hexagonal-phase-forming propensity likely plays a major role. There are also reports that (*38, 39*) the inclusion of DOPE in the cationic lipid formulation increases transfection activity by enhancing mixing and fusion of liposomes and cell membranes. DOPE forms inverted hexagonal phase structures at ambient temperature (*40*); inclusion of DOPE is presumed to enhance endosomal escape of the lipoplexes into the cytoplasm, as DOPE is thought to have fusogenic properties important for endosomal membrane disruption.

Another example of single-tailed cationic lipid is RPR 228091 (see Figure 7) that was composed of a spermine derived amino acid, coupled to a single C_{18} alkyl chain, and it was suitable for transfection (*41*).

Cationic lipids with three aliphatic chains usually show lower transfection efficiency than lipids with two chains (*34*). However, the transfection can be greatly improved when the third chain is short or could be removed by intracellular reduction of a disulfide bond (*42*−*44*). Rosenzweig et al. (*43*) synthesized a series of *O*-alkyl dioleoylphosphatidylcholinium cationic analogues (see Figure 8) ranging from methyl to octadecyl, and tested them for transfection activity. These compounds could show phase behavior changing with the length of the third chain,

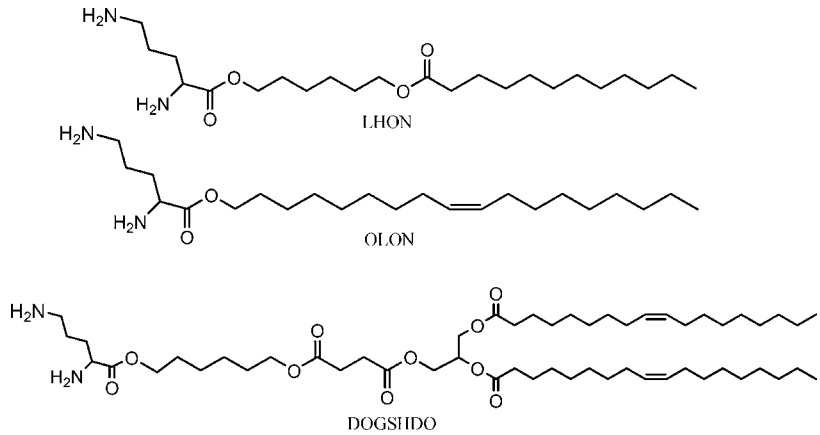


Figure 5. Chemical structures of LHON, OLON, and DOGSHDO.

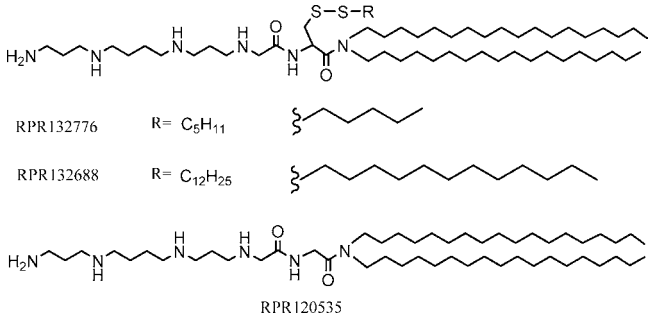


Figure 9. Chemical structures of RPR 132776, PRP 132688, and PRP 120535.

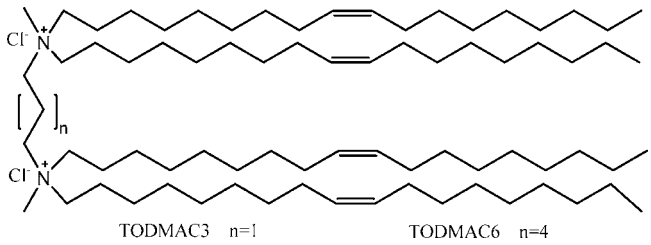


Figure 10. Chemical structures of TODMAC.

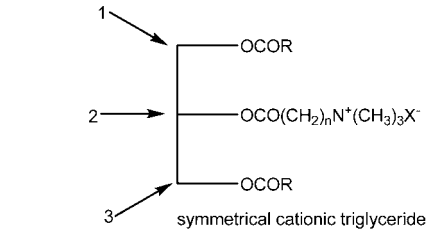
which was an alkyl group linked as phosphate triester. The short-chain (ethyl and propyl) derivatives, which formed a lamellar phase after hydration, were most effective in DNA transfection. The intermediate chain (hexyl) compound, which also formed a lamellar phase in aqueous solution, had approximately the same transfection efficiency as ethyl and propyl. However, hexyl compound assumed a cubic phase in high salt concentrations and became capable of mediating transfection only when vigorously dispersed by sonication. The octyl and octadecyl derivatives formed an inverted hexagonal phase in excess water and exhibited good transfection activity after sonication (*43*).

Byk et al. (*42, 44*) prepared a series of lipopolyamines. They found that the lipid with a dithiol connecting the additional side chain to the vector body showed better transfection activity than the equivalent lipid missing the additional third side chain. Moreover, shorter chains (C_5) showed better transfection activity than longer chain (C_{12}) trilipids (see Figure 9).

A few researchers were interested in novel tetraalkyl cationic lipids (*45*−*47*). Gaucheron et al. (*46*) synthesized a new class of divalent tetraalkyl cationic lipids. These cationic lipids are dimers of DODAC (see Figure 10) joined by a hydrocarbon of three or six carbons in length (TODMAC3 and TODMAC6, respectively). It was concluded that TODMAC6 exhibited potential as a transfection agent as compared to DODAC for in vitro and in vivo use and that the design of cationic lipids according to their ability to induce nonbilayer structure provided a useful guide for synthesis of new cationic lipids. However, TODMAC3 exhibited lower transfection efficiency than that achieved with DODAC.

Generally speaking, for aliphatic chains, single-tailed and three-tailed cationic lipids are better known as surfactants because of their ability to form micelles in solution, but they are more toxic and less efficient than their double-tailed counterparts. Therefore, most of the aliphatic chains in the cationic lipids are double-tailed.

Unsaturation and Branching of Aliphatic Chains. To rationally design and to optimize cationic lipid formulations for efficient gene delivery in therapeutics, many investigations aim at defining a structure−function relationship for cationic lipids. The solid geometry of the unsaturated aliphatic chains is an important variation. A few investigators found that the trans geometry was more favorable to transfection (*48*). However,



1Aa	R $-(CH_2)_7CH{=}CH(CH_2)_7CH_3$	(Z)	n 1
1Ba	$-(CH_2)_7CH{=}CH(CH_2)_7CH_3$	(E)	1
1Ca	$-(CH_2)_{16}CH_3$		1
1Ab	$-(CH_2)_7CH{=}CH(CH_2)_7CH_3$	(Z)	3
1Bb	$-(CH_2)_7CH{=}CH(CH_2)_7CH_3$	(E)	3
1Cb	$-(CH_2)_{16}CH_3$		3
1Ac	$-(CH_2)_7CH{=}CH(CH_2)_7CH_3$	(Z)	4

Figure 11. Chemical structures of symmetrical cationic triglyceride.

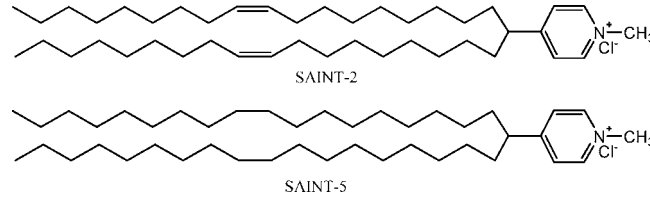


Figure 12. Chemical structures of SAINT-2 and SAINT-5 amphiphiles.

Obika et al. (*49*) obtained an opposite result by synthesizing and evaluating a series of triglycerides **1Aa**−**1Cb** (see Figure 11). They found the cis oleoyl chain (**1Ab**) to be more active in transfection than the trans elaidoyl one (**1Bb**) in quaternary ammonium lipids.

At the same time, they found that the transfection efficiency depends upon both the structure of the acyl chain at the 1- and 3-position of glycerol backbone and the length of the linker connecting the hydrophilic headgroup with the glycerol backbone. The transfection activity was increased when the unsaturated structure was introduced in the middle of a long acyl chain (**1Aa** > **1Bb** > **1Cb**).

The overwhelming majority of the results showed that the unsaturated C18:1 oleyl was the optimal aliphatic chain, which was frequently the best choice for good transfection (*31, 48, 50, 51*). Zuhorn et al. (*52*) synthesized two pyridinium-based lipid analogues with identical headgroups but differing in alkyl chain unsaturation, i.e., SAINT-5 (C18:0) and SAINT-2 (C18:1) (see Figure 12). Their data indicated that at a charge ratio of 2.5/1 the enhancing effect of DOPE on transfection efficiency was highest and the unsaturated C18:1 oleyl SAINT-2/DOPE was more active in transfection than saturated C18:0 SAINT-5/DOPE, which might rely on the relative efficiencies of DNA release from the lipoplexes upon encounter with (intra) cellular membranes.

Koynova et al. (*53*) synthesized two cationic phospholipid derivatives with asymmetric hydrocarbon chains: ethyl esters of oleoyldecanoylethylphosphatidylcholine (C18:1/C10-EPC) and stearoyldecanoylethylphosphatidylcholine (C18:0/C10-EPC). The former was more effective as a DNA transfection agent (human umbilical artery endothelial cells) than the latter, despite their similar chemical structure and virtually identical lipoplex organization. However, an opposite result was obtained by Roosgen and co-workers (*54*), showing that the saturated

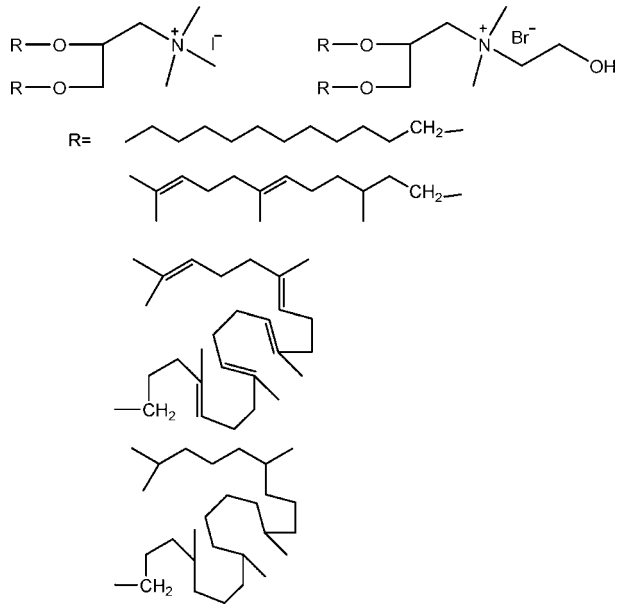


Figure 13. Chemical structures of cationic lipids analogous to DOTMA and DMRIE.

C18:0 performed better than the equivalent C18:1 counterpart; it probably involved other effects like the easier hydrolysis of the headgroup−hydrophobic chain ester linker for saturated than for unsaturated chains.

There are some examples that monoacetylenic or diacetylenic cationic lipids were useful as transfection agents (*30, 31*). Fletcher et al. (*31*) reported the modification of the hydrophobic region of the monovalent cationic lipid DOTAP, by substituting the cis double bonds of the oleate tails with C−C triple bonds in varying positions, in an effort to alter the membrane properties of the lipoplexes with minimal change to the liposome/micelle−DNA interaction. Replacement of the cis double bonds of DOTAP with triple bonds forms more stable liposomes and lipoplex systems near physiological temperatures in comparison to DOTAP by X-ray diffraction studies, perhaps thereby providing enhanced protection to pDNA from extracellular DNA endonucleases. At the same time, the lipid transition is on the cusp of physiologically relevant temperatures, hence preventing overstability and excess rigidity that could otherwise hinder desired cell membrane−lipoplex interactions. It is anticipated that fatty acid tails with triple bonds rather than cis double bonds would exhibit a substantially reduced tangle and consequently afford more rigid liposomal bilayers.

Membrane fluidity may be important for proper assembly of the lipoplexes and is thought to affect endosomal membrane fusion, an essential step required for the DNA to escape from the endosomes; thus, it also has influence on the transfection

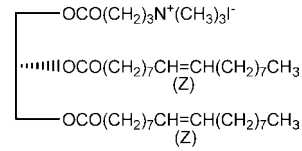


Figure 15. Chemical structures of asymmetrical triglyceride.

efficiency (*55−61*). It is known that the membrane fluidity increased when an unsaturated structure was introduced into the hydrophobic chain of the lipid, by disrupting membrane packaging and facilitating DNA escape inside the cells. The best chains in terms of benefit to transfection are frequently the unsaturated ones: one reason lies in their effect on the membrane fluidity. A few typical cases have been enumerated in which unsaturated and branched chains help to fluidize the bilayer (*29, 62*). Arpicco et al. (*62*) synthesized a C_{15} dihydro farnesyl derivative (see Figure 13) with an unusual branched structure, which was less active than the C_{12} saturated lipids but, interestingly, more active than commercial lipids, such as DOTMA in almost all cell lines tested.

Similarly, a formulation containing a short unsaturated C14:1 lipid and a branched C_{16} colipid, with very high fluidity, was found to be the best transfectant in vitro from a series of combinations of lipid and co-lipid chains by Ferrari et al. (*29*). These systems should be more fluid than their corresponding fully saturated analogues. A disadvantage of the unsaturation is the reduced stability in storage, because it is susceptible to oxidation (*63*).

Asymmetry of the Hydrophobic Domain. One of the important factors which can affect the efficacy of cationic lipids is the asymmetry of the hydrophobic domain. Some researchers synthesized a series of cationic lipids that were based on glycerol backbone, which was constructed not only in symmetrical structure (see Figure 14) but asymmetrical structure as well (see Figure 14) (*49*).

To compare the transfection ability of a symmetrical cationic triglyceride (**1Ab**) (see Figure 11) with that of an asymmetric triglyceride counterpart (see Figure 15), they were formulated into cationic liposomes with DOPE. It was found that symmetrical cationic triglycerides worked as well as the asymmetrical triglyceride counterpart for transfection efficiency, but showed an obvious advantage over their asymmetric counterparts in the synthesis (*49*).

Several researchers found that the identical alkyl chains are liable to transfect in the lipid structure (*48, 67, 68*). However, most researchers have found that transfection efficiency can be increased either by using the different alkyl chains in the same lipid or by using cationic lipids of asymmetrical backbone (*69*). Cationic lipids which contain different alkyl chains were difficult to synthesize; therefore, only a few examples of cationic lipids with different alkyl chains can be seen in the literature. Heyes

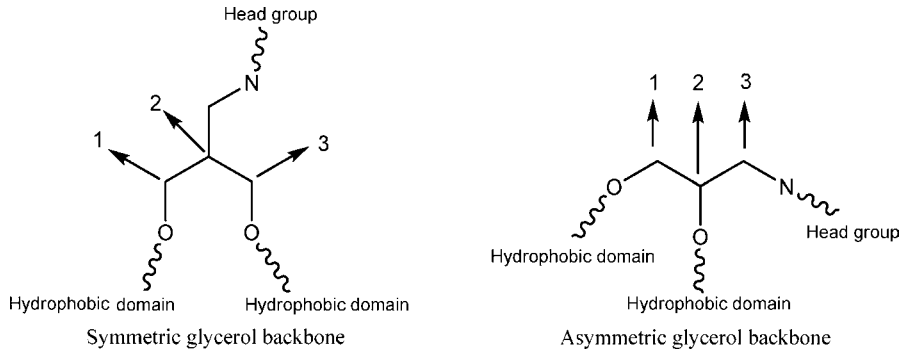
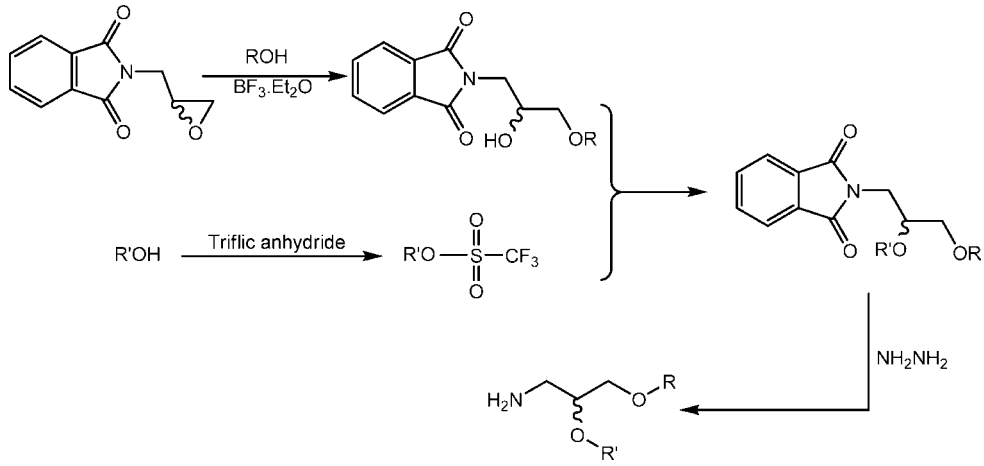


Figure 14. Lipids with glycerol-type backbone.

Scheme 1. Synthesis of Diether Lipids with Symmetric and Asymmetric Hydrophobic Domain



et al. (*69*) synthesized a series of diether lipids of identical or different alkyl chains with primary amino headgroups and showed a convenient route for the synthesis of asymmetric lipids (see Scheme 1). Two of the most effective diether lipids, hydrophobic domain with the shortest identical chains ($R{=}R'{=}C_{12}$) and with particularly different chains ($R{=}C_{12}$, $R'{=}C_{18}$), were chosen.

Ferrari et al. (*29*) found that the hydrocarbon chains of lipid−co-lipid pairs with a high level of asymmetry (C18:1 in lipid−C12:0 in co-lipid) and high symmetry (C16:0 in lipid−C16:0 in co-lipid) had the best transfection efficiency (see Figure 16). Regarding the above explanation, the asymmetry of the hydrophobic domains may afford better intermembrane mixing and the pDNA may be more weakly associated with high symmetry, thus leading to higher transfection levels.

Numerous investigations have also succeeded in developing a highly efficient series of non-glycerol-based novel symmetrical transfection lipids (*64*−*66*). Recently, it was reported that the symmetrical disulfide lipid RPR 128522 (see Figure 17) without glycerol backbone formulated into cationic liposomes with DOPE had obtained significant transfection activity (*62*).

Hyvonen et al. (*64*) synthesized a series of novel symmetrical cationic amphiphilic double-charged 1,4-dihydropyridine derivatives (1,4-DHP) (see Figure 18), which have been shown to condense DNA and efficiently transfect it into cells in vitro, and they were based on dihydropyridine ring backbone.

Although there are many cationic lipids of the symmetrical structure for gene transfection, the in vitro activities of asymmetric lipids are usually superior to the symmetric analogues.

Length of Aliphatic Chains. Much work has been carried out on modifying cationic lipids for use in gene transfection in order to determine if there is a "best" length of chain (*29, 42, 45, 48, 51, 55, 60, 61, 64, 65, 70*−*77*). However, solid conclusions are rarely obtained, for the conclusions of these studies are frequently contradictory. Most of the studies have indicated that cationic lipids with shorter chain length (for saturated chains) were generally important for acquiring high transfection efficiency, since they are responsible for membrane fluidity and good lipid mixing within the bilayer.

For a series of 1,4-dihydropyridine amphiphiles with alkyl chains from C_{10} to C_{16} mentioned above, the C_{10} compound had the highest membrane destabilization activity and achieved the best delivery of DNA in the cytosol, but it did not transfect actively. The equivalent C_{12} compound, although a weaker endosomal disruptor, showed the highest transfection (*64*). In analyzing a series of cationic lipids that differ only by chain length (for saturated chains), most of the studies consider the suitable length to be C_{12} and C_{14}.

Gilot et al. (*77*) synthesized a set of polyvalent cationic lipids (GB compounds) (see Figure 19) derived from natural glycine betaine compounds covalently linked to acyl chains by enzymatically hydrolyzable peptide and ester bonds. Their data indicated that GB compounds allowed high gene transfer efficiency in cultured hepatocytes without cytotoxicity, and

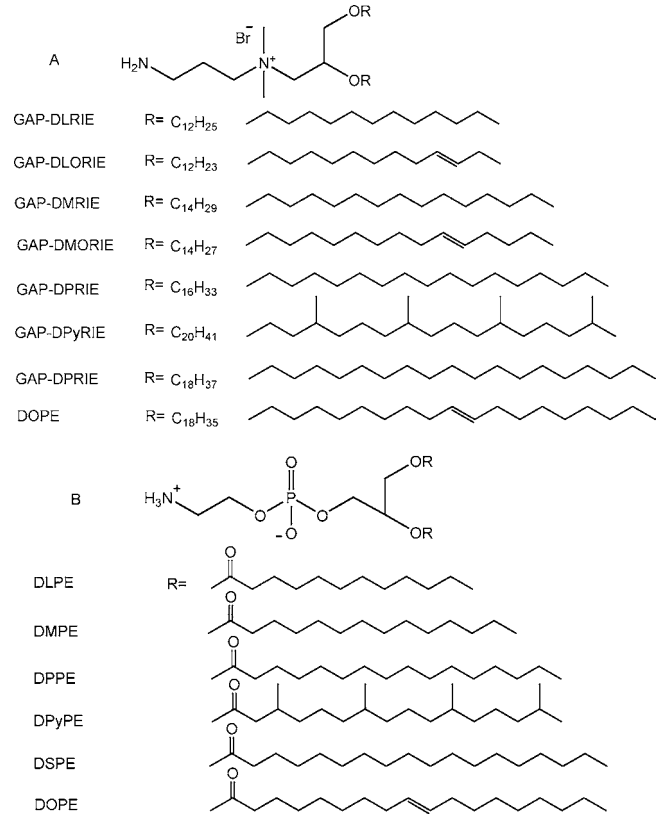


Figure 16. (A) Structures of the cytofectins used in this study (from top to bottom): GAP-DLRIE (C12:0); GAP-DLORIE (C12:1); GAP-DMRIE (C14:0); GAP-DMORIE (C14:1); GAP-DPRIE (C16:0); GAP-DPyRIE (16:0); GAP-DSRIE (C18:0); GAP-DORIE (C18:1). (B) Structures of co-lipids used in this study (from top to bottom): DLPE (C12:0); DMPE (C14:0); DPPE (C16:0); DPyPE (C16:0); DSPE (C18:0); DOPE (C18:1).

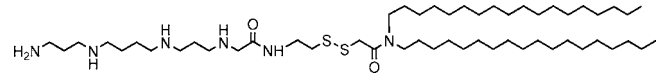


Figure 17. Chemical structures of RPR 128522.

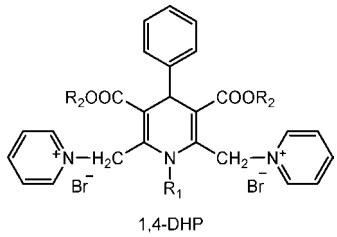


Figure 18. Chemical structures of 1,4-dihydropyridine derivatives.

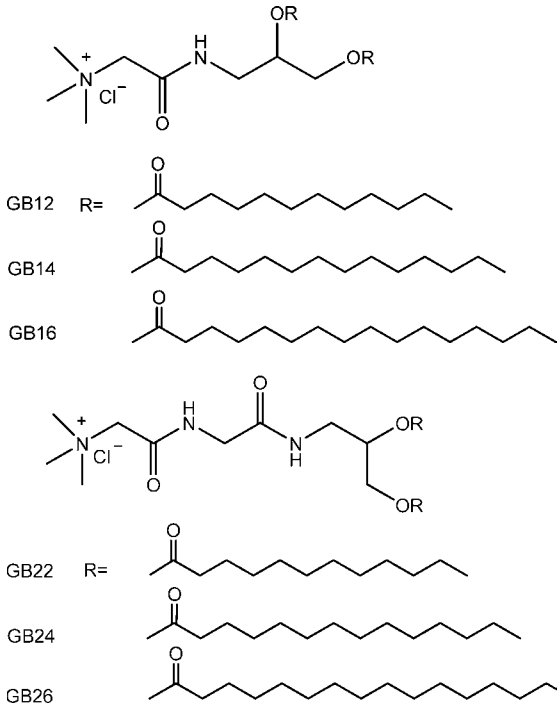


Figure 19. Chemical structures of GB compounds.

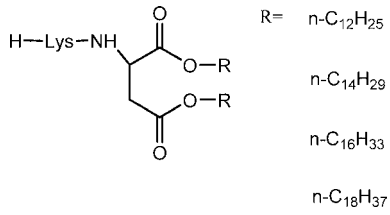


Figure 20. Chemical structures of KD compounds.

unexpectedly, GB12/GB22 characterized by short acyl chains (C_{12}) was most efficient.

In the absence of serum, all cationic lipids tested with hydrocarbon chains in vicinal configuration esterified to a glycerol backbone (the respective *N*-(1,2-diacyldihydroxypropyl)-*N*,*N*,*N*-trimethylammonium chlorides or *N*-(1,2-diacyldihydroxypropyl)-*N*-(hydroxyethyl)-*N*,*N*-dimethylammonium chlorides, as well as *N*-(1,2-diacyldihydroxypropyl)-*N*-(1,2-dihydroxypropyl)-*N*,*N*-dimethylammonium chlorides with l-auroyl, myristoyl, palmitoyl, stearoyl, and erucoyl chains) were able to transfect cells when combined with DOPE. It was found that the cationic lipid with dimyristoyl chains demonstrated the highest transfection efficiency of plasmid DNA (*78*).

A series of cationic lipids based on lysylaspartate (KD) (see Figure 20), diacyl derivatives with hydrocarbon chains of differing lengths (C_{12}, C_{14}, C_{16}, and C_{18}) exhibited different DNA-binding affinities which were correlated with their in vitro gene transferring capabilities. The KD derivatives with shorter acyl chains (C_{12} and C_{14}) exhibited stronger DNA binding

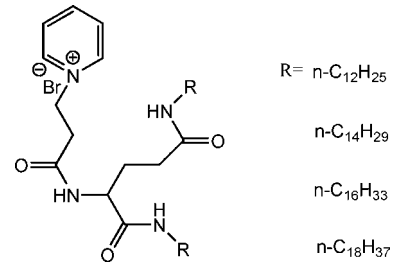


Figure 21. Chemical structures of the glutamide lipids.

affinity and more efficient transfection than those with longer (C_{16} and C_{18}) acyl chains (*79, 80*).

At the same time, the efficiency of cationic lipids with alkyls in the range 12−16 carbons in length was well-documented by Gopal et al. (*81*), and 14-carbon-length lipids were most efficient among several cationic lipids with different chemical structures (see Figure 21).

Felgner et al. (*59*) reported the synthesis and assay results for several series of homologous lipids. They found that, as the length of the saturated aliphatic chain increased from 14 to 18 carbon atoms, the transfection activity of the resulting cationic lipids progressively declined.

In order to understand the relationship between the length of aliphatic chains and transfection activity better, Floch et al. (*82*) synthesized a homologous series of cationic phosphonolipids with different alkyl chain substitutions. The order of transfection efficiency was disteryl (di-C18:0) < dipalmityl (di-C16:0) < dimyristyl (di-C14:0). The transfection efficiency and membrane fluidity of the analogues increased as the length of the aliphatic chains decreased.

However, some degree of rigidity for the membrane is also required, in order to stabilize the liposome (*74, 80*). Long-chain lipids would probably strengthen the stability (*42, 56, 74*). From the interplay of these opposite trends, the optimal chain length depends on the specifics of a given overall cationic lipid structure to achieve the best balance. It should be mentioned that the shorter aliphatic chains allow for better transfection in vitro, whereas the longer aliphatic chains allow for better transfection in vivo (*60, 82*). Whatever the quaternary trimethylonium used for cationic phosphonolipids by using different neutral lipids in the transfection process, in vivo transfection efficiency of compounds involving a C18:1 chain was higher than with the C14:0 analogues and with the reverse in vitro (*60, 82*). It may be that the function of the neutral lipid is different in vitro from that in vivo in the formation of lipoplexes and depends on the nature of the quaternary trimethylonium used.

In general, cationic lipids with the shorter aliphatic chains (C_{12} and C_{14}) were more efficient than the longer (C_{16} and C_{18}) counterparts in transfection efficiency. It is possible that shorter hydrocarbon chains increase the fluidity of the bilayer and favor a higher rate of intermembrane transfer of lipid monomers and lipid membrane mixing, resulting in potential disruption of the endosome and consequent DNA escape from endosomal degradation.

Special Moieties at the Hydrophobic Chains. Some new vectors were designed to covalently connect some special moieties at the end of the hydrophobic chains, in order to get the relationship between hydrophobic chains and transfection efficiency.

Jacopin et al. (*83*) synthesized a glycosylated analogue (see Figure 22) of the dialkylamidoglycylcarboxyspermines, which formed stable particles at low charge ratio and was efficient for gene delivery.

Many groups also reported a few other glycosylated cationic bolaamphiphiles similar to the compound. Brunelle et al. (*84*)

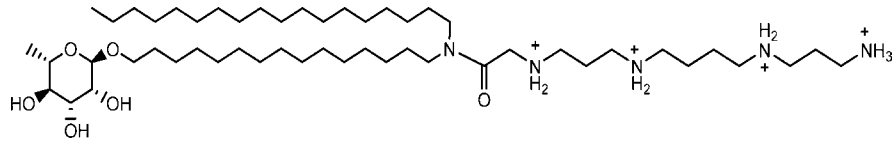


Figure 22. Glycosylated analogue of lipopolyamines.

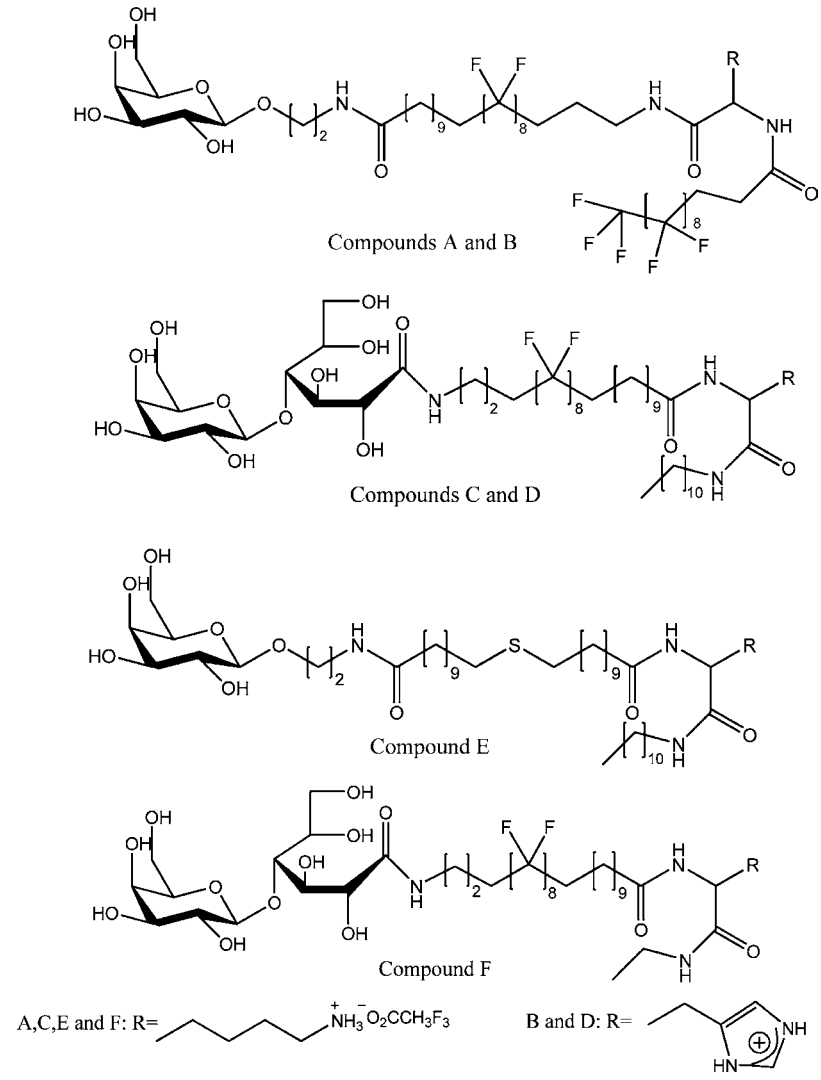


Figure 23. Set of dissymmetric hemifluorocarbon bolaamphiphiles.

synthesized a new series of dissymmetric hemifluorocarbon bolaamphiphiles (see Figure 23), and the dissymmetric functionalization of diiodoperfluorooctane led to bolaamphiphile molecules composed of a partially fluorocarbon core end-capped with a glycoside and an ammonium salt. They found that the incorporation of two fluorinated segments in the molecular structure of the bolaamphiphiles is detrimental for an efficient DNA condensation. In contrast, a partial fluorination of the hydrophobic core of bolas increased not only the DNA complexation abilities, but also the DNA transfection efficiency. Relatively high transfection activity was obtained for the bolaamphiphile possessing a lysine headgroup and one fluorinated segment close to the carbohydrate moiety. This result could be explained by the small size and the positive surface charge of the bolaplex. Vierling's group (*85*) described the synthesis of three new α-galacto-ω-polyamine double-chain bolaamphiphiles (Gal-CL) (see Figure 24), and their design combines a hydrophilic galactosyl residue (which serves as a molecular signal for cell targeting) linked through a long spacer to various hydrophilic linear or branched polyamine polar heads (for the interactions with DNA and its compaction) and to a hydrophobic tail constituted by two long alkyl chains. The three new double-chain bolaamphiphiles, whether used with DOPE or with pcTG90/DOPE, were found to be more efficient nonspecific gene transfer agents than the single-chain head GalSper compound.

A particular example has been found by Abe and co-workers, who reported two hydrophobic chains of a cationic lipid connected two ferrocenes, respectively (*86, 87*). Abbott et al. (*88*) demonstrated that a ferrocene-containing, redox-active cationic lipid (see Figure 25) can be used to offer either high (on) or very low (off) levels of cell transfection depending on a reduced or oxidized state. If successfully developed through future studies, the ability to activate lipoplexes toward transfection and "on demand" could create new opportunities to deliver DNA in vitro and in vivo.

Balakirev et al. (*89*) synthesized a new cationic amphiphilic vector for gene delivery made from the natural provitamin, lipoic

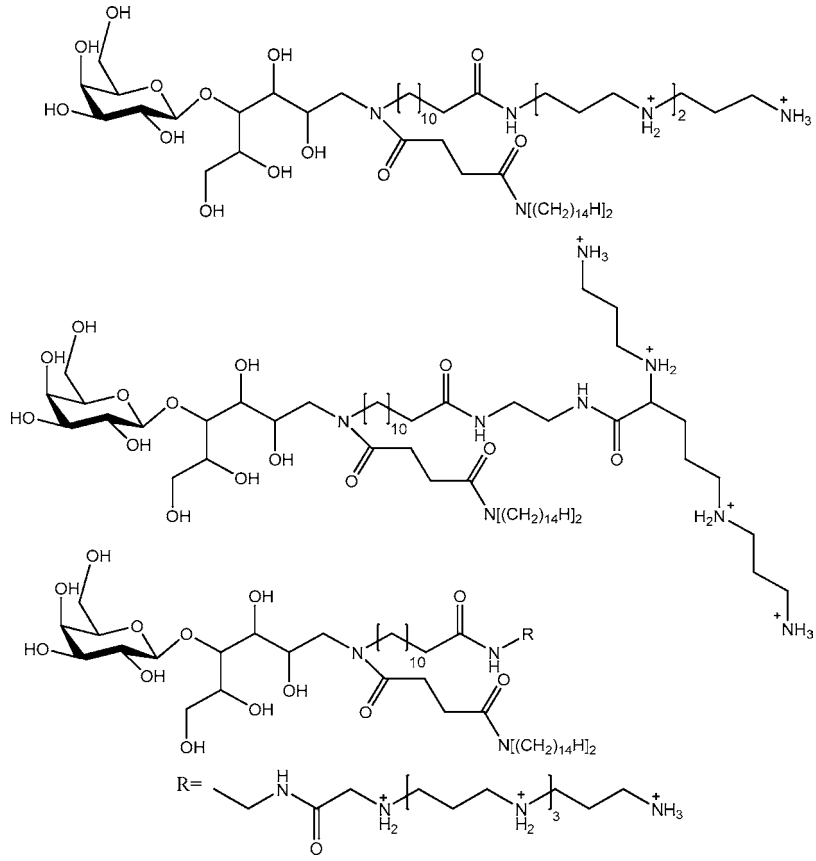


Figure 24. Chemical structures of Gal-CL.

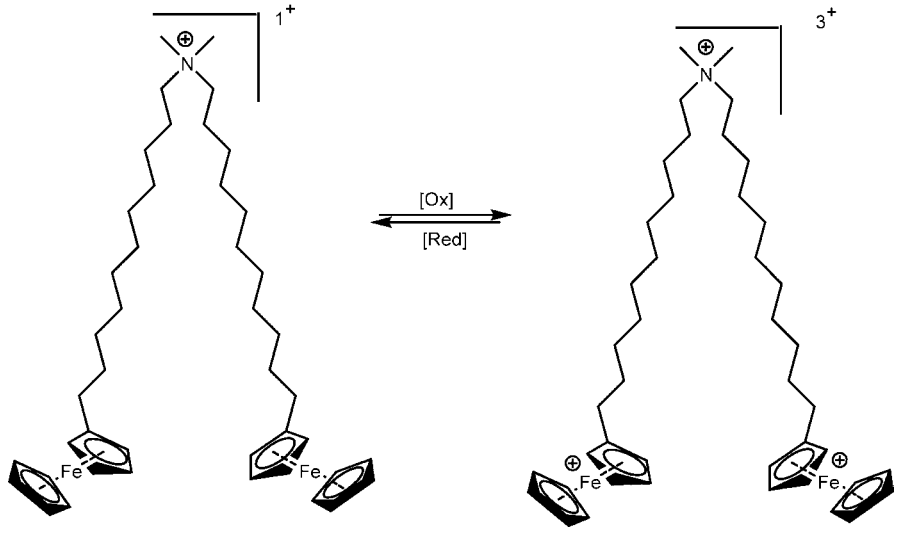


Figure 25. Chemical structures of ferrocene-containing dimethyldioctadecylammonium bromide.

acid. In addition, they demonstrated the principle of a redox-controlled gene delivery system that uses the reversibility of the thiol−disulfide exchange reaction. In the oxidized state, these amphiphiles condensed DNA into stable virus-sized complexes, which efficiently enter cells and released DNA in a reducing intracellular environment by various thiols as well as enzymatically, by thioredoxin reductase. Their data suggested that amphiphile−DNA complexes for gene transfection in vitro showed a several-fold increase of transgene expression compared with DOTAP. Their transfection efficiency can be further augmented by attachment of the nucleus-targeting peptide to the amphiphile. Having been formed from the natural compound lipoic acid, these cationic amphiphiles might be biodegradable and nontoxic.

Grinberg et al. (*90*) introduced the synthesis of a series of amphiphilic derivatives based on vernonia oil (see Figure 26). These compounds with three vernolic acid moieties bound together through a glycerol backbone proved to have good gene transfection properties, their structure is symmetrical, and their chains with some special moieties are branched and unsaturated. It is all these structure in cationic lipid that makes a combination

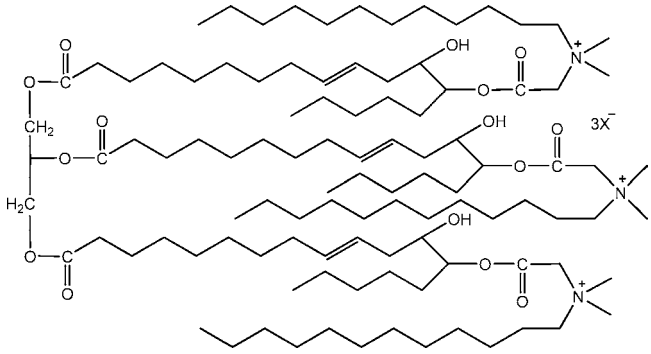


Figure 26. Chemical structures of amphiphilic derivatives based on vernonia oil.

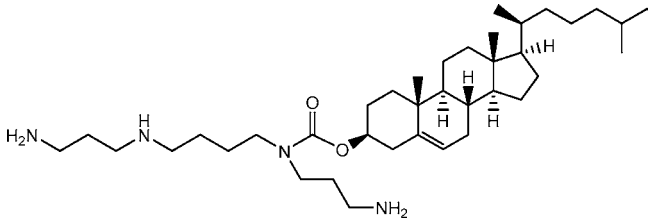


Figure 27. Chemical structure of GL-67.

that facilitated the complexation of DNA and its transport across biological barriers.

STEROID HYDROPHOBIC DOMAIN

In 1991, Gao et al. (*58*) reported the synthesis and application of the cholesterol-based cationic lipid DC-Chol, which was combined with DOPE to tranfect mammalian cells. Since then, considerable effort has been made in the synthesis of steroidal cationic lipids due to their potential applications in gene therapy (*55, 57, 58, 91*−*100*). Among the steroid groups, cholesteryl is by far the most frequently encountered.

For cholesterol-containing cationic lipids, it has been shown that those with the cholesterol hydrophobic domain linked to a multivalent T-shaped headgroup were most efficient when instilled into murine lungs (*91*). An example is cationic lipid GL-67 (see Figure 27), one of the multivalent T-shaped headgroups, which has been found to be particularly efficient for gene transfer to cultured cells and in murine lungs (*91*).

Then, Wu et al. (*101*) reported three cationic cholesterol derivatives differing in their types of amine and bearing a hydroxyethyl group at the amine group, synthesized and formulated into liposomes and nanoparticles as gene delivery vectors, and their formulations were optimized for gene transfection of the human lung adenocarcinoma A549 cell line. They found that the use of cationic lipids with a hydroxyethyl group at the tertiary amine headgroup showed the highest gene expression among cationic cholesterol derivatives lipids.

Otherwise, Philippe Belmont and co-workers (*102*) demonstrated that they synthesized a cationic cholesterol derivative characterized by an aminoglycoside headgroup. The amino-sugar-based cationic lipid was highly efficient for gene transfection into a variety of mammalian cell lines when used either alone or as a liposomal formulation with the neutral phospholipid DOPE. Their results showed the usefulness of cationic lipids composed of an aminoglycoside headgroup and cholesterol tail for gene transfection in vitro and in vivo.

Other steroid compounds used as hydrophobic moieties for cationic lipids include vitamin D (*103*), bile acids (*104*), antibiotic (*105*), cholestane, and litocholic acid (*63*).

Ren et al. (*103*) claimed that a new panel of steroidal cationic lipids (see Figure 26) using commercially available vitamin D_2

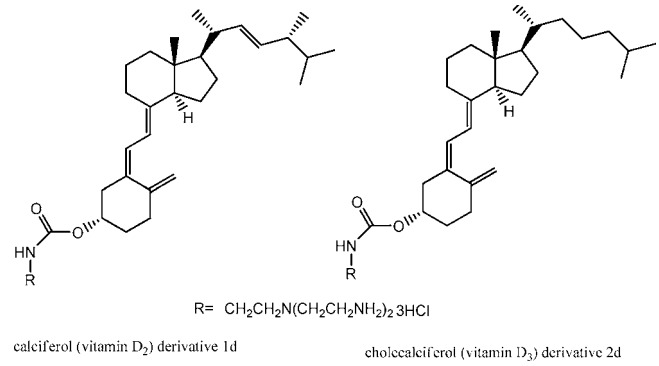


Figure 28. Vitamin D-based cationic lipids.

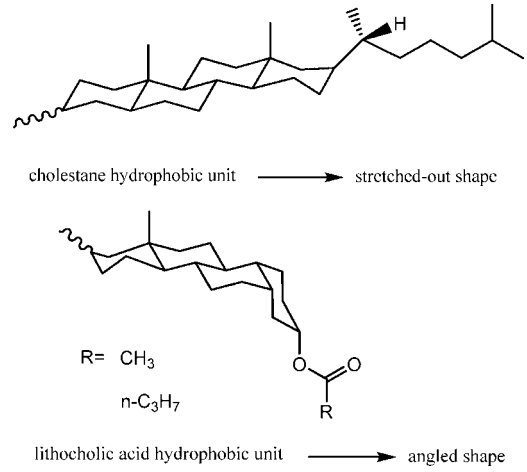


Figure 29. Chlolestane and lithocholic acid-based cationic lipids.

(calciferol) or vitamin D_3 (chole-calciferol) as hydrophobic motifs was synthesized for gene delivery. They found that the synthetic vitamin D-based cationic lipids **1d** and **2d** (see Figure 28) formulated with DOPE as a colipid exhibited superior transfection activity. Transfection results obtained from the experimentation suggested that these new vitamin D-based cationic lipids were useful for transfection reagents in vitro gene transfer studies.

Kichler et al. (*105*) showed that a class of facial amphiphiles, which were made by conjugating different amines to a steroid nucleus, were able to efficiently mediate gene transfer when associated with DOPE and shown to possess significant antibacterial activity even on bacteria strains such as *S. aureus* while being poorly hemolytic. Therefore, they thought that this study could serve as a starting point for the development of new compounds which are able at the same time to deliver a gene medicine and kill bacteria. Fujiwara et al. (*63*) designed a novel potent class of DNA delivery agents based on cholestane and lithocolic acid, of which the former had a *trans*-decaline structure and the latter, a *cis*-decaline structure, different space-filling character. The structure of the former was stretched, and the latter was angled-shaped. The former performed better in transfection efficiency than the latter (see Figure 29).

A few examples showing cationic lipids using a bile acid scaffold had a similar shape to cholesterol but were more hydrophilic due to the presence of polyhydroxyl groups (*104*). A particular example has been found by Randazzo and co-workers (*106*), who reported that incorporation of a double bond in the bile acid moiety enhanced transfection efficiency significantly and produced two compounds with little cytotoxicity and transfection potency comparable to Lipofectamine 2000.

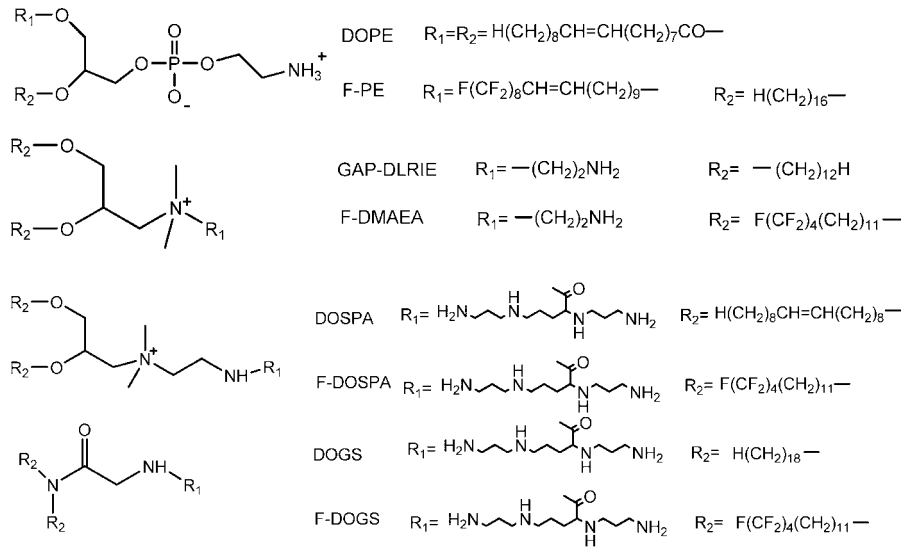


Figure 30. Chemical structure of the fluorinated and conventional cationic and helper lipids used and/or mentioned in this study. F-DOSPA, F-DMAEA, and F-DOGS F-PE are fluorinated lipids.

Lipids with steroid hydrophobic domain tend to rigidify the bilayers and are more stable in the bilayer structure.

FLUORINATED HYDROPHOBIC DOMAIN

The fluorinated part of the hydrophobic chain can also influence the transfection efficiency of cationic lipids in vivo and in vitro. Many varieties of fluorinated cationic lipids have been developed as transfecting agents, which are very efficient in compacting DNA and delivering it to cells in vitro and in vivo cationic lipid-mediated gene delivery (*107*−*111*). Gaucheron et al. (*111*) described the synthesis of fluorinated glycerophosphoethanolamines (F-PEs) helper lipids, which showed a significantly higher transfection helper potential as compared with that of DOPE. Two fluorinated cationic lipids F-DMAEA and F-DOSPA (see Figure 28) were designed by Boulanger et al. (*107*). Their hydrophobic part consisted of two $F(CF_2)_4(CH_2)_{11}$ chains, which led to one of the most efficient gene transfer agents in the fluorinated DOGS series (with either both chains fluorinated to varying degrees or just a single chain fluorinated) (see Figure 30) (*109, 110*). Lipoplexes from the above compounds were very stable to storage and more resistant to detergent in vivo. Their data demonstrated that fluorinated lipids had higher transfection efficiency in vivo and in vitro. It also suggested that their enhanced hydrophobic and lipophobic character prevented them from disintegration and, consequently, from DNA degradation and from interactions with lipophilic and hydrophilic biocompounds. Vierling's group (*112*) also described the synthesis of new perfluorinated dimerizable detergents with a tricationic or tetracationic (linear or branched spermine, respectively) polar head, which exhibited a higher in vitro and in vivo transfection potential than conventional lipoplexes or even than PEI polyplexes. Their production resulted in the development of tiny, monomolecular DNA nanoparticles that were obtained using new perfluorinated dimerizable detergents.

CONCLUSIONS

In recent years, considerable progress has been made in defining conditions that favor or promote lipoplex-mediated transfection, particularly with regard to the structural features of cationic lipids. The extent of gene therapy using synthetic vectors depends on the development of new approaches to improve the features of cationic lipids for the purpose of facilitating their use in vivo. From the chemistry point of view, the structure of cationic lipids is an important factor for their transfection activity and toxicity. Some common conclusions can be achieved by comparing the different structures and their transfection activity in the same family or different families of lipids. The transfection efficiency is not determined solely by one domain of cationic lipids but by the combination of them (*35*). The hydrophobic domain of cationic lipids mainly includes aliphatic chains, steroid domain, and fluorinated domain, which determines the phase transition temperature and the fluidity of the bilayer, and influences the stability of liposomes, the DNA protection from nucleases, amd the DNA release from complex. In the process of DNA transfer, cationic lipids protect DNA against degradation by nucleases and serum components, create a less negative surface charge, can be designed to target delivery to specific cell types through receptor−ligand interactions, and can also facilitate intracellular trafficking, which includes endosomal escape, cytoplasmic transport, and nuclear entry, while also having an important influence on the release of DNA to allow expression (*113, 114*).

Some traditional cationic lipids have been used in gene therapy, many of which have two hydrophobic tails. The chain length, asymmetry, branching, and unsaturation affect transfection activity in vivo and in vitro. Most studies suggest that transfection increases with decrease of chain length or increase of chain asymmetry, branching, or unsaturation. It is possible that shorter, asymmetrical, branched, and unsaturated hydrocarbon chains decrease the phase transition temperature, increase the fluidity of the bilayer, and favor a higher intermembrane transfer rate and lipid mixing, resulting in potential disruption of the endosome and consequent DNA releasing from endosomal degradation (*115*). The introduction of some special groups (such as ferrocene, lipoic acid) in the tail of the lipid can improve the efficiency of transfection and reduce toxicity, and would be worth exploring further as an in vivo delivery system for gene therapy. There is a new strategy which is introducing some special chemical bounds (such as ester linkage) upon traditional hydrophobic tails of cationic lipids that show low toxicity level (*3*) and high transfection efficiency and may provide an optimistic outlook for the development of lipid-based systems that are more applicable for human gene therapy. It might be development trends for cationic lipids that hydrophobic chains with some special moieties are branched and unsaturated.

Cationic lipids using cholesterol as a hydrophobic tail can also improve the efficiency of transfection. This is because the

formation of cholesterol offers rigidity and very stable bilayer structure, as well as its endogenous biodegradability and fusion activity. The hydrophobic domain of cationic lipids can not only directly affect the efficiency of transfection, but also indirectly influence transfection efficiency by the properties of the membrane (membrane fluidity and rigidity) that was formed from them. Further development in structure and properties of membrane will certainly rely on better understanding of vector interaction with plasmid and cellular components. Another trend of cationic lipid development is the substitution of some fluorinated groups for the hydrogens of two hydrophobic tails, which can improve transfection efficiency in vitro and in vivo. Fluorinated liposomes made from highly fluorinated double-chain phospho- or glycolipids, as well as fluorinated lipoplexes made from highly fluorinated polycationic lipospermines and reporter genes, have displayed a number of interesting physicochemical and biological properties (*110*). In general, it seems that, when researchers design cationic lipids for gene delivery, the balances between the opposing factors including fluidity and rigidity, symmetry and asymmetry, saturation and unsaturation, linearity and branching, short chain and long chain, and hydrophilicity and lipophilicity of lipids should be taken into great consideration. It would be very important for scientists to have a good understanding about the effect of the different hydrophobic domains of cationic lipids on transfection efficiency, which would be helpful to prepare novel cationic lipids and design novel formulations with high transfection efficiency.

ACKNOWLEDGMENT

The study was supported by Program for New Century Excellent Talents in University (NCET-08-0654) and the National Natural Science Foundation of China (20876027).

LITERATURE CITED

(1) El-Aneed, A. (2004) An overview of current delivery systems in cancer gene therapy. *J. Controlled Release 94*, 1–14.
(2) Blau, H. M., and Springer, M. L. (1995) Gene therapy-a novel form of drug delivery. *N. Engl. J. Med. 333*, 1204–1207.
(3) Lv, H. T., Zhang, S. B., Wang, B., Cui, S. H., and Yan, J. (2006) Toxicity of cationic lipids and cationic polymers in gene delivery. *J. Controlled Release 114*, 100–109.
(4) Kay, M. A., Glorioso, J. C., and Naldini, L. (2001) Viral vectors for gene therapy: the art of turning infectious agents into vehicles of therapeutics. *Nat. Med. 7*, 33–40.
(5) Zhang, S. B., Xu, Y. M., Wang, B., Qiao, W. H., Liu, D. L., and Li, Z. S. (2004) Cationic compounds used in lipoplexes and polyplexes for gene delivery. *J. Controlled Release 100*, 165–180.
(6) Liu, F., and Huang, L. (2002) Development of non-viral vectors for systemic gene delivery. *J. Controlled Release 78*, 259–266.
(7) Duan, Y., Zhang, S. B., Wang, B., Yang, B. L., and Zhi, D. F. (2009) The biological routes of gene delivery mediated by lipid-based non-viral vectors. *Expert Opin. Drug Delivery 6*, 1351–1361.
(8) Mrsny, R. J. (1999) Special feature: a survey of the recent patent literature on the delivery of genes and oligonucleotides. *J. Drug Targeting 7*, 1–10.
(9) Roth, J. A., Nguyen, D., Lawrence, D. D., Kemp, B. L., Carrasco, C. H., Ferson, D. Z., Hong, W. K., Komaki, R., Lee, J. J., Nesbitt, J. C., Pisters, K. M. W., Putnam, J. B., Schea, R., Shin, D. M., Walsh, G. L., Dolormente, M. M., Han, C. I., Martin, F. D., Yen, N., Xu, K., Stephen, L. C., cDonnell, T. J., Mukhopadhyay, T., and Cai, D. (1996) Retrovirus-mediated wild-type P_{53} gene transfer to tumors of patients with lung cancer. *Nat. Med. 2*, 985–991.
(10) Dass, C. R. (2002) Biochemical and biophysical characteristics of lipoplexes pertinent to solid tumour gene therapy. *Int. J. Pharm. 241*, 1–25.
(11) Anderson, W. F. (1992) Human gene therapy. *Science 256*, 808–813.
(12) Mukherjee, K., Sen, J., and Chaudhuri, A. (2005) Common co-lipids, in synergy, impart high gene transfer properties to transfection-incompetent cationic lipids. *FEBS Lett. 579*, 1291–1300.
(13) Verma, I. M., and Weitzman, M. D. (2005) Gene therapy: twenty-first century medicine. *Annu. Rev. Biochem. 74*, 711–738.
(14) Ma, B. C., Zhang, S. B., Jiang, H. M., Zhao, B. D., and Lv, H. T. (2007) Lipoplex morphologies and their influences on transfection efficiency in gene delivery. *J. Controlled Release 123*, 184–194.
(15) Tsukamoto, M., Ochiya, T., Sugimura, S. T., and Terada, M. (1995) Gene transfer and expression in progeny after intravenous DNA injection into pregnant mice. *Nat. Genet. 9*, 243–248.
(16) Felgner, P. L., Gadek, T. R., Holm, M., Roman, R., Chan, H. S., Wenz, M., Northrop, J. P., Ringgold, G. M., and Danielson, M. (1987) Lipofection: a highly efficient, lipid-mediated DNA-transfection procedure. *Proc. Natl. Acad. Sci. U.S.A. 84*, 7413–7417.
(17) Malone, R. W., Felgner, P. L., and Verma, I. M. (1989) Cationic liposome-mediated RNA transfection. *Proc. Natl. Acad. Sci. U.S.A. 86*, 6077–6081.
(18) Felgner, P. L., and Ringold, G. M. (1989) Cationic liposome-mediated transfection. *Nature 337*, 387–388.
(19) Leventis, R., and Silvius, J. R. (1990) Interactions of mammalian cells with lipid dispersions containing novel metabolizable cationic amphiphiles. *Biochim. Biophys. Acta, Biomembr. 1023*, 124–132.
(20) Gebeyehu, G., Jessee, J. A., Ciccarone, V. C., Hawley-Nelson, P., and Thytil, A. (1994) A cationic lipid containing an N-(2-bromoethyl) moiety has been reported, U.S. Patent 5,334,761.
(21) Dodds, E., Dunckley, M. G., Naujoks, K., Michaelis, U., and Dickson, G. (1998) Lipofection of cultured mouse muscle cells: a direct comparison of Lipofectamine and DOSPER. *Gene Ther. 5*, 542–551.
(22) Kunitake, T., Okahata, Y., Shimomura, M., Yasunami, S., and Takarabe, K. (1981) Formation of stable bilayer assemblies in water from single-chain amphiphiles. Relationship between the amphiphile structure and the aggregate morphology. *J. Am. Chem. Soc. 103*, 5401–5413.
(23) Krishnudu, K., Ahmad, M. U., Ali, S. M., and Ahmad, I. (2004) Synthesis of novel cationic cardiolipin analogues for the optimal delivery of therapeutic agents. *Tetrahedron Lett. 45*, 2743–2746.
(24) Niculescu-Duvaz, D., Heyes, J., and Springer, C. J. (2003) Structure-activity relationship in cationic lipid mediated gene transfection. *Curr. Med. Chem. 10*, 1233–1261.
(25) Hirko, A., Tang, F., and Hughes, J. A. (2003) Cationic lipid vectors for plasmid DNA delivery. *Curr. Med. Chem. 10*, 1185–1193.
(26) Tranchant, I., Thompson, B., Nicolazzi, C., Mignet, N., and Scherman, D. (2004) Physicochemical optimization of plasmid delivery by cationic lipids. *J. Gene. Med. 6*, S24–S35.
(27) Martin, B., Sainlos, M., Aissaoui, A., Oudrhiri, N., Hauchecorne, M., Vigneron, J. P., Lehn, J. M., and Lehn, P. (2005) The design of cationic lipids for gene delivery. *Curr. Pharm. Des. 11*, 375–394.
(28) Behr, J. P. (1994) Gene transfer with synthetic cationic amphiphiles: prospects for gene therapy. *Bioconjugate Chem. 5*, 382–389.
(29) Ferrari, M. E., Rusalov, D., Enas, J., and Wheeler, C. J. (2002) Synergy between cationic lipid and co-lipid determines the macroscopic structure and transfection activity of lipoplexes. *Nucleic Acids Res. 30*, 1808–1816.
(30) Patel, M., Vivien, E., Hauchecorne, M., Oudrhiri, N., Ramasawmy, R., Vigneron, J. P., Lehn, P., and Lehn, J. M. (2001) Efficient gene transfection by bisguanylated diacetylene lipid formulations. *Biochem. Biophys. Res. Commun. 281*, 536–543.

(31) Fletcher, S., Ahmad, A., Perouzel, E., Heron, A., Miller, A. D., and Jorgensen, M. R. (2006) In vivo studies of dialkynoyl analogues of DOTAP demonstrate improved gene transfer efficiency of cationic liposomes in mouse lung. *J. Med. Chem. 49*, 349–357.

(32) Bennett, M. J., Aberle, A. M., Balasubramaniam, R. P., Malone, J. G., Malone, R. W., and Nantz, M. H. (1997) Cationic lipid-mediated gene delivery to murine lung: correlation of lipid hydration with in vivo transfection activity. *J. Med. Chem. 40*, 4069–4078.

(33) Pinnaduwage, P., Schmitt, L., and Huang, L. (1989) Use of a quaternary ammonium detergent in liposome mediated DNA transfection of mouse L-cells. *Biochim. Biophys. Acta, Biomembr. 985*, 33–37.

(34) Cameron, F. H., Moghaddam, M. J., Bender, V. J., Whittaker, R. G., Mott, M., and Lockett, T. (1999) A transfection compound series based on a versatile Tris linkage. *Biochim. Biophys. Acta, Biomembr. 1417*, 37–50.

(35) Tang, F., and Hughes, J. A. (1999) Synthesis of a single-tailed cationic lipid and investigation of its transfection. *J. Controlled Release 62*, 345–358.

(36) Gao, X., and Huang, L. (1995) Cationic liposome-mediated gene transfer. *Gene Ther. 2*, 710–722.

(37) Rolland, A. P. (1998) From genes to gene medicines: recent advances in nonviral gene delivery. *Crit. Rev. Ther. Drug Carrier Syst. 15*, 143–198.

(38) Farhood, H., Serbina, N., and Huang, L. (1994) The role of dioleoyl phosphatidylethanolamine in cationic liposome mediated gene transfer. *Biochim. Biophys. Acta, Biomembr. 1235*, 289–295.

(39) Felgner, J. N., Kummar, R., Sridhar, C. N., Wheeler, C., Tsai, Y. K. J. K., Border, R., Ramsay, P., Martin, M., and Felgner, P. (1994) Enhanced gene delivery and mechanism studies with a novel series of cationic lipid formulations. *J. Biol. Chem. 269*, 2550–2561.

(40) Cullis, P. R., and de Kruijff, B. (1979) Lipid polymorphism and the functional roles of lipids in biological membranes. *Biochim. Biophys. Acta, Biomembr. 559*, 399–420.

(41) Wetzer, B., Byk, G., Frederic, M., Airiau, M., Blanche, F., Pitard, B., and Scherman, D. (2001) Reducible cationic lipids for gene transfer. *Biochem. J. 356*, 747–756.

(42) Byk, G., Dubertret, C., Escriou, V., Frederic, M., Jaslin, G., Rangara, R., Pitard, B., Crouzet, J., Wils, P., Schwartz, B., and Scherman, D. (1998) Synthesis, activity, and structure-activity relationship studies of novel cationic lipids for DNA transfer. *J. Med. Chem. 41*, 224–235.

(43) Rosenzweig, H. S., Rakhmanova, V. A., McIntosh, T. J., and MacDonald, R. C. (2000) O-Alkyl dioleoylphosphatidylcholinium compounds: the effect of varying alkyl chain length on their physical properties and in vitro DNA transfection activity. *Bioconjugate Chem. 11*, 306–313.

(44) Byk, G., Wetzer, B., Frederic, M., Dubertret, C., Pitard, B., Jaslin, G., and Scherman, D. (2000) Reduction-sensitive lipopolyamines as a novel nonviral gene delivery system for modulated release of DNA with improved transgene expression. *J. Med. Chem. 43*, 4377–4387.

(45) Kasireddy, K. S., Ali, M., Ahmad, M. U., Choudhury, S., Chien, P. Y., Sheikh, S., and Ahmad, I. (2005) Synthesis of cationic cardiolipin analogues. *Bioorg. Chem. 33*, 345–362.

(46) Gaucheron, J., Wong, T., Wong, K. F., Maurer, N., and Cullis, P. R. (2002) Synthesis and properties of novel tetraalkyl cationic lipids. *Bioconjugate Chem. 13*, 671–675.

(47) Bajaj, A., Paul, B., Indi, S. S., Kondaiah, P., and Bhattacharya, S. (2007) Effect of the hydrocarbon chain and polymethylene spacer lengths on gene transfection efficacies of gemini lipids based on aromatic backbone. *Bioconjugate Chem. 18*, 2144–2158.

(48) Woude, I., Wagenaar, A., Meekel, A. A. P., ter Beest, M. B. A., Ruiters, M. H. J., Engberts, J. B. F. N., and Hoekstra, D. (1997) Novel pyridinium surfactants for efficient, nontoxic in vitro gene delivery. *Proc. Natl. Acad. Sci. U.S.A. 94*, 1160–1165.

(49) Obika, S., Yu, W., Shimoyama, A., Uneda, T., Miyashita, K., Doi, T., and Imanishi, T. (2001) Symmetrical cationic triglycerides an efficient synthesis and application to gene transfer. *Bioorg. Med. Chem. 9*, 245–254.

(50) Loisel, S., Floch, V., Le Gall, C., and Ferec, C. (2001) Factors influencing the efficiency of lipoplexes mediated gene transfer in lungs after intravenous administration. *J. Liposome Res. 11*, 127–138.

(51) Delepine, P., Guillaume, C., Floch, V., Loisel, S., Yaouanc, L. L., Clement, J. C., and Abbayes, H. D. (2000) Cationic phosphonolipids as nonviral vectors: In vitro and in vivo applications. *J. Pharm. Sci. 89*, 629–638.

(52) Zuhorn, I. S., Oberle, V., Visser, W. H., Engberts, J. B. F. N., Bakowsky, U., Polushkin, E., and Hoekstra, D. (2002) Phase behavior of cationic amphiphiles and their mixtures with helper lipid influences lipoplex shape, DNA translocation, and transfection efficiency. *Biophys. J. 83*, 2096–2108.

(53) Koynova, R., Wang, L., and MacDonald, R. C. (2006) An intracellular lamellar-nonlamellar phase transition rationalizes the superior performance of some cationic lipid transfection agents. *Proc. Natl. Acad. Sci. U.S.A. 103*, 14373–14378.

(54) Roosjen, A., Smisterová, J., Driessen, C., Anders, J. T., Wagenaar, A., Hoekstra, D., Hulst, R., and Engberts, J. B. F. N. (2002) Synthesis and characteristics of biodegradable pyridinium amphiphiles used for in vitro DNA delivery. *Eur. J. Org. Chem.* 1271–1277.

(55) Ren, T., Song, Y. K., Zhang, G., and Liu, D. (2000) Structural basis of DOTMA for its high intravenous transfection activity in mouse. *Gene Ther. 7*, 764–768.

(56) Vigneron, J. P., Oudrhiri, N., Fauquet, M., Vergely, L., Bradley, J. C., Basseville, M., Lehn, P., and Lehn, J. M. (1996) Guanidinium-cholesterol cationic lipids: efficient vectors for the transfection of eukaryotic cells. *Proc. Natl. Acad. Sci. U.S.A. 93*, 9682–9686.

(57) Cooper, R. G., Etheridge, C. J., Stewart, L., Marshall, J., Rudginsky, S., Cheng, S. H., and Miller, A. D. (1998) Polyamine analogues of 3β-(N-(N', N'-dimethylaminoethane)carbamoyl-)cholesterol (DC-Chol) as agents for gene delivery. *Chem.—Eur. J. 4*, 137–151.

(58) Gao, X., and Huang, L. (1991) A novel cationic liposome reagent for efficient transfection of mammalian cells. *Biochem. Biophys. Res. Commun. 179*, 280–285.

(59) Felgner, J. H., Kumar, R., Sridhar, C. N., Wheeler, C. J., Tsai, Y. J., Border, R., Ramsey, P., Martin, M., and Felgner, P. L. (1994) Enhanced gene delivery and mechanism studies with a novel series of cationic lipid formulations. *J. Biol. Chem. 269*, 2550–2561.

(60) Floch, V., Loisel, S., Guenin, E., Hervé, A. C., Clément, J. C., Yaouanc, J. J., Abbayes, H., and Férec, C. (2000) Cation substitution in cationic phosphonolipids: a new concept to improve transfection activity and decrease cellular toxicity. *J. Med. Chem. 43*, 4617–4628.

(61) Zhdanov, R. I., Podobed, O. V., and Vlassov, V. V. (2002) Cationic lipid-DNA complexes-lipoplexes for gene transfer and therapy. *Bioelectrochemistry 58*, 53–64.

(62) Arpicco, S., Canevari, S., Ceruti, M., Galmozzi, E., Rocco, F., and Cattel, L. (2004) Synthesis, characterization and transfection activity of new saturated and unsaturated cationic lipids. *II Farmaco 59*, 869–878.

(63) Fujiwara, T., Hasegawa, S., Hirashima, N., Nakanishi, M., and Ohwada, T. (2000) Gene transfection activities of amphiphilic steroid-polyamine conjugates. *Biochim. Biophys. Acta, Biomembr. 1468*, 396–402.

(64) Hyvönena, Z., Plotnieceb, A., Reineb, I., Chekavichusb, B., Dubursb, G., and Urttia, A. (2000) Novel cationic amphiphilic 1,4-dihydropyridine derivatives for DNA delivery. *Biochim. Biophys. Acta, Biomembr. 1509*, 451–466.

(65) Ren, T., Zhang, G., Song, Y. K., and Liu, D. (1999) Synthesis and characterization of aromatic ring-based cationic lipids for

gene delivery in vitro and in vivo. *J. Drug Targeting 7*, 285–292.

(66) Banerjee, R., Das, P. K., Srilakshmi, G. V., and Chaudhuri, A. (1999) Novel series of non-glycerol-based cationic transfection lipids for use in liposomal gene delivery. *J. Med. Chem. 42*, 4292–4299.

(67) Floch, V., Audrezet, M. P., Guillaume, C., Gobin, E., Le Bolch, G., Clement, J. C., Yaouanc, J. J., Des Abbayes, H., Mercier, B., Leroy, J. P., Abgrall, J. F., and Ferec, C. (1998) Transgene expression kinetics after transfection with cationic phosphonolipids in hematopoietic non adherent cells. *Biochim. Biophys. Acta, Biomembr. 1371*, 53–70.

(68) Dileep, P. V., Antony, A., and Bhattacharya, S. (2001) Incorporation of oxyethylene units between hydrocarbon chain and pseudoglyceryl backbone in cationic lipid potentiates gene transfection efficiency in the presence of serum. *FEBS Lett. 509*, 327–331.

(69) Heyes, J. A., Niculescu-Duvaz, D., Cooper, R. G., and Springer, C. J. (2002) Synthesis of novel cationic lipids: effect of structural modification on the efficiency of gene transfer. *J. Med. Chem. 45*, 99–114.

(70) McGregor, C., Perrin, C., Monck, M., Camilleri, P., and Kirkby, A. J. (2001) Rational approaches to the design of cationic gemini surfactants for gene delivery. *J. Am. Chem. Soc. 123*, 6215–6220.

(71) Regelin, A. E., Fankhaenel, S., Gürtesch, L., Prinz, C., von Kiedrowski, G., and Massing, U. (2000) Biophysical and lipofection studies of DOTAP analogs. *Biochim. Biophys. Acta, Biomembr. 1464*, 151–164.

(72) Ren, T., and Liu, D. (1999) Synthesis of diether-linked cationic lipids for gene delivery. *Bioorg. Med. Chem. Lett. 9*, 1247–1250.

(73) Fichert, T., Regelin, A., and Massing, U. (2000) Synthesis and transfection properties of novel non-toxic monocationic lipids. variation of lipid anchor, spacer and head group structure. *Bioorg. Med. Chem. Lett. 10*, 787–791.

(74) Srilakshmi, G. V., Sen, J., Chauduri, A., Ramadas, Y., and Rao, N. M. (2002) Anchor-dependent lipofection with non-glycerol based cytofectins containing single 2-hydroxyethyl head groups. *Biochim. Biophys. Acta, Biomembr. 1559*, 87–95.

(75) Sen, J., and Chaudhuri, A. (2005) Design, syntheses, and transfection biology of novel non-cholesterol- based guanidinylated cationic lipids. *J. Med. Chem. 48*, 812–820.

(76) Kim, H. S., Moon, J., Kim, K. S., Choi, M. M., Lee, J. E., Heo, Y., Cho, D. H., Jang, D. O., and Park, Y. S. (2004) Gene-transferring efficiencies of novel diamino cationic lipids with varied hydrocarbon chains. *Bioconjugate Chem. 15*, 1095–1101.

(77) Gilot, D., Miramon, M. L., Benvegnu, T., Ferrieres, V., Loreal, O., Guguen-Guillouzo, C., Plusquellec, D., and Loyer, P. (2002) Cationic lipids derived from glycine betaine promote efficient and non-toxic gene transfection in cultured hepatocytes. *J. Gene Med. 4*, 415–427.

(78) Lindner, L. H., Brock, R., Arndt-Jovin, D., and Eibl, H. (2006) Structural variation of cationic lipids: Minimum requirement for improved oligonucleotide delivery into cells. *J. Controlled Release 110*, 444–456.

(79) Kim, H. S., Song, I. H., Kim, J. C., Kim, E. J., Jang, D. O., and Park, Y. S. (2006) In vitro and in vivo gene-transferring characteristics of novel cationic lipids, DMKD (O, O'-dimyristyl-N-lysyl aspartate) and DMKE (O, O'-dimyristyl-N-lysyl glutamate). *J. Controlled Release 115*, 234–241.

(80) Balasubramanian, R. P., Bennet, M. J., Aberle, A. M., Malone, J. G., Nantz, M. H., and Malone, R. W. (1996) Structural and functional analysis of cationic transfection lipids: the hydrophobic domain. *Gene Ther. 3*, 163–172.

(81) Gopal, V., Prasad, T. K., Rao, N. M., Takafuji, M., Rahman, M. M., and Ihara, H. (2006) Synthesis and in vitro evaluation of glutamide-containing cationic lipids for gene delivery. *Bioconjugate Chem. 17*, 1530–1536.

(82) Flocha, V., Le Bolc'hb, G., Audrézeta, M. P., Yaouancb, J. J., Clémentb, J. C., des Abbayesb, H., Merciera, B., Abgrallc, J. F., and Férec, C. (1997) Cationic phosphonolipids as non viral vectors for DNAtransfection in hematopoietic cell lines and CD34+cells. *Blood Cells Mol. Dis. 23*, 69–87.

(83) Jacopin, C., Hofland, H., Scherman, D., and Herscovici, J. (2001) Synthesis and transfecting properties of a glycosylated polycationic DNA vector. *Bioorg. Med. Chem. Lett. 11*, 419–422.

(84) Brunelle, M., Polidori, A., Denoyelle, S., Fabiano, A. S., Vuillaume, P. Y., Laurent-Lewandowski, S., and Pucci, B. (2009) A structure-activity investigation of hemifluorinated bifunctional bolaamphiphiles designed for gene delivery. *C. R. Chimie 12*, 188–208.

(85) Fabio, K., Gaucheron, J., Giorgio, C. D., and Vierling, P. (2003) Novel galactosylated polyamine bolaamphiphiles for gene delivery. *Bioconjugate Chem. 14*, 358–367.

(86) Kakizawa, Y., Sakai, H., Nishiyama, K., Abe, M., Shoji, H., Kondo, Y., and Yoshino, N. (1996) Solution properties of double-tailed cationic surfactants having ferrocenyl groups in their hydrophobic moieties. *Langmuir 12*, 921–924.

(87) Kakizawa, Y., Sakai, H., Yamaguchi, A., Kondo, Y., Yoshino, N., and Abe, M. (2001) Electrochemical control of vesicle formation with a double-tailed cationic surfactant bearing ferrocenyl moieties. *Langmuir 17*, 8044–8048.

(88) Abbott, N. L., Jewell, C. M., Hays, M. E., Kondo, Y., and Lynn, D. M. (2005) Ferrocene-containing cationic lipids: influence of redox state on cell transfection. *J. Am. Chem. Soc. 127*, 11576–11577.

(89) Balakirev, M., Schoehn, G., and Chroboczek, J. (2000) Lipoic acid-derived amphiphiles for redox-controlled DNA delivery. *Chem. Biol. 7*, 813–819.

(90) Grinberg, S., Linder, C., Kolot, V., Waner, T., Wiesman, Z., Shaubi, E., and Heldman, E. (2005) Novel cationic amphiphilic derivatives from vernonia oil: synthesis and self-aggregation into bilayer vesicles, nanoparticles, and DNA complexants. *Langmuir 21*, 7638–7645.

(91) Lee, E. R., Marshall, J., Siegel, C. S., Jiang, C., Yew, N. S., Nichols, M. R., Nietupski, J. B., Ziegler, R. J., Lane, M. B., Wang, K. X., Wan, N. C., Scheule, R. K., Harris, D. J., Smith, A. E., and Cheng, S. H. (1996) Detailed analysis of structures and formulations of cationic lipids for efficient gene transfer to the lung. *Hum. Gene Ther. 7*, 1701–1717.

(92) Takeuchi, K., Ishihara, M., Kawaura, C., Noji, M., Furuno, T., and Nakanishi, M. (1996) Effect of zeta potential of cationic liposomes containing cationic cholesterol derivatives on gene transfection. *FEBS Lett. 397*, 207–209.

(93) Okayama, R., Noji, M., and Nakanishi, M. (1997) Cationic cholesterol with a hydroxyethylamino head group promotes significantly liposome-mediated gene transfection. *FEBS Lett. 408*, 232–234.

(94) Ghosh, Y. K., Visweswariah, S. S., and Bhattacharya, S. (2000) Nature of linkage between the cationic headgroup and cholesteryl skeleton controls gene transfection efficiency. *FEBS Lett. 473*, 341–344.

(95) Percot, A., Briane, D., Coudert, R., Reynier, P., Bouchemal, N., Lièvre, N., Hantz, E., Salzmann, J. L., and Cao, A. (2004) A hydroxyethylated cholesterol-based cationic lipid for DNA delivery: effect of conditioning. *Int. J. Pharm. 278*, 143–163.

(96) Geall, A. J., Taylor, R. J., Earll, M. E., Eaton, M. A. W., and Blagbrough, I. S. (2000) Synthesis of cholesterol-polyamine carbamates: pKa studies and condensation of calf thymus DNA. *Bioconjugate Chem. 11*, 314–326.

(97) Geall, A. J., Eaton, M. A. W., Baker, T., Catterall, C., and Blagbrough, I. S. (1999) The regiochemical distribution of positive charges along cholesterol polyamine carbamates plays significant roles in modulating DNA binding affinity and lipofection. *FEBS Lett. 459*, 337–342.

(98) Choi, J. S., Lee, E. J., Jang, H. S., and Park, J. S. (2001) New cationic liposomes for gene transfer into mammalian cells with high efficiency and low toxicity. *Bioconjugate Chem. 12*, 108–113.

(99) Gao, H., and Hui, K. M. (2001) Synthesis of a novel series of cationic lipids that can act as efficient gene delivery vehicles through systematic heterocyclic substitution of cholesterol derivatives. *Gene Ther. 8*, 855–863.

(100) Zhdanov, R. I., Kutsenko, N. G., Podobed, O. V., Buneeva, O. A., Tsvetkova, T. A., Konevets, D. N., and Vlassov, V. V. (1998) Cholesterol polyethylen/propylen/imines as mediators of transfection of eukaryotic cells for gene therapy. *Dokl. Akad. Nauk 361*, 695–699.

(101) Ding, W. X., Hattori, Y., Higashiyama, K., and Maitani, Y. (2008) Hydroxyethylated cationic cholesterol derivatives in liposome vectors promote gene expression in the lung. *Int. J. Pharm. 354*, 196–203.

(102) Belmont, P., Aissaoui, A., Hauchecorne, M., Oudrhiri, N., Petit, L., Vigneron, J. P., Lehn, J. M., and Lehn, P. (2002) Aminoglycoside-derived cationic lipids as efficient vectors for gene transfection in vitro and in vivo. *J. Gene Med. 4*, 517–526.

(103) Ren, T., Zhang, G., Liu, F., and Liu, D. (2000) Synthesis and evaluation of vitamin D-based cationic lipids for gene delivery in vitro. *Bioorg. Med. Chem. Lett. 10*, 891–894.

(104) Walker, S., Sofia, M. J., Kakarla, R., Kogan, N. A., Wierichs, L., Longley, C. B., Bruker, K., Axelrod, H. R., Midha, S., Babu, S., and Kahne, D. (1996) Cationic facial amphiphiles: a promising class of transfection agents. *Proc. Natl. Acad. Sci. U.S.A. 93*, 1585–1590.

(105) Kichler, A., Leborgne, C., Savage, P. B., and Danos, O. (2005) Cationic steroid antibiotics demonstrate DNA delivery properties. *J. Controlled Release 107*, 174–182.

(106) Randazzo, R. A. S., Bucki, R., Janmey, P. A., and Diamond, S. L. (2009) A series of cationic sterol lipids with gene transfer and bactericidal activity. *Bioorg. Med. Chem. 17*, 3257–3265.

(107) Gaucheron, J., Santaella, C., and Vierling, P. (2001) In vitro gene transfer with a novel galactosylated spermine bolaamphiphile. *Bioconjugate Chem. 12*, 569–575.

(108) Vierling, P., Santaella, C., and Greiner, J. (2000) Highly fluorinated amphiphiles as drug and gene carrier and delivery systems. *J. Fluorine Chem. 107*, 337–354.

(109) Gaucheron, J., Santaella, C., and Vierling, P. (2001) Highly fluorinated lipospermines for gene transfer: synthesis and evaluation of their in vitro transfection efficiency. *Bioconjugate Chem. 12*, 114–128.

(110) Gaucheron, J., Santaella, C., and Vierling, P. (2001) Improved in vitro gene transfer mediated by fluorinated lipoplexes in the presence of a bile salt surfactant. *J. Gene Med. 3*, 338–344.

(111) Gaucheron, J., Boulanger, C., Santaella, C., Sbirrazzuoli, N., Boussif, O., and Vierling, P. (2001) In vitro cationic lipid-mediated gene delivery with fluorinated glycerophosphoethanolamine helper lipids. *Bioconjugate Chem. 12*, 949–963.

(112) Fabio, K., Giorgio, C. D., and Vierling, P. (2005) New perfluorinated polycationic dimerizable detergents for the formulation of monomolecular DNA nanoparticles and their in vitro transfection efficiency. *Biochim. Biophys. Acta. Biomembr. 1724*, 203–214.

(113) Niidome, T., and Huang, L. (2002) Gene therapy progress and prospects: nonviral vectors. *Gene Ther. 9*, 1647–1652.

(114) Varga, C. M., Hong, K., and Lauffenburger, D. A. (2001) Quantitative analysis of synthetic gene delivery vector design properties. *Mol. Ther. 4*, 438–446.

(115) Xu, Y., Jr. (1996) Mechanism of DNA release from cationic liposome/DNA complexes used in cell transfection. *Biochemistry 35*, 5616–5623.

BC900393R

Tumor Targeting Chitosan Nanoparticles for Dual-Modality Optical/MR Cancer Imaging

Taehwan Nam,[†,‡,§] Sangjin Park,[†,§] Seung-Young Lee,[§] Kyeongsoon Park,[§] Kuiwon Choi,[§] In Chan Song,[||] Moon Hee Han,[||] James J. Leary,[⊥] Simseok Andrew Yuk,[§,#] Ick Chan Kwon,[§] Kwangmeyung Kim,*[,§] and Seo Young Jeong*[,‡]

Department of Life and Nanopharmaceutical Science, Kyung Hee University, 1 Hoegi-dong, Dongdaemun-gu, Seoul, 130-701, Korea, Biomedical Research Center, Korea Institute of Science and Technology, 39-1 Hawolgok-dong, Seongbuk-gu, Seoul, 136-791, Korea, Department of Radiology, Seoul National University College of Medicine, 101 Daehangno, Chongno-Ko, 110-744, Korea, and Weldon School of Biomedical Engineering and School of Chemical Engineering, Purdue University, West Lafayette, Indiana. Received September 16, 2009; Revised Manuscript Received January 26, 2010

We report tumor targeting nanoparticles for optical/MR dual imaging based on self-assembled glycol chitosan to be a potential multimodal imaging probe. To develop an optical/MR dual imaging probe, biocompatible and water-soluble glycol chitosan (M_w = 50 kDa) were chemically modified with 5β-cholanic acid (CA), resulting in amphiphilic glycol chitosan-5β-cholanic acid conjugates (GC-CA). For optical imaging near-infrared fluorescence (NIRF) dye, Cy5.5, was conjugated to GC-CA resulting in Cy5-labeled GC-CA conjugates (Cy5.5-GC-CA). Moreover, in order to chelate gadolinium (Gd(III)) in the Cy5.5-GC-CA conjugates, 1,4,7,10-tetraazacyclododecane-1,4,7,10-tetraacetic acid (DOTA) was directly conjugated in Cy5.5-GC-CA. Finally, the excess $GdCl_3$ was added to DOTA modified Cy5.5-GC-CA conjugates in distilled water (pH 5.5). The freshly prepared Gd(III) encapsulated Cy5.5-GC-CA conjugates were spontaneously self-assembled into stable Cy5.5 labeled and Gd(III) encapsulated chitosan nanoparticles (Cy5.5-CNP-Gd(III)). The Cy5.5-CNP-Gd(III) was spherical in shape and approximately 350 nm in size. From the cellular experiment, it was demonstrated that Cy5.5-CNP-Gd(III) were efficiently taken up and distributed in cytoplasm (NIRF filter; red). When the Cy5.5-GC-Gd(III) were systemically administrated into the tail vein of tumor-bearing mice, large amounts of nanoparticles were successfully localized within the tumor, which was confirmed by noninvasive near-infrared fluorescence and MR imaging system simultaneously. These results revealed that the dual-modal imaging probe of Cy5.5-CNP-Gd(III) has the potential to be used as an optical/MR dual imaging agent for cancer treatment.

Recently, nanotechnology and molecular imaging have been combined to generate multifunctional nanoparticles that simultaneously facilitate early-stage cancer diagnosis, target drug delivery with minimal toxicity, and monitor cancer treatment (*1*−*3*). In particular, various multimodal nanoparticle imaging probes have been tested to overcome the limitations of either imaging method when used alone (*4, 5*). The combination of magnetic resonance (MR) imaging and near-infrared fluorescence (NIRF) optical imaging for cancer diagnosis have several attractive attributes that have driven the development of molecular imaging strategies for these modalities (*6*−*8*).

The major advantage of NIRF optical imaging is the capability of visualizing target biological molecules (peptides, drugs, DNA, siRNA, proteins, etc.) in vivo with a higher sensitivity (*9*−*15*). However, the spatial resolution of NIRF optical imaging is not enough to show the location of a three-dimensional target molecule with anatomical resolution. MR imaging is one of the imaging techniques used to obtain three-dimensional information. Besides the excellent spatial resolution, one limitation of MRI is its low sensitivity to contrast agents, which are important for the detection of cellular or molecular changes on a nanomolar scale. Therefore, the limited sensitivity of MR imaging can be overcome by combination with NIRF optical imaging methods.

Of note, polymeric nanoparticles are known to accumulate at the solid tumor site by the so-called enhanced permeation and retention (EPR) effect, resulting in efficient accumulation in solid tumor tissues (*16*). Therefore, polymeric nanoparticles have been applied as effective multifunctional nanoparticles capable of enhancing the diagnostic and therapeutic efficacy of imaging probes and therapeutic agents in cancer treatment. This is due to the fact that polymeric nanoparticles exhibited ideal in vivo characteristics, such as biocompatibility and biodegradability, and prolonged circulation time the bloodstream. For example, Doiron et al. recently reported optical/T1 dual imaging agent based on PLGA which encapsulated Gd(III) and rhodamine (*17*). However, it did not describe biodistribution or in vivo tumor targeting. As an optical/T2 dual imaging agent, Yu et al prepared polymer-coated iron oxide nanoparticles with drug loading (*18*). Doxorubicin was used as an anticancer agent that exhibited fluorescence as an optical imaging agent. It efficiently targeted and showed antitumor effects in vivo. However, the imaging probe was still distributed in other major organs such as the liver.

Herein, we introduce tumor targeting chitosan nanoparticles for optical/MR dual imaging that was based on polymeric nanoparticle technology and molecular imaging. Previously, we have developed hydrophobically modified glycol chitosan nanoparticles (HGC) as novel nanosized drug carriers in cancer

* Corresponding author. Tel: +82-2-958-5912; Fax: +82-2-958-5909; E-mail: kim@kist.re.kr (K. Kim). Tel: +82-2-966-3885; Fax: +82-2-961-0356; E-mail: syjeong@khu.ac.kr (S. Y. Jeong).

[†] These authors contributed equally to this paper.

[‡] Kyung Hee University.

[§] Korea Institute of Science and Technology.

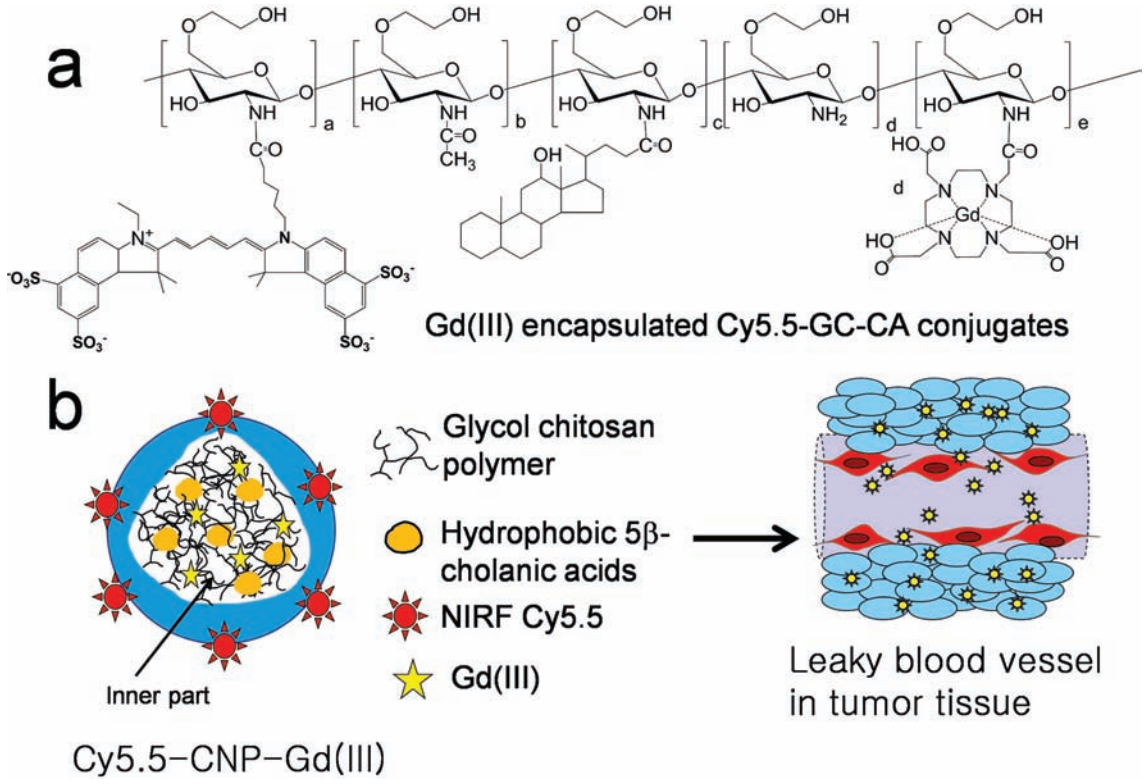
[||] Seoul National University College of Medicine.

[⊥] Weldon School of Biomedical Engineering, Purdue University.

[#] School of Chemical Engineering, Purdue University.

10.1021/bc900408z © 2010 American Chemical Society
Published on Web 03/04/2010

Scheme 1. (a) Chemical Structure of Cy5.5-CNP-Gd(III) and (b) Schematic Illustration of Self-Assembled Chitosan Nanoparticles (Blue Color, Glycol Chitosan Shell; White Color, Inner Part of Chitosan Nanoparticle) and Tumor Targeting for Dual-Modal NIRF Optical/MR Imaging Probes



treatment that can self-assemble in aqueous solution to form stable nanoparticles (*19*−*21*). Selective accumulation of HGC nanoparticles in the tumor interstitium by the EPR effect was exhibited when systemically administered to deliver various types of therapeutic agents (*19, 21*). To make new optical/MR dual imaging agents, we designed tumor targeting chitosan-based nanoparticles (CNPs) containing dual imaging agents (NIRF dye, Cy5.5 (*20*), and gadolinium (Gd(III)) ions) (*16, 22, 23*) (Scheme 1). The tumor targeting profile and cancer imaging potential of dual imaging probes of chitosan nanoparticles were evaluated in tumor-bearing mice.

To make optical/MR dual imaging nanoparticles biocompatible and water-soluble, glycol chitosan (GC, M_w = 50 kDa) was chemically modified with 5β-cholanic acid (CA) in the presence of EDC and NHS, which promoted amide linkage formation between the amine group of chitosan and carboxyl acid of CA, resulting in GC-CA (*24*−*26*). A colloidal titration method showed that GC-CA had an average molecular weight of 54 kDa, indicating that 11 ± 2 of CA molecules were chemically conjugated to GC (*20*). For the optical/MR dual-modal cancer imaging, 0.5 ± 0.1 of NIRF dye, monohydroxysuccinimide Cy5.5-NHS, was conjugated to GC-CA (Cy5.5-GC-CA). In order to chelate Gd(III) in the conjugates, monoreactive hydroxysuccinimide-DOTA was directly conjugated to the amine groups in the Cy5.5-GC-CA. The degrees of conjugation were in the range from 13 to 45, confirmed by ^{1}H NMR (Table 1). Finally, the excess of $GdCl_3$ was added to DOTA modified Cy5.5-GC-CA in distilled water (pH 5.5). After the reaction, EDTA tetrasodium salt was used to remove the unreacted Gd(III) ions. The weight ratio of Gd(III) in the conjugates was maximized to approximately 6 ± 0.28%, measured by energy dispersive spectroscopy (EDS) and inductively coupled plasma−atomic emission spectrometer (ICP-AES) (Table 1; see Supporting Information). In this study, maximum Gd(III) encapsulated Cy5.5-labled chitosan nanoparticles (Cy5.5-CNP-Gd(III); 6.28 wt %) were used to analyze their characteristics in vitro and in vivo.

Table 1. Characterization of the Weight Ratio of Gd(III) in CNPs

sample	Ds of DOTA[a]	wt (%) of Gd(III)	diameter (nm)
Cy5.5-CNPs	−	−	250 ± 18
Cy5.5-CNPs-[Gd(III)-2%]	13	2.39	260 ± 28
Cy5.5-CNPs-[Gd(III)-4%]	34	4.22	320 ± 35
Cy5.5-CNPs-[Gd(III)-6%]	45	6.28	350 ± 42

[a] Degree of substitution of the number of DOTA per on CNPs.

The dried Gd(III) encapsulated chitosan conjugates, when dissolved in aqueous solutions, spontaneously self-assembled into stable Cy5.5 labeled and Gd(III) encapsulated chitosan nanoparticles (Cy5.5-CNP-Gd(III)). Dynamic light scattering and transmission electron microscopy (TEM) analyses revealed that Cy5.5-CNP-Gd(III) were spherical and approximately 350 nm in size (Figure 1a). In phosphate buffered saline (PBS) at 37 °C, the Cy5.5-CNP-Gd(III) remained dispersed and maintained their original nanoparticle size for up to 40 days, indicating the excellent stability of nanoparticle probes in aqueous conditions (Figure 1b). Also, Cy5.5-CNP-Gd(III) were rapidly taken up within one hour by HeLa cells expressing a green fluorescence protein-tagged histone 2B (HeLa H2B-GFP), but free Cy5.5 molecules were not taken up by the cells within same time. Of note, most of the internalized particles were found in the cytoplasm (NIRF filter; red), not in the GFP-labeled nuclear compartment (FITC filter; green) (Figure 1c). This rapid cellular uptake characteristic of Cy5.5-CNP-Gd(III) facilitated delivery of anticancer drugs and imaging agents into the cytoplasmic compartment of target tumor cells. Moreover, Cy5.5-CNP-Gd(III) exhibited almost 100% of cell viability (Figure 1d), even at the relative high concentration up to 250 μg/mL.

To demonstrate the ability of Cy5.5-CNP-Gd(III) as an optical/MR dual-modal imaging probe, we obtained the NIRF

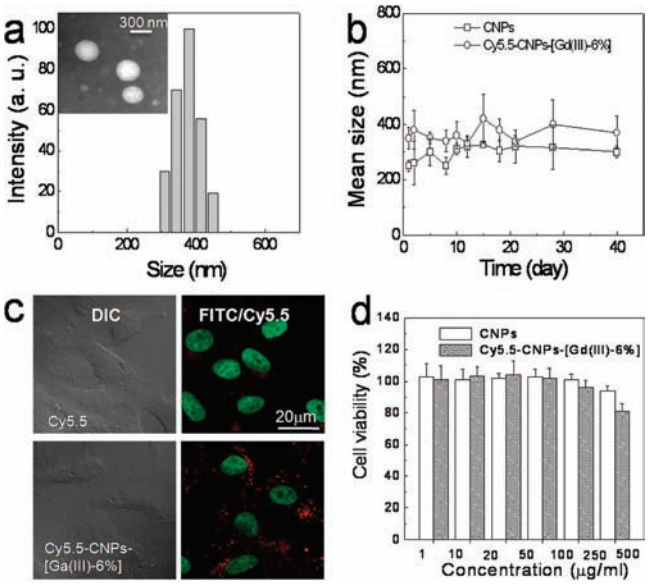


Figure 1. (a) Average size of Cy5.5-CNP-Gd(III) in PBS (pH 7.4, 37C), confirmed with dynamic light scattering. (b) In vitro stability of Cy5.5-CNP-Gd(III) in PBS for 40 days. (c) Cellular uptake profiles of free Cy5.5 and Cy5.5-CNP-Gd(III) in a cell culture system. Each sample was incubated with HeLa H2B-GFP cells for 1 h (original magnification × 400). (d) Cell viability of Cy5.5-CNP-Gd(III) in SCC7 cells for 1 day.

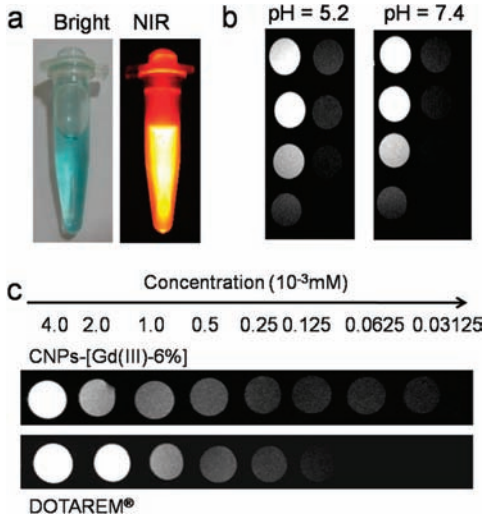


Figure 2. (a) Bright and NIRF images of the Cy5.5-CNP-Gd(III) in PBS. (b) T1-weighted spin−echo images of Cy5.5-CNP-Gd(III) in acidic (pH 5.2) and physiological condition (pH7.4). (c) T1-weighted spin−echo MR image (1.5T) showing bright MR signals of DOTEM and Cy5.5-CNP-Gd(III) in PBS.

optical and MR images from the optical or MR phantom test, respectively. Cy5.5-CNP-Gd(III) solution (1 mg/mL in PBS) produced a strong NIRF signal when we used a Cy5.5 filter set (Figure 2a), facilitating noninvasive imaging of the nanoparticles in live animals. The bright signal enhancement in the T1-weighted MR images revealed a progressive increase as the concentration of Cy5.5-CNP-Gd(III) increased. In particular, they showed the same T-1 weight MR image at the different pH conditions, indicating the stability of chelated Gd(III) ions in the nanoparticles (Figure 2b). As a comparison, we obtained MR images of commercialized MR contrast agent DOTAREM. The contrast efficiency of Cy5.5-CNP-Gd(III) was less than that of DOTAREM, at the higher Gd(III) concentration (>2.0 × 10^{-3} mM) (Figure 2c). It is deduced that the encapsulated Gd(III) in the hydrophobic inner part of nanoparticles decreased the

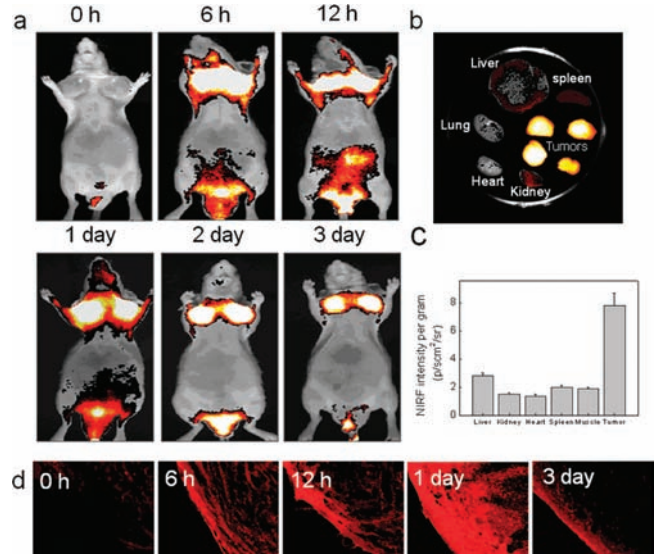


Figure 3. In vivo time-dependent biodistribution of Cy5.5-CNP-Gd(III) in SCC7 tumor-bearing mice (diameter = 8−10 mm). (a) In vivo time-dependent whole body imaging after i.v. injection of Cy5.5-CNP-Gd(III) (5 mg/kg). (b) Ex vivo images of normal organs (liver, lung, spleen, heart, and kidney) and tumors excised at 1 day postinjection. (c) A quantification of in vivo biodistribution of Cy5.5-CNP-Gd(III) was recorded as total photon counts per centimeter squared per steradian (p/s/cm^2/sr) per each excised organ at 1 day postinjection. All data represent mean ± s.e. (d) NIRF microscopic images of tumors excised from Cy5.5 (5 mg/kg)-labeled CNPs-treated SCC7 tumor-bearing mice. The NIRF microscopic image of each sample was viewed using an NIRF microscope with Cy5.5 filter set. Original magnification is × 100.

relaxivity of Gd(III), resulted in the reduction of accessibility in aqueous condition. Interestingly, it retained higher contrast signal at the lower concentration. This phantom study demonstrated the potential value of Cy5.5-CNP-Gd(III) as a contrast agent for optical and MR imaging, simultaneously.

We subsequently monitored the time-dependent in vivo biodistribution of Cy5.5-CNP-Gd(III) after intravenous injection into nude mice bearing pectoral subcutaneous murine squamous carcinoma cells (SCC7) tumors of about 8−10 mm in diameter by using Kodak Image Station; with a special C-mount lens and Cy5.5 bandpass emission filter (Figure 3a). Cy5.5-CNP-Gd(III)-treated mice (5 mg/kg) presented a strong NIRF signal throughout the whole body within 6 h of injection, indicating that the nanoparticles rapidly circulated in the bloodstream. From the NIRF optical images, we could delineate subcutaneous tumors from the surrounding background tissue at 6 h postinjection, and they exhibited a maximum NIRF signal beginning at 12 h postinjection. It should be noted that the tumors maintained this maximal NIRF intensity for 3 days, but the NIRF signal persisted for up to 5 days postinjection, with a gradual decrease in signal in the tumor. Of note, ex vivo NIRF images of excised tissues (liver, lung, kidney, heart, and the tumors) provided substantial evidence for the EPR effect-based tumor targeting ability of Cy5.5-CNP-Gd(III) in SCC7 tumor-bearing mice (Figure 3b) at 1 day postinjection of Cy5.5-CNP-Gd(III). The image revealed that Cy5.5-CNP-Gd(III) were mainly taken up by the tumor tissues, whereas their uptake in normal tissues was not significant. Furthermore, the NIRF total photon counts per gram of each organ from the tumor tissues were 3- to 7-fold higher than those from other organs, providing decisive evidence that Cy5.5-CNP-Gd(III) specifically targeted tumor tissues (Figure 3c). Via microscale images, Cy5.5-CNP-Gd(III) initially localized in the peripheral region of tumors after 6 h postinjection in mice, and the

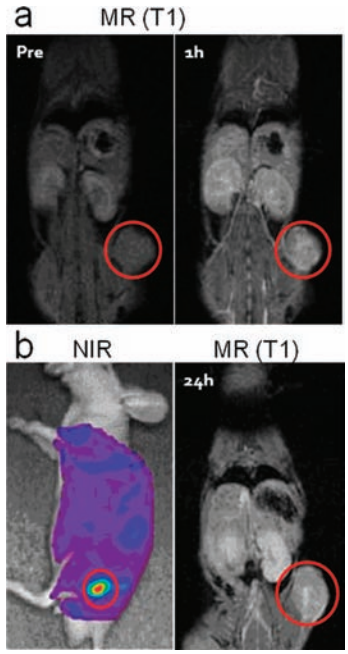


Figure 4. Tumor target specificity of Cy5.5-CNP-Gd(III) in SCC7 tumor-bearing mice (diameter = 8−10 mm). (a) Coronal slices of T1-weighted MR images of Cy5.5-CNP-Gd(III) in SCC7 tumor-bearing mice at 0 and 1 h postinjection. Red circles indicate that SCC-7 tumor tissue. (b) Both NIRF and T1-weighted MR images were simultaneously observed after 1 day postinjection of Cy5.5-CNP-Gd(III) (5 mg/kg).

maximum NIRF intensity was observed throughout the entire tumor after 12 h postinjection (Figure 3d). All images were reproducible and revealed the feasibility as a targeted optimal imaging probe for in vivo cases. On the basis of this imaging data, our glycol chitosan nanoparticles showed higher tumor homing ability in tumor-bearing mice. Until the exact mechanism of the higher tumor homing ability is completely evaluated, the unique characteristics of the glycol chitosan nanoparticles that we observed in vitro (i.e., stability in blood, deformability, and rapid cellular uptake) may have contributed significantly to their tumor targeting by the EPR effect in vivo (*19, 24*−*26*). Furthermore, when the Cy5.5-CNP-Gd(III) was injected into the tumor-bearing mice, it presented a prolonged blood lifetime, in which 50% glycol chitosan nanoparticles could circulate for 23 h, compared to free Cy5.5 (Supporting Information Figure SI1).

Next, we investigated whether optical/MR dual imaging could be used to detect tumor tissues in live animals. In SCC7 tumor-bearing mice (8−10 mm in diameter), both NIRF optical and MR imaging readily detected the inoculated tumor tissues after 1 day postinjection of Cy5.5-CNP-Gd(III) (5 mg/kg). First of all, MR imaging showed tumor tissues. In particular, coronal T1-weight MR images showed a high spatial resolution of tumor tissues after 1 day postinjection (Figure 4a). The clear margin of tumor tissue in soft tissue could be completely delineated by the bright T1-weight MR image, indicating the excellent nanoparticle accumulation at the tumor site. The relative signal enhancement (RSE, %) was calculated in the region of interests (ROIs) of the T1-weighted images. After 1 day postinjection of Cy5.5-CNP-Gd(III), the ROI value at tumor strongly increased from 70 to 162, compared to that of muscle (65 to 95). Noticeable brightening appeared at tumor with the RSE value of 231%, indicating the higher tumor targeting ability of glycol chitosan nanoparticles. However, the sensitivity was not higher compared to that of optical imaging. As we expected, NIRF imaging showed a strong and sensitive fluorescence image under explore Optix system, indicating high sensitivity of NIRF imaging, but the high-resolution histological and spatial image was not enough to clearly delineate the exact tumor site (Figure 4b). As NIRF optical imaging offers high sensitivity and the prospect of real-time intraoperative monitoring of tumor biopsy, on the other hand, MR imaging offers excellent spatial resolution and intrinsic soft-tissue contract. Thus, the combination of NIRF optical imaging and MR imaging for cancer imaging may overcome the limitations of either imaging method when used alone.

In conclusion, we prepared tumor targeting nanoparticles for optical/MR dual imaging that was based on self-assembled glycol chitosan nanoparticles. For the optical/MR dual imaging, Cy5.5 as NIRF and DOTA to chelate Gd(III) were directly conjugated in the chitosan conjugates. In tumor-bearing mice, Cy5.5-labeled and Gd(III) ion-chelated chitosan nanoparticles showed long and stable blood circulation characteristics, and they demonstrated excellent tumor targeting ability based on the EPR effects. More importantly, the combination of NIRF optical imaging and MR imaging for cancer imaging not only offered high sensitivity, but also presented excellent spatial resolution of target tumor tissue. Therefore, Cy5.5-CNP-Gd(III) has the potential to be used as optical/MR dual imaging agents for cancer imaging.

ACKNOWLEDGMENT

This work was financially supported by the Real-Time Molecular Imaging Project, 2009K 001594, Seoul R&BD Program (10524), Pioneer Research Program (2009-0081523), and Global Research Laboratory Project of MEST and by a grant from the Intramural Research Program of the KIST, and by a grant (A062254) from the Korea Health 21 R&D Project.

Supporting Information Available: Experimental procedures. This material is available free of charge via the Internet at http://pubs.acs.org.

LITERATURE CITED

(1) Kircher, M. F., Mahmood, U., King, R. S., Weissleder, R., and Josephson, L. (2003) A multimodal nanoparticle for preoperative magnetic resonance imaging and intraoperative optical brain tumor delineation. *Cancer Res. 63*, 8122–5.

(2) Banerjee, S. S., and Chen, D. H. (2009) A multifunctional magnetic nanocarrier bearing fluorescent dye for targeted drug delivery by enhanced two-photon triggered release. *Nanotechnology 20*, 185103.

(3) Torchilin, V. P. (2006) Multifunctional nanocarriers. *Adv. Drug Delivery Rev. 58*, 1532–55.

(4) Bagalkot, V., Zhang, L., Levy-Nissenbaum, E., Jon, S., Kantoff, P. W., Langer, R., and Farokhzad, O. C. (2007) Quantum dot-aptamer conjugates for synchronous cancer imaging, therapy, and sensing of drug delivery based on bi-fluorescence resonance energy transfer. *Nano Lett. 7*, 3065–70.

(5) Lim, Y. T., Cho, M. Y., Choi, B. S., Lee, J. M., and Chung, B. H. (2008) Paramagnetic gold nanostructures for dual modal bioimaging and phototherapy of cancer cells. *Chem. Commun. (Camb.)* 4930–2.

(6) Josephson, L., Kircher, M. F., Mahmood, U., Tang, Y., and Weissleder, R. (2002) Near-infrared fluorescent nanoparticles as combined MR/optical imaging probes. *Bioconjugate Chem. 13*, 554–60.

(7) Kim, S., Lim, Y. T., Soltesz, E. G., De Grand, A. M., Lee, J., Nakayama, A., Parker, J. A., Mihaljevic, T., Laurence, R. G., Dor, D. M., Cohn, L. H., Bawendi, M. G., and Frangioni, J. V. (2004) Near-infrared fluorescent type II quantum dots for sentinel lymph node mapping. *Nat. Biotechnol. 22*, 93–7.

(8) Lisy, M. R., Hartung, A., Lang, C., Schuler, D., Richter, W., Reichenbach, J. R., Kaiser, W. A., and Hilger, I. (2007) Fluorescent bacterial magnetic nanoparticles as bimodal contrast agents. *Invest. Radiol. 42*, 235–41.

(9) Persigehl, T., Heindel, W., and Bremer, C. (2005) MR and optical approaches to molecular imaging. *Abdom. Imaging 30*, 342–54.

(10) Santra, S., Kaittanis, C., Grimm, J., Perez, J. M. (2009) Drug/dye-loaded, multifunctional iron oxide nanoparticles for combined targeted cancer therapy and dual optical/magnetic resonance imaging. *Small*.

(11) Yang, J., Lim, E. K., Lee, H. J., Park, J., Lee, S. C., Lee, K., Yoon, H. G., Suh, J. S., Huh, Y. M., and Haam, S. (2008) Fluorescent magnetic nanohybrids as multimodal imaging agents for human epithelial cancer detection. *Biomaterials 29*, 2548–55.

(12) Zhang, Y., Wang, S. N., Ma, S., Guan, J. J., Li, D., Zhang, X. D., and Zhang, Z. D. (2008) Self-assembly multifunctional nanocomposites with Fe3O4 magnetic core and CdSe/ZnS quantum dots shell. *J. Biomed. Mater. Res. A 85*, 840–6.

(13) Jin, T., Yoshioka, Y., Fujii, F., Komai, Y., Seki, J., and Seiyama, A. (2008) Gd(3+)-functionalized near-infrared quantum dots for in vivo dual modal (fluorescence/magnetic resonance) imaging. *Chem. Commun. (Camb.)* 5764–6.

(14) Veiseh, O., Sun, C., Gunn, J., Kohler, N., Gabikian, P., Lee, D., Bhattarai, N., Ellenbogen, R., Sze, R., Hallahan, A., Olson, J., and Zhang, M. (2005) Optical and MRI multifunctional nanoprobe for targeting gliomas. *Nano Lett. 5*, 1003–8.

(15) Xu, H. N., Zhou, R., Nioka, S., Chance, B., Glickson, J. D., and Li, L. Z. (2009) Histological basis of MR/optical imaging of human melanoma mouse xenografts spanning a range of metastatic potentials. *Adv. Exp. Med. Biol. 645*, 247–53.

(16) Reddy, L. H. (2005) Drug delivery to tumours: recent strategies. *J. Pharm. Pharmacol. 57*, 1231–42.

(17) Doiron, A. L., Homan, K. A., Emelianov, S., and Brannon-Peppas, L. (2009) Poly(lactic-co-glycolic) acid as a carrier for imaging contrast agents. *Pharm. Res. 26*, 674–82.

(18) Yu, M. K., Jeong, Y. Y., Park, J., Park, S., Kim, J. W., Min, J. J., Kim, K., and Jon, S. (2008) Drug-loaded superparamagnetic iron oxide nanoparticles for combined cancer imaging and therapy in vivo. *Angew. Chem., Int. Ed. Engl. 47*, 5362–5.

(19) Hwang, H. Y., Kim, I. S., Kwon, I. C., and Kim, Y. H. (2008) Tumor targetability and antitumor effect of docetaxel-loaded hydrophobically modified glycol chitosan nanoparticles. *J. Controlled Release 128*, 23–31.

(20) Hyung Park, J., Kwon, S., Lee, M., Chung, H., Kim, J. H., Kim, Y. S., Park, R. W., Kim, I. S., Bong Seo, S., Kwon, I. C., and Young Jeong, S. (2006) Self-assembled nanoparticles based on glycol chitosan bearing hydrophobic moieties as carriers for doxorubicin: in vivo biodistribution and anti-tumor activity. *Biomaterials 27*, 119–26.

(21) Kim, J. H., Kim, Y. S., Kim, S., Park, J. H., Kim, K., Choi, K., Chung, H., Jeong, S. Y., Park, R. W., Kim, I. S., and Kwon, I. C. (2006) Hydrophobically modified glycol chitosan nanoparticles as carriers for paclitaxel. *J. Controlled Release 111*, 228–34.

(22) Mishra, A., Pfeuffer, J., Mishra, R., Engelmann, J., Mishra, A. K., Ugurbil, K., and Logothetis, N. K. (2006) A new class of Gd-based DO3A-ethylamine-derived targeted contrast agents for MR and optical imaging. *Bioconjugate Chem. 17*, 773–80.

(23) Oudkerk, M., Sijens, P. E., Van Beek, E. J., and Kuijpers, T. J. (1995) Safety and efficacy of Dotarem (Gd-DOTA) versus magnevist (Gd-DTPA) in magnetic resonance imaging of the central nervous system. *Invest. Radiol. 30*, 75–8.

(24) Nam, H. Y., Kwon, S. M., Chung, H., Lee, S. Y., Kwon, S. H., Jeon, H., Kim, Y., Park, J. H., Kim, J., Her, S., Oh, Y. K., Kwon, I. C., Kim, K., and Jeong, S. Y. (2009) Cellular uptake mechanism and intracellular fate of hydrophobically modified glycol chitosan nanoparticles. *J. Controlled Release 135*, 259–67.

(25) Park, K., Hong, H. Y., Moon, H. J., Lee, B. H., Kim, I. S., Kwon, I. C., and Rhee, K. (2008) A new atherosclerotic lesion probe based on hydrophobically modified chitosan nanoparticles functionalized by the atherosclerotic plaque targeted peptides. *J. Controlled Release 128*, 217–23.

(26) Min, K. H., Park, K., Kim, Y. S., Bae, S. M., Lee, S., Jo, H. G., Park, R. W., Kim, I. S., Jeong, S. Y., Kim, K., and Kwon, I. C. (2008) Hydrophobically modified glycol chitosan nanoparticles-encapsulated camptothecin enhance the drug stability and tumor targeting in cancer therapy. *J. Controlled Release 127*, 208–18.

BC900408Z

Copper-Free Click Chemistry for Highly Luminescent Quantum Dot Conjugates: Application to *in Vivo* Metabolic Imaging

Aude Bernardin,[†] Aurélie Cazet,[‡] Laurent Guyon,[†] Philippe Delannoy,[‡] Françoise Vinet,[†] David Bonnaffé,[§] and Isabelle Texier*[,†]

CEA, LETI-MINATEC, Département des Technologies pour la Biologie et la Santé, 17 rue des Martyrs, F-38054 Grenoble, France, Université des Sciences et Technologies de Lille, UMR 8576, Unité de Glycobiologie Structurale et Fonctionnelle, 59655 Villeneuve d'Ascq, France, and Université Paris-Sud 11, ICMMO UMR 8182, Laboratoire de Chimie Organique Multifonctionnelle, 91405 Orsay, France. Received December 18, 2009; Revised Manuscript Received February 9, 2010

Quantum dots (QD) are inorganic nanocrystals with outstanding optical properties, specially suited for biological imaging applications. Their attachment to biomolecules in mild aqueous conditions for the design of bioconjugates is therefore highly desirable. 1,3-dipolar [3 + 2] cycloaddition between azides and terminal alkynes ("click chemistry") could represent an attractive QD functionalization method. Unfortunately, the use of the popular Cu(I)-catalyzed version of this reaction is not applicable for achieving this goal, since the presence of copper dramatically alters the luminescence properties of QD dispersions. We demonstrate here that copper-free click chemistry, between strained cyclooctyne functionalized QD and azido-biomolecules, leads to highly luminescent conjugates. In addition, we show that QD-cyclooctyne can be used at previously unreported low concentration (250 nM) for imaging the incorporation of azido-modified sialic acid in cell membrane glycoproteins.

Fluorescence imaging, from the cellular to the macroscopic range, is an invaluable tool to improve our knowledge of complex biological pathways, in particular, those not ruled by genomics, such as post-transcriptional modifications (e.g., phosphorylation, glycosylation). In the last ten years, inorganic semiconductor nanocrystals known as quantum dots (QD) have drawn attention as a potential alternative to classical organic fluorophores for imaging purposes (*1*−*3*). Their tunable, narrow, and symmetric emission band, long luminescence lifetime, and good photostability make them attractive objects for fluorescence in vitro diagnostics and in vivo imaging (*4*−*9*). Conjugation of QD with biomolecules such as antibodies, proteins, enzymes, DNA, and oligosaccharides is a prerequisite to their use as biological probes for fluorescence imaging. Therefore, the presence on QD surfaces of reactive moieties allowing further mild, selective, bioorthogonal, and water-compatible ligation with biomolecules, while keeping the outstanding optical properties of the nanoparticle, is of crucial importance. In this regard, Cu(I)-catalyzed 1,3-dipolar [3 + 2] cycloadditions between azides and terminal alkynes, considered by Sharpless "the cream of the crop" among "click" reactions that can be carried out in water (*10*−*13*), seems to be an attractive method for QD bioderivatization. Indeed, Cu(I) promoted click chemistry has been extensively used for the modification of numerous bio- or synthetic polymers (*14*−*18*) and capsules (*18*−*20*), as well as the functionalization of gold (*21*−*23*), silica (*24*), and iron oxide (*18, 25*−*27*) nanoparticles, as well as carbon nanotubes (*18, 24*). The selective and orthogonal reactivity of the azido and terminal alkyne groups has been used for the conjugation of a number of these materials with a wide range of synthetic molecules and biomolecules (peptides, proteins, enzymes, drugs, saccharides, dyes, organometallic compounds, and so forth) while keeping their functionalities (*22, 23, 25, 27, 28*). Moreover, the reaction leads to the formation of a very stable triazole linker, quantitatively, with a limited number of byproduct, and in mild conditions.

Quite surprisingly, however, the use of Cu(I) promoted click chemistry for QD functionalization has only been sparingly reported (*29*). This may be accounted for by the fact that a strong inhibition of the QD luminescence has been observed for bare CdS nanocrystals in the presence of copper ions (*29*−*31*). It has been proposed that isolated Cu^+ or ultrasmall Cu_xS (x = 1−2) aggregates form on the QD surface, inhibiting their emission properties (*30, 31*). Despite their poly(ethylene glycol) (PEG) organic coating and their protective inorganic ZnS shell, commercial CdSe/ZnS/PEG_{2000}-NH_2 QD (Invitrogen ITK 545 aminoPEG, noted as QD-amine **1**) used in this study also suffer a dramatic irreversible luminescence inhibition whenever incubated in the presence of $CuSO_4$/sodium ascorbate (NaAsc), the Cu(I) catalyst classically described for Huisgen cycloadditions in water (Figure 1). Two main mechanisms can account for the QD luminescence inhibition in the presence of copper, either (i) luminescence quenching due to nondestructive energy transfer or photoinduced electron transfer between the semiconductor nanomaterial and the Cu cations, which could actually be chelated by the PEG chains coating the nanoparticles; or (ii) chemical reaction between copper and the CdSe/ZnS particles themselves, leading to a partial or complete destruction of the core−shell structure responsible for the luminescence properties (reduction of the number of luminescent dots and/or their intrinsic luminescence intensity). In addition to the formation of Cu_xS aggregates on the surface of CdS nanocrystals (*30, 31*), rapidly occurring cation exchange altering the inner core structure of CdS and CdSe quantum dots has been reported (*32, 33*). In this latter case, the modification of the crystalline structure and shape of the small particles, accompanied by the modification of their optical properties, has been observed (*32, 33*). More thorough studies on the copper-induced luminescence inhibition mechanism of QD-amine **1** are in progress and will be detailed elsewhere. However, evidence supporting hypothesis (ii) has already appeared: (1) Energy and

* E-mail: isabelle.texier-nogues@cea.fr. Tel: +33 438 784 670, fax: +33 438 785 787.

[†] CEA, LETI-MINATEC, DTBS.

[‡] USTL, UMR 8576, UGSF.

[§] UPS-11, UMR 8182, LCOM.

10.1021/bc900564w © 2010 American Chemical Society
Published on Web 03/11/2010

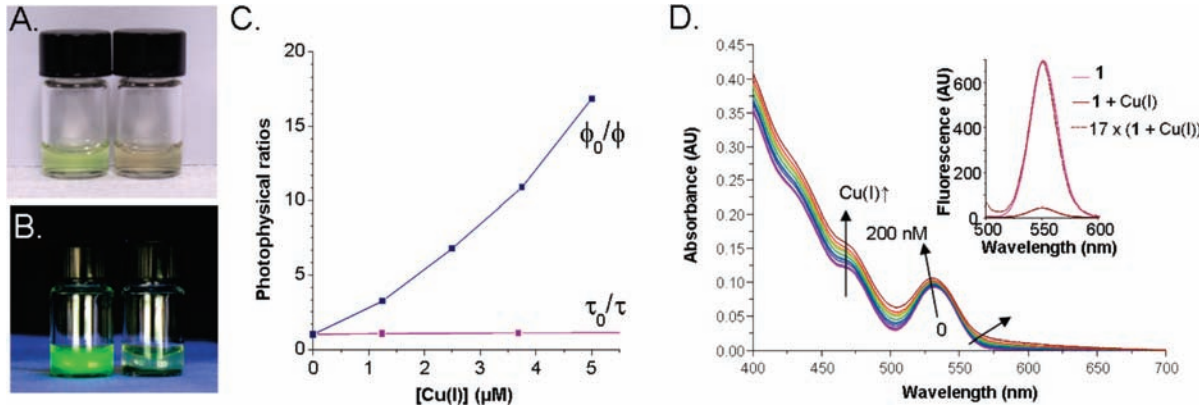
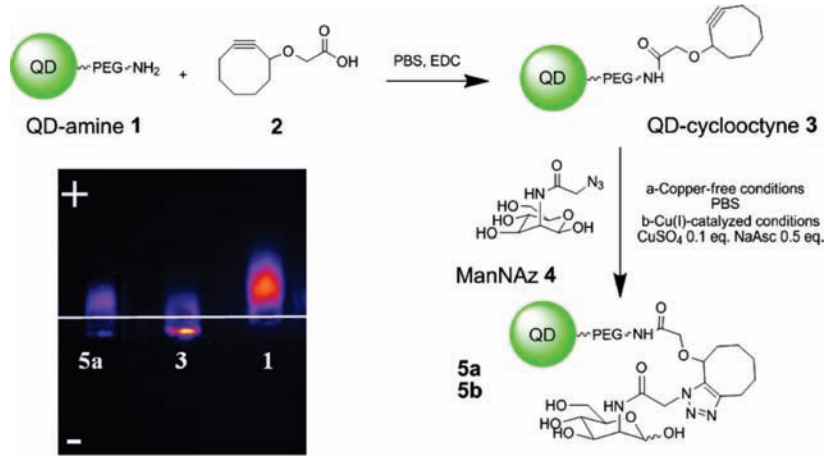


Figure 1. Cu-induced luminescence inhibition of QD-amine **1** (17 nM) in 1× PBS. (A,B) Photographs of the suspensions under white (A) and UV (B) light before (left) and after (right) NaAsc/$CuSO_4$ addition (25 μM). (C) Stern−Volmer plots depicting the luminescence inhibition of QD-amine **1**. Φ (respectively τ) is QD luminescence quantum yield (respectively luminescence lifetime). 0-subscript stands for values in the absence of Cu (I). (D) Absorption spectra of QD-amine **1** (17 nM) in the presence of increasing concentrations of Cu(I). Inset: luminescence spectra of QD-amine **1** (17 nM) in the absence and in the presence of 5 μM Cu(I).

electron transfer has always been reported to affect both nanoparticle luminescence quantum yield (Φ) and lifetime (τ) (*34*−*36*). The Stern−Volmer plot Φ_0/Φ depicting the ratio of the luminescence quantum yield of QD-amine **1** before (Φ_0) and after (Φ) addition of Cu(I) solution (Figure 1) evidence strong luminescence inhibition (decrease by 50% for usual click conditions: 0.1 equiv Cu(I) per functional group). Moreover, even after five washes with PBS, which should have eliminated residual copper in solution or copper tied by weak interaction to the QD surface, Φ is not restored. The nature of the copper-related QD luminescence inhibition is further investigated by performing luminescence lifetime measurement. As already accounted for in the literature, CdSe dispersions observed as a macroscopic sample display multiexponential luminescence decays (*37, 38*). However, biexponential fit of the data most often provides a satisfactory description in order to account for QD luminescence quenching by electron or energy transfer (*34*−*36*). The luminescence decays in 1× PBS buffer of the core−shell CdSe/ZnS QD-amine **1** used in this study can indeed be satisfactorily fitted by biexponential decays, with a major "long" component $\tau \approx 20$ ns and a minor short-lived component (2.7 ns), both insensitive to copper concentration (see details in Supporting Information). Since only modifications of Φ and not τ are observed, it suggests that it is the number of emitting nanocrystals that is affected by copper addition, rather than the involvement of QD exciton interactions. (2) Cu(I) or Cu(II) solutions do not display absorption bands in the 500−600 nm range that would overlap with the absorption and emission spectra of the particles and induce energy transfer, and the redox potentials of the species involved should not lead to electron transfer according to the study reported by Mattoussi et al. (*36*). (3) Only slight spectral modifications are observed upon copper addition in quantum dot dispersion: 2 nm blue shift for the plasmon absorption band, in addition to a global increase of the solution absorbance (Figure 1). These spectral modifications are similar to those observed by Isarov et al. (*31*), who accounted them for by the formation of small Cu_xS aggregates on the nanocrystal surface. (4) The possible exchange of shell Zn^{2+} by Cu^{2+} cations is highly thermodynamically favorable due to the lower solubility of CuS ($K_s = 8 \times 10^{-37}$) in comparison to ZnS ($K_s = 2 \times 10^{-25}$ (wurtzite) to 3×10^{-23} (zinc blende)) (*39*), whereas the number of copper ions added in the solution is in the same range as those of zinc cations constituting the QD shell (calculated using 4 nm as the CdSe/ZnS diameter according to the supplier, and 2.7 nm diameter CdSe core according to the emission wavelength (*40*)). Moreover, the ionic diameter of Cu^{2+} (0.72 Å) is identical to that of Zn^{2+} (0.72 Å), and both ZnS and CuS can crystallize with a hexagonal structure, which should facilitate the exchange in the QD shell (*33, 39, 41*). The small size of the nanocrystals (4 nm total diameter, 2.7 nm core) means that only 5 to 6 atomic layers constitute the core−shell QD, which moreover display a high surface to volume ratio, which could account for an important solid reactivity (*33*).

If the presence of copper induces the irreversible formation of nonemissive nanocrystals with a different composition and structure than the starting QD particles, Cu(I) click chemistry cannot be used for the functionalization of these objects while preserving their inner structure integrity. Copper-free click reactions are therefore highly desirable for QD derivatization in biological media. The possibility to use the Bertozzi's modification of the 1,3-dipolar [3 + 2] cycloaddition between azides and alkynes, known as "copper-free click chemistry", has been investigated to achieve this goal (*42*−*47*). The principle of copper-free click chemistry relies on the use of cycle's strain, such as in the cyclooctyne moiety present in compounds **2** and **3** (Scheme 1), to replace the Cu(I) catalysis as the reaction's driving force. Moreover, copper-free click chemistry avoids the presence of the metallic cation, potentially toxic for living cells, the presence of which can therefore be restrictive for in vivo reactions (*43*). In order to investigate the impact of the functionalizing conditions (classical and copper-free click chemistry) on QD luminescence, QD-amine **1** are derivatized with cycloot-1-yn-3-glycolic acid **2** by EDC coupling to afford QD-cyclooctyne **3** after size exclusion chromatography (Scheme 1). QD-cyclooctyne **3** are then reacted with a DMSO solution of azido-tagged mannosamine (ManNAz **4**), a good model for further in vivo imaging studies, in the absence (leading to **5a**) or in the presence (leading to **5b**) of a "Cu-click buffer". After purification by size-exclusion chromatography, the success of the coupling reactions is qualitatively assessed by agarose gel electrophoresis (Scheme 1), since the migration pattern of the nanoparticles are dependent on the QD size, charge, and coating (*48*). QD functionalization is further evidenced by modification of the particle hydrodynamic diameter and zeta potential measured using dynamic light scattering in PBS buffer (Table 1). QD-amine **1** has an inner negative polymer coating, which is partly counterbalanced by the terminal protonated amino groups at the end of the PEG chains. Overall, the zeta potential of QD-amine **1** is slightly negative (−3.5 ± 5.6 mV), and particles migrate toward the positive pole in the gel (Scheme 1). Alkyne derivatization induces a negative shift of the zeta potential of QD-cyclooctyne **3** (−25.6 ± 7.6 mV), as surface positive ammonium groups of QD-amine **1** are replaced by

Scheme 1. Functionalization of QD Surface by Copper-Free (a) and Cu(I)-Catalyzed (b) Click Chemistries[a]



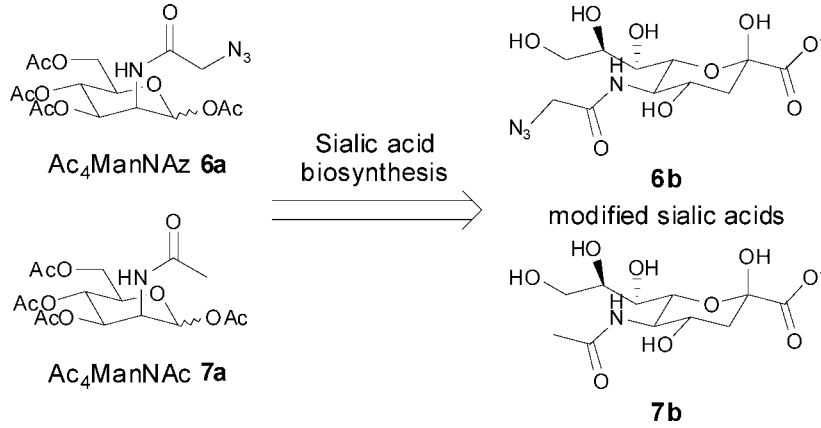
[a] Modifications of the QD surface are qualitatively assessed by electrophoretic migration of the particles on agarose gel.

Table 1. Physical and Optical Properties of QD in Phosphate Buffer

nanoparticles	hydrodynamic diameter (nm)[a,b]	zeta potential (mV)[a,c]	absorption maximum (nm)[b]	emission maximum (nm)[b,d]	luminescence quantum yield[a,b,d]
QD-amine **1**	14.7 ± 0.4	−3.5 ± 5.6	530	552	100
QD-cyclooctyne **3**	9.6 ± 0.7	−25.6 ± 7.6	531	552	137 ± 14
5a	16.3 ± 2.0	−41.4 ± 2.1	530	551	127 ± 13
5b	16.9 ± 1.2	−39.5 ± 3.7	530	550	47 ± 5

[a] Standard deviation for three different measures. [b] Measures are performed in 1× PBS buffer (10 mM phosphate, 137 mM NaCl, pH 7.3). [c] Measures are carried out in 0.1× PBS buffer (1 mM phosphate, 13.7 mM NaCl, pH 7.3) in order to limit the buffer conductivity. Several peaks are observed in zeta potential analysis, even with commercial QD-amine **1**. The values indicated refer to the main peak (>65%). [d] Excitation at 488 nm.

Scheme 2. Cell Machinery Modification of Mannosamines Ac_4ManNAz 6a and Ac_4ManNAc 7a to Biosynthesize Sialic Acids 6b and 7b, Respectively



neutral alkyne groups. Interestingly, the hydrodynamic diameter of particles **3** (9.6 ± 0.7 nm) is reduced in comparison to that of QD-amine **1** (14.7 ± 0.4 nm), probably because the rather hydrophobic ending groups prefer to retract in the PEG chains of the QD-coating polymer than remain in aqueous solution. Moreover, QD-cyclooctyne **3** migrate in the agarose gel toward the negative pole. Such a migration pattern has already been reported for gold (*49*) and CdSeTe/ZnS (*50*) nanoparticles coated by poly(ethylene glycol) chains. It has been accounted for by the association of positively charged cations, such as sodium and potassium cations present in PBS or TBE buffer, with the ethyleneoxide motif (*51*). Therefore, PEG chains associated with positive charges would be the entities that appear on the particle surface for QD-cyclooctyne **3**, accounting for their electrophoretic migration toward the negative pole. As previously suggested for other quantum dot conjugates, gel migration orientation would be mainly governed by the charges on the external surface of the particles, whereas zeta potential might rather reflect the overall charges of the QDs (taking into account their inner negative charges) (*50*). ManNAz **4** grafting onto the QD **5a** and **5b** is evidenced by an important increase of the particle hydrodynamic diameter (∼16−17 nm) and a shift of the zeta potential (∼ −40 mV) (Table 1), along with an electrophoretic migration toward the positive pole. The presence of negative charges on the QD-ManNAz particles **5a** and **5b** might be due to the long-known reaction between carbohydrate diols and the borate ions of the electrophoresis buffer. Indeed, neutral carbohydrates are known to migrate toward the positive pole in such electrophoretic conditions (*52*). The two QD-ManNAz conjugates **5a** and **5b** display similar structural properties (size and zeta potential), regardless of the functionalization method used. In particular, the increase of the hydrodynamic diameter of the particles can certainly be attributed to the stretching of the highly hydrophilic PEG-saccharide chains in the aqueous phase. However, if alkyne derivatization does not alter the QD luminescence and integrity

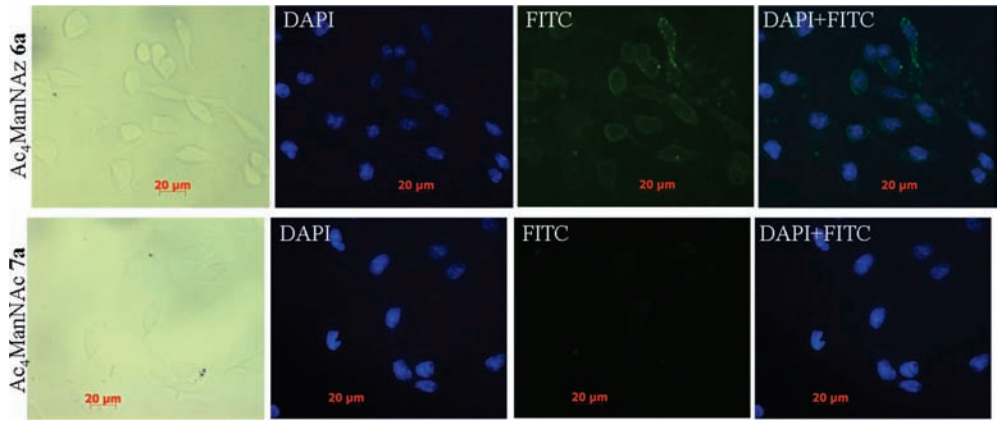


Figure 2. Fluorescence microscopy images of CHO cells treated with Ac_4ManNAz **6a** or Ac_4ManNAc **7a** (negative control) at 200 μM for 3 days, incubated with QD-cyclooctyne **3** (green) at 250 nM for 4 h at 4 °C, and fixed with paraformaldehyde 4%. Nuclei have been stained with DAPI (blue).

(QD-cyclooctyne **3** display even ~30% improved Φ in comparison to QD-amine **1**), the presence of copper for QD modified by classical click chemistry (conditions **b**) induces a loss of about half of the luminescence for the QD suspension (Table 1). Interestingly, copper-free click chemistry (conditions **a**) allows the modification of the QD surface with a high remaining luminescent quantum yield (Table 1). Strain-promoted Huisgens cycloaddition thus appears as a method of choice for the functionalization of QD using such a bioorthogonal and biocompatible "click" reaction.

To outline the interest of QD modified by cyclooctynes for biological applications, the possibility to use QD-cyclooctyne **3** for the in vivo imaging of the metabolic incorporation of sialic acids on cell membrane glycoconjugates is investigated. The development of new fluorescent tools for the in vivo imaging of the biosynthesis of glycoconjugates is of tremendous interest. The modification of cell surface glycosylation is a common phenotypic change that occurs in a number of pathologies, including carcinogenesis (*53*−*55*). It mainly affects the outer part of the carbohydrate moiety of glycoproteins and glycolipids, leading to the expression of tumor associated carbohydrate antigens (TACA). Most of TACA are sialylated and the expression of TACA such as sialyl-Lewis^x or sialyl-Tn is usually linked to tumor aggressiveness (*56, 57*). Acetylated azidomannosamine Ac_4ManNAz **6a** (or peracetylated mannosamine Ac_4ManNAc **7a** used as a negative control) is incubated with CHO (Chinese Hamster Ovary) cells for incorporation in membrane glycoconjugates via a metabolic savage pathway (*58*). Acetylated Ac_4ManNAz **6a** is used instead of ManNAz **4**, since acetylation allows for a better cellular internalization and incorporation in glycoconjugates (*59*). Briefly, cells treated with Ac_4ManNAz **6a** (200 μM) or with Ac_4ManNAc **7a** (200 μM) for 3 days metabolize the mannosamine moiety into sialic acids **6b** and **7b**, which can subsequently be used by the cell machinery and be incorporated in the newly synthesized glycoproteins exposed on the cell membrane (Scheme 2) (*60*). The incorporation of the azido-modified metabolite **6b** transferred to the cell's membrane epitope is revealed using copper-free click chemistry with QD-cyclooctyne **3** as labeling agent (incubation at 250 nM for 4 h at 4 °C, to avoid particle endocytosis). Epi-fluorescence microscopy images are recorded and are displayed in Figure 2. Cell membranes are clearly labeled by the QD conjugate **3** when CHO cells have been incubated with Ac_4ManNAz **6a**, contrary to the negative control Ac_4ManNAc **7a** for which no background signal is detected, indicating the absence of QD agglomeration or precipitation at the cell surface. The low photobleaching rate of QD under microscopic illumination, as well as the multimeric presentation of cyclooctyne moieties on their surface, could account for the improved detection sensitivity (250 nM of QD-cyclooctyne **3**) in comparison to other organic dye based probes, used at >50 μM concentrations (*43*). The copper-free click reaction is therefore successfully performed in biological media and allows labeling with QD at submicromolar concentrations with a good signal/noise ratio.

We have demonstrated that copper-free click chemistry offers a great opportunity for QD facile bioorthogonal derivatization, while bypassing the luminescence inhibition of the particles observed in the presence of Cu(I), the catalyst classically used for alcyne-azide conjugation. Because of their excellent optical properties in general, and their reduced photobleaching rate during microscopic observations in particular, QD modified by cyclooctyne groups prove to be an interesting alternative to organic fluorescent probes usually used for in vivo metabolic imaging (*43*). Numerous other applications, especially in the field of biology, can be envisioned using this new functionalization process of QD, taking benefit of both the outstanding optical properties of the nanocrystals as labeling agents and the versatile chemistry of copper-free azido/constraint alkyne cycloaddition that circumvent the impossibility of using the popular Cu(I)-catalyzed version of this reaction.

ACKNOWLEDGMENT

We acknowledge Peter Reiss (CEA, INAC) for fruitful discussion of the results. This work is supported by the Commissariat à l'Energie Atomique, France, through the "Technologies pour la santé'" program (TIMOMA2).

Supporting Information Available: Experimental procedures, QD absorption and emission spectra, luminescence lifetime measurement details, hydrodynamic diameter measurements. This material is available free of charge via the Internet at http://pubs.acs.org.

LITERATURE CITED

(1) Medintz, I. L., Uyeda, H. T., Goldman, E. R., and Mattoussi, H. (2005) Quantum dot bioconjugates for imaging, labelling and sensing. *Nat. Mater. 4*, 435–446.
(2) Michalet, X., Pinaud, F. F., Bentolila, L. A., Tsay, J. M., Doose, S., Li, J. J., Sundaresan, G., Wu, A. M., Gambhir, S. S., and Weiss, S. (2005) Quantum dots for live cells, in vivo imaging, and diagnostics. *Science 307*, 538–544.
(3) Smith, A. M., Gao, X., and Nie, S. (2004) Quantum dot nanocrystals for in vivo molecular and cellular imaging. *Photochem. Photobiol. 80*, 377–385.

(4) Azzazy, H. M. E., Mansour, M. M. H., and Kazmierczak, S. C. (2007) From diagnostics to therapy: propects of quantum dots. *Clin. Biochem. 40*, 917–927.

(5) Medintz, I. L., Mattoussi, H., and Clapp, A. R. (2008) Potential clinical applications of quantum dots. *Int. J. Nanomed. 3*, 151–167.

(6) Smith, A. M., Duan, H., Mohs, A. M., and Nie, S. (2008) Bioconjugated quantum dots for in vivo molecular and cellular imaging. *Adv. Drug Delivery Rev. 60*, 1226–1240.

(7) Xing, Y., and Rao, J. (2008) Quantum dot bioconjugates for *in vitro* diagnostics & *in vivo* imaging. *Cancer Biomarkers 4*, 307–319.

(8) Alivisatos, A. P., Gu, W., and Larabell, C. (2005) Quantum dots as cellular probes. *Annu. Rev. Biomed. Eng. 7*, 55–76.

(9) Pinaud, F., Michalet, X., Bentolila, L. A., Tsay, J. M., Doose, S., Li, J. J., Iyer, G., and Weiss, S. (2006) Advances in fluorescence imaging with quantum dot bio-probes. *Biomaterials 27*, 1679–1687.

(10) Kolb, H. C., Finn, M. G., and Sharpless, K. B. (2001) Click chemistry: diverse chemical function from a few good reactions. *Angew. Chem., Int. Ed. 40*, 2004–2021.

(11) Kolb, H. C., and Sharpless, K. B. (2003) The growing impact of click chemistry on drug discovery. *Drug Discovery Today 8*, 1128–1137.

(12) Moses, J. E., and Moorhouse, A. D. (2007) The growing applications of click chemistry. *Chem. Soc. Rev. 36*, 1249–1262.

(13) Meldal, M., and Tornoe, C. W. (2008) Cu-catalyzed azide-alkyne cycloaddition. *Chem. Rev. 108*, 2952–3015.

(14) Dedola, S., Nepogodiev, S. A., and Field, R. A. (2007) Recent applications of the CuI-catalysed Huisgen azide-alkyne 1,3 dipolar cycloaddition reaction in carbohydrate chemistry. *Org. Biomol. Chem. 5*, 1006–1017.

(15) Pieters, R. J., Rijkers, T. S., and Liskamp, R. M. J. (2007) Application of the 1,3-dipolar cycloaddition reaction in chemical biology: approaches toward multivalent carbohydrates and peptides and peptide-based polymers. *QSAR Comb. Sci. 26*, 1181–1190.

(16) Iha, R. K., Wooley, K. L., Nyström, A. M., Burke, D. J., Kade, M. J., and Hawker, C. J. (2009) Applications of orthogonal "click" chemistries in the synthesis of functional soft materials. *Chem. Rev. 109*, 5620–5686.

(17) van Dijk, M., Rijkers, D. T. S., Liskamp, R. M. J., van Nostrum, C. F., and Hennink, W. E. (2009) Synthesis and applications of biomedical and pharmaceutical polymers via click chemistry methodologies. *Bioconjugate Chem. 20*, 2001–2016.

(18) Binder, W. H., and Sachsenhofer, R. (2008) 'Click' chemistry in polymer and material science: an update. *Macromol. Rapid Commun. 29*, 952–981.

(19) Ochs, C. J., Such, G. K., Städler, B., and Caruso, F. (2008) Low-fouling, biofunctionalize, and biodegradable click capsules. *Biomacromolecules 9*, 3389–3396.

(20) Wang, Q., Chan, T. R., Hilgraf, R., Fokin, V. V., Sharpless, K. B., and Finn, M. G. (2003) Bioconjugation by copper(I)-catalyzed azide-alkyne [3 + 2] cycloaddition. *J. Am. Chem. Soc. 125*, 3192–3193.

(21) Boisselier, E., Salmon, L., Ruiz, J., and Astruc, D. (2008) How to very efficiently functionalize gold nanoparticles by "click" chemistry. *Chem. Commun.* 5788–5790.

(22) Brennan, J. L., Hatzakis, N. S., Tshikhudo, T. R., Dirvianskyte, N., Razumas, V., Patkar, S., Vind, J., Svendsen, A., Nolte, R. J. M., Rowan, A. E., and Brust, M. (2006) Bionanoconjugation via click chemistry: the creation of functional hybrids of lipases and gold nanoparticles. *Bioconjugate Chem. 17*, 1373–1375.

(23) Fleming, D. A., Thode, C. J., and Williams, M. E. (2006) Triazole cycloaddition as a general route for functionalization of Au nanoparticles. *Chem. Mater. 18*, 2327–2334.

(24) Nebhani, L., and Barner-Kowollik, C. (2009) Orthogonal transformations on solid substrates: efficient avenues to surface modification. *Adv. Mater. 21*, 3442–3468.

(25) Polito, L., Monti, D., Caneva, E., Delnevo, E., Russo, G., and Prosperi, D. (2008) One-step bioengineering of magnetic nanoparticles via a surface diazo transfer/azide-alkyne click reaction sequence. *Chem. Commun.* 621–623.

(26) von Maltzahn, G., Ren, Y., Park, J.-H., Min, D.-H., Kotamraju, V. R., Jayakumar, J., Fogal, V., Sailor, M. J., Ruoslahti, E., and Bhatia, S. N. (2008) In vivo tumor cell targeting with "click" nanoparticles. *Bioconjugate Chem. 19*, 1570–1578.

(27) Sun, E. Y., Josephson, L., and Weissleder, R. (2006) Clickable" nanoparticles for targeted imaging. *Mol. Imaging 5*, 122–128.

(28) O'Reilly, R. K., Joralemon, M. J., Wooley, K. L., and Hawker, C. J. (2005) Functionalization of micelles and shell cross-linked nanoparticles using click chemistry. *Chem. Mater. 17*, 5976–5988.

(29) Binder, W. H., Sachsenhofer, R., Straif, C. J., and Zirbs, R. (2007) Surface-modified nanoparticles via thermal and Cu(I)-mediated "click" chemistry: generation of luminescent CdSe nanoparticles with polar ligands guiding supramolecular recognition. *J. Mater. Chem. 17*, 2125–2132.

(30) Chen, Y., and Rosenzwaig, Z. (2002) Luminescent CdS quantum dots as selective ion probes. *Anal. Chem. 74*, 5132–5138.

(31) Isarov, A. V., and Chrysochoos, J. (1997) Optical and photochemical properties of nonstoiechiometric cadmium sulfide nanoparticles: surface modification with copper (II) ions. *Langmuir 13*, 3142–3149.

(32) Klimov, V., Bolivar, P. H., Kurz, H., Karavanskii, V., Krasovskii, V., and Korkishko, Y. (1995) Limnear and nonlinear transmission of Cu_xS quantum dots. *Appl. Phys. Lett. 67*, 653–655.

(33) Son, D. H., Hughes, S. M., Yin, Y., and Alivisatos, A. P. (2004) Cation exchange reactions in ionic nanocrystals. *Science 306*, 1009–1012.

(34) Clapp, A. R., Medintz, I. L., Mauro, J. M., Fischer, B. R., Bawendi, M. G., and Mattoussi, H. (2004) Fluorescence resonance energy transfer between quantum dot donors and dye-labeled protein acceptors. *J. Am. Chem. Soc. 126*, 301–310.

(35) Medintz, I. L., Clapp, A. R., Mattoussi, H., Goldman, E. R., Fischer, B. R., and Mauro, J. M. (2003) Self-assembled nanoscale biosensors based on quantum dot FRET donors. *Nat. Mater. 2*, 630–638.

(36) Medintz, I. L., Pons, T., Trammell, S. A., Grimes, A. F., English, D. S., Blanco-Canosa, J. B., Dawson, P. E., and Mattoussi, H. (2008) Interactions between redox complexes and semiconductor quantum dots coupled via a peptide bridge. *J. Am. Chem. Soc. 130*, 16745–16756.

(37) Fischer, B. R., Eisler, H.-J., Stott, N. E., and Bawendi, M. G. (2004) Emission intensity dependance and single-exponential behavior in single colloidal quantum dot fluorescence lifetimes. *J. Phys. Chem. B 108*, 143–148.

(38) Meijerink, A. (2008) Exciton Dynamics and energy transfer processes in semiconductor nanocrystals, in *Semiconductor nanocrystal quantum dots* (Rogach, A., Ed.) pp 277−310, Springer-Verlag, Wien.

(39) *Handbook of chemistry and physics*, 70th ed. (1989−1990) CRC Press, Boca Raton.

(40) Yu, W. W., Qu, L., Guo, W., and Peng, X. (2003) Experimental determination of the extinction coefficient of CdTe, CdSe, and CdS nanocrystals. *Chem. Mater. 15*, 2854–2860.

(41) Kudera, S., Carbone, L., Manna, L., and Parak, W. J. (2008) Growth mechanism, shape and composition control of semiconductor nanocrystals, in *Semiconductor nanocrystal quantum dots* (Rogach, A., Ed.) pp 1−34, Springer-Verlag, Berlin.

(42) Agard, N. J., Baskin, J. M., Prescher, J. A., Lo, A., and Bertozzi, C. R. (2006) A comparative study of bioorthogonal reactions with azides. *ACS Chem. Biol. 1*, 644–648.

(43) Agard, N. J., Prescher, J. A., and Bertozzi, C. R. (2004) A strain-promoted [3 + 2] azide-alkyne cycloaddition for covalent modification of biomolecules in living systems. *J. Am. Chem. Soc. 126*, 15046–15047.

(44) Baskins, J. M., Prescher, J. A., Laughlin, S. T., Agard, N. J., Chang, P. V., Miller, I. A., Lo, A., Codelli, J. A., and Bertozzi, C. R. (2007) Copper-free click chemistry for dynamic in vivo imaging. *Proc. Natl. Acad. Sci. U.S.A. 104*, 16793–16797.

(45) Codelli, J. A., Baskin, J. M., Agard, N. J., and Bertozzi, C. R. (2008) Second-generation difluorinated cyclooctynes for copper-free click chemistry. *J. Am. Chem. Soc. 130*, 11486–11493.

(46) Ning, X., Guo, J., Wolfert, M. A., and Boons, G.-J. (2008) Visualizing metabolically labeled glycoconjugates of living cells by copper-free and fast Huisgen cycloadditions. *Angew. Chem., Int. Ed. 47*, 2253–2255.

(47) Sletten, E. M., and Bertozzi, C. R. (2008) A hydrophilic azacyclooctyne for Cu-free click chemistry. *Org. Lett. 10*, 3097–3099.

(48) Pons, T., Uyeda, H. T., Medintz, I. L., and Mattoussi, H. (2006) Hydrodynamic dimensions, electrophoretic mobility, and stability of hydrophilic quantum dots. *J. Phys. Chem. B 110*, 20308–20316.

(49) Sperling, R. A., Pellegrino, T., Li, J. K., Chang, W. H., and Parak, W. J. (2006) Electrophoretic separation of nanoparticles with a discrete number of functional groups. *Adv. Funct. Mater. 16*, 943–948.

(50) Daou, T. J., Li, L., Reiss, P., Josserand, V., and Texier, I. (2009) Effect of poly(ethylene glycol) length on the in vivo behavior of coated quantum dots. *Langmuir 25*, 3040–3044.

(51) Sartori, R., Sepulveda, L., Quina, F., Lissi, E., and Abuin, E. (1990) Binding of electrolytes to poly(ethylene oxide) in aqueous solutions. *Macromolecules 23*, 3878.

(52) Foster, A. B. (1957) Zone electrophoresis of carbohydrates. *Adv. Carbohydrate Chem. 12*, 81–115.

(53) Dennis, J. W., Granovsky, M., and Warren, C. E. (1999) Glycoprotein glycosylation and cancer progression. *Biochim. Biophys. Acta-Gen. Subj. 1473*, 21–34.

(54) Hakomori, S., and Zhang, Y. M. (1997) Glycosphingolipid antigens and cancer therapy. *Chem. Biol. 4*, 97–104.

(55) Laughlin, S. T., and Bertozzi, C. R. (2009) Imaging the glycome. *Proc. Natl. Acad. Sci. U.S.A. 106*, 12–17.

(56) Dall'Olio, F. (2000) The sialyl-alpha2,6-lactosaminyl-structure: biosynthesis and functional role. *Glycoconjugate J. 17*, 669–676.

(57) Wang, P. H. (2005) Altered glycosylation in cancer: sialic acids and sialyltransferases. *J Cancer Mol. 1*, 73–81.

(58) Schauer, R., and Kamerling, J. P. (1997) in *Glycoproteins II* pp 243−402, Elsevier, Amsterdam.

(59) Sarkar, A. K., et al. (1997) Fucosylation of disaccharide precursors of sialyl Lewis(X) inhibit selectin-mediated cell adhesion. *J. Biol. Chem. 272*, 25608–25616.

(60) Keppler, O. T. (2001) Biochemical engineering of the N-acyl side chain of sialic acid: biological implications. *Glycobiology 11*, 11r–18r.

BC900564W

Synthesis and Application of Lactosylated, ^{99m}Tc Chelating Albumin for Measurement of Liver Function

Philippe Chaumet-Riffaud,*[,†,‡] Ivan Martinez-Duncker,[#] Anne-Laure Marty,[§] Cyrille Richard,[§] Alain Prigent,[†,‡] Frederic Moati,[†,‡] Laure Sarda-Mantel,[||,⊥] Daniel Scherman,[§] Michel Bessodes,[§] and Nathalie Mignet[§]

Université Paris-Sud 11, EA4046, Kremlin-Bicêtre, F-94275, AP-HP, CHU de Bicêtre, Le Kremlin-Bicêtre, F-94275, Unité de Pharmacologie Chimique et Génétique, U640 INSERM, UMR8151 CNRS, Université Paris Descartes, Paris, France, F-75006, Université Paris 7, U733 INSERM, CRB3, Faculté Xavier Bichat, Paris, France, AP-HP, Hôpital Bichat, Paris, F-75018, and Faculty of Science, Morelos State Autonomous University, Cuernavaca, Mexico. Received June 24, 2009; Revised Manuscript Received December 15, 2009

Neogalactosylated and neolactosylated albumins are currently used as radiopharmaceutical agents for imaging the liver asialoglycoprotein receptors, which allows the quantification of hepatic liver function in various diseases and also in healthy liver transplant donors. We developed an original process for synthesizing a chelating neolactosylated human albumin using maleimidopropyl-lactose and maleimidopropyl-diethylene triamine pentaacetic acid (DTPA) derivatives. The lactosylated protein (LACTAL) conjugate showed excellent liver uptake compared to nonlactosylated protein and a very high signal-to-noise ratio, based on functional assessment of biodistribution in mice using ^{99m}Tc-scintigraphy.

INTRODUCTION

The evaluation of hepatic function is required to determine the physiological status of the liver, particularly for patients with liver disease whose treatment of choice is hepatectomy or liver transplantation (*1*). Therefore, determination of the hepatic function is crucial to predict patient outcome before and after hepatectomy or liver transplantation (*2*), as well as for healthy liver donor assessment. Asialoglycoproteins are internalized into hepatocytes via the asialoglycoprotein receptors which recognize galactose and *N*-acetyl-galactosamine moieties bound to proteins. The number of asialoglycoprotein receptors on the hepatocytes of patients with liver disease is reduced and is thus considered a good indicator for the evaluation of liver function (*3, 4*). In addition, noninvasive quantification of the liver uptake of radiolabeled asialoglycoproteins also provides useful information, especially in terms of spatial distribution of hepatic function. The asialoglycoprotein receptors are localized mainly on liver parenchymal cells (*5*) and play a major role in the hepatic clearance of serum proteins (*6*). Most of the receptors (90%) are located on sinusoidal faces of hepatocytes with only 10% on lateral faces (*7*). Non-hepatic cells such as endothelial and Kupffer cells have no or few asialoglycoprotein receptors (*8*), and hepatocytes are the most represented cells in the liver. Therefore, targeting the asialoglycoprotein receptors results in targeting mainly hepatocytes.

The measurement of the hepatic functional reserve by kinetic studies of liver binding and blood clearance of galactosylated ligands to the asialoglycoprotein receptors is validated and directly reflects the number of functional hepatocytes (*9, 10*). Quite a few reports of procedures for the preparation of a modified human serum albumin (HSA) have been described for use as a liver radiopharmaceutical agent (*11*−*14*). For instance, de Graaf et al. (*11*) recently showed that ^{99m}Tc-DTPA-galactosylalbumin (^{99m}Tc-GSA) scintigraphy combined with SPECT (single photon emission computed tomography) is a feasible noninvasive method to assess hepatic functional volume in normal rat liver, as well as during liver regeneration in a rat model with partial hepatectomy. However, these procedures have a number of limitations: long reaction times, reduction of structural disulfide bonds, alterations of the neat charge of the protein, or reactions involving toxic reagents such as sodium cyanoborohydride for reductive amination. Therefore, the aim of our study was to develop an alternate process to prepare a DTPA-lactosyl albumin (LACTAL), using a quick single-step reaction involving maleimido-derivatized reagents, and perform preclinical studies to validate its use as a radiopharmaceutical for liver function imaging (*15*).

MATERIAL AND METHODS

Material. Chemical reagents were obtained from Sigma-Aldrich company, and solvents from SDS (France). 4-Nitrophenylcarbonate Wang resin was obtained from Novabiochem. 3-(Maleimido) propionic acid *N*-hydroxysuccinimide ester and lactosylamine were obtained using described procedures (*16, 17*). Human serum albumin compliant with European safety regulations was purchased from LFB (France) as a 40 mg/mL solution in normal saline (Vialebex). Vasculocis (i.e., ^{99m}Tc human albumin) was obtained from Cisbio IBA (France). Disposable aseptic 0.22 μm filters were purchased from Millipore Company. The ^{99}Mo/^{99m}Tc-generators were purchased from Mallinckrodt Company. The ITLC SG plates were purchased from PALL Corporation (France). Tin salts were purchased from Sigma-Aldrich Company (99.995% purity). Bicinchonic acid assay for protein quantitation was purchased from Pierce by Perbio Scientific. Quantichrom Calcium Assay Kit for DTPA determination was from Gentaur (Belgium). Grafting on HSA, preparation of the ready to use mixture with $SnCl_2$, and lyophilization were performed under sterile conditions. Analyti-

* Corresponding author. Fax: +33(0)145212112; e-mail: philippe.chaumet-riffaud@bct.aphp.fr.
† Université Paris-Sud 11, EA4046.
‡ AP-HP, CHU de Bicêtre.
§ Unité de Pharmacologie Chimique et Génétique, U640 INSERM, UMR8151 CNRS.
|| Université Paris 7, U733 INSERM.
⊥ AP-HP, Hôpital Bichat.
Morelos State Autonomous University.

10.1021/bc900275f © 2010 American Chemical Society
Published on Web 03/04/2010

cal HPLC was performed on a Merck-Hitachi gradient pump equipped with a L-6200A intelligent pump and a UV−visible detector L-4000 Merck. Electrophoresis of proteins was performed on NuPage 10% Bis-Tris Gel from InVitrogen.

1-(β-D-Lactosyl)-3-maleimidopropionamide or Maleimidopropyl-Lactose (1). β-D-lactosylamine (100 mg; 0.25 mmol, ref *16*) was dissolved in DMF (2 mL), 3-(maleimido)propionic acid *N*-hydroxysuccinimide ester (73 mg; 0.28 mmol) was added and the mixture was stirred overnight at room temperature. The reaction medium was evaporated and the residue precipitated in acetone. The white solid obtained by centrifugation was washed several times with acetone and dried to give **1** (73 mg; 60%). This product is hygroscopic and should be stored accordingly. MS: *m/z* 515 for [M + Na]. ^{1}H NMR (400 MHz, DMSO, δ ppm): 8.55 (d, J = 12 Hz, 1H), 7.01 (s, 2H), 5.12 (d, J = 4 Hz, 1H), 5.02 (d, J = 8 Hz, 1H), 4.80 (d, J = 4 Hz, 1H), 4.76−4.71 (m, 2H), 4.66 (dd, J = 4 Hz, 1H), 4.55−4.52 (m, 2H), 4.2 (d, J = 8 Hz, 1H), 3.69 (dd, J = 4 Hz, J = 12 Hz, 1H), 3.63−3.44 (m, 6H), 3.35−3.29 (m, 8H), 3.10 (m, 1H). ^{13}C NMR (100 MHz, DMSO, δ ppm): 170.61; 169.71; 134.42; 103.67; 80.36; 79.02; 76.29; 75.53; 75.41; 73.09; 71.92; 70.47; 68.00; 60.26. Anal. Calcd for $C_{19}H_{28}N_2O_{13}$; H_2O: C 44.70, H 5.88, N 5.49. Found: C 44.24, H 6.08, N 4.88.

{Carboxymethyl-[2-(carboxymethyl-{2-[carboxymethyl-({2-[3-(2,5-dioxo-2,5-dihydro-pyrrol-1-yl)-propionylamino]-ethylcarbamoyl}-methyl)-amino]-ethyl}-amino)-ethyl]-amino}-acetic acid or Maleimidopropyl-DTPA (3). 4-Nitrophenyl carbonate Wang resin (1 g; 0.54 mmol/g) was swollen in *N*-methylpyrrolidone (NMP) and ethylenediamine was added in excess (0.36 mL; 10 equiv). It was left under gentle shaking overnight. It was then thoroughly rinsed with NMP and a solution of diethylene triamine pentacetic dianhydride (1.9 g; 5.4 mmol; 10 equiv) in NMP (20 mL) was added, followed by triethylamine (0.8 mL; 10 equiv). The suspension was shaken overnight. The resin was washed with NMP (3 × 10 mL), H_2O (1 × 10 mL; contact 30 min), absolute ethanol (3 × 10 mL), and ether (2 × 10 mL), and dried in air.

A solution of trifluoroacetic acid (TFA) (9 mL), H_2O (1 mL), and triisopropyl silane (200 μL) was added to the dry resin and allowed to react 3 h at 30 °C. The eluate was concentrated and the residue washed with ether to give (**2**) as a white powder (0.268 g; 84% crude).

The powder was dissolved in DMSO (1 mL), then 3-(maleimido)propionic acid *N*-hydroxysuccinimide ester (0.14 g; 1.1 equiv) and triethylamine (0.14 mL; 2 equiv) were added. The mixture was left at room temperature overnight then diluted with ethyl acetate to induce precipitation. The precipitate was centrifuged, rinsed with ethyl acetate and ether, and dried to give **3** (0.16 g; 51% overall yield; hygroscopic). MS: *m/z* 587. ^{1}H NMR (400 MHz, DMSO, δ ppm): 7.28 (s, 2H), 4.55 (m, 2H), 4.40−4.10 (m, 7H), 3.86−3.57 (m, 9H), 3.15 (m, 2H), 2.92 (m, 2H). ^{13}C NMR (100 MHz, D_2O, δ ppm MeOH): 176.72; 174.00; 172.77; 170.6; 134.65; 57.59; 57.36; 57.29; 57.11; 52.10; 51.35; 38.88; 38.67; 34.87; 34.60. Anal. Calcd for $C_{23}H_{34}N_6O_{12}$; H_2O: C 45.69, H 5.96, N 13.90. Found C 45.59, H 5.74, N 13.30.

LACTAL Synthesis. Instruments and solutions were sterilized using a Getinge Vertical Sterilizer AVOR 130. Buffer was degassed by sonication in a US cleaning bath (Branson 1510). Iminothiolane (6 mg, 64 μmol in 200 μL PBS/EDTA 5 mM pH 7.8), maleimido-propyl-lactose (3.3 mg, 6.8 μmol in 100 μL PBS/EDTA 5 mM), and buffered maleimido-propyl-DTPA (2 mg, 3.4 μmol in 100 μL PBS/EDTA 5 mM) were added to the solution of HSA (100 μL, 4 mg, 59 nmol, 3.2 μmol NH_2). All components were gently mixed during 1 h at room temperature. Then, the mixture was diluted to 4 mL with NaCl 0.9% (degassed with N_2 and filtered under 0.22 μm) and transferred to a centrifuge ultrafiltration system with a molecular weight cutoff of 30 kDa. The mixture was centrifuged at 4000 rpm (3000 *g*) during 10 min, until the filtrate did not contain any DTPA. The absence of residual DTPA reagent was controlled by taking a sample of the filtrate (180 μL) and adding an excess of $EuCl_3$, $6H_2O$ (20 μL, 1 g/L). Measurement of the europium signal by time-resolved fluorescence at 616 nm with a spectrofluorimeter (Victor2, Perkin-Elmer) indicated the diminution of the DTPA content as washes proceeded.

The total protein amount recovered from the experiment was quantified by the BCA reagent. The modified HSA (10 μL of a solution estimated to be at 1 mg/mL) was mixed with 200 μL of the BCA reagent and incubated for 30 min at 37 °C. The concentration was obtained from a standard concentration range of unmodified HSA taken at 562 nm. 98 ± 1% of protein was recovered from the process.

The amount of lactose coupled to the protein was determined by the method of Dubois (*18*). The modified HSA (10 μL, 1 mg/mL) was introduced in a glass vial, then phenol (5% in water, 190 μL) and concentrated sulfuric acid (200 μL) were added. The vial was heated at 90 °C during 5 min then left to cool down at room temperature. Measurements were done at 490 nm; the concentration was calculated from a standard concentration range of lactose and indicated 30 ± 3 lactose/HSA (mol/mol).

The amount of DTPA coupled to the protein was determined by the Quantichrom Calcium Assay Kit (Gentaur). The modified HSA (100 μL, 1 mg/mL) was introduced in a 1 mL cuvette, then $CaCl_2$ (20 μL, 1 M) was added, and the volume was completed with 500 μL of the calcium working solution provided by the kit. After 3 min, the optical density was measured at 612 nm giving the free calcium concentration from which the amount of DTPA could be deduced. 5 ± 1 DTPA/HSA (mol/mol) was found.

The modified and unmodified albumin were analyzed by HPLC using a Vydac column C4−214TP5415 (4.6 mm × 150 mm) (Interchim, Montluçon, France), eluted with a gradient from 90/10 A/B to 10/90 A/B during 20 min with a flow rate of 1 mL/min (solvent A: H_2O + 0.1% TFA, solvent B: acetonitrile) and detection at 220 nm. HSA elution time: 12.1 ± 0.1 min. LACTAL elution time: 11.8 ± 0.1 min. (Despite the small difference in elution time, a shoulder was clearly observed when a mixture of the two compounds were injected.) Electrophoresis (MOPS buffer, 150 V) was performed with LACTAL and HSA and compared with the SeeBlue Plus2 Pre-Stained Standard (Invitrogen, 4−250 kDa). The modified protein appeared as a single band. The estimated mass for LACTAL was 93 kDa, which corresponded to 29 lactose units and 5 DTPA (Figure 1).

Preparation of LACTAL Lyophilisate and Labeling. The pH of a modified protein solution (500 μL, 15 mg/mL) was carefully adjusted to 1.5 with HCl 1 N, then a solution of stannous chloride in HCl 1 N (10 mg/mL, 20 μL, 28 μg/mg protein) was added and the mixture was left 20 min protected from light at room temperature. The volume was adjusted to 1 mL and aliquoted in 5 × 2 mL serum vials (200 μL, 1.44 mg/vial), frozen in liquid nitrogen, and lyophilized. The system was then equilibrated to atmospheric pressure by nitrogen. The vials were sealed under nitrogen using a glovebox.

The lyophilized product was redissolved in NaCl solution (0.9%; 1 mL). A saline solution of ^{99m}Tc (pertechnetate) freshly eluted from a ^{99}Mb generator was added (5−7 × 10^6 Bq/200 μg prot), and the mixture was incubated for 30 min at 50 °C. Radio-TLC chromatograms were obtained using a BIOSCAN Miniscan system. The radiochemical purity was checked using ITLC methods to determine the amounts of unbound and hydrolyzed ^{99m}Tc. ITLC/Umezawa (ethanol/10% ammonium

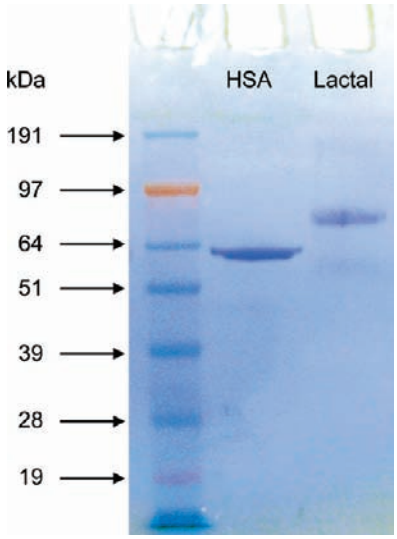


Figure 1. Gel electrophoresis of HSA and LACTAL with the Invitrogen NuPAGE Novex kit (MOPS buffer, 150 V).

acetate = 1:1) was used to check the labeling efficiencies. Unbound ^{99m}Tc moved to the solvent front, and LACTAL-bound ^{99m}Tc stayed at the origin on ITLC/Umezawa. The solution of ^{99m}Tc-LACTAL was stable at room temperature for 20 h.

Biodistribution Studies. A gamma scintillation counter Wizard 1480 automatic model from Perkin-Elmer Company was used for counting radioactivity of mouse organs in biodistribution studies. Male mice (26−28 g) were injected via the tail vein with 0.55 MBq of ^{99m}Tc-labeled ligand. Animals were anesthetized and sacrificed at planned time-points (three per time point; 10, 30, and 90 min). Blood and organ samples (heart, blood, kidney, spleen, lung, and liver) were collected, weighed with an electronic balance, and counted in a gamma scintillation counter.

In Vivo Imaging Studies. A small-animal dedicated gamma camera from BIOSPACE Lab (France) equipped with a low-energy high-resolution parallel collimator was used for imaging rats (field of view: 8 cm). Following anesthesia with pentobarbital, male Wistar rats (n = 9, 220−240 g) were injected intravenously through the penis vein with 200 μL of tracer (5−10 MBq). The rats were then placed on their back on the gamma camera where posterior planar acquisitions were recorded.

RESULTS

Synthesis of the Maleimidopropyl-Lactose. D-Lactose was first reacted with ammonium carbamate in methanol/water to give the carbamate salt of the amino-lactoside which was treated just before use with triethylamine to give the 1-aminosugar as described in the literature (*16*). This product was reacted with 3-(maleimido)-propionic acid *N*-hydroxysuccinimide ester (*17*) to give the final maleimidopropyl-lactose **1** (Scheme 1). This product could be stored for months at 4 °C in dry atmosphere.

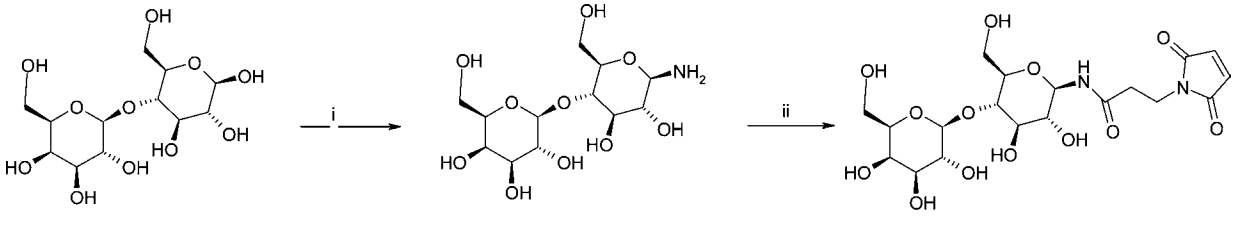
Synthesis of the Maleimidopropyl-DTPA. For a better regioselective reaction of the multifunctional DTPA, we developed a solid-phase synthesis (Scheme 2). 4-Nitrophenylcarbonate Wang resin was reacted with excess ethylene diamine in NMP. The reaction progress could be monitored in UV by the release of 4-nitrophenol (410 nm). After thorough washings, DTPA anhydride was added in excess and the mixture swirled for 1 h. End of reaction was monitored by negative Kaiser and TNBS tests. Successive washings with NMP, water, methanol, and diethyl ether were performed to eliminate the excess of DTPA, hydrolyze the remaining anhydride function, and dry the resin. The resin was dried in air, and a mixture of trifluoroacetic acid/water/triisopropylsilane was added as a degrafting reagent. The solution was thoroughly evaporated to give pure ethylenediamine-DTPA (**2**) which was condensed without further purification with 3-(maleimido)-propionic acid *N*-hydroxysuccinimide ester to give maleimidopropyl-DTPA (**3**).

Synthesis of the Modified Albumin (LACTAL). In preliminary studies, the modified protein was prepared in two separated steps: first, introduction of the thiol functions with iminothiolane (*19*), then addition of the maleimido-lactose (**1**) and maleimido-DTPA (**3**). This allowed quantitation of the intermediate thiol groups with the Ellman reagent. However, this first step was unreliable, leading to unreproducible amounts of thiol groups which was probably due to rearrangement of the iminothiolane moiety with time (*20*) or oxidation. The protocol was then modified to a single-step process (Scheme 3). The successive addition of iminothiolane, lactose, and DTPA derived maleimide compounds allowed achieving the reproducible HSA modification. The lactose and DTPA derivatives (**1** and **3**) were introduced on the ε-amino groups of the protein lysines without significant changes in the ionic balance of the protein (*21*); the presence of EDTA avoided thiol oxidation. There was no evidence in favor of the formation of aggregates which could induce changes in surface properties of the protein molecule.

Stability of the Solution and of the Lyophilisate. Stability of the solution of LACTAL was checked after a one-year storage at 4 °C and 32 months for the lyophilized kit. There were no differences from freshly prepared material, no aggregates were observed, and the imaging properties were identical.

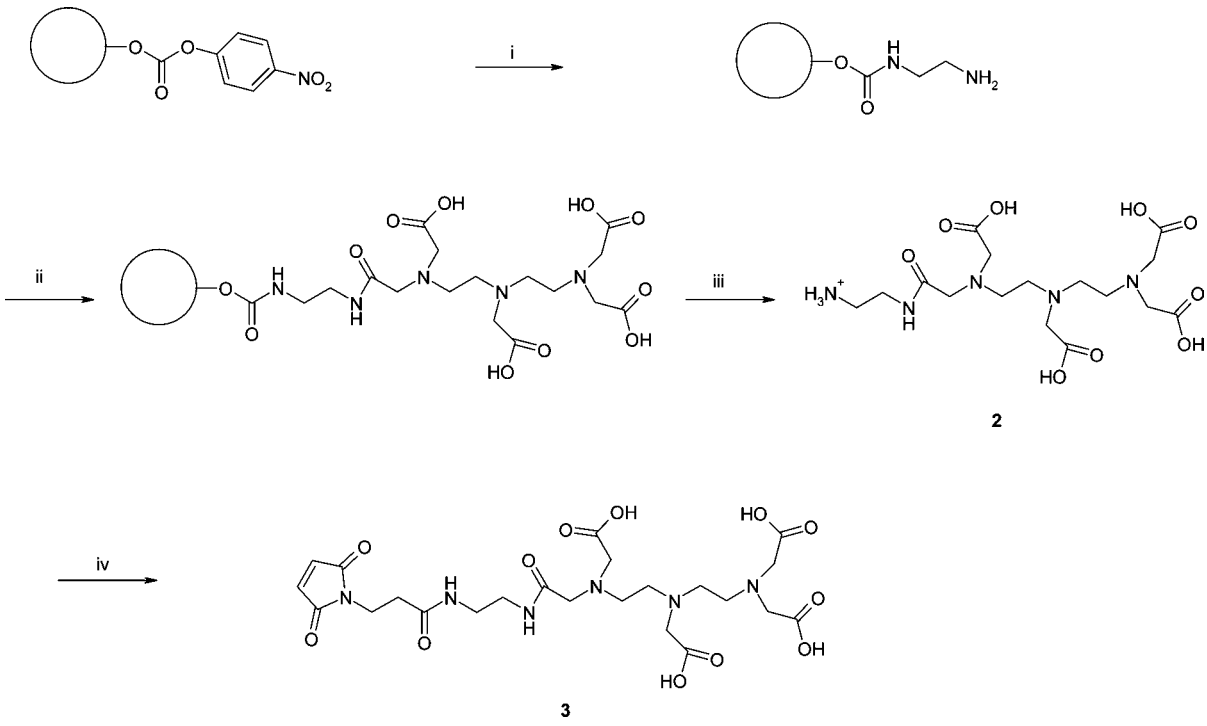
In Vivo Imaging in Rats. The biodistribution of the tracer was studied through the completion of an acquisition in list mode over an extended period up to 2 h in some rats. Figure 2 shows a sequence of 15 dynamic images of 2 min each, corresponding to the first 30 min post iv administration. Just after injection, the distribution of LACTAL resembled an intravascular tracer and the anatomical regions showing high activity at this stage corresponded to highly vascularized organs. Then, the images highlighted an early and predominantly hepatic uptake with a plateau that was reached between 2−6 min and continued for

Scheme 1[a]



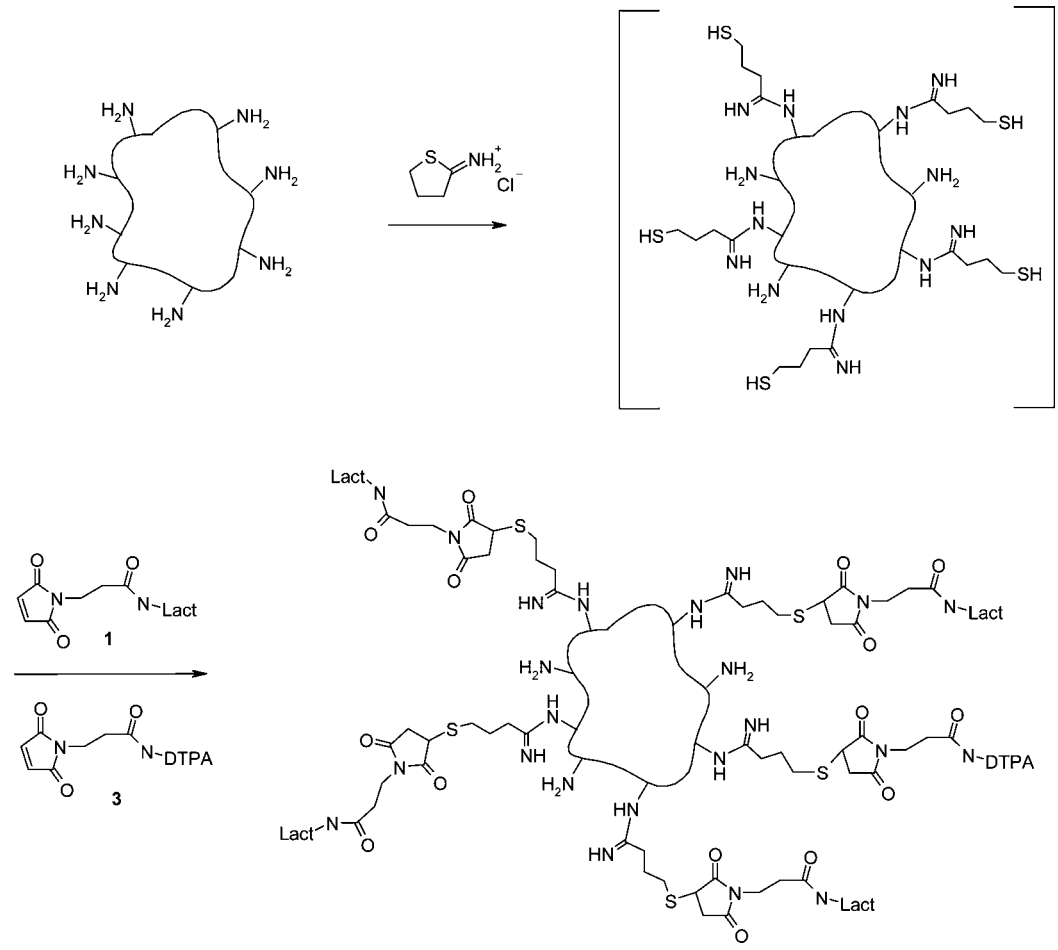
[a] Synthesis of maleimidopropyl-lactose (**1**): i, NH_4OH, NH_2-COO^-; NH_4^+; ii, Et_3N, MeOH (0.5), EtOH/water (1:0.4), see ref *16*; ii, 3-(maleimido)propionic acid *N*-hydroxysuccinimide ester, DMF.

Scheme 2[a]



[a] Synthesis of maleimidopropyl-DTPA (**3**): i, ethylene diamine, NMP; ii, DTPA anhydride, triethylamine; iii, TFA, triisopropylsilane; iv, 3-(maleimido)propionic acid *N*-hydroxysuccinimide ester, Et_3N, DMSO.

Scheme 3. One-Step Preparation of LACTAL: Human Serum Albumin Modified by Simultaneous Introduction of Maleimidopropyl-Lactose and -DTPA Derivatives



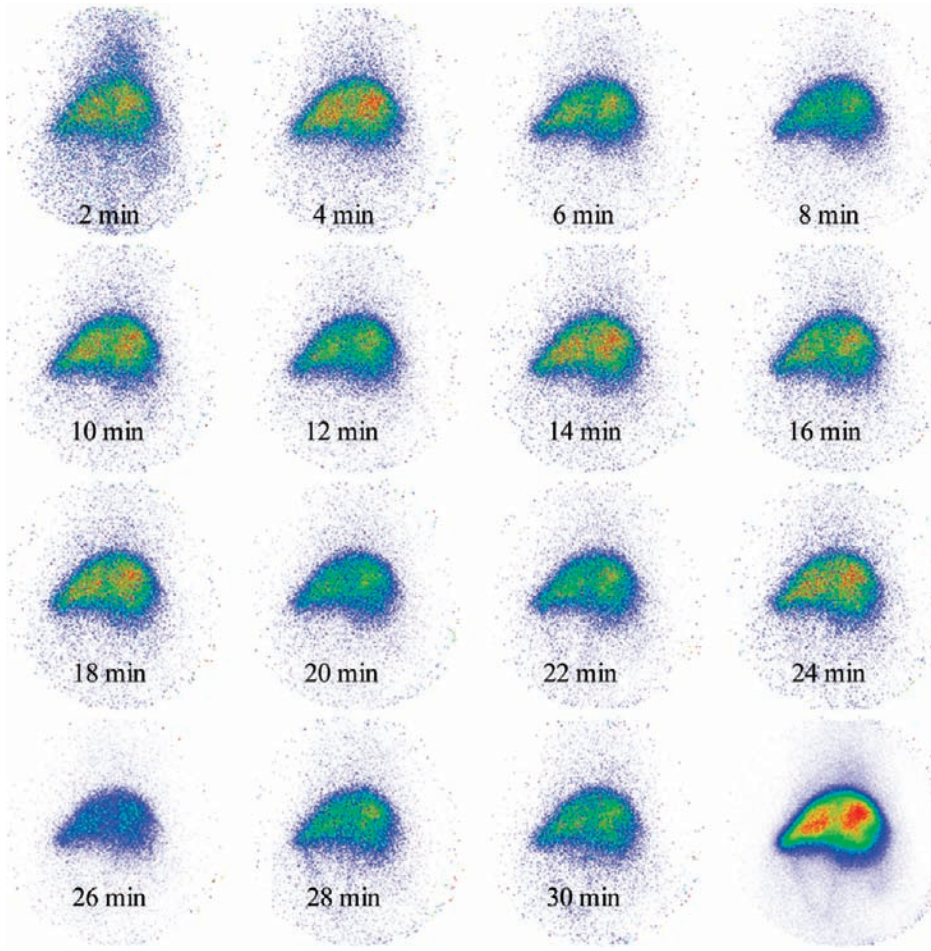


Figure 2. Posterior planar scintigraphic acquisition was started immediately after intravenous injection of 200 μL of ^{99m}Tc labeled LACTAL (5−10 MBq). List-mode data were acquired for at least 30 min for all animals. Using Biospace software, the list-mode data were reformated into fifteen 2 min frames. The last image on the bottom right is a summed image (0−30 min).

at least 20 min in this animal species. After 30 min, the liver uptake began to decrease, and analysis of dynamic images such as those in Figure 3 (12 images of 5 min each between 30 and 90 min after iv injection) referred to a disposal of the product by the bile ducts. An important passage in the gastrointestinal tract most likely in the form of degradation products was also visible. The last picture showed predominant radioactivity in the digestive tube and some traces in the bladder indicating the modes of degradation and elimination of the tracer.

Biodistribution in Mice. The biodistribution of LACTAL in mice is illustrated in Table 1. The activities were measured in different organs and expressed as the percentage of the injected dose per gram of organ. Non-lactosylated ^{99m}Tc human serum albumin (Vascolucis) was used as a control. The biodistribution data confirmed the results of the visual analysis of scintigraphic acquisitions. The liver uptake was very early and intense. Splenic fixation was much lower, confirming the specificity of the radiolabeled molecule for ASGP hepatic receptors. Blood levels were very low after 10 min reflecting the very high plasma clearance; a slight rise to late time is likely to reflect intrahepatic degradation of the tracer leading to release of ^{99m}Tc labeled catabolites in the bloodstream. Contrary to what was observed with LACTAL, the activity in hepatic tissue of the control (Vascolucis) one hour after the injection was much lower than the blood activity. These results are consistent with the fact that this tracer remains mainly in the intravascular compartment (Table 1).

DISCUSSION

Although the indocyanine green clearance test is widely used to assess the hepatic functional reserve before hepatectomy, discrepancies between indocyanine green clearance values and histological observations in the liver are noted in given instances. Volumetric measurements may not be relevant in patients with advanced chronic liver disease requiring major liver resection (*22*). In a similar way, iminodiacetic acid ^{99m}Tc labeled derivatives are good tracers of the hepatic biliary clearance and are mostly dedicated to the diagnosis of gall bladder dysfunctions by cholescintigraphy (*23*). These tracers are not specifically targeted to the asialoglycoprotein receptors.

Previously reported work indicated that the measurement of the hepatic functional reserve could be very useful before hepatectomy as well as for the evaluation of the post-transplantation residual hepatic functional reserve in donors. It could also be useful for the follow-up and functional prognosis of the hepatic graft, staging, and preoperative evaluation. Furthermore, a precise assessment of functional hepatic reserve would also be useful for the follow-up and prognosis of hepatic function in cirrhotic patients, the evaluation of surgical resection extension in patients with hepatocellular carcinoma, and prognosis in acute hepatitis. The preoperative estimation of the maximal removal rate of ^{99m}Tc GSA radioligand in the predicted liver remnant has proved useful for determining the hepatectomy procedure (*24*).

There are at least 5 different glycosylated tracers identified, based on a literature search. ^{99m}Tc-Galactosyl-neoglycoalbumin

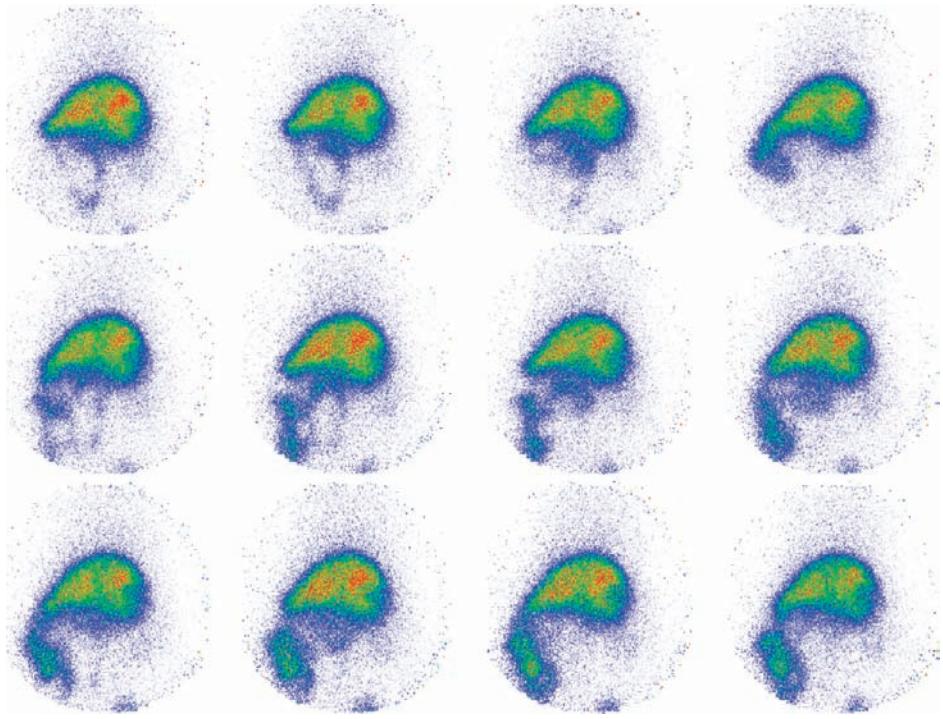


Figure 3. Posterior planar scintigraphic acquisition was performed between 30 and 90 min after intravenous injection of 200 μL of ^{99m}Tc labeled LACTAL (5−10 MBq). Using Biospace software, the list-mode data were reformated into twelve 5 min dynamic frames.

Table 1. Biodistribution Results after 10 min ($n = 3$), 30 min ($n = 3$), and 90 min ($n = 3$) following Intravenous Injection of ^{99m}Tc-Labeled LACTAL or Vasculosis (60 min, $n = 3$) into Healthy Mice[a]

	heart	liver	spleen	kidneys	blood	lung
Lactal [$t = 10$ min]	0.88 ± 0.24	51.3 ± 4.27	3.77 ± 0.35	3.89 ± 0.59	1.98 ± 0.60	1.76 ± 0.55
Lactal [$t = 30$ min]	0.26 ± 0.10	36.7 ± 6.68	0.25 ± 0.15	1.21 ± 0.54	0.59 ± 0.24	0.34 ± 0.16
Lactal [$t = 90$ min]	0.52 ± 0.12	24.3 ± 3.19	1.74 ± 1.16	2.82 ± 0.48	0.82 ± 0.03	0.72 ± 0.09
Vasculosis 60 min	4.13 ± 1.05	5.10 ± 1.55	3.31 ± 0.84	6.77 ± 1.92	35.3 ± 4.04	6.17 ± 2.03

[a] Results were expressed as the percentage of injected dose per gram of organ (% of ID/g of organ) at the different times.

(^{99m}Tc-NGA) was prepared by the covalent coupling of 2-imino-2-ethyloxymethyl-1-thiogalactose to human serum albumin (*13*) (about 24 galactose units per albumin molecule). Labeling of this compound with ^{99m}Tc was achieved by an electrolytic method. Biodistribution studies in rabbits demonstrated that the liver is the only site with ^{99m}Tc-NGA uptake (*25*). As for ^{99m}Tc-GSA (*11*), preclinical studies demonstrated its diagnostic efficiency, the safety and the stability of ^{99m}Tc-NGA, but the labeling method is difficult to implement in most clinical departments. This is why a diethylenetriaminepentaacetic acid conjugated neogalactosylated albumin was developed later on (*26*). The reaction is very quick and yields HSA derivatives containing 4.5 to 7 DTPA per mole of protein. The combination of galactosylated albumin to DTPA enabled the production of an instant kit (*27*). Numerous publications are available concerning the use of this radiopharmaceutical, which is distributed only in Japan and not commercially available in European countries. Besides, the chemical process for synthesis is a derivatization with cyanomethyl-thiogalactose which may lead to toxic byproduct.

^{67}Ga-desferoxamine-galactosyl-neoglycoalbumin (^{67}Ga-DF-NGA) is a galactosylated human serum albumin molecule. It is similar to NGA, as described above except for a covalent coupling of a desferoxamin molecule. Thus, DF-NGA indirectly binds to ^{67}Ga. This radiomarker has demonstrated high liver uptake in rabbits, but it has never been administered to humans (*14*). ^{99m}Tc-Neolactosylated-albumin (^{99m}Tc-LSA) is the only glycosylated human albumin synthesized by conjugating lactose to HSA using a reductive amination process (*12*). However, the use of sodium cyanoborohydride in this reaction is questionable for human use. Direct labeling with ^{99m}Tc was possible due to the adjunction of medronate and stannous chloride to the reduced LSA.

We have developed a new synthetic process for a lactosylated albumin which involves a simultaneous set of reactions with the protein. Thiol functions were generated by reaction of iminothiolane with the ε-amines of lysines, in the presence of the maleimides derivatives (lactose and DTPA). This avoided the formation of byproduct induced by the rearrangement of the iminothiol moiety (*20*) or by oxidation. The same conjugation chemistry was used for the introduction of both the ligand (lactose) and the cryptant (DTPA), leading to reliable and reproducible results and the control of the two entity ratio.

This new process involved five simple steps: (1) synthesis of a maleimide derivative of the targeting ligand (in the example, lactose) and of a technetium chelate (diethylene triamine pentaacetic acid, DTPA); (2) introduction of thiol functions by reaction of iminothiolane on the ε-amino groups of the protein lysines and simultaneous covalent grafting of the ligand and chelate moieties on the protein carrier (this smoothly provided functionalization without significant changes in the ionic balance of the protein (*21*)); (3) purification of the modified protein by ultrafiltration; (4) lyophilization after addition of the correct amount of stannous chloride (for technetium reduction); (5) prior to injection, association with technetium or another radioligand or contrast agent by chelation. This chemistry can easily be

adapted to the conjugation of many other ligands, including sugars, peptides or vitamins, and other markers can be introduced into the DTPA cryptants for other modes of detection (i.e., magnetic resonance imaging or fluorescence). Furthermore, the reaction times are considerably shorter than the above-mentioned protocols thus avoiding bacteria growth.

Asialoglycoproteins are internalized into hepatocytes via a receptor that recognizes the terminal galactose and *N*-acetyl-galactosamine residues of carbohydrate chains. The uptake and the intracellular processing of ^{125}I and ^{99m} Tc NGA were studied in an isolated perfused rat liver model (*28*). After a 1 min pulse administration of iodine NGA, 40% of the radioactivity was taken up at first pass by the liver, and after 15−20 min, 82% of the ^{125}I was released at the sinusoidal pole of the hepatocyte, predominantly as small catabolites. In contrast, only 4% of ^{99m}Tc galactosylated albumin taken up by the liver reappeared in the perfusate, and 40% of the radioactivity was found in the bile one hour after injection. Our results confirmed that liver captation was very high after first pass (80% of injected dose) and that the majority of the injected activity was eliminated by the biliary track. The residual activity in the liver was 34% ID after 90 min. Unlike colloidal tracers, the liver uptake was not accompanied by a splenic uptake suggesting a specific hepatocyte captation as also shown by Kim et al. (*29*). No or very little activity was visible in the urinary tract.

CONCLUSION

A receptor-specific ligand for the asialoglycoprotein hepatic receptor was developed using a straightforward, cyanide-free conjugation with human serum albumin. The pharmaceutical validation of the process will need complementary studies. Imaging and biodistribution studies demonstrated hepatic targeting and rapid blood clearance for this tracer. ^{99m}Tc-LACTAL accumulated mainly in the liver, and there was negligible uptake in the spleen. Kinetic parameters provided by these experiments will be useful for the design and the implementation of supplementary non clinical studies and phase I trials in healthy volunteers. In addition, this process could enable efficient and fast modification of protein templates with other ligands and chelated nuclei for use in nuclear medicine or magnetic resonance imaging of different targets.

ACKNOWLEDGMENT

We thank the CNRS for a one-year support for a valorisation engineer (M. A-L.). We would like to thank Mr. Abdelhakand Jallane for his technical assistance in biodistribution studies and Dr. Anne Gruaz-Guyon for her scientific advice.

LITERATURE CITED

(1) Clavien, P. A., Petrowsky, H., De Oliveira, M. L., and Graf, R. (2007) Strategies for safer liver surgery and partial liver transplantation. *New. Engl. J. Med. 356*, 1545–1559.

(2) Ishikawa, M., Yogita, S., Miyake, H., Fukuda, Y., Harada, M., Wada, D., and Tashiro, S. (2007) Differential diagnosis of small hepatocellular carcinoma and borderline lesions and therapeutic strategy. *Hepato-gastroenterol. 49*, 1591–1596.

(3) Sawamura, T., Nakada, H., Hazama, H., Shiozaki, Y., Sameshima, Y., and Tashiro, Y. (1984) Hyperasialoglycoproteinemia in patients with chronic liver diseases and/or liver cell carcinoma. Asialoglycoprotein receptor in cirrhosis and liver cell carcinoma. *Gastroenterology 87*, 1217–1221.

(4) Stockert, R. J. (1995) The asialoglycoprotein receptor: relationships between structure, function, and expression. *Physiol. Rev. 75*, 591–609.

(5) Aschwell, G., and Morell, A. G. (1981) The role of surface carbohydrates in the hepatic recognition and transport of circulating proteins. *Adv. Enzymol. 41*, 99–128.

(6) Aschwell, G., and Streer, C. J. (1981) Hepatic recognition and catabolism of serum glycoprotein. *JAMA 246*, 2358–2364.

(7) Stockert, R. J., and Morell, A. G. (1983) Hepatic binding protein: the galactose-specific receptor of mammalian hepatocytes. *Hepatology 3*, 750–757.

(8) Matsuura, S., Nakada, H., Sawamura, T., and Tashiro, Y. (1982) Distribution of an asialoglycoprotein receptor on rat hepatocyte cell surface. *J. Cell Biol. 95*, 864–875.

(9) Lee, J. (1998) Quantitative evaluation of liver function with hepatic receptor scintigraphy using Tc-99m galactosylated serum albumin (GSA). *Korean J. Nucl. Med. 32*, 305–313.

(10) Miki, K., Kubota, K., Inoue, Y., Vera, D. R., and Makuuchi, M. (2001) Receptor measurements via Tc-GSA kinetic modeling are proportional to functional hepatocellular mass. *J. Nucl. Med. 42*, 733–737.

(11) de Graaf, W., Veteläinen, R. L., de Bruin, K., van Vliet, A. K., van Gulik, T. M., and Bennink, R. J. (2008) 99mTc-GSA scintigraphy with SPECT for assessment of hepatic function and functional volume during liver regeneration in a rat model of partial hepatectomy. *J. Nucl. Med. 49*, 122–128.

(12) Jeong, J. M., Hong, M. K., Lee, J., Son, M., So, Y., Lee, D. S., Chung, J. K., and Lee, M. C. (2004) 99mTc-Neolactosylated human serum albumin for imaging the hepatic asialoglycoprotein receptor. *Bioconjugate Chem. 15*, 850–855.

(13) Vera, D. R., Stadalnik, R. C., and Krohn, K. A. (1985) Technetium-99m galactosyl-neoglycoalbumin: preparation and preclinical studies. *J. Nucl. Med. 26*, 1157–1167.

(14) Vera, D. R. (1992) Gallium-labeled deferoxamine-galactosyl-neoglycoalbumin: a radiopharmaceutical for regional measurement of hepatic receptor. *J. Nucl. Med. 33*, 1160–1166.

(15) Scherman, D., Bessodes, M., Chaumet-Riffaud, P., and Mignet, N. (2008)New conjugates for therapeutic purposes, and/or as a diagnostic and/or imaging agent, and methods for preparing the same. PCT/FR2007/052517; WO/2008/074960 A3

(16) Likhosherstov, L. M., Novikova, O. S., and Shibaev, V. N. (2002) New efficient synthesis of β-glucosylamines of mono and disaccharides with the use of ammonium carbamate. *Dokl. Chem. 383*, 89–92.

(17) Nielsen, O., and Buchardt, O. (1991) Facile synthesis of reagents containing a terminal maleimido ligand linked to an active ester. *Synthesis* 819–821.

(18) Dubois, M., Gilles, K. A., Hamilton, J. K., Rebers, P. A., and Smith, F. (1956) Colorimetric method for determination of sugars and related substances. *Anal. Chem. 28*, 350–356.

(19) Weber, C., Reiss, S., and Langer, K. (2000) Preparation of surface modified protein nanoparticles by introduction of sulfhydryl groups. *Int. J. Pharm. 211*, 67–78.

(20) Singh, R., Kats, L., Blättler, W. A., and Lambert, J. M. (1996) Formation of N-substituted 2-iminothiolanes when amino groups in proteins and peptides are modified by 2-iminothiolane. *Anal. Biochem. 236*, 114–125.

(21) Jue, R., Lambert, J. M., Pierce, L. R., and Traut, R. R. (1978) Addition of sulfhydryl groups to Escherichia Coli ribosomes by protein modification with 2-iminothiolane (methyl 4-mercaptobutyrimidate). *Biochemistry 17*, 5399–5405.

(22) Vauthey, J. N., Chaoui, A., Do, K. A., Bilimoria, M. M., Fenstermacher, M. J., Charnsangavej, C., Hicks, M., Alsfasser, G., Lauwers, G., Hawkins, I. F., and Caridi, J. (2000) Standardized measurement of the future liver remnant prior to extended liver resection: Methodology and clinical associations. *Surgery 127*, 512–519.

(23) Krishnamurthy, G. T., and Krishnamurthy, S. (2002) Hepatic bile entry into and transit pattern within the gallbladder lumen: a new quantitative cholescintigraphic technique for measurement of its concentration function. *J. Nucl. Med. 43*, 901–908.

(24) Kwon, A.-H., Matsui, Y., Kaibori, M., and Ha-Kawa, S. K. (2006) Preoperative regional maximal removal rate of technetium-99m-galactosyl human serum albumin (GSA-Rmax) is useful for judging the safety of hepatic resection. *Surgery 140*, 379–386.

(25) Kudo, M., Vera, D. R., Stadalnik, R. C., Trudeau, W. L., Ikekubo, K., and Todo, A. (1990) In vivo estimates of hepatic binding protein concentration: correlation with classical indicators of hepatic functional reserve. *Am. J. Gastroenterol. 85*, 1142–1148.

(26) Kudo, M., Todo, A., Ikekubo, K., Hino, M., Yonekura, Y., Yamamoto, K., and Torizuka, K. (1991) Functional hepatic imaging with receptor-binding radiopharmaceutical: clinical potential as a measure of functioning hepatocyte mass. *Gastroenterol. Jpn. 26*, 734–741.

(27) Kubota, Y., Kojima, M., Hazama, H., Kawa, S., Nakazawa, M., Nishiyama, Y., Nakagawa, S., Murase, T., Okuno, H., et al. (1986) A new liver function test using the asialoglycoprotein-receptor system on the liver cell membrane. I. Evaluation of liver imaging using the technetium-99m-neoglycoprotein. *Kaku Igaku 23*, 899–905.

(28) Gore, S., Morris, A. I., Gilmore, I. T., Maltby, P. J., Thornback, J. R., and Billington, D. (1991) Differences in the intracellular processing of the radiolabel following the uptake of iodine-125- and technetium-99m-neogalactosyl albumin by the isolated perfused rat liver. *J. Nucl. Med. 32*, 506–511.

(29) Kim, S., Jeong, J. M., Hong, M. K., Jang, J.-J., Lee, J., Lee, D. S., Chung, J.-K., and Lee, M. C. (2008) Differential receptor targeting of liver cells using 99mTc- neoglycosylated human serum albumins. *Arch. Pharm. Res. 31*, 60–66.

BC900275F

Detection of TrkB Receptors Distributed in Cultured Hippocampal Neurons through Bioconjugation between Highly Luminescent (Quantum Dot-Neutravidin) and (Biotinylated Anti-TrkB Antibody) on Neurons by Combined Atomic Force Microscope and Confocal Laser Scanning Microscope

Ji Won Park,[†] Aee-Young Park,[†] Seonghoon Lee,*[,†] Nam-Kyung Yu,[‡] Seung-Hee Lee,[‡] and Bong-Kiun Kaang[‡]

Molecular Electronics and NanoStructures Laboratory, School of Chemistry, NS60, National Creative Research Initiative Center for Memory, Department of Biological Sciences, College of Natural Sciences, Seoul National University, Seoul 151-747, Republic of Korea. Received July 9, 2009; Revised Manuscript Received February 26, 2010

We developed highly luminescent and cost-effective quantum dot (QD)-neutravidin (NTV) bioconjugates to detect the tyrosine kinase B (TrkB) receptors distributed in the cultured hippocampus neurons. Hippocampal neurons were incubated with biotinylated anti-TrkB antibody, followed by further incubation with QD-NTV bioconjugates. QD-NTV biomarkers on the extracellular domain of TrkB receptors were imaged by the combined atomic force microscope and confocal laser scanning microscope (AFM-CLSM) providing resolved (nanometer-scale) structural and fluorescent images. We found that TrkB receptors were distributed over the neuronal cell bodies (soma) and neurites. TrkB receptors in the somata looked more concentrated, but those in the neurites appeared punctate. Thus, our QD-based immunocytochemistry technique combined with an AFM-CLSM can be used for three-dimensional morphology of neurons on nanometer-scale structural resolution and their fluorescence images with QDs. Furthermore, this technique can be applied for real-time fluorescence imaging or long-term study of live neurons.

INTRODUCTION

Currently, researches in neuroscience have been focused on the fundamental understanding of ligand (or neurotrophins)−receptor interaction mechanism, the localization of receptors on the surface of neurons, and receptor-bound signal trafficking. Neurotrophins are a family of growth factors regulating differentiation, maturity, and survival of neurons. The diverse functions of neurotrophins are mediated by their specific interaction with tyrosine kinase receptors (*1*). The tyrosine kinase receptors (Trks) include TrkA (a receptor for nerve growth factor (NGF)), TrkB (a receptor for brain-derived neurotrophic factor (BDNF) and neurotrophin-4/5 (NT-4/5)), and TrkC (a receptor for neurotrophin-3 (NT3)). Specially, TrkB (Tyrosine Kinase B), expressed in the developing nervous system including the forebrain, caudal midbrain, hindbrain, spinal cord, the trigeminal ganglion, and differentiating neural crest cells, possesses high binding affinity to brain-derived neurotrophic factor (BDNF) and neurotrophin-4(NT-4) (*2*). The binding of BDNF to TrkB receptor activates downstream intracellular cascades, regulating neuronal development and plasticity, long-term potentiation, and apoptosis (*3*). It was also reported that short-term physical exercise stimulates BDNF and TrkB gene expression in the brain (*4*). It was recently revealed that signaling through TrkB receptors appears to be related to Alzheimer's disease (*5*). Genetic ablation of TrkB gene in the forebrain changes hippocampal spine density and length in an age- and region-specific manner, which in turn may affect synaptic transmission and plasticity. The hippocampus is best recognized for its role in declarative memory and spatial learning (*6*). To understand the pathogenic mechanism related to the TrkB receptors as well as the development and regulation of the nervous system, it is important to monitor the localization of TrkB receptors in hippocampal neurons.

For several decades, an immunocytochemical method has been developed to detect antigens (e.g., extracellular surface of membrane receptors) using antigen−antibody reaction. To visualize antigens with an optical microscope, antibodies have to be labeled with various and multiple fluorescent dyes simultaneously (*7*). Optical microscopy provides selective and specific visualization of labeled species in the sample, and renders it possible to monitor the process and dynamics of living cells with high temporal resolution. The lateral resolution of optical microscopy is usually limited by the diffraction to about half the wavelength of the light used, thus restricting to achieve a detailed structural image. Great advances in optical microscopy such as near field scanning optical microscopy (NSOM), stimulated emission depletion microscopy (STED), photoactivated localization microscopy (PALM), and stochastic optical reconstruction microscopy (STORM) have been achieved to overcome the optical diffraction limit, but there still are constraints for realizing time-resolved dynamics or three-dimensional imaging (*8*).

Electron microscopy (EM) is a well-established technique identifying highly resolved structural features of targets in the sample on subnanometer-scale resolution. However, EM can be applied to only fixed cells (*9*). Our integrated AFM and CLSM (AFM-CLSM) has advantages over EM or OM in that nanometer-scale spatial resolution, frame/second temporal resolution, and chemical identification through fluorescence detection can be done simultaneously for live cells. Using AFM-CLSM, we can easily get optical and spatial images of targets on the cells. We can also take the depth-resolved (*z*-stack) fluorescent images of antigens by CLSM together with their nanometer-

* Corresponding author. Tel: + 82-2-880-1456. Fax: +82-2-889-1568. E-mail address: shnlee@snu.ac.kr.

[†] School of Chemistry.

[‡] Department of Biological Sciences.

10.1021/bc900304b © 2010 American Chemical Society
Published on Web 03/29/2010

scale cellular structural images by AFM. AFM is a subnanometer resolution scanning-probe device in which a sharp tip at the end of a flexible cantilever is scanned over the samples' surface (*10*). AFM has been used to take three-dimensional images of live biological samples, because it can provides structural details at subnanometer resolution in an ambient air or under liquid environment (*11*). Over the past few years, various efforts have been made to combine optical microscopy and AFM in order to study a range of biological processes in terms of a 3D structural and fluorescent image (*12*−*17*). CLSM offers high-quality three-dimensional fluorescent images over conventional wide-field optical microscopy, due to its ability to control the depth of a focal plane to eliminate out-of-focus light or glares in specimens and its capability to collect serial (i.e., *z*-stack) optical images for thick specimens.

In order to investigate the localization of TrkB receptors, we labeled them with highly luminescent, no-photobleaching, and photostable fluorescent QDs. Semiconductor quantum dots with broad absorption, high extinction coefficient, high luminance, narrow, and tunable emission wavelength through the adjustment of their size are ideal fluorophores as biological tagging materials (*18*−*20*). In addition, compared with conventional organic dyes or GFPs, QDs have high photostability and can resist to photobleaching for a prolonged time of AFM-CLSM measurement (*21*−*23*). QDs have been used for protein and DNA immunoassays, fluorescence resonance energy transfer (FRET), diagnostics, live cell imaging through bioconjugation, and high-throughput screening. At present, bioconjugates of QDs bound to ligands such as streptavidins, neutravidins, and biotinylated proteins are excellent tools for the study of neuroscience. In our study, we report the synthesis of highly luminescent water-soluble QD-neutravidin (NTV) bioconjugates and the spatial and optical characterization of TrkB receptors in cultured hippocampal neurons using combined atomic force and confocal microscopy. We synthesized semiconductor QDs with a high photoluminescence quantum yield (∼80% PL QY at room temperature) and a narrow size distribution and a chemical composition gradient in a radial direction of a spherically shaped QD (*25*). Our QDs with a chemical composition gradient have better structural stability and quantum efficiency. Water-soluble quantum dots were prepared by replacing the oleic acid (OA) attached to the surface of QDs with mercaptopropionic acid (MPA). Even after the surface modification with MPA, our QDs still maintain high quantum efficiency due to our original QD structure of chemical composition gradients in a radial direction. Water-soluble QDs kept at 4 °C have been stable for up to one year. We conjugated QDs in phosphate buffered saline (PBS) of pH 7.4 with NTVs which bound with biotinylated anti-TrkB antibody. NTV has more advantages over commonly used streptavidin (STV) in that NTV is more cost-effective and reduces nonspecific binding because of more neutral pI (pH at isoelectric point) (*24*). Water-soluble QD-NTV bioconjugates interact with TrkB receptors, pretreated with biotinylated anti-TrkB receptor antibody and located in cultured hippocampal neurons, via a high affinity between avidin and biotin. The distribution of TrkB receptors in cultured hippocampal neurons was observed three-dimensionally by AFM-CLSM at nanometer-scale spatial resolution combined with optical fluorescence images.

MATERIALS AND METHODS

Reagents. Cadmium oxide (CdO, 99.99%), zinc acetate (99.9%, powder), selenium (99.9%, powder), sulfur (99.9%, powder), trioctylphosphine (TOP, 90%), oleic acid (OA, 90%), 1-octadecene (ODE, 90%), mercaptopropionic acid (MPA, 99.8%), 1-ethyl-3-(3-dimethylaminopropyl)carbodiimide (EDC), *N*-hydroxysuccinimide (NHS), sephadex G-25 (beads for gel-filtration), agarose for gel electrophoresis, sodium phosphate dibasic heptahydrate (for PBS buffer solutions, ACS reagent grade), sodium dihydrogen phosphate dehydrate (for PBS buffer solutions), Trizma base (minimum 99.9% titration) and acetic acid (glacial) for Tris-Acetate EDTA (TAE) buffer solutions, brilliant blue R and bromophenol blue sodium salt for electrophoresis and biological analysis, ethylene diamine tetra acetic acid sodium salt (EDTA sodium salt), paraformaldehyde were purchased from Sigma Aldrich. Neutravidin (NTV) was purchased from Pierce.

Biotinylated antibody against mouse TrkB extracellular domain (BAF1494), which is polyclonal full length goat IgG, was purchased from R&D system. Hexane, methanol, ethanol, acetone, and chloroform were purchased from Daejung chemicals. All chemicals were used as purchased without further purification. Buffer solutions are homemade.

Single-Step Synthesis of Quantum Dots with Chemical Composition Gradients. The highly luminescent green-emitting (the emission wavelength is 520 nm with a fwhm of less than 30 nm) CdSe/ZnS quantum dots with chemical composition gradients were produced by our previously reported single-step synthetic method (*25*). The size of green-emitting CdSe/ZnS QDs with chemical composition gradients were measured to be 6 nm (with a size distribution of less than 5%) by transmission electron microscopy (TEM).

Preparation of Water-Soluble Quantum Dots. We prepared water-soluble quantum dots by replacing the oleic acid (OA, originally coordinated ligand to QDs as they were produced) with mercaptopropionic acid (MPA) (*25, 26*).

Measurement of Quantum Yield (QY) of QDs. The photoluminescence quantum yield (PL QY) of CdSe/ZnS QDs with chemical composition gradients dispersed in 0.2 M PBS buffer of pH 7.4 was measured and estimated by comparing their photoluminescence intensities with those of primary standard dye solutions (emission close to the QDs, Coumarin 545 with the QY of 0.95 in ethanol) at the same optical density (0.05) at the same excitation wavelength of 465 nm. The room temperature PL QY of the green-emitting QDs is typically ∼80%.

Measurement of the Concentration of QDs. In this study, the concentration of green-emitting CdSe/ZnS QDs was measured using an Agilent 8454 UV−vis spectrometer and was calculated based upon a previously reported method (*27*).

Water-Soluble Quantum Dot-Bound Neutravidin (QD-NTV). The conjugation was carried out through a coupling reaction between the carboxyl group of MPA and an amino group of NTV using EDC as the coupling activator (*28*). The concentration ratio of QDs to NTV is 1:40 in moles. The conjugation of QDs dispersed in PBS buffer with NTV was done as follows. The 100 μL of 2 mM EDC dissolved in 0.2 M of 2-(morpholino) ethanesulfonic acid (MES) of pH 6.0 was added to the QD solution, and then the resulting solution was stirred mildly for 5 min. The 50 μL of 5 mM NHS dissolved in 0.2 M of MES of pH 6.0 was added to the e-tube mixture with a 30 min mild stirring at room temperature. After 30 min stirring, the mixture was purified by size exclusion chromatography using sephadex G-25. Only QDs reacted with EDC and NHS were collected. Then, 5 μL of NTV taken from the stock solution (stock solution: 10 mg dissolved in 1 mL of 0.2 M borate of pH 9.5) was diluted with 95 μL of 0.2 M borate of pH 9.5, and then this solution was added to the solution containing QDs reacted with EDC and NHS. The solution was stirred at room temperature for 2 h, and QD-NTV was purified by a Sephacryl S-400 HR size exclusion spin column (GE healthcare, Sweden).

Cell Culture. Primary hippocampal neurons were cultured from mice embryo E18 (ICR strain) by modified protocol from Baker et al. (*29*). Briefly, pregnant ICR mice were euthanized

to decapitate fetus and dissect out the fetal brains. Hippocampi were removed under a dissecting microscope and trypsinized with 2.5% trypsin solution in distilled water. Then, neurons were dissociated and plated on the poly(L-lysine)-coated glass bottom culture dishes in a concentration of 50,000/cm^2. Neurons were grown for two weeks in maintenance medium (neurobasal medium containing 2% B-27, 1 mM glutamine, and penicillin/streptomycin) before fixation.

Cell Fixation. For the detection of TrkB receptors, mouse hippocampal neurons were fixed with 4% paraformaldehyde on ice for 10 min. Then, we washed the cells with PBS more than 3 times. In order to reduce the nonspecific binding, the cells were blocked with 2% (wt/vol) of BSA dissolved in PBS for overnight at 4 °C. Next day, we washed the cells with PBS more than 3 times.

Detection of TrkB Receptors on a Mouse Hippocampus Neuron Cell Surface. Biotinylated anti-TrkB antibodies and QD-NTV were diluted in PBS. Fixed and BSA-blocked primary neurons were incubated with 5 μg/mL of a mouse anti-TrkB antibody that recognized the external domain of a TrkB receptor (catalog no. BAF 1494; R&D systems) for 2 h at room temperature. Then, the neurons were washed with PBS several times to eliminate the nonspecific binding of biotinylated anti-TrkB antibody. Next, we sequentially incubated the neurons with 160 nM of QD-NTV for 2 h at room temperature. During this incubation, final bioconjugation of biotinylated anti-TrkB antibody with QD-NTV via avidin−biotin coupling was made at the cell surface where TrkB receptors were located. For an optical microscope measurement, neuron cells were examined just right after a QD-labeling step. For combined atomic force and confocal microscopy measurements, neuron cells were dehydrated with 75%, 90%, and 100% of ethanol in series, and then they were air-dried.

MEASUREMENTS AND ANALYSIS

Optical Characterization. Room-temperature optical absorption spectra of CdSe/ZnS core/shell QDs with chemical composition gradient were measured with an Agilent 8454 UV−vis diode array spectrometer. QDs were diluted in hexane or PBS. Photoluminescence spectra were collected on an ACTON spectrometer connected with a photomultiplier tube (Acton Research).

Gel Electrophoresis. The conjugation of water-soluble QDs with NTVs was confirmed by gel electrophoresis (Mupid-2 plus model). Gels were 1% agarose in Tris-Acetate EDTA (TAE) buffer. Gels were run at 100 V for 80 min with TAE buffer as the running buffer. Gel images were taken on an Olympus EX 140 with a UV lamp (VL-4LC, made in EEC).

Fourier Transform Infrared (FT-IR) Spectroscopy. To confirm an amide bonding of QDs with NTVs, we carried out the analysis of FT-IR vibration spectra of samples of QD-NTV (JASCO FT/IR-660 plus, made by JASCO).

Confocal Laser Scanning Microscopy. The confocal fluorescent images and differential interference contrast (DIC) images of QD-labeled hippocampus neurons were obtained using Fluoview FV1000 confocal laser scanning microscope (CLSM; Olympus, Tokyo, Japan) connected to an IX 81 inverted microscope (Olympus, Tokyo, Japan) with a UPLAPO 60X waterproof objective (its numerical aperture (NA) was 1.20). QDs were excited with a 488 nm Ar^+ ion laser line and detected in the wavelength range 510−530 nm. The confocal fluorescence images were overlaid with DIC images in order to locate the components of neuron cells in more informative way.

Combined Atomic Force Microscopy and Confocal Laser Scanning Microscopy (AFM-CLSM). Fluorescent and nanometer-scale spatially resolved structural images of QD-labeled cells were obtained with a combined AFM-CLSM. A MFP-3D (atomic force microscope, Asylum Research) was placed on an IX 81 inverted microscope (Olympus) coupled to a Fluoview FV 1000 confocal laser scanning microscope (CLSM; Olympus). The combined AFM-CLSM setup was placed on a TS-140 antivibration optical table, and then the whole thing was enclosed in an acoustically isolated chamber. In order to get a three-dimensional fluorescence image of neurons by CLSM, we collected the depth-resolved (i.e., z-stack) fluorescence images of neurons in every 0.3 μm. The whole image of neurons was reconstructed from all the z-stack fluorescence images. Neurons were imaged at a scan rate of 1.0 Hz in the contact mode with an Asylum Research AFM. A 200-μm-long PNP-TR cantilever (NanoWorld, Switzerland) with a spring constant of 0.08 N/m and a resonant frequency of 17 kHz was used. The tip radius of curvature is smaller than 10 nm. The force of 1.0 nN was maintained during imaging. We positioned the cantilever tip in the AFM head over the optical axis of the CLSM by manually adjusting the AFM stage in the combined AFM and CLSM instrument.

RESULTS AND DISCUSSION

We produced highly luminescent semiconductor quantum dots (QY ~80%) by our single-step synthesis of QDs with chemical composition gradients (*25*). In the bioconjugation study, we used green CdSe/ZnS core/shell QDs with chemical composition gradients emitting at 520 nm with a fwhm less than 30 nm. The size distribution of the QDs is within 5%. The average size of the QDs is 6 nm in diameter. The unique structure of our QDs (QDs with gradual chemical composition gradient outward) has good merits: the relaxation of the strain caused by the lattice mismatch between the CdSe core and the ZnS shell even though the thickness of the outer part of the QDs is more than two atomic layers, funneling the excitons toward the cores of QDs due to chemical composition gradients (i.e., energy-gradient structure) and thus enhancing the photoluminescence (PL QY ~80%). In order to use QDs for biological applications, we need to have water-soluble QDs. The QDs as produced by our single-step synthetic method were originally surface-passivated with oleic acid that functioned as a solvent and coordinating ligand. Water-soluble QDs were prepared by replacing the oleic acid coordinated to their surfaces with mercaptopropionic acid (MPA) via a conventional ligand exchange reaction (*25, 26*). The MPA-capped QD precipitates are collected out from the turbid mixture by several centrifugal purifications. We disperse MPA-capped QDs in PBS. Figure 1a shows the photoluminescence spectra of green-emitting CdSe/ZnS core/shell QDs with chemical composition gradient (high quantum yield ~80%) capped with oleic acids (OA) and dispersed in hexane (denoted with solid line) and those capped with MPAs and dispersed in PBS (denoted with dotted line). As shown in Figure 1a, water-soluble QDs capped with MPAs still maintain high quantum efficiency. Figure 1b shows high luminance of both QD-OAs dispersed in hexane and QD-MPAs dispersed in PBS under an indoor common fluorescent lamp. Figure 1c shows the photoimages of the same QDs irradiated with a UV lamp under the indoor common fluorescent lamp off. Our green-emitting CdSe/ZnS core/shell QDs with chemical composition gradients either capped with oleic acids (OA) or capped with MPAs are highly luminescent (measured to be ~80% QY, using a reference dye of coumarin 545 with 95% of QY in ethanol). Water-soluble QD-MPAs dispersed in PBS have been stable for more than a year at 4 °C. Eventually, in order to detect TrkB receptors on the neuron cells through the interaction between QD-neutravidin (QD-NTV) and biotinylated anti-TrkB antibody, we need to generate QD-NTV. A solution of NTV powder dissolved in 0.2 M borate of pH 9.5 is mixed with QD-MPAs dispersed in PBS. The concentration of QD-MPAs turns out 0.42 μM and 10 mg

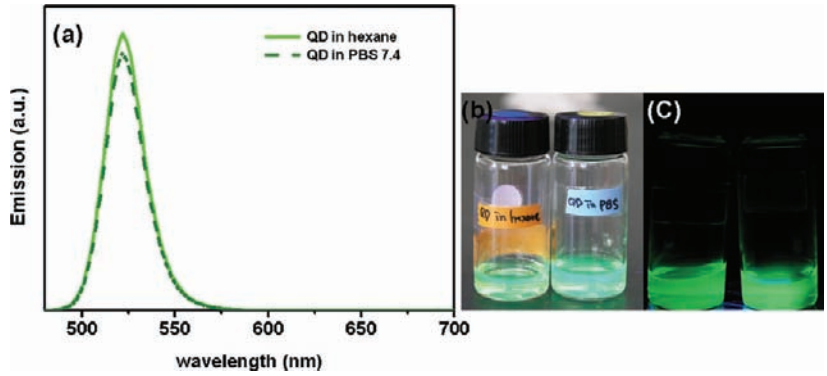


Figure 1. (a) Photoluminescence spectra of green-emitting CdSe/ZnS core/shell QDs with chemical composition gradient capped with oleic acids and dispersed in hexane (denoted with solid line) and those capped with MPAs and dispersed in PBS (denoted with dotted line). (b) It shows high luminance of both QD-OAs dispersed in hexane and QD-MPAs dispersed in PBS under an indoor common fluorescent lamp. (c) It shows the photo of the same QDs irradiated with a UV lamp under the fluorescent lamp off.

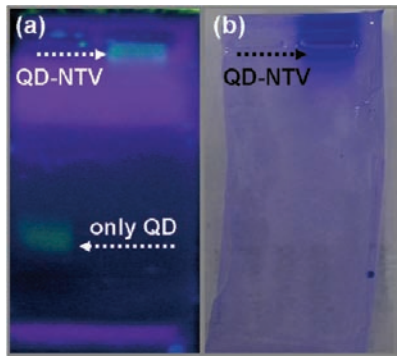


Figure 2. (a) Fluorescent images of MPA-capped QDs and NTV-conjugated QDs in 1% agarose gel after gel electrophoresis. (b) QD-NTV stained by Coomassie blue. The blue band confirms the existence of NTV proteins in QD-NTV.

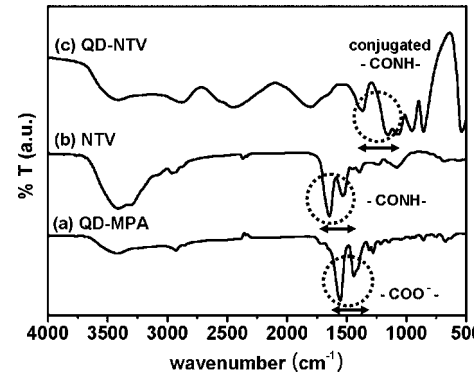


Figure 3. Fourier transform infrared (FT-IR) spectra of (a) MPA-capped QD, (b) NTV, and (c) QD-NTV.

of NTV is dissolved in 1 mL of 0.2 M borate of pH 9.5, and thus that of NTV turns out to be 167 μM. The conjugation is made through a coupling reaction between the carboxyl group of MPA and an amino group of NTV using EDC as the coupling activator (*28*). After the coupling reaction, the mixture of QD-MPA, NTV, and QD-NTV was purified through gel filtration. QD-NTV conjugates are confirmed by the two following methods. In one way, samples were analyzed by electrophoresis on a 1% agarose gel in Tris acetate EDTA (TAE) buffer. Gels are run at 100 V for 80 min with TAE buffer as the running buffer. Figure 2a shows the green fluorescent images of a gel plate with well-resolved separation of QD-NTVs from QDs. The top band is QD-NTVs and the bottom band is QDs only. In the other way, as shown in the Figure 2b, the left well in the gel plate is loaded only water-soluble QDs, the right well is loaded with water-soluble QD-NTV. The interaction between SO_3^- functional group of brilliant blue R (or called Coomassie blue) and NH_3^+ amino functional group of amino acids such as tyrosine, histidine, and phenyl alanine causes the blue stain in the protein moiety under the solution of pH 4.3. In the destaining solution (pH < 2), gel becomes transparent except for the bands containing protein moieties. The blue stain confirms there is a protein moiety. The right well in the gel plate is indeed QD-NTVs. Using a Fourier transform infrared (FT-IR) spectrometer, we obtained vibration spectra of functional groups of QD-MPA, NTV, and QD-NTV. The FT-IR spectra were shown in Figure 3. The IR bands at 1554 and 1440 cm^{-1}, at 3405 and 3350 cm^{-1}, and at 3413 cm^{-1} are characteristic bands of asymmetric and symmetric stretching bands of $-COO^-$ functional group in QD-MPA, primary amine N−H stretching bands of free NTV, and N−H stretching bands of conjugated QD-NTV, respectively (*30, 31*). The amide bands I and II of NTV itself are shown at 1644 cm^{-1} and at 1526 cm^{-1}. The conjugated amide bands of −CONH− functional group in QD-NTV are located 1366 cm^{-1} and 1154 cm^{-1} (red-shifted from those of QD-MPA). Next, the avidin−biotin interaction was used for the detection of TrkB receptors through ligand−receptor binding. In our study, neutravidin [MW 60kD, pI 6.3] instead of streptavidin [MW 53kD, pI 6.8−7.5] or avidin [MW 67kD, pI 10] was used because neutravidin with lysine-rich residues available to amide bondings with carboxylic groups of QD-MPA does not have an Arg-Tyr-Asp (RYD) sequence, which may cause nonspecific bindings, and because deglycosylated neutravidin reduces oligosaccharide-based lectin binding with biotin-binding affinity retained (*26*). We used biotinylated anti-TrkB antibody (R&D systems) as a binding moiety to QD-NTV. The scheme we took for fluorescence imaging was the binding via avidin−biotin coupling between TrkB receptors attached with biotinylated anti-TrkB antibodies on the neuron cells through antigen−antibody interaction and QD-NTV (a fluorescent tag).

We prepared biotinylated anti-TrkB antibody dissolved in PBS (5 μg/mL). The two-week-grown hippocampal neurons were plated at a density of 50,000 cells/cm^2 onto poly(L-lysine)-coated glass-bottomed culture dish. Cultured hippocampal neurons were fixed with 4% paraformaldehyde on ice for 10 min, and the cells were washed with PBS more than 3 times. In order to reduce the nonspecific binding, the cells were blocked with 2% (wt/vol) of BSA dissolved in PBS for overnight at 4 °C, and then, we washed the cells with PBS more than 3 times. There are some reports that the conjugates of QDs with antibodies bind specifically to membrane receptors in both fixed and live cells (*32*−*34*). In the first step, we checked nonspecific binding of QD-NTV to cultured primary mouse hippocampal neurons. The conjugation of QD-NTV to cultured hippocampal neurons was carried out in PBS. Mouse hippocampal neurons

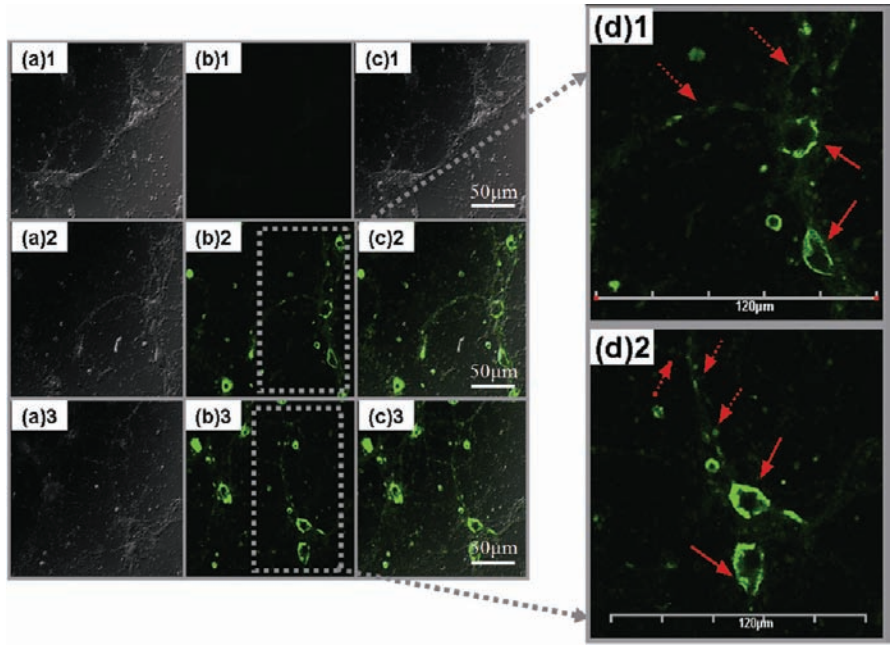


Figure 4. DIC and confocal fluorescence microscopic images of mouse hippocampal neuron. (a) 1−2: DIC images of the neuron cell with biotinylated anti-TrkB antibody unattached and that with biotinylated anti-TrkB antibody attached, respectively. (a) 3: DIC image of other region of the neuron cell with biotinylated anti-TrkB antibody attached. (b) 1: fluorescent image of the neuron cell without any biotinylated anti-TrkB antibody treated with QD-NTV and shows no fluorescence. (b) 2−3: fluorescent images of two different regions of the cultured hippocampal neurons with biotinylated anti-TrkB antibody treated with QD-NTV. (c) 1−3: the overlapped images of (a) 1−3 and (b) 1−3, respectively. (d) 1−2: enlarged images of some part of (b) 2−3, the neuron cell bodies and neurites are marked with solid and dashed arrows, respectively.

were incubated with 160 nM of QD-NTV for 2 h, and then we washed the cells with PBS more than 3 times. After washing the cell many times, QD fluorescence signal does not appear on the surface of the cells (Figure 4(b)1). Thus, we confirm that QD-NTV rarely binds nonspecifically to the cell membrane in fixed hippocampal neurons. In the second step, in order to detect endogenous TrkB receptors on cultured hippocampal neurons, we treated the cells with biotinylated anti-TrkB antibody (5 μg/mL) dissolved in PBS buffer for 2 h. To eliminate nonspecific binding of biotinylated anti-TrkB antibody, the cells were washed with PBS several times. Biotinylated anti-TrkB antibodies were specifically located at the TrkB receptors on the neuron cells through antigen−antibody interaction. Then, we incubated cultured hippocampus neurons attached with biotinylated anti-TrkB antibody with 160 nM of QD-NTV for 2 h. QD-NTV specifically bound to biotinylated anti-TrkB antibody of the neuron cells via avidin−biotin coupling. Finally, the bioconjugation via avidin−biotin coupling between biotinylated anti-TrkB antibody located at the TrkB receptors on the neurons and QD-NTV were made for fluorescence imaging.

In Figure 4, (a)1−3 are DIC (differential interference contrast) images of the neuron cells, (b)1−3 are fluorescent images of the neuron cells, (c)1−3 are overlapped images of DIC images (a)1−3 with fluorescent images (b)1−3. Figure 4(a)1 shows a DIC image of the neuron cell without any biotinylated anti-TrkB antibody treated with QD-NTV; the (b)1 panel is a fluorescent image of the neuron cell without any biotinylated anti-TrkB antibody treated with QD-NTV and shows no fluorescence, and thus confirms no nonspecific binding between the neuron cell and QD-NTV. Nonspecifically bound QD-NTV to the cells has been eliminated through washing with PBS buffer. Figure 4(a)2−3 and (b)2−3 are DIC images and fluorescent images of two different regions of the cultured hippocampus neuron cells with biotinylated anti-TrkB antibody treated with QD-NTV, respectively. QD-NTV specifically binds to biotinylated anti-TrkB antibody of the neuron cells via avidin−biotin coupling. From the overlapped images of Figure 4(a)1−3 and (b)1−3 shown in (c)1−3 panels, we clearly see QD green fluorescence present on the neuron cell bodies and neurites. Figure 4(c)2 and (c)3 shows QD green fluorescence signals from the neuron cell bodies and neurites. More green fluorescence signal came from the neuron cell bodies. Thus, more TrkB receptors were distributed over the cell bodies (soma) than the neurites within neurons. Enlarged images of some part of Figure 4(b)2−3 are shown in part (d)1−2. The neuron cell bodies and neurites are marked with solid and dashed arrows, respectively. TrkB receptors in the cell bodies (soma) were distributed in a highly concentrated manner, whereas those in the neurites were distributed in a punctuate manner, as shown enlarged images (Figure 4(d)1−2). The location of TrkB receptors has been previously studied by Swanwick et al. (*35*). However, the fluorescence images were not enough to show three-dimensional structures. Drake et al. reported the localization of TrkB receptors in hippocampal neurons with EM (*36*), but due to the limitation to prepare samples, their results did not properly reflect the distribution of TrkB receptors over the whole neuronal structure. Our homemade combined atomic force microscope and confocal laser scanning microscope (AFM-CLSM) instrument enables the three-dimensional imaging of neurons on nanometer-scale structural resolution and fluorescent chemical identification. With the homemade AFM-CLSM, we obtained 3-D images of QD-labeled TrkB receptors in hippocampal neurons, and these were shown in Figure 5. We obtained AFM-CLSM images after dehydration and air-drying of QD-labeled neuron cells. The three-dimensional cell surface topography (Figure 5b) is obtained by the three-dimensional surface-plotting of the height-contrast image (Figure 5a). The topographical image of the cell surface was shown on nanometer scale, and the cell's maximal height was ~1.5 μm. The 3-D cellular structures, such as somata and neurites, were clearly visualized. We obtained the depth-resolved (i.e., z-stack) fluorescence images of neurons in every 0.3 μm and reconstructed them (x, y, z = every 0.3 μm) to get a three-dimensional fluorescence image of neurons. The merged 3-D neuron image of the structural image by AFM and the fluorescent image by CLSM is shown in Figure 5d. Thus, the whole fluorescent TrkB signals

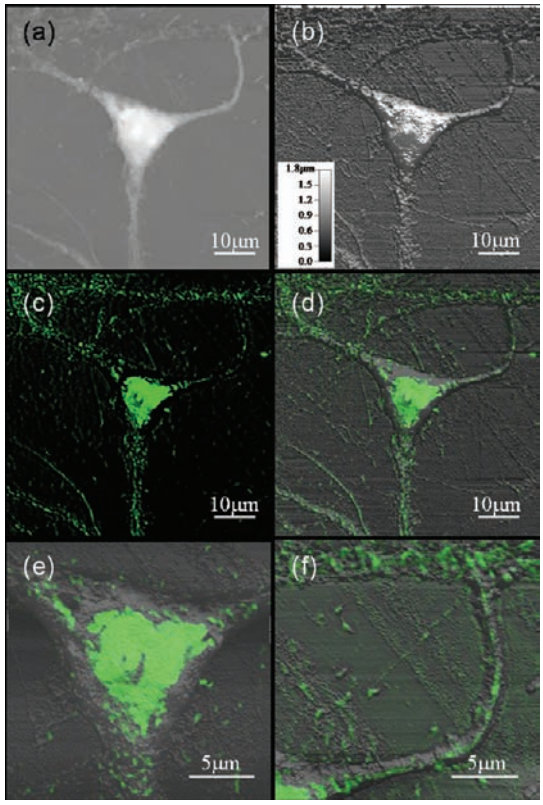


Figure 5. Image of cultured hippocampal neurons acquired with combined AFM-CLSM. (a) Height contrast image. (b) 3-D surface plot of height image. (c) CLSM fluorescence image. This is two-dimensional projection fluorescence image. (d) 3-D surface plot of height image combined with a CLSM projection image given in (c). (e) Magnified image of soma region shown in (d). (f) Magnified image of neurite region shown in (d).

over the cell surface can be correlated to the cellular ultrastructure resolved by AFM. Magnified AFM-CLSM image shows that TrkB receptors are distributed in a highly concentrated manner in the central soma but punctately at the edge of soma (Figure 5e). Furthermore, TrkB receptors appeared to be punctate in the neurites, consistent with the report from Swanwick et al. (*35*). Additionally, most punctate TrkB receptors in the neurites were located on the high ridges of neurites. Thus, our AFM-CLSM analysis using QD enabled us to discover precise correlation between immunocytochemically fluorescent signals and cellular structures, which could not be done with a conventional fluorescent image analysis system.

CONCLUSION

We have demonstrated that the highly luminescent bioconjugates of QD-neutravidin and biotinylated anti-TrkB antibody are available to acquire the distribution of TrkB receptors by depth-resolved fluorescent signals, which are highly correlated with nanoscale cellular structural images. We synthesized nearly monodispersed water-soluble CdSe/ZnS core/shell QDs (QY ~80% at room temperature) with chemical composition gradients emitting at 520 nm with a fwhm less than 30 nm. QD-NTV is made through a coupling reaction between the carboxyl group of water-soluble QD-MPA and the amino group of NTV using EDC as the coupling activator. In order to study the neurons through AFM-CLSM, we generated the bioconjugates of biotinylated anti-TrkB antibody, which detect the TrkB receptors on the surface of neurons with QD-NTV via avidin−biotin coupling. We compared the conjugated QD-NTV fluorescent signals between neurons treated with biotinylated anti-TrkB antibody and QD-NTV and neurons treated with only QD-NTV. QD fluorescence is present only on the cells treated with biotinylated anti-TrkB antibody. This result confirms the successful bioconjugation between QD-NTV and biotinylated anti-TrkB antibody. From the fluorescence study, we find that TrkB receptors are distributed widely over the neuron cell bodies (soma), whereas they are distributed as a punctate structure on the neurites. We further discover the precise localization of TrkB receptors by correlating the fluorescent image with nanoscale cellular structures resolved by AFM. AFM-CLSM images show that TrkB receptors are located broadly in the central soma but showing punctate structures at the edge of soma. Interestingly, punctate signals of TrkB receptors on the neurites are located on the high ridges of neurites. Over the repeated scans by AFM-CLSM imaging, the bioconjugates show no photobleaching. Thus, we suggest that our QD-based immunocytochemistry technique can be utilized for stable structural and fluorescent imaging in neurons by AFM-CLSM. Furthermore, our bioconjugate, QD-NTV-biotin-TrkB, can be applied for real-time fluorescence signal trafficking or long-term imaging in live neurons.

ACKNOWLEDGMENT

This work was supported in part by MOE through BK21 program and Seoul R&BD program (10543). We thank NRF (for Artificial Atoms Research) and CNNC for supporting this research. We also acknowledge the student support from the NRF through Systems Institute-National Core Research Center (NCRC). This work was supported by National Creative Research Initiative Center for Memory and WCU program (to B.K.K).

Note Added after ASAP Publication: This paper was published on the Web on Mar 29, 2010, with an error in the last paragraph in the Results and Discussion section. The corrected version was reposted on Apr 1, 2010.

LITERATURE CITED

(1) Zheng, J., Shen, W., Lu, T., Zhou, Y., Chen, Q., Wang, Z., Xiang, T., Zhu, Y., Zhang, C., Duan, S., and Xiong, Z. (2008) Clathrin-dependent endocytosis is required for TrkB-dependent Akt-mediated neuronal protection and dendritic growth. *J. Biol. Chem. 283*, 13280–13288.

(2) Chao, M. V. (1992) Neurotrophin receptors: A window into neuronal differentiation. *Neuron 9*, 583–593.

(3) Xu, B., Gottschalk, W., Chow, A., Wilson, R. I., Schnell, E., Zang, K., Wang, D., Nicoll, R. A., Lu, B., and Reichardt, L. F. (2000) The role of brain-derived neurotrophic factor receptors in the mature hippocampus: modulation of long-term potentiation through a presynaptic mechanism involving TrkB. *J. Neurosci. 20*, 6888–6897.

(4) Neeper, S. A., Gomez-Pinilla, F., Choi, J., and Cotman, C. W. (1996) Physical activity increases mRNA for brain-derived neurotrophic factor and nerve growth factor in rat brain. *Brain Res. 726*, 49–56.

(5) Chen, Z., Simmons, M. S., Perry, R. T., Wiener, H. W., Harrell, L. E., and Go, R. C. P. (2008) Genetic association of neurotrophic tyrosine kinase receptor type 2 (NTRK2) with Alzheimer's disease. *Am. J. Med. Genet. Part B Neuropsychiatr. Genet. 147B*, 363–369.

(6) von Bohlen und Halbach, O., Krause, S., Medina, D., Sciarretta, C., Minichiello, L., and Unsicker, K. (2006) Regional- and age-dependent reduction in trkB receptor expression in the hippocampus is associated with altered spine morphologies. *Biol. Psychiatry 59*, 793–800.

(7) Larsson, L. I. (1988) Immunocytochemical detection systems. in *Immunocytochemistry: Theory and practice*, pp 77−145, Chapter 3, CRC Press, Inc., Boca Raton, FL.

(8) Hellriegel, C., and Gratton, E. (2009) Real-time multi-parameter spectroscopy and localization in three-dimensional single-particle tracking. *J. R. Soc. Interface 6*, S3–S14.

(9) Venkatesan, C., Song, X Z., Go, C. G., Kurose, H., and Aoki, C. (1996) Cellular and subcellular distribution of α_{2A}-adrenergic receptors in the visual cortex of neonatal and adult rats. *J. Comp. Neurol. 365*, 79–95.

(10) Binnig, G., Quate, C. F., and Gerber, C. (1986) Atomic force microscope. *Phys. Rev. Lett. 56*, 930–933.

(11) Trach, A., and Meininger, G. A. (2008) Atomic force microscopy. *Curr. Protoc. Microbiol. 8*, 2C.2.12C.2.17.

(12) Lieberman, K., Ben-Ami, N., and Lewis, A. (1996) A fully integrated near-field optical, far-field optical, and normal-force scanned probe microscope. *Rev. Sci. Instrum. 67*, 3567–3572.

(13) Lal, R., and Proksch, R. (1997) Multimodal atomic force microscopy: biological imaging using atomic force microscopy combined with light fluorescence and confocal microscopies and electrophysiologic recording. *Int. J. Imaging Syst. Technol. 8*, 293–300.

(14) Horton, M., Charras, G., Ballestrem, C., and Lehenkari, P. (2000) Integration of atomic force and confocal microscopy. *Single Mol. 1*, 135–137.

(15) Noy, A., and Huser, T. R. (2003) Combined force and photonic probe microscope with single molecule sensitivity. *Rev. Sci. Instrum. 74*, 1217–1221.

(16) Kellermayer, M. S. Z., Karsai, A., Kengyel, A., Nagy, A., Bianco, P., Huber, T., Kulcsar, A., Niedetzky, C., Proksch, R., and Grama, L. (2006) Spatially and temporally synchronized atomic force and total internal reflection fluorescence microscopy for imaging and manipulating cells and biomolecules. *Biophy. J. 91*, 2665–2677.

(17) Doak, S. H., Rogers, D., Jones, B., Francis, L., Conlan, R. S., and Wright, C. (2008) High-resolution imaging using a novel atomic force microscope and confocal laser scanning microscope hybrid instrument: essential sample preparation aspects. *Histochem. Cell. Biol. 130*, 909–916.

(18) Weller, H. (1993) Colloidal semiconductor q-particles: Chemistry in the transition region between solid state and molecules. *Angew. Chem., Int. Ed. Engl. 32*, 41–53.

(19) Alivisatos, A. P. (1996) Semiconductor clusters, nanocrystals, and quantum dots. *Science 271*, 933–937.

(20) Lidke, D. S., Nagy, P., Heintzmann, R., Arndt-Jovin, D. J., Post, J. N., Grecco, H. E., Jares-Erijman, E. A., and Jovin, T. M. (2004) Quantum dot ligands provide new insights into erbB/HER receptor-mediated signal transduction. *Nat. Biotechnol. 22*, 198–203.

(21) Michalet, X., Pinaud, F., Lacoste, T. D., Dahan, M., Bruchez, M. P., Alivisatos, A. P., and Weiss, S. (2001) Properties of fluorescent semiconductor nanocrystals and their application to biological labeling. *Single Mol. 2*, 261–276.

(22) Bruchez, M., Moronne, M., Gin, P., Weiss, S., and Alivisatos, A. P. (1998) Semiconductor nanocrystals as fluorescent biological labels. *Science 281*, 2013–2016.

(23) Chan, W. C. W., and Nie, S. (1998) Quantum dot bioconjugates for ultrasensitive nonisotopic detection. *Science 281*, 2016–2018.

(24) Meyer, S. C., Gaj, T., and Ghosh, I. (2008) Highly selective cyclic peptide ligands for neutravidin and avidin identified by phage display. *Chem. Biol. Drug. Des. 68*, 3.

(25) Bae, W. K., Char, K., Hur, H., and Lee, S. (2008) Single step synthesis of quantum dots with chemical composition gradients. *Chem. Mater. 20*, 531–539.

(26) Mattoussi, H., Mauro, J. M., Goldman, E. R., Anderson, G. P., Sundar, V. C., Mikulec, F. V., and Bawendi, M. G. (2000) Self-assembly of CdSe-ZnS quantum dot bioconjugates using an engineered recombinant protein. *J. Am. Chem. Soc. 122*, 12142–12150.

(27) Yu, W. W., Qu, L., Guo, W., and Peng, X. (2003) Experimental determination of the extinction coefficient of CdTe, CdSe, and CdS nanocrystals. *Chem. Mater. 15*, 2854–2860.

(28) Hermanson, G. T. (1996) *Bioconjugate techniques*, pp 169−176, Chapter 3, Academic Press, New York.

(29) Baker, G., and Goslin, K. (1998) *Culturing nerve cells*, 2nd ed., pp 339−370, MIT Press, Cambridge, MA.

(30) Chen, B., Yu, Y., Zhou, Z., and Zhong, P. (2004) Synthesis of novel nanocrystals as fluorescent sensors for Hg^{2+} Ions. *Chem. Lett. 33*, 1608–1609.

(31) Pavia, D. L., Lampman, G. M., and Kriz, G. S. (2001) *Introduction to spectroscopy*, 3rd ed., pp 26−52, Chapter 2, Harcourt Press, Washington.

(32) Rajan, S. S., and Vu, T. Q. (2006) Quantum dots monitor TrkA receptor dynamics in the interior of neural PC12 cells. *Nano Lett. 9*, 2049–2059.

(33) Dahan, M., Levi, S., Luccardini, C., Rostaing, P., Riveau, B., and Triller, A. (2003) Diffusion dynamics of glycine receptors revealed by single-quantum dot tracking. *Science 302*, 442–444.

(34) Wu, X., Liu, H., Liu, J., Haley, K. N., Treadway, J. A., Larson, J. P., Ge, N., Peale, F., and Bruchez, M. P. (2003) Immunofluorescent labeling of cancer marker Her2 and other cellular targets with semiconductor quantum dots. *Nat. Biotechnol. 21*, 41–46.

(35) Swanwick, C. C., Harrison, M. B., and Kapur, J. (2004) Synaptic and extrasynaptic localization of brain-derived neurotrophic factor and the tyrosine kinase B receptor in cultured hippocampal neurons. *J. Comp. Neurol. 478*, 405–417.

(36) Drake, C. T., Milner, T. A., and Patterson, S. L. (1999) Ultrastructural localization of full-length trkB immunoreactivity in rat hippocampus suggests multiple roles in modulating activity-dependent synaptic plasticity. *J. Neurosci. 19*, 8009 8026.

BC900304B

In Vivo Tumor-Targeted Fluorescence Imaging Using Near-Infrared Non-Cadmium Quantum Dots

Jinhao Gao,*,† Kai Chen,† Renguo Xie,‡ Jin Xie,† Yongjun Yan,† Zhen Cheng,† Xiaogang Peng,‡ and Xiaoyuan Chen*,†,§

Molecular Imaging Program at Stanford, Department of Radiology and Bio-X Program, School of Medicine, Stanford University, 1201 Welch Road, Stanford, California 94305-5484, Department of Chemistry and Biochemistry, University of Arkansas, Fayetteville, Arkansas 72701, and Laboratory for Molecular Imaging and Nanomedicine, National Institute of Biomedical Imaging and Bioengineering, National Institutes of Health, Bethesda, Maryland 20892. Received July 21, 2009; Revised Manuscript Received February 10, 2010

This article reported the high tumor targeting efficacy of RGD peptide labeled near-infrared (NIR) non-cadmium quantum dots (QDs). After using poly(ethylene glycol) to encapsulate InAs/InP/ZnSe QDs (emission maximum at about 800 nm), QD800-PEG dispersed well in PBS buffer with the hydrodynamic diameter (HD) of 15.9 nm and the circulation half-life of ~29 min. After coupling QD800-PEG with arginine−glycine−aspartic acid (RGD) or arginine−alanine−aspartic acid (RAD) peptides, we used nude mice bearing subcutaneous U87MG tumor as models to test tumor-targeted fluorescence imaging. The results indicated that the tumor uptake of QD800-RGD is much higher than those of QD800-PEG and QD800-RAD. The semiquantitative analysis of the region of interest (ROI) showed a high tumor uptake of 10.7 ± 1.5%ID/g in mice injected with QD800-RGD, while the tumor uptakes of QD800-PEG and QD800-RAD were 2.9 ± 0.3%ID/g and 4.0 ± 0.5%ID/g, respectively, indicating the specific tumor targeting of QD800-RGD. The high reproducibility of bioconjunction between QDs and the RGD peptide and the feasibility of QD-RGD bioconjugates as tumor-targeted fluorescence probes warrant the successful application of QDs for in vivo molecular imaging.

INTRODUCTION

The integration of nanotechnology with molecular biology and medicine has resulted in active developments of a new emerging research area-nanobiotechnology (*1*). This technological innovation, referred to as nanomedicine by the National Institutes of Health (NIH), has great potential to offer exciting and abundant opportunities for discovering new materials, processes, and phenomena in biomedicine. Nanoscale materials have now been widely exploited in many biomedical applications, such as biosensor, disease detection, molecular imaging, and disease treatment (*2*−*7*). The basic rationale is that the metal, metal oxide, semiconductor, or self-assembled molecular nanostrucuters have novel properties and functions that are not available from bulk counterparts or individual molecules. One of the most advanced and exciting forefronts of nanobiotechnology is the application of quantum dots (QDs) in biology and medicine (*8*). After surface functionalization using peptides, proteins, and antibodies, QDs indeed showed great ability to target and detect specific tissues in living subjects by the rapid readout of fluorescence imaging (*9*−*16*). Compared with the organic dyes and fluorescent proteins, QDs show many unique optical properties, such as narrow and tunable emission spectra, superior photostability, high quantum yields, and the capacity of simultaneous excitation of multiple fluorescence colors. Moreover, there are many more alternatives in QDs with NIR emission for in vivo imaging than organic dyes, such as CdTe/CdSe (*17*), $InAs_xP_{1-x}$/InP/ZnSe (*18*), CuInSe (*19*), and Cu-doped InP/ZnSe (*20*) QDs. The QDs emitting at above 700 nm in the NIR region minimize the problems of indigenous fluorescence of tissues and meet the requirements of in vivo biological imaging applications. However, it is reported that Cd-containing QDs indeed showed cytotoxicity under extreme conditions (*21, 22*). Several studies have shown that QDs may be systemically distributed in organs and tissues. The absorption, distribution, metabolism, and excretion characteristics are highly variable for QDs because of the wide variation in QD physicochemical properties (*23*−*25*). For in vivo applications, metabolic clearance of the nanoparticles remains an issue, that is, it is hard to know about how these nanoparticles would be completely cleared out of the body. To avoid such a dilemma, one strategy is to replace the Cd metal by other more benign elements. For example, $CuInS_2$/ZnS core/shell QDs do not contain any Class A elements (Cd, Pb, and Hg) or Class B elements (Se and As) (*26*), which may show great potential as biocompatible probes for biomedical applications. Recently, carbon dots (C-dots) as new emerging optical probes have aroused research interest because of their nontoxicity compared with semiconductor QDs (*27*). Another important strategy is the surface coating and modification of QDs, which improve water solubility, stability, and biocompatibility, and assign a desired bioactivity (*24*). For example, QDs can be coated with hydrophilic poly(ethylene glycol) (PEG) groups or a cross-linked silica shell (*8, 28*) to render QDs biocompatible and can be further conjugated with bioactive moieties to target specific biologic tissues or cells.

Cancer is a class of diseases in which a number of cells display uncontrolled growth, invasion, and sometimes metastasis. Cell adhesion molecule integrin $\alpha_v\beta_3$ is a key player in tumor angiogenesis, progression, and spread. Integrin $\alpha_v\beta_3$ specifically binds the arginine−glycine−aspartic acid (RGD)-containing components in the interstitial matrix (*29*). Integrins expressed on endothelial cells modulate cell migration and survival during angiogenesis, while integrins expressed on carcinoma cells

* Corresponding author. Email: gaojh@stanford.edu (J.G.); shawn.chen@nih.gov (X.C.).
† Stanford University.
‡ University of Arkansas.
§ National Institutes of Health.

10.1021/bc900323v © 2010 American Chemical Society
Published on Web 04/06/2010

potentiate metastasis by facilitating the invasion and movement across blood vessels (*30*). Tumor expression of integrin $\alpha_v\beta_3$ correlates well with the tumor progression in several malignancies, such as melanoma, glioma, and breast cancer (*31*−*33*). In this work, we chose non-cadmium and NIR QDs as the low-toxic and efficient fluorescence probe to image the integrin $\alpha_v\beta_3$-positive tumor vasculature in vivo after the surface modification of RGD peptide.

EXPERIMENTAL SECTION

Preparation of QD800-PEG. The synthesis of InAs/InP/ZnSe core/shell/shell QDs (emission maximum at about 800 nm) is similar to that described in the previous publication (*34*). We used the conjugate of phospholipid and poly(ethylene glycol) (DSPE-PEG2000 amine: 1,2-distearoyl-*sn*-glycero-3-phosphoethanolamine-*N*-[amino(polyethylene glycol)-2000], Avanti Polar Lipids, Inc.) to encapsulate QD800 and make the nanoparticles water-dispersible (*28, 35*). Typically, we mixed as-synthesized QD800 (10 nmol) and DSPE-PEG2000 amine (∼1.8 μmol) in 200 μL of chloroform and left the container open in a fume hood to evaporate the chloroform solvent slowly at room temperature. The dry sample was pumped under vacuum for about 4 h to remove chloroform completely and then redispersed in water by gentle sonication. The as-prepared QD800-PEG was purified by centrifugation using Millipore (Centrifugal filter devices, 100 K) at 4000 rpm for 20 min to remove the excess amount of DSPE-PEG2000 amine. The final concentration of QD800-PEG in PBS buffer (1×) was about 10 μM ready for further bioconjugation.

Synthesis of QD800-RGD and QD800-RAD. The procedure for surface functionalization of QD800-PEG with amine terminal groups is similar to that used in our previous report with a minor modification (*36*). We mixed QD800-PEG (1 nmol) and 4-maleimidobutyric acid *N*-succinimidyl ester (1 μmol) in borate buffer (pH ∼8.5) and incubated the mixture at room temperature for about 2 h with gentle shaking. After purification by a NAP-10 column (GE Healthcare Life Sciences), we added thiolated RGD peptide (c(RGDy(ε-acetylthiol)K), denoted as RGD-SH, 1 μmol) (*36*) into the activated QD800 sample and kept shaking for about 2 h at room temperature. After further purification by the NAP-10 column, we stored the QD800-RGD conjugate in PBS buffer with a concentration of 1 μM ready for animal use. For comparison, we added thiolated RAD peptide (c(RADy(ε-acetylthiol)K), denoted as RAD-SH, 1 μmol) instead to synthesize the QD800-RAD conjugate as a control.

Animal Model. Animal experiments were performed according to a protocol approved by the Stanford University Institutional Animal Care and Use Committee. The U87MG human glioblastoma tumor model was established by subcutaneous injection of U87MG cells (∼5×10^6 in 50 μL of PBS) into the front flank of female athymic nude mice (Harlan). The mice were subjected to imaging studies when the tumor volume reached 200−500 mm^3 (about 3 weeks after inoculation).

Half-Life Measurement. After the tail vein injection of QD800-PEG (200 pmol) in normal nude mice, we collected blood samples (∼15 mg each) at intervals of about 10 min and repeated them about 5 times. The blood samples were mixed with 20 μL of heparin (Sigma-Aldrich) solution (4 units/mL) and subjected to fluorescence imaging immediately using IVIS Imaging System (IVIS 100 Series; Cy5.5 excitation filter, 605−665 nm; ICG emission filter, 800−875 nm). Under the assistance of Living Image software, we recorded the information of the region of interest (ROI) for each blood sample.

In Vivo and Ex Vivo Fluorescence Imaging. After the tail vein injection of QD800-RGD, QD800-PEG, and QD800-RAD (∼200 pmol in each mouse), the mice were monitored at multiple time points (e.g., 0.5, 1, 4, 5, 6, 18, and 24 h) using IVIS Imaging System (IVIS 100 Series; Cy5.5 excitation filter, 605−665 nm; ICG emission filter, 800−875 nm). For ex vivo imaging, after the tumors and major organs were harvested, we immediately subjected the tissues to fluorescence imaging using IVIS Imaging System.

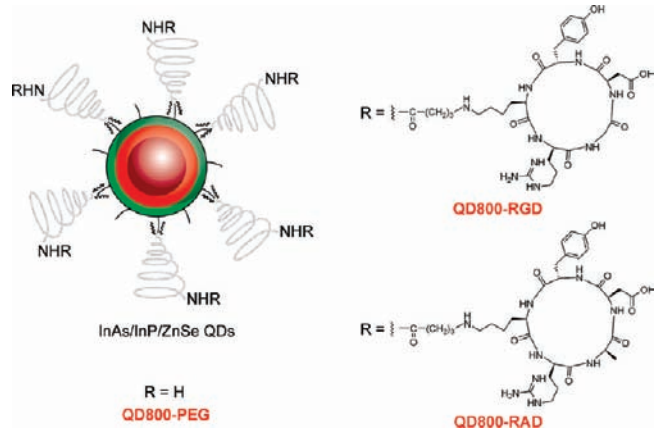


Figure 1. Structure of QD800-PEG, QD800-RGD, and QD800-RAD.

Immunofluorescence Staining. After 4 h p.i. of QD800-RGD, QD800-PEG, and QD800-RAD, the mice were sacrificed, and the tumors were harvested and frozen in OCT medium (Sakura Finetek) immediately. The tissues were cut into 5-μm-thick slices using microtome for fluorescence microscopy studies. U87MG tumor frozen tissue slices were fixed in cold acetone for about 10 min and dried in air for about 30 min. The sections were blocked with 10% donkey serum for about 10 min and then incubated with a rat antimouse CD31 monoclonal antibody (1:50; BD BioSciences) for 30 min at room temperature. After incubation with a Cy3-conjugated donkey antirat secondary antibody (1:100; Jackson ImmunoResearch Laboratories, Inc.) for another 30 min, we examined the tumor sections under fluorescence microscopes.

RESULTS AND DISCUSSION

Peptide-Labeled QDs. The as-synthesized InAs/InP/ZnSe core/shell/shell QDs (emission maximum at about 800 nm) with TOPO as surfactant only dispersed in nonpolar organic solvents, such as hexane and chloroform (Figure 2A,B). Poly(ethylene glycol) phosphatidylethanolamine (e.g., DSPE-PEG2000 amine) is one kind of micelle-forming hydrophilic polymer-grafted lipids (*28*). Therefore, the TOPO capped QDs could be encapsulated in the hydrophobic core of this micelle. We used DSPE-PEG2000 amine to coat QDs to make the QDs become water-dispersible and improve their biocompability. The procedure of coating is very facile and highly repeatable. The water-dispersible QD800-PEG (∼19% in QY) with an amine terminal group allows further modification and bioconjugation on the surface of nanoparticles. In order to maintain the binding activity of the circle (RGDyK), we used 4-maleimidobutyric acid *N*-succinimidyl ester as the heterodimeric cross-linker to conjugate QD800-PEG with the thiolated RGD peptide c(RGDy(ε-acethylthiol)K) to yield QD800-RGD (Figure 1). We also conjugated QD800-PEG with the thiolated RAD peptide c(RADy(ε-acethylthiol)K) to produce QD800-RAD as the negative control.

Analysis of Hydrodynamic Diameter (HD) and Circulation Half-Life. After surface coating and modification, all three samples (QD800-PEG, QD800-RGD, and QD800-RAD) could disperse well in PBS buffer. The absorbance and fluorescence emission spectra indicated that these water-dispersible QD samples maintain the optical properties with an emission

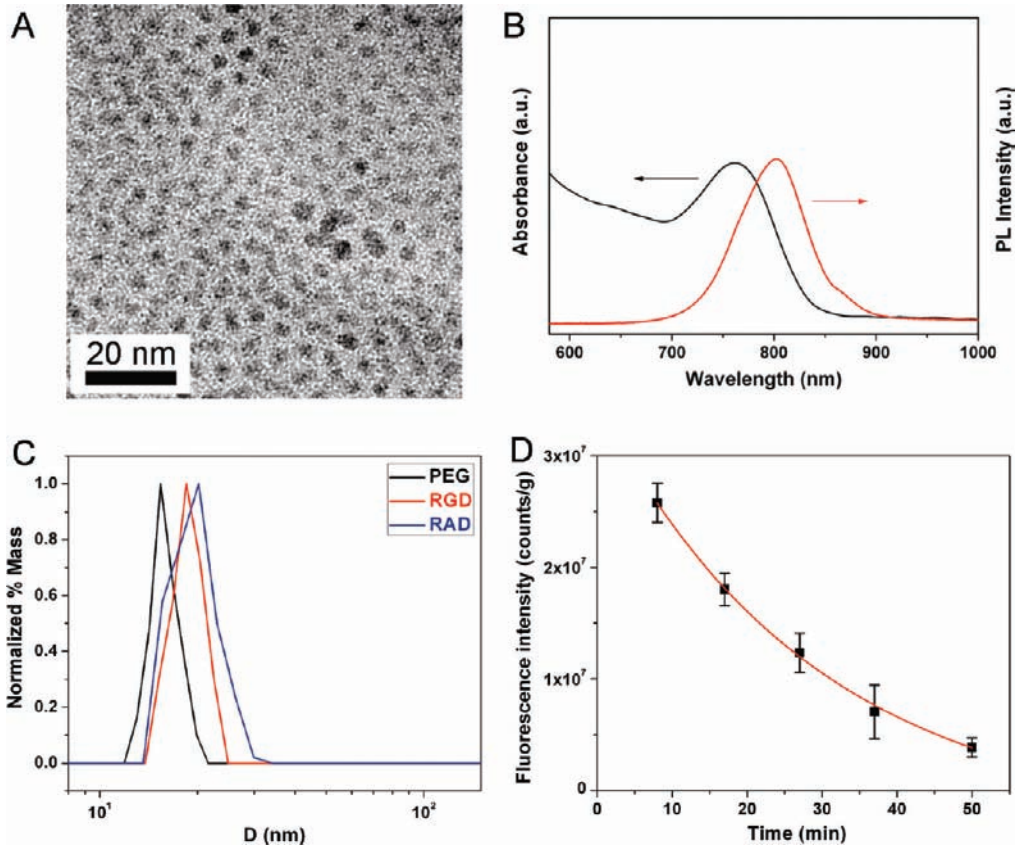


Figure 2. (A) TEM image and (B) absorbance and fluorescence emission spectra of InAs/InP/ZnSe core/shell/shell nanoparticles dispersed in chloroform, showing that the size of QDs is about 5 nm in diameter with the maximum emission peak at about 800 nm. (C) DLS analysis of QD800-PEG, QD800-RGD, and QD800-RAD with the HDs in PBS buffer of 16.5 nm, 19.6 nm, and 20.1 nm, respectively. (D) Circulation half-life analysis of QD800-PEG in nude mice, showing that the half-life of QD800-PEG is 29.0 ± 9.1 min.

maximum at ~800 nm in PBS buffer or 90% mouse serum (Figures S1 and S2, Supporting Information). After incubation of QD samples in mouse serum under typical body temperature (37 °C) for 24 h, over 80% of the emission intensity of QD800-RGD and QD800-RAD remained (Figure S3, Supporting Information), suggesting the good physiological stability of these peptide-labeled QDs. Dynamic light scattering (DLS) analysis showed that the HDs of QD800-PEG, QD800-RGD, and QD800-RAD are about 16.5 nm, 19.6 nm, and 20.1 nm, respectively (Figure 2C). On the basis of the size of these QD samples, the number of amine groups on the surface of each QD800-PEG (60−70 free amine groups) and the maximum ligand conjugation efficiency (40%−50%) (*37*), we estimated that there are 20−35 RGD peptides or RAD peptides on each peptide-labeled QD. In comparison with the small molecule mercaptopropionic acid (MPA) capped QD800-MPA (about 10 nm in HD) (*34*), QD800-PEG has a larger size in HD because of polymer coating. After the bioconjugation of RGD or RAD peptides on the surface of nanoparticles, the HDs of nanoparticles were slightly increased. In order to test the circulation half-life of QD800-PEG, we collected the blood samples within 1 h after the tail vein injection of QD particles in nude mice. Following the one-phase exponential decay, the analysis of the decrease in fluorescence intensity (i.e., ROI measurement) per gram of blood sample during blood circulation indicated that the half-life of QD800-PEG is about 29 min (Figure 2D). With the increase of HDs after peptide coupling, we estimated that the half-lives of QD800-RGD and QD800-RAD might be slightly shorter than that of QD800-PEG.

In Vivo Tumor-Targeted Imaging. After the preparation of these three samples (QD800-PEG, QD800-RGD, and QD800-RAD) with the final concentration of 1 μM in PBS buffer, we

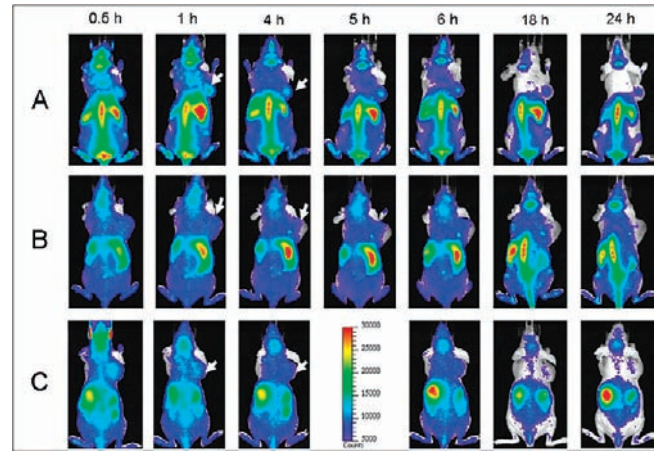


Figure 3. In vivo fluorescence imaging of U87MG tumor-bearing mice (arrows) injected with (A) QD800-RGD, (B) QD800-PEG, and (C) QD800-RAD.

administered intravenous injections (200 μL per mouse) into the athymic nude mice bearing subcutaneous U87MG human glioblastoma tumors. We used an IVIS 100 series to take the fluorescence images at multiple time points (0.5, 1, 4, 5, 6, 18, and 24 h). We set the Cy5.5 excitation filter (615−665 nm) and the ICG emission filter (800−875 nm) to take the fluorescence images with a strong fluorescent signal and low background signal. As shown in Figure 3, as early as 0.5 h postinjection (p.i.), the fluorescence signal derived from QD800-RGD and QD800-RAD both appeared in the tumors. After about 1 h, the tumors were very distinguishable from other tissues with good fluorescence contrast (arrows) in the mice injected

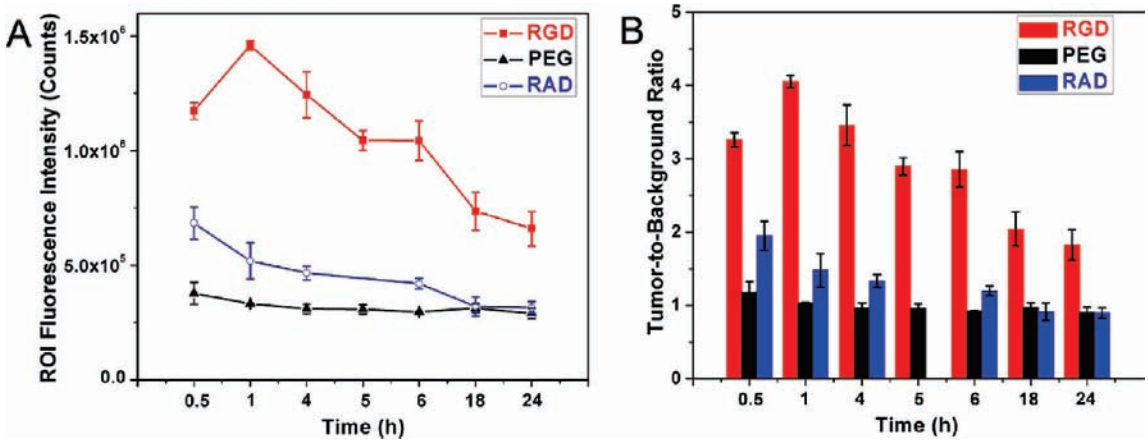


Figure 4. (A) Tumor fluorescence intensity-time and (B) tumor-to-background ratios of mice injected with QD800-RGD, QD800-PEG, and QD800-RAD. The data are represented as mean ± standard deviation (SD), $n = 3$/group.

with QD800-RGD (Figure 3A), indicating highly specific tumor targeting of QD800-RGD. However, the tumor fluorescence intensity decreased over the time in the mice injected with QD800-RAD (arrows, Figure 3C). We did not observe the tumor contrast in the mice injected with QD800-PEG (Figure 3B). The particularly bright fluorescence from the liver, spleen, and bone marrow reflected the reticuloendothelial system (RES)'s accumulation of QDs at these sites, which accounts for the relatively short half-lives of these QDs. The rapid uptake of QDs by the RES may significantly reduce their half-lives. It is noticed that the tumor contrast was still obvious even after 24 h in the mice injected with QD800-RGD, indicating that the tumor targeting of QD800-RGD induces high retention of QDs in the tumor site, which was further confirmed by the analysis of ROI. Under the assistance of Living Image software, we recorded the information of ROI and computed the statistical data for the ROI measurements. As shown in Figure 4A, after about 1 h p.i. of QD800-RGD, the fluorescence signal of the tumor reached the maximum and then slightly decreased over time (tumor-to-background ratios were 3.26 ± 0.10, 4.26 ± 0.08, 3.46 ± 0.27, 2.90 ± 0.12, 2.85 ± 0.24, 2.04 ± 0.23, and 1.83 ± 0.21 at 0.5, 1, 4, 5, 6, 18, and 24 h p.i., respectively, $n = 3$/group; Figure 4B), while there was little to no tumor contrast in the mice injected with QD800-PEG or QD800-RAD (Figure 4B).

Ex Vivo Fluorescence Imaging and Semiquantitative Analysis. At 4 h p.i., the mice injected with QD800-RGD, QD800-PEG, or QD800-RAD were sacrificed. We collected the tumors and major organs to acquire fluorescence images under the same conditions as those in immediate in vivo imaging. As shown in Figure 5, ex vivo imaging further confirmed the obvious fluorescence signal in the U87MG tumor of mice injected with QD800-RGD (Figure 5A), whereas there was virtually no fluorescence signal in the tumors of mice injected with QD800-PEG or QD800-RAD (Figure 5B,C). Although the fluorescence intensity of the liver was highest among all of the organs, the difference between tumor fluorescence signals indicated that only QD800-RGD has the capability to specifically target and detect the U87MG tumor.

The fluorescence signal intensity of ex vivo imaging is close to a true reflection of the QDs retained inside the organs because of deep penetration in the NIR region and no antofluorescence in ex vivo images. Then, we performed the ROI analysis on the ex vivo fluorescence images to semiquantitatively study the uptake ratio of QDs in each organ. As shown in Figure 5D, the ROI analysis showed high tumor uptake of 10.7 ± 1.5%ID/g in the mice injected with QD800-RGD, while the tumor uptakes of QD800-PEG and QD800-RAD under the same conditions

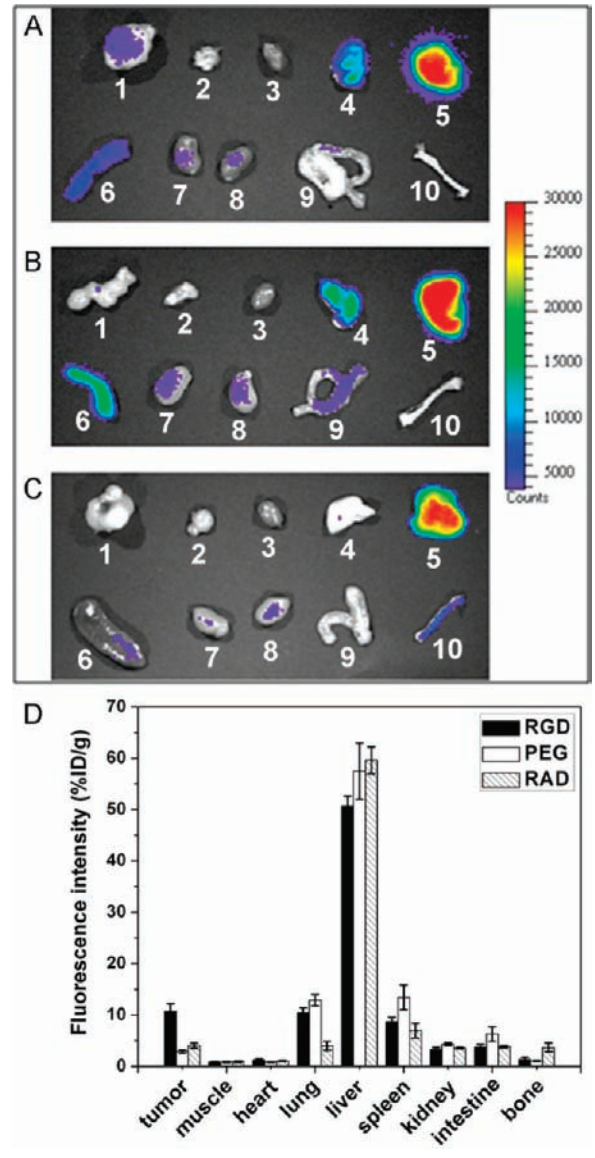


Figure 5. Ex vivo NIR fluorescence imaging after 4 h p.i. of (A) QD800-RGD, (B) QD800-PEG, and (C) QD800-RAD. In each image 1, U87MG tumor; 2, muscle; 3, heart; 4, lung; 5, liver; 6, spleen; 7, kidney (left); 8, kidney (right); 9, intestine; and 10, bone. (D) ROI analysis of major organs in ex vivo fluorescence imaging after 4 h p.i. of QD800-RGD, QD800-PEG, and QD800-RAD. The data are represented as mean ± standard deviation (SD), $n = 3$/group.

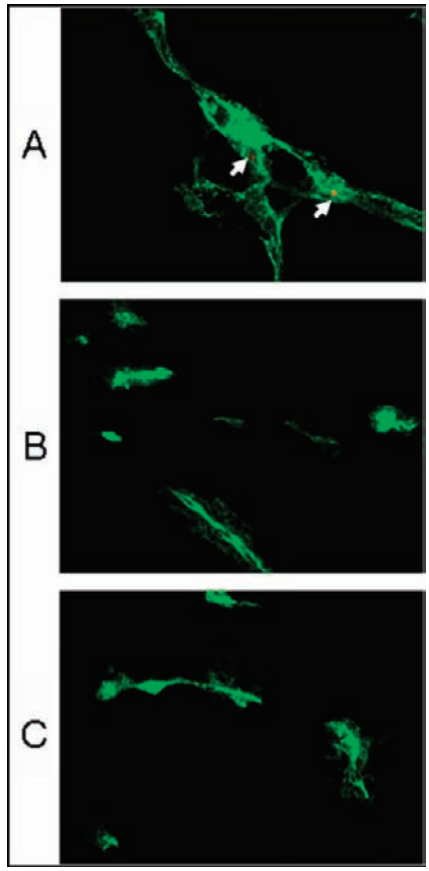


Figure 6. Immunofluorescence staining (CD31, green) of frozen U87MG tumor tissue slices from mice after 4 h p.i. of (A) QD800-RGD, (B) QD800-PEG, or (C) QD800-RAD. Arrows point to QD800-RGD nanoparticles staying within the tumor angiogenic vessel. Magnification: 400×.

were 2.9 ± 0.3%ID/g and 4.0 ± 0.5%ID/g, respectively. The semiquantitative ROI analysis further confirmed that QD800-RGD could be an excellent candidate as a probe for tumor-targeted fluorescence imaging. In order to verify the highly specific targeting of QD800-RGD to the integrin $\alpha_v\beta_3$-positive tumor, we used the LS174T tumor model with very low $\alpha_v\beta_3$ overexpression (*38*) as the negative control to do the fluorescence imaging (Figure S4, Supporting Information). The low LS174T tumor uptake of QD800-RGD (~2.8%ID/g at 4 h p.i.) indicated that QD800-RGD specifically targets integrin $\alpha_v\beta_3$ in living mice.

Histology Study. In order to investigate the microscopic localization of QDs in the tumors, CD31 immunostaining of tumor tissue slides would allow the visualization of tumor vasculature. From the fluorescence overlay images (Figure 6), we indeed found the presence of QD800-RGD in the tumor vessels (arrows, Figure 6A) but no QD fluorescence signal in the tumor vessels of mice injected with QD800-PEG or QD800-RAD (Figure 6B,C). The excellent overlay between QD fluorescence and CD31 staining of tumor vessels confirmed that QD800-RGD did not extravasate the tumor vessels, suggesting that these QDs with big size (about 20 nm in HD) could only target vascular integrin but not tumor cell integrin (*9, 10, 39*). However, the QDs with smaller size (<10 nm in HD) may facilitate extravasation due to the enhanced permeability and retention (EPR) effect, enhance the specific targeting to tumor cells, and minimize the RES uptake (*40*−*43*). Indeed, the coating, size, and surface charge of NIR QDs are three key features to influence the in vivo behavior of QDs and should be considered for future designs of QDs as imaging probes for clinical uses (*43*−*45*).

CONCLUSIONS

In this work, we have investigated in vivo tumor-targeted fluorescence imaging using QD800-RGD. The QD800-RGD nanoparticles are NIR fluorescent (emission wavelength higher than 750 nm), non-cadmium containing (lower toxic than Cd-based QDs (*34*)), and specific to target integrin $\alpha_v\beta_3$. In comparison with QD800-PEG and QD800-RAD, the tumor uptake of QD800-RGD is much higher with good contrast from the surrounding tissues, indicating specific tumor targeting of QD800-RGD. The results shown here, together with our previous work (*9, 10, 36*), fully demonstrated the reproducibility of bioconjugation between QDs and RGD peptide, the feasibility of QD-RGD bioconjugates as tumor-targeted fluorescence probes, and the possibility of QDs in the applications of molecular imaging and diagnosis.

ACKNOWLEDGMENT

This work was partially supported by NCI/NIH R21 CA121842 and U54 CA119367.

Supporting Information Available: Absorbance and fluorescence emission spectra, serum stability, fluorescence imaging, and fluorescence microscopic images. This material is available free of charge via the Internet at http://pubs.acs.org.

LITERATURE CITED

(1) Whitesides, G. M. (2003) The 'right' size in nanobiotechnology. *Nat. Biotechnol. 21*, 1161–1165.
(2) Rosler, A., Vandermeulen, G. W. M., and Klok, H. A. (2001) Advanced drug delivery devices via self-assembly of amphiphilic block copolymers. *Adv. Drug Delivery Rev. 53*, 95–108.
(3) Corot, C., Robert, P., Idee, J. M., and Port, M. (2006) Recent advances in iron oxide nanocrystal technology for medical imaging. *Adv. Drug Delivery Rev. 58*, 1471–1504.
(4) Cai, W. B., and Chen, X. Y. (2007) Nanoplatforms for targeted molecular imaging in living subjects. *Small 3*, 1840–1854.
(5) McCarthy, J. R., and Weissleder, R. (2008) Multifunctional magnetic nanoparticles for targeted imaging and therapy. *Adv. Drug Delivery Rev. 60*, 1241–1251.
(6) Gao, J. H., and Xu, B. (2009) Applications of nanomaterials inside cells. *Nano Today 4*, 37–51.
(7) Gao, J. H., Gu, H. W., and Xu, B. (2009) Multifunctional magnetic nanoparticles: design, synthesis, and biomedical applications. *Acc. Chem. Res. 42*, 1097–1107.
(8) Bruchez, M., Moronne, M., Gin, P., Weiss, S., and Alivisatos, A. P. (1998) Semiconductor nanocrystals as fluorescent biological labels. *Science 281*, 2013–2016.
(9) Cai, W. B., Shin, D. W., Chen, K., Gheysens, O., Cao, Q. Z., Wang, S. X., Gambhir, S. S., and Chen, X. Y. (2006) Peptide-labeled near-infrared quantum dots for imaging tumor vasculature in living subjects. *Nano Lett. 6*, 669–676.
(10) Cai, W. B., Chen, K., Li, Z. B., Gambhir, S. S., and Chen, X. Y. (2007) Dual-function probe for PET and near-infrared fluorescence imaging of tumor vasculature. *J. Nucl. Med. 48*, 1862–1870.
(11) Jayagopal, A., Russ, P. K., and Haselton, F. R. (2007) Surface engineering of quantum dots for in vivo vascular Imaging. *Bioconjugate Chem. 18*, 1424–1433.
(12) Diagaradjane, P., Orenstein-Cardona, J. M., Colon-Casasnovas, N. E., Deorukhkar, A., Shentu, S., Kuno, N., Schwartz, D. L., Gelovani, J. G., and Krishnan, S. (2008) Imaging epidermal growth factor receptor expression in vivo: Pharmacokinetic and biodistribution characterization of a bioconjugated quantum dot nanoprobe. *Clin. Cancer Res. 14*, 731–741.

(13) Chen, K., Li, Z. B., Wang, H., Cai, W. B., and Chen, X. Y. (2008) Dual-modality optical and positron emission tomography imaging of vascular endothelial growth factor receptor on tumor vasculature using quantum dots. *Eur. J. Nucl. Med. Mol. Imaging 35*, 2235–2244.

(14) Lei, Y., Tang, H., Yao, L., Yu, R., Feng, M., and Zou, B. (2008) Applications of mesenchymal stem cells labeled with Tat peptide conjugated quantum dots to cell tracking in mouse body. *Bioconjugate Chem. 19*, 421–427.

(15) Smith, A. M., Duan, H. W., Mohs, A. M., and Nie, S. M. (2008) Bioconjugated quantum dots for in vivo molecular and cellular imaging. *Adv. Drug Delivery Rev. 60*, 1226–1240.

(16) Gao, X. L., Chen, J., Chen, J. Y., Wu, B. X., Chen, H. Z., and Jiang, X. G. (2008) Quantum dots bearing lectin-functionalized nanoparticles as a platform for in vivo brain imaging. *Bioconjugate Chem. 19*, 2189–2195.

(17) Kim, S., Lim, Y. T., Soltesz, E. G., De Grand, A. M., Lee, J., Nakayama, A., Parker, J. A., Mihaljevic, T., Laurence, R. G., Dor, D. M., Cohn, L. H., Bawendi, M. G., and Frangioni, J. V. (2004) Near-infrared fluorescent type II quantum dots for sentinel lymph node mapping. *Nat. Biotechnol. 22*, 93–97.

(18) Kim, S. W., Zimmer, J. P., Ohnishi, S., Tracy, J. B., Frangioni, J. V., and Bawendi, M. G. (2005) Engineering $InAs_xP_{1-x}$/InP/ZnSe III-V alloyed core/shell quantum dots for the near-infrared. *J. Am. Chem. Soc. 127*, 10526–10532.

(19) Allen, P. M., and Bawendi, M. G. (2008) Ternary I-III-VI quantum dots luminescent in the red to near-infrared. *J. Am. Chem. Soc. 130*, 9240–9241.

(20) Xie, R. G., and Peng, X. G. (2009) Synthesis of Cu-doped InP nanocrystals (d-dots) with ZnSe diffusion barrier as efficient and color-tunable NIR emitters. *J. Am. Chem. Soc. 131*, 10645–10651.

(21) Derfus, A. M., Chan, W. C. W., and Bhatia, S. N. (2004) Probing the cytotoxicity of semiconductor quantum dots. *Nano Lett. 4*, 11–18.

(22) Kirchner, C., Liedl, T., Kudera, S., Pellegrino, T., Javier, A. M., Gaub, H. E., Stolzle, S., Fertig, N., and Parak, W. J. (2005) Cytotoxicity of colloidal CdSe and CdSe/ZnS nanoparticles. *Nano Lett. 5*, 331–338.

(23) Hoshino, A., Fujioka, K., Oku, T., Suga, M., Sasaki, Y. F., Ohta, T., Yasuhara, M., Suzuki, K., and Yamamoto, K. (2004) Physicochemical properties and cellular toxicity of nanocrystal quantum dots depend on their surface modification. *Nano Lett. 4*, 2163–2169.

(24) Hardman, R. (2006) A toxicologic review of quantum dots: Toxicity depends on physicochemical and environmental factors. *Environ. Health Perspect. 114*, 165–172.

(25) Lewinski, N., Colvin, V., and Drezek, R. (2008) Cytotoxicity of nanoparticles. *Small 4*, 26–49.

(26) Xie, R. G., Rutherford, M., and Peng, X. G. (2009) Formation of high-quality I-III-VI semiconductor nanocrystals by tuning relative reactivity of cationic precursors. *J. Am. Chem. Soc. 131*, 5691–5697.

(27) Sun, Y. P., Zhou, B., Lin, Y., Wang, W., Fernando, K. A. S., Pathak, P., Meziani, M. J., Harruff, B. A., Wang, X., Wang, H. F., Luo, P. J. G., Yang, H., Kose, M. E., Chen, B. L., Veca, L. M., and Xie, S. Y. (2006) Quantum-sized carbon dots for bright and colorful photoluminescence. *J. Am. Chem. Soc. 128*, 7756–7757.

(28) Dubertret, B., Skourides, P., Norris, D. J., Noireaux, V., Brivanlou, A. H., and Libchaber, A. (2002) In vivo imaging of quantum dots encapsulated in phospholipid micelles. *Science 298*, 1759–1762.

(29) Xiong, J. P., Stehle, T., Zhang, R. G., Joachimiak, A., Frech, M., Goodman, S. L., and Aranout, M. A. (2002) Crystal structure of the extracellular segment of integrin alpha V beta 3 in complex with an Arg-Gly-Asp ligand. *Science 296*, 151–155.

(30) Felding-Habermann, B., O'Toole, T. E., Smith, J. W., Fransvea, E., Ruggeri, Z. M., Ginsberg, M. H., Hughes, P. E., Pampori, N., Shattil, S. J., Saven, A., and Mueller, B. M. (2001) Integrin activation controls metastasis in human breast cancer. *Proc. Natl. Acad. Sci. U.S.A. 98*, 1853–1858.

(31) Albelda, S. M., Mette, S. A., Elder, D. E., Stewart, R. M., Damjanovich, L., Herlyn, M., and Buck, C. A. (1990) Integrin distribution in malignant melanoma: association of the beta 3 subunit with tumor progression. *Cancer Res. 50*, 6757–6764.

(32) Kanamori, M., Vanden Berg, S. R., Bergers, G., Berger, M. S., and Pieper, R. O. (2004) Integrin beta 3 overexpression suppresses tumor growth in a human model of gliomagenesis: Implications for the role of beta 3 overexpression in glioblastoma multiforme. *Cancer Res. 64*, 2751–2758.

(33) Gasparini, G., Brooks, P. C., Biganzoli, E., Vermeulen, P. B., Bonoldi, E., Dirix, L. Y., Ranieri, G., Miceli, R., and Cheresh, D. A. (1998) Vascular integrin alpha(v)beta(3): A new prognostic indicator in breast cancer. *Clin. Cancer Res. 4*, 2625–2634.

(34) Xie, R. G., Chen, K., Chen, X. Y., and Peng, X. G. (2008) InAs/InP/ZnSe core/shell/shell quantum dots as near-infrared emitters: bright, narrow-band, non-cadmium containing, and biocompatible. *Nano Res. 1*, 457–464.

(35) Carion, O., Mahler, B., Pons, T., and Dubertret, B. (2007) Synthesis, encapsulation, purification and coupling of single quantum dots in phospholipid micelles for their use in cellular and in vivo imaging. *Nat. Protoc. 2*, 2383–2390.

(36) Cai, W. B., and Chen, X. Y. (2008) Preparation of peptide-conjugated quantum dots for tumor vasculature-targeted imaging. *Nat. Protoc. 3*, 89–96.

(37) Gao, X. H., Cui, Y. Y., Levenson, R. M., Chung, L. W. K., and Nie, S. M. (2004) In vivo cancer targeting and imaging with semiconductor quantum dots. *Nat. Biotechnol. 22*, 969–976.

(38) Su, Z. F., Liu, G. Z., Gupta, S., Zhu, Z. H., Rusckowski, M., and Hnatowich, D. J. (2002) In vitro and in vivo evaluation of a technetium-99m-labeled cyclic RGD peptide as a specific marker of alpha(V)beta(3) integrin for tumor imaging. *Bioconjugate Chem. 13*, 561–570.

(39) Akerman, M. E., Chan, W. C. W., Laakkonen, P., Bhatia, S. N., and Ruoslahti, E. (2002) Nanocrystal targeting in vivo. *Proc. Natl. Acad. Sci. U.S.A. 99*, 12617–12621.

(40) Choi, H. S., Liu, W. H., Misra, P., Tanaka, E., Zimmer, J. P., Ipe, B. I., Bawendi, M. G., and Frangioni, J. V. (2007) Renal clearance of quantum dots. *Nat. Biotechnol. 25*, 1165–1170.

(41) Park, J. H., Gu, L., von Maltzahn, G., Ruoslahti, E., Bhatia, S. N., and Sailor, M. J. (2009) Biodegradable luminescent porous silicon nanoparticles for in vivo applications. *Nat. Mater. 8*, 331–336.

(42) Gao, J. H., Chen, K., Xie, R. G., Xie, J., Lee, S., Cheng, Z., Peng, X. G., and Chen, X. Y. (2010) Ultrasmall near-infrared non-cadmium quantum dots for in vivo tumor imaging. *Small 6*, 256–261.

(43) Choi, H. S., Liu, W., Liu, F., Nasr, K., Misra, P., Bawendi, M. G., and Frangioni, J. V. (2010) Design considerations for tumour-targeted nanoparticles. *Nat. Nanotechnol. 5*, 42–47.

(44) Schipper, M. L., Cheng, Z., Lee, S. W., Bentolila, L. A., Iyer, G., Rao, J. H., Chen, X. Y., Wu, A. M., Weiss, S., and Gambhir, S. S. (2007) MicroPET-based biodistribution of quantum dots in living mice. *J. Nucl. Med. 48*, 1511–1518.

(45) Schipper, M. L., Iyer, G., Koh, A. L., Cheng, Z., Ebenstein, Y., Aharoni, A., Keren, S., Bentolila, L. A., Li, J. Q., Rao, J. H., Chen, X. Y., Banin, U., Wu, A. M., Sinclair, R., Weiss, S., and Gambhir, S. S. (2009) Particle size, surface coating, and PEGylation influence the biodistribution of quantum dots in living mice. *Small 5*, 126–134.

BC900323V

High Relaxivity Trimetallic Nitride (Gd_3N) Metallofullerene MRI Contrast Agents with Optimized Functionality

Jianfei Zhang,[†] Panos P. Fatouros,[‡] Chunying Shu,[†] Jonathan Reid,[†] Lesley Shantell Owens,[†] Ting Cai,[†] Harry W. Gibson,[†] Gary L. Long,[†] Frank D. Corwin,[‡] Zhi-Jian Chen,[§] and Harry C. Dorn*,[†]

Department of Chemistry, Virginia Polytechnic Institute and State University, Blacksburg, Virginia 24060, and Department of Radiology and Department of Neurosurgery, Virginia Commonwealth University, Richmond, Virginia 23298. Received August 23, 2009; Revised Manuscript Received November 20, 2009

Water-soluble poly(ethylene glycol) (PEG) functionalized and hydroxylated endohedral trimetallic nitride metallofullerene derivatives, $Gd_3N@C_{80}[DiPEG(OH)_x]$, have been synthesized and characterized. The ^1H MRI relaxivities in aqueous solution were measured for the derivatives with four different molecular weights of PEG (350−5000 Da) at 0.35, 2.4, and 9.4 T. The 350/750 Da PEG derivatives have the highest relaxivities among the derivatives, 237/232 mM^{-1} s^{-1} for r_1 and 460/398 mM^{-1} s^{-1} for r_2 (79/77 mM^{-1} s^{-1} and 153/133 mM^{-1} s^{-1} based on Gd^{3+} ion), respectively, at a clinical-range magnetic field of 2.4 T. These represent some of the highest relaxivities reported for commercial or investigational MRI contrast agents. Dynamic light scattering results confirm a larger average size for 350/750 Da PEGs derivatives (95/96 nm) relative to longer chain length derivatives, 5000 Da PEG derivatives (37 nm). Direct infusion of the optimized 350 Da PEG derivatives into live tumor-bearing rat brains demonstrated an initial uniform distribution, and hence, the potential for effective brachytherapy applications when the encapsulated Gd^{3+} ions are replaced with radioactive ^{177}Lu.

INTRODUCTION

Magnetic resonance imaging (MRI) is widely used in the clinical diagnosis of cancer and other diseases. Improved contrast can be obtained by the use of intravenously injected paramagnetic contrast agents due to their extravasation across leaking vasculature and subsequent accumulation in lesions. Since contrast agents are widely employed in clinical MRI studies, these agents must be biologically safe and have a high relaxivity in order to minimize the amount delivered. Currently, the most widely used MRI contrast agents are gadolinium chelates: the large number of unpaired electrons (seven) per Gd^{3+} ion and favorably long electron spin−lattice relaxation time significantly increase the relaxation rate of water hydrogens (*1, 2*). However, it has been recently reported that nephrogenic systemic fibrosis (NSF), a painful and debilitating disorder of the skin and systemic tissues in patients with renal insufficiency, is associated with exposure to Gd^{3+} ions from contrast agents (*3, 4*). New contrast agents with higher relaxivity and lower toxicity are an important target of current investigations.

Because of their shape, capacity for multiple *endo* encapsulants and isolation of the Gd^{3+} ions from the bioenvironment, endohedral metallofullerenes (EMFs) represent ideal next generation nanoparticles as diagnostic biomedical nanoprobes. Several new classes of MRI contrast agents, water-soluble endohedral metallofullerenes, have been reported (*5*−*17*). EMFs have been functionalized with hydrophilic groups, e.g., −OH or −COOH (*8*−*12*). These water-soluble EMF derivatives show significantly greater relaxivities than the chelated Gd^{3+} compounds in current clinical use.

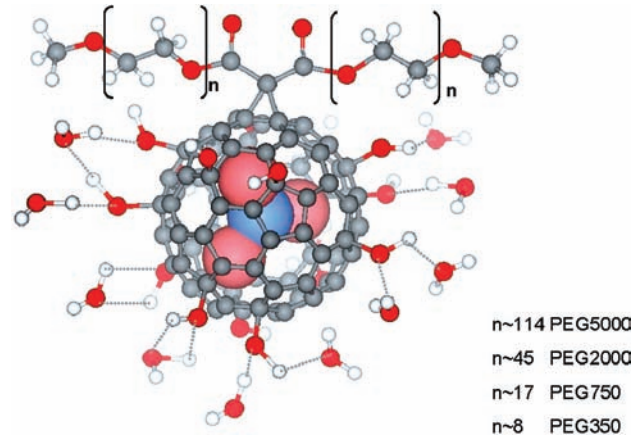


Figure 1. The $Gd_3N@C_{80}[DiPEG(OH)_x]$ nanoparticle with several hydrogen-bonded water molecules shown.

We have previously reported the synthesis of trimetallic nitride templated (TNT) EMFs, $A_xB_{3-x}N@C_{80}$ (A,B = metal, x = 0−3) (*18*). The TNT EMFs have an additional advantage: they can encapsulate up to three Gd^{3+} ions inside the cage, resulting in higher relaxivity. If different metal atoms/ions are encapsulated, e.g., Lu, Tb, Ho, and so forth, TNT EMFs can also act as multimodal (MRI and radiotherapy) platforms with the same biodistribution. We previously reported the synthesis of $Gd_3N@C_{80}[DiPEG5000(OH)_x]$ (PEG = poly(ethylene glycol)) (*7*), which is water-soluble and exhibits high relaxivity. *In vitro* and *in vivo* studies demonstrated the potential applicability of this MRI contrast agent. More recent studies have also demonstrated high relaxivity for related TNT EMFs with different functionalities (*13, 15, 16*). The high relaxivity of the TNT EMFs derivative arises from the following factors: (1) the large number of exchangeable water molecules coordinated to the hydroxyl groups which are attached to the carbon cage (Figure 1) and are simultaneously relaxed by the $(Gd_3N)^{6+}$

* Corresponding author. Harry C. Dorn, Department of Chemistry, Virginia Polytechnic Institute and State University, Blacksburg, VA, 24060; E-Mail: hdorn@vt.edu; Phone: 540-231-5953; Fax: 540- 231-3255.

[†] Virginia Polytechnic Institute and State University.

[‡] Department of Radiology, Virginia Commonwealth University.

[§] Department of Neurosurgery, Virginia Commonwealth University.

10.1021/bc900375n © 2010 American Chemical Society
Published on Web 03/10/2010

endohedral cluster, (2) the slow rotational correlation time caused by the long PEG chain and aggregation effects.

In the current study, we synthesized pegylated and hydroxylated $Gd_3N@C_{80}$ with different PEG chain lengths (350−5000 MW), and the relaxivities of these derivatives were measured at three different magnetic field strengths. The optimum PEG chain of these pegylated and hydroxylated $Gd_3N@C_{80}$ derivatives is an important structural property for potential MRI studies at different magnetic field strengths. To demonstrate the *in vivo* applicability of these high-relaxivity contrast agents, a convection-enhanced delivery (CED) method was used to infuse $Gd_3N@C_{80}$[DiPEG(OH)$_x$] directly into a brain-tumor-bearing rat.

MATERIALS AND METHODS

Synthesis of $Gd_3N@C_{80}$[DiPEG(OH)$_x$]. $Gd_3N@C_{80}$ was produced by the standard Krätschmer-Huffman (K−H) method with the introduction of nitrogen gas into the K−H generator (*18*). The product was purified by HPLC as previously reported (*19*). 1,8-Diazabicyclo(5.4.0)undec-7-ene (DBU, FW 152.24), 98%, was purchased from Sigma-Aldrich; 99% CBr_4, 99% 18-crown-6, 50% sodium hydroxide solution, and 30 wt % hydrogen peroxide were used as obtained from Aldrich Chemical Co. Di{ω-methyl-poly(ethylene glycol)} malonate (DiPEG) 350, 750, 2000, and 5000 (MW. 768, 1568, 4068, 10 068, respectively) were prepared from ω-methyl-poly(ethylene glycol)s (PEGs) as follows: To a solution of PEG and triethylamine (TEA) in CH_2Cl_2, a solution of malonyl dichloride in CH_2Cl_2 was added dropwise. The molar ratio of PEG/TEA/malonyl dichloride was 2:2:1. The solution was stirred at room temperature under N_2 protection for 3 h, concentrated and dropped into a large amount of ethyl ether, and then fractionated by a silica gel column.

$Gd_3N@C_{80}$, DiPEG, DBU, and CBr_4 were dissolved in chlorobenzene in molar ratio 1:20:20:67. After deaeration with bubbling argon for 30 min, the solution was stirred overnight at room temperature. The resultant mixture was evaporated, and the residue was dissolved in toluene. To this solution, 18-crown-6 and 50% sodium hydroxide solution were added, and the resultant solution was stirred for 4 h. 1.5 mL hydrogen peroxide was added drop by drop, and more water was added. The mixture was stirred overnight at room temperature. The resultant solution was concentrated and separated on a Sephadex G25 (Pharmacia) size-exclusion gel column with distilled water as eluent to afford a narrow golden band (first fraction, pH ≤ 7). (See Supporting Information Figure 1.)The yield was up to 95%.

Relaxivity Measurements. The concentrations of Gd^{3+} ions were determined by inductively coupled plasma optical emission spectroscopy (ICP-OES, Perkin-Elmer Optima 5300DV) at 342.247 nm. The instrument was calibrated by a 10 ppm ICP standard solution. Each molecule was assumed to encapsulate three Gd^{3+} ions, so the concentration of $Gd_3N@C_{80}$[DiPEG(OH)$_x$] was assumed to be one-third of the Gd^{3+} ion concentration.

The proton relaxation times were measured at three different magnetic field strengths: 0.35 T (TEACH SPIN PS1-B), 2.4 T (Bruker/Biospec), and 9.4 T (Varian Inova 400). The inversion−recovery method was used to measure T_1 and the Carr-Pucell-Meiboom-Gill method was used for measurement of T_2. The relaxivities were extracted from linear fits of plots of relaxation rates ($1/T_1$ and $1/T_2$) vs the concentrations of the paramagnetic species.

Dynamic Light Scattering. Dynamic light scattering (DLS) measurements were carried out with an ALV/CGS-3 compact goniometer system and ALV/LSE-5003 multi-τ digital correlator at 25 °C. He−Ne laser producing vertically polarized light of λ_0 = 632.8 nm was used as a light source. Each sample was filtered with a 0.5 μm cellulose acetate membrane filter.

Animal Studies. We used a convection-enhanced delivery method (*7*) to infuse 0.0235 mM $Gd_3N@C_{80}$[DiPEG350(OH)$_x$] into a live rat brain tumor and followed the functionalized EMF redistribution over the course of several days. Infusion was applied for 180 min at a rate of 0.2 μL/min with a total infusion volume of 36 μL.

RESULTS AND DISCUSSION

^{1}H NMR. ^{1}H NMR spectra of $Gd_3N@C_{80}$[DiPEG(OH)$_x$] was performed on an Inova 400. Figure 2a displays the ^{1}H NMR spectra of $Gd_3N@C_{80}$[DiPEG350(OH)$_x$] and malonyl DiPEG350 in D_2O. In $Gd_3N@C_{80}$[DiPEG350(OH)$_x$] the $-OCH_3$ and $-OCH_2CH_2-$ signals appeared at δ3.35 ppm (s, 6H) and 3.67 ppm (m, 52H), respectively; the signals for $-COOCH_2-$ and $COOCH_2CH_2-$ centered at 4.32 ppm (t, 4H) and 3.78 ppm (t, 4H) in the malonate disappeared in the TNT EMFs derivative apparently due to the strong paramagnetic effect of the Gd^{3+} ions. The NMR spectra of other PEG derivatives gave similar results.

UV−Vis. The UV−Vis spectra of $Gd_3N@C_{80}$ and $Gd_3N@C_{80}$[DiPEG2000(OH)$_x$] are shown in Figure 2b. For $Gd_3N@C_{80}$, there is an absorption peak at about 710 nm and a second absorption occurs at 410 nm (*20*). These absorptions are attributed to the $\Pi\rightarrow\Pi^*$ transitions (*21*). For the functionalized metallofullerenes, however, these characteristic features are significantly reduced. This indicates that the conjugated π structure of the carbon cage has been significantly altered. Similar results were obtained with other samples with different molecular weights ($Gd_3N@C_{80}$[DiPEG5000, 750, 350(OH)$_x$]).

Mass Spectra. To confirm the functionalization, MALDI-TOF mass spectra were obtained for DiPEG750, $Gd_3N@C_{80}$[DiPEG750], and $Gd_3N@C_{80}$[DiPEG750(OH)$_x$] (see Supporting Information Figure 2). The spectrum for DiPEG 750 was a series of peaks centered at about *m*/*z* 1388. The peaks were separated by *m*/*z* 44, which is the mass of the (CH_2CH_2O) unit. The spectrum of $Gd_3N@C_{80}$[DiPEG750] was a series of peaks centered at about *m*/*z* 2907. The separation of *m*/*z* 1 is attributed to the isotope effect of $Gd_3N@C_{80}$. We can clearly see that $Gd_3N@C_{80}$ was successfully functionalized with DiPEG750. However, in the mass spectrum of $Gd_3N@C_{80}$[DiPEG750(OH)$_x$] we only observed peaks for metallofullerene (*m*/*z* 1447) and PEG fragments (centered at *m*/*z* 759 and separated by 44). Even though the molecular ion peak was not observed, the metallofullerene and PEG fragments indicate successful functionalization.

MRI Relaxivity. The ability of paramagnetic compounds to enhance the relaxation rate can be described by the following equation (*1, 2*):

$$\frac{1}{T_{i,\mathrm{obs}}} = \frac{1}{T_{i,\mathrm{H_2O}}} + \frac{1}{T_{i,\mathrm{para}}} = \frac{1}{T_{i,\mathrm{H_2O}}} + r_i[\mathrm{M}] \quad i = 1,2 \quad (1)$$

$1/T_1$ and $1/T_2$ are the longitudinal and transverse relaxation rates. $1/T_{i,\mathrm{obs}}$ is the observed value of the solution and $1/T_{i,\mathrm{para}}$ is the contribution of the paramagnetic compound. [M] is the concentration of the paramagnetic species. r_1 and r_2 are defined as longitudinal and transverse relaxivities, respectively, which are expressed in $(\mathrm{mM}\cdot\mathrm{s})^{-1}$.

A major contribution to $1/T_{i,\mathrm{para}}$ arises from the simultaneous relaxation of multiple water molecules. This is the result of the dipolar electron−nuclear spin interaction between the large fluctuating Gd^{3+} electron magnetic moment and the water hydrogen nucleus. These relaxed water molecules undergo subsequent rapid exchange with bulk water. Dipole−dipole interactions are described by the Solomon-Bloembergen-Morgan

(SBM) equations. In the high-field region (above 10 MHz), these equations reduce to (*1, 2*)

$$\frac{1}{T_{1M}} = \frac{6}{15}\frac{\gamma_I^2 g^2 \mu_B^2 S(S+1)}{r_H^6}\left(\frac{\tau_C}{1+\omega_H^2\tau_c^2}\right) \quad (2)$$

$$\frac{1}{T_{2M}} = \frac{1}{15}\frac{\gamma_I^2 g^2 \mu_B^2 S(S+1)}{r_H^6}\left(4\tau_c + \frac{3\tau_C}{1+\omega_H^2\tau_c^2}\right) \quad (3)$$

$$\tau_C^{-1} = \tau_M^{-1} + \tau_R^{-1} + \tau_{1e}^{-1} \quad (4)$$

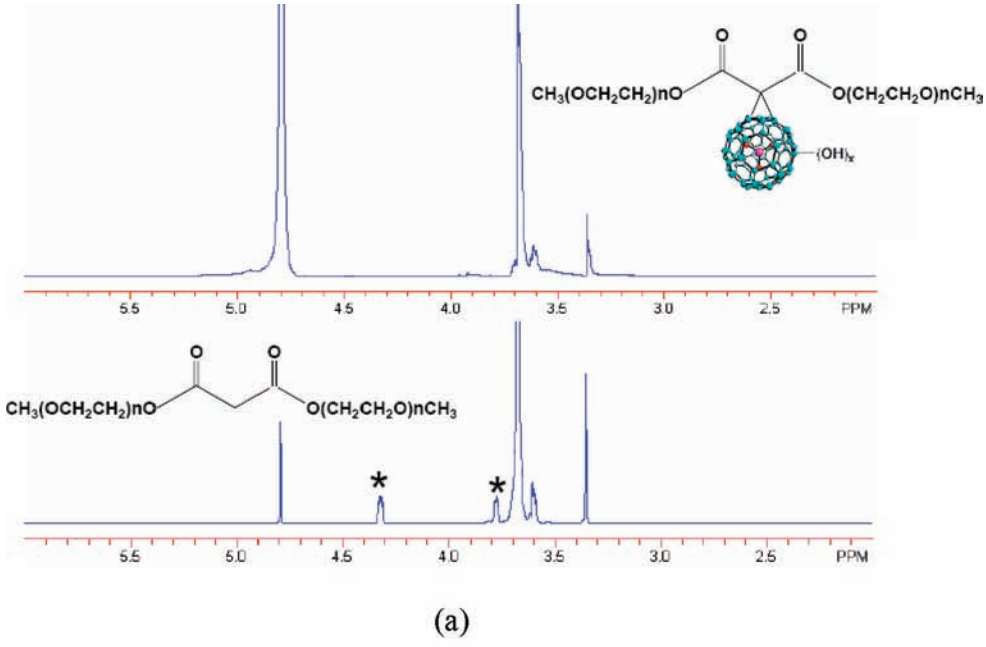
If a water exchange process exists, then the relaxation rates are (*1, 2*):

$$\frac{1}{T_{1,para}} = \frac{q[M]/55600}{T_{1M}+\tau_M} \quad (5)$$

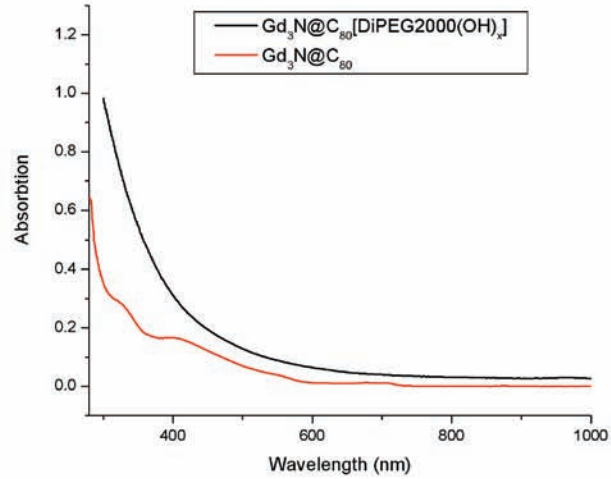
$$\frac{1}{T_{2,para}} = \frac{q[M]/55600}{T_{2M}+\tau_M} \quad (6)$$

[M] is in units of mM, τ_R is the rotational correlation time, τ_M is the residence time of the coordinated water molecules, ω_H is the Larmor frequency of proton, τ_{1e} is the longitudinal relaxation time of electron, and q is the number of the water molecules that coordinate to the paramagnetic molecules. τ_C is dominated by the shortest correlation time among τ_R, τ_M, and τ_{1e}. If τ_R is the dominant time, the relaxivity as a function of frequency shows a broad maximum peak that increases with increasing τ_R (*1*).

In the present investigation, the relaxivities of all the $Gd_3N@C_{80}$[DiPEG(OH)$_x$] samples were measured. The results are summarized in Table 1. Our previously reported relaxivities for $Gd_3N@C_{80}$[DiPEG5000(OH)$_x$] (*7*) are also listed, and they agree with the current data. All the $Gd_3N@C_{80}$[DiPEG(OH)$_x$] samples have high r_1 and r_2 values at all three magnetic field strengths. The r_1 values range from



(a)



(b)

Figure 2. (a) 400 MHz ^{1}H NMR spectra of $Gd_3N@C_{80}$[DiPEG350(OH)$_x$] (top) in comparison with DiPEGM350 malonate (bottom) in D_2O; (b) UV−Vis spectra of $Gd_3N@C_{80}$ and $Gd_3N@C_{80}$[DiPEG2000(OH)$_x$]. Note the disappearance of the characteristic peaks at 330 and 410 nm in the derivative.

Table 1. Relaxivity Data of $Gd_3N@C_{80}$[DiPEG(OH)$_x$] Series[a]

mol. weight of PEG	conc. range (μM)	r_1 (0.35 T) (mM^{-1} s^{-1})	r_2 (0.35 T) (mM^{-1} s^{-1})	r_1 (2.4 T) (mM^{-1} s^{-1})	r_2 (2.4 T) (mM^{-1} s^{-1})	r_1 (9.4 T) (mM^{-1} s^{-1})	r_2 (9.4 T) (mM^{-1} s^{-1})
5000	0.4−6.5	107 ± 8	127 ± 36	139 ± 6	221 ± 11	52.5 ± 2.4	186 ± 12
5000 (*7*)	1.6−12.6	102	144	143	222	32	137
2000	1.0−15.2	130 ± 4	148 ± 8	158 ± 6	249 ± 12	41.9 ± 3.0	218 ± 11
750	1.1−17.4	152 ± 5	169 ± 20	232 ± 10	398 ± 22	63.3 ± 1.8	274 ± 9
350	1.5−23.5	227 ± 31	268 ± 19	237 ± 9	460 ± 23	68.2 ± 3.3	438 ± 5

[a] The relaxivities were measured at room temperature in water.

Table 2. Relaxivity Data of $Gd_3N@C_{80}$[DiPEG(OH)$_x$] Series[a]

metallofullerene derivatives	r_1 (mM^{-1} s^{-1})	magnetic field strength (T)
$Gd@C_{82}O_6(OH)_{16}(NH_2CH_2CH_2COOH)_8$ (*6*)	9.1	1.5
Gadofullerenol (*22*)	47	9.4
$Gd@C_{82}(OH)_{40}$ (*12*)	67	0.47
	81	1.0
	31	4.7
$Gd@C_{60}(OH)_x$ (*26*)	83.2	1.4
$Gd@C_{60}[C(COOH)_2]_{10}$ (*11, 26*)	24.0	1.4
	4.6	0.47
$Gd_3N@C_{80}$[DiPEG350(OH)$_x$]	227 (75.7 Gd^{3+} based)	0.35
	237 (79.0 Gd^{3+} based)	2.4
	68.2 (22.7 Gd^{3+} based)	9.4

[a] The relaxivities were measured at room temperature in water.

139 mM^{-1} s^{-1} (Gd^{3+} based relaxivity 46.3 mM^{-1} s^{-1}) to 237 mM^{-1} s^{-1} (Gd^{3+}-based relaxivity 79.0 mM^{-1} s^{-1}) for the different PEG chains at 2.4 T compared to the value of about 4 mM^{-1} s^{-1} for commercially available Gd^{3+} ion chelated contrast agents. Several other groups have also reported r_1 values of mono gadofullerene derivatives, that is, one Gd^{3+} ion per fullerene cage. These r_1 values are typically higher than those of commercial MRI contrast agents. In our work, the relaxivities of all the $Gd_3N@C_{80}$[DiPEG(OH)$_x$] samples are significantly higher on a per molecule basis. A summary of these other studies and the relaxivities of $Gd_3N@C_{80}$[DiPEG350(OH)$_x$] in the current study are presented in Table 2 (*6, 8, 9, 11, 12, 22*).

As previously indicated, a primary reason for the high molar relaxivity of the $Gd_3N@C_{80}$[DiPEG(OH)$_x$] samples in comparison with other endohedral metallofullerenes derivatives originates from the presence of three Gd^{3+} ions within the cage: the charge transfer between the $(Gd_3N)^{6+}$ cluster and the $(C_{80})^{6-}$ cage leads to a very stable nanoparticle. Previous studies have confirmed that ferromagnetic coupling in this cluster gives rise to a large magnetic moment, 21 μB (*23*). The dipolar electron−nuclear spin interaction between the fluctuating Gd^{3+} electron magnetic moment and the large number of exchangeable water hydrogen atoms induces efficient proton relaxation. This is in contrast with the conventional Gd-DTPA complex, which has a single water molecule bound in the first coordination sphere of the metal ion, exchanges rather slowly with the bulk water, and the entire complex tumbles very rapidly.

Further factors contributing to the relaxation process relate to the unique property of the fullerenes to aggregate and form large nanoclusters. Aggregation occurs frequently for water-soluble metallofullerenes and affects the relaxivity significantly as previous studies have shown (*5, 9*). For the low molar mass $Gd_3N@C_{80}$[DiPEG(OH)$_x$] samples, the aggregates are formed by hydrogen bonding between −OH groups; however, the hydrophobic fullerene−fullerene interactions are also strong. Hence, fullerene aggregates can be formed. According to the Debye-Stokes equation for rigid spherical particles

$$\tau_R = 4\pi\eta r_{eff}^3/3k_BT$$

the rotational correlation time τ_R increases as the particle radius increases, which is an important parameter influencing relaxivity as a function of magnetic field strength. It has also been postulated that the presence of these aggregates might lead to a "confined" pool of water molecules in the interstitial spaces between individual gadofullerenes, which exchanges rapidly with the bulk water increasing again the relaxivity (*24*). Depending on the PEG length and aggregate size, different restricted pools of water would be created as mentioned above influencing the measured overall relaxivities.

Table 3. r_2/r_1 Ratios of the Pegylated/Hydroxylated Samples

sample	r_2/r_1 (0.35 T)	r_2/r_1 (2.4 T)	r_2/r_1 (9.4 T)
5000	1.19	1.59	3.54
2000	1.14	1.58	5.20
750	1.11	1.72	4.33
350	1.18	1.94	6.42

In the limit of $\tau_M \ll T_{1M}$, T_{2M} for eqs 2 and 3, we obtain

$$r_2/r_1 = [3 + 4(1 + \omega_H^2\tau_C^2)]/6 \quad (7)$$

At low field, $\omega_H^2\tau_C^2 \ll 1$ and the ratio approaches the value $7/6 = 1.17$. Our measured ratios of r_2/r_1 are listed in Table 3. On the basis of eq 7, the ratios at 0.35 T are consistent with the predicted value. Another result of the SBM equations is $\omega_H\tau_C \approx 1$ at maximum r_1. According to eq 7, this leads to $r_2/r_1 \approx 11/6 = 1.83$ for the peak. The ratios for the 750 and 350 PEGs at 2.4 T are close to $11/6 = 1.83$ and hence the maximum r_1 values should occur near 100 MHz (2.4 T). We can also see that at 2.4 T the 750/350 Da species has the maximum r_1 of all the samples. Hence, at 2.4 T for the 750/350 samples we obtain $\tau_C = 1/\omega_H = 1.59$ ns, which is significantly longer than the commercial contrast agent, e.g., $\tau_R = 66$ ps for the [Gd(DTPA-BMA)] (*1*). This assumes that τ_C is dominated by a rotational component.

The aggregation behavior was studied by DLS experiments. The DLS results for all $Gd_3N@C_{80}$[DiPEG(OH)$_x$] samples are shown in Figure 3. The mean peak positions are 75 nm, 76 nm, 58 nm, and 37 nm for $Gd_3N@C_{80}$[DiPEG350(OH)$_x$], $Gd_3N@C_{80}$[DiPEG750(OH)$_x$], $Gd_3N@C_{80}$[DiPEG2000(OH)$_x$], and $Gd_3N@C_{80}$[DiPEG5000(OH)$_x$], respectively. The 350PEG and 750PEG samples have the largest average aggregation size (∼75 nm), while the 5000PEG sample is much smaller (∼37 nm). The trend of decreasing aggregation size with increasing molecular weight is consistent with the relaxivity trend. It should

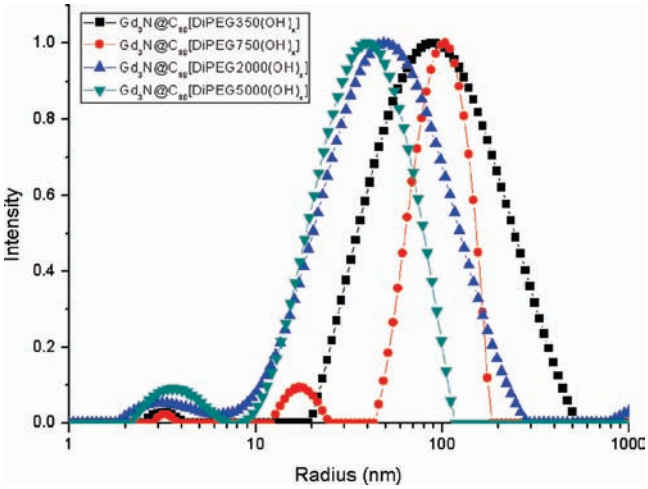


Figure 3. Size distribution of $Gd_3N@C_{80}$[DiPEG(OH)$_x$] from DLS experiments. The mean peak positions are 75 nm, 76 nm, 58 nm, and 37 nm for $Gd_3N@C_{80}$[DiPEG350(OH)$_x$], $Gd_3N@C_{80}$[DiPEG750(OH)$_x$], $Gd_3N@C_{80}$[DiPEG2000(OH)$_x$] and $Gd_3N@C_{80}$[DiPEG5000(OH)$_x$], respectively.

also be noted that these pegylated particles clearly deviate from spherical shape and the ones with longer PEG chains might exhibit internal flexibility. This could be an important additional factor for the observed reduced relaxivities for these larger molecules due to increased anisotropic rotation described by a fast local motion component that controls relaxivity and a slow global motional component (*25*).

Animal Infusion Study. Pure T_1 computed images of three consecutive brain slices of a live rat brain following infusion of 0.0235 mM $Gd_3N@C_{80}$[DiPEG350(OH)$_x$] into the brain tumor are shown in Figure 4. The middle column indicates the slice with the tumor, while the left and the right columns are slices without tumor used as controls. Immediately after the infusion is terminated ("3.5 h"), the $Gd_3N@C_{80}$[DiPEG350(OH)$_x$] nanoparticles have been distributed throughout the tumor, reducing the tissue T_1 values. The tumor appears as a dark area, as the white circle indicates. As time progresses, the brain tumor grows and the $Gd_3N@C_{80}$[DiPEG350(OH)$_x$] nanoparticles appear to be pushed out into the tumor periphery. This is illustrated at day 7 in the T_1 map, which shows aggregates on the surface, and the T_1-weighted image shows an enhancement ring around the tumor. These results illustrate the enhanced *in vivo* relaxivity of this optimized $Gd_3N@C_{80}$-[DiPEG350(OH)$_x$] system at low molar concentrations. It should also be noted that after 7 days the nanoparticles can still enhance the MRI contrast, which indicates that these metallofullerene agents can be used for long-term imaging diagnostic applications. In addition, these metallofullerene agents provide a platform for effective brachytherapy applications when Gd is replaced and/or combined with other radioactive agents (^{177}Lu).

CONCLUSIONS

We synthesized hydroxylated and pegylated Gd-containing TNT EMFs, $Gd_3N@C_{80}$[DiPEG(OH)$_x$], with different chain lengths of PEG. The relaxivities were measured at three magnetic field strengths. All the samples show significantly higher r_1 and r_2 compared to commercially available Gd-chelates and show considerable promise as a new class of contrast agents. They represent some of the highest relaxivities reported in the literature for commercial and investigational MRI contrast agents. Analyzing the field dependence of r_1, r_2, and r_2/r_1 indicates reasonable agreement with the predictions of the SBM theory under the assumption that the rotational correlation time τ_R dominates the relaxation process. Direct infusion of these particles into the live tumor-bearing rat brain demonstrates an initial uniform distribution and hence the potential for effective brachytherapy applications when Gd is replaced with radioactive ^{177}Lu.

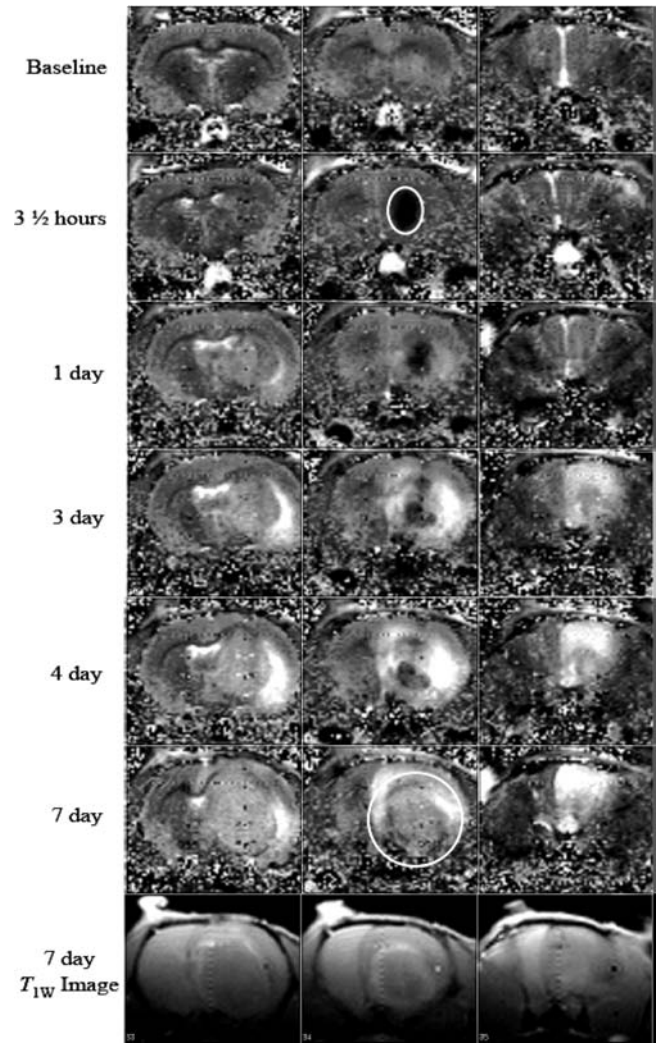


Figure 4. T_1 computed images and T_{1w} image of a live rat brain after direct infusion of 0.0235 mM $Gd_3N@C_{80}$[DiPEG350(OH)$_x$] into the tumor.

ACKNOWLEDGMENT

We thank the National Science Foundation [DMR-0507083] and the National Institute of Health [1R01-CA119371-01] for support. The authors thank Dr. William Keith Ray and Kim C. Harich for the help with the mass spectra.

Supporting Information Available: Additional information as described in the text. This material is available free of charge via the Internet at http://pubs.acs.org.

LITERATURE CITED

(1) Caravan, P., Ellison, J. J., McMurry, T. J., and Lauffer, R. B. (1999) Gadolinium(III) chelates as MRI contrast agents: structure, dynamics, and applications. *Chem. Rev. 99*, 2293–2352.
(2) Lauffer, R. B. (1987) Paramagnetic metal complexes as water proton relaxation agents for NMR imaging: theory and design. *Chem. Rev. 87*, 901–927.
(3) Sieber, M. A., Pietsch, H., Walter, J., Haider, W., Frenzel, T., and Weinmann, H. J. (2008) A preclinical study to investigate the development of nephrogenic systemic fibrosis: A possible

role for gadolinium-based contrast media. *Invest. Radiol. 43*, 65–75.

(4) Grobner, T. (2006) Gadolinium - a specific trigger for the development of nephrogenic fibrosing dermopathy and nephrogenic systemic fibrosis? *Nephrol., Dial., Transplant. 21*, 1104–1108.

(5) Shu, C. Y., Zhang, E. Y., Xiang, J. F., Zhu, C. F., Wang, C. R., Pei, X. L., and Han, H. B. (2006) Aggregation studies of the water-soluble gadofullerene magnetic resonance imaging contrast agent: $[Gd@C_{82}O_6(OH)_{16}(NHCH_2CH_2COOH)_8]_x$. *J. Phys. Chem. B 110*, 15597–15601.

(6) Shu, C. Y., Gan, L. H., Wang, C. R., Pei, X. L., and Han, H. B. (2006) Synthesis and characterization of a new water-soluble endohedral metallofullerene for MRI contrast agents. *Carbon 44*, 496–500.

(7) Fatouros, P. P., Corwin, F. D., Chen, Z. J., Broaddus, W. C., Tatum, J. L., Kettenmann, B., Ge, Z., Gibson, H. W., Russ, J. L., Leonard, A. P., Duchamp, J. C., and Dorn, H. C. (2006) In vitro and in vivo imaging studies of a new endohedral metallofullerene nanoparticle. *Radiology 240*, 756–764.

(8) Toth, E., Bolskar, R. D., Borel, A., Gonzalez, G., Helm, L., Merbach, A. E., Sitharaman, B., and Wilson, L. J. (2005) Water-soluble gadofullerenes: Toward high-relaxivity, pH-responsive MRI contrast agents. *J. Am. Chem. Soc. 127*, 799–805.

(9) Sitharaman, B., Bolskar, R. D., Rusakova, I., and Wilson, L. J. (2004) $Gd@C_{60}[C(COOH)_2]_{10}$ and $Gd@C_{60}(OH)_x$: nanoscale aggregation studies of two metallofullerene MRI contrast agents in aqueous solution. *Nano Lett. 4*, 2373–2378.

(10) Kato, H., Kanazawa, Y., Okumura, M., Taninaka, A., Yokawa, T., and Shinohara, H. (2003) Lanthanoid endohedral metallofullerenols for MRI contrast agents. *J. Am. Chem. Soc. 125*, 4391–4397.

(11) Bolskar, R. D., Benedetto, A. F., Husebo, L. O., Price, R. E., Jackson, E. F., Wallace, S., Wilson, L. J., and Alford, J. M. (2003) First soluble $M@C_{60}$ derivatives provide enhanced access to metallofullerenes and permit in vivo evaluation of $Gd@C_{60}[C(COOH)_2]_{10}$ as a MRI contrast agent. *J. Am. Chem. Soc. 125*, 5471–5478.

(12) Mikawa, M., Kato, H., Okumura, M., Narazaki, M., Kanazawa, Y., Miwa, N., and Shinohara, H. (2001) Paramagnetic water-soluble metallofullerenes having the highest relaxivity for MRI contrast agents. *Bioconjugate Chem. 12*, 510–514.

(13) Shu, C. Y., Corwin, F. D., Zhang, J. F., Chen, Z. J., Reid, J. E., Sun, M. H., Xu, W., Sim, J. H., Wang, C. R., Fatouros, P. P., Esker, A. R., Gibson, H. W., and Dorn, H. C. (2009) Facile preparation of a new gadofullerene-based magnetic resonance imaging contrast agent with high H-1 relaxivity. *Bioconjugate Chem. 20*, 1186–1193.

(14) Shu, C. Y., Wang, C. R., Zhang, J. F., Gibson, H. W., Dorn, H. C., Corwin, F. D., Fatouros, P. P., and Dennis, T. J. S. (2008) Organophosphonate functionalized $Gd@C_{82}$ as a magnetic resonance imaging contrast agent. *Chem. Mater. 20*, 2106–2109.

(15) Shu, C. Y., Ma, X. Y., Zhang, J. F., Corwin, F. D., Sim, J. H., Zhang, E. Y., Dorn, H. C., Gibson, H. W., Fatouros, P. P., Wang, C. R., and Fang, X. H. (2008) Conjugation of a water-soluble gadolinium endohedral fulleride with an antibody as a magnetic resonance imaging contrast agent. *Bioconjugate Chem. 19*, 651–655.

(16) MacFarland, D. K., Walker, K. L., Lenk, R. P., Wilson, S. R., Kumar, K., Kepley, C. L., and Garbow, J. R. (2008) Hydrochalarones: A novel endohedral metallofullerene platform for enhancing magnetic resonance imaging contrast. *J. Med. Chem. 51*, 3681–3683.

(17) Zhang, E. Y., Shu, C. Y., Feng, L., and Wang, C. R. (2007) Preparation and characterization of two new water-soluble endohedral metallofullerenes as magnetic resonance imaging contrast agents. *J. Phys. Chem. B 111*, 14223–14226.

(18) Stevenson, S., Rice, G., Glass, T., Harich, K., Cromer, F., Jordan, M. R., Craft, J., Hadju, E., Bible, R., Olmstead, M. M., Maitra, K., Fisher, A. J., Balch, A. L., and Dorn, H. C. (1999) Small-bandgap endohedral metallofullerenes in high yield and purity. *Nature 401*, 55–57.

(19) Ge, Z. X., Duchamp, J. C., Cai, T., Gibson, H. W., and Dorn, H. C. (2005) Purification of endohedral trimetallic nitride fullerenes in a single, facile step. *J. Am. Chem. Soc. 127*, 16292–16298.

(20) Krause, M., and Dunsch, L. (2005) Gadolinium nitride Gd_3N in carbon cages: The influence of cluster size and bond strength. *Angew. Chem., Int. Ed. 44*, 1557–1560.

(21) Yang, S. F., Kalbac, M., Popov, A., and Dunsch, L. (2006) Gadolinium-based mixed metal nitride clusterfullerenes $Gd_xSc_{3-x}N@C_{80}$ ($x = 1, 2$). *ChemPhysChem 7*, 1990–1995.

(22) Zhang, S., Sun, D., Li, X., Pei, F., and Liu, S. (1997) Synthesis and solvent enhanced relaxation property of water-soluble endohedral metallofullerenols. *Fullerene Sci. Technol. 5*, 1635–1643.

(23) Qian, M. C., Ong, S. V., Khanna, S. N., and Knickelbein, M. B. (2007) Magnetic endohedral metallofullerenes with floppy interiors. *Phys. Rev. B: Condens. Matter 75*, 104424.

(24) Laus, S., Sitharaman, B., Toth, E., Bolskar, R. D., Helm, L., Wilson, L. J., and Merbach, A. E. (2007) Understanding paramagnetic relaxation phenomena for water-soluble gadofullerenes. *J. Phys. Chem. C 111*, 5633–5639.

(25) Lipari, G., and Szabo, A. (1982) Model-free approach to the interpretation of nuclear magnetic-resonance relaxation in macromolecules 0.1. theory and range of validity. *J. Am. Chem. Soc. 104*, 4546–4559.

(26) Laus, S., Sitharaman, B., Toth, E., Bolskar, R. D., Helm, L., Asokan, S., Wong, M. S., Wilson, L. J., and Merbach, A. E. (2005) Destroying gadofullerene aggregates by salt addition in aqueous solution of $Gd@C_{60}(OH)_x$ and $Gd@C_{60}[C(COOH)_2]_{10}$. *J. Am. Chem. Soc. 127*, 9368–9369.

BC900375N

DNA Photocleavage by DNA and DNA−LNA Amino Acid−Dye Conjugates

Adva Biton, Aviva Ezra, Jana Kasparkova, Viktor Brabec, and Eylon Yavin*

Department of Medicinal Chemistry, The Institute for Drug Research, The School of Pharmacy, The Hebrew University of Jerusalem, Hadassah Ein-Karem, Jerusalem 91120, Israel, and Institute of Biophysics, Academy of Sciences of the Czech Republic, v.v.i., 61265 Brno, Czech Republic. Received August 26, 2009; Revised Manuscript Received December 28, 2009

DNA photocleavage by triplex forming oligonucleotides (TFO) has potential implications in both biotechnology and medicine. We have synthesized a series of homopurine DNA and DNA/LNA 14-mers to which an amino acid (glycine or L-tryptophan) and a cyanine dye are covalently linked. Two cyanine dyes were examined that include a quinolinium ring linked to a benzothiazolium ring through a monomethine (TO1) or trimethine (TO2) linker. The 14-mer sequence was chosen to target mdm2, a ubiquitin ligase (E3) that regulates p53 by promoting its ubiquitylation and proteosomal degradation. Such inhibition has been previously proposed as a therapeutic approach to target wild-type p53-expressing cancers. To examine whether our TFO conjugates photocleave the mdm2 target, we incubated the various conjugates with the mdm2 plasmid and irradiated the samples with visible light. We show that only the TFO with the complementary sequence and with an intervening L-tryptophan leads to the linearization of the plasmid after a short irradiation time (10 min) exciting the dye (λ_{max}(TO1) = 500 nm and λ_{max}(TO2) = 630 nm) with visible light. Furthermore, the photoreactivity is more pronounced for the LNA/DNA conjugate, an observation that is consistent with improved hybridization to the DNA target. Sequence specificity of the photoreaction is further corroborated on a synthetic 44-mer duplex containing the TFO site. Evidence for a ROS-dependent mechanism is also given and discussed.

INTRODUCTION

The selective photocleavage of DNA holds great therapeutic potential as means of down-regulating gene expression in a controlled and persistent manner (*1*−*4*). A common and attractive approach depends on light activation of a DNA−dye conjugate, leading to the formation of reactive oxygen species (ROS) that are localized at the target site (*2, 3, 5*). Such an approach merits from the control in localizing the damage at a given area (e.g., tissue) and at a timely fashion.

Several studies have shown that such site-specific selectivity is achievable. Notable are extensive studies with psoralen-conjugates, that upon UV irradiation lead to stable cross-links on the target duplex DNA (*6*−*24*). Some ODN-conjugates have shown site-specific photoreactivity upon irradiation in the visible region (*25*−*32*), and only very few reports have applied dyes that have relevant wavelengths for in vivo applications (i.e. over 600 nm) (*33*−*35*).

For example, a lutetium (III) texaphyrin complex tethered to a 2′-OMe RNA analogue was shown to selectively photocleave a complementary DNA strand after sample irradiation (λ = 732 nm) followed by piperidine treatment, resulting in DNA strand breaks primarily at guanine residues (*34*). Such reactivity is a consequence of singlet oxygen generation that preferably oxidizes guanine, the base with the lowest oxidation potential of all four natural DNA bases. Piperidine is then required in order to promote DNA scission at oxidized sites.

The use of visible light to achieve direct DNA strand breaks would be advantageous, since (1) there would be no toxicity due to irradiation (as opposed to UV) and (2) DNA damage would be more deleterious (strand break as opposed to nucleobase oxidation). Thiazole orange (TO) is a highly fluorescent intercalating dye and an efficient singlet oxygen sensitizer (*36*). TO has negligible fluorescence in solution, and obtains intense fluorescence when bound to nucleic acids. Kelley and co-workers have shown that, upon tethering TO to a dipeptide having either L-tryptophan (W) or L-tyrosine (Y), photoactivation of the dye (at 500 nm) resulted in the generation of a stable peroxide on the aromatic ring promoting nonselective DNA cleavage (*37, 38*). It was also shown that Y and W were required for the observed DNA cleavage (as determined by supercoiled plasmid nicking) and that replacing these amino acids with glycine or L-phenylalanine resulted in a peptide−dye conjugate that had no apparent photoinduced activity toward plasmid DNA.

Inspired by the photoreactivity of TO-peptides discovered by the Kelley group, we decided to explore the possibility of tethering TO-tryptophan to a TFO in order to achieve frank DNA strand breaks after visible light irradiation of the conjugate in the presence of the target plasmid DNA. In addition to monomethine TO-conjugates, we synthesized a series of DNA conjugates that include a cyanine dye with a trimethine linker (TO2) (*39*), as this dye is photoexcited at a wavelength (630 nm) that is relevant for tissue penetration (i.e., photodynamic therapy) in an in vivo setting.

Furthermore, we explored the outcome of introducing LNA bases in the TFO in order to improve the hybridization of such TFOs to the targeted DNA (*40*−*46*). We chose a TFO consisting of the homopurine sequence 5′-AAAGGAAAGGGAAA to target the Mdm2 oncogene. Mdm2 acts as an inhibitor of p53 by accelerating its intracellular degradation. As Mdm2 is overexpressed in many cancer cells, it is an attractive anticancer target (*47*−*49*).

Herein, we report on the synthesis of the TFO conjugates and their photoreactivity toward the mdm2 gene in its DNA plasmid form and in a synthetic DNA duplex containing the TFO binding site.

EXPERIMENTAL PROCEDURES

Irradiation with Plasmid PCMV-MDM2. Photoinduced DNA cleavage experiments were done using the MDM2 plasmid

* eylony@ekmd.huji.ac.il, tel: 972-2-6758692, fax: 972-2-6757076.

10.1021/bc900372h © 2010 American Chemical Society
Published on Web 03/26/2010

(8427 bp's) containing the target sequence that was incubated with the various DNA conjugates overnight at 37 °C. For DNA conjugates, the following buffer was used for incubation: 2 mM EDTA, 20 mM Tris, and 200 mM NaCl (pH = 7.4). For DNA/LNA conjugates, the following buffer was used for incubation: 10 mM NaH_2PO_4 and 50 mM NaCl (pH = 7.4).

Each of the conjugates were irradiated (in a dark room) for the indicated time with visible light. The light source used was a 150 W halogen lamp. This lamp (mrc) has a fiber optic that allows us to aim the light source onto the sample. Samples were placed in an eppendorf tube and the light source (from the filament) was about 1 cm away from the sample. Visible light was filtered with a cutoff filter (passing light between 400 to 600 nm for TO1 and 500 to 750 nm for TO2).

Irradiation with Synthetic 44-mer Duplex. The 44-mer duplex DNA as well as ssDNA markers were purchased from Synthezza (Jerusalem, Israel) and used as received. These sequences are as follows: 44-mers (with TFO target underlined), 3′ TCGGTCCGAAAGTAGTTTCCTTTCCCTT-TATGATAGTCTAAACA-5′; and its complementary sequence, 5′-AGCCAGGCTTTCATCAAAGGAAAGGGAAA-TACTATCAGATTTGT-3′. 23-mers: 3′-TTCCCTTTATGAT-AGTCTAAACA-5′ and 5′-AAGGGAAATACTATCAGA-TTTGT-3′. 20-mers: 3′-CCTTTATGATAGTCTAAACA-5′ and 5′-GGAAATACTATCAGATTTGT-3′. 17-mer: 3′-CCTTTAT-GATAGTCTAAACA-5′. 14-mer: 3′-TTATGATAGTCTAAA-CA-5′.

The 44-mer duplex containing the 14 base targeting sequence at its center was incubated (37 °C, 16 h) with an equimolar concentration (100 μM) of conjugate **3a**. The following buffer was used for incubation: 10 mM Tris, 100 mM NaCl, and 1 mM EDTA. All the samples were irradiated (in a dark room) for the indicated time (30 min) with visible light as described for plasmid irradiation.

Gel Electrophoresis. Agarose (1%) gel electrophoresis was carried out using Tris-acetate-EDTA (TAE) buffer. Running conditions: 60 min at 100 V. Denaturing (15% Urea) PAGE (19:1 acrylamide/bis-acrylamide) was carried out in Tris-borate-EDTA (TBE) buffer. Running conditions: 120 min at 100 V. The gels were stained with EB for 15 min and washed with DDW.

T_m Measurements. All thermal denaturation studies were carried out using quartz cuvettes with an optical path length of 1 cm on a Cary 300 UV/vis spectrophotometer interfaced with a computer for data collection and analysis. The temperature was increased and decreased from 20 to 80 °C at the rate of 1 °C/min. Samples were heated at 90 °C for 5 min and cooled down to room temperature for several hours prior measuring the melting profile of the dsDNA (44-mer). For triplex formation, the LNA-TFO (conjugate **3a**) was incubated with the dsDNA at 37 °C for 16 h.

Thermal denaturation experiments were carried out on a sample containing 1 μM duplex and same concentration of TFO for the triplex study. All samples were prepared in 10 mM Tris, 100 mM NaCl, and 1 mM EDTA. The melting temperature was determined by plotting the first derivative of the absorbance versus temperature profile and is accurate to ±1 °C.

Solid-Phase Synthesis of DNA and DNA/LNA Conjugates. The DNA (or DNA/LNA) oligomers were synthesized on an automated DNA synthesizer (ABI 3400) using standard phosphoramidite chemistry removing the DMT group at the 5′ end. All subsequent coupling reactions were performed on the solid phase (CPG resin (Glen Research), 2 μmol scale). The 5′-OH end of the oligos were extended with an ethylenediamine spacer by reacting the 5′-OH group with carbonyldiimidazole (CDI) (50 μmol CDI in 1 mL CH_3CN) for 1 h. After washing resin with CH_3CN (3 × 1 mL), ethylenediamine (10 μmol) and diisopropylethylamine (DIEA, 12 μmol) were added, and the reaction vessel was shacked overnight at RT. After washing the resin with dioxane (3 × 1 mL), CH_3CN (2 × 1 mL), and DCM (2 × 1 mL), coupling reactions with NPS (*O*-nitrophenylsulphenyl)-protected amino acids (L-tryptophan and glycine) were carried out using 4 equiv NPS-a.a. (8 μmol), 4.8 equiv HOBT (9.6 μmol), 4.8 equiv (9.6 μmol) HATU, and 8 equiv (16 μmol) DIEA in dry *N*,*N*-dimethylformamide (DMF, 1 mL) for 3 h. The NPS protecting group was removed with 2% dichloroacetic acid (DCA) in thioacetamide (TAA) (dissolved in 1 mL *N*-methylpyrrolidone ((NMP)) for 15 min. The free amine was finally coupled to the carboxy functionalized thiazole orange (TO1 or TO2, 4 equiv (8 μmol) under conditions as described for amino acid coupling.

DNA and DNA/LNA conjugates were removed from the resin by treating solid support with a 33% solution of NH_4OH for 1−2 h at room temperature. The supernatant was removed and incubated at 37 °C for 24 h to ensure the removal of all protecting groups from DNA and LNA bases. The NH_4OH solution was dried under vacuum and the resulting solid was purified by RP-HPLC (Shimatzu LC2010) using a semipreparative C18 reverse-phase column (Phenomenex, Jupiter 300 A) at a flow rate of 3.5 mL/min. Conditions for HPLC separation of DNA and DNA/LNA conjugates are described in detail in Supporting Information. Mobile phase A was either 50 mM NH_4OAc (pH 5.5) or 50 mM TEAA (pH = 7) with 5% CH_3CN; mobile phase B was either CH_3CN or MeOH. HPLC purified DNA and DNA/LNA conjugates were characterized by MALDI-TOF MS (see Table 1).

Table 1

conjugate	% nicked[a] (form II)	% linear[a] (form III)	MALDI-TOF MS obs./calc. (M + 1)
1a	41.7	11.9	5063.4/5064.0
1b	36		4932.0/4934.0
1c	12		5063.7/5064.0
2a	51.3	6.4	5116.4/5114.8
2b	21.6		4831.8/4833.0
2c	14.5		5116.2/5114.8
3a	55.4	20.4	5234.5/5232.2
3b	33		5103.0/5102.2
3c	9.8		5234.3/5232.2

[a] Values are for 30 min irradiation.

RESULTS

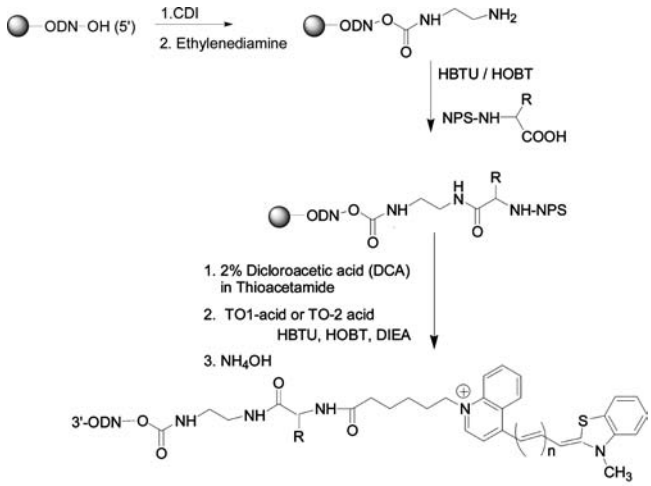
Synthesis of DNA and DNA/LNA-Amino Acid-Dye Conjugates. Scheme 1 shows the synthetic strategy for the synthesis of DNA and DNA/LNA-amino acid-dye conjugates with two cyanine dyes having either a monomethine linker (TO1) or a trimethine linker (TO2). Upon photoexcitation of such dye conjugates, the following processes are expected: (1) generation of singlet oxygen and/or peroxide upon photoactivation according to the choice of the intervening amino acid and (2) selective cleavage of the target DNA by conjugating a complementary TFO strand to the amino acid−dye moiety.

The possible photochemically induced reactions are depicted in Scheme 2.

Synthesis of cyanine dyes (TO1 and TO2) with pendant carboxylic acid moieties was accomplished according to the literature (*39*). Initially, the oligomer (14-mer homopurine, vide post) was synthesized on an automated DNA/RNA synthesizer on a standard CPG solid support. All subsequent reactions were carried out on the solid support including linker extension, as well as amino acid and dye conjugations.

NPS protected amino acids (glycine and L-tryptophan) were used for all conjugates. As the removal of NPS is achievable at mild reducing acidolysis conditions (*50*), this type of chemistry should be suitable for peptide-ODN synthesis. Indeed, we have

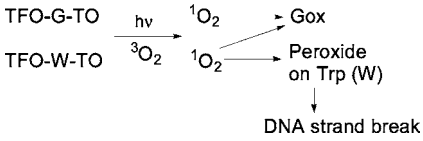
Scheme 1. Solid-Phase Synthesis of DNA and DNA/LNA-Amino Acid-Dye Conjugates



Conjugate 1a: DNA = 3'-AAAGGAAAGGGAAA-5', R = CH2-indole, n=0 (TO1)
Conjugate 1b: DNA = 3'-AAAGGAAAGGGAAA-5', R = H, n=0 (TO1)
Conjugate 1c: DNA = 3'-AAGGAAGAGAGAAA-5', R = CH2-indole, n=0 (TO1)
Conjugate 2a: DNA = 3'-AAAGGAAAGGGAAA-5', R = CH2-indole, n=1 (TO2)
Conjugate 2b: DNA = 3'-AAAGGAAAGGGAAA-5', R = H, n=1 (TO2)
Conjugate 2c: DNA = 3'-AAGGAAGAGAGAAA-5', R = CH2-indole, n=1 (TO2)
Conjugate 3a: DNA/LNA = 3'-AAAGGAAAGGGAAA-5', R = CH2-indole, n=0 (TO1)
Conjugate 3b: DNA/LNA = 3'-AAAGGAAAGGGAAA-5', R = H, n=0 (TO1)
Conjugate 3c: DNA/LNA = 3'-AAGGAAGAGAGAAA-5', R = CH2-indole, n=0 (TO1)

Underlined bases = LNA's for conjugates **3a-c**

Scheme 2. Possible Photochemical Pathways of DNA and DNA/LNA-Amino Acid-Dye Conjugates



found that using NPS-protected amino acids is superior to that of Fmoc protected amino acids (based on HPLC analysis; data not shown). Finally, DNA and DNA/LNA conjugates were removed from the solid support by treating resins with a 33% solution of NH_4OH for 1−2 h. Subsequently, base protecting groups were removed by incubating the ammonia solution at 37 °C for 24 h. All DNA conjugates were then HPLC purified on a reverse phase C18 column and analyzed by Maldi-TOF MS (see Supporting Information for HPLC chromatograms).

Choice of Amino Acid and DNA Sequence. The introduction of L-tryptophan in close proximity to the dye is expected to lead to its oxidation via singlet oxygen sensitization yielding a peroxide on the indole ring (*37, 38*). Such an ROS is anticipated to cause direct DNA strand breaks. Of all the aromatic amino acids that exert such reactivity (Trp, Tyr, and His), L-tryptophan has been shown to yield the highest peroxide levels (*51*). A 14-mer homopurine sequence (5′-AAAGGAAAGGGAAA-3′) was chosen as a triplex-forming oligonucleotide (TFO) that has the propensity of forming a triplex with the sense strand of the mdm2 gene in an antiparallel fashion (*4*). A plasmid of this gene (P-CMV-mdm2) was used as the DNA target; this plasmid includes the 14-mer TFO target.

Thus, the "wild-type" TFO includes an intervening L-tryptophan between the ODN and the dye (conjugate **1a**, Scheme 1). As a comparison, we chose to introduce glycine at this position, as it is not expected to react with singlet oxygen, and in turn, such a conjugate should exclusively yield singlet oxygen upon photoactivation (conjugate **1b**, Scheme 1). In addition, we synthesized a scrambled TFO sequence with an intervening L-tryptophan as a control conjugate that potentially may form a peroxide on the indole ring but is not expected to form a triplex with the target DNA (conjugate **1c**, Scheme 1).

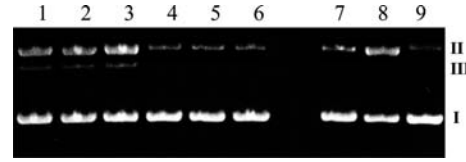


Figure 1. Photocleavage activity of conjugates **1a**−**1c** on the PCMV-MDM2 (8427 bp) plasmid in a buffer consisting of 2 mM EDTA, 20 mM Tris, and 200 mM NaCl (pH = 7.4) as determined by agarose gel electrophoresis. Solutions contained 2 μg plasmid and 10 μM TFO. Lanes 1−4: plasmid + conjugate **1a** (with L-tryptophan) after 15, 20, and 30 min of irradiation and in the dark, respectively. Lanes 5−6: plasmid + conjugate **1b** (scrambled) after 30 min of irradiation and in the dark. Lanes 7−8: plasmid + conjugate **1c** (with glycine) in the dark and after 30 min of irradiation. Lane 9: plasmid after 30 min irradiation.

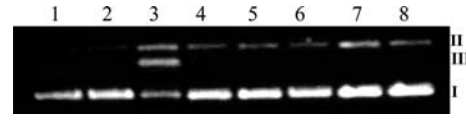


Figure 2. Oxygen dependence of photocleavage reaction of conjugates **1a** and **1b** with PCMV-MDM2 plasmid as determined by agarose gel electrophoresis. Solutions contained 2 μg plasmid and 10 μM TFO. Lanes 1 and 2, plasmid in the dark and after 30 min of irradiation; lanes 3−5, plasmid + conjugate **1a** without inhibitor, with NaN_3 (1 mM), and with Trolox (0.1 mM), respectively; lanes 6−8, plasmid + conjugate **1b** with NaN_3 (1 mM), without inhibitor and with Trolox (0.1 mM), respectively. The same buffer was used as in Figure 1.

Conjugates **1a**−**1c** all contain TO1 that is photoexcited at 500 nm. As a comparison, the analogous conjugates (conjugates **2a**−**2c**) were synthesized that include TO2; a dye that is excited at a longer wavelength, namely, 630 nm.

Finally a set of conjugates were synthesized with TO1 that included several LNA's as means to improve triplex formation (conjugates **3a**−**3c**).

Photocleavage of Plasmid DNA by DNA Conjugates. Prior to irradiation, DNA conjugates were incubated for 16 h with the plasmid DNA at 37 °C. In the case of the all-DNA TFO conjugates (**1a**−**c**, **2a**−**c**) a 100-fold molar excess of TFO was used to ensure triplex formation (*24*). As shown on the agarose gel (Figure 1), visible light irradiation of DNA conjugate **1a** with TO1 leads to some DNA relaxation of the supercoiled form (I) to the relaxed form (II) with a faint band corresponding to the linearized form (III) (lanes 1−3). Photoirradiation of the DNA conjugate with glycine (**1b**) results in some DNA relaxation of the plasmid with no indication of linearization (lane 8). Finally, the conjugate with the scrambled sequence (conjugate **1c**) has no apparent effect on the target plasmid DNA (lanes 5−6). Clearly, the photoreaction is sequence-specific, as the conjugate with the scrambled sequence (conjugate **1c**) does not lead to any detectable DNA photocleavage.

The DNA conjugates (**2a**−**2c**) with the TO2 dye were next examined for their photoactivity toward the mdm2 plasmid. As shown in Figure 3, a similar behavior was seen with these conjugates (**2a**−**2c**) as for the previous set (conjugates **1a**−**1c**). Thus, conjugate **2a** (with L-tryptophan) leads to extensive nicking of the supercoiled plasmid (lanes 6 and 7) with some indication for linearized plasmid (form III). Conjugate **2c** (scrambled) shows no photoactivity (lanes 2−4), similar to the behavior observed for conjugate **1c**. Finally, conjugate **2b** (with glycine) leads to some DNA relaxation (form II) (lanes 9−10) with no sign of the linear form (III).

Photocleavage of Plasmid DNA by DNA/LNA Conjugates. Prior to irradiation, DNA/LNA conjugates (**3a**−**3c**) were incubated for 16 h with the plasmid DNA at 37 °C. With

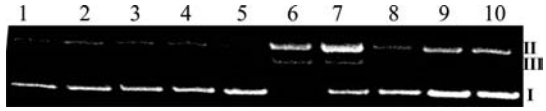


Figure 3. Photocleavage of PCMV-MDM2 plasmid by DNA conjugates with an appended cyanine dye TO2 as determined by agarose gel electrophoresis. Solutions contained 2 μg plasmid and 10 μM TFO. Lane 1, plasmid irradiated for 1 h (DNA only); lanes 2−4, plasmid + conjugate **2c** (scrambled) in the dark and after 1 h and 30 min irradiation, respectively; lanes 5−7, plasmid + conjugate **2a** (with L-tryptophan) in the dark and after 1 h and 30 min of irradiation, respectively; lanes 8−10, plasmid + conjugate **2b** (with glycine) in the dark and after 1 h and 30 min of irradiation, respectively. The same buffer was used as in Figure 1.

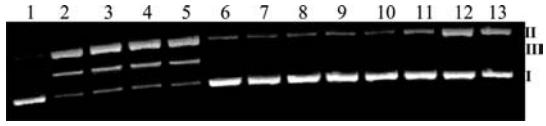


Figure 4. Photocleavage of PCMV-MDM2 plasmid by TFO containing LNA conjugates **3a**−**3c** (with TO1) in phosphate buffer (10 mM NaH_2PO_4, 50 mM NaCl, pH = 7.4), as determined by agarose gel electrophoresis. Lane 1, plasmid irradiated for 30 min (DNA only); lanes 2−6, plasmid + conjugate **3a** (with L-tryptophan) after 10, 15, 20, and 30 min irradiation and in the dark, respectively; lanes 7−9, plasmid + conjugate **3c** after 15 and 30 min irradiation and in dark, respectively; lanes 10−3, plasmid + TFO conjugate **3b** in the dark and after 10, 15, and 30 min irradiation, respectively.

the LNA/DNA hybrid (conjugates **3a**−**3c**), only a 2-fold access was used as such TFOs have been shown to readily from a triplex at such molar ratios. In order to verify triplex formation by the LNA conjugates, a synthetic 44-mer duplex containing the 14 base targeting sequence at its center was incubated (37 °C, 16 h) with an equimolar concentration (100 μM) of conjugate **3a**. Thermal denaturation profiles of the duplex and the triplex were carried out (see Supporting Information for thermal denaturation curves). A T_m value of 52 °C was determined by subtracting the triplex profile from that of the duplex profile. This value is similar (T_m = 50 °C) to that reported for a homopyrimidine 15-mer TFO containing 6 LNA's (*52*). The photoactivity of these set of conjugates is shown in Figure 4. Conjugate **3a** is shown to cause substantial linearization of the mdm2 plasmid after a short irradiation period of 10 min (lane 2). No significant change in the amount of nicked and linearized plasmid is observed at longer periods of irradiation (lanes 3−5). The scrambled LNA/DNA conjugate (**3c**) has no apparent photoactivity, whereas the conjugate with glycine (**3b**) leads only to plasmid DNA relaxation (form II).

Photocleavage of a Synthetic 44-mer Duplex DNA by DNA/LNA Conjugate 3a. To gain insight into the selectivity of DNA photocleavage by the LNA TFO (conjugate **3a**), a synthetic 44-mer duplex containing the 14-mer target site of conjugate **3a** was utilized as the DNA target. The 44-mer strands were chosen from the mdm2 plasmid with 15-mers flanking both sides of the central 14-mer target (underlined) as follows: 3′-TCGGTCCGAAAGTAGTTTCCTTTCCCTT-TATGATAGTCTAAACA-5′,5′-AGCCAGGCTTTCATCAAAG-GAAAGGGAAATACTATCAGATTTGT-3′.

A denaturing polyacrylamide gel (subsequently stained with EtBr) was used to follow the photoreaction (Figure 5). In lanes 1−6, various lengths of ssDNA were added as DNA markers in order to estimate the length of the DNA photoproduct formation. As shown in lane 9, a new migrating band is seen above the faster migrating TFO (**3a**) after sample irradiation (30 min); a product that is not observed in the dark control (lane 10: TFO + 44-mer duplex DNA without irradiation). This band migrates similarly to the 17-mer (lane 5). Thus, this gel is indicative of a site-specific photoreaction leading to a distinct

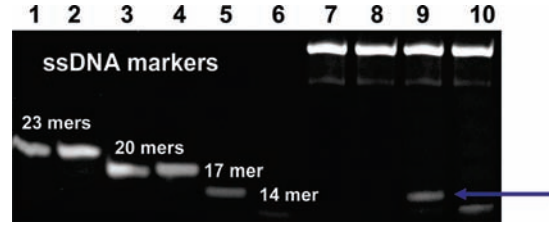


Figure 5. Photocleavage of a synthetic duplex DNA (a 44-mer containing the TFO targeting site at its center) by the TFO containing LNA conjugate **3a** (with TO1) in phosphate buffer (10 mM NaH_2PO_4, 50 mM NaCl, pH = 7.4), as determined by 15% denaturing polyacrylamide gel electrophoresis. Lanes 1−6: ssDNA markers with the same sequence composition as the 44-mer. 20- and 23-mers are from the 5′-end of the TC-rich 44-mer and from the 3′-end of the AG-rich 44-mer, respectively. 14- and 17-mers are from the 5′-end of the TC-rich 44-mer. Lanes 7 and 8: 44-mer duplex DNA in the dark and after irradiation (30′), respectively. Lanes 9 and 10: 44-mer duplex DNA and the LNA conjugate **3a** after 30′ irradiation and in the dark, respectively. Blue arrow indicates the formation of a new photoinduced DNA product. The gel was run in Tris-borate-EDTA (TBE) buffer for 120 min at 100 V and stained with ethidium bromide.

band that is in the range of 16−18 bases. It is not clear as to the fate of the remaining duplex (ca. 29 base pairs). We assume that this duplex is not well resolved and remains with the original 44-mer duplex at the upper part of the gel.

Photocleavage Activity Is Oxygen Dependent. In order to verify the involvement of reactive oxygen species (ROS) in the DNA photocleavage reaction, two ROS scavengers were used. Inhibition of cleavage in the presence of singlet oxygen quencher NaN_3 indicates the involvement of singlet oxygen as the reactive species (*53*) whereas a radical scavenger such as Trolox (*37, 54*) indicates the involvement of a peroxide.

As shown in Figure 2, there is a clear indication that the photoactivity depends on reactive oxygen species (ROS). Both NaN_3 and Trolox almost completely shut down photoreactivity of conjugate **1a** (Figure 2, lanes 4 and 5, respectively). These data are in agreement with both singlet oxygen and peroxide as the ROS involved in the observed photoactivity. In the case of conjugate **1b**, some attenuation in photoinduced DNA nicking is observed in the presence of NaN_3 (Figure 2, compare lanes 6 and 7). In the presence of Trolox (Figure 2, lane 8), DNA nicking is attenuated but to a lesser extent. As the photoactivity of this conjugate (**1b**) is generally not substantial, it is difficult to conclude on the inhibitory effect of Trolox on the photoactivity of conjugate **1b**.

DISCUSSION

Photocleavage of a specific gene at a PDT-relevant wavelength may be a powerful tool for genetic modifications both in biotechnology and in gene therapy. Toward this goal, we have studied a series of TFO conjugates that differ in several characteristics: (1) the choice of sequence (i.e., wild type vs scrambled), (2) the intervening amino acid (i.e., Gly vs Trp), (3) the dye molecule (i.e., TO1 vs TO2), and (4) the ODN type (i.e., DNA vs DNA/LNA). Table 1 summarizes the photoactivity of the various conjugates.

It is important to stress the contribution of the intervening amino acid. When glycine is placed between TFO and dye (conjugates **1b**, **2b**, and **3b**), the only photoinduced DNA damage to the mdm2-plasmid is nicking of supercoiled DNA (form I) to its relaxed form (form II), an observation that is consistent with singlet oxygen reactivity. However, when L-tryptophan is introduced, photoactivation of the conjugates (**1a**, **2a**, and **3a**) in the presence of the mdm2 plasmid leads to its linearization; particularly for the LNA/DNA conjugate (conjugate **3a**, Figure 4, lanes 2−5, and Table 1). This

observation is highly relevant in the context of the cell as such DNA damage (i.e., double strand breaks) is less manageable by the cellular DNA repair mechanism (*55*).

As Trolox inhibits this photoreaction (Figure 2, lanes 6) and in accordance with studies on the photoactivity of peptide-TO1 (*37, 38*), we conclude that a peroxide is formed on the indole ring of L-tryptophan leading to a radical reaction (most likely by 5′-hydrogen abstraction (*51*)). It is this mechanism that distinguishes the photoactivity of L-tryptophan containing conjugates (**1a**, **2a**, and **3a**) from their glycine counterparts (**1b**, **2b**, and **3b**).

The fact that linearization is more pronounced in the LNA/DNA TFO could be related to the superior hybridization that is expected from such a TFO in comparison to DNA-only TFO's. All conjugates with a scrambled TFO sequence (**1c**, **2c**, and **3c**) did not produce any detectable DNA damage upon photoactivation. This is indicative of a photoinduced reaction that is sequence-dependent. This is further supported by the photocleaved DNA product (lane 9, Figure 5) formed after irradiation of a synthetic 44-mer DNA duplex with the LNA TFO (conjugate **3a**).

Finally, when comparing both cyanine dyes (TO1 and TO2) we observe a similar photoactivity for all DNA conjugates (see Table 1). This is encouraging since, as opposed to TO1, TO2 has not been studied in the context of DNA damage. Thus, we have established the potential of utilizing cyanine dyes with longer absorption wavelengths for site-specific DNA photocleavage by TFO-Trp-Dye conjugates.

ACKNOWLEDGMENT

We thank the Alex Grass Center for Drug Design and Synthesis of Novel Therapeutics for financial support. The PCMV-MDM2 plasmid was generously provided by Prof. Matthias Dobbelstein. We thank Shimon Steingart for technical assistance. J.K. and V.B. were supported by the Grant Agency of the Academy of Sciences of the Czech Republic (IAA400040803).

Supporting Information Available: HPLC chromatograms of DNA and DNA/LNA conjugates and thermal denaturation curves of duplex (44-mer) and triplex (44-mer duplex and 14-mer TFO). This material is available free of charge via the Internet at http://pubs.acs.org.

LITERATURE CITED

(1) Besch, R., Giovannangeli, C., and Degitz, K. (2004) Triplex-forming oligonucleotides - Sequence-specific DNA ligands as tools for gene inhibition and for modulation of DNA-associated functions. *Curr. Drug Targets 5*, 691–703.

(2) Boerner, L. J. K., and Zaleski, J. M. (2005) Metal complex-DNA interactions: from transcription inhibition to photoactivated cleavage. *Curr. Opin. Chem. Biol. 9*, 135–144.

(3) Da Ros, T., Spalluto, G., Boutorine, A. S., Bensasson, R. V., and Prato, M. (2001) DNA-photocleavage agents. *Curr. Pharm. Des. 7*, 1781–1821.

(4) Rogers, F. A., Lloyd, J. A., and Glazer, P. M. (2005) Triplex-forming oligonucleotides as potential tools for modulation of gene expression. *Curr. Med. Chem. Anti-Cancer Agents 5*, 319–326.

(5) Thuong, N. T., and Helene, C. (1993) Sequence-specific recognition and modification of double-helical DNA by oligonucleotides. *Angew. Chem., Int. Ed. 32*, 666–690.

(6) Barre, F. X., Giovannangeli, C., Helene, C., and Harel-Bellan, A. (1999) Covalent crosslinks introduced via a triple helix-forming oligonucleotide coupled to psoralen are inefficiently repaired. *Nucleic Acids Res. 27*, 743–749.

(7) Cassidy, R. A., Kondo, N. S., and Miller, P. S. (2000) Triplex formation by psoralen-conjugated chimeric oligonucleoside methylphosphonates. *Biochemistry 39*, 8683–8691.

(8) Christensen, L. A., Wang, H., Van Houten, B., and Vasquez, K. M. (2008) Efficient processing of TFO-directed psoralen DNA interstrand crosslinks by the UvrABC nuclease. *Nucleic Acids Res. 36*, 7136–7145.

(9) Diviacco, S., Rapozzi, V., Xodo, L., Helene, C., Quadrifoglio, F., and Giovannangeli, C. (2001) Site-directed inhibition of DNA replication by triple helix formation. *FEBS Lett. 15*, 2660–2668.

(10) Giovannangeli, C., Diviacco, S., Labrousse, V., Gryaznov, S., Charneau, P., and Helene, C. (1997) Accessibility of nuclear DNA to triplex-forming oligonucleotides: The integrated HIV-1 provirus as a target. *Proc. Natl. Acad. Sci. U.S.A. 94*, 79–84.

(11) Higuchi, M., Kobori, A., Yamayoshi, A., and Murakami, A. (2009) Synthesis of antisense oligonucleotides containing 2′-O-psoralenylmethoxyalkyl adenosine for photodynamic regulation of point mutations in RNA. *Bioorg. Med. Chem. 17*, 475–483.

(12) Kim, K. H., Nielsen, P. E., and Glazer, P. M. (2006) Site-specific gene modification by PNAs conjugated to psoralen. *Biochemistry 45*, 314–323.

(13) Kim, K. H., Nielsen, P. E., and Glazer, P. M. (2007) Site-directed gene mutation at mixed sequence targets by psoralen-conjugated pseudo-complementary peptide nucleic acids. *Nucleic Acids Res. 35*, 7604–7613.

(14) Li, H., Broughton-Head, V. J., Peng, G. M., Powers, V. E. C., Ovens, M. J., Fox, K. R., and Brown, T. (2006) Triplex staples: DNA double-strand cross-linking at internal and terminal sites using psoralen-containing triplex-forming oligonucleotides. *Bioconjugate Chem. 17*, 1561–1567.

(15) Majumdar, A., Khorlin, A., Dyatkina, N., Lin, F. L. M., Powell, J., Liu, J., Feiz, Z. Z., Khripine, Y., Watanabe, K. A., George, J., Glazer, P. M., and Seidman, M. M. (1998) Targeted gene knockout mediated by triple helix forming oligonucleotides. *Nat. Genet. 20*, 212–214.

(16) Majumdar, A., Muniandy, P. A., Liu, J., Liu, J. I., Liu, S. T., Cuenoud, B., and Seidman, M. M. (2008) Targeted gene knock in and sequence modulation mediated by a psoralen-linked triplex-forming oligonucleotide. *J. Biol. Chem. 283*, 11244–11252.

(17) Musso, M., Wang, J. C., and VanDyke, M. W. (1996) In vivo persistence of DNA triple helices containing psoralen-conjugated oligodeoxyribonucleotides. *Nucleic Acids Res. 24*, 4924–4932.

(18) Oh, D. H., Suzara, V., and Krishnan, R. (2008) Modulation of psoralen DNA crosslinking kinetics associated with a triplex-forming oligonucleotide. *Photochem. Photobiol. 84*, 727–733.

(19) Shahid, K. A., Majumdar, A., Alam, R., Liu, S. T., Kuan, J. Y., Sui, X. F., Cuenoud, B., Glazer, P. M., Miller, P. S., and Seidman, M. M. (2006) Targeted cross-linking of the human beta-globin gene in living cells mediated by a triple helix forming oligonucleotide. *Biochemistry 45*, 1970–1978.

(20) Takasugi, M., Guendouz, A., Chassignol, M., Decout, J. L., Lhomme, J., Thuong, N. T., and Helene, C. (1991) Sequence-specific photoinduced cross-linking of the 2 strands of double-helical DNA by a psoralen covalently linked to a triple helix-forming oligonucleotide. *Proc. Natl. Acad. Sci. U.S.A. 88*, 5602–5606.

(21) Vasquez, K. M., Wang, G., Havre, P. A., and Glazer, P. M. (1999) Chromosomal mutations induced by triplex-forming oligonucleotides in mammalian cells. *Nucleic Acids Res. 27*, 1176–1181.

(22) Vasquez, K. M., Wensel, T. G., Hogan, M. E., and Wilson, J. H. (1996) High-efficiency triple-helix-mediated photo-cross-linking at a targeted site within a selectable mammalian gene. *Biochemistry 35*, 10712–10719.

(23) Yamayoshi, A., Kato, K., Suga, S., Ichinoe, A., Arima, T., Matsuda, T., Kato, H., Murakami, A., and Wake, N. (2007) Specific apoptosis induction in human papillomavirus-positive cervical carcinoma cells by photodynamic antisense regulation. *Oligonucleotides 17*, 66–79.

(24) Ye, Z. Y., Guntaka, R. V., and Mahato, R. I. (2007) Sequence-specific triple helix formation with genomic DNA. *Biochemistry 46*, 11240–11252.
(25) Crean, C. W., Kavanagh, Y. T., O'Keeffe, C. M., Lawler, M. P., Stevenson, C., Davies, R. J. H., Boyle, P. H., and Kelly, J. M. (2002) Targeting of photooxidative damage on single-stranded DNA representing the bcr-abl chimeric gene using oligonucleotide-conjugates containing [Ru(phen)(3)](2+)-like photosensitiser groups. *Photochem. Photobiol. Sci. 1*, 1024–1033.
(26) Doan, T. L., Perrouault, L., Praseuth, D., Habhoub, N., Decout, J. L., Thuong, N. T., Lhomme, J., and Helene, C. (1987) Sequence-specific recognition, photo-cross-linking and cleavage of the DNA double helix by an oligo-[alpha]-thymidylate covalently linked to an azidoproflavine derivative. *Nucleic Acids Res. 15*, 7749–7760.
(27) Inoue, T., Sugiura, Y., Saitoh, J., Ishiguro, T., and Otsuka, M. (1999) Fluorescence property of oxazole yellow-linked oligonucleotide. Triple helix formation and photocleavage of double-stranded DNA in the presence of spermine. *Bioorg. Med. Chem. 7*, 1207–1211.
(28) Le Doan, T., Praseuth, D., Perrouault, L., Chassignol, M., Thuong, N. T., and Helene, C. (1990) Sequence-targeted photochemical modifications of nucleic acids by complementary oligonucleotides covalently linked to porphyrins. *Bioconjugate Chem. 1*, 108–113.
(29) Le Gac, S., Rickling, S., Gerbaux, P., Defrancq, E., Moucheron, C., and, and Kirsch-De Mesmaeker, A. (2009) A photoreactive ruthenium(II) complex tethered to a guanine-containing oligonucleotide: A biomolecular tool that behaves as a "seppuku molecule. *Angew. Chem., Int. Ed. 48*, 1122–1125.
(30) Lentzen, O., Constant, J. F., Defrancq, E., Prevost, M., Schumm, S., Moucheron, C., Dumy, P., and Kirsch-De Mesmaeker, A. (2003) Photocrosslinking in ruthenium-labelled duplex oligonucleotides. *ChemBioChem 4*, 195–202.
(31) Ortmans, I., Content, S., Boutonnet, N., Kirsch-De Mesmaeker, A., Bannwarth, W., Constant, J. F., Defrancq, E., and, and Lhomme, J. (1999) Ru-labeled oligonucleotides for photoinduced reactions on targeted DNA guanines. *Chem.−Eur. J. 5*, 2712–2721.
(32) Perrouault, L., Asseline, U., Rivalle, C., Thuong, N. T., Bisagni, E., Giovannangeli, C., Ledoan, T., and Helene, C. (1990) Sequence-specific artificial photo-induced endonucleases based on triple helix-forming oligonucleotides. *Nature 344*, 358–360.
(33) Boutorine, A. S., Brault, D., Takasugi, M., Delgado, O., and Helene, C. (1996) Chlorin-oligonucleotide conjugates: Synthesis, properties, and red light-induced photochemical sequence-specific DNA cleavage in duplexes and triplexes. *J. Am. Chem. Soc. 118*, 9469–9476.
(34) Magda, D., Wright, M., Miller, R. A., Sessler, J. L., and Sansom, P. I. (1995) Sequence-specific photocleavage of DNA by an expanded porphyrin with irradiation above 700 nm. *J. Am. Chem. Soc. 117*, 3629–3630.
(35) Sessler, J. L., Sansom, P. I., Kral, V., Oconnor, D., and Iverson, B. L. (1996) Sapphyrin-oligonucleotide conjugates. Novel sequence-specific DNA photomodifying agents with increased binding affinity. *J. Am. Chem. Soc. 118*, 12322–12330.
(36) Nygren, J., Svanvik, N., and Kubista, M. (1998) The interactions between the fluorescent dye thiazole orange and DNA. *Biopolymers 46*, 39–51.
(37) Mahon, K. P., Ortiz-Meoz, R. F., Prestwich, E. G., and Kelley, S. O. (2003) Photosensitized DNA cleavage promoted by amino acids. *Chem. Commun.* 1956–1957.
(38) Mahon, K. P., Roy, M. D., Carreon, J. R., Prestwich, E. G., Rouge, J. L., Shin, S., and Kelley, S. O. (2006) Tunable DNA cleavage by intercalating peptidoconjugates. *ChemBioChem 7*, 766–773.
(39) Carreon, J. R., Stewart, K. M., Mahon, K. P., Shin, S., and Kelley, S. O. (2007) Cyanine dye conjugates as probes for live cell imaging. *Bioorg. Med. Chem. Lett. 17*, 5182–5185.
(40) Brunet, E., Alberti, P., Perrouault, L. C., Babu, R., Wengel, J., and Giovannangeli, C. (2005) Exploring cellular activity of locked nucleic acid-modified triplex-forming oligonucleotides and defining its molecular basis. *J. Biol. Chem. 280*, 20076–20085.
(41) Kumar, N., Nielsen, K. E., Maiti, S., and Petersen, M. (2006) Triplex formation with alpha-L-LNA (alpha-L-ribo-configured locked nucleic acid). *J. Am. Chem. Soc. 128*, 14–15.
(42) Kumar, N., Patowary, A., Sivasubbu, S., Petersen, M., and Maiti, S. (2008) Silencing c-MYC expression by targeting quadruplex in P1 promoter using locked nucleic acid trap. *Biochemistry 47*, 13179–13188.
(43) Petersen, M., and Wengel, J. (2003) LNA: a versatile tool for therapeutics and genomics. *Trends Biotechnol. 21*, 74–81.
(44) Rahman, S. M. A., Seki, S., Obika, S., Haitani, S., Miyashita, K., and Imanishi, T. (2007) Highly stable pyrimidine-motif triplex formation at physiological pH values by a bridged nucleic acid analogue. *Angew. Chem., Int. Ed. 46*, 4306–4309.
(45) Sun, B. W., Babu, B. R., Sorensen, M. D., Zakrzewska, K., Wengel, J., and Sun, J. S. (2004) Sequence and pH effects of LNA-containing triple helix-forming oligonucleotides: Physical chemistry, biochemistry, and modeling studies. *Biochemistry 43*, 4160–4169.
(46) Torigoe, H., Hari, Y., Sekiguchi, M., Obika, S., and Imanishi, T. (2001) 2′-O,4′-C-methylene bridged nucleic acid modification promotes pyrimidine motif tripler DNA formation at physiological pH - Thermodynamic and kinetic studies. *J. Biol. Chem. 276*, 2354–2360.
(47) Bianco, R., Ciardiello, F., and Tortora, G. (2005) Chemosensitization by antisense oligonucleotides targeting MDM2. *Curr. Cancer Drug Targets 5*, 51–56.
(48) Rayburn, E., Zhang, R. W., He, J., and Wang, H. (2005) MDM2 and human malignancies: Expression, clinical pathology, prognostic markers, and implications for chemotherapy. *Curr. Cancer Drug Targets 5*, 27–41.
(49) Toledo, F., and Wahl, G. M. (2006) Regulating the p53 pathway: in vitro hypotheses, in vivo veritas. *Nat. Rev. Cancer 6*, 909–923.
(50) Stern, M., Warshawsky, A., and Fridkin, M. (1979) Facile thiolytic removal of the ortho-nitrophenylsulfenyl amino-protecting group. *Int. J. Pept. Protein Res. 13*, 315–319.
(51) Prestwich, E. G., Roy, M. D., Rego, J., and Kelley, S. O. (2005) Oxidative DNA strand scission induced by peptides. *Chem. Biol. 12*, 695–701.
(52) Sau, S. P., Kumar, P., Anderson, B. A., Østergaard, M. E., Deoblad, L., Paszczynski, A., Sharma, P. K., and Hrdlicka, P. J. (2009) Optimized DNA-targeting using triplex forming C5-alkynyl functionalized LNA. *Chem. Commun.* 6756–6758.
(53) Hasty, N., Merkel, P. B., Radlick, P., and Kearns, D. R. (1972) Role of azide in singlet oxygen reactions - reaction of azide with singlet oxygen. *Tetrahedron Lett.* 49–52.
(54) Sarker, A. H., Watanabe, S., Seki, S., Akiyama, T., and Okada, S. (1995) Oxygen radical-induced single-strand DNA breaks and repair of the damage in a cell-free system. *Mutation Res. DNA Repair 337*, 85–95.
(55) Pardo, B., Gomez-Gonzalez, B., and Aguilera, A. (2009) DNA repair in mammalian cells. *CMLS 66*, 1039–1056.

BC900372H

Charge Dependent Substrate Activity of C3′ and N3 Functionalized, Organometallic Technetium and Rhenium-Labeled Thymidine Derivatives toward Human Thymidine Kinase 1

Harriet Struthers,[†] David Viertl,[‡] Marek Kosinski,[‡] Bernhard Spingler,[§] Franz Buchegger,[‡] and Roger Schibli*,[†]

Department of Chemistry and Applied Biosciences, ETH Zurich, 8093 Zurich, Switzerland, Division of Nuclear Medicine, Centre Hospitalier Universitaire Vaudois, 1011 Lausanne, Switzerland, and Institute of Inorganic Chemistry, University of Zurich, 8057 Zurich, Switzerland. Received August 27, 2009; Revised Manuscript Received March 9, 2010

Human cytosolic thymidine kinase (hTK1) has proven to be a suitable target for the noninvasive imaging of cancer cell proliferation using radiolabeled thymidine analogues such as [^{18}F]3′-fluoro-3′-deoxythymidine ([^{18}F]FLT). A thymidine analogue for single photon emission computed tomography (SPECT), which incorporates the readily available and inexpensive nuclide technetium-99m, would be of considerable practical interest. hTK1 is known to accommodate modification of the structure of the natural substrate thymidine at the positions N3 and C3′ and, to a lesser extent, C5. In this work, we used the copper-catalyzed azide−alkyne cycloaddition to synthesize two series of derivatives in which thymidine is functionalized at either the C3′ or N3 position with chelating systems suitable for the $M(CO)_3$ core (M = ^{99m}Tc, Re). The click chemistry approach enabled complexes with different structures and overall charges to be synthesized from a common precursor. Using this strategy, the first organometallic hTK1 substrates in which thymidine is modified at the C3′ position were identified. Phosphorylation of the organometallic derivatives was measured relative to thymidine. We have shown that the influence of the overall charge of the derivatives is dependent on the position of functionalization. In the case of the C3′-functionalized derivatives, neutral and anionic substrates were most readily phosphorylated (20−28% of the value for the parent ligand thymidine), whereas for the N3-functionalized derivatives, cationic and neutral complexes were apparently better substrates for the enzyme (14−18%) than anionic derivatives (9%).

INTRODUCTION

Human thymidine kinase 1 (hTK1[1]) is a cytosolic enzyme which catalyzes the γ-phosphate transfer from ATP to the 5′-hydroxyl groups of thymidine (dT) and 2′-deoxyuridine (dUrd). Other hTK1 substrates include 3′-azido-3′-deoxythymdine, AZT, and 3′-fluoro-3′-deoxythymidine, FLT, where thymidine has been modified at the C3′-position, and the phosphorylation of which is the first step in their activation as anti-HIV prodrugs (*1, 2*). It is well documented, however, that hTK1 is among the most selective of the nucleoside kinases and is particularly sensitive to changes in the structure of the natural substrates dT and dUrd (*3*). Eriksson et al. have shown that minor modification of the structure at the 5-position is possible, for example, 5-halo and 5-ethyl substitutions are tolerated, but substitution with bulkier groups such as 5-propenyl or 5-(2-chloroethyl) are not (*1, 4*). More recently, Tjarks and co-workers have shown that hTK1 is also amenable to modification of thymidine at the N3-position (*5, 6*). Functionalization with a series of bulky carborane derivatives, tethered from N3 of the pyrimidine base with varying spacer length, does not prevent phosphorylation of the nucleoside analogue. The experimental results of substrate activity investigations have all since been rationalized by the determination of the 3-D structure of hTK1, which confirms that hTK1 has a much smaller binding site than other nucleoside kinases (*7*).

Unlike the activity of other mammalian deoxyribonucleoside kinases, hTK1 activity is stringently cell cycle regulated (*3*). Active enzyme is not found in resting cells, but activity increases dramatically by the time cells reach the S-phase, to coincide with DNA synthesis. A number of thymidine analogues, which aim to target the high hTK1 activity in proliferating cells, have been developed. As potential agents for boron neutron capture therapy, thymidine derivatives incorporating *closo-o-* and *nido-m*-carboranes have been extensively investigated (*5, 6, 8, 9*). Similarly, thymidine derivatives labeled with radionuclides suitable for positron emission tomography (PET) have been developed with the goal of monitoring tumor growth and response to therapy (*10−12*). However, PET nuclides typically have very short half-lives and their production is expensive, usually requiring an onsite cyclotron. A thymidine analogue labeled with technetium for in vivo single photon emission computed tomography (SPECT) would be of considerable interest. Technetium has nearly perfect decay characteristics for diagnostic applications ($T_{1/2}$ = 6 h, 140 keV γ-radiation); moreover, it is readily available at low cost from a ^{99}Mo/^{99m}Tc generator system.

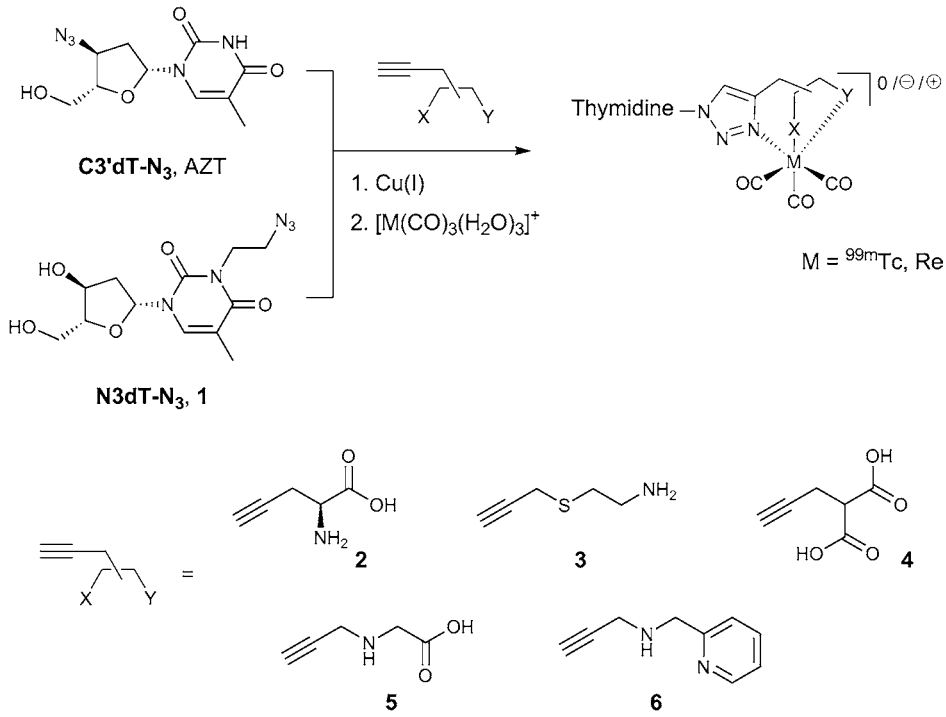
Given the promising reports of the retained substrate activity of N3-functionalized carborane thymidine derivatives (*5, 6, 9*), the N3 position is appealing for functionalization with a technetium complex. We recently reported the synthesis and in vitro evaluation of two series of technetium-labeled thymidine

* E-mail: roger.schibli@pharma.ethz.ch.
[†] ETH Zurich.
[‡] Centre Hospitalier Universitaire Vaudois.
[§] University of Zurich.

[1] Abbreviations: hTK1, human thymidine kinase 1; ATP, adenosine triphosphate; dT, thymidine; dUrd, uridine; AZT, 3′-azido-3′-deoxythymdine; FLT, 3′-fluoro-3′-deoxythymdine; PET, positron emission tomography; SPECT, single photon emission tomography; TBDMS, *tertiary*-butyldimethylsilyl; Boc, *tertiary*-butoxycarbonyl; dTTP, thymidine 5′-triphosphate; hENT1, human equilibrative nucleoside transporter; IdUrd, 5-iododeoxyuridine; FdUrd, 5-fluorodeoxyuridine; Glut1, glucose transporter 1; LAT, large neutral amino acid transporter 1; PBS, phosphate buffered saline; HEPES, 4-(2-hydroxyethyl)-1-piperazineethanesulfonic acid; NADH, nicotinamide adenine dinucleotide hydrate; PK, pyruvate kinase; LDH, lactate dehydrogenase; DTT, dithiothreitol; PEP, phospho(enol)pyruvate.

10.1021/bc900380n © 2010 American Chemical Society
Published on Web 04/01/2010

Scheme 1



derivatives in which the nucleoside was functionalized at the N3 position and could qualitatively show that all of the compounds retained activity toward hTK1 (*13, 14*). It has also been reported that minor structural modifications at the C3′ position do not dramatically lower affinity toward hTK1 (*4*). From the elucidation of the structure of hTK1, Welin et al. suggest that tolerance of C3′ modification could be a result of the open nature of the C3′/C4′ environment and the proximity of the C3′ substituent to the surface of the enzyme (*7*). However, to our knowledge there have not been any systematic investigations into the steric tolerance of hTK1 at this position. Tjarks' group report a small series of compounds in which thymidine has been functionalized at the 3′ position with a carborane (*15*). Unfortunately, the poor stability of these compounds prevented their thorough characterization with respect to their activity toward hTK1.

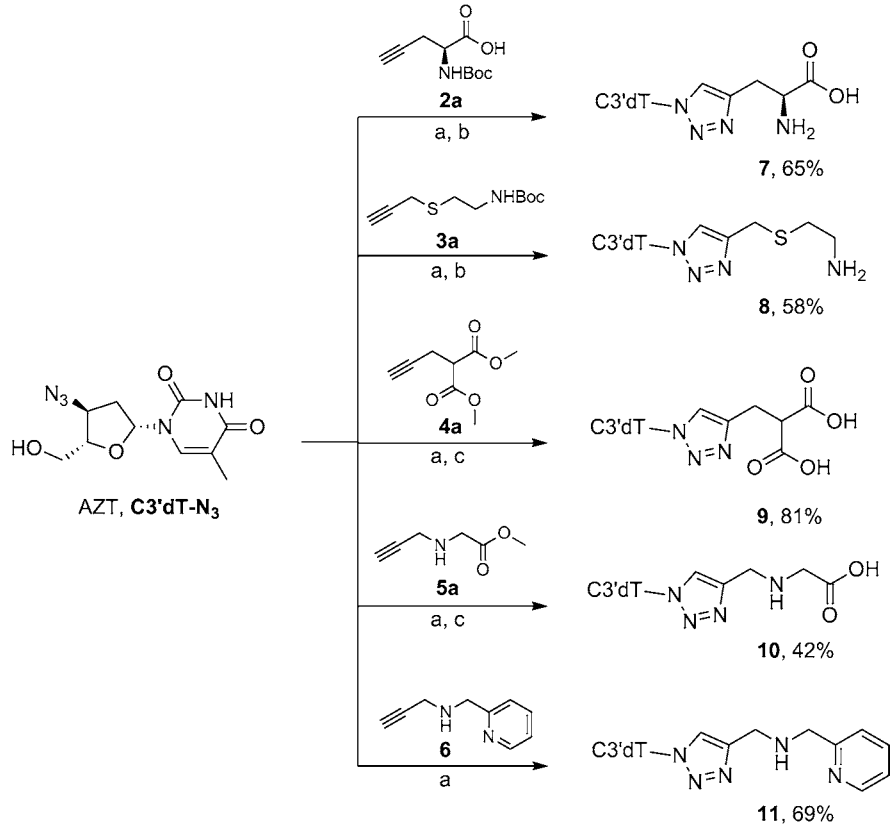
The aim of the current investigation was the synthesis of technetium-labeled thymidine analogues, which have the potential to be used in radiopharmacy as proliferation markers. We chose to investigate the substrate activity of C3′-functionalized thymidine analogues, and to compare these with N3-functionalized derivatives, particularly with regard to their overall charge. We used the "click-to-chelate" approach (*14, 16*) for the parallel synthesis of two series of derivatives which could be labeled with technetium and rhenium (Scheme 1). This strategy exploits the remarkable features of the copper catalyzed azide−alkyne cycloaddition (*17, 18*) and enables simultaneous formation of the chelating system and conjugation to a biologically relevant molecule in a single, high-yielding step. In the present study, a series of bidentate alkynes (Scheme 1, **2**−**6**) were reacted with either the commercial C3′-azido thymidine derivative AZT (C3′dT-N_3) or an N3 azido-thymidine derivative (N3dT-N_3, **1**) to yield two sets of conjugates with efficient tridentate triazole-containing chelators for the $M(CO)_3$ core (M = ^{99m}Tc, Re). This enabled us to identify novel organometallic substrates for hTK1 and qualitatively analyze structure−activity relationships. Preliminary investigations were also carried out into the cell-internalizing ability of representative complexes in two human glioblastoma cell lines.

RESULTS AND DISCUSSION

Chemistry. Thymidine can be readily functionalized at the C3′ position using the "click-to-chelate" approach starting from the commercially available azide 3′-azido-3′-deoxythymidine, AZT. Tridentate chelators for the $M(CO)_3$ core were incorporated by reaction of AZT with a suitable alkyne (Scheme 2). Suitable alkynes (Scheme 1) were prepared by alkylation of propargylamine with bromoacetate (**5**), alkylation of commercial amines with propargyl bromide (**3** and **6**), or are commercially available (**2** and **4**). Full details of the synthesis of the alkyne components used were recently reported (*14*). The copper catalyzed azide−alkyne cycloaddition was performed using standard Sharpless conditions: 1 equiv of alkyne and 1 equiv of azide were stirred at room temperature for 12 h in a mixture of *t*BuOH and water with catalytic amounts of copper acetate (0.1 equiv) and sodium ascorbate (0.2 equiv) (*19*). For ease of purification of the products, alkynes **2**−**5** were substituted with compounds **2a**−**5a**, in which carboxylic acids were protected as methyl esters and primary amines were Boc-protected. However, in previous studies we have shown that for radiolabeling purposes it is not necessary to use protected substrates or indeed to purify the ligands prior to radiolabeling (*14, 16*).

Thymidine derivatives **7** and **8** were prepared from the reactions of AZT with alkynes **2a** and **3a**, respectively. In both cases, the Boc-protected triazole products were purified by silica gel chromatography using mixtures of CH_2Cl_2 and MeOH before the Boc protecting groups were removed in a mixture of trifluoroacetic acid (10%) and CH_2Cl_2. Compounds **7** and **8** were purified by solid-phase extraction using Sep-Pak columns. Thymidine derivatives **9** and **10** were prepared from the reactions of AZT with alkynes **4a** and **5a**, respectively. The intermediates were purified by silica gel chromatography before the methyl esters were removed with aqueous NaOH. Compounds **9** and **10** were purified by solid-phase extraction using Sep-Pak columns. Compound **11** was purified by silica gel

Scheme 2[a]



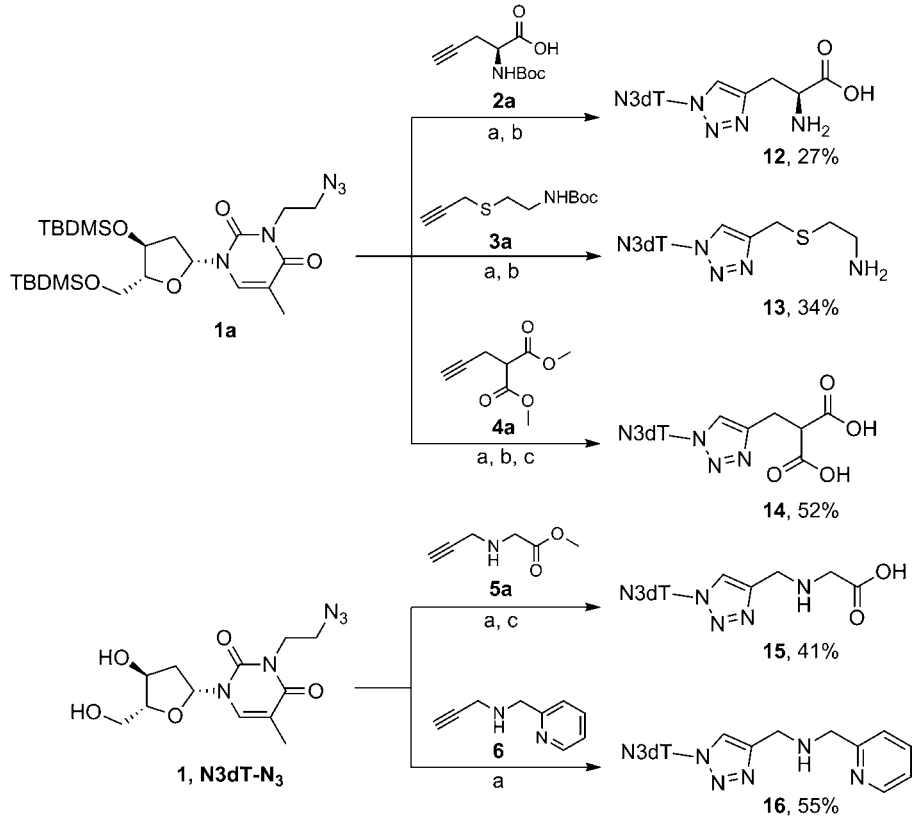
[a] (a) $Cu(OAc)_2.H_2O$, Na(ascorbate), *t*BuOH/H_2O; (b) TFA, CH_2Cl_2; (c) NaOH, H_2O, followed by HCl.

chromatography after the reaction of AZT and *N*-propargyl-pyridine-2-methylamine, **6**.

The N3-functionalized thymidine derivatives **12**, **13**, **15**, and **16** have been reported previously, however, they were only characterized via mass spectrometry (*14*). For their synthesis, thymidine was functionalized at the N3 position with an azido-ethyl group following the recently reported procedure (*14*) (Note: In an evaluation of the "click-to-chelate" approach, the compounds were synthesized using stock solutions (10^{-2} M) of the deprotected analogues of alkynes **2**, **3**, **5**, and **6**, compound **1**, copper(II) acetate, and sodium ascorbate (*14*)). In analogous procedures to the synthesis of the C3′-functionalized derivatives described above, tridentate chelators for the $M(CO)_3$ core (M = ^{99m}Tc, Re) were installed at the N3 position by reacting the N3-functionalized azido-thymidine derivative **1** or the *O*-TBDMS protected precursor **1a** with alkynes **2**−**6** using standard conditions for the click reaction and as outlined in Scheme 3. Thymidine derivatives **12** and **13** were prepared from the reactions of the *O*-TBDMS protected N3-functionalized thymidine precursor, **1a**, and alkynes **2a** and **3a**, respectively. The protected triazole intermediates were purified by silica gel chromatography using mixtures of CH_2Cl_2 and MeOH. In both cases, the Boc and TBDMS protecting groups of the products were removed in a single step with HCl in MeOH. Compounds **12** and **13** were purified by solid-phase extraction, although compound **12** could also be recrystallized from MeOH. Similarly, derivative **14** was prepared from the reaction of **1a** with alkyne **4a**. The protected intermediate was stirred in HCl/MeOH to remove the TBDMS protecting groups, followed by aqueous NaOH to remove the methyl esters. Thymidine derivative **15** was prepared from the reaction of **1** and alkyne **5a**. The intermediate was purified by silica gel chromatography before the methyl ester was removed with aqueous NaOH. In this case, removal of the TBDMS protecting groups from the azido-thymidine derivative **1a** with NBu_4F proved more efficient before the click reaction, as **1** could more easily be separated from excess NBu_4^+ salts than the more hydrophilic triazole product **15**. Both compounds **14** and **15** were purified by solid-phase extraction using Sep-Pak columns. Compound **16** was purified by silica gel chromatography after the reaction of **1** and *N*-propargyl-pyridine-2-methylamine, **6**.

The $Re(CO)_3$ complexes of all of the functionalized thymidine derivatives were prepared from the precursor $[ReBr_3(CO)_3][NEt_4]_2$ and a stoichiometric amount of the corresponding ligand in a mixture of MeOH and water at 50 °C. In each case, the quantitative formation of the product was observed by HPLC. The crude products were purified by solid-phase extraction using Sep-Pak columns and a water−MeOH gradient. The IR spectra of all of the rhenium complexes revealed the typical *fac*-$Re(CO)_3$ pattern with significantly blue-shifted, intense CO stretching frequencies (around 2020 cm^{-1} and 1880 cm^{-1}) compared with the starting material $[ReBr_3(CO)_3]^{2-}$ (2000 cm^{-1} and 1868 cm^{-1}). NMR analyses provided evidence that in each case the metal core is site specifically coordinated to the tridentate metal chelating system introduced at either the C3′ or N3 position, and showed similar features to model complexes which were synthesized with benzyl azide and characterized previously (*14*). Typically, the proton NMR spectra showed low field shifts of the protons in the chelating system after metal chelation. Independent resonances are observed for each proton in the CH_2 groups of the chelating system; they become distinguishable due to a lack of symmetry in the metal chelate. As was the case with the model complexes, signals for the protons of coordinated primary and secondary amines were also observed in the NMR spectra of the thymidine complexes as a result of the decrease in rate of H/D exchange. A key difference between the thymidine chelates and the analogous model complexes is the appearance of diastereoisomers, which can be distinguished in some cases by NMR and/or HPLC. For the C3′ complexes, HPLC analyses revealed two isomeric products for both

Scheme 3[a]



[a] (a) $Cu(OAc)_2 \cdot H_2O$, Na(ascorbate), *t*BuOH/H_2O; (b) HCl, MeOH; (c) NaOH, H_2O, followed by HCl.

$[Re(CO)_3\mathbf{8}]Br$ and $[Re(CO)_3\mathbf{10}]$, but only in the case of $[Re(CO)_3\mathbf{11}]Br$ were two isomers apparent in the ^1H NMR spectrum. For the N3-functionalized complexes $[Re(CO)_3\mathbf{13/16}]Br$ and $[Re(CO)_3\mathbf{15}]$, two diastereoisomers can be distinguished by NMR. The differences in chemical shifts of the two isomers are most pronounced for the complex $[Re(CO)_3\mathbf{13}]Br$, and HPLC analysis also revealed two product peaks in this case. In analogous model complexes, where a benzyl group substitutes the thymidine residue, isomers were not distinguishable by either HPLC or NMR (*14*). All of the complexes were readily water-soluble, which is a prerequisite for in vitro assessment.

Crystals of the complex $[Re(CO)_3\mathbf{11}][CF_3CO_2]$ suitable for X-ray crystallography were prepared by exchange of the bromide anion with the more bulky $CF_3CO_2^-$ anion using the corresponding silver salt. The final crystals were grown by diffusion of diethyl ether into a solution of the complex in methanol. Structural analysis revealed that the counterion was a mixture of Br^- and $CF_3CO_2^-$ as a result of incomplete precipitation of AgBr. The structure of the complex cation confirmed the expected tridentate, facial coordination of the κN,κN,κN chelator, which has not previously been structurally characterized (Figure 1). The Re−N3 bond length (2.146 (3) Å) is in agreement with the Re−N (triazole) bond length in other $Re(CO)_3$ complexes with triazole-containing ligands (*14*). Similarly, the Re−N4 (2.218(4) Å) and Re−N5 (2.181(3) Å) bond lengths are consistent with those found in $Re(CO)_3$ complexes with amine and pyridine containing chelators (*20*−*22*). For example, Banerjee et al. report the crystallographic characterization of a series of tridentate chelating systems for the $M(CO)_3$ core (M = ^{99m}Tc, Re) which incorporate an aliphatic amine with pyridyl and/or imidazoyl donor groups and are structurally similar to the chelator in compound **11** (*20*). The Re−N bond lengths in the novel triazole-containing chelating system were consistent with the values reported for the coordinated aliphatic amines (2.23−2.29 Å), pyridyl (2.16−2.18 Å), and imidazoyl (2.14−2.16 Å) groups. Crystallographic data are reported in the Supporting Information.

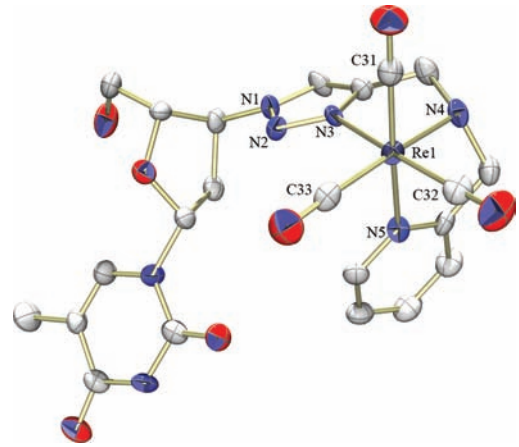


Figure 1. ORTEP-3 (*23*) representation of the complex cation $[Re(CO)_3\mathbf{11}]^+$ with thermal ellipsoids shown at 50% probability. Hydrogen atoms are omitted for clarity. Selected bond lengths [Å] and angles [°]: Re(1)−N(3) 2.146(3), Re(1)−N(4) 2.218(4), Re(1)−C(31) 1.915(4), Re(1)−C(32) 1.929(5), Re(1)−N(5) 2.181(3), Re(1)−C(33) 1.900(5), C(33)−Re(1)−C(31) 91.46(18), C(33)−Re(1)−C(32) 88.3(2), C(31)−Re(1)−C(32) 87.17(19), C(32)−Re(1)−N(3) 172.83(16), C(31)−Re(1)−N(5) 171.65(19), C(33)−Re(1)−N(4) 170.51(16).

Radioactive technetium-99 m complexes were prepared with the ligands **7**, **8**, **10**, **11**, **12**, **13**, **15**, and **16**. The complexes were prepared quantitatively by adding the organometallic precursor $[^{99m}Tc(CO)_3(H_2O)_3]^+$ (*24*) to a solution of the ligand in physiological phosphate buffer (PBS; pH 7.4) and heating for 45 min at 95 °C. In each case, a single product was observed. Characterization of the radioactive complexes was accomplished by comparison of the retention times observed in the γ-HPLC

Scheme 4

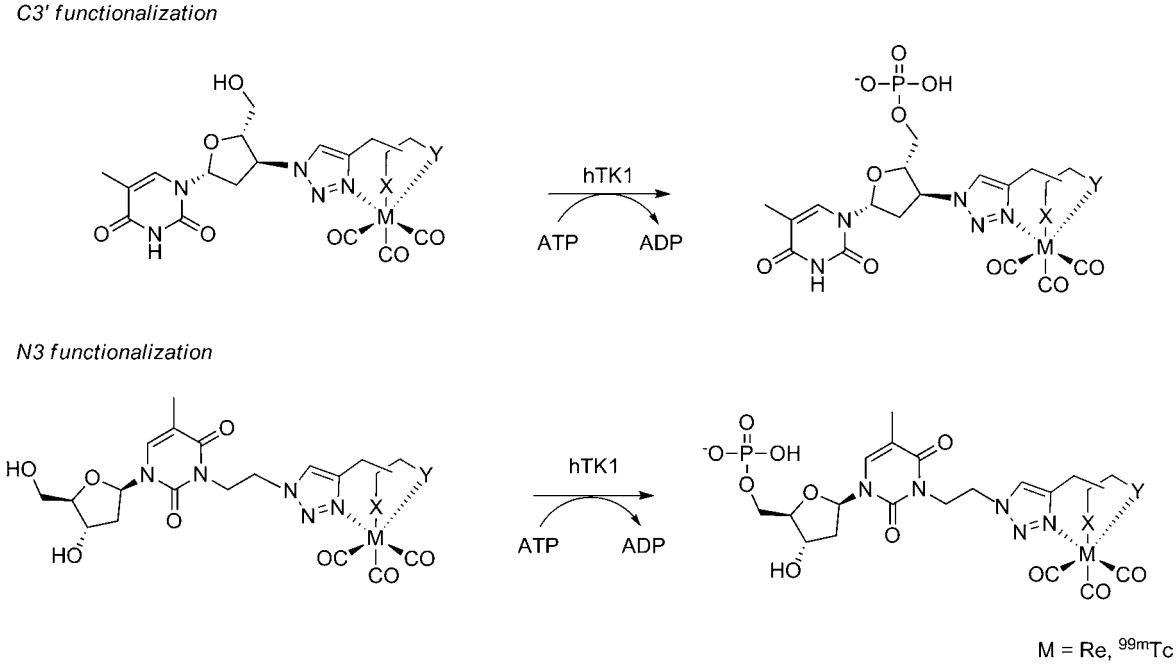


Table 1. Phosphorylation of Organometallic Thymidine Complexes [Re(CO)$_3$7−16]

compound	position of functionalization	overall charge	phosphorylation [%][a]
[Re(CO)$_3$**7**]	C3′	neutral	20.3 ± 0.8
[Re(CO)$_3$**10**]	C3′	neutral	27.6 ± 1.9
[Re(CO)$_3$**9**]NEt$_4$	C3′	anionic	23.1 ± 1.8
[Re(CO)$_3$**8**]Br	C3′	cationic	12.5 ± 0.5
[Re(CO)$_3$**11**]Br	C3′	cationic	14.2 ± 0.2
[Re(CO)$_3$**12**]	N3	neutral	17.9 ± 0.1
[Re(CO)$_3$**15**]	N3	neutral	14.1 ± 0.2
[Re(CO)$_3$**14**]NEt$_4$	N3	anionic	9.0 ± 0.4
[Re(CO)$_3$**13**]Br	N3	cationic	10.9 ± 0.4
[Re(CO)$_3$**16**]Br	N3	cationic	16.8 ± 0.2
Thymidine	-	-	100[a]

[a] The phosphorylation of thymidine was arbitrarily set to 100%.

trace with those in the UV-trace of the corresponding rhenium complexes. Given the experimental limitations, the retention times matched for all pairs of complexes. For in vitro and enzymatic studies, ^{99m}Tc complexes were separated from unreacted thymidine derivatives by HPLC.

In Vitro Evaluation of the Organometallic Thymidine Derivatives. *Substrate Activity toward Human Thymidine Kinase.* By incubating solutions of the complexes with ATP in the presence of hTK1, we have shown previously that the ^{99m}Tc-labeled complexes [^{99m}Tc(CO)$_3$**12**] and [^{99m}Tc(CO)$_3$**15**] are substrates for the enzyme (*14*). Under the same conditions, substrate activity was not observed with the complexes [^{99m}Tc(CO)$_3$**13**]$^+$ and [^{99m}Tc(CO)$_3$**16**]$^+$ (*14*). In the current investigation, the hTK1 substrate activities of all target rhenium complexes were assessed using a coupled thymidine kinase-pyruvate kinase-lactate dehydrogenase UV assay ($\lambda = 340$ nm) as previously described (*6, 25*). We were able to show that all of the C3′-functionalized and N3-functionalized rhenium complexes were substrates for hTK1 (Scheme 4). The results with both series of compounds are presented in Table 1. The phosphorylation of thymidine was arbitrarily set to 100%.

In the first series of complexes, the ribose of thymidine is functionalized directly at the C3′ position and there is no spacer between the thymidine and metal chelate. The metal-labeled compounds have varying overall charges depending on the functional groups of the chelating system. The relative rates of phosphorylation ranged from 13−28%. The neutral complex [Re(CO)$_3$**10**] had the highest relative phosphorylation of 27.6 ± 1.9%. There is a clear trend in phosphorylation rate as a function of overall charge. The anionic C3′-functionalized compound (23.1 ± 1.8%) has a comparable rate of phosphorylation to the neutral C3′-functionalized compounds (27.6 ± 1.9% and 20.3 ± 0.8%), whereas the cationic complexes appear to be much less readily phosphorylated (12.5 ± 0.5% and 14.2 ± 0.2% for [Re(CO)$_3$**8**]Br and [Re(CO)$_3$**11**]Br, respectively). This is perhaps surprising given that the structure of hTK1 co-crystallized with the feedback inhibitor thymidine triphosphate (dTTP) shows the proximity and suspected interaction of the C3′ substituent (in the case of dTTP, a hydroxyl group) with a glycine residue and an aspartic acid residue (*7*). There is, however, an arginine residue in the same region of the active site. Interaction between the C3′ substituent and the cationic side chain of arginine may compensate for the loss of interaction with the C3′ hydroxyl group of thymidine, and thus be an explanation for the greater substrate efficiency of the anionic complex compared to the cationic complexes. However, at the moment this remains purely speculative, and only co-crystallization of the complex with the enzyme would provide further insight into the observed trend.

In the second series of compounds, thymidine was functionalized at the N3 position. As for the C3′-functionalized complexes, the overall charges of the derivatives vary, but in all cases, there is an ethyl spacer between thymidine and the metal complex. The phosphorylation data show that in general the C3′-functionalized compounds are better substrates for hTK1 than the N3-functionalized compounds. The phosphorylation is relatively low compared to thymidine for all of the complexes (9−18%), although interestingly, in this series of compounds the neutral and cationic complexes appear to be better substrates than the anionic complex. This is consistent with results from Tjarks et al., which show that zwitterionic NH_3^+-*nido-m*-carborane-substituted thymidine analogues (with a propyl spacer) have high substrate activity (*26*). However, the variation in the phosphorylation of the two cationic complexes (10.9 ± 0.4% and 16.8 ± 0.2% for [Re(CO)$_3$**13**]Br and [Re(CO)$_3$**16**]Br, respectively) suggests that, in addition to overall charge,

Table 2. Internalization into the Human Glioblastoma Cell Lines U251 and LN229, with and without Pretreatment with 5-Fluorodeoxyuridine, as a Percentage of the Initial Activity Added

	U251		LN229	
	internalization [%]	pretreated with FdUrd[a] [%]	internalization [%]	pretreated with FdUrd[a] [%]
^{125}IdUrd	14.03 ± 1.69	59.29 ± 2.80	8.81 ± 0.43	39.40 ± 1.39
[^{99m}Tc(CO)$_3$**7**]	0.01 ± 0.00	0.02 ± 0.00	0.01 ± 0.00	0.01 ± 0.00
[^{99m}Tc(CO)$_3$**16**]$^+$	0.13 ± 0.01	0.14 ± 0.01	0.12 ± 0.01	0.15 ± 0.01

[a] Cells were incubated with 1 μM FdUrd for 1 h before addition of the radioactive dT analogue.

structural differences in the metal chelate also affect the substrate affinity for hTK1. It is not possible, therefore, to rule out structural differences in addition to overall charge as the reason for the lower substrate affinity of the complex [Re(CO)$_3$**14**]NEt$_4$, which in contrast to the anionic C3′-functionalized compound had the lowest phosphorylation rate in the series (9.0 ± 0.4%).

In a second, direct assay, the radioactive and nonradioactive complexes [^{99m}Tc/Re(CO)$_3$**X**] (**X** = **7**, **10**, **11**, **15**) were incubated with ATP and recombinant hTK1 only. The enzymatic reactions were analyzed by HPLC (UV-trace at λ = 254 nm for the rhenium complexes, γ-trace in the case of the radioactive Tc-99m complexes). For both the ^{99m}Tc and the Re compounds, phosphorylation resulted in a measurable shift in retention time on a C_{18} reversed phase column and the monophosphorylated products [^{99m}Tc/Re(CO)$_3$**X**]-**P** (**X** = **7**, **10**, **11**, **15**) were distinguished clearly from the starting material. In the case of the complex [Re(CO)$_3$**7**], the reaction mixture was purified by HPLC, and the fractions collected were analyzed by mass spectroscopy. The fraction corresponding to the starting material showed a mass peak at m/z = 651.09, $[C_{18}H_{19}N_6O_9Re]H^+$. The more hydrophilic phosphorylated complex, [Re(CO)$_3$**7**]-**P**, revealed a mass peak at m/z = 731.03 $[C_{18}H_{20}N_6O_{12}PRe]H^+$. In time dependent HPLC experiments monitoring the phosphorylation of complex [Re(CO)$_3$**7**], an increase in the concentration of the monophosphorylated species, [Re(CO)$_3$**7**]-**P**, and corresponding decrease in the concentration of the starting complex was observed.

Cell Internalization Experiments. hTK1 is located in the cytosol, and therefore, a potential substrate has to pass through the cell membrane before it can be phosphorylated. If this transport is not achieved actively via nucleoside transporters, then it must occur by passive diffusion (*27*). This has been suggested as the major cell internalization route for the carborane-thymidine derivatives reported by Tjarks et al. (*26*) Similarly, AZT is not recognized by the ubiquitously expressed human equilibrative nucleoside transporter type 1 (hENT1) and is transported primarily by passive diffusion (*28*). By analogy to the N3-functionalized carborane derivatives and AZT, we suspected passive diffusion would be the most likely cell internalization route of our C3′/N3-functionalized complexes.

In a preliminary study of the cell internalizing ability of the organometallic thymidine derivatives, we investigated the internalization of one ^{99m}Tc(CO)$_3$-labeled complex from each series of compounds. We expected the neutral complexes to be the most likely to be internalized based on our previous experience (*13*). We therefore chose to investigate the neutral complex [^{99m}Tc(CO)$_3$**7**] from the series of C3′-functionalized compounds. To complete a previous series of N3-functionalized thymidine analogues, we chose to investigate the cationic complex [^{99m}Tc(CO)$_3$**16**]$^+$, (internalization of anionic and neutral N3-functionalized thymidine analogues has been observed previously) (*13*). The incorporation of both complexes into two human glioblastoma cell lines was measured and compared with the incorporation of ^{125}I-iododeoxyuridine (^{125}IdUrd), using cell lines and conditions established for the incorporation of ^{125}IdUrd (*29, 30*). Internalization was measured with and without pretreatment with 5-fluorodeoxyuridine (FdUrd), which is known to increase uptake of 5-iododeoxyuridine by inhibiting endogenous thymidine synthesis and inducing upregulation of nucleoside transporters (*29, 31*−*33*). The results for both cell lines, U251 and LN229, and with and without 5-fluorodeoxyuridine pretreatment are presented in Table 2.

The data show that there was only minor cell-associated radioactivity after incubation of both cell lines with [^{99m}Tc(CO)$_3$**7**] and [^{99m}Tc(CO)$_3$**16**]$^+$. This can be rationalized either as a lack of uptake or as a lack of intracellular retention of the radioactive probes. Assuming that the complexes are stable in vitro and are intracellularly phosphorylated, the data suggest that neither of the ^{99m}Tc-labeled derivatives are able to enter the cells. The fact that pretreatment with 5-fluorodeoxyuridine (FdUrd), which should stimulate nucleoside transport, had no effect on the amount of radioactivity associated with the cells, provides further evidence that uptake is not mediated by nucleoside transporters. It is likely that the structural modification at either the C3′ or the N3 position is significant enough to prohibit active incorporation mediated by nucleoside transporters. This is in agreement with our previous experience of organometallic thymidine derivates. Although we reported moderate cell uptake of N3-functionalized thymidine derivatives (0.6−4.8%) into SKNMC tumor cells, uptake increased with increasing lipophilicity (*13*). We assume, therefore, that factors such as hydrophilicity, charge, and/or size prevent [^{99m}Tc(CO)$_3$**7**] or [^{99m}Tc(CO)$_3$**16**]$^+$ exhibiting any significant internalization via passive diffusion. An alternative explanation for the negligible accumulation of radioactivity is that either the compounds are not sufficiently phosphorylated or they are susceptible to intracellular degradation. It has been shown for a number of N3-functionalized carboranyl thymidine analogues that the compounds cannot compete intracellularly with endogenous thymidine (*34*).

CONCLUSIONS

Starting from two azido-functionalized thymidine derivatives, we were able to investigate the influence of the position of the metal complex on the substrate affinity, as well as the influence of charge on the relative phosporylation of two series of novel M(CO)$_3$-labeled thymidine derivatives. The "click-to-chelate" approach was used to synthesize thymidine derivatives functionalized with a tridentate chelator for the M(CO)$_3$ core at either the C3′ or N3 position of thymidine. All of the conjugates could be readily labeled with the M(CO)$_3$ precursors to form well-defined organometallic complexes, with differing structures and overall charges. Incubation of the Re(CO)$_3$ derivatives with ATP in the presence of hTK1 led to the formation of monophosphorylated organometallic thymidine derivatives, which were observed by HPLC and unambiguously identified by mass spectroscopy. In this way, we were able to show that all of the compounds tested, which vary in the position of the metal chelate and overall charge, were substrates for hTK1. For each of the complexes, the rate of phosphorylation was measured quantitatively relative to thymidine, the natural substrate for hTK1. We could show that for the two sets of compounds investigated the C3′-functionalized thymidine derivatives were on average more readily phosphorylated by hTK1 than the N3-

functionalized derivatives. Furthermore, we have shown that the effect of the overall charge of the substrate is dependent on the position of the metal complex. For the C3′-functionalized complexes, the rates of phosphorylation followed the trend neutral ≈ anionic > cationic. In the case of the N3-functionalized derivatives, the trend neutral ≈ cationic > anionic was observed for the relative phosphorylation rates of the complexes.

The first cell internalization experiments did not give promising results. Neither of the C3′ or N3 functionalized derivatives tested were either actively or passively transported into cells. It seems unlikely that any of the current set of compounds will be useful as a proliferation marker. The incorporation of, for example, a cell penetrating peptide sequence may improve uptake, however, introduction of an additional targeting group would induce further structural changes that in turn would decrease the substrate activity of compounds which already show significantly lower activity than the natural substrate. As we have shown and noted before in a similar study of technetium-labeled glucose analogues, it is possible to develop ^{99m}Tc-based, small molecular substrates for a given enzyme (such as hexokinase, or in the present case hTK1). However, a critical point during the development of such compounds is their active transport by transporters with further substrate specificity (such as Glut1 or a nucleoside transporter) to their intracellular targets. Although there have been recent reports of organometallic pseudoamino acids which target the LAT transporter (*35*), in general it would appear that ^{99m}Tc and metal-based radiopharmaceuticals which target receptors which themselves facilitate internalization show much more promise for the future.

EXPERIMENTAL DETAILS

Chemistry. All chemicals were purchased from Sigma-Aldrich or Fluka, Buchs, Switzerland. All chemicals and solvents were of reagent grade and were used without further purification unless otherwise stated. The precursor *fac*-$[Re(CO)_3Br_3][NEt_4]_2$ (*36*) was prepared according to the published procedure. $[Na][^{99m}TcO_4]$ was eluted from a ^{99}Mo/^{99m}Tc-generator (Covidien, Petten) with a 0.9% saline solution. Reactions were monitored by HPLC or by thin-layer chromatography (TLC) using precoated silica gel 60 F_{254} aluminum sheets (Merck), and visualized by UV absorption or stained with a solution of ninhydrin in EtOH. Column chromatography was performed using silica gel 60 (Fluka; particle size 0.04−0.063 mm). Analytical HPLC was performed using a Merck-Hitachi L-7000 system equipped with an L-7400 tunable absorption detector and an XBridge C-18 reverse phase column (5 μM, 4.6 × 150 mm, Waters). HPLC solvents were either water with 0.1% TFA (solvent A) and MeCN (solvent B) or water (solvent A) and MeOH (solvent B) (for purification of ^{99m}Tc complexes) with a flow rate of 1 mL/min. The gradient was as follows: 0−15 min, gradient from 95% A to 20% A; 15−20 min, gradient from 20% A to 95% A; 20−25 min, 95% A. Sep-Pak columns (Waters) were washed with methanol and water prior to use. Products were eluted using water or a water−methanol gradient. Nuclear magnetic resonance spectra were recorded on a 400 MHz Bruker spectrometer. ^{1}H and ^{13}C chemical shifts are reported relative to residual solvent peaks or water as a reference. Values of the coupling constant, *J*, are given in hertz (Hz). The following abbreviations are used for the description of ^{1}H NMR spectra: singlet (s), doublet (d), triplet (t), quartet (q), multiplet (m), doublet of doublets (dd), broad singlet (bs). The chemical shifts of complex multiplets are given as the range of their occurrence. Infrared spectra were recorded on a Perkin-Elmer Spectrum 100 FT-IR, with a universal ATR sampling accessory. Low resolution mass spectra were recorded with a Micromass Quattro micro API LC-ESI using either the negative or positive ionization mode. High-resolution mass spectra were recorded with a Bruker FTMS 4.7T BioAPEXII.

^{125}I-IdUrd of high radiochemical purity was prepared from the precursor 5-tri-*n*-butyl-stannyl-2′-deoxyuridine and purified by SepPak RP-18 cartridges using a modified version of a method originally described by Foulon et al. (*37, 38*) Radiochemical purity was repeatedly verified by TLC using polyethyleneimine cellulose F strips (Merck, Darmstadt, Germany) with a mobile phase of 0.2 M ammonium bicarbonate and radioactivity reading on a Tracemaster 20 (Berthold, Bad Wildbad, Germany). In all experiments, ^{125}I-IdUrd represented >98% of overall ^{125}I activity. Contamination with unlabeled IdUrd was avoided in the production of ^{125}I-IdUrd. It was calculated that the standard activity of 5 kBq ^{125}I-IdUrd in 0.5 mL used in the incorporation experiments represented a concentration of 0.2 nM, though this is only an indicative value, as it has not been experimentally verified.

3′,5′-Di-*O*-(*tert*-butyl-dimethyl-silanyl)thymidine and 3-(2-bromoethyl)-3′,5′-di-*O*-(*tert*-butyl-dimethyl-silanyl)thymidine were synthesized according to previously published procedures (*13*). All analytical data were in accordance with those already published (*13*).

3-(2-Azidoethyl)-3′,5′-di-O-(tert-butyl-dimethyl-silanyl)thymidine, **1a.** 3-(2-Bromoethyl)-3′,5′-di-*O*-(*tert*-butyl-dimethyl-silanyl)thymidine (1.03 g, 1.78 mmol) was dissolved in MeCN (20 mL) and 10 equiv of NaN_3 (1.16 g 17.8 mmol) were added. The reaction mixture was stirred at 80 °C for 16 h and followed by TLC. After cooling to room temperature, the solvent was removed under reduced pressure and the product extracted into EtOAc and washed twice with water and once with saturated NaCl. The aqueous phases were re-extracted with EtOAc. The organic phases were combined, dried over Na_2SO_4, and evaporated under reduced pressure to give the pure product as a colorless liquid (750 mg, 80%). ^{1}H NMR ($CDCl_3$) δ 7.48 (d, J = 0.9, 1H); 6.36 (m, J = 7.9, 5.8, 1H); 4.40 (m, 1H); 4.19 (m, J = 6.3, 1.9, 2H); 3.94 (m, J = 2.4, 1H); 3.87 (dd, J = 11.4, 2.6, 1H); 3.76 (dd, J = 11.4, 2.3, 1H); 3.54 (t, J = 6.3, 2H); 2.30−2.23 (m, 1H); 2.02−1.95 (m, 1H); 1.93 (s, 3H); 0.92 (s, 9H); 0.89 (s, 9H); 0.19 (s, 6H); 0.08 (s, 3H); 0.07 (s, 3H) ppm. ^{13}C NMR ($CDCl_3$) δ 163.5, 151.0, 134.0, 110.1, 88.0, 85.7, 72.4, 63.1, 48.6, 41.6, 40.0, 26.1, 25.9, 18.5, 18.1, 13.2, −4.5, −4.7, −5.2, −5.3 ppm. High res. MS (ESI) *m/z* 562.2851 $[C_{24}H_{45}N_5O_5Si_2]Na^+$ (calc. 562.2851).

3-(2-Azidoethyl)thymidine (N3dT-N$_3$), **1.** 3-(2-Azidoethyl)-3′,5′-di-*O*-(*tert*-butyl-dimethyl-silanyl)thymidine (900 mg, 1.67 mmol) was dissolved in THF (20 mL). NBu_4F (1.16 g, 3.68 mmol) was added and the reaction was stirred at room temperature and followed by TLC. After two hours, the solvent was removed under reduced pressure and a 1:1 mixture of water and EtOAc (40 mL) was added. The solvent was evaporated from the aqueous phase under reduced pressure and the crude product was purified by column chromatography with a mixture of CH_2Cl_2 and methanol (9%) to give the product as a colorless liquid (500 mg, 96%). ^{1}H NMR (D_2O) δ 7.69 (d, J = 1.1, 1H); 6.30 (m, J = 6.7, 1H); 4.47 (m, J = 6.4, 4.2, 1H); 4.18 (m, J = 7.0, 5.4, 2H); 4.04 (m, J = 8.7, 3.8, 1H); 3.85 (dd, J = 12.5, 5.0, 1H); 3.77 (dd, J = 12.5, 3.6, 1H); 3.56 (t, J = 5.8, 2H); 2.44−2.32 (m, 2H); 1.92 (d, J = 0.98, 3H). ^{13}C NMR ($CDCl_3$) δ 166.03, 152.21, 136.44, 111.16, 87.24, 86.61, 71.01, 61.76, 49.50 (MeOH), 48.90, 40.94, 39.41, 12.88 ppm. High res. MS (ESI) *m/z* 312.1299 $[C_{12}H_{17}N_5O_5]H^+$ (calc. 312.1302).

Alkynes, **2−6.** 2-propargyl glycine, **2**, *N*-Boc-2-propargyl glycine, **2a**, and 2-propargyl dimethyl malonate, **4a**, are commercially available. Alkynes **3** and **5** were prepared according to published procedures (*14*), alkyne **6** was prepared from the reaction of pyridine-2-methylamine (0.53 g, 4.89 mmol), and propargyl bromide (0.58 g, 4.89 mmol) in a solution of triethylamine (1.02 mL, 7.34 mmol) in MeCN (50 mL). The reaction mixture was stirred at 50 °C and followed by TLC.

After 4 h, the solvent was removed and the reaction mixture purified by column chromatography with CH_2Cl_2 and MeOH (5%). The product was isolated as a yellow liquid (178 mg, 25%). Full analytical data for compounds **2**−**6** and **2a**−**5a** can be found in the Supporting Information. Data were in agreement with those already published (*14*).

Copper Catalyzed Azide−*Alkyne Cyclycloaddition. General Procedure A.* The alkyne (1−2 equiv) and azide (1 equiv) were added to a 1:1 mixture of *t*BuOH and water to form a 0.1 mM solution. 0.1 equiv of $Cu(OAc)_2 \cdot H_2O$ and 0.2 equiv of sodium ascorbate were added and the mixture stirred at room temperature for 12 h.

Compound **7.** As per general procedure A, with AZT (130 mg, 0.49 mmol) and **2a** (137 mg, 0.64 mmol). The solvent was removed and the residue redissolved in a mixture of CH_2Cl_2 and MeOH (10%). The crude product was purified by column chromatography with a mixture of CH_2Cl_2 and MeOH (10%) to give the Boc protected triazole product (183 mg, 77%). ^{1}H NMR (CD_3OD) δ 7.91 (s, 1H), 7.89 (s, 1H), 6.49 (t, J = 6.5, 1H), 5.39 (m, 1H), 4.33 (m, 1H), 4.25 (t, J = 5.4, 1H), 3.89 (dd, J = 12.2, 2.9, 1H), 3.77 (dd, J = 12.2, 3.1, 1H), 3.24 (dd, J = 14.6, 5.1, 1H), 3.13 (dd, J = 14.6, 6.6, 1H), 2.93−2.83 (m, 1H), 2.77−2.64 (m, 1H), 1.91 (s, 3H), 1.41 (s, 9H) ppm. ^{13}C NMR (CD_3OD) δ 166.29, 152.10, 137.98, 124.35, 111.50, 86.66, 86.40, 80.54, 62.14, 61.07, 38.88, 28.82, 12.51 ppm. High res. MS (ESI) *m*/*z* 481.2039 $[C_{20}H_{28}N_6O_8]H^+$ (calc. 481.2041). The intermediate (120 mg, 0.25 mmol) was dissolved in a mixture of CH_2Cl_2 (12.5 mL) and TFA (1.25 mL) and stirred overnight at rt. The solvent was removed under reduced pressure, and the residue redissolved in water (1 mL) and neutralized with 5 M NaOH. The crude product was purified by solid phase extraction using a Sep-Pak column. The fractions containing the product were evaporated under reduced pressure to give **12** as a colorless oil (81 mg, 85%).^{1}H NMR ($CDCl_3$) δ ^{1}H NMR (400 MHz, MeOD) δ 8.01 (s, 1H), 7.91 (s, 1H), 6.49 (t, J = 6.6, 1H), 5.42 (m, 1H), 4.36 (m, 2H), 3.91 (dd, J = 12.1, 3.0, 1H), 3.78 (dd, J = 12.1, 3.2, 1H), 3.43 (dd, J = 15.7, 5.0, 1H), 3.35 (d, J = 15.7, 7.3, 1H), 2.94−2.82 (m, 1H), 2.79−2.65 (m, 1H), 1.91 (s, 3H) ppm. ^{13}C NMR (CD_3OD) δ 170.88, 166.50, 152.48, 142.79, 138.29, 124.79, 111.94, 86.90, 86.55, 62.44, 61.49, 53.79, 39.18, 27.32, 12.61 ppm. High res. MS (ESI) *m*/*z* 381.1515 $[C_{15}H_{20}N_6O_6]H^+$ (calc. 381.1517).

Compound **8.** As per general procedure A, with AZT (100 mg, 0.37 mmol) and **3a** (150 mg, 0.70 mmol). The solvent was removed and the residue redissolved in a mixture of CH_2Cl_2 and MeOH (10%). The crude product was purified by column chromatography with a mixture of CH_2Cl_2 and MeOH (10%) to give the Boc protected triazole product (142 mg, 79%). ^{1}H NMR (CD_3OD) δ H NMR (400 MHz, MeOD) δ 8.07 (s, 1H), 7.92 (d, J = 0.8, 1H), 6.48 (t, J = 6.4, 1H), 5.41 (dt, J = 8.6, 5.6, 1H), 4.37 (dt, J = 5.7, 3.0, 1H), 3.91 (dd, J = 12.3, 3.0, 1H), 3.84 (s, 2H), 3.78 (dd, J = 12.3, 3.2, 1H), 3.21 (t, J = 7.0, 2H), 2.92 (dt, J = 12.5, 6.1, 1H), 2.81−2.65 (m, 1H), 2.58 (t, J = 7.0, 2H), 1.91 (d, J = 0.8, 3H), 1.43 (s, 9H). ppm. ^{13}C NMR (CD_3OD) δ 166.29, 152.39, 137.97, 111.50, 102.16, 86.67, 86.39, 62.12, 60.79, 38.89, 28.72, 12.50 ppm. High res. MS (ESI) *m*/*z* 483.2018 $[C_{20}H_{30}N_6O_6S]H^+$ (calc. 483.2020). The intermediate (130 mg, 0.27 mmol) was dissolved in a mixture of CH_2Cl_2 (13.5 mL) and TFA (1.35 mL) and stirred overnight at rt. The solvent was removed under reduced pressure, and the residue redissolved in water (1 mL) and neutralized with 5 M NaOH. The crude product was purified by solid phase extraction using a Sep-Pak column. The fractions containing the product were evaporated under reduced pressure to give **13** as a white powder (77 mg, 74%).^{1}H NMR (CD_3OD) δ 8.08 (s, 1H), 7.90 (d, J = 0.8, 1H), 6.49 (t, J = 6.5, 1H), 5.42 (dt, J = 8.7, 5.2, 1H), 4.44−4.28 (m, 1H), 3.90 (dd, J = 12.2, 3.0, 1H), 3.85 (s, 2H), 3.79 (dd, J = 12.2, 3.2, 1H), 2.91 (t, J = 6.6, 2H), 2.93−2.86 (m, 1H), 2.78−2.72 (m, 1H), 2.69 (t, J = 6.6, 2H), 1.89 (d, J = 0.8, 3H). ppm. ^{13}C NMR (CD_3OD) δ 167.49, 153.22, 146.98, 138.33, 124.15, 111.92, 86.84, 86.49, 62.41, 61.39, 50.00, 49.79, 49.58, 49.36, 49.15, 48.94, 48.72, 48.51, 40.92, 39.16, 33.91, 26.14, 12.72 ppm. High res MS (ESI) *m*/*z* 383.1498 $[C_{15}H_{22}O_4N_6S]H^+$ (calc. 383.1496).

Compound **9.** As per general procedure A, with AZT (70 mg, 0.26 mmol) and **4a** (45 mg, 0.26 mmol). The solvent was removed and the residue redissolved in a mixture of CH_2Cl_2 and MeOH (10%). The crude product was purified by column chromatography with a mixture of CH_2Cl_2 and MeOH (5%) to give the ester protected triazole product (109 mg, 95%). ^{1}H NMR (CD_3OD) δ 7.90 (s, 1H), 7.90 (d, J = 1.1, 1H), 6.46 (t, J = 6.5, 1H), 5.38 (dt, J = 8.7, 5.5, 1H), 4.33 (dt, J = 5.9, 3.2, 1H), 3.92−3.85 (m, 2H), 3.75 (dd, J = 12.2, 3.2, 1H), 3.71 (s, 6H), 3.28 (d, J = 7.6, 2H), 2.88 (ddd, J = 13.9, 6.6, 5.6, 1H), 2.72 (ddd, J = 14.3, 8.5, 6.3, 1H), 1.91 (d, J = 1.1, 3H). ppm. ^{13}C NMR (CD_3OD) δ 170.76, 166.69, 152.57, 145.56, 138.53, 124.12, 111.75, 86.89, 86.64, 62.42, 61.14, 53.35, 39.28, 25.85, 12.65 ppm. High res. MS (ESI) *m*/*z* 438.1622 $[C_{18}H_{23}N_5O_8]H^+$ (calc. 438.1619). The intermediate (100 mg, 0.23 mmol) was dissolved in a mixture of MeOH (1 mL) and 1 M NaOH (1 mL) and stirred for 2 h at rt. The mixture was neutralized by addition of 1 M HCl, before being concentrated under reduced pressure. The crude product was purified by solid phase extraction using a Sep-Pak column. The fractions containing the product were evaporated under reduced pressure to give **14** as a white solid (90 mg, 85%). ^{1}H NMR (D_2O) δ 7.81 (s, 1H), 7.71 (d, J = 1.1, 1H), 6.42 (dd, J = 7.0, 6.0, 1H), 5.35 (dt, J = 8.7, 6.3, 1H), 4.42 (m, 1H), 3.87 (dd, J = 12.8, 3.2, 1H), 3.76 (dd, J = 12.8, 4.4, 1H), 3.37 (t, J = 7.8, 1H), 3.09 (d, J = 7.8, 2H), 2.95 (ddd, J = 13.0, 6.9, 1H), 2.79 (ddd, J = 13.0, 8.8, 5.7, 1H), 1.88 (d, J = 1.1, 3H) ppm. ^{13}C NMR (D_2O) δ 177.87, 151.46, 146.98, 137.65, 122.60, 111.25, 85.47, 84.36, 60.53, 59.25, 58.31, 36.94, 26.39 ppm. MS (ESI) *m*/*z* 408.17 $[C_{16}H_{18}N_5O_8]^-$.

Compound **10.** As per general procedure A, with AZT (200 mg, 0.74 mmol) and **5a** (142 mg, 1.12 mmol). The solvent was removed and the residue redissolved in a mixture of CH_2Cl_2 and MeOH (10%). The crude product was purified by column chromatography with a mixture of CH_2Cl_2 and MeOH (10%) to give the ester protected triazole product (140 mg, 48%). ^{1}H NMR (CD_3OD) δ 8.03 (s, 1H), 7.91 (d, J = 0.9, 1H), 6.48 (t, J = 6.5, 1H), 5.42 (dt, J = 8.6, 5.4, 1H), 4.36 (m, 1H), 3.92 (s, 2H), 3.90 (dd, J = 12.2, 3.0, 1H), 3.77 (dd, J = 12.2, 3.2, 1H), 3.72 (s, 3H), 3.46 (s, 2H), 2.97−2.83 (m, 1H), 2.80−2.66 (m, 1H), 1.91 (d, J = 0.9, 3H) ppm. ^{13}C NMR (CD_3OD) δ 173.68, 166.61, 152.50, 147.09, 138.39, 124.29, 111.82, 86.85, 86.55, 62.29, 61.18, 52.45, 50.19, 44.39, 39.19, 12.62 ppm. High res. MS (ESI) *m*/*z* 395.1674 $[C_{16}H_{22}N_6O_6]H^+$ (calc. 395.1674). The intermediate (100 mg, 0.25 mmol) was dissolved in a mixture of H_2O (2 mL) and 1 M NaOH (0.5 mL) and stirred for 2 h at rt. The mixture was neutralized by addition of 1 M HCl, before being concentrated under reduced pressure. The crude product was purified by solid phase extraction using a Sep-Pak column. The fractions containing the product were evaporated under reduced pressure to give **15** as a white solid (84 mg, 88%). ^{1}H NMR (D_2O) δ 8.26 (s, 1H), 7.69 (s, 1H), 6.41 (t, J = 6.6, 1H), 5.42 (dt, J = 8.7, 5.8, 1H), 4.44 (dd, J = 9.5, 4.0, 1H), 4.39 (s, 2H), 3.87 (dd, J = 12.7, 3.3, 1H), 3.77 (dd, J = 12.7, 4.3, 1H), 3.60 (s, 2H), 2.94 (ddd, J = 13.0, 6.6, 1H), 2.80 (ddd, J = 14.7, 8.7, 6.2, 1H), 1.86 (s, 3H). ppm. ^{13}C NMR (D_2O) δ 171.62, 167.14, 152.22, 138.98, 138.36, 126.49, 112.13, 86.24, 84.89, 61.21, 60.47, 49.50 (MeOH) 49.12, 41.69, 37.50, 12.15 ppm. High res. MS (ESI) *m*/*z* 381.1519 $[C_{15}H_{20}N_6O_6]H^+$ (calc. 381.1517).

Compound **11.** As per general procedure A, with AZT (85 mg, 0.32 mmol) and **6** (100 mg, 0.68 mmol). The product was extracted into EtOAc and washed twice with saturated NaCl. The aqueous phases were re-extracted with EtOAc. The organic phases were combined, dried over Na_2SO_4, and evaporated under reduced pressure. The crude product was purified by column chromatography with a mixture of CH_2Cl_2 and MeOH (5%) to give the pure triazole product as a crystalline yellow solid (92 mg, 69%). ^{1}H NMR (CD_3OD) δ 8.53 (d, J = 4.5, 1H), 7.96 (s, 1H), 7.86−7.77 (m, 2H), 7.48 (d, J = 7.8, 1H), 7.36−7.29 (m, 1H), 6.17 (t, J = 6.6, 1H), 4.69 (t, J = 5.6, 2H), 4.38 (t, J = 5.6, 3H), 3.96 (s, 4H), 3.87 (q, J = 3.4, 1H), 3.78 (dd, J = 12.0, 3.1, 1H), 3.71 (dd, J = 12.0, 3.7, 1H), 2.26−2.11 (m, 2H), 1.84 (s, 3H) ppm. ^{13}C NMR (CD_3OD) δ 166.76, 152.71, 138.36, 124.62, 111.90, 86.86, 86.58, 62.43, 61.46, 39.18, 12.63 ppm. High res MS (ESI) m/z $[C_{19}H_{23}N_7O_4]H^+$. (calc. 414.1890).

Compound **12.** As per general procedure A, with **1a** (487 mg, 0.90 mmol) and **2a** (192 mg, 0.90 mmol). The product was extracted into EtOAc and washed twice with saturated NaCl. The aqueous phases were re-extracted with EtOAc. The organic phases were combined, dried over Na_2SO_4, and evaporated under reduced pressure. The crude product was purified by column chromatography with a mixture of CH_2Cl_2 and MeOH (5%) to give the Boc-protected triazole product as a colorless oil (335 mg, 49%). ^{1}H NMR (CD_3OD) δ 7.79 (s, 1H), 7.56 (s, 1H), 6.22 (t, J = 6.7, 1H), 4.85 (s, 4H), 4.62 (t, J = 5.8, 2H), 4.46 (m, 1H), 4.36 (m, 2H), 4.25 (s, 1H), 3.92 (m, 1H), 3.84 (ddd, J = 23.7, 11.4, 3.2, 2H), 3.17 (s, 2H), 2.27−2.21 (m, 1H), 2.18−2.02 (m, 1H), 1.87 (s, 4H), 1.42 (s, 9H), 0.94 (s, 9H), 0.93 (s, 9H), 0.14 (s, 6H), 0.12 (s, 6H) ppm. ^{13}C NMR (CD_3OD) δ 164.99, 152.00, 135.98, 110.61, 89.33, 87.16, 73.64, 64.16, 42.03, 28.85, 26.55, 26.34, 19.34, 18.92, 13.48, −4.38, −4.55, −5.12, −5.15 ppm. MS (ESI) m/z 753.29 $[C_{34}H_{60}N_6O_9Si_2]H^+$. The intermediate (300 mg, 0.40 mmol) was dissolved in MeOH (20 mL). Concentrated HCl (0.4 mL) was added and the mixture was stirred overnight at rt. The solvent was removed under reduced pressure, and the residue redissolved in a mixture of water and EtOAc (1:1, 15 mL). The aqueous phase was neutralized with 1 M NaOH and concentrated under reduced pressure. The crude product was purified by solid phase extraction using a Sep-Pak column. The fractions containing the product were evaporated under reduced pressure to give **7** as a white powder (95 mg, 56%).^{1}H NMR (D_2O) δ 7.75 (s, 1H), 7.47 (d, J = 0.9, 1H), 6.01 (t, J = 6.6, 1H), 4.53 (m, 2H), 4.27 (m, J = 6.4, 4.4, 1H), 4.19 (t, J = 5.4, 2H), 3.85 (m, 2H), 3.67 (dd, J = 12.5, 3.5, 1H), 3.58 (dd, J = 12.5, 5.1, 1H), 3.18 (dd, J = 15.7, 4.9, 1H), 3.09 (dd, J = 15.7, 7.3, 1H), 2.26−2.05 (m, 2H), 1.68 (s, 3H).ppm. ^{13}C NMR (D_2O) δ 173.72, 165.71, 151.81, 142.76, 136.62, 125.91, 110.93, 87.46, 86.68, 70.91, 61.85, 55.14, 49.50 (MeOH), 48.70, 41.81, 39.38, 27.11, 12.70 ppm. High res. MS (ESI) m/z 425.1776 $[C_{17}H_{24}N_6O_7]H^+$ (calc. 425.1779).

Compound **13.** As per general procedure A, with **1a** (488 mg, 0.90 mmol) and **3a** (180 mg, 0.84 mmol). The product was extracted into EtOAc and washed twice with saturated NaCl. The aqueous phases were re-extracted with EtOAc. The organic phases were combined, dried over Na_2SO_4, and evaporated under reduced pressure. The crude product was purified by column chromatography with a mixture of CH_2Cl_2 and MeOH (5%) to give the Boc-protected triazole product as a colorless oil (240 mg, 38%). ^{1}H NMR ($CDCl_3$) δ 7.58 (s, 1H), 7.44 (d, J = 1.0, 1H), 6.23 (m, 1H), 4.61 (t, J = 6.0, 2H), 4.38 (m, 3H), 3.91 (q, J = 2.5, 1H), 3.84 (dd, J = 11.3, 2.5, 2H), 3.77 (s, 2H), 3.73 (dd, J = 11.3, 2.5, 1H), 3.29 (m, 2H), 2.61 (t, J = 6.6, 2H), 2.24−2.19 (m, 1H), 1.97−192 (m, 1H), 1.86 (d, J = 1.0, 3H), 1.42 (s, 9H), 0.91 (s, 9H), 0.87 (s, 9H), 0.09 (s, 6H), 0.07 (s, 3H), 0.06 (s, 3H) ppm. ^{13}C NMR ($CDCl_3$) δ 162.96, 150.46, 134.14, 122.15, 109.59, 87.69, 85.28, 71.93, 62.58, 53.51, 47.37, 41.43, 40.39, 39.32, 31.33, 28.11, 25.90, 25.71, 18.39, 17.95, 13.17, −4.64, −4.90, −5.40, −5.49 ppm. High res. MS (ESI) m/z 777.3826 $[C_{34}H_{62}O_7N_6S]Na^+$ (calc. 777.3831). The intermediate (200 mg, 0.27 mmol) was dissolved in MeOH (14 mL). Concentrated HCl (0.28 mL) was added and the mixture was stirred overnight at rt. The solvent was removed under reduced pressure and the residue redissolved in a mixture of water and EtOAc (1:1, 15 mL). The aqueous phase was neutralized with 1 M NaOH and concentrated under reduced pressure. The crude product was purified by solid phase extraction using a Sep-Pak column. The fractions containing the product were evaporated under reduced pressure to give **8** as a colorless oil (100 mg, 89%).^{1}H NMR (CD_3OD) δ 7.92 (s, 1H), 7.83 (d, J = 0.9, 1H), 6.17 (t, J = 6.6, 1H), 4.68 (t, 2H), 4.45−4.29 (m, 3H), 3.89 (m, 1H), 3.79 (dd, J = 12.0, 3.1, 1H), 3.76 (s, 2H), 3.72 (dd, J = 12.0, 3.7, 1H), 2.78 (t, J = 6.6, 2H), 2.59 (t, J = 6.6, 2H), 2.27−2.21 (m, 2H), 2.19−2.12 (m, 2H), 1.86 (d, J = 0.9, 3H) ppm. ^{13}C NMR (CD_3OD) δ 165.18, 152.22, 146.90, 136.83, 125.10, 110.57, 89.06, 87.35, 72.07, 62.84, 42.01, 41.59, 41.37, 35.27, 25.94, 13.26 ppm. High res. MS (ESI) m/z 427.1755 $[C_{17}H_{26}O_5N_6S]H^+$ (calc. 427.1758).

Compound **14.** As per general procedure A, with **1a** (200 mg, 0.37 mmol) and **4a** (63 mg, 0.37 mmol). The product was extracted into EtOAc and washed twice with saturated NaCl. The aqueous phases were re-extracted with EtOAc. The organic phases were combined, dried over Na_2SO_4, and evaporated under reduced pressure. The crude product was purified by column chromatography with a mixture of CH_2Cl_2 and MeOH (3%) to give the TBDMS and ester protected triazole product (194 mg, 74%). ^{1}H NMR (CD_3OD) δ 7.43 (s, 1H), 6.24 (dd, J = 7.8, 5.8, 1H), 4.56 (t, J = 6.3, 2H), 4.37 (dd, J = 7.6, 4.9, 3H), 3.91 (q, J = 2.5, 1H), 3.84 (dt, J = 5.8, 5.1, 2H), 3.75 (t, J = 2.2, 1H), 3.72 (s, 7H), 3.28 (d, J = 7.6, 2H), 2.22 (ddd, J = 13.2, 5.8, 2.7, 1H), 1.95 (ddd, J = 13.2, 7.8, 6.1, 1H), 1.87 (d, J = 1.1, 3H), 0.91 (s, 9H), 0.88 (s, 9H), 0.09 (s, 6H), 0.06 (d, J = 3.8, 6H) ppm. ^{13}C NMR (CD_3OD) δ 168.87, 162.94, 150.46, 143.77, 133.89, 122.44, 109.86, 87.69, 85.26, 71.93, 62.86, 52.46, 51.09, 47.38, 41.25, 25.78, 25.69, 24.70, 18.26, 17.69, 12.92, −4.99, −5.79 ppm. High Res. MS (ESI) m/z 732.3428 $[C_{32}H_{55}N_5O_9Si_2]Na^+$ (calc. 732.3431). The intermediate (190 mg, 0.27 mmol) was dissolved in MeOH (15 mL). Concentrated HCl (0.3 mL) was added and the mixture was stirred overnight at rt. The solvent was removed under reduced pressure, and the residue redissolved in a mixture of water and EtOAc (1:1, 15 mL). The pH of the aqueous phase was increased to 12 with 1 M NaOH and stirred for a further 2 h at rt. After this time, the mixture was neutralized with 1 M HCl before the solvent was removed under reduced pressure. The crude product was purified by solid phase extraction using a Sep-Pak column. The fractions containing the product were evaporated under reduced pressure to give **9** as a white powder (86 mg, 70%). ^{1}H NMR (CD_3OD) δ 7.69 (s, 1H), 7.61 (s, 1H), 6.13 (t, J = 6.5, 1H), 4.64 (m, 2H), 4.42 (dt, J = 6.4, 4.2, 1H), 4.34 (m, 2H), 4.05−3.94 (m, 1H), 3.82 (dd, J = 12.5, 3.5, 1H), 3.73 (dd, J = 12.5, 5.2, 1H), 3.35 (t, J = 7.8, 1H), 3.06 (d, J = 7.8, 2H), 2.40−2.17 (m, 2H), 1.84 (s, 3H) ppm. ^{13}C NMR (D_2O) δ 146.94, 136.31, 124.25, 110.63, 87.10, 86.74, 70.80, 61.67, 49.50 (MeOH) 39.35, 12.67. High res. MS (ESI) m/z 476.1378 $[C_{18}H_{23}N_5O_9]Na^+$ (calc. 476.1388).

Compound **15.** As per general procedure A, with **1** (144 mg, 0.46 mmol) and **5a** (59 mg, 0.46 mmol). The solvent was removed and the residue redissolved in a mixture of CH_2Cl_2 and MeOH (10%). The crude product was purified by column chromatography with a mixture of CH_2Cl_2 and MeOH (10%) to give the ester protected triazole product (135 mg, 67%). ^{1}H NMR (CD_3OD) δ 7.90 (s, 1H), 7.83 (d, J = 1.0, 1H), 6.17 (t,

J = 6.6, 1H), 4.68 (t, J = 5.7, 2H), 4.37 (t, J = 5.6, 3H), 3.92−3.85 (m, 3H), 3.80 (dd, J = 12.0, 3.1, 1H), 3.74−3.70 (dd, J = 12.0, 3.8, 1H), 3.72 (s, 3H), 2.24 (ddd, J = 13.6, 6.2, 3.9, 1H), 2.16 (ddd, J = 11.4, 6.6, 1H), 1.85 (d, J = 1.0, 3H) ppm. ^{13}C NMR (CD_3OD) δ 165.08, 152.25, 136.76, 125.04, 110.37, 88.96, 87.10, 71.92, 62.57, 43.87, 42.08, 41.54, 13.13 ppm. High res. MS (ESI) *m/z* 439.1933 $[C_{18}H_{26}N_6O_7]H^+$ (calc. 439.1936). The intermediate (112 mg, 0.26 mmol) was dissolved in a mixture of H_2O (2 mL) and 1 M NaOH (0.5 mL) and stirred for 2 h at rt. The mixture was neutralized by addition of 1 M HCl, before being concentrated under reduced pressure. The crude product was purified by solid phase extraction using a Sep-Pak column. The fractions containing the product were evaporated under reduced pressure to give **10** as a white solid (70 mg, 61%). ^{1}H NMR (CD_3OD) δ 7.97 (s, 1H), 7.82 (s, 1H), 6.16 (t, J = 6.6, 1H), 4.68 (t, J = 5.6, 2H), 4.37 (m, 3H), 3.98 (s, 2H), 3.90 (q, J = 3.4, 1H), 3.79 (dd, J = 12.0, 3.1, 1H), 3.72 (dd, J = 12.0, 3.8, 1H), 3.31 (s, 2H), 2.25 (ddd, J = 13.5, 6.1, 3.8, 1H), 2.15 (ddd, J = 13.5, 6.6, 1H), 1.86 (s, 3H) ppm. ^{13}C NMR (CD_3OD) δ 176.69, 165.06, 152.03, 145.19, 136.79, 125.45, 110.43, 88.81, 87.25, 71.77, 62.64, 52.00, 43.92, 41.88, 41.34, 13.07 ppm. High res. MS (ESI) *m/z* 425.1776 $[C_{17}H_{24}N_6O_7]H^+$ (calc. 425.1779).

Compound **16.** As per general procedure A, with **1** (280 mg, 0.90 mmol) and **6** (131 mg, 0.88 mmol). The product was extracted into EtOAc and washed twice with saturated NaCl. The aqueous phases were re-extracted with EtOAc. The organic phases were combined, dried over Na_2SO_4, and evaporated under reduced pressure. The crude product was purified by column chromatography with a mixture of CH_2Cl_2 and MeOH (5%) to give the pure triazole product as a yellow solid (220 mg, 55%).^{1}H NMR (CD_3OD) δ 8.53 (d, J = 4.5, 1H), 7.96 (s, 1H), 7.86−7.77 (m, 2H), 7.48 (d, J = 7.8, 1H), 7.33 (m, 1H), 6.17 (t, J = 6.6, 1H), 4.69 (t, J = 5.6, 2H), 4.38 (t, J = 5.6, 2H), 4.37 (m, 1H), 3.96 (s, 4H), 3.87 (q, J = 3.4, 1H), 3.78 (dd, J = 12.0, 3.1, 1H), 3.71 (dd, J = 12.0, 3.7, 1H), 2.26−2.11 (m, 2H), 1.84 (s, 3H) ppm. ^{13}C NMR (CD_3OD) δ 165.20, 159.35, 152.25, 150.18, 146.37, 138.93, 136.91, 125.44, 124.40, 124.12, 110.58, 89.06, 87.36, 72.07, 62.84, 53.95, 44.26, 42.13, 41.52, 18.52, 13.22 ppm. High res. MS (ESI) *m/z* 458.2149 $[C_{21}H_{27}N_7O_5]H^+$ (calc. 458.2146).

Rhenium Complexes. Tricarbonyl rhenium complexes were synthesized according to the following general procedure: 1 equiv of thymidine containing ligand and 1 equiv of $[ReBr_3(CO)_3][NEt_4]_2$ were dissolved in a 1:1 mixture of MeOH and water to form a 0.1 M solution. In the reactions with ligands **9** and **14**, the pH of the reaction mixture was adjusted to 7 with aqueous NEt_4OH. The reaction was stirred at 50 °C for 2 h and followed by HPLC. The solvents were removed under vacuum and the residue was purified by solid phase extraction using a Sep-Pak column and a water-MeOH gradient to give the $Re(CO)_3$ complex as a white or off-white powder.

[$Re(CO)_3$**7**]. (41 mg, 59%). ^{1}H NMR (CD_3OD) δ 8.20 (s, 1H), 7.86 (s, 1H), 6.44 (t, J = 6.4, 1H), 5.90 (dd, J = 11.0, 5.8, 1H), 5.58−5.44 (m, 1H), 5.18 (d, J = 11.4, 1H), 4.45−4.32 (m, 1H), 4.11 (d, J = 3.9, 1H), 3.92 (dd, J = 12.2, 2.9, 1H), 3.81 (dd, J = 12.2, 3.1, 1H), 3.38 (dd, J = 16.0, 1H), 3.26 (dd, J = 4.2, 1H), 3.02−2.73 (m, 2H), 1.91 (s, 3H) ppm. ^{13}C NMR (CD_3OD) δ 197.39, 196.67, 184.57, 166.45, 152.22, 144.06, 138.43, 126.48, 111.81, 86.97, 85.89, 62.30, 62.01, 52.78, 38.68, 27.39, 12.19 ppm. High res. MS (ESI) *m/z* 651.0846 $[C_{18}H_{19}N_6O_9Re]H^+$ (calc. 651.0844).

[$Re(CO)_3$**8**]Br. (17 mg, 61%). ^{1}H NMR (CD_3OD) δ 8.41 (s, 1H), 7.88 (s, 1H), 6.48 (t, J = 6.3, 1H), 5.55 (m, 1H), 5.32 (bs, 1H), 4.60 (bs, 1H), 4.53 (d, J = 17.2, 1H), 4.56−4.47 (m, 1H), 4.24 (d, J = 17.2, 1H), 3.93 (dd, J = 12.0, 3.1, 1H), 3.86 (dd, J = 12.0, 1H), 3.04−2.96 (m, 1H), 2.95−2.87 (m, 1H), 2.92 (m, 2H), 2.86−2.74 (m, 1H), 2.27 (m, 1H) ppm. ^{13}C NMR (CD_3OD) δ 166.42, 152.40, 151.52, 138.40, 125.44, 111.65, 87.03, 86.92, 86.23, 85.88, 63.81, 63.66, 62.60, 62.37, 44.65, 39.03, 34.23, 12.61 ppm. High res. MS (ESI) *m/z* 653.0818 $[C_{18}H_{22}N_6O_7ReS]^+$ (calc. 653.0822).

[$Re(CO)_3$**9**]NEt_4. (30 mg, 45%). ^{1}H NMR (CD_3OD) δ 8.20 (s, 1H), 7.89 (d, J = 1.1, 1H), 6.46 (t, J = 6.4, 1H), 5.57−5.47 (m, 1H), 4.43 (dt, J = 6.1, 3.2, 1H), 3.95 (dd, J = 12.4, 3.0, 1H), 3.85 (dd, J = 12.4, 3.3, 1H), 3.61 (t, J = 4.7, 1H), 3.44 (d, J = 4.7, 2H), 3.37−3.28 (m, 8H), 3.06−2.93 (m, 1H), 2.84 (ddd, J = 14.3, 8.7, 5.8, 1H), 1.93 (d, J = 1.1, 3H), 1.35−1.27 (m, 12H) ppm. ^{13}C NMR (CD_3OD) δ 198.32, 179.91, 179.88, 166.42, 152.23, 147.36, 138.48, 126.96, 111.65, 86.92, 86.10, 62.05, 62.03, 53.82, 53.31, 53.28, 53.25, 38.79, 27.02, 12.46, 7.59 ppm. High res. MS (ESI) *m/z* 680.00629 $[C_{19}H_{19}N_5O_{11}Re]^+$ (calc. 680.0634).

[$Re(CO)_3$**10**]. (58 mg, 83%). ^{1}H NMR (CD_3OD) δ ^{1}H NMR (400 MHz, MeOD) δ 8.32 (s, 1H), 7.86 (d, J = 5.6, 1H), 6.46 (q, J = 6.8, 1H), 5.62−5.47 (m, 1H), 4.40 (dd, J = 5.2, 3.2, 1H), 4.36−4.22 (m, 2H), 3.88 (dd, 1H), 3.83−3.77 (m, 1H), 3.81 (d, J = 17.3, 1H), 3.38 (d, J = 17.3, 1H), 3.04−2.93 (m, 1H), 2.85−2.76 (m, 1H), 1.91 (s, 3H) ppm. ^{13}C NMR (CD_3OD) δ 197.37, 196.71, 183.78, 166.35, 152.20, 149.87, 138.37, 124.04, 111.79, 86.68, 85.88, 62.93, 61.86, 56.29, 53.09, 38.38, 12.50 ppm. High res. MS (ESI) *m/z* 651.0838 $[C_{18}H_{19}N_6O_9Re]H^+$ (calc. 651.0844).

[$Re(CO)_3$**11**]Br. (64 mg, 55%). ^{1}H NMR (CD_3OD) δ ^{1}H NMR (400 MHz, MeOD) δ 8.83 (t, J = 5.9, 1H), 8.15 (s, 1H, isomer A), 8.14 (s, 1H, isomer B), 8.00−7.91 (m, 1H), 7.82 (s, 1H), 7.60 (d, J = 7.9, 1H), 7.39 (dd, J = 13.2, 6.6, 1H), 6.38 (td, J = 6.6, 2.2, 1H), 5.40 (dt, J = 9.4, 4.9, 1H), 4.78 (d, J = 17.0, 1H), 4.69 (d, J = 17.0, 1H), 4.52 (d, J = 16.5, 1H), 4.40−4.31 (m, 1H, isomer B), 4.36 (d, J = 16.5, 1H), 4.17−4.05 (m, 1H, isomer A), 3.84 (dd, J = 12.1, 3.3, 1H, isomer B), 3.79 (dd, J = 12.2, 3.3, 1H, isomer A), 3.70 (dd, J = 12.1, 3.1, 1H, isomer B), 3.60 (dd, J = 12.2, 3.2, 1H, isomer A), 2.90−2.80 (m, 1H, isomer A), 2.72 (ddd, J = 14.4, 8.3, 6.4, 1H, isomer A), 2.63 (dd, J = 14.0, 7.2, 1H, isomer B), 2.48 (ddd, J = 14.1, 6.4, 4.8, 1H, isomer B), 1.90 (s, 3H) ppm. ^{13}C NMR (CD_3OD) δ 166.27, 161.70, 153.16, 151.89, 150.24, 140.91, 137.97, 126.77, 124.37, 124.07, 111.80, 86.69, 86.48, 85.91, 85.65, 63.87, 63.45, 63.15, 62.27, 62.00, 52.77, 39.16, 38.39, 12.19 ppm. High res. MS (ESI) *m/z* 684.1214 $[C_{22}H_{23}N_7O_7Re]^+$ (calc. 684.1212).

[$Re(CO)_3$**12**]. (55 mg, 95%). ^{1}H NMR (CD_3OD) δ 8.08 (s, 1H), 7.85 (s, 1H), 6.20 (t, J = 6.6, 1H), 5.91−5.77 (m, 1H), 5.15 (d, J = 11.2, 1H), 4.78 (m, 2H), 4.48−4.34 (m, 2H), 4.08 (m, 1H), 3.92 (m, J = 3.3, 1H), 3.80 (dd, J = 12.0, 3.0, 1H), 3.73 (dd, J = 12.0, 3.8, 1H), 3.38 (m, 1H), 3.27 (dd, J = 17.6, 4.3, 1H), 2.39 (ddd, J = 13.6, 5.9, 3.6, 1H), 2.24−2.18 (m, 1H), 1.89 (s, 3H) ppm. ^{13}C NMR (DMSO) δ 198.26, 197.44, 196.44, 180.16, 162.49, 150.18, 142.22, 135.08, 126.16, 108.26, 87.38, 84.99, 69.95, 61.07, 50.69, 50.60, 48.57, 48.05, 25.97, 12.84 ppm. High res MS (ESI) *m/z* 695.1106 $[C_{20}H_{23}N_6O_{10}Re]H^+$ (calc. 695.1107).

[$Re(CO)_3$**13**]Br. (20 mg, 74%). ^{1}H NMR (CD_3OD) δ 8.26 (s, 1H), 8.22 (s, 1H), 7.88 (d, J = 0.9, 1H), 7.87 (d, J = 0.9, 1H), 6.27−6.22 (m, 1H), 6.21 (t, J = 6.5, 1H), 5.43 (bs, 1H), 5.37 (bs, 1H), 4.87−4.79 (m, 2H), 4.79−4.69 (m, 2H), 4.55−4.47 (m, 2H), 4.47−4.42 (m, 2H), 4.43−4.36 (m, 2H), 4.34 (dd, J = 7.6, 4.5, 1H), 4.30 (d, J = 3.5, 1H), 4.20 (d, J = 11.3, 1H), 4.16 (d, J = 11.2, 1H), 4.10 (bs, 2H), 3.93 (dd, J = 6.6, 3.3, 1H), 3.91 (dd, J = 6.7, 3.4, 1H), 3.81 (t, J = 2.8, 1H), 3.78 (t, J = 2.7, 1H), 3.76−3.72 (m, 1H), 3.72−3.68 (m, 1H), 3.05−2.88 (m, 3H), 2.88−2.76 (m, 2H), 2.76−2.61 (m, 1H), 2.47 (m, 1H), 2.41−2.29 (m, 1H), 2.27−2.19 (m, 4H), 1.88 (s, 3H), 1.87 (s, 3H) ppm. ^{13}C NMR (CD_3OD) δ 165.44 (165.29), 152.51, 151.23 (150.97), 137.22 (137.04), 126.03 (125.90),

110.87, 89.10, 87.02, 72.50 (72.37), 63.06 (62.99), 51.44 (51.32), 44.90 (44.38), 42.82 (42.65), 41.14 (41.06), 38.92 (38.59), 34.38 (34.27), 13.11 ppm. High res MS (ESI) *m/z* 697.1086 $[C_{20}H_{26}N_6O_8ReS]^+$ (calc. 697.1084).

$[Re(CO)_3$**14**$]NEt_4$. (67 mg, 65%). ^{1}H NMR (CD_3OD) δ 8.06 (s, 1H), 7.76 (d, $J = 1.0$, 1H), 6.04 (t, $J = 6.4$, 1H), 4.79−4.68 (m, 2H), 4.51−4.42 (m, 1H), 4.40−4.34 (m, 2H), 3.88 (m, 1H), 3.78 (dd, $J = 12.1$, 3.3, 1H), 3.70 (dd, $J = 12.1$, 4.3, 1H), 3.56 (t, $J = 4.3$, 1H), 3.39 (d, $J = 4.3$, 2H), 3.34−3.25 (m, 8H), 2.28 (ddd, $J = 13.8$, 6.3, 4.0, 1H), 2.14−2.05 (m, 1H), 1.87 (d, $J = 0.9$, 3H), 1.33−1.25 (m, 12H) ppm. ^{13}C NMR (CD_3OD) δ 164.66, 152.10, 147.03, 137.40, 128.06, 88.54, 87.76, 71.76, 62.64, 53.08, 41.86, 41.31, 12.99, 7.42 ppm. High res. MS (ESI) *m/z* 721.90 $[C_{21}H_{21}N_5O_{12}Re]^-$ (calc.).

$[Re(CO)_3$**15**$]$. (96 mg, 84%). ^{1}H NMR (CD_3OD) δ 8.18 (s, 1H), 7.84 (m, 1H), 7.23−7.12 (m, 1H), 6.26 (m, 1H), 4.81−4.69 (m, 2H), 4.55−4.28 (m, 3H), 3.91 (m, 1H), 3.84−3.68 (m, 3H), 3.35−3.30 (m, 2H), 2.42−2.26 (m, 1H), 2.21 (m, 1H), 1.92−1.84 (m, 3H) ppm. ^{13}C NMR (CD_3OD) δ 183.90, 165.23, 151.88, 149.46, 136.63, 124.91, 110.45, 88.82, 87.25, 86.96, 71.99, 62.64, 55.73, 53.58, 41.28, 12.98 ppm. High res MS (ESI) *m/z* 695.1117 $[C_{20}H_{23}N_6O_{10}Re]H^+$ (calc. 695.1107).

$[Re(CO)_3$**16**$]$Br. (110 mg, 73%). ^{1}H NMR (CD_3OD) δ 8.77 (t, $J = 5.0$, 1H), 8.01−7.93 (m, 2H), 7.97 (s, 1H), 7.84 (d, 1H), 7.63 (d, $J = 8.0$, 1H), 7.38 (t, $J = 6.6$, 1H), 6.12 (t, $J = 6.8$, 1H), 4.80−4.55 (m, 4H), 4.49 (dd, $J = 16.7$, 8.1, 1H), 4.41 (dt, $J = 6.1$, 3.2, 1H), 4.37−4.21 (m, 3H), 3.99−3.92 (m, 1H), 3.81 (dd, $J = 12.0$, 3.1, 2H), 3.74 (dd, $J = 12.0$, 3.7, 2H), 2.28−2.12 (m, 2H), 1.84 (d, 3H) ppm. ^{13}C NMR (CD_3OD) δ 164.98 (164.96), 161.85 (161.79), 153.48 (153.46), 152.12 (152.02), 150.64 (150.61), 141.48 (141.45), 136.86, 126.66, 124.57 (124.55), 124.49 (124.43), 110.58 (110.53), 89.10 (89.07), 87.08 (86.92), 72.33 (72.31), 63.96, 62.93 (62.91), 53.13 (53.07), 50.79 (50.56), 41.87 (41.67), 41.27 (41.19), 13.17 ppm. High res MS (ESI) *m/z* 728.1470 $[C_{24}H_{27}N_7O_8Re]^+$ (calc. 728.1474).

Technetium-99m Complexes. The 99 m-technetium tricarbonyl complexes of ligands **7**, **8**, **10**, **11**, **12**, **13**, **15**, and **16**, were synthesized according to the following general procedure: A solution of $[^{99m}Tc(CO)_3(H_2O)_3]^+$ (50 μL; ~500 MBq mL^{-1}) was added to a 10^{-3} M solution of the relevant ligand (50 μL) diluted with PBS (400 μL; pH 7.4) to give a final ligand concentration of 10^{-4} M. The reaction mixtures were heated for 45 min at 95 °C. The radioactive product was separated from unlabeled ligand by HPLC. The complexes were characterized by comparison of their HPLC retention times (γ-trace) with those of their rhenium analogues (UV-trace).

X-ray Crystallography. Crystallographic data were collected at 183(2) K on an Oxford Diffraction Xcalibur system with a Ruby detector (Mo K_α radiation, $\lambda = 0.7107$ Å) using graphite-monochromated radiation. A suitable crystal was covered with oil (Infineum V8512, formerly known as Paratone N), mounted on top of a glass fiber and immediately transferred to the diffractometer. The program suite CrysAlis^{Pro} (*CrysAlis*^{Pro} software system (2007), Oxford Diffraction Ltd., Oxford, UK) was used for data collection, semiempirical absorption correction and data reduction. The structure was solved with direct methods using SIR97 (*39*) and refined by full-matrix least-squares methods on F^2 with SHELXL-97 (*40*). The final model was checked with the help of the program Platon (*41*). CCDC-743723 contains the supplementary crystallographic data for this paper. This data are presented in the Supporting Information or can be obtained free of charge from The Cambridge Crystallographic Data Centre via www.ccdc.cam.ac.uk/data_request/cif.

In Vitro Analysis. *Phosphorylation Transfer Assays.* Thymidine and thymidine analogues $[Re(CO)_3$**7**$-$**16**$]^{0/+/-}$ were assayed at 25 °C for 15 min in 200 μL of a mixture containing 155.38 μL water, 10 μL 1 M HEPES buffer (pH 7.5), 0.2 μL 1 M DTT, 0.42 μL 100 mM PEP, 0.5 μL 1 M $MgCl_2$, 7.2 μL 5 mM NADH, 2 μL 100 mM ATP, 0.6 μL pyruvate kinase (1350 U/mL), 0.7 μL lactate dehydrogenase (1420 U/mL), 5 μL hTK1 (~0.5 mg/mL), and 20 μL of a 10 mM solution of thymidine or the thymidine analogue $[Re(CO)_3$**7**$-$**16**$]^{0/+/-}$.

For each substrate, the linear decrease in UV absorption at 340 nm was measured from 0 to 15 min. The gradients of the regression lines between 6 and 12 min were compared to thymidine, the phosphorylation of which was assumed to be 100%.

Thymidine analogues $[Re(CO)_3$**X**$]^{0/+}$ (**X** = **7**, **10**, **11**, **15**) were also assayed at 37 °C for 1 h in 200 μL of a mixture containing 112.3 μL water, 10 μL 1 M HEPES buffer (pH 7.5), 0.2 μL 1 M DTT, 0.5 μL 1 M $MgCl_2$, 2 μL 100 mM ATP, 5 μL hTK1 (~0.5 mg/mL), 20 μL of a 10 mM solution of $[Re(CO)_3$**X**$]^{0/+}$ (**X** = **7**, **10**, **11**, **15**), and 50 μL of an aqueous solution of $[^{99m}Tc(CO)_3$**X**$]^{0/+}$ (**X** = **7**, **10**, **11**, **15**) (~100 kBq). The reaction mixtures were quenched by addition of 800 μL 5 mM EDTA solution and analyzed by HPLC.

Cell Lines and Culture. Two human glioblastoma cell lines were used: U251 (American Type Culture Collection, ATCC) and LN229 (a gift from Prof. N. de Tribolet, Service of Neurosurgery, University Hospital, Geneva, Switzerland). Cells were cultured at 37 °C and 5% CO_2 in RPMI 1640 with glutamax I (Invitrogen AG, Basel Switzerland), supplemented with 10% heat-inactivated fetal bovine serum (Chemie Brunschwig AG, Basel, Switzerland), penicillin (50 units/mL), and streptomycin (0.05 mg/mL; Life Technologies Inc., Grand Island, NY, USA), which was changed twice a week. Because mycoplasma contamination is a potential source of increased nucleoside turnover and could therefore modulate FdUrd efficacy, the cell lines were regularly tested for four major potential mycoplasma contaminations (Mycoplasma Detection Kit, F. Hoffmann-La Roche Ltd., Basel, Switzerland).

Radioactive dT Analogue Incorporation Assay. 24-well culture dishes were plated with 20 000 cells for LN229 and with 15 000 cells for U251. After 3 days, the exponentially growing cells were incubated for 2 h at 37 °C and 5% CO_2 with either 5 kBq ^{125}I-IdUrd, 10 kBq $[^{99m}Tc(CO)_3$**7**$]$, or 10 kBq $[^{99m}Tc(CO)_3$**16**$]^+$ in 0.5 mL medium. After this time, the supernatant was removed and the cells were washed three times with PBS. The cells were detached with 300 μL of 1 M NaOH. Radioactivity was measured in a gamma counter (Wizard 3" 1480 automatic gamma counter, Wallac Oy, Turku, Finland) and the results expressed as a percentage of the initial activity added. In the FdUrd pretreatment assay, cells were pretreated with 1 μM FdUrd and incubated for 1 h at 37 °C and 5% CO_2. After this time, the supernatant was removed and the cells were washed twice with PBS before either 5 kBq ^{125}I-IdUrd, 10 kBq $[^{99m}Tc(CO)_3$**7**$]$, or 10 kBq $[^{99m}Tc(CO)_3$**16**$]^+$ was added in 0.5 mL fresh medium.

Supporting Information Available: NMR and HPLC analysis of target complexes, crystal data and structure refinement for $[Re(CO)_3$**11**$][CF_3CO_2]_{0.8}[Br]_{0.2}$, and further details of the phosphorylation assay. This material is available free of charge via the Internet at http://pubs.acs.org.

LITERATURE CITED

(1) Eriksson, S., Kierdaszuk, B., Munch-Petersen, B., Oberg, B., and Johansson, N. G. (1991) Comparison of the substrate specificities of human thymidine kinase-1 and kinase-2 and deoxycytidine kinase toward antiviral and cytostatic nucleoside analogs. *Biochem. Biophys. Res. Commun. 176*, 586–592.

(2) Schinazi, R. F., Mead, J. R., and Feorino, P. M. (1992) Insights into HIV chemotherapy. *AIDS Res. Hum. Retrov. 8*, 963–990.

(3) Eriksson, S., Munch-Petersen, B., Johansson, K., and Eklund, H. (2002) Structure and function of cellular deoxyribonucleoside kinases. *Cell. Mol. Life Sci. 59*, 1327–1346.

(4) Eriksson, S., and Wang, J. H. (1995) Substrate specificities of mitochondrial thymidine kinase and cytosolic deoxycytidine kinase against 5-aryl substituted pyrimidine-2′-deoxyribose analogs. *Nucleosides Nucleotides 14*, 507–510.

(5) Al-Madhoun, A. S., Johnsamuel, J., Yan, J. H., Ji, W. H., Wang, J. H., Zhuo, J. C., Lunato, A. J., Woollard, J. E., Hawk, A. E., Cosquer, G. Y., Blue, T. E., Eriksson, S., and Tjarks, W. (2002) Synthesis of a small library of 3-(carboranylalkyl)thymidines and their biological evaluation as substrates for human thymidine kinases 1 and 2. *J. Med. Chem. 45*, 4018–4028.

(6) Byun, Y., Thirumamagal, B. T. S., Yang, W., Eriksson, S., Barth, R. F., and Tjarks, W. (2006) Preparation and biological evaluation of 10B-enriched 3-[5-{2-(2,3-dihydroxyprop-1-yl)-o-carboran-1-yl}pentan-1-yl]thymidine (N5−2OH), a new boron delivery agent for boron neutron capture therapy of brain tumors. *J. Med. Chem. 49*, 5513–5523.

(7) Welin, M., Kosinska, U., Mikkelsen, N. E., Carnrot, C., Zhu, C. Y., Wang, L. Y., Eriksson, S., Munch-Petersen, B., and Eklund, H. (2004) Structures of thymidine kinase 1 of human and mycoplasmic origin. *Proc. Natl. Acad. Sci. U.S.A. 101*, 17970–17975.

(8) Lunato, A. J., Wang, J. H., Woollard, J. E., Anisuzzaman, A. K. M., Ji, W. H., Rong, F. G., Ikeda, S., Soloway, A. H., Eriksson, S., Ives, D. H., Blue, T. E., and Tjarks, W. (1999) Synthesis of 5-(carboranylalkylmercapto)-2 ′-deoxyuridines and 3-(carboranylalkyl)thymidines and their evaluation as substrates for human thymidine kinases 1 and 2. *J. Med. Chem. 42*, 3378–3389.

(9) Johnsamuel, J., Lakhi, N., Al-Madhoun, A. S., Byun, Y., Yan, J. H., Eriksson, S., and Tjarks, W. (2004) Synthesis of ethyleneoxide modified 3-carboranyl thymidine analogues and evaluation of their biochemical, physicochemical, and structural properties. *Bioorg. Med. Chem. 12*, 4769–4781.

(10) Conti, P. S., Alauddin, M. M., Fissekis, J. R., Schmall, B., and Watanabe, K. A. (1995) Synthesis of 2′-fluoro-5-[C-11]-methyl-1-b-D-arabinofuranosyluracil ([C-11]-Fmau) - a potential nucleoside analog for in-vivo study of cellular proliferation with PET. *Nucl. Med. Biol. 22*, 783–789.

(11) Shields, A. F., Grierson, J. R., Dohmen, B. M., Machulla, H. J., Stayanoff, J. C., Lawhorn-Crews, J. M., Obradovich, J. E., Muzik, O., and Mangner, T. J. (1998) Imaging proliferation in vivo with [F-18]FLT and positron emission tomography. *Nat. Med. 4*, 1334–1336.

(12) Gardelle, O., Roelcke, U., Vontobel, P., Crompton, N. E. A., Guenther, I., Blauenstein, P., Schubiger, A. P., Blattmann, H., Ryser, J. E., Leenders, K. L., and Kaser-Hotz, B. (2001) [^{76}Br]Bromodeoxyuridine PET in tumor-bearing animals. *Nucl. Med. Biol. 28*, 51–57.

(13) Desbouis, D., Struthers, H., Spiwok, V., Küster, T., and Schibli, R. (2008) Synthesis, in vitro, and in silico evaluation of organometallic technetium and rhenium thymidine complexes with retained substrate activity toward human thymidine kinase type 1. *J. Med. Chem. 51*, 6689–6698.

(14) Struthers, H., Spingler, B., Mindt, T. L., and Schibli, R. (2008) Click-to-Chelate": Design and incorporation of triazole-containing metal-chelating systems into biomolecules of diagnostic and therapeutic interest. *Chem.—Eur. J. 14*, 6173–6183.

(15) Yan, J. H., Naeslund, C., Al-Madhoun, A. S., Wang, J. H., Ji, W. H., Cosquer, G. Y., Johnsamuel, J., Sjoberg, S., Eriksson, S., and Tjarks, W. (2002) Synthesis and biological evaluation of 3′-carboranyl thymidine analogues. *Bioorg. Med. Chem. Lett. 12*, 2209–2212.

(16) Mindt, T. L., Struthers, H., Brans, L., Anguelov, T., Schweinsberg, C., Maes, V., Tourwe, D., and Schibli, R. (2006) Click to Chelate": Synthesis and installation of metal chelates into biomolecules in a single step. *J. Am. Chem. Soc. 128*, 15096–15097.

(17) Tornøe, C. W., Christensen, C., and Meldal, M. (2002) Peptidotriazoles on solid phase: [1,2,3]-triazoles by regiospecific copper(I)-catalyzed 1,3-dipolar cycloadditions of terminal alkynes to azides. *J. Org. Chem. 67*, 3057–3064.

(18) Kolb, H. C., and Sharpless, K. B. (2003) The growing impact of click chemistry on drug discovery. *Drug Discovery Today 8*, 1128–1137.

(19) Rostovtsev, V. V., Green, L. G., Fokin, V. V., and Sharpless, K. B. (2002) A stepwise Huisgen cycloaddition process: Copper(I)-catalyzed regioselective "ligation" of azides and terminal alkynes. *Angew. Chem., Int. Ed. 41*, 2596–2599.

(20) Banerjee, S. R., Levadala, M. K., Lazarova, N., Wei, L., Valliant, J. F., Stephenson, K. A., Babich, J. W., Maresca, K. P., and Zubieta, J. (2002) Bifunctional single amino acid chelates for labeling of biomolecules with the $\{Tc(CO)_3\}^+$ and $\{Re(CO)_3\}^+$ cores. Crystal and molecular structures of $[ReBr(CO)_3(H_2NCH_2C_5H_4N)]$, $[Re(CO)_3\{(C_5H_4NCH_2)_2NH\}]Br$, $[Re(CO)_3\{(C_5H_4NCH_2)_2NCH_2CO_2H\}]Br$, $[Re(CO)_3\{X(Y)NCH_2CO_2CH_2CH_3\}]Br$ (X = Y = 2-pyridylmethyl; X = 2-pyridylmethyl, Y = 2-(1-methylimidazolyl)methyl; X = Y = 2-(1-methylimidazolyl)methyl), $[ReBr(CO)_3\{(C_5H_4NCH_2)NH(CH_2C_4H_3S)\}]$, and $[Re(CO)_3\{(C_5H_4NCH_2)N(CH_2C_4H_3S)(CH_2CO_2)\}]$. *Inorg. Chem. 41*, 6417–6425.

(21) Lazarova, N., Babich, J., Valliant, J., Schaffer, P., James, S., and Zubieta, J. (2005) Thiol- and thioether-based bifunctional chelates for the $\{M(CO)_3\}^+$ core (M = Tc, Re). *Inorg. Chem. 44*, 6763–6770.

(22) Schibli, R., La Bella, R., Alberto, R., Garcia-Garayoa, E., Ortner, K., Abram, U., and Schubiger, P. A. (2000) Influence of the denticity of ligand systems on the in vitro and in vivo behavior of 99mTc(I)-tricarbonyl complexes: a hint for the future functionalization of biomolecules. *Bioconjugate Chem. 11*, 345–351.

(23) Farrugia, L. J. (1997) ORTEP-3 for Windows - a version of ORTEP-III with a Graphical User Interface (GUI). *J. Appl. Crystallogr. 30*, 565.

(24) Alberto, R., Ortner, K., Wheatley, N., Schibli, R., and Schubiger, A. P. (2001) Synthesis and properties of boranocarbonate: A convenient in situ CO source for the aqueous preparation of $[^{99m}Tc(H_2O)_3(CO)_3]^+$. *J. Am. Chem. Soc. 123*, 3135–3136.

(25) Kornberg, A., and Pricer, W. E. (1951) Enzymatic phosphorylation of adenosine and 2,6-diaminopurine riboside. *J. Biol. Chem. 193*, 481–495.

(26) Byun, Y., Yan, J. H., Al-Madhoun, A. S., Johnsamuel, J., Yang, W. L., Barth, R. F., Eriksson, S., and Tjarks, W. (2005) Synthesis and biological evaluation of neutral and zwitterionic 3-carboranyl thymidine analogues for boron neutron capture therapy. *J. Med. Chem. 48*, 1188–1198.

(27) Zhang, J., Visser, F., King, K. M., Baldwin, S. A., Young, J. D., and Cass, C. E. (2007) The role of nucleoside transporters in cancer chemotherapy with nucleoside drugs. *Cancer Metastasis Rev. 26*, 85–110.

(28) Yao, S. Y. M., Ng, A. M. L., Sundaram, M., Cass, C. E., Baldwin, S. A., and Young, J. D. (2001) Transport of antiviral 3′-deoxy-nucleoside drugs by recombinant human and rat equilibrative, nitrobenzylthioinosine (NBMPR)-insensitive (ENT2) nucleoside transporter proteins produced in Xenopus oocytes. *Mol. Membr. Biol. 18*, 161–167.

(29) Dupertuis, Y. M., Vazquez, M., Mach, J. P., De Tribolet, N., Pichard, C., Slosman, D. O., and Buchegger, F. (2001) Fluorodeoxyuridine improves imaging of human glioblastoma xenografts with radiolabeled iododeoxyuridine. *Cancer Res. 61*, 7971–7977.

(30) Perillo-Adamer, F., Delaloye, A. B., Genton, C. S., Schaffland, A. O., Dupertuis, Y. M., and Buchegger, F. (2006) Short fluorodeoxyuridine exposure of different human glioblastoma lines induces high-level accumulation of S-phase cells that avidly incorporate I-125-iododeoxyuridine. *Eur. J. Nucl. Med. Mol. Imaging 33*, 613–620.

(31) Perumal, M., Pillai, R. G., Barthel, H., Leyton, J., Latigo, J. R., Forster, M., Mitchell, F., Jackman, A. L., and Aboagye, E. O.

(2006) Redistribution of nucleoside transporters to the cell membrane provides a novel approach for imaging thymidylate synthase inhibition by positron emission tomography. *Cancer Res. 66*, 8558–8564.
(32) Pressacco, J., Mitrovski, B., Erlichman, C., and Hedley, D. W. (1995) Effects of thymidylate synthase inhibition on thymidine kinase activity and nucleoside transporter expression. *Cancer Res. 55*, 1505–1508.
(33) Armstrong, R. D., and Diasio, R. B. (1980) Metabolism and biological activity of 5′-deoxy-5-fluorouridine, a novel fluoropyrimidine. *Cancer Res. 40*, 3333–3338.
(34) Tjarks, W., Tiwari, R., Byun, Y., Narayanasamy, S., and Barth, R. F. (2007) Carboranyl thymidine analogues for neutron capture therapy. *Chem. Commun.* 4978–4991.
(35) Liu, Y., Pak, J. K., Schmutz, P., Bauwens, M., Mertens, J., Knight, H., and Alberto, R. (2006) Amino acids labeled with $[^{99m}Tc(CO)_3]^+$ and recognized by the L-type amino acid transporter LAT1. *J. Am. Chem. Soc. 128*, 15996–15997.
(36) Alberto, R., Egli, A., Abram, U., Hegetschweiler, K., Gramlich, V., and Schubiger, P. A. (1994) Synthesis and reactivity of $[NEt_4]_2[ReBr_3(CO)_3]$. Formation and structural characterization of the clusters $[NEt_4][Re_3(\mu_3\text{-}OH)(\mu\text{-}OH)_3(CO)_9]$ and $[NEt_4][Re_2(\mu\text{-}OH)_3(CO)_6]$ by alkaline titration. *J. Chem. Soc., Dalton Trans.* 2815–2820.
(37) Foulon, C. F., Adelstein, S. J., and Kassis, A. I. (1996) Kit formulation for the preparation of radiolabeled iododeoxyuridine by demetallation. *J. Nucl. Med. 37*, S1–S3.
(38) Schaffland, A. O., Delaloye, A. B., Kosinski, M., Dupertuis, Y. M., and Buchegger, F. (2004) The prearation of clinical grade 5-[I-123]iodo-2′-deoxyuridine and 5-[I-125]iodo-2′-deoxyuridine with high in vitro stability and the potential for early proliferation scintigraphy. *Nucl. Med. Commun. 25*, 461–468.
(39) Altomare, A., Burla, M. C., Camalli, M., Cascarano, G. L., Giacovazzo, C., Guagliardi, A., Moliterni, A. G. G., Polidori, G., and Spagna, R. (1999) SIR97: a new tool for crystal structure determination and refinement. *J. Appl. Crystallogr. 32*, 115–119.
(40) Sheldrick, G. M. (2008) A short history of SHELX. *Acta Crystallogr., Sect. A: Found. Crystallogr. 64*, 112–122.
(41) Spek, A. L. (2003) Single-crystal structure validation with the program PLATON. *J. Appl. Crystallogr. 36*, 7–13.

BC900380N

"Zero-Length" Dimers of Ribonuclease A: Further Characterization and No Evidence of Cytotoxicity

Francesca Vottariello, Chiara Costanzo, Giovanni Gotte, and Massimo Libonati*

Dipartimento di Scienze Morfologico-Biomediche, Sezione di Chimica Biologica, Facoltà di Medicina e Chirurgia, Università di Verona, Strada Le Grazie 8, I-37134 Verona, Italy. Received September 15, 2009; Revised Manuscript Received February 10, 2010

"Zero-length" dimers of ribonuclease A, a novel type of dimers formed by two RNase A molecules bound to each other through a zero-length amide bond [Simons, B. L., et al. (2007) *Proteins 66*, 183−195], were further characterized and tested for their possible in vitro cytotoxic activity. Results obtained are the following. Besides dimers, also trimers and higher oligomers could be identified among the products of the covalently linking reaction, and the "zero-length" dimers prepared by us appear not to be a unique species. The product was indeed heterogeneous, and results obtained with two RNase A mutants, E9A and K66A, indicated that amino and carboxyl groups others than those belonging to Lys66 and Glu9 are involved in the amide bond. As for their functional properties, the "zero-length" dimers degrade poly(A)·poly(U) (dsRNA) with an activity that increases with the increase of the oligomer's basicity and yeast RNA (ssRNA) with an activity that instead decreases with the increase of oligomer's basicity, which is in agreement with previous data. No cytotoxicity of the RNase A "zero-length" dimers could be evidenced in assays performed with various tumor cells lines; the dimers, instead, become cytotoxic if cationized by conjugation with polyethylenimine (PEI) [Futami et al. (2005) *J. Biosci. Bioengin. 99*, 95−103]. However, PEI derivatives of RNase A "zero-length" dimers and PEI derivatives of native RNase A resulted to be equally cytotoxic. In other words, protein "dimericity" does not play any role in this case. Moreover, the acquired cytotoxicity does not seem to be specific for tumor cells: PEI-cationized native RNase A was also cytotoxic toward human monocytes.

INTRODUCTION

Many ribonucleases were found to be endowed with remarkable biological activities, among which an interesting in vitro and in vivo cytotoxic action against tumor cells (*1*−*5*). This finding aroused new interest in this class of enzymes and opened a new chapter in the field of potential anticancer therapy. Among cytotoxic monomeric ribonucleases, a well-known example is onconase, an enzyme found in the oocytes and early embryos of *Rana pipiens* (*2*). Among mammalian pancreatic-type ribonucleases, well-known is the ribonuclease from bovine semen, BS-RNase[1]. Bovine seminal RNase is a unique natural dimer, with its two subunits sharing 83% identity with bovine pancreatic ribonuclease (*6, 7*). This dimeric RNase is endowed with various biological activities, among which is a strong antitumor action (*7, 8*).

Artificial dimers of RNase A were casually obtained for the first time in 1962 by Crestfield, Stein, and Moore (*9*). These authors envisaged the way in which an RNase A dimer could form and proposed a model consisting in the exchange between two ribonuclease molecules of their N-terminal ends (*9, 10*). This mechanism was later identified and confirmed by Eisenberg and colleagues in studying the structure of the diphtheria toxin (*11, 12*), and named "three-dimensional (3D) domain swapping". In 1998, Eisenberg et al. (*13*) found it to determine the structure of one (the N-dimer, as it was called later) of the two dimeric conformers of RNase A that had been identified by Crestfield and colleagues (*10*). Dimerization of RNase A had also been obtained by cross-linking two enzyme molecules with the bifunctional reagent dimethyl suberimidate, which reacts with the ε-amino group of one lysine residue of each protein molecule (*14*). These cross-linked RNase A dimers exhibited antitumor action similar to that of BS-RNase (*15, 16*). All ribonuclease dimers, natural or artificial, degrade double-stranded RNA (*14, 17*), DNA/RNA hybrids (*18*), and poly(A) (*19*) under conditions where native, monomeric RNase A does not. On this basis, the idea grew that "dimericity" could be a determinant factor in conferring novel and functionally important side properties to a ribonuclease (*14*−*19*). Evidence further supporting this idea also came from dimeric mutants of human pancreatic RNase (*20*) or bovine pancreatic RNase A (*21*), which were shown to be selectively cytotoxic toward tumor cells, while the corresponding native, monomeric proteins are devoid of any biological activity.

With the procedure described by Crestfield et al. (*9*), i.e., by lyophilizing RNase A from 40−50% acetic acid solutions, trimers, tetramers, and higher-order oligomers also form besides dimers, each species comprising, like dimeric RNase A (*10*), at least two conformers, one more basic, one less basic, one more abundant, and one less (*22*−*27*). The structure of the second, more abundant and more basic RNase A dimer (C-dimer), formed through the exchange of the C-termini between two protein molecules (*28*), and the structure of the

* Corresponding author. Tel: +39-045-8027166. Fax: +39-045-8027170. E-mail: massimo.libonati@univr.it.

[1]Abbreviations: BS-RNase, bovine seminal ribonuclease; RNase A, bovine pancreatic ribonuclease A; N-dimer (N_D) or C-dimer (C_D), N-terminal or C-terminal swapped dimer of RNase A; C-trimer (C_T), cyclic RNase A trimer; zl, "zero-length"; zl-D, zl-T or zl-HO, "zero-length" dimers, trimers or higher oligomers of RNase A; H-wt M, H-E9A M, H-K66A M, heated native (monomeric) RNase A and RNase A variants; PEI, polyethylenimine; PEI-M, PEI-conjugated wt (monomeric) RNase A; PEI-RNase A-zl-D, PEI-conjugated RNase A zero-length dimers; NaP, sodium phosphate buffer; TNBS, trinitrobenzensulfonic acid; ssRNA, single-stranded RNA; dsRNA, double-stranded RNA; dsRNase, an RNase active on dsRNA; IPTG, isopropyl β-D-1-thiogalactopyranoside; PMSF, phenylmethylsulfonyl fluoride; EDC, 1-ethyl-3-(dimethylaminopropyl)-carbodiimide; cRI, cytosolic ribonuclease inhibitor; LB, lysogenic broth; FBS, fetal bovine serum.

10.1021/bc900407v © 2010 American Chemical Society
Published on Web 03/04/2010

C-terminal domain-swapped cyclic trimer (C-trimer) (*25, 26, 28*) have been solved, and plausible models were proposed for another trimer and several other RNase A oligomers (*23*−*29*). The 3D domain-swapped RNase A oligomers larger than dimers are also able to degrade dsRNA (*22, 24, 27*). Dimers and higher oligomers of RNase A are cytotoxic (*30*) like BS-RNase (*7, 8*) and the RNase A cross-linked dimers (*15, 16*) and trimers (*31*), the extent of these activities increasing as a function of the oligomers' complexity (*24, 30, 32*). Therefore, not only the "dimericity", but in general the "oligomericity" of a ribonuclease, characterized by the increase of the basicity of the complex, was thought to be an important structural determinant for the acquisition by the enzyme of novel functional properties (*24, 32*). In 2006, Leich et al. designed a fusion protein consisting of two RNase A molecules bound to each other by a peptide linker of varying length and composition between the C-terminus of one and the N-terminus of a second ribonuclease molecule by gene duplication (*33*). This tandem RNase A dimer is a potent cytotoxic agent against human erytroleukemia cells (further evidence of the importance of ribonuclease dimericity), although its ribonucleolytic activity is severely reduced. More recently, Simons et al. prepared a novel type of covalently linked RNase A dimer, which consists of two enzyme molecules bound to each other through a zero-length amide bond (*34*). This dimer also is able to degrade double-stranded poly(A)·poly(U) besides ssRNA (*34*).

We do not know whether the cytotoxic tandem dimer of Leich et al. is also able to attack double-helical polyribonucleotides. On the other hand, Simons et al. did not show whether their "zero-length" RNase A dimers might acquire cytotoxic activity in parallel with their ability to degrade double-stranded RNA. Theoretically, both an additional enzymatic activity for the tandem dimer of Leich et al. and a biological action for the "zero-length" dimer of Simons et al. could reasonably be expected. Here, we have examined the latter possibility, i.e., whether RNase A dimerized through the zero-length amide bond, according to the procedure of Simons et al. (*34*), could show a cytotoxic action. The results we obtained were negative, i.e., the "zero-length" dimers do not show, at least under the experimental conditions and with the cell lines used by us, any significant cytotoxicity. They acquire a high cytotoxic activity against tumor cells cultures if cationized with polyethylenimine (PEI) according to the procedure outlined by Futami et al. (*35*). The extent of this cytotoxicity is, however, not higher than that, already evidenced by Futami et al. (*35*), exerted by PEI-cationized monomeric RNase A. Moreover, the latter appears to be cytotoxic also against human monocytes, i.e., normal cells.

EXPERIMENTAL PROCEDURES

Materials. All chemicals were of the highest purity available. Their origin is specified in text and legends to figures and tables. Bovine seminal ribonuclease was a kind gift of Dr. J. Matousek (Institute of Animal Physiology and Genetics, The Academy of Sciences of the Czech Republic, Libechov 27721, Czech Republic). Isolation and purification of the enzyme were performed as described elsewhere (*30*).

In Vacuo Cross Linking of RNase A. According to the procedure outlined by Simons et al. (*34, 36*), bovine pancreatic RNase A (Type XII-A, purchased from Sigma Chem. Co., lot no. 124K7680, R5500) was dissolved in ddH_2O at a concentration of 5−40 mg/mL (when necessary, the pH of the solution was adjusted to 7.0 with 1 N NaOH) and lyophilized. The glass tube was sealed under vacuum (∼0.5 mBar) and incubated in an oven at 85 °C for 96−144 h. After releasing the vacuum, the protein sample was reconstituted with 40 mM sodium phosphate buffer, pH 6.7, to obtain a final protein concentration of 10 mg/mL. Then, the sample was incubated at 50 °C for 24 h to dissociate RNase A noncovalent oligomers formed.

Conjugation of Bovine RNase A and Its "Zero-Length" Dimers to Polyethylenimine. We followed the procedure described by Futami et al. (*35*). Native RNase A was dissolved in a 60 mg/mL solution of polyethylenimine (PEI, M_n 1200, M.W. 1300 Da, Sigma #482595, lot no. 05329KH), pH 5.0; protein final concentration, 1 mg/mL. EDC (Sigma #E7750, lot no. 107K0664) was added, final concentration, 0.1 mg/mL. The mixture was incubated for 16−24 h at room temperature. The same procedure was followed for the conjugation of the zero-length dimers. Then, the mixture was dyalized against water, and concentrated with Amicon Ultra filters (Millipore), cutoff 3000 Da. At the end, the material was lyophilized. Otherwise, it was partially purified performing two-step cation-exchange chromatography (see next paragraph).

Purification and Analysis of the Covalent RNase A Oligomers. *Size-Exclusion Chromatography.* Purification of the covalent RNase A oligomers was accomplished by two size-exclusion chromatography steps performed with a Superdex 75 26/60 column (GE-Healthcare) attached to an äKTA FPLC system, at room temperature. The column was equilibrated with 0.2 or 0.4 M NaP (pH 6.7)/0.15 M NaCl. The flow rate was 1 mL/min. To determine the yield of the reaction and the purity of the products the mixture of oligomers was analyzed with two size-exclusion chromatography steps using a Superdex 75 HR 10/300 column (GE-Healthcare) attached to an äKTA FPLC system, at room temperature. The column was equilibrated with 0.2 and 0.4 NaP, pH 6.7, in the first and second purification step, respectively. Elution was performed at a flow rate of 0.15 mL/min in the first and 0.07 mL/min in the second purification step.

Ion-Exchange Chromatography. Analyses of the covalent RNase A "zero-length" oligomers were also performed with cation-exchange chromatography using either Source 15S HR 10/10 or Mono S strong cationic columns (GE-Healthcare) and the same äKTA FPLC system mentioned above, at room temperature. Three different gradients were applied to the columns. The first was a preliminary stepwise gradient of NaP (70−90 mM, pH 6.7), followed by a linear (90−200 mM, pH 6.7) gradient at a flow rate of 1 mL/min (total, 44 min). The second was a linear 40−200 mM NaP (pH 6.7) gradient at a flow rate of 1 mL/min (total, 60 min). The third was a stepwise 40−200 mM NaP (pH 6.7) gradient.

To separate the RNase A-PEI conjugate(s) from nonconjugated RNase A and purify the products, two different elution schemes of cation-exchange chromatography were used: (i) a stepwise procedure, increasing by 30 mM, from 70 to 400 mM, the NaP (pH 6.7) concentration, and (ii) a two-step cation-exchange chromatography, each step under isocratic conditions (first step: 70 mM NaP, pH 6.7, to elute the nonconjugated protein; second step: 400 mM NaP, pH 6.7).

Quantification of the "Zero-Length" Oligomers. Each oligomeric species produced was quantified by measuring the area of its peak appearing in the gel filtration pattern of the first size-exclusion purification step and calculating its percentage relative to the sum of the areas of all peaks eluted. The purity of the "zero-length" species was also determined by measuring the intensity of the corresponding gel band with the use of the *ImageJ* program and calculating its percentage relative to the sum of the intensities of all bands.

Gel Electrophoresis. Cathodic gel electrophoresis under nondenaturing conditions was performed according to Goldenberg (*37*), with slight modifications (*22*), using β-alanine/acetic acid buffer, pH 4.0. 12.5−15% polyacrylamide gels were run at 20 mA for 100−140 min at 4 °C. Fixing and staining were performed with 12% trichloroacetic acid and 0.1% Coomassie Blue R-250.

SDS PAGE was performed according to Laemmli (*38*) using Tris/glycine buffer, pH 8.3. 12.5−15% polyacrylamide gels and 18% acrylamide gels were used to analyze the "zero-length" species or the products conjugated to PEI. Gels were run at 20−22 mA for 100−120 min at room temperature. Staining was made with a solution containing 0.025% Coomassie Blue R-250, 40% methanol, and 7% acetic acid.

DNA gel electrophoresis was performed with a 1% agarose gel, using 0.04 M Tris-acetate buffer, pH 8, containing 1 mM EDTA (TAE buffer). Gels were run at 100 V for 60 min, and a 500 bp Molecular Ruler (Bio-Rad #170−8203) was used as a molecular weight standard.

Production of RNase A mutants. *Construction of the Mutants.* The gene coding for wild-type RNase A, cloned into the expression vector pT7−7 (containing also the gene that codes for ampicillin resistance) between the *NdeI* and *Hin*dIII restriction enzyme sites, was kindly provided by Professor A. Di Donato (Faculty of Sciences, the University of Naples). Two mutants of the RNase A gene (E9A and K66A) were obtained using the QuikChange II Site-Directed Mutagenesis Kit (Stratagene, #200523, lot no. 1260135). pT7−7 template (with the RNase A wt gene) was added to the reaction buffer containing dNTPs and mutagenic primers.

The sequences of the primers were as follows:

Mutant E9A	FW 5′-GCAGCAGCCAAGTTTG*CC*GCGGCAGCACATGGAC-3′
	RV 5′- GTCCATGTGCTGCCGC*G*CAAACTTGGCTGCTGC-3′
Mutant K66A	FW 5′-CCCAGAAAAATGTTGCCTGC*GC*GAATGGGCAGACC-3′
	RV 5′-GGTCTGCCCATTC*GC*GCAGGCAACATTTTTCTGGG-3′

DNA polymerase was added and PCR performed. After denaturation of the double-stranded DNA template at 95 °C for 30 s, the first cycle was started: 95 °C for 30 s, annealing at 57 °C for 1 min, and polymerization at 68 °C for 12 min. These steps were repeated 16 times. Finally, the sample was cooled to 4 °C.

The DNA template was digested with *DpnI*, and the mutated and amplified plasmid was used to transform the XL1-Blue supercompetent cells. A colony of these cells was isolated and inoculated in 5 mL of LB containing Ampicillin (100 μg/mL). This overnight culture was used for plasmid DNA miniprep purification, using the Wizard Plus SV Minipreps DNA Purification System (Promega, #A1330, lot no. 182970). A DNA gel electrophoresis was performed to verify the presence of the amplified pT7−7 plasmid after PCR and DNA miniprep purification. Furthermore, the plasmidic DNA was sequenced and the presence of the desired mutation confirmed.

Production and Purification of RNase A from E. coli Inclusion Bodies. The PT7−7 plasmid containing the RNase A mutated gene was added to *E. coli* strain BL21-Gold (DE3) cells and incubated on an ice bath for 30 min. Cells were then transformed by thermal shock at 42 °C for 20 s. After 1 min on ice, the transformed *E. coli* was regenerated in 1 mL of LB (without ampicillin) and incubated at 37 °C for 1 h with shaking. After centrifugation of the culture, the pellet was resuspended in 100 μL of LB broth. Cells were seeded on LB Agar plates containing 100 μg/mL ampicillin, and incubated at 37 °C overnight. A colony was then isolated and inoculated in 5 mL of LB with 50 μg/mL ampicillin. This culture was incubated at 37 °C with shaking for at least 6 h, then inoculated in 150 mL of LB with 50 μg/mL ampicillin and incubated overnight at 37 °C with shaking. Fifteen milliters of this culture was used to inoculate 500 mL of LB containing 50 μg/mL ampicillin. The inoculated culture was shaken at 37 °C until the early log phase (A_{600} = 0.6 O.D.) was reached. It was then induced to express the cDNA coding for RNase A by adding IPTG (0.5 mM, final concentration). Induction of protein expression was performed overnight under the same conditions of the incubation.

The culture was centrifuged at 5500 rpm for 10 min and bacteria were resuspended in 0.1 M Tris-acetate buffer, pH 8.4 (10 mL/1000 OD_{600} units), containing PMSF as inhibitor of serine proteases and cysteine protease (4 μL of 0.1 M PMSF/g *E. coli*).

To verify the presence of RNase A in the cell culture before starting protein extraction, an analysis with SDS PAGE was performed (18% polyacrylamide gel, Tris/glycine buffer, pH 8.3). Amounts corresponding to 0.126 OD_{600} of *E. coli* collected before and after induction with IPTG were run at 20−22 mA at room temperature.

Cell lysis and inclusion bodies extraction were performed by incubation with lysozyme (0.8 mg/g *E. coli*) at room temperature for 20 min, and by freezing (in liquid nitrogen) and thawing (at 37 °C). After these last steps, the extract was treated as described elsewhere (*39*) to perform RNase A renaturation. To verify the presence of RNase A in the fractions eluted during these two purification steps, a Kunitz assay (*40*) was performed (purified yeast RNA as substrate), using native RNase A (Sigma Aldrich, type XII-A, R5500) as a control.

Determination of Free Amino Groups. 150 μg of protein were dissolved in 1 mL of 0.15 M sodium tetraborate ($Na_2B_4O_7$), pH 9.5. 0.2 mL of 0.015 M TNBS was added to the solution ("blank" consisted in 1 mL of 0.15 M sodium tetraborate, pH 9.5, and 0.2 mL of TNBS (*14*)). The reaction mixtures were maintained in the dark at 37 °C for 45 min. Reaction was stopped by adding 2 mL of 85−90% formic acid. Spectrophotometric measurements were performed at 340 nm, and the native, monomeric RNase A value was taken as a standard corresponding to 11 free amino groups (*14*).

Enzymatic Assays.

A. Ribonucleolytic activity on ssRNA (purified yeast RNA) as substrate was determined spectrophotometrically at 300 nm, according to Kunitz (*40*). One unit is the amount of enzyme that is capable of causing a decrease of the RNA absorbance at 300 nm (measured in the initial linear tract) per minute at 25 °C. The substrate is a 0.05% solution of purified yeast RNA in 0.05 M sodium acetate, pH 5.0.

B. The activity of the various RNase A species on the double-helical poly(A)·poly(U) complex (Sigma-Aldrich, P1537) as substrate (40 μg/mL) was determined spectrophotometrically at room temperature by measuring, as described elsewhere (*17*), the increase of the absorbance at 260 nm after addition of the various RNase species to the assay mixtures. One enzyme unit is the amount of enzyme that catalyzes the cleavage of one μmol of phosphodiester linkages of the double helical substrate per minute at 25 °C (*22, 45*).

Specific activities are expressed as units per milligram protein.

Cell Lines and Proliferation Assays. PSN1 (human pancreas adenocarcinoma), K562 (human chronic myelogenous leukemia), and U937 (human leukemic monocyte lymphoma) cell lines were grown in RPMI 1640 medium supplemented with 2 mM L-glutamine, 10% FBS, and 50 mg/mL gentamicin sulfate (BioWhittaker, Cambrex). Human cervix carcinoma HeLa cells were cultured in DMEM supplemented with 2 mM glutamine, 10% FBS, and 50 mg/mL gentamicin sulfate. All mentioned cell lines were incubated at 37 °C with 5% CO_2. Human monocytes were separated by centrifugation on Ficoll-Paque Plus under endotoxin-free conditions from buffy coats of healthy donors. Monocytes (99.8% pure), obtained as described in ref *41* and with the MACS Human Monocyte Isolation Kit II (Miltenyi Biotec), were resuspended in RPMI 1640 supplemented with 10% low endotoxin FBS and 2 mM L-glutamine (BioWhittaker).

At the beginning of each experiment, PSN1 cells were plated at 4×10^3 cells/well, K562 cells at 8×10^3 cells/well, and monocytes at 2×10^4 cells/well. All cell lines were plated in

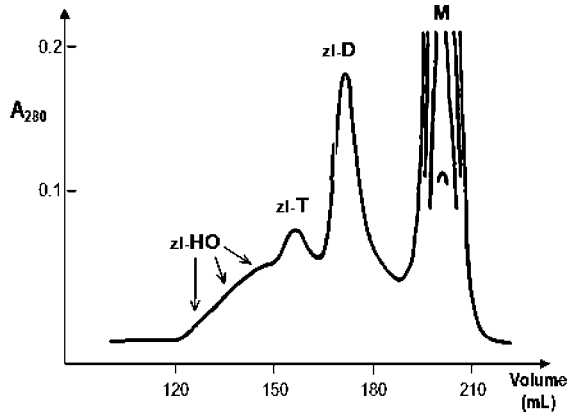


Figure 1. Purification and analysis of RNase A "zero-length" oligomers by size-exclusion chromatography. Twenty milligrams of the oligomers' mixture prepared by the procedure outlined by Simons et al. (*34, 36*) were applied onto a Superdex 75 26/60 (GE-Healthcare) column. Buffer: 0.2 M NaP, pH 6.7/0.15 M NaCl (*34*). Flow rate: 1 mL/min, room temperature. M: monomeric RNase A. zl-D, zl-T, zl-HO: "zero-length" dimer, trimer, and higher oligomers of RNase A.

96-well plates and after 24 h treated as described in the figure legends. At the end of the treatments, cell viability was determined by a metabolic assay using the CellTiter 96 AQ_{ueous} One Solution reagent (Promega) following the manufacturer instructions. Cultures were incubated for 2 h at 37 °C with 5% CO_2, and conversion of MTS into formazan was read at 490 nm.

RESULTS AND DISCUSSION

Preparation of "Zero-Length" Dimers of RNase A. RNase A "zero-length" dimers were obtained with the procedure described by Simons et al. (*34*). The products of the reaction were heated at 50 °C for 24 h to dissociate the noncovalent aggregates possibly formed, purified, and analyzed by gel filtration and SDS PAGE. The gel filtration profile (Figure 1) shows the elution of a great amount of monomeric protein (M), preceded by a clear peak of dimer (zl-D), a smaller peak of trimer (zl-T), and a region of unidentified higher oligomers (zl-HO). By measuring the areas of the peaks and/or the intensity of the bands, the following amounts could be calculated: 15.2 ± 1.9% for the dimer, 5.3 ± 2.0% for the trimer, and 3.7 ± 2.6% for the higher oligomers. The SDS PAGE analysis (Figure 2A) shows several clearly visible bands, of which the densest one is the residual monomeric RNase A. After gel filtration, the purity of the various oligomeric species was determined by electrophoretic analyses. Their purity values decreased as a function of the oligomers' sizes (Figure 2B): the dimer was 76.8 ± 6.9% pure, the trimer 46.9 ± 6.7%, and the higher oligomers 44.8 ± 14.8%. The dimeric species, isolated from the gel filtration pattern, was subjected to an ion-exchange chromatographic purification (*22, 24, 34*), the results of which indicated that the product was actually very heterogeneous (data not shown). All species collected from the gel filtration were also analyzed by cathodic gel electrophoresis (Figure 2C). It is clearly visible that they display an electrophoretic mobility similar to that of the corresponding domain-swapped oligomers, but their spreading bands suggest that the material is heterogeneous. Focusing on zl-D, its heterogeneity could be due to the presence of not only a single dimer (*34*), but to more than one product of the reaction. In other words, this could mean the possible involvement of amino and carboxyl groups other than only those belonging to Lys66 and Glu9.

Are Lys66 and Glu9 the Only Reactive Residues? An Answer from Two RNase A Mutants. To test this hypothesis, we prepared two mutants of RNase A, E9A and K66A, through site-directed mutagenesis (see Experimental Procedures). On the basis of the work of Simons et al. (*34*), these two protein species should not react in the cross-linking reaction developed by these authors, that is, no "zero-length" dimers of RNase A should form. Before testing this possibility, we verified the nature of the two mutants by sequencing their plasmidic DNA. In addition, the elution profiles of the two mutants obtained with a cation-exchange chromatography performed under isocratic conditions (Supporting Information Figure 1) confirmed that the site-directed mutagenesis had been successful. Indeed, the K66A variant is more acid than the wild type lacking one basic amino acid residue and elutes before native RNase A, whereas the E9A mutant, lacking an acid residue, becomes more basic and elutes definitely later. The two mutants were now subjected to the identical experimental conditions used with native RNase A to produce "zero-length" dimers, and the results obtained are shown in Figure 3 and Table 1. It clearly appears that the two variants (Figure 3A,B) are capable of forming dimers, trimers, and higher oligomers in amounts and relative proportions (Table 1) similar to those obtained with native RNase A (Figure 3C). Therefore, differently from what observed by Simons et al. (*34*), Lys66 and Glu9 are not the only residues of RNase A reacting in the procedure.

Determination of Free Amino Groups. To improve the understanding of the results presented above, we determined (by the reaction with TNBS; see Experimental Procedures, and ref *14*) the number of free amino groups present in the protein species deriving from the two variants. They were analyzed before (monomers) and after (monomers M, and dimers, zl-D) subjecting them to the in vacuo heating reaction outlined by Simons et al. (*34*). Table 2 shows the results obtained. On the basis of the eleven NH_2 groups present in native, monomeric RNase A (*14*), it clearly appears that between two and four lysine residues are involved in the amide bond(s) forming in the procedure (*34*) in all types of dimers examined. The analysis was also performed on the monomers (M) of the three RNase A species. In the case of the monomeric K66A variant, both the unheated and heated (H, i.e., subjected to the in vacuo heating reaction) mutant have one NH_2 group less than native RNase A. The missing amino group is obviously that of the Lys66 residue which was mutated in to alanine. Notably, no intramolecular bonds form in the K66A variant. On the contrary, in the E9A variant one amino group is missing only after the in vacuo heating reaction (H E9A M), as it occurs in native RNase A (H-wt M). This might suggest that an intramolecular amide bond could form in these species, involving the Lys66 ε-NH_2 (*34*). The acid partner to react should be the carboxyl group of Asp121 (*42*), whose distance from Lys66 (*42, 43*) is suitable for the reaction to occur.

Enzymatic Assays. All RNase A oligomers obtained so far, either by cross-linking reactions or by one of the other ways by which the enzyme protein can aggregate (*24, 44*), acquire the ability to degrade double-stranded polyribonucleotides. The extent of the degrading activity increases with the size of the oligomer, i.e., with the number or density of positive charges present on the molecule (*24, 45*). The ability of a ribonuclease to digest dsRNA was in fact ascribed to the occurrence of a high protein basicity (*17, 45, 46*). Along with this novel catalytic action, basic ribonucleases and the RNase A oligomers maintain their activity against ss-RNA, the extent of which, however, decreases as the size and/or the basicity of the protein molecule increase (*24, 45, 47*), this being just the opposite of what happens with double-helical RNA substrates. On this basis, we tested the "zero-length" dimers and trimers, and the higher, indistinct oligomers for their action on dsRNA. Table 3 shows the activities of the "zero-length" oligomers of native RNase A (wt zl-D, wt zl-T, wt zl-HO) and of the "zero-length" dimers

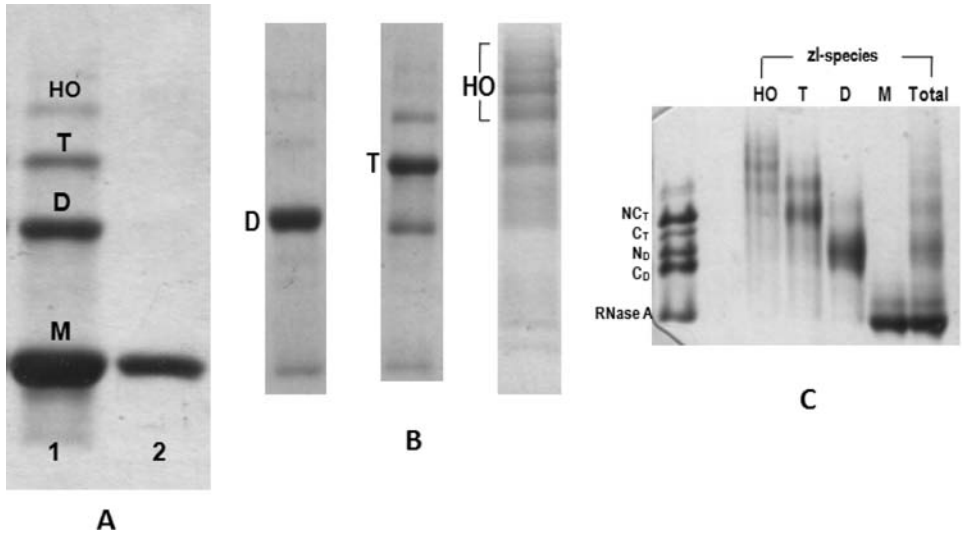


Figure 2. Denaturing and nondenaturing PAGE analysis of the RNase A "zero-length" oligomers. (A) 12.5% polyacrylamide SDS PAGE. Lane 1, 12 μg of the total mixture obtained by the procedure outlined by Simons et al. (*34*); see also Experimental Procedures; lane 2, 2 μg of native RNase A (Sigma Type XII-A) as a standard. (B) 12.5% polyacrylamide SDS PAGE purity assay of the various oligomeric species. Oligomers were purified by two successive gel filtrations. Densities of bands were determined by the *ImageJ* (1.36−6 MB) program. (C) 12.5% polyacrylamide cathodic PAGE of the RNase A "zero-length" species collected from gel filtration and compared with the domain swapped RNase A oligomers (*22, 23*). "Zero-length" RNase A oligomers: M = monomer; D = dimer; T = trimer; HO = higher-order oligomers. In cathodic PAGE: RNase A, native monomer (2 μg); N_D, C_D, N- or C-terminus swapped RNase A dimers (3 μg each); NC_T, N+C-termini swapped trimer (3 μg); C_T, cyclic C-terminus swapped trimer (2 μg).

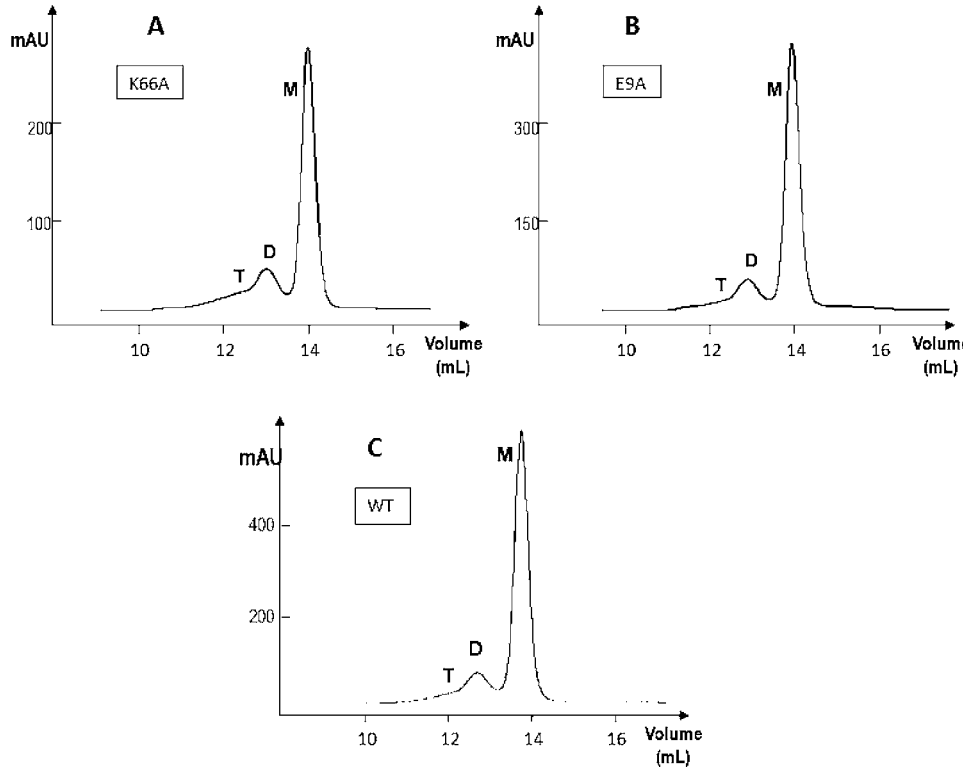


Figure 3. Size-exclusion chromatography of "zero-length" oligomers formed by the two RNase A mutants. The reaction mixture, after heating at 50 °C and cooling, was applied on to a Superdex 75 10/300 (GE-Healthcare) column; buffer, 0.2 M NaP, pH 6.7, containing 0.15 M NaCl; flow rate, 0.15 mL/min, at room temperature. (A) K66A, 1 mg applied; (B) E9A, 1.5 mg applied. (C) WT (wt RNase A), 2 mg applied.

obtained from its two variants (E9A zl-D, K66A zl-D) on dsRNA (poly(A)·poly(U)) or ssRNA (yeast RNA), compared to the action of the corresponding monomeric species. The activities of BS-RNase and of the 3D domain-swapped RNase A oligomers are also included for comparison. The activity values determined with both the ds- and ssRNAs as substrates are in agreement with previous results (*23, 24, 42, 45, 47*); however, it is worth pointing out the lower capacity of degrading dsRNA shown by the K66A variant and its oligomers, compared with native RNase A, which can be ascribed to the one positive charge missing in the mutant. While the activity values of the "zero-length" dimers against poly(A)·poly(U) determined by Simons et al. (*34*) and by us here are similar, we could not confirm the activity values on ssRNA as reported in ref *34*: in our hands, the zl-D, zl-T, and zl-HO are progressively less active as a function of the increase of their size (or positive charges

Table 1. Yields (%) of the "Zero-Length" Oligomers formed by the RNase A Species[a]

oligomers[b]	WT	K66A	E9A
zl-D	15.2 ± 1.9	17.0 ± 0.2	14.7 ± 0.9
zl-T + zl-HO	9.0 ± 2.9	10.6 ± 0.8	5.9 ± 0.1

[a] Yields were determined by measuring the area of each peak and calculating its percentage relative to the sum of the areas of all peaks eluted. The values reported for the two mutants are means of the measured areas from three different gel filtration experiments ± s.d., while the values relative to the wt are means of 11 gel filtration experiments (see Experimental Procedures) ± s.d. [b] WT, native RNase A; zl-D, "zero-length" dimer; zl-T, "zero-length" trimer; zl-HO, "zero-length" higher oligomers.

Table 2. Free Amino Groups Present in Each RNase A Species

RNase A species	free NH_2 groups[a]
RNase A	11.0[a]
H-wt M[b]	10.3 ± 1.2
wt zl-D	7.5 ± 0.9
E9A M	11.4 ± 0.9
H-E9A M	10.0 ± 1.0
E9A zl-D	7.9 ± 0.9
K66A M	9.3 ± 0.8
H−K66A M	10.0 ± 0.8
K66A zl-D	7.9 ± 0.7

[a] In each experiment, the absorbance value determined for native, monomeric RNase A was made equal to 11 amino groups, based on 11 free amino groups present in the native protein (*14*). The values reported are means of four experimental values ± s.d. [b] H, "heated", i.e., RNase A monomeric species recovered after being subjected to the in vacuo heating procedure reported (*34*) and used to prepare the cross-linked, "zero-length" oligomers. wt, native RNase A; M, monomeric species; zl-D, "zero-length" dimers.

Table 3. Enzymatic Activities of the Various RNase A Monomeric and "Zero-Length" or Domain-Swapped Oligomeric Species on Single-Stranded (Yeast) or Double-Stranded (poly(A)·poly(U)) RNA

RNase species	specific activity,[a] poly(A)·poly(U) as substrate	specific activity,[a] Yeast RNA as substrate
BS-RNase	7.8 ± 1.3	15.5 ± 3.4
RNase A	2.4 ± 0.5	70.3 ± 8.8
H-wt M	1.3 ± 0.5	62.9 ± 8.6
wt zl-D	4.6 ± 1.1	44.7 ± 6.3
wt zl-T	6.3 ± 2.1	29.0 ± 4.4
wt zl-HO	11.3 ± 2.7	5.1 ± 0.6
E9A M	1.1 ± 0.2	73.6 ± 7.0
H-E9A M	n.d.[b]	66.4 ± 8.3
E9A zl-D	2.0 ± 0.2	36.0 ± 8.4
K66A M	0.5 ± 0.1	66.8 ± 6.2
H−K66A M	n.d.[b]	68.5 ± 4.1
K66A zl-D	0.6 ± 0.2	40.4 ± 5.6
N_D	2.8 ± 0.1	40.7 ± 18.1
C_D	8.6 ± 0.7	16.0 ± 3.5
NC_T	16.1 ± 3.6	33.2 ± 7.7
C_T	20.5 ± 2.2	25.7 ± 2.2
HO	24.2 ± 2.1	15.5 ± 2.7

[a] Specific activity values were calculated as described in refs *17*, *45* (see also Experimental Procedures). Each value is the mean of results obtained in several different assays ± s.d. Amounts of enzyme used with poly(A)·poly(U) as substrate: monomer, 10 μg; dimer, 5 μg; trimer, 2.5 μg; higher oligomers, 1 μg. Amounts of enzyme used with yeast RNA as substrate: monomer or dimers, 0.5 μg; trimer, 1.0 μg; higher oligomers (HO), 1.5 μg. N_D, C_D, N- or C-terminus swapped RNase A dimers; NC_T, N+C-termini swapped trimer; C_T, cyclic C-terminus swapped trimer; HO, mixture of N+C-swapped higher-order RNase A oligomers. [b] Not determined. H (heated) wt M: see legend to Table 2.

density), which agrees with all previous results (*24, 42, 45, 47*). The enzymatic activity values of the three RNase A monomeric variants determined with yeast RNA as substrate before and after the in vacuo heating reaction show that the activities of the wt enzyme and E9A monomeric variant slightly decrease after the reaction, while the activity of the K66A variant does not. Although modest, that lowering in activity might be ascribed to the modification of D121, whose catalytic role in RNase A is well-known (*48*). The activity of monomeric K66A, on the contrary, does not substantially change, remaining slightly lower than that of the wt enzyme and E9A mutant either before or after the reaction. This is in line with the known catalytic role of K66 P0 subsite (*49*). Although the differences of the enzymatic activities (see Table 3) are modest and lower than what could be expected for species that potentially lose D121 (*48*), it has to be taken into account that possibly yeast RNA is not the most appropriate ssRNA substrate to highlight them (*48*). Nevertheless, the trend shown by the enzymatic activity of the three RNase A monomeric variants agrees with the hypothesis that the K66-D121 intramolecular bond could form in the in vacuo heating of wt RNase A.

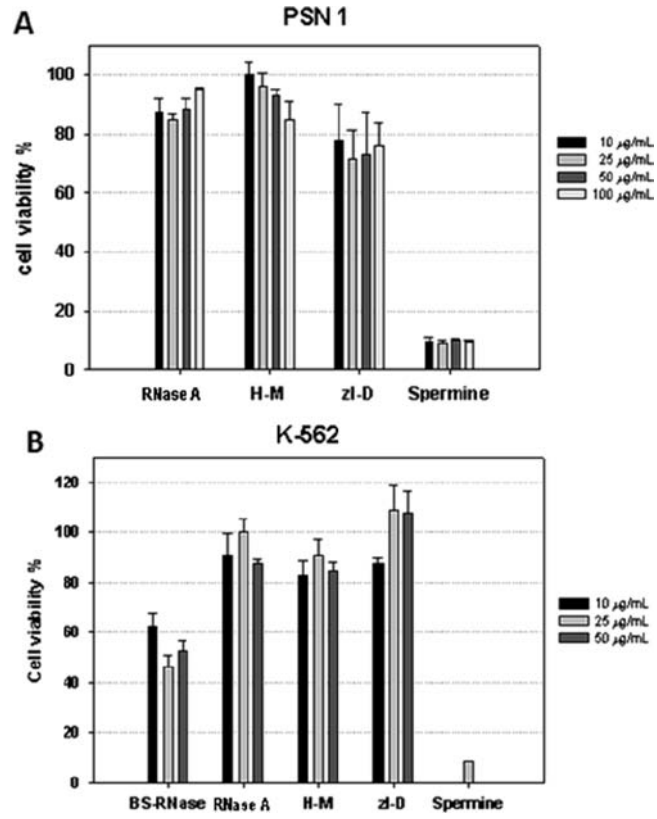


Figure 4. Cytotoxic activity of the various RNase A "zero-length" species on two different tumor cell lines. The various "zero length" oligomers were purified, lyophilized, and dissolved in sterile, twice-distilled water just before their addition to the cell cultures for 48 h (see Experimental Procedures). H-M indicates native, monomeric RNase A subjected to, and recovered after, the in vacuo heating (H) procedure of Simons et al. (*34*); zl-D, "zero-length" dimers of RNase A. (A) PSN1 cell cultures. The various "zero length" oligomers and spermine were used at 10 μg/mL, 25 μg/mL, 50 μg/mL, and 100 μg/mL. (B) K562 cell cultures. The various RNase A "zero-length" species were used at 10 μg/mL, 25 μg/mL, 50 μg/mL, and spermine at 20 μg/mL. Cell viability was calculated as a percentage of treated versus untreated cells. Each value shown is the mean of three measures from three independent experiments ± s.d.

Are the RNase A "Zero-Length" Dimers Cytotoxic? This novel type of dimers was tested on PSN1 human adenocarcinoma cell line grown in culture. The results are shown in Figure 4A. We tested various concentrations of (i) native RNase A (NH-M), (ii) the RNase A that was recovered from the in vacuo heating reaction, indicated as H-M, (iii) the "zero-length" dimers (zl-D), and in addition (iv) spermine as a positive control. After 48 h incubation, no significantly higher cytotoxic action of the "zero-length" dimers, compared to that of the two monomeric

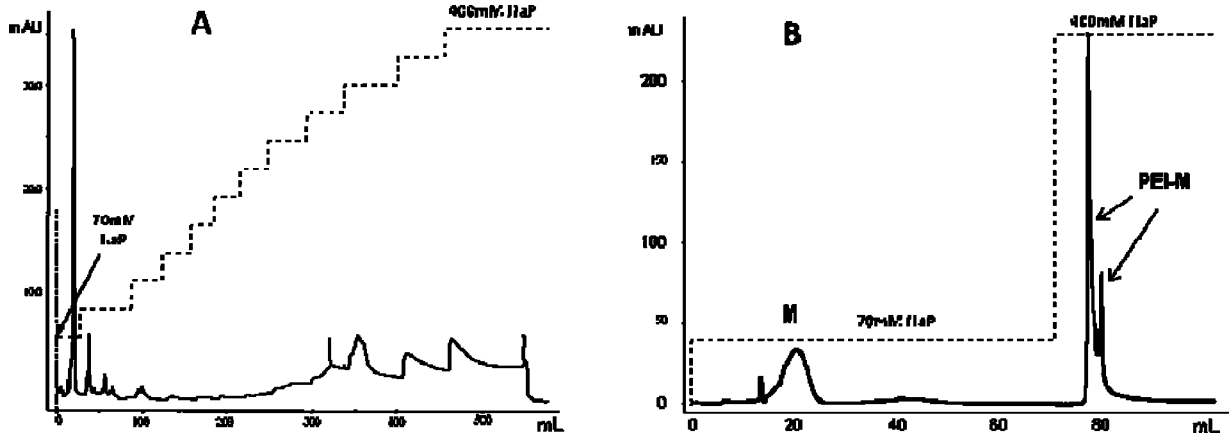


Figure 5. Purification and analysis of monomeric RNase A conjugated with polyethylenimine. (A) Stepwise cation-exchange chromatography of the PEI-RNase A complex. The reaction mixture was dialyzed against Milli-Q water and concentrated by Amicon filters (cut off 3000 Da). 750 μg of material were applied on to a Source 15S HR 10/10 (Ge-Healthcare) column. Eluting buffer, NaP, pH 6.7. Starting NaP concentration, 70 mM; at each step, it was raised by 30 mM. Final NaP concentration, 400 mM. Before the end of chromatography, 1 M NaCl was also added to ensure a complete elution of all conjugated species. (B) Partial purification of the PEI-RNase A complex (1 mg): cation-exchange chromatography with a Source 15S HR 10/10 (GE-Healthcare) column. Buffer: NaP, pH 6.7. Two-step chromatography under isocratic conditions: first step, 70 mM NaP buffer, with elution of nonconjugated monomeric RNase A; second step, 400 mM NaP buffer, with elution of the PEI-conjugated species. Percentage values were calculated by measuring the areas of single peaks (see Experimental Procedures). M, RNase A monomer; D, dimer; T, trimer; HO, higher oligomers of RNase A; PEI-M, polyethylenimine-conjugated monomeric RNase A.

species, could be evidenced, while the unspecific cytotoxicity of spermine was remarkably high.

A second experiment was carried out with K562 cells, which previously were shown to be susceptible to the action of BS-RNase (*50*). The cells were subjected for 48 h to the action of all RNase A species at the concentrations indicated (see Figure 4B), but the zl-D were inactive, while BS-RNase and spermine were considerably cytotoxic. By extending this experiment up to 72 h, the results did not change (data not shown).

Further experiments were performed with HeLa and U937 cells using the same protein concentrations and times of incubation tested with PSN1 cells. In these cases also, the various RNase A species resulted to be totally inactive (data not shown), while spermine was cytotoxic like in the previous experiment. In conclusion, therefore, the "zero-length" oligomers of RNase A appear to be devoid, at least under the experimental conditions and with the cell lines used by us, of any significant cytotoxic activity.

Cationization of Native RNase A and Its "Zero-Length" Dimers with Polyethylenimine and Analysis of the Products of the Conjugation Reaction. The cytotoxicity of RNase A cationized with polyethylenimine (PEI) has been shown by Futami et al. (*35*). Could the PEI-cationized RNase A "zero-length" dimer(s) acquire a cytotoxic action higher than that of the PEI-cationized monomer, which could be ascribable to the dimericity of the RNase A molecule? To answer this question, we used the procedure outlined by Futami et al. (ref *35*; see also Experimental Procedures) to cationize with PEI the zl-D prepared by us. The reaction was first carried out with native, monomeric RNase A, to obtain the species called PEI-M. The products of the reaction were purified and analyzed by cation-exchange chromatography and SDS PAGE. Figure 5A shows the profile of a cation-exchange chromatogram in which a stepwise increase of NaP concentration was applied (see Experimental Procedures). A sharp peak appeared at a NaP concentration of 70 mM (pH 6.7). From its position, it can be deduced that it corresponds to unreacted RNase A contained in the reaction mixture. At higher salt concentration, several irregular peaks emerged successively. This in turn suggests that the product of the PEI-RNase A conjugation is a heterogeneous mixture of PEI-M species deriving from the reaction of the various carboxyl groups available on the protein. To make the isolation of the PEI-RNase A products easier, a different chromatographic approach was followed (Figure 5B): after the elution of monomeric unreacted RNase A at 70 mM NaP, pH 6.7 (*22*−*24*), the NaP concentration was brought to 400 mM. Two sharp, but not completely resolved, peaks of conjugated species eluted immediately. They were collected, dialyzed against water, concentrated with Amicon ultrafilters, and electrophoresed or kept at 4 °C until use. The SDS-PAGE analysis carried out on these PEI-M products (Supporting Information Figure 2) confirmed that they were heterogeneous. Now, we carried out the conjugation reaction of the RNase A "zero-length" dimers with polyethylenimine. The results (data not shown) were qualitatively similar to those obtained with native RNase A. Considering that the starting dimeric protein species to be PEI-conjugated was actually a mixture of "zero-length" dimers and not the only E9-K66 zl-D as described in ref *34*, the product of the conjugation reaction could have obviously been even more heterogeneous than the one obtained with monomeric RNase A. We decided therefore to use the entire, unpurified mixture of PEI-RNase A "zero-length" dimer(s) (PEI-zl-D) to determine its enzymatic and biological activity.

Table 4. Enzymatic Activity of PEI-Conjugated or Not Conjugated RNase A on Double-Stranded (poly(A)·poly(U)) or Single-Stranded (yeast) RNA

RNase species	Specific activity[a], poly(A)·poly(U) as substrate	Specific activity[a], yeast RNA as substrate
BS-RNase	6.9 ± 0.8	14.0 ± 1.6
RNase A	1.9 ± 0.1	75.3 ± 8.4
PEI-M (NP[b])	2.6 ± 0.5	41.3 ± 5.3
zl-D	4.3 ± 0.3	59.7 ± 2.5
PEI-zl-D (NP[b])	8.4 ± 1.1	38.0 ± 8.2

[a] Specific activity values calculated as described (refs *17*, *45*; see also Experimental Procedures). Each value is the mean of three different assays ± s.d. Concentrations of the various enzyme species in the assay: 10 μg monomer, and 5 μg dimer with poly(A)·poly(U) as substrate; 0.5 μg monomer or dimer with yeast RNA as substrate. [b] NP: not purified, total reaction mixture (*35*) dialyzed against water, concentrated, and then dissolved (1 mg/mL) in Milli-Q water.

Enzymatic Assay of the "Zero-Length" RNase A Dimers Conjugated to Polyethylenimine. Table 4 shows the enzymatic activities of the PEI-zl-D on dsRNA and ssRNA. The assay comprised the action of (i) native RNase A, (ii) the PEI-native RNase A complex (PEI-M), (iii) the unconjugated

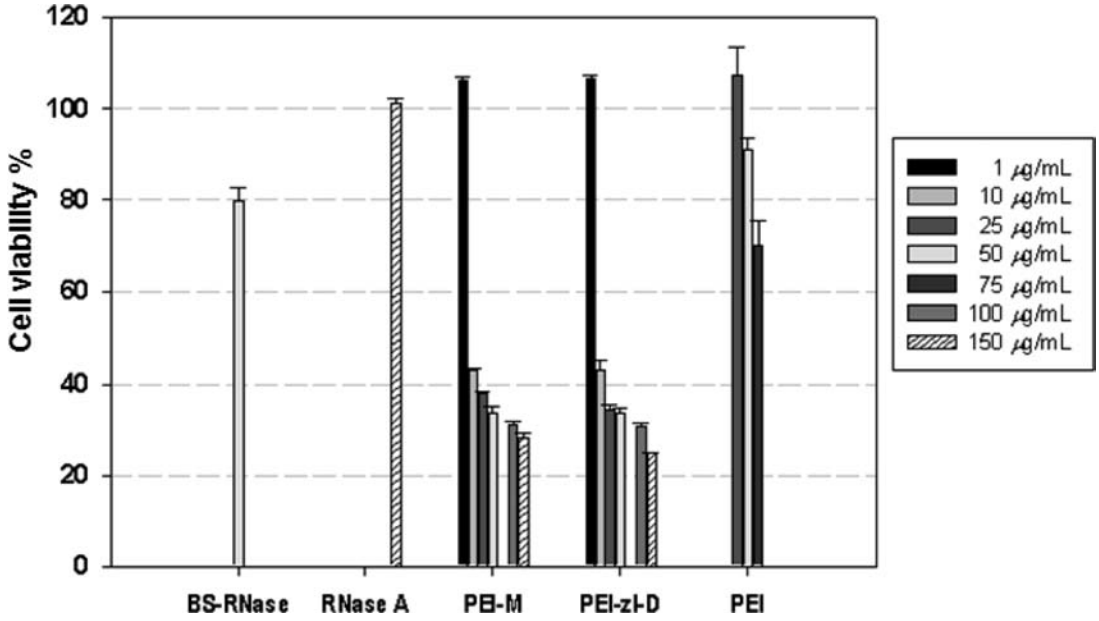


Figure 6. Cytotoxic action of the PEI-RNase A monomeric and dimeric complexes on K562 cell line, as a function of protein concentration. Interaction of the various RNase species with cells lasted 24 h. The two RNase A species (PEI-M and PEI-zl-D) were not purified samples. M, monomeric RNase A; zl-D, RNase A "zero-length" dimers. BS-RNase, bovine seminal RNase, PEI-M, PEI-conjugated monomeric RNase A; PEI-zl-D, PEI-conjugated RNase A "zero-length" dimers; PEI, polyethylenimine. PEI alone was used at 50% concentration that of the RNase A species, as it had been estimated to represent about half of the mass of the PEI-RNase A complexes (see text for details). Cell viability was calculated as a percentage of treated versus untreated cells. Each value shown is the mean of three measures from three independent experiments ± s.d.

"zero-length" RNase A dimers (zl-D), (iv) the PEI-RNase A "zero-length" dimers (PEI-zl-D) complex(es), and (v) BS-RNase for comparison. As for the dsRNase activity, while that of PEI-M was only about 30% higher than the activity of native RNase A, the degrading actions of the "zero-length" dimers as such (220% higher), BS-RNase (360% higher), and PEI-zl-D (440% higher) were remarkable, and in line with results presented in this work or elsewhere (*22*−*24, 27, 45, 47*). The same is true for the results obtained with yeast RNA as a substrate, i.e., all RNase A derivatives and BS-RNase showed lower activity values in comparison with the activity of native RNase A. This result is also in agreement with all previous available data, and with the interpretations advanced elsewhere (*24, 42, 47*). PEI alone (not shown) was absolutely inactive.

In conclusion, the relationship between the RNase basicity and the increased activity on dsRNA or the decreased activity on ssRNA was once again confirmed here. Indeed, the RNase A derivatives are more basic than native RNase A, as demonstrated by the chromatographic pattern of Figure 5, although their pI values are missing. Instead, the pI of BS-RNase is known to be at pH 10.3 (versus the RNase A pI at pH 9.6) as shown in 1972 by D'Alessio et al. (*6*), who demonstrated the higher basicity of BS-RNase compard to RNase A.

Cytotoxicity on K562 Cells of RNase A Monomers and "Zero-Length" Dimers Cationized by Conjugation with Polyethylenimine. The cell line used in the following experiments was K562, which, as mentioned above, is sensitive to BS-RNase. Figure 6 shows the results obtained in a 24 h test by comparing the cytotoxic actions of various concentrations of the PEI-M and the PEI-zl-D complexes with the cytotoxic actions of native RNase A, BS-RNase (both tested in single doses), and three concentrations of PEI alone. We have chosen the amount of PEI (MW 1300 Da) to be tested alone as the one theoretically corresponding to the amount of the substance (five molecules) bound to 50% of the side-chain carboxyl groups present in RNase A. It clearly appears that PEI-M and PEI-zl-D showed strong but quite similar cytotoxicity values, whereas PEI alone was inactive at 25 μg/mL and slightly cytotoxic at 50 or 75 μg/mL. RNase A (150 μg/mL) was inactive and BS-RNase slightly active at 50 μg/mL. Additional experiments as a function of time were performed using two different doses of all agents tested above, i.e., 10 μg/mL (Supporting Information Figure 3A) and 25 μg/mL (Supporting Information Figure 3B). Only PEI-M and PEI-zl-D showed a significant but quite similar cytotoxic action at a concentration of 10 μg/mL, while very modest, if any, was the cytotoxic activity of BS-RNase under identical conditions. At the concentration of 25 μg/mL, stronger but again quite similar to each other were the actions of both PEI-M and PEI-zl-D, whereas the cytotoxic activity of BS-RNase was now evident but still rather modest. In conclusion, the RNase A "zero-length" dimers cationized with polyethylenimine did not acquire a cytotoxic action higher than that of the PEI-cationized monomeric RNase A.

Moreover, we also tested the latter complex on human monocytes, and Figure 7 shows the results obtained. It is quite clear that both the unpurified and purified PEI-RNase A complexes, at the concentration of 25 μg/mL, showed a remarkable cytotoxicity toward monocytes under conditions where BS-RNase (50 μg/mL), native RNase A (100 μg/mL) or PEI alone (12.5 μg/mL) were substantially inactive. Therefore, the cytotoxic action of monomeric RNase A (and presumably that of its "zero-length" dimers) conjugated to PEI appears not to be specific for tumor cells, which drastically decreases the significance of a potential therapeutic use of ribonucleases cationized with polyethylenimine.

Why are the Non-Cationized "Zero-Length" Dimers of RNase A Not Cytotoxic? While native, monomeric RNase A is not cytotoxic (*24, 30*−*32*), other members of the pancreatic-type ribonuclease superfamily display, often along with other biological actions, remarkable activity against malignant tumor cells (*1, 7, 8, 51*−*55*). Cytotoxic RNases usually present a high basic charge density and the ability to evade the cytosolic ribonuclease inhibitor (cRI). The former is a feature also linked to the ability of a ribonuclease to attack dsRNA: the higher the number of positive charges present in the proximity of the

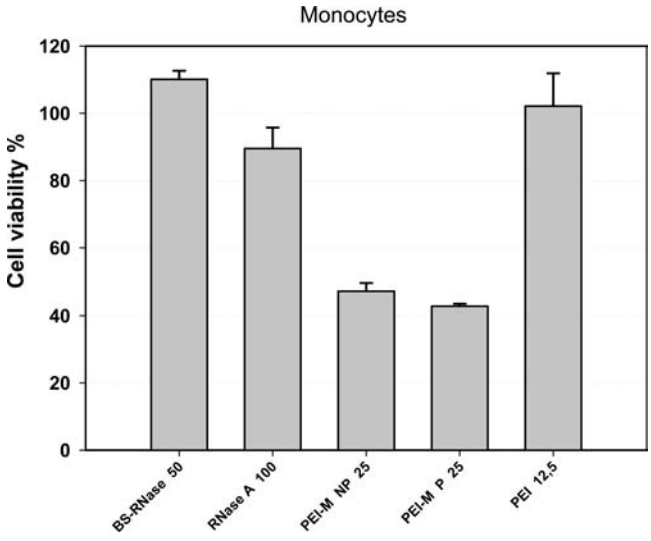


Figure 7. Action of polyethylenimine-cationized RNase A on human monocytes. Monocytes were plated in 96-well plates at 2×10^4/well and incubated overnight. Then, the following substances were added: BS-RNase, 50 μg/mL; native RNase A, 100 μg/mL; purified or unpurified native PEI-RNase A complex(es), 25 μg/mL; PEI, 12.5 μg/mL. The cells were treated for 24 h at 37 °C. Cell viability was calculated as a percentage of treated versus untreated cells. Each value shown is the mean of three measures from three independent experiments ± s.d.

enzyme active site, the higher the ability of the RNase to degrade dsRNA (*17, 22, 24, 27, 32, 45*). It has to be recalled here that the preservation of enzymatic activity also seems to be mandatory for a ribonuclease to be cytotoxic or, generally, biologically active (*24, 30, 33, 56*). It is also worth mentioning that enzymatic activity and cytotoxicity cannot be proportionally related to each other (*57, 58*). This evidence suggests that ribonuclease cytotoxicity could actually be ruled by several factors, among which is the possibility for the enzyme protein to evade interaction with the cytosolic ribonuclease inhibitor. However, several exceptions to the "rule" that only RNases able to evade interaction with cRI are cytotoxic were recently found (*33, 59, 60*). Therefore, it could not be surprising that the "zero-length" dimers of RNase A are ineffective against tumor cells notwithstanding they are not trapped by cRI (*34*) and are enzymatically active toward ss- and dsRNA (ref *34*, and present work). The conformational stability (*61*) and, above all, the location of the positive charges on an RNase molecule (*62*) can be determinant for it to be biologically active (*61, 62*) considering either the efficacy of the RNase−RNA interaction (*32, 45, 61, 62*) or the productive interactions that the protein can build with the cell membrane in order to be internalized (*62−64*). As far as the RNase A zl-D (*34, 36*) are concerned, it must be recalled that their molecular structure is unknown. On the basis of the study of Simons et al., it appears improbable for their structure to be similar to any of the well-known dimeric structures of RNase A (*9−11, 13, 23−28*) or even to that of the cross-linked dimers constructed by Wang, Wilson, and Moore in 1976 (*14*). Indeed, in this last case the diimidoester linker leaves remarkable freedom to the two protein molecules linked to each other. Instead, the amide bond of the RNase A zl-D makes the vicinity of the two protein subunits quite tight. In other words, these novel dimers should be characterized by a relatively strong immobility, high rigidity, and lower symmetry compared to other known dimeric ribonuclease structures (*13, 28, 29*). The structural characteristics of the RNase A zl-D might be a key in understanding why this novel type of RNase A dimer is not cytotoxic. On the other hand, the evident accessibility of its active site to substrates, and the positive charge density of the protein, which could maintain its enzymatic activity against both ss- and dsRNA, are facts that point out the substantial complexity of the matter (*65*). Moreover, since from the present work it appears that the amide bond induced by the procedure outlined by Simons et al. (*34, 36*) may intervene not only between Lys66 and Glu9 (*34*), but also between amino and carboxyl groups of other amino acid residues, the reciprocal location of the protein subunits in the dimer can vary remarkably.

Therefore and in conclusion, the compactness and the possibly variable features of the structure of the RNase A "zero-length" dimers may be their most characteristic structural aspect, responsible, at least partly, for the absence of cytotoxicity in them, making these dimers different in this respect from other natural or artificial ribonuclease dimers.

ACKNOWLEDGMENT

This work was supported by the Italian Ministero per l'Istruzione e la Ricerca Scientifica and the University of Verona, Verona, Italy (Grant: ex60%-Gotte07). We deeply thank Dr. Monica Vincenzi, the Medical Faculty of the University of Verona, for the DNA sequencing experiments.

Supporting Information Available: Supporting graphs showing (*1*) Superimposed Cation-Exchange chromatographies of native RNase A and its two mutants (K66A and E9A); (*2*) SDS PAGE (18% polyacrilamide) of PEI-RNase A complex(es); (*3*) Kinetics of the cytotoxic action of monomeric or PEI-"zero-length" dimeric RNase A complexes on cultures of K562 cell line. This material is available free of charge via the Internet at http://pubs.acs.org.

LITERATURE CITED

(1) Leland, P. A., and Raines, R. T. (2001) Cancer chemotherapy - ribonucleases to the rescue. *Chem. Biol. 8*, 405–413.
(2) Ardelt, W., Mikulski, S. M., and Shogen, K. (1991) Amino acid sequence of an anti-tumor protein from *Rana pipiens* oocytes and early embryos. Homology to pancreatic ribonucleases. *J. Biol. Chem. 266*, 245–251.
(3) Makarov, A. A., and Ilinskaya, O. N. (2003) Cytotoxic ribonucleases: molecular weapons and their targets. *FEBS Lett. 540*, 15–20.
(4) Ardelt, B., Ardelt, W., and Darzynkiewicz, Z. (2003) Cytotoxic ribonucleases and RNA interference (RNAi). *Cell Cycle 2*, 22–24.
(5) Ilinskaya, O. N., and Makarov, A. A. (2005) Why ribonucleases cause death of cancer cells? *Mol. Biol. 39*, 3–13.
(6) D'Alessio, G., Floridi, A., De Prisco, R., Pignero, A., and Leone, E. (1972) Bull semen ribonucleases. 1. Purification and physico-chemical properties of the major component. *Eur. J. Biochem. 26*, 153–161.
(7) D'Alessio, G., Di Donato, A., Piccoli, R., and Russo, N. (2001) Seminal ribonuclease: preparation of natural and recombinant enzyme, quaternary isoforms, isoenzymes, monomeric forms; assay for selective cytotoxicity of the enzyme. *Methods Enzymol. 341*, 248–263.
(8) Matousek, J. (2001) Ribonucleases and their antitumor activity. *Comp. Biochem. Physiol. C Toxicol. Pharmacol. 129*, 175–191.
(9) Crestfield, A. M., Stein, W. H., and Moore, S. (1962) On the aggregation of bovine pancreatic ribonuclease. *Arch. Biochem. Biophys. Suppl. 1*, 217–222.
(10) Fruchter, R. G., and Crestfield, A. M. (1965) Preparation and properties of two active forms of ribonuclease dimer. *J. Biol. Chem. 240*, 3868–3874.
(11) Bennett, M. J., Choe, S., and Eisenberg, D. (1994) Domain swapping: entangling alliances between proteins. *Proc. Natl. Acad. Sci. U.S.A. 91*, 3127–3131.
(12) Bennett, M. J., Schlunegger, M. P., and Eisenberg, D. (1995) 3D Domain swapping: A mechanism for oligomer assembly. *Protein Sci. 4*, 2455–2468.

(13) Liu, Y., Hart, P. J., Schlunegger, M. P., and Eisenberg, D. (1998) The crystal structure of a 3D domain-swapped dimer of RNase A at 2.1 Å resolution. *Proc. Natl. Acad. Sci. U.S.A. 95*, 3437–3442.
(14) Wang, D., Wilson, G., and Moore, S. (1976) Preparation of cross-linked dimers of pancreatic ribonuclease. *Biochemistry 15*, 660–665.
(15) Bartholeyns, J., and Baudhuin, P. (1976) Inhibition of tumor cell proliferation by dimerized ribonuclease. *Proc. Natl. Acad. Sci. U.S.A. 73*, 573–576.
(16) Tarnowski, G. S., Kassel, R. L., Mountain, I. M., Blackburn, P., Wilson, G., and Wang, D. (1976) Comparison of antitumor activities of pancreatic ribonuclease and its cross-linked dimer. *Cancer Res. 36*, 4074–4078.
(17) Libonati, M., and Floridi, A. (1969) Breakdown of double-stranded RNA by bull semen ribonuclease. *Eur. J. Biochem. 8*, 81–87.
(18) Libonati, M., Sorrentino, S., Galli, R., La Montagna, R., and Di Donato, A. (1975) Degradation of DNA.RNA hybrids by aggregates of pancreatic ribonuclease. *Biochim. Biophys. Acta 407*, 292–298.
(19) Libonati, M. (1971) Degradation of poly(A) and double-stranded RNA by aggregates of pancreatic ribonuclease. *Biochim. Biophys. Acta 228*, 440–445.
(20) Piccoli, R., Di Gaetano, S., De Lorenzo, C., Grauso, M., Monaco, C., Spalletti-Cernia, D., Laccetti, P., Cinatl, J., Matousek, J., and D'Alessio, G. (1999) A dimeric mutant of human pancreatic ribonuclease with selective cytotoxicity toward malignant cells. *Proc. Natl. Acad. Sci. U.S.A. 96*, 7768–7773.
(21) Di Donato, A., Cafaro, V., and D'Alessio, G. (1994) Ribonuclease A can be transformed into a dimeric ribonuclease with antitumor activity. *J. Biol. Chem. 269*, 17394–17396.
(22) Gotte, G., Bertoldi, M., and Libonati, M. (1999) Structural versatility of bovine ribonuclease A. Distinct conformers of trimeric and tetrameric aggregates of the enzyme. *Eur. J. Biochem. 265*, 680–687.
(23) Gotte, G., and Libonati, M. (2004) Oligomerization of ribonuclease A. Two novel three-dimensional domain-swapped tetramers. *J. Biol. Chem. 279*, 36670–36679.
(24) Libonati, M., and Gotte, G. (2004) Oligomerization of bovine ribonuclease A: structural and functional features of its multimers. *Biochem. J. 380*, 311–327.
(25) Nenci, A., Gotte, G., Bertoldi, M., and Libonati, M. (2001) Structural properties of trimers and tetramers of ribonuclease A. *Protein Sci. 10*, 2017–2027.
(26) Liu, Y., Gotte, G., Libonati, M., and Eisenberg, D. (2002) Structures of the two 3D domain-swapped RNase A trimers. *Protein Sci. 11*, 371–380.
(27) Gotte, G., Laurents, D. V., and Libonati, M. (2006) Three-dimensional domain-swapped oligomers of ribonuclease A: identification of a fifth tetramer, pentamers and hexamers, and detection of trace heptameric, octameric and nonameric species. *Biochim. Biophys. Acta 1764*, 44–54.
(28) Liu, Y., Gotte, G., Libonati, M., and Eisenberg, D. (2001) A domain-swapped RNase A dimer with implications for amyloid formation. *Nat. Struct. Biol. 8*, 211–214.
(29) Cozza, G., Moro, S., and Gotte, G. (2008) Elucidation of the ribonuclease A aggregation process mediated by 3D domain swapping: A computational approach reveals possible new multimeric structures. *Biopolymers 89*, 26–39.
(30) Matousek, J., Gotte, G., Pouckova, P., Soucek, J., Slavik, T., Vottariello, F., and Libonati, M. (2003) Antitumor and other biological actions of oligomers of ribonuclease A. *J. Biol. Chem. 278*, 23817–23822.
(31) Gotte, G., Testolin, L., Costanzo, C., Sorrentino, S., Armato, U., and Libonati, M. (1997) Cross-linked trimers of bovine ribonuclease A: activity on double-stranded RNA and antitumor action. *FEBS Lett. 415*, 308–312.
(32) Libonati, M. (2004) Biological actions of the oligomers of ribonuclease A. *Cell. Mol. Life Sci. 61*, 2431–2436.
(33) Leich, F., Koeditz, J., Ulbrich-Hofmann, R., and Arnold, U. (2006) Tandemization endows bovine pancreatic ribonuclease with cytotoxic activity. *J. Mol. Biol. 358*, 1305–1313.
(34) Simons, B. L., Kaplan, H., Fournier, S. M., Cyr, T., and Hefford, M. A. (2007) A novel crosslinked RNase A dimer with enhanced enzymatic properties. *Proteins: Struct., Funct., Bioinformatics 66*, 183–195.
(35) Futami, J., Kitazoe, M., Maeda, T., Nukui, E., Sakaguchi, M., Kosaka, J., Miyazaki, M., Kosaka., M., Tada, H., Seno, M., Sasaki, J., Huh, N-H, Namba, M, and Yamada, H. (2005) Intracellular delivery of proteins into mammalian living cells by polyethylenimine-cationization. *J. Biosci. Bioeng. 99*, 95–103.
(36) Simons, B. L., King, M. C., Cyr, T., Hefford, M. A., and Kaplan, H. (2002) Covalent cross-linking of proteins without chemical reagents. *Protein Sci. 11*, 1558–1564.
(37) Goldenberg, D. P. (1989) Analysis of protein conformation by gel electrophoresis. In *Protein structure: a practical approach* (Creighton, T. E., Ed.) pp 225−250, Chapter 10, Oxford University Press, IRL Press, Oxford, U.K.
(38) Laemmli, U. K. (1970) Cleavage of structural proteins during the assembly of the head of bacteriophage T4. *Nature 227*, 680–685.
(39) Gotte, G., Donadelli, M., Laurents, D. V., Vottariello, F., Morbio, M., and Libonati, M. (2006) Increase of RNase A N-terminus polarity or C-terminus apolarity changes the two domains' propensity to swap and form the two dimeric conformers of the protein. *Biochemistry 45*, 10795–10806.
(40) Kunitz, M. (1946) A spectrophotometric method for the measurement of ribonuclease activity. *J. Biol. Chem. 164*, 563–568.
(41) Tamassia, N., Le Moigne, V., Rossato, M., Donini, M., McCartney, S., Calzetti, F., Colonna, M., Bazzoni, F., and Cassatella, M. A. (2008) Activation of an immunoregulatory and antiviral gene expression program in poly(I:C)-transfected human neutrophils. *J. Immunol. 181*, 6563–6573.
(42) Lopez-Alonso, J. P., Diez-Garcia, F., Font, J., Ribo, M., Vilanova, M., Scholtz, J. M., Gonzalez, C., Vottariello, F., Gotte, G., Libonati, M., and Laurents, D. V. (2009) Carbodiimide EDC induces cross-links that stabilize RNase A C-dimer against dissociation: EDC adducts can affect protein net charge, conformation, and activity. *Bioconjugate Chem. 20*, 1459–1473.
(43) Wlodawer, A., Svensson, L. A., Sjoelin, L., and Gilliland, L. (1988) Structure of phosphate-free ribonuclease A refined at 1.26 Å. *Biochemistry 27*, 2705–2717.
(44) Gotte, G., Vottariello, F., and Libonati, M. (2003) Thermal aggregation of ribonuclease A. A contribution to the understanding of the role of 3D domain swapping in protein aggregation. *J. Biol. Chem. 278*, 10763–10769.
(45) Libonati, M., and Sorrentino, S. (2001) Degradation of double-stranded RNA by mammalian pancreatic-type ribonucleases. *Methods Enzymol. 341*, 234–248.
(46) Libonati, M., Furia, A., and Beintema, J. J. (1976) Basic charges on mammalian ribonuclease molecules and the ability to attack double-stranded RNA. *Eur. J. Biochem. 69*, 445–451.
(47) Libonati, M., Bertoldi, M., and Sorrentino, S. (1996) The activity on double-stranded RNA of aggregates of ribonuclease A higher than dimers increases as a function of the size of the aggregates. *Biochem. J. 318*, 287–290.
(48) Schultz, L. W., Quirk, D. J., and Raines, R. T. (1998) His. .Asp catalytic dyad of ribonuclease A: structure and function of the wild-type, D121N, and D121A enzymes. *Biochemistry 37*, 8886–8898.
(49) Fisher, B. M., Ha, J.-H., and Raines, R. T. (1998) Coulombic forces in protein-RNA interactions: binding and cleavage by Ribonuclease A and variants at Lys7, Arg10, and Lys66. *Biochemistry 37*, 12121–12132.
(50) Pouckova, P., Morbio, M., Vottariello, F., Laurents, D. V., Matousek, J., Soucek, J., Gotte, G., Donadelli, M., Costanzo, C., and Libonati, M. (2007) Cytotoxicity of polyspermine-ribonuclease A and polyspermine-dimeric ribonuclease A. *Bioconjugate Chem. 18*, 1946–1955.

(51) Matousek, J., Kim, J.-S., Soucek, J., Riha, J., Ribo', M., Leland, P. A., and Raines, R. T. (1997) Ribonucleases endowed with specific toxicity for spermatogenic layers. *Comp. Biochem. Physiol. 118B*, 881–888.

(52) Matousek, J. (1973) The effect of bovine seminal ribonuclease (BS RNase) on cells of Crocker tumour in mice. *Experientia 29*, 858–859.

(53) Laccetti, P., Spalletti-Cernia, D., Portella, G., De Corato, P., D'Alessio, G., and Vecchio, G. (1994) Seminal ribonuclease inhibits tumor growth and reduces the metastatic potential of Lewis lung carcinoma. *Cancer Res. 54*, 4253–4256.

(54) D'Alessio, G. (1993) New and cryptic biological messages from RNases. *Trends Cell Biol. 3*, 106–109.

(55) Boix, E., Wu, Y., Vasandani, V. M., Saxena, S. K., Ardelt, W., Ladner, J., and Youle, R. J. (1996) Role of the N terminus in RNase A homologues: differences in catalytic activity, ribonuclease inhibitor interaction and cytotoxicity. *J. Mol. Biol. 257*, 992–1007.

(56) Shapiro, R., Fox, E. A., and Riordan, J. F. (1989) Role of Lysines in human angiogenin: chemical modification and site-directed mutagenesis. *Biochemistry 28*, 1726–1732.

(57) Bretscher, L. E., Abel, R. A., and Raines, R. T. (2000) A Ribonuclease A variant with low catalytic activity but high cytototoxicity. *J. Biol. Chem. 275*, 9893–9896.

(58) Lee, J. E., Bae, E., Bingman, C. A., Jr., and Raines, R. T. (2008) Structural basis for catalysis by onconase. *J. Mol. Biol. 375*, 165–177.

(59) De Lorenzo, C., Di Malta, C., Cali, G., Troise, F., Nitsch, L., and D'Alessio, G. (2007) Intracellular route and mechanism of action of ERB-h RNase, a human anti-ErbB2 anticancer immunoagent. *FEBS Lett. 581*, 296–300.

(60) Bosch, M., Benito, A., Ribó, M., Puig, T., Beaumelle, B., and Vilanova, M. (2004) A nuclear localization sequence endows human pancreatic ribonuclease with cytotoxic activity. *Biochemistry 43*, 2167–2177.

(61) Schulenburg, C, Ardelt, B., Ardelt, W., Arnold, U., Shogen, K., Ulbrich-Hofmann, R., and Darzynkiewicz, Z. (2007) The interdependence between catalytic activity, conformational stability, and cytotoxicity of onconase. *Cancer Biol. Ther. 6*, 1233–1239.

(62) Turcotte, R. F., Lavis, L. D., and Raines, R. T. (2009) Onconase cytotoxicity relies on the distribution of its positive charge. *FEBS J. 276*, 3846–3857.

(63) Notomista, E., Mancheño, J. M., Crescenzi, O., Di Donato, A., Gavilanes, J., and D'Alessio, G. (2006) The role of electrostatic interactions in the antitumor activity of dimeric RNases. *FEBS J. 273*, 3687–3697.

(64) Ercole, C., Colamarino, R. A., Pizzo, E., Fogolari, F., Spadaccini, R., and Picone, D. (2009) Comparison of the structural and functional properties of RNase A and BS-RNase: A stepwise mutagenesis approach. *Biopolymers 91*, 1009–1017.

(65) Johnson, R. J, Chao, T. Y., Lavis, L. D., and Raines, R. T. (2007) Cytotoxic ribonucleases: the dichotomy of Coulombic forces. *Biochemistry 46*, 10308–10316.

BC900407V

Synthesis and Characterization of Alkylated Poly(1-vinylimidazole) to Control the Stability of its DNA Polyion Complexes for Gene Delivery

Shoichiro Asayama,* Tomoe Hakamatani, and Hiroyoshi Kawakami

Department of Applied Chemistry, Tokyo Metropolitan University, 1-1 Minami-Osawa, Hachioji, Tokyo 192-0397, Japan.
Received September 17, 2009; Revised Manuscript Received March 25, 2010

Poly(1-vinylimidazole) (PVIm) with alkylated imidazole groups has been synthesized as a pH-sensitive polycation to control the stability of its DNA polyion complexes for gene delivery. The resulting alkylated PVIm (PVIm-R) was water-soluble despite deprotonation of the imidazole groups at physiological pH, as determined by acid−base titration and solution turbidity measurements. Agarose gel retardation assay proved that the alkylated imidazole groups worked as anchor groups to retain DNA. Pyrene fluorescence measurement showed that the hydrophobic domain of the DNA complex with butylated PVIm (PVIm-Bu) increased after the protonation of imidazole groups of the PVIm-Bu to enhance the membrane disruptive activity. The PVIm-Bu exhibited no significant cytotoxicity in spite of the existence of cationic groups. The resulting PVIm-Bu/DNA complexes easily released DNA, as compared with the octylated PVIm, which was examined by competitive exchange with dextran sulfate. As a result, the PVIm-R/DNA complexes mediated efficient gene delivery, and the gene expression depended on the length and density of the alkyl chains. These results suggest that pH-sensitive PVIm-R's control of the stability of DNA polyion complexes enhanced noncytotoxic gene delivery by the optimized alkylated imidazole groups.

INTRODUCTION

In gene delivery systems, the formation of polycation/DNA polyion complexes is a key factor for the new design of efficient delivery (*1*−*3*). The polyion complexes on the cell plasma membrane are internalized into acidic endosomal vesicles where they are subjected to a significant pH change from pH 7 to 5 (*4*). Endosomal escape is one of the critical factors for efficient gene delivery. pH-sensitive polymers such as poly(ethylenimine) (PEI[1]), which is able to capture protons entering an endosome, have been used to achieve efficient release of the delivered material from endosomes (*5*−*7*). PEI induces swelling of the endosomes that leads to membrane disruption, that is, the proton sponge effect.

Recently, polymers modified with histidine or other moieties containing an imidazole group have shown significant enhancement of gene expression without increasing cytotoxicity compared with that of nonmodified polymers (*8*−*12*). In this case, histidine or other moieties containing an imidazole group have made polycation/DNA complexes escape from an endosome by a proton sponge mechanism. The imidazole heterocycles displaying a pK_a around 6 possess buffering capacity in endosomal pH, inducing membrane destabilization after their protonation. The resulting imidazole groups facilitate the release of polycation/DNA complexes to cytosol.

However, we have already reported a poly(1-vinylimidazole) (PVIm) with several aminoethyl groups, that is, aminated PVIm (PVIm-NH_2), for a pH-sensitive polycation to enhance cell-specific gene delivery (*13*). By using PVIm-NH_2 as a pH-sensitive DNA carrier, as well as a lactosylated poly(L-lysine) as a cell-targeting DNA carrier, the resulting ternary complexes specifically mediate gene expression. Gene expression depends on our new concept that DNA ternary complexes dissociate ligand polycations in response to endosomal pH (*13, 14*). However, PVIm-NH_2/DNA binary complexes mediate no significant gene expression.

In this study, to develop PVIm-NH_2 for the realization of efficient gene expression, we have synthesized PVIm with several alkylated imidazole groups, that is, alkylated PVIm (PVIm-R). PVIm is a water-soluble homopolymer possessing many imidazole groups. In spite of a large capacity for H^+ buffering at endosomal pH, PVIm has difficulty in forming complexes with DNA at physiological pH because its imidazole groups are negligibly charged at physiological pH. The introduced alkylated imidazole groups with a quaternary nitrogen atom are expected to work as new anchor groups to retain DNA and to control the stability of polyion complexes. The control of the stability of the polyion complexes by the length and density of the alkylated imidazole groups has no precedent, to the best of our knowledge. Consequently, pH-sensitive PVIm-R's control of the stability of DNA polyion complexes is expected to mediate efficient gene expression by optimizing the length and density of the alkylated imidazole groups.

EXPERIMENTAL PROCEDURES

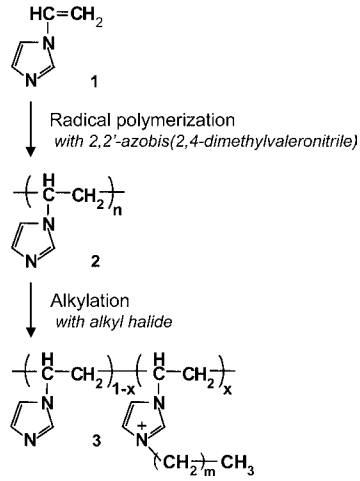
Materials. 1-Vinylimidazole (VIm), 1-bromobutane, 1-bromooctane, and pyrene were purchased from Aldrich Chemical Co. (Milwaukee, WI). VIm was distilled under reduced pressure. 2,2′-Azobis(2,4-dimethylvaleronitrile) (V-65) and bromoethane were purchased from Wako Pure Chemical Industries, Ltd. (Osaka, Japan), and V-65 was recrystallized from ethanol. Iodomethane was purchased from Kanto Chemical Co., Inc. (Tokyo, Japan). PEI solution (M_n = ∼60,000) and salmon testis deoxyribonucleic acid (DNA) sodium salt were from Sigma Chemical Co. (St. Louis, MO). All other chemicals of a special grade were used without further purification.

* To whom correspondence should be addressed. Tel: +81-42-677-1111 (ext.) 4976. Fax: +81-42-677-2821. E-mail: asayama-shoichiro@c.metro-u.ac.jp.

[1]Abbreviations: PEI, poly(ethylenimine); PVIm, poly(1-vinylimidazole); PVIm-NH_2, aminated poly(1-vinylimidazole); PVIm-R, alkylated poly(1-vinylimidazole); VIm, 1-vinylimidazole; V-65, 2,2′-azobis(2,4-dimethylvaleronitrile); GFC, gel filtration chromatography; FBS, fetal bovine serum; EtBr, ethidium bromide; RLU, relative light unit; DS, dextran sulfate.

10.1021/bc900411m © 2010 American Chemical Society
Published on Web 04/05/2010

Scheme 1. Synthesis of Alkylated Poly(1-vinylimidazole)



Synthesis of PVIm-R. The synthetic route of PVIm-R is shown in Scheme 1. VIm (**1**) (300 μL) and V-65 (15.8 mg) as an initiator were dissolved in 2.7 mL of *N*,*N*-dimethylformamide (DMF). The radical polymerization reaction was carried out at 45 °C for 1 day. After the reaction, the content was poured into a large excess of acetone, and the precipitate was dried *in vacuo*. The resulting polymer (**2**) (25 mg) and various amounts of alkyl halide (iodomethane, bromoethane, 1-bromobutane, or 1-bromooctane) (3−100 μL) were dissolved in 2 mL of DMF. The reaction was carried out at 40 °C for 1−6 days according to each case. The reaction mixture was poured into a large excess of diethyl ether. The precipitate was dried *in vacuo* and dissolved in water. After dialysis against distilled water using a Spectra/Por 7 membrane (molecular weight cutoff = 10^3), the resulting polymer (**3**) was obtained by freeze-drying.

Gel Filtration Chromatography (GFC). GFC was carried out using a JASCO PU-980 pumping system (Tokyo, Japan) at the flow rate of 1.0 mL/min with a Shodex OHpak SB-804 HQ column (Showa Denko K. K., Tokyo, Japan). The aqueous solution containing 0.5 M CH_3COOH and 0.2 M $NaNO_3$ was used as a mobile phase. One hundred microliters of 1 mg/mL samples were injected into the column. Eluate was detected by a refractive index detector (RI-1530, JASCO). Calibration was made with polyethylene glycol standards.

^{1}H NMR Spectroscopy. Each polymer (3 mg) was dissolved in 700 μL of D_2O (99.8 atom % deuterium; Acros, NJ). The ^{1}H NMR spectra (400 MHz) were obtained by a JEOL JNM-AL400 spectrometer (Tokyo, Japan).

Acid−Base Titration and Turbidity Measurement of PVIm-R. To 1.5 mL of an aqueous solution of the polymer (3.3 mg/mL) was added a 1 M HCl solution, and the acidic polymer solution (pH 4) was titrated with a 0.2 M NaOH solution. The pH value was checked with a pH meter (model F-52T, Horiba, Kyoto, Japan). The titration was carried out by the stepwise addition of 0.2 M NaOH and stopped at pH 10. The turbidity of the solution during the titration was measured by monitoring the absorbance at 500 nm with a spectrophotometer (model Ubest-55, JASCO, Tokyo, Japan).

Agarose Gel Retardation Assay. Salmon testis DNA was dissolved in PBS (−) at 1.1 mg/mL. The resulting DNA stock solution was added to the polymer solutions in 50 mM sodium phosphate buffer (pH 7.5 or pH 6.0) at various polymer/DNA ratios. The final diluted concentration of DNA was adjusted to 66.7 μg/mL. After 30 min of incubation at room temperature, each sample (corresponding to 1 μg of DNA) was mixed with a loading buffer and loaded onto a 1% agarose gel containing 1 μg/mL of ethidium bromide (EtBr). Gel electrophoresis was run at room temperature in 50 mM sodium phosphate buffer (pH 7.5 or pH 6.0) at 50 V for 15 min. The DNA bands were visualized under UV irradiation. In the case of the assay for the stability of the PVIm-R/DNA complexes, gel electrophoresis was run in the presence of dextran sulfate (1−20 mM as sulfate group) incubated with each sample at room temperature for 10 min.

Pyrene Fluorescence. A known amount of pyrene in acetone solution was added to PBS (−), resulting in the solution at a final concentration of 6.0×10^{-7} M. The pyrene solution (1 mL) was mixed with the PVIm-R/DNA complexes in 1 mL of PBS (−) where 29 μg/mL DNA was used at a +/− ratio of 1, 4, or 12. The sample solution was incubated overnight at room temperature, and emission spectra with excitation at 337 nm were recorded. The fluorescence intensity ratio of the first band at 373 nm to the third band at 384 nm (I_1/I_3) was analyzed at pH 7.4 or pH 6.0.

Hemolysis Assay. The PVIm-R/DNA complexes were prepared at a +/− ratio of 12 with 10 mM sodium phosphate buffer (pH 7.4 or pH 6.0) containing 130 mM NaCl. Then, 150 μL of the resulting sample containing 186 μg of PVIm-R was incubated with 20 μL of preserved sheep blood (Cosmo Bio Co., Ltd., Tokyo, Japan) for 120 mim at 37 °C. After centrifugation (13000 rpm, 1 min, 4 °C), the released hemoglobin was determined by measuring the absorbance at 570 nm with a Model-550 microplate reader (Bio-Rad Laboratories, Inc., Tokyo, Japan).

Cell Viability Assay. HepG2 cells (a gift from the Japan Health Sciences Foundation), human hepatoma cell line, were cultured in tissue culture flasks containing Dulbecco's modified Eagle's medium supplemented with 10% heat-inactivated FBS. The cells were seeded at 1×10^4 cells/well in a 96-well plate and incubated overnight at 37 °C in a 5% CO_2 incubator. The cells were treated with each polymer (0−400 μg/mL) and incubated for 24 h at 37 °C. By further incubation for 4 h, the cell viability was measured using the Alamar Blue assay (*15*) in triplicate.

Transfection Procedure. In a typical 96-well plate experiment, 1×10^4 cells/well HepG2 cells were transfected in Dulbecco's modified Eagle's medium supplemented with 10% heat-inactivated FBS by the addition of 15 μL of PBS (−) containing 200 ng of plasmid DNA encoding the modified firefly luciferase (pGL3-Control Vector; from Promega Co.) and complexed with polycations. After 1 day of incubation, the medium was removed, and the cells were further incubated for 2 days in Dulbecco's modified Eagle's medium supplemented with 10% FBS. Then, the cells were subjected to the luciferase assay (Promega kit) according to the manufacturer's instructions. Luciferase activities were normalized by protein concentrations and are presented as relative light units (RLU). Protein concentrations were determined by the BCA protein assay kit (Pierce) according to the manufacturer's instructions.

RESULTS AND DISCUSSION

Synthesis of PVIm-R. As shown in Scheme 1, PVIm (**2**) was reacted with an alkyl halide such as 1-bromobutane for alkylation to obtain quaternary imidazole groups. The number-average molecular weight of each resulting polymer (**3**) determined by GFC was about 8.8×10^3. The ^{1}H NMR spectrum of the resulting polymers showed the characteristic signals of both PVIm (*16*) [δ 1.8−2.2 (methylene), 2.3−3.7 (methine), and 6.4−7.2 (imidazole) ppm] and alkyl [δ 0.7−0.8 (terminal-methyl), 1.0−1.2 (3-methylene of butyl or 3,4,5,6,7-methylene of octyl), and 1.4−1.7 (2-methylene) ppm] moieties. From the signal ratio, the content (density) of alkylated imidazole groups was calculated. Thus, we have synthesized PVIm with quaternary imidazole groups, that is, PVIm-R.

pH-Dependent Behavior of PVIm-R in Water. To examine the ionic properties of the remaining imidazole groups, we

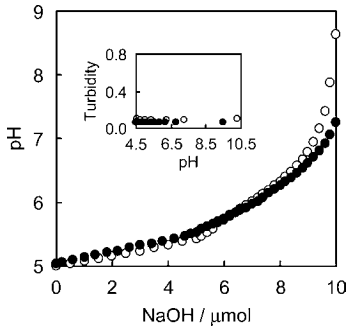


Figure 1. Acid−base titration curves of PVIm-R: (●) 18 mol % butylated PVIm; (○) 40 mol % butylated PVIm. Acidic polymer solutions (3.3 mg/mL) were titrated with the stepwise addition of 0.2 M NaOH. (Inset) Effect of pH on the solubility of the PVIm-R in water (3.3 mg/mL): (●) 18 mol % butylated PVIm; (○) 40 mol % butylated PVIm. The turbidity was measured by monitoring the absorbance at 500 nm of the polymer aqueous solution during acid−base titration.

carried out the acid−base titration of the resulting PVIm-R solution, as shown in Figure 1. Butylated PVIm, that is, PVIm-Bu, was chosen for representative PVIm-R. The imidazole protons of the PVIm-Bu were gently dissociated around pH 6 so that the pK_a of the PVIm-Bu was considered to be around 6. The proton dissociation profile approximately depended on the content of butylated imidazole groups. Namely, the 18 mol % butylated PVIm exhibited larger capacity of proton buffering around pH 6 because PVIm-Bu had more unmodified imidazole groups with a pK_a around 6. However, proton buffering of the 40 mol % butylated PVIm occurred in a little lower region of pH, suggesting that proton dissociation occurred easily because of the more hydrophobic environment near the imidazole groups. It should be noted that the aqueous solution of PVIm-Bu exhibited no significant turbidity above pH 6 in spite of the deprotonation of imidazole groups (Figure 1, inset). These results suggest that PVIm-R such as PVIm-Bu possessed a large capacity of proton buffering at endosomal pH and that the PVIm-R was water-soluble despite the deprotonation of the imidazole groups.

pH-dependent Complex Formation between DNA and PVIm-R. We examined whether the PVIm-Bu, as representative PVIm-R, formed the polyion complexes with DNA by agarose gel electrophoresis (Figure 2A). At pH 7.4, no band was observed when the DNA was mixed with an excess of PVIm-Bu (lanes 4−6). The band disappearance is considered to be attributed to the induction of the coil−globule transition of DNA and the resulting inhibition of the intercalation of EtBr (*17, 18*). In particular, almost no free DNA was observed at the [butylated imidazole]$_{PVIm\text{-}Bu}$/[phosphate]$_{DNA}$ ratio of 1 (lane 3), where the amount of the cationic butylated imidazole groups of PVIm-Bu was equal to the anionic phosphate groups of DNA. The excess PVIm-Bu polymers are considered to remain in the free state (Figure S-1, Supporting Information). Even in the presence of an excess amount of the unmodified PVIm at pH 7.4, it is reported that most of the DNA migrated into the plus pole of the gel owing to the complete deprotonation of the imidazole groups (*13, 19*). These results suggest that the PVIm-Bu formed the DNA complexes at the stoichiometric charge ratio of DNA to butylated imidazole groups; that is, the butylated imidazole groups worked as unique anchor groups to retain DNA. Furthermore, the free DNA observed at the [butylated imidazole]$_{PVIm\text{-}Bu}$/[phosphate]$_{DNA}$ ratio of 0.5 at pH 7.4 (lane 2) completely disappeared at pH 6.0 (lane 2′). This is due to the protonation of the unmodified imidazole groups of the PVIm backbone.

To examine further the pH-dependent behavior of the DNA complexes with PVIm-Bu, we investigated the hydrophobicity

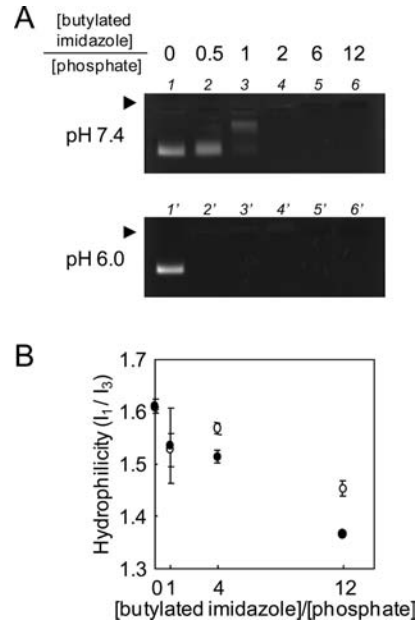


Figure 2. (A) Analysis of the pH-dependent formation of the complexes between DNA and PVIm-R by agarose gel electrophoresis. Interaction of 18 mol % butylated PVIm with DNA at pH 7.4 (lanes 1−6) or pH 6.0 (lanes 1′−6′): lanes 1 and 1′, DNA alone; lanes 2−6 and 2′−6′, PVIm-Bu/DNA mixtures at different unit ratios relative to butylated imidazole groups of PVIm-Bu per phosphate group of DNA ([butylated imidazole]/[phosphate] = *0.5*, *1*, *2*, *6*, or *12*), lanes 2 and 2′, *0.5*; lanes 3 and 3′, *1*; lanes 4 and 4′, *2*; lanes 5 and 5′, *6*; lanes 6 and 6′, *12*. The solid arrowhead indicates the well where each sample was loaded. (B) I_1/I_3 of pyrene fluorescence in PBS(−) with PVIm-Bu/DNA complexes at pH 7.4 (○) or pH 6.0 (●). The complexes were formed at +/− ratio of 1, 4, or 12 where the final concentration of DNA was 14.5 μg/mL. I_1/I_3 was defined as the fluorescence intensity ratio of the first band at 373 nm to the third band at 384 nm where the final concentration of pyrene was 0.3 μM.

of the complexes by using the fluorescence of pyrene. An emission intensity ratio of the first (373 nm) to the third (384 nm) peaks of pyrene, I_1/I_3, is known to be sensitive to the microenvironmental polarity surrounding the pyrene molecule (*20*). Consequently, this ratio has been widely used to estimate the hydrophobic nature (*21−23*). Namely, since this parameter decreases with an increase of hydrophobicity, it represents hydrophilicity. Figure 2B depicts the I_1/I_3 ratio of pyrene fluorescence in the buffer containing various PVIm-Bu/DNA complexes at pH 7.4 or pH 6.0. In buffers dissolving DNA, the I_1/I_3 ratios of pyrene were approximately 1.6 at pH 7.4 and pH 6.0. The presence of PVIm-Bu affected hydrophilicity (I_1/I_3 ratio), which tended to decrease as the [butylated imidazole]$_{PVIm\text{-}Bu}$/[phosphate]$_{DNA}$ ratio increased. These results suggest that the PVIm-Bu/DNA complexes formed the domain with a hydrophobic nature. Furthermore, it should be noted that hydrophilicity (I_1/I_3 ratio) in the presence of the excess amount of PVIm-Bu ([butylated imidazole]$_{PVIm\text{-}Bu}$/[phosphate]$_{DNA}$ = 4 or 12) at pH 6.0 was lower than that at pH 7.4. The resulting hydrophobic nature is therefore considered to increase even after the protonation of imidazole groups of the PVIm-Bu. These results suggest that the protonated PVIm-Bu enhanced the micelle formation which consisted of the shell of the protonated imidazole groups and the core of the butylated imidazole groups. It can be said that the PVIm-Bu/DNA complexes were capable of varying their hydrophobic−hydrophilic balance in response to endosomal pH.

Biochemical Properties of the PVIm-R/DNA Complexes. To examine the effect of the resulting pH-dependent change of the hydrophobic−hydrophilic balance on the interaction with the real cell membranes, we measured the hemolytic activity

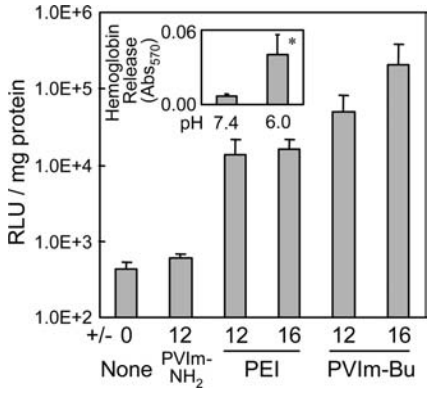


Figure 3. Transfection of luciferase gene to HepG2 cells by the DNA complexes with PVIm-R. As PVIm-R, 18 mol % butylated PVIm was used at the +/− ratio of 12 or 16. The PVIm-NH_2/DNA complexes at +/− ratio of 12 and the PEI/DNA complexes at +/− ratio of 12 or 16 were used as the control. The cells (1×10^4 cells/well) were transfected by adding 200 ng of plasmid DNA complexed with polycations for 1 day in the presence of 10% FBS. Gene expression was determined 2 days later as RLU normalized by protein concentrations. Symbols and error bars represent the mean and standard deviation of the measurements made in paired samples ($n = 3$). (Inset) Effect of pH on the hemolytic activity of PVIm-R/DNA complexes. Erythrocytes were incubated with the PVIm-Bu/DNA complexes at the +/− ratio of 12 for 120 min at 37 °C in 10 mM sodium phosphate buffer (pH 7.4 or pH 6.0) containing 130 mM NaCl. The released hemoglobin was determined by measuring the absorbance at 570 nm (Abs_{570}), where the Abs_{570} in the absence of the PVIm-Bu/DNA complexes (pH 7.4 or pH 6.0) was used as a baseline. Symbols and error bars represent the mean and standard deviation of the measurements made in paired samples ($n = 3$). * indicates statistical significance ($p < 0.02$) when compared to the pH 7.4 value.

of the PVIm-Bu/DNA complexes as representative PVIm-R/DNA complexes (Figure 3, inset). The complexes caused negligible hemolysis at pH 7.4, whereas the hemolytic activity significantly increased at pH 6.0. These results suggest that the membrane disruptive activity of the PVIm-Bu/DNA complexes increased at endosomal pH. The hydrophobic−hydrophilic balance of the PVIm-Bu/DNA complexes at endosomal pH is considered to enhance membrane disruptive activity. It is therefore expected that PVIm-Bu enhances the ability to escape from acidic endosomal vesicles.

As a result of the membrane disruptive activity at endosomal pH, we first examined the gene expression mediated by the PVIm-Bu/DNA complexes. As shown in Figure 3, the PVIm-Bu/DNA complexes mediated remarkable gene expression, which was higher than that mediated by the control PEI. It should be noted that the PVIm-Bu/DNA complexes showed gene expression values approximately 100 times higher than that of the PVIm-NH_2/DNA complexes. These results suggest that not PVIm-NH_2 but PVIm-Bu possessed the required properties as a gene carrier. A main property is considered to be the stabilization of the DNA complexes, not the proton buffering, by the introduced alkyl groups such as butyl groups.

Stability of PVIm-R/DNA Complexes. To confirm the stability of the PVIm-R/DNA complexes, we attempted to release DNA from the polyion complexes by competitive exchange with other polyanions (*24*). For effective transfection, the release of DNA should not happen outside the target cell, whereas that must occur somewhere inside to allow the binding of the transcription machinery. In biological fluids, the proteins borne by various anionic polysaccharides circulate. As an extreme case, dextran sulfate was used as a polyanion; namely, the agarose gel electrophoresis was carried out after the PVIm-R/DNA complexes were incubated with dextran sulfates. The results are shown in Figure 4. As the concentration of the dextran sulfate increased, the DNA increasingly migrated (lanes 4−6)

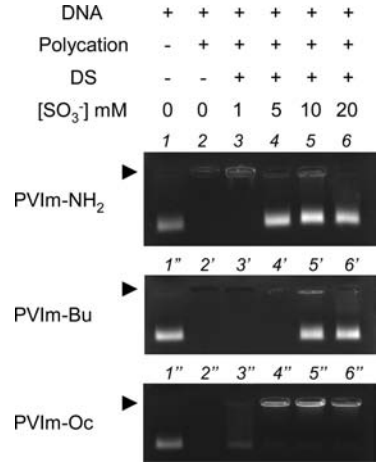


Figure 4. Release of DNA from PVIm-R/DNA complexes by dextran sulfates (DS) as assessed by agarose gel electrophoresis: lanes 1, 1′, and 1″, DNA alone; lanes 2, 2′, and 2″, 0 mM; lanes 3, 3′, and 3″, 1 mM; lanes 4, 4′, and 4″, 5 mM; lanes 5, 5′, and 5″, 10 mM; lanes 6, 6′, and 6″, 20 mM. The DNA mixtures with 18 mol % butylated PVIm (PVIm-Bu) or 18 mol % octylated PVIm (PVIm-Oc) at the +/− ratio of 12 were incubated for 10 min at room temperature in the presence (lanes 3′−6′ and 3″−6″) or absence (lanes 2′ and 2″) of DS (1−20 mM as sulfate group), followed by loading to the gel. As the control, the DNA mixture with PVIm-NH_2 at the +/− ratio of 12 was used in the presence (lanes 3−6) or absence (lane 2) of DS. The solid arrowhead indicates the well where each sample was loaded.

in the case of PVIm-NH_2/DNA complexes. However, in case of DNA complexes with octylated PVIm, that is, PVIm-Oc, almost no DNA migrated even in the presence of a higher concentration of dextran sulfate (lane 6″). These results suggest that PVIm-NH_2/DNA complexes easily released DNA by exposure to polyanions and that PVIm-Oc/DNA complexes stably retained DNA. It is worth noting that it was hard to migrate the DNA in the case of the PVIm-Bu/DNA complexes, as compared with the PVIm-NH_2/DNA complexes (lane 4′). This is probably caused by an adequate length of alkyl chains to stabilize the electrostatic interaction between PVIm-R and DNA. It is reported that the stability of polycation/DNA complexes depends on the chain length of a whole polymer; namely, the longer polycation is found to interact with DNA more strongly than the shorter one (*25*−*27*). In this study, the stability of polycation/DNA complexes has depended on the chain length of introduced alkyl chains in the polycation, which promises a unique design of polycation/DNA complexes. We have therefore considered that PVIm-Bu/DNA complexes have the ability to retain DNA stably outside the target cell and to release DNA adequately inside the cell for transcription.

Cytotoxicity of PVIm-R/DNA Complexes. Cytotoxicity of a gene carrier is an important factor for clinical applications. Free polycations exist solely when DNA is released from the polyion complexes (*28*). Furthermore, the overall cytotoxicity of free polycations is higher than that of the corresponding complexes. Accordingly, we chose the cytotoxicity assay of the free polycations to give a worst case estimating the interaction of the polycations with cells rather than that of the polyion complexes with DNA. As shown in Figure 5, we therefore examine the effect of PVIm-R on cell viability. The viability of HepG2 hepatoma cells did not significantly decrease when PVIm-Bu was added up to the concentration of 400 μg/mL, which was higher than the transfection conditions. Consequently, it is worth noting that PVIm-Bu exhibited no apparent cytotoxicity. The control methylated and ethylated PVIm, that is, PVIm-Me and PVIm-Et, respectively, exhibited the same tendency as PVIm-Bu. However, little viability was observed when PVIm-Oc, as well as the control PEI, was added up to 50

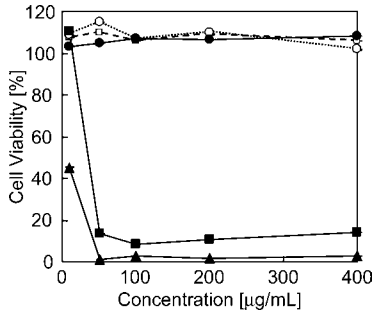


Figure 5. Effect of PVIm-R on the viability of HepG2 cells after 1 day of incubation: (●) 20 mol % butylated PVIm (PVIm-Bu); (■) 20 mol % octylated PVIm (PVIm-Oc); (○) 20 mol % ethylated PVIm (PVIm-Et); (□) 20 mol % methylated PVIm (PVIm-Me); (▲) PEI. Symbols and error bars represent the mean and standard deviation of the measurements made in triplicate wells.

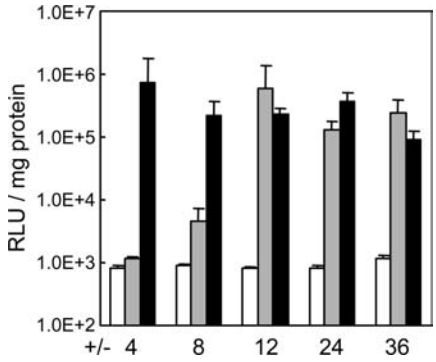


Figure 6. Effect of the density of the alkylated imidazole groups on the transfection activity mediated by PVIm-R/DNA complexes. As PVIm-R, 7 mol % butylated PVIm (white bars), 23 mol % butylated PVIm (gray bars), or 38 mol % butylated PVIm (black bars) was used for the transfection. The PVIm-Bu/DNA complexes were prepared at the +/− ratio of 4, 8, 12, 24, or 36. Other experimental conditions are the same as those described in Figure 3.

μg/mL. These results suggest that PVIm-R with a relatively short length of alkyl groups such as butyl, ethyl, or methyl groups promises to be a noncytotoxic gene carrier. The noncytotoxic property may be attributed to the partial shielding of surface charge, as poly(ethylene glycol) (*29*), by unmodified imidazole groups. However, PVIm-R with a relatively long length of alkyl groups such as octyl groups is considered to cause significant cytotoxicity by the presence of the more amphiphilic property for cell membrane damage. Actually, a little significant cytotoxicity was observed when PVIm-Bu was added up to the concentration of 1000 μg/mL, where PVIm-Me and PVIm-Et exhibited no significant cytotoxicity (Figure S-2, Supporting Information).

Gene Delivery by PVIm-R/DNA Complexes. As a result of no apparent cytotoxicity, we further examined the gene expression mediated by PVIm-R/DNA complexes in view of the density of alkylated imidazole groups. As shown in Figure 6, the PVIm-Bu polycations with different densities of butylated imidazole groups were used as representative PVIm-R for DNA complex formation. Little gene expression was observed at any +/− ratio when we used the DNA complexes with PVIm-Bu with a lower density (7 mol %) of butylated imidazole groups. In case of the PVIm-Bu with a higher density (38 mol %) of butylated imidazole groups, however, the DNA complexes mediated remarkable gene expression even if the complexes at the +/− ratio of 4 was used. Although the DNA complexes with PVIm-Bu with a middle density (23 mol %) of butylated imidazole groups mediated little gene expression at the +/− ratio of 4, the DNA complexes at higher +/− ratios succeeded

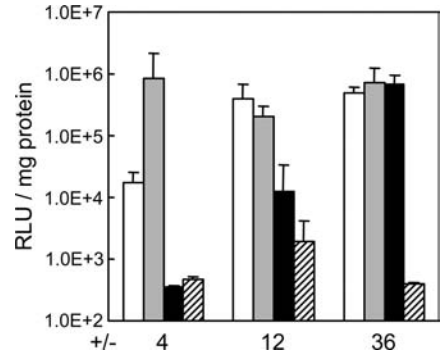


Figure 7. Effect of the length of the alkylated imidazole groups on the transfection activity mediated by PVIm-R/DNA complexes. As PVIm-R, 20 mol % methylated PVIm (PVIm-Me) (white bars), 20 mol % ethylated PVIm (PVIm-Et) (gray bars), 20 mol % butylated PVIm (PVIm-Bu) (black bars), or 20 mol % octylated PVIm (PVIm-Oc) (hatched bars) were used for the transfection. The PVIm-R/DNA complexes were prepared at the +/− ratio of 4, 12, or 36. Other experimental conditions are the same those described in Figure 3.

in remarkable gene expression. These results suggest that the density of the butylated imidazole groups in PVIm-Bu was an important factor for gene delivery.

As a result of the dependency of the density of the butylated imidazole groups, we finally examined the gene expression mediated by the PVIm-R/DNA complexes in view of the alkyl chain length of alkylated imidazole groups. Figure 7 shows the effect of the alkyl chain length of PVIm-R with a middle density (20 mol %) of alkylated imidazole groups on gene expression. As expected, PVIm-Oc mediated little gene expression because of too stable retention of DNA (Figure 4) and significant cytotoxicity (Figure 5). As a result of PVIm-Bu with a middle density (18 mol %, Figure 3; 23 mol %, Figure 6) of alkylated imidazole groups, the gene expression mediated by the PVIm-Bu/DNA complexes depended on the +/− ratio. It should be noted that PVIm-Me and PVIm-Et mediated higher gene expression than PVIm-Bu at lower +/− ratios. Especially, the gene expression mediated by the PVIm-Et/DNA complexes did not depend on the +/− ratio. These results suggest that the alkyl chain length of the alkylated imidazole groups was also an important factor for gene delivery.

Gene expression decreased with a decrease in the density of the alkylated (butylated) imidazole groups (Figure 6). The higher gene expression mediated by PVIm-Me and PVIm-Et is therefore unexpected (Figure 7) because the shorter length of the alkyl chain decreased the apparent density of the alkylated imidazole groups. However, it is surprising that the PVIm-Bu/DNA complex with a middle density of butylated imidazole groups was more stable than that with higher density (Figure S-3, Supporting Information). The excess butylated imidazole groups are therefore considered to enhance the membrane disruptive activity to escape from acidic endosomal vesicles. Furthermore, it is also surprising that the DNA complex with PVIm-Me or PVIm-Et was more stable than that with PVIm-Bu (Figure S-4, Supporting Information). At present, the stability mechanism is unclear; analysis is now in progress for more detailed investigations. Nevertheless, it can be said that the PVIm-Et/DNA complex as well as the PVIm-Me complex has more adequate retention of DNA for gene delivery, as compared with the PVIm-Bu/DNA complex. Although amphiphilic imidazolinium compounds for gene delivery were previously reported, the compounds form liposomes whose stability depends on the length of the dialkyl groups of imidazolinium (*30*). In this study, many alkyl groups in PVIm-R are considered to be intertwined with DNA grooves and the degree of intertwining may affect the transcription of the delivered gene.

Taking these results into account, alkylated imidazole groups are essential and unique functional groups in PVIm-R for efficient gene delivery.

Conclusions. We have synthesized a unique pH-sensitive polycation PVIm-R and evaluated the physicochemical and biochemical properties of the pH-sensitive gene carrier. The resulting PVIm-R was water-soluble in spite of the deprotonation of the imidazole groups at physiological pH. PVIm-R/DNA complex formation was mediated by alkylated imidazole groups working as anchor groups to retain DNA. The DNA complex with butylated PVIm (PVIm-Bu) formed the domain with a hydrophobic nature, which increased after the protonation of imidazole groups of PVIm-Bu. The increased hydrophobic−hydrophilic incline of the PVIm-R/DNA complexes at endosomal pH enhanced membrane disruptive activity. PVIm-Bu exhibited no significant cytotoxicity in spite of the existence of cationic groups and easily released DNA, as compared with PVIm-Oc. By using PVIm-R as a pH-sensitive DNA carrier, PVIm-R/DNA complexes mediated efficient gene delivery attributed to the alkylated imidazole groups, and gene expression depended on the length and density of the alkyl chains. Consequently, PVIm-R's control of the stability of DNA polyion complexes enhanced noncytotoxic gene delivery by optimized alkylated imidazole groups. The control of the polycation/DNA complex properties by varying the length and density of the alkyl chains grafted onto PVIm is expected to offer unique designs for gene delivery systems.

Supporting Information Available: Analysis of the formation of the complex between DNA and PVIm-Bu by agarose gel electrophoresis in the absence of EtBr; effect of PVIm-R on the viability of HepG2 cells after 1 day incubation; release of DNA from PVIm-Bu/DNA complexes by dextran sulfates (DS) as assessed by agarose gel electrophoresis; and release of DNA from PVIm-R/DNA complexes by dextran sulfates (DS) as assessed by agarose gel electrophoresis. This material is available free of charge via the Internet at http://pubs.acs.org.

LITERATURE CITED

(1) Fukushima, S., Miyata, K., Nishiyama, N., Yamasaki, Y., and Kataoka, K. (2005) PEGylated polyplex micelles from triblock catiomers with spatially ordered layering of condensed pDNA and buffering units for enhanced intracellular gene delivery. *J. Am. Chem. Soc. 127*, 2810–2811.

(2) Zugates, G. T., Anderson, D. G., Little, S. R., Lowhorn, I. E. B., and Ranger, R. (2006) Synthesis of poly(β-amino ester)s with thiol-reactive side chains for DNA delivery. *J. Am. Chem. Soc. 128*, 12726–12734.

(3) Liu, Y., and Reineke, T. M. (2007) Poly(glycoamidoamine)s for gene delivery. Structural effects on cellular internalization, buffering capacity, and gene expression. *Bioconjugate Chem. 18*, 19–30.

(4) Steinman, R. M., Mellman, I. S., Muller, W. A., and Cohn, Z. A. (1983) Endocytosis and the recycling of plasma membrane. *J. Cell Biol. 96*, 1–27.

(5) Boussif, O., Lezoualc'h, F., Zanta, M. A., Margny, M. D., Scherman, D., Demeneix, B., and Behr, J. P. (1995) A versatile vector for gene and oligonucleotide transfer into cells in culture and *in vivo*: Polyethylenimine. *Proc. Natl. Acad. Sci. U.S.A. 92*, 7297–7301.

(6) Thomas, M., and Klibanov, A. M. (2002) Enhancing polyethylenimine's delivery of plasmid DNA into mammalian cells. *Proc. Natl. Acad. Sci. U.S.A. 99*, 14640–14645.

(7) Sonawane, N. D., Szoka, F. C., Jr., and Verkman, A. S. (2003) Chloride accumulation and swelling in endosomes enhances DNA transfer by polyamine-DNA polyplexes. *J. Biol. Chem. 278*, 44826–44831.

(8) Roufaï, M. B., and Midoux, P. (2001) Histidylated polylysine as DNA vector: Elevation of the imidazole protonation and reduced cellular uptake without change in the polyfection efficiency of serum stabilized negative polyplexes. *Bioconjugate Chem. 12*, 92–99.

(9) Kim, T. H., Ihm, J. E., Choi, Y. J., Nah, J. W., and Cho, C. S. (2003) Efficient gene delivery by urocanic acid-modified chitosan. *J. Controlled Release 93*, 389–402.

(10) Park, J. S., Han, T. H., Lee, K. Y., Han, S. S., Hwang, J. J., Moon, D. H., Kim, S. Y., and Cho, Y. W. (2006) N-acetyl histidine conjugated glycol chitosan self-assembled nanoparticles for intracytoplasmic delivery of drugs: Endocytosis, exocytosis and drug release. *J. Controlled Release 115*, 37–45.

(11) Mishra, S., Heidel, J. D., Webster, P., and Davis, M. E. (2006) Imidazole groups on a linear, cyclodextrin-containing polycation produce enhanced gene delivery via multiple processes. *J. Controlled Release 116*, 179–192.

(12) Swami, A., Aggarwal, A., Pathak, A., Patnaik, S., Kumar, P., Singh, Y., and Gupta, K. C. (2007) Imidazolyl-PEI modified nanoparticles for enhanced gene delivery. *Int. J. Pharm. 335*, 180–192.

(13) Asayama, S., Sekine, T., Kawakami, H., and Nagaoka, S. (2007) Design of aminated poly(1-vinylimidazole) for a new pH-sensitive polycation to enhance cell-specific gene delivery. *Bioconjugate Chem. 18*, 1662–1667.

(14) Asayama, S., Sekine, T., Kawakami, H., and Nagaoka, S. (2006) pH-Dependent dissociation of carbohydrate ligand polycations from DNA ternary complexes. *Chem. Lett. 35*, 100–101.

(15) Unsworth, J. M., Rose, F. R. A. J., Wright, E., Scotchford, C. A., and Shakesheff, K. M. (2003) Seeding cells into needled felt scaffolds for tissue engineering applications. *J. Biomed. Mater. Res. 53*, 617–620.

(16) Henrichs, P. M., Whitlock, L. R., Sochor, A. R., and Tan, J. S. (1980) Conformational behavior of poly(*N*-vinylimidazole). Potentiometric titration, viscosity, and proton nuclear magnetic resonance studies. *Macromolecules 13*, 1375–1381.

(17) Shuai, X., Merdan, T., Unger, F., and Kissel, T. (2005) Supramolecular gene delivery vectors showing enhanced transgene expression and good biocompatibility. *Bioconjugate Chem. 16*, 322–329.

(18) Pouton, C. W., Lucas, P., Thomas, B. J., Uduehi, A. N., Milroy, D. A., and Moss, S. H. (1998) Polycation-DNA complexes for gene delivery: a comparison of the biopharmaceutical properties of cationic polypeptides and cationic lipids. *J. Controlled Release 53*, 289–299.

(19) Asayama, S., Akaike, T., and Maruyama, A. (2001) Bi-phasic polycation for the DNA carrier responding to endosomal pH. *Colloids Surf., B 22*, 183–191.

(20) Kalyanasundaram, K., and Thomas, J. K. (1977) Environmental effects on vibronic band intensities in pyrene monomer fluorescence and their application in studies of micellar systems. *J. Am. Chem. Soc. 99*, 2039–2044.

(21) Schild, H. G., and Tirrell, D. A. (1991) Microheterogeneous solutions of amphiphilic copolymers of N-isopropylacrylamide. An imvestigation via fluorescence methods. *Langmuir 7*, 1319–1324.

(22) Tamano, K., Imae, T., Yusa, S., and Shimada, Y. (2005) Structure-selective dye uptake into an aggregate of a copolymer with linear polyelectrolyte block and hydrophobic block carrying pendant dendritic moiety in water. *J. Phys. Chem. B 109*, 1226–1230.

(23) Sakaguchi, N., Kojima, C., Harada, A., and Kono, K. (2008) Preparation of pH-sensitive poly(glycidol) derivatives with varying hydrophobicities: Their ability to sensitize stable liposomes to pH. *Bioconjugate Chem. 19*, 1040–1048.

(24) Chittimalla, C., Zammut-Italiano, L., Zuber, G., and Behr, J. P. (2005) Monomolecular DNA nanoparticles for intravenous delivery of genes. *J. Am. Chem. Soc. 127*, 11436–11441.

(25) Wang, S., Cheng, L., Yu, F., Pan, W., and Zhang, J. (2006) Delivery of different length poly(L-lysine)-conjugated ODN to HepG2 cells using N-stearyllactobionamide-modified liposomes

and their enhanced cellular biological effects. *Int. J. Pharm. 311*, 82–88.
(26) Higashi, N., Uchino, A., Mizuguchi, Y., and Niwa, M. (2006) Chain length effects of oligo(L-lysine)-shelled dendrimers on interaction with DNA. *Int. J. Biol. Macromol. 38*, 120–125.
(27) Srinivasachari, S., Liu, Y., Prevette, L. E., and Reineke, T. M. (2007) Effects of trehalose click polymer length on pDNA complex stability and delivery efficacy. *Biomaterials 28*, 2885–2898.
(28) Tian, H., Xiong, W., Wei, J., Wang, Y., Chen, X., Jing, X., and Zhu, Q. (2007) Gene transfection of hyperbranched PEI grafted by hydrophobic amino acid segment PBLG. *Biomaterials 28*, 2899–2907.
(29) Ahn, C. H., Chae, S. Y., Bae, Y. H., and Kim, S. W. (2004) Synthesis of biodegradable multi-block copolymers of poly(L-lysine) and poly(ethylene glycol) as a non-viral gene carrier. *J. Controlled Release 97*, 567–574.
(30) Solodin, I., Brown, C. S., Bruno, M. S., Chow, C. Y., Jang, E. H., Debs, R. J., and Heath, T. D. (1995) A novel series of amphiphilic imidazolinium compounds for in vitro and in vivo gene delivery. *Biochemistry 34*, 13537–13544.

BC900411M

Synthesis of Pyridyl Disulfide-Functionalized Nanoparticles for Conjugating Thiol-Containing Small Molecules, Peptides, and Proteins

André J. van der Vlies,[†] Conlin P. O'Neil,[†] Urara Hasegawa,[†] Nathan Hammond,[†] and Jeffrey A. Hubbell*[,†,‡]

Institute of Bioengineering (IBI) and Institute of Chemical Sciences and Engineering (ISIC), Ecole Polytechnique Fédérale de Lausanne (EPFL), Lausanne CH-1015, Switzerland. Received October 10, 2009; Revised Manuscript Received March 25, 2010

Previously we reported emulsion polymerization of propylene sulfide with Pluronic F127 as an emulsifier, yielding nanoparticles (NPs) in the 25 nm size range. Immunologically functional NPs were prepared by adding an antigen−Pluronic conjugate to the polymerization mixture (Reddy, S. T., et al. (2007) *Nat. Biotechnol. 25*, 1159). We sought a more flexible scheme for conjugation of antigens and other biomolecules to the NP surfaces that would allow for milder reaction conditions than achievable during the polymerization step. Here, we present the synthesis of such functionalizable NPs in the form of NPs that carry thiol-reactive groups, to which thiol-containing antigens (peptide or protein) or other biomolecules can be conjugated under mild conditions to yield immunofunctional NPs. The Pluronic-stabilized poly(propylene sulfide) (PPS) NPs with thiol-reactive pyridyl disulfide groups are prepared in two steps by (1) emulsion polymerization of propylene sulfide in the presence of a carboxylate-Pluronic and (2) reaction of the carboxylic acid groups on the NP surface with cysteamine pyridyl disulfide and a water-soluble carbodiimide reagent. We choose pyridyl disulfide groups to have a reduction-sensitive disulfide bond linking the antigen to the NP surface, allowing efficient release of antigen inside the cell in response to the reductive conditions within the endosome. The functionalizable NPs are characterized by proton NMR, dynamic light scattering (DLS), UV/vis spectroscopy, and transmission electron microscopy (TEM). Conjugation of small molecules and protein to the NP surface is presented.

INTRODUCTION

In the field of immunotherapy, one aims to either elicit or repress an immune response by directly affecting the immune system. Antigen-presenting cells (APCs[§]) patrol the body for antigens, the most powerful APCs being dendritic cells (DCs) (*1, 2*). After taking up the antigen, the DCs move to the draining lymph node to present peptides processed from the antigen and stimulate naive CD4 and CD8 T cells for induction of humoral and cell-mediated immunity (*3*). In order to induce an adaptive immune response, the DC should mature before presenting antigen to T cells. Maturation of DCs is induced by the presence of a danger signal, also referred to as an adjuvant, often selected as a ligand of Toll-like receptors (*4*).

On the basis of the above-mentioned needs, there has been growing interest in the use of biomaterials in both antigen and adjuvant delivery (*5*). Immobilizing an antigen onto or encapsulating it within the polymeric vehicle can protect the antigen from enzymatic degradation, and the carrier itself can be delivered intracellularly, enabling antigen processing and presentation to take place. Most work has focused on targeting peripheral immature DCs using polymeric poly(lactide-*co*-glycolide) (PLGA) microparticles (*6*−*12*) and polyelectrolyte microcapsules (*13*). However, these cells must travel to the draining lymph nodes to present the antigen to T cells. We previously showed that immature DCs in the lymph node can be targeted efficiently using ultrasmall nanoparticles (NPs) of about 25 nm in diameter exploiting the interstitial flow from the blood capillaries to the lymphatic capillaries and then draining lymph nodes (*14*). In this way the most potent APCs in the lymph node are targeted directly and very efficiently.

Poly(propylene sulfide) (PPS) NPs are synthesized by emulsion polymerization of propylene sulfide using Pluronic F127 an emulsifier surfactant (*15, 16*). The NPs consist of a hydrophobic rubbery cross-linked PPS core with a Pluronic-coated surface. The hydrophobic PPS core allows for encapsulation of hydrophobic drugs, should it be desired, and is stimulus-responsive toward oxidation (*16, 17*). We showed that exposure to hydrogen peroxide as a model intracellular oxidant leads to oxidation of the thioether groups leading to sulfoxide and sulfone structures, making the initial hydrophobic PPS core hydrophilic and thus soluble (*16*). This allows the incorporated drug to be released and offers a mechanism for particle clearance from the body (*17*). To show that these NPs are not only taken up by lymph-node-resident DCs but also induce adaptive immunity, we used ovalbumin (OVA) as a model antigen. OVA-NPs, prepared by incorporating an OVA−Pluronic conjugate into the NP polymerization mixture, induced both a humoral and cell-mediated immune response when injected into mice (*18*), the terminal Pluronic hydroxyl groups on the surface of the NPs activating complement to serve as an adjuvant (*18*).

* To whom correspondence should be addressed. Address: Laboratory for Regenerative Medicine and Pharmacobiology, Institute of Bioengineering, Station 15, Ecole Polytechnique Fédérale de Lausanne (EPFL), Lausanne, CH-1015, Switzerland. E-mail: jeffrey.hubbell@epfl.ch. Phone: +41 21 693 9681. Fax: +41 21 693 9665.

[†] Institute of Bioengineering (IBI).

[‡] Institute of Chemical Sciences and Engineering (ISIC).

[§]Abbreviations: APC, antigen presenting cell; DBU, 1,8-diazabicyclo-[5.4.0]undec-7-ene; DC, dendritic cell; DLS, dynamic light scattering; DMF, dimethylformamide; DMSO, dimethyl sulfoxide; DTT, dithiothreitol; EDC, *N*-(3-dimethylaminopropyl)-*N*′-ethylcarbodiimide; HEPES, hydroxyethylpiperazineethanesulfonic acid; HPLC, high performance liquid chromatography; HRMS, high resolution mass spectra; NMR, nuclear magnetic resonance; MeOH, methanol; MES, morpholineethanesulfonic acid; MWCO, molecular weight cut-off; NHS, *N*-hydroxysuccinimide; NP, nanoparticle; OVA, ovalbumin; PLGA, poly(lactide-*co*-glycolide); PO, propylene oxide; PPO, polypropylene oxide; PPS, polypropylene sulfide; sulfo-NHS, *N*-hydroxysulfosuccinimide sodium salt; TCEP·HCl, tris(2-carboxyethyl)phosphine hydrochloride; TEM, transmission electron microscopy; TFA, trifluoroacetic acid; TIS, triisopropylsilane.

10.1021/bc9004443 © 2010 American Chemical Society
Published on Web 04/06/2010

A limitation of the scheme described above is the need for synthesizing a Pluronic−antigen conjugate for each antigen to be bound to the NP surface. Furthermore, the antigen is linked to the NP with a bond that is not cleavable under biological conditions, which could be problematic for antigen release, especially of peptides, within DCs. We therefore sought a scheme by which to provide NPs with a reactive group that would allow straightforward conjugation of antigens and further allow release upon endocytosis by DCs. We choose thiol-reactive pyridyl disulfide groups at the surface of the NP, as antigens such as peptides and proteins can be easily engineered to contain free cysteine groups. The formed disulfide bond between the antigen and NP would allow efficient release of antigen within the cell in response to the reductive conditions within the endosome. This report describes the concept, synthesis, and characterization of thiol-reactive, reductively sensitive NPs and the conjugation with low molecular weight compounds and proteins.

EXPERIMENTAL PROCEDURES

Materials and Methods. Pluronic F127, hydroxyethylpiperazineethanesulfonic acid (HEPES) (Sigma), streptavidin-Alexa488 (Invitrogen), (+)-D-biotin (Applichem), aldrithiol, fluorescamine, trifluoracetic acid (TFA), triisopropylsilane (TIS), phenol, 0.5 M $NaOCH_3$ in methanol, propylene sulfide, 1,8-diazabicyclo[5.4.0]undec-7-ene (DBU), *N*-hydroxysuccinimide (NHS), Tris(2-carboxyethyl)phosphine hydrochloride (TCEP·HCl), iodoacetamide, potassium hydroxide, CaH_2 (Aldrich), dithiothreitol (DTT) (Biorad), Sephadex G50, Sepharose 6B, Sepharose CL-6B (Sigma), Ellman reagent (Pierce), cysteamine hydrochloride, potassium carbonate, mercaptopropionic acid methyl ester, triphenylphosphine, acetic acid, methanesulfonyl chloride, sodium hydroxide, *N*-(3-dimethylaminopropyl)-*N*′-ethylcarbodiimide (EDC), *N*-hydroxysulfosuccinimide sodium salt (sulfo-NHS), triphenylmethanol, $BF_3 \cdot Et_2O$ (Fluka), and morpholineethanesulfonic acid (MES) (Calbiochem) were used as received. All chemicals relating to peptide synthesis were from Novabiochem. Molecular sieves (3 Å, Fluka) were heated at 180 °C under reduced pressure for at least 16 h. Diethyl ether, methanol, and toluene were used as received. Dimethylformamide (DMF) was distilled over CaH_2 under reduced pressure at 40 °C and kept over molecular sieves. Dichloromethane was dried over molecular sieves. Water was distilled twice or freed from salt using the Milli-Q water system. All reactions were done under argon (Messer) atmosphere.

^1H NMR. Spectra were measured on a Bruker 400 Ultrashield spectrometer. NMR was performed in deuterated chloroform ($CDCl_3$), deuterated methanol (CD_3OD), or deuterated dimethyl sulfoxide (DMSO-d_6). Peaks are referenced against residual solvent at 7.26 ppm ($CDCl_3$), 3.35 ppm (CH_3OD), or 2.50 ppm (DMSO-d_6). For each sample 32 scans were collected and the D1 was set at 10 s.

UV/Visible Spectroscopy. Spectra were obtained on a Shimadzu UV mini 1240 UV/visible spectrophotometer using 1.0 cm quartz cuvettes or a Tecan Safire^2 well plate reader using polystyrene well plates.

Dynamic Light Scattering. Data were obtained on a Malvern Nanoseries Zetasizer instrument with 632 nm laser using PMMA cuvettes by diluting NP solutions with PBS (10 mM, pH 7.4) to a final NP concentration of 2 mg/mL. Sizes are given in nm and are obtained as the *Z*-average by fitting the correlation function using the cumulant method.

High Resolution Mass Spectrometry. Spectra were collected by the Institute of Chemical Sciences and Engineering (ISIC) at the Ecole Polytechnique Fédérale de Lausanne (EPFL), Switzerland. ESI-TOF-MS data were acquired on a Q-Tof Ultima mass spectrometer (Waters) fitted with a LockSpray dual electrospay ion source and operating in the positive ionization mode. The samples were diluted in methanol acidified with 0.1% HCOOH and introduced into the mass spectrometer by infusion at a flow rate of 20 mL/min. External calibration was carried out with a solution of phosphoric acid at 0.01%. Data were processed using the MassLynx 4.1 software.

Transmission Electron Microscopy. Carbon coated 400 mesh copper grids (Agar Scientific, Stansted, U.K.) were prepared under glow discharge, and 5 μL of NP solution was placed onto the grid. After 60 s, the grid was washed with H_2O and then dried by blotting the side of the grid with filter paper. To stain, 5 μL of 2% uranyl acetate solution was added to the grid. After 30 s, the stain was blotted off the same as above and was allowed to dry for 5 min at room temperature before analysis. Microscope images were acquired on a Philips CM-12 TEM (Koninklijke Philips Electronics, Eindhoven, The Netherlands). Images were captured using a Gatan MSC CCD camera (Gatan Inc., Grandchamp, France) and processed using Adobe Photoshop software (Adobe Systems, San Jose, CA). TEM images were analyzed with Scion image analysis software, and size results are given as the mean diameter ± SD and number of particles measured in parentheses.

Preparative HPLC. Purification by HPLC was done by reverse phase HPLC chromatography using a C18 column. Separation and collection were performed by UV and mass directed software (Waters, Baden-Daettwil, Switzerland).

SDS−PAGE. The 10% gels were run at 300 V for 2 h. Protein bands were visualized by UV.

Ellman Assay (19). Ellman solution was prepared by dissolving 4.0 mg of Ellman reagent in 1.0 mL of Ellman buffer (1 mM EDTA, 100 mM phosphate, pH 8.0). Thiol concentrations were measured by reacting 20 μL of Ellman solution with 20 μL of sample. After 15 min the mixture was diluted by the addition of 960 μL of Ellman buffer and the absorbance at 412 nm read. Thiol concentrations were calculated from a standard curve using thiomaleic acid. In the range 1−4 mM measurements were done in a well plate using 200 μL of sample. For thiol concentrations in the range 50−1000 μM, measurements were done using a quartz cuvette.

Fluorescamine Assay (20). Fractions from the Sepharose 6B and Sepharose CL-6B column (50 μL) were mixed with 100 μL of 100 mM HEPES, pH 8, and 20 μL of a solution of fluorescamine (5 mg/mL) in acetone. The sample was reacted at room temperature for 15 min and the fluorescence (λ_{ex} = 390 nm, λ_{em} = 475 nm) read using black polystyrene Nunc plates.

Pyridyl Disulfide Loading NPs. Pyridyl-NP solutions were mixed 1:1 by volume with a 5 mM TCEP·HCl solution in 100 mM HEPES, pH 8, and reacted for 15 min. The absorbance at 340 nm was read, and after correction for the absorbance of pyridyl-NP and TCEP·HCl the concentration of pyridyl disulfide calculated from a standard curve of pyridine thione (**8**) in HEPES, pH 8. If the concentration was too high, NP solutions were diluted with H_2O.

Compound Synthesis. *Pluronic Bromide (1).* **1** was prepared as reported before (*21*).

Pluronic Mesylate (2). An amount of 23.6 g (1.86 mmol) of Pluronic F127 was dissolved in 500 mL of toluene, and 100 mL of toluene was removed by azeotropic distillation using a Dean−Stark trap. The solution was cooled to room temperature, and 2.6 mL (18.6 mmol, 10 equiv) of triethylamine and 1.4 mL (18.6 mmol) of methanesulfonyl chloride was added. After 18 h the yellow suspension was filtered and the clear yellow filtrate concentrated under reduced pressure. The residue was dissolved in 100 mL of CH_2Cl_2, filtered over a SiO_2 bed (1.0 cm (diameter) × 5.0 cm (height)), and the SiO_2 was washed with CH_2Cl_2 (3 × 50 mL). The filtrate was concentrated to a

volume of about 50 mL and precipitated in 1000 mL of Et_2O. The white precipitate was filtered off, washed with 100 mL of Et_2O, and dried under reduced pressure to yield 21.0 g (89%) of white powder. The degree of functionalization was 100% according to ^{1}H NMR. ^{1}H NMR ($CDCl_3$): $\delta = 4.35-4.38$ (m, CH_2-O-SO_2-), 3.60−3.67 (m, CH_2, PEG), 3.47−3.58 (m, CH_2, PPO), 3.34−3.42 (m, CH, PPO), 3.07 (*s*, -SO_2-C$\underline{H}_3$), 1.11−1.15 (CH_3, PPO).

*Pluronic Thioether Propionic Acid Methyl Ester (**3**).* An amount of 21.0 g (**2**) was dissolved in 100 mL of DMF, and to the clear solution was added 2.29 g (16.5 mmol) of potassium carbonate followed by 2 mL (16.5 mmol) of mercaptopropionic acid methyl ester. The mixture was stirred for 20 h and concentrated under reduced pressure. The residue was dissolved in 100 mL of CH_2Cl_2 and mixed with 11 g of activated carbon. The mixture was filtered over a filter cell and the residue washed with CH_2Cl_2 (3 × 100 mL). The clear colorless filtrate was reduced to about 50 mL by evaporation and precipitated in 1000 mL of Et_2O. The white solid was filtered, washed with 100 mL of Et_2O, and dried under reduced pressure to yield 18.2 g (87%). The degree of functionalization was 92% according to ^{1}H NMR. ^{1}H NMR ($CDCl_3$): $\delta = 3.70$ (s, OCH_3), 3.59−3.63 (m, CH_2, PEG), 3.46−3.58 (m, CH_2, PPO), 3.36−3.44 (m, CH, PPO), 2.83 (*t*, $J = 7.6$ Hz, -O-CH_2-C$\underline{H}_2$-S-), 2.73 (*t*, $J = 7.2$ Hz, −S-C$\underline{H}_2$-CH_2-CO-), 2.63 (t, $J = 7.2$ Hz, -CH_2-CO-), 1.12−1.16 (CH_3, PPO).

*Pluronic Thioether Propionic Acid Sodium Salt (**4**).* An amount of 18.0 g (**3**) (2.83 mmol) was dissolved in 200 mL of Milli-Q water, and to the clear solution added a solution of 0.57 g (14.1 mmol) of sodium hydroxide in 5 mL of Milli-Q water. After 21 h the solution was transferred into a regenerated cellulose dialysis tube, molecular weight cut-off (MWCO) of 3.5 kDa, and dialyzed against 5 L of Milli-Q for 29 h with replacement of the water three times. The solution was lyophilized to yield 12.2 g (68%) of white solid. The degree of functionalization according to ^{1}H NMR was 95%. NMR ($CDCl_3$): $\delta = 3.59-3.63$ (m, CH_2, PEG), 3.46−3.58 (m, CH_2, PPO), 3.35−3.44 (m, CH, PPO), 2.83 (t, $J = 6.4$ Hz, -O-CH_2-C$\underline{H}_2$-S-), 2.73 (t, $J = 6.8$ Hz, -S-C$\underline{H}_2$-CH_2-CO-), 2.50, (t, $J = 6.8$ Hz, -CH_2-CO-), 1.13−1.16 (CH_3, PPO).

*Pyridyl Disulfide Cysteamine HCl Salt (**5**).* An amount of 0.57 g (0.5 mmol) of cysteamine·HCl was added to a solution of 3.3 g (15.0 mmol) of aldrithiol in 10 mL of methanol. The yellow solution was stirred overnight and the product obtained by precipitation in 500 mL of Et_2O. After filtration, the residue was dissolved in 15 mL of MeOH and again precipitated in 500 mL of Et_2O. The white solid was dried under reduced pressure to yield 0.94 g (84%). ^{1}H NMR (DMSO-d_6): $\delta = 8.51-8.50$ (m, 1H), 8.30 (bs, 3H), 7.86−7.82 (m, 1H), 7.75 (d, 1H), 7.31−7.28 (m, 1H), 3.13−3.05 (m, 4H). HRMS $[M + H]^+$ calculated for $C_7H_{10}N_2S_2$ 187.0364, found 187.0358.

*Pluronic Pyridyl Disulfide (**6**).* Amounts of 0.25 g (0.02 mmol) of **4** and 22.8 mg (0.2 mmol) of NHS were dissolved in 5 mL of CH_2Cl_2. To the clear solution were added 38 mg (0.2 mmol) of EDC, 44 mg (0.2 mmol) of **5**, and 38 μL (0.2 mmol) of triethylamine, and the turbid mixture was stirred for 18 h at room temperature. The yellow solution was concentrated in a flow of N_2 and the residue dissolved in 5 mL of H_2O. The milky solution was transferred to a dialysis bag (MWCO = 3.5 kDa) and dialyzed against 2 L of H_2O for 1 day. The polymer was recovered by lyophilization to yield 0.19 g (76%). The degree of functionalization according to ^{1}H NMR was 95%. ^{1}H NMR ($CDCl_3$): $\delta = 8.51$ (m, CH_{aromat}), 7.64 (m, CH_{aromat}), 7.55 (m, CH_{aromat}), 7.33 (bs, NH), 7.13 (m, CH_{aromat}), 3.69−3.59 (m, CH_2, PEG), 3.58−3.44 (m, CH_2, PPO), 3.42−3.33 (m, CH, PPO), 2.94 (t, CH_2, $J = 5.6$ and 6.0 Hz), 2.88 (t, CH_2, $J = 7.2$ Hz), 2.74 (t, CH_2, $J = 6.8$ and 6.4 Hz), 2.51 (t, CH_2, $J = 7.2$ and 7.6 Hz), 1.14 (m, CH_3, PPO).

Table 1. Dynamic Light Scattering Results for the Different NP Formulations[a]

	carboxylate-NP		pyridyl disulfide-NP	
wt % COOH	*Z*-avg[b] (SD)	PDI[c] (SD)	*Z*-Avg[b] (SD)	PDI[c] (SD)
0	31.8 (0.80)	0.260 (0.003)		
10	33.0 (0.31)	0.142 (0.006)	35.7 (0.13)	0.207 (0.005)
25	31.0 (0.24)	0.168 (0.013)	33.7 (0.71)	0.175 (0.003)
50	32.6 (0.08)	0.147 (0.004)	42.5 (0.30)	0.225 (0.009)
75	32.9 (0.18)	0.145 (0.006)	42.0 (0.15)	0.219 (0.002)
100	31.3 (0.22)	0.113 (0.001)	42.4 (0.17)	0.209 (0.004)

[a] Values are the average of three measurements of the same sample. [b] Size in nm as measured by the *Z*-average obtained by fitting the correlation function using the cumulant method. [c] Polydispersity index (PDI) calculated from fitting the correlation function using the cumulant method.

*Thioacetic Acid S-[3-[3-(3-Acetylsulfanylpropoxy)-2,2-bis-(3-acetylsulfanylpropoxymethyl)propoxy]propyl] Ester (**7**).* The four-arm initiator was synthesized as reported (*16*).

NP Synthesis. This was adapted from that reported (*16*). An amount of 10 mL of Milli-Q H_2O was freed from oxygen by three evacuation/purge (Ar) cycles, and under Ar flow the hydroxyl- and carboxylate Pluronic (500 mg total) were added. After all the Pluronic was dissolved the resulting solution was again evacuated and purged with Ar three times, and under Ar flow 400 μL (5.0 mmol) of propylene sulfide was added. The emulsion was stirred for 30 min after which 24.3 mg (0.04 mmol) of the four-arm initiator **7**, previously reacted for 15 min with 322 μL of 0.5 M $NaOCH_3$ (0.16 mmol) solution in MeOH, was added under Ar. The mixture was stirred for another 15 min, and then an amount of 60 μL of DBU (0.4 mmol) was added. The mixture was stirred for 24 h and exposed to air for 2 h to cross-link, and the remaining thiolates were quenched by the addition of 47.5 mg (0.26 mmol) of iodoacetamide and stirred for 2 h. Ellman assay of the NP solution confirmed the absence of thiolate anions, and the mixture was dialyzed (MWCO = 100 kDa) against 5 L of Milli-Q water for at least 2 days with regular replacement of the water. After filtration (0.22 μm filter) the size of the NPs was measured by dynamic light scattering and a small volume was lyophilized to obtain the NP concentration in mg/mL. NMR of the solid was used to calculate the weight % of Pluronic in the NPs.

*Pyridinethione (**8**).* The ether fractions of **5** were combined and concentrated under reduced pressure, and the residue was dissolved in 10 mL of MeOH and reacted with 1.74 g (15.0 mmol) of cysteamine·HCl overnight. The turbid mixture was diluted with 100 mL of EtOAc and washed with 100 mL of H_2O. After the organic phase was dried over Na_2SO_4 the mixture was filtered and the clear solution concentrated under reduced pressure. The residue was purified by SiO_2 column chromatography, $R_f = 0.46$ (EtOAc). ^{1}H NMR ($CDCl_3$): $\delta = 7.61-7.56$ (m, 1H), 7.43−7.39 (m, 1H), 6.81−6.78 (m, 1H), 1.79 (bs, 1H). HRMS $[M + H]^+$ calculated for C_5H_5NS 112.0221, found 112.0297.

Synthesis of Pyridyl Disulfide-NPs, General Procedure. To the carboxylate-NP solution is added solid MES to a final concentration of 100 mM and the pH adjusted to 4.0−4.5 with a pH meter. To the clear solution are added pyridyl disulfide cysteamine·HCl, sulfo-NHS, and EDC all at an excess of 20 equiv relative to the amount of Pluronic as calculated from NMR. After reaction for 2−24 h the solution is dialyzed for at least 2 days to remove unreacted reagents using MWCO = 3.5−10 kDa. The pyridyl disulfide-NPs in Table 1 and Figures 2−4 were made by reacting for 24 h and then purified using MWCO = 3.5 kDa dialysis tubing. Below follows the detailed reaction for functionalization of 100 wt % carboxylate-NPs. To

3.0 mL of 100 wt % carboxylate-NP solution (50.4 mg/mL), corresponding to 28.7 mg/mL of Pluronic according to NMR, was added 60 mg of MES (final concentration 102 mM), and the pH was adjusted to 4.4. To the NP solution containing 86.1 mg of carboxylate-Pluronic (0.014 mmol of carboxylate groups) were added 30.1 mg (0.14 mmol, 10 equiv) pyridyl disulfide cysteamine·HCl salt, 30.1 mg of sulfo-NHS (0.14 mmol, 10 equiv), and 33.1 mg (0.17 mmol, 12 equiv) of EDC. After 22 h the NP solutions were dialyzed against 5 L of Milli-Q water (MWCO = 3.5 kDa) for 2 days. After filtration through 0.22 μm filter, the size was measured by dynamic light scattering. The concentration of the pyridyl disulfide groups was determined by measuring the absorbance at 340 nm after reducing the NPs with TCEP·HCl. Lyophilization of a small sample yields the concentration of the NP solution.

*Trityl Cysteamine (**9**).* An amount of 11.4 g (100 mmol) of cysteamine·HCl and 27.3 g (105 mmol) of triphenylmethanol was added to 100 mL of DMF, and the mixture was heated at 60 °C for 15 min to obtain a clear-yellow solution. The solution was cooled, 14 mL of BF_3·Et_2O (110 mmol) was added, and the mixture was heated at 80 °C. After 14 h the mixture was concentrated under reduced pressure and the oil was dissolved in 500 mL of EtOAc. Upon standing a white solid precipitated that was filtered off. The remaining clear EtOAc solution was washed with saturated NaCl (aq) solution, causing more solid to precipitate that was filtered off. Both solids were combined and dried under reduced pressure, yielding 33.1 g (93 mmol, 93%) of tritylcysteamine·HCl salt. The free base was prepared by treating 2.9 g (8.1 mmol) of the HCl salt with 150 mL of saturated KOH (aq) solution and 500 mL of Et_2O. The clear layers were separated, and the organic phase was dried over Na_2SO_4 and concentrated under reduced pressure. This yielded after drying under reduced pressure 2.0 g (8.3 mmol, 78%) of the free salt. NMR ($CDCl_3$): δ = 7.44 (m, 6H, CH_{aromat}), 7.27 (m, 9H, CH_{aromat}), 2.60 (t, 2H, CH_2−N, J = 6.4 and 6.6 Hz), 2.34 (t, 2H, CH_2-S, J = 6.4 and 6.6 Hz), 1.48 (br, 2H, NH_2). HRMS $[M + H]^+$ calculated for $C_{21}H_{21}NS$ 320.1473, found 320.1466.

*Biotin Cysteamine (**10**).* Amounts of 0.49 g (2.0 mmol) of D-(+)-biotin, 0.47 g (2.0 mmol) of EDC, and 0.96 g (5.0 mmol) of *N*-hydroxysuccinimide were suspended in 10 mL of DMF. After the addition of 0.58 g (5.0 mmol) of **9** and 278 μL (2.0 mmol) of triethylamine the mixture was stirred for 2 days at room temperature. The mixture was concentrated under reduced pressure and taken up in 50 mL of EtOAc and washed with H_2O (3 × 50 mL). After drying over Na_2SO_4 and solvent removal the residue was dissolved in a mixture of 10 mL of CF_3COOH and 10 mL of CH_2Cl_2, and 431 μL (2.1 mmol) triisopropylsilane was added. After 4 h the volatiles were removed in a flow of N_2 and the residue was dissolved in 25 mL of EtOAc and extracted with H_2O (3 × 10 mL). The aqueous extracts were combined and lyophilized. The compound was purified by HPLC to yield 0.091 g of white solid (15% overall yield). ^{1}H NMR (CD_3OD): δ = 4.53 (m, 1H), 4.34 (m, 1H), 3.37 (t, 2H, J = 6.8 Hz), 3.25 (m, 1H), 2.97 (dd, 1H, J = 4.8 and 12.81 Hz), 2.74 (d, 1H, J = 12.8 Hz), 2.64 (t, 2H, J = 7.2 Hz), 2.25 (t, 2H, J = 7.2 Hz), 1.82−1.58 (m, 4H), 1.54−1.42 (m, 2H). HRMS $[M + H]^+$ calculated for $C_{12}H_{21}N_3O_2S_2$ 304.1154, found 304.1157.

Biotin-NPs. Pyridyl disulfide-NPs (500 μL, 35.2 mg/mL, 75% NP) with a pyridyl disulfide loading of 1.9 mM were diluted with 500 μL of HEPES solution (200 mM, pH 8.0) and added to 1.1 mg (3.6 μmol, 1.8 equiv) of biotin cysteamine. The reaction was followed by measuring the absorbance at 340 nm in a quartz cuvette. After 1 h the absorbance was stable and the NPs were purified by dialysis (MWCO = 10 kDa) against 5 L of H_2O for 24 h with regular replacement of water. The presence of biotin on the NPs was confirmed by the HABA/avidin displacement assay (*22*). The number of biotin molecules per NP was estimated to be approximately 800 (see Supporting Information).

*Ac-SDKDSLKCG-OH Peptide (**11**).* Fmoc-Gly (0.65 mmol, 194.0 mg, 3 equiv) was coupled to NovaPEG Wang resin (250 mg, loading 0.87 mmol/g) with 134.6 mg (0.65 mmol, 3 equiv) of DCC and 13.2 mg (0.11 mmol, 0.5 equiv) of DMAP in 10 mL of DMF. After the resin was washed with DMF (5 × 10 mL) the Fmoc group was removed with 20% piperidine in DMF (10 mL) and after washing with DMF (5 × 10 mL) used to couple the other amino acids using standard Fmoc-amino acid/HBTU/HOBt/DIPEA (0.5 M/0.5 M/0.5 M/1.0 M, 5 equiv solutions in DMF) double coupling Fmoc chemistry on a Chemspeed peptide synthesizer. After Fmoc removal of the last amino acid serine the N-terminus was acetylated by reaction with acetic acid/HBTU/HOBt/DIPEA. The peptide was cleaved from the resin using 4 mL of TFA/TIS/phenol/H_2O, 35:2:2:1, for 4 h and precipitated in diethyl ether to yield the crude peptide that was purified by reverse phase HPLC to yield 71 mg (0.064 mmol, 29%) of white solid. HRMS $[M + H]^+$ calculated for $C_{43}H_{12}N_2O_{20}S$ 1109.4785, found 1109.4803.

Peptide-NPs. A solution of the peptide was prepared at a thiol concentration of 2.1 mM, and 100 μL of this solution was diluted with 100 μL of 100 mM acetate buffer, pH 4, and added to 200 μL of pyridyl-NP solution (58.8 mg/mL, 25% NP) with a pyridyl disulfide loading of 0.93 mM. The excess of thiol to pyridyl disulfide was 10%. The reaction was followed by measuring the absorbance at 340 nm in a well plate reader. After 2 h the absorbance was stable and the peptide-NPs were purified by gel filtration over Sepharose 6B beads eluting in water (200 μL sample and 10 mL bed volume). Presence of the peptide on the NPs was measured with fluorescamine. The number of Ac-SDKDSLKCG-OH peptide molecules per NP was estimated to be approximately 160 (see Supporting Information).

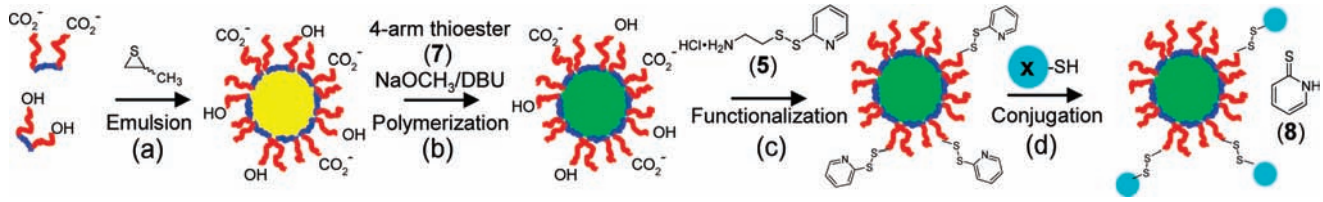
Reduction of Peptide-NPs. An amount of 200 μL of purified peptide-NPs was mixed with 10 μL of a solution of 57.2 mg/mL TCEP·HCl, resulting in a final concentration of 9.5 mM reducing agent. The mixture was incubated for 2 h, and the NPs were purified by gel filtration over Sepharose 6B beads eluting in water (200 μL sample and 10 mL bed volume). As a control, 200 μL of purified peptide-NPs mixed with 10 μL of H_2O was purified as well.

OVA-Functionalized NPs. OVA (12.5 mg/mL) in 10 mM PBS was reduced with DTT at a final concentration of 32 mM for 4 h. Excess reducing agent was removed by gel filtration over Sephadex G50 eluting with H_2O. The fractions were analyzed by Ellman assay prior to lyophilization to quantify the amount of OVA; it was assumed that all cysteines were present in the thiol form. Pyridyl disulfide-NPs with a pyridyl disulfide loading of 547 μM (41 mg/mL, 25% NP) were added to 750 μL of lyophilized 100 mM HEPES, pH 8.0, solution, and the clear solution was added to 7.85 mg of lyophilized OVA resulting in a final OVA concentration of 10.4 mg/mL (236 μM). The reaction mixture was incubated overnight at 4 °C and purified by gel filtration over Sepharose CL-6B beads eluting in water (180 μL sample and 12 mL bed volume). As a control, nonreduced OVA was reacted in the same way. Presence of the OVA protein was measured with fluorescamine. The number of OVA protein molecules per NP was estimated to be approximately 75 (see Supporting Information).

RESULTS

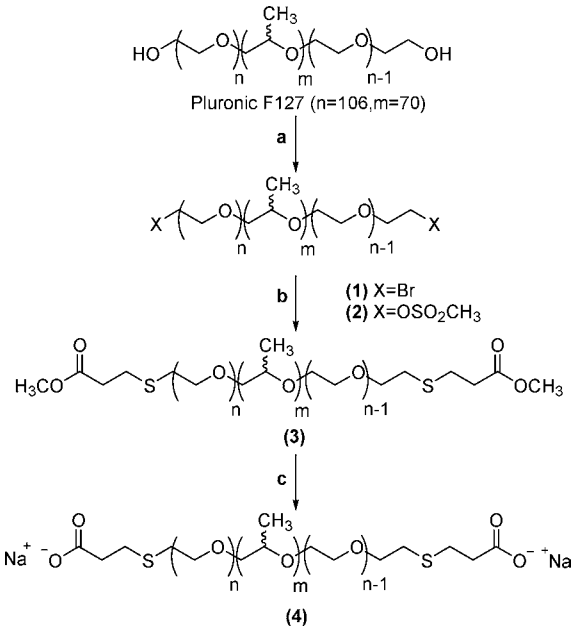
In Scheme 1, the design concept of the functionalizable NPs is shown. When a carboxylate-Pluronic is mixed with the hydroxyl-Pluronic into the propylene sulfide emulsion, NPs can be prepared with surface carboxylate groups. These carboxylate

Scheme 1. Synthesis of Funtionalizable Nanoparticles[a]



[a] (a) Hydroxyl-Pluronic and carboxylate-Pluronic are used to make an emulsion with propylene sulfide. (b) To the emulsion is added four-arm thiol initiator, and polymerization is started by addition of base. After polymerization, particles are exposed to air to cross-link, and the remaining thiolates are end-capped with iodoacetamide. (c) The carboxylate-nanoparticles are reacted with pyridyl disulfide cysteamine (**5**) to yield thiol-reactive functionalizable nanoparticles. (d) Conjugation of thiol-containing biotin (**10**), AcSDKDSLKCGOH peptide (**11**), and OVA protein gives biological-functional nanoparticles.

Scheme 2. Synthesis of Carboxyl-Functionalized Pluronic[a]



[a] (a) $SOBr_2$, toluene, reflux 4 h (**1**) or CH_3SO_2Cl, Et_3N, toluene, overnight (**2**); (b) thiopropionic acid methyl ester, K_2CO_3, DMF, overnight; (c) NaOH (aq), overnight.

groups on the NP surface can then be converted into pyridyl disulfide groups. The thiol-reactive pyridyl disulfide group allows for conjugation with thiol-containing small molecules, peptides, and proteins. The first step is synthesis of carboxylate group-carrying NPs. To accomplish this, a Pluronic-carboxylate was synthesized as shown in Scheme 2.

As the first step of Pluronic carboxylation, both hydroxyl groups were converted into either the bromide by reaction with thionyl bromide or the mesylate with methanesulfonyl chloride in toluene. The degree of functionalization was 100% for both the bromide and mesylate according to NMR, as no OH groups were visible in deuterated DMSO. Harris et al. showed that the OH group of PEG occurs as a triplet at $\delta = 4.58$ ppm in this aprotic solvent and can be used to determine the degree of functionalization reliably (*23*). Nucleophilic substitution of the bromide or mesylate with mercaptomethyl propionate in the presence of potassium carbonate in DMF afforded the corresponding methyl ester in high yield. Hydrolysis of the ester in aqueous NaOH yielded the carboxylate-Pluronic, as was shown by the disappearance of the CH_3 group at 3.7 ppm. The presence of the carboxylate groups was furthermore confirmed by reaction with pyridyl disulfide cysteamine·HCl in the presence of EDC and NHS (Scheme 3) to yield the corresponding pyridyl disulfide-Pluronic. In addition, the degree of functionalization was calculated by reducing the pyridyl disulfide groups with TCEP·HCl in aqueous HEPES, pH 8, and reading the absorbance at 340 due to pyridinethione release. The degree of functionalization was 100% on a mass basis.

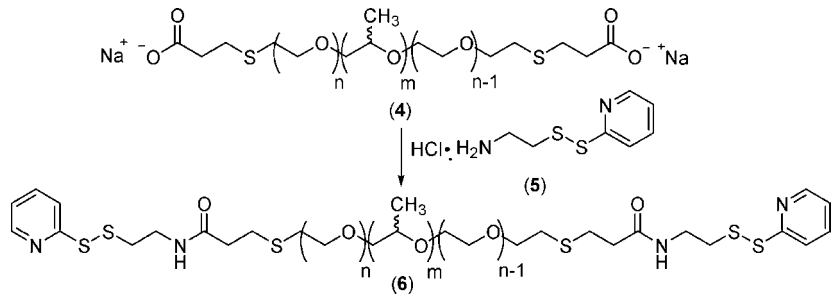
The synthesized carboxylate-Pluronic was used for NP synthesis. To gain information on how it would affect NP synthesis, the weight ratio of carboxylate-Pluronic to hydroxyl-Pluronic in the polymerization mixture was varied between 0% and 100%. (For some applications, retention of surface hydroxyl groups on the NPs is important (*18*).) DLS and TEM show that the addition of carboxylate-Pluronic does not significantly affect the size of NPs compared to the NPs with hydroxyl-Pluronic alone, as can be seen from Table 1 and Figure 1, panels A and B. However, the polydispersity index (PDI) was lower than for NPs with hydroxyl-Pluronic alone, which is reflected by the absence of the larger particles in 100% carboxylate-NPs (Figure 1B) and their presence in the hydroxyl-NPs (Figure 1A).

From NMR, the degree of polymerization of propylene sulfide can be calculated by comparing the integral ratio after normalizing of the propylene sulfide CH_3 group at 1.3 ppm and that of the four-arm initiator methylene group -CH_2- at 1.8 ppm. Figure 2 shows the degree of polymerization as a function of weight percentage carboxylate-Pluronic present in the polymerization mixture. The average degree of polymerization for the different carboxylate-NPs is 63 ± 3 propylene sulfide monomer units, which corresponds to 16 ± 1 units per initiator arm in average. These values are quite similar to those (58 and 14 units, respectively) calculated for hydroxyl-NPs. NMR also allows calculation of the weight contributions of Pluronic, PPS, and initiator to the total NP mass (see Supporting Information). From Figure 3 it can be seen that the different carboxylate-NPs all have a similar composition. The average values are $57 \pm 2.1\%$ for Pluronic, $39 \pm 2.0\%$ for PPS, and $3.6 \pm 0.2\%$ for the initiator. These values agree well with those found for hydroxyl-Pluronic alone NPs (55%, 41%, and 4.1%, respectively).

Having established that NPs can be made using the carboxylate-Pluronic, the next step was reacting them with pyridyl disulfide cysteamine·HCl, obtained in a single step from cysteamine·HCl and aldrithiol in methanol, using standard EDC/sulfo-NHS coupling chemistry at pH 4.0−4.5. The amount of Pluronic was calculated from NMR data of lyophilized carboxylate-NPs. Since it was not clear what the amount of carboxylate-Pluronic in the 10−75% carboxylate-NPs was, calculations of coupling reagents were based on the total amount Pluronic in the NP solutions (as measured by NMR), which was similar for all carboxylate-NPs solutions. The number of equivalents of EDC (24 equiv), sulfo-NHS (20 equiv), and pyridyl disulfide cysteamine·HCl (20 equiv) relative to Pluronic was fixed, and the reactions were carried out at the same time.

After functionalization, the NPs were dialyzed and characterized by DLS (Table 1) and TEM (Figure 1C). The PDI slightly increased, and TEM supports the DLS data, as larger particles are present as well. NMR of the different NPs revealed the presence of the pyridyl disulfide group by the four characteristic signals of the pyridyl disulfide group as observed for the pyridyl

Scheme 3. Synthesis of Pyridyl Disulfide-Functionalized Pluronic[a]



[a] EDC, NHS, CH_2Cl_2, overnight.

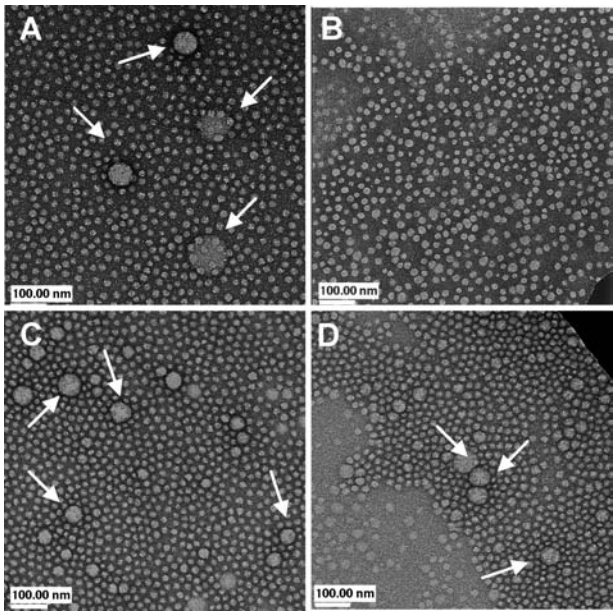


Figure 1. TEM images of aqueous nanoparticle (NP) suspensions. Size ± SD is given in nm, and number of particles measured is indicated in parentheses: (A) hydroxyl-NPs, 17.4 ± 4.5 (691); (B) 100% carboxylate-NPs, 16.0 ± 3.6 (570); (C) 50% pyridyl disulfide-NPs, 16.2 ± 4.5 (986); (D) 75% biotin-NPs, 16.7 ± 5.3 (849). Some larger particles as mentioned in the text are indicated by white arrows.

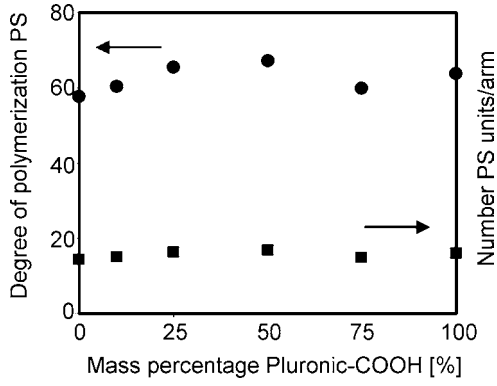


Figure 2. Degree of polymerization of propylene sulfide (circles) and number of propylene sulfide units per initiator arm (squares) as a function of weight percentage carboxylate-Pluronic in the polymerization mixture.

disulfide-Pluronic (**6**). More importantly, the presence of a broad signal at 7.3 ppm assigned to the NH of the amide bond, and also present in the above-mentioned pyridyl disulfide-Pluronic, confirmed successful conjugation (see Supporting Information). In Figure 4 the number of pyridyl disulfide groups relative to the number of propylene glycol repeating units on the Pluronic

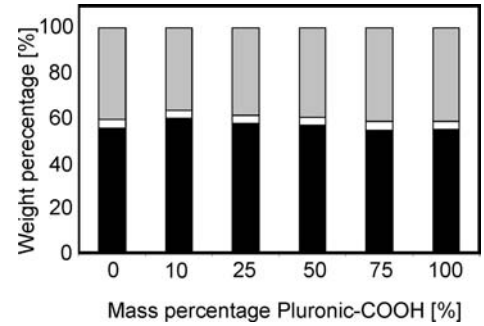


Figure 3. Mass percentage of Pluronic (black), poly(propylene sulfide) (gray), and initiator (white) of total NP weight as a function of weight percentage carboxylate-Pluronic in the polymerization mixture as calculated from NMR.

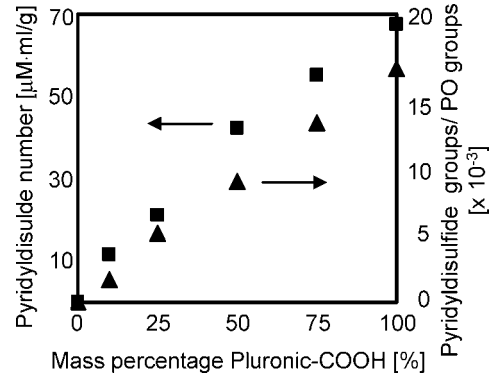
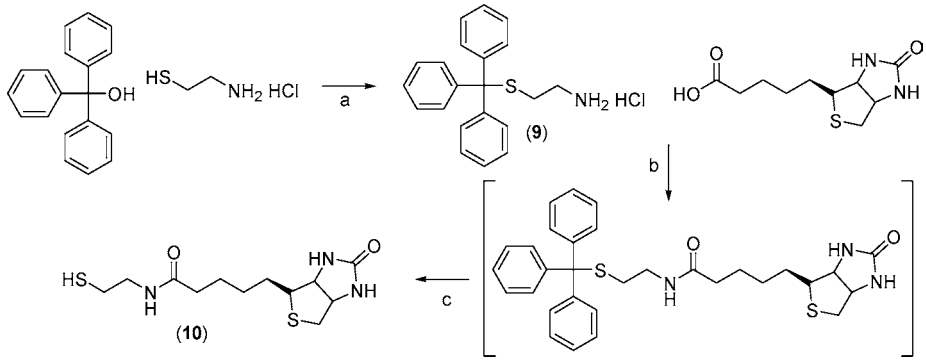


Figure 4. Number of pyridyl disulfide groups divided by the number of repeating propylene oxide (PO) units (triangles) as calculated from NMR from the ratio of pyridyl disulfide groups in μM (as measured by release of pyridine thione after reduction with TCEP·HCl) and NP concentration in mg/mL. The pyridyl disulfide number (squares) is a linear function of weight percentage carboxylate-Pluronic in the polymerization mixture.

as measured with NMR shows that there is a linear relationship between the feed ratio of carboxylate-Pluronic and the amount of pyridyl disulfide-Pluronic present on the NP. However, the reaction does not lead to full conversion of all carboxylate into pyridyl disulfide groups, as can be calculated from the carboxylate-Pluronic feed ratio at 100%. By comparison of the experimentally determined ratio of pyridyl disulfide groups to propylene glycol groups with that theoretically calculated, about 57% of carboxylate groups were determined to have reacted. A similar value of 61% is obtained by measuring the release of pyridine thione after reduction with TCEP·HCl and comparing this concentration with that calculated from the NP concentration and weight percentage of Pluronic in the NP solution. This low functionalization degree is not due to loss and/or modification of carboxylic acid groups during NP synthesis. Control experiments with the carboxylate-Pluronic under conditions used for

Scheme 4. Synthesis of Thiolated Biotin[a]



[a] (a) $BF_3 \cdot Et_2O$, DMF, 80°C, 16 h; (b) EDC, NHS, Et_3N, 2 days; (c) CF_3COOH/TIS, CH_2Cl_2, 4 h.

Table 2. Dynamic Light Scattering Results for the Different Conjugated NPs[a]

compd	*Z*-Avg[b] (SD)	PDI[c] (SD)
biotin	36.4 (0.26)	0.201 (0.003)
peptide	36.7 (0.21)	0.209 (0.003)
OVA	56.0 (0.32)	0.267 (0.006)

[a] Values are the average of three measurements of the same sample. [b] Size in nm as measured by the *Z*-average obtained by fitting the correlation function using the cumulant method. [c] Polydispersity index (PDI) calculated from fitting the correlation function using the cumulant method.

polymerization but without the addition of propylene sulfide did not lead to changes in the NMR spectrum (data not shown). The same linear trend is observed if the total pyridyl disulfide loading in μM is normalized by the NP concentration in mg/mL, the pyridyl disulfide number (Figure 4). Both DLS and TEM confirmed that the NPs kept their small size but that some aggregation occurred as shown by the increase in PDI (Table 1) and the presence of bigger particles in TEM (Figure 1C).

With the pyridyl disulfide-NPs at hand, we wanted to show that we could easily conjugate small molecules, peptides, and proteins. We first considered conjugation of a thiol-containing biotin to the NPs. In Scheme 4, the synthesis of this compound is outlined. After purification by HPLC, the biotin cysteamine was conjugated to pyridyl disulfide-NPs and purified by dialysis. DLS (Table 2) and TEM (Figure 1D) both show that the NPs kept their size. Successful conjugation was shown by adding the biotin-NPs to streptavidin Alexa488 and loading the NP solutions on a SDS−PAGE gel. From Figure 5 (lanes 4−6) it can be seen that above a certain biotin/streptavidin molar ratio, all streptavidin was bound to the NP surface and was no longer able to move into the gel. The reductive sensitivity of the biotin-NP disulfide linkage is clearly illustrated by running the gel (lanes 8−10) in the presence of mercaptoethanol, a reducing agent that leads to cleavage of the disulfide bond between biotin and the NP.

To see the effect of molecular size on conjugation, a model peptide was synthesized with a cysteine added at the C-terminus. Conjugation of the peptide was done at pH 4, and excess peptide was removed by gel filtration on Sepharose 6B beads. Figure 6A shows the elution profile for pyridyl disulfide-NP after reducing the fractions with TCEP·HCl and measuring the absorbance at 340 nm due to pyridinethione release. As can be seen from Figure 6A, the NPs elute as a sharp peak and DLS confirmed the presence of NPs in the fractions. Figure 6B shows the elution profile of peptide-NP after gel filtration as measured after reaction of the lysine residues on the peptide with fluorescamine and measuring the fluorescence intensity. As can be seen, the peptide is bound to the NPs, as the elution profile is practically the same as that measured for the pyridyl disulfide-

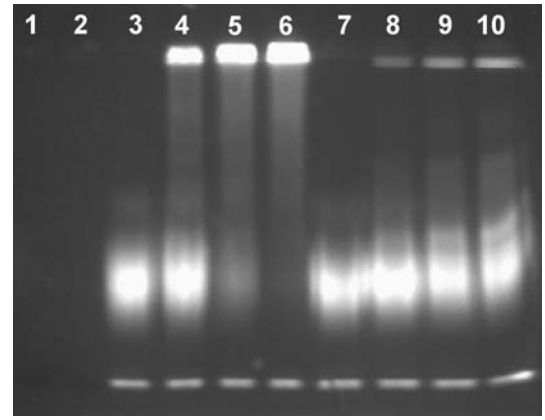


Figure 5. SDS−PAGE gel showing the interaction between biotin-NPs and streptavidin-Alexa488: (lane 1) ladder; (lane 2) biotin-NPs (15 μL); (lane 3) streptavidin-Alexa488 (10 μg); (lanes 4−6) streptavidin-Alexa488 (10 μg) with increasing volumes (5, 10, and 15 μL) of biotin-NPs; (lanes 7−10) same as for lanes 3−6 but in the presence of β-mercaptoethanol.

NP. DLS (Table 2) shows that the NPs still have similar size relative to the pyridyl disulfide-NP. To show that this peptide is linked by a disulfide bond, the peptide-NPs were reduced with TCEP·HCl prior to gel filtration. In Figure 6C it can be seen that the peak in Figure 5B is completely gone and that a new peak can be observed at higher elution volume, which is due to free peptide.

Having shown that a small molecule and a larger peptide can be conjugated to the pyridyl disulfide-NPs, we were also interested in conjugating proteins. We choose OVA, a 44 000 Da protein that after full reduction has six cysteine residues, and we conjugated it to the NPs. From the elution profile shown in Figure 7A, it can be seen that all OVA has been conjugated. Reduction of OVA is necessary, as shown for the elution profile of the reaction mixture of OVA that had not been reduced prior to conjugation (Figure 7B). Clearly OVA elutes much later than when bound to the NPs.

DISCUSSION

We previously reported the emulsion polymerization of propylene sulfide/Pluronic F127 by anionic ring-opening polymerization (*16*). The presence of the two hydroxyl groups of the Pluronic F127 on the surface of the cross-linked polypropylene sulfide core opens the possibility of introducing biological functionality onto the NPs by modifying the α,ω hydroxyl groups. However, this should be done prior to making the NPs, as commonly used hydroxyl activation chemistries are not compatible with the aqueous solution of the NPs. For this reason, Pluronic F127 has been modified with reactive groups and

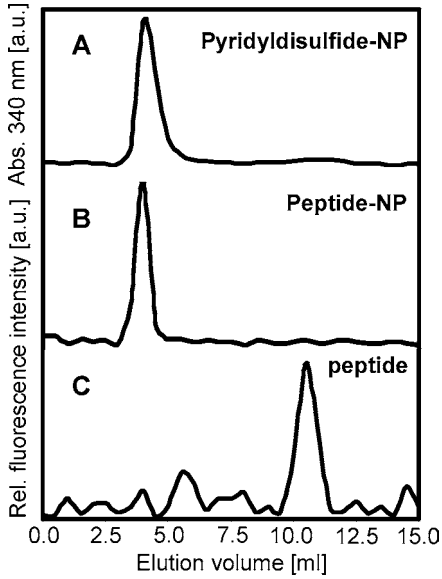


Figure 6. (A) Elution profile of pyridyl disulfide-NPs. Fractions were reduced with TCEP·HCl, and the absorbance at 340 nm due to pyridine thione was measured. (B) Elution profile of peptide-NPs after purification. (C) Elution profile peptide-NPs after reduction with TCEP·HCl. Fractions were reacted with fluorescamine, and the fluorescence intensity was measured.

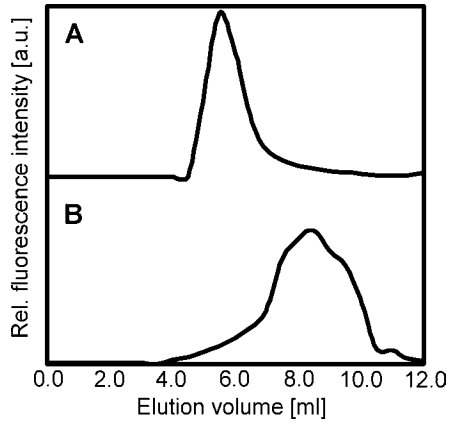


Figure 7. Elution profile after reacting pyridyl disulfide-NPs at pH 8 with (A) reduced and (B) nonreduced ovalbumin. Fractions were analyzed by addition of fluorescamine and measurement of the fluorescence intensity.

reacted with molecules prior to nanoparticle synthesis to obtain biologically functional nanoparticles. Previously we have modified Pluronic F127 with *p*-nitrophenol (*17*) and vinylsulfone (*18*) groups that allow conjugation of peptides (*24*) and proteins (*16, 18*) using amines and thiols.

Despite the successful applications described above, there remains a disadvantage in our previous scheme, in that for making biological-functional NPs each time the corresponding functionalized Pluronic has to be synthesized, which may limit the scope of use of the biological-functional NPs. Furthermore, the polymerization conditions during NP synthesis might be deleterious for the bioactivity of, for example, proteins for which the conservation of sensitive native three-dimensional structure is highly important. Indeed, in the case of the GOx-NPs, despite careful optimization of the synthesis, more than 30% loss of enzyme activity after NP synthesis was observed.

For these reasons, we sought to develop a more flexible system that would allow for mild reaction conditions and broad pH range to conjugate small molecules, peptides, and proteins to the NP surface. We reasoned that a thiol-reactive group on the surface of the NP for binding to the NPs might be most advantageous, as peptides and proteins can be easily engineered to have a free thiol group. In this way with only one NP batch, functionalizable NPs, one would have access to a number of biological-functional NPs.

Chart 1. Commonly Available Thiol-Reactive Groups (A) Vinylsulfone, (B) Acrylate, (C) Maleimide, (D) Alkyl Bromide or Iodide, (E) Pyridyl Disulfide

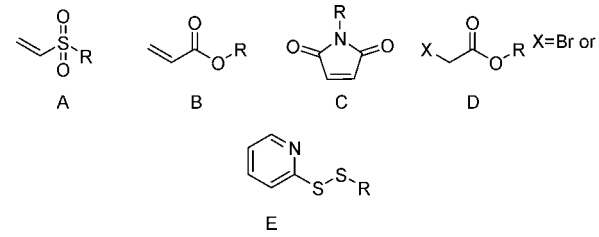


Chart 2. Reaction between Pyridyl Disulfide and a Thiol To Give a Mixed Disulfide with Release of Pyridine Thione



For the thiol-reactive group on the NP surface, there are several options, as shown in Chart 1. First are the Michael acceptors vinylsulfone (**A**), acrylate (**B**), and maleimide (**C**). These groups react with thiols in a conjugate Michael addition to form a thioether bond between the thiol and double bond. A thioether bond is also formed when the thiol reacts in a nucleophilic substitution reaction with bromo and iodo derivatives (**D**). The disadvantage of these thiol-reactive groups is that a physiologically irreversible thioether bond is formed. In the case of antigen delivery, this might be problematic, as the antigen is not released from the NP after being taken up by the cell unless first proteolytically processed. Despite the fact that the acrylate-based conjugate is cleavable by ester hydrolysis, this group is problematic for long-term storage of the aqueous antigen-NPs solution.

Another thiol-reactive group is the pyridyl disulfide group (**E**) that reacts with thiols to give a disulfide bond and releases pyridine thione as shown in Chart 2. This disulfide exchange reaction is practically irreversible because of the formation of the very stable pyridine thione which has a anomalously low pK_a value (*25*). This is also the reason why this reaction takes place over a broad pH range between 4 and 8 (data not shown). In addition to the broad pH range, conjugation using the pyridyl disulfide group has two other advantages: the amount of protein or peptide conjugated can be quantified by measuring the release of pyridine thione, and the peptide or protein is linked to the NP surface via a reduction-sensitive disulfide bond, which allows a cellular mechanism for antigen release after endocytosis due to the reductive potential early during endolysosomal processing. This increase in reducing environment will result in cleavage of the peptide/protein-NP disulfide bond and allow for release of the peptide or protein from the NP to affect its biological activity. This antigen release mechanism was not possible in the original scheme using the vinylsulfone coupling; rather, proteolytic release was required. For this reason we functionalized the NPs with this pyridyl disulfide group. The most straightforward approach is synthesis of a pyridyl disulfide-Pluronic and adding this to the polymerization mixture to make pyridyl disulfide-NPs. However, a problem is that the thiolate species that are responsible for the polymerization of propylene sulfide could also react with the pyridyl disulfide groups on the Pluronic. Indeed, after synthesizing pyridyl disulfide-Pluronic (*21*) and addition to the polymerization mixture, NMR showed that the pyridyl disulfide group was not present after NP

synthesis (data not shown). To circumvent this problem, i.e., introducing the thiol-reactive pyridyl disulfide group in the presence of thiolate species, we came to the following approach as outlined in Scheme 1. As the first step, carboxylate-functionalized NPs are synthesized and, in the second step, functionalized with a pyridyl disulfide containing a free amine to introduce the thiol reactive groups. Note that we choose the NPs to have a negative charge instead of positive (amines) to avoid the potential toxic effects of cationic charges that could arise from unreacted amine groups. The carboxylate-Pluronic was therefore synthesized in three steps from Pluronic F127 as outlined in Scheme 1. The use of the methyl ester was necessary, as reaction of mercaptopropionic acid also led to substitution at the carboxylic acid leading to an ester bond as was visible from ^{1}H NMR by the occurrence of a triplet around 4.2 ppm. After alkaline hydrolysis, the carboxylate-Pluronic was kept as its sodium salt so as to not interfere during NPs synthesis by lowering the pH. As the final step in characterizing the carboxylate-Pluronic, the polymer was reacted with pyridyl disulfide·HCl to give pyridyl disulfide-Pluronic. This polymer would serve as a reference for characterization of the pyridyl disulfide NPs.

With the carboxylate-Pluronic at hand, NPs were synthesized by emulsion polymerization with different COOH-to-OH Pluronic mass ratios. After exposure to air for 2 h to form disulfides, the remaining free thiolate anions that were spatially too far apart to form disulfides were blocked by the addition of iodoacetamide. Previous work had shown that this is effective in blocking thiolates (*15*) and capping was quantitative as measured by Ellman assay. This blocking is important to avoid a disulfide exchange reaction when the pyridyl disulfide groups are introduced onto the NPs. From the DLS and TEM data, it can be seen that the addition of carboxylate-Pluronic did not significantly affect the size of the final NPs. The PDI, however, dropped significantly (Table 1), suggesting that the negatively charged NP surface stabilizes the particles, which can be explained by DLVO theory, which states that like charge stabilizes colloid particles (*26*). In addition, the carboxylate-Pluronic did not influence the ring-opening polymerization of propylene sulfide to a significant extent as shown by the degree of polymerization and weight composition of the NPs. This shows that the NP synthesis is not affected significantly by the presence of the carboxylate-Pluronic in the polymerization mixture. Because of overlap of the characteristic signals of the carboxylate-Pluronic at 2.5, 2.7, and 2.8 ppm with the broad CH and CH_2 signals at 2.5−2.7 and 2.8−3.0 ppm of the PPS, it was not possible to determine the percentage of carboxylate-Pluronic present in the 10−75% carboxylate-NPs by NMR. For this reason we used the conjugation with pyridyl disulfide cysteamine·HCl as an indirect measurement to obtain insight into how the carboxylate-Pluronic was incorporated into NP surface as a function of the feed ratio in the polymerization mixture. From the 100% carboxylate-NPs, it was calculated that only about 60% functionalization was achieved, even though the carboxylate-Pluronic alone could be functionalized almost quantitatively. This lower degree of functionalization is not due to loss of carboxylate groups as was shown in control experiments. An explanation could be that some carboxylate groups remain inaccessible during functionalization, though how that would happen is unclear: interaction of the negatively charged carboxylate group with the hydrophobic PPS is unlikely. It is therefore more likely that the EDC/sulfo-NHS coupling chemistry itself limits the degree of functionalization because of its inherent water sensitivity. Indeed model experiments in which pyridyl disulfide cysteamine·HCl was coupled (using NHS) to the carboxylate-Pluronic that had been used in NP synthesis led to almost quantitative conversions in CH_2Cl_2 but only 45% in MES (aq) buffer (data not shown). The linear trend in Figure 4 suggests that the percentage of carboxylate-Pluronic on the NP surface is the same as that in the polymerizing mixture but that only about 60% can be functionalized. This finding enables the control of surface density of pyridyl disulfide groups on the NP surface by adjusting the feed ratio in the polymerization mixture of carboxylate- to hydroxyl-Pluronic.

Having shown that pyridyl disulfide groups could be introduced onto the NPs, it was important to show that these are actually in contact with the aqueous phase and available for conjugating with peptides and proteins. To explore this, we synthesized a thiol-containing biotin molecule and reacted it with the pyridyl disulfide-NPs. With this biotin molecule at both ends of the Pluronic, it would also be possible to see whether after conjugating biotin on the Pluronic ends the NP surface would be still accessible for interaction with large proteins. Biotin interacts with streptavidin, a 66 000 Da protein, to form the strongest noncovalent bond known in nature. Indeed biotin on the NPs is able to interact with the binding pockets of streptavidin, as shown in Figure 5. This result shows that the pyridyl disulfide groups on the NP surface are accessible in the aqueous phase for conjugation and that streptavidin is able to interact with the conjugated biotin on the NP surface. The biotin-NPs are furthermore interesting from a staining point of view. Having biotin bound to the NPs enables us the ability to probe the presence of the NPs in tissues by cryosectioning and staining with fluorescently labeled streptavidin.

For immunotherapy applications normally whole immunogenic proteins are used; however, they typically lead to release of a limited number of antigenic peptides when processed within DCs. For example the OVA protein yields two (SIINFEKL and ISQAVHAAHAEINE) antigenic peptide sequences upon processing by DCs (*27*). Since peptides are easily accessible by solid phase peptide synthesis, they can be made to have a free cysteine residue, enabling conjugation to NPs. As a model, we synthesized a nine amino acid peptide containing a cysteine and conjugated it to the NP. For purification of the peptide-NP, gel filtration was used because it is time saving and a better purification method compared to dialysis, especially with increasing size of the molecule to be conjugated. The presence of the peptide on the NPs was confirmed with DLS and fluorescamine (*20*). Important in our concept of antigen-bearing NPs is the reductive sensitivity of the antigen-NP disulfide bond. For this reason, we exposed both the biotin-NPs and peptide-NPs to a reducing agent to demonstrate sensitivity to reduction. In the case of biotin, mercaptoethanol led to a cleavage of the disulfide bond at room temperature as shown by SDS−PAGE gel where the streptavidin was no longer bound to the NP surface and freely moved into the gel. For the peptide-NP, addition of TCEP·HCl also led to disulfide cleavage as could be shown after gel filtration.

Finally we wanted to show that it is also possible to conjugate a larger protein. We choose OVA because it is a model antigen that is used frequently in immunotherapy studies. OVA has four free cysteine residues and one disulfide bond that would allow easy conjugation using our functionalization scheme. The problem is that these four cysteine residues are buried in the native state and are not reactive toward iodoacetic acid at pH 8.2, an alkylation agent (*28*). For this reason we reduced OVA to expose all six cysteine residues (four free and two in a disulfide). This, however, leads to a potential problem of cross-linking, as the NP surface is decorated with several pyridyl disulfide groups. With careful optimization, we managed to conjugate OVA to pyridyl disulfide-NPs. From Figure 6A it can be seen that all OVA eluted in one peak and that free OVA was not detected. DLS indicated an increase in size but the OVA nanoparticles still remained small (Table 2). That practically

no free OVA was present is clearly illustrated in Figure 6B by elution nonreduced OVA, which elutes at a much higher elution volume and shows the need for reducing OVA prior to conjugation. Indeed, if conjugation of reduced OVA is not quantitative, the elution profile shows both peaks (data not shown).

To conclude, we have presented a scheme by which to make thiol-reactive Pluronic-stabilized poly(propylene sulfide) NPs by incorporating a carboxylate-Pluronic into the hydroxyl-Pluronic/propylene sulfide mixture that was subsequently reacted with pyridyl disulfide cysteamine to yield pyridyl disulfide-NPs. The polymerization and NP composition were not affected by the presence of the carboxylate-Pluronic, and the number of pyridyl disulfide groups on the NP surface could be controlled by changing the weight ratio of carboxylate-Pluronic to hydroxyl-Pluronic in the mixture. We further showed that we could conjugate biotin, a nine amino acid peptide, as well as the larger protein OVA. Currently we are exploring the functionalizable NPs scheme for immunological application by conjugating antigenic peptides, proteins, and protein structures with adjuvant activity.

ACKNOWLEDGMENT

We thank the Competence Centre for Materials Science and Technology (CCMX) of the ETH-Board Switzerland for partial funding of this research.

Supporting Information Available: Calculation of NP composition, NMR spectra of **6** and pyridyl disulfide-NP, and estimation of numbers of biotin, peptide, and OVA molecules per NP. This material is available free of charge via the Internet at http://pubs.acs.org.

LITERATURE CITED

(1) Nestle, F. O., Banchereau, J., and Hart, D. (2001) Dendritic cells: on the move from bench to bedside. *Nat. Med. 7*, 761–765.

(2) Banchereau, J., and Steinman, R. M. (1998) Dendritic cells and the control of immunity. *Nature 392*, 245–252.

(3) Randolph, G. J., Angeli, V., and Swartz, M. A. (2005) Dendritic-cell trafficking to lymph nodes through lymphatic vessels. *Nat. Rev. Immunol. 5*, 617–628.

(4) Gay, N. J., Gangloff, M., and Weber, A. N. R. (2006) Toll-like receptors as molecular switches. *Nat. Rev. Immunol. 6*, 693–698.

(5) Hubbell, J. A., Thomas, S. N., and Swartz, M. A. (2009) Materials engineering for immunomodulation. *Nature 462*, 449–460.

(6) Singh, M., Briones, M., Ott, G., and O'Hagan, D. (2000) Cationic microparticles: a potent delivery system for DNA vaccines. *Proc. Natl. Acad. Sci. U.S.A. 97*, 811–816.

(7) Newman, K. D., Samuel, J., and Kwon, G. (1998) Ovalbumin peptide encapsulated in poly(D,L lactic-*co*-glycolic acid) microspheres is capable of inducing a T helper type 1 immune response. *J. Controlled Release 54*, 49–59.

(8) Newman, K. D., Sosnowski, D. L., Kwon, G. S., and Samuel, J. (1998) Delivery of MUC1 mucin peptide by poly(D,L-lactic-*co*-glycolic acid) microspheres induces type 1 T helper immune responses. *J. Pharm. Sci. 87*, 1421–1427.

(9) Newman, K. D., Elamanchili, P., Kwon, G. S., and, and Samuel, J. (2002) Uptake of poly(D,L-lactic-*co*-glycolic acid) microspheres by antigen-presenting cells in vivo. *J. Biomed. Mater. Res. 60*, 480–486.

(10) McKeever, U., Barman, S., Hao, T., Chambers, P., Song, S., Lunsford, L., Hsu, Y. Y., Roy, K., and Hedley, M. L. (2002) Protective immune responses elicited in mice by immunization with formulations of poly(lactide-*co*-glycolide) microparticles. *Vaccine 20*, 1524–1531.

(11) Jiang, W., Gupta, R. K., Deshpande, M. C., and Schwendeman, S. P. (2005) Biodegradable poly(lactic-*co*-glycolic acid) microparticles for injectable delivery of vaccine antigens. *Adv. Drug Delivery Rev. 57*, 391–410.

(12) Bennewitz, N. L., and Babensee, J. E. (2005) The effect of the physical form of poly(lactic-*co*-glycolic acid) carriers on the humoral immune response to co-delivered antigen. *Biomaterials 26*, 2991–2999.

(13) De Koker, S., Naessens, T., De Geest, B. G., Bogaert, P., Demeester, J., De Smedt, S., and Grooten, J. (2010) Biodegradable polyelectrolyte microcapsules: antigen delivery tools with Th17 skewing activity after pulmonary delivery. *J. Immunol. 184*, 203–211.

(14) Reddy, S. T., Rehor, A., Schmoekel, H. G., Hubbell, J. A., and Swartz, M. A. (2006) In vivo targeting of dendritic cells in lymph nodes with poly(propylene sulfide) nanoparticles. *J. Controlled Release 112*, 26–34.

(15) Rehor, A., Tirelli, N., and Hubbell, J. A. (2002) A new living emulsion polymerization mechanism: episulfide anionic polymerization. *Macromolecules 35*, 8688–8693.

(16) Rehor, A., Hubbell, J. A., and Tirelli, N. (2004) Oxidation-sensitive polymeric nanoparticles. *Langmuir 21*, 411–417.

(17) Rehor, A., Botterhuis, N. E., Hubbell, J. A., Sommerdijk, N., and Tirelli, N. (2005) Glucose sensitivity through oxidation responsiveness. An example of cascade-responsive nano-sensors. *J. Mater. Chem. 15*, 4006–4009.

(18) Reddy, S. T., van der Vlies, A. J., Simeoni, E., Angeli, V., Randolph, G. J., O'Neil, C. P., Lee, L. K., Swartz, M. A., and Hubbell, J. A. (2007) Exploiting lymphatic transport and complement activation in nanoparticle vaccines. *Nat. Biotechnol. 25*, 1159–1164.

(19) Ellman, G. L. (1959) Tissue sulfhydryl groups. *Arch. Biochem. Biophys. 82*, 70–77.

(20) Udenfriend, S., Stein, S., Bohlen, P., Dairman, W., Leimgruber, W., and Weigele, M. (1972) Fluorescamine: a reagent for assay of amino acids, peptides, proteins, and primary amines in the picomole range. *Science 178*, 871–872.

(21) O'Neil, C. P., van der Vlies, A. J., Velluto, D., Wandrey, C., Demurtas, D., Dubochet, J., and Hubbell, J. A. (2009) Extracellular matrix binding mixed micelles for drug delivery applications. *J. Controlled Release 137*, 146–151.

(22) Green, N. M. (1970) Spectrophotometric determination of avidin and biotin. *Methods Enzymol. 18* (Part 1), 418–424.

(23) Dust, J. M., Fang, Z. H., and Harris, J. M. (2002) Proton NMR characterization of poly(ethylene glycols) and derivatives. *Macromolecules 23*, 3742–3746.

(24) Rothenfluh, D. A., Bermudez, H., O'Neil, C. P., and Hubbell, J. A. (2008) Biofunctional polymer nanoparticles for intra-articular targeting and retention in cartilage. *Nat. Mater. 7*, 248–254.

(25) Tatsumi, E., and Hirose, M. (1997) Highly ordered molten globule-like state of ovalbumin at acidic pH: native-like fragmentation by protease and selective modification of Cys367 with dithiodipyridine. *J. Biochem. 122*, 300–308.

(26) Verwey, E. J. W., Overbeek, J. T. G. (1948) *Theory of the Stability of Lyophobic Colloids* Elsevier, New York.

(27) Burgdorf, S., Kautz, A., Bohnert, V., Knolle, P. A., and Kurts, C. (2007) Distinct pathways of antigen uptake and intracellular routing in CD4 and CD8 T cell activation. *Science 316*, 612–616.

(28) Takahashi, N., and Hirose, M. (1990) Determination of sulfhydryl groups and disulfide bonds in a protein by polyacrylamide gel electrophoresis. *Anal. Biochem. 188*, 359–365.

BC9004443

Stabilized ^{111}In-Labeled sCCK8 Analogues for Targeting CCK2-Receptor Positive Tumors: Synthesis and Evaluation

Susan Roosenburg,[#,‡] Peter Laverman,[#] Lieke Joosten,[#] Annemarie Eek,[#] Wim J. G. Oyen,[#] Marion de Jong,[§] Floris P. J. T. Rutjes,[‡] Floris L. van Delft,[‡,*] and Otto C. Boerman[#]

Department of Nuclear Medicine, Radboud University Nijmegen Medical Center, The Netherlands, Institute for Molecules and Materials, Radboud University Nijmegen, Nijmegen, The Netherlands, and Department of Nuclear Medicine, Erasmus MC, Rotterdam, The Netherlands. Received October 25, 2009; Revised Manuscript Received January 15, 2010

Radiolabeled cholecystokinin-8 (CCK8) peptide analogues can be used for peptide receptor radionuclide imaging and therapy for tumors expressing CCK2/gastrin receptors. Earlier findings indicated that sulfated CCK8 (sCCK8, Asp-Tyr(OSO_3H)-Met-Gly-Trp-Met-Asp-Phe-NH_2) may have better characteristics for peptide receptor radionuclide therapy (PRRT) than gastrin analogues. However, sCCK8 contains an easily hydrolyzable sulfated tyrosine residue and two methionine residues which are prone to oxidation. Here, we describe the synthesis of stabilized sCCK8 analogues, resistant to hydrolysis and oxidation. Hydrolytic stability was achieved by replacement of the Tyr(OSO_3H) moiety by a robust isosteric sulfonate, Phe(p-CH_2SO_3H). Replacement of methionine by norleucine (Nle) or homopropargylglycine (HPG) avoided undesired oxidation side-reactions. The phenylalanine analogue Phe(p-CH_2SO_3H) of L-tyrosine, synthesized by a modification of known synthetic routes, was incorporated in three peptides: sCCK8[Phe^2(p-CH_2SO_3H),Met^{3,6}], sCCK8[Phe^2(p-CH_2SO_3H),Nle^{3,6}], and sCCK8[Phe^2(p-CH_2SO_3H),HPG^{3,6}]. All peptides were *N*-terminally conjugated with the macrocyclic chelator DOTA (1,4,7,10-tetraazacyclododecane-*N*,*N*′,*N*″,*N*‴-tetraacetic acid) and radiolabeled with In-111. In vitro binding assays on CCK2R-expressing HEK293 cells revealed that all three peptides showed specific binding and receptor-mediated internalization, with binding affinity values (IC_{50}) in the nanomolar range. In vitro oxidation studies demonstrated that peptides with Nle or HPG indeed were resistant to oxidation. In vivo targeting studies in mice with AR42J tumors showed that tumor uptake was highest for ^{111}In-DOTA-sCCK8 and ^{111}In-DOTA-sCCK8[Phe^2(p-CH_2SO_3H),Nle^{3,6}] (4.78 ± 0.64 and 4.54 ± 1.15%ID/g, respectively, 2 h p.i.). The peptide with the methionine residues replaced by norleucine (^{111}In-DOTA-sCCK8[Phe^2(p-CH_2SO_3H), Nle^{3,6}]) showed promising in vivo characteristics and will be further investigated for radionuclide imaging and therapy of CCK2R-expressing tumors.

INTRODUCTION

Cholecystokinin (CCK), a functional peptide hormone in the gastrointestinal tract and the brain, mediates a variety of hormonal and neuromodulatory functions mediated by two receptors, CCK1R and CCK2R (*1*). In addition, a splice variant of the CCK2R was identified, CCK2i4svR, which is expressed at relatively low levels in human colorectal cancer and in pancreatic cancer, but not in normal tissue (*2*). All three receptors belong to the superfamily of G-protein coupled receptors. Several tumor types, such as small cell lung cancers (SCLC) and medullary thyroid carcinomas (MTC), abundantly express CCK2/gastrin receptors (CCK2R) (*3*).

Since both gastrin and CCK8 display a high affinity for these receptors (*3*), radiolabeled analogues of these peptides may be considered for peptide receptor imaging and peptide receptor radionuclide therapy (PRRT). We have previously shown that sCCK8 (Asp-Tyr(OSO_3H)-Met-Gly-Trp-Met-Asp-Phe-NH_2) has good characteristics for PRRT compared to gastrin analogues (*4*). Sulfated CCK8 has affinity for both the CCK1 and CCK2 receptor, and shows better CCK2R targeting characteristics as compared to nonsulfated CCK8 (nsCCK8). Behr et al. found that minigastrin analogues showed extremely high kidney uptake, whereas CCK8 exhibited low kidney uptake (*5*). The high kidney uptake was shown to be related to the pentaglutamate sequence of minigastrin, and was found to be reduced by coinjection of poly-Glu-containing peptides (*6, 7*). Unlike gastrin, sCCK8 includes a sulfated tyrosine (Tyr) residue that is easily hydrolyzable. Moreover, an Fmoc-Tyr(SO_3H)-OH building block is difficult to use in solid-phase peptide synthesis (SPPS), as it is acid labile (*8*). Another pitfall of sCCK8 is the presence of two methionines (Met) that are prone to oxidation to sulfoxides during radiolabeling and potentially also in vivo, leading to loss of receptor binding (*9, 10*). Therefore, we aimed to develop new and stabilized sCCK8 analogues, resistant to both hydrolysis and oxidation. To this end, we envisaged replacement of the Tyr sulfate moiety by a robust isosteric sulfonate. Since sulfonate isosteres of tyrosine sulfate are not commercially available, synthetic preparation of the phenylalanine analogue Phe(p-CH_2SO_3H) from L-tyrosine was required, to afford a Phe(p-CH_2SO_3H) building block that can be incorporated in peptide sequences under normal coupling conditions in SPPS without additional side chain protection (*11*). Second, to prevent oxidation, two sCCK8 analogues were designed with the Met residues replaced by norleucine (Nle) or homopropargylglycine (HPG) (*12, 13*). All peptides were *N*-terminally conjugated with the macrocyclic chelator DOTA (1,4,7,10-tetraazacyclododecane-*N*,*N*′,*N*″,*N*‴-tetraacetic acid) to allow radiola-

* Author for correspondence: Dr. F.L. van Delft, Institute for Molecules and Materials, Radboud University Nijmegen, Heyendaalseweg 135, 6525 AJ Nijmegen, The Netherlands, e-mail: F.vanDelft@science.ru.nl.

[#] Department of Nuclear Medicine, Radboud University Nijmegen Medical Centre.

[‡] Institute for Molecules and Materials, Radboud University Nijmegen.

[§] Department of Nuclear Medicine, Erasmus MC.

10.1021/bc900465y © 2010 American Chemical Society
Published on Web 03/19/2010

beling. Finally, the three sCCK8 analogues were characterized both in vitro and in vivo and compared to DOTA-sCCK8.

EXPERIMENTAL PROCEDURES

Synthesis of Fmoc-Phe(p-CH_2SO_3Na)-OH. *General Methods.* Solvents were distilled from appropriate drying agents prior to use and stored under nitrogen. Chemicals were purchased from Sigma-Aldrich and used as received, unless stated otherwise. Reactions were carried out under inert atmosphere of dry nitrogen or argon. Standard syringe techniques were applied for the transfer of dry solvents and air- or moisture-sensitive reagents. Reactions were followed, and R_F values were obtained using thin-layer chromatography (TLC) on silica gel-coated plates (Merck 60 F254) with the indicated solvent mixture. Detection was performed with UV-light. NMR spectra were recorded on a Bruker DMX 300 (300 MHz) spectrometer in $CDCl_3$ solutions (unless otherwise reported). Chemical shifts are given in ppm with respect to tetramethylsilane (TMS) as internal standard. Coupling constants are reported as *J*-values in Hz. Mass was determined by LCQ measurement. Column or flash chromatography was carried out using ACROS silica gel (0.035−0.070 mm, and ca. 6 nm pore diameter).

*N-tert-Butyloxycarbonyl-L-tyrosine Methyl Ester (**1**).* 30.0 g (165.55 mmol) L-tyrosine was dissolved in 1.1 L MeOH and cooled on an ice bath. 15.65 mL (215.24 mmol, 1.3 equiv) $SOCl_2$ was added dropwise and the reaction mixture was refluxed at 75 °C overnight. The solvent was evaporated, and the crude product (38.2 g white solid) was used in the next step. ^{1}H NMR (D_2O) δ 3.25 (dq, 2H, Ar-CH_2-CH), 3.86 (s, 3H, -OCH_3), 4.39 (t, 1H, α-C*H*), 6.91−7.21 (dd, 4H, Ar-*H*).

Next, 38.2 g crude product was dissolved in 500 mL dioxane/H_2O (1/1). 34.65 g (412.5 mmol, 3 equiv) $NaHCO_3$ and 43.21 g (198 mmol, 1.2 equiv) Boc_2O were added and the mixture was stirred at RT for 2 h. Dioxane was removed in vacuo and EtOAc was added. The organic layer was washed with water and brine, dried on $MgSO_4$, filtered, and concentrated to yield an orange oil, that crystallized overnight, yielding 44.52 g (150.7 mmol, 91% over 2 steps) of white crystals. R_F (EtOAc/heptane 1/1) 0.49; mp 95 °C; ^{1}H NMR ($CDCl_3$) δ 1.42 (s, 9H, −C(CH_3)$_3$), 3.02 (dq, 2H, Ar-CH_2-CH), 3.71 (s, 3H, -OCH_3), 4.53 (m, 1H, α-C*H*), 4.98 (m, 1H, -N*H*), 5.50 (bs, 1H, -O*H*), 6.72−6.99 (dd, 4H, Ar-*H*).

*N-tert-Butyloxycarbonyl-O-trifluoromethylsulfonyl-L-tyrosine Methyl Ester (**2**).* (*14, 15*) 1.0 g (3.39 mmol) of compound **1** was dissolved in 40 mL CH_2Cl_2 and cooled on an ice bath. Then, 720 μL (4.23 mmol, 1.25 equiv) DIPEA and 1.45 g (4.23 mmol, 1.25 equiv) phenyltriflimide were added, before stirring the mixture at RT overnight. Solvent was removed in vacuo, and the remaining colorless oil was dissolved in 40 mL EtOAc. The solution was washed with H_2O, 0.1 M HCl, and brine, dried on $MgSO_4$, and concentrated. The crude product was purified by flash column chromatography (EtOAc/heptane 15/85). Yield: 1.095 g (2.56 mmol, 79%) white crystals (after drying in vacuo). R_F (EtOAc/heptane 1/1) 0.65; mp 48 °C (lit.48−49 °C); ^{1}H NMR ($CDCl_3$) δ 1.41 (s, 9H, -C(CH_3)$_3$), 3.00−3.20 (dq, 2H, Ar-CH_2-CH), 3.71 (s, 3H, -OCH_3), 4.61 (m, 1H, α-C*H*), 5.00 (m, 1H, -N*H*), 7.22 (s, 4H, Ar-*H*). MS(ESI-TOF): 392.0 ($M+H^+$), calcd 392 ($M+H^+$).

*N-tert-Butyloxycarbonyl-p-vinyl-L-phenylalanine Methyl Ester (**3**).* 1.43 g (30.4 mmol, 1.2 equiv) of LiCl in a 250 mL flask was flame-dried in vacuo. 100 mL of dry DMF, 10.95 g (25.6 mmol) of compound **2**, and 8.23 mL (28.2 mmol, 1.1 equiv) tri-*n*-butyl vinyl tin were added. The mixture was stirred at RT for 10 min. $(PPh_3)_2PdCl_2$ (0.91 g, 3 mol %) was added, and the mixture was heated up to 90 °C and stirred overnight in sealed flask. Water was added and the product was extracted with EtOAc/heptane (1/1, 3 × 20 mL). Organic layers were dried on $MgSO_4$ and concentrated in vacuo. The crude product was purified by flash column chromatography (CH_2Cl_2, EtOAc/heptane 1/1). Yield: 6.12 g (19.8 mmol, 68%) colorless oil. R_F (EtOAc/heptane 1/3) 0.42; ^{1}H NMR ($CDCl_3$) δ 1.42 (s, 9H, −C(CH_3)$_3$), 3.05−3.14 (m, 2H, Ar-CH_2-CH), 3.71 (s, 3H, -OCH_3), 4.58 (m, 1H, α-C*H*), 4.97 (m, 1H, -N*H*), 5.22 (d, J = 10.88, 1H, CH=CH*H*), 5.71 (d, J = 17.61, 1H, CH=C*H*H), 6.68 (dd, J = 17.61, 1H, C*H*=CH_2), 7.07 (d, J = 9.17, 2H, Ar-*H*), 7.33 (d, J = 8.06, 2H, Ar-*H*).

*N-tert-Butyloxycarbonyl-(p-hydroxymethyl)-L-phenylalanine Methyl Ester (**4**).* (*11*) Ozone was bubbled through a solution of the vinyl compound **3** (4.26 g, 13.96 mmol) in 60 mL MeOH at −60 °C until the solution turned blue. The mixture was stirred under N_2 for 10 min at −60 °C and 10.3 mL (139.6 mmol, 10 equiv) of Me_2S was added. The mixture was stirred for 1 h at −60 °C. Then, $NaBH_4$ (2.64 g, 69.8 mmol, 5 equiv) was added. The mixture was stirred at −60 °C for 10 min, then allowed to warm to 0 °C and stirred for an additional 45 min. Saturated NH_4Cl (60 mL) was added, and the product was extracted with EtOAc (2 × 100 mL). The organic layers were dried on $MgSO_4$, filtered, and concentrated to give a yellow−brown oil. The crude product was purified by flash column chromatography (EtOAc/heptane 2/3 → EtOAc 100%). Yield: 8.18 g (26.5 mmol, 50.4% over 2 steps, 74%) of white/yellow crystals. R_F (EtOAc/heptane 1/1) 0.31; mp 81 °C; ^{1}H NMR ($CDCl_3$) δ 1.42 (s, 9H, −C(CH_3)$_3$), 3.08 (dd, J = 10.36, 2H, Ar-CH_2-CH), 3.72 (s, 3H, -OCH_3), 4.57 (m, 1H, α-C*H*), 4.67 (d, J = 5.85, 2H, -CH_2OH), 4.97 (m, 1H, -N*H*), 7.11 (d, J = 8.02, 2H, Ar-*H*), 7.29 (d, J = 8.02, 2H, Ar-*H*). MS(ESI-TOF): 332.2 ($M+Na^+$), calcd 332.16 ($M+H^+$).

*(p-Chloromethyl)-L-phenylalanine Methyl Ester (**5**).* (*16*) Compound **4** (10.03 g) was dissolved in 350 mL of CH_2Cl_2 and $SOCl_2$ (25−30 equiv) was added dropwise, before refluxing overnight. After evaporation to dryness, the remaining solid was rinsed twice with Et_2O and dried. The product was used in the next step without further purification. Yield: 4.59 g (62%) of an off-white solid. R_F (CH_2Cl_2/MeOH/AcOH 9/1/0.1) 0.34; mp 178 °C (lit. 180 °C); ^{1}H NMR (MeOD) δ 3.15−3.32 (dq, 2H, Ar-CH_2-CH), 3.81 (s, 3H, -OCH_3), 4.33 (m, 1H, α-C*H*), 4.65 (s, 2H, -CH_2Cl), 7.28 (d, 2H, Ar-*H*), 7.43 (d, 2H, Ar-*H*); MS(ESI-TOF): 228.0 ($M+H^+$), calcd 228.07 ($M+H^+$).

*(p-Sulfomethyl)-L-phenylalanine (**6**).* (*11, 16*) Compound **5** (4.59 g, 20.2 mmol) was dissolved in 200 mL H_2O and 20.3 g (161.6 mmol, 8 equiv) Na_2SO_3 was added. The mixture was refluxed at 100 °C for 3 h. The solvent was removed in vacuo and the crude product was washed with EtOH, yielding 32.25 g of a white solid after drying in vacuo. The crude product was used in the next step. ^{1}H NMR (D_2O) δ 3.08−3.12 (dq, 2H, Ar-CH_2-CH), 3.97 (m, 1H, α-C*H*), 4.20 (s, 2H, -CH_2SO_3Na), 7.33 (d, 2H, Ar-*H*), 7.43 (d, 2H, *H*). MS(ESI-TOF): 280.3 ($M+H^+$), calcd 280.3 ($M+H^+$).

*N-Fluorenyl-9-methoxycarbonyl-(p-sulfomethyl)-L-phenylalanine (**7**).* (*16*) The sulfonate product **6** (5 mmol) was dissolved in 40 mL H_2O, cooled on an ice-bath and pH was set to 9.0 with 0.1 M NaOH. Next, 2.11 g (6.25 mmol, 1.25 equiv) Fmoc-OSu was dissolved in 50 mL dioxane and added to the mixture. The mixture was stirred on an ice-bath for 30 min, then at RT for 6 h while maintaining the pH between 8.5 and 9.0 with an automatic titrator filled with 0.1 M NaOH. Dioxane was evaporated and the excess Fmoc-OSu was extracted with diethyl ether. The aqueous solution was acidified to pH 5 with 1 M HCl and concentrated to dryness. The crude product was dissolved in methanol, the insoluble material was removed by filtration, and the methanol was evaporated. The residue was dissolved in water and was washed with ethyl acetate before concentration. This product was purified by column chroma-

tography (MeCN/H_2O 9/1), yielding 1.04 g of white solid (2.07 mmol, 41.4% over 2 steps). R_F (ACN/H_2O 9/1) 0.24; mp 185 °C (lit. 184 °C); ^{1}H NMR (MeOD) δ 2.93−3.18 (dq, 2H, Ar-CH_2-CH), 3.99 (m, 1H, α-C*H*), 4.20 (s, 2H, -CH_2SO_3Na), 7.15−7.41 (m, 8H, Ar-*H* (Fmoc)), 7.61 (d, 2H, Ar-*H*), 7.78 (d, 2H, Ar-*H*); MS(ESI-TOF): 480.1 (M−H$^+$), calcd 480.11 (M−H$^+$).

Synthesis of DOTA−Peptides. Peptides were synthesized on a peptide synthesizer (Peptide Synthesizer SP 4000-LAB, Labortec AG) by applying the Fmoc-strategy. In all coupling steps, DIPCDI and HOBt were used, except for coupling of Fmoc-Phe(*p*-CH_2SO_3H) and DOTA(*t*-Bu)$_3$, which was performed in the presence of HBTU and DIPEA. After completion of the synthesis of the peptide on the resin, the peptide was cleaved off by stirring in TFA/ethanedithiol (EDT)/triisopropyl silane (TIS)/H_2O (92.5/2.5/2.5/2.5) for 3−5 h. The mixture was filtered, the filtrate centrifuged with Et_2O. The precipitated peptide was washed with Et_2O and centrifuged several times. Formation of the correct product was corroborated with mass spectrometry (ESI-TOF).

The remaining *t*-Bu protecting groups of the chelator were removed by stirring the product in TFA in the presence of a few drops of concentrated HCl, leading to complete removal of all protecting groups within 1 h. Three peptides were synthesized: DOTA-sCCK8[Phe^2(*p*-CH_2SO_3H)] (DOTA-D-Asp-Phe(CH_2SO_3H)-Met-Gly-Trp-Met-Asp-Phe-NH_2), DOTA-sCCK8[Phe^2(*p*-CH_2SO_3H), Nle^{3,6}] (DOTA-D-Asp-Phe(CH_2SO_3H)-Nle-Gly-Trp-Nle-Asp-Phe-NH_2), and DOTA-sCCK8[Phe^2(*p*-CH_2SO_3H), HPG^{3,6}] (DOTA-D-Asp-Phe(CH_2SO_3H)-HPG-Gly-Trp-HPG-Asp-Phe-NH_2).

Peptides were analyzed by analytical HPLC (Alltima C18 5 μm, 3.2 × 150 mm, Alltech, USA) with 5−75% ACN 0.1% TFA in H_2O 0.1% TFA as an eluent. DOTA-sCCK8[Phe^2(*p*-CH_2SO_3H)] and DOTA-sCCK8[Phe^2(*p*-CH_2SO_3H), Nle^{3,6}] were further purified by SP RP-HPLC (ReproSil 100 C18 250 mm × 10 mm, Dr. A. Maisch HPLC-GmbH, Germany), using ACN 0.1% TFA (5−75% over 30 min) in H_2O 0.1% TFA as an eluent. Peptide-containing fractions (detected by UV-light) were lyophilized and analyzed by HPLC and mass spectrometry. DOTA-sCCK8[Phe^2(*p*-CH_2SO_3H)] = 1525.7 (M−H$^+$), calcd = 1526.55. DOTA-sCCK8[Phe^2(*p*-CH_2SO_3H), Nle^{3,6}] = 1489.8 (M−H$^+$) calcd = 1490.64. DOTA-sCCK8[Phe^2(*p*-CH_2SO_3H), HPG^{3,6}] = 1481.8 (M−H$^+$) calcd = 1482.58.

DOTA-sCCK8 was prepared as described before (*17*).

Radiolabeling. The DOTA-conjugated peptides were radiolabeled with $^{111}InCl_3$ (Covidien, Petten, The Netherlands) in 0.25 M ammonium acetate buffer, pH 5.0, for 30 min at 95 °C. Labeling efficiency and radiochemical purity were checked by HPLC (1100 series LC system, Agilent Technologies, Palo Alto, CA, USA, RP-C18 column 5 μm, 4.6 × 250 mm) with a gradient of H_2O containing 0.1% TFA and ACN containing 0.1% TFA, and ITLC on ITLC-SG strips (Pall Life Sciences, Milford, MA, USA) with 0.1 M NH_4OAc/0.1 M EDTA (1/1 v/v) (R_F labeled peptide = 0, R_F unbound ^{111}In = 1), as well as MeOH/3.5% NH_3 (1/1 v/v) (R_F colloid = 0, R_F unbound ^{111}In or labeled peptide >0.8) as eluents. The radiochemical purities of peptides used in the studies described here were always above 95%. Maximum specific activity was 5.5 GBq/μmol.

Determination of Partition Coefficient (log P). To determine the lipophilicity of the radiolabeled peptides, approximately 60 000 dpm ^{111}In-DOTA-peptide was diluted in 3 mL PBS. An equal volume of 1-octanol was added to obtain a binary system. The system was vortexed for 10 s and mixed more gently for another 4 min. The two layers were separated by centrifugation (3000 *g*, 5 min). Three samples of 250 μL were taken of both layers and the radioactivity was determined in a 3″ well-type gamma-counter (Wallac 1480-Wizard 3, Perkin-Elmer, Boston, MA, USA). The log P value was calculated with the following formula:

$$\text{Log P}_{\text{octanol/water}} = \log(\text{cpm}_{\text{octanol}}/\text{cpm}_{\text{water}})$$

Oxidation Experiments. To study the susceptibility of the peptide analogues to oxidation, the ^{111}In-labeled peptides were incubated with oxidation buffer (H_2O_2/acetic acid/NH_4OAc 1/3/36) for 10 min at RT. Before and after incubation, the peptides were analyzed using RP-HPLC.

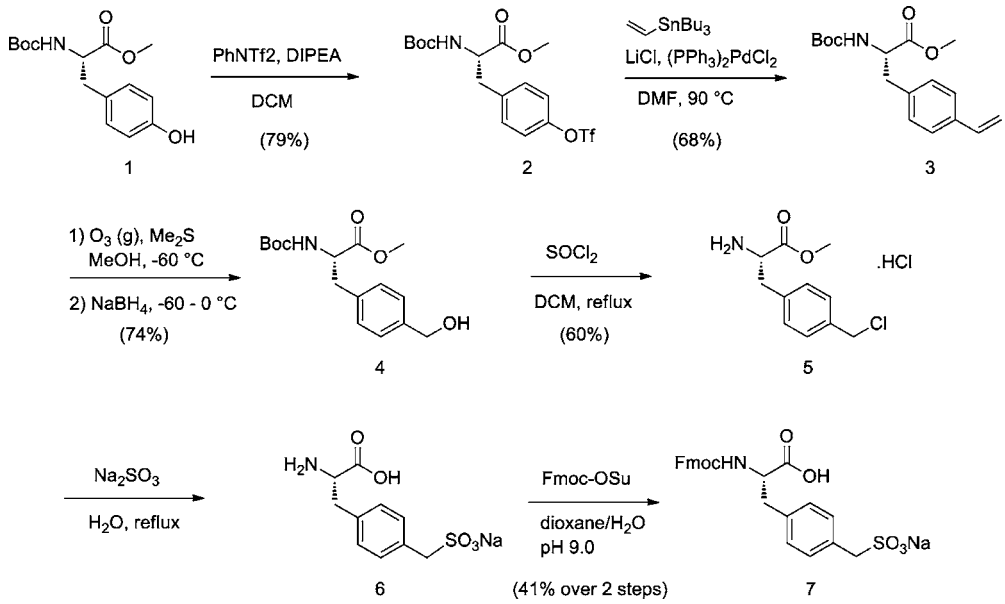
Stability Experiments. To study the stability of the peptide analogues, the ^{111}In-labeled peptides were incubated in human serum for 4 h at 37 °C. The samples were centrifuged at 3000 *g* for 5 min. The plasma was removed and mixed with acetonitrile. Before and after incubation, the peptides were analyzed using RP-HPLC.

Internalization Experiments. The internalization of the radiolabeled DOTA−peptides was investigated using HEK293-CCK2R cells (obtained from M. Hellmich, Univ. of Texas Medical Branch, Galveston, USA). Cells were cultured in Dulbecco's Modified Eagle's medium (DMEM) and supplemented with 10% fetal calf serum (FCS) and G418 (400 μg/mL). Cells were grown in a humidified atmosphere with 5% CO_2 at 37 °C. Cells were grown to confluency in 6-well plates. Radiolabeled peptide was added at a concentration of 4.4 × 10^{-2} nM (12 000 dpm/well). Cells were incubated for 0.5−2 h at either 0 or 37 °C, medium was removed, and cells were washed with ice-cold binding buffer (DMEM supplemented with 0.5% w/v bovine serum albumin (BSA)). To remove receptor-bound radiolabeled peptide, cells were incubated with acid buffer (0.1 M acetic acid, 154 mM NaCl, pH 2.0) for 10 min at 0 °C. After washing the cells twice with ice-cold PBS, the internalized fraction was determined by counting the cells in a gamma counter. The receptor-bound activity was also determined by counting the acid wash fractions.

Determination of IC_{50} Values. The 50% inhibitory concentration (IC_{50}) of the peptides for binding the CCK2R was determined on HEK293-CCK2R cells in a competitive binding assay. Cells were grown to confluency in 6-well plates. Cells were washed with binding buffer and incubated at RT for 10 min in binding buffer. Subsequently, unlabeled peptide was added in the range 0.1−100 nM together with a trace amount of ^{111}In-DOTA-sCCK8[Phe^2(*p*-CH_2SO_3H), HPG^{3,6}] (12 000 dpm). After incubation at RT for 1 h, binding buffer was removed and cells were washed twice with binding buffer. Cell-associated radioactivity was determined. The IC_{50} was defined as the peptide concentration at which 50% of binding without competitor was reached. IC_{50} values (including standard deviations) were calculated using *GraphPad Prism* software (version 4.00 for Windows, GraphPad Software, San Diego, CA, USA).

Biodistribution Studies. The in vivo tumor targeting potential of the ^{111}In-DOTA-peptides was investigated in female athymic BALB/c mice. Subcutaneous tumors were induced by inoculation with CCK2R expressing AR42J cells (rat tumor of the exocrine pancreas). Cells were cultured in DMEM with 4500 mg/L D-glucose (Gibco, Invitrogen, Breda, The Netherlands), supplemented with 10% FCS and 1% penicillin/streptomycin. Mice were inoculated s.c. with 4 × 10^6 AR42J cells (200 μL) in the left flank. When tumors had reached a weight of 0.2 g, mice were divided in groups of 5 mice each and 370 kBq ^{111}In-DOTA-peptide (0.1 μg) was injected intravenously. Specificity was studied in groups (n = 5) which received a 1000-fold molar excess of unlabeled sCCK8. Mice were killed 2 h postinjection (p.i.), a blood sample was drawn, and tissues of interest were dissected, weighed, and counted in a gamma-counter along with a standard of the injected activity to allow calculation of the injected dose per gram tissue (% ID/g). Animal experiments

Scheme 1. Synthesis Route of Fmoc-Phe(p-CH_2SO_3H)-OH



were approved by the local animal welfare committee and carried out according to national regulations.

Statistical Analysis. All mean values are expressed as mean ± standard deviation (SD). Statistical analysis was performed using one-way analysis of variance using *GraphPad InStat* software (version 3.10, Graphpad software). The level of significance was set at $p < 0.05$.

RESULTS

Synthesis of Phe(p-CH_2SO_3H) and Peptides. Since sulfonate building blocks are not commercially available, Fmoc-Phe(*p*-CH_2SO_3H)-OH was synthesized starting from L-tyrosine, by modification of known routes (Scheme 1). First, the amino group and the acid functionality were protected by a Boc- and a methyl group, respectively. The hydroxy group of **1** was activated by triflation using phenyltriflimide and DIPEA, giving the triflate **2** in 79% yield (*14*). The next step, a Stille vinylation (*14, 18*), was performed under strictly dry conditions and required careful workup and rapid purification to obtain the vinylated product **3**. Ozonolysis and reduction of the vinyl compound was performed immediately to obtain the hydroxymethylated compound **4** (*15, 18*). The chloromethyl derivative **5**, obtained from alcohol **4** by treatment with thionyl chloride, was converted into the sulfonate **6** by refluxing in water in the presence of a large excess of Na_2SO_3 (*9*). NMR spectra showed that the methyl group was concomitantly removed in this reaction, thereby obviating a separate deprotection step. The final step in the synthesis of the sulfonate building block was Fmoc-protection of the amine under basic conditions (*16*). The overall yield of the synthesis starting from L-tyrosine was 9% (*19*).

Having the phenylalanine sulfonate building block **7** at hand, we investigated the synthesis of sCCK8 analogues by solid-phase peptide synthesis. Initial application of standard coupling conditions (HOBt, DIPCDI) to Fmoc-Phe(*p*-CH_2SO_3H)-OH failed to afford incorporation of Phe(*p*-CH_2SO_3H)-OH in the peptide. Fortunately, switching of reagents to HBTU and DIPEA led to the desired octapeptide uneventfully. To obtain other more stable sCCK8 peptide analogues not susceptible to oxidation, methionine residues were replaced by either norleucine (Nle) or homopropargylglycine (HPG) residues. After incorporation of the final amino acid, the macrocyclic chelator DOTA was coupled on the resin as tri-*tert*-butyl protected derivative. The latter coupling reaction was found to proceed optimally under the action of HBTU and DIPEA. After cleavage from the resin with TFA/H_2O (92.5/2.5, v/v) in the presence of ethanedithiol (EDT) and triisopropyl silane (TIS), with simultaneous protective group removal, the peptides were purified by RP-HPLC. Molecular structures of the peptides are depicted in Figure 1.

Partition Coefficient. For ^{111}In-DOTA-sCCK8[Phe^2(*p*-CH_2SO_3H] and ^{111}In-DOTA-sCCK8[Phe^2(*p*-CH_2SO_3H,Nle^{3,6}], the log P values were -2.97 ± 0.02 and -2.93 ± 0.13, respectively. The log P value for ^{111}In-DOTA-sCCK8[Phe^2(*p*-CH_2SO_3H,HPG^{3,6}] was -2.86 ± 0.14. These values were comparable to that of the lead compound, ^{111}In-DOTA-sCCK8: -2.91 ± 0.20. All compounds were relatively hydrophilic, and the molecular changes did not affect the hydrophilicity of the peptide significantly.

Oxidation Experiments. After 10 min incubation in oxidation buffer (containing hydrogen peroxide and acetic acid), about 66% of the ^{111}In-labeled DOTA-sCCK8[Phe^2(*p*-CH_2SO_3H), Met^{3,6}] was oxidized, as judged by RP-HPLC. Both ^{111}In-DOTA-sCCK8[Phe^2(*p*-CH_2SO_3H),Nle^{3,6}] and ^{111}In-DOTA-sCCK8[Phe^2(*p*-CH_2SO_3H,HPG^{3,6}] did not show any oxidation.

Stability Experiments. In vivo, the peptide analogues should remain intact long enough to target the gastrin/CCK2 receptors. After 4 h incubation in human serum at 37 °C, peptides remained intact. Of the ^{111}In-labeled DOTA-sCCK8[Phe^2(*p*-CH_2SO_3H), Met^{3,6}] 2.3% was oxidized after incubation in the serum.

Internalization Experiments. Internalization of the peptides by HEK293-CCK2R cells was investigated in vitro. After 2 h incubation at 37 °C, 35.2 ± 2.1% of the added ^{111}In-DOTA-sCCK8 was internalized by the cells, most of it during the first 30 min (Figure 2). Receptor bound fraction after 2 h was 11.6 ± 0.7%. Of both ^{111}In-DOTA-sCCK8[Phe^2(*p*-CH_2SO_3H)] and ^{111}In-DOTA-sCCK8[Phe^2(*p*-CH_2SO_3H,HPG^{3,6}], about 13% of the added radiolabeled compound was internalized by the CCK2R after 2 h at 37 °C, while 10−12% was still receptor-bound. The internalized fraction of ^{111}In-DOTA-sCCK8[Phe^2(*p*-CH_2SO_3H,Nle^{3,6}] after 2 h was 26.8 ± 1.4% with a receptor-bound fraction of 9.4 ± 0.6% (Figure 2). Internalization kinetics of ^{111}In-DOTA-sCCK8 and ^{111}In-DOTA-sCCK8[Phe^2(*p*-CH_2SO_3H,Nle^{3,6}] showed to be similar, although the percentage of internalized fraction was about 7% lower for the synthetic peptide ($P < 0.05$). Similar data were found using AR42J cells (data not shown).

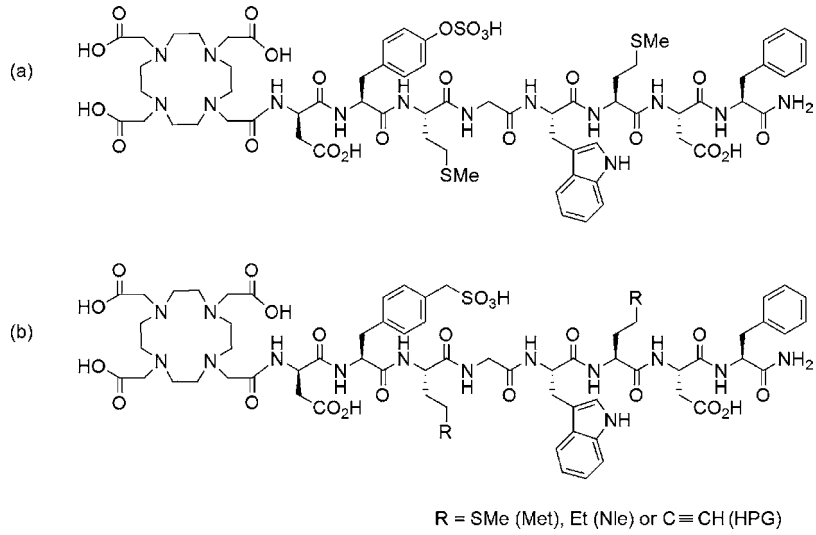


Figure 1. Molecular structures of (a) DOTA-sCCK8 and (b) synthetic DOTA-peptides.

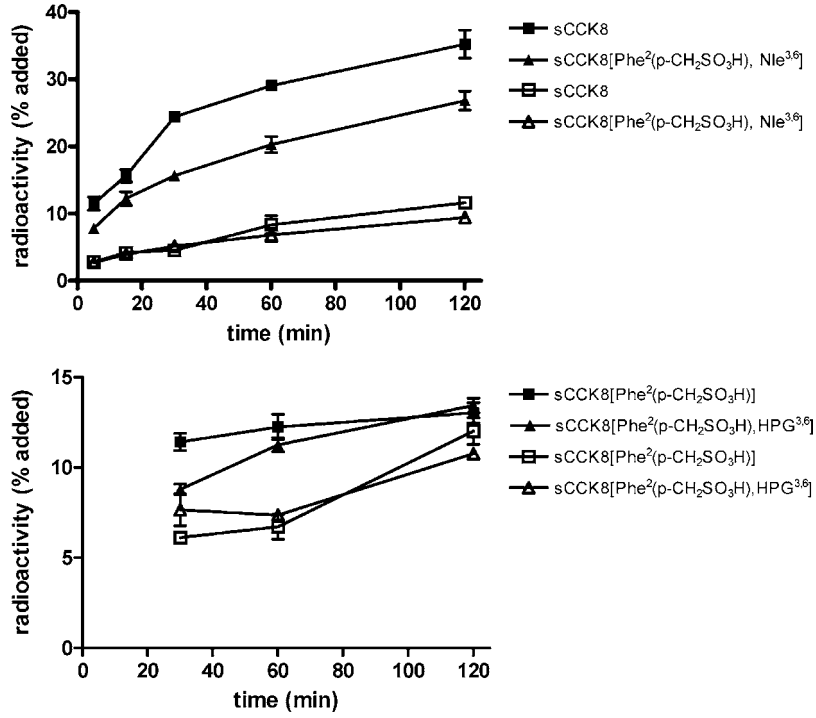


Figure 2. Internalization and receptor bound fractions in HEK293-CCK2R cells. Closed symbols indicate internalized fraction and open symbols indicate receptor-bound fraction. Values are expressed as percentage of the total amount added.

Determination of IC_{50} Values. The apparent IC_{50} values for binding CCK2R were determined for all peptides, using HEK293-CCK2R cells in a solid-phase competitive binding assay (Figure 3). All peptides showed an IC_{50} in the low nanomolar range, although the apparent IC_{50} values of the three synthesized peptides were approximately 10-fold higher than that of the lead compound. The apparent IC_{50} value for sCCK8 was 1.16 ± 0.06 nM, for DOTA-sCCK8[Phe^2(*p*-CH_2SO_3H)] 27.2 ± 1.44 nM, for DOTA-sCCK8[Phe^2(*p*-CH_2SO_3H), Nle^{3,6}] 11.6 ± 1.06 nM, and for DOTA-sCCK8[Phe^2(*p*-CH_2SO_3H), HPG^{3,6}] 13.2 ± 1.12 nM.

Biodistribution. The potential of the radiolabeled DOTA-peptides for in vivo targeting of CCK2R expressing tumors was investigated in athymic mice with AR42J tumors. The biodistribution 2 h p.i. for each of the four ^{111}In-labeled peptides is summarized in Figure 4.

Tumor uptake of ^{111}In-DOTA-sCCK8 and ^{111}In-DOTA-sCCK8[Phe^2(*p*-CH_2SO_3H,Nle^{3,6}] were comparable (4.78 ± 0.64 and 4.54 ± 1.15% ID/g, respectively). The radioactivity concentration of these peptides in the tumor was the highest of all tissues studied ($P < 0.001$). For both other compounds, the tumor uptake was significantly lower (2.18 ± 0.18% ID/g for ^{111}In-DOTA-sCCK8[Phe^2(*p*-CH_2SO_3H], $P < 0.001$) and 1.92 ± 0.31% ID/g for ^{111}In-DOTA-sCCK8[Phe^2(*p*-CH_2SO_3H,HPG^{3,6}], $P < 0.001$), and pancreatic concentration for these peptides was at the same level as the concentration in the tumor. Tumor uptake of all compounds could be blocked by coinjection of an excess of unlabeled sCCK8, indicating receptor-mediated uptake. For all compounds tested, the uptake in the normal tissues, such as the blood, lungs, muscle, spleen, and small intestine was low. Specific uptake was also found in the pancreas and, to a lesser extent, in the stomach. Most likely, this is due to relatively high CCK2R

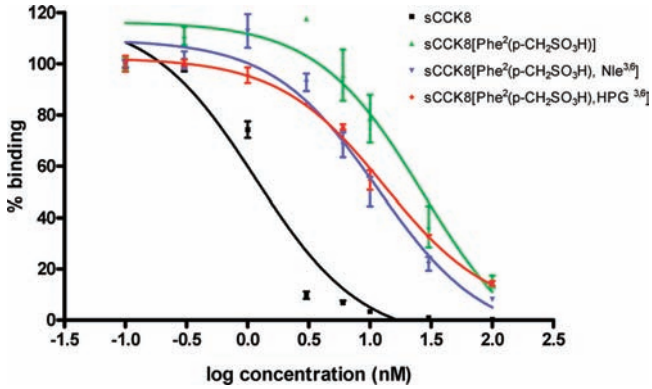


Figure 3. Competition binding analyses (IC_{50}) of four peptides using HEK293-CCK2R cells.

expression in murine pancreatic tissue en stomach. Kidney uptake of all peptides was low (<1.5% ID/g).

DISCUSSION

In earlier studies, we as well as others have shown that radiolabeled CCK8 peptide analogues show promise for peptide receptor radionuclide targeting of small cell lung cancers and medullary thyroid carcinomas (*4, 5, 8, 12*). In particular, sCCK8 was found to possess better CCK-receptor targeting behavior (*4*). An important drawback of the peptides used to date, however, is the intrinsic hydrolytic instability of the tyrosine sulfate ester. Moreover, since CCK8 contains two methionine residues, radiolabeling inevitably leads to varying amounts of thioether oxidation, which negates the binding affinity of the peptide to CCKR. Having these drawbacks in mind, we aimed for sCCK8 peptide analogues with improved stability as compared to the lead compound sCCK8. This study describes the characterization of three DOTA-conjugated analogues of the sCCK8 peptide.

A promising method to avoid the instability of the sulfate ester is the replacement of the sulfated tyrosine by a phenylalanine sulfonate isostere, featuring a covalent C−S bond that is fully resistant to water. However, lack of commercial availability of such an unnatural amino acid necessitated a suitable synthetic preparation.

Synthesis started with a tyrosine triflate derivative (**2**), which is readily available from the corresponding protected tyrosine **1** by reaction with phenyl triflimide. For the synthesis of the hydroxymethylphenylalanines, we investigated different routes: the palladium-catalyzed coupling of the tyrosine triflate with *tert*-butyl acrylate (Heck reaction) and the coupling of the tyrosine triflate to vinyltributylstannane in the presence of metallic palladium and lithium chloride (Stille reaction), leading to styrene derivative **3**. The latter reaction was found to give the best results, which is similar to the published data (*14, 18*). Both Tilley et al. and the group of Larsen described this reaction with slightly different tyrosine derivatives and they could obtain the allylated compounds in good yields (65−82%) after purification (*14, 18*). We found that careful workup and immediate ozonolysis and reduction were essential to obtain the hydroxymethylated product **4** in acceptable yields. We also attempted to follow the four-step synthesis route described by Miranda et al. (*16*), but the chloromethylation of phenylalanine, the first step in this route, also failed to succeed in our hands, as reported earlier (*19*). In addition, a third attempt involved synthesis of the hydroxymethylphenylalanine directly by a Stille reaction with (tributylstannyl)methanol (*20*). Several palladium complexes and solvents were investigated, but the desired compound could not be produced.

The chloromethyl derivative **5** was obtained from the alcohol **4** by treatment with thionyl chloride. We found that during this

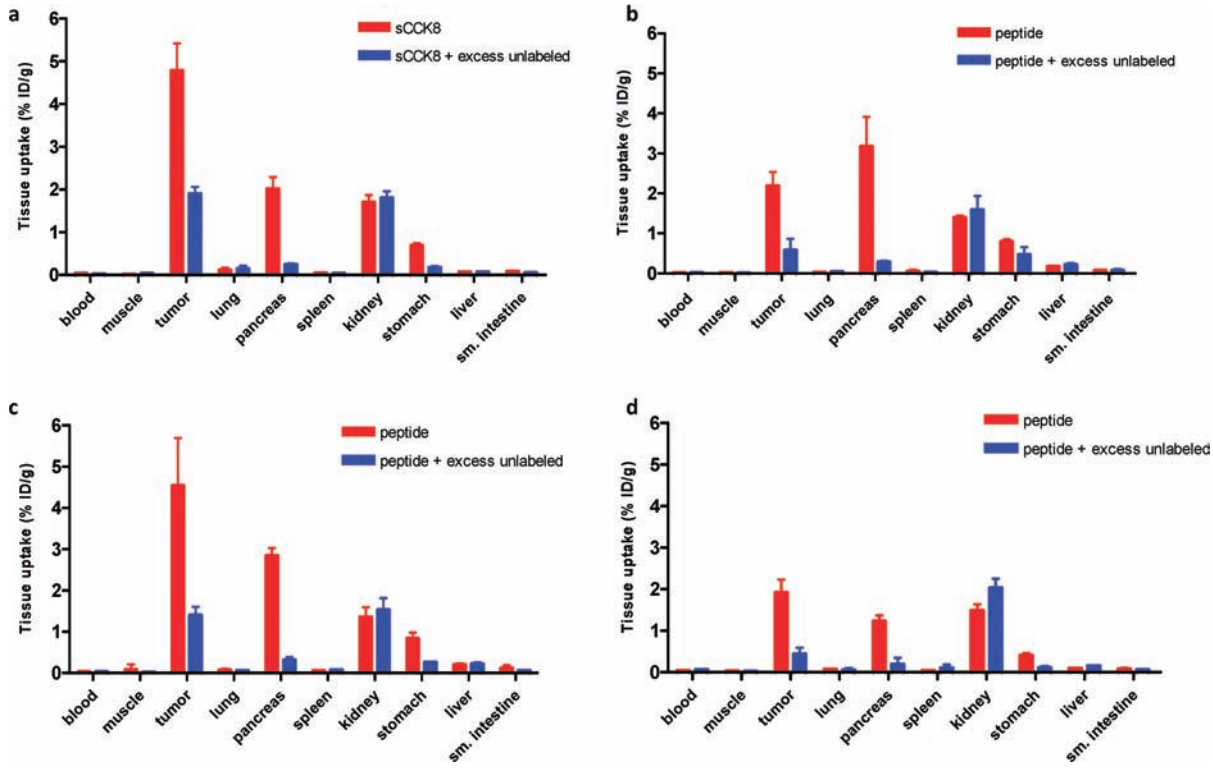


Figure 4. Biodistribution of (a) DOTA-sCCK8, (b) DOTA-sCCK8[Phe^2(p-CH_2SO_3H)], (c) DOTA-sCCK8[Phe^2(p-CH_2SO_3H), $Nle^{3,6}$], and (d) DOTA-sCCK8[Phe^2(p-CH_2SO_3H), $HPG^{3,6}$] in athymic mice bearing CCK2R expressing tumors in the left flank. Values are expressed as percentage of the injected dose per gram tissue ($n = 5$ mice/group). Blocking was performed by coinjection of a 1000-fold molar excess of unlabeled sCCK8. Mice were dissected at 2 h p.i.

reaction the Boc-protective group was conveniently removed as well, probably due to the formation of HCl in this reaction. The next step, conversion to the sulfonate **6**, was also accompanied by an unintended but useful side reaction, i.e., hydrolysis of the methyl ester, thereby saving another deprotection step. On the basis of the whole sequence, it can be concluded that a practical, multigram-scale procedure has been developed in only 8 steps starting from L-tyrosine, leading to the final Fmoc-protected sulfonate building block **7** in an acceptable yield (9%).

The Fmoc-Phe(*p*-CH_2SO_3H)-OH building block was smoothly incorporated in the peptide sequence on solid phase, but required replacement of the typical DIPCDI/HOBt mixture with HBTU and DIPEA as coupling reagents. Three peptides were synthesized with the sulfonate building block, differing in the presence of Met, Nle, or HPG residues on both positions 3 and 6. Finally, all peptides were N-terminally conjugated with the macrocyclic chelator DOTA, also requiring HBTU/DIPEA for activation.

Receptor binding studies and internalization studies were performed on HEK293 cells stably expressing the CCK2 receptor. Substituting the tyrosine sulfate by its phenylalanine isostere resulted in sCCK8 analogues with apparent affinities for the CCK2 receptor in the low nanomolar range. When the Met residues were replaced by Nle residues, a more stable peptide was obtained with comparable tumor uptake in CCK2R positive tumors. Reubi et al. also found that replacement of methionine by norleucine in a DTPA-conjugated nonsulfated CCK8-peptide does not affect the binding affinity for the CCK2 receptor, but increases the plasma stability of the compound (*12*). In contrast, Mather et al. found that substitution of the methionine residue with norleucine in gastrin peptide analogues lowered both in vitro binding affinity and tumor uptake in vivo. As Mather synthesized gastrin analogues and not CCK8 analogues, these peptides may be affected differently by substitution of methionine by norleucine. This difference may also be due to the two additional histidines on the N-terminus (*9*). The group of Aloj synthesized and evaluated a series of cyclic sCCK8 peptide analogues, in which the tyrosine sulfate and both methionines were preserved. They found that cyclization of the peptides caused a 1000-fold decrease in affinity for both the CCK1 and CCK2 receptor (*21, 22*).

Homopropargylglycine has not earlier been applied in tumor-targeting peptides, but has been generally shown to be a suitable and stable substitute for methionine (*13*). We found that replacement of methionine by homopropargylglycine caused reduction of CCK2R affinity resulting in reduced uptake of the radiolabeled peptide in the AR42J tumor.

The CCK2 receptor belongs to the family of G-protein-coupled receptors. When gastrin or CCK8 binds to the receptor, the complex is internalized, after which the receptor can be recycled or metabolized. After binding and internalization of ^{111}In-labeled peptides, the radiometal is retained intracellularly in the lysozomes. The peptides in this study all showed time-dependent internalization. About 27% of ^{111}In-DOTA-sCCK8[Phe^2(*p*-CH_2SO_3H), Nle^{3,6}] was internalized after 2 h, where ^{111}In-DOTA-sCCK8 showed 35% internalization ($P < 0.05$).

The peptides in this study showed very low kidney retention (1.5% ID/g, 2 h p.i.) and display also low uptake in the main peripheral tissue. This is in contrast with ^{111}In-labeled minigastrin analogues, which display a very high kidney uptake, 40−60% ID/g (*5*). Derivatives of minigastrin, lacking the pentaglutamate sequence, showed a comparably low kidney uptake compared to CCK8 analogues (*23*). Low kidney and peripheral tissue retention are prerequisites for receptor-targeted imaging and therapeutic agents. The observed specific uptake in the pancreas can be explained by the fact that in rodents the pancreas expresses the CCK-receptor, whereas in human pancreatic tissue, the CCK2 receptor is not expressed. Therefore, in a clinical setting, pancreatic uptake of radiolabeled sCCK8 analogues is not expected.

In summary, DOTA-sCCK8[Phe^2(*p*-CH_2SO_3H), Nle^{3,6}] is a peptide with receptor affinity and tumor uptake comparable to sCCK8, but with an increased stability and therefore is a promising peptide for use in PRRT.

CONCLUSION

A successful synthetic route was developed to a tyrosine isostere that is not susceptible to hydrolysis of the sulfate ester linkage and therefore is a valuable building block for the preparation of medicinally relevant peptides. A series of radiolabeled sCCK8 analogues with increased stability over the natural peptide was successfully synthesized by solid-phase peptide synthesis. The peptide with methionine residues replaced by norleucine (DOTA-sCCK8[Phe^2(*p*-CH_2SO_3H), Nle^{3,6}]) showed promising characteristics for CCK2R targeting and will be further investigated for its potency in imaging and therapy.

Supporting Information Available: NMR-spectra, HPLC-spectra, biodistribution studies. This material is available free of charge via the Internet at http://pubs.acs.org.

ACKNOWLEDGMENT

Bianca Lemmers is kindly acknowledged for her assistance with the animal experiments. The study was financially supported by the Dutch Cancer Society grant KUN 2006-3575.

LITERATURE CITED

(1) Noble, F., Wank, S. A., Crawley, J. N., Bradwejn, J., Seroogy, K. B., Hamon, M., and Roques, B. P. (1999) International Union of Pharmacology. XXI. Structure, distribution and functions of cholecystokinin receptors. *Pharmacol. Rev. 51*, 745–781.

(2) Hellmich, M. R., Rui, X. L., Hellmich, H. L., Fleming, R. Y. D., Evers, B. M., and Townsend, Jr., C. M. (2000) Human colorectal cancers express a constitutively active cholecystokinin-B/gastrin receptor that stimulates cell growth. *J. Biol. Chem. 275*, 32122–32128.

(3) Reubi, J. C., Schaer, J. C., and Waser, B. (1997) Cholecystokinin(CCK)-A and CCK-B/gastrin receptors in human tumors. *Cancer Res. 57*, 1377–1386.

(4) Laverman, P., Béhé, M., Oyen, W. J. G., Willems, P. H. G., Corstens, F. H. M., Behr, T. M., and Boerman, O. C. (2004) Two technetium-99m-labeled cholecystokinin-8 (CCK8) peptides for scintigraphic imaging of CCK receptors. *Bioconjugate Chem. 15*, 561–568.

(5) Behr, T. M., Jenner, N., Béhé, M., Angerstein, C., Gratz, S., Raue, F., and Becker, W. (1999) Radiolabeled peptides for targeting cholecystokinin-B/gastrin receptor-expressing tumors. *J. Nucl. Med. 40*, 1029–1044.

(6) Béhé, M. P., Kluge, G., Becker, W., Gotthardt, M., and Behr, T. M. (2005) Use of polyglutamic acids to reduce uptake of radiometal-labeled minigastrin in the kidneys. *J. Nucl. Med. 46*, 1012–1015.

(7) Nock, B. A., Maina, T., Béhé, M. P., Nikolopoulou, A., Gotthardt, M., Schmitt, J. S., Behr, T. M., and Maecke, H. R. (2005) CCK-2/gastrin receptor-targeted tumor imaging with 99mTc-labeled minigastrin analogs. *J. Nucl. Med. 46*, 1727–1736.

(8) De Luca, S., and Morelli, G. (2004) Synthesis and characterization of a sulfated and a non-sulfated cyclic CCK8 analogue functionalized with a chelating group for metal labeling. *J. Pept. Sci. 10*, 265–273.

(9) Mather, S. J., McKenzie, A. J., Sosabowski, J. K., Morris, T. M., Ellison, D., and Watson, S. A. (2007) Selection of radiolabeled gastrin analogs for peptide receptor-targeted radionuclide therapy. *J. Nucl. Med. 48*, 615–622.

(10) Breeman, W. A. P., Fröberg, A. C., de Blois, E., van Gameren, A., Melis, M., de Jong, M., Maina, T., Nock, B. A., Erion, J. L., Maecke, H. R., and Krenning, E. P. (2008) Optimised labeling, preclinical and initial clinical aspects of CCK-2 receptor-targeting with 3 radiolabeled peptides. *Nucl. Med. Biol. 35*, 839–849.

(11) Gonzalez-Muniz, R., Cornille, F., Bergeron, F., Ficheux, D., Pothier, J., Durieux, C., and Roques, B. P. (1991) Solid phase synthesis of a fully active analogue of cholecystokinin using the acid-stable Boc-Phe(*p*-CH_2SO_3H) as a substitute for Boc-Tyr(SO_3H) in CCK8. *Int. J. Pept. Protein Res. 37*, 331–340.

(12) Reubi, J. C., Waser, B., Schaer, J. C., Laederach, U., Erion, J., Srinivasan, A., Schmidt, M. A., and Bugaj, J. E. (1998) Unsulfated DTPA- and DOTA-CCK analogs as specific high-affinity ligands for CCK-B receptor-expressing human and rat tissues in vitro and in vivo. *Eur. J. Nucl. Med. 25*, 481–490.

(13) van Hest, J. C. M., Kiick, K. L., and Tirrell, D. A. (2000) Efficient incorporation of unsaturated methionine analogues into proteins in vivo. *J. Am. Chem. Soc. 122*, 1282–1288.

(14) Tilley, J. W., Sarabu, R., Wagner, R., and Mulkerins, K. (1990) Preparation of carboalkoxyalkylphenylalanine derivatives from tyrosine. *J. Org. Chem. 55*, 906–910.

(15) Chen, P., Cheng, P. T. W., Alam, M., Beyer, B. D., Bisacchi, G. S., Dejneka, A. T., Evans, A. J., Gerytok, J. A., Hermsmeier, M. A., Humphreys, W. G., Jacobs, G. A., Kocy, O., Lin, P.-F., Lis, A., Marella, M. A., Ryono, D. E., Sheaffer, A. K., Spergel, S. H., Syn, C.-Q., Tino, J. A., Vite, G., Colonno, R. J., Zahler, R., and Barrish, J. C. (1996) Aminodiol HIV protease inhibitors Synthesis and structure-activity relationships of P1/P1' compounds: correlation between lipophilicity and cytotoxicity. *J. Med. Chem. 39*, 1991–2007.

(16) Miranda, M. T. M., Liddle, R. A., and Rivier, J. E. (1993) Synthesis of human CCK26−33 and CCK-33 related analogues on 2,4-DMBHA and TMBHA. *J. Med. Chem. 36*, 1681–1688.

(17) Laverman, P., Roosenburg, S., Gotthardt, M., Park, J., Oyen, W. J. G., de Jong, M., Hellmich, M. R., Rutjes, F. P. J. T., van Delft, F. L., and Boerman, O. C. (2007) Targeting of a CCK2 receptor splice variant with 111In-labelled cholecystokinin-8 (CCK8) and 111In-labelled minigastrin. *Eur. J. Nucl. Med. Mol. Imaging 35*, 386–392.

(18) Larsen, S. D., Barf, T., Liljebris, C., May, P. D., Ogg, D., O'Sullivan, T. J., Palazuk, B., Schostarez, H. J., Craig Stevens, F., and Bleasdale, J. E. (2002) Synthesis and biological activity of a novel class of small molecular weight peptidomimetic competitive inhibitors of protein tyrosine phosphatase 1B. *J. Med. Chem. 45*, 598–622.

(19) Herzner, H., and Kunz, H. (2007) (p-Sulfomethyl)phenylalanine as a mimic of O-sulfatyl-tyrosine in synthetic partial sequences of P-Selectin glycoprotein ligand 1 (PSGL-1). *Tetrahedron 63*, 6423–6436.

(20) Danheiser, R. L., Romines, K. R., Koyama, H., Gee, S. K., Johnson, C. R., and Medich, J. R. (1998) A hydroxymethyl anion equivalent: tributyl[(methoxymethoxy)methyl]stannane. *Org. Synth. 9*, 704–708.

(21) De Luca, S., Saviano, M., Della Moglie, R., Digilio, G., Bracco, C., Aloj, L., Tarallo, L., Pedone, C., and Morelli, G. (2006) Conformationally constrained CCK8 analogues obtained from a rationally designed peptide library as ligands for cholecystokinin type B receptor. *ChemMedChem 1*, 997–1006.

(22) De Luca, S., De Capua, A., Saviano, M., Della Moglie, R., Aloj, L., Tarallo, L., Pedone, C., and Morelli, G. (2007) Synthesis and biological evaluation of cyclic and branched peptide analogues as ligands for cholecystokinin type 1 receptor. *Bioorg. Med. Chem. 15*, 5845–5853.

(23) Good, S., Walter, M. A., Waser, B., Wang, X., Müller-Brand, J., Béhé, M. P., Reubi, J.-C., and Maecke, H. R. (2008) Macrocyclic chelator-coupled gastrin-based radiopharmaceuticals for targeting of gastrin receptor-expressing tumours. *Eur. J. Nucl. Med. Mol. Imaging 35*, 1868–1877.

BC900465Y

In Situ Growth of Side-Chain PEG Polymers from Functionalized Human Growth Hormone—A New Technique for Preparation of Enhanced Protein−Polymer Conjugates

Johannes Pall Magnusson,[†] Sara Bersani,[‡] Stefano Salmaso,[‡] Cameron Alexander,[†] and Paolo Caliceti*,[‡]

School of Pharmacy, University of Nottingham, University Park, Nottingham NG7 2RD, United Kingdom, and Department of Pharmaceutical Sciences, University of Padua - Via F. Marzolo 5, 35131, Padova, Italy. Received October 29, 2009; Revised Manuscript Received February 12, 2010

The application of atom transfer radical polymerization (ATRP) for preparation of a novel class of protein−polymer bioconjugates is described, exemplified by the synthesis of a recombinant human growth hormone (rh-GH) poly(ethylene glycol) methyl ether methacrylate (PEGMA) hybrid. The rh-GH protein was activated via a bromoester functionalized linker and used as a macroinitiator to polymerize the hydrophilic monomer PEGMA under solely aqueous conditions at 4 °C. ATRP conditions resulted in controlled polymer growth from rh-GH with low-polydispersity polyPEGMA chains. The rh-GH PEGMA product exhibited properties consistent with the presence of attached hydrophilic polymer chains, namely, high stability to denaturation and proteolysis. The polymerization conditions and conjugation proceeded with retention of the biological activity of the hormone. The rh-GH PEGMA was administered subcutaneously to rats and the activity compared to native rh-GH. The rh-GH PEGMA exhibited similar activity as the native rh-GH in vivo when a daily dose of 40 μg was administered. However, when a higher dose of 120 μg was administered with 3 days between injections the bioavailability of the rh-GH PEGMA was significantly better than that of the native. The results therefore demonstrate that ATRP can be successfully used as a general alternative approach to direct polymer conjugation, namely, PEGylation, to produce PEG-like protein conjugates. This technique can be exploited to design and synthesize protein−polymer derivatives with tailored therapeutic properties.

INTRODUCTION

Proteins are of increasing interest in medicine (*1–3*) and the emerging field of bionanotechnology (*4, 5*). Advances in recombinant DNA techniques have made possible the production of therapeutic proteins in large quantities (*6*). However, the potential for applying proteins in clinical and technological settings has been limited since they are prone to denaturation and aggregation in vitro (*7*), while in vivo, proteins administered by standard routes exhibit poor pharmacokinetic properties (*8*). In efforts to circumvent these problems, proteins have been selectively modified by tailoring their amino acid sequences (*9, 10*) and/or by attachment of polymer chains (*11–13*). Of the latter, the attachment of poly(ethylene glycol) (PEG) polymers (PEGylation) has been most extensively studied (*14*) and has already created numerous successful products for the clinic (*15*). Attached PEG enhances the stability of the protein, increases the hydrodynamic volume, and makes the surface less accessible to proteases and the immune system (*16*). This leads to better retention times in the body and improved bioavailability (*17*). However, PEGylation is not without certain limitations. PEG is difficult to modify after conjugation to a protein—for example, when a cell-targeting ligand or a fluorophore is needed—and the purification of unreacted PEG from a protein polymer mixture can be highly problematic. The alternative option to attaching a preformed polymer to a protein is to grow a polymer from a protein such that no free polymer in solution is formed. The benefits of the "growing from" approach are not limited to ease of purification and addition of targeting ligands or other chemical moieties, physicochemical or biological modifiers, after growth of polymer from the protein. If the polymerization can be controlled, a wide variety of bioconjugates with potentially "tunable" activity can be prepared from a single protein precursor: these might include block copolymers wherein different segments of the polymer chain confer specific properties such as response to pH or other microenvironmental stimuli, tightly defined hydrophilic/hydrophobic character, membrane insertion, cell recognition properties, or resistance to proteases. However, the chemical strategies needed to grow PEG and related substituted oxiranes from a protein in a controllable manner, such as living anionic polymerization, are not compatible with retaining protein structure and activity.

In recent years, controlled radical polymerization techniques (*18–21*) have enabled the growth of polymers with highly defined molar masses and functional group content from a wide variety of commercially available monomers. Methacrylate monomers with oligo(ethylene glycol) side chains can be prepared using these routes to form comb polymer analogues of PEG. As a consequence, there is now considerable interest in evaluating whether these polymers might replace PEG in biomedical settings. One such possibility is to generate polymer−protein conjugates by growing PEG-analogue polymers such as PEGmethacrylate (PEGMA) from proteins functionalized with a polymerization-initiating site. A number of recent papers have demonstrated the feasibility of using proteins as macroinitiators from which to grow polymers (*22, 23*). To date, while there have been recent reports of postpolymerization attachment of poly(PEGmethacrylates) [polyPEGMA)] to peptides and proteins (*24–28*), reports of growing these polymers directly from proteins have been quite scarce (*23, 29*).

Here, we describe the synthesis of a poly(PEGMA) conjugate of recombinant human growth hormone (rh-GH) by controlled radical polymerization from an initiator-functionalized rh-GH

* Corresponding author e-mail: paolo.calceti@unipd.it.
[†] University of Nottingham.
[‡] University of Padua.

10.1021/bc900468v © 2010 American Chemical Society
Published on Web 03/04/2010

precursor. We chose rh-GH as the protein model because the native protein is the drug of choice for treatment of growth deficiency and PEGylated GH forms have been developed either by nonspecific or, recently, by selective polymer conjugation (*30–32*). We activated rh-GH by a lysine reactive linker, and then, poly(PEGMA) was grown from the protein under solely aqueous conditions at low temperature. The rh-GH polymer hybrid was characterized and tested in an in vivo model and was found to exhibit increased activity in comparison to the native protein. The combination of mild conditions for bioconjugation and polymer synthesis makes this technique favorable as a generic approach for the modification of biomacromolecules. In addition, the good biocompatibility profile of poly(PEGMA) (*33*), the enhanced stability of the rh-GH bioconjugate, and the desire to reduce the daily injection profile currently adopted for rh-GH in the clinic suggest that the conjugate is promising for therapeutic applications.

MATERIALS AND METHODS

Materials. The recombinant human growth hormone (rh-GH) was a kind gift of Bio-Ker srl (Pula, Italy). α-Br-isobutyryl bromide (98%), copper(II) bromide ($CuBr_2$, 99%), L-ascorbic acid (99%), and triethylamine (Et_3N, 99.5%) were used as received from Sigma Aldrich (St. Louis, MO, USA). Poly(ethylene glycol) methyl ether methacrylate (PEGMA, M_n 475) was purchased from Sigma Aldrich and purified before use by passing through a column filled with neutral alumina. Water used for the polymerizations was of ELGA grade. Tris(2-pyridyl) methylamine (TPMA) was prepared as described elsewhere (*34*). Dialysis membrane (MWCO 6−8000, regenerated cellulose) was used as received from Spectrapor (Tempe, AZ, USA). All solvents and reagents were of analytical or HPLC grade and purchased from Sigma or Fisher Scientific (Loughborough, UK) unless otherwise stated. Deuterated solvents were obtained from Sigma. Tetra(ethylene glycol) (TEG, 99%) was dried via three cycles of distillation with anhydrous toluene.

Animals. Four-week-old hypophysectomized female Sprague−Dawley rats, weighing 70−80 g, were obtained from Charles River (Como, Italy). Animal care and handling were performed in accordance with the provisions of the European Economic Community Council Directive 86/209 (recognized and adopted by the Italian Government with the approval decree D.M. No. 230/95-B) and the NIH publication no. 85−23, revised in 1985.

Initiator Synthesis. *Compound* **1***: 2-[2-[2-(2-Hydroxyethoxy-)ethoxy]ethoxy]-ethyl-α-bromo-2-isobutyrate (HO-TEG-Br).* Anhydrous tetra(ethylene glycol) (TEG, 100 g, 0.51 mol) and triethylamine (Et_3N, 5.7 g, 0.05 mol) were dissolved in 100 mL of tetrahydrofuran (THF), and the mixture was placed in an ice bath. α-Br-isobutyryl bromide (11.9 g, 0.05 mol) was added dropwise to the mixture under vigorous stirring. The reaction was left for 1 h in the ice bath and at room temperature for 16 h. The mixture was filtered and the THF was removed under vacuum; the remaining oily residue was dissolved in 150 mL of water and extracted twice with 150 mL of dichloromethane. The organic solution was dried by addition of anhydrous Na_2SO_4 and filtered. The solvent was removed under vacuum and the resultant oily residue was purified by silica chromatography using 10:90 methanol:diethyl ether as eluent to give HO-TEG-Br (compound **1**, Figure 1). The synthesis resulted in HO-TEG-Br as a pale yellow oil in 80% yield. The purity and the product identity were verified by high-resolution mass spectrometry (HRMS) and NMR spectroscopy. HRMS spectra were recorded on an ESI-TOF Waters 2795 separation module/micromass LCT platform.^{1}H and ^{13}C NMR spectra (Supporting Information, Figures S1 and S2) were recorded on a Bruker 400 spectrometer at 399.8 MHz (^{1}H) and 100.5 MHz (^{13}C) in chloroform-*d*. Chemical shifts are reported in ppm relative to TMS.

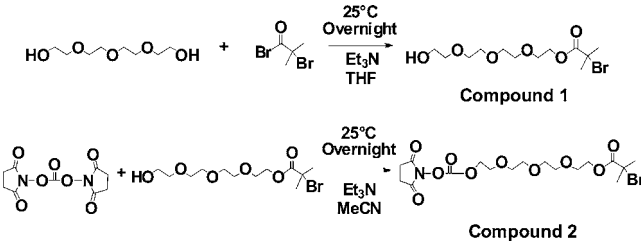


Figure 1. Synthesis of a TEG-based amine-reactive ATRP initiator.

HRMS: calcd for (M^+) 342.0678 and (M+Na) 365.0576; found (M+Na^+) 364.8483. ^{1}H NMR ($CDCl_3$, 400 MHz): δ 4.32 (m, 2H), 3.76−3.51 (m, 14H), 2.66 (s, 1H), 1.92 (m, 6H). ^{13}C NMR ($CDCl_3$): δ 171.57, 72.49, 70.63, 70.56, 70.33, 68.73, 65.09, 61.67, 55.72, 30.53. The NMR spectra are reported in the Supporting Information.

Compound **2***: 1-(2,5-Dioxopyrrolidin-1-yloxy)-1-oxo-2,5,8,11-tetraoxatridecan-13-yl-α-bromo-2-isobutyrrate (succinimidyl-TEG-Br).* Anhydrous HO-TEG-Br (2.45 g, 7.1 mmol) was dissolved in 5 mL of acetonitrile (MeCN). *N*,*N*′-Disuccinimidyl carbonate (DSC, 2.16 g, 8.5 mmol) and Et_3N (0.87 g, 8.5 mmol) were added. The reaction mixture was left at room temperature for 16 h. The MeCN was evaporated and the oily residue dissolved in chloroform and washed 3 times with an equivalent amount of water. The final organic solution was dried by addition of anhydrous Na_2SO_4 and filtered. The chloroform was evaporated and the oily residue purified by silica chromatography as reported above to give succinimidyl-TEG-Br (compound **2,** Figure 1) as a yellow oil in 70% yield. The purity and the product identity were verified by high-resolution mass spectrometry (HRMS) and nuclear magnetic resonance. The ^{1}H and ^{13}C NMR spectra (Supporting Information, Figure S3 and S4) were recorded as reported above.

HRMS: calcd for (M^+): 483.0740 and (M+Na^+) 506.0638; found (M+Na^+) 506.0536. (Note, presence of (M+H_2O) peak at 503.1014 indicated NHS-hydroxylation under MS conditions.) ^{1}H NMR ($CDCl_3$, 400 MHz): δ 4.48−4.46 (m, 2H), 4.36−4.33 (m, 2H), 3.85−3.67 (m, 12H), 2.85 (s, 4H), 1.96 (m, 6H). ^{13}C NMR ($CDCl_3$): δ 171.60, 168.59, 151.62, 70.87, 70.69, 70.62, 70.59, 70.21, 68.71, 68.32, 65.15, 55.81, 30.74, 25.54.

Conjugation of Initiator to rh-GH. Recombinant human growth hormone (rh-GH, 90 mg, 0.004 mmol) was dissolved in 40 mL of 1 mM phosphate buffer, 0.15 M NaCl, pH 7.5. Succinimidyl-TEG-Br (100 mg, 0.20 mmol) was dissolved in 1 mL of DMSO and added dropwise; the reaction was left for 90 min at room temperature. The mixture was dialyzed for 3 days at 4 °C, and then lyophilized to yield the rh-GH-TEG-Br conjugate (macroinitiator) (90 mg) as a powdery solid.

MALDI-TOF. MALDI-TOF (Matrix-assisted laser desorption/ionization (time-of-flight)) analysis was carried out on a Bruker MALDI TOF Ultraflex II machine. Briefly, an aqueous solution of the conjugate (1.0 mg/mL) was mixed with an equal volume of matrix material (8 mg sinapic acid, 0.5 mL water and 0.5 mL MeCN). An aliquot (2 μL) of the resulting mixture was spotted onto a plate target and allowed to dry. The level of conjugation was determined by comparing the molar mass of the conjugate to the native protein.

Polymer Growth from rh-GH. The macroiniator rh-GH-TEG-Br (30 mg, 0.0014 mmol) was dissolved in 4.5 mL of 1 mM phosphate buffer, 0.15 M NaCl, pH 8.0. PEGMA 475 (475 mg, 1 mmol), $CuBr_2$ (11.2 mg, 0.05 mmol), and TPMA (14.5 mg, 0.05 mmol) were added to the protein solution. The mixture was placed in an ice bath at 4 °C and bubbled through with argon. After 15 min, ascorbic acid (1.32 mg, 0.0075 mmol) was added to initiate polymerization. The reaction was stopped after 16 h, and the free monomers, copper, and ligand were removed

by dialysis, which was carried out for 3 days at 4 °C in 4 mM EDTA. The protein solution was then dialyzed against water, frozen with liquid nitrogen, and lyophilized. Two hundred milligrams of product (rh-GH-PEGMA) was collected.

SDS PAGE. Sodium dodecyl sulfate polyacrylamide gel electrophoresis (SDS-PAGE) was carried out at 100 mV using 8% acrylamide gel prepared by the standard method and visualized by Coomassie staining (*35*). The gels were additionally stained for PEG by Iodine (*36*).

Circular Dichroism Analysis. Circular dichroism (CD) spectra were recorded in the far UV region (195−250 nm) using rh-GH solutions (0.1 mg/mL, 4.5 μM) or an equimolar quantity of rh-GH-PEGMA in 20 mM phosphate buffer, 0.15 M NaCl, pH 7.2. A J-810 Jasco spectrodichrograph (Tokyo, Japan) instrument was used.

Protein and PEG Content in the rh-GH-PEGMA Conjugate. Protein concentrations of the native and the rh-GH-PEGMA were evaluated spectrophotometrically using the calculated molar coefficient extinction at 280 nm of rh-GH ($\varepsilon = 16\,170\ M^{-1}\ cm^{-1}$). The concentration was also confirmed by BCA Protein Assay (Pierce, Rockford IL, USA) (*32*) using native rh-GH solutions as standard for the calibration curve [Abs = 0.7926 (Protein conc, mg/mL) + 0.0317, $R^2 = 0.9997$]. PEG [poly(ethylene glycol)] content in the rh-PEGMA solution was determined by an iodine assay (*33*) using a calibration curve obtained by plotting the absorbance at 535 nm against PEG concentration in the range 2−5 μg/mL, [Abs = 0.0664 (PEG conc, μg/mL) + 0.001, $R^2 = 0.99$].

The polymer/protein molar ratio in the rh-GH-PEGMA derivative was spectrophotometrically evaluated by a trinitrobenzensulfonic acid (TNBS) colorimetric method (*37*).

Molar Mass Analysis. Polymers were cleaved from protein specifically by adopting a method from Jaquemard et al. (*38*). The protein−polymer hybrid (10 mg), anhydrous THF (10 mL), and tetra-*n*-butylammonium fluoride (TBAF, 100 μL) were placed in a round-bottom flask with a condenser, and the mixture was refluxed for 6 h. The THF was evaporated and the polymer extracted into DMF and analyzed by gel permeation chromatography (GPC).

Molar masses and molar mass distributions of the polymer species were determined using a Varian Laboratories GPC-50 instrument with triple detection (RI, viscometry and MALLS). Chromatograms were run at 50 °C using dimethylformamide (DMF) as eluent with a flow rate of 1 mL/min. The columns used were Polargel L; detection was performed by a Refractive Index detector (RI). The GPC was calibrated with linear PMMA (poly(methyl methacrylate)) standards.

High-Performance Liquid Chromatography Analysis. Size-exclusion analyses (SEC-HPLC) were run on a Shimadzu LC-10AS pump with the SPD-10A detector set at 214 nm. The system was equipped with a Bio-Gel SEC 40-XL column (5 μm, 300 × 7.8 mm; BioRad, Milan, Italy) and isocratically eluted with 63 mM phosphate buffer, 3% isopropanol, pH 7.0, at a flow rate of 0.6 mL/min.

Stability Studies. Stability studies were performed by incubation of rh-GH (1 mg/mL) or equimolar rh-GH-PEGMA solutions in 20 mM phosphate buffer, 0.15 M NaCl, pH 7.4, at 37 °C. Parallel samples were incubated at 37 °C under magnetic stirring in order to simulate stress conditions. At scheduled times, aliquots (50 μL) were taken and diluted with buffer (50 μL), centrifuged at 5000 rpm for 5 min, and analyzed by SEC-HPLC as reported above. The area under the curve corresponding to native or rh-GH-PEGMA bioconjugate was compared with standard titration curves obtained with the rh-GH and rh-GH-PEGMA, to evaluate the remaining protein content in the PBS solution.

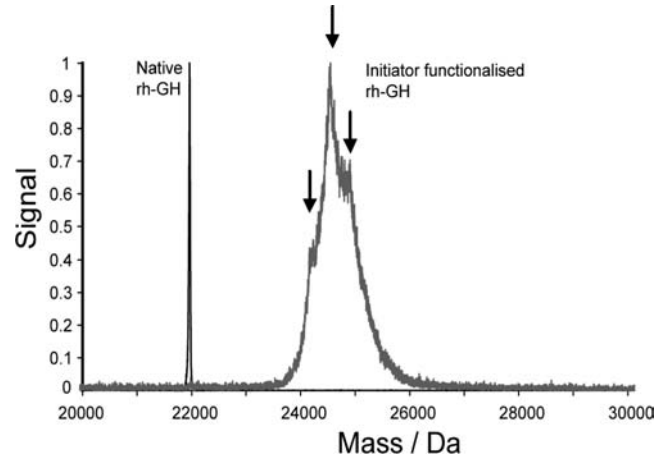


Figure 2. MALDI-TOF analysis: native rh-GH and α-Br isobutyryl-tetra(ethylene glycol)-functionalized rh-GH conjugate (initiator functionalized rh-GH). The arrows indicate the rh-GH forms functionalized with 6, 7, and 8 α-Br isobutyryl-tetra(ethylene glycol) moieties.

Pepsin Proteolysis. Native rh-GH (400 μg) or equimolar amounts of rh-GH-PEGMA were dissolved in 2 mL of 0.01 M HCl and added to 1 mL of 25 μg/mL pepsin solution in 0.01 M HCl (25:1 rh-GH/pepsin molar ratio). The solutions were maintained at 25 °C. At scheduled times (0, 15, 30, 60, 90, 120 min), samples (250 μL) were removed and analyzed by the TNBS assay to determine the protein amino groups released by protein hydrolysis. The degradation degree was calculated on the basis of the optical density values obtained at the experimental time points, which were referred to the maximal optical density obtained with the native protein (100%) achieved as a plateau after 9 h incubation with the proteolytic enzyme.

In Vivo Activity. Forty hypophysectomized female Sprague Dowley rats weighing 70−80 g were randomly divided into five groups of eight animals. Animals of Group A were treated on days 0, 1, 2, 3, 4, and 5 by subcutaneous injection of a physiological solution (200 μL); animals of Groups B and C were treated on days 0, 1, 2, 3, 4, and 5 by subcutaneous injection of native rh-GH (40 μg) or equimolar of rh-GH-PEGMA in physiological solutions (200 μL), respectively; animals of Groups D and E were subcutaneously injected at days 0 and 3 with native rh-GH (120 μg) or equimolar of rh-GH-PEGMA in physiological solutions (200 μL), respectively. The animals were weighed daily, and the weight increase was recorded. The activity of the hormone was estimated by changes in the body mass of the animals as described previously by Clark et al. (*32*).

RESULTS

rh-GH-PEGMA Preparation. The synthetic strategy adopted to prepare compound **1** (Figure 1) employed a large excess of tetraethylene glycol to favor its monoacylation. Silica chromatography yielded compound **1** in high purity and good yield (80%). Compound **1** was reacted subsequently at the free hydroxyl terminus to generate compound **2** as a heterobifunctional spacer with an amine-reactive component at one end and an ATRP initiating site at the opposite end. The yield of product **2** following purification was 70%.

The ATRP initiator linker (compound **2**) was reacted with rh-GH at pH 7.5 in order to ensure conjugation at the terminal amine and lysine residues (*39*). Modification of the all accessible amino groups was achieved by using a large excess of compound **2** compared to rh-GH.

MALDI-TOF spectra of the native rh-GH and the conjugated protein reported in Figure 2 revealed that the linker conjugation yielded three main species corresponding to conjugates bearing

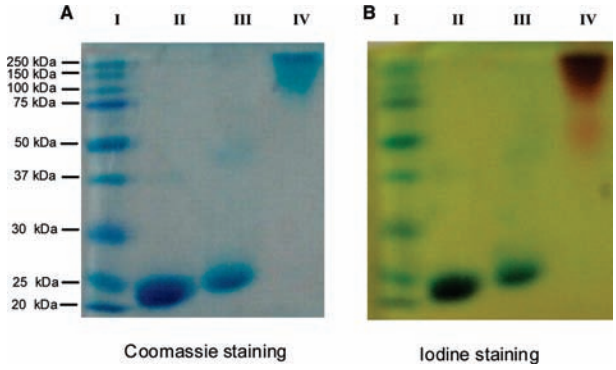


Figure 3. SDS PAGE stained with Coomassie blue (A) and iodine (B): Lane I, protein marker; Lane II, native rh-GH; Lane III, initiator functionalized rh-GH; Lane IV, rh-GH-PEGMA.

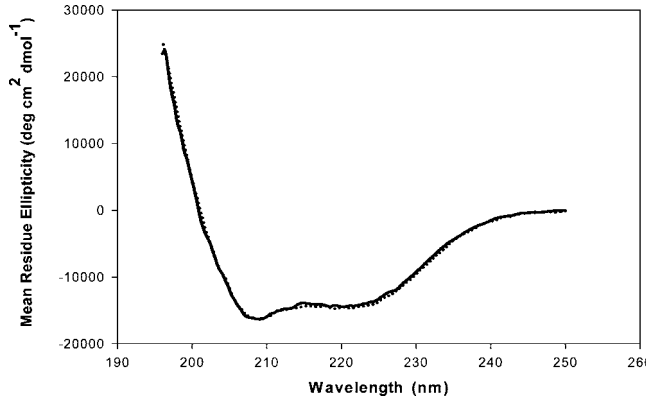


Figure 4. CD profiles of native rh-GH (—) and rh-GH-PEGMA (•••).

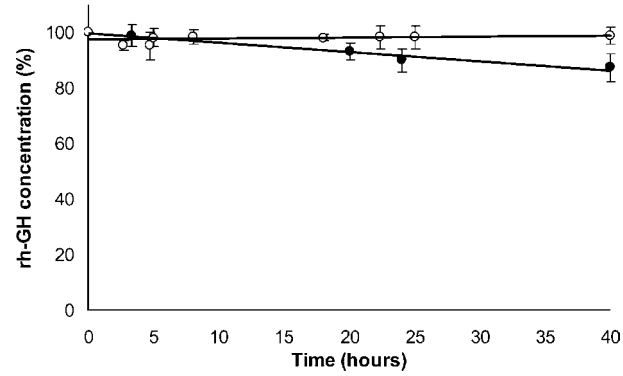


Figure 5. Stability profile of native rh-GH (●) and rh-GH-PEGMA (○) at 37 °C.

6, 7, and 8 tetra(ethylene glycol)-α-Br-isobutyryl functions (mol wt 24 130, 24 485, and 24 840 Da, respectively). This result indicates that the majority of the 10 protein amino groups (9 Lys and 1 amino terminal Phe) were modified. The species with 7 initiator-modified moieties was predominant. After PEGMA polymerization, the TNBS analysis gave a mean of 9 modified amino residues per protein, corresponding to 90% of available amino groups. The higher value for the colorimetric assay was most likely due to the fact that the assay is dependent on the accessibility of TNBS to the amines, which results in an overestimation of the number of modified amines in the conjugate compared to the native protein (*40*). Therefore, it is more likely that the MALDI TOF results gave a better indication of the degree of conjugation of the initiator and the polymer to rh-GH.

SDS PAGE analysis of the native rh-GH (Lane II), initiator-functionalized rh-GH (Lane III), and the rh-GH-PEGMA conjugate (Lane IV) illustrated that after the polymerization neither native nor macroinitiator (rh-GH-TEG-Br) were present (Figure 3). The polymerization resulted in the protein-containing fractions of the polymer-conjugate migrating less through the gel and remaining at the top (higher molar mass regions) of the gel (Figure 3A). Iodine staining confirmed the presence of PEG in the same regions (Figure 3B), providing further support for the formation of the PEGMA-rh-GH conjugate.

Structural Characterization of rh-GH-PEGMA. The protein−polymer hybrid composition was evaluated by UV absorbance at 280 nm and BCA assay for protein determination and by an iodine assay for PEG quantification. The spectroscopic analysis of rh-GH-PEGMA solutions showed that the conjugate consisted of 15% protein and 85% polymer by mass. This was equivalent to a total molar mass of 147 kDa for the protein polymer hybrid. Therefore, the molar mass of the polymer chains calculated by combining the number of modified amino groups obtained by the MALDI-TOF analysis, and the molar mass obtained by the spectroscopic assays was 19.5 kDa. Additionally, the molar mass of polymer species liberated from the conjugate by acidic hydrolysis of the conjugate was measured by gel permeation chromatography (GPC profiles reported in the Supporting Information, Figure S5). A molar mass peak (M_p) of 22 kDa with a polydispersity index of 1.2 was obtained, which is in reasonable agreement with results obtained by the other methods. The slight variation in the molar mass determined by GPC and the spectrometric assays was most probably a function of the GPC calibration with poly(methyl methacrylate) standards which have different hydrodynamic properties from the comb-type PEGMA polymers. More importantly, the GPC analysis demonstrated that all the polymer species on the protein were narrowly and equally distributed around the M_p. Therefore, it can be assumed that all of the activated amines had similar accessibility and efficiency to propagate the polymerization. According to the number of polymer chains and their molar mass, the monomer conversion after 16 h reaction was 38%.

Size-exclusion HPLC chromatography (HPLC profiles reported in the Supporting Information, Figure S6) confirmed the higher molar mass of rh-GH-PEGMA compared to native protein. Dynamic light scattering indicated the presence of species of R_H 10−12 nm in buffer, which is consistent with the modified protein size, but no larger aggregates or precipitates were observed under the concentrations and conditions employed for DLS.

Both CD and UV−vis spectra obtained with rh-GH-PEGMA conjugate overlaid the spectra recorded with the native protein indicating that no significant alterations in the protein conformation were induced by polymer conjugation. The CD profiles reported in Figure 4 show that conjugation did not induce alteration in the secondary structure of rh-GH. The α-helix content calculated according to the k2D method was 57% in the conjugate and 58% in the native protein, which is in agreement with the data reported in the literature.

Stability of rh-GH-PEGMA. The stability profiles obtained for rh-GH and rh-GH-PEGMA at 37 °C in solution are shown in Figure 5. The concentration of rh-GH in the solution slightly decreased throughout the experiment time indicating that the protein slowly denatured, leading to aggregation and precipitation. The concentration of rh-GH-PEGMA on the other hand did not change during the experiment, demonstrating that the attached polymer chains enhanced the physical stability of the protein thus preventing aggregation and precipitation phenomena.

The stability of rh-GH and rh-GH-PEGMA was also investigated under stress conditions produced by high solution agitation. The stability profiles depicted in Figure 6 demonstrated that the PEGMA conjugation prevented protein aggregation and

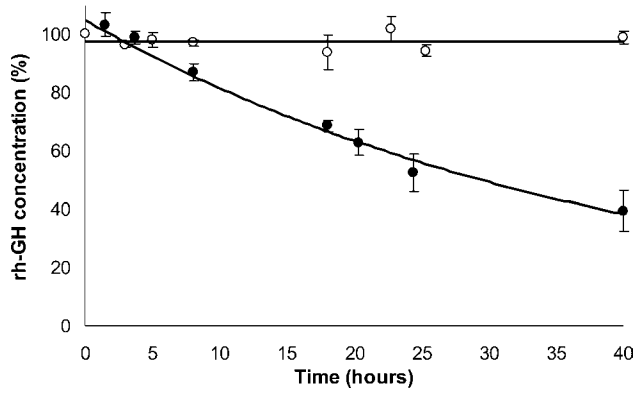


Figure 6. Stability profile of native rh-GH (●) and rh-GH-PEGMA (○) at 37 °C under stress conditions.

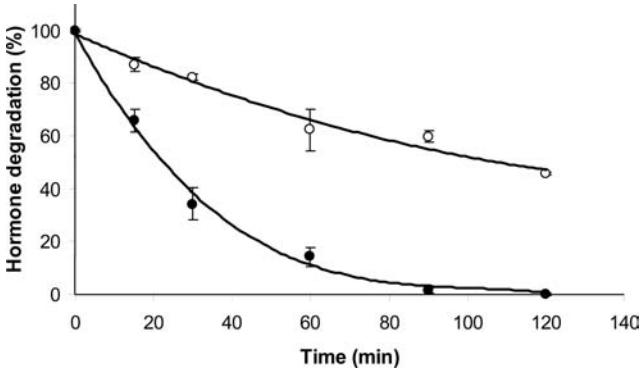


Figure 7. Degradation profiles of native rh-GH (●) and rh-GH-PEGMA (○) incubated with pepsin.

precipitation in an even more pronounced fashion under agitation than in solution. Indeed, under stress the native protein rapidly aggregated and precipitated when stirred, which was reflected by a first-order concentration decrease of the native protein. The rh-GH-PEGMA concentration by contrast was not significantly affected by the agitation.

Under proteolytic conditions, the native rh-GH was rapidly degraded. Figure 7 shows that the concentration of native rh-GH was reduced by 50% in 20 min and complete degradation of protein occurred by 120 min. In contrast, 50% degradation of rh-GH PEGMA required at least 120 min in the presence of pepsin. We attribute this to the PEGMA chains on the surface of the rh-GH polymer conjugate preventing access for the protease, which in turn led to improved stability.

Biological Investigations. The biological activity of native and rh-GH-PEGMA were examined in vivo by subcutaneous administration of equimolar doses of the two protein forms to hypophysectomized rats. Two different dosage protocols were used: daily administration of 40 μg rh-GH equivalent dose for 6 days and 120 μg rh-GH equivalent dose twice a week. The daily weight increase of the animals was monitored for 9 days as shown in Figure 8.

Figure 8a shows that daily administration of 40 μg hormone equivalent dose of rh-GH-PEGMA elicited similar body weight profiles to those obtained with the same dosage regimen of native hormone. A few days after the final injection of the protein, the weight of the animals in both groups started to decline.

Higher doses of 120 μg were administered to other groups of animals in a dosing regime involving 3 days between the injections (Figure 8b). The native rh-GH elicited a single day dose response. The weight of the animals increased the day following an injection of the native rh-GH but afterward the

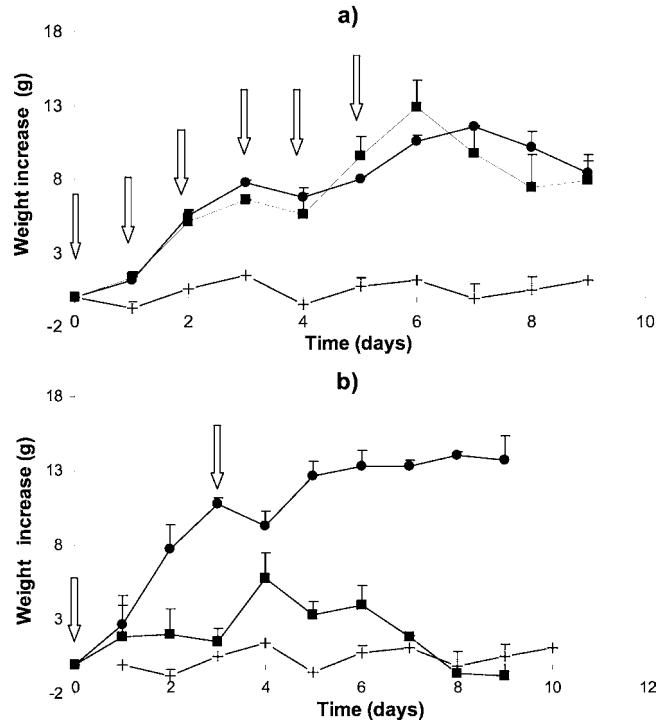


Figure 8. Rat weight increase (%) after administration of rh-GH and rh-GH-PEGMA. In (a), 40 μg daily treatment (arrows) of native rh-GH (■), rh-GH-PEGMA (●), and buffer (+) (Control); in (b), rat weight increase (%) after administration 120 μg twice a week treatment (arrows) of native rh-GH (■), rh-GH-PEGMA (●), and buffer (+) (Control).

weight of the animals remained constant or declined. The rh-GH PEGMA injections, on the other hand, exhibited a sustained response for a few days following the injections. At that point in time, the weights of the animals that had received the native rh-GH injections were not significantly different from the control group. The weights gained by the animals following injections of the rh-GH PEGMA were maintained for the remainder of the study.

DISCUSSION

The aim of this work was to evaluate whether the "growing from" polymerization could be used as an alternative approach to conventional direct PEGylation for production of pharmaceutically active polymer−protein conjugates. Controlled radical polymerization related protocols possess a number of potential advantages compared to "grafting to" polymer conjugation. These include high versatility and tunability, control of polymer molar mass and polydispersity, as well as reduced purification drawbacks. These advantages, together with the easier and versatile site-selective conjugation of low molecular weight anchoring functions (initiators), as compared to site-selective large bulky polymer conjugation, potentially allow a much greater diversity of polymer−protein conjugates to be prepared. However, it is important to consider carefully the method by which the polymer can be grown from a protein and the means by which an initiating group can best be attached.

Our primary aim was to demonstrate proof of concept of the "growing from" approach to obtain active protein−polymer bioconjugates in a controlled way. We thus prepared an α,ω-heterobifunctional ATRP initiator linked via a tetra(ethylene glycol) spacer to an active ester (Compound **2**), so that polymer growth sites could be generated from derivatized accessible amino groups on rh-GH. MALDI-TOF and SDS-PAGE confirmed reaction of the linker with rh-GH and the modified

protein was found to be an active macroinitiator for polymer growth. The derivatization degree of rh-GH with the linker was in fair agreement with data reported for prior modifications with other polymers in the literature (*31*), which have indicated that Lys-115 is unreactive and four other lysines of the ten present on rh-GH are poorly reactive. We chose an ATRP route for polymer growth, as this method is advantageous for generating a very wide range of molar masses with good control. Also, ATRP can operate under mild conditions, which is important to prevent protein denaturation and inactivation. Finally, we wanted to establish an all-aqueous protocol, as the flexibility inherent to the ATRP approach allows for the introduction of many different monomers, each of which might contribute to a desired property or activity. Surprisingly, there have been relatively few reports to date of ATRP polymerizations from proteins, and none have reported "grafting from" proteins at low temperature in water. The success of the grafting-from procedure we adopted here was shown by the narrow molar mass range of the polymers grown from the protein and the complete conversion of macroinitiator to polymer−protein conjugate as shown by SDS-PAGE, iodine staining, gel permeation chromatography, and titrations. Importantly, all the initiator domains on the protein structure were involved in the polymerization process. This was a relevant finding, as it indicated the robustness of the polymer-growth methodology. Although all the lysines derivatized were close to the surface of rh-GH, they were in subtly different environments; the fact that the polymers grew to a molar mass of about 20 kDa with narrow polydispersity ($M_w/M_n = 1.2$) is indicative that the initiator termini were free to react equally and that chain growth occurred smoothly from all the sites. The low polydispersity and the homogeneous product features are important requisites from a regulatory viewpoint, as the resulting conjugates are less heterogeneous than polymer−protein conjugates generated with polymers obtained through conventional free-radical routes.

The improved stability of the rh-GH to aggregation and precipitation from solutions as a consequence of bioconjugation is attributable to the presence of the PEGMA comb polymer shell. PEGMA chains, with their dense hydrophilic surface layer, have in fact been reported to reduce aggregation compared to conventional PEG (*41*). The presence of about 7 polyPEGMA chains on the rh-GH conjugate was most likely to have been responsible for the enhanced protein stability. Although the PEG side chains on the PEGMA systems we used were smaller (8−9 ethylene glycol repeat units, $M_n \sim 475$) compared to those used by Ryan et al. (*24*) for direct salmon calcitonin conjugation ($M_n \sim 1100$), the hydrated polymer shell around the protein is still likely to present a strong entropic barrier to aggregation processes.

Increased resistance to pepsin degradation also occurred after polymer conjugation. This resistance to pepsin activity is due to reduced access of the protease to the rh-GH target confirming the steric shielding of the conjugated polymer chains. There is of course a trade-off between steric shielding to protect against proteases while not shielding the active site of the prepared bioconjugate to the extent that functionality is lost (*42*).

The in vivo data on the effect of rh-GH and rh-GH-PEGMA indicated that the functional activity of the hormone was not affected significantly by polymer conjugation. Administration daily of 40 μg equivalent doses of rh-GH and rh-GH-PEGMA over 6 days resulted in similar weight growth profiles. However, for a higher equivalent dose (120 μg), introduced at day 0 and day 3 only, there was a significant enhancement in the weight gain of the animals, indicative of enhanced and sustained bioactivity.

The enhanced bioactivity obtained with rh-GH-PEGMA was similar to that reported for rh-GH analogues obtained by site-specific 20 kDa PEG monoconjugation (*30*) and multiple 5 kDa PEG attachment (*32*). Intriguingly, our data with the PEGMA-modified rh-GH showed enhanced activity compared to the native rh-GH over the same dosing regime as the previously reported mono-PEGylated analogue, despite the more extensive derivatization on multiple amino group residues for the rh-GH-PEGMA. Clark et al. (*32*) demonstrated that all the rh-GH derivatives obtained by random modification with several PEG chains displayed higher pharmacological activity than the parent molecule. Nevertheless, it was shown that the in vivo activity of PEGylated rh-GH was affected by the number of the attached polymer molecules, PEG size, and shape (*43*). This result is probably due to a balance of effects bestowed by the polymer conjugation. Indeed, the rh-GH in vitro activity was found to significantly decrease as the polymer size or number of polymer chains increase, while the protein stability and the pharmacokinetic behavior are known to improve as the polymer content in the conjugate increases (*44*). In vivo, the activity decrease may be counterbalanced by the increased stability and enhanced pharmacokinetic profile of the conjugate that, depending on its structural composition of the conjugate, may display improved therapeutic efficacy compared to the native counterpart as observed with other proteins (*44, 45*). Therefore, it is possible that a derivative containing several high molecular weight polymer chains displays a better pharmacological performance than derivatives obtained with higher numbers of polymers each of lower molar mass. Additionally, it should be considered that polyPEGMA has a different structure than linear PEG. The polyPEGMA in this study contains short PEG side chains attached to a polymethacrylate backbone via an ester bond. This structural difference may be an important factor in maintaining the high biological activity. Indeed, polyPEGMA chains are less flexible than linear PEG owing to their "bottle brush" structure and, therefore, may have a lower masking effect. Furthermore, PEG can be slowly released in vivo from the PEGMA side chains by ester bond cleavage. In both cases, the accessibility of the protein for receptor recognition would be enhanced compared to the conformationally highly mobile linear PEGs of similar molar mass.

Overall, the obtained data reported in the present paper are supportive of a novel GH bioconjugate with enhanced stability and pharmacodynamic properties compared to the native protein. Similarly to other protein drugs, the clinical need for daily injections of GH has already led to the development of new PEGylated derivatives, but the ATRP−polymer conjugates we have prepared here have a number of potential advantages over the PEGylated counterparts. The combination of synthetic polymers with natural biomolecules has been shown to be beneficial in many areas (*46*) due to the ability to tailor the properties of the synthetic component while exploiting, for example, the specificity of the natural polymer. However, the synthetic part of a bioconjugate produced via ATRP might also contain blocks that further enhance activity compared to conventional linear or branched PEG conjugates. PEGMA analogues are more easily modified via copolymerization with components that can change conformation in response to pH, temperature, redox, or other stimuli, enabling the activity of the protein to be controlled by the attached polymer. Responsive polymer−protein conjugates have been prepared previously (*47–49*), but the detailed study of such systems in vivo is still unexplored. In addition, PEGMA polymers created via this route can be end-functionalized or reacted at side-chains (*50*) in a way not possible for conventional PEG reagents, and thus, addition of targeting agents, cell penetrating peptides, and so forth would be more simple to accomplish than for conventional PEGylated

proteins. ATRP routes to these new "smart" bioconjugates are under active investigation in our laboratories.

CONCLUSIONS

We have demonstrated that "grafting from" polymerization methodologies can be successfully exploited to produce new protein−polymer bioconjugates with tunable properties. This approach opens new perspectives in optimization of protein bioconjugates for pharmaceutical applications. The synthesis and characterization of a novel rh-GH PEGMA polymer conjugate using a living polymerization technique was carried out under wholly aqueous conditions that ensure protein stability during the conjugate polymer growth process. The aqueous ATRP polymerization method offers great versatility for controlling the polymer topology and creates materials with well-defined properties and customizable functionalities. The latter is especially important for biomedical applications. The growth of the polymers from the protein generated a conjugate material with improved stability of the proteinaceous component in solution and more importantly enhanced the pharmacokinetics of the protein. The data indicate that proteins modified with ATRP-grown polymer might be administered less frequently than native proteins, thus offering the possibility of increased patient compliance and more cost-effective treatment.

ACKNOWLEDGMENT

We thank the Engineering and Physical Sciences Research Council (EPSRC) and the European Union (NanoSci E+) for financial support, Drs. George Pasparakis and Wenxin Wang for many helpful discussions, Christine Grainger-Boultby for technical support.

Supporting Information Available: ^{1}HNMR and ^{13}C NMR spectra of Compounds **1** and **2**, the GPC chromatograph of the PEGMA polymer grown from rh-GH and the HPLC profiles of native rh-GH and rh-GH-PEGMA. This material is available free of charge via the Internet at http://pubs.acs.org.

LITERATURE CITED

(1) Veronese, F. M., Sacca, B., De Laureto, P. P., Sergi, M., Caliceti, P., Schiavon, O., and Orsolini, P. (2001) New pegs for peptide and protein modification, suitable for identification of the pegylation Site. *Bioconjugate Chem. 12*, 62–70.

(2) Pavlou, A. K., and Reichert, J. M. (2004) Recombinant protein therapeutics success rates, market trends and values to 2010. *Nat. Biotechnol. 22*, 1513–1519.

(3) Gao, W., Liu, W., Mackay, J. A., Zalutsky, M. R., Toone, E. J., and Chilkoti, A. (2009) In situ growth of a stoichiometric PEG-like conjugate at a protein's N-terminus with significantly improved pharmacokinetics. *Proc. Natl. Acad. Sci. U.S.A. 106*, 15231–15236.

(4) Sarikaya, M., Tamerler, C., Jen, A. K. Y., Schulten, K., and Baneyx, F. (2003) Molecular biomimetics: nanotechnology through biology. *Nat. Mater. 2*, 577–585.

(5) Tachibana, Y., Kurisawa, M., Uyama, H., and Kobayashi, S. (2003) Thermo- and pH-responsive biodegradable poly(alpha-N-substituted gamma-glutamine)s. *Biomacromolecules 4*, 1132–1134.

(6) Moks, T., Abrahmsen, L., Osterlof, B., Josephson, S., Ostling, M., Enfors, S. O., Persson, I., Nilsson, B., and Uhlen, M. (1987) Large-scale affinity purification of human insulin-like growth factor-I from culture-medium of Escherichia-Coli. *Bio-Technology 5*, 379–382.

(7) Kiefhaber, T., Rudolph, R., Kohler, H.-H., and Buchner, J. (1991) Protein aggregation in vitro and in vivo: a quantitative model of the kinetic competition between folding and aggregation. *Nat. Biotechnol. 9*, 825–829.

(8) Veronese, F. M., and Pasut, G. (2005) PEGylation, successful approach to drug delivery. *Drug Discovery Today 10*, 1451–1458.

(9) Meyer, D. E., and Chilkoti, A. (2002) Genetically encoded synthesis of protein-based polymers with precisely specified molecular weight and sequence by recursive directional ligation: examples from the elastin-like polypeptide system. *Biomacromolecules 3*, 357–367.

(10) Ng, S. P., Billings, K. S., Ohashi, T., Allen, M. D., Best, R. B., Randles, L. G., Erickson, H. P., and Clarke, J. (2007) Designing an extracellular matrix protein with enhanced mechanical stability. *Proc. Natl. Acad. Sci. U.S.A. 104*, 9633–9637.

(11) Pasut, G., Mero, A., Caboi, F., Scaramuzza, S., Sollai, L., and Veronese, F. M. (2008) A new PEG-beta-alanine active derivative for releasable protein conjugation. *Bioconjugate Chem. 19*, 2427–2431.

(12) Lee, S., Greenwald, R. B., Mcguire, J., Yang, K., and Shi, C. (2001) Drug delivery systems employing 1,6-elimination: releasable poly(ethylene glycol) conjugates of proteins. *Bioconjugate Chem. 12*, 163–169.

(13) Shaunak, S., Godwin, A., Choi, J.-W., Balan, S., Pedone, E., Vijayarangam, D., Heidelberger, S., Teo, I., Zloh, M., and Brocchini, S. (2006) Site-specific PEGylation of native disulfide bonds in therapeutic proteins. *Nat. Chem. Biol. 2*, 312.

(14) Webster, R., Didier, E., Harris, P., Siegel, N., Stadler, J., Tilbury, L., and Smith, D. (2007) PEGylated proteins: Evaluation of their safety in the absence of definitive metabolism studies. *Drug Metab. Dispos. 35*, 9–16.

(15) Harris, J. M., and Veronese, F. M. (2003) Peptide and protein pegylation II - clinical evaluation - preface. *Adv. Drug Delivery Rev. 55*, 1259–1260.

(16) Harris, J. M., and Chess, R. B. (2003) Effect of pegylation on pharmaceuticals. *Nat. Rev. Drug Discovery 2*, 214–221.

(17) Filpula, D., and Zhao, H. (2008) Releasable PEGylation of proteins with customized linkers. *Adv. Drug Delivery Rev. 60*, 29–49.

(18) Braunecker, W. A., and Matyjaszewski, K. (2007) Controlled/living radical polymerization: Features, developments, and perspectives. *Prog. Polym. Sci. 32*, 93–146.

(19) Noda, T., Grice, A. J., Levere, M. E., and Haddleton, D. M. (2007) Continuous process for ATRP: Synthesis of homo and block copolymers. *Eur. Polym. J. 43*, 2321–2330.

(20) Bories-Azeau, X., Armes, S. P., and Van Den Haak, H. J. W. (2004) Facile synthesis of zwitterionic diblock copolymers without protecting group chemistry. *Macromolecules 37*, 2348–2352.

(21) Vo, C. D., Rosselgong, J., Armes, S. P., and Billingham, N. C. (2007) RAFT synthesis of branched acrylic copolymers. *Macromolecules 40*, 7119–7125.

(22) Bontempo, D., and Maynard, H. D. (2005) Streptavidin as a macroinitiator for polymerization: in situ protein and polymer conjugate formation. *J. Am. Chem. Soc. 127*, 6508–6509.

(23) Boyer, C., Bulmus, V., Liu, J. Q., Davis, T. P., Stenzel, M. H., and Barner-Kowollik, C. (2007) Well-defined protein-polymer conjugates via in situ RAFT polymerization. *J. Am. Chem. Soc. 129*, 7145–7154.

(24) Ryan, S. M., Wang, X. X., Mantovani, G., Sayers, C. T., Haddleton, D. M., and Brayden, D. J. (2009) Conjugation of salmon calcitonin to a combed-shaped end functionalized poly(poly(ethylene glycol) methyl ether methacrylate) yields a bioactive stable conjugate. *J. Controlled Release 135*, 51–59.

(25) Nicolas, J., Mantovani, G., and Haddleton, D. M. (2007) Living radical polymerization as a tool for the synthesis of polymer-protein/peptide bioconjugates. *Macromol. Rapid Commun. 28*, 1083–1111.

(26) Bays, E., Tao, L., Chang, C.-W., and Maynard, H. D. (2009) Synthesis of semitelechelic maleimide Poly(PEGA) for protein conjugation By RAFT polymerization. *Biomacromolecules 10*, 1777–1781.

(27) Heredia, K. L., Tolstyka, Z. P., and Maynard, H. D. (2007) Aminooxy end-functionalized polymers synthesized by ATRP

for chemoselective conjugation to proteins. *Macromolecules 40*, 4772–4779.
(28) Nicolas, J., San Miguel, V., Mantovani, G., and Haddleton, D. M. (2006) Fluorescently tagged polymer bioconjugates from protein derived macroinitiators. *Chem. Commun.* 4697–4699.
(29) Lele, B. S., Murata, H., Matyjaszewski, K., and Russell, A. J. (2005) Synthesis of uniform protein-polymer conjugates. *Biomacromolecules 6*, 3380–3387.
(30) Cox, G. N., Rosendahl, M. S., Chlipala, E. A., Smith, D. J., Carlson, S. J., and Doherty, D. H. (2007) A long-acting, mono-PEGylated human growth hormone analog is a potent stimulator of weight gain and bone growth in hypophysectomized rats. *Endocrinology 148*, 1590–1597.
(31) Mero, A., Spolaore, B., Veronese, F. M., and Fontana, A. (2009) Transglutaminase-mediated PEGylation of proteins: direct identification of the sites of protein modification by mass spectrometry using a novel monodisperse PEG. *Bioconjugate Chem. 20*, 384–389.
(32) Clark, R., Olson, K., Fuh, G., Marian, M., Mortensen, D., Teshima, F., Chang, S., Chu, H., Mukku, V., CanovaDavis, E., Somer, T., Cronin, M., Winkler, M., and Wells, J. A. (1996) Long-acting growth hormones produced by conjugation with polyethylene glycol. *J. Biol. Chem. 271*, 21969–21977.
(33) Abraham, S., Brahim, S., and Guiseppi-Elie, A. (2004) Molecularly engineered hydrogels for implant biocompatibility. *Proc. 26th Annu. Int. Conf. IEEE Eng. Med. Biol. Soc. 1−7* (26), 5036–5039.
(34) Tyeklar, Z., Jacobson, R. R., Wei, N., Murthy, N. N., Zubieta, J., and Karlin, K. D. (1993) Reversible reaction of dioxygen (and carbon monoxide) with a copper(I) complex. X-ray structures of relevant mononuclear Cu(I) precursor adducts and the trans-(.mu.-1,2-peroxo)dicopper(II) product. *J. Am. Chem. Soc. 115*, 2677–2689.
(35) Ausubel, F. M. B., R., Kingston, R. E., Moore, D. D., Seidman, J. G., Smith, J. A., and Struhl, K. (2002) *Short Protocols in Molecular Biology*, 5th ed., Vol. 1, Wiley, New York.
(36) Kurfürst, M. M. (1992) Detection and molecular weight determination of polyethylene glycol-modified hirudin by staining after sodium dodecyl sulfate-polyacrylamide gel electrophoresis. *Anal. Biochem. 200*, 244–248.
(37) Habeeb, A. F. S. (1966) Determination of free amino groups in proteins by trinitrobenzenesulfonic acid. *Anal. Biochem. 14*, 328.
(38) Jacquemard, U., Bénéteau, V., Lefoix, M., Routier, S., Mérour, J.-Y., and Coudert, G. (2004) Mild and selective deprotection of carbamates with Bu_4NF. *Tetrahedron 60*, 10039–10047.
(39) Hermanson, G. T. (2008) *Bioconjugate techniques*, 2nd ed., Academic Press, New York.
(40) Sartore, L., Caliceti, P., Schiavon, O., Monfardini, C., and Veronese, F. M. (1991) Accurate evaluation method of the polymer content in monomethoxy(polyethylene glycol) modified proteins based on amino-acid-analysis. *Appl. Biochem. Biotechnol. 31*, 213–222.
(41) Schramm, O. G., Pavlov, G. M., van Erp, H. P., Meier, M. A. R., Hoogenboom, R., and Schubert, U. S. (2009) A versatile approach to unimolecular water-soluble carriers: ATRP of PEGMA with hydrophobic star-shaped polymeric core molecules as an alternative for PEGylation. *Macromolecules 42*, 1808–1816.
(42) Pradhananga, S., Wilkinson, I., and Ross, R. J. M. (2002) Pegvisomant: structure and function. *J. Mol. Endocrinol.* 29.
(43) Peschke, B., Zundel, M., Bak, S., Clausen, T. R., Blume, N., Pedersen, A., Zaragoza, F., and Madsen, K. (2007) C-terminally PEGylated hGH-derivatives. *Bioorg. Med. Chem. 15*, 4382–4395.
(44) Salmaso, S., Bersani, S., Semenzato, A., and Caliceti, P. (2006) Nanotechnologies in protein delivery. *J. Nanosci. Nanotechnol. 6*, 2736–2753.
(45) Kinstler, O., Molineux, G., Treuheit, M., Ladd, D., and Gegg, C. (2002) Mono-N-terminal poly(ethylene glycol)-protein conjugates. *Adv. Drug Delivery Rev. 54*, 477–485.
(46) Cunliffe, D., Pennadam, S., and Alexander, C. (2004) Synthetic and biological polymers - merging the interface. *Eur. Polym. J. 40*, 5–25.
(47) Hoffman, A. S., and Stayton, P. S. (2007) Conjugates of stimuli-responsive polymers and proteins. *Prog. Polym. Sci. 32*, 922–932.
(48) Maynard, H. D., Heredia, K. L., Li, R. C., Parra, D. P., and Vazquez-Dorbatt, V. (2007) Thermoresponsive biohybrid materials synthesized by ATRP. *J. Mater. Chem. 17*, 4015–4017.
(49) Pennadam, S. S., Lavigne, M. D., Dutta, C. F., Firman, K., Mernagh, D., Gorecki, D. C., and Alexander, C. (2004) Control of a multisubunit DNA motor by a thermoresponsive polymer switch. *J. Am. Chem. Soc. 126*, 13208–13209.
(50) Geng, J., Mantovani, G., Tao, L., Nicolas, J., Chen, G. J., Wallis, R., Mitchell, D. A., Johnson, B. R. G., Evans, S. D., and Haddleton, D. M. (2007) Site-directed conjugation of "Clicked" glycopolymers to form glycoprotein mimics: Binding to mammalian lectin and induction of immunological function. *J. Am. Chem. Soc. 129*, 15156–15163.

BC900468V

Folic Acid-Conjugated Chitosan Nanoparticles Enhanced Protoporphyrin IX Accumulation in Colorectal Cancer Cells

Shu-Jyuan Yang,[§] Feng-Huei Lin,[§] Kun-Che Tsai,[§] Ming-Feng Wei,[§] Han-Min Tsai,[§] Jau-Min Wong,[§] and Ming-Jium Shieh*[,§,‡]

Institute of Biomedical Engineering, College of Medicine and College of Engineering, National Taiwan University, Taipei 10051, Taiwan, and Department of Oncology, National Taiwan University Hospital and College of Medicine, Taipei 10002, Taiwan. Received November 2, 2009; Revised Manuscript Received February 11, 2010

Folic acid can be covalently conjugated to chitosan molecules via its γ-carboxyl moiety and thus retain a high affinity for colorectal cancer cells bearing folate receptor overexpression. Colorectal cancer is one of the leading causes of malignant death and often goes undetected with current colonoscopy practices. Improved methods of detecting dysplasia and tumors during colonoscopy will improve mortality. A folic acid conjugated chitosan nanoparticle as a suitable vehicle for carrying 5-aminolaevulinic acid (5-ALA) is developed to enhance the detection of colorectal cancer cells in vivo after a short-term uptake period. Chitosan can be successfully conjugated with folic acid to produce folic acid−chitosan conjugate, which is then loaded with 5-ALA to create nanoparticles (fCNA). The loading efficiency of 5-ALA in fCNA particles and the *z*-average diameter were in the range 35−40% and 100 nm, respectively. The zeta-potential for fCNA was 20 mV, enough to keep the nanoparticle stable without aggregation. The fCNA is then incubated with HT29 and Caco-2 colorectal cancer cell lines overexpressing folate receptor on the surface of the cell membrane to determine the rate of accumulation of protoporphyrin IX (PpIX). The results show that fCNA can be taken up more easily by HT29 and Caco-2 cell lines after short-term uptake period, most likely via receptor-mediated endocytosis, and the PpIX accumulates in cancer cells as a function of the folate receptor expression and the folic acid modification. Therefore, the folic acid−chitosan conjugate appears to be an ideal vector for colorectal-specific delivery of 5-ALA for fluorescent endoscopic detection.

INTRODUCTION

Folic acid is a ligand that is useful for targeting cell membrane and enhancing nanoparticle endocytosis via the folate receptor. It is a stable, inexpensive, and generally poorly immunogenic chemical with a high affinity for the folate receptor (*1, 2*). Because the folate receptor overexpresses on many human epithelial cancer cell surfaces, including cancers of the ovary, kidney, uterus, colon, and lung, conjugation of drugs and macromolecules with folic acid can enhance their uptake and targeting ability (*3*−*9*). Folic acid conjugates, which are covalently derivative via folate's γ-carboxyl moiety, can maintain a high affinity to the folate receptor, and the mechanism of cellular uptake of folic acid conjugates by folate receptors is as effective as that of folic acid chemical (*2*). They can enter cells by folate receptor-mediated endocytosis and move through many organelles by vesicular trafficking, which can supply materials to release into cell cytoplasm. Later, the unligated folate receptor may recycle to the cell surface to transport more folic acid conjugates (*2, 3*). This process has more advantages for the efficient intracellular delivery of anticancer agents or macromolecules than the one that relies on cell membrane markers.

The incidence of colorectal cancer is increasing worldwide and its prognosis remains poor (*10*). In general, survival is inversely related to extent of tumor spread at time of detection. Relative rates of survival of 50% at three years and 40% at five years have remained unchanged since the 1960s (*11*). Prognosis is excellent with detection at an early stage. Unfortunately, small colorectal neoplasia and early cancer are frequently overlooked during endoscopy. Therefore, a powerful and highly sensitive tool for the detection of precancerous lesions would be of great value.

Photodiagnosis is one of the most promising and noninvasive methods for detecting malignant or premalignant tissue (*12*). Currently, detection of abnormal tissue usually involves the use of an exogenous chromophore, such as protoporphyrin IX (PpIX), excited by optima light to generate fluorescence in cancer lesions (*13*). The 5-aminolevulinic acid (5-ALA) used in the study, a precursor in heme group synthesis, is totally degraded intracellularly and converted to PpIX. Because the decomposition rate of PpIX in cancer cells differs from that in normal cells, the photosensitive fluorophore, PpIX, can be used to detect cancer lesions (*14, 15*). Protoporphyrin IX in normal cells is usually maintained at a constant level and quickly degraded if it exceeds the equilibrium level. However, this feedback mechanism does not function well in cancer cells, where PpIX degrades at a slow pace and accumulates at very high concentrations. In addition, ferrochelatase, one of the major enzymes involved in converting PpIX into heme, remains at low activity in cancer cells and results in the limited availability of iron that partially contributes to the high concentration of PpIX in those abnormal cells (*16*). Generally, PpIX can be totally degraded within 2 to 4 h in normal cells and 12−24 h in cancer cells (*17*).

Because unprotected 5-ALA is easily engulfed by bacteria in the gastrointestinal tract (GI tract), its presence is open to misinterpretation and it has not been suitable as a marker during endoscopy (*18*). We have developed a chitosan nanoparticle vehicle for carrying 5-ALA that prevents bacterial uptake (*19*). Chitosan is the polymer of 2-amino-2-deoxy-β-D-glucan by

* Corresponding author. Shieh, M.-J., Tel: 886-2-23123456 ext 67512; Fax: 886-2-23940049; E-mail: soloman@ntu.edu.tw; image_0120@yahoo.com.tw.

[§] National Taiwan University.

[‡] National Taiwan University Hospital and College of Medicine.

10.1021/bc9004798 © 2010 American Chemical Society
Published on Web 03/11/2010

glycosidic linkages. The primary amino groups on the molecular chain of chitosan have special properties that make chitosan more useful in pharmaceutical applications. Compared with other biological polymers, chitosan is more cationic, which allows it to approach cell membranes more easily. In addition, it has muco-adhesive properties that prolong its retention to targeted substrates (*20*−*24*). Additionally, chitosan induces no allergic reactions or immuno-rejections. Also, its bacteriostatic properties discourage bacterial uptake in the GI tract (*25*). Furthermore, chitosan is a linear polyamine with an abundance of free amino groups that promote cross-linkage. Its cationic nature also promotes ionic cross-linkage with multivalent anions, such as sodium tripolyphosphate (STPP) (*26*).

Our previous study using chitosan as a vehicle for 5-ALA has shown that the accumulation of PpIX in colorectal cancer cells could be detected after 24 h incubation (*19*). In order to enhance the uptake and targeting ability of nanoparticles into targeted cells, target-specific ligands are usually used to conjugate to the surface of the polymer carrier. The main aim of this study was to determine the suitability of the synthesized folic acid−chitosan conjugates for carrying 5-ALA and to determine its targeting and uptake efficiency in different human colorectal cancer cell lines (HT29 and Caco-2) by folate receptor-mediated endocytosis after a short-term uptake period for the clinical practice.

EXPERIMENTAL PROCEDURES

Materials. Chitosan (99% deacetylation and 150 kDa M.W.) and 5-aminolevulinic acid (5-ALA) were purchased from Fluka (Germany). Sodium tripolyphosphate (STPP) was purchased from Wako Pure Chemical Industries (Osaka, Japan). Folic acid was purchased from TCI (Tokyo, Japan). 1-(3-Dimethylaminopropyl)-3-ethylcarbodiimide hydrochloride (EDC) was purchased from Acros Organics (New Jersey, USA); anhydrous dimethyl sulfoxide (DMSO) was purchased from Riedel-de Haën (Germany). They were all reagent grade and used without further purification.

Conjugation of Folic Acid with Chitosan. The process of conjugation of folic acid to chitosan molecules is described as follows: A solution of folic acid and EDC in 20 mL anhydrous DMSO (molar ratio was 1:1) was prepared and stirred at room temperature until EDC and folic acid were well-dissolved and mixed. The mixture was then added slowly to 0.5% (w/v) chitosan in acetic acid aqueous solution (0.1 M, pH 4.7) and stirred at room temperature in the dark for 16 h to let folic acid conjugate onto chitosan molecules. The solution was brought to pH 9.0 by dripping with NaOH aqueous solution (1.0 M) and centrifuged at 2500 rpm to spin down the folic acid−chitosan conjugate. The precipitate was dialyzed first against phosphate buffered saline (PBS, pH 7.4) for 3 days and then against water for 4 days. Finally, the folic acid conjugated chitosan was isolated as a sponge by lyophilization and kept for follow-up study (*6, 7*). Folic acid−chitosan conjugates were formed at selected amino groups of chitosan to folic acid molar ratios from 1:0.02 to 1:0.2. Abbreviations for different folic acid−chitosan conjugates are shown in Table 1.

Characterization of the Folic Acid−Chitosan Conjugates. The chemical compositions of chitosan, folic acid−chitosan conjugates, and folic acid were characterized with an ATR-FT-IR spectrometer (VARIAN UMA600; Palo Alto, CA) to determine the characteristics of the folic acid−chitosan conjugates. The ^{1}H NMR spectra of folic acid−chitosan conjugates were recorded on a Bruker Avance-400 MHz NMR spectrometer (Bruker BioSpin, MA, USA) using deuterium acetic acid-d_4/deuterium oxide solution (1/4 v/v) as a solvent.

The folic acid to amino groups molar ratios in folic acid−chitosan conjugates were estimated by determining the intensity of absorption maximum (285 nm) of folate derivative in 0.02% folic acid−chitosan conjugate solution with an ultraviolet−visible (UV−vis) spectrophotometry (Cary 50 Conc, Varian; Australia). In this study, folic acid powder was dissolved in 0.1 M NaOH solution and diluted to a series of gradient folic acid standard solutions that were used to prepare the calibration curve in the range 0.0025−0.05 mg/mL for further analysis.

Table 1. Molar Ratio of Folic Acid/Amino Groups in Folic Acid−Chitosan Conjugates and Yield of the Synthesis Conjugates[a]

folic acid−chitosan conjugates abbreviation	formulated molar ratio of folic acid/NH_2	molar ratio of folic acid/NH_2 in folic acid−chitosan conjugate mean ± SD	yield (%)
f02Chi	0.02	0.008 ± 0.0003	81.6 ± 2.02
f04Chi	0.04	0.015 ± 0.0008	77.0 ± 0.27
f06Chi	0.06	0.018 ± 0.0007	71.2 ± 2.73
f08Chi	0.08	0.028 ± 0.0011	68.7 ± 3.13
f10Chi	0.10	0.033 ± 0.0018	67.5 ± 0.39
f20Chi	0.2	0.059 ± 0.0039	53.2 ± 1.15

[a] ($n = 5$).

Synthesis of Nanoparticles. The preparation of chitosan nanoparticles loaded with 5-ALA was based on the ionic gelation interaction between positively charged chitosan and negatively charged STPP at room temperature (*27*). The negative charge of ionized 5-ALA also partially contributed to the gelation interactions in this study. The preparation process is briefly described as follows: 0.05% chitosan and folic acid−chitosan conjugate solutions were prepared by dissolving 0.5 mg chitosan powder and folic acid−chitosan conjugate sponge in 1 mL 0.01 M acetic acid solution at pH 4.0, respectively. 0.15% 5-ALA solution was prepared by dissolving 1.5 mg 5-ALA powder in 1 mL 0.05% STPP solution, where STPP were dissolved in PBS beforehand. Either 2 mL of STPP solution or 2 mL of 5-ALA solution was added to 5 mL of chitosan or folic acid−chitosan conjugate solution with a peristaltic pump at a flow rate of 0.5 mL/min to prepare the CN, CNA, fCN, and fCNA nanoparticle suspended solutions, where CN and fCN were represented as chitosan and folic acid conjugated chitosan nanoparticles without 5-ALA loading, and chitosan and folic acid conjugated chitosan nanoparticles loaded with 5-ALA were termed CNA and fCNA. The preparation of fCNA was schematically illustrated in Figure 1. The prepared nanoparticle suspended solutions were later used directly without further treatment.

Particle Size and the Zeta-Potential of CN, CNA, fCN, and fCNA. Measurements of particle size and zeta-potential of various nanoparticles were performed on the Zetasizer-3000 (Malvern Instruments; Westborough, MA) by dynamic light scattering measurements and laser Doppler electrophoresis, respectively. Particle size was measured at 25 °C with a 90° scattering angle based on the Zetasizer-3000 internal setting. The cumulative curve was used to present the mean hydrodynamic diameter. Measurements of zeta-potential were made using the aqueous flow cell in the automatic mode at 25 °C (*28*).

Loading Efficiency of 5-ALA in CNA and fCNA. Loading efficiency of 5-ALA in nanoparticles was assessed by centrifuging the particle solution at a 20 000 *g* force to spin down the particles. The suspension was collected and then reacted with 2,4,6-trinitrobenzene sulfonic acid (TNBS) as an assay reagent to detect 5-ALA in the suspension. Assay was performed by using a TNBS kit (Pierce Chemical Company; Rockford, IL) according to the manufacturer's instructions. In the study, 5-ALA powder was dissolved in reaction buffer (0.1 M sodium bicarbonate, pH 8.5) and diluted to a serial of gradient 5-ALA standard solutions that were used to prepare the calibration curve in the range of 2−20 μg/mL for further analysis. The loading

efficiency of 5-ALA in the nanoparticles was calculated with the following equation:

$$\text{loading efficiency (\%)} = \frac{C_t - C_f}{C_t} \times 100\%$$

where C_t and C_f were total amount of 5-ALA and free amount of 5-ALA in the suspension, respectively.

Transmission Electron Microscope Examination. Carbon-coated 200 mesh copper grids were immersed in CN, CNA, fCN, and fCNA solutions. Grids were placed on delicate-task-wipers to absorb excess liquid and then dried in a desiccator overnight. The dried copper grids with CN, CNA, fCN, and fCNA were examined under the Hitachi TEM H-7500 (Tokyo, Japan).

Determining Expression of Folate Receptor among Colorectal Cancer Cell Lines. Expression content of folate receptor on cell membrane was determined by Western blot method. Two colorectal cancer cell lines (HT29 and Caco-2) were pretreated by scraping the cell cultures into cold lysis buffer (RIPA buffer) containing protease inhibitors. Whole cell lysate was assayed for the protein concentration by using the DC protein assay (Bio-Rad; Hercules, CA) with bovine serum albumin as standard. Total protein (30 μg) was separated on 10% SDS−polyacrylamide gel electrophoresis (SDS-PAGE) gels, and then transferred to polyvinylidene fluoride (PVDF) membranes (Amersham Biosciences; Sweden). The PVDF membranes were incubated in blocking buffer (5% nonfat dry milk, 0.1% Tween20 in TBS) at room temperature for 60 min, and subsequently treated with primary antibody, rabbit antihuman folate receptor (1:1000 dilution, Santa Cruz Biotechnology; CA, USA), in blocking buffer overnight at 4 °C. Membranes were washed with Tris-buffered saline (TBS) containing 0.1% Tween20 (USB Corporation; Cleveland, OH), and further incubated with the horseradish peroxidase-conjugated antirabbit IgG (1:5000 dilution, Sigma) as secondary antibody at room temperature for 60 min. Finally, membranes were incubated in blocking buffer at room temperature for 60 min, and then washed with PBS containing 0.1% Tween20. The bands of proteins were visualized by using chemiluminescence enhancing (Amersham Parmacia Biotech; Piscataway, NJ) and exposed to Hyperfilm MP. The signals of antihuman folate receptor in the Western blotting were quantified with the software *ImageQuant 5.1*, and the data were normalized to β-actin expression.

Measurement of Accumulated PpIX. Cell lines HT29 and Caco-2 were cultured in Dulbecco's Modified Eagle's Medium (GIBCO; Grand Island, NY) supplement with 10% (v/v) fetal bovine serum, 2 mM glutamine, 10 mM nonessential amino acids, 50 IU/mL penicillin, and 50 Ag/mL streptomycin, at 37 °C and in an atmosphere of 5% CO_2, respectively. Cultured medium was changed on alternate days until confluent.

The following quantities of cells were seeded onto 24-well culture plates: 1.2×10^5/well HT29 and 3×10^4/well Caco-2. After cell lines were cultured for 24 h, the medium was replaced with fresh medium containing CNA and fCNA. The CNA and fCNA solutions were concentrated to 10× by Amicon Ultra (Centrifugal Filter Devices, Millipore) to remove the unloaded 5-ALA beforehand. Moreover, because of no blood supplement in the GI tract, the fresh medium without serum supplement was used. Cells were further cultured for 3, 6, and 12 h to allow uptake of nanoparticles and to convert 5-ALA to PpIX. In order to determine the effect of folic acid−folate receptor mediated

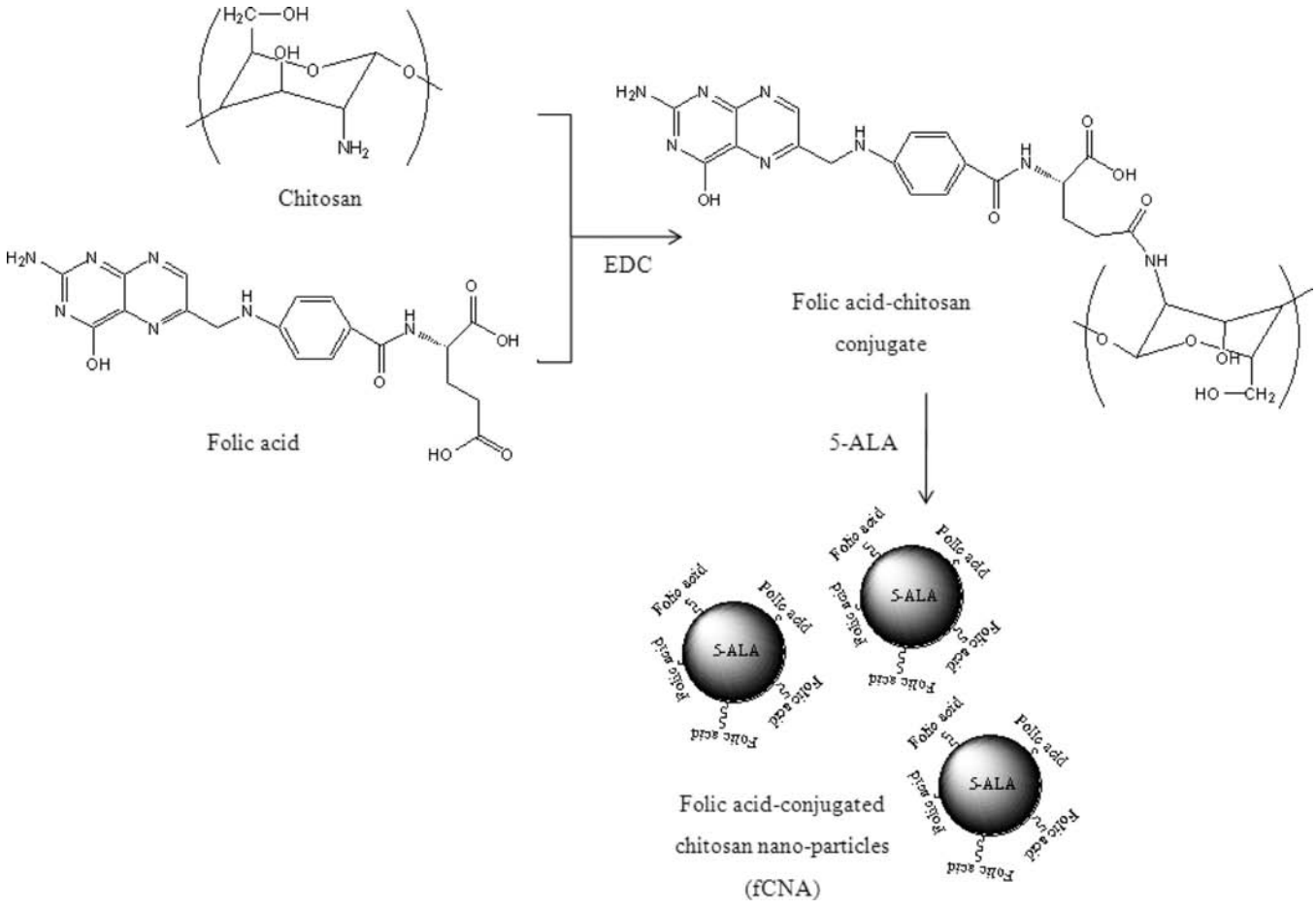


Figure 1. Schematic illustration of the preparation folic acid-conjugated chitosan nanoparticles for PpIX accumulation in colorectal cancer cells.

endocytosis on the endogenously synthesized PpIX, fresh culture media, both with or without free folic acid, were tested at the same time. The concentration of free folic acid (5 mM) used was expected to result in complete saturation of folate receptors (*5*). After removal of the cultured medium, plates were washed with PBS three times. The PpIX were extracted with DMSO, and the fluorescent intensity of PpIX was determined by the spectrofluorometer (Molecular Device Spectra Max Gemine XS; Sunnyvale, CA) with the excitation wavelength of 405 nm and the emission wavelength at 635 nm. The fluorescent intensity was expressed as accumulative percentage.

In order to evaluate the feasibility of the prepared fCNA on colorectal cancer cells detection after short-term uptake period, the glass plate was placed in a Petri dish and seeded with HT29, Caco-2, or a normal cell line (human colon fibroblast (CCD112)). After cells were cultured for 24 h, medium was replaced with fresh medium containing CAN, fCNA, and 5-ALA. To confirm the nanoparticle uptake content as a function of the folate receptor expression and the folic acid modification, a fluorescent compound, calcein, was incorporated simultaneously into CNA and fCNA as a fluorescent marker. Cells were further cultured for 12 h to allow for uptake of nanoparticles and conversion of 5-ALA to PpIX. After the cultured medium was removed, the glass plate was washed three times with PBS and the cells were fixed with 10% formalin and then examined under a spectral confocal and multiphoton system (Leica TCS SP5, Wetzlar, Germany). The average fluorescent intensity of calcein in cells was quantified with the *MetaMorph* imaging software (v 7.5, Molecular Devices, USA) to demonstrate the content of nanoparticle uptake. The data represented an average of five regions obtained from randomly chosen areas of each sample, and the brightness of the green emission light of the CNA group was designated as 100% for the individual colorectal cancer cell lines.

Statistical Analysis. Mean plus/minus standard deviation (SD) and graphs were used to describe the data. One-way analysis of variance (ANOVA) with post hoc muti-comparison methods, such as Fisher's LSD test and Tamhane's T2 test, was used to assess the differences in the fluorescent intensity of PpIX and calcein in colorectal cancer cells fed with CNA and fCNA. All p values were two-sided, and their significance level was 0.05. The software of statistic package for social science 11.0 (SPSS 11.0) was used to conduct all statistical analysis.

RESULTS

Characterization of Folic Acid−Chitosan Conjugates. Folate acid−chitosan conjugates could be synthesized by chemically linking folic acid to chitosan via EDC as a carboxyl activating agent. They were formed at the selected amino groups of chitosan to folic acid molar ratios from 1:0.02 to 1:0.2. Abbreviations for different folic acid−chitosan conjugates are shown in Table 1. The FT-IR spectra of the chitosan, folic acid−chitosan conjugates (f06Chi, f20Chi), and pure folic acid were shown in Figure 2. Because the folic acid modification in the folic acid-chitosan conjugate, f02Chi, was too low to easily determine the difference between chitosan and folic acid−chitosan conjugate in FT-IR spectra, it was not shown in Figure 2. Characteristic FT-IR absorption peaks of folic acid at 1450, 1520, and 1605 cm^{-1} were observed in the spectrum of folic acid−chitosan conjugates. In the pure folic acid and folic acid−chitosan conjugates, the absorption bands at 1450 and 1605 cm^{-1} were assigned to the stretching vibrations of C═C in the backbone of the aromatic ring (*29*). Furthermore, chitosan and folic acid−chitosan conjugates all contained the −CONH− group. The carbonyl absorption band, C═O, is known as the amide I band, and N−H is termed the amide II band. Their position depends on the degree of hydrogen bonding and, thus, the physical state of the compound. The most significant IR frequencies of the chitosan and folic acid−chitosan conjugates are the amide I band (carbonyl stretching) and the amide II band

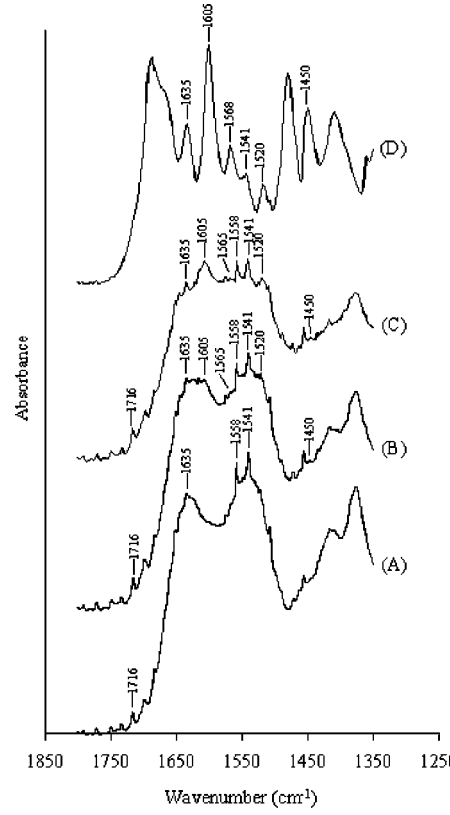


Figure 2. FT-IR spectra of folic acid−chitosan conjugates (A) chitosan, (B) f06Chi, (C) f20Chi, and (D) pure folic acid.

Table 2. Relative Intensity Ratio of the N−H Bending over C═O Stretching in Chitosan and Folic Acid−Chitosan Conjugates

sample	band		wavenumber (cm^{-1})	intensity ratio (Amide II/ Amide I)
chitosan	Amide II	free N−H	1541	1.813
			1558	
	Amide I	bonded C═O	1635	1
		free C═O	1716	
f06Chi	Amide II	free N−H	1541	2.267
			1558	
		bonded N−H	1565	
	Amide I	bonded C═O	1635	1
		free C═O	1716	
f20Chi	Amide II	free N−H	1541	2.276
			1558	
		bonded N−H	1565	
	Amide I	bonded C═O	1635	1
		free C═O	1716	

Table 3. z-Average Diameter, Zeta-Potential, and Loading Efficiency of Chitosan Nanoparticles Prepared in Different Conditions

sample	z-average diameter[a] mean ± SD (nm)	PDI[b]	zeta-potential (mV)	loading efficiency mean ± SD (%)
CN	102.4 ± 7.74	0.252	25.0 ± 1.84	−
CNA	96.0 ± 4.82	0.392	24.4 ± 1.78	43.1 ± 5.71
f02CN	100.1 ± 10.75	0.434	22.6 ± 1.54	−
f02CNA	93.6 ± 5.80	0.381	21.9 ± 2.09	38.9 ± 3.52
f06CN	99.0 ± 7.00	0.444	21.1 ± 2.19	−
f06CNA	112.8 ± 13.19	0.457	20.1 ± 1.76	35.5 ± 1.40

[a] z-average diameter is the mean diameter based on the intensity of scattered light. [b] PDI = polydispersity index (ratio of weight- to number-average particle diameter).

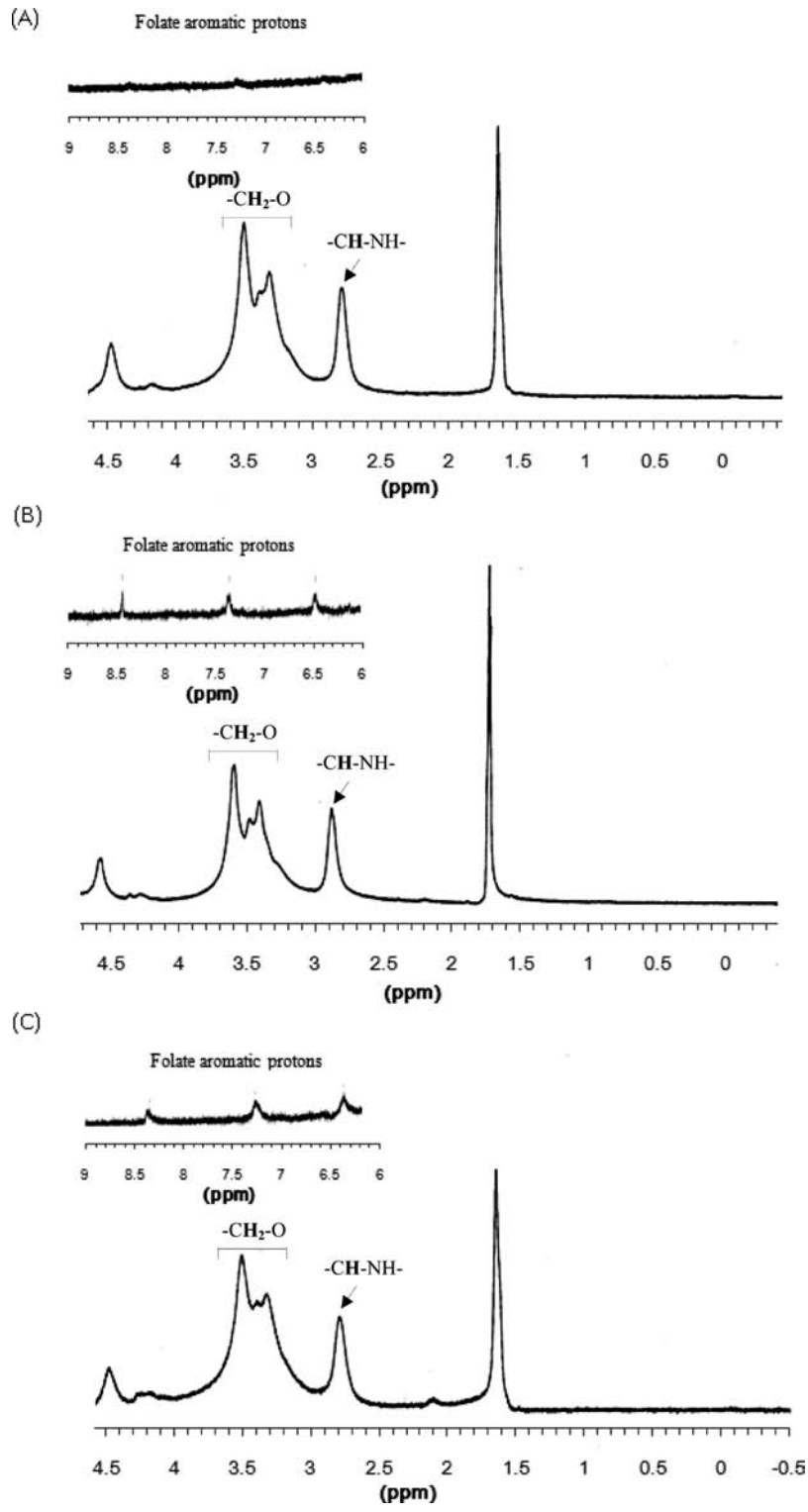


Figure 3. ^{1}H NMR spectrum of f02Chi (A), f06Chi (B), and f20Chi (C) folic acid−chitosan conjugates in an acetic acid-d_4/D_2O solution (1/4 v/v).

(N−H deformation mode) vibration. The former is typically around 1720−1740 cm^{-1} and is shifted to lower frequencies by hydrogen bonding (weakening of the force constant due to partial single-bond character). The latter is typically between 1500 and 1550 cm^{-1} and is believed to shift to the higher frequencies upon hydrogen-bond formation (strengthening of the force constant for deformation vibrations) (*30*). Figure 2 shows that there were two absorption peaks for the C═O group. The peak at about 1635 cm^{-1} represented the bonded C═O stretching and the peak at about 1716 cm^{-1} represented the free C═O stretching (*31*). The amide II band was observed at a relatively high frequency (1565 cm^{-1}), most probably due to the hydrogen-bond formation. The peaks at about 1541 and 1558 cm^{-1} were related to free N−H bending. In Table 2, it can be seen that the amide II/I intensity ratio increased with increasing folic acid conjugation in folic acid−chitosan conjugates.

Successful synthesis of folic acid−chitosan conjugates was also confirmed by a ^{1}H NMR spectroscopy, and the ^{1}H NMR spectra of folic acid−chitosan conjugates are shown in Figure 3. The signals at δ 1.65, 2.88, and 3.08−3.64 ppm were assigned

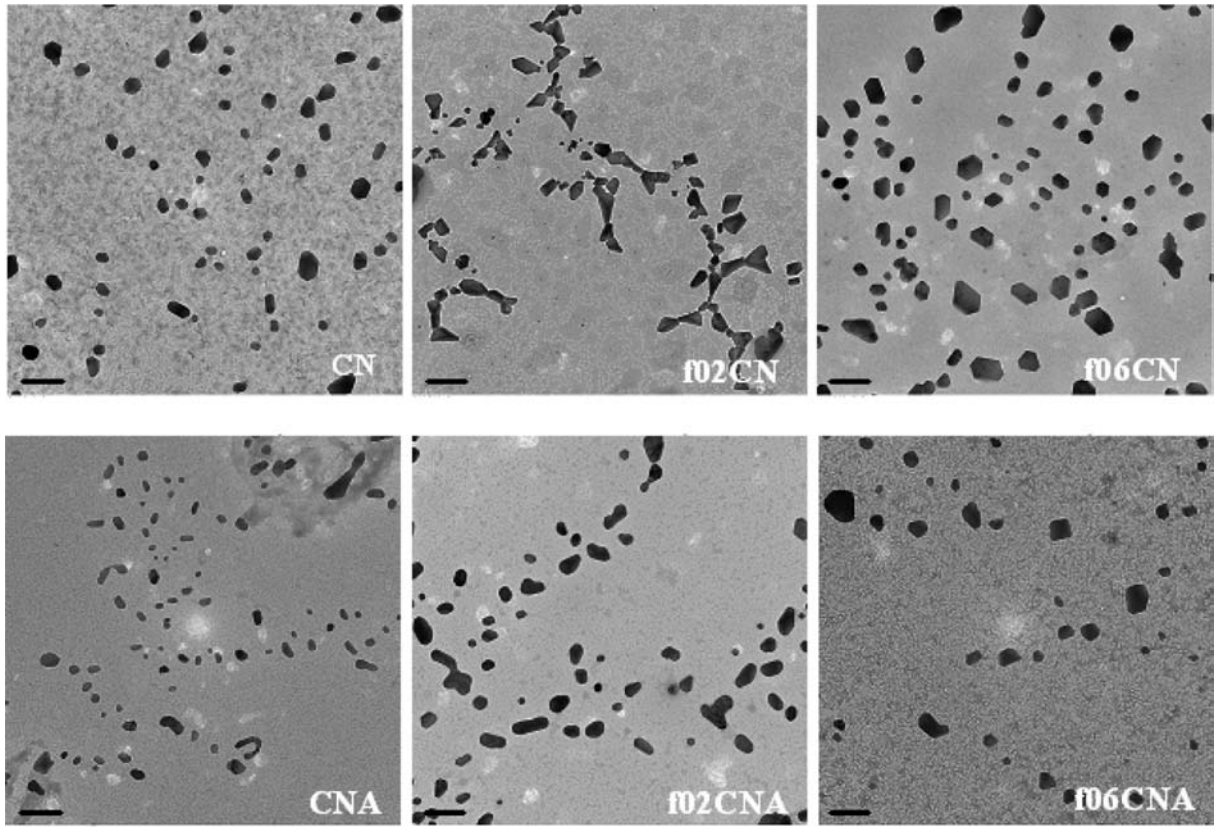


Figure 4. Photos from TEM for CN and CNA modified with folic acid or without. The scale bar in the picture is 1 μm.

to the resonance of the monosaccharide residue protons, $-COCH_3$, $-CH-NH-$, and $-CH_2-O-$, respectively (*2, 7*). The signals appearing at δ 6.3−8.5 ppm in the ^1H NMR spectra of folic acid−chitosan conjugates attributed to the resonance of the folate aromatic protons, and they revealed that the couple of the folate residue to the chitosan could be achieved via EDC-mediated reaction (*7, 32*).

Table 1 shows the molar ratio of folic acid to amino groups in folic acid−chitosan conjugates evaluated by an absorbance at $\lambda = 285$ nm in the UV−vis spectra of the conjugates. The lowest molar ratio was 0.008 in f02Chi, which was two-fifths of the formulated molar ratio; however, the highest molar ratio was up to 0.059 (f20Chi), three-tenths of the formulated molar ratio only. The incremental trend of the folic acid conjugation in the folic acid−chitosan conjugates matched that of folic acid addition, but it was still lower than the formulated molar ratio. Moreover, the yield of f02Chi was 81.6%, and decreased to 53.2% as the folic acid addition in the reaction increased (f20Chi) (Table 1).

Particle Size, Zeta-Potential, and Loading Efficiency of 5-ALA in Nanoparticles. Table 3 shows the *z*-average diameter, zeta-potential, and loading efficiency of chitosan nanoparticles, which were prepared in different conditions. When chitosan was conjugated with an abundance of folic acid molecules (f08Chi, f10Chi, and f20Chi), it was difficult to dissolve it into 0.01 M acetic acid solution completely, most likely due to the unsolvable property of folic acid in acetic acid (*33*). Accordingly, folic acid−chitosan conjugates with large folic acid modification were not suitable for use as a carrier for 5-ALA in the present prepared nanoparticle condition. As shown in Table 3, the *z*-average diameter of the prepared nanoparticles did not vary significantly with change of folic acid on chitosan polymer (CN and fCN) or 5-ALA loading (CNA and fCNA). Also, the *z*-average diameter of prepared nanoparticles was about 100 nm. The zeta-potential analysis revealed that the nanoparticles prepared in different conditions all bore a positive charge (in the range 20−25 mV). However, when the CN was modified with folic acid, as was so-called fCN, the zeta-potential of particles decreased with increase in the percentage with folic acid conjugation. If the CN and fCN were loaded with 5-ALA, the zeta-potential of the CNA and fCNA decreased slightly as compared with CN and fCN, respectively. The loading efficiency of 5-ALA in CNA was 43% and decreased to 35% with increasing percentage of folic acid conjugation.

Figure 4 shows the particle sizes of CN, CNA, fCN, and fCNA as determined by transmission electron microscopic examination (TEM). The particle size distribution of CN and CNA was major in the range 60−200 nm, but fell into the range 100−600 nm for f06CN and f06CNA. Therefore, the particle size distribution strongly depended on and increased with the increase of percentage of conjugated folic acid. These results are in agreement with the polydispersity index (PDI) values of the prepared nanoparticles measured by dynamic light scattering measurements using the Zetasizer-3000.

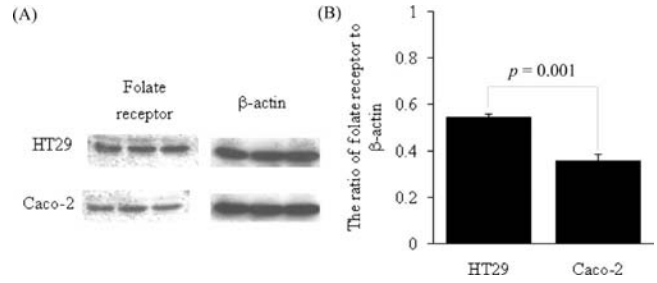


Figure 5. (A) Western blot analysis of folate receptor expression and (B) the ratio of folate receptor to β-actin quantified with the software *ImageQuant 5.1* on HT29 and Caco-2 colorectal cancer cell membrane ($n = 3$).

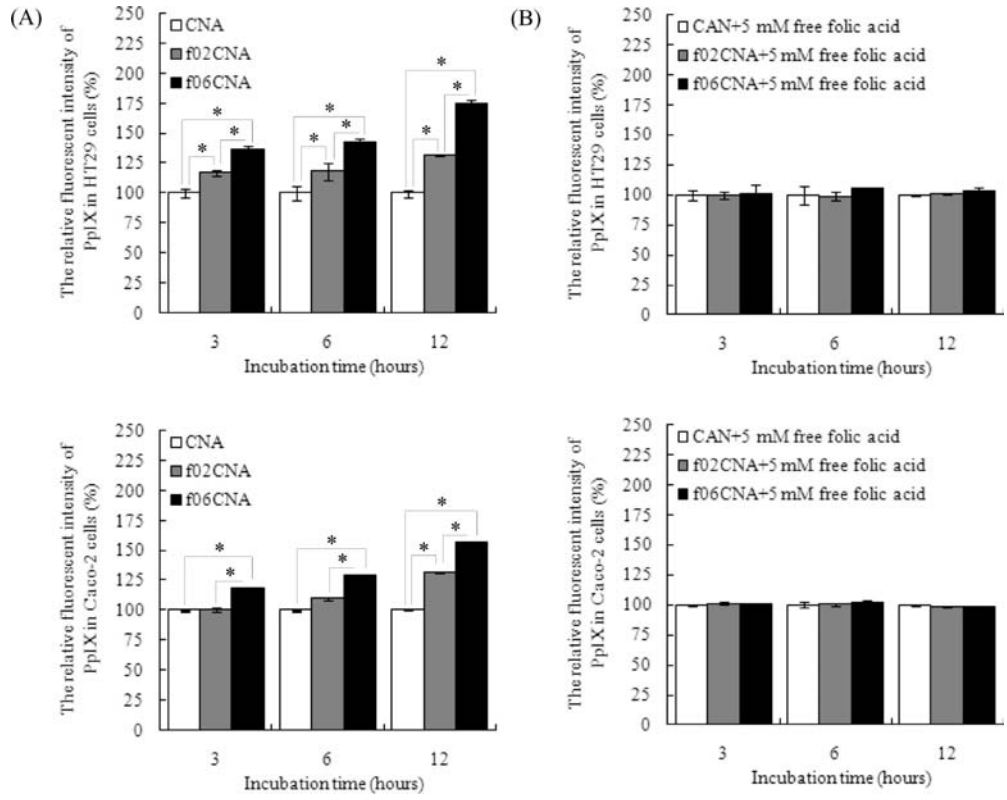


Figure 6. (A) Relative fluorescent intensity of PpIX in HT29 and Caco-2 cells when fed with the prepared CNA, f02CNA, and f06CNA for 3, 6, and 12 h. (B) In order to determine the effect of folic acid−folate receptor mediated endocytosis on the endogenously synthesized PpIX, the relative fluorescent intensity of PpIX in HT29 and Caco-2 cells was also be estimated when cultured in a fresh medium with the nanoparticle suspension and 5 mM free folic acid addition for 3, 6, and 12 h. *: $p < 0.05$.

Expression of Folate Receptor among Colorectal Cancer Cell Lines. Because folate receptors are known to be overexpressed and actively internalized through folate receptor-mediated endocytosis in various types of colorectal cancer cells, folic acid has been considered to be a suitable ligand for improving the cellular uptake of drugs and macromolecules into cells (*3*). Therefore, the expression of folate receptor on HT29 and Caco-2 colorectal cancer cells was examined by the Western blot method and shown in Figure 5. It was apparent that expression of folate receptor depended on the cell line: expression of folate receptor was of a low level for Caco-2 cells, whereas HT29 cells exhibited 1.5-fold higher expression of folate receptors than did Caco-2 cells.

Measurement of PpIX in Colorectal Cancer Cells. Figure 6 shows the relative fluorescent intensity of PpIX in HT29 and Caco-2 cells cultured in a medium with or without free folic acid addition. The brightness of the emission light of the CNA group was designated as 100% for the individual colorectal cancer cell lines. Figure 6A shows that increase of bright red emission light of PpIX in HT29 and Caco-2 cells was only 31.3% and 31.2%, respectively, when the cells were cultured with f02CNA for 12 h. However, when f06CNA was fed to HT29 and Caco-2 cells, increases in intensity of brightness were 42.5% and 28.8% after 6 h of incubation and significantly up to 74.8% and 57.2% after incubating for 12 h, respectively.

In order to evaluate the role of folic acid in the cellular uptake of folic acid-conjugated chitosan nanoparticles, CNA, f02CNA, and f06CNA coincubated with free folic acid were fed to the HT29 and Caco-2 cells. Figure 6B shows that there were no significant brightness intensity differences among CNA, f02CNA, and f06CNA groups and that free folic acid molecules could compete with f02CNA and f06CNA for folate receptors and suppress the receptor-mediated endocytosis of the prepared particles. These results showed that folic acid−chitosan conjugates could significantly enhance the cell uptake of 5-ALA and the accumulation of PpIX in HT29 and Caco-2 cells via the folate receptor-mediated endocytosis.

Figure 7 shows the red fluorescence of PpIX excited by a green laser and observed under a spectral confocal and multiphoton system in HT29, Caco-2, and CCD112 cells, which were fed with CNA, f02CNA, f06CNA, or 5-ALA for 12 h. Pure 5-ALA or 5-ALA in the prepared nanoparticles has been released in colorectal cancer cell lysosomes and then converted into PpIX, which accumulated in cells and then was excited by a green laser and emitted red light. Figure 7 shows CNA, fCNA, and 5-ALA taken up by CCD112 cells. Because of the quick degradation rate of PpIX in the normal cell, no red light was emitted and interference with malignant cell identification was unlikely.

A compound, calcein, is a membrane-impermeant fluorescent dye and can be incorporated into the prepared CNA and fCNA simultaneously by the electrostatic interaction between negatively charged calcein and positively charged chitosan. When HT29 and Caco-2 cells were fed with the calcein-incorporated CNA and fCNA nanoparticles for 12 h, the green brightness of calcein excited by a UV light increased with the increasing folic acid modification in the prepared nanoparticles (Figure 8A). As presented in Figure 8B, HT29 cells fed with the highest folic acid conjugated nanoparticles (f06CNA) exhibited a substantial calcein fluorescent intensity, suggesting the high activity for folate receptor-mediated endocytosis in HT29 cells with higher folate receptor expression. These results also demonstrated that enhancement of cellular association and uptake was induced by the specific interaction of folic acid conjugated nanoparticle with its receptor on the cellular surface and by

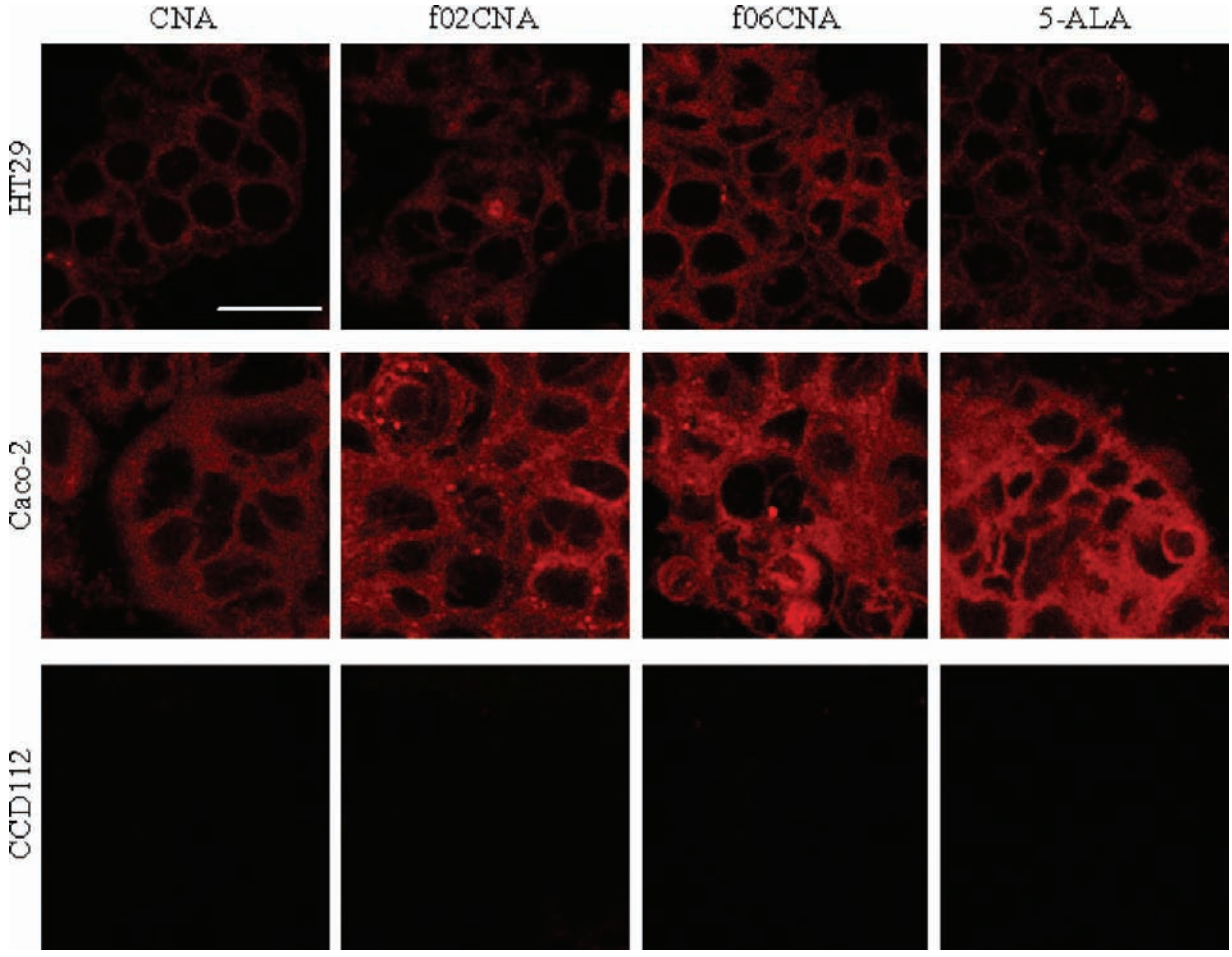


Figure 7. Spectral confocal and multiphoton system images of PpIX in HT29, Caco-2, and CCD112 cells when incubated with the prepared CNA, f02CNA, f06CNA, and pure drug 5-ALA for 12 h. The scale bar in the image is 25 μm.

subsequent internalization through the receptor-mediated endocytosis.

DISCUSSION

Folic acid is a stable, inexpensive, and generally poorly immunogenic chemical. It can be covalently conjugated to chitosan molecules via its γ-carboxyl moiety and thus retain a high affinity for folate receptors. Moreover, the ability of cellular uptake of folic acid−chitosan conjugate via folate receptor-mediated endocytosis is still as good as that of folic acid (*6*). In this study, the folic acid−chitosan conjugates bearing different content of folate derivatives could be fabricated by varying the folic acid to amino groups of chitosan molar ratios in the synthesis procedure (Table 1). The FT-IR and ^{1}H NMR spectra of the folic acid−chitosan conjugates confirmed that folic acid could be conjugated onto chitosan molecules successfully, but the relevant signals in ^{1}H NMR spectra, which were recommended by Wang et al. (*32*) and could be used to ascertain the regiochemistry of the linkage of folate derivatives and chitosan, were masked by the strong and broad signals owing to the resonances of the protons associated to chitosan monosaccharide residues (Figures 2 and 3). Thus, we were unable to determine the regiochemistry of the folate linkage in folic acid−chitosan conjugates from ^{1}H NMR spectra, but it could be inferred that folic acid was conjugated to an amino group via its γ-carboxyl moiety mostly due to the reaction conditions chosen and the steric constraints.

Chitosan was chosen as the cationic polymer because it provides many free amino groups that can be quickly gelled to form micro/nanoparticles once it contacts polyanions (*34*). In this study, we found a weak association between the particle size of the prepared nanoparticles and the folic acid conjugation or 5-ALA load. However, the zeta-potential and loading efficiency of 5-ALA depended on the folic acid conjugation. Zeta-potential can greatly influence particle stability through electrostatic repulsion between particles. Greater zeta-potential resulted in improved stability of nanoparticles in the solution and a narrower size distribution, presumably because the charged particles repelled one another and therefore overcame the natural tendency to aggregate (*35*).

As shown in Table 3, the zeta-potential of the CN and CNA was about 25 mV. This provided enough surface charge to stabilize the particles from aggregation, which was decreased when CN and CNA were conjugated with folic acid. When the more electroneutral folate derivatives displaced the protoned amino groups (f06CN and f06CNA), the zeta-potential was even down to 20 mV, and therefore it might not provide enough repulsive force to stabilize the particles from aggregation for long-term storage. These results are consistent with the Zeta-sizer-3000 measurements and TEM observations. When the prepared particles conjugated with folic acid, they got a large PDI value (Table 3) and a wide particle size distribution in the range 100−600 nm (Figure 4).

When CNA was conjugated with folic acid (fCNA), the loading efficiency of 5-ALA decreased to 38% and 35% for f02CNA and f06CNA particles, respectively (Table 3). In f02CNA and f06CNA particles, a number of amino groups were replaced by folic acid and reduced the positive charges on chitosan molecules to attract 5-ALA molecules. Moreover, the spatial hinder of folate derivatives on chitosan backbone might

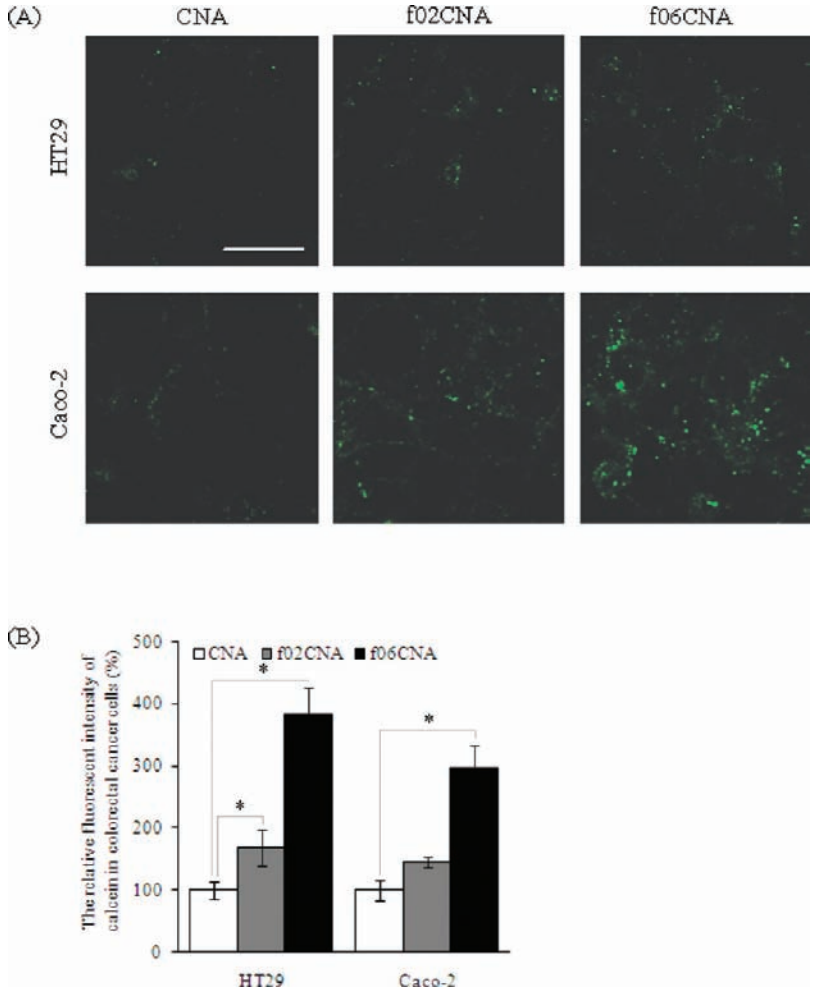


Figure 8. (A) Green fluorescent images of calcein in HT29 and Caco-2 cells when fed with the calcein-incorporated CNA, f02CNA, and f06CNA nanoparticles for 12 h. The scale bar in the image is 25 μm. (B) The relative fluorescent intensity of calcein in HT29 and Caco-2 cells. *: $p < 0.05$.

resist the interaction between chitosan and 5-ALA molecules. On the basis of these reasons, the loading efficiency appeared strongly dependent on the content of folic acid conjugation. In the previous studies (*19*), no red fluorescence of PpIX could be observed in *E. coli* when fed with the prepared CNA nanoparticles, and it pointed out that the uptake of 5-ALA in *E. coli* could be precluded by encapsulating 5-ALA in an antibacterial material, such as chitosan. Furthermore, the incorporation of 5-ALA in the CNA would be stable because of the lack of 5-ALA release from the particle and uptake by *E. coli*. Therefore, it was feasible to load 5-ALA in the CNA and fCNA nanoparticles and then deliver them into colorectal cancer cells via folate receptor-mediated endocytosis.

Folate receptor is frequently overexpressed on the surface of many human cancer cell types, such as carcinomas of the kidney, ovary, uterus, testis, and adenocarcinomas of the colon (*4*). For this reason, many studies have used folic acid as a ligand with cationic liposomes and other polymers to target cells with folate receptor expression and promote its entry into malignant cells via folate receptor-mediated endocytosis. Figure 6A shows that, for f06CNA group, much more PpIX accumulated in HT29 and Caco-2 cells than that for CNA group. This enhancement of PpIX accumulation might be due to the high folic acid conjugation on f06CNA, which could result in stronger affinity to the folate receptor on HT29 and Caco-2 cell membrane and higher efficacy of internalization via folate receptor-mediated endocytosis. Moreover, variation in the degree of folate receptor among various colorectal cancer cell lines will result in variation in degree of target uptake efficiency. The folate receptor expression on HT29 cell membrane was remarkable higher than that on Caco-2 cell membrane (Figure 5), and this resulted in a lower f06CNA engulfment and a lower difference in the enhanced PpIX accumulation in Caco-2 cells than in HT29 cells (Figure 6A). In addition, the improvement of cell uptake via electrostatic attraction between particles and cell membrane was not conspicuous for HT29 and Caco-2 cells due to no difference of PpIX accumulation in HT29 and Caco-2 cells when cultured in a fresh medium suspending with the prepared nanoparticles bearing different surface charge and free folic acid (Figure 6B).

In previous studies, 5-ALA was encapsulated in chitosan nanoparticles and taken up by cells but not bacteria, which could interfere with the efficacy of detection of cancer cells. However, culturing the 5-ALA loading chitosan nanoparticle with cancer cells for 24 h would result in an observable fluorescent intensity (*19*). The conjugation of folic acid onto a chitosan molecular backbone via amide bond could promote the uptake of particles into a cell after only 12 h of incubation time. The HT29 and Caco-2 cells showed a stronger uptake of f06CNA nanoparticles than those of pure 5-ALA alone (Figure 7). When HT29 and Caco-2 cells were fed with f06CNA, the f06CNA was easily engulfed via folate receptor-mediated endocytosis, and then 5-ALA could be converted into to PpIX intracellularly to reach the visual fluorescent intensity noted after 12 h of incubation. Since PpIX in normal cells is always maintained at a constant level (*16*), no red fluorescence suggesting interference with the diagnostic results could be observed inside CCD112 cells

(Figure 7). The results shown in Figure 8 confirmed that the f06CNA was easily taken up either in HT29 cells or in Caco-2 cells as against the CNA. However, the difference in the enhanced particle uptake evaluated from the calcein fluorescence intensity was much higher than that determined by PpIX accumulation, suggesting that the release of 5-ALA from f02CNA and f06CNA was slow and sustained and resulted in a lower improvement of PpIX accumulation. These findings suggest that 5-ALA would be a perfect precursor exogenous chromophore for detecting cancer lesions and that chitosan conjugated with folic acid could be a suitable vehicle for carrying 5-ALA.

In clinical applications, because employing folic acid conjugated with chitosan nanoparticles only in oral form might result in dissolution in the stomach at a pH that is lower than that of the pK_a of chitosan (*34*), coating the conjugate with a pH-sensitive polymer, such as poly(acrylic acid) (*35*), would be necessary. Furthermore, the usage of STPP and acetic acid solution in the particle preparation process will not cause any distress to the blood circulation or other part of human systems when the folic acid-conjugated chitosan nanoparticles are applied as an oral form for the colon-specific drug delivery system.

CONCLUSIONS

In this study, a chitosan nanoparticle that was successfully conjugated with folic acid and loaded with 5-ALA was taken up by HT29 and Caco-2 cell lines, most likely via receptor-mediated endocytosis. Chitosan conjugated with folic acid appears to be an ideal vector for colorectal-specific drug delivery of 5-ALA for fluorescent endoscopic detection of colorectal cancer.

ACKNOWLEDGMENT

This research work was funded by National Science Council, ROC (NSC98-2120-M-002-008).

LITERATURE CITED

(1) Park, E. K., Lee, S. B., and Lee, Y. M. (2005) Preparation and characterization of methoxy poly(ethylene glycol)/poly(e-caprolactone) amphiphilic block copolymeric nanospheres for tumor-specific folate-mediated targeting of anticancer drugs. *Biomaterials 26*, 1053–1061.

(2) Chan, P., Kurisawa, M., Chung, J. E., and Yang, Y. Y. (2007) Synthesis and characterization of chitosan-g-poly(ethylene glycol)-folate as a non-viral carrier for tumor-targeted gene delivery. *Biomaterials 28*, 540–549.

(3) Wang, S., and Low, P. S. (1998) Folate-mediated targeting of antineoplastic drugs, imaging agents, and nucleic acids to cancer cells. *J. Controlled Release 53*, 39–48.

(4) Quintana, A., Raczka, E., Piehler, L., Lee, I., Myc, A., Majoros, I., Patri, A. K., Thomas, T., Mulé, J., Jr, and Baker, J. R. (2002) Design and function of a dendrimer-based therapeutic nanodevice targeted to tumor cells through the folate receptor. *Pharm. Res. 19*, 1310–1316.

(5) Oyewumi, M. O., Yokel, R. A., Jay, M., Coakley, T., and Mumper, R. J. (2004) Comparison of cell uptake, biodistribution and tumor retention of folate-coated and PEG-coated gadolinium nanoparticles in tumor-bearing mice. *J. Controlled Release 95*, 613–626.

(6) Mansouri, S., Cuie, Y., Winnik, F., Shi, Q., Lavigne, P., Benderdour, M., Beaumont, E., and Fernandes, J. C. (2006) Characterization of folate-chitosan-DNA nanoparticles for gene therapy. *Biomaterials 27*, 2060–2065.

(7) Dubé, D., Francis, M., Leroux, J. C., and Winnik, F. M. (2002) Preparation and tumor cell uptake of poly(N-isopropylacrylamide) folate conjugates. *Bioconjugate Chem. 13*, 6856–6892.

(8) Liu, S. Q., Wiradharma, N., Gao, S. J., Tong, Y. W., and Yang, Y. Y. (2007) Bio-functional micelles self-assembled from a folate-conjugated block copolymer for targeted intracellular delivery of anticancer drugs. *Biomaterials 28*, 1423–1433.

(9) Zhang, Y., Kohler, N., and Zhang, M. (2002) Surface modification of superparamagnetic magnetite nanoparticles and their intracellular uptake. *Biomaterials 23*, 1553–1561.

(10) Rembacken, B., Fujii, T., and Kondo, H. (2001) The recognition and endoscopic treatment of early gastric and colonic cancer. *Best Pract. Res. Clin. Gastroenterol. 15*, 317–336.

(11) Mountney, L., Sanderson, H., and Harris, J. (1994) *Health Care Needs Assessment* (Stevens, A., and Raftery, J., Eds.) Chapter 7, Vol 1, Radcliffe Medical Press, Oxford.

(12) Allison, R. R., Mota, H. C., and Sibata, C. H. (2004) Clinical PD/PDT in North America: An historica review. *Photodiagnosis Photodyn. Ther. 1*, 263–277.

(13) Allison, R. R., Cuenca, R., Downie, G. H., Randall, M. E., Bagnato, V. S., and Sibata, C. H. (2005) PD/PDT for gynecological disease: A clinical review. *Photodiagnosis Photodyn. Ther. 2*, 51–63.

(14) Pottier, R. H., Chow, Y. F., LaPlante, J. P., Truscott, T. G., Kennedy, J. C., and Beiner, L. A. (1986) Non-invasivetech technique for obtaining fluorescence excitation and emission spectra in vivo. *Photochem. Photobiol. 44*, 679–687.

(15) Kennedy, J. C., Pottier, R. H., and Ross, D. C. (1990) Photodynamic therapy with endogenous protoporphyrin IX: basic principles and present clinical experience. *J. Photochem. Photobiol. B 6*, 143–148.

(16) Grimbergen, M. C., van Swol, C. F., Jonges, T. G., Boon, T. A., and van Moorselaar, R. J. (2003) Reduced specificity of 5-ALA induced fluorescence in photodynamic diagnosis of transitional cell carcinoma after previous intravesical therapy. *Eur. Urol. 44*, 51–56.

(17) Steluti, R., De Rosa, F. S., Collett, J., Tedesco, A. C., and Bentley, M. V. (2005) Topical glycerol monooleate/propylene glycol formulations enhance 5-aminolevulinic acid in vitro skin delivery and in vivo protophorphyrin IX accumulation in hairless mouse skin. *Eur. J. Pharm. Biopharm. 60*, 439–444.

(18) Gederaas, O. A., Rasch, M. H., Berg, K., Lagerberg, J. W., and Dubbelman, T. M. (1999) Photodynamically induced effects in colon carcinoma cells (WiDr) by endogenous photosensitizers generated by incubation with 5-aminolaevulinic acid. *J. Photochem. Photobiol. B 49*, 162–170.

(19) Yang, S. J., Shieh, M. J., Lin, F. H., Lou, P. J., Peng, C. L., Wei, M. F., Yao, C. J., Lai, P. S., and Young, T. H. (2009) Colorectal cancer cell detection by 5-aminolaevulinic acid-loaded chitosan nano-particles. *Cancer Lett. 273*, 210–220.

(20) Berscht, P. C., Nies, B., Liebendorfer, A., and Kreuter, J. (1994) Incorporation of basic fibroblast growth factor into methylpyrrolidinone chitosan fleeces and determination of the in vitro release characteristics. *Biomaterials 15*, 593–600.

(21) Thanou, M., Verhoef, J. C., and Junginger, H. E. (2001) Chitosan and its derivatives as intestinal absorption enhancers. *Adv. Drug. Delivery Rev. 50*, S91–S101.

(22) Thanou, M., Verhoef, J. C., and Junginger, H. E. (2001) Oral drug absorption enhancement by chitosan and its derivatives. *Adv. Drug. Delivery Rev. 52*, 117–126.

(23) Agnihotri, S. A., Mallikarjuna, N. N., and Aminabhavi, T. M. (2004) Recent advances on chitosan-based micro- and nanoparticles in drug delivery. *J. Controlled Release 100*, 5–28.

(24) Qi, L., Xu, Z., Jiang, X., Hu, C., and Zou, X. (2004) Preparation and antibacterial activity of chitosan nanoparticles. *Carbohydr. Res. 339*, 2693–2700.

(25) Du, J., Zhang, S., Sun, R., Zhang, L. F., Xiong, C. D., and Peng, Y. X. (2005) Novel polyelectrolyte carboxymethyl konjac glucomannan-chitosan nanoparticles for drug delivery. II. Release of albumin in vitro. *J. Biomed. Mater. Res. Part B 72B*, 299–304.

(26) Xu, Y., Du, Y., Huang, R., and Gao, L. (2003) Preparation and modification of N-(2-hydroxyl) propyl-3-trimethyl ammonium chitosan chloride nanoparticle as a protein carrier. *Biomaterials 24*, 5015–5022.

(27) Kiang, T., Wen, J., Lim, H. W., and Leong, K. W. (2004) The effect of the degree of chitosan deacetylation on the efficiency of gene transfection. *Biomaterials 25*, 5293–5301.

(28) Gan, Q., Wang, T., Cochrane, C., and McCarron, P. (2005) Modulation of surface charge, particle size and morphological properties of chitosan-TPP nanoparticles intended for gene delivery. *Colloid Surf., B 44*, 65–73.

(29) Choy, J. H., Jung, J. S., Oh, J. M., Park, M., Jeong, J., Kang, Y. K., and Han, O. J. (2004) Layered double hydroxide as an efficient drug reservoir for folate derivatives. *Biomaterials 25*, 3059–3064.

(30) Akasaka, K., Gyimesi-Forrás, K., Lämmerhofer, M., Fujita, T., Watanabe, M., Harada, N., and Lindner, W. (2005) Investigations of molecular recognition aspects related to the enantiomer separation of 2-methoxy-2-(1-naphthyl)propionic acid using quinine carbamate as chiral selector: An NMR and FT-IR spectroscopic as well as X-ray crystallographic study. *Chirality 17*, 544–555.

(31) Yang, J. M., Lin, H. T., and Yang, S. J. (2005) Evaluation of poly(*N*-isopropylacrylamide) modified hydroxyl-terminated polybutadiene based polyurethane membrane. *J. Membr. Sci. 258*, 97–105.

(32) Wang, S., Luo, J., Lantrip, D. A., Waters, D. J., Mathias, C. J., Green, M. A., Fuchs, P. L., and Low, P. S. (1997) Design and synthesis of [^{111}In]DTPA-folate for use as a tumor-targeted radiopharmaceutical. *Bioconjugate Chem. 8*, 673–679.

(33) Dawson, R. M. C., Elliott, D. C., Elliott, W. H., and Jones, K. M. (1986) *Data for Biochemical Research*, pp 134−135, Oxford University Press, New York.

(34) Qi, L., Xu, Z., Jiang, X., Li, Y., and Wang, M. (2005) Cytotoxic activities of chitosan nanoparticles and copper-loaded nanoparticles. *Bioorg. Med. Chem. Lett. 15*, 1397–1399.

(35) Hu, Y., Jiang, X., Ding, Y., Ge, H., Yuan, Y., and Yang, C. (2002) Synthesis and characterization of chitosan-poly(acrylic acid) nanoparticles. *Biomaterials 23*, 3193–3201.

BC9004798

Considerations of Solid-Phase DNA Amplification

Ramkumar Palanisamy,† Ashley R. Connolly,† and Matt Trau*

Centre for Biomarker Research and Development, Australian Institute for Bioengineering and Nanotechnology (AIBN), The University of Queensland, Brisbane Qld-4072, Australia. Received November 10, 2009; Revised Manuscript Received February 3, 2010

Solid-phase (SP) polymerase chain reaction (PCR) is an increasingly popular tool used to produce immobilized DNA for a variety of applications, including high-throughput DNA sequencing and SNP analysis. Despite its usefulness, the mechanism of DNA amplification using immobilized primers has not been thoroughly explored. Herein, we describe a SP-PCR process that was designed to explore and better understand some limitations of SP-DNA amplification. The rate of SP-DNA amplification was measured, and the ability to exponentially amplify DNA on a surface was demonstrated. Approximately 50 amol of DNA was amplified to detectable levels using SP-PCR. The mechanism and some limitations of the reaction were investigated by measuring the density of the primer on the surface prior to amplification and the amount of immobilized amplicon produced after SP-PCR. This enabled some of the practical limitations of the reaction to be addressed within a logical theoretical framework.

INTRODUCTION

The polymerase chain reaction (PCR) has revolutionized the field of molecular biology by enabling a specific fragment of DNA in a heterogeneous mixture to be amplified in excess of one million fold. This very sensitive technique enables DNA to be amplified to levels that are detectable and useful in a wide range of biological applications (*1, 2*).

Conventionally, PCR is performed in solution using two primers that are each designed to hybridize to the 3′ ends of a denatured DNA duplex. A thermostable DNA polymerase is used to extend the 3′ end of each primer to replicate the duplex, which accumulates exponentially with repetitive rounds of thermal cycling. PCR can also be used to generate an immobilized amplicon in a process called solid-phase (SP) PCR. There are two common forms of SP-PCR. In one form, DNA amplification is initiated with both primers in solution to enable the amplicon to be produced in an amount sufficient to extend an immobilized primer (*3*−*6*). The second form involves generating an immobilized amplicon by grafting both primers on a surface (*6, 7*). The primer(s) can be immobilized on a microtiter plate (*8, 9*), a flat surface (*10*−*12*), or a microbead encased in a micelle. In each case, enzymatic extension of the primer produces a tethered amplicon that can be easily detected, quantified, and manipulated for subsequent applications including cloning, high-throughput DNA sequencing and SNP detection (*13, 14*).

Despite its potential, the amount of immobilized amplicon produced using SP-PCR is limited. Although the surface itself reduces the yield of amplicon, numerous nonfouling surfaces and strategies to project the primer away from the surface have had only limited success (*15, 16*). To better understand the factors that reduce the yield of amplified DNA, a SP-PCR assay on silica microbeads was developed. This enabled the mechanism of SP-DNA amplification to be thoroughly investigated. The detection limit of the SP-PCR system was determined, and the kinetics of DNA amplification on the surface of a microbead were investigated. The amount of immobilized primer extended during the amplification reaction was also quantified and the accuracy of the assay was assessed. These data provide an insight into the mechanism and some of the fundamental limitations of SP-DNA amplification.

Table 1. PCR Primer and DNA Template Sequences

	Oligonucleotide Sequences (5′-3′)
Forward primer	NH_2 TTG ATC CTG GGA GTT GAC AGC CAA AGA TGG GTC CAG TTC A
Primer probe	Cy5-T GAA CTG GAC CCA TCT TTG GCT GTC AAC TCC CAG GAT CAA
DNA Template	GGC ATC CAC GGG CGC ATC TCC GTT GAG GGC CAG GAA GTG AAC TGG ACC CAT CTT TGG
Reverse primer	ALEXA 488-GAA ACC CAT CAG TCA AGG AGG CAT CCA CGG GCG CAT CTC C

MATERIALS AND METHODS

Fluorescently Encoded Microbeads. Preparation of 6 μm diameter silica microbeads has been previously described (*17*). The microbeads were coated with aminopropylsilane, and the surface was derivatized with adipic acid (*18*).

Coupling of Oligonucleotides to Microbeads. The 5′ end of the forward primer was coupled to 6 μm adipic acid coated microbeads using standard 1-ethyl-3-(3-dimethylaminopropyl)-carbodiimide (EDC) chemistry (*18*). The DNA coupled microbeads were pelleted by centrifugation at 10 000 G for 30 s and washed three times with 1 mL of 0.1 M 2-morpholinoethane sulfonic acid (MES buffer supplemented with 0.01% SDS) and stored at 4 °C.

Oligonucleotides. Unlabeled oligonucleotides were purchased from GeneWorks (GeneWorks Pty. Ltd., Adelaide, Australia), and fluorescently labeled oligonucleotides were purchased from Invitrogen (Invitrogen Corporation, California, USA). The oligonucleotides used in this study are listed in Table 1.

Solid-Phase Polymerase Chain Reaction. 50 pg of single-stranded (ss) DNA template was amplified in a 30 μL reaction containing 1.25 U of Taq DNA polymerase (GoTaq Flexi DNA polymerase, Promega Corporation, Wisconsin, USA), 0.2 mM

* Correspondence to Matt Trau, m.trau@uq.edu.au, Centre for Biomarker Research and Development, Australian Institute for Bioengineering and Nanotechnology, The University of Queensland, Brisbane Qld-4072. Phone: +61 7 3346 4173, fax: +61 7 3346 3973.

† These authors contributed equally to this work.

10.1021/bc900491s © 2010 American Chemical Society
Published on Web 03/23/2010

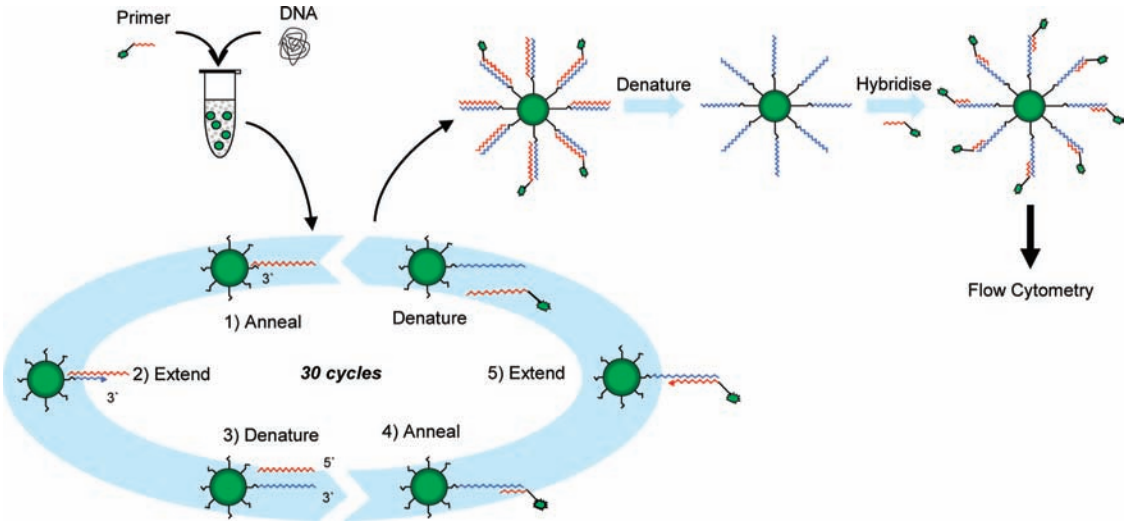


Figure 1. SP-PCR. Microbeads containing the immobilized forward primer were suspended in a solution containing the reverse primer and the DNA template. The template annealed to the immobilized forward primer (1) enabling the 3′ end of the primer to be extended by Taq polymerase (2) to generate dsDNA. The DNA duplex was thermally denatured (3) to allow the reverse primer to anneal to the newly synthesized immobilized amplicon. (4). Extension of the reverse primer regenerated dsDNA duplex (5) which was subjected to repetitive cycles of denaturation, annealing, and extension to produce many immobilized amplicons. The extent of SP-PCR was determined by denaturing the amplicon and probing the surface immobilized ssDNA with a fluorescent reverse primer. The level of fluorescence was quantified using a flow cytometer.

of each dNTPs, 2.5 mM $MgCl_2$, 1× PCR buffer (GoTaq PCR buffer, Promega), 0.1% Tween 20, 0.5 μM of A488 reverse primer, and approximately 4×10^4 microbeads containing the immobilized forward primer. Cycling was carried out in a Corbett Research thermocycler using the following conditions: denaturation at 94 °C for 1 min, followed by 30 cycles of 94 °C for 1 min, 55 °C for 2 min, and 72 °C for 1 min.

DNA Hybridization. Following PCR, the immobilized amplicon was denatured at 100 °C for 90 s in 400 μL of 4× SSC buffer (0.6 M NaCl, 0.06 M sodium citrate). The microbeads were pelleted and denaturation was repeated twice. 50 ng of A488 reverse primer was hybridized to the immobilized ssDNA in 10 μL milli Q and 4 μL hybridization buffer (50 mM $NaHPO_3$, 0.5 M NaCl, and 0.5% SDS). Hybridization was performed at 55 °C for 60 min in a vessel shaking at 1400 rpm. The microbeads were then washed and suspended in 100 μL of 0.01% SDS in preparation for analysis using flow cytometry.

Flow Cytometry. Fluorescence on the surface of the microbeads was measured using a DakoCytomation Moflo flow cytometer. The Alexa 488 (A488) fluorophore (Invitrogen Corporation, CA, USA) was excited with a 488 nm laser and emission monitored at 530 nm. The Cy5 fluorophore (GE Healthcare Bio-Sciences, Uppsala, Sweden) was excited with a 635 nm laser and emission monitored at 670 nm. Data were collected on a logarithmic scale and analyzed using *Summit* v 4.0 software.

RESULTS

Assay Design. The mechanism of SP-PCR was investigated using a PCR assay designed to exclusively amplify surface immobilized DNA. The assay was initiated by hybridization of a ssDNA template to an immobilized forward primer. Enzymatic extension of the immobilized primer generated an immobilized amplicon. A reverse primer could then hybridize to the immobilized amplicon and undergo extension to produce a copy of the ssDNA template (Figure 1). Therefore, SP-PCR will only progress after enzymatic extension of the immobilized forward primer. This enabled the mechanism of SP-PCR to be analyzed in the absence of any amplification of DNA in solution, which will inevitably occur if amplification is initiated with a dsDNA template.

Following amplification, the amount of PCR product on the surface was measured by denaturing the amplicon and hybridizing a fluorescently labeled DNA probe to the immobilized ssDNA. The intensity of the fluorescent signal on surface of the microbead was measured using a flow cytometer to reveal the amount of SP-DNA synthesis.

Assay Optimisation. Several parameters likely to affect SP-PCR were optimized to ensure efficient DNA amplification. Washing the microbeads with PCR buffer prior to amplification was essential for successful SP-PCR. The concentration of magnesium was varied between 2 and 3 mM and amplification was optimal at 2.5 mM. To ensure amplification was not limited by the amount of the reverse primer in the reaction, its concentration was the doubled from 0.5 μM which produced only 15% increase in the amount of immobilized amplicon. Subsequent increases in concentration had no effect on the yield of SP-DNA amplification. 4×10^4 microbeads were used in the SP-PCR. The amount of forward primer in the PCR was changed by varying the number of microbeads added to the reaction. Halving the number had no significant effect on the yield of the immobilized amplicon, while an excess number of microbeads reduced the yield of immobilized amplicon, which was attributed to sedimentation of the microbeads.

The rate of hybridization of a complementary strand of DNA to the immobilized primer will dictate the duration of the annealing step during PCR. This was determined by directly hybridizing a complementary fluorescent probe to the immobilized forward primer at 55 °C in PCR buffer. The extent of hybridization to the immobilized primer was determined by measuring the fluorescence using flow cytometry. After hybridization for 1.5 min, the fluorescence on the surface of the microbead reached 70% of the maximum level measured after 10 min. This indicated an annealing time of approximately 2 min during SP-PCR cycling was sufficient for the DNA template to hybridize to the immobilized primer.

Detection Limit. Fluorescently encoded microbeads have been used for sensitive detection of PCR products (*19*−*22*). However, amplification of DNA directly on a surface is considerably less sensitive (*6, 7*). Therefore, we investigated some factors that were likely to influence SP-DNA amplification

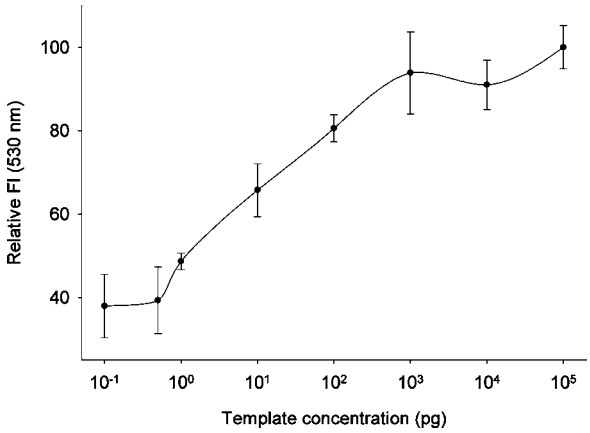


Figure 2. Replicate SP-PCR were prepared each containing approximately 4×10^4 microbeads with the forward primer immobilized on their surface, the reverse primer in solution, and the specified amount of DNA template. Following amplification, the immobilized dsDNA was denatured and the extent of SP-PCR was determined by hybridizing a fluorescent probe to the immobilized ssDNA amplicon. Values represent the mean fluorescence ± standard deviation of triplicate reactions (*y*-axis) for each template concentration (*x* axis) which was determined by flow cytometric analysis of the microbeads.

in an attempt to characterize and better understand the limitations of the reaction.

The detection limit and analytical range of this SP-PCR was assessed by amplifying serial dilutions of the DNA template (from 100 ng to 100 fg) in triplicate reactions containing the immobilized forward primer and the reverse primer in solution. The extent of SP-DNA amplification was determined by hybridizing a fluorescent probe to the ssDNA immobilized on the surface after denaturation of the amplicon. The fluorescence increased with template concentration (Figure 2), indicating that more DNA amplification occurred on the surface at higher template concentration. When the DNA template was present in excess of 1 ng, there was no significant increase in the amount of immobilized amplicon produced, suggesting the surface became saturated with the with PCR products. The coefficient of variation of the replicate reactions varied from 4% to 20% and was, on average, 10% throughout the analytical range of template concentrations.

Amplification Mode. The amount of SP-PCR product increased as more DNA template was added to the reaction (Figure 2). However, it is unclear if this increase was the result of linear amplification or inefficient exponential amplification of the template. When a single primer is used in a PCR, the amount of template will only double after each cycle resulting in linear amplification of DNA. In the presence of both primers, DNA amplification progresses exponentially and the amount of amplicon produced is maximized. Therefore, the mode of SP-DNA amplification was investigated by omitting the reverse primer to ensure linear amplification of the template. The reverse primer was then added to a replicate reaction to enable it to proceed exponentially. The extent of DNA amplification was determined by hybridizing a fluorescent probe to the ssDNA remaining on the surface after denaturation of the amplicon. After 25 cycles of linear amplification, there was a 2.3-fold increase in the amount of PCR product on the surface. After 25 cycles of exponential PCR, there was a 7.8-fold increase in the amount of PCR product, which was 3.4-fold more than linear amplification (Figure 3). This demonstrates that the reverse primer is utilized during SP-PCR to increase the amount of SP-DNA produced during amplification.

The change in fluorescence on the surface of the bead at different cycle numbers was used to determine the efficiency of SP-DNA amplification. In a PCR, the initial amount of DNA template (T_o) amplifies with an efficiency (E_t) over (j) cycles to produce an amount of product (T_j) according to eq 1 (*23*).

$$T_j = T_o(1 + E_t)^j \quad (1)$$

Equation 1 was solved for different values of E_t to produce a curve that approximated the experimentally acquired data (Figure 3). This revealed that exponential SP-PCR progressed with an amplification efficiency (E_t) of approximately 9%, before the reaction reached a plateau after 17 cycles.

Quantification. The amplification efficiency of SP-PCR is approximately 91% lower than PCR performed in solution. This inefficiency may be attributed to a low primer concentration, its inability to diffuse through solution, or inefficient enzymatic extension. However, attempts to overcome these inefficiencies by projecting primers away from the surface or modifying surface have had only limited success (*15, 16*). In an attempt to better understand the factors that limit SP-PCR, the amount of DNA amplification on the surface was accurately measured.

Initially, the amount of forward primer immobilized on the surface of each microbead was quantified. Different amounts of a fluorescently labeled DNA strand complementary to the immobilized primer were prepared and incubated with replicate samples containing 4×10^4 microbeads. The fluorescence on the surface of each bead was plotted as a function of DNA concentration to produce a curve indicative of a Langmuir isotherm (*24*) (Figure 4). The amount of immobilized primer was determined by calculating the amount of fluorescent DNA that saturated the surface of 4×10^4 microbeads. A 6.0 ± 0.5 μm diameter microbead was found to contain $(2.6 \pm 0.2) \times 10^6$ primers or $(2.3 \pm 0.3) \times 10^{10}$ primers per mm^2. Therefore, approximately 0.17 pmol of forward primer was added to each PCR with the addition of 4×10^4 microbeads.

The amount of immobilized amplicon produced after 30 cycles of SP-PCR was also measured. Following amplification, the immobilized amplicon was denatured to generate immobilized ssDNA. Different amounts of the fluorescently labeled

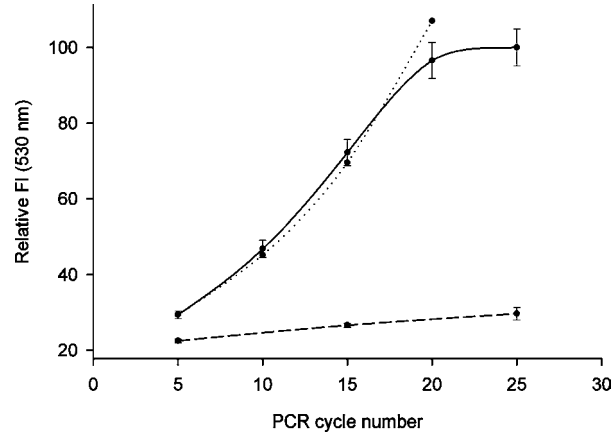


Figure 3. Replicate SP-PCRs were prepared each containing approximately 4×10^4 microbeads with the forward primer immobilized on their surface and 1 ng of DNA template. The reverse primer was either omitted from the SP-PCR (dashed line) or added to the reaction (solid line). Amplification progressed for the indicated number of cycles. Following amplification, the immobilized dsDNA was denatured, and the extent of SP-PCR was determined by hybridizing a fluorescent probe to the immobilized ssDNA amplicon. Values represent the mean fluorescence ± standard deviation of triplicate reactions (*y*-axis) for each template concentration (*x* axis), which was determined by flow cytometric analysis of the microbeads. The efficiency of exponential SP-PCR was calculated by solving eq 1 for different values of E_t. An amplification efficiency of 9% ($E_t = 0.09$) and an arbitrary T_o value of 72.17 were substituted into eq 1 to calculate T_j at different cycle numbers to obtain a line (dotted) that best fits the experimental data.

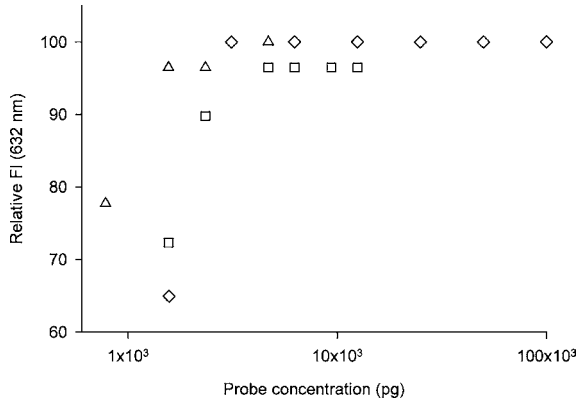


Figure 4. Replicate samples containing 4×10^4 microbeads with the forward primer immobilized on the surface were prepared. Each sample was hybridized with the specified concentration of fluorescently labeled oligonucleotide probe (◇), complementary to the immobilized primer. The experiment was repeated (□) and performed with fewer microbeads (2×10^4 (Δ)). The fluorescence on the surface of each bead was measured using flow cytometry. The values represent the average fluorescence on the surface of each microbead (*y*-axis) for each concentration of the complementary fluorescent probe (*x*-axis) measured by flow cytometry. The amount of immobilized primer was determined by calculating the amount of fluorescent DNA that saturated the surface of the microbeads.

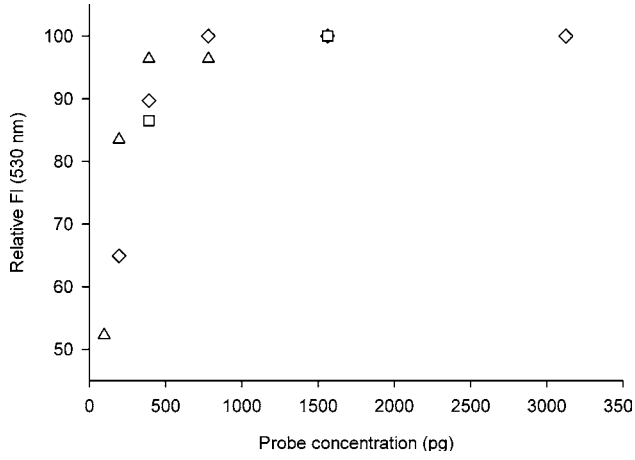


Figure 5. SP-PCR amplification of 1 μg of DNA template was performed in replicate reactions containing 2×10^4 microbeads, then the immobilized amplicons were denatured. Each sample was hybridized with the specified concentration of fluorescently labeled oligonucleotide probe (◇), complementary to the immobilized amplicon. The experiment was repeated (Δ) and performed with fewer microbeads (1×10^4 (□)). The fluorescence on the surface of each microbead was measured using flow cytometry. The values represent the average fluorescence on the surface of each microbead (*y*-axis) for each concentration of the complementary fluorescent probe (*x*-axis). The amount of immobilized amplicon produced by SP-PCR was determined by calculating the amount of fluorescent DNA that saturated the surface of the microbeads.

reverse primer were prepared and incubated with replicate samples containing 2×10^4 microbeads. The fluorescence on the surface of each microbead after hybridization is depicted in Figure 5. The amount of immobilized PCR product was measured and it was calculated that each microbead contained $(9.5 \pm 0.7) \times 10^5$ amplicons, or $(8.4 \pm 1.1) \times 10^9$ amplicons per mm^2. Therefore, only (36 ± 7)% of the primers immobilized on the surface were extended after 30 cycles of SP-PCR.

The molecular geometry of ssDNA in solution has been modeled. The theoretical radius of gyration of a 96 base ssDNA amplicon was calculated to be approximately 3.0 nm with a cross section area of 28.8 nm^2. Therefore, each 6.0 ± 0.5 μm bead can ideally contain $(3.5 \pm 0.4) \times 10^{10}$ amplicons per mm^2. Therefore, only (24 ± 4)% of the available surface was covered with the amplicon after 30 cycles of SP-PCR.

DISCUSSION

We have devised a SP-PCR assay on a microbead that enabled the mechanism of SP-DNA amplification to be explored. The assay described herein was performed using only the reverse primer in solution to generate an immobilized amplicon. This enabled the mechanism of SP-PCR to be analyzed in the absence of any amplification of DNA in solution. DNA was amplified exponentially on the surface and the amount of amplicon produced was quantified.

Reaction conditions for optimal SP-DNA amplification were elucidated and found to be similar to those of conventional PCR, despite the reported use of lengthy cycling parameters (*5*). Conditioning the DNA-coated surface with the PCR reaction buffer was essential for successful amplification and hybridization of the template to the immobilized primer occurred rapidly during thermal cycling. The forward primer was found to be securely immobilized on the surface despite reports of primer detachment during thermal cycling (*6*). The stability was attributed to the covalent attachment of the forward primer and the molecular stability of the silica microbeads. As a result, the coefficient of variation was on average 10% between replicate amplification reactions. This level of reproducibility was obtained without agitating the microbeads during thermal cycling, which has been reported to retard SP-DNA amplification (*25*). It is unclear if the microbeads remain in suspension during the reaction, but it is clear that they all contain a consistent amount of surface immobilized amplicon. Therefore, the template was not locally sequestered on the surface but diffused freely in solution initiating DNA polymerization on different microbeads in the reaction.

The amount of PCR product generated on the surface of each microbead increased when more template was added to the reaction (Figure 2). However, when the template concentration was in excess of 1 ng there was no appreciable increase in the amount of amplicon produced. This may be due to the DNA template saturating the surface or other factors may be acting to retard amplification. It is generally accepted that lack of diffusion, proximity to the surface, and low concentration of the immobilized primer most likely inhibit SP-DNA amplification (*15, 16, 25, 26*). However, *Taq* polymerase was enzymatically active while in close proximity to the surface and was able to perform both forward and reverse priming reactions effectively. Moreover, the DNA template was shown to undergo exponential amplification during the reaction. The efficiency of exponential SP-PCR was approximately 9% (i.e., $E_t = 0.09$) indicating that only 9 of 100 primers were extended during each cycle of PCR. This is substantially lower than solution PCR where the efficiency approaches 90−100% (i.e., $E_t = 0.9-1.0$) (*27*). Attempts to increase the overall yield of the immobilized amplicon by increasing PCR cycle number and reducing the number of microbeads had no measurable impact on the detection limit. Approximately 3×10^7 copies of DNA could be amplified to detectable levels by SP-PCR.

Only a fraction (36%) of the immobilized primers were extended during SP-PCR. This suggests amplification was not limited by the amount of the immobilized primer, but more likely by the generation of the amplicon itself. The immobilized amplicon (96 bases) was 2.4-fold longer than the primer (40 bases) and could conceivably "mask" adjacent primers after amplification. More specifically, primers within approximately one gyration radius of the amplicon would experience this masking effect. This will predominate when the primers are immobilized at high density, while at low density, amplification will be limited by insufficient primers.

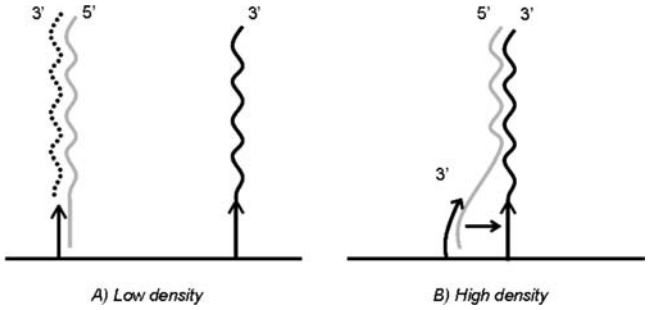


Figure 6. Neighboring DNA interactions during SP-PCR. (A) When the DNA amplicons (black line) are at low density, the 3′ end of the immobilized primer (arrow) will undergo extension by Taq polymerase to produce a new immobilized amplicon. (B) As SP-PCR progresses, the amplicon density increases and it is proposed that extension of the immobilized primer is retarded because the DNA template (gray line) will hybridize to an adjacent amplicon in preference to the primer.

A 96-base amplicon has a theoretical gyration radius of 3.0 nm and a cross-sectional area of approximately 28.8 nm^2. This would enable approximately 3.5×10^{10} amplicons to be produced per mm^2, on the surface of each 6 μm bead. However, only 8.4×10^9 amplicons were generated per mm^2, which is substantially lower than expected. The amount of product produced during SP-PCR may not be limited exclusively by primer "masking", other factors may also retard amplification.

SP PCR progressed exponentially, but amplification was retarded during the later cycles (Figure 3) which suggests the progress of the reaction was inhibiting amplification. As the amount of immobilized PCR product increased, the DNA template may be likely to hybridize to the immobilized amplicon in preference to the primer. This will prevent primer extension and limit the amount of SP-DNA amplification. This inhibitory effect is more likely to occur when the immobilized primer and amplicon are in close proximity. More specifically, when separated by the approximate gyration diameter of the template, the PCR template is more likely to hybridize to the immobilized amplicon in preference to the immobilized primer (Figure 6). Under these conditions, it is predicted that SP-DNA amplification will reach a "plateau" when the immobilized amplicon density is 75% lower than that predicted theoretically. This is equivalent to $(8.7 \pm 1.0) \times 10^9$ amplicons per mm^2, which is similar ($97 \pm 17\%$) to the experimentally determined value of $(8.4 \pm 1.1) \times 10^9$ amplicons per mm^2. The inhibitory effect of SP-PCR is likely to be enhanced by factors that increase the gyration radius of the amplicon. Larger amplicons have an increased gyration radius and are predicted to have a lower yield during SP-PCR, which is consistent with experimental findings (*28*). "Spacers" designed to project the primers from the surface will make the primers more accessible to the polymerase, but will also increase the gyration radius of the amplicon and may limit the yield of SP-PCR.

In summary, we have characterized some factors that influence SP-DNA amplification and have identified other factors that are likely to limit the yield of DNA during amplification. It has been demonstrated that DNA polymerase retained catalytic activity in close proximity to a surface. SP-PCR was used to exponentially amplify ssDNA to generate a unique homogeneous amplicon on a surface. However, the amplification efficiency was substantially lower than that of solution-phase PCR. The amount of amplicon produced was not exclusively limited by a lack of diffusion and concentration of the immobilized primer, but more likely by the production of the immobilized amplicon during the reaction. The data presented here provide insight into the mechanism of SP-DNA amplification and highlight some factors that may need to be addressed in order to achieve efficient DNA amplification on a surface.

ACKNOWLEDGMENT

We gratefully acknowledge funding and support from the NBCF through the National Collaborative Breast Cancer Research Grant Program.

LITERATURE CITED

(1) Mullis, K., Faloona, F., Scharf, S., Saiki, R., Horn, G., and Erlich, H. (1986) Specific enzymatic amplification of DNA in vitro: the polymerase chain reaction. *Cold Spring Harb. Symp. Quant. Biol. 51 Pt 1*, 263–73.

(2) Saiki, R. K., Gelfand, D. H., Stoffel, S., Scharf, S. J., Higuchi, R., Horn, G. T., Mullis, K. B., and Erlich, H. A. (1988) Primer-directed enzymatic amplification of DNA with a thermostable DNA polymerase. *Science 239*, 487–91.

(3) Diehl, F., Li, M., He, Y., Kinzler, K. W., Vogelstein, B., and Dressman, D. (2006) BEAMing: single-molecule PCR on microparticles in water-in-oil emulsions. *Nat. Methods 3*, 551–9.

(4) Nakano, M., Nakai, N., Kurita, H., Komatsu, J., Takashima, K., Katsura, S., and Mizuno, A. (2005) Single-molecule reverse transcription polymerase chain reaction using water-in-oil emulsion. *J. Biosci. Bioeng. 99*, 293–5.

(5) Kojima, T., Takei, Y., Ohtsuka, M., Kawarasaki, Y., Yamane, T., and Nakano, H. (2005) PCR amplification from single DNA molecules on magnetic beads in emulsion: application for high-throughput screening of transcription factor targets. *Nucleic Acids Res. 33*, e150.

(6) Adessi, C., Matton, G., Ayala, G., Turcatti, G., Mermod, J. J., Mayer, P., and Kawashima, E. (2000) Solid phase DNA amplification: characterisation of primer attachment and amplification mechanisms. *Nucleic Acids Res. 28*, E87.

(7) Shapero, M. H., Leuther, K. K., Nguyen, A., Scott, M., and Jones, K. W. (2001) SNP genotyping by multiplexed solid-phase amplification and fluorescent minisequencing. *Genome Res. 11*, 1926–34.

(8) Niemeyer, C. M., Adler, M., and Wacker, R. (2007) Detecting antigens by quantitative immuno-PCR. *Nat. Protoc. 2*, 1918–30.

(9) Sjoroos, M., Ilonen, J., and Lovgren, T. (2001) Solid-phase PCR with hybridization and time-resolved fluorometry for detection of HLA-B27. *Clin. Chem. 47*, 498–504.

(10) Kim, J. H., Hong, J. A., Yoon, M., Yoon, M. Y., Jeong, H. S., and Hwang, H. J. (2002) Solid-phase genetic engineering with DNA immobilized on a gold surface. *J. Biotechnol. 96*, 213–21.

(11) Levesque, G., Bharucha, A. D., and Murthy, M. R. (1993) Reverse transcription and PCR amplification of rare mRNAs immobilized on oligo(dT) cellulose. *Anal. Biochem. 213*, 170–1.

(12) von Nickisch-Rosenegk, M., Marschan, X., Andresen, D., and Bier, F. F. (2008) Reverse transcription-polymerase chain reaction on a microarray: the integrating concept of active arrays. *Anal. Bioanal. Chem. 391*, 1671–8.

(13) Brenner, S., Williams, S. R., Vermaas, E. H., Storck, T., Moon, K., McCollum, C., Mao, J. I., Luo, S., Kirchner, J. J., Eletr, S., DuBridge, R. B., Burcham, T., and Albrecht, G. (2000) In vitro cloning of complex mixtures of DNA on microbeads: physical separation of differentially expressed cDNAs. *Proc. Natl. Acad. Sci. U.S.A. 97*, 1665–70.

(14) Shendure, J., Porreca, G. J., Reppas, N. B., Lin, X., McCutcheon, J. P., Rosenbaum, A. M., Wang, M. D., Zhang, K., Mitra, R. D., and Church, G. M. (2005) Accurate multiplex polony sequencing of an evolved bacterial genome. *Science 309*, 1728–32.

(15) Carmon, A., Vision, T. J., Mitchell, S. E., Thannhauser, T. W., Muller, U., and Kresovich, S. (2002) Solid-phase PCR in microwells: effects of linker length and composition on tethering, hybridization, and extension. *Biotechniques 32*, 410–412, 414−8, 420.

(16) Shchepinov, M. S., Case-Green, S. C., and Southern, E. M. (1997) Steric factors influencing hybridisation of nucleic acids to oligonucleotide arrays. *Nucleic Acids Res. 25*, 1155–61.
(17) Miller, C. R., Vogel, R., Surawski, P. P., Jack, K. S., Corrie, S. R., and Trau, M. (2005) Functionalized organosilica microspheres via a novel emulsion-based route. *Langmuir 21*, 9733–40.
(18) Corrie, S. R., Lawrie, G. A., and Trau, M. (2006) Quantitative analysis and characterization of biofunctionalized fluorescent silica particles. *Langmuir 22*, 2731–7.
(19) Wilson, W. J., Erler, A. M., Nasarabadi, S. L., Skowronski, E. W., and Imbro, P. M. (2005) A multiplexed PCR-coupled liquid bead array for the simultaneous detection of four biothreat agents. *Mol. Cell Probes 19*, 137–44.
(20) Kalogianni, D. P., Elenis, D. S., Christopoulos, T. K., and Ioannou, P. C. (2007) Multiplex quantitative competitive polymerase chain reaction based on a multianalyte hybridization assay performed on spectrally encoded microspheres. *Anal. Chem. 79*, 6655–61.
(21) Song, L., Ahn, S., and Walt, D. R. (2006) Fiber-optic microsphere-based arrays for multiplexed biological warfare agent detection. *Anal. Chem. 78*, 1023–33.
(22) Li, S., Liu, H., Wang, Z., Hou, P., Guo, Y., He, Q., and He, N. (2006) Magnetic-particles-based high-throughput genotyping method with dual-color fluorescence hybridization. *Anal. Biochem. 359*, 277–9.
(23) Raeymaekers, L. (1993) Quantitative PCR: theoretical considerations with practical implications. *Anal. Biochem. 214*, 582–5.
(24) Chatelier, R. C., and Ashcroft, R. G. (1987) Calibration of flow cytometric fluorescence standards using the isoparametric analysis of ligand binding. *Cytometry 8*, 632–6.
(25) Andreadis, J. D., and Chrisey, L. A. (2000) Use of immobilized PCR primers to generate covalently immobilized DNAs for in vitro transcription/translation reactions. *Nucleic Acids Res. 28*, e5.
(26) Guo, Z., Guilfoyle, R. A., Thiel, A. J., Wang, R., and Smith, L. M. (1994) Direct fluorescence analysis of genetic polymorphisms by hybridization with oligonucleotide arrays on glass supports. *Nucleic Acids Res. 22*, 5456–65.
(27) Connolly, A. R., Cleland, L. G., and Kirkham, B. W. (1995) Mathematical considerations of competitive polymerase chain reaction. *J. Immunol. Methods 187*, 201–11.
(28) Tiemann-Boege, I., Curtis, C., Shinde, D. N., Goodman, D. B., Tavare, S., and Arnheim, N. (2009) Product length, dye choice, and detection chemistry in the bead-emulsion amplification of millions of single DNA molecules in parallel. *Anal. Chem. 81*, 5770–6.

BC900491S

Novel Cationic Lipids Based on Malonic Acid Amides Backbone: Transfection Efficacy and Cell Toxicity Properties

Martin Heinze,[†] Gerald Brezesinski,[‡] Bodo Dobner,[†] and Andreas Langner*[,†]

Institute of Pharmacy, Department of Biochemical Pharmacy, Martin-Luther-University, Wolfgang-Langenbeck-Strasse 4, 06120 Halle (Saale), Germany, and Max Planck Institute of Colloids and Interfaces, Am Muehlenberg 1, 14476 Potsdam, Germany. Received November 11, 2009; Revised Manuscript Received December 23, 2009

Gene delivery using nonviral approaches has been extensively studied as a basic tool for intracellular gene transfer. Despite intensive research activity, the aim of creating a vector which meets all necessary demands has still not been reached. One possibility to solve the nonviral vector associated problem of low transfection efficacy is the development of new cationic amphiphiles. Therefore, the non-glycerol-based cationic lipids **1**−**9** have been synthesized and tested for in vitro gene delivery experiments. The backbone structure of the lipids consists of a malonic acid diamide with two long hydrophobic chains. The degree of saturation of the hydrophobic chains and the structure of the polar cationic headgroup were varied. The preparation follows an easy process and facilitates the trouble-free insertion of different alkyl chains. By studying in vitro gene delivery an increase of transfection efficacy was observed when using at least one unsaturated alkyl chain in the hydrophobic part and lysine or bis(2-aminoethyl)aminoethylamid as hydrophilic headgroup. This leads to cationic lipids exhibiting comparable or even higher transfection efficacies compared to the commercially available LipofectAmine and SuperFect.

INTRODUCTION

Without doubt, gene therapy is a very promising method for the treatment of cancer and genetic diseases which are still insufficiently treatable (*1–3*). Although a lot of work has been done creating efficient gene shuttles and progress has been made over the past years, there exists no satisfying gene transfer system. In addition to the application of viral vectors, the design and synthesis of new cationic lipids is a very promising tool for gene therapy. While the transduction with modified viruses is very efficient especially for in vivo gene transfer, viruses have eminent disadvantages due to their immunogenic potential and their possibility to induce cancer (*4–7*). Nonviral gene delivery systems have, on one hand, been demonstrated as standard tools for in vitro transfection with currently more than 60 commercially available kits (*8*). On the other hand, they are regarded as a promising approach for the treatment of genetic diseases (*9, 10*) and cancer (*11–13*). However, nonviral gene delivery suffers from low transfection efficiency. Surely this is the main reason that these gene delivery systems have just a marginal stake in clinical trials (*14*). For this reason, it is of great importance to advance nonviral gene transfer systems. One possibility is the development of new, efficient, and nontoxic cationic lipids.

There are mainly three structures of cationic amphiphiles used for gene delivery: glycerol derived lipids and cholesterol-based and non-glycerol-based compounds. The group of glycerol derived lipids includes in addition to *N*-[1-(2,3-dioleyloxy)propyl]-*N,N,N*-trimethylammoniumchloride (DOTMA)[1] , first described by Felgner in his pioneering work (*15*), 1,2-dioleoyloxy-3-(trimethylammonio)propane (DOTAP), 1,2-dimyristyloxypropyl-3-dimethyl(hydroxyethyl)ammoniumbromide (DMRIE), and 2,3-dioleyloxy-*N*-[2-(spermincarboxamido)ethyl]-*N,N*-dimethyl-1-propane-ammoniumtrifluoracetate (DOSPA) (*16–18*). Substances that exhibit no glycerol backbone are also capable of transfering genes into cells, especially by the usage of *N*-methyl-4-(dioleyl)methylpyridiniumchloride (SAINT-2) or 1-[2-(oleoyloxy)ethyl]-2-oeyl-3-(2-hydroxyethyl)imidazoliniumchloride (DOTIM) (*19, 20*).

For a number of these and other cationic amphiphiles, it was shown that hydrophobic chains as well as the polar head and even the connecting backbone have a great influence on the transfection efficiency (*16, 19, 21–23*). Several groups have been working on establishment of a structure−function relationship to define the requirements for safe and efficient gene transfer with cationic lipids (*16, 19–26*).

We have now designed a new class of cationic lipids consisting of the diamide structure of malonic acid as anchor group for the hydrocarbon chains as well as the cationic headgroup inclusive spacer molecules. The idea for the preparation of these new substances is mainly based on three characteristics: First, the new compounds are easy to produce starting from cost-effective materials, and the syntheses facilitate the trouble-free insertion of different alkyl chains. Second, it may be accepted that the compounds should have biocompatibility due to the amide bond as a connection between polar headgroup, linker moiety, and partially the hydrophobic chains. Third, a positive effect may result from the ability of the malonic diamide structure to build an H-bonded network, which could stabilize the complex formation especially under neutral conditions.

* Corresponding author footnote. Phone: +49-(0)345-5525080. Fax: +49 -(0)345-5527018. E-mail: andreas.langner@pharmazie.uni-halle.de.
[†] Martin-Luther-University.
[‡] Max Planck Institute of Colloids and Interfaces.

[1]Abbreviations: DOTMA, *N*-[1-(2,3-dioleyloxy)propyl]-*N,N,N*-trimethylammoniumchloride; DOTAP, 1,2-dioleoyloxy-3-(trimethylammonio)propane; DMRIE, 1,2-dimyristyloxypropyl-3-dimethyl(hydroxyethyl)ammoniumbromide; DOSPA, 2,3-dioleyloxy-*N*-[2-(spermincarboxamido)ethyl]-*N,N*-dimethyl-1-propane-ammoniumtrifluoracetate; SAINT-2, *N*-methyl-4-(dioleyl)methylpyridiniumchloride; DOTIM, 1-[2-(oleoyloxy)ethyl]-2-oeyl-3-(2-hydroxyethyl)imidazoliniumchloride; EEDQ, 2-ethoxy-1-ethoxycarbonyl-1,2-dihydrochinoline; BOP, (benzotriazol-1-yloxy)-tris-(dimethylamino)-phosphoniumhexafluorophosphate; DCC, *N,N′*-dicyclohexylcarbondiimid; ONPG, O-nitrophenyl-*β*-galactopyranoside; DOPE, 1,2-dioleoyl-*sn*-glycero-3-phosphoethanolamine; MTT, 3-(4,5-dimethylthiazol-2-yl)-2,5-diphenyltetrazolium bromide.

10.1021/bc9004624 © 2010 American Chemical Society
Published on Web 03/23/2010

The characteristic of the compounds is the specific feature of hydrophobic chain bound to malonic acid amides backbone. One alkyl chain is bound to C2 of the malonic acid, whereas the second hydrophobic chain was linked via an amide bond to one of the carboxylic groups of the diacid. The two alkyl chains that are necessary for satisfying gene delivery vary in the degree of saturation. Starting from two C16 chains, we replaced them by successive substitution with the oleyl residue whereby the chain was elongated. According to the generally accepted finding that spacer molecules enhance the efficacy of transfection (*27*), at first we used only ethylene diamine and tris(aminoethyl)amine as spacer molecules. These compounds were connected with the malonic acid backbone by a second amide bond. Lipids **1**−**3** with the ethylene amine spacer itself were capable of transfering DNA into cells in culture, admittedly to a minor degree. However, this molecule residue was introduced for binding a proper cationic headgroup. The primary amino group was then transformed into a further amide function with boc-lysine resulting in two protonable amine residues after elimination of the protective groups. On the other hand, the tris(aminoethyl)-amine comprises both the spacer and the headgroup resulting from the two aminoethyl residues at the tertiary amine. This branched structure is suitable for the creation of dendrimer-like headgroups (*28*).

The main focus of attention for the new lipids was concentrated on transfection efficacy and toxicity properties compared with LipofectAmine and SuperFect, as they are the frequently used nonviral gene delivery systems. In first tests with these new transfection reagents, we have observed enhanced gene transfection activity with regard to commercially available vectors.

EXPERIMENTAL PROCEDURES

General Procedures and Materials. All materials and reagents were purchased from SigmaAldrich Co. Ltd. unless otherwise stated. All solvents were analytically pure and dried before use. The reactions were performed under argon. TLC was carried out on aluminum sheets precoated with silica gel 60 F254 (Merck) and developed with bromothymol blue dip. Column chromatography was performed using silica gel 60 (0.04−0.063 mm) for middle-pressure liquid chromatography (MPLC, Büchi, Germany) or silica gel 60 (0.063−0.200 mm) for normal-pressure procedure. The ESI−mass spectra were recorded with a Finnigan MAT 710 C (Thermo Separation Products, San Jose, USA) with electron spray ionization energy of 4.5 kV in negative and positive modus. EI−mass spectra were prepared with an AMD 402 (70 eV, AMD Intecta GmbH, Harpstedt, Germany). The ^{1}H NMR and the ^{13}C NMR spectra were recorded on a Varian Gemini 2000. For performing the elemental analysis, a Leco apparatus was used. The final products were fully characterized by ^{1}H NMR, ^{13}C NMR, mass spectrometry, and elemental analysis. p-CMV-SPORT-β-Gal plasmid and LipofectAmine reagent were purchased from Invitrogene Life technologies (Germany). SuperFect and plasmid isolation kit were purchased from QIAGEN (QIAGEN, Hilden, Germany). LLC PK1 cells (ATCC CL−101) were purchased from the American Type Culture Collection (ATCC USA) and A549 cells from German Collection of Microorganisms and Cell Cultures (DSMZ GmbH). Cell culture media, fetal bovine serum, and phosphate buffered saline were supplied from PAA Laboratories (PAA Laboratories GmbH Germany). Antibiotics and 3-(4,5-dimethylthiazol-2-yl)-2,5-diphenyltetrazolium bromide (MTT) were purchased from Sigma (Sigma Aldrich, Germany). DOPE was purchased from Fluka (Switzerland), and cholesterol was supplied from Roth (Carl Roth GmbH Germany).

Alkyl Malonic Acid Monoethyl Ester IIa,b. The alkyl malonic acid diethyl ester **I** (0.045 mol) was dissolved in ethanol (30 mL). Then, potassium hydroxide (2.92 g, in 30 mL ethanol) was added dropwise during 1 h into the solution with stirring. The mixture was stirred for further 3 h and was then allowed to stand overnight at room temperature. The mixture was heated for a short time to reflux, and the hot solution was filtered to remove bis-potassium salt. From the cooled mixture, the monopotassium salt of hexadecyl malonic acid monoethyl ester was separated by filtration. The salt was dissolved in water and acidified with equimolar amount of 0.1 M hydrochloric acid. The crude monoester was then extracted three times with 30 mL ether. The combined etheral solutions were washed with water and brine, dried over sodium sulfate, and evaporated to dryness. The compound was purified by crystallization from heptane or by column chromatography using silica gel 60.

In the case of **IIb**, no salt precipitates. Therefore, the mixture was concentrated under vacuum to the half of the volume and acidified after cooling. Compound **IIb** was then extracted 3 times with ether, and the combined etheral phase was washed and dried as described above. **IIb** was purified by column chromatography.

Hexadecyl Malonic Acid Monoethyl Ester (IIa). The experimental data were in agreement with the literature (*29*).

(9*Z*)-Octadec-9-enyl Malonic Acid Monoethyl Ester (IIb). Yield: 68%, colorless oil, $C_{23}H_{42}O_4$, 382.57 g/mol, EI−MS: 382 (M^+).^{1}H NMR (400 MHz, $CDCl_3$) δ: 0.85 (t, 3H, [−C*H*$_3$]), 1.20−1.90 (m, 29H, [$H_3C(CH_2)_6CH_2CH$═$CHCH_2(CH_2)_7$−], [−OCH_2CH_3]), 1.95−2.05 (m, 4H, [−CH_2CH═$CHCH_2$−]), 3.38−3.40 (t, 1H, [−C*H*−]), 4.22 (q, 2H, [−OCH_2CH_3]), 5.30−5.39 (m, 2H, [−C*H*═C*H*−]). Anal. Calcd.: C, 72.20; H, 11.06. Found: C, 71.92; H, 11.17.

2-[(Alkylamino)carbonyl]octadecanoic Acid Ethyl Ester IIIa,b. *Procedure 1.* Compound **IIa** (0.014 mol) and 10 mL thionyl chloride were given into a flask, and the mixture was allowed to stand overnight at room temperature until a clear solution appears. Then, the excess thionyl chloride was removed under vacuo. The residue was dried under vacuum over potassium hydroxide. After that, the crude malonic ester chloride was dissolved in 50 mL dry $CHCl_3$ and cooled down to 0 °C. Hexadecylamine or oleylamine (0.013 mol) and triethyl amine (1.3 g, 0.013 mol), dissolved in 10 mL dry $CHCl_3$, were dropped into the solution with stirring at the same temperature. After 2 h stirring at room temperature, the $CHCl_3$ solution was washed three times with ice water and dried over sodium sulfate. The crude product was crystallized from acetone.

Procedure 2. A suspension of compound **II** (0.014 mol), hexadecylamine or oleylamine (0.014 mol), and 3.5 g (0.014 mol) EEDQ in 100 mL ethanol was heated for 24 h at 50 °C. The solvent was then reduced to half of the volume, diluted with 100 mL $CHCl_3$, and washed with water. After drying the organic layer over sodium sulfate, the solvent was evaporated and the residue recrystallized from acetone.

2-[(Hexadecylamino)carbonyl]octandecanoic Acid Ethyl Ester (IIIa). Yield: 91% (procedure 1), 86% (procedure 2), $C_{37}H_{73}NO_3$, 580.0 g/mol, mp: 72−73 °C. ESI−MS: (M^++Na).^{1}H NMR (400 MHz, $CDCl_3$) δ: 0.85 (t, 6H, 2[−C*H*$_3$]), 1.23−1.86 (m, 61H, [−OCH_2CH_3], [$H_3C(CH_2)_{15}$−], [$H_3C(CH_2)_{14}CH_2NH$−]), 3.14−3.18 (m, 2H, [−CH_2NHCO−]), 3.22−3.28 (m, 1H, [−C*H*−]), 4.16 (q, 2H, [−OCH_2CH_3]), 6.52−6,55 (m, 1H, [−N*H*−]). Anal. Calcd.: C, 76.62; H, 12.69; N, 2.41. Found: C, 76.58; H, 12.70; N, 12.37.

2-{[(9*Z*)-Octadec-9-enylamino]carbonyl}octadecanoic Acid Ethyl Ester (IIIb). Yield: 83% (procedure 1), 83% (procedure 2), $C_{39}H_{75}NO_3$, 606.03 g/mol, mp: 45−47 °C. ESI−MS: (M^++H). ^{1}H NMR (400 MHz, $CDCl_3$) δ: 0.85 (t, 6H, 2[−C*H*$_3$]), 1.18−1.86 (m, 57H, [$H_3C(CH_2)_{15}$−], [$H_3C(CH_2)_6CH_2CH$═$CHCH_2(CH_2)_6CH_2NH$−], [−OCH_2CH_3]), 1.90−2.04 (m, 4H, [−CH_2CH═$CHCH_2$−]), 3.14−3.27 (m, 3H, [−CH_2NHCO−], [−C*H*−]), 4.17 (q, 2H, [−OCH_2CH_3]),

5.30−5.35 (m, 2H, [−C*H*═C*H*−]), 6.53−6.56 (m, 1H, [−N*H*−]). Anal. Calcd.: C, 77.29; H, 12.47; N, 2.31. Found: C, 76.96; H, 12.43; N, 2.37.

2-{[(9*Z*)-Octadec-9-enylamino]carbonyl}-(11*Z*)-icos-11-enoic Acid Ethyl Ester (IIIc). Yield: 83% (procedure 2), $C_{41}H_{77}NO_3$, 632.04 g/mol, EI−MS: 632 (M^+, 100), mp: 32−35 °C. ^{1}H NMR (400 MHz, $CDCl_3$) δ: 0.87 (2t, 6H, 2[−CH_3]), 1.17−1.88 (m, 51 H, [$H_3C(CH_2)_6CH_2CH$═$CHCH_2(CH_2)_7$−], [$H_3C(CH_2)_6CH_2CH$═$CHCH_2(CH_2)_6CH_2NH$−], [−OCH_2CH_3]), 1.90−2.05 (m, 8H, 2[−CH_2CH═$CHCH_2$−]), 3.15−3.19 (m, 2H, [−CH_2NHCO−]), 3.20−3.27 (m, 1H, [−C*H*−]), 4.19 (q, 2H, [−OCH_2CH_3]), 5.30−5.40 (m, 4H, 2[−C*H*═C*H*−]), 6.50−6.54 (m, 1H, [−N*H*−]). Anal. Calcd.: C, 77.91; H, 12.28; N, 2.21. Found: C, 77.83; H, 12.38; N, 2.30.

Saponification of IIIa−c. *General Procedure.* Potassium hydroxide (0.56 g, 0.01 mol) was added to a suspension of compound **III** (2.9 g, 0.005 mol) in ethanol (50 mL), and the mixture was heated under reflux for 5 h. After cooling to room temperature, the precipitated potassium salt was filtered by suction, washed with ether, and dried in vacuum. The salt (3.0 g, 0.0049 mol) was then suspended in 50 mL water containing 1.25 mL conc. HCl under cooling with ice and stirring. After 1 h, the acid **IV** was thrice extracted with $CHCl_3$. The combined $CHCl_3$ layers were dried and evaporated and the residue was crystallized from heptane.

2-[(Hexadecylamino)carbonyl]octadecanoic Acid (IVa). Yield: 85%, white crystals, $C_{35}H_{69}NO_3$, 577.96 g/mol, mp: 74−76 °C. ESI−MS: (M-H).^{1}H NMR (400 MHz, $CDCl_3$/CD_3OD) δ: 0.86 (t, 6H, 2[−CH_3]), 1.23−1.95 (m, 58 H, [$H_3C(CH_2)_{15}$−], [$H_3C(CH_2)_{14}CH_2NH$−]), 3.09−3.18 (m, 2H, [−CH_2NHCO−]), 3.26−3.35 (m, 1H, [−C*H*−]), 5.89−5.94 (m, 1H, [−N*H*−]). Anal. Calcd.: C, 76.16; H, 12.60; N, 2.54. Found: C, 76.16; H, 12.67, N, 2.54.

2-{[(9*Z*)-Octadec-9-enylamino]carbonyl}octadecanoic Acid (IVb). Yield: 82%, white crystals, $C_{37}H_{71}NO_3$, 577.96 g/mol, mp: 74−76 °C. ESI−MS: (M-H).^{1}H NMR (400 MHz, $CDCl_3$/CD_3OD) δ: 0.86 (t, 6H, 2[−CH_3], 1.18−1.89 (m, 54H, [$H_3C(CH_2)_{15}$−], [$H_3C(CH_2)_6CH_2CH$═$CHCH_2(CH_2)_6CH_2NH$−]), 1.92−2.05 (m, 4H, [−CH_2CH═$CHCH_2$−]), 3.14−3.30 (m, 3H, [−CH_2NHCO−], [−C*H*−]), 5.30−5.36 (m, 2H, −C*H*═C*H*−]), 6.45−6.50 (m, 1H, [−N*H*−]). Anal. Calcd.: C, 76.89; H, 12.38; N, 2.42. Found: C, 76.91; H, 12.36; N, 2.42.

2-{[(9*Z*)-Octadec-9-enylamino]carbonyl}-(11*Z*)-icos-11-enoic Acid (IVc). Yield: 85%, white waxy substance, $C_{39}H_{73}NO_3$, 604.00 g/mol, mp: 70−72 °C. ESI−MS: (M-H).^{1}H NMR (400 MHz, $CDCl_3$) δ: 0.80−0.89 (t, 6H, 2 [−CH_3]), 1.20−1.90 (m, 50H, [$H_3C(CH_2)_6CH_2CH$═$CHCH_2(CH_2)_7$−], [$H_3C(CH_2)_6CH_2CH$═$CHCH_2(CH_2)_6CH_2NH$−]), 1.92−2.08 (m, 8H, 2[−CH_2CH═$CHCH_2$−]), 3.08−3.30 (m, 3H, [−CH_2NHCO−], [−C*H*−]), 5.34−5.40 (m, 4H, 2[−C*H*═C*H*−]), 6.05−6.15 (m, 1H, [−N*H*−]). Anal. Calcd.: C, 77.54; H, 12.18; N, 2.32. Found: C, 77.44; H, 12.36; N, 2.30.

Reaction of IVa−c with the Spacer Molecules to Va−f. *Procedure 1.* Compound **IV** (1 mmol) was dissolved in 50 mL CH_2Cl_2 and 140 mg (1.2 mmol) *N*-hydroxysuccinimide were added. Then, 288 mg (1.4 mmol) DCC was added to the slurry, and the mixture was allowed to stir for 12 h at room temperature. After that time, the precipitate of dicyclohexyl urea was filtered off and ethylene diamine or tris(aminoethyl)amine (20 mmol) was added to the solution. The mixture was stirred for 4 h at room temperature. The organic layer was then filtered, washed with water and brine, and dried over sodium sulfate. After evaporation of the solvent, the crude product was purified by column chromatography on silica gel 60 and $CHCl_3$/methanol using gradient technique.

Procedure 2. Triethylamine (0.152 g, 1.5 mmol) was added to a solution of compound **IV** (1 mmol), ethylene diamine or tris(aminoethyl)amine (20 mmol), and BOP (0.442 g, 1 mmol) in CH_2Cl_2 (20 mL). The mixture was stirred at room temperature overnight. The solution was filtered, washed with water, dried over sodium sulfate, and evaporated. The residue was purified by crystallization from heptane.

***N*-(2-Aminoethyl)-*N*′,2-dihexadecyl Propane Diamide (Va).** Yield: 65% (procedure 1), 83% (procedure 2), white substance, 594.01 g/mol, mp: 74−76 °C. ESI−MS: (M^++H), ^{1}H NMR (400 MHz, $CDCl_3$/CD_3OD) δ: 0.87 (t, 6H, 2[−CH_3]), 1.00−1.57 (m, 58H, [$H_3C(CH_2)_{15}$−], [$H_3C(CH_2)_{14}CH_2NH$−]), 2.72 (m, 2H, [H_2NCH_2−]), 2.90−3.10 (m, 4H, [−CH_2NHCO−], [$H_2NCH_2CH_2NHCO$−]), 3.25−3.31 (m, 1H, [−C*H*−]), 4.15−4.20 (m, 2H, 2[−N*H*−]). Anal. Calcd.: C, 74.81; H, 12.73; N, 7.07. Found: C, 74.75; H, 12.69; N, 7.05.

***N*-(2-Aminoethyl)-2-hexadecyl-*N*′-[(9*Z*)-octadec-9-enyl]-propane Diamide (Vb).** Yield: 68% (procedure 1), 80% (procedure 2), white substance, $C_{39}H_{77}N_3O_2$, 620.05 g/mol, mp: 68−71 °C. ESI−MS: (M^++H).^{1}H NMR (400 MHz, $CDCl_3$/CD_3OD) δ: 0.85 (t, 6H, 2[−CH_3]), 1.20−1.88 (m, 54H, [$H_3C(CH_2)_{15}$−], [$H_3C(CH_2)_6CH_2CH$═$CHCH_2(CH_2)_6CH_2NH$−]), 1.92−2.03 (m, 4H, [−CH_2CH═$CHCH_2$−]), 2.79−2.81 (m, 2H, [H_2NCH_2−]), 2.94−3.23 (m, 4H, [−CH_2NHCO−], [$H_2NCH_2CH_2NHCO$−]), 3.26−3.30 (m, 1H, [−C*H*−]), 5.29−5.35 (m, 2H, [−C*H*═C*H*−]), 5.77−5.80 (m, 2H, 2[−CON*H*−]). Anal. Calcd.: C, 75.55; H, 12.52; N, 6.78. Found: C, 75.43; H, 12.37; N, 6.69.

***N*-(2-Aminoethyl)-*N*′,2-di[(9*Z*)-octadec-9-enyl]propane Diamide (Vc).** Yield: 82% (procedure 2), white substance, $C_{41}H_{79}N_3O_2$, 646.06 g/mol, ESI−MS: (M^++H). ^{1}H NMR (400 MHz, $CDCl_3$) δ: 0.86 (t, 6H, 2[−CH_3]), 1.20−1.90 (m, 48H, [$H_3C(CH_2)_6CH_2CH$═$CHCH_2(CH_2)_7$−], [$H_3C(CH_2)_6CH_2CH$═$CHCH_2(CH_2)_6CH_2NH$−]), 1.92−2.05 (m, 8H, 2[−CH_2CH═$CHCH_2$−]), 2.78−2.82 (m, 2H, [$H_2NCH_2CH_2NH$−]), 3.18−3.22 (m, 4H, −CH_2NHCO−], [$H_2NCH_2CH_2NHCO$−], 3.25−3.32 (m, 1H, [−C*H*−]), 5.25−5.40 (m, 4H, 2[−C*H*═C*H*−]), 5.80−5.89 (m, 2H, 2[−CON*H*−]). Anal. Calcd.: C, 76.22; H, 12.32; N, 6.50. Found: C, 76.22; H, 12.38; N, 6.42.

***N*-[Bis(2-aminoethyl)amino]ethyl-*N*′,2-dihexadecylpropane Diamide (Vd).** Yield: 49% (procedure 1), 76% (procedure 2), white substance, $C_{41}H_{85}N_5O_2$, 680.15 g/mol, mp: 84−86 °C. ESI−MS: (M^++H). ^{1}H NMR (400 MHz, $CDCl_3$/CD_3OD) δ: 0.84 (t, 6H, 2[−CH_3]), 1.22−1.79 (m, 58H, [$H_3C(CH_2)_{15}$−], [$H_3C(CH_2)_{14}CH_2NH$−]), 2.51−2.56 (m, 4H, 2[$H_2NCH_2CH_2$−]), 2.73−2.76 (m, 4H, 2[$H_2NCH_2CH_2$−]), 2.96 (t, 2H, [−NCH_2CH_2NH−]), 3.13−3.20 (m, 2H, [−CH_2NHCO−]), 3.21−3.35 (m, 2H, [−NCH_2CH_2NHCO−]), 3.60−3.63 (m, 1H, [−C*H*−]), 5,77−5.89 (m, 2H, [−CON*H*−]). ^{13}C NMR (100 MHz, $CDCl_3$) δ: 14.56, 23.22, 27.48, 28.13, 29.83, 29.88, 30.00, 30.15, 30.17, 30.20, 30.24, 32.47, 33.33, 38.01, 39.59, 40.05, 40.18, 54.02, 54.87, 56.98, 172.00, 172.16. Anal. Calcd. for $C_{41}H_{85}N_5O_2 \times H_2O$: C, 70.53; H, 12.56; N, 10.03. Found: C, 70.37; H, 12.64; N, 9.95.

***N*-[Bis(2-aminoethyl)amino]ethyl-2-hexadecyl-*N*′-[(9*Z*)-octadec-9-enyl]propane Diamide (Ve).** Yield: 49% (procedure 1), 71% (procedure 2), white waxy substance, $C_{43}H_{87}N_5O_2$, 706.18 g/mol, mp: 35 °C. ESI−MS: (M^++H). ^{1}H NMR (400 MHz, $CDCl_3$/CD_3OD) δ: 0.85 (t, 6H, 2[−CH_3], 1.20−1.89 (m, 54H, [$H_3C(CH_2)_{15}$−], [$H_3C(CH_2)_6CH_2CH$═$CHCH_2(CH_2)_6CH_2NH$−]), 1.95−2.05 (m, 4H, [−CH_2CH═$CHCH_2$−]), 2.50−2.56 (m, 4H, 2[$H_2NCH_2CH_2$−]), 2.79−2.81 (m, 4H, 2[$H_2NCH_2CH_2$−]), 2.94−3.23 (m, 4H, [−CH_2NHCO−], [−NCH_2CH_2NHCO−]), 3.26−3.30 (m, 1H, [−C*H*−]), 5.29−5.35 (m, 2H, [−C*H*═C*H*−]), 5.77−5.86 (m, 2H, 2[−CON*H*−]). ^{13}C NMR (100 MHz, $CDCl_3$) δ: 14.31, 23.14, 25.84, 27.48, 27.67, 28.00, 29.69, 29.77, 29.79, 29.84, 29.91, 30.01, 30.10, 30.14, 30.19, 30.24, 30.28, 31.04, 31.40, 32.42, 33.05, 37.72, 37.97, 40.20, 52.35, 54.19, 54.39, 54.56, 130.14, 130.34, 172.12,

172.24. Anal. Calcd. for $C_{43}H_{87}N_5O_2 \times H_2O$: C, 71.31; H, 12.38; N, 9.67. Found: C, 71.03; H, 12.45; N, 9.52.

***N*-[Bis(2-aminoethyl)amino]ethyl-*N′*,2-di[(9*Z*)-octadec-9-enyl]propane Diamide (Vf).** Yield: 74% (procedure 2), white waxy substance, $C_{45}H_{89}N_5O_2$, 732.22 g/mol. ESI−MS: $(M^+ + H)$. ^{1}H NMR (400 MHz, $CDCl_3$) δ: 0.87 (t, 6H, 2[−C*H*$_3$]), 1.20−1.90 (m, 50H, [$H_3C(CH_2)_6CH_2CH$═$CHCH_2(CH_2)_6CH_2NH$−], [$H_3C(CH_2)_6CH_2CH$═$CHCH_2(CH_2)_7$−), 1.90−2.05 (m, 8H, 2[−C*H*$_2$CH═CHC*H*$_2$−]), 2.49−2.6 (m, 4H, 2[$H_2NCH_2CH_2N$−]), 2.80−2.92 (m, 6H, 2[$H_2NCH_2CH_2N$−], [−N*CH*$_2$CH$_2$NH−), 3.16−3.30 (m, 4H, [−C*H*$_2$NHCO−], [−NCH$_2$C*H*$_2$NHCO−]), 3.50−3.59 (m, 1H, [−C*H*−]), 5.30−5.38 (m, 2H, [−C*H*═C*H*−]), 5.80−5.89 (m, 2H, [−CON*H*−]). ^{13}C NMR (100 MHz, $CDCl_3$) δ: 13.93, 22.50, 26.81, 27.05, 27.50, 29.00, 29.13, 29.23, 29.27, 29.31, 29.34, 29.36, 29.43, 29.48, 29.52, 29.59, 31.72, 32.41, 32.66, 37.70, 39.32, 39.41, 53.40, 54.49, 56.46, 129.36, 129.38, 129.53, 129.55, 170.78, 171.11. Anal. Calcd. for $C_{45}H_{89}N_5O_2 \times H_2O$: C, 72.04; H, 12.22; N, 9.34. Found: C, 72.38; H, 12.17; N, 9.25.

Reaction Va−c to Compounds VIa−c. *General Procedure.* 0.84 mmol of compound **V** was dissolved in 30 mL CH_2Cl_2. 0.9 mmol (0.4 g) diboc-lysin-*N*-hydroxysuccinimid ester was given to this solution. The mixture was stirred for 1 h at room temperature and then for another 10 h under reflux. After that time, the solvent was evaporated, the residue was chromatographed using a short column and dry silicagel with $CHCl_3$/methanol (98:2, v/v) as eluent. The so-purified product was dissolved in 15 mL CH_2Cl_2, and 1 mL trifluoro acetic acid was added. The mixture was allowed to stir for 4 h, then mixture was diluted with 60 mL $CHCl_3$. 100 mL diluted ammonia was poured into the mixture, which was shaken until two clear phases evolved. The organic layer was separated, dried over sodium sulfate, and evaporated. The crude products **VI** were then purified by column chromatography using silicagel 60 and $CHCl_3$/methanol/NH_3 with gradient technique.

***N′*-2[(2,6-Diamino-1-oxohexyl)amino]ethyl-2,*N*-(dihexadecyl)propane Diamide (VIa).** Yield: 54%, white waxy substance, $C_{43}H_{87}N_5O_3$, 722.18 g/mol, mp: 111−112 °C. ESI−MS: $(M^+ + H)$.^{1}H NMR (400 MHz, $CDCl_3$) δ: 0.86 (t, 6H, [−C*H*$_3$]), 1.18−1.88 (m, 64H, [$H_3C(CH_2)_{15}$−], [$H_3C(CH_2)_{14}CH_2NH$−], [−$(CH_2)_3CH_2NH_2$]), 2.82−2.87 (m, 2H, [−C*H*$_2$NH$_2$]), 3.05−3.09 (m, 1H, [−C*H*−]), 3.20−3.38 (m, 5H, [−CONHC*H*$_2$CH$_2$NHCO−], [−CONHCH$_2$C*H*$_2$NHCO−], [−COC*H*(NH$_2$)CH$_2$−]), 6.58−6.70 (m, 2H, 2[−CON*H*−]). ^{13}C NMR (100 MHz, $CDCl_3$/CD_3OD) δ: 13.11, 22.03, 22.08, 22.11, 26.32, 26.85, 28.61, 28.73, 28.85, 28.96, 29.00, 29.03, 29.07, 30.18, 31.16, 31.24, 31.32, 34.03, 38.26, 38.42, 38.95, 40.00, 53.62, 54.26, 170.51, 171.35. Anal. Calcd. for $C_{43}H_{87}N_5O_3 \times H_2O$: C, 69.77; H, 12.12; N, 9.46. Found: C, 70.05; H, 12.16; N, 9.39.

***N′*-2-[(2,6-Diamino-1-oxo-hexyl)amino]ethyl-2-hexadecyl-*N*-[(9*Z*)-octadec-9-enyl]propane Diamide (VIb).** Yield: 56%, white waxy substance, $C_{45}H_{89}N_5O_3$, 748.22 g/mol, mp: 104−105 °C, ESI−MS: $(M^+ + H)$. ^{1}H NMR (400 MHz, $CDCl_3$) δ: 0.85 (2t, 6H, [−C*H*$_3$]), 1.20−1.80 (m, 60H, [$H_3C(CH_2)_{15}$−], [$H_3C(CH_2)_6CH_2CH$═$CHCH_2(CH_2)_6CH_2NH$−], [−$(CH_2)_3CH_2NH_2$]), 1.92−2.04, (m, 4H, [−C*H*$_2$CH═CHC*H*$_2$−]), 2.80−2.85 (m, 2H, [−C*H*$_2$NH$_2$]), 3.05−3.10 (m, 1H, [−C*H*−]), 3.22−3.43 (m, 5H, [−CONHC*H*$_2$CH$_2$NHCO−], [−CONHCH$_2$C*H*$_2$NHCO−], [−COC*H*(NH$_2$)CH$_2$−]), 5.33−5.41 (m, 2H, [−C*H*═C*H*−]), 6.55−6.65 (2m, 2H, 2[−CON*H*−]). ^{13}C NMR (100 MHz, $CDCl_3$/CD_3OD) δ: 13.99, 22.38, 26.66, 26.91, 27.20, 28.94, 29.01, 29.06, 29.16, 29.22, 29.31, 29.36, 29.40, 29.47, 31.63, 31.91, 32.28, 34.32, 38.58, 39.32, 40.30, 53.97, 54.45, 129.29, 129.51, 170.68, 171.70. Anal. Calcd. for $C_{45}H_{89}N_5O_3 \times H_2O$: C, 70.54; H, 11.97; N, 9.14. Found: C, 70.71; H, 11.63; N, 9.17.

***N′*-2-[(2,6-Diamino-1-oxo-hexyl)amino]ethyl-2,*N*-di[(9*Z*)-octadec-9-enyl]propane Diamide (VIc).** Yield: 53%, white pasty substance, $C_{47}H_{91}N_5O_3$, 774.26 g/mol, mp: 109−111 °C. ESI−MS: $(M^+ + H)$. ^{1}H NMR (400 MHz, $CDCl_3$) δ: 0.86 (t, 6H, 2[−C*H*$_3$]), 1.15−1.88 (m, 56H, [$H_3C(CH_2)_6CH_2CH$═$CHCH_2(CH_2)_7$−], [$H_3C(CH_2)_6CH_2CH$═$CHCH_2(CH_2)_6CH_2NH$−], [−$(CH_2)_3CH_2NH_2$]), 1.90−2.05 (m, 8H, 2[−C*H*$_2$CH═CHC*H*$_2$−]), 2.80−2.85 (m, 2H, [H_2NCH_2−]), 3.05−3.10 (m, 1H, [−C*H*−]), 3.15−3.25 (m, 2H, [−C*H*$_2$NHCO−]), 3.25−3.40 (m, 5H, [−CONHC*H*$_2$CH$_2$NHCO−], [−CONHCH$_2$C*H*$_2$NHCO−], [−COC*H*(NH$_2$)CH$_2$−]), 5.30−5.40 (m, 4H, 2[−C*H*═C*H*−]), 6.60−6.65 (2 m, 2H, 2[−CON*H*−]). ^{13}C NMR (100 MHz, $CDCl_3$/CD_3OD) δ: 13.66, 22.38, 26.67, 26.92, 27.21, 28.94, 29.01, 29.14, 29.22, 29.41, 29.47, 30.62, 31.62, 32.29, 34.32, 38.58, 39.32, 40.35, 53.99, 54.47, 129.31, 129.50, 170.67, 171.70. Anal. Calcd. for $C_{47}H_{91}N_5O_3 \times H_2O$: C, 71.25; H, 11.83; N, 8.84. Found: C, 71.37; H, 11.57; N, 8.86.

Preparation of Liposomes. A $CHCl_3$/methanol solution (9/1, v/v) of the pure cationic lipid was combined with a $CHCl_3$ solution of DOPE or cholesterol. The mixtures were dried under reduced pressure to remove the organic solvent, and the dried film was vacuum-desiccated for 3 h. The lipid film was dissolved in distilled water at room temperature to a final concentration of 2 mg lipid/mL. The film was allowed to swell in a water bath at 40 °C for at least 15 min. Subsequently, the lipid formulations were vortexed and sonicated to clarity in a bath sonicator. The samples were stored in the refrigerator at 4 °C before experiments.

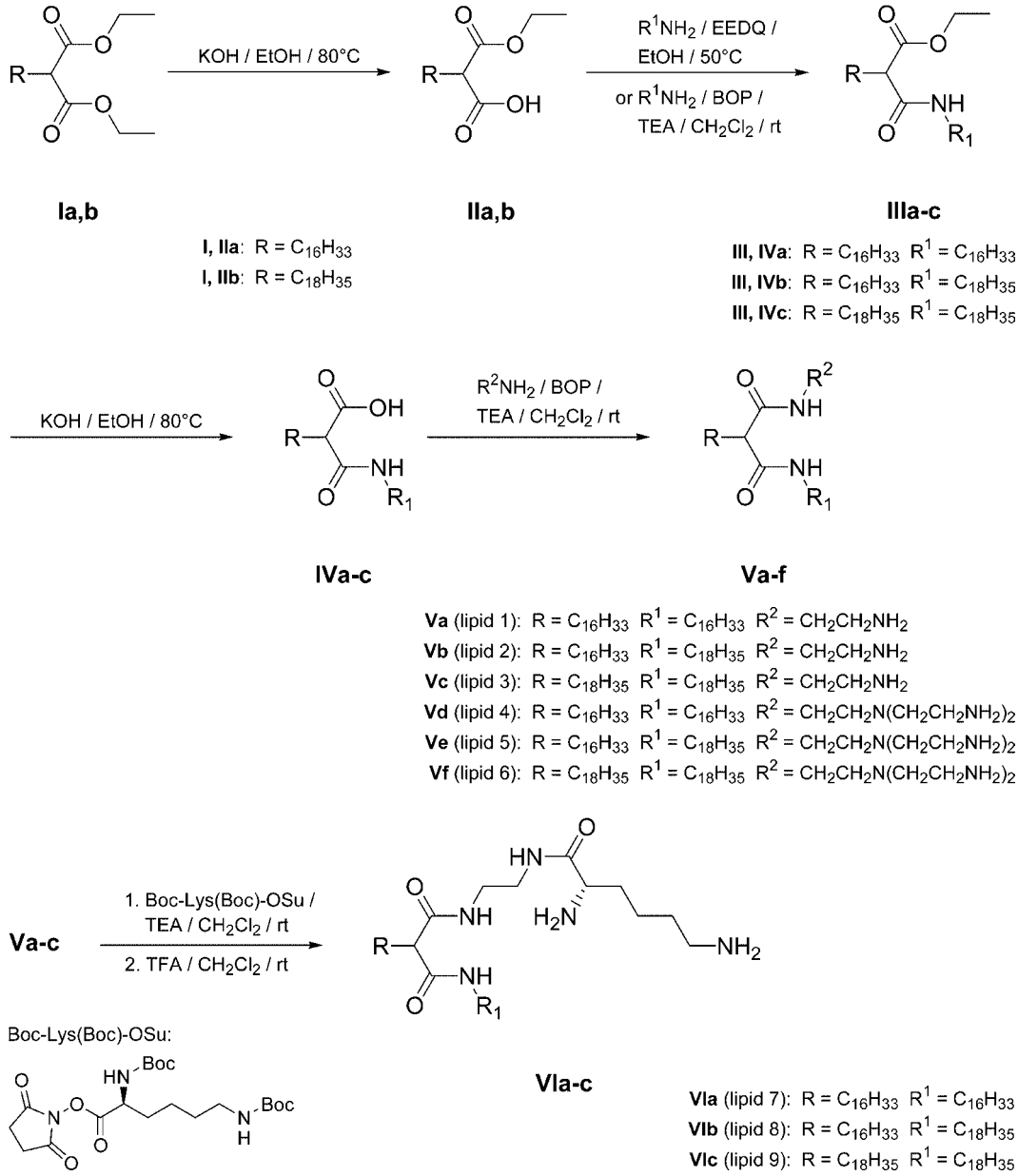
Preparation of Plasmid DNA. pCMV Sport β-Gal was isolated from *Escherichia coli* DH5α (Invitrogene life technologies) using a Quiagen plasmid mega kit (Quiagen) following the manufacturer's instructions (*30*). DNA with an $OD_{260}/OD_{280} = 1.94$ was used for experiments.

Cell Culture. LLC PK1 cells (porcine kidney epithelial cells) were cultured in 75 cm^2 tissue culture flasks in Medium 199 adjusted to contain 2.2 g/L sodium bicarbonate, 10% fetal bovine serum (FBS), and 0.05 mg/mL gentamycin at 37 °C and 5% CO_2. The cells were grown confluently and were regularly split twice a week. Only cells that had undergone fewer than 30 passages were used for transfection and MTT experiments.

A549 cells (human lung carcinoma cells) were cultured in 75 cm^2 tissue culture flasks in Dulbecos's modified eagle medium (DMEM) adjusted to contain 4.5 g/L glucose, 10% FBS, and 0.05 mg/mL gentamycin at 37 °C and 5% CO_2. The cells were grown confluently and were regularly split twice a week. For experiments, only cells in the range of passages 20−60 were used.

Transfection Biology. 16−24 h before transfection, cells were seeded into a 96 well plate at a density of 8000−10 000 cells/well by usage of LLC PK1 and 18 000−20 000 in the case of A549 cells. Lipoplex mixtures were prepared by combining plasmid DNA (0.1 μg per well = 2.5 μg/mL) with varying amounts of cationic liposome suspension in the absence or presence of 10% serum in Medium 199 or DMEM. The samples were incubated for 15 min at room temperature (total volume 40 μL/well). The N/P ratios were varied from 1:1 to 4:1 or even higher in cases when the results of experiments foreshadow increasing transfection efficacies at higher charge ratios. During this time, cells were washed once with phosphate buffered saline (PBS). Then the complexes were added to the cells. After 4 h of incubation, 160 μL of Medium 199 or DMEM was added to the cells in a way that the final concentration of FBS reached 10%. The medium was refreshed after 24 h, and the reporter gene activity was estimated after 48 h. Therefore, the cells were washed with PBS lysed for 15 min in lysis buffer (5 mM Chaps in 50 mM Hepes buffer). The solution was taken out of the wells, reunited in safe-lock tubes (Eppendorf), centrifuged, and stored on ice. It was pipeted again in a 96 well plate and substrate solution [1.33 mg/mL of *O*-nitrophenyl-β-galactopyranoside (ONPG), $MgCl_2$ 2 mM, β-mercaptoethanol 100 mM in 0.2 M sodium phosphate pH 7.3] was added and incubated for 30 min at 37 °C. The reaction was stopped with 1 M sodium carbonate. Absorption at 405 nm was converted to β-galactosi-

Scheme 1. Synthesis of Lipids 1−9 Starting from Alkyl Malonic Acid Diethyl Ester



dase units using a calibration curve constructed with pure commercial β-galactosidase enzyme. Protein concentration was detected with bichinonic acid reaction (*31*). Absorption at 570 nm was converted by using a calibration curve made of bovine serum albumin. All experiments were carried out sixfold. Every experiment was repeated three to five times on different days.

Toxicity Assay. Cytotoxicity of the lipoplexes was assessed by the MTT reduction assay (*32*). The cytotoxicity assays were performed in 96 well plates by maintaining the same ratio and number of cells and lipoplexes as used in the transfection experiments. MTT was added after refreshing the medium (24 h after addition of lipoplexes to the cells) and incubated for 3 h at 37 °C. Afterward, the cells were lysed with a mixture of 10% sodium dodecyl sulfate in acetic acid/dimethyl sulfoxide. Absorption was measured at 570 nm. The results were expressed as percent viability = [A_{570} (treated cells) − background]/[A_{570} (untreated cells) − background] × 100.

Size Measurements. The sizes of liposomes and lipoplexes were measured in distilled water by photon correlation spectroscopy on a HPPS−ET (Malvern, U.K.) with sample refractive index of 1.25 and a viscosity of 0.8872 at 25 °C. Lipoplexes were prepared by following the instructions used for transfection experiments and measured with 2.5 μg DNA/mL sample. The *z*-average and PDI were calculated by using the automatic mode. Every sample was measured by three spectroscopic runs consisting of ten consecutive scans, each of 10 s in duration. Results shown are the average of these three values.

X-Gal Staining. To estimate a successful transfection, cells were histochemically stained with 5-bromo-4-chloro-3-indolyl-β-D-galactopyranoside (X-Gal). β-Galactosidase expressing cells can be indicated by blue color. The experiments were carried out in 24 well plates with a density of 40 000−50 000 cells per well and DNA concentration of 2.5 μg/mL (1.25 μg/well in 24 well plate). 48 h after transfection, cells were washed two times with PBS (2 × 500 μL) and fixed with 0.2% glutaraldehyde and 2.0% formaldehyde in PBS for 10 min at room temperature. Afterward, the cells were washed with PBS again (2 × 500 μL) and were stained subsequently with 1 mg/mL X-gal in PBS containing 2 mM $MgSO_4$ and 4 mM $K_3[Fe(CN)_6]$ and 4 mM $K_4[Fe(CN)_6]$ for 3 h at 37 °C.

Statistical Analysis. All measurements were collected (n = 3−9) and expressed as means ± standard deviation. One-way

ANOVA was used in conjunction with Bonferoni's multiple comparison test to assess the statistical significance.

RESULTS

Synthesis of Malonic Acid Amides Cationic Lipids. The synthesis of the compounds is shown in Scheme 1. Starting from long-chain monoalkylated malonic acid esters, which are easy to prepare by alkylation reaction of malonic acid diesters (*33*) with the corresponding alkyl halides or methansulfonates, one of the ester groups was saponified according to published methods (*34*). We have also studied the preparation of the monoester starting from malonic esters with different alcoholic residues followed by a selective saponification. Because of the simplicity of the first reaction, this procedure was used. Compounds **IIa**,**b** were then transformed into the 2-alkylmalonic acid ester amides **IIIa**−**c** by reaction with hexadecyl or oleyl amine using condensing reagents. The most effective reagents were 2-ethoxy-1-ethoxycarbonyl-1,2-dihydrochinoline (EEDQ) and the benzotriazole derived compounds known from peptide synthesis, like (benzotriazol-1-yloxy)-tris-(dimethylamino)-phosphoniumhexaflourophospahte (BOP), leading to the products in high yield.

For the synthesis of **IIIa**,**b**, the activation via the corresponding acid chloride was also a high-yield procedure, but in the case of the unsaturated chain of **IIb**, we used only the modern condensation agents. The saponification of the ester with potassium hydroxide yields the acids. For the second coupling reaction with ethylene diamine or tris(aminoethyl)amine to **Va**−**f**, *N*-hydroxysuccinimide/*N,N*′-dicyclohexylcarbondiimid (DCC) or better BOP was used as condensing reagent. We found that a 20-fold excess of the di- or triamine is necessary. This ensures yields of more than 70%. On the other hand, the reaction with only a 5- to 10-fold excess leads only to a yield of 20%, also in the case of BOP as the most effective condensing reagent. The introduction of a lysine residue into compounds **Va**−**c** was realized in good yields using the commercially available diboc-lysine-*N*-hydroxysuccinimide ester. The crude products were purified to some extent by filtration using silica gel. For the removal of the protective groups, trifluoroacetic acid in methylene chloride was used. The yields after the two steps were more than 50%.

In Vitro Transfection and Cell Toxicity of Malonic Acid Amides Cationic Liposomes. To form liposomes for gene transfer experiments, cationic amphiphiles are usually mixed with colipids. Most frequently, 1,2-dioleoyl-*sn*-glycero-3-phosphoethanolamine (DOPE) and cholesterol are used (*26, 35–37*). Their influence on transfection is ascribed to their tendency to adopt the inverted hexagonal H_{II} phase that seems to be necessary for the DNA release from the endosomal compartment (*36, 38–42*). For that reason, all of the lipids **1**−**9** were mixed in different molar ratios with DOPE or cholesterol to determine the most auspicious combination. To identify the kind of structure/activity relationship for the malonic acid amides, nearly 60 samples were prepared and tested for their ability to transfect cells in culture.

Figure 1 summarizes the relative in vitro gene delivery efficiencies of lipid **8** mixed with colipids. Lipoplex (cationic liposome/DNA complex) mixtures were prepared by combining plasmid DNA (0.1 μg per well = 2.5 μg/mL) with varying amounts of cationic liposome suspension in plain Medium 199. The N/P ratios were varied from 1:1 to 4:1. Lipid **8** has been proven to be successful for gene transfer into cells in culture. The majority of the analyzed samples exhibit high transfection efficacies. All tested combinations of this lipid with cholesterol show equal or higher transfection efficacy than LipofectAmine and SuperFect. Merely the maximum values were found at different N/P ratios. The use of DOPE as colipid decreases the transfection efficiencies. Only lipid **8**/DOPE 1:1 (*n*/*n*) is comparable to commercially available gene transfer kits.

Table 1 summarizes the results of all lipids **1**−**9** in combination with the used helper lipids. It shows the most auspicious combination of any lipid with any colipid in gene transfer experiments. Furthermore, the N/P ratio, the MTT based percent cell viability, and the results of size measurements are listed. Apart from four samples, for all new lipids transfection was detected, but only lipid **6**, lipid **8**, and lipid **9** exhibit transfection efficacies that make them comparable to commercially available vectors. Liposomes that consist of lipid **6** or lipid **8** and cholesterol as colipid lead to increasing transfection efficacies. As shown in Figure 2, this effect is statistically significant compared to LipofectAmine (*) or SuperFect (^), whereas the effects on cell survival are similar.

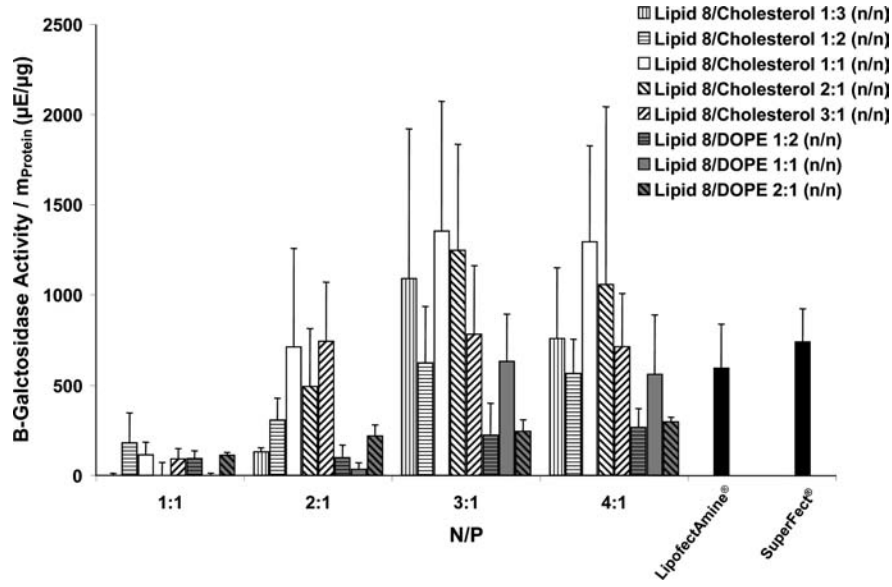


Figure 1. In vitro transfection efficacies of lipid **8** in LLC PK1 cells using cholesterol and DOPE as colipid (at different lipid/cholesterol or lipid/DOPE molar ratios). Micro units of β-galactosidase related to cell protein concentration were plotted against the varying N/P ratios. The transfection efficiencies of the liposome samples were compared to those of the commercially available LipofectAmine and SuperFect. The experiments were performed as described in the text. The transfection values shown are the average of at least three experiments carried out on three different days.

Table 1. In Vitro Transfection Efficacies, Size Measurements, and MTT Assays of Lipids 1−9 in LLC PK1 Cells Using DOPE and Cholesterol as Colipid (at Different Lipid/Colipid Molar Ratios)[a]

sample	N/P ratio	*z*-average ± *s* [nm] liposomes	*z*-average ± *s* [nm] lipoplexes	activity$_{\beta\text{-gal}}$/m_{protein} ± *s* [μE/μg]	viability ± *s* [%]
Lipid 1/DOPE 2:1 (*n*/*n*)	4:1	50 ± 1	185 ± 1	no transfection	86 ± 11
Lipid 1/Cholesterol 1:1 (*n*/*n*)	3:1	147 ± 5	330 ± 11	no transfection	69 ± 9
Lipid 2/DOPE 1:1 (*n*/*n*)	4:1	99 ± 10	205 ± 2	no transfection	91 ± 7
Lipid 2/Cholesterol 1:1 (*n*/*n*)	1:1	108 ± 3	136 ± 1	352 ± 191	93 ± 17
Lipid 3/DOPE 2:1 (*n*/*n*)	4:1	120 ± 1	171 ± 2	276 ± 157	85 ± 13
Lipid 3/Cholesterol 2:1 (*n*/*n*)	1:1	151 ± 2	681 ± 33	29 ± 13	94 ± 13
Lipid 4/DOPE 1:2 (*n*/*n*)	3:1	104 ± 7	423 ± 6	190 ± 69	84 ± 14
Lipid 4/Cholesterol 1:2 (*n*/*n*)	6:1	120 ± 7	189 ± 6	16 ± 7	94 ± 11
Lipid 5/DOPE 3:1 (*n*/*n*)	6:1	112 ± 50	113 ± 1	156 ± 38	92 ± 6
Lipid 5/Cholesterol 1:1 (*n*/*n*)	2:1	100 ± 3	116 ± 1	31 ± 25	102 ± 13
Lipid 6/DOPE 2:1 (*n*/*n*)	6:1	87 ± 16	189 ± 1	335 ± 104	77 ± 15
Lipid 6/Cholesterol 2:1 (*n*/*n*)	7:1	88 ± 17	134 ± 1	1018 ± 206	82 ± 8
Lipid 7/DOPE 1:1 (*n*/*n*)	2:1	108 ± 1	1132 ± 114	no transfection	84 ± 9
Lipid 7/Cholesterol 1:1 (*n*/*n*)	2.5:1	139 ± 1	642 ± 12	117 ± 37	83 ± 7
Lipid 8/DOPE 1:1 (*n*/*n*)	3:1	131 ± 46	268 ± 7	633 ± 263	89 ± 11
Lipid 8/Cholesterol 1:1 (*n*/*n*)	4:1	90 ± 4	137 ± 1	1294 ± 511	85 ± 14
Lipid 9/DOPE 2:1 (*n*/*n*)	2:1	121 ± 2	583 ± 2	309 ± 211	86 ± 10
Lipid 9/Cholesterol 1:1 (*n*/*n*)	2:1	94 ± 1	258 ± 1	692 ± 190	90 ± 8

[a] The transfection and viability values listed are the average of at least three experiments carried out on different days.

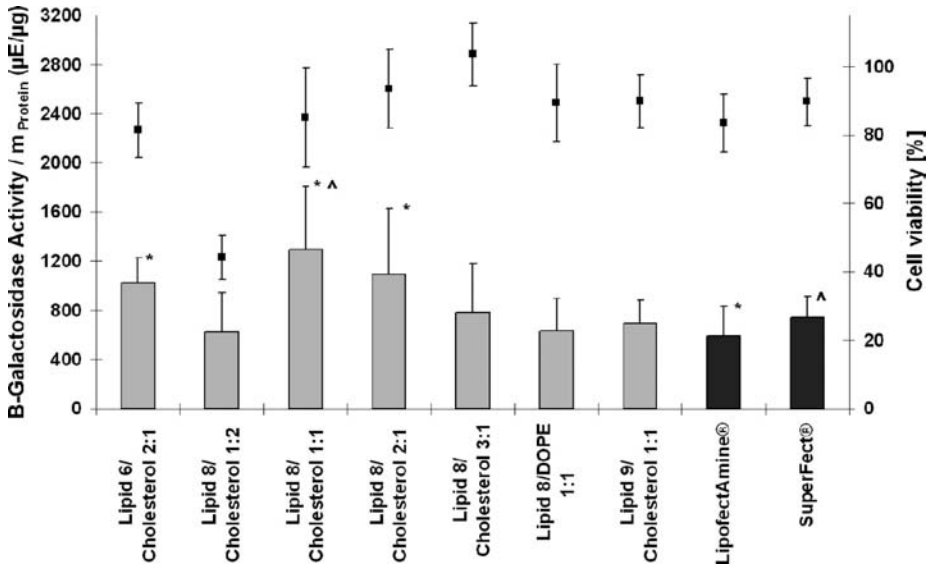


Figure 2. In vitro transfection efficacies and cell viability values of lipids **6**, **8**, and **9** in LLC PK1 cells using cholesterol or DOPE as colipid (at different lipid/cholesterol or lipid/DOPE molar ratios). Micro units of β-galactosidase related to cell protein concentration and cell viability in % were plotted against different samples. The transfection efficiencies of the liposomes were compared to that of commercially available LipofectAmine and SuperFect. Percent cell viability is plotted on secondary *y*-axis via scatter diagram. The transfection and cytotoxicity values shown are the average of at least three experiments carried out on three different days. Statistical analyses were carried out with $p < 0.05$, one-way ANOVA, and Bonferoni's multiple comparison tests (*^).

Figure 3 summarizes the results of gene transfer experiments in LLC PK1 cells with LipofectAmine (A), lipid **1** (B), and lipid **6** (C) visualized by histochemical staining (X-Gal assay). Whereas LipofectAmine and lipid **6**/cholesterol 2:1 (*n*/*n*) lead to considerable staining of wells, no colored cells were found when using lipoplexes consisting of lipid **1** as gene transfer reagent.

In the majority of cases, the cell viability fluctuates between 80% and 90% (cf. Table 1). These results suggest that the applied liposomes have an influence on the cell survival but that the efficacy of the gene transfer is not directly coupled with the toxicity. For instance, lipid **1** and lipid **7** with no or low transfection efficacy have similar or even stronger influence on the cell viability than lipid **6**, lipid **8**, or lipid **9**, although those are proven to be successful for the transfection process.

Figure 4 shows the results of 3-(4,5-dimethylthiazol-2-yl)-2,5-diphenyltetrazolium bromide (MTT) measurements of lipid **1**, lipid **7**, and lipid **8** and lipid **9** lipoplexes. The addition of lipoplexes decreases the cell viability. This effect was observed for all lipids and all N/P ratios. Furthermore, there is no statistically significant difference between the charge ratios of one sample, which suggests that the cell viability is already decreased at low lipid concentrations. An increase of cationic lipid concentration shows little effect on the toxicity at least in applied N/P ratios. Interestingly, the influence on cell viability of lipid **1** in combination with cholesterol is more distinct than that of lipid **8** or lipid **9**. Liposomes, which are not qualified for in vitro gene delivery, influence cell survival to the same degree or even more than efficiently transfecting samples. By comparing lipoplexes that consist of lipid **9** with those of lipid **1** and lipid **7**, the differences in cell viability are statistically significant just like the comparison of lipid **1** and lipid **8**. The results suggest that the chemical structure of the cationic lipid and the composition of liposomes play a major role in cell damaging characteristics, as well as in the ability to transfer nucleic acids. It was observed that the addition of lipoplexes leads to derogation of LLC PK1 cell survival independent of successful or unsuccessful gene transfer. Transfection of cells in culture is to a certain level connected with toxicity, but the reverse is not compulsory. To look for other parameters, which

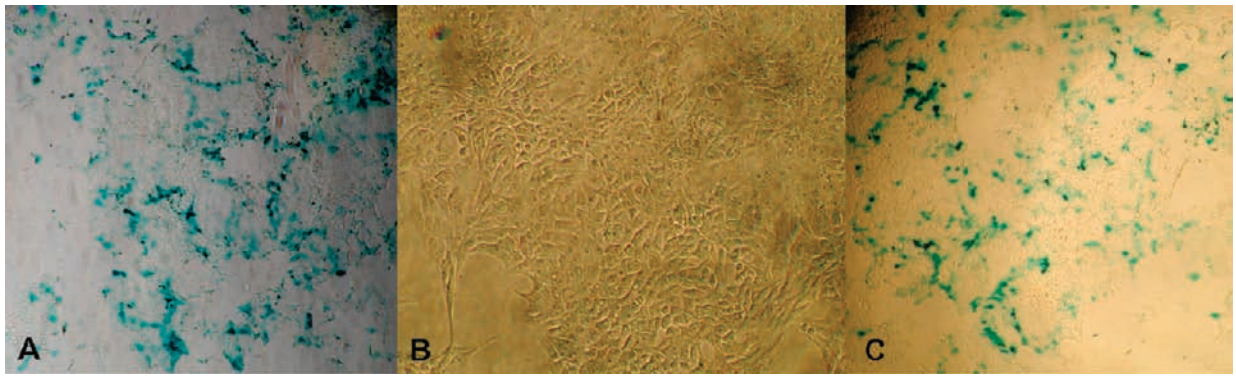


Figure 3. Pictures of X-Gal assay in LLC PK1 cells using lipid **1**, lipid **6**, and LipofectAmine. Cells were incubated with 2.5 μg/mL of DNA and stained 48 h after starting transfection. (A) LipofectAmine, magnification 1:10. (B) Lipid 1/DOPE 1:1 (*n*/*n*), magnification 1:200. (C) Lipid 6/Cholesterol 2:1 (*n*/*n*), magnification 1:10.

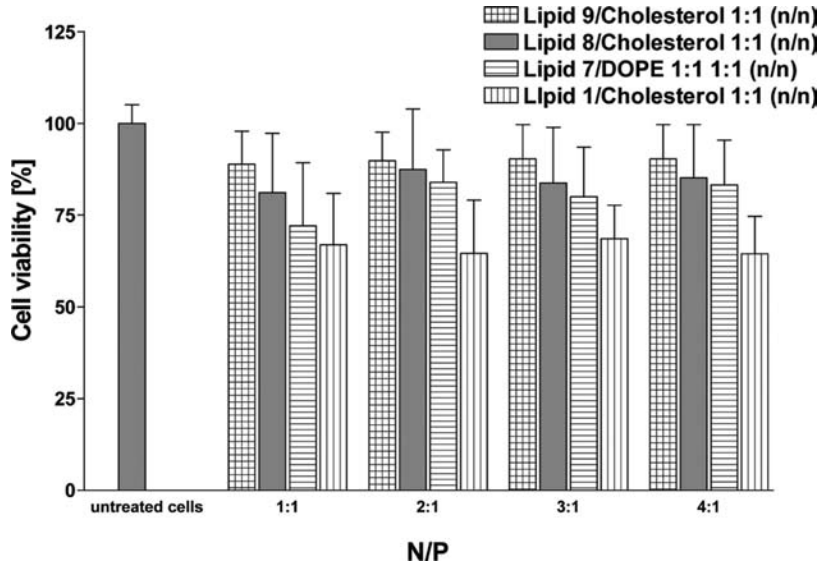


Figure 4. MTT-based cellular cytotoxicities of lipids **1**, **7**, **8**, and **9** in LLC PK1 cells using DOPE or cholesterol as colipid (at a lipid/colipid molar ratio of 1:1). The percent cell viability was plotted against the varying N/P ratios. The experiments were performed as described in the text. The cytotoxicity values shown are the average of at least three experiments carried out on different days.

are important for cell damaging characteristics of cationic liposomes, MTT measurements of lipoplexes consisting of lipid **8** were specified.

Figure 5 summarizes these results in LLC PK1 cells. As shown, the N/P ratios are varied from 1:1 to 4:1 for all applied lipoplexes. The concentration of lipid **8** is the same in all samples and increases merely with increasing N/P ratios (in the range 4.05−16.2 μmol/L). It is shown that lipoplexes consisting of a larger percentage of colipids exhibit more cytotoxic potential as lipoplexes consisting of larger percentage of lipid **8**. With increasing concentration of the helper-lipid, cell survival decreases. This effect is highly pronounced using cholesterol, but also visible using DOPE as colipid. The concentration of the colipid also seems to play a decisive role in cell damaging characteristics of cationic liposomes. As the mixed liposomes influence the shape and structure of lipoplexes, variances in the ratio between the cationic and the helper lipids has an impact not only on transfection efficacy, but also on compatibility and consequently the cell viability.

Figure 6 summarizes the results of PCS measurements for selected malonic acid amides. Since particle size seems to be crucial for transfection efficiencies compared with lipoplex charge or zeta potential (*41*), the size measurements of all lipoplexes were used to find a correlation of transfection efficacy and particle size. For DOTAP lipoplexes, it was shown that particles with 500 nm sizes were more effective in cell culture experiments than 100 nm lipoplexes (*41, 43*). For successful in vivo gene transfer, particles should have a size less than 150 nm, because larger ones are quickly cleared from blood (*44, 45*).

The results of size measurements of six liposomes and lipoplexes consisting of lipid **1**, lipid **2**, lipid **7**, lipid **8**, and lipid **9** are plotted. They were chosen to distinguish between well-transfecting and nontransfecting lipoplexes. All of them disclose some similarities. The increasing particle size in connection with increasing cationic lipid concentrations has a maximum value at charge equalization (*17*). The displaced maximum values are presumably due to varied capability to condense DNA. By comparing lipoplexes consisting of lipid **7**, lipid **8**, and lipid **9**, it is conspicuous that not only the number of amine residues and the cationic lipid concentration but also the fluidity of liposome membranes is important for charge equalization. Unfortunately, the differences in particle size between transfecting and nontransfecting liposomes are marginal, so that differentiations between the samples are hardly assessable. Certainly, it should be noted that lipoplexes, which exhibit appreciable transfection features, have *z*-average values which are only slightly larger than those of the pure liposomes. The particle size of the majority of lipoplexes is less than 500 nm (cf. Table 1).

As a matter of course, lipid **6**, lipid **8**, and lipid **9** were analyzed for their ability to transfer genes in another cell strain. Figure 7 summarizes the results of in vitro gene delivery and

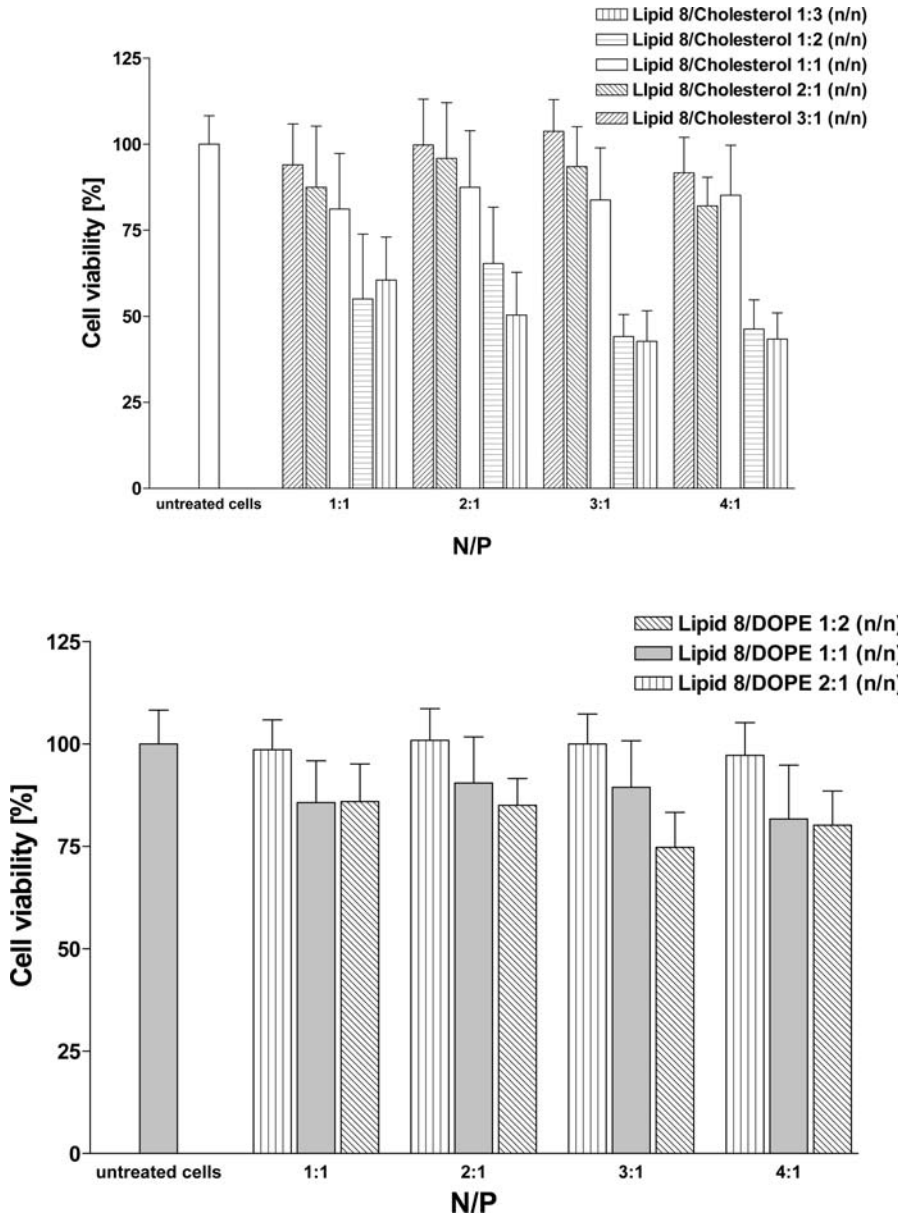


Figure 5. MTT-based cellular cytotoxicities of lipid **8** in LLC PK1 cells using cholesterol and DOPE as colipid (at different lipid/colipid molar ratios). The percent cell viability was plotted against the varying N/P ratios.

MTT based cell viability assays in A549 cells. Even if transfection efficacy of lipid **8** is not as appreciable as in LLC PK1 cells, it is still comparable to LipofectAmine and SuperFect. In human lung carcinoma cells, the multivalent cationic lipids **6** and **9** with two unsaturated alkyl chains were found to transfer DNA statistically significantly better than commercially available vectors at similar cell viability values (*).

Figure 8 summarizes the experiments of gene transfer in the presence of FBS in LLC PK1 cells. Lipoplexes were incubated with the cells as described in the Experimental Procedures section, certainly the concentration of serum was adjusted to 10% from the outset of experiments and kept for 48 h. Admittedly, total protein concentration of human serum that is between 66 and 83 g/L (*46*) is just reached with a level of 60%, but information about serum compatibility of applied lipoplexes is still possible. A slight influence of serum was observed for SuperFect and lipid **8**/cholesterol 2:1 (*n*/*n*), whereas lipid **8**/cholesterol 2:1 (*n*/*n*) offers nearly twice the amount of transfection efficacy. Notably, for LipofectAmine, which contains DOPE, a decrease of gene transfer was observed. Lipoplexes consisting of lipid **6** and lipid **9** deteriorate in transfection efficacy in regard to gene transfer without serum over a period of 4 h. Nevertheless, these samples exhibit gene transfer rates in excess of LipofectAmine that are partially statistically significant (*).

DISCUSSION

Since their introduction as gene carriers in 1987 (*15*), cationic liposomes have become well-studied nonviral vectors (*47*). Lipoplex mediated gene delivery systems are currently the most favorable means to achieve transgene expression in cells in culture. In the meantime, about 1300 clinical trials in gene therapy research have been carried out (*14*). Although hundreds of cationic lipids have been studied (*48*), there is still a need to develop new gene transfer systems.

By engineering new lipids for nonviral gene delivery, it is important to investigate structure/activity relationships to expedite the reasonable development of these substances. In the case of malonic acid amides, several effects of structure−function relationships were demonstrated. Independent of the chemical structure of the hydrophilic molecule part or the colipid, it was observed that the insertion of at

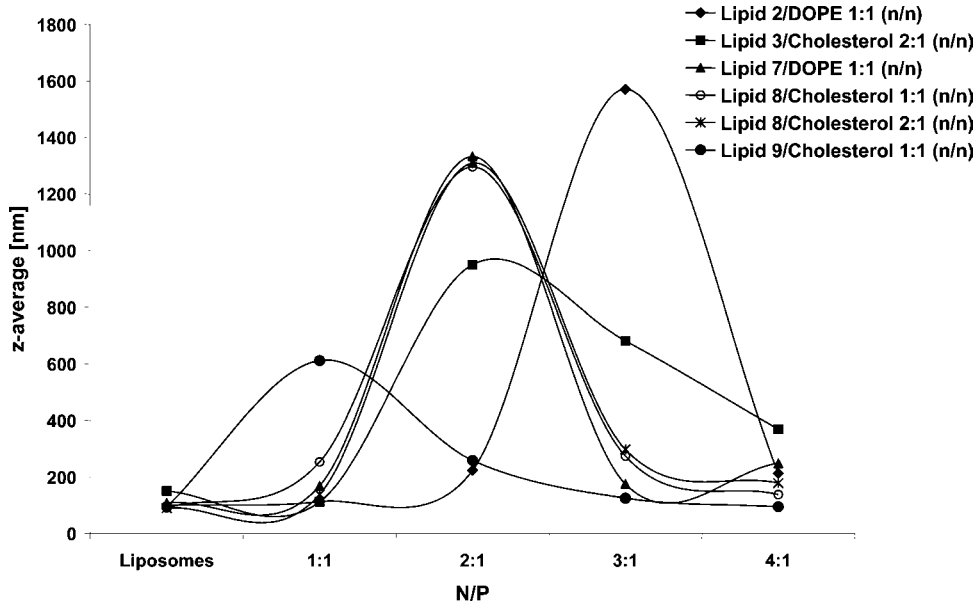


Figure 6. Photon correlation spectroscopy analyses of liposomes and lipoplex mixtures: Changes of particle size as a function of increasing lipid concentration (concentration of DNA = 2.5 μg/mL). The average diameters of lipoplex particles in each set of lipoplex mixtures were determined by three spectroscopic runs comprising ten consecutive scans, each of 10 s in duration.

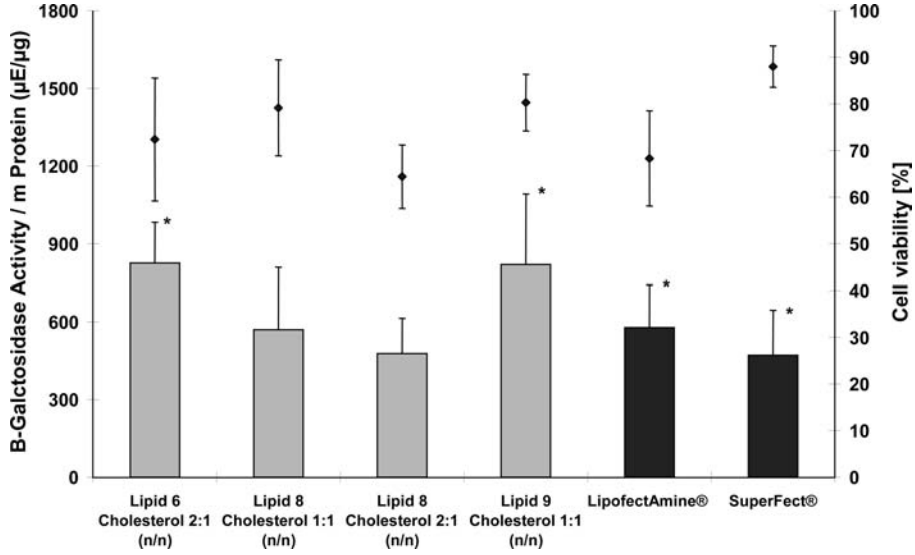


Figure 7. In vitro transfection efficacies and MTT based cell viability values of lipids **6**, **8**, and **9** in A549 cells using cholesterol as colipid. The transfection efficacies and percent cell viability values were compared with LipofectAmine and SuperFect. Percent cell viability is plotted on a secondary *y*-axis via scatter diagram. The transfection and cell viability values shown are the averages of at least three experiments carried out on different days. Statistical analyses were carried out with $p < 0.05$, one-way ANOVA, and Bonferoni's multiple comparison tests (*).

least one unsaturated alkyl chain leads to higher transfection efficacies. Already, Felgner et al. could demonstrate that increasing membrane fluidity often leads to increasing transfection efficacies (*16*). This effect has been attributed to an enhanced capability of fluid amphiphiles to condense DNA (*16, 49*). Besides the electrostatic interaction of cationic lipids and DNA, packing properties of the lipids seem to be important for the condensation of DNA (*40*). It was shown that the insertion of tris(aminoethyl)amine and lysine as hydrophilic headgroup increase transfection efficacy. Although lipids **1**−**3** are able to adsorb DNA in monolayer experiments and protect partially nucleic acids in ethidium bromide exclusion assay (data not shown), multivalent headgroups seem to be more suitable for lipoplex-mediated gene transfer. Except for monovalent substances, all lipids exhibit higher transfection efficacies in combination with cholesterol as colipid. Helper lipids mainly affect the tertiary structure of the plasmid DNA in lipoplexes (*8*). Although this does not affect the transfection effiency (*39, 50*), the influence of colipids for gene transfection is indisputable. As mentioned above, colipids influence the transfection because of their tendency to adopt the inverted hexagonal H_{II} phase that seems to be necessary for the DNA release from the endosomal compartment. Furthermore, DOPE promotes the lipid exchange between liposome and the endosome membrane, which is also crucial for the endosome releasing process (*51, 52*).

The fact that cholesterol was found to be a more efficacious colipid than DOPE is an encouraging result in regard to in vivo gene transfer experiments. Although the application of cationic liposomes as gene delivery systems in cells in culture is popular, the in vivo application still has serious drawbacks (*53*). Due to the chemical structure of the lipids used, liposomes interact with different components of the human

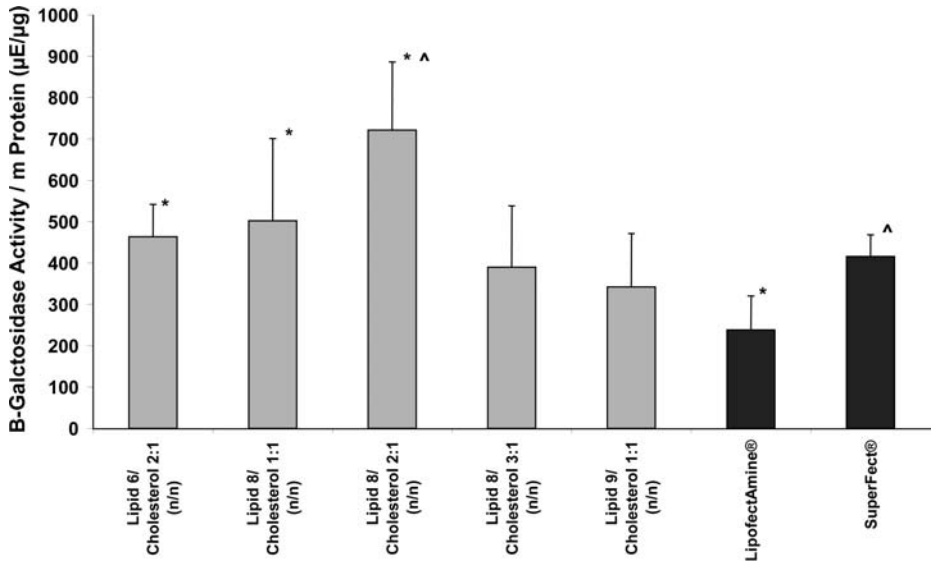


Figure 8. In vitro transfection efficacies of lipids **6**, **8**, and **9** in LLC PK1 cells in the presence of serum compared with LipofectAmine and SuperFect. Concentration of FBS was adjusted to 10% from the outset of experiment and kept up for 48 h. N/P ratios: lipid **6**, 6:1; lipid **8**, 4:1 and 4:1; lipid **9**, 3:1. The transfection values shown are the average of leastwise three experiments carried out on three different days. Statistical analyses were carried out with $p < 0.05$, one-way ANOVA, and Bonferoni's multiple comparison tests (*^).

organism, especially negatively charged amphipathic proteins and polysaccharides that are present in blood, mucus, or tissue matrix (*47*). Plasma proteins like albumin adsorb on the liposome surface and make them recognizable for cells of the reticuloendothelial system (*54*). For liposomes consisting of phospholipids, it is well-known that lipoproteins lead to membrane disintegrations as a consequence of lipid exchange. Mainly liposomes containing lipids with unsaturated fatty acids interact notably with lipoproteins (*55*). For that reason, DOPE is unsuitable for in vivo gene transfer (*56*). On the contrary, cholesterol was found to stabilize the lipoplex structure in blood (*57, 58*). To minimize disadvantageous effects of nonviral vectors in systemic gene delivery, PEG−lipid conjugates were successfully incorporated in lipoplexes (*59*). On the other hand, lipoplexes exhibiting certain serum stability without modification could advance in vivo gene delivery. As shown, cationic liposomes that consist of malonic acid amides have the ability to transfer nucleic acids even in the presence of FBS.

Malonic acid amides describe an interesting novel group of cationic amphiphiles. Nine substances were synthesized and mixed with DOPE or cholesterol, and liposomes were tested for their ability to transfect cells in culture. It was shown that three of them transfect cells at comparable or even higher levels than commercially available LipofectAmine and SuperFect. Thereby, it was observed that lipids containing at least one unsaturated alkyl chain in the hydrophobic molecule part and multivalent headgroups are very successful in gene transfer experiments. Along with this, the cell damaging characteristics of lipoplexes were analyzed. Although the addition of lipoplexes is connected with decreasing cell survival, in the majority of cases the applied lipoplexes show remarkably high cell viability (>80%).

Furthermore, some lipids proved to be successful in gene transfer experiments notwithstanding the presence of serum. Certainly, despite these promising results, further research is clearly needed to clarify the complex mechanism of cationic lipid mediated gene transfer. The presented malonic acid amides are qualified for these requirements. The preparation facilitates the trouble-free variation of alkyl chain length. In addition, multivalent hydrophilic molecule parts are suited to link other cationic residues or molecules for functionalization. Thereby, we expect further developments from this kind of cationic lipids toward successful in vivo gene transfer.

ACKNOWLEDGMENT

We thank the Max Planck Institute of Colloids and Interfaces Potsdam for financial support.

LITERATURE CITED

(1) Rubanyi, G. M. (2001) The future of human gene therapy. *Mol. Aspects Med. 22*, 113–142.
(2) Anderson, W. F. (1998) Human gene therapy. *Nature 392*, 25–30.
(3) Hunt, K. K., and Vorburger, S. A. (2002) Tech.Sight. Gene therapy. Hurdles and hopes for cancer treatment. *Science 297*, 415–416.
(4) El-Aneed, A. (2004) An overview of current delivery systems in cancer gene therapy. *J. Controlled Release 94*, 1–14.
(5) Hacein-Bey-Abina, S., Garrigue, A., Wang, G. P., Soulier, J., Lim, A., Morillon, E., Clappier, E., Caccavelli, L., Delabesse, E., Beldjord, K., Asnafi, V., MacIntyre, E., Dal Cortivo, L., Radford, I., Brousse, N., Sigaux, F., Moshous, D., Hauer, J., Borkhardt, A., Belohradsky, B. H., Wintergerst, U., Velez, M. C., Leiva, L., Sorensen, R., Wulffraat, N., Blanche, S., Bushman, F. D., Fischer, A., and Cavazzana-Calvo, M. (2008) Insertional oncogenesis in 4 patients after retrovirus-mediated gene therapy of SCID-X1. *J. Clin. Invest. 118*, 3132–3142.
(6) Howe, S. J., Mansour, M. R., Schwarzwaelder, K., Bartholomae, C., Hubank, M., Kempski, H., Brugman, M. H., Pike-Overzet, K., Chatters, S. J., de Ridder, D., Gilmour, K. C., Adams, S., Thornhill, S. I., Parsley, K. L., Staal, F. J., Gale, R. E., Linch, D. C., Bayford, J., Brown, L., Quaye, M., Kinnon, C., Ancliff, P., Webb, D. K., Schmidt, M., von Kalle, C., Gaspar, H. B., and Thrasher, A. J. (2008) Insertional mutagenesis combined with acquired somatic mutations causes leukemogenesis following gene therapy of SCID-X1 patients. *J. Clin. Invest. 118*, 3143–3150.
(7) Walther, W., and Stein, U. (2000) Viral vectors for gene transfer: a review of their use in the treatment of human diseases. *Drugs 60*, 249–271.
(8) Boktov, J., Hirsch-Lerner, D., and Barenholz, Y. (2007) Characterization of the interplay between the main factors contributing to lipoplex-mediated transfection in cell cultures. *J. Gene Med. 9*, 884–893.

(9) Hyde, S. C., Southern, K. W., Gileadi, U., Fitzjohn, E. M., Mofford, K. A., Waddell, B. E., Gooi, H. C., Goddard, C. A., Hannavy, K., Smyth, S. E., Egan, J. J., Sorgi, F. L., Huang, L., Cuthbert, A. W., Evans, M. J., Colledge, W. H., Higgins, C. F., Webb, A. K., and Gill, D. R. (2000) Repeat administration of DNA/liposomes to the nasal epithelium of patients with cystic fibrosis. *Gene Ther. 7*, 1156–1165.

(10) Noone, P. G., Hohneker, K. W., Zhou, Z., Johnson, L. G., Foy, C., Gipson, C., Jones, K., Noah, T. L., Leigh, M. W., Schwartzbach, C., Efthimiou, J., Pearlman, R., Boucher, R. C., and Knowles, M. R. (2000) Safety and biological efficacy of a lipid-CFTR complex for gene transfer in the nasal epithelium of adult patients with cystic fibrosis. *Mol. Ther. 1*, 105–114.

(11) Veelken, H., Mackensen, A., Lahn, M., Kohler, G., Becker, D., Franke, B., Brennscheidt, U., Kulmburg, P., Rosenthal, F. M., Keller, H., Hasse, J., Schultze-Seemann, W., Farthmann, E. H., Mertelsmann, R., and Lindemann, A. (1997) A phase-I clinical study of autologous tumor cells plus interleukin-2-gene-transfected allogeneic fibroblasts as a vaccine in patients with cancer. *Int. J. Cancer 70*, 269–277.

(12) Hui, K. M., Ang, P. T., Huang, L., and Tay, S. K. (1997) Phase I study of immunotherapy of cutaneous metastases of human carcinoma using allogeneic and xenogeneic MHC DNA-liposome complexes. *Gene Ther. 4*, 783–790.

(13) Stopeck, A. T., Jones, A., Hersh, E. M., Thompson, J. A., Finucane, D. M., Gutheil, J. C., and Gonzalez, R. (2001) Phase II study of direct intralesional gene transfer of allovectin-7, an HLA-B7/beta2-microglobulin DNA-liposome complex, in patients with metastatic melanoma. *Clin. Cancer Res. 7*, 2285–2291.

(14) Edelstein, M. L., Abedi, M. R., and Wixon, J. (2007) Gene therapy clinical trials worldwide to 2007--an update. *J. Gene Med. 9*, 833–842.

(15) Felgner, P. L., Gadek, T. R., Holm, M., Roman, R., Chan, H. W., Wenz, M., Northrop, J. P., Ringold, G. M., and Danielsen, M. (1987) Lipofection: a highly efficient, lipid-mediated DNA-transfection procedure. *Proc. Natl. Acad. Sci. U.S.A. 84*, 7413–7417.

(16) Felgner, J. H., Kumar, R., Sridhar, C. N., Wheeler, C. J., Tsai, Y. J., Border, R., Ramsey, P., Martin, M., and Felgner, P. L. (1994) Enhanced gene delivery and mechanism studies with a novel series of cationic lipid formulations. *J. Biol. Chem. 269*, 2550–2561.

(17) Lasic, D. D. (1997) *Liposomes in Gene Delivery*, CRC Press, New York.

(18) Leventis, R., and Silvius, J. R. (1990) Interactions of mammalian cells with lipid dispersions containing novel metabolizable cationic amphiphiles. *Biochim. Biophys. Acta 1023*, 124–132.

(19) van der Woude, I., Wagenaar, A., Meekel, A. A., ter Beest, M. B., Ruiters, M. H., Engberts, J. B., and Hoekstra, D. (1997) Novel pyridinium surfactants for efficient, nontoxic in vitro gene delivery. *Proc. Natl. Acad. Sci. U.S.A. 94*, 1160–1165.

(20) Solodin, I., Brown, C. S., Bruno, M. S., Chow, C. Y., Jang, E. H., Debs, R. J., and Heath, T. D. (1995) A novel series of amphiphilic imidazolinium compounds for in vitro and in vivo gene delivery. *Biochemistry 34*, 13537–13544.

(21) Bajaj, A., Kondiah, P., and Bhattacharya, S. (2007) Design, synthesis, and in vitro gene delivery efficacies of novel cholesterol-based gemini cationic lipids and their serum compatibility: a structure-activity investigation. *J. Med. Chem. 50*, 2432–2442.

(22) Heyes, J. A., Niculescu-Duvaz, D., Cooper, R. G., and Springer, C. J. (2002) Synthesis of novel cationic lipids: effect of structural modification on the efficiency of gene transfer. *J. Med. Chem. 45*, 99–114.

(23) Sen, J., and Chaudhuri, A. (2005) Design, syntheses, and transfection biology of novel non-cholesterol-based guanidinylated cationic lipids. *J. Med. Chem. 48*, 812–820.

(24) Choi, J. S., Lee, E. J., Jang, H. S., and Park, J. S. (2001) New cationic liposomes for gene transfer into mammalian cells with high efficiency and low toxicity. *Bioconjugate Chem. 12*, 108–113.

(25) Haas, M., Audouy, S., Muizebelt, I., Smisterova, J., Engberts, J. B., Hoekstra, D., Storm, G., and Hulst, R. (2005) In-vivo delivery of DNA and protein using conceptually new cationic, sunfish', amphiphiles. *J. Controlled Release 101*, 401.

(26) Kim, H. S., Moon, J., Kim, K. S., Choi, M. M., Lee, J. E., Heo, Y., Cho, D. H., Jang, D. O., and Park, Y. S. (2004) Gene-transferring efficiencies of novel diamino cationic lipids with varied hydrocarbon chains. *Bioconjugate Chem. 15*, 1095–1101.

(27) Karmali, P. P., Kumar, V. V., and Chaudhuri, A. (2004) Design, syntheses and in vitro gene delivery efficacies of novel mono-, di- and trilysinated cationic lipids: a structure-activity investigation. *J. Med. Chem. 47*, 2123–2132.

(28) Ewert, K. K., Evans, H. M., Zidovska, A., Bouxsein, N. F., Ahmad, A., and Safinya, C. R. (2006) A columnar phase of dendritic lipid-based cationic liposome-DNA complexes for gene delivery: hexagonally ordered cylindrical micelles embedded in a DNA honeycomb lattice. *J. Am. Chem. Soc. 128*, 3998–4006.

(29) Eisner, U., Polonsky, M. J., and Lederer, E. (1955) *Bull. Soc. Chem. Fr.* 212–218.

(30) Quiagen® Plasmid Purification handbook. www1.qiagen.com/Plasmid/handbooks.aspx.

(31) Rosenberg, I. M. (1996) *Protein Analysis and Prurification: Benchtop techniques*, Birkenhäuser, Boston.

(32) Mosmann, T. (1983) Rapid colorimetric assay for cellular growth and survival: application to proliferation and cytotoxicity assays. *J. Immunol. Methods 65*, 55–63.

(33) Schmidt, R. R., and Jankowsky, K. (1996) Newtypes of nonionic surfactants with sugar head groups. *Liebigs Ann. 6*, 867–879.

(34) Breslow, D. S., Baumgarten, E., and Hauser, C. R. (1944) A new synthesis of β-Ketoesters of the type $RCOCH_2COOC_2H_5$. *J. Am. Chem. Soc. 66*, 1286.

(35) Mukherjee, K., Sen, J., and Chaudhuri, A. (2005) Common co-lipids, in synergy, impart high gene transfer properties to transfection-incompetent cationic lipids. *FEBS Lett. 579*, 1291–1300.

(36) Ma, B., Zhang, S., Jiang, H., Zhao, B., and Lv, H. (2007) Lipoplex morphologies and their influences on transfection efficiency in gene delivery. *J. Controlled Release 123*, 184–194.

(37) Patil, S. D., Rhodes, D. G., and Burgess, D. J. (2005) DNA-based therapeutics and DNA delivery systems: a comprehensive review. *Aaps J 7*, E61−77.

(38) Koltover, I., Salditt, T., Radler, J. O., and Safinya, C. R. (1998) An inverted hexagonal phase of cationic liposome-DNA complexes related to DNA release and delivery. *Science 281*, 78–81.

(39) Simberg, D., Danino, D., Talmon, Y., Minsky, A., Ferrari, M. E., Wheeler, C. J., and Barenholz, Y. (2001) Phase behavior, DNA ordering, and size instability of cationic lipoplexes. Relevance to optimal transfection activity. *J. Biol. Chem. 276*, 47453–47459.

(40) Zuhorn, I. S., Oberle, V., Visser, W. H., Engberts, J. B., Bakowsky, U., Polushkin, E., and Hoekstra, D. (2002) Phase behavior of cationic amphiphiles and their mixtures with helper lipid influences lipoplex shape, DNA translocation, and transfection efficiency. *Biophys. J. 83*, 2096–2108.

(41) Zuhorn, I. S., Engberts, J. B., and Hoekstra, D. (2007) Gene delivery by cationic lipid vectors: overcoming cellular barriers. *Eur. Biophys. J. 36*, 349–362.

(42) Zuhorn, I. S., Bakowsky, U., Polushkin, E., Visser, W. H., Stuart, M. C., Engberts, J. B., and Hoekstra, D. (2005) Nonbilayer phase of lipoplex-membrane mixture determines endosomal escape of genetic cargo and transfection efficiency. *Mol. Ther. 11*, 801–810.

(43) Simberg, D., Weisman, S., Talmon, Y., and Barenholz, Y. (2004) DOTAP (and other cationic lipids): chemistry, biophysics, and transfection. *Crit. Rev. Ther. Drug Carrier Syst. 21*, 257–317.

(44) Kayser, O., and Kiderlen, A. F. (2004) *Non Viral Gene Delivery Systems. In Pharmaceutical Biotechnology*, Kayser and Müller, Eds. WileyVCH, Weinheim.

(45) Li, W., and Szoka, F. C., Jr. (2007) Lipid-based nanoparticles for nucleic acid delivery. *Pharm. Res. 24*, 438–449.
(46) Schaller, J., Gerber, S., Kaempfer, U., Lejon, S., and Trachsel, C. (2008) *Human Blood Plasma Proteins*, John Wiley & Sons Ltd., Chichester-West Sussex.
(47) Gao, X., Kim, K. S., and Liu, D. (2007) Nonviral gene delivery: what we know and what is next. *Aaps J. 9*, E92−104.
(48) Liu, D., Ren, T., and Gao, X. (2003) Cationic transfection lipids. *Curr. Med. Chem. 10*, 1307–1315.
(49) Spector, M. S., and Schnur, J. M. (1997) DNA ordering on a lipid membrane. *Science 275*, 791–792.
(50) Zuidam, N. J., Barenholz, Y., and Minsky, A. (1999) Chiral DNA packaging in DNA-cationic liposome assemblies. *FEBS Lett. 457*, 419–422.
(51) Xu, Y., and Szoka, F. C., Jr. (1996) Mechanism of DNA release from cationic liposome/DNA complexes used in cell transfection. *Biochemistry 35*, 5616–5623.
(52) Farhood, H., Serbina, N., and Huang, L. (1995) The role of dioleoyl phosphatidylethanolamine in cationic liposome mediated gene transfer. *Biochim. Biophys. Acta 1235*, 289–295.
(53) Mintzer, M. A., and Simanek, E. E. (2009) Nonviral vectors for gene delivery. *Chem. Rev. 109*, 259–302.
(54) Oja, C. D., Semple, S. C., Chonn, A., and Cullis, P. R. (1996) Influence of dose on liposome clearance: critical role of blood proteins. *Biochim. Biophys. Acta 1281*, 31–37.
(55) Hain, I., and Pepen, G. (1990) *Phospholipids: Biochemical, Pharmaceutical and Analytical Concideration*s, Plenum Press, New York.
(56) Matsuura, M., Yamazaki, Y., Sugiyama, M., Kondo, M., Ori, H., Nango, M., and Oku, N. (2003) Polycation liposome-mediated gene transfer in vivo. *Biochim. Biophys. Acta 1612*, 136–143.
(57) Song, Y. K., Liu, F., Chu, S., and Liu, D. (1997) Characterization of cationic liposome-mediated gene transfer in vivo by intravenous administration. *Hum. Gene Ther. 8*, 1585–1594.
(58) Li, S., Tseng, W. C., Stolz, D. B., Wu, S. P., Watkins, S. C., and Huang, L. (1999) Dynamic changes in the characteristics of cationic lipidic vectors after exposure to mouse serum: implications for intravenous lipofection. *Gene Ther. 6*, 585–594.
(59) Ambegia, E., Ansell, S., Cullis, P., Heyes, J., Palmer, L., and MacLachlan, I. (2005) Stabilized plasmid-lipid particles containing PEG-diacylglycerols exhibit extended circulation lifetimes and tumor selective gene expression. *Biochim. Biophys. Acta 1669*, 155–163.

BC9004624

Remodeling of Dynamic Structures of HIV-1 Envelope Proteins Leads to Synthetic Antigen Molecules Inducing Neutralizing Antibodies

Toru Nakahara,[†] Wataru Nomura,*[,†] Kenji Ohba,[‡] Aki Ohya,[†] Tomohiro Tanaka,[†] Chie Hashimoto,[†] Tetsuo Narumi,[†] Tsutomu Murakami,[‡] Naoki Yamamoto,[‡] and Hirokazu Tamamura*[,†]

Department of Medicinal Chemistry, Institute of Biomaterials and Bioengineering, Tokyo Medical and Dental University, 2-3-10 Kandasurugadai, Chiyoda-ku, Tokyo 101-0062, Japan, and AIDS Research Center, National Institute of Infectious Diseases, 1-23-1 Toyama, Shinjuku-ku, Tokyo 162-8640, Japan. Received November 16, 2009; Revised Manuscript Received February 28, 2010

A synthetic antigen targeting membrane-fusion mechanism of HIV-1 has a newly designed template with C3-symmetric linkers mimicking N36 trimeric form. The antiserum produced by immunization of the N36 trimeric form antigen showed structural preference in binding to N36 trimer and stronger inhibitory activity against HIV-1 infection than the N36 monomer. Our results suggest an effective strategy of HIV vaccine design based on a relationship to the native structure of proteins involved in HIV fusion mechanisms.

INTRODUCTION

Antibody-based therapy is one of the promising treatments for AIDS. In recent years, AIDS antibodies have been produced by immunization (*1*) and by de novo engineering of monoclonal antibodies (mAb) with molecular evolution tactics such as phage display (*2*). Despite enormous efforts, however, only a limited number of highly and broadly HIV-neutralizing human mAbs have been isolated and characterized. These antibodies include gp41 Abs, 2F5 (*3*−*6*) and 4E10 (*5*−*7*), and gp120 Abs, 2G12 (*8*) and b12 (*9*). gp41 is a transmembrane envelope glycoprotein, which is divided into an endodomain and an ectodomain by the transmembrane region; the latter contains a hydrophobic amino-terminal fusion peptide, followed by amino-terminal and carboxy-terminal leucine/isoleucine heptad repeat domains with helical structures (HR1 and HR2, respectively). In the membrane fusion process of HIV-1, these subunits form a "pre-bundle" complex. The HR1 and HR2 regions are termed the N-terminal helix (N36) and C-terminal helix (C34), respectively. These helices form a six-helical bundle consisting of a central parallel trimeric coiled-coil of N36 surrounded by C34 in an antiparallel hairpin fashion. In design of immunogens that elicit broadly neutralizing antibodies, a useful strategy is to produce molecules that mimic the natural trimer on the virion surface. Previous studies show that these molecules could be proteins expressed as a recombinant form or on the surface of particles such as pseudovirions or proteoliposomes (*10*−*12*). The X-ray crystallographic study of gp41 shows that the distances between any two residues at the N-terminus of N-region are almost equal at approximately 10 Å (Figure 1A). A chemically synthetic template could be useful in connection with the design of a peptidomimetic corresponding to the native structure of gp41. To date, several gp41 mimetics have been synthesized as inhibitors or antigens and subjected to inhibition or neutralization assays (*13*−*16*). However, the templates for assembly of these helical peptides contain branched peptide linkers, which are not exactly equivalent in length (*14*). The N-terminal peptides constrained by another threefold linker showed high affinity for C-terminal peptides, although its biological advantages have not been determined (*15*). The mimicry can be estimated using the broadly neutralizing mAbs; suitable mimetics will bind neutralizing mAbs efficiently, but they will bind non-neutralizing mAbs poorly. In the present study, we designed and synthesized a novel three-helical bundle mimetic, which corresponds to the trimeric form of N36. We investigated whether mice immunized with the equivalent trimeric form of N36 mimetic can produce antibodies with stronger binding affinity for N36 trimer than for N36 monomer. This approach demonstrates the possibility of producing structure-specific antibodies by immunization of synthetic antigens corresponding to the natural form of viral proteins.

EXPERIMENTAL PROCEDURES

Conjugation of N36REGC and the Template to Produce triN36e. Compound **6** (100 μg, 0.174 μmol) and N36REGC (3.4 mg, 0.574 μmol) were dissolved in a mixture of 300 μL of 200 mM acetate buffer (pH 5.2) and 300 μL of TFE under a nitrogen atmosphere, then TCEP·HCl was added. The reaction was stirred for 72 h at room temperature and monitored by HPLC. The ligation product (triN36e) was separated as an HPLC peak and was characterized by ESI-TOF-MS, *m*/*z* calcd for $C_{690}H_{1160}N_{226}O_{201}S_3$ 15933.1, found 15933.8. The purification was performed by reverse phase HPLC (YMC-Pack ODS-A column, 10 × 250 mm). Elution was carried out with a 40−50% linear gradient of acetonitrile (0.1% TFA) over 50 min. Purified triN36e, obtained in 16% yield, was identified by ESI-TOF-MS. The detailed synthesis of peptides is described in the Supporting Information (SI).

CD Spectra. CD measurements were performed with a J-720 circular dichroism spectrolarimeter equipped with a thermoregulator (JASCO). The wavelength dependence of molar ellipticity [θ] was monitored at 25 °C from 190 to 250 nm. Peptides were dissolved in 20 mM acetate buffer (pH 4.0) containing 40% MeOH (*23, 24*). The experimental helicity was calculated as reported previously (*17*−*19*).

Immunization and Sample Collection. Six-week-old male BALB/c mice were purchased from Sankyo Laboratory Service Corp. (Tokyo, Japan) and maintained under specific pathogen-free conditions in an animal facility. The experimental protocol was approved by the ethical review committee of Tokyo Medical and Dental University. Freund incomplete adjuvant and PBS

* To whom correspondence should be addressed. E-mail: nomura.mr@tmd.ac.jp; tamamura.mr@tmd.ac.jp. phone: +81-3-5280-8036, fax: +81-3-5280-8039.

[†] Tokyo Medical and Dental University.

[‡] National Institute of Infectious Diseases.

10.1021/bc900502z © 2010 American Chemical Society
Published on Web 04/01/2010

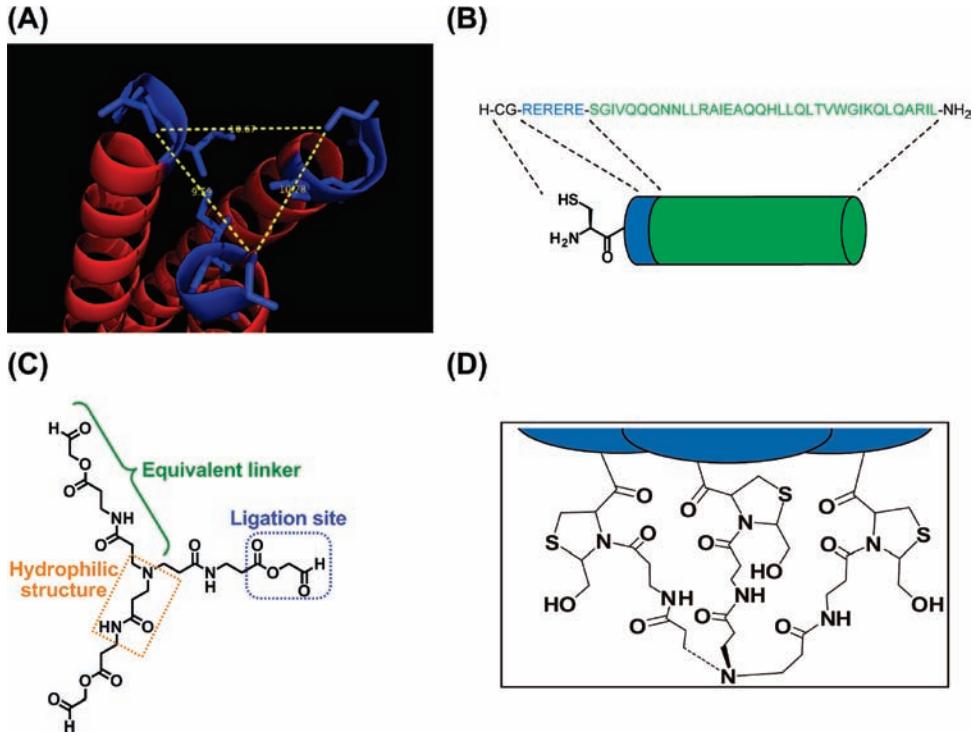


Figure 1. (A) Distances between hydrogen atoms for hydroxyl groups in N-terminal serine residues of N36 helices in trimeric form. The distances were evaluated by PyMOL (*21*). (B) Cartoon presentation of each N36 derived peptide, N36REGC. (C) Design of a C3-symmetric template. The amino acid residues are described in single letters. (D) Conjugated structure of trimeric N36 after thiazolidine ligation.

were purchased from Wako Pure Chemical Industries (Osaka, Japan). DMSO (endotoxin free) was purchased from Sigma-Aldrich (St. Louis, MO).

All mice were bled one week before immunization. One hundred micrograms of antigen was dissolved in 1 μL of DMSO. The solution was mixed with 50 μL of PBS and 50 μL of Freund incomplete adjuvant. The mixture was injected subcutaneously under anesthesia on days 0, 14, 28, 42, and 58. Mice were bled on days 21, 35, 49, and 65. Serum was separated by centrifugation (15 000 rpm) at 4 °C for 15 min and inactivated at 56 °C for 30 min. Sera were stored at −80 °C before use.

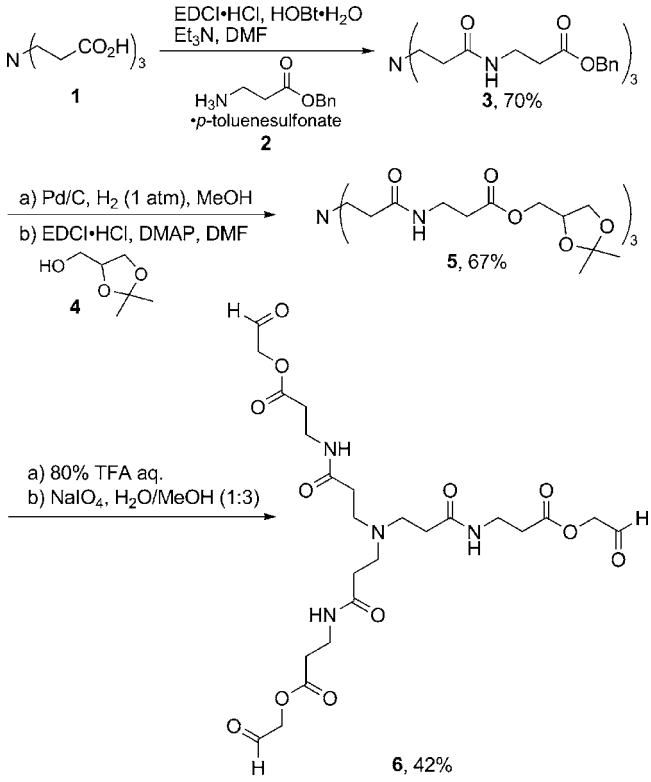
Serum Titer ELISA. Tween-20 (polyoxyethylene (20) sorbitan monolaurate) and hydrogen peroxide (30%) were purchased from Wako. ABTS (2,2-azino-bis(3-ethylbenzothiazoline-6-sulfonic acid) diammonium salt) was purchased from Sigma-Aldrich. Antimouse IgG (H+L)(goat)-HRP was purchased from EMD Chemicals (San Diego, CA). Ninty-six-well microplates were coated with 25 μL of a synthetic peptide at 10 μg/mL in PBS at 4 °C for overnight. The coated plates were washed 10 times with deionized water and blocked with 150 μL of blocking buffer (0.02% PBST, PBS with 0.02% Tween 20, containing 5% skim milk) at 37 °C for 1 h. The plates were washed with deionized water 10 times. Mice sera were diluted in 0.02% PBST with 1% skim milk, and 50 μL of 2-fold serial dilutions of sera from 1/200 to 1/102400 were added to the wells and allowed to incubate at 37 °C for 2 h. The plates were washed 10 times with deionized water. Twenty-five microliters of HRP-conjugated antimouse IgG, diluted 1:2000 in 0.02% PBST, was added to each well. After 45 min incubation, the plates were washed 10 times and 25 μL of HRP substrate, prepared by dissolving 10 mg ABTS to 200 μLof HRP staining buffer—a mixture of 0.5 M citrate buffer (pH 4.0, 1 mL), H_2O_2 (3 μL), and H_2O (8.8 mL)—was added. After 30 min incubation, the reaction was stopped by addition of 25 μL/well 0.5 M H_2SO_4, and optical densities were measured at 405 nm.

Virus Preparation. The pNL4-3 construct (8 μg) was transfected into 293T cells by Lipofectamine LTX (Invitrogen, Carlsbad, CA) followed by changing medium at 12 h after transfection. At 48 h after changing medium, the supernatant was collected, passed through a 0.45 μm filter, and stored at −80 °C as HIV-1_{NL4-3} strain before use. For titration, MT-4 cells were infected with serially 3-fold diluted virus from 1/10 to 1/196830, and cultured for 7 days. HIV-1 p24 levels in supernatants were measured, and then the titer of virus solution was calculated.

Anti-HIV Assay. Virus was prepared as described above except that the transfection of pNL4-3 was performed by the calcium phosphate method. Anti-HIV-1 activity was determined on the basis of protection against HIV-1-induced cytopathogenicity in MT-4 cells. Various concentrations of AZT, N36RE, and triN36e (The starting concentrations are 100, 10, and 1 μM, respectively) were added to HIV-1-infected MT-4 cells (MOI = 0.01) by 2-fold serial dilution and placed in wells of a flat-bottomed microtiter plate (2.0×10^4 cells/well). After 5 days' incubation at 37 °C in a CO_2 incubator, the number of viable cells was determined using the 3-(4,5-dimethylthiazol-2-yl)-2,5-diphenyltetrazolium bromide (MTT) method (EC_{50}). Cytotoxicity of compounds was determined on the basis of viability of mock-infected cells using the MTT method (CC_{50}). Each experiment was performed three times independently.

Neutralizing Assay. MT4-cells (1×10^5 cells/100 μL) were incubated in 100 μL medium containing 10 μL sera from immunized or preimmunized mice for 1 h at 37 °C, then pretreated MT-4 cells were infected with HIV-1_{NL4-3} (MOI = 0.05). At 3 days after infection, cells were collected by centrifuge at 4000 rpm for 10 min at 4 °C. After discarding supernatant, pellets were lysed with 30 μL of lysis buffer (50 mM Tris·HCl (pH 7.5), 150 mM NaCl, 1% NP-40), then 30 μL of 2 × SDS buffer (125 mM Tris·HCl (pH 6.8), 4% SDS, 20% glycerol, 10% 2-ME, 0.004% BPB) were added and boiled for 10 min. The samples (5 μL) were subjected to SDS-page to perform Western blotting. The HIV-1 gag p24 was detected by using Western lightning ECL kit (PerkinElmer, MA) according to manufacturer's instruction after treatment of HIV-1 p24

Scheme 1. Synthesis of the Equivalently Branched Template 6



antibody (2C2; 1:2000 dilution) (*20*) and anti- mouse IgG (H+L)-HRP (Millipore, MA). The band intensity of p24 was calculated with post/pre-immunized samples by using *ImageJ* image analyzing software.

RESULTS AND DISCUSSION

The N-region of gp41 is known to be an aggregation site involving a trimeric coiled-coil conformation. In design of an N36-derived peptide (N36RE), the triplet repeat of arginine and glutamic acid was fused to the N-terminus to increase the solubility in buffer solution (Figure 1B). In order to form a triple helix corresponding precisely to the gp41 prefusion form, we designed the novel C3-symmetric template depicted in Figure 1C. This designed template linker has three branches of equal length and possesses the hydrophilic structure and ligation site for coupling with N36RE. The template was synthesized from the commercially available 3-[bis(2-carboxyethyl)amino]propanoic acid **1** as shown in Scheme 1. Coupling of **1** with β-alanine benzyl ester **2** gave the corresponding triamide **3** in 77% yield. Cleavage of three benzyl esters by hydrogenation and coupling with solketal **4** produced the corresponding triester **5**. Deprotection of the acetonides with aqueous 80% TFA followed by oxidative cleavage of diol group led to the desired template **6**. This approach uses thiazolidine ligation for chemoselective coupling of Cys-containing unprotected N36RE (N36REGC) with a three-armed aldehyde scaffold producing triN36e (Figure 1D). Thiazolidine ligation is a peptide segment coupling strategy which does not require side chain protecting groups (*22*−*26*). The reaction consists of three steps: (i) aldehyde introduction, in which a masked glycolaldehyde ester is linked to the carboxyl terminus of an unprotected peptide by reverse proteolysis; (ii) ring formation, in which the unmasked aldehyde reacts at acidic pH with the α-amino group of an N-terminal cysteine residue of the second unprotected peptide forming a thiazolidine ring; and (iii) rearrangement at higher pH in which O-acyl ester linkage is converted to an N-acyl amide linkage forming a peptide bond with a pseudoproline structure (Figure 2).

Circular dichroism (CD) spectra of triN36e and N36RE, which is a monomer form without N-terminal Cys-Gly residues, are shown in Figure 3A. The peptides were dissolved in 20 mM acetate buffer with 40% MeOH, pH4.0, suitable for measurement of CD spectra of membrane proteins (*27, 28*). Both spectra display double minima at 208 and 222 nm and showed high molar ellipticity as absolute values (Table 1). The results indicate that these peptides form a highly structured α-helix and that the helical content of the trimer triN36e is higher than that of the monomer N36RE. Furthermore, to assess the interaction of triN36e with C34, CD spectra of the peptide mixture with C34-derived peptide, C34RE, were measured (Figure 3B,C). The spectrum of triN36e and C34RE mixture showed high molecular ellipticity as an absolute value comparable with that of triN36e alone. This supports the conclusion that C34RE interacts with tri36e and thereby induces a higher helical form as shown previously (*29*).

Mice were immunized with these synthetic gp41 mimetics and antibody production was successfully induced (the detailed titer increase in 5 weeks' immunization is given in the Supporting Information). Two out of three mice showed induction of antibodies against either antigen (N36RE or triN36e). Antibody titers and selectivity of antisera isolated from mice immunized with N36RE or triN36e were evaluated by serum titer ELISA against coated synthetic antigens. The most active antiserum for each antigen was utilized for the evaluation of binding activity by ELISA (Figure 4). The N36RE-induced antibody showed approximately 5 times higher affinity for N36RE than for triN36e, as 50% bound serum dilutions are 3.88×10^{-4} and 2.14×10^{-3} to N36RE and triN36e, respectively. It is noteworthy that the triN36e-induced antibody showed approximately 30 times higher preference in binding affinity for triN36e antigen than for N36RE (serum dilutions at 50% bound are 3.83×10^{-3} to N36RE and 1.33×10^{-4} to triN36e). Although this evaluation was not determined with purified mAbs, it is clear that the antibodies produced exploit a structural preference for antigens. The mechanism of induction

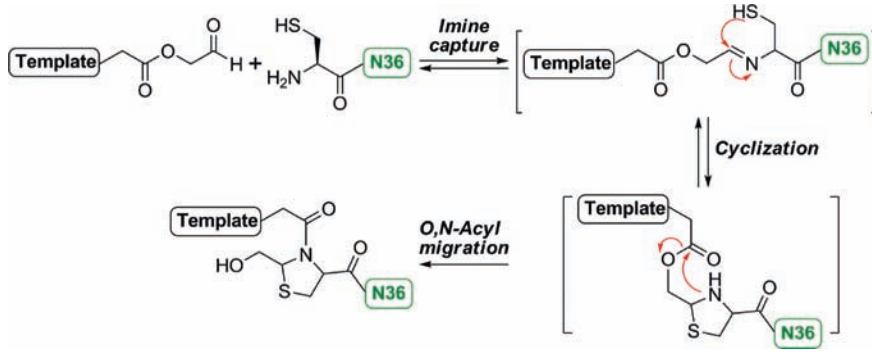


Figure 2. Reaction mechanisms of thiazolidine ligation utilized for assembly of N36RE helices on the template.

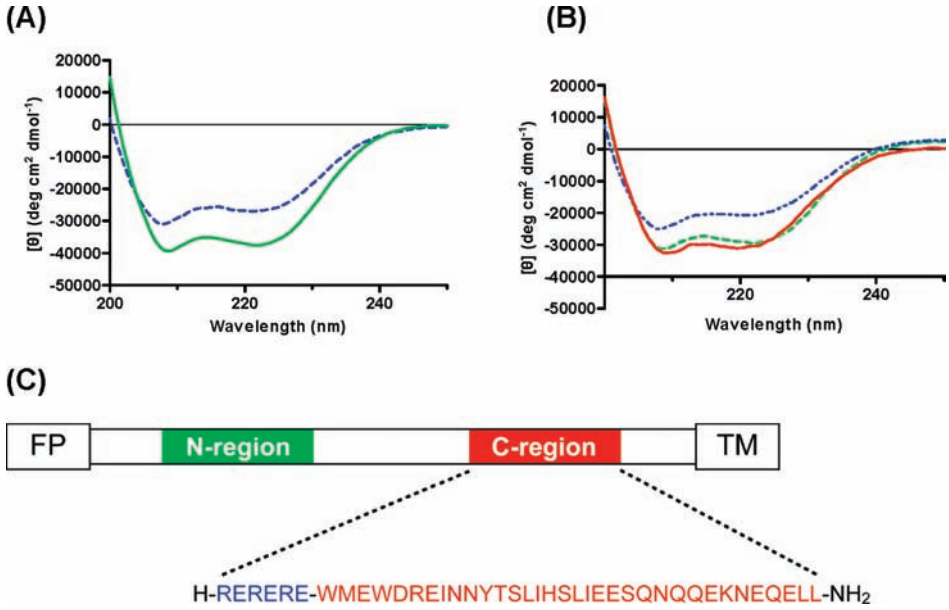


Figure 3. (A) Circular dichroism (CD) spectra of N36RE and triN36e. In the spectra, a blue dashed line and a green line show N36RE (monomer) and triN36e (trimer), respectively. Concentrations of the peptides are 10 and 3.3 μM for N36RE and triN36e, respectively. (B) CD spectra in the presence or absence of C34RE peptide. The spectra show the following: a dashed green line, triN36e; a dashed blue line, C34RE; a red line, triN36e+C34RE, respectively. The concentrations of peptides were as follows: triN36e (2.3 μM), C34-derived peptide C34RE (7 μM), and mixture of both peptides (3.5 μM each). (C) The amino acid sequence of C34RE described in single letters. FP and TM represent hydrophobic fusion peptide and transmembrane domain, respectively.

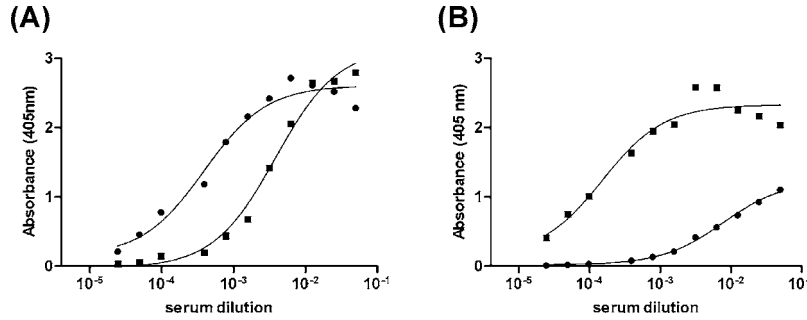


Figure 4. Serum titers of antibodies produced by N36 monomer and conformationally constrained N36 trimeric antigen. The titers were evaluated against N36RE (monomer) (A) and triN36e (trimer) (B). The plots indicate the results of sera obtained from N36RE-immunized mouse (•) and triN36e-immunized mouse (■).

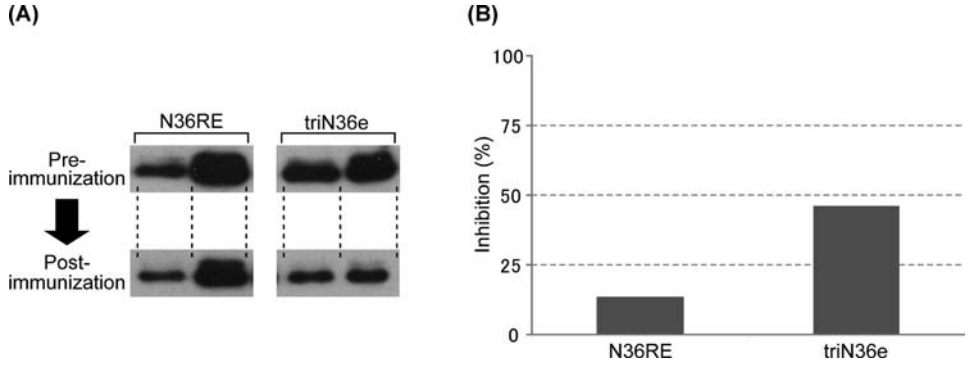


Figure 5. Determination of neutralization activity of the antibodies produced by immunization of peptidomimetic antigens. (A) Results of p24 assay to evaluate inhibition for HIV-1 infection by produced antibodies. Preimmunization sera were used as control. Experiments were duplicated. (B) Average % inhibition of p24 production calculated from the band intensities in panel (A).

of structure-specific antibody is still not clear, but the results could suggest the efficacy of producing antibodies with structural specificity and that the synthesis of structure-involving antigens is an effective strategy when higher specificity is required.

Neutralizing activity of sera against HIV-1 infection was assessed by p24 assays utilizing antisera from two mice that showed antibody production for each antigen (Figure 5). Sera

Table 1. Differences of α-Helicities between N36RE and triN36e Calculated from CD Spectra in Figure [3]

	$[\theta]_{222}$	$[\theta]_{222}/[\theta]_{208}$	α-helicity
N36RE	−30 957	0.87	73%
triN36e	−38 998	0.96	95%

Table 2. EC_{50} and CC_{50} Values Calculated from Inhibition Assays of Peptidomimetics

	AZT	triN36e	N36RE
EC_{50} (μM)[a]	0.047	0.49	1.4
CC_{50} (μM)[b]	>50	>1	>10

[a] EC_{50} values are based on the inhibition of HIV-induced cytopathogenicity in MT-4 cells. [b] CC_{50} values are based on the reduction of the viability of MT-4 cells. All data are the mean values for at least three experiments.

from mice immunized with the same antigen showed similar inhibitory activity against viral infection (12.5% and 14.8% for N36RE, 40.3% and 52.1% for triN36e). A trend was observed that the sera from triN36e immunization shows higher inhibition than those from N36RE immunization. This suggests that the synthetic antigen corresponding to the N36 trimeric form induces antibody with neutralization activity superior to that of the monomer peptide antigen and implies a restricted response of B-cells upon immunization to the trimeric form of N36RE. In order to assess the compatibility of induced antibodies in HIV-1 entry inhibition, the HIV-1 inhibitory activities of peptidomimetics (N36RE and triN36e) have been evaluated by viral infection and cytotoxicity assays. A C-terminal region peptide known as Enfuvirtide (T20, Roche/Trimeris) has been used clinically as a fusion inhibitor, and its success indicates that gp41-derived peptides might be potent inhibitors, useful against HIV-1 infection (*30*). In the development of anti-HIV peptides, several mimetics such as Enfuvirtide, CD4 binding site of gp120 (*31*), and protein-nucleic acid interactions (*32*), which disrupt protein−protein interactions, have been produced. As indicated in Table 2, N36 and triN36e showed modest inhibitory activity as reported in previous studies (*33*−*35*). The potency of triN36e was three times higher than that of N36RE indicating that the active structure of monomer N36RE is a trimeric form. Cytotoxicity of the antigens was not observed at concentrations of 1 μM of triN36e and 10 μM of N36RE.

CONCLUSIONS

In summary, a mimic of HIV-1 gp41-N36 designed as a new vaccine has been synthesized utilizing a novel template with three branched linkers of equal lengths. Thiazolidine-forming ligation attached the esteraldehyde of three-branched template with N-terminal cysteine of peptides in an aqueous medium. The resulting peptide antigen successfully induces antibodies with neutralization activity against HIV-1 infection. It is of special interest that the antibody produced acquires structural preference to antigen, which showed 30 times higher binding affinity for trimer than for monomer. This indicates the effectiveness of the design based on the structural dynamics of HIV-1 fusion mechanism of an antigen which could elicit neutralizing antibodies. In a design based on the N36 region of gp41, the exposed timing of epitopes is limited during HIV-1 entry (*36*), and carbohydrates, which could make accession of antibodies to epitopes difficult, are not associated with the amino acid residues of the native protein. These two advantages could further enhance the potential of a vaccine design based on the N36 region. During preparation of the manuscript, a new HIV vaccine strategy was reported by Burton's group (*37*). The report describes the importance of antibody recognition for the trimer form of surface protein. The trimer-specific antibodies indicate broad and potent neutralization. The gp41 trimer-form specific antibody produced in this study could also obtain the corresponding properties. The elucidation of antibody-producing mechanisms and epitope recognition mode of antibodies in antiserum during HIV-1 entry will be addressed in future studies.

ACKNOWLEDGMENT

The authors deeply thank Prof. K. Akiyoshi (Tokyo Medical and Dental Univ.) for allowing access to CD spectroporalimeter.

Supporting Information Available: HPLC chromatograms and NMR charts of compounds **3**, **5**, and **6**. Results of ESI-TOF-MS, and HPLC chromatograms of peptides N36RE, N36REGC, and triN36e. Results of serum titer ELISA of antisera collected during immunization. This material is available free of charge via the Internet at http://pubs.acs.org.

LITERATURE CITED

(1) Cabezas, E., Wang, M., Parren, P. W. H. I., Stanfield, R. L., and Satterthwait, A. C. (2000) A structure-based approach to a synthetic vaccine for HIV-1. *Biochemistry 39*, 14377–14391.

(2) Burton, D. R., Barbas, C. F., III, Persson, M. A. A., Koenig, S., Chanock, R. M., and Lerner, R. A. (1991) A large array of human monoclonal antibodies to type 1 human immunodeficiency virus from combinatorial libraries of asymptomatic seropositive individuals. *Proc. Natl. Acad. Sci. U.S.A. 88*, 10134–10137.

(3) Conley, A. J., Kessler, J. A. II, Boots, L. J., Tung, J. S., Arnold, B. A., Keller, P. M., Shaw, A. R., and Emini, R. A. (1994) Neutralization of divergent human immunodeficiency virus type 1 variants and primary isolates by IAM-41−2F5, an anti-gp41 human monoclonal antibody. *Proc. Natl. Acad. Sci. U.S.A. 91*, 3348–3352.

(4) Ofek, G., Tang, M., Sambor, A., Katinger, H., Mascola, J. R., Wyatt, R., and Kwong, P. D. (2004) Structure and mechanistic analysis of the anti-human immunodeficiency virus type 1 antibody 2F5 in complex with its gp41 epitope. *J. Virol. 78*, 10724–10737.

(5) Alam, S. M., McAdams, M., Boren, D., Rak, M., Scearce, R. M., Gao, F., Camacho, Z. T., Gewirth, D., Kelsoe, G., Chen, P., and Haynes, B. F. (2007) The role of antibody polyspecificity and lipid reactivity in binding of broadly neutralizing anti-HIV-1 envelope human monoclonal antibodies 2F5 and 4E10 to glycoprotein 41 membrane proximal envelope epitopes. *J. Immunol. 178*, 4424–4435.

(6) Nelson, J. D., Brunel, F. M., Jensen, R., Crooks, E. T., Cardoso, R. M. F., Wang, M., Hessell, A., Wilson, I. A., Binley, J. M., Dawson, P. E., Burton, D. R., and Zwick, M. B. (2007) An affinity-enhanced neutralizing antibody against the membrane-proximal external region of human immunodeficiency virus type 1 gp41 recognizes an epitope between those of 2F5 and 4E10. *J. Virol. 81*, 4033–4043.

(7) Cardoso, R. M. F., Zwick, M. B., Stanfield, R. L., Kunert, R., Binley, J. M., Katinger, H., Burton, D. R., and Wilson, I. A. (2005) Broadly neutralizing anti-HIV antibody 4E10 recognizes a helical conformation of a highly conserved fusion-associated motif in gp41. *Immunity 22*, 163–173.

(8) Trkola, A., Purtscher, M., Muster, T., Ballaun, C., Buchacher, A., Sullivan, N., Srinivasan, K., Sodroski, J., Moore, J. P., and Katinger, H. (1996) Human monoclonal antibody 2G12 defines a distinctive neutralization epitope on the gp120 glycoprotein of human immunodeficiency virus type 1. *J. Virol. 70*, 1100–1108.

(9) Pantophlet, R., Saphire, E. O., Poignard, P., Parren, P. W. H. I., Wilson, I. A., and Burton, D. R. (2003) Fine mapping of the interaction of neutralizing and nonneutralizing monoclonal antibodies with the CD4 binding site of human immunodeficiency virus type 1 gp120. *J. Virol. 77*, 642–658.

(10) Sanders, R. W., Vesanen, M., Schuelke, N., Master, A., Schiffner, L., Kalyanaraman, R., Paluch, M., Berkhout, B., Maddon, P. J., Olson, W. C., Lu, M., and Moore, J. P. (2002) Stabilization of the soluble, cleaved, trimeric form of the envelope glycoprotein complex of human immunodeficiency virus type 1. *J. Virol. 76*, 8875–8889.

(11) Yang, X., Wyatt, R., and Sodroski, J. (2001) Improved elicitation of neutralizing antibodies against primary human immunodeficiency viruses by soluble stabilized envelope glycoprotein trimers. *J. Virol. 75*, 1165–1171.
(12) Grundner, C., Mirzabekov, T., Sodroski, J., and Wyatt, R. (2002) Solid-phase proteoliposomes containing human immunodeficiency virus envelope glycoproteins. *J. Virol. 76*, 3511–3521.
(13) De Rosny, E., Vassell, R., Wingfield, R. T., Wild, C. T., and Weiss, C. D. (2001) Peptides corresponding to the heptad repeat motifs in the transmembrane protein (gp41) of human immunodeficiency virus type 1 elicit antibodies to receptor-activated conformations of the envelope glycoprotein. *J. Virol. 75*, 8859–8863.
(14) Tam, J. P., and Yu, Q. (2002) A facile ligation approach to prepare three-helix bundles of HIV fusion-state protein mimetics. *Org. Lett. 4*, 4167–4170.
(15) Xu, W., and Taylor, J. W. (2007) A template-assembled model of the N-peptide helix bundle from HIV-1 gp-41 with high affinity for C-peptide. *Chem. Biol. Drug Des. 70*, 319–328.
(16) Louis, J. M., Nesheiwat, I., Chang, L., Clore, G. M., and Bewlet, C. A. (2003) Covalent trimers of the internal N-terminal trimeric coiled-coil of gp41 and antibodies directed against them are potent inhibitors of HIV envelope-mediated cell fusion. *J. Biol. Chem. 278*, 20278–20285.
(17) Chen, Y.-H., Yang, J. T., and Chau, K. H. (1974) Determination of the helix and β form of proteins in aqueous solution by circular dichroism. *Biochemistry 13*, 3350–3359.
(18) Gans, P. J., Lyu, P. C., Manning, M. C., Woody, R. W., and Kallenbach, N. R. (1991) The helix-coil transition in heterogeneous peptides with specific side-chain interactions: theory and comparison with CD spectral data. *Biopolymers 13*, 1605–1614.
(19) Jackson, D. Y., King, D. S., Chmielewski, J., Singh, S., and Schultz, P. G. (1991) A general approach to the synthesis of short alpha-helical peptides. *J. Am. Chem. Soc. 113*, 9391–9392.
(20) Ohba, K., Ryo, A., Dewan, M. Z., Nishi, M., Naito, T., Qi, X., Inagaki, Y., Nagashima, Y., Tanaka, Y., Okamoto, T., Terashima, K., and Yamamoto, N. (2009) Follicular dendritic cells activate HIV-1 replication in monocytes/macrophages through a juxtacrine mechanism mediated by P-selectin glycoprotein ligand 1. *J. Immunol. 183*, 524–532.
(21) Liu, J., Shu, W., Fagan, M. B., Nunberg, J. H., and Lu, H. (2001) Structural and functional analysis of the HIV gp41 core containing an Ile573 to Thr substitution: implications for membrane fusion. *Biochemistry 40*, 2797–2807.
(22) Liu, C. F., and Tam, J. P. (1994) Peptide segment ligation strategy without use of protecting groups. *Proc. Natl. Acad. Sci. U.S.A. 91*, 6584–6588.
(23) Tam, J. P., and Miao, Z. (1999) Stereospecific pseudoproline ligation of N-terminal serine, threonine, or cysteine-containing unprotected peptides. *J. Am. Chem. Soc. 121*, 9013–9022.
(24) Tam, J. P., Yu, Q., and Yang, J.-L. (2001) Tandem ligation of unprotected peptides through thiaprolyl and cysteinyl bonds in water. *J. Am. Chem. Soc. 123*, 2487–94.
(25) Eom, K. D., Miao, Z., Yang, J.-L., and Tam, J. P. (2003) Tandem ligation of multipartite peptides with cell-permeable activity. *J. Am. Chem. Soc. 125*, 73–82.
(26) Sadler, K., Zhang, Y., Xu, J., Yu, Q., and Tam, J. P. (2008) Quaternary protein mimetics of gp41 elicit neutralizing antibodies against HIV fusion-active intermediate state. *Biopolym. (Pept. Sci.) 90*, 320–329.
(27) Bychkova, V. E., Dujsekina, A. E., Klenin, S. I., Tiktopulo, E. I., Uversky, V. N., and Ptitsyn, O. B. (1996) Molten globule-like state of cytochrome *c* under conditions simulating those near the membrane surface. *Biochemistry 35*, 6058–6063.
(28) Nishi, K., Komine, Y., Sakai, N., Maruyama, T., and Otagiri, M. (2005) Cooperative effect of hydrophobic and electrostatic forces on alcohol-induced α-helix formation of α_1-acid glycoprotein. *FEBS Lett. 579*, 3596–3600.
(29) Chan, D. C., Chutkowski, C. T., and Kim, P. S. (1998) Evidence that a prominent cavity in the coiled coil of HIV type 1 gp41 is an attractive drug target. *Proc. Natl. Acad. Sci. U.S.A. 95*, 15613–15617.
(30) Liu, S., Jing, W., Cheng, B., Lu, H., Sun, J., Yan, X., Niu, J., Farmar, J., Wu, S., and Jiang, S. (2007) HIV gp41 C-terminal heptad repeat contains multifunctional domains: relation to mechanism of action of anti-HIV peptides. *J. Biol. Chem. 282*, 9612–9620.
(31) Franke, R., Hirsch, T., Overwin, H., and Eichler, J. (2007) Synthetic mimetics of the CD4 binding site of HIV-1 gp120 for the design of immunogens. *Angew. Chem., Int. Ed. 46*, 1253–1255.
(32) Robinson, J. A. (2008) β-hairpin peptidomimetics: design, structures and biological activities. *Acc. Chem. Res. 41*, 1278–1288.
(33) Lu, M., Ji, H., and Shen, S. (1999) Subdomain folding and biological activity of the core structure from human immunodeficiency virus type 1 gp41: implications for viral membrane fusion. *J. Virol. 73*, 4433–4438.
(34) Eckert, D. M., and Kim, P. S. (2001) Design of potent inhibitors of HIV-1 entry from the gp41 N-peptide region. *Proc. Natl. Acad. Sci. U.S.A. 98*, 11187–11192.
(35) Bianchi, E., Finotto, M., Ingallinella, P., Hrin, R., Carella, A. V., Hous, X. S., Schleif, W. A., and Miller, M. D. (2005) Covalent stabilization of coiled coils of the HIV gp41 N region yields extreamely potent and broad inhibitors of viral infection. *Proc. Natl. Acad. Sci. U.S.A. 102*, 12903–12908.
(36) Zwick, M. B., Saphire, E. O., and Burton, D. R. (2004) gp41: HIV's shy protein. *Nat. Med. 10*, 133–134.
(37) Walker, L. M., Phogat, S. K., Chan-Hui, P.-Y., Wagner, D., Phung, P., Goss, J. L., Wrin, T., Simek, M. D., Fling, S., Mitcham, J. L., Lehrman, J. K., Priddy, F. H., Olsen, O. A., Frey, S. M., Hammond, P. W., Kaminsky, S., Zamb, T., Moyle, M., Koff, W. C., Poignard, P., and Burton, D. R. (2009) Broad and potent neutralizing antibodies from an African donor reveal a new HIV-1 vaccine target. *Science 326*, 285–289.

BC900502Z

In Vivo Evaluation of ^{64}Cu-Labeled Magnetic Nanoparticles as a Dual-Modality PET/MR Imaging Agent

Charles Glaus,[†] Raffaella Rossin,[‡] Michael J. Welch,[‡] and Gang Bao*,[†]

Department of Biomedical Engineering, Georgia Institute of Technology and Emory University, Atlanta, Georgia, and Mallinckrodt Institute of Radiology, Washington University School of Medicine, St. Louis, Missouri. Received November 19, 2009; Revised Manuscript Received February 25, 2010

A novel nanoparticle-based dual-modality positron emission tomograph/magnetic resonance imaging (PET/MRI) contrast agent was developed. The probe consisted of a superparamagnetic iron oxide (SPIO) core coated with PEGylated phospholipids. The chelator 1,4,7,10-tetraazacyclo-dodecane-1,4,7,10-tetraacetic acid (DOTA) was conjugated to PEG termini to allow labeling with positron-emitting ^{64}Cu. Radiolabeling with ^{64}Cu at high yield and high purity was readily achieved. The ^{64}Cu-SPIO probes produced strong MR and PET signals and were stable in mouse serum for 24 h at 37 °C. Biodistribution and in vivo PET/CT imaging studies of the probes showed a circulation half-life of 143 min and high initial blood retention with moderate liver uptake, making them an attractive contrast agent for disease studies.

INTRODUCTION

Multimodality imaging combines two or more distinct imaging modalities in a way that leverages the respective strengths and weaknesses of each imaging technology. Examples include combined PET-CT (*1*), PET-MR (*2, 3*), and MR-fluorescence imaging (*4, 5*), which often generate results superior to both modalities operating separately. The combination of positron emission tomography (PET) with X-ray computed tomography (CT) has become the gold standard in oncologic imaging (*1*). Positron emission tomography is the most sensitive human molecular imaging modality and produces whole body images of functional and molecular information. CT rapidly acquires whole-body images at high resolution but exposes patients and experimental animals to substantial doses of ionizing radiation. Magnetic resonance imaging (MRI), in comparison, uses no ionizing radiation and provides soft tissue contrast superior to CT. Combining PET with the high-resolution, spectroscopic, or contrast enhanced abilities of MRI would produce a breakthrough in the detection and monitoring of disease (*2*).

Nanoparticles possess unique characteristics that make them well-suited as probes for molecular imaging (*6*). Particles can be synthesized in a systematic fashion with tight control over nanoparticle diameter to produce particles with narrow size distributions. As particles become smaller, their surface area to volume ratio increases significantly. Engineering of nanoparticle surface chemistry allows the surface area to be decorated with therapeutic molecules, imaging agents, targeting ligands, or nucleic acids. Distinct ligands and reporters can be attached to a single particle to allow multiplexing and multifunctionality. A single nanoparticle can be conjugated with a large number of targeting ligands, increasing the affinity of the nanoparticle to its biological target through a phenomenon known as multivalency. Additionally, a nanoparticle can be conjugated with a large number of reporter molecules (e.g., fluorophores, radionuclides), increasing signal-to-noise in imaging applications.

The unique qualities of nanoparticles described above make them superior in many ways to traditional low molecular weight MRI contrast agents and PET probes (*7*). Compared to gadolinium-based MRI contrast agents, nanoparticle MRI contrast agents circulate in the blood for longer periods of time, offer greater sensitivity, and may produce fewer side effects (*8*). Radiolabeled nanoparticles can circulate for longer periods of time than small molecule PET tracers and can carry greater numbers of radionuclides (*9*). Nanoparticles are therefore a promising material for the construction and evaluation of combined PET/MRI probes.

Herein, we report the development of a novel dual-modality nanoparticle for PET/MR imaging. The probe in this work has a superparamagnetic iron oxide nanoparticle (SPIO) core with a micelle coating composed of functionalized PEGylated lipids. The nanoparticles were modified with DOTA to allow chelation of copper-64 for PET imaging. The nanoparticles were labeled at high specific activity and produced strong PET and MRI contrast. The pharmacokinetics of this novel probe was measured using microPET/CT and organ biodistribution.

EXPERIMENTAL PROCEDURES

Materials. Superparamagnetic iron oxide (SPIO) crystalline cores (generously provided by Dr. Charles O'Connor, University of New Orleans) were synthesized using a reverse micelle process (*10, 11*). 1,2-Distearoyl-*sn*-glycero-3-phosphoethanolamine-*N*-[amino(polyethylene glycol)2000] (DSPE-PEG2000-amine) and 1,2-distearoyl-*sn*-glycero-3-phosphoethanolamine-*N*-[methoxy(polyethylene glycol)-5000] (DSPE-mPEG5000) were purchased from Avanti Polar Lipids Inc. (Alabaster, AL). 1,4,7,10-Tetraazacyclododecane-1,4,7,10-tetraacetic acid mono(*N*-hydroxysuccinimide ester) (DOTA-NHS) was purchased from Macrocyclics Inc. (Dallas, TX). ^{64}Cu was produced on a Washington University School of Medicine Cyclotron (Model CS-15, Cyclotron Corp.) by the ^{64}Ni(p,n)^{64}Cu reaction with the nuclide having a specific activity of 220 ± 55 mCi/μg at the end of bombardment, as previously described (*12*). All buffers used for ^{64}Cu labeling were passed through a Chelex 100 column before use. Water was deionized to 18 MΩ cm using an E-Pure water filtration system (Barnstead International, Dubuque, IA). Wiretrol II capillary micropipets were purchased from the

* Corresponding author. Tel: 1-404-385-0373. Fax: 1-404-894-4243. E-mail: gang.bao@bme.gatech.edu.

[†] Georgia Institute of Technology and Emory University.

[‡] Washington University School of Medicine.

10.1021/bc900511j © 2010 American Chemical Society
Published on Web 03/30/2010

Drummond Scientific Company (Broomall, PA). Chelex 100 resin (50−100 mesh), hydrochloric acid, hydroxylamine hydrochloride, ferrous ammonium sulfate hexahydrate, 1,10-phenanthroline, ethylenediaminetetraacetic acid (EDTA), 10 mM phosphate buffered saline (PBS), chloroform, and mouse serum were purchased from Sigma-Aldrich Inc. (St. Louis, MO).

Preparation of Micelle-Coated SPIOs. Micelle-coated SPIOs (mSPIOs) were prepared as previously described (*13*) with slight modifications. DSPE-PEG2000-amine and DSPE-mPEG5000 were individually dispersed in chloroform at 25 mg/mL and stored at −20 °C prior to the coating procedure. To prepare amino-functionalized mSPIOs, DSPE-PEG2000-amine (9 μmol) and DSPE-mPEG5000 (34 μmol) were added to 24 mL chloroform in a round-bottomed flask. Uncoated SPIOs suspended in toluene (20 mg Fe) were then added to the flask, and the mixture was placed in a rotary evaporator. Pressure was slowly reduced to 10 mTorr to remove all solvents, resulting in a dry film of nanoparticles and PEG-phospholipids. The physical adsorption of PEGylated lipids onto particles was due to a hydrophobic interaction between cetyltrimethylammonium bromide capping ligands on the nanoparticle surface and acyl chains of phospholipids. The film was heated at 60 °C for 30 min under vacuum. Next, the flask was removed from vacuum and the film hydrated using deionized water with gentle agitation followed by sonication, producing a clear, brown solution of mSPIOs. Empty PEG-phospholipid micelles were separated from mSPIOs by ultracentrifugation (Optima XL-100K; Beckman Coulter Inc., Fullerton, CA) for 10 h at 280 000 *g* (4 °C). The supernatant containing empty micelles was removed and the nanoparticle pellet was resuspended in PBS to 10 mg Fe/mL and passed through a 0.1 μm Anotop syringe filter (Whatman International Ltd., UK).

Conjugation of mSPIOs with DOTA-NHS-Ester. DOTA-NHS-ester was reacted with 1 mL of 10 mg Fe/mL amino-functionalized mSPIOs at 1 mM in PBS (pH 7.5) overnight at 4 °C. The product, DOTA-mSPIO, was separated from excess DOTA-NHS-ester by dialysis using a 100 kD Float-A-Lyzer (Spectrum Laboratories, Inc., Rancho Dominguez, CA) against 2 L of phosphate buffer for 48 h at 4 °C with a total of 8 buffer changes. The number of DOTA groups per mSPIO, estimated at 5−10, is proportional to the percentage of initial DSPE-PEG2000-amine present during the micelle coating procedure (*14, 15*).

Iron Concentration Determination. Iron concentration of DOTA-mSPIO solutions were determined using a 1,10-phenanthroline assay after conjugation of DOTA to mSPIOs (*16, 17*). Solutions of hydroxylamine hydrochloride (10 mg/mL), sodium acetate (125 mg/mL), 1,10-phenanthroline (1 mg/mL), and hydrochloric acid (6 M) were freshly prepared using deionized water. In a 200 μL PCR tube, 17 μL of hydrochloric acid was added to 18 μL of dilute nanoparticles and incubated in a thermocycler at 100 °C for 10 min. The resulting solution of dissolved mSPIOs was combined with 10 μL of hydroxylamine hydrochloride and 855 μL of sodium acetate, followed by addition of 100 μL 1,10-phenanthroline. After 10 min, the absorbance of the sample at 510 nm was measured using a Safire microplate reader (Tecan Group Ltd., Männedorf, Switzerland) and compared to the absorbance of a standard curve created using a ferrous ammonium sulfate hexahydrate solution.

Relaxation Measurement. Relaxation measurements were carried out using a 0.47 T Minispec mq20 (Bruker Optics, Billerica, MA) according to previous studies (*13*). Briefly, transverse magnetization decay curves were acquired using a Carr-Purcell-Meiboom-Gill sequence, while longitudinal magnetization recovery curves were acquired using an inversion−recovery sequence. Curves were fit using *Origin 6* analysis software (OriginLab Corp., Northampton, MA) to obtain T_2 time constants. Relaxivity values (r_2) were calculated using T_2 time constants and the iron concentration of measured samples.

Radiolabeling of DOTA-mSPIO with ^{64}Cu. In general, DOTA-mSPIOs were labeled with ^{64}Cu and analyzed according to Rossin et al (*18*). DOTA-mSPIOs (5 mg in 610 μL) were incubated with $^{64}CuCl_2$ (3 mCi in 2.2 μL, 0.1 M HCl) in 0.1 M ammonium acetate buffer (pH 5.5) at 37 °C for 1 h in a thermomixer. The solution was then challenged with 5 μL of 10 mM EDTA or DTPA at 37 °C for 5 min with mixing to remove nonspecifically bound ^{64}Cu. Labeling yield was determined by radiochemical thin layer chromatography (radio-TLC). A small amount of the ^{64}Cu-labeled mSPIO (^{64}Cu-mSPIO) solution was applied to an ITLC-SG plate (Pall Corporation, East Hills, NY) and developed using a 1:1 mixture (v/v) of 10% (w/v) ammonium acetate and methanol. The TLC plate was then measured using a Bioscan 200 imaging scanner (Bioscan Inc., Washington, DC, and the labeling yield was found to be 94%. The ^{64}Cu-labeled mSPIOs were then passed through a centrifugal desalting column (Pierce Biotechnology, Inc., Rockford, IL) to remove the small amount of unbound ^{64}Cu contained in the sample.

Radiochemical purity (RCP, the percentage of the total radioactivity that was due to DOTA-mSPIOs) of ^{64}Cu-mSPIO was evaluated by radio-fast protein liquid chromatography (radio-FPLC) using an Amersham Biosciences ÄKTA FLPC system (GE Healthcare, Piscataway, NJ) equipped with a UV detector (280 nm) and fitted with an in-line model 170 radioisotope detector (Beckman Coulter Inc., Fullerton, CA). A 100 μL sample of dilute ^{64}Cu-mSPIO was applied to a Superose 12 gel filtration column (GE Healthcare, Piscataway, NJ) and eluted with 20 mM HEPES and 150 mM NaCl at a flow rate of 0.8 mL/min. The RCP of ^{64}Cu-labeled mSPIO was found to be >95%, indicating that less than 5% of the total radioactivity present in the sample was due to free ^{64}Cu. The nanoparticle solution was then diluted with PBS to obtain doses suitable for biodistribution and imaging studies. The serum stability of ^{64}Cu-mSPIO was determined by incubating labeled nanoparticles in mouse serum at 37 °C with constant shaking for up to 24 h. The samples were subjected to radio-TLC analysis after 0, 1, 3, 6, and 24 h incubation to measure the amount of radioactivity due to ^{64}Cu dissociated from ^{64}Cu-mSPIOs.

Size Determination. Dynamic light scattering (DLS) was used to measure the hydrodynamic diameter of uncoated SPIOs and DOTA-mSPIOs using a NICOMP 380 ZLS Submicrometer Particle Sizer (Particle Sizing Systems, Inc., Santa Barbara, CA) equipped with a 632.8 nm He−Ne laser and an Avalanche Photodiode detector at a fixed 90° scattering angle. DLS measurements were performed on DOTA-mSPIO samples chelated with "cold" (i.e., stable) isotopes of copper (Cu-mSPIO) according to the same procedure used for radiolabeling with copper-64. DLS of uncoated, hydrophobic SPIOs was performed in toluene. Dilute nanoparticle samples (0.4 mL) were placed in prewashed cylindrical optical cells and incident laser light was adjusted using a neutral density filter to obtain a scattering intensity of 300 kHz. Samples were scanned at 23 °C for 30 min in a temperature-controlled sample chamber, and data are reported as the volume-weighted hydrodynamic diameter.

Uncoated SPIOs were stored in toluene prior to surface modification and were analyzed using transmission electron microscopy (TEM) to ensure monodispersity. TEM micrographs were produced by applying dilute SPIO samples to copper TEM grids allowing the organic solvent to evaporate. Grids were then imaged using a Hitachi H-7500 TEM. Micrographs were analyzed for particle size and distribution using NIH *ImageJ*.

Biodistribution. All animal studies were performed in compliance with guidelines set by the Washington University

Animal Studies Committee. Female BALB/c mice (Charles River Laboratories, Inc., Wilmington, MA) weighing approximately 20 g were anesthetized using 1−2% isoflurane and given tail vein injections of 100 μCi of purified ^{64}Cu-mSPIO at a dose of 10 mg Fe/kg body weight. Mice ($n = 4$ per time point) were sacrificed by cervical dislocation at 10 min, 1 h, 4 h, and 24 h postinjection, and organs of interest were collected, blotted dry, weighed, and assessed for radioactivity by counting for one minute in a Gamma 8000 scintillation counter (Beckman Coulter Inc., Fullerton, CA). A standard dose was prepared and measured along with the samples to allow calculation of the percentage injected dose (%ID) for the various tissues and organs. Data were corrected for ^{64}Cu decay and the percentage injected dose per gram of tissue (%ID/g) and the percentage injected dose per organ (%ID/organ) were calculated according to the following equations:

$$\%\text{ID/g} = \frac{(\text{cpm in sample} - \text{background}) \times 10^2}{(\text{decay correction factor}) \times (\text{sample weight}) \times (\text{cpm in standard dose})} \quad (1)$$

$$\%\text{ID/organ} = \frac{(\text{cpm in sample} - \text{background}) \times 10^2}{(\text{decay correction factor}) \times (\text{cpm in standard dose})} \quad (2)$$

Small-Animal PET/CT Imaging Studies of ^{64}Cu-mSPIOs. MicroPET imaging scans were performed using a microPET Focus 120 (Siemens Medical Solutions USA, Inc., Malvern, PA). Female BALB/c mice (20−25 g) were anesthetized using 1−2% isoflurane and given tail vein injections with 100 μCi of purified ^{64}Cu-mSPIO (10 mg Fe/kg body weight) in 100 μL PBS. The anesthetized animals were monitored for physiological signs. Mice were reanesthetized and imaged in the supine position at 1 h, 4 h, and 24 h postinjection. PET scan acquisition time for the 10 min, 1 h, and 4 h images was 10 min, while the PET scan acquisition time for the 24 h image was 20 min. Mice were scanned on a microCAT II (Siemens Medical Solutions USA, Inc., Malvern, PA) immediately after microPET. Analysis of microPET images was accomplished using vendor software (ASIPro, Siemens Medical Solutions USA, Inc.) on decay-corrected images. Coregistration of microPET and microCT images was performed using fiducial markers in the animal transfer bed and the *Amira* software package (Mercury Computer Systems, Inc., Chelmsford, MA). The small animal studies were performed following an IACUC-approved protocol.

Phantom Study. To demonstrate the ability of mSPIOs to function as a dual imaging agent, we prepared microcentrifuge tubes of ^{64}Cu-mSPIOs for PET and MR imaging. Radiolabeled nanoparticles were added to a tubes containing PBS to a final concentrations of 10 and 25 μg Fe/mL. The tubes were placed upright in the bed of a Focus 120 microPET and scanned for 10 min. After a sufficient amount of time to allow ^{64}Cu to decay, the samples were then imaged in a 7.0-T Pharmascan magnet (Bruker BioSpin, Billerica, MA). A T_2-weighted proton density scan was obtained using a multislice multiecho sequence (MSME-PD-T2, Bruker Paravision 4) using the following parameters: 1000 ms repetition time (TR); 12 echo times (TE) ranging from 12−144 ms; 180° flip angle, 3 cm FOV; 1 mm slice thickness, 2 averages.

RESULTS

Nanoparticle Formation and Characterization. Dual PET/MRI nanoparticles (Figure 1A) were prepared by first encapsulating monocrystalline superparamagnetic iron oxide nanoparticles (SPIOs) in PEG-phospholipid micelles (*13, 19, 20*). This technique exploited the hydrophobic interaction between

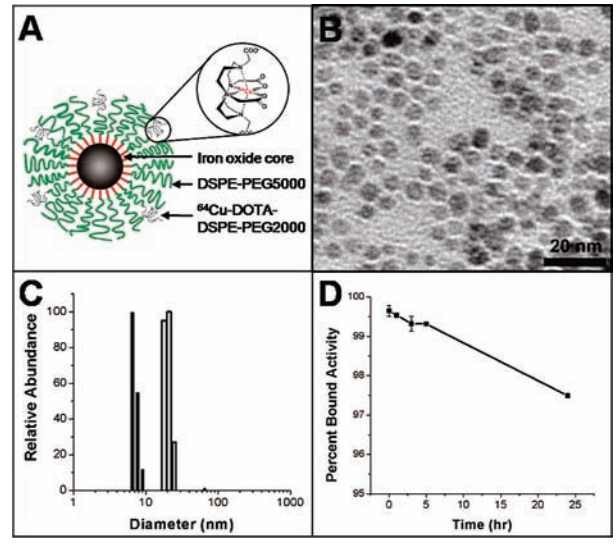


Figure 1. (A) Schematic representation of dual-modality ^{64}Cu-mSPIO. (B) Transmission electron micrograph of uniform monocrystalline superparamagnetic iron oxide nanoparticles. (C) Dynamic light scattering showing highly monodisperse populations of SPIO before (closed bars) and after (open bars) encapsulation in PEGylated lipid micelle. (D) In vitro stability of ^{64}Cu-mSPIO over the course of 24 h incubation in mouse serum at 37 °C.

capping ligands on the nanoparticle surface and hydrocarbon chains of PEGylated phospholipids, leaving the PEG moieties exposed to confer water solubility and reduce protein absorption. High magnetic field gradients surround the surface of the iron oxide core, allowing sensitive detection by MRI. The DOTA-functionalized PEG-phospholipid coating permits labeling with ^{64}Cu for sensitive detection by PET imaging. SPIOs used in this experiment were highly monodisperse (Figure 1B), having an average diameter of 6.2 nm with size variation of 9%, as determined by TEM. Functionalized micelle-coated SPIOs (mSPIOs) were prepared by coating nanoparticles with a 1:5 molar ratio of amino-PEG2000 phospholipids to methoxy-terminated mPEG5000 phospholipids. Empty micelles were separated from mSPIOs using ultracentrifugation, and the yield, calculated from Fe concentration measurements, was found to be 44%. The r_2 relaxivity of mSPIOs, measured using a 0.47 T Bruker Minispec, was 209 ± 26 mM^{-1} s^{-1}.

Amine-modified mSPIOs were conjugated with DOTA-NHS-ester to allow incorporation of PET imaging isotopes. Dialysis was used to separate DOTA-mSPIOs from excess DOTA-NHS-ester, and dynamic light scattering was employed to measure the hydrodynamic diameter of the DOTA-mSPIO (Figure 1C). We found that DOTA-mSPIOs had a hydrodynamic diameter of 20.3 ± 1.9 nm as determined by dynamic light scattering, while prior to lipid-PEG encapsulation, the SPIO cores had an average diameter of 7.1 ± 0.7 nm, consistent with the TEM measurement.

^{64}Cu-Radiolabeling of DOTA-mSPIO. To construct the dual-modality PET/MR contrast agent, the positron-emitting radionuclide ^{64}Cu ($t_{1/2} = 12.7$ h; $\beta^+ = 0.653$ MeV, 17.4%; $\beta^- = 0.578$ MeV, 39%) was used to radiolabel mSPIOs to allow small animal PET imaging and biodistribution studies. Copper-64 is commonly used in PET imaging and radiopharmaceuticals (*21*) because it can be produced at high specific activity in biomedical cyclotrons (*22, 23*), and chelation of ^{64}Cu to various macrocyclic ligands can provide an efficient route for radiolabeling a wide variety of macromolecules and nanoparticles.

Labeling of DOTA-mSPIOs was achieved by incubation with ^{64}Cu at 37 °C for 1 h in 0.1 M ammonium acetate buffer, pH 5.5 (radiolabeling in acetate buffer was found to be superior to

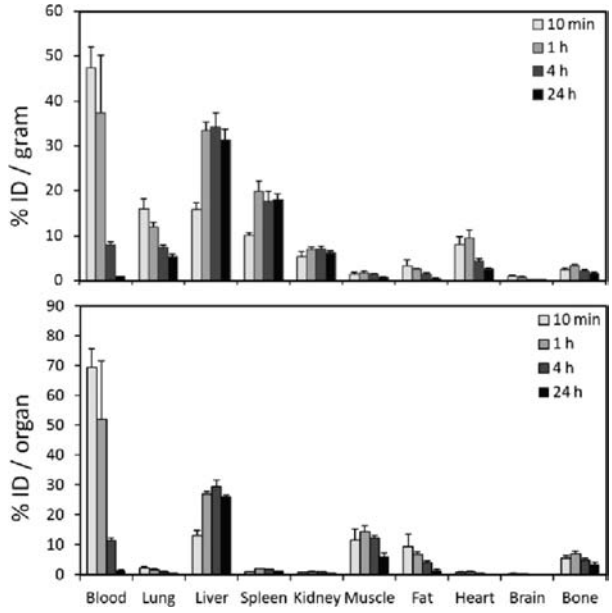


Figure 2. Biodistribution data of dual-PET/MRI ^{64}Cu-mSPIO (10 mg Fe/kg body weight) in BALB/c mice. Groups of mice ($n = 4$) were sacrificed at 10 min, 1 h, 4 h, and 24 h, and select organs were measured for activity. Data are expressed as percent injected dose per gram tissue (%ID/g, top) and percent injected dose per organ (%ID/organ, bottom) ± one standard deviation.

Table 1. Organ Biodistribution as Percent Injected Dose per Gram Tissue

organ	10 min	1 h	4 h	24 h
blood	47.47 ± 4.64	37.31 ± 12.87	7.89 ± 0.76	1.01 ± 0.05
lung	16.06 ± 2.03	11.98 ± 1.01	7.29 ± 0.64	5.37 ± 0.52
liver	15.85 ± 1.41	33.42 ± 1.85	34.20 ± 3.08	31.33 ± 2.33
spleen	10.07 ± 0.56	19.96 ± 2.27	17.52 ± 2.32	18.05 ± 1.27
kidney	5.26 ± 1.16	6.87 ± 0.63	7.03 ± 0.65	6.20 ± 0.38
muscle	1.37 ± 0.49	1.78 ± 0.30	1.45 ± 0.14	0.72 ± 0.13
fat	3.23 ± 1.40	2.51 ± 0.16	1.41 ± 0.28	0.49 ± 0.12
heart	8.00 ± 1.72	9.46 ± 1.76	4.29 ± 0.66	2.52 ± 0.35
brain	0.95 ± 0.14	0.77 ± 0.20	0.31 ± 0.01	0.30 ± 0.02
bone	2.47 ± 0.39	3.28 ± 0.29	2.17 ± 0.28	1.62 ± 0.27

labeling in 0.1 mM ammonium citrate buffer, pH 5.5). It was found that DOTA-mSPIOs could be labeled to a specific activity of at least 2−4 GBq/mmol Fe (10−20 μCi/μg Fe) with a yield of 94%. Nonspecifically bound ^{64}Cu was removed from ^{64}Cu-mSPIOs by addition of excess EDTA following completion of the labeling reaction, and ^{64}Cu-EDTA was separated from ^{64}Cu-mSPIOs using a desalting column. The radiochemical purity of the labeled nanoparticles, defined as the percentage of the total radioactivity that was bound to DOTA-mSPIOs, was determined by radio-FPLC to be >95%. Incubation of ^{64}Cu-mSPIOs at 37 °C for 24 h in mouse serum indicated high in vitro stability of ^{64}Cu radiolabeling (Figure 1D).

Biodistribution Studies. The pharmacokinetics and biodistribution of ^{64}Cu-mSPIO were studied to evaluate the nanoparticle's potential as a dual-PET/MRI in vivo imaging probe. Radiolabeled nanoparticles were administered via tail vein injection, and circulation half-life and accumulation in major organs were investigated; the results of organ biodistribution, presented as percent injected dose per gram tissue, are shown in Figure 2 and Table 1. To allow dual PET/MR imaging with ^{64}Cu-mSPIOs, the dose of particles administered needed to be within the detection limits of both modalities. Because PET is more sensitive than MRI (*24*), the amount of administered iron oxide was the limiting factor when formulating doses for injection. Mice ($n = 4$) weighing approximately 20 g were injected with a 10 mg Fe/kg dose of ^{64}Cu-mSPIOs (100 μCi, radiochemical purity >95%), an amount of iron oxide used for typical in vivo magnetic resonance imaging experiments. Each dose of particles contained 100 μCi of ^{64}Cu ($t_{1/2} = 12.7$ h) to allow imaging up to 24 h postinjection. ^{64}Cu-labeled mSPIOs exhibited high blood retention at 10 min and 1 h postinjection of 47.5 ± 4.6 and 37.3 ± 12.9%ID/g, respectively. Blood retention of ^{64}Cu-labeled mSPIOs decreased to 7.9 ± 0.8%ID/g at 4 h postinjection and to 1.0 ± 0.05%ID/g by 24 h postinjection. Accumulation in the heavily vascularized tissues of the heart and lungs generally followed the pattern of blood retention. The circulation half-life of labeled nanoparticles was 143 ± 21 min, substantially longer than ^{64}Cu-DOTA alone, which undergoes rapid renal excretion (circulation half-life ~6 min) (*25, 26*).

Organs of the reticuloendothelial system (RES) experienced moderate nanoparticle uptake. The liver and spleen showed a low initial accumulation of 15.8 ± 1.4 and 10.1 ± 0.6%ID/g, respectively. At 1 h postinjection, the liver and spleen uptake reached 33.4 ± 1.8 and 20.0 ± 2.3%ID/g, respectively, and generally maintained those values for the remainder of the study. It has been shown previously that ^{64}Cu dissociated from the ^{64}Cu-DOTA complex will undergo transchelation by proteins such as superoxide dismutase, metallothionein, and ceruloplasmin (*27–29*) in the liver. Therefore, while liver uptake at later time points was prominent, some contribution may have been due to an accumulation of disassociated ^{64}Cu.

Kidney uptake remained relatively constant, averaging 5−7%ID/g for all time points. Renal excretion of ^{64}Cu-labeled mSPIOs was assessed by measuring urine activity using a metabolism cage. The activity of urine at 4 h postinjection was 1.1%ID/g at 4 h postinjection and 5.0%ID/g at 24 h postinjection. This implies that although ^{64}Cu-labeled mSPIOs were larger than the cutoff for glomerular filtration (*30*), their individual ^{64}Cu-DOTA-PEGylated lipids were able to traverse the fenestrae of glomerular capillaries when disassociated from the nanoparticle surface. All other organs evaluated showed low (muscle, fat, bone) or negligible (brain) uptake. Animals were not perfused prior to counting, so some contribution of activity in the harvested organs may have been due to remaining blood.

Small Animal PET Imaging Studies. The PET imaging capabilities of dual-modality ^{64}Cu-labled mSPIOs were analyzed by small animal microPET imaging performed using a microPET Focus 120. In this study, BALB/c mice were administered 100 μCi of ^{64}Cu-mSPIO (10 mg Fe/kg body weight) in 100 μL PBS via tail vein injection and imaged at 1 h, 4 h, and 24 h postinjection. Accurate comparison of microPET images with ex vivo biodistribution data required additional anatomical information that was provided by microCT scans. Mice were scanned on a microCAT II immediately after acquisition of microPET images, and coregistration was accomplished using fiducial landmarks on the animal bed. Examples of coregistered images obtained after administration of ^{64}Cu-mSPIO are shown in Figure 3.

MicroPET images showed general agreement with the results of the nanoparticle biodistribution studies. High levels of activity were observed in the heart and carotid arteries at 1 h postinjection (Figure 3A,B), indicating a large amount of nanoparticles in circulation. The strong presence of circulating nanoparticles was also observed in the descending abdominal aorta, aortic bifurcation, and common iliac arteries. Less activity was observed in the heart at 4 h postinjection (Figure 3C,D). This absence of activity in the heart indicated a marked decrease in circulating nanoparticles relative to levels at 1 h postinjection, corresponding well to the decrease in blood activity observed from the 1 to 4 h ex vivo biodistribution. Uptake of ^{64}Cu-mSPIOs by the liver was also clearly apparent, suggesting that

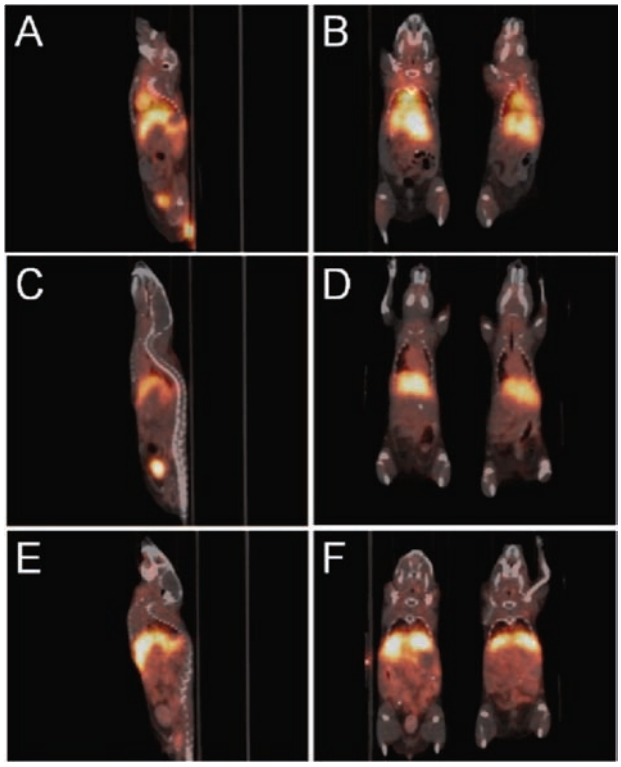


Figure 3. Coregistered microPET/microCT of BALB/c mice administered 100 μCi of ^{64}Cu-mSPIOs (10 mg Fe/kg body weight, 100 μL injection volume). Whole body sagittal (A−E) and coronal (B−F) PET images are decay corrected and scaled by min/max frame: (A, B) 1 h; (C, D) 4 h; and (E, F) 24 h postinjection.

significant amounts of nanoparticles were sequestered by the RES at 4 h postinjection.

By 24 h postinjection, microPET images showed little activity in the heart (Figure 3E,F), corresponding to negligible amounts of circulating nanoparticles. While the liver and spleen showed high uptake at 24 h, widespread activity could also be observed in gastrointestinal (GI) tract. This activity indicated that ^{64}Cu-mSPIOs (and their metabolic products) present in the liver underwent biliary excretion into the GI tract to be eliminated in the feces.

Phantom Studies. To verify the dual imaging capability of ^{64}Cu-mSPIOs, nanoparticle samples underwent PET and MR scans using standard techniques. Figure 4 shows T_2-weighted and microPET images of 10 and 25 μg Fe/mL samples of labeled magnetic nanoparticles. Iron oxide cores in ^{64}Cu-mSPIO produced a characteristic darkening (signal hypointensity) at increasing iron concentrations, seen in Figure 4A. A strong PET signal was produced from ^{64}Cu chelated to PEG-phospholipid micelle coating (Figure 4B).

DISCUSSION

The combination of positron emission tomography (PET) with magnetic resonance imaging (MRI) offers many opportunities (*31–34*). MRI produces high-resolution soft tissue images as well as functional and spectroscopic information. PET provides quantitative, whole-body imaging with high sensitivity. Interest in combining PET with MRI has surged (*2, 35–37*), and structured nanomaterials have emerged as a possible platform for the development of dual-PET/MR imaging agents. Although dual modality PET/MRI imaging does not necessarily require a combined PET/MRI contrast agent, the use of ^{64}Cu-mSPIO in dual modality PET/MRI imaging offers certain potential advantages, including enhanced PET contrast, better circulation half-life, and better correlation between functional (PET) and

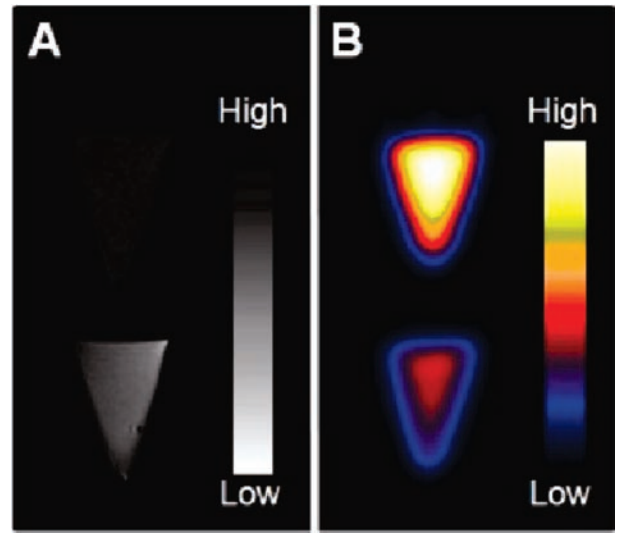


Figure 4. PET and MR imaging of ^{64}Cu-mSPIO phantoms. (A) T_2-weighted image of 25 μg Fe/mL (top) and 10 μg Fe/mL (bottom) of ^{64}Cu-labeled magnetic nanoparticles (scale bar corresponds to high and low iron concentration). (B) Decay-corrected microPET image of 25 μg Fe/mL (top) and 10 μg Fe/mL (bottom) of ^{64}Cu-labeled magnetic nanoparticles (scale bar corresponds to high and low copper-64 concentration).

morphological (MRI) information. While magnetic nanoparticles have been used extensively with MRI to study a wide range of biological phenomena such stem cell tracking (*13, 38*), cancer detection (*39–41*), and atherosclerotic monitoring (*42–44*), the synthesis and use of nanoparticles as PET molecular imaging agents have only recently been explored in detail (*45–48*). Nanoparticles are well-suited to the design of PET probes, because their relatively large surface area (as compared with small-molecule PET agents) can be labeled to a high specific activity, allowing for increased sensitivity of detection and increased payload of targeting ligands and therapeutic isotopes.

Encapsulation of magnetic nanoparticles in micelles of PEGylated lipids has many advantages over traditional polymer- and carbohydrate-based approaches. Unlike polymeric encapsulation, the modular nature of this coating scheme allows the functionalization of nanoparticle surfaces with multiple lipid species and alternative chemical groups on PEG termini to be achieved in situ by simple adjustment of the stoichiometry of the initial lipid solution. Additionally, polymer coatings commonly applied to nanoparticles are relatively bulky and possess surface chemistry that results in nanoparticles that experience high RES uptake (*26*). Carbohydrate coatings traditionally used in precipitation-based nanoparticle synthesis limit the core size that can be encapsulated (*49*) and generally require postsynthesis surface functionalization. Several functionalized PEG-phospholipids are commercially available and inexpensive, and PEGylated lipid coatings have been applied to nanoparticles ranging from 3 nm (*50*) to 35 nm (*51*) using multiple chemical functionalities (*20, 52*).

^{64}Cu-mSPIOs produced strong MR and PET signals (Figure 4) and were found to be stable in serum for 24 h (Figure 1D). The potential of this nanoparticle as a novel imaging agent was investigated by ex vivo biodistribution and in vivo PET imaging. Biodistribution results showed high initial blood retention with moderate liver uptake (Figure 2). ^{64}Cu-mSPIO had a circulation lifetime of 143 min, a value that compares well with previous reports of quantum dots and silica nanoparticles with PEGylated lipid coatings (*53, 54*). This result suggests that the circulation profile is dominated by the coating and that lipid-PEG coatings can be generalized to other classes of nanoparticle cores with differing chemistries.

PET/CT imaging showed high levels of ^{64}Cu in several regions. In general, microPET imaging correlated well with biodistribution findings. The heart and carotid arteries were clearly visible at early time points, indicating a high level of ^{64}Cu-mSPIO blood retention (Figure 3A,B). While the liver and spleen showed high uptake at 24 h postinjection, widespread activity could also be observed in gastrointestinal (GI) tract (Figure 3E,F). This activity was an indication that ^{64}Cu-mSPIOs (and their metabolic products) sequestered in the liver at earlier time points underwent biliary excretion into the GI tract to be eliminated in the feces. Since iron oxide nanoparticles have been used in humans with few observed side effects (*55, 56*), and ^{64}Cu has been used in patients (*57–60*) and showed no toxicity, ^{64}Cu-mSPIO probes have a high potential for clinical applications.

In summary, we report the development and in vivo evaluation of a novel dual-PET/MRI nanoparticle probe composed of a monocrystalline superparamagnetic iron oxide (SPIO) core and a physically adsorbed layer of PEGylated lipids. This is in contrast to the published reports of dual-modality PET/MRI nanoparticles that used either dextran-based (*61, 62*) or protein-based (*7, 63*) coatings. We have characterized the physical and pharmacokinetic properties of ^{64}Cu-mSPIO probes and evaluated their potential as a dual-modality imaging agent using quantitative ex vivo biodistribution and in vivo microPET/CT imaging. We are currently investigating the targeting abilities of these and other dual-PET/MRI nanoparticle probes and their application to disease detection and treatment in atherosclerosis and cancer models.

ACKNOWLEDGMENT

This work was supported by the National Heart Lung and Blood Institute of the NIH as Programs of Excellence in Nanotechnology (HL80711 to G.B. and HL080729 to M.J.W.), and as a Center of Cancer Nanotechnology Excellence (CA119338 to G.B.). The production of ^{64}Cu was supported by the National Cancer Institute (CA86307 to M.J.W.).

LITERATURE CITED

(1) Czernin, J., Allen-Auerbach, M., and Schelbert, H. (2007) Improvements in cancer staging with PET/CT: literature-based evidence as of September 2006. *J. Nucl. Med. 48*, 78S.

(2) Judenhofer, M. S., Wehrl, H. F., Newport, D. F., Catana, C., Siegel, S. B., Becker, M., Thielscher, A., Kneilling, M., Lichy, M. P., Eichner, M., Klingel, K., Reischl, G., Widmaier, S., Rocken, M., Nutt, R. E., Machulla, H. J., Uludag, K., Cherry, S. R., Claussen, C. D., and Pichler, B. J. (2008) Simultaneous PET-MRI: a new approach for functional and morphological imaging. *Nat. Med. 14*, 459–465.

(3) Higuchi, T., Anton, M., Dumler, K., Seidl, S., Pelisek, J., Saraste, A., Welling, A., Hofmann, F., Oostendorp, R. A., Gansbacher, B., Nekolla, S. G., Bengel, F. M., Botnar, R. M., and Schwaiger, M. (2009) Combined reporter gene PET and iron oxide MRI for monitoring survival and localization of transplanted cells in the rat heart. *J. Nucl. Med. 50*, 1088–1094.

(4) Xu, H., Regino, C. A., Koyama, Y., Hama, Y., Gunn, A. J., Bernardo, M., Kobayashi, H., Choyke, P. L., and Brechbiel, M. W. (2007) Preparation and preliminary evaluation of a biotin-targeted, lectin-targeted dendrimer-based probe for dual-modality magnetic resonance and fluorescence imaging. *Bioconjugate Chem. 18*, 1474–1482.

(5) Koyama, Y., Talanov, V. S., Bernardo, M., Hama, Y., Regino, C. A., Brechbiel, M. W., Choyke, P. L., and Kobayashi, H. (2007) A dendrimer-based nanosized contrast agent dual-labeled for magnetic resonance and optical fluorescence imaging to localize the sentinel lymph node in mice. *J. Magn. Reson. Imaging 25*, 866–871.

(6) Lee, S. K., and Chen, X. (2009) Dual-modality probes for in vivo molecular imaging. *Mol. Imaging 8*, 87–100.

(7) Lee, H. Y., Li, Z., Chen, K., Hsu, A. R., Xu, C., Xie, J., Sun, S., and Chen, X. (2008) PET/MRI dual-modality tumor imaging using arginine-glycine-aspartic (RGD)-conjugated radiolabeled iron oxide nanoparticles. *J. Nucl. Med. 49*, 1371–1379.

(8) Xie, J., Huang, J., Li, X., Sun, S., and Chen, X. (2009) Iron oxide nanoparticle platform for biomedical applications. *Curr. Med. Chem. 16*, 1278–1294.

(9) Shokeen, M., Fettig, N. M., and Rossin, R. (2008) Synthesis, in vitro and in vivo evaluation of radiolabeled nanoparticles. *Q. J. Nucl. Med. Mol. Imaging 52*, 267–277.

(10) Feltin, N., and Pileni, M. P. (1997) New technique for synthesizing iron ferrite magnetic nanosized particles. *Langmuir 13*, 3927–3933.

(11) Seip, C. T., and O'Connor, C. J. (1999) The fabrication and organization of self-assembled metallic nanoparticles formed in reverse micelles. *Nanostruct. Mater. 12*, 183–186.

(12) McCarthy, D. W., Shefer, R. E., Klinkowstein, R. E., Bass, L. A., Margeneau, W. H., Cutler, C. S., Anderson, C. J., and Welch, M. J. (1997) Efficient production of high specific activity 64Cu using a biomedical cyclotron. *Nucl. Med. Biol. 24*, 35–43.

(13) Laconte, L. E., Nitin, N., Zurkiya, O., Caruntu, D., O'Connor, C. J., Hu, X., and Bao, G. (2007) Coating thickness of magnetic iron oxide nanoparticles affects R(2) relaxivity. *J. Magn. Reson. Imaging 26*, 1634–1641.

(14) Ducongé, F., Pons, T., Pestourie, C., Hérin, L., Thézé, B., Gombert, K., Mahler, B., Hinnen, F., Kühnast, B., Dollé, F., Dubertret, B., and Tavitian, B. (2008) Fluorine-18-labeled phospholipid quantum dot micelles for in vivo multimodal imaging from whole body to cellular scales. *Bioconjugate Chem. 19*, 1921–1926.

(15) Johnsson, M., Hansson, P., and Edwards, K. (2001) Spherical micelles and other self-assembled structures in dilute aqueous mixtures of poly(ethylene glycol) lipids. *J. Phys. Chem. B 105*, 8420–8430.

(16) Yu, Z. (2006) in *Klinik für Kardiologie*, p 60, Charité-Universitätsmedizin Berlin, Berlin.

(17) Yu, Z., Grafe, M., Meyborg, H., Fleck, E., and Li, Y. (2006) *In vitro* characterization of magnetic resonance imaging contrast agents for molecular imaging. *ASH Annu. Meeting Abstr. 108*, 3944.

(18) Rossin, R., Pan, D., Qi, K., Turner, J. L., Sun, X., Wooley, K. L., and Welch, M. J. (2005) 64Cu-labeled folate-conjugated shell cross-linked nanoparticles for tumor imaging and radiotherapy: synthesis, radiolabeling, and biologic evaluation. *J. Nucl. Med. 46*, 1210–1218.

(19) van Tilborg, G., Mulder, W., Deckers, N., Storm, G., Reutelingsperger, C., Strijkers, G., and Nicolay, K. (2006) Annexin A5-functionalized bimodal lipid-based contrast agents for the detection of apoptosis. *Bioconjugate Chem. 17*, 741–749.

(20) Nitin, N., LaConte, L. E., Zurkiya, O., Hu, X., and Bao, G. (2004) Functionalization and peptide-based delivery of magnetic nanoparticles as an intracellular MRI contrast agent. *J. Biol. Inorg. Chem. 9*, 706–712.

(21) Sun, X., and Anderson, C. (2004) Production and applications of copper-64 radiopharmaceuticals. *Methods Enzymol. 386*, 237–61.

(22) McCarthy, D., Shefer, R., Klinkowstein, R., Bass, L., Margeneau, W., Cutler, C., Anderson, C., and Welch, M. (1997) Efficient production of high specific activity 64Cu using a biomedical cyclotron. *Nucl. Med. Biol. 24*, 35–43.

(23) McCarthy, D., Bass, L., Cutler, P., Shefer, R., Klinkowstein, R., Herrero, P., Lewis, J., Cutler, C., Anderson, C., and Welch, M. (1999) High purity production and potential applications of copper-60 and copper-61. *Nucl. Med. Biol. 26*, 351–358.

(24) Frangioni, J. (2008) New technologies for human cancer imaging. *J. Clin. Oncol. 26*, 4012.

(25) Jones-Wilson, T., Deal, K., Anderson, C., McCarthy, D., Kovacs, Z., Motekaitis, R., Sherry, A., Martell, A., and Welch, M. (1998) The in vivo behavior of copper-64-labeled azamacrocyclic complexes. *Nucl. Med. Biol. 25*, 523–530.

(26) Schipper, M. L., Cheng, Z., Lee, S. W., Bentolila, L. A., Iyer, G., Rao, J., Chen, X., Wu, A. M., Weiss, S., and Gambhir, S. S. (2007) microPET-based biodistribution of quantum dots in living mice. *J. Nucl. Med. 48*, 1511–1518.

(27) Bass, L., Wang, M., Welch, M., and Anderson, C. (2000) In vivo transchelation of copper-64 from TETA-octreotide to superoxide dismutase in rat liver. *Bioconjugate Chem. 11*, 527–532.

(28) Woodin, K., Heroux, K., Boswell, C., Wong, E., Weisman, G., Niu, W., Tomellini, S., Anderson, C., Zakharov, L., and Rheingold, A. (2005) Kinetic inertness and electrochemical behavior of Copper (II) tetraazamacrocyclic complexes: possible implications for in vivo stability. *Eur. J. Inorg. Chem. 23*, 4829–4833.

(29) Mirick, G., O'Donnell, R., DeNardo, S., Shen, S., Meares, C., and DeNardo, G. (1999) Transfer of copper from a chelated 67Cu-antibody conjugate to ceruloplasmin in lymphoma patients. *Nucl. Med. Biol. 26*, 841–845.

(30) Choi, H., Liu, W., Misra, P., Tanaka, E., Zimmer, J., Ipe, B., Bawendi, M., and Frangioni, J. (2007) Renal clearance of quantum dots. *Nat. Biotechnol. 25*, 1165–1170.

(31) Seemann, M. D. (2005) Whole-body PET/MRI: the future in oncological imaging. *Technol. Cancer Res. Treat. 4*, 577–582.

(32) Cherry, S. R. (2006) The 2006 Henry N. Wagner Lecture: Of mice and men (and positrons)--advances in PET imaging technology. *J. Nucl. Med. 47*, 1735–1745.

(33) Ruf, J., Lopez Hanninen, E., Bohmig, M., Koch, I., Denecke, T., Plotkin, M., Langrehr, J., Wiedenmann, B., Felix, R., and Amthauer, H. (2006) Impact of FDG-PET/MRI image fusion on the detection of pancreatic cancer. *Pancreatology 6*, 512–519.

(34) Seemann, M. D., Meisetschlaeger, G., Gaa, J., and Rummeny, E. J. (2006) Assessment of the extent of metastases of gastrointestinal carcinoid tumors using whole-body PET, CT, MRI, PET/CT and PET/MRI. *Eur. J. Med. Res. 11*, 58–65.

(35) Catana, C., Procissi, D., Wu, Y., Judenhofer, M. S., Qi, J., Pichler, B. J., Jacobs, R. E., and Cherry, S. R. (2008) Simultaneous in vivo positron emission tomography and magnetic resonance imaging. *Proc. Natl. Acad. Sci. U.S.A. 105*, 3705–3710.

(36) Pichler, B. J., Judenhofer, M. S., and Wehrl, H. F. (2008) PET/MRI hybrid imaging: devices and initial results. *Eur. Radiol. 18*, 1077–1086.

(37) Pichler, B. J., Wehrl, H. F., Kolb, A., and Judenhofer, M. S. (2008) Positron emission tomography/magnetic resonance imaging: the next generation of multimodality imaging? *Semin. Nucl. Med. 38*, 199–208.

(38) Walczak, P., Ruiz-Cabello, J., Kedziorek, D. A., Gilad, A. A., Lin, S., Barnett, B., Qin, L., Levitsky, H., and Bulte, J. W. (2006) Magnetoelectroporation: improved labeling of neural stem cells and leukocytes for cellular magnetic resonance imaging using a single FDA-approved agent. *Nanomedicine 2*, 89–94.

(39) Walczak, P., Kedziorek, D. A., Gilad, A. A., Barnett, B. P., and Bulte, J. W. (2007) Applicability and limitations of MR tracking of neural stem cells with asymmetric cell division and rapid turnover: the case of the shiverer dysmyelinated mouse brain. *Magn. Reson. Med. 58*, 261–269.

(40) Montet, X., Montet-Abou, K., Reynolds, F., Weissleder, R., and Josephson, L. (2006) Nanoparticle imaging of integrins on tumor cells. *Neoplasia 8*, 214–222.

(41) Lee, J. H., Huh, Y. M., Jun, Y. W., Seo, J. W., Jang, J. T., Song, H. T., Kim, S., Cho, E. J., Yoon, H. G., Suh, J. S., and Cheon, J. (2007) Artificially engineered magnetic nanoparticles for ultra-sensitive molecular imaging. *Nat. Med. 13*, 95–99.

(42) Wickline, S. A., and Lanza, G. M. (2003) Nanotechnology for molecular imaging and targeted therapy. *Circulation 107*, 1092–1095.

(43) Winter, P. M., Morawski, A. M., Caruthers, S. D., Fuhrhop, R. W., Zhang, H., Williams, T. A., Allen, J. S., Lacy, E. K., Robertson, J. D., Lanza, G. M., and Wickline, S. A. (2003) Molecular imaging of angiogenesis in early-stage atherosclerosis with alpha(v)beta3-integrin-targeted nanoparticles. *Circulation 108*, 2270–2274.

(44) Nahrendorf, M., Jaffer, F. A., Kelly, K. A., Sosnovik, D. E., Aikawa, E., Libby, P., and Weissleder, R. (2006) Noninvasive vascular cell adhesion molecule-1 imaging identifies inflammatory activation of cells in atherosclerosis. *Circulation 114*, 1504–1511.

(45) Fukukawa, K., Rossin, R., Hagooly, A., Pressly, E. D., Hunt, J. N., Messmore, B. W., Wooley, K. L., Welch, M. J., and Hawker, C. J. (2008) Synthesis and characterization of core-shell star copolymers for in vivo PET imaging applications. *Biomacromolecules 9*, 1329–1339.

(46) Rossin, R., Muro, S., Welch, M. J., Muzykantov, V. R., and Schuster, D. P. (2008) In vivo imaging of 64Cu-labeled polymer nanoparticles targeted to the lung endothelium. *J. Nucl. Med. 49*, 103–111.

(47) Sun, G., Hagooly, A., Xu, J., Nystrom, A. M., Li, Z., Rossin, R., Moore, D. A., Wooley, K. L., and Welch, M. J. (2008) Facile, efficient approach to accomplish tunable chemistries and variable biodistributions for shell cross-linked nanoparticles. *Biomacromolecules 9*, 1997–2006.

(48) Sun, X., Rossin, R., Turner, J. L., Becker, M. L., Joralemon, M. J., Welch, M. J., and Wooley, K. L. (2005) An assessment of the effects of shell cross-linked nanoparticle size, core composition, and surface PEGylation on in vivo biodistribution. *Biomacromolecules 6*, 2541–2554.

(49) Jarrett, B., Frendo, M., Vogan, J., and Louie, A. (2007) Size-controlled synthesis of dextran sulfate coated iron oxide nanoparticles for magnetic resonance imaging. *Nanotechnology 18*, 35603.

(50) Dubertret, B., Skourides, P., Norris, D., Noireaux, V., Brivanlou, A., and Libchaber, A. (2002) In vivo imaging of quantum dots encapsulated in phospholipid micelles. *Science 298*, 1759–1762.

(51) van Schooneveld, M. M., Vucic, E., Koole, R., Zhou, Y., Stocks, J., Cormode, D. P., Tang, C. Y., Gordon, R. E., Nicolay, K., Meijerink, A., Fayad, Z. A., and Mulder, W. J. M. (2008) Improved biocompatibility and pharmacokinetics of silica nanoparticles by means of a lipid coating: a multimodality investigation. *Nano Lett. 8*, 2517–2525.

(52) Mulder, W. J. M., Koole, R., Brandwijk, R. J., Storm, G., Chin, P. T. K., Strijkers, G. J., de Mello Donega, C., Nicolay, K., and Griffioen, A. W. (2006) Quantum dots with a paramagnetic coating as a bimodal molecular imaging probe. *Nano Lett. 6*, 1–6.

(53) Duconge', F., Pons, T., Pestourie, C., He'rin, L., The'ze', B., Gombert, K., Mahler, B., Hinnen, F., Kühnast, B., and Dolle', F. (2008) Fluorine-18-labeled phospholipid quantum dot micelles for in vivo multimodal imaging from whole body to cellular scales. *Bioconjugate Chem. 19*, 1921–1926.

(54) van Schooneveld, M., Vucic, E., Koole, R., Zhou, Y., Stocks, J., Cormode, D., Tang, C., Gordon, R., Nicolay, K., and Meijerink, A. (2008) Improved biocompatibility and pharmacokinetics of silica nanoparticles by means of a lipid coating: a multimodality investigation. *Nano Lett. 8*, 2517–2525.

(55) Anzai, Y., Blackwell, K. E., Hirschowitz, S. L., Rogers, J. W., Sato, Y., Yuh, W. T., Runge, V. M., Morris, M. R., McLachlan, S. J., and Lufkin, R. B. (1994) Initial clinical experience with dextran-coated superparamagnetic iron oxide for detection of lymph node metastases in patients with head and neck cancer. *Radiology 192*, 709–715.

(56) Heesakkers, R., Hövels, A., Jager, G., van den Bosch, H., Witjes, J., Raat, H., Severens, J., Adang, E., van der Kaa, C., and Fütterer, J., J. B. (2008) MRI with a lymph-node-specific contrast agent as an alternative to CT scan and lymph-node dissection in patients with prostate cancer: a prospective multicohort study. *Lancet Oncol. 9*, 850–856.

(57) Anderson, C. J., Dehdashti, F., Cutler, P. D., Schwarz, S. W., Laforest, R., Bass, L. A., Lewis, J. S., and McCarthy, D. W. (2001) 64Cu-TETA-octreotide as a PET imaging agent for patients with neuroendocrine tumors. *J. Nucl. Med. 42*, 213–221.

(58) Lewis, J. S., Laforest, R., Dehdashti, F., Grigsby, P. W., Welch, M. J., and Siegel, B. A. (2008) An imaging comparison of 64Cu-ATSM and 60Cu-ATSM in cancer of the uterine cervix. *J. Nucl. Med. 49*, 1177–1182.

(59) Osborn, S. B., Szaz, K. F., and Walshe, J. M. (1969) Studies with radioactive copper (64Cu and 67Cu): abdominal scintiscans in patients with Wilson's disease. *Q. J. Med. 38*, 467–474.

(60) Walshe, J. M., and Potter, G. (1977) The pattern of the whole body distribution of radioactive copper (67Cu, 64Cu) in Wilson's disease and various control groups. *Q. J. Med. 46*, 445–462.

(61) Nahrendorf, M., Zhang, H., Hembrador, S., Panizzi, P., Sosnovik, D. E., Aikawa, E., Libby, P., Swirski, F. K., and Weissleder, R. (2008) Nanoparticle PET-CT imaging of macrophages in inflammatory atherosclerosis. *Circulation 117*, 379–387.

(62) Jarrett, B. R., Gustafsson, B., Kukis, D. L., and Louie, A. Y. (2008) Synthesis of 64Cu-labeled magnetic nanoparticles for multimodal imaging. *Bioconjugate Chem. 19*, 1496−1504.

(63) Choi, J. S., Park, J. C., Nah, H., Woo, S., Oh, J., Kim, K. M., Cheon, G. J., Chang, Y., Yoo, J., and Cheon, J. (2008) A hybrid nanoparticle probe for dual-modality positron emission tomography and magnetic resonance imaging. *Angew. Chem., Int. Ed. Engl. 47*, 6259–6262.

BC900511J

Discovery of Metabolically Stabilized Electronegative Polyacridine-PEG Peptide DNA Open Polyplexes

Christian A. Fernandez, Nicholas J. Baumhover, Kevin Anderson, and Kevin G. Rice*

Divisions of Pharmaceutics and Medicinal & Natural Products Chemistry, College of Pharmacy, University of Iowa, Iowa City, Iowa 52242. Received November 20, 2009; Revised Manuscript Received January 29, 2010

Cationic condensing peptides and polymers bind electrostatically to DNA to form cationic polyplexes. While many cationic polyplexes are able to achieve in vitro transfection mediated through electrostatic interactions, few have been able to mediate gene transfer in vivo. The present study describes the development and testing of polyacridine PEG-peptides that bind to plasmid DNA by intercalation resulting in electronegative open polyplex DNA. Polyacridine PEG-peptides were prepared by chemically conjugating 6-(9-acridinylamino) hexanoic acid onto side chains of Lys in PEG-Cys-Trp-$(Lys)_{3, 4, or 5}$. The resulting PEG-Cys-Trp-$(Lys\text{-}(Acr))_{3, 4, or 5}$ peptides bound tightly to DNA by polyintercalation, rather than electrostatic binding. Unlike polycationic polyplexes, polyacridine PEG-peptide polyplexes were anionic and open coiled, as revealed by zeta potential and atomic force microscopy. PEG-Cys-Trp-$(Lys\text{-}(Acr))_5$ showed the highest DNA binding affinity and the greatest ability to protect DNA from metabolism by DNase. Polyacridine PEG-peptide DNA open polyplexes were dosed intramuscularly and electroporated in mice to demonstrate their functional activity in gene transfer. These results establish polyacridine PEG-peptide DNA open polyplexes as a novel gene delivery method for in vivo use.

INTRODUCTION

Nonviral gene delivery systems have traditionally relied on reversible binding between cationic carriers and anionic oligonucleotides (*1*−*3*). The resulting lipoplexes and polyplexes typically possess a positive surface charge as determined by zeta potential measurements. While cationic DNA lipoplexes and polyplexes have shown the ability to mediate in vitro gene transfer through electrostatic binding to cell surfaces, they exhibit poor gene transfer properties in vivo, in part due to their overall cationic charge (*4, 5*). There have been many attempts to mask the positive charge of cationic polyplexes with polyethylene glycol (PEG) to improve blood compatibility (*6*−*11*).

Alternatively, it is difficult to prepare an electronegative DNA polyplex using cationic polymers. This has been attempted by either partially titrating a polycationic polymer with plasmid DNA or using a layer-by-layer addition of oppositely charged polymers in an attempt to reverse the charge of polyplexes (*12*−*14*). The resulting electronegative polyplexes are formed in a delicate and unstable equilibrium (*15*). Attempting to reverse the charge of a cationic polyplex with the addition of an anionic polymer can lead to dissociation of the DNA. Similarly, if titrated to below the charge equivalency point, the polyplex is not completely protected against DNase, whereas if titrated to charge equivalency, the resulting neutral polyplexes are hydrophobic and aggregate. Titration past the equivalency point results in collapse of a polyplex into a cationic colloidal particle that is relatively stable but highly cationic and thereby less compatible with blood components (*5*). Consequently, we sought to find an alternative approach to ionic binding to DNA that would result in stable electronegative polyplexes.

In principle, the high affinity DNA binding achieved by polyintercalation could result in metabolically stable electronegative polyplexes (*16*). Electronegative polyplexes may bind to fewer proteins and thereby be more blood and tissue compatible to allow delivery via intramuscle electroporation (IM-EP) (*17*−*20*).

Polyacridine containing polymers have been previously investigated as gene transfer agents by Szoka, Vierling, and Neilsen (*21*−*23*). Their studies utilized polyacridine polymers possessing one, two, or three acridine units conjugated to either a neoglycopeptide or a nuclear localizing sequence. While these polyacridine carriers could bind to DNA, they possessed modest gene transfer activity in vitro (*22, 23*). Alternatively, we have recently reported that a polyacridine peptide modified with a melittin fusogenic peptide is a potent in vitro gene transfer agent (*24*). The most potent polyacridine-melittin gene delivery peptide contained four acridines and possessed a sequence of Lys(Acr)-Arg-Lys(Acr)-Arg-Lys(Acr)-Arg-Lys(Acr)-Arg-Cys joined to melittin by a disulfide bond. Polyacridine-melittin bioconjugates formed electropositive DNA polyplexes in which their potency was dependent upon the number of acridines, the identity of the spacing amino acid, and the presence of a reducible disulfide bond between polyacridine and melittin.

To date, there are no reports of polyacridine peptides modified with PEG. The present study demonstrates a synthetic strategy to modify the side chains of Lys in PEG-Cys-Trp-$(Lys)_n$ peptides with acridine. The resulting PEG-Cys-Trp-$(Lys(Acr))_n$ peptides bind reversibly to DNA through intercalation and demonstrate the ability to form a unique electronegative open polyplex DNA structure that is protected from DNase and maintains transfection competency in vivo. The unique properties of PEGylated polyacridine DNA electronegative open polyplexes afford desirable characteristics that are more compatible with in vivo nonviral gene delivery compared to cationic polyplexes.

MATERIALS AND METHODS

N-terminal Fmoc protected amino acids, 9-hydroxybenzotriazole (HOBt), diisopropylcarbodiimide (DIC), and Wang resin were purchased from Advanced ChemTech (Lexington, KY). Sephadex G-25, HEPES buffer, tris(2-carboxyethyl)-phosphine hydrochloride (TCEP), diisopropylethylamine (DIPEA), piperdine, acetic anhydride, triisopropylsilane (TIS), DNase I (EC

* To whom correspondence should be addressed. Tel: 319-335-9903. Fax: 319-335-8766. E-mail: kevin-rice@uiowa.edu.

10.1021/bc900514s © 2010 American Chemical Society
Published on Web 03/10/2010

3.1.21.1), 9-chloroacridine, and thiazole orange were obtained from Sigma Chemical Co (St. Louis, MO). Acetonitrile, *N*,*N*-dimethylformamide (DMF), and trifluoroacetic acid (TFA) were purchased from Fisher Scientific (Pittsburgh, PA). Agarose was obtained from Gibco-BRL. mPEG-maleimide 5000 Da was purchased from Nektar (Huntsville, AL), mPEG-amine (5000 Da) was purchased from Creative Biotechnology (Winston-Salem, NC), and bis-amino PEG (2000 Da) was purchased from Iris Biotech GmbH (Marktredwitz, Germany). The 5.3 kb luciferase plasmid, pGL3 control vector, containing a SV40 promoter and enhancer was obtained from Promega (Madison, WI). Plasmid DNA was amplified in DH5α strain of *E. coli* and purified according to the manufacturer's instructions.

Synthesis and Characterization of PEGylated Cys-Trp-Lys$_n$ Peptides. Cys-Trp-Lys$_n$ synthesis was carried out using standard Fmoc chemistry on a computer interfaced Advanced Chemtech APEX 396 solid-phase peptide synthesizer with 9-hydroxybenzotriazole and diisopropylcarbodiimide double couplings followed by N-capping with acetic anhydride as described previously (*25*). Cleavage and deprotection were accomplished by reacting the resin with TFA/TIS/water (95:2.5:2.5) at RT for 3 h. The crude peptide was precipitated in cold diethyl ether, centrifuged, and the supernatant was decanted. Crude peptides were reconstituted in 0.1% TFA and purified on a preparatory RP-HPLC using a Vydac C18 column (2 × 25 cm) eluted at 10 mL/min with 0.1 v/v % TFA and a gradient of acetonitrile of 5−25% over 30 min while monitoring Abs 280 nm. Purified peptides were reconstituted in 0.1% TFA and quantified by Abs (Trp $\varepsilon_{280nm} = 5600\ M^{-1}\ cm^{-1}$) to determine the isolated yield of 30%. The purified peptides were characterized using LC-MS by separation on a Vydac C18 analytical column (0.47 × 25 cm) eluted at 0.7 mL/min with 0.1% TFA and a gradient of acetonitrile of 5−25% over 30 min while detecting ESI-MS in the positive ion mode.

PEGylation of the Cys residue on Cys-Trp-Lys$_{3,4and5}$ was achieved by reacting 0.9 mol equiv of peptide with 1 mol equiv of PEG$_{5000Da}$-maleimide in 100 mM sodium phosphate buffer pH 7 for 1 h at RT (*25*). PEGylated peptides were purified on a G-25 column (2.5 × 50 cm) eluted with 0.1% acetic acid while monitoring Abs 280 nm. The peak corresponding to the PEG-peptide eluted in the void volume (100 mL), was pooled, concentrated by rotary evaporation, and freeze−dried. The PEG-peptide was reconstituted in 0.1% TFA, and quantified by Abs (Trp $\varepsilon_{280nm} = 5600\ M^{-1}\ cm^{-1}$) to determine an isolated yield of 80%. PEG-peptides were characterized by MALDI-TOF MS by combining 1 nmol with α-cyano-4-hydroxycinnamic acid (CHCA) prepared in 50% (v/v) acetonitrile and 0.1% TFA. Samples were spotted onto the target and ionized on a Bruker Biflex III mass spectrometer operated in the positive ion mode.

Synthesis of Polyacridine PEG Peptides and Mono- and Bis-Acridine PEGs. 6-(9-Acridinylamino)hexanoic acid was prepared according to a prior published procedure (*26*). The carboxyl group on 6-(9-acridinylamino) hexanoic acid was activated with 1.1 mol equiv of DIC and HOBt in DMF. Activated 6-(9-acridinylamino) hexanoic acid (12 mol equiv) was reacted with 2.5 μmol of PEG-Cys-Trp-Lys$_{3,4,and5}$ in 3 mL of DMF at RT for 24 h. The PEG-Cys-Trp-(Lys(Acr))$_{3,4,and5}$ peptides were purified using a G-25 column (2.5 × 50 cm) eluted with 0.1% acetic acid while monitoring Abs 280 nm. The product peak eluting at 100 mL was pooled, freeze−dried, and characterized using MALDI-TOF MS as described above. A yield of 42% of PEG-Cys-Trp-(Lys(Acr))$_{3,4,and5}$ peptides was determined by acridine Abs ($\varepsilon_{409nm} = 9266\ M^{-1}\ cm^{-1}$) assuming additivity of acridine molar absorptivity and complete conjugation to the ϵ-amine of Lys. Similarly, mono- and bis-acridinylated PEGs were prepared by reacting 6 mol equiv of activated 6-(9-acridinylamino) hexanoic acid with PEG-amine or bis-amino PEG (2 μmol) in 2 mL of DMF. The acridinylated PEGs were purified by G-25 column and characterized by MALDI-TOF MS.

Thiazole Orange Displacement Assay. The binding of polyacridine PEG-peptides to DNA was determined using an intercalator dye displacement assay (*27*). pGL3 (1 μg) was prepared in 5 mM Hepes pH 7.4 containing 40 nM thiazole orange. Polyacridine PEG-peptides were added to pGL3 to prepare samples of 0, 0.25, 0.5, 1, 2, 3, and 4 nmol per μg of DNA in a final volume of 500 μL. The fluorescence intensity of each sample was measured using an LS50B fluorometer (Perkin-Elmer, UK) with an excitation wavelength of 500 nm while monitoring emission at 530 nm. The data were converted to percent by comparison to the fluorescence intensity of thiazole orange in buffer (0%) and pGL3 with fully bound thiazole orange (100%).

Gel Band Shift and DNase Protection Assay. pGL3 (1 μg) or DNA polyplexed (1 μg) prepared in 18 μL of normal saline were combined with 1 nmol of mono-acridine PEG, bis-acridine PEG, PEG-Cys-(Lys-Acr)$_3$, PEG-Cys-(Lys-Acr)$_4$, or PEG-Cys-(Lys-Acr)$_5$ and 2 μL of loading buffer (*28*). The samples were loaded onto a 1% agarose gel (50 mL) and electrophoresed in TAE buffer at 80 V for 90 min. The gel was stained in 2 mg/mL ethidium bromide at 5 °C overnight, and the transilluminated gels were photographed using Polaroid 667 film. pGL3 (1 μg) or DNA polyplexes (1 μg) prepared with 1 nmol of mono-acridine PEG, bis-acridine PEG, PEG-Cys-(Lys-Acr)$_3$, PEG-Cys-(Lys-Acr)$_4$, or PEG-Cys-(Lys-Acr)$_5$ in 20 μL of normal saline was incubated with 0.06 U of DNase I at 37 °C for 0−20 min (*29*). The samples were applied to a 1% agarose gel and electrophoresed as described above.

Particle Size and Zeta Potential of Polyacridine PEG-Peptide DNA Open Polyplexes. Polyacridine PEG-peptide DNA polyplexes were formed by combining 10 μg of pGL3 (in 500 μL of 5 mM Hepes pH 7.4) with an equal volume containing 1, 2, 4, 8, 12, 16, or 20 nmol of polyacridine PEG-peptide while vortexing. The polyplexes were equilibrated at RT for 30 min prior to analysis of particle size (QELS) and zeta potential using a Brookhaven ZetaPlus (Brookhaven Instruments, Holtsville, NY). The particle size diameter and zeta potential are reported as the mean and standard deviation of ten measurements.

Atomic Force Microscopic Analysis of Polyacridine PEG-Peptide DNA Open Polyplexes. pGL3 was prepared at a concentration of 100 μg per ml in 10 mM Tris containing 1 mM EDTA pH 8. DNA polyplexes were prepared identically with the addition of PEG-Cys-Trp-(Lys(Acr))$_5$ at either 0.2 or 1 nmol per μg of DNA. pGL3 and DNA polyplexes were diluted 10-fold in 40 mM Hepes containing 5 mM nickel chloride pH 6.7, then deposited on a freshly cleaved mica surface and incubated for 10 min, followed by washing with deionized water (*30*). Alternatively, polyacridine-melittin DNA polyplexes were prepared at 0.5 nmol of peptide per μg of DNA at a concentration of 100 μg per ml of DNA and directly deposited on a freshly cleaved mica surface and allowed to bind for 10 min prior to washing with deionized water (*24*). Images were captured using an Asylum atomic force microscope (AFM) MFP3D (Santa Barbara, CA) operated in ac-mode using a silicon cantilever (Ultrasharp NSC15/AIBS, Mikro Masch).

Intramuscle-Electroporation Dosing. Male ICR mice (Harlan), weighing 25−30 g, were prepared for IM-EP dosing by anesthetization with an intraperitoneal dose of 200 μL of ketamine/xylazine (20 mg/mL and 2 mg/mL, respectively). The hamstring muscles were sheared and swabbed with 70% ethanol prior to administering a 50 μL dose over 10 s in normal saline to both gastrocnemius muscles in 2 mice by a 1 mL monoject syringe (1 cm^3, 28 G × 1/2). After dosing, the BTX 2-Needle

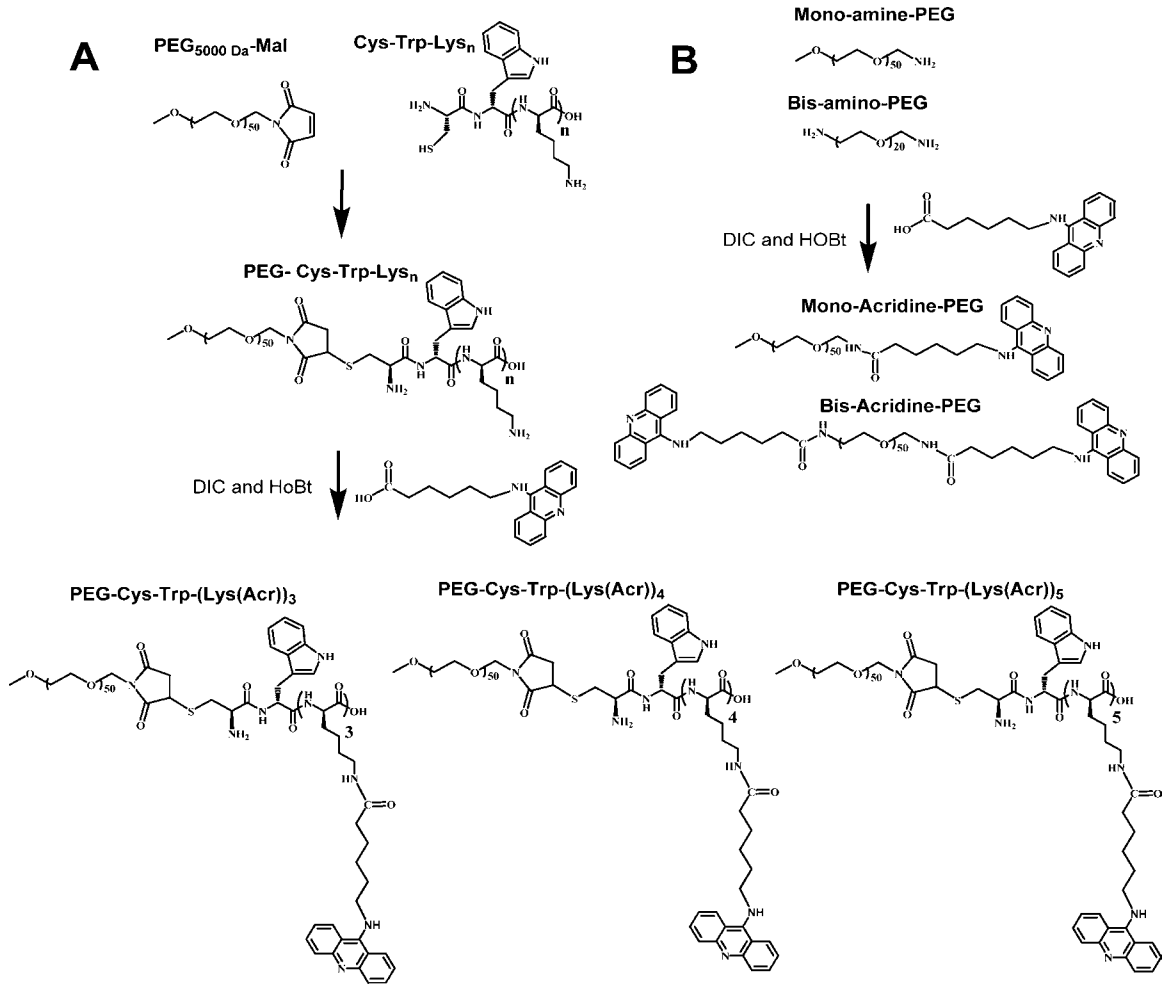


Figure 1. Preparation of PEGylated polyacridine bioconjugates. PEG_{5000Da}-maleimide was reacted with the Cys residue on Cys-Trp-Lys_3, Cys-Trp-Lys_4, and Cys-Trp-Lys_5 to form PEG-Cys-Trp-$(Lys)_{3,\,4,\,\text{and}\,5}$. Activated 6-(9-acridinylamino) hexanoic acid was reacted with ε-amines of Lys to form PEG-Cys-Trp-$(Lys\text{-}(Acr))_{3,\,4,\,\text{and}\,5}$. Alternatively, mono and bis PEG-amine were reacted with activated 6-(9-acridinylamino) hexanoic acid to prepare mono-Acr-PEG and bis-Acr-PEG.

Array Electrode was inserted into the skin with the electrodes straddling the dosing site. Successive electronic stimulation was generated by the EMC BTX 830, Square-Wave Pulse Generator (BTX, Harvard Apparatus) as the power source. At 1 min postadministration of the DNA dose, the pulse generator delivered six successive 100 V pulses over 20 ms with a 100 ms interval between pulses (*31*).

Bioluminescence Imaging. Luciferase reporter gene expression was quantified by bioluminescence imaging (BLI) at 2−14 days following IM-EP using an IVIS Imaging System 200 series (Xenogen) (*32*). Mice were anesthetized by isofluorane (2% flow with oxygen) and dosed intramuscularly with 40 μL of 30 mg per ml D-luciferin (GoldBio). Bioluminescent images were acquired 5 min post substrate administration and acquired for 1 min with a 24.6 cm field of view. The resultant grayscale images with a colormap overlay were analyzed using the *IgorPro 4.09* software (LivingImage). Luciferase expression is reported as photons/s/cm^2/steradian within a uniformly defined region of interest.

RESULTS

Several polyintercalator constructs that bind to double-stranded DNA have been reported in prior studies aimed at delivering plasmid DNA (*21*−*23*). These studies designed and tested delivery molecules possessing one to three acridine dyes displayed on a branched polymer modified with a neoglycopeptide or a nuclear localizing peptide, the later of which were shown to mediate in vitro gene expression (*22, 23*). These studies established that two to three acridines were required to achieved sufficient DNA binding affinity for in vitro transfection.

In the present study, we sought to use a synthetic strategy that would allow for the incorporation of more than three acridines by covalent modification of the side chain of PEGylated polylysine. This was accomplished by first modifying acridine to possess a 6-amino hexanoic acid and then activating the carboxyl group to allow coupling to the ϵ-amines of PEG-Cys-Trp-$(Lys)_{3,\,4,\,\text{and}\,5}$ to afford PEG-Cys-Trp-$(Lys(Acr))_{3,\,4,\,\text{and}\,5}$ (Figure 1). In addition, conjugation of acridine 6-amino hexanoic acid directly to PEG-amine and bis amino PEG afforded constructs with either one or two acridines (Figure 1). This strategy provided an advantage by allowing the comparison of DNA binding affinity with PEGs modified with 1−5 acridines.

Chromatographic evidence supporting the synthesis of PEG-Cys-Trp-$(Lys(Acr))_5$ is illustrated in Figure 2. Modification of Cys-Trp-$(Lys)_5$ with PEG results in a significant delay in elution on RP-HPLC compared to Cys-Trp-$(Lys)_5$. However, upon conjugation of five acridines to PEG-Cys-Trp-$(Lys)_5$, the resulting PEG-Cys-Trp-$(Lys(Acr))_5$ elutes only slightly later, and is detected at Abs $_{409nm}$.

The complete conjugation of acridine to the each Lys side chain was established using MALDI-TOF MS analysis. Conjugation of Cys-Trp-$(Lys)_5$ (948.8 g/mol) with polydisperse PEG of average mass of 5425 Da results in a PEG-Cys-Trp-$(Lys)_5$ with an apparent average mass of 6546 Da (Figure 3A−C).

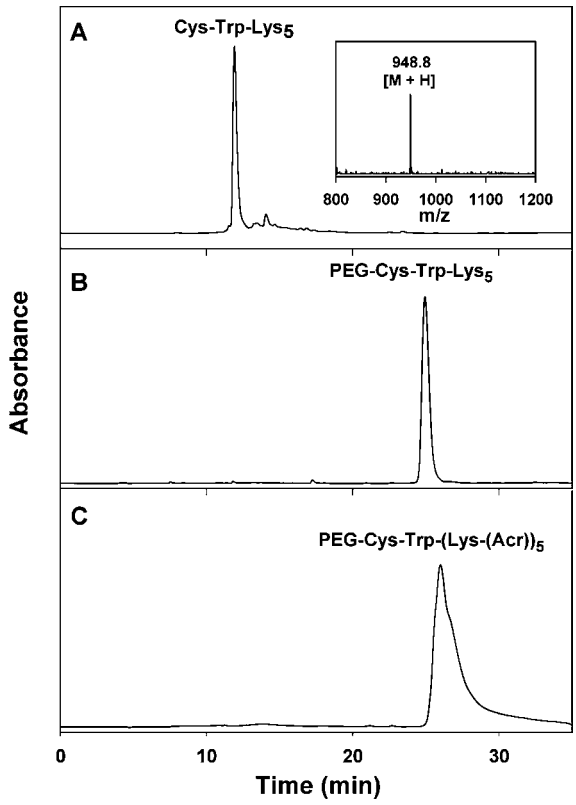


Figure 2. RP-HPLC Analysis of PEG-Cys-Trp-(Lys-(Acr))$_5$. Cys-Trp-(Lys)$_5$ elutes at 10 min on RP-HPLC eluted with 0.1% TFA and an acetonitrile gradient 5−60% over 30 min while detecting Trp by Abs at 280 nm (panel A). The inset shows the ESI-MS of Cys-Trp-Lys$_5$ with an [M+H] = 982.8 Da. Purified PEG-Cys-Trp-(Lys)$_5$ elutes at 24 min under identical gradient and detection (panel B). Purified PEG-Cys-Trp-(Lys(Acr))$_5$ elutes as a broad peak at 25 min and is detected by Abs 409 nm due to acridine (panel C).

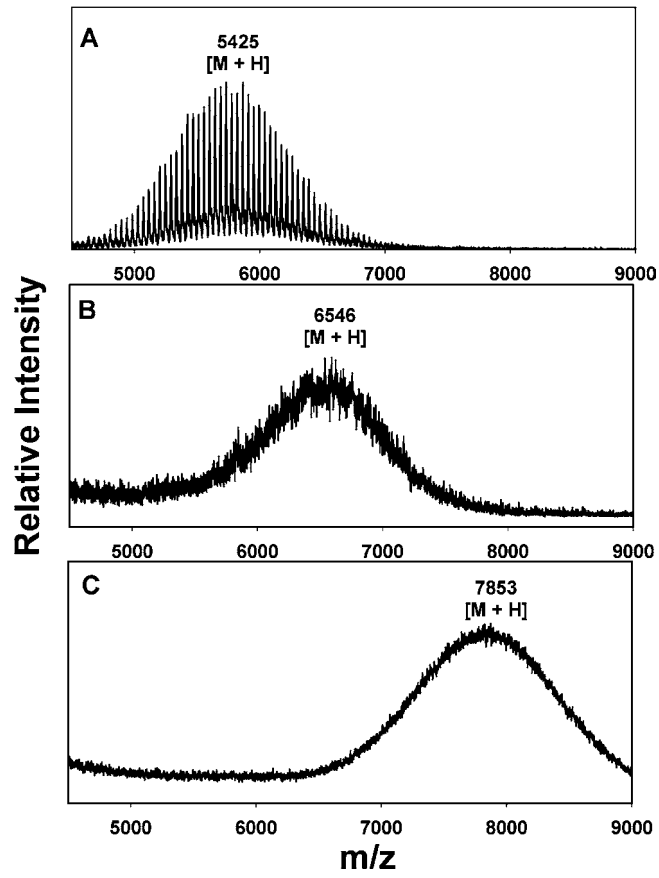


Figure 3. Mass spectral analysis of PEG-Cys-Trp-(Lys(Acr))$_5$. MALDI-TOF MS analysis PEG$_{5000Da}$-maleimide resulted in an average mass with *m/z* of 5425 (panel A). MS analysis of PEG-Cys-Trp-(Lys)$_5$ resulted in a mass shift of 1121 Da, consistent with the formation of the PEG-peptide with *m/z* of 6546 (panel B). Following conjugation of five 6-(9-acridinylamino) hexanoic acid residues (290 g/mol), the average mass increases by 1307 Da, consistent with the formation of PEG-Cys-Trp-(Lys(Acr))$_5$ with *m/z* of 7853 (panel C).

Purified PEG-Cys-Trp-(Lys(Acr))$_5$ produced an average mass of 7853 Da (Figure 3D), consistent with the conjugation of 4.4 acridines. Similar mass spectral results were obtained when preparing PEG-Cys-Trp-(Lys(Acr))$_3$ and PEG-Cys-Trp-(Lys(Acr))$_4$ as summarized in Table 1.

The relative DNA binding affinity of mono and bis-acridine PEG compared to polyacridine PEG-peptides was established using a thiazole orange displacement assay (*33*) (Figure 4A). Titration of 0.2−4 nmols of mono-acridine PEG with 1 μg of pGL3 resulted in minimal displacement of thiazole orange. By comparison, bis-acridine PEG demonstrated higher affinity, resulting in a decrease in fluorescence intensity by approximately 40% at 1 nmol per μg of DNA. The apparent DNA binding affinity of PEG-Cys-Trp-(Lys(Acr))$_{3-5}$ was higher than either mono- or bis-acridine PEG, resulting in approximately 10% fluorescence intensity at a stoichiometry of 1 nmol per μg of DNA (Figure 4A).

The DNA binding affinity was also compared by a band shift assay performed at a constant stoichiometry of 1 nmol per μg of DNA (Figure 4B). Monoacridine PEG failed to produce a band shift relative to plasmid DNA (Figure 4B, lanes 1 and 2), whereas bis-acridine PEG partially retarded the migration of DNA (Figure 4B, lane 3). PEG-Cys-Trp-(Lys(Acr))$_{3and4}$ both further retarded DNA migration to a similar extent (lanes 4 and 5), whereas PEG-Cys-Trp-(Lys(Acr))$_5$ led to complete retardation of DNA migration and also inhibited intense ethidium staining (Figure 4B, lane 6). Conversely, PEG-Cys-Trp-(Lys)$_5$ was unable to cause a band DNA shift (not shown).

A further demonstration of polyacridine binding to DNA binding utilized a titration experiment while monitoring both the particle size and zeta potential of DNA polyplexes as a function of increasing concentration of polyacridine (Figure 5). The titration of PEG-Cys-Trp-(Lys(Acr))$_3$ with pGL3 results in a decrease in the apparent particle diameter to approximately 200 at 0.2 nmols per μg of DNA but then plateaued at higher stoichiometries. The zeta potential gradually increased from −15 to −5 mV when titrating with 0.1 to 2 nmol of PEG-Cys-Trp-(Lys(Acr))$_3$ per μg of DNA, indicating that the polyplexes remained electronegative (Figure 5A). A nearly identical trend was observed when titrating pGL3 with PEG-Cys-Trp-

Table 1. MS Analysis of Polyacridine PEG-Peptides and Mono- and Bis-Acridine PEG.

sample	mass (g/mol)	mass difference[b]
Mono-amine-PEG	5385	
Mono-acridine-PEG	5626	241 (0.8)[c]
Bis-amine-PEG	2000	
Bis-acridine-PEG	2813	813 (2.8)[c]
Cys-Trp-Lys$_3$[a]	691.4	
PEG-Cys-Trp-Lys$_3$	6524	
PEG-Cys-Trp-(Lys(Acr))$_3$	7238	714 (2.5)[c]
Cys-Trp-Lys$_4$[a]	819.5	
PEG-Cys-Trp-Lys$_4$	6623	
PEG-Cys-Trp-(Lys(Acr))$_4$	7533	910 (3.1)[c]
Cys-Trp-Lys$_5$[a]	948.5	
PEG-Cys-Trp-Lys$_5$	6555	
PEG-Cys-Trp-(Lys(Acr))$_5$	7822	1267 (4.4)[c]

[a] Determined by ESI-MS. [b] Measured mean difference in MALDI-TOF mass due to the addition of acridine. [c] Calculated number of acridine-6-amino-hexanoic acids based on 291 g/mol.

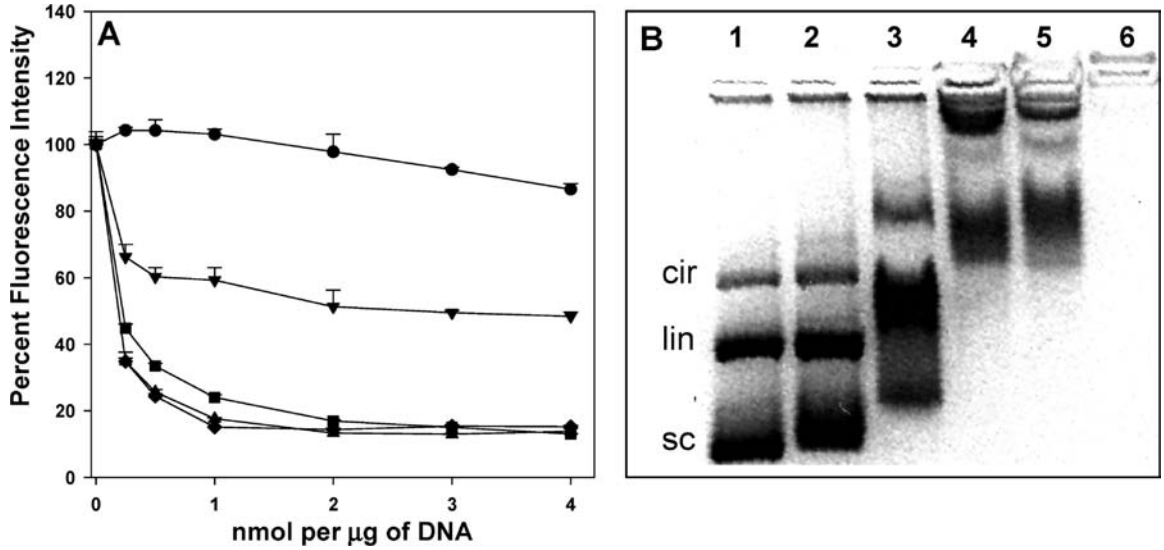


Figure 4. Relative binding affinity of mono-acridine-PEG, bis-acridine-PEG, and polyacridine peptides with DNA. The relative binding affinity of mono- and bis-acridine-PEG, and PEG-Cys-Trp-(Lys(Acr))$_{3,\ 4,\ \text{and}\ 5}$ for DNA was determined using a thiazole orange dye displacement assay and agarose gel band shift assay. Thiazole orange displacement established weak DNA binding for mono- (•) and bis-acridine-PEG (▼), with higher and indistinguishable affinity determined for PEG-Cys-Trp-(Lys(Acr))$_3$ (■), 4 (▲), and 5 (♦) (panel A). The DNA binding affinity was also compared by agarose gel electrophoresis DNA migration (1 μg) (lane 1) relative to polyplexes prepared with 1 nmol each of mono-acridine PEG (lane 2), bis-acridine PEG (lane 3), PEG-Cys-(Lys(Acr))$_3$ (lane 4), PEG-Cys-(Lys(Acr))$_4$ (lane 5), or PEG-Cys-(Lys(Acr))$_5$ (lane 6) (panel B). The results established maximal binding affinity with PEG-Cys-(Lys(Acr))$_5$ (lane 6).

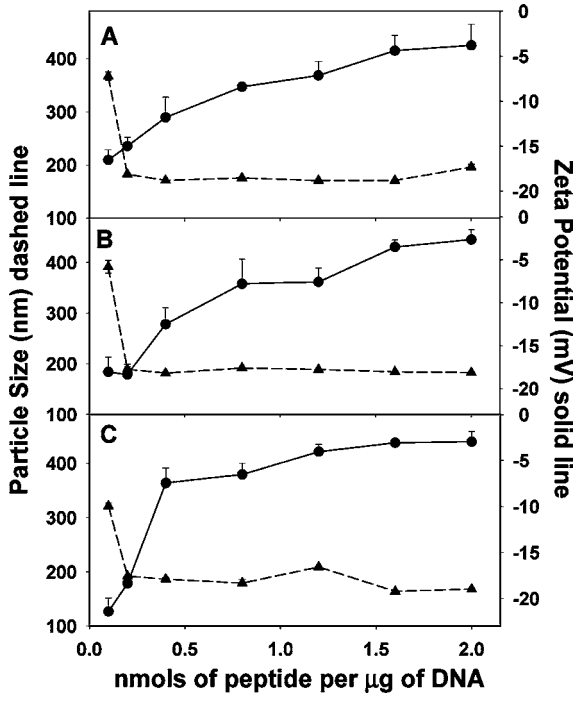


Figure 5. Particle size and zeta potential of polyacridine-peptide DNA polyplexes. The mean diameter size and zeta potential of DNA polyplexes prepared with 0.1, 0.2, 0.4, 0.8, 1.2, 1.6, or 2 nmol of PEG-Cys-(Lys(Acr))$_{3,\ 4,\ \text{and}\ 5}$ per μg of DNA were compared. At 0.2 nmol of polyacridine peptide or higher, PEG-Cys-(Lys(Acr))$_3$ formed polyplexes of apparent mean diameter of 200 nm that remained unchanged throughout the titration (panel A, dashed line). In contrast, the zeta potential progressively increased from −15 mV to approximately −2 mV when titrating from 0.1−2 nmol per μg of DNA (panel A, solid line). Nearly identical results were obtained when titrating with PEG-Cys-(Lys(Acr))$_4$ (panel B) and PEG-Cys-(Lys(Acr))$_5$ (panel C).

(Lys(Acr))$_4$ and PEG-Cys-Trp-(Lys(Acr))$_5$ (Figure 5B,C), with the exception that the latter reached an asymptote of −5 mV at 1 nmol per μg of DNA due to its greater DNA binding affinity.

The unusual zeta potential properties of the polyacridine DNA polyplexes prompted an investigation into their morphology using atomic force microscopy. Under analysis by AFM, plasmid DNA is observed as an open circular structure when immobilized onto electropositive mica prepared with immobilized Ni (Figure 6A). By comparison, PEG-Cys-Trp-(Lys(Acr))$_5$ DNA polyplexes prepared at either 0.2 or 1 nmol per μg of DNA also resulted in a open circular structure, which we term open polyplexes (Figure 6B,C). Comparison of the size and shape of open polyplexes with plasmid DNA reveals a slightly more compact structure that becomes progressively more tightly wound at higher stoichiometry of polyacridine. The appearance of smaller particles in Figure 6B,C is the result of AFM tip irregularities (*34*). Finer analysis of the data in Figure 6B,C suggests that the thickness of the open polyplex DNA is reduced by 20% relative to naked DNA. The open polyplex structure observed by AFM is quite unique when compared to an electropositive polyplex prepared with polyacridine melittin (Figure 6D).

We conjectured that the DNA in open polyplexes may be protected from metabolic degradation by serum endonucleases. The metabolic stability was evaluated by treating pGL3 with DNase followed by gel electrophoresis. Unprotected pGL3 is significantly degraded by DNase in 5 min and completely degraded by 10 min (Figure 7A, lanes 2 and 3). The weak binding affinity afforded by mono- or bis-acridine PEG failed to protect DNA from metabolism (Figure 7B,C). Comparison of the metabolic stability of PEG-Cys-Trp-(Lys(Acr))$_{3,4\text{and}5}$ DNA open polyplexes demonstrated that PEG-Cys-Trp-(Lys(Acr))$_3$ and PEG-Cys-Trp-(Lys(Acr))$_4$ provided partial protection (Figure 7D,E), whereas PEG-Cys-Trp-(Lys(Acr))$_5$ provided complete protection (Figure 7F). Decreasing the stoichiometry from 1 nmol of PEG-Cys-Trp-(Lys(Acr))$_5$ to 0.4 or 0.2 nmol per μg of DNA established that at lower stoichiometries the DNA was more susceptible to metabolism (Figure 7G,H).

The in vivo gene transfer properties of PEG-Cys-(Lys-(Acr))$_5$-DNA open polyplexes were evaluated in mice following IM-EP. pGL3 and pGL3 PEG-Cys-(Lys-(Acr))$_5$ open polyplexes prepared at 0.2, 2, and 4 nmol per μg of DNA formulations were administered by IM-EP, and the expression was monitored

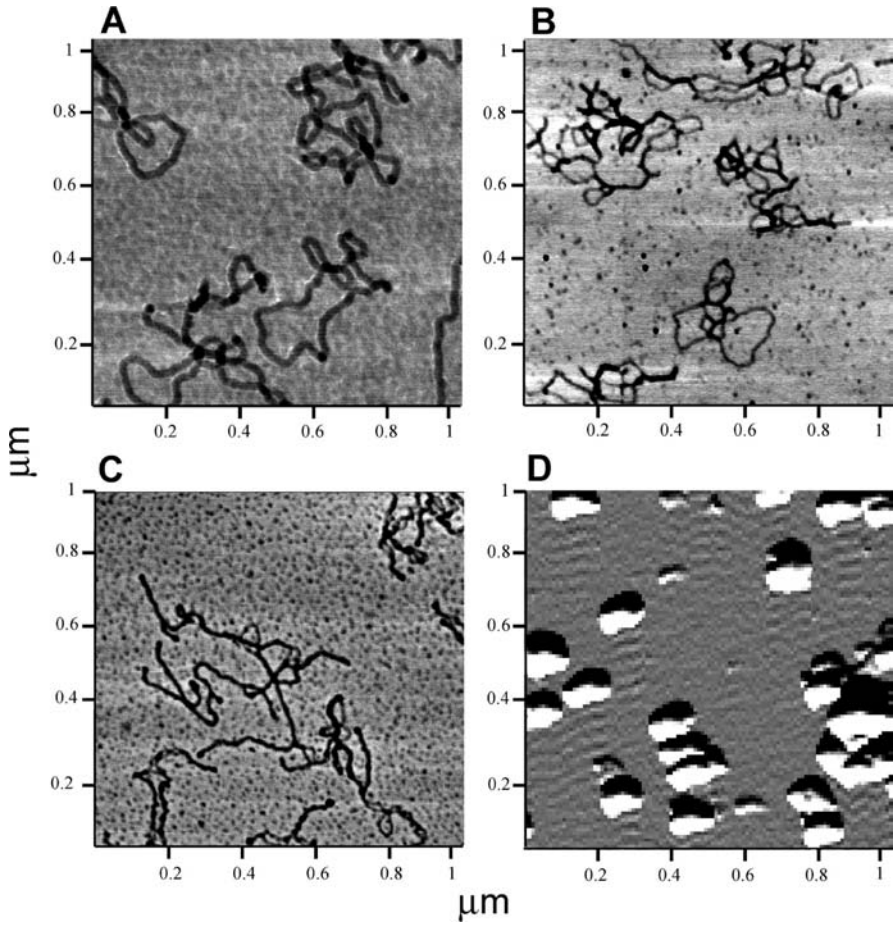


Figure 6. Atomic force microscopy analysis of plasmid DNA and polyacridine DNA polyplexes. AFM was used to compare the relative morphology of plasmid DNA or PEG-Cys-Trp-(Lys(Acr))$_5$ DNA polyplexes bound to electropositively charged mica in panels A−C. Plasmid DNA appears as an open circular structure (panel A) of comparable dimensions relative to PEG-Cys-Trp-(Lys-Acr)$_5$ DNA polyplexes prepared at either 0.2 nmol per μg of DNA (panel B) or 1 nmol per μg of DNA (panel C). Alternatively, a cationic polyplex prepared with polyacridine melittin binds to electronegative mica and appears as a collapsed structure (panel D). The results establish polyacridine PEG peptides bind to DNA to form electronegative open polyplexes that possess similar morphology as plasmid DNA.

for two weeks by bioluminescence imaging (Figure 8). At day 2 following dosing, pGL3 and the DNA open polyplexes prepared at 2 nmol per μg of DNA produced identical expression levels. Open polyplexes prepared at 4 nmol per μg of DNA showed approximately 10-fold lower expression, whereas a formulation prepared with 0.2 nmol per μg of DNA resulted in a 100-fold decrease in expression. A similar expression time course was observed for pGL3 and DNA open polyplexes prepared with 0.2 and 2 nmol of PEG-Cys-(Lys-(Acr))$_5$ per μg of DNA resulting in a 10-fold decrease over 14 days. The expression time-course for open polyplexes prepared at 4 nmol of PEG-Cys-(Lys-(Acr))$_5$ per μg of DNA was extended, resulting in only a 2−3-fold loss in expression across the 14 day sampling period.

DISCUSSION

An important function of a gene delivery carrier is to protect DNA from premature metabolism during transit (*35*). The present study demonstrates that polyintercalation provides strong and reversible binding to DNA that delays metabolic degradation. The main advantage of this approach over polycationic polymer binding to DNA is that high affinity can be achieved with a short polyacridine and that the charge of the resulting DNA polyplexes can be controlled to be either positive or negative, depending on intended applications in vitro or in vivo (*24*). Prior reports of the cellular toxicity of known intercalators demonstrate a dependency on both chemical structure and dose (*36*). Little or no information is available regarding the toxicity of PEGylated polyacridine peptides.

To evaluate the relationship between DNA binding affinity and metabolic stability, five DNA carriers were prepared that varied the number of acridines from 1 to 5. The synthetic strategy conjugated 6-(9-acridinylamino) hexanoic acid with the primary amine(s) on PEG-amine, bis-amino PEG, and the ε-amines on PEG-Cys-Trp-(Lys)$_{3,\ 4,\ \text{or}\ 5}$. This strategy not only simplified the chemical preparation of the delivery molecules, but also allowed for a long 12 atom tether between each acridine and the peptide backbone to facilitate flexible multivalent binding of acridine with DNA.

The DNA binding affinity significantly increased for PEG-Cys-(Lys-(Acr))$_{3,\ 4,\ \text{and}\ 5}$ compared to mono- and bis-acridine PEG as determined by both fluorophore displacement and DNA band shift on agarose gel electrophoresis (Figure 4A,B). While the QELS particle size suggested the formation of large polyplexes with an apparent diameter of 200 nm, the zeta potential revealed that for PEG-Cys-(Lys-(Acr))$_{3,\ 4,\ \text{and}\ 5}$ polyplexes were negatively charged. AFM images established that the shape of PEG-Cys-(Lys-(Acr))$_{3,\ 4,\ \text{and}\ 5}$ DNA polyplexes were open-coiled structures that closely resemble plasmid DNA (Figure 6). The observed electronegative open polyplexes are distinct from electropositive condensed polyplexes that are formed by polycation binding with DNA. The metabolic stability afforded by comparing PEG-Cys-(Lys-(Acr))$_{3,\ 4,\ \text{and}\ 5}$ establish a relationship between the apparent DNA binding affinity and the degree of protection from

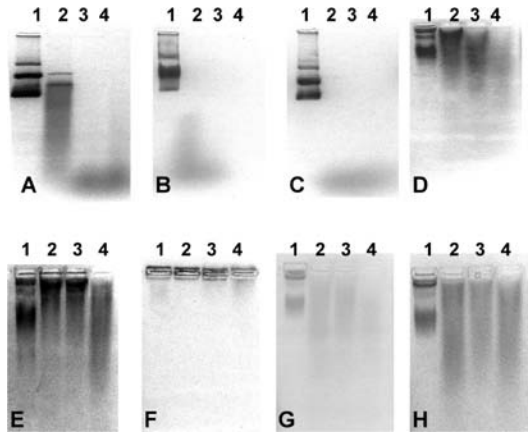


Figure 7. Relative metabolic stability of mono-acridine-PEG, bis-acridine-PEG, and polyacridine peptides DNA polyplexes. The relative metabolic stability of DNA polyplexes was compared with plasmid DNA by agarose gel electrophoresis. Plasmid DNA (1 μg) (panel A), or DNA polyplexes prepared with 1 nmol each of mono-acridine PEG (panel B), bis-acridine PEG (panel C), PEG-Cys-(Lys(Acr))$_3$ (panel D), PEG-Cys-(Lys(Acr))$_4$ (panel E), or PEG-Cys-(Lys-(Acr))$_5$ (panel) were incubated with 0.06 U of DNase at 37 °C for 0 (lane 1), 5 (lane 2), 10 (lane 3), and 20 (lane 4) min. PEG-Cys-(Lys(Acr))$_5$ DNA polyplexes were also prepared at 0.2 (panel G) and 0.4 (panel H) nmol of polyacridine peptide per μg of DNA and digested with DNase. The results demonstrate that PEG-Cys-(Lys-(Acr))$_5$ provided the greatest protection at 1 nmol per μg of DNA, (panel F) while the lower stoichiometries of 0.2 or 0.4 nmol per μg of DNA (panel G and H) resulted in less stability.

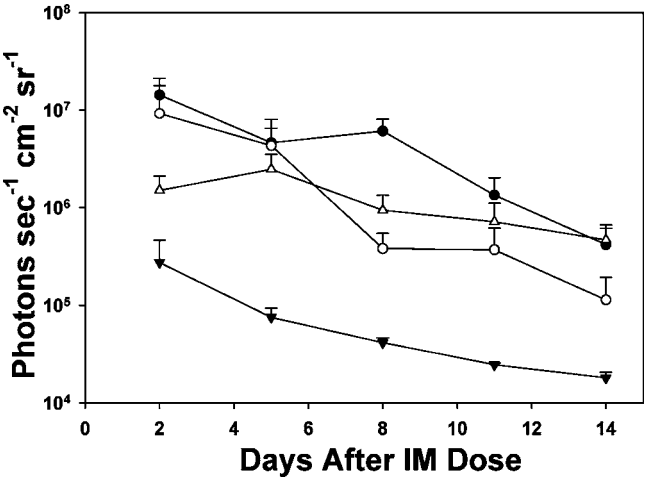


Figure 8. In vivo gene expression mediated by polyacridine peptide DNA polyplexes. The gene transfer efficiencies of naked DNA (•) or polyacridine peptide DNA polyplexes prepared with 0.2 (▲), 2 (○), or 4 (Δ) nmol of PEG-Cys-(Lys-(Acr))$_5$ per μg of DNA were determined following i.m. dosing and electroporation of 1 μg of pGL3 in the gastrocnemius muscle of ICR male mice (n = 4). The luciferase expression was quantified at times ranging from 2−14 days by bioluminescence imaging (BLI) following an i.m. dose of luciferin. Open polyplexes prepared at 0.2 nmol (▲) of PEG-Cys-(Lys-(Acr))$_5$ per μg of DNA showed the lowest transfection efficiency, while polyplexes prepared at 2 nmol (○) of PEG-Cys-(Lys-(Acr))$_5$ per μg of DNA showed similar expression levels to that of naked DNA. Increasing the stoichiometry to 4 nmol (Δ) PEG-Cys-(Lys-(Acr))$_5$ per μg of DNA resulted in a more sustained expression. The results represent the mean and standard deviation of four doses.

DNase. Additionally, the metabolic protection of DNA afforded by PEG-Cys-(Lys-(Acr))$_5$ was concentration-dependent.

IM-EP of cationic DNA polyplexes results in lower gene expression levels compared to naked DNA alone (*20, 37, 38*). This may be due to the charge of cationic polyplexes that are unable to electromigrate through the transient pore formed during electroporation (*20*). In contrast, the IM-EP of DNA versus PEG-Cys-(Lys-(Acr))$_5$ DNA open polyplexes resulted in very similar levels and duration of expression in mice over two weeks. However, at an elevated stoichiometry of PEG-Cys-(Lys-(Acr))$_5$, a lower but more sustained expression was determined, perhaps due to the metabolic protection afforded by the peptide at higher stoichiometries.

The results of this study establish a new family of PEGylated polyacridine gene delivery carriers that bind to DNA and provide protection against DNase. The unique anionic open polyplex structure is compatible with IM-EP. Given the flexibility of design, polyacridine gene delivery systems could be optimized for a variety of other nonviral gene delivery applications.

ACKNOWLEDGMENT

We gratefully acknowledge support for this work from the NIH Grant DK066212 and NIH Predoctoral Training Grant Support for KA (T32 GM067795).

LITERATURE CITED

(1) Wu, G. Y., and Wu, C. H. (1988) Evidence for targeted gene delivery to Hep G2 hepatoma cells in vitro. *Biochemistry 27*, 887–892.

(2) Boussif, O., Lezoualc'h, F., Zanta, M. A., Mergny, M. D., Scherman, D., Demeneix, B., and Behr, J. P. (1995) A versatile vector for gene and oligonucleotide transfer into cells in culture and in vivo: polyethylenimine. *Proc. Natl. Acad. Sci. U.S.A. 92*, 7297–301.

(3) Gao, X., and Huang, L. (1991) A novel cationic liposome reagent for efficient transfection of mammalian cells. *Biochem. Biophys. Res. Commun. 179*, 280–5.

(4) Yang, J. P., and Huang, L. (1997) Overcoming the inhibitory effect of serum on lipofection by increasing the charge ratio of cationic liposome to DNA. *Gene Ther. 4*, 950–60.

(5) Wolfert, M. A., Dash, P. R., Nazarova, O., Oupicky, D., Seymour, L. W., Smart, S., Strohalm, J., and Ulbrich, K. (1999) Polyelectrolyte vectors for gene delivery: influence of cationic polymer on biophysical properties of complexes formed with DNA. *Bioconjugate Chem. 10*, 993–1004.

(6) Choi, Y. H., Liu, F., Park, J. S., and Kim, S. W. (1998) Lactose-poly(ethylene glycol)-grafted poly-L-lysine as hepatoma cell-tapgeted gene carrier. *Bioconjugate Chem. 9*, 708–18.

(7) Choi, Y. H., Liu, F., Choi, J. S., Kim, S. W., and Park, J. S. (1999) Characterization of a targeted gene carrier, lactose-polyethylene glycol-grafted poly-L-lysine and its complex with plasmid DNA. *Hum. Gene Ther. 10*, 2657–65.

(8) Ogris, M., Brunner, S., Schuller, S., Kircheis, R., and Wagner, E. (1999) PEGylated DNA/transferrin-PEI complexes: reduced interaction with blood components, extended circulation in blood and potential for systemic gene delivery. *Gene Ther. 6*, 595–605.

(9) Peracchia, M. T., Fattal, E., Desmaele, D., Besnard, M., Noel, J. P., Gomis, J. M., Appel, M., d'Angelo, J., and Couvreur, P. (1999) Stealth PEGylated polycyanoacrylate nanoparticles for intravenous administration and splenic targeting. *J. Controlled Release 60*, 121–128.

(10) Lee, H., Jeong, J. H., and Park, T. G. (2002) PEG grafted polylysine with fusogenic peptide for gene delivery: high transfection efficiency with low cytotoxicity. *J. Controlled Release 79*, 283–91.

(11) Hosseinkhani, H., and Tabata, Y. (2004) PEGylation enhances tumor targeting of plasmid DNA by an artificial cationized protein with repeated RGD sequences, Pronectin*R*. *J. Controlled Release 97*, 157–171.

(12) Trubetskoy VS, L. A., Hagstrom, J. E., Budker, V. G., and Wolff, J. A. (1999) Layer-by-layer deposition of oppositely charged polyelectrolytes on the surface of condensed DNA particles. *Nucleic Acid Res. 27*, 3090–3095.

(13) Taori, V. P., Liu, Y., and TM, R. (2009) DNA delivery in vitro via surface release from multilayer assemblies with poly-(glycoamidoamine)s. *Acta Biomater. 5*, 925–33.
(14) Blacklock, J., You, Y. Z., Zhou, Q. H., Mao, G., and D., O. (2009) Gene delivery in vitro and in vivo from bioreducible multilayered polyelectrolyte films of plasmid DNA. *Biomaterials 30*, 939–50.
(15) Wu, G. Y., and Wu, C. H. (1988) Receptor-mediated Gene Delivery and Expression In Vivo. *J. Biol. Chem. 263*, 14621–14624.
(16) Ueyama, H., Waki, M., Takagi, M., and Takenaka, S. (2000) Novel synthesis of a tetra-acridinyl peptide as a new DNA polyintercalator. *Nucleic Acids Symp. Ser.* 133–4.
(17) Satkauskas, S., Bureau, M. F., Puc, M., Mahfoudi, A., Scherman, D., Miklavcic, D., and Mir, L. M. (2002) Mechanisms of in vivo DNA electrotransfer: respective contributions of cell electropermeabilization and DNA electrophoresis. *Mol. Ther. 5*, 133–40.
(18) Molnar, M. J., Gilbert, R., Lu, Y., Liu, A. B., Guo, A., Larochelle, N., Orlopp, K., Lochmuller, H., Petrof, B. J., Nalbantoglu, J., and Karpati, G. (2004) Factors influencing the efficacy, longevity, and safety of electroporation-assisted plasmid-based gene transfer into mouse muscles. *Mol. Ther. 10*, 447–55.
(19) van der Aa, M. A., Koning, G. A., d'Oliveira, C., Oosting, R. S., Wilschut, K. J., Hennink, W. E., and Crommelin, D. J. A. (2005) An NLS peptide covalently linked to linear DNA does not enhance transfection efficiency of cationic polymer based gene delivery systems. *J. Gene Med. 7*, 208–217.
(20) Weecharangsan, W., Opanasopit, P., and Lee, R. J. (2007) In vitro gene transfer using cationic vectors, electroporation and their combination. *Anticancer Res. 27*, 309–13.
(21) Haensler, J., and Szoka, J. F. C. (1993) Synthesis and characterization of a trigalactosylated bisacridine compound to target DNA to hepatocytes. *Bioconjugate Chem. 4*, 85–93.
(22) Boulanger, C., Di Giorgio, C., and Vierling, P. (2005) Synthesis of acridine-nuclear localization signal (NLS) conjugates and evaluation of their impact on lipoplex and polyplex-based transfection. *Eur. J. Med. Chem. 40*, 1295–306.
(23) Shiraishi, T., Hamzavi, R., and Nielsen, P. E. (2005) Targeted delivery of plasmid DNA into the nucleus of cells via nuclear localization signal peptide conjugated to DNA intercalating bis- and trisacridines. *Bioconjugate Chem. 16*, 1112–1116.
(24) Baumhover, N. J., Anderson, K., Fernandez, C. A., and Rice, K. G. (2009) Synthesis and in vitro testing of new potent polyacridine-melittin gene delivery peptides. *Bioconjugate Chem.*, In Press.
(25) Chen, C. P., Park, Y., and Rice, K. G. (2004) An improved large-scale synthesis of PEG-peptides for gene delivery. *J. Pept. Res. 64*, 237–43.
(26) Karup, G., Meldal, M., Nielsen, P. E., and Buchardt, O. (1988) 9-Acridinylpeptides and 9-acridinyl-4-nitrophenylsulfonylpeptides. Synthesis, binding to DNA, and photoinduced DNA cleavage. *Int. J. Pept. Protein Res. 32*, 331–343.
(27) McKenzie, D. L., Kwok, K. Y., and Rice, K. G. (2000) A potent new class of reductively activated peptide gene delivery agents. *J. Biol. Chem. 275*, 9970–9977.
(28) Adami, R. C., and Rice, K. G. (1999) Metabolic stability of glutaraldehyde cross-linked peptide DNA condensates. *J. Pharm. Sci. 88*, 739–746.
(29) Adami, R. C., Collard, W. T., Gupta, S. A., Kwok, K. Y., Bonadio, J., and Rice, K. G. (1998) Stability of peptide-condensed plasmid DNA formulations. *J. Pharm. Sci. 87*, 678–683.
(30) Bezanilla, M., Drake, B., Nudler, E., Kashlev, M., Hansma, P. K., and Hansma, H. G. (1994) Motion and enzymatic degreadation of DNA in the atomic force microscope. *Biophys. J. 67*, 2454–9.
(31) Liu, F., and L, H. (2002) A syringe electrode device for simultaneous injection of DNA and electrotransfer. *Mol. Ther. 5*, 323–328.
(32) Wu, J. C., Sundaresan, G., Iyer, M., and Gambhir, S. S. (2001) Noninvasive optical imaging of firefly luciferase reporter gene expression in skeletal muscles of living mice. *Mol. Ther. 4*, 297–306.
(33) Wadhwa, M. S., Collard, W. T., Adami, R. C., McKenzie, D. L., and Rice, K. G. (1997) Peptide-mediated gene delivery: influence of peptide structure on gene expression. *Bioconjugate Chem. 8*, 81–8.
(34) Camesano, T. A., Natan, M. J., and Logan, B. E. (2000) Observation of changes in bacterial cell morphology using tapping mode atomic force microscopy. *Langmuir 16*, 4563–4572.
(35) Collard, W. T., Yang, Y., Kwok, K. Y., Park, Y., and Rice, K. G. (2000) Biodistribution, metabolism, and in vivo gene expression of low molecular weight glycopeptide polyethylene glycol peptide DNA co-condensates. *J. Pharm. Sci. 89*, 499–512.
(36) Ferguson, L. R., and Denny, W. A. (2007) Genotoxicity of non-covalent interactions: DNA intercalators. *Mutat. Res. 623*, 14–23.
(37) Sakai, M., Nishikawa, M., Thankaketpaisarn, O., Yamashita, F., and Hahida, M. (2005) Hepatocyte-targeted gene transfer by combination of vascularly delivered plasmid DNA and in vivo electroporation. *Gene Ther. 12*, 607–616.
(38) Kawano, T., Yamagata, M., Takahashi, H., Niidome, Y., Yamada, S., Katayama, Y., and Niidome, T. (2006) Stabilizing of plasmid DNA in vivo by PEG-modified cationic gold nanoparticles and the gene expression assisted with electrical pulses. *J. Controlled Release 111*, 382–389.

BC900514S

Imaging Human Pancreatic Cancer Xenografts by Targeting Mutant *KRAS2* mRNA with [^{111}In]DOTA$_n$-Poly(diamidopropanoyl)^m-*KRAS2* PNA-D(Cys-Ser-Lys-Cys) Nanoparticles

Nariman V. Amirkhanov,[†,‡] Kaijun Zhang,[§] Mohan R. Aruva,[§] Mathew L. Thakur,[§,||] and Eric Wickstrom*[,‡,||]

Laboratory of Nucleic Acids Chemistry, Institute of Chemical Biology and Fundamental Medicine, Novosibirsk 630090, Russia, and Departments of Biochemistry & Molecular Biology and Radiology, and Kimmel Cancer Center, Thomas Jefferson University, Philadelphia, Pennsylvania 19107. Received November 27, 2009; Revised Manuscript Received February 16, 2010

95% of patients with ductal pancreatic cancer carry 12th codon activating mutations in their *KRAS2* oncogenes. Early whole body imaging of mutant *KRAS2* mRNA activation in pancreatic cancer would contribute to disease management. Scintigraphic hybridization probes to visualize gene activity in vivo constitute a new paradigm in molecular imaging. We have previously imaged mutant *KRAS2* mRNA activation in pancreatic cancer xenografts by positron emission tomography (PET) based on a single radiometal, ^{64}Cu, chelated to a 1,4,7,10-tetra(carboxymethylaza)cyclododecane (DOTA) chelator, connected via a flexible, hydrophilic spacer, aminoethoxyethoxyacetate (AEEA), to the N-terminus of a mutant *KRAS2* peptide nucleic acid (PNA) hybridization probe. A peptide analogue of insulin-like growth factor 1 (IGF1), connected to a C-terminal AEEA, enabled receptor-mediated endocytosis. We hypothesized that a polydiamidopropanoyl (PDAP) dendrimer (generation *m*), with increasing numbers (*n*) of DOTA chelators, extended via an N-terminal AEEA from a mutant *KRAS2* PNA with a C-terminal AEEA and IGF1 analogue could enable more intense external imaging of pancreatic cancer xenografts that overexpress IGF1 receptor and mutant *KRAS2* mRNA. ([^{111}In]DOTA-AEEA)$_n$-PDAP^m-AEEA$_2$-*KRAS2* PNA-AEEA-IGF1 analogues were prepared and administered intravenously into immunocompromised mice bearing human AsPC1 (G12D) pancreatic cancer xenografts. CAPAN2 (G12 V) pancreatic cancer xenografts served as a cellular *KRAS2* mismatch control. Scintigraphic tumor/muscle image intensity ratios for complementary [^{111}In]$_n$-PDAP^m-*KRAS2* G12D probes increased from 3.1 ± 0.2 at $n = 2$, $m = 1$, to 4.1 ± 0.3 at $n = 8$, $m = 3$, to 6.2 ± 0.4 at $n = 16$, $m = 4$, in AsPC1 (G12D) xenografts. Single mismatch [^{111}In]$_n$-PDAP^m-*KRAS2* G12 V control probes showed lower tumor/muscle ratios (3.0 ± 0.6 at $n = 2$, $m = 1$, 2.6 ± 0.9 at $n = 8$, $m = 3$, and 3.7 ± 0.3 at $n = 16$, $m = 4$). The mismatch results were comparable to the PNA-free [^{111}In]DOTA control results. Simultaneous administration of nonradioactive Gd$_n$-*KRAS2* G12 V probes ($n = 2$ or 8) increased accumulation of [^{111}In]$_8$*KRAS2* G12 V probes 3−6-fold in pancreatic cancer CAPAN2 xenografts and other tissues, except for a 2-fold decrease in the kidneys. As a result, tissue distribution tumor/muscle ratios of ^{111}In uptake increased from 3.1 ± 0.5 to 6.5 ± 1.0, and the kidney/tumor ratio of ^{111}In uptake decreased by more than 5-fold from 174.8 ± 17.5 to 30.8 ± 3.1. Thus, PDAP dendrimers with up to 16 DOTA chelators attached to PNA-IGF1 analogs, as well as simultaneous administration of the elevated dose of nonradioactive Gd$_n$-*KRAS2* G12 V probes, enhanced tumor uptake of [^{111}In]$_n$*KRAS2* PNA probes. These results also imply that Gd(III) dendrimeric hybridization probes might be suitable for magnetic resonance imaging of gene expression in tumors, because the higher generations of the dendrimers, including the NMR contrast Gd$_n$-*KRAS2* G12 V probes, improved tumor accumulation of the probes and specificity of tumor imaging.

INTRODUCTION

Pancreatic cancer will kill over 30 000 US men and women in 2010 (*1*). The vast majority of patients with pancreatic cancer present at an advanced, incurable stage. Even before an enlarged mass can be seen by magnetic resonance imaging (MRI) or computerized tomography (CT), early stage pancreatic intraepithelial neoplasia cells contain high levels of mRNAs copied from hyperactive cancer genes such as *KRAS2* and *HER2* (*2*). 95% of patients with ductal pancreatic cancer carry 12th codon activating mutations in their *KRAS2* oncogenes (*2*). Specific detection of pancreatic intraepithelial neoplasia by molecular imaging would enable resection of ductal pancreatic cancer at a survivable stage. Monitoring oncogene expression by radiohybridization imaging might also provide the earliest possible evidence for therapeutic efficacy, or resistance, sooner than FDG-PET.

Scintigraphic imaging, such as planar or PET, is very sensitive, but only appropriate in a human subject when suspect masses are evident or highly likely. Nonradioactive fluorescent imaging and luminescent imaging are impractical for any suspect mass more than 2 cm below the surface of the skin. Nonradioactive MRI could be effective for molecular imaging of deep-seated malignant foci, particularly due to the high spatial resolution (up to 25−100 μm) of MRI (*3*). However, disadvantages of MRI include relatively low specificity and the requirement for large quantities of the injected probes containing gadolinium.

Noninvasive scintigraphic imaging of gene expression by detection of specific mRNAs in cells to diagnose cancer and

Corresponding author. Dr. Eric Wickstrom, Department of Biochemistry & Molecular Biology, Thomas Jefferson University, 233 S. 10th Street, Suite 219, Philadelphia, PA 19107, voice: 215-955-4578; fax: 215-955-4580; e-mail: eric@tesla.jci.tju.edu.

[†] Institute of Chemical Biology and Fundamental Medicine.

[‡] Biochemistry and Molecular Biology, Thomas Jefferson University.

[§] Radiology, Thomas Jefferson University.

[||] Kimmel Cancer Center, Thomas Jefferson University.

10.1021/bc900523c © 2010 American Chemical Society
Published on Web 03/16/2010

other diseases in living systems has been attempted with antisense oligonucleotides (*3*−*14*). Specific imaging of target gene mRNA requires multiple steps: probe permeation into tissue, endocytosis into the cells, probe hybridization with the target mRNA, probe:mRNA accumulation in the specific cells, and effluxing of unbound probes. Nonhybridized probes must efflux from cells with little or no expression of the target mRNA in order to permit a specific image in the targeted cells.

We used peptide nucleic acids (PNA[1]) (*15*) because PNA is resistant to biological degradation and binds complementary mRNA with affinity, specificity, and stability exceeding those of corresponding DNA/RNA duplexes (*16*). PNA oligomers are uncharged, resulting in poor cellular uptake, which minimizes nonspecific binding to cells (*17*).

Receptor-mediated endocytosis of PNA drugs or diagnostic probes into malignant cells that overexpress insulin-like growth factor 1 (IGF1) receptors can be accomplished with a short, cyclized IGF1 peptide analogue, D(Cys-Ser-Lys-Cys), separated from the C-terminus of the PNA by a flexible, hydrophilic aminoethoxyethoxyacetic acid (AEEA) spacer (*9, 10, 13, 18*). Alanine replacements in the peptide (*9, 10, 12, 13, 18*), or peptide blocking by native IGF1 (*13*), minimized internalization. Bonding radioactive metal cations to specific chelator-PNA-IGF1 analogues enabled their delivery to cells for radioimaging in xenografts in living subjects (*9, 10, 12, 13*).

In the case of activated *KRAS2* G12D mRNA overexpressed in pancreatic cancer AsPC1 cells, the melting temperature, T_m, of the complementary *KRAS2* G12D PNA 12-mer with a *KRAS2* G12D RNA 20-mer was 80 °C, independent of the peptide ligand sequence (*12*), following the typical behavior of PNA:RNA duplexes (*19, 20*). A single mismatch, corresponding to the difference between the *KRAS2* G12D mutant sequence and the *KRAS2* G12 wild-type sequence, lowered the T_m by 20 °C. Three mismatches lowered the T_m by 30 °C. Those thermodynamic results predicted single mismatch hybridization specificity under intracellular conditions.

Uptake of [^{99m}Tc]SBTG$_2$-DAP-AEEA-*KRAS2* PNA-AEEA-IGF1 analogue by AsPC1 cells at 37 °C was 3-fold greater than accumulation of a corresponding *CCND1* probe (*21*). Those results are consistent with greater cellular retention due to *KRAS2* complementarity. Confocal fluorescence microscopic measurements of the mass transfer coefficients of AsPC1 cellular uptake of fluorescent analogues of the *KRAS2* G12D PNA probes revealed 10-fold less uptake by dual amino acid mismatch probes (*22*).

[^{64}Cu]DOTA-AEEA-*KRAS2* PNA-AEEA-IGF1 analogues enabled PET imaging in pancreatic cancer AsPC1 G12D xenografts, with single base mismatch precision in the PNA. Tumor core PET contrast intensities were 8-fold greater than contralateral muscle PET intensities for the *KRAS2* G12D complementary probe. Much lower tumor core PET intensities in the cases of G12 wild-type (one mismatch), G12 V (one mismatch), G12K (two mismatches), and G12E (three mismatches) sequence controls implied that PET imaging intensity depended upon accurate mRNA hybridization (*12*).

Similarly, a dual amino acid mismatch sequence in the IGF1 analogue, with a fully matched PNA sequence, reduced PET contrast intensities (*12*). Furthermore, reduced PET intensities were observed in G12 V single mismatch pancreatic CAPAN2 xenografts, after administration of the G12D probe, and in *KRAS2*$^-$ breast cancer BT474 xenografts. Four hours of distribution, cellular efflux, and systemic excretion were necessary before clear images could be obtained (*12*).

Those *KRAS2* PET imaging experiments all depended on probes with a single chelator binding a single radionuclide. To increase mRNA-specific contrast by genetic probes, particularly for less abundant mRNAs, it would be desirable to increase the number of metal ions per hybridization probe. For that purpose, we designed novel polydiamidopropanoyl (PDAP) dendrimers with increasing numbers of primary amines by coupling Fmoc-AEEA monomers and Fmoc-diaminopropanoate (DAP) monomers to the N-terminus of PNA−peptide chimeras extended from polymer supports (*23*). To each amine, we coupled a DOTA chelator by one of its carboxylates, converting it into a DOTA moiety.

Recently, we reported the synthesis of (Gd-DOTA-AEEA)$_n$-PDAP^m-AEEA$_2$-*KRAS2* PNA-AEEA-IGF1 analogue MRI contrast agents (*24*). MRI phantom experiments showed proportional increase of the MRI intensity and T1 relaxivity with increases in the number of Gd(III) chelated to those probes. To estimate the fraction of internalized Gd$_n$*KRAS2* PNA agents that would be hybridized to available *KRAS2* mRNAs in live tumor cells, the T_m of each probe was measured with increasing generations of the PDAP dendrimers hybridized to *KRAS2* G12D 20-mer RNA. Fully matched (Gd-DOTA-AEEA)$_n$-PDAP^m-AEEA$_2$-*KRAS* G12D PNA-IGF1 analogues formed stable complementary PNA/RNA hybrid complexes with melting temperatures (T_m) of 79−80 °C. The generation of the PDAP dendrimers did not influence the T_m values of PNA/RNA hybrid duplexes. A single mismatch, corresponding to the single base difference between the G12D mutant sequence and the G12 V mutant sequence, lowered the T_m by 12 °C (*24*). These thermodynamic results predict single mismatch hybridization specificity for the dendrimeric PNA probes under intracellular conditions.

However, before evaluation of such dendrimeric probes for noninvasive molecular imaging of intracellular mRNA and oncogene expression, several questions must be addressed. First of all, how does the number of metal cations chelated to the PNA probes or the generation of PDAP dendrimers influence their uptake and accumulation in the tumor-targeted tissue and in other tissues? Second, how does the concentration of the dendrimeric PNA probes influence the imaging of the tumor? As a result of the sensitivity limitations of MRI with Gd(III) contrast, we chose to label the dendrimeric hybridization probes with ^{111}In(III) [γ, 0.171, 0.245 MeV, half-life 67.32 h (2.8 d)] for scintigraphic imaging. Free, unchelated ^{111}In(III) accumulates nonspecifically in the kidneys, liver, spleen, bone, and tumors of mice bearing colon, lung, or neuroblastoma xenografts (*25*). However, chelated ^{111}In(III) is exceedingly stable, dissociating by no more than 1% in 10 days at 37 °C in the presence of serum, correlating with a binding constant of $\sim 10^{24}$ (*26*).

Here, we report the sensitivity of noninvasive scintigraphic imaging of overexpressed oncogene *KRAS2* mRNA with γ-emitting ([^{111}In]DOTA-AEEA)$_n$-PDAP^m-AEEA$_2$-*KRAS2* PNA-IGF1 analogues, **WT5195**, **WT8900**, and **WT13842**, specific for *KRAS2* G12D or *KRAS2* G12 V mRNA, with up to $n = 16$ ^{111}In(III) per probe. We investigated the accumulation of the [^{111}In]$_n$*KRAS2* probes in immunocompromised mice bearing human AsPC1 (G12D) or CAPAN2 (G12 V) pancreatic cancer xenografts. We also investigated the effect of administering mixtures of ^{111}In(III)-chelated PNA hybridization probes with increasing doses of nonradioactive Gd(III)-chelated hybridization probes in order to saturate nonspecific tissue binding sites. This approach permitted us to determine how the concentration and

[1]Abbreviations: AEEA, aminoethoxyethoxyacetate linker; DAP, diamidopropanoyl; DOTA, 1,4,7,10-tetra(carboxymethylaza)cyclododecane; HATU, 2-(7-aza-1*H*-benzotriazole-1-yl)-1,1,3,3-tetramethyl-uronium hexa-fluorophosphate; PDAP, polydiamidopropanoyl; PET, positron emission tomography; PNA, peptide nucleic acid; SBTG, S-benzoyl-thioglycoloyl; T_m, melting temperature.

Scheme 1. (Metal-DOTA-AEEA)$_n$-PDAP^m-AEEA$_2$-*KRAS2* PNA-AEEA-IGF1 Analogues

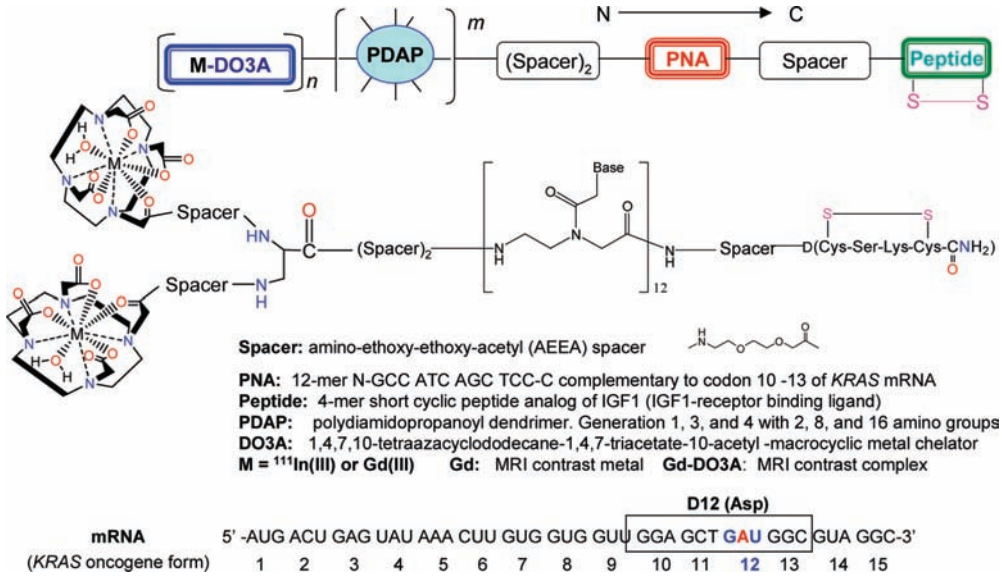


Table 1. (DOTA-AEEA)$_n$-PDAP^m-AEEA$_2$-*KRAS2* PNA-AEEA-IGF1 Analogues [from ref *24*]^a

name	label	sequence	calc. mass, Da.	obs. mass, Da	% yield	T_m, °C
$DOTA_2$ G12D	WT5195	(DOTA-AEEA)$_2$-PDAP^1-AEEA$_2$-**GCCAtCAGCTCC**-AEEA-D(Cys-Ser-Lys-Cys)	5194.65	5195.63	12.6	78.7 ± 0.6
$DOTA_8$ G12D	WT8900	(DOTA-AEEA)$_8$-PDAP^3-AEEA$_2$-**GCCAtCAGCTCC**-AEEA-D(Cys-Ser-Lys-Cys)	8900.47	8901.06	2.4	75.9 ± 0.5
$DOTA_{16}$ G12D	WT13842	(DOTA-AEEA)$_{16}$-PDAP^4-AEEA$_2$-**GCCAtCAGCTCC**-AEEA-D(Cys-Ser-Lys-Cys)	13841.57	13843.50	0.57	74.1 ± 1.0
$DOTA_2$ G12 V	WT5204	(DOTA-AEEA)$_2$-PDAP^1-AEEA$_2$-**GCCAaCAGCTCC**-AEEA-D(Cys-Ser-Lys-Cys)	5203.7	5204.6	20.2	68.0 ± 1.2
$DOTA_8$ G12 V	WT8910	(DOTA-AEEA)$_8$-PDAP^3-AEEA$_2$-**GCCAaCAGCTCC**-AEEA-D(Cys-Ser-Lys-Cys)	8909.5	8911.9	11.5	66.9 ± 0.5
$DOTA_{16}$ G12 V	WT13851	(DOTA-AEEA)$_{16}$-PDAP^4-AEEA$_2$-**GCCAaCAGCTCC**-AEEA-D(Cys-Ser-Lys-Cys)	13850.6	ND	6.8	68.8 ± 0.5
Gd_2 G12 V	WT5512	(Gd-DOTA-AEEA)$_2$-PDAP^1-AEEA$_2$-**GCCAaCAGCTCC**-AEEA-D(Cys-Ser-Lys-Cys)	5512.2	5514.0	16.6	68.0 ± 1.0
Gd_8 G12 V	WT10144	(Gd-DOTA-AEEA)$_8$-PDAP^3-AEEA$_2$-**GCCAaCAGCTCC**-AEEA-D(Cys-Ser-Lys-Cys)	10143.5	10143.6	5.8	66.8 ± 0.9

^{a} Masses were measured by MALDI TOF MS or ESI-MS. Yields were calculated with respect to initial amino acid loading of the resin beads. Melting temperatures are shown ± standard errors of the means. ND: not done.

dendrimer generation of our Gd(III)-chelated agents influenced the specificity and intensity of *KRAS2* mRNA scintigraphic imaging.

MATERIALS AND METHODS

Synthesis of (DOTA-AEEA)$_n$-PDAP^m-AEEA$_2$-KRAS2 PNA-AEEA-IGF1 Analogue Nanoparticles. The unlabeled hybridization probes (Scheme 1, Table 1) containing 12-base PNAs flanked by the dendrimeric radionuclide chelators $DOTA_2$, $DOTA_8$, or $DOTA_{16}$ at the N-terminus, and a short retro-inverso cyclized fragment of IGF1, D(Cys-Ser-Lys-Cys), at the C-terminus (Figure 1), were assembled by solid-phase synthesis from Fmoc-monomers, purified, and characterized as described (*24*), and in the Supporting Information.

Radiolabeling of DOTA$_n$-KRAS2 PNA Probes with ^{111}In(III). DOTA$_n$-*KRAS2* PNA probes (n = 2, 8, 16; G12D and G12 V *KRAS2* mutants, Table 1) were labeled with ^{111}In(III) essentially as described (*6*). Briefly, 5−10 μL of $^{111}InCl_3$ at 3.7−7.4 MBq/μL (100−200 μCi/μL) in 0.05 M HCl (MDS Nordion, Kanata, ON, Canada) containing 37 MBq (1 mCi) (~21 pmol, assuming the specific activity for carrier-free $^{111}InCl_3$, 1.723 GBq/nmol, 46.6 Ci/μmol), were incubated with 45 μL of 0.10−0.15 mM (~6 nmol) of the indicated DOTA$_n$-*KRAS2* PNA probes in 0.10 M NaOAc, pH 7.0, for 15 min at 80 °C. The radiolabeling yield (typically >95%) was analyzed by HPLC as below. Thus, the final specific activity of the PNA probes, assuming stoichiometric chelation, was ~6 MBq/nmol (0.17 Ci/μmol). Similarly, 500 nmol of DOTA was labeled with 74 MBq (2 mCi) (~42 pmol) of ^{111}In as a control probe, with a calculated specific activity of ~0.15 MBq/nmol (0.004 Ci/μmol) in a final volume of 100 μL.

Solutions were diluted with 100 μL of 0.9% saline. Aliquots of each labeling mixture (10−14 μCi, 0.37−0.52 MBq) were analyzed by reversed-phase HPLC on a 4.6 × 150 mm C_{18} column (Altima, Alltech) coupled to a UV detector, NaI (Tl) radioactivity monitor, and a rate meter. The column was eluted with a 30 min gradient from 4% to 72% CH_3CN in aqueous 0.1% CF_3CO_2H, at 1 mL/min, at 23 °C. Other aliquots of the labeling mixtures (250−350 μCi, 9.0−13.0 MBq) after dilution with 0.9% saline up to a total volume of 200 μL were used for tail vein administration into mice to image tumors.

In Vitro Stability. Labeled probes were tested for stability in 0.9% saline, and with 100-fold molar excesses of diethylenetriaminepentaacetic acid (DTPA), human serum albumin, or cysteine at 22 °C for more than 2 days. Stability was determined by HPLC as above.

Chelation of DOTA$_n$-KRAS2 PNA Probes with Gd(III). DOTA$_n$-*KRAS2* PNA probes (n = 2, 8, 16; G12 V *KRAS2* mutants, Table 1), 0.5 mM in 0.1 M NaOAc, pH 6.0, were incubated with at least a 10-fold excess of $GdCl_3$ at 80 °C for 15 min to maximize chelation, as described (*24*). Spectrophotometric quantitation of remaining unchelated Gd(III) ions was carried out by titration with 1 mM DTPA solution in water in the presence of arsenazo III dye, which changes from a cherry-red color with a peak at 665 nm to a blue color after forming a specific Gd(arsenazo III)$_2$ complex in 0.15 M NaOAc, pH 4 (*27, 28*). 90−98% of the DOTA residues in the hybridization probes were occupied by Gd(III) ions. The final Gd-chelated products were purified on a 22 × 250 mm Alltima C_{18} column eluted with a linear 30 min gradient from 0% to 30% CH_3CN in aqueous 0.1% CF_3CO_2H, at 10 mL/min, at 50 °C, monitored at 260 nm (*24*).

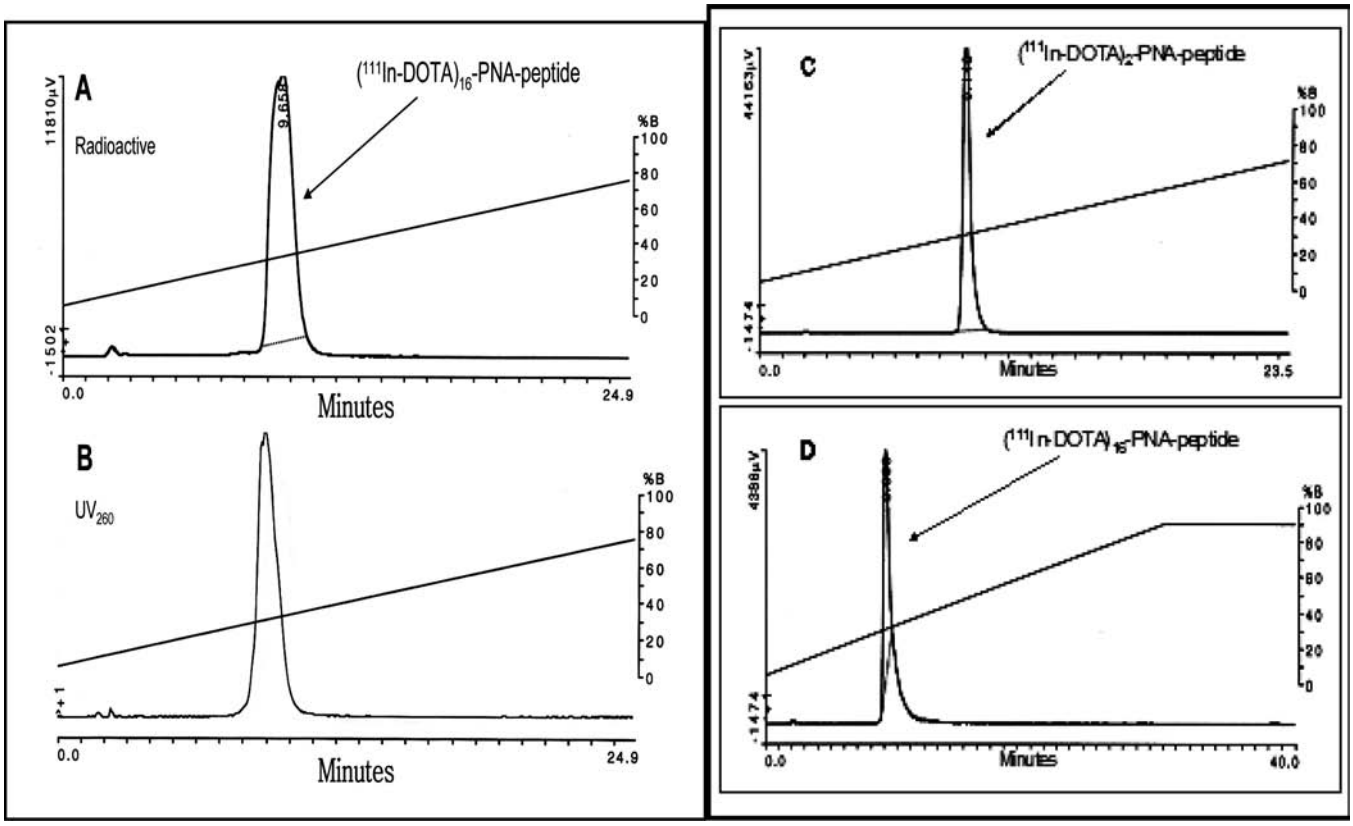


Figure 1. C_{18} HPLC profiles of $[^{111}In]_n$*KRAS2* G12D probes, eluted as described in Materials and Methods. (A) Analytical radioactivity profile of $[^{111}In]_{16}$*KRAS2* G12D, **WT13842**. (B) Analytical absorbance profile at 260 nm of $[^{111}In]_{16}$*KRAS2* G12D, **WT13842**. (C) Analytical radioactivity profile of $[^{111}In]_2$*KRAS2* G12D, **WT5195**, in the combined urine from 3 immunocompromised mice bearing AsPC1 xenografts 3.5 h after tail vein administration. (D) Analytical radioactivity profile of $[^{111}In]_{16}$*KRAS2* G12D, **WT13842**, in the combined urine from 3 immunocompromised mice bearing AsPC1 xenografts 3.5 h after tail vein administration.

Cell Culture and Xenografts. The human pancreatic cancer cell line AsPC1 (American Type Culture Collection, Rockville, MD), isolated from ascites of a female patient with invasive pancreatic adenocarcinoma (*29*), expresses a 12th codon GGT→GAT, G12D mutant *KRAS2* oncogene (*30*), and overexpresses IGF1R (*31*). As a *KRAS2* sequence control, the human pancreatic cancer cell line CAPAN2 (American Type Culture Collection, Rockville, MD), which was isolated from a male patient with invasive pancreatic adenocarcinoma (*32*), expresses a 12th codon GGT→GTT, G12 V mutant *KRAS2* oncogene (*33*), and overexpresses IGF1R (*34*). Pancreatic cancer cells were maintained in log phase in RPMI 1640 (AsPC1) or McCoy's 5a (CAPAN2) media supplemented with 2 mM glutamine, 5000 U/mL penicillin, 50 μg/mL streptomycin, 10% fetal bovine serum (Sigma Chemical Co., St. Louis, MO), incubated at 37 °C in a humidified incubator containing 5% CO_2/95% air and cultured to 80% confluence prior to splitting or implantation. Quantitative RT-PCR analysis of total RNA from AsPC1 cells yielded about 20 000 *KRAS2* mRNA per cell (*12*).

For tumor induction, approximately (5−6) × 10^6 cells in 0.2 mL of culture medium were implanted intramuscularly through a sterile 27 gauge needle into the thighs of 6−8-week-old 20−25 g female immunocompromised NCR mice obtained from NCI. Tumors were grown to no more than 1 cm in diameter. All animal studies were conducted in accordance with federal and state guidelines governing the laboratory use of animals, and under approved protocols reviewed by the Animal Care and Use Committee at Thomas Jefferson University. All animals were anesthetized by approved methods, and when required, the animals were restrained using methods and devices specifically designed to provide a minimum of discomfort to the animal. Animals were euthanized in a halothane chamber, consistent with USDA regulations and American Veterinary Medical Association recommendations.

Systematic Administration and Tissue Distribution of Labeled Probes. To assess *KRAS2* probe imaging and distribution, 7.4−11.1 MBq (200−300 μCi), ∼2 nmol, of the $[^{111}In]_n$-*KRAS2* G12D and G12 V probes in 0.2 mL of sterile 0.14 M NaCl, pH 7, was administered to groups of 3−5 mice with xenografts each through a lateral tail vein using a sterile 27 gauge needle. Distributions were also measured for mixtures of $[^{111}In]_n$*KRAS2* G12 V probes with an additional 11, 48, or 94 nmol of Gd_n-*KRAS2* G12 V probes. ∼11 MBq (∼300 μCi), 80 nmol, of [^{111}In]DOTA was administered as a control. Free, unchelated ^{111}In(III) was not used as a control due to its nonspecific accumulation in the kidneys, liver, spleen, bone, and tumors of mice bearing a variety of xenografts (*25*).

At 4, 8, and 24 h postinjection, mice were lightly anesthetized with a mixture of ketamine (200 mg/kg), xylazine (10 mg/kg), and acetopromazine (2 mg/kg), then imaged using a Starcam (GE Medical, Milwaukee, WI) gamma camera equipped with a parallel hole collimator. For each image, 300 000 counts were collected. Digital scanning of region-of-interest intensities with the interfaced Integra computer (GE Medical) across each scintigraphic image from the tumor-free left flank to the tumor-bearing right flank provided quantitation of tumor images. Statistical significance was assessed by standard error of the means, assuming normal distributions.

After 24 h, mice were euthanized. Portions of muscle, intestine, heart, lungs, blood, spleen, kidneys, liver, and tumor were collected. We did not attempt to dissect out the pancreas, because in mice, the pancreas is remarkably small and wrapped tightly around the small intestine. Portions of tail were not collected separately from muscle, because previous imaging

experiments had not shown excess residual probe remaining in the tails. The dissected tissues were washed free of blood, blotted dry, and weighed, and radioactivity associated with each tissue was counted in an automatic gamma counter (Packard Series 5000, Meridien, CT), together with a standard radioactive solution of a known quantity prepared at the time of injection. Results were expressed as percent of injected dose per gram of tissue (% ID/g). Null probabilities were calculated by Student's *t* test.

In Vivo Stability. Analysis of urine samples will reveal catabolism of labeled probes occurring throughout the body of the animals. [^{111}In]chelates are so strong as to preclude transchelation to serum proteins (*26*). Urine was collected up to 3.5 h postinjection from groups of 3−5 mice injected with radiohybridization probes for assessment of probe stability. The urine samples were combined, sedimented at 2000 × *g* for 10 min, filtered through Millipore HAWP 025 membranes with 0.22 μm pores, and analyzed by RP-HPLC as described in Radiolabeling.

RESULTS

Characterization of (DOTA-AEEA)$_n$-PDAP^m-AEEA$_2$-KRAS2 PNA-AEEA-IGF1 Nanoparticles. Theoretically, the number of free amino groups on the growing PDAP dendrimers on the polymer support at each generation should double at each coupling. The number of amino groups available at each generation was determined by measuring the absorbance of the dibenzofulvene-piperidine adduct (ε_{301} = 7800 M^{-1} cm^{-1}) released upon Fmoc deprotection after each coupling of (Fmoc)$_2$-DAP-COOH as described (*24*). The number of Fmoc deprotection residues released from the growing PDAP dendrimers at each step increased from 1.00 to 2.00, 3.98, then 7.61 (95.0% yield) for PDAP^3 with 8 theoretical amines, as reported (*24*). For PDAP^4 dendrimers with 16 theoretical amines, Fmoc deprotection residues released increased from 1.00 to 1.95, 3.82, 7.58, then 14.16 (88.5% yield) (*24*).

Analysis of [^{111}In]$_n$KRAS2 PNA Probes. A ≥600-fold excess of DOTA residues (≥15 nmol) over ∼21 pmol of $^{111}InCl_3$ promoted chelation of ^{111}In(III) to DOTA-dendrimer PNA probes. The lack of free ^{111}In(III) permitted administration of [^{111}In]$_n$*KRAS2* PNA probes directly after labeling. Before administration to mice, aliquots of radiolabeled probes were analyzed by HPLC, monitoring with both UV detector at 260 nm and with NaI (Tl) radioactivity monitoring detector. Analytical HPLC of the [^{111}In]$_{16}$*KRAS2* G12D probe **WT13842** is shown as an example (Figure 1AB). Generations 1 and 3 are shown in Figures S1 and S2 in the Supporting Information. On the basis of the HPLC results, routine radiochemical yields of more than 95% with specific activities of ∼6 MBq/nmol (0.17 mCi/nmol) of [^{111}In]$_n$*KRAS2* PNA probes were obtained. Theoretically, >600-fold greater specific activity of [^{111}In]$_n$-*KRAS2* PNA probes could be obtained, if stoichiometric amounts of $^{111}InCl_3$ were used.

Radiohybridization Probe Stability in Vitro. These preparations were stable at 22 °C for more than 2 days, as determined by HPLC, and were stable to challenges with 100-fold molar excesses of diethylenetriaminepentaacetic acid (DTPA), human serum albumin, or cysteine. The analyses indicated that essentially all of the ^{111}In(III) was bound to DOTA$_n$-*KRAS2* PNA probes. These results made it possible to administer the labeled probes directly without the necessity for further purification. Due to the efficiency of labeling observed, each labeled probe was used directly for administration into the tail veins of immunocompromised mice bearing AsPC1 xenografts.

Radiohybridization Probe Stability in Vivo. To check the in vivo stability of radiohybridization probe, [^{111}In]$_n$*KRAS2* PNA probes were injected into the tail veins of immunocompromised mice bearing AsPC1 pancreatic cancer xenografts. HPLC analysis of radioactivity in the combined 3.5 h urine sample from mice injected with [^{111}In]$_2$*KRAS2* G12D probe, **WT5195** (Figure 1C) and [^{111}In]$_{16}$*KRAS2* G12D probe, **WT13842** (Figure 1D) revealed a void volume peak of free ^{111}In that included less than 1% of radioactivity and a probe peak eluting at 9 min with more than 99% of the radioactivity.

Breakdown fragments of [^{111}In]**WT5195** and [^{111}In]**WT13842** were not detected. In a comparable study with [^{64}Cu]DOTA-AEEA-*CCND1* PNA-AEEA-IGF1 analogue in immunocompromised mice bearing breast cancer xenografts, no evidence was seen for transchelation to serum or tissue proteins (*13*).

Systemic Administration of Radiohybridization Probes. Scintigraphic images of γ-particles emitted from immunocompromised mice bearing pancreatic cancer xenografts 24 h after administration of [^{111}In]$_n$*KRAS2* PNA probes are shown in Figure 2A for the fully matched [^{111}In]$_n$*KRAS2* G12D probes and in Figure 2B for the single mismatch [^{111}In]$_n$*KRAS2* G12 V probes. Imaging of PNA-free [^{111}In]DOTA as a control is also presented in Figure 2A.

Digital scanning of the xenograft region-of-interest on the right flank vs the mirror image tumor-free region-of-interest on the left flank (muscle) was carried out to determine the tumor/muscle (T/M) intensity ratios of each subject. The intensity averages and standard deviations of the T/M ratios are shown at the bottoms of each image in Figure 2 and in Table S1 in the Supporting Information.

In the case of imaging with fully matched [^{111}In]$_n$*KRAS2* G12D PNA sequences, the T/M ratios increased from 3.1 ± 0.2 at n = 2, **WT5195**; to 4.1 ± 0.3 at n = 8, **WT8900**; to 6.2 ± 0.4 at n = 16, **WT13842**. Kruskal−Wallis one-way analysis of variance on ranks indicated that the differences in the mean values among the four treatment groups were greater than would be expected by chance ($p < 0.001$). Comparison of each treatment group with every other treatment group by the Holm-Sidak all-pairwise multiple comparison procedure revealed that each group was statistically significantly different from the others ($p \leq 0.05$).

On the other hand, imaging with single mismatch [^{111}In]$_n$-*KRAS2* G12 V PNA control probes showed lower T/M ratios (3.0 ± 0.6 at n = 2, **WT5204**; 2.6 ± 0.9 at n = 8, **WT8910**; and 3.7 ± 0.3 at n = 16, **WT13851**). Kruskal−Wallis one-way analysis of variance on ranks indicated that the three treatment groups were indistinguishable from each other. T/M ratios from single mismatch [^{111}In]$_n$*KRAS2* G12 V control probes were comparable to the T/M ratios for the PNA-free [^{111}In]DOTA control (Figure 2A). The single mismatch control results established a basis for determination of PNA sequence specificity for the accumulation of fully matched [^{111}In]$_n$*KRAS2* G12D probes in the xenografts.

Upon comparing the image intensity T/M ratios obtained for fully matched [^{111}In]$_n$*KRAS2* G12D probes in AsPC1 xenografts in mice (Figure 2C), it is apparent that the T/M ratio for [^{111}In]$_2$*KRAS2* G12D remained at ∼3 at 4, 8, and 24 h after injection, while T/M for [^{111}In]$_8$*KRAS2* G12D remained at ∼4, and T/M for [^{111}In]$_{16}$*KRAS2* G12D remained at ∼6. This result implies that the avidity of the xenografts for the [^{111}In]$_n$*KRAS2* G12D probes, relative to the avidity of the contralateral muscle, had already leveled out by 4 h after administration.

Dose Dependence of Radiohybridization Probe Administration. In view of our intent to use Gd(III)-chelated probes for MRI of mRNA expression (*24*), we assessed the effect of elevated doses of Gd$_n$*KRAS2* G12 V probes with constant doses of [^{111}In]$_8$*KRAS2* G12 V probes on scintigraphic image intensity. Nonradioactive Gd$_n$*KRAS2* G12 V probes (n = 2 or 8) (1.9, 11, 48, and 94 nmol) were mixed with ∼2 nmol (300−350 μCi, 11−13 MBq) of fully matched [^{111}In]$_8$*KRAS2* G12 V probe, then admin-

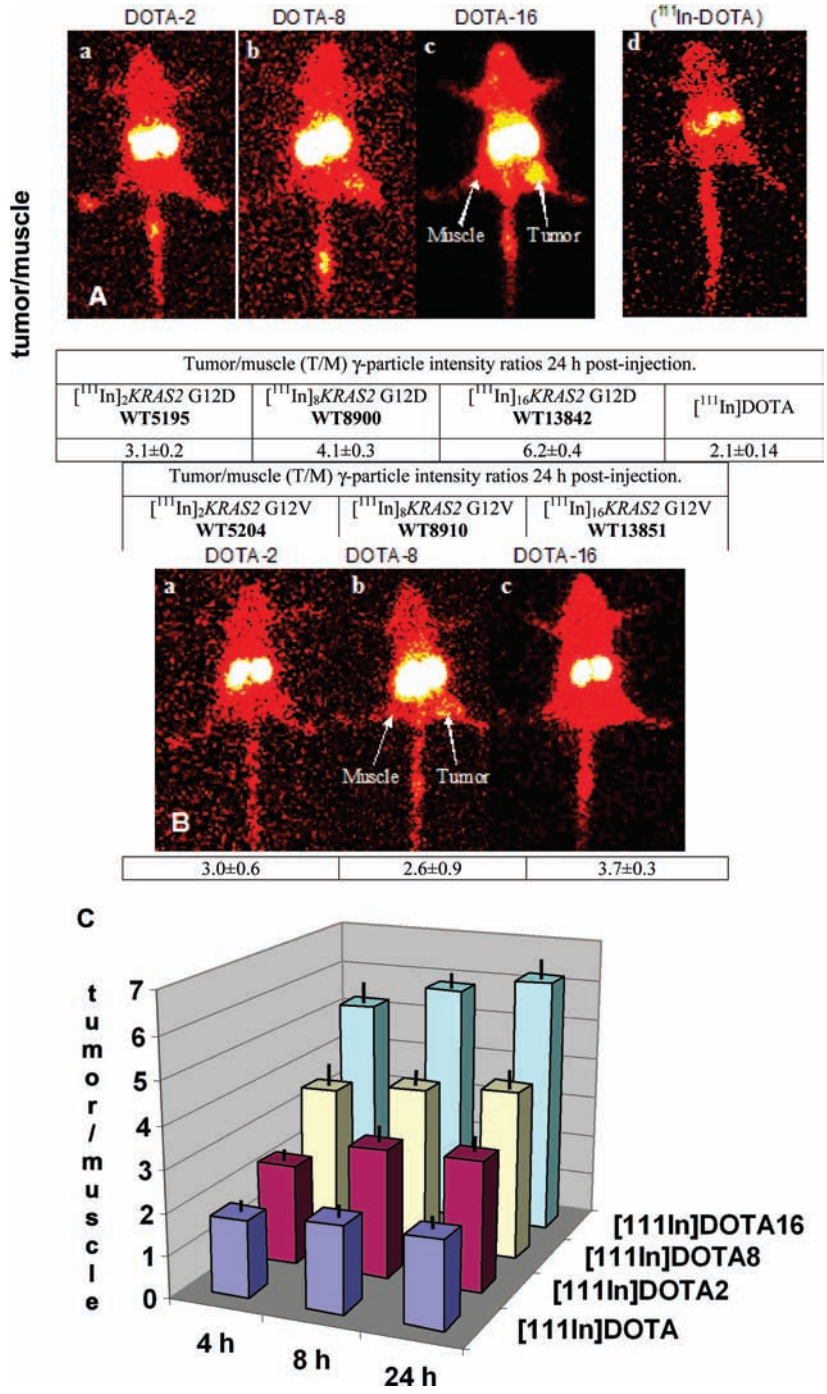
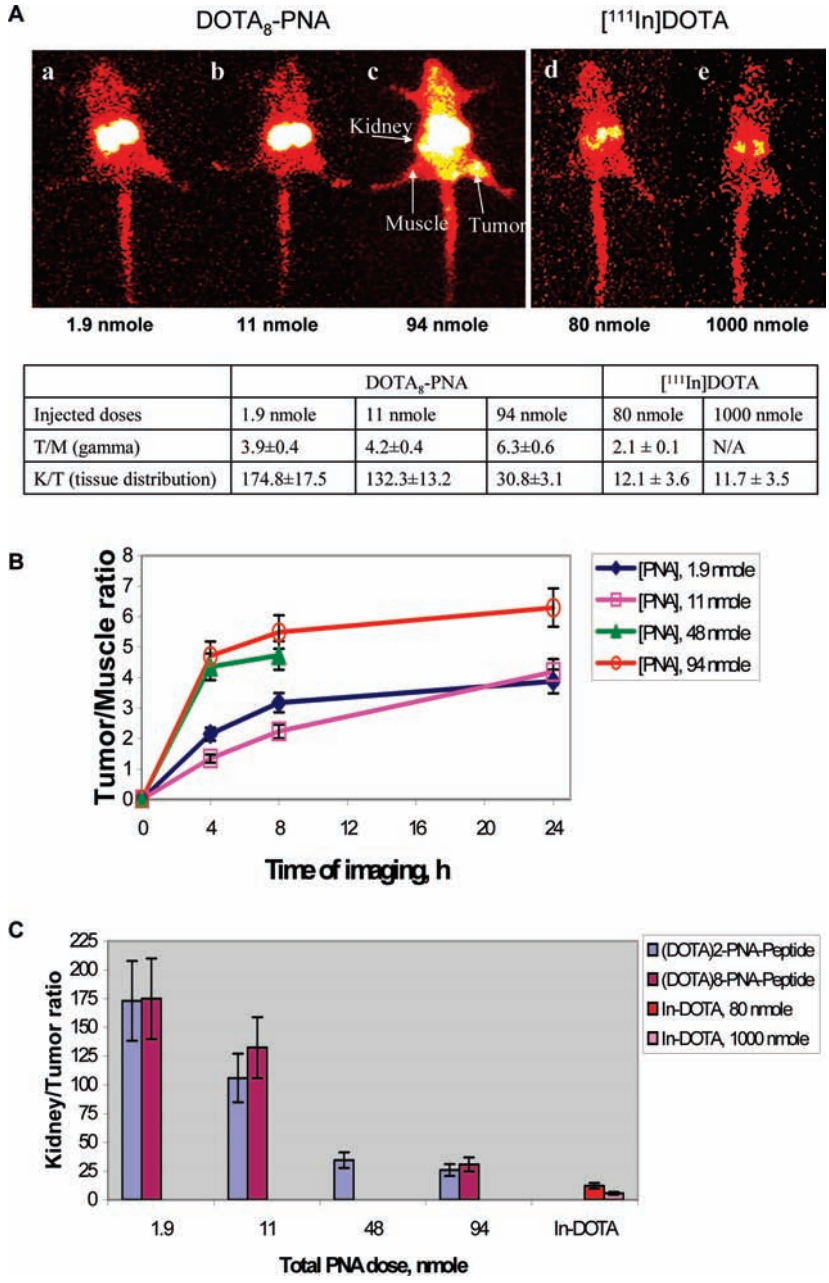


Figure 2. Scintigraphic images of immunocompromised mice bearing human AsPC1 pancreatic cancer xenografts at 24 h after tail vein administration of ~2 nmol (300−350 μCi, 11−13 MBq) of $[^{111}In]_n$*KRAS2* probes to groups of 3 mice. (A) Fully matched G12D probe images (a) $[^{111}In]_2$*KRAS2* G12D, **WT5195**; (b) $[^{111}In]_8$*KRAS2* G12D, **WT8900**; (c) $[^{111}In]_{16}$*KRAS2* G12D, **WT13842**; (d) 80 nmol [^{111}In]DOTA (~11 MBq, ~300 μCi) control. Tumor/Muscle (T/M) γ-particle intensity ratios were calculated for each group of 3 mice. Holm-Sidak all pairwise multiple comparison revealed that each group was statistically significantly different from the others ($p \leq 0.05$). (B) Single mismatch G12 V probes images (a) $[^{111}In]_2$*KRAS2* G12 V, **WT5204**; (b) $[^{111}In]_8$*KRAS2* G12 V, **WT8910**; (c) $[^{111}In]_{16}$*KRAS2* G12 V, **WT13851**. Kruskal−Wallis one-way analysis of variance on ranks indicated that the three treatment groups were indistinguishable from each other. (C) Histograms of tumor/muscle (T/M) γ-particle intensity ratios of G12D fully matched probes calculated from scintigraphic image intensities. Solid black lines show standard deviations. Each group was statistically significantly different from the other three ($p \leq 0.05$).

istered to immunocompromised mice bearing CAPAN2 (G12 V) pancreatic cancer xenografts. Scintigraphic images recorded 24 h after administration of $[^{111}In]_8$*KRAS2* G12 V probes are shown in Figure 3A for added Gd_8*KRAS2* G12 V probe, **WT8910**, and in Figure S3 of the Supporting Information for Gd_2*KRAS2* G12 V probe, **WT5204**. Elevated doses of Gd_8*KRAS2* G12 V probes increased accumulation of the fully matched $[^{111}In]_8$*KRAS2* G12 V probe in CAPAN2 (G12 V) xenografts, thereby increasing the T/M ratio from 3.9 ± 0.4 to 6.3 ± 0.6 (Figure 3A).

The time courses of $[^{111}In]_8$*KRAS2* G12 V probe accumulation in tumor and muscle were similar for 1.9 and 11 additional nanomoles of nonradioactive probe, but shifted up markedly for 48 and 94 additional nanomoles (Figure 3B). The effect of additional nonradioactive probe was apparent as early as 4 h after administration. Tissue distribution data for all time points are shown in Table S2 in Supporting Information.

Tissue Distribution of Radiohybridization Probes. Tissue distribution of each of the $[^{111}In]_n$*KRAS2* PNA probes in



	DOTA$_8$-PNA			[^{111}In]DOTA	
Injected doses	1.9 nmole	11 nmole	94 nmole	80 nmole	1000 nmole
T/M (gamma)	3.9±0.4	4.2±0.4	6.3±0.6	2.1 ± 0.1	N/A
K/T (tissue distribution)	174.8±17.5	132.3±13.2	30.8±3.1	12.1 ± 3.6	11.7 ± 3.5

Figure 3. Immunocompromised mice bearing human CAPAN2 (G12 V) pancreatic cancer xenografts at 24 h after tail vein administration of ~2 nmol (300−350 μCi, 11−13 MBq) of fully matched [^{111}In]$_8$-*KRAS2* G12 V, **WT8910**, mixed with increasing doses of Gd$_2$-*KRAS2* G12 V, **WT5512**, or Gd$_8$-*KRAS2* G12 V, **WT10144**. (A) Scintigraphic images of mice that received (a) 1.9 nmol, (b) 11 nmol, or (c) 94 nmol of nonradioactive Gd$_8$ probes. Additional tumor-bearing mice were injected with (d) 80 nmol (~11 MBq, ~300 μCi) or (e) 1000 nmol (~11 MBq, ~300 μCi) of [^{111}In]DOTA as controls. Tumor/Muscle (T/M) ratios were calculated from γ-particle intensity data. Kidney/Tumor (K/T) ratios were calculated from tissue distribution data. (B) Time course of Tumor/Muscle (T/M) ratios from γ-particle intensity data. (C) Dependence of kidney/tumor (K/T) tissue distribution ratios on elevated Gd$_n$ probe dose. The decrease of K/T with added nonradioactive Gd$_n$ probes were the same for Gd$_2$ probes or Gd$_8$ probes. The Mann−Whitney rank sum test indicated that there was not a statistically significant difference ($p = 0.886$).

immunocompromised mice bearing human AsPC1 pancreatic cancer xenografts was measured at 24 h after administration. The measured tissue distribution data are presented in Table 2. Tissue distribution data for [^{111}In]$_n$*KRAS2* G12 V probes in CAPAN2 xenografts are presented in Table S2 in the Supporting Information. Probe distribution into the mouse pancreas was not measured, because it is wrapped around the intestine in a thin layer, unlike the human pancreas.

In addition to typical measurements of percent of injected dose per gram of tissue (%ID/g) for individual tissues, we calculated the total percent of injected dose per gram of tissue. The total percent of injected dose per gram of tissue informs us of the total radioactivity that remains in the body after injection. That number reports how quickly the radioactive probes can be utilized or excreted. Interestingly, we found that this value, total percent of injected dose per gram of tissue, is different for different generations of dendrimers and different kinds of radioactive probes.

At 24 h after injection, the total %ID/g increased in all tissues with the size of the dendrimer and number of ^{111}In per probe, which implies that larger probes are retained longer in the tissues prior to renal excretion. This phenomenon was seen with both the fully matched [^{111}In]$_n$*KRAS2* G12D probes (Table 2A) and with the single mismatch [^{111}In]$_n$*KRAS2* G12 V probes (Table 2B). Tumor %ID also increased with dendrimer size, particularly for $n = 16$ (Table 2A). The muscle %ID also increased in the

Table 2. Tissue Distribution (% injected dose/g) of [^{111}In]$_n$*KRAS2* PNA Probes vs [^{111}In]DOTA, in Immunocompromised Mice Bearing Human AsPC1 (G12D) Pancreatic Cancer Xenografts[a]

A. Fully Matched [^{111}In]$_n$*KRAS2* G12D Probes

tissues	[^{111}In]$_2$ **WT5195**	null prob.	[^{111}In]$_8$ **WT8900**	null prob.	[^{111}In]$_{16}$ **WT13842**	null prob.	[^{111}In]DOTA
muscle	0.038 ± 0.007	0.0034	0.040 ± 0.010	0.0125	0.267 ± 0.052	0.0009	0.012 ± 0.003
intestine	0.048 ± 0.007	0.0025	0.048 ± 0.004	0.0004	0.201 ± 0.041	0.0014	0.018 ± 0.003
heart	0.028 ± 0.008	0.0150	0.035 ± 0.005	0.0013	0.189 ± 0.047	0.0019	0.008 ± 0.002
lungs	0.217 ± 0.257	0.2951	0.096 ± 0.021	0.0122	0.175 ± 0.048	0.0076	0.038 ± 0.009
blood	0.020 ± 0.010	0.2988	0.018 ± 0.001	0.0517	0.042 ± 0.007	0.0110	0.013 ± 0.003
spleen	0.079 ± 0.006	0.0003	0.075 ± 0.005	0.0002	0.279 ± 0.037	0.0004	0.032 ± 0.003
kidneys	18.367 ± 1.892	0.0001	29.615 ± 9.207	0.0054	42.609 ± 7.619	0.0007	0.500 ± 0.099
liver	0.147 ± 0.015	0.0005	0.152 ± 0.012	0.0002	0.584 ± 0.063	0.0001	0.055 ± 0.005
tumor	0.135 ± 0.034	0.0093	0.143 ± 0.011	0.0001	0.676 ± 0.030	0.000005	0.041 ± 0.005
total %	19.08 ± 1.91	0.0001	30.22 ± 9.19	0.0124	45.02 ± 7.62	0.0001	0.72 ± 0.14
T/M	3.59 ± 0.95	0.8015	3.72 ± 0.66	0.5985	2.6 ± 0.56	0.2091	3.40 ± 0.74
T/B	7.12 ± 1.59	0.0145	7.8 ± 0.64	0.0005	16.39 ± 1.96	0.0003	3.18 ± 0.45
K/T	142.67 ± 41.47	0.0056	210.8 ± 79.68	0.0048	63.43 ± 14.42	0.0048	12.12 ± 3.62

B. Single Mismatch [^{111}In]$_n$*KRAS2* G12 V Probes

tissues	[^{111}In]$_2$ **WT5204**	null prob.	[^{111}In]$_8$ **WT8910**	null prob.	[^{111}In]$_{16}$ **WT13851**	null prob.	[^{111}In]DOTA
muscle	0.046 ± 0.006	0.0009	0.030 ± 0.004	0.0034	0.201 ± 0.030	0.0004	0.012 ± 0.003
intestine	0.079 ± 0.008	0.0002	0.043 ± 0.006	0.0030	0.156 ± 0.023	0.0005	0.018 ± 0.003
heart	0.042 ± 0.004	0.0002	0.037 ± 0.006	0.0014	0.333 ± 0.042	0.0002	0.008 ± 0.002
lungs	0.093 ± 0.009	0.0017	0.207 ± 0.031	0.0008	0.371 ± 0.055	0.0005	0.038 ± 0.009
blood	0.049 ± 0.005	0.0004	0.012 ± 0.002	0.6560	0.213 ± 0.032	0.0004	0.013 ± 0.003
spleen	0.105 ± 0.012	0.0005	0.056 ± 0.009	0.0119	0.559 ± 0.087	0.0005	0.032 ± 0.003
kidneys	19.04 ± 2.34	0.0002	13.89 ± 2.11	0.0004	55.41 ± 12.85	0.0018	0.500 ± 0.099
liver	0.248 ± 0.033	0.0006	0.104 ± 0.015	0.0058	0.979 ± 0.150	0.0004	0.055 ± 0.005
tumor	0.144 ± 0.014	0.0003	0.113 ± 0.014	0.0011	1.309 ± 0.211	0.0005	0.041 ± 0.005
total %	19.85 ± 3.22	0.00006	14.5 ± 2.18	0.0004	59.53 ± 10.32	0.0109	0.72 ± 0.14
T/M	3.11 ± 0.46	0.5952	3.72 ± 0.007	0.4955	6.51 ± 0.97	0.0115	3.40 ± 0.74
T/B	2.96 ± 0.45	0.5816	9.28 ± 0.007	0.00002	6.15 ± 0.88	0.0065	3.18 ± 0.45
K/T	132.2 ± 26.1	0.0014	122.8 ± 35.2	0.0056	42.3 ± 8.4	0.0046	12.12 ± 3.62

[a] Tissue samples were analyzed 24 h after tail vein administration of ~2 nmol doses of each [^{111}In]$_n$*KRAS2* probe, or 80 nmol (~11 MBq, 300 μCi) of [^{111}In]DOTA control, to immunocompromised mice bearing human AsPC1 (G12D) pancreatic cancer xenografts (n = 3).

same order, which correlates with little change in the tumor/muscle (T/M) ratios as a function of n (Table 2A). On the other hand, the kidney/tumor ratios (K/T) were least for n = 16 (Table 2AB).

In contrast, the total %ID/g for the PNA-free [^{111}In]DOTA control was 26−83 times less than the total %ID/g for the [^{111}In]$_n$*KRAS2* PNA probes (Table 2A), which implies that the low molecular mass [^{111}In]DOTA does not accumulate readily in tissues, unlike the significant nonspecific organ accumulation of free ^{111}In(III) (*25*), and is cleared much more rapidly than high molecular weight probes like [^{111}In]$_n$*KRAS2* PNA probes. The [^{111}In]DOTA complex does not dissociate appreciably over the time course of the experiment, precluding redistribution to naturally occurring proteins in blood and tissues. As a result, the chemically stable and neutral [^{111}In]DOTA complex exits the body quickly by renal excretion. The T/M ratios for [^{111}In]DOTA were comparable to that for [^{111}In]$_n$*KRAS2* PNA probes (Table 2).

Elevated doses of nonradioactive Gd$_8$-*KRAS2* G12 V probe, 1.9 to 94 nmol, added to [^{111}In]$_8$*KRAS2* G12 V probe, increased image intensity of the fully matched [^{111}In]$_8$PNA probe in CAPAN2 (G12 V) xenografts 24 h after administration (Figure 3A). As a result, T/M ratios of ^{111}In image intensity at 24 h increased from 3.9 ± 0.4 to 6.3 ± 0.6 (Figure 3A). T/M ratios for all time points increased upon addition of Gd$_{2,8}$-*KRAS2* G12 V probes (Figure 3B, and Table S2 in Supporting Information).

Tissue distribution measurements (Table S2 in Supporting Information) showed increased accumulation of the fully matched [^{111}In]$_8$PNA probe, in combination with elevated doses of nonradioactive Gd$_{2,8}$-*KRAS2* G12 V probe in CAPAN2 (G12 V) xenografts, as well as in other tissues, by 3−6-fold, except for a 2-fold decrease in kidney accumulation. The K/T ratio decreased dramatically and significantly, more than 5-fold, from 174 ± 17 to 28 ± 3, 24 h after coinjecting 94 nmol of nonradioactive Gd$_{2,8}$-*KRAS2* G12 V probe with 2 nmol of [^{111}In]$_8$*KRAS2* G12 V probe (Figure 3C). K/T reduction by the Gd$_2$-*KRAS2* G12 V probe vs the Gd$_8$-*KRAS2* G12 V probe, analyzed by the Mann−Whitney rank sum test, was not significantly different (p = 0.886).

DISCUSSION

These studies revealed that [^{111}In]$_n$*KRAS2* PNA-IGF1 analogue nanoparticles permeated xenografts, entered cancer cells, and accumulated in a sequence-specific manner. We observed that the relative T/M intensity of scintigraphic images of AsPC1 pancreatic cancer xenografts increased with the size of the dendrimer and the number of DOTA chelating groups, up to n = 16, but only for fully matched [^{111}In]$_n$*KRAS2* G12D probes. In contrast, the relative T/M intensity of scintigraphic images of AsPC1 pancreatic cancer xenografts stayed constant for single mismatch [^{111}In]$_n$*KRAS2* G12 V probes, independent of size and number of chelated ^{111}In cations.

Tissue distribution measurements of total %ID/g, reaching 45−60%, imply that the largest [^{111}In]$_{16}$*KRAS2* PNA probes exhibit longer clearance times than the smaller probes. In the n = 16 case, renal excretion was apparently reduced, relative to smaller probes. That hypothesis agrees with the reduction in K/T ratios with increasing "n" of DOTA residues per PNA probe. For MRI, as well as for scintigraphic imaging, extended retention will increase signal intensity over 24−48 h, for which we already observed a preliminary indication (*24*).

The average diameter of gyration for the Gd$_{16}$-*KRAS2* G12D probe, g/mol, was previously calculated to be 3.3 ± 0.1 nm (*24*). In contrast, the single chelator [^{64}Cu]*KRAS2* G12D probe, g/mol, was previously calculated to be 2.2 ± 0.1 nm (*12*). On the nanoparticle scale, 2−3 nm is still small, minimizing the probability of nanoparticle toxicity. DOTA holds Gd(III) so

strongly (*35*) that toxicity by transchelation is most unlikely. In practice, Gd-chelator toxicity occurs only in the context of poor kidney function (*36*). Considering potential toxicity of the PNA, no hepatic or renal toxicity was observed in mice after administration of 2.5 mg/kg of PNA (*37*), nor immunogenicity (*38*), mutagenicity, or clastogenicity (*39*).

In our previous report (*24*), we noted that concentration of *KRAS2* PNA hybridization probes in AsPC1 cells should approach a maximum, based on our QRT-PCR analysis (*12*), of 2×10^4 *KRAS2* mRNAs in a 1 pL pancreas cancer cell, or ~30 nM. At 1 ^{111}In(III) or Gd(III) per DOTA chelator, 480 nM intracellular ^{111}In(III) or Gd(III) might thus be achieved at 16 Gd(III) per probe. These calculated concentrations of intracellular Gd(III) are in accord with the minimum concentration of 300 nM Gd-nanoparticle calculated for molecular MR visualization in T1-weighted imaging (*40*). That estimate was confirmed in turn for fourth-generation polyamidoamine dendrimers conjugated with 40 Gd(III)-DTPA chelators and a fluorescently labeled anti-EGFR antibody. That large, slowly rotating probe displayed a relaxivity of 323.5/mM•s (*40*). Furthermore, we discussed at length (*24*) the phenomena of restricted mobility and degrees of freedom for Gd_n-*KRAS2* PNA probes bound to high molecular mass *KRAS2* mRNA/polyribosome complexes in viscous cytoplasm that would all contribute to increased relaxivity, relative to Gd-DTPA. This analysis predicts favorable tumor accumulation of the Gd_8-chelated *KRAS2* probe at elevated doses, which correlates with the positive preliminary MRI result we reported earlier (*24*).

After finding sequence-specific images of *KRAS2* mRNA expression in pancreatic cancer xenografts with 2 nmol doses of complementary [^{111}In]$_n$*KRAS2* G12D probes, we modeled the circumstances of MRI, requiring higher doses of nonradioactive Gd-chelated probes. Upon mixing increasing doses of Gd_n-*KRAS2* G12 V probe with constant [^{111}In]$_8$*KRAS2* G12 V probe prior to administration, we observed more intense CAPAN2 G12 V xenograft ^{111}In images, and less intense kidney images, as the nonradioactive Gd_n-*KRAS2* G12 V probe dose increased. In parallel, elevated doses of $Gd_{2.8}$-*KRAS2* G12 V probe added to [^{111}In]$_8$*KRAS2* G12 V probe significantly decreased K/T.

This phenomenon suggests that nonspecific binding sites in the kidney consume a significant portion of the 2 nmol doses of undiluted [^{111}In]$_8$*KRAS2* G12 V probes, but only a small portion of the 96 nmol doses of the [^{111}In]$_8$*KRAS2* G12 V-Gd_n-*KRAS2* G12 V mixture. In the AsPC1 xenograft, however, IGF1R turns over continuously over the 48 h of these experiments, continually delivering probes with IGF1 analogues into the cytoplasm of AsPC1 cells. Furthermore, continuous transcription of new *KRAS2* mRNAs over the 48 h of these experiments suggests that available *KRAS2* mRNA binding sites are not saturated. If the intracellular *KRAS2* mRNAs are not saturated, then both labeled and unlabeled PNA probes can accumulate inside pancreatic cancer cells over time, yielding our observation of significantly decreased K/T at 24−48 h.

CONCLUSIONS

(1) mRNA expression in pancreatic cancer xenografts can be selectively imaged with ([^{111}In]DOTA-AEEA)$_n$-PDAP^m-$AEEA_2$-*KRAS2* PNA-AEEA-IGF1 analogue probes with single mismatch specificity. (2) Tumor/Muscle image intensity ratios for ([^{111}In]DOTA)$_n$*KRAS2* G12D PNA probes increased from 3 to 6, in the order $DOTA_2 < DOTA_8 < DOTA_{16}$. (3) Elevated doses of Gd_8-*KRAS2* G12 V probes increased the image intensity of [^{111}In]$_8$*KRAS2* G12 V probes in xenografts, thereby increasing the tumor-to-muscle ratios from 3.9 ± 0.4 to 6.3 ± 0.6. Elevated doses of $Gd_{2,8}$-*KRAS2* G12 V probes decreased the kidney-to-tumor ratios more than 5-fold from 174 ± 17 to 28 ± 3.

These experiments supported the hypothesis that PDAP dendrimers with up to 16 DOTA chelators coupled to PNA-IGF1 analogue probes do not inhibit tumor uptake of PNA-IGF1 analogue probes. Thus, dendrimeric PNA genetic imaging agents can be used directly for preclinical scintigraphic imaging. In addition, dendrimeric PNA genetic imaging agents can be used for preliminary radionuclide testing of targeting specificity prior to full preclinical development of Gd-chelated PNA agents for magnetic resonance imaging (MRI) of pathogenic mRNA in vivo.

ACKNOWLEDGMENT

We thank Dr. Richard Wassell for assistance in measuring mass spectra of DOTA-PDAP-PNA-IGF1 analogues. Grant support: This work was supported in part by NCI contract N01 CO27175 and NCI subaward CA105008 to E.W., and NCI grant CA109231 to M.L.T. Conflicts of interest: E.W. and MLT founded GeneSeen LLC, which might ultimately benefit from the results of this investigation, but did not support the work.

Supporting Information Available: Additional data on synthesis and experimental results with additional *KRAS2* probes. This material is available free of charge via the Internet at http://pubs.acs.org.

LITERATURE CITED

(1) American Cancer Society. (2009) Cancer Facts and Figures American Cancer Society, Atlanta, GA.
(2) Kern, S. E., Hruban, R. H., Hidalgo, M., and Yeo, C. J. (2002) An introduction to pancreatic adenocarcinoma genetics, pathology and therapy. *Cancer Biol. Ther. 1*, 607–13.
(3) Massoud, T. F., and Gambhir, S. S. (2003) Molecular imaging in living subjects: seeing fundamental biological processes in a new light. *Genes Dev. 17*, 545–80.
(4) Tavitian, B., Terrazzino, S., Kuhnast, B., Marzabal, S., Stettler, O., Dolle, F., Deverre, J. R., Jobert, A., Hinnen, F., Bendriem, B., Crouzel, C., and Di Giamberardino, L. (1998) In vivo imaging of oligonucleotides with positron emission tomography. *Nat. Med. 4*, 467–71.
(5) Shi, N., Boado, R. J., and Pardridge, W. M. (2000) Antisense imaging of gene expression in the brain in vivo. *Proc. Natl. Acad. Sci. U.S.A. 97*, 14709–14714.
(6) Gallazzi, F., Wang, Y., Jia, F., Shenoy, N., Landon, L. A., Hannink, M., Lever, S. Z., and Lewis, M. R. (2003) Synthesis of radiometal-labeled and fluorescent cell-permeating peptide-PNA conjugates for targeting the bcl-2 proto-oncogene. *Bioconjugate Chem. 14*, 1083–95.
(7) Blasberg, R. G. (2003) Molecular imaging and cancer. *Mol. Cancer Ther. 2*, 335–43.
(8) Roivainen, A., Tolvanen, T., Salomaki, S., Lendvai, G., Velikyan, I., Numminen, P., Valila, M., Sipila, H., Bergstrom, M., Harkonen, P., Lonnberg, H., and Langstrom, B. (2004) 68Ga-labeled oligonucleotides for in vivo imaging with PET. *J. Nucl. Med. 45*, 347–355.
(9) Tian, X., Aruva, M. R., Qin, W., Zhu, W., Duffy, K. T., Sauter, E. R., Thakur, M. L., and Wickstrom, E. (2004) External imaging of CCND1 cancer gene activity in experimental human breast cancer xenografts with 99mTc-peptide-peptide nucleic acid-peptide chimeras. *J. Nucl. Med. 45*, 2070–2082.
(10) Tian, X., Aruva, M. R., Qin, W., Zhu, W., Sauter, E. R., Thakur, M. L., and Wickstrom, E. (2005) Noninvasive molecular imaging of *MYC* mRNA expression in human breast cancer xenografts with a [^{99m}Tc]peptide-peptide nucleic acid-peptide chimera. *Bioconjugate Chem. 16*, 70–79.
(11) Sun, X., Fang, H., Li, X., Rossin, R., Welch, M. J., and Taylor, J. S. (2005) MicroPET imaging of MCF-7 tumors in mice via unr mRNA-targeted peptide nucleic acids. *Bioconjugate Chem. 16*, 294–305.
(12) Chakrabarti, A., Zhang, K., Aruva, M. R., Cardi, C. A., Opitz, A. W., Wagner, N. J., Thakur, M. L., and Wickstrom, E. (2007)

Radiohybridization PET imaging of *KRAS* G12D mRNA expression in human pancreas cancer xenografts with [^{64}Cu]DO3A-peptide nucleic acid-peptide nanoparticles. *Cancer Biol, Ther. 6*, 948–956.

(13) Tian, X., Aruva, M. R., Zhang, K., Cardi, C. A., Thakur, M. L., and Wickstrom, E. (2007) PET imaging of *CCND1* mRNA in human MCF7 estrogen receptor-positive breast cancer xenografts with an oncogene-specific [^{64}Cu]DO3A-PNA-peptide radiohybridization probe. *J. Nucl. Med. 48*, 1699–1707.

(14) Jia, F., Figueroa, S. D., Gallazzi, F., Balaji, B. S., Hannink, M., Lever, S. Z., Hoffman, T. J., and Lewis, M. R. (2008) Molecular imaging of bcl-2 expression in small lymphocytic lymphoma using 111In-labeled PNA-peptide conjugates. *J. Nucl. Med. 49*, 430–8.

(15) Nielsen, P. E., Egholm, M., Berg, R. H., and Buchardt, O. (1991) Sequence-selective recognition of DNA by strand displacement with a thymine-substituted polyamide. *Science 254*, 1497–500.

(16) Larsen, H. J., Bentin, T., and Nielsen, P. E. (1999) Antisense properties of peptide nucleic acid. *Biochim. Biophys. Acta 1489*, 159–66.

(17) Gray, G. D., Basu, S., and Wickstrom, E. (1997) Transformed and immortalized cellular uptake of oligodeoxynucleoside phosphorothioates, 3′-alkylamino oligodeoxynucleotides, 2′-O-methyl oligoribonucleotides, oligodeoxynucleoside methylphosphonates, and peptide nucleic acids. *Biochem. Pharmacol. 53*, 1465–1476.

(18) Basu, S., and Wickstrom, E. (1997) Synthesis and characterization of a peptide nucleic acid conjugated to a D-peptide analog of insulin-like growth factor 1 for increased cellular uptake. *Bioconjugate Chem. 8*, 481–488.

(19) Egholm, M., Buchardt, O., Christensen, L., Behrens, C., Freier, S. M., Driver, D. A., Berg, R. H., Kim, S. K., Norden, B., and Nielsen, P. E. (1993) PNA hybridizes to complementary oligonucleotides obeying the Watson- Crick hydrogen-bonding rules. *Nature 365*, 566–568.

(20) Tian, X., and Wickstrom, E. (2002) Continuous solid-phase synthesis and disulfide cyclization of peptide-PNA-peptide chimeras. *Org. Lett. 4*, 4013–4016.

(21) Tian, X., Chakrabarti, A., Amirkhanov, N. V., Aruva, M. R., Zhang, K., Mathew, B., Cardi, C., Qin, W., Sauter, E. R., Thakur, M. L., and Wickstrom, E. (2005) External imaging of CCND1, MYC, and KRAS oncogene mRNAs with tumor-targeted radionuclide-PNA-peptide chimeras. *Ann. N.Y. Acad. Sci. 1059*, 106–44.

(22) Opitz, A. W. (2008) in *Chemical Engineering*, p 457, University of Delaware, Newark.

(23) Amirkhanov, N. V., and Wickstrom, E. (2005) Synthesis of novel polydiamidopropanoate dendrimer PNA-peptide chimeras for non-invasive magnetic resonance imaging of cancer. *Nucleosides Nucleotides Nucleic Acids 24*, 423–6.

(24) Amirkhanov, N. V., Dimitrov, I., Opitz, A. W., Zhang, K., Lackey, J. P., Cardi, C. A., Lai, S., Wagner, N. J., Thakur, M. L., and Wickstrom, E. (2008) Design of (Gd-DO3A)$_n$-polydiamidopropanoate-peptide nucleic acid-D(Cys-Ser-Lys-Cys) magnetic resonance contrast agents. *Biopolymers 89*, 1061–1076.

(25) Watanabe, N., Oriuchi, N., Endo, K., Inoue, T., Tanada, S., Murata, H., Kim, E. E., and Sasaki, Y. (1999) Localization of indium-111 in human malignant tumor xenografts and control by chelators. *Nucl. Med. Biol. 26*, 853–8.

(26) Cole, W. C., DeNardo, S. J., Meares, C. F., McCall, M. J., DeNardo, G. L., Epstein, A. L., O'Brien, H. A., and Moi, M. K. (1987) Comparative serum stability of radiochelates for antibody radiopharmaceuticals. *J. Nucl. Med. 28*, 83–90.

(27) Pippin, C. G., Parker, T. A., McMurry, T. J., and Brechbiel, M. W. (1992) Spectrophotometric method for the determination of a bifunctional DTPA ligand in DTPA-monoclonal antibody conjugates. *Bioconjugate Chem. 3*, 342–5.

(28) Bryant, L. H., Jr., Brechbiel, M. W., Wu, C., Bulte, J. W., Herynek, V., and Frank, J. A. (1999) Synthesis and relaxometry of high-generation (G = 5, 7, 9, and 10) PAMAM dendrimer-DOTA-gadolinium chelates. *J. Magn. Reson. Imaging 9*, 348–52.

(29) Tan, M. H., and Chu, T. M. (1985) Characterization of the tumorigenic and metastatic properties of a human pancreatic tumor cell line (AsPC-1) implanted orthotopically into nude mice. *Tumour Biol. 6*, 89–98.

(30) Yasuda, D., Iguchi, H., Ikeda, Y., Nishimura, S., Steeg, P., Misawa, T., Nasawa, H., and Kono, A. (1993) Possible association of nm23 gene expression and Ki-ras point mutations with metastatic potential in human pancreatic cancer-derived cell lines. *Int. J. Oncol. 3*, 641–4.

(31) Neid, M., Datta, K., Stephan, S., Khanna, I., Pal, S., Shaw, L., White, M., and Mukhopadhyay, D. (2004) Role of insulin receptor substrates and protein kinase C-zeta in vascular permeability factor/vascular endothelial growth factor expression in pancreatic cancer cells. *J. Biol. Chem. 279*, 3941–8.

(32) Fogh, J., Fogh, J. M., and Orfeo, T. (1977) One hundred and twenty-seven cultured human tumor cell lines producing tumors in nude mice. *J. Natl. Cancer Inst. 59*, 221–6.

(33) Sun, C., Yamato, T., Furukawa, T., Ohnishi, Y., Kijima, H., and Horii, A. (2001) Characterization of the mutations of the K-ras, p53, p16, and SMAD4 genes in 15 human pancreatic cancer cell lines. *Oncol. Rep. 8*, 89–92.

(34) Yendluri, V., Wright, J. R., Coppola, D., Buck, E., Iwata, K. K., Mokenze, M., Sebti, S., and Springett, G. M. (2008) in *Gastrointestinal Cancers Symposium*, p 184, American Society of Clinical Oncology, Orlando, FL.

(35) Tweedle, M. F., Hagan, J. J., Kumar, K., Mantha, S., and Chang, C. A. (1991) Reaction of gadolinium chelates with endogenously available ions. *Mag. Reson. Imaging 9*, 409–415.

(36) Briguori, C., Colombo, A., Airoldi, F., Melzi, G., Michev, I., Carlino, M., Montorfano, M., Chieffo, A., Bellanca, R., and Ricciardelli, B. (2006) Gadolinium-based contrast agents and nephrotoxicity in patients undergoing coronary artery procedures. *Catheter Cardiovasc. Interv. 67*, 175–80.

(37) Rembach, A., Turner, B. J., Bruce, S., Cheah, I. K., Scott, R. L., Lopes, E. C., Zagami, C. J., Beart, P. M., Cheung, N. S., Langford, S. J., and Cheema, S. S. (2004) Antisense peptide nucleic acid targeting GluR3 delays disease onset and progression in the SOD1 G93A mouse model of familial ALS. *J. Neurosci. Res. 77*, 573–82.

(38) Cutrona, G., Boffa, L. C., Mariani, M. R., Matis, S., Damonte, G., Millo, E., Roncella, S., and Ferrarini, M. (2007) The peptide nucleic acid targeted to a regulatory sequence of the translocated c-myc oncogene in Burkitt's lymphoma lacks immunogenicity: follow-up characterization of PNAEmu-NLS. *Oligonucleotides 17*, 146–50.

(39) Boffa, L. C., Cutrona, G., Cilli, M., Matis, S., Damonte, G., Mariani, M. R., Millo, E., Moroni, M., Roncella, S., Fedeli, F., and Ferrarini, M. (2007) Inhibition of Burkitt's lymphoma cells growth in SCID mice by a PNA specific for a regulatory sequence of the translocated c-myc. *Cancer Gene Ther. 14*, 220–6.

(40) Wang, E., Isaacman, S., Chang, Y.-T., Deans, A., Johnson, G., and Canary, J. (2005) Radiological Society of North America Annual Meeting, p TA35, Chicago IL.

BC900523C

Synthesis of a Novel α-Galactosyl Ceramide Haptenated-Lipid Antigen, a Useful Tool in Demonstrating the Involvement of *i*NKT Cells in the Production of Antilipid Antibodies

Natacha Veerapen,[†] Elizabeth A. Leadbetter,[‡] Michael B. Brenner,[‡] Liam R. Cox,[§] and Gurdyal S. Besra*[,†]

School of Biosciences and School of Chemistry, University of Birmingham, Edgbaston, Birmingham, B15 2TT, United Kingdom, Division of Rheumatology, Immunology, and Allergy, Brigham and Women's Hospital, Harvard Medical School, 1 Jimmy Fund Way, Boston, Massachusetts 02115. Received November 30, 2009; Revised Manuscript Received March 4, 2010

A new haptenated derivative of α-galactosyl ceramide (α-GalCer) has been synthesized to assist in the study of the mechanism of T cell help for the production of B cell antibodies. Our synthetic route provides access to an amine intermediate which can easily be extended to generate an array of compounds, useful in various ongoing studies. Herein, we also describe the biological evaluation of the nitrophenyl (NP) haptenated α-GalCer and demonstrate its importance in such mechanistic studies. For instance, *in vitro* studies showed that NP-α-GalCer stimulates both T and B cell proliferation while *in vivo* studies in immunized mice showed the production of IgG anti-NP antibodies after exposure to NP-α-GalCer. The interpretation of these results helps toward a better understanding of T cell help for the production of antibodies.

INTRODUCTION

Antigen-presenting cells (APC) [1]and lymphocytes are two major cell types that work together to ensure an effective immune response through the recognition and elimination or neutralization of pathogenic organisms and other foreign invaders in mammals (*1*−*4*). APC include macrophages, B lymphocytes, and dendritic cells, while T cells, invariant natural killer (*i*NKT), and natural killer (NK) cells are three major types of lymphocytes important for immune defense. Specifically, B cells recognize their epitopes as a part of either an intact protein, lipid molecule, or polysaccharide, whereas T cells only recognize epitopes which are subcomponents of an intact molecule and are found in association with antigen-presenting molecules, such as MHC class II or CD1.

A distinctive class of T cells, known as invariant Natural Killer T (*i*NKT) cells, display characteristics of both T cells and NK cells and play a crucial role in diverse immune responses and other pathologic conditions (*5*). The synthetic glycolipid α-galactosyl ceramide (α-GalCer) (*6*), known as KRN7000 (**1**), is a powerful agonist for these cells. When it is presented by CD1d, it activates *i*NKT cells to release diverse cytokines, including both Th1 and Th2 cytokines (*7*−*9*). It is believed that the release of Th1 cytokines may contribute to antitumor and antimicrobial functions, while Th2 cytokines may help alleviate autoimmune diseases (*10*−*12*), such as multiple sclerosis (*13*) and arthritis (*14*) or helminth infections. Once stimulated, *i*NKT cells also activate other cells, such as dendritic cells, NK cells, peptide-reactive T cells, and B cells (*2*).

The detection of IgG antilipid antibodies, generated by lipid-specific B cells during infection and autoimmune disease, such as malaria (*15*) and systemic lupus erythematosus (*16*), respectively, suggests the existence of cooperation between *i*NKT cells and B cells (*17*). To better understand the mechanism of *i*NKT cell help for the production of antilipid antibodies, haptenated lipid antigens, containing both a B cell recognition component and an *i*NKT cell agonist are useful tools (Figure 1) (*17*). As part of ongoing studies on the emerging role for CD1d and *i*NKT cells/B cell responses that are crucial in defense against infection, autoimmunity, and tumor immunity, easy access to hybrid haptenated lipids is therefore desired. Here, we propose that the modified α-GalCer derivative **2** (Figure 2) represents an ideal template which is easily amenable to such molecules. We believe that the amine functionality in compound **2** allows conjugation to different haptens, e.g., biotin or 4-hydroxy-3-nitrophenyl (NP) to yield substrates such as compound **3**, thereby making it an ideal scaffold. In this paper, we describe the syntheses of compounds **2** and **3** and describe the biological activities of compounds **3** and **4** (Figure 2). The hapten, 4-hydroxy-3-nitrophenyl (NP), was chosen as the B cell recognition component because the anti-NP B cell response has been extensively studied in mice and there are a number of B-cell specific immunologic tools available to investigate this response (*18*−*20*). Conversely, α-GalCer was selected as the *i*NKT cell component of this conjugated molecule because it is also a well-studied antigen which stimulates robust activation

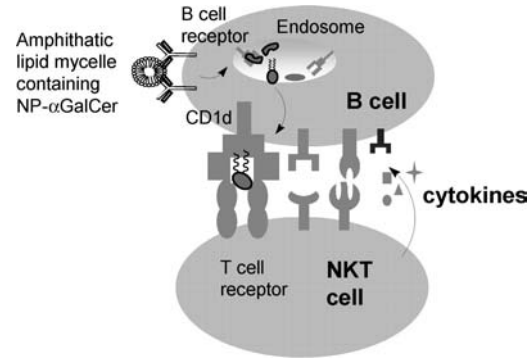


Figure 1. *i*NKT cells provide cognate help for lipid-specific B cells.

* To whom correspondence should be addressed. Phone: (44)1214158123; E-mail: g.besra@bham.ac.uk.

[†] School of Biosciences, University of Birmingham.

[‡] Harvard Medical School.

[§] School of Chemistry, University of Birmingham.

[1]Abbreviations: APC, antigen-presenting cell; IgG, immunoglobin G; IgM, immunoglobin M; DMF, dimethylformamide; CFSE, carboxyfluorescein succinimidyl ester.

10.1021/bc9005255 © 2010 American Chemical Society
Published on Web 03/26/2010

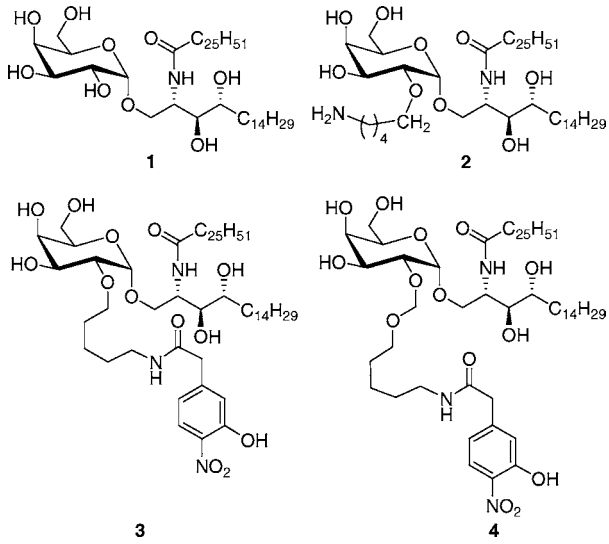


Figure 2. CD1d agonist KRN7000 and analogues.

of *i*NKT cells and for which there are a number of important immunologic tools available.

EXPERIMENTAL PROCEDURES

General Experimental Procedures. ^{1}H NMR spectra were recorded at 400 or 300 MHz, using Bruker AMX 400, Bruker AV 400, Bruker AV 300, and Bruker AC 300 spectrometers. ^{13}C NMR spectra were recorded at 100 or 75 MHz, respectively, using Bruker AMX 400, Bruker AV 400, Bruker AV 300, and Bruker AC 300 spectrometers. Chemical shifts are reported as δ values (ppm) referenced to the following solvent signals: $CHCl_3$, δ H 7.26; $CDCl_3$, δ C 77.0; CH_3OH, δ H 3.34; CD_3OD, δ C 49.9. Quaternary carbons were reported only when observed. HRMS were recorded on a Micromass LCT spectrometer using a lock mass incorporated into the mobile phase. All reagents were obtained from commercial sources and were used without further purification unless stated otherwise. Anhydrous solvents were purchased from Sigma-Aldrich, U.K., stored over 4 Å molecular sieves and under an argon atmosphere. Analytical thin layer chromatography (TLC) was performed on aluminum plates precoated with Merck silica gel 60A F-254 as adsorbent. The developed plates were air-dried, visualized by UV detection (at 254 nm) and/or stained with 5% phosphomolybdic acid in EtOH (MPA spray). Compounds were purified by flash column chromatography on Merck silica gel (particle size 40−63 lm mesh) or Fluka 60 (40−60 lm mesh) silica gel.

Phenyl 3,4-*O*-Isopropylidene-6-*O*-*tert*-butyldiphenylsilyl-2-*O*-(5-azapentyl)-1-thio-β-D-galactopyranoside 13. To a cold solution of phenyl 3,4-*O*-isopropylidene-6-*O*-*tert*-butyldiphenylsilyl-1-thio-β-D-galactopyranoside **12** (2.00 g, 3.64 mmol) in dry DMF (30 mL) was added sodium hydride (0.44 g, 18.2 mmol, 5 equiv) in small amounts at 0 °C. The solution was allowed to stir for 20 min before the addition of 1,5-dibromopentane (4 mL, 18.2 mmol, 5 equiv). The reaction mixture was stirred at room temperature for two hours, and then taken up in water (50 mL). The resulting mixture was then extracted with CH_2Cl_2 (3 × 20 mL). The combined organic layers were washed with brine (30 mL), dried over anhydrous Na_2SO_4, and concentrated in vacuo. The crude bromide was further dissolved in DMSO (30 mL) and sodium azide (1.20 g, 18.2 mmol, 5 equiv) was added. The reaction was stirred overnight at 60 °C, after which it was taken up in water (50 mL) and extracted with CH_2Cl_2 (3 × 20 mL). The combined organic layers were then washed with brine (30 mL), dried over anhydrous Na_2SO_4, and evaporated. The residue was then purified by flash chromatography using hexanes/EtOAc (4:1) to give the desired product as a colorless oil (1.80 g, 2.72 mmol, 75%). ^{1}H NMR ($CDCl_3$): δ 7.65−7.75 (3H, m, Ar-*H*), 7.49−7.55 (2H, m, Ar-*H*), 7.32−7.44 (8H, m, Ar-*H*), 7.19−7.27 (2H, m, Ar-*H*), 4.55 (1H, d, $J_{1,2}$ = 9.72 Hz, H-1), 4.28 (1H, dd, $J_{4,3}$ = 5.6, $J_{4,5}$ = 1.9 Hz, H-4), 4.15 (1H, dd, $J_{3,2}$ = 6.5 Hz, H-3), 3.96−3.83 (3H, m, H-5, H-6a, H-6b), 3.72 (1H, ddd, $J_{1a',1b'}$ = 10.7, $J_{1a',2a'}$ = $J_{1a',2b'}$ = 6.1 Hz, $OCH_2C_3H_6CH_2N_3$), 3.59 (1H, ddd, $J_{1b',2a'}$ = 8.1, $J_{1b',2b'}$= 5.2 Hz, $OCH_2C_3H_6CH_2N_3$), 3.34−3.39 (1H, m, H-2), 3.26−3.31 (2H, m, $OCH_2C_3H_6CH_2N_3$), 1.56−1.70 (4H, m, CH_2), 1.34, 1.47 (6H, 2s, $C(CH_3)_2$), 1.09 (2H, s, CH_2), 1.06 (9H, s, *t*-Bu). ^{13}C NMR (75 MHz, $CDCl_3$): δ 135.6, 134.8, 133.4, 131.4, 131.5, 129.7, 128.8, 127.7, 127.6, 127.2 (18 C_{Ar}), 109.8 ($O_2C(CH3)_2$), 86.6 (C-1), 79.7, 79.2, 76.7, 73.4 (C-2, C-3, C-4, C-5), 71.7 ($OCH_2C_3H_6CH_2N_3$), 63.0 (C-6), 51.4 ($OCH_2C_3H_6CH_2N_3$), 29.5, 28.6 (2 × CH_2), 28.0, 26.8, 26.6, 26.3 ($C(CH_3)_3$, $C(CH_3)_2$), 23.3 (CH_2), 19.2 ($C(CH_3)_3$). HRMS calcd for $C_{36}H_{47}N_3O_5SiS$ $[M+Na]^+$: 684.2904, found 684.2908.

Phenyl 2-*O*-(5-Azapentyl)-1-thio-β-D-galactopyranoside 10. To a solution of **13** (1.50 g, 2.27 mmol) in THF (30 mL) was added a 1 M solution of tetrabutylammonium fluoride (4.50 mL, 2 equiv). The reaction mixture was stirred at room temperature for 4 h. Upon completion of the reaction, the reaction mixture was diluted with EtOAc (20 mL) and washed successively with water (20 mL) and brine (20 mL). The organic layer was dried over anhydrous Na_2SO_4 and evaporated. The residue was then dissolved in CH_2Cl_2, and TFA (5 mL) was added. The mixture was stirred at room temperature for 2 h, after which time TLC analysis indicated that the reaction was complete. The solvents were removed in vacuo, and the residue was purified by flash chromatography using EtOAc to give the desired product as a colorless oil (0.68 g, 1.78 mmol, 78%). ^{1}H NMR ($CDCl_3$): δ 7.48−7.54 (2H, m, Ar-*H*), 7.26−7.35 (3H, m, Ar-*H*), 4.59 (1H, d, H-1, $J_{1,2}$ = 9.7 Hz), 4.06 (1H, d, $J_{4,3}$ = 3.1 Hz, H-4), 3.95 (1H, dd, $J_{6a,6b}$ = 11.9, $J_{6a,5}$ = 5.9 Hz, H-6a), 3.90 (1H, dd, H-6b), 3.80−3.69 (2H, m, $OCH_2C_3H_6CH_2N_3$), 3.63 (1H, dd, $J_{3,2}$ = 8.9 Hz, H-3), 3.58 (1H, m, H-5), 3.45 (1H, t, H-2), 3.28 (2H, t, $OCH_2C_3H_6CH_2N_3$), 1.56−1.71 (4H, m, CH_2), 1.07 (2H, s, CH_2). ^{13}C NMR (75 MHz, $CDCl_3$): δ 134.0, 131.1, 129.0, 127.4 (6 C_{Ar}), 87.7 (C-1), 78.5, 77.9, 75.1, 69.8 (C-2, C-3, C-4, C-5), 73.2 ($OCH_2C_3H_6CH_2N_3$), 62.6 (C-6), 51.4 ($OCH_2C_3H_6CH_2N_3$), 29.7, 28.6 (2 × CH_2), 23.2 (CH_2), 19.2 ($C(CH_3)_3$). HRMS calcd for $C_{17}H_{25}N_3O_5S$ $[M+Na]^+$: 406.1413, found 406.1426.

Phenyl 3-*O*-Benzyloxy-4,6-*O*-di-*tert*-butylsilylene-2-*O*-(5-azapentyl)-1-thio-β-D-galactopyranoside 8. To a solution of **10** (0.52 g, 1.36 mmol) in dry DMF (15 mL) was added di-*tert*-butylsilyl bis(trifluoromethanesulfonate) (0.90 g, 2.04 mmol, 1.5 equiv) at 0 °C, and the mixture was stirred for 30 min, then neutralized with Et_3N. The solution was taken up in water and extracted with EtOAc (3 × 20 mL). The organic layers were combined, washed with brine (20 mL), dried over anhydrous Na_2SO_4, and evaporated. The residue was then dissolved in pyridine (20 mL) and benzoyl chloride (0.27 g, 1.92 mmol, 1.4 equiv) was added. The mixture was stirred at room temperature for 2 h, after which time TLC analysis indicated that the reaction was complete. The reaction was quenched with methanol, diluted with CH_2Cl_2 (30 mL), washed successively with 1 M HCl (3 × 20 mL), water (2 × 20 mL), brine (20 mL), dried over anhydrous Na_2SO_4, and concentrated in vacuo. The residue was finally purified by flash chromatography using hexanes/EtOAc (4:1) to give the desired product as a colorless oil (0.82 g, 1.31 mmol, 96%). ^{1}H NMR ($CDCl_3$): δ 8.06−8.13 (2H, m, Ar-*H*), 7.41−7.65 (6H, m, Ar-*H*), 7.27−7.34 (2H, m, Ar-*H*), 5.03 (1H, dd, $J_{3,2}$ = 9.4, $J_{3,2}$ = 3.1 Hz, H-3), 4.69−4.75 (2H, m, H-1, H-4), 4.22−4.28 (2H, m, H-6a, H-6b), 3.82−3.94 (2H, m, H-2, $OCH_2C_3H_6CH_2N_3$), 3.66 (1H, ddd, $J_{1a',1b'}$ = 9.0, $J_{1a',2a'}$ = $J_{1a',2b'}$

= 6.2 Hz, $OCH_2C_3H_6CH_2N_3$), 3.50 (1H, s, H-5), 3.05−3.18 (2H, m, $OCH_2C_3H_6CH_2N_3$) 1.26−1.57 (4H, m, CH_2), 1.09 (2H, s, CH_2), 1.16, 0.97 (18H, 2s, 2 × *t*-Bu). ^{13}C NMR (75 MHz, $CDCl_3$): δ 133.2, 132.0, 131.9, 129.6, 128.8, 128.5, 127.4 (12 C_{Ar}), 88.5 (C-1), 77.3 (C-3), 76.7, 74.6, 70.6 (C-2, C-4, C-5), 73.3 ($OCH_2C_3H_6CH_2N_3$), 67.2 (C-6), 51.2 ($OCH_2C_3H_6CH_2N_3$), 29.7, 28.5 (2 × CH_2), 27.7, 27.4 (2 × $C(CH_3)_3$), 23.3, 20.7 (2 × $C(CH_3)_3$). HRMS calcd for $C_{32}H_{45}N_3O_6SiS$ $[M+Na]^+$: 650.2696, found 650.2693.

(2*S*,3*S*,4*R*)-2-*N*-*tert*-Butoxycarbonylamino-3,4-di(benzyloxy)1-[3-*O*-benzyloxy-4,6-*O*-di-*tert*-butylsilylene-2-*O*-(5-azapentyl)-α-D-galactopyranosyloxy)]-octadecane 14. A suspension of **10** (0.75 g, 1.20 mmol), **9** (0.90 g, 1.44 mmol, 1.2 equiv), silver triflate (0.18 g, 2.4 mmol), and 4 Å molecular sieves in anhydrous CH_2Cl_2 (10 mL) was stirred, with the exclusion of light for 10 min at room temperature under Ar before it was cooled to −78 °C. A solution of *p*-nitrobenzenesulfenyl chloride (0.24 g, 1.20 mmol, 95% purity) in anhydrous CH_2Cl_2 (2 mL) was dropped into the above suspension at −78 °C. The reaction mixture was maintained at −78 °C for 30 min and allowed to warm up to 0 °C over the following 30 min, after which TLC analysis showed that the reaction was complete. The reaction was quenched with saturated $NaHCO_3$ (2 mL) and diluted with CH_2Cl_2 (5 mL) to give a suspension, which was filtered through Celite, and the Celite pad was washed with CH_2Cl_2 (10 mL). The filtrate was separated, and the organic phase was dried over anhydrous Na_2SO_4 and evaporated. The residue was purified by flash chromatography using hexanes/EtOAc (5:1) to give the glycosylated compound **14** as a light yellow oil (1.02 g, 0.89 mmol, 75%). ^{1}H NMR ($CDCl_3$): δ 7.89−8.13 (6H, m, Ar-*H*), 7.32−7.64 (12H, m, Ar-*H*), 5.64 (1H, dd, $J_{3,2}$ = 8.5, $J_{3,4}$ = 3.4 Hz, H-3^{Cer}), 5.39−5.52 (2H, m, N*H*BOC, H-4^{Cer}), 5.24 (1H, dd, $J_{3,2}$ = 10.3, $J_{3,2}$ = 3.1 Hz, H-3), 5.00 (1H, d, $J_{1,2}$ = 3.5 Hz, H-1), 4.27 (1H, d, H-4), 4.06−4.32 (3H, m, H-6a, H-6b, H-2^{Cer}), 4.00 (1H, dd, H-2), 3.73−3.84 (2H, m, H-5, H-1a^{Cer}), 3.60−3.71 (2H, m, $OCH_2C_3H_6CH_2N_3$, H-1b^{Cer}), 3.44 (1H, ddd, $J_{1a',1b'}$ = 8.9, $J_{1a',2a'}$ = $J_{1a',2b'}$ = 6.6 Hz, $OCH_2C_3H_6CH_2N_3$), 2.84−3.06 (2H, m, $OCH_2C_3H_6CH_2N_3$), 1.80−2.02 (2H, m, H-5a^{Cer}, H-5b^{Cer}), 1.49 (9H, s, $NHCO_2C(CH_3)_3$), 1.15−1.13 (24H, m, CH_2), 1.06−1.14 (2H, m, CH_2), 0.94−098 (2H, m, CH_2), 1.03, 0.92 (18H, 2s, 2 × *t*-Bu), 0.87 (3H, t, CH_3). ^{13}C NMR (75 MHz, $CDCl_3$): δ 133.3, 132.9, 133.2, 132.0, 131.9, 129.9, 129.7, 129.6, 129.4, 128.8, 128.5, 127.4 (18 C_{Ar}), 97.4 (C-1), 80.3 ($NHCOOC(CH_3)_3$), 77.1 (C-3), 76.5, 74.8, 70.2 (C-2, C-4, C-5), 73.8 (C-3^{Cer}), 73.2 ($OCH_2C_3H_6CH_2N_3$), 71.8 (C-4^{Cer}), 67.0 (C-6), 61.7 (C-1^{Cer}), 51.2 ($OCH_2C_3H_6CH_2N_3$), 49.9 (C-2^{Cer}), 32.1−22.8 (13 × CH_2^{Cer}), 29.8, 28.4 (2 × CH_2), 27.6, 27.3 (2 × $C(CH_3)_3$), 23.1, 20.5 (2 × $C(CH_3)_3$), 14.8 (CH_3^{Cer}). HRMS calcd for $C_{63}H_{94}N_4O_{13}Si[M+Na]^+$: 1165.6484, found 1165.6488.

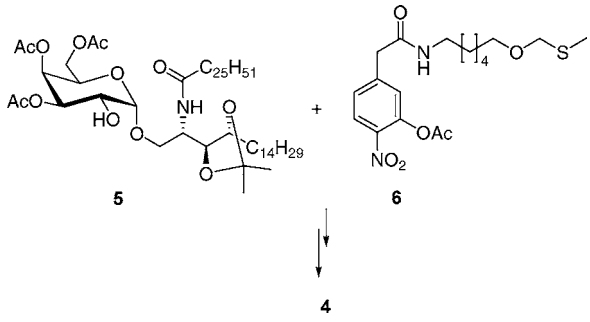
(2*S*,3*S*,4*R*)-2-*N*-*tert*-Butoxycarbonylamino-1-[2-*O*-(5-azapentyl)-α-D-galactopyranosyloxy)]-octadecanediol 15. To a solution of **14** (0.93 g, 0.814 mmol) in THF was added a 1 M solution of tetrabutylammonium fluoride (2 mL, 2 equiv). The reaction mixture was stirred at room temperature for 6 h. Upon completion of the reaction, the reaction mixture was diluted with EtOAc (20 mL) and washed successively with water (20 mL) and brine (20 mL). The organic layer was dried over anhydrous Na_2SO_4 and evaporated. The residue was then dissolved in MeOH and a 1 M solution of NaOMe (5 mL) was added. The mixture was stirred at room temperature for 2 h, after which time TLC analysis indicated that the reaction was complete. The reaction was neutralized by the addition of Dowex 50WX8−200 resin. The latter was then filtered and the filtrate concentrated to give a residue, which was purified by flash chromatography using EtOAc/MeOH (7:1) to give the title compound as a colorless syrup (0.49 g, 0.710 mmol, 88%). ^{1}H NMR ($CDCl_3$): δ 4.90 (1H, d, $J_{1,2}$ = 3.8 Hz, H-1), 3.81 (1H, d, $J_{4,3}$ = 3.1 Hz, H-4), 3.70 (1H, dd, $J_{1a',1b'}$ = 10.9, $J_{1a',2a'}$ = 4.4 Hz, H-1a^{Cer}), 3.65 (1H, dd $J_{3,2}$ = 9.8 Hz, H-3), 3.54−3.62 (5H, m, H-1b^{Cer}, H-2^{Cer}, H-3^{Cer}, H-4^{Cer}, H-5), 3.43 (1H, dd, H-2), 3.31−3.37 (2H, m, H-6a, H-6b), 3.20 (2H, ddd, $J_{1a',1b'}$ = 8.9, $J_{1a',2a'}$ = $J_{1a',2b'}$ = 6.8 Hz, $OCH_2C_3H_6CH_2N_3$), 2.02−2.11 (2H, m, $OCH_2C_3H_6CH_2N_3$), 1.50 (9H, s, $NHCO_2C(CH_3)_3$) 1.35−1.60 (m, 8H, CH_2), 1.22−1.32 (2H, m, CH_2), 1.20−1.23 (68H, m, CH_2), 0.71 (6H, t, *J* = 6.8 Hz, CH_3). ^{13}C NMR (75 MHz, $CDCl_3$): δ 98.1 (C-1), 78.2, 76.1, 75.2, 71.4, 70.2, 69.2 (C-2, C-3, C-4, C-5, C-4^{Cer}, C-3^{Cer}), 71.2 ($OCH_2C_3H_6CH_2N_3$), 68.2 (C-1^{Cer}), 61.4 (C-6), 51.3 ($OCH_2C_3H_6CH_2N_3$), 50.1 (C-2^{Cer}), 36.5−22.0 (17 × CH_2), 27.5, 27.3 (2 × $C(CH_3)_3$), 14.0 (CH_3^{Cer}). HRMS calcd for $C_{34}H_{66}N_4O_{10}[M+Na]^+$: 713.4677, found 713.4676.

(2*S*,3*S*,4*R*)-2-Amino-*N*-hexacosanoyl-1-[2-*O*-(5-azapentyl)-α-D-galactopyranosyloxy)]-3,4-octadecanediol 16. Compound **15** (0.38 g, 0.550 mmol) was dissolved in CH_2Cl_2/MeOH (2:1) (10 mL) and TFA (2 mL) was added. The reaction was stirred for 2 h and concentrated in vacuo to give the crude amine which was used in the next step without purification. The crude amine was then dissolved in a 1:1 mixture of THF/NaOAC (saturated solution) (5 mL) and the freshly prepared acid chloride of hexacosanoic acid (0.25 g, 0.603 mmol, 1.1 equiv) was added. The reaction was allowed to stir overnight at room temperature. The organic phase was then concentrated, and the residue was purified by flash chromatography (gradient from $CHCl_3$ to 15% MeOH in $CHCl_3$) to give the acylated compound **16** as a white solid (0.38 g, 0.39 mmol, 71%). ^{1}H NMR ($CDCl_3$/CD_3OD 2:1): δ 4.86 (1H, d, $J_{1,2}$ = 3.6 Hz, H-1), 3.79 (1H, d, $J_{4,3}$ = 3.2 Hz, H-4), 3.72 (1H, dd, $J_{1a',1b'}$ = 10.9, $J_{1a',2a'}$ = 4.6 Hz, H-1a^{Cer}), 3.64 (1H, dd $J_{3,2}$ = 9.8 Hz, H-3), 3.52−3.60 (5H, m, H-1b^{Cer}, H-2^{Cer}, H-3^{Cer}, H-4^{Cer}, H-5), 3.43 (1H, dd, H-2), 3.31−3.37 (2H, m, H-6a, H-6b), 3.20 (2H, ddd, $J_{1a',1b'}$ = 8.9, $J_{1a',2a'}$ = $J_{1a',2b'}$ = 6.8 Hz, $OCH_2C_3H_6CH_2N_3$), 2.00−2.10 (2H, m, $OCH_2C_3H_6CH_2N_3$), 1.36−1.59 (m, 8H, CH_2), 1.25−1.35 (2H, m, CH_2), 1.20−1.24 (68H, m, CH_2), 0.73 (6H, t, *J* = 6.8 Hz, CH_3). ^{13}C NMR (75 MHz, $CDCl_3$): δ 97.7 (C-1), 77.2, 75.2, 72.1, 70.4, 69.6, 69.3 (C-2, C-3, C-4, C-5, C-4^{Cer}, C-3^{Cer}), 71.2 ($OCH_2C_3H_6CH_2N_3$), 67.4 (C-1^{Cer}), 61.5 (C-6), 51.1 ($OCH_2C_3H_6CH_2N_3$), 49.8 (C-2^{Cer}), 36.2, 32.9, 31.6, 29.4, 29.1, 28.3, 25.6, 22.8, 22.4 (CH_2), 13.7(CH_3^{Cer}). HRMS calcd for $C_{55}H_{108}N_4O_9$ $[M+Na]^+$: 991.8014, found 991.8018.

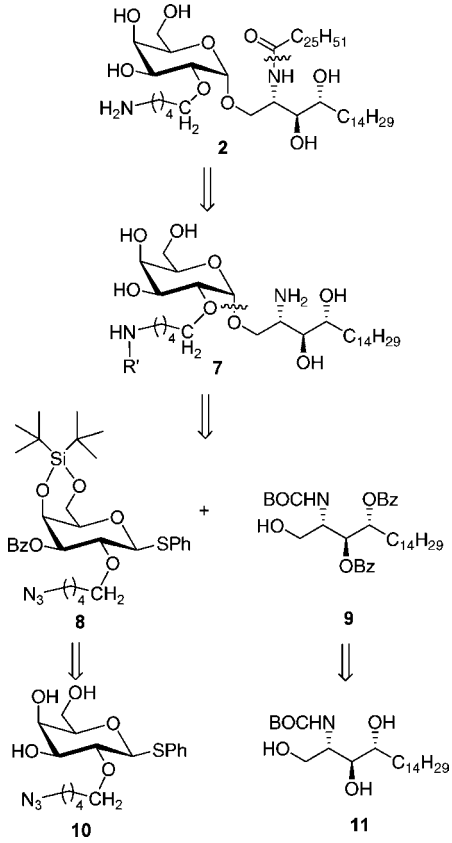
(2*S*,3*S*,4*R*)-2-Amino-*N*-hexacosanoyl-1-[2-*O*-(5-aminopentyl)-α-D-galactopyranosyloxy)]-3,4-octadecanediol 3. Compound **16** (0.32 g, 0.33 mmol) was dissolved in MeOH (10 mL) and stirred with Pd−C (5 mg) under H_2 overnight, after which time it was filtered through a pad of Celite, which was subsequently washed with MeOH. The combined filtrates were concentrated and the target compound **3** was obtained as a white solid (0.28 g, 0.297 mmol, 90%). The crude amine was used without any further purification in the following acylation reactions. **Acylation to give compound 3:** (3-hydroxy-4-nitrophenyl) acetic acid (17 mg, 0.09 mmol) was added to neat oxalyl chloride (1 mL) and stirred at 70 °C for 2 h, after which time the solution was cooled to rt and the unreacted oxalyl chloride was removed under a stream of argon. The residual volatiles were removed under reduced pressure. The resulting crude acyl chloride was dissolved in THF (1 mL) and added to a solution of amine **3** (50 mg, 0.05 mmol) in THF/NaOAc(sat) (1:1, 1 mL). The reaction was stirred vigorously overnight after which the organic phase was removed. The aqueous phase was further extracted with THF (2 × 1 mL), and the combined organic phases were concentrated. The residue was finally purified by flash chromatography (gradient from $CHCl_3$ to 15% MeOH in $CHCl_3$) to give the acylated compound **17** as a yellow solid (42 mg, 0.39 mmol, 71%). ^{1}H NMR ($CDCl_3$/CD_3OD 2:1): δ 7.85 (1H, d, *J* = 2.4 Hz), 7.36 (1H, dd, *J* = 8.6, *J* = 2.4 Hz), 6.90 (1H, d, *J*

= 8.6 Hz), 4.81 (1H, d, $J_{1,2}$ = 3.6 Hz, H-1), 3.74 (1H, d, $J_{4,3}$ = 3.1 Hz, H-4), 3.25−3.69 (10H, m, H-1a^{Cer}, H-1b^{Cer}, H-2^{Cer}, H-3^{Cer}, H-4^{Cer}, H-2, H-3, H-5, H-6a, H-6b), 3.00 (2H, t, $J_{1a',2a'}$ = $J_{1a',2b'}$ = 6.4 Hz, OCH_2C$_3$H$_6$CH$_2$NHCO), 2.00−2.06 (2H, m, OCH$_2$C$_3$H$_6$CH_2NHCO), 1.32−1.50 (m, 8H, CH_2), 1.20−1.24 (68H, m, CH_2), 0.68 (6H, t, J = 6.5 Hz, CH_3). ^{13}C NMR (75 MHz, CDCl$_3$): δ 173.2 (C═O), 138.8, 125.1, 120.4 (C$_{Ar}$), 98.1 (C-1), 77.3, 75.2, 72.9, 70.5, 69.8, 69.2 (C-2, C-3, C-4, C-5, C-4^{Cer}, C-3^{Cer}), 71.1 (OCH_2C$_3$H$_6$CH$_2$NHCO), 63.1 (C-1^{Cer}), 60.4 (C-6), 49.9 (C-2^{Cer}), 42.0 (COCH_2Ar), 39.5 (OCH$_2$C$_3$H$_6$CH_2NHCO), 31.9−21.1 (CH_2), 14.1 (CH_3^{Cer}). HRMS calcd for C$_{63}$H$_{115}$N$_3$O$_{13}$ [M+Na]$^+$: 1144.8328, found 1144.8326.

Scheme 1. Synthesis of Compound 4



Scheme 2. Retrosynthetic Ananlysis of Target Compound 3



Mice. All mice were maintained in Dana Farber Animal Facility according to IACUC guidelines. C57BL/6 WT were obtained from Jackson Laboratories. C57BL/6 Vα14 Tg mice (iNK T TcR Tg) created by A. Bendelac (University of Chicago, Chicago) were provided by Mark Exley (Beth Israel Hospital, Boston). C57BL/6.SJL congenic B1−8^{hi} B cell receptor knock-in mice, previously created by insertion of a high-affinity NP-specific BcR transgene into the BCR coding region to maintain class switch components, were provided by M. Nussenzweig (Rockefeller University, New York). Mice were immunized as noted with 200 μL intraperitoneally (IP) in PBS/0.1%BSA. Serum was collected by retro-orbital bleed and stored at −20 °C until evaluation.

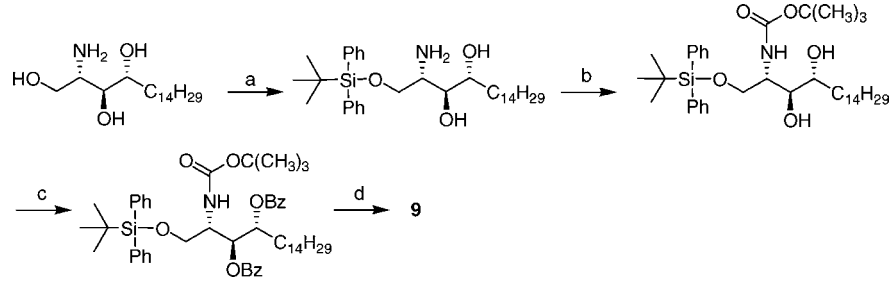
Murine Serum Antibody ELISA. NP-conjugated antigen challenge induces a heteroclitic response, where the resulting antibodies have higher affinity for NIP, so antibody is detected with an NIP-specific ELISA. Plates (Immulon 2 HB) were coated with 1 mg NIP (5)-OVAL in PBS and blocked with 10% soy milk/0.05% Tween/PBS. Serum was serially diluted in 0.1% soy milk/PBS and antibody detected with HRP-labeled goat antimouse IgG, IgM (Southern Biotech) developed with ABTS (Sigma A-1888). Concentration was extrapolated from IgG anti-NP (clone Pevchγ1) or IgM anti-NP (clone J558) (provided by A. Ferguson, Boston University School of Medicine, Boston) standard curves.

In Vitro Proliferation Assay. B and T cells were purified by pan-B or pan-T MACS bead separation (Milteny-Biotec) according to the manufacturer's instructions. iNK T TcR Tg total splenic T cells were approx 40% iNK T cells (data not shown). Purified B and T cells were mixed at 1:1 ratio (1×10^5 cells per well each) and labeled with 0.5 μM CFSE (Sigma 21888) for 9 min in PBS, then quenched with FCS and washed extensively before culture. Proliferation was assessed by FACs as CFSE dilution on day 3. Murine-specific antibodies were anti-CD19 PerCP-Cy5.5 (1D3), anti-Thy1.2 APC(53−2.1), NA/LE anti-CD3 (145−2C11), and isotype controls (all BD Biosciences PharMingen). Cells were preblocked with unlabeled anti-FcγRIII, II (clone 2.4G2).

RESULTS AND DISCUSSION

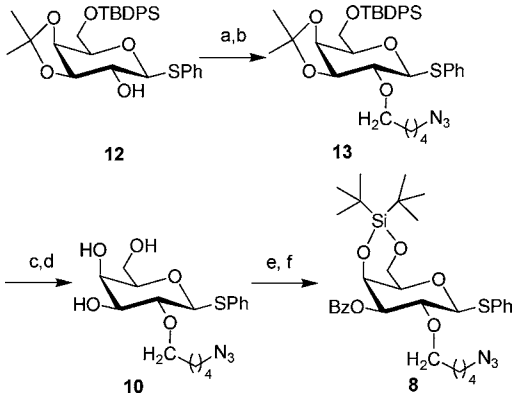
Compound **4** was synthesized as reported via a pseudoglycosylation reaction of compound **6** with a suitably protected α-GalCer **5** (Scheme 1) (*17*). In this route, the six-carbon linker was first attached to the hapten (*p*-nitrophenol) before being added onto the sugar residue. While this remains an effective strategy for synthesizing derivatives of α-GalCer, we have observed that glycosylation reactions at this slightly hindered C-2 position can sometimes be tricky and dependent upon various factors, such as the reactivity of the donor, thus offering

Scheme 3. [a]



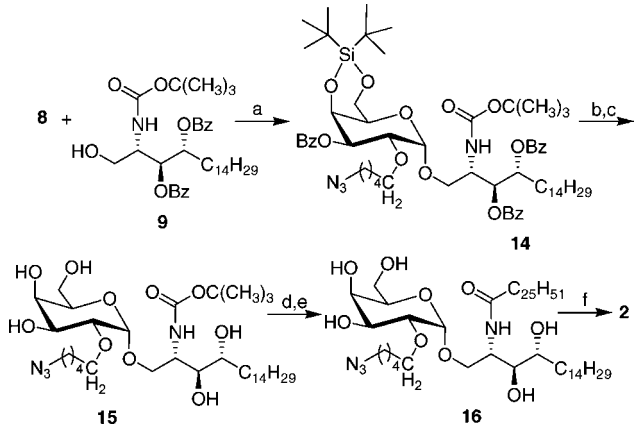
[a] (a) $C_4H_9Si(C_6H_5)_2Cl$, Pyridine, quant; (b) $(BOC)_2O$, CH_3CN, Et_3N, 72%; (c) BzCl, Pyridine, 84%; (d) TBAF, THF, 82%.

Scheme 4. [a]



[a] (a) DMF, NaH, $(CH_2)_5Br_2$, quant; (b) NaN_3, DMSO, 60 °C, 75%; (c) TBAF, THF, quant; (d) TFA, CH_2Cl_2, 78%; (e) $Si(OTf)_2(C_4H_9)_2$, DMF, Et_3N, quant; (f) BzCl, Pyridine, 96%.

Scheme 5. [a]

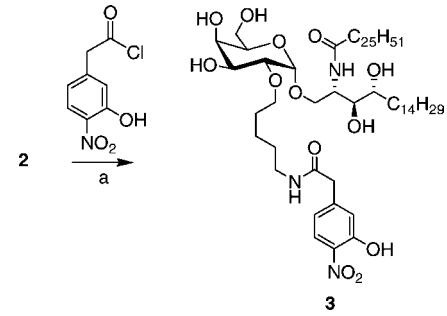


[a] (a) *p*-NO_2PhSCl, AgOTf, CH_2Cl_2, −78 °C, 75%; (b) TBAF, THF, quant; (c) NaOMe/MeOH, 88%; (d) TFA, CH_2Cl_2, quant; (e) $C_{25}H_{51}COCl$, THF/NaOAc (1:1), 71%; (f) H_2, Pd, MeOH, 90%.

limited scope for hapten diversity. Therefore, we reason that the introduction of a linker into the sugar residue via a reaction other than glycosylation is worth exploring. Also, in the interest of adaptability, the linker should facilitate the introduction of different haptens or other molecules via simple and diverse reactions.

Retrosynthetic analysis (Scheme 2) indicated that target compound **3** can be obtained by acylation of compound **7**, which in turn can be accessed from the coupling of sugar donor **8** with the sphingosine derivative **9**. This route is quite efficient as it entails the introduction of the linker at C-2 prior to glycosylation via an alkylation reaction, thereby eliminating the complications discussed above. It is noteworthy that compound **7** bears amine functionalities on both the sugar and the sphingosine base moieties. Judicious orthogonal protection of the two amino groups is therefore required, as they are to be acylated with different carboxylic acids at distinct stages in the course of the synthetic route. Since the sugar moiety is to be subjected to a wider range of chemical reactions, we chose to protect the amino group as the corresponding azide. The latter is known to be very stable and compliant to diverse reaction conditions. As for the amino group on the sphingosine moiety, we opted for the acid-sensitive BOC protecting group, which is also compatible with the benzoate protecting group. To ensure α-selectivity in the crucial glycosylation step, we relied on the directing effect of the bulky 4,6-*O*-di-*tert*-butylsilylene (DTBS) group on the sugar moiety (*21*).

Scheme 6. [a]



[a] (a) THF/NaOAc (1:1), 71%.

The phytosphingosine acceptor **9** (*22*) was synthesized from (2*S*,3*S*,4*R*)-2-amino-1,3,4-octadecanetriol using standard procedures summarized in Scheme 3. The spectroscopic data of compound **9** matched those previously reported (*22*). Regarding the synthesis of **10**, an appropriately protected galactosyl derivative had to be carefully chosen at the outset. Importantly, the protecting groups should withstand the basic reaction conditions for the formation of an alkoxide at C-2. In galactose, the cis-orientation of the hydroxyl groups at C-3 and C-4 facilitate their simultaneous protection as the acetonide, while the primary hydroxyl group at C-6 can be selectively blocked using diphenyltertiarybutylsilyl chloride, thereby leaving C-2 free for modification.

The crucial intermediate **12** was thus synthesized from β-D-galactopyranose pentaacetate according to published report (*23*). The alkoxide of **12**, which was generated in situ by treatment with NaH in DMF, was then reacted with commercially available 1,5-dibromopentane to afford the bromide. The amine functional group was then introduced into the molecule by an S_N2 displacement of the bromide with sodium azide in DMSO. With the linker in place at C-2, we then proceeded to the preparation of the glycosyl donor **8**. The protecting groups were sequentially removed to give **10** in quantitative yields. Finally, introduction of the α-directing bulky DTBS group at C-4 and C-6, followed by benzoylation at C-3, gave compound **8** as colorless syrup in 96% yield after purification.

With both the donor **8** and the acceptor **9** in hand, we next turned our attention to the glycosylation reaction. Because of the possible cleavage of the acid-sensitive BOC group on the acceptor, we preferred avoiding the usual method of activation of the thioglycoside with NIS/TfOH. When using Crich's (*24*) relatively new method of activation with the commercially available *p*-nitrobenzenesulfenyl chloride (*p*-NO_2PhSCl) in conjunction with silver triflate in anhydrous CH_2Cl_2 at −78 °C over 2 h, we were pleased to observe that the desired glycoslated product **14** was obtained as the α-anomer exclusively in 75% yield after purification by flash chromatography. The formation of the α-linkage was confirmed by the H-1 and C-1 signals in ^1H and ^{13}C NMR, respectively.

Stepwise deprotection of compound **14** was then carried out. To avoid any probable base-induced migration of the benzoate to the free amine, we chose to remove the BOC protecting group on the aglycon last. Hence, treatment with TBAF and Zemplen's deprotection of the benzoate protecting groups produced the intermediate **15** as a thick syrup in quantitative yields. The BOC group was subsequently cleaved with TFA and the resulting free amine was acylated with the fully saturated fatty acid, hexacosanoic acid. This was achieved by the reaction of the corresponding acid chloride with the free amine in a 1:1 mixture of THF and saturated sodium acetate solution. The azide intermediate **16** was obtained as a white solid after concentration of the organic phase and purification of the residue by flash

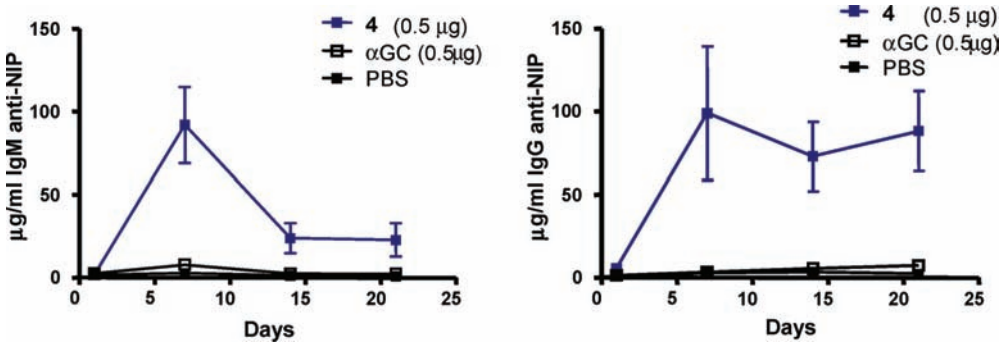


Figure 3. NP-haptenated derivative (**4**) of αGalCer, but not αGalCer, stimulates in vivo production of NP-specific IgM (left panel) and IgG (right panel) by B1−8 BcR Tg mice. (n = 2−4 mice/group, representative example from more than 2 experiments).

chromatography. Ultimately, hydrogenation of the azide in methanol provided the desired scaffold **2**. Conjugation of the amine with the NP hapten was then accomplished by acylation with its corresponding activated carboxylic acid group. Compound **3** was obtained after stirring freshly prepared acid chloride of the (3-hydroxy-4-nitrophenyl) acetic acid with **2** in a 1:1 mixture of THF and saturated sodium acetate solution for 12 h (Scheme 6).

Following successful synthesis, the NP-derivatives (**3** and **4**) were tested *in vivo* and *in vitro* for recognition by *i*NKT and B cells. Mice expressing an increased frequency of B cells with an NP-specific B cell receptor (B1−8 BcR Tg) were found to develop high titers of both IgM and IgG anti-NP antibodies in their serum (Figure 3) when immunized with **4**, but not αGalCer or PBS/0.1%BSA. Because T cell help is required for class switch to IgG, the presence of NP-specific IgG antibodies following immunization with **4** suggests T cell help is being provided, most likely by *i*NKT cells recognizing the α-GalCer component of the compound (Figure 1). In depth investigations of this immunologic cooperation have been published elsewhere (*17*). Furthermore, the requirement of *i*NKT activation and response for both the specific antibody production and class-switch was demonstrated by Batista et al. (*25*) in their *in vivo* studies using α-GalCer conjugated with the antigen CGG (chicken gamma globulin). Therefore, it can be inferred that *i*NKT cells help anti-lipid antibody production.

The biological functions of **3** and **4** haptenated with NP (3-hydroxy-4-nitrophenyl) using the two different approaches described above were then compared in vitro. To compare functional recognition of **3** and **4** by *i*NKT cells and B cells, isolated cell populations were mixed, labeled with CFSE, incubated in vitro, and then assessed for proliferation after three days of culture. Proliferation in response to control stimuli (Figure 4, lower panel) confirms the specificity of the assay, since only B cells respond to the B cell stimulus, LPS (*Salmonella enterica,* Sigma); *i*NKT cells respond more strongly to the T cell stimulus, anti-CD3; and neither cell type responds to the media alone. *i*NKT cells respond to αGalCer, and while there is no selective advantage for NP-specific B cells, there are likely some B cells specific for α-GalCer in any population which contribute to the low level of proliferation observed in the αGalCer stimulated group. Our data show that proliferative responses by *i*NKT cells and B cells were predominantly comparable following stimulation with **3** and **4** despite their slight structural differences. (Figure 4, upper panel). Importantly, previous in vitro experiments (*17*) showed that NP-α-GalCer **4** stimulated 3.2 μg/mL anti-NP IgG by day 7, whereas α-GalCer

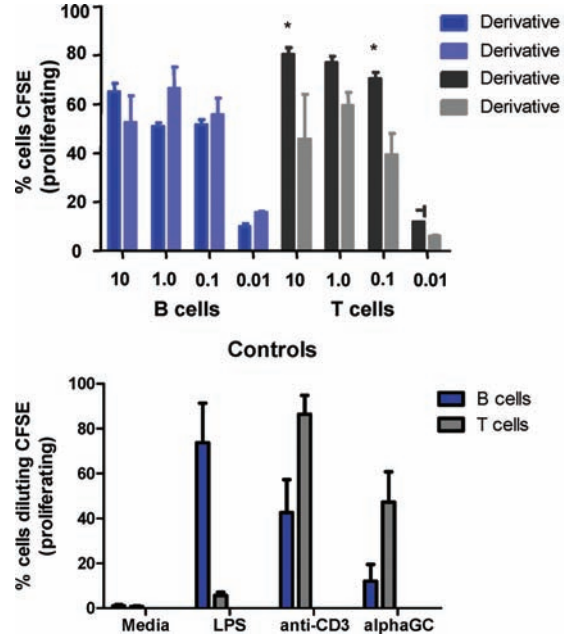


Figure 4. Alternatively synthesized NP-haptenated compounds **3** and **4** stimulate similar levels of iNKT and B cell proliferation. Mixtures of T cells from Vα14 Tg mouse and B cells from B1−8 BcR Tg mouse were stimulated with 10−0.01 ng/mL NP-αGalCer (top panel), or media, 1 μg/mLLPS, 10 μg/mL anti-CD3, 10 ng/mL αGalCer as controls (bottom panel). Proliferation is measured as % B and T cells diluting CFSE. Statistics performed by *Prism* software ANOVA analysis (* = $p < 0.05$ for 2 vs 17). Each bar represents the mean of pools of triplicate wells from two experiments.

stimulated <0.05 μg/mL IgG anti NP, clearly indicating that both **3** and **4** induce substantial proliferation of both B and T cells.

CONCLUSION

We have described the synthesis of a highly biologically attractive glycolipid template **2**, which can be conjugated to multiple molecules, exemplified by the synthesis of compound **3**. Furthermore, the biological evaluation of the haptenated derivatives of α-GalCer showed that the biologic recognition of **3** and **4** is virtually the same and that they are both important tools in studying the mechanism of *i*NKT cell help for the production of anti-lipid antibodies.

ACKNOWLEDGMENT

We thank Michel Nussenzweig and Mark Exley for generously providing transgenic mice. This work was supported by the Irvington Institute for Immunological Research (E.A.L.) and National Institutes of Health Grant T32 AR007530-21(to

M.B.B.). G.S.B acknowledges support in the form of a personal research chair from Mr. James Badrick, Royal Society Wolfson Research Merit Award, as a former Lister Institute-Jenner Research Fellow, the Medical Council and the Wellcome Trust (084923/B/08/7).

LITERATURE CITED

(1) Bendelac, A., Bonneville, M., and Kearney, J. F. (2001) Autoreactivity by design: innate B and T lymphocytes. *Nat. Rev. Immunol. 1*, 177–186.

(2) Kronenberg, M. (2005) Toward an understanding of NKT cell biology: progress and paradoxes. *Annu. Rev. Immnunol. 23*, 877–900.

(3) Brutkiewicz, R. R. (2006) CD1d ligands: the good, the bad, and the ugly. *J. Immunol. 177*, 769–775.

(4) Bendelac, A., Rivera, M. N., Park, S. H., and Roark, J. H. (1997) Mouse CD1-specific NK1 T cells: development, specificity, and function. *Annu. Rev. Immunol. 15*, 535–562.

(5) Hong, S., Scherer, D. C., Mendiratta, S. K., Serizawa, I., Koezuka, Y., and Van Kaer, L. (1999) Lipid antigen presentation in the immune system: lessons learned from CD1d knockout mice. *Immunol. Rev. 169*, 31–44.

(6) Kawano, T., Cui, J., Koezuka, Y., Toura, I., Kaneko, Y., Motoki, K., Ueno, H., Nakagawa, R., Sato, H., Kondo, E., Koseki, H., and Taniguchi, M. (1997) CD1d-restricted and TCR-mediated activation of valpha14 NKT cells by glycosylceramides. *Science 278*, 1626–1629.

(7) Crowe, N. Y., Uldrich, A. P., Kyparissoudis, K., Hammond, K. J. L., Hayakawa, Y., Sidobre, S., Keating, R., Kronenberg, M., Smyth, M. J., and Godfrey, D. I. (2003) Glycolipid antigen drives rapid expansion and sustained cytokine production by NK T cells. *J. Immunol. 171*, 4020–4027.

(8) Burdin, N., Brossay, L., and Kronenberg, M. (1999) Immunization with alpha-galactosylceramide polarizes CD1-reactive NK T cells towards Th2 cytokine synthesis. *Eur. J. Immunol. 29*, 2014–2025.

(9) Carnaud, C., Lee, D., Donnars, O., Park, S. H., Beavis, A., Koezuka, Y., and Bendelac, A. (1999) Cutting edge: Cross-talk between cells of the innate immune system: NKT cells rapidly activate NK cells. *J. Immunol. 163*, 4647–4650.

(10) Taniguchi, M., Harada, M., Kojo, S., Nakayama, T., and Wakao, H. (2003) The regulatory role of Valpha14 NKT cells in innate and acquired immune response. *Annu. Rev. Immnunol. 21*, 483–513.

(11) Godfrey, D. I., MacDonald, H. R., Kronenberg, M., Smyth, M. J., and Van Kaer, L. (2004) NKT cells: what's in a name? *Nat. Rev. Immunol. 4*, 231–237.

(12) Gonzalez-Aseguinolaza, G., Van Kaer, L., Bergmann, C. C., Wilson, J. M., Schmieg, J., Kronenberg, M., Nakayama, T., Taniguchi, M., Koezuka, Y., and Tsuji, M. (2002) Natural killer T cell ligand alpha-galactosylceramide enhances protective immunity induced by malaria vaccines. *J. Exp. Med. 195*, 617–624.

(13) Miyamoto, K., Miyake, S., and Yamamura, T. (2001) A synthetic glycolipid prevents autoimmune encephalomyelitis by inducing TH2 bias of natural killer T cells. *Nature 413*, 531–534.

(14) Chiba, A., Oki, S., Miyamoto, K., Hashimoto, H., Yamamura, T., and Miyake, S. (2004) Suppression of collagen-induced arthritis by natural killer T cell activation with OCH, a sphingosine-truncated analog of alpha-galactosylceramide. *Arthritis Rheum. 50*, 305–313.

(15) Naik, R. S., Branch, O. L. H., Woods, A. S., Vijaykumar, M., Perkins, D. J., Nahlen, B. L., Lal, A. A., Cotter, R. J., Costello, C. E., Ockenhouse, C. F., Davidson, E. A., and Gowda, D. C. (2000) Glycosylphosphatidylinositol anchors of Plasmodium falciparum: molecular characterization and naturally elicited antibody response that may provide immunity to malaria pathogenesis. *J. Exp. Med. 192*, 1563–1575.

(16) Gourley, I. S., McMillan, S. A., and Bell, A. L. (1996) Clinical features associated with a positive anticardiolipin antibody in Irish patients with systemic lupus erythematosus. *Clin. Rheumatol. 15*, 457–460.

(17) Leadbetter, E. A., Brigl, M., Illarionov, P., Cohen, N., Luteran, M. C., Pillai, S., Besra, G. S., and Brenner, M. B. (2008) NK T cells provide lipid antigen-specific cognate help for B cells. *Proc. Natl. Acad. Sci. U.S.A. 105*, 8339–8344.

(18) Boscardin, S. B., Hafalla, J. C., Masilamani, R. F., Kamphorst, A. O., Zebroski, H. A., Rai, U., Morrot, A., Zavala, F., Steinman, R. M., Nussenzweig, R. S., and Nussenzweig, M. C. (2006) Antigen targeting to dendritic cells elicits long-lived T cell help for antibody responses. *J. Exp. Med. 203*, 599–606.

(19) Wolniak, K. L., Noelle, R. J., and Waldschmidt, T. J. (2006) Characterization of (4-hydroxy-3-nitrophenyl) acetyl (NP)-specific germinal center B cells and antigen-binding B220- cells after primary NP challenge in mice. *J. Immunol. 177*, 2072–2079.

(20) Furukawa, K., Shimizu, T., Murakami, A., Kono, R., Nakagawa, M., Sagawa, T., Yamato, I., and Azuma, T. (2007) Strategy for affinity maturation of an antibody with high evolvability to (4-hydroxy-3-nitrophenyl) acetyl hapten. *Mol. Immunol. 44*, 2436–2445.

(21) Kimura, A., Imamura, A., Ando, H., Ishida, H., and Kiso, M. (2006) A novel synthetic route to α-galactosyl ceramides and iGb3 using DTBS-directed α-selective galactosylation. *Synlett. 15*, 2379–2382.

(22) Fujio, M., Wu, D., Garcia-Navarro, R., Ho, D. D., Tsuji, M., and Wong, C. H. (2006) Structure-based discovery of glycolipids for CD1d-mediated NKT cell activation: tuning the adjuvant versus immunosuppression activity. *J. Am. Chem. Soc. 128*, 9022–9023.

(23) Broddefalk, J., Bergquist, K. E., and Kihlberg, J. (1998) Use of acid-labile protective groups for carbohydrate moieties in synthesis of glycopeptides related to type II collagen. *Tetrahedron 54*, 12047–12070.

(24) Crich, D., Cai, F., and Yang, F. (2008) A stable, commercially available sulfenyl chloride for the activation of thioglycosides in conjunction with silver trifluoromethanesulfonate. *Carbohydr. Res. 343*, 1858–1862.

(25) Barral, P., Eckl-Dorna, J., Harwood, N. E., De Santo, C., Salio, M., Illarionov, P., Besra, G. S., Cerundolo, V., and Batista, F. D. (2008) B cell receptor-mediated uptake of CD1d-restricted antigen augments antibody responses by recruiting invariant NKT cell help *in vivo*. *Proc. Natl. Acad. Sci. U.S.A. 105*, 8345–8350.

BC9005255

Synthesis of Oligonucleotide Glycoconjugates Using Sequential Click and Oximation Ligations

Marika Karskela,* Mia Helkearo, Pasi Virta, and Harri Lönnberg

Department of Chemistry, University of Turku, FIN-20014 Turku, Finland. Received December 2, 2009; Revised Manuscript Received January 7, 2010

Oligodeoxyribonucleotide glycoconjugates bearing two trivalent glycoclusters have been synthesized by two alternative methods based on solid-supported oximation of aminooxy functionalized oligonucleotides with glycoclusters constructed by click chemistry. In more detail, the trivalent glycoclusters (**5** and **6**) bearing three sugar pendants were first assembled by treating a 4-[tri-*O*-propargylpentaerythrityloxy]benzaldehyde scaffold with methyl 6-azido-6-deoxyglycopyranoside under the click reaction conditions. Two phosphoramidite reagents containing a phthaloyl protected aminooxy function, viz., 2-cyanoethyl *N*,*N*-diisopropylphosphoramidites derived from 3-[3,5-bis(phthalimidoxymethyl)phenoxy]propanol (**12**) and 5-(4,4′-dimethoxytrityl)-1,2-dideoxy-1-*C*-(2-phthalimidoxyethyl)-*β*-D-*erythro*-pentofuranose (**16**), were synthesized and incorporated as branching units in appropriate places of the oligonucleotide chains. On using **12**, the phthaloyl protections of the branching unit were removed and two identical glycoclusters were attached via oxime linkage to the 5′-terminus of the support-bound oligonucleotide chain. With branching unit **16**, the phosphoramidite coupling and the oximation were carried out alternately, allowing introduction of two dissimilar trivalent glycoclusters close to the 3′-end of the oligonucleotide chain. The products (**20**, **26**) were released and deprotected by ammonolysis and purified by HPLC chromatography.

INTRODUCTION

Oligonucleotide-based drugs show promise as a novel form of chemotherapy, although several thresholds must still be overcome on the way to applicable nucleic acid therapeutics (*1–14*). Poor cellular uptake, in particular, limits the applicability of both antisense oligonucleotides and siRNA. A possible way to combat this drawback is to conjugate the therapeutic oligonucleotide to an agent expected to exhibit cell-type organ specificity (*15–20*). The oligonucleotide conjugate, hence, is enriched on the cell-surface and internalized by endocytosis. It is well-known that carbohydrate−protein interactions play a major role in recognition of cells by pathogens (*21–23*). These interactions are multipodal; high-affinity binding is achieved by multiple simultaneous interactions, a phenomenon known as a glycocluster effect (*24–26*). Usually, multiantennary carbohydrates anchored to cell membranes recognize extracellular proteins (*27–29*), but the opposite is also possible. Trivalent *N*-acetylgalactosamine conjugate of oligodeoxynucleotide methylphosphonate (*30*) and phosphorothioate (*31*), tetravalent galactose conjugates of oligodeoxynucleotides (*32, 33*), and monovalent galactose conjugates of oligodeoxynucleotide phosphorothioates (*34*) have all shown enhanced uptake in liver via the galactose-specific asialoglycoprotein receptor-mediated endocytosis. It has also been shown that a transmembrane glycoprotein CD44 recognizes hyaluronic oligomers (*35*) and glycoconjugation may be exploited to target antigenic peptides to dendritic cells (*36*). Accordingly, glycotargeting appears to be a feasible approach (*37*) and development of reproducible methods for convenient preparation of various types of oligonucleotide glycoconjugates appears worthwhile. Workable chemistry is a prerequisite for extensive biological studies.

* Corresponding author. Phone +358-2-333 6787, Fax +358-2-333 6700, E-mail: marika.karskela@utu.fi.

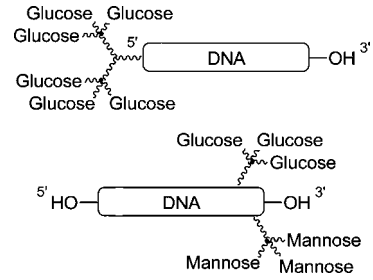


Figure 1. Oligonucleotide glycoconjugates prepared.

Solid-phase oximation, click chemistry, and phosphoramidite coupling are the methods most extensively applied to preparation of oligonucleotide glycoconjugates on a solid support (*19, 38, 39*). Apart from coupling of some aminoglycosides (*40, 41*) and trigalactosylated tetrahydroxycholane (*42*) by phosphoramidite chemistry, the approaches described so far allow attachment of mono- or disaccharides along the oligonucleotide chain using either nucleosidic (*43–45*) or non-nucleosidic (*46–49*) branching units or their conjugation to the internucleosidic phosphodiester linkages (*50*). The examples of oligonucleotide conjugates bearing a multiantennary terminal glycocluster are limited to prepration of a spruce-like tetramannosyl 5′-conjugate (*51*), a trivalent 5′-terminal conjugate containing three different sugars (*52*), and a 3′-cyclodextrin conjugate (*53*). High-affinity binding to membrane lectins may, however, require simultaneous interaction with even more than three or four appropriately situated sugar ligands. For this reason, we now report a protocol for solid-phase synthesis of an oligonucleotide conjugate bearing a hexavalent cluster at the 5′-terminus (Figure 1). In addition, we describe a protocol for attachment of various prefabricated trivalent clusters at desired sites of the oligonucleotide chain. Both methods are based on preparation of aldehyde functionalized trivalent clusters in

10.1021/bc900529g © 2010 American Chemical Society
Published on Web 03/12/2010

solution by click chemistry and attachment of these clusters to the support-anchored oligonucleotide by oximation.

EXPERIMENTAL PROCEDURES

General Methods and Materials. CH_2Cl_2, 1,4-dioxane, and MeCN were dried over 4 Å molecular sieves, THF over 3 Å sieves. Diethyl ether was dried over sodium. Triethylamine was dried by consecutive distillations from ninhydrin and potassium hydroxide, and then stored over CaH_2. The NMR spectra were recorded at 500 MHz. The chemical shifts are given in ppm using internal TMS as a reference. Appropriate 2D NMR methods (COSY, HSQC, and HMBC) were used for peak assignment. The mass spectra were recorded using EI and ESI ionization methods. C18 RP HPLC analyses of oligonucleotide conjugates were performed using Thermo ODS Hypersil (250 × 4.6 mm, 5 μm) analytical column, a gradient elution from 0% to 50% MeCN in 0.05 mol L^{-1} NH_4OAc (aq) buffer over 30 min (conjugates **20**, **23**, and purified **26**) or 60 min (conjugates **25** and crude **26**), flow rate 1 mL min^{-1}, and detection at 260 nm. For purifications, Thermo ODS Hypersil (250 × 10 mm, 5 μm) column and flow rate 3 mL min^{-1} were used.

4-(Tri-*O*-propargylpentaerythrityloxy)benzaldehyde (2). To a solution of tri-*O*-propargyl pentaerythritol (*54*) (**1**, 0.50 g, 2.0 mmol) in dry THF (10 mL), 4-hydroxybenzaldehyde (0.29 g, 2.4 mmol) and triphenylphosphine (0.63 g, 2.4 mmol) were added. The mixture was cooled to 0 °C and diisopropylazodicarboxylate (DIAD, 0.50 mL, 2.4 mmol) was added dropwise. The mixture was stirred at 70 °C for 10 h and evaporated to dryness. Crude product was purified by silica gel chromatography (30% ethyl acetate in petroleum ether) to yield 0.38 g (53%) of **2.** ^{1}H NMR 500 MHz, $CDCl_3$): δ_{ppm} 9.88 (s, 1H, CHO), 7.82 (m, 2H, Ar), 7.02 (m, 2H, Ar), 4.14 (d, 6H, J = 2.4 Hz, 3 × CH_2CCH), 4.08 (s, 2H, CH_2OAr), 3.66 (s, 6H, 3 × CH_2O), 2.40 (t, 3H, J = 2.4 Hz, 3 × CH_2CCH); ^{13}C NMR (125 MHz, $CDCl_3$): δ_{ppm} 190.8, 164.2, 131.9, 129.9, 115.0, 79.8, 74.3, 68.5, 67.1, 58.8, 44.7; HRMS (EI): M^+ $C_{21}H_{22}O_5$ requires 354.1467, found 354.1455.

Glucoside Cluster (5). Compound **2** (64 mg, 0.18 mmol) was dissolved in 1,4-dioxane (1.3 mL) together with methyl 2,3,4-tri-*O*-acetyl-6-azido-6-deoxy-α-D-glucopyranoside (**3**, 310 mg, 0.90 mmol). $CuSO_4$ as 0.05 mol L^{-1} aqueous solution (36 μL 1.8 μmol) and sodium ascorbate as 0.1 mol L^{-1} aqueous solution (0.90 mL, 0.090 mmol) were added. The mixture was stirred at 50 °C for 4.5 h and then at room temperature overnight. The volatiles were evaporated and the residue was dissolved in ethyl acetate and washed twice with brine. The aqueous layer was extracted twice with ethyl acetate. The combined organic layers were dried with Na_2SO_4 and evaporated to dryness. The residue was purified by silica gel chromatography (5% MeOH in CH_2Cl_2) to yield 140 mg (56%) of **5**. ^{1}H NMR (500 MHz, $CDCl_3$): δ_{ppm} 9.89 (s, 1H, CHO), 7.83 (m, 2H, Ar), 7.64 (s, 3H, 3 × CH triazole), 6.95 (m, 2H, Ar), 5.47 (m, 3H, 3 × H-3 Glc), 4.88−4.81 [m, 9H, 3 × (H-1, H-4, and H-2 Glc)], 4.58 (s, 6H, 3 × OCH_2C═), 4.56 (dd, 3H, J = 2.4 and 14.4 Hz, 3 × H-6a Glc), 4.38 (dd, 3H, J = 8.3 and 14.4 Hz, 3 × H-6b Glc), 4.17 (m, 3H, 3 × H-5 Glc), 3.99 (s, 2H, CH_2OAr), 3.56 (s, 6H, 3 × CCH_2O), 3.09 (s, 9H, 3 × OCH_3), 2.10 (s, 9H, 3 × CH_3), 2.07 (s, 9H, 3 × CH_3), 2.01 (s, 9H, 3 × CH_3); ^{13}C NMR (125 MHz, $CDCl_3$): δ_{ppm} 190.7, 170.1, 169.8, 169.8, 163.9, 145.0, 131.9, 129.9, 124.1, 114.7, 96.5, 70.6, 69.9, 69.7, 68.5, 67.7, 67.0, 64.8, 55.3, 50.5, 45.0, 20.6, 20.6; HRMS (ESI): $[M + Na]^+$ $C_{60}H_{79}N_9NaO_{29}$ requires 1412.4882, found 1412.4879.

Mannoside Cluster (6). was synthesized from **2** (64 mg, 0.18 mmol) and methyl 2,3,4-tri-*O*-acetyl-6-azido-6-deoxy-α-D-mannopyranoside (*55*) (**4**, 310 mg, 0.90 mmol) as described for **5** to yield 142 mg (57%) of **6**. ^{1}H NMR (500 MHz, $CDCl_3$): δ_{ppm} 9.90 (s, 1H, CHO), 7.83 (m, 2H, Ar), 7.65 (s, 3H, 3 × CH triazole), 6.93 (m, 2H, Ar), 5.32 (dd, 3H, J = 3.4 and 10.0 Hz, 3 × H-3 Man), 5.21 (dd, 3H, J = 1.6 and 3.4 Hz, 3 × H-2 Man), 5.14 (m, 3H, 3 × H-4 Man), 4.62 (d, 3H, J = 1.6 Hz, 3 × H-1 Man), 4.59−4.56 [m, 9H, 3 × (H-6a Man and OCH_2C═)], 4.36 (dd, 3H, J = 9.1 and 14.3 Hz, 3 × H-6b Man), 4.15−4.11 (m, 3H, 3 × H-5 Man), 3.96 (s, 2H, CH_2OAr), 3.54 (s, 6H, 3 × CCH_2O), 3.04 (s, 9H, 3 × OCH_3), 2.14 (s, 9H, 3 × CH_3), 2.11 (s, 9H, 3 × CH_3), 2.00 (s, 9H, 3 × CH_3); ^{13}C NMR (125 MHz, $CDCl_3$): δ_{ppm} 190.7, 170.1, 169.8, 169.7, 163.9, 144.8, 131.9, 130.0, 124.1, 114.8, 98.4, 69.4, 69.1, 68.7, 68.6, 67.5, 67.0, 64.8, 55.1, 50.9, 45.0, 20.8, 20.8, 20.6; HRMS (ESI): $[M + H]^+$ $C_{60}H_{80}N_9O_{29}$ requires 1390.5062, found 1390.5033.

Dimethyl 5-[3-(4-Methoxytrityl)propoxy]isophthalate (8). Dimethyl 5-hydroxyisophthalate (**7**, 2.10 g, 10.0 mmol) and 3-(4-methoxytrityl)propan-1-ol [prepared as corresponding tritylated propanediol (*56*)] (3.78 g, 10.8 mmol) were dissolved in dry THF (70 mL) and triphenylphosphine (2.85 g, 10.8 mmol) was added. The mixture was cooled to 0 °C and diethylazodicarboxylate (DEAD, 1.68 mL, 10.8 mmol) in dry THF (7 mL) was added dropwise. The reaction was allowed to proceed at room temperature for 19 h, followed by addition of triphenylphosphine (0.53 g, 2.0 mmol) and DEAD (0.31 mL, 2.0 mmol) and the stirring was continued for 2 h. The mixture was evaporated to dryness and the residue was purified by silica gel chromatography (25% ethyl acetate in petroleum ether) to yield 4.14 g (77%) of **8** as colorless oil. ^{1}H NMR (500 MHz, $CDCl_3$): δ_{ppm} 8.27 (m, 1H, Ar), 7.71 (br d, 2H, Ar), 7.43 (m, 4H, MMTr), 7.30 (m, 2H, MMTr), 7.25 (m, 4H, MMTr), 7.20 (m, 2H, MMTr), 6.79 (m, 2H, MMTr), 4.19 (t, 2H, J = 6.2 Hz, CH_2OAr), 3.94 (s, 6H, 2 × $COOCH_3$), 3.77 (s, 3H, OCH_3), 3.30 (t, 2H, J = 6.0 Hz, MMTrOCH_2), 2.07 (tt, 2H, J = 6.0 and 6.2 Hz, $CH_2CH_2CH_2$); ^{13}C NMR (125 MHz, $CDCl_3$): δ_{ppm} 166.2, 159.0, 158.5, 144.6, 135.8, 131.7, 130.3, 128.4, 127.7, 126.8, 122.8, 119.8, 113.0, 86.2, 65.5, 59.5, 55.2, 52.4, 29.8; HRMS (ESI): $[M + Na]^+$ $C_{33}H_{32}NaO_7$ requires 563.2046, found 563.2043.

5-[3-(4-Methoxytrityl)propoxy]-1,3-phenylenedimethanol (9). Compound **8** (4.14 g, 7.66 mmol) was dried over P_2O_5, dissolved in dry diethyl ether (80 mL), and cooled to 0 °C. Lithium aluminum hydride (0.87 g, 23 mmol) was slowly added and stirring was continued for 2.5 h at room temperature. The excess hydride was destroyed by careful addition of water and the solids were filtered. The product containing filtrate was diluted with ethyl acetate and washed with brine. The organic layer was dried with Na_2SO_4 and evaporated to dryness to yield 3.50 g (94%) of **9** as colorless oil. ^{1}H NMR (500 MHz, $CDCl_3$): δ_{ppm} 7.42 (m, 4H, MMTr), 7.29 (m, 2H, MMTr), 7.25 (m, 4H, MMTr), 7.20 (m, 2H, MMTr), 6.91 (br s, 1H, Ar), 6.79 (br s, 2H, Ar), 6.77 (m, 2H, MMTr), 4.63 (s, 4H, 2 × CH_2OH), 4.12 (t, 2H, J = 6.2 Hz, CH_2OAr), 3.77 (s, 3H, OCH_3), 3.27 (t, 2H, J = 6.0 Hz, MMTrOCH_2), 2.05 (tt, 2H, J = 6.0 and 6.2 Hz, $CH_2CH_2CH_2$), 1.90 (br s, 2H, 2 × OH); ^{13}C NMR (125 MHz, $CDCl_3$): δ_{ppm} 159.5, 158.4, 144.7, 142.7, 135.9, 130.4, 128.4, 127.7, 126.8, 117.4, 113.0, 112.2, 86.2, 65.2, 64.9, 59.8, 55.2, 29.9; HRMS (ESI) $[M + Na]^+$ $C_{31}H_{32}NaO_5$ requires 507.2147, found 507.2169.

5-[3-(4-Methoxytrityl)propoxy]-1,3-phenylenebis(methyleneoxyphthalimide) (10). To a solution of **9** (3.50 g, 7.22 mmol) in dry THF (80 mL) *N*-hydroxyphthalimide (2.35 g, 14.4 mmol) and triphenylphosphine (3.77 g, 14.4 mmol) were added. The mixture was cooled to 0 °C and diethylazodicarboxylate (DEAD, 2.24 mL, 14.4 mmol) in dry THF (10 mL) was added dropwise. The mixture was stirred for 20 h

at room temperature and evaporated to dryness. Crude product was purified by silica gel chromatography (1% MeOH in CH_2Cl_2) to yield 3.01 g (53%) of **10** as white foam. ^{1}H NMR (500 MHz, $CDCl_3$): δ_{ppm} 7.71 (m, 8H, Pht), 7.44 (m, 4H, MMTr), 7.31 (m, 2H, MMTr), 7.26−7.16 (m, 7H, MMTr and Ar), 7.12 (br d, 2H, Ar), 6.78 (m, 2H, MMTr), 5.18 (s, 4H, 2 × CH_2ON), 4.19 (t, 2H, J = 6.2 Hz, CH_2OAr), 3.76 (s, 3H, CH_3), 3.27 (t, 2H, J = 6.0 Hz, MMTrOCH_2), 2.06 (tt, 2H, J = 6.0 and 6.2 Hz, $CH_2CH_2CH_2$); ^{13}C NMR (125 MHz, $CDCl_3$): δ_{ppm} 163.4, 159.2, 158.4, 144.7, 136.0, 135.4, 134.4, 130.3, 128.9, 128.4, 127.7, 126.7, 123.5, 122.7, 116.5, 113.0, 86.2, 79.4, 65.0, 59.8, 55.2, 29.9; HRMS (ESI) $[M + Na]^+$ $C_{47}H_{38}N_2NaO_9$ requires 797.2475, found 797.2512.

3-[3,5-Bis(phthalimidoxymethyl)phenoxy]propanol (11). Compound **10** (3.01 g, 3.88 mmol) was suspended in 80% aqueous acetic acid (40 mL) and stirred for 4.5 h. The mixture was evaporated to dryness, and the residue was dissolved in CH_2Cl_2 and washed with saturated $NaHCO_3$. The organic layer was separated and the aqueous layer was extracted four times with CH_2Cl_2. The combined organic layers were dried with Na_2SO_4 and evaporated to dryness. The residue was purified by silica gel chromatography (4−5% MeOH in CH_2Cl_2) to yield 1.61 g (82%) of **11** as white powder. ^{1}H NMR [500 MHz, $(CD_3)_2SO$]: δ_{ppm} 7.86 (s, 8H, Pht), 7.22 (br s, 1H, Ar), 7.15 (br d, 2H, Ar), 5.16 (s, 4H, 2 × CH_2ON), 4.58 (t, 1H, J = 5.2 Hz, OH), 4.08 (t, 2H, J = 6.4 Hz, CH_2OAr), 3.56 (dt, 2H, J = 5.2 and 6.2 Hz, CH_2OH), 1.87 (tt, 2H, J = 6.2 and 6.4 Hz, $CH_2CH_2CH_2$); ^{13}C NMR [125 MHz, $(CD_3)_2SO$]: δ_{ppm} 163.6, 159.1, 136.4, 135.3, 129.0, 123.7, 122.8, 116.4, 79.3, 65.3, 57.7, 32.5; HRMS (ESI): $[M + Na]^+$ $C_{27}H_{22}N_2NaO_8$ requires 525.1274, found 525.1305.

3-[3,5-Bis(phthalimidoxymethyl)phenoxy]propyl 2-cyanoethyl *N,N*-Diisopropylphosphoramidite (12). Compound **11** (290 mg, 0.578 mmol) was dried over P_2O_5 and suspended in dry 1,4-dioxane (3 mL). Dry triethylamine (287 μL, 2.07 mmol) and 2-cyanoethyl *N,N*-diisopropylphosphonamidic chloride (141 μL, 0.632 mmol) were added under nitrogen. The mixture was stirred for 2.5 h and then subjected directly to a silica gel column. Elution with 1% triethylamine and 29% petroleum ether in ethyl acetate yielded 284 mg (70%) of **12** as white powder. ^{1}H NMR (500 MHz, $CDCl_3$): δ_{ppm} 7.81 (m, 4H, Pht), 7.73 (m, 4H, Pht), 7.21 (m, 1H, Ar), 7.16 (br d, 2H, Ar), 5.17 (s, 4H, 2 × CH_2ON), 4.15 (t, 2H, J = 6.1 Hz, CH_2OAr), 3.91−3.76 (m, 4H, 2 × $POCH_2$), 3.61 [m, 2H, 2 × CH(CH_3)$_2$], 2.64 (t, 2H, J = 6.5 Hz, CH_2CN), 2.10 (m, 2H, $CH_2CH_2CH_2$), 1.19 (s, 3H, CH_3), 1.18 (s, 3H, CH_3), 1.18 (s, 3H, CH_3), 1.17 (s, 3H, CH_3); ^{13}C NMR (125 MHz, $CDCl_3$): δ_{ppm} 163.4, 159.2, 135.4, 134.4, 128.9, 123.5, 122.7, 117.7, 116.5, 79.5, 64.7, 60.1 [d, J(^{13}C, ^{31}P) = 17.6 Hz], 58.4 [d, J(^{13}C, ^{31}P) = 19.2 Hz], 43.0 [d, J(^{13}C, ^{31}P) = 12.5 Hz], 30.9 [d, J(^{13}C, ^{31}P) = 7.2 Hz], 24.6 (m), 20.4 [d, J(^{13}C, ^{31}P) = 7.1 Hz]; ^{31}P NMR (200 MHz, $CDCl_3$): δ_{ppm} 147.7; HRMS (ESI): $[M + Na]^+$ $C_{36}H_{39}N_4NaO_9P$ requires 725.2353, found 725.2371.

5-(4,4′-Dimethoxytrityl)-3-*O*-*tert*-butyldimethylsilyloxy-1,2-dideoxy-1-C-(2-phthalimidoxyethyl)-β-D-erythro-pentofuranose (14). 5-(4,4′-Dimethoxytrityl)-3-*O*-*tert*-butyldimethylsilyloxy-1,2-dideoxy-1-*C*-(2-hydroxyethyl)-β-D-*erythro*-pentofuranose (*40*) (**13**, 1.64 g, 2.84 mmol), *N*-hydroxyphthalimide (0.557 g, 3.42 mmol), and triphenylphosphine (0.896 g, 3.41 mmol) were dissolved in dry THF (40 mL). Diethylazodicarboxylate (DEAD, 573 μL, 3.68 mmol) was added dropwise and the mixture was stirred for 89 h at room temperature. After evaporation, the residue was dissolved in CH_2Cl_2 and washed three times with saturated $NaHCO_3$. The combined aqueous layers were extracted with CH_2Cl_2, and then the organic layers were combined, dried with Na_2SO_4, and evaporated. Crude product was purified by silica gel chromatography (0.1% triethylamine and 3% MeOH in CH_2Cl_2) to yield 1.90 g (93%) of **14**. ^{1}H NMR (500 MHz, $CDCl_3$): δ_{ppm} 7.82 (m, 2H, Pht), 7.73 (m, 2H, Pht), 7.44 (m, 2H, DMTr), 7.33 (m, 4H, DMTr), 7.27 (m, 2H, DMTr), 7.18 (m, 1H, DMTr), 6.82 (m, 4H, DMTr), 4.40−4.31 (m, 3H, CH_2ON and H-1), 4.25 (m, 1H, H-3), 3.88 (m, 1H, H-4), 3.79 (s, 6H, 2 × OCH_3), 3.07 (m, 2H, H-5), 2.08 (m, 2H, CH_2CH_2ON), 1.94 (m, 1H, H-2a), 1.74 (m, 1H, H-2b), 0.84 [s, 9H, C(CH_3)$_3$], 0.01 (s, 3H, CH_3Si), −0.02 (s, 3H, CH_3Si); ^{13}C NMR (125 MHz, $CDCl_3$): δ_{ppm} 163.6, 158.4, 145.0, 136.2, 134.4, 130.1, 128.9, 128.2, 127.7, 126.6, 123.5, 113.0, 86.4, 85.9, 76.1, 75.2, 74.3, 64.3, 55.2, 41.3, 34.2, 25.8, 18.0, −4.6, −4.8; HRMS (ESI) $[M + Na]^+$ $C_{42}H_{49}NNaO_8Si$ requires 746.3125, found 746.3147.

5-(4,4′-Dimethoxytrityl)-1,2-dideoxy-1-*C*-(2-phthalimidoxyethyl)-β-D-erythro-pentofuranose (15). Triethylamine trihydrofluoride (409 μL, 2.51 mmol) was added to a solution of **14** (1.21 g, 1.67 mmol) in dry THF (15 mL). The mixture was stirred at room temperature for 24 h, after which another portion of triethylamine trihydrofluoride (408 μL, 2.50 mmol) was added. The reaction was allowed to proceed for another 24 h, followed by addition of triethylamine (200 μL, 1.43 mmol) and evaporation. The crude product was purified by silica gel chromatography (0.1% triethylamine and 3% MeOH in CH_2Cl_2) to yield 0.538 g (53%) of **15**. ^{1}H NMR (500 MHz, $CDCl_3$): δ_{ppm} 7.82 (m, 2H, Pht), 7.73 (m, 2H, Pht), 7.42 (m, 2H, DMTr), 7.32 (m, 4H, DMTr), 7.27 (m, 2H, DMTr), 7.19 (m, 1H, DMTr), 6.82 (m, 4H, DMTr), 4.42−4.29 (m, 4H, CH_2ON, H-1, and H-3), 3.91 (m, 1H, H-4), 3.79 (s, 6H, 2 × OCH_3), 3.23 (dd, 1H, J = 4.6 and 9.6 Hz, H-5a), 3.08 (dd, 1H, J = 5.9 and 9.6 Hz, H-5b), 2.10−2.05 (m, 3H, CH_2CH_2ON and H-2a), 1.90−1.84 (m, 2H, H-2b and OH); ^{13}C NMR (125 MHz, $CDCl_3$): δ_{ppm} 163.6, 158.5, 144.9, 136.1, 134.5, 130.1, 128.9, 128.2, 127.8, 126.8, 123.5, 113.1, 86.1, 85.8, 75.9, 75.3, 74.7, 64.7, 55.2, 40.9, 34.2; HRMS (ESI): $[M + Na]^+$ $C_{36}H_{35}NNaO_8$ requires 632.2261, found 632.2268.

5-(4,4′-Dimethoxytrityl)-1,2-dideoxy-1-*C*-(2-phthalimidoxyethyl)-β-D-erythro-pentofuranosyl-3-(2-cyanoethyl-*N,N*-diisopropylphosphoramidite) (16). 2-Cyanoethyl *N,N,N′,N′*-tetraisopropylphosphordiamidite (365 μL, 1.15 mmol) was added to a solution of **15** (0.538 g, 0.884 mmol) in dry MeCN (1 mL), followed by addition of tetrazole as 0.45 mol L^{-1} solution in MeCN (2.0 mL, 0.90 mmol). After 80 min, the mixture was evaporated to dryness, saturated $NaHCO_3$ was added, and the product was extracted twice with CH_2Cl_2. The combined organic layers were dried with Na_2SO_4 and evaporated to yield 0.618 g (86%) of **16**. ^{1}H NMR (500 MHz, CD_3CN): δ_{ppm} 7.83 (m, 4H, Pht), 7.49−7.46 (m, 2H, DMTr), 7.37−7.30 (m, 6H, DMTr), 7.25−7.21 (m, 1H, DMTr), 6.91−6.86 (m, 4H, DMTr), 4.42 (m, 1H, CHHON), 4.38−4.32 (m, 3H, CHHON, H-1, and H-3), 4.01 (m, 1H, H-4), 3.84−3.67 (m, 8H, $POCH_2$ and 2 × OCH_3), 3.60 (m, 2H, H-2), 3.15 (m, 1H, H-5a), 3.05 (m, 1H, H-5b), 2.66 (t, 1H, J = 6.0 Hz, CHHCN), 2.55 (t, 1H, J = 6.0 Hz, CHHCN), 2.24−2.00 [m, 3H, CH(CH_3)$_3$ and CH_2CH_2ON], 1.93−1.85 [m, 1H, CH(CH_3)$_3$], 1.19−1.03 (m, 12H, 4 × CH_3); ^{31}P NMR (200 MHz, CD_3CN): δ_{ppm} 147.2; HRMS (ESI): $[M + Na]^+$ $C_{45}H_{52}N_3NaO_9P$ requires 832.3339, found 832.3311.

Synthesis of Oligodeoxyribonucleotide 5′-Glycoconjugate (20). The oligodeoxyribonucleotide **18** was synthesized on an Applied Biosystems 392 DNA synthesizer on 1.0 μmol scale using commercial 1000 Å CPG-succinyl-thymidine support and conventional phosphoramidite chemistry. Standard DNA coupling protocol was used except for a prolonged coupling time for phosphoramidite **12** (600 s, 0.13 mol L^{-1} solution in dry MeCN). After the oligonucleotide assembly, the support-bound material was removed from the synthesizer

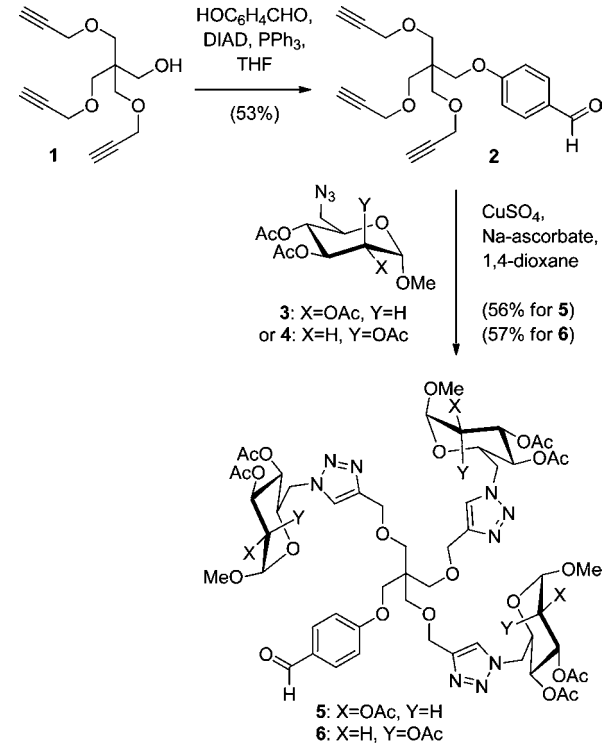
and the phthaloyl protections were removed by 0.5 mol L^{-1} hydrazinium acetate treatment; i.e., the support was suspended in a mixture of $NH_2NH_2 \cdot H_2O$, pyridine, and AcOH (0.124/4/1 v/v/v) for 30 min, washed with pyridine and MeCN, and dried. An aliquot of the support **19** (6.9 mg, 0.21 μmol) was transferred to microcentrifuge tube, and the glucoside cluster **5** was coupled to the aminooxy groups by adding the glycocluster as a 0.08 mol L^{-1} solution (55 μL, 4.2 μmol) in MeCN to the support. The mixture was shaken at ambient temperature for 24 h, filtered, washed with MeCN, and dried. To ensure the completeness of the reaction, oximation was repeated twice. The unreacted aminooxy groups were capped with acetone (1 h), and the support was dried. The oligodeoxyribonucleotide glycoconjugate was released from the support and deprotected with concentrated ammonia (33% aqueous NH_3, 16 h at 55 °C). The crude product was evaporated, dissolved in 30% aqueous MeCN, and purified by C18 RP HPLC. The authenticity of the conjugate **20** was verified by MS (ESI) spectroscopy: required 6817.2, found 6816.5.

Synthesis of Oligodeoxyribonucleotide 3′-Glycoconjugate (26). The general procedures were as described for **20**. Phosphoramidite **16** (0.11 mol L^{-1} solution in dry MeCN) was coupled to CPG-succinyl-thymidine support using a prolonged coupling time of 1200 s and 6 extra detritylations. The support-bound material **22** was removed from the synthesizer, and the phthaloyl protection was removed by hydrazinium acetate treatment as described for **20**. The support (18.8 mg, 0.56 μmol) was transferred to microcentrifuge tube, and the mannoside cluster **6** was coupled to the aminooxy group by adding the glycocluster as a 0.07 mol L^{-1} solution (80 μL, 5.7 μmol) in MeCN to the support. The mixture was shaken at ambient temperature for 24 h, filtered, washed with MeCN, and dried. Oximation with the glycocluster was repeated twice, followed by acetone treatment (1 h). The support **23** was dried and reloaded to the DNA synthesizer. The oligonucleotide chain assembly was continued by coupling of a thymidine residue (two consecutive couplings, 600 s each) and phosphoramidite **16** (three consecutive couplings, 1200 s each). The support-bound **24** was again removed from the synthesizer, the phthaloyl protection was removed, and the glucoside cluster **5** was coupled three times as a 0.09 mol L^{-1} solution (60 μL, 5.1 μmol) in MeCN to the support as described above. After acetone treatment (1 h) and drying, the support **25** was reloaded to the DNA synthesizer for the assembly of the remaining chain. Two consecutive couplings were again performed with the adjacent thymidine residue, whereas the rest of the chain was assembled using standard DNA coupling protocol. The oligodeoxyribonucleotide glycoconjugate was released from the support and deprotected with concentrated ammonia (33% aqueous NH_3, 16 h at 55 °C). The crude product was evaporated, dissolved in 30% aqueous MeCN, and purified by C18 RP HPLC. The authenticity of the conjugate **26** was verified by MS (ESI) spectroscopy: required 7599.6, found 7599.0.

RESULTS AND DISCUSSION

Synthesis of Glycoclusters (5,6). Previously (*54*) published tri-*O*-propargyl pentaerythritol (**1**) was used as a core molecule in the synthesis of trivalent glycoclusters (Scheme 1). First, an aldehyde functionality was introduced in the core to allow ligation of the clusters to aminooxy functionalized oligonucleotides. For this purpose, the free hydroxyl group of **1** was subjected to Mitsunobu reaction with 4-hydroxybenzaldehyde, which gave the desired scaffold **2** in 53% yield. Methyl 6-azido-6-deoxy-α-D-gluco- (**3**) and -α-D-mannopyranoside (**4**) (*55*) were used for construction of the clusters. Accordingly, copper(I)-catalyzed 1,3-dipolar cycloaddition (*57, 58*), the so-called click reaction, was applied to attach the sugarazide units to scaffold **2** to obtain glycoclusters **5** (56%) and **6** (57%). The advantage of clustering the sugars via the 6-position of the carbohydrate ring is that it allows variation of the aglycone moiety, which may in some cases affect the efficiency of lectin binding (*29*).

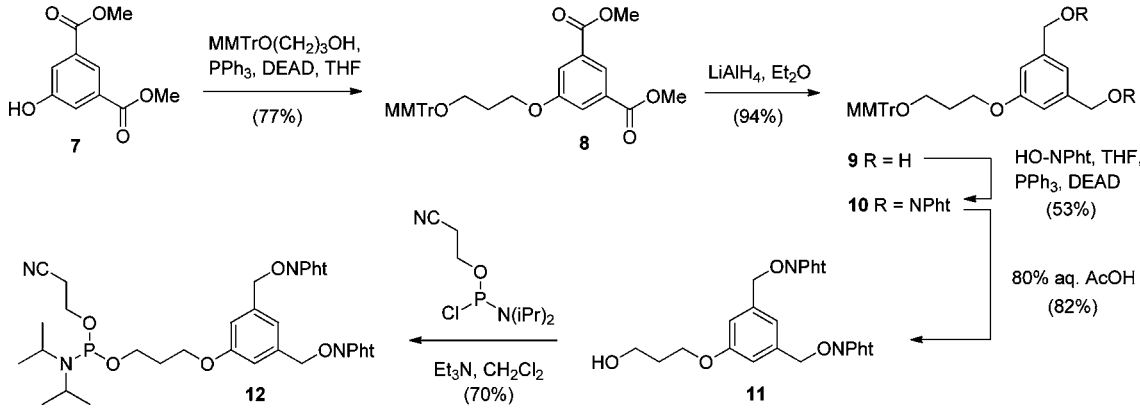
Scheme 1. Synthesis of Glycoclusters 5 and 6



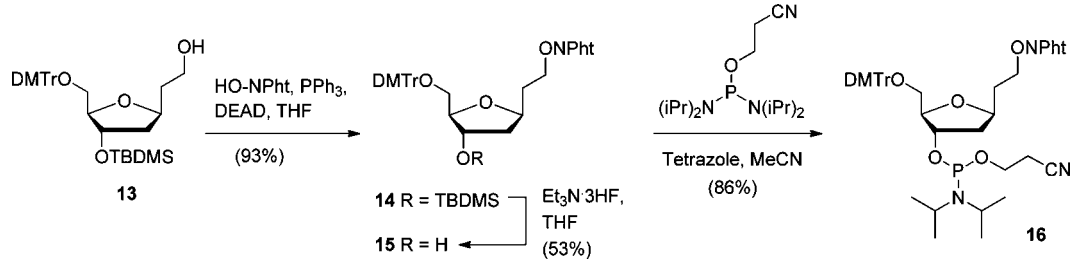
Synthesis of the 5′-Branching Unit (12). To enable conjugation of two trivalent glycoclusters to the 5′-end of an oligonucleotide, a phosphoramidite reagent bearing two phthaloyl-protected aminooxy functions (**12**, Scheme 2) was synthesized. This building block is compatible with conventional solid-phase oligonucleotide synthesis by the phosphoramidite strategy and it can be attached to the oligonucleotide chain by a somewhat elongated coupling cycle. Commercially available dimethyl 5-hydroxyisophthalate **7** was used as the starting material to which 4-methoxytrityl protected propanediol arm (prepared as corresponding tritylated propanediol (*56*)) was attached by Mitsunobu reaction (→ **8**, 77%). The methyl ester functions were then reduced to primary alcohols with lithium aluminum hydride to obtain **9** (94%). The phthaloyl protected aminooxy groups were generated by Mitsunobu reaction with *N*-hydroxyphthalimide (→ **10**, 53%). The 4-methoxytrityl protection was finally removed with acetic acid (→ **11**, 82%) and the exposed hydroxyl group was phosphitylated to give **12** (70%).

Synthesis of the Intrachain Branching Unit (16). To enable conjugation of trivalent clusters in desired positions within the oligonucleotide chain and, in particular, to allow introduction of dissimilar glycoclusters in different sites within the chain, a deoxyribose-derived C-glycosidic phosphoramidite reagent **16** (Scheme 3) bearing a phthaloyl protected aminooxy function was synthesized. Previously (*40*) prepared 5-(4,4′-dimethoxytrityl)-3-*O*-*tert*-butyldimethylsilyloxy-1,2-dideoxy-1-*C*-(2-hydroxyethyl)-β-D-*erythro*-pentofuranose (**13**) was used as a starting material. The primary hydroxyl group was converted to a phthaloyl protected aminooxy group by the Mitsunobu reaction to obtain **14** (93%). *tert-*

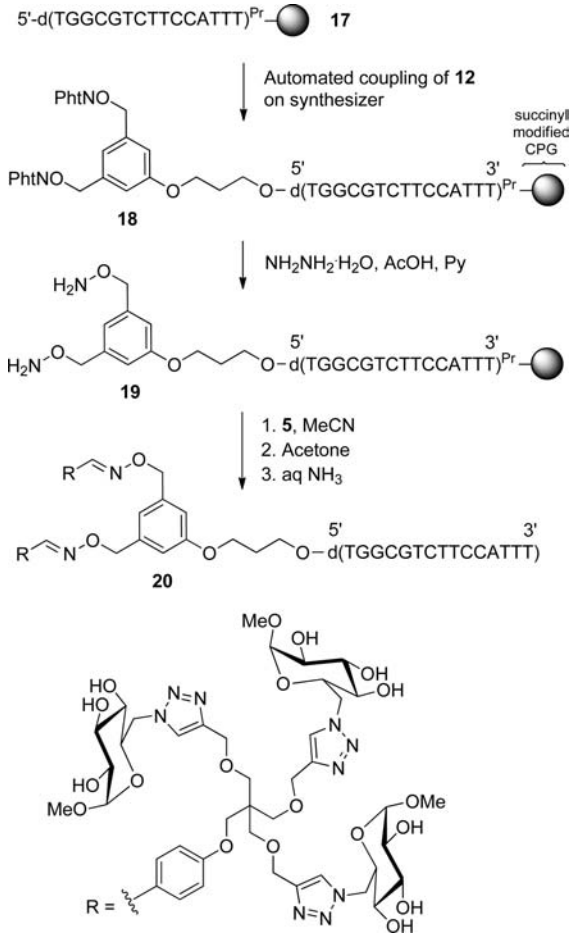
Scheme 2. Synthesis of the 5′ Branching Unit 12



Scheme 3. Synthesis of the Intrachain Branching Unit 16



Scheme 4. Synthesis of Oligonucleotide 5′-Glycoconjugate 20[a]



[a] Abbreviation Pr used for the fully protected oligodeoxyribonucleotide.

Butyldimethylsilyl protection was removed (→ **15**, 53%), and the hydroxyl group was phosphitylated to give **16** (86%).

Preparation of an Oligonucleotide 5′-Glycoconjugate (20). The synthesis of the oligonucleotide conjugate containing two trivalent glucopyranosyl clusters at the 5′-terminus was initiated by coupling phosphoramidite **12** to the 5′-hydroxy of otherwise fully protected support-bound oligonucleotide (**17**, Scheme 4). The support was removed from the synthesizer and the phthaloyl protections were removed from the solid-supported oligomer (**18**) by treatment with hydrazinium acetate in pyridine. The exposed aminooxy groups of **19** were then oximated with 20 equiv of the aldehyde functionalized glucoside cluster **5** in acetonitrile for 24 h. To ensure the efficiency of oximation, the treatment was repeated twice. The remaining

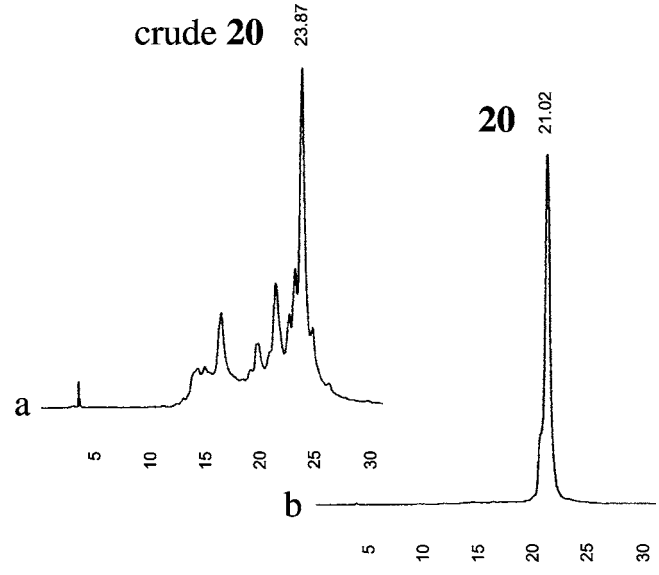
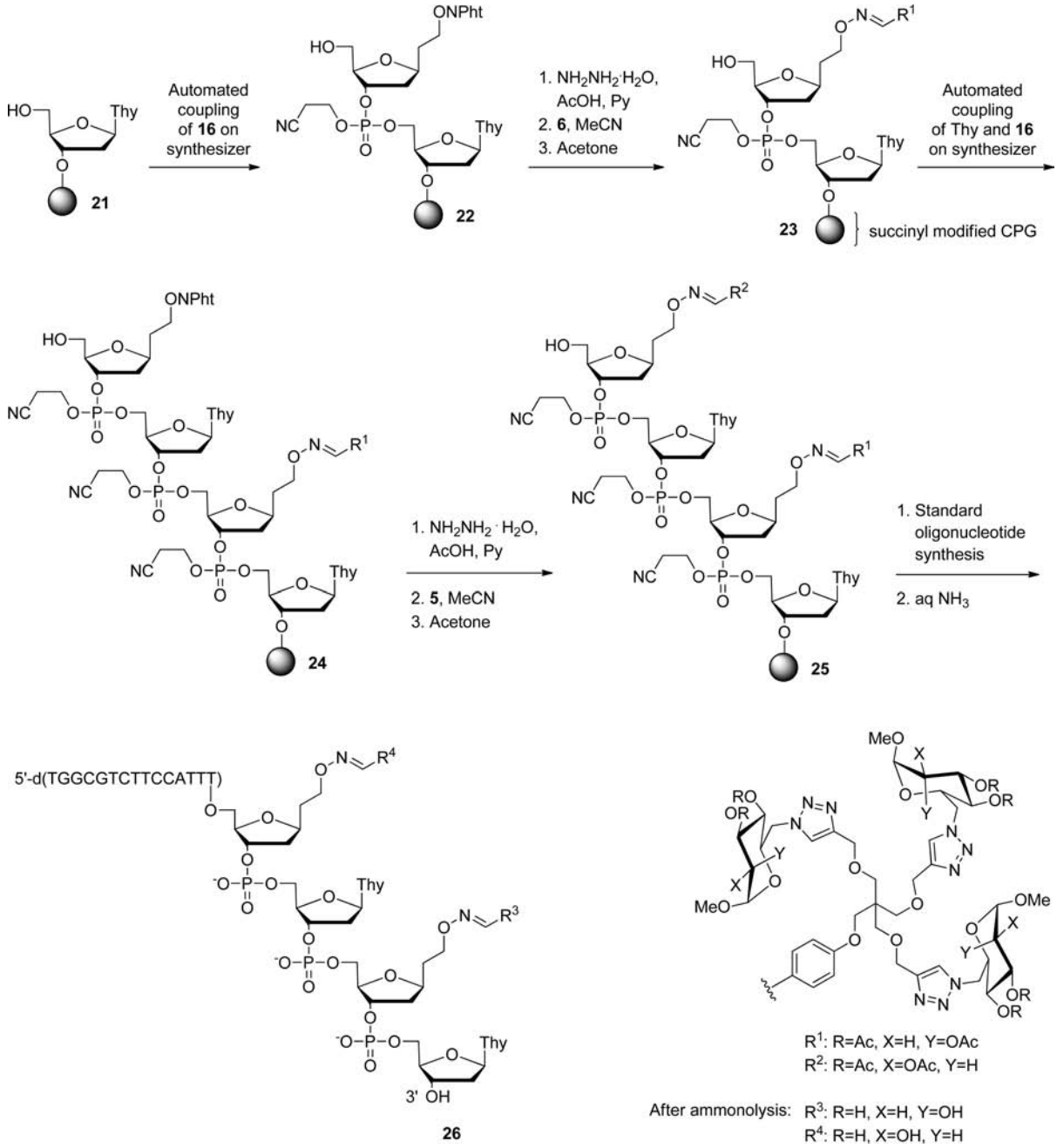


Figure 2. RP HPLC trace of the crude (a) and purified (b) oligonucleotide glycoconjugate **20**. For the chromatographic conditions, see experimental procedures.

Scheme 5. Synthesis of Oligonucleotide 3′-Glycoconjugate 26



unreacted aminooxy groups were capped with acetone, after which the conjugate was released from the support and deprotected by standard ammonolysis (16 h, at 55 °C). The crude product was purified by RP HPLC (Figure 2) and analyzed by MS (ESI) spectroscopy. As seen from the HPLC trace, the desired conjugate **20** was the main product. In addition, an incompletely oximated conjugate, i.e., conjugate having only one sugar cluster attached, was detected in a minor amount. All in all, the method proved to be successful in the preparation of glycoconjugates bearing six sugars that may adopt a more or less parallel orientation in space.

Preparation of an Intrachain Oligonucleotide Glycoconjugate (26). Intrachain branching unit **16** was used for preparation of a glycoconjugate with two dissimilar glycoclusters attached close to the 3′-terminus of the oligonucleotide (**26**, Scheme 5). The first branching unit was coupled to CPG-succinyl-thymidine support after which the support (**22**) was removed from the synthesizer and the phthaloyl protection was removed by the hydrazinium acetate treatment discussed above. The exposed aminooxy group was oximated with 10 equiv of the mannoside cluster **6** in acetonitrile for 24 h. Oximation was repeated twice followed by capping with acetone. HPLC trace of the crude conjugate released by ammonolysis from an aliquot of support **23** can be seen in Figure 3. The support (**23**) was reloaded to the synthesizer and one thymidine unit and another branching unit **16** were coupled using consecutive couplings for both compounds to enhance the coupling efficiency. The support was again removed from the synthesizer and the phthaloyl protection was removed from the tetrameric structure (**24**) as before. The second oximation step was carried out three times using now the glucoside cluster **5**. After acetone capping, the support **25** was again reloaded to the synthesizer. The first thymidine residue following the branching unit was introduced by two consecutive couplings, while the rest of the oligonucleotide chain was assembled by standard DNA coupling protocol. The conjugate was released and deprotected by ammonolysis (16 h, at

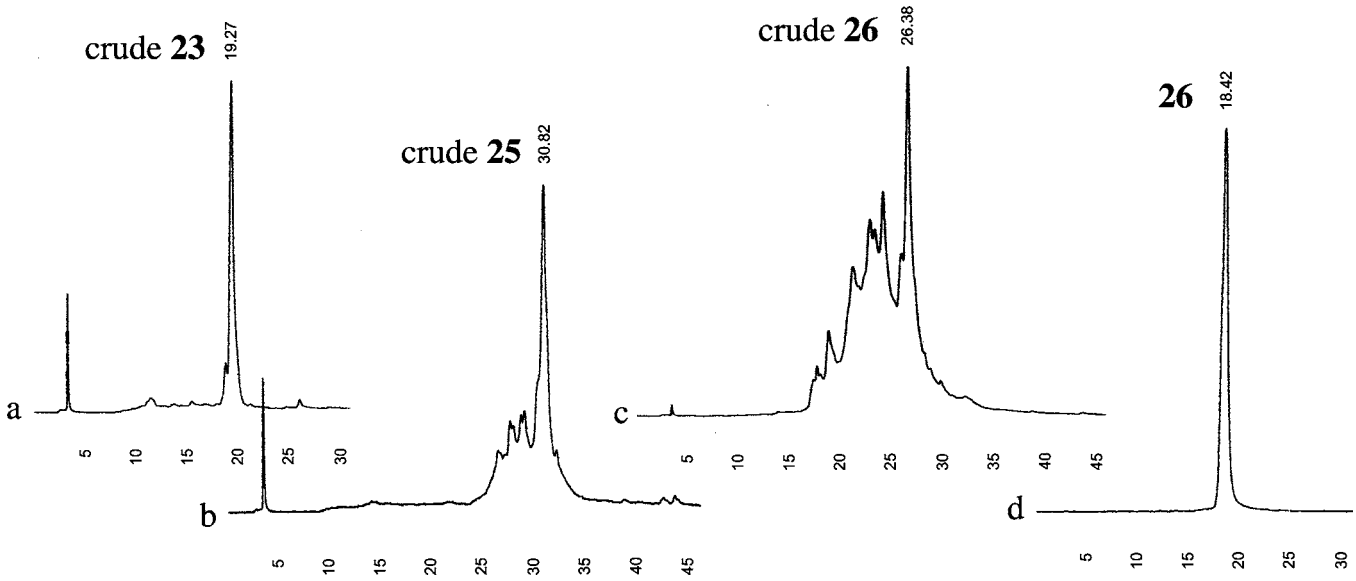


Figure 3. RP HPLC traces of the crude oligonucleotide glycoconjugates released by ammonolysis from aliquots of supports **23** (a), and **25** (b), and the HPLC trace of the crude (c) and purified (d) oligonucleotide glycoconjugate **26**. For the chromatographic conditions, see experimental procedures.

55 °C), followed by purification by RP HPLC (Figure 3) and analysis by MS (ESI) spectroscopy. Conjugate **26** was the main product although numerous side products could be detected, especially due to incomplete coupling of the second branching unit. Oxidation on the other hand seemed to proceed almost to completion on the basis of the HPLC traces of the crude intermediates released by ammonolysis from aliquots of supports **23** and **25** (Figure 3).

CONCLUSION

It has been shown that trivalent glycoclusters bearing a benzaldehyde moiety for subsequent conjugation (**5**, **6**) may be conveniently prepared from tri-*O*-propargylpentaerythritol in two steps by applying sequentially the Mitsunobu and click reactions. These clusters may rather efficiently be conjugated to solid supported oligonucleotides incorporating aminooxy functionalized branching units. On using a 5′-terminal 3,5-bis(aminooxymethyl)phenyl group (**12**) for branching, a conjugate bearing six sugars having a more or less parallel orientation is conveniently obtained. When a 2′-deoxyribose-derived aminooxyethyl *C*-glycoside (**16**) is inserted into the oligonucleotide chain, the prefabricated clusters may be attached to desired sites within the chain. This can be done in a stepwise manner, and hence, more than one type of clusters may be introduced.

ACKNOWLEDGMENT

The authors thank M.Sc. Teija Niittymäki and Ms. Miriam von Usedom for their help in preparation of some of the compounds. The Graduate School of Organic Chemistry and Chemical Biology is gratefully acknowledged for financial support.

Supporting Information Available: NMR spectral data for **2**, **5**, **6**, **8**−**12**, **14**−**16**, and MS spectral data for **20** and **26**. This material is available free of charge via the Internet at http://pubs.acs.org.

LITERATURE CITED

(1) Kurreck, J. (2009) RNA interference: from basic research to therapeutic applications. *Angew. Chem., Int. Ed. 48*, 1378–1398.
(2) Castanotto, D., and Rossi, J. J. (2009) The promises and pitfalls of RNA-interference-based therapeutics. *Nature 457*, 426–433.
(3) Bauman, J., Jearawiriyapaisarn, N., and Kole, R. (2009) Therapeutic potential of splice-switching oligonucleotides. *Oligonucleotides 19*, 1–13.
(4) Sasaki, S., and Nagatsuki, F. (2006) Application of unnatural oligonucleotides to chemical modification of gene expression. *Curr. Opin. Chem. Biol. 10*, 615–621.
(5) Aboul-Fadl, T. (2005) Antisense oligonucleotides: the state of the art. *Curr. Med. Chem. 12*, 2193–2214.
(6) Grosshans, H., and Filipowicz, W. (2008) Molecular biology: the expanding world of small RNAs. *Nature 451*, 414–416.
(7) Corey, D. R. (2007) RNA learns from antisense. *Nat. Chem. Biol. 3*, 8–11.
(8) Wilson, C., and Keefe, A. D. (2006) Building oligonucleotide therapeutics using non-natural chemistries. *Curr. Opin. Chem. Biol. 10*, 607–614.
(9) Haasnoot, J., Westerhout, E. M., and Berkhout, B. (2007) RNA interference against viruses: strike and counterstrike. *Nat. Biotechnol. 25*, 1435–1443.
(10) Kim, D. H., and Rossi, J. J. (2007) Strategies for silencing human disease using RNA interference. *Nat. Rev. Gen. 8*, 173–184.
(11) Bumcrot, D., Manoharan, M., Koteliansky, V., and Sah, D. W. Y. (2006) RNAi therapeutics: a potential new class of pharmaceutical drugs. *Nat. Chem. Biol. 2*, 711–719.
(12) Dykxhoorn, D. M., Palliser, D., and Lieberman, J. (2006) The silent treatment: siRNAs as small molecule drugs. *Gene Ther. 13*, 541–552.
(13) de Fougerolles, A., Vornlocher, H.-P., Maraganore, J., and Lieberman, J. (2007) Interfering with disease: a progress report on siRNA-based therapeutics. *Nat. Rev. Drug Discovery 6*, 443–453.
(14) Leung, R. K. M., and Whittaker, P. A. (2005) RNA interference: from gene silencing to gene-specific therapeutics. *Pharm. Ther. 107*, 222–239.
(15) Manoharan, M. (2002) Oligonucleotide conjugates as potential antisense drugs with improved uptake, biodistribution, targeted delivery, and mechanism of action. *Antisense Nucleic Acids Drug Dev. 12*, 103–128.
(16) Gilmore, I. R., Fox, S. P., Hollins, A. J., and Akhtar, S. (2006) Delivery strategies for siRNA-mediated gene silencing. *Curr. Drug Delivery 3*, 147–155.
(17) Jeong, J. H., Mok, H., Oh, Y.-K., and Park, T. G. (2009) siRNA conjugate delivery systems. *Bioconjugate Chem. 20*, 5–14.
(18) Da Ros, T., Spalluto, G., Prato, M., Saison-Behmoaras, T., Boutorine, A., and Cacciari, B. (2005) Oligonucleotides and oligonucleotide

conjugates: a new approach for cancer treatment. *Curr. Med. Chem. 12*, 71–78.
(19) Lönnberg, H. (2009) Solid-phase synthesis of oligonucleotide conjugates useful for delivery and targeting of potential nucleic acid therapeutics. *Bioconjugate Chem. 20*, 1065–1094.
(20) Akhtar, S., Hughes, M. D., Khan, A., Bibby, M., Hussain, M., Nawaz, Q., Double, J., and Sayyed, P. (2000) The delivery of antisense therapeutics. *Adv. Drug Delivery Rev. 44*, 3–21.
(21) Ernst, B., and Magnani, J. L. (2009) From carbohydrate leads to glycomimetic drugs. *Nat. Rev. Drug Discovery 8*, 661–677.
(22) Gabius, H.-J., Siebert, H.-C., André, S., Jiménez-Barbero, J., and Rüdiger, H. (2004) Chemical biology of the sugar code. *ChemBioChem 5*, 740–764.
(23) Dwek, R. A. (1996) Glycobiology: Toward understanding the function of sugars. *Chem. Rev. 96*, 683–720.
(24) Mammen, M., Choi, S.-K., and Whitesides, G. M. (1998) Polyvalent interactions in biological systems: implications for design and use of multivalent ligands and inhibitors. *Angew. Chem., Int. Ed. 37*, 2755–2794.
(25) Lundquist, J. J., and Toone, E. J. (2002) The cluster glycoside effect. *Chem. Rev. 102*, 555–578.
(26) Collins, B. E., and Paulson, J. C. (2004) Cell surface biology mediated by low affinity multivalent protein-glycan interactions. *Curr. Opin. Chem. Biol. 8*, 617–625.
(27) Doores, K. J., Gamblin, D. P., and Davis, B. G. (2006) Exploring and exploiting the therapeutic potential of glycoconjugates. *Chem.—Eur. J. 12*, 656–665.
(28) Kiessling, L. L., Gestwicki, J. E., and Strong, L. E. (2006) Synthetic multivalent ligands as probes of signal transduction. *Angew. Chem., Int. Ed. 45*, 2348–2368.
(29) Ambrosi, M., Cameron, N. R., and Davis, B. G. (2005) Lectins: tools for the molecular understanding of the glycocode. *Org. Biomol. Chem. 3*, 1593–1608.
(30) Hangeland, J. J., Flesher, J. E., Deamond, S. F., Lee, Y. C., Ts'O, P. O. P., and Frost, J. J. (1997) Tissue distribution and metabolism of the [^{32}P]-labeled oligodeoxynucleoside methylphosphonate-neoglycopeptide conjugate, [YEE(ah-GalNAc)$_3$]-SMCC-AET-pU^{m}pT$_7$, in the mouse. *Antisense Nucleic Acids Drug Dev. 7*, 141–149.
(31) Duff, R. J., Deamond, S. F., Roby, C., Zhou, Y., and Ts'O, P. O. P. (2000) Intrabody tissue-specific delivery of antisense conjugates in animals: ligand-linker-antisense oligomer conjugates. *Methods Enzymol. 313*, 297–321.
(32) Biessen, E. A., Vietsch, H., Rump, E. T., Fluiter, K., Kuiper, J., Bijsterbosch, M. K., and van Berkel, T. J. C. (1999) Targeted delivery of oligodeoxynucleotides to parenchymal liver cells in vivo. *Biochem. J. 340*, 783–792.
(33) Biessen, E. A. L., Vietsch, H., Rump, E. T., Fluiter, K., Bijsterbosch, M. K., and van Berkel, T. J. C. (2000) Targeted delivery of antisense oligonucleotides to parenchymal liver cells *in vivo*. *Methods Enzymol. 314*, 324–342.
(34) Zhu, L., Ye, Z., Cheng, K., Miller, D. D., and Mahato, R. I. (2008) Site-specific delivery of oligonucleotides to hepatocytes after systemic administration. *Bioconjugate Chem. 19*, 290–298.
(35) Toole, B. P. (2004) Hyaluronan: from extracellular glue to pericellular cue. *Nat. Rev. Cancer 4*, 528–539.
(36) Srinivas, O., Larrieu, P., Duverger, E., Boccaccio, C., Bousser, M.-T., Monsigny, M., Fonteneau, J.-F., Jotereau, F., and Roche, A.-C. (2007) Synthesis of glycocluster-tumor antigenic peptide conjugates for dendritic cell targeting. *Bioconjugate Chem. 18*, 1547–1554.
(37) Yan, H., and Tram, K. (2007) Glycotargeting to improve cellular delivery efficiency of nucleic acids. *Glycoconj. J. 24*, 107–123.
(38) Lönnberg, H. (2009) Solid-supported synthesis of glycoconjugates. *Curr. Org. Synth. 6*, 400–425.
(39) Zatsepin, T. S., and Oretskaya, T. S. (2004) Synthesis and applications of oligonucleotide-carbohydrate conjugates. *Chem Biodivers. 1*, 1401–1417.
(40) Ketomäki, K., and Virta, P. (2008) Synthesis of aminoglycoside conjugates of 2′-*O*-methyl oligoribonucleotides. *Bioconjugate Chem. 19*, 766–777.
(41) Charles, I., Xi, H., and Arya, D. P. (2007) Sequence-specific targeting of RNA with an oligonucleotide-neomycin conjugate. *Bioconjugate Chem. 18*, 160–169.
(42) Maier, M. A., Yannopoulos, C. G., Mohamed, N., Roland, A., Fritz, H., Mohan, V., Just, G., and Manoharan, M. (2003) Synthesis of antisense oligonucleotides conjugated to a multilalent carbohydrate cluster for cellular targeting. *Bioconjugate Chem. 14*, 18–29.
(43) Kiviniemi, A., Virta, P., and Lönnberg, H. (2008) Utilization of intrachain 4′-*C*-azidomethylthymidine for preparation of oligonucleotide conjugates by click chemistry in solution and on a solid support. *Bioconjugate Chem. 19*, 1726–1734.
(44) Matsuura, K., Hibino, M., Yamada, Y., and Kobayashi, K. (2001) Construction of glycol-clusters by self-organization of site-specifically glycosylated oligonucleotides and their cooperative amplification of lectin recognition. *J. Am. Chem. Soc. 123*, 357–358.
(45) Turner, J. J., Meeuwenoord, N. J., Rood, A., Borst, P., van der Marel, G. A., and van Boom, J. H. (2003) Reinvestigation into the synthesis of oligonucleotides containing 5-(β-D-glucopyranosyloxymethyl)-2′-deoxyuridine. *Eur. J. Org. Chem.* 3832–3839.
(46) Katajisto, J., Virta, P., and Lönnberg, H. (2004) Solid-phase synthesis of multiantennary oligonucleotide glycoconjugates utilizing on-support oximation. *Bioconjugate Chem. 15*, 890–896.
(47) Karskela, M., Virta, P., Malinen, M., Urtti, A., and Lönnberg, H. (2008) Synthesis and cellular uptake of fluorescently labeled multivalent hyaluronan disaccharide conjugates of oligonucleotide phosphorotioates. *Bioconjugate Chem. 19*, 2549–2558.
(48) Pourceau, G., Meyer, A., Vasseur, J.-J., and Morvan, F. (2009) Synthesis of mannose and galactose oligonucleotide conjugates by bi-click chemistry. *J. Org. Chem. 74*, 1218–1222.
(49) Matulic-Adamic, J., Serebryany, V., Haeberli, P., Mokler, V. R., and Beigelman, L. (2002) Synthesis of *N*-acetyl-D-galactosamine and folic acid conjugated ribozymes. *Bioconjugate Chem. 13*, 1071–1078.
(50) Bouillon, C., Meyer, A., Vidal, S., Jochum, A., Chevolot, Y., Cloarec, J.-P., Praly, J.-P., Vasseur, J.-J., and Morvan, F. (2006) Microwave assisted click chemistry for the synthesis of multiple labeled-carbohydrate oligonucleotides on solid support. *J. Org. Chem. 71*, 4700–4702.
(51) Dubber, M., and Fréchet, J. M. J. (2003) Solid-phase synthesis of multivalent glycoconjugates on a DNA synthesizer. *Bioconjugate Chem. 14*, 239–246.
(52) Katajisto, J., Heinonen, P., and Lönnberg, H. (2004) Solid-phase synthesis of oligonucleotide glycoconjugates bearing three different glycosyl groups: orthogonally protected bis(hydroxymethyl)-*N, N*′-bis(3-hydroxypropyl)malondiamide phosphoramidite as key building block. *J. Org. Chem. 69*, 7609–7615.
(53) D'Onofrio, J., Montesarchio, D., De Napoli, L., and Di Fabio, G. (2005) An efficient and versatile solid-phase synthesis of 5′- and 3′-conjugated oligonucleotides. *Org. Lett. 7*, 4927–4930.
(54) Calvo-Flores, F. G., Isac-García, J., Hernández-Mateo, F., Pérez-Balderas, F., Calvo-Asín, J. A., Sanchéz-Vaquero, E., and Santoyo-González, F. (2000) 1,3-Dipolar cycloadditions as a tool for the preparation of multivalent structures. *Org. Lett. 2*, 2499–2502.
(55) Ito, Y., and Okuda, T. (1967) 6-Amino-6-deoxy-D-mannose. Jpn. Tokkyo Koho/JP patent 42008003 19670331.
(56) Hernández, A.-I., Familiar, O., Negri, A., Rodriguez-Barrios, F., Gago, F., Karlsson, A., Camarasa, M.-J., Balzarini, J., and Pérez-Pérez, M.-J. (2006) N^1 Substituted thymine derivatives as mitochondrial thymidine kinase (TK-2) inhibitors. *J. Med. Chem. 49*, 7766–7773.
(57) Rostovtsev, V. V., Green, L. G., Fokin, V. V., and Sharpless, K. B. (2002) A stepwise Huisgen cycloaddition process: copper(I)-catalyzed regioselective "ligation" of azides and terminal alkynes. *Angew. Chem., Int. Ed. 41*, 2596–2599.
(58) Tornoe, C. W., Christensen, C., and Meldal, M. (2002) Peptidotriazoles on solid phase: [1,2,3]-triazoles by regiospecific copper(I)-catalyzed 1,3-dipolar cycloadditions of terminal alkynes to azides. *J. Org. Chem. 67*, 3057–3064.

BC900529G

Development of Double-Stranded siRNA Labeling Method Using Positron Emitter and Its In Vivo Trafficking Analyzed by Positron Emission Tomography

Kentaro Hatanaka,[†] Tomohiro Asai,[†] Hiroyuki Koide,[†] Eriya Kenjo,[†] Takuma Tsuzuku,[†] Norihiro Harada,[‡] Hideo Tsukada,[‡] and Naoto Oku*,[†]

Department of Medical Biochemistry and Global COE Program, Graduate School of Pharmaceutical Sciences, University of Shizuoka, 52-1 Yada, Suruga-ku, Shizuoka-city, Shizuoka 422-8526, Japan, and PET Center, Central Research Laboratory, Hamamatsu Photonics K.K., 5000 Hirakuchi, Hamakita-ku, Hamamatsu-city, Shizuoka 434-8601, Japan. Received December 7, 2009; Revised Manuscript Received February 8, 2010

Pharmacokinetic study of small interfering RNA (siRNA) is an important issue for the development of siRNAs for use as a medicine. For this purpose, a novel and favorable positron emitter-labeled siRNA was prepared by amino group-modification using *N*-succinimidyl 4-[fluorine-18] fluorobenzoate ([^{18}F]SFB), and real-time analysis of siRNA trafficking was performed by using positron emission tomography (PET). Naked [^{18}F]-labeled siRNA or cationic liposome/[^{18}F]-labeled siRNA complexes were administered to mice, and differential biodistribution of the label was imaged by PET. The former was cleared quite rapidly from the bloodstream and excreted from the kidneys; but in contrast, the latter tended to accumulate in the lungs. We also confirmed the biodistribution of fluorescence-labeled naked siRNA and cationic liposome/siRNA complexes by use of a near-infrared fluorescence imaging system. As a result, a similar biodistribution was observed, although quantitative data were obtained only by planar positron imaging system (PPIS) analysis but not by fluorescence in vivo imaging. Our results indicate that PET imaging of siRNA provides important information for the development of siRNA medicines.

INTRODUCTION

Small interfering RNA (siRNA) is a short double-stranded nucleic acid molecule that induces sequence-dependent gene silencing (*1, 2*), and gene therapy using siRNA is expected to be a novel treatment strategy for various diseases (*3*). However, the degradation of naked siRNA after administration into the bloodstream of human and animals readily occurs due to nucleases in the blood. Furthermore, siRNA poorly penetrates the plasma membranes of target cells, thus making difficult the delivery to the cytosol of targeted cells for effective gene knockdown. Therefore, a delivery system of siRNA molecules is considered to be indispensable for establishing siRNA therapy. Many studies on the in vivo application of siRNA using chemical modification (*4*) or drug delivery system (DDS) carriers such as liposomes (*5*) and micelles (*6*) for efficacious delivery and gene silencing have been reported. Cationic liposomes or micelles are representative carriers having electric charges on their surface. Because siRNA possesses polyanionic charges, it electrostatically interacts with cationic carriers used for RNA interference (RNAi). Pharmacokinetic studies on siRNA/carrier complexes have been performed by using fluorescence- or radioisotope-labeled carriers or carrier-entrapped imaging agents for magnetic resonance imaging. The techniques of carrier-labeling, however, do not always reflect the biodistribution of siRNA, since there is a chance that the siRNA may become detached from the carrier in the bloodstream, especially when the siRNA is bound to the surface of cationic carriers. To evaluate the in vivo behavior of siRNA itself, the trafficking of it is carried out by near-infrared fluorescence (NIRF) imaging (*7*). However, like fluorescence imaging, NIRF imaging is affected by tissue depth to some extent, and therefore, quantitative data are difficult to obtain. In addition, although the NIRF imaging method is applicable for use on nonhuman primates, the method for human use has not yet been established.

To obtain precise pharmacokinetic information on siRNA molecules or their carriers in vivo, positron emission tomography (PET) is one of the ideal techniques. PET enables the determination of the real-time biodistribution and topical accumulation of positron emitter-labeled compound noninvasively. This technique can be applied in preclinical studies, in which a drug candidate labeled with a positron emitter is injected into animals. The circulation profile, biodistribution in various tissues, and eventual elimination of the drug candidate from the body can be monitored noninvasively in the same animal. Furthermore, certain positron emitter-labeled new drug candidates can be used for microdosing studies in humans. Such phase zero studies enable the investigator to reduce the rate of dropout of drug candidates in further clinical studies. For the pharmacokinetic study of DDS carriers, we previously reported a novel [^{18}F]-probe for labeling the lipid assembly carriers for PET analysis (*8*). As mentioned above, since siRNA may possibly dissociate from its carrier and be degraded by plasma nucleases after injection into the bloodstream, we have sought to label siRNA with a positron emitter for the analysis of siRNA trafficking in vivo. The pharmacokinetic information on siRNA molecules, like that of the carrier, is considered to be critical and indispensable for the development of siRNA medicines.

Recently, Bartlett et al. labeled the sense strand of siRNA with copper-64 by using 1,4,7,10-tetraazacyclododecane-*N,N′,N″,N‴*-tetraacetic acid (DOTA) and then annealed this modified strand with the unmodified antisense strand for the determining biodistribution of siRNA in micellar carriers (*9*).

* Corresponding author. Naoto Oku, Department of Medical Biochemistry, University of Shizuoka School of Pharmaceutical Sciences, 52-1 Yada, Suruga-ku, Shizuoka 422-8526, Telephone number: +81-54-264-5701, Fax number: +81-54-264-5705, E-mail address: oku@u-shizuoka-ken.ac.jp.

[†] University of Shizuoka.

[‡] Hamamatsu Photonics K.K.

10.1021/bc9005267 © 2010 American Chemical Society
Published on Web 03/08/2010

Viel et al. reported the conjugation of ^{18}F to oligonucleotide by using (*N*-[3-(2-[^{18}F]fluoropyridin-3-yloxy)-propyl]-2-bromoacetamide ([^{18}F]FRyBrA), and this method also required the annealing process (*10, 11*). In spite of their efforts, detail pharmacokinetic information about naked siRNA or siRNA in DDS carriers is still largely lacking.

In the present study, we developed a novel technique for labeling siRNA with a positron emitter, ^{18}F, in which double-stranded siRNA was labeled to gain conformational accuracy for examining the pharmacokinetics of siRNA by using [^{18}F]SFB as an ^{18}F labeling reagent. [^{18}F]SFB have been widely used to form a stable amide bond by reacting with primary amino groups for a short time and very easily for labeling certain peptides (*12*), antibodies (*13*), or DNA oligonucleotides (*14*). Because ^{18}F has an extremely short half-life (109 min), avoidance of the annealing process by labeling of double-stranded siRNA is favorable. [^{18}F]-labeled siRNA thus prepared was identified by ESI-TOF-MS, HPLC, and autoradiography after electrophoresis. By use of this positron emitter-labeled siRNA, we actually examined the biodistribution of siRNA by PPIS in the presence or absence of cationic liposome, a DDS carrier of siRNA. We also performed NIRF imaging for verifying the in vivo behavior of siRNA and discussed the correspondence of the imaging results obtained from NIRF imaging and PPIS imaging.

EXPERIMENTAL PROCEDURES

Materials. 4,7,13,16,21,24-Hexaoxa-1,10-diazabicyclo[8.8.8]-hexacosane (K[2.2.2]), tetra-*n*-propyl-ammonium hydroxide (Pr_4NOH), *N*,*N*,*N*′,*N*′-tetramethyl-*O*-(*N*-succinimidyl)uronium tetrafluoroborate (TSTU), CH_3CN (anhydrous), and fetal bovine serum were obtained from Sigma-Aldrich (Saint Louis, MO, USA). Potassium carbonate·$1.5H_2O$ was purchased from Merck (Darmstadt, Germany). Anion-exchange resin AG1-X8 (OH^- form, 100−200 mesh) was from Bio-Rad Laboratories (Hercules, USA). *N,N*-Dimethylformamide (DMF) was purchased from Wako Pure Chemical Industries, Ltd. (Osaka, Japan). A cationic lipid for transgene use, 1,2-dioleoyl-3-trimethylammonium-propane (DOTAP), was purchased from Avanti Polar Lipids Inc. (Alabaster, AL, USA). Cholesterol was kindly provided by Nippon Fine Chemical Co., Ltd. (Takasago, Hyogo, Japan). Trizol reagent was obtained from Invitrogen Co. (Carlsbad, CA). An alfalfa-free feed was purchased from Oriental Yeast co. Ltd. (Tokyo, Japan). Escain was purchased from Mylan Pharmaceuticals (Morgantown, WV). All other chemicals and solvents were analytical grade and were used without further purification unless otherwise stated. [^{18}F]Fluoride was produced with a cyclotron (HM-18, Sumitomo Heavy Industries, Tokyo, Japan) at Hamamatsu Photonics PET Center by the ^{18}O(p,n)^{18}F nuclear reaction using [^{18}O]H_2O. Labeled compounds were synthesized by using modified CUPID system (Sumitomo Heavy Industries, Tokyo, Japan). The HPLC column used for the purification of succinimidyl 4-[^{18}F] fluorobenzoate ([^{18}F]SFB) was an Inertsil ODS3 (10 × 250 mm, 5 μm, GL Sciences Inc., Tokyo, JAPAN). Nonradioactive fluorine-conjugated siRNA was identified by using a UPLC/ESI-QTOF-MS system, which consisted of an ACQUITY ultraperformance liquid chromatography (UPLC) system and an electrospray ionization quadrupole time-of-flight mass spectrometer (SYNAPT High Definition Mass Spectrometry system; Waters, Milford, MA, USA). An ultraviolet−visible (UV/vis) detector (ACQUITY TUV, Waters) was used. The UPLC column used for the identification of fluorine-labeled siRNA was an Acquity UPLC BEH C18 column (2.1 × 100 mm, 1.7 μm, Waters Corp.). The particle size and zeta-potential of nanoparticles were measured by using a Zetasizer Nano ZS (Malvern, Worcs, UK). Gel for obtaining an autoradiogram of ^{18}F and siRNA after electrophoresis was used an FLA-7000 (FUJIFILM Corporation, Tokyo, Japan) and LAS-3000 mini system (Fuji Film, Tokyo, Japan), respectively. Fluorescence imaging was performed by using a Xenogen IVIS Lumina System coupled to *Living Image* software for data acquisition (Xenogen Corp., Alameda, CA). PET imaging was performed by using a planar positron imaging system (PPIS, Hamamatsu Photonics, Shizuoka, Japan). Radioactivities in each organs were measured by gamma-counter (ARC-2000, Aloka, Tokyo, Japan).

Experimental Animals. Five-week-old male BALB/c mice male were purchased from Japan SLC Inc. (Shizuoka, Japan). The animals were cared for according to the Animal Facility Guidelines of the University of Shizuoka. All animal experiments were approved by the Animal and Ethics Review Committee of the University of Shizuoka.

siRNA Sequence. Alexa Fluor 750-labeled siRNA (AF750-siRNA) was purchased from Japan Bio Services Co., Ltd. (Saitama, Japan). Antisense strand contained a fluorescence at the 3′ end of the strand. siRNA for positron emitter-labeling was synthesized and purified by Hokkaido System Science. The nucleotide sequences of the siRNA were those of an unspecific scrambled RNA, and the antisense strand contained a 3′ amino C6 linker for the radioactive labeling of the siRNA duplex (Scheme 1). The sequences of the siRNA used were 5′-CGAUUCGCUAGACCGGCUUCAUUGCAG-3′ (sense) and 5′-GCAAUGAAGCCGGUCUAGCGAAUCGAU-3′ (antisense).

Synthesis of Ethyl-(4-Trimethylammonium)benzoate Trifluoromethanesulfonate. Ethyl 4-dimethylaminobenzoate was synthesized according to the procedure reported by Haka et al. (*15*). The synthetic compound was assigned by ^{1}H NMR and ^{13}C NMR. Ethyl 4-dimethylaminobenzoate 11.4 g (59 mmol) was dissolved in 70 mL anhydrous CH_2Cl_2. Ten grams of $CF_3SO_3CH_3$ (64.9 mmol) was added dropwise to the solution, and the mixture was stirred overnight at room temperature. A crystalline precipitate was formed by the addition of Et_2O (100 mL) and collected by suction filtration. Recrystallization from CH_2Cl_2/Et_2O gave 10.2 g (48%) of ethyl 4-trimethylammoniumbenzoate trifluoromethanesulfonate.

Radiosynthesis of [^{18}F]KF/K[2,2,2] Complex. [^{18}F]KF/K-[2,2,2] was obtained by use of a previously reported method (*16*). In brief, [^{18}F]fluoride was trapped by ion-exchange resin AG1-X8 and eluted from the resin by 0.5 mL of 40 mM K_2CO_3. To this fluoride solution, 15 mg of K[2,2,2] in CH_3CN (2 mL) was added. Water was removed by azeotropic distillation at 110 °C under He flow (400 mL/min) for 5 min. To the residue, the addition of CH_3CN (1 mL) and azeotropic distillation were repeated twice. Then, the residue was dried under reduced pressure for 1 min, and the reaction vessel was purged with a flow of He (50 mL/min) for 1 min to ensure complete dryness. Finally, the reaction vessel was cooled to room temperature and used for further labeling.

Preparation of Succinimidyl 4-[^{18}F]fluorobenzoate ([^{18}F]-SFB). [^{18}F]SFB was prepared according to the one-pot procedure of Tang et al. (*17*) with some modifications. The precursor (5 mg) in 1.5 mL of CH_3CN was added to the dried [^{18}F]KF/K[2,2,2] complex mentioned above and reacted at 80 °C for 10 min. After the reaction mixture had been cooled, 20 μL of 1 M Pr_4NOH in 0.5 mL of CH_3CN was added; and hydrolysis was carried out at 120 °C for 5 min. Then, to the reaction mixture, TSTU (15 mg) in 0.5 mL of CH_3CN was added and converted to [^{18}F]SFB at 80 °C for 5 min. The reaction mixture was diluted with 2.0 mL of 5% CH_3COOH and transferred to the HPLC injector. Crude product was purified by semipreparative HPLC (CH_3CN:H_2O = 300:700, 6 mL/min, 254 nm). The radioactive peak eluted at 25.7 min was collected, diluted with 30 mL of H_2O, and passed through a Sep-Pak C18 cartridge (Waters). [^{18}F]SFB retained on the cartridge was released with 4 mL of CH_2Cl_2 and recovered into a V-vial by passage through a Sep-Pak Dry cartridge (Waters). Then, the [^{18}F]SFB was concen-

Scheme 1. Synthesis of the [^{18}F]SFB and [^{18}F]-Labeled siRNA

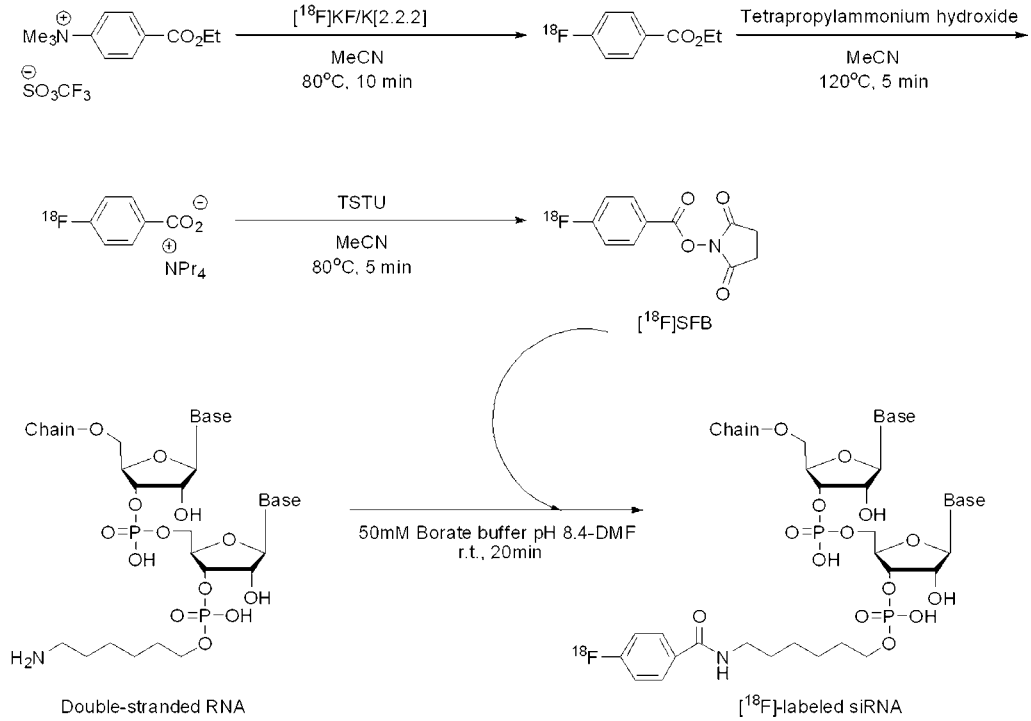


Table 1. Gradient Flow Table

time (min)	0.1 M TEAA (%)	CH_3CN (%)	flow rate (mL/min)
0−2	95−90	5−10	0.3
2−3	90−75	10−25	0.3
3−7	75−60	25−40	0.3
7−10	60−0	40−100	0.3

trated by a flow of He (200 mL/min) at 60 °C and used for labeling. [^{18}F]SFB with (a specific radioactivity of 51.4 GBq/μmol, a radiochemical yield of 21.1%) was obtained.

Radiolabeling of siRNA with [^{18}F]SFB. siRNA (40 nmol) in 16 μL of 50 mM borate buffer, pH 8.5, was added to the [^{18}F]SFB (60 nmol) in 3.6 μL of DMF. The mixture was vortexed for a few seconds and then incubated at room temperature for 20 min. The reaction mixture was purified and concentrated by ultrafiltration through a 10 000 molecular weight cutoff filter (Amicon, Millipore, Bedford, MA, USA). The mixture was centrifuged at 4000 × *g* with RNase-free phosphate-buffered saline (PBS). [^{18}F]-labeled siRNA with a radiochemical yield of 37.9% and a specific activity of 25.5 GBq/μmol was obtained. Nonradioactive fluorine-conjugated siRNA was synthesized in a similar manner except that 150 nmol cold SFB was used instead of 60 nmol [^{18}F]SFB.

Analytical Methods. Nonradioactive fluorine-conjugated siRNA was identified by using a UPLC/ESI-QTOF-MS system. The analytical column was maintained at 40 °C. A ultraviolet−visible (UV/vis) detector, equipped with a 500 nL flow cell, was also directly connected between the column outlet and the QTOF-MS instrument. Fractionation of fluorine-conjugated siRNA was performed at a flow rate of 0.3 mL/min using as the eluent the gradient of 0.1 M triethylammonium acetate (TEAA, pH 7.0) and CH_3CN. Gradient profile is presented in the Table 1.

Evaluation of siRNA Labeling. Precursor siRNA, fluorine-conjugated siRNA (non-RI), and [^{18}F]-labeled siRNA (0.5 μg) were applied to a 15% polyacrylamide gel and electrophoresed. Then, the gel was exposed to an imaging plate for obtaining an autoradiogram of ^{18}F by using an FLA-7000; the gel was stained for 5 min in ethidium bromide (EtBr), and siRNA was detected by using a LAS-3000 mini system.

Preparation of Cationic Liposomes and Their Complexes with siRNA. DOTAP and cholesterol (1:1 as a molar ratio) were dissolved in *tert*-butyl alcohol for freeze−drying and hydrated in RNase-free PBS. The liposomes were frozen and thawed for 3 cycles using liquid nitrogen and extruded 10 times through a polycarbonate membrane filter having a pore size of 100 nm (Nucleopore, Maidstone, UK). Then, the cationic liposome and siRNA were mixed gently and incubated for 10 min at room temperature to form liposome/siRNA complexes. The nitrogen moiety of cationic liposome to the phosphorus of siRNA (N/P ratio) was 24:1 in the complexes. The particle size and zeta-potential of liposome/siRNA complexes diluted with RNase-free PBS were measured. The particle size of liposome/siRNA complexes was 218 ± 3.0 nm (n = 3), and the particles showed monodispersion (polydispersity index = 0.16). The zeta-potential was 36.3 ± 1.9 mV.

Near-Infrared Fluorescence Imaging in Vivo. The biodistribution of AF750-siRNA was assessed by using an IVIS Lumina System. Mice were fed an alfalfa-free feed to reduce the effect of background fluorescence. The animals were anesthetized continuously via inhalation of 2% escain. siRNA or liposome/siRNA complexes containing 15 μg AF750-siRNA were injected via a tail vein under anesthesia. Alexa Fluor 750 fluorescence was acquired every 10 min for up to 60 min after the injection. After monitoring, the mice were sacrificed under anesthesia. Then, the organs, namely, heart, lungs, liver, spleen, and kidneys, were collected and imaged ex vivo with the IVIS.

PPIS Imaging of [^{18}F]-Labeled siRNA. Biodistribution of [^{18}F]-labeled siRNA was imaged noninvasively by using a PPIS (*18*−*20*). Animals were anesthetized with an intraperitoneal injection of pentobarbital at 50 mg/kg, and then fixed on an animal holder. To determine the whole-body biodistribution of siRNA, we administered the [^{18}F]-labeled siRNA intravenously (2.5 MBq/mouse). The scan was started immediately after the administration and performed for 60 min. Images were analyzed by using software *ImageJ*. After the PPIS scan, the mice were sacrificed for the collection of the blood from a carotid artery under anesthesia. Then, the heart, lungs, liver, spleen, and kidneys were removed, and the biodistribution of

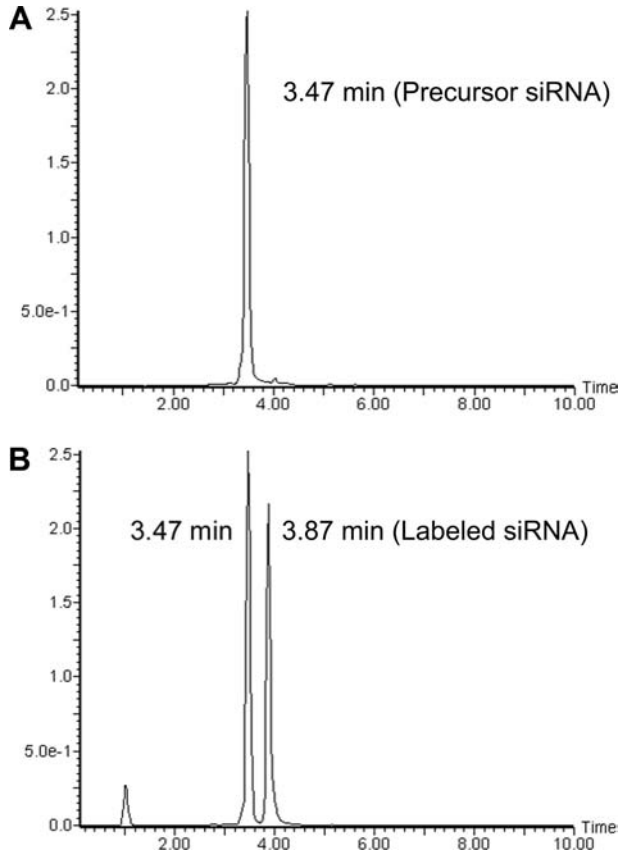


Figure 1. UPLC analysis of fluorine-conjugated siRNA. Nonradioactive fluorine was conjugated to siRNA and separated with the UPLC system. (A) Peak of precursor siRNA at 3.47 min. (B) Peaks of unreacted siRNA at 3.47 min and fluorine-labeled siRNA at 3.87 min after the reaction.

[18F]-labeled siRNA was measured with a gamma counter. Distribution data were presented as percent dose per wet tissue. The total volume of blood was assumed to be 7.56% of the body weight. A time−activity curve was obtained from the mean pixel radioactivity in the region of interest (ROI) of the PPIS images.

Evaluation of siRNA Stability against Serum-Mediated Degradation. Fluorine-conjugated (0.5 μg) naked siRNA or that complexed with liposomes was incubated in 90% fetal bovine serum for 60 min at 37 °C. The siRNA was extracted from the serum by using Trizol reagent and subjected to 15% polyacrylamide gel electrophoresis. The gel was stained for 5 min in EtBr, and siRNA was detected by using a LAS-3000 mini system.

RESULTS

[18F]-Labeling of siRNA and Its Radiochemistry. The methods for synthesis of [18F]SFB and [18F]-labeling of siRNA are shown in Scheme 1. At first, we prepared non-radioisotope (non-RI) fluorine-conjugated siRNA and identified the compound by using LC/ESI-TOF-MS (Table 1). Unreacted siRNA showed a peak at 3.47 min (Figure 1A). After the reaction, HPLC analysis indicated 2 main peaks, namely, labeled siRNA at 3.87 min and precursor siRNA at 3.47 min, respectively (Figure 1B). These peaks were fractionated by HPLC and analyzed by ESI-TOF-MS, giving multiply charged ion peaks of *m*/*z* $[M\text{-}8H]^{8-}$ 2196.1, $[M\text{-}7H]^{7-}$ 2510.9, and $[M\text{-}6H]^{6-}$ 2930.0 (data not shown), which corresponded to the labeled siRNA (expected mass of *m*/*z* $[M\text{-}8H]^{8-}$ 2196.7, $[M\text{-}7H]^{7-}$ 2510.7, and $[M\text{-}6H]^{6-}$ 2929.3). The overall yield of labeled siRNA was greater than 30% based on the peak area. On the basis of the result from non-RI fluorine-grafting to siRNA, [18F]-labeled siRNA was prepared according to the same procedure, and then electrophoresis assay and subsequent autoradiography were performed to confirm the production of [18F]-labeled siRNA. Electrophoresis assay with an imaging plate showed that the siRNA was labeled with [18F]-fluorine without any other exposure bands (Figure 2). In addition, the main band visualized by EtBr staining showed the same position as the band on the same polyacrylamide gel observed by autoradiography. As a result, [18F]-labeled siRNA was successfully prepared without any positron emitter-labeled byproducts, and the labeled siRNA was not degraded under the experimental conditions used.

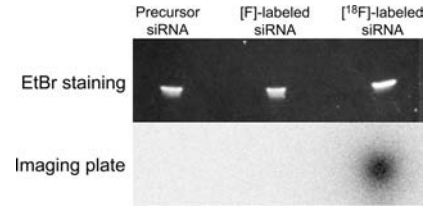


Figure 2. Demonstration of [18F] labeling of siRNA. Precursor siRNA, fluorine-conjugated siRNA, and [18F]-labeled siRNA were applied to a 15% polyacrylamide gel, electrophoresed, and stained with ethidium bromide. The gel was exposed to an imaging plate for detecting 18F.

Biodistribution of siRNA Determined with near-Infrared Fluorescence Imaging in Vivo. We examined the in vivo behavior of siRNA by use of the NIRF imaging system. Mice were intravenously administered naked AF750-siRNA or liposome/AF750-siRNA complexes via a tail vein. The fluorescence imaging of AF750-siRNA was started immediately after the injection and monitored for 60 min. The biodistribution of AF750-siRNA is shown in Figure 3. The results indicated that the fluorescence compound was accumulated in the bladder immediately after the administration of naked AF750-siRNA and then excreted in the urine (Figure 3A). On the contrary, fluorescence was observed at the upper part of the body where the lung was positioned after the administration of liposome/AF750-siRNA complexes. The total fluorescence intensity of the image of mice injected with naked AF750-siRNA was apparently higher than that obtained with the liposomal formulation: Fluorescence in bladder after injection of naked siRNA was quite intense because bladder is located near the body surface, while that in lungs after injection of cationic liposome complexes was weak because lungs are located more deep from body surface compared with bladder.

The ex vivo imaging showed that a small amount of fluorescence remained in the kidneys but that no fluorescence was detected in the other tissues examined (Figure 3B). In contrast, the fluorescence of the cationic liposome/AF750-siRNA complexes accumulated in the lungs, being consistent with the in vivo imaging data.

Stability of Fluorine-Conjugated siRNA against Serum-Mediated Degradation. We evaluated the stability of naked fluorine-conjugated siRNA and cationic liposome/fluorine-conjugated siRNA complexes in serum for 60 min (Figure 4). The naked fluorine-conjugated siRNA incubated in PBS (control) was not decomposed. However, the band of naked siRNA obtained by electrophoresis of the sample that had been incubated in the presence of serum disappeared, indicating that the siRNA had been degraded by RNase within 60 min. In contrast, the band of siRNA was detected in the case of the cationic liposome/siRNA complexes exposed to the serum, indicating that complex formation protected siRNA from RNase in the serum.

In Vivo PPIS Imaging of siRNA Trafficking. Next, we examined [18F]-labeled siRNA trafficking by use of PPIS. Mice were intravenously administered naked [18F]-labeled siRNA in

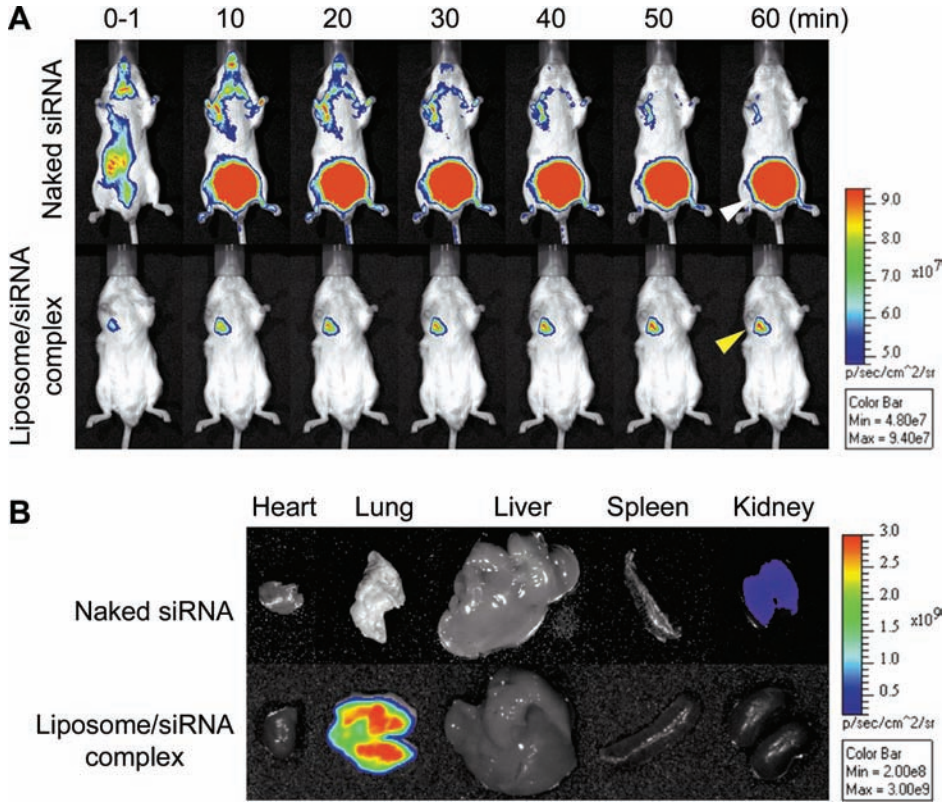


Figure 3. NIRF in vivo imaging with AF750-siRNA and liposome/AF750-siRNA complexes. (A) AF750- siRNA (top) or liposome/AF750-siRNA complexes (bottom) were intravenously administered to BALB/c mice. Images were acquired every 10 min for up to 60 min after the administration. The white arrowhead shows the bladder region, and the yellow arrowhead, the lung region. (B) Ex vivo imaging of AF750-siRNA and liposome/AF750-siRNA complexes at 60 min after administration.

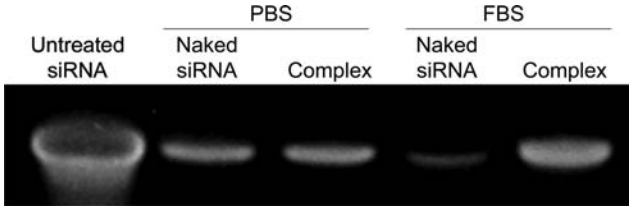


Figure 4. Stability of naked siRNA or liposome/siRNA complexes in FBS. siRNA (0.5 μg) was incubated with PBS (−) or 90% FBS at 37 °C for 60 min. siRNA was extracted and electrophoresed on a 15% polyacrylamide gel after a 60 min incubation and stained with EtBr. Untreated siRNA was used as a control marker.

PBS (−) or liposome/[^{18}F]-labeled siRNA complexes via a tail vein. The real-time imaging of [^{18}F]-labeled siRNA using PPIS was acquired for 60 min, and images were integrated every 5 min (Figure 5A). The ^{18}F radioactivity of the naked [^{18}F]-labeled siRNA accumulated inside the kidneys immediately after administration. This accumulation was not detected in NIRF in vivo imaging because of the influence of tissue depth. Then, ^{18}F was transferred to the bladder and subsequently excreted in the urine. In contrast, most of the ^{18}F radioactivity after the administration of cationic liposome/[^{18}F]-labeled siRNA complexes were retained in the lungs for 60 min, and only insignificant accumulation of them was observed in the bladder. The time−activity curve of ^{18}F in naked siRNA showed transient accumulation in kidney immediately after injection (19% injected dose/tissue at 2 min), and half of that was transferred to bladder at 21 min, and then the excretion of ^{18}F to bladder was gradually increased (Figure 5B). In contrast, the most of the ^{18}F after injection of liposome/siRNA complexes immediately accumulated in lungs and was maintained up to 60 min (76% injected dose/tissue). The biodistribution data obtained with a gamma counter after organ dissection showed that the ^{18}F after administration of naked [^{18}F]-labeled siRNA had not been distributed in any tissues tested, whereas the radioactivity after the injection of the cationic liposome/[^{18}F]-labeled siRNA complexes was highly distributed in the lungs (Figure 5C). These results corresponded roughly to the data obtained from the fluorescence ex vivo imaging.

Moreover, to confirm whether the accumulation of ^{18}F in the lungs after administration of cationic liposome/[^{18}F]-labeled siRNA reflected the accumulation of the liposomes of the complex, we examined the biodistribution of cationic liposome/siRNA complexes prepared with [^{3}H]cholesterylhexadecyl ether as a component. As a result, the liposomal complexes with siRNA were distributed in the lungs quite similarly to the distribution of the ^{18}F, suggesting that cationic liposome/siRNA accumulated in lungs as the complex form (Supporting Information Figure S1).

DISCUSSION

Recently, the topical application of siRNA medicines has reached clinical trial, and siRNA delivery systems for systemic injection have been extensively studied for the next generation of siRNA medicines (*21*). Pharmacokinetic information on siRNA molecules is considered to be particularly important for the acceleration of the development of siRNA medicine. Among the technologies for pharmacokinetic analysis, PET imaging technique is considered to be applicable to both preclinical trial and microdosing study (human phase 0 study). Using subtoxic and subpharmacologic doses, PET microdosing studies can be performed to screen for drug candidates for clinical trials on the basis of their pharmacokinetic properties (*22, 23*).

In the present study, we labeled double-stranded siRNA with^{18}F to obtain pharmacokinetics information about siRNA and siRNA in DDS carriers. We used [^{18}F]-fluorine as a short-

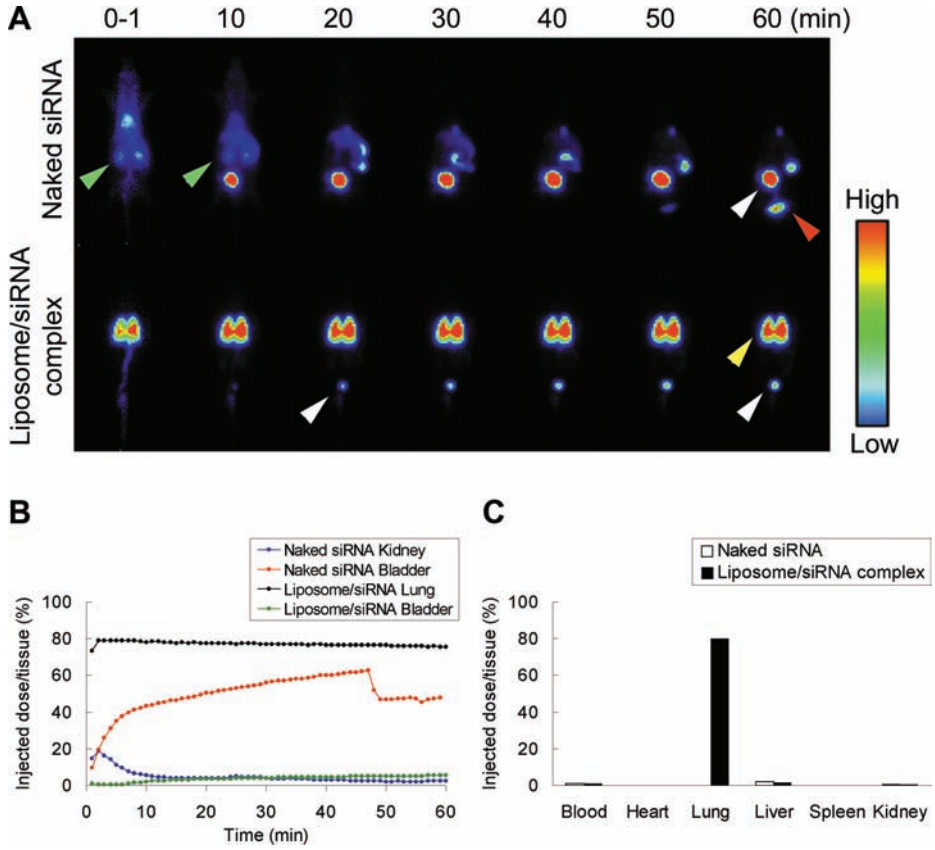


Figure 5. PPIS imaging with [18F]-labeled siRNA and liposome/[18F]-labeled siRNA complexes. (A) Naked siRNA (top) or liposome/siRNA complexes (bottom) at 2.5 MBq in 0.2 mL were intravenously administered to BALB/c mice. Images were acquired with a 1 min frame at 1, 10, 20, 30, 40, 50, and 60 min after the administration. The green arrowhead shows kidneys; the white one, the bladder; the red one, urine; and the yellow one, the lungs. (B) Real-time changes in [18F]-labeled siRNA and liposomal [18F]-labeled siRNA. Time activity curves of 18F with naked siRNA shows kidney (blue) and bladder (red) and that of 18F with cationic liposome/siRNA shows lung (black) and bladder (green). (C) After the PPIS scan, the mice were sacrificed, and biodistribution of 18F in each organ was then measured with a gamma counter.

lived positron-emitting radionuclide (half-life: 109 min), which has been applied to humans for cancer diagnosis in the form of [2-18F]2-deoxy-2-fluoroglucose ([18F]FDG). The advantages of the present methodology to label siRNA are that (1) the modification of double-stranded RNA with amino group enables fast preparation and purification without the time-consuming process of annealing and (2) the methodology maintains the conformational accuracy of the siRNA. Indeed, reaction of siRNA and [18F]SFB was complete within 20 min. In addition, fluorine-conjugated siRNA was identified by LC and ESI-TOF-MS (Figure 1) and did not decompose during the reaction or purification process (Figure 2).

It is well-known that one of the most important factors regarding the biodistribution of liposomes in vivo is the charge of the liposomal surface. Positively charged complexes aggregate in the presence of serum proteins (*24*), are entrapped in the lung capillaries, and thus accumulate in the lung tissue (*25, 26*) after intravenous administration. In fact, when liposomes were labeled with [3H]cholesterylhexadecyl ether, the radioactivity of cationic liposome/siRNA complexes accumulated in the lungs (Supporting Information Figure S1). However, since nucleic acids such as siRNAs and oligodeoxynucleotides (ODNs) are known to be eliminated from the circulation via the kidneys and excreted into the urine 60 min after administration via a tail vein (*27, 28*), distribution studies on siRNAs or ODNs besides on their carriers are important for the development of nucleic acid medicines. In the distribution study, [3H]cholesterylhexadecyl ether was accumulated in the liver to some extent, although the accumulation of siRNA was not observed after injection of cationic liposome/siRNA complex. We speculate that siRNA was degraded in the liver and excreted, while cholesterylhexadecyl ether did not.

In the present study, we first used AF750-siRNA and examined its in vivo behavior by using NIRF fluorescence imaging. NIRF fluorescence was rapidly cleared from the bloodstream and excreted in the bladder after the administration of naked AF750-siRNA (Figure 3). In contrast, the fluorescence of cationic liposome/siRNA complexes accumulated in the lungs. However, the differential fluorescence intensities between in vivo images and ex vivo ones indicated the limitation of NIRF imaging. Quantitative analysis could not be applied due to the influence of tissue depth on the fluorescence intensity. Moreover, it is possible that fluorescence self-quenching and/or resonance energy transfer affect the intensity.

In contrast to NIRF imaging, PPIS or PET technology provides quantitative analytic data with high spatial resolution. 18F was observed in the kidneys until 10 min after the administration of naked [18F]-labeled siRNA, and subsequently, it was transferred to the bladder and excreted into urine (Figure 5). This result is consistent with previous result reported by Viel et al. who used 18F-labeled naked siRNA (*11*). Other reports also presented the renal excretion of siRNA (*27, 29, 30*). In addition, Bartlett et al. reported that the excretion of 64Cu-labeled naked siRNA was quite fast (*9*). They indicated that the siRNA in a complex with cyclodextrin-containing polycation excreted quite rapidly and suggested the instability of the complex. Therefore, determination of siRNA trafficking instead of carrier trafficking is important for the development of siRNA medicines. In contrast to the in vivo fate of naked siRNA, the 18F of

cationic liposome/[^{18}F]-labeled siRNA complexes was spread throughout the lungs and was retained in them at least up to 60 min.

Next, we investigated the stability of siRNA in the presence of serum by performing an electrophoresis assay. The data indicated that naked siRNA was degraded when incubated for 60 min in serum, whereas the liposome/siRNA complexes were not (Figure 4). These results suggest that naked siRNA has a short half-life in vivo and is rapidly eliminated by renal excretion as a degraded form. However, further study is needed to clarify whether the excreted siRNA is in the intact form or degraded form. On the other hand, a part of the ^{18}F showed enterohepatic circulation. This enterohepatic circulation would be mediated by some of the fragmented siRNA having the polar moiety (the alkyl chain on the 3′ end of the antisense strand) and nonpolar moiety (siRNA).

As indicated above, the serum stability study showed that the liposomal siRNA was not degraded in the presence of serum. Furthermore, the ^{18}F distribution of liposomal [^{18}F]-labeled siRNA was similar to the distribution of the [^{3}H]-labeled liposome carrier: Both were accumulated in the lungs after intravenous administration. Taken together, our data strongly suggest that liposomal siRNA would be delivered to the lungs in its intact form. In conclusion, we developed a novel positron emitter-labeling methodology for siRNA and evaluated the in vivo trafficking of [^{18}F]-labeled siRNA by PPIS. The results of present study suggest that siRNA is stable as a complex with liposomes and should be deliverable specific tissues depending on the characteristics of the carrier. Therefore, designing the DDS carrier expands the usefulness of siRNA in vivo, and the present technology might support the development of siRNA medicines.

ACKNOWLEDGMENT

This study was financially supported by the Health and Labor Sciences Research Grants from the Ministry of Health, Labour, and Welfare of Japan. Synthesis of positron emitter-labeled siRNA was supported in part by Hokkaido System Science Co. Ltd. We thank Drs. T. Kakiuchi and H. Uchida at Hamamatsu Photonics K.K. PET Center for PET study for their technical assistance. They also thank Drs. S. Akai and T. Toyo'oka at the University Shizuoka for their valuable discussions as well as for allowing us to use their facilities. We also acknowledge Dr. S. Inagaki for helpful discussions and excellent technical assistance.

Supporting Information Available: Preparation of [^{3}H]-labeled liposome and complex. Biodistribution of liposomes and complexes. This material is available free of charge via the Internet at http://pubs.acs.org.

LITERATURE CITED

(1) Fire, A., Xu, S., Montgomery, M. K., Kostas, S. A., Driver, S. E., and Mello, C. C. (1998) Potent and specific genetic interference by double-stranded RNA in Caenorhabditis elegans. *Nature 391*, 806–811.

(2) Elbashir, S. M., Harborth, J., Lendeckel, W., Yalcin, A., Weber, K., and Tuschl, T. (2001) Duplexes of 21-nucleotide RNAs mediate RNA interference in cultured mammalian cells. *Nature 411*, 494–498.

(3) Pai, S. I., Lin, Y. Y., Macaes, B., Meneshian, A., Hung, C. F., and Wu, T. C. (2006) Prospects of RNA interference therapy for cancer. *Gene Ther. 13*, 464–477.

(4) Jeong, J. H., Mok, H., Oh, Y. K., and Park, T. G. (2009) siRNA conjugate delivery systems. *Bioconjugate Chem. 20*, 5–14.

(5) Zimmermann, T. S., Lee, A. C. H., Akinc, A., Bramlage, B., Bumcrot, D., Fedoruk, M. N., Harborth, J., Heyes, J. A., Jeffs, L. B., John, M., Judge, A. D., Lam, K., McClintock, K., Nechev, L. V., Palmer, L. R., Racie, T., Rohl, I., Seiffert, S., Shanmugam, S., Sood, V., Soutschek, J., Toudjarska, I., Wheat, A. J., Yaworski, E., Zedalis, W., Koteliansky, V., Manoharan, M., Vornlocher, H. P., and MacLachlan, I. (2006) RNAi-mediated gene silencing in non-human primates. *Nature 441*, 111–114.

(6) Kim, S. H., Jeong, J. H., Lee, S. H., Kim, S. W., and Park, T. G. (2008) LHRH receptor-mediated delivery of siRNA using polyelectrolyte complex micelles self-assembled from siRNA-PEG-LHRH conjugate and PEI. *Bioconjugate Chem. 19*, 2156–2162.

(7) Medarova, Z., Pham, W., Farrar, C., Petkova, V., and Moore, A. (2007) In vivo imaging of siRNA delivery and silencing in tumors. *Nat. Med. 13*, 372–377.

(8) Urakami, T., Akai, S., Katayama, Y., Harada, N., Tsukada, H., and Oku, N. (2007) Novel amphiphilic probes for [^{18}F]-radiolabeling preformed liposomes and determination of liposomal trafficking by positron emission tomography. *J. Med. Chem. 50*, 6454–6457.

(9) Bartlett, D. W., Su, H., Hildebrandt, I. J., Weber, W. A., and Davis, M. E. (2007) Impact of tumor-specific targeting on the biodistribution and efficacy of siRNA nanoparticles measured by multimodality *in vivo* imaging. *Proc. Natl. Acad. Sci. U.S.A. 104*, 15549–15554.

(10) Viel, T., Kuhnast, B., Hinnen, F., Boisgard, R., Tavitian, B., and Dolle, F. (2007) Fluorine-18 labelling of small interfering RNAs (siRNAs) for PET imaging. *J. Labelled Compd. Radiopharm. 50*, 1159–1168.

(11) Viel, T., Boisgard, R., Kuhnast, B., Jego, B., Siquier-Pernet, K., Hinnen, F., Dolle, F., and Tavitian, B. (2008) Molecular imaging study on *in vivo* distribution and pharmacokinetics of modified small interfering RNAs (siRNAs). *Oligonucleotides 18*, 201–212.

(12) Chen, X., Park, R., Shahinian, A. H., Tohme, M., Khankaldyyan, V., Bozorgzadeh, M. H., Bading, J. R., Moats, R., Laug, W. E., and Conti, P. S. (2004) 18F-labeled RGD peptide: initial evaluation for imaging brain tumor angiogenesis. *Nucl. Med. Biol. 31*, 179–189.

(13) Vaidyanathan, G., and Zalutsky, M. R. (1994) Improved synthesis of N-succinimidyl 4-[^{18}F]fluorobenzoate and its application to the labeling of a monoclonal-antibody fragment. *Bioconjugate Chem. 5*, 352–356.

(14) Li, J., Trent, J. O., Bates, P. J., and Ng, C. K. (2006) Labeling G-rich oligonucleotides (GROs) with N-succinimidyl 4-[^{18}F]fluorobenzoate (S18FB). *J. Labelled Compd. Radiopharm. 49*, 1213–1221.

(15) Haka, M. S., Kilbourn, M. R., Watkins, G. L., and Toorongian, S. A. (1989) Aryltrimethylammonium trifluoromethanesulfonates as precursors to aryl [^{18}F] fluorides: improved synthesis of [^{18}F] GBR-13119. *J. Labelled Compd. Radiopharm. 27*, 823–833.

(16) Harada, N., Ohba, H., Fukumoto, D., Kakiuchi, T., and Tsukada, H. (2004) Potential of [^{18}F]β-CFT-FE (2β-carbomethoxy-3β-(4-fluorophenyl)-8-(2-[^{18}F]fluoroethyl)nortropane) as a dopamine transporter ligand: A PET study in the conscious monkey brain. *Synapse 54*, 37–45.

(17) Tang, G., Zeng, W. B., Yu, M. X., and Kabalka, G. (2008) Facile synthesis of N-succinimidyl 4-[^{18}F]fluorobenzoate ([^{18}F]SFB) for protein labeling. *J. Labelled Compd. Radiopharm. 51*, 68–71.

(18) Takamatsu, H., Kakiuchi, T., Noda, A., Uchida, H., Nishiyama, S., Ichise, R., Iwashita, A., Mihara, K., Yamazaki, S., Matsuoka, N., Tsukada, H., and Nishimura, S. (2004) An application of a new planar positron imaging system (PPIS) in a small animal: MPTP-induced parkinsonism in mouse. *Ann. Nucl. Med. 18*, 427–431.

(19) Uchida, H., Okamoto, T., Ohmura, T., Shimizu, K., Satoh, N., Koike, T., and Yamashita, T. (2004) A compact planar positron imaging system. *Nucl. Instrum. Methods Phys. Res., Sect. A 516*, 564–574.

(20) Uchida, H., Sato, K., Kakiuchi, T., Fukumoto, D., and Tsukada, H. (2008) Feasibility study of quantitative radioactivity monitoring of tumor tissues inoculated into mice with a planar positron imaging system (PPIS). *Ann. Nucl. Med. 22*, 57–63.
(21) de Fougerolles, A. R. (2008) Delivery vehicles for small interfering RNA *in vivo*. *Hum. Gene Ther. 19*, 125–32.
(22) Bauer, M., Wagner, C. C., and Langer, O. (2008) Microdosing studies in humans: the role of positron emission tomography. *Drugs in R&D 9*, 73–81.
(23) Wagner, C. C., Muller, M., Lappin, G., and Langer, O. (2008) Positron emission tomography for use in microdosing studies. *Curr. Opin. Drug Discovery Dev. 11*, 104–110.
(24) Litzinger, D. C., Brown, J. M., Wala, I., Kaufman, S. A., Van, G. Y., Farrell, C. L., and Collins, D. (1996) Fate of cationic liposomes and their complex with oligonucleotide *in vivo*. *Biochim. Biophys. Acta, Biomembr. 1281*, 139–149.
(25) Li, S., Tseng, W. C., Stolz, D. B., Wu, S. P., Watkins, S. C., and Huang, L. (1999) Dynamic changes in the characteristics of cationic lipidic vectors after exposure to mouse serum: implications for intravenous lipofection. *Gene Ther. 6*, 585–594.
(26) McLean, J. W., Fox, E. A., Baluk, P., Bolton, P. B., Haskell, A., Pearlman, R., Thurston, G., Umemoto, E. Y., and McDonald, D. M. (1997) Organ-specific endothelial cell uptake of cationic liposome-DNA complexes in mice. *Am. J. Physiol. 273*, H387–404.
(27) van de Water, F. M., Boerman, O. C., Wouterse, A. C., Peters, J. G., Russel, F. G., and Masereeuw, R. (2006) Intravenously administered short interfering RNA accumulates in the kidney and selectively suppresses gene function in renal proximal tubules. *Drug Metab. Dispos. 34*, 1393–1397.
(28) Lendvai, G., Velikyan, I., Bergstrom, M., Estrada, S., Laryea, D., Valila, M., Salomaki, S., Langstrom, B., and Roivainen, A. (2005) Biodistribution of 68Ga-labelled phosphodiester, phosphorothioate, and 2′-O-methyl phosphodiester oligonucleotides in normal rats. *Eur. J. Pharm. Sci. 26*, 26–38.
(29) Braasch, D. A., Paroo, Z., Constantinescu, A., Ren, G., Oz, O. K., Mason, R. P., and Corey, D. R. (2004) Biodistribution of phosphodiester and phosphorothioate siRNA. *Bioorg. Med. Chem. Lett. 14*, 1139–1143.
(30) Liu, N., Ding, H., Vanderheyden, J. L., Zhu, Z., and Zhang, Y. (2007) Radiolabeling small RNA with technetium-99m for visualizing cellular delivery and mouse biodistribution. *Nucl. Med. Biol. 34*, 399–404.

BC9005267

Design, Synthesis, and Biological Evaluation of a Robust, Biodegradable Dendrimer

Derek G. van der Poll,[†] Heidi M. Kieler-Ferguson,[†] William C. Floyd,[†] Steven J. Guillaudeu,[†] Katherine Jerger,[‡] Francis C. Szoka,*[,‡] and Jean M. Fréchet*[,†]

College of Chemistry, University of California, Berkeley, California 94720-1460, Department of Biopharmaceutical Sciences and Pharmaceutical Chemistry, University of California, San Francisco, California 94143-0446. Received December 11, 2009; Revised Manuscript Received February 17, 2010

PEGylated dendrimers are attractive for biological applications due to their tunable pharmacokinetics and ability to carry multiple copies of bioactive molecules. The rapid and efficient synthesis of a robust and biodegradable PEGylated dendrimer based on a polyester−polyamide hybrid core is described. The architecture is designed to avoid destructive side reactions during dendrimer preparation while maintaining biodegradability. Therefore, a dendrimer functionalized with doxorubicin (Dox) was prepared from commercial starting materials in nine, high-yielding linear steps. Both the dendrimer and Doxil were evaluated in parallel using equimolar dosage in the treatment of C26 murine colon carcinoma, leading to statistically equivalent results with most mice tumor-free at the end of the 60 day experiment. The attractive features of this dendritic drug carrier are its simple synthesis, biodegradability, and versatility for application to a variety of drug payloads with high drug loadings.

INTRODUCTION

The use of macromolecular carriers for the delivery of chemotherapeutics originated from the hypothesis that polymers may be used to improve both the solubility and the blood circulation time of small molecule drugs (*1, 2*). It was later discovered that macromolecules have the additional benefit of increased accumulation in tumor tissue as a result of the leaky vasculature surrounding rapidly growing neoplasm—a concept known as the enhanced permeation and retention (EPR) effect (*3, 4*). Thus, macromolecular carriers can provide both enhanced pharmacokinetics and a passive targeting mechanism, characteristics that may be used to increase the efficacy of small molecule drugs. To this end, carrier systems such as linear polymers, micellar assemblies, liposomes, polymersomes, and dendrimers have been studied in an effort to identify an ideal drug carrier (*5*−*14*). Important design features (*9*) include a long blood circulation time, high tumor accumulation, high drug loading, low toxicity, low polydispersity index, and simple preparation. Considering the above criteria, PEGylated dendrimers (*15, 16*) constitute an attractive platform, because their size and degree of branching can be precisely controlled and they possess multiple functional appendages for the attachment of both drugs and solubilizing groups. Dendritic drug carriers based on polyesters (*17*−*19*), polyamines (*20, 21*), melamines or triazines (*22*−*24*), PAMAM (*25*−*30*), and other polyamides (*31*−*33*) have all been explored and recently reviewed (*14*). Polyesters constitute a very attractive class of materials because they are biodegradable; however, the hydrolytic susceptibility of the ester bond can make the synthesis of drug conjugates somewhat challenging. The hydrolysis rates of polyesters can vary dramatically depending on the hydrophobicity of the monomer, steric environment, and the reactivity of functional groups located within the dendrimer (*34*). In contrast, polyamide and polyamine dendrimers can withstand a much wider selection of synthetic manipulations, but they do not degrade as easily in the body and thus they may be more prone to long-term accumulation in vivo (*35*). Currently, challenges facing the biological application of dendrimers are their lengthy syntheses and the need to develop nontoxic, biodegradable dendrimers that are still resilient to the reaction conditions encountered during their synthesis and modification. As a result, accessing a universal, biodegradable, highly soluble, unimolecular carrier capable of achieving a high drug loading and low polydispersity has remained a challenge.

In recent studies, we have determined that a family of polyester-core dendrimer based on a 2,2-bis(hydroxymethyl) propanoic acid (bis-HMPA) monomer unit, typically functionalized with eight 5 kDa poly(ethylene glycol) (PEG) chains (*18*), is biocompatible and that it is capable of high drug loading while facilitating high tumor accumulation through its long circulation half-life. An asymmetric bis-HMPA PEGylated dendrimer functionalized with doxorubicin via a pH-sensitive acyl hydrazone bond demonstrated outstanding antitumor activity in mice bearing murine C26 colon carcinoma (*17*). Despite these promising in vivo results, further evaluation of this asymmetric carrier in biological models was slowed by its lengthy synthesis (*37*). Therefore, we sought to transpose the beneficial features (*9*) of this PEGylated dendrimer onto a simpler and more readily prepared carrier. Initial approaches involved simplified multifunctional dendrimers based on bis-HMPA (*38, 39*); however, some issues still remained, as undesired degradation of the polyester backbone was observed during the attachment of certain drugs.

Herein, we describe the design evolution of three dendrimers that resulted in the creation of a new PEGylated dendrimer, which circumvented the synthetic and biological limitations uncovered in previous studies. We report a very efficient synthesis that combines the biocompatibility of bis-HMPA dendrimers with the robustness of polyamide dendrimers, yielding a hybrid scaffold capable of translation into clinical studies.

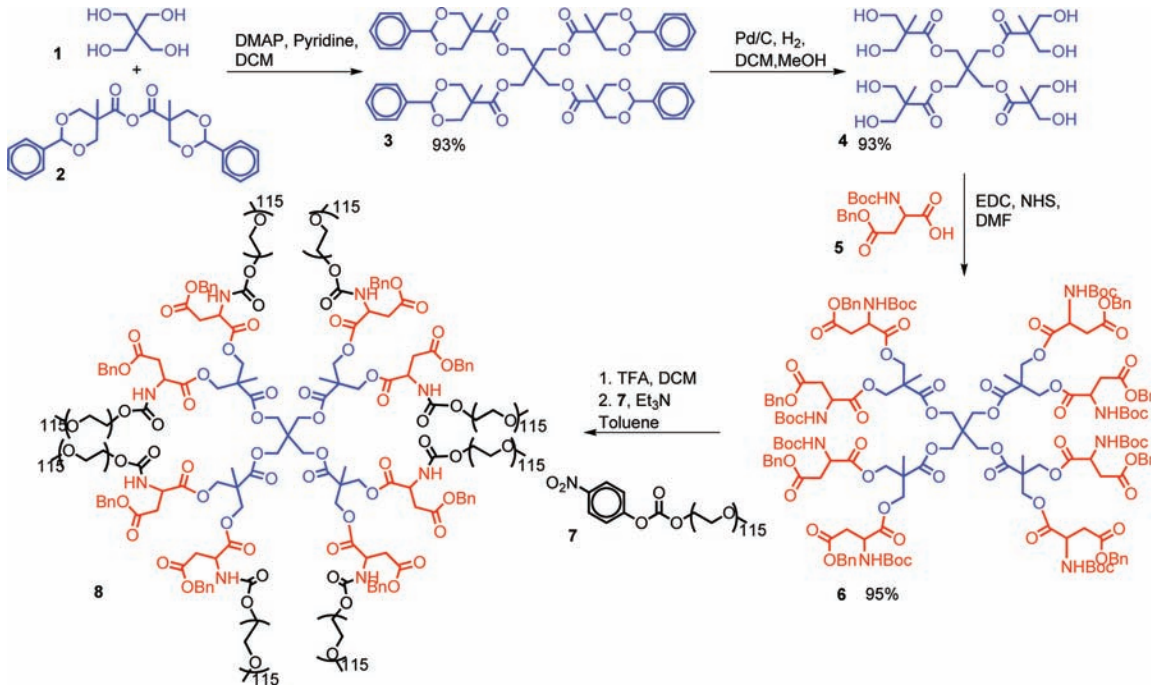
MATERIALS AND METHODS

Materials. Materials were used as obtained from commercial sources unless otherwise noted. Poly(ethylene glycol) was purchased from Laysan Biosciences Inc. Amino acid derivatives

* Corresponding authors. E-mail addresses: szoka@cgl.ucsf.edu and frechet@berkeley.edu.
[†] University of California, Berkeley.
[‡] University of California, San Francisco.

10.1021/bc900553n © 2010 American Chemical Society
Published on Web 03/30/2010

Scheme 1. Synthesis of Symmetrically PEGylated Dendrimer



were purchased from Bachem. Dimethylformamide (DMF), pyridine, and dichloromethane (DCM) for syntheses were purged 1 h with nitrogen and further dried by passing them through commercially available push stills (Glass Contour). Solvents were removed under reduced pressure using a rotary evaporator or by vacuum pump evacuation. Compounds **2**, **3**, **4** (*19*), **6**, **8**, **9** (*39*), **10** (*40*), **15**, **17**, **18**, and **19** (*41*) were synthesized according to published procedures.

Characterization. NMR spectra were recorded on Bruker AV 300, AVB 400, AVQ 400, or DRX 500 MHz instruments. Spectra were recorded in $CDCl_3$ or D_2O solutions and were referenced to TMS or the solvent residual peak and taken at ambient temperature. Elemental analyses were performed at the UC Berkeley Mass Spectrometry Facility. MALDI-TOF MS was performed on a PerSeptive Biosystems Voyager-DE using the following matrices: *trans*-3-indoleacrylic acid (IAA) for *tert*-butyloxycarbonyl (Boc) protected dendrimers; or 2,5-dihyroxybenzoic acid (DHB) for amine-terminated dendrimers. Samples were prepared by diluting dendrimer solutions (~1 M) 40-fold in 100 mM matrix solutions in tetrahydrofuran and spotting 0.5 μL on the sample plate. Size exclusion chromatography (SEC) was performed using one of three systems:

SEC System A: a Waters 515 pump, a Waters 717 auto sampler, a Waters 996 Photodiode Array detector (210−600 nm), and a Waters 2414 differential refractive index (RI) detector. SEC was performed at 1.0 mL/min in a PLgel Mixed B (10 μm) and a PLgel Mixed C (5 μm) column (Polymer Laboratories, both 300 × 7.5 mm), in that order, using DMF with 0.2% LiBr as the mobile phase and linear PEO (4200−478 000 MW) as the calibration standards. The columns were thermostatted at 70 °C.

SEC System B: The same equipment as System A, but performed at 1.0 mL/min in two SDV Linear S (5 μm) columns (Polymer Standards Service, 300 × 8 mm) using DMF with 0.2% LiBr as the mobile phase.

SEC System C: A Waters Alliance separation module 2695 (sample compartment maintained at 37.0 ± 3.0 °C), a Waters 410 differential RI detector, a Waters 996 photodiode array detector (λ = 486 nm), and a Shodex OHpak SB-804 HQ SEC column. An isocratic flow rate of 0.7 mL/min was used with a mobile phase composed of 70%/30%/0.05% water/acetonitrile/formic acid.

Doxorubicin loading was quantified using a Lambda 35 UV−vis spectrometer (PerkinElmer, Wellesley, MA). Measurements were performed in sealed, standard 1 cm quartz cells in Millipore water at room temperature.

Animal and Tumor Models. All animal experiments were performed in compliance with National Institutes of Health guidelines for animal research under a protocol approved by the Committee on Animal Research at the University of California (San Francisco, CA) (UCSF). C26 colon carcinoma cells obtained from the UCSF cell culture facility were cultured in RPMI medium 1640 containing 10% FBS. Female BALB/c mice were obtained from Simonsen Laboratories, Inc. (Gilroy, CA).

EA-G$_1$-Lys(Boc)$_8$ (22). Pentaerythritol (353 mg, 2.6 mmol), BocLys(Boc)-ONp (5.500 g, 11.8 mmol), and 4-dimethylaminopyridine (DMAP) (125 mg, 1.0 mmol) were added to a 20 mL reaction vial. Under a nitrogen atmosphere, DMF (5.5 mL) and triethylamine (1.6 mL, 11.5 mmol) were added and the reaction stirred for 48 h. MALDI-TOF analysis confirmed the reaction had gone to completion. *N,N*-Dimethylethylene diamine (300 μL, 4.1 mmol) was added to quench excess PNP esters. After 10 min, the mixture was diluted with ether (200 mL) and washed with three 100 mL portions of 1 M NaOH, three 100 mL portions of 1 M $NaHSO_4$, 100 mL DI water, and 100 mL of brine. The organic layer was dried over Na_2SO_4 and evaporated to dryness to give **22** (3.455 g, 93% yield) as a white foam. ^{1}H NMR (400 MHz, $CDCl_3$): δ 1.26−1.49 (m, 88H), 1.58−1.83 (m, 8H), 3.09−3.11 (m, 8H), 4.08−4.18 (m, 12H), 4.80 (s, 4H), 5.3−5.6 (br d, 4H). ^{13}C NMR (100 MHz, $CDCl_3$): δ 22.5, 28.3, 28.4, 29.6, 31.5, 39.9, 53.4, 62.2, 79.0, 79.8, 155.7, 156.1. Calc $[M]^+$ ($C_{69}H_{124}N_8O_{24}$) m/z = 1448.87. Found MALDI-TOF $[M+Na]^+$ m/z = 1470.0.

EA-G$_1$-Lys(NH$_3$TFA)$_8$ (22a). Compound **22** (209 mg, 144 μmol) was dissolved in 1:1 trifluoroacetic acid (TFA)/DCM for 1 h. Quantitative deprotection was confirmed by MALDI-TOF analysis. The solvents were removed under reduced pressure to give **22a** as a gummy solid in quantitative yield. ^{1}H NMR

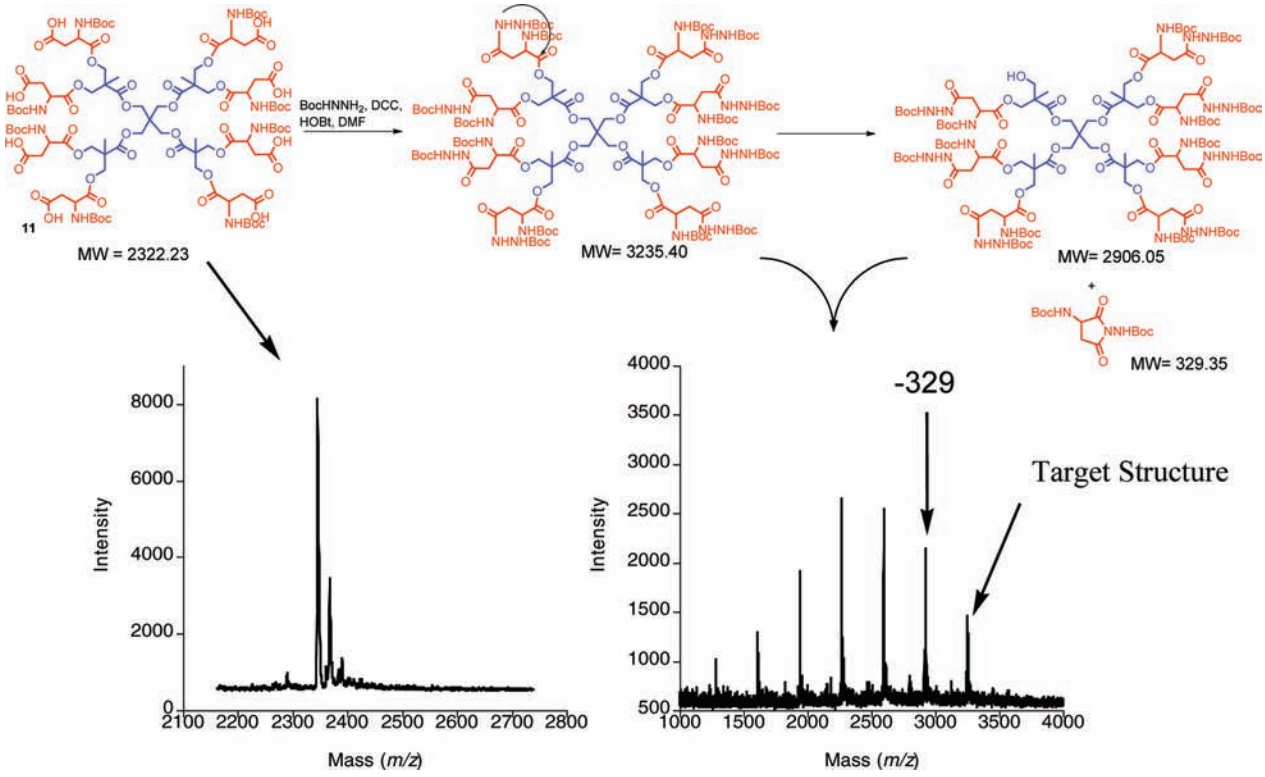


Figure 1. Proposed degradation pathway for polyester dendrimer.

(400 MHz, MeOD): δ 1.40−1.60 (m, 8H), 1.67−1.75 (m, 8H), 1.87−2.10 (m, 8H), 2.99 (t, J = 8 Hz, 8H), 4.21 (t, J = 6 Hz, 4H), 4.40 (s, 8H). ^{13}C NMR (100 MHz, MeOD): δ 21.8, 26.5, 29.5, 38.7, 42.5, 52.3, 62.9, 161.4, 161.7, 168.6. Calc $[M]^+$ ($C_{29}H_{60}N_8O_8$) m/z = 648.45. Found MALDI-TOF $[M+H]^+$ m/z = 649.6.

EA-G$_1$-Lys(Glu(Bn)Boc)$_8$ (24). Compound **22a** (89 mg, 63 μmol) and BocGlu(OBz)-ONp (290 mg, 632 μmol) were added to a 20 mL reaction vial. Under a nitrogen atmosphere, DMF (1 mL) and triethylamine (140 μL, 1.0 mmol) were added and the reaction was allowed to stir for 4 h. MALDI-TOF analysis showed a single peak corresponding to the fully functionalized dendrimer. *N,N*-Dimethylethylene diamine (50 μL, 690 μmol) was added to quench excess PNP esters. The reaction was diluted with ethyl acetate (100 mL) and washed with three 50 mL portions of 1 M $NaHSO_4$, three 50 mL portions of saturated K_2CO_3, 50 mL of DI water, and 50 mL brine. The organic layer was dried over Na_2SO_4 and evaporated to dryness to give **24** (171 mg, 87% yield) as a white foam. ^{1}H NMR (400 MHz, MeOD): δ 1.41−1.56 (bm, 96H), 1.60−1.75 (m, 4H), 1.70−2.13 (m, 16H), 2.25−2.40 (m, 4H), 2.44−2.51 (m, 12H), 2.58−2.61 (m, 4H), 3.10−3.20 (m, 8H), 4.09−4.25 (m, 12H), 4.35−4.40 (m, 4H) 5.08−5.09 (2s, 16H), 7.28−7.38 (m, 40H). ^{13}C NMR (100 MHz, MeOD): δ 23.8, 28.6, 31.5, 40.8, 44.6, 49.0, 54.4, 64.9, 163.4, 163.8, 170.7. Calc $[M]^+$ ($C_{165}H_{228}N_{16}O_{48}$) m/z = 3201.59. Found MALDI-TOF $[M+Na]^+$ m/z = 3223.3.

EA-G$_1$-Lys(Glu(Bn)NH$_3$TFA)$_8$ (24a). Compound **24** (100 mg, 31 μmol) was dissolved in 1:1 TFA/DCM for 1 h. Quantitative deprotection was confirmed by MALDI-TOF analysis. The solvents were removed under reduced pressure to give **24a** as a gummy solid in quantitative yield. ^{1}H NMR (400 MHz, MeOD): δ 1.19−1.35 (m, 16H), 1.45−1.65 (m, 8H), 2.04−2.20 (m, 16H), 2.38−2.46 (m, 8H), 2.51−2.63 (m, 8H), 2.89−2.93 (m, 4H), 3.09−3.12 (m, 4H), 3.89−3.96 (m, 12H), 4.11 (t, J = 4.4 Hz, 4H), 4.30−4.33 (m, 4H), 4.80−5.00 (m, 16H), 7.17−7.26 (m, 40H). ^{13}C NMR (100 MHz, MeOD): δ = 24.1, 27.7, 29.7, 30.3, 30.5, 31.6, 40.2, 53.5, 53.9, 54.1, 63.9, 67.8, 116.7, 119.6, 129.2, 129.3, 129.6, 137.3, 162.8, 163.2, 169.8, 170.3, 172.7, 173.6, 173.8. Calc $[M]^+$ ($C_{125}H_{164}N_{16}O_{32}$) m/z = 2402.73. Found MALDI-TOF $[M+Na]^+$ m/z = 2424.8.

EA-G$_1$-Lys(Glu(Bn)PEO)$_8$ (25). PNP-PEG carbonate (986 mg, 192 μmol) and **24a** (81 mg, 203 μmol NH_3) were added to a 20 mL reaction vial. Under a nitrogen atmosphere, DMF (3 mL) was added. After using a warm water bath to dissolve the starting material, triethylamine (120 μL, 0.863 mmol) was added. After stirring for 48 h (reaction monitored by SEC analysis), no further increase in the molecular weight was observed and the reaction was considered complete. Piperidine (50 μL, 0.506 mmol) was added to quench remaining PNP carbonate. After 1 h, acetic anhydride (400 μL, 4.24 mmol) was added to acylate any remaining primary amines on the dendrimer that had not reacted with the PNP-PEG carbonate. After stirring an additional hour, the reaction mixture was precipitated into ether (300 mL) and **25** (999 mg) was collected by filtration as a fluffy white solid. In some cases, residual 5 kDa PEG was observed after the PEGylation was considered complete. This could be removed by dialysis using 100 000 MWCO tubing against water for 24 h. ^{1}H NMR (500 MHz, D_2O): δ 1.20−1.80 (br m, 24H), 1.80−2.10 (br d, 16H), 2.35−2.55 (br s, 16H), 3.05−3.20 (br s, 8H), 3.38 (s, 24H), 3.40−3.90 (br m, ∼3900H), 4.00−4.40 (br m, 36H), 5.09−5.15 (br s, 16H), 7.25−7.40 (br m, 40H). DMF SEC: M_n: 32 000 Da, M_w: 35 000 Da, PDI: 1.09.

EA-G$_1$-Lys(GluPEO)$_8$ (25a). Compound **25** (402 mg, 10.1 μmol) was added to a 20 mL reaction vial and dissolved in MeOH (9 mL). Activated Pd/C (10 wt %, 50 mg) was added and the reaction put under hydrogen atmosphere. The reaction was stirred overnight, then filtered and solvent removed via rotary evaporation to give **25a** (387 mg) as a white solid. ^{1}H NMR (500 MHz, D_2O): δ 1.20−1.80 (br m, 24H), 1.80−2.1 (br d, 16H), 2.40−2.51 (m, 16H), 3.15−3.25 (br s, 8H), 3.38 (s, 24H), 3.40−3.90 (br m, ∼3900H), 4.00−4.40 (br m, ∼36H).

EA-G$_1$-Lys(Glu(NNBoc)PEO)$_8$ (26). Compound **25a** (710 mg, 142 μmol COOH), *t*-butyl carbazate (94 mg, 711 μmol), and DMAP (10 mg, 81 μmol) was added to a 20 mL reaction

vial. Under a nitrogen atmosphere, DCM (8 mL) was added dropwise. The solution was cooled to 0 °C followed by the addition of 1-ethyl-3-(3-dimethylaminopropyl)carbodiimide (EDC) (136 mg, 709 μmol). The reaction was allowed to warm to room temperature and stirred overnight. The reaction was dialyzed against MeOH in 12 kDa−14 kDa MWCO dialysis with 3 solvent changes over 18 h. Concentration of the bag contents in vacuo gave **26** (660 mg) as a white solid. ^{1}H NMR (500 MHz, D_2O): δ 1.30−1.60 (br m, 100H), 1.65−2.20 (br m, 20H), 2.30−2.45 (br s, 16H), 3.15−3.25 (br s, 8H), 3.38 (s, 24H), 3.50−3.90 (br m, ∼3900H), 4.00−4.45 (br m, 40H).

EA-G$_1$-Lys(Glu(NNH$_3$TFA)PEO)$_8$ (26a). Compound **26** (102 mg) was dissolved in 1:1 TFA/DCM for 1 h. The solvents were removed under reduced pressure to give 100 mg of **26a** as a gummy solid. ^{1}H NMR (500 MHz, D_2O): δ 1.15−1.80 (br m, 24H), 1.85−2.00 (br m,16), 2.05−2.15 (br m, 16H), 2.15−2.25 (br m, 16H), 3.05−3.15 (br s,8H), 3.38 (s, 24H), 3.50−3.90 (br m, ∼3900H), 4.00−4.45 (br m, 40H).

EA-G$_1$-Lys(Glu(NNDox)PEO)$_8$ (27). Compound **26a** (72 mg, 14 μmol NNBoc) and doxorubicin (50 mg, 92 μmol) were added to a 20 mL reaction vial and were dissolved in MeOH (3 mL), pyridine (100 μL), and acetic acid (100 μL). The reaction was purged with nitrogen and stirred at 60 °C in the dark for 18 h. The reaction mixture was loaded directly onto a Sephadex LH-20 column and eluted with methanol. The first dark red band was collected and the solvent removed by rotary evaporation. The solid material was further purified using a Biorad PD-10 column with water as the eluent. After lyophilization, 67.2 mg of red powder remained. The Dox loading was quantified using the absorbance at 486 nm (ε = 11 500) (*42*) to be 9.6 wt %, or 88% of the maximum theoretical loading.

Polymer Degradation Study. Compound **26** (20 mg) was dissolved in 1.5 mL of 1× PBS buffer and incubated at 37 °C. At t = 0, 1, 2, 3, 6, 15, and 20 days, 100 μL aliquots were taken out and immediately frozen followed by lyophilization. At the end of the experiment, each sample was dissolved in 0.5 mL DMF from the System A mobile phase, filtered though a 0.2 μm PVTF filter, and measured by the RI detector on system A.

Hydrolysis of Dox from Compound 27 at pH 7.4 and pH 5. Drug release rates were determined by a modified published procedure (*43*). Compound **27** was dissolved in either 1× PBS or pH 5 acetate buffer (30 mM with 70 mM $NaNO_3$), at 1 mg/mL. Buffers were preheated to 37 °C before dissolving polymer and maintained at this temperature throughout the experiment. At each time point, 25 μL was injected onto SEC system C for analysis.

Cytotoxicity Studies in Cells. The cytotoxicities of free Dox, **26**, and **27** were determined by using the MTT assay with C26 cells. Cells were seeded onto a 96-well plate at a density of 5.0 × 10^3 cells per well in 100 μL of medium and incubated overnight (37 °C, 5% CO_2, and 80% humidity). An additional 100 μL of new medium (RPMI medium 1640, 10% FBS, 1% penicillin−streptomycin, 1% Glutamax) containing varying concentrations of Dox, **26**, or **27** were added to each well. After incubation for 72 h, 40 μL of media containing thiazolyl blue tetrazolium bromide (5 mg/mL) was added. The cells were incubated for 3 h, after which time the medium was carefully removed. To the resulting purple crystals was added 200 μL of DMSO and 25 μL of pH 10.5 glycine buffer (0.1 M glycine/0.1 M NaCl). Optical densities were measure at 570 nm by a SpectraMAX 190 microplate reader (Molecular Devices, Sunnyvale, CA). Optical densities measured for wells containing cells that received neither dendrimer nor drug were considered to represent 100% viability. IC_{50} values were obtained from sigmoidal fits of the data using *Origin 7* SR4 8.0552 software (OriginLab, Northampton, MA).

Biodistribution Study in Xenograph Mice. Six- to eight-week-old female Balb/C mice were injected in the right hind flank with 3 × 10^5 C26 cells. Twelve days after tumor inoculation, mice were randomized into two groups. Mice were injected by means of the tail vein either with Doxil (8 mg Dox eq/kg; 3 mice) or with **27** (8 mg Dox eq/kg; 6 mice) in ∼200 μL of PBS. Blood was collected from half of the mice injected with polymer by submandibular bleeds 60 and 1440 min after dosing (data not shown); after 2880 min, the three mice were sacrificed. The remaining six mice were sacrificed at 1 wk postinjection. The blood (collected by heart puncture), heart, liver, spleen, kidney, muscle, and tumor were collected for analysis. Each organ was weighed and 200−300 mg of the collected organs were homogenized with zirconium beads and 1 mL acidified isopropyl alcohol (0.075 M HCl, 90% IPA). The samples then incubated at 4 °C for 24 h. Serum was collected using Microtainer serum separator vials and processed in the same manner as the organs. The samples were frozen in a −80 °C freezer until measurements could be made. At measurement time, samples were thawed, briefly vortexed, and centrifuged for 3 min at 8000 rpm. Then, 80 μL of supernatant was combined with 920 μL of acidified IPA for fluorescence measurements. Dox fluorescence (excitation 490 nm; emission 590 nm) was measured on a PTI fluorimeter (Birmingham, NJ). Calibration curves were made from organ samples collected from an untreated mouse.

Chemotherapy Experiments. While under anesthesia, female Balb/C mice were shaved, and C26 cells (3 × 10^5 cells in 50 μL) were injected subcutaneously in the right-hand flank. At eight days post-tumor implantation, mice were randomly distributed into treatment groups of 10 animals. Mice were injected by means of the tail vein with Doxil (20 mg Dox/kg) or **27** (10, 15, and 20 mg Dox/kg) in approximately 200 μL of solution. Mice were weighed and tumors measured every other day. The tumor volume was estimated by measuring the tumor volume in three dimensions with calipers and calculated using the formula tumor volume = length × width × height. Mice were removed from the study when (i) a mouse lost 15% of its initial weight, (ii) any tumor dimension was >20 mm, or (iii) the mouse was found dead. The mice were followed until day 60 post-tumor inoculation. Statistical analysis was performed as previously described (*41*) using *MedCalc 8.2.1.0* for Windows (MedCalc Software, Mariakerke, Belgium). The tumor growth delay was calculated based upon a designated tumor volume of 400 mm^3.

RESULTS AND DISCUSSION

Exploring Polyester-Core Dendrimers. Polyester dendrimers based on bis(HMPA) monomer units are an attractive scaffold for biological applications because they are nonimmunogenic, biodegradable, and nontoxic (*36*). Scheme 1 outlines the synthesis of a core-functionalized PEGylated dendrimer we have developed earlier (*39*). Briefly, the tetrafunctional pentaerythritol core **1** was modified with a benzylidene-protected bis(HMPA) monomer **2** to afford the first-generation dendrimer **3**. After removal of the protecting groups via hydrogenolysis, the eight peripheral hydroxyl groups were functionalized with orthogonally protected aspartic acid to give **6**. Subsequent deprotection of the amino groups of **6** followed by PEGylation with the 5 kDa PEG electrophiles gave dendrimer **8**. Removal of the benzyl ester protecting groups of **8** via hydrogenolysis afforded dendrimer **9** with eight carboxylic acids moieties available for potential drug attachment. However, early attempts at the functionalization of this dendrimer with *t*-butyl carbazate or glutamic acid derivative **10** were unsuccessful as degradation of the dendrimer was observed during this reaction.

In order to gain insight into the degradation pathway, we prepared the dendrimer probe **11** and attempted to functionalize

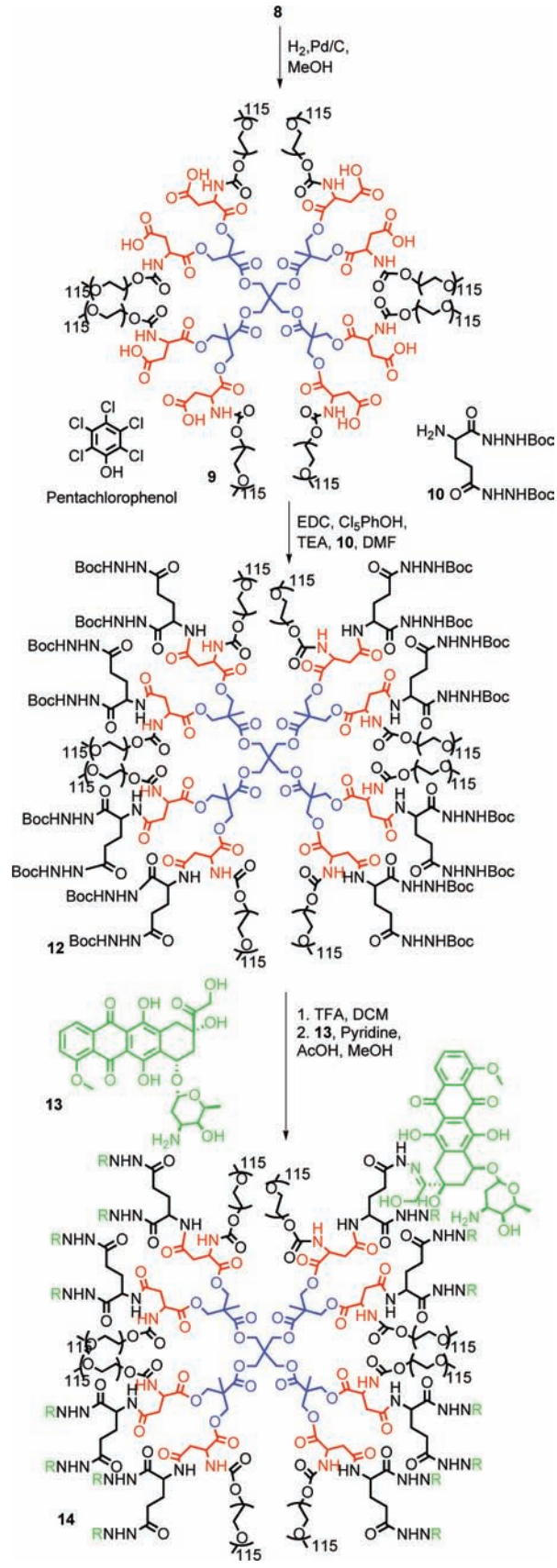
its aspartic acid chain-ends with *t*-butyl carbazate. Probe molecule **11** was selected instead of PEGylated dendrimer **9** as progress of its reaction could be more easily monitored by MALDI-TOF since it does not contain PEG chains (Figure 1). As a result of a degradation side reaction, only a small amount of the target product was formed, leading to the appearance of lower molecular weight products with molecular weights that decreased in increments of 329 amu, likely as a result of intramolecular cyclization reactions as proposed in Figure 1. This type of cyclization reaction on benzyl ester-protected aspartic acid residues is documented in the peptide literature and additives have been developed to suppress such reactions (*44*). For example, pentachlorophenol (PCP) has been used to decrease the production of the aminosuccinyl byproduct by inhibiting amide deprotonation. Under these buffered conditions, the primary amines are still available to react with *p*-nitrophenyl (PNP) carbonates and other electrophiles. The use of PCP as an additive proved beneficial in our hands as it allowed the functionalization of the carboxylic acid side chains of dendrimer **9** with protected nucleophile**10** to give dendrimer **12** (Scheme 2). Finally, doxorubicin hydrazone conjugate **14** was obtained after removal of the Boc groups from the hydrazide linkers in **12** and condensation of the resulting amines with the ketone group of doxorubicin **13**. In order to determine how rapidly this polyester architecture breaks down under physiological conditions, **12** was incubated in PBS buffer at 37 °C and the evolution of its molecular weight with time was monitored by SEC. This revealed that the α-amino esters located did not survive long enough for use of **12** in vivo as significant degradation was observed after only 10 h. For this reason, we began exploring alternative dendrimer scaffolds based on more robust polyamide cores.

Exploring Polylysine-Core Dendrimers. In contrast to polyester dendrimers, polyamide dendrimers are less susceptible to hydrolysis, but this increased stability may hamper their break down in vivo. Recently, Fox et al. functionalized a PEGylated polylysine with camptothecin and observed 100% survival in transgenic mice with HT-29 human colon carcinoma over a 70 day experiment (*41*). While the degradation of amide bonds in linear peptides in vivo is well established, the fate of branched, acylated, and PEGylated polyamide dendrimers is less certain as proteases may not be able to access amide bonds near the core of the structure. However, even slow or incomplete degradation of the carrier may be permissible for drug delivery applications if the byproduct are nontoxic and small in size (*45, 46*). In order to apply the polylysine carrier used by Fox (*41*) to the delivery of doxorubicin, dendrimer **18** with a protected hydrazide had to be prepared.

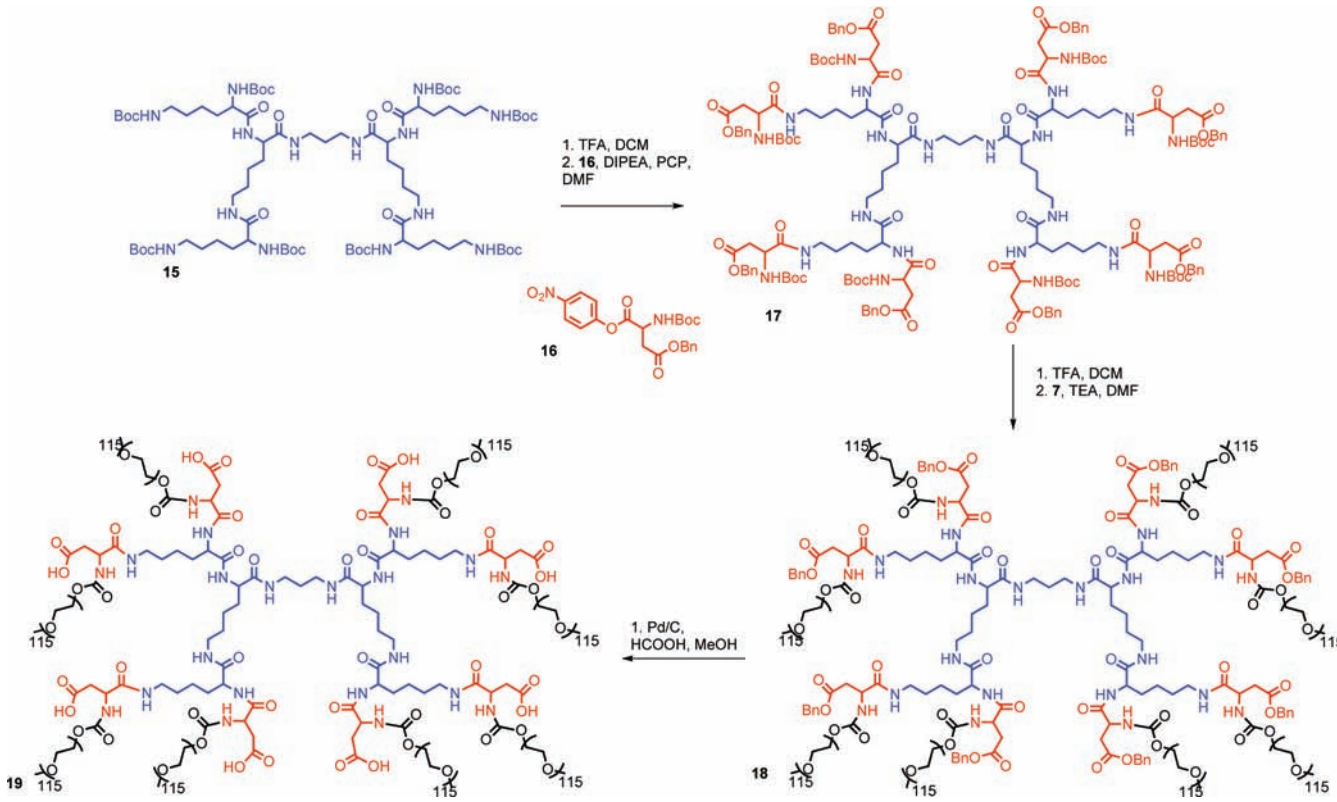
Lysine dendrimer **15**, first described by Denkewalter (*47*) in 1982, was used as the starting material. Its peripheral amines were acylated with PNP-Asp(Bn)Boc to afford dendrimer **17** (Scheme 3). It is worth noting that the PCP additive was also needed when attaching aspartic acid to the G_2 lysine periphery. Otherwise, a five-membered amino succinyl byproduct can form via amidolysis of the benzyl ester protected side chain. Deprotection of the amino groups of the aspartate termini and PEGylation with PEG-*p*-nitrophenyl carbonate afforded **18**. Unfortunately, the coupling of *t*-butyl carbazate to the deprotected side chain carboxylic acid terminal moieties (*19*) led to the appearance of degradation byproducts such as **20** (Figure 2). Monitoring of the reaction by size exclusion chromatography (Figure 2) showed the formation of lower molecular weight by products—presumably formed as a result of attack of the hydrazide nitrogens onto the carbamate linkers to PEG, thus forming a six-membered cyclic byproduct and releasing PEG.

This side reaction could be circumvented in two ways (see Supporting Information): (i) replacement of the carbamate in **18** with a more stable amide linkage by using carboxymethyl terminated PEG instead of a PNP carbamate; or (ii) use of a glutamic acid spacer between the nucleophilic hydrazides and the relatively labile carbamate linkages to PEG. The latter route requires more synthetic operations, but has the added benefit

Scheme 2. Linker Attachment and Dox Loading



Scheme 3. PEGylated Polylysine Synthesis



of doubling the number of hydrazides through which drug molecules can be attached. Overall, while feasible, this route did not fully meet our criteria for an optimized dendritic drug carrier.

Exploring Hybrid Ester-Amide-Core Dendrimers. The important lessons learned from the synthesis of both the polyester and polyamide carriers ultimately led us to consider a hybrid approach that combines their separate virtues in one scaffold. It appears that the combination of a hydrolytically degradable ester core and a more chemically resistant amide periphery might be ideal for the construction of PEGylated drug conjugates. Furthermore, the early designs we tested (vide supra) also underscored the importance of avoiding the positioning nucleophilic sites at a 5- or 6-atom distance from potential leaving groups (*43*). Hybrid dendrimer **24** (Scheme 4), representing such an architecture was obtained in three simple steps and 81% overall yield without any chromatographic purification.

Synthesis of the hybrid carrier began by treatment of pentaerythritol **1** with the *p*-nitrophenyl ester of lysine **21** (Scheme 4). The amine protecting groups of the resulting dendrimer **22** were then removed and the molecule was provided with "differentiated end functionalities" by reacting each of its eight primary amino groups with orthogonally protected PNP-glutamic acid **23**. Glutamic acid was selected over aspartic acid for the following reasons: (i) pentachlorophenol was no longer needed to prevent amidolysis of the benzyl ester group, since formation of the 6-membered amino succinyl byproduct was not observed; and (ii) *t*-butyl carbazate could be attached directly to the glutamic acid side chain without any degradation as cyclization of the acyl hydrazide onto the carbamate to form a seven-membered ring was not an issue. Eight 5 kDa PEG chains were then installed on the dendrimer periphery via a carbamate linkage. This was accomplished by quantitative removal of the Boc protecting groups and subsequent PEGylation with 1 equiv (per amine) of PNP-PEG (Scheme 4). The PEGylation reaction was extended over two days, at which time, piperidine was added to quench any unreacted PNP-PEG, and then acetic anhydride was added to acylate any remaining primary amines on the dendrimer scaffold. The resulting PEGylated dendrimer **25** was purified via precipitation into ether to give a polymer with MW ~40 000 Da and PDI < 1.1, with an average particle size of 12 nm as determined by dynamic light scattering (DLS). Finally, residual linear PEG could be removed by dialysis using 100 000 MW cutoff dialysis tubing in water.

The benzyl ester protected side chains of the glutamic acid moieties in **25** were removed via hydrogenolysis, and the resultant carboxylic acids were treated with *t*-butyl carbazate and 1-ethyl-3-(3-dimethylaminopropyl)carbodiimide (EDC) to give dendrimer **26** with eight protected hydrazides available for drug attachment. Finally, target drug conjugate **27** was successfully obtained from the protected precursor **26** by removal of the Boc groups and subsequent condensation with doxorubicin in 5% pyridine/acetic acid solution of methanol at 60 °C.

The degradation profile of the ester-amide dendrimer hybrid was evaluated under physiological conditions. Polymer **26** was incubated at 37 °C in phosphate buffer at physiological pH and the molecular weight was monitored over 20 days by size exclusion chromatography (Figure 3a). As expected, the polymer degraded into 10 kDa and 5 kDa fragments as a result of the slow hydrolysis of both ester and carbamate moieties. Given that the threshold for renal clearance for linear polymers is estimated to be near 45 000 Da (*48*), cleavage of the 40 000 Da branched polymer following delivery of its payload contributes to prevent its long-term accumulation. The observed degradation profile is promising, as it suggests that hybrid dendrimer **26** is sufficiently stable to allow for selective tumor uptake, yet can be eventually broken down and cleared (*9*). It is also noteworthy that the drug is attached to a narrow population of polymeric material and that no significant amount of free drug is present as confirmed by the absence of a peak corresponding to free drug at 590 nm in the UV−vis trace of the conjugate (Figure 3b).

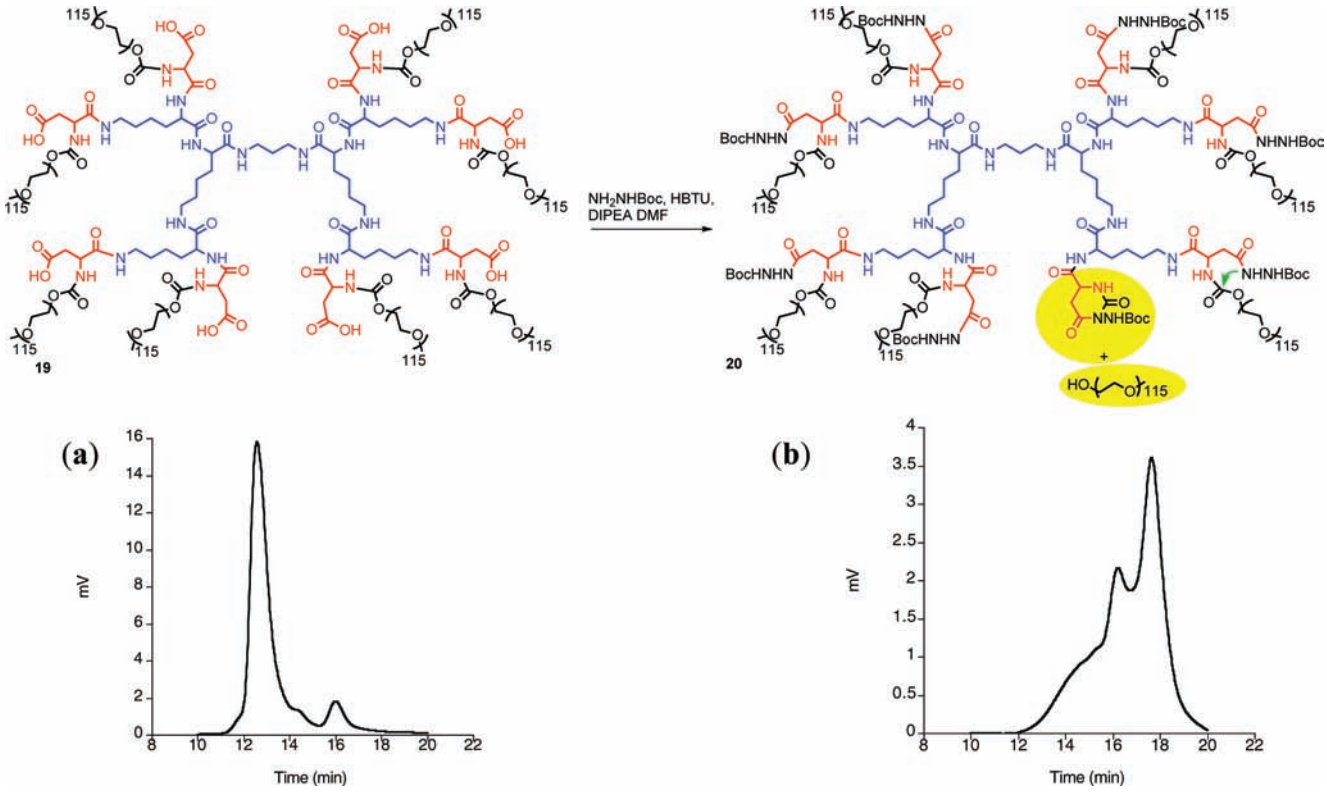
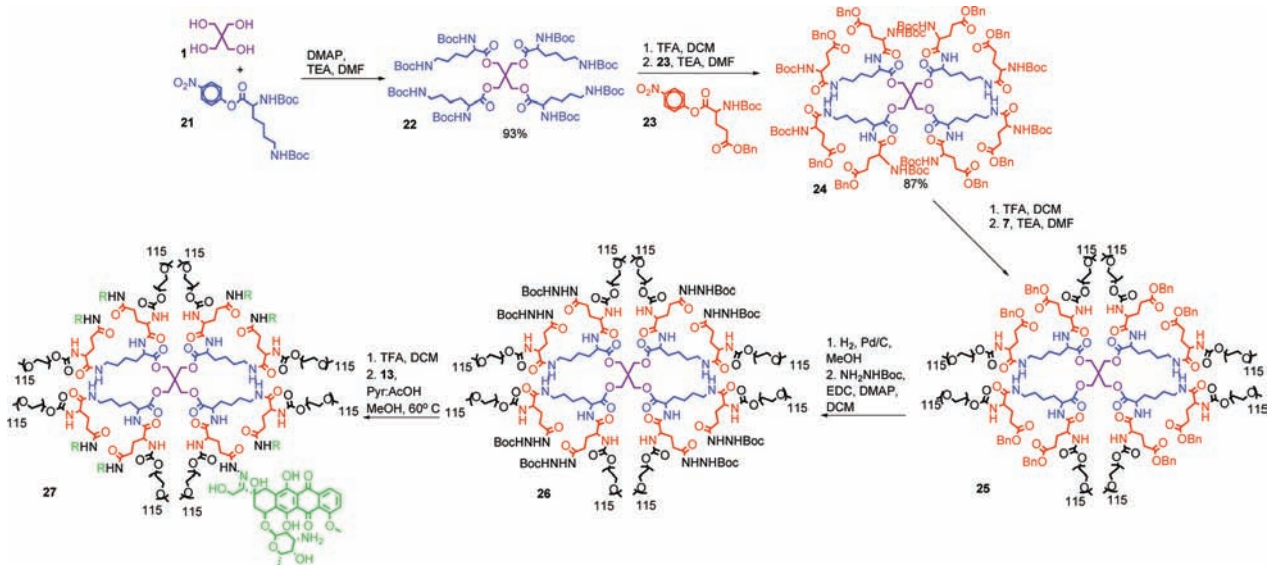


Figure 2. PEGylated polylysine degradation: (a) SEC of compound **19**, (b) SEC of reaction mixture with byproduct **20**.

Scheme 4. Synthesis of Drug Loaded PEGylated Ester-Amide Dendrimer



Carrier drug loading was determined via UV−vis spectroscopy and could be varied from 6−10 wt/wt% depending on how many equivalents of doxorubicin were used in the loading step. This correlates to 55−92% of the theoretical maximum doxorubicin loading for a ~40 kDa polymer with 8 sites for drug attachment. Doxorubicin was chosen for attachment because it is a well-established and highly effective chemotherapeutic agent (*49*) that can benefit from conjugation to a carrier to decrease its innate cardiotoxicity. It is important to note that a variety of drugs, prodrugs, or other biological agents may potentially be attached to dendritic carriers based on **25** through its latent carboxylic acid side chains. The pH-dependence for the rate of hydrolysis of the hydrazone bond we formed is well-studied (*43, 50, 51*), and we could confirm that the drug would be selectively released under acidic conditions similar to those found in the lysosome (*43*). At pH 7.4, less than 5% of drug was released over 48 h, while the half-life of hydrolysis at pH 5 was 22 h.

In Vitro Toxicity of Ester-Amide Dendrimer. The in vitro cytotoxicity tests showed that **26** remained nontoxic toward C26 cells at a concentration of 5 mg/mL. When Dox was conjugated to the carrier, a 10-fold decrease in toxicity was observed over the free Dox ($IC_{50(27)}$ = 529.6 ± 3.8 nM; $IC_{50(Dox)}$ = 52.4 ± 12.7 nM). The decrease in toxicity may be attributed to the slower rate of uptake of the ester-amide carrier compared to free Dox and the slow hydrolysis of the drug from the carrier.

Biodistribution in Tumored Mice. The biodistribution of the ester-amide dendrimer was determined in C26 tumored female Balb/C mice (Figure 4). Mice were injected with 8 mg Dox eq/kg, formulated as Doxil or **27**. After 48 h, Dox

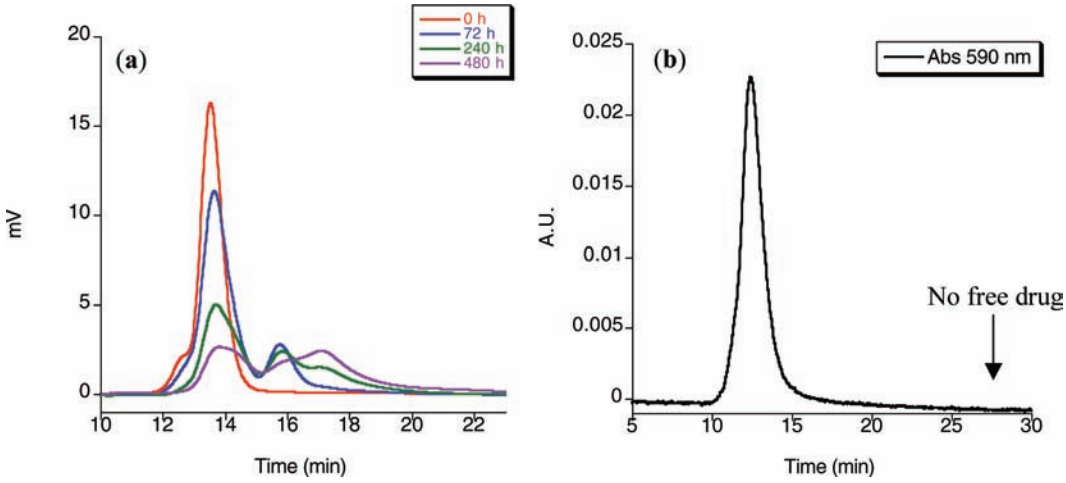


Figure 3. (a) Size exclusion chromatographs of **26** in pH 7.4 PBS buffer at 37 °C. (b) UV−vis size exclusion chromatograph of **27** at 590 nm.

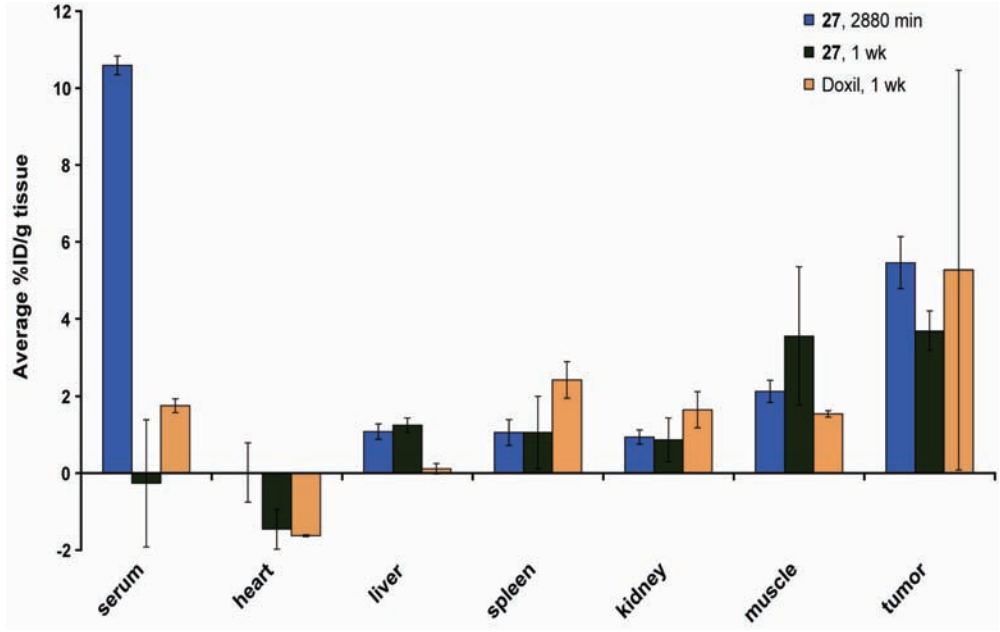


Figure 4. 48 h and 1 week biodistribution of **27** and 1 week biodistribution of Doxil in mice with s.c. C26 colon carcinoma.

accumulation within the tumor was 5.5 ± 0.7% ID/g of tissue (compared to vital organs, $p < 0.001$), whereas accumulation in the vital organs was less than 2% ID/g of tissue. This result is comparable to the levels of accumulation we have previously observed for related macromolecules (*36, 39*). Furthermore, we were pleased to find a measurable level of Dox still remained within the tumor tissue (compared to vital organs, $p < 0.05$) after one week with little accumulation within the vital organs. Mice injected with **27** or Doxil had comparable tumor accumulation after one week, 3.7 ± 0.51% ID/g of tissue and 5.27 ± 5.19% ID/g of tissue respectively. The ester-amide dendrimer showed lower accumulation within the spleen than Doxil. Lowering Dox accumulation in the vital organs is important for reducing systemic toxicity, while uptake by tumor tissue must be maintained to promote treatment efficacy.

Chemotherapy Study in Tumored Mice. A dose−response experiment was performed in C26 tumored Balb/C mice; four treatment groups were investigated, Doxil (20 mg Dox/kg) and **27** (10, 15, and 20 mg Dox/kg). Dose-dependent survival was observed and all three groups treated with **27** showed significant tumor growth delay (TGD) and prolonged survival (Table 1, Figure 5). Mice treated with **27** at 20 mg Dox/kg had 9 out of 10 mice tumor free at the end of the study (day 60), with TGD of 229% ($p < 0.0001$) and median survival time of 60 days. For **27** administered at 15 mg Dox/kg and 10 mg Dox/kg, the treatment groups had 175% ($p < 0.0001$) and 74% TGD ($p < 0.0001$) and a median survival time of 60 and 33 days, respectively. Doxil had 8 out of 10 mice alive at day 60, but the two deaths appeared to be due to treatment-related toxicity. Weight loss due to treatment toxicity was on average not severe, with a mean weight loss of 6.4% for Doxil and 4.3% for **27** (20 mg Dox/kg). This result is comparable to the chemotherapy experiment with the asymmetrically PEGylated dendrimer vs Doxil, both administered at 20 mg Dox/kg (*17*). In this earlier study, there was complete tumor regression with the asymmetrically PEGylated dendrimer carrier with a single toxic death observed in the parallel Doxil experiment. Therefore, both the current and the earlier studies confirm that Dox-loaded PEGylated dendrimer carriers are as effective as Doxil against the C26 tumor model. The ester-amide dendrimer **27** may exhibit less toxicity than Doxil at equivalent Dox dosages and its biodegradability, streamlined synthesis, and facile

Table 1. In Vivo Efficacy of Ester Amide Dendrimer Conjugate and Controls against Balb/C Mice with C26 Colon Carcinoma[a]

treatment group	no. mice	dose (mg/kg)	mean TGD (%)	median survival time (days)	TRD	LTS
PBS	10			20	0	0
Doxil	10	20	245[b]	60[b]	2	8
27	10	20	229[b]	60[b]	0	9
27	10	15	175[b]	60[b]	0	6
27	10	10	74[c]	33[b]	0	1

[a] TGD, tumor growth delay, calculate from time of growth to 400 mm^3; TRD, treatment-related death; LTS, long term survivors. [b] Compared to PBS, $P \leq 0.0001$. [c] Compared to PBS, $P = 0.004$.

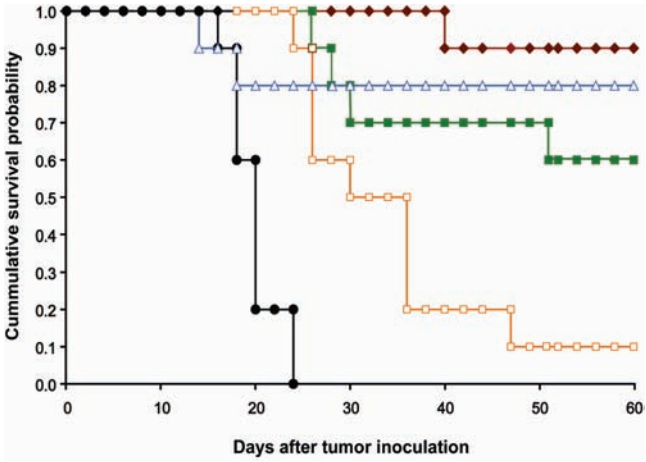


Figure 5. Survival probability versus time for Balb/C mice bearing s.c. C26 colon carcinoma after a single injection of PEGylated polyester-amide Dox conjugate or control. Mice were treated 8 days after tumoring. ◆, **27** (20 mg Dox equiv/kg); ■, **27** (15 mg Dox equiv/kg); □, **27** (10 mg Dox equiv/kg); Δ, Doxil (20 mg Dox equiv/kg); •, PBS.

storage as a dry powder offer significant advantages over existing treatments.

CONCLUSION

In conclusion, the attractive features of polyester and polyamide dendrimers have been combined to form a robust yet degradable polyvalent macromolecular scaffold that can be prepared in a scalable fashion. The final drug-loaded dendrimer is made entirely from commercial starting materials in nine high-yielding steps, four of which are near-quantitative deprotection steps. No chromatographic steps are required during the dendrimer preparation. This scaffold will be studied with additional tumor models and drugs as it shows promise as a clinically relevant delivery vehicle.

ACKNOWLEDGMENT

Financial support of this research by the National Institutes of Health (RO1 EB 002047) is gratefully acknowledged. We thank Dr. Megan Fox for insightful discussions.

Supporting Information Available: Additional synthetic details and characterization. This material is available free of charge via the Internet at http://pubs.acs.org.

LITERATURE CITED

(1) Kopecek, J. (1977) Soluble biomedical polymers. *Polym. Med. 7*, 191–221.
(2) Bader, H., Ringsdorf, H., and Schmidt, B. (1984) Water-soluble polymers in medicine. *Angew. Makromol. Chem. 123*, 457–485.
(3) Seymour, L. W. (1992) Passive tumor targeting of soluble macromolecules and drug conjugates. *Crit. Rev. Ther. Drug 9*, 135–187.
(4) Matsumura, Y., and Maeda, H. (1986) A new concept for macromolecular therapeutics in cancer-chemotherapy - mechanism of tumoritropic accumulation of proteins and the antitumor agent smancs. *Cancer Res. 46*, 6387–6392.
(5) Liu, S., Maheshwari, R., and Kiick, K. L. (2009) Polymer-based therapeutics. *Macromolecules 42*, 3–13.
(6) Kataoka, K., Harada, A., and Nagasaki, Y. (2001) Block copolymer micelles for drug delivery: design, characterization and biological significance. *Adv. Drug Delivery Rev. 47*, 113–131.
(7) Guo, X., and Szoka, F. C. (2003) Chemical approaches to triggerable lipid vesicles for drug and gene delivery. *Acc. Chem. Res. 36*, 335–341.
(8) Christian, D. A., Cai, S., Bowen, D. M., Kim, Y., Pajerowski, J. D., and Discher, D. E. (2009) Polymersome carriers: From self-assembly to siRNA and protein therapeutics. *Eur. J. Pharm. Biopharm. 71*, 463–474.
(9) Fox, M. E., Szoka, F. C., and Fréchet, J. M. J. (2009) Soluble polymer carriers for the treatment of cancer: the importance of molecular architecture. *Acc. Chem. Res. 42*, 1141–1151.
(10) Li, M. H., and Keller, P. (2009) Stimuli-responsive polymer vesicles. *Soft Matter 5*, 927–937.
(11) Green, J. J., Langer, R., and Anderson, D. G. (2008) A combinatorial polymer library approach yields insight into nonviral gene delivery. *Acc. Chem. Res. 41*, 749–759.
(12) Haag, R., and Kratz, F. (2006) Polymer therapeutics: Concepts and applications. *Angew. Chem., Int. Ed. 45*, 1198–1215.
(13) Peer, D., Karp, J. M., Hong, S., Farokhzad, O. C., Margalit, R., and Langer, R. (2007) Nanocarriers as an emerging platform for cancer therapy. *Nat. Nanotechnol. 2*, 751–760.
(14) Medina, S. H., and El-Sayed, M. E. H. (2009) Dendrimers as carriers for delivery of chemotherapeutic agents. *Chem. Rev. 109*, 3141–3157.
(15) Gillies, E. R., and Fréchet, J. M. J. (2005) Dendrimers and dendritic polymers in drug delivery. *Drug Discovery Today 10*, 35–43.
(16) Lee, C. C., MacKay, J. A., Fréchet, J. M. J., and Szoka, F. C. (2005) Designing dendrimers for biological applications. *Nat. Biotechnol. 23*, 1517–1526.
(17) Lee, C. C., Gillies, E. R., Fox, M. E., Guillaudeu, S. J., Fréchet, J. M. J., Dy, E. E., and Szoka, F. C. (2006) A single dose of doxorubicin-functionalized bow-tie dendrimer cures mice bearing C-26 colon carcinomas. *Proc. Natl. Acad. Sci. U.S.A. 103*, 16649–16654.
(18) De Jesus, O. L. P., Ihre, H. R., Gagne, L., Fréchet, J. M. J., and Szoka, F. C. (2002) Polyester dendritic systems for drug delivery applications: In vitro and in vivo evaluation. *Bioconjugate Chem. 13*, 453–461.
(19) Parrott, M. C., Marchington, E. B., Valliant, J. F., and Adronov, A. (2005) Synthesis and properties of carborane-functionalized aliphatic polyester dendrimers. *J. Am. Chem. Soc. 127*, 12081–12089.
(20) Bellis, E., Hajba, L., Kovacs, B., Sandor, K., Kollar, L., and Kokotos, G. (2006) Three generations of alpha,gamma-diaminobutyric acid modified poly(propyleneimine) dendrimers and their cisplatin-type platinum complexes. *J. Biochem. Biophys. Meth. 69*, 151–161.
(21) Krishna, T. R., Jain, S., Tatu, U. S., and Jayaraman, N. (2005) Synthesis and biological evaluation of 3-amino-propan-1-ol based poly(ether imine) dendrimers. *Tetrahedron 61*, 4281–4288.
(22) Chen, H. T., Neerman, M. F., Parrish, A. R., and Simanek, E. E. (2004) Cytotoxicity, hemolysis, and acute in vivo toxicity of dendrimers based on melamine, candidate vehicles for drug delivery. *J. Am. Chem. Soc. 126*, 10044–10048.
(23) Lim, J. D., and Simanek, E. E. (2008) Synthesis of water-soluble dendrimers based on melamine bearing 16 paclitaxel groups. *Org. Lett. 10*, 201–204.

(24) Lim, J., Guo, Y., Rostollan, C. L., Stanfield, J., Hsieh, J. T., Sun, X. K., and Simanek, E. E. (2008) The role of the size and number of polyethylene glycol chains in the biodistribution and tumor localization of triazine dendrimers. *Mol. Pharmaceut. 5*, 540–547.
(25) Esfand, R., and Tomalia, D. (2001) Poly(amidoamine) (PAMAM) dendrimers: from biomimicry to drug delivery and biomedical applications. *Drug Discovery Today 6*, 427–436.
(26) Khandare, J. J., Jayant, S., Singh, A., Chandna, P., Wang, Y., Vorsa, N., and Minko, T. (2006) Dendrimer versus linear conjugate: Influence of polymeric architecture on the delivery and anticancer effect of paclitaxel. *Bioconjugate Chem. 17*, 1464–1472.
(27) Kono, K., Kojima, C., Hayashi, N., Nishisaka, E., Kiura, K., Wataral, S., and Harada, A. (2008) Preparation and cytotoxic activity of poly(ethylene glycol)-modified poly(amidoamine) dendrimers bearing adriamycin. *Biomaterials 29*, 1664–1675.
(28) Bhadra, D., Bhadra, S., Jain, S., and Jain, N. K. (2003) A PEGylated dendritic nanoparticulate carrier of fluorouracil. *Int. J. Pharm. 257*, 111–124.
(29) Patri, A. K., Myc, A., Beals, J., Thomas, T. P., Bander, N. H., and Baker, J. R. (2004) Synthesis and in vitro testing of J591 antibody-dendrimer conjugates for targeted prostate cancer therapy. *Bioconjugate Chem. 15*, 1174–1181.
(30) Malik, N., Evagorou, E. G., and Duncan, R. (1999) Dendrimer-platinate: a novel approach to cancer chemotherapy. *Anti-Cancer Drugs 10*, 767–776.
(31) Kaminskas, L. M., Kelly, B. D., McLeod, V. M., Boyd, B. J., Krippner, G. Y., Williams, E. D., and Porter, C. J. H. (2009) Pharmacokinetics and tumor disposition of PEGylated, methotrexate conjugated poly-L-lysine dendrimers. *Mol. Pharmaceut. 6*, 1190–1204.
(32) Kaneshiro, T. L., Wang, X., and Lu, Z. R. (2007) Synthesis, characterization, and gene delivery of poly-L-lysine octa(3-aminopropyl)silsesquioxane dendrimers: nanoglobular drug carriers with precisely defined molecular architectures. *Mol. Pharmaceut. 4*, 759–768.
(33) Okuda, T., Kawakami, S., Akimoto, N., Niidome, T., Yamashita, F., and Hashida, M. (2006) PEGylated lysine dendrimers for tumor-selective targeting after intravenous injection in tumor-bearing mice. *J. Controlled Release 116*, 330–336.
(34) Grinstaff, M. W. (2002) Biodendrimers: New polymeric biomaterials for tissues engineering. *Chem.—Eur. J. 8*, 2838–2846.
(35) Malik, N., Wiwattanapatapee, R., Klopsch, R., Lorenz, K., Frey, H., Weener, J. W., Meijer, E. W., Paulus, W., and Duncan, R. (2000) Dendrimers: Relationship between structure and biocompatibility in vitro, and preliminary studies on the biodistribution of I-125-labelled polyamidoamine dendrimers in vivo (vol 65, pg 133, 2000). *J. Controlled Release 68*, 299–302.
(36) Gillies, E. R., Dy, E., Fréchet, J. M. J., and Szoka, F. C. (2005) Biological evaluation of polyester dendrimer: Poly(ethylene oxide) "Bow-Tie" hybrids with tunable molecular weight and architecture. *Mol. Pharmaceut. 2*, 129–138.
(37) Gillies, E. R., and Fréchet, J. M. J. (2002) Designing macromolecules for therapeutic applications: Polyester dendrimer-poly(ethylene oxide) "bow-tie" hybrids with tunable molecular weight and architecture. *J. Am. Chem. Soc. 124*, 14137–14146.
(38) Goodwin, a. P., Lam, S. S., and Fréchet, J. M. J. (2007) Rapid, efficient synthesis of heterobifunctional biodegradable dendrimers. *J. Am. Chem. Soc. 129*, 6994–6995.
(39) Guillaudeu, S. J., Fox, M. E., Haidar, Y. M., Dy, E. E., Szoka, F. C., and Fréchet, J. M. J. (2008) PEGylated dendrimers with core functionality for biological applications. *Bioconjugate Chem. 19*, 461–469.
(40) King, H. D., Yurgaitis, D., Willner, D., Firestone, R. A., Yang, M. B., Lasch, S. J., Hellstrom, K. E., and Trail, P. A. (1999) Monoclonal antibody conjugates of doxorubicin prepared with branched linkers: A novel method for increasing the potency of doxorubicin immunoconjugates. *Bioconjugate Chem. 10*, 279–288.
(41) Fox, M. E., Guillaudeu, S., Fréchet, J. M. J., Jerger, K., Macaraeg, N., and Szoka, F. C. (2009) Synthesis and in vivo antitumor efficacy of PEGylated poly(l-lysine) dendrimer-camptothecin conjugates. *Mol. Pharmaceut. 6*, 1562–1572.
(42) Gabbay, E. J., Grier, D., Fingerle, R. E., Reimer, R., Levy, R., Pearce, S. W., and Wilson, W. D. (1976) Interaction specificity of anthracyclines with deoxyribonucleic-acid. *Biochemistry 15*, 2062–2070.
(43) Lee, C. C., Cramer, A. T., Szoka, F. C., and Fréchet, J. M. J. (2006) An intramolecular cyclization reaction is responsible for the in vivo inefficacy and apparent pH insensitive hydrolysis kinetics of hydrazone carboxylate derivatives of doxorubicin. *Bioconjugate Chem. 17*, 1364–1368.
(44) Martinez, J., and Bodanszky, M. (1978) Side reactions in peptide-synthesis.9. suppression of the formation of aminosuccinyl peptides with additives. *Int. J. Pept. Protein Res. 12*, 277–283.
(45) Tekade, R. K., Kumar, P. V., and Jain, N. K. (2009) Dendrimers in oncology: an expanding horizon. *Chem. Rev. 109*, 49–87.
(46) Kaminskas, L. M., Boyd, B. J., Karellas, P., Krippner, G. Y., Lessene, R., Kelly, B., and Porter, C. J. H. (2008) The impact of molecular weight and PEG chain length on the systemic pharmacokinetics of PEGylated poly L-lysine dendrimers. *Mol. Pharmaceut. 5*, 449–463.
(47) Denkewalter. (1982) U.S. Patent, 4, 360,646.
(48) Seymour, L. W., Duncan, R., Strohalm, J., and Kopecek, J. (1987) Effect of molecular-weight (Mw) of n-(2-hydroxypropyl) methacrylamide copolymers on body distribution and rate of excretion after subcutaneous, intraperitoneal, and intravenous administration to rats. *J. Biomed. Mater. Res. 21*, 1341–1358.
(49) Kratz, F., Warnecke, A., Schmid, B., Chung, D. E., and Gitzel, M. (2006) Prodrugs of anthracyclines in cancer chemotherapy. *Curr. Med. Chem. 13*, 477–523.
(50) Bae, Y., Nishiyama, N., Fukushima, S., Koyama, H., Yasuhiro, M., and Kataoka, K. (2005) Preparation and biological characterization of polymeric micelle drug carriers with intracellular pH-triggered drug release property: Tumor permeability, controlled subcellular drug distribution, and enhanced in vivo antitumor efficacy. *Bioconjugate Chem. 16*, 122–130.
(51) Ulbrich, K., Etrych, T., Chytil, P., Jelinkova, M., and Rihova, B. (2003) HPMA copolymers with pH-controlled release of doxorubicin - In vitro cytotoxicity and in vivo antitumor activity. *J. Controlled Release 87*, 33–47.

BC900553N

$S4_{13}$-PV Cell-Penetrating Peptide Forms Nanoparticle-Like Structures to Gain Entry Into Cells

Kärt Padari,[‡,†] Kaida Koppel,[‡,†] Annely Lorents,[†] Mattias Hällbrink,[§] Miguel Mano,[||] Maria C. Pedroso de Lima,[||] and Margus Pooga*[,†,⊥]

Department of Developmental Biology, Institute of Molecular and Cell Biology, University of Tartu, EE51010 Tartu, Estonia, Department of Neurochemistry, Stockholm University, SE10691 Stockholm, Sweden, Center for Neuroscience and Cell Biology and Department of Biochemistry, University of Coimbra, 3001-401 Coimbra, Portugal, and Estonian Biocentre, EE51010 Tartu, Estonia. Received December 30, 2009; Revised Manuscript Received February 17, 2010

Despite increasing interest in cell-penetrating peptides (CPPs) as carriers for drugs and in gene therapy, the current understanding of their exact internalization mechanism is still far from complete. The cellular translocation of CPPs and their payloads has been mostly described by fluorescence- and activity-based methods, leaving the more detailed characterization at the ultrastructural level almost out of attention. Herein, we used transmission electron microscopy to characterize the membrane interaction and internalization of a cell-penetrating peptide $S4_{13}$-PV. We demonstrate that $S4_{13}$-PV peptide forms spherical nanoparticle-like regular structures upon association with cell surface glycosaminoglycans on the plasma membrane. Insertion of $S4_{13}$-PV particles into plasma membrane induces disturbances and leads to the vesicular uptake of peptides by cells. We propose that for efficient cellular translocation $S4_{13}$-PV peptides have to assemble into particles of specific size and shape. The spherical peptide particles are not dissociated in intracellular vesicles but often retain their organization and remain associated with the membrane of vesicles, destabilizing them and promoting the escape of peptides into cytosol. Lowering the temperature and inhibition of dynamins' activity reduce the internalization of $S4_{13}$-PV peptides, but do not block it completely. Our results provide an ultrastructural insight into the interaction mode of CPPs with the plasma membrane and the distribution in cells, which might help to better understand how CPPs cross the biological membranes and gain access into cells.

INTRODUCTION

Cell-penetrating peptides (CPPs) [1]constitute an expanding peptide family with a common denominator—the ability to cross biological membranes and gain access into living cells. These peptides have been applied to drag various molecules into cells, like siRNA (*1, 2*), PNA oligomers (*3, 4*), peptides (*5*), proteins (*6, 7*), plasmids (*8*), and bigger particles (*9–11*). Although the mechanism of CPP cellular uptake is far from being fully understood yet, their potential to target cargo molecules into cells has been widely appreciated and used. Nevertheless, unraveling of the uptake mechanism of CPPs is of high importance for both achieving the specific targeting and increasing the biological response, i.e., the activity of delivered cargo in the cellular interior.

Initially, the internalization of CPPs was suggested to occur by direct translocation across the plasma membrane and not by receptor-mediated endocytosis. After the discovery of artifactual redistribution of membrane-associated CPPs into cells and nucleus upon fixation, the "endocytosis only" concept was introduced, and ideas about passage of peptides directly across the plasma membrane were neglected (*12, 13*). Experiments in living nonfixed cells implicated the involvement of different endocytic pathways in the internalization of CPPs and their conjugates: clathrin-mediated endocytosis (*14*), lipid raft/caveolae-mediated endocytosis (*15, 16*), and macropinocytosis (*17, 18*). However, a number of recent studies demonstrated the switching between different cellular distribution patterns of CPPs (from the punctuate/vesicular to the diffuse/uniform characteristic to penetration mechanism) in response to the shift of experimental conditions, like the concentration of CPP, the temperature, and the size of cargo (*5, 19–21*). Currently, CPPs are considered to use a combination of multiple mechanisms for cell entry—direct translocation and endocytosis.

Due to the high positive charge, CPPs interact electrostatically with the negatively charged extracellular matrix, probably glycosaminogycans (GAG) at the cell surface. Membrane-associated heparan sulfate containing proteoglycans has been shown to be a primary interaction site of CPPs with the plasma membrane mediating their uptake by cells (*14, 18, 22, 23*). Moreover, recent investigations indicate that cationic peptides reorganize the extracellular matrix and the binding of CPPs to the negatively charged GAGs induces their clustering at the surface of cells thereby stimulating the endocytotic uptake of formed aggregates (*24, 25*). Although it is generally appreciated that GAGs are essential for cellular translocation of CPPs, information about other anionic molecules, which are also suggested as possible uptake mediators of CPPs, is still lacking.

In our study, we focused on the $S4_{13}$-PV peptide, its interaction with the cell surface, and translocation into cells. $S4_{13}$-PV is a chimeric CPP that contains a 13 amino acid sequence derived from dermaseptin S4 and the nuclear localization signal

* Correspondence should be addressed to Prof. Margus Pooga, Institute of Molecular and Cell Biology, Riia 23, 51010 Tartu, Estonia, Tel: (372)7 375 049, Fax: (372)7 420 286, E-mail: mpooga@ebc.ee.

‡ These authors contributed equally to this work

† University of Tartu.

§ Stockholm University.

|| University of Coimbra.

⊥ Estonian Biocentre.

[1]Abbreviations: CPP, cell-penetrating peptide; GAG, glycosaminoglycan; HSPG, heparan sulfate proteoglycan; LAMP-2, lysosome associated membrane protein 2; MRR, membrane repair response; RR, ruthenium red; TEM, transmission electron microscopy; MVB, multivesicular body.

10.1021/bc900577e © 2010 American Chemical Society
Published on Web 03/05/2010

of the simian virus 40 (SV40) large T antigen (*26*). We have previously shown that the $S4_{13}$-PV peptide is efficiently taken up by cells in a rapid dose-dependent manner, which is distinct from endocytosis and most likely involves direct penetration across cell membranes (*19, 27*). Circular dichroism analysis and the change in fluorescence emission spectra of the $S4_{13}$-PV peptide upon interaction with target membranes implicated that the peptide acquires a helical conformation in the presence of target membranes and is partially inserted in the hydrophobic environment of lipid bilayer (*28*). The high translocation ability and the cellular delivery potential of $S4_{13}$-PV peptide was recently corroborated by successful transfection of cells with plasmid DNA (*8*).

The vast majority of studies examining the CPPs' uptake and cellular localization have used fluorophore-labeled peptides. Fluorescence microscopy is a very powerful technique for visualizing the uptake and location of peptides in cells. However, it does not provide sufficiently detailed information regarding whether CPPs associate first with the extracellular matrix or directly with the plasma membrane, what is the size and shape of loci of initial contacts of CPPs with cells, which type of vesicles mediate the uptake, and so forth. In addition, the fluorescence signal might be quenched in the cellular environment, especially in vesicles with low pH or when associated with polyanions, as well as on the cell surface upon interaction with heparan sulfate proteoglycans (HSPGs) (*29*) complicating the interpretation of fluorescence microscopy results. Transmission electron microscopy, on the other hand, provides resolution necessary to unambiguously assign the localization of CPPs in relation to subcellular compartments and, moreover, to examine how peptides interact with the plasma membrane and extracellular matrix components. Still, quite a few studies have used electron microscopy to assess the mechanism of CPP uptake.

In this study, we used transmission electron microscopy to characterize the cellular uptake of a cell-penetrating peptide $S4_{13}$-PV and its analogues with reversed NLS and scrambled sequence. We demonstrate that $S4_{13}$-PV peptides form nanoparticle-like regular spheric structures on the cell surface to enter HeLa cells. Our data indicate that these CPPs associate first with the cell surface anionic glycosaminoglycans and assemble in spherical clusters followed by the interaction with the plasma membrane. Accumulation of $S4_{13}$-PV particles on/in the plasma membrane leads to their cell entry and membrane repair response, which is only induced at high peptide concentrations. The cellular uptake of $S4_{13}$-PV peptide is markedly reduced at low temperature or by the inhibition of dynamins' activity, but not completely ceased. We provide ultrastructural insight into the membrane interaction and cellular uptake of $S4_{13}$-PV peptides, which will contribute to our current understanding of how CPPs cross biological membranes and enter cells.

EXPERIMENTAL PROCEDURES

Cell Culture. Human cervical carcinoma cell line HeLa was cultured in Iscove's Modified Dulbecco's Medium (IMDM) (Gibco, Invitrogen, UK) supplemented with 10% fetal bovine serum (FBS) (PAA Laboratories, Austria), 100 IU/mL penicillin, and 100 μg/mL streptomycin (Gibco, Invitrogen, UK). Wild-type CHO-K1 and glycosaminoglycan mutant CHO cell line pgsA-745 was cultured in Ham's F12 culture medium (Gibco, Invitrogen, UK) containing 10% FBS, 100 IU/mL penicillin, and 100 μg/mL streptomycin. Cells were grown in a humidified atmosphere containing 5% CO_2 at 37 °C.

Peptides. High-purity (>95%) $S4_{13}$-PV peptide (ALWKTLLKKVLKAPKKKRKVC), reverse NLS peptide (ALWKTLLKKVLKAVKRKKKPC), and scrambled sequence (KTLKVAKWLKKAKPLRKLVKC) were obtained from Thermo Electron (Thermo Electron GmbH, Karlsruhe, Germany). The peptides were modified with an acetyl group at the N-terminus and had an amide group at the C-terminus. Peptides were tagged with Nanogold (Monomaleimido Nanogold, Nanoprobes, NY, *d* 1.4 nm) by forming a covalent bond between the thiol group of peptide and the maleimide group of label by incubation at a molar ratio 2.5:1 in 50% methanol at 30 °C for 90 min. Methanol was removed and the conjugate concentrated by speed-vac to reach 50−100 μM concentration of labeled peptide. The conjugate with 1:1 peptide/Nanogold ratio was purified to homogeneity by size-exclusion chromatography on Superdex Peptide HR10/30 in buffer containing 35 mM Tris-HCl pH 7.5, 105 mM NaCl, and 30% (v/v) acetonitrile or by reversed phase chromatography on Pro RPC HR5/2 (Pharmacia, Sweden) in water−acetonitrile gradient in the presence of 0.1% TFA and concentrated again. The analysis of conjugate by both above-mentioned chromatography methods yielded a single peak.

Treatment of Cells with Peptides. Cells were seeded onto glass coverslips in 24-well plates, grown to 80−90% confluence, and incubated with culture medium containing 0.1−3 μM gold-labeled peptides at 37 °C for 10 min to 24 h depending on the experimental setup. After incubation, the cells were washed twice with cell culture medium and processed for electron microscopy (see below). For low-temperature experiments, cells were preincubated in culture medium at 10 °C for 30 min, followed by treatment with peptides at the same temperature for 1 h.

Staining of Cell Surface Acidic Mucopolysaccharides with Ruthenium Red. After incubation with Nanogold-labeled peptides, cells were washed twice with cell culture medium and fixed with 2.5% glutaraldehyde containing 1 mg/mL ruthenium red (Sigma-Aldrich, Germany) in the cacodylate buffer (0.1 M sodium cacodylate, pH 7.4) for 1 h. The ruthenium red-stained cells were then washed twice for 10 min with the cacodylate buffer and processed for TEM as described below.

Treatment of Cells with Hyaluronidase. Hyaluronan chains were removed from the surface of pgsA-745 CHO cells by treating with 300 μg/mL hyaluronidase (Sigma-Aldrich, Germany) in serum-free (SF) medium at 37 °C for 30 min. Thereafter, the cells were incubated with 1 μM gold-labeled peptides for 1 h in fresh SF medium containing 300 μg/mL hyaluronidase.

Plasma Membrane Repair Assay. Cells were washed with SF culture medium and incubated with 0.5−10 μM peptides in SF medium for 30 min at 37 °C. Treated cells were washed with PBS, fixed with 3% paraformaldehyde in phosphate buffer (0.1 M, pH 7.4) for 30 min, and washed with PBS. The control cells were permeabilized with methanol at −20 °C for 15 min to expose all intracellular LAMP-2 antigens. The sites of unspecific binding were blocked with 10% nonfat dry milk in PBS for 1 h. LAMP-2 was stained with monoclonal antibody (H4B4, DSHB, 1:100) for 1 h and Alexa Fluor 488-conjugated goat antimouse antibody (Invitrogen, 1:400) for 30 min at room temperature in dark. The solution of secondary antibody was supplemented with 1 μg/mL propidium iodide to assess the intactness of plasma membrane. The coverslips were washed, mounted on glass slides with Fluoromount G (Electron Microscopy Sciences, Hatfield, PA, USA), and analyzed with fluorescence microscopy. Images were recorded using an Olympus BX61 microscope equipped with CCD camera DP70 or Olympus FV1000 confocal microscope (Olympus, Tokyo, Japan). Obtained images were processed with *Adobe Photoshop 7.0* (Adobe Systems, San Jose, CA, USA).

Transmission Electron Microscopy. After treatment with Nanogold-labeled or unlabeled peptides, the cells were fixed with 2.5% glutaraldehyde in cacodylate buffer at room temperature for 1 h and washed two times for 10 min with cacodylate buffer. The Nanogold label of peptides was magnified

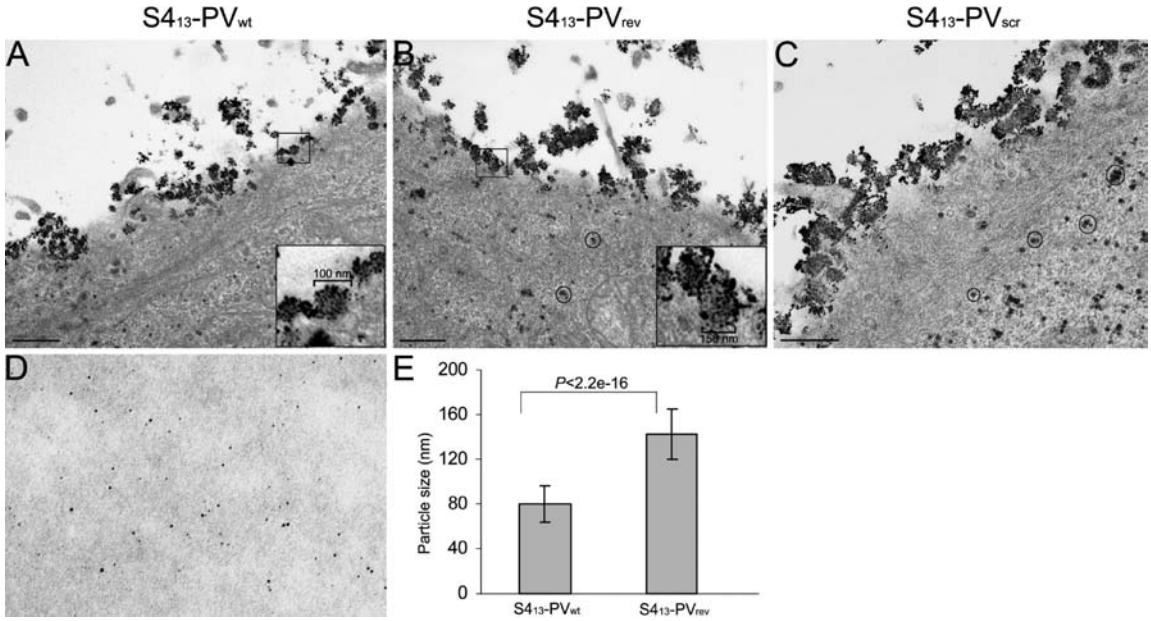


Figure 1. Interaction of S4$_{13}$-PV$_{wt}$ and its analogues with the plasma membrane of HeLa cells. Cells were incubated with 1 μM Nanogold-labeled S4$_{13}$-PV$_{wt}$ (A), S4$_{13}$-PV$_{rev}$ (B), and S4$_{13}$-PV$_{scr}$ (C) for 30 min. Insets in A and B illustrate the enlarged nanoparticles of S4$_{13}$-PV$_{wt}$ (100 nm) and S4$_{13}$-PV$_{rev}$ (150 nm) peptides, respectively. For clarity, note that the black circles in B and C indicate some glycogen granules, which may misleadingly be referred to as the peptide nanoparticles. (D) Distribution of S4$_{13}$-PV$_{wt}$ peptide in cell-free system. Two micromolar Nanogold-labeled S4$_{13}$-PV$_{wt}$ in cell culture medium was placed onto blank sections on TEM grid and allowed to air-dry. The Nanogold (1.4 nm) particles were magnified by silver deposition to ~10 nm. (E) Quantitative analysis of the size of the nanoparticles formed by S4$_{13}$-PV$_{wt}$ and S4$_{13}$-PV$_{rev}$ peptide. Scale bars 0.5 μm.

by silver enhancement for 2−5 min with HQ Silver kit from Nanoprobes (Yaphank, NY, USA) following the protocol suggested by manufacturers. The silver deposition was stabilized by toning with 0.05% gold chloride (*30*). Cells were postfixed with 1% osmium tetroxide in the cacodylate buffer containing 15 mg/mL potassium ferrocyanate at room temperature for 1 h. After osmification, the cells were washed three times for 5 min with cacodylate buffer and dehydrated with 70%, 96%, and twice with 100% ethanol. Finally, the coverslips were dipped into acetone and embedded in epoxy resin (TAAB Laboratories Equipment Ltd., UK). Ultrathin sections were cut in parallel with the coverslip and contrasted in 2% uranyl acetate in 50% ethanol for 2 min and in lead citrate for 2 min. The sections were examined with a JEM-100S (JEOL, Tokyo, Japan) transmission electron microscope at 80 kV. The scanned electron microphotos were analyzed and processed with *Adobe Photoshop 7.0* software. Statistical analysis was performed using program R 2.6.0.

Treatment of Cells with Dynasore and Transferrin. For electron microscopy, the activity of dynamins was inhibited by pretreating cells with 80 μM dynasore (AKos GmbH, Steinen, Germany) in SF culture medium at 37 °C for 30 min (*31*). The peptides were diluted to the concentration of 1 μM in the same solution and incubated for 1 h.

For transferrin uptake, 5×10^4 HeLa cells were seeded onto glass coverslips in 24-well plate one day before experiment. Cells were washed twice with SF medium and pretreated for 30 min at 37 °C with 80 μM dynasore in SF culture medium or SF medium only. For visualizing endosomes, cells were incubated with 10 μg/mL transferrin labeled with Alexa Fluor 594 (Molecular Probes, Invitrogen, OR, USA) in the corresponding medium for 2 min at room temperature, washed 3 times with the corresponding medium without transferrin, and incubated for an additional 15 min at 37 °C. Treated cells were washed twice with cold 0.2 M glycine buffer containing 0.15 M NaCl (pH 3.0) for 30 s, followed by washing with cold PBS, and fixed with 4% paraformaldehyde in PBS on ice for 30 min. Fixed cells were washed with PBS and mounted to microscope slides with 30% glycerol in PBS. The images were recorded and processed as described above.

RESULTS

S4$_{13}$-PV Peptides Assemble into Small Nanoparticle-Like Spherical Structures Upon Interaction with the Plasma Membrane of HeLa Cells. In order to characterize the cellular uptake of the S4$_{13}$-PV peptides at the ultrastructural level, we tagged the original "wild-type" peptide (S4$_{13}$-PV$_{wt}$) and its analogues with reversed NLS (S4$_{13}$-PV$_{rev}$) and scrambled sequence (S4$_{13}$-PV$_{scr}$) covalently with Nanogold clusters of 1.4 nm in diameter. Incubation of HeLa cells with 1 μM S4$_{13}$-PV$_{wt}$-nanogold conjugates led to the association of peptides into spherical structures, which accumulated on the plasma membrane and entered cells. These structures had regular shape and relatively uniform size of about 80−100 nm reminiscent of nanoparticles (Figure 1A). The assembly of wild-type peptide into nanoparticles was rather prevailing, but still a fraction of peptides bound to the extracellular matrix without formation of spherical structures. S4$_{13}$-PV$_{rev}$ peptide formed similar nanoparticle-like structures, albeit somewhat bigger and more variable in size and shape (Figure 1B). Quantitative analysis revealed that the average size of particles formed by S4$_{13}$-PV$_{rev}$ peptide was about 1.8 times bigger (142.6 ± 22.7 nm) than those formed by wild-type peptide (79.8 ± 16.4 nm) (Figure 1E). In contrast to S4$_{13}$-PV$_{wt}$ and S4$_{13}$-PV$_{rev}$, the peptide with scrambled sequence (S4$_{13}$-PV$_{scr}$) could not assemble into spherical structures and typically formed bigger irregular aggregates on the plasma membrane of cells (Figure 1C). This suggests that the peptide with scrambled sequence cannot acquire a regular structure similar to the wild-type and reverse NLS peptides.

The spherical structures of wild-type and reversed NLS peptides seem to form only in the presence of cell membranes, since the incubation of peptides in the cell culture medium (Figure 1D) with or without calf serum did not lead to assembly of nanoparticles. Next, we assessed whether the characteristic spherical assemblies are induced by the Nanogold cluster used

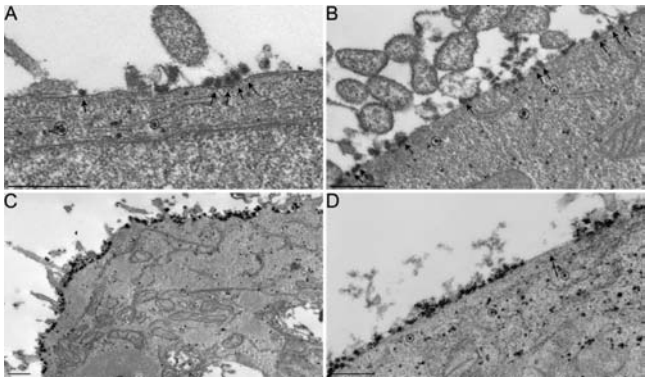


Figure 2. Association of the nanoparticles of $S4_{13}$-PV_{wt} with cell surface mucopolysaccharides. Nanoparticles on the surface of HeLa cells after incubation with 4 μM unlabeled (A,B) or 1 μM Nanogold-labeled (C,D) $S4_{13}$-PV_{wt} peptides for 1 h and stained with ruthenium red (RR). Arrows in A and B indicate the $S4_{13}$-PV_{wt} nanoparticles formed by unlabeled peptide. Arrow in D points to the surface region lacking both the binding of $S4_{13}$-PV_{wt} peptides and RR-staining. Note that the glycogen granules in the cytoplasm (some of them surrounded by black circles in A, B, and C) may look similar to the peptide nanoparticles. Scale bars 0.5 μm.

for peptide labeling and not by the peptide. As expected, the cationized Nanogold was rarely detected in association with cells after incubation in identical conditions, and no spherical assemblies were ever detected (data not shown), showing that the specific clustering was indeed induced by the peptides. To further confirm this, we incubated cells with 1 μM of gold-labeled peptide and added unlabeled peptide at 2, 4, or 9 μM concentration. At all used concentrations, similar regular structures formed on/in the cell surface in analogy with the gold-labeled peptides only. However, in the presence of unlabeled peptide the number of gold labels per nanosphere was lower than in nanostructures obtained by incubating cells with Nanogold-labeled peptide only (data not shown). This demonstrates that both the gold-labeled and unlabeled $S4_{13}$-PV_{wt} peptides are capable of forming nanoparticles and intermix with one another. In line with this, when we incubated cells with unlabeled peptides only, either at 4 (Figure 2A,B) or 10 μM concentration, we also detected similar distinct electron-dense spherical structures on the surface of HeLa cells, which probably represent the same particles. Analogous results were also obtained with $S4_{13}$-PV peptide with reversed NLS sequence (data not shown).

Cell Surface Glycosaminoglycans Are Involved in the Formation of Peptide Nanostructures. The electron microphotos revealed that the peptide nanoparticles always had an electron-dense background. Binding of polycationic molecules, e.g., cell-penetrating peptides, to the HSPGs is known to induce the clustering and concentration of peptides to the cell surface as dense aggregates followed by their internalization (*24, 25*). Therefore, we visualized the extracellular matrix with ruthenium red (RR), a polycationic cytochemical stain for cell surface mucopolysaccharides. Ruthenium red markedly increased the staining of the plasma membrane and especially the extracellular matrix surrounding cells. In line with the staining of extracellular matrix, the electron density of $S4_{13}$-PV clusters' background was markedly increased by RR treatment (Figure 2C,D). In addition, we noticed that $S4_{13}$-PV peptides associated preferentially with the membrane areas marked with ruthenium red, but not with regions lacking the intense stain of RR (arrow in Figure 2D).

To further assess the involvement of glycosaminoglycans, we analyzed the association of $S4_{13}$-PV_{wt} with the cell surface and internalization in wild-type and glycosaminoglycan-deficient Chinese hamster ovary (CHO) cells. In wild-type CHO cells,

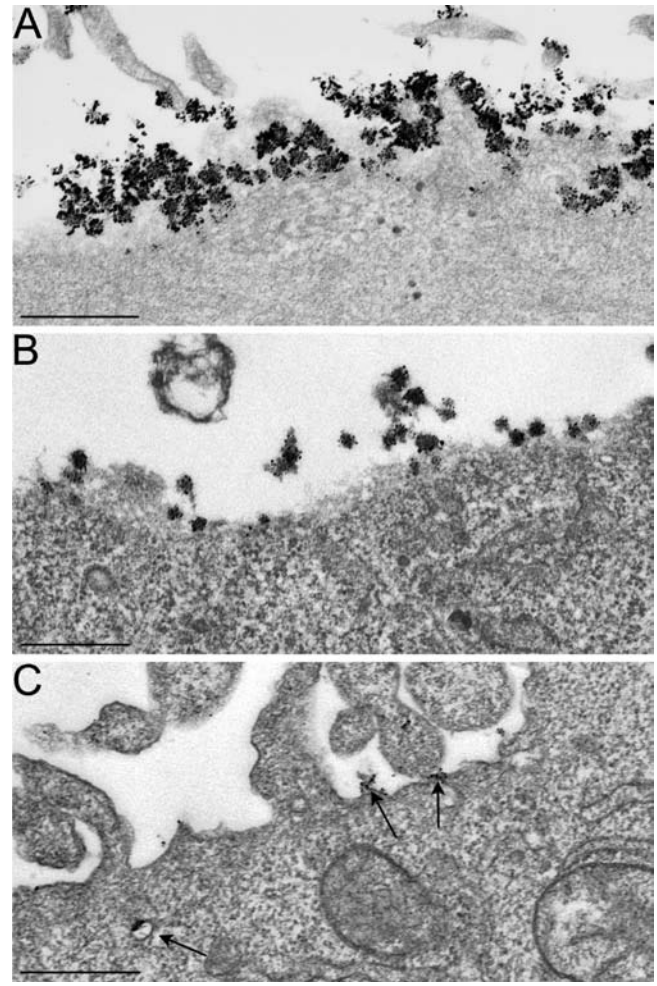


Figure 3. Effect of hyaluronidase treatment on the formation of $S4_{13}$-PV nanostructures. Wild-type CHO-K1 (A) and glycosaminoglycan (GAG) mutant CHO cells (pgsA-745) (B,C) were incubated with 1 μM Nanogold-labeled $S4_{13}$-PV_{wt} peptide for 1 h. (C) The GAG-deficient CHO cells were pretreated with 300 μg/mL hyaluronidase in serum-free medium for 30 min at 37 °C to remove hyaluronan chains from the cell surface and incubated with 1 μM gold-labeled $S4_{13}$-PV_{wt} in the same solution for 1 h. Arrows in C indicate the few peptides that bound to the plasma membrane and internalize into cells after hyaluronidase treatment. Scale bars 0.5 μm.

the peptide accumulated extensively to the cell surface and formed nanospheres with similar size and shape as in HeLa cells (Figure 3A). The nanoparticles of $S4_{13}$-PV were also present at the surface of mutant CHO-pgsA-745 cells, which are defective in glycosaminoglycan biosynthesis (*32*) and lack specific GAG assemblies (Figure 3B). However, the amount of peptide particles on the surface of GAG deficient cells was markedly reduced in comparison to the wild-type CHO. Treatment of mutant CHO cells with hyaluronidase, which specifically cleaves glycosidic bonds in hyaluronic acid and thereby removes the hyaluronan strands and the hyaluronan filament-associated proteoglycans from the cell surface abolished the formation of $S4_{13}$-PV nanoparticles. However, some peptide particles were able to associate with the cell surface and internalize into cells even after treatment with hyaluronidase (arrows in Figure 3C).

In order to determine more specifically the electron-dense membrane constituents associating with $S4_{13}$-PV nanostructures on the cell surface, we incubated peptides in a cell-free system with different isolated acidic glycosaminoglycans (i.e., chondroitin sulfate, heparin, hyaluronan) in the cell culture medium. Unexpectedly, under these conditions none of the examined

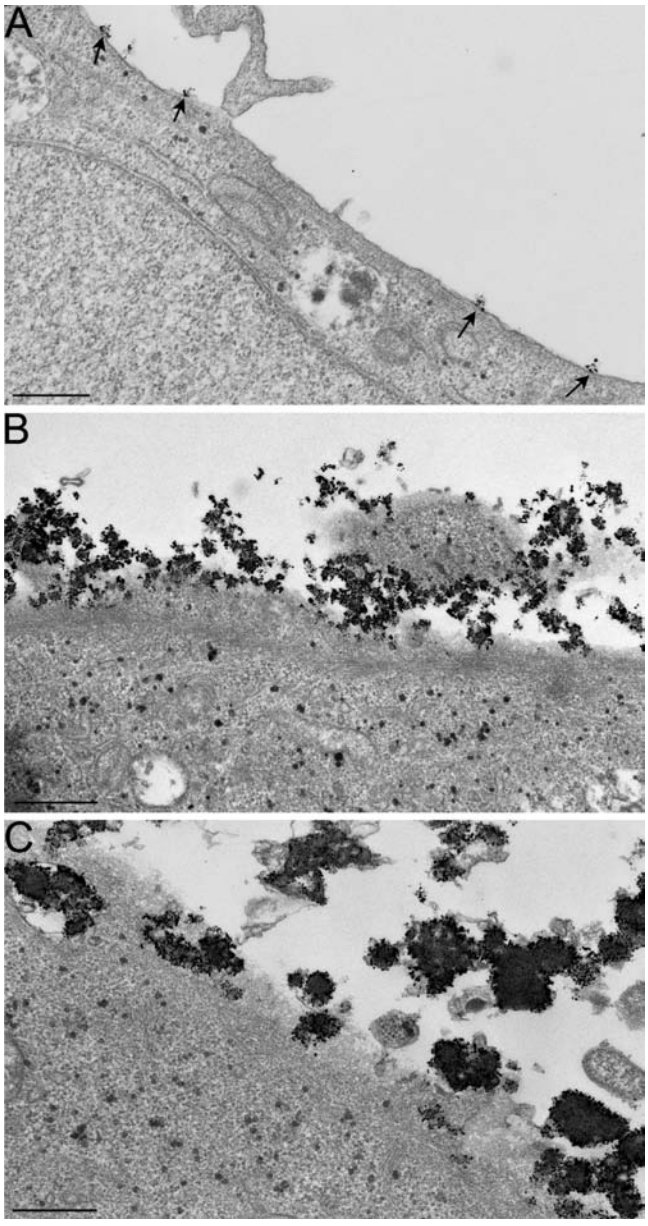


Figure 4. Concentration- and time-dependent formation of $S4_{13}$-PV nanostructures. HeLa cells were incubated with 0.1 μM $S4_{13}$-PV_{wt} for 10 min (A), 0.5 μM (B) or 3 μM $S4_{13}$-PV_{wt} (C) for 1 h. Single clusters of $S4_{13}$-PV_{wt} (arrows in A) at the cell surface formed at a lower concentration; peptide particles of typical size (B) and large irregular aggregates (C) formed at higher concentrations, 0.5 μM and 3 μM respectively. Scale bars 0.5 μm.

GAGs alone were sufficient to induce the formation of nanoparticle-like structures of this peptide (data not shown).

Formation of $S4_{13}$-PV Nanostructures Is Dependent on the Peptide Concentration and Incubation Time. The clusters of $S4_{13}$-PV were detectable by electron microscopy as early as 10 min after the addition of peptides to HeLa cells at the concentration of 0.1 μM. As expected, at low concentration only the "germs" of the nanostructures were detected attached to the cell membrane (arrows in Figure 4A). The peptide-containing structures were small and contained only a few gold particles per cluster. Peptides were taken up by cells also at this concentration and they localized in small ($\leq$50 nm) vesicles under the plasma membrane. Longer incubation (1 h) at this peptide concentration resulted in a slight increase in the surface-bound as well as internalized $S4_{13}$-PV particles. Upon longer incubation, the size of peptide-containing structures did not increase and remained similar to that observed after 10 min incubation. However, at 0.5 and 1 μM concentrations the assemblies of $S4_{13}$-PV peptides exhibited a characteristic spherical shape and size, had higher background density, and comprised more gold particles (Figure 4B). These peptide nanoparticles accumulated extensively at the plasma membrane during 1 to 24 h of continuous incubation with cells. A negligible fraction of peptide particles at 1 μM concentration formed bigger conglomerates during 4 to 24 h, but most of these still retained regularity and a uniform size in bigger structures. However, when we increased the concentration of labeled peptides to 2−3 μM, the large aggregates (up to 0.5−1 μm diameter) started to form already in 1 h (Figure 4C).

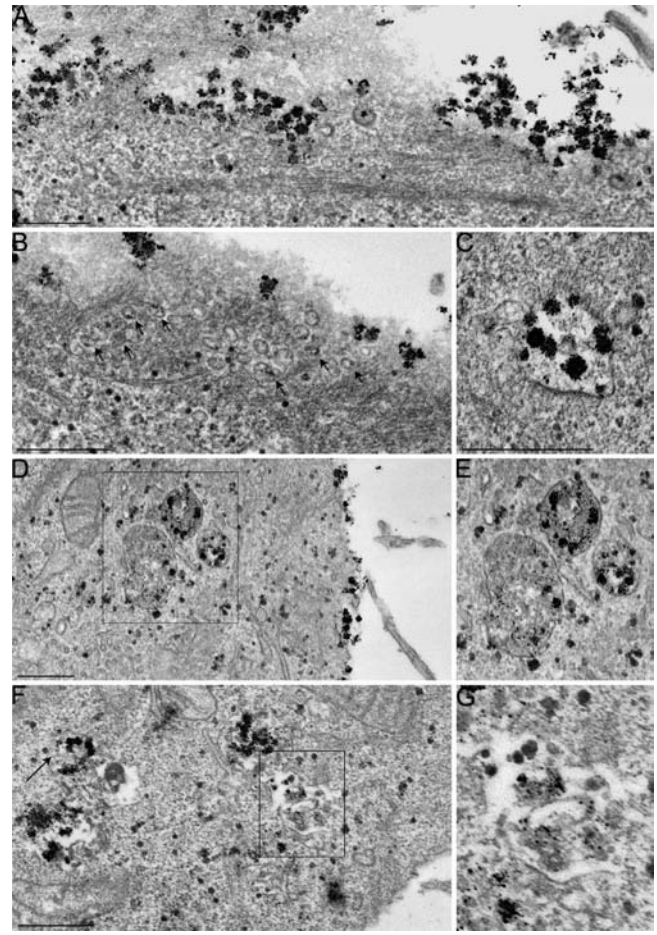


Figure 5. Translocation and intracellular localization of $S4_{13}$-PV_{wt} peptide. HeLa cells were incubated with 0.5 μM (A,B) or 1 μM $S4_{13}$-PV_{wt} (D,E) for 1 h, and with 1 μM $S4_{13}$-PV_{wt} for 24 h (C,F). Accumulation of $S4_{13}$-PV_{wt} nanoparticles to the cell surface (A), internalization in small vesicles (arrows in B), and localization in caveosome-like structures (C) or multivesicular bodies (D,E). Arrow in F and enlarged section (G) indicate the peptide-containing vesicles with a discontinuous membrane after 24 h of $S4_{13}$-PV_{wt} incubation with cells. Scale bars 0.5 μm.

$S4_{13}$-PV Peptides Interfere with the Organization of the Plasma Membrane and Efficiently Enter the Cells. The $S4_{13}$-PV_{wt} and $S4_{13}$-PV_{rev} peptides associated preferentially with specific loci on the plasma membrane. Upon longer incubation, the peptide nanostructures continued to accumulate in these particular regions on the cell surface. Accumulation of peptides interfered with the distinct ultrastructure of the lipid bilayer turning it hardly detectable by electron microscopy. In parallel with the destabilization of the lipid bilayer, the peptide particles inserted into the cortical cytoplasm (Figure 5A) and entered deeper into cells.

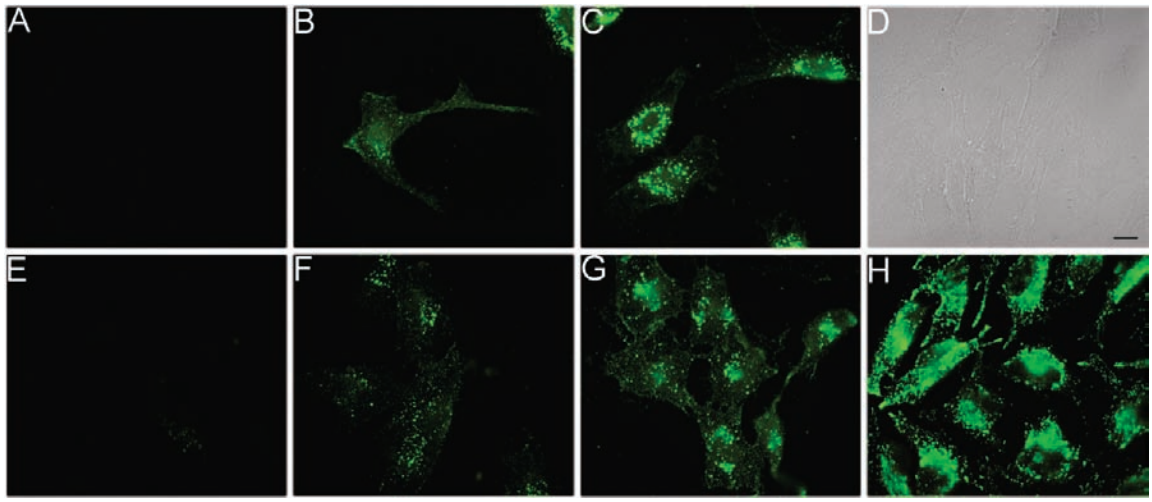


Figure 6. Induction of the membrane repair response by $S4_{13}$-PV peptide. HeLa cells were incubated with 1 μM (A), 3 μM (B), 5 μM (C) $S4_{13}$-PV_{wt} or 1 μM (E), 3 μM (F), 5 μM (G) $S4_{13}$-PV_{rev} at 37 °C for 30 min. LAMP-2 was visualized with monoclonal LAMP-2 antibody and Alexa Flour 488-conjugated antimouse antibody. The membrane repair response is not induced at lower concentration of $S4_{13}$-PV_{wt} (A) and $S4_{13}$-PV_{rev} (E) peptides. LAMP-2 signal appeared at the plasma membrane higher concentrations of $S4_{13}$-PV_{wt} (B,C) and $S4_{13}$-PV_{rev} (F,G) peptides. (D) DIC image of cells in panel A. Localization of LAMP-2 protein in control cells permeabilized with methanol (H). Scale bar 10 μm.

In parallel with the interaction of $S4_{13}$-PV nanostructures with the plasma membrane, the formation and pinching off of small vesicles with diameter of 50−100 nm into cells was induced and some of these also contained peptides (Figure 5B). In addition, peptides were found in bigger rosette-like structures, morphologically reminiscent of caveosomes (Figure 5C). The peptide nanoparticles were present also in multivesicular bodies (MVB), especially after longer incubation. Interestingly, even inside the MVB the distinct spherical organization of peptides was retained for at least 1−4 h (Figure 5D,E). The peptide structures usually located on the inner surface of the vesicle and were mostly in direct contact with the membrane of vesicles. Continuous uptake of $S4_{13}$-PV peptides by cells during 24 h led to their high accumulation in large vacuoles (Figure 5F). This was accompanied by impaired membrane integrity of some peptide-containing vesicles (arrow in Figure 5F,G) indicating that the high concentration of $S4_{13}$-PV can destabilize the membrane and induce the escape of peptides into the cytosol.

$S4_{13}$-PV Peptides Enter Cells without Triggering the Membrane Repair Response, which Requires Higher Peptide Concentrations. Next, we assessed whether $S4_{13}$-PV peptides caused plasma membrane disturbances at the extent of enabling calcium influx into cells and thereby triggering the plasma membrane repair response (MRR). Under these circumstances, the intracellular vesicles donate membranes to reseal the injured plasma membrane, and this can be detected by the exposure of lysosomal membrane protein LAMP-2 to the plasma membrane of intact cells (*33*).

Incubation of HeLa cells with 0.5−1 μM wild-type $S4_{13}$-PV did not trigger the plasma membrane repair response (Figure 6A). It is remarkable that efficient cellular uptake of $S4_{13}$-PV_{wt} peptide takes place without disturbing the ordered packing of the plasma membrane or evoking the membrane repair response. Higher concentrations of peptide starting from 3 μM led to marked fusion of lysosomal membranes with the plasma membrane, and LAMP-2 was detected all over the plasma membrane as distinct punctae (Figure 6B,C). At 10 μM concentration, the plasma membrane resealing was triggered in more than 80% of cells.

The peptide with reversed NLS sequence induced MRR at somewhat lower concentration than the wild-type peptide. LAMP-2 was targeted to the plasma membrane in about 10% of cells already after incubation with 2 μM peptide (data not shown). At 3 μM peptide concentration, LAMP-2 was present at the plasma membrane of 50% of cells (Figure 6F). Increasing the $S4_{13}$-PV_{rev} concentration to 5 μM induced appearance of LAMP-2 on the plasma membrane of almost all cells in specimen (Figure 6G). However, even at 5 μM $S4_{13}$-PV_{rev} concentration the integrity of the plasma membrane was not impaired since propidium iodide could not enter cells (data not shown).

$S4_{13}$-PV analogue with scrambled sequence was the least potent to induce targeting of LAMP-2 to the outer leaflet of the plasma membrane. Very few cells became positive for the lysosomal protein at the cell surface starting from 5 μM concentration and reaching a maximum at 10 μM concentration where almost all of the population was stained. However, not all LAMP-2 antigens became accessible to antibodies at the peptide concentration with the highest induction ability (in case of all used peptides), because the removal of membrane lipids by methanol fixation led to a drastically elevated staining of this lysosomal protein all over the cell (Figure 6H).

Cellular Uptake of $S4_{13}$-PV Peptides Is Reduced at Low Temperature. At 10 °C, the $S4_{13}$-PV_{wt} and both of its analogues associated with the plasma membrane to a lesser extent than at the physiological temperature, and their translocation into cells was diminished. The $S4_{13}$-PV_{wt} and $S4_{13}$-PV_{rev} peptides were still able to assemble into nanostructures, although the size of peptide clusters was more variable and their shape less uniform (Figure 7A,B). At low-temperature condition, the peptides associated with the plasma membrane/extracellular matrix as either irregular aggregates or single clusters. Surprisingly, despite the markedly decreased amount of surface-bound peptides the vesicular uptake of $S4_{13}$-PV peptides was not blocked at 10 °C. However, only a few or single gold particles were in small vesicles or bigger vesicular structures (arrows in Figure 7B,C), which located in the cortical cytoplasm or in the close proximity of the plasma membrane but not deeper in cells.

Dynamin Inhibition Does Not Abolish the Vesicular Uptake of $S4_{13}$-PV by HeLa Cells. Dynasore, an inhibitor of dynamin GTPase activity, blocks the formation and fission of endocytic vesicles in most pathways (*31*). Therefore, we examined the effect of dynasore on the translocation efficiency of $S4_{13}$-PV. Inhibition of dynamins decreased but did not abolish the vesicular uptake of $S4_{13}$-PV nanoparticles. Even in the presence of dynasore, the $S4_{13}$-PV peptides induced the formation and

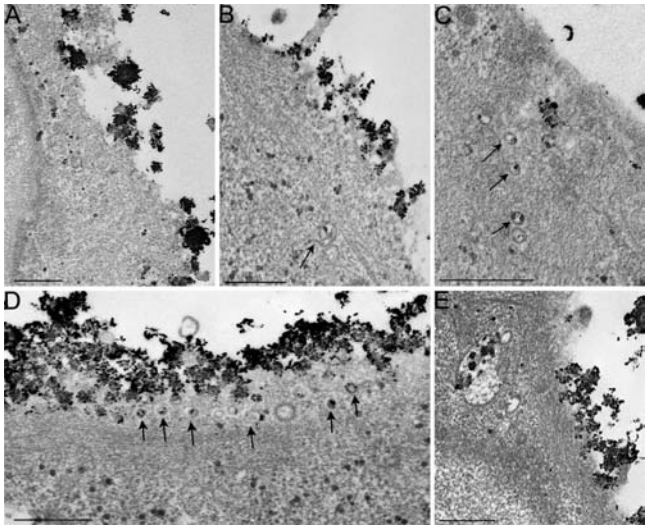


Figure 7. Effect of low temperature and dynamin inhibition on cellular translocation of $S4_{13}$-PV peptides. HeLa cells were incubated with 1 μM $S4_{13}$-PV_{wt} (A), $S4_{13}$-PV_{rev} (B), or $S4_{13}$-PV_{scr} (C) at 10 °C for 1 h. HeLa cells incubated with 1 μM $S4_{13}$-PV_{wt} for 1 h in the presence of dynasore (80 μM) at 37 °C (D,E). Arrows indicate internalized peptides in small vesicles formed at low temperature (B,C) and in dynasore-treated cells (D). Scale bars 0.5 μm.

fission of small vesicles. The formed small vesicles localized mainly in the cortical cytoplasm near the plasma membrane and contained typically a few labeled peptides (Figure 7D). Remarkably, $S4_{13}$-PV_{wt} peptides were also taken up into large endosomal structures ($\geq$0.5 μm) despite the presence of dynasore (Figure 7E). The control cells incubated with Alexa Fluor 594 conjugated transferrin, as a marker for dynamin-dependent endocytic pathway, corroborated the inhibition of endocytosis by dynasore, since only a negligible part of protein was taken up by cells (Supporting Information Figure S1). These findings suggest that $S4_{13}$-PV peptides can also gain entry into cells by endocytic processes that do not necessarily require dynamin.

DISCUSSION

Cell-penetrating peptides have been under intense investigation from the moment of their discovery 15 years ago, but the discussion about their mechanism of association with cells, uptake, and cargo delivery is still continuing, and consensus has not yet been reached in some key questions. Currently, a growing number of studies support the view that CPPs enter cells by different mechanisms, which act in parallel, and for most CPPs, more than one cellular pathway exists. Previously, we have shown that the internalization of $S4_{13}$-PV cell-penetrating peptide proceeds by at least two different mechanisms: an endocytic pathway, which prevails at lower peptide concentrations, and an alternative endocytosis-independent mechanism that is induced preferentially at higher peptide concentrations (*19*). In addition, we demonstrated that the localization of this peptide is not markedly changed upon fixation with aldehydes (*19*), which enables studies at an ultrastructural level by transmission electron microscopy in fixed specimen.

Electron microphotos revealed that the Nanogold-labeled (1.4 nm gold cluster) $S4_{13}$-PV_{wt} peptide assembles into small spherical structures at the plasma membrane of HeLa cells. Considering the relatively uniform size of 80−100 nm and regular shape of the particles formed by $S4_{13}$-PV peptides, we called these structures "nanoparticles" for brevity. The ability to form nanoparticles was also observed for analog of $S4_{13}$-PV peptide with reversed NLS sequence, which clustered in regular spherical structures although with bigger and less uniform size (~140 nm). In contrast, the peptide with scrambled sequence, $S4_{13}$-PV_{scr}, failed to form such spherical structures despite having an identical amino acid composition. The scrambled analogue of $S4_{13}$-PV formed bigger irregular aggregates and entered cells less efficiently than $S4_{13}$-PV_{wt} and $S4_{13}$-PV_{rev} peptides, indicating that not only the amino acid composition, but also their positions influence the mode of interaction with cell surface and subsequent internalization. In general, we observed that the formation of small and regular peptide-containing structures is in good correlation with their ability to enter cells, i.e., the peptides forming regular particles are more efficiently taken into cells. This observation could explain our earlier reports (*27, 28*) demonstrating that the cellular uptake of the scrambled peptide was significantly less efficient than that of $S4_{13}$-PV_{wt} or with reversed NLS peptides. On the basis of the study of peptide conformational changes, we have previously attributed the better internalization properties of the $S4_{13}$-PV and reverse NLS peptide, compared to the scrambled peptide, to the ability of these peptides to adopt an amphipathic α-helical conformation upon interaction with the negatively charged membranes. The changes in the secondary structure of CPPs could in turn induce rearrangement of the plasma membrane lipids leading to peptide internalization (*27*). The electron microscopy results described here are quite well in line with this concept—the plasma membrane of HeLa cells becomes less distinct upon interaction with $S4_{13}$-PV_{wt} or $S4_{13}$-PV_{rev} but not with $S4_{13}$-PV_{scr}. Both the modulation of plasma membrane properties and the different size of peptide assemblies on the cell surface might be responsible for differences in cell-translocation ability of $S4_{13}$-PV peptides.

The first hint that CPPs may assemble in clusters upon association with cells can be found in a publication demonstrating the receptor-independent internalization of the third helix of the Antennapedia homeodomain in 1996 (*34*). Although it was not discussed by the authors at that time, the visualization of Antp(43−58) by colloidal gold particles in electron microscopy reveals that this peptide tends to localize in cells as small clusters in parallel to its even/diffuse distribution. The clustering of peptides to produce particles or aggregates has also been described for other CPPs. Some amphipathic CPPs, like SAP and Pep-1, self-assemble in aqueous solution (*35–37*). On the other hand, the aggregation and clustering can be induced by the binding of CPPs to HSPGs on the cell surface (*24*). Remarkably, not only CPPs, but also some amyloidogenic polypeptides form aggregates to gain access into cells. For example, the large fibrillar polyglutamine peptide aggregates (0.2−0.5 μm in diameter) are able to penetrate the cytosolic compartment of mammalian cells where they can nucleate the aggregation of other soluble proteins containing polyglutamine sequence (*38*).

The cell-penetrating peptide Pep-1, which analogously to $S4_{13}$-PV peptide is amphipathic and comprises a NLS sequence, forms discrete nanometer-sized particles when complexed with cargo protein in solution (*37*). The Pep-1/cargo nanoparticles were of about 80−120 nm diameter as characterized by scanning electron microscopy and light scattering measurements. Analogously to Pep-1, some other short amphipathic peptides, e.g., MPG and CADY, have been demonstrated to form stable nanoparticles with proteins and/or nucleic acids in solution (*39*). Considering these results and taking into account that different cargo molecules can influence the properties of its carrier peptide (*40*), we assessed whether the Nanogold tag, which we conjugated to the peptide could induce/facilitate the assembly of $S4_{13}$-PV nanoparticles or determine their size and structure. The Nanogold cluster is very stable, has no overall charge, and is considered of no affinity to proteins. Still, its diameter is 1.4

nm, and it could alter the bulk properties of peptide more than typically used fluorophores. Although we cannot completely exclude some impact of the gold label on the formation of $S4_{13}$-PV nanoparticles, it cannot be the main assembling force, since after incubation of cells with unlabeled peptides, we were still able to clearly detect the distinct spherical structures. The particles of "naked" $S4_{13}$-PV were reminiscent of structures formed with $S4_{13}$-PV-Nanogold conjugates. The similar size of formed particles suggests that the Nanogold tag does not contribute markedly to the assembly of $S4_{13}$-PV nanoparticle-like structures. It remains nonetheless unclear whether the formation of the nanoparticle-like structures by the $S4_{13}$-PV_{wt} or $S4_{13}$-PV_{rev} peptides is somehow related to the ability of these peptides to adopt a helical conformation.

CPPs may also bunch on the surface of cultured mammalian cells. Ziegler et al. demonstrated that peptides and other cationic compounds can cluster GAGs and induce formation of particles on the surface of cells (*24, 25*). The initial study revealed the presence of strongly absorbing aggregates (<5 μm) of Tat peptide bound to membrane-associated HS on the surface of mouse fibroblasts in fluorescence microscopy experiments (*24*). Moreover, the interaction of CPPs with heparin in cell-free system produced particles, which size ranged from 80 to 130 nm depending on peptide as revealed by light scattering (*25*). In order to distinguish whether the formation of $S4_{13}$-PV peptide nanoparticles is taking place in solution or on the cell surface only, we first examined peptides in a cell-free system. Nanogold-labeled $S4_{13}$-PV did not form nanoparticles in culture medium either in the presence or in the absence of fetal bovine serum and peptides were detected by TEM as single dots distributed evenly on the grid. Somewhat surprisingly, the incubation of $S4_{13}$-PV peptides with different anionic glycosaminoglycans, like heparin, chondroitin sulfate, and hyaluronan, did not lead to the formation of nanoparticles. The absence of $S4_{13}$-PV nanoparticles in solution suggests that a specific environment or a direct interaction with the cell surface is required for the clustering of this peptide. We have shown that the presence of heparan sulfate proteoglycans at cell surface facilitates the cellular uptake of the $S4_{13}$-PV peptide at lower concentration (*27*). By now, the convincing evidence of HSPGs as true internalizing receptors of macromolecular cargo has been provided (*41*). Wittrup et al. showed that the sorting of cell-surface HSPGs to endocytic vesicles is heparan sulfate epitope specific and mediated by both PG core proteins, a transmembrane syndecan, as well as GPI-anchored glypican. Moreover, HIV-1 Tat CPP competes for the internalizing PG population and delivers its cargo through the same vesicular compartments as HSPGs ligands (*41*). To probe the presence of glycosaminoglycans in the content of $S4_{13}$-PV nanoparticles, we used ruthenium red, a polycationic stain for the visualization of acidic polysaccharides on the outer surface of cells. The increase in the electron density of $S4_{13}$-PV nanoparticles after ruthenium red staining corroborated the presence of carbohydrate components in particles and their significance in accumulation of CPPs at the cell membrane and uptake. However, the fact that $S4_{13}$-PV peptide was able to form nanoparticles even on the surface of glycosaminoglycan mutant CHO cells (pgsA-745) lacking xylosyltransferase suggests that the formation of nanoparticles is not merely dependent on the presence of heparan sulfate and/or chondroitin sulfate. Surprisingly, enzymatic cleavage of hyaluronan filaments from the surface of glycan-deficient CHO cells completely abolished the formation of $S4_{13}$-PV nanoparticles, and only a negligible part of peptide was taken up by cells. These data further confirm that the glycosidic component is required for the formation of peptide nanoparticles, and the hyaluronic acid together with hyaluronan-associated proteoglycans might contribute to the formation of these particles.

Experiments with model membranes have demonstrated that $S4_{13}$-PV peptides become buried in the lipid bilayer upon interaction with negatively charged lipid vesicles (*28*). Our electron microscopy results revealed that the clearly distinguishable lipid bilayer of the plasma membrane becomes hazy and is mostly undetectable at the accumulation sites of peptides, suggesting that the association of $S4_{13}$-PV nanoparticles to the plasma membrane interferes with the ordered packing of lipids in the membrane. We demonstrated recently that the accumulation of some CPPs on/in the plasma membrane introduces disturbances, which might be compensated by the membrane repair response (MRR) mechanism (*33*). The plasma membrane resealing is usually activated by the influx of calcium ions from the exterior into cytoplasm, which triggers the exocytosis of intracellular vesicles to reseal the injured plasma membrane or replace the damaged regions. Most commonly, lysosomes donate their membrane for plasma membrane repair, which is accompanied with the exposure of lysosomal lumenal proteins, like LAMP-1 or LAMP-2, to cell surface (*42, 43*). The fluorescence microscopy results demonstrate that $S4_{13}$-PV peptides can indeed induce the membrane repair response, since LAMP-2 protein is targeted to plasma membrane and is detectable in nonpermeabilized cells, but this only occurs at high peptide concentrations. However, the very efficient uptake of $S4_{13}$-PV wild-type and reversed NLS peptides takes place also at lower concentrations than those necessary for triggering the MRR at considerable extent. The emergence of LAMP-2 on the plasma membrane correlates with the size and heterogeneity of $S4_{13}$-PV particles recorded by TEM. More specifically, the $S4_{13}$-PV_{wt} peptide forms the uniform particles with 80−100 nm diameters and evokes MRR only in a small population of cells starting from 3 μM concentration. $S4_{13}$-PV_{rev} formed somewhat bigger and more heterogeneous nanoparticles than wild-type peptide and induced emergence of LAMP-2 already from 2 μM peptide concentration, suggesting higher interference with the membrane integrity by bigger and more variable particles. At the higher concentrations, both these peptides produced large particles with highly varying size and induced MRR all over the plasma membrane in all cells in culture. $S4_{13}$-PV with the scrambled sequence associated with cells without disturbing the integrity of lipid bilayer, and as expected, no induction of MRR was detected up to 10 μM concentration.

The association of $S4_{13}$-PV nanoparticles with the plasma membrane also induced vesicle formation and a partial uptake of $S4_{13}$-PV peptides by small vesicles, which resemble caveosomal structures. Later, the $S4_{13}$-PV peptides were targeted to multivesicular bodies, suggesting that this pathway leads to late endosomal structures. On the other hand, the association of other CPPs with glycosaminoglycans was shown to induce their energy-dependent uptake via clathrin-mediated endocytic pathway (*12, 14*). Both these pathways are dynamin-dependent and could be inhibited with the small cell-permeable drug dynasore (*31*) or by lowering temperature below 18 °C. As expected, the presence of dynasore did not markedly interfere with the assembly of $S4_{13}$-PV nanoparticles, their insertion into plasma membrane, or its destabilization and blurring detected by TEM. However, treatment with dynasore drastically decreased the vesicle formation, but still did not completely abolish it, suggesting that mostly dynamin-dependent processes are active in the uptake of $S4_{13}$-PV peptide, in analogy with Tat and oligoarginine as shown earlier (*21*). Several endocytosis pathways, for example, macropinocytosis, fluid-phase endocytosis, and some other less well understood uptake mechanisms, are dynamin-independent (*44–47*). Although the vesicles, which could by morphology be assigned to these pathways, were present in electron microphotos of dynasore-treated cells, their impact to the uptake of $S4_{13}$-PV_{wt} peptides remained low.

Lowering of incubation temperature, which decreases the plasma membrane fluidity and flexibility, and abolishes most endocytic processes, had a contrasting effect. The association of $S4_{13}$-PV peptide with the extracellular matrix, the formation of nanoparticles, as well as the uniformity of latter were markedly decreased. The cellular uptake of $S4_{13}$-PV peptide was diminished at 10 °C but still not completely stopped, in analogy with our earlier study of other CPPs (*48*). These results support the endocytic uptake mechanism of $S4_{13}$-PV peptides by cells and emphasize the significance of plasma membrane fluidity and dynamic rearrangement of underlying cytoskeleton for the internalization of peptide nanoparticles.

Interestingly, the $S4_{13}$-PV nanoparticles retained their spherical organization within endocytic vesicles for at least 1−4 h, suggesting that the peptide is not dissociated from anionic GAG molecules and its degradation is inhibited. This is also consistent with the observation about HSPGs, which cointernalize with their ligands and remain intact in isolated vesicles for more than three hours (*41*). When the MVBs fuse with lysosomes, their lumenal content is usually degraded or condensed. However, the $S4_{13}$-PV nanoparticles were rather intact even after 24 h incubation. In some vesicles, the high concentration of CPPs had interfered with the integrity of their membrane, since a fraction of vesicles were broken or had lost the continuous membrane and peptides had escaped to the cytosol.

In conclusion, our data demonstrate that $S4_{13}$-PV peptides assemble into spherical structures with diameter of 80−100 nm clustering acidic polysaccharides on cell surface. These nanoparticle-like structures insert into the plasma membrane and by destabilizing and rearranging it induce formation and fission of small endocytic vesicles, but are conveyed toward cell center in large vesicles. The ability of $S4_{13}$-PV peptides to form nanoparticles with about 80−100 nm diameter correlates with the efficacy of their cellular uptake.

ACKNOWLEDGMENT

We thank M. Kure for an excellent technical assistance in electron microscopy and H. Räägel for fruitful discussions and critical reading of manuscript. The work was supported by grants from Estonian Science Foundation (ESF 7058) and from Portuguese Science Foundation (PTDC/BIO/65627/2006).

Supporting Information Available: Effect of dynamin inhibition on transferrin uptake by HeLa cells. This material is available free of charge via the Internet at http://pubs.acs.org.

LITERATURE CITED

(1) Lundberg, P., El-Andaloussi, S., Sutlu, T., Johansson, H., and Langel, Ü. (2007) Delivery of short interfering RNA using endoso molyti c cell-penetrating peptides. *FASEB J. 21*, 2664–2671.

(2) Crombez, L., Aldrian-Herrada, G., Konate, K., Nguyen, Q. N., McMaster, G. K., Brasseur, R., Heitz, F., and Divita, G. (2009) A new potent secondary amphipathic cell-penetrating peptide for siRNA delivery into mammalian cells. *Mol. Ther. 17*, 95–103.

(3) Lundin, P., Johansson, H., Guterstam, P., Holm, T., Hansen, M., Langel, Ü., and El-Andaloussi, S. (2008) Distinct uptake routes of cell-penetrating peptide conjugates. *Bioconjugate Chem. 19*, 2535–2542.

(4) Ivanova, G. D., Arzumanov, A., Abes, R., Yin, H., Wood, M. J., Lebleu, B., and Gait, M. J. (2008) Improved cell-penetrating peptide-PNA conjugates for splicing redirection in HeLa cells and exon skipping in mdx mouse muscle. *Nucleic Acids Res. 36*, 6418–6428.

(5) Tünnemann, G., Martin, R. M., Haupt, S., Patsch, C., Edenhofer, F., and Cardoso, M. C. (2006) Cargo-dependent mode of uptake and bioavailability of TAT-containing proteins and peptides in living cells. *FASEB J. 20*, 1775–1784.

(6) Wadia, J. S., Stan, R. V., and Dowdy, S. F. (2004) Transducible TAT-HA fusogenic peptide enhances escape of TAT-fusion proteins after lipid raft macropinocytosis. *Nat. Med. 10*, 310–315.

(7) Rinne, J., Albarran, B., Jylhava, J., Ihalainen, T. O., Kankaanpaa, P., Hytonen, V. P., Stayton, P. S., Kulomaa, M. S., and Vihinen-Ranta, M. (2007) Internalization of novel non-viral vector TAT-streptavidin into human cells. *BMC Biotechnol. 7*, 1.

(8) Trabulo, S., Mano, M., Faneca, H., Cardoso, A. L., Duarte, S., Henriques, A., Paiva, A., Gomes, P., Simoes, S., and de Lima, M. C. (2008) S4(13)-PV cell penetrating peptide and cationic liposomes act synergistically to mediate intracellular delivery of plasmid DNA. *J Gene Med. 10*, 1210–1222.

(9) Lewin, M., Carlesso, N., Tung, C. H., Tang, X. W., Cory, D., Scadden, D. T., and Weissleder, R. (2000) Tat peptide-derivatized magnetic nanoparticles allow in vivo tracking and recovery of progenitor cells. *Nat. Biotechnol. 18*, 410–414.

(10) Zhao, M., Kircher, M. F., Josephson, L., and Weissleder, R. (2002) Differential conjugation of tat peptide to superparamagnetic nanoparticles and its effect on cellular uptake. *Bioconjugate Chem. 13*, 840–844.

(11) Iwasa, A., Akita, H., Khalil, I., Kogure, K., Futaki, S., and Harashima, H. (2006) Cellular uptake and subsequent intracellular trafficking of R8-liposomes introduced at low temperature. *Biochim. Biophys. Acta 1758*, 713–720.

(12) Richard, J. P., Melikov, K., Vivés, E., Ramos, C., Verbeure, B., Gait, M. J., Chernomordik, L. V., and Lebleu, B. (2003) Cell penetrating peptides: A reevaluation of the mechanism of cellular uptake. *J. Biol. Chem. 278*, 585–590.

(13) Lundberg, M., and Johansson, M. (2001) Is VP22 nuclear homing an artifact? *Nat. Biotechnol. 19*, 713–714.

(14) Richard, J. P., Melikov, K., Brooks, H., Prevot, P., Lebleu, B., and Chernomordik, L. V. (2005) Cellular uptake of unconjugated TAT peptide involves clathrin-dependent endocytosis and heparan sulfate receptors. *J. Biol. Chem. 280*, 15300–15306.

(15) Fittipaldi, A., Ferrari, A., Zoppe, M., Arcangeli, C., Pellegrini, V., Beltram, F., and Giacca, M. (2003) Cell membrane lipid rafts mediate caveolar endocytosis of HIV-1 Tat fusion proteins. *J. Biol. Chem. 278*, 34141–34149.

(16) Ferrari, A., Pellegrini, V., Arcangeli, C., Fittipaldi, A., Giacca, M., and Beltram, F. (2003) Caveolae-mediated internalization of extracellular HIV-1 tat fusion proteins visualized in real time. *Mol. Ther. 8*, 284–294.

(17) Kaplan, I. M., Wadia, J. S., and Dowdy, S. F. (2005) Cationic TAT peptide transduction domain enters cells by macropinocytosis. *J. Controlled Release 102*, 247–253.

(18) Nakase, I., Tadokoro, A., Kawabata, N., Takeuchi, T., Katoh, H., Hiramoto, K., Negishi, M., Nomizu, M., Sugiura, Y., and Futaki, S. (2007) Interaction of arginine-rich peptides with membrane-associated proteoglycans is crucial for induction of actin organization and macropinocytosis. *Biochemistry. 46*, 492–501.

(19) Mano, M., Teodosio, C., Paiva, A., Simoes, S., and Pedroso de Lima, M. C. (2005) On the mechanisms of the internalization of S4(13)-PV cell-penetrating peptide. *Biochem. J. 390*, 603–612.

(20) Fretz, M. M., Penning, N. A., Al-Taei, S., Futaki, S., Takeuchi, T., Nakase, I., Storm, G., and Jones, A. T. (2007) Temperature-, concentration- and cholesterol-dependent translocation of L- and D-octa-arginine across the plasma and nuclear membrane of CD34+ leukaemia cells. *Biochem. J. 403*, 335–342.

(21) Duchardt, F., Fotin-Mleczek, M., Schwarz, H., Fischer, R., and Brock, R. (2007) A comprehensive model for the cellular uptake of cationic cell-penetrating peptides. *Traffic 8*, 848–866.

(22) Tyagi, M., Rusnati, M., Presta, M., and Giacca, M. (2001) Internalization of HIV-1 tat requires cell surface heparan sulfate proteoglycans. *J. Biol. Chem. 276*, 3254–3261.

(23) Poon, G. M., and Gariepy, J. (2007) Cell-surface proteoglycans as molecular portals for cationic peptide and polymer entry into cells. *Biochem. Soc. Trans. 35*, 788–793.

(24) Ziegler, A., Nervi, P., Dürrenberger, M., and Seelig, J. (2005) The cationic cell-penetrating peptide CPP(TAT) derived from the HIV-1 protein TAT is rapidly transported into living fibroblasts: optical, biophysical, and metabolic evidence. *Biochemistry. 44*, 138–148.

(25) Ziegler, A., and Seelig, J. (2008) Binding and clustering of glycosaminoglycans: a common property of mono- and multivalent cell-penetrating compounds. *Biophys. J. 94*, 2142–2149.

(26) Hariton-Gazal, E., Feder, R., Mor, A., Graessmann, A., Brack-Werner, R., Jans, D., Gilon, C., and Loyter, A. (2002) Targeting of nonkaryophilic cell-permeable peptides into the nuclei of intact cells by covalently attached nuclear localization signals. *Biochemistry. 41*, 9208–9214.

(27) Mano, M., Henriques, A., Paiva, A., Prieto, M., Gavilanes, F., Simoes, S., and Pedroso de Lima, M. C. (2006) Cellular uptake of S413-PV peptide occurs upon conformational changes induced by peptide-membrane interactions. *Biochim. Biophys. Acta 1758*, 336–346.

(28) Mano, M., Henriques, A., Paiva, A., Prieto, M., Gavilanes, F., Simoes, S., and de Lima, M. C. (2007) Interaction of S413-PV cell penetrating peptide with model membranes: relevance to peptide translocation across biological membranes. *J. Pept. Sci. 13*, 301–313.

(29) Ziegler, A., and Seelig, J. (2007) High affinity of the cell-penetrating peptide HIV-1 Tat-PTD for DNA. *Biochemistry 46*, 8138–8145.

(30) Arai, R., Geffard, M., and Calas, A. (1992) Intensification of labelings of the immunogold silver staining method by gold toning. *Brain Res. Bull. 28*, 343–345.

(31) Macia, E., Ehrlich, M., Massol, R., Boucrot, E., Brunner, C., and Kirchhausen, T. (2006) Dynasore, a cell-permeable inhibitor of dynamin. *Dev. Cell 10*, 839–850.

(32) Esko, J. D., Stewart, T. E., and Taylor, W. H. (1985) Animal cell mutants defective in glycosaminoglycan biosynthesis. *Proc. Natl. Acad. Sci. U.S.A. 82*, 3197–3201.

(33) Palm-Apergi, C., Lorents, A., Padari, K., Pooga, M., and Hällbrink, M. (2009) The membrane repair response masks membrane disturbances caused by cell-penetrating peptide uptake. *FASEB J. 23*, 214–223.

(34) Derossi, D., Calvet, S., Trembleau, A., Brunissen, A., Chassaing, G., and Prochiantz, A. (1996) Cell internalization of the third helix of the Antennapedia homeodomain is receptor-independent. *J. Biol. Chem. 271*, 18188–18193.

(35) Pujals, S., Fernandez-Carneado, J., Lopez-Iglesias, C., Kogan, M. J., and Giralt, E. (2006) Mechanistic aspects of CPP-mediated intracellular drug delivery: relevance of CPP self-assembly. *Biochim. Biophys. Acta 1758*, 264–279.

(36) Henriques, S. T., and Castanho, M. A. (2005) Environmental factors that enhance the action of the cell penetrating peptide pep-1 A spectroscopic study using lipidic vesicles. *Biochim. Biophys. Acta 1669*, 75–86.

(37) Munoz-Morris, M. A., Heitz, F., Divita, G., and Morris, M. C. (2007) The peptide carrier Pep-1 forms biologically efficient nanoparticle complexes. *Biochem. Biophys. Res. Commun. 355*, 877–882.

(38) Ren, P. H., Lauckner, J. E., Kachirskaia, I., Heuser, J. E., Melki, R., and Kopito, R. R. (2009) Cytoplasmic penetration and persistent infection of mammalian cells by polyglutamine aggregates. *Nat. Cell Biol. 11*, 219–225.

(39) Crombez, L., Morris, M. C., Deshayes, S., Heitz, F., and Divita, G. (2008) Peptide-based nanoparticle for ex vivo and in vivo drug delivery. *Curr. Pharm. Des. 14*, 3656–3665.

(40) El-Andaloussi, S., Järver, P., Johansson, H. J., and Langel, Ü. (2007) Cargo-dependent cytotoxicity and delivery efficacy of cell-penetrating peptides: a comparative study. *Biochem. J. 407*, 285–292.

(41) Wittrup, A., Zhang, S. H., ten Dam, G. B., van Kuppevelt, T. H., Bengtson, P., Johansson, M., Welch, J., Morgelin, M., and Belting, M. (2009) ScFv antibody-induced translocation of cell-surface heparan sulfate proteoglycan to endocytic vesicles: evidence for heparan sulfate epitope specificity and role of both syndecan and glypican. *J. Biol. Chem. 284*, 32959–32967.

(42) McNeil, P. L., and Steinhardt, R. A. (2003) Plasma membrane disruption: repair, prevention, adaptation. *Annu. Rev. Cell Dev. Biol. 19*, 697–731.

(43) McNeil, P. L. (2002) Repairing a torn cell surface: make way, lysosomes to the rescue. *J. Cell Sci. 115*, 873–879.

(44) Pelkmans, L., and Helenius, A. (2003) Insider information: what viruses tell us about endocytosis. *Curr. Opin. Cell Biol. 15*, 414–422.

(45) Bonazzi, M., Spano, S., Turacchio, G., Cericola, C., Valente, C., Colanzi, A., Kweon, H. S., Hsu, V. W., Polishchuck, E. V., Polishchuck, R. S., Sallese, M., Pulvirenti, T., Corda, D., and Luini, A. (2005) CtBP3/BARS drives membrane fission in dynamin-independent transport pathways. *Nat. Cell Biol. 7*, 570–580.

(46) Kirkham, M., and Parton, R. G. (2005) Clathrin-independent endocytosis: new insights into caveolae and non-caveolar lipid raft carriers. *Biochim. Biophys. Acta 1746*, 349–363.

(47) Glebov, O. O., Bright, N. A., and Nichols, B. J. (2006) Flotillin-1 defines a clathrin-independent endocytic pathway in mammalian cells. *Nat. Cell Biol. 8*, 46–54.

(48) Padari, K., Säälik, P., Hansen, M., Koppel, K., Raid, R., Langel, Ü., and Pooga, M. (2005) Cell transduction pathways of transportans. *Bioconjugate Chem. 16*, 1399–1410.

BC900577E

Rates and Equilibria for Probe Capture by an Antibody with Infinite Affinity

Tolulope A. Aweda[†], Heather E. Beck[†], Anna M. Wu[‡], Liu H. Wei[‡], Wolfgang A. Weber[§], and Claude F. Meares*[,†]

Chemistry Department, University of California, Davis, California, Department of Molecular and Medical Pharmacology, David Geffen School of Medicine, University of California, Los Angeles, California, and Department of Nuclear Medicine, University of Freiburg, Freiburg, Germany. Received January 23, 2010; Revised Manuscript Received March 11, 2010

Probe-capture systems based on proteins and synthetic ligands have become important for new analytical and imaging applications. We have used kinetic measurements of luminescence and measurements of binding by isothermal calorimetry to determine essential rate and equilibrium constants for a system that permanently captures modified DOTA chelates for positron imaging. We used that information along with previous results to quantitatively characterize the behavior of this system in vitro and in vivo. Under physiological conditions at 37 °C, the equilibrium dissociation constant for yttrium *S*-2-(4-aminobenzyl)-1,4,7,10-tetraazacyclododecanetetraacetate from antibody 2D12.5 is 2.0 (± 0.4) × 10^{-9} M and the dissociation rate constant is 7.0 (± 0.7) × 10^{-3} s^{-1}, leading to an inferred association rate constant of 3.5 × 10^{6} M^{-1} s^{-1}. Using these values to interpret data from earlier experiments leads to the rate constant 2.5 × 10^{-2} s^{-1} for covalent attachment of bound yttrium *S*-2-(4-acrylamidobenzyl)-1,4,7,10-tetraazacyclododecanetetraacetate to the G54C mutant of antibody 2D12.5. These values lead to a model for the detailed behavior of the latter system for tumor imaging in vivo that is consistent with experimental observations.

INTRODUCTION

The capture of probe molecules by receptors has an established and increasing role in the biomedical applications of bioconjugate chemistry. Biotinylated probes bind to avidin or streptavidin (*1*); hexahistidine tags bind to NTA[1]chelates (*2*); antibodies bind to haptens (*3*); and a number of engineered proteins bind to synthetic tags (*4*). These systems display a variety of properties, which dictate their applicability to specific problems. Their quantitative rates and equilibria of binding—and, if applicable, attachment—are fundamentally important but not always known. Here, we describe measurements and interpretation of a set of values for the engineered antibody binding site 2D12.5 G54C, which captures labeled acrylamidobenzyl-DOTA (AABD) metal chelates with infinite affinity. This system is highly promising for pretargeted imaging and therapy applications in vivo, and has recently been demonstrated to have potential as a reporter gene (*5*).

EXPERIMENTAL PROCEDURES

Reagents. DOTA and aminobenzyl-DOTA (ABD) were purchased from Macrocyclics (Dallas, TX). TEA and plastic backed thin layer silica (TLC) plates were purchased from EMD Chemicals. Rare earth salts were purchased from Sigma Aldrich (St Louis, MO). Fetal bovine serum and G418 selection antibiotic were also purchased from Sigma Aldrich. Biotechnical grade glycine, DEAE-cellulose, lithium dodecyl sulfate, and glycerol were purchased from Fisher Scientific (Waltham, MA). DTPA and EDTA were purchased from Acros Organics (Geel, Belgium). Microtiter plates were purchased from Greiner Bio-One (Monroe, NC). DMEM, PBS based enzyme-free cell dissociation buffer, and 4−20% Tris-glycine Novex gels were purchased from Invitrogen (Carlsbad, CA). PVDF membrane was purchased from Millipore (Billerica, MA) and SuperSignal West Dura Extended Duration substrate was purchased from Thermo Scientific (Waltham, MA). All buffers were made using 18 mΩ cm water and thoroughly degassed for all experiments. Rabbit antihuman Fc fragment antibody was purchased from Jackson Immuno Research (West Grove, PA), while the horseradish peroxidase conjugated goat antirabbit antibody was purchased from Pierce (Rockford, IL). Tris-HCl was purchased from USB (Cleveland, OH). Bromophenol Blue was purchased from Bio-Rad (Hercules, CA).

Metalation of Chelates. The concentration of stock ABD and DOTA was measured using a Co-57 metal binding assay as previously described (*6*). Briefly, 200 μM stock YCl_3 and $Co(NO_3)_2$ were prepared in metal-free 0.05 N HCl. Next, 80 mM ABD (0.048 mmol, 600 μL) was chelated with 1.5 equiv of YCl_3 or $Co(NO_3)_2$ at 37 °C for 2 h in 0.5 M triethylamine acetate, pH 6.0. Also, 80 mM DOTA (0.048 mmol, 600 μL) was chelated with 1.5 equiv $TbCl_3$ using the same conditions. The percent chelation was measured using competitive metal-binding assay with Co-57. The unreacted excess metal was scavenged with DTPA (0.2 M, 300 μL). In order to remove excess salts, the metal chelates were passed through an anionic DEAE-cellulose column, eluted in ammonium acetate (gradient: 0.1 to 1 M), and then lyophilized four times to remove ammonium acetate, being redissolved in water and re-lyophilized each day. The dry, desalted metal chelate was dissolved in 0.1

* Address correspondence to Claude Meares, Department of Chemistry, University of California, Davis, One Shields Ave, Davis, CA 95616, Phone: 530-752-0936, Fax: 530-752-8938, E-mail: cfmeares@ucdavis.edu.

† University of California, Davis.

‡ University of California, Los Angeles.

§ University of Freiburg.

[1]Abbreviations: NTA, Nitrilotriacetic acid; ABD, *S*-2-(4-Aminobenzyl)-1,4,7,10-tetraazacyclododecanetetraacetic acid; AABD, *S*-2-(4-acrylamidobenzyl)-1,4,7,10-tetraazacyclododecanetetraacetic acid; DOTA, 1,4,7,10-tetraazacyclododecane *N*,*N*′,*N*″,*N*‴-tetraacetate; DTPA, Diethylenetriaminepentaacetic acid; DMEM, Dulbecco's modified Eagle's medium; TEA, Triethylamine; DTPA, Diethylenetriaminepentaacetic acid; DAbR1, DOTA antibody reporter 1; PVDF, Polyvinylidine difluoride; TBST, Tris-buffered saline with 0.05% (v/v) Tween 20.

10.1021/bc100046p © 2010 American Chemical Society
Published on Web 04/02/2010

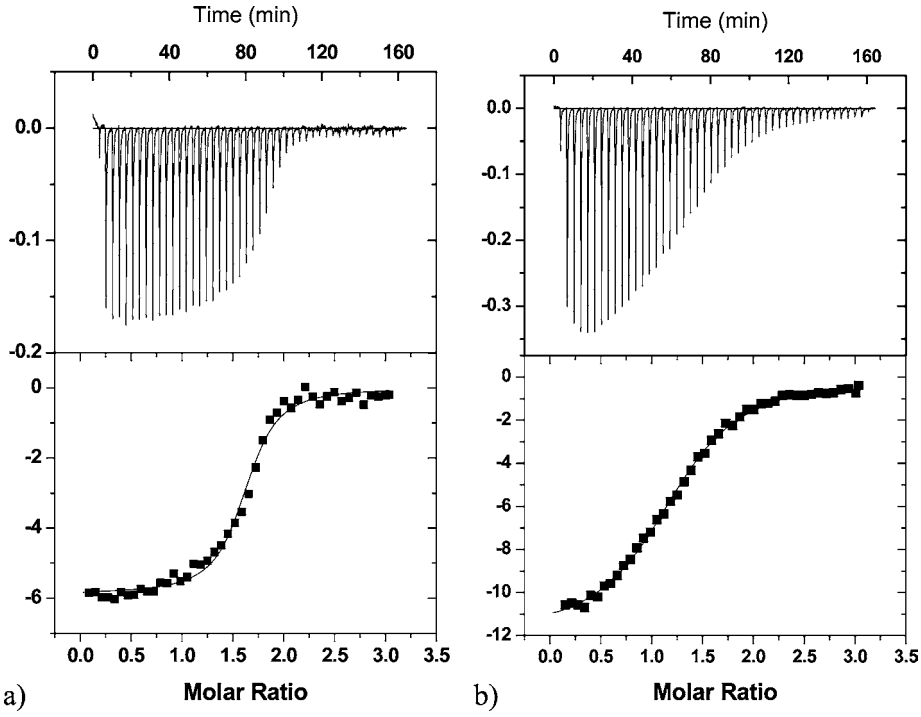


Figure 1. Calorimetric titrations of wild-type 2D12.5 monoclonal antibody (12.5 μM for ABD(Co) or 16.1 μM for competitive titration) with (a) the chelate ABD(Y) (150 μM) in the presence of ABD(Co) (100 μM) (competitive titration), (b) chelate ABD(Co) (150 μM). The upper vertical axis represents the raw differential power in μcal/s between the reference and sample cells, while the lower vertical axis represents the normalized kcal/mol of injected ABD chelate. The experiments were performed at 30 °C in 0.1 M sodium phosphate, pH 7.0.

M sodium phosphate buffer, pH 7.0. The concentration of the metal chelate was confirmed by measuring its absorbance at 286 nm using $\varepsilon_{286} = 1430\ M^{-1}\ cm^{-1}$, as determined from titrations of ABD with standard metal solutions.

Protein Preparation. Wild-type 2D12.5 monoclonal antibody (whole IgG, 50 μM) was dialyzed into the same buffer as the chelates and filtered through a 0.22 μm. The concentration was measured by A_{280} as 48.3 μM ($\varepsilon_{280} = 194\ 900$) and diluted to the appropriate concentration in the sodium phosphate buffer.

Isothermal Titration Calorimetry. This was carried out according to the manufacturer's instructions, using a VP-ITC titration calorimeter (Microcal Inc., Northampton, MA). All thermodynamic data were analyzed with MicroCal software, *Origin 7.0*, which performs nonlinear least-squares curve fitting.

Blank Experiment. ABD(Co) (150 μM) or ABD(Y) (128 μM) in the syringe was titrated in 46 injections into the sample buffer, 0.1 M sodium phosphate (pH 7.0). The small heat change produced was used for blank subtraction from the analyte-ligand experiments.

Competitive Binding Experiments. The high affinity between ABD(Y) and 2D12.5 mAb led to results from direct binding experiments that were not sufficiently accurate to yield a reliable value for the equilibrium constant. The method of Velazquez et al. (*7*) employs a competitive or displacement method using a competing weaker ligand to lower the apparent affinity of the stronger ligand. This approach involves two sets of experiments, as described below.

Direct Titration of Weak Competitor with 2D12.5 mAb. ABD(Co) (150 μM, 12 times molar concentration of the antibody) placed in the syringe was titrated in 45 injections into 12.5 μM 2D12.5 mAb (analyte in the cell, 1.45 mL). The volume for each injection was 6 μL. This experiment was carried out at 30 and 37 °C.

Competitive Binding with Excess of Stronger Competitor in the Syringe. After the first direct titration of the monoclonal antibody 2D12.5 with ABD(Co), the cell was cleaned out and a second titration involving the strong ligand was carried out. 150 μM ABD(Y) in the syringe was titrated in 46 injections against a mixture of 100 μM ABD(Co)−16.1 μM 2D12.5 (analyte in the cell, 1.45 mL). The volume for each injection was 6 μL. Experiments were carried out at 30 and 37 °C. Titrations are shown in Figure 1 and Figure 2.

Time-Resolved Fluorescence. Time-resolved fluorescence measurements were made on a Fluostar Fluorescence microplate reader (BMG Lab Technologies) using the 280 nm excitation and 550 nm emission filters, each with ±10 nm bandpass.

Off-Rate Determination Using 2D12.5 Enhanced Luminescence of Tb^{3+}. The UV excitation of the 2D12.5-DOTA(Tb) complex at 280 nm leads to energy transfer from aromatic amino acid side chains in the antibody to the bound DOTA(Tb), producing an enhanced green Tb luminescence at 545 nm (*8*). We used this phenomenon to measure the dissociation rate of ABD(Y) from the antibody. Monoclonal antibody 2D12.5 (10 μM) was incubated with 100 μM ABD(Y) overnight to ensure that equilibrium association was attained. At the beginning of the luminescence experiment, the DOTA(Tb) complex was quickly added in large excess, so that each ABD(Y) dissociating from the 2D12.5 antibody binding pocket would be replaced immediately by DOTA(Tb). In the experiment, 50 μL of 2 mM DOTA(Tb) was autoinjected into 50 μL of 10 μM 2D12.5+ABD(Y) in TBS (50 mM Tris-HCl, 150 mM NaCl), pH 7.4.This was done at 30 °C and also at 37 °C in 96-well black round-bottom microplates with 5 sets of controls: 2D12.5, 2D12.5+ ABD(Y), 2D12.5+DOTA(Tb), DOTA(Tb) only, and TBS buffer only. In all the wells, total volume was kept at 100 μL and the final concentration of 2D12.5 mAb kept at 5 μM in the appropriate wells. The time-resolved fluorescence was read at 550 ± 10 nm, 40 μs delay, with 200 scans every 15 s. Each reading was blanked with the buffer and DOTA(Tb) readings. Also, increasing concentrations of DOTA(Tb) (2 mM and 4 mM final concentrations) were evaluated in order to ensure that sufficient excess was being used. The experiments were carried

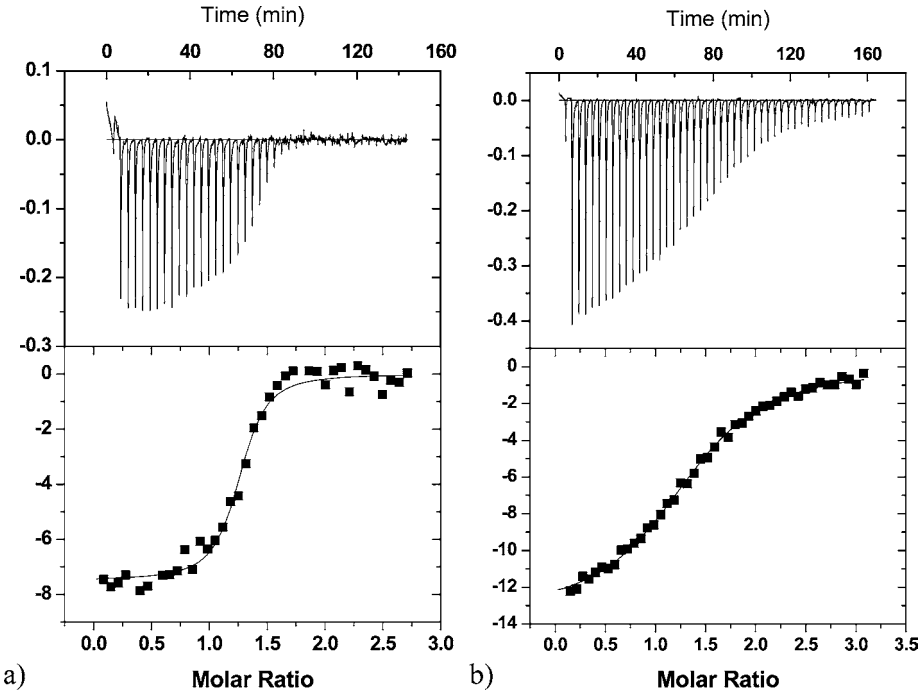


Figure 2. Calorimetric titrations of wild-type 2D12.5 monoclonal antibody (15.6 μM for ABD(Co) or 12.4 μM for competitive titration) with (a) the chelate ABD(Y) (150 μM) in the presence of ABD(Co) (100 μM) (competitive titration) and (b) the chelate ABD(Co) (150 μM). The upper vertical axis represents the raw differential power in μcal/s between the reference and sample cells, while the lower vertical axis represents the normalized kcal/mol of injected ABD chelate. The experiments were performed at 37 °C in 0.1 M sodium phosphate, pH 7.0.

out in triplicate. As a control, nonspecific mouse IgG was incubated with ABD(Y) and analyzed the same way as 2D12.5 mAb. Data are presented in Figure 3.

Western Blots to Evaluate the Number of Binding Sites on DAbR1-Transfected U-87 Glioma Cells. Glioblastoma (U87) cells stably transfected with the DAbR1 gene and the scFv-human Fc minibody standard protein were prepared as described (*5*). Cells were maintained at 37 °C in a humidified CO_2 incubator (5% CO_2) in complete Dulbecco's modified Eagle's medium containing 10% (v/v) heat inactivated fetal bovine serum and G418 selection antibiotic (250 μg/mL). Cells were dissociated for Western blots using PBS based enzyme-free cell dissociation buffer and pelleted by centrifugation (1000 × *g* for 5 min). Cell pellets were resuspended in phosphate-buffered saline and diluted 1:1 with 5× concentrated SDS PAGE sample application buffer consisting of 125 mM Tris-HCl pH 8, 25 M EDTA, 10% (w/v) lithium dodecyl sulfate, 50% (v/v) glycerol, 0.05% (w/v) bromophenol blue, and 0.5% (v/v) β-mercaptoethanol. Resuspended cells were boiled for 10 min and sonicated in an ice bath in 5 s bursts until samples were completely soluble (5 to 6 min). Reduced whole cell lysates were loaded into 4−20% Tris-glycine Novex gel and electrophoresed at 150 V for 1.5 h. Protein was transferred to a polyvinylidene difluoride membrane and blocked overnight at 4 °C in Tris-buffered saline, pH 7.4, with 5% nonfat milk. The membranes were probed for 2 h with rabbit antihuman Fc antibody (1:5000) in TBST. The membranes were washed 6× with 50 mL of TBST and probed for 2 h with a horseradish peroxidase conjugated goat antirabbit antibody (1:5000). Blots were washed 6× with 50 mL of TBST and were treated with SuperSignal West Dura Extended Duration substrate according to manufacturer instructions and imaged with a Typhoon Trio variable mode imaging system (GE Healthcare Life Sciences) using the chemiluminescent setting. The band density of triplicate whole cell lysate samples were measured and compared with a human IgG Fc standard curve using Bio-Rad Quantity One software. Results are shown in Figure 4.

Mathematical Modeling of Kinetic Behavior. The systems of differential eqs 1−4 and 5−9 (see below) were solved numerically, and Figures 5−8 were prepared, using Mathematica 7 software.

RESULTS AND DISCUSSION

In what follows, we build up a simple mathematical description of the behavior of this probe-capture system that is consistent with all the data available. This begins with calorimetric measurements of the equilibrium thermodynamics of reversible binding of aminobenzyl-DOTA(Y) to mouse 2D12.5 IgG. We turned to calorimetry after surface plasmon resonance experiments failed to give reliable results; this appeared to result primarily from the small size of the DOTA chelate, which led to a lack of sensitivity to binding. Alternative surface plasmon resonance strategies were not successful in our hands. On the other hand, calorimetry generally is suitable for small molecules as well as macromolecules.

Thermodynamic Parameters Obtained from ITC. Using isothermal titration calorimetry, we measured the binding affinity

Table 1. Thermodynamic Parameters for the Reversible Association of Aminobenzyl-DOTA Chelates to Antibody 2D12.5 at 30 and 37 °C[a]

chelate	T, °C	K_A, M^{-1}	ΔG, kcal/mol	ΔH, kcal/mol	ΔS, cal/(mol K)	K_D, M
ABD(Co)	30	$8.2(\pm0.9) \times 10^5$	−8.2(±0.1)	−12.2(±0.4)	−13.2(±1.3)	$1.2(\pm0.1) \times 10^{-6}$
ABD(Co)	37	$7.1(\pm0.4) \times 10^5$	−8.3(±0.1)	−12.4(±4.8)	−13.3(±4.8)	$1.4(\pm0.1) \times 10^{-6}$
ABD(Y)	30	$3.3(\pm2.1) \times 10^8$	−11.7(±0.4)	−18.2(±0.5)	−21.5(±2.9)	$3.1(\pm2.0) \times 10^{-9}$
ABD(Y)	37	$5.2(\pm0.9) \times 10^8$	−12.4(±0.2)	−20.1(±1.2)	−24.9(±4.1)	$2.0(\pm0.4) \times 10^{-9}$

[a] Data from ITC experiments in Figure 1 and Figure 2. (Standard deviations in parentheses.)

Table 2. Kinetic Parameters for the Dissociation of ABD(Y) Ligand from Antibody 2D12.5[a]

	37 °C			30 °C		
experiment	k_{off}, s^{-1}	half-life, s	calc k_{on}, M^{-1} s^{-1}	k_{off}, s^{-1}	half-life, s	calc k_{on}, M^{-1} s^{-1}
Avg(SD)	$7.0(\pm0.7) \times 10^{-3}$	97 ± 9	3.5×10^6	$4.0(\pm0.3) \times 10^{-3}$	161 ± 13	1.3×10^6

[a] Data from luminescence experiments in Figure 3.

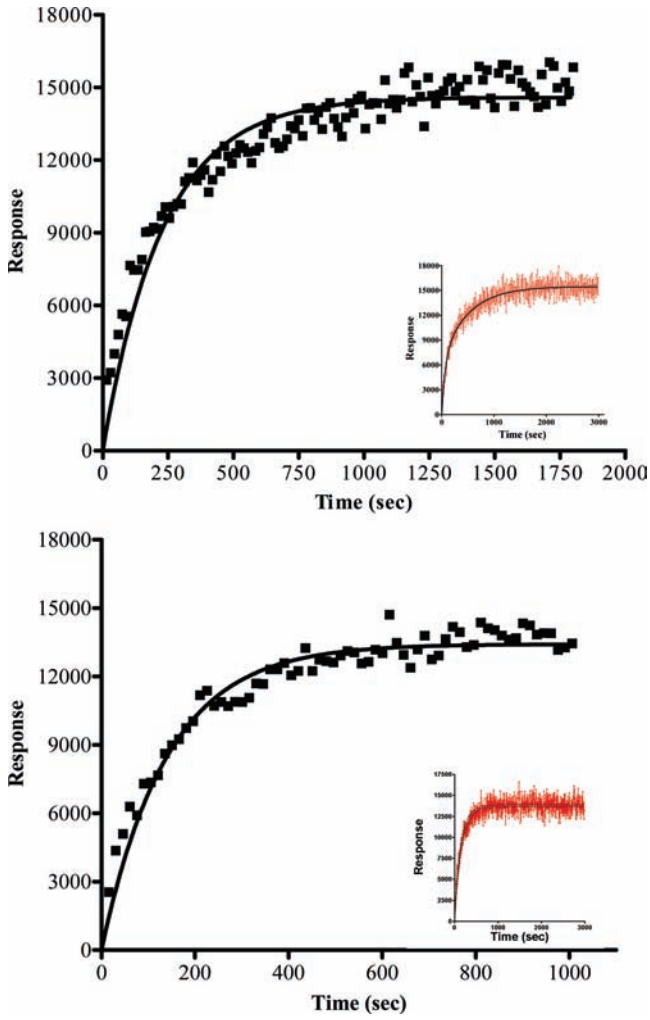
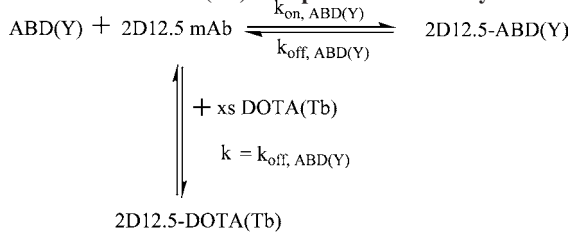


Figure 3. Curve fits from the determination of the dissociation rate constant between ABD(Y) and parental 2D12.5 antibody. Upper panel, 30 °C; lower panel 37 °C (note: time scales are different). 1, 2, and 4 mM DOTA(Tb) was used to competitively replace the ABD(Y) when it dissociated from the 2D12.5 binding site. Triplicate experiments were done at each DOTA(Tb) concentration, and all the data were combined for the fits and plots. Insets show longer total time courses, which indicate that equilibrium has been reached.

Scheme 1. Competition Experiment to Measure k_{off} by Forming the Luminescent DOTA(Tb) Complex with Antibody 2D12.5[a]



[a] First, the antibody was saturated with ABD(Y), then it was mixed with a large excess of DOTA(Tb).

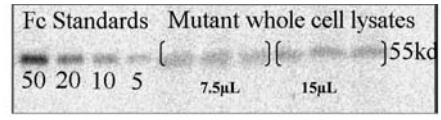
and other thermodynamic parameters involved in the reversible interaction of ABD(Y) and parental 2D12.5 monoclonal antibody. From previous reports (*9*), we expected that the K_D should be on the order of 10^{-8} M, indicating that the binding interaction is strong. In the direct titration of ABD(Y) with 2D12.5, the binding curve was difficult to fit because of high binding affinity. However, as shown by Velazquez et al. (*7*), the apparent affinity of a strong ligand can be lowered by the presence of a weaker ligand so that a more accurate binding affinity can be measured for the strong ligand. Sigurskjold (*10*) provides a complete mathematical analysis of the displacement or competitive isothermal titration calorimetric technique. These experiments were carried out at 30 °C (Figure 1) and 37 °C (Figure 2); results are summarized in Table 1.

Having the equilibrium constant in hand, we measured the dissociation rate constant k_{off} at 30 and 37 °C; we did this indirectly, by measuring the luminescence of DOTA(Tb) as it bound to the antibody when ABD(Y) dissociated, as described below.

Statistical Analysis of Fluorescence Time-Resolved Data. As shown in Scheme 1, the rate of association of the excess DOTA(Tb) with 2D12.5 was taken to equal the rate of dissociation of ABD(Y) from 2D12.5 mAb. The terbium luminescence response at 545 nm for DOTA(Tb) bound to 2D12.5 mAb (*8*) was monitored as a function of time. To ensure that excess DOTA(Tb) was present, three different concentrations were used. Similar results were obtained in all cases, and all three sets of triplicate results were fitted to one curve. The k_{off} was obtained from a fit of the following equation that describes the pseudo-first-order association kinetics: $Y = Y_{max}(1 - e^{-kt})$, where Y is the terbium luminescence intensity and the pseudo-first-order rate constant for binding DOTA(Tb) is $k = k_{off}$ s^{-1} (with t in seconds).

The dissociation rate constant of ABD(Y) with 2D12.5 antibody was determined from the plot of the fluorescence signal growth of 2D12.5-DOTA(Tb) complex with time (Figure 3). Attempts to fit the data to more than one rate constant gave inferior results. Having measured k_{off} and K_D, we can calculate $k_{on} = (k_{off}/K_D)$ M^{-1} s^{-1} (Table 2).

With these results, we are now able to model the behavior of this infinite affinity system, explaining previous observations in vitro and in vivo. Corneillie et al. (*11*) studied the rate of formation of the covalent bond between the acryloyl group of



Whole cell lysate	Band Density ODu/mm^2	Average band density ODu/mm^2	Average Band mass in ng	Average # Fc/cell ±SD
7.5µL samples	4924; 4944; 4367	4745 (±328)	3.4 (± 1.3)	$5.5(\pm2.2)\times10^4$
15µL samples	5435; 5708; 5737	5626 (±167)	6.9 (±0.7)	$5.7(\pm0.6)\times10^4$

Figure 4. Western blot of reduced whole cell lysate vs human Fc standard. Calculations were performed for 4.4×10^4cell/μL and a formula weight of 110 kDa for the protein, using the equation $y = 0.004x - 15.63$ obtained by fitting the standards. There are 2 binding sites per 110 kDa protein, implying $\sim10^5$ binding sites per cell.

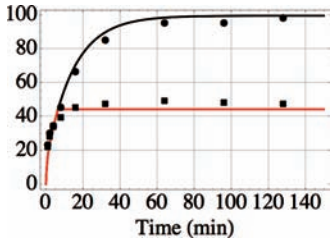


Figure 5. Formation of the covalent bond between AABD(Y) and the G54C mutant of DOTA-binding Fab 2D12.5 in vitro at 37 °C, pH 7.5, as a function of time; nonlinear least-squares fit of data from ref *11* using eqs 1−4. The top data (●) are for bond formation in the absence of competitor, while the bottom data (■) are the result of adding excess unlabeled competitor after 6 min. The values $k_{on} = 3.5 \times 10^6$ M^{-1} s^{-1} and $k_{off} = 7.0 \times 10^{-3}$ M^{-3} s^{-1} determined in this work lead to the nonlinear least-squares value $k_{irr} = 2.5 \times 10^{-2}$ s^{-1} for formation of the covalent bond, and probability $x = 0.2$ of binding in a reactive conformation, all of which were used to construct the black curve. The red curve was drawn using the same values, with the added constraint of no association or reassociation after 6 min.

AABD(Y) and the cysteine of the G54C mutant of antibody 2D12.5. As shown in Figure 5, we were able to fit Corneillie's results with the following set of kinetic equations:

$$\frac{d[AABD(Y)]}{dt} = \frac{d[G54C]}{dt} = k_{on}[AABD(Y)][G54C] + k_{off}[C_R] + k_{off}[C_{NR}] \quad (1)$$

$$\frac{d[C_R]}{dt} = xk_{on}[AABD(Y)][G54C] - k_{off}[C_R] - k_{irr}[C_R] \quad (2)$$

$$\frac{d[C_{NR}]}{dt} = (1 - x)k_{on}[AABD(Y)][G54C] - k_{off}[C_{NR}] \quad (3)$$

$$\frac{d[P]}{dt} = k_{irr}[C_R] \quad (4)$$

In order to fit the complex kinetic behavior observed in ref *11*, it is necessary to assume that AABD(Y) can form either a reactive complex C_R (which can form the product P) or a nonreactive complex C_{NR} with the G54C antibody binding site. This is consistent with the observation of two modes of binding in crystal structures of the parental antibody complex (*12*). The fit in Figure 5 gives the value $k_{irr} = 1.5$ min $^{-1} = 2.5 \times 10^{-2}$ s^{-1} derived using the nonlinear least-squares method. The partitioning of complex formation between the nonreactive C_{NR}, with probability $1 - x = 0.8$, and the reactive C_R, with probability $x = 0.2$, is also necessary to fit these data.

It is expected that the different binding modes should have different values for k_{on} and k_{off}. However, the values of k_{on} and k_{off} are not sufficiently different to be measured separately by the methods available to us. The crystal structures show two binding modes in which the antibody−DOTA interactions are almost identical but the DOTA side chain is oriented differently (*12*). On the basis of the proximity of the DOTA side chain to residue 54 in one structure but not the other, these could plausibly correspond to the reactive and unreactive binding observed kinetically in ref *11*. The goodness of fit in Figure 5 justifies the use of this minimal set of rate constants to model the processes of tumor uptake discussed below.

We have found that the 2D12.5 G54C Fab expressed in *D. melanogaster* S2 cells (*11*) is largely cysteinylated (has a cysteine monomer attached to Cys-54 by a disulfide bond), which protects the Cys-54 side chain from reaction with electrophiles such as AABD(Y) (*13*). The experiments in ref *11* were carried out using an excess of radiolabeled AABD(Y) to detect the rate of covalent bond formation by Michael addition; thus, the results were sensitive only to protein with a free thiol at G54C, and the value of k_{irr} is not affected by the presence of cysteinylated protein.

Reviewing the values of these new rate constants shows that the second-order association reaction controlled by $k_{on} = 3.5 \times 10^6$ M^{-1} s^{-1} is rather rapid compared to the more typical values of $k_{on} \approx 10^5$ M^{-1} s^{-1} observed for antibody−protein association (*14*). However, it is not as fast as the biotin−streptavidin association, for which the rate constant is reported to be $k_{on} = 7.5 \times 10^7$ M^{-1} s^{-1} at 25 °C (*15*). This comparison is important because the streptavidin−biotin system has been widely used for pretargeted delivery of small probes for imaging and therapy of cancer (*16*). However, streptavidin is immunogenic in human patients (*17*), so the irreversible antibody capture system may provide a desirable alternative: currently, making antibodies minimally immunogenic is less challenging than doing the same for streptavidin (*5*).

The rate constant for reversible dissociation of nonelectrophilic ABD(Y) from parental antibody 2D12.5, $k_{off} = (7.0 \pm 0.7) \times 10^{-3}$ s^{-1}, is quite fast compared to that for dissociation of biotin from streptavidin, which is reported to be $k_{off} = (4.1 \pm 0.3) \times 10^{-5}$ s^{-1} at 37 °C under comparable conditions (*18*). This rapid dissociation, combined with the effects of irreversible binding and the branching between reactive and nonreactive complexes, makes the behavior of the reactive AABD(Y) with the G54C binding site quite unusual. The results above imply that in a homogeneous solution approximately $x \cdot (k_{irr})/(k_{irr} + k_{off}) = 0.2 \cdot (25)/(25 + 7) \cong 16\%$ of the AABD(Y) molecules will form permanent bonds with the receptor site the first time they bind, without ever dissociating, while the majority (~80%) will dissociate, diffuse, and rebind. Because the results in vivo will depend on additional factors such as effective target site concentration on cell surfaces and transport behavior of the probe in a tumor, it was important to observe this system in an animal model to see if it would exhibit biological properties useful for imaging and perhaps therapy.

Wei et al. (*5*) prepared an engineered version of the 2D12.5 G54C antibody with infinite affinity, termed DAbR1, in which the binding site was expressed as part of an scFv-Fc fusion protein on the surface of U-87 human glioma cells implanted in the flanks of SCID mice. The behavior of AABD(^{86}Y) after injection into the tail vein was monitored by microPET imaging, with highly successful results; some experimental data from ref *5* are used in Figure 6. Having determined values for k_{on}, k_{off}, k_{irr}, and x under physiological conditions in vitro, we sought to use these numbers to fit the data for in vivo tumor uptake in order to understand how this system behaves relative to reversible ligand−receptor pairs.

It is convenient to describe the basic unit of a glioma tumor as a "cord", a cylindrical array of cancer cells surrounding a blood capillary (*19*), from which the tumor tissue receives nutrients and also small molecules such as the PET probe AABD(^{86}Y). Characterizing the behavior of cells around one capillary can lead to a useful description of the main features of the tumor (*20*). Our goal here is to consider the major consequences of irreversible binding of the probe to its receptor, in order to gain insight into the essentials of this chemistry in a living organism.

The immediate requirement is the formulation and solution of a set of partial differential equations to describe not only the chemistry already considered in vitro but also the diffusion of the AABD(Y) probe in vivo to its receptors on the tumor cell surface. Assuming cylindrical symmetry and considering a small segment of a long cylinder reduces the geometry to one

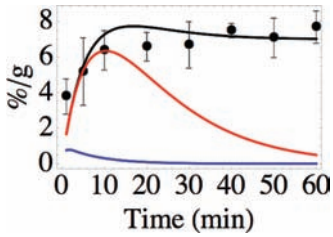


Figure 6. Experimental tumor uptake data (● ± SD) from ref *5*, showing the results of injection of AABD(^{86}Y) into the tail veins of SCID mice bearing xenograft U-87 human glioma tumors expressing the DAbR1 reporter gene, plotted as average % dose per gram tissue vs time. The black curve shows how these data are fit by the solutions to the concentrations of all labeled species in eqs 5−9. The red curve shows the behavior predicted if irreversible binding did not occur ($k_{irr}\rightarrow 0$), and the blue curve shows the behavior predicted if there were no binding of the probe at all ($k_{on}\rightarrow 0$), which is consistent with experimental observations of mice bearing xenograft U-87 human glioma tumors that do not carry the DAbR1 gene.

dimension: the radial distance r from the center of the capillary (*20*). The appropriate reaction-diffusion equations are given below as eqs 5−9; only the probe diffuses, but the concentration of each species depends on both r and t:

$$\frac{\partial[\mathrm{AABD(Y)}]}{\partial t} = D\left\{\frac{\partial^2[\mathrm{AABD(Y)}]}{\partial r^2} + r^{-1}\cdot\frac{\partial[\mathrm{AABD(Y)}]}{\partial r}\right\} - k_{on}[\mathrm{AABD(Y)}][\mathrm{DAbR1}] + k_{off}[C_R] + k_{off}[C_{NR}] \quad (5)$$

$$\frac{\partial[\mathrm{DAbR1}]}{\partial t} = -k_{on}[\mathrm{AABD(Y)}][\mathrm{DAbR1}] + k_{off}[C_R] + k_{off}[C_{NR}] \quad (6)$$

$$\frac{\partial[C_{NR}]}{\partial t} = (1 - x)k_{on}[\mathrm{AABD(Y)}][\mathrm{DAbR1}] - k_{off}[C_{NR}] \quad (7)$$

$$\frac{\partial[C_R]}{\partial t} = xk_{on}[\mathrm{AABD(Y)}][\mathrm{DAbR1}] - k_{off}[C_{NR}] - k_{irr}[C_R] \quad (8)$$

$$\frac{\partial[P]}{\partial t} = k_{irr}[C_R] \quad (9)$$

We sought realistic solutions to these equations by fitting the in vivo tumor uptake data from ref *5*, using nonlinear least-squares with the concentration of AABD(Y) at the periphery of the capillary as the only adjustable parameter, along with literature values for the typical radius of a capillary (10 μ) and a tumor cord (∼100 μ) (*20, 21*), the diffusion coefficient of a metal chelate in brain tissue (3.4×10^{-6}cm^2/s) (*22*), and the observed ∼5 min circulatory half-life of the AABD(Y) probe (*5*). The calculated behavior is compared to experimental data in Figure 6; it is important to emphasize that the values for k_{on}, k_{off}, k_{irr}, and x were those determined from in vitro experiments described above, with no adjustments. An important underlying assumption throughout is that, consistent with the crystal structures of parental Fab-DOTA complexes (*12*), the complex tolerates molecular changes at positions peripheral to the sites of van der Waals contact between protein and DOTA. Thus, the most important interactions between receptor and ligand persist through genetic substitution of Cys for Gly at position 54, reformatting of the mouse IgG to chimeric G54C Fab or to G54C scFv, and chemical changes at the *para* position of the DOTA side chain.

Figure 6 also illustrates the predicted effects of eliminating irreversible binding of the AABD(Y) probe in the tumor while

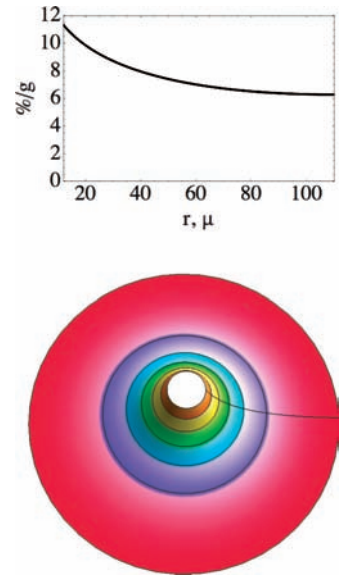


Figure 7. Top: predicted concentration of the probe 60 min after injection, as a function of distance from just outside the boundary of the capillary (12 μ) to the outer periphery of the tumor cord (110 μ from the center of the coordinate system). Bottom: contour plot of probe concentration in a transaxial slice of the tumor from 12 μ (∼12%/g) to 110 μ (∼6%/g); color of contour changes at approximately 1%/g intervals. The capillary (radius 10 μ) is within the empty space in the center, and the concentration profile along the radial line is given by the graph above.

maintaining reversible binding (setting $k_{irr}\rightarrow 0$) or eliminating probe binding altogether (setting $k_{on}\rightarrow 0$). The fit to the in vivo experimental data in Figure 6 was made with the assumption that all the G54C binding sites expressed on cell surfaces have the side chain of Cys-54 free to react with the acryloyl group of AABD(Y), which would not be true for the highly cysteinylated antibody expressed in S2 cells (*13*). Changing the calculation to assume a significant degree of blocked Cys-54 leads to curves that resemble the red curve ($k_{irr}\rightarrow 0$) in Figure 6, diverging markedly from experimental observation. Thus, the binding sites expressed on the surface of U-87 cells in vivo exhibit little or no blockage of the Cys-54 side chain. Because there is no established way to change the oxidation state of the expressed G54C side chain on cell surfaces in vivo, this information is crucial to the design of future experiments. It also illustrates the diversity of post-translational modification in eukaryotic cells.

One of the central issues of molecular targeting is the transport of probe molecules, whether large or small, from the blood into the target tissue (*21*). A number of interesting experiments have been carried out to demonstrate the effects of various parameters on this process (e.g., *refs* 23, 24). The results in ref *5* demonstrate rapid, durable uptake in a xenograft tumor but lack the spatial resolution to provide information about whether the irreversible binding occurs at the edge of the capillary or throughout the tumor. The model developed here predicts that probe molecules present in the tumor 1 h after administration will all be irreversibly bound to the engineered receptor, with a spatial distribution plotted in Figure 7. While the average concentration of probe in the tumor at 1 h was observed to be approximately 7%/g, the predicted concentration near the capillary is almost 12%/g, declining to slightly more than 6%/g near the periphery of the tumor cord.

It is informative to use the solutions of eqs 5−9 to gain a sense of how the concentrations of the different probe-containing species vary with time and position in the tissue. The curves in Figure 8 imply that the free probe AABD(Y) is quickly incorporated into complexes C_{NR} and C_R, with the latter rapidly

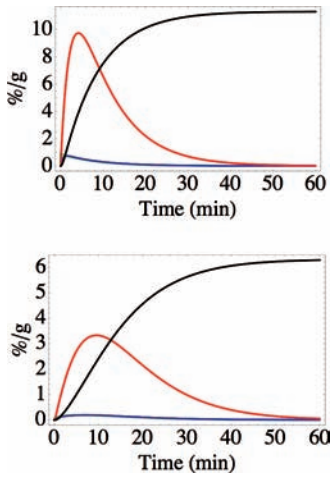


Figure 8. Predicted speciation of the probe in the tumor at two positions, as a function of time. Top: near the capillary surface (12 μ from the center of the coordinate system, for which the capillary radius is 10 μ). Bottom: near the outer periphery of the tumor cord (distance 110 μ from the center of the coordinate system, 100 μ from the edge of the capillary). The curves represent product P (black), nonreactive complex C_{NR} (red), and, practically superimposed, the reactive complex C_R (blue) and free probe AABD(Y) (green). The product P dominates the concentrations of the other species after about 20 min.

converted to P. Because of the short lifetime of either complex, the product P becomes the dominant species within a short period. Rapid clearance of the probe from the circulation leads to disappearance of the other species from the tumor before 60 min has elapsed. The behavior illustrated in Figure 8 for positions near the capillary and near the outer periphery of the tumor cord is predicted to be qualitatively similar at intermediate distances from the capillary, with no remarkable differences except that the final concentration of P varies with r according to Figure 7, and the concentrations of all the species are predicted to change more slowly farther from the capillary.

The interplay between molecular transport and ligand−receptor binding provides an almost inexhaustible range of possibilities for molecular imaging probes. This is true when irreversible binding may take place, as in the case of antibodies with infinite affinity (*3, 25*). In the most extreme manifestation, an irreversible probe molecule would encounter its receptor and become permanently attached immediately after entering tumor tissue; in that case, the curve in Figure 7 would be a narrow peak at the left side, falling to zero with increasing distance. In the case examined here, the probe has both reactive and nonreactive modes of binding to the receptor, and the latter is more probable; nonreactive binding and dissociation can serve to further spread the probe through the tissue before it becomes permanently fixed on a receptor.

If we compare this to purely reversible binding, we see the possibility that it can offer a useful middle ground encompassing the most desirable aspects of opposing extremes. Very strong (though reversible) binding such as provided by the streptavidin−biotin pair would be expected to yield a zone of stably bound probe molecules near the capillary, as long as streptavidin is in excess over biotinylated probe molecules. This nonuniform distribution of probes in tissue, referred to as the binding-site barrier, could be ameliorated if the concentration of avidin molecules were too low to efficiently capture the probes or if the concentration of probe molecules was large enough to saturate the streptavidin sites, allowing other probe molecules to diffuse past. On the other hand, weaker reversible binding naturally allows small probe molecules to penetrate into tissue by virtue of repeated dissociation, diffusion, and association. This might eventually lead to uniform distribution in tissue, but since the binding is not durable, the concentration of the probe falls to zero in an inconveniently short time. The contour plot in Figure 7 implies a combination of durable binding and broad distribution that would be difficult to produce by other means.

ACKNOWLEDGMENT

We thank Dr. Andrew Fisher for sharing his isothermal calorimeter and instructions for its use, Dr. Mark McCoy and Dr. Michael Toney for insightful discussion and help on the kinetics experiments, and Dr. Tove Olafsen for the human IgG standard. Supported by Research Grants CA016861 and CA136639 to C.F.M. from the National Cancer Institute, National Institutes of Health.

Supporting Information Available: Key Mathematica instructions for solving eqs 1−9. This material is available free of charge via the Internet at http://pubs.acs.org.

LITERATURE CITED

(1) Liu, G., and Hnatowich, D. J. (2008) A semiempirical model of tumor pretargeting. *Bioconjugate Chem. 19*, 2095–2104.
(2) Huang, Z., Hwang, P., Watson, D. S., Cao, L., and Szoka, F. C., Jr. (2009) Tris-nitrilotriacetic acids of subnanomolar affinity toward hexahistidine tagged molecules. *Bioconjugate Chem. 20*, 1667–1672.
(3) Chmura, A. J., Orton, M. S., and Meares, C. F. (2001) Antibodies with infinite affinity. *Proc. Natl. Acad. Sci. U.S.A. 98*, 8480–8484.
(4) Chidley, C., Mosiewicz, K., and Johnsson, K. (2008) A designed protein for the specific and covalent heteroconjugation of biomolecules. *Bioconjugate Chem. 19*, 1753–1756.
(5) Wei, L. H., Olafsen, T., Radu, C., Hildebrandt, I. J., McCoy, M. R., Phelps, M. E., Meares, C. F., Wu, A. M., Czernin, J., and Weber, W. A. (2008) Engineered antibody fragments with infinite affinity as reporter genes for PET imaging. *J. Nucl. Med. 49*, 1828–1835.
(6) Meares, C. F., McCall, M. J., Reardan, D. T., Goodwin, D. A., Diamanti, C. I., and McTigue, M. (1984) Conjugation of antibodies with bifunctional chelating agents: isothiocyanate and bromoacetamide reagents, methods of analysis, and subsequent addition of metal ions. *Anal. Biochem. 142*, 68–78.
(7) Velazquez-Campoy, A., and Freire, E. (2006) Isothermal titration calorimetry to determine association constants for high-affinity ligands. *Nat. Protoc. 1*, 186–191.
(8) Corneillie, T. M., Whetstone, P. A., Fisher, A. J., and Meares, C. F. (2003) A rare earth-DOTA-binding antibody: probe properties and binding affinity across the lanthanide series. *J. Am. Chem. Soc. 125*, 3436–3437.
(9) Goodwin, D. A., Meares, C. F., Watanabe, N., McTigue, M., Chaovapong, W., Ransone, C. M., Renn, O., Greiner, D. P., Kukis, D. L., and Kronenberger, S. I. (1994) Pharmacokinetics of pretargeted monoclonal antibody 2D12.5 and Y-88-Janus-2-(p-nitrobenzyl)-1,4,7,10-tetraazacyclododecanetetraacetic acid (DOTA) in balb/c mice with KHJJ mouse adenocarcinoma - a model for Y-90 radioimmunotherapy. *Cancer Res. 54*, 5937–5946.
(10) Sigurskjold, B. W. (2000) Exact analysis of competition ligand binding by displacement isothermal titration calorimetry. *Anal. Biochem. 277*, 260–266.
(11) Corneillie, T. M., Lee, K. C., Whetstone, P. A., Wong, J. P., and Meares, C. F. (2004) Irreversible engineering of the multielement-binding antibody 2D12.5 and its complementary ligands. *Bioconjugate Chem. 15*, 1392–1402.
(12) Corneillie, T. M., Fisher, A. J., and Meares, C. F. (2003) Crystal structures of two complexes of the rare-earth-DOTA-binding antibody 2D12.5: ligand generality from a chiral system. *J. Am. Chem. Soc. 125*, 15039–15048.
(13) Miao, Z., McCoy, M. R., Singh, D. D., Barrios, B., Hsu, O. L., Cheal, S. M., and Meares, C. F. (2008) Cysteinylated protein as reactive disulfide: an alternative route to affinity labeling. *Bioconjugate Chem. 19*, 15–19.

(14) Ramakrishnan, M., Kandimalla, K. K., Wengenack, T. M., Howell, K. G., and Poduslo, J. F. (2009) Surface plasmon resonance binding kinetics of Alzheimer's disease amyloid â peptide-capturing and plaque-binding monoclonal antibodies. *Biochemistry 48*, 10405–10415.

(15) Hyre, D. E., Le Trong, I., Merritt, E. A., Eccleston, J. F., Green, N. M., Stenkamp, R. E., and Stayton, P. S. (2006) Cooperative hydrogen bond interactions in the streptavidin-biotin system. *Protein Sci. 15*, 459–67.

(16) Pagel, J. M., Orgun, N., Hamlin, D. K., Wilbur, D. S., Gooley, T. A., Gopal, A. K., Park, S. I., Green, D. J., Lin, Y., and Press, O. W. (2009) A comparative analysis of conventional and pretargeted radioimmunotherapy of B-cell lymphomas by targeting CD20, CD22, and HLA-DR singly and in combinations. *Blood 113*, 4903–4913.

(17) Pagel, J. M., Hedin, N., Subbiah, K., Meyer, D., Mallet, R., Axworthy, D., Theodore, L. J., Wilbur, D. S., Matthews, D. C., and Press, O. W. (2003) Comparison of anti-CD20 and anti-CD45 antibodies for conventional and pretargeted radioimmunotherapy of B-cell lymphomas. *Blood 101*, 2340–2348.

(18) Klumb, L. A., Chu, V., and Stayton, P. S. (1998) Energetic roles of hydrogen bonds at the ureido oxygen binding pocket in the streptavidin-biotin complex. *Biochemistry 37*, 7657–7663.

(19) Thalhauser, C. J., Sankar, T., Preul, M. C., and Kuang, Y. (2009) Explicit separation of growth and motility in a new tumor cord model. *Bull. Math. Biol. 71*, 585–601.

(20) Eikenberry, S. (2009) A tumor cord model for Doxorubicin delivery and dose optimization in solid tumors. *Theor. Biol. Med. Model. 6*, 16.

(21) Fujimori, K., Covell, D. G., Fletcher, J. E., and Weinstein, J. N. (1989) Modeling analysis of the global and microscopic distribution of immunoglobulin G, F(ab')2, and Fab in tumors. *Cancer Res. 49*, 5656–5663.

(22) Syková, E., and Nicholson, C. (2008) Diffusion in brain extracellular space. *Physiol. Rev. 88*, 1277–1340.

(23) Adams, G. P., Schier, R., McCall, A. M., Simmons, H. H., Horak, E. M., Alpaugh, R. K., Marks, J. D., and Weiner, L. M. (2001) High affinity restricts the localization and tumor penetration of single-chain Fv antibody molecules. *Cancer Res. 61*, 4750–4755.

(24) Dennis, M. S., Jin, H., Dugger, D., Yang, R., McFarland, L., Ogasawara, A., Williams, S., Mary J., Cole, Ross, S., and Schwall, R. (2007) Imaging tumors with an albumin-binding Fab, a novel tumor-targeting agent. *Cancer Res. 67*, 254–261.

(25) Butlin, N. G., and Meares, C. F. (2006) Antibodies with infinite affinity: origins and applications. *Acc. Chem. Res. 39*, 780–787.

BC100046P

Microencapsulation of Islets with Living Cells Using PolyDNA-PEG-Lipid Conjugate

Yuji Teramura, Luan Nguyen Minh, Takuo Kawamoto, and Hiroo Iwata*

Radioisotope Research Center, Kyoto University, Yoshida-Konoe-Cho, Sakyo-ku, Kyoto, 606-8501, Japan, and Department of Reparative Materials, Institute for Frontier Medical Sciences, Kyoto University, 53 Kawara-Cho, Shogoin, Sakyo-ku, Kyoto, 606-8507, Japan. Received November 10, 2009; Revised Manuscript Received February 25, 2010

Microencapsulation of islets with a semipermeable membrane, i.e., bioartificial pancreas, is a promising way to transplant islets without the need for immunosuppressive therapy for insulin-dependent diabetes mellitus (type I diabetes). However, materials composing a bioartificial pancreas are not ideal and might activate defense reactions against foreign materials. In this study, we propose an original method for microencapsulation of islets with living cells using an amphiphilic poly(ethylene glyocol)-conjugated phospholipid derivative (PEG-lipid) and DNA hybridization. PolyA and polyT were introduced onto the surfaces of the islets and HEK 293 cells, respectively, using amphiphilic PEG-lipid derivatives. PolyA20 modified HEK cells were immobilized onto the islet surface where polyT20-PEG-lipid was incorporated. The cells spread and proliferated on the islet surface, and the islet surface was completely encapsulated with a cell layer after culture. The encapsulated islets retained the ability to control insulin release in response to glucose concentration changes.

INTRODUCTION

The bioartificial pancreas, which encapsulates islets of Langerhans (islets) within a semipermeable membrane, is one of the therapeutic devices for patients with insulin-dependent diabetes mellitus (type I diabetes). It is a safe and simple way to transplant islets without the need for immunosuppressive therapy. The semipermeable membrane protects the islets from the immune system of a recipient patient, and thus, the islets are expected to survive and release insulin for a long period of time and thereby control glucose metabolism. Various types of bioartificial pancreas have been proposed and developed (*1*−*3*), with the microencapsulated type being a promising model. In this example, islets are microencapsulated within an alginate/poly(L-lysine) polyion complex membrane (*4*) or an agarose hydrogel (*5*−*8*). Our group has used the agarose system and has demonstrated its efficacy in diabetic animals (*5*−*8*). Recently, we also have developed an original design for a bioartificial pancreas for transplantation into the liver through the portal vein (*9*−*15*). However, materials composing a bioartificial pancreas have not been ideal and might activate defense reactions against foreign materials. Compatibility of the membrane with the recipient patient should be improved.

We proposed to enclose islets from a donor under a layer of cells from a recipient to increase compatibility with the patient. Since the outermost surface is the recipient's own cells, the host immune defense system will not be provoked. In our previous study, we developed a method to enclose islets with living cells (*15*). Amphiphilic poly(ethylene glycol)-conjugated phospholipid derivatives (PEG-lipid) and biotin/streptavidin reactions were employed (*15*). Although the biotin/streptavidin reaction worked well to cover the islets with living cells, streptavidin is a xenogeneic protein and is expected to activate the host immune system. We sought to improve this technique with the use of biocompatible materials.

In this study, we employed DNA hybridization instead of the biotin/streptavidin reaction. Polyadenine (polyA) and polythymine (polyT) were introduced onto the surfaces of the islets and HEK 293 cells, respectively, by using polyA or polyT-conjugated PEG-lipid. We already succeeded in the cell−cell attachment induced by hybridization of DNA-conjugated PEG-lipid (*18*). The hybridization of DNA-conjugated PEG-lipid was effectively used for the cell−cell attachment and cell-immobilization to the substrate. The HEK 293 cells were thereby immobilized on the surface of the islets through hybridization of polyA and polyT. A layer of living HEK cells was formed on the surface of islets.

EXPERIMENTAL PROCEDURES

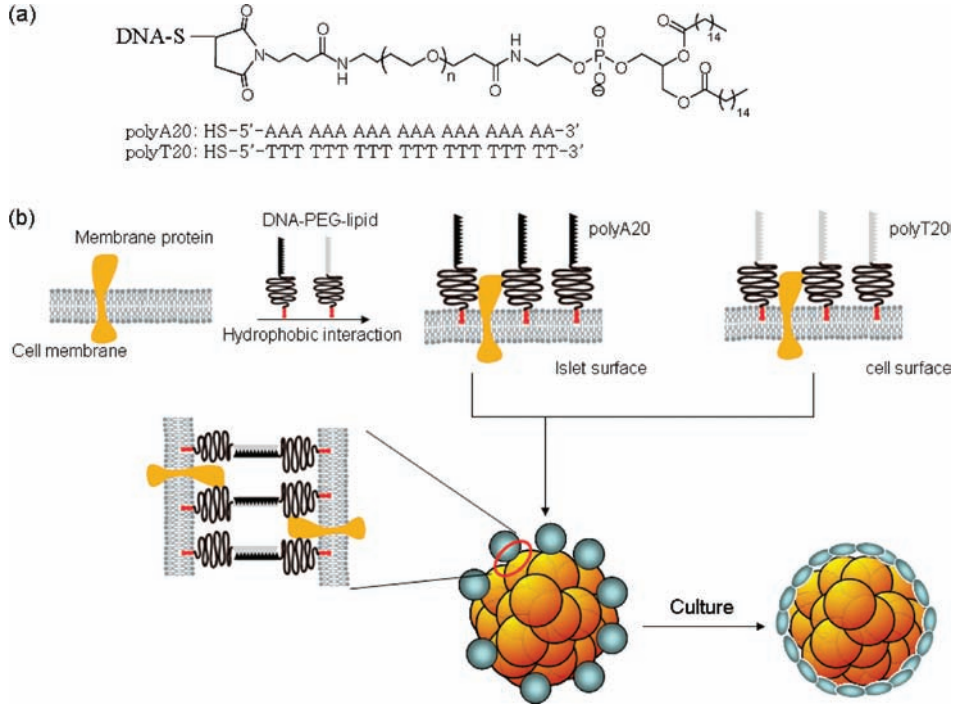
Materials. α-*N*-Hydroxysuccinimidyl-*ω*-maleimidyl poly(ethylene glycol) (NHS-PEG-Mal, M_w: 5000) was purchased from Nektar Therapeutics (San Carlos, USA). 1, 2-Dipalmitoyl-*sn*-glycerol-3-phosphatidylethanolamine (DPPE) was purchased from NOF Corporation (Tokyo, Japan). Dichloromethane, triethylamine, sucrose, and diethyl ether were purchased from Nacalai Tesuque (Kyoto, Japan). Hoechst 33342 nuclear stain was purchased from Dojindo Laboratories (Kumamoto, Japan). Alexa 488-labeled goat antiguinea pig IgG, minimum essential medium (MEM), HEPES buffer solution, Hanks' balanced salt solution(HBSS), Medium 199, RPMI-1640 medium, penicillin, and streptomycin were purchased from Invitrogen Co. (Carlsbad, CA, USA). Fetal bovine serum (FBS) was obtained from Equitech-Bio, Inc. (TX, USA), and phosphate-buffered saline (PBS) from Nissui Pharmaceutical Co. Ltd. (Tokyo, Japan). Enzyme-linked immunosorbent assay (ELISA) kits for the insulin assay were purchased from Shibayagi Co., Ltd. (Gunma, Japan). Tissue-Tek was purchased from Sakura Fine Technical Co. Ltd. (Tokyo, Japan). Goat normal serum and polyclonal guinea pig anti-insulin serum were purchased from Dako (Glostrup, Denmark). The 10% formalin solution, dithiothreitol (DTT), and Triton X-100 were purchased from Wako Pure Chemical (Osaka, Japan). NAP-5 column was purchased from GE health care (GE Healthcare UK Ltd., Buckinghamshire, UK).

Synthesis of polyDNA-PEG-Phospholipid Conjugate (polyDNA-PEG-lipid). Mal-PEG-lipid was synthesized by first dissolving NHS-PEG-Mal (180 mg), triethylamine (50 μL) and

* Address correspondence and reprint requests to Hiroo Iwata, Ph.D. E-mail: iwata@frontier.kyoto-u.ac.jp, phone/fax: +81-75-751-4119.

10.1021/bc900494x © 2010 American Chemical Society
Published on Web 03/08/2010

Scheme 1[a]



[a] (a) Chemical structure of DNA-conjugated PEG-DPPE (polyDNA-PEG-lipid) and the DNA sequence of polyA20 and polyT20. (b) Schematic illustration of interaction between polyDNA-PEG-lipid and a lipid bilayer of the cell membrane, and immobilization of living cells to the islet surface. DNA (polyA20 or polyT20)-PEG-lipid has hydrophobic acyl chains which anchor into the cell membrane. After mixing polyT-PEG-lipid-modified GFP-HEK cells and polyA-PEG-lipid-modified islets, they were suspended in medium and cultured at 37 °C and 5% CO_2. During culture, GFP-HEK cells spread and grew on the islet surface.

DPPE (20 mg) in dichloromethane and stirring for 36 h at room temperature as shown in Scheme S1 (Supporting Information) (rt) (*12*). After precipitation with diethyl ether, Mal-PEG-lipid was obtained as a white powder (190 mg, yield 80%). ^{1}H NMR ($CDCl_3$, 400 MHz, δ ppm): 0.88 (t, 6H, $-CH_3$), 1.25 (br, 56H, $-CH_2-$) 3.64 (br, 480H, PEG), 6.71 (s, 2H, $-HC{=}CH-$, maleimide).

The structure of polyDNA-PEG-lipid was shown in Scheme 1a. PolyA20 and polyT20 which carry $(CH_2)_6$-SS-$(CH_2)_6$-OH at 5′ end were purchased from Sigma-Aldrich Chemical Co (see Scheme S1 in Supporting Information). PolyDNA-SH was prepared by reduction of the disulfide bond with DTT in accordance with the instructions of the manufacturer. Briefly, polyDNA-disulfide conjugate (in 10 mM Tris-HCl, 1 mM EDTA, pH 8.0) was mixed with DTT (0.04 M) for 16 h at rt for removal of protection group for thiol. After purification with NAP-5 column, polyDNA-SH was obtained.

The SH groups at the 5′-ends of polyDNAs were used to form conjugates with the Mal-PEG-lipid. A PBS solution of polyDNA-SH (1.0 mg) was mixed with Mal-PEG-lipid (5.0 mg) and the reaction mixture was left for 24 h at rt to form conjugations. polyDNA-PEG-lipid (500 μg/mL in PBS) was used for surface modification of cells and islets without any further purification.

Encapsulation of Islets with GFP-HEK Cells. HEK293, which stably expressed enhanced green fluorescence protein (EGFP) (GFP-HEK), was kindly supplied by Dr. K. Kato (Institute for Frontier Medical Sciences, Kyoto University). The GFP-HEK cells were routinely maintained in MEM supplemented with 10% FBS, 100 U/mL penicillin, and 0.1 mg/mL streptomycin. GFP-HEK cells were collected by centrifugation (180 × *g*, 5 min, rt) after treatment with trypsin. The cells were washed with HBSS to remove the medium. A cell pellet (2×10^6 cells) was obtained by centrifugation. After the addition of polyT20-PEG-lipid solution (50 μL, 500 μg/mL) to the cell suspension, the suspension was incubated for 1 h with gentle agitation at rt. The cells were then suspended in 10 mL HBSS and collected by centrifugation (180 × *g*, 5 min, 25 °C, twice) to obtain polyT20-PEG-lipid-modified cells.

Islets were isolated from the pancreas of female Syrian hamsters (7−8 weeks old, Japan SLC, Inc., Shizuoka, Japan) using the collagenase digestion method. The islets were cultured for 7 d after isolation to remove cells damaged by the isolation procedure. The islets were maintained in culture medium (Medium 199 with 10% FBS, 8.8 mM HEPES buffer, 100 units/mL penicillin, 100 μg/mL streptomycin, and 8.8 U/mL heparin). A solution of polyA20-PEG-lipid solution (500 μg/mL, 100 μL of PBS) was added to suspension of the islets in serum-free medium (200 islets), and the mixture was incubated at rt for 1 h. After washing three times with serum-free medium, polyA20-PEG-lipid-modified islets were obtained. Finally, polyT20-PEG-lipid-modified GFP-HEK cells (2×10^6) and polyA20-PEG-lipid-modified islets (200 islets) were mixed in serum-free medium (300 μL), and the mixture was incubated for 60 min with gentle agitation at rt. The GFP-HEK cell-immobilized islets were picked up by hand using a Pasteur pipet (inside diameter: 1 mm) under a stereomicroscope and cultured on a nontreated dish at 37 °C under 5% CO_2 in Medium 199 supplemented with 10% FBS. Islets were observed by a confocal laser scanning microscope (FLUOVIEW, FV500, Olympus Optical Co. Ltd., Tokyo, Japan) and a phase-contrast microscope (IX71, Olympus). The FITC and GFP were excited by an argon laser (488 nm) and the fluorescence was detected though a bandpass filter (510−550 nm).

Histochemical Analysis. GFP-HEK cells-immobilized islets were washed with PBS and then transferred to 10% formalin solution and incubated for 1 d at rt. The formalin solution was removed, and the islets were sequentially kept in 3% and 10% sucrose in PBS for 1 d, followed by incubation in 20% sucrose in PBS for an additional 1 d at rt. The islets were embedded in

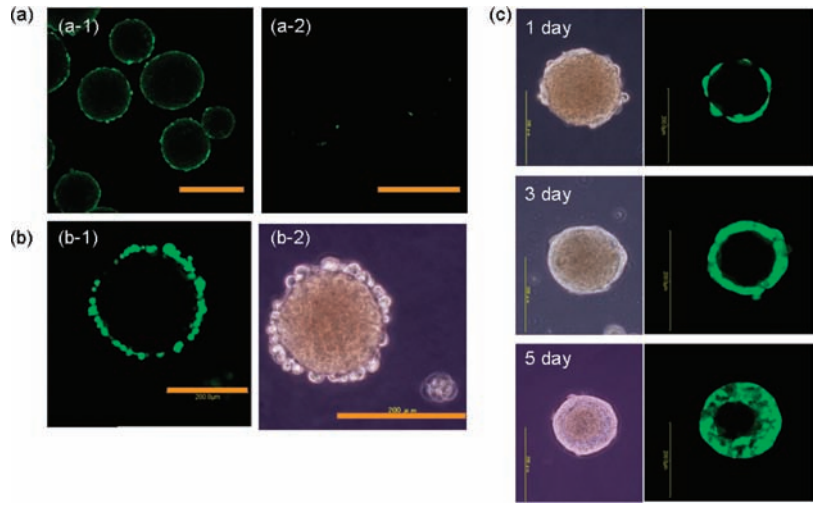


Figure 1. Encapsulation of islets with living cells. (a) Hamster islets modified with polyA20-PEG-lipid were treated with (a-1, FITC) FITC-labeled polyT20. (a-2) Naked islets were treated with FITC-labeled polyT20. These islets were observed by a confocal laser scanning microscope. (b) Attachment of polyT20-PEG-lipid modified GFP-HEK cells onto the surface of polyA20-PEG-lipid modified hamster islets. An islet was observed by a confocal laser scanning microscope for (b-1, GFP) and a phase contrast microscope (b-2). (c) GFP-HEK cells-immobilized islets were cultured in Medium 199 supplemented 10% FBS at 37 °C under 5% CO_2 for 1, 3, and 5 days. Islets were observed by a phase contrast microscope (left panels) and a confocal laser scanning microscope (right panels, GFP). Scale bars: 200 μm.

Tissue-Tek for freezing. The frozen specimens were sliced (6 μm thick) using a cryostat (CM 3050S IV, Leica, Solms, Germany). The sliced sections were permeabilized by treatment with 0.2% Triton X-100 in PBS at rt for 15 min. The samples were first treated with a 10% normal goat serum in PBS for 1 h to block the nonspecific binding of antibodies. The samples were then treated with 1% guinea pig anti-insulin serum in PBS containing 3% goat normal serum for 3.5 h at rt, and then washed with PBS. The samples were incubated with fluorescently labeled secondary antibody, 0.2% Alexa 488 Goat antiguinea pig IgG in PBS containing 3% goat normal serum, at rt for 1.5 h. Cell nuclei were counterstained with Hoechst 33342. The localization of secondary antibodies and the Hoechst dye was analyzed by a fluorescence upright microscope (BX51, Olympus). The sliced sections were also stained with hematoxylin-eosin (HE) using a conventional staining method.

Insulin Secretion from GFP-HEK Cell-Encapsulated Islets on Glucose Stimulation. Static insulin secretion tests were performed on GFP-HEK cell-immobilized islets (50 islets) after culturing for 3 days to evaluate their insulin-secreting ability in response to changes in glucose concentration. As a control experiment, this assay was performed on islets without enclosure with HEK cells (naïve islets). GFP-HEK cell-immobilized islets and naïve islets were exposed to solutions of glucose in Krebs-Ringer's buffer (KRB) at concentrations of 0.1 g/dL, then 0.3 g/dL, and finally 0.1 g/dL glucose for intervals of 1 h in each solution at 37 °C. The supernatants were collected after each 1 h incubation, and the insulin concentrations in the KRB solutions were determined by ELISA.

Statistical Analysis. Comparisons between two groups were made using Student's *t*-tests. $p < 0.05$ was considered statistically significant. All statistical calculations were performed using the software *KaleidaGraph 4.0J*.

RESULTS

Islet Encapsulation with Living GFP-HEK Cells. Islets were treated with polyA20-PEG-lipid, followed by treatment with FITC-labeled polyT20 (Figure 1a). Fluorescence from FITC-labeled polyT20 was clearly seen at the periphery of each islet (Figure 1a-1). No fluorescence was observed in naked islets treated with FITC-labeled polyT20 (Figure 1a-2). Thus, polyA20 can be immobilized onto the surface of islets using polyA20-PEG-lipid without damaging islet morphology, and polyA20 on the cell surface can hybridized with polyT20.

GFP-HEK cells were immobilized onto the surface of islets by DNA hybridization between polyA20 on the islets and polyT20 on the GFP-HEK cells. Figure 1b shows a microscopic image of a GFP-HEK cell-islet complex just after preparation. The HEK cells on the islet surface appeared as white cells under a phase contrast microsope (Figure 1b-2) and were more clearly identified as green cells of GFP-HEK under a confocal laser scanning microscope (Figure 1,b-1). Single HEK cells were recognized on the islets, indicating that the GFP-HEK cells had become immobilized on the islet surface by DNA hybridization. The inhibition study was also performed. When polyA20-islets and polyT20-GFP-HEK were previously incubated with polyT20 and polyA20, respectively, no specific immobilization of GFP-HEK cells on islets was observed (see Figure S1 of Supporting Information).

The modified islets were cultured in medium in a culture dish and observed at 1, 3, and 5 days after the complex was formed (Figure 1c). Although GFP-HEK cells were attached and spread on the surface after 1 day of culture, the islet surface was not completely covered with cells. The HEK cells spread and gradually proliferated on the islet surface, and by 3 days in culture, the islet surface was fully covered with a layer of HEK cells (Figure 1c). As seen Figure 1c and Figure 2, HEK cells proliferated continuously and form a thicker multicell layer due to lack of contact inhibition as the culture period proceeded.

Histochemical Analysis. The GFP-HEK cell-encapsulated islets were histochemically analyzed by HE and insulin staining (Figure 2). In HE staining, a layer of GFP-HEK cells was observed around the islet surface after culturing for 3 and 5 days (left panel in Figure 2). The nuclei of GFP-HEK cells were slightly larger than that of islets. The multilayers of GFP-HEK cells were formed on the islet surface after culturing for 3 and 5 days. Necrosis of islet cells was not observed even at the center of the complex at 5 days. Figure 2 also shows images of insulin-stained GFP-HEK cell-encapsulated islets (right panel). Islets stained green with anti-insulin antibody were found in a core cell aggregate. These results indicate that GFP-HEK cell-encapsulation did not impair the morphology of islets.

Insulin Secretion by Glucose Stimulation. We examined the abilities of the islets modified with or without HEK cell-

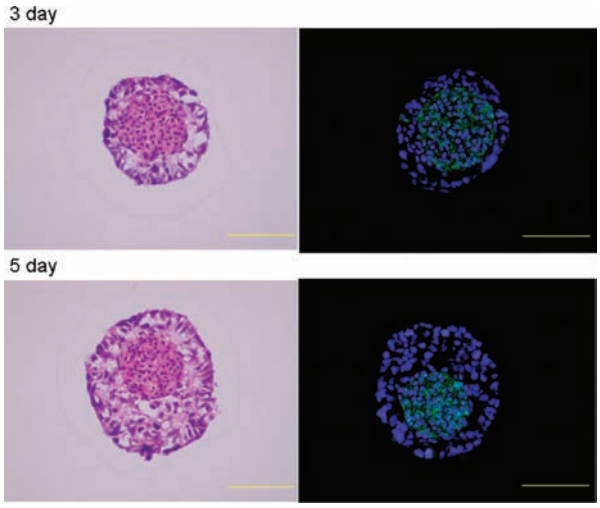


Figure 2. Histochemical analyses of GFP-HEK cell-immobilized islets cultured for 3 and 5 days. Frozen sections of GFP-HEK cell-immobilized islets were stained with (left panels) hematoxylin-eosin (HE) or (right panels) Alexa 488-labeled anti-insulin antibody and Hoechst 33342 dye for nuclear staining. Right panels show merged microscopic images of insulin (green fluorescence) and Hoechst 33342 staining (blue fluorescence). Scale bars: 100 μm.

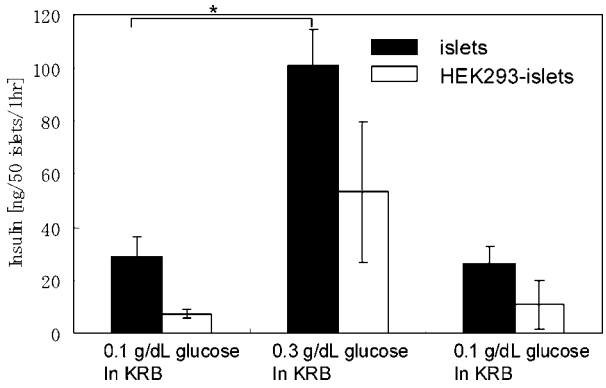


Figure 3. Glucose stimulation test of islets encapsulated HEK cells after 3 days culture. As a control experiment, the assay was performed on naive islets. The amounts of insulin secreted from the islets in response to glucose concentration changes (0.1, 0.3, 0.1 g/dL) were determined by ELISA. Results are expressed as mean ± SD for $n = 3$. KRB: Krebs-Ringer buffer. An asterisk represents a significant difference ($p < 0.05$) between two groups.

encapsulation to release insulin. At the basal glucose concentration, 0.1 g/dL, insulin release by the encapsulated islets was less than that by naïve islets. We also performed a glucose stimulation test to examine the ability of the modified islets to regulate insulin release in response to changes in the glucose level. When the glucose concentration in the medium was increased from 0.1 g/dL to 0.3 g/dL, islets of both groups increased insulin release above basal levels (Figure 3). Insulin release returned to basal levels when the islets were re-exposed to 0.1 g/dL glucose. Glucose stimulation indexes (insulin release at 0.3 g/dL glucose/insulin release at 0.1 g/dL glucose) calculated from these results were 7.3 ± 5.3 and 3.6 ± 1.0 for the encapsulated islets and naïve islets, respectively. Although there was no significant difference between two groups for glucose stimulation index, the amount of insulin secretion of the encapsulated islets tended to be lower than that of native islets at 0.1 g/dL and 0.3 g/dL glucose in KRB. These results indicate that the HEK cell layer did not influence the islets' ability to regulate insulin release in response to glucose concentration, although the cause of decreased insulin release by encapsulated islets was not clear. It might be attributed to the oxygen consumption by the HEK293 cells since low oxygen tension can decrease islet cell function. The decrease of basal insulin release in encapsulated islets is a topic that requires further study.

DISCUSSION

There were some fundamental studies on improvement of biocompatibility by using cells such as chondrocyte (*16, 17*). Pollok et al. first reported the macroencapsulation of rat islets with porcine chondrocyte membrane (*16*). Porcine chondrocytes were cultured to form a confluent monolayer for use as a matrix upon which to deposit islets. After the islets were attached to poly(glycolic acid) polymer fibers, the islet−polymer composite was wrapped with chondrocyte membrane by hand. Lee et al. also demonstrated enclosure of islets with chondrocyte membranes using the cell sheet engineering technique (*17*). However, the increase of total volume after enclosure and aggregate formation of islets inside the membrane led to necrosis of islet cells at the center. Lee et al. also demonstrated enclosure of islets with chondrocyte membranes using the cell sheet engineering technique (*17*). The issue of islet necrosis still remains to be resolved. They expected that chondrocyte membrane would work as an immuno-isolation membrane of bioartificial pancreas, although unfortunately, they have not yet reported results of animal experiments.

To overcome this problem, we studied methods to enclose islets singly with living cells. Herein, we have used amphiphilic polyDNA-PEG-lipid to immobilize GFP-HEK cells on the surface of islets through hybridization between polyA20 and polyT20. The surface of the islets was completely covered with a cell layer after 3 to 5 days in culture without central necrosis of the islet cells (Figure 2). Insulin secretion upon glucose stimulation was well maintained in the cell-encapsulated islets complex, although total insulin secretion was reduced as compared to normal islets (Figure 3). HEK cells which formed a multicell layer on islets consume oxygen and thus islet cells were exposed to low concentration of oxygen. We thought that the reduction of insulin secretion was due to the insufficient oxygen supply to β-cells of islets. The same phenomena were observed in islets encapsulated with HEK cells using the biotin/streptavidin reaction. However, we might evade this issue by encapsulation with endothelial cells because they are expected to form a single cell layer.

We have reported immobilization of cells onto the islet surface by using biotin/streptavidin reaction (*15*). Although the specific biotin/streptavidin reaction worked well to cover the islets with living cells, streptavidin is expected to activate the host immune system because it is a xenogeneic protein isolated from bacteria. Therefore, we improved the technique compatible to future clinical application. There was no difference in islet encapsulation efficiency between these two techniques.

Many shortcomings remain to be overcome prior to clinical application. The cells employed are HEK293 cells, which proliferate rapidly and form a multicellular layer. Most primary cells, that is, cells isolated from normal animals, proliferate much more slowly than HEK cells and cannot form a multicellular layer. Thus, we should select types of primary cells which can effectively form a cell layer on islets. The short- and long-term effects of the covered cells on islet functions should be carefully examined. We also should follow the fate of cells after transplantation. In addition, the efficiency and biocompatibility of cell-based microencapsulation should be examined carefully by using animal experiments early. Although these issues should be addressed, the technology developed in this study will be

useful in preparation of future bioartificial pancreas and studies on cell−cell interaction.

CONCLUSIONS

Islets can be individually encapsulated with living cells through hybridization between polyA and polyT which can be introduced onto the surfaces of islets and cells, respectively, using amphiphilic PEG-lipid derivatives. No central necrosis was observed after encapsulation. The encapsulated islets still retained the ability to control insulin release in response to changes in glucose concentration.

ACKNOWLEDGMENT

This study was supported in part by a Grant-in-Aid for Scientific Research (A) (No. 21240051) and a Challenging Exploratory Research grant (No. 21650118) from the Ministry of Education, Culture, Sports, Science, and Technology (MEXT) of Japan and by the Ministry of Health, Labor, and Welfare of Japan (H20-007).

Supporting Information Available: Chemical scheme for preparation of polyDNA-SH and polyDNA-PEG-DPPE is shown in Scheme S1. The result of inhibition experiment for immobilization of polyT20-GFP-HEK onto polyA20-islets is shown in Figure S1. This material is available free of charge via the Internet at http://pubs.acs.org.

LITERATURE CITED

(1) Lanza, R. P., Sullivan, S. J., and Chick, W. L. (1992) Treatment of severely diabetic pancreatectomized dogs using a diffusion-based hybrid pancreas. *Diabetes 41*, 886–889.

(2) Altman, J. J., Houlbert, D., Callard, P., McMillan, P., Solomon, B. A., Rosen, J, and Galletti, P. M. (1986) Long-term plasma glucose normalization in experimental diabetic rats with macroencapsulated implants of benign human insulinomas. *Diabetes 35*, 625–633.

(3) Lacy, P. E., Hegre, O. D., Gerasimidi-Vazeou, A., Gentile, F. T., and Dionne, K. E. (1991) Maintenance of normoglycemia in diabetic mice by subcutaneous xenografts of encapsulated islets. *Science 254*, 1782–1784.

(4) Lin, F., and Sun, A. M. (1980) Microencapsulated islets as bioartificial endocrine pancreas. *Science 210*, 908–910.

(5) Iwata, H., Takagi, T., Shimizu, H., Yamashita, K., Kobayashi, K., and Akutsu, T. (1992) Agarose for bioartificial pancreas. *J. Biomed. Mater. Res. 26*, 967–977.

(6) Iwata, H., Kobayashi, K., Takagi, T., Oka, T., Yang, H., Amemiya, H., Tsuji, T., and Ito, F. (1994) Feasibility of agarose microbeads with xenogeneic islets as a bioartificial pancreas. *J. Biomed. Mater. Res. 28*, 1003–1011.

(7) Kobayashi, T., Aomatsu, Y., and Iwata, H. (2003) Indefinite islet protection from autoimmune destruction in nonobese diabetic mice by agarose microencasulation without immunosupression. *Transplantation 75*, 619–625.

(8) Agudelo, C. A., Teramura, Y., and Iwata, H. (2009) Cryopreserved agarose-encapsulated islets as bioartificial pancreas: a feasibility study. *Transplantation 87*, 29–34.

(9) Teramura, Y., and Iwata, H. (2008) Islets surface modification prevents blood-mediated inflammatory responses. *Bioconjugate Chem 19*, 1389–1395.

(10) Totani, T., Teramura, Y., and Iwata, H. (2008) Immobilization of urokinase to islet surface by amphiphilic poly (vinyl alcohol) carrying alkyl side chains. *Biomaterials 29*, 2878–2883.

(11) Miura, S., Teramura, Y., and Iwata, H. (2006) Encapsulation of islets with ultra-thin polyion complex membrane through poly(ethylene glycol)-phospholipids anchored to cell membrane. *Biomaterials 27*, 5828–5835.

(12) Teramura, Y., Kaneda, Y., and Iwata, H. (2007) Islet-encapsulation in ultra-thin layer-by-layer membranes of poly-(vinyl alcohol) anchored to poly(ethylene glycol)-lipids in the cell membrane. *Biomaterials 28*, 4818–4825.

(13) Teramura, Y., Kaneda, Y., Totani, T., and Iwata, H. (2008) Behavior of synthetic polymers immobilized on cell membrane. *Biomaterials 29*, 1345–1355.

(14) Teramura, Y., and Iwata, H. (2009) Surface modification of islets with PEG-lipid for improvement of graft survival in intraportal transplantation. *Transplantation 88*, 624–630.

(15) Teramura, Y., and Iwata, H. (2009) Islet encapsulation with living cells for improvement of biocompatibility. *Biomaterials 30*, 2270–2275.

(16) Pollok, J. M., Lorenzen, M., Kölln, P. A., Török, E., Kaufmann, P. M., Kluth, D., Bohuslavizki, K. H., Gundlach, M., and Rogiers, X. (2001) In vitro function of islets of Langerhans encapsulated with a membrane of porcine chondrocytes for immunoisolation. *Dig. Surg. 18*, 204–210.

(17) Lee, J. I., Nishimura, R., Sakai, H., Sasaki, N., and Kenmochi, T. (2008) A newly developed immunoisolated bioartificial pancreas with cell sheet engineering. *Cell Transplant 17*, 51–59.

(18) Teramura, Y., Chen, H., Kawamoto, T., and Iwata, H. (2010) Control of cell attachment through polyDNA hybridization. *Biomaterials 31*, 2229–2235.

BC900494X

Tumor-Selective Delivery of Macromolecular Drugs via the EPR Effect: Background and Future Prospects

Hiroshi Maeda*

Laboratory of Microbiology and Oncology, Faculty of Pharmaceutical Sciences, and Division of Applied Chemistry, Graduate School of Engineering, Sojo University, Kumamoto, 860-0082 Japan. Received February 5, 2010; Revised Manuscript Received March 29, 2010

This paper briefly documents the history of the discovery of the EPR (enhanced permeability and retention) effect and elucidates an analogy between bacterial infection involving proteases that trigger kinin generation and cancer. The EPR effect of macromolecules in cancer tissues is defined, and the distinction between the EPR effect (with reference to clearance of macromolecules from the interstitial space of tumor tissues) and the simple passive targeting of drugs to tumors is described. Additional points of discussion include the uniqueness of tumor vessels, the influence of kinin and other vascular mediators such as nitric oxide (NO) and prostaglandins, and the heterogeneity of the EPR effect. Two different strategies to augment the EPR effect that were discovered are elevating blood pressure artificially via slow infusion of angiotensin II and applying nitroglycerin or other NO donors. Use of the nitroagent increased not only the blood flow of the tumor, but also the delivery of drug to the tumor and the drug's therapeutic effect. This finding shows an intriguing analogy to hypoxic cardiac infarct tissue, in that both are improved by NO. These two methods were applied to treatment of rodents and human cancers, in combination with other anticancer agents, with successful results achieved in rodents as well as humans. These data suggest very appealing prospects for utilization of the EPR effect in future development of cancer therapeutics.

NATURE OF THE EPR EFFECT AND FACTORS AFFECTING THE EPR EFFECT

In 1964, I had started to work on a proteinaceous anticancer agent called neocarzinostatin (NCS[1]; MW = 12 kDa) (*1*). My initial research on NCS was extended to the development of an NCS conjugate with a polymer (styrene-maleic acid, or SMA), which I named SMANCS (MW of about 16 kDa) (*2*, *3*). SMANCS could bind to plasma albumin (67 kDa), so that it would become a larger molecule, about 83 kDa (*3*, *4*). This development of the albumin-bound SMANCS formed the basis for my continuing work on what would be now called the EPR (enhanced permeability and retention) effect (see later).

Another focus of my research was the molecular mechanism of bacterial infection involving bacterial proteases, because of their pathogenic potential. During this work, we demonstrated that bacterial proteases could activate the bradykinin-generating cascade called the kallikrein-kinin cascade (*5–10*), which facilitated vascular leakage.

Human blood plasma contains no effective inhibitors of bacterial proteases. As a result, a number of precursor proteases (proenzymes) could be activated by limited proteolysis such as that occurring in the coagulation system (which forms fibrin gel or blood clots) (*7–9*). We found that bacterial proteases in blood plasma could generate the endogenous nonapeptide bradykinin (a member of the kinin family); the bradykinin was liberated from its precursor kininogen in the plasma via limited proteolysis. This kinin causes very potent pain and induces vascular permeability (or edema) in vivo at the site of its generation (*5–10*) (Figure 1A). This vascular permeability, or extravasation of this dye out of the vessels and into interstitial tissue space, can be quantified by determining the amount of dye extracted from the tissue. The Evans blue is so tightly bound to albumin that the extravasation can be regarded as macromolecular extravasation from the vasculature. We also found that similar extravasation occurred in most experimental solid tumors via bradykinin generation (*10–15*) (Figure 1B). Both normal inflammatory and tumor tissues exhibit similar enhanced vascular permeability (Figure 1). The difference between these tissues is related to the clearance rates of the Evans blue−albumin complex from each tissue, which are quite dissimilar. Clearance of Evans blue−albumin complex from normal tissue is much faster (usually within 1 wk) than clearance from tumor tissue, which is much slower and takes more than 3−4 wk (*11–20*). I named the enhanced permeability and retention (EPR) effect of macromolecules in tumor tissues (*11*).

The EPR effect was more marked when the lipid contrast agent Lipiodol (with SMANCS dissolved in it) was injected via the tumor-feeding artery (*16–20*). In the clinical setting, this EPR effect has been observed with gamma ray-emitting gallium in radioscintigraphy, in which gallium-67 bound to the plasma protein transferrin (MW = 90 kDa) demonstrated the EPR effect, as shown in radioscintigraphic images of tumors.

During the past 25 years, considerable evidence supporting the EPR effect has been accumulated. The EPR effect has been

* Corresponding author. Tel.: +81 96-326-4114; Fax: +81 96-326-3185. E-mail address: hirmaeda@ph.sojo-u.ac.jp.

[1]Abbreviations: NCS, neocarzinostatin; SMA, styrene-maleic acid copolymer; EPR, enhanced permeability and retention; NO, nitric oxide; CT, computed tomography; AT-II, angiotensin II.

[2]Biocompatible in this case means being inert with reference to the immune system, that is, free from removal by macrophages or the reticuloendothelial system. Polycations are readily captured by the negatively charged laminar surface of blood vessels or by the liver or kidney. Conformational changes (denaturation) of plasma proteins or other biocompatible molecules are detected, and they can be rapidly cleared. For instance, α_2-macroglobulin has a $t_{1/2}$ in mice of more than 144 h, but when it is complexed with a protease, its $t_{1/2}$ is only 2.5 min (*47*).

10.1021/bc100070g © 2010 American Chemical Society
Published on Web 04/16/2010

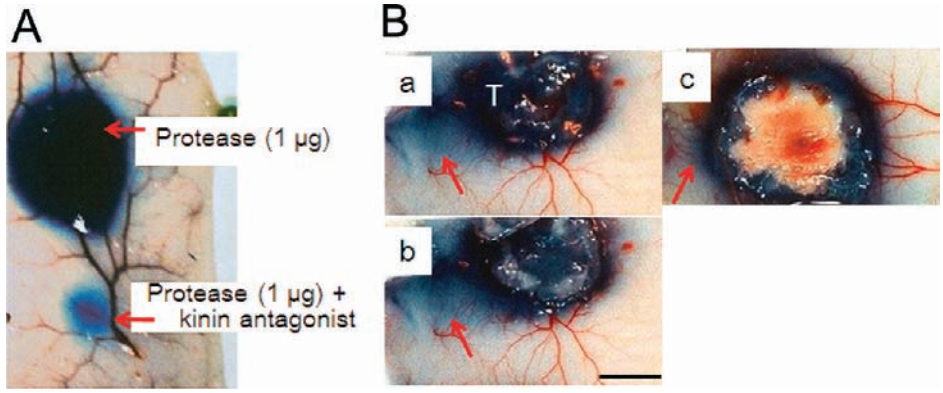


Figure 1. (A) Extravasation of Evans blue−albumin induced by 1 μg of bacterial protease (serratial 56 kDa) as a result of kinin generation or 1 μg of protease plus the kinin antagonist SQ 20881 (50 μmol), injected at the site of protease injection. The protease-induced vascular permeability was inhibited by the kinin antagonist. (B) Extravasation in murine S-180 solid tumor. (a) Macroscopic tumor (T) under the skin, after intravenous (i.v.) Evans blue injection. (b) Horizontally cut surface of the same tumor, also after i.v. Evans blue injection. In (b), the tumor tissue shows heterogeneous staining of Evans blue as inhomogeneous extravasation of the blue dye−albumin complex. (c) Another example of a horizontally cut surface of an S-180 tumor. The center of the tumor shows no EPR effect, but the intense permeability of tumor vessels is clear at the periphery, which has a pattern similar to that found in human metastatic liver cancer (see Figure 4 Case 2B and ref *19*). This type of peripheral uptake of SMANCS/Lipiodol is seen via computed tomography (CT) in metastatic human tumors and is classified as B-type staining (see ref *19* and Figure 4 Case 2B). Arrows in B point to areas in which the EPR effect also occurred in normal tissue as a result of the generation of vascular mediators such as bradykinin. Figure 1B is adapted with permission from ref *14*.

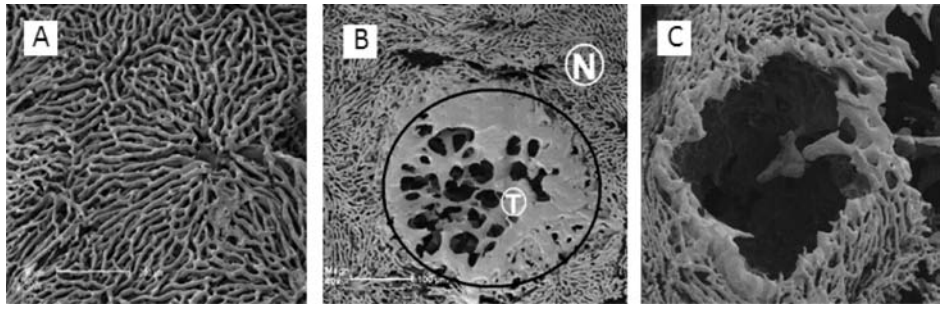


Figure 2. Scanning electron micrographs of vascular casts of plastic resin in the liver. (A) Normal capillary structure. (B) Vascular structure of the liver with a metastatic microtumor nodule, as indicated by T. Polymer resin extravasated only into the vascular bed of the tumor, whereas the normal vasculature (N) did not show such polymer leakage. (C) In the same murine tumor model as that used for B, a macromolecular drug (SMA-pirarubicin micelles) (*23*) had been injected i.v. 1 week earlier, and that caused selective disintegration of the tumor blood vessel bed (seen as an empty void, equivalent to the circled area containing the T in B). The tumor had been chemically induced by dimethylhydrazine in the colon of CBA mice, and a metastasis model was generated (*45*). Tumor-selective drug delivery and damage could be achieved in the mouse even with a tumor size as small as 200 μm, i.e., micronodules. Tumor nodules as small as 200 μm already have unique blood vasculature, which is evidence of tumor angiogenesis. These pictures are courtesy of Prof. C. Christophi and Ms. J. Daruwalla, University of Melbourne. Parts A and B are adapted with permission from ref *45*.

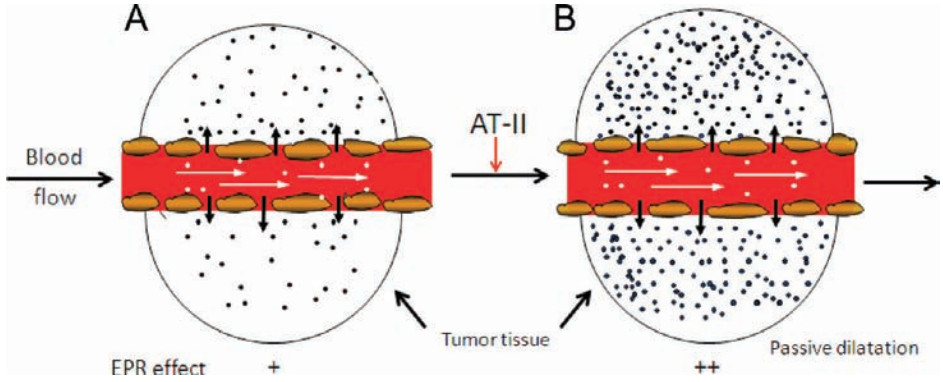


Figure 3. Diagrammatic representation of blood vasculature in tumor tissue under normotensive (A) and hypertensive (B) conditions (adapted from ref *20* with permission). Angiotensin II (AT-II)-induced enhanced extravasation of macromolecular drugs (dark dots) is shown in B. A greater EPR effect occurred in tumor tissue after AT-II-induced systemic hypertension, with tumor vessels opening wider, whereas normal blood vessels constricted and showed small openings of endothelial cell−cell gaps.

observed with biocompatible[2] macromolecules or nanoparticles with a molecular size of more than 40 kDa and up to the size of bacteria (approximately 1 μm) in most experimental solid tumor (see Figure 2). Professor Folkman first observed neoangiogenesis in tumor tissue when a tumor cell cluster (nodule) reached a size of about 2−3 mm (*21*). More detailed

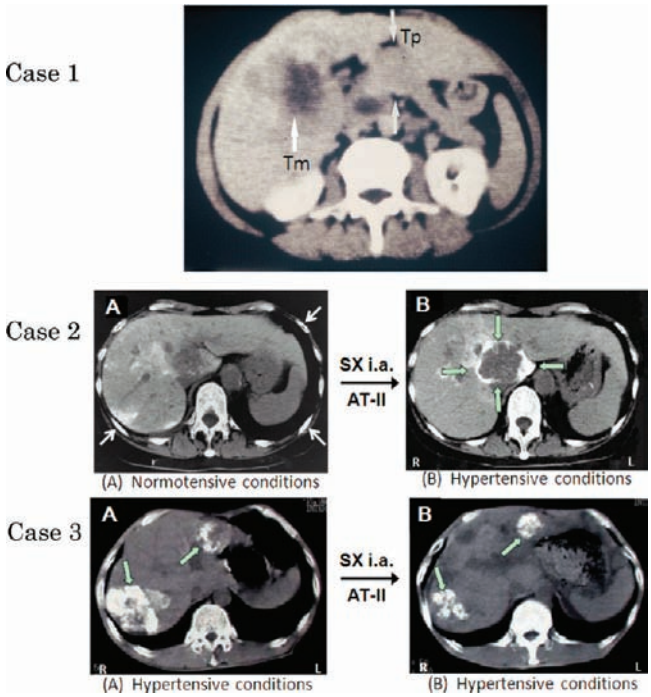


Figure 4. CT scans showing metastatic liver cancer in humans. Case 1. Metastatic tumor originating from pancreatic cancer. Arrows indicate dark low-density areas or hypovascular tumor areas; Tp points to the site of the primary pancreatic tumor, and Tm, the metastatic tumor in the liver. Case 2. CT scans demonstrating colon cancer metastasized to the liver. Arrows at the periphery of Case 2A are ribs (bones). (A) SMANCS/Lipiodol was infused via the hepatic artery under normotension. (B) SMANCS/Lipiodol was infused via the hepatic artery but under AT-II-induced hypertension (*20*). The arrows point to the main metastatic tumor in the liver. Note the more effective drug delivery only in the periphery of the tumor mass, which was defined as type B staining (*19*) (see Figure 1Bc). The intensity of the SMANCS/Lipiodol staining (white area) at the periphery of the tumor depended on the dose, the pressure applied, and the duration of the induced hypertension during arterial infusion, among other factors. Case 3. CT scans of stomach cancer metastatic to the liver. Note the white high-density areas (arrows) in which accumulation of SMANCS/Lipiodol was tumor-selective. This SMANCS/Lipiodol infusion was also performed under AT-II-induced hypertension (*20*) (see text). The CT scan in B was obtained 8 months after the scan in A. Note the considerable tumor size reduction (white areas), even in the liver metastatic lesion. The staining seen in A somewhat resembles the B-type staining seen in Case 2B (*19*), that is, circumferential low-density staining after AT-II infusion induced hypertension. As in Case 2, more complete filling of tumor with drug was achieved with AT-II-induced hypertension. Figure 4 is adapted with permission from ref *20*.

scanning electron microscopic observations of metastatic tumor nodules in the liver, in which vascular casts of blood vessels were obtained with plastic resin, indicated that tumor nodules of 100 μm have a highly permeable vascular bed (ref *22* and others) that is not seen in normal blood vasculature (Figure 2). Administration of a micellar drug (SMA-pirarubicin) (*23*) selectively destroyed the tumor micronodules by means of the EPR effect and did not damage normal blood vessels (Figure 2c).

The EPR effect with macromolecular drugs or lipid particles is clearly different from the so-called passive targeting of drugs to tumors, in that the drug retention period in tumors showing the EPR effect is more than days to weeks, whereas that of passive targeting may be only a few minutes, or no more than 10 min, as routinely observed during tumor angiography. Radiology clinics normally use low-molecular-weight angiographic contrast agents, which usually do not remain in tumor tissues for more than 10 min, so that the radiographic image is visible for only a short time, and no retention as seen in the case of the EPR effect.

One of our review articles in *Bioconjugate Chemistry* with good numbers of citations on this matter appeared in 1992 (*24*). The EPR effect was observed not only with plasma proteins, but also with micelles composed of block copolymers of n(PEG-poly Asp), as reported by Yokoyama et al. (*25*); with HPMA (hydroxypropyl methacrylate) copolymer conjugated with drugs (*26*); and with our micelles composed of SMA copolymer and various encapsulated drugs (*23, 27*). In addition, similar results have been obtained with liposomes (*28*), IgG and other plasma proteins (*11*), DNA-complexes, PEGylated proteins (ref *29* and others), and bacteria with diameters of 1−2 μm (*30, 31*).

In additional studies, we identified nitric oxide (NO), prostaglandins, peroxynitrite, collagenase, and bradykinin, among others, as factors facilitating the EPR effect (*33–36*).

INDUCED ARTIFICIAL AUGMENTATION OF THE EPR EFFECT, OVERCOMING OF THE HETEROGENEITY, AND CLINICAL OUTLOOK

Our interest is now focused on the artificial augmentation of the EPR effect for more efficient tumor-selective drug delivery. One method that we utilized for this purpose of enhancing drug delivery is elevation of systemic blood pressure by means of angiotensin II (AT-II) (*20, 37*) (Figure 3). The method was originally described by Suzuki et al. (*38*). Indeed, we discovered that this method improved drug delivery as well as therapeutic efficacy markedly against highly refractory solid tumors such as metastatic liver cancer, and even cancers of the gallbladder and pancreas (*20*) (Figures 3 and 4).

The second method used to enhance drug delivery involved nitroglycerin and other NO-releasing agents (*39, 40*). This method is unique because in hypoxic tumor tissue nitroglycerin can be converted into nitrite, which can then be reduced to NO (*41*) (Figure 5A). As stated above, NO is one of the potent mediators of vascular extravasation. Thus, topical application of nitroglycerin at any skin site resulted in a 2−3-fold increase in drug delivery (Figure 5B,C), which also potentiated the therapeutic effect in experimental tumors (*39, 40*) as well as in human cancers (*42, 43*).

Both Yasuda et al. (*42, 43*) and Graham's group (*44*), in agreement with our findings, independently reported an advantage of nitroglycerin or nitroagents for improving therapeutic efficacy. It is interesting to note that hypoxia and the low pH of tumor tissues are analogous to conditions in cardiac tissue in the presence of angina pectoris (*41*). In such cardiac tissues, release of nitrite from nitroglycerin and conversion of nitrite to NO (Figure 5A) facilitated vascular blood flow and hence elevated pO_2, with a consequent enhancement of the EPR effect and drug delivery (*39, 40*).

Despite the heterogeneity of drug distribution (on the EPR effect) in tumor tissues (Figure 1B,b and c), the just-described methods of augmenting the EPR effect, i.e., elevation of blood pressure and use of nitroglycerin, did indeed enhance drug delivery and therapeutic efficacy in a more ubiquitous manner, that is, for solid tumors in general. The EPR effect may therefore become increasingly realized as useful for cancer therapy and diagnosis that would have more universal application than the antibody-dependent selectivity of a single molecular target species. Furthermore, this enhanced EPR effect, induced by either elevating blood pressure or utilizing nitroglycerin, appears to be effective in apparently hypovascular tumors, such as metastatic liver cancer and pancreatic cancer; in tumors refractory to radiotherapy and most of chemotherapy (*39, 40, 42, 43*); and even in minute tumor nodules as small as 100 μm (Figure

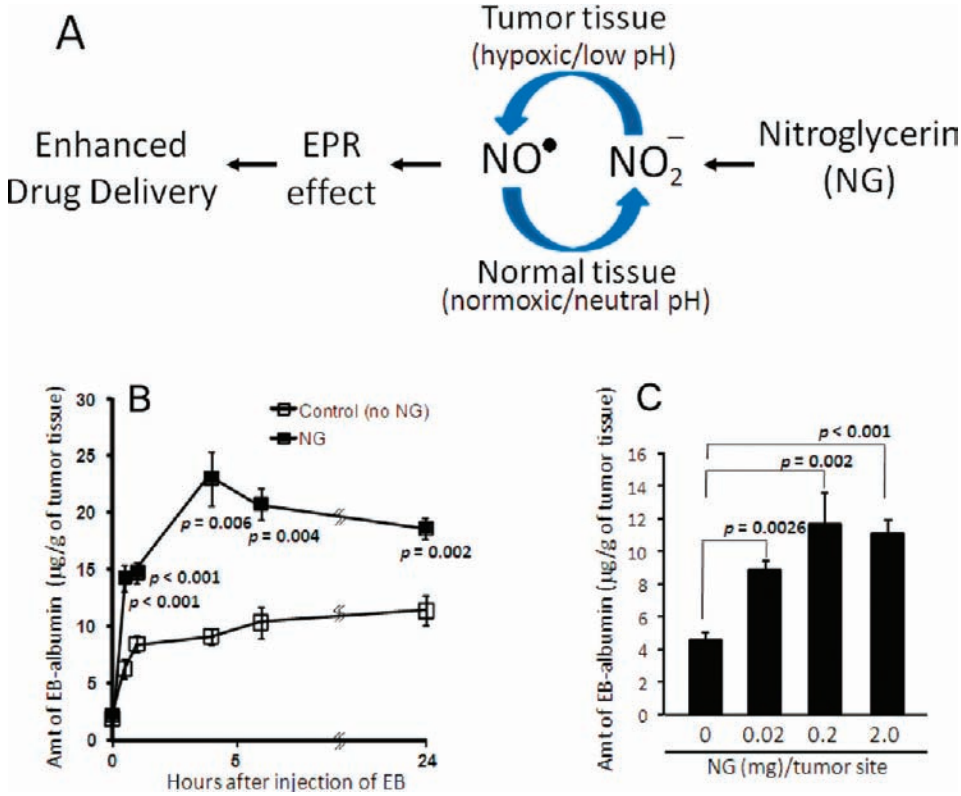


Figure 5. (A) Mechanism of NO generation from nitroglycerin (NG). NO_2^- is generated from NG, to a greater degree in hypoxic tumor tissues than in normal tissues. NO_2^- is then reduced to NO˙ in tumor and hypoxic tissues, which contributes to the EPR effect (*14*, *33*). (B) Time-dependent increase in delivery of Evans blue (EB)-albumin to tumors after topical application of NG ointment to the skin (1 mg/mouse). This effect lasted more than 24 h. (C) Dose-dependent increase in delivery of Evans blue-albumin to tumors in mice. Tumor diameters were 5−8 mm; dye concentration was determined after extraction of the dye and measuring absorption. Adapted with permission from ref *40*.

2), so that invisible metastatic tumor foci in the liver may be more selectively targeted (*45*, *46*).

CONCLUSIONS

The EPR effect is mediated by various vascular mediators including bradykinin and NO, among others. Some tumors undergo active angiogenesis, which results in high vascular density, whereas others are dormant or hypovascular. Many other tumors exhibit heterogeneous vascular features. However, we can effectively enhance drug delivery to most of these tumors, if not all, via augmenting the EPR effect, by elevating systemic blood pressure with AT-II. Another method of enhancing drug delivery is application of nitroglycerin, which we discovered generates NO in hypoxic tumor tissues and facilitates drug delivery. Both methods have been demonstrated to work in clinical settings.

ACKNOWLEDGMENT

The author would like to thank the generosity of Ms. J. Daruwella and Prof. C. Christophi of University of Melbourne, Australia, for providing the electron micrographs of Figure 2, and my colleagues, the late Dr. T. Konno of Kumamoto University for Figure 1, Case 1, and Dr. A. Nagamitsu of Nagamitsu Clinic, Fukuoka, for Figure 4, Cases 2 and 3. I also acknowledge the help and assistance of my previous and present colleagues including Ms. A. Takaki and Ms. J. Gandy for their typing and editing of the manuscript.

LITERATURE CITED

(1) Maeda, H., Edo, K., and Ishida, N., Eds. (1997) *Neocarzinostatin: The Past, Present, and Future of an Anticancer Drug*, pp 1−289, Springer-Verlag, Tokyo.

(2) Maeda, H., and Konno, T. (1997) Metamorphosis of neocarzinostatin to SMANCS-chemistry, pharmacology and clinical effect of the first prototype anticancer polymer therapeutic. In *Neocarzinostatin: The Past, Present, and Future of an Anticancer Drug* (Maeda, H., Edo, K., and Ishida, N., Eds.) pp 227−267, Springer-Verlag, Tokyo.

(3) Maeda, H., Ueda, M., Morinaga, T., and Matsumoto, T. (1985) Conjugation of poly(styrene-co-maleic acid) derivatives to the antitumor protein neocarzinostatin: Pronounced improvements in pharmacological properties. *J. Med. Chem. 28*, 455–461.

(4) Kobayashi, A., Oda, T., and, and Maeda, H. (1988) Protein binding of macromolecular anticancer agent SMANCS: Characterization of poly(styrene-co-maleic acid) derivatives as an albumin binding ligand. *J. Bioact. Compat. Polym. 3*, 319–333.

(5) Matsumoto, K., Yamamoto, T., Kamata, R., and Maeda, H. (1984) Pathogenesis of serratial infection: Activation of the Hageman factor-prekallikrein cascade by serratial protease. *J. Biochem. 96*, 739–749.

(6) Molla, A., Yamamoto, T., Akaike, T., Miyoshi, S., and Maeda, H. (1989) Activation of Hageman factor and prekallikrein and generation of kinin by various microbial proteinases. *J. Biol. Chem. 264*, 10589–10594.

(7) Maeda, H. (1996) Role of microbial proteases in pathogenesis. *Microbiol. Immunol. 40*, 685–699.

(8) Maeda, H. (2002) Microbial proteinases and pathogenesis of infection. In *Wiley Encyclopedia of Molecular Medicine* (Creighton, T. E., Ed.) pp 2663−2668, Vol *4*, John Wiley & Sons, New York.

(9) Maeda, H., Akaike, T., Sakata, Y., Maruo, K. (1993) Role of bradykinin in microbial infection: Enhancement of septicemia by microbial proteinases and kinin. In *Proteases, Proteases Inhibitor and Protease-Derived Peptides: Importance in Human Pathophysiology and Therapeutics. Agents Actions Supplement* (Chironis, J. C., and Repine, J. E., Eds.) pp 159−165, Vol *42*, Birkhauser-Verlag AG, Basel.

(10) Maeda, H., Matsumura, Y., and Kato, H. (1988) Purification and identification of [hydroxprolyl^3]bradykinin in ascetic fluid from a patient with gastric cancer. *J. Biol. Chem. 263*, 16051–16054.
(11) Matsumura, Y., and Maeda, H. (1986) A new concept for macromolecular therapeutics in cancer chemotherapy: Mechanism of tumoritropic accumulation of proteins and the antitumor agent smancs. *Cancer Res. 46*, 6387–6392.
(12) Matsumura, Y., Kimura, M., Yamamoto, T., and Maeda, H. (1988) Involvement of the kinin-generating cascade in enhanced vascular permeability in tumor tissue. *Jpn. J. Cancer Res. 79*, 1327–1334.
(13) Matsumura, Y., Maruo, K., Kimura, M., Yamamoto, T., Konno, T., and Maeda, H. (1991) Kinin-generating cascade in advanced cancer patients and in vitro study. *Jpn. J. Cancer Res. 82*, 732–741.
(14) Wu, J., Akaike, T., and Maeda, H. (1998) Modulation of enhanced vascular permeability in tumors by a bradykinin antagonist, a cyclooxygenase inhibitor, and a nitric oxide scavenger. *Cancer Res. 58*, 159–165.
(15) Maeda, H., Wu, J., Okamoto, T., Maruo, K., and Akaike, T. (1999) Kallikrein-kinin in infection and cancer. *Immunopharmacology 43*, 115–128.
(16) Maeda, H. (1991) SMANCS and polymer-conjugated macromolecular drugs: Advantages in cancer chemotherapy. *Adv. Drug Delivery Rev. 6*, 181–202.
(17) Iwai, K., Maeda, H., and Konno, T. (1984) Use of oily contrast medium for selective drug targeting to tumor: Enhanced therapeutic effect and X-ray image. *Cancer Res. 44*, 2115–2121.
(18) Konno, T., Maeda, H., Iwai, K., Maki, S., Tashiro, S., Uchida, M., and Miyauchi, Y. (1984) Selective targeting of anti-cancer drug and simultaneous image enhancement in solid tumors by arterially administered lipid contrast medium. *Cancer 54*, 2367–2374.
(19) Maki, S., Konno, T., and Maeda, H. (1985) Image enhancement in computerized tomography for sensitive diagnosis of liver cancer and semiquantitation of tumor selective drug targeting with oily contrast medium. *Cancer 56*, 751–757.
(20) Nagamitsu, A., Greish, K., and Maeda, H. (2009) Elevating blood pressure as a strategy to increase tumor-targeted delivery of macromolecular drug SMANCS: Cases of advanced solid tumors. *Jpn. J. Clin. Oncol. 39*, 756–766.
(21) Folkman, J. (1974) Tumor angiogenesis. *Adv. Cancer Res. 19*, 331–358.
(22) Skinner, S. A., Tutton, P. J., and O'Brien, P. E. (1990) Microvascular architecture of experimental colon tumors in the rat. *Cancer Res. 50*, 2411–2417.
(23) Greish, K., Nagamitsu, A., Fang, J., and Maeda, H. (2005) Copoly(styrene-maleic acid)-pirarubicin micelles: High tumor-targeting efficiency with little toxicity. *Bioconjugate Chem. 16*, 230–236.
(24) Maeda, H., Seymour, L. W., and Miyamoto, Y. (1992) Conjugates of anticancer agents and polymers: Advantages of macromolecular therapeutics in vivo. *Bioconjugate Chem. 3*, 351–362.
(25) Yokoyama, M., Okano, T., Sakurai, Y., and Kataoka, K. (1994) Improved synthesis of adriamycin-conjugated poly(ethylene oxide)-poly(aspartic acid) block copolymer and formation of unimodal micellar structure with controlled amount of physically entrapped adriamycin. *J. Controlled Release 32*, 269–277.
(26) Duncan, R. (2009) Development of HPMA copolymer-anticancer conjugates: Clinical experience and lessons learnt. *Adv. Drug Delivery Rev. 61*, 1131–1148.
(27) Iyer, A., Greish, K., Seki, T., Okazaki, S., Fang, J., Takeshita, K., and Maeda, H. (2007) Polymeric micelles of zinc protoporphyrin for tumor targeted delivery based on EPR effect and singlet oxygen generation. *J. Drug Targeting 15*, 496–506.
(28) Zalipsky, S., Saad, M., Kiwan, R., Ber, E., Yu, N., and Minko, T. (2007) Antitumor activity of new liposomal prodrug of mitomycin C in multidrug resistant solid tumor: Insights of the mechanism of action. *J. Drug Targeting 15*, 518–530.
(29) Fang, J., Nakamura, H., and Iyer, A. K. (2007) Tumor-targeted induction of oxystress for cancer therapy. *J. Drug Targeting 15*, 475–486.
(30) Kimura, N. T., Taniguchi, S., Aoki, K., and Baba, T. (1980) Selective localization and growth of *Bifidobacterium bifidum* in mouse tumors following intravenous administration. *Cancer Res. 96*, 739–749.
(31) Zhao, M., Yang, M., Ma, H., Li, X., Tan, X., Li, S., Yang, Z., and Hoffman, R. (2006) Targeted therapy with a *Salmonella typhimurium* leucine-arginine auxotroph cures orthotopic human breast tumors in nude mice. *Cancer Res. 66*, 7647–7652.
(32) Torchilin, V. (2010) Tumor delivery of macromolecular drugs based on the EPR effect, *Adv. Drug Delivery Rev.*, in press.
(33) Maeda, H., Noguchi, Y., Sato, K., and Akaike, T. (1994) Enhanced vascular permeability in solid tumor is mediated by nitric oxide and inhibited by both new nitric oxide scavenger and nitric oxide synthase inhibitor. *Jpn. J. Cancer Res. 85*, 331–334.
(34) Wu, J., Akaike, T., Hayashida, K., Okamoto, T., Okuyama, A., and Maeda, H. (2001) Enhanced vascular permeability in solid tumor involving peroxynitrite and matrix metalloproteinase. *Jpn. J. Cancer Res. 92*, 439–451.
(35) Tanaka, S., Akaike, T., Wu, S. J., Fang, J., Sawa, T., Ogawa, M., Beppu, T., and Maeda, H. (2003) Modulation of tumor-selective vascular blood flow and extravasation by the stable prostaglandin I_2 analogue beraprost sodium. *J. Drug Targeting 11*, 45–52.
(36) Maeda, H. (2001) The enhanced permeability and retention (EPR) effect in tumor vasculature: The key role of tumor-selective macromolecular drug targeting. *Adv. Enzyme Regul. 41*, 189–207.
(37) Suzuki, M., Hori, K., Abe, I., Saito, S., and Saito, H. (1981) A new approach to cancer chemotherapy: A selective enhancement of tumor blood flow with angiotensin II. *J. Natl. Cancer Inst. 67*, 663–669.
(38) Li, C. J., Miyamoto, Y., Kojima, Y., and Maeda, H. (1993) Augmentation of tumor delivery of macromolecular drugs with reduced bone marrow delivery by elevating blood pressure. *Br. J. Cancer 67*, 975–980.
(39) Maeda, H., Seki, T., and Fang, J. (2008) Enhanced tumor delivery of macromolecular antitumor-drugs by topical application of nitroglycerin on superficial tumors, Abstract #P-518 in the 67th Annual Meeting of the Japanese Cancer Association, Nagoya, p 213.
(40) Seki, T., Fang, J., and Maeda, H. (2009) Enhanced delivery of macromolecular antitumor drugs to tumors by nitroglycerin application. *Cancer Sci. 100*, 2426–2430.
(41) Feelisch, M., and Noack, E. A. (1987) Correlation between nitric oxide formation during degradation of organic nitrates and activation of guanylate cyclase. *Eur. J. Pharmacol. 139*, 19–30.
(42) Yasuda, H., Yamaya, M., Nakayama, K., Sasaki, T., Ebihara, S., Kanda, A., Asada, M., Inoue, D., Suzuki, T., Okazaki, T., Takahashi, H., Yoshida, M., Kaneta, T., Ishizawa, K., Yamanda, S., Tomita, N., Yamasaki, M., Kikuchi, A., Kubo, H., and Sasaki, H. (2006) Randomized phase II trial comparing nitroglycerin plus vinorelbine and cisplatin with vinorelbine and cisplatin alone in previously untreated stage IIIB/IV non-small-cell lung cancer. *J. Clin. Oncol. 24*, 688–694.
(43) Yasuda, H., Nakayama, K., Watanabe, M., Suzuki, S., Fuji, H., Okinaga, S., Kanda, A., Zayasu, K., Sasaki, T., Asada, M., Suzuki, T., Yoshida, M., Yamanda, S., Inoue, D., Kaneta, T., Kondo, T., Takai, Y., Sasaki, H., Yanagihara, K., and Yamaya, M. (2006) Nitroglycerin treatment may enhance chemosensitivity to docetaxel and carboplatin in patients with lung adenocarcinoma. *Clin. Cancer Res. 12*, 6748–6757.
(44) Siemens, D. R., Heaton, J. P. W., Adams, M. A., Kawakami, J., and Graham, C. H. (2009) Phase II study of nitric oxide donor for men with increasing prostate-specific antigen level after

surgery or radiotherapy for prostate cancer. *Urology 74*, 878–883.

(45) Maeda, H., Bharate, G. Y., and Daruwalla, J. (2009) Polymeric drugs and nanomedicines for efficient tumor targeted drug delivery based on EPR-effect. *Eur. J. Pharm. Biopharm. 71*, 409–419.

(46) Daruwalla, J., Greish, K., Wilson, C. M., Muralidharan, V., Iyer, A., Maeda, H., and Christophi, C. (2009) Styrene maleic acid-pirarubicin disrupts tumor microcirculation and enhances the permeability of colorectal liver metastases. *J. Vasc. Res. 46*, 218–228.

(47) Maeda, H., Matsumura, Y., Oda, T., and Sasamoto, K. (1986) Cancer selective macromolecular therapeusis: Tailoring of an antitumor protein drug. In *Protein Tailoring for Food and Medical Uses* (Feeney, R. E., and Whitaker, J. R., Eds.) pp 353−382, Marcel Dekker, Inc., New York.

BC100070G

siRNA Delivery to CNS Cells using a Membrane Translocation Peptide

Marytheresa A. Ifediba,[†,§,||] Zdravka Medarova,[†] Shu-wing Ng,[‡] Junzheng Yang,[‡] and Anna Moore*[,†]

Molecular Imaging Laboratory, MGH/MIT/HMS Athinoula A. Martinos Center for Biomedical Imaging, Massachusetts General Hospital and Harvard Medical School, Charlestown, Massachusetts 02129, Department of Obstetrics, Gynecology, and Reproductive Biology, Division of Gynecologic Oncology, Brigham and Women's Hospital, 221 Longwood Avenue, Boston, Massachusetts 02115, School of Engineering and Applied Sciences, Harvard University, Cambridge, Massachusetts 02138, and Harvard-MIT Division of Health Sciences and Technology (HST), Massachusetts Institute of Technology, Cambridge, Massachusetts 02139. Received November 6, 2009; Revised Manuscript Received March 30, 2010

RNA interference (RNAi) is a sequence-specific gene silencing technique that has been applied to multiple pathological conditions. In this report, we describe the generation and in vitro characterization of an RNAi-based fluorescent probe for use as a therapeutic in the setting of ischemic stroke. Probe delivery to bEnd.3 brain endothelial cells and primary cortical neurons and astrocytes was promoted by incorporating small interfering RNA (siRNA) into complexes with fluorescently labeled myristoylated polyarginine peptides. The resulting probe was partially protected from serum nuclease degradation and was efficiently internalized by cells as confirmed by flow cytometry and confocal microscopy. In addition, application of the siRNA probe directed against c-Src, a protein implicated in stroke pathology, led to statistically significant reduction of endogenous *c-src* mRNA levels in all cell types tested. Results demonstrate the proof-of-principle that functionalized peptide−siRNA probes can be used as potential tools for dual imaging and therapeutic applications.

INTRODUCTION

In the past decade, RNA interference (RNAi) technology has been rapidly integrated into basic biomedical research, emerging as a premier method for regulating gene expression in a variety of model systems. As RNAi-based therapies progress to clinical trials and are applied to increasingly complex human diseases, the need for more robust strategies for small RNA delivery and monitoring becomes critical (*1*). These considerations are particularly relevant in neurological pathologies, for which an intact blood brain barrier (BBB) opposes direct contact between diseased cells and most systemically administered agents. One approach for overcoming biological membranes exploits naturally occurring membrane translocation peptides (*2, 3*) known as cell penetrating peptides (CPPs), cationic peptides that have been adapted to accommodate diverse molecular cargoes, including proteins (*4*), liposomes (*5*), and nanoparticles (*6*). Recently, it was demonstrated that intravenously injected small interfering RNA (siRNA), when used in conjunction with a peptide sequence from rabies virus glycoprotein, is delivered to the brain and retains its gene silencing capabilities (*7*).

In the present study, we utilized optically labeled polyarginine peptides modified with a 14-carbon myristic acid moiety (MPAP) for siRNA delivery. It has been shown previously that myristoylation increases the affinity of the peptide for lipid bilayer membranes, enhancing peptide entry into cells by several-fold relative to Tat and unmodified polyarginine cell penetrating peptides (*8*). This peptide was used by us to promote cellular delivery of nanoparticle imaging agents to solid tumors after intravenous injection (*9, 10*). Furthermore, MPAP is BBB permeable in vivo, where it was shown to localize to neurons, astrocytes, and endothelial cells after intravascular administration (*11*). These properties make MPAP ideally suited for use with siRNA to form a dual optical imaging and therapeutic probe for neurological applications, provided that a method of complexation is developed that does not interfere with the bioactivity of siRNA molecules.

This work details the generation and in vitro testing of an MPAP and siRNA (MPAP-siRNA) imaging probe complex for the treatment of ischemic stroke. In the setting of ischemic stroke, disruption of blood flow to the brain induces a cascade of pathological cell signaling events, culminating in widespread death of neurons and supporting cells (*12*). We hypothesize that if siRNA directed against proteins implicated in stroke pathology were effectively delivered to primary neurons and astrocytes to intercede in this process, neuroprotection could be elicited. With this in mind, we developed dual MPAP-siRNA optical imaging probes directed against c-Src, a protein tyrosine kinase that becomes upregulated after stroke and is associated with increased tissue damage in cerebral ischemia models (*13, 14*). Probes were assembled by utilizing the natural affinity of cationic peptides for oligonucleotides, a process that was optimized to ensure maximum siRNA incorporation. MPAP-siRNA complexes were tested for stability and their internalization by primary cells and an endothelial cell line was monitored by flow cytometry and confocal microscopy. The probes were also evaluated for their cytotoxic effects and siRNA silencing efficiency. Results confirm that MPAP-siRNA complexes become internalized by cells and cause statistically significant reductions in endogenous *c-src* levels without significantly affecting cell viability, paving the way for the future studies of the dual imaging and therapeutic probe in vivo.

EXPERIMENTAL PROCEDURES

Myristoylated polyarginine peptide (MPAP), C14-βAla-$(Arg)_7$-Cys(SH)-NH_2, was synthesized as described previously

* Address correspondence and reprint requests to Anna Moore, Ph.D., Molecular Imaging Laboratory, MGH/MIT/HMS Athinoula A. Martinos Center for Biomedical Imaging, Massachusetts General Hospital/ Harvard Medical School, Bldg. 75, 13th St., Charlestown, MA 02129. E-mail: amoore@helix.mgh.harvard.edu. Tel. 617-724-0540, Fax. 617-643-4865.

[†] Massachusetts General Hospital and Harvard Medical School.

[‡] Brigham and Women's Hospital.

[§] Harvard University.

[||] Massachusetts Institute of Technology.

10.1021/bc900488e © 2010 American Chemical Society
Published on Web 04/26/2010

(*11*) and conjugated to Cy5.5 fluorescent dye (Amersham, Piscataway, NJ) to form MPAP−Cy5.5. To promote probe complex formation, MPAP−Cy5.5 was mixed through gentle aspiration with a solution of siRNA conjugated to Dy547 (siRNA−Dy547), a fluorescent tag with absorbance/emission max of 548/562 nm. The resulting probe mixture was incubated for 20 min at room temperature to induce complete complexation of the two components.

To optimize stoichiometry of MPAP−Cy5.5 and siRNA−Dy547 complexes, we performed polyacrylamide gel electrophoresis. Various dilutions of MPAP−Cy5.5 solution were added to siRNA−Dy547 (20 pmol) to obtain 1:10, 1:5, 1:2.5, 1:1, 2.5:1, 5:1, and 10:1 siRNA-to-peptide molar ratios. Samples were run on polyacrylamide gels and stained with ethidium bromide for visualization of uncomplexed siRNA.

Solutions of free siRNA−Dy547 or complexes of siRNA−Dy547 and MPAP−Cy5.5, hereafter termed MPAP-Src, were incubated in mouse serum to evaluate the protective effect of MPAP−Cy5.5 on nuclease digestion of siRNA. MPAP−Cy5.5 and c-Src siRNA were combined at a 1:5 siRNA-to-peptide molar ratio to form MPAP-Src. MPAP-Src was incubated in fresh mouse serum for 0, 0.5, 1, 2, 4, or 8 h. The amount of siRNA spared from nuclease digestion was determined by gel electrophoresis, SYBR Gold (Molecular Probes, Invitrogen, Eugene OR) staining, and quantification using *ImageJ* software (NIH).

Cortical neuron cultures were generated from embryonic day 18 C57BL/6 mouse fetuses (see Supporting Information). Cell culture of cortical astrocytes was performed using a slight modification of the procedure for neurons, with cortices dissected from C57BL/6 mouse pups, postnatal days 1−2 (see Supporting Information). A brain endothelial cell line, bEnd.3, was obtained from American Type Culture Collection (Manassas, VA) and maintained according to the vendor's instructions (see Supporting Information). To promote probe internalization by cells, MPAP-Src solutions were added to primary astrocytes, primary neurons, or bEnd.3 cells plated in 12-well plates in serum-free media and incubated for 24 h. To determine the cytotoxicity of probe incubation, cells exposed to MPAP-Src for 48 h or untreated cells were processed using MTT and CASP-3-C (Sigma, St. Louis, MO) caspase-3 assays (see Supporting Information).

The extent of probe internalization by cells was investigated using FACS analysis and confocal microscopy (see Supporting Information). Confocal microscopy was also used in conjunction with LysoSensor Green staining of living cells to evaluate the mechanism of MPAP-Src uptake. To assess the effect of MPAP-Src internalization, total RNA was purified from cells treated with MPAP-Src or scrambled control siRNA probes (MPAP-ctrl) and subjected to real-time quantitative RT-PCR (TaqMan) to determine relative levels of *c-src* mRNA.

RESULTS AND DISCUSSION

MPAP has proven effective as a membrane translocation moiety when covalently linked to optical probes and iron oxide nanoparticles (*9, 10*). In this report, we wished to extend the use of optically labeled MPAP further, by taking advantage of the potential for its polyarginine residues to electrostatically interact with negatively charged siRNA molecules. To promote the formation of siRNA dual optical imaging probes, c-Src siRNA−Dy547 and MPAP−Cy5.5 were mixed in several molar ratios. The efficiency of MPAP binding to siRNA was determined by performing gel electrophoresis on the resulting MPAP-Src solutions to assess the proportion of free siRNA in each mixture. MPAP-Src complexes remained in the loading well during gel electrophoresis, while uncomplexed siRNA readily entered the gel and stained with ethidium bromide (Figure 1).

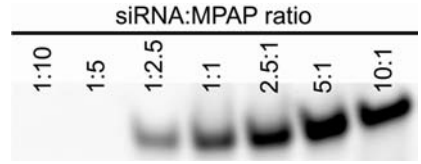


Figure 1. Gel mobility shift assay. MPAP-Cy5.5 was incubated with c-Src siRNA at several molar ratios to form MPAP-Src probes. At the 1:5 siRNA-to-MPAP ratio, most siRNA was incorporated into complexes.

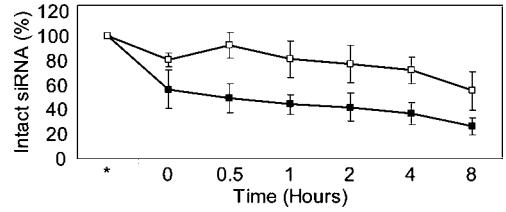


Figure 2. Serum stability. Stability of MPAP-Src (open squares) in serum relative to Dy547-labeled c-Src siRNA alone (closed squares) was investigated by incubating probes in 75% mouse serum for 0−8 h. MPAP complexation to siRNA confers partial protection from serum nucleases, yielding a higher percentage of intact siRNA after incubation in serum than siRNA alone (mean ± s.d.) relative to undigested controls (*).

In solutions containing a 1:5 siRNA-to-MPAP molar ratio or higher peptide content, the vast majority of siRNA was associated with MPAP. Full incorporation of siRNA into probes was deemed important to maximize siRNA internalization and silencing potential. Thus, the siRNA-to-peptide ratio at which no discernible siRNA remained unassociated with MPAP−Cy5.5, 1:5, was used for subsequent experiments.

Ultimate utility of MPAP-Src in vivo requires protection of siRNA from nucleases in the bloodstream. Generally, siRNAs are chemically modified to extend their serum half-life relative to naked siRNA, which becomes degraded and inactivated within minutes of blood exposure (*15, 16*). To investigate the stability of the siRNA incorporated into MPAP-Src, siRNA complexes and naked siRNA−Dy547 were exposed to serum for up to 8 h. Following removal of serum proteins and MPAP with proteinase K (1 mg/mL), intact siRNA was analyzed by gel electrophoresis and quantified (Figure 2). It was observed that the optical label Dy547 conjugated to c-Src siRNA partially protects it from degradation by nucleases, with just over 25% of the total siRNA retained after 8 h. The presence of MPAP appears to confer an additional measure of protection, such that the amount of free siRNA after 8 h of MPAP-Src incubation in serum was close to 55%. These results indicate that MPAP complexation has a stabilizing effect on c-Src siRNA.

Internalization of MPAP-Src probes was evaluated in vitro in a variety of cell types implicated in ischemic stroke pathology, including primary cortical neurons, astrocytes, and the bEnd.3 brain endothelial cell line. Cells incubated for 24 h with MPAP-Src or MPAP associated with scrambled control siRNA (MPAP-ctrl) were subjected to flow cytometry and monitored for Cy5.5 and Dy547 fluorescence. Figure 3 shows significant signal from both siRNA and MPAP relative to untreated controls in all cell types. Internalization of MPAP-Src and MPAP-ctrl occurred in similar patterns, indicating that MPAP association with c-Src siRNA is not sequence-dependent. Furthermore, flow cytometry scatter plots (data not shown) showed that roughly 46% of bEnd3 cells, 77% of neurons, and 78% of astrocytes with MPAP uptake also contained c-Src siRNA, suggesting that siRNA did not dissociate from MPAP but formed a stable complex in solution.

To confirm that MPAP-Src probe was internalized by cells and not passively associated with the cell membrane, confocal

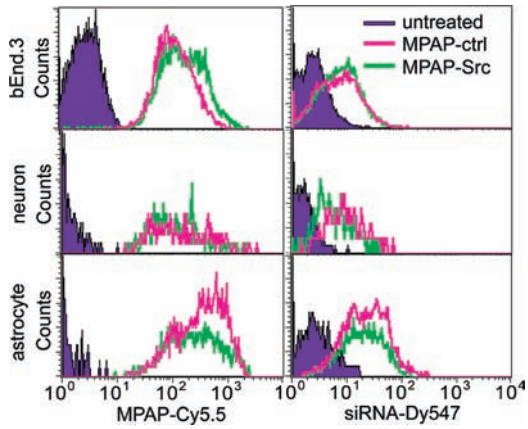


Figure 3. Flow cytometry. Astrocytes, neurons, and bEnd.3 cells were subjected to MPAP-Src or MPAP-ctrl incubation for 24 h, followed by flow cytometry. All cell types were positive for the presence of both MPAP−Cy5.5 and siRNA−Dy547.

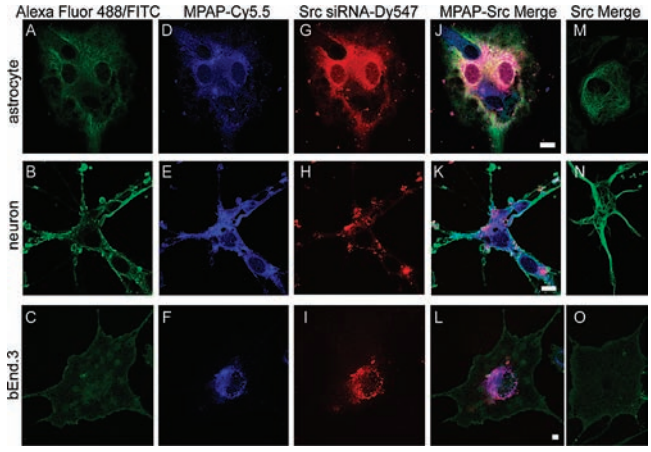


Figure 4. Confocal microscopy of astrocytes, neurons, and bEnd.3 stained with GFAP (A), β-III tubulin (B), and CD31 (C), respectively. Following incubation with MPAP-Src probe for 24 h and cell-specific staining, cells were visualized by confocal microscopy. MPAP (D−F) and c-SRC siRNA (G−I) were taken up by cells following MPAP-Src incubation, whereas incubation with 100 pmol of c-Src siRNA alone resulted in no significant siRNA uptake (M−O). Scale bar = 10 μm.

microscopy was performed. Neurons, astrocytes, and bEnd.3 cells stained with cell-specific antibodies (Figure 4A−C) were positive for the presence of both MPAP (Figure 4D−F) and c-Src siRNA (Figure 4G−I). In general, c-Src siRNA colocalized with MPAP (Figure 4J−L), though, for neurons in particular, there was evidence that MPAP and siRNA become dissociated to some degree when taken up by cells (Figure 4K). The presence of MPAP was crucial for internalization, as is evident by the complete absence of c-Src siRNA uptake relative to MPAP-Src when cells were incubated with equivalent quantities of siRNA alone (Figure 4M−O).

The mechanism of cellular internalization was investigated in unfixed astrocytes, bEnd.3 cells, and neurons using Lysosensor Green staining that is specific for endosomal vesicles (Figure 5D−F). As in fixed cells, MPAP-Src substantially entered cells (Figure 5M−O). A significant portion of c-Src and MPAP signal appeared to originate from vesicles in all cell types, suggesting that a dominant mechanism of MPAP uptake is endocytosis. These findings prompt concerns that MPAP-Src becomes sequestered in vesicles where it would be unable to access RNAi machinery to achieve successful c-Src silencing. To address this, expression levels of endogenous *c-src* mRNA were evaluated by RT-PCR following MPAP-Src uptake. Total

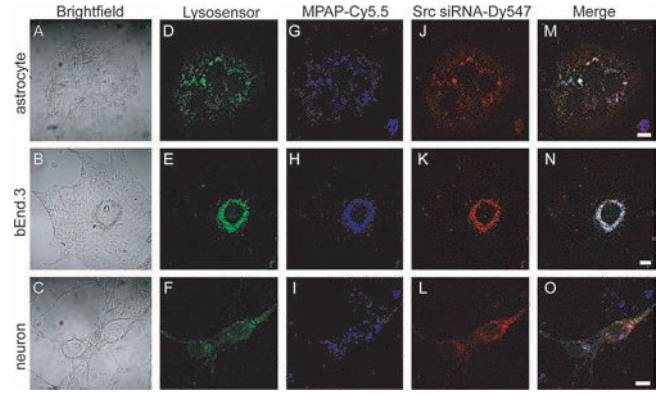


Figure 5. Cells were visualized using confocal microscopy following Lysosensor Green staining of unfixed astrocytes, bEnd.3 cells, and neurons (D−F) to determine the mechanism of cellular uptake of MPAP-Src. MPAP (G−I) and c-Src siRNA (J−L) generally colocalize with endosomal vesicles. Scale bar = 10 μm.

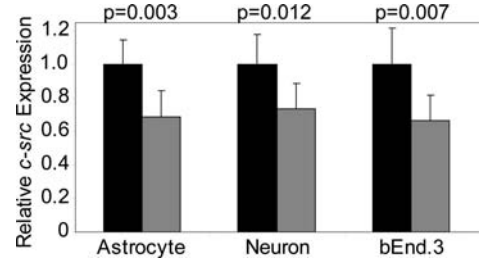


Figure 6. Quantitative RT-PCR analysis of endogenous *c-src* mRNA expression levels (mean ± s.d., $n = 7$) in astrocytes, neurons, and bEnd.3 cells treated with MPAP-ctrl (black bars) or MPAP-Src (gray bars) for 48 h. After administration of MPAP-Src, there was a significant reduction in *c-src* levels in all cell types tested.

c-src expression after MPAP-Src treatment was compared to expression after treatment with MPAP-ctrl, a control used to differentiate siRNA-induced *c-src* inhibition from off-target effects potentially caused by the MPAP method of siRNA delivery. Endogenous *c-src* levels were reduced to a statistically significant degree in all cell types subjected to MPAP-Src treatment for 48 h relative to controls (Figure 6). For astrocytes and bEnd.3 cells, *c-src* expression decreased to approximately 66% of controls, while in neurons, the decrease was to 75%. Similar reductions in *c-src* levels were achieved following 24-h MPAP-Src treatment in astrocytes and bEnd.3 cells (data not shown). Thus, despite the observation that MPAP-Src appears to traffic to some extent in endosomal vesicles, the endosomal escape of siRNA and its separation from MPAP is sufficient to mediate a significant degree of endogenous gene inhibition. To determine if MPAP-Src mediated siRNA delivery was cytotoxic, MTT and caspase-3 assays were performed (Figure 7). MPAP-Src treatment resulted in no discernible increase in cytotoxicity in either astrocytes or bEnd.3 cells relative to untreated controls as assessed by MTT and caspase-3 analysis. Likewise, MTT analysis showed no relative decrease in viability in neurons. Although caspase-3 levels appeared elevated in neurons, suggesting the presence of apoptosis following 48 h of MPAP incubation, the effect was not statistically significant. These data indicate that MPAP-Src treatment induced partial endogenous gene silencing without the cytotoxic effects that are often observed in other peptide-based delivery systems (*17*).

This report details the characterization and in vitro testing of a fluorescent siRNA imaging probe for application to ischemic stroke. MPAP, an amphipathic membrane translocation peptide derivative capable of crossing the blood−brain barrier, was shown to form stable complexes with siRNA and mediate cell

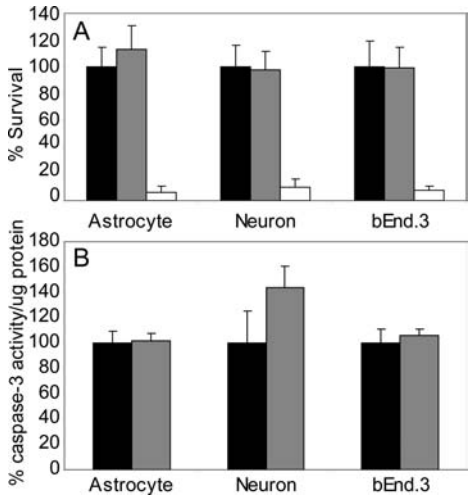


Figure 7. A. The percent survival (mean ± s.d.) of cells treated with MPAP-Src or staurosporine (gray and white bars, respectively) relative to untreated controls (black bars) was obtained by MTT analysis. MPAP-Src treatment resulted in no significant increase in cytotoxicity in any of the cell types. B. Caspase-3 activity (mean ± s.d.) in cells treated with MPAP-Src (gray bars) presented relative to activity in untreated cells (black bars). Though slight increases in caspase-3 signal were apparent, particularly in neurons, these were not statistically significant in any of the cells tested.

entry in primary neurons and astrocytes and an endothelial cell line without significant cytotoxicity. The internalized probe was biologically active, reducing endogenous levels of *c-src* mRNA that codes for a protein associated with detrimental outcome following ischemic stroke.

Previous studies have shown successful noncovalent complexation of siRNA to cell penetrating peptides for delivery to model and therapeutic targets (*7, 18*−*20*). Here, we demonstrate the proof-of-principle that simple complexation techniques can be employed to produce a dual optical imaging and therapeutic probe. We intend to investigate the probe as a method of monitoring siRNA delivery and treatment of cerebral ischemia in vivo.

ACKNOWLEDGMENT

This publication was made possible through partial grant support by grant T32 EB001680 from the National Institute of Biomedical Imaging and Bioengineering (NIBIB).

Supporting Information Available: Detailed experimental procedures. This material is available free of charge via the Internet at http://pubs.acs.org.

LITERATURE CITED

(1) Castanotto, D., and Rossi, J. J. (2009) The promises and pitfalls of RNA-interference-based therapeutics. *Nature 457*, 426–33.
(2) Vives, E., Brodin, P., and Lebleu, B. (1997) A truncated HIV-1 Tat protein basic domain rapidly translocates through the plasma membrane and accumulates in the cell nucleus. *J. Biol. Chem. 272*, 16010–7.
(3) Derossi, D., Joliot, A. H., Chassaing, G., and Prochiantz, A. (1994) The third helix of the Antennapedia homeodomain translocates through biological membranes. *J. Biol. Chem. 269*, 10444–50.
(4) Schwarze, S. R., Ho, A., Vocero-Akbani, A., and Dowdy, S. F. (1999) In vivo protein transduction: delivery of a biologically active protein into the mouse. *Science 285*, 1569–72.
(5) Torchilin, V. P., Levchenko, T. S., Rammohan, R., Volodina, N., Papahadjopoulos-Sternberg, B., and D'Souza, G. G. (2003) Cell transfection in vitro and in vivo with nontoxic TAT peptide-liposome-DNA complexes. *Proc. Natl. Acad. Sci. U.S.A. 100*, 1972–7.
(6) Lewin, M., Carlesso, N., Tung, C. H., Tang, X. W., Cory, D., Scadden, D. T., and Weissleder, R. (2000) Tat peptide-derivatized magnetic nanoparticles allow in vivo tracking and recovery of progenitor cells. *Nat. Biotechnol. 18*, 410–4.
(7) Kumar, P., Wu, H., McBride, J. L., Jung, K. E., Kim, M. H., Davidson, B. L., Lee, S. K., Shankar, P., and Manjunath, N. (2007) Transvascular delivery of small interfering RNA to the central nervous system. *Nature 448*, 39–43.
(8) Pham, W., Kircher, M. F., Weissleder, R., and Tung, C. H. (2004) Enhancing membrane permeability by fatty acylation of oligoarginine peptides. *ChemBioChem 5*, 1148–51.
(9) Kumar, M., Medarova, Z., Pantazopoulos, P., Dai, G., Moore, A. (2010) Novel membrane permeable contrast agent for brain tumor detection by MRI. *Magn. Reson. Med. 63*, 617−624.
(10) Medarova, Z., Pham, W., Farrar, C., Petkova, V., and Moore, A. (2007) In vivo imaging of siRNA delivery and silencing in tumors. *Nat. Med. 13*, 372–7.
(11) Pham, W., Zhao, B. Q., Lo, E. H., Medarova, Z., Rosen, B., and Moore, A. (2005) Crossing the blood-brain barrier: a potential application of myristoylated polyarginine for in vivo neuroimaging. *Neuroimage 28*, 287–92.
(12) Lipton, P. (1999) Ischemic cell death in brain neurons. *Physiol. Rev. 79*, 1431–568.
(13) Korematsu, K., Goto, S., Nagahiro, S., and Ushio, Y. (1994) Microglial response to transient focal cerebral ischemia: an immunocytochemical study on the rat cerebral cortex using anti-phosphotyrosine antibody. *J. Cereb. Blood Flow Metab. 14*, 825–30.
(14) Paul, R., Zhang, Z. G., Eliceiri, B. P., Jiang, Q., Boccia, A. D., Zhang, R. L., Chopp, M., and Cheresh, D. A. (2001) Src deficiency or blockade of Src activity in mice provides cerebral protection following stroke. *Nat. Med. 7*, 222–7.
(15) Braasch, D. A., Jensen, S., Liu, Y., Kaur, K., Arar, K., White, M. A., and Corey, D. R. (2003) RNA interference in mammalian cells by chemically-modified RNA. *Biochemistry 42*, 7967–75.
(16) Soutschek, J., Akinc, A., Bramlage, B., Charisse, K., Constien, R., Donoghue, M., Elbashir, S., Geick, A., Hadwiger, P., Harborth, J., John, M., Kesavan, V., Lavine, G., Pandey, R. K., Racie, T., Rajeev, K. G., Rohl, I., Toudjarska, I., Wang, G., Wuschko, S., Bumcrot, D., Koteliansky, V., Limmer, S., Manoharan, M., and Vornlocher, H. P. (2004) Therapeutic silencing of an endogenous gene by systemic administration of modified siRNAs. *Nature 432*, 173–8.
(17) Saar, K., Lindgren, M., Hansen, M., Eiriksdottir, E., Jiang, Y., Rosenthal-Aizman, K., Sassian, M., and Langel, U. (2005) Cell-penetrating peptides: a comparative membrane toxicity study. *Anal. Biochem. 345*, 55–65.
(18) Simeoni, F., Morris, M. C., Heitz, F., and Divita, G. (2003) Insight into the mechanism of the peptide-based gene delivery system MPG: implications for delivery of siRNA into mammalian cells. *Nucleic Acids Res. 31*, 2717–24.
(19) Kim, W. J., Christensen, L. V., Jo, S., Yockman, J. W., Jeong, J. H., Kim, Y. H., and Kim, S. W. (2006) Cholesteryl oligoarginine delivering vascular endothelial growth factor siRNA effectively inhibits tumor growth in colon adenocarcinoma. *Mol. Ther. 14*, 343–50.
(20) Lundberg, P., El-Andaloussi, S., Sutlu, T., Johansson, H., and Langel, U. (2007) Delivery of short interfering RNA using endosomolytic cell-penetrating peptides. *Faseb J. 21*, 2664–71.

BC900488E

Solid-Phase Synthesis of PEGylated Lipopeptides Using Click Chemistry

Rasmus I. Jølck, Rolf H. Berg, and Thomas L. Andresen*

Technical University of Denmark, DTU Nanotech, Department of Micro- and Nanotechnology, Frederiksborgvej 399, 4000 Roskilde, Denmark. Received January 2, 2010; Revised Manuscript Received March 29, 2010

A versatile methodology for efficient synthesis of PEGylated lipopeptides via CuAAC "Click" conjugation between alkyne-bearing solid-supported lipopeptides and azido-functionalized PEGs is described. This new and very robust method offers a unique platform for synthesizing PEGylated lipopeptides with a high level of complexity. These molecules, obtained in a single purification step, are ideally suited for functionalization of solid-supported lipid bilayers and liposomal drug delivery systems and are particularly valuable in enzyme activation strategies.

We report for the first time a highly efficient and versatile methodology for the synthesis of PEGylated lipopeptides on solid-phase support by use of the Cu(I) catalyzed azide/alkyne Huisgen 1,3-dipolar cycloaddition (CuAAC "Click" conjugation) developed by the Meldal (*1*) and the Sharpless (*2*) laboratories. This approach allows for an efficient synthesis of highly functionalized PEGylated lipopeptides, which are particularly interesting in the field of drug delivery. Current research in advanced liposomal drug delivery systems is increasingly focused on materials with a high complexity and functionality. Functionalized lipids can be difficult and expensive to synthesize, which is highly problematic for their utilization in drug delivery systems in a clinical setting. This creates a crucial need for the development of new approaches for obtaining complex lipids efficiently. Conjugates with the general composition of lipid-peptide-PEG have drawn particular interest due to their use as triggering molecules in enzymatically sensitive drug delivery systems (*3*−*7*). Such conjugates are particularly difficult to synthesize due to the diverse properties of the peptidyl side chains, the high molecular mass of the poly(ethylene glycol) (PEG) polymer, and the amphiphilic character of the compounds, which results in difficult purification procedures. Currently, such molecules are predominantly synthesized by postassembly of the lipid, peptide, and PEG-polymer fragments using *N*-hydroxysuccinimide (NHS) and *N*,*N*″-dicyclohexylcarboiimide (DCC) chemistry in solution (*3*, *4*). This approach may result in unspecific binding if multiple binding sites are present within the peptide. Furthermore, it often results in moderate yields and time-consuming purification steps.

In the present communication, we report a novel approach for the synthesis of complex PEGylated lipopeptides solely on solid-phase support. The method is based on the known advantages of solid phase peptide synthesis (SPPS) (*8*) and the unique features of the CuAAC reaction. By adopting SPPS methodology, excess reagents can easily be removed by washing and the required purification steps are greatly reduced. In addition, the CuAAC reaction is one of the most useful and robust ligation reactions available and offers unique flexibility due to the high level of orthogonality to other chemical functionalities. We have developed a general methodology for achieving PEGylated lipopeptides on solid-phase support by using the CuAAC reaction with the solvent, the choice of resin, and the reaction time as the optimization parameters.

* Corresponding author. Tel: +45 46775480; Fax. +45 46774791; E-mail: thomas.andresen@nanotech.dtu.dk.

The resin-bound diacylated lipopeptide **1** (Figure 1) was chosen as an immobilized model substrate for the on-resin CuAAC reaction. A bulky peptide with large side-chain protection groups was chosen in order to demonstrate the versatility of the developed method. The alkyne functionality at the C-terminal of the peptide serves as a site specific conjugation site, whereas the tryptophan residue was chosen as a UV-marker for HPLC monitoring at 280 nm. The model lipopeptide **1** was synthesized on both PS (1% DVB cross-linked) resin and NovaSyn TentaGel resin both equipped with the Rink amide linker in order to elucidate the effect of the solid-phase support.

Lipopeptide **1** was synthesized manually by employing standard Fmoc chemistry (*9*) (see Supporting Information). The alkyne functionality was introduced at the C-terminal of the lipopeptide by using (*S*)-2-(Fmoc-amino)-4-pentynoic acid. The diacyl lipid anchor was achieved by conjugation of N_{α},N_{β}-di-Fmoc-L-2,3-diaminopropionic acid (Fmoc-dap(Fmoc)-OH) to the *N*-terminal of the peptide followed by diacylation with myristic acid (Scheme 1). After diacylation with myristic acid, a test cleavage of **1** from the resin was conducted in order to confirm the peptide sequence by MALDI-TOF MS and RP-HPLC (see Supporting Information).

The methoxy poly(ethylene glycol) azides **3a**−**c** needed for the on-resin CuAAC reaction were synthesized from the commercially available corresponding monomethoxy poly(ethylene glycol)s by either tosylation or mesylation of the alcohol, followed by a nucleophilic substitution with sodium azide, as illustrated in Scheme 2. This approach was easily scaled up and resulted in good yields. Azide formation was confirmed by ^{1}H NMR, ^{13}C NMR, MALDI-TOF MS, and FT-IR (see Supporting Information).

The efficiency of the CuAAC reaction between the resin-bound lipopeptide **1** and the monomethoxy poly(ethylene glycol) azides **3a**−**c** was studied as a function of time, choice of resin, and solvent. The reactions were carried out in 2.5 mL reaction vessels by using 50 mg lipopeptide modified resin (12.5−15 μmol lipopeptide), 5 equiv of the azide functionalized polymer, 5 equiv copper(I) iodide, and 5 equiv sodium ascorbate in either DMF/piperidine (4:1) or CH_2Cl_2/piperidine (4:1). The total reaction volume was adjusted in all cases to give a final concentration of the above-mentioned reagents of 61.25 mM (Scheme 3).

Small samples of resin were taken out after 1, 2, 5, 24, 48, and 72 h respectively. The PEGylated lipopeptides were cleaved from the resin with a mixture of TFA/TIS/H_2O, lyophilized, and analyzed by analytical RP-HPLC, employing a Waters XTerra RP_{18} 5 μm (4.6 × 150 mm) column with water/

10.1021/bc100002a © 2010 American Chemical Society
Published on Web 04/26/2010

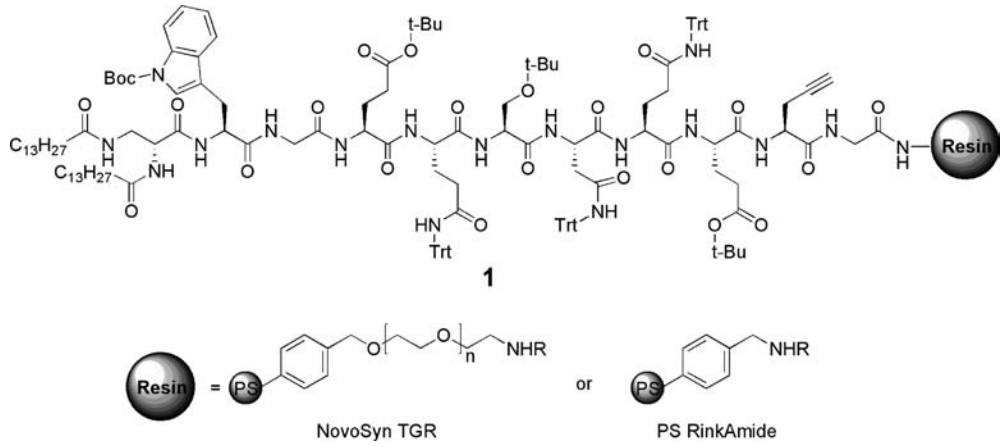
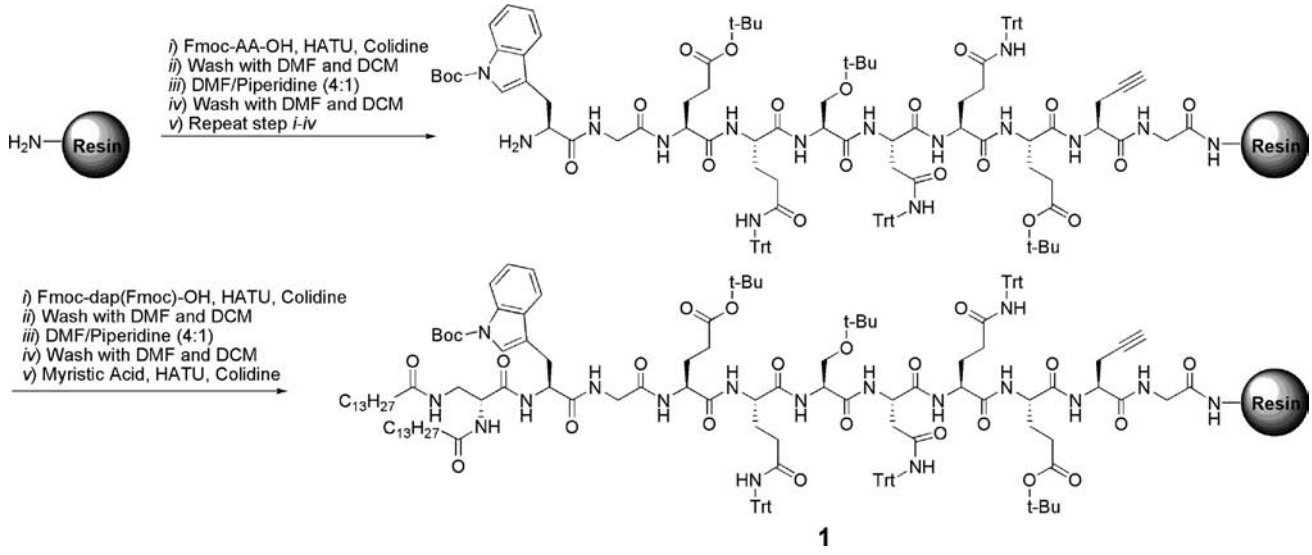
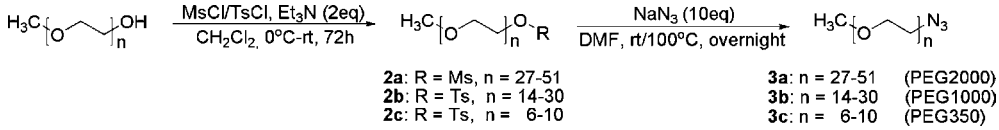


Figure 1. Fully protected diacylated lipopeptide **1** was employed as an immobilized model substrate for the on-resin CuAAC "Click" reaction with PEG. **1** was synthesized on both PS- and TentaGel resin equipped with Rink amide linker.

Scheme 1. Synthetic Pathway to the Resin-Bound Lipopeptide 1



Scheme 2. Synthetic Pathway to the Methoxy Poly(Ethylene Glycol) Azides 3a−c Used for On-Resin CuAAC Reaction

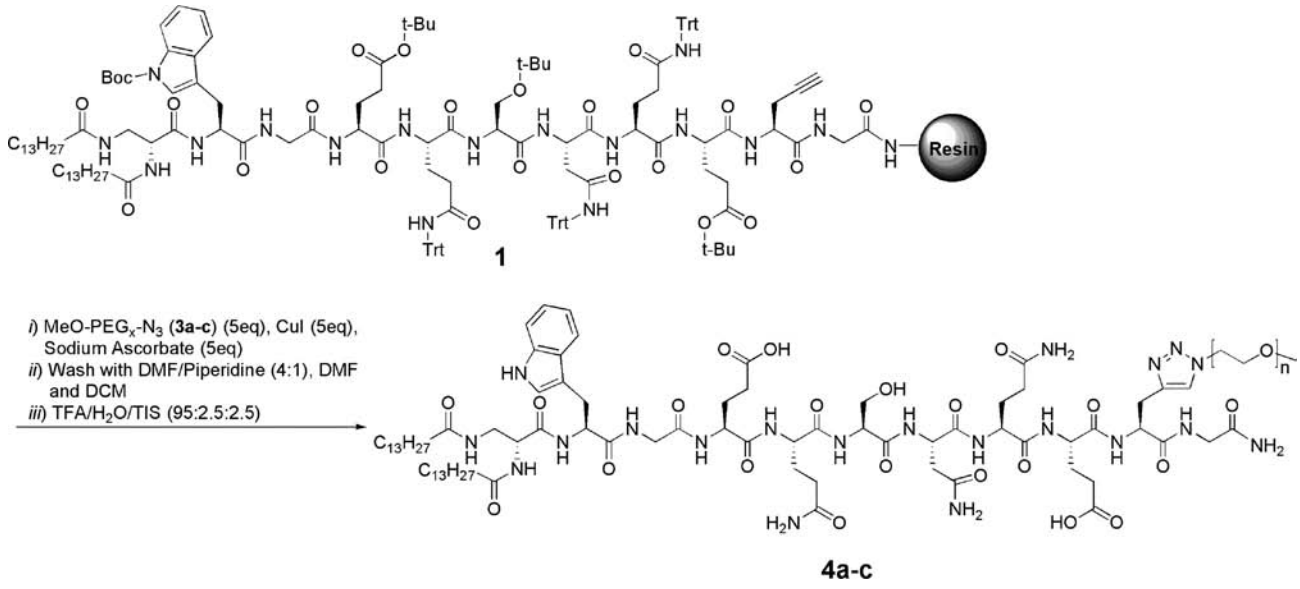


acetonitrile as the mobile phase. The degree of PEGylation was calculated from the area under the curve (AUC) from the two peaks corresponding to the lipopeptide and the PEGylated lipopeptide, respectively, at 280 nm by the formula given in eq 1.

$$\text{PEGylation degree} = \frac{\text{AUC}_{\text{lipid-peptide-PEG}}}{\text{AUC}_{\text{lipid-peptide-PEG}} + \text{AUC}_{\text{lipid-peptide}}} \times 100\% \quad (1)$$

The obtained results from the on-resin CuAAC on PS-RinkAmide resin with the synthesized PEG azides **3a**−**c** are given in Figure 2a. As Figure 2a clearly illustrates, the average size of the PEG-azide used for the CuAAC reaction has a significant influence on both the reaction rate and the degree of conversion. Complete PEGylation with MeO-PEG_{350}-N_3 (**3c**) was observed within the first hour, whereas MeO-PEG_{1000}-N_3 (**3b**) and MeO-PEG_{2000}-N_3 (**3a**) resulted in 80% and 50% PEGylation degree in 48 h, respectively. Since 99% of the available reaction sites on the resin are present inside the polystyrene matrix, diffusion of the reacting species is usually the limiting factor (*10*). This effect gets progressively more dominant with higher molecular weight polymers, which is clearly illustrated by the observed conversion. Similar observations have been reported by Klok et al. (*11*) and Mutter et al. (*12*), who studied *N*-terminal PEGylation with α-methoxy-*ω*-carbonyl functionalized PEG to PS-supported peptides. They reported quantitative conversion with MeO-PEG_{700}-COOH, whereas only 40% conversion was achieved when the average molecular weight was increased to 1800 Da. The strong decrease in the conversion degree was explained by the lower reactivity of the polymer, by the

Scheme 3. Employed Reaction Conditions for the On-Resin PEGylation of 1, Followed by Deprotection and Cleavage from Solid Support



decrease in diffusion into the PS-matrix, and by the increasing incompatibility of the polymer with the solid support. We have therefore compared the coupling efficiency of PEG on the PS-RinkAmide resin with the efficiency on NovaSyn TentaGel resin. The TentaGel resin was chosen because of its hydrophilic character due to the high content of PEG (approximately 70 mass%), which should improve the compatibility of the PEG-azides with the solid support. Furthermore, enzymes such as porcine pancreatic trypsin (23.5 kDa) and various lipases (30−40 kDa) have been reported to be able to penetrate to the core of TentaGel resins (*13, 14*), which clearly illustrates the easy accessibility of this class of resins. However, although the TentaGel resin should be more compatible and accessible to the reacting PEG-azides, no significant improvement of the PEGylation degree was observed (Figure 2b). Again, complete PEGylation with MeO-PEG_{350}-N_3 (**3c**) was observed within the first hour, whereas MeO-PEG_{1000}-N_3 (**3b**) and MeO-PEG_{2000}-N_3 (**3a**) resulted in 85% and 55% PEGylation degree in 48 h, respectively. Due to the lack of success in increasing the yield for the longer PEGs by choice of resin, we attempted to improve the degree of conversion by changing the solvent mixture for the on-resin CuAAC reaction. The swelling behavior of the resin is highly dependent on the solvent polarity, which will affect the diffusion of solute molecules within the matrix (*10*, *15*). By changing the solvent system from DMF/piperidine (4:1) to CH_2Cl_2/piperidine (4:1), the degree of conversion was improved from 85% to quantitative yield for MeO-PEG_{1000}-N_3 (**3b**) and from 55% to 85% for MeO-PEG_{2000}-N_3 (**3a**) (Figure 2c). Precipitation of a small amount of 1-(chloromethyl)-piperidine was observed, but did not effect the CuAAC reaction. Furthermore, addition of the Cu(I)-stabilizing ligand bathophenanthroline disulfonic acid (*16*) or an increase of temperature to 50 °C did not result in an improved conversion degree (data not shown). No evidence of alkyne−alkyne homocoupling (Glaser-coupling) was observed by MALDI-TOF MS at any time during the reaction, most likely due to the pseudo dilution effect (*17*). Excess of reagents and Cu(I) was easily washed away resulting in high purity of the crude products.

In conclusion, we have demonstrated a novel approach for the synthesis of PEGylated lipopeptides via the CuAAC "Click" reaction between an alkyne-bearing solid-supported diacylated lipopeptide and α-methoxy-*ω*-azido functionalized PEGs. The alkyne functionality was easily inserted into the peptide and served as a site-specific conjugation site, without the need for complex protective group strategies. The α-methoxy-*ω*-azido functionalized PEGs were readily available from the corresponding alcohols, and the on-resin CuAAC with the large polymers proved to be fully compatible with Fmoc-SPPS methodology. HPLC analysis of the cycloaddition products demonstrated a clear polymer size dependent conversion degree. Small polymers such as MeO-PEG_{350}-N_3 (**3c**) reacted readily and resulted in full conversion regardless of the choice of resin and solvent mixture. Full conversion was also achieved after 24 h with MeO-PEG_{1000}-N_3 (**3b**) when applying the NovaSyn TentaGel resin in a mixture of CH_2Cl_2/piperidine (4:1), whereas 85% conversion was achieved with MeO-PEG_{2000}-N_3 (**3a**) under the same conditions. The employed strategy allows for PEG insertion (and other molecules) in the final step of the synthesis to any position that is desired in the peptide, and importantly provides the possibility of verifying possible amino acid deletions before PEGylation, which can otherwise be very difficult to detect.

The method described here enables easy synthesis of molecules with a high level of complexity which, after a single purification step, is ideally suited for functionalization of solid-supported lipid bilayers and liposomal drug delivery systems and is particularly valuable in enzyme activation strategies. Additional targeting ligands or functional groups can easily be attached to the distal end of the PEG-azide, resulting in an even higher level of complexity, if needed. Furthermore, this method also enables easy synthesis of asymmetric diacyl lipopeptides by choosing a 2,3-diaminopropionic acid derivate with two orthogonal amine protection groups. This allows for optimization of the lipopeptide properties with respect to its integration and compatibility with lipid bilayers, which has been shown to be a crucial parameter in controlling the release of encapsulated content in liposomal drug delivery systems (*18*).

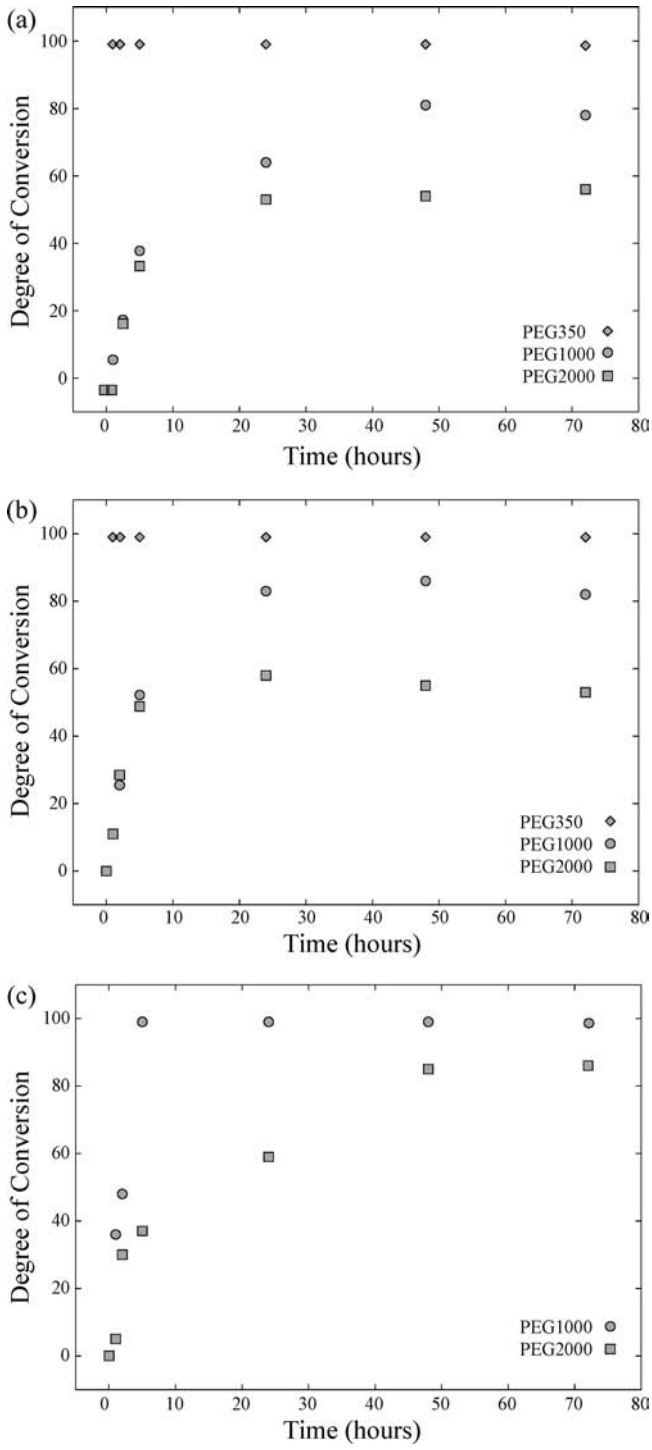


Figure 2. Measured degree of conversion of the CuAAC reaction between the resin bound lipopeptide **1** and the methoxy poly(ethylene glycol) azides (□) MeO-PEG_{2000}-N_3 (**3a**), (○) MeO-PEG_{1000}-N_3 (**3b**), and (◇) MeO-PEG_{350}-N_3 (**3c**). (a) PS-resin in DMF/piperidine (4:1), (b) TentaGel-resin in DMF/piperidine (4:1), and (c) TentaGel-resin in CH_2Cl_2/piperidine (4:1).

ACKNOWLEDGMENT

Financial support was kindly provided by the Danish Strategic Research Council (NABIIT) ref. 2106-07-0033 and the Technical University of Denmark (DTU).

Supporting Information Available: Detailed description of the synthetic approach to compound **1**, **3a**−**3c**, and **4a**−**c**, HPLC data, and characterization of the synthetic compounds (^{1}H NMR, ^{13}C NMR, IR, MALDI-TOF MS). This material is available free of charge via the Internet at http://pubs.acs.org.

LITERATURE CITED

(1) Tornøe, C. W. and Meldal, M. (2001) Peptidotriazoles: Copper(I)-catalyzed 1,3-dipolar cycloadditions on solid-phase. *Peptides: The Wave of the Future, Proceedings of the 17th American Peptide Symposium* (Houghten, R. A. and Lebl, M., Eds.), pp 263−264, American Peptide Society, San Diego, CA.

(2) Rostovtsev, V. V., Green, L. G., Fokin, V. V., and Sharpless, K. B. (2002) A stepwise Huisgen cycloaddition process: copper(I)-catalyzed regioselective "ligation" of azides and terminal alkynes. *Angew. Chem., Int. Ed. 41*, 2596–2599.

(3) Terada, T., Iwai, M., Kawakami, S., Yamashita, F., and Hashida, M. (2006) Novel PEG-matrix metalloproteinase-2 cleavable peptide-lipid containing galactosylated liposomes for hepatocellular carcinoma-selective targeting. *J. Controlled Release 111*, 333–342.

(4) Hatakeyama, H., Akita, H., Kogure, K., Oishi, M., Nagasaki, Y., Kihira, Y., Ueno, M., Kobayashi, H., Kikuchi, H., and Harashima, H. (2007) Development of a novel systemic gene delivery system for cancer therapy with a tumor-specific cleavable PEG-lipid. *Gene Ther. 14*, 68–77.

(5) Zhang, J. X., Zalipsky, S., Mullah, N., Pechar, M., and Allen, T. M. (2004) Pharmaco attributes of dioleoylphosphatidylethanolamine/cholesterylhemisuccinate liposomes containing different types of cleavable lipopolymers. *Pharmacol. Res. 49*, 185–198.

(6) Meers, P. (2001) Enzyme-activated targeting of liposomes. *Adv. Drug Delivery Rev. 53*, 265–272.

(7) Hatakeyama, H., Ito, E., Akita, H., Oishi, M., Nagasaki, Y., Futaki, S., and Harashima, H. (2009) A pH-sensitive fusogenic peptide facilitates endosomal escape and greatly enhances the gene silencing of siRNA-containing nanoparticles *in vitro* and *in vivo*. *J. Controlled Release 139*, 127–132.

(8) Merrifield, R. B. (1963) Solid phase synthesis. I. The synthesis of a tetrapeptide. *J. Am. Chem. Soc. 85*, 2149–2154.

(9) Fields, G. B., and Noble, R. L. (1990) Solid phase peptide synthesis utilizing 9-fluorenylmethoxycarbonyl amino acids. *Int. J. Pept. Protein Res. 35*, 161–214.

(10) Sucholeiki, I. (1999) New developments in solid phase synthesis supports. *Mol. Diversity 4*, 25–30.

(11) Vandermeulen, G. W. M., Tziatzios, C., and Klok, H. A. (2003) Reversible self-organization of poly(ethylene glycol)-based hybrid block copolymers mediated by a De Novo four-stranded alpha-helical coiled coil motif. *Macromolecules 36*, 4107–4114.

(12) Becker, H., Lucas, H. W., Maul, J., Pillai, V. N. R., Anzinger, H., and Mutter, M. (1982) Polyethyleneglycols grafted onto crosslinked polystyrenes - a new class of hydrophilic polymeric supports for peptide synthesis. *Makromol. Chem. Rapid Commun. 3*, 217–223.

(13) Quarrell, R., Claridge, T. D. W., Weaver, G. W., and Lowe, G. (1995) Structure and properties of TentaGel resin beads: Implications for combinatorial library chemistry. *Mol. Diversity 1*, 223–232.

(14) Sauerbrei, B., Jungmann, V., and Waldmann, H. (1998) An enzyme-labile linker group for organic syntheses on solid supports. *Angew. Chem., Int. Ed. 37*, 1143–1146.

(15) Park, B., and Lee, Y. (2000) The effect of PEG groups on swelling properties of PEG-grafted-polystyrene resins in various solvents. *React. Funct. Polym. 44*, 41–46.

(16) Lewis, W. G., Magallon, F. G., Fokin, V. V., and Finn, M. G. (2004) Discovery and characterization of catalysts for azide-alkyne cycloaddition by fluorescence quenching. *J. Am. Chem. Soc. 126*, 9152–9153.

(17) Scott, L. T., Rebek, J., Ovsyanko, L., and Sims, C. L. (1977) Organic chemistry on the solid phase. Site-site interactions on functionalized polystyrene. *J. Am. Chem. Soc. 99*, 625–626.

(18) Banejee, J., Hanson, A. J., Gadam, B., Elegbede, A. I., Tobwala, S., Ganuly, B., Wagh, A. V., Muhonen, W. W., Law, B., Shabb, J. B., Srivastava, D. K., and Mallik, S. (2009) Release of liposomal contents by cell-secreted matrix metalloproteinase-9. *Bioconjugate Chem. 20*, 1332–1339.

BC100002A

$^{188}Re(CO)_3$-Dipicolylamine-Alendronate: A New Bisphosphonate Conjugate for the Radiotherapy of Bone Metastases

Rafael Torres Martin de Rosales,[†] Ciara Finucane,[‡] Julie Foster,[‡] Stephen J. Mather,[‡] and Philip J. Blower*[,†]

King's College London, Division of Imaging Sciences, 4th Floor Lambeth Wing, St. Thomas' Hospital, SE1 7EH, London, United Kingdom, Centre for Molecular Oncology and Imaging, Institute of Cancer, Barts and The London School of Medicine, John Vane Science Centre, Charterhouse Square, EC1M 6BQ, London, United Kingdom. Received February 5, 2010; Revised Manuscript Received March 31, 2010

The palliation of pain due to bone metastases using targeted compounds containing β-emitters such as rhenium-188 (^{188}Re) is an accepted and effective form of treatment. Here, we describe the efficient synthesis and preclinical evaluation of $^{188}Re(CO)_3$-dipicolylamine(DPA)-alendronate, a novel bifunctional bisphosphonate for the palliative treatment of bone metastases. $^{188}Re(CO)_3$-DPA-alendronate can be easily synthesized with high specific activities and yields (18.8 GBq/mg, radiochemical yield $\geq$96%) in two steps using kit-based methodology, and in contrast with the clinically approved bisphosphonate $^{186/188}$Re-HEDP, it forms inert, single species that have been well-characterized. In vivo imaging and biodistribution studies demonstrate that $^{188}Re(CO)_3$-DPA-alendronate is superior to ^{188}Re-HEDP in targeting and accumulating in areas of high metabolic bone activity while having low soft-tissue uptake. In addition to these studies, a simple and convenient new method for purifying its precursor, *fac*-$[^{188}Re(CO)_3(H_2O)_3]^+$, is described.

Bone metastases arise most commonly from malignancy of breast, prostate, and lung cancers with an estimated 80% of patients eventually developing these secondary tumors (*1*). Other types of cancers such as melanoma, ovarian, thyroid, kidney, and head and neck are also likely to present these complications. One of the most distressing effects of bone metastases is extensive pain which severely impairs the quality of life of these patients. Palliation of the pain is usually managed by using strong opioid analgesics such as morphine. With ongoing administration, however, these drugs may induce severe side effects such as nausea, respiratory depression, and addiction/withdrawal syndrome. Palliative treatment using external beam radiation therapy is also commonly employed. This modality, however, is not recommended when the metastases have spread to several distant sites of the skeleton, as harmful radiation of essential organs cannot be avoided.

A very effective way of palliating the pain of these tumors is by internal radiotherapy using β^--emitting radionuclides (*2*). In this modality, a targeted radioactive pharmaceutical is taken up selectively by the bone metastases giving a high localized dose of radiotherapy to these areas. Several clinical trials have demonstrated its usefulness. In fact, several β^--emitting radiopharmaceuticals are currently being used in the clinic, of which the most popular are $^{89}SrCl_2$ (Metastron) and ^{153}Sm-ethylenediamine tetra(methylene phosphonic acid) (^{153}Sm-EDTMP or Quadramet) (*3*−*5*). Their clinical efficacy is proven, but they are not without disadvantages. ^{89}Sr and ^{153}Sm can only be produced in specialized nuclear reactors which are decreasing in number. Another concern is economic, as a single dose of one of these agents costs ca. $2900 per dose (*6*). Furthermore, neither is carrier-free, and the low stability of ^{153}Sm-EDTMP requires coadministration of a high concentration of unlabeled EDTMP. As a consequence, there has been a growing interest in developing therapeutic bone-seeking radiopharmaceuticals using generator-produced isotopes. Generator technologies not only provide straightforward availability of radioisotopes in any laboratory or clinical center around the world, but also reduce costs dramatically, as a single generator can potentially provide hundreds of doses.

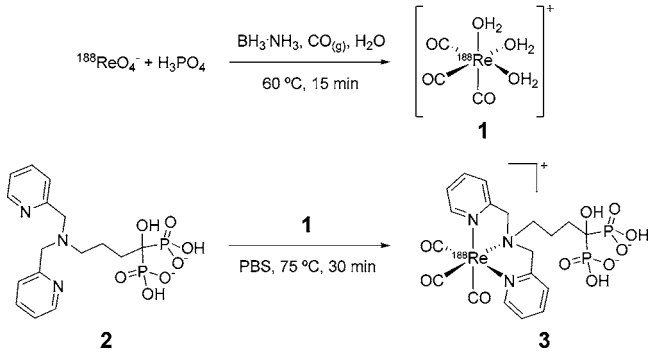
Rhenium-188 (^{188}Re) is arguably the most promising generator-produced β^--emitting radionuclide for the radiotherapy of bone metastases. ^{188}Re (E_{max} 2.12 MeV, 100%) is readily available using commercially available generators and shows favorable therapeutic properties. It also emits γ-photons (155 keV, 15%) that allow imaging using single photon emission computed tomography (SPECT) (*7, 8*). It has a medium-short half-life (16.9 h) and similar chemistry to technetium-99m (^{99m}Tc), the most widely used radionuclide in biomedical imaging. It was this Tc−Re analogy that drove forward the development of $^{186/188}$Rehydroxyethylidene-1,1-diphosphonate ($^{186/188}$Re-HEDP), the therapeutic "analogues" of the ^{99m}Tc-bisphosphonates (^{99m}Tc-BPs) routinely used as bone imaging agents. ^{186}Re-HEDP and ^{188}Re-HEDP have shown promise as palliative and therapeutic agents for bone metastases in recent clinical trials (*9*−*14*), but their properties are far from optimal from a chemical and pharmaceutical point of view. Their main drawback is that their chemical structures and compositions remain unidentified, although there are clear indications that they are composed of a mixture of anionic polymers (*15*). Also, these complexes are not entirely analogous to their technetium "analogues" since additional nonradioactive Re needs to be added as a "carrier" to achieve bone targeting (*14, 16, 17*). Furthermore, a large fraction of the injected complexes degrade to perrhenate (ReO_4^-) in vivo within 24 h and thus are not retained in bone metastases.

These drawbacks are attributable to poor chemical design. In these complexes, the BP acts as both radionuclide-binding ligand and targeting group, compromising both roles. We believe that to improve upon current Re-BPs a more logical approach is the use of targeted bifunctional ligands in which the targeting (BP) and metal chelating groups are separated within the molecule so that they can each function independently and effectively. A few recent reports describe such a bifunctional

* Corresponding author. E-mail: philip.blower@kcl.ac.uk.
[†] King's College London.
[‡] Centre for Molecular Oncology and Imaging.

10.1021/bc100071k © 2010 American Chemical Society
Published on Web 04/13/2010

Scheme 1



approach based on BPs (*18*−*20*). These BP conjugates, however, require complicated multistep synthetic strategies, show high plasma protein binding, and often form enantiomeric mixtures. To address these issues, we recently developed dipicolylamine(DPA)-alendronate (**2**, Scheme 1), an easily synthesized and well-characterized bifunctional bisphosphonate that forms single, well-defined isostructural Tc(I) and Re(I) tricarbonyl complexes that efficiently accumulate in bone tissue in vivo (*21*). Herein, we describe the synthesis, characterization, and preclinical in vivo studies of its ^{188}Re complex, $^{188}Re(CO)_3$-DPA-alendronate (**3**, Scheme 1), in comparison with ^{188}Re-HEDP to evaluate its potential as a new improved radiopharmaceutical for the therapy of bone metastases.

3 was easily made from generator-eluted $^{188}ReO_4^-$ in two steps (Scheme 1). The precursor *fac*-$[^{188}Re(CO)_3(H_2O)_3]^+$ (**1**, Scheme 1) was synthesized following the method of Schibli et al. (*22*). The radiochemical yields of **1** ranged between 80% and 85%, in agreement with the published method, with the remaining byproduct being unreduced and/or reoxidized $^{188}ReO_4^-$ and colloidal "$^{188}ReO_2$". A new purification method was required, since none was described in the original report. We reasoned that ionic chromatography could be used to separate the two byproducts based on their ionic and colloidal character. Thus, the crude solution was passed through a system composed of two solid-phase extraction columns connected in series, an OnGuard II Ag column (Dionex) to remove chloride ions from the saline solution, followed by a strong anion exchange (SAX) column (SAX Varian Bond Elut 100 mg) to retain $^{188}ReO_4^-$. Using this system, **1** is obtained in the eluate in good radiochemical yields (65%, based on initial $^{188}ReO_4^-$ activity) and excellent purities (≥99%) (Figure 1). The OnGuard II Ag column was proven necessary in order to remove the chloride ions from the saline solution that otherwise compete with $^{188}ReO_4^-$ in the SAX column, at the expense of **1** being retained to some extent in the OnGuard II Ag column (10%). Attempts to release trapped **1** using increasing concentrations of NaCl were unsuccessful, suggesting that the interaction between **1** and the OnGuard II Ag column is not ionic.

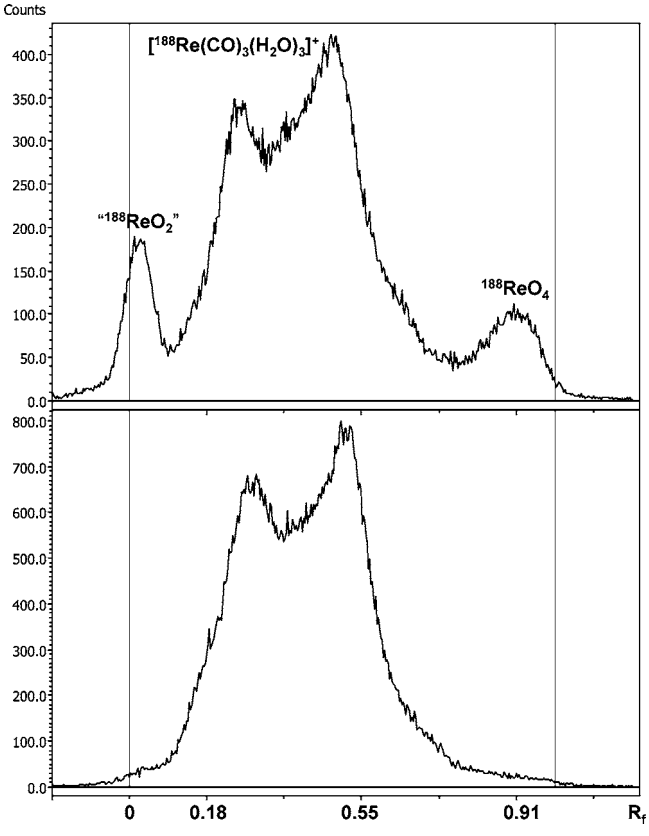


Figure 1. Silica gel TLC analyses of $[^{188}Re(CO)_3(H_2O)_3]^+$ (**1**) in the crude reaction solution (top) and after purification (bottom). Vertical lines indicate origin and solvent front. Using MeOH/HCl_{conc} (99%:1%) as the mobile phase, "$^{188}ReO_2$" colloids appear at $R_F = 0.05$, **1** appears as two broad peaks with $R_F = 0.20-0.50$, and $^{188}ReO_4^-$ appears at $R_F = 0.90$).

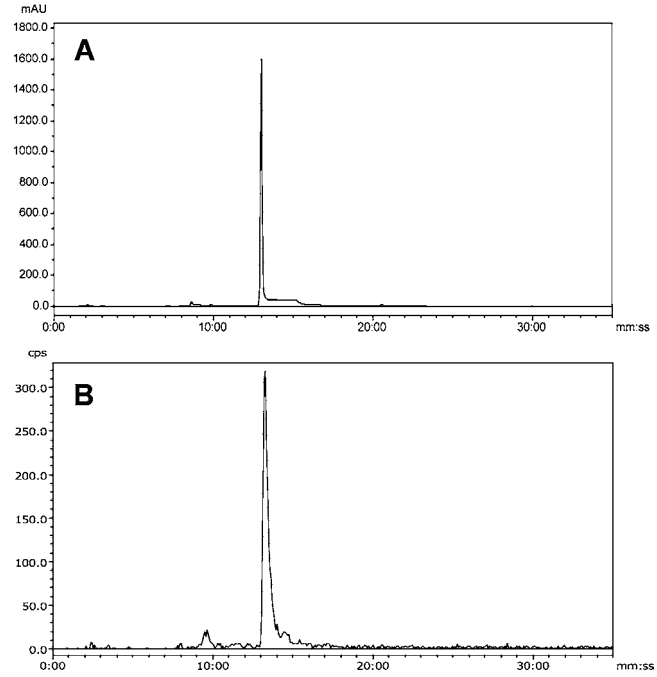


Figure 2. RP-HPLC chromatograms of nonradioactive $Re(CO)_3$-DPA-alendronate (A, UV detection (254 nm), t_R = 13:12 mm:ss) and **3** (B, β detection, t_R = 13:12 mm:ss). The difference in peak width is due to the larger cell volume of the γ/β^- detector.

3 was synthesized by mixing a solution of freshly made **1** (100 μL, 150 MBq) with **2** (0.01 mg/mL in PBS, 100 μL) in a N_2-purged vial followed by heating at 75 °C for 30 min. RP-HPLC analysis of the reaction solution revealed the formation of **3** with a specific activity of 18.8 GBq/mg and ≥96% radiochemical yield with the remainder of the activity being $^{188}ReO_4^-$. In contrast to $[^{99m}Tc(CO)_3(OH_2)_3]^+$, reoxidation of **1** to $^{188}ReO_4^-$ during labeling conditions has been observed previously with other ligands and can be rationalized to be the result of the lower redox potential of Re compared to that of Tc (*22*). Longer reaction times (up to 60 min) and lower reaction temperatures (60 °C) led to lower yields of **3**. A comparison with the chromatogram of the well-characterized nonradioactive $Re(CO)_3$-DPA-alendronate complex, and its ^{99m}Tc analogue, demonstrates the formation of the desired compound as a single species (Figure 2) (*21*).

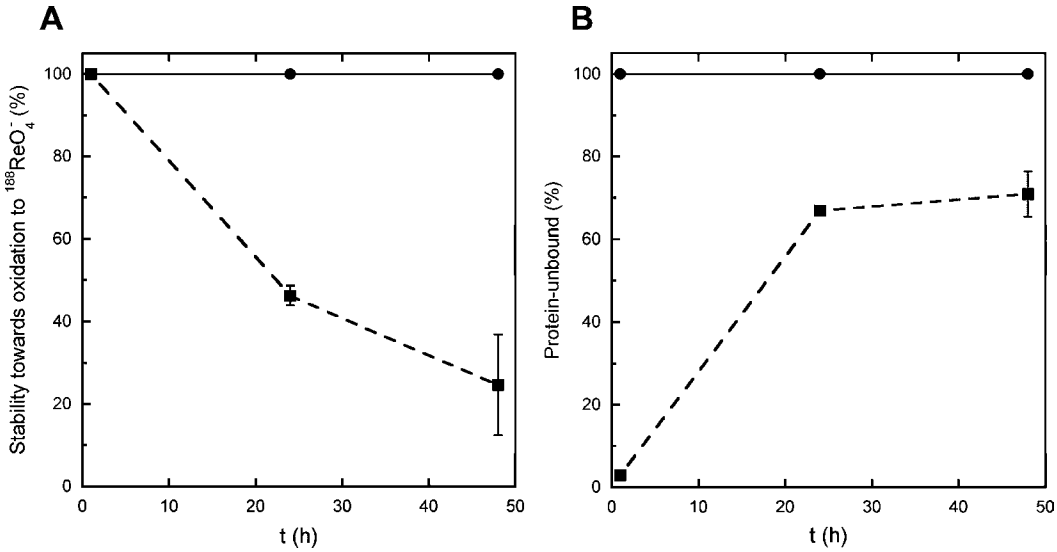


Figure 3. Stability study (toward oxidation to $^{188}ReO_4^-$) in PBS (A) and serum protein binding study (B), of **3** (black circles) and ^{188}Re-HEDP (black squares). See Supporting Information for methods.

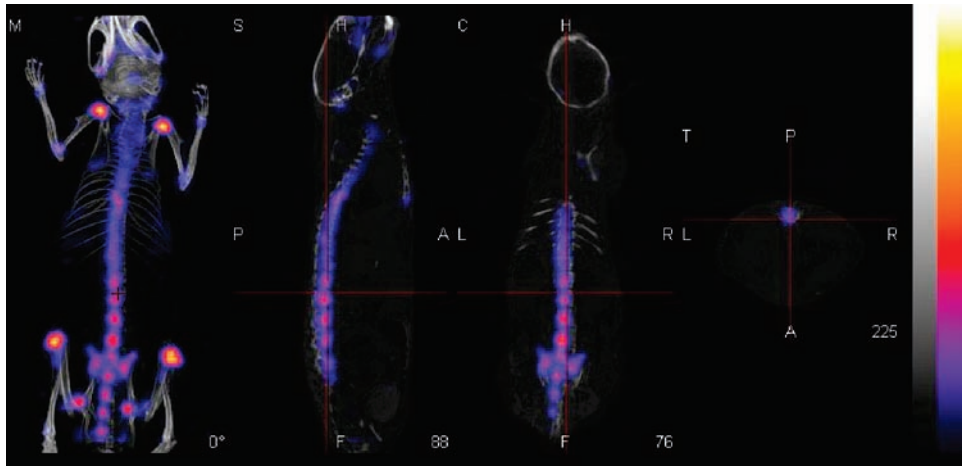


Figure 4. SPECT (color)/CT (grayscale) image taken 24 h postinjection showing the high uptake of **3** in bone tissue, particularly at the joints. From left to right, maximum intensity projection (M), sagittal (S), coronal (C), and transverse (T) sections.

In order to achieve the maximum therapeutic efficiency, ^{188}Re compounds must remain stable and bound to the target during at least one to three half-lives of ^{188}Re (16.9 h). One of the most important drawbacks of ^{188}Re-HEDP is its lack of stability both in vivo and in vitro. In order to assess the in vitro stability of **3** in comparison with ^{188}Re-HEDP, both compounds were incubated in PBS for 48 h at 37 °C. RP-HPLC and TLC analyses demonstrated that **3** did not degrade over this time, whereas most of ^{188}Re-HEDP oxidized to $^{188}ReO_4^-$ (up to 75%) (Figure 3A). Incubation of both compounds in human serum show most of the radioactivity from the ^{188}Re-HEDP sample remains bound to serum proteins during the first 24 h. After this time, ~70% of the radioactivity was free in solution. ITLC analyses demonstrated, however, that the non-protein-bound radioactivity was $^{188}ReO_4^-$, the decomposition product of ^{188}Re-HEDP. **3**, on the other hand, remained non-protein-bound and unmodified throughout the 48 h incubation period (Figure 3B).

In vivo imaging studies with **3** and ^{188}Re-HEDP were carried out at 1, 5, 24, and 48 h postinjection with adult BALB/c female mice (9 weeks old for **3** and 8 weeks old for ^{188}Re-HEDP) using a nanoSPECT/CT scanner (Figure 4). These studies confirmed the ability of **3** to accumulate in areas of metabolically active bone such as the joints, while soft-tissue organ uptake was very low throughout the experiment. Quantification of the images provided an interesting comparison of the pharmacokinetics of each compound (Figure 5). Thus, both compounds show an increase in uptake in the knee for the first 5 h. After this time, however, the uptake of **3** increased during the next 24 h, whereas that of ^{188}Re-HEDP diminished until the end of the 48 h experiment. We speculate that the increased uptake in bone of **3** during the first 24 h is the result of recycling of the unmetabolized, chemically intact complex from soft tissues, coupled with its excellent retention and slow release from bone compared to ^{188}Re-HEDP. This is in agreement with the biodistribution profiles at 48 h (vide infra) as well as with previous in vitro experiments with its ^{99m}Tc analogue, demonstrating the superior capabilities of Re/Tc-DPA-alendronate for binding and remaining bound to the main component of bone mineral (hydroxyapatite) (*21*). Further experiments, however, would be needed to confirm this hypothesis.

Ex vivo biodistribution studies at 48 h demonstrate that **3** exhibits higher uptake in bone tissue than ^{188}Re-HEDP (percentage of injected dose per gram of tissue (% ID/g) in one whole femur: 21.2 ± 6.6% for **3**; cf. 13.4 ± 0.2% for ^{188}Re-HEDP), consistent with its higher stability and/or better targeting properties (Figure 6). As shown in the above-mentioned imaging studies, soft-tissue uptake was very low for both compounds with most organs having an uptake of less than 0.6% ID/g. **3** consistently shows higher uptake than ^{188}Re-HEDP in these organs, especially in the liver (0.96 ± 0.2% ID/g). This may

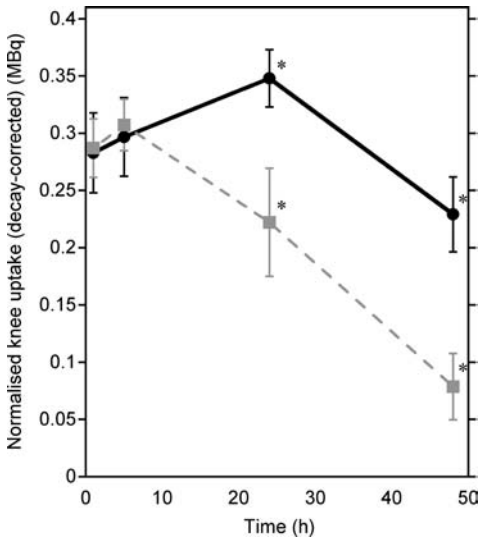


Figure 5. Uptake in the left knee (decay-corrected) after injection of **3** (33 MBq, black circles, continuous line) or ^{188}Re-HEDP (29 MBq, gray squares, dashed line) obtained from ROI analysis of the imaging data. The data from **3** were scaled by a factor of 29/33 to take into account the different injected activity. Values represent the mean ± SD (n = 3 mice). * indicates a significant difference ($P < 0.05$, Student's paired t-test) between the two radiotracers.

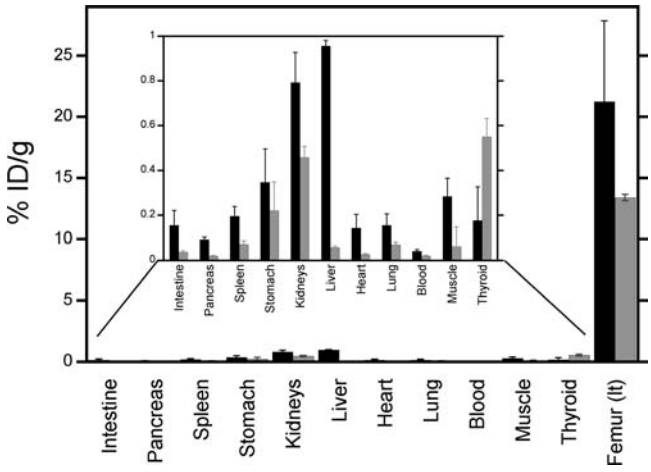


Figure 6. Biodistribution profile of **3** (black bars) and ^{188}Re-HEDP (gray bars) at t = 48 h postinjection. Values represent the mean ± SD (n = 3 mice).

be explained by the lipophilic nature of the carbonyl and dipicolylamine groups. An interesting exception, however, is the lower uptake of **3** in the thyroid. We attribute this to the tendency of ^{188}Re-HEDP, but not **3**, to decompose into $^{188}ReO_4^-$, which is known to be taken up by sodium-iodide symporter (NIS)-expressing organs such as the thyroid (*23*).

In conclusion, we have described a simple and convenient method to purify **1** that will facilitate the labeling of other small molecules and biomolecules such as His-tagged peptides/proteins with ^{188}Re in high radiochemical yields and purities (*24*). We have also described the synthesis of **3** as a new radiopharmaceutical for the radionuclide therapy of bone metastases. **3** can be easily synthesized with high specific activities in two steps using kit-based methodology, and in contrast with the clinically approved $^{186/188}$Re-HEDP, it forms an inert, single species that has been well-characterized. The strategy of using a designed chelating agent for rhenium rather than relying on the chelating properties of the bisphosphonate group is vindicated in that **3** displays superior stability, bone targeting, and retention properties. **3** is therefore an attractive candidate for further clinical studies.

ACKNOWLEDGMENT

This work was supported by Cancer Research UK (Grant C789/A7649) and conducted within the King's College London-UCL Comprehensive Cancer Imaging Centre supported by CRUK & EPSRC, in association with the MRC and DoH (England). This collaborative study was performed within the framework of the COST Action BM0607 on Targeted Radionuclide Therapy.

Supporting Information Available: Detailed experimental details for the synthesis of **1** and **3** and in vitro and in vivo procedures. This material is available free of charge via the Internet at http://pubs.acs.org.

LITERATURE CITED

(1) Jasmin, C. (2005) *Textbook of bone metastases*, J. Wiley & Sons, Hoboken, NJ.

(2) Lewington, V. J. (2005) Bone-seeking radionuclides for therapy. *J. Nucl. Med. 46*, 38s–47s.

(3) Lewington, V. J., McEwan, A. J., Ackery, D. M., Bayly, R. J., Keeling, D. H., Macleod, P. M., Porter, A. T., and Zivanovic, M. A. (1991) A prospective, randomized double-blind crossover study to examine the efficacy of Sr-89 in pain palliation in patients with advanced prostate-cancer metastatic to bone. *Eur. J. Cancer 27*, 954–958.

(4) Resche, I., Chatal, J. F., Pecking, A., Ell, P., Duchesne, G., Rubens, R., Fogelman, I., Houston, S., Fauser, A., Fischer, M., and Wilkins, D. (1997) A dose-controlled study of Sm-153-ethylenediaminetetramethylenephosphonate (EDTMP) in the treatment of patients with painful bone metastases. *Eur. J. Cancer 33*, 1583–1591.

(5) Tian, J. H., Zhang, J. M., Hou, Q. T., Oyang, Q. H., Wang, J. M., Luan, Z. S., Chuan, L., and He, Y. J. (1999) Multicentre trial on the efficacy and toxicity of single-dose samarium-153-ethylene diamine tetramethylene phosphonate as a palliative treatment for painful skeletal metastases in China. *Eur. J. Nucl. Med. 26*, 2–7.

(6) Krishnamurthy, G. T., and Krishnamurthy, S. (2000) Invited commentary - Radionuclides for metastatic bone pain palliation: A need for rational re-evaluation in the new millennium. *J. Nucl. Med. 41*, 688–691.

(7) Blower, P. J., Kettle, A. G., O'Doherty, M. J., Coakley, A. J., and Knapp, F. F. (2000) Tc-99m(V)DMSA quantitatively predicts Re-188(V)DMSA distribution in patients with prostate cancer metastatic to bone. *Eur. J. Nucl. Med. 27*, 1405–1409.

(8) Blower, P. J., Lam, A. S. K., O'Doherty, M. J., Kettle, A. G., Coakley, A. J., and Knapp, F. F. (1998) Pentavalent rhenium-188 dimercaptosuccinic acid for targeted radiotherapy: synthesis and preliminary animal and human studies. *Eur. J. Nucl. Med. 25*, 613–621.

(9) Tian, M., Zhang, H., Li, S., Endo, K., and Tanada, S. (2004) Rhenium-188-HEDP for the palliation of painful bone metastases. *J. Clin. Oncol. 22*, 766S–766S.

(10) Liepe, K., Kropp, J., Runge, R., and Kotzerke, J. (2003) Therapeutic efficiency of rhenium-188-HEDP in human prostate cancer skeletal metastases. *Br. J. Cancer 89*, 625–629.

(11) Palmedo, H., Grunwald, F., Wagner, U., Kohler, S., Krebs, D., and Biersack, H. J. (1998) Remission of bone metastases after combined chemotherapy and radionuclide therapy with Re-186-HEDP. *Clin. Nucl. Med. 23*, 501–504.

(12) de Klerk, J. M. H., van het Schip, A. D., Zonnenberg, B. A., van Dijk, A., Quirijnen, J., Blijham, G. H., and van Rijk, P. P. (1996) Phase I study of rhenium-186-HEDP in patients with bone metastases originating from breast cancer. *J. Nucl. Med. 37*, 244–249.

(13) Maxon, H. R., Schroder, L. E., Hertzberg, V. S., Thomas, S. R., Englaro, E. E., Samaratunga, R., Smith, H., Moulton, J. S., Williams, C. C., Ehrhardt, G. J., and Schneider, H. J. (1991) Rhenium-186(Sn)HEDP for treatment of painful osseous metastases - results of a double-blind crossover comparison with placebo. *J. Nucl. Med. 32*, 1877–1881.

(14) Palmedo, H., Guhlke, S., Bender, H., Sartor, J., Schoeneich, G., Risse, J., Grunwald, F., Knapp, F. F., and Biersack, H. J. (2000) Dose escalation study with rhenium-188 hydroxyethylidene diphosphonate in prostate cancer patients with osseous metastases. *Eur. J. Nucl. Med. 27*, 123–130.

(15) Handeland, Å., Lindegaard, M. W., and Heggli, D.-E. (1989) Biodistribution of anionic separated MDP complexes from different MDP preparations. *Eur. J. Nucl. Med. Mol. Imaging 15*, 609–611.

(16) de Klerk, J. M. H., van Dijk, A., van het Schip, A. D., Zonnenberg, B. A., and van Rijk, P. P. (1992) Pharmacokinetics of 186Re after administration of 186Re-HEDP to patients with bone metastases. *J. Nucl. Med. 33*, 646–651.

(17) Hsieh, B. T., Hsieh, J. F., Tsai, S. C., Lin, W. Y., Wang, S. J., and Ting, G. (1999) Comparison of various rhenium-188-labeled diphosphonates for the treatment of bone metastases. *Nucl. Med. Biol. 26*, 973–976.

(18) Ogawa, K., Mukai, T., Arano, Y., Ono, M., Hanaoka, H., Ishino, S., Hashimoto, K., Nishimura, H., and Saji, H. (2005) Development of a rhenium-186-labeled MAG_3-conjugated bisphosphonate for the palliation of metastatic bone pain based on the concept of bifunctional radiopharmaceuticals. *Bioconjugate Chem. 16*, 751–757.

(19) El-Mabhouh, A., Angelov, C., McEwan, A., Jia, G., and Mercer, J. (2004) Preclinical investigations of drug and radionuclide conjugates of bisphosphonates for the treatment of metastatic bone cancer. *Cancer Biother. Radiopharm. 19*, 627–640.

(20) Ogawa, K., Mukai, T., Arano, Y., Otaka, A., Ueda, M., Uehara, T., Magata, Y., Hashimoto, K., and Saji, H. (2006) Rhenium-186-monoaminemonoamidedithiol-conjugated bisphosphonate derivatives for bone pain palliation. *Nucl. Med. Biol. 33*, 513–520.

(21) Torres Martin de Rosales, R., Finucane, C., Mather, S. J., and Blower, P. J. (2009) Bifunctional bisphosphonate complexes for the diagnosis and therapy of bone metastases. *Chem. Commun.* 4847–4849.

(22) Schibli, R., Schwarzbach, R., Alberto, R., Ortner, K., Schmalle, H., Dumas, C., Egli, A., and Schubiger, P. A. (2002) Steps toward high specific activity labeling of biomolecules for therapeutic application: Preparation of precursor $[^{188}Re(H_2O)_3(CO)_3]^+$ and synthesis of tailor-made bifunctional ligand systems. *Bioconjugate Chem. 13*, 750–756.

(23) Riese, C., Seitz, S., Schipper, M., and Behr, T. (2009) Effective treatment of pancreatic neuroendocrine tumours transfected with the sodium iodide symporter gene by 186Re-perrhenate in mice. *Eur. J. Nucl. Med. Mol. Imaging 36*, 1767–1773.

(24) Waibel, R., Alberto, R., Willuda, J., Finnern, R., Schibli, R., Stichelberger, A., Egli, A., Abram, U., Mach, J. P., Pluckthun, A., and Schubiger, P. A. (1999) Stable one-step technetium-99m labeling of His-tagged recombinant proteins with a novel Tc(I)-carbonyl complex. *Nat. Biotechnol. 17*, 897–901.

BC100071K

Synthesis of Tumor-Avid Photosensitizer−Gd(III)DTPA Conjugates: Impact of the Number of Gadolinium Units in T_1/T_2 Relaxivity, Intracellular localization, and Photosensitizing Efficacy

Lalit N. Goswami,[†] William H. White III,[†] Joseph A. Spernyak,[‡] Manivannan Ethirajan,[†] Yihui Chen,[†] Joseph R. Missert,[†] Janet Morgan,[§] Richard Mazurchuk,[‡] and Ravindra K. Pandey*,[†]

PDT Center, Cell Stress Biology, Preclinical Imaging Facility, and Department of Dermatology, Roswell Park Cancer Institute, Buffalo, New York 14263. Received December 2, 2009; Revised Manuscript Received March 8, 2010

To develop novel bifunctional agents for tumor imaging (MR) and photodynamic therapy (PDT), certain tumor-avid photosensitizers derived from chlorophyll-a were conjugated with variable number of Gd(III)aminobenzyl DTPA moieties. All the conjugates containing three or six gadolinium units showed significant T_1 and T_2 relaxivities. However, as a bifunctional agent, the 3-(1′-hexyloxyethyl)pyropheophorbide-a (HPPH) containing 3Gd(III) aminophenyl DTPA was most promising with possible applications in tumor-imaging and PDT. Compared to HPPH, the corresponding 3- and 6Gd(III)aminobenzyl DTPA conjugates exhibited similar electronic absorption characteristics with a slightly decreased intensity of the absorption band at 660 nm. However, compared to HPPH, the excitation of the broad "Soret" band (near 400 nm) of the corresponding 3Gd(III)aminobenzyl-DTPA analogues showed a significant decrease in the fluorescence intensity at 667 nm.

INTRODUCTION

Magnetic resonance imaging (MRI) is a medical imaging technique commonly used in radiology to visualize the internal structure and function of the body (*1*). MRI provides greater contrast between the different soft tissues of the body than computed tomography (CT), making it especially useful in neurological (brain), musculoskeletal, cardiovascular, and oncological (cancer) imaging (*2*). However, MR imaging has some practical disadvantages. For example, benign tumors may be difficult to distinguish from malignant lesions. The fibrocystic disease of the breast, fibroadenomas, sclerosing adenosis, atypical hyperplasia, lobular carcinoma in situ (LCIS), and breast papillomas can all produce contrast enhancement patterns that are hard to distinguish from malignant processes. In addition, some benign processes such as proliferative dysplasia, inflammation, wounds, and benign tumors can enhance in a similar fashion to malignant tumors (*3*). These shortcomings of MRI in measuring tissue properties offer opportunities that may be satisfied with information provided by optical fluorescence imaging with near-infrared light (*4*). Optical techniques offer the potential to contribute greatly to the expansion of clinical multimodality techniques. Their ability to image structural, functional, and molecular information at different spatial and temporal scales makes them very attractive. In this case, the multimodality approach can be used as the combination of multiple optical techniques in one instrument and/or the fusion of an optical technique with another well-established clinical modality, such as PET, CT, or MRI (*5, 6*).

Clinically, optical imaging modality has been employed to enable or improve PDT (*7*). Most of the porphyrin-based photosensitizers generally fluoresce and the fluorescent nature of these porphyrins has been exploited for the detection of early stage cancers in the lung, bladder, and other sites (*8*). In addition, for treatment of early disease or for deep-seated tumors the fluorescence can be used to guide the activated light. Most of the porphyrin-based compounds are not optimal fluorophores for tumor detection for several reasons, especially a small shift between the long-wavelength absorption and emission bands, which make it technically difficult to separate the fluorescence from excitation wavelength (*9*). However, certain pyropheophorbide-a analogues (e.g., HPPH) produce very high fluorescence quantum yields and exciting them at their long-wavelength absorption (665 nm) produces two emission bands: a strong peak at 670 nm, and a weaker band at 720 nm. This characteristic of HPPH has been used for in vivo fluorescence imaging of canine and other tumors (*10*). In recent years, integrating the strengths of each imaging modality has become a major research area. The research in our laboratory has also been focused on designing certain porphyrin-based compounds as "multifunctional agents" for tumor imaging and photodynamic therapy (PDT) (*11*−*15*).

We have previously shown that HPPH (*16*−*21*) a tumor-avid photosensitizer (currently undergoing phase I/II human clinical trials) on conjugating with Gd(III)aminobenzyl DTPA [Gd(III)ADTPA] can be used for both tumor MR imaging and PDT (*22, 23*). In our initial study, among the compounds investigated, the conjugates with two Gd(III)ADTPA moieties showed greater tumor contrast than the corresponding mono-Gd(III)ADTPA derivative. However, poor solubility of these agents in various clinically acceptable formulations restricted their use for detailed in vivo studies, including toxicity. To investigate the effect of increased number of GD(III)ADTPA moieties in tumor imaging/PDT and also to improve water solubility, we decided to extend this approach further, and a series of tumor-avid long-wavelength absorbing chlorophyll-a analogues (pyropheophorbide-a and purpurinimide) containing three or six Gd(III)ADTPA moieties with variable lipophilicity were synthesized. For developing "bifunctional agents" with longer wavelength absorption than HPPH (λ_{max}: 660 nm), a related conjugate containing a highly tumor-avid purpurinimide (λ_{max}: 700 nm) (*24*) was also prepared. In this manuscript, the synthesis, photophysical properties, T_1/T_2 relaxivity, and in vitro photosensitizing efficacy of a series of novel photosensitizer-

[†] PDT Center, Cell Stress Biology.
[‡] Preclinical Imaging Facility.
[§] Department of Dermatology.

10.1021/bc9005305 © 2010 American Chemical Society
Published on Web 04/13/2010

Gd(III)ADTPA conjugates are discussed. The second part of our study (see the following paper in this issue) is focused on selecting the optimal "multifunctional agent" for tumor-imaging (MRI, fluorescence imaging) and PDT. In vivo PDT response is discussed in terms of long-term cure rate and monitoring of the vascular response via immunohistochemistry. Finally, the biodistribution and organ-specific toxicity of the lead compound (C-14 labeled) at variable time points is also discussed.

EXPERIMENTAL PROCEDURES

Chemistry. The synthetic intermediates and the final products were characterized by NMR (400 MHz), mass spectrometry (EIMS and HRMS) and elemental analysis. ^{1}H NMR spectra were recorded on a Bruker AMX-400 spectrometer. Chemical shifts are expressed in δ ppm. All photophysical experiments were carried out using spectroscopic-grade solvents. The reactions were monitored by TLC and/or spectrophotometrically. Column chromatography was performed either over Silica Gel 60 (70−230 mesh) or neutral Alumina (Brockmann grade III, 50 mesh). UV−visible spectra were recorded on Varian Cary 50 Bio UV−visible spectrophotometer using dichloromethane as solvent unless otherwise specified. Fluorescence spectra were recorded on a Varian Cary Eclipse fluorescence spectrophotometer with an excitation wavelength in the "Soret" band region between 410 and 425 nm.

Compound 1. HPPH (100.0 mg, 0.157 mmol), amine **A** (97.8 mg, 0.235 mmol), EDCI (1-ethyl-3-(3-dimethylaminopropyl)-carbodiimide hydrochloride) (60.2 mg, 0.314 mmol), and DMAP (4-dimethylaminopyridine) (38.36 mg, 0.314 mmol) were taken in a dry, round-bottom flask (100 mL). Dry dichloromethane (30 mL) was added and the reaction mixture was stirred at room temperature for 16 h under N_2 atm. The reaction mixture was diluted with dichloromethane (100 mL), washed with brine solution, organic layer separated, dried over sodium sulfate, and concentrated. The crude mixture was chromatographed over silica gel using 1−3% methanol/dichloromethane mixture as eluent to give product **1**. Yield: 130.0 mg (80.0%). UV−vis (λ_{max}, dichloromethane): 318, 412, 506, 537, 604, and 660 nm. ^{1}H NMR (400 MHz, $CDCl_3$): δ 9.78 (s, 1H, H-5), 9.41 (s, 1H, H-10), 8.54 (s, 1H, H-20), 5.96−5.91 (m, 2H, $CH_3\underline{CH}$Ohexyl, NH), 5.33 (d, 1H, CH-15^1, J = 19.6 Hz), 5.14 (d, 1H, CH-15^1, J = 19.6 Hz), 4.53 (q, 1H, H-17, J = 7.2 Hz), 4.32 (m, 1H, H-18), 3.71−3.67 (m, 2H, -O$\underline{CH_2}$-hexyl), 3.63−3.60 (m, 2H, 8-$\underline{CH_2}CH_3$), 3.52 (s, 3H, 7-CH_3), 3.39 (s, 3H, 2-CH_3), 3.27 (s, 3H, 12-CH_3), 2.67 (m, 1H, CH-17^2), 2.37 (m, 1H, H-17^2), 2.26 (m, 1H, H-17^1), 2.15−2.13 (m, 9H, 3CH_2-chain and $\underline{CH_3}$CHOhexyl), 1.97 (m, 1H, H-17^1), 1.92 (t, 6H, 3CH_2-chain, J = 7.6 Hz), 1.80 (d, 3H, 18-CH_3, J = 7.2 Hz), 1.73 (m, 2H, CH_2hexyl), 1.66 (t, 3H, 8-$CH_2\underline{CH_3}$, J = 7.6 Hz), 1.44 (m, 2H, CH_2hexyl), 1.30 (s, 27H, 3$CO_2{}^t$Bu), 1.24 (m, 4H, 2CH_2hexyl), 0.78 (t, 3H, CH_3hexyl, J = 6.8 Hz), 0.04 (brs, 1H, NH), −1.68 (brs, 1H, NH). EIMS: 1035 (MH^+). HRMS: Calcd for $C_{61}H_{87}N_5O_9$, 1033.6503; found 1034.6564 (MH^+).

Compound 2. Compound **1** (73.0 mg, 0.07 mmol) was stirred with 70% trifluoroacetic acid (TFA)/dichloromethane (DCM, 5.0 mL) at room temperature for 3 h. The resultant mixture was concentrated and dried under high vacuum to remove traces of TFA. To this crude preparation were added amino-benzyl-DTPA-penta-*tert*-butyl ester (219.0 mg, 0.282 mmol), EDCI (67.0 mg, 0.352 mmol), and DMAP (43.0 mg, 0.352 mmol). Dry dichloromethane (30 mL) was added and the reaction mixture was stirred at RT for 16 h under N_2 atm. The reaction mixture was diluted with dichloromethane (100 mL), washed with brine solution, organic layer separated, dried over sodium sulfate, and concentrated. The crude mixture was chromatographed over alumina G (III) using 1−3% methanol/dichloromethane mixture as eluent to give product **2**. Yield: 130.0 mg (58.47%). UV−vis (λ_{max}, dichloromethane): 319, 411, 506, 537, 604, 661. ^{1}HNMR (400 MHz, $CDCl_3$): δ 9.74 (splitted s, 1H, H-5), 9.36 (splitted s, 1H, H-10), 8.54 (splitted s, 1H, H-20), 8.17 (brs, 1H, NH), 7.74 (m, 1H, Ph-DTPA), 7.61−7.56 (m, 2H, Ph-DTPA), 7.43 (m, 4H, Ph-DTPA), 7.12 (m, 5H, Ph-DTPA), 6.96 (brs, 1H, NH), 5.96 (m, 1H, $CH_3\underline{CH}$Ohexyl), 5.29 (d, 1H, CH-15^1, J = 19.2 Hz), 5.11 (d, 1H, CH-15^1, J = 19.2 Hz), 4.47 (m, 1H, H-17), 4.26 (m, 1H, H-18), 3.64 (m, 2H, and O$\underline{CH_2}$hexyl), 3.54 (m, 2H, 8-$\underline{CH_2}CH_3$), 3.45−3.38 (m, 30H, 15CH_2-DTPA), 3.36 (s, 3H, 7-CH_3), 3.32 (s, 3H, 2-CH_3), 3.22 (s, 3H, 12-CH_3), 3.12 (m, 3H, CH-DTPA), 2.84−2.70 (m, 19H, 9CH_2-DTPA and CH-17^2), 2.59 (m, 6H, 6CH_2-benzyl), 2.47−2.41 (m, 8H, 3CH_2-chain, CH-17^2 and CH-17^1), 2.19−2.15 (m, 9H, 3CH_2-chain, $\underline{CH_3}$CH−Ohexyl), 2.06 (d, 3H, 18-CH_3, J = 7.6 Hz), 2.00 (m, 1H, CH-17^1), 1.74 (m, 4H, 2CH_2-hexyl), 1.66 (t, 3H, 8-$CH_2\underline{CH_3}$, J = 7.2 Hz), 1.60 (m, 135H for 15 $CO_2{}^t$Bu), 1.26 (m, 4H, 2CH_2-hexyl), 0.77 (m, 3H, CH_3-Ohexyl), 0.55 (brs, 1H, NH), −0.24 (brs, 1H, NH). HRMS: Calcd for $C_{172}H_{267}N_{17}O_{36}$, 3149.053; found 3150.10 (MH^+).

Compound 3. Compound **2** (110.0 mg, 0.034 mmol) was stirred with 70% TFA/DCM (5.0 mL) at room temperature for 3 h. The resultant mixture was concentrated and dried under high vacuum to remove trace TFA. The crude preparation thus obtained was dissolved in pyridine (10 mL), and while stirring, $GdCl_3 \cdot 6H_2O$ (77.9 mg, 0.21 mmol) in 1 mL of water was added slowly, and the resultant mixture was stirred for 16 h. The reaction mixture was concentrated to dryness under high vacuum. The residue was washed with water (10 mL × 3) and acetone (10 mL × 3) and finally dried under high vacuum using P_2O_5 as drying agent. Yield: 75.0 mg (77.55%). UV−vis (λ_{max}, MeOH): 620, 408, 504, 537, 604, and 660 nm. Elemental analysis: Calcd for $C_{113}H_{151}Gd_3N_{17}O_{36}$: C, 48.55; H, 5.44; Gd, 16.88; N, 8.52; O, 20.61. Found: C, 48.68; H, 5.49; N, 8.57.

Compound 5. Acid **4** (100.0 mg, 0.143 mmol), amine **A** (89.1 mg, 0.214 mmol), EDCI (54.9 mg, 0.28 mmol), and DMAP (34.9 mg, 0.28 mmol) were taken in a dry, round-bottom flask (RBF, 100 mL). Dry dichloromethane (30 mL) was added to it, and the reaction mixture was stirred at RT for 16 h under N_2 atm. The reaction mixture was diluted with dichloromethane (100 mL), washed with brine solution, the organic layer separated, dried over sodium sulfate, and concentrated. The crude mixture was chromatographed over silica gel using 1−2% methanol/dichloromethane mixture as eluent to give product **5**. Yield: 134.0 mg (85.3%). UV−vis (λ_{max} nm, dichloromethane): 318, 411, 506, 536, 604, and 661. ^{1}H NMR (400 MHz, $CDCl_3$): δ 9.76 (splitted s, 1H, H-5), 9.38 (splitted s, 1H, H-10), 8.55 (s, 1H, H-20), 6.02 (d, 1H, $CH_3\underline{CH}$OTEG, J = 6.4 Hz), 5.99 (brs, 1H, NH), 5.34 (d, 1H, CH-15^1, J = 20.0 Hz), 5.15 (d, 1H, CH-15^1, J = 20.0 Hz), 4.58 (q, 1H, H-17, J = 6.8 Hz), 4.33 (m, 1H, H-18), 3.88−3.75 (m, 4H, 2$\underline{CH_2}$-O-TEG), 3.70−3.62 (m, 6H, 3$\underline{CH_2}$-O-TEG), 3.55 (m, 2H, 8-$\underline{CH_2}CH_3$), 3.47−3.44 (m, 2H, $\underline{CH_2}$-O-TEG), 3.40 (s, 3H, 7-CH_3), 3.39 (s, 3H, 2-CH_3), 3.29 (s, 3H, 12-CH_3), 3.27 (s, 3H, $\underline{CH_3}$-O-TEG), 2.69 (m, 1H, CH-17^2), 2.39 (m, 1H, CH-17^2), 2.31 (m, 1H, CH-17^1), 2.14 (m, 8H, 4CH_2-chain), 2.00 (m, 1H, CH-17^1), 1.92 (m, 7H, 2CH_2-chain, $\underline{CH_3}$CHOTEG), 1.82 (d, 3H, 18-CH_3, J = 7.2 Hz), 1.68 (t, 3H, 8-$CH_2\underline{CH_3}$, J = 7.6 Hz), 1.31 (s, 27H, 3$CO_2{}^t$Bu), 0.42 (brs, 1H, NH), −1.69 (brs, 1H, NH). EIMS: 1097 (MH^+). Calcd for $C_{62}H_{89}N_5O_{12}$, 1095.6507; found 1096.6571 (MH^+).

Compound 6. Compound **5** (100.0 mg, 0.091 mmol) was stirred with 80% TFA/DCM (5.0 mL) at room temperature for 3 h. The resultant mixture was concentrated and dried under high vacuum to remove trace TFA. To this crude preparation were added amino-benzyl-DTPA-penta-*tert*-butyl ester (285.0 mg, 0.365 mmol), EDCI (105.0 mg, 0.54 mmol), and DMAP (66.8 mg, 0.54 mmol). Dry dichloromethane (30 mL) was added, and the reaction mixture was stirred at RT for 16 h under N_2

atm. The reaction mixture was diluted with dichloromethane (100 mL), washed with brine solution, the organic layer separated, dried over sodium sulfate, and concentrated. The crude mixture was chromatographed over alumina Gr(III) using 1−3% methanol/dichloromethane mixture as eluent to give product **6**. Yield: 250.0 mg (85.3%). UV−vis (λ_{max} nm, dichloromethane): 319, 411, 506, 537, 606, 661. ^{1}HNMR (400 MHz, $CDCl_3$): δ 9.70 (splitted s, 1H, H-5), 9.44 (splitted s, 1H, H-10), 9.37 (brs, 1H, NH), 9.20 (brs, 1H, NH), 8.56 (m, 1H, NH), 8.47 (s, 1H, H-20), 7.77 (m, 1H, Ph-DTPA), 7.59 (m, 2H, Ph-DTPA), 7.44 (m, 2H, Ph-DTPA), 7.10 (m, 6H, Ph-DTPA), 6.81 (m, 1H, Ph-DTPA), 5.97 (m, 1H, $CH_3\underline{CH}$OTEG), 5.20 (m, 2H, CH_2-15^1), 4.60 (m, 1H, H-17), 4.22 (m, 1H, H-18), 3.81−3.64 (m, 4H, 2CH_2−OTEG), 3.57−3.50 (m, 4H, 8-$\underline{CH_2}CH_3$, $\underline{CH_2}$-OTEG), 3.60 (m, 6H, 3CH_2OTEG), 3.38 (s, 30H, 15CH_2-DTPA), 3.35 (s, 3H, 7-CH_3), 3.23 (m, 6H, 12-CH_3, OCH_3-TEG), 3.04 (m, 3H, 3CH-DTPA), 2.70 (m, 19H, 9CH_2-DTPA, CH-17^2), 2.55 (m, 7H, 3CH_2-benzyl and CH-17^2), 2.32 (t, 6H, 3CH_2-chain, J = 6.8 Hz), 2.23 (m, 1H, CH-17^1), 2.10 (d, 3H, $\underline{CH_3}$CH−OTEG, J = 6.4 Hz), 2.01 (m, 1H, CH-17^1), 1.77 (d, 3H, 18-CH_3, J = 7.2 Hz), 1.68 (t, 3H, 8-$CH_2\underline{CH_3}$, J = 7.6 Hz), 1.59 (t, 6H, 3CH_2-chain, J = 6.4 Hz), 1.44 (m, 135H, 15CO_2^{t}Bu), −1.75 (brs, 1H, NH). HRMS: Calcd for $C_{173}H_{269}N_{17}O_{39}$, 3211.077; found 3212.20 (MH^+).

Compound 7. Compound **6** (226.0 mg, 0.07 mmol) was stirred with 80% TFA/DCM (5.0 mL) at room temperature for 3 h. The resultant mixture was concentrated and dried under high vacuum to remove trace TFA. The crude mixture thus obtained was dissolved in pyridine (10 mL), and while stirring, $GdCl_3\cdot 6H_2O$ (156.9 mg, 0.422 mmol) in 1 mL of water was added slowly, and the resultant mixture was stirred for 16 h. The reaction mixture was concentrated to dryness under high vacuum. The residue was washed with water (10 mL × 3) and acetone (10 mL × 3) and finally dried under high vacuum using P_2O_5 as drying agent. Yield: 165.0 mg (82.5%). UV−vis (λ_{max} nm, MeOH): 320, 408, 505, 537, 605, and 660 nm. Elemental analysis: Calcd for $C_{113}H_{149}Gd_3N_{17}O_{39}$: C, 47.77; H, 5.29; Gd, 16.60; N, 8.38; O, 21.96. Found: C, 47.85; H, 5.30; N, 8.43.

Compound 9. Acid **8** (82.0 mg, 0.118 mmol), amine **A** (73.6 mg, 0.177 mmol), EDCI (45.3 mg, 0.236 mmol), and DMAP (28.8 mg, 0.236 mmol) were taken in a dry RBF (100 mL). Dry dichloromethane (30 mL) was added and the reaction mixture was stirred at RT for 16 h under N_2 atm. The reaction mixture was diluted with dichloromethane (100 mL), washed with brine solution, the organic layer separated, dried over sodium sulfate, and concentrated. The crude mixture was chromatographed over silica gel using 1−2% methanol/dichloromethane mixture as eluent to give product **9**. Yield: 90.0 mg (69.8%). UV−vis (λ_{max}, dichloromethane): 365, 418, 509, 545, and 699 nm. ^{1}H NMR (400 MHz, $CDCl_3$): δ 9.75 (splitted s, 1H, meso-H), 9.64 (s, 1H, meso-H), 8.55 (s, 1H, meso-H), 6.25 (m, 1H, CONH), 5.79 (q, 1H, $CH_3\underline{CH}$Obutyl, J = 6.4 Hz), 5.34 (m, 1H, H-17), 4.52 (t, 2H, -N$\underline{CH_2}$butyl, J = 7.2 Hz), 4.42 (m, 1H, H-18), 3.84 (s, 3H, ring-CH_3), 3.70−3.59 (m, 4H, -O$\underline{CH_2}$-butyl, 8-$\underline{CH_2}CH_3$), 3.32 (s, 3H, ring-CH_3), 3.17 (s, 3H, ring-CH_3), 2.61 (m, 1H, CH-17^2), 2.43 (m, 1H, H-17^2), 2.27 (m, 1H, H-17^1), 2.20 (t, 6H, 3$\underline{CH_2}$-chain, J = 7.2 Hz), 2.06 (m, 3H, $\underline{CH_3}$CHObutyl), 2.01 (t, 6H, 3$\underline{CH_2}$-chain, J = 7.6 Hz), 1.82 (m, 1H, H-17^1), 1.75 (d, 3H, 18-CH_3, J = 6.0 Hz), 1.68 (t, 3H, 8-$CH_2\underline{CH_3}$, J = 7.6 Hz), 1.62 (m, 8H, 4$\underline{CH_2}$butyl), 1.34 (s, 27H, 3CO_2^{t}Bu), 1.10 (t, 3H, $\underline{CH_3}$-obutyl, J = 7.2 Hz), 0.87 (t, 3H, $\underline{CH_3}$-Nbutyl, J = 7.2 Hz), 0.40 (brs, 1H, NH), −0.06 (brs, 1H, NH). EIMS: 1092 (MH^+). HRMS: Calcd for $C_{63}H_{90}N_6O_{10}$, 1090.6718; found 1091.6823 (MH^+).

Compound 10. Compound **9** (80.0 mg, 0.073 mmol) was stirred with 70% TFA/DCM (5.0 mL) at room temperature for 3 h. The resultant mixture was concentrated and dried under high vacuum to remove trace TFA. To this crude mixture were added, amino-benzyl-DTPA-penta-*tert*-butyl ester (286.0 mg, 0.366 mmol), EDCI (84.4 mg, 0.44 mmol), and DMAP (53.7 mg, 0.44 mmol). Dry dichloromethane (30 mL) was added, and the reaction mixture was stirred at RT for 16 h under N_2 atm. The reaction mixture was diluted with dichloromethane (100 mL), washed with brine solution, the organic layer separated, dried over sodium sulfate, and concentrated. The crude mixture was chromatographed over alumina G (III) using 1−3% methanol/dichloromethane mixture as eluent to give product **10**. Yield: 140.0 mg (59.57%). UV−vis (λ_{max}, dichloromethane): 365, 418, 509, 546, 699 nm. ^{1}H NMR (400 MHz, $CDCl_3$): δ 9.75 (splitted s, 1H, meso-H), 9.63 (splitted s, 1H, meso-H), 9.33 (brs, 1H, NH), 8.60 (splitted s, 1H, meso-H), 7.61 (m, 2H, Ph-DTPA), 7.58 (m, 1H, Ph-DTPA), 7.37 (m, 3H, Ph-DTPA), 7.12 (m, 5H, Ph-DTPA), 6.84 (m, 1H, Ph-DTPA), 5.76 (m, 1H, $CH_3\underline{CH}$Obutyl), 5.39 (m, 1H, H-17), 4.45 (m, 3H, H-18 and N$\underline{CH_2}$butyl), 3.82 (s, 3H, ring-CH_3), 3.65 (m, 4H, 8-$\underline{CH_2}CH_3$ and O$\underline{CH_2}$butyl), 3.38 (m, 22H, 11CH_2-DTPA), 3.31 (m, 11H, 4CH_2-DTPA and ring-CH_3), 3.17 (s, 3H, ring-CH_3), 3.03 (m, 3H, CH-DTPA), 2.84−2.61 (m, 19H, 9CH_2-DTPA and CH-17^2), 2.47 (m, 8H, 6CH_2-benzyl and CH-17^2 and CH-17^1), 2.20 (m, 6H, 3CH_2-chain), 2.04 (d, 3H, $\underline{CH_3}$CHObutyl, J = 6.8 Hz), 1.96 (m, 6H, 3CH_2-chain), 1.84 (m, 1H, CH-17^1), 1.73 (s, 3H, 17-CH_3), 1.67 (t, 3H, 8-$CH_2\underline{CH_3}$, J = 7.2 Hz), 1.60 (m, 4H, 2CH_2-Obutyl), 1.41 (m, 135H for 15 CO_2^{t}Bu), 1.37 (m, 4H, 2CH_2-N-butyl), 1.03 (t, 3H, CH_3-Obutyl, J = 6.8 Hz), 0.86 (t, 3H, CH_3-N-butyl, J = 6.8 Hz), −0.09 (brs, 1H, NH). HRMS: Calcd for $C_{174}H_{270}N_{18}O_{37}$, 3206.104; found 3207.250 (MH^+).

Compound 11. Compound **10** (130.0 mg, 0.04 mmol) was stirred with 70% TFA/DCM (5.0 mL) at room temperature for 3 h. The resultant mixture was concentrated and dried under high vacuum to remove trace TFA. The crude preparation thus obtained was dissolved in pyridine (10 mL), and while stirring, $GdCl_3\cdot 6H_2O$ (90.3 mg, 0.243 mmol) in 1 mL of water was added slowly and the resultant mixture was stirred for 16 h. The reaction mixture was concentrated to dryness under high vacuum. The residue was washed with water (10 mL × 3), acetone (10 mL × 3), and finally dried under high vacuum using P_2O_5 as drying agent. Yield: 80.0 mg (69.9%). UV−vis (λ_{max}, MeOH): 364, 415, 546, and 700 nm. Elemental analysis: Calcd for $C_{114}H_{150}Gd_3N_{18}O_{37}$: C, 48.28; H, 5.33; Gd, 16.63; N, 8.89; O, 20.87. Found: C, 48.14; H, 5.40; N, 8.93.

Compound 12. HPPH (100.0 mg, 0.157 mmol), di-*tert*-butyl iminodiacetate (77.0 mg, 0.314 mmol), EDCI (60.2 mg, 0.314 mmol), and DMAP (38.36 mg, 0.314 mmol) were taken in a dry RBF (100 mL). Dry dichloromethane (30 mL) was added and the reaction mixture was stirred at room temperature for 16 h under N_2 atm. The reaction mixture was diluted with dichloromethane (100 mL), washed with brine solution, the organic layer separated, dried over sodium sulfate, and concentrated. The crude mixture was chromatographed over silica gel using 1−1.5% methanol/dichloromethane mixture as eluent to give product **12**. Yield: 120.0 mg (88.3%). UV−vis (λ_{max} nm, dichloromethane): 317, 411, 506, 538, 605, and 660 nm. ^{1}H NMR (400 MHz, $CDCl_3$): δ 9.80 (s, 1H, H-5), 9.51 (s, 1H, H-10), 8.55 (s, 1H, H-20), 5.94 (q, 1H, $CH_3\underline{CH}$Ohexyl, J = 6.4 Hz), 5.33 (d, 1H, CH-15^1, J = 20.0 Hz), 5.17 (d, 1H, CH-15^1, J = 20.0 Hz), 4.52 (q, 1H, H-17, J = 7.6 Hz), 4.41 (m, 1H, H-18), 4.04 (m, 2H, CH_2chain), 3.75 (m, 2H, -O$\underline{CH_2}$-hexyl), 3.67 (s, 3H, 7-CH_3), 3.62 (m, 2H, 8-$\underline{CH_2}CH_3$), 3.42 (s, 3H, 2-CH_3), 3.37 (m, 2H, CH_2chain), 3.29 (s, 3H, 12-CH_3), 2.77 (m, 1H, CH-17^2), 2.46 (m, 1H, CH-17^2), 2.16 (m, 1H, CH-17^1), 2.13 (m, 3H, and $\underline{CH_3}$CHOhexyl), 1.97 (m, 1H, CH-17^1), 1.84 (d, 3H, 18-CH_3, J = 7.2 Hz), 1.78 (m, 2H, CH_2hexyl), 1.72 (t, 3H, 8-$CH_2\underline{CH_3}$, J = 7.6 Hz), 1.49 (s, 9H, CO_2^{t}Bu), 1.46 (m, 2H, CH_2hexyl), 1.45 (s, 9H, CO_2^{t}Bu), 1.25 (m, 4H,

2CH_2hexyl), 0.8 (t, 3H, CH_3hexyl, $J = 6.8$ Hz), 0.42 (brs, 1H, NH), −1.7 (brs, 1H, NH). EIMS: 865 (MH^+) (*25*).

Compound 13. Compound **12** (120.0 mg, 0.139 mmol) was stirred with 70% TFA/DCM (5.0 mL) at room temperature for 3 h. The resultant mixture was concentrated and dried under high vacuum to remove trace TFA. To this crude preparation were added amine **A** (144.2 mg, 0.34 mmol), EDCI (106.6 mg, 0.556 mmol), and DMAP (67.8 mg, 0.556 mmol). Dry dichloromethane (30 mL) was added, and the reaction mixture was stirred at RT for 16 h under N_2 atm. The reaction mixture was diluted with dichloromethane (100 mL), washed with brine solution, the organic layer separated, dried over sodium sulfate, and concentrated. The cude mixture was chromatographed over silica gel using 2−6% methanol/dichloromethane mixture as eluent to give product **13**. Yield: 190.0 mg (88.3%). UV−vis (λ_{max}, dichloromethane): 318, 411, 506, 537, 605, and 660 nm. ^{1}H NMR (400 MHz, $CDCl_3$): δ 9.78 (s, 1H, H-5), 9.52 (s, 1H, H-10), 8.3 (s, 1H, H-20), 8.27 (brs, 1H, NH), 8.17 (brs, 1H, NH), 6.59 (brs, 1H, NH), 5.90 (m, 1H, $CH_3\underline{CH}$Ohexyl), 5.34 (d, 1H, CH-15^1, $J = 20.0$ Hz), 5.15 (d, 1H, CH-15^1, $J = 20.0$ Hz), 4.53 (q, 1H, H-17, $J = 6.0$ Hz), 4.36 (m, 1H, H-18), 3.77 (m, 2H, -O$\underline{CH_2}$-hexyl), 3.69 (m, 2H, 8-$\underline{CH_2}CH_3$), 3.67 (s, 3H, 7-CH_3), 3.61 (m, 4H, 2CH_2chain), 3.36 (s, 3H, 2-CH_3), 3.26 (s, 3H, 12-CH_3), 2.77 (m, 1H, CH-17^2), 2.66 (m, 1H, CH-17^2), 2.52 (m, 1H, CH-17^1), 2.23 (m, 12H, 6CH_2-chain), 2.11 (d, 3H, $\underline{CH_3}$CHOhexyl, $J = 6.4$ Hz), 2.07 (m, 6H, 3CH_2-chain), 1.95 (m, 6H, 3CH_2-chain), 1.93 (m, 1H, CH-17^1), 1.81 (d, 3H, 18-CH_3, $J = 7.2$ Hz), 1.75 (m, 2H, CH_2hexyl), 1.71 (t, 3H, 8-$CH_2\underline{CH_3}$, $J = 8.0$ Hz), 1.43 (m, 2H, CH_2hexyl), 1.41 (s, 27H, 3$CO_2{}^t$Bu), 1.32 (s, 27H, 3$CO_2{}^t$Bu), 1.24 (m, 4H, 2CH_2hexyl), 0.77 (t, 3H, CH_3hexyl, $J = 6.8$ Hz). EIMS: 1548 (MH^+). HRMS: Calculated for $C_{87}H_{131}N_7O_{17}$, 1545.9601, found 1545.9574 (M^+).

Compound 14. Compound **13** (100.0 mg, 0.064 mmol) was stirred with 80% TFA/DCM (5.0 mL) at room temperature for 3 h. The resultant mixture was concentrated and dried under high vacuum to remove trace TFA. To this crude preparation were added amino-benzyl-DTPA-penta-*tert*-butyl ester (503.5 mg, 0.64 mmol), EDCI (123.9 mg, 0.64 mmol), and DMAP (78.8 mg, 0.64 mmol). Dry *N*,*N*-dimethylformamide (15 mL) was added and reaction mixture was stirred at RT for 16 h under N_2 atm. The reaction mixture was concentrated under vacuum, dichloromethane added (100 mL), washed with brine solution, the organic layer separated, dried over sodium sulfate, and concentrated. The crude mixture was chromatographed over alumina G (III) using 1−3% methanol/dichloromethane mixture as eluent to give product **14**. Yield: 250.0 mg (70.0%). UV−vis (λ_{max}, dichloromethane): 318, 413, 507, 539, 606, and 660. Elemental analysis: Calcd for $C_{309}H_{491}N_{31}O_{71}$: C, 64.25; H, 8.57; N, 7.52; O, 19.67. Found: C, 64.30; H, 8.59; N, 7.56.

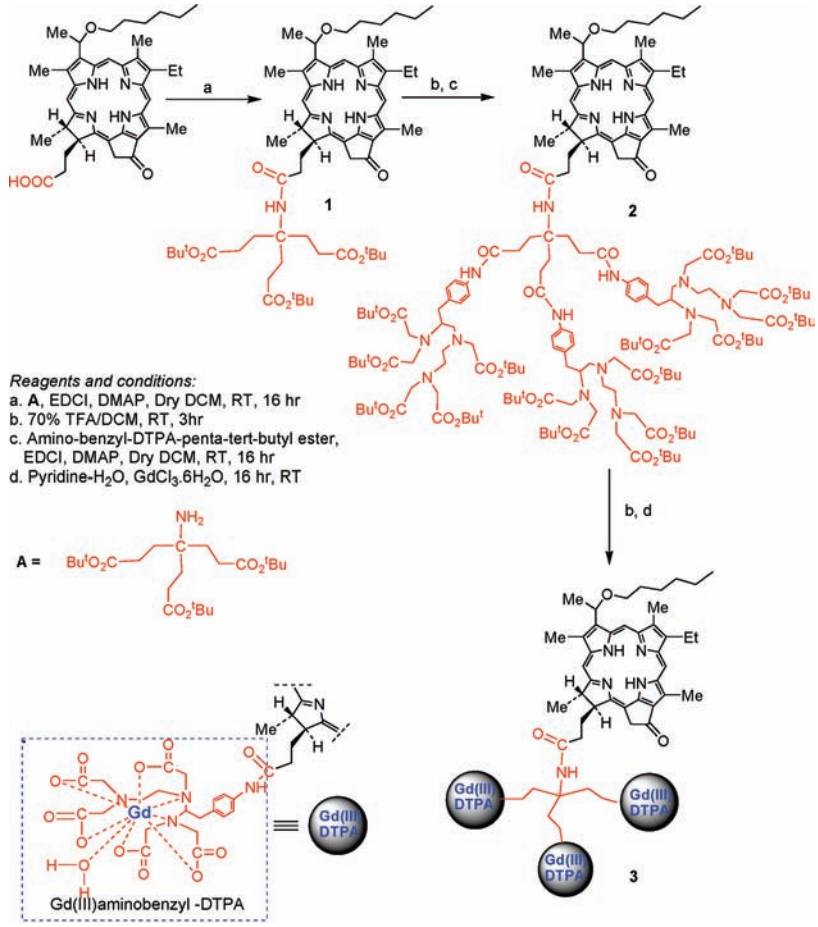
Compound 15. Compound **14** (225.0 mg, 0.038 mmol) was stirred with 70% TFA/DCM (5.0 mL) at room temperature for 3 h. The resultant mixture was concentrated and dried under high vacuum to remove trace TFA. The crude preparation thus obtained was dissolved in pyridine (10 mL), and while stirring, $GdCl_3 \cdot 6H_2O$ (173.7 mg, 0.46 mmol) in 1 mL of water was added slowly, and the resultant mixture was stirred for 16 h. The reaction mixture was concentrated to dryness under high vacuum. The residue was washed with water (10 mL × 3) and acetone (10 mL × 3) and finally dried under high vacuum using P_2O_5 as drying agent. Yield: 170.0 mg (86.7%). UV−vis (λ_{max}, MeOH): 320, 411, 507, 539, 606, and 660 nm. Elemental analysis: Calcd for $C_{189}H_{251}Gd_6N_{31}O_{71}$: C, 45.07; H, 5.02; Gd, 18.73; N, 8.62; O, 22.55. Found: C, 45.15; H, 5.10; N, 8.58.

Compound 16. Acid **4** (150.0 mg, 0.214 mmol), di-*tert*-butyl iminodiacetate (105.0 mg, 0.429 mmol), EDCI (82.3 mg, 0.429 mmol), and DMAP (52.0 mg, 0.429 mmol) were taken into a dry RBF (100 mL). Dry dichloromethane (30 mL) was added and the reaction mixture was stirred at RT for 16 h under N_2 atm. The reaction mixture was diluted with dichloromethane (100 mL), washed with brine solution, the organic layer was separated, dried over sodium sulfate, and concentrated. The crude mixture was chromatographed over silica gel using 1−1.5% methanol/dichloromethane mixture as eluent to give product **16**. Yield: 165.0 mg (82.9%). UV−vis (λ_{max}, dichloromethane): 318, 411, 506, 536, 605, and 661 nm. ^{1}H NMR (400 MHz, $CDCl_3$): δ 9.75 (splitted s, 1H, H-5), 9.52 (splitted s, 1H, H-10), 8.53 (s, 1H, H-20), 6.01 (m, 1H, $CH_3\underline{CH}$OTEG), 5.31 (d, 1H, CH-15^1, $J = 20.0$ Hz), 5.13 (d, 1H, CH-15^1, $J = 20.0$ Hz), 4.50 (q, 1H, H-17, $J = 7.2$ Hz), 4.36 (m, 1H, H-18), 4.02 (m, 2H, CH_2chain), 3.85 (m, 2H, $\underline{CH_2}$-O-TEG), 3.79 (m, 2H, $\underline{CH_2}$-O-TEG), 3.73 (m, 4H, 3$\underline{CH_2}$-O-TEG), 3.68 (s, 3H, 7-CH_3), 3.66 (m, 2H, 8-$\underline{CH_2}CH_3$), 3.55 (m, 2H, $\underline{CH_2}$-O-TEG), 3.39 (s, 3H, 2-CH_3), 3.27 (s, 6H, 12-CH_3 and $\underline{OCH_3}$-TEG), 2.75 (m, 1H, CH-17^2), 2.44 (m, 1H, CH-17^2), 2.41 (m, 1H, CH-17^1), 2.16 (m, 1H, CH-17^1), 2.14 (d, 3H, $\underline{CH_3}$CHOTEG, $J = 6.4$ Hz), 1.81 (d, 3H, 18-CH_3, $J = 7.6$ Hz), 1.71 (t, 3H, 8-$CH_2\underline{CH_3}$, $J = 7.6$ Hz), 1.44 (splitted s, 9H, $CO_2{}^t$Bu), 1.06 (splitted s, 9H, $CO_2{}^t$Bu), 0.39 (brs, 1H, NH), −1.80 (brs, 1H, NH). EIMS: 927 (MH^+). HRMS: Calcd for $C_{52}H_{71}N_5O_{10}$, 925.5201, found 926.5288 (MH^+).

Compound 17. Compound **16** (140.0 mg, 0.151 mmol) was stirred with 70% TFA/DCM (5.0 mL) at room temperature for 3 h. The resultant mixture was concentrated and dried under high vacuum to remove trace TFA. To this crude preparation were added amine **A** (188.2 mg, 0.453 mmol), EDCI (115.9 mg, 0.604 mmol), and DMAP (73.7 mg, 0.604 mmol). Dry dichloromethane (30 mL) was added and the reaction mixture was stirred at RT for 16 h under N_2 atm. The reaction mixture was diluted with dichloromethane (100 mL), washed with brine solution, the organic layer separated, dried over sodium sulfate, and concentrated. The crude mixture was chromatographed over silica gel using 3−7% methanol/dichloromethane mixture as eluent to give product **17**. Yield: 210.0 mg (86.4%). UV−vis (λ_{max}, dichloromethane): 318, 411, 506, 536, 604, and 661 nm. ^{1}H NMR (400 MHz, $CDCl_3$): δ 9.76 (splitted s, 1H, H-5), 9.53 (s, 1H, H-10), 8.63 (s, 1H, H-20), 8.31 (splitted s, 1H, CONH), 6.56 (splitted s, 1H, CONH), 6.00 (m, 1H, $CH_3\underline{CH}$OTEG), 5.35 (d, 1H, CH-15^1, $J = 20.0$ Hz), 5.16 (d, 1H, CH-15^1, $J = 20.0$ Hz), 4.53 (q, 1H, H-17, $J = 7.6$ Hz), 4.36 (d, 1H, H-18, $J = 10.4$ Hz), 3.85−3.80 (m, 4H, 2$\underline{CH_2}$-O-TEG), 3.74−3.71 (m, 6H, 2CH_2chain, $\underline{CH_2}$-O-TEG), 3.67 (s, 3H, 7-CH_3), 3.66 (m, 4H, 8-$\underline{CH_2}CH_3$, $\underline{CH_2}$-O-TEG), 3.53 (m, 2H, $\underline{CH_2}$-O-TEG), 3.42−3.39 (m, 5H, $\underline{CH_2}$-O-TEG, 2-CH_3), 3.27−3.26 (m, 6H, 12-CH_3, $\underline{OCH_3}$TEG), 2.75 (m, 1H, CH-17^2), 2.67 (m, 1H, CH-17^2), 2.52 (m, 1H, CH-17^1), 2.24−2.22 (m, 13H, 6$\underline{CH_2}$-chain, CH-17^1), 2.14 (d, 3H, $\underline{CH_3}$CHOTEG, $J = 6.8$ Hz), 2.09−2.04 (m, 6H, 3$\underline{CH_2}$-chain), 1.96 (m, 6H, 3$\underline{CH_2}$-chain), 1.81 (d, 3H, 18-CH_3, $J = 7.2$ Hz), 1.71 (t, 3H, 8-$CH_2\underline{CH_3}$, $J = 8.0$ Hz), 1.41 (s, 27H, 3$CO_2{}^t$Bu), 1.33 (s, 27H, 3$CO_2{}^t$Bu), 0.39 (brs, 1H, NH), −1.79 (brs, 1H, NH). EIMS: 1610 (MH^+). HRMS: Calcd for $C_{88}H_{133}N_7O_{20}$, 1607.9605, found: 1607.9650 (M^+).

Compound 18. Compound **17** (100.0 mg, 0.06 mmol) was stirred with 80% TFA/DCM (5.0 mL) at room temperature for 3 h. The resultant mixture was concentrated and dried under high vacuum to remove trace TFA. To this crude preparation were added amino-benzyl-DTPA-penta-*tert*-butyl ester (471.0 mg, 0.60 mmol), EDCI (115.9 mg, 0.60 mmol), and DMAP (73.8 mg, 0.60 mmol). Dry *N*,*N*-dimethylformamide (15 mL) was added and the reaction mixture was stirred at RT for 16 h under N_2 atm. The reaction mixture was concentrated under vacuum, dichloromethane added (100 mL), washed with brine solution, the organic layer separated, dried over sodium sulfate, and concentrated. The crude mixture was chromatographed over alumina G (III) using 1−3% methanol/dichloromethane mixture

Scheme 1



as eluent to give product **18**. Yield: 250.0 mg (69.0%). UV−vis (λ_{max}, dichloromethane): 319, 412, 508, 538, 606, and 661 nm. Elemental analysis: Calcd for $C_{309}H_{491}N_{31}O_{74}$: C, 63.72; H, 8.50; N, 7.46; O, 20.33. Found: C, 63.67; H, 8.57; N, 7.46.

Compound 19. Compound **18** (215.0 mg, 0.0369 mmol) was stirred with 80% TFA/DCM (5.0 mL) at room temperature for 3 h. The resultant mixture was concentrated and dried under high vacuum to remove trace TFA. The crude preparation thus obtained was dissolved in pyridine (10 mL), and while stirring, $GdCl_3 \cdot 6H_2O$ (164.6 mg, 0.44 mmol) in 1 mL of water was added slowly, and the resultant mixture was stirred for 16 h. The reaction mixture was concentrated to dryness under high vacuum. The residue was washed with water (10 mL × 3) and acetone (10 mL × 3), and finally dried under high vacuum using P_2O_5 as drying agent. Yield: 160.0 mg (85.0%). UV−vis (λ_{max}, MeOH): 320, 410, 507, 539, 606, and 661 nm. Elemental analysis: Calcd for $C_{190}H_{253}Gd_6N_{31}O_{74}$: C, 44.76; H, 5.00; Gd, 18.50; N, 8.52; O. Found: C, 44.80; H, 5.07; N, 8.51.

Calculation of In Vitro Relaxivities. MRI acquisitions were performed using a General Electric 4.7T/33 cm horizontal bore magnet (GE NMR instruments, Fremont, CA) incorporating AVANCE digital electronics (Bruker BioSpec platform with *ParaVision* v 3.0.2 acquisition software, Bruker Medical, Billerica, MA).

Each conjugate was diluted with phosphate-buffered saline (pH 7.4) to a concentration ranging from 0.02 mM to 0.10 mM and imaged at 25 °C. T_1 relaxation rates (R_1) were acquired utilizing a saturation recovery, spin−echo (SE) sequence with a fixed echo time (T_E) = 10 ms and repetition times (T_R) ranging from 75 to 8000 ms. Additional MR acquisition parameters were as follows: field of view (FOV) 32 × 32 mm^2, slice thickness = 1 mm, slices = 3, interslice gap = 2 mm, matrix = 192 × 192, number of averages (NEX) = 1. Signal intensities at each repetition time were sampled by taking the mean intensity within regions of interest (ROI's) using commercially available image processing software (*Analyze 7.0*, AnalyzeDirect, Overland, KS), and R_1 and S_{MAX} were calculated by nonlinear fitting of the equation

$$S_{(TR)} = S_{MAX}(1 - e^{-(R1 \cdot TR)}) + \text{background noise}$$

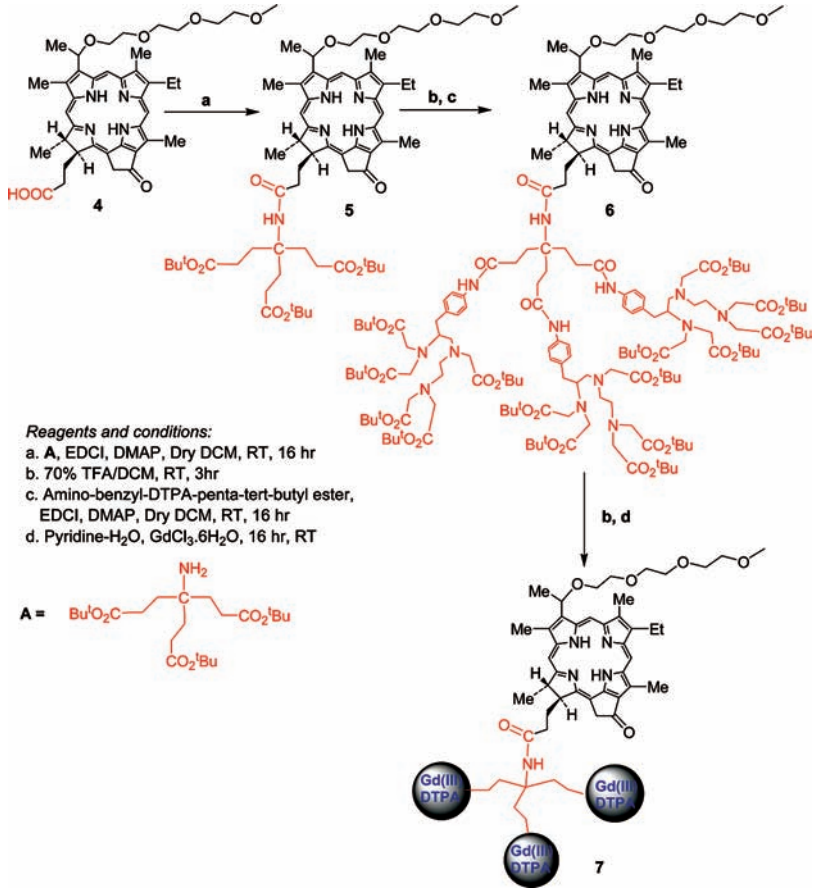
using Matlab's Curve Fitting Toolbox (*Matlab 7.0*, MathWorks Inc., Natick, MA). The T_1 relaxivity for each conjugate was then determined by obtaining the slope of the compound's molar concentration vs R_1 via linear regression fitting of the data. Similarly, T_2 relaxation rates (R_2) were acquired using a multiecho, Carr-Purcell-Meiboom Gill (CPMG) SE sequence with a fixed T_R of 2500 ms and T_E times ranging from 15 to 300 ms, NEX = 2. R_2 and S_{MAX} were calculated as described above using the equation

$$S_{(TE)} = S_{MAX}(e^{-(R2 \cdot TE)}) + \text{background noise}$$

As before, the T_2 relaxivity was determined by obtaining the slope of concentration vs R_2 via linear regression fitting of the data.

Determination of in Vitro Photobleaching. In vitro photobleaching (*26*) of each compound was performed using a continuous light source at 665 nm at a power of 500 mW and a dose rate of 75 mW/cm^2. Samples were prepared in 17% bovine calf serum. Individual 2.5 mL samples in 17% bovine calf serum were irradiated in quartz cuvettes and monitored via UV−vis spectroscopy (Varian Cary Bio 50 spectrophotometer,

Scheme 2



Palo Alto, CA) at 665 nm until the peak had been reduced to a minimum of 70%.

Evaluation of Phototoxicity Viability. The compounds were tested for photodynamic efficacy at 4 μM and variable light doses (at 665 nm for HPPH analogues and 705 nm for purpurinimides) after incubating for 24 h with (Colon26) cells seeded in 96 well plates. Viability was measured 48 h later using the 3-[4,5-dimethylthiazol-2-yl]-2,5-diphenyltetrazoliumbromide (MTT) assay (*26*). The results were plotted as percent survival compared with the untreated dark control (no drug, no light) at each light dose (in J/cm^2).

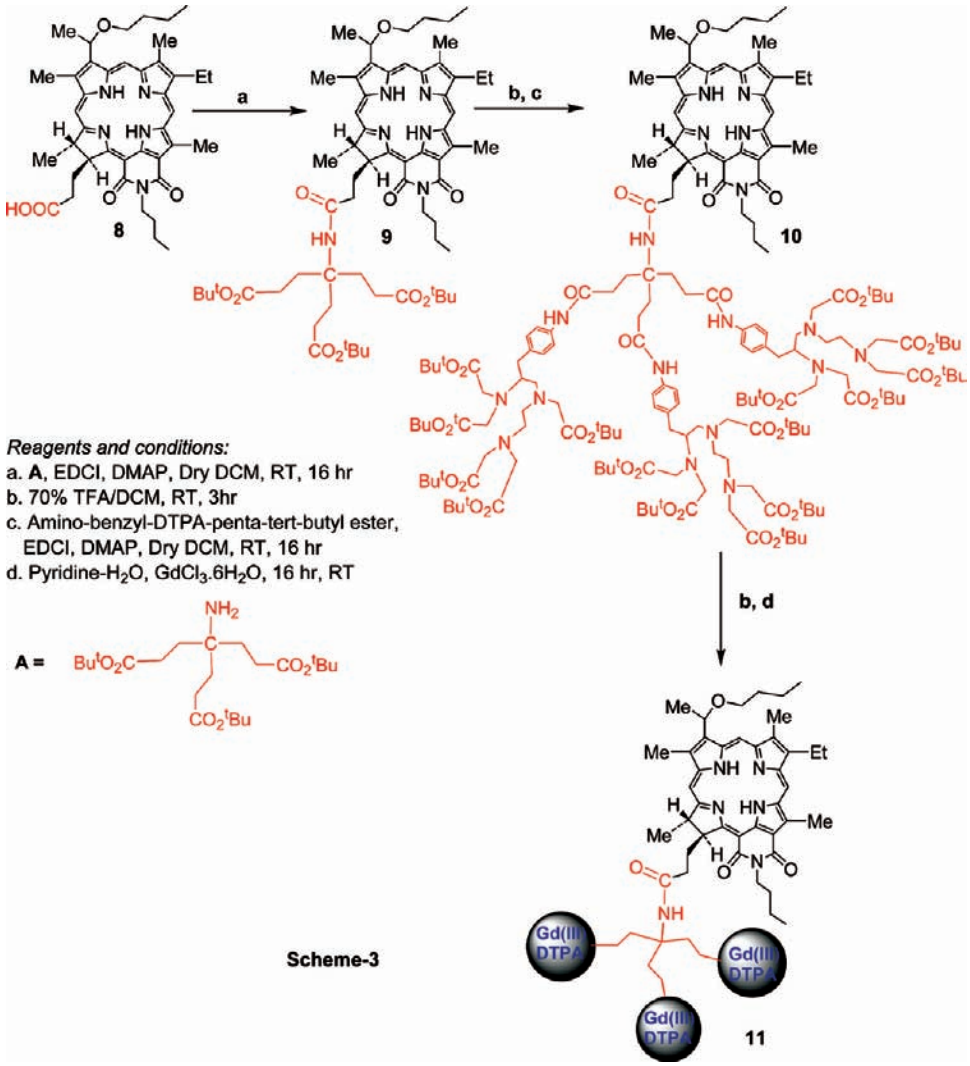
Determination of in Vitro Intracellular Localization. Colon26 cells were seeded at 1×10^5 cells in 2 mL growth medium on poly(L-lysine) coated glass coverslips in 6-well plates and cultured for 48 h to allow attachment and spreading. The photosensitizer (1.0 μM) was incubated with the cells in the dark at 37 °C for 4 or 24 h. The cells were coincubated with organelle specific dyes MitoTracker Green FM for 30 min at 0.5 μM, Lysotracker Green at 1 μM for 2 h, and Bodipy Ceramide C5-albumin complexes at 5 μM (*27*) according to manufacturer's instructions (Invitrogen). Prior to microscopy, the cells were rinsed with PBS and mounted with PBS containing 1 μM DAPI. Live cells were examined with a Zeiss Axiovert 200 inverted fluorescence with a Fluoarc mercury vapor shortarc lamp as light source. Fluorescent images from the same fields were captured successively in detector channels using suitable filter sets (Chromatechnology) for the PS and the organelle probes with an AxioCam MR-MRGrab frame grabber and a monochromatic CCD camera (Zeiss AxioCam MRm). Filter cubes contained 410/40 nm excitation, beamsplitter 505, and bandpass emission 675/50 nm for the PS; excitation bandpass 470/40 nm, beamsplitter 495, and bandpass emission 525/50 nm for MitoTracker Green and Lysotracker Green; excitation bandpass 565/30 nm, beamsplitter 585, and bandpass emission 620/60 nm for the Bodipy C5 ceramide and excitation 390/22 nm, beamsplitter 420 nm, and bandpass emission 460/50 nm. Images were digitally processed with the Zeiss *AxioVision LE* v 4.1 software.

Statistical Evaluation. In vitro PDT of the compounds was presented as the mean and standard deviation of three replicate experiments. In vivo PDT of the compounds was compared in Kaplan−Meier plots. *GraphPad Prism 5.0* was utilized to compare tumor response curves.

RESULTS AND DISCUSSION

Chemistry. For the preparation of photosensitizer-Gd(III) ADTPA conjugates, 3-(1′-hexyloxyethyl)-3-devinylpyropheophorbide-a (HPPH) HPPH and 3-(1′-butyloxyethyl)3-devinyl-purpurin-18-*N*-butylbutylimide **8** were synthesized by following the methodologies developed in our laboratory (*28*). For the synthesis of HPPH-3Gd(III)ADTPA **3**, HPPH was reacted with aminotriester **1** (Scheme 1which on treating with trifluoroacetic acid (TFA) and further reaction with aminobenzylDTPA butyl ester gave the desired conjugate. To investigate the effect of lipophilicity of the conjugate in tumor-imaging (MRI) and PDT, we synthesized a series of compounds with increasing/decreasing lipophilicity/hydrophilicity by modifying the position-17 of pyropheophorbide with alkyl ether (butyl or hexyl) or poly-(ethylene glycol) moieties. We started with compound **4** containing an ethylene glycol group at position-3, which on a sequence of reactions illustrated in Scheme 2 produced the corresponding 3Gd(III)aminobenzyl DTPA conjugate **7** in modest yield. For the synthesis of a bifunctional agent with longer wavelength absorption, pyropheophorbide-a analogues (HPPH or compound **4**) were replaced with a highly effective photosensitizer **8** (Scheme 3) (developed on the basis of structure−activity relationships studies) exhibiting longer wave-

Scheme 3



length absorption near 700 nm, and the corresponding 3Gd(III)-ADTPA conjugate **11** was synthesized. To further investigate the effect of increased Gd(III) units in MR imaging ability and the effect of overall lipophilicity in pharmacokinetic/pharmacodynamic characteristics, pyropheophorbide-6Gd(III)aminobenzyl conjugates **15** and **19** containing a hexyl ether or an ethylene glycol group at position-3 were synthesized by following the methodology as depicted in Schemes 4 and 5, respectively. The structures of all the intermediates and the final products were confirmed by NMR, mass spectrometry, and elemental analyses.

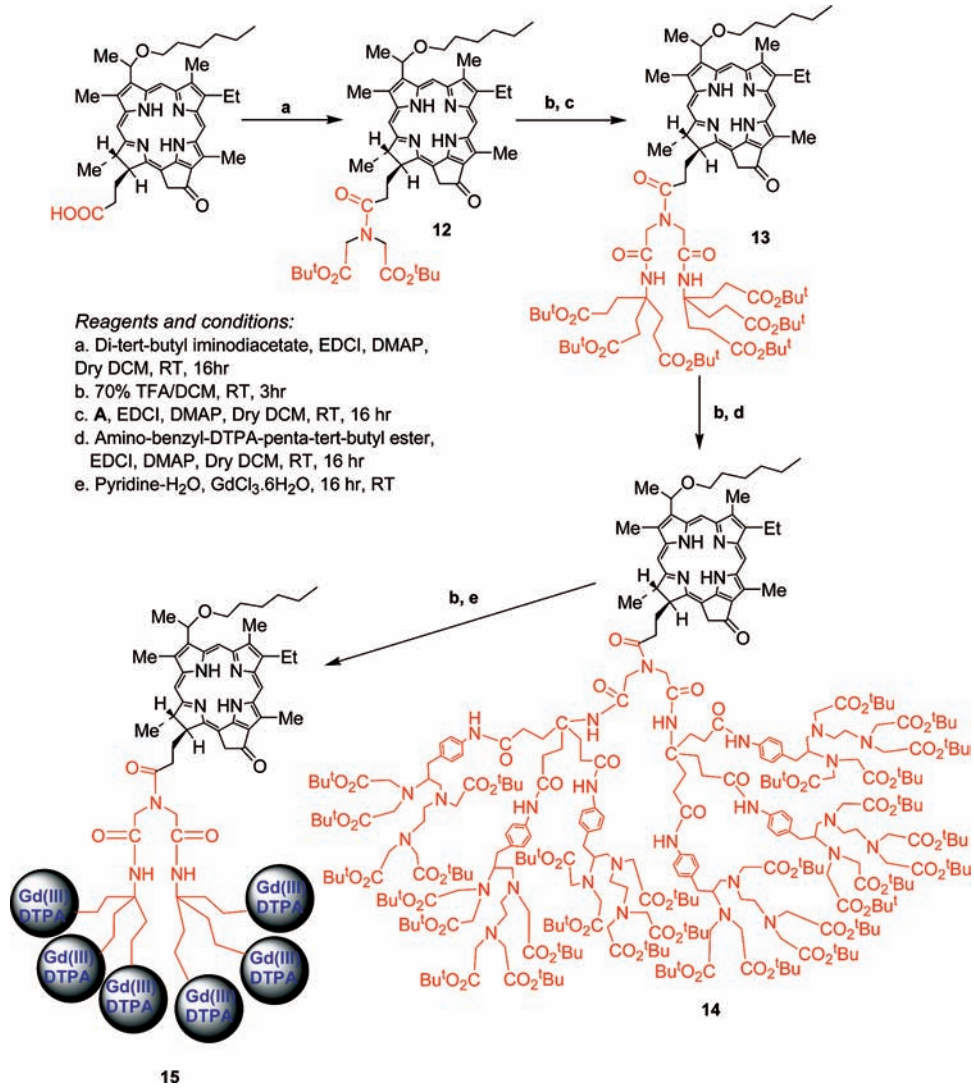
Effect of Gadolinium Chelates in Absorption and Fluorescence Properties of HPPH. To investigate the effect of the number of Gd(III) units in absorption and fluorescence properties of the conjugates, HPPH and the corresponding conjugates **3** and **15** containing three- and six gadolinium chelates were dissolved in methanol, and the electronic absorption spectra and fluorescence spectra were measured at equimolar concentrations. As can be seen from Figure 1A, subtle deviations were observed among the UV−vis spectra of HPPH, **3** (HPPH-3Gd(III) chelate, and **15** (HPPH-6Gd(III)chelate). The Soret band region in compound **15** was much broader. The long wavelength absorption intensity at 660 nm for conjugates **3** and **15** was slightly lower (ε = 35 000, 33 000, respectively) than that observed for HPPH (ε = 45 000).

Compared to HPPH, the emission spectra (Figure 1B) of the metalated analogues **3** and **15** showed a significant decrease in fluorescence intensity. Excitations of these compounds in the "Soret" band region (410−425 nm) exhibited an emission peak at 667 nm, and as can be seen from Figure 1B, compared to HPPH the corresponding Gd(ADTPA) analogues decrease the fluorescence intensity. A sharp decrease in fluorescence intensity indicates a possible interaction between the gadolinium chelates and the HPPH moiety, and detailed photophysical studies of this phenomenon are currently in progress.

Effect of Gd(III)aminobenzyl DTPA Moiety in Photobleaching of HPPH. The singlet oxygen produced on exposing photosensitizer within a tumor to light is responsible for the destruction of tumor and also the photosensitizer (*29, 30*). In order to achieve an optimal PDT response, it is extremely important to make the maximum use of the tumor oxygen supply and also to understand the photobleaching characteristics of the photosensitizer by the single oxygen produced in situ. In this study, HPPH and the corresponding gadolinium analogues **3** and **15** with 3 and 6 Gd(III)aminobenzyl DTPA units, respectively, were dissolved in 17% bovine calf serum (BCS) solution and irradiated with laser light at 665 nm. The absorption spectra were measured at regular intervals and the observed peak intensity values at λ_{max} 665 nm were plotted against the light exposure time.

As can be seen from the results summarized in Figure 2, the presence of Gd(III)aminobenzl DTPA moieties in both conjugates **3** and **15** significantly reduced the rate of photobleaching of the HPPH. The longer stability of the Gd(III) containing photosensitizers provides an opportunity for an additional light

Scheme 4



treatment to those cancer patients, which did not produce a satisfactory response after initial treatment without injecting more PDT agent.

T_1 and T_2 Relaxivity of HPPH-Gd(III)aminobenzylDTPA Conjugates. The T_1 and T_2 relaxivity values of the photosensitizer-Gd(III)ADTPA conjugates are summarized in Table 1. Compared to Magnevist, the relaxivity values were higher for compounds containing 3- or 6Gd-ADTPA moieties. However, the increase in relaxivity was nonlinear with the increase in the number of Gd(III) units. The reason for the lack of linearity is attributed to the relative close proximity of Gd-ADTPA groups, which may be reducing the degree of relaxation enhancement by limiting the hydration of the molecule.

In selection of a lead candidate, T_1 relaxivity was favored over T_2, as an increase in T_1 relaxation rate reduces saturation of signal, leading to brighter intensity in tumors, while an increase in T_2 relaxation rate causes loss of signal intensity, producing poorer contrast. Although all compounds exhibited adequate T_1/T_2 ratios, compounds **15** and **19** displayed the highest T_1/T_2 ratios but limited photosensitizing efficacy.

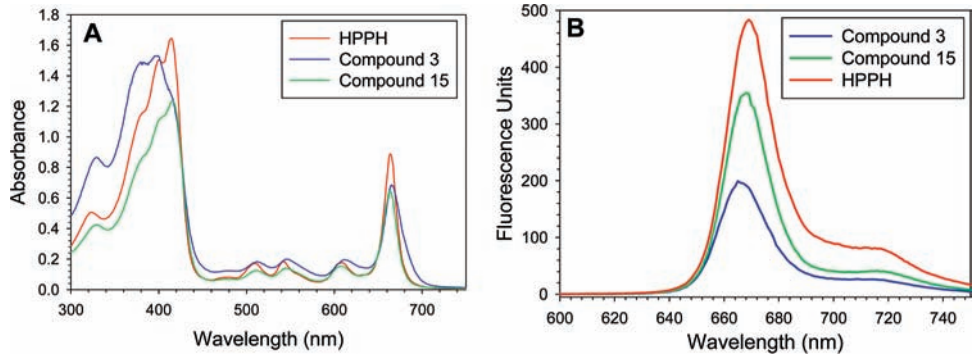
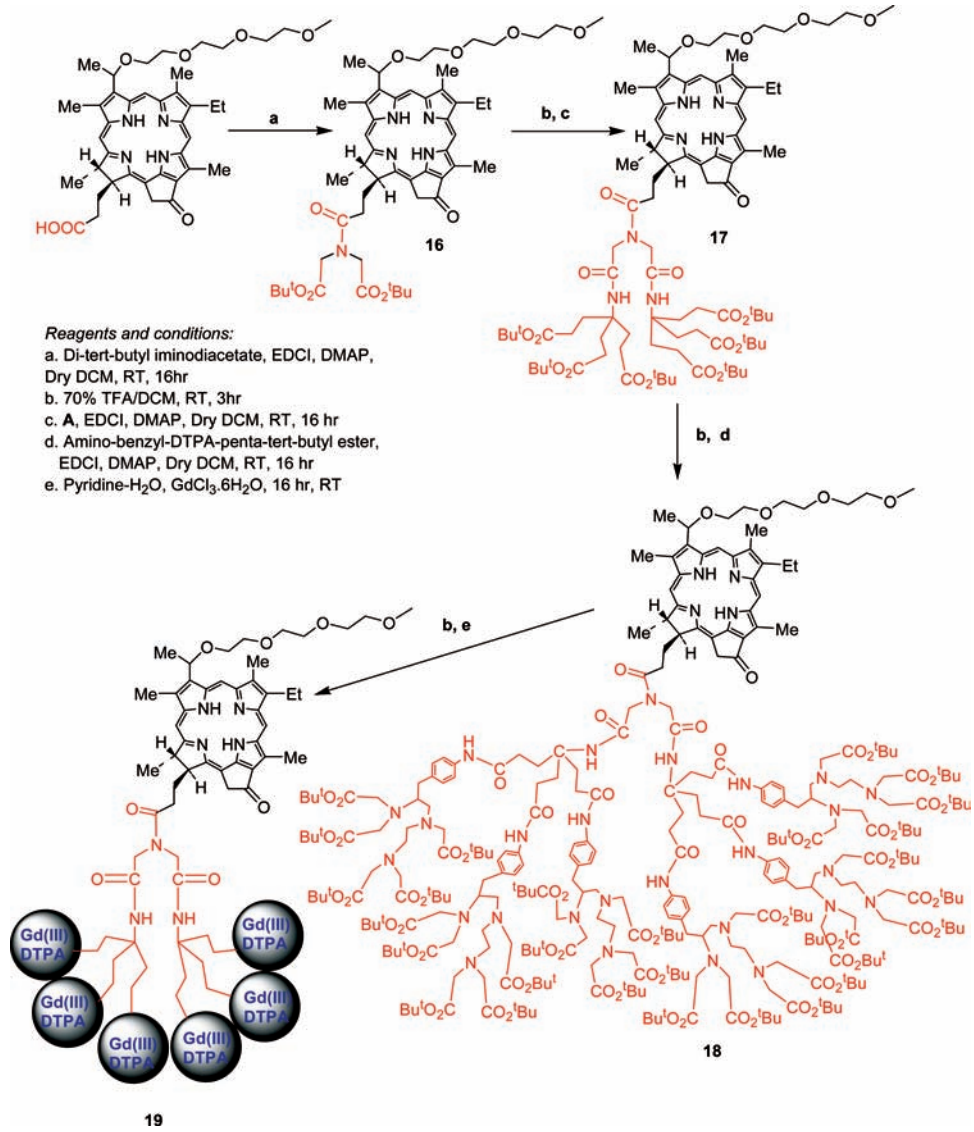


Figure 1. Comparative absorption (A) and fluorescence spectra (B) of HPPH and the corresponding 3 Gd(III)aminobenzyl DTPA **3** and 6Gd(III)aminobenzyl DTPA conjugate **15** in methanol (conc. 19.6 μM).

Scheme 5



In Vitro Photosensitizing Activity. To determine the effect of the nature of photosensitizer and the number of Gd(III)-ADTPA moieties on photosensitizing efficacy, conjugates **3**, **7**, **11**, **15**, and **19** were evaluated in RIF cells at various concentrations and light doses. The results obtained at a fixed concentration of the conjugates (4.0 μM) but at variable light doses are shown in Figure 3. As can be seen, among all the derivatives both HPPH and purpurinimide linked with 3Gd(III)ADTPA moieties (**3** and **11**, respectively) were more effective than those containing 6Gd(III)ADTPA moieties (**15** and **19**, respectively). Interestingly, replacing the hexyl ether functionality at position-3 with PEG (**7** and **19**) reduced the in vitro efficacy.

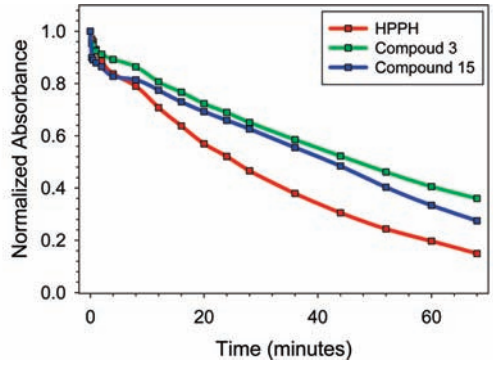


Figure 2. Comparative photobleaching characteristics of HPPH and the corresponding 3 and 6Gd(III) aminobenzyl DTPA **3** and **15**, respectively, at (9.8 μM) in 17% BCS. The solutions were exposed with a laser light (500 mW, 665 nm, 75 mW/cm^2) and the absorption peak at 665 nm were recorded at variable time points.

Table 1. Comparative T_1 and T_2 Relaxivity Values of the Conjugates and Magnevist

	$(mM \cdot s)^{-1}$	
Compound	T_1	T_2
3	13.50	81.37
15	24.72	66.54
11	14.14	85.32
7	13.58	40.11
Magnevist	4.33	5.10
19	25.09	69.19

Intracellular Localization of HPPH vs HPPH-3Gd(III)ADTPA Conjugate. Most of the porphyrin-based compounds can be observed intracellularly with a fluorescence microscope. It has been shown that photosensitizers localize to cytosolic targets such as Golgi, endoplasmic reticulum, mitochondria, lysosomes, and membranes (*31*, *32*). Efforts have been made to investigate a correlation between the site(s) of localization and PDT activity

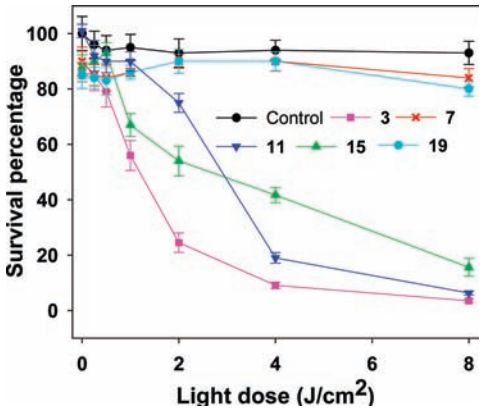


Figure 3. In vitro photosensitizing activity of photosensitizer-Gd(III)ADTPA conjugates (4.0 μM) in RIF cells. The cells were incubated for 24 h and then exposed to light at a dose of 3.2 mW/cm^2. Control cells were exposed to light only.

of photosensitizers. Moan et al. (*33*) suggested that lysosomes are a primary localization site but not the photodynamic target. However, it has not been determined whether the lysosomes rupture after PDT damage and release the compound or whether some other cellular damage, caused by unobservable functions of the photosensitizer elsewhere in the cell, cause the lysosome to rupture and subsequently release the photosensitizer. We have previously shown that most of the effective PDT agents, including HPPH developed in our laboratory, localize either in mitochondria or in lysosomes (*34*). We have also observed that, besides the overall lipophilicity, the nature of the substituents introduced in photosensitizers also makes a remarkable difference in intracellular localization characteristics (*35*).

To determine the impact of Gd(III)ADTPA moieties in site of localization of HPPH, the intracellular localization of both the compounds was investigated by using various site-specific probes. Although some of the conjugates were also found in the mitochondra and lysosomes (see Figure 4 and the Supporting Information), localization of the lead Gd-containing compound **3** appeared to be primarily in the Golgi apparatus as determined by its colocalization with a probe for that organelle. Addition of Gd alone may not account for the shift from mitochondria observed with HPPH to the Golgi, but may be partly due to the position at which the additional moieties are attached and a significant change in overall lipophilicity of the molecule. Primarily, photosensitizers which localize to the mitochondria are more effective at evoking cell death (*34*); however, photosensitizers which localize to alternative cellular organelles also exhibit the ability to induce cell mortality upon light irradiation (*36*). Further studies to establish a correlation between the site(s) of localization and cell death (apoptosis vs necrosis) are currently in progress.

CONCLUSION

Our studies indicate that tumor-avid photosensitizers can be used as vehicles for delivering the MR imaging agents to tumors. Compared to Magnevist, a clinical standard, most of the conjugates showed enhanced tumor-imaging potential (T_1/T_2 relaxivity) which increased by increasing the number of Gd(III)ADTPA units. However, as a "multifunctional agent" for tumor-imaging (MR and fluorescence) and PDT, HPPH containing 3Gd(III)ADTPA showed the best PDT efficacy (in vivo results are presented in the following paper of this journal). Our approach has great potential for developing dual-function agents for MR imaging and phototherapy with increased sensitivity by reducing false-positive and false-negative results in screening, diagnosis, treatment monitoring, or image-guided intervention.

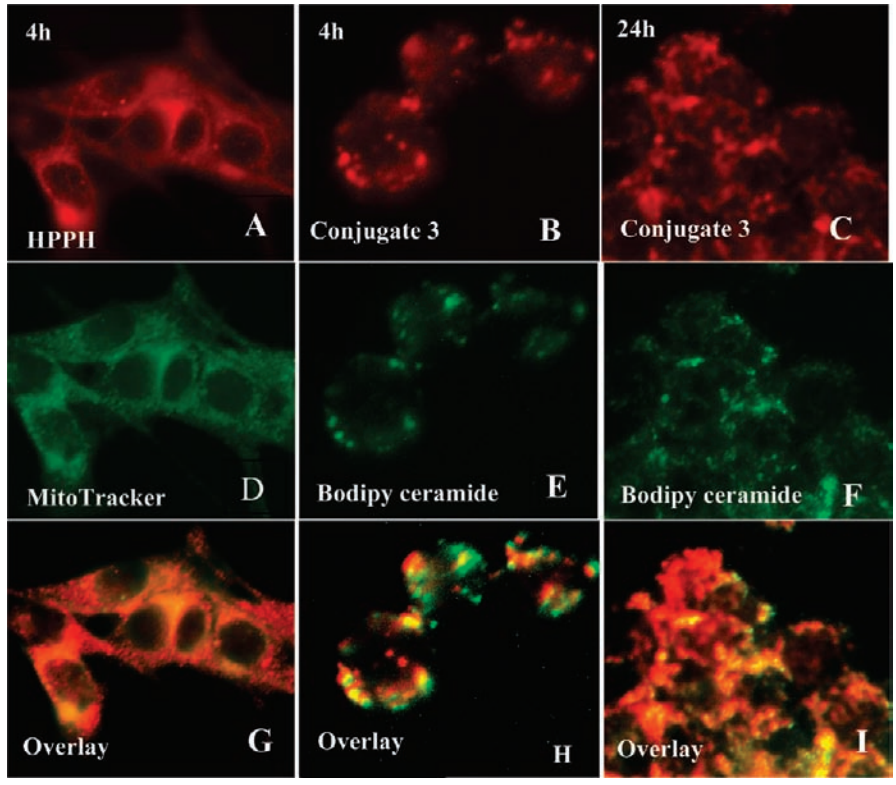


Figure 4. False-color images showing subcellular localization of HPPH and compound **3** (red) in Colon26 cells after 4 h (B) or 24 h incubations (A and C), respectively. Localization was determined by fluorescence microscopy by coincubation with fluorescent organelle probes (green). Subcellular areas of colocalization in the overlay of compound **3** or HPPH with the probes are yellowish orange. A, HPPH; B,C, compound **3**; D, MitoTracker Green; E,F, Bodipy ceramide C5-albumin complex; G, overlay of HPPH and MitoTracker Green; H,I, overlays of compound **3** and Bodipy ceramide C5-albumin complex.

ACKNOWLEDGMENT

The financial support from the NIH (R21/R33 Grant CA109914) and the shared resources of the RPCI support grant (P30CA16056) is highly appreciated.

Supporting Information Available: The ^{1}H NMR spectra of selected compounds and the intracellular localization profiles of the conjugates. This material is available free of charge via the Internet at http://pubs.acs.org.

LITERATURE CITED

(1) Caravan, P., Ellison, J. J., McMurry, T. J., and Lauffer, R. B. (1999) Gadolinium(III) chelates as MRI contrast agents: Structure, dynamics and applications. *Chem. Rev. 99*, 2293–2352.

(2) Kolokythas, O., Shibata, D. K., and Dubinsky, T. J. (2009) *Medical Imaging in Image-Guided Therapy Systems* (Vaezy, S., and Zderic, V., Eds.) pp 17−57, Artech House, Boston.

(3) Hamblin, M. R., and Mroz, P., Eds. (2008) *Advances in Photodynamic Therapy*, Artech House, Norwood, MA.

(4) Carpenter, C. M., and Pogue, B. W. (2008), *Difuse Optical Spectroscopy with Magnetic Resonance Imaging in Translational Multimodality Optical Imaging* (Azar, F. S., and Intes, X., Eds.) pp 125−162, Artech House, Boston.

(5) Povoski, S. P., Hall, N. C., Marin, E. W., and Walker, M. J. (2008) Multimodality approach of perioperative ^{18}F-FDG PET/CT imaging, intraoperative ^{18}F-FDG handheld gamma probe detection, and intraoperative ultrasound for tumor localization and verification of resection of all sites of hypermetabolic activity in case of occult recurrent metastatic melanoma. *World J. Surg. Oncol. 6*, 1.

(6) Shah, N. J., Gibbs, J., Wolverton, D., Cerussi, A., Hylton, N., and Tromberg, B. J. (2005) Combined diffuse optical spectroscopy and contrast-enhanced magnetic resonance imaging for monitoring breast cancer neoadjuvant chemotherapy: A case study. *J. Biomed. Opt. 10*, 051503.

(7) Ruck, A., Dolp, F., Hulshoff, C., Hauser, C., and Scaffi-Happ, C. (2005) Fluorescence lifetime in PDT. An overview. *Med. Las. Appl. 20*, 125–129.

(8) Van den Bergh, H. (2003) Early detection of lung cancer and the role of endoscopic fluorescence imaging. *Med. Las. Appl. 18*, 20–26.

(9) Smith, K. M., Ed. (1975) *Porphyrins and metalloporphyrins*, Elsevier Scientific Publishing Company, Amsterdam.

(10) Gurfinkel, M., Thompson, A. B., Ralston, W., Troy, T. L., Reynolds, S. R., Muggenberger, B., Nikula, K., Pandey, R. K., Mayer, R., Hawrysz, D. J., and Sevick-Muraca, E. M. (2000) Pharmacokinetics of indocyanine green and carotene-HPPH-conjugate for detection of normal and tumor tissue using fluorescence near infrared continuous wave imaging. *Photochem. Photobiol. 72*, 94–102.

(11) Li, G., Slansky, A., Dobhal, M. P., Goswami, L. N., Graham, A., Chen, Y., Kanter, P., Aleberico, R. A., Spernyak, J., Morgan, J., Mazurchuk, R., Oseroff, A., Grossman, Z., and Pandey, R. K. (2005) Chlorophyll-a analogues conjugated with aminobenzyl DTPA as potential bifunctional agents for magnetic resonance imaging and photodynamic therapy. *Bioconjugate Chem. 16*, 32–42.

(12) Chen, Y., Gryshuk, A., Achilefu, S., Ohulchanskyy, T., Potter, W., Zhong, T., Morgan, J., Chance, B., Prasad, P. N., Henderson, B. W., Oseroff, A., and Pandey, R. K. (2005) A novel approach to a bifunctional photosensitizer for tumor imaging and phototherapy. *Bioconjugate Chem. 16*, 1264–1274.

(13) Pandey, S. K., Gryshuk, A. L., Sajjad, M., Zgeng, X., Chen, Y., Abouzeid, M. M., Morgan, J., Nabi, H. A., Oseroff, A., and Pandey, R. K. (2005) Multimodality agents for tumor imaging (PET, fluorescence) and PDT. A possible "see and treat" approach. *J. Med. Chem. 48*, 6286–6295.

(14) Pandey, S. K., Chen, Y., Zawada, R. H., Oseroff, A., and Pandey, R. K. (2006) Utility of tumor-avid photosensitizers in developing bifunctional agents for tumor-imaging and phototherapy. *Proc. SPIE 6139*, 6139051–57.

(15) Chen, Y., Ohkubo, K., Zhang, M., Liu, W., Pandey, S. K., Ciesielski, M., Baumann, H., Fukuzumi, S., Kadish, K. M., Fenstermaker, R., Oseroff, A., and Pandey, R. K. (2007) Photophysical, electrochemical characteristics and cross linking of STAT-3 proteins by an efficient bifunctional agent for fluorescence image-guided photodynamic therapy. *Photochem. Photobiol. Sci. 6*, 1257–1267.

(16) Pandey, R. K., Sumlin, A. B., Potter, W. R., Bellnier, D. A., Henderson, B. W., Constantine, S., Aoudia, M., Rodgers, M. A., Smith, K. M., and Dougherty, T. J. (1996) Structure and photodynamic efficacy among alkyl ether analogues of chlorophyll-a derivatives. *Photochem. Photobiol. 63*, 194–205.

(17) Henderson, B. W., Bellnier, D. A., Graco, W. R., Sharma, A., Pandey, R. K., Vaughan, L., Weishaupt, K. R., and Dougherty, T. J. (1997) A quantitative structure-activity relationship for a congeneric series of pyropheophorbide derivatives as photosensitizers for photodynamic therapy. *Cancer Res. 57*, 4000–4007.

(18) Dougherty, T. J., Pandey, R. K., Nava, H. R., Smith, J. A., Douglass, H. O., Edge, S. B., Bellnier, D. A., O'Malley, L., and Cooper, M. (2000) Preliminary clinical data on a new photodynamic therapy photosensitizer, HPPH for treatment of obstructive esophageal cancer. *Proc. SPIE 3909*, 25–27.

(19) Bellnier, D. A., Greco, W. R., Loewen, G. M., Nava, V., Oseroff, A., Pandey, R. K., Tsuchida, T., and Dougherty, T. J. (2003) Population pharmacokinetics of the photodynamic therapy agent HPPH in cancer patients. *Cancer Res. 63*, 1806–1813.

(20) Loewen, G. M., Pandey, R. K., Bellnier, D. A., Henderson, B. W., and Pandey, R. K. (2006) Endobronchial photodynamic therapy for lung cancer. *Las. Surg. Med. 38*, 364–370.

(21) Bellnier, D. A., Greco, W. R., Nava, H., Loewen, G. M., Oseroff, A. R., and Dougherty, T. J. (2005) Mild skin phototoxicity in cancer patients following injection of Photochlor (HPPH) for photodynamic therapy. *Cancer Chemother. Pharmacol. 57*, 40–45.

(22) Pandey, R. K., Goswami, L. N., Chen, Y., Gryshuk, A., Missert, J. R., Oseroff, A., and Dougherty, T. J. (2006) Nature: A rich source for developing multifunctional agents. Tumor-imaging and photodynamic therapy. *Las. Surg. Med. 38*, 445–467.

(23) Spernyak, J., White, W. H., Ethirajan, M., Patel, N., Goswami, L., Chen, Y., Turowski, S., Missert, J. R., Batt, C., Mazurchuk, R., and Pandey, R. K. (2009) Hexylether Derivative of Pyropheophorbide-a (HPPH) on Conjugating with 3Gadolinium(III) Aminobenzyl diethylenetriaminopentaacetic Acid Shows Potential for *In vivo* Tumor-Imaging (MR, Fluorescence) and Photodynamic Therapy. *Bioconjugate Chem.* Submitted for publication.

(24) Zheng, G., Camacho, S., Potter, W., Bellnier, D. A., Henderson, B. W., Dougherty, T. J., and Pandey, R. K. (2001) Synthesis, tumor-uptake and in vivo photosensitizing efficacy of a homologues series of 3-(1′-alkoxyethyl)purpurin-18-N-alkylimides. *J. Med. Chem. 44*, 1540–1559.

(25) Pandey, R. K. Unpublished results.

(26) Merlin, J. L., Azzi, S., Lignon, D., Ramacci, C., Zeghari, N., and Guillemin, F. (1992) MTT assays allow quick and reliable measurement of the response of human tumour cells to photodynamic therapy. *Eur. J. Can. 28A*, 1452–1458.

(27) Kessel, D., and Castelli, M. (2001) Evidence that bcl-2 is the target of three photosensitizers that induce a rapid apoptotic response. *Photochem. Photobiol. 74*, 318–322.

(28) Pandey, R. K. Unpublished results.

(29) Finlay, J. C., Mitra, S., and Foster, T. H. (2002) In vivo mTHPC photobleaching in normal rat skin exhibits irradiance dependent features. *Photochem. Photobiol. 75*, 282–288.

(30) Sharman, W. M., Allen, C. M., and Van Lier, J. E. (2000) Role of activated oxygen species in photodynamic therapy. *Enzymology 319*, 57.

(31) Kessel, D., and Woodburn, K. (1993) Biodistribution of photosensitizing agents. *Int. J. Biochem. 10*, 1377–1383.
(32) Malik, Z., Amit, I., and Rothmann, C. (1997) Subcellular localization of sulfonated tetraphenyl porphines in colon carcinoma cells by spectrally resolved imaging. *Photochem. Photobiol. 65*, 389–396.
(33) Moan, J., Berg, K., Anholt, A., and Madslien, K. (1994) Sulfonated aluminum phthalocyanines as sensitizers for photochemotherapy. Effects of small doses on localization, dye fluorescence and photosensitivity in V79 cells. *Int. J. Cancer 58*, 865–870.
(34) Morgan, J., Oseroff, A. O., and Torchilin, V. P. (2001) Mitochondrial based anti-cancer photodynamic therapy. *Adv. Drug Delivery Rev. 49*, 71–86.
(35) Zheng, X., Morgan, J., Pandey, S. K., Chen, Y., Tracy, E., Baumann, H., Missert, J. R., Batt, C., Jackson, J., Bellnier, D. A., Henderson, B. W., and Pandey, R. K. (2009) Conjugation of HPPH to carbohydrates changes its subcellular distribution and enhances photodynamic activity in vivo. *J. Med. Chem. 52*, 4306–4318.
(36) Sibrian-Vazquez, M., Ortiz, J., Nesterova, I. V., Fernandez-Lazaro, F., Sastre-Sanstos, A., Soper, S. A., and Vicente, G. H. (2007) Synthesis and properties of cell-targeted Zn(II)-phthalocyanine-peptide conjugates. *Bioconjugate Chem. 18*, 410–420.

BC9005305

Hexylether Derivative of Pyropheophorbide-a (HPPH) on Conjugating with 3Gadolinium(III) Aminobenzyldiethylenetriaminepentaacetic Acid Shows Potential for in Vivo Tumor Imaging (MR, Fluorescence) and Photodynamic Therapy

Joseph A. Spernyak,[†] William H. White III,[‡] Manivannan Ethirajan,[‡] Nayan J. Patel,[‡,§] Lalit Goswami,[‡] Yihui Chen,[‡] Steven Turowski,[†] Joseph R. Missert,[‡] Carrie Batt,[‡] Richard Mazurchuk,[†] and Ravindra K. Pandey*[,‡]

Preclinical Imaging Facility, PDT Center, Cell Stress Biology, and Molecular Pharmacology and Cancer Therapeutics, Roswell Park Cancer Institute, Buffalo, New York 14263. Received December 2, 2009; Revised Manuscript Received March 8, 2010

Conjugates of 3-(1′-hexyloxyethyl)-3-devinyl pyropheophorbide-a (HPPH) with multiple Gd(III)aminobenzyl diethylenetriamine pentacetic acid (ADTPA) moieties were evaluated for tumor imaging and photodynamic therapy (PDT). In vivo studies performed in both mice and rat tumor models resulted in a significant MR signal enhancement of tumors relative to surrounding tissues at 24 h postinjection. The water-soluble (pH: 7.4) HPPH-3Gd(III) ADTPA conjugate demonstrated high potential for tumor imaging by MR and fluorescence. This agent also produced long-term tumor cures via PDT. An in vivo biodistribution study with the corresponding ^{14}C-analogue also showed significant tumor uptake 24 h postinjection. Toxicological evaluations of HPHH-3Gd(III)ADTPA administered at and above imaging/therapeutic doses did not show any evidence of organ toxicity. Our present study illustrates a novel approach for the development of water-soluble "multifunctional agents", demonstrating efficacy for tumor imaging (MR and fluorescence) and phototherapy.

INTRODUCTION

Early detection and treatment of cancer presents numerous clinical benefits. While the disease is well-localized and neoplastic growths are small, highly localized therapies have the potential advantage of reduced side effects and minimal damage to normal tissues (as opposed to systemic chemotherapy or invasive surgery). One example of localized therapy is photodynamic therapy, or PDT. PDT works via the creation of cytotoxic singlet oxygen formed by exposing a photosensitizing agent with an appropriate wavelength of a laser light (*1*).

One of the first photosensitizing agents approved for treatment of cancer was porfimir sodium (Photofrin). Photofrin is considered a first-generation photosensitizer and has been used in the treatment of Barrett's esophagus (*2*), cervical cancer (*3*), endobronchial cancer (*4*), and papillary bladder cancer (*5*). However, Photofrin has several inherent limitations, namely, its low molar absorption coefficient (1170 M^{-1} cm^{-1}) (*6*), as well as skin photosensitivity resulting from residual photosensitizer delocalized throughout the skin (*7*). These limitations have led to the development of "second generation" sensitizers which absorb energy efficiently at longer wavelengths and localize more effectively within the tumor. One such compound is 3-[1′-hexyloxyethyl]-3-devinyl pyropheophorbide-a (HPPH), which has a peak absorbance at 665 nm (in vivo absorption) and is currently in phase II clinical trials for the treatment of esophageal, lung, and cutaneous tumors (*8*, *9*). In contrast to most porphyrin-based agents, HPPH does not show any significant skin phototoxicity in patients.

A typical treatment regimen involves the single injection of agent followed by light illumination of the tumor after time has passed to allow for tumor uptake of the PDT agent. As PDT requires direct illumination of light onto the photosensitizer, image-guided therapy may be an effective way to efficiently (a) determine the size and extent of the tumor and (b) assist the clinician in localizing the light source onto the tumor. While still relatively novel in application, image-guided PDT has shown efficacy as a primary treatment in head and neck cancer (*10*) or as an adjuvant treatment to fluorescence-guided resection in high-grade gliomas (*11*) and melanomas that have metastasized to the brain (*12*). To this end, we have explored the feasibility of incorporating imaging functionality into porphyrin-based PDT agents to develop compounds that can be used in both diagnosis and therapy.

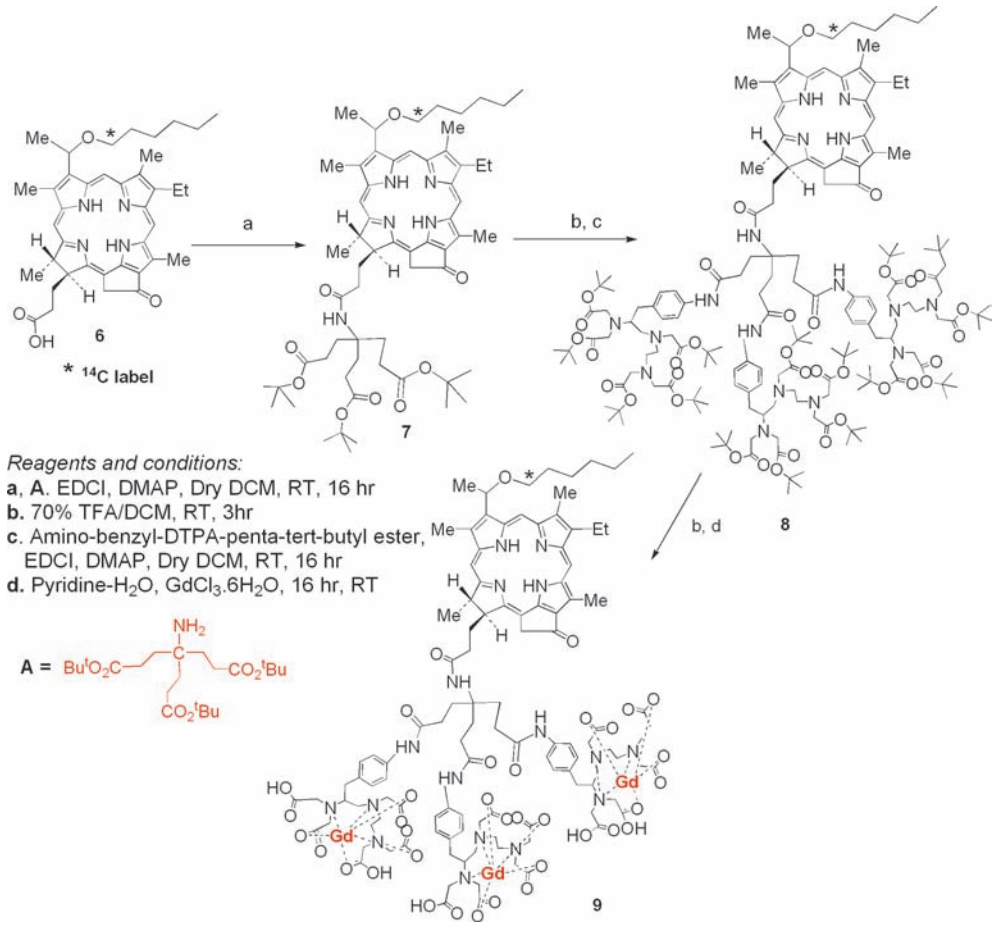
Magnetic resonance imaging (MRI) is well-suited for image guided therapy, as it does not require ionizing radiation, is noninvasive, and provides three-dimensional tomographic data sets with excellent soft tissue contrast. Use of gadolinium-based contrast agents has shown utility in the diagnosis of cancer (*13*−*16*) and in the study of numerous other disease states (*17*, *18*). Gadolinium, or Gd(III), has seven unpaired electrons within inner orbital shells, giving it a high degree of paramagnetism, which causes an increase in the T_1 relaxation rates (R_1) of nearby water molecules, thereby enhancing the MR signal.

Magnetic resonance imaging has numerous limitations, however. Detection sensitivity of MR contrast agents is relatively poor, requiring levels of Gd(III) to be at micromolar concentrations within the tissues. Determination of the degree of tissue signal enhancement requires comparison of preinjection and postinjection images. In comparison to contrast-enhanced MRI, fluorescence imaging has a much higher sensitivity in the detection of imaging agents and does not require multiple imaging time points. Fluorescence imaging is relatively inexpensive and can be employed in situations where MRI is ill-suited for use, such as such imaging subjects with metal embedded within their bodies or who cannot remain motionless. Therefore, incorporating both optical and MR imaging functionality into an effective photosensitizer allows one to incorporate the complementary strengths of each imaging modality.

[†] Preclinical Imaging Facility.
[‡] PDT Center.
[§] Molecular Pharmacology and Cancer Therapeutics.

10.1021/bc9005317 © 2010 American Chemical Society
Published on Web 04/13/2010

Scheme 1. Synthesis of ^{14}C-Labeled HPPH-3Gd(III)ADTPA



Previously, we reported on the utility of tumor-avid HPPH in developing "multifunctional agents" (*19*) where HPPH was conjugated with Gd(III)-DTPA and showed in vivo tumor enhancement at 24 h postinjection on MR images. However, due to its low water solubility it was difficult to formulate at higher concentrations.

In this report, we describe the comparative in vivo tumor imaging and PDT efficacy of a series of conjugates containing 3- or 6-Gd(III)aminobenzyl DTPA units with the expectation that the additional number of Gd(III) units would improve solubility and increase tumor conspicuity. Among the compounds evaluated, the HPPH-3 Gd(III)aminobenzyl DTPA was selected as a lead compound on the basis of its imaging potential, in vitro PDT efficacy, and ease of synthesis. The utility of the conjugate was further evaluated for in vivo fluorescence imaging, in vivo PDT efficacy, organ toxicity, and PDT-induced mechanism of action. In addition, an in vivo biodistribution study of the lead conjugate was performed with the corresponding ^{14}C-labeled analogue.

EXPERIMENTAL PROCEDURES

Chemistry. A detailed report on the synthesis, characterization, in vitro intracellular localization, and T_1 relaxivity of the multifunctional agents is reported in our preceding publication of this journal. In brief, three groups of compounds were synthesized (Figure 1): (i) HPPH with 3- or 6-Gd(III)-aminobenzylDTPA, (ii) Pyro-based photosensitizer with 3- or 6-Gd(III)-aminobenzylDTPA groups in which the hexyl chain of HPPH is replaced with an ether-linked tri(ethylene glycol) functionality (OTEG), (iii) a purpurinimide analogue [longer wavelength photosensitizer (λ_{max}: 700 nm)] linked with 3-Gd(III)-aminobenzylDTPA. Although all the conjugates showed potential for tumor imaging (MRI), HPPH conjugated with 3Gd(III)ADTPA (Figure 1) was found to be most promising as a multifunctional agent for tumor imaging and phototherapy, and therefore was investigated further for detailed biological evaluation.

Selection Criteria of the Best Candidate for Tumor Imaging and PDT. In our preceding paper, we discussed the synthesis, photophysical characteristics, in vitro T_1/T_2 MR relaxivity, and in vitro/in vivo PDT efficacy of a series of HPPH-Gd(III)ADTPA conjugates. Some of the analogues showed enhanced tumor contrast, but limited PDT efficacy. Because the objective of our research was focused on developing "multifunctional agents" for tumor imaging and phototherapy, we selected only those candidates which showed both imaging and therapeutic potential. The selection criteria we used for identification of the lead compound are summarized in Figure 2.

Synthesis of ^{14}C-Labeled HPPH Aminotriester Derivative 7. ^{14}C-HPPH **6** (15.0 mg, 0.023 mmol; specific activity: 5.2 μCi/μmol), aminotriester (15 mg, 0.036 mmol), EDCI (1-ethyl-3-(3-dimethylaminopropyl)carbodiimide hydrochloride) (9 mg, 0.05 mmol), and DMAP (4-dimethylaminopyridine) (6 mg, 0.05 mmol) were taken in a dry, round-bottom flask (25 mL). Dry dichloromethane (DCM, 5 mL) was added and reaction mixture was stirred at room temperature (RT) for 12 h under N_2 atm. Reaction mixture was diluted with DCM (10 mL), washed with brine solution, organic layer separated, dried over sodium sulfate, and concentrated. Crude mixture was purified over preparative thin layer chromatography (silica gel) using 1% MeOH/DCM mixture to give the desired product **7**. Yield: 18.0 mg (76.0%).

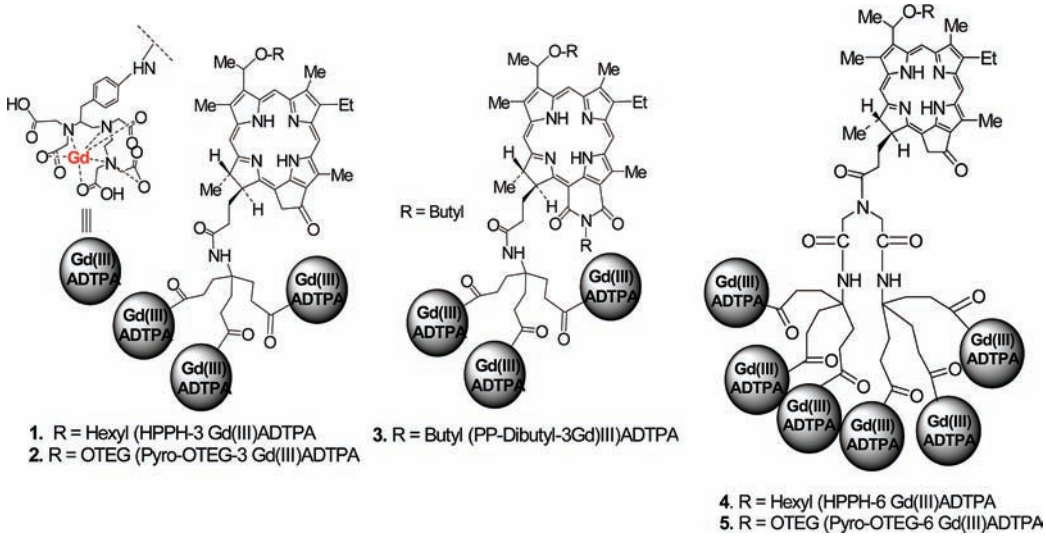


Figure 1. Gd(III)ADTPA conjugates of photosensitizers with variable lipophilicity.

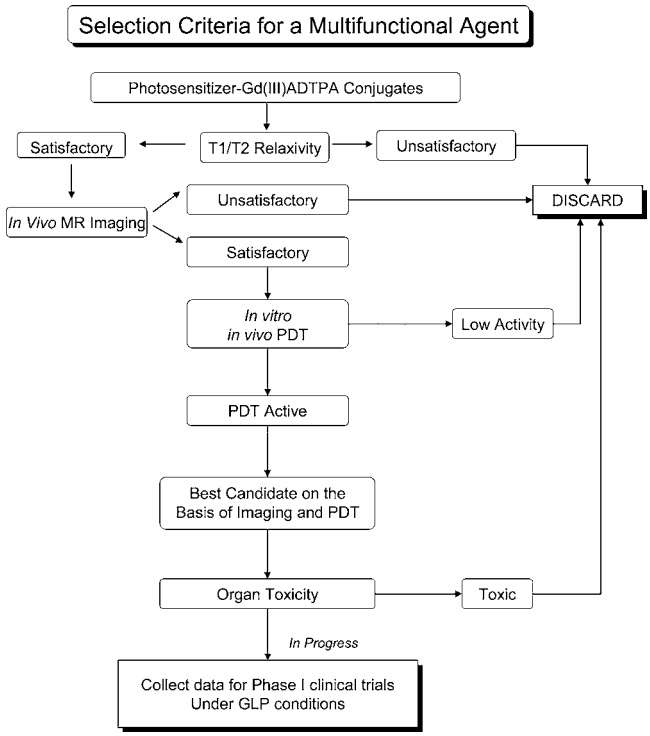


Figure 2. Selection criteria for identifying the best candidate for MR imaging and therapy.

Synthesis of ^{14}C-Labeled HPPH tri-AminobenzylDTPA Ester 8. Compound **7** (17.0 mg, 0.016 mmol) was stirred with 70% trifluoroacetic acid (TFA) / DCM (2.0 mL) at room temperature for 5 h. Resultant mixture was concentrated and dried under high vacuum to remove trace TFA. To this crude were added amino-benzyl-DTPA-penta-*tert*-butyl ester (54.0 mg, 0.069 mmol), EDCI (20.0 mg, 0.103 mmol), and DMAP (12.0 mg, 0.103 mmol). Dry dichloromethane (5 mL) was added and reaction mixture was stirred at RT for 16 h under N_2 atm. Reaction mixture was further diluted with dichloromethane (10 mL), washed with brine solution, organic layer separated, dried over sodium sulfate, and concentrated. Crude mixture was purified over short column (0.5 cm width, 12 cm height) containing grade-III alumina as a stationary phase and a 3% MeOH/DCM mixture as eluent to give product **8**. Yield (2 steps): 31.0 mg (61.0%).

Synthesis of ^{14}C-Labeled HPPH 3Gd(III)-AminobenzylDTPA Complex 9. Compound **8** (30.0 mg, 0.009 mmol) was stirred with 70% TFA/DCM (2.0 mL) at RT for 5 h. Resultant mixture was concentrated and dried under high vacuum to remove trace TFA. The crude obtained was dissolved in pyridine (2 mL) and put under continuous stirring. $GdCl_3 \cdot 6H_2O$ (20.0 mg, 0.054 mmol) in 0.5 mL of water was slowly added to this solution and resultant mixture was stirred for an additional 16 h. Reaction mixture was filtered and the residue obtained was washed with water (10 mL $\times$ 3) and acetone (10 mL $\times$ 3) and then dried under high vacuum to yield gadolinium complex **9**. Yield: 18.0 mg (72.0%). Specific activity: 3.9 μCi/μmol.

Animal Models. In vivo PDT experiments were performed in two tumor models, C3H mice bearing radiation induced fibroblast (RIF) tumors and BALB/c mice bearing Colon 26 tumors (NCI, Bethesda, MD). These tumor models were chosen as they have been extensively characterized in our lab in determining the PDT efficacy of numerous photosensitizers. In both models, tumor cells (1×10^6 Colon 26 cells in 50 μL PBS, 4×10^5 RIF cells in 50 μL PBS) were implanted subcutaneously and were allowed to grow to an approximate diameter of 5−7 mm. For MR imaging of the most promising candidates, Ward tumor cells were implanted subcutaneously above the intraperitoneal cavity of adolescent Fischer 344 rats (Harlan Laboratories) (150−200 g). Tumors were allowed to grow to ~1 cm in diameter prior to MR imaging. The in vivo biodistribution of the ^{14}C-labeled lead compound was also performed in rats bearing Ward tumors. Due to the size limitation of the in vivo fluorescence instrument, the fluorescence imaging of the lead compound was performed in BALB/c mice bearing Colon 26 tumors. All animal procedures were carried out in accordance with guidelines approved by the Institute Animal Use and Care Committee.

MR Imaging Potential of the Conjugates. Among the compounds investigated, the conjugates containing three Gd(III)-ADTPA moieties had better in vitro PDT activity than those containing six Gd(III)ADTPA (see the preceding paper in this issue). Therefore, only those conjugates bearing three Gd(III)-ADTPA chelates were examined for detailed in vivo MR imaging ability (tumor contrast enhancement) in rats bearing Ward tumors. Prior to imaging, anesthesia was induced in the animals with 4% isoflurane and maintained with 2% isoflurane during imaging. Animal temperature and respiration rate were monitored with an MR-compatible small animal monitoring system (model 1025, SAII, Stony Brook, NY), and temperature

was maintained at 32 °C with warm air. A sealed tube containing 150 μM Gd(III)-DTPA (Magnevist, Bayer HealthCare Pharmaceuticals) was placed on each side of each animal to serve as an MR signal intensity calibration standard.

Prior to tail vein administration of each agent (dose:10 μmol/kg), MRI data sets were acquired for each animal to serve as baseline controls, and then animals were rescanned 24 h after injection. An additional MRI data set was acquired at 8 h post injection of conjugate **2** (Pyro-OTEG-3Gd) because a faster clearance rate from the body was anticipated. For comparison to clinically administered MRI contrast agents, two separate groups of rats ($n = 3$ per group) were imaged immediately before and after the administration of Gd(III)-DTPA via tail vein catheter at the clinically recommended dose of 100 μmol/kg, as well as at 10 μmol/kg to compare imaging results with our multifunctional agents.

Two SE imaging protocols were used with identical slice prescription parameters [5−6 axial slices, 1.5 mm slice thickness, 6 × 6 cm FOV(field of view), 256 × 192 acquisition matrix zero-filled to 256 × 256]: first, a moderately T_1-weighted scan acquired with a T_E/T_R of 10/1200 ms (echo and repetition time, respectively) and, second, a heavily T_1-weighted scan acquired with chemical shift selective (CHESS) fat suppression with a T_E/T_R of 10/356 ms.

Additionally, T_1 relaxation rates for tissues were determined by acquiring a series of 6 fast spin−echo encoded scans with T_R's ranging from 360 to 6000 ms.

Last, in vivo testing of HPPH-3Gd(III)ADTPA was performed with an orthotopic RIF tumor model implanted into the thigh muscle of C57bl/6 mice. Imaging parameters were modified to achieve higher resolution required for imaging mice (FOV = 32 mm, matrix size =160 × 160, slice thickness =1 mm). All other data acquisition parameters were identical to the MR imaging protocol described above.

In vivo MR data sets were processed with commercially available software (*Analyze 7.0*, Analyze Direct, Overland Park, KS) by defining a region of interest (ROI) for tumor, muscle surrounding the backbone, and the 150 μM Gd-DTPA calibration standards. Following segmentation, the mean signal intensities for each ROI were sampled. To normalize signal intensity values acquired at different time points, all signal intensity values were divided by the average intensity value of the two Gd-DTPA phantoms. Normalized contrast between tumor and muscle was then determined by subtraction of the mean signal intensity of the two regions. T_1 relaxation rates of tumor and back muscle were calculated by taking the mean intensity within ROI's, and R_1 and S_{MAX} were calculated by nonlinear fitting of the equation

$$S_{(TR)} = S_{MAX}(1 - e^{-(R1 \cdot TR)}) + \text{background noise}$$

using Matlab's Curve Fitting Toolbox (*Matlab 7.0*, MathWorks Inc., Natick, MA). Tissue concentrations of agents were estimated using the following equation

$$[CA] = (R_{1post\text{-}inj} - R_{1pre\text{-}inj}) \div \text{relaxivity}$$

where the compound relaxivity was determined and reported in the accompanying paper.

Fluorescence Imaging. Fluorescence imaging of photosensitizer accumulation in the tumor was carried out using a Nuance optical imaging camera system (Cambridge Research Inc., Woburn, MA). When the tumor reached 4−5 mm in diameter, mice were anesthetized with either a ketamine/xylene mixture (100/10 mg/kg) or 8 mg/kg of pentobarbitol sodium. Prior to imaging, Nair was used to remove hair from the skin surrounding the Colon 26 tumors. Fluorescent excitation was achieved using a spectrum between 525−555 nm using a tungsten−halogen light source. Spectral emission images were acquired from the range 550−700 nm prior to and 24 h postadministration of HPPH-3Gd(III)ADTPA. HPPH-specific images were spectrally unmixed using the Nuance software and represented in false color images.

In Vivo PDT Efficacy and Assessment of Response. When tumor reached 4−5 mm in diameter, the mice were injected with HPPH-3Gd(III)ADTPA at the imaging dose (10 μmol/kg). Prior to PDT treatment, Nair was used to remove all hair surrounding the tumor site. At 24 h postinjection, the mice were restrained in plastic plexiglass holders without anesthesia, treated with a laser light (70 J/cm^2, 70 mW/cm^2). Following treatment, mice were observed daily for tumor regrowth or tumor cure. Visible tumors were measured using two orthogonal measurements, L and W (L perpendicular to W) and the volumes were calculated using the Microsoft *Excel* formula $V = L \times W^2/2$ and recorded. Mice were considered cured if there was no palpable tumor by day 60. Mice were euthanized if the tumor reached 400 mm^3 due to tumor burden.

In Vivo Biodistribution Studies. The ^{14}C-labeled photosensitizers (0.2 mL/0.08 μCi) were individually administered to mice through a lateral tail vein [3 mice/group (BALB/c mice bearing Colon 26 tumors and C3H mice bearing RIF tumors)]. At 24 and 48 h postinjection, 3 mice per time point were sacrificed by CO_2 asphyxiation. The blood was collected into heparinized syringes and immediately centrifuged to obtain plasma. The plasma was transferred to a scintillation vial for ^{14}C counting. The organs of interest (skin, muscle, tumor, heart, lung, liver, kidney, and spleen) were removed. Sample weights were recorded and 1 mL of Solvable (PerkinElmer, Waltham, Massachusetts) was added to each sample and incubated overnight at 53 °C. The samples were allowed to dissolve before adding 80 μL of peroxide (20 μL at a time). After samples were sufficiently bleached, 15 mL of scintillation fluid was added and the samples were run on a Beckman LS 6000LL scintillation counter. Raw data were then converted to counts per gram tissue weight and plotted using *SigmaPlot 10.0* software.

Toxicology Study. To assess the possible toxicity effects of our lead imaging agent, HPPH-3Gd(III)ADTPA was injected into 27 rats (9 rats/group) at concentrations of 5 μmol/kg (lower than the imaging dose), 10 μmol/kg (imaging dose), and 25 μmol/kg (higher than the imaging dose). An additional 3 rats were used as control. Animals were sacrificed 14 days postinjection; liver, spleen, kidney, skin, heart, and lung were collected and fixed in formalin. Fixed tissue specimens were embedded in paraffin, sectioned, and subsequently stained with hematoxylin and eosin (H&E). Individual tissue sections were examined by light-field microscopy for evidence of toxicity.

RESULTS

^{14}C-Labeled HPPH-3GD(III)-DTPA 9. The ^{14}C-labeled HPPH was synthesized from methyl pyropheophorbide-a by following the reported procedure. It was then converted into the corresponding 3Gd(III)-ADTPA (specific activity: 3.9 μCi/μmol) analogue by following the methodology reported for the nonlabeled conjugate in our preceding paper in this issue.

In Vivo Tumor Enhancement by MR Imaging. All HPPH-Gd(III)-ADTPA conjugates containing either three or six gadolinium units showed tumor contrast enhancement 24 h after administration. However, our objective was to develop dual-function agents which could be used for both tumor imaging and therapy. Unfortunately, the conjugates with six gadolinium units showed limited photosensitizing efficacy. Therefore, only those conjugates containing 3Gd(III)-ADTPA groups were investigated for in vivo assessment of tumor contrast enhancement. Figure 3 shows the increase in the normalized contrast between tumor and muscle at 24 h postinjection of each of the

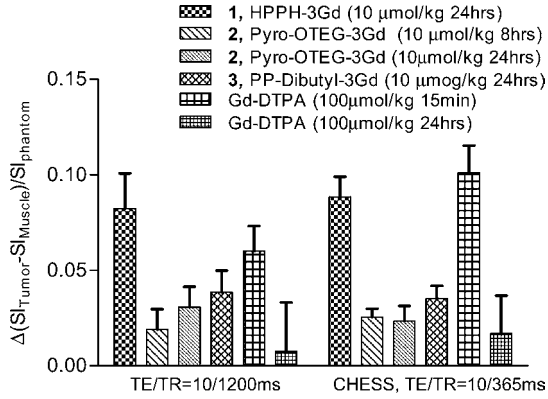


Figure 3. Comparison of the relative increases in contrast between tumor and back muscle for the MR contrast/PDT agents and a clinical dose of Gd(III)-DTPA. The tumor-to-muscle-contrast enhancement caused by the HPPH-3Gd(III)ADTPA (10 μmol/kg) was comparable to the enhancement from clinical Gd(III)-DTPA (100 μmol/kg) seen immediately after injections, despite HPPH-3Gd(III)ADTPA being administered at one-tenth the concentration of Gd(III)-DTPA, and imaged 24 h postinjection.

Table 1. Dose Dependence of HPPH-3Gd(III) ADTPA on Increase in Contrast and T_1 Relaxation Rate

Scan Protocol	10 μmol/kg	5 μmol/kg	2.5 μmol/kg
T_E/T_R = 10/1200 ms (% increase of contrast)	101.5	40.1	−2.71
CHESS fat saturation (% increase of contrast)	130.3	51.4	8.60
ΔR_1 $(s)^{-1}$	0.12	0.08	0.05

3Gd(III)-ADTPA containing agents (Pyro-OTEG-3Gd(III)-ADTPA was also imaged at 8 h postinjection).

All of the multifunctional agents showed increased tumor-to-muscle contrast as compared to baseline values. HPPH-3Gd(III)ADTPA showed the greatest increase in tumor conspicuity administered at 10 μmol/kg (C) at 24 h postinjection in both T_1-weighted scans. As a result, HPPH-3Gd(III)ADTPA was

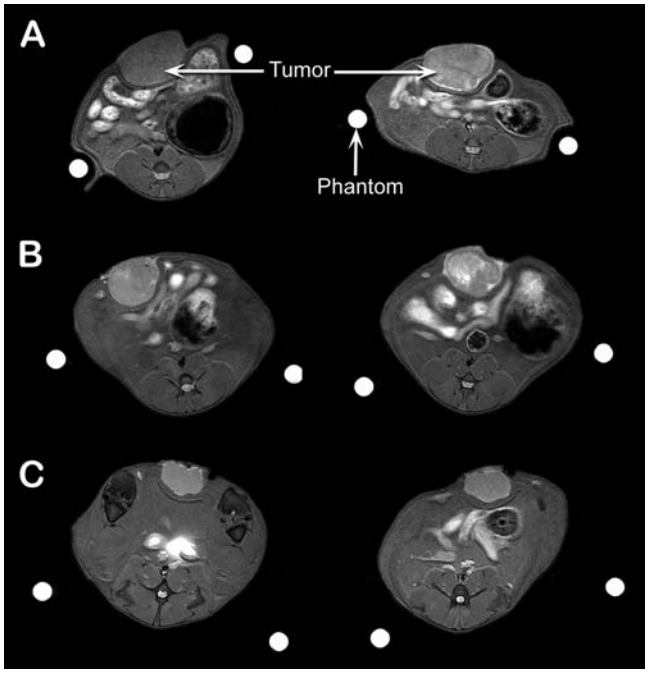


Figure 4. Visible increase in signal intensity was seen in rat Ward Colon tumors (arrow) from preinjection (left) to postinjection (right, 24 h postinjection) of conjugate **1** (HPPH-3Gd) at 10 μmol/kg (A) and at 5 μmol/kg (B). Tumor contrast enhancement of HPPH-3Gd compares favorably to Gd-DTPA.

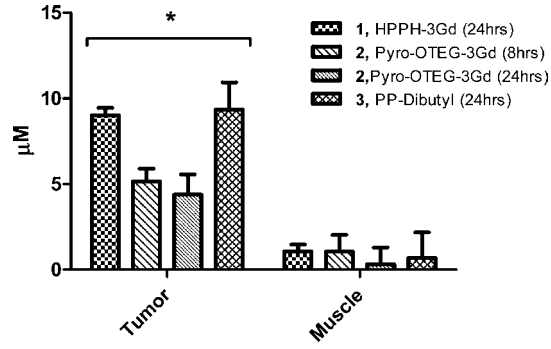


Figure 5. Preferential tumor uptake of multifunctional agents was seen 24 h post administration as compared to muscle (dose = 10 μmol/kg of each conjugate). Concentrations of agents were determined by dividing by change in T_1 relaxation rate by the relaxivity of each agent as determined in vitro. Each compound showed a statistically greater amount of uptake in the tumor as compared to muscle (* $p < 0.05$, unpaired Student's t test.)

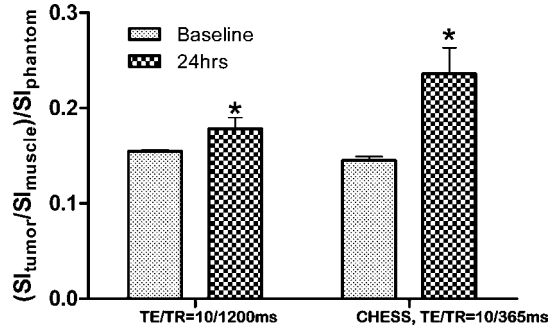


Figure 6. Increase in contrast between RIF tumor and leg muscle was significant for conjugate **1**, HPPH-3Gd (dose = 10 μmol/kg; * $p < 0.05$, paired, one-way Student's t test.)

selected for further characterization at lower doses and in an additional tumor model.

HPPH-3Gd(III)ADTPA also showed quantifiable increases in tumor to muscle contrast and T_1 relaxation rates at 5 and 2.5 μmol/kg, albeit lower than the increases from the 10 μmol/kg dose. Percent increases in tumor to muscle contrast from baseline values for each dose are shown in Table 1, as well as the average increase in T_1 relaxation rate of the tumor. At administered doses of 10 and 5 μmol/kg of HPPH-3Gd(III)ADTPA, the increase in tumor signal intensity could be seen clearly (Figure 4). However, at a dose of 2.5 μmol/kg, tumor signal enhancement was not discernible visually (not shown). T_1 relaxometry of tumor and muscle before and after injection showed preferential tumor uptake of all of the 3Gd(III)ADTPA conjugates tested (Figure 5). Only minimal increases in T_1 relaxation rates compared to baseline values were observed in normal tissue (muscle) 24 h after injection. Tumor-specific enhancement by HPPH-3Gd(III)ADTPA was also seen in an orthotopic RIF tumor model. A significant increase in contrast between tumor and adjacent leg muscle was exhibited (Figure 6). Contrast between tumor and leg muscle increased an average of 36% for the two scan protocols employed.

In Vivo Fluorescence Imaging. Fluorescence imaging potential of HPPH-3Gd(III)ADTPA was evaluated at the imaging dose (10 μmol/kg) in BALB/c mice bearing Colon 26 tumors at 24, 48, and 72 h postinjection. The fluorescence intensity measured in the tumor was maximum at the 24 h postinjection, but was still visible at 48 h. At 72 h, the majority of the drug has cleared out leaving only minimal fluorescence. Tumor enhancement was highest in the 24 h image with a tumor to skin intensity ratio of 3.79 compared with only 2.73 at 48 h (Figure 7).

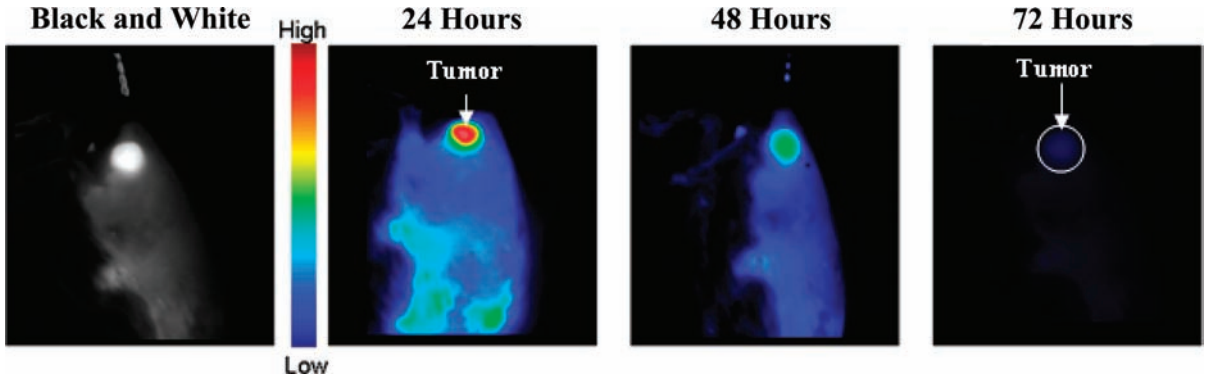


Figure 7. In vivo fluorescent images of conjugate **1** (HPPH-3Gd) in BALB/c mice at 24, 48, and 72 h with an imaging/therapeutic dose of 10 μmol/kg. Spectrally unmixed images are presented with a false color representing fluorescence intensity of the imaging agent. Best tumor images were obtained at 24 h post injection. A preanalysis black and white image at 24 h is given for comparison with the false color images provided.

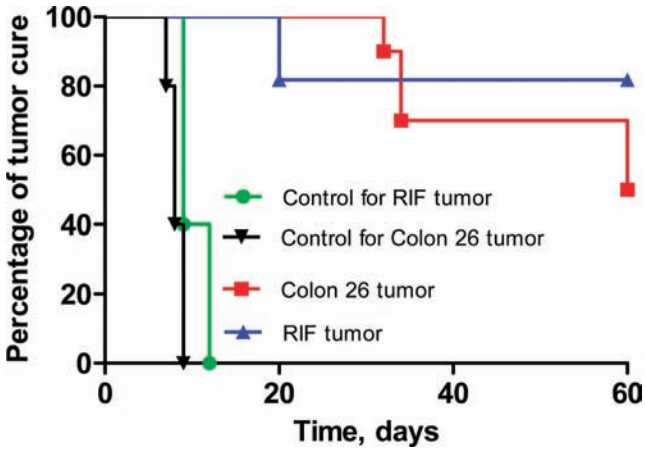


Figure 8. In vivo PDT efficacy of HPPH-3GD(III)ADTPA **1** in (A) C3H mice bearing RIF tumors and (B) BALB/c mice bearing Colon 26 tumors at an imaging dose (10 μmol/kg). Mice were irradiated with a laser light (70 J/cm^2, 70 mW/cm^2) and the tumor size was measured daily.

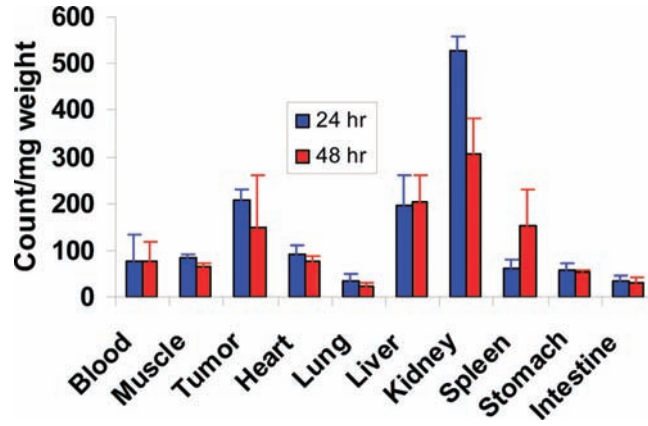


Figure 9. In vivo biodistribution of ^{14}C-labeled HPPH-3Gd(III)ADTPA in Ward colon tumors (3 rats/group): The ^{14}C-labeled conjugate (0.2 mL/0.8 μCi) was administered to 3 rats/group. At 24 and 48 h after injection, 3 rats/time point were sacrificed. Preferable uptake of conjugate **1** in the tumor was seen at 24 and 48 h compared to most normal tissues.

In Vivo PDT Efficacy. For in vivo screening, 6Gd(III)-ADTPA-HPPH conjugate **4** which showed the best T_1 and T_2 relaxivity was initially evaluated at variable doses (2.5, 5.0, and 10.0 μmol/kg) in mice bearing RIF tumors.

Tumors were exposed to a laser light (135 J/cm^2, 75 mW/cm^2) at 24 h postinjection, and tumor growth was recorded daily. Even at such a higher dose, conjugate **4** did not show any significant photosensitizing efficacy. Under similar treatment parameters, conjugates **1**−**3** and **5** were also evaluated. Interestingly, compounds **2** and **5** produced minimal tumor response, whereas the mice injected with **1** and **3** on exposure to light produced 100% mortality. This could possibly be due to high singlet oxygen formation in organs such as liver and spleen (due to high uptake of conjugates) on exposing the tumor (which is in close proximity to tumors) to the light. However, at the same imaging dose (10 μmol/kg), but at a lower light dose compared to **3**, conjugate **1** [HPPH-3Gd(III)aminobenzyl DTPA] was quite effective in both RIF and Colon 26 tumor models. The best tumor response was obtained after exposing the tumors to a laser light (665 nm at 70 J/cm^2, 70 mW/cm^2) at 24 h post treatment (Figure 8).

In Vivo Biodistribution of HPPH-3Gd(III)ADTPA Conjugate. The biodistribution of HPPH-3Gd(III)ADTPA conjugate was evaluated in vivo using Ward tumors in Fischer 344 rats. The distribution of the conjugate to tumor was higher than blood, muscle, heart, lung, spleen, stomach, and intestine, and similar to that of liver (Figure 9). However, kidney showed a significant uptake of the conjugate at 24 h, with a considerable decrease seen at 48 h postinjection, suggesting glomerular filtration of the conjugate by the kidneys.

Toxicological Study (a Range-Finding Study). For a 14 day range-finding toxicity study, male and female SD rats (3 per sex per group) were treated with vehicle (phosphate buffered saline), 5, 10, and 25 μmol HPPH-3Gd(III)ADTPA/kg (a total of 24 rats). The lowest dose chosen coincided with lowest dose required for MR imaging efficacy, and the upper dose was five times that. Higher doses could not be obtained because of solubility limitations. No infusional toxicities were seen, and the rats showed no acute toxicities. As is standard in single dose studies, the rats were sacrificed 14 days after treatment.

Full hematological and serum chemistry evaluation was conducted on an individual animal basis at the time of necropsy, and histopathological evaluation of all major organs (20 tissues per rat) was carried out. Representative toxicological results in tissues of an animal that received 25 μmol/kg (2.5× higher than the imaging/therapeutic dose) are shown in Figure 10. H&E results obtained from liver, spleen, kidney, skin, heart, and lungs following HPPH-3Gd(III)ADTPA administration demonstrated that each tissue appeared normal, well-preserved, and devoid of toxicological lesions.

DISCUSSION

With advances in the early detection of cancerous lesions, highly localized therapies such as photodynamic therapy present a favorable alternative to invasive surgery or systemic chemo-

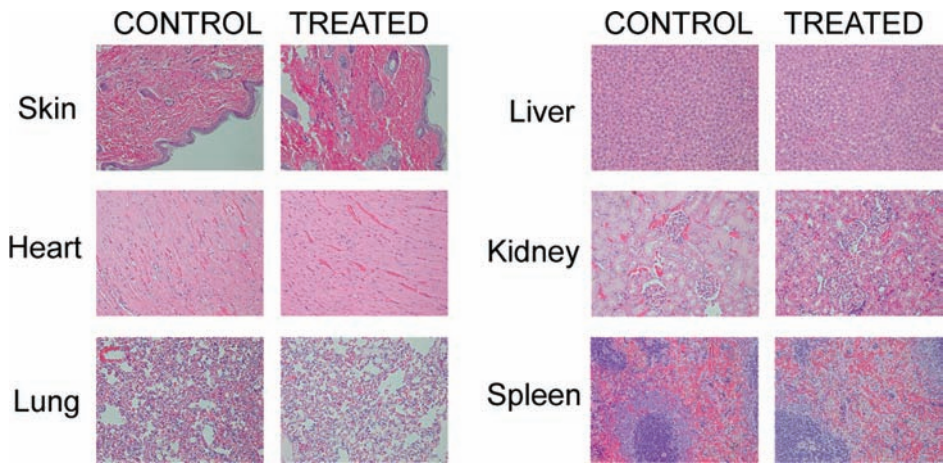


Figure 10. In vivo histochemical staining of HPPH-3Gd(III)-ADTPA conjugate. No histologic evidence of toxicity was observed in the animals (rats) administered with HPPH-3Gd(III)-ADTPA at a dose of 25 μmol/kg (2.5-fold higher than the imaging dose). Histological structure of every organ was preserved.

therapy. In this paper, we report the advancement of combined MR contrast/PDT agents. The combination of diagnostic and therapeutic efficacy into a single compound offers multiple advantages. In the case of deep-seated tumors, the ability to use noninvasive imaging to better delineate tumor boundaries or metastatic spread immediately prior to or during PDT would be a valuable tool to the clinician. Furthermore, the inclusion of MR contrast enhancing groups into the therapeutic agent provides a probe to determine intratumoral concentration of the PDT agent. To a first approximation, the T_1 relaxation rate (R_1) of tissue increases linearly with contrast agent concentration within the tissue (*20*). Therefore, measuring baseline relaxation rates and monitoring the increase in R_1 allows for individualized measurements of the pharmacokinetics of the agent within the tumor. In the past, the time requirements for in vivo T_1 relaxometry were prohibitive for routine assessment of changes in T_1 rates. However, through rapid measurement techniques, T_1 rates can be measured well under 5 min in a patient (*21*−*23*). These advances, as well as the lack of nonionizing radiation associated with MRI, allow for serial assessment of multifunctional agent concentration. Thus, light dosing parameters may potentially be adjusted on a per patient basis, maximizing efficacy while reducing phototoxicity to surrounding normal tissue. Furthermore, if these multifunctional agents can be modified for more effective uptake into tumors, MRI may be used serially to measure individual tumor uptake at variable time points, and PDT treatment can begin as soon as intratumoral levels reach a predetermined threshold.

As determined by T_1 relaxometry, there was minimal uptake in muscle at 24 h postinjection. Biodistribution studies of ^{14}C labeled compound displayed similar preferential uptake of HPPH-3Gd(III)ADTPA in the tumor. Using the relaxivity 13.50 $(mM \cdot s)^{-1}$ for HPPH-3Gd(III)ADTPA (as determined in vitro), mean tumor concentration of the conjugate at 24 h was 9.0 μM. The primary cause of preferential tumor accumulation is believed to be the result of the enhanced permeability and retention effect associated with tumor vasculature. It has been reported that Gadophrin-2, another porphyrin-based compound, binds with the serum protein albumin and accumulates preferentially in the rim of necrotic regions (*24*, *25*).

At the MR imaging dose (10 μmol/kg), the utility of the conjugate **1** was also investigated for in vivo fluorescence imaging and PDT. As can be seen from Figures 7 and 8, the conjugate produced significant tumor contrast and long-term PDT activity in two tumor models. However, HPPH-3Gd(III)-ADTPA produced excellent PDT response and tumor-imaging potential at lower doses as well (data not shown). The difference between the MR imaging dose required for HPPH-Gd(III)-ADTPA is 10- to 20-fold less than the clinical MR imaging agent Gd(III)-DTPA in mice and rat models. This study further indicates that the conjugates in which tumor-avid photosensitizer (HPPH) was used as a vehicle for MR imaging require a much higher dose than required for fluorescence imaging and therapy. However, even at higher doses required for MR imaging, no histologic evidence of toxicity was seen by detailed in vivo organ toxicological studies in rats. Thus, the development of such multifunctional conjugates with tumor-avid photosensitizer presents a clear potential for a "see and treat" approach in photodynamic therapy.

CONCLUSION

In summary, our study indicates that tumor-avid photosensitizers can be used as vehicles to deliver the desired imaging agent to tumor. The presence of three Gd(III)ADTPA moieties increased tumor conspicuity during MR imaging while maintaining antitumor PDT efficacy. The fluorescent characteristic of the HPPH-based conjugate (Ex: 665 nm, Em: 715 nm) also showed a great potential for complementary optical imaging of the tumor. Thus, the HPPH-3Gd(III)ADTPA as a single moiety can be used for tumor imaging by MR and fluorescence with an option of photodynamic therapy. Our next goal is to increase the tumor specificity of these multifunctional agents by introducing variable number of tumor-targeting moieties such as (a) cyclic RGD peptide which binds preferably to the $\alpha_v\beta_3$ integrin expressed in the neoangiogenic vasculatures of tumors (*7*, *26*, *27*), (b) folic acid to target folate receptors known for their high expressions in breast cancers, and (c) certain β-galactosides for binding to integrin-3 to target metastatic brain tumors. A target-specific approach may help to reduce the dose required for MR imaging efficacy, which is already 10-fold less than that of the typical dose of Gd-DTPA (100 μmol/kg) used clinically.

ACKNOWLEDGMENT

The authors are highly thankful to Dr. Peter Kanter for animal toxicological studies, Dr. Toth, pathologist (RPCI) for analyzing the in vivo toxicological data, and Dr. Rustum (Chair, Department of Cancer Biology) for valuable discussions. Financial support from the NIH (Grants R21/33 CA109914 and PO1, CA55791), Roswell Park Alliance Foundation, and the shared resources of the RPCI Support Grant (P30CA16056) is highly appreciated.

Supporting Information Available: In vivo MR images of conjugates **1**−**5** and the intracellular localization of HPPH-

3Gd(III)aminobenzyl DTPA **3**.This material is available free of charge via the Internet at http://pubs.acs.org.

LITERATURE CITED

(1) Dougherty, T. J., Gomer, C. J., Henderson, B. W., Jori, G., Kessel, D., Korbelik, M., Moan, J., and Peng, Q. (1998) Photodynamic therapy. *J. Natl. Cancer Inst. 90*, 889–905.

(2) Overholt, B. F., Wang, K. K., Burdick, J. S., Lightdale, C. J., Kimmey, M., Nava, H. R., Sivak, M. V., Jr., Nishioka, N., Barr, H., Marcon, N., Pedrosa, M., Bronner, M. P., Grace, M., and Depot, M. (2007) Five-year efficacy and safety of photodynamic therapy with photofrin in barrett's high-grade dysplasia. *Gastrointest. Endosc. 66*, 460–468.

(3) Yamaguchi, S., Tsuda, H., Takemori, M., Nakata, S., Nishimura, S., Kawamura, N., Hanioka, K., Inoue, T., and Nishimura, R. (2005) Photodynamic therapy for cervical intraepithelial neoplasia. *Oncology 69*, 110–116.

(4) Loewen, G. M., Pandey, R., Bellnier, D., Henderson, B., and Dougherty, T. (2006) Endobronchial photodynamic therapy for lung cancer. *Lasers Surg. Med. 38*, 364–370.

(5) Nseyo, U. O., DeHaven, J., Dougherty, T. J., Potter, W. R., Merrill, D. L., Lundahl, S. L., and Lamm, D. L. (1998) Photodynamic therapy (PDT) in the treatment of patients with resistant superficial bladder cancer: A long-term experience. *J. Clin. Laser Med. Surg. 16*, 61–68.

(6) Dolmans, D. E., Fukumura, D., and Jain, R. K. (2003) Photodynamic therapy for cancer. *Nat. Rev. Cancer 3*, 380–387.

(7) Sibata, C. H., Colussi, V. C., Oleinick, N. L., and Kinsella, T. J. (2001) Photodynamic therapy in oncology. *Expert Opin. Pharmacother. 2*, 917–927.

(8) Dougherty, T. J., Pandey, R. K., Nava, H. R., Smith, J. A., Douglass, H. O., Edge, S. B., Bellnier, D., O'Malley, L., and Cooper, M. (2000) Preliminary clinical data on a new photodynamic therapy photosensitizer: 2-[1-hexyloxyethyl]-2-devinylpyropheophorbide-a (HPPH) for treatment of obstructive esophageal cancer. *Proc. SPIE 3909*, 25–27.

(9) Bellnier, D., Greco, W., Loewen, G., Nava, H., Oseroff, A., Pandey, R., Tsuchida, T., and Dougherty, T. (2003) Population pharmacokinetics of the photodynamic therapy agent 2-[1-hexyloxyethyl]-2-devinyl pyropheophorbide-a in cancer patients. *Cancer Res. 63*, 1806–1813.

(10) Jäger, H. R., Taylor, M. N., Theodossy, T., and Hopper, C. (2005) MR imaging-guided interstitial photodynamic laser therapy for advanced head and neck tumors. *Am. J. Neuroradiol. 26*, 1193–1200.

(11) Eljamel, M. S., Goodman, C., and Moseley, H. (2008) ALA and photofrin® fluorescence-guided resection and repetitive PDT in glioblastoma multiforme: A single centre phase III randomised controlled trial. *Lasers Med. Sci. 23*, 361–367.

(12) Zilidis, G., Aziz, F., Telara, S., and Eljamel, M. S. (2008) Fluorescence image-guided surgery and repetitive photodynamic therapy in brain metastatic malignant melanoma. *Photodiagn. Photodyn. Ther. 5*, 264–266.

(13) Tanimoto, A., Nakashima, J., Kohno, H., Shinmoto, H., and Kuribayashi, S. (2007) Prostate cancer screening: The clinical value of diffusion-weighted imaging and dynamic MR imaging in combination with T2-weighted imaging. *J. Magn. Reson. Imaging I 25*, 146–152.

(14) Yuh, W., Fisher, D., Nguyen, H., Tali, E., and Mayr, N. (1992) The application of contrast agents in the evaluation of neoplasms of the central nervous system. *Top. Magn. Reson. Imaging 4*, 1–6.

(15) Safir, J., Zito, J., Gershwind, M., Faegenburg, D., Tobin, C., Cayea, P., Wortman, W., Sclafani, L., and Maurer, V. (1998) Contrast-enhanced breast MRI for cancer detection using a commercially available system--a perspective. *Clin. Imaging 22*, 162–179.

(16) Ward, J. (2006) New MR techniques for the detection of liver metastases. *Cancer Imaging 6*, 33–42.

(17) Sakuma, H. (2007) Magnetic resonance imaging for ischemic heart disease. *J. Magn. Reson. Imaging 26*, 3–13.

(18) Runge, V. M., Muroff, L. R., and Jinkins, J. R. (2001) Central nervous system: Review of clinical use of contrast media. *Top. Magn. Reson. Imaging. 12*, 231–263.

(19) Li, G., Slansky, A., Dobhal, M. P., Goswami, L. N., Graham, A., Chen, Y., Kanter, P., Alberico, R. A., Spernyak, J., Morgan, J., Mazurchuk, R., Oseroff, A., Grossman, Z., and Pandey, R. K. (2005) Chlorophyll-a analogues conjugated with aminobenzyl-DTPA as potential bifunctional agents for magnetic resonance imaging and photodynamic therapy. *Bioconjugate Chem. 16*, 32–42.

(20) Shuter, B., Wang, S., Roche, J., Briggs, G., and Pope, J. M. (1998) Relaxivity of Gd-EOB-DTPA in the normal and biliary obstructed guinea pig. *J. Magn. Reson. Imaging. 8*, 853–861.

(21) Schmitt, P., Griswold, M. A., Jakob, P. M., Kotas, M., Gulani, V., Flentje, M., and Haase, A. (2004) Inversion recovery TrueFISP: Quantification of T1, T 2, and spin density. *Magn. Reson. Med. 51*, 661–667.

(22) Bellamy, D. D., Pereira, R. S., McKenzie, C. A., Prato, F. S., Drost, D. J., Sykes, J., and Wisenberg, G. (2001) Gd-DTPA bolus tracking in the myocardium using T1 fast acquisition relaxation mapping (T1 FARM). *Magn. Reson. Med. 46*, 555–564.

(23) Cheng, H. M., and Wright, G. A. (2006) Rapid high-resolution T1 mapping by variable flip angles: Accurate and precise measurements in the presence of radiofrequency field inhomogeneity. *Magn. Reson. Med. 55*, 566–574.

(24) Ni, Y., Marchal, G., Yu, J., Lukito, G., Petre, C., Wevers, M., Baert, A. L., Ebert, W., Hilger, C. S., and Maier, F. K. (1995) Localization of metalloporphyrin-induced "specific" enhancement in experimental liver tumors: Comparison of magnetic resonance imaging, microangiographic, and histologic findings. *Acad. Radiol. 2*, 687–699.

(25) Hofmann, B., Bogdanov, A., Jr., Marecos, E., Ebert, W., Semmler, W., and Weissleder, R. (1999) Mechanism of gadophrin-2 accumulation in tumor necrosis. *J. Magn. Reson. Imaging 9*, 336–341.

(26) Brooks, P. C., Clark, R. A., and Cheresh, D. A. (1994) Requirement of vascular integrin alpha v beta 3 for angiogenesis. *Science 79*, 1157–1164.

(27) Anderson, S. A., Rader, R. K., Westlin, W. F., Null, C., Jackson, D., Lanza, G. M., Wickline, S. A., and Kotyk, J. J. (2000) Magnetic resonance contrast enhancement neovasculature with $\alpha(v)\beta 3$-targeted nanoparticles. *Magn. Reson. Med. 44*, 433–439.

BC9005317

Low Molecular Weight Polyethylenimine Conjugated Gold Nanoparticles as Efficient Gene Vectors

Chu Hu, Qi Peng, Fujie Chen, Zhenlin Zhong,* and Renxi Zhuo*

Key Laboratory of Biomedical Polymers of Ministry of Education, Department of Chemistry, Wuhan University, Wuhan 430072, P. R. China. Received August 22, 2009; Revised Manuscript Received March 7, 2010

Gold nanoparticles (GNPs) conjugated with low molecular weight polyethylenimine (PEI 800 Da) were synthesized, and their characteristics as gene transfection vectors were investigated. The polyethylenimine conjugated GNPs (GNP-PEI800s) can retard plasmid DNA completely at N/P ratios above 4 in electrophoresis on agarose gel, and they also render effective protection of DNA from attack by DNase. TEM imaging revealed that GNP-PEI800s with higher PEI grafting density resulted in more compact and smaller complexes with plasmid DNA, compared to those obtained with lower grafting density ones. These complexes showed high efficiency in gene delivery in monkey kidney cells in vitro. In the absence of serum, GNP-PEI800s can transfect pGL-3 to COS-7 cells 3 to 4 orders more efficient than unmodified PEI800, reaching almost the same magnitude of PEI 25 kDa. More importantly, in contrast to the dramatically lowered efficiency of high molecular weight PEIs such as PEI 25 kDa in the presence of serum, the efficiency of GNP-PEI800s can be retained or even enhanced in serum-containing media. GNP-PEI800 1.3 exhibited transfection efficiency exceeding 60-fold that of PEI 25 kDa in 10% serum medium. All GNP-PEI800s exhibit mild cytotoxicity in comparison with that of PEI 25 kDa.

INTRODUCTION

Substantial effort has been focused on synthetic nonviral vector systems such as cationic lipids (*1*), dendrimers (*2*), and cationic polymers (*3*). Among them, polyethylenimine (PEI) is one of the most extensively studied polycations (*4*). The relatively high transfection efficiency of PEI has led to intense research in terms of both understanding (*5, 6*) and improving (*7, 8*) gene delivery by PEI. The efficiency and toxicity of PEI are strongly correlated with its molecular weight (MW) (*9*). High molecular weight PEI such as PEI with molecular weight of 25 000 Da (PEI 25 kDa) leads to high transgene expression, but its acute cytotoxicity and significantly lower efficiency in the presence of serum (*10*) has restricted its clinical development (*11*). Meanwhile, low molecular weight PEI, which has been demonstrated to be nontoxic in cell culture studies, displays very poor transfection activity (*12*), presumably because of its inability to condense DNA effectively (*13*). To achieve a useful level of transfection efficiency while minimizing the toxicity, low molecular weight PEIs such as PEI with molecular weight of 800 Da (PEI800) are modified by cross-linking via biodegradable linkages (*14*−*16*).

Recently, efforts have been made for construction of inorganic nanoparticles as alternate nonviral vectors including silica (*17*), iron oxide (*18*), carbon nanotube (*19*), and gold nanoparticles (GNPs) (*20*−*24*). GNPs provide attractive scaffolds for gene delivery vectors (*25*−*29*). GNPs can be readily synthesized varying in diameter from about 5 nm to around 150 nm and conjugated with targeting molecules through thiol linkages. GNPs of small size provide a high surface-to-volume ratio, maximizing grafting density of target molecules, which allow further tuning of the surface charge and hydrophobicity. Moreover, GNPs are bioinert and nontoxic (*30*). Various GNPs functionalized with cationic quaternary ammonium (*20*), cationic lipid (*21*), chitosans (*22*), amino acids (*23*), and polyethylenimine (*24*) were demonstrated to be excellent vehicles for the delivery of genetic material into cells.

Thomas and Klibanov covalently conjugated branched PEI of 2 kDa to GNPs and found that conjugation to GNPs greatly enhances PEI's transfer of plasmid DNA into mammalian cells (*24*). We recently reported a convenient procedure for preparation of thiolated PEI with controllable amounts of thiol groups by ring-opening reaction of thiiranes (*16a*) and found that disulfide cross-linked PEI800 is superior to the cross-linked PEI 1.8 kDa and 25 kDa for use as gene vectors (*16b*). Efficient gene delivery systems based on low molecular weight PEIs such as PEI800 are attractive because of lower toxicity and easier clearance from body than higher molecular weight ones. In the present study, we devised a series of PEI800 conjugated GNPs (GNP-PEI800) at different PEI/Au molar ratios as nonviral vectors. The effect of PEI grafting density on DNA binding capacity, DNA protection ability, surface charge and size of GNP-PEI800s/DNA complexes, cytotoxicity, and in vitro transfection efficiency of nanoparticles were investigated.

MATERIALS AND METHODS

Materials. Branched PEI with molecular weights of 25 kDa and 800 Da were purchased from Aldrich. Methylthiirane was synthesized by literature procedure (*31*). $HAuCl_4$ tetrahydrate and $NaBH_4$ were obtained from Shanghai Chemical Co (China). GelRed was purchased from Biotium (CA, USA). Dulbecco's Modified Eagle's Medium (DMEM), fetal bovine serum (FBS), Dulbecco's phosphate buffered saline (PBS), and 3-[4,5-dimethylthiazol-2-yl]-2,5-diphenyltetrazolium bromide (MTT) were purchased from Invitrogen Corp. The Micro BCA protein assay kit was purchased from Pierce. DNase, DNase reaction buffer, and stop reaction buffer were purchased from (Promega, USA). Ultrapure water (18.0 MΩ, Millipore) was used throughout the experiment. Plasmid pGL3 was propagated at 37 °C in *Escherichia colia* in Luria−Bertani (LB) medium containing 50 μg/mL kanamycin or 60 μg/mL ampicillin. The mixture was shaken overnight at 250 rpm. The plasmid was purified using E.Z.N.A. Fastfilter Endo-Free Plasmid Midi Kits (Omega)

* To whom correspondence and reprint requests should be addressed. Phone: +86-27-6875-4061. Fax: +86-27-6875-4509. E-mail: zlzhong@whu.edu.cn.

10.1021/bc900374d © 2010 American Chemical Society
Published on Web 05/03/2010

Table 1. Composition and Characteristics of PEI Conjugated Gold Nanoparticles GNP-PEI800

		composition						
sample	molar feed ratio[a] (Au:PEI)	PEI[b](wt%)	Au[c](wt%)	molar ratio (Au:PEI)	gold core size[d] (nm)	number of PEI800 molecules per particle	number of gold atoms per particle	grafting density (N_{PEI}/nm^2)
GNP-PEI800 5.6	1:1.6	21.7	28.4	5.6:1	5.7	1000	5600	10
GNP-PEI800 4.3	1:3.1	25.2	25.4	4.3:1	5.4	1100	4900	12
GNP-PEI800 1.3	1:15	35.6	10.3	1.3:1	7.7	11000	14000	57

[a] Molar feed ratio of $HAuCl_4 \cdot 4H_2O$ to PEI 800 Da. [b] Calculated on the basis of nitrogen content from elemental analysis. [c] Based on ICP-AES measurement. [d] Based on TEM images.

according to the manufacturer's instruction. The DNA concentration was determined by measuring the UV absorbance at 260 nm. The purity of DNA was assessed spectrophotometrically by measuring absorbance at wavelengths of 260 and 280 nm (OD_{260}/OD_{280} 1.8 or greater). DNA aliquots were stored at −20 °C prior to use.

Synthesis of Thiolated PEI (PEI-SH). In a 25 mL flask, 1.00 g of PEI800 was dissolved in 5 mL of deionized water. Hydrochloric acid (0.1 M) was added to the PEI solution until pH was regulated to 7.2. After removal of water, the neutralized PEI was redissolved in 10 mL of CH_3OH. The assigned amount of thiirane was added after the container was purged with argon. The flask was kept in a 50 °C oil bath for 24 h under magnetic stirring. The solution was evaporated to remove CH_3OH and the yellow solid thus obtained was kept under argon. Two kinds of thiolated PEIs varying in thiol group content were synthesized, and the thiol group contents were determined to be 0.8 and 1.7, respectively, by Ellman's method (*32*, *33*).

General Procedure for the Synthesis of GNP-PEI800. $HAuCl_4$ (tetrahydrate, 0.10 g, 0.24 mmol) was mixed with calculated amount of PEI-SH in 10 mL of water and stirred for 15 min; then, freshly prepared $NaBH_4$ solution (0.45 g, 12 mmol in 5 mL of water) was added dropwise. Within 90 s, the solution turned dark purple signaling the onset of gold nanoparticles formation. The mixture was stirred at room temperature for an extra 24 h. The conjugates were dialyzed extensively against water with 12 kDa cutoff dialysis tubes. The solution was filtered through a 0.22 mm pore size polyether sulfone membrane and stored at room temperature for use. A measured portion was lyophilized and submitted for elemental analysis. On the basis of nitrogen content from elemental analysis and gold content from ICP measurements, the ratios of gold/PEI800 were calculated and summarized in Table 1.

Instrumentation. Elemental analysis was performed by using Vario EL III (Germany). UV−vis spectra were recorded on a Perkin Elmer UV−vis spectrophotometer with a quartz cuvette with a 10 mm optical path length. The ICP-AES was carried on a Thermo IRIS Intrepid II XSP spectrometer (USA). The morphologies of GNP-PEI800s and GNP-PEI800/DNA complexes were observed on transmission electron microscope (TEM JEM-100CXa) with an acceleration voltage of 100 kV.

Particle Size and Zeta Potential Measurements. The particle size and zeta potential were measured with a Nano-ZS ZEN3600 (Malvern) at room temperature. The relative amount of GNP-PEI800s/DNA was express as N/P molar ratio which is calculated with the N content in GNP-PEI800s based on the elemental analysis and the P content in the DNA solution of known concentration. The GNP-PEI800s/DNA complexes at various N/P ratios ranging from 30 to 180 were prepared by adding appropriate volumes of GNP-PEI800s to 50 μL of pGL-3 DNA (20 ng/mL in 40 mM Tris-HCl buffer solution), and then the complexes were diluted to a total volume of 1 mL with 150 mM NaCl and vortexed for 15 s. After that, the complexes were incubated at room temperature for 30 min before measurements of particle sizes or zeta potentials.

Agarose Gel Retardation Assay. GNP-PEI800/DNA complexes at predetermined N/P ratios were loaded on 0.7% (w/v) agarose gel containing GelRed and electrophoresed with Tris-acetate (TAE) running buffer at 80 V for 80 min. DNA was visualized with a UV lamp using a Vilber Lourmat imaging system (France).

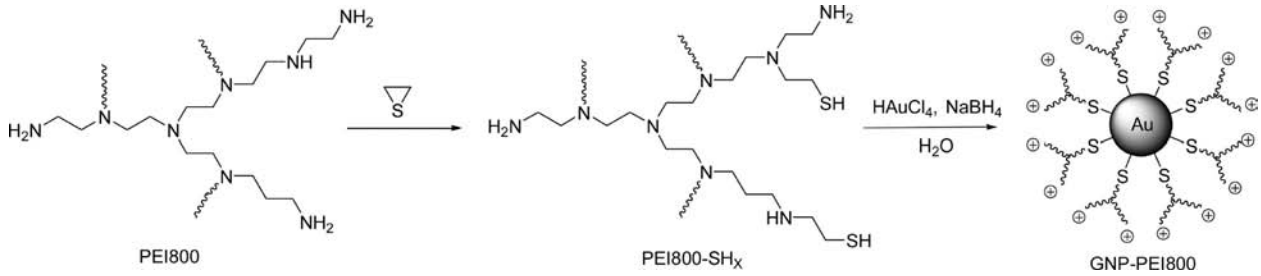
DNase Protection Assay. The concentration of DNase enzyme was 1 U/μg DNA. Reaction mixture for DNase digestion contained 1.0 μL of 10× reaction buffers, 8.0 μL of either DNA or GNP-PEI800s/DNA complex with an amount of DNA of 0.2 μg, and 1.0 μL of DNase enzyme (1 U/μL). The digestions were incubated at 37 °C for 30 min and halted by addition of 1.0 μL of stop solution followed by heating at 65 °C for 30 min. The complexes were then analyzed by agarose gel electrophoresis. The integrity of DNA in each formulation was compared with untreated DNA as a control.

Cytotoxicity Assay. The cytotoxicity assay was carried out on the basis of an MTT assay on COS-7 cells. Cells were seeded in 96-well plates at an initial density of 5000 cells/well in DMEM complete medium. The cells were allowed to grow for 24 h. The original media were then replaced with 100 μL of fresh DMEM complete media. The GNP-PEI800s, PEI 800 Da, or PEI 25 kDa solution were added to the media. Each dosage was replicated in 4 wells. Treated cells were incubated at 37 °C under a humidified atmosphere of 95% air and 5% CO_2 for 24 h. MTT reagent (20 μL in PBS, 5 mg/mL) was added to each well, and the cells were incubated for another 4 h at 37 °C. The liquid in each well was removed with cautions to avoid disturbing the crystals on the well wall. 100 μL of DMSO was added to each well to dissolve the crystals. The absorbance at 570 nm of the solution in each well was recorded using a Microplate Reader (Bio-Rad model 550).

In addition to the general control experiment of cell culturing in the absence of the polycation samples, control experiment using GNP-PEI800s in medium without cells was carried out to exclude the interference caused by the absorbance of gold nanoparticles at 570 nm. Cell viability was calculated according to the following equation: Cell viability (%) = $(OD_{sample} - OD_{GNP} - OD_{blank})/(OD_{control} - OD_{blank}) \times 100$ where OD_{sample} is the absorbance of the solution of the cells cultured with GNP-PEIs and PEI; OD_{blank} is the absorbance of the medium, $OD_{control}$ is the absorbance of the solution of the cells cultured with the medium only, and OD_{GNP} is the absorbance of the control solution of GNP-PEI800s in medium without cells.

Luciferase Assay. For in vitro transfection study, COS-7 cells were plated in 24-well plates at a density of 5×10^4 cells/well. They were incubated at 37 °C in a humidified atmosphere of 95% air and 5% CO_2 until the cells reached about 70% confluence. At the time of transfection, the medium in each well was replaced with 1 mL of DMEM without FBS. The cells were transfected with gene-loaded complexes containing 1 μg of plasmid DNA at 37 °C for 4 h. Then, the complexes were removed, and the cells were washed by PBS three times. The cells were then incubated in fresh DMEM with 10% FBS at 37 °C for another 48 h and lysed with the reporter lysis buffer (Promega, USA). The luciferase activity in cell extracts was measured using a luciferase assay kit (Promega, USA). The relative light units (RLU) were normalized by the total protein concentration of the cell extracts, and the total protein was

Scheme 1



measured with a BCA protein assay kit (PERBIO, USA). Luciferase activity was expressed as RLU/mg protein.

Cell Uptake Tracing Assay. GelRed was used as molecular probe to label pGL-3. The GNP-PEI800s/DNA complexes at N/P ratio of 90 were prepared. After the complexes were incubated for 4 h at 37 °C, the medium was replaced with GelRed solution (in 1/10 000 (v/v) DMEM with 10% FBS) and incubated for 10 min at 37 °C. Then, the GelRed solution was replaced with fresh DMEM with 10% FBS. After incubating for an extra 4 h, the cells were directly visualized on a laser confocal scanning microscope (Eclipse C1Si, Nikon, Japan).

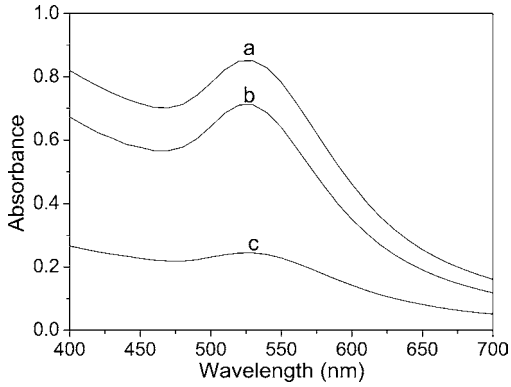


Figure 1. Absorption spectra of (a) GNP-PEI800 5.6, (b) GNP-PEI800 4.3, and (c) GNP-PEI800 1.3 at concentration of 0.15 mg/mL.

RESULTS AND DISCUSSION

Preparation and Characterization of GNP-PEI800s. As shown in Scheme 1, thiolated PEIs (PEI-SH) were synthesized via the ring-opening reaction of methylthiirane on low molecular weight PEI with an M_w of 800 Da. PEI conjugated golden nanoparticles (GNP-PEI800s) were prepared by the simple one-pot reduction of tetrachloroaurate with sodium borohydrate in the presence of PEI-SH. To explore the effect of PEI grafting density on transfection efficiency, we fabricated GNPs with varied Au/PEI molar feed ratios. The elemental composition of the GNP-PEI800s was measured by using a Vario EL III elemental analyzer (for CHN) and ICP-AES measurement (for Au). On the basis of the nitrogen and gold contents, the molar ratio composition of the GNP-PEI800s was calculated and summarized in Table 1. The UV−vis spectra of GNP-PEI800s were shown in Figure 1. These spectra have a strong absorption feature at 520 nm due to the characteristic surface plasmon resonance of GNPs (*34*). Though the GNP-PEI800s were at the same weight concentration of 0.15 mg/mL, the absorbance strength was different, because the absorbance of the conjugates is proportional to the content of GNP cores other than the weight of the total conjugates. Actually, the absorbance strength in Figure 1 is in good agreement with the Au/PEI composition ratios in Table 1. Electron micrographs of GNP-PEI800s and those of their complexes with the plasmid pGL3 DNA are presented in Figure 2. All PEI800-GNPs exhibited no apparent

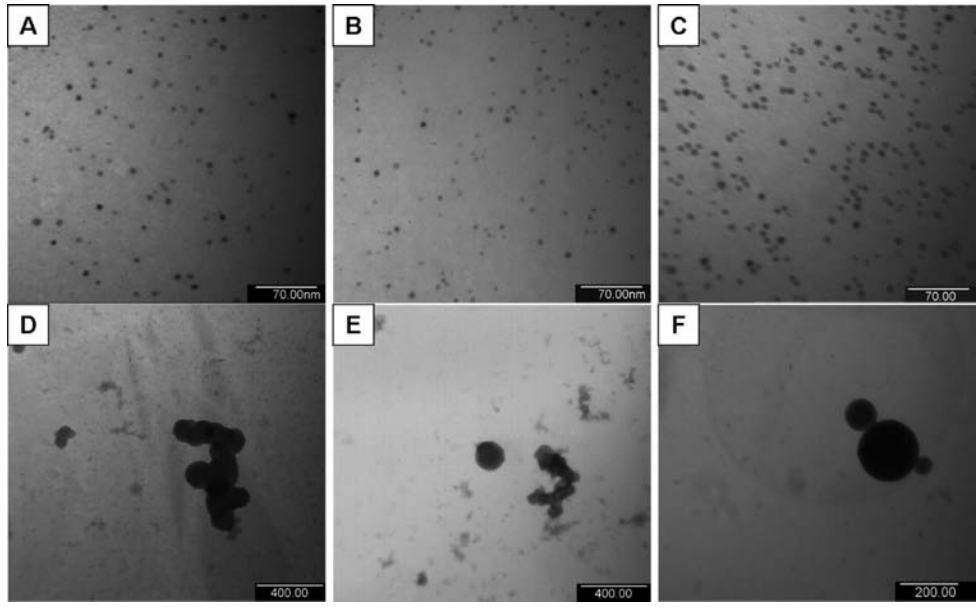


Figure 2. TEM micrographs of (A) GNP-PEI800 5.6, (B) GNP-PEI800 4.3, (C) GNP-PEI800 1.3, (D) GNP-PEI800 5.6/pGL3 complex, (E) GNP-PEI800 4.3/pGL3 complex, and (F) GNP-PEI800 1.3/pGL3 complex. The GNP−PEI800/pGL3 complexes were prepared at N/P ratio of 30.

signs of aggregation. The sizes of the gold core deduced from TEM were 5.7 ± 1.5 nm for GNP-PEI800 5.6, 5.4 ± 0.8 nm for GNP-PEI800 4.3, and 7.7 ± 1.8 nm for GNP-PEI800 1.3, respectively.

GNP conjugates with thiolated PEI 2 kDa were previously prepared and studied for enhanced gene tansfection (*24*). Compared with the literature procedure of making thiolated PEI by reduction of disulfide cross-linked PEI, our thiirane ring-opening procedure is more direct and controllable without need of time-consuming dialysis. The GNP-PEI800s have higher PEI content that is beneficial to higher gene loading capacity. It is worth noting that GNP-PEI800s are very stable. After 6 months of stocking at room temperature, no obvious changes were observed with GNP-PEI800 solutions.

Determination of Graft Density of PEI800 on GNPs. The number of gold atoms in each nanoparticle (U) was calculated according to eq 1 (*35*).The number of PEI molecules per nanoparticle (N) and grafting density of PEI (δ) can be determined using eqs 2−5, and the results are shown in Table 1.

$$U = \frac{2}{3}\pi\left(\frac{D}{\alpha}\right)^3 \tag{1}$$

$$N_{\mathrm{GNPs}} = \frac{W_{\mathrm{Au}}}{M_{\mathrm{Au}}U} \tag{2}$$

$$N_{\mathrm{PEI}} = \frac{W_{\mathrm{PEI}}}{MW_{\mathrm{PEI}}} \tag{3}$$

$$N = \frac{N_{\mathrm{PEI}}}{N_{\mathrm{GNPs}}} \tag{4}$$

$$\delta = \frac{N}{\pi D^2} \tag{5}$$

where α refers to the edge of a unit cell, which has a value of 4.0786 Å on the edge; there are four gold atoms per unit cell. D is the diameter of nanoparticles. W_{Au} and W_{PEI} are the gold content and PEI content, and N_{GNPs} and N_{PEI} are the molar number of gold nanoparticles and PEI. MW_{PEI} and M_{Au} are the molecular weight of PEI and gold.

Characterization of Complexes. The morphology of the complexes was also monitored by TEM. Upon the addition of DNA, GNP−PEI conjugates tended to aggregate with DNA forming submicrometer particles. At N/P ratio of 30, all of the complexes exhibited diameters below 400 nm. The structure of the complexes varied as a function of PEI grafting density on the GNPs. While mainly anomalous loose aggregations with a size of around 400 nm were observed in the images of GNP-PEI800 5.6/DNA (Figure 2D), both anomalous loose and spherical structures were found in GNP-PEI800 4.3/DNA (Figure 2E), and when GNP-PEI800 1.3/DNA complexes were formed, compact and ordered spherical granules were the primary structure as shown in Figure 2F.

The particle sizes of the complexes were further determined by DLS (Figure 3). At low N/P ratios, the complex size decreases rapidly with the increase in the amount of GNP-PEI800. At higher N/P ratios, however, the size becomes less sensitive or even independent of the ratio. As for GNP-PEI800 4.3 and GNP-PEI800 1.3, the sizes were around 200 nm and fairly consistent at N/P ratios ranging from 30 to 180. For complexes with GNP-PEI800 5.6, the particle size showed no obvious differences at high N/P ratios over 90. This phenomenon could be interpreted as the complexation of DNA by the GNP-PEI800 conjugate is saturated above a certain N/P ratio. The results of size measurement by DLS were in accordance with

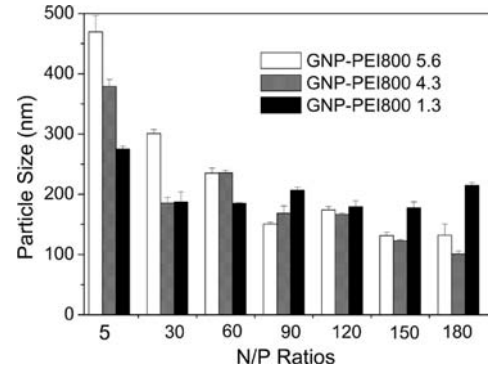


Figure 3. Particle size of GNP-PEI800/pGL3 complexes at various N/P ratios in 150 mM NaCl solution.

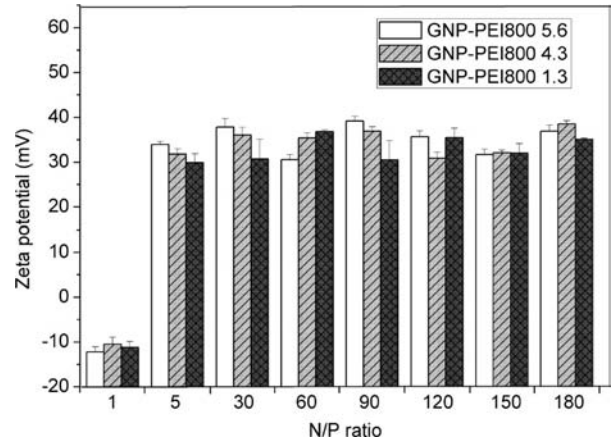


Figure 4. Surface charge of GNP-PEI800/pGL3 complexes at various N/P ratios with fixed pGL3 concentration of 1 μg/mL.

TEM results that a higher PEI grafting density would promote condensation more efficiently.

Surface charge of DNA complexes is another important parameter in determining the efficiency of cellular uptake. Zeta potentials of the complexes were shown in Figure 4. Regardless of the Au/PEI composition, all DNA complexes of the three GNP-PEI800 conjugates showed very similar surface charge profiles. At very low N/P ratio of 1, the particles had zeta potential of about −10 mV, implying that the negative charge of DNA is not completely neutralized. With increasing N/P ratio, zeta potentials of the complexes increased and reached plateaus between +30 and +40 mV at N/P ratios above 5. Complexes of GNP-PEI800s bearing positive surface potentials that should promote initial adhesion on a negatively charged cell surface (*31*).

The ability of GNP-PEI800s to interact with DNA was characterized by agarose gel electrophoresis. In good agreement with zeta potential measurements, the migration of pDNA was completely retarded at a relatively low N/P ratio of 4 (Figure 5), which indicated high DNA binding capacity of all the conjugates. Intensities of DNA staining decreased obviously at higher N/P ratios. Condensation of DNA with GNP-PEI800s might result in exclusion of the dye due to alterations in the double helix leading to reduced fluorescence emission (*37*). As a result, the intensities of DNA staining decrease with increasing DNA condensation ability at higher N/P ratios.

To investigate whether GNP-PEI800s are efficient in protecting DNA from enzyme cleavage, an in vitro DNase protection assay was performed by agarose gel electrophoresis. An amount of enzyme equal to 5 units (1 U/μg DNA) was fixed in the experiment. DNase was added to naked plasmid DNA and GNP-PEI800/DNA complexes (N/P = 20), followed by incubation

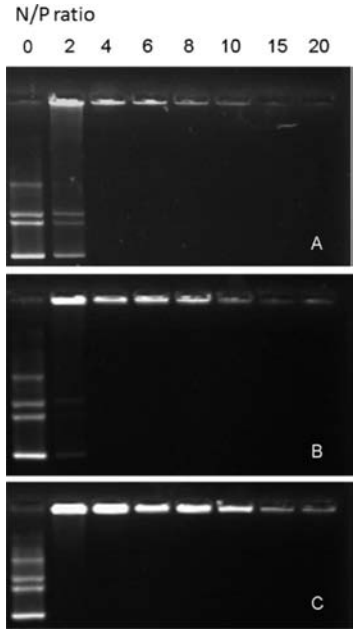


Figure 5. Agarose gel electrophoresis assay of the complexes of pGL3 plasmid DNA (100 ng/well) with (A) GNP-PEI800 5.6, (B) GNP-PEI800 4.3, and (C) GNP-PEI800 1.3 at various N/P ratios. The line of N/P = 0 refers to pGL3 in the absence of GNP-PEI800.

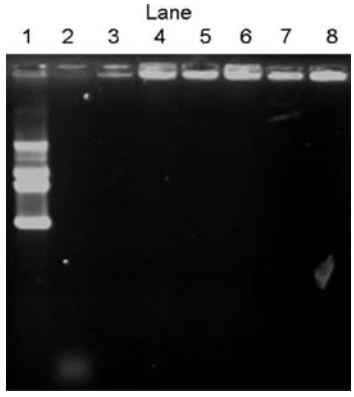


Figure 6. Agarose gel showing DNase digestion results. Lanes 1, 3, 5, 7 are undigested samples of naked DNA, GNP-PEI800 5.6/DNA, GNP-PEI800 4.3/DNA, and GNP-PEI800 1.3/DNA, respectively. Lanes 2, 4, 6, 8 are the above samples exposed to enzyme. Five units of enzyme were used for each reaction. The amount of DNA was 200 ng/well.

for 15 min at 37 °C. As shown in Figure 6 (lane 2), when exposed to the same amount of enzyme under the same conditions, free plasmid DNA alone was digested thoroughly, while plasmid DNA complexed with GNP-PEI800s remained intact.

Cytotoxicity. The cytotoxicity of GNP-PEI800s was evaluated by MTT assay. It should be noted that the absorbance of GNP obviously affects the assay accuracy especially at high concentration. Control experiment using GNP-PEI800s in medium without cells was carried out to get rid of the interference of the absorbance of gold nanoparticles on the color intensity of the assay at 570 nm. The results are presented in Figure 7. In the case of GNP-PEI800 5.6 and GNP-PEI800 4.3, half of the cells were still metabolically active when exposed to a concentration of 300 mg/L, which was almost the same as unmodified PEI 800 Da. In contrast, GNP-PEI800 1.3 with higher PEI content showed greatly increased cytotoxicity compared to the other two GNP-PEI800s, though its half-cell viability concentration was still three times higher than that of PEI 25 kDa. The relatively higher cytotoxicity of GNP-PEI 1.3 may be caused by its high PEI grafting density of 57 chains/nm^2. High cationic charge densities and compact structure, as well as high molecular weight, usually result in high cytotoxicity.

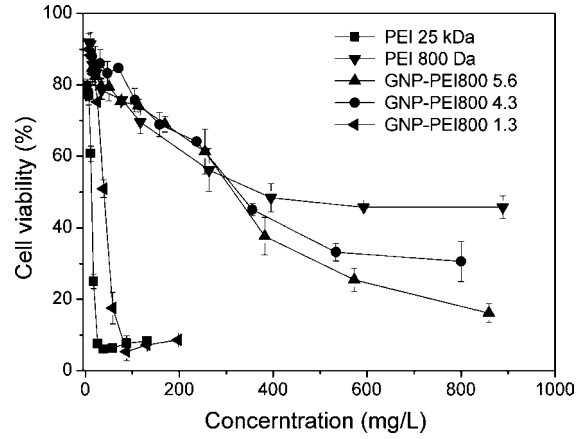


Figure 7. Cell viability at 24 h after the addition of GNPs, PEI 25 kDa, and PEI 800 Da.

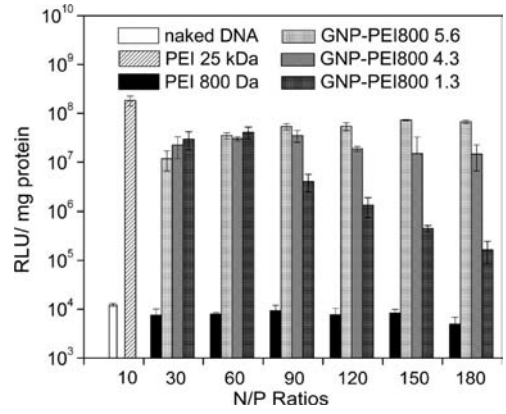


Figure 8. In vitro transfection efficiency of complexes of pGL3 with GNPs in COS-7 cells in comparison with PEI 25 kDa and PEI 800 Da in serum-free medium.

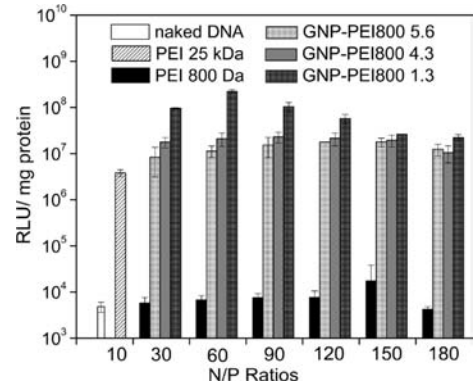


Figure 9. In vitro transfection efficiency of complexes of pGL3 with GNPs in COS-7 cells in comparison with PEI 25 kDa and PEI 800 Da in medium containing 10% serum.

GNP-PEI800 Conjugates Mediated in Vitro Transfection. Transfection efficiency of GNP-PEI800 conjugates was evaluated by luciferase expression of pGL3 plasmid DNA in monkey kidney (COS-7) cells. Complexes were prepared with N/P ratios ranging from 30 to 180, among which the optimal ratio of each complex was determined. Branched PEI 25 kDa at its optimal N/P ratio of 10 and unmodified PEI 800 Da were used for comparison.

Figure 8 shows luciferase expression mediated by the conjugates in the serum-free medium. Under this condition,

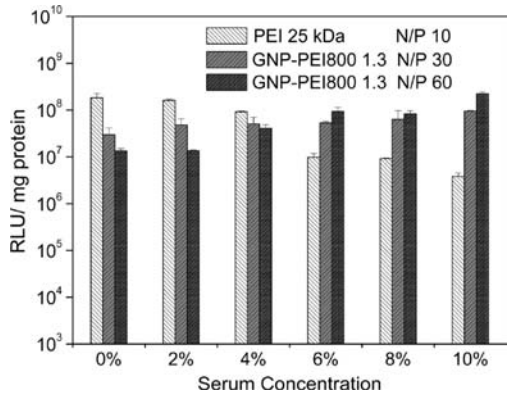


Figure 10. In vitro transfection efficiency of complexes of pGL3 with GNP-PEI800 1.3 at different serum concentrations (v/v) in comparison with PEI 25 kDa.

GNP-PEI800 4.3/DNA complexes at N/P ratio of 90 exhibited the highest efficiency, while GNP-PEI800 5.6 and GNP-PEI800 1.3 reached their maxima at N/P ratio of 150 and 60, respectively. The optimal N/P ratio of each GNP-PEI800 decreased with the increase of PEI grafting density on the GNPs, indicating that GNPs with higher PEI density may achieve efficient transfection at lower N/P ratios. At its best ratio, GNP-PEI800 4.3 achieved nearly half the luciferase expression of PEI 25 kDa, which was worth mentioning, since unmodified PEI 800 was 1000 times less efficient even at a relatively high N/P ratio of 150. In the case of GNP-PEI800 1.3, complexes prepared at N/P ratio of 90 or higher ratios led to abnormal sharply reduced efficiency, possibly ascribed to the increased cytotoxicity, which may also explain why its efficiency was not the highest among the three.

It is known that transfection efficiency of high molecular weight PEI decreased in serum supplemented medium (*31*). Therefore, the development of nonviral gene vectors that can retain efficiency in serum is important. Thus, we tested transfection efficiency of GNP-PEI800s in the presence of serum. As shown in Figure 9, when 10% serum was supplemented in the media, the strong dependence of transfection activity on PEI grafting density became more obvious. The transfection efficiencies declined in the order GNP-PEI800

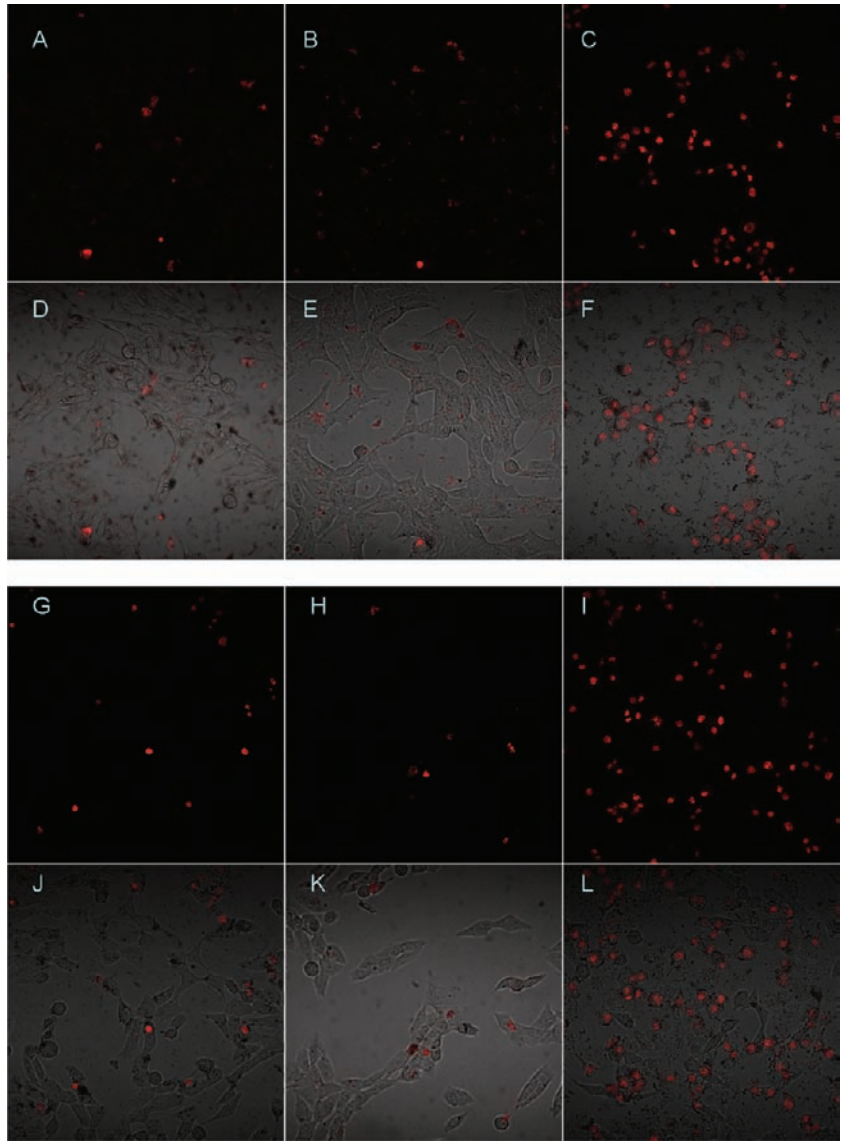


Figure 11. Confocal cell images showing tracking of GelRed labeled GNP-PEI800/DNA complexes. (A−C) Complexes of GNP-PEI800 5.6/DNA, GNP-PEI800 4.3/DNA, and GNP-PEI800 1.3/DNA at N/P ratio of 90 after 4 h post-transfection in serum-free medium. (G−I) Complexes of GNP-PEI800 5.6/DNA, GNP-PEI800 4.3/DNA, and GNP-PEI800 1.3/DNA at N/P ratio of 90 after 4 h post-transfection in medium containing 10% serum. The light inverted micrographs are D−F and J−L, respectively. The micrographs were obtained at magnification of 400×.

1.3 > GNP-PEI800 4.3 > GNP-PEI 800 5.6 (at optimal N/P ratios of 60, 90, and 150, respectively). This sequence is consistent with the PEI grafting density of the GNP-PEI800 conjugates. Specifically, GNP-PEI800 1.3 exhibited efficiency 10 times higher than that of GNP-PEI800 4.3 and PEI800-GNP 5.6 at their optimal N/P ratios. Moreover, the efficiency of GNP-PEI800 1.3 was found to significantly exceed that of PEI 25 kDa. It is interesting that the presence of serum resulted in significant enhancement of gene transfer efficiency of GNP-PEI800 1.3, while GNP-PEI800 4.3 and PEI800-GNP 5.6 could also retain their efficiency under the same conditions. In contrast, the efficiency of PEI 25 kDa was greatly decreased by the presence of serum.

To get further insight into the effect of serum on efficiency, we performed transfection at different serum concentrations. Since GNP-PEI800 1.3 exhibited the most striking distinction between its efficiency in the absence and presence of serum, it was selected for the subsequent experiment. Two N/P ratios of 30 and 60 were chosen to exclude the impact of cytotoxicity at higher ratios. Branched PEI 25 kDa at the optimal N/P ratio of 10 was used for comparison. Figure 10 shows the comparative gene transfection efficiencies of GNP-PEI800 1.3 and PEI 25 kDa in the presence of various percentages of serum. There was a gradual decrease in the transfection efficacy with increase in serum concentrations in the case of PEI 25 kDa, while GNP-PEI800 1.3 showed a completely opposite tendency. For example, at 6% serum concentration, only 5% of its transfection efficiency in serum-free medium was observed for PEI 25 kDa, whereas gene expression with GNP-PEI800 1.3 was promoted about 7 times higher than that without serum. The result clearly shows that GNP-PEI800 1.3 is a better transfection agent in the presence of serum than PEI 25 kDa.

The enhancement of transfection efficiency of GNP-PEI800 1.3 in serum might be related to lowered cytotoxicity. The high PEI grafting density in GNP-PEI800 1.3 can largely increase the effective molecular weight of PEI 800 Da, which consequently leads to more efficient DNA condensation and thus more efficient transfection. However, it induced inevitable cytotoxicity simultaneously. At the same concentration as in its complex, the cell viability of GNP-PEI800 1.3 alone decreased with an increase in N/P ratio, which was greater than 80% cell viability at N/P ratios of 30 and 60, nearly 60% at N/P ratios of 90 and 120, and 20% at N/P ratios of 150 and 180. These results revealed that the cytotoxicity of the GNP-PEI800 conjugates is remarkable under the transfection conditions. Thus, the enhancement of transfection efficiency in serum-containing medium might be related to the cell function raised by the addition of serum.

Cell Uptake Tracing. The capacity of GNP-PEI800s to internalize plasmid DNA into cells was additionally observed by confocal laser scanning microscopy (CLSM). GelRed was used as a molecular probe to label pGL-3. Complexes of all three GNP-PEI800 samples at N/P ratio of 90 were incubated in the medium in the absence and presence of serum, respectively, and examined at 4 h post-transfection. Control experiments with labeled naked DNA showed no signs of cellular uptake (data not shown). As shown in Figure 11, the uptake of complexes in the absence and presence of serum exhibited subtle differences. In the case of GNP-PEI800 1.3, the percentage of cells showing complex uptake was high, which probably contributed to its high transfection efficiency. However, the high absorption of GNP-PEI800 1.3 may also impair plasma membrane dramatically and result in high cytotoxicity. In fact, a significant level of cellular dysfunction or even cell death was observed in the images. By comparison of the two images in Figure 11F and L, it is obvious the cells in the serum-containing medium were better in morphology than those in serum-free medium. The results imply that the cytotoxicity of the PEI conjugated GNP was reduced by the presence of serum, while the cell uptake capacity was retained. Generally, the qualitative results of CLSM are in good agreement with the results of luciferase assay and cytotoxicity assay.

CONCLUSION

In closing, we have synthesized a series of hybrid GNP-PEI800s by conjugating PEI 800 Da to gold nanoparticles at three PEI/Au molar ratios. GNP-PEI800s possesses many outstanding features in favor of polycation-mediated gene delivery, including efficient DNA condensation, high DNA binding capability and DNA protection against degradation by DNase. In consequence, GNP-PEI800s can transfect COS-7 cells 3 to 4 orders more efficient than unmodified PEI800, reaching almost the same magnitude of PEI 25 kDa. Moreover, in contrast to the dramatically lowered efficiency of high molecular weight PEIs such as PEI 25 kDa in the presence of serum, the efficiency of GNP-PEI800s can be retained or even enhanced, reaching 60-fold higher than that of PEI 25 kDa in 10% serum medium. The research demonstrated that GNP−PEI conjugates are very promising as gene delivery vectors.

ACKNOWLEDGMENT

This research was financially supported by National Natural Science Foundation of China (20774067) and National Basic Research Program of China (2005CB623903 and 2009CB930300).

LITERATURE CITED

(1) de Lima, M. C. P., Neves, S., Filipe, A., Duzgunes, N., and Simoes, S. (2003) Cationic liposomes for gene delivery: from biophysics to biological applications. *Curr. Med. Chem. 10*, 1221–1231.

(2) Dufes, C., Uchegbu, I. F., and Schatzlein, A. G. (2005) Dendrimers in gene delivery. *Adv. Drug Delivery Rev. 57*, 2177–2202.

(3) Pack, D. W., Hoffman, A. S., Pun, S., and Stayton, P. S. (2005) Design and development of polymers for gene delivery. *Nat. Rev. Drug Discovery 4*, 581–593.

(4) Boussif, O., Lezoualc'h, F., Zanta, M. A., Mergny, M. D., Scherman, D., Demeneix, B., and Behr, J.-P. (1995) A versatile vector for gene and oligonucleotide transfer into cells in culture and in vivo: polyethylenimine. *Proc. Natl. Acad. Sci. U.S.A. 92*, 7297–7301.

(5) Godbey, W. T., Wu, K. K., and Mikos, A. G. (1999) Tracking the intracellular path of poly(ethylenimine)/DNA complexes for gene delivery. *Proc. Natl. Acad. Sci. U.S.A. 96*, 5177–5181.

(6) Suh, J., Wirtz, D., and Hanes, J. (2003) Efficient active transport of gene nanocarriers to the cell nucleus. *Proc. Natl. Acad. Sci. U.S.A. 100*, 3878–3882.

(7) Kircheis, R., Wightman, L., and Wagner, E. (2001) Design and gene delivery activity of modified polyethylenimines. *Adv. Drug Delivery Rev. 53*, 341–358.

(8) Forrest, M. L., Meister, G. E., Koerber, J. T., and Pack, D. W. (2004) Partial acetylation of polyethylenimine enhances *in vitro* gene delivery. *Pharm. Res. 21*, 365–371.

(9) Godbey, W. T., Wu, K. K., and Mikos, A. G. (2001) Poly(ethylenimine)-mediated gene delivery affects endothelial cell function and viability. *Biomaterials 22*, 471–480.

(10) Boussif, O., Zanta, M. A., and Behr, J. P. (1996) Optimized galenics improve in vitro gene transfer with cationic molecules up to 1000-fold. *Gene Ther. 3*, 1074–1080.

(11) Godbey, W. T., Wu, K. K., and Mikos, A. G. (1999) Poly(ethylenimine) and its role in gene delivery. *J. Controlled Release 60*, 149–160.

(12) Kunath, K., Harpe, A. V., Fischer, D., Peterson, H., Bickel, U., Voigt, K., and Kissel, T. (2003) Low-molecular-weight polyethylenimine as a non-viral vector for DNA delivery,

comparison of physicochemical properties, transfection efficiency and in vivo distribution with high-molecular-weight polyethylenimine. *J. Controlled Release 89*, 113–125.
(13) Petersen, H., Kunath, K., Martin, A. L., Stolnik, S., Roberts, C. J., Davies, M. C., and Kissel, T. (2002) Star-shaped poly(ethylene glycol)-block-polyethylenimine copolymers enhance DNA condensation of low molecular weight polyethylenimines. *Biomacromolecules 3*, 926–936.
(14) Gosselin, M. A., Guo, W., and Lee, R. J. (2001) Efficient gene transfer using reversibly crosslinked low molecular weight polyethylenimine. *Bioconjugate Chem. 12*, 989–994.
(15) Thomas, M., Ge, Q., Lu, J. J., Chen, J. Z., and Klibanov, A. M. (2005) Crosslinked small polyethylenimine, while still nontoxic, deliver DNA efficiently to mammalian cells in vitro and in vivo. *Pharm. Res. 22*, 373–380.
(16) (a) Peng, Q., Zhong, Z., and Zhuo, R. (2008) Disulfide cross-linked polyethylenimines (PEI) prepared via thiolation of low molecular weight PEI as highly efficient gene vectors. *Bioconjugate Chem. 19*, 499–506. (b) Peng, Q., Hu, C., Cheng, J., Zhong, Z., and Zhuo, R. (2009) Influence of disulfide density and molecular weight on disulfide cross-linked polyethylenimine as gene vectors. *Bioconjugate Chem. 20*, 340–346.
(17) Luo, D., and Saltzman, W. M. (2000) Enhancement of transfection by physical concentration of DNA at the cell surface. *Nat. Biotechnol. 18*, 893–895.
(18) Xiang, J. J., Tang, J. Q., Zhu, S. G., Nie, X. M., Lu, H. B., Shen, S. R., Li, X. L., Tang, K., Zhou, M., and Li, G. Y. (2003) IONP-PLL, a novel non-viral vector for efficient gene delivery. *J. Gene Med. 5*, 803–817.
(19) Cai, D., Mataraza, J. M., Qin, Z. H., Huang, Z., Huang, J., Chiles, T. C., Carnahan, D., Kempa, K., and Ren, Z. (2005) Highly efficiency molecular delivery into mammalian cells using carbon nanotube spearing. *Nat. Methods 2*, 449–454.
(20) Sandhu, K. K., McIntosh, C. M., Simard, J. M., Smith, S. W., and Rotello, V. M. (2002) Gold nanoparticle-mediated transfection of mammalian cells. *Bioconjugate Chem. 13*, 3–6.
(21) Li, D., Li, P., Li, G., Wang, J., and Wang, E. (2009) The effect of nocodazole on the transfection efficiency of lipid-bilayer coated gold nanoparticles. *Biomaterials 30*, 1382–1388.
(22) Zhou, X., Zhang, X., Yua, X., Zha, X., Fu, Q., Liu, B., Wang, X., Chen, Y., Chen, Y., Shan, Y., Jin, Y., Wu, Y., Liu, J., Kong, W., and Shen, J. (2008) The effect of conjugation to gold nanoparticles on the ability of low molecular weight chitosan to transfer DNA vaccine. *Biomaterials 29*, 111–117.
(23) Ghosh, P. S., Kim, C.-K., Han, G., Forbes, N. S., and Rotello, W. M. (2008) Efficient gene delivery vectors by tuning the surface charge density of amino acid-functionalized gold nanoparticles. *ACS Nano 2*, 2213–2218.
(24) Thomas, M., and Klibanov, A. M. (2003) Conjugation to gold nanoparticles enhances polyethylenimine's transfer of plasmid DNA into mammalian cells. *Proc. Natl. Acad. Sci. U.S.A. 100*, 9138–9143.
(25) Rosi, N. L., Giljohann, D. A., Thaxton, C. S., Lytton-Jean, A. K. R., Han, M. S., and Mirkin, C. A. (2006) Oligonucleotide-modified gold nanoparticles for intracellular gene regulation. *Science 312*, 1027–1030.
(26) Yamauchi, F., Koyamatsu, Y., Kato, K., and Iwata, H. (2006) Layer-by-layer assembly of cationic lipid and plasmid DNA onto gold surface for stent-assisted gene transfer. *Biomaterials 27*, 3497–3504.
(27) Elbakry, A., Zaky, A., Liebkl, R., Rachel, R., Goepferich, A., and Breunig, M. (2009) Layer-by-layer assembled gold nanoparticles for siRNA delivery. *Nano Lett. 9*, 2059–2064.
(28) Lee, J. S., Green, J. J., Love, K. T., Sunshine, J., Langer, R., and Anderson, D. G. (2009) Gold, poly(beta-amino ester) nanoparticles for small interfering RNA delivery. *Nano Lett. 9*, 2402–2406.
(29) Giljohann, D. A., Seferos, D. S., Prigodich, A. E., Patel, P. C., and Mirkin, C. A. (2009) Gene regulation with polyvalent siRNA-nanoparticle conjugates. *J. Am. Chem. Soc. 131*, 2072–2073.
(30) Connor, E. E., Mwamuka, J., Gole, A., Murphy, C. J., and Wyatt, M. D. (2005) Gold nanoparticles are taken up by human cells but do not cause acute cytotoxicity. *Small 1*, 325–327.
(31) Bordwell, F. G., and Andersen, H. M. (1953) The reaction of epoxides with thiourea. *J. Am. Chem. Soc. 75*, 4959–4962.
(32) Eyer, P., Worek, F., Kiderlen, D., Sinko, G., Stuglin, A., Rudolf, V. S., and Reiner, E. (2003) Molar absorption coefficients for the reduced Ellman reagent: reassessment. *Anal. Biochem. 312*, 224–227.
(33) Riddles, P. W., Blakeley, R. L., and Zerner, B. (1979) Ellman's reagent: 5, 5′-dithiobis(2-nitrobenzoic acid)-a reexamination. *Anal. Chem. 94*, 75–81.
(34) Daniel, M.-C., and Astruc, D. (2004) Gold nanoparticles: Assembly, supramolecular chemistry, quantum-size-related properties, and applications toward biology, catalysis, and nanotechnology. *Chem. Rev. 104*, 293–346.
(35) Chithrani, B. D., Ghazani, A. A., and Chan, W. C. W. (2006) Determining the size and shape dependence of gold nanoparticle uptake into mammalian cells. *Nano Lett. 6*, 662–668.
(36) Mansouri, S., Cuie, Y., Winnik, F., Shi, Q., Lavigne, P., Benderdour, M., Beaumont, E., and Fernandes, J. C. (2006) Characterization of folate-chitosan-DNA nanoparticles for gene therapy. *Biomaterials 27*, 2060–2065.
(37) Akinc, A., Thomas, M., Klibanov, A. M., and Langer, R. (2005) Exploring polyethylenimine-mediated DNA transfection and the proton sponge hypothesis. *J. Gene Med. 7*, 657–663.

BC900374D

Liposomal Polyamine−Dialkyl Phosphate Conjugates as Effective Gene Carriers: Chemical Structure, Morphology, and Gene Transfer Activity

Takehisa Dewa,*,† Tomohiro Asai,⊥ Yuka Tsunoda,⊥ Kiyoshi Kato,† Daisuke Baba,† Misa Uchida,† Ayumi Sumino,† Kayoko Niwata,⊥ Takuya Umemoto,⊥ Kouji Iida,# Naoto Oku,⊥ and Mamoru Nango*,†

Department of Life and Materials Engineering, Nagoya Institute of Technology, Gokiso-cho, Showa-ku, Nagoya 466-8555 Japan, Department of Medical Biochemistry and Global COE, University of Shizuoka School of Pharmaceutical Sciences, 52-1 Yada, Suruga-ku, Shizuoka, 422-8526 Japan, and Nagoya Municipal Industrial Research Institute, 3-4-41 Rokuban-cho, Atsuta-ku, Nagoya 456-0058 Japan. Received August 24, 2009; Revised Manuscript Received January 5, 2010

Synthetic cationic lipids are promising transfection agents for gene therapy. We report here that polyamine conjugates of dialkyl phosphates, combined with natural lipids and assembled in the form of liposomes (polycationic liposome: PCL), possess high transfection activity in the COS-1 cell line. Furthermore, we describe the functional morphology of the PCL/DNA complexes as revealed by atomic force microscopy (AFM). The conjugates were synthesized from dialkyl phosphates (with alkyl chain lengths of 12, 14, or 16 carbons) by reaction with the polyamine molecules, spermidine, spermine, or polyethylenimine (PEI(1800)). [Dewa, T., et al. *Bioconjugate Chem.* **2004**, *15*, 824]. The PCL composed of the spermidine and C16 conjugate combined with phospholipid and cholesterol (conjugate/phospholipid/cholesterol = 1/1/1 as a molar ratio) exhibited 3.6 times higher activity than that of a popular commercial product. Systematic tests revealed clear correlations of the transgene activity with physical properties of the polyamine, in particular, that longer alkyl chains and the lower molecular weight polyamines (spermidine, spermine) favor high efficacy at the higher nitrogen/phosphate ratio = 24 (N/P, stoichiometric ratio of nitrogen in the conjugate to phosphate in DNA). The low molecular weight polyamine-based PCLs, which formed 150−400 nm particles with plasmid DNA (lipoplexes), exhibited ∼3-fold higher gene transfer activity than micellar aggregates (lacking phospholipid and cholesterol) of the corresponding conjugate. In contrast, the PEI-based PCL formed large aggregates (∼1 μm), that, like the micellar aggregate form, had low activity. Activity of the low molecular weight polyamine-based PCLs increased linearly with the N/P of the lipoplex up to N/P = 24. Formation of lipoplexes was examined by agarose gel electrophoresis, dynamic light scattering (DLS), and AFM. At the lower N/P = 5, large aggregates of complex (∼1 μm), in which DNA molecules were loosely packed, were observed. At higher N/P, lipoplexes were converted into smaller particles (150−400 nm) having a lamellar structure, in which DNA molecules were tightly packed. Such morphological features of the lipoplex correlate with the dependence of transfection on the N/P in that the lamellar structures gave superior transfection. AFM also indicated that the lipoplexes disassembled significantly, releasing DNA, when the lipoplexes were exposed to acidic conditions (pH 4). The significance for transfection activity of the metamorphosis of bilayer lipoplexes is discussed relative to that of the less active micellar aggregate form, which is unresponsive to pH change.

INTRODUCTION

Development of more efficient and safer gene carriers using nonviral compounds is one of the most challenging aspects of gene therapy (*1, 2*). Compared to viral carrier systems, nonviral gene carrier systems have advantages in simplicity of use, lack of specific immune response, and ease of mass production due to the low cost of preparation; however, they have the disadvantage of low transfection efficiency, which needs to be overcome (*3, 4*). To improve the efficiency of nonviral carriers, many synthetic organic compounds, including cationic lipids (*5*−*9*), polycations (*10*−*15*), and combinations thereof (*16*−*22*), have been developed as nonviral gene carriers (*23*). Substantial research has been reported on structure−activity relationships for cationic amphiphiles concerning the cationic and hydrophobic portions (*24*−*28*). Such amphiphiles form self-assembling micelles and liposomes in an aqueous phase, the structures of which have been investigated using small-angle X-ray scattering (SAXS)[1], transmission electron microscopy (TEM), and atomic force microscopy (AFM) to gain knowledge about structure−activity relationship, particularly those involving ordered structures (lamellar, inverted hexagonal, and cubic phases) and their morphological changes (*29*, *30*) as well as about the size of complexes (*31*).

The mechanism of gene delivery by such cationic carriers probably involves an endosomal pathway (*32*): (i) cellular uptake via endocytosis, (ii) DNA release from endosome, and (iii) entry

* To whom correspondence should be addressed. Department of Life and Materials Engineering, Nagoya Institute of Technology, Gokiso-cho, Showa-ku, Nagoya 466-8555 Japan (T.D.) Tel/Fax: +81-52-735-5144. (M.N.) Tel/Fax: +81-52-735-5226. E-mail: takedewa@nitech.ac.jp, nango@nitech.ac.jp.

† Nagoya Institute of Technology.

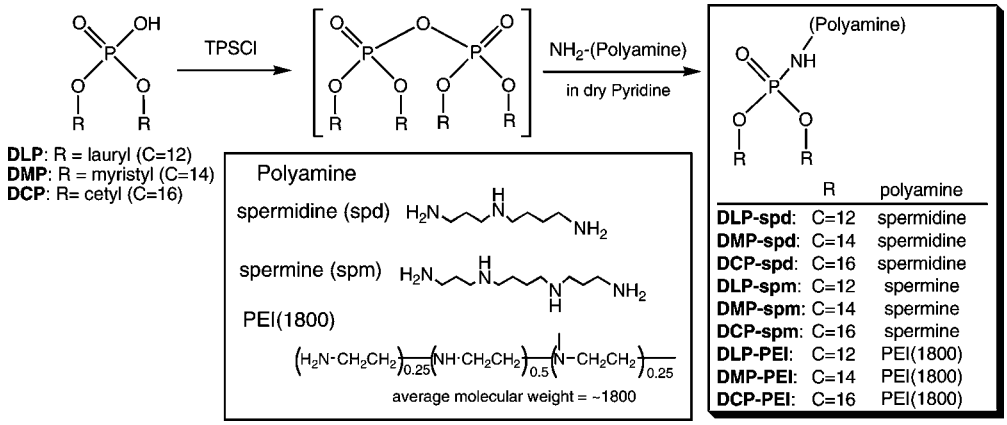
⊥ University of Shizuoka.

Nagoya Municipal Industrial Research Institute.

[1]Abbreviations: SAXS, small-angle X-ray scattering: TEM, transmission electron microscopy; AFM, atomic force microscopy; NLS, nuclear localization signal peptide; PCL, polycation liposome; PEI, polyethylenimine; MALDI-TOF-MS, matrix assisted laser desorption ionization-time-of-flight-mass spectroscopy; DOPE, 1,2-dioleoyl-*sn*-glycero-3-phosphoethanolamine; DPPC, 1,2-dipalmitoyl-*sn*-glycero-3-phosphoethanolamine; PLL, poly(L-lysine); FBS, fetal bovine serum; DMEM, Dulbecco's Modified Eagle Medium; N/P, nitrogen/phosphate ratio.

10.1021/bc900376y © 2010 American Chemical Society
Published on Web 04/08/2010

Scheme 1. Polyamine-Dialkyl Phosphate Conjugates As Gene Carriers[a]



[a] NH_2-(Polyamine) represents polyamines and their primary amine portion that reacts with the phosphate portion.

into the nucleus. Many researchers have devised cationic compounds that facilitate the process, for example, ligand-conjugated molecules targeting a receptor such as integrin (*33, 34*), pH-responsive or cleavable molecules that enable escape of DNA from endosome (*13, 35*−*38*), and conjugation of nuclear localization signal peptides (NLS) (*39, 40*) for steps (i)−(iii), respectively. For cationic lipids/DNA complexes (lipoplexes), it has been proposed that a morphological change from lamellar to inverted hexagonal phase in the acidic endosomal environment facilitates the endosomal release and escape of DNA (*41, 42*). In addition to investigation of intracellular trafficking of polycation−DNA complexes (polyplexes and lipoplexes), observation of morphology and metamorphosis of the complexes is very important to shed light on the mechanism of gene transfer and provide information for development of novel synthetic carriers (*30, 43, 44*).

We have reported that polycationic liposomes (PCL) containing cetylated polyethylenimine (cetyl-PEI) possess high gene transfer activity (*45*−*47*). The cetyl-PEI molecule is anchored by the hydrophobic cetyl portion and is distributed over the liposomal surface. In our previous report, we proposed a possible mechanism of PCL-mediated gene transfer, in which PCL/DNA complexes are taken up by the endosomal pathway (based on tracking of fluorescence-labeled components, PCL lipid, cetyl-PEI, and DNA), after which the cetyl-PEI/DNA complex is released and transferred into the nucleus via the cytosol (*48*). Compaction of DNA is therefore crucial, and both electrostatic and hydrophobic interactions in the cetyl-PEI/DNA complex are responsible for its effective compaction.

We have previously described novel polyamine (spermidine, spermine, or PEI)-dicetyl phosphate conjugates, prepared via a facile synthetic route (Scheme 1) (*49*) in which the polyamine and phosphate portions are linked through a P−N bond. When suspended in aqueous solution, they form micellar aggregates and exhibit moderate gene-transfer activity, the magnitude of which is relatively insensitive to the modification of the polyamine portion. In the present report, we present (1) evidence demonstrating that the transgene activity is dramatically enhanced when the conjugates are assembled into liposomes containing cholesterol and phospholipid and that the activity is susceptible to the chemical modification of the conjugate both in the polyamine and in the hydrophobic chain portions (Scheme 1). We show further that (2) gene transfer activity of the corresponding PCLs strongly depends on the type of polyamine in the conjugate, with notable differences between the lower molecular weight polyamines (spermidine and spermine) on one hand and the polymer type (PEI(1800)) on the other.

We also examined (3) the morphology of the lipoplexes by AFM and discuss the relationship between the structure of lipoplexes and their transfection efficiency. AFM analysis has a considerable advantage for observation of lipoplex morphology, especially for less ordered structures (*50*); however, until now little clear evidence has been reported on the relationship between morphological change and DNA release. In this research, DNA release as a result of disassociation of the complex was revealed by AFM. We discuss morphology−activity relationships on the basis of electrophoresis analysis, dynamic light scattering (DLS), and AFM observation.

EXPERIMENTAL PROCEDURES

General Methods. Unless stated otherwise, all chemicals and reagents were obtained commercially and used without further purification. Dialkyl phosphates, dilauryl phosphate (DLP), dimyristyl phosphate (DMP), and dicetyl phosphate (DCP) were synthesized from corresponding alcohols, i.e., lauryl (C12), myristyl (C14), and cetyl (C16) alcohols, and $POCl_3$ in accordance with the reported method (*51*). The polyamine−dicetyl phosphate conjugates, DCP-spermidine (**DCP-spd**), DCP-spermine (**DCP-spm**), and DCP-PEI(1800) (**DCP-PEI**) were synthesized as described previously (*49*). Other conjugates, DLP-spermidine (**DLP-spd**), DLP-spermine (**DLP-spm**), DLP-PEI(1800) (**DLP-PEI**), DMP-spermidine (**DMP-spd**), DMP-spermine (**DMP-spm**), and DMP-PEI(1800) (**DMP-PEI**), were also synthesized using analogous procedures. Spectral data are given below. (Note: The asymmetric molecule, spermidine, has two distinguishable primary amines. Products, **DLP-spd**, **DMP-spd**, and **DCP-spd**, bearing a spermidine moiety, have two isomers, which, to date, have not been identified spectroscopically. Similarly, the content of primary amine of PEI(1800) in the products DLP-PEI, DMP-PEI, and DCP-PEI is 25% in total amino moieties (on the basis of theoretical calculation); thus, some structural uncertainty cannot be avoided.)

DLP-spermidine conjugate (**DLP-spd**). ^{1}H NMR (300 MHz, $CDCl_3$): δ 0.88 (t, 6H), 1.26 (s, 36H), 1.51−1.95 (br m, 12H), 2.65−3.05 (br m, 6H), 3.98 (br m, 4H), 4.50 (br s, 4H). MALDI-TOF-MS for $(C_{31}H_{69}N_3O_3P)^+$: calcd 562.9, found 563.0.

DLP-spermine conjugate (**DLP-spm**). ^{1}H NMR (300 MHz, $CDCl_3$): δ 0.88 (t, 6H), 1.26 (s, 36H), 1.49−2.00 (br m, 15H), 2.63−3.05 (br m, 14H), 3.95 (br m, 4H). MALDI-TOF-MS for $(C_{34}H_{76}N_4O_3P)^+$: calcd 620.0, found 620.2.

DLP-PEI(1800) conjugate (**DLP-PEI**). ^{1}H NMR (300 MHz, $CDCl_3$): δ 0.88 (t, 6H), 1.26 (s, 36H), 1.58−1.65 (br m, 4H), 2.55−3.80 (br m, 209H), 3.95 (br m, 4H).

DMP-spermidine conjugate (**DMP-spd**). ^{1}H NMR (300 MHz, $CDCl_3$): δ 0.88 (t, 6H), 1.26 (s, 44H), 1.50−1.71 (br m, 10H), 2.61−3.02 (br m, 12H), 3.98 (br m, 4H). MALDI-TOF-MS for $(C_{35}H_{77}N_3O_3P)^+$: calcd 619.0, found 618.9.

DMP-spermine conjugate (**DMP-spm**). ^{1}H NMR (300 MHz, $CDCl_3$): δ 0.88 (t, 6H), 1.26 (s, 44H), 1.61−2.00 (br m, 17H), 2.63−3.04 (br m, 12H), 3.97 (br m, 4H). MALDI-TOF-MS for $(C_{38}H_{84}N_4O_3P)^+$: calcd 676.1, found 676.1.

DMP-PEI(1800) conjugate (**DMP-PEI**). ^{1}H NMR (300 MHz, $CDCl_3$): δ 0.88 (t, 6H), 1.26 (s, 44H), 1.56−1.65 (br m, 4H), 2.55−3.82 (br m, 209H), 3.95 (br m, 4H).

Preparation of Polycation Liposome (PCL). Polycation liposome suspensions were typically prepared as follows: polyamine conjugate, phospholipid (either 1,2-dioleoyl-*sn*-glycero-3-phosphoethanolamine (DOPE) or 1,2-dipalmitoyl-*sn*-glycero-3-phosphocholine (DPPC)), and cholesterol (1/1/1 as a molar ratio) were dissolved in chloroform/*t*-butyl alcohol (2/1). After removal of chloroform under reduced pressure, the residual solvent was removed by freeze−drying overnight. The lyophilized powder was hydrated with Tris-HCl buffer (20 mM, pH 8.0) followed by three freeze−thaw cycles, and the resultant suspension was then subsequently extruded through polycarbonate membranes of 0.4, 0.2, and 0.1 μm pore diameter at room temperature. For vesicles composed of DPPC, the hydration and extrusion were carried out at 60 °C. Unless stated otherwise, PCL refers to the DOPE-based polycation liposome. A suspension of the polyamine conjugate alone was prepared in the Tris-HCl buffer (20 mM, pH 8.0) by ultrasonication for 3 min. For convenience, particles so prepared are termed "micellar aggregates". Hereafter, polycation liposomes (PCL) and micellar aggregates (M) composed of the conjugates are described as "**conjugate**(PCL)", such as **DCP-spd**(PCL), and "**conjugate**(M)", such as **DCP-spd**(M), respectively.

Lipoplex Formation with Plasmid DNA. A plasmid encoding luciferase gene, pCAG-luc3 (6480 bp, a gift of DNAVEC Institute, Tsukuba, Japan), was amplified in *E. coli* JM109 (Nippon Gene, Toyama, Japan) and purified as described before (*47*). One microgram of the plasmid DNA in a TE buffer was added to a suspension of PCL containing 1 mM of polyamine conjugate so as to give the desired nitrogen/phosphate ratio, N/P. The mixture was incubated for 20 min at room temperature when used for transfection. A plasmid, ColE1 DNA (6646 bp, Nippon Gene), was used for an assay of ethidium bromide intercalation and morphological observation of lipoplexes with AFMs (JSPM-4210, JEOL, and PicoPlus, Molecular Imaging), using the AC mode under ambient air conditions. A sample was deposited on a mica surface by spin coating, followed by drying in a desiccator for 1 h under reduced pressure to remove water from the mica surface. A freshly cleaved mica surface is negatively charged. As appropriate, the mica was treated with poly(L-lysine) (PLL) to provide positively charged surface. Hereafter, the negatively and positively charged mica substrates are described as bare mica and PLL-mica, respectively.

The sizes of PCLs, micellar aggregates, and their lipoplexes were analyzed by dynamic light scattering (DLS) with a NICOMP particle sizing system (model 370, Santa Barbara, CA, USA). The ζ-potentials of the cationic vectors were measured with ZETA SIZER Nano-ZS (MALVERN, Worcestershire, U.K.). Agarose-gel electrophoretic analysis was conducted by using 0.8% agarose (UltraPure agarose, Invitrogen) and 1 kb DNA ladder marker (Invitrogen). Electrophoresed DNA bands were stained with ethidium bromide.

For observation of morphological change of lipoplex by acidification, to a solution of lipoplex (pH 8.0) was added acetic acid so as to acidify down to pH 4. The solution was incubated for 1 h at room temperature.

Transfection Procedure. COS-1 cells were cultured in Dulbecco's modified Eagle medium (DMEM) supplemented with 10% fetal bovine serum (FBS, Japan Bioserum Co. Ltd.) under a humidified atmosphere of 5% CO_2 in air. One day before a transfection experiment, 1×10^5 COS-1 cells were seeded onto each of several 35 mm dishes and incubated overnight in a CO_2 incubator. Then, the cells were washed twice with DMEM, and a suspension of lipoplex (1 μg DNA) was added to them in the presence of 10% FBS-DMEM. After 3 h incubation (37 °C, 5% CO_2), the cells were washed twice with DMEM and cultured for another 48 h in 10% FBS-DMEM. The cells in the 35 mm dishes were washed twice with phosphate-buffered saline at 37 °C, and 200 μL of cell lysis buffer (LC-β, TOYO B-Net Co. Ltd., Tokyo) was added. After 15 min incubation, the cells were collected with a cell scraper, frozen at −80 °C, and then thawed at room temperature. The lysate was centrifuged at 15 000 rpm for 5 min at 4 °C. The supernatant was subjected to the luciferase assay (Pica Gene, TOYO B-Net Co. Ltd., Tokyo) using a luminophotometer (Luminescencer-PSN AB-2200, ATTO). The observed intensity in instrument light units was normalized to the amount of protein determined by BCA protein assay kit (PIERCE) to give relative light units (RLU/mg protein).

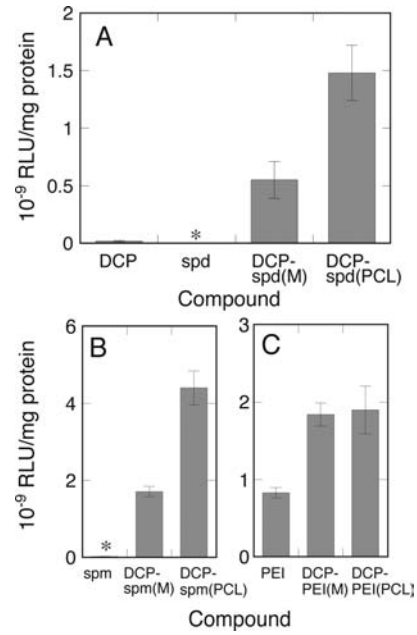


Figure 1. Transfection efficacy of polyamine−lipid conjugates, **DCP-spd** (A), **DCP-spm** (B), and **DCP-PEI** (C), and their constituents, DCP (A) and polyamines, spermidine (spd, A), spermine (spm, B), and PEI(1800) (PEI, C), on COS-1 cells. Efficacy was evaluated with the luciferase activity. The observed values for spermidine and spermine indicated by the asterisks (*) were apparently negligible on the activity scale shown. The conjugates **DCP-spd**(M), **DCP-spm**(M), and **DCP-PEI**(M) represent their micellar aggregate forms, and **DCP-spd**(PCL), **DCP-spm**(PCL), and **DCP-PEI**(PCL) represent the conjugate-based PCLs (conjugate/DOPE/cholesterol = 1/1/1 (mol/mol/mol)). The nitrogen/phosphate (N/P) ratio was 16/1 for the polyamine conjugate/DNA complexes. For the monoanionic DCP, the molar ratio, DCP/nucleotide = 16/1, was applied as a negative control experiment. Transfection was conducted in the presence of 10% FBS.

RESULTS

Transfection Efficacy of Micellar Aggregates and PCL Vectors: Comparison of the Dicetyl Phosphate Derivatives of Spermidine, Spermine, and Polyamine. Figure 1A shows the transfection efficacy of the polyamine conjugate, **DCP-spd**(M), and its constituent molecules, DCP and spermidine (spd). The conjugate (in this case an aqueous micellar suspension) shows greatly increased efficacy relative to the constituent molecules, DCP and spermidine. For these polyamine/DNA complexes, the nitrogen/phosphorus ratio (N/P) was 16. The data of the figure indicate that coupling the lipophilic and cationic portions is essential to obtain gene transfer. Such an

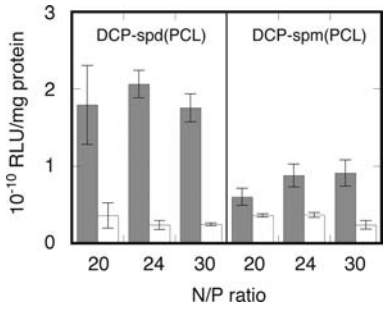


Figure 2. Transfection efficacy of spermidine and spermine conjugates (**DCP-spd** and **DCP-spm**, respectively) incorporated into DOPE-based (closed bar) and DPPC-based (open bar) liposomes. Polyamine conjugate/phospholipid/cholesterol = 1/1/1 (mol/mol/mol). Transfection was conducted in the presence of 10% FBS.

effect of conjugating these two moieties was also observed for the spermine conjugate, **DCP-spm**(M) (Figure 1B). When the conjugates were further formulated with DOPE and cholesterol (conjugate/DOPE/cholesterol = 1/1/1 (mol/mol/mol)) to generate polycation liposomes (PCL) (**DCP-spd**(PCL) and **DCP-spm**(PCL)), efficacies were further enhanced by a factor of 2−3 relative to the micellar aggregate suspensions (**DCP-spd**(M) and **DCP-spm**(M)). The polycation PEI(1800) itself showed moderate activity and the conjugate, **DCP-PEI**(M), exhibited even greater activity. However, in contrast to the other conjugates, the activity of the liposomal form, **DCP-PEI**(PCL), was comparable to that of the micellar version, **DCP-PEI**(M). The cytotoxicity of the conjugates, as both micellar aggregates and PCLs, was low; the latter vectors, which exhibited higher activity, also had slightly higher toxicity than the former (Supporting Information Figure S1).

Effect of the Phospholipid Components of PCLs on Their Transfection Efficacy. Figure 2 shows the transfection efficacy of **DCP-spd**(PCL) and **DCP-spm**(PCL) composed of either DOPE (dark bar) or DPPC (bright bar) in the N/P range 20−30. It is clear that the DOPE-based PCL exhibits significantly greater activity than the DPPC-based compound for both the **DCP-spd**(PCL) and the **DCP-spm**(PCL). This is indicative of a lipid-mediated gene transfer mechanism; DOPE is well-known as a "helper" lipid, which is believed to facilitate membrane fusion and endosomal escape of the DNA (*52*). DOPE in the present PCL systems presumably also plays a role in the mechanism to expedite membrane fusion and destabilization of the endosomal membrane. DPPC, whose T_m is 41.5 °C (*53*), renders the PCL more stable and more rigid than does DOPE. Thus, it is likely that the fusogenic property of DOPE is responsible for the enhanced transfection activity of its complexes relative to those containing DPPC.

Optimal Structure of the Conjugate Molecules for Gene Transfer. The facile synthetic route provides a variety of polycationic compounds that can be exploited to examine the effect of the polycationic and hydrophobic portions on transfection efficiency. We hence examined the effect on transfection activity of different polyamine conjugates incorporated into PCLs: C12, C14, or C16 alkyl chain in the lipophilic portion and spermidine, spermine, or PEI(1800) as the polycationic headgroup of the conjugate. The data on these compounds are shown in Figure 3. This result reveals clear tendencies of longer length of the alkyl group and the lower molecular weight of the polyamines (spermidine, spermine) to enhance transfection. When compared with a commercial product, Lipofectamine 2000, the **DCP-spd**(PCL) possessed 3.6-fold higher activity. The transfection activity of **DCP-spd**(PCL) and **DCP-spm**(PCL) depends on cell lines tested (Figure 3B): **DCP-spd**(PCL) < **DCP-spm**(PCL) for Lewis lung carcinoma (LLC) and **DCP-spd**(PCL) > **DCP-spm**(PCL) for B16BL6.

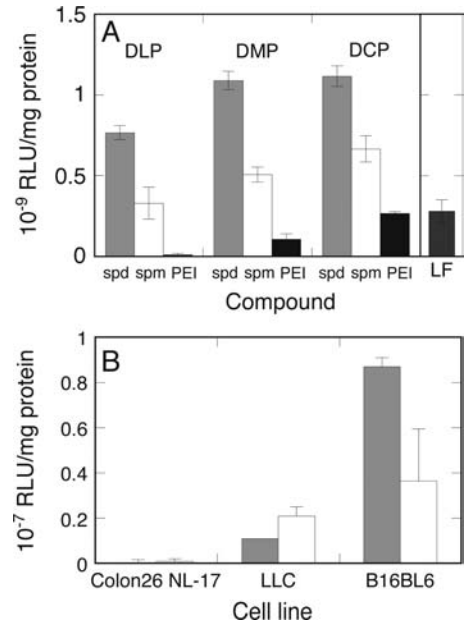


Figure 3. (A) Effect of polyamine and hydrophobic portions on PCL-mediated gene transfer efficiency. PCL were composed of polyamine conjugate/DOPE/cholesterol (1/1/1 (mol/mol/mol)). N/P ratio was 24. Transfection was done in the presence of 10% FBS. LF represents Lipofectamine 2000 as a positive control experiment. (B) Transfection efficiency of **DCP-spd**(PCL) (dark bar) and **DCP-spm**(PCL) (open bar) for various murine cancer cells. In the presence of 10% serum, lipoplexes (N/P = 24) were applied to Colon26 NL-17, Lewis lung carcinoma (LLC), and B16BL6 melanoma cells. Transfection procedure was carried out as described in the Experimental Section.

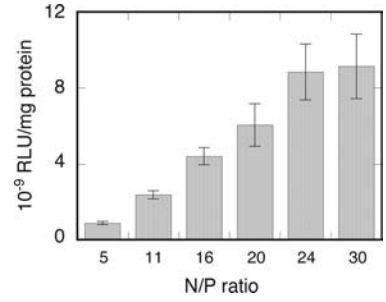


Figure 4. Effect of the N/P ratio on the transfection efficacy of **DCP-spm**(PCL) (**DCP-spm**/DOPE/cholesterol = 1/1/1 (mol/mol/mol)). Transfection was in the presence of 10% FBS.

N/P-Dependent Efficacy and Complexation of PCL with DNA. Figure 4 shows the dependence of **DCP-spm**(PCL) efficacy on the ratio of the number of nitrogen atoms in the conjugate to that of phosphate in the DNA (N/P). The efficacy increases with the N/P ratio essentially linearly up to 24. A similar N/P dependence has been also observed for **DCP-spd**(PCL) (data not shown for clarity), indicating that excess polyamine relative to DNA is needed for effective gene transfer by PCLs. In contrast, the transfection activity of micellar aggregates **DCP-spd**(M) and **DCP-spm**(M) reaches plateau values in the N/P range 11−16 ($1-2 \times 10^9$ of RLU/mg protein). This tendency is consistent with our previous data obtained with the β-galactosidase expression system (*49*).

To elucidate the characteristics of N/P dependence, formation of **DCP-spd**(PCL)/DNA and **DCP-spm**(PCL)/DNA lipoplexes was analyzed by agarose gel electrophoreses (Figure 5A,B) and DLS analysis (Table 1). In Figure 5, lane 2 of the plasmid DNA (pCAG-luc3) shows free-DNA bands (supercoiled and open circular DNAs). Lane 3 represents **DCP-spd**(PCL) and **DCP-spm**(PCL) alone as a control experiment. In the lower N/P range

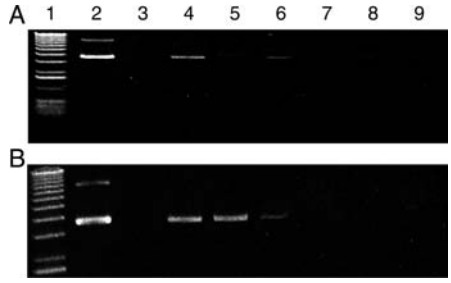


Figure 5. Agarose gel electrophoresis of PCL/plasmid DNA (pCAG-luc3: 6480 bp) lipoplexes. **DCP-spd**(PCL) (A) and **DCP-spm**(PCL) (B) were mixed with the DNA in the N/P range 5−30. Lane 1, 1 kb DNA ladder marker; lane 2, plasmid DNA (6480 bp) alone; lane 3, PCL alone. Lanes 4−9 represent PCL/DNA lipoplexes at N/P = 5, 11, 16, 20, 24, and 30, respectively.

Table 1. DLS Analysis of Various Polyamine-Dialkyl Phosphate Conjugate/DNA Complexes

				size (nm)	
entry	compound	N/P ratio	pH	PCL	micelle
1	**DCP-spd**	−	8	158 ± 56	249 ± 106
2		2	8	231 ± 89	
3		5	8	651 ± 501	1181 ± 1057
4		16	8	190 ± 83	
5		24	8	261 ± 114	1791 ± 1630
6		24	4	985 ± 1437	1624 ± 1566
7	**DCP-spm**	−	8	159 ± 30	225 ± 102
8		2	8	293 ± 112	
9		5	8	764 ± 378	321 ± 181
10		16	8	296 ± 168	
11		24	8	256 ± 116	1767 ± 1284
12		24	4	1033 ± 1060	1209 ± 949
13	**DCP-PEI**	−	8	214 ± 90	275 ± 184
14		24	8	1062 ± 783	317 ± 243

5−16 (lanes 4−6), the open circular DNA band vanished and the supercoiled DNA band gradually faded for both of **DCP-spd**(PCL) and **DCP-spm**(PCL). In the higher N/P range (20−30, lanes 7−9), the latter DNA band totally disappeared, indicating that the DNA molecules are completely entrapped within the lipoplex. Ethidium bromide (EtBr) replacement experiments also reveal condensation of DNA in the N/P range 5−30 (Supporting Information Figure S2).

The particle size of lipoplexes estimated by DLS analysis is summarized in Table 1. The diameters of the **DCP-spd**(PCL) and **DCP-spm**(PCL) alone are 158 ± 56 and 159 ± 30 nm, respectively (entries 1 and 7). Lipoplexes were larger and their size increased with increasing N/P up to 5 (entries 2 and 8 at N/P = 2 and entries 3 and 9 at N/P = 5). At N/P = 5, the PCL/DNA lipoplexes became larger with a broad distribution from 650 nm to over 1 μm (entries 3 and 9). In the higher N/P range (N/P = 16−24), sizes were reduced, converging at 261 ± 114 nm (**DCP-spd**(PCL), entry 5) and 256 ± 116 nm (**DCP-spm**(PCL), entry 11). ζ-potential measurements indicated the polarity of surface charge of lipoplexes inverts from negative in the lower N/P (5−11) to positive in the higher N/P (>16) regions.

AFM images revealed characteristic morphologies of lipoplexes in the both low and high N/P ranges (Figure 6A−D). When the **DCP-spd**(PCL)/DNA and **DCP-spm**(PCL)/DNA lipoplexes at N/P = 5 were put on PLL-treated mica (positively charged surface), large aggregates in the sub-micrometer size range (600−1200 nm, Figure 6A,B) were observed. These structures resembled by bead-like aggregates (*54*) composed of small particles (80−120 nm in diameter, 8−20 nm in height) connected to one another. Such aggregates were not observed on a negatively charged bare mica. This is understandable since the lipoplex at N/P = 5 is negatively charged, and the lipoplex

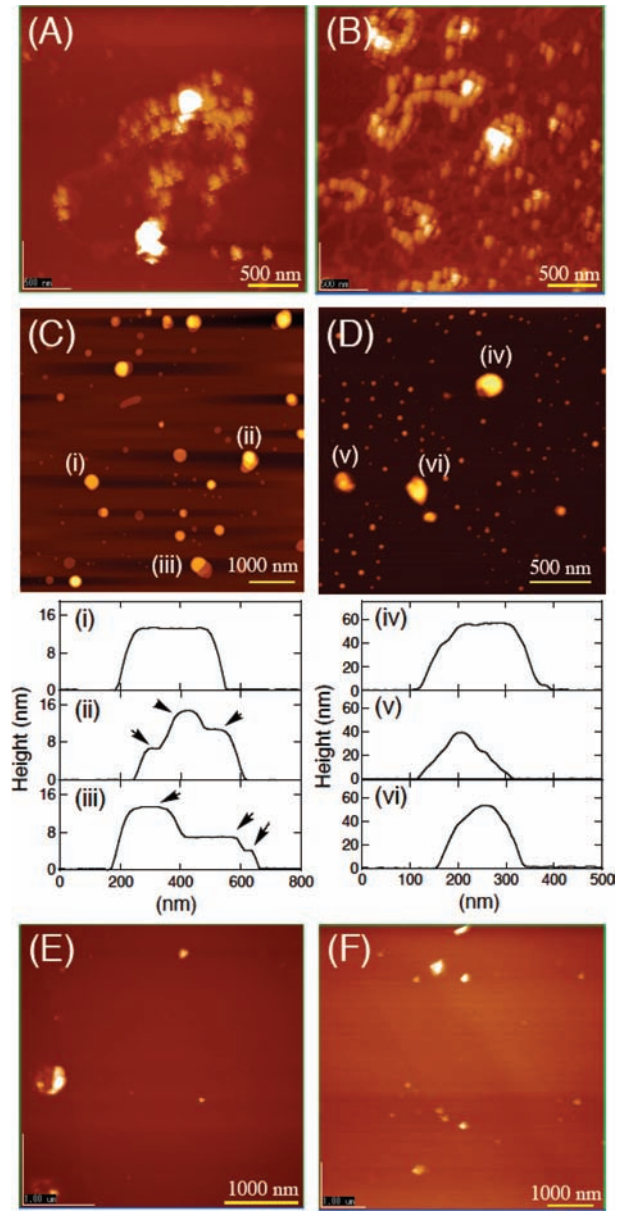


Figure 6. AFM images of PCL/plasmid DNA (ColE1; 6646 bp) lipoplexes: (A), **DCP-spd**(PCL)/DNA (N/P = 5); (B), **DCP-spm**(PCL)/DNA (N/P = 5); (C), **DCP-spd**(PCL)/DNA (N/P = 24); (D), **DCP-spm**(PCL)/DNA (N/P = 24); (E and F), **DCP-PEI**(PCL)/DNA complex (N/P = 24). Scale bars shown in the images are 500 nm (A,B,D) and 1000 nm (C,E,F). The PCL/DNA complexes were applied to PLL-mica (A,B) and bare mica (C,D,E,F). All images were taken under an ambient air conditions. Height profiles of the objects (i)−(iii) in C and (iv)−(v) in D are shown below these images. Arrows in (ii) and (iii) indicate step-like profiles discussed in the text. Images E and F for **DCP-PEI**(PCL)/DNA were taken from a different area of the bare mica surface.

must be adsorbed on the PLL-mica surface through electrostatic interaction to be imaged. The outer periphery of the large aggregates is rich in DNA molecules, presumably those were so loosely attached that they were liberated from the aggregates during electrophoresis.

At the high N/P = 24, spherical complexes were observed for **DCP-spd**(PCL) and **DCP-spm**(PCL) complexes; their diameters were 200−400 nm for **DCP-spd**(PCL)/DNA (C) and 150−250 nm for **DCP-spm**(PCL)/DNA lipoplexes (D), and their heights were 12−30 and 27−60 nm, respectively. The size of the complexes is in good agreement with the values observed by DLS. The detailed topography of these **DCP-spd**(PCL)/DNA

and **DCP-spm**(PCL)/DNA lipoplexes showed flat-topped spheres and spherical structures (line profiles (i)−(iii) for (C) and (iv)−(vi) for (D)). The profiles (ii) and (iii) are characteristically "step-like" (arrows). The heights indicated in (ii) are 6, 10, and 14 nm. Considering the thickness of lipid bilayer (4 nm) and the diameter of DNA (2 nm), these three values correspond to one bilayer (4 nm) + DNA (2 nm) = 6 nm, a double bilayer (8 nm) + DNA = 10 nm, and a triple bilayer (12 nm) + DNA = 14 nm, respectively. Thus, the step-like structure is reasonably indicative of a smectic lamellar assembly, where DNA molecules are laminated between bilayers.

Compared with **DCP-spd**(PCL) and **DCP-spm**(PCL) lipoplexes, the size of the **DCP-PEI**(PCL)/DNA lipoplex (N/P = 24) is large and has a broad distribution (1062 ± 783 nm, Table 1, entry 14). AFM images of the **DCP-PEI**(PCL)/DNA lipoplex show aggregates with heterogeneous and featureless shapes (Figure 6E,F). EtBr replacement experiments revealed DNA condensation in a similar manner to that of **DCP-spd**(PCL) and **DCP-spm**(PCL) (Supporting Information Figure S2).

Disruption of the PCL/DNA Lipoplexes. When the **DCP-spd**(PCL)/DNA and **DCP-spm**(PCL)/DNA lipoplexes (N/P = 24) were incubated in acidic solution (down to pH 4), the particle sizes measured by DLS became significantly larger and exhibited broad distributions (Table 1, entries 6 and 12). AFM imaging revealed morphological transformation of the PCL/DNA complexes upon acidification. When the dispersion of **DCP-spd**(PCL)/DNA lipoplexes (N/P = 24) was acidified at pH 4 for 1 h by addition of acetic acid, deformed structures were observed on bare mica (Figure 7A). Relative to the original structure (Figure 6C), the complex is decisively deformed by the acid treatment. Although some of the flat-topped sphere complexes remain, the predominant morphology is particles connected with strings. The height of the clusters is 25−53 nm and they are connected with string portions that are 6−10 nm high. When the acid-treated complex solution was put on PLL-mica, additional deformed objects appeared on the surface (Figure 7B). A "beads on a string" deformed structure is composed of very small particles (50−100 nm in diameter) and string parts (∼70 nm in width and 2−5 nm in height). The beads on a string structure observed on the positively charged surface must consist of DNA-rich fragments associated with some lipid components. The **DCP-spm**(PCL)/DNA lipoplex maintains its spherical structure on bare mica (Figure 7C). On the PLL-mica, on the other hand, deformed structures were observed as in the case of **DCP-spm**(PCL)/DNA lipoplex (Figure 7D). Such morphological changes upon acidification result from disassembly of the lipoplexes and the accompanying DNA release. Gel electrophoretic analysis provided evidence for the DNA release; the released plasmid band increased with the acidification from pH 8 to pH 4 (Supporting Information Figure S4). In sharp contrast, such a morphological change was not observed for the micellar aggregate **DCP-spd**(M) (Figure 7E,F). DLS analysis indicates an insensitivity of the micellar aggregates to acidification (Table 1, entries 6 and 12).

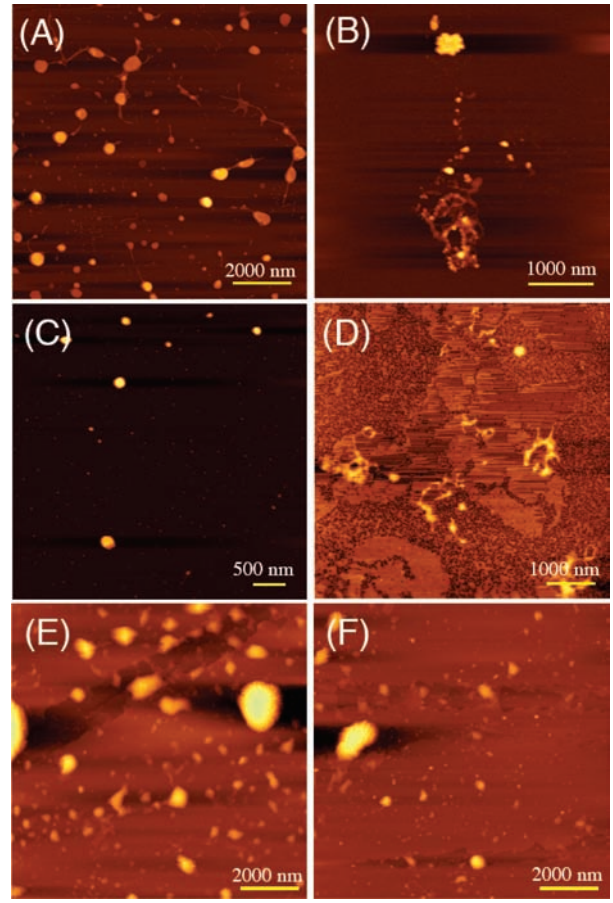


Figure 7. AFM images of disassembled lipoplexes, **DCP-spd**(PCL)/DNA (A and B) and **DCP-spm**(PCL)/DNA (C and D) by acidification at pH 4. Images (E) and (F) represent the micellar aggregate **DCP-spd**(M)/DNA complex before and after the acid treatment, respectively. The acid-treated suspensions of complexes were put on bare mica (A,C,E,F) and PLL-mica (B,D). After removal of the solution, the images were acquired. Scale bars: 2000 nm (A), 1000 nm (B), 500 nm (C), 1000 nm (D), 2000 nm (E) and (F).

DISCUSSION

Chemical Structure of the Polyamine Conjugates. The polyamine-dialkyl phosphate conjugates can be readily synthesized via a two-step reaction: (i) formation of dimerized dialkyl phosphate anhydride and (ii) its nucleophilic substitution with polyamines. The synthetic strategy gives access to a wide variety of polyamine−dialkyl phosphate derivatives. Conjugation of the polyamine and hydrophobic portions is required for an effective gene carrier (Figure 1). Such amphiphilicity is essential to condense DNA molecules, which requires both electrostatic and hydrophobic interactions (*45*, *49*). We tested a number of combinations of dialkyl and polyamine portions for their activity in gene transfection. The longer alkyl chain exhibited higher efficiency (Figure 3). The ζ-potential of the DOPE-based PCL increased with alkyl chain length, for example, 27.6, 33.4, and 37.1 mV for **DLP-spd**, **DMP-spd**, and **DCP-spd**, respectively, showing that the conjugate with the longer chain length provides the higher positive potential. The hydrophobic interaction results in stable incorporation of the conjugate into the PCL, consistent with transfection activity in the order of C16 ≥ C14 > C12. We found that the micellar aggregate of **DCP-PEI** conjugate exhibited slightly higher transfection activity than the low-molecular-weight amine conjugates, **DCP-spd**(M) and **DCP-spm**(M); however, the activity of **DCP-PEI**(PCL) was marginal. The size of **DCP-PEI**(PCL)/DNA lipoplex is significantly greater than that of the other lipoplexes (Table 1, entry 14). The **DCP-PEI** conjugate is composed of DCP/PEI(1800) = ∼1/1, judged by ^{1}H NMR (*49*). As previously reported, the cetyl-PEI, whose PCL possesses high transfection activity, consists of 10 cetyl portions in the polymer (*47*). The cetyl-PEI can attach to the PCL surface via the anchoring of cetyl portions in the lipid bilayer. However, that is not the case for **DCP-PEI**(PCL); the single hydrophobic portion in the conjugate is not enough to provide adequate covering of PEI over the PCL surface. This may cause "PEI-protrusion" from the surface, which gives rise to the large and heterogeneous aggregation seen upon combination with DNA molecules. This is likely the reason for the lower activity of the **DCP-PEI**(PCL). Taken together, these consid-

erations suggest that a homogeneous positive charge distribution on the PCL surface is important to the transfection activity.

Effect of Bilayer Structure on the Transfection Activity. In the series of polyamines tested in this study, the low-molecular-weight polyamines were found to be more effective gene carriers when these conjugates were assembled into PCLs. The transfection activity of the PCL was ~3 times larger than as the corresponding micellar aggregate (Figure 1). The effect of the helper lipid, DOPE, was clearly substantial, as is shown in Figure 2. DOPE, a predominantly nonlamellar lipid, is thought to facilitate fusion and destabilization of the endosomal membrane after uptake of cationic lipid/DNA complexes into a cell. In our previous report, we described intercellular trafficking of PCL (composed of cetyl-PEI and DOPE)-DNA complexes, which were taken up into cells by endosomal pathway (*48*), followed by endosomal escape. In fact, transfection activity of the present PCLs was inhibited by nigericin, which is able to dissipate the pH gradient across the endosomal membranes, by 30−50%, suggesting that endosomal pathway is likely involved in the mechanism in the present lipoplex system. It appears, therefore, that the mechanism of the lipofection by the compounds in this study may be similar to that of this and other agents known to be enhanced by DOPE. The lipoplexes made from the bilayer-structured PCLs evidently involve lamellar assemblies, given that AFM images reveal the presence of step-like profiles ((ii) and (iii) in Figure 6). The step-like profiles imply a lamellar complex, in which DNA rods (2 nm in diameter) are laminated between bilayers (4 nm thickness). Such an intrinsic bilayer structure may predispose lipoplexes to interact with cell and endosomal membranes. This is not the case for micellar aggregates, whose morphology is large spheres (Figure 7E and Table 1 entry 5), in which polyamine conjugate and DNA molecules likely aggregate randomly. This may be one of the reasons for the higher activity of PCL-based lipoplex, whose size is more favorable to transfection.

The linear dependence of activity on N/P (Figure 4) is related to the morphology of the lipoplex. The electrophoresis experiment (Figure 5) and AFM images (Figure 6A−D) suggest a reasonable explanation of the dependence, namely, the following: In the low N/P range (~5), the PCLs inadequately condense DNA molecules, giving the bead-like structures (Figure 6A,B). The DNA molecules loosely packed in the complex are readily released during electrophoresis. Such a complex, whose ζ-potential is negative, is too large to be introduced into the cell membrane via endocytosis; therefore, the transfection level is low. With increasing N/P ratio, the morphology of the lipoplex transforms from large bead-like structure into smaller particles, wherein DNA molecules are condensed more tightly (Figure 6C,D). The size of the lipoplexes, whose ζ-potential is positive, is 150−400 nm, more favorable for cellular uptake via endocytosis (*30*). Given that the lamellar assembly in the lipoplex is responsible for its effectiveness as a gene carrier (*29*, *30*), the population of active species for gene transfer would increase with increasing in the N/P. Although highly positive-charged carriers are generally toxic, the PCL described here exhibit low cytotoxicity, an advantage for in vitro and in vivo applications.

Disassembly of the Lipoplexes and DNA Release. Facile escape from the acidic endosomal compartment is necessary for efficient gene transfer. Disassembly of the lipoplex associated with DNA release has been clearly observed by AFM imaging (Figure 7) and by electrophoretic analyses (Supporting Information Figure S3). Upon acidification (down to pH 4), the extent of protonation of the polyamine portion is increased. Assuming that the lipoplex forms smectic lamella, electrostatic repulsion between layers must be increased with such protonation, resulting in the disruption of the lipoplex. For lipoplexes composed of **DCP-spd**(PCL) and **DCP-spm**(PCL), disruption accompanying DNA release has been confirmed. In sharp contrast, the size and shape of micellar aggregate/DNA complexes composed of **DCP-spd** and **DCP-spm** are insensitive to acidification (Figure 7F and Table 1, entries 6 and 12). This would be due to their amorphous structure, which does not respond to pH change. Thus, the disassembly of the lipoplex composed of the bilayer-structured PCL is essential in effective gene transfer, especially in the process of endosomal escape, where lipid exchange and flip−flop are involved in disrupting the membrane and leading to DNA release (*42*). Although the acidity of this experimental condition (pH 4) seems higher than that in endosome (pH 5.5), such a protonation process on the polyamines should be involved in the endosomal environment, because the protonation on the polyamines whose pK_a values are >8 may proceed rather gradually in the acidic region, especially in the self-assembled lamellar structure, where polyamines are densely packed. This finding suggests a strategy for molecular design—especially in the polyamine portion—in which a morphological transformation of lipoplexes is taken advantage of for new nonviral transfection strategies.

CONCLUSION

We have demonstrated that PCL composed of the low-molecular-weight polyamine conjugates, DCP-spermidine (**DCP-spd**) and DCP-spermine (**DCP-spm**), exhibit much higher gene transfer activity than PEI(1800) conjugate-based **DCP-PEI**(PCL). The former compounds generate 150−400 nm diameter lipoplexes, whereas the latter gives rise to large aggregates. In the case of the former compounds, AFM images clearly reveal a morphological change upon acidification, indicating DNA release from the lipoplexes, whereas in contrast, the morphology of micellar aggregates is insensitive to pH change. A pH-dependent transformation is crucial in gene transfer, and the chemical structure of the polyamine portion may therefore play an important role in the acidification-induced transformation. We have also described the relation between the N/P dependence of transfection activity and the morphology of the lipoplexes as revealed by AFM. Morphological study with AFM provided useful information for understanding the basis of lipoplexes with superior activity and for design strategies leading to optimally efficient gene carriers.

ACKNOWLEDGMENT

The authors thank Dr. Robert C. MacDonald for helpful comments and discussion. The present work was partially supported by "Grant-in-Aid for Scientific Research on Innovative Areas 2006 (Molecular Science of Fluctuations toward Biological Functions)" (21107510) from the Ministry of Education, Culture, Sports, Science and Technology (MEXT) of the Japanese Government.

Supporting Information Available: Evaluation of cytotoxicity polyamine conjugates and their PCLs (Figure S1), changes in fluorescence intensity of ethidium bromide intercalated into ColE1 plasmid DNA-PCLs (Figure S2), and electrophoretic analysis of DNA release from the lipoplex (Figure S3). This material is available free of charge via the Internet at http://pubs.acs.org.

LITERATURE CITED

(1) Kay, M. A., Liu, D., and Hoogerbrugge, P. M. (1997) Gene therapy. *Proc. Natl. Acad. Sci. U.S.A. 94*, 12744–12746.
(2) Lasic, D. D. (1997) *Liposomes in Gene Derivary*, CRC Press, New York.
(3) Miller, A. D. (1998) Cationic liposomes for gene therapy. *Angew. Chem., Int. Ed. 37*, 1768–1785.

(4) Li, S., and Huang, L. (2000) Nonviral gene therapy: promises and challenges. *Gene Ther. 7*, 31–34.

(5) Felgner, P. L., and Ringold, G. M. (1989) Cationic liposome-mediated transfection. *Nature 337*, 387–388.

(6) MacDonald, R. C., Ashley, G. W., Shida, M. M., Rakhmanova, V. A., Tarahovsky, Y. S., Pantazatos, D. P., Kennedy, M. T., Pozharski, E. V., Baker, K. A., Jones, R. D., Rosenzweig, H. S., Choi, K. L., Qiu, R., and McIntosh, T. J. (1999) Physical and biological properties of cationic triesters of phosphatidylcholine. *Biophys. J. 77*, 2612–2629.

(7) Felgner, P. L., Gadek, T. R., Holm, M., Roman, R., Chan, H. W., Wenz, M., Northrop, J. P., Ringold, G. M., and Danielsen, M. (1987) Lipofection: A highly efficient, lipid-mediated DNA-transfection procedure. *Proc. Natl. Acad. Sci. U.S.A. 84*, 7413–7417.

(8) Behr, J.-P., Demeneix, B., Loeffler, J. P., and Perez-Mutul, J. (1989) Efficient gene transfer into mammalian primary endocrine cells with lipopolyamine-coated DNA. *Proc. Natl. Acad. Sci. U.S.A. 86*, 6982–6986.

(9) Meyer, O., Kirpotin, D., Hong, K., Sternberg, B., Park, J. W., Woodle, M. C., and Papahadjopoulos, D. (1998) Cationic liposomes coated with polyethylene glycol as carriers for oligonucleotides. *J. Biol. Chem. 273*, 15621–15627.

(10) Boussif, O., Lezoulch, F., Zanta, M. A., Mergny, M. D., Scherman, D., Demeneix, B., and Behr, J.-P. (1995) A versatile vector for gene and oligonucleotide transfer into cells in culture and in vivo: Polyethylenimine. *Proc. Natl. Acad. Sci. U.S.A. 92*, 7297–7301.

(11) Petersen, H., Fechner, P. M., Martin, A. L., Kunath, K., Stolnik, S., Roberts, C. J., Fischer, D., Davies, M. C., and Kissel, T. (2002) Polyethylenimine-graft-poly(ethylene glycol) copolymers: influence of copolymer block structure on DNA complexation and biological activities as gene delivery system. *Bioconjugate Chem. 13*, 845–854.

(12) Koide, A., Kishimura, A., Osada, K., Jang, W.-D., Yamasaki, Y., Kataoka, K., Harada, A., and Nagasaki, Y. (2006) Semipermeable polymer vesicle (PICsome) self-assembled in aqueous medium from a pair of oppositely charged block copolymers: Physiologically stable micro-/nanocontainers of water-soluble macromolecules. *J. Am. Chem. Soc. 128*, 5988–5989.

(13) Russ, V., Elfberg, H., Thoma, C., Kloeckner, J., Ogris, M., and Wagner, E. (2008) Novel degradable oligoethylenimine acrylate ester-based pseudodendrimers for in vitro and in vivo gene transfer. *Gene Ther. 15*, 18–29.

(14) Haensler, J., and Szoka, F. C., Jr. (1993) Polyamidoamine cascade polymers mediate efficient transfection of cells in culture. *Bioconjugate Chem. 4*, 372–379.

(15) Shim, M. S., and Kwon, Y. J. (2009) Acid-responsive linear polyethylenimine for efficient, specific, and biocompatible siRNA delivery. *Bioconjugate Chem. 20*, 488–499.

(16) Guillot-Nieckowski, M., Joester, D., Stöhr, M., Losson, M., Adrian, M., Wagner, B., Kansy, M., Heinzelmann, H., Pugin, R., Diederich, F., and Gallani, J.-L. (2007) Self-assembly, DNA complexation, and pH response of amphiphilic dendrimers for gene transfection. *Langmuir 23*, 737–746.

(17) Wu, J., Lizarzaburu, M. E., Kurth, M. J., Liu, L., Wege, H., Zern, M. A., and Nantz, M. H. (2001) Cationic lipid polymerization as a novel approach for constructing new DNA delivery agents. *Bioconjugate Chem. 12*, 251–257.

(18) Ewert, K. K., Evans, H. M., Zidovska, A., Bouxsein, N. F., Ahmad, A., and Safinya, C. R. (2006) A columnar phase of dendritic lipid-based cationic liposome-DNA complexes for gene delivery: Hexagonally ordered cylindrical micelles embedded in a DNA honeycomb lattice. *J. Am. Chem. Soc. 128*, 3998–4006.

(19) Takahashi, T., Hirose, J., Kojima, C., Harada, A., and Kono, K. (2007) Synthesis of poly(amidoamine) dendron-bearing lipids with poly(ethylene glycol) grafts and their use for stabilization of nonviral gene vectors. *Bioconjugate Chem. 18*, 1163–1169.

(20) Matsui, K., Sando, S., Sera, T., Aoyama, Y., Sasaki, Y., Komatsu, T., Terashima, T., and Kikuchi, J. (2006) Cerasome as an infusible, cell-friendly, and serum-compatible transfection agent in a viral size. *J. Am. Chem. Soc. 128*, 3114–3115.

(21) Mustapa, M. F. M., Grosse, S. M., Kudsiova, L., Elbs, M., Raiber, E.-A., Wong, J. B., Brain, A. P. R., Armer, H. E. J., Warley, A., Keppler, M., Ng, T., Lawrence, M. J., Hart, S. L., Hailes, H. C., and Tabor, A. B. (2009) Stabilized integrin-targeting ternary LPD (Lipopolyplex) vectors for gene delivery designed to disassemble within the target cell. *Bioconjugate Chem. 20*, 518–532.

(22) Kogure, K., Akita, H., Yamada, Y., and Harashima, H. (2008) Multifunctional envelope-type nano device (MEND) as a non-viral gene delivery system. *Adv. Drug Delivery Rev. 60*, 559–571.

(23) Mintzer, M. A., and Simanek, E. E. (2009) Nonviral vectors for gene delivery. *Chem. Rev. 109*, 259–302, Also references citied therein.

(24) Remy, J.-S., Sirlin, C., Vierling, P., and Behr, J.-P. (1994) Gene transfer with a series of lipophilic DNA-binding molecules. *Bioconjugate Chem. 5*, 647–654.

(25) Geall, A. J., Eaton, M. A. W., Baker, T., Catterall, C., and Blagbrough, I. S. (1999) The regiochemical distribution of positive charges along cholesterol polyamine carbamates plays significant roles in modulating DNA binding affinity and lipofection. *FEBS Lett. 459*, 337–342.

(26) Ewert, K., Ahmad, A., Evans, H. M., Schmidt, H.-W., and Safinya, C. R. (2002) Efficient synthesis and cell-transfection properties of a new multivalent cationic lipid for nonviral gene delivery. *J. Med. Chem. 45*, 5023–5029.

(27) Byk, G., Dubertret, C., Escriou, V., Frederic, M., Jaslin, G., Rangara, R., Pitard, B., Crouzet, J., Wils, P., Schwartz, B., and Scherman, D. (1998) Synthesis, activity, and structure-activity relationship studies of novel cationic lipids for DNA transfer. *J. Med. Chem. 41*, 224–235.

(28) McGregor, C., Perrin, C., Monck, M., Camilleri, P., and Kirby, A. J. (2001) Rational approaches to the design of cationic gemini surfactants for gene delivery. *J. Am. Chem. Soc. 123*, 6215–6220.

(29) Koltover, I., Salditt, T., Rädler, J. O., and Safinya, C. R. (1998) An inverted hexagonal phase of cationic liposome-DNA complexes related to DNA release and delivery. *Science 281*, 78–81.

(30) Koynova, R., Wang, L., and MacDonald, R. C. (2006) An intracellular lamellar-nonlamellar phase transition rationalizes the superior performance of some cationic lipid transfection agents. *Proc. Natl. Acad. Sci. U.S.A. 103*, 14373–14378.

(31) Aoyama, Y., Kanamori, T., Nakai, T., Sasaki, T., Horiuchi, S., Sando, S., and Niidome, T. (2003) Artificial viruses and their application to gene delivery. Size-controlled gene coating with glycocluster nanoparticles. *J. Am. Chem. Soc. 125*, 3455–3457.

(32) Wrobel, I., and Collins, D. (1995) Fusion of cationic liposomes with mammalian cells occurs after endocytosis. *Biochim. Biophys. Acta 1235*, 296–304.

(33) Mustapa, M. F. M., Bell, P. C., Hurley, C. A., Nicol, A., Guénin, E., Sarkar, S., Writer, M. J., Barker, S. E., Wong, J. B., Pilkington-Miksa, M. A., Papahadjopoulos-Sternberg, B., Shamlou, P. A., Hailes, H. C., Hart, S. L., Zicha, D., and Tabor, A. B. (2007) Biophysical characterization of an integrin-targeted lipopolyplex gene delivery vector. *Biochemistry 46*, 12930–12944.

(34) Varga, C. M., Wickham, T. J., and Lauffenburger, D. A. (2000) Receptor-mediated targeting of gene delivery vectors: Insights from molecular mechanisms for improved vehicle design. *Biotechnol. Bioeng. 70*, 593–605.

(35) Oupicky, D., Parker, A. L., and Seymour, L. W. (2002) Laterally stabilized complexes of DNA with linear reducible polycations: Strategy for triggered intracellular activation of DNA delivery vectors. *J. Am. Chem. Soc. 124*, 8–9.

(36) Dauty, E., Remy, J.-S., Blessing, T., and Behr, J.-P. (2001) Dimerizable cationic detergents with a low cmc condense plasmid DNA into nanometric particles and transfect cells in culture. *J. Am. Chem. Soc. 123*, 9227–9234.

(37) Miyata, K., Kakizawa, Y., Nishiyama, N., Harada, A., Yamasaki, Y., Koyama, H., and Kataoka, K. (2004) Block catiomer polyplexes with regulated densities of charge and disulfide cross-linking directed to enhance gene expression. *J. Am. Chem. Soc. 126*, 2355–2361.

(38) Anderson, D. G., Lynn, D. M., and Lange, R. (2003) Semi-automated synthesis and screening of a large library of degradable cationic polymers for gene delivery. *Angew. Chem., Int. Ed. 42*, 3153–3158.

(39) Zanta, M. A., Beleguise-Valladier, P., and Behr, J.-P. (1999) Gene delivery: A single nuclear localization signal peptide is sufficient to carry DNA to the cell nucleus. *Proc. Natl. Acad. Sci. U.S.A. 96*, 91–96.

(40) Manickam, D. S., and Oupicky, D. (2006) Multiblock reducible copolypeptides containing histidine-rich and nuclear localization sequences for gene delivery. *Bioconjugate Chem. 17*, 1395–1403.

(41) Bell, Paul C., Bergsma, M., Dolbnya, I. P., Bras, W., Stuart, M. C. A., Rowan, A. E., Feiters, M. C., and Engberts, J. B. F. N. (2003) Transfection mediated by gemini surfactants: Engineered escape from the endosomal compartment. *J. Am. Chem. Soc. 125*, 1551–1558.

(42) Xu, Y., and Szoka, F. C., Jr. (1996) Mechanism of DNA release from cationic liposome/DNA complexes used in cell transfection. *Biochemistry 35*, 5616–5623.

(43) Wan, L., Manickam, D. S., Oupicky, D., and Mao, G. (2008) DNA release dynamics from reducible polyplexes by atomic force microscopy. *Langmuir 24*, 12474–12482.

(44) Tarahovsky, Y. S., Koynova, R., and MacDonald, R. C. (2004) DNA release from lipoplexes by anionic lipids: Correlation with lipid mesomorphism, interfacial curvature, and membrane fusion. *Biophys. J. 87*, 1054–1064.

(45) Yamazaki, Y., Nango, M., Matsuura, M., Hasegawa, Y., Hasegawa, M., and Oku, N. (2000) Polyamine liposomes, a novel nonviral gene transfer system, constructed drom cetylated polyethyleninine. *Gene Ther. 7*, 1148–1155.

(46) Oku, N., Yamazaki, M., Matsuura, M., Sugiyama, M., Hasegawa, M., and Nango, M. (2001) A novel non-viral gene transfer system, polycation liposomes. *Adv. Drug Delivery Rev. 52*, 209–218.

(47) Matsuura, M., Yamazaki, Y., Sugiyama, M., Kondo, M., Ori, H., Nango, M., and Oku, N. (2003) Polycation liposome-mediated gene transfer in vivo. *Biochim. Biophys. Acta 1612*, 136–143.

(48) Sugiyama, M., Matsuura, M., Takeuchi, Y., Kosaka, J., Nango, M., and Oku, N. (2004) Possible mechanism of polycation liposome (PCL)-mediated gene transfer. *Biochim. Biophys. Acta 1660*, 24–30.

(49) Dewa, T., Ieda, Y., Morita, K., Wang, L., MacDonald, R. C., Iida, K., Yamashita, K., Oku, N., and Nango, M. (2004) Novel polyamine-dialkyl phosphate conjugates for gene carriers. Facile synthetic route via an unprecedented dialkyl phosphate. *Bioconjugate Chem. 15*, 824–830.

(50) Oberle, V., Bakowsky, U., Zuhorn, I. S., and Hoekstra, D. (2000) Lipoplex formation under equilibrium conditions reveals a three-step mechanism. *Biophys. J. 79*, 1447–1454.

(51) Kunitake, T., and Okahata, Y. (1978) Synthetic bilayer membranes with anionic head groups. *Bull. Chem. Soc. Jpn. 51*, 1877–1879.

(52) Felgner, J. H., Kumar, R., Sridhar, C. N., Wheeler, C. J., Tsai, Y. J., Border, R., Ramsey, P., Martin, M., and Felgner, P. L. (1994) Enhanced gene delivery and mechanism studies with a novel series of cationic lipid formulations. *J. Biol. Chem. 269*, 2550–2561.

(53) Cevc, G. (1993) *Phospholipids Handbook*, Marcel Dekker, Inc., New York.

(54) Yoshikawa, Y., Emi, N., Kanbe, T., Yoshikawa, K., and Saito, H. (1996) Folding and aggregation of DNA chains induced by complexation with lipospermine: formation of a nucleosome-like structure and network assembly. *FEBS Lett. 396*, 71–76.

BC900376Y

Site-Specific, Orthogonal Labeling of Proteins in Intact Cells with Two Small Biarsenical Fluorophores

Alexander Zürn,[§] Christoph Klenk,[§] Ulrike Zabel,[§,#] Susanne Reiner,[§] Martin J. Lohse,*[,§,#] and Carsten Hoffmann[§]

Institute of Pharmacology and Toxicology, Rudolf Virchow Center University of Würzburg, Versbacher Strasse 9, 97078 Würzburg, Germany. Received September 7, 2009; Revised Manuscript Received January 19, 2010

The fusion of fluorescent proteins to proteins of interest has greatly advanced fluorescence microscopy, but is often limited by their large size. Here, we report site-specific, orthogonal labeling of two cellular proteins in intact cells with two small fluorescent dyes: fluorescein arsenical hairpin binder, FlAsH, and its red analogue, ReAsH, which bind to tetracysteine motifs. Development of a sequential labeling method to two different motifs, CCPGCC and FLNCCPGCCMEP, allowed site-specific labeling with FlAsH and ReAsH, respectively. Using the cell surface receptor for parathyroid hormone and its cytosolic binding protein, β-arrestin2, we show their selective visualization in intact cells and analyze their interaction by colocalization and fluorescence resonance energy transfer (FRET). We propose that this method may be widely applied to label intracellular proteins and to study their interactions in intact cells with minimal disturbance of their function.

INTRODUCTION

Fluorescence microscopy of cellular and subcellular structures generally requires the use of fluorophores. These fluorophores can be attached, for example, to antibodies in order to visualize specific proteins and structures. However, in intact cells this approach is mostly limited to cell surface proteins, because the labeled antibodies cannot pass the cell membrane. This situation has been greatly advanced by the discovery of the green fluorescent protein (GFP) and its many colored variants, which can be fused to proteins of interest and permit their visualization (*1*). To date, numerous variants of GFP and other fluorescent proteins, characterized by different fluorescent properties, have been described, and permit various fluorescence techniques to study the localization and interaction of proteins in intact cells, including fluorescence resonance energy transfer (FRET) (*2*). However, protein function may be disturbed by fusion with the ~27 kDa GFP molecule and limit their use for in vivo imaging (*3–5*). Moreover, GFPs are often fused to proteins via a flexible linker, and this together with the size of GFPs makes it difficult to predict the exact position of the central fluorophore in relation to the protein of interest.

Alternatives to GFPs include fusions with an O^6-alkylguanine-DNA-alkyltransferase (AGT), which binds covalently O^6-benzylguanine that can be chemically coupled with various fluorescent dyes. While this technique offers the advantage of using highly fluorescent dyes, the AGT tags are also of considerable size (~20 kDa). Depending on the dye used and its membrane permeability, this method can be used to label cell surface as well as intracellular proteins (*6–9*). Other enzymes that can be fused to proteins and permit labeling with a variety of fluorescent dyes include dihydrofolate reductase (together with fluorescent trimethoprim derivatives (*10*)) and a modified haloalkane dehalogenase designed to covalently bind to synthetic ligands (*11*).

A technique to minimize the size of the fluorescent dyes involves the insertion of an oligo-histidine tag into the target protein. This motif can form a complex with a nitrilo triacetic acid (NTA)-Ni^{2+}, which can again be coupled to fluorophores. By combining different fluorescently labeled NTA-variants, FRET measurements have been done with purified proteins (*12*). Labeling of proteins at the extracellular face of intact cells has also been shown, but the fluorophores did not cross the cell membrane and thus did not permit labeling of intracellular proteins (*13*). With sizes of 2−5 kDa, these complexes are much smaller than the GFP-variants or the AGT-tag, but their low affinity results in a low stability of the complex (*14*).

To circumvent these problems, a much smaller, chemical fluorescent label was reported as an alternative. The 700 Da fluorescein derivative FlAsH (fluorescein arsenical hairpin binder) and the resorufin derivative ReAsH (red arsenical hairpin binder) have been shown to bind to a tetracysteine motif (CCPGCC) with high affinity and specificity (*15, 16*). Such tetracysteine motifs can be genetically introduced into proteins. Labeling of tetracysteine-motif containing proteins requires a labeling step that results in a complex formation between the label and the tetracysteine motif. This needs to be followed by a washing procedure to minimize unspecific background staining. This labeling technique has been used for cytosolic as well as membrane proteins (*17, 18*). FlAsH can be used as an alternative to YFP and forms a FRET pair with CFP. Using FlAsH instead of YFP, we were able to rescue the functionality of a G-protein coupled receptor (GPCR), which was inactive when labeled with YFP in its third intracellular loop (*3*).

However, for FRET (or colocalization) studies, this approach still required CFP (or a similar protein) as a second label, and it would seem attractive to also replace this second label by a small one. Therefore, further studies have been undertaken to simultaneously label and visualize two different proteins within a cell using two small fluorophores. Different approaches for simultaneous labeling with FlAsH and ReAsH have been described. Robia et al. (*19*) cloned two CCPGCC sequences into the sarcoplasmic reticulum protein phospholamban and stained cells expressing this construct by simultaneous incubation with ReAsH and FlAsH; this resulted in random labeling of phospholamban with either FlAsH or ReAsH. Interestingly,

* Corresponding author. Institute of Pharmacology and Toxicology, University of Würzburg, Versbacher Str. 9, 97078 Würzburg. Phone: ++49 931 20148400, Fax: ++49 931 20148411, E-mail lohse@toxi.uni-wuerzburg.de.

[§] Institute of Pharmacology and Toxicology.

[#] Rudolf Virchow Center.

10.1021/bc900394j © 2010 American Chemical Society
Published on Web 04/29/2010

phospholamban, a small protein of 5 kDa, still formed pentamers after labeling, indicating that the protein had remained functional (*19*). Roberti et al. (*20*) performed nondirected labeling with the two small fluorophores of α-synuclein aggregates in vitro and in cells. Finally, Squier et al. presented a tetracysteine motif, CCKACC, with different binding rates and affinities for FlAsH and ReAsH compared to the CCPGCC motif; this allowed sequential labeling, but this approach has so far been done only with purified proteins (*21*).

Despite these studies demonstrating the value of biarsenical dyes, site-specific labeling of two different proteins with FlAsH and ReAsH in intact cells has not yet been achieved. However, such specific labeling would be necessary to distinguish two different proteins by different labels in order to achieve the full power of fluorescence microscopy and FRET techniques. Therefore, we set out to develop such specific labeling of intracellular proteins. To do so, we utilized different tetracysteine motifs (*22*) and developed a selective and specific labeling protocol. We show that a cell surface and a cytosolic protein—the parathyroid hormone (PTH) receptor and its binding protein β-arrestin2—can be specifically labeled with FlAsH and ReAsH in the same cell and their known interaction (*23*) can then be visualized by colocalization and FRET studies.

EXPERIMENTAL PROCEDURES

Reagents. FlAsH and ReAsH are commercially available from Invitrogen as TC-FlAsH and TC-ReAsH, respectively. Human [$Nle^{8,18}$,Tyr^{34}]PTH(1−34), abbreviated as PTH(1−34), was obtained from Bachem. 1,2-Ethane dithiol (EDT) was from Sigma-Aldrich and British anti-Lewisite (BAL; 1,2-dimercaptopropanol) from Fluka. All other reagents were of the highest available grade from standard sources, generally from Sigma-Aldrich.

Molecular Biology. cDNA-sequences coding for a FLNCCPGCCMEP or a HRWCCPGCCKTF sequence (*22*) followed by those for CFP or YFP were fused to the very C-terminus of the A_{2A}-receptor cDNA. These constructs served for the analysis of the affinities for the twelve amino acid FlAsH binding motifs. The six amino acid motif CCPGCC was inserted in the third intracellular loop the A_{2A}-receptor after the position 215 (*3*), resulting in a sequence MESCCPGCCARS, and a CFP or YFP was fused to the receptor sequence after position 340.

Similarly, a FLNCCPGCCMEP motif (or a CCPGCC motif) was inserted into the C-terminus of the human PTH receptor following amino acid position 515. Likewise, a CCPGCC motif (or a FLNCCPGCCMEP motif) with a linker sequence was fused to the very C-terminus of β-arrestin2, resulting in an addition of KQMESCCPGCCARSTLQ (or KQMESFLNCCPGCCMEPARSTLQ), i.e., the same amino acid motifs as above. Site-directed mutagenesis was achieved using standard polymerase chain reaction techniques followed by DNA-sequencing for verification. For transient expression in mammalian cells, all cDNAs were cloned into the pcDNA3 vector (Invitrogen).

Cell Culture. HEK cells were maintained in Dulbecco's modified Eagle's medium (DMEM) supplemented with 10% fetal calf serum, 100 000 U/L penicillin and 100 mg/L streptomycin at 37 °C and 7% CO_2. For fluorescence measurements, cells were seeded on round polylysine-coated coverslips in 6-well plates 6 h prior to transfection. Cells were transfected using Effectene (Quiagen) according to the manufacturer's instructions. Assays were performed 48 h after transfection.

FlAsH and ReAsH Labeling. Transfected cells grown on polylysine-coated 24 mm coverslips to a confluence of about 70% were washed twice with 1 mL Phenol red-free Hank's balanced salt solution containing 1.8 g/L glucose (HBSS; Invitrogen) and incubated at 37 °C and 7% CO_2 for 1 h with 1 mL 2.5 μM ReAsH, 12.5 μM EDT in HBSS. Subsequently, cells were washed once with 1 mL HBSS. To reduce nonspecific labeling, cells were next incubated for 10 min at 37 °C and 7% CO_2 with 1 mL 250 μM BAL in HBSS and washed again with 1 mL HBSS. Subsequently, cells were incubated at 37 °C and 7% CO_2 for 1 h with 1 mL 250 nM FlAsH, 12.5 μM EDT in HBSS, washed again with HBSS, incubated for 10 min with 1 mL 250 μM EDT in HBSS, and finally washed twice with HBSS.

Determination of FlAsH and ReAsH Affinities. As a measure of the affinity of FlAsH and ReAsH to different binding motifs, we determined the concentration−response curves of the removal of the fluorophore by BAL. After labeling of transfected HEK cells, crude cell membranes were prepared by lysis with an Ultra-Turrax device and centrifugation at 120 000 × *g*. The membranes were resuspended in 500 μL of 50 mM Tris-buffer, pH 7.4, and FlAsH or ReAsH fluorescence were measured in a spectrofluorometer (Perkin-Elmer LS50B) in a 600 μL cuvette. The excitation wavelength for the CFP-FlAsH constructs was 436 nm and the emission spectrum was measured at 460−600 nm. For the YFP-ReAsH constructs, the excitation wavelength was 490 nm and the emission spectrum was measured at 500−700 nm. To determine the affinity of the fluorophores to the individual binding motifs, the concentration of BAL was increased stepwise. FRET between the two labels in a given construct was determined as the ratio between the emission of the donor (CFP or YFP; at 490 or 525 nm) and the emission of the acceptor (FlAsH or ReAsH; at 525 or 608 nm).

Confocal Microscopy. HEK cells were transfected with cDNA constructs coding for the PTH receptor or β-arrestin2, respectively, and labeled with FlAsH and ReAsH as described above. Coverslips were mounted using an Attofluor holder (Molecular Probes).

Images were taken on a Leica TCS SP5 confocal microscope with a 63 × 1.4 oil objective. For excitation of FlAsH, the 514 nm line of an argon laser was used, and fluorescence intensities were recorded from 520 to 560 nm. ReAsH was excited using a 594 nm laser line, and fluorescence intensities were recorded from 600 to 700 nm. Settings for image acquisition were kept constant at 1024 × 1024 pixel format and 400 Hz. Time series were recorded using the standard Leica software package. The pictures were taken sequentially at 3 min intervals. For the β-arrestin2 translocation, the time series were stopped after 9 min, and for receptor internalization, image acquisition was terminated after 18 min.

Measurement of Intracellular Free Calcium Responses. HEK cells were grown on polylysine-coated 24 mm coverslips to a confluence of about 70%. The cells were transfected with PTH-receptor cDNA constructs using Effectene (Quiagen) according to the manufacturer's instructions. Assays were performed 48 h after transfection. To load the calcium indicator, cells were incubated for 35 min at 37 °C in loading buffer (10 mM HEPES, 140 mM NaCl, 5.4 mM KCl, 1 mM $MgCl_2$, 2 mM $CaCl_2$) containing the calcium-sensitive dye, Fura-2 a.m. (1 μM), washed three times with loading buffer, and incubated at room temperature in the dark for 40 min. To determine Fura-2-fluorescence, an inverted fluorescence microscope was used (dichroic mirror, 455DCLP; filter set, 340 and 380 nm excitation filters and 520/20 emission filter), and the Ca^{2+} responses in single cells to stimulation with 10 nM PTH (1−34), added with a pipet, were measured by recording the Fura-2 fluorescence using *MetaMorph/MetaFluor* software (Visitron) and calculating the ratio of Fura-2 emission when excited at 340 nm and at 380 nm.

FRET Measurements with FlAsH and ReAsH. Dynamic FRET measurements using FlAsH as the donor and ReAsH as the acceptor were performed with a custom-built Zeiss Observ-

er.Z1 microscope equipped with a Visitron dual view, a DCLP 565 nm beam splitter, and 535/30 nm and 595/70 nm emission filters to monitor the FlAsH and ReAsH signals, respectively. An EXFO X-cite 120 lamp was used as the excitation source at a wavelength of 500 nm. Under these conditions, no direct excitation of ReAsH was measured. For bleedthrough of FlAsH into the ReAsH channel, a correction of 25% was determined in control experiments and applied. Data were measured using the *MetaFluor* software (Visitron), and *Origin6.1* (OriginLab) was used for analysis.

RESULTS

Affinity Measurements. In order to achieve selective binding of two small fluorophores to specific motifs, we aimed to identify motifs with different affinities toward FlAsH and ReAsH. Initially, we set out to assess the individual binding affinities of two recently described (*22*) 12-amino-acid high-affinity motifs (FLNCCPGCCMEP and HRWCCPGCCKTF). In order to study labeling and affinities in intact cells, we assessed these motifs in the context of the A_{2A} adenosine receptor, a prototypical G-protein coupled receptor (*3*). The two motifs were fused to C-terminus of the receptor, followed directly by CFP or YFP, respectively (Figure 1A). All constructs were expressed in HEK cells and showed specific membrane localization as measured by confocal microscopy (data not shown). In addition, to introduce a second label (for FRET studies) to a site with lower affinity, we expressed the similar A_{2A} adenosine receptor constructs carrying the core CCPGCC motif in their third intracellular loop (Figure 1A).

All constructs were labeled in HEK cells with either FlAsH or ReAsH, respectively, in order to allow intramolecular FRET between either CFP and FlAsH or YFP and ReAsH. Membranes were then prepared from the cells, and the emission spectra of each construct were measured. Figure 1B shows the emission spectra of a CFP- and FlAsH-labeled A_{2A} adenosine receptor (construct #5). The emission of both fluorophores, CFP (emission maximum at 480 nm) and FlAsH (emission maximum at 525 nm), were both clearly detectable in this spectrum when CFP was excited (436 nm). The strong emission of FlAsH under these conditions is indicative of FRET. Similarly, FRET was detected in membranes with an A_{2A} adenosine receptor labeled with YFP and ReAsH (construct #6; Supporting Information Figure 1).

FlAsH and ReAsH are fluorescent only when bound covalently to their tetracysteine motifs. British anti-Lewisite (BAL, dimercaptopropanol) can compete for binding and thus reduce their fluorescence signals (*22*). As a consequence, in the FRET-reporter constructs increasing BAL concentrations should decrease the emission of FlAsH or ReAsH, respectively, and because of ensuing lack of FRET increase the emission of the respective GFP-variant. This was indeed observed, with increasing concentrations of BAL causing the spectrum to shift progressively from two peaks of equal height (green curve) to one with a dominant CFP-emission and lacking FlAsH emission (cyan curve) (Figure 1B). The ratio between the emissions of CFP/FlAsH (or YFP/ReAsH) can be used to generate a kind of "competition curve" for BAL, and the IC_{50} value reflect the stability of FlAsH and ReAsH binding to the respective motif (i.e., a high IC_{50} value of BAL corresponds to a high stability).

These IC_{50} values were ~5.6 mM of BAL for FlAsH at the FLNCCPGCCMEP-motif, whereas the affinity for FlAsH at the HRWCCPGCCKTF motif was 2.3 mM of BAL. A clearly lower affinity for FlAsH was determined for the 6-amino-acid motif CCPGCC with 0.7 mM of BAL. For ReAsH, 3-fold lower affinities were determined for each motif, with IC_{50} values of 2.0 mM, 0.8 mM, and 0.2 mM of BAL, respectively (Supporting Information Table 1). Thus, the three tetracysteine motifs can be exploited for the development of a selective labeling protocol.

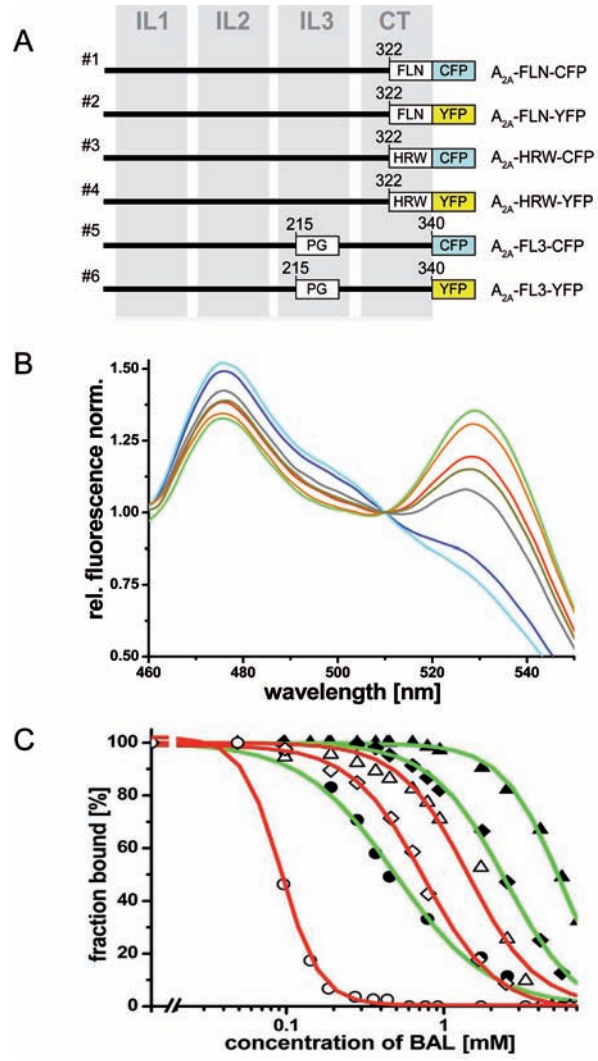


Figure 1. Characterization of FlAsH and ReAsH binding motifs in A2A-adenosine receptors. (A) Schematic representation of the different constructs. CFP or YFP were attached C-terminally after the indicated amino acid position. The 12-amino-acid tetracysteine motifs are denoted "FLN"for FLNCCPGCCMEP and "HRW" for HRWCCPGCCKTF. The 6-amino-acid tetracysteine motif CCPGCC is denoted "PG". Additional numbers denote the sites (amino acid number) of motif insertion. IL and CT denote intracellular loops and C-terminus, respectively. (B) Fluorescence emission spectrum of FlAsH-labeled A2A-FL3-CFP (construct #5) and disruption of FRET by increasing concentrations of BAL (0−4 mM), measured with 436 nm excitation. (C) Reduction of ReAsH and FlAsH binding to the different tetracysteine motifs by BAL. Shown is the fraction of the indicated motifs occupied by the respective label (FlAsH green curves, ReAsH red curves) as a function of the BAL concentration used to displace binding. Data are derived from experiments as shown in (B). Symbols denote: open circle, A2A-Fl3-YFP (construct #6), filled circle, A2A-Fl3-CFP (construct #5); open diamond, A2AHRW-YFP (construct #4); filled diamond, A2A-HRW-CFP (construct #3); open triangle, A2A-FLN-YFP (construct #2); filled triangle, A2A-FLN-CFP (construct #1). Data are representative measurements of three independent experiments. IC_{50} values are given in Supporting Information Table 1.

Selective Labeling in Intact Cells. In order to develop a double labeling protocol, we used two proteins, localized in two different cellular compartments in resting cells, that display a well-described, agonist dependent interaction: the cell surface parathyroid hormone receptor (PTH receptor, a G-protein coupled receptor) and its cytosolic binding protein β-arrestin2 (*23*). The motif with the highest affinity, FLNCCPGCCMEP, was inserted into the C-terminus of the PTH receptor, and the motif with the lowest affinity, CCPGCC, was fused to the

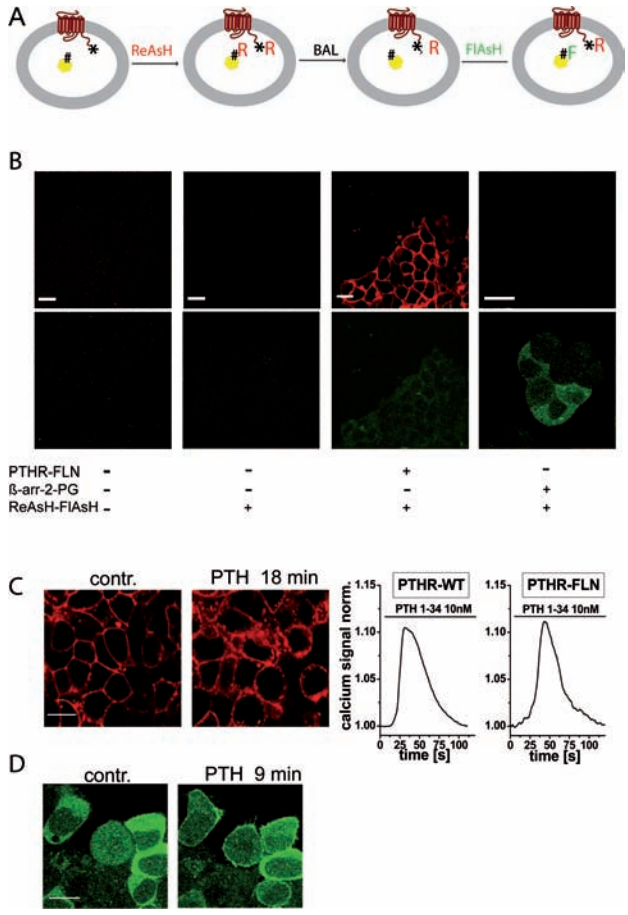


Figure 2. Specific labeling of the PTH receptor and β-arrestin2 in intact cells with ReAsH and FlAsH. (A) Schematic representation of the labeling protocol. Initially, the FLNCCPGCCMEP motif in the PTH receptor (*) as well as the CCPGCC motif in β-arrestin2 (#) were both covalently labeled with ReAsH (R). In a washing step with BAL, ReAsH was selectively removed from the CCPGCC motif in β-arrestin2. Finally, the latter motif was again labeled with FlAsH (F). (B) Specificity and completeness of labeling. The upper row of panels shows the ReAsH emission (594 nm laser line excitation, 600−700 nm emission); the lower row shows the FlAsH fluorescence (514 nm laser line excitation, 520−560 nm emission). The panels (from left to right) show nontransfected HEK cells before (left) and after (second from left) the labeling protocol (as depicted in (A)), HEK cells expressing only the PTH receptor construct (second from right) or the β-arrestin2 construct (both labeled as depicted in (A)). (C) Functional integrity of the ReAsH labeled PTH receptor. The left panels show receptor internalization in HEK cells in response to PTH (1 μM, 18 min; right) compared to unstimulated controls (left). The right panels show Ca^{2+}-responses to PTH (measured with Fura-2) in HEK cells transiently expressing wild-type or FLNCCPGCCMEP labeled receptors. (D) Functional integrity of FlAsH-labeled β-arrestin2. HEK cells transiently expressing unlabeled PTH receptors and FlAsH-labeled β-arrestin2 were stimulated with PTH (1 μM, 9 min; right) to induce translocation of β arrestin2 to the plasma membrane. White scale bars represent 10 μm.

C-terminus of β-arrestin2. HEK cells expressing both constructs were sequentially labeled with FlAsH and ReAsH with various protocols, resulting in the following optimal procedure (Figure 2A; see Experimental Procedures for further details). First, cells were incubated with 2.5 μM ReAsH for 1 h and then washed with 250 μM BAL for 10 min. This BAL concentration left >95% of FLNCCPGCCMEP motif in the PTH receptor bound with ReAsH, while almost all ReAsH was removed from the CCPGCC motif in β-arrestin2 (compare open circles and open triangles in Figure 1C). Subsequently, cells were incubated for another hour with 250 nM FlAsH, which allowed full labeling of the CCPGCC motif, while the FLNCCPGCCMEP motif remained "protected" by the already bound ReAsH. Finally, cells were subjected to a washing procedure using 250 μM 1,2-ethane dithiol (EDT) to reduce nonspecific labeling.

The specificity of this labeling protocol was ascertained in various control experiments (Figure 2B). First, we showed that background labeling, i.e., when no tetracysteine containing proteins were transfected, was negligible (Figure 2B, second from left), and in fact, fluorescence in both channels was not much different from totally unlabeled cells (Figure 2B, left). Furthermore, we confirmed that the two labels were bound to the correct sites, i.e., that indeed ReAsH already bound to the FLNCCPGCCMEP motif would protect this motif from subsequent labeling with FlAsH. To do so, we transfected HEK cells with the PTH receptor-FLNCCPGCCMEP construct alone and subjected these cells to the labeling protocol. Figure 2B (second from right) shows that indeed this resulted in clear cell surface staining with ReAsH, but essentially no labeling with FlAsH. This illustrates that despite its higher affinity FlAsH does not displace ReAsH from the FLNCCPGCCMEP motif and confirms the site specificity of the labeling procedure. Conversely, when HEK cells were transfected with the β-arrestin-2-CCPGCC construct alone and then labeled, this resulted in clear labeling of the cytosolic β-arrestin-2 with FlAsH but essentially no labeling with ReAsH (Figure 2B, right). Protein synthesis ongoing during the labeling process did not appear to cause a significant resynthesis of the first labeling motifs, as evidenced by very low background staining (Figure 2B, second from left), low FlAsH binding to receptors nearing the ReAsH motif (Figure 2B, second from right) and a lack of improvement when the labeling was done in the presence of the protein synthesis inhibitor cycloheximide (not shown). Taken together, these data indicate both negligible background staining and highly specific, orthogonal labeling of the two tetracysteine motifs with FlAsH or ReAsH, respectively.

The functional integrity of the labeled proteins after this labeling procedure was verified along several lines. First, the ReAsH-labeled PTH receptors were localized at the cell surface and internalized in response to stimulation with PTH (Figure 2C), indicating an intact activation switch and internalization process of the receptor construct. Second, the ReAsH-labeled receptors generated intracellular Ca^{2+} signals that were not different from the signals mediated by wild-type receptors (Figure 2C**)**, indicating intact coupling to G-proteins and downstream signaling. Finally, FlAsH-labeled β-arrestin2 translocated from the cytosol to the cell surface in response to stimulation of the PTH receptor (Figure 2D**)**, indicating an intact interaction between the two proteins and normal β-arrestin2 behavior (*23*).

Co-Localization and FRET Measurements. A number of experiments were then carried out to assess whether this site-specific labeling protocol allowed the study of protein colocalization and protein−protein interactions, using again the PTH receptor/β-arrestin2 interaction as a model. HEK cells, expressing PTH receptor-LNCCPGCCMEP and β-arrestin2-CCPGCC, were labeled as above. Analysis by confocal microscopy with the appropriate wavelengths showed the ReAsH-labeled receptors at the cell surface and the FlAsH-labeled β-arrestin2 in the cytosol. Stimulation of the cells with PTH caused translocation of β-arrestin to the cell surface, and this was visualized by an overlay of the ReAsH and FlAsH emissions (Figure 3A).

Scanning of such cells expressing the two labeled proteins allowed a quantification of the ReAsH label at the cell surface and of the cytosolic (control) vs cell surface (PTH-stimulated) localization of β-arrestin2 (Figure 3B). While the PTH receptors were primarily localized to the cell surface under both conditions, β-arrestin2 was evenly distributed throughout the cell under control conditions, but showed a preferential localization

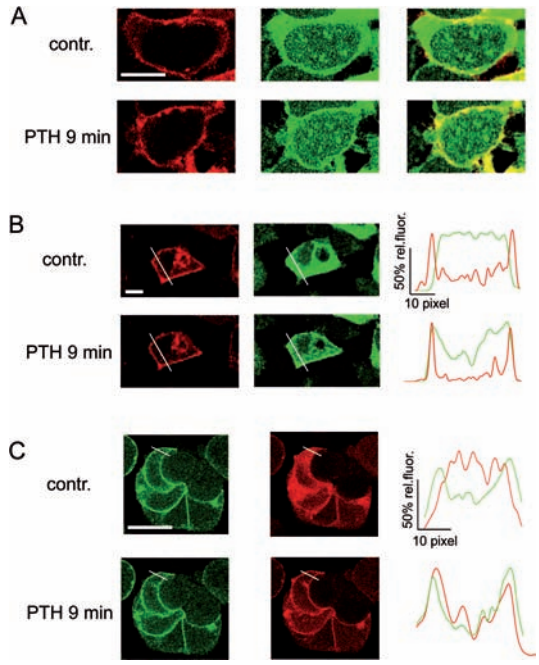


Figure 3. Interaction of ReAsH-labeled PTH receptors with FlAsH-labeled β-arrestin2 in HEK cells. (A) PTH-induced colocalization of receptors and β-arrestin2 at the plasma membrane. HEK cells expressing both ReAsH-labeled PTH receptors (FLNCCPGCCMEP motif) and FlAsH-labeled β-arrestin2 (CCPGCC motif) are shown prior to stimulation (top) or 9 min after stimulation with PTH (1 μM, bottom). Shown are the images of ReAsH emission (left), FlAsH emission (center), and the corresponding overlay images. The yellow color in the overlay images indicates co-localization of FlAsH and ReAsH labeled proteins. (B) PTH-induced translocation of β-arrestin2 to the plasma membrane represented by relative distribution of fluorescence intensity. FlAsH or ReAsH emission coming from labeled β-arrestin2 or labeled PTH receptor was quantified along the indicated white line before (top right) and after (bottom right) stimulation of the cells with PTH as in (A). The relative fluorescence intensity traces indicate a uniform distribution of FlAsH under control conditions and clear plasma membrane preponderance after receptor stimulation. (C) Same experiment as in (B), but with β-arrestin2 equipped with the FLNCCPGCCMEP motif and labeled with ReAsH, and the PTH receptor with the lower-affinity CCPGCC motif labeled with FlAsH. PTH-induced translocation of β-arrestin2 to the plasma membrane represented by confocal images (left) and relative distribution of fluorescence intensity (right). The relative fluorescence intensity traces indicate a uniform distribution of ReAsH under control conditions, and clear cell surface preponderance after receptor stimulation.

at the cell surface after stimulation with PTH. These experiments document that ReAsH and FlAsH can be used for selective labeling of specific proteins and to visualize their intracelluar (co)localization.

To demonstrate the versatility of our technique, we exchanged the tetracysteine tags, i.e., β-arrestin2 was equipped with the FLNCCPGCCMEP sequence (ReAsH motif), and the PTH receptor with the lower affinity CCPGCC sequence (FlAsH motif). Labeling was done as before and resulted in clear cytosolic ReAsH-labeling of β-arrestin2 and cell surface labeling of the PTH receptor with FlAsH (Figure 3C). The ReAsH-labeled β-arrestin2 again translocated to the cell surface upon receptor stimulation as visualized by confocal imaging (Figure 3C, left) and fluorescence quantification (Figure 3C, right).

To show that FRET can be measured between FlAsH and ReAsH, we first studied intramolecular FRET and labeled again an A_{2A}-adenosine receptor (as in Figure 1), carrying a CCPGCC sequence (FlAsH motif) in the third intracellular loop, and a FLNCCPGCCMEP sequence at the C-terminus, which was labeled at both sites as before. Partial acceptor photobleaching (550 nm, 500 s) caused an increase of donor fluorescence by almost 10%, indicative of FRET (Supporting Information Figure 2). Ratiometric quantification of agonist-induced changes in FRET was then used to study the dynamics of the interaction between β-arrestin2 and PTH receptors and to show that direct protein−protein interactions were the basis for their colocalization in cells stimulated with PTH (Figure 4). HEK cells transfected and labeled as in Figure 3A were excited at the appropriate wavelength for FlAsH (500 nm) and observed under wide-field conditions equipped to simultaneously image emission of FlAsH (535/30 nm) and ReAsH (595/70 nm). Addition of the agonist PTH caused a decrease of the FlAsH fluorescence, while the ReAsH fluorescence increased in a reciprocal manner with the same time course (Figure 4, left). As a consequence, the FRET ratio increased (Figure 4, right) and the time course of this increase corresponded to the previously described kinetics of the PTH receptor/β-arrestin2 interaction (*23, 24*). This behavior is indicative of the progressive development of FRET and illustrates that site-selective labeling with ReAsH and FlAsH can be used for specific FRET measurements.

DISCUSSION

Labeling of intracellular proteins with GFP and other fluorescent proteins variants has become an extremely popular tool in fluorescence microscopy. However, the limitations mentioned above have prompted a search for alternatives, most

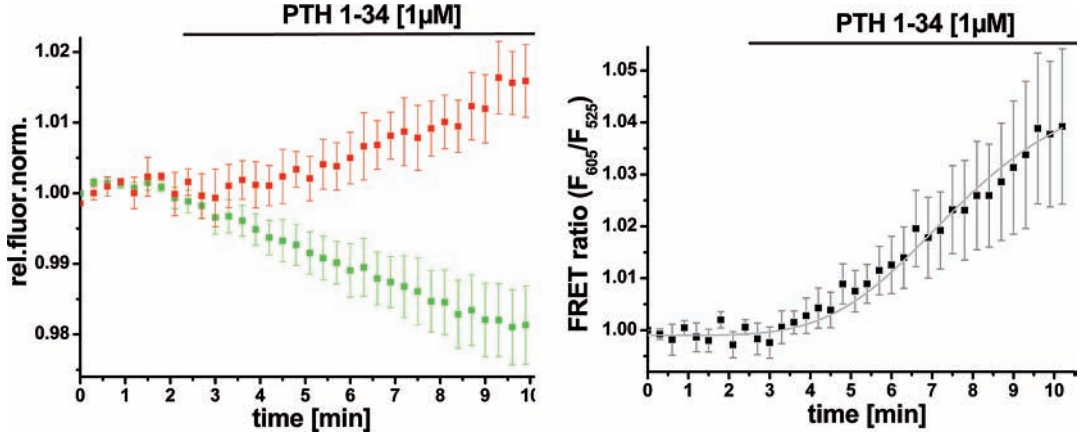


Figure 4. FRET between ReAsH-labeled PTH receptors (FLNCCPGCCMEP motif) and FlAsH-labeled β-arrestin2 (CCPGCC motif) in HEK cells. Exposure to PTH (1 μM) causes a decrease in FlAsH emission and a simultaneous increase in ReAsH emission (left), resulting in an increase in the emission ratio (595 nm/535 nm), which is indicative for FRET (right). Every time point shows the mean of five independent measurements and the SEM.

notably smaller labels, an issue that appears particularly important when labeling small and/or multifunctional proteins (*25, 26*). To achieve labeling of intracellular proteins with small labels in intact cells, the technique of tetracysteine motif labeling with FlAsH (or ReAsH) appears at present the most attractive approach, due to the small size of the labels (~0.7 kDa). An additional, and particularly useful property of these dyes is that they become fluorescent only when bound to these tetracysteine motifs (*2, 15*). Analogues with brighter fluorescence have also been synthesized (*27, 28*) and will add to the attractiveness of this technology. Applied to GPCRs, FlAsH-labels have not only been used to report agonist-induced conformational changes of receptors (*3, 29*), but also to pick up differences in agonist-induced changes in different positions of the third intracellular loop (*30*), illustrating the versatility of this label and the usefulness of its small size and the fixed binding to its recognition sequence.

In FRET studies using FlAsH, usually CFP (or a similar variant) is employed as the second label. Attempts to measure FRET between FlAsH and ReAsH have been reported, but they were based on nonselective, i.e., random labeling of tetracysteine motifs by the two labels (*20*). Such random labeling does not permit the identification of different proteins by specific labels; furthermore, it reduces the signal/noise ratio and complicates the molecular interpretation of FRET changes. With an isolated protein in vitro, Wilkins et al. (*31*) have recently achieved site-specific labeling with FlAsH using protection of sites with photocaged amino acids, but this approach has so far been used only with in vitro translated proteins and a single label.

To overcome these problems, we have developed here a sequential labeling procedure that results in site-specific, orthogonal labeling of two different tetracysteine motifs in intact cells. Applying this procedure to a cell surface GPCR and its cytosolic binding protein, β-arrestin2, we observed that the labeled proteins retained essential functions. Furthermore, we showed that the labeling was clearly site-specific, as evidenced by the cell surface vs cytosolic localization of the two labels and their distinct movements upon receptor stimulation. Finally, the specific labeling permitted the demonstration of the agonist-dependent interaction of the two proteins by co-localization and by FRET between the labels; the kinetics of this translocation and interaction agree with the well-known time course, which occurs over several minutes (*24, 32*).

The labeling procedure resulted in virtually no background labeling, but essentially complete labeling of the two sites, as evidenced by our inability to label the "ReAsH-site" with FlAsH after the ReAsH labeling step (see Figure 2B). The specificity and wide applicability of this method should also make the development of FlAsH analogues with improved fluorescent properties an attractive goal, to achieve wider variability of colors and combinations of different fluorophores. Our data suggest that with this method specific labeling of intracellular proteins may be generally achievable and may permit the study of intracellular proteins with minimal disturbance of their function.

ACKNOWLEDGMENT

We thank Moritz Bünemann, Kristina Lorenz, Joachim Schmitt, and Gregory Harms for helpful discussions and Nicole Ziegler for expert technical assistance. This work was funded by the Deutsche Forschungsgemeinschaft (SFB487 TPA1; to MJL and CH) and the European Research Council (Advanced Investigator Grant to MJL).

Supporting Information Available: Table 1 reflectsBAL concentrations that were needed to reduce binding of FlAsH or ReAsH to the indicated tetracystein motif by 50%. Figure 1 shows fluorescence excitation and emission spectra of YFP and ReAsH. Figure 2 shows photobleaching of a FlAsH and ReAsH labeled A_{2A}-PG3-FLN33 construct. This material is available free of charge via the Internet at http://pubs.acs.org.

LITERATURE CITED

(1) Tsien, R. Y. (1998) The green fluorescent protein. *Annu. Rev. Biochem. 67*, 509–44.

(2) Shaner, N. C., Steinbach, P. A., and Tsien, R. Y. (2005) A guide to choosing fluorescent proteins. *Nat. Methods 2*, 905–909.

(3) Hoffmann, C., Gaietta, G., Bünemann, M., Adams, S. R., Oberdorff-Maass, S., Behr, B., Vilardaga, J. P., Tsien, R. Y., Ellisman, M. H., and Lohse, M. J. (2005) A FlAsH-based FRET approach to determine G protein-coupled receptor activation in living cells. *Nat. Methods 2*, 171–176.

(4) Lisenbee, C. S., Karnik, S. K., and Trelease, R. N. (2003) Overexpression and mislocalization of a tail-anchored GFP redefines the identity of peroxisomal ER. *Traffic 4*, 491–501.

(5) Andresen, M., Schmitz-Salue, R., and Jakobs, S. (2004) Short tetracysteine tags to beta-tubulin demonstrate the significance of small labels for live cell imaging. *Mol. Biol. Cell 15*, 5616–22.

(6) Gautier, A., Juillerat, A., Heinis, C., Correa, I. R., Jr., Kindermann, M., Beaufils, F., and Johnsson, K. (2008) An engineered protein tag for multiprotein labeling in living cells. *Chem. Biol. 15*, 128–36.

(7) Gronemeyer, T., Chidley, C., Juillerat, A., Heinis, C., and Johnsson, K. (2006) Directed evolution of O6-alkylguanine-DNA alkyltransferase for applications in protein labeling. *Protein Eng. Des. Sel. 19*, 309–16.

(8) Keppler, A., Pick, H., Arrivoli, C., Vogel, H., and Johnsson, K. (2004) Labeling of fusion proteins with synthetic fluorophores in live cells. *Proc. Natl. Acad. Sci. U.S.A. 101*, 9955–9.

(9) Maurel, D., Comps-Agrar, L., Brock, C., Rives, M. L., Bourrier, E., Ayoub, M. A., Bazin, H., Tinel, N., Durroux, T., Prezeau, L., Trinquet, E., and Pin, J. P. (2008) Cell-surface protein-protein interaction analysis with time-resolved FRET and snap-tag technologies: application to GPCR oligomerization. *Nat. Methods 5*, 561–7.

(10) Miller, L. W., Cai, Y., Sheetz, M. P., and Cornish, V. W. (2005) In vivo protein labeling with trimethoprim conjugates: a flexible chemical tag. *Nat. Methods 2*, 255–7.

(11) Los, G. V., and Wood, K. (2007) The HaloTag: a novel technology for cell imaging and protein analysis. *Methods Mol. Biol. 356*, 195–208.

(12) Kapanidis, A. N., Ebright, Y. W., and Ebright, R. H. (2001) Site-specific incorporation of fluorescent probes into protein: hexahistidine-tag-mediated fluorescent labeling with $(Ni^{(2+)})$:nitrilotriacetic Acid (n)-fluorochrome conjugates. *J. Am. Chem. Soc. 123*, 12123–5.

(13) Guignet, E. G., Hovius, R., and Vogel, H. (2004) Reversible site-selective labeling of membrane proteins in live cells. *Nat. Biotechnol. 22*, 440–4.

(14) Soh, N. (2008) Selective chemical labeling of proteins with small fluorescent molecules based on metal-chelation Methodology. *Sensors 8* (2), 1004–102.

(15) Griffin, B. A., Adams, S. R., and Tsien, R. Y. (1998) Specific covalent labeling of recombinant protein molecules inside live cells. *Science 281*, 269–72.

(16) Adams, S. R., Campbell, R. E., Gross, L. A., Martin, B. R., Walkup, G. K., Yao, Y., Llopis, J., and Tsien, R. Y. (2002) New biarsenical ligands and tetracysteine motifs for protein labeling in vitro and in vivo: synthesis and biological applications. *J. Am. Chem. Soc. 124*, 6063–76.

(17) Nikolaev, V. O., Hoffmann, C., Bunemann, M., Lohse, M. J., and Vilardaga, J. P. (2006) Molecular basis of partial agonism at the neurotransmitter α_{2A}-adrenergic receptor and G_i-protein heterotrimer. *J. Biol. Chem. 281*, 24506–11.

(18) Jost, C. A., Reither, G., Hoffmann, C., and Schultz, C. (2008) Contribution of fluorophores to protein kinase C FRET probe performance. *ChemBioChem 9*, 1379–84.

(19) Robia, S. L., Campbell, K. S., Kelly, E. M., Hou, Z., Winters, D. L., and Thomas, D. D. (2007) Forster transfer recovery reveals that phospholamban exchanges slowly from pentamers but rapidly from the SERCA regulatory complex. *Circ. Res. 101*, 1123–9.

(20) Roberti, M. J., Bertoncini, C. W., Klement, R., Jares-Erijman, E. A., and Jovin, T. M. (2007) Fluorescence imaging of amyloid formation in living cells by a functional, tetracysteine-tagged alpha-synuclein. *Nat. Methods 4*, 345–51.

(21) Chen, B., Cao, H., Yan, P., Mayer, M. U., and Squier, T. C. (2007) Identification of an orthogonal peptide binding motif for biarsenical multiuse affinity probes. *Bioconjugate Chem. 18*, 1259–65.

(22) Martin, B. R., Giepmans, B. N., Adams, S. R., and Tsien, R. Y. (2005) Mammalian cell-based optimization of the biarsenical-binding tetracysteine motif for improved fluorescence and affinity. *Nat. Biotechnol. 23*, 1308–1314.

(23) Vilardaga, J. P., Frank, M., Krasel, C., Dees, C., Nissenson, R. A., and Lohse, M. J. (2001) Differential conformational requirements for activation of G proteins and the regulatory proteins arrestin and G protein-coupled receptor kinase in the G protein-coupled receptor for parathyroid hormone (PTH)/PTH-related protein. *J. Biol. Chem. 276*, 33435–43.

(24) Vilardaga, J. P., Bünemann, M., Krasel, C., Castro, M., and Lohse, M. J. (2003) Measurement of the millisecond activation switch of G protein-coupled receptors in living cells. *Nat. Biotechnol. 21*, 807–12.

(25) Robia, S. L., Flohr, N. C., and Thomas, D. D. (2005) Phospholamban pentamer quaternary conformation determined by in-gel fluorescence anisotropy. *Biochemistry 44*, 4302–11.

(26) Marks, K. M., and Nolan, G. P. (2006) Chemical labeling strategies for cell biology. *Nat. Methods 3*, 591–6.

(27) Cao, H., Xiong, Y., Wang, T., Chen, B., Squier, T. C., and Mayer, M. U. (2007) A red cy3-based biarsenical fluorescent probe targeted to a complementary binding peptide. *J. Am. Chem. Soc. 129*, 8672–3.

(28) Spagnuolo, C. C., Vermeij, R. J., and Jares-Erijman, E. A. (2006) Improved photostable FRET-competent biarsenical-tetracysteine probes based on fluorinated fluoresceins. *J. Am. Chem. Soc. 128*, 12040–1.

(29) Vilardaga, J. P., Nikolaev, V. O., Lorenz, K., Ferrandon, S., Zhuang, Z., and Lohse, M. J. (2008) Conformational cross-talk between α_{2A}-adrenergic and μ-opioid receptors controls cell signaling. *Nat. Chem. Biol. 4*, 126–31.

(30) Zürn, A., Zabel, U., Vilardaga, J. P., Schindelin, H., Lohse, M. J., and Hoffmann, C. (2009) Fluorescence resonance energy transfer analysis of α_{2A} -adrenergic receptor activation reveals distinct agonist-specific conformational changes. *Mol. Pharmacol. 75*, 534–41.

(31) Wilkins, B. J., Yang, X., and Cropp, T. A. (2009) Photochemical control of FlAsH labeling of proteins. *Bioorg. Med. Chem. Lett. 19*, 4296–8.

(32) Krasel, C., Bunemann, M., Lorenz, K., and Lohse, M. J. (2005) β-Arrestin binding to the β_2-adrenergic receptor requires both receptor phosphorylation and receptor activation. *J. Biol. Chem. 280*, 9528–35.

BC900394J

Exchange Kinetics of Protein-Functionalized Micelles and Liposomes Studied by Förster Resonance Energy Transfer

Sanne W. A. Reulen and Maarten Merkx*

Laboratory of Chemical Biology, Department of Biomedical Engineering, Eindhoven University of Technology, P.O. Box 513, 5600 MB Eindhoven, The Netherlands. Received September 13, 2009; Revised Manuscript Received April 2, 2010

Protein-functionalized micelles and liposomes are attractive delivery systems for applications ranging from targeted drug delivery to molecular imaging. In particular, systems that use pegylated phospholipids have become popular, but little is known about the stability of these lipid-functionalized proteins toward exchange. In this study, Förster resonance energy transfer (FRET) between the fluorescent proteins ECFP and EYFP was used to investigate the lipid exchange behavior of protein-functionalized liposomes and micelles. Native chemical ligation was used as an efficient method to site-specifically couple varying amounts of proteins to pegylated phospholipids. No exchange was observed between protein-functionalized phospholipids in sterically stabilized liposomes. In micelles, however, protein-functionalized lipids were found to exchange with a half-time of exchange ranging from almost 2 h at room temperature to 4 min at 37 °C. These pegylated micelles remained intact at lipid concentrations down to 0.15 μM, indicating that they are even more stable than previously assumed. The results obtained in this study provide a useful frame of reference for assessing the potential role of protein exchange in biomedical applications of these lipid-based nanoparticles.

INTRODUCTION

Lipid-based nanoparticles such as micelles and liposomes are attractive delivery systems in a variety of biomedical applications including targeted drug delivery and molecular imaging (*1, 2*). An important development in this area has been the use of poly(ethylene glycol) (PEG) modified phospholipids. Incorporation of PEG-modified phospholipids in liposomes was shown to improve their biodistribution and half-time of circulation (*3*), most likely because the PEG shell prevents adsorption of proteins and cells. Pegylated phospholipids are also known to form relatively stable and well-defined micelles, allowing applications ranging from targeted delivery of hydrophobic drugs to their use as relatively small, macromolecular MRI contrast agents (*4*−*6*). Active targeting of micelles and liposomes has been accomplished by coupling targeting ligands such as proteins (*4, 7, 8*), peptides (*9, 10*), and carbohydrates (*11*−*13*) to the end of the PEG-chain, ensuring good accessibility of the targeting ligand. Typically, peptides and proteins are coupled to pegylated phospholipids by reaction of lysine or cysteine side chains to active esters or maleimide functionalities. However, the limited control of these classical bioconjugation reactions often yields heterogeneous conjugates and sometimes leads to protein inactivation.

An important property of protein-functionalized micelles and liposomes that has received little attention is their stability toward exchange of lipidated proteins. Successful therapeutic application of liposomes and micelles requires that the protein-functionalized phospholipids remain associated with the nanoparticle within the time frame of the experiment. While exchange of lipidated proteins has been studied previously for vesicles and other biologically relevant bilayer systems (*14*−*16*), such studies have not been reported for protein-functionalized micelles or sterically stabilized liposomes. Work by Silvius et al. showed that derivatization of phospholipids with PEG chains or protein domains can substantially enhance phospholipid transfer rates between egg phosphatidyl choline vesicles (*14*). However, phospholipid exchange was found to be much slower in the liposome preparations that are typically used for molecular imaging applications, which are stabilized by the incorporation of PEG-modified phospholipids and high concentrations of cholesterol (>30%). Exchange rates were also found to be highly dependent on the acyl chain length, with Li and co-workers reporting essentially no exchange for PEG2000-DSPE (*17*). The latter study used biotinylated PEG2000-DSPE, however, and the effect of protein conjugation was not taken into account. Desorption rates of pegylated phospholipids in PEG2000-DSPE micelles have recently been shown to be highly temperature dependent, with half-lives ranging from several days at 5 °C to less than 1 h at 30 °C (*6*).

We and others have recently explored the use of native chemical ligation (NCL) as an attractive chemoselective conjugation reaction to couple proteins site-specifically via their C-terminus to supported lipid bilayers, micelles, and liposomes (*18*−*20*). In this study, we applied Förster resonance energy transfer (FRET) between donor and acceptor fluorescent proteins (ECFP and EYFP, respectively) as a tool to study protein exchange in protein-functionalized micelles and liposomes. Micelles and liposomes with high and tunable protein/particle ratios were obtained by NCL of fluorescent proteins to cysteine-functionalized PEG2000-distearoylphosphatidyl-ethanolamine (DSPE) phospholipids (Figure 1a). The availability of these well-defined protein-functionalized micelles and liposomes allowed an in-depth characterization of the exchange kinetics of lipidated proteins under a variety of conditions (Figure 1b). Micelles containing a 1:1 ratio of ECFP and EYFP also provided an opportunity to investigate structural properties of micelles such as aggregation number and stability (Figure 1c,d).

EXPERIMENTAL PROCEDURES

General. Unless stated otherwise, all reagents and chemicals were obtained from commercial sources and used without further purification. 1,2-Dipalmitoyl-*sn*-glycero-3-phosphoethanolamine-

* Corresponding author. Maarten Merkx, Laboratory of Chemical Biology, Department of Biomedical Engineering, Eindhoven University of Technology, P.O. Box 513, 5600 MB Eindhoven, The Netherlands. E-mail: m.merkx@tue.nl. Fax: (+31) 40-245-1036; Tel: (+31) 40-247-4728.

10.1021/bc900398p © 2010 American Chemical Society
Published on Web 04/16/2010

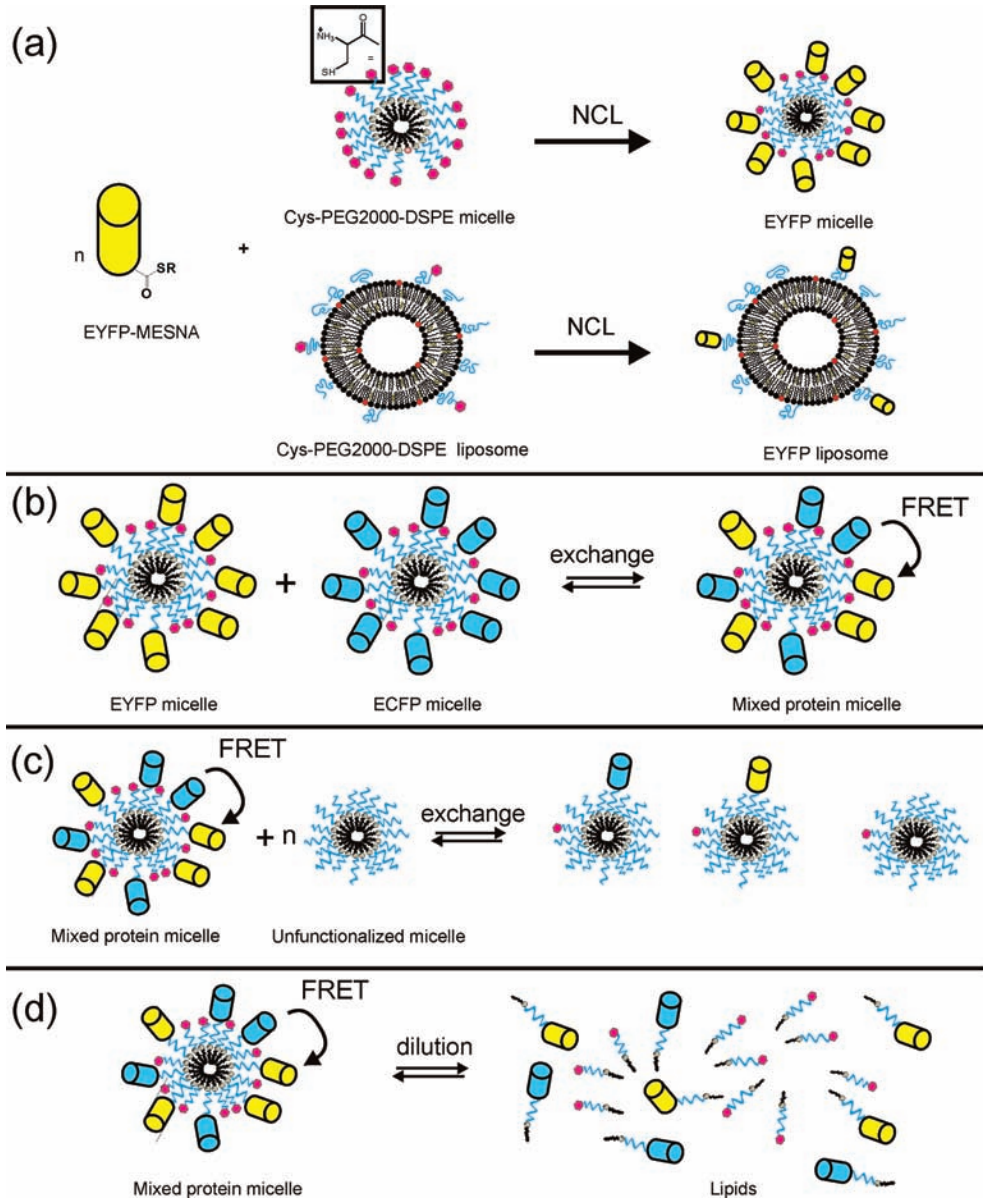


Figure 1. Förster resonance energy transfer (FRET) between donor (ECFP) and acceptor (EYFP) fluorescent domains allows characterization of protein transfer kinetics and various other structural aspects of protein functionalized micelles and liposomes. (a) Preparation of fluorescent protein micelles and liposomes by native chemical ligation of fluorescent proteins with a C-terminal MESNA-thioester to cysteine-functionalized micelles and liposomes. (b) The kinetics of lipidated protein exchange can be studied by monitoring the increase in FRET upon mixing ECFP- and EYFP micelles or liposomes. (c) Dilution of mixed ECFP-EYFP micelles with increasing amounts of nonfunctionalized pegylated phospholipids informs about the average aggregation number. (d) Determination of critical micelle concentration by stepwise dilution of mixed ECFP-EYFP-micelles in buffer.

N-(Lissamine rhodamine B sulfonyl) (rhodamine-DPPE), 1,2-dipalmitoyl-*sn*-glycero-3-phosphoethanolamine-*N*-(7-nitro-2-1,3-benzoxadiazol-4-yl) (NBD-DPPE), and 1,2-distearoyl-*sn*-glycero-3-phosphoethanolamine-*N*-[methoxy(poly(ethylene glycol))-2000] (PEG2000-DSPE) were purchased from Avanti Polar Lipids. Cysteine-functionalized 1,2-distearoyl-*sn*-glycero-3-phosphoethanolamine-*N*-[amino(poly(ethylene glycol))2000] (Cys-PEG2000-DSPE) was synthesized as described previously (*19*). 4-(Carboxylmethyl) thiophenol (MPAA), Tris(2-carboxyethyl) phosphine hydrochloride (TCEP), and sodium 2-mercaptoethanesulfonate (MESNA) were purchased from Sigma.

Protein Expression and Purification. ECFP and EYFP with a C-terminal thioester were expressed using the IMPACT system (New England Biolabs) as previously described (*21*). Briefly, proteins were expressed in *E. coli BL21* (DE3) cells using IPTG induction. After protein expression, the cell pellet was harvested and proteins were extracted using the BugBuster protocol (Novagen). The proteins were obtained with C-terminal MESNA thioester using chitin affinity chromatography, followed by MESNA-induced cleavage of the protein−intein bond. The concentrations of ECFP with a C-terminal MESNA thioester (ECFP-MESNA) and EYFP with a C-terminal MESNA thioester (EYFP-MESNA) were determined by UV−vis using $\varepsilon_{434\ nm} = 29\,000\ M^{-1}\ cm^{-1}$ (*22*) and $\varepsilon_{514\ nm} = 84\,000\ M^{-1}\ cm^{-1}$ (*23*), respectively.

Cysteine−Liposome Preparation. Liposomes were prepared by lipid film hydration as described previously (*19*). A mixture of DSPC (37 μmol), Gd-DTPA-bis(stearylamide) (25 μmol), cholesterol (33 μmol), PEG2000-DSPE (2.5 μmol), and Cys-PEG2000-DSPE (2.5 μmol) was dissolved in $CHCl_3$/MeOH 4:1 (v/v) and concentrated under reduced pressure at room temperature. The obtained lipid film was hydrated in 2.5 mL HBS (10 mM HEPES, 135 mM NaCl, pH 7.4). This dispersion was extruded five times at 65 °C through 200 nm polycarbonate

membrane filters. Cysteine−liposomes were stored at 4 °C before further modification.

Synthesis of Protein-Functionalized Liposomes. Native chemical ligation of EYFP-MESNA (97 μM) to cysteine−liposomes (581 μM Cys-PEG2000-DSPE) was done for 24 h at 20 °C in HBS containing 50 mM MPAA and 10 mM TCEP and pH of 6.2. Similar conditions were used to ligate ECFP-MESNA (103 μM) to cysteine−liposomes (620 μM Cys-PEG2000-DSPE). The amount of lipidated protein was determined from SDS-PAGE analysis by integration of the bands of unreacted and lipidated protein. The liposome concentration was calculated from the lipid concentration that was determined via phosphate analysis, using the assumption of unilamellar liposomes and a lipid surface area of 0.6 nm^2 (*24, 25*). The number of proteins per liposome was then obtained by dividing the concentration of lipidated protein by the liposome concentration. The protein-functionalized liposomes were separated from nonreacted protein by ultracentrifugation for 1 h at 270 000 *g* and 20 °C using a Kontron Centrikon T-2060 ultracentrifuge with a TFT 70.38 rotor. The liposomal pellet was resuspended in HBS pH 7.4, and pellet and supernatant were analyzed using SDS-PAGE to confirm the separation between lipidated and unreacted protein. Protein-functionalized liposomes were stored at 4 °C.

Synthesis of Protein-Functionalized Micelles. 0.3 μmol Cys-PEG2000-DSPE was dissolved in chloroform and placed in a glass vial. After chloroform evaporation, the obtained lipid film was rehydrated in 0.1 M sodium phosphate pH 8.5 with 50 mM MPAA and 10 mM TCEP, vortexed for 2 min, followed by 5 min sonication. ECFP-MESNA and EYFP-MESNA were added in varying amounts depending on the required protein load per micelle and the pH was adjusted to ∼6.5 with 1 M sodium phosphate pH 9.2. After overnight incubation at room temperature, the protein micelles were analyzed using SDS-PAGE to check for complete conversion to the lipidated protein. Upon complete conversion, the average amount of proteins per micelle was calculated by simply dividing the protein concentration over the micelle concentration. The latter was calculated from the total amount of lipids and the previously reported aggregation number of 90 lipids per micelle. Protein-functionalized micelles were stored at 4 °C.

Preparation of NBD and Rhodamine-Containing Micelles. 0.9 μmol of Cys-PEG2000-DSPE and 0.02 μmol NBD-DPPE or 0.02 μmol rhodamine-DPPE in chloroform were placed in a vial. After chloroform evaporation, the obtained lipid film was rehydrated in HBS with 50 mM MPAA and 10 mM TCEP and vortexed for 2 min, followed by 5 min sonication. Micelles were stored at 4 °C.

Fluorescence Spectroscopy. Fluorescence emission spectra were recorded on a Varian Cary Eclipse photoluminescence spectrometer, equipped with a cuvette holder that was temperature controlled by a Peltier element. Liposomes and micelles were diluted separately and prewarmed in cuvettes. The liposomes or micelles were mixed in a 1:1 ratio, and protein−lipid or dye−lipid transfer was monitored by exciting the donor and monitoring the emission of the donor and acceptor for a certain time period. All spectra were corrected for wavelength-dependent efficiency of the instrument. The observed rates of exchange were obtained by fitting the emission ratio as a function of time using eq 1

$$\text{ratio}(t) = (\text{ratio}_{\text{end}} - \text{ratio}_{\text{start}}) \times (1 - \exp^{-kt}) + \text{ratio}_{\text{start}} \quad (1)$$

RESULTS AND DISCUSSION

Protein−Phospholipid Exchange between Liposomes. Liposomes were prepared containing 2.5% Cys-PEG2000-DSPE, 2.5% PEG2000-DSPE, 25% Gd-DTPA-bis(stearylamide), 37% DSPC, and 33% cholesterol by lipid film hydration as described previously (*19*). These sterically stabilized liposomes have previously been thoroughly characterized using both DLS and cryoTEM, showing very stable liposomes with an average diameter of 200 nm (*26*). The liposomes obtained in this manner were subsequently functionalized with thioester-modified ECFP or EYFP using native chemical ligation in the presence of the thiol MPAA (*27*) as a catalyst. After removal of unreacted proteins via ultracentrifugation, protein-functionalized liposomes were obtained containing ∼1300 ECFP/liposome or ∼1000 EYFP/liposome (Supporting Information Figure S1).

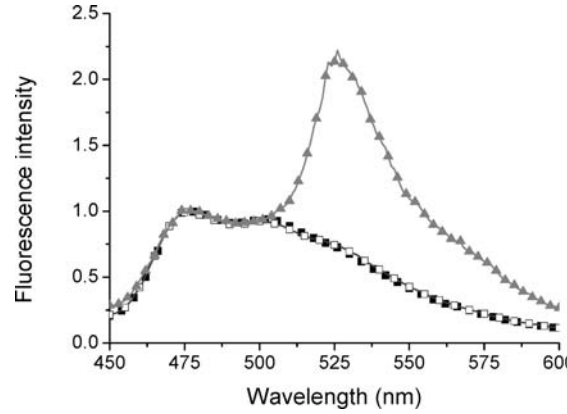


Figure 2. Characterization of protein−phospholipid transfer between ECFP-liposomes and EYFP/liposomes using steady-state fluorescence spectroscopy. All measurements were performed at 37 °C in 10 mM HEPES, 135 mM NaCl, pH 7.4, with a total protein concentration of 2.3 μM ([liposome] = 1.9 nM). Emission spectra were obtained using an excitation wavelength of 420 nm with a slit width of 10 nm, monitoring the emission from 450 to 600 nm with a slit width of 5 nm. The plot with the black squares shows a summation of the emission spectra of ECFP and EYFP liposomes measured before mixing (black squares). The spectrum labeled with open squares shows the emission spectrum obtained 23 h after mixing, while the emission spectrum labeled with gray triangles is from liposomes that contained approx 630 copies of ECFP and 630 copies of EYFP per liposome. All spectra were normalized to ECFP emission at 475 nm.

ECFP and EYFP liposomes were mixed at a 1:1 ratio, and emission spectra were monitored in time (Figure 2). Even after 24 h of incubation at 37 °C, the emission spectrum remained identical to the summation of the emission spectra of the separate ECFP and EYFP liposomes, consistent with the absence of any protein exchange between the liposomes under these conditions. Experiments at higher temperatures (55 °C) were hampered by the instability of the ECFP domain under these conditions, which prevented reliable measurements over prolonged periods of time. To establish that the surface density of proteins used here was sufficient to allow significant energy transfer between ECFP and EYFP when present on the same liposome, we also prepared liposomes that were reacted with a 1:1 mixture of ECFP- and EYFP-thioester. The emission spectrum of this control liposome, which contained approx 630 copies of ECFP and 630 copies of EYFP, indeed showed an intense EYFP peak at 527 nm when excited at 420 nm, providing clear evidence for energy transfer between ECFP and EYFP (Figure 2). Li et al. previously also did not observe any lipid exchange when monitoring the reaction at 37 °C for up to 25 h for biotinylated PEG2000-DSPE using a more indirect assay in the same type of liposomes (*17*). We thus conclude that in these liposomes protein functionalization does not result in an enhanced exchange of PEG2000-DSPE, at least not under the conditions and the time scale that are relevant for molecular imaging applications.

Protein−phospholipid Exchange between Micelles. Several studies have reported efficient transfer of pegylated phospholids from micelles to liposomes (*17, 28, 29*). In addition, Tirrell and

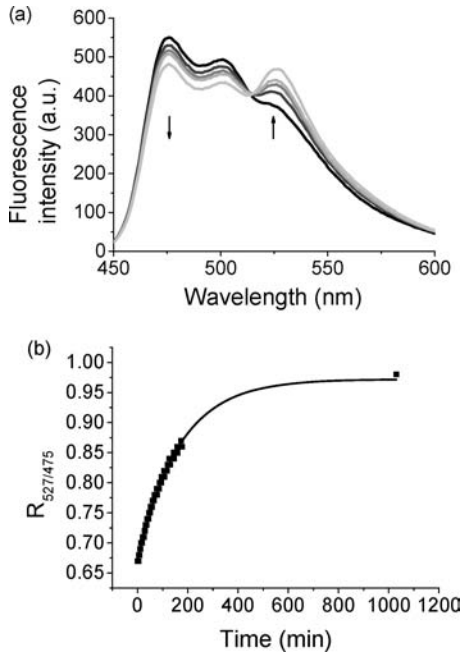


Figure 3. Monitoring protein exchange between ECFP-micelles and EYFP-micelles at 20 °C using steady-state fluorescence spectroscopy. All measurements were performed in HBS pH 7.4 with a protein−lipid concentration of 4.8 μM and a total lipid concentration of 40 μM. Emission spectra were obtained using an excitation wavelength of 420 nm with a slit width of 5 nm. Emission spectra (a) are shown after 0 min (black), 60 min (dark gray), 120 min (medium gray), 178 min (gray), and overnight incubation (light gray). (b) Plot showing the increase in emission ratio R527/475 as a function of time. The solid line represents a fit to eq 1 using a rate constant $k_{obs} = 1.0 \times 10^{-4}$ s^{-1}.

co-workers recently showed a desorption rate of ~3 h^{-1} at 30 °C for PEG2000-DSPE micelles (*6*). However, as far as we know exchange of pegylated phospholipids between micelles has not been studied for protein functionalized systems. Micelles containing an average of 11 copies of EYFP or ECFP were prepared via native chemical ligation with MPAA as the catalyst (*20*). SDS-PAGE analysis showed essentially complete conversion of ECFP and EYFP to their lipidated forms (Supporting Information Figure S2). Structural characterization of these preparations using dynamic light scattering (DLS) showed the presence of well-defined protein micelles with an average diameter of 14 nm and only a very small amount of larger aggregates (Supporting Information Figure S3). These ECFP- and EYFP-functionalized micelles are thus similar to the previously characterized CNA35-micelles, and do not show a higher tendency to form other aggregates (*20*). Protein exchange was observed after mixing the ECFP and EYFP micelles at room temperature as evidenced by the decrease in ECFP emission at 475 nm and the concomitant increase in EYFP emission at 527 nm (Figure 3). However, at 20 °C the exchange is still slow. A fit of the emission ratio as a function of time yielded an observed rate of 1.0×10^{-4} s^{-1}, corresponding to a half-life of almost 2 h at room temperature (Table 1). Since protein micelles are typically used at higher temperatures, we also monitored the exchange reaction at 28 and 37 °C (Figure 4). Protein exchange was strongly dependent on the temperature, showing a half-life of only 4 min at 37 °C. Please note that the final emission ratio that is reached at equilibrium is different at various temperatures, probably reflecting differences in temperature-dependent fluorescent properties of ECFP and EYFP. Exchange experiments were also performed at lower protein functionalization levels to exclude the possibility that interactions between donor and acceptor proteins influenced the exchange kinetics. Similar exchange rates were observed for micelles carrying on average 5 and 2 proteins per micelle (Table 1), suggesting that protein−protein interactions did not affect the rate-limiting step in the exchange reaction. (Supporting Information Figure S4).

To understand the contribution of the protein and the PEG chain on the protein−phospholipid transfer rate, we also studied the exchange of phospholipids that contained nitrobenzoxazole (NBD) and rhodamine as donor and acceptor dyes directly attached to the phosphate ester headgroup. Cys-PEG2000-DSPE micelles were prepared containing either 2.5 mol % of rhodamine-DPPE or NBD-DPPE and exchange was monitored at 37 and 55 °C (Supporting Information Figure S5). At 37 °C, the exchange of the dye-labeled phospholipids was observed to be 50× slower than the exchange of the protein-PEG2000-DSPE conjugates under otherwise similar conditions (Table 1). Very similar exchange rates were observed for micelles containing PEG2000-DSPE lacking the cysteine functionality, thus excluding the possibility that the slow exchange rate was affected by possible disulfide bond formation. Direct comparison of the exchange rates between the dye−lipid system and the protein-PEG2000-lipid system is difficult because the acyl tail in the dye−lipid system is two carbon atoms shorter. Since lipid exchange rates are highly dependent on the acyl length of the lipid tail and exhibit slower transfer rates upon increasing tail lengths (*30*), we expect that the half-time of exchange of dye−DSPE lipids would be even slower. This in turn implies that introduction of protein and PEG chain together enhanced the rate of phospholipid exchange more than 50-fold.

Concentration Dependence of Protein−Phospholipid Transfer between Micelles. Dissociation of amphiphiles from micelles into solution is generally considered to be the rate limiting step in phospholipid exchange (*31*). However, some studies on mixed micelles have found an increase in exchange rates at high micelle concentrations, suggesting a role for micelle collisions in the transfer reaction (*32*). To investigate the role of such collisions on the exchange rate of protein−phospholipid in micelles, additional exchange experiments were performed at higher lipid concentrations. Micelles containing an equimolar amount of ECFP and EYFP were first prepared by mixing ECFP and EYFP micelles at 37 °C until full exchange was reached. Next, a large excess of nonfunctionalized PEG2000-DSPE micelles was added and the transfer of fluorescent proteins was monitored by the decrease in FRET. Figure 5 shows the emission ratio as a function of time after adding PEG2000-DSPE micelles (594 μM PEG2000-DSPE) to the mixed ECFP−EYFP micelles (40 μM Cys-PEG2000-DSPE) at 20 °C, 28 °C, and 37 °C. The exchange rates observed at these high PEG2000-DSPE concentrations are similar to the rates obtained in the initial experiments where the formation of mixed micelles was monitored at 15-fold lower PEG2000-DSPE concentrations (Table 1). This observation shows that collisions between micelles do not play a significant role in protein exchange, rendering dissociation of the protein-PEG2000-DSPE from the micelle the most likely rate-limiting step in the transfer reaction. In addition, the exchange rates observed in this study for ECFP- and EYFP-functionalized Cys-PEG2000-DSPE micelles are similar to the desorption rates reported by Tirrell and co-workers for PEG2000-DSPE micelles at 20 and 28 °C (*6*). This finding thus confirms that desorption of protein-functionalized PEG2000-DSPE is the rate-limiting step in the exchange process and suggests that protein functionalization does not significantly increase exchange rates for these pegylated phospholipids.

Structural Properties of Protein-Functionalized Micelles. Micelles functionalized with ECFP and EYFP not only provide a straightforward manner to study the kinetics of protein exchange, but they also offer an opportunity to probe structural properties of these micelles. The protein−micelle ratios reported

Table 1. Characteristics of the Transfer Process between Micelles Using ECFP and EYFP or Rhodamine and NBD as Probes

mixing process between	[total lipid] (μM)	T (°C)	k_{obs} (s^{-1})[a]	$t_{1/2}$ (min)[b]
ECFP ($n = 11$) + EYFP ($n = 11$) micelles	40	20	$1.0 \times 10^{-4} \pm 1.5 \times 10^{-6}$	115.5
ECFP ($n = 11$) + EYFP ($n = 11$) micelles	40	28	$6.0 \times 10^{-4} \pm 8.1 \times 10^{-6}$	19.3
ECFP ($n = 11$) + EYFP ($n = 11$) micelles	40	37	$2.9 \times 10^{-3} \pm 6.9 \times 10^{-5}$	4.0
ECFP ($n = 5$) + EYFP ($n = 5$) micelles	40	37	$1.7 \times 10^{-3} \pm 5.2 \times 10^{-5}$	6.8
ECFP ($n = 2$) + EYFP ($n = 2$) micelles	40	37	$2.2 \times 10^{-3} \pm 2.6 \times 10^{-4}$	5.3
rhodamine + NBD micelles	40	37	$5.6 \times 10^{-5} \pm 1.3 \times 10^{-6}$	206.3
rhodamine + NBD micelles	40	55	$8.8 \times 10^{-4} \pm 2.1 \times 10^{-5}$	13.1
ECFP-EYFP micel + unfunctionalized micelles	627	20	$1.7 \times 10^{-4} \pm 3.8 \times 10^{-6}$	68.0
ECFP-EYFP micel + unfunctionalized micelles	627	28	$4.7 \times 10^{-4} \pm 2.9 \times 10^{-6}$	24.6
ECFP-EYFP micel + unfunctionalized micelles	627	37	$2.6 \times 10^{-3} \pm 2.6 \times 10^{-5}$	4.5

[a] The observed rate constants (k_{obs}) were calculated using eq 1. [b] The half-times of decay ($t_{1/2}$) were calculated using the relation $\ln 2/k_{obs}$.

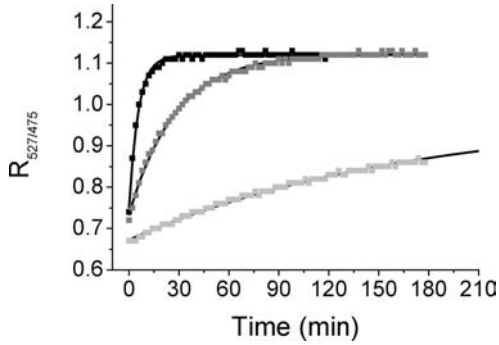


Figure 4. Comparison of protein exchange between ECFP-micelles and EYFP-micelles at 20 °C (light gray), 28 °C (dark gray), and 37 °C (black) using steady-state fluorescence spectroscopy. All measurements were performed in HBS pH 7.4 with a protein−lipid concentration of 4.8 μM and a total lipid concentration of 40 μM. The exchange was monitored by exciting ECFP at 420 nm and monitoring the EYFP to ECFP ratio (527 nm/475 nm) over time with excitation and emission slit widths of 5 nm. Plots of the emission ratio as a function of time were fitted to eq 1 (black lines).

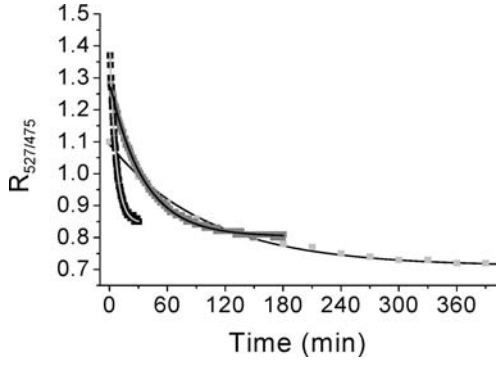


Figure 5. Exchange of ECFP-EYFP micelles with high concentrations of unfunctionalized PEG2000-DSPE micelles monitored using steady-state fluorescence spectroscopy. All measurements were performed in HBS pH 7.4 with a protein−lipid concentration of 4.0 μM and a total lipid concentration of 627 μM. The exchange was monitored by exciting ECFP at 420 nm and monitoring the EYFP to ECFP ratio (R527 nm/475 nm) over time at 20 °C (light gray), 28 °C (gray), and 37 °C (black). Plots of the emission ratio as a function of time were fitted to eq 1 (solid lines).

here were calculated assuming an aggregation number (N_a) of 90 lipids per micelle, a number that is based on previous SANS measurements on (nonfunctionalized) PEG2000-DSPE micelles (*33*). Since the amount of energy transfer is correlated to the presence of ECFP and EYFP on a single micelle, titration of PEG2000-DSPE to mixed ECFP−EYFP micelles should result in a decrease in emission ratio until a regime is reached where the average protein−micelle ratio is less than two. Figure 6A shows the results of such a titration experiment in which increasing concentrations of PEG2000-DSPE were added to ECFP−EYFP micelles. Indeed, a strong decrease in FRET is

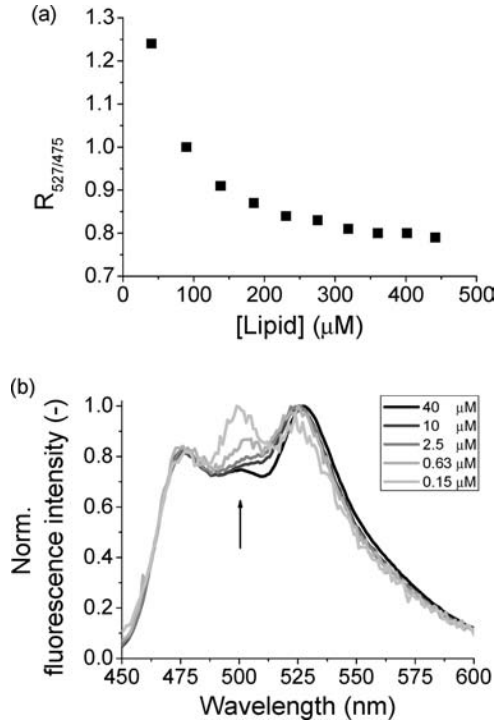


Figure 6. Structural properties of mixed ECFP−EYFP micelles studied using FRET. Mixed ECFP−EYFP micelles were prepared by mixing ECFP-micelles and EYFP-micelles in a 1:1 ratio yielding a starting concentration of 2.4 μM ECFP-PEG2000-DSPE, 2.4 μM EYFP-PEG2000-DSPE, and 35 μM Cys-PEG2000-DSPE. All measurements were performed in HBS pH 7.4 at 37 °C. (A) Decrease of FRET observed in ECFP−EYFP micelles by the addition of increasing concentrations of PEG2000-DSPE. Emission spectra were measured after 20 min incubation at 37 °C to allow complete exchange of lipidated proteins. (B) Determination of the CMC by stepwise dilution of mixed ECFP−EYFP-micelles in buffer. After each dilution step, micelles were left to equilibrate for 30 min before measuring an emission spectrum using an excitation wavelength of 430 nm. The arrow indicates the appearance of a Raman scatter band that increases in relative intensity at low protein concentrations.

observed up to a total PEG2000-DSPE concentration of 150−200 μM, after which the ratio stabilizes. The observation of an inflection point around 200 μM is consistent with the aggregation numbers of 72−90 that were reported in previous studies, suggesting that protein functionalization did not significantly alter the aggregation number (*33*−*35*).

Micelles functionalized with a combination of donor and acceptor fluorescent proteins also provide an alternative method to assess the stability of protein-functionalized micelles by monitoring FRET upon dilution of these micelles in buffer. The critical micelle concentration is typically measured by employing methods that rely on solubilization of fluorescent dyes in the micellar interior, but it has been argued that these methods could be less reliable for stable micelles (*36*). The ratio of EYFP and

ECFP emission was determined as a function of Cys-PEG2000-DSPE concentration after time was taken to allow equilibration at 37 °C. Figure 6B shows the emission spectra normalized for dilution up to a Cys-PEG2000-DSPE concentration of 0.15 μM. Surprisingly, no significant change was observed in the ratio between EYFP emission and ECFP emission, showing that micelles remained intact under these conditions even at 0.15 μM PEG2000-DSPE. Unfortunately, no reliable measurements could be obtained at concentrations below lipid concentrations of 0.15 μM (corresponding to 10 nM ECFP and EYFP) due to the increasing intensity of a Raman scatter at 500 nm. Nonetheless, the CMC determined in this manner is at least 10-fold lower than the 1−10 μM CMC values that were previously reported for (protein functionalized) PEG2000-DSPE micelles (*20, 33, 37*). It is unclear whether this difference is being caused by the more direct measurement of the CMC or reflects a possible stabilization of the micelles induced by the presence of ECFP and EYFP.

CONCLUSION

Functionalization of pegylated phospholipids with donor and acceptor fluorescent domains provides a straightforward approach to study the stability of protein-functionalized liposomes and micelles with respect to protein−lipid transfer. Even after incubation for 24 h at 37 °C, no protein exchange is observed for sterically stabilized liposomes. Protein exchange is relatively fast for PEG2000-DSPE micelles at 37 °C, but much slower at room temperature. The similar exchange rates obtained for protein-functionalized PEG2000-DSPE found here and non-functionalized PEG2000-DSPE micelles reported previously suggest that protein functionalization does not result in an additional enhancement of lipid-exchange rates. Nonetheless, the short half-life of 4 min observed at 37 °C shows that these micellar systems are kinetically unstable under physiological conditions and might rapidly exchange their protein-functionalized lipids with other lipid pools such as cellular membranes.

ACKNOWLEDGMENT

The authors thank Wouter Habraken for his help with DLS, Marcel Rooijackers for initial exploratory research with the fluorescent protein micelles, Ilmar Kruis for exploratory work with the fluorescent protein liposomes, Erik Sanders for liposome preparation, and Bert Meijer and Luc Brunsveld for support and useful discussions. This work was supported by an NWO VIDI grant 700.56.428 to M.M. and the BSIK program entitled Molecular Imaging of Ischemic Heart Disease (project number BSIK03033).

Supporting Information Available: SDS-PAGE analysis of protein conjugation to liposomes and micelles (Figures S1−S2), DLS characterization of the ECFP-and EYFP micelles (Figure S3), the effect of protein-loading on protein exchange kinetics of the protein-micelles (Figure S4) and exchange between NBD-DPPE and Rhodamine-DPPE in Cys-PEG2000-DSPE micelles (Figure S5). This material is available free of charge via the Internet at http://pubs.acs.org.

LITERATURE CITED

(1) Allen, T. M., and Cullis, P. R. (2004) Drug delivery systems: entering the mainstream. *Science 303*, 1818–1822.

(2) Mulder, W. J., Strijkers, G. J., van Tilborg, G. A., Griffioen, A. W., and Nicolay, K. (2006) Lipid-based nanoparticles for contrast-enhanced MRI and molecular imaging. *NMR Biomed. 19*, 142–164.

(3) Allen, T. M., and Hansen, C. (1991) Pharmacokinetics of stealth versus conventional liposomes: effect of dose. *Biochim. Biophys. Acta 1068*, 133–141.

(4) Torchilin, V. P., Lukyanov, A. N., Gao, Z., and Papahadjopoulos-Sternberg, B. (2003) Immunomicelles: targeted pharmaceutical carriers for poorly soluble drugs. *Proc. Natl. Acad. Sci. U.S.A. 100*, 6039–6044.

(5) Trubetskoy, V. S., and Torchilin, V. P. (1996) Polyethyleneglycol based micelles as carriers of therapeutic and diagnostic agents. *STP Pharma Sci. 6*, 79–86.

(6) Kastantin, M., Ananthanarayanan, B., Karmali, P., Ruoslahti, E., and Tirrell, M. (2009) Effect of the lipid chain melting transition on the stability of DSPE-PEG(2000) micelles. *Langmuir 25*, 7279–7286.

(7) Park, J. W., Hong, K., Carter, P., Asgari, H., Guo, L. Y., Keller, G. A., Wirth, C., Shalaby, R., Kotts, C., and Wood, W. I. (1995) Development of anti-p185HER2 immunoliposomes for cancer therapy. *Proc. Natl. Acad. Sci. U.S.A. 92*, 1327–1331.

(8) Briley-Saebo, K. C., Shaw, P. X., Mulder, W. J. M., Choi, S.-H., Vucic, E., Aguinaldo, J. G. S., Witztum, J. L., Fuster, V., Tsimikas, S., and Fayad, Z. A. (2008) Targeted molecular probes for imaging atherosclerotic lesions with magnetic resonance using antibodies that recognize oxidation-specific epitopes. *Circulation 117*, 3206–3215.

(9) Nasongkla, N., Shuai, X., Ai, H., Weinberg, B. D., Pink, J., Boothman, D. A., and Gao, J. (2004) cRGD-functionalized polymer micelles for targeted doxorubicin delivery. *Angew. Chem., Int. Ed. Engl. 43*, 6323–6327.

(10) Zalipsky, S., Puntambekar, B., Boulikas, P., Engbers, C. M., and Woodle, M. C. (1995) Peptide attachment to extremities of liposomal surface grafted PEG chains: Preparation of the long-circulating form of laminin pentapeptide, YIGSR. *Bioconjugate Chem. 6*, 705–708.

(11) Jule, E., Nagasaki, Y., and Kataoka, K. (2002) Surface plasmon resonance study on the interaction between lactose-installed poly(ethylene glycol)-poly(D, L-lactide) block copolymer micelles and lectins immobilized on a gold surface. *Langmuir 18*, 10334–10339.

(12) Murthy, B. N., Voelcker, N. H., and Jayaraman, N. (2006) Evaluation of alpha-D-mannopyranoside glycolipid micelles-lectin interactions by surface plasmon resonance method. *Glycobiology 16*, 822–832.

(13) DeFrees, S. A., Phillips, L., Guo, L., and Zalipsky, S. (1996) Sialyl Lewis x liposomes as a multivalent ligand and inhibitor of E-selectin mediated cellular adhesion. *J. Am. Chem. Soc. 118*, 6101–6104.

(14) Silvius, J. R., and Zuckermann, M. J. (1993) Interbilayer transfer of phospholipid-anchored macromolecules via monomer diffusion. *Biochemistry 32*, 3153–3161.

(15) Zacharias, D. A., Violin, J. D., Newton, A. C., and Tsien, R. Y. (2002) Partitioning of lipid-modified monomeric GFPs into membrane microdomains of live cells. *Science 296*, 913–916.

(16) Brunsveld, L., Waldmann, H., and Huster, D. (2009) Membrane binding of lipidated Ras peptides and proteins - The structural point of view. *Biochim. Biophys. Acta, Biomembr. 1788*, 273–288.

(17) Li, W. M., Xue, L., Mayer, L. D., and Bally, M. B. (2001) Intermembrane transfer of polyethylene glycol-modified phosphatidylethanolamine as a means to reveal surface-associated binding ligands on liposomes. *Biochim. Biophys. Acta, Biomembr. 1513*, 193–206.

(18) Grogan, M. J., Kaizuka, Y., Conrad, R. M., Groves, J. T., and Bertozzi, C. R. (2005) Synthesis of lipidated green fluorescent protein and its incorporation in supported lipid bilayers. *J. Am. Chem. Soc. 127*, 14383–14387.

(19) Reulen, S. W. A., Brusselaars, W. W. T., Langereis, S., Mulder, W. J. M., Breurken, M., and Merkx, M. (2007) Protein-liposome conjugates using cysteine-lipids and native chemical ligation. *Bioconjugate Chem. 18*, 590–596.

(20) Reulen, S. W. A., Dankers, P. Y. W., Bomans, P. H. H., Meijer, E. W., and Merkx, M. (2009) Collagen targeting using protein-functionalized micelles: the strength of multiple weak interactions. *J. Am. Chem. Soc. 131*, 7304–7312.

(21) Evers, T. H., van Dongen, E. M. W. M., Faesen, A. C., Meijer, E. W., and Merkx, M. (2006) Quantitative understanding of the energy transfer between fluorescent proteins connected via flexible peptide linkers. *Biochemistry 45*, 13183–13192.

(22) Rizzo, M. A., Springer, G. H., Granada, B., and Piston, D. W. (2004) An improved cyan fluorescent protein variant useful for FRET. *Nat. Biotechnol. 22*, 445–449.

(23) Patterson, G., Day, R. N., and Piston, D. (2001) Fluorescent protein spectra. *J. Cell Sci. 114*, 837–838.

(24) Rouser, G., Fkeischer, S., and Yamamoto, A. (1970) Two dimensional thin layer chromatographic separation of polar lipids and determination of phospholipids by phosphorus analysis of spots. *Lipids 5*, 494–496.

(25) Strijkers, G. J., Mulder, W. J., van Heeswijk, R. B., Frederik, P. M., Bomans, P., Magusin, P. C., and Nicolay, K. (2005) Relaxivity of liposomal paramagnetic MRI contrast agents. *Magma 18*, 186–192.

(26) Sanders, H., Strijkers, G., Mulder, W., Huinink, H., Erich, S., Adan, O., Sommerdijk, N., Merkx, M., and Nicolay, K. (2009) Morphology, binding behavior and MR-properties of paramagnetic collagen-binding liposomes. *Contr. Med. Mol. Imaging 4*, 81–88.

(27) Johnson, E. C., and Kent, S. B. (2006) Insights into the mechanism and catalysis of the native chemical ligation reaction. *J. Am. Chem. Soc. 128*, 6640–6646.

(28) Zalipsky, S., Mullah, N., Harding, J. A., Gittelman, J., Guo, L., and DeFrees, S. A. (1997) Poly(ethylene glycol)-grafted liposomes with oligopeptide or oligosaccharide ligands appended to the termini of the polymer chains. *Bioconjugate Chem. 8*, 111–118.

(29) Uster, P. S., Allen, T. M., Daniel, B. E., Mendez, C. J., Newman, M. S., and Zhu, G. Z. (1996) Insertion of poly(ethylene glycol) derivatized phospholipid into pre-formed liposomes results in prolonged in vivo circulation time. *FEBS Lett. 386*, 243–246.

(30) Fullington, D. A., and Nichols, J. W. (1993) Kinetic analysis of phospholipid exchange between phosphatidylcholine/taurocholate mixed micelles: Effect of the acyl chain moiety of the micellar phosphatidylcholine. *Biochemistry 32*, 12678–12684.

(31) Roseman, M. A., and Thompson, T. E. (1980) Mechanism of the spontaneous transfer of phospholipids between bilayers. *Biochemistry 19*, 439–444.

(32) Jones, J. D., and Thompson, T. E. (1990) Mechanism of spontaneous, concentration-dependent phospholipid transfer between bilayers. *Biochemistry 29*, 1593–1600.

(33) Ashok, B., Arleth, L., Hjelm, R. P., Rubinstein, I., and Onyuksel, H. (2004) In vitro characterization of PEGylated phospholipid micelles for improved drug solubilization: effects of PEG chain length and PC incorporation. *J. Pharm. Sci. 93*, 2476–2487.

(34) Sato, T., Sakai, H., Sou, K., Buchner, R., and Tsuchida, E. (2007) Poly(ethylene glycol)-conjugated phospholipids in aqueous micellar solutions: hydration, static structure, and interparticle interactions. *J. Phys. Chem. B 111*, 1393–1401.

(35) Johnsson, M., Hansson, P., and Edwards, K. (2001) Spherical micelles and other self-assembled structures in dilute aqueous mixtures of poly(ethylene glycol) lipids. *J. Phys. Chem. B 105*, 8420–8430.

(36) Lukyanov, A. N., Gao, Z., Mazzola, L., and Torchilin, V. P. (2002) Polyethylene glycol-diacyllipid micelles demonstrate increased acculumation in subcutaneous tumors in mice. *Pharm. Res. 19*, 1424–1429.

(37) Lukyanov, A. N., and Torchilin, V. P. (2004) Micelles from lipid derivatives of water-soluble polymers as delivery systems for poorly soluble drugs. *Adv. Drug Delivery Rev. 56*, 1273–1289.

BC900398P

Surfactant-Free Poly(styrene-*co*-glycidyl methacrylate) Particles with Surface-Bound Antibodies for Activation and Proliferation of Human T Cells

Katja Thümmler,*[,†] Nadine Häntzschel,[‡] Alla Skapenko,[†] Hendrik Schulze-Koops,[†] and Andrij Pich[§]

Division of Rheumatology, Medizinische Poliklinik, Ludwig-Maximilians-Universität Munich, D-80336 Munich, Germany, and Department of Macromolecular Chemistry and Textile Chemistry, Technische Universität Dresden, D-01062 Dresden, Germany.
Received September 14, 2009; Revised Manuscript Received March 18, 2010

In this article, we present our results on the design of new polymeric carriers for antibodies. Polymer colloids based on poly(styrene-*co*-glycidyl methacrylate) were synthesized by surfactant-free emulsion polymerization. Obtained polymer particles stabilized by grafted poly(ethylene glycol) (PEG) chains and carrying active epoxy groups were used for the covalent immobilization of activating antibodies against the human surface proteins CD (cluster of differentiation) 3 and CD28. The particle−antibody conjugates were employed for the stimulation of human CD4 memory T cells. This was analyzed by the up-regulation of the activation markers CD69 and CD25 on T cells and T cell proliferation as assessed by the dilution of a fluorescent dye on dividing daughter T cells. The particle−antibody conjugates were able to stimulate T cells at least as efficiently as conventional methods, e.g., surface-immobilized antibodies. Furthermore, an increase of the PEG chain length of the particles decreased the efficiency of the particle−antibody conjugates to activate T cells.

INTRODUCTION

Polymeric particles are very versatile objects whose properties can be tailor-made during synthesis by varying different parameters such as the nature of the monomer, the polymerization procedure, or additives. In biomedicine, for example, particles can be used as carriers in drug delivery systems, as well as for agglutination tests and in the area of biosensors. However, due to the complexity of biological systems there is still a need for the development of new reactive polymeric carriers.

Most synthesis strategies employ surfactants that are noncovalently bound. Therefore, they can desorb under certain circumstances like high ionic strength, freezing, or mechanical stress leading to unstable dispersions and undesired interactions with other substances. One aim of this work was the synthesis of highly reactive particles avoiding classical surfactants by using surfactant-free heterophase polymerization. This technique employs functional monomers such as acetoacetoxyethyl methacrylate (*1*) or poly(ethylene glycol) methacrylate (*2*) that are able to stabilize the prepared particles. Furthermore, PEG derivatives are known for their biocompatibility and the reduction of unspecific protein adsorption and cell adhesion (*3*−*5*).

The covalent attachment of biomolecules can be realized by a posterior grafting of molecules with desired functionalities or by direct functionalization during polymerization (*6*). The use of glycidyl methacrylate (GMA) for immobilization of biomolecules has been known for a long time because its epoxy groups are able to react with several functional groups such as thiol, amino, or hydroxy groups without further activation. A lot of work in this area has been done by Horák and co-workers (*7, 8*) who synthesized magnetic particles containing GMA and used these for the immobilization of biomolecules.

Several other publications deal with copolymers of GMA and 2-hydroxyethyl methacrylate and their use for the immobilization of enzymes (*9*−*12*). In contrast, little research has so far been done in the field of immobilization of antibodies using GMA. Faure et al. (*13*) prepared miniaturized immunoextraction columns by bonding of anti-ochratoxin A antibodies on poly(glycidyl methacrylate-*co*-ethylene dimethacrylate) monoliths. Iwata et al. (*14*) immobilized goat anti-mouse immunglobulin-(Ig) G Fab′ fragments on GMA-containing polymer brushes in a defined orientation.

To explain processes of the human immune system, it is necessary to examine single steps of an immune response in vitro. Furthermore, the amount of primary cells from blood donations is limited. Analysis of immunological systems in vitro frequently requires expansion and activation of the desired cell species, e.g., T cells. Another application for T cell expansion is for therapeutic purposes, e.g., for the treatment of cancer (*15*) or autoimmune diseases (*16*−*18*).

Stimulation of T cells with immobilized antibodies to surface proteins, such as the polymorphic T cell receptor (TCR) or the nonpolymorphic CD (cluster of differentiation) 3 complex, mimics binding of the major histocompatibility class II/peptide complex (MHC class II/peptide) on the surface of antigen-presenting cells to T cells and hence initiates the T cell activation program (*19*). To stimulate T cells effectively, two activation signals are required. The first signal occurs via the T cell receptor complex, whereas the second, so-called co-stimulatory signal, can be provided by engaging the nonpolymorphic surface receptor CD28. A conventional method for polyclonal stimulation of memory T cells (T_{mem}) in vitro employs antibodies to CD3 adsorbed on plastic cell culture plates in combination with

* Author to whom correspondence should be addressed. E-mail: katja.thuemmler@med.uni-muenchen.de, Ludwig-Maximilians-Universität Munich, Medizinische Poliklinik, Division of Rheumatology, Pettenkoferstr. 8a, D-80336 Munich, Germany. Tel.: +49 89 516 034 53. Fax: +49 89 516 034 74.

† Ludwig-Maximilians-Universität Munich.

‡ Technische Universität Dresden. Current address: Centre for BioNano Interactions, School of Chemistry and Chemical Biology, University College Dublin, Belfield, Dublin 4, Ireland.

§ Technische Universität Dresden. Current address: Deutsches Wollforschungsinstitut, RWTH Aachen University, Pauwelsstrasse 8, D-52056 Aachen, Germany.

10.1021/bc900402d © 2010 American Chemical Society
Published on Web 04/28/2010

antibodies to CD28. The immobilization of the antibodies to CD3 is necessary, as it effectively permits cross-linking of the CD3 complexes on the surface of T cells, a prerequisite for T cell activation. Soluble antibodies to CD3, in fact, are not sufficient to induce T cell activation in most experimental settings (*20*−*22*). In contrast, CD28 mediated signals are rather independent of cross-linking, and stimulation of CD28 can be provided by soluble or immobilized antibodies to CD28. As cross-linking of CD3 can be employed upon contact with any carrier on which antibodies to CD3 can be immobilized in adequate densities, effective T cell activation can be initiated by CD3 and CD28 antibodies immobilized on polymeric particles.

The aim of the present work was the development of a simple and cheap polymeric carrier system for antibodies. The important challenge was a proper design of the particle surface, e.g., the presence of reactive functional groups able to bind antibodies, the presence of hydrophilic polymer chains for enhanced colloidal stability to avoid particle aggregation, as well as adjustment of particle size in submicrometer range. In the present study, we used particles immobilized with anti-CD3 and anti-CD28 antibodies to stimulate T cells and compared this method to the activating effect of plate bound antibodies to CD3 in concert with soluble anti-CD28 (control sample). Furthermore, we assessed whether particle−antibody conjugates without poly(ethylene glycol) methyl ether methacrylate (PEGMEMA) chains or with PEGMEMA chains of different length vary in their capacity to stimulate T cells.

EXPERIMENTAL PROCEDURES

Materials. Styrene (S, Fluka) was purified using an inhibitor remover (Aldrich) according to the manufacturer's description. Glycidyl methacrylate (GMA, Fluka) was purified by vacuum distillation. Poly(ethylene glycol) methyl ether methacrylate (PEGMEMA, Aldrich), 2,2′-azobis(2-methylpropionamidine) dihydrochloride (AMPA, Aldrich), dimethyl sulfoxide (Merck), 5-(and 6-) carboxyfluoresceine-diacetate-succinimidylester (CFSE, Molecular Probes), tris(hydroxymethyl)-aminomethane (Tris, Merck), ethanol (Aldrich), sodium azide (Merck), cresol red (Chemapol Praha), 1,4-dioxane (Riedel-de Haën), hydrogen chloride dioxane solution (Fluka), potassium chloride solution in methanol (Grüssing), tris(hydroxymethyl)-aminomethane (Merck), Hanks' solution (Apotheke Innenstadt, LMU Munich), phosphate buffer solution (PBS, Invitrogen), Ficoll-Hypaque-solution/Lymphoflot (Biotest), fetal calf serum (FCS, Invitrogen), sheep erythrocytes (SBRC, Fiebig-Nährstofftechnik), Penicillin G/Streptomycin (Invitrogen), L-glutamine (Invitrogen), Interleukin 2 (Chiron), and RPMI 1640 (Invitrogen) were used as received. For the preparation of FACS (fluorescence activated cell sorting)−PBS, 500 mL PBS, 10 mL FCS, and 0.5 mL of NaN_3 solution in water (10%) were mixed. Deionized water was employed as reaction medium for emulsion polymerization.

The following monoclonal antibodies (mAbs) were used for cell purification and cell culture: anti-CD3 (OKT3), anti-CD8 (OKT8), anti-CD16 (3g8FcIII), anti-HLA-DR (L243; all from American Type Culture Collection), anti-CD28 (28.2; BD Pharmigen), anti-CD19 (HD37, Dako Diagnostika), anti-CD45RA (111.1 C5; a gift from Dr. R. Vilella, Barcelona, Spain), anti-CD56 (MOC-1, Dako Cytomation), and polyclonal antimouse IgG (MP Biomedicals).

For cell staining, fluorescein isothiocyanate (FITC)-conjugated or phycoerythrin (PE)-conjugated mAbs were applied: FITC-anti-CD3 (UCHT1), PE-anti-CD4 (Q4120), FITC-anti-CD4 (Q4120, all from Sigma), and PE-anti-CD3 (UCHT1), PE-anti-CD28 (CD28.2), PE-anti-CD25 (M-A251), FITC-anti-CD27 (M-T271), PE-anti-CD45RO (UCHL1), FITC-anti-CD69 (FN50, all from BD Pharmigen).

Synthesis of Polymeric Particles. A monomer mixture containing appropriate amounts of styrene and GMA was prepared. A double-walled glass reactor equipped with stirrer was filled with 170 mL distilled water. For the preparation of PEGMEMA containing particles, appropriate amounts of PEGMEMA were previously dissolved in the water. Then, the monomer mixture was added to the water phase under stirring. The obtained pre-emulsion was heated to 60 °C and stirred for 1 h while purging with nitrogen. To start the polymerization process, 10 mL of water with 1.5 wt % of initiator was added. Latexes were prepared at 10% solid content. The reaction time was 8 h at 60 °C.

Titration of Epoxy Groups. Water-based particle dispersions were freeze−dried. 0.5 g of dried particles were redispersed in 20 mL 1,4-dioxane. Then, 5 mL of a solution of hydrogen chloride in dioxane were added. The mixture was stirred for 8 h at room temperature. Remaining hydrogen chloride was determined by titration with a solution of potassium hydroxide in methanol. The equivalence point was determined by either potentiometric titration or with 1 mL of a solution of 0.1 g cresol red in 100 mL ethanol−water mixture (volume ratio = 1:1) as color indicator.

Attachment of Antibodies to Polymeric Particles. *Fluorescence-Labeled Antibodies.* The particle dispersions were diluted 1:100 with 50 mM Tris-HCl (pH 9.5). 25 μL of fluorescence-labeled antibodies were added to 100 μL of diluted particle dispersion. Then, the samples were incubated at 37 °C for 2 h. After washing with 50 mM Tris buffer, the particle−antibody conjugates were resuspended in 150 μL FACS-PBS and analyzed by flow cytometry.

Antibodies for Cell Activation. The particle dispersions were sterilized by washing with ethanol twice and diluted with 50 mM Tris (pH 9.5) 1:500. 150 μL of the antibody solution in 50 mM Tris with the desired antibody concentrations was added. The final concentration of antibodies was 1 μg/mL. The samples were incubated at 37 °C for 2 h, afterward washed twice with deionized water, and transferred to the cell culture medium. The particle amount in each sample corresponded to the surface area of one well of the cell culture plate.

Attachment of Antibodies to Cell Culture Plates (Control Sample). Each well of a 48-well plate was filled with 150 μL of an antibody solution of appropriate concentration (1 μg/mL in 50 mM Tris-HCl) and incubated at 37 °C in a humidified atmosphere containing 5% CO_2 for 2 h. The plates were washed twice with Hanks' solution to remove unbound antibodies and obtain a neutral pH and used for further cell culture.

Cell Purification. Mononuclear cells were obtained from heparinized peripheral blood of one healthy individual. Ethical approval was obtained by the local Institutional Review Board, and all subjects enrolled gave their written informed consent. After gradient centrifugation (20 min, 400*g*) over a Ficoll-Hypaque layer followed by washing with PBS, cells were incubated with sheep red blood cells (rosetting) (*23*). The rosette-positive cells were further purified by negative selection using saturating amounts of mAbs against CD8, CD16, and CD19, followed by panning on plastic Petri dishes coated with goat antimouse IgG for 15 min at room temperature as previously described (*24*, *25*). CD4 T cells were harvested by gently washing the dishes with a solution of 4% NHS (normal human serum)/RPMI 1640 in PBS and centrifugation. In the last step, resting CD4 T_{mem} were isolated by negative selection using anti-HLA-DR, anti-CD45RA, anti-CD56, and anti-CD8 antibodies. Recovered cells were washed with PBS and resuspended in 10% NHS/RPMI 1640. The homogeneity and purity of isolated T cells were assessed by flow cytometry. Routinely, ≥90% T cells were positive for CD3 and CD4.

Table 1. Ingredients Used in Emulsion Polymerization (Reaction Temperature: 60 °C)

N	*S* [g]	GMA [g]	GMA [wt%]	PEGMEMA [g]	PEGMEMA [wt%]	M_n, [g/mol] PEGMEMA	initiator [g]	water [g]
1	19	1	5	-	-	-	0.3	180
2	19	0.5	2.5	0.5	2.5	~475	0.3	180
3	19	0.5	2.5	0.5	2.5	~1100	0.3	180
4	19	0.5	2.5	0.5	2.5	~2080	0.3	180

Cell Culture. Culturing of the cells was carried out in RPMI 1640 medium supplemented with penicillin G/streptomycin (50 U/mL), L-glutamine (2 mM), 10% NHS, and 10 ng/mL IL-2. Cell cultures were maintained at 37 °C in a humidified atmosphere containing 5% CO_2. Memory CD4 T cells were aliquoted at a concentration of 0.75×10^6 cells/mL in the cell culture medium. 300 μL of the cell suspension were pipetted in each well of a 48-well cell culture plate (Costar) and diluted with the same volume of cell culture medium containing the particle−antibody conjugates.

Alternatively, the same amount of T cells was stimulated with Dynabeads CD3/CD28 T Cell Expander beads (Dynal Biotech) according to the manufacturer instruction at a 3:1 beads per T cell ratio.

Flow Cytometry. 1×10^5 T cells/sample were washed with FACS-PBS, resuspended in 50 μL FACS-PBS, and incubated with saturating amounts of directly fluorochrome labeled mAb against different surface molecules (CD25 or CD69) for 15 min at 4 °C in the dark. Afterward, cells were washed twice with 1 mL FACS-PBS and resuspended in 300 μL FACS-PBS. To obtain quantitative data with very high reliability, at least 1×10^4 T cells/sample were analyzed as recommended (*26*) and the mean fluorescence intensity (MFI) and standard deviation were calculated for the entire population of 1×10^4 T cells.

Analysis of Cell Division. 1 μL of the CD4 T_{mem} cell suspension (10×10^6 cells/mL) in PBS was incubated with a 10 mM solution of CFSE in dimethyl sulfoxide for 8 min at room temperature, with a final CFSE concentration of 10 μM. Labeling was stopped by adding of 1 mL NHS. Cells were washed twice with RPMI 1640 supplemented as described above. At indicated time points of cell culture, cells were harvested, washed with FACS-PBS, resuspended with 250 μL FACS-PBS, and analyzed by flow cytometry. The proliferation index of the cells was calculated as 1/MFI × 100%.

Characterization Methods. SEM images were taken with a Gemini microscope (Zeiss, Germany). For sample preparation, particle dispersions were diluted with deionized water, dropped onto aluminum support, and dried at room temperature. Samples were coated with a thin Au/Pd layer to increase the contrast and quality of the images. Images were obtained at a voltage of 4 kV. Dynamic light scattering measurements were performed with a Zetasizer Nanoseries ZEN3600 (Malvern Instruments, UK). Stability measurements of particle dispersions were performed with the separation analyzer LUMiFuge 114 (LUM GmbH, Germany). Measurements were made in glass tubes at an acceleration velocity of 3000 rpm. The slopes of the sedimentation curves were used to calculate the sedimentation velocities and to get information about the stability of the samples. Flow cytometry analysis was done with a Cytomics FC500, Beckman Coulter. Fluorescence was excited with an Ar-ion laser at a wavelength of 488 nm. Fluorescence signals were determined using appropriate electronic compensation to exclude emission spectra overlap. For extracellular staining, 0.1×10^6 cells/staining were washed with 1 mL FACS-PBS, resuspended in 50 μL FACS-PBS, and incubated with saturating amounts of PE- or FITC-labeled antibodies for 15 min at 4 °C in the dark. Afterward, the cells were washed twice with 1 mL FACS-PBS, resuspended with 250 μL FACS-PBS, and analyzed by flow cytometry. Light microscopy was performed with an Axiovert 25 microscope (Zeiss, Germany).

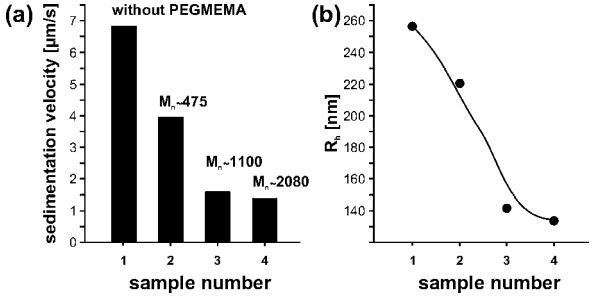


Figure 1. Sedimentation velocities (a) and hydrodynamic radius (b) of polymer particles prepared with PEGMEMA macromonomers of different molecular weights.

RESULTS AND DISCUSSION

Particle Size and Morphology. Poly(styrene-*co*-glycidyl methacrylate) (PS-PGMA) and PS-PEGMEMA-PGMA particles were prepared by surfactant-free heterophase polymerization. Interestingly, this technique could be used although GMA is regarded as a rather hydrophobic monomer. But in comparison to styrene, the difference in hydrophobicity is big enough for sufficient particle stabilization. Hence, the obtained dispersions were stable and showed no precipitation during storage. In all runs, the final monomer conversion was between 80% and 85%. An overview of the reaction recipes for emulsion polymerization is given in Table 1.

For further evaluation of colloidal stability, sedimentation experiments with an analytical centrifuge were performed (Figure 1a). As expected, the best stability (lowest sedimentation velocity) was observed for dispersions with the highest molecular weight of PEGMEMA, because poly(ethylene glycol) and its derivatives are known as effective sterical stabilizers (*27*, *28*).

Figure 1b shows results of dynamic light scattering indicating that the molecular weight of the PEGMEMA macromonomer has a strong influence on the final size of polymer colloids. It is obvious that the particle size decreases with an increase of the PEGMEMA molecular weight. Obtained polymer particles are monodisperse and possess a spherical shape as shown in SEM images (Figure 2).

Furthermore, it is believed that the particles possess a core−shell structure due to different hydrophilicity and reactivity of monomers. In the presence of a water-soluble initiator, polymerization in the water phase likely involves a homogeneous nucleation mechanism because the functional monomer has a low ability to form defined micelles in water. As both functional monomers, PEGMEMA and GMA, are more reactive than styrene, formed oligoradicals will contain more GMA and PEGMEMA units leading to enhanced heterogeneity of copolymers. Addition of styrene leads to the formation of amphiphilic polymer chains which can act as stabilizers during polymerization of residual styrene. Thus, final particles probably consist of a polystyrene-rich dense core and a more diffuse shell containing PEGMEMA and GMA units, respectively, as confirmed for similar particles (*2*). This leads to the assumption that the epoxy groups should be mainly located in the outer region of synthesized particles.

The amount of reactive epoxy groups of polymerized particles was determined by titration using the HCl−dioxane method (*29*). About 85% of the epoxy groups were still intact and available

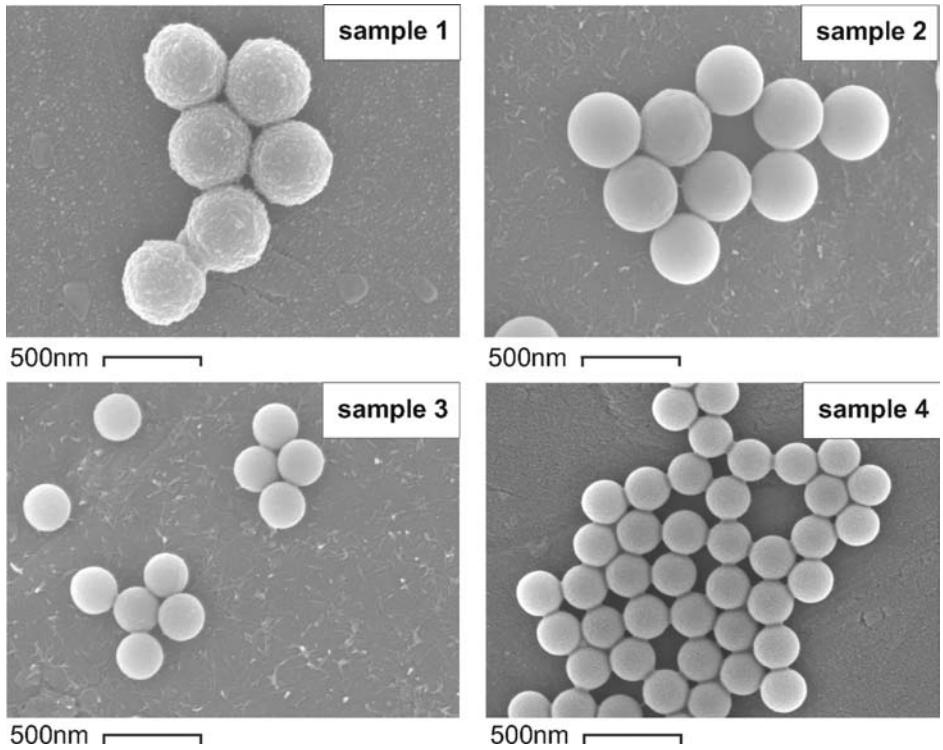


Figure 2. SEM images of polymer colloids (numbers correspond to sample numbers in Table 1).

for further reactions, e.g., immobilization of antibodies after polymerization.

Immobilization of Antibodies. Most standard methods bind proteins only by adsorption which usually leads to a high degree of protein denaturation (*30, 31*). In order to enhance the activity of bound antibodies and therefore minimize the amount needed for a certain cell activation, we chose to immobilize antibodies by covalent bonding via epoxy groups. In this context, PEGMEMA was incorporated into the particles not only for enhanced stability, but also for the prevention of protein adsorption. The ability of the synthesized polymeric particles to bind antibodies was demonstrated by immobilization of fluorescence-labeled antibodies (FITC labeled anti-CD3 and PE labeled anti-CD28) followed by flow cytometry analysis. As shown in Figure 3a, light scattering provides information about the size (forward scatter) and the surface characteristics (sideward scatter) of the particles. The scatter plots are then used to gate on the particle population of interest, and fluorescence signals of this population are measured in the different channels according to the fluorescent dye. Figure 3b,c demonstrates the corresponding flow cytometry plots of pure PS-PGMA particles. The particles did not show signals themselves, in either the FITC or the PE channel, verifying that the particles have no significant autofluorescence.

In contrast, Figures 3d,e presents the flow cytometry plots for PS-PGMA particles after immobilization of saturating amounts of fluorescence-labeled antibodies to CD3 (FITC) and to CD28 (PE), respectively. The peaks in Figure 3d,e are shifted to higher fluorescence signals in FITC/PE channels compared to Figure 3b,c indicating fluorescent particle−antibody conjugates. FACS analysis showed that 99.5% of the particles were FITC-positive and 98.7% of the particles were positive for PE. Therefore, PS-PGMA particles are able to immobilize both antibodies to CD3 and CD28 effectively. Similar results were obtained for PS-PEGMEMA-PGMA particles (data not shown).

Light Microscopy Investigation of Cell Culture. Since the particles effectively bind fluorescending antibodies as demonstrated by flow cytometric analysis, we immobilized particles with activating antibodies (1 μg/mL) against human CD3 and CD28 and analyzed their effect on human T cells by light microscopy. As shown in Figure 4a, purified T cells alone exhibit a round shape and an equal distribution throughout the cell culture plate. The conventional T cell stimulation by plate-bound antibodies in the control sample results in the characteristic pattern of activated T cells (*32*) (Figure 4b). T cell activation induces the formation of cell clusters and changed cell morphology. Upon contact with particle−antibody conjugates (Figure 4c), the same effects can be observed as compared with conventional plate-bound antibodies confirming a proper T cell activation by particle−antibody conjugates. Interestingly, endocytosis of the particles by the human T cells was not observed in contrast to human monocytes, which show strong endocytotic activity when incubated with the particles (data not shown).

Assessment of T Cell Stimulation. After antibody immobilization on the particles, we furthermore studied the influence of the particle surface properties on the ability of the antibodies to stimulate human CD4 memory T cells as monitored by their expression of the activation markers CD69 and CD25 and by their proliferation upon contact with the particle−antibody conjugates. The amount of activated T cells expressing the T cell activation markers CD69 and CD25 was determined by specific labeling of the T cells with fluorescent antibodies and further flow cytometric analysis of T cells on days 2, 3, and 4 after contact with particle−antibody conjugates. As already shown in other studies, expression of CD69 in activated T cells starts earlier than that of CD25 (*33, 34*). Figure 5 confirms successful cell activation in case of samples 1 and 2, whereas samples 3 and 4 (higher molecular weight of PEGMEMA) comprise significantly less activated cells. As all different particles (samples 1−4) were immobilized with the same amounts of antibodies, a comparable antibody density on the surface of the different particle is supposed. Therefore, the lower capacity of samples 3 and 4 to activate T cells possibly occurs due to restricted antibody−cell contact because longer PEGMEMA chains on the particle surface may prevent contact

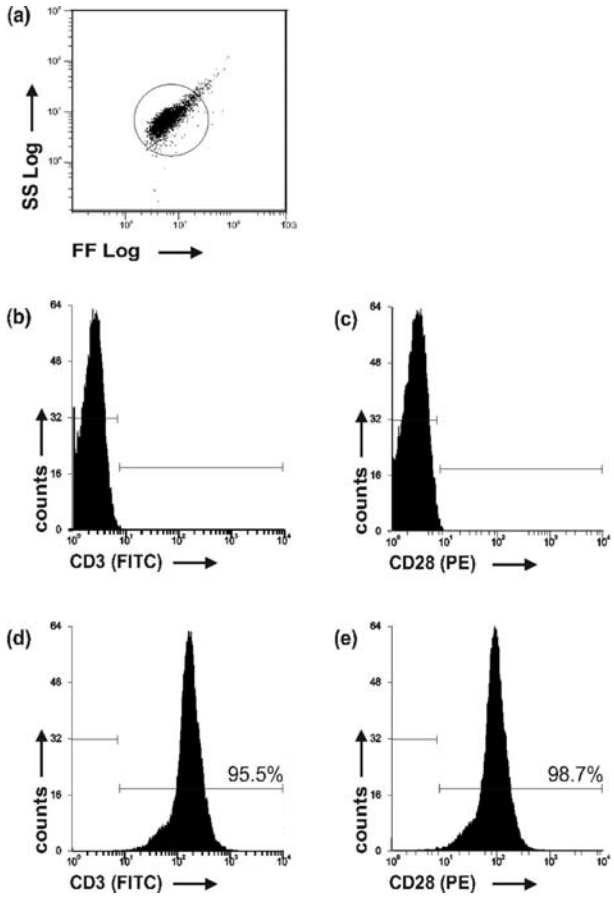


Figure 3. Flow cytometry analysis was performed for PS-PGMA particles (sample 1). (a) Forward scatter (FF) and sideward scatter (SS) of the PS-PGMA particles are plotted on a logarithmic scale, and the region of interest was selected based on the size and surface structure of the particles. Fluorescence signals in the FITC (b) or PE (c) channel of PS-PGMA particles alone or for PSPGMA particles with immobilized fluorescence-labeled anti-CD3-FITC (d) and anti-CD28-PE (e) are shown for the population selected in (a).

with the T cells. Of note, particles alone without antibodies on the surface have no influence on T cell activation or proliferation at all, because the measured data for CD69, CD25, and proliferation were similar to the data observed for T cells alone (blank). T cell activation by PS-PGMA particle−antibody conjugates (sample 1) is at least as sufficient as activation by conventional methods. In comparison to plate-bound antibodies (control sample), the frequencies of activated T cells were slightly enhanced after stimulation with particle−antibody conjugates especially at early time points of T cell activation. Since the surface areas of the particles and the cell culture plate in the control samples are identical, the applied polymeric particles may possess a higher density or better cross-linking of CD3 compared to the conventional method.

For our study, we used the same antibody concentration that is routinely used for the immobilization of activating antibodies on plastic (1 μg/mL) (*25, 35*). However, our interest was also to evaluate if different amounts of antibodies on the surface of the particles or on the cell culture plate may have an influence on the activation of the T cells. As shown in Supporting Information Figure S1, the chosen antibody concentration of 1 μg/mL is in the saturating region for an appropriate activation of T cells. Interestingly, higher amounts of antibody did not increase cell activation, but rather showed a tendency to decrease the activation of memory T cells. This observation is in correlation with reports from the literature, that high levels of anti-CD3 antibodies and prolonged T cell receptor stimulation

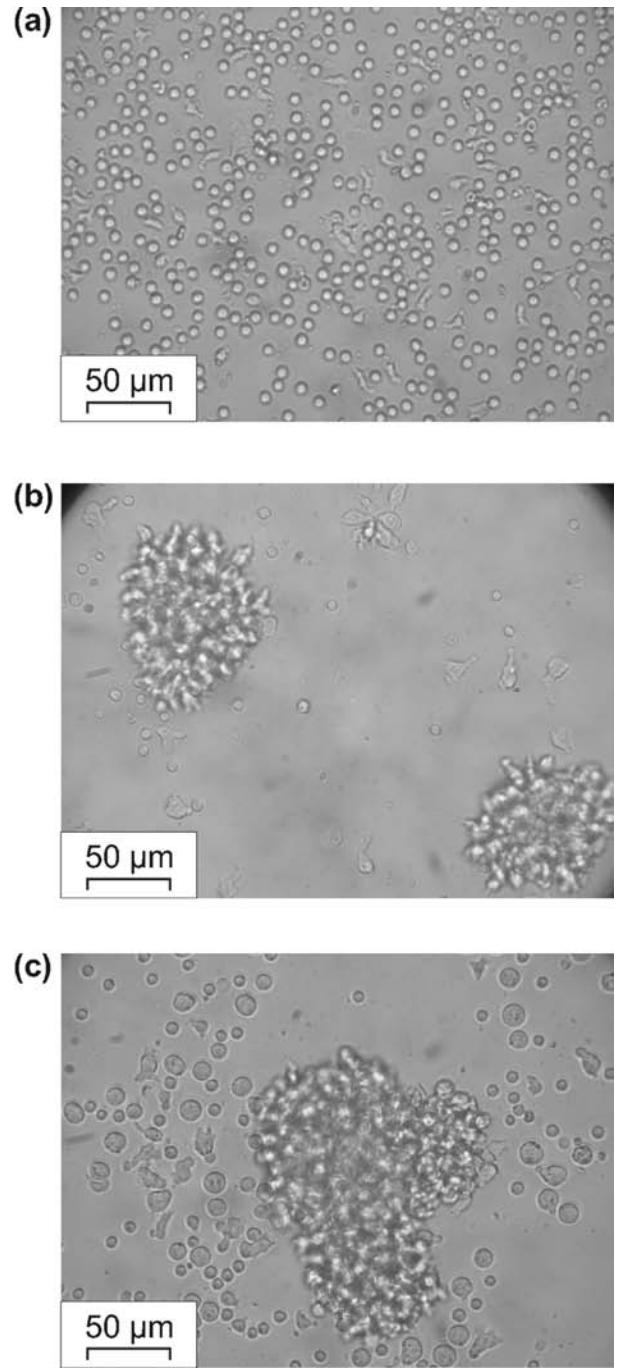


Figure 4. Light microscopy image of T cell culture: (a) purified nonstimulated T cells, (b) T cells conventionally stimulated with plate-bound antibodies (control sample), (c) T cells after contact with PS-PGMA particles with bound antibodies (note that particle−antibody conjugates are too small to be visualized by light microscopy).

may reduce T cell expansion and increase activation-induced apoptosis (*36, 37*).

Cell proliferation was analyzed by equal distribution of the dye CFSE to daughter cells after cell division. The corresponding fluorescence signal was investigated by flow cytometry. Analysis of cell proliferation revealed similar tendencies (Figure 6) and, therefore, is in line with the results from the determination of activation markers. In addition, we compared the proliferation of T cells stimulated with plate-bound antibodies to CD3 or with antibodies bound to different particles with the effects of commercially available Dynabeads CD3/CD28 T Cell Expander beads on T cell proliferation. Dynabeads are 4.5 μm

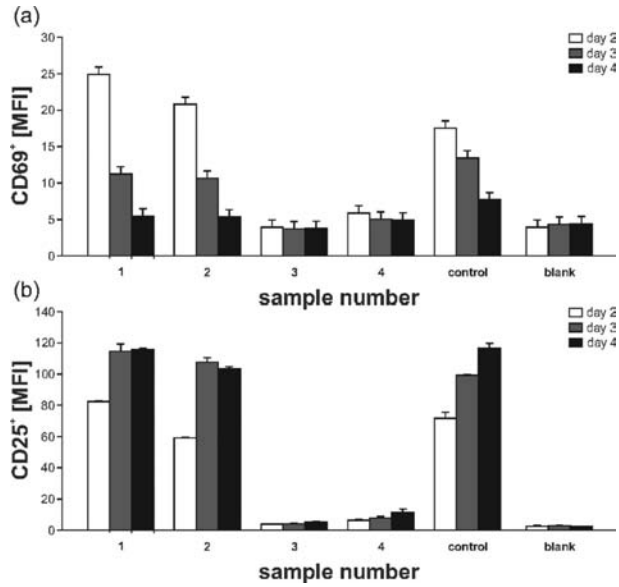


Figure 5. Mean fluorescence intensity of cells exhibiting the T cell activation markers CD69 (a) and CD25 (b) after contact with particle-bound antibodies. Sample numbers correspond to Table 1. The control represents conventional activation of T cells with plate-bound antibodies to CD3 and soluble anti-CD28. The blank denotes nonstimulated T cells without contact to antibodies or particles.

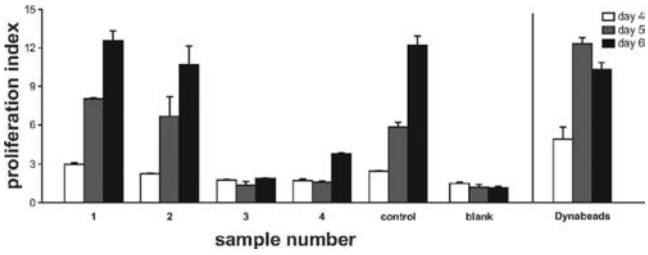


Figure 6. Proliferation of cells after contact with particle-bound antibodies. Sample numbers correspond to Table 1. The control represents conventional activation of T cells with plate-bound antibodies to CD3 and soluble anti-CD28. Blank denotes nonstimulated T cells without contact to antibodies or particles. Dynabeads represents T cells stimulated with Dynabeads CD3/CD28 T Cell Expander beads.

superparamagnetic microparticles with covalently bound antibodies available for different applications. Here, we used CD3/CD28 T Cell Expander Dynabeads for the expansion of human T cells, with antibodies to CD3 and CD28 coupled to the beads. Of note, the Dynabeads indeed showed an increased proliferation at early time points but reaching a plateau at later time points.

CONCLUSIONS

Up to now, most methods for T cell expansion are time-consuming, and large amounts of cells are needed. Improvements were achieved by using Dynabeads for the expansion of human T cells (*38*), but one potential disadvantage of these particles are surfactant residues. With regard to an application in complex biological systems, the negative effects of surfactants on skin permeability (*39*), on cell membrane structure (*40*), or on their cytotoxic effects (*41*) should be considered. Besides, normal microparticles must be separated from the cell population before flow cytometry analysis due to their large size. The benefit of Dynabeads for the expansion of T cells is undoubted, and this technique is now routinely used for the expansion of distinct T cell subsets with regulatory functions (*42*). We could also observe a robust proliferation induced by the Dynabeads, but excessive proliferation is often linked to a decreased differentiation of cells (*43*). Indeed, we observed reduced cytokine levels in T cells stimulated with Dynabeads (data not shown). Therefore, other tools for specific applications such as expansion of highly differentiated effector T cells would be desirable.

To overcome those limitations, surfactant-free emulsion polymerization was used to synthesize poly(styrene-*co*-glycidyl methacrylate) particles. Employing this technique, particles with size in the submicrometer range could be obtained. The use of glycidyl methacrylate as a functional co-monomer ensured incorporation of reactive epoxy-groups into particle surface. The use of poly(ethylene glycol) methyl ether methacrylate (PEGMEMA) macromonomers in the polymerization process improved the colloidal stability of particles. Additionally, the size of polymer colloids could be adjusted by varying the PEGMEMA molecular weight. Active epoxy groups on the particle surface were applied for immobilization of antibodies to CD3 and CD28 by covalent bonding. By flow cytometric analysis, we could demonstrate that more than 95% of the particles effectively bound the antibodies. These particle−antibody conjugates were used for stimulation of human CD4 memory T cells. Effective T cell responses after contact with particle−antibody conjugates were assessed by light microscopy of the T cells showing a characteristic pattern of activation. Furthermore, T cell activation was observed by evaluating the expression of the activation markers CD69 and CD25 and cell proliferation. For the PGMA particle−antibody conjugates, T cell activation is at least as sufficient as activation by conventional methods. Interestingly, at early time points frequencies of activated T cells were enhanced after stimulation with PGMA particle−antibody conjugates as compared with conventional activation (25 MFI vs 17.6 MFI for CD69 and 82.8 MFI vs 72 MFI for CD25). At higher PEG chain lengths, cell activation with particle−antibody conjugates was less efficient, possibly due to restricted antibody−cell contact.

In summary synthesized particle−antibody conjugates can be used as an alternative for other techniques of T cell activation and therefore may have potential for therapeutic applications.

ACKNOWLEDGMENT

Katja Thümmler and Nadine Häntzschel contributed equally to this work. The authors thank Dr. Iryna Prots and Dr. Wolfgang Kuon for helpful discussions and comments. This work was supported by Deutsche Forschungsgemeinschaft (DFG: SCHU 786/8-1, SK 59/4-1 and SFB 287).

Supporting Information Available: T cell activation (CD25 expression) is compared in response to stimulation with different amounts of antibodies bound to the particles (sample 1) or to the cell culture plate (control). This material is available free of charge via the Internet at http://pubs.acs.org.

LITERATURE CITED

(1) Pich, A., Bhattacharya, S., and Adler, H.-J. P. (2005) Composite magnetic particles: 1. Deposition of magnetite by heterocoagulation method. *Polymer 46*, 1077–1086.
(2) Pich, A., Lu, Y., and Adler, H.-J. (2003) Preparation of PEGMA-functionalized latex particles. 1. System styrene/PEGMA. *Colloid Polym. Sci. 281*, 907–915.
(3) Lee, J. H., Kopecek, J., and Andrade, J. D. (1989) Protein-resistant surfaces prepared by PEO-containing block copolymer surfactants. *J. Biomed. Mater. Res. 23*, 351–368.
(4) Lee, J. H., Kopeckova, P., Kopecek, J., and Andrade, J. D. (1990) Surface properties of copolymers of alkyl methacrylates with methoxy (polyethylene oxide) methacrylates and their

application as protein-resistant coatings. *Biomaterials 11*, 455–464.

(5) VandeVondele, S., Vörös, J., and Hubbell, J. A. (2003) RGD-grafted poly-L-lysine-graft-(polyethylene glycol) copolymers block non-specific protein adsorption while promoting cell adhesion. *Biotechnol. Bioeng. 82*, 784–790.

(6) Pichot, C. (1990) Recent developments in the functionalization of latex particles. *Makromol. Chem. Macromol. Symp. 35/36*, 327–347.

(7) Horák, D., Rittich, B., Španová, A., and Beneš, M. J. (2005) Magnetic microparticulate carriers with immobilized selective ligands in DNA diagnostics. *Polymer 46*, 1245–1255.

(8) Horák, D., and Benedyk, N. (2004) Magnetic poly(glycidyl methacrylate) microspheres prepared by dispersion polymerization in the presence of electrostatically stabilized ferrofluids. *J. Polym. Sci., Part A: Polym. Chem. 42*, 5827–5837.

(9) Akgöl, S., Bayramoğlu, G., Kacar, Y., Denizli, A., and YakupArıca, M. (2002) Poly(hydroxyethyl methacrylate-*co*-glycidyl methacrylate) reactive membrane utilised for cholesterol oxidase immobilization. *Polym. Int. 51*, 1316–1322.

(10) Bayramoğlu, G., Altınok, H., Bulut, A., Denizli, A., and YakupArıca, M. (2003) Preparation and application of spacer-arm-attached poly(hydroxyethyl methacrylate-*co*-glycidyl methacrylate) films for urease immobilization. *React. Funct. Polym. 56*, 111–121.

(11) Doretti, L., Ferrara, D., Gattolin, P., and Lora, S. (1996) Covalently immobilized enzymes on biocompatible polymers for amperometric sensor applications. *Biosens. Bioelectron. 11*, 365–373.

(12) Di Nino, G., Turacchio, M., D'Archivio, A. A., Lora, S., Corain, B., and Antonini, G. (2004) Catalytic activity of bovine lactoperoxidase supported on macroporous poly(2-hydroxyethyl methacrylate-*co*-glycidyl methacrylate). *React. Funct. Polym. 61*, 411–419.

(13) Faure, K., Delaunay, N., Allonclе, G., Cotte, S., and Rocca, J.-L. (2007) Optimization of *in-situ* monolithic synthesis for immunopreconcentration in capillary. *J. Chromatogr., A 1149*, 145–150.

(14) Iwata, R., Satoh, R., Iwasaki, Y., and Akiyoshi, K. (2008) Covalent immobilization of antibody fragments on well-defined polymer brushes via site-directed method. *Colloids Surf., B: Biointerfaces 62*, 288–298.

(15) Thompson, J. A., Figlin, R. A., Sifri-Steele, C., Berenson, R. J., and Frohlich, M. W. (2003) A phase I trial of CD3/CD28-activated T cells (Xcellerated T cells) and interleukin-2 in patients with metastatic renal cell carcinoma. *Clin. Cancer Res. 9*, 3562–3570.

(16) Earle, K. E., Tang, Q., Zhou, X., Liu, W., Zhu, S., Bonyhadi, M. L., and Bluestone, J. A. (2005) In vitro expanded human CD4+CD25+ regulatory T cells suppress effector T cell proliferation. *Clin. Immunol. 115*, 3–9.

(17) Dudley, M. E., Wunderlich, J. R., Robbins, P. F., Yang, J. C., Hwu, P., Schwartzentruber, D. J., Topalian, S. L., Sherry, R., Restifo, N. P., Hubicki, A. M., Robinson, M. R., Raffeld, M., Duray, P., Seipp, C. A., Rogers-Freezer, L., Morton, K. E., Mavroukakis, S. A., White, D. A., and Rosenberg, S. A. (2002) Cancer regression and autoimmunity in patients after clonal repopulation with antitumor lymphocytes. *Science 298*, 850–854.

(18) Bonyhadi, M., Frohlich, M., Rasmussen, A., Ferrand, C., Grosmaire, L., Robinet, E., Leis, J., Maziarz, R. T., Tiberghien, P., and Berenson, R. J. (2005) In vitro engagement of CD3 and CD28 corrects T cell defects in chronic lymphocytic leukemia. *J. Immunol. 174*, 2366–2375.

(19) Trickett, A., and Kwan, Y. L. (2003) T cell stimulation and expansion using anti-CD3/CD28 beads. *J. Immunol. Meth. 275*, 251–255.

(20) Kawaguchi, M., and Eckels, D. D. (1995) Differential activation through the TCR-CD3 complex affects the requirement for costimulation of human T cells. *Hum. Immunol. 43*, 136–148.

(21) Geppert, T. D., and Lipsky, P. E. (1988) Activation of T lymphocytes by immobilized monoclonal antibodies to CD3. Regulatory influences of monoclonal antibodies to additional T cell surface determinants. *J. Clin. Invest. 81*, 1497–1505.

(22) Geppert, T. D., and Lipsky, P. E. (1987) Accessory cell independent proliferation of human T4 cells stimulated by immobilized monoclonal antibodies to CD3. *J. Immunol. 138*, 1660–1666.

(23) Rosenberg, S. A., and Lipsky, P. E. (1979) Monocyte dependence of pokeweed mitogen-induced differentiation of immunoglobulin-secreting cells from human peripheral blood mononuclear cells. *J. Immunol. 122*, 926–931.

(24) Schulze-Koops, H., Lipsky, P. E., and Davis, L. S. (1998) Human memory T cell differentiation into Th2-like effector cells is dependent on IL-4 and CD28 stimulation and inhibited by TCR ligation. *Eur. J. Immunol. 28*, 2517–2529.

(25) Skapenko, A., Wendler, J., Lipsky, P. E., Kalden, J. R., and Schulze-Koops, H. (1999) Altered memory T cell differentiation in patients with early rheumatoid arthritis. *J. Immunol. 163*, 491–499.

(26) Faint, J. M., Pilling, D., Akbar, A. N., Kitas, G. D., Bacon, P. A., and Salmon, M. (1999) Quantitative flow cytometry for the analysis of T cell receptor V 102 chain expression. *J. Immunol. Meth 225*, 53–60.

(27) Napper, D. H. (1983) In *Polymeric Stabilization of Colloidal Dispersions*, 3rd ed., pp 18−30, Academic Press, New York.

(28) Morrison, I. D., and Ross, S. (2002) In *Colloidal Dispersions: Suspensions, Emulsions and Foams*, Wiley-Interscience, New York.

(29) Falk, B., and Crivello, J. V. (2005) Synthesis and modification of epoxy- and hydroxy-functional microspheres. *J. Appl. Polym. Sci. 97*, 1574–1585.

(30) Butler, J. E., Ni, L., Nessler, R., Joshi, K. S., Suter, M., Rosenberg, B., Chang, J., Brown, W. R., and Cantarero, L. A. (1992) The physical and functional behaviour of capture antibodies adsorbed on polystyrene. *J. Immunol. Meth. 150*, 77–90.

(31) Butler, J. E, Ni, L., Brown, W. R., Joshi, K. S., Chang, J., and Rosenberg, B., Jr (1993) The immunochemistry of sandwich ELISAs-VI. Greater than 90% of monoclonal and 75% of polyclonal anti-fluorescyl capture antibodies (Cabs) are denaturated by passive adsorption. *Mol. Immunol. 30*, 1165–1175.

(32) Sabatos, C. A., Doh, J., Chakravarti, S., Friedman, R. S., Pandurangi, P. G., Tooley, A. J., and Krummel, M. F. (2008) A synaptic basis for paracrine interleukin-2 signaling during homotypic T cell interaction. *Immunity 29*, 238–248.

(33) Schuurman, H. J., van Wichen, D., de Weger, R. A., and López-Botet, M. (1989) Expression of activation antigens on thymocytes in the 'common thymocyte' stage of differentiation. *Thymus 14*, 43–53.

(34) Tugores, A., Alonso, M. A., Sánchez-Madrid, F., and De Landázuri, M. O. (1992) Human T cell activation through the activation-inducer molecule/CD69 enhances the activity of transcription factor AP-1. *J. Immunol. 148*, 2300–2306.

(35) Coligan, J. E, Kruisbeek, A. M., Margulies, D. H., Shevach, E. M., and Strober, W. (2006) Proliferative Assays for T Cell Function. *Curr. Protoc. Immunol. 1*, 3.12.23.12.5.

(36) Iezzi, G., Karjalainen, K., and Lanzavecchia, A. (1998) The Duration of antigenic stimulation determines the fate of naive and effector T cells. *Immunity 8*, 89–95.

(37) Xue-Zhong, Y., Martin, P. J., and Anasetti, C. (2003) CD28 Signal enhances apoptosis of CD8 T cells after strong TCR ligation. *J. Immunol. 170*, 3002–3006.

(38) Kalamasz, D., Long, S. A., Taniguchi, R., Buckner, J. H., Berenson, R. J., and Bonyhadi, M. J. (2004) Optimization of human T-cell expansion ex vivo using magnetic beads conjugated with anti-CD3 and Anti-CD28 antibodies. *Immunotherapy 27*, 405–418.

(39) Lopez, A., Llinares, F., Cortell, C., and Herraez, M. (2000) Comparative enhancer effects of Span20 with Tween20 and Azone on the in vitro percutaneous penetration of compounds with different lipophilicities. *Int. J. Pharm. 202*, 133–140.

(40) Oberle, R., Moore, T., and Krummel, D. (1995) Evaluation of mucosal damage of surfactants in rat jejunum and colon. *J. Pharmacol. Toxicol. Methods 33*, 75–81.

(41) Grant, R., Yao, C., Gabaldon, D., and Acosta, D. (1992) Evaluation of surfactant cytotoxicity potential by primary cultures of ocular tissues: I. Characterization of rabbit corneal epithelial cells and initial injury and delayed toxicity studies. *Toxicology 76*, 153–176.

(42) Oberg, H.-H., Wesch, D., Lenke, J., and Kabelitz, D. (2006) An optimized method for the functional analysis of human regulatory T cells. *Scand. J. Immunol. 64*, 353–360.

(43) Mayer, L. (1986) Terminal maturation of resting B cells by proliferation-independent B cell differentiation factors. *J. Exp. Med. 164*, 383–392.

BC900402D

Expression, Glycoform Characterization, and Antibody-Binding of HIV-1 V3 Glycopeptide Domain Fused with Human IgG1-Fc

Qiang Yang, Cishan Li, Yadong Wei, Wei Huang, and Lai-Xi Wang*

Institute of Human Virology and Department of Biochemistry and Molecular Biology, University of Maryland School of Medicine, 725 West Lombard Street, Baltimore, Maryland 21201. Received September 24, 2009; Revised Manuscript Received March 18, 2010

The third variable (V3) domain of HIV-1 gp120 envelope glycoprotein is critical for HIV-1 entry and represents an attractive target for vaccine design. There are three conserved *N*-glycans within or around the V3 loop. The N295 and N332 glycans at the base of V3 are usually characterized as high-mannose type in gp120, and the N301 glycan is a complex type. We report in this paper the expression and characterization of glycosylated, full-size V3 domain derived from HIV-1_{Bal} strain as an IgG1-Fc fusion protein, including its binding to two broadly HIV-neutralizing antibodies 2G12 and 447-52D. It was found that expressing the V3-Fc fusion protein in the HEK293T cells resulted in the production of a glycoform in which all the *N*-glycans were complex type, in contrast to the glycosylation pattern of V3 in the context of gp120, where the N295 and N332 glycans are high-mannose type. Controlling the glycosylation to restore an epitope of antibody 2G12 was achieved by using an inhibitor of glycan processing enzymes. Mutational studies indicate that the glycan at N301 slightly decreases the binding of V3-Fc to antibody 447-52D, but it can significantly enhance the binding of the V3-Fc to antibody 2G12 when it is changed to a high-mannose type *N*-glycan. The high-mannose type V3-Fc fusion protein that includes both the 2G12 and 447-52D epitopes represents an interesting immunogen that may be able to raise anti-HIV neutralizing antibodies.

INTRODUCTION

Neutralizing antibodies are an important component of protective immunity against HIV-1 infection (*1–3*). So far, a few human monoclonal antibodies (MAbs) have been characterized, suggesting the presence of conserved neutralizing epitopes in the HIV-1 envelope glycoproteins. Thus, characterization and reconstitution of the neutralizing epitopes for these broadly neutralizing antibodies constitute an important step for HIV-1 vaccine design. The third variable (V3) domain of HIV-1 gp120 envelope glycoprotein was once considered "the principal neutralization determinant (PND)" for vaccine development (*4, 5*). While the sequence variation resulted in the production of most anti-V3 antibodies that are strain-specific and neutralize only T-cell line adapted viruses or a very narrow range of primary isolates, there is accumulating evidence showing that broadly reactive anti-V3 antibodies capable of neutralizing HIV-1 primary isolates across clades do exist (*2*). For example, the anti-V3 monoclonal antibody (mAb) 447-52D is able to neutralize HIV-1 primary isolates of clades A, B, and F, regardless of the sequence variability of the V3 loop (*6–8*). In fact, despite the sequence variations flanking the tip of the loop, V3 domains from different viral strains do share conserved sequence and structural features in order to function as a key determinant in recognizing chemokine coreceptor (CCR5 or CXCR4) during HIV-1 infection (*9–12*). In addition to those conserved elements, such as a fixed size (30−35 amino acids) of the loop, a conserved disulfide bond at the base, and a β-turn structure at the conserved tip (GPGR or GPGQ) (*5, 13*), V3 domains from many different strains also carry three conserved *N*-glycans, within or adjacent to the loop, at the N295, N301, and N332 glycosylation sites (HXB2 numbering, http://hiv-web.lanl.gov). In the context of gp120, the N301 glycosylation site within the V3 loop usually carries a complex type *N*-glycan, while the N295 and N332 sites at the base normally bear high-mannose type *N*-glycans (*14, 15*). The two high-mannose type *N*-glycans at N295 and N332 sites are particularly interesting, as they were proposed to be an essential component of the epitope of the broadly neutralizing antibody 2G12 (*16, 17*). The human mAb 2G12 is the only broadly neutralizing antibody so far discovered that recognizes a novel cluster of high-mannose type *N*-glycans with terminal Manα1,2Man motifs in gp120 (*16–19*).

As part of our research program on HIV-1 vaccine, we are interested in reconstituting a V3 domain immunogen that integrates both the carbohydrate and peptide epitopes of the broadly neutralizing antibodies 2G12 and 447-52D. V3 domain has been previously expressed in the context of different fusion proteins for biochemical and immunological studies (*20–24*). But most of the V3 fusion proteins previously described were not glycosylated, as they were usually overproduced in *E. coli* that lacks protein glycosylation machinery (*20–23*). A large outdomain (aa 251−481) of a clade C gp120, which consists of V3 and other domains (C3, V4, C4, V5, and C5), was expressed in baculovirus infected insect cells as a glycosylated Fc-fusion protein (*24*). This study confirms the importance of the *N*-glycans around the V3 domain for 2G12 recognition, but the nature of the glycans (complex type vs high-mannose type) attached to V3 and other domains in the recombinant protein is yet to be characterized. We describe in this paper the expression of a glycosylated V3 domain as an IgG1-Fc fusion protein in the human embryonic kidney 293T (HEK293T) cell line. A V3 domain corresponding to the sequence aa 291−336 (46 amino acid residues) of HIV-1_{Bal} gp120 was chosen, which was fused to the C-terminus of the human IgG1-Fc domain (232 amino acid residues). The resulting V3-Fc fusion protein contains four glycosylation sites: three (N295, N301, and N332) are in the V3 domain and one is in the Fc domain (Fc-N297) (Figure 1). The advantage of making the IgG1-Fc fusion protein was

* To whom correspondence should be addressed. E-mail: LWang@som.umaryland.edu.

10.1021/bc9004238 © 2010 American Chemical Society
Published on Web 04/06/2010

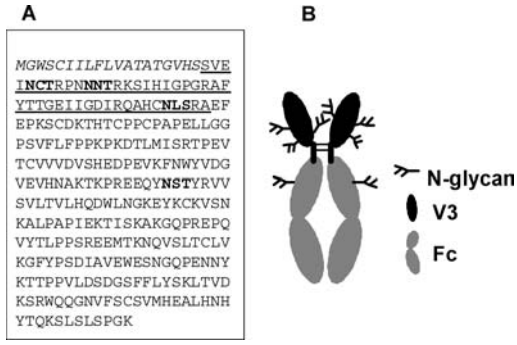


Figure 1. Schematic presentation of the glycosylated V3-Fc fusion protein. (A) Amino acid sequence of the V3-Fc fusion protein. The signal peptide sequence is italic, the V3 domain is underlined, and the glycosylation sites are in bold. (B) Homodimer of V3-Fc, in which the *N*-glycans at the N295 and N332 glycosylation sites in V3 domain are expected to be high-mannose type (HM), the glycan at N301 site in V3 domain is expected to be complex type (CT), and the *N*-glycan at the Fc region is expected to be complex type (CT).

several-fold. In addition to the easiness of purification of the Fc-tagged fusion protein via protein A affinity chromatography, fusing the small V3 polypeptide to the Fc is likely to stabilize the resulting recombinant protein and prevent degradation, as previously demonstrated for the Fc-fused gp41 ectodomain (*25*). Moreover, it has been suggested that the Fc domain could enhance the immunogenicity of the Fc-fusion protein by facilitating the uptake of antigens via Fc-mediated interactions with Fcγ receptors on antigen presenting cells (*24–26*). We report here the expression, characterization, and antibody-binding of different glycoforms of the recombinant V3-Fc fusion protein. Our results suggest that the high-mannose type V3-Fc fusion protein, which constitutes the epitopes of both the neutralizing antibodies 2G12 and 447-52D, may be a valuable immunogen for raising broadly neutralizing antibodies against HIV-1.

EXPERIMENTAL PROCEDURES

Strains, Cell Line, Media, and Enzymes. *Escherichia coli* DH5α was used for all molecular cloning steps. It was grown in LB broth (1% casein peptone, 0.5% yeast extract, and 1% NaCl). Human HEK293T cell line was used for the expression of V3-Fc fusion protein. It was cultured in DMEM medium supplemented with 10% low IgG fetal bovine serum (HyClone, Logan, UT) and 12.5 mM HEPES buffer.

Construction of pcDNA-LV3Fc Expression Vector and Site-Directed Mutagenesis. A 46 amino acid V3 domain was chosen from the sequence (aa 291−336, HXB2 numbering) of the gp120 derived from the HIV-1 BAL strain (R5 tropic). This domain includes the two glycosylation sites at the base of the V3 loop. The fusion protein was arranged by adding the Fc domain of human IgG1 to the C-terminus of the V3 domain. The human CD5 antigen leader sequence (*27*) was added to the N-terminus of fusion protein. The whole fusion construct was assembled in pGEM-T vector (Promega, Madison, WI). First, the coding fragments for human IgG1-Fc, V3, and CD5 leader were amplified by PCR with respective primer pairs and cloned into pGEM-T vector. The Fc coding fragment was amplified by a primer pair, (forward) CGA ATT CGA GCC CAA ATC TTG TGA C, (reverse) GTA GCG GCC GCT TAT TTA CCC GGG GAC AGG GAG. V3 fragment was amplified by the following primers, (forward) TCT CGA GCG TGG AGA TCA ACT GCA C and (reverse) TGA ATT CGG CGC GGC TCA GGT TGC. CD5 leader was amplified with (forward) CGG TAC CAT GGG ATG GTC ATG TAT CAT C and (reverse) GCT CGA GTG TAC ACC GGT TGC AGT. Each fragment was inserted into the pGEM-T vector, resulting in three plasmids: pT-Fc, pT-V3, and pT-CD5. To assemble the final expression construct, the Fc fragment was released from pT-Fc with *Eco*R I and *Not* I and cloned into corresponding sites of pT-V3, resulting in pT-V3Fc. Subsequently, V3Fc fragment was released with *Xho* I and *Not* I from the pT-V3Fc and cloned into corresponding site of pT-L, resulting in pT-LV3Fc. Finally, the assembled LV3Fc fragment was released from pT-LV3Fc and cloned into *Kpn*I and Not I site of mammalian expression vector pcDNA3.1+ (Invitrogen, Carlsbad, CA), resulting in the expression vector pcDNA-LV3Fc. To generate the single mutants of N-glycosylation sites in fusion protein, site-directed mutagenesis was carried out by using a commercial site-directed mutagenesis kit (QuickChange, Stratagene). All mutants were confirmed by DNA sequencing.

Transfection and Expression of V3-Fc in HEK293T Cells. The phenol-free pcDNA-LV3Fc plasmid for transfection was prepared with HiSpeed Plasmid Midi Kit or QIAfilter Maxi Kit (Qiagen). Transient transfection was performed using Fugene6 transfection reagent (Roche) following the manufacture's protocol. After transfection, the expression of fusion protein was periodically monitored using an antihuman IgG1 Fc ELISA assay kit (human IgG ELISA quantitation kit, BETHYL Laboratories Inc., Montgomery, TX). Complex type V3-Fc was expressed without the addition of mannosidase inhibitor. For generation of HM type V3-Fc, kifunensine (Caltech), the mannosidase inhibitor, was added into the culture system immediately after the transfection.

Purification of the Fusion Glycoprotein. The culture supernatant was collected 4 days after transfection. The fusion protein was purified by affinity chromatography using a protein A-agarose resin (Pierce). The cell-free culture supernatant was loaded on the protein A column pre-equilibrated with the binding buffer (pH 8.0, Thermo Scientific, Rockford, IL). After an extensive wash with the same buffer, V3-Fc was eluted with IgG elution buffer (pH3.0, Thermo Scientific, Rockford, IL). Each elution fraction was immediately neutralized with 1 M Tris-HCl, pH 8.8. Subsequently, all fractions were combined and concentrated with centrifugal filtration (Amicon Ultra centrifugal filter, Millipore, Billerica, MA). The integrity and purity of protein were checked by SDS−PAGE. The protein A column was regenerated with the elution buffer.

Size Exclusion Chromatography (SEC). The SEC chromatography was performed on an AKTA FPLC system (GE Healthcare) at 4 °C. The purified V3-Fc was loaded on a Superdex 200 10/300 GL size exclusion column (GE Healthcare). The column was eluted with a buffer containing 150 mM NaCl and 20 mM Tris-HCl (pH 8.0) at a flow rate of 0.5 mL/min. The sizes of proteins were estimated by using thyroglobulin (670 kDa) γ-globulin (158 kDa), ovalbumin (44 kDa), and myoglobin (17 kDa) as standards.

Enzymatic Deglycosylation. Purified V3-Fc proteins in various glycoforms were deglycosylated by different glycosidase treatment. PNGase F and Endo H (New England Biolabs) treatments were performed according to the manufacture's instruction, respectively. Deglycosyaltion of high mannose type V3-Fc was carried out by incubation of the V3-Fc fusion protein with endo-β-*N*-acetylglucosaminidase from *Arthrobacter* (Endo-A) (1/100, by weight) in a 25 mM Tris-Cl buffer (pH 8.0) at 37 °C for 2 h. Endo-A was expressed according to the reported method (*28*).

MALDI-TOF Mass Spectrometry. For the MALDI-TOF MS analysis of *N*-glycans, the total *N*-glycans of V3-Fc were released from 60 μg of glycoprotein by 10 U of PNGase F with incubation at 37 °C for 48 h. The reaction mixture was then treated with 10 mU of neuraminidase (from *Clostridium perfringens*, Sigma) and incubation at 37 °C for 2 h for

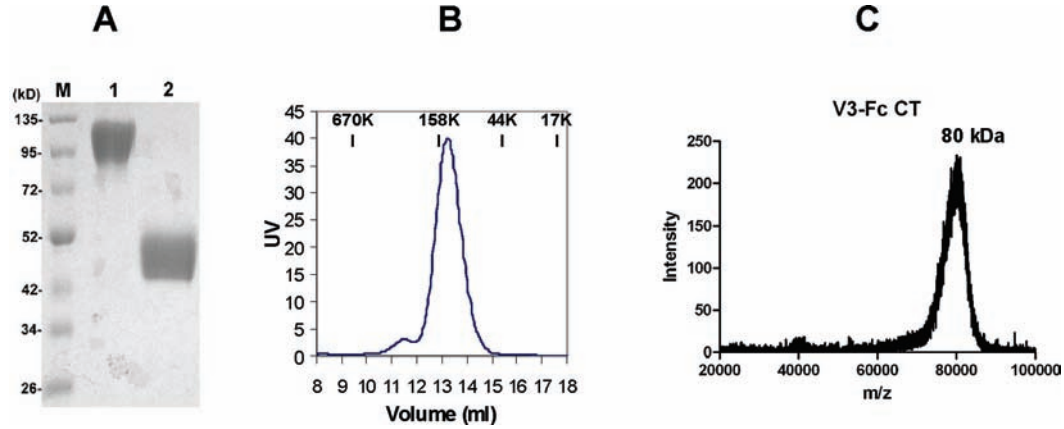


Figure 2. Analysis of the expressed V3-Fc fusion protein: (A) SDS−PAGE of the V3-Fc fusion protein under nonreducing (lane 1) and reducing conditions (lane 2); (B) gel-filtration chromatography of the V3-Fc under native condition; (C) MALDI-TOF MS analysis of the native V3-Fc.

desialylation. The released *N*-glycans were separated with centrifuge filtration (Microcon centrifugal filter, 10 KDa cutoff, Millipore), desalted by treatment with anion-exchange resin (DOWEX 1X2-100, Sigma-Aldrich) and cation-exchange resin (DOWEX 50WX8-100, Sigma-Aldrich), and finally lyophilized. The *N*-glycans were analyzed using a Bruker Autoflex II linear MALDI-TOF mass spectrometer (Bruker Daltonics) with 2,5-dihydroxybenzoic acid (DHB) as the matrix. The MALDI-TOF analysis of V3-Fc fusion protein was performed with the same machine, with sinapinic acid as matrix.

Surface Plasmon Resonance (SPR) Measurement. The interactions between the glycoforms of V3-Fc fusion protein and antibodies 2G12 and 447-52D were evaluated using a BIAcore T100 system (GE Healthcare). Monoclonal antibodies 2G12 and 447-52D (NIH AIDS Research and Reference reagent program) were immobilized respectively on CM5 sensor chips in an acetate buffer (10 mM, pH 5.0) by use of the amine coupling kit provided by the manufacturer, until the targeted response unit (RU) was reached. The reaction was quenched by the addition of ethanolamine HCl (1 M, pH 8.5). A reference cell without the antibody was prepared by similar procedures. Analyses were performed at 25 °C by injecting a solution of the respective V3-Fc glycoforms in a HBS-P buffer (10 mM HEPES, 150 mM NaCl, and 0.05% surfactant P20, pH 7.4) at a flow rate of 30 μL/min for 2 min, followed by wash for 5 min with HBS-P buffer for dissociation. The sensor surface was regenerated through a two-step wash (first wash, 3.5 M $MgCl_2$ for 0.5 min; second wash, HBS-P for 1 min). Data processing was carried out using the BIAcore T100 software.

RESULTS AND DISCUSSION

Expression, Purification, and Characterization of the V3-Fc Fusion Protein. The expression vector encoding the fusion protein was introduced into HEK293T cells by transient transfection. The culture supernatant was collected 4 days after transfection, and the V3-Fc fusion protein was purified with protein A affinity chromatography. The fusion protein appeared as a broad band at ∼49 kDa under reduced conditions (Figure 2A, lane 2) on SDS−PAGE. The broad band implicates a significant heterogeneity in the *N*-glycans attached. Under nonreducing (native) conditions, the fusion protein migrated on SDS−PAGE as a broad band at 110 kDa (Figure 2A, lane 1). These results suggest that the fusion protein is present as a homodimer in aqueous solution. This is expected, as the hinge-containing IgG-Fc turns to form a covalently linked homodimer through the formation of two pairs of disulfide bonds (*29*). The dimer format of the fusion protein under native conditions was further confirmed by size-exclusion chromatography. The V3-Fc fusion protein was eluted as a peak at ∼110 kDa, suggesting that it exists as a homodimer (Figure 2B). However, it was observed that the apparent molecular weight of the fusion protein was significantly bigger than the calculated molecular weight. On the basis of the assumption that the V3-Fc fusion protein (31 kDa for the protein backbone) carries four *N*-glycans and each *N*-glycan has an average molecular weight of 2 kDa, the estimated molecular weight should be around 39 kDa. The apparent molecular size (∼49 kDa) of the monomeric fusion protein on SDS−PAGE was clearly larger than the calculated data. The homodimer also showed a much larger size on SDS−PADE (under native condition) as well as in size-exclusion chromatography. One possible explanation is that the heavily glycosylated protein might have an extensive hydration to give a large hydration volume. To verify the actual molecular mass, the native V3-Fc fusion protein was subject to MALDI-TOF MS analysis (Figure 2C). While the fusion protein appeared as a broad signal, indicating the heterogeneity of the attached *N*-glycans, the average molecular mass is ∼80 kDa, which is consistent with the expected molecular weight of the heterogeneous dimeric V3-Fc glycoprotein (78−82 kDa).

To characterize the N-glycosylation status of the V3-Fc, the fusion protein was treated with PNGase F, which would remove all *N*-glycans attached. SDS−PAGE showed that the deglycosylated V3-Fc appeared as a sharp band with a size of ∼38 kDa (Figure 3A, lane 2). An 11 kDa difference between the glycosylated V3-Fc (∼49 kDa) and deglycosylated V3-Fc (∼38 kDa) suggests that the monomeric V3-Fc carries at least four *N*-glycans. Thus, all the glycosylation sites (three in the V3 domain and one in the Fc domain) in the expressed fusion protein should be glycosylated. Treatment of the fusion protein with Endo-H, an endo-glycosidase that cleaves only high-mannose type or hybrid type *N*-glycans, did not cause any change in the molecular size of the protein (comparing lane 3 and lane 1, Figure 3A). These results suggest that the V3-Fc fusion protein does not contain any high-mannose type or hybrid type *N*-glycans.

To validate the glycan profiles of the expressed fusion protein, the total *N*-glycans were released by PNGase F treatment. The released *N*-glycans were subjected to MALDI-TOF MS analysis after desialylation by sialidase, which simplifies the profiles of complex type *N*-glycans and also enhances the detection sensitivity. It was found that all the *N*-glycans in the V3-Fc fusion protein were complex type composed of bi-, tri-, and tetraantennary complex *N*-glycans, and no high-mannose type or hybrid type sugars were present (Figure 3B). The found molecular mass and proposed structures of the released *N*-glycans were listed in Table 1. These MS analysis data

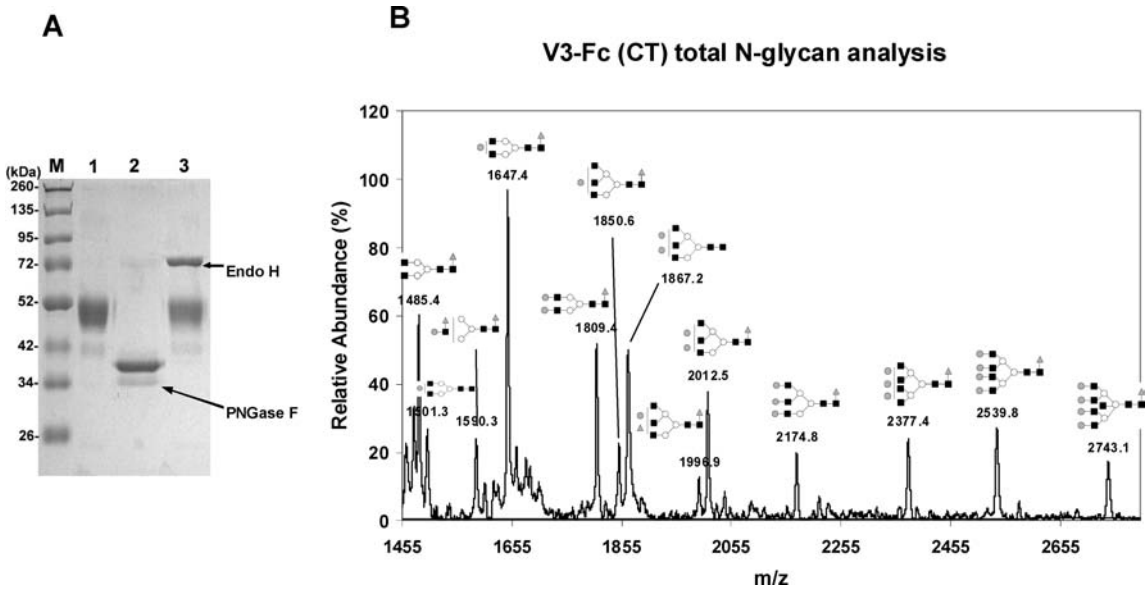


Figure 3. Characterization of the glycan profile of complex type fusion protein V3-Fc CT: (A) SDS−PAGE of the fusion proteins before and after enzymatic treatment (lane 1, untreated V3-Fc; lane 2, treated by PNGase F; lane 3, treated by Endo H); (B) MALDI-TOF MS analysis of total *N*-glycans released by PNGase F.

Table 1. Molecular Mass and Proposed Structures of the Desialylated *N*-Glycans Released from the Complex Type V3-Fc[a]

Calculated ($M+Na^+$)	Found ($M+Na^+$)	Composition	Suggested structures
1485.5	1485.2	Hex3HexNAc4dHex1	
1501.5	1501.1	Hex4HexNAc4	
1590.6	1590.3	Hex4HexNAc3dHex2	
1647.6	1647.2	Hex4HexNAc4dHex1	
1809.6	1809.0	Hex5HexNAc4dHex1	
1850.7	1849.7	Hex4HexNAc5dHex1	
1866.7	1866.3	Hex5HexNAc5	
1996.7	1996.9	Hex4HexNAc5dHex2	
2012.7	2012.1	Hex5HexNAc5dHex1	
2174.8	2174.0	Hex6HexNAc5dHex1	
2377.9	2377.2	Hex6HexNAc6dHex1	
2539.9	2538.9	Hex7HexNAc6dHex1	
2743.0	2741.9	Hex7HexNAc7dHex1	

[a] Gray triangle, fucose; gray circle, galactose; black square,, *N*-acetylglucosamine; open circle, mannose; Hex, hexose; HexNAc, *N*-acetylhexosamine; dHex, monodeoxyhexose.

confirmed the results from the Endo-H treatment. This is an interesting observation. In HIV-1 gp120, the two conserved *N*-glycans at the base of the V3 loop, N295 and N332, are usually high-mannose type, and the one within the V3 loop (N301) is conserved as a complex type *N*-glycan (*14*, *15*). We have shown here that when the V3 domain was expressed in the context of Fc-fusion protein, all the *N*-glycans were processed to form complex type sugars. These results suggest that the two *N*-glycans at N295 and N332 might be inaccessible for further processing by ER and Golgi α-mannosidases in the context of gp120, but in the Fc-fusion protein, the *N*-glycans at the two sites are more exposed so that further trimming and modifications could be achieved to form complex type sugars. These results also suggest that the microenvironment of the N-glycosylation sites, e.g., the steric hindrance around the sites due to the presence of other proximal domains, is critical for determining the nature of the *N*-glycans attached. This glycoform of the V3-Fc fusion protein, in which all the *N*-glycans are complex type, is named as V3-Fc-CT.

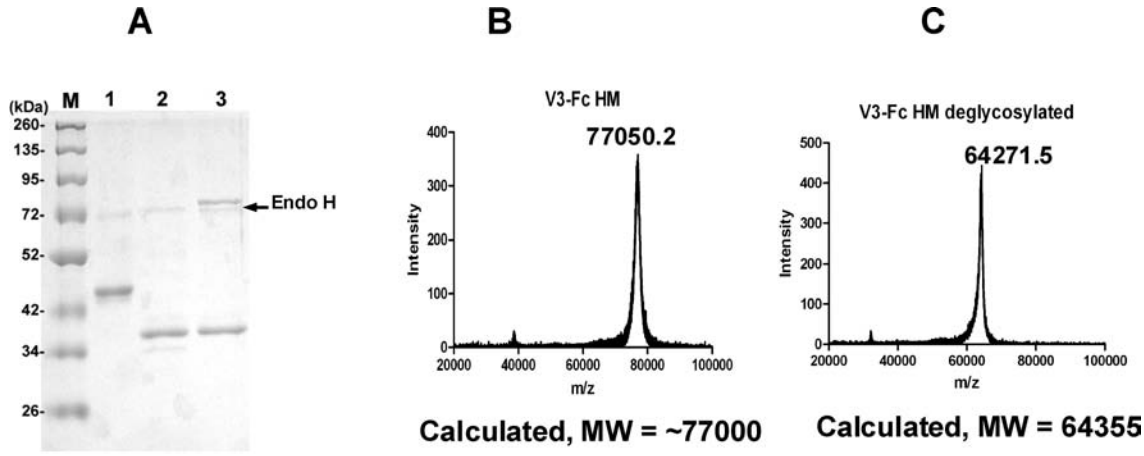


Figure 4. Characterization of the fusion protein V3-Fc expressed in the presence of α-mannosidase inhibitor kifunensine (2 μg/mL): (A) SDS−PAGE of the fusion proteins before and after deglycosylation (lane 1, untreated V3-Fc; lane 2, treated by PNGase F; lane 3, treated by Endo H); (B) MALDI-TOF MS analysis of intact fusion protein as a homodimer; (C) MALDI-TOF MS analysis of intact fusion protein after deglycosylation with Endo-H.

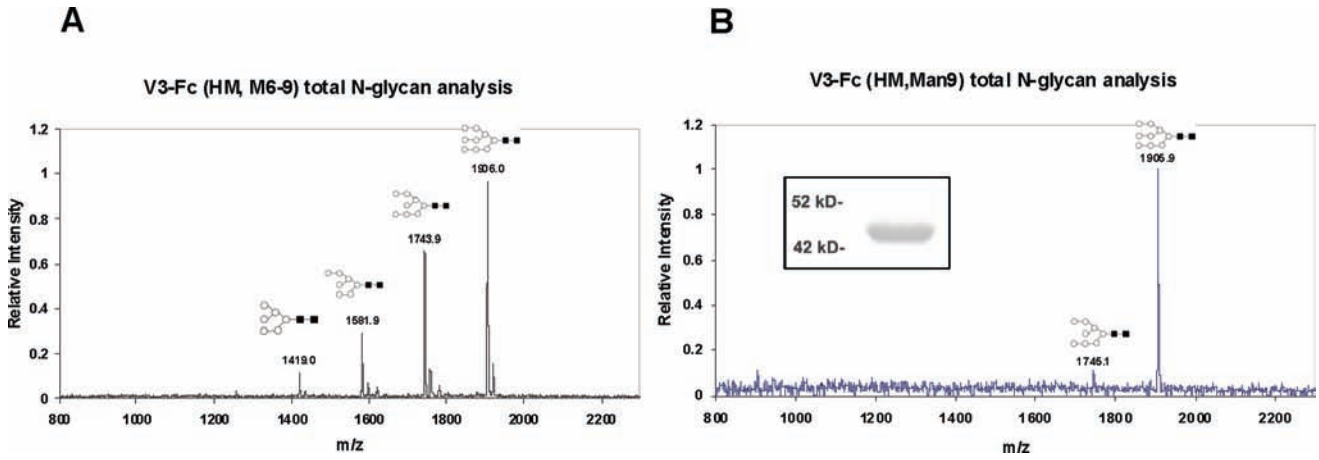


Figure 5. MALDI-TOF MS profiles of the *N*-glycans released from the HM type V3-Fc by PNGase F treatment: (A) *N*-glycans from the V3-Fc fusion protein expressed in the presence of kifunensine at 2 μg/mL; (B) *N*-glycans from the V3-Fc fusion protein expressed in the presence of kifunensine at 10 μg/mL. Inset: SDS−PAGE of V3-Fc expressed in the presence of kifunensine at 10 μg/mL.

Table 2. Molecular Mass and Proposed Structures of the High-Mannose Type *N*-Glycans Released from the HM-V3-Fc[a]

Calculated ($M+Na^+$)	Found ($M+Na^+$)	Composition	Suggested structures
1419.5	1418.9	Hex6HexNAc2	
1581.5	1581.8	Hex7HexNAc2	
1743.6	1743.9	Hex8HexNAc2	
1905.6	1905.9	Hex9HexNAc2	

[a] Black square, *N*-acetylglucosamine; open circle, mannose; Hex, hexose; HexNAc, *N*-acetylhexosamine.

Expression and Characterization of High-Mannose Glycoforms of V3-Fc and Its Selected N-Glycosylation Mutants. It is known that antibody 2G12 recognizes a cluster of high-mannose type *N*-glycans around the V3 domain, and the *N*-glycans at the N295 and N332 sites of HIV-1 gp120 are the essential components for the epitope (*16*, *17*, *30*, *31*). The unexpected results that all the *N*-glycans attached to the V3-Fc fusion protein are complex type sugars when expressed in the HEK293 cell line prompted us to restore high-mannose type *N*-glycans in the V3-Fc fusion protein by controlling the glycan processing with a specific glycosidase inhibitor. It was previously reported that expression of glycoproteins in HEK293 cell lines in the presence of kifunensine, a potent α-mannosidase inhibitor, could efficiently control the glycosylation at the high-mannose type stage, thus leading to the formation of high-mannose glycoforms of recombinant glycoproteins (*32*–*34*). In particular, Scanlan and co-workers have successfully expressed HIV-1_{IIIB} gp120 in CHO cell line in the presence of kifunensine, which produced a novel glycoform of HIV-1_{IIIB} gp120 that carries high-mannose type sugars (*33*). Thus, we expressed the V3-Fc fusion protein in the HEK293T culture system in the presence of kifunensine (2 μg/mL). The expressed fusion protein, named as V3-Fc-HM, appeared at ∼95 kDa in SDS−PAGE under nonreducing condition (data not shown) and at ∼45 kDa under reduced condition as a clear band (Figure 4A, lane 1). This result indicates that the fusion protein

expressed is a homodimer. The dimeric form of the fusion protein was also confirmed by size-exclusion chromatography, which appeared as a single peak larger than 90 kDa (data not shown). In contrast to the complex type fusion protein V3-Fc-CT that appeared as a broad band in SDS−PAGE, the high-mannose type fusion protein V3-Fc HM appeared as a much sharper band, suggesting that the glycans attached are more uniformed. Removal of the V3-Fc-HM by PNGase F gave the deglycosylated fusion protein that appeared as a single band at 38 kDa (Figure 4A, lane 2), which is at the same size of the deglycosylated fusion protein from V3-Fc-CT. In addition, treatment of V3-Fc-HM with Endo-H resulted in a single band in SDS−PAGE (Figure 4A, lane 3) that had a similar size of the PNGase-F treated protein. This result indicates that all the glycans attached in V3-Fc-HM are Endo-H-sensitive, high-mannose type *N*-glycans. The MALDI-TOF MS of the V3-Fc-HM (Figure 4B) showed an average molecular mass of 77 050 Da, which is consistent with a V3-Fc homodimer carrying four high-mannose *N*-glycans (calculated, $M = 77\,000$ Da, for the Man8GlcNAc2 glycofrom). The observed *m*/*z* data from the MALDI-TOF MS of the Endo-H deglycosylated fusion protein (Figure 4C) are also in agreement with the calculated molecular weight of the deglycosylated protein (observed, 64 271 Da, calculated, $M = 64\,355$ Da). Finally the *N*-glycans released from the V3-Fc-HM by PNGase F were analyzed by MS. It was found that most of the glycoforms were Man9GlcNAc2 and Man8GlcNAc2, together with minor fractions of Man7GlcNAc2 and Man6GlcNAc2 glycoforms (Figure 5A and Table 2). Thus, the use of 2 μg/mL of kifunensine in the expression system could efficiently control the glycosylation processing at the high-mannose stage. To produce a homogeneous high-mannose type glycoform of V3-Fc, we increased the concentration of kifunensine in the HEK293 expression system to 10 μg/mL. Interestingly, we found that the fusion protein obtained under this condition was almost the Man9GlcNAc2 glycoform, with only a minor amount of the Man8GlcNAc2 (Figure 5B). No glycans smaller than Man8GlcNAc2 were formed under this expression condition. Thus, a new glycoform, V3-Fc-Man9 was obtained that appeared as a homogeneous glycoprotein, as indicated by SDS−PAGE (Figure 5B, inlet).

We also produced two mutants, N301A and Fc-N297A, in which the N301 glycosylation site in the V3 and the N297 site in the Fc domain were deleted, respectively. Both mutants were expressed in HEK293T cells in the presence of 2 μg/mL kifunensine to provide the high-mannose type glycoforms. SDS−PAGE analysis indicated that the two mutants were about 2 kDa smaller in size than that of the high-mannose glycoform of the wild type fusion protein (V3-Fc-HM) (Figure 6A, lane 1, V3-Fc-HM; lane 2, N301A; lane 3, Fc-N297A). These data suggest the deletion of one *N*-glycan in the two mutants. The *N*-glycan profiles of the two mutants are shown in Figure 6B and Figure 6C. Both have very similar profiles as that of the V3-Fc-HM, with Man9GlcNAc2 and Man8GlcNAc2 as the major glycoforms.

Binding of V3-Fc Glycoforms with Broadly Neutralizing Antibody 2G12. Monoclonal antibody 2G12 is a broadly HIV-neutralizing antibody that recognizes a cluster of high-mannose type *N*-glycans in HIV-1 gp120 (*16–18, 30*). We measured the interactions between 2G12 and the various glycoforms of V3-Fc with Biacore surface plasmon resonance (SPR) technology. 2G12 was immobilized on the SPR chip, and its real-time association and dissociation with V3-Fc at various concentrations were examined. It was observed that the complex type glycoform V3-Fc-CT did not show measurable interaction with 2G12 (Figure 7A). This result was expected, as 2G12 was previously shown to recognize only those *N*-glycans that bear terminal Manα1,2Man motifs (*16–19*). In contrast, the high-

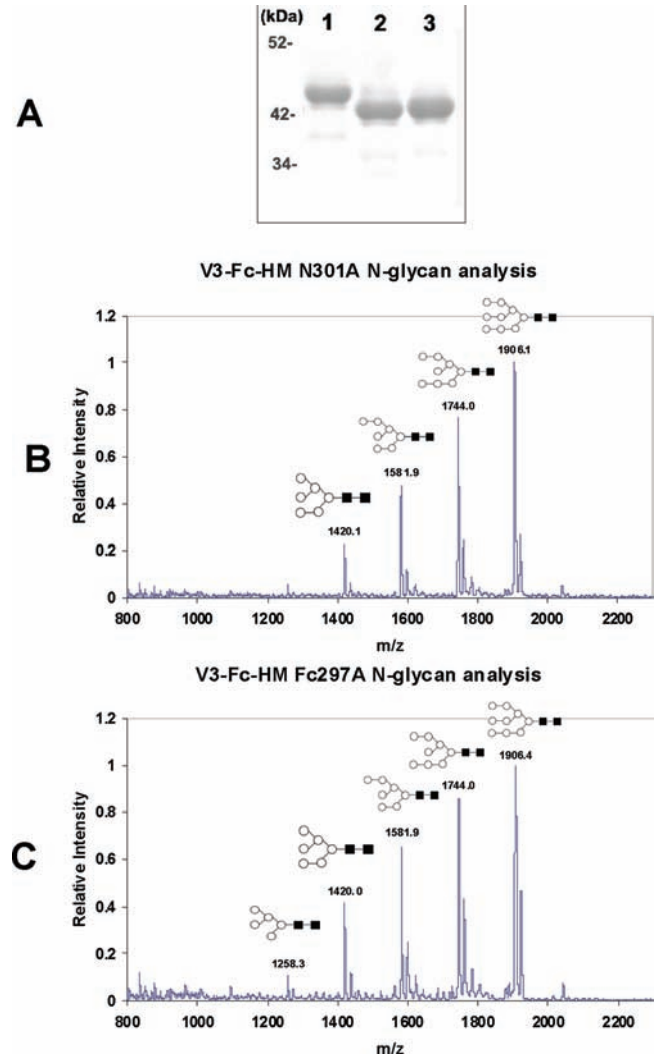


Figure 6. Characterization of V3-Fc mutants and their glycoprofiles. (A) SDS−PAGE analysis of V3-Fc mutants: lane 1, wild type V3-Fc HM); lane 2, V3-Fc N301A; lane 3, V3-Fc Fc-N297A. (B, C) MALDI-TOF MS analysis of PNGase F released *N*-glycan from N301A and Fc-N297A mutants, respectively.

mannose type glycoforms of V3-Fc demonstrated significant affinity to 2G12. The binding profiles of the V3-Fc-HM, V3-Fc-M9, and the two mutants (N301A and Fc-N297A) are shown in Figure 7B−E, respectively. The binding profile of gp120 derived from the HIV-1_{Bal} strain is shown in Figure 7F. It was found that the binding of antibody 2G12 to the four high-mannose glycoforms of V3-Fc fusion protein (including the two mutants) followed a quick association/dissociation kinetic process. Unfortunately, an attempt to fit the SPR data to possible kinetic equations failed to provide an accurate dissociation constant (K_d), making it difficult to have a quantitative comparison of the binding of 2G12 with different V3-Fc glycoforms. Nevertheless, a comparison of the sensorgrams of the various glycoforms indicated that the V3-Fc-HM and V3-Fc-M9 had a comparable affinity to 2G12 and followed a very similar kinetic profile (Figure 7B vs Figure 7C). Since both glycoforms carry Man9GlcNAc2 and Man8GlcNAc2 as the major *N*-glycans, these results are consistent with previous observations that Man9GlcNAc2 and Man8GlcNAc2 interacted with 2G12 equally efficiently through the D1 arm contact (*18, 19*). Interestingly, removal of the *N*-glycan at the N301 site significantly reduced the affinity to antibody 2G12 (Figure 7D). In native HIV-1 gp120, the glycan at the N301 site of V3 is a conserved complex type sugar that did not positively contribute

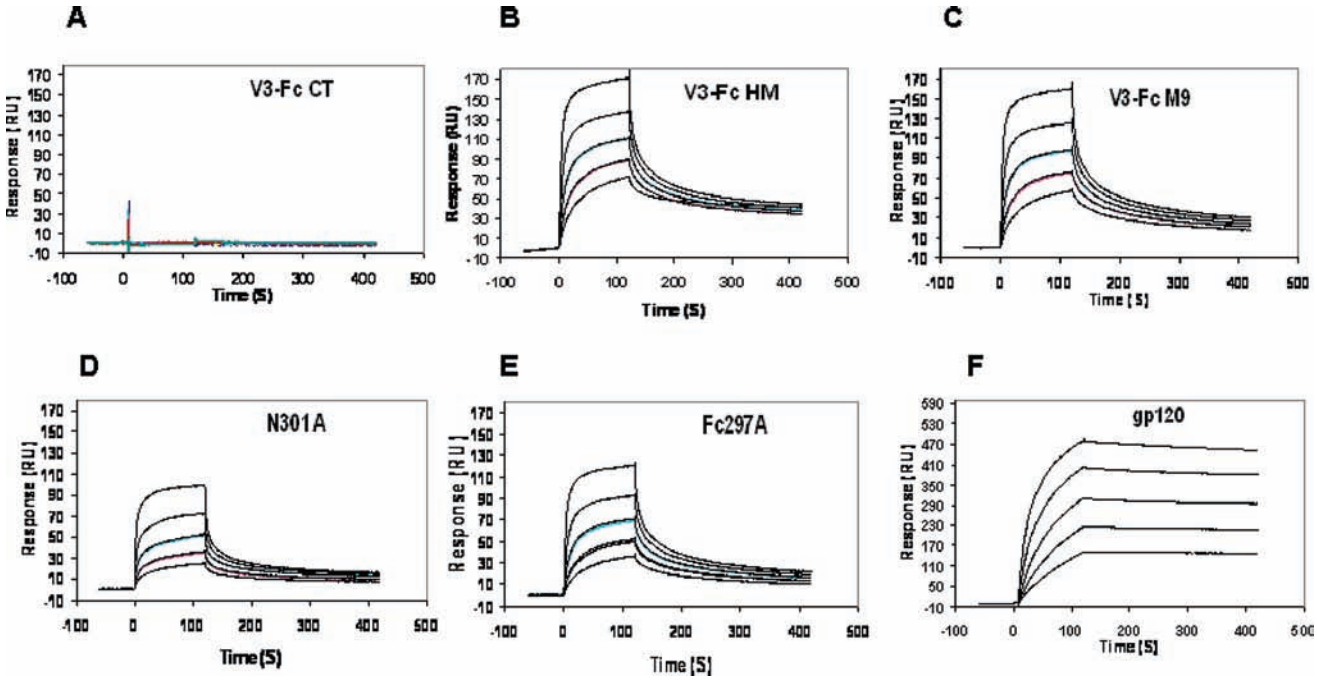


Figure 7. SPR sensorgram of the binding of different glycoforms of V3-Fc and its mutants with immobilized 2G12 antibody. V3-Fc was applied to analysis with a serial concentration of 2-fold dilution, with the highest concentration set at 2 μM. The interaction between gp120 and immobilized 2G12 was analyzed in a similar manner except that the highest concentration of gp120 was set at 1 μM.

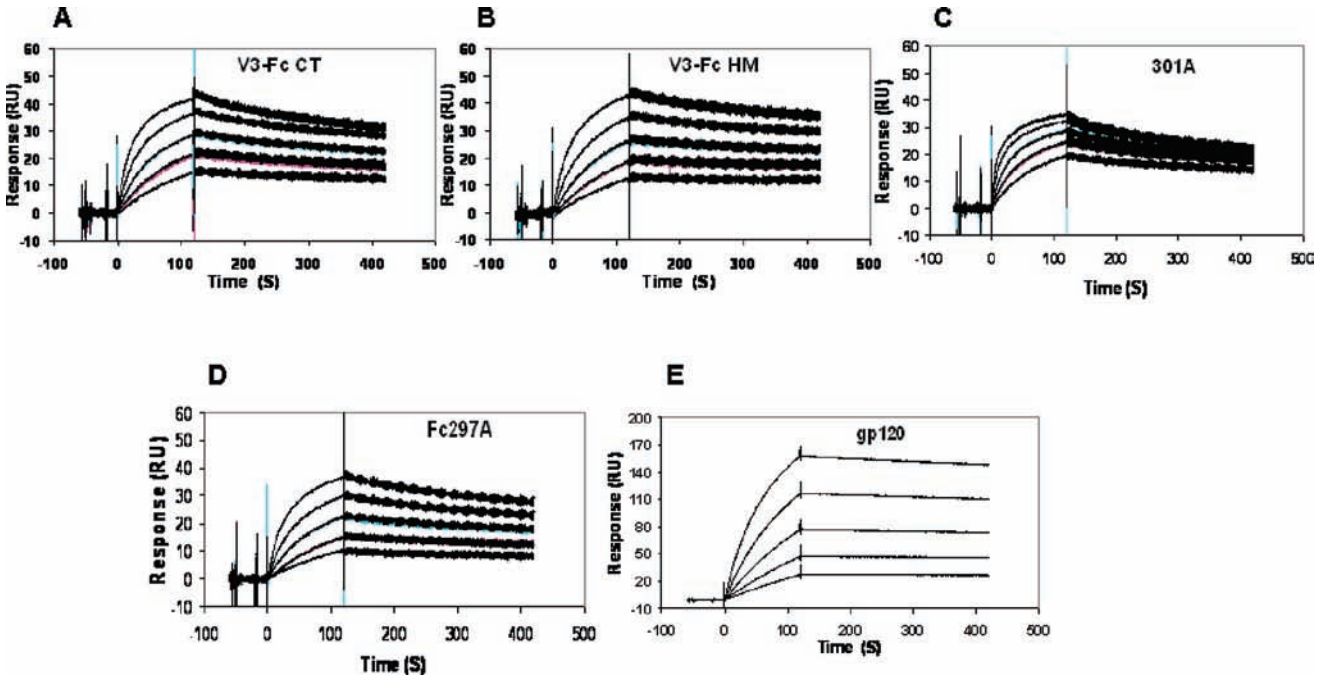


Figure 8. SPR sensorgram of the binding of different glycoforms of V3-Fc with immobilized 447-52D antibody. Both V3-Fc and gp120 were applied to the analysis with a serial concentration of 2-fold dilution. The highest concentration was set at 200 nM.

to the binding of 2G12 (*14*, *15*). Thus, changing this *N*-glycan to a high-mannose type glycan seemed to create a new epitope (likely a cluster of the three *N*-glycans at N295, N301, and N332) for 2G12 that has a much higher affinity to 2G12 than the epitope formed only by the two glycans at N295 and N332. As for the Fc glycosylation, we also observed that removal of the *N*-glycan at the Fc domain resulted in the reduction of the binding of the resulting mutant (Fc-N297A) to 2G12 (Figure 7E), albeit to a lesser extent than the N301A mutant. This result implicated that the Fc domain *N*-glycan was also involved in the interaction of the V3-Fc fusion protein with 2G12. In contrast to those recombinant V3-Fc fusion proteins, the dissociation between gp120 and 2G12 was found to be extremely slow (Figure 7F), although its association rate was comparable to those of the V3-Fc fusion proteins (Figure 7F). A typical HIV-1 gp120 carries 24 *N*-glycans, among which 11 are high-mannose type and 13 are complex type *N*-glycans (*14*, *15*). The extremely slow dissociation rate for the gp120-2G12 interaction suggests that other key elements, e.g., some protein domains or additional high-mannose type *N*-glycans in the context of gp120, might be also be involved in subsequent interactions to strengthen the binding, after initiate recognition with gp120. The difficulty of fitting the binding data to any appropriate kinetic equations also implicates a complex process for the 2G12−glycan interactions.

Although the high-mannose *N*-glycans at the N295 and N332 sites in gp120 are essential for 2G12 recognition, the precise epitope of antibody 2G12 is still not fully characterized.

Binding of V3-Fc Glycoforms with Broadly Neutralizing Antibody 447-52D. Monoclonal antibody 447-52D is another broadly neutralizing antibody that is specific for the V3 loop. It is a conformation-sensitive antibody. X-ray structural studies indicated that 447-52D Fab recognized the V3 peptide by binding to two domains: the conserved β-turn at the tip (GPGR) of the V3 loop and the peptide amide backbone, rather than the variable side chains of the surrounding sequence (*35*). Although extensive structural and biochemical studies have been performed for the interactions between 447-52D and various V3 antigens, it is hitherto not clear how the conserved *N*-glycans within or around the V3 loop affect the antibody−epitope interaction. This is partly attributed to the difficulty of obtaining structurally defined, glycosylated full-size V3 domains. To examine the effects of glycosylation on the antibody binding, we tested the interaction of different glycoforms of V3-Fc with antibody 447-52D using SPR technology. Interestingly, both the complex type (V3-Fc-CT) and the high-mannose type glycoforms (V3-Fc-HM) of the fusion protein could bind 447-52D with a high affinity and with a very similar association/dissociation pattern (Figure 8A and Figure 8B). Fitting of the binding data to a steady-state mode equation gave an estimated K_d of 46 and 72 nM for the V3-Fc-CT and V3-Fc-HM, respectively. The data suggest that the nature of the glycosylations at the N295, N301, and N332 sites did not significantly affect the recognition of the antibody to its epitope. On the other hand, the binding of the N301A and F-N297A mutants with 447-52D was assessed by SPR (Figure 8C and Figure 8D) and the dissociation constants (K_d) for N301A and Fc-N297A were estimated to be 21 and 67 nM, respectively. Interestingly, the N301A mutant (K_d = 21 nM) showed a 2-fold increase in affinity to 447-52D in comparison with the V3-Fc-CT (K_d = 46 nM), while the Fc-N297A (K_d = 67 nM) had essentially the same affinity as V3-Fc-HM (K_d = 72 nM). These data suggest that an *N*-glycan at N301 might partially hinder the interaction between antibody 447-52D and the V3 antigen. Nevertheless, all the glycoforms of V3-Fc could still bind antibody 447-52D with very high affinity at nanomolar concentrations. The affinity of the glycosylated V3-Fc with 447-52D is comparable to that of the nonglycosylated V3 inserted at the surface loop location of *E. coli* thioredoxin (*22*). For comparison, we measured the binding of HIV-1_{Bal} gp120 to 447-52D (Figure 8E). The K_d was estimated to be 23 nM. Taken together, these data suggest that the nature and the presence of the three conserved *N*-glycans at N295, N301, and N332 sites that are near the epitope do not significantly affect the antibody recognition of its epitope, although deletion of the *N*-glycan at N301 does increase the affinity to some extent. Moreover, the comparable binding affinity among the various Fc fusion proteins and the HIV-1 gp120 suggests that the fusion protein could present a similar conformational epitope of 447-52D as that existing in native gp120. Thus, the high-mannose type fusion proteins (V3-Fc-HM and V3-Fc-M9), which include both the epitopes of 2G12 and 447-52D, could represent an interesting immunogen that may be used to elicit neutralizing antibodies against HIV-1.

CONCLUSION

Several glycoforms of the V3-Fc fusion protein were successfully expressed and characterized. Our studies demonstrate that the nature of the V3 glycosylation depends on the protein context where the V3 domain is present. Antibody binding studies revealed that the nature and presence of the glycan at N301 within the V3 loop did not significantly affect the recognition of antibody 447-52D with the V3 domain. On the other hand, controlling the glycosylation at the three sites (N295, N301, and N332) at high-mannose type *N*-glycans could partially reconstitute the epitope of antibody 2G12. In particular, mutational studies indicate that installing a high-mannose type *N*-glycan at the N301, which is usually occupied by a complex type *N*-glycan in gp120, significantly enhances the binding to 2G12. The resulting high-mannose type V3-Fc fusion protein that includes both the 2G12 and 447-52D epitopes thus represents an interesting immunogen that may be able to raise neutralizing antibodies against HIV-1.

ACKNOWLEDGMENT

We thank Drs. Anthony L. DeVico, George K. Lewis, and Yongjun Guan for helpful discussions during the work. The human antibodies 2G12 and 447-52D were provided by the National Institutes of Health (NIH)'s AIDS Research and Reference Reagent Program. This work was supported by the National Institutes of Health (NIH Grant R01 AI067111).

LITERATURE CITED

(1) Burton, D. R., Desrosiers, R. C., Doms, R. W., Koff, W. C., Kwong, P. D., Moore, J. P., Nabel, G. J., Sodroski, J., Wilson, I. A., and Wyatt, R. T. (2004) HIV vaccine design and the neutralizing antibody problem. *Nat. Immunol. 5*, 233–236.

(2) Zolla-Pazner, S. (2004) Identifying epitopes of HIV-1 that induce protective antibodies. *Nat. Rev. Immunol. 4*, 199–210.

(3) Karlsson Hedestam, G. B., Fouchier, R. A., Phogat, S., Burton, D. R., Sodroski, J., and Wyatt, R. T. (2008) The challenges of eliciting neutralizing antibodies to HIV-1 and to influenza virus. *Nat. Rev. Microbiol. 6*, 143–155.

(4) Ghiara, J. B., Stura, E. A., Stanfield, R. L., Profy, A. T., and Wilson, I. A. (1994) Crystal structure of the principal neutralization site of HIV-1. *Science 264*, 82–85.

(5) Huang, C. C., Tang, M., Zhang, M. Y., Majeed, S., Montabana, E., Stanfield, R. L., Dimitrov, D. S., Korber, B., Sodroski, J., Wilson, I. A., Wyatt, R., and Kwong, P. D. (2005) Structure of a V3-containing HIV-1 gp120 core. *Science 310*, 1025–1028.

(6) Gorny, M. K., Conley, A. J., Karwowska, S., Buchbinder, A., Xu, J. Y., Emini, E. A., Koenig, S., and Zolla-Pazner, S. (1992) Neutralization of diverse human immunodeficiency virus type 1 variants by an anti-V3 human monoclonal antibody. *J. Virol. 66*, 7538–7542.

(7) Gorny, M. K., Williams, C., Volsky, B., Revesz, K., Cohen, S., Polonis, V. R., Honnen, W. J., Kayman, S. C., Krachmarov, C., Pinter, A., and Zolla-Pazner, S. (2002) Human monoclonal antibodies specific for conformation-sensitive epitopes of V3 neutralize human immunodeficiency virus type 1 primary isolates from various clades. *J. Virol. 76*, 9035–9045.

(8) Zolla-Pazner, S., Zhong, P., Revesz, K., Volsky, B., Williams, C., Nyambi, P., and Gorny, M. K. (2004) The cross-clade neutralizing activity of a human monoclonal antibody is determined by the GPGR V3 motif of HIV type 1. *AIDS Res. Hum. Retroviruses 20*, 1254–1258.

(9) Rizzuto, C. D., Wyatt, R., Hernandez-Ramos, N., Sun, Y., Kwong, P. D., Hendrickson, W. A., and Sodroski, J. (1998) A conserved HIV gp120 glycoprotein structure involved in chemokine receptor binding. *Science 280*, 1949–1953.

(10) Hoffman, T. L., and Doms, R. W. (1999) HIV-1 envelope determinants for cell tropism and chemokine receptor use. *Mol. Membr. Biol. 16*, 57–65.

(11) Rizzuto, C., and Sodroski, J. (2000) Fine definition of a conserved CCR5-binding region on the human immunodeficiency virus type 1 glycoprotein 120. *AIDS Res. Hum. Retroviruses 16*, 741–749.

(12) Basmaciogullari, S., Babcock, G. J., Van Ryk, D., Wojtowicz, W., and Sodroski, J. (2002) Identification of conserved and variable structures in the human immunodeficiency virus gp120 glycoprotein of importance for CXCR4 binding. *J. Virol. 76*, 10791–10800.

(13) Hartley, O., Klasse, P. J., Sattentau, Q. J., and Moore, J. P. (2005) V3: HIV's switch-hitter. *AIDS Res. Hum. Retroviruses 21*, 171–189.

(14) Leonard, C. K., Spellman, M. W., Riddle, L., Harris, R. J., Thomas, J. N., and Gregory, T. J. (1990) Assignment of intrachain disulfide bonds and characterization of potential glycosylation sites of the type 1 recombinant human immunodeficiency virus envelope glycoprotein (gp120) expressed in Chinese hamster ovary cells. *J. Biol. Chem. 265*, 10373–10382.

(15) Zhu, X., Borchers, C., Bienstock, R. J., and Tomer, K. B. (2000) Mass spectrometric characterization of the glycosylation pattern of HIV-gp120 expressed in CHO cells. *Biochemistry 39*, 11194–11204.

(16) Sanders, R. W., Venturi, M., Schiffner, L., Kalyanaraman, R., Katinger, H., Lloyd, K. O., Kwong, P. D., and Moore, J. P. (2002) The mannose-dependent epitope for neutralizing antibody 2G12 on human immunodeficiency virus type 1 glycoprotein gp120. *J. Virol. 76*, 7293–7305.

(17) Scanlan, C. N., Pantophlet, R., Wormald, M. R., Ollmann Saphire, E., Stanfield, R., Wilson, I. A., Katinger, H., Dwek, R. A., Rudd, P. M., and Burton, D. R. (2002) The broadly neutralizing anti-human immunodeficiency virus type 1 antibody 2G12 recognizes a cluster of alpha1→2 mannose residues on the outer face of gp120. *J. Virol. 76*, 7306–7321.

(18) Calarese, D. A., Scanlan, C. N., Zwick, M. B., Deechongkit, S., Mimura, Y., Kunert, R., Zhu, P., Wormald, M. R., Stanfield, R. L., Roux, K. H., Kelly, J. W., Rudd, P. M., Dwek, R. A., Katinger, H., Burton, D. R., and Wilson, I. A. (2003) Antibody domain exchange is an immunological solution to carbohydrate cluster recognition. *Science 300*, 2065–2071.

(19) Calarese, D. A., Lee, H. K., Huang, C. Y., Best, M. D., Astronomo, R. D., Stanfield, R. L., Katinger, H., Burton, D. R., Wong, C. H., and Wilson, I. A. (2005) Dissection of the carbohydrate specificity of the broadly neutralizing anti-HIV-1 antibody 2G12. *Proc. Natl. Acad. Sci. U.S.A. 102*, 13372–13377.

(20) Sharon, M., Gorlach, M., Levy, R., Hayek, Y., and Anglister, J. (2002) Expression, purification, and isotope labeling of a gp120 V3 peptide and production of a Fab from a HIV-1 neutralizing antibody for NMR studies. *Protein Expression Purif. 24*, 374–383.

(21) Gorny, M. K., Revesz, K., Williams, C., Volsky, B., Louder, M. K., Anyangwe, C. A., Krachmarov, C., Kayman, S. C., Pinter, A., Nadas, A., Nyambi, P. N., Mascola, J. R., and Zolla-Pazner, S. (2004) The V3 loop is accessible on the surface of most human immunodeficiency virus type 1 primary isolates and serves as a neutralization epitope. *J. Virol. 78*, 2394–2404.

(22) Chakraborty, K., Durani, V., Miranda, E. R., Citron, M., Liang, X., Schleif, W., Joyce, J. G., and Varadarajan, R. (2006) Design of immunogens that present the crown of the HIV-1 V3 loop in a conformation competent to generate 447-52D-like antibodies. *Biochem. J. 399*, 483–491.

(23) Varona-Santos, J. T., Vazquez-Padron, R. I., and Moreno-Fierros, L. (2006) Production of a short recombinant C4V3 HIV-1 immunogen that induces strong anti-HIV responses by systemic and mucosal routes without the need of adjuvants. *Viral Immunol. 19*, 237–249.

(24) Chen, H., Xu, X., and Jones, I. M. (2007) Immunogenicity of the outer domain of a HIV-1 clade C gp120. *Retrovirology 4*, 33.

(25) Zhang, M. Y., Wang, Y., Mankowski, M. K., Ptak, R. G., and Dimitrov, D. S. (2009) Cross-reactive HIV-1-neutralizing activity of serum IgG from a rabbit immunized with gp41 fused to IgG1 Fc: possible role of the prolonged half-life of the immunogen. *Vaccine 27*, 857–863.

(26) Guyre, P. M., Graziano, R. F., Goldstein, J., Wallace, P. K., Morganelli, P. M., Wardwell, K., and Howell, A. L. (1997) Increased potency of Fc-receptor-targeted antigens. *Cancer Immunol. Immunother. 45*, 146–148.

(27) Haas, J., Park, E. C., and Seed, B. (1996) Codon usage limitation in the expression of HIV-1 envelope glycoprotein. *Curr. Biol. 6*, 315–324.

(28) Fujita, K., and Takegawa, K. (2001) Chemoenzymatic synthesis of neoglycoproteins using transglycosylation with endo-beta-*N*-acetylglucosaminidase A. *Biochem. Biophys. Res. Commun. 282*, 678–682.

(29) Lund, J., Takahashi, N., Popplewell, A., Goodall, M., Pound, J. D., Tyler, R., King, D. J., and Jefferis, R. (2000) Expression and characterization of truncated forms of humanized L243 IgG1. Architectural features can influence synthesis of its oligosaccharide chains and affect superoxide production triggered through human Fc-gamma receptor I. *Eur. J. Biochem. 267*, 7246–7257.

(30) Trkola, A., Purtscher, M., Muster, T., Ballaun, C., Buchacher, A., Sullivan, N., Srinivasan, K., Sodroski, J., Moore, J. P., and Katinger, H. (1996) Human monoclonal antibody 2G12 defines a distinctive neutralization epitope on the gp120 glycoprotein of human immunodeficiency virus type 1. *J. Virol. 70*, 1100–1108.

(31) Chen, H., Xu, X., Bishop, A., and Jones, I. M. (2005) Reintroduction of the 2G12 epitope in an HIV-1 clade C gp120. *AIDS 19*, 833–835.

(32) Chang, V. T., Crispin, M., Aricescu, A. R., Harvey, D. J., Nettleship, J. E., Fennelly, J. A., Yu, C., Boles, K. S., Evans, E. J., Stuart, D. I., Dwek, R. A., Jones, E. Y., Owens, R. J., and Davis, S. J. (2007) Glycoprotein structural genomics: solving the glycosylation problem. *Structure 15*, 267–273.

(33) Scanlan, C. N., Ritchie, G. E., Baruah, K., Crispin, M., Harvey, D. J., Singer, B. B., Lucka, L., Wormald, M. R., Wentworth, P., Jr., Zitzmann, N., Rudd, P. M., Burton, D. R., and Dwek, R. A. (2007) Inhibition of mammalian glycan biosynthesis produces non-self antigens for a broadly neutralising, HIV-1 specific antibody. *J. Mol. Biol. 372*, 16–22.

(34) Zhou, Q., Shankara, S., Roy, A., Qiu, H., Estes, S., McVie-Wylie, A., Culm-Merdek, K., Park, A., Pan, C., and Edmunds, T. (2008) Development of a simple and rapid method for producing non-fucosylated oligomannose containing antibodies with increased effector function. *Biotechnol. Bioeng. 99*, 652–665.

(35) Stanfield, R. L., Gorny, M. K., Williams, C., Zolla-Pazner, S., and Wilson, I. A. (2004) Structural rationale for the broad neutralization of HIV-1 by human monoclonal antibody 447-52D. *Structure 12*, 193–204.

BC9004238

Comparison of the C2A Domain of Synaptotagmin-I and Annexin-V As Probes for Detecting Cell Death

Israt S. Alam,[†,§] Andre A. Neves,[†,§] Timothy H. Witney,[‡] Joan Boren,[§] and Kevin M. Brindle*[,‡,§]

Department of Biochemistry, University of Cambridge, 80 Tennis Court Road, Cambridge CB2 1GA, United Kingdom, and Cancer Research UK Cambridge Research Institute, Li-Ka Shing Centre, Robinson Way, Cambridge CB2 0RE, United Kingdom.
Received October 8, 2009; Revised Manuscript Received March 9, 2010

The induction of apoptosis is frequently accompanied by the exposure of phosphatidylserine (PS) on the cell surface, which has been detected using radionuclide and fluorescently labeled derivatives of the PS-binding protein, Annexin V. The fluorescently labeled protein has been used extensively in vitro as a diagnostic reagent for detecting cell death, and radionuclide-labeled derivatives have undergone clinical trials for detecting tumor cell death in vivo following treatment. We show here that the C2A domain of Synaptotagmin-I, which had been fluorescently labeled at a single cysteine residue introduced by site-directed mutagenesis, detected the same levels of cell death as a similarly labeled Annexin-V derivative, in drug-treated murine lymphoma and human breast cancer cell lines in vitro. However, the C2A derivative showed significantly less binding to viable cells and, as a consequence, up to 4-fold more specific binding to apoptotic and necrotic cells when compared with Annexin-V. C2A offers a potential route for the development of a new generation of more specific imaging probes for the detection of tumor cell death in the clinic.

INTRODUCTION

The detection of cell death in the clinic is of considerable interest for assessing the effectiveness of therapy and for determining the progression of disease (*1, 2*). In oncology, the induction of tumor cell death following treatment can be a good predictive indicator of treatment outcome, a positive correlation having been observed, for example, between the levels of tumor cell death post treatment and patient survival rates, in human breast cancer (*3, 4*). Apoptosis is frequently associated with the externalization of negatively charged phospholipids, such as phosphatidylserine (PS), on the outer leaflet of the plasma membrane bilayer, where they direct engulfment of the apoptotic cell by neighboring phagocytes (*5*). PS is also exposed during subsequent necrosis, due to disruption of plasma membrane integrity. The detection of PS exposure by Annexin V (AnxV) has often been used to detect apoptosis. AnxV is a 36 kDa protein that binds with high affinity and in a Ca^{2+}-dependent manner to the PS exposed on dying cells. Radionuclide derivatives of AnxV reached early-stage clinical trials and were shown to detect cell death in patients with myocardial infarcts (*6*), lymphoma, and lung cancer (*7, 8*). There were, however, problems with biodistribution (*9, 10*).

The C2A domain of Synaptotagmin I is a 14.7 kDa protein, which like AnxV binds to PS in a Ca^{2+}-dependent manner (*11, 12*). A glutathione-S-transferase (GST)-tagged version of C2A was shown to detect cell death in vitro and in vivo using radionuclide and MR imaging techniques (*13*−*15*). The protein is of interest since, due to its smaller size, it may show better penetration of tumor tissue than AnxV and also better clearance of unbound material, thus generating better tissue contrast.

In previous studies with the C2A domain of synaptotagmin, an MRI contrast agent was attached to the ε-amino group of surface lysine residues (*13, 15, 16*). There are 14 lysine residues in C2A and a total of 35 in the C2A-GST fusion protein (*15*). Attachment of labels to multiple lysine residues inevitably results in a reagent that consists of a heterogeneous mixture of molecular species. Moreover, in the case of an MRI agent based on C2A-GST, modification of these lysine residues with MR-detectable Gd^{3+}-chelates was shown to lower the affinity of the protein for phosphatidylserine (PS) (*15*). We describe here a site-directed mutant of C2A, C2Am, in which we have replaced a serine residue that is distant from the PS-binding site, with a single cysteine residue (S78C). Since there are no other cysteine residues in the protein, this provides a unique site for the modification of the protein with fluorescent, radionuclide, or MR-detectable labels. In this study, we have assessed the potential of a fluorescent derivative of C2Am to detect cell death in murine lymphoma and human breast cancer cell lines, by comparing both its sensitivity and specificity for detection of apoptotic and necrotic cells with that of a fluorescent derivative of AnxV that is available commercially.

EXPERIMENTAL PROCEDURES

Materials. All tissue culture reagents, SYTOX Green dead cell stain, and Annexin V-Alexa Fluor647 (AnxV-AlxF647) were from Invitrogen (Paisley, Renfrewshire, UK). The green Polycaspases FLICA kit was from Immunochemistry Technologies LLC (Bloomington, MN, USA). All chemicals were of analytical grade from Sigma-Aldrich Co. Ltd. (Poole, Dorset, UK), unless stated otherwise. Etoposide (EPOSIN) was from PCH Pharmachemie, (Haarlem, Netherlands). Murine lymphoma (EL-4) cells were obtained from the American Type Culture Collection (Teddington, Middlesex, UK) and MDA-MB-231 cells were from European Collection of Cell Cultures (Salisbury, Wiltshire, UK).

Construction, Overexpression, and Purification of C2A(S78C). The *Rattus norvegicus* synaptotagmin I sequence was obtained from the NCBI Genbank service (sequence NM_001033680).

* Corresponding author. Kevin M. Brindle, Department of Biochemistry, University of Cambridge, 80 Tennis Court Road, Cambridge CB2 1GA, UK., Tel: +44 (0)1223 333674, Fax: +44 (0)1223 766002, Email: kmb1001@cam.ac.uk.

† Equal contributions.

§ Cancer Research UK Cambridge Research Institute.

‡ University of Cambridge.

10.1021/bc9004415 © 2010 American Chemical Society
Published on Web 04/19/2010

Appropriate primers for mutagenesis were designed using Quikchange Primer Design software. The C2A-containing pGEX-2T vector (GE Healthcare, Chalfont St Giles, UK) was isolated from *E. coli* BL21 cells and mutagenesis performed using the QuikChange Site-Directed Mutagenesis kit (Stratagene, La Jolla, CA, USA). *E. coli* DH5a competent cells were transformed with the mutant plasmid by heat shock and the amplified vector then isolated and sequenced. Finally, *E. coli* BL21 cells were transformed with the vector by electroporation. The proteins were expressed as 42-kDa GST-tagged fusion proteins, following induction using isopropyl-β-D-thiogalactoside (IPTG), and the S78C mutant was purified using affinity chromatography (see Methods 1 in Supporting Information). The extent of purification was analyzed using SDS-PAGE. Protein concentrations were determined using a Non-Interfering Protein AssayTM kit (NIPA from Merck Chemicals Ltd., Nottingham, UK) and by densitometry for AnxV-AlxF647 (see Methods 2 in Supporting Information).

Production of Fluorescently Labeled Protein. The mutant protein (C2Am) was covalently labeled with the fluorophore Alexa Fluor 647 (AF647), by reaction of the cysteine-78 residue with the maleimide group of Alexa Fluor 647 C2 maleimide (Invitrogen). Briefly, the protein was reduced using 10 mM DTT for half an hour at room temperature. The protein was then washed in a 5 kDa vivaspin concentrator (Sartorius, Epsom, UK) in HNE buffer (20 mM HEPES, 100 mM NaCl, 5 mM EDTA, pH 7.4). The protein was kept at a concentration in the range 50−100 μM, and an approximately 10-fold molar excess of the fluorescent maleimide dye was added. The reaction was allowed to proceed on a magnetic stirrer at 4 °C overnight. The modified protein was separated from unreacted dye by gel filtration using a Hi Load Superdex 75 26/60 prep grade column (GE Healthcare). Electrospray ionization (ESI) mass spectrometry was used to confirm modification of the protein, which showed a single species of approximately 17 204 Da (C2Am-AF647) (see Methods 3 and Figure S1 in Supporting Information).

Surface Plasmon Resonance (SPR). Protein affinity of C2Am and C2Am-AF647 for PS-containing liposomes was estimated using the Biacore T100 (Biacore, GE Healthcare). (See Methods 4 in Supporting Information).

Cell Culture. EL4 murine lymphoma and MDA-MB-231 human breast cancer cells were propagated in RPMI 1640 media, supplemented with 10% fetal calf serum and 2 mM L-glutamine. Cell number and viability were monitored using Trypan blue dye staining. EL4 cell death was induced by addition of 5 μM etoposide for up to 24 h and MDA cell death by treatment with doxorubicin (1 μg/mL) for up to 96 h.

Detection of Cell Death Using Flow Cytometry. Cell pellets (10^6 cells) were washed in ice-cold HEPES-buffered saline (10 mM HEPES, 150 mM NaCl, 2 mM $CaCl_2$, pH 7.4) with 1% fetal calf serum and resuspended in 100 μL of the same buffer containing C2Am-AF647, which was used at concentrations between 50 nM to 1.0 μM, or AnnexinV-AF647 (Invitrogen), which was used at concentrations between 1 and 20 nM, in combination with SYTOX Green (Invitrogen; 50 nM), and incubated for 15 min at 37 °C. The resulting mixture was washed twice, kept briefly on ice, and then analyzed in an LSRII cytometer (BD Biosciences, Rockville, MD USA), with 20 000 cells counted per event.

For detection of active caspases, EL4 or MDA cells were washed and then incubated with Poly Caspases FLICA for 30 min at 37 °C (300-fold diluted stock). A further wash step was performed before incubation with C2Am and AnxV. The same washing steps were applied as in all the other flow cytometry studies. All experiments were performed at least three times.

Image Analysis of C2Am and AnxV Binding to Dying Cells. EL4 cell pellets (5×10^6 cells) were washed in ice-cold HEPES-buffered saline. The pellets were resuspended in 1 mL of warm buffer containing the mitochondrial stain MitoTracker Orange CMTMRos (Invitrogen, 100 nM) and incubated for 30 min at 37 °C. Cells were washed once and resuspended in ice-cold HEPES-buffered saline with 3% BSA for 30 min at 4 °C. Cells were then resuspended in 100 μL HEPES-buffered saline containing either C2Am-AF647 or AnxV-AF647 (Invitrogen), which were used at concentrations of 200 nM and 4 nM, respectively, and incubated for 15 min at 37 °C. The resulting mixture was then washed twice and resuspended in 100 μL ice-cold buffer containing the nucleic acid stain, 7-amino-actinomycin D (7-AAD) (Invitrogen, 20 μg/mL) and kept on ice briefly before samples were loaded into an ImageStream system (Amnis Corporation, Seattle, WA, USA), and a file of 5000 cells was collected in the standard collection mode. Data files were analyzed using *IDEAS* software (Amnis, Seattle, WA) to obtain fluorescence images of individual cells.

Statistical Analysis. Two-way ANOVA and subsequent Mann−Whitney's test were used for all analyses. *P*-values below 0.05 were considered to be statistically significant.

RESULTS

Preparation of C2A(S78C). The serine residue at position 78 of the C2A domain of Synaptotagmin-I (position 217 of Synaptotagmin-I), was replaced with a cysteine residue, using site-directed mutagenesis. Three candidate amino acid residues were selected for replacement: Ser217, Gln154, Asn248. SDS PAGE of the three GST-C2A mutants (S217C, N248C, and Q154C) was used to assess the levels of expression before and after IPTG induction. All vector-transformed bacteria expressed the mutant proteins to some degree, but a much higher level of overexpression was obtained for S217C. The isolated C2A domain [C2A(S78C)] was prepared as described in Experimental Procedures.

Synthesis and Characterization of C2A(S78C)-Alexa Fluor 647. C2A(S78C) was reacted with a maleimide derivative of Alexa Fluor 647. The modified protein (C2Am), gave a single peak on electrospray ionization mass spectrometry, with the expected mass of 17 204 Da (see Figure S1 in Supporting Information). SDS-PAGE also showed a single band of the expected mass (see Figure S2 in Supporting Information). Surface plasmon resonance (SPR) measurements gave similar dissociation constants (K_d) for the unmodified and modified proteins for PS of 55.4 ± 3.5 nM and 71.0 ± 6.9 nM, respectively. The dissociation constant of wild-type C2A for PS is approximately 20 nM (*16*). These dissociation constants were corroborated by kinetic analysis of the SPR data (see Table ST1 in Supporting Information). The k_{on} values determined from the kinetic analysis for the unmodified and modified proteins were 2.01×10^6 M^{-1} s^{-1} and 2.14×10^6 M^{-1} s^{-1}, respectively, and the k_{off} values were 0.110 s^{-1} and 0.188 s^{-1}, respectively.

Analysis of Fluorescently Labeled Annexin V. A commercial preparation of Annexin V (AnxV), that had been labeled with the same fluorophore (Alexa Fluor 647, or AF647) as C2Am, was analyzed by SDS-PAGE, which showed bands at ca. 35 kDa and ca. 65 kDa, which were thought to be AnxV and BSA, respectively (see Figure S3a in Supporting Information). The latter is an additive in the preparation, at 0.1% (w/v). Fluorescent imaging of the same gel showed that the band at ca. 35 kDa was fluorescent (647 nm excitation), confirming it as AF647-labeled AnxV (see Figure S3b in Supporting Information). The intensity of this band indicated that it was approximately 2% (w/w) of the total protein concentration (determined to be 800 μg/mL), and therefore, the concentration of AnxV was estimated to be approximately 460 nM in this commercial preparation of the protein.

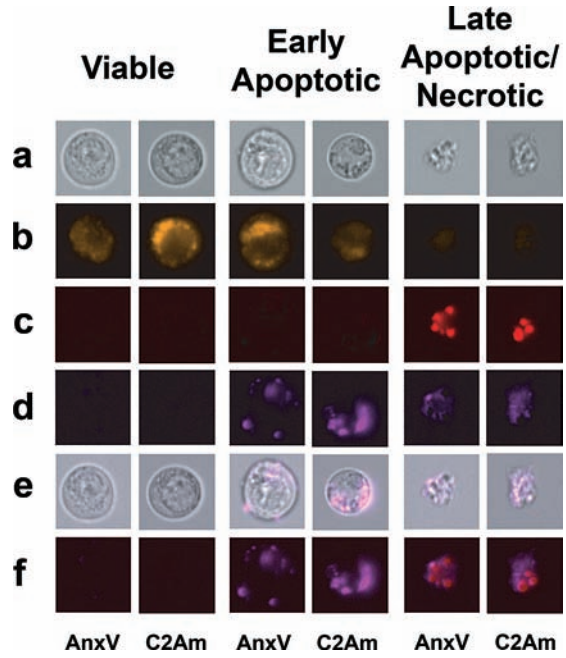


Figure 1. Images of EL4 cells at different stages of cell death. Bright field images (A); fluorescent images of cells stained with MitoTracker orange (B); fluorescent images of cells stained with the DNA stain, 7AAD (7-amino-actinomycin) (C); fluorescent images of cells stained with AnxV-AF647 or C2Am-AF647 (D); overlays of images shown in A and D (E); overlays of images shown in C and D (F). C2Am was used at a concentration of 200 nM and AnxV at 4 nM.

Flow Cytometry of Dying Cells Stained with C2Am or AnxV. Images were acquired from etoposide-treated EL4 cells that had been sorted according to the level of binding of C2Am or AnxV. Viable cells, which did not stain with C2Am or AnxV (Figure 1d), had a rounded morphology and an intact plasma membrane (Figure 1a), showed mitochondrial activity (Figure 1b) and no nucleic acid staining (Figure 1c). In contrast, early apoptotic cells that stained with C2Am or AnxV (Figure 1d) appeared irregular, with blebbing of the plasma membrane (Figure 1a), but still showed mitochondrial activity (Figure 1b) and no nucleic acid staining (Figure 1c). Late apoptotic/necrotic cells showed no detectable mitochondrial activity (Figure 1b), pronounced nucleic acid staining (Figure 1c), which demonstrated loss of plasma membrane integrity, and C2Am or AnxV staining (Figure 1d). Overlays of C2Am or AnxV staining with the bright field images are shown in Figure 1e, demonstrating that both probes stain the EL4 cell membrane of early apoptotic cells. Overlays of nucleic acid staining with the corresponding images of C2Am and AnxV staining are shown in Figure 1f, demonstrating that both C2Am and AnxV accumulate intracellularly in late apoptotic/necrotic EL4 cells.

Detection of Cell Death Using Flow Cytometry and C2Am or AnxV. The facility of C2Am to detect cell death by flow cytometry in drug-treated murine lymphoma (EL4) and human breast cancer (MDA-MB-231, hereafter referred to as MDA) cell lines was compared with detection using AnxV. Cell death was induced by treatment of EL4 and MDA cells with etoposide or doxorubicin, respectively (Figures 2 and 3).

Treatment of cells with DNA damaging agents, such as etoposide and doxorubicin, results in activation of poly ADP-ribose polymerase (PARP) and, since NAD^+ is a substrate for PARP, depletion of the cellular NAD(H) pool (*17*). As a consequence, NADH autofluorescence is decreased considerably upon the induction of cell death using DNA damaging agents, and this decrease occurs relatively early after etoposide treatment in EL4 cells (*18*). Therefore, we identified apoptotic cells by their low NADH autofluorescence (green symbols), necrotic cells by their low NADH autofluorescence and high SYTOX green fluorescence (SYTOX green is a marker of cell necrosis) (orange symbols), and viable cells by their high NADH autofluorescence and low SYTOX green fluorescence (blue symbols) (Figure 3a,b and i,j). In this study, we have not tried to distinguish between primary necrosis, that is cells that have become necrotic without engaging the apoptotic pathway, and secondary necrosis, in which late apoptotic cells have become necrotic (*19*). Instead, when we refer to late apoptotic or necrotic cells, we are referring to cells with compromised plasma

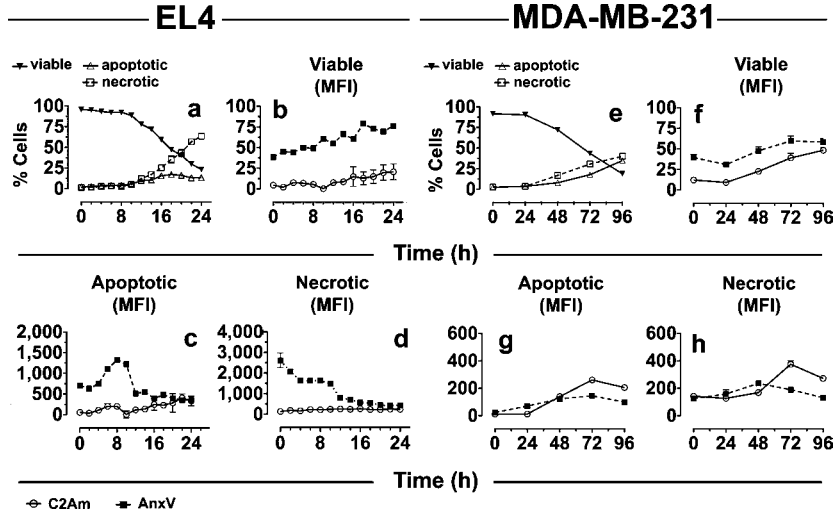


Figure 2. Binding of C2Am and AnxV to viable, apoptotic, and necrotic EL4 and MDA cell populations. Cell death was induced in EL4 and MDA cells by treatment with etoposide or doxorubicin, respectively, for the specified times. The fractions of apoptotic (△), necrotic (□), and viable cells (▼) were assessed by flow cytometric measurements of NADH autofluorescence (Exc, $\lambda = 350$; Em, $\lambda = 475$ nm) and Sytox green staining (Exc, $\lambda = 504$; Em, $\lambda = 523$ nm) (a and e). Binding of fluorescently labeled derivatives of C2Am (○) and AnxV (■) to the viable (b,f), apoptotic (c,g), and necrotic (d,h) cell populations was also assessed by flow cytometry, where binding is expressed as the mean fluorescence intensity (the total fluorescent signal for this population was divided by the number of cells and is expressed in arbitrary units). The fluorescence intensities used to calculate the MFIs were standardized to autofluorescence levels in the Alexa Fluor 647 channel. Data shown are means ± SEM ($n = 3$; error bars lie within the symbols when not visible) for each time point. C2Am was used at a concentration of 200 nM and AnxV at a concentration of 4 nM. Differences were significant at the following: $^*P < 0.05$, plot a-6 and 12 h, b-2 h, c-24 h; $^{**}P < 0.01$, a-8 h, b-4 and 14 h, d-48 h; $^{***}P < 0.001$, a-10 and 14 to 24 h, b-0 and 12 h, c-48 to 96 h, d-0, 24, 72, and 96 h.

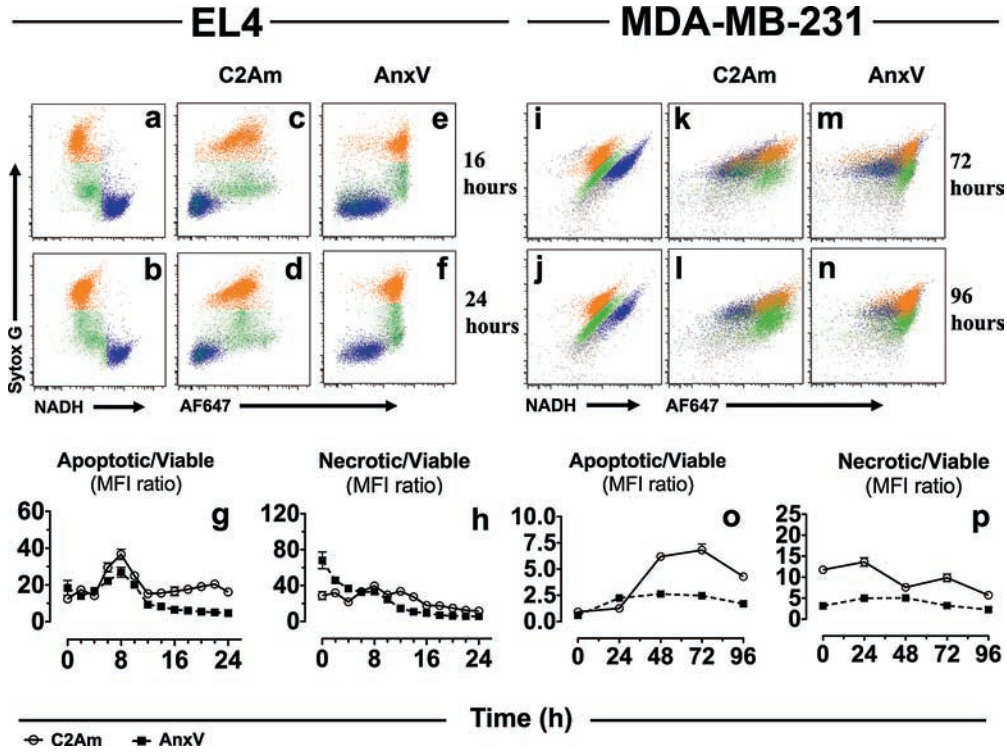


Figure 3. Specificity of C2Am and AnxV binding to viable, apoptotic, and necrotic EL4 and MDA cell populations. Cell death was induced by treatment of EL4 and MDA cells with etoposide or doxorubicin, respectively, for the specified times. The fractions of apoptotic (green symbols), necrotic (orange symbols), and viable cells (blue symbols) were assessed by flow cytometric measurements of NADH autofluorescence (Exc, λ = 350; Em, λ = 475 nm, *x*-axis) and Sytox green nuclear staining (Exc, λ = 504; Em, λ = 523 nm, *y*-axis) (a, b, i, and j). Binding of Alexa Fluor 647-labeled C2Am or AnxV (Exc, λ = 647; Em, λ = 670 nm, *x*-axis) to these cell populations is shown in c and d and k and l for C2Am and in e and f and m and n for AnxV. The specificity of binding was assessed by plotting the mean fluorescence intensity (MFI) ratios for the Alexa Fluor 647 following binding of C2Am (○) and AnxV (■) to the indicated cell populations, where these cell populations were identified by their NADH autofluorescence and Sytox green nuclear staining (g,h and o,p). The fluorescence intensities used to calculate the MFIs were standardized to autofluorescence levels in the Alexa Fluor 647 channel. Data shown are means ± SEM (n = 3, error bars lie within the symbols when not visible) for each time point. Differences were significant at the following: *$P < 0.05$, plot s-48 h; **$P < 0.01$, h-12 h, i-14 h, q-24 and 72 h, r-24 h; ***$P < 0.001$, g-0 to 24 h, h-0 to 10 and 14 h, i-0 to 12 h, q-0 and 48 h, r-72 and 96 h, s-72 and 96 h. Sytox SYTOX green; AF647 = Alexa Fluor 647.

Table 1. Correlation Factors (R^2) for Best Fit of EL4 or MDA Cell Populations (% Cells) Identified by C2Am or AnxV and by Measurements of NADH UV Autofluorescence and SYTOX Green Staining

	viable	apoptotic	necrotic
	C2Am vs AnxV		
EL4	0.9641	0.9333	0.9919
MDA	0.9947	0.9913	0.9936
	C2Am vs NADH and SYTOX Green		
EL4	0.9983	0.9859	0.9969
MDA	0.9734	0.9965	0.9840
	AnxV vs NADH and SYTOX Green		
EL4	0.9975	0.9568	0.9986
MDA	0.9677	0.9913	0.9936

membrane integrity and which therefore stain with the nucleic acid stains SYTOX green or 7-AAD.

Both C2Am (Figure 3c,d and k,l) and AnxV (Figure 3e,f and m,n) bound to the apoptotic and necrotic cell fractions identified by measurements of NADH autofluorescence and SYTOX green staining. Moreover, the cell populations identified by either protein were well-correlated with each other and with the cell populations identified by measurements of NADH autofluorescence and SYTOX green staining (Table 1). However, C2Am showed better specificity for detecting apoptotic and necrotic cells, when compared with AnxV, which can be explained by the greater binding of AnxV to viable cells. Viable EL4 and MDA cells (Figure 2b and f, respectively) showed consistently higher absolute staining with AnxV (up to 4-fold, $P < 0.001$, for EL4 cells and up to 2-fold, $P < 0.01$, for MDA cells) when compared with C2Am, despite being used at a 50-fold lower concentration (4 nM AnxV and 200 nM C2Am). Although apoptotic and necrotic EL4 and MDA cells generally showed more labeling with AnxV than C2Am (Figure 2c,d and g,h), the effects of this on the specificity of detection of apoptotic and necrotic cells was more than offset by the greater binding of AnxV to the viable cells. This improved specificity can readily be appreciated from plots of the ratios of the mean fluorescence intensities (apoptotic and necrotic versus viable) following binding of C2Am and AnxV. The ratios of the mean fluorescence intensities (MFI) for apoptotic/viable (Figure 3g and o) and necrotic/viable (Figures 3 h and p) cells were higher for C2Am than for AnxV for the majority of the time following drug treatment, for both EL4 and MDA cells. C2Am showed greater specificity for apoptotic cells ($P < 0.05$ for EL4 and MDA cells) and necrotic cells ($P < 0.05$ for EL4 cells and $P < 0.01$ for MDA cells) when compared to AnxV.

Apoptotic and necrotic MDA cells (Figure 3i and j, represented by the green and orange symbols) showed similar levels of SYTOX green staining to viable cells (in blue). Compare Figure 3a and b for EL4 cells with Figure 3i and j for MDA cells. However, doxorubicin is fluorescent and its emission overlaps with that of SYTOX Green (*20*), and therefore, this effect was probably due to the presence of the drug in the viable MDA cells in this particular experiment.

Comparison of Cell Labeling with C2A and AnxV with Caspase Activation. As a further independent measure of cell death, we assessed caspase activation using a Poly Caspases

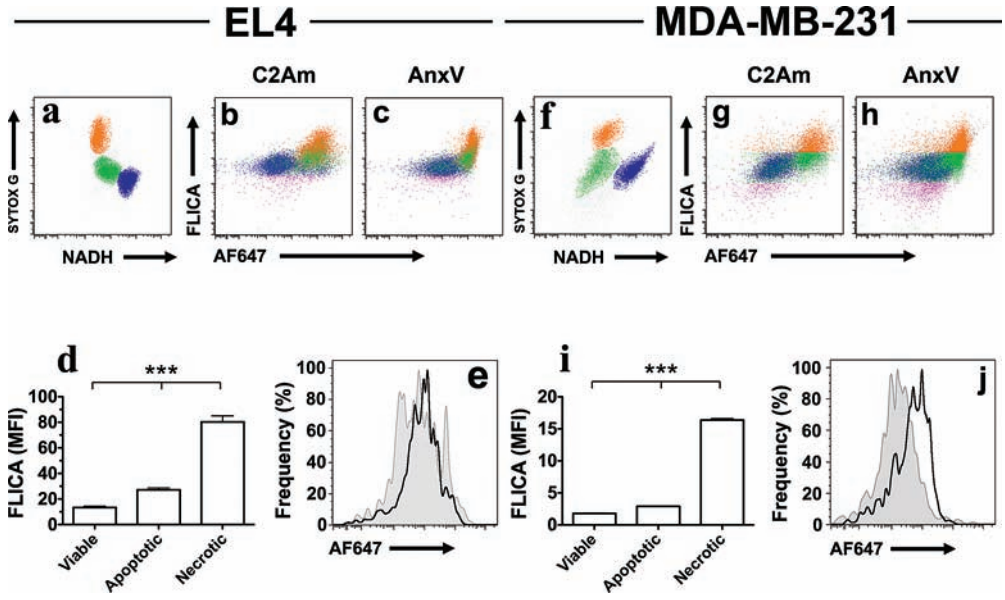


Figure 4. Dual scatter plots of active caspase labeling (Poly Caspases FLICA carboxyfluorescein; Exc, $\lambda = 490$; Em, $\lambda = 530$ nm, *y*-axis) versus labeling with C2Am (b and g) or AnxV (c and h) (Alexa Fluor 647; Exc, $\lambda = 647$; Em, $\lambda = 670$ nm, *x*-axis) of EL4 cells treated with etoposide (5 μM) for 16 h (a−c) and MDA cells treated with doxorubicin (1 μg/mL) for 72 h (f−h). Apoptotic (green), late apoptotic/necrotic (orange), and viable (blue) EL4 or MDA cells were identified based on their levels of NADH autofluorescence and staining with SYTOX green (a, EL4 cells; f, MDA cells). Mean fluorescence intensities (MFI) following FLICA-labeling of the different EL4 and MDA cell populations is shown in (d) and (i), respectively. Data shown are means ± SEM ($n = 3$) (***$P < 0.001$). C2Am and AnxV labeling (Alexa Fluor 647; Exc, $\lambda = 647$; Em, $\lambda = 670$ nm, *x*-axis) of the 5% of the viable cell population (purple in b and c and g and h) that showed the lowest FLICA labeling are shown for EL4 (e) and MDA (j) cells against the frequency of events. Viable EL4 and MDA cells stained more with AnxV (black line) than C2Am (shaded gray area) ($P < 0.05$, for EL4 and $P < 0.001$, for MDA). MFI values, in arbitrary units (a.u.), were standardized to green autofluorescence levels. C2Am was used at a concentration of 200 nM and AnxV at a concentration of 4 nM.

FLICA (fluorescent-labeled inhibitor of caspases) kit, which is based on caspase inhibitors that are linked to a green (carboxyfluorescein) fluorophore. FLICA is cell-permeant and is thought to bind only to active caspases within cells. Plots of SYTOX Green labeling as a function of NAD(H) autofluorescence were used, as before, to identify three cell populations: apoptotic cells (represented by the green symbols), late apoptotic/necrotic cells (orange symbols), and viable cells (blue symbols) (Figure 4). Dual scatter plots of drug-treated EL4 and MDA cells stained with FLICA and C2Am are shown in Figure 4b and g, respectively, and with FLICA and AnxV in Figure 4c and h, respectively. In EL4 cell populations treated with etoposide for 24 h, the MFIs for apoptotic and late apoptotic/necrotic cells stained with FLICA were up to 2-fold ($P < 0.001$) and 6-fold ($P < 0.01$) more, respectively, when compared with viable cells (Figure 4d). In MDA cells treated for 72 h with doxorubicin, these differences were up to 2-fold ($P < 0.01$) and 10-fold ($P < 0.001$) more for apoptotic and late apoptotic/necrotic cells, respectively, when compared with viable cells (Figure 4i). The binding of C2Am and AnxV to the viable cell population was examined by selecting the 5% of the viable cell population that showed the lowest FLICA labeling (Figure 4b,c and g,h) and analyzing the binding of C2Am and AnxV to this population. This is shown for EL4 cells in Figure 4e and for MDA cells in Figure 4j. This analysis confirmed that both C2Am and AnxV show low levels of binding to viable cells, which show the lowest FLICA labeling, but that AnxV binding to these cells was significantly greater than that of C2Am ($P < 0.05$, EL4 and $P < 0.001$, MDA).

Effects of C2Am and AnxV Concentration on Their Binding to Drug-Treated Cells. The proteins were used at concentrations of between 0.05 and 1.0 μM for C2Am and 1−20 nM, for AnxV. The AnxV concentration recommended by the manufacturer is approximately 20 nM. Again, the three different cell populations, viable, apoptotic, and late apoptotic/necrotic, were selected based on SYTOX Green staining and NAD(H)

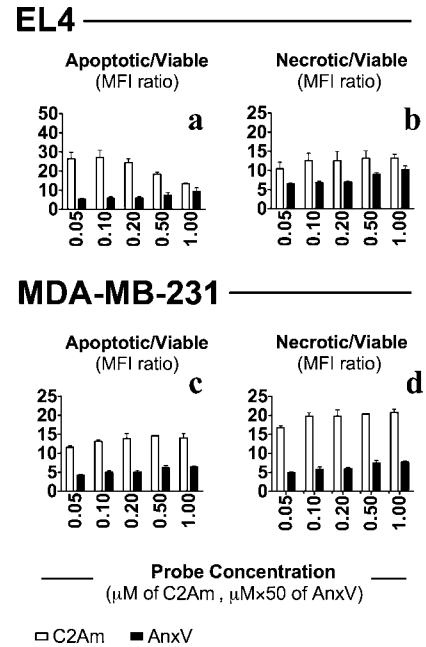


Figure 5. Effect of probe concentration on the specificity of labeling with C2Am and AnxV. C2Am was used at concentrations between 0.05 and 1.0 μM. AnxV was used at 50× lower concentrations, between 1 and 20 nM. EL4 cells were treated with etoposide (5 μM) for 16 h and MDA cells were treated with doxorubicin (1 μg/mL) for 72 h. MFI ratios for apoptotic/viable and necrotic/viable are shown for EL4 cells (a and b) and for MDA cells (c and d) following labeling with C2Am (open bars) or AnxV (closed bars). The different cell populations were identified based on their NADH autofluorescence and staining with SYTOX green, as in Figures 2−4. Data are shown as means ± SEM ($n = 3$). The differences in MFI ratios between C2Am and AnxV were significant at *$P < 0.05$, plot b-0.1 and 0.2 μM; **$P < 0.01$, a-0.5 μM; ***$P < 0.001$, a-0.05 to 0.2 μM, c-0.05 to 1.0 μM, d-0.05 to 1.0 μM.

autofluorescence. The levels of AnxV staining were consistently higher ($P < 0.05$) than C2Am for all cell populations (see Figure S4a−c in Supporting Information), above a concentration of 0.5 μM for C2Am and 10 nM for AnxV. This included the viable cell population, where the mean fluorescence intensity (MFI) for cells stained with AnxV was significantly higher ($P < 0.01$) than for those stained with C2Am (see Figure S4a in Supporting Information), despite AnxV being used at 50-fold lower concentrations. As a consequence, the mean fluorescence intensity (MFI) ratios for apoptotic/viable (Figure 5a) and necrotic/viable (Figure 5b) EL4 cells were significantly higher for C2Am than AnxV, at all the concentrations tested, indicating more specific labeling of both apoptotic ($P < 0.01$) and necrotic cells ($P < 0.05$) by C2Am. Similar results were obtained for the MDA line, for which the MFI of viable cells stained by AnxV was also significantly higher ($P < 0.01$) than for those stained with C2Am (see Figure S4d in Supporting Information), again despite being used at 50-fold lower concentrations. The levels of AnxV and C2Am staining of apoptotic and necrotic MDA cells were similar at these concentrations (see Figure S4e,f in Supporting Information), and like EL4 cells, the ratios of apoptotic/viable (Figure 5c) and necrotic/viable (Figure 5d) MDA cell staining were significantly higher for C2Am ($P < 0.001$), indicating again more specific labeling of both apoptotic and necrotic cells compared to viable cells.

On the basis of the concentration dependency of C2Am binding to apoptotic EL4 (see Figure S4b in Supporting Information) and MDA cells (see Figure S4e in Supporting Information), which shows partial or total saturation of the MFI value, we estimated the concentration of PS exposed on these dying cells. Assuming a 1:1 binding model of C2Am to PS, this gave values of 277 ± 42 and 127 ± 10 pmol of PS per million apoptotic EL4 and MDA cells, respectively.

Ca^{2+}-Dependence of C2Am and AnxV Binding to Dying Cells. Binding of C2Am and AnxV to the PS exposed on dying cells is calcium-dependent. However, both proteins are also known to bind other plasma membrane phospholipids in a Ca^{2+}-independent manner (*21, 22*). Drug-treated EL4 and MDA cells were incubated in the presence of Ca^{2+} (2 mM) or EDTA (10 mM) and binding of C2Am (200 nM) and AnxV (4 nM) was assessed by flow cytometry. The MFI ratios for binding to apoptotic versus viable and necrotic versus viable cells are shown in Figure 6. Binding to apoptotic EL4 cells was largely Ca^{2+}-dependent for both proteins, and significantly higher than in the absence of Ca^{2+} (Figure 6a) ($P < 0.001$ and $P < 0.05$, for C2Am and AnxV, respectively). The mean MFI ratio for apoptotic/viable in the absence of Ca^{2+} was 0.04 and 0.12 for C2Am and AnxV, respectively. C2Am, however, showed a more pronounced Ca^{2+}-independent binding to necrotic EL4 cells (Figure 6b) (a mean MFI ratio for necrotic/viable of 0.52 versus 0.16 for AnxV). This was also the case for necrotic MDA cells, where C2Am showed more Ca^{2+}-independent binding (with a MFI ratio for necrotic/viable of 0.58 versus 0.08 for AnxV). However, in these cells, C2Am also showed relatively high levels of Ca^{2+}-independent binding to apoptotic cells as well.

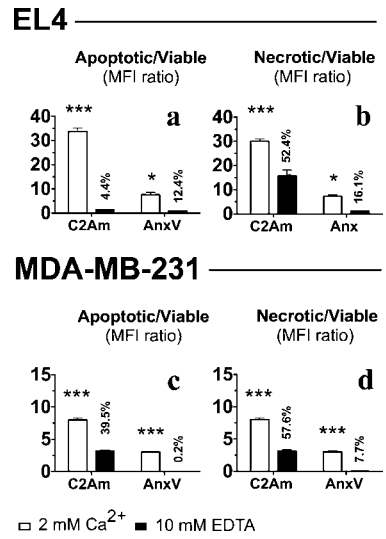


Figure 6. Effect of Ca^{2+} concentration on binding of C2Am and AnxV to apoptotic and necrotic cells. EL4 cells were treated with etoposide (5 μM) for 16 h and MDA cells were treated for 72 h with doxorubicin (1 μg/ml). MFI ratios for apoptotic/viable and necrotic/viable cells are shown for EL4 cells (a and b) and for MDA cells (c and d) following labeling with C2Am or AnxV in the presence of 2 mM Ca^{2+} (open bars) or 10 mM EDTA (filled bars). The different cell populations were identified based on their NADH autofluorescence and staining with SYTOX green, as in Figures 2−4. The ratios obtained in the absence of Ca^{2+} are also shown as a percentage of the ratios obtained in the presence of Ca^{2+}. The data are shown as means ± SEM ($n = 3$). *$P < 0.05$, ***$P < 0.001$.

DISCUSSION

Detection of PS with fluorescently labeled AnxV is a commonly used method for detecting apoptotic cell death in vitro (*23, 24*). Fluorescent, paramagnetic, and radionuclide-labeled derivatives of AnxV have also been used to detect cell death in vivo (*25−30*). In this study, we have evaluated, in comparison with AnxV, a novel probe for cell death detection based on the C2A domain of Synaptotagmin-I (*11, 31*). A GST-C2A fusion protein has been labeled previously with paramagnetic and radionuclide labels and used to detect apoptotic cells in vivo using magnetic resonance and radionuclide imaging, respectively (*13−15, 32*). A problem with these early derivatives of C2A was that they were labeled on one or more of the ε-amino groups of the 35 lysine residues in the fusion protein, and thus, the imaging agent was a heterogeneous mixture of labeled molecules (*15, 32*). Moreover, in the case of the agent labeled with Gd^{3+}-chelates, increased labeling led to a loss of affinity for PS and increased nonspecific binding (*15*). In this study, we have produced a site-directed mutant of C2A, containing a single cysteine residue C2A(S78C), which was labeled stoichiometrically with a fluorophore to yield a single chemical species (C2Am). The unmodified protein showed a comparable dissociation constant to the wild-type protein for PS (55 nM vs 20 nM, respectively) (*16*), and this was increased only slightly by modification of the cysteine residue with the fluorophore ($K_d = 71$ nM). We have shown that this fluorescently labeled derivative was able to detect PS on apoptotic and necrotic murine lymphoma and human breast cancer cells in vitro by flow cytometry. Although the C2Am derivative showed less labeling of apoptotic and necrotic cells than a similarly labeled commercial preparation of AnxV, the C2Am derivative showed lower binding to viable cells, despite being used at 50-fold higher concentrations and, as a consequence, better specificity for the detection of apoptotic and necrotic cells. This was reflected in the consistently higher ratios for the apoptotic/viable and necrotic/viable mean fluorescence intensities (MFI) for cells labeled with C2Am as compared with AnxV.

Titration of apoptotic EL4 and MDA cells with increasing concentrations of C2Am led to saturation of the bound fluorescence intensity and enabled us to estimate the abundance of PS, which for EL4 was 277 ± 42 pmol/10^6 cells and for MDA 127 ± 10 pmol/10^6 cells. The concentration of PS on EL4 cells is comparable to the level reported for apoptotic Jurkat cells of 240 pmol/10^6 cells, which is a human lymphoid cell line (*33*).

In order to investigate further the apparent binding of AnxV to viable cells, we used a fluorescently labeled inhibitor of

activated caspases (FLICA) to confirm that this cell population, which was identified as viable from measurements of NADH autofluorescence, was indeed viable. There has been some discussion as to whether FLICA detects activated caspases or the cell damage mediated by activated caspases (*34*, *35*). Regardless of the mechanism responsible, we expect viable cells to show only low levels of FLICA staining. The viable cell population, identified from measurements of NADH autofluorescence in drug-treated cell preparations, showed 2-fold and 6-fold less labeling with FLICA, when compared with apoptotic and late apoptotic/necrotic cells, respectively, in EL4 cells and 2-fold and 10-fold less labeling, respectively, in MDA cells, confirming that this was a genuinely viable cell population. When we analyzed C2m and AnxV binding to the 5% of the viable cell population that showed the lowest labeling with FLICA, there was considerably more labeling with AnxV (up to 5-fold) than with C2Am.

The Ca^{2+}-dependent binding of C2A and AnxV to PS is well-documented (*12*, *23*). Binding of both probes to the apoptotic cell fraction was largely quenched (60−99%) by the addition of EDTA (10 mM). This was also the case for AnxV binding to necrotic cells (8−16% of Ca^{2+}-independent binding). However, a large component of C2Am binding to necrotic cells was Ca^{2+}-independent (53% for EL4 and 58% for MDA). Since there is no evidence that C2A has any detectable affinity for PS in the absence of Ca^{2+} (*36*), the reason for this binding is unclear, although it could relate to the smaller size of C2Am making it better able to cross the ruptured cell membranes of necrotic cells. The Ca^{2+}-independent binding observed for both proteins may be due to binding to other phospholipids that are externalized during apoptosis (e.g., phosphatidylethanolamine or phosphatidylinositol) (*37*).

Although both proteins exhibit Ca^{2+}-dependent binding of anionic phospholipids, their three-dimensional structures, mechanisms of binding, and ultimately their affinities for PS differ appreciably. The C2A domain is a compact eight-stranded β-sheet structure interconnected by seven loops (*31*). The Ca^{2+} and PS binding sites are formed by the three loops at the top of the domain. There are three sites for Ca^{2+} in the Ca^{2+} binding pocket of C2A, and this binding stabilizes the loops but produces no significant conformational changes (*38*). The empty coordination sites on the bound Ca^{2+} ions are filled by direct interaction with anionic phospholipids. In contrast, AnxV is composed of four compact α-helical domains. Each domain contains a Ca^{2+} and phospholipid binding site (*39*). Two Ca^{2+} ions are bound at each binding site (*40*) and Ca^{2+}-induced conformational changes allow these multiple PS binding sites to interact in a cooperative manner, giving rise to the high affinity for PS (*41*). Furthermore, chemical cross-linking studies have shown that Annexin-V can form calcium-induced trimers, hexamers, and larger aggregates on phospholipid membranes (*42*). This multivalent binding likely explains the very high affinities reported for AnxV binding to PS, in the range 0.03−15 nM (*43*, *44*). This range is considerably lower than that reported previously for C2A (*16*) and that measured here. The much higher affinity of AnxV for PS may explain the binding of this protein to viable cells, which could express low levels of PS. The lower affinity of C2Am for PS may reduce binding to viable cells and hence explain why it is a more specific probe for cell death detection than AnxV.

CONCLUSIONS

We have synthesized a chemically well-defined fluorescent derivative of a site-directed mutant of the C2A domain of Synaptotagmin-I (S78C), which shows lower binding to viable cells than a similarly labeled Annexin V derivative and consequently has better specificity for detecting cell death. The lower binding to viable cells may be due to the lower affinity of C2A for PS. The lower binding of C2A to viable cells may be important when radionuclide derivatives of this protein are used to detect cell death in vivo, since this may reduce the nonspecific tissue accumulation observed with radionuclide-labeled derivatives of Annexin-V.

ACKNOWLEDGMENT

The work was supported by a Cancer Research UK Programme grant (to K.M.B.; C197/A3514) and by a Translational Research Program Award from The Leukemia & Lymphoma Society. T.H.W. was in receipt of BBSRC CASE studentship with GE Healthcare. We thank Dr. Len Packman at the Department of Biochemistry, University of Cambridge, for mass spectrometric analysis and Dr. Maaike de Backer, also at the Department of Biochemistry, for suggesting candidate mutations.

Supporting Information Available: Expression and purification of C2A(S78C), the protein assay, electrospray ionization (ESI) mass spectrometry, and surface plasmon resonance (SPR) measurements are described in more detail. There is a table showing the dissociation constants derived from affinity and kinetic analysis of the SPR data, a figure showing the ESI−mass spectrum of the C2Am-AlxF647 conjugate, figures showing the SDS-PAGE gels of the C2Am-AlxF647 and AnxV-AlxF647 conjugates and a figure demonstrating the effect of probe concentration on the specificity of labeling with C2Am and AnxV. This material is available free of charge via the Internet at http://pubs.acs.org.

LITERATURE CITED

(1) Blankenberg, F. G. (2008) In vivo detection of apoptosis. *J. Nucl. Med. 49*, 81S–95S.

(2) Brindle, K. (2008) New approaches for imaging tumour responses to treatment. *Nat. Rev. Cancer 8*, 1–14.

(3) Chang, J., Ormerod, M., Powles, T. J., Allred, D. C., Ashley, S. E., and Dowsett, M. (2000) Apoptosis and proliferation as predictors of chemotherapy response in patients with breast carcinoma. *Cancer 2000*, 2145–2152.

(4) Buchholz, T. A., Davis, D. W., McConkey, D. J., Symmans, W. F., Valero, V., Jhingran, A., Tucker, S. L., Pusztai, L., Cristofanilli, M., Esteva, F. J., Hortobagyi, G. N., and Sahin, A. A. (2003) Chemotherapy-induced apoptosis and Bcl-2 levels correlate with breast cancer response to chemotherapy. *Cancer J. 9*, 33–41.

(5) Savill, J., Fadok, V., Henson, P., and Haslett, C. (1993) Phagocyte recognition of cells undergoing apoptosis. *Immunol. Today 14*, 131–136.

(6) Hofstra, L., Liem, I. H., Dumont, E. A., Boersma, H., van Heerde, W. L., Doevendans, P. A., DeMuinck, E., Wellens, H. J. J., Kemerink, G. J., Reutelingsperger, C. P. M., and Heidendal, G. A. (2000) Visualisation of cell death in vivo in patients with acute myocardial infarction. *Lancet 356*, 209–212.

(7) Belhocine, T., Steinmetz, N., Hustinx, R., Bartsch, P., Jerusalem, G., Seidel, L., Rigo, P., and Green, A. (2002) Increased uptake of the apoptosis-imaging agent $^{(99m)}$Tc recombinant human Annexin V in human tumors after one course of chemotherapy as a predictor of tumor response and patient prognosis. *Clin. Cancer Res. 8*, 2766–2774.

(8) Boersma, H. H., Kietselaer, B. L., Stolk, L. M., Bennaghmouch, A., Hofstra, L., Narula, J., Heidendal, G. A., and Reutelingsperger, C. P. (2005) Past, present, and future of annexin A5: from protein discovery to clinical applications. *J. Nucl. Med. 46*, 2035–2050.

(9) Kemerink, G. J., Boersma, H. H., Thimister, P. W. L., Hofstra, L., Liem, I. H., Pakbiers, M. T. W., Janssen, D., Reutelingsperger, C. P. M., and Heidendal, G. A. K. (2001) Biodistribution and

dosimetry of Tc-99m-BTAP-annexin-V in humans. *Eur. J. Nuc. Med. 28*, 1373–1378.
(10) Boersma, H. H., Liem, I. H., Kemerink, G. J., Thimister, P. W. L., Hofstra, L., Stolk, L. M. L., van Heerde, W. L., Pakbiers, M. T. W., Janssen, D., Beysens, A. J., Reutelingsperger, C. P. M., and Heidendal, G. A. K. (2003) Comparison between human pharmacokinetics and imaging properties of two conjugation methods for Tc-99m-Annexin A5. *Brit. J. Radiol. 76*, 553–560.
(11) Davletov, B. A., and Sudhof, T. C. (1993) A single C2 domain from synaptotagmin I is sufficient for high affinity Ca2+/phospholipid binding. *J. Biol. Chem. 268*, 26386–26390.
(12) Sudhof, T. C., De Camilli, P., Niemann, H., and Jahn, R. (1993) Membrane fusion machinery: insights from synaptic proteins. *Cell 75*, 1–4.
(13) Zhao, M., Beauregard, D. A., Loizou, L., Davletov, B., and Brindle, K. M. (2001) Non-invasive detection of apoptosis using magnetic resonance imaging and a targeted contrast agent. *Nat. Med. 7*, 1241–1244.
(14) Zhao, M., Zhu, X., Ji, S., Zhou, J., Ozker, K. S., Fang, W., Molthen, R. C., and Hellman, R. S. (2006) 99mTc-labeled C2A domain of synaptotagmin I as a target-specific molecular probe for noninvasive imaging of acute myocardial infarction. *J. Nucl. Med. 47*, 1367–1374.
(15) Krishnan, A. S., Neves, A. A., de Backer, M. M., Hu, D.-E., Davletov, B., Kettunen, M. I., and Brindle, K. M. (2008) Detection of cell death in tumors using MRI and a gadolinium-based targeted contrast agent. *Radiology 246*, 854–862.
(16) Neves, A. A., Krishnan, A. S., Kettunen, M. I., Hu, D.-E., deBacker, M. M., Davletov, B., and Brindle, K. M. (2007) A paramagnetic nanoprobe to detect tumor cell death using magnetic resonance imaging. *Nano Lett. 7*, 1419–1423.
(17) Sims, J. L., Berger, S. J., and Berger, N. A. (1983) Poly(ADP-ribose) polymerase inhibitors preserve nicotinamide adenine dinucleotide and adenosine 5′-triphosphate pools in DNA-damaged cells: mechanism of stimulation of unscheduled DNA synthesis. *Biochemistry 22*, 5188–5194.
(18) Witney, T. H., Kettunen, M. I., Day, S. E., Hu, D. E., Neves, A. A., Gallagher, F. A., Fulton, S. M., and Brindle, K. M. (2009) A comparison between radiolabeled fluorodeoxyglucose uptake and hyperpolarized C-13-labeled pyruvate utilization as methods for detecting tumor response to treatment. *Neoplasia 6*, 574–582.
(19) Krysko, D. V., Berghe, T. V., D'Herde, K., and Vandenabeele, P. (2008) Apoptosis and necrosis: detection, discrimination and phagocytosis. *Methods 44*, 205–221.
(20) Primeau, A. J., Rendon, A., Hedley, D., Lilge, L., and Tannock, I. F. (2005) The distribution of the anticancer drug doxorubicin in relation to blood vessels in solid tumors. *Clin. Cancer Res. 11*, 8782–8788.
(21) Almeida, P. F. F., Sohma, H., Rasch, K. A., Wieser, C. M., and Hinderliter, A. (2005) Allosterism in membrane binding: A common motif of the annexins? *Biochemistry 44*, 10905–10913.
(22) Fernandez-Chacon, R., Shin, O. H., Konigstorfer, A., Matos, M. F., Meyer, A. C., Garcia, J., Gerber, S. H., Rizo, J., Sudhof, T. C., and Rosenmund, C. (2002) Structure/function analysis of Ca^{2+} binding to the C(2)A domain of synaptotagmin 1. *J. Neurosci. 22*, 8438–8446.
(23) Vermes, I., Haanen, C., Steffens-Nakken, H., and Reutelingsperger, C. P. (1995) A novel assay for apoptosis. Flow cytometric detection of phosphatidylserine expression on early apoptotic cells using fluorescein labelled Annexin V. *J. Immunol. Methods 184*, 39–51.
(24) van Genderen, H., Kenis, H., Lux, P., Ungethum, L., Maassen, C., Deckers, N., Narula, J., Hofstra, L., and Reutelingsperger, C. (2006) In vitro measurement of cell death with the annexin A5 affinity assay. *Nat. Protoc. 1*, 363–367.
(25) Cauchon, N., Langlois, R., Rousseau, J. A., Tessier, G., Cadorette, J., Lecomte, R., Hunting, D. J., Pavan, R. A., Zeisler, S. K., and van Lier, J. E. (2007) PET imaging of apoptosis with ^{64}Cu-labeled streptavidin following pretargeting of phosphatidylserine with biotinylated annexin-V. *Eur. J. Nucl. Med. Mol. Imaging 34*, 247–258.
(26) Keen, H. G., Dekker, B. A., Disley, L., Hastings, D., Lyons, S., Reader, A. J., Ottewell, P., Watson, A., and Zweit, J. (2005) Imaging apoptosis in vivo using I-124-annexin V and PET. *Nucl. Med. Biol. 32*, 395–402.
(27) Petrovsky, A., Schellenberger, E., Josephson, L., Weissleder, R., and Bogdanov, A. (2003) Near-infrared fluorescent imaging of tumor apoptosis. *Cancer Res. 63*, 1936–1942.
(28) Schellenberger, E. A., Bogdanov, A., Jr., Petrovsky, A., Ntziachristos, V., Weissleder, R., and Josephson, L. (2003) Optical imaging of apoptosis as a biomarker of tumor response to chemotherapy. *Neoplasia 5*, 187–192.
(29) Yagle, K. J., Eary, J. F., Tait, J. F., Grierson, J. R., Link, J. M., Lewellen, B., Gibson, D. F., and Krohn, K. A. (2005) Evaluation of F-18-annexin V as a PET imaging agent in an animal model of apoptosis. *J. Nucl. Med. 46*, 658–666.
(30) Schellenberger, E. A., Bogdanov, A., Jr., Hogemann, D., Tait, J., Weissleder, R., and Josephson, L. (2002) Annexin V-CLIO: a nanoparticle for detecting apoptosis by MRI. *Mol. Imaging 1*, 102–107.
(31) Sutton, R. B., Davletov, B. A., Berghuis, A. M., Sudhof, T. C., and Sprang, S. R. (1995) Structure of the first C2 domain of synaptotagmin I: a novel Ca2+/phospholipid-binding fold. *Cell 80*, 929–938.
(32) Jung, H. I., Kettunen, M. I., Davletov, B., and Brindle, K. M. (2004) Detection of apoptosis using the C2A domain of synaptotagmin I. *Bioconjugate Chem. 15*, 983–987.
(33) Borisenko, G. G., Matsura, T., Liu, S. X., Tyurin, V. A., Jianfei, J., Serinkan, F. B., and Kagan, V. E. (2003) Macrophage recognition of externalized phosphatidylserine and phagocytosis of apoptotic Jurkat cells--existence of a threshold. *Arch. Biochem. Biophys. 413*, 41–52.
(34) Smolewski, P., Grabarek, J., Halicka, D. H., and Darzynkiewicz, Z. (2002) Assay of caspase activation in situ combined with probing plasma membrane integrity to detect three distinct stages of apoptosis. *J. Immunol. Methods 265*, 111–121.
(35) Pozarowski, P., Huang, X., Halicka, D. H., Lee, B., Johnson, G., and Darzynkiewicz, Z. (2003) Interactions of fluorochrome-labeled caspase inhibitors with apoptotic cells: a caution in data interpretation. *Cytometry, Part A 55A*, 50–60.
(36) Kuo, W. W., Herrick, D. Z., Ellena, J. F., and Cafiso, D. S. (2009) The calcium-dependent and calcium-independent membrane binding of Synaptotagmin 1: Two modes of C2B binding. *J. Mol. Biol. 387*, 284–294.
(37) Emoto, K., Toyama-Sorimachi, N., Karasuyama, H., Inoue, K., and Umeda, M. (1997) Exposure of phosphatidylethanolamine on the surface of apoptotic cells. *Exp. Cell Res. 232*, 430–434.
(38) Shao, X. G., Fernandez, I., Sudhof, T. C., and Rizo, J. (1998) Solution structures of the Ca^{2+}-free and Ca^{2+}-bound C(2)A domain of synaptotagmin I: Does Ca^{2+} induce a conformational change? *Biochemistry 37*, 16106–16115.
(39) Liemann, S., and Huber, R. (1997) Three-dimensional structure of annexins. *Cell. Mol. Life Sci. 53*, 516–521.
(40) Silvestro, L., and Axelsen, P. H. (1999) Fourier transform infrared linked analysis of conformational changes in annexin V upon membrane binding. *Biochemistry 38*, 113–121.
(41) Concha, N. O., Head, J. F., Kaetzel, M. A., Dedman, J. R., and Seaton, B. A. (1993) Rat annexin-V crystal-structure - Ca^{2+}-induced conformational-changes. *Science 261*, 1321–1324.
(42) Concha, N. O., Head, J. F., Kaetzel, M. A., Dedman, J. R., and Seaton, B. A. (1992) Annexin-V forms calcium-dependent trimeric units on phospholipid-vesicles. *FEBS Lett. 314*, 159–162.
(43) Appelt, U., Sheriff, A., Gaipl, U. S., Kalden, J. R., Voll, R. E., and Herrmann, M. (2005) Viable, apoptotic and necrotic monocytes expose phosphatidylserine: cooperative binding of the ligand Annexin V to dying but not viable cells and implications for PS-dependent clearance. *Cell Death Differ. 12*, 194–196.
(44) Tait, J. F., and Gibson, D. (1992) Phospholipid binding of annexin-V-effects of calcium and membrane phosphatidylserine content. *Arch. Biochem. Biophys. 298*, 187–191.

BC9004415

Influence of Multivalent Nitrilotriacetic Acid Lipid−Ligand Affinity on the Circulation Half-Life in Mice of a Liposome-Attached His_6-Protein

Virginia Platt, Zhaohua Huang, Limin Cao, Matthew Tiffany, Kareen Riviere, and Francis C. Szoka, Jr.*

Joint Graduate Group in Bioengineering, University of California at San Francisco and Berkeley, San Francisco, California 94143, and Departments of Bioengineering and Therapeutic Sciences and Pharmaceutical Chemistry, School of Pharmacy, University of California, San Francisco, California 94143-0912. Received October 13, 2009; Revised Manuscript Received March 23, 2010

Metal chelation−ligand interactions, such as occur between nitrilotriacetic acid (NTA)-nickel and multihistidines, enable the noncovalent attachment of histidine-modified proteins to liposomes and other particles. We compared three lipids: a mono-NTA lipid (ca. 10 μM affinity) and two tris-NTA lipid derivatives (ca. 3 nM and 0.2 nM affinity) in their ability to retain two different his_6-containing proteins on NTA-liposomes in the presence of serum or plasma and after intravenous injection in mice. At nanomolar affinities, the off-rate of a his_6-ligand is sufficiently long so that his_6-proteins attached to particle surfaces will remain with the particle for hours; thus, we hypothesized that the increased his_6 affinity of multivalent NTA-modified liposomes would retain his_6-proteins longer both *in vitro* and *in vivo*. For each of the three lipids, we found a robust association and complete activity retention of two his_6-modified proteins: a far red-fluorescent protein, monomeric Katushka (mKate), and a prodrug-converting enzyme, yeast cytosine deaminase (yCD). Proteins associated more tightly *in vitro* with tris-NTA liposomes than with mono-NTA liposomes in the presence of refiltered fetal calf serum and mouse plasma. Free yCD exchanged with previously associated mKate for tris-NTA binding sites on the liposome surface. This exchange was due to the exchange of the proteins for NTA occupancy and not due to the exchange of tris-NTA lipid out of the liposome. The amount of yCD on the surface was similar if the proteins were co-associated or if mKate was pre-associated. This exchange confirms that NTA associated proteins are in a dynamic state and can exchange with multihistidine proteins in the biological milieu. There was no difference in circulation time of the protein when it was intravenously administered by itself or attached to any of the NTA-modified liposomes because *in vivo* the protein was rapidly released from the NTA liposomes. Upon recovery from blood, liposomes containing tris-NTA accumulated a different plasma protein profile than control liposomes, suggesting that Ni-NTA specifically interacts with some plasma proteins. The reason for the rapid protein dissociation from the liposome *in vivo* is not clear; it could be due to displacement by endogenous histidine-containing proteins or to natural chelators that remove nickel from the NTA. Regardless of the cause, improvements in chelator or ligand design are needed before metal chelation will be capable of retaining histidine-modified proteins on NTA liposomes after *in vivo* administration.

INTRODUCTION

Nickel chelation chromatography, and similar technologies that depend upon noncovalent interactions between a nickel chelator and a multihistidine-ligand, are widely used to purify proteins and associate proteins with surfaces (*1, 2*). The affinity of first-generation nitrilotriacetic acid (NTAs) is about 10 μM, whereas affinities of newer trivalent-NTAs (tris-NTAs) are in the nanomolar range (*3*−*6*).

NTA-mediated protein association is a useful investigative tool that is mild enough to retain protein activity and requires only a simple modification of the amino acid sequence—the addition of a string of histidines (*1, 7*). This interaction is reversible by stripping the chelated nickel from the NTA or allowing molecules to compete with the protein for NTA association (*2*). Proteins remain in a lateral surface orientation (*8*−*10*) and free of surface involvement (*11*). The stable, well-defined orientation allows proteins to be imaged and their structure or function investigated (*12, 13*). NTA coated surfaces improve AFM-based protein imaging and have been used to measure real-time substrate degradation (*14*). Active, surface-immobilized proteins can also be used to exploit the activity of these proteins in microarrays and biosensors (*7, 8, 15, 16*).

Modifications to the linkage area of the NTA headgroups change the molecules affinity for his-tagged proteins. The addition of poly(ethylene glycol) (PEG) increases protein capture efficiency (*15, 16*). Multivalent NTAs improve affinity by allowing multiple chelated nickels within the NTA cluster to interact with a single his-tag (*6, 17*−*19*).

Advances in protein production by recombinant techniques have largely removed protein availability as a limitation for protein-related therapies (*20*). The stability and rapid clearance of proteins *in vivo* are barriers that can reduce their therapeutic potential (*21*). These limitations can be overcome, in part, by using nanocarriers to alter protein pharmacokinetics or increase protein stability (*22*−*24*). Additional problems arise as chemical conjugation of proteins to carrier surfaces can damage the protein and the percent of protein attached to the carrier can be low (*25*). Multivalent NTAs have the potential to increase the efficiency, simplify the modification of nanocarriers and enable a "toolkit" approach for *in vivo* therapeutic use. Coupling proteins to carriers using a noncovalent NTA also avoids harsh conjugation chemistries. At low nanomolar affinities, the off-rate of a his_6 ligand from an NTA-nickel is sufficiently long so that the his_6-proteins bound to particle surfaces will remain with

* Corresponding author. HSE 1145, 513 Parnassus Avenue, University of California, San Francisco, CA 94141-0912, USA. Fax 415 476 0688. E-mail: szoka@cgl.ucsf.edu.

10.1021/bc900448f © 2010 American Chemical Society
Published on Web 04/12/2010

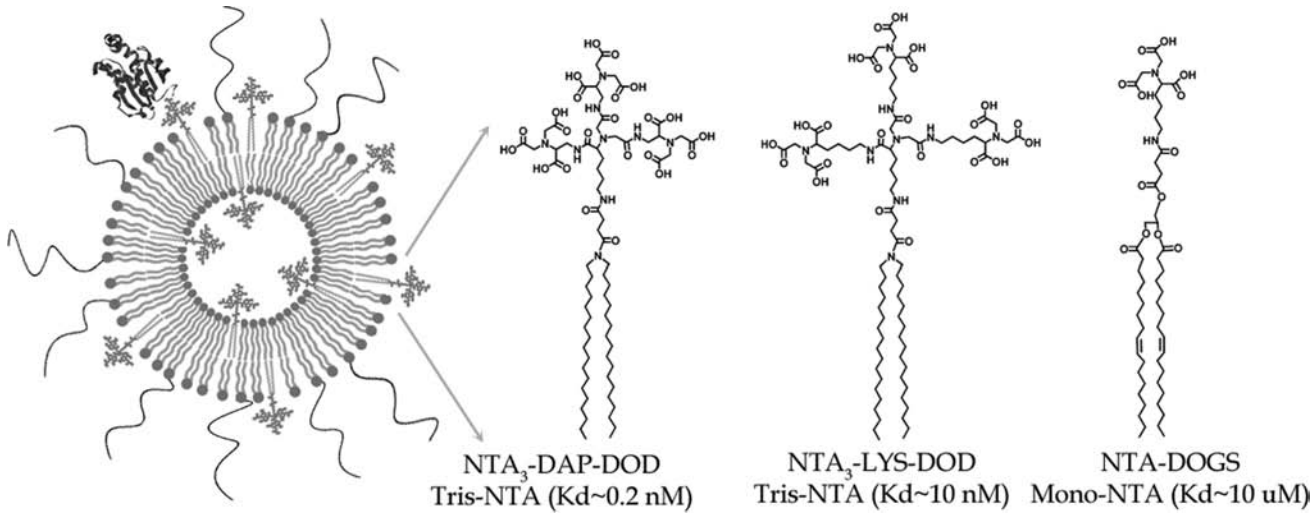


Figure 1. Illustration of nitrilotriacetic acid (NTA)-containing PEGylated liposomes with an associated his-tagged protein. Reported equilibrium dissociation constants are given for a his_6 peptide ligand (*5, 18*).

the particle for hours. Thus, an appropriate NTA-lipid would enable the creation of NTA-modified liposomes that could be functionalized with any his_6-containing protein.

The increased affinity of a multivalent NTA for a his-tagged protein is strong enough to make the interactions stable *in vitro* (*3*−*5*, *18*, *19*, *26*−*28*). Immunoliposomes generated by associating single-chain antibody fragments to liposomes with mono-NTA lipids were found to be suitable for rapid *in vitro* screening (*27*, *28*). However, incubation with human plasma as a surrogate for *in vivo* studies caused the protein to dissociate from the mono-NTA (*29*).

Other groups have shown success *in vivo*. His-tagged epitopes have been associated with both mono- and multivalent-NTA nanoparticles to mediate immunotherapies (*3*, *26*, *30*). A his-tagged peptide designed to be membrane penetrating and immunostimulatory was shown to induce splenocytic immune stimulation in BALB/c mice when associated with NTA-DOGS-liposomes (*26*). Using the same NTA-DOGS-lipid, an NTA-wax nanoparticle induced immune response against an HIV Gag protein (*30*). Potential vaccines were also formulated from plasma membrane vesicles derived from tumor cells modified to contain tris-NTA lipid (*3*). When mice were immunized by subcutaneous injection of these vesicles, containing encapsulated cytokines, they exhibited decreased tumor growth when challenged two weeks after immunization (*3*). In all three studies, the nanoparticles were injected subcutaneously and were not exposed to blood. The stability of the protein−vesicle association *in vivo* was not monitored, so the duration of protein retention is not known.

In this study, we compare the behavior of liposomes modified with three different NTA-lipids of increasing affinities for his-tagged proteins: mono-NTA-DOGS, tris-NTA-LYS-DOD, and tris-NTA-DAP-DOD (Figure 1). Liposome formulations containing NTA-lipids robustly associated both yCD and mKate without decreasing protein activity but association with the NTA liposomes did not increase the protein's circulation time.

EXPERIMENTAL PROCEDURES

Materials. All reagents and solvents obtained from commercial suppliers were used without further purification. Palmitoyloleoylphosphatidyl choline (POPC), palmitoyloleoylphosphatidyl glycerol (POPG), methoxy poly(ethylene glycol) 2000 disteroylphosphatidyl ethanolamine (mPEG (2000)-DSPE), 1,2-dioleoyl-*sn*-glycero-3-phosphoethanolamine-*N*-(Lissamine Rhodamine B Sulfonyl) (rhodamine-DOPE) and cholesterol were obtained from Avanti Polar Lipids (Alabaster, AL). Ni-NTA-DOGS (1,2-dioleoyl-*sn*-glycero-3-{(*N*-(5-amino-1-carboxypentyl)iminodiacetic acid)succinyl}) was purchased from Avanti Polar Lipids preloaded with nickel. Frozen, refiltered fetal calf serum (FCS) was obtained from the UCSF Cell Culture Facility and was prepared by filter-purifying serum, not heat inactivation, thus retaining active portions of the complement cascade.

Synthesis of Tris-NTA-LYS-DOD and Tris-NTA-DAP-DOD. The tris-NTA-lipids were synthesized via the methods described by Huang et al. (*4*, *5*). Tris-NTA-lipids are constructed from a base of dioctadececyl (DOD) lipid chains and diaminopropionic acid (DAP) or lysine (LYS) for tris-NTA-DAP-DOD and tris-NTA-LYS-DOD, respectively (Figure 1). Lipids were stored dry and dissolved in organic solvents immediately prior to use. To load the NTA_3 head groups with nickel, $NiCl_2$ was dissolved in minimal H_2O followed by methanol. NTA_3-lipids were incubated with nickel in the methanol−water solution (3 mol equiv $NiCl_2$ per mol NTA_3) at 60 °C for 15 min. The solution was allowed to cool to room temperature before adding it to the lipid formulation mixture. Preloading the nickel prior to liposome formation prevented dilution during removal of the excess nickel. Ni-NTA-DOGS was used as received from Avanti Polar Lipids.

Synthesis of FITC-DSPE. The fluorescent lipid was synthesized via direct coupling of FITC to DSPE. To a solution of DSPE (50 mg) in dry chloroform (5 mL) and triethylamine (37.3 μL) was added FITC (52.1 mg, 2 equiv) in minimal dimethyl sulfoxide (DSMO). The mixture reacted overnight at room temperature in the dark. Crude product solution was concentrated by rotary evaporation and purified on a Biotage Horizon HPFC system with prepacked silica columns (Biotage; Charlottesville, VA). The elution gradient consisted of 3 segments (solvent A, chloroform; B, methanol); 0−20% B, 24 mL; 20−20% B, 48 mL; 20−30% B, 72 mL. Fractions of pure product were pooled, evaporated, and dried under high vacuum overnight. Rf = 0.38 in chloroform/methanol (4:1 v/v). The product was dissolved and stored in chloroform at −40 °C. During synthesis, handling, and use, FITC-DSPE was protected from photobleaching by minimizing exposure to light and heat. Structure of the product was confirmed with ^{1}H NMR and MALDI mass spectrometry.

Formation of Liposomes. Liposomes were prepared by the sonication and extrusion method (*31*). Briefly, lipids dissolved in organic solvents were added to depyrogenated borosilicate glass tubes. Solvent was evaporated while rotating under reduced pressure at room temperature to form a lipid film. Residual

solvent was removed under high vacuum overnight. Films were then rehydrated in 1 mL HEPES buffer (20 mM HEPES, 140 mM NaCl, pH 7.4) with intermittent vortexing and sonicated under argon for 10 min at 23 °C to form vesicles. Liposome diameter was reduced by serially extruding 11 times through 200, 100, and 80 nm polycarbonate membranes with a hand-held extruder (Avestin; Ontario, Canada). Formulations contained either NTA_3-LYS-DOD, NTA_3-DAP-DOD, or NTA-Ni-DOGS (POPC/Chol/mPEG/NTA 55:40:5:*n*, molar ratio, where *n* corresponds to the mole percent NTA for each formulation). All liposomes contained 5 mol % mPEG(2000), unless noted. Control liposomes contained 1.5 mol % POPG to mimic the charge density of a 0.3% NTA_3-containing liposome formulation.

In some experiments, a tris-NTA-containing formulation without nickel was also used as a negative control. Liposome diameter and zeta potential were measured using a Zetasizer 3000 (Malvern Instruments; UK) for 3 or more liposome preparations of each formulation. The fluorescent signal from FITC-DSPE lipid, incorporated into the formulation to allow for tracking of the liposome (at 0.05 mol % unless noted), was not significantly decreased once liposomes formed. Lipid concentration in solution was calculated from the FITC signal based on control liposomes containing the same NTA concentration. Inclusion of NTA lipids caused both a slight fluorescence decrease and a negative charge.

Transfer of Tris-NTA Lipids between Lipid Membranes. Liposomes were prepared as described above (20 μmol/mL total lipid) that contained 3% tris-NTA-DAP, POPC, cholesterol, and 0.1 mol % FITC-DSPE (3:60:40:0.1 mol ratio) or POPC, cholesterol, and rhodamine-DOPE (60:40:0.05 mol ratio). Liposomes containing tris-NTA-DAP were mixed with liposomes without NTA lipids (1:1 v/v) and incubated at 37 °C for 3 h. Liposome mixtures (3 μmol total lipid) were then passed over an AG 1-X2 anion exchange column (1 × 6 cm bed volume, Bio-Rad Laboratories, Inc.; Hercules, CA) pre-equilibrated with 20 mM HEPES, 140 mM NaCl (pH 7.4). Uncharged rhodamine-containing liposomes were not retained by the column and appeared in the void volume fractions. Negatively charged, tris-NTA-DAP, FITC-containing liposomes were retained by the column and eluted with 20 mM Tris-HCl, 1 M NaCl (pH 9.5). Presence of liposomes was determined on the basis of rhodamine or FITC fluorescence (excitation/emission 544/590 nm and 490/520 nm, respectively). The charge of neutral, rhodamine-containing liposomes was monitored (Zetasizer 3000, Malvern Instruments; UK) before and after incubation with NTA-liposomes.

Protein Production. Genes for thermostabilized yeast cytosine deaminase (yCD; 18 kDa) (*32*) and monomeric Katushka (mKate; 27 kDa) (*33*) were constructed from gene fragments. Briefly, an optimized gene sequence for *E. coli* K12 (high) codon bias was designed and 27 or 32 primers (for yCD and mKate respectively) were used to construct a complete gene sequence using PCR. PCR was performed with GoTaq DNA polymerase (Promega; Madison, WI) in a GeneAmp PCR system 2400 thermal cycler (Perkin-Elmer; Waltham, MA). Synthesized genes were then ligated into pET15b vector for amplification and expression.

Protein was expressed in BL21-Codon Plus (DE3)-RIPL *E. coli* cells (Stratagene; La Jolla, CA). *E. coli* were grown in LB culture medium containing 30 μg/mL kanamycin and 50 μg/mL chloramphenicol at 37 °C until the OD600 nm reached 0.6−0.9. Protein expression was induced with 1 mM isopropyl α-D-1-thiogalactopyranoside (IPTG) with 0.5 mM zinc acetate. After overnight expression at room temperature, protein was purified from the cell supernatant by lysing the cells using freeze−thaw followed by sonication. His-tagged proteins were purified from other cellular proteins on a HisTrapFF affinity column (Amersham Biosciences; Piscataway, NJ) and eluted with 300 mM imidazole. The remaining yCD protein contaminants were removed by size exclusion chromatography on a HiPrep Sepharose S-100HR 16/60 size exclusion column (Amersham Biosciences; Piscataway, NJ). Buffers were exchanged using a PD10 desalting column (GE Healthcare; UK). OD280 nm was measured to obtain the fractions containing protein.

Liposome−Protein Association. His-tagged proteins were associated with liposomes at room temperature. Liposomes (2 μmol total lipid) were incubated with 270 μg mKate-his_6 or 180 μg yCD-his_6 in 0.2 mL HEPES buffer. For a 1% NTA containing formulation, this solution corresponds to a 1:1 molar ratio of surface NTA to his_6. To quantitate the extent of protein−liposome association, samples containing at least 2 μmol total lipid were passed through a pre-equilibrated 1 × 20 cm Sepharose CL-4B column under gravity flow. Fractions collected every 20 s (0.5 mL) were assayed for the presence of protein and liposomes. Liposomes eluted in the void volume and were measured by fluorescence (excitation/emission 490/520 nm). Protein concentration was quantified with a Bradford Protein Assay (Biorad Laboratories; Hercules, CA). This experiment was performed in triplicate for each protein/liposome formulation to ensure reproducibility.

Protein Activity. mKate activity was measured by fluorescence (excitation/emission 544/590 nm) in a Fluorostar 403 microplate reader (BMG Lab Technologies; Durham, NC). Enzymatic conversion of 5-FC to 5-FU per microgram of yCD was measured using previously described methods (*34*). Briefly, 1 μg yCD or yCD on liposomes was incubated in 1 mL PBS containing 5 mM 5-FC at 37 °C. Aliquots of the reaction mixture (20 μL) were removed at 10, 20, and 30 min and enzymatic conversion quenched by dilution to 1 mL in 0.1 M HCl in PBS. The amount of 5-FU formed in the reaction was determined by measuring the UV absorbance at 255 and 290 nm. Concentration (mM) of 5-FU was calculated as 0.185 × (Abs 255) − 0.049 × (Abs 290) to adjust for the presence of unconverted 5-FC. The activity of each sample was measured in triplicate.

Amount of enzyme activity per unit of lipid was measured after free protein was removed to ensure that all active protein was associated with the surface of the liposome. Liposome concentration was estimated on the basis of the presence of a FITC-DSPE fluorophore within the membrane.

Protein Dissociation in Serum or Plasma. The dissociation of protein from liposomes was measured by challenging already associated protein with refiltered fetal calf serum (FCS). Liposomes with associated protein were mixed 1:1 in refiltered FCS and incubated at 37 °C for a predetermined time. After incubation, samples were passed through a 1 × 20 cm Sepharose CL-4B column under gravity flow to separate free from bound protein. Liposome-containing fractions were collected and yCD concentrations were measured on the basis of conversion activity. mKate activity was measured by fluorescence. The experiment, including liposome formulation, was performed in triplicate.

For studies using mouse plasma, whole blood was collected using a heart puncture technique in BALB/c mice with a heparin (Sigma Aldrich; St. Louis, MO) loaded syringe. Plasma was clarified at 14 000 × *g* (Eppendorf Centrifuge 5415C, Brinkman Instruments, Inc.; Westbury, NY) for 20 min and stored at 4 °C for no longer than 2 days. Liposomes containing 1% tris-NTA-DAP were incubated with mKate for 1 h prior to addition of mouse plasma. Liposomes, with preassociated mKate, were mixed 1:1 with mouse plasma and incubated at 37 °C for 24 h. Samples were prepared in triplicate.

His-Tagged Protein Competition. Liposomes were prepared as described above and incubated to give 1:1 surface NTA to

mKate ratio. After 1 h, surface association was challenged with yCD. Proteins were allowed to equilibrate for an additional hour at room temperature and then passed over a Sepharose CL-4B column. Total protein was measured using the Bradford Protein Assay. Fluorescence of mKate and liposomes were monitored as described above. The competition assay was performed in triplicate for each formulation.

Protein Half-Life *in Vivo.* Liposomes were prepared at 20 mM lipid by hydrating films in sterile PBS, as described above. Once liposome diameter was reduced to approximately 80 nm, liposomes were sterilized with 0.2 μm filters. Each protein was iodinated following the Iodogen iodination protocol (Pierce Biotechnology; Rockford IL). Briefly, an iodination tube was washed with 1 mL PBS. To the tube was added 0.1 mL 0.2 M HEPES, pH 7.4, and 10 μL NaI^{125} ($\sim$1 mCi). Approximately 0.5 mg protein was added to the tube and the solution was reacted at room temperature for 10 min. The reaction mixture was diluted with nonradioactive protein and serially purified on a prepacked PD10 desalting column followed by a 1 $\times$ 15 cm Sephadex G-50 column. Fractions containing radioactive protein were collected and reaction efficiency calculated. The protein was then further diluted to give one million counts per dose of protein. Diluted, iodinated protein was mixed with liposomes to give one protein per surface available NTA and incubated for 1 h at room temperature prior to injection.

All animal procedures were conducted in accordance with the policies of the UCSF Institutional Animal Care and Use Committee. Mice (Jackson Laboratories; Bar Harbor, ME) were housed in an official UCSF facility. For periods of less than 48 h, during experimentation, mice were housed in UCSF approved laboratory conditions. BALB/c or Swiss-Webster mice (6−8 weeks old) were divided into treatment groups of 3 animals. Each group received 10 mM total lipid with 1.35 mg/mL iodinated mKate or 0.89 mg/mL iodinate yCD in 200 μL PBS via tail vein injection (one million I^{125} counts per dose; injection accounts for approximately a 15% increase in total blood volume).

Radioactivity in the blood obtained from submandibular cheek pouch bleeds at 5 min and 1 h (50 μL; less than 5% total blood volume) with a final bleed at 6 h (0.5 to 1 mL; 30−60% total blood volume) was quantified by gamma scintillation counting (Wallac Wizard, Perkin-Elmer; Waltham, MA). Liver, lung, and spleen were collected and analyzed for accumulation of radioactivity.

Noniodinated mKate and liposomes containing 0.5% FITC-DSPE were monitored in the blood by heart puncture at 15 min. Plasma was collected by centrifugation at 14 000 $\times$ *g* and liposomes were separated from the bulk free protein with a Sepharose CL-4B column. mKate fluorescence was measured (excitation/emission 544/590 nm) to quantify mKate remaining with the liposomes.

Association of Endogenous Proteins with NTA-Liposomes After Intravenous Administration. Liposomes containing either 1% tris-NTA-DAP or 1.5% POPG and 0.5% FITC-DSPE, 5% mPEG-DSPE were recovered from the blood of BALB/c mice. Whole blood was collected 10 min after liposome injection (2 μmol lipid in 200 μL PBS) by heart puncture using a heparin loaded syringe. Plasma was collected by sedimenting blood cells at 14 000 $\times$ *g* and liposomes were separated from unassociated protein using a Sepharose CL-4B column. Fractions containing liposomes were collected on the basis of FITC fluorescence (excitation/emission 490/520 nm). Liposome concentration was calculated on the basis of a FITC fluorescence standard curve constructed from serially diluted liposomes of the same lipid formulation. Protein concentration was measured using the Bradford Protein Assay (Biorad Laboratories; Hercules, CA).

Liposome fractions containing liposome-associated proteins were mixed with SDS gel-loading buffer (1:1 v/v) (*35*) and boiled for 10 min. Approximately 5 μg protein was loaded per well onto a 15-well, 4−15% tris-Glycine, SDS-PAGE gel (Biorad Laboratories; Hercules, CA). Protein bands were separated at 120 V for approximately 1 h and the gel was stained (Silver Stain Plus, Biorad Laboratories; Hercules, CA). Prestained protein ladders (10−230 kDa, New England Biolabs; Ipswich, MA) were included to estimate protein molecular weight. Relative protein quantity in each band was estimated using *ImageJ* gel analysis software (NIH *ImageJ* 1.42q; Bethesda, MD). For statistical comparisons, lanes were equalized to the 37 kDa protein band.

mKate Association with NTA-Liposomes Recovered after Intravenous Administration. BALB/c mice were injected with liposomes containing 1.0% tris-NTA-DAP and 5% mPEG-DSPE. Whole blood was collected and plasma was clarified via centrifugation as described previously. Free protein was separated from liposome-bound protein and liposome-containing fractions were collected on the basis of fluorescence. Liposomes were concentrated using a microcon concentrator (YM10, 10 000 MWCO, Millipore; Bedford, MA) pre-equilibrated with untreated tris-NTA-DAP-containing liposomes. Liposome fractions were concentrated for 30 min at 14 000 $\times$ *g*. Final liposome concentration was estimated on the basis of liposome fluorescence. Liposomes were then incubated with 5-fold excess of mKate (5 mKate per 1 surface available tris-NTA-DAP) for 3 h at room temperature. Free mKate was separated from liposome-associated mKate on a Sepharose CL-4B column. mKate fluorescence was measured (excitation/emission 544/590 nm) in liposome-containing fractions.

Hemopexin Interactions with NTA-Liposomes *in Vitro.* Hemopexin (HPX, Human, 70 kDa, Cell Sciences; Canton, MA) was dissolved in PBS (to 1 mg/mL) and incubated with liposomes (5 μmol/mL) containing 1.0% tris-NTA-DAP and 5% mPEG-DSPE for 3 h at room temperature. The final ratio of HPX to tris-NTA-DAP available on the liposome surface was 1:2 (a 2-fold excess tris-NTA-DAP). Following incubation, free HPX was separated from liposome-associated protein on a Sepharose CL-4B column pre-equilibrated in PBS. Liposome concentration was determined by FITC-fluorescence. Protein concentration in each fraction was determined by Bradford Protein Assay.

The dissociation of mKate from liposomes was measured by challenging liposomes containing preassociated mKate with HPX. Liposomes were incubated with mKate for 1 h prior to HPX addition. Liposomes containing preassociated mKate (3 μmol/mL with 0.4 mg/mL mKate) were incubated with a 1.5 volume excess HPX (at 1 mg/mL). The final ratio of HPX to tris-NTA-DAP available on the liposome surface was 1.5:1. The molar ratio of HPX to mKate in solution was also 1.5:1. Samples were incubated at 37 °C for 3 h. After incubation, samples were passed through a 1 $\times$ 20 cm Sepharose CL-4B column under gravity flow to separate free from bound protein. Fractions containing mKate were assayed on the basis of fluorescence (excitation/emission 544/590 nm). The ratio of mKate fluorescence to μmol/lipid was based upon a FITC standard curve prepared from liposomes of the same lipid formulation. Samples were assayed in triplicate.

RESULTS

Liposome Formulation and Construction. An illustration of a liposome and the NTA lipids used in this study is shown in Figure 1. The reported equilibrium dissociation constants for each lipid with a multihistidine peptide are also given (*4, 18*). Liposome diameter and stability was largely unaffected by the presence of NTA lipids (up to 3 mol %). We estimated, using

Table 1. Liposome Diameter and Zeta-Potential of NTA-Containing Liposomes with 3%, 1%, or 0.3% NTA and 5 mol % mPEG or 1% NTA without mPEG[a]

	3% NTA, 5% mPEG	1% NTA, 5% mPEG	1% NTA, 0% mPEG	0.3% NTA, 5% mPEG
		Tris-NTA-DAP		
diameter (nm)	88.0 ± 6.4	82.1 ± 2.5	88.3 ± 6.6	95.2 ± 15.1
ζ potential (mV)	−21.0	−18.3 ± 2.7	−18.6 ± 1.3	−19.3
		Tris-NTA-LYS		
diameter (nm)	107.9 ± 3.8	96.0 ± 11.5	96.6 ± 12.1	82.9 ± 7.6
ζ potential (mV)	−22.8	−18.6 ± 0.2	−20.1	−15.3
		NTA-DOGS		
diameter (nm)	78.7 ± 14.7	75.4 ± 12.3	85.0 ± 7.8	71.5 ± 1.0
ζ potential (mV)	−18.9	−16.9 ± 0.6	−16.1	−12.6
		Control (1.5% POPG, 5% mPEG)		
diameter (nm)		80.5 ± 6.5		
ζ potential (mV)		−15.6 ± 1.6		

[a] Control liposomes contained 1.5 mol % POPG to mimic the charge of 0.3% NTA-containing liposomes. ($n = 3$).

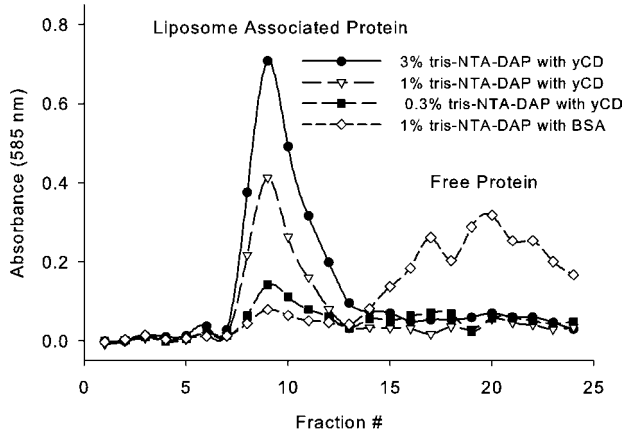


Figure 2. Representative association of proteins with the surface of NTA-liposomes. Liposomes bearing tris-NTA-DAP at 3% (circles), 1% (triangles), or 0.3% (squares) were associated with his-tagged yCD to saturate the available surface NTA. BSA was associated with 1% tris-NTA-DAP liposomes as a control (diamonds).

the protein diameter (UCSF Chimera; San Francisco, California) and NTA-lipid surface density on the liposome (*36*), that steric hindrance between adjacent NTA binding sites should effect association around 3% NTA with a 1:1 surface NTA to protein loading ratio. The liposome diameter and charge as measured by the zeta potential were similar for all formulations (Table 1).

His-Tagged Protein Association with Surface Displayed NTA on Liposomes. Liposomes containing any of the three NTA-lipids associated with protein to near the maximal expected amount. Free protein was separated from liposome-bound protein to determine the extent of association. Liposomes, along with their associated protein, elute in the void volume of a Sepharose CL-4B size exclusion column; nonassociated protein elutes at a larger volume. A representative example of protein separation in each fraction is shown in Figure 2. Liposomes with 3%, 1%, or 0.3% NTA_3-DAP associated with yCD to near saturation, with no free yCD visible in later fractions. BSA did not associate with 1% NTA_3-DAP liposomes.

The concentration of liposomes in each fraction was calculated on the basis of FITC-DSPE fluorescence. It was assumed that NTA lipids would distribute evenly between the inner and outer liposome surfaces. Hence, complete association was deemed to be a 1:1 ratio of his-tagged protein to expected surface-available NTA (Table 2).

Liposomes that contained NTA but not nickel did not associate with protein. BSA, which does not contain a his-tag, did not associate with NTA-nickel-containing liposomes. Control liposomes, containing both mPEG and POPG and having a similar surface charge as 0.3% NTA liposomes, associated with a minor amount of protein. The addition of EDTA, a strong chelator for nickel, to any NTA-containing liposome eliminated protein binding. Thus, a chelated nickel on the liposome surface and a his-tagged protein are necessary for this technology to be effective. When those elements are present, the amount of bound protein is stoichiometric with the amount of Ni-NTA on the liposome surface. yCD is a dimer, so it might be expected that greater than 100% association would occur, but this was rarely seen. This indicates that both his-tags of the dimer are engaged to the NTAs on the liposome surface. The amounts of mKate associated with 3, 1, and 0.3 mol % NTA containing liposomes are given in Figure 3.

Activity Retention of Surface Associated Proteins. Covalent attachment methods often partially or fully inactivate proteins (*25*). We measured the retention of activity of both yCD and mKate after binding to the NTA liposome. yCD converts the prodrug 5-FC to the cytotoxic drug 5-FU and the association of yCD with the surface of liposomes does not hinder 5-FC prodrug conversion. yCD retains full enzymatic activity when on the surface of a liposome (Figure 4A). Some proteins exhibit increased function and experience less product inhibition (to which yCD is susceptible) when in close proximity to a lipid bilayer (*22*); a slight increase in activity is observed in the liposome-bound yCD.

mKate also completely occupied all of the available sites on NTA-bearing liposomes at the NTA surface densities studied (Figure 4B). The activity of these liposomes was based on the fluorescence of the mKate. Unlike the observed increase in yCD activity when associated with the NTA-liposome, there was no increase in fluorescence for mKate.

Protein Dissociation in the Presence of Serum or Plasma. Liposomes bearing NTA preassociated with mKate or yCD were mixed at a 1:1 volume ratio with refiltered FCS. Figure 5 shows the retained protein on the surface of 1% NTA, 5% mPEG liposomes. The estimated amount of protein retained by the liposome is based on active protein and thermostabilized yCD has an activity half-life of over 50 h (*32*). The decrease in fluorescent activity of mKate over 24 h in FCS corresponds to approximately 5−10% of the total mKate fluorescence. This fluorescence decrease is equivalent to that seen in the loss of total fluorescence from free mKate in FCS at 37 °C over the same time period.

Dissociation of mKate from tris-NTA-DAP containing liposomes was also measured in the presence of mouse plasma. Plasma was prepared, stored at 4 °C, and used within 2 days. More mKate disassociated from the surface of NTA-

Table 2. yCD Association with NTA-Containing Liposomes[a]

mol % NTA with 5% mPEG (NTA:protein) ratio		tris-NTA-DAP mg/μmol lipid	tris-NTA-DAP % of expected	tris-NTA-LYS mg/μmol lipid	tris-NTA-LYS % of expected	NTA-DOGS mg/μmol lipid	NTA-DOGS % of expected
3.0% (1:1)		0.28 ± 0.02	103 ± 7	0.28 ± 0.03	102 ± 12	0.27 ± 0.05	99 ± 16.8
3.0% (3:1)		0.09 ± 0.02	91 ± 16	0.10 ± 0.01	105 ± 9	0.09 ± 0.01	94 ± 7.3
1.0% (1:1)		0.10 ± 0.02	103 ± 16	0.12 ± 0.01	128 ± 11	0.10 ± 0.01	108 ± 12.2
0.3% (1:1)		0.04 ± 0.01	108 ± 15	0.04 ± 0.00	131 ± 1	0.03 ± 0.00	94 ± 12.9
0.3% (1:3)		0.03 ± 0.01	118 ± 21	0.04 ± 0.00	118 ± 3	0.06 ± 0.01	189 ± 16.4
1.0% (1:1)	No mPEG[b]	0.09 ± 0.01	104 ± 14	0.11 ± 0.01	119 ± 6	0.10 ± 0.02	104.2 ± 23.8
1.0% (1:1)	BSA[c]	0.01 ± 0.00	11 ± 3	0.01 ± 0.00	12 ± 4	0.01 ± 0.00	8.6 ± 1.0
1.0% (1:1)	No nickel[d]	0.02 ± 0.01	20 ± 6	0.02 ± 0.00	23 ± 2		
1.5% POPG	No NTA[e]	0.01 ± 0.00	13 ± 3				

[a] Protein association was measured using the Bradford Protein Assay after unbound protein removal on a Sepharose CL-4B size exclusion column. Two variables are indicated for each NTA formulation: percent NTA present in the liposome is indicated by mol % NTA, protein added to formed liposomes is indicated as a ratio (NTA:protein). Data represent analysis of liposome-containing fractions. Control liposomes of various formulations were used to validate NTA-nickel-his-tag interactions. [b] Liposomes formulated without a 5% mPEG coat associated similar amounts of yCD as those containing mPEG. [c] BSA, a control protein that does not contain a his-tag, had limited association with liposomes containing NTA-nickel. [d] Liposomes formulated with NTA, but without nickel, associated less yCD than those with nickel. [e] Liposomes containing POPG, to mimic the charge of NTA-containing liposomes, had minimal yCD association.

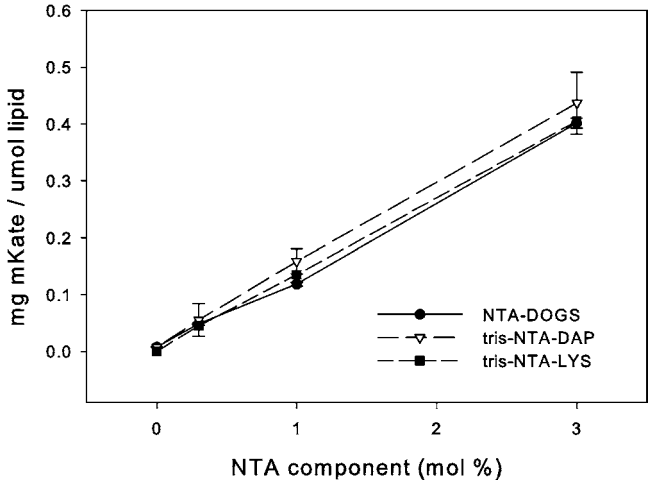


Figure 3. Association of mKate with the surface of NTA-liposomes. The amount of protein per μmol liposomes containing 3, 1, and 0.3 mol % NTA-DOGS (circles), tris-NTA-DAP (triangles), or tris-NTA-LYS (squares) ($n = 3$).

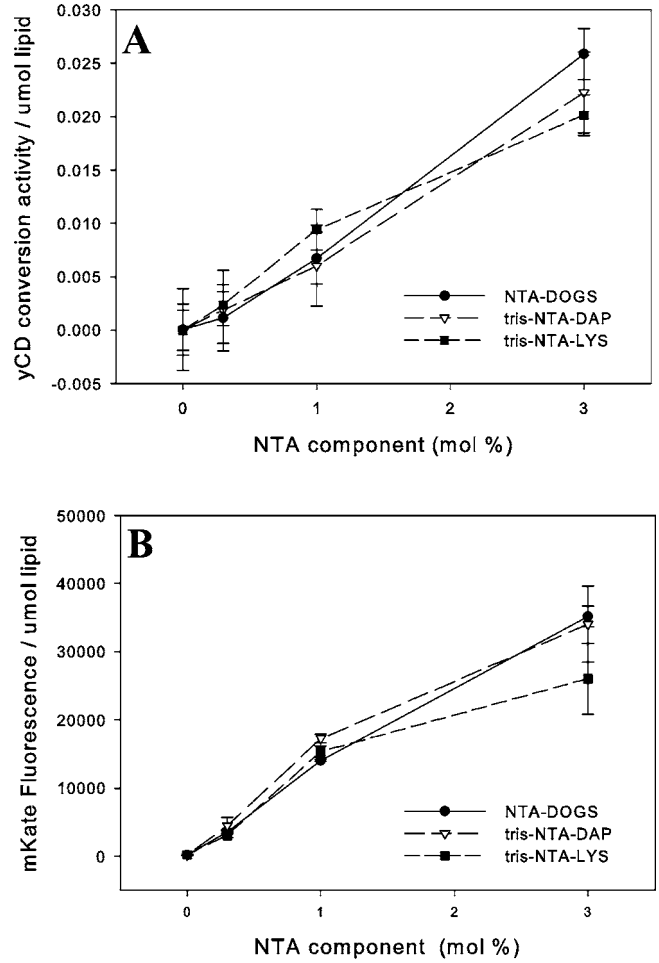


Figure 4. Retained protein activity of yCD (A) or mKate (B) on the surface of NTA-liposomes. The protein activity per μmol liposomes containing 3, 1, and 0.3 mol % NTA-DOGS (circles), tris-NTA-DAP (triangles), or tris-NTA-LYS (squares) ($n = 3$).

containing liposomes after 24 h (Figure 5C) than disassociated from liposomes exposed to FCS (Figure 5B). Tris-NTA-DAP-liposomes exposed to mouse plasma retained 30 ± 4% of the initial mKate after 24 h.

NTA_3-DAP has a higher affinity for histidine-tags than does NTA_3-LYS (*5*). Tris-NTAs in turn have significantly higher affinity (0.2−10 nM) than mono-NTA (10 μM) (*18*). For both yCD and mKate, retention in refiltered FCS or mouse plasma is related, but not directly proportional to, the relative affinity for the NTA lipids.

Competition between NTA-Liposome Bound His_6-Proteins and Subsequently Added His_6-Proteins. mKate that was stably associated with the liposome surface was challenged with added his_6-yCD. Despite the slightly higher affinity of tris-NTA-lipids for mKate ($K_d = 0.69$ nM) than for yCD ($K_d = 3.02$ nM) (*5*), yCD exchanged with preassociated mKate for positions on the liposome surface (Figure 6). Upon addition of a competing protein, proteins redistributed to yield the stoichiometric distribution of proteins on the surface of the liposome regardless of their reported affinity. For example, if yCD and mKate are at the same final concentration in solution, there will be an equal amount of yCD and mKate on the surface of the liposome and in solution. This arrangement will occur regardless of which protein is first incubated with the liposomes. When prebound mKate was challenged with BSA, which lacked a his-tag, no mKate dissociated; however, BSA nonspecifically associated with the liposome so that the total amount of liposome-bound protein increased.

Retention of Tris-NTA-Lipids in Liposomes. Liposomes containing 3% tris-NTA-DAP (−23.6 mV) were retained on a highly charged anion exchange column, while neutral liposomes (−4.1 mV) passed through the column in the void volume. The tris-NTA-DAP-DOD lipid did not transfer between labile lipid bilayers to a measurable degree. After 3 h at 37 °C, the neutral

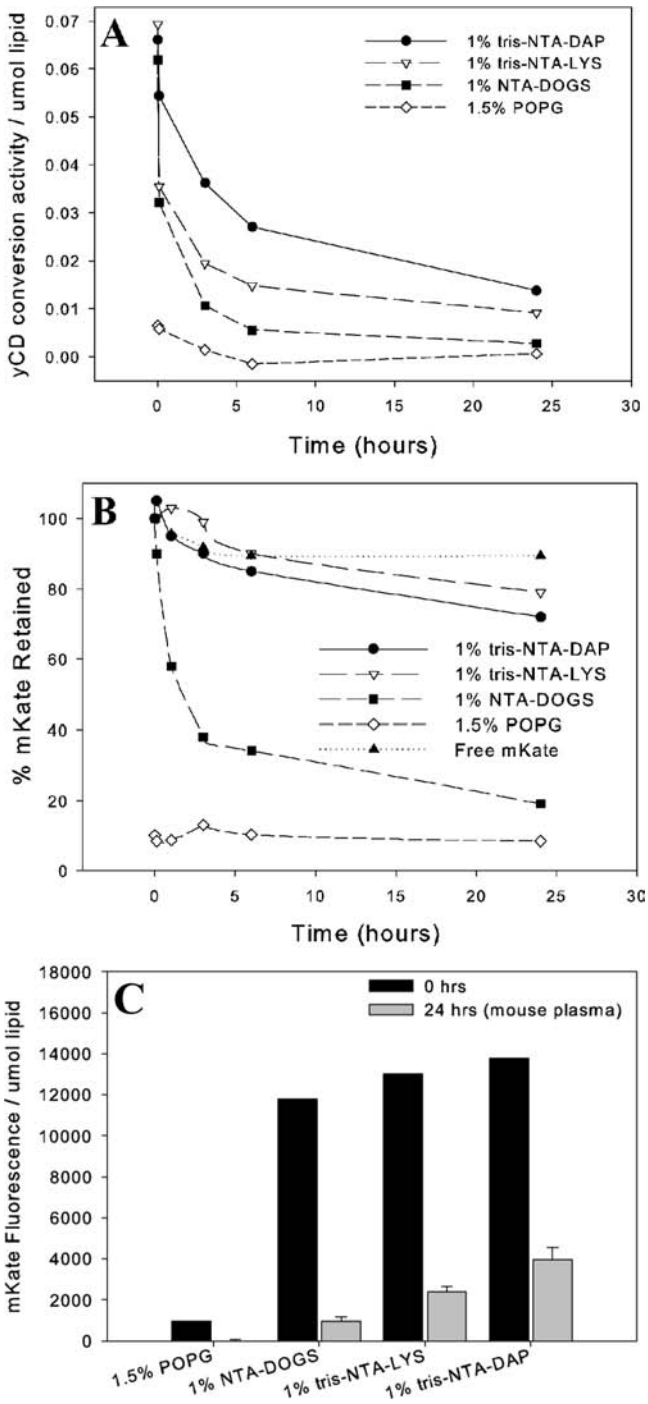


Figure 5. Dissociation of yCD (A) or mKate (B,C) from NTA-liposomes in serum or plasma. Enzyme activity per unit of liposome (for yCD) or percent retained mKate fluorescence after unbound protein has been removed for each of four liposome types: 1% tris-NTA-DAP (circles), 1% tris-NTA-LYS (triangles), 1% NTA-DOGS (filled squares), and control liposomes containing 1.5% POPG (diamonds). Time-course studies were done in the presence of refiltered fetal calf serum (A,B). Dissociation in the presences of mouse plasma was studied at 24 h (C) (yCD, $n = 1$; mKate, $n = 3$).

liposomes passed through the anion exchange column in the same fraction and retained the same surface charge (-4.8 ± 1.3) as neutral liposomes that were not incubated with NTA-containing liposomes (-3.8 ± 1.4). Neutral liposomes were fully recovered in the void volume (105 537 ± 13 546 au fluorescence or 105 ± 14% of the expected fluorescence based on untreated, neutral liposomes).

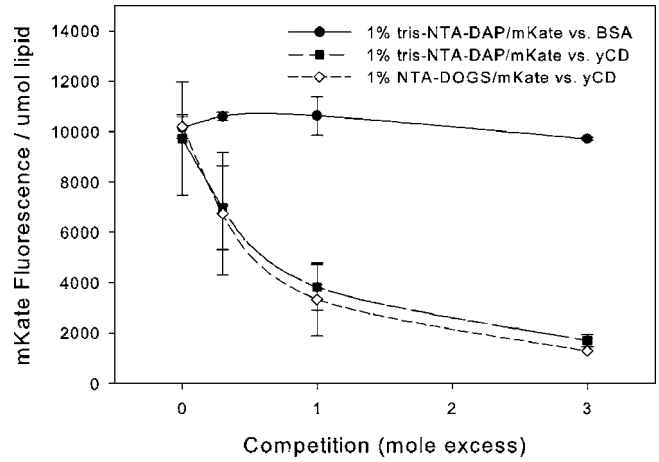


Figure 6. Competition of proteins with pre-associated mKate. Competition of BSA for pre-associated mKate on 1% tris-NTA-DAP (circles) or yCD for pre-associated mKate on 1% tris-NTA-DAP (squares) and 1% NTA-DOGS (diamonds) ($n = 3$).

Half-Life of NTA-Liposome Associated Proteins Upon Intravenous Administration. The association of iodinated protein with NTA-liposomes did not increase the residence time of either protein in the blood after intravenous injection (Figure 7). To ensure that iodination was not responsible for protein loss from the liposome, noniodinated mKate was associated with fluorescent tris-DAP-NTA-liposomes and injected into mice. After 15 min, blood was collected and the mKate-NTA liposomes remaining in plasma were separated on a Sepharose CL-4B column. A majority of the liposomes remained in circulation, but only a small fraction of the injected mKate was associated with the liposome fractions from the column (Figure 7B, inset). This verified that the mKate rapidly dissociated from the liposome upon contact with blood.

Endogenous Protein Binding to NTA-Liposomes Upon Intravenous Administration. When recovered from blood, tris-NTA-DAP containing liposomes had a different protein profile than liposomes with a similar charge (1.5% POPG, Figure 8A). In this experiment, three mice were injected per group with each liposome formulation. Unassociated plasma proteins were removed from liposome fractions based on size exclusion on a Sepharose CL-4B column. Tris-NTA-DAP-containing liposomes associated more protein (420 ± 90 μg/μmol lipid) than did POPG-containing liposomes (320 ± 60 μg/μmol lipid); however, this difference was not significant ($p = 0.19$). Lower molecular weight bands at approximately 12, 28, 58−60, and 75−90 kDa were enriched in tris-NTA-DAP-containing liposomes compared to POPG-containing liposomes (Figure 8A).

The quantity of protein present in the bands at approximately 12, 27, 37, and 60 (as a doublet) kDa was estimated using *ImageJ* gel analysis software and the area under the histogram peaks was calculated (Figure 8B). Equalizing the values based on the protein band at 37 kDa suggests that tris-NTA-DAP liposomes associate the 12 kDa and 60 kDa proteins significantly more than POPG containing liposomes ($p = 0.048$, 0.040, respectively). Association of the 27 kDa protein was higher with tris-NTA-liposomes than POPG; however, the difference was not significant.

Liposomes recovered from the blood of mice associated mKate after separation from plasma proteins. Liposomes containing tris-NTA-DAP were purified from unassociated plasma proteins, concentrated, and then mixed with a 5-fold excess of mKate. Liposomes associated approximately 70% of the mKate that would be expected based on liposome fluorescence (7000 units fluorescent/μmol lipid) compared to liposomes that were not exposed to mouse blood. This confirms that the

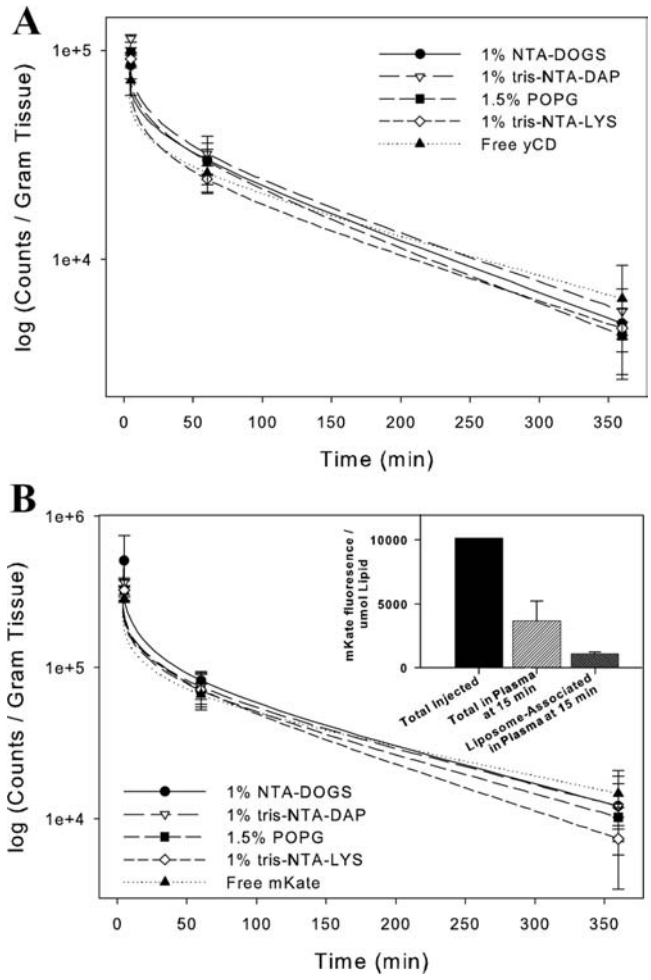


Figure 7. Disappearance of iodinated yCD (A) or mKate (B) after intravenous injection in mice (filled triangles) on four liposome types: 1% tris-NTA-DAP (open triangles), 1% tris-NTA-LYS (diamonds), 1% NTA-DOGS (circles), or control liposomes containing 1.5% POPG (squares). Each animal was injected with one million I^{125} counts per dose. Non-iodinated mKate (B**,** inset) fluorescence remaining bound 15 min after injection on 1% tris-NTA-DAP liposomes ($n = 3$).

tris-NTA lipid was not removed from the liposome during circulation in mice.

Hemopexin, a plasma protein which scavenges heme from the blood, was identified as a candidate for removing nickel from tris-NTA containing liposomes (*37*). Exposure of tris-NTA-DAP-liposomes to hemopexin did not effect mKate association. Hemopexin bound to tris-NTA-DAP-liposomes at approximately 25 μg/μmol lipid; this binding quantity (approximately 8% of 1:1 surface available NTA:HPX) is considered nonspecific binding and is similar to the quantity seen for BSA association to NTA-liposomes or his-tagged protein association to POPG control liposomes.

DISCUSSION

We characterized the effect of increasing affinity in a series of Ni-NTA/his_6 pairs, on his_6-protein-NTA liposome association, his_6-protein activity, and his_6-protein retention on NTA-liposomes under a variety of conditions. The surprising finding is that, despite the retention of the his_6-proteins on the NTA liposomes in FCS and mouse plasma, the NTA-liposome-attached protein rapidly dissociated from the liposome upon intravenous administration and hence was eliminated from circulation as rapidly as the injected "free" protein. The rapid elimination occurred regardless of whether the liposome contained a low affinity NTA lipid or a high affinity NTA lipid and was not consistent with the measured off-rates of the same protein on a NTA Biacore chip.

Our experiments were enabled by the synthesis of a series of tris-NTA chelators with increasing affinity for the his_6-tag (*5*). We synthesized tris-NTA-lipids with two different carbon lengths between each NTA headgroup to examine the effect of linker spacing on binding affinity. yCD and mKate retained activity when associated with the surface of NTA-containing liposomes, so the interaction holds forth the prospect of a modular system for easily constructing liposomes modified with any protein that has a his_6-tag.

Retention time for the his_6-proteins on the surface of a Biacore chip modified with the various NTA derivatives increased as NTA linker length decreased. Dissociation rates for the same NTA derivative also varied between his_6-proteins; this was ascribed to differences in the accessibility of the his-tag (*5*). Assuming that the protein is rapidly eliminated when released from the liposome, the blood residence time of a his_6-protein attached to an NTA-liposome after intravenous administration can be calculated from the dissociation rate. For the tris-NTA-LYS headgroup, with four carbons in the linker region, the half-time of release from the surface of a Biacore chip was 14 min with yCD ($k_d = 0.83 \times 10^{-3}$/s). If the linker is decreased by one carbon, the half-time was 20 min with yCD ($k_d = 0.59 \times 10^{-3}$/s) and 50 min with mKate ($k_d = 0.22 \times 10^{-3}$/s). When the linker region was decreased by another carbon, the computed half-time with mKate increased to over 2 h ($k_d = 0.89 \times 10^{-3}$/s) (*5*).

Proteins associated with the higher affinity NTA-liposomes were retained on the liposome much better when exposed to FCS than when on the mono-NTA modified liposomes (Figure 5). The magnitude of this increased association time is related to the affinity of each NTA−protein pair (Figure 5). At 24 h, approximately 80% of the initially bound mKate remained associated with either the tris-NTA-LYS and tris-NTA-DAP liposomes, whereas only 20% mKate remained bound to liposomes containing NTA-DOGS. yCD dissociated to a greater extent from the surface of the liposome than did mKate, which is consistent with the difference in affinity ($K_d = 0.69$ and 3.02 nM) for mKate and yCD, respectively. When plasma was obtained from mice, approximately 30% of the initially bound mKate remained associated with the tris-NTA-DAP liposomes at 24 h (Figure 5C). However, as expected for a reversible interaction, his_6-proteins could exchange with proteins in solution even from the lipid with the highest affinity, the tris-NTA-DAP. This reflects the dynamic nature of this system (Figure 6).

While tris-NTA-DAP increased retention of both proteins as compared to NTA-DOGS in FCS, it did not improve protein association *in vivo* (Figure 7). All of the formulations studied exhibited a similar clearance rate to that of free protein. PEGylated liposomes of this diameter have a circulation half-life of half a day or more (*38*). If the dissociation rate was the prime determinant of protein loss from the liposome, tris-NTA association should have afforded some improvement in circulation time for the liposome-bound protein over the free protein. The dynamic nature of noncovalent protein association with NTA may allow any multihistidine-containing protein in the body to actively compete with the associated protein, even if the affinity of the nascent, competing protein is much lower than that of the associated protein. However, if loss of protein is a simple equilibrium phenomenon, the off rate would still control the residence time of the protein on the liposome. Therefore, there must be other factors that contribute to the rapid dissociation after intravenous injection.

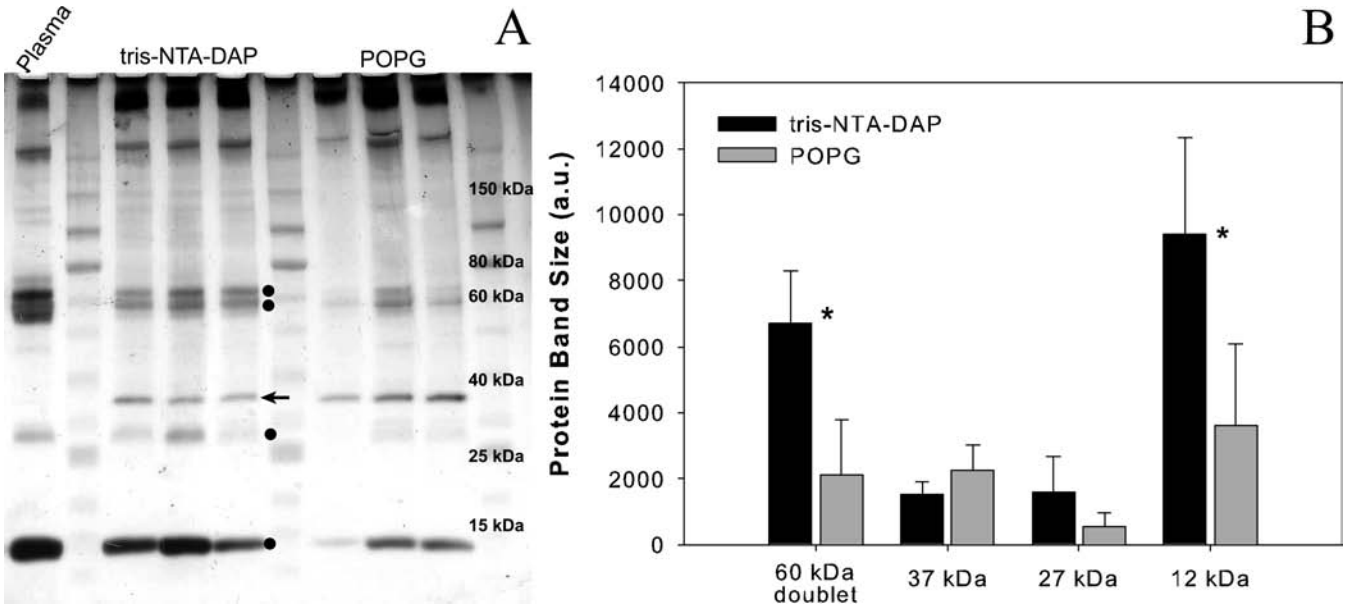


Figure 8. Analysis of protein interactions with NTA-modified and control liposomes. Liposomes containing either 1% tris-NTA-DAP or 1.5% POPG with 5% mPEG were recovered from the plasma of mice after intravenous injection. Each lane represents recovery of liposomes from an individual mouse, which accounts for the variable amount of total protein per well. Liposomes were purified to remove unassociated proteins and run on a 4−15% tris-Glycine SDS Page Gel. Circles (•) denote proteins that were substantially more visible in tris-NTA-DAP containing fractions than in control fractions after silver staining (A). The relative amount of protein in each band was quantified using *ImageJ* software. Association of the proteins at 60 kDa and 12 kDa are statistically greater for the tris-NTA-DAP-liposome than control liposomes (* $p < 0.05$) (B).

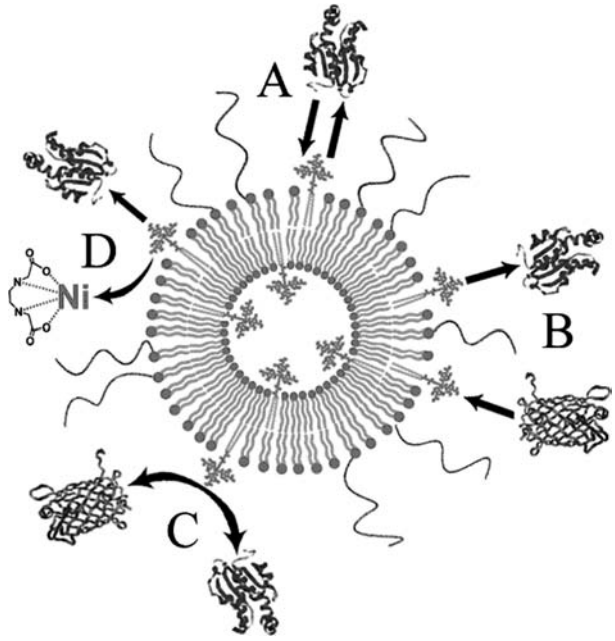


Figure 9. Modes of interaction of His-tagged proteins with NTA-containing PEGylated liposomes. Proteins bearing a his-tag associate and dissociate from the liposome surface (A). Upon dissociation, other proteins may associate with the newly available NTAs (B), proteins may directly compete for NTA binding (C), or nickel may be removed by endogenous chelators (D).

Plasma proteins may play a crucial role in the disruption of his_6-NTA association (Figure 9). Some plasma proteins may interact preferentially with the surface of NTA-liposomes (Figure 8A) (*29*) and may contribute to protein dissociation or loss of nickel from the chelator. Tris-NTA-DAP-containing liposomes recovered from mouse blood contained several proteins that were less present on liposomes containing POPG. These proteins may include metal-scavenging and histidine-rich plasma proteins, such as thioredoxin (12 kDa), Hemopexin (HPX, approximately 60 kDa) and histidine-rich glycoprotein (HRG, 75−95 kDa) (*37*, *39*, *40*). HPX scavenges heme within the blood, partially due to a high-affinity binding site containing eight histidines (*37*). This protein also binds divalent metal ions, including nickel (*41*), and has been shown to interact with immobilized metal-affinity columns (*42*). Although HPX did not bind tris-NTA-DAP liposomes or cause mKate dissociation under the conditions studied, similar metal-scavenging plasma proteins may interact with liposome-displayed NTA *in vivo*. HRG, another abundant plasma protein, has also been shown to scavenge heme, interact with metal ions, and bind to nickel-NTA with high affinity (*39*, *43*). Endogenous biochelators may act as an additional destabilizing factor by removing bound nickel from the NTA (*44*). Although NTA-liposomes recovered from blood could associate mKate (Figure 8C) without addition of exogenous nickel, removal of nickel from the NTA in blood may act to partially disassociate proteins. Competition for NTA occupancy by endogenous histidine-rich proteins, along with loss of nickel, may cause the initial protein dissociation from the liposome upon exposure to blood.

Several groups have published the robust association of his-tagged proteins with NTA containing nano-lipoparticles (*3*, *4*, *26*, *29*, *30*, *45*). Our findings must be reconciled with a number of papers where proteins associated with liposomes or lipid particles containing mono-NTA or tris-NTA mediate a number of immune responses (*3*, *26*, *30*). Protein-NTA particles generated a measurable immune response based on specific serum IgG levels (*30*) or an increase in splenocytes secreting cytokines (*26*). Mice immunized with tris-NTA containing plasma membrane vesicles showed decreased tumor growth (*3*). In these studies, the NTA particle was injected via the subcutaneous route. After subcutaneous administration, the particles are exposed to an order of magnitude lower concentration of endogenous proteins and the NTA liposome and its attached protein are eliminated more slowly than after intravenous administration. Second, the immune response is exquisitely sensitive to a protein antigen and even small quantities of protein that remained associated with the particle might have been responsible for the observed effects. Thus, it is not possible to

deduce the amount of protein that these various particles delivered from the observed immune responses.

Many *in vitro* cellular studies using protein-his_6/NTA-lipooparticles are performed in the presence of FCS-rich cell culture media. Under these conditions, Herringson et al. state that the his_6-protein/tris-NTA association is sufficiently robust so that *in vitro* retention will translate to *in vivo* protein/particle stability (*46*). However, our results indicate that improvements in metal chelation methodologies are required if metal chelation technology is to be useful for *in vivo* particle applications. Our group is exploring methods to improve the affinity of the system and reduce loss of nickel chelation. One approach is to increase the shielding in the vicinity of the acetic acid moiety by incorporating branched methyl groups. This might provide a hydrophobic wall that impedes removal of the chelated metal. An alternative approach is to synthesize a "clamp" for the chelated nickel. Chemically, this can be easily accomplished by covalently attaching histamines to a triacetic acid scaffold, such as the building blocks used to synthesize tris-NTA. The imidazole groups would then form a triad complementary structure to interact with the chelated nickel on the lipids. Although the triad histamine could not be incorporated into a recombinant protein, it could be used as a high-affinity binding partner for the chelated nickel. It remains to be discovered whether such improvements will be sufficient to stabilize NTA-protein-his_6 complexes *in vivo*.

ACKNOWLEDGMENT

We gratefully thank Katherine Jerger for her assistance with animal experiments. This work was supported by grant NIH R01 GM061851. Protein production and the salary of Dr. Cao were supported by UC discovery grant Bio 60−10618 and Halozyme, Inc. Our appreciation is extended to Greg Frost for suggesting hemopexin might interfere with his_6/NTA interactions in plasma and Christopher Cullander for helpful discussions regarding this manuscript.

LITERATURE CITED

(1) Sigal, G. B., Bamdad, C., Barberis, A., Strominger, J., and Whitesides, G. M. (1996) A self-assembled monolayer for the binding and study of histidine-tagged proteins by surface plasmon resonance. *Anal. Chem. 68*, 490–497.

(2) Ueda, E. K., Gout, P. W., and Morganti, L. (2003) Current and prospective applications of metal ion-protein binding. *J. Chromatogr., A 988*, 1–23.

(3) van Broekhoven, C. L., and Altin, J. G. (2005) The novel chelator lipid 3(nitrilotriacetic acid)-ditetradecylamine (NTA(3)-DTDA) promotes stable binding of His-tagged proteins to liposomal membranes: potent anti-tumor responses induced by simultaneously targeting antigen, cytokine and costimulatory signals to T cells. *Biochim. Biophys. Acta 1716*, 104–116.

(4) Huang, Z., Park, J. I., Watson, D. S., Hwang, P., and Szoka, F. C., Jr. (2006) Facile synthesis of multivalent nitrilotriacetic acid (NTA) and NTA conjugates for analytical and drug delivery applications. *Bioconjugate Chem. 17*, 1592–1600.

(5) Huang, Z., Hwang, P., Watson, D. S., Cao, L., and Szoka, F. C. (2009) Tris-nitrilotriacetic acids of subnanomolar affinity toward hexahistidine tagged molecules. *Bioconjugate Chem. 20*, 1667–1672.

(6) Altin, J. G., Banwell, M. G., Coghlan, P. A., Easton, C. J., Nairn, M. R., and Offermann, D. A. (2006) Synthesis of NTA(3)-DTDA - A chelator-lipid that promotes stable binding of His-tagged proteins to membranes. *Aust. J. Chem. 59*, 302–306.

(7) Balland, V., Hureau, C., Cusano, A. M., Liu, Y., Tron, T., and Limoges, B. (2008) Oriented immobilization of a fully active monolayer of histidine-tagged recombinant laccase on modified gold electrodes. *Chemistry 14*, 7186–7192.

(8) Dietrich, C., Schmitt, L., and Tampe, R. (1995) Molecular organization of histidine-tagged biomolecules at self-assembled lipid interfaces using a novel class of chelator lipids. *Proc. Natl. Acad. Sci. U.S.A. 92*, 9014–9018.

(9) Dorn, I. T., Pawlitschko, K., Pettinger, S. C., and Tampe, R. (1998) Orientation and two-dimensional organization of proteins at chelator lipid interfaces. *Biol. Chem. 379*, 1151–1159.

(10) Tinazli, A., Tang, J., Valiokas, R., Picuric, S., Lata, S., Piehler, J., Liedberg, B., and Tampe, R. (2005) High-affinity chelator thiols for switchable and oriented immobilization of histidine-tagged proteins: a generic platform for protein chip technologies. *Chemistry 11*, 5249–5259.

(11) Schuy, S., Treutlein, B., Pietuch, A., and Janshoff, A. (2008) In situ synthesis of lipopeptides as versatile receptors for the specific binding of nanoparticles and liposomes to solid-supported membranes. *Small 4*, 970–981.

(12) Keller, T. A., Duschl, C., Kröger, D., Sévin-Landais, A.-F., Vogel, H., Cervigni, S. E., and Dumy, P. (1995) Reversible oriented immobilization of histidine-tagged proteins on gold surfaces using a chelator thioalkane. *Supramol. Sci. 2*, 155–160.

(13) Barklis, E., McDermott, J., Wilkens, S., Schabtach, E., Schmid, M. F., Fuller, S., Karanjia, S., Love, Z., Jones, R., Rui, Y., Zhao, X., and Thompson, D. (1997) Structural analysis of membrane-bound retrovirus capsid proteins. *Embo J. 16*, 1199–1213.

(14) Dorn, I. T., Eschrich, R., Seemuller, E., Guckenberger, R., and Tampe, R. (1999) High-resolution AFM-imaging and mechanistic analysis of the 20 S proteasome. *J. Mol. Biol. 288*, 1027–1036.

(15) Zhen, G., Zurcher, S., Falconnet, D., Xu, F., Kuennemann, E., and Textor, M. (2005) NTA-functionalized Poly(L-lysine)-g-Poly(ethylene glycol): A polymeric interface for binding and studying 6 his-tagged proteins. *Conf. Proc. IEEE Eng. Med. Biol. Soc. 1*, 1036–1038.

(16) Kang, E., Park, J. W., McClellan, S. J., Kim, J. M., Holland, D. P., Lee, G. U., Franses, E. I., Park, K., and Thompson, D. H. (2007) Specific adsorption of histidine-tagged proteins on silica surfaces modified with Ni2+/NTA-derivatized poly(ethylene glycol). *Langmuir 23*, 6281–6288.

(17) Guignet, E. G., Hovius, R., and Vogel, H. (2004) Reversible site-selective labeling of membrane proteins in live cells. *Nat. Biotechnol. 22*, 440–444.

(18) Lata, S., Reichel, A., Brock, R., Tampe, R., and Piehler, J. (2005) High-affinity adaptors for switchable recognition of histidine-tagged proteins. *J. Am. Chem. Soc. 127*, 10205–10215.

(19) Lata, S., Gavutis, M., Tampe, R., and Piehler, J. (2006) Specific and stable fluorescence labeling of histidine-tagged proteins for dissecting multi-protein complex formation. *J. Am. Chem. Soc. 128*, 2365–2372.

(20) Leader, B., Baca, Q. J., and Golan, D. E. (2008) Protein therapeutics: a summary and pharmacological classification. *Nat. Rev. Drug Discovery 7*, 21–39.

(21) Werle, M., and Bernkop-Schnurch, A. (2006) Strategies to improve plasma half life time of peptide and protein drugs. *Amino Acids 30*, 351–367.

(22) Nagami, H., Yoshimoto, N., Umakoshi, H., Shimanouchi, T., and Kuboi, R. (2005) Liposome-assisted activity of superoxide dismutase under oxidative stress. *J. Biosci. Bioeng. 99*, 423–428.

(23) Spira, J., Plyushch, O. P., Andreeva, T. A., and Andreev, Y. (2006) Prolonged bleeding-free period following prophylactic infusion of recombinant factor VIII reconstituted with pegylated liposomes. *Blood 108*, 3668–3673.

(24) Yatuv, R., Dayan, I., Carmel-Goren, L., Robinson, M., Aviv, I., Goldenberg-Furmanov, M., and Baru, M. (2008) Enhancement of factor VIIa haemostatic efficacy by formulation with PEGylated liposomes. *Haemophilia 14*, 476–483.

(25) Colletier, J. P., Chaize, B., Winterhalter, M., and Fournier, D. (2002) Protein encapsulation in liposomes: efficiency depends on interactions between protein and phospholipid bilayer. *BMC Biotechnol. 2*, 9.

(26) Chikh, G. G., Li, W. M., Schutze-Redelmeier, M. P., Meunier, J. C., and Bally, M. B. (2002) Attaching histidine-tagged peptides and proteins to lipid-based carriers through use of metal-ion-chelating lipids. *Biochim. Biophys. Acta 1567*, 204–212.

(27) Nielsen, U. B., Kirpotin, D. B., Pickering, E. M., Drummond, D. C., and Marks, J. D. (2006) A novel assay for monitoring internalization of nanocarrier coupled antibodies. *BMC Immunol. 7*, 24.

(28) Ruger, R., Muller, D., Fahr, A., and Kontermann, R. E. (2005) Generation of immunoliposomes using recombinant single-chain Fv fragments bound to Ni-NTA-liposomes. *J. Drug Targeting 13*, 399–406.

(29) Ruger, R., Muller, D., Fahr, A., and Kontermann, R. E. (2006) In vitro characterization of binding and stability of single-chain Fv Ni-NTA-liposomes. *J. Drug Targeting 14*, 576–582.

(30) Patel, J. D., O'Carra, R., Jones, J., Woodward, J. G., and Mumper, R. J. (2007) Preparation and characterization of nickel nanoparticles for binding to his-tag proteins and antigens. *Pharm. Res. 24*, 343–352.

(31) Szoka, F., Olson, F., Heath, T., Vail, W., Mayhew, E., and Papahadjopoulos, D. (1980) Preparation of unilamellar liposomes of intermediate size (0.1−0.2 umol) by a combination of reverse phase evaporation and extrusion through polycarbonate membranes. *Biochim. Biophys. Acta 601*, 559–571.

(32) Korkegian, A., Black, M. E., Baker, D., and Stoddard, B. L. (2005) Computational thermostabilization of an enzyme. *Science 308*, 857–860.

(33) Shcherbo, D., Merzlyak, E. M., Chepurnykh, T. V., Fradkov, A. F., Ermakova, G. V., Solovieva, E. A., Lukyanov, K. A., Bogdanova, E. A., Zaraisky, A. G., Lukyanov, S., and Chudakov, D. M. (2007) Bright far-red fluorescent protein for whole-body imaging. *Nat. Methods 4*, 741–746.

(34) Senter, P. D., Su, P. C., Katsuragi, T., Sakai, T., Cosand, W. L., Hellstrom, I., and Hellstrom, K. E. (1991) Generation of 5-fluorouracil from 5-fluorocytosine by monoclonal antibody-cytosine deaminase conjugates. *Bioconjugate Chem. 2*, 447–451.

(35) Sambrook, J., and Russell, D. W. (2001) *Molecular cloning: a laboratory manual*, Cold Spring Harbor Laboratory, Cold Spring Harbor, NY.

(36) Scherer, J. R. (1989) Dependence of lipid chain and head group packing of the inverted hexagonal phase on hydration. *Biophys. J. 55*, 965–971.

(37) Paoli, M., Anderson, B. F., Baker, H. M., Morgan, W. T., Smith, A., and Baker, E. N. (1999) Crystal structure of hemopexin reveals a novel high-affinity heme site formed between two beta-propeller domains. *Nat. Struct. Biol. 6*, 926–931.

(38) Lasic, D. D., Martin, F. J., Gabizon, A., Huang, S. K., and Papahadjopoulos, D. (1991) Sterically stabilized liposomes: a hypothesis on the molecular origin of the extended circulation times. *Biochim. Biophys. Acta 1070*, 187–192.

(39) Mori, S., Takahashi, H. K., Yamaoka, K., Okamoto, M., and Nishibori, M. (2003) High affinity binding of serum histidine-rich glycoprotein to nickel-nitrilotriacetic acid: the application to microquantification. *Life Sci. 73*, 93–102.

(40) Powis, G., and Montfort, W. R. (2001) Properties and biological activities of thioredoxins. *Annu. Rev. Biophys. Biomol. Struct. 30*, 421–455.

(41) Mauk, M. R., Rosell, F. I., Lelj-Garolla, B., Moore, G. R., and Mauk, A. G. (2005) Metal ion binding to human hemopexin. *Biochemistry 44*, 1864–1871.

(42) Porath, J., and Olin, B. (1983) Immobilized metal ion affinity adsorption and immobilized metal ion affinity chromatography of biomaterials. Serum protein affinities for gel-immobilized iron and nickel ions. *Biochemistry 22*, 1621–1630.

(43) Morgan, W. T. (1985) The histidine-rich glycoprotein of serum has a domain rich in histidine, proline, and glycine that binds heme and metals. *Biochemistry 24*, 1496–1501.

(44) Bell, S. G., and Vallee, B. L. (2009) The metallothionein/thionein system: an oxidoreductive metabolic zinc link. *ChemBioChem 10*, 55–62.

(45) Fischer, N. O., Blanchette, C. D., Chromy, B. A., Kuhn, E. A., Segelke, B. W., Corzett, M., Bench, G., Mason, P. W., and Hoeprich, P. D. (2009) Immobilization of his-tagged proteins on nickel-chelating nanolipoprotein particles. *Bioconjugate Chem. 20*, 460–465.

(46) Herringson, T. P., and Altin, J. G. (2009) Convenient targeting of stealth siRNA-lipoplexes to cells with chelator lipid-anchored molecules. *J. Controlled Release 139*, 229–238.

BC900448F

Synthesis and Characterization of Fluorescent 4-Hydroxytamoxifen Conjugates with Unique Antiestrogenic Properties

Emily L. Rickert,[‡] Sean Oriana,[‡] Cori Hartman-Frey,[§] Xinghua Long,[§] Timothy T. Webb,[§] Kenneth P. Nephew,[§] and Ross V. Weatherman*[,†]

Department of Chemistry and Biochemistry, Rose-Hulman Institute of Technology, Terre Haute, Indiana, Department of Medicinal Chemistry and Molecular Pharmacology, Purdue University, West Lafayette, Indiana, and Medical Sciences and the Department of Cellular and Integrative Physiology, Indiana University School of Medicine, Bloomington, Indiana. Received October 21, 2009; Revised Manuscript Received March 1, 2010

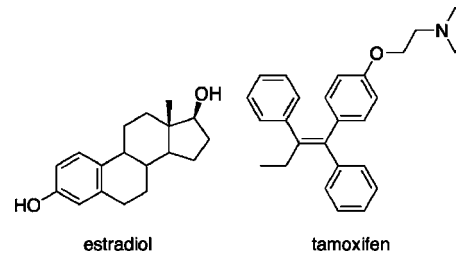
Membrane receptors for steroid hormones are currently a subject of considerable debate. One approach to selectively target these putative receptors has been to couple ligands to substances that restrict cell permeability. Using this approach, an analogue of the estrogen receptor ligand 4-hydroxytamoxifen was attached to fluorescent dyes with differing degrees of predicted cell permeability. The conjugates bound to estrogen receptor in vitro, but all three conjugates, including one predicted to be cell-impermeable, inhibited estradiol-induced transcriptional activation. Fluorescence microscopy revealed cytoplasmic localization for all three conjugates. We further characterized a 4-hydroxytamoxifen analogue conjugated to a BODIPY fluorophore in breast cancer cell lines. Those experiments suggested a similar, but not identical, mode of action to 4-hydroxytamoxifen, as the fluorescent conjugate was equally effective at inhibiting proliferation of both tamoxifen-sensitive and tamoxifen-resistant breast cancer cell lines. While these findings point to significant complicating factors in designing steroid hormone mimics targeted to the plasma membrane, the results also reveal a possible new direction for designing estrogen receptor modulators.

INTRODUCTION

Estrogens, including 17β-estradiol (Scheme 1), are known to play key roles in female reproductive tissues such as the breast and uterus (*1*), and compounds that modulate estrogen signaling are clinically valuable for relieving menopausal symptoms or treating diseases such as breast cancer (*2*). However, current estrogen-based therapies have serious side effects in nontarget tissues, presenting significant therapeutic challenges. Breast cancer therapies such as tamoxifen (Scheme 1) can cause hot flashes in patients, and estrogen replacement therapies can increase the risk of breast cancer to unacceptable levels (*3, 4*). As a result, in order for progress in the field of estrogen drug design and discovery to continue to move forward, the key mechanisms of estrogen signaling and their roles in specific physiological responses to estrogen signaling modulators need to be identified.

There are multiple types of receptors in a cell that bind estrogens (*5*). The classical estrogen receptors and two major subtypes of the nuclear receptors are estrogen receptor (ER) alpha and ER beta (*6, 7*). Other receptors that can bind to estrogen ligands include the G-protein coupled receptor (GPCR) known as GPR30 (*8*) and variants of ER alpha (*9*). The possibility that some of these receptors may be associated with the plasma membrane has been an area of considerable debate, especially since certain cellular responses to estrogen such as the activation of kinase signaling cascades are typical downstream events of membrane receptor activation (*10*). Additional receptors have been identified based on homology with the classical estrogen receptors, but their activity does not appear to be directly regulated by physiological estrogens (*11*).

Scheme 1



Membrane-associated ERs have been postulated for a long time (*12*), but identifying and characterizing those receptors has been difficult and controversial (*13*). One strategy to selectively target membrane ERs has been to increase the polarity of known ER ligands until they become cell-impermeable, but confirming the localization of these molecules has proven to be difficult (*14,15*). Conjugating the ligand to proteins such as bovine serum albumin allows for tracking, since a fluorescent tag can also be attached to the protein (*16, 17*), but the use of the protein conjugates has been controversial for a number of reasons, including the purity of the conjugates and their unusual binding kinetics for ER (*18, 19*).

A potentially useful strategy that combines the ability to alter cell permeability with the ability to track localization is the conjugation of ER ligands to fluorescent dyes. Fluorescent ER ligand conjugates have been used for quite some time to try to determine the ER content of the cell (*20, 21*), but the growing library of available fluorophores now includes compounds that are cell-impermeable, making it possible to generate cell-impermeable fluorescent conjugates to target membrane steroid hormone receptors. Toward this objective, a cell-impermeable fluorescent estradiol conjugate has recently been used to

* Address correspondence to Ross V. Weatherman, Department of Chemistry and Biochemistry, Rose-Hulman Institute of Technology, CM 67, 5500 Wabash Avenue, Terre Haute, IN, 47803-3999, e-mail: weatherm@rose-hulman.edu. Phone (812) 877-8718, FAX (812) 872-6019.

[‡] Purdue University.

[§] Indiana University School of Medicine.

[†] Rose-Hulman Institute of Technology.

10.1021/bc900461h © 2010 American Chemical Society
Published on Web 04/26/2010

determine GPR30 localization of the estrogen-binding GPCR (*22*). In the current study, we use a similar strategy with a well-known ER ligand, 4-hydroxytamoxifen, to develop a novel set of fluorescent conjugates. These conjugates bind with good affinity to the estrogen receptor in vitro, and show remarkable differences in receptor localization and effects on estrogen signaling in cell-based assays when compared to the previously reported estradiol conjugate. We also show for the first time that even the ethinyl estradiol conjugate displays significant uptake over time, complicating the use of this type of chemical probe for longer-term studies of plasma membrane-initiated, estrogen signaling.

EXPERIMENTAL PROCEDURES

General Procedures. All reagents were purchased from Sigma-Aldrich. Routine proton nuclear magnetic resonance spectra (^{1}H NMR) were obtained on a Bruker DRX500 (500 MHz) instrument. ^{1}H NMR chemical shifts are reported as δ values in parts per million (ppm) downfield from internal tetramethylsilane. NMR instruments were provided by the Shared Resource Center of the Purdue Cancer Center. The plasmids used in the reporter gene assays, pSG5-ERalpha, pSG5-ERbeta, and estrogen response element (ERE)-luciferase, have been described elsewhere (*23, 24*). Analytical HPLC was performed using a 4.6 × 150 mm Agilent Eclipse XDB-C8 5 μm reverse-phase column with UV signal detection at 280 nm and fluorescence detection at excitation/emission of 488/508 nm. Preparative HPLC was performed using a 25 × 250 mm Vydac C8 15 μm semipreparative column with signal detection at 280 nm. Nonlinear regression analysis of binding and reporter assay curves was performed using *Prism 4* software. Images were acquired using either a Nikon TE2000 inverted microscope or a Zeiss LSM 710 upright microscope. Images on both microscopes were acquired sequentially using a 60× oil 1.4 NA lens. OHT-6C-BODIPY images were obtained by exciting with the 488 nm line of a 4-line argon laser. Alexa Fluor 546-labeled conjugates were excited at 543 nm using a green HeNe laser, and emission wavelengths greater than 560 nm were collected.

Conjugate Synthesis. The synthesis of OHT-6C has been described elsewhere (*25*). The ethinyl estradiol Alexa Fluor 546 was made by following a previously reported procedure (*22*). For the conjugation reactions, the commercially available *N*-hydroxysuccinimide ester of each fluorophore (5 mg for the carboxyfluorescein and BODIPY-FL esters and 2.5 mg for each of the Alexa Fluor esters) was dissolved in DMSO (0.25 mL). To each solution was added 10 mg of OHT-6C dissolved in DMSO (0.25 mL). The reaction proceeded in the dark at room temperature overnight. The sample was then purified by preparative HPLC with a water/acetonitrile eluent gradient starting at 20% acetonitrile and ending at 100% acetonitrile at 70 min. The eluent also contained 0.1% trifluoroacetic acid. The fractions containing the appropriate product were then freeze−dried using a lyophilizer. Characterization of each conjugate is included in the Supporting Information.

Radiolabeled Ligand Receptor Binding Assay. In each well of a 96 well plate, 25 μL of a solution containing binding buffer (100 mM potassium phosphate (pH 7.4), 100 μg/mL bovine gamma globulin, and 0.02% sodium azide) plus 2 nM [2,4,6,7,16,17-^{3}H] estradiol (GE Healthcare) and different concentrations of competitor were added to a 25 μL solution containing 30 nM of full-length recombinant estrogen receptor alpha or beta (Invitrogen) in binding buffer. After 2 h incubation at room temperature, the mixture was transferred to a MultiScreen HTS Filter Plate (Millipore) and washed with binding buffer to remove unbound ligand. Plates were allowed to dry overnight. Microscint 0 scintillation fluid (Perkin-Elmer) was added, and the radioactivity was counted on a Packard TopCount scintillation counter. Each drug concentration was tested three times each in three different experiments. Data were analyzed using *Prism* software.

Cell Culture. The ER-positive MCF-7 cell line was grown in phenol red free DMEM F-12 HAM medium supplemented with 0.876 g/L glutamine, 100 mg/L streptomycin sulfate, 100 units/mL of penicillin G, and 10% fetal bovine serum (FBS) at 37 °C in an air/carbon dioxide (95:5) atmosphere. MDA-MB-231 and SKBR3 breast cell lines were grown in phenol red free RPMI 1640 medium supplemented with 0.876 g/L glutamine, 100 mg/L streptomycin sulfate, 100 units/mL of penicillin G, and 10% fetal bovine serum (FBS) at 37 °C in an air/carbon dioxide (95:5) atmosphere. Transfection assays were run with the same media conditions except serum free media was used.

Luciferase Reporter Assays. Cells were plated in 24 well plates (2×10^6 cells per plate). Transfections were performed according to the protocol for Lipofectamine 2000. In order to normalize for the transfection efficiency in each well, the dual luciferase system was used in which a constitutively expressed, chemically orthogonal luciferase expression vector was also transfected. The total amount of DNA/well for each plasmid was as follows: ERE-luciferase 0.3 μg/well, and *Renilla*-luciferase 0.1 μg/well. The ratio of total DNA/Lipofectamine 2000 ratio was 1:3. After transfection, the plates were incubated at 37 °C for 6 h before replacing the media with serum free media for 24 h. The serum free media was then replaced with fresh serum free media and the ligands. All ligands were delivered in DMSO or ethanol and the total concentration of organic solvent in each was 0.1% or less. For competition experiments with 4-hydroxytamoxifen compounds, the ligand was added to media already containing 10 nM estradiol. For the ethinyl estradiol conjugates, ligand was added to media containing 5 nM raloxifene, an antagonist of ER in the ERE assay. After 18 h, the cells were lysed and assayed for dual luciferase activity in a Packard TopCount luminometer according to the protocol provided by Promega. The relative light units (RLU) were then calculated by dividing the output of the ERE-driven luciferase in each well by the output of the *Renilla* luciferase. For antagonist experiments, the percent transcriptional activation was calculated using the RLU value obtained with 10 nM estradiol as 100% and the RLU value obtained with 1 μM fulvestrant as 0%. Each drug concentration was tested in triplicate, and each experiment was repeated at least three times.

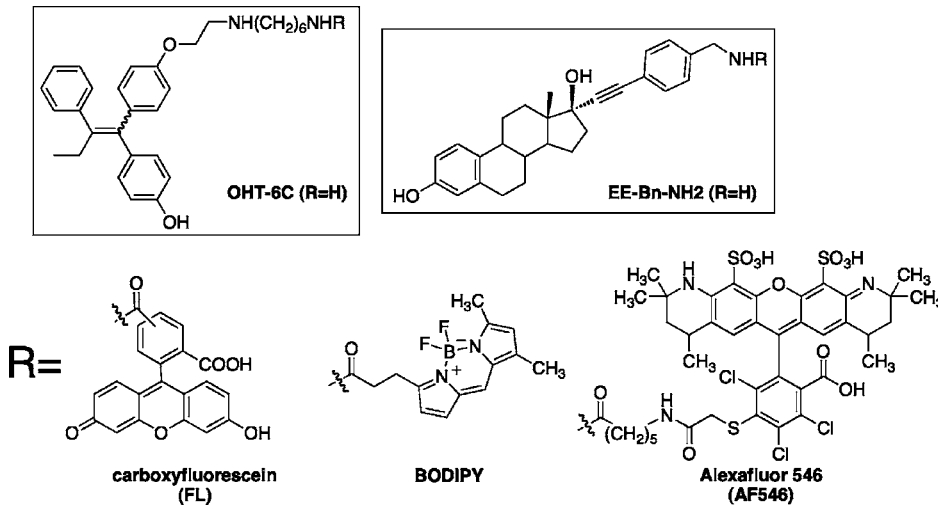
Uptake Studies. MCF-7 (ER-positive cell line) and MDA-MB-231 and SKBR3 (both ER-negative cell lines) were seeded on poly(L-lysine) coverslips and grown to 90% confluency. Drugs were dosed in serum free medium for the appropriate time point. Cells were washed and fixed using 4% paraformaldehyde. Coverslips were washed and mounted using ProLong Gold Antifade Reagent containing DAPI and then imaged.

Timed Uptake Studies. For the timed uptake studies in Figure 3, 3×10^5 MCF7 cells were seeded into each chamber of an 8-chambered, CC2-coated LabTek slide and grown to 90% confluency. The timed conjugate uptake assay was performed following a previously reported procedure (*22*).

Proliferation Studies. MCF-7 or tamoxifen-resistant MCF-7 cells (*26*) were plated in 96 well dishes (2000 cells per well) in steroid-free medium and treated with 1 nM of estradiol and various doses of 4-hydroxytamoxifen or OHT-6C-BODIPY. Cell numbers were determined by MTT assay after 7 days of treatment.

Receptor Stability Studies. MCF7 cells (5×10^5/dish) were plated in 60 mm dishes in steroid-free medium for 3 days prior to drug exposure. Whole cell extracts were prepared by suspending cells in 0.1 mL of lysis buffer (62 mM Tris, pH 6.8, 2% sodium dodecyl sulfate; 10% glycerol; 10 μL protease inhibitor cocktail set III). After sonication (3 × 10 s), insoluble

Scheme 2



material was removed by centrifugation (15 min at 12 000 *g*), and protein concentration in the supernatant was determined using a protein assay kit (Bio-Rad Laboratories, Inc.). The protein extracts were mixed with 1/4 vol of 5× electrophoresis sample buffer and boiled for 5 min at 90 °C. Protein extract (50 μg per lane) was then fractionated by SDS-PAGE, transferred to polyvinylidene difluoride membrane, and probed with antibodies. Primary antibody was detected by horseradish peroxidase-conjugated second antibody and visualized using enhanced SuperSignal West Pico Chemiluminescent Substrate (Pierce Chemical Co., Rockford, IL). The band density of exposed films was evaluated with *ImageJ* software (http://rsb.info.nih.gov/ij/).

RESULTS

Design and Synthesis of the Conjugates. While there has been success in generating inherently fluorescent ER ligands (*27*), we opted for the traditional conjugation strategy of attaching the fluorescent dye to an ER ligand through a flexible linker. The keys to success with this strategy are (1) the choice of the ER ligand and (2) identifying a location on the drug where linker attachment is well-tolerated. Tamoxifen, one of the most studied ER ligands, shows a mixed agonist/antagonist profile therapeutically (*3*) and has long been associated with possible plasma membrane binding sites, including some that might not bind estradiol itself (*28*). We have previously shown that potential linkers can be attached to the more potent tamoxifen metabolite, 4-hydroxytamoxifen (OHT), through the basic side chain with only small losses in binding affinity for ER and inhibitory potency in cell-based gene reporter assays (*29*). We have also shown that an analogue with a 1,6-diaminohexane linker known as OHT-6C (Scheme 2), showed strong ER binding affinity when coupled to a poly(methacrylic acid) polymer (*25*). For the cell-impermeable fluorescent dye, Alexa Fluor 546 was chosen. For comparison, we also chose two dyes, carboxyfluorescein and BODIPY FL, that have been well-characterized as cell-permeable fluorophores. Amine-reactive analogues of all three fluorophores were purchased as activated *N*-hydroxysuccinimide esters and linked to the primary amine of the OHT-6C analogue to generate three different conjugates (Scheme 2). The resulting conjugates (and OHT-6C itself) are generated as mixtures of *E* and *Z* isomers—the two forms readily interconvert at room temperature. Previous work with 4-hydroxytamoxifen has shown that, despite this interconversion, the *Z* isomer is almost exclusively bound by the receptor both in vitro and in vivo (*30*, *31*). All three of the conjugates showed nearly identical fluorescence spectra in solution as their parent fluorophores, although the overall fluorescence intensity of each conjugate was somewhat decreased (likely due to a change in the overall chemical environment of the fluorophore).

ER Binding and Effects on ER-Mediated Transcription. The conjugates were compared for their ability to bind to ER in solution using competition binding experiments with tritium-labeled estradiol. As predicted, all of the conjugates still retained their ability to bind to both ER alpha and ER beta in vitro at submicromolar concentrations, although there was some loss in affinity compared to the parent compound and to estradiol and OHT (Figure 1A and Table 1). In the published structures of the ER ligand binding domain bound to OHT, the basic side chain extends away from the binding pocket and into solution (*32*), which could explain the general tolerance in binding for the bulky OHT substitutions conjugates, although the weaker binding affinity suggests that there could be some somewhat unfavorable interactions with the fluorophore. This possibility seems likely considering that the largest fluorophore, Alexa Fluor 546, has the worst binding potency.

The conjugates were also tested for their ability to inhibit estradiol-induced activation of ER-mediated transcription using a cell-based luciferase reporter gene assay. In this assay, ER-positive MCF7 cells were transiently transfected with a reporter plasmid containing the luciferase gene under the control of a consensus estrogen response element-containing promoter. In this reporter system, dosing the cells with estradiol typically activates transcription of the reporter gene, while OHT acts as an antagonist. On the basis of the predicted cell permeability of the conjugates, we expected the carboxyfluorescein and BODIPY-labeled conjugates to still act as antagonists and the Alexa Fluor 546-labeled conjugate to have no effect due to its inability to enter the cell and interact with the ER. As shown in Figure 1B, all three conjugates antagonized ER-mediated transcription with roughly the same inhibitory IC_{50} (100−900 nM concentration range), 10−50-fold worse than OHT or OHT-6C. The conjugates were also rechecked for purity by analytical HPLC. No free OHT ligand was detected, suggesting that the conjugates enter the cell and modulate receptor function by an undetermined mechanism.

Conjugate Uptake and Localization. Confocal laser scanning microscopy was used to monitor the cellular uptake and localization of the conjugates at different time points. Previous studies using fluorescent ER ligands capable of modulating ER-mediated transcription reported observing the fluorescence in the nucleus (*33*). In addition, our work (*34*) along with multiple

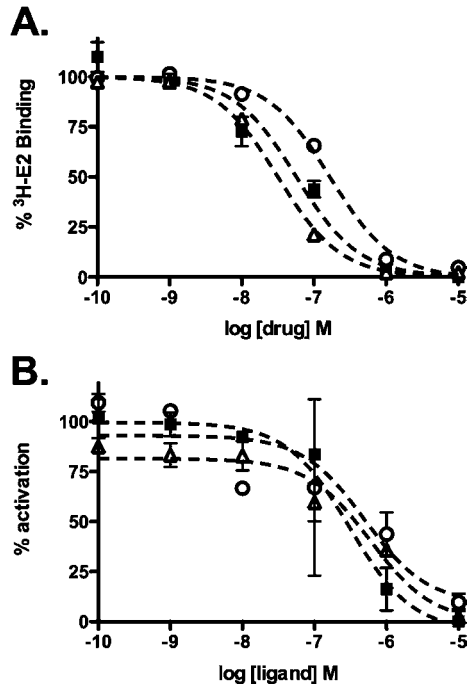


Figure 1. ER-modulatory activities of OHT conjugates. A. Effects of conjugates on the binding of purified ER alpha to 2 nM ^{3}H-labeled estradiol. B. Effects of conjugates on ER-mediated transcription in MCF7 cells transiently transfected with a luciferase reporter plasmid under the control of ERE-containing promoter. The drugs were added in the presence of 10 nM estradiol. Luciferase activity was examined at 24 h after drug treatment and percent activation calculated relative to cells treated with estradiol only. In both graphs, open circles = OHT-6C-AF; solid squares = OHT-6C-BODIPY; open triangles = OHT-6C−CF.

Table 1. Estrogen Receptor Modulation Properties of Conjugates

compound	ER alpha IC_{50} (nM)[a]	ER beta IC_{50} (nM)[a]	ERE IC_{50} (nM)[b]
estradiol	2.5 ± 0.2	3.7 ± 1.0	16 ± 10[d]
OHT	8.5 ± 3.9	13 ± 7	40 ± 10[c]
OHT-6C (R = H)	15 ± 5	9 ± 5	85 ± 50[c]
OHT-6C-FL	25 ± 10	35 ± 20	900 ± 600[c]
OHT-6C-BODIPY	30 ± 10	40 ± 20	250 ± 110[c]
OHT-6C-AF546	180 ± 30	240 ± 70	600 ± 350[c]
EE-Bn-NH_2	7 ± 4	6 ± 4	150 ± 20[d]
EE-Bn-AF546	10 ± 2	35 ± 20	140 ± 90[d]

[a] ER binding determined using competition experiments with purified ER and ^{3}H-labeled estradiol as described in the experimental procedures. [b] ERE activity determined using MCF7 cells transfected with luciferase reporter plasmid under control of consensus ERE as described in the experimental procedures. [c] IC_{50} values determined in the presence of 10 nM estradiol. [d] IC_{50} values determined in the presence of 5 nM raloxifene.

other studies demonstrated that ER localizes to the nucleus in the presence of agonists or antagonists (reviewed in *refs* 35, 36). Since all three conjugates were ER antagonists, we expected to see similar nuclear localization patterns; however, the fluorescence localized to the cytoplasm in a number of the ER-positive MCF7 cell lines and was clearly excluded from the nucleus at 100 nM and 10 μM (Figure 2). To our knowledge, this pattern of cellular localization has not been previously reported for any fluorescent ER ligand.

Comparison with 17α-Ethynyl Estradiol Conjugates. In order to compare the unusual localization of the OHT-derived conjugates to a conjugate with a known localization pattern, we also synthesized the previously reported 17α-ethinyl estradiol analogue conjugated to Alexa Fluor 546. This conjugate which has been reported to be cell impermeable (*22*) was first tested

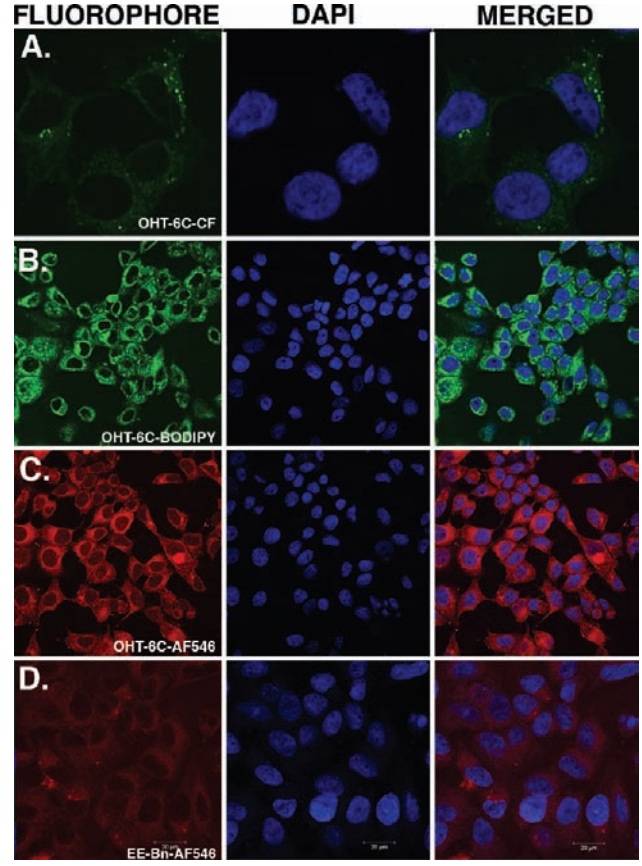


Figure 2. Images of uptake of conjugates by ER-positive MCF7 cell line after 6 h of dosing. Row A, 10 μM OHT-6C−CF; Row B, 100 nM OHT-6C-BODIPY; Row C, 10 μM OHT-6C-AF546; Row D, 1 μM EE-Bn-AF546. The first image of each row is the emission of the fluorophore. The second image of each row is the image of the DAPI nuclear stain, and the third image is the merged picture of the first two images. Due to the relatively low brightness of the carboxyfluorescein conjugate, we have shown an image at higher magnification than the other fluorophores.

for its ability to bind to ER alpha and ER beta in vitro. We observed sufficient binding affinity for both receptor subtypes (Table 1) and subsequently tested the conjugate for its effect on ER-mediated transcription in the ER-positive MCF7 breast cancer cell line. Surprisingly, the conjugate, at submicromolar concentrations, activated ER-mediated transcription from a consensus estrogen response element (Supporting Information Figure S1), in contrast to the original report describing the 17α-ethinyl estradiol−Alexa Fluor conjugate as a cell-impermeable probe (*22*). It should be noted, however, that, in the first report, the conjugate was tested at lower concentrations and for much shorter time periods than used for the transcriptional activation assays in the present study.

In order to attempt to reconcile the apparent differences in the permeability of our ethinyl estradiol conjugate compared to the previous report, we examined the cellular localization of both the OHT and ethinyl estradiol−Alexa Fluor 546 conjugates, as well as the Alexa Fluor546 dye itself, at different time periods using the original experimental conditions in the MCF7 breast cancer cell line (ref *22* and described in the Experimental Procedures). After 15 min, no uptake was apparent for either the ethinyl estradiol conjugate or the Alexa Fluor dye; however, significant uptake of the OHT-6C conjugate was observed (Figure 3). Thus, the results for the ethinyl estradiol conjugate are consistent with a previous report (*22*), although after a 2 h incubation, cytoplasmic localization was seen for all of the compounds (Figure 3).

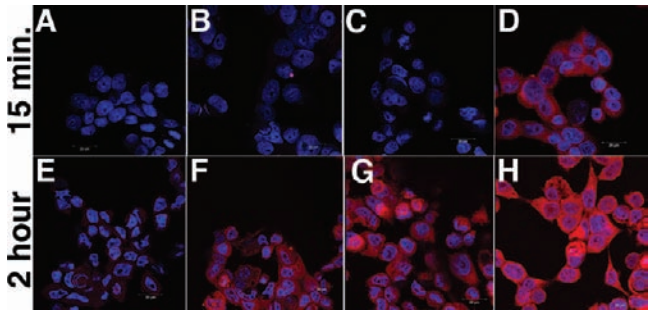


Figure 3. MCF7 cells were treated with different Alexa Fluor 546 conjugates for either 15 min (A−D) or 2 h (E−H) and imaged as described in the experimental procedures. The conjugates used are as follows: images A and E, DMSO; images B and F, 1 μM Alexa Fluor 546 dye alone; images C and G, 1 μM EE-Bn-AF; images D and H, 1 μM OHT-6C-AF. The images represent merged images of the emission from the DAPI stain of the nucleus (blue) and the emission of the Alexa Fluor dye (red).

Characterization of Conjugate Uptake and Localization. On the basis of brightness and potency qualities, the OHT-6C-BODIPY conjugate was chosen to further examine the mechanisms of uptake and cytoplasmic localization. Similar to the OHT-6C-AF conjugate, uptake of the OHT-6C-BODIPY by ER positive MCF7 cells could be detected as soon as 15 min after dosing using confocal laser microscopy and uptake increased over time (Supporting Information Figure S2). The fluorescence in the cytoplasm was stable, as no conspicuous change in fluorescence was observed 12 h after the media containing the conjugate with conjugate-free media was replaced (data not shown).

Uptake of the BODIPY-labeled conjugate in the ER-positive MCF7 breast cell line was compared to the ER-negative MDA-MB-231 and SKBR3 breast cell lines using confocal laser microscopy. No difference in the degree of uptake was seen (Supporting Information Figure S3), suggesting that ER does not play a significant role in conjugate uptake or localization. Moreover, uptake and localization were not altered in the presence of the ER ligands estradiol or OHT (Figure 4), suggesting a "non-receptor mediated" mechanism of uptake. We also considered the possibility of an endocytic mechanism. However, even at the earliest time points, fluorescence from the conjugate was seen in the cytoplasm, and the fluorescence did not colocalize with a commercially available, fluorescent endosomal or lysosomal markers (data not shown). Taken together, these observations suggest that, while there may be some endocytic conjugate uptake, the majority of the conjugate appears to enter the cell through either passive diffusion or pinocytosis.

Effects of the Conjugate on ER Activity. The unusual cytoplasmic localization of the OHT-6C-BODIPY conjugate prompted us to investigate whether this localization had any effect on ER function. To address this key question, we first compared classical ER responses to OHT-6C-BODIPY and tamoxifen. The effect of the conjugate on proliferation of both tamoxifen-sensitive and tamoxifen-resistant breast cancer cell lines were measured. The growth of ER-positive MCF7 breast cancer cells are stimulated by estradiol, and either tamoxifen or OHT block that stimulation. As shown in Figure 5, both OHT and OHT-6C-BODIPY were able to block estradiol-induced growth in tamoxifen-sensitive MCF7 cells, indicating that the conjugate is still capable of classic ER antagonism. The compounds were also tested against a subline of MCF7 cells that were grown in the presence of tamoxifen until they developed a resistance to the drug (*26*). The conjugate, in contrast to OHT, showed equal effectiveness in the tamoxifen-resistant line as it did in the parental MCF7 cell line (Figure 5), suggesting that the conjugate has an overlapping, but not identical, mechanism of action to 4-hydroxytamoxifen.

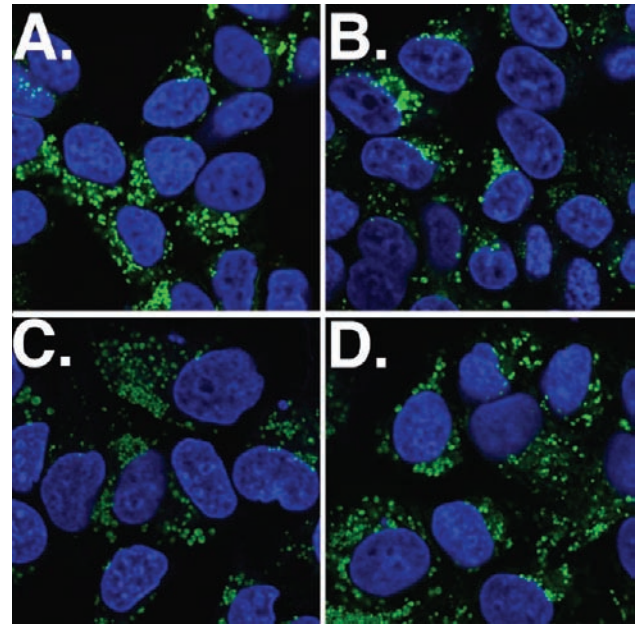


Figure 4. Uptake by MCF7 cells of 100 nM OHT-6C-BODIPY in the presence of competing ER ligands as analyzed by confocal scanning laser microscopy. The competing drugs are as follows: A, DMSO; B, 1 μM estradiol; C, 1 μM 4-hydroxytamoxifen; D, 1 μM OHT-6C. Images represent merged fluorescent images of emission from DAPI nuclear stain (blue) and the emission from the BODIPY fluorophore (green).

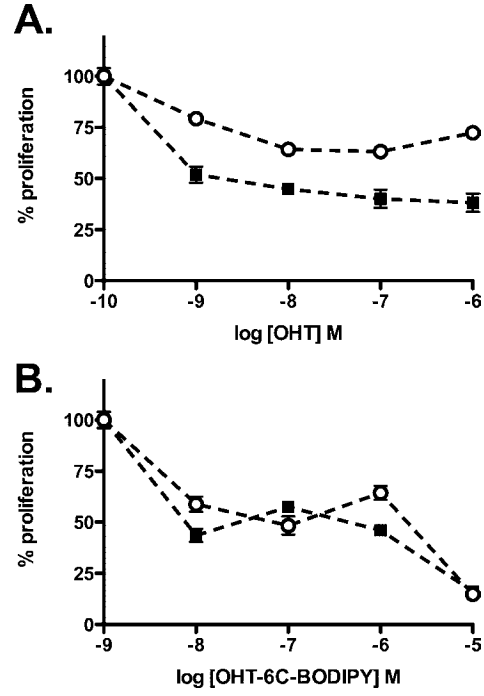


Figure 5. Effect of OHT (A) and OHT-6C-BODIPY (B) on proliferation of tamoxifen-sensitive, parental MCF7 cells (closed squares) and a tamoxifen-resistant MCF7 cell subline (open circles). Cells were seeded in hormone-free medium and treated in the presence of 1 nM E2. Seven days after treatment, cell number was determined by MTT assay. Experiments were performed twice in triplicate.

We next examined the effect of these conjugates on cellular ER levels, a key determinant of hormone sensitivity. One of the critical differences between the mechanism of action of selective estrogen receptor modulators (SERMs) like OHT and

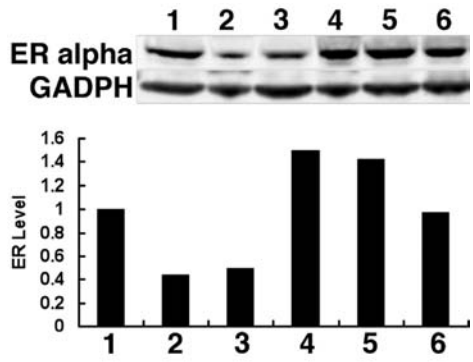


Figure 6. Effects of the OHT-6C-BODIPY conjugate on ER alpha stability. MCF7 cells were seeded in hormone-free medium for three days, then treated with different compounds for 24 h. Lane 1, DMSO; lane 2, 10 nM estradiol; lane 3, 100 nM fulvestrant; lane 4, 100 nM 4-hydroxytamoxifen; lane 5, 1 μM OHT-6C; lane 6, 10 μM OHT-6C-BODIPY. ER alpha levels in whole cell extracts were determined by immunoblotting with anti-ERα antibody. GAPDH was used as the loading control. Relative ER alpha levels (versus untreated cells) are shown in the corresponding histogram.

another class of drugs known as SERDs (selective ER down-regulators) such as fulvestrant is that OHT stabilizes cellular ER levels, while fulvestrant causes rapid receptor degradation (*37,38*). Whereas both estradiol and fulvestrant induced marked receptor downregulation in MCF7 cells after a 24 h incubation, no receptor degradation was observed after treatment with the OHT-6C-BODIPY conjugate (Figure 6), indicating that OHT-6C-BODIPY is more similar in mechanism of action to SERMs rather than compounds in the SERD class.

DISCUSSION

The design and synthesis of fluorescent conjugates for estrogen signaling modulators has previously focused on targeting activity either in the nucleus or the membrane. Although the compounds described in this paper were intended to target either of these locations, they instead localized to the cytoplasm. The only compounds for which specific cytoplasmic localization has been previously reported are a highly useful set of dendrimer-based estradiol analogues (*39, 40*). The uptake of those analogues appears to be mediated by ER and nuclear exclusion and seems to derive from the overall size and charge of the dendrimers (*39, 40*). For the fluorescent conjugates described in this current study, the mechanism of conjugate uptake and apparent exclusion from the nucleus is not as clear. ER does not appear to play a significant role in cellular uptake of the conjugates, which was similar in ER± breast cancer cell lines and not affected by the addition of competing ER ligands in ER+ cells (Figures 2−4, Supporting Information Figure S3). Furthermore, it is unlikely that conjugate size is a contributing factor to the observed cytoplasmic accumulation, as all of the conjugates are small enough to easily enter the nucleus.

We also found that the ethinyl estradiol Alexa Fluor conjugate, previously reported to be cell-impermeable (*22*), showed similar uptake to the OHT conjugates, with accumulation time being the only difference between these conjugates (Figure 3), indicating a slower mode of uptake. Although this observation would apparently contradict earlier claims regarding cell impermeability of the ethinyl estradiol conjugate, by using the reported concentrations and time intervals (*22*), we also found that no uptake was detected, consistent with those previous results. This lag in uptake has been indirectly seen with other highly polar ethinyl estradiol analogues. In ER alpha expressing COS7 cells, a longer time period was required to observe cellular uptake of compounds that did not stimulate rapid calcium mobilization, as these more polar ethinyl estradiol analogues showed a slower increase in mobilization (*15*).

It is difficult to exactly rationalize why the fluorescent conjugates all showed similar levels of cellular uptake and why the localization was almost entirely in the cytoplasm of the cells. One of the difficulties in trying to understand uptake is the fact that the conjugates are not particularly potent compared to their in vitro binding affinity. In addition, the fluorescence of the conjugates cannot be detected easily at lower nanomolar concetration ranges. As a result, localization only can be studied at higher concentrations where events such as aggregation could be playing a role. Aggregate formation would be consistent with the long-term stability and general punctate pattern of fluorescence seen in OHT-6C-BODIPY fluorophore treated cells, providing a possible reason the conjugate is excluded from the nucleus. Tamoxifen is known to interact with membranes (*41*), which could serve or initiate a nucleation event, leading to internalization of even the relatively more polar Alexa Fluor conjugates. Evidence for aggregation was not seen using standard fluorimetry of conjugates in solution, although we acknowledge that the level of sensitivity of the fluorimeters available to us does not approach that of confocal laser scanning microscopy.

A mechanism that also explains why the fluorescent conjugates are able to inhibit ER-mediated transcription is unclear. The dendrimer conjugates described by the Katzenellenbogen laboratories localize to the cytoplasm and have little to no effect on ER-mediated transcription (*39, 42*). The antagonist activity of the fluorescent OHT conjugates could arise from ER binding to the conjugate in the cytoplasm and being sequestered away from the nucleus. Alternatively, conjugate degradation within the cell could release free ligand from the fluorescent dye and subsequent transport of ligand to the nucleus. Toward these possibilities, we determined the hydrolytic susceptibility of the amide bond common to all of the conjugates by performing pH stability experiments in solution (various pHs at 37 °C for multiple days; data not shown). No release of OHT-6C was detected by HPLC, and no other nonfluorescent products were observed, but it is always possible with ligands as potent as OHT-6C that some level of hydrolysis undetectable by HPLC or any other standard analytical technique is still occurring and is responsible for the transcriptional inhibition. In addition, subcellular fractionation studies performed in ER-positive MCF7 cells dosed with OHT-6C-BODIPY revealed the presence of ER only in the nucleus, thereby contradicting the sequestration hypothesis. Another explanation is that, despite the apparent nuclear exclusion of the fluorescent conjugate, a small amount of nonaggregated conjugate is free to enter the nucleus. The concentration of this soluble conjugate is below detection sensitivity by microscopy in the presence of the much brighter cytoplasmic aggregates but able to inhibit ER transcription in a manner similar to the nonconjugated OHT6C ligand itself.

Overall, our findings indicate that a hydrophobic and planar drug portion of a conjugate can significantly complicate the use of fluorescent dyes to dictate subcellular localization. Considering that most drugs targeting steroid hormone receptors fit this description, care should be taken when using this type of approach to selectively target plasma membrane-initiated steroid hormone signaling. While it may be possible to obtain the desired localization by only studying very rapid signaling or by connecting the drug and fluorophore with a linker that prevents aggregation, we contend that thorough testing of the conjugates at different concentrations and time points is necessary before conclusions about selectivity can be drawn.

In addition to the unusual localization pattern, another unique property of the OHT conjugates is their ability to effectively inhibit proliferation of ER-positive, tamoxifen-resistant breast

cancer cells. Whether this activity is the result of altered ER function due to the added bulk of the fluorophore attachment in a manner similar to but distinct from compounds like fulvestrant or to changes in the intracellular drug concentrations due to the aggregate is unknown at this time. At this point, ongoing work to improve the potency of the compounds is necessary before more detailed mechanistic work can be pursued. Nonetheless, either mechanism could have significant impact on the discovery and development of hormone therapies for ER-positive, antiestrogen resistant breast cancer, the focus of our ongoing studies.

ACKNOWLEDGMENT

The Army Breast Cancer Research Program (BC030507) and the National Institutes of Health (R01 DK075376) supported RVW, and National Cancer Institute CA113001 supported KPN. Purdue Research Foundation supported ELR with a predoctoral fellowship.

Supporting Information Available: Mass spectrometry data for all of the conjugates, further NMR characterization of the OHT-6C-BODIPY conjugate, and additional graphs and images. This material is available free of charge via the Internet at http://pubs.acs.org.

LITERATURE CITED

(1) Katzenellenbogen, B. S., Tsai, T. S., Tatee, T., and Katzenellenbogen, J. A. (1979) Estrogen and antiestrogen action: studies in reproductive target tissues and tumors. *Adv. Exp. Med. Biol. 117*, 111–32.

(2) Jordan, V. C. (2004) Selective estrogen receptor modulation: concept and consequences in cancer. *Cancer Cell 5*, 207–13.

(3) Jordan, V. C. (2007) SERMs: meeting the promise of multifunctional medicines. *J. Natl. Cancer Inst. 99*, 350–6.

(4) Jordan, V. C. (2007) Chemoprevention of breast cancer with selective oestrogen-receptor modulators. *Nat. Rev. Cancer 7*, 46–53.

(5) Weatherman, R. V. (2008) Untangling the Estrogen Receptor Web: Tools to Selectively Study Estrogen binding Receptors, in *Nuclear Receptors as Drug Targets* (Ottow, E., and Weinmann, H., Eds.) pp 47−64, Wiley-VCH, Weinhem.

(6) Hewitt, S. C., Harrell, J. C., and Korach, K. S. (2005) Lessons in estrogen biology from knockout and transgenic animals. *Annu. Rev. Physiol. 67*, 285–308.

(7) Koehler, K. F., Helguero, L. A., Haldosen, L. A., Warner, M., and Gustafsson, J. A. (2005) Reflections on the discovery and significance of estrogen receptor beta. *Endocr. Rev. 26*, 465–78.

(8) Prossnitz, E. R., and Maggiolini, M. (2009) Mechanisms of estrogen signaling and gene expression via GPR30. *Mol. Cell. Endocrinol. 308*, 32–8.

(9) Li, L., Haynes, M. P., and Bender, J. R. (2003) Plasma membrane localization and function of the estrogen receptor alpha variant (ER46) in human endothelial cells. *Proc. Natl. Acad. Sci. U.S.A. 100*, 4807–12.

(10) Wehling, M., and Losel, R. (2006) Non-genomic steroid hormone effects: Membrane or intracellular receptors? *J. Steroid Biochem. Mol. Biol. 102*, 180–3.

(11) Giguère, V., Yang, N., Segui, P., and Evans, R. (1988) Identification of a new class of steroid hormone receptors. *Nature 331*, 91–4.

(12) Pietras, R. J., and Szego, C. M. (1977) Specific binding sites for oestrogen at the outer surfaces of isolated endometrial cells. *Nature 265*, 69–72.

(13) Levin, E. R. (2009) Membrane ER{alpha} signaling to cell functions, *J Physiol*.

(14) Jarman, M., Leung, O. T., Leclercq, G., Devleeschouwer, N., Stoessel, S., Coombes, R. C., and Skilton, R. A. (1986) Analogues of tamoxifen: the role of the basic side-chain. Applications of a whole-cell oestrogen-receptor binding assay to N-oxides and quaternary salts. *Anti-Cancer Drug Des. 1*, 259–68.

(15) Revankar, C. M., Mitchell, H. D., Field, A. S., Burai, R., Corona, C., Ramesh, C., Sklar, L. A., Arterburn, J. B., and Prossnitz, E. R. (2007) Synthetic estrogen derivatives demonstrate the functionality of intracellular GPR30. *ACS Chem. Biol. 2*, 536–44.

(16) Berthois, Y., Pourreau-Schneider, N., Gandilhon, P., Mittre, H., Tubiana, N., and Martin, P. M. (1986) Estradiol membrane binding sites on human breast cancer cell lines. Use of a fluorescent estradiol conjugate to demonstrate plasma membrane binding systems. *J. Steroid Biochem. 25*, 963–72.

(17) Jansson, S. E., Gripenberg, J., Karonen, S. L., Wasenius, V. M., Pantzar, P., Kontula, K., Karkkainen, J., and Adlercreutz, H. (1985) Cytochemical demonstration of estrogen binding sites in breast cancer by estradiol covalently linked to horseradish peroxidase. *Eur. J. Cancer Clin. Oncol. 21*, 625–30.

(18) Stevis, P. E., Deecher, D. C., Suhadolnik, L., Mallis, L. M., and Frail, D. E. (1999) Differential effects of estradiol and estradiol-BSA conjugates. *Endocrinology 140*, 5455–5458.

(19) Taguchi, Y., Koslowski, M., and Bodenner, D. L. (2004) Binding of estrogen receptor with estrogen conjugated to bovine serum albumin (BSA). *Nucl. Recept. 2*, 5.

(20) Carlson, K. E., Coppey, M., Magdelenat, H., and Katzenellenbogen, J. A. (1989) Receptor binding of NBD-labeled fluorescent estrogens and progestins in whole cells and cell-free preparations. *J. Steroid Biochem. 32*, 345–55.

(21) Fisher, B., Gunduz, N., Zheng, S., and Saffer, E. A. (1982) Fluoresceinated estrone binding by human and mouse breast cancer cells. *Cancer Res. 42*, 540–9.

(22) Revankar, C. M., Cimino, D. F., Sklar, L. A., Arterburn, J. B., and Prossnitz, E. R. (2005) A transmembrane intracellular estrogen receptor mediates rapid cell signaling. *Science 307*, 1625–30.

(23) Weatherman, R. V., Carroll, D. C., and Scanlan, T. S. (2001) Activity of a tamoxifen-raloxifene hybrid ligand for estrogen receptors at an AP-1 site. *Bioorg. Med. Chem. Lett. 11*, 3129–31.

(24) Weatherman, R. V., Clegg, N. J., and Scanlan, T. S. (2001) Differential SERM activation of the estrogen receptors (ERalpha and ERbeta) at AP-1 sites. *Chem. Biol. 8*, 427–36.

(25) Rickert, E. L., Trebley, J. P., Peterson, A. C., Morrell, M. M., and Weatherman, R. V. (2007) Synthesis and characterization of bioactive tamoxifen-conjugated polymers. *Biomacromolecules 8*, 3608–12.

(26) Fan, M., Yan, P. S., Hartman-Frey, C., Chen, L., Paik, H., Oyer, S. L., Salisbury, J. D., Cheng, A. S., Li, L., Abbosh, P. H., Huang, T. H., and Nephew, K. P. (2006) Diverse gene expression and DNA methylation profiles correlate with differential adaptation of breast cancer cells to the antiestrogens tamoxifen and fulvestrant. *Cancer Res. 66*, 11954–66.

(27) Hwang, K. J., Carlson, K. E., Anstead, G. M., and Katzenellenbogen, J. A. (1992) Donor-acceptor tetrahydrochrysenes, inherently fluorescent, high-affinity ligands for the estrogen receptor: binding and fluorescence characteristics and fluorometric assay of receptor. *Biochemistry 31*, 11536–45.

(28) de Medina, P., Favre, G., and Poirot, M. (2004) Multiple targeting by the antitumor drug tamoxifen: a structure-activity study. *Curr. Med. Chem. Anticancer Agents 4*, 491–508.

(29) Trebley, J. P., Rickert, E. L., Reyes, P. T., and Weatherman, R. V. (2006) Tamoxifen-based probes for the study of estrogen receptor-mediated transcription. *Ernst Schering Res. Found Workshop* 75–87.

(30) Katzenellenbogen, J. A., Carlson, K. E., and Katzenellenbogen, B. S. (1985) Facile geometric isomerization of phenolic nonsteroidal estrogens and antiestrogens: limitations to the interpretation of experiments characterizing the activity of individual isomers. *J. Steroid Biochem. 22*, 589–96.

(31) Robertson, D. W., Katzenellenbogen, J. A., Hayes, J. R., and Katzenellenbogen, B. S. (1982) Antiestrogen basicity--activity relationships: a comparison of the estrogen receptor binding and antiuterotrophic potencies of several analogues of (Z)-1,2-diphenyl-1-[4-[2-(dimethylamino)ethoxy]phenyl]-1-butene (tamoxifen, Nolvadex) having altered basicity. *J. Med. Chem. 25*, 167–71.

(32) Shiau, A. K., Barstad, D., Loria, P. M., Cheng, L., Kushner, P. J., Agard, D. A., and Greene, G. L. (1998) The structural basis of estrogen receptor/coactivator recognition and the antagonism of this interaction by tamoxifen. *Cell 95*, 927–937.

(33) Miksicek, R. J., Carlson, K. E., Hwang, K. J., and Katzenellenbogen, J. A. (1995) Studies using fluorescent tetrahydrochrysene estrogens for in situ visualization of the estrogen receptor in living cells. *Mol. Endocrinol. 9*, 592–604.

(34) Long, X., and Nephew, K. P. (2006) Fulvestrant (ICI 182,780)-dependent interacting proteins mediate immobilization and degradation of estrogen receptor-alpha. *J. Biol. Chem. 281*, 9607–15.

(35) Kawata, M., Matsuda, K., Nishi, M., Ogawa, H., and Ochiai, I. (2001) Intracellular dynamics of steroid hormone receptor. *Neurosci. Res. 40*, 197–203.

(36) Leclercq, G., Lacroix, M., Laios, I., and Laurent, G. (2006) Estrogen receptor alpha: impact of ligands on intracellular shuttling and turnover rate in breast cancer cells. *Curr. Cancer Drug Targets 6*, 39–64.

(37) Berry, N. B., Fan, M., and Nephew, K. P. (2008) Estrogen receptor alpha (ER{alpha}) hinge-region lysines 302 and 303 regulate receptor degradation by the proteasome, *Mol. Endocrinol.*

(38) Fan, M., Rickert, E. L., Chen, L., Aftab, S. A., Nephew, K. P., and Weatherman, R. V. (2007) Characterization of molecular and structural determinants of selective estrogen receptor down-regulators. *Breast Cancer Res. Treat. 103*, 37–44.

(39) Harrington, W. R., Kim, S. H., Funk, C. C., Madak-Erdogan, Z., Schiff, R., Katzenellenbogen, J. A., and Katzenellenbogen, B. S. (2006) Estrogen dendrimer conjugates that preferentially activate extranuclear, nongenomic versus genomic pathways of estrogen action. *Mol. Endocrinol. 20*, 491–502.

(40) Kim, S. H., and Katzenellenbogen, J. A. (2006) Hormone-PAMAM dendrimer conjugates: polymer dynamics and tether structure affect ligand access to receptors. *Angew. Chem., Int. Ed. Engl. 45*, 7243–8.

(41) Engelk, M., Bojarski, P., Bloss, R., and Diehl, H. (2001) Tamoxifen perturbs lipid bilayer order and permeability: comparison of DSC, fluorescence anisotropy, laurdan generalized polarization and carboxyfluorescein leakage studies. *Biophys. Chem. 90*, 157–73.

(42) Madak-Erdogan, Z., Kieser, K. J., Kim, S. H., Komm, B., Katzenellenbogen, J. A., and Katzenellenbogen, B. S. (2008) Nuclear and extranuclear pathway inputs in the regulation of global gene expression by estrogen receptors. *Mol. Endocrinol. 22*, 2116–27.

BC900461H

Synthesis and Evaluation of [^{18}F]-FEAnGA as a PET Tracer for β-Glucuronidase Activity

Inês F. Antunes,*[,†] Hidde J. Haisma,[‡] Philip H. Elsinga,[†] Rudi A. Dierckx,[†] and Erik F. J. de Vries[†]

Department of Nuclear Medicine and Molecular Imaging, University Medical Center Groningen, University of Groningen, P.O. Box 30.001, 9700 RB Groningen, The Netherlands, and Department of Pharmaceutical Gene Modulation, University Center for Pharmacy, University of Groningen, A. Deusinglaan 1, 9713 AV Groningen, The Netherlands. Received October 21, 2009; Revised Manuscript Received January 29, 2010

To increase the therapeutic index of chemotherapeutic drugs, prodrugs have been investigated as anticancer agents, as they may present fewer cytotoxic side effects than conventional cytotoxic drugs, while therapeutic efficacy is maintained or even increased. Extracellular β-glucuronidase (β-GUS) in the tumors has been investigated as a target enzyme for prodrug therapy, as it can convert nontoxic prodrugs into cytostatic drugs. To optimize β-GUS-based prodrug therapies, PET imaging could be a useful tool by providing information regarding the localization and quantification of β-GUS. Here, we describe our first PET tracer for extracellular β-GUS, [^{18}F]-FEAnGA, which consists of a 2-[^{18}F]fluoroethylamine ([^{18}F]-FEA) group bound to a glucuronic acid via a self-immolative nitrophenyl spacer. [^{18}F]-FEAnGA was synthesized by alkylation of its imidazole carbamate precursor with [^{18}F]-FEA, followed by deprotection of the sugar moiety with NaOH in 10−20% overall radiochemical yield. [^{18}F]-FEAnGA is about 10-fold more hydrophilic than the cleavage product [^{18}F]-FEA, and it is stable in PBS and rat plasma for at least 3 h. In the presence of either *Escherichia coli* β-GUS or bovine liver β-GUS, in vitro cleavage of [^{18}F]-FEAnGA with complete release of [^{18}F]-FEA was observed within 30 min. C6 glioma cells incubated with the tracer and *Escherichia coli* β-GUS or bovine liver β-GUS showed a 4- and 1.5-fold higher uptake of radioactivity, respectively, as compared to control C6 cells without β-GUS. Incubation of CT26 murine colon adenocarcinoma cells or the genetically engineered CT26mβGUS cells, which expressed membrane-anchored GUS on the outer cell membrane, with the tracer, resulted in a 3-fold higher uptake into GUS-expressing cells as compared to control cells. In a preliminary microPET study in mice bearing both CT26 and CT26mβGUS tumors, [^{18}F]-FEAnGA exhibited a 2-fold higher retention of radioactivity in the tumor expressing β-GUS than in the control tumor. [^{18}F]-FEA did not show any difference in tracer uptake between tumors. These results suggest that [^{18}F]-FEAnGA may be a suitable PET tracer for evaluation of β-GUS activity, since it is specifically cleaved by β-GUS and the released [^{18}F]-FEA remains attached to targeted cells.

INTRODUCTION

To overcome the limitation of toxicity associated with chemotherapeutic drugs, local conversion of a nontoxic prodrug (PD) to the active cytotoxic drug in or in the vicinity of tumors provides a means for delivering active drugs selectively to tumor cells while sparing the normal cells of a host.

β-glucuronidase (β-GUS) (EC 3.2.1.31) belongs to a group of isoenzymes that catalyze the hydrolysis of β-D-glucuronides to the corresponding alcohol and D-glucuronate. The enzyme is present in virtually all tissues and can be found in microsomes (endoplasmic reticulum) and lysosomes (Fishman). The human enzyme has a pH optimum of 4 to 5. Under normal tissue pH, only about 10% of the maximum activity is retained. β-GUS concentrations are low in human serum and the extracellular compartment of normal tissue (*1*). However, increased levels of extracellular β-GUS have been reported in a number of pathological conditions, such as rheumatoid arthritis, leprosy, myocardial infarction, liver fibrosis, bacterial infection, and various inflammatory processes (*2*). It is also known that tumors have high extracellular levels of β-GUS, due to invading monocytes and granulocytes (*3*). Extracellular β-GUS is also associated with tumor invasiveness and metastatic potential (*3*). Therefore, β-GUS seems to be a promising candidate for a PD-converting enzyme.

Glucuronide−drug conjugates exhibit improved water solubility, stability, and lower toxicity toward normal cells than the native drug. However, glucuronide−drug conjugates are susceptible to enzymatic cleavage by β-GUS, resulting in the in situ generation of highly cytotoxic drugs that can selective incorporate into targeted tumor cells (*1, 4, 5*). A number of prodrugs for β-GUS have been designed. These prodrugs generally consist of three distinct parts: a trigger, a linker, and an effector unit. For β-GUS targeted prodrugs, the trigger and effector units consist of a glucuronide moiety and the cytostatic drug, respectively. They are joined together by the linker unit, which should release the drug as fast as possible after prodrug activation via a chemical breakdown (*6*−*8*).

Encouraging results were obtained with the prodrugs DOX-GA3 and HMR1826 both carrying para-substituted aromatic spacers, which were able to release doxorubicin after enzymatic cleavage of the glucuronide moiety by extracellular β-GUS (Scheme 1).

As follows from the above, bioactivation of the glucuronide prodrug by β-GUS is an attractive approach in prodrug therapy.

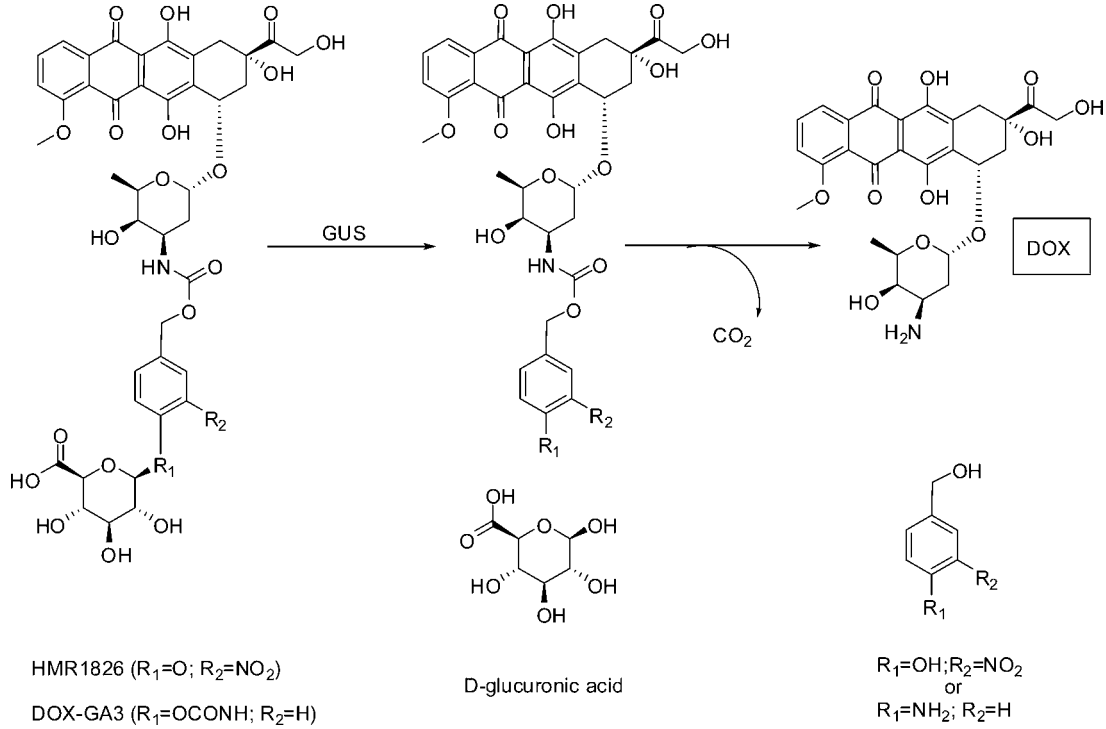
* Author for correspondence: Inês Antunes, Department of Nuclear Medicine and Molecular Imaging, University Medical Center Groningen, University of Groningen, PO Box 30.001, 9700 RB Groningen, The Netherlands, Tel.: +31-50-3619309, FAX: +31-50-3611687, E-mail: i.farinha.antunes@ngmb.umcg.nl.

† University Medical Center Groningen.

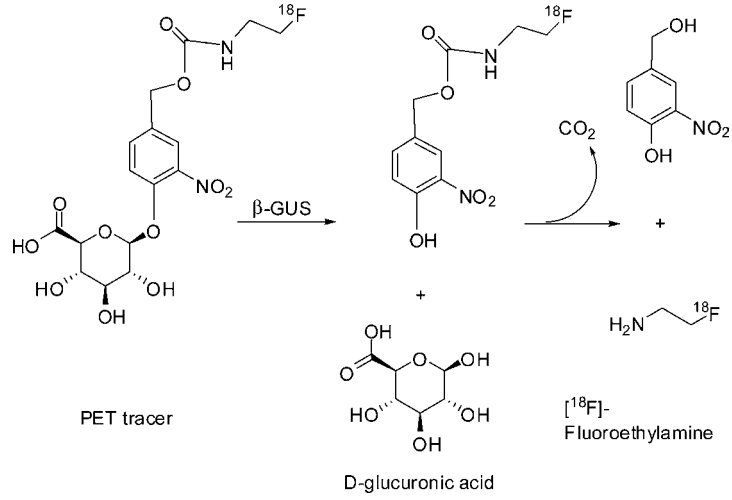
‡ University Center for Pharmacy, University of Groningen.

10.1021/bc9004602 © 2010 American Chemical Society
Published on Web 04/23/2010

Scheme 1. Mechanism of Activation of the Prodrugs HMR1826 and DOX-GA3 by β-GUS



Scheme 2. General Structure of the PET Tracer and Its Mechanism of Activation



However, interindividual and intertissue variability of β-GUS activity, as well as factors modulating the enzyme's expression and activity, are key determinants for the success of these therapeutic strategies (*9*, *10*).

For a better understanding of the mechanisms of action and metabolic conversion of these PD, some in vivo optical measurements of gene/enzyme expression have been done using substrates with fluorescent or bioluminescent properties. These optical imaging modalities are useful in superficial tissues and have extensive application in small animals, but application to larger animals or humans is limited by the depth of light penetration (*11*−*13*). Monitoring enzyme or gene expression in larger animals and ultimately in humans is possible with the use of specific radiotracers combined with nuclear imaging techniques like PET or SPECT (*14*−*17*). Among these techniques, PET is of particular interest for drug development because of its high sensitivity and ability to provide quantitative kinetic data (*18*, *19*).

For PET imaging of β-GUS activity, a suitable tracer is necessary (*20*). Therefore, we aimed to develop a PET tracer that allows repetitive noninvasive imaging of β-GUS activity in living subjects. Thus, we designed a potential PET tracer with a structure based on HMR1826. In the PET tracer, the doxorubicin moiety is replaced by a [^{18}F]-fluoroalkylamine group.

Due to the highly hydrophilic character of the glucuronide, the intact tracer will be rapidly cleared from plasma and from tissues that do not have extracellular β-GUS. However, in tissues with high levels of β-GUS, the enzyme should cleave the glucuronic acid moiety from the PET tracer. As a result, the less hydrophilic [^{18}F]-fluoroethylamine will be released after self-immolation of the spacer, and we hypothesized that [^{18}F]-fluoroethylamine will be trapped in the target tissue (Scheme 2).

This study aimed to provide a proof of principle of this tracer design. The tracer may be further optimized by replacing the

[18F]-fluoroethylamine moiety with, for example, a more lipophilic or targeted moiety in order to increase trapping efficiency as a result of increased nonspecific binding.

MATERIALS AND METHODS

Reagents and solvents were obtained from commercial suppliers (Aldrich, Fluka, Sigma, and Merck) and used without further purification. A glucose, magnesium, and calcium solution (GMC-PBS) was prepared by adding 5.6 mM D-glucose, 0.49 mM $MgCl_2$, and 0.68 mM $CaCl_2$ to 100 mL phosphate-buffered saline (PBS). Flash chromatography was performed on silica gel 60 (0.040−0.063, Merck). All reactions were monitored by thin layer chromatography on Merck F-254 silica gel plates. Detection of the compounds on the TLC plates was performed with UV light (254 nm). Sugar compounds were additionally visualized by staining the TLC strip with 8% H_2SO_4 followed by heating. For radiolabeled compounds, the detection on the TLC was performed with Cyclone phosphor storage screens (multisensitive, Packard). These screens were exposed to the TLC strips for a few seconds and subsequently read out using a Cyclone phosphor storage imager (PerkinElmer) and analyzed with OptiQuant software. ^{1}H and ^{19}F NMR were recorded on a Varian 300 and 200 MHz, respectively. Chemical shifts were determined relative to the signal of the solvent, converted to the TMS scale, and expressed in δ units (ppm) downfield from TMS. Coupling constants were reported in Hertz (Hz). Splitting patterns are defined as s (singlet), d (doublet), dd (double−doublet), t (triplet), dt (double−triplet), or m (multiplet). HPLC purifications were performed with an Elite LaChrom VWR Hitachi L-2130 pump system using a Phenomenex Prodigy C18-column, connected to a UV-spectrometer (Elite LaChrom VWR Hitachi L-2400 UV detector) set at 254 nm and a Bicron frisk-tech radiation detector. Radioactivity measurements for log *D* determination and cell studies were done using an automated gamma counter (Compugamma, LKB Wallac). Absorbance measurements in the enzyme assays were obtained with a UV spectrophotometer (Waters 2487 dual wavelength absorbance detector). CT26mβGUS murine colon adenocarcinoma cells were kindly provided by Steve Roffler (*11*), Institute of Biomedical Science, Academia Sinica, Academia Road, Section 2 No128, 11529 Taipei, Taiwan.

Synthesis. *Methyl 1-O-(4-((2-Fluoroethylcarbamoyloxy) methyl)-2-nitrophenyl)-2,3,4-tri-O-acetyl-β-D-glucopyronuronate (***2***).* Methyl 1-O-(4-(1*H*-imidazole-carbamoyloxymethyl)-2-nitrophenyl)-2,3,4-tri-*O*-acetyl-β-D-glucopyronuronate (**1**) was synthesized in 3 steps according to the procedure described by Duimstra et al. (*21*). Carbamate **1** (0.2 g, 0.35 mmol) was dissolved in 3 mL anhydrous CH_2Cl_2 under a N_2 atmosphere and cooled to 0 °C. Methyl triflate (45 μL, 0.40 mmol) was added to the reaction mixture. After stirring for 30 min at 0 °C, the reaction mixture was diluted with 2 mL Et_2O and cooled to −20 °C to allow the methylated product to precipitate. The white solid was collected by filtration, washed with Et_2O, and dried in vacuo. The methylated compound was resuspended in 2.5 mL CH_2Cl_2 under a N_2 atmosphere, and 2-fluoroethylamine hydrochloride (0.05 g, 0.54 mmol) and tryethylamine (75 μL, 0.54 mmol) were added. The slurry was stirred for 5 h at room temperature and then washed with water and brine. The organic layer was dried on Na_2SO_4, concentrated in vacuo, and purified by flash chromatography (silica, EtOAc−Hex 1:1 + 0.1% Et_3N) to give 81 mg (41%) of **2** as a white solid. ^{1}H NMR (300 MHz, DMSO-d_6) δ 1.97 (s, 3H, OAc), 1.99 (s. 6H, OAc), 3.23 (m, 2H, CH_2N), 3.61 (s, 3H, $COOCH_3$), 4.38 (dt, 2H, J = 47.2 Hz, J = 10 Hz, CH_2F), 4.71 (d, 1H, J = 9.5 Hz, H-5), 5.01−5.12 (m, 4H, benzylic CH_2, H-2, H-4), 5.43 (t, 1H, J = 19 Hz, H-3), 5.71 (d, 1H, J = 7.7 Hz, H-1), 7.40 (d, 1H, J = 8.4 Hz, ArH), 7.56 (m, 1H, NH), 7.65 (d, 1H, J = 9.5 Hz, ArH), 7.87 (s. 1H, ArH). ^{19}F NMR (200 MHz, DMSO-d_6) δ −217.84. ESI-MS *m/z* 592.3 $[M+NH_4]^+$, 597.3 $[M+Na]^+$.

*Methyl 1-O-(4-((2-Fluoroethylcarbamoyloxy)methyl)-2-nitrophenyl)-β-D-glucopyronuronate (***3***).* 12.6 μL 30% w/v NaOMe in MeOH was added to a solution of **2** (50 mg, 0.087 mmol) in anhydrous MeOH at 0 °C. After 2 h of stirring under nitrogen atmosphere, the reaction was quenched with acetic acid and concentrated in vacuo. The crude residue was purified by flask column chromatography (silica, 10% MeOH in CH_2Cl_2). The resulting solid was dissolved in acetone and filtered through a 0.2 μm PTFE filter to remove any remaining silica. Trituration of the solid in diethyl ether yielded 30.3 mg of **3** (78%) as a white solid.

^{1}H NMR (300 MHz, DMSO-d_6) δ 3.2 (m, 2H, CH_2N, 3.63 (s, 3H, $COOCH_3$), 4.10 (d, 1H, J = 9.1 Hz, H-5), 4.38 (dt, 2H, J = 47.6 Hz, J = 10 Hz, CH_2F), 5.00 (s, 2H, benzylic CH_2), 5.3 (d, 2H, J = 7 Hz, H-2, H-4), 5.51 (s, 2H, H-3, H-1), 7.42 (d, 1H, J = 8.8 Hz, ArH), 7.56 (m, 1H, NH), 7.65 (m, 2H, NH, ArH), 7.84 (s, 1H, ArH). ^{19}F NMR (200 MHz, DMSO-d_6) δ −232. ESI-MS *m/z* 455.3 $[M+Li]^+$.

*1-O-(4-(2-Fluoroethyl-carbamoyloxymethyl)-2-nitrophenyl)-O-β-D-glucopyronuronate (FEAnGA) (***4***).* A solution of **3** (20 mg, 0.047 mmol) in acetone (1 mL) was stirred in the presence of a 1 M NaOH (380 μL) solution at 0 °C. After 10 min, the mixture was neutralized with 1 M HCl, concentrated in vacuo, and purified by flash chromatography (Silica, MeCN/H_2O 7:3) to give 17.3 mg of a light yellow solid (91%).

^{1}H NMR (300 MHz, DMSO-d_6) δ 3.2 (m, 2H, CH_2N), 3.55 (d, 1H, J = 9.4 Hz, H-5), 4.38 (dt, 2H, J = 47.6 and 10 Hz, CH_2F), 5.01 (s, 2H, benzylic CH_2), 5.11 (d, 2H, J = 6.8 Hz, H-2, H-4), 5.30 (d, 2H, J = 4.4 Hz, H-3, H-1), 7.41 (d, 1H, J = 9.1 Hz, ArH), 7.60 (m, 2H, NH, ArH), 7.83 (s. 1H, ArH). ^{19}F NMR (200 MHz, DMSO-d_6) δ −225; *m/z* 457.2 $[M+Na]^+$.

Radiolabeling. *Radiosynthesis of [*^{18}*F]-FEAnGA ([*^{18}*F]-***4***).* Aqueous [18F]-fluoride was produced by irradiation of [18O] water with a Scanditronix MC-17 cyclotron via the ^{18}O (p,n)^{18}F nuclear reaction. The [18F]-fluoride solution was passed through a SepPak Light Accell plus QMA anion exchange cartridge (Waters) to recover the ^{18}O-enriched water. The [18F]-fluoride was eluted from the cartridge with 1 mL of K_2CO_3 (5 mg/mL) and collected in a vial with 20 mg Kryptofix 2.2.2. To this solution, 1 mL acetonitrile was added and the solvents were evaporated at 130 °C. The ^{18}F-KF/Kryptofix complex was dried 3 times by the addition of 0.5 mL acetonitrile, followed by evaporation of the solvent.

[18F]-FEA ([18F]-7) was prepared by fluorination of *N*-[2-(toluene-4-sulfonyloxy)ethyl]phthalimide (30 mg, 0.09 mmol) in acetonitrile at 110 °C, followed by deprotection with hydrazine hydrate (50 μL, 1.03 mmol) as described in the literature (*22*). The resulting amine was distilled at 75 °C into an ice-cold solution of **1** (5 mg, 0.009 mmol) in acetonitrile (0.2 mL). The mixture was allowed to react at room temperature for 30 min. The product was diluted with 20 mL of water and passed through a tC18 cartridge (activated with 5 mL EtOH and 10 mL H_2O). Deprotection of the hydroxyl groups was done on the tC18 cartridge by addition of 1 mL 2 M NaOH and incubation for 7 min at room temperature. The product was eluted from the cartridge with 4 mL of water and purified by HPLC (10% EtOH in NaH_2PO_4 0.025 M (pH 6.3); 4 mL/min; retention time: [18F]-FEAnGA = 10 min).

The radiolabeled compound [18F]-FEAnGA ([18F]-**4**) was obtained in 5−20% radiochemical yield from [18F]-fluoride (decay-corrected) in 150 min. At the end of synthesis (EOS), the specific activity was 5−10 GBq/μmol and the radiochemical purity was >95%.

Stability of [$^{18/19}$F]-FEAnGA. Samples of [$^{18/19}$F]-FEAnGA were taken for stability testing. The sample of FEAnGA was dissolved in PBS (1 mL) and incubated at 37 °C. After 60 min, the solution was analyzed by HPLC (retention time: FEAnGA = 3.2 min, HNBA = 10.4 min) (20% CH_3CN/NaH_2PO_4 0.025 M (pH 6.3); 4 mL/min).

A sample of radiolabeled [^{18}F]-FEAnGA was dissolved in PBS (1 mL) and rat plasma (1 mL) and incubated at 37 °C. After 1 h and 3 h of incubation, respectively, the stability of the radiolabeled [^{18}F]-FEAnGA was followed by Radio-TLC (R_f FEA = 0.0, R_f FEAnGA = 0.4) (eluent: MeOH/CH_2Cl_2 2:8 + 0.1% Et_3N). After elution, the TLCs were analyzed by phosphor storage imaging. The screens were scanned with Cyclone phosphor storage system (PerkinElmer), and the percentage of conversion of [^{18}F]-FEAnGA as a function of the incubation period was calculated by ROI analysis using Opti-Quant software.

In order to not underestimate the amounts of [^{18}F]-FEA due to its volatile nature, we created a calibration curve of the amount of [^{18}F]-FEA evaporated over time in the radio TLC ($y = -0.2141x + 103.11$, $R^2 = 0.72$, $P = 0.03$) and corrected all values. The calibration curve was prepared by pipetting 1.5 μL of a stock [^{18}F]-FEA solution at different time points in a TLC plate. The TLC was read out by storage phosphorus imaging. Images were analyzed by Optiquant software and the percentage of evaporated activity was calculated. At 60 min, approximately 10% of [^{18}F]-FEA has evaporated.

Distribution Coefficient (Log $D_{7.4}$). To determine the Log $D_{7.4}$ of [^{18}F]-FEA and [^{18}F]-FEAnGA, an aliquot of 1 mL of HPLC purified [^{18}F]-FEA or [^{18}F]-FEAnGA solution was added to a mixture of *n*-octanol/PBS (5 mL/5 mL) at pH 3 and 7 for [^{18}F]-FEAnGA and at pH 7 and 10 for [^{18}F]-FEA. The tubes were vortexed at room temperature for 1 min, followed by 30 min shaking in a water bath at 37 °C. Aliquots of 1000 and 25 μL were drawn from the *n*-octanol and aqueous phase, respectively, and the radioactivity was counted using an automated gamma counter. The experiments were performed at least in triplicate.

In Vitro Hydrolysis of FEAnGA. To assess the kinetics parameters for the β-GUS-catalyzed hydrolysis of FEAnGA, aliquots of FEAnGA were prepared with concentrations ranging from 0.001 to 0.01 M in PBS buffer (pH 7.4). To a 0.950 mL solution containing 0.1% BSA in PBS (pH = 7.4), 3.7 μg (74U) *Escherichia coli* β-GUS (E.C.3.2.1.31, 20 000 U/mg Aldrich) and 50 μL of FEAnGA were added. The solution was incubated at 37 °C in a water bath, and 75 μL samples were collected at different time points ranging from 30 s to 30 min after the start of incubation. Each sample was immediately added to 500 μL acetonitrile in ice to stop the reaction. The release of 4-hydroxy-3-nitrobenzyl alcohol (HNBA) ($\varepsilon = 3460\ M^{-1}\ cm^{-1}$) was monitored by measuring the UV absorbance at 420 nm. The initial velocities of the reactions were determined from the slope of the absorbance curve at time = 0.The kinetic parameters K_M and V_{max} were obtained from a Lineweaver−Burk plot (*12, 23, 24*).

The kinetic parameters of the hydrolysis of FEAnGA by bovine liver β-GUS were determined as described above, but with minor modifications. Briefly, to a 0.8 mL solution containing 0.1% BSA in PBS (pH = 5), 95.2 μg (952U) bovine liver β-GUS (B-10, E.C.3.2.1.31, 10 000 U/mg Sigma) and 200 μL of FEAnGA were added. The same assay was also performed for a control sample solution (without enzyme) under the same conditions, and it showed negligible absorption for the duration of the experiment. For comparison, the kinetic parameters of a reference substrate, *p*-nitrophenyl-β-D-glucuronide (PNPG) ($\varepsilon = 7578\ M^{-1}\ cm^{-1}$) were determined using the same conditions as for FEAnGA. The experiment was preformed in triplicate.

In Vitro Hydrolysis of [^{18}F]-FEAnGA. To a 0.6 mL solution of 0.1% BSA in PBS (pH = 7), 3.7 μg (74U) *Escherichia coli* β-GUS or 95.2 μg (952U) bovine liver β-GUS and 0.4 mL of HPLC purified [^{18}F]-FEAnGA (0.68−1.28 MBq) were added. The solutions were incubated in a water bath at 37 °C, and 75 μL samples were collected at different time points ranging from 30 s to 30 min after the start of incubation. The enzymatic activity was stopped by dilution of the samples in 0.5 mL of acetonitrile and cooling of the samples in ice. The degradation of the radiolabeled [^{18}F]-FEAnGA was followed by Radio-TLC (eluent: MeOH/CH_2Cl_2 2:8 + 0.1% Et_3N). After elution, the TLCs were analyzed by phosphor storage imaging as described earlier.

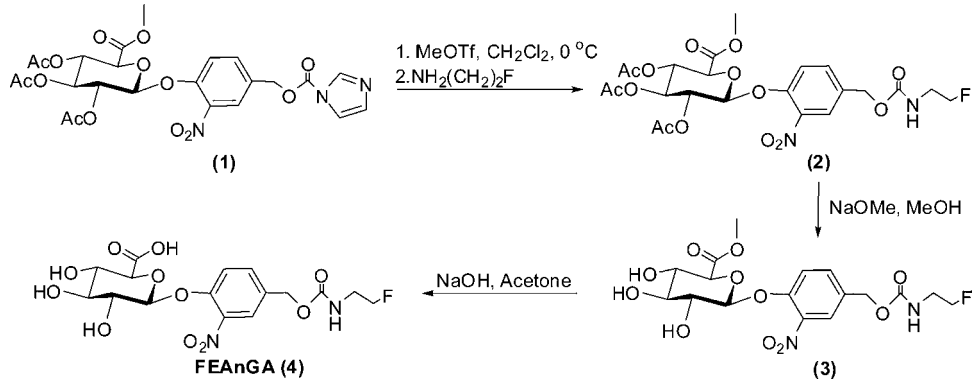
Cellular Uptake of [^{18}F]-FEAnGA in C6 Glioma Cells. C6 glioma cells were maintained in 5 mL Dulbecco's Modified Eagle Medium (DMEM) supplemented with 7.5% fetal bovine serum (FBS) in 25 cm^3 culture flasks. Cells were grown in a humidified atmosphere containing 5% CO_2 and were passaged every 3−4 days. For uptake experiments, cells were plated in triplicate in a 12-well plate at a density of 7×10^5 cells per well. After 24 h, the medium was discarded and 1 mL of PBS-GMC buffer per well was added, followed by the addition of 200 μL [^{18}F]-FEAnGA (ca. 250 kBq) or 10 μL [^{18}F]-FEA (ca. 125 kBq). In 2 series of 3 wells, an excess of *E. coli* β-GUS (740U) or bovine liver β-GUS (340U) was added, respectively. After 60 min of incubation at 37 °C, the medium was collected and the cells washed with cold PBS (3 × 1 mL/well), harvested with trypsin (250 μL), and resuspended in 1750 μL of DMEM. The cell suspensions as well as the supernatant fractions were collected separately for each well, and the radioactivity was measured using a gamma counter. For each well, the medium was analyzed for conversion of [^{18}F]-FEAnGA into [^{18}F]-FEA as described earlier.

Cellular Uptake of [^{18}F]-FEAnGA in CT26 Adenocarcinoma Cells. CT26 control cells as well as the genetically engineered CT26mβGUS murine colon adenocarcinoma cells that express membrane-anchored GUS on the outer cell membrane were maintained in 10 mL DMEM medium supplemented with 10% FBS and 1% penicillin−streptomycin in 75 cm^3 culture flasks. Cells were grown in a humidified atmosphere containing 5% CO_2 and were passaged every 3−4 days. For uptake experiments, cells were plated in triplicate in a 12-well plate at a density of 7×10^5 cells per well. After 24 h, the medium was discarded and 1 mL of PBS-GMC buffer per well was added followed by the addition of 200 μL [^{18}F]-FEAnGA (ca. 250 kBq) or 10 μL [^{18}F]-FEA (ca. 125 kBq). The rest of the tracer uptake experiment was performed as described above.

Efflux Analysis of [^{18}F]-FEA in C6 Glioma Cells. C6 glioma cells were plated in triplicate in a 12-well plate at a density of 7×10^5 cells per well. After 24 h, the medium was discarded and 1 mL of PBS-GMC buffer per well was added, followed by the addition of 10 μL [^{18}F]-FEA (ca. 1.3 MBq). After 60 min of incubation at 37 °C, the medium was discarded, the cells washed with cold PBS (3 × 1 mL/well), and 1 mL of PBS-GMC buffer per well was added. At different time points, the medium was collected and the cells harvested with trypsin (250 μL) and resuspended in 1750 μL of DMEM. The cell suspensions as well as the supernatant fractions were collected separately for each well, and the radioactivity was measured using a gamma counter.

MicroPET Imaging in a β-GUS Expressing Tumor (CT26mβGUS) Mouse Model. The animals were provided with standard laboratory chow and tap water ad libitum. All studies were carried out in compliance with the local ethical guidelines for animal experiments. The protocol was approved by the local

Scheme 3. Synthesis of Compound FEAnGA



Animal Ethics Committee. CT26 and CT26mβGUS cells [(1−1.6) × 10^6, in a 1:1 mixture of Matrigel and DMEM with 10% FBS] were subcutaneously injected into the right and left shoulders of two male Balb/c mice (6−8 weeks old), respectively. On day 7 after inoculation of the mice with CT26 and CT26mβGUS cells, the mice were anesthetized with 2% Isoflurane and fixed to the bed in the small animal PET camera in transaxial position. A 20 min transmission scan with a Co-57 point source was obtained for the correction of attenuation of 511 keV photons by tissue. After the transmission scan was completed, the PET tracer [18F]-FEAnGA (4.4 MBq) or [18F]-FEA (4.2 MBq) was injected via the penile vein of the animal. A 60 min static image was acquired with a Focus 220 rodent scanner (CTI Siemens, Munich, Germany). Emission sinograms were iteratively reconstructed (OSEM2D) after being normalized, corrected for attenuation, and corrected for decay of radioactivity. Subsequent to the μPET imaging, the animal fixed to the bed was positioned in the microCT scanner (MicroCT II, CTI Siemens) and a microCT image (exposure time = 1050 ms; X-ray voltage = 55 kvp; anode current = 500 μA; number of rotation steps = 500; total rotation = 360°) was acquired for 15 min for anatomic localization. From the difference in bed positions from the PET to the CT, a transformation matrix was constructed, which describes the translation between both images. This transformation matrix was used for precise fusion of both images, using Inveon Research Workplace (Siemens) software.

Data Analysis. Apparent kinetic constants (V_{max} and K_M) were determined from Lineweaver-Buck plots of the initial rates ($1/V_0$) against the reciprocal substrate concentration 1/[S] generated in *Sigmaplot* software. The comparison between cells with and without β-GUS was performed using a two-sided *t* test that was paired for the different conditions in a single experiment. In all cases, $P \leq 0.05$ was considered significant.

RESULTS AND DISCUSSION

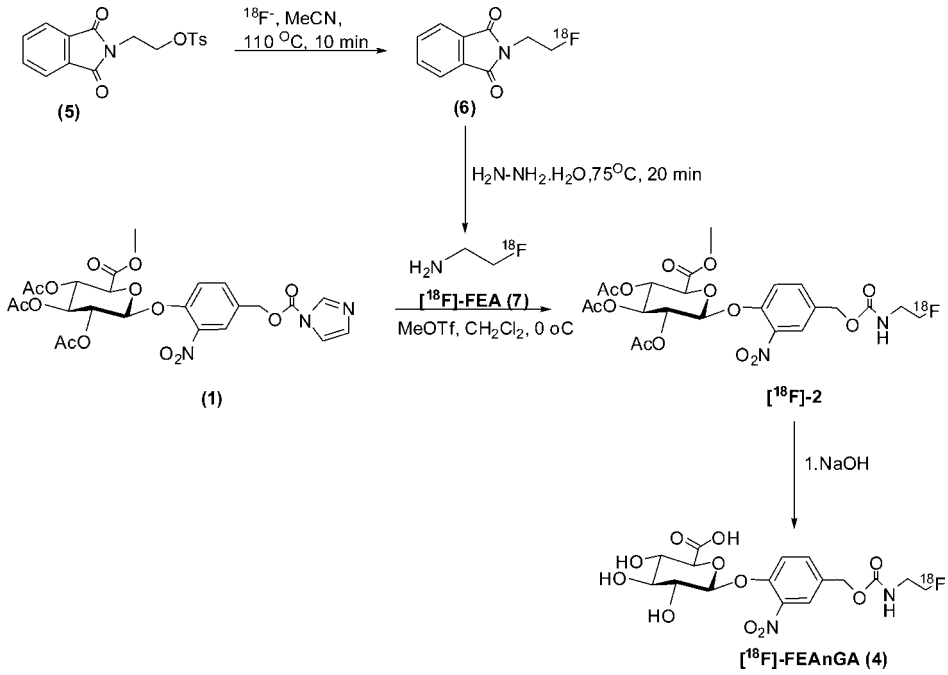
Prior studies with DOX-GA3 and HMR 1826, which have a β-glucuronyl group attached to doxorubicin via a para-substituted aromatic group showed promising preclinical results for PD therapy. Their low general toxicity has been clearly demonstrated in mice and rats studies with human tumor xenografts such as lungs, colon, breast, ovary, stomach, and pancreatic cancer. Experiments in ex vivo human lung tumor specimens have demonstrated that HMR1826 leads to increased levels of free DOX in tumor tissues and decreased levels in normal tissues compared to native DOX, while DOX-GA3 showed enhanced efficacy in ovarian cancer xenografts in comparison to native DOX. Inspired by the structures of the doxorubicin prodrugs, we designed an 18F-labeled PET tracer for imaging of β-GUS (Scheme 2). In this PET tracer, the DOX moiety is replaced by a lipophilic labeled molecule; after cleavage of the PET tracer by β-GUS, the labeled lipophilic part of the molecule is supposed to be trapped at the cleavage site by nonspecific binding.

Compound **1** was prepared in 3 steps from methyl 1-bromo-2,3,4-tri-*O*-acetyl-α-D-glucopyronuronate according to the procedure described by Duimstra et al. (*21*). Activation of the imidazole intermediate with methyltriflate followed by the reaction with fluoroethylamine gave compound **2** in 30% yield. It was observed that the amount of methyl triflate used was critical in this step, since higher amounts than 1.1 mol equiv led to lower yields of compound **2**. This could be due to the reaction of fluorethylamine with the excess of methyl triflate instead of compound **1**. The deprotection of the sugar moiety in 2 in a single step did not give product **4** in the desired yield, as the reaction was incomplete and led to the formation of multiple side products. Moreover, the purification of product FEAnGA by flash chromatography proved difficult, and consequently, it was decided to perform the synthesis of FEAnGA by a two-step procedure as depicted in Scheme 3. First, deacetylation of the hydroxyl groups was achieved using sodium methoxide. Then, the basic hydrolysis of the carboxylic ester was performed with NaOH, which afforded the unlabeled reference compound FEAnGA in 50% yield. The overall yield of this procedure was 23%. The identity of the compound was confirmed by low-resolution mass spectroscopy (LRMS) and the disappearance of the methoxy and acetyl groups of the glucuronic moiety in ^{1}H NMR.

The anomeric β-configuration, essential for substrate affinity for β-GUS, was confirmed by the NMR, which showed the H-1 proton as a doublet at a chemical shift $\delta_{H\text{-}1}$ of 5.71 ppm with a characteristic coupling constant J_{H1-H2} of 7.7 Hz. Typically, the H1−H2 coupling constants of the α anomer are 2−5 Hz, whereas the coupling constant of the β anomer is between 6 and 10 Hz (*19*, *25*, *26*).

The synthesis of [18F]-FEAnGA is a 3-step procedure consisting of the preparation of [18F]-FEA followed by the coupling of the amine with compound **1** and the removal of the protecting groups. [18F]-FEA was prepared according to the procedure described by Tewson (*22*) by reaction of the tosylate **5** with [18F]fluoride and subsequent removal of the phthalimide group **6** with hydrazine. This last step is of critical importance with regard to the final labeling yield. In order to obtain distilled [18F]-FEA in 48 ± 9% (n = 8) yield, it is necessary to use hydrated hydrazine in a reaction mixture that is free of acetonitrile to avoid the evaporation of the hydrazine associated water, which is required for the hydrolysis of the phthalimide moiety. On the other hand, distillation should not be performed at higher temperatures than 75 °C or longer than 15 min to avoid the distillation of hydrazine into the second reaction vial. Hydrazine competes with [18F]-FEA in the carbamate formation reaction, thus

Scheme 4. Radiosynthesis of Compound [^{18}F]FEAnGA



decreasing the final yield. The carbamate formation of compound **1** with the distilled [^{18}F]-FEA gives compound [^{18}F]-FEAnGA in 33 ± 19% (n = 8) yield after 30 min of reaction at room temperature. Deprotection of the hydroxyl groups was done on the tC18 cartridge by addition of 1 mL 2 M NaOH and incubation for 7 min at room temperature. The product was eluted from the cartridge with 4 mL of water and was purified by HPLC in 79 ± 9% (n = 8) yield. In contrast to the deprotection of the reference compound **2** which was obtained in 2 steps, surprisingly it was possible to deprotect [^{18}F]-**2** in a single step giving our final product in good yield. Thus, the final product [^{18}F]-FEAnGA was obtained in 13 ± 7% (n = 8) overall radiochemical yield (corrected for decay, based on [^{18}F]-fluoride) with a total synthesis time of 150 min (Scheme 4). The identity of the tracer was confirmed by coelution with an authentic sample of the nonradioactive compound by RP-HPLC.

The stability of [$^{18/19}$F]-FEAnGA in PBS was determined at 37 °C. After 1 h of incubation, HPLC analysis showed that 98% of the tracer was still intact. The stability of [^{18}F]-FEAnGA in PBS and rat plasma were also determined at 37 °C. After 1 and 3 h of incubation, 98% and 99% (Radio-TLC) of the radioactivity still corresponded to the intact tracer, respectively. This indicates that the tracer is highly stable in vitro.

The lipophilicities of [^{18}F]-FEAnGA and [^{18}F]-FEA were determined by measuring their *n*-octanol/water distribution coefficient at pH 7.4; the Log D was found to be −1.61 ± 0.01 for [^{18}F]-FEAnGA and −0.69 ± 0.02 for [^{18}F]-FEA. As expected, [^{18}F]-FEAnGA is about 10 times more hydrophilic than [^{18}F]-FEA due to the presence of the glucuronic acid moiety. Moreover, [^{18}F]-FEAnGA is less hydrophilic at pH 3 (Log $D_{3.0}$ −1.01 ± 0.03) than at pH 7.4, because the glucuronic acid is partially protonated at acidic pH (pK_a ≈ 3). In contrast,

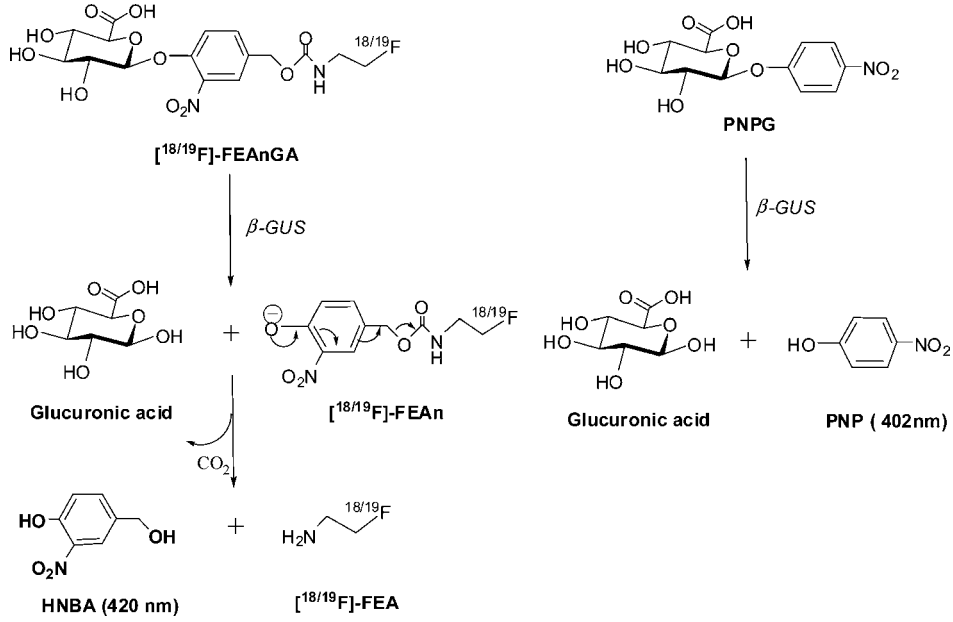


Figure 1. Mechanism of activation of [$^{18/19}$F]-FEAnGA and PNPG by β-GUS.

Table 1. Enzyme Kinetic Parameters for FEAnGA Represented by the Mean Values of Triplicate Samples ± SD

enzyme	substrate	K_M (μM)	V_{max} (μmol min^{-1} mg^{-1})	k_{cat} (s^{-1})	k_{cat}/K_M (10^6 M^{-1} s^{-1})
E. coli β-GUS	PNPG	8.2 ± 1.6	1366 ± 68	660	80.3
	FEAnGA	7.1 ± 0.9	348 ± 24	134	24.6
bovine liver β-GUS	PNPG	34.0 ± 16.5	56.9 ± 23	19	0.6
	FEAnGA	5.7 ± 2.7	25.8 ± 9	10	1.8

the log *D* of [^{18}F]-FEA was increased at pH 10 (−0.42 ± 0.03) as compared to pH 7.4, due to the fact that [^{18}F]-FEA is no longer protonated at basic pH (p$K_a \approx 8.8$) (*15*, *19*, *27*−*30*).

The enzymatic processing of FEAnGA was studied using commercially available bacterial *Escherichia coli* β-GUS and mammalian bovine liver β-GUS. The water-soluble FEAnGA is stable in aqueous buffer in the absence of β-GUS, and as a result, a solution of FEAnGA remains colorless. However, in the presence of β-GUS it undergoes rapid hydrolysis, resulting in the spontaneous release of [^{18}F]-FEA and the self-immolating spacer, which immediately colors the solution yellow. The liberation of 4-hydroxy-3-nitrobenzyl alcohol (HNBA) can be measured with a UV spectrophotometer at 420 nm. In a similar manner, the commercially available reference substrate, PNPG, is cleaved by β-GUS, producing *p*-nitrophenol (PNP) which can also be measured by UV spectrophotometer at 402 nm (Figure 1.)

Thus, the kinetic parameters for the hydrolysis of FEAnGA were determined by measuring the release of HNBA under physiological conditions. The kinetic parameters of PNPG were also determined under the same conditions for comparison. In general, the kinetic parameters of FEAnGA are on the same order of magnitude as those of PNPG, which indicates that FEAnGA is a good substrate of β-GUS as well. The maximum hydrolysis rate (V_{max}) of PNPG by *Escherichia coli* β-GUS and bovine liver β-GUS was 4 and 2 times higher than that of FEAnGA, respectively (Table 1). FEAnGA and PNPG show similar affinity for *E. coli* β-GUS ($K_M \approx 7$ μM). However, FEAnGA ($K_M = 5.8$ μM) has 6 times higher affinity than PNPG ($K_M = 34$ μM) toward bovine liver-β-GUS. Thus, despite the slightly lower turnover (K_{cat}) of FEAnGA by bovine liver-β-GUS as compared to PNPG, FEAnGA will still undergo relatively fast hydrolysis at low concentrations of substrate and enzyme, as is demonstrated by higher catalytic efficiency, K_{cat}/K_M. Although FEAnGA is a slightly less efficient substrate for *E. coli* β-GUS compared to PNPG, it proves to be a better

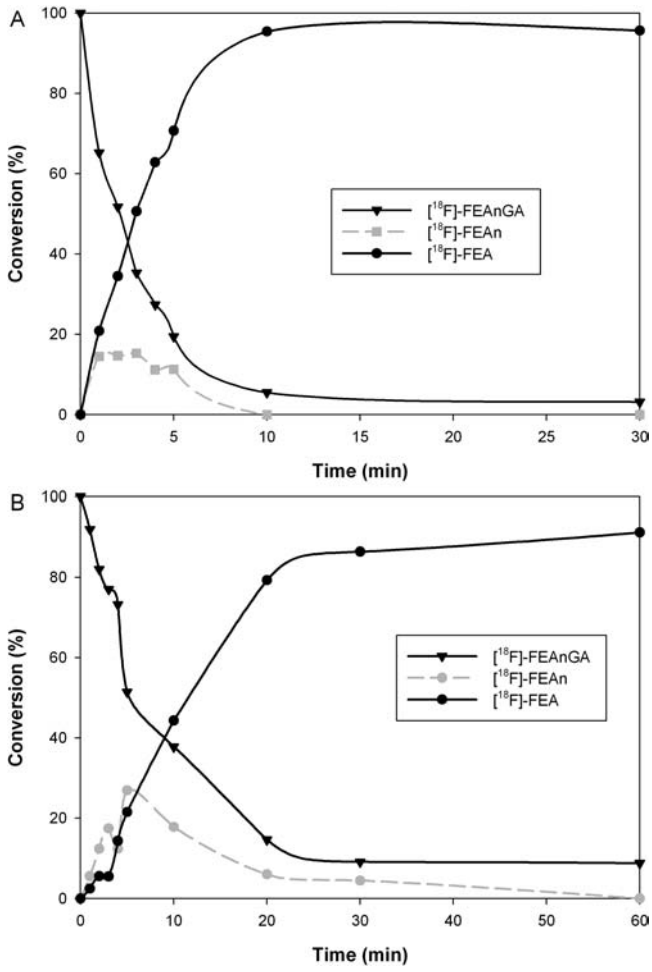


Figure 2. Cleavage of [^{18}F]-FEAnGA by (A) *E. coli* β-GUS ($n = 1$), (B) bovine liver β-GUS ($n = 1$).

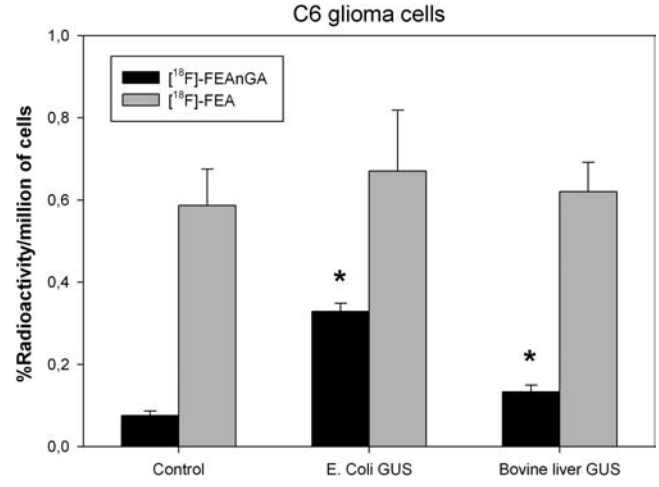


Figure 3. Cell-associated radioactivity of [^{18}F]-FEAnGA and [^{18}F]-FEA in control C6 cells and in C6 cells in the presence of *E. coli* β-GUS and bovine liver β-GUS. Data are expressed as % radioactivity/million cells and are mean values of triplicate samples ± SD.* $P < 0.05$, paired bidirectional Student's *t* test.

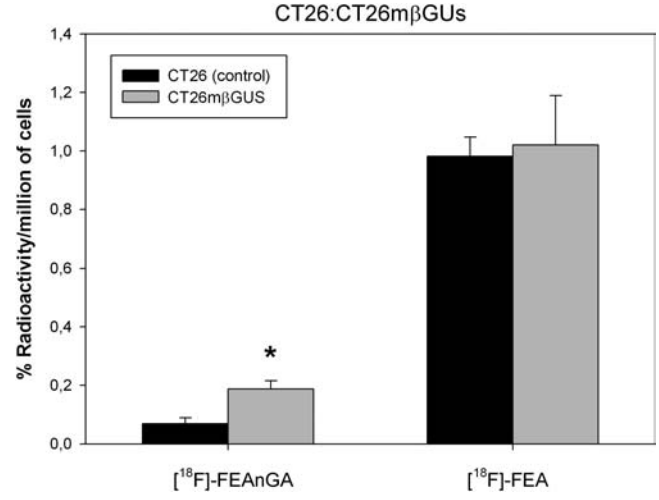


Figure 4. Cell-associated radioactivity of [^{18}F]-FEAnGA and [^{18}F]-FEA in control (CT26) and CT26mβGUS cells. Data are expressed as % radioactivity/million cells and are mean values of triplicate samples ± SD. *$P < 0.05$, paired bidirectional Student's *t* test.

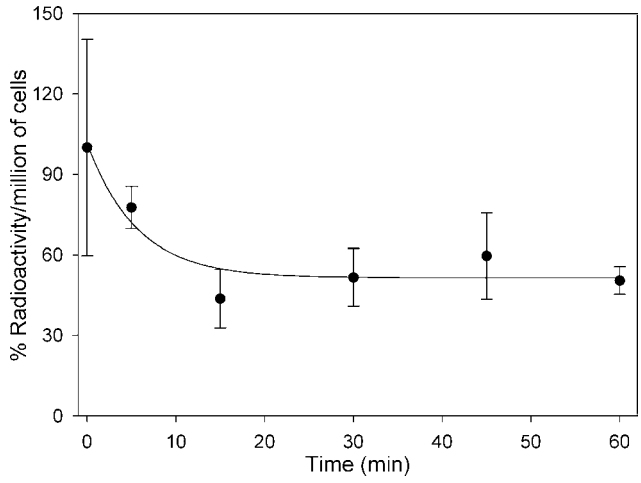


Figure 5. Cell-associated radioactivity of [^{18}F]-FEA in C6 cells. Data are expressed as % radioactivity/million cells and are mean values of triplicate samples ± SD. The efflux follows an exponential decay ($y = 51.47 + 50.06\ e^{(-0.18x)}$, $R^2 = 0.90$; $P = 0.03$).

substrate for bovine liver β-GUS (high K_{cat}/K_M) (Table 1). In a control experiment under identical conditions, but in the absence of β-GUS, no hydrolysis of FEAnGA was observed. These results indicate that FEAnGA is specifically hydrolyzed by β-GUS (*21*, *27*, *31*, *32*).

Radiolabeled [^{18}F]-FEAnGA was rapidly cleaved by both *Escherichia coli* β-GUS and bovine liver β-GUS. Radio-TLC analysis confirmed that the cleavage of [^{18}F]-FEAnGA by both enzymes is a two-step process (*33*). The consumption of [^{18}F]-FEAnGA leads to the formation of an intermediate which we hypothesized being the 4-(hydroxymethyl)-2-nitrophenol self-immolative spacer attached to [^{18}F]-FEA ([^{18}F]-FEAn). The intermediate ([^{18}F]-FEAn) is subsequently converted to [^{18}F]-FEA resulting in almost complete cleavage of the tracer into [^{18}F]-FEA within 10 min of incubation with *Escherichia coli* β-GUS (95% conversion) and 30 min of incubation with bovine liver β-GUS (86% conversion) (Figure 2).

C6 glioma cells were incubated with [^{18}F]-FEAnGA or [^{18}F]-FEA for 60 min at 37 °C, in the presence of either *E. coli* β-GUS (740 U) or bovine liver β-GUS (340 U) or in the absence of the enzyme (control). As depicted in Figure 3, the cell associated radioactivity was 6 times higher when C6 cells are incubated with [^{18}F]-FEA than when the C6 cells were incubated with [^{18}F]-FEAnGA in the absence of β-GUS. This increase in uptake is most likely due to the small size of [^{18}F]-FEA that enables the crossing of the cell membrane by passive diffusion. As expected, there is no significant difference in the cell-associated radioactivity of C6 cells incubated with [^{18}F]-FEA in the presence or absence of β-GUS. However, when C6 cells are incubated with [^{18}F]-FEAnGA the cell-associated radioactivity increases 4 and 1.5 times in the presence of *E. coli* β-GUS and bovine liver β-GUS, respectively. The higher tracer uptake in the presence of *E. coli* β-GUS compared to the uptake in the presence of bovine liver β-GUS could be explained by the fact that the catalytic rate of bovine liver β-GUS toward [^{18}F]-FEAnGA is 13 times lower than the catalytic rate of *E. coli* β-GUS.

Indeed, the radio-TLC of the medium samples shows that in the presence of *E. coli* β-GUS the conversion of [^{18}F]-FEAnGA into [^{18}F]-FEA is 99%, while with bovine liver β-GUS, there is only 37% of conversion into [^{18}F]-FEA (Supporting Information). These results suggest that the increase in cell-associated radioactivity is associated with the conversion of [^{18}F]-FEAnGA into [^{18}F]-FEA.

In addition to the uptake in C6 cells, [^{18}F]-FEAnGA and [^{18}F]-FEA were evaluated in genetically engineered CT26mβGUS murine colon adenocarcinoma cells that expressed membrane-anchored β-GUS on the outer cell membrane. Therefore, CT26 cells and CT26mβGUS were incubated with [^{18}F]-FEAnGA or [^{18}F]-FEA for 60 min at 37 °C. Incubation with [^{18}F]-FEA resulted in a 14-fold higher cell-associated radioactivity in

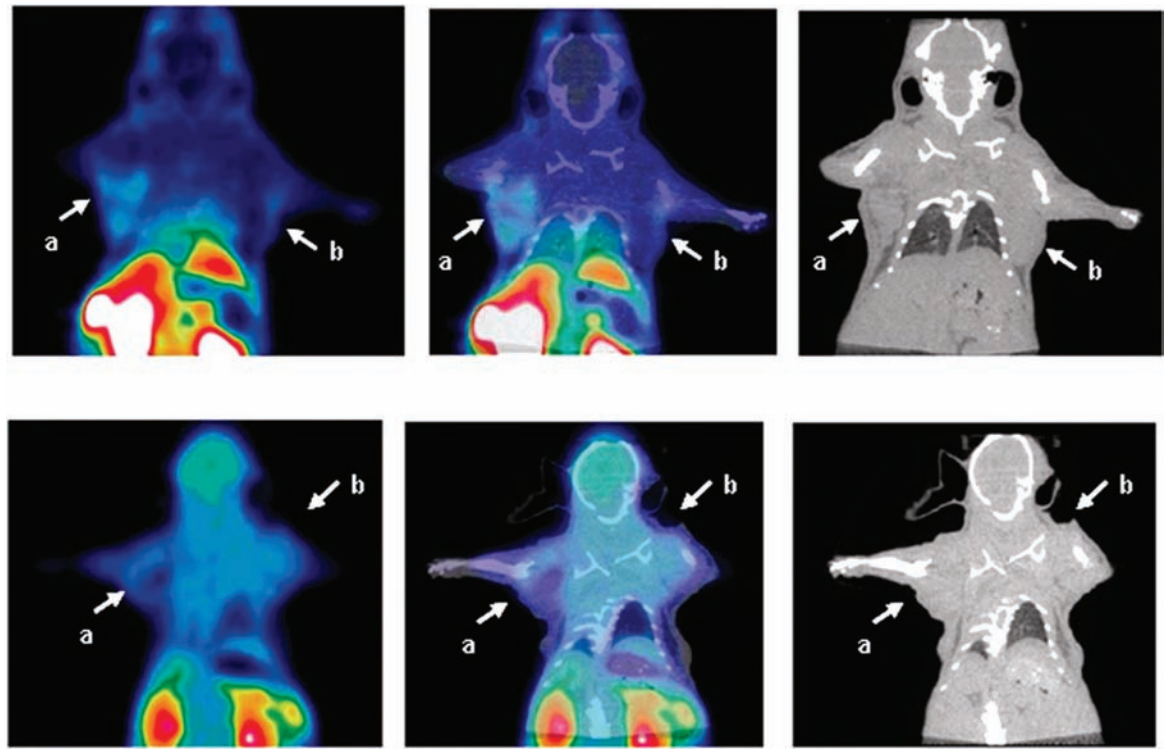


Figure 6. MicroPET image (left), microPET/CT fusion image (middle), and microCT image (right) of a mouse bearing a CT26mβGUS tumor (a) and a CT26 tumor (b) injected with either [^{18}F]-FEAnGA (upper row) or [^{18}F]-FEA (lower row).

control CT26 cells than incubation with [^{18}F]-FEAnGA. There is no significant difference between CT26 and CT26mβGUS associated radioactivity when incubated with [^{18}F]-FEA, while incubation with [^{18}F]-FEAnGA caused 3-fold higher uptake in β-glucuronidase expressing cells (CT26mβGUS) than control CT26 cells (Figure 4). Radio-TLC of the medium showed that [^{18}F]-FEAnGA was converted into [^{18}F]-FEA (20%) by the enzyme expressing cells only (Supporting Information).

For a good PET tracer, not only tracer uptake, but also its retention is important. To evaluate whether the tracer after cleavage of β-GUS is retained by C6 cells, the efflux of [^{18}F]-FEA was investigated as shown in Figure 5, the efflux analysis seems to indicate that 50% of the cell-associated radioactivity is bound loosely to the extracellular domain. Nevertheless, it was observed that, in the absence of radioactivity in the medium, 50% of the radioactivity still remains trapped in the cells.

To test the potential of [^{18}F]-FEAnGA as a PET tracer probe for detecting β-GUS expression in vivo, a preliminary PET study was performed in two mice bearing CT26 and CT26mβGUS tumors. Mice were injected with either [^{18}F]-FEAnGA or [^{18}F]-FEA, and a microPET scan was acquired for 60 min followed by a 15 min microCT scan.

When injected with [^{18}F]-FEAnGA, the CT26mβGUS tumor had more retention of radioactivity than the control tumor (CT26). The tracer uptake ratio between the CT26mβGUS tumor and the control CT26 tumor was 2 at 1 h post injection. This enhanced tumor uptake was ascribed to the selective production of [^{18}F]-FEA due to the cleavage of [^{18}F]-FEAnGA by β-GUS that is expressed extracellularly in the CT26mβGUS tumor only. The uncleaved [^{18}F]-FEAnGA was rapidly excreted out of the body through the kidneys leading to a very clear image with a good tumor-to-background ratio. On the other hand, the animal injected with [^{18}F]-FEA did not show specific accumulation in the CT26mβGUS tumor (Figure 6). It is possible to observe an absence of uptake in the center of the CT26mβGUS tumor due to the advanced necrosis of the tumor.

These preliminary imaging results suggest that extracellular β-GUS efficiently cleaves the tracer, resulting in the formation of [^{18}F]-FEA, which is retained in the tumor. The increased retention of radioactivity in the tumor that expresses β-glucuronidase extracellularly can be visualized in the image; additional animal experiments are in progress to further evaluate the properties of [^{18}F]-FEAnGA in vivo.

CONCLUSION

[^{18}F]-FEAnGA was efficiently labeled with [^{18}F]-fluoride in good yield. [$^{18/19}$F]-FEAnGA showed high in vitro stability in PBS and rat plasma. Kinetic studies indicate that [$^{18/19}$F]-FEAnGA is a good substrate for *E. coli* β-GUS and bovine liver β-GUS. Cleavage of the tracer by β-GUS caused an increase in cell-associated radioactivity in rodent tumor cells. Initial animal studies showed that [^{18}F]-FEAnGA is specially retained in CT26mβGUS tumors with high tumor uptake and good tumor-to-background ratio. Therefore, [^{18}F]-FEAnGA has proven to be a promising PET tracer for imaging of extracellular β-glucuronidase activity.

ACKNOWLEDGMENT

We gratefully thank Annie van Dam and Margot Jeronimus-Stratingh for performing all LRMS analysis, Katica Stojanov for her help in the C6 glioma cell studies, Dr. Steve Roffler for providing the CT26mβGUS cells, and Jurgen Sijbesma for the help in the in vivo study.

Supporting Information Available: ^{1}H NMR, ^{19}F NMR spectra, and the raw LRMS of compounds **2**, **3**, and **4**. Radio-TLC of the medium of C6 glioma cells and CT26/CT26mβGUS. This material is available free of charge via the Internet at http://pubs.acs.org.

LITERATURE CITED

(1) de Graaf, M., Boven, E., Scheeren, H. W., Haisma, H. J., and Pinedo, H. M. (2002) Beta-glucuronidase-mediated drug release. *Curr. Pharm. Des. 8*, 1391–1403.

(2) George, J. (2008) Elevated serum beta-glucuronidase reflects hepatic lysosomal fragility following toxic liver injury in rats. *Biochem. Cell Biol. 86*, 235–243.

(3) Boyer, M. J., and Tannock, I. F. (1993) Lysosomes, lysosomal enzymes, and cancer. *Adv. Cancer Res. 60*, 269–291.

(4) Chen, X., Wu, B., and Wang, P. G. (2003) Glucuronides in anti-cancer therapy. *Curr. Med. Chem. Anticancer Agents 3*, 139–150.

(5) de Groot, F. M., Damen, E. W., and Scheeren, H. W. (2001) Anticancer prodrugs for application in monotherapy: targeting hypoxia, tumor-associated enzymes, and receptors. *Curr. Med. Chem. 8*, 1093–1122.

(6) Denny, W. A. (2003) Prodrugs for gene-directed enzyme-prodrug therapy (suicide gene therapy). *J. Biomed. Biotechnol.* 48–70.

(7) Papot, S., Tranoy, I., Tillequin, F., Florent, J. C., and Gesson, J. P. (2002) Design of selectively activated anticancer prodrugs: elimination and cyclization strategies. *Curr. Med. Chem. Anti-cancer Agents 2*, 155–185.

(8) Rivault, F., Tranoy-Opalinski, I., and Gesson, J. P. (2004) A new linker for glucuronylated anticancer prodrugs. *Bioorg. Med. Chem. 12*, 675–682.

(9) Sperker, B., Murdter, T. E., Schick, M., Eckhardt, K., Bosslet, K., and Kroemer, H. K. (1997) Interindividual variability in expression and activity of human beta-glucuronidase in liver and kidney: consequences for drug metabolism. *J. Pharmacol. Exp. Ther. 281*, 914–920.

(10) Sperker, B., Werner, U., Murdter, T. E., Tekkaya, C., Fritz, P., Wacke, R., Adam, U., Gerken, M., Drewelow, B., and Kroemer, H. K. (2000) Expression and function of beta-glucuronidase in pancreatic cancer: potential role in drug targeting. *Naunyn Schmiedebergs Arch. Pharmacol. 362*, 110–115.

(11) Chen, K. C., Cheng, T. L., Leu, Y. L., Prijovich, Z. M., Chuang, C. H., Chen, B. M., and Roffler, S. R. (2007) Membrane-localized activation of glucuronide prodrugs by beta-glucuronidase enzymes. *Cancer Gene Ther. 14*, 187–200.

(12) Ho, N. H., Weissleder, R., and Tung, C. H. (2007) A self-immolative reporter for beta-galactosidase sensing. *ChemBioChem 8*, 560–566.

(13) Su, Y. C., Chuang, K. H., Wang, Y. M., Cheng, C. M., Lin, S. R., Wang, J. Y., Hwang, J. J., Chen, B. M., Chen, K. C., Roffler, S., and Cheng, T. L. (2007) Gene expression imaging by enzymatic catalysis of a fluorescent probe via membrane-anchored beta-glucuronidase. *Gene Ther. 14*, 565–574.

(14) Biber, F. Z., Unak, P., Ertay, T., Medine, E. I., Zihnioglu, F., Tasci, C., and Durak, H. (2006) Synthesis of an estradiol glucuronide derivative and investigation of its radiopharmaceutical potential. *Appl. Radiat. Isot. 64*, 778–788.

(15) Celen, S., Deroose, C., de Groot, T., Chitneni, S. K., Gijsbers, R., Debyser, Z., Mortelmans, L., Verbruggen, A., and Bormans, G. (2008) Synthesis and evaluation of F-18- and C-11-labeled phenyl-galactopyranosides as potential probes for in vivo visualization of LacZ gene expression using positron emission tomography. *Bioconjugate Chem. 19*, 441–449.

(16) Ertay, T., Unak, P., Biber, F. Z., Tasci, C., Zihnioglu, F., and Durak, H. (2007) Scintigraphic imaging with a peptide glucuronide in rabbits: Tc-99m-exorphin C glucuronide. *Appl. Radiat. Isot. 65*, 170–175.

(17) Kumar, P., Wiebe, L. I., Mannan, R. H., Zhang, Z., Xia, H. Y., and Mcewan, A. J. (2002) [Tc-99m]Technetium labelled PnAo-azomycin glucuronides: a novel class of imaging markers of tissue hypoxia. *Appl. Radiat. Isot. 57*, 719–728.

(18) Brady, F., Luthra, S. K., Brown, G. D., Osman, S., Aboagye, E., Saleem, A., and Price, P. M. (2001) Radiolabelled tracers and anticancer drugs for assessment of therapeutic efficacy using PET. *Curr. Pharm. Des. 7*, 1863–1892.

(19) Rukhman, I., and Gutman, A. L. (2000) Synthesis of morphine 6-alpha-D-glucuronide. *Tetrahedron Lett. 41*, 6889–6892.

(20) Antunes, I. F., Haisma, H. J., and de Vries, E. F. (2008) Tumor-specific activation of prodrugs: is there a role for nuclear medicine? *Nucl. Med. Commun. 29*, 845–846.

(21) Duimstra, J. A., Femia, F. J., and Meade, T. J. (2005) A gadolinium chelate for detection of beta-glucuronidase: A self-immolative approach. *J. Am. Chem. Soc. 127*, 12847–12855.

(22) Tewson, T. J. (1997) Synthesis of [F-18]fluoroetanidazole: A potential new tracer for imaging hypoxia. *Nucl. Med. Biol. 24*, 755–760.

(23) Combaud, D., Thomas, M., Papot, S., and Gesson, J. P. (2005) Synthesis and evaluation of p-nitrophenyl beta-D-glucopyranosiduronic analogues as new triggers for beta-glucuronidase mediated prodrug monotherapy. *Lett. Drug Des. Discovery 2*, 631–637.

(24) Tomasic, J., and Keglevic, D. (1973) Kinetics of hydrolysis of synthetic glucuronic esters and glucuronic ethers by bovine liver and Escherichia-coli beta-glucuronidase. *Biochem. J. 133*, 789–795.

(25) Chittaboina, S., Hodges, B., and Wang, Q. (2006) A facile route for the regioselective deacetylation of peracetylated carbohydrates at anomeric position. *Lett. Org. Chem. 3*, 35–38.

(26) Stachulski, A. V., and Jenkins, G. N. (1998) The synthesis of O-glucuronides. *Nat. Prod. Rep. 15*, 173–186.

(27) Houba, P. H., Leenders, R. G., Boven, E., Scheeren, J. W., Pinedo, H. M., and Haisma, H. J. (1996) Characterization of novel anthracycline prodrugs activated by human beta-glucuronidase for use in antibody-directed enzyme prodrug therapy. *Biochem. Pharmacol. 52*, 455–463.

(28) Huwyler, J., Drewe, J., Klusemann, C., and Fricker, G. (1996) Evidence for P-glycoprotein-modulated penetration of morphine-6-glucuronide into brain capillary endothelium. *Br. J. Pharmacol. 118*, 1879–1885.

(29) Huwyler, J., Drewe, J., Gutmann, H., Thole, M., and Fricker, G. (1998) Modulation of morphine-6-glucuronide penetration into the brain by P-glycoprotein. *Int. J. Clin. Pharmacol. Ther. 36*, 69–70.

(30) Leu, Y. L., Chen, C. S., Wu, Y. J., and Chern, J. W. (2008) Benzyl ether-linked glucuronide derivative of 10-hydroxycamptothecin designed for selective camptothecin-based anticancer therapy. *J. Med. Chem. 51*, 1740–1746.

(31) Bosslet, K., Czech, J., and Hoffmann, D. (1994) Tumor-selective prodrug activation by fusion protein-mediated catalysis. *Cancer Res. 54*, 2151–2159.

(32) Wei, G. P., Loktionova, N. A., Pegg, A. E., and Moschel, R. C. (2005) beta-glucuronidase-cleavable prodrugs of O-6-benzylguanine and O-6-benzyl-2′-deoxyguanosine. *J. Med. Chem. 48*, 256–261.

(33) Bakina, E., Wu, Z., Rosenblum, M., and Farquhar, D. (1997) Intensely cytotoxic anthracycline prodrugs: glucuronides. *J. Med. Chem. 40*, 4013–4018.

BC9004602

Conjugation of Fluorescent Proteins with DNA Oligonucleotides

Vidmantas Lapiene, Florian Kukolka,* Kathrin Kiko, Andreas Arndt, and Christof M. Niemeyer*

Technische Universität Dortmund, Fakultät Chemie, Biologisch-Chemische Mikrostrukturtechnik, Otto-Hahn Str. 6, D-44227 Dortmund, Germany. Received October 28, 2009; Revised Manuscript Received March 1, 2010

This work describes the synthesis of covalent ssDNA conjugates of six fluorescent proteins, ECFP, EGFP, E^2GFP, mDsRed, Dronpa, and mCherry, which were cloned with an accessible C-terminal cystein residue to enable site-selective coupling using a heterobispecific cross-linker. The resulting conjugates revealed similar fluorescence emission intensity to the unconjugated proteins, and the functionality of the tethered oligonucleotide was proven by specific Watson−Crick base pairing to cDNA-modified gold nanoparticles. Fluorescence spectroscopy analysis indicated that the fluorescence of the FP is quenched by the gold particle, and the extent of quenching varied with the intrinsic spectroscopic properties of FP as well as with the configuration of surface attachment. Since this study demonstrates that biological fluorophores can be selectively incorporated into and optically coupled with nanoparticle-based devices, applications in DNA-based nanofabrication can be foreseen.

INTRODUCTION

The investigation of the fundamental principles of photosynthesis is of great current interest. In this context, the synthesis of artificial light harvesting devices from multiple chromophoric units and the study of energy transfer processes occurring in these systems aims to mimic natural photosynthesis and to develop materials and devices with complex spectroscopic properties. Recent approaches to assemble light harvesting complexes included the use of small molecule chromophors, such as porphyrin derivatives (*1*), polypyridine complexes of d^6 metal ions (*2*), perylene-based polyphenyl dendrimers (*3, 4*), or supramolecular assemblies of functional dyes (*5*). On the other hand, significant research is currently devoted to the exploitation of biomolecules for the assembly of functional devices. In this young field of science, the bioconjugation of short DNA oligonucleotides to various molecular compounds and materials has already been established as a means to fabricate nanoscaled functional devices (*6*). The approach is based on the extraordinary specific molecular recognition properties of short ssDNA oligonucleotides, which can be harnessed as structure-directing agents for the rational assembly of proteins, nanoparticles, and other components (*7*−*9*).

In view of synthetic energy transfer systems, the naturally occurring family of fluorescent proteins (FPs) is currently attracting increasing interest (*6*). Starting with the initial discovery of naturally occurring *Aequorea victoria* green fluorescent protein (GFP) (*10*), nowadays a large number of structural variants of GFP are available and they are routinely used as genetically encoded markers for cell biology and the study of biomolecular interactions by means of Förster resonance energy transfer (FRET) (*11*−*14*). Moreover, FPs are currently being exploited in materials research as chromophors for the fabrication of nanoscaled optically addressable devices. For instance, FPs have been used to decorate semiconductor nanoparticles, often termed "quantum dots" (QD), to study FRET mechanisms occurring in such light-addressable nanodevices (*15*−*19*). Also, it has recently been demonstrated that the color of natural fluorescent proteins can be controlled by photonic crystals (*20*).

In these examples, the decoration of the inorganic materials with FPs was achieved by adsorption and electrostatic interactions (*21*), thus allowing only limited control of the assembly process. To extend controlability of supramolecular FP assembly and enable rational design of FP-based FRET systems, we have previously established the synthesis of a covalent ssDNA conjugate, using the enhanced yellow fluorescent protein (EYFP) (*22*). The use of this conjugate indeed enabled the DNA-based assembly of FRET systems, in which the spatial proximity of the chromophors can be controlled by the helicity of the dsDNA carrier backbone (*23, 24*). Moreover, the ssDNA−EYFP conjugate was used to explore FRET processes in three-chromophore QD assemblages (*17*) and to investigate particle−protein interactions, taking advantage of EYFP fluorescence emission quenching by gold nanoparticles (*25*). Very recently, a ssDNA conjugate of the photoswitchable FP Dronpa, one of the conjugates developed in the course of the work reported here, was used in a single-molecule FRET study (*26*).

In this full paper, we describe the synthesis of six novel DNA oligonucleotide−FP conjugates, based on mutant variants of the native FPs (Figure 1). In particular, the fluorescent proteins ECFP, a cyan mutant of jellyfish *Aequorea victoria* GFP (*27*), EGFP (*28*), E^2GFP (*29*), mDsRed, a monomeric variant of tetrameric DsRed (*30, 31*), available from Clontech, photoswitchable Dronpa (*32*), and mCherry (*33*) were cloned with an N-terminal hexahistidine sequence and a C-terminal cystein residue. The engineered cystein residue was positioned at the C-terminal region of the FPs because known crystal structures suggest that this region is easily accessible for chemical conjugation. Indeed, all six proteins could be derivatized with maleimide-activated DNA oligomers to yield the desired ssDNA−FP conjugates. These hybrid molecules were characterized and then used for the investigation of fluorescence emission quenching as a result of their specific hybridization with ssDNA-modified gold nanoparticles (DNA-AuNP), bearing the complementary oligonucleotides. Determination of hybridization kinetics and quenching efficiency revealed slight but distinct differences between the six DNA−FP conjugates, as a consequence of the optical and steric properties of the individual FPs.

EXPERIMENTAL PROCEDURES

Molecular cloning and overexpression of the recombinant FPs was carried out similar to previously described methods (*22, 34*).

* Telefax: Int. + 49 (0)231/755 7082, E-mail: christof.niemeyer@tu-dortmund.de.

10.1021/bc900471q © 2010 American Chemical Society
Published on Web 04/30/2010

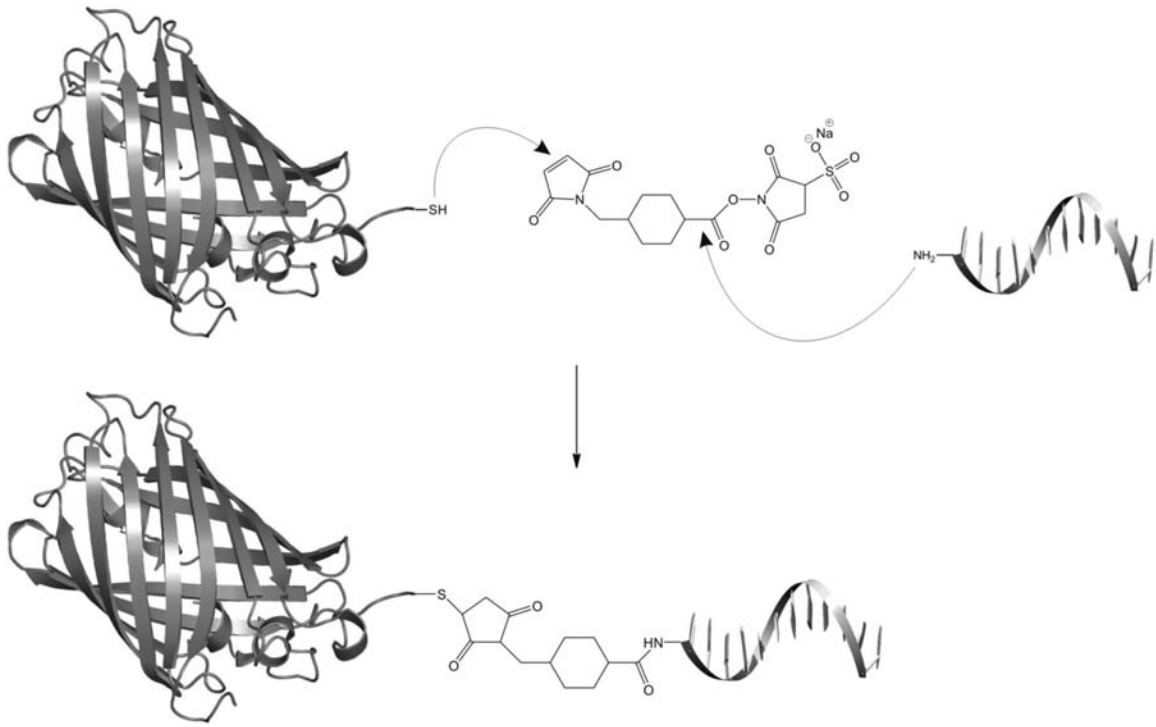


Figure 1. Schematic representation of the cross-linking of alkylamino-modified DNA with mutant ^{Cys}FP by initial maleimide activation of the DNA cA24 and subsequent reaction with the genetically engineered cystein residue of the FP.

Table 1. Spectroscopic Properties and Yields Obtained from Overexpression and Covalent ssDNA-Conjugation of the Various Fluorescent Proteins Described in This Study

entry	protein	λ_{Exc} [nm]	λ_{EM} [nm]	vector	expression yield [μg/mL]	conjugation yield [%][a]
1	ECFP-Cys	434	476	pQE30	76	33
2	EGFP-Cys	488	508	pQE30	156	22
3	Dronpa-Cys	503	518	pQE30	258	28
4	E^2GFP-Cys	514	528	pQE30	71	36
5	mDsRed-Cys	558	583	pQE30	215	18
6	mCherry-Cys	587	615	pEXP17-N-mCherry-Cys	105	15

[a] Calculated with respect to the amount of ssDNA oligonucleotide.

Synthesis of ssDNA−FP conjugates was achieved from 5′-alkylamino-modified DNA using the heterobispecific cross-linker sulfosuccinimidyl-4-(*N*-maleimidomethyl) cyclohexane-1-carboxylate (sSMCC) (*22*). Preparation of 23 nm diameter ssDNA-modified gold nanoparticles and hybridization with ssDNA−FP conjugates was carried out as described before (*25*). Full details on cloning and expression of FPs, experimental protocols for conjugate synthesis, and binding studies with DNA-AuNP are available in the Supporting Information.

RESULTS AND DISCUSSION

To facilitate site-selective conjugation with DNA oligonucleotides, we followed the bioconjugation approach previously explored for the coupling of the fluorescent protein EYFP with alkylamino-modified DNA (*22*). This method is based on the cloning and heterologous expression of a mutant FP, containing an N-terminal hexahistidine sequence and a C-terminal cystein residue. While the His_6-tag allows for convenient purification of the recombinant FP, the accessible C-terminal Cys residue enabled conjugation with thiol-reactive DNA oligonucleotides. Genetic engineering of the cystein residue into the FP genes was achieved by PCR techniques. Detailed information on the cloning of the expression vectors is given in the Supporting Information. Transformation of *E. coli* BL21 and overexpression of the recombinant FPs was followed by Ni-NTA affinity chromatography. Expression yields obtained ranged 70−260 μg/mL cell culture (Table 1). Gel electrophoretic analysis of the recombinant FPs revealed that the proteins were sufficiently pure (>85%) to enable chemical coupling with DNA oligomers.

Site-selective chemical coupling of the mutant FPs with DNA oligomers was achieved by using the heterobispecific cross-linker sulfosuccinimidyl-4-(*N*-maleimidomethyl) cyclohexane-1-carboxylate (sSMCC), which contains a thiol-reactive maleimide functionality in addition to an amino-reactive NHS group (Figure 1). To this end, commercially available alkylamino-modified oligonucleotide cA24 was reacted with an excess of sSMCC to install a maleimide group at the 5′-end of the oligomer. Subsequent to purification by gel filtration chromatography, the oligomer was allowed to react with the recombinant FP, and crude reaction products were purified by ultrafiltration and anion-exchange chromatography (Figure S1, in the Supporting Information). Isolated yields, determined by UV/vis spectroscopy after alkaline denaturation (*35*−*37*), ranging 15−36% (Table 1), thus indicating that the synthetic protocol allows ready production of the desired DNA−FP conjugates. Gel electrophoretic analysis of the conjugates (Figure 2) showed that the products essentially contained a single molecular species, with only slight impurities of the unconjugated protein. Denaturing SDS-gel electrophoresis indicated the expected increase in molecular weight of ∼8 kDa due to the attachement of one oligonucleotide per FP molecule (Figure 2A). This result was also obtained for Dronpa, which contains an additional Cys residue at position 113. We assume that the exclusive generation of the monoconjugated cA24-Dronpa is due to our optimized

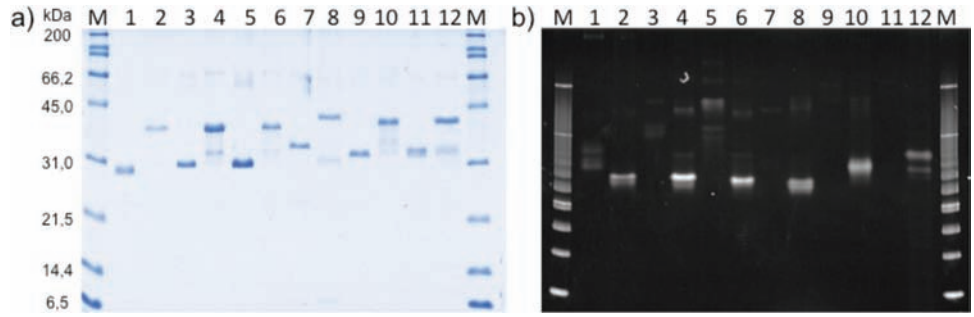


Figure 2. Gel electrophoretic analysis of recombinant FPs and their respective ssDNA conjugates. (A) 14% denaturing SDS polyacrylamide gel, stained with Coomassie: lane M, SDS Broadrange Marker (Bio-Rad); lane 1, EGFP; 2, cA24-EGFP; 3, E^2GFP; 4, cA24-E^2GFP; 5, ECFP; 6, cA24-ECFP; 7, mDsRed; 8, cA24-mDsRed; 9, Dronpa; 10, cA24-Dronpa; 11, mCherry; 12, cA24-mCherry. (B) 14% nondenaturing polyacrylamide gel after DNA staining with SybrGold: lane M, O'RangeRuler 50bp DNA ladder (Fermentas); lanes 1−12, same samples as in (A). Note that, although SybrGold dye is usually selective for nucleic acid staining, some FPs are visible as weak bands (e.g., lanes 1, 5, 7). This phenomenon has previously been observed (*22*), and it results from the native FP fluorescence at the filter settings used for SybrGold imaging (λ_{Exc} = 365 nm, λ_{Em} = 520 nm, see also Figure S7 in the Supporting Information).

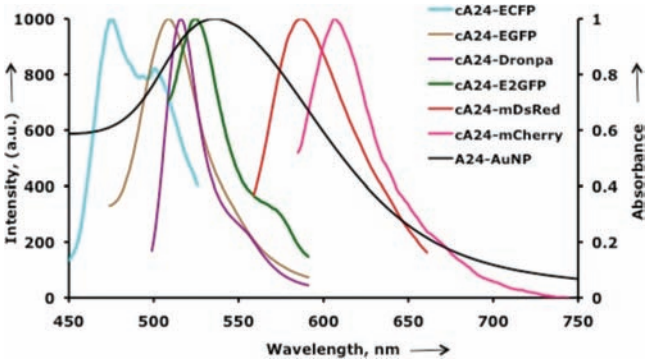


Figure 3. Fluorescence emission spectra of the DNA−FP conjugates cA24-ECFP (cyan), cA24-EGFP (brown), cA24-Dronpa (purple), cA24-E^2GFP green), cA24-mDsRed (red), and cA24-mCherry (pink). For comparison, the absorbance spectrum of AuNP is shown as the black curve.

reaction conditions (i.e., excess of protein and short reaction time) in addition to careful purification by gradient anion-exchange chromatography. Analysis under nondenaturing conditions (Figure 2B) showed that the electrophoretic mobility of the DNA−FP conjugates was increased, as compared to the individual native FPs, due to the appended negatively charged oligonucleotide.

The DNA−FP conjugates were analyzed by fluorescence spectroscopy (Figure 3), their fluorescence emission and UV/vis absorbance spectra were compared to those of the native FPs (Figures S2, S3, in the Supporting Information), and quantum yields were determined (Table S3, in the Supporting Information). The spectroscopic properties of all DNA−FP conjugates were basically identical to those of the unconjugated FPs, thus confirming that (i) all FPs under investigation here were fully maturated and (ii) conjugation with ssDNA did not significantly affected the chromophore of the native FP.

With the desired DNA−FP conjugates in hand, we investigated their nucleic acid hybridization with gold nanoparticles (AuNPs), containing the complementary ssDNA oligomer A24. It should be noted that the generation of protein-functionalized gold nanoparticles is of great current interest, due to their applications in biosensing and diagnostics (*8*, *9*). While protein−AuNPs are long known as versatile probes in immunohistochemistry and related techniques (*7*), mixed hybrid nanoparticles containing both nucleic acid fragments and proteins have only recently been established (*25*, *38*−*42*), because they offer additional functionality due to the presence of both classes of biomolecular recognition elements. We had previously demonstrated that such hybrid particles can be readily prepared by specific DNA hybridization using DNA−AuNPs and appropriate ssDNA−protein conjugates bearing the complementary sequence (*25*, *38*, *41*, *43*), and here we applied this method to investigate whether the various ssDNA−FP conjugates are functional with respect to both the FP fluorescence and their specific Watson−Crick hybridization capability.

Similar to that reported for small-molecule organic fluorescent dyes (*44*−*50*), the FP fluorescence should be quenched upon binding to the AuNP, and it was interesting to see whether and how quenching would be influenced by the optical properties of the various FPs under investigation here. To this end, binding of the various covalent DNA−FP conjugates was investigated, using three different kinds of DNA-coated 23 nm AuNPs (Figure 4a). 5′A24-AuNP contained the complementary oligomer A24 bound via its 5′-end, while 3′A24-AuNP contained the A24 sequence attached via its 3′-end. Due to the directionality of the DNA double helical spacer, the distance between the gold surface and the FP is greater in the case of 5′A24-AuNP than for 3′A24-AuNP. Moreover, the noncomplementary oligonucleotide AuNP-dT124b was used as control. Gel electrophoretic analysis was used to initially confirm specificity of binding (Figure S4, in the Supporting Information). In the case of DNA−AuNPs bearing complementary oligomers, a decrease in electrophoretic mobility of the nanoparticle bands indicated formation of the respective FP−AuNPs, while incubation with dT124b-AuNP only revealed very small shifts of the particle bands (lanes 11−15, in Supporting Information Figure S4; see also Figure S6). This confirmed that the binding of all ssDNA−FP conjugates to the DNA−AuNPs primarily occurred due to specific Watson−Crick base-pairing of the oligonucleotides.

We then investigated whether and to what extent the binding of the various ssDNA−FP conjugates to the DNA−AuNP leads to the quenching of FP fluorescence. In an initial set of experiments, solutions of the DNA−FP conjugate (1.2 pmol in TETBS buffer, pH 7.3, containing 150 mM NaCl) were mixed with solutions of the various DNA−AuNP (36 fmol in TETBS buffer containing 150 mM NaCl, corresponding to 32 mol equiv of DNA−FP to DNA−AuNP) and incubated for 6 h at room temperature. While the entire data is represented in Supporting Information Figure S4, it is examplified here for cA24-EGFP and cA24-mCherry (Figure 4b) that end-point determination of the fluorescence showed marked differences between the samples. The fluorescence of the pure ssDNA−FP conjugates (blue curves) is significantly decreased upon addition of noncomplementary dT124b-AuNP, and this effect occurrs due to strong absorption and scattering caused by the AuNPs. The extent of decrease differed clearly for the various FPs under investigation, which is a logical consequence of the different wavelenghts used for FP excitation. The absorption spectrum of AuNP (Figure 3) indicates that the particle's broad plasmon

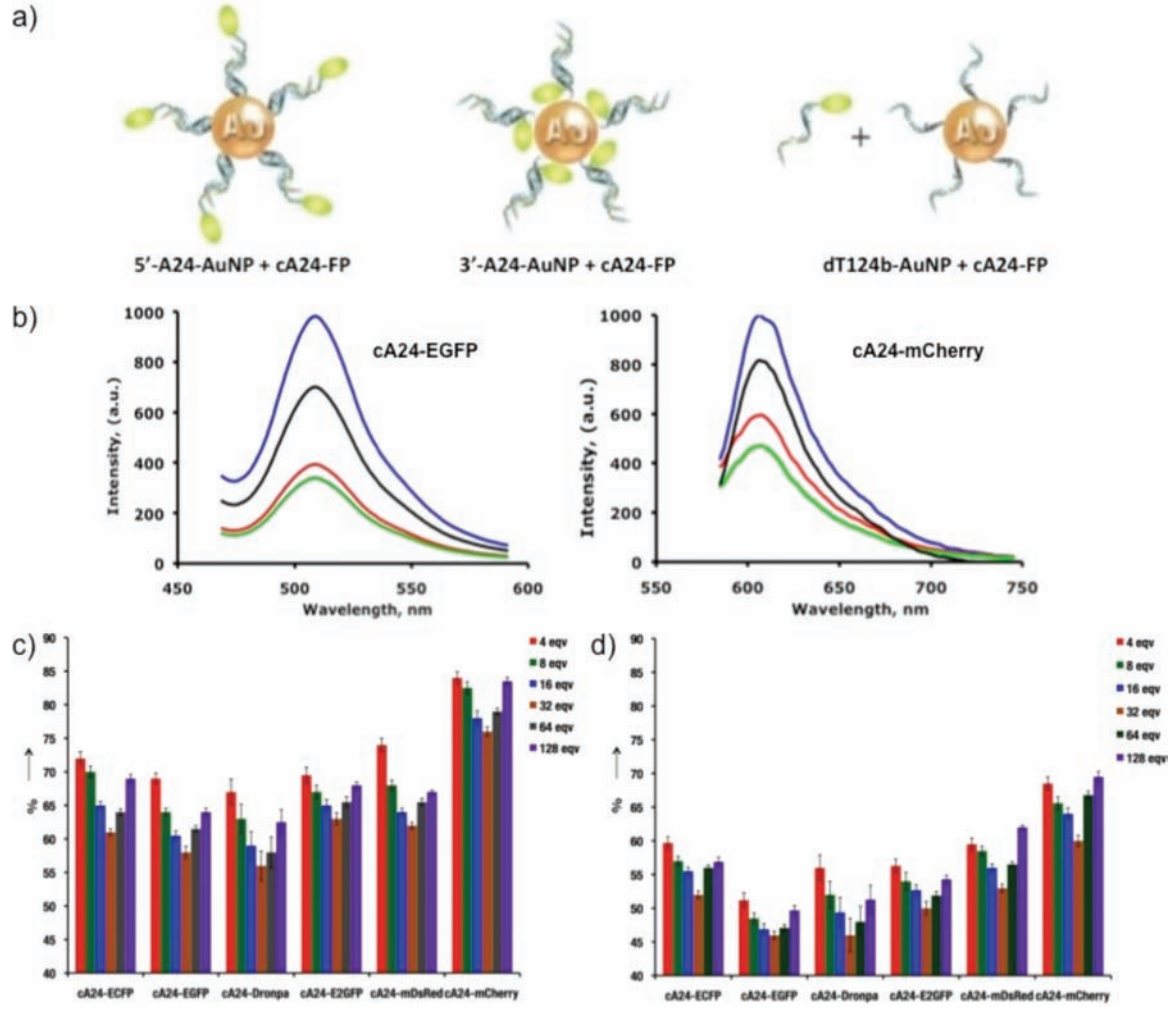


Figure 4. AuNP-induced quenching of FP fluoresence. (A) Schematic representations of DNA-directed binding of ssDNA−FP conjugates to DNA−AuNPs and the DNA−AuNPs used for immobilization of cA24−FP conjugates to DNA−AuNPs and the DNA−AuNPs used for immobilization of cA24−FP conjugates. (B) End point determination of the fluorescence measured for cA24-EGFP and cA24-mCherry before (blue curves) and after incubation with 5′A24-AuNP (red), 3′A24-AuNP (green), or dT124b-AuNP (black). (C,D) Variation of coupling ratio FP/AuNP; fluorescence values of the ssDNA−FP conjugates after binding to 5′A24-AuNP (C) or 3′A24-AuNP (D) were normalized with respect to the fluorescence of analogous samples after incubation with noncomplementary dT124b-AuNP.

absorption has its maximum at about 540 nm. This wavelength almost coincides with the excitation/emission wavelenghts of mDsRed (558/583 nm). In contrast, plasmon absorption is significantly less effective at the excitation/emission wavelenghts of ECFP (434/476 nm), EGFP (488/508 nm), or mCherry (587/615 nm). Consequently, the amount of scattering induced by addition of dT124b-AuNP, and thus immediate decrease in FP fluorescence, is much higher for mDsRed than for ECFP, EGFP, or mCherry.

Normalized values of ssDNA−FP conjugate's fluorescence, measured in the presence of dT124b-AuNP, 5′A24-AuNP, or 3′A24-AuNP, are summarized in Table 2. To account for the aforementioned wavelength-dependent differences in scattering, fluorescence of the ssDNA−FP conjugate in the presence 5′A24-AuNP or 3′A24-AuNP was normalized with respect to the value measured in the presence of noncomplementary dT124b-AuNP, set as 100%. It is clearly evident from the data of Table 2 as well as from the original data (Figure 4b and Supporting Information Figure S5) that addition of the complementary AuNPs led to a significantly higher quenching of the fluorescence of the FP, and this effect was markedly different for particles 5′A24-AuNP and 3′A24-AuNP (red and green curves, in Figure 4b). This result is in aggreement with the expectation that Watson−Crick hybridization with 5′A24-AuNP should lead to the formation of a 24 base-pair dsDNA spacer of approximately 8.5 nm in length between the protein and the gold surface, while the hybridization with 3′A24-AuNP should localize the protein in closer proximity to the particle's surface.

Table 2. Numerical Values of ssDNA−FP Conjugate Fluorescence, Measured in the Presence of Gold Nanoparticles[a]

entry	conjugate	dT124b-AuNP[b]	5′A24-AuNP[c]	3′A24-AuNP[c]
1	cA24-ECFP	70	61	52
2	cA24-EGFP	72	58	46
3	cA24-Dronpa	61	56	45
4	cA24-E^{2}GFP	55	63	50
5	cA24-mDsRed	42	62	53
6	cA24-mCherry	82	76	60

[a] End point determination after 6 h of incubation with 32 mol equiv of AuNP. [b] Normalized values [%] with respect to the fluorescence of pure cA24-FP in the absence of AuNP (100%). [c] Normalized values [%] with respect to the fluorescence of cA24-FP in the presence of noncomplementary dT124b-AuNP set as 100%.

The difference in quenching efficiency observed for the two different configurations, however, is relatively small. This suggests that binding and quenching aspects are involved. The fundamental mechanisms of the quenching of organic fluorophores by metal nanoparticles are still under investigation (*44*−*50*), and one important factor concerns the knowledge of real distances between the chromophore and the metal surface. The AuNP-bound DNA should be able to adopt a number of different conformations, such as being fully stretched and

pointing perpendicular from the surface, adopting a random coil shape, or possibly being tilted and interacting with the AuNP surface (*51*). Hence, the aforementioned nominal difference in distance of about 8.5 nm is most likely affected by the presence of various conformational states. Moreover, slight changes in protein loading should also induce different distances and/or different dynamics and, thus, might affect the quenching efficiency.

To further analyze the system, we also studied the influence of surface coverage of AuNP with ssDNA−FP conjugate on the quenching efficiency. To this end, particles 5′A24-AuNP (Figure 4c) and 3′A24-AuNP (Figure 4d) were incubated with various molar equivalents of ssDNA−FP conjugate, and fluorescence emission was determined after 15 h. The fluorescence emission values measured were normalized to that of similar samples incubated with noncomplementary dT124b-AuNP. It is evident that the nature of FP did not markedly influence the stoichiometry of binding. In all cases, the fluorescence decreased for the binding of up to about 32 mol equiv of ssDNA−FP conjugate, and a further increase led to an increase in fluorescence, due to increasing amounts of free conjugate in the solution. It should be noted that the about 32 mol equiv of ssDNA−FP conjugate, which hybridizes to the 25 nm AuNP, correlates with an approximately 18% hybridization efficiency of the in total about 175 oligonucleotide molecules bound at the AuNP (see Supporting Information). This result is in good agreement with earlier studies concerning the hybridization efficiency of DNA−AuNPs (*52*,*53*).

As expected, the extent of quenching differed significantly with the configuration of binding (Figure 4c vs d), and interestingly, the quenching efficiency was different for the various FPs studied (see also Table 2). In particular, strongest quenching was observed for binding of EGFP- and Dronpa-conjugate to either 5′A24-AuNP or 3′A24-AuNP, and this maximum was slightly more pronounced in the case of 3′A24-AuNP. The relative quenching efficiency observed for the six ssDNA−FP conjugates is in good aggreement with what one would expect from the overlap of FP fluorescence emission and AuNP plasmon absorption (Figure 3).

It was also analyzed whether the two different configurations, realized in the binding to either 5′A24-AuNP or 3′A24-AuNP, affect the kinetics of protein immobilization (Supporting Information Figure S5). Time-dependent fluorescence measurements showed that the ssDNA−FP conjugates rapidly hybridize with 5′A24-AuNP, and the reaction was completed within less than 4 h. The curves also suggest that the binding of ssDNA-FP to 3′A24-AuNP was slightly slower than binding to 5′A24-AuNP. This observation is in agreement with the proposed configuration, since binding to 3′A24-AuNP requires the bulky FP to penetrate, at least partially, the dense layer of DNA oligomers attached to the particle's surface.

In conclusion, we have shown that fluorescent proteins can be effectively conjugated with DNA oligonucleotides, using a combination of genetic engineering and heterobispecific cross-linking chemistry. The resulting ssDNA−FP conjugates revealed similar spectroscopic properties than the unconjugated FPs. Moreover, the functionality of the tethered oligonucleotide was proven by specific Watson−Crick base pairing to cDNA-modified gold nanoparticles. Fluorescence spectroscopy analysis indicated that the FP fluorescence is quenched by the gold particle and the extent of quenching varied with the intrinsic spectroscopic properties of FP as well as with the configuration of surface attachement. Thus, this study demonstrates that these biological fluorophores can be incorporated into and optically coupled with nanoparticle-based devices using DNA-based assembly schemes. Given the enormous power of structural DNA nanotechnology and nanofabrication, we therefore anticipate that further elaboration on covalent DNA−FP conjugates might open up ways toward nanostructured materials with programmable functionalities for a broad range of applications in nanobiotechnology.

ACKNOWLEDGMENT

This work was supported in part by Deutsche Forschungsgemeinschaft (DFG, grants Ni-399/6-1/6-2) Max-Planck Research School in Chemical Biology (IMPRS-CB), Dortmund, and the project SMD in the course of FP7-NMP-2008-SMALL-2, founded by European Comission. We thank Martina Reibner for preparation of DNA-conjugated gold nanoparticles. We are also grateful to the reviewer for very important comments on the manuscript.

Supporting Information Available: Full details on experimental protocols for molecular cloning of FPs, conjugate and nanoparticle synthesis, hybridization assays, characterization of ssDNA−FP conjugates, and spectroscopic analysis of their binding to DNA−AuNP. This material is available free of charge via the Internet at http://pubs.acs.org.

LITERATURE CITED

(1) Nakamura, Y., Aratani, N., and Osuka, A. (2007) Cyclic porphyrin arrays as artificial photosynthetic antenna: synthesis and excitation energy transfer. *Chem. Soc. Rev. 36*, 831–845.
(2) Hammarstrom, L. (2003) Towards artificial photosynthesis: ruthenium-manganese chemistry mimicking photosystem II reactions. *Curr. Opin. Chem. Biol. 7*, 666–673.
(3) Hofkens, J., Cotlet, M., Vosch, T., Tinnefeld, P., Weston, K. D., Ego, C., Grimsdale, A., Mullen, K., Beljonne, D., Bredas, J. L., Jordens, S., Schweitzer, G., Sauer, M., and De Schryver, F. (2003) Revealing competitive Forster-type resonance energy-transfer pathways in single bichromophoric molecules. *Proc. Natl. Acad. Sci. U.S.A. 100*, 13146–13151.
(4) Weil, T., Reuther, E., Beer, C., and Mullen, K. (2004) Synthesis and characterization of dendritic multichromophores based on rylene dyes for vectorial transduction of excitation energy. *Chem.—Eur. J. 10*, 1398–1414.
(5) Chen, Z., Lohr, A., Saha-Moller, C. R., and Wurthner, F. (2009) Self-assembled pi-stacks of functional dyes in solution: structural and thermodynamic features. *Chem. Soc. Rev. 38*, 564–584.
(6) Niemeyer, C. M. (2010) Semisynthetic DNA-protein conjugates for biosensing and nanofabrication. *Angew. Chem. Int. Ed. 49*, 1200–1216.
(7) Niemeyer, C. M. (2001) Nanoparticles, proteins, and nucleic acids: biotechnology meets materials science. *Angew. Chem., Int. Ed. 40*, 4128–4158.
(8) Katz, E., and Willner, I. (2004) Integrated nanoparticle-biomolecule hybrid systems: synthesis, properties, and applications. *Angew. Chem., Int. Ed. 43*, 6042–6108.
(9) Rosi, N. L., and Mirkin, C. A. (2005) Nanostructures in Biodiagnostics. *Chem. Rev. 105*, 1547–1562.
(10) Tsien, R. Y. (1998) The green fluorescent protein. *Annu. Rev. Biochem. 67*, 509–544.
(11) Chudakov, D. M., Lukyanov, S., and Lukyanov, K. A. (2005) Fluorescent proteins as a toolkit for in vivo imaging. *Trends Biotechnol. 23*, 605–613.
(12) Merzlyak, E. M., Goedhart, J., Shcherbo, D., Bulina, M. E., Shcheglov, A. S., Fradkov, A. F., Gaintzeva, A., Lukyanov, K. A., Lukyanov, S., Gadella, T. W., and Chudakov, D. M. (2007) Bright monomeric red fluorescent protein with an extended fluorescence lifetime. *Nat. Methods 4*, 555–557.
(13) Shcherbo, D., Merzlyak, E. M., Chepurnykh, T. V., Fradkov, A. F., Ermakova, G. V., Solovieva, E. A., Lukyanov, K. A., Bogdanova, E. A., Zaraisky, A. G., Lukyanov, S., and Chudakov, D. M. (2007) Bright far-red fluorescent protein for whole-body imaging. *Nat. Methods 4*, 741–746.

(14) Tsien, R. Y. (2009) Constructing and exploiting the fluorescent protein paintbox (Nobel Lecture). *Angew. Chem., Int. Ed. Engl. 48*, 5612–5626.
(15) Geissbuehler, I., Hovius, R., Martinez, K. L., Adrian, M., Thampi, K. R., and Vogel, H. (2005) Lipid-coated nanocrystals as multifunctionalized luminescent scaffolds for supramolecular biological assemblies. *Angew. Chem., Int. Ed. 44*, 1388–1392.
(16) Hering, V. R., Gibson, G., Schumacher, R. I., Faljoni-Alario, A., and Politi, M. J. (2007) Energy transfer between CdSe/ZnS core/shell quantum dots and fluorescent proteins. *Bioconjugate Chem. 18*, 1705–1708.
(17) Lu, H., Schoeps, O., Woggon, U., and Niemeyer, C. M. (2008) A self-assembled donor comprising quantum dots and fluorescent proteins for long-range fluorescence resonance energy transfer. *J. Am. Chem. Soc. 130*, 4815–4827.
(18) Dennis, A. M., and Bao, G. (2008) Quantum dot-fluorescent protein pairs as novel fluorescence resonance energy transfer probes. *Nano Lett. 8*, 1439–1445.
(19) Hering, V. R., Faulin, T. E., Triboni, E. R., Rodriguez, S. D., Bernik, D. L., Schumacher, R. I., Mammana, V. P., Faljoni-Alario, A., Abdalla, D. S., Gibson, G., and Politi, M. J. (2009) Violet ZnSe/ZnS as an alternative to green CdSe/ZnS in nanocrystal-fluorescent protein FRET systems. *Bioconjugate Chem. 20*, 1237–1241.
(20) Blum, C., Mosk, A. P., Nikolaev, I. S., Subramaniam, V., and Vos, W. L. (2008) Color control of natural fluorescent proteins by photonic crystals. *Small 4*, 492–496.
(21) Irrgang, J., Ksienczyk, J., Lapiene, V., and Niemeyer, C. M. (2009) Analysis of non-covalent bioconjugation of colloidal nanoparticles by means of atomic force microscopy and data clustering. *ChemPhysChem 10*, 1483–1491.
(22) Kukolka, F., and Niemeyer, C. M. (2004) Synthesis of fluorescent oligonucleotide- EYFP conjugate: Towards supramolecular construction of semisynthetic biomolecular antennae. *Org. Biomol. Chem. 2*, 2203–2206.
(23) Kukolka, F., Mueller, B. K., Paternoster, S., Arndt, A., Niemeyer, C. M., Braeuchle, C., and Lamb, D. C. (2006) A single molecule FRET analysis of fluorescent DNA-protein conjugates for nanobiotechnology. *Small 2*, 1083–1089.
(24) Kukolka, F., Schoeps, O., Woggon, U., and Niemeyer, C. M. (2007) DNA-directed assembly of supramolecular fluorescent-protein energy-transfer systems. *Bioconjugate Chem. 18*, 621–627.
(25) Hazarika, P., Kukolka, F., and Niemeyer, C. M. (2006) Reversible binding of fluorescent proteins at DNA-gold nanoparticles. *Angew. Chem., Int. Ed. 45*, 6827–6830.
(26) Heiss, G., Lapiene, V., Kukolka, F., Niemeyer, C. M., Braeuchle, C., and Lamb, D. C. (2009) Single-molecule investigations of a photoswitchable nanodevice. *Small 5*, 1169–1175.
(27) Heim, R., and Tsien, R. Y. (1996) Engineering green fluorescent protein for improved brightness, longer wavelengths and fluorescence resonance energy transfer. *Curr. Biol. 6*, 178–182.
(28) Yang, T. T., Cheng, L., and Kain, S. R. (1996) Optimized codon usage and chromophore mutations provide enhanced sensitivity with the green fluorescent protein. *Nucleic Acids Res. 24*, 4592–4593.
(29) Cinelli, R. A. G., Pellegrini, V., Ferrari, A., Faraci, P., Nifosì, R., Tyagi, M., Giacca, M., and Beltram, F. (2001) Green fluorescent protein as optically-controllable elements in bioelectronics. *Appl. Phys. Lett. 79*, 3353–3355.
(30) Matz, M. V., Fradkov, A. F., Labas, Y. A., Savitsky, A. P., Zaraisky, A. G., Markelov, M. L., and Lukyanov, S. A. (1999) Fluorescent proteins from nonbioluminescent Anthozoa species. *Nat. Biotechnol. 17*, 969–973.
(31) Baird, G. S., Zacharias, D. A., and Tsien, R. Y. (2000) Biochemistry, mutagenesis, and oligomerization of DsRed, a red fluorescent protein from coral. *Proc. Natl. Acad. Sci. U.S.A. 97*, 11984–11989.
(32) Ando, R., Mizuno, H., and Miyawaki, A. (2004) Regulated fast nucleocytoplasmic shuttling observed by reversible protein highlighting. *Science 306*, 1370–1373.
(33) Shaner, N. C., Campbell, R. E., Steinbach, P. A., Giepmans, B. N., Palmer, A. E., and Tsien, R. Y. (2004) Improved monomeric red, orange and yellow fluorescent proteins derived from Discosoma sp. red fluorescent protein. *Nat. Biotechnol. 22*, 1567–1572.
(34) Rabe, K. S., Kiko, K., and Niemeyer, C. M. (2008) Characterization of the Peroxidaseacitivtiy of Cyp119, a thermostable P450 from Sulfolobus acidocaldarius. *ChemBioChem 9*, 420–425.
(35) Patterson, G. H., Knobel, S. M., Sharif, W. D., Kain, S. R., and Piston, D. W. (1997) Use of the green fluorescent protein and its mutants in quantitative fluorescence microscopy. *Biophys. J. 73*, 2782–2790.
(36) Kredel, S., Nienhaus, K., Oswald, F., Wolff, M., Ivanchenko, S., Cymer, F., Jeromin, A., Michel, F. J., Spindler, K. D., Heilker, R., Nienhaus, G. U., and Wiedenmann, J. (2008) Optimized and far-red-emitting variants of fluorescent protein eqFP611. *Chem. Biol. 15*, 224–233.
(37) Lelimousin, M., Noirclerc-Savoye, M., Lazareno-Saez, C., Paetzold, B., Le Vot, S., Chazal, R., Macheboeuf, P., Field, M. J., Bourgeois, D., and Royant, A. (2009) Intrinsic dynamics in ECFP and Cerulean control fluorescence quantum yield. *Biochemistry 48*, 10038–10046.
(38) Niemeyer, C. M., and Ceyhan, B. (2001) DNA-directed functionalization of colloidal gold with proteins. *Angew. Chem., Int. Ed. 40*, 3685–3688.
(39) Nam, J. M., Thaxton, C. S., and Mirkin, C. A. (2003) Nanoparticle-based bio-bar codes for the ultrasensitive detection of proteins. *Science 301*, 1884–1886.
(40) Georganopoulou, D. G., Chang, L., Nam, J. M., Thaxton, C. S., Mufson, E. J., Klein, W. L., and Mirkin, C. A. (2005) Nanoparticle-based detection in cerebral spinal fluid of a soluble pathogenic biomarker for Alzheimer's disease. *Proc. Natl. Acad. Sci. U.S.A. 102*, 2273–2276.
(41) Hazarika, P., Ceyhan, B., and Niemeyer, C. M. (2005) Sensitive detection of proteins using difunctional DNA-gold nanoparticles. *Small 1*, 844–848.
(42) Becker, C. F. W., Marsac, Y., Hazarika, P., Moser, J., Goody, R. S., and Niemeyer, C. M. (2007) Functional immobilization of the small GTPase Rab6A on DNA-gold-nanoparticles using a site-specifically attached polyethylene glycol linker and thiol place exchange reaction. *ChemBioChem 8*, 32–36.
(43) Schroeder, H., Adler, M., Gerigk, K., Müller-Chorus, B., Götz, F., and Niemeyer, C. M. (2009) A user configurable microfluidic device for multiplexed immunoassays based on DNA-directed assembly. *Anal. Chem. 81*, 1275–1279.
(44) Dubertret, B., Calame, M., and Libchaber, A. J. (2001) Single-mismatch detection using gold-quenched fluorescent oligonucleotides. *Nat. Biotechnol. 19*, 365–370.
(45) Dulkeith, E., Morteani, A. C., Niedereichholz, T., Klar, T. A., Feldmann, J., Levi, S. A., van Veggel, F. C., Reinhoudt, D. N., Moller, M., and Gittins, D. I. (2002) Fluorescence quenching of dye molecules near gold nanoparticles: radiative and nonradiative effects. *Phys. Rev. Lett. 89*, 203002.
(46) Gueroui, Z., and Libchaber, A. (2004) Single-molecule measurements of gold-quenched quantum dots. *Phys. Rev. Lett. 93*, 166108.
(47) Yun, C. S., Javier, A., Jennings, T., Fisher, M., Hira, S., Peterson, S., Hopkins, B., Reich, N. O., and Strouse, G. F. (2005) Nanometal surface energy transfer in optical rulers, breaking the FRET barrier. *J. Am. Chem. Soc. 127*, 3115–3119.
(48) Dulkeith, E., Ringler, M., Klar, T. A., Feldmann, J., Munoz Javier, A., and Parak, W. J. (2005) Gold nanoparticles quench fluorescence by phase induced radiative rate suppression. *Nano Lett. 5*, 585–589.
(49) Ray, P. C., Fortner, A., Griffin, J., Kim, C. K., Singh, J. P., and Yu, H. (2005) Laser-induced fuorescence quenching of tagged oligonucleotide probes by gold nanoparticles. *Chem. Phys. Lett. 414*, 259–264.

(50) Lakowicz, J. R. (2005) Radiative decay engineering 5: metal-enhanced fluorescence and plasmon emission. *Anal. Biochem. 337*, 171–194.

(51) Parak, W. J., Pellegrino, T., Micheel, C. M., Gerion, D., Williams, S. C., and Alivisatos, A. P. (2003) Conformation of oligonucleotides attached to gold nanocrystals probed by gel electrophoresis. *Nano Lett. 3*, 33–36.

(52) Demers, L. M., Mirkin, C. A., Mucic, R. C., Reynolds, R. A., Letsinger, R. L., Elghanian, R., and Viswanadham, G. (2000) A fluorescence-based method for determining the surface coverage and hybridization efficiency of thiol-capped oligonucleotides bound to gold thin films and nanoparticles. *Anal. Chem. 72*, 5535–5541.

(53) Niemeyer, C. M., Ceyhan, B., and Hazarika, P. (2003) Oligofunctional DNA-gold nanoparticle conjugates. *Angew. Chem., Int. Ed. 42*, 5766–5770.

BC900471Q

Biological *in Vitro* and *in Vivo* Studies of a Series of New Asymmetrical Cationic $[^{99m}Tc(N)(DTC\text{-}Ln)(PNP)]^+$ Complex (DTC-Ln = Alicyclic Dithiocarbamate and PNP = Diphosphinoamine)

Cristina Bolzati,*[,†,‡] Mario Cavazza-Ceccato,[‡] Stefania Agostini,[‡] Fiorenzo Refosco,[†] Yoshihiro Yamamichi,[§] Shinji Tokunaga,[§] Davide Carta,[‡] Nicola Salvarese,[‡] Daniele Bernardini,[||] and Giuliano Bandoli[‡]

ICIS-CNR, Corso Stati Uniti, 4, 35127 Padova, Italy, Department of Pharmaceutical Sciences, University of Padua, Via Marzolo, 5, 35131 Padova, Italy, Research Center, Nihon Medi-Physics Co., Ltd., 3-1 Kitasode, Sodegaura, Chiba 299-0266, Japan, and Department of Veterinary Clinical Science, University of Padua, Viale dell'Università 16, 35020 Legnaro, Padua, Italy. Received November 10, 2009; Revised Manuscript Received January 18, 2010

$^{99m}Tc(N)$-DBODC5 is a cationic mixed compound under clinical investigation as potential myocardial imaging agent. In spite of this, analogously to the other cationic ^{99m}Tc-agents, presents a *relatively* low first-pass extraction. Thus, modification of $^{99m}Tc(N)$-DBODC(5) direct to increase its first-pass extraction keeping unaltered the favorable imaging properties would be desirable. This work describes the synthesis and biological evaluation of a series of novel cationic ^{99m}Tc-nitrido complexes, of general formula $[^{99m}TcN(DTC\text{-}Ln)(PNP)]^+$ (DTC-Ln= alicyclic dithiocarbamates; PNP = diphosphinoamine), as potential radiotracers for myocardial perfusion imaging. The synthesis of cationic ^{99m}Tc-(N)-complexes were accomplished in two steps. Biodistribution studies were performed in rats and compared with the distribution profiles of $^{99m}Tc(N)$-DBODC5 and ^{99m}Tc-Sestamibi. The metabolisms of the most promising compounds were evaluated by HPLC methods. Biological studies revealed that most of the complexes have a high initial and persistent heart uptake with rapid clearance from nontarget tissues. Among tested compounds, **2** and **12** showed improved heart uptake with respect to the gold standard ^{99m}Tc-complexes with favorable heart-to-liver and slightly lower heart-to-lung ratios. Chromatographic profiles of $^{99m}Tc(N)$-radioactivity extracted from tissues and fluids were coincident with the native compound evidencing remarkable *in vivo* stability of these agents. This study shows that the incorporation of alicyclic dithiocarbamate in the $[^{99m}Tc(N)(PNP)]^+$ building block yields to a significant increase of the heart uptake at early injection point suggesting that the first-pass extraction fraction of these novel complexes may be increased with respect to the other cationic ^{99m}Tc-agents keeping almost unaltered the favorable target/nontarget ratios.

INTRODUCTION

In spite of the great strides in developing myocardial perfusion scintigraphy, there is a general agreement about the fact that an improved myocardial agent having imaging characteristics much closer to those of an ideal perfusion indicator still needs to be found (*1*). An ideal perfusion imaging agent should possess a few important properties, such as a high first-pass extraction, a rapid elimination from critical nontarget tissues such as lungs and liver, and a rapid blood clearance to allow a clear visualization of the cardiac region. Moreover, the myocardial uptake should be linear over the whole range of blood flow passing through the organ (*2*). Despite their widespread clinical application, ^{99m}Tc-Sestamibi (Cardiolite) and ^{99m}Tc-Tetrofosmin (Myoview) do not meet all these requirements, in part due to their high liver uptake which makes it very difficult to interpret heart activity in the inferior and left ventricular wall (*3*−*5*).

Over the past few years, novel examples of myocardial tracers, characterized by the presence of a terminal technetium–nitrogen multiple bond, have been reported (*6, 7*). One of these included a new class of monocationic compounds of the type $[^{99m}Tc(N)(DTC)(PNP)]^+$, where DTC is an aliphatic dithiocarbamate ligand and PNP a diphosphinoamine. Among the tested compounds, $[^{99m}Tc(N)(DBODC)(PNP5)]^+$ and $[^{99m}Tc(N)(DBODC)(PNP3)]^+$ [DBODC = bis(*N*-ethoxyethyl)-dithiocarbamato; PNP5 = bis(dimethoxypropylphosphinoethyl)-ethoxyethylamine]; PNP3 = bis(dimethoxypropylphosphinoethyl)-methoxyethylamine)] complexes, namely, ^{99m}Tc-(N)-DBODC5 and ^{99m}Tc-(N)-DBODC3, respectively, showed the most interesting biodistribution properties (*8, 9*). In particular, animal studies of ^{99m}Tc-(N)-DBODC5 revealed singular biodistribution profiles characterized by a high and persistent myocardial accumulation, with an uptake mechanism and a kinetic behavior identical to those of the commercially available myocardial imaging agents (*10*). The most interesting properties lie in its rapid lungs and liver clearance and consequently in its favorable heart/lungs and heart/liver ratios, thus exhibiting unprecedented imaging characteristics with respect to the commercially available myocardial imaging agents, ^{99m}Tc-Sestamibi and ^{99m}Tc-Tetrofosmin (*8*−*12*).

Similar results were found in humans. Preliminary phase I study data in healthy volunteers showed that both rest and peak stress administration of ^{99m}Tc-(N)-DBODC5 can yield high-quality myocardial images starting from 5 min p.i., suggesting a promising diagnostic value of this new tracer (*13*).

As for other cationic ^{99m}Tc-complexes, the favorable properties of ^{99m}Tc-(N)-DBODC5 are somehow negatively counterbalanced by its *relatively* low first-pass extraction (approximately 60%) and minimal redistribution (*12, 14*−*16*), if compared to those of neutral ^{99m}Tc-complexes, such as ^{99m}Tc-Teboroxime

* To whom correspondence should be addressed. ICIS-CNR, Corso Stati Uniti, 4, 35127 Padova, Italy. Phone: +39 049 8275352. Fax: +39 049 8275366. E-mail: bolzati@icis.cnr.it.

† ICIS-CNR.

‡ Department of Pharmaceutical Sciences, University of Padua.

§ Nihon Medi-Physics Co., Ltd.

|| Department of Veterinary Clinical Science, University of Padua.

10.1021/bc900493e © 2010 American Chemical Society
Published on Web 04/19/2010

(88−91%) and ^{99m}Tc(N)NOET (NOET = *N*-ethoxy,*N*-ethyl dithiocarbamate) (∼80−90%) (*17*−*19*). For the two latter compounds, the high initial heart extraction [3.44 ± 0.32% ID/organ at 1 min p.i. for ^{99m}Tc-Teboroxime and 4.28 ± 0.18% ID/organ at 5 min p.i. for ^{99m}Tc(N)NOET] and the redistribution properties seem to be correlated to the higher lipophilic character which allows, through a passive diffusion mechanism, a rapid diffusion/penetration of the complexes across the cell membrane and to the higher circulating blood activity with respect to those exhibited by monocationic compounds (*6*, *20*, *21*). Tracers with higher first-pass extraction will accurately track blood flows over a wide range than tracers with lower first-pass extraction, and thus, they may potentially be more sensitive for the quantitative evaluation of milder flow-limiting coronary stenosis under stress conditions; in addition, a nonlinear behavior could be preferred for a qualitative assessment.

On the basis of these considerations, a rational modification of the ^{99m}Tc-(N)-DBODC5 compound directly to produce new ^{99m}Tc-agents with high initial heart uptake, which is correlated with the first-pass extraction, but maintaining the favorable pharmacokinetic properties of ^{99m}Tc-(N)-DBODC5 can be considered.

Over the last years, different ^{99m}Tc-mixed compounds containing alkoxy-alkyl amino-diphosphine ligands such as [^{99m}Tc(N)-(L)(PNP)]$^{+}$ (L = linear-chain- or crown ether-containing dithiocarbamate or thiomaltol derivates), [^{99m}Tc(NNPh)(L)-(PNP)]$^{+}$ (DTC = crown ether-containing dithiocarbamate), and [^{99m}Tc(CO)$_3$(PNP)]$^{+}$ have been reported as potential myocardial imaging agents (*8*, *22*−*28*). The evidence that all of these compounds maintain similar favorable biodistribution patterns, characterized by a rapid elimination of the activity from nontarget tissues, regardless of the presence of the terminal technetium−nitrogen multiple bond and regardless of the nature of the dithiocarbamate, maltol, or the CO coligand suggests that this behavior may be mainly correlated to the [Tc(PNP)]$^{n+}$ scaffold and in particular to the chemical structure of the PNP ligand as well as to the presence of alkoxy-alkyl pendant groups.

Recently, we reported a new class of neutral nitrido mixed ligand complexes of the type [^{99m}Tc(N)(DTC-Ln)(PS)] where (PS) is a branched phosphinoethanethiolate ligand and (DTC-Ln) an alicyclic dithiocarbamate. Biodistribution studies carried out in rats of some of these lipophilic compounds exhibited remarkably high, but transient, myocardial uptake (*29*). Comparison of the myocardial uptakes at early injection times (2 min, which may correspond to a certain extent to a first-pass extraction) evidenced that [^{99m}Tc(N)(DTC-Ln)(PS)] complexes with dithiocarbamates containing pyrrolidine (4.78 ± 0.76% ID/g), piperidine (3.79 ± 1.99% ID/g), and *N*-ethyl-piperazine (4.81 ± 0.73% ID/g) substituents showed higher initial heart activity than those exhibited by compounds incorporating dithiocarbamate with linear chains such as diethyldithiocarbamate (2.48 ± 0.35% ID/g) or DBODC (2.93 ± 0.72% ID/g).

The prominent back diffusion of these [^{99m}Tc(N)(DTC-Ln)(PS)] compounds is likely related to their neutral and lipophilic properties and to the fact that they are not joined intracellularly owing to the lack of an appropriate trapping mechanism that may be connected to the absence of the cationic charge. These observations prompted us to combine the biological properties of the well studied monocationic [^{99m}Tc(N)(DTC)(P-NP)]$^{+}$ with those of the neutral [^{99m}Tc(N)(DTC-Ln)(PS)] complexes by introducing a dithiocarbamate containing pyrrolidine, piperidine, or *N*-ethylpiperazine into the [^{99m}Tc(N)-(PNP)]$^{2+}$ building block.

In this preliminary study, our goal was to verify if the novelty to include alicyclic dithiocarbamates into a cationic species of the type [^{99m}Tc(N)(DTC)(PNP)]$^{+}$ may favor high initial heart uptake, as observed for neutral [^{99m}Tc(N)(DTC-Ln)(PS)] compounds, along with a prolonged retention. Moreover, considering that in these asymmetrical compounds variation of both DTC and PNP showed significant impact on their distribution properties (*8*, *23*) additional newly synthesized diphosphine ligands were evaluated.

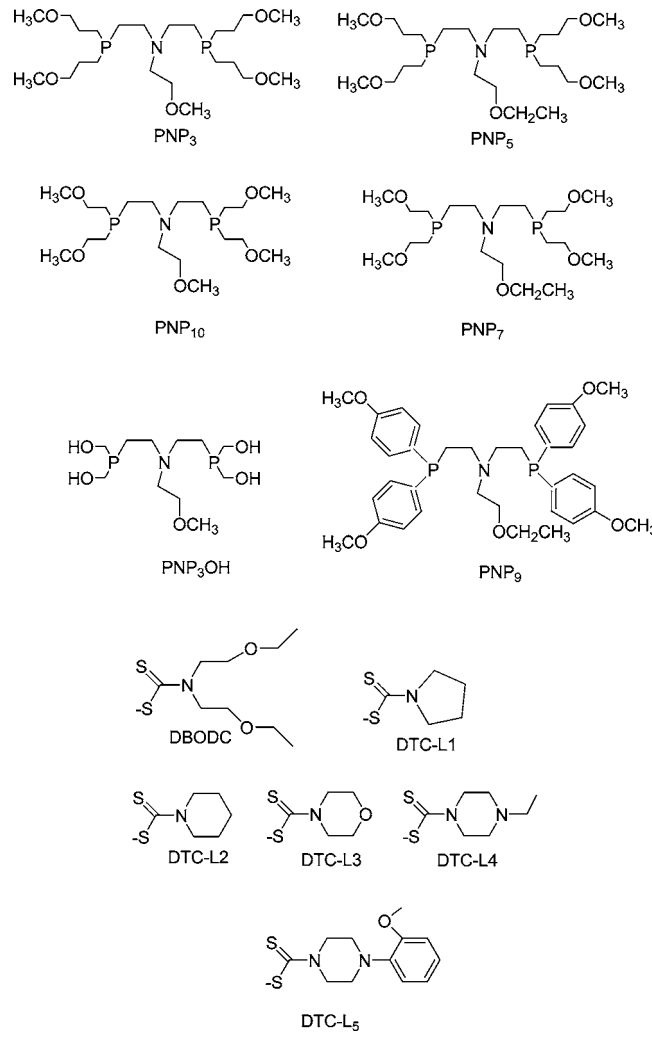


Figure 1. Diphosphinoamine and dithiocarbamate used in our experiments.

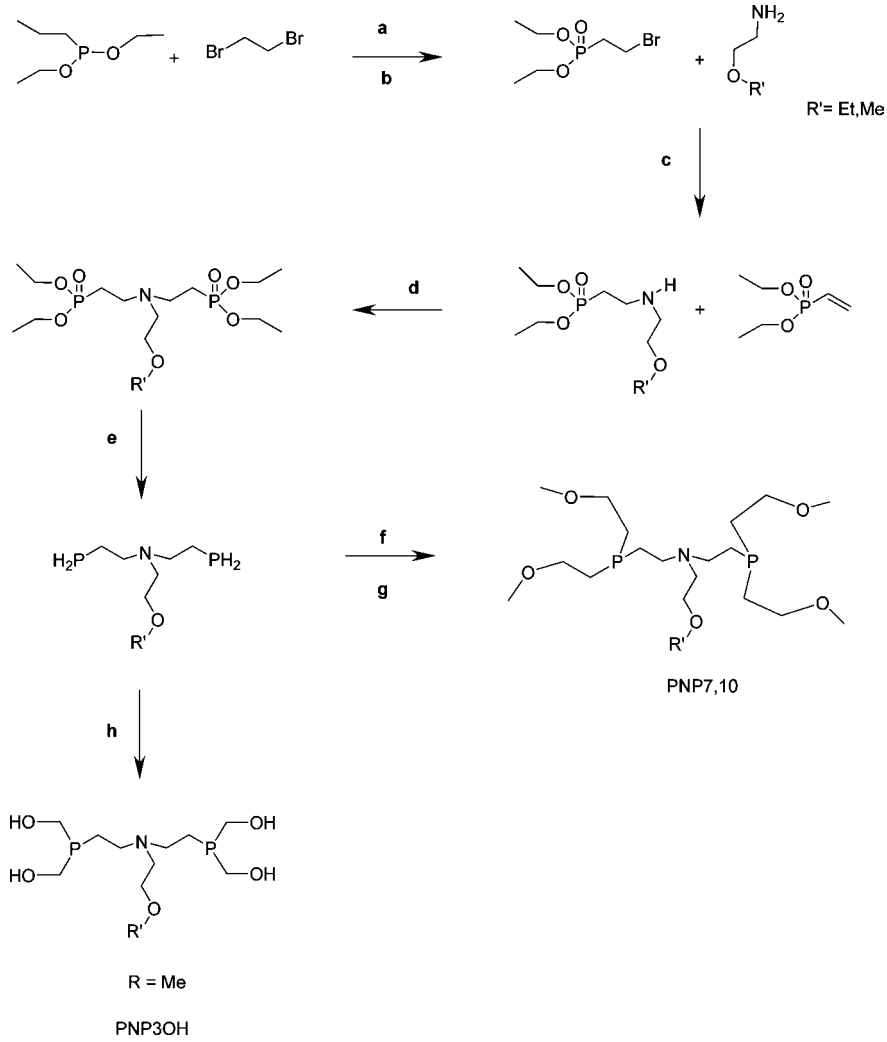
In this article, we describe the synthesis and chromatographic characterization of a series of new monocationic mixed compounds of the general formula [^{99m}Tc(N)(DTC-Ln)(PNP)]$^{+}$. Diphosphinoamine (PNP) and dithiocarbamate (DTC-Ln) ligands utilized in this investigation are illustrated in Figure 1.

The *in vitro* stability and transchelation toward an excess of cysteine of all synthesized compounds were evaluated. Comparison of the biodistribution data of these new compounds with the biological profiles of the ^{99m}Tc-(N)-DBODC5,3 complexes and of the commercially available ^{99m}Tc-Sestamibi is presented. In addition the *in vitro* and *in vivo* stability of the most promising compounds of the new series was assessed.

EXPERIMENTAL PROCEDURES

General. All chemicals and reagents were purchased from Aldrich Chemicals (Milano, Italy). All solvents were of reagent grade and were used without further purification. PNP3 and PNP5 were purchased from Argus Chemicals (Prato, Italy). Diphosphinoamine PNP7 (bis(dimethoxyethylphosphinoethyl)-ethoxyethylamine), PNP9 (bis(*p*-methoxyphenylphosphinoethyl)-methoxyethylamine), PNP10 (bis(dimethoxyethylphosphinoethyl)-methoxyethylamine), and PNP3OH (bis(2-

Scheme 1[a]



[a] Reagents and conditions: (a) Δ, 2 h; (b) distil. 1 mm Hg, 75 °C; (c) MeCN, K_2CO_3, 65 °C, 3 h; (d) $LiClO_4$, 75 °C, 7 h; (e) $LiAlH_4$, Et_2O_{dry}, 0 °C; (f) *n*-BuLi, THF_{dry}, −78 °C, N_2; g) Cl-$CH_2CH_2OCH_3$, 0 °C, N_2; (h) EtOH, CH_2O.

dihydroxymethylene)phosphinoethyl)-methoxyethylamine) were synthesized according to reported procedures (*30*, *31*). The general way of synthesis of the ligands is exemplified in Scheme 1. PNP3OH was utilized as the phosphonium salt PNP3OH × HCl and converted *in situ* into the corresponding diphosphinoamine.

To avoid oxidation, all of the solvents used in reactions with the alkyl diphosphinoamine were previously degassed. DBODC, as sodium salt, was acquired from Alchemy (Bologna, Italy). DTC-L1 (pyrrolidinedithiocarbamate) as ammonium salt was purchased from Merck (Milano, Italy). Other DTC-Ln were prepared as detailed below. ^{99m}Tc as Na[$^{99m}TcO_4$] was eluted from a Drytec ^{99} Mo/^{99m}Tc generator provided by GE Healthcare (Milano, Italy).

For comparison studies, both ^{99m}Tc-(N)-DBODC5,3 complexes were synthesized according to the literature methods (*7*, *8*), whereas ^{99m}Tc-Sestamibi (Bristol-Myers Squibb) was prepared through reconstitution of the commercially available kits.

Analysis. Elemental analyses (C, H, N, and S) were performed on a Carlo Erba 1106 elemental analyzer. ^{1}H and ^{13}C NMR spectra were collected on a Bruker 300 instrument, using $SiMe_4$ as internal reference (^{1}H and ^{13}C).

Thin-layer chromatography (TLC) and high performance liquid chromatography (HPLC) analyses were used to evaluate the radiochemical purity (RCP) and the stability of the compounds. TLC analysis was performed on C18 F_{254S} plates (Merck, Milano, Italy) using a mixture of Saline/MeOH/THF/$HAc_{(g)}$ (2/8/1/1) as mobile phase or alternatively on SiO_2 F_{254} plates (Merck, Milano, Italy) using a mixture of EtOH/$CHCl_3$/Tol/NH_4Ac 0.5 M (5/3/3/1). The activity on the plates was detected and measured using a Cyclone Instrument equipped with a phosphorus imaging screen and OptiQuant image analysis software (Packard, Meridian, CT).

HPLC was performed on a Beckman System Gold instrument equipped with a programmable solvent Model 126, a sample injection valve 210A, a scanning detector Module 166, and a radioisotope detector Model B-FC-3200 Bioscan. HPLC analysis was carried out using a reversed-phase Beckman ODS precolumn (5 μm, 4.6 × 45 mm), and a reversed-phase Beckman ODS column (5 μm, 4.6 × 250 mm). log k'_0 of the complexes were determined by HPLC chromatography as previously reported (*8*) and compared with the log k'_0 value of ^{99m}Tc-Sestamibi.

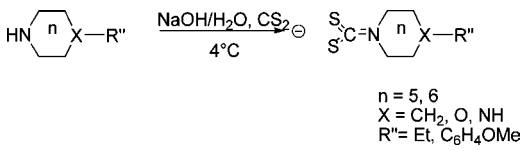
Serum protein binding affinity was evaluated through chromatographic methods using HPLC and a size-exclusion Microspin G50 column (Amersham Biosciences). Analytical RP HPLC was performed with a Symmetry 300 C4 precolumn (5 μm, 3.9 × 20 mm) and a Symmetry 300 C4 column (5 μm, 4.6 × 150 mm). Solvent A = H_2O (0.1% TFA; pH 3.0), solvent B = CH_3CN (0.1% TFA). Gradient: 0−2 min B 15%; 2−20 min B 65%; 20−22 B 15%; 22−25 B 15%. The flow rate was 1 mL/min.

Table 1

complex	no	TLC C18 R_F	TLC SiO_2 R_F	HPLC R_T(min)	% RCY	log k'_0	protein bound (%)
[^{99m}Tc(N)(DTC-L1)(PNP3)]$^{+}$	**1**	0.50	0.58	11.24[a]	95	2.51	1.13 ± 0.04
[^{99m}Tc(N)(DTC-L2)(PNP3)]$^{+}$	**2**	0.52	0.54	11.73[a]	95	3.09	2.13 ± 0.03
[^{99m}Tc(N)(DTC-L2)(PNP5)]$^{+}$	**3**	0.48	0.52	14.82[a]	92	3.20	1.64 ± 0.05
[^{99m}Tc(N)(DTC-L2)(PNP7)]$^{+}$	**4**	0.49	0.6	14.52[a]	72	3.11	1.54 ± 0.05
[^{99m}Tc(N)(DTC-L2)(PNP10)]$^{+}$	**5**	0.44	0.62	11.87[a]	75	2.25	2.15 ± 0.13
[^{99m}Tc(N)(DTC-L3)(PNP3)]$^{+}$	**6**	0.65	0.41	7.89[a]	95	2.29	0.56 ± 0.03
[^{99m}Tc(N)(DTC-L4)(PNP3)]$^{+}$	**7**	0.31	0.44	10.93[a]	94	2.71	2.19 ± 0.09
[^{99m}Tc(N)(DTC-L5)(PNP3)]$^{+}$	**8**	0.41	0.57	17.33[a]	95	3.47	4.13 ± 0.03
[^{99m}Tc(N)(DBODC)(PNP3OH)]$^{+}$	**9**	0.81		18.32[b]	58	1.09	0.90 ± 0.03
[^{99m}Tc(N)(DBODC)(PNP7)]$^{+}$	**10**	0.55	0.61	14.90[a]	79	3.38	2.11 ± 0.03
[^{99m}Tc(N)(DBODC)(PNP9)]$^{+}$	**11**	0.34	0.81	13.80[c]	76	4.73	15.13 ± 0.10
[^{99m}Tc(N)(DBODC)(PNP10)]$^{+}$	**12**	0.57	0.59	11.90[a]	70	3.25	2.43 ± 0.07
[^{99m}Tc(N)(DBODC)(PNP3)]$^{+}$		0.43	0.78	16.06[a], 31.06[b]	95	3.35	0.53 ± 0.04
[^{99m}Tc(N)(DBODC)(PNP5)]$^{+}$		0.61	0.80	18.13[a]	93	3.68	1.10 ± 0.09
^{99m}Tc-Sestamibi				9.15[a]	95	3.22	

[a] HPLC: solvent A = phosphate buffer 0.02 M at pH 7.4. Solvent B = MeOH (20: 80). Flow rate of 1 mL/min for 30 min. [b] A = NH_4Ac 0.05 M. B = CH_3CN. Gradient: 0−5 min B 20%; 5−15 min B 40%; 15−20 min B 90%; 20−30 min B 90%; 30−33 min B 20%; 33−35 min B 20%. Flow rate of 1 mL/min. [c] A = 0.1%TFA H_2O at pH 3.0. B = 0.1% TFA MeCN. Gradient: 0 min B 50%; 0−8 min B 100%; 8−20 min B 100%. Flow rate of 0.9 mL/min.

Scheme 2



Measured physical properties of [^{99m}Tc(N)(DTC-Ln)(PNP)]$^{+}$ agents are reported in Table 1, including HPLC capacity factors and rat plasma protein binding. Images were collected using a gamma camera PRISM 3000 XP.

Ligands Synthesis. *Dithiocarbamate DTC-Ln.* Basically, the dithiocarbamate ligands DTC-L2−5 were prepared by reaction of the relevant secondary amine with an equivalent amount of carbon disulfide in NaOH solution, as detailed below. The general pathway of synthesis is shown in Scheme 2.

In a water-bath cooled vessel, 1.6 mmol of the appropriate secondary amine were suspended in water (10 mL), and an aqueous solution of NaOH (1.6 mmol/1.5 mL) was slowly added followed by dropwise addition of carbon disulfide (1.6 mmol/, 100 μL, 4 × 25 μL). The reaction mixture was stirred at room temperature for 1 h to obtain a yellow−orange solution. The solvent was removed under reduced pressure, and the resulting crude residue was recrystallized from ethanol/diethyl ether to give white crystals of the corresponding dithiocarbamate as sodium salt.

DTC-L2 (Piperidin Dithiocarbamate). The yield was 41%. Anal. Calcd for $C_6H_{10}NNaS_2$ (MW 183.27): C 39.32, H 5.50, N 7.64, S 34.99. Found: C 40.97, H 6.01, N 7.56, S 35.24. IR (KBr cm^{-1}) 2930 (−CH_2); 2852 (−CH_2); 1449 (CH_2); 1409 (C−N); 1218 (C═S). ^{1}H NMR (D_2O) δ: 4.19−4.15 (t, 4H, J = 5.3 Hz −$CH_2CH_2C\underline{H_2}$N-), 1.72−1.65 (m, 4H, −$CH_2C\underline{H_2}$-CH_2N-), 1.58−1.64 (m, 2H, -$C\underline{H_2}CH_2CH_2$N-).^{13}C NMR (D_2O) δ: 202.2 (C═S), 52.6 ($CH_2CH_2\underline{C}H_2$N-), 25.2 (−$CH_2\underline{C}H_2$-CH_2N-), 21.9 ($\underline{C}H_2CH_2CH_2$N-).

DTC-L3 (Morfolin Dithiocarbamate). The yield was 48%. Calcd for $C_5H_8NNaOS_2$ (MW 185.25): C 32.42, H 4.35, N 7.56, O 8.64, S 34.62. Found: C 31.97, H 4.58, N 7.06, O 8.94, S 35.24. IR (KBr cm^{-1}) 2930 (−CH_2); 1418 (C−N); 1219 (C═S). ^{1}H NMR (D_2O) δ: 4.24 (m, 4H, -$OCH_2C\underline{H_2}$N-), 3.62 (m, 4H, -$OC\underline{H_2}CH_2$N-). ^{13}C NMR (D_2O) δ: 212.0 (C═S), 68.91 (−OCH_2-$\underline{C}H_2$N-), 54.15 (-$O\underline{C}H_2CH_2$N-).

DTC-L4 (1-Ethyl-piperazine Dithiocarbamate). The yield was 60%. Calcd for $C_7H_{13}N_2NaS_2$ (MW 212.04): C 39.60, H 6.17, N 13.19, S 30.21. Found: C 40.97, H 7.58, N 13.86, S 30.54. IR (KBr cm^{-1}) 2969(−CH_3); 2818 (−CH_2); 1415 (C−N); 1227 (C═S). ^{1}H NMR (D_2O) δ: 4.32−4.16 (m, b, 4H, $CH_2C\underline{H_2}$N(CS_2)), 2.52 (m, b, 4H (CH_3CH_2)N$C\underline{H_2}CH_2$N-), 2.47−2.39 (q, b, 2H, J = 7.3 Hz $CH_3C\underline{H_2}N$ <), 1.05−0.98 (t, 3H, $C\underline{H_3}CH_2N$ <).^{13}C NMR (D_2O) δ: 202,10 (C═S), 50,91 ((CH_3CH_2)N$\underline{C}H_2CH_2$), 50.75 ($CH_3\underline{C}H_2N$ <), 49.81 (−CH_2-$\underline{C}H_2$N(CS_2)), 10.00 ($\underline{C}H_3CH_2N$ <).

DTC-L5 (4-N-(2 Methoxyphenyl)-piperazine Dithiocarbamate). The yield was 76%. Calcd for $C_{12}H_{15}N_2NaOS_2$ (MW 290.05): C 49.63, H 5.21, N 9.65, O 5.51, S 22.08. Found: C 50.97, H 5.99, N 9.89, O 5.94, S 23.24. IR (KBr cm^{-1}) 1464 (F, C−N); 1236 (F, C═S). ^{1}H NMR (D_2O) δ: 7.01−6.96 (m, 4H, Ar), 4.37 (m, 4H, $CH_2C\underline{H_2}$N(CS_2)), 3.74 (s, 3H, O$C\underline{H3}$), 2.95 (m, 4H, $CH_2C\underline{H_2}$N−Ar).^{13}C NMR (D_2O) δ: 214,10 (C═S), 155.21, 143.42 (2C, -*Ar*) 125.35−115.53 (4C, -*Ar*), 62.03 (2C, $CH_2\underline{C}H_2$N(CS_2)), 57.95 (-O$\underline{C}$H3), 53.21 (−$CH_2\underline{C}H_2$N−Ar).

Preparation of the ^{99m}Tc(N)-Complexes. Na[^{99m}TcO_4] (0.25 mL, 50.0 MBq−2.2 GBq) was added to a vial containing 5.0 mg of succinic dihydrazide (SDH = $NH_2NHC(O)CH_2CH_2$-$C(O)NHNH_2$), 5.0 mg of ethylenediamine tetraacetic acid (EDTA), and 0.1 mg of $SnCl_2$ (tin chloride) suspended in 0.1 mL of saline and 1 mL of EtOH. The vial was kept at room temperature for 30 min giving a mixture of ^{99m}Tc-nitrido precursors, [^{99m}Tc≡N]$_{mix}^{2+}$. Then, 1.0 mg of the selected diphosphinoamine (dissolved in 0.1 mL of EtOH) and 2.0 mg of the appropriate dithiocarbamate (dissolved in 0.2 mL of saline) were simultaneously added to the reaction vial. The radiochemical yield (RCY), of each compound, determined by TLC and HPLC chromatography, after 15 min at 80 °C, is reported in Table 1.

*Preparation of [^{99m}Tc(N)(DBODC)(PNP3OH)]$^{+}$ (**9**).* To a mixture of [^{99m}Tc≡N]$_{mix}^{2+}$ prepared as described above, 2.0 mg of PNP3OH × HCl dissolved in 0.5 mL of phosphate buffer (0.1 M and pH 7.4) and 1.0 mg of DBODC dissolved in 0.2 mL of saline were simultaneously added. The radiochemical yield (RCY) determined by TLC and HPLC, after 15 min at 80 °C, is reported in Table 1.

Dose Preparation of ^{99m}Tc(N)-Complexes. A Sep-Pak C18 cartridge (Waters) was activated with 5 mL of EtOH and 5 mL of deionized water. Then, the reaction solution containing the selected ^{99m}Tc(N)-complex was diluted with 8.0 mL of deionized water and loaded on the cartridge. Approximately 90% of the initial activity was retained on the cartridge. After washing the cartridge with water (20.0 mL) and 35% ethanol (5.0 mL), the complex was eluted using a mixture of ethanol and saline 90/10 (0.250 mL × 1; 0.750 mL × 1). Ninety percent of the loaded activity was collected in the second fraction. The solvent was eliminated under dinitrogen stream; the complex was dissolved in saline and utilized for *in vitro* and *in vivo* stability studies.

Compound **9.** For biodistribution studies, the complex was purified by HPLC, concentrated on a preactivated Sep Pak C18 cartridge, rinsed with H_2O (10 mL), and eluted using a mixture of EtOH/NBu_4Br (0.1 M) 50/50 (0.5 mL × 2). The second fraction containing all of the activity was diluted with saline and utilized for *in vitro* and *in vivo* studies. After purification, the radiochemical purity (RCP), evaluated by HPLC chromatography, was >95%. The stability of the isolated complex was evaluated over time.

In Vitro Studies. *Solution Stability of the ^{99m}Tc(N)-Complexes.* Aliquots of each reaction mixture containing the relevant ^{99m}Tc(N)-complex were analyzed by HPLC at 1, 2, and 18 h postlabeling.

For the cysteine (Cys) challenge experiment, an aliquot (50.0 μL) of a 10.0 mM stock aqueous solution of Cys was added to a polypropylene test tube (5.0 mL) containing 0.2 M phosphate buffer (250.0 μL and pH 7.4), water (100.0 μL), and the selected ^{99m}Tc(N)-complex (100.0 μL). The mixture was vortexed and incubated at 37 °C for 18 h. A blank reaction containing an equal volume of water instead of Cys was also accomplished. At 15 min, 1, 2, and 18 h aliquots of the reaction mixture were withdrawn and analyzed by TLC and HPLC chromatography.

Protein Binding. Considering the rapid blood clearance of these compounds, the affinity of the complexes toward the serum protein was evaluated after 2, 10, and 60 min of incubation at 37 °C in human and in rat serum by chromatographic methods using the procedures reported below.

Purified ^{99m}Tc(N)-complex (100.0 μL) (50−100 MBq) was added to 900.0 μL of human or rat serum; 150.0 μL of each sample was withdrawn and diluted in 1350.0 μL of phosphate buffer (0.02 M and pH 7.4). Aliquots of this solution were treated and analyzed as follows:

Method a. 100.0 μL was analyzed by HPLC, without further purification, using a RP Symmetry C4.

Method b. 25.0 μL was loaded on a prespun (2,000*g* for 1 min) Sephadex G-50 mini-column. The column was centrifuged at 2,000*g* for 1 min. The collected eluate and the column were counted in a γ-counter. The protein-bound complex was calculated as the percentage of total activity. HPLC analysis performed on the eluate revealed only the presence of the proteic fraction. All activity was found associated to the column.

As the blank 25.0 μL of the ^{99m}Tc(N)-complex was controlled after incubation in PBS at 37 °C for 60 min.

Metabolism. The *in vitro* metabolism studies of the agents were evaluated by monitoring the radiochemical purity (RCP) at different time points using the following procedures. In a polypropylene test tube, 50.0 μL of the purified Tc-99 m complex (50−100 MBq) was added to (a) 450.0 μL of rat serum, (b) 450.0 μL of human serum, (c) 450.0 μL of rat liver homogenate, and (d) 950.0 μL of saline as a blank. The resulting mixtures were incubated at 37 °C for 2 h. At 15 min, 1 and 2 h aliquots (200.0 μL) of each solution were withdrawn, diluted with 800.0 μL of phosphate buffer (0.2 M and pH 7.4), and filtered using an OASIS HLB extraction cartridge before HPLC injection. In detail, the sample was loaded on cartridges conditioned with MeOH (1 mL) and equilibrated with water (1 mL) and washed with MeOH 5% (3.0 mL). Ninety percent of the starting activity was eluted using a mixture of ethanol and an aqueous solution of 90/10 (1.0 mL) NBu_4Br (0.1 M); 100.0 μL of this fraction was analyzed by TLC and HPLC chromatography.

In Vivo Studies. Animal experiments were carried out in compliance with the national laws relating to the conduct of animal experimentation.

Biodistribution Studies. Before injection, each ^{99m}Tc(N)-complex was purified using the procedure outlined above. After purification, the activity recovered was further diluted with saline to obtain a final solution which was <5% in ethanol content. Female Sprague−Dawley rats weighing 180−200 g were anesthetized with an intraperitoneal injection of a mixture of Zoletil (40 mg kg^{-1}) and xilazine (2 mg kg^{-1}). The jugular vein was surgically exposed, and 100.0 μL (300−370 kBq) of the solution containing the radioactive complex was injected. The animals (n = 3) were sacrificed by cervical dislocation at different times postinjection. The blood was withdrawn from the heart through a syringe immediately after sacrifice, weighed, and counted. Organs were excised, rinsed in saline, weighed, and counted in a γ-counter. Results normalized as percent injected dose per gram (% ID/g) are reported in Tables 1S−3S (see Supporting Information). For comparison purposes, ^{99m}Tc-(N)(DBODC)(3/5), ^{99m}Tc-Sestamibi, and ^{99m}Tc-Tetrofosmin were evaluated using the same procedure.

In Vivo Stability and Metabolism. For the most promising compounds **2** and **12**, the extraction of the complex from rat tissues and urine was performed using the following procedure. One hundred microliters of the solution containing the radioactive complex (370−500 MBq) was injected into the jugular vein of anesthetized rats (200−250 g). At 30 and 120 min postinjection, the animals were sacrificed. The heart, kidneys, and small intestine were excised, rinsed with water, weighed, and counted in a NaI well counter. Results were normalized as percent injected dose per gram (% ID/g).

Extraction from the Heart and from the Kidneys. The extraction of the complex from the myocardial and renal tissue was performed following the previously reported procedures (*10*).

Metabolites in the Intestine. The intestinal lumen was rinsed with 2 mL of water; 90% of the total activity was collected in the endoluminal content. The liquid fraction was separated from the intestinal content by centrifugation (3.000*g* for 10 min) and counted. Fifty percent of the activity was found in the first liquid fraction (Fraction I). Exhaustive extraction of the residual activity from the solid fraction was performed by using MeCN (2 mL) followed by centrifugation (3.000*g* for 10 min) (Fraction II). An aliquot of each fraction (1 mL) was eluted through an OASIS HLB extraction cartridge and the eluate analyzed by TLC and HPLC.

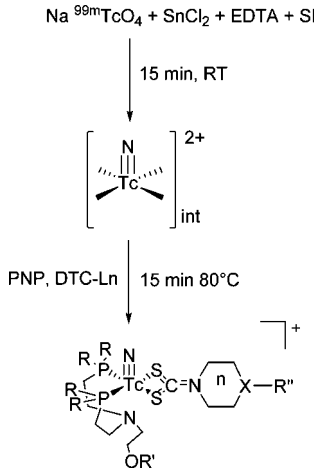
Metabolites in the Urine. The urine was collected from the bladder and loaded directly onto an activated OASIS HLB extraction cartridge. The complex was eluted with a mixture of EtOH and saline 90/10 (0.5 mL) and analyzed by TLC and HPLC.

In Vivo Whole-Body γ-Camera Imaging. Serial *in vivo* γ-camera imaging was performed in 12 additional anesthetized rats. Compound **2** (n = 3) (44.4−59.2 MBq), **12** (n = 3), ^{99m}Tc(N)(DBODC)(5) (n = 3), or ^{99m}Tc-Sestamibi (n= *3*) was injected via the jugular vein, after which the rats were placed supine directly on the surface of the collimator. Whole body images where acquired at 2, 30, and 60 min postinjection using a 15% window centered on the 140 keV ^{99m}Tc photopeak. Imaging acquisition time was 5 min at each time point, resulting in approximately 1.2−1.0 × 10^6 counts in each image. The images were then quantified by regions of interest drawn on the heart, lung, and liver regions on each image.

RESULTS

$[^{99m}Tc(N)(DTC\text{-}Ln)(PNP)]^+$ mixed compounds were efficiently prepared, starting from $[Na^{99m}TcO_4]$ following the synthesis pathway sketched in Scheme 3. The labeling procedure entailed the preliminary formation of a mixture of $[^{99m}Tc{\equiv}N]^{2+}$nitrido precursors, through the reduction of ^{99m}Tc pertechnetate with tin(II) chloride in the presence of SDH as a nitride nitrogen donor. In the second step, the mixture was transformed, at 80 °C, into the final heterocomplex, by simultaneous addition of the two ligands at neutral pH.

Scheme 3



In all cases, the reactions were completed after 15 min of heating at 80 °C, and no improvement of the RCY was obtained modifying the reactions conditions. The RCY of all synthesized compounds, along with their chromatographic properties are reported in Table 1. log k'_0 values were determined for each compound by reversed-phase HPLC and compared with the log k'_0 of the analogous mixed-compounds ^{99m}Tc-(N)-DBODC(3/5) and commercially available ^{99m}Tc-Sestamibi (Table 1). Excluding **11**, all of the compounds are less lipophilic than ^{99m}Tc-(N)-DBODC(3/5). As expected, in [^{99m}Tc(N)(DBODC)(PNP)]$^{+}$ the replacement of PNP3 or PNP5 with a more hydrophilic diphosphinoamine such as PNP3OH, PNP7, and PNP10 had a significant impact on the lipophilicity of the final heterocomplexes. In accordance, the retention times (R_t) of the corresponding complexes moved consistently to lower values (Table 1) according to their variation in log k'_0 values.

The complexes remained stable in reaction solution for >8 h postlabeling and for 18 h after purification in injectable solution. No significant change of radiochemical purity (RCP) was observed after 18 h of incubation at 37 °C with an excess of cysteine. No ^{99m}Tc activity was coeluted with any protein, and essentially all activity was eluted in a single peak as the native compound showing that no degradation processes had occurred (HPLC profiles of rat serum incubated with the more representative ^{99m}Tc(N)-complexes at 1 h are shown in Figure 1S, Supporting Information).

These results were confirmed by size exclusion chromatography experiments (Table 1). In both cases, no significant serum protein binding was found by chromatographic methods in both human and rat sera. This behavior was in agreement with the extremely rapid blood clearance of these agents.

Biodistribution studies of all asymmetrical complexes were carried out in rats. Before the injection, the radiolabeled compounds were purified following the procedure described in the Experimental Procedures section. The RCP and the stability of the purified complexes were evaluated at 15 min prior to *in vivo* administration and for the succeeding 18 h. The tissue uptake and the target-to-background ratio of the complexes are reported in Table 2 and Tables S1−S3 (see Supporting Information).

In general, the ^{99m}Tc(N)-compounds evidenced high and persistent heart uptake (3.98 ± 0.34−1.74 ± 0.06% ID/g at 2 min p.i.; 3.67 ± 0.55−2.40 ± 0.08% ID/g at 120 min p.i.) (Figure 2). Only **9** and **11** presented a low myocardial activity followed by rapid washout: 0.30 ± 0.04% ID/g at 2 min p.i.; 0.06 ± 0.00% ID/g at 10 min p.i. for **9**; 0.52 ± 0.07% ID/g at 2 min. p.i.; 0.28 ± 0.04% ID/g at 120 min p.i. for **11**.

The blood clearance was rapid (in the ranges 0.64 ± 0.13−0.16 ± 0.04% ID/g at 2 min p.i.; 0.28 ± 0.01−0.01 ± 0.00% ID/g at 60 min p.i.), and the activity was eliminated through both the hepatic system and urinary tract.

More accurately, a low lung uptake followed by a rapid washout was observed for the two [^{99m}Tc(N)(DBODC)(PNP)]$^{+}$compounds (PNP = PNP7(**10**), PNP10(**12**)). Similar low lung accumulation was shown by the other complexes but without detectable washout. The liver uptake was transient, and the elimination of the activity from this tissue was fast and quantitative for all complexes with the exception of the most lipophilic complexes of the series **8** (1.43 ± 0.11 ID/g at 120 min p.i.) and **11** (9.93 ± 0.78 ID/g at 120 min p.i.). It is interesting to note that, in spite of the enhanced hydrophilicity of **9**, biodistribution data showed a greater excretion of the tracer into the intestine (i.e., 30.53 ± 1.36% ID/g at 120 min p.i.) than into the urine (13.53 ± 2.33% ID/g at 120 min p.i.). A less favorable kinetic of elimination from the nontarget tissues with corresponding low heart-to-lung and heart-to-liver ratios was observed for **5**.

***In Vivo* Whole-Body γ-Camera Imaging.** Although the *ex vivo* biodistribution studies give a quantitative assessment of the organ uptake of a specific tracer, whole-body imaging allows a direct comparison of both the imaging quality and T/B ratio of the different tracers in living animals.

Considering their high myocardial uptake and heart/liver ratio, we selected **2** and **12** for imaging studies in rats (Table 2). For comparative purposes, we also collected the images of ^{99m}Tc-(N)-DBODC5 and ^{99m}Tc-Sestamibi.

Figure 3 displays *in vivo* whole body planar images acquired at different time points after injection. On all images acquired at 2 min p.i., high liver uptake was observed neighboring the heart, but the lung activity was low for all tracers. After 30 min, the liver uptake of the Tc(N)-complexes was visibly decreased and nearly disappeared at 60 min p.i., while the level of the liver activity for ^{99m}Tc-Sestamibi remained high.

Metabolism Studies of 2 and 12. Because of the fast blood clearance and the low liver uptake followed by rapid washout, extraction of the complexes from these tissues was not accomplished at the same times of interest. Thus, the stability of the two most promising agents in these tissues was evaluated *in vitro*, incubating the purified compounds both in human and rat sera as well as in the rat liver homogenate, at 37 °C for 120 min. The complexes were stable in all conditions; in particular, no transformation of the native compounds into more hydrophilic species as a result of metabolic actions was observed.

Extraction of the activity localized in the heart tissue after endovenous injection of the tracer was accomplished using the procedure reported in the Experimental Procedures section. In both cases, approximately 90% of the activity initially localized in the myocardial tissue was recovered in the organic phase (MeCN) and analyzed by TLC and HPLC, in order to investigate the influence of the uptake process on the chemical identity of the complexes (Figure 4b). The myocardial uptake/trapping process did not involve a change in the chemical nature of the tracer; indeed, the activity extracted from the myocardial tissue coincided exactly with the control peak.

The *in vivo* stability and metabolism of these agents were evaluated comparing the chromatographic profiles of the injected compounds with that of the activity extracted from the endoluminal content of the small intestine, kidneys, and urine from animals administrated 30 and 120 min earlier.

Approximately, 80% of the initial activity localized in the tissues or in the liquids was taken out and analyzed. The chromatographic profiles evidenced the presence of a single peak

Table 2. Selected Biodistribution Data for the Most Promising Cationic ^{99m}Tc(N)complexes, 2 and 12, Compared with the Biodistribution Data of the Gold Standard ^{99m}Tc-(N)-DBODC5 and ^{99m}Tc-Sestamibi[a]

complex	organ	2 min	10 min	30 min	60 min	120 min
2	blood	0.21 ± 0.02	0.04 ± 0.01	0.02 ± 0.00	0.01 ± 0.00	0.00 ± 0.00
	heart	3.79 ± 0.36	4.16 ± 0.32	3.40 ± 0.13	3.77 ± 0.55	3.67 ± 0.30
	lungs	1.06 ± 0.08	0.87 ± 0.12	0.97 ± 0.15	1.04 ± 0.35	0.79 ± 0.05
	liver	2.39 ± 0.32	0.54 ± 0.09	0.23 ± 0.12	0.18 ± 0.05	0.13 ± 0.05
	kidneys	12.81 ± 0.29	11.74 ± 0.15	6.19 ± 0.66	5.81 ± 0.28	4.07 ± 0.11
	small intestine	1.99 ± 0.11	4.48 ± 0.21	10.56 ± 0.80	12.36 ± 1.10	13.20 ± 0.71
	muscle	0.19 ± 0.02	0.21 ± 0.01	0.28 ± 0.00	0.29 ± 0.01	0.25 ± 0.00
	urine		46.84	22.04 ± 0.58	9.82 ± 1.19	9.29 ± 0.73
	heart/lung	3.57	4.78	3.50	3.62	4.64
	heart/liver	1.58	7.70	14.78	20.94	28.23
12	blood	0.35 ± 0.06	0.05 ± 0.00	0.02 ± 0.01	0.01 ± 0.00	0.01 ± 0.00
	heart	3.45 ± 0.31	3.50 ± 0.18	3.61 ± 0.26	3.33 ± 0.13	3.24 ± 0.13
	lungs	1.25 ± 0.13	0.96 ± 0.18	0.71 ± 0.06	0.54 ± 0.02	0.38 ± 0.00
	liver	2.14 ± 0.12	0.90 ± 0.31	0.40 ± 0.07	0.18 ± 0.03	0.12 ± 0.00
	kidneys	16.15 ± 0.74	8.09 ± 0.55	6.37 ± 0.19	4.75 ± 0.50	2.75 ± 0.50
	small intestine	3.22 ± 0.13	4.41 ± 0.63	5.83 ± 0.36	5.79 ± 0.25	5.45 ± 0.45
	muscle	0.35 ± 0.00	0.30 ± 0.01	0.20 ± 0.01	0.18 ± 0.00	0.16 ± 0.01
	urine		15.63 ± 3.64	20.19 ± 0.54	19.08 ± 0.35	34.21 ± 3.23
	heart/lung	2.76	3.64	5.08	6.17	8.52
	heart/liver	1.61	3.89	9.02	18.50	27.00
DBODC(5)	blood	0.14 ± 0.05	0.03 ± 0.01	0.02 ± 0.00	0.02 ± 0.01	0.01 ± 0.00
	heart	2.95 ± 0.09	2.84 ± 0.05	3.02 ± 0.30	2.91 ± 0.04	2.75 ± 0.04
	lungs	0.88 ± 0.06	0.64 ± 0.05	0.57 ± 0.02	0.39 ± 0.01	0.29 ± 0.02
	liver	2.53 ± 0.25	1.43 ± 0.12	0.64 ± 0.02	0.20 ± 0.01	0.11 ± 0.01
	heart/lung	3.35	4.43	5.29	7.46	9.48
	heart/liver	1.16	1.98	4.71	14.55	25.00
Sestamibi	blood	0.13 ± 0.04			0.01 ± 0.00	
	heart	3.09 ± 0.17			3.29 ± 0.39	
	lungs	1.71 ± 0.09			0.45 ± 0.02	
	liver	3.03 ± 0.29			1.28 ± 0.15	
	heart/lung	1.81			7.31	
	heart/liver	1.02			2.57	

[a] The organ uptake is expressed as % ID/g.

which perfectly overlapped the control compounds indicating that any metabolic transformation occurred (Figure 4c,d,e).

DISCUSSION

In this study, a new series of monocationic mixed ^{99m}Tc(N)-compounds incorporating alicyclic dithiocarbamate and alternative diphosphinoamine ligand was reported. These compounds were stable in solution and inert toward transchelation with an excess of free cysteine, demonstrating their remarkable stability and kinetic inertness.

The complexes appeared to possess promising biological properties exhibiting high and persistent heart localization, low lungs accumulation, and rapid blood clearance. The liver washout was fast, and the activity of the excreted tracer quickly moved from the hepatic tissue to the gastrointestinal area showing high activity in the intestine at 10 min p.i. The fast decrease of the circulating activity, due to high intestinal accumulation, led to rapid elimination from blood and from critical nontarget tissues such as lungs and liver, resulting in high heart-to-lung and heart-to-liver ratios. As observed in other

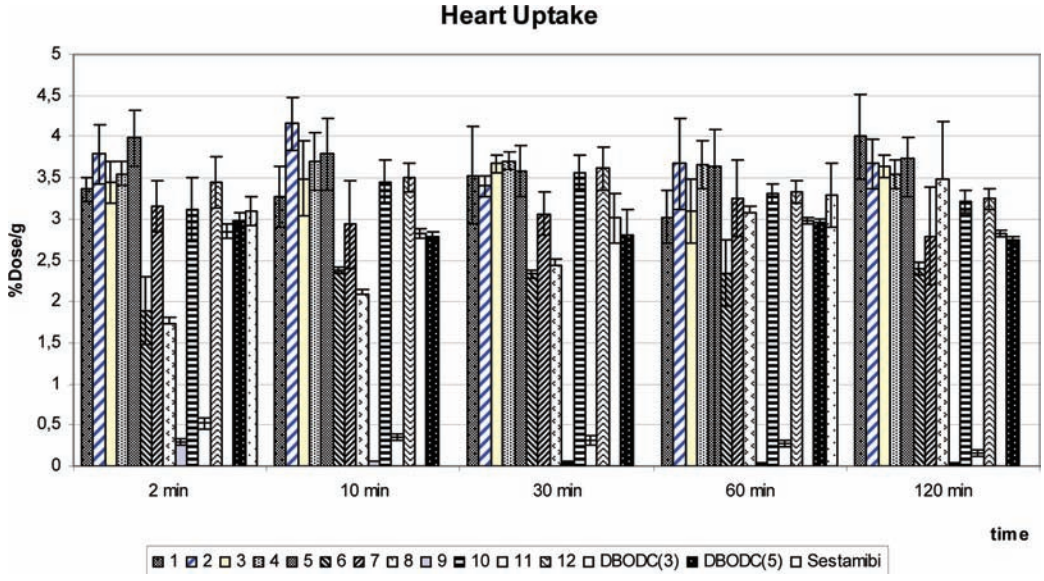


Figure 2. Comparison of heart activity over time of ^{99m}Tc-complexes.

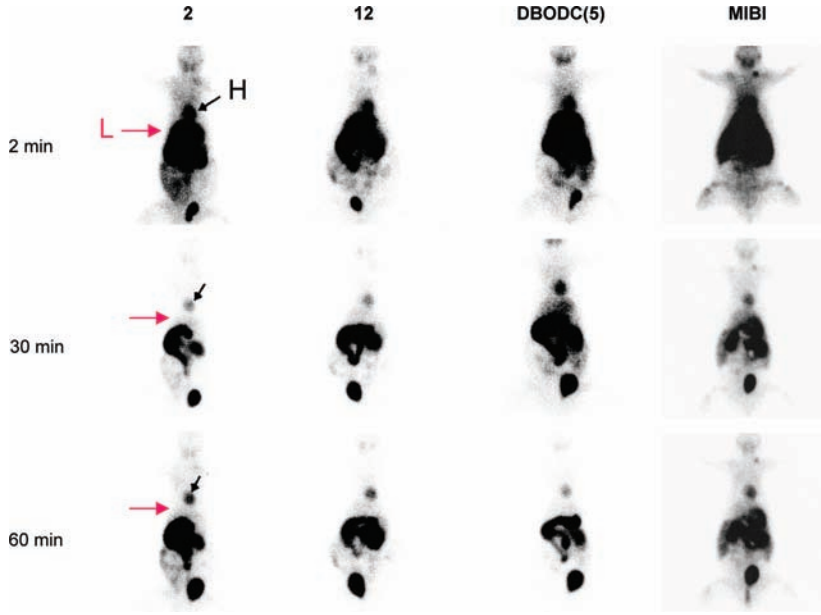


Figure 3. Planar imaging of the rats administrated with 55.0 MBq of **2**, **12**, ^{99m}Tc-DBODC5, and ^{99m}Tc-Sestamibi.

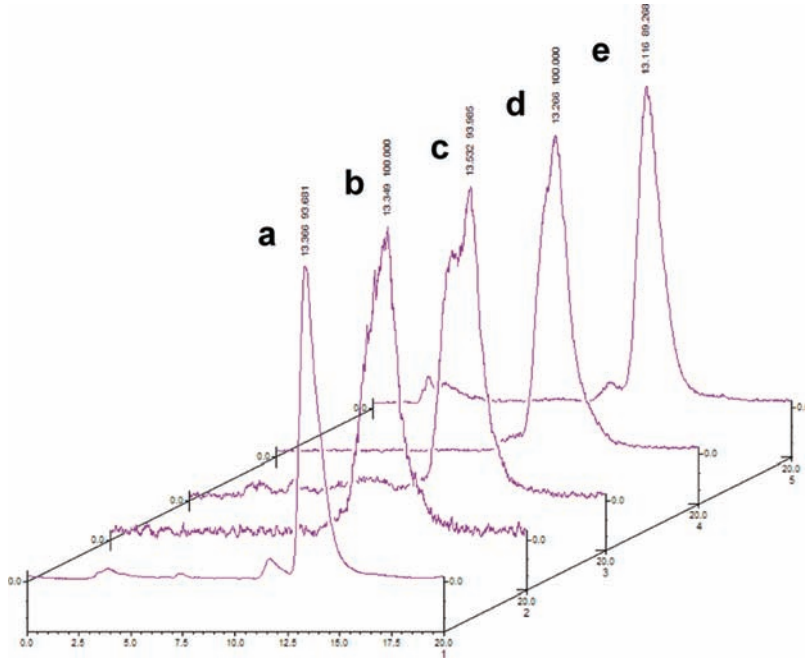


Figure 4. HPLC profile of **2** after tissue extraction: (a) control; (b) activity extracted from myocardial tissue; (c) activity extracted from endoluminal content; (d) activity extracted from kidneys; (e) urine. Similar results were obtained for **12**.

[^{99m}Tc(N)(DTC)(PNP)]$^{+}$ compounds, differences in biological behavior were found to be dependent on the nature of the dithiocarbamate ligands and on the modifications of the functional group attached either to the phosphorus or to the nitrogen atom of the PNP ligand (*8, 23*).

Considering the [^{99m}Tc(N)(DTC-Ln)(PNP3)]$^{+}$ series of complexes, we observed that variations in distribution properties were related to the nature of the dithiocarbamate ligand. The most important effects of modifications were changes in heart accumulation. In particular, the replacement in DBODC of the linear chain with alicyclic groups was responsible, in spite of their low log k'_0 values, for a significant increase in myocardial uptake (in the order DTC-L2 > DTC-L1 > DTC-L4) which resulted, at 2 min p.i., in 10−20% higher accumulation than that of both ^{99m}Tc-(N)-DBODC(3/5) and ^{99m}Tc-Sestamibi (Figure 2). Meanwhile, a considerable decrease of heart activity was observed after the administration of **6** and of **8** which correspond to the least and most lipophilic compounds, respectively.

A parallel increase in myocardial accumulation was also detected for [^{99m}Tc(N)(DBODC)(PNP)]$^{+}$ series of complexes, where PNP was PNP5,7 or PNP10 alternatively, when the linear dithiocarbamate ligand (DBODC) was replaced with the alicyclic DTC-L2.

The incorporation, in the [^{99m}Tc(N)(PNP)]$^{2+}$ synthon, of alicyclic dithiocarbamates should be consistent with a significant variation of the hydration sphere of the final mixed compounds and probably with an enhancement of their asymmetry.

In particular, the lack of a polar center (O, N) in saturated alicyclic dithiocarbamate such as DTC-L1 and DTC-L2 reduced the hydration possibility of this domain of the complex which therefore should appear less hydrated with respect to the (more polar) diphosphinoamine fragment. As a result, the exposition

of the less hydrated portion of the molecule to the hydrophobic cellular components may facilitate the interaction and the diffusion of the agents through the cellular membrane, increasing their extraction from the myocytes at early injection point.

In view of the series of the $[^{99m}Tc(N)(DBODC)(PNP)]^+$ complexes, the replacement of the diphosphine ligands PNP3 or PNP5 with PNP7 or PNP10 (replacement of four methoxypropyl with four methoxyethyl pendant groups at P donors) caused a considerable reduction of liver activity and consequently a reduction in activity in the intestinal tract, and a concomitant increased uptake in the urinary tract. This outcome is due to the enhanced hydrophilic properties of the molecules as a result of the shortening of the ether groups.

For both compounds, myocardial uptake was high and invariable over time; in particular, **12** showed heart activity comparable to that of **2** and was consequently higher with respect to the lead $^{99m}Tc(N)$-compounds, and showed favorable heart-to-lung and heart-to-liver ratios.

Unexpectedly, in **9** (log k'_0 1.09) the introduction of the highly hydrophilic hydroxymethyl groups in the PNP3OH ligand, led to a greater intestinal excretion of the activity with respect to urine. The heart uptake was initially very low, with additional wash-out.

These findings evidenced that lipophilicity remains an important factor influencing the biodistribution profile of these classes of tracers. In addition, slight differences in tissue biodistribution were also found depending on the nature of the chain attached to the tertiary amino group of the PNP ligand (PNP3/PNP10 = $-CH_2CH_2OCH_3$; PNP5/PNP7 = $-CH_2CH_2OCH_2CH_3$). Meanwhile, the heart uptake of these complexes was almost the same, and differences in lungs and liver uptake and washout were evidenced. In fact, as previously observed for $^{99m}Tc(N)(DBODC)(3/5)$ or for other cationic asymmetrical dithiocarbamate $^{99m}Tc(N)$-compounds bearing PNP3 or PNP5 diphosphinoamine (*8*), the replacement of the terminal $-OCH_3$ group on the nitrogen chain of PNP ligand with the $-OCH_2CH_3$ one led to a slight enhancement of the nontarget tissue uptake and to a reduction of the rate of elimination of the complex from the pulmonary and hepatic districts corresponding to a reduction of the heart-to-lung or the heart-to-liver ratios.

On the basis of all these results, we thought to combine in **5** the best pharmacokinetic properties of the corresponding homologue compounds **2** and **12**. Actually, the placing of DTC-L2 instead of DBODC produced a notable increase of myocardial uptake in comparison with that of complex **12** (3.98 ± 0.34 vs 3.45 ± 0.31), but its biodistributive pattern was affected by an augmented activity accumulation in nontarget tissues, such as lungs and liver, followed by a reduced washout, thus giving low target-to-nontarget ratios if compared with those of **2** and

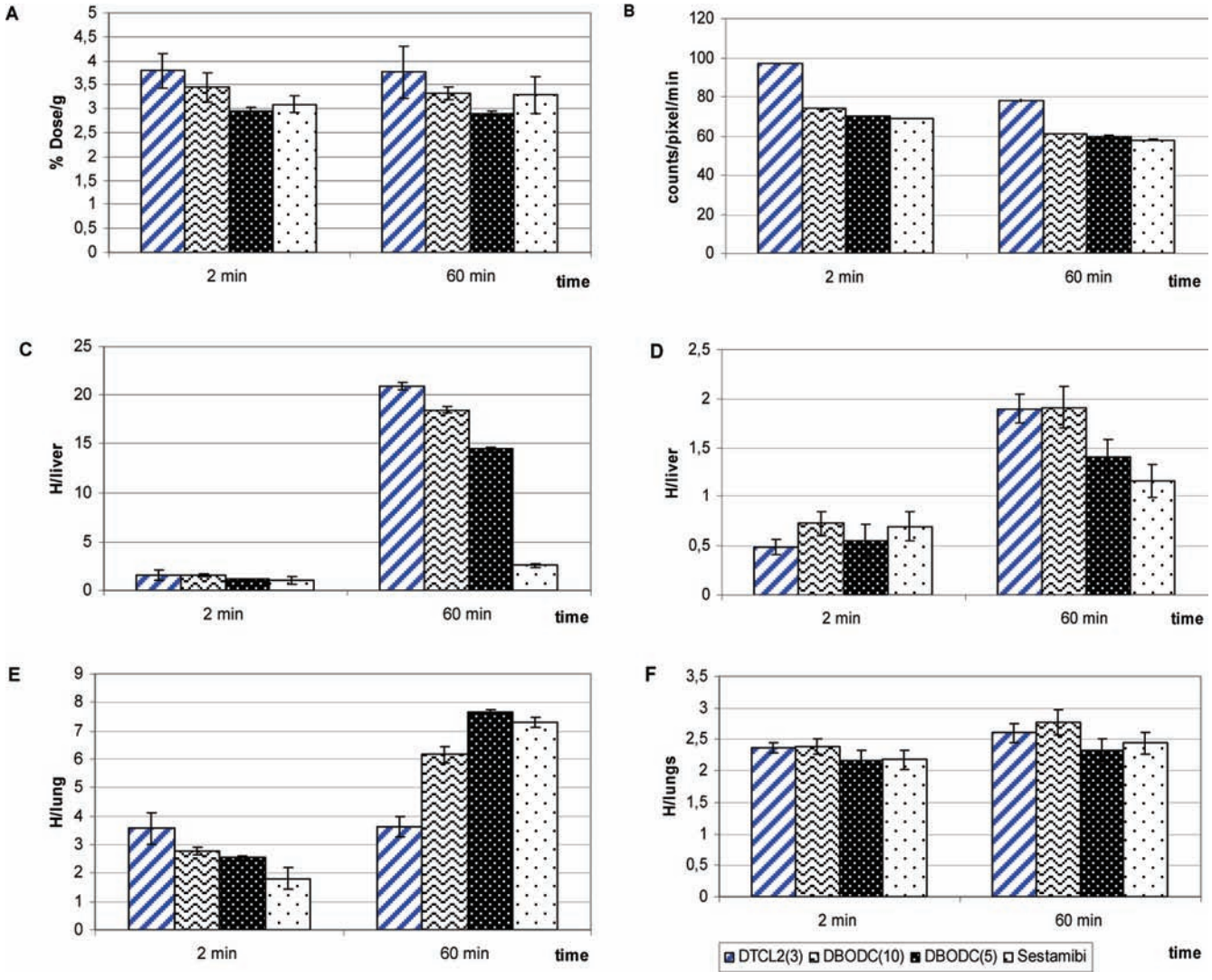


Figure 5. Comparison of (a) heart activity; (b) heart-to-liver activity ratios; and (c) heart-to-lung activity ratios over time from γ-well counting (A, C, and E); and *in vivo* image quantification (B, D, and F) of the most promising $^{99m}Tc(N)$compounds [**2**-DTC-L2(3) and **12**-DBODC(10)] with ^{99m}Tc-DBODC5 and ^{99m}Tc-Sestamibi.

12. This fact suggested for **5** a different clearance pathway with respect to the other complexes, thus evidencing that dimension and shape can significantly affect the biodistribution properties of this class of tracers.

Comparison with Gold Standard ^{99m}Tc-Agents. As previously indicated, among a series of several properties an ideal perfusion tracer should have a high first-pass extraction fraction with stable myocardial retention. Since the first-pass extraction takes place within the first 2 min after injection, the 2 min heart uptake may be used for a rough assessment of the first-pass extraction fraction of these new compounds. In general, higher heart uptake at 2 min p.i. suggests a better first-pass extraction fraction.

Amid the tested compounds, **2** and **12** presented superior biological profiles. Comparison of the heart activity uptake over time of the best candidates with respect to ^{99m}Tc-(N)-DBODC5 and to the commercially available agent ^{99m}Tc-Sestamibi is reported in Figure 5a. Variations of the heart-to-liver uptake and the heart-to-lung uptake are reported in Figure 5b,c.

Data at 2 min p.i. showed that the myocardial uptakes of both **2** and **12** were higher than the accumulation of ^{99m}Tc-(N)-DBODC5 and ^{99m}Tc-Sestamibi. These findings prompted us to believe that these new compounds might possess a first-pass extraction fraction superior to that of the standard cationic ^{99m}Tc-(N)-DBODC5, ^{99m}Tc-Sestamibi, and ^{99m}Tc-Tetrofosmin tracers. Accurate determination should be performed in more appropriate animal models.

For both **2** and **12**, the heart-to-liver ratio, at 1 h p.i., was much more favorable in comparison with ^{99m}Tc-Sestamibi ratios and similar to that found for ^{99m}Tc-(N)-DBODC5 (Figure 5 c). From a clinical point of view, the remarkably rapid efflux of these new agents from the liver without reducing myocardial uptake would be a great advance, allowing a more accurate assessment of myocardial perfusion. In fact, fast liver clearance may significantly reduce photon scatter from the liver into the inferior and in the inferoapical walls on myocardial perfusion images, thus reducing artifacts and potentially improving the diagnostic accuracy for the detection of coronary artery disease compared with that of the other ^{99m}Tc-perfusion tracers (*11*).

The heart-to-lung ratio of **12** was comparable with those of the reference tracers, whereas the **2** ratios were slight lower. In spite of this, the collected whole-body imaging of this latter complex showed a good heart-to-lung contrast comparable to those of the other compounds.

Recently, we investigated the mechanism of distribution, retention, and excretion of ^{99m}Tc-(N)-DBODC5 (*10*). Considering the close equivalence in chemical structure of these novel ^{99m}Tc(N)-complexes (**2** and **12**) with ^{99m}Tc-(N)-DBODC5, it is reasonable to assume for these tracers a similar mechanism of heart accumulation: lipophilicity modulates the penetration of the complexes into the cellular membrane, while electronic charge is responsible for irreversible tissue uptake, which is mediated by the negative mitochondrial transmembrane potential. Consequently, it is also realistic to believe that the better myocardial uptake of these agents was likely caused by the enhanced capability to cross the plasma membrane. In general, the aptitude of a monocationic compound to diffuse freely through the cell membrane is correlated with the lipophilicity of the complexes evaluated as log *P* values (*23, 24, 32*−*34*). Data obtained in this investigation suggested that despite the fact that lipophilicity remained an important factor influencing the pharmacokinetic properties of these agents, dimension, shape, and changes in the hydration sphere of the molecules have an important role in heart uptake.

In addition, metabolic studies aimed to clarify the reasons behind the rapid excretion of these new ^{99m}Tc(N)-complexes from nontarget tissues revealed that the agents were eliminated in the native (unmetabolized) form, indicating that metabolization of these ^{99m}Tc(N)-compounds cannot explain their favorable pharmacokinetic properties and rapid efflux from nontarget tissues.

Pgp and MRP are important determinants of the pharmacokinetic profile of different drugs. In addition to their overexpression in tumors, Pgp/MRP are normally located in several tissues involved in excretory functions, including the biliary surface of hepatocytes, the apical surface of mucosal cells in the small intestine and colon, and the brush border of proximal tubule cells in the kidney (*35*−*37*). In a recent study, we found that the rapid efflux of ^{99m}Tc-(N)-DBODC5 from nontarget tissues is correlated to Pgp/MRP function (*10*). Thus, the close equivalence in the metabolic profile of **2**, **12**, and ^{99m}Tc-(N)-DBODC5 suggested that the markedly rapid efflux from the principal organs of metabolism may be correlated to the Pgp/MRP transport function of these sites (*10*). This common behavior supports the possibility that the diagnostic application of this class of ^{99m}Tc(N)-complexes could be extended to oncology as in tumor and in MDR imaging studies (*38*).

CONCLUSIONS

The synthesis and the biological evaluation of novel cationic mixed ligand compounds of the type [^{99m}Tc(N)(DTC)-(PNP)]$^{+}$(DTC = DTC-Ln or DBODC) as potential myocardial imaging agents were described. In these compounds, modifications of the dithiocarbamate and PNP ligands led to a fine modulation of the lipophilic properties of the final complex. Notably, the introduction of alicyclic dithiocarbamate determined a significant increase of the heart uptake at early injection point, suggesting that the first-pass extraction fraction of such complexes may be augmented with respect to the other cationic ^{99m}Tc-agents.

This preliminary study clearly shows that through an appropriate modification of molecular properties such as lipophilicity, volume, and shape it is possible to design and develop new myocardial imaging agents with improved biodistribution profile with respect to the ^{99m}Tc-(N)-DBODC5 lead compound.

ACKNOWLEDGMENT

We thank Dr. G. Gerardi from the Department of Veterinary Clinical Science of Padua and Dr. G. Saladini from the Nuclear Medicine Service, Istituto Oncologico Veneto (IOV) of Padua for their collaboration in imaging studies, Mr. Mariano Schiavon for his assistance in the biological studies, and Mrs. Anna Rosa Moresco for her work in the elemental analysis. We also thank Nihon Medi-Physic, Tokyo, Japan, for the financial support of this work.

Supporting Information Available: HPLC chromatograms of **2** and **12** incubated at 37 °C for 60 min in rat serum, along with selected biodistribution data for cationic [^{99m}Tc(N)(DTC-Ln)(PNP)]$^{+}$ and [^{99m}Tc(N)(DBODC)(PNP)]$^{+}$ complexes and heart-to-background ratios for all cationic ^{99m}Tc(N)-complexes. This material is available free of charge via the Internet at http://pubs.acs.org.

LITERATURE CITED

(1) Llaurado, J. G. (2001) The quest for the perfect myocardial perfusion indicator… still a long way to go. *J. Nucl. Med. 42*, 282–284.

(2) Schwaiger, M., and Melin, J. (1999) Cardiological applications of nuclear medicine. *Lancet 354*, 661–666.
(3) Parker, J. A. (2001) Cardiac nuclear medicine in monitoring patients with coronary heart disease. *Semin. Nucl. Med. 31*, 223–237.
(4) Kapur, A., Latus, K. A., Davies, G., Dhawan, R. T., Eastick, S., Jarritt, P. H., Roussakis, G., Young, M. C., Anagnostopoulos, C., Bomanji, J., Costa, D. C., Pennell, D. J., Prvulovich, E. M., Ell, P. J., and Underwood, R. S. (2002) A comparison of three radionuclide myocardial perfusion tracers in clinical practice: the ROBUST study. *Eur. J. Nucl. Med. 29*, 1608–1616.
(5) Kailasnath, P., and Sinusus, A. J. (2001) Comparison of Tl-201 with Tc-99m-labeled myocardial perfusion agents: technical, physiological, and clinic issues. *J. Nucl. Cardiol. 8*, 482–498.
(6) Pasqualini, R., Duatti, A., Bellande, E., Comazzi, V., Brucato, V., Hoffschir, D., Fagret, D., and Comet, M. (1994) Bis (dithiocarbamato) nitrido technetium-99m radiopharmaceuticals: a class of neutral myocardial imaging agents. *J. Nucl. Med. 35*, 334–341.
(7) Boschi, A., Bolzati, C., Uccelli, L., Duatti, A., Benini, E., Refosco, F., Tisato, F., and Piffanelli, A. (2002) A class of asymmetrical nitrido ^{99m}Tc heterocomplexes as heart imaging agents with improved biological properties. *Nucl. Med. Commun. 23*, 689–693.
(8) Boschi, A., Uccelli, L., Bolzati, C., Duatti, A., Sabba, N., Moretti, E., Di Domenico, G., Zavattini, G., Refosco, F., and Giganti, M. (2003) Synthesis and biologic evaluation of monocationic asymmetrical ^{99m}Tc-nitride heterocomplexes showing high heart uptake and improved imaging properties. *J. Nucl. Med. 44*, 806–814.
(9) Bolzati, C., Refosco, F., Cagnolini, A., Tisato, F., Boschi, A., Duatti, A., Uccelli, L., Dolmella, A., Marotta, E., and Tubaro, M. (2004) Synthesis, solution-state and solid-state structural characterization on monocationic nitrido heterocomplex [M(N)(DTC)(PNP)] + (M=99Tc, Re; DTC = dithiocarbammate; PNP = heterodiphosphine). *Eur. J. Inorg. Chem. 9*, 1902–1913.
(10) Bolzati, C., Cavazza-Ceccato, M., Agostini, S., Tokunaga, S., Casara, D., and Bandoli, G. (2008) Subcellular distribution and metabolism studies of the potential myocardial imaging agent [^{99m}Tc(N)(DBODC)(PNP5)]$^{+}$. *J. Nucl. Med. 49*, 1336–1344.
(11) Hatada, K., Riou, L. M., Ruiz, M., Yamamichi, Y., Duatti, A., Lima, R. L., Allen, R., Goode, A. R., Watson, D. D., Beller, G. A., and Glover, D. K. (2004) ^{99m}Tc-N-DBODC5, a new myocardial perfusion imaging agent with rapid liver clearance: comparison with ^{99m}Tc-Sestamibi and ^{99m}Tc-Tetrofosmin in rats. *J. Nucl. Med. 45*, 2095–2101.
(12) Hatada, K., Ruiz, M., Riou, L. M., Lima, R. L., Goode, A. R., Watson, D. D., Beller, G. A., and Glover, D. K. (2006) Organ biodistribution and myocardial uptake, washout, and redistribution kinetics of Tc-99m N-DBODC5 when injected during vasodilator stress in canine models of coronary stenoses. *J. Nucl. Cardiol. 6*, 779–790.
(13) Cittanti, C., Uccelli, L., Pasquali, M., Boschi, A., Flammia, C., Bagatin, E., Casali, M., Stabin, M. G., Feggi, L., Giganti, M., and Duatti, A. (2008) Whole-body biodistribution and radiation dosimetry of the new cardiac tracer ^{99m}Tc-N-DBODC. *J. Nucl. Med. 49*, 1299–1304.
(14) Glover, D. K., Ruiz, M., Yang, J. Y., Smith, W. H., Watson, D. D., and Beller, G. A. (1997) Myocardial ^{99m}Tc-tetrofosmin uptake during adenosine-induced vasodilatation with either a critical or mild coronary stenosis: comparison with 201Tl and regional myocardial blood flow. *Circulation 96*, 2332–2338.
(15) Glover, D. K., Ruiz, M., Takehana, K., Petruzella, F. D., Riou, L. M., Rieger, J. M., Macdonald, T. L., Watson, D. D., Linden, J., and Beller, G. A. (2001) Pharmacological stress myocardial perfusion imaging with the potent and selective A(2A) adenosine receptor agonists ATL193 and ATL146e administered by either intravenous infusion or bolus injection. *Circulation 104*, 1181–1187.
(16) Glover, D. K., Ruiz, M., Edwards, N. C., Cunningham, M., Simanis, J. P., Smith, W. H., Watson, D. D., and Beller, G. A. (1995) Comparison between 201Tl and ^{99m}Tc sestamibi uptake during adenosine-induced vasodilatation as a function of coronary stenosis severity. *Circulation 91*, 813–820.
(17) Rumsey, W. L., Rosenspire, K. C., and Nunn, A. D. (1992) Myocardial extraction of teboroxime: effects of teboroxime interaction with blood. *J. Nucl. Med. 33*, 94–101.
(18) Fagret, D., Ghezzi, C., and Vanzetto, G. (2001) ^{99m}Tc-N-NOET imaging for myocardial perfusion: can it offer more than we already have? *J. Nucl. Med. 42*, 1395–1396.
(19) Uccelli, L., Giganti, M., Duatti, A., Bolzati, C., Pasqualini, R., Cittanti, C., Colamussi, P., and Piffanelli, A. (1995) Subcellular distribution of technetium-99m-NOEt in rat myocardium. *J. Nucl. Med. 36*, 2075–2079.
(20) Vanzetto, G., Calnon, D. A., Ruiz, M., Watson, D. D., Pasqualini, R., Beller, G. A., and Glover, D. K. (1997) Myocardial uptake and redistribution of ^{99m}Tc-N-NOET in dogs with either sustained coronary low flow or transient coronary occlusion: comparison with 201Tl and myocardial blood flow. *Circulation 96*, 2325–2331.
(21) Narra, R. K., Nunn, A. D., Kuczynski, B. L., Feld, T., Wedeking, P., and Eckelman, W. C. (1989) A neutral Technetium-99m complex for myocardial imaging. *J. Nucl. Med. 30*, 1830–1837.
(22) Kim, Y. S., He, Z., Hsieh, W. Y., and Liu, S. (2006) A novel ternary ligand system useful for the preparation of cationic ^{99m}Tc-diazenido complexes and ^{99m}Tc-labelling small biomolecules. *Bioconjugate Chem. 17*, 473–484.
(23) Liu, S., He, Z., Hsieh, W. Y., and Kim, Y. S. (2006) Evaluation of novel cationic ^{99m}Tc-nitrido complexes as radiopharmaceuticals for heart imaging: improving liver clearance with crown ether groups. *Nucl. Med. Biol. 33*, 419–432.
(24) He, Z., Hsieh, W. Y., Kim, Y. S., and Liu, S. (2006) Evaluation of novel cationic ^{99m}Tc(I)-tricarbonyl complexes as potential radiotracers for myocardial perfusion imaging. *Nucl. Med. Biol. 33*, 1045–1053.
(25) Kim, Y. S., He, Z., Hsieh, W. Y., and Liu, S. (2007) Impact of bidentate chelators on lipophilicity, stability, and biodistribution characteristics of cationic ^{99m}Tc-nitrido complexes. *Bioconjugate Chem. 18*, 929–936.
(26) Fang, W., Liu, Y. J., Zhu, L., Kim, Y. S., Liu, S., and He, Z. X. (2008) Evaluation of (TcN)-Tc-99m-15C5 as a new myocardial perfusion imaging agent in normal dogs and canines with coronary stenosis. *Nucl. Med. Com. 29*, 775–781.
(27) Kim, Y. S., Wang, J. J., Broisat, A., Glover, D. K., and Liu, S. (2008) Tc-99m-N-MPO: Novel cationic Tc-99m radiotracer for myocardial perfusion imaging. *J. Nucl. Cardiol. 15*, 535–546.
(28) Kim, Y. S., Shi, J. Y., Zhai, S. Z., Hou, G. H., and Liu, S. (2009) Mechanism for myocardial localization and rapid liver clearance of Tc-99m-N-MPO: A new perfusion radiotracer for heart imaging. *J. Nucl. Cardiol. 16*, 571–579.
(29) Bolzati, C., Benini, E., Cavazza-Ceccato, M., Cazzola, E., Malagò, E., Agostini, S., Tisato, F., Refosco, F., and Bandoli, G. (2006) From symmetrical to asymmetrical nitrido phosphinothiol complexes: A new class of neutral mixed-ligand ^{99m}Tc-complexes as potential brain imaging agents. *Bioconjugate Chem. 17*, 419–428.
(30) Tisato, F., Refosco, F., Bolzati, C., Agostini, S., Porchia, M., Cavazza-Ceccato, M., and Tokunaga, S. (2006) Intermediate compound of technetium nitride complex for radiodiagnostic imaging, patent n PCT/JP2006/301260.
(31) Kothari, K. K., Raghuraman, K., Pillarsetty, N. K., Hoffman, T. J., Owen, N. K., Katti, K. V., and Volkert, W. A. (2003) Syntheses, *in vitro* and *in vivo* characterization of a Tc-99m-(I)-tricarbonyl-benzylamino-dihydroxymethyl phosphine (NP_2)chelate. *Appl. Radiat. Isot. 58*, 543–549.
(32) Marmion, M. E., Woulfe, S. R., Neumann, W. L., Nosco, D. L., and Deutsch, E. (1999) Preparation and characterization of technetium complexes with Schiff base and phosphine coordination: Complexes of technetium-99g and -99m with substituted acac2en and trialkyl phosphines (where acac2en=N,

NV-ethylenebis[acetylacetone iminato]). *Nucl. Med. Biol. 26*, 755–770.

(33) Lisic, E. C., Heeg, M. J., and Deutsch, E. (1999) ^{99m}Tc(L-L) $^{3+}$ complexes containing ether analogs of DMPE. *Nucl. Med. Biol. 26*, 563–571.

(34) Tisato, F., Maina, T., Shao, L. R., Heeg, M. J., and Deutsch, E. (1996) Cationic [^{99m}TcIII(DIARS)2(SR)2] + complexes as potential myocardial perfusion imaging agents (DIARS = o-phenylenebis(dimethylarsine), SR = thiolate). *J. Med. Chem. 39*, 1253–1261.

(35) Ford, J. M., and Hait, W. N. (1990) Pharmacology of drugs that alter multidrug resistance in cancer. *Pharmacol. Rev. 42*, 155–199.

(36) Gatmaitan, Z. C., and Arias, I. M. (1993) Structure and function of P-glycoprotein in normal liver and small intestine. *Adv. Pharmacol. 24*, 77–97.

(37) Fricker, G., and Miller, D. S. (2002) Relevance of mutidrug resistance protein for intestinal drug absorption *in vitro* and *in vivo*. *Pharmacol. Toxicol. 90*, 5–13.

(38) Bolzati, C., Cavazza-Ceccato, M., Gandin, V., Marzano, C., Refosco, F., Dolmella, A., Colabufo, N. A., Berardi, F., Perrone, R., and Bandoli, G. (2009) ^{99m}Tc-(N)-DBODC5 from cardiology to oncology. Preliminary *in vitro* study [PW142]. *Eur. J. Nucl. Med. Mol. Imaging 36* (Suppl 2), S309.

BC900493E

Characterization and Cancer Cell Specific Binding Properties of Anti-EGFR Antibody Conjugated Quantum Dots

Junghan Lee,[†] Youngseon Choi,[†] Keumhyun Kim,[†] Sukmin Hong,[†] Hye-Young Park,[†] Taesup Lee,[‡] Gi Jeong Cheon,[‡] and Rita Song*[,†]

Nano/Bio Chemistry Laboratory, Institut Pasteur Korea (IP-K), 696 Sampyeong-dong, Bundang-gu, Seongnam-si, Gyeonggi-do, 463-400, South Korea, and Molecular Imaging Laboratory, Korea Institute of Radiological & Medical Sciences (KIRAMS), 215-4 Gongneung-dong, Nowon-gu, Seoul, 139-706, South Korea. Received November 11, 2009; Revised Manuscript Received January 15, 2010

Synthesis of biologically active antibody conjugated quantum dots (QDs) has been of great importance in cellular imaging and diagnostics. Cetuximab (or Erbitux) is the first monoclonal antibody drug which targets the epidermal growth factor receptor (EGFR) overexpressed in most cancer cells. In the present work, we investigated three different conjugation strategies to obtain the biologically functional QD−cetuximab conjugates for the tumor-specific imaging. Successful conjugation of cetuximab to QDs was achieved using PEG conjugated polymer-coated QDs and two long-chain heterobifunctional linkers, sulfo-LC-SPDP and sulfo-SMCC. The dissociation constant of the QD−cetuximab conjugates to EGFR was determined to be 0.61 ± 0.28 nM. The cancer cell-specific binding ability of the QD−cetuximab conjugates was evaluated in vitro, and the cellular internalization of the QD−cetuximab conjugates was clearly demonstrated in live cells by confocal microscopy. The cellular imaging experiments using the QD−cetuximab conjugates showed a clear endocytosis pathway, which was evidenced by the colocalization of the QD−cetuximab conjugates with dye-labeled transferrin. These results suggest that the QD−cetuximab conjugates as an imaging modality for tumor EGFR overexpression can be expected to provide important information on the expression levels of EGFR on the cancer cells.

INTRODUCTION

Synthesis of biologically active quantum dot (QD) conjugates with a variety of biomolecules has been of great importance in cellular imaging and diagnostics (*1–3*). The conventional labeling methods using organic fluorophores or fluorescent proteins have exhibited several problems such as photobleaching or low quantum yield despite their great success. Semiconductor QD nanocrystals with unique photochemical properties such as high photoluminescence and photostability have shown great potential to overcome currently existing shortcomings for a cellular labeling agent in biological and medical applications (*4*). QD bioconjugates have demonstrated successful application in various cellular targeting and imaging studies (*3*). Optimized methodologies for obtaining biofunctional QD−antibody conjugates have become more important. Recently, Pathak et al. (*5*) claimed that the conjugation and blocking conditions for antibodies should be optimized in order to avoid nonspecific artifact labeling and maintain their original binding affinity.

Recently, commercially available activators or functional linkers have been routinely used to perform various conjugation reactions. Among them, a covalent cross-linking agent, 1-ethyl-3-(3-dimethylaminoprophyl)carbodiimide hydrochloride (EDC) has been extensively used to prepare antibody-conjugated nanoparticles (*6*). However, this method has sometimes been found to result in low quantum yield and aggregates of the final nanoparticle conjugate. To improve this chemical-induced instability, a variety of conjugation reactions should be optimized depending on the nature of antibodies and characteristics of the nanoparticles.

Cetuximab (or Erbitux) is the first monoclonal antibody (mAb) drug which targets the epidermal growth factor receptor (EGFR) overexpressed in most cancer cells (*7*) and has been widely used for the treatment of patients with metastatic colorectal carcinoma (*8, 9*). EGFR has been recognized as a biomarker of cancer cells since activation of EGFR is associated with the tumorigenic mechanisms such as autonomous cell growth, invasion, angiogenesis, and metastasis (*10, 11*). Elevated levels of EGFR are found on various types of tumors, such as breast, ovarian, lung, prostate, and colorectal cancers, and have been proposed as a prognostic marker. In this context, the recent reports exploiting cetuximab as a targeting modality for cancer diagnostics have been of great interest (*12–14*).

In the present work, we investigated three different conjugation strategies to obtain the biologically functional QD−cetuximab conjugates for the tumor-specific imaging. The conjugation efficiency, binding specificity, and cellular internalization process were also compared according to the conjugation methods. The cancer cell-specific binding ability of the QD−cetuximab conjugates was evaluated in vitro, and the cellular internalization of the QD−cetuximab conjugates was clearly demonstrated in live cells by confocal laser scanning fluorescence microscope.

EXPERIMENTAL PROCEDURES

Materials. 2,2′-(Ethylenedioxy) bis-(ethylamine), (*N*-(3-dimethylaminopropyl)-*N*′-ethylcarbodiimide hydrochloride (EDC), and dithiothreitol (DTT) were purchased from Sigma. Sulfosuccinimidyl 6-[3′-(2-pyridyldithio)propionamido]hexanoate (Sulfo-LC-SPDP) and sulfosuccinimidyl-*trans*-4-(*N*-maleimidomethyl)cyclohexane-1-carboxylate (Sulfo-SMCC) were purchased from Pierce. *O*,*O*′-Bis(2-aminoethyl) octadecaethylene glycol was

* Corresponding author. Rita Song, Ph.D., Nano/Bio Chemistry Laboratory, Institut Pasteur Korea, Tel: +82-31-8018-8230, Fax: +82-31-8018-8014, E-mail: rsong@ip-korea.org.
[†] IP-K.
[‡] KIRAMS.

10.1021/bc9004975 © 2010 American Chemical Society
Published on Web 04/26/2010

purchased from Fluka and poly(ethylene glycol) (PEG) diamines (M_w = 2000 and 5000) were obtained from SunBio. Dulbecco's Modification of Eagle's Medium (DMEM), Roswell Park Memorial Institute (RPMI), fetal bovin serum, penicillin−streptomysin, and phosphate buffered saline (PBS, pH 7.4) were obtained from Gibco. Cy5 mono-NHS ester was purchased from Amersham, and Alexa Fluor 633 conjugated transferrin was purchased from Molecular Probe. Cetuximab (Erbitux) was purchased from Merck. The cancer cell lines (A549 and CT26.WT) were kindly provided by KIRAMS (Korea Institute of Radiological & Medical Sciences).

Preparation of CdSe/ZnS Nanocrystals. The starting core/shell CdSe/ZnS nanocrystals were prepared by the previously reported method (*15, 16*) with a slight modification (see Supporting Information S1).

Preparation of PEG-Conjugated Polymer Coated QDs 2. To the solution of the polymer coated QDs **1** (500 μL of 3 μM) were added diamino poly(ethylene glycol) and EDC to obtain amine functionalized QDs (see Supporting Information S2).

Preparation of QD−Cetuximab Conjugates Using Two Bifunctional Cross-Linkers. Amine functionalized QDs **2** reacted with 1000 equiv of sulfo-LC-SPDP. DTT (3.5 μL of 1 M) was then added to the solution under nitrogen flow to reduce the disulfide bond of LC-SPDP attached to QDs **3**. After 3 h of the reaction at room temperature, the excess of sulfo-LC-SPDP was removed using a NAP-5 desalting column pre-equilibrated with a conjugation buffer (1× PBS, pH 7.4). At the same time, cetuximab antibody **5** (500 μL of 2 mg/mL) was activated by 1000 equiv of sulfo-SMCC to give SMCC activated antibody **6**. After 30 min of the reaction, the excess of sulfo-SMCC was removed by membrane filtration (MWCO, 30 kDa). Finally, the LC-SPDP modified QD **4** and the SMCC activated cetuximab **6** were mixed and incubated at room temperature for 3 h. This reaction mixture was purified by removing the unreacted antibodies using a Superdex 200 size exclusion column. The final concentration of the resulting QD−cetuximab conjugates **7** was determined by measuring the absorbance using a reported extinction coefficient (ε_{600}, 1.7×10^7 M^{-1} cm^{-1}) of the QD (*17*).

Preparation of QD−Cetuximab Conjugates 8 Using Zero-Order Cross-Linker, EDC. Another type of QD−cetuximab conjugates was prepared using a widely used coupling reagent, EDC. To 500 μL of cetuximab solution (2 mg/mL), 1000 equiv of EDC was added. After 30 min incubation, excess EDC was removed by membrane filtration (MWCO, 30 kDa). Amine-functionalized QDs were then added and incubated at room temperature for 3 h. Finally, QD−cetuximab conjugates were purified using the Superdex 200 size exclusion column.

Preparation of QD−Cetuximab Conjugates 9 Using a Short Chain Cross-Linker, Sulfo-SMCC. Cetuximab antibody (500 μL of 2 mg/mL) was reacted with DTT (65 μL of 1 M) for 2 h to reduce the disulfide bond, and excess DTT was removed by membrane filtration (MWCO, 30 kDa). 200 μL of amine functionalized QDs (3.5 μM) was reacted with 1000 equiv of sulfo-SMCC for 30 min, and SMCC-modified QDs were purified using a NAP-5 desalting column. SMCC modified QDs and reduced cetuximab antibodies were mixed and reacted at room temperature for 3 h and the final mixture was purified by using the Superdex 200 size exclusion column.

Preparation of Cy5-Labeled Cetuximab Antibody. Cy5-labeled cetuximab was prepared to study the binding affinity of cetuximab in comparison with Cy5 and nanoparticle conjugates. To 600 μL of cetuximab antibody solution (2 mg/mL), 400 μL of Cy5-mono *N*-hydroxysuccinimide (NHS) solution (2.5 mg/mL in DMSO) was added and incubated at room temperature for 3 h. Then, the Cy5-labeled cetuximab was purified by membrane filtration (MWCO, 30 kDa). The concentration of Cy5-labeled cetuximab conjugate was determined at the protein absorption peak (280 nm).

General Characterization Methods. All absorption spectra were obtained in a quartz cuvette using Cary 5000 UV−vis spectrometer (Varian Inc., CA, USA) with a spectral range 200−800 nm, a scan rate of 600 nm/min, and a slit width of 2 nm. Photoluminescence was measured by a Fluorolog−3 spectrofluorimeter (HORIBA, Jobin Yvon, UK) with excitation at 480 nm at an integration time of 0.1 s and an excitation and emission slit width of 1 nm. Agarose gel electrophoresis was performed in 1% agarose in 0.5× Tris-borate EDTA buffer (pH 8.0) at 50 V cm^{-1} for 40 min. The resulting gel image was obtained on LAS 3000 gel imager (Fuji, Japan). For identification of antibodies, the gel was poststained with Colloidal Blue solution (Invitrogen, USA). The number of cetuximab antibodies per QDs was determined by BCA protein assay, following the protocol suggested by the supplier (Thermo). For the hydrodynamic size measurement of the QD−antibody conjugates, dynamic light scattering (DLS) analysis was performed using Nano-ZS (Malvern, UK) at room temperature.

Cell Culture. The human lung carcinoma cell line, A549, which overexpresses the epidermal grow factor receptor (EGFR) was grown in Dulbeco's modified Eagle's medium (DMEM) with 10% heat-inactivated fetal bovine serum (FBS) and 0.5% penicillin (100 units/mL)−streptomycin (100 μg/mL). As a control cell line that does not express EGFR, the mouse colon carcinoma cell line CT26.WT was cultured in supplemented RPMI with 10% heat-inactivated FBS and 0.5% penicillin (100 units/mL)−streptomycin (100 μg/mL).

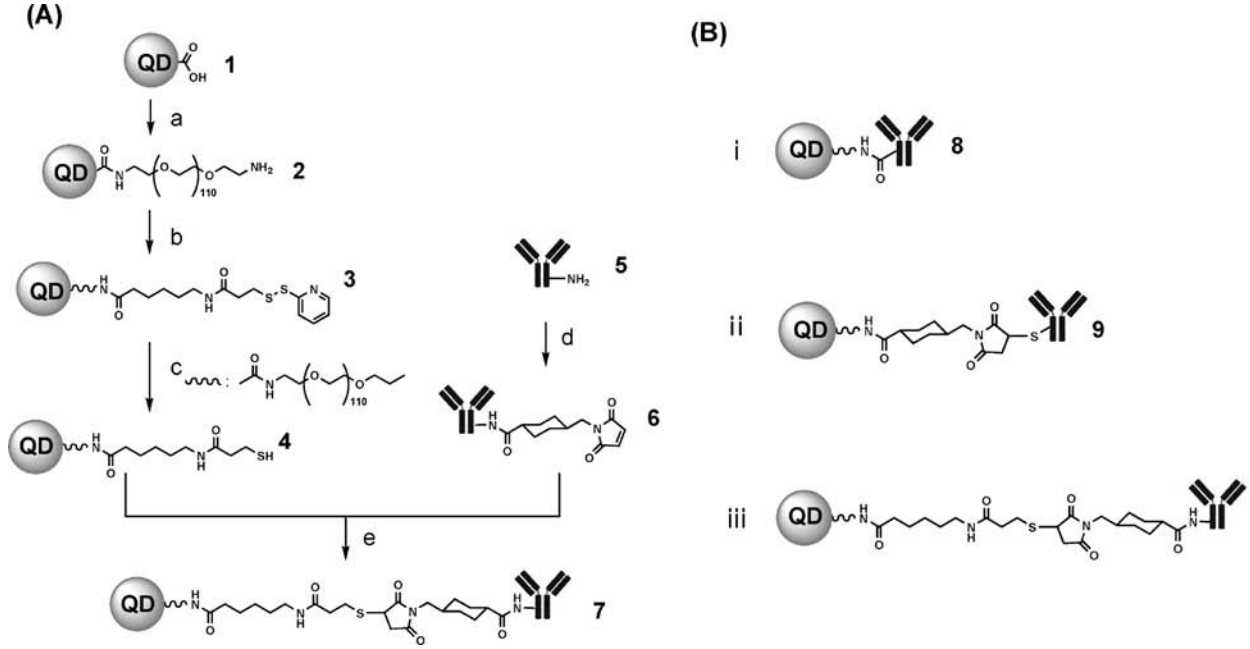
Flow Cytometry. For the specific cellular binding study, both A549 and CT26.WT cells (6×10^5 cells per tube) were incubated at 4 °C for 1 h with the solution of QD or QD−cetuximab conjugates in the final concentration of 10 nM. For the quantitative binding study, different concentrations of QD−cetuximab conjugates (0−50 nM) or Cy5-labeled cetuximab conjugates were used. The cells were then fixed with 4% paraformaldehyde at room temperature, followed by washing with fresh FACS buffer (1× PBS with 5% BSA). Cell-associated fluorescence intensity was measured using a Beckton Dickinson FACS Canto II (BD Bioscience, USA) through the PE channel (564−606 nm band-pass filter) for QD600 and APC channel (650−670 nm bandpass filter) for Cy5. FL1 fluorescence of at least 10 000 cells per sample was acquired and the mean fluorescence of the viable cells was analyzed in triplets. The data processing for K_d determination was done with *GraphPad Prism 5* software.

Cell Imaging. Cellular uptake of QD−cetuximab conjugates was investigated by confocal fluorescence microscope (Zeiss LSM5 Live). A549 cells (5000 cells/well) were seeded in glass-bottomed 8-well chamber slide (Lab-Tek) with 0.4 mL DMEM medium. After 24 h incubation at 37 °C, the cells were treated with 1 μM QD−cetuximab conjugate solution (QD final concentration = 2.5 nM). Consecutively, 1 μL of AlexaFluor (AF) 633-labeled transferrin (1 mg/mL in PBS; Invitrogen) was also added to the cell medium as an endosomal labeling reagent. After incubation at 37 °C for 20 min, the cells were washed with fresh DMEM medium three times. Fluorescence images of the cells were obtained with confocal microscope at 37 °C using a 63× oil immersion objective and a scan speed of 1 frame/s. For the excitation of QD, 488 Ar-ion laser line was used with emission bandpass filer (550−615 nm), while the AF633−transferrin conjugate was excited with 633 He−Ne laser and observed with long pass filter (650 nm).

RESULTS AND DISCUSSION

Preparation and Characterization of QD−Cetuximab Conjugates. The conjugation of biomolecules to QDs has been often a challenge due to the decreased water-solubility, quantum yield, and stability of the resulting conjugates, and the con-

Scheme 1. Synthesis of QD−Cetuximab Conjugates[a]



[a] (A) Carboxylated polymer-coated QDs were modified to amine-functionalized QDs by reacting with diamino-PEG (MW = 5000) and EDC; amine-functionalized QDs were produced by reacting with diamino-PEG molecules (a) and first activated with sulfo-LC-SPDP (b) and thiolated by a reducing reagent, DTT (c). At the same time, the cetuximab antibody was activated by sulfo-SMCC (d). After mixing two solutions, QD−cetuximab conjugates were produced (e). (B) The structures of three QD−cetuximab conjugates were presented.

comitant loss of binding affinity of biomolecules due to the steric hindrance of the nanoparticles (*18*). In this regard, our major effort was concentrated to prepare stable QD−antibody conjugates to maintain the original solubility and high binding affinity of the antibody. We prepared PEG conjugated QDs by reacting amino PEG5000 moiety with the polymer-coated QDs to improve the solubility and stability in the biological medium. This reaction allowed to introduce the amine functional groups on the QD surface (see Supporting Information S2). Many reports have demonstrated successful conjugation of protein to the nanoparticles by using EDC or sulfo-SMCC (*1, 19–21*). However, the conjugation efficiency, reactivity, and binding affinity of the resulting conjugates varied considerably depending on the reactivity of the reagents, nanoparticles, and antibodies used. Therefore, various conjugation strategies need to be tested and optimized, considering the different reactivity of the reagents and molecular characteristics of antibodies. In addition to the EDC and sulfo-SMCC for the conjugation, two different heterobifunctional linkers were also employed in order to obtain optimal antibody−QDs conjugates. This coupling strategy by using sulfo-LC-SPDP and sulfo-SMCC linkers was chosen to reduce the antibody stress and the steric hindrance of the bulky QD nanoparticles (Scheme 1). First, 10 000 equiv of sulfo-LC-SPDP were reacted with the amino PEG-functionalized QD **2** at room temperature for 1 h to give the linker attached QD **3**. After finishing the reaction, the disulfide bond at the end of the linker was cleaved by adding an excess amount of DTT. The resulting QDs **4** having the monothiol functionality were purified using a desalting column (NAP-5) equilibrated with PBS buffer (pH 7.4) to remove unreacted sulfo-LC-SPDP and DTT molecules. On the other hand, to introduce the thiol-reactive maleimido group, the amine groups of cetuximab **5** were also activated by using 10 equiv of sulfo-SMCC. Excess SMCC linker was removed by membrane filtration (MWCO 30 kDa) using 1× PBS. Finally, the maleimido-functionalized cetuximab **6** was reacted with the monothiolated QDs **4** with 10:1 molar ratio for 1 h in PBS (pH 7.4). The resulting QD−cetuximab conjugates **7** were purified by size exclusion column chromatography using the Superdex 200 equilibrated with 1× PBS (pH 7.4). Approximately 70% of the first elution fraction was collected under ultraviolet lamp (365 nm wavelength).

The first evidence of successful conjugation of QD with cetuximab was obtained from agarose gel electrophoresis (Figure 1). In gel running conditions (pH 8.5), the starting QDs barely moved on the gel because of the decreased negative charges due to the amino-PEG5k conjugation (see Supporting Information). Cetuximab antibodies (pI = 8.48) (http://www.drugbank.ca/drugs/DB00002) are slightly positively charged in the gel running buffer condition, migrating toward the negative electrode (lane 5; lower panel). On the other hand, sulfo SMCC-activated cetuximab showed net negative charges (lane 6; lower panel). The reaction of the sulfo LC-SPDP modified QDs with the sulfo SMCC activated cetuximab via thiol-maleimide coupling chemistry resulted in the formation of negatively charged QD-cetuximab conjugate. The colocalization of QDs fluorescence and cetuximab stained by Colloidal Blue (lane 3) indicated the successful attachment of QDs to the cetuximab. The simple mixture of QDs and the cetuximab did not show any migration changes (data not shown). DLS analysis indicated that the hydrodynamic size of the QD-cetuximab (27.9 ± 7.8 nm) increased compared with the starting QDs (18.4 ± 5.4 nm) (Figure 1B). The number of cetuximab bound per QD was determined to be 6.27 ± 0.62 based on the BCA protein assay with 63% conjugation efficiency.

We also tried two other conjugation methods to prepare QD−cetuximab conjugates. The reaction with EDC proved to be unsuccessful in our case as shown in the gel electrophoresis analysis (Figure 1A, lane 4). This may be due to the fact that the carboxyl residues of the cetuximab are not readily available for EDC activation or due to the accessibility issue of the amino groups of the bulky QD nanoparticles to the carboxyl residues of the antibody (the number of amino groups is ∼1.5× more than that of carboxyl group on the cetuximab antibody molecule: histidine, 26; lysine, 88; arginine, 36; aspartic acid, 52; glutamic acid, 60). In addition, these experiments sometimes resulted in

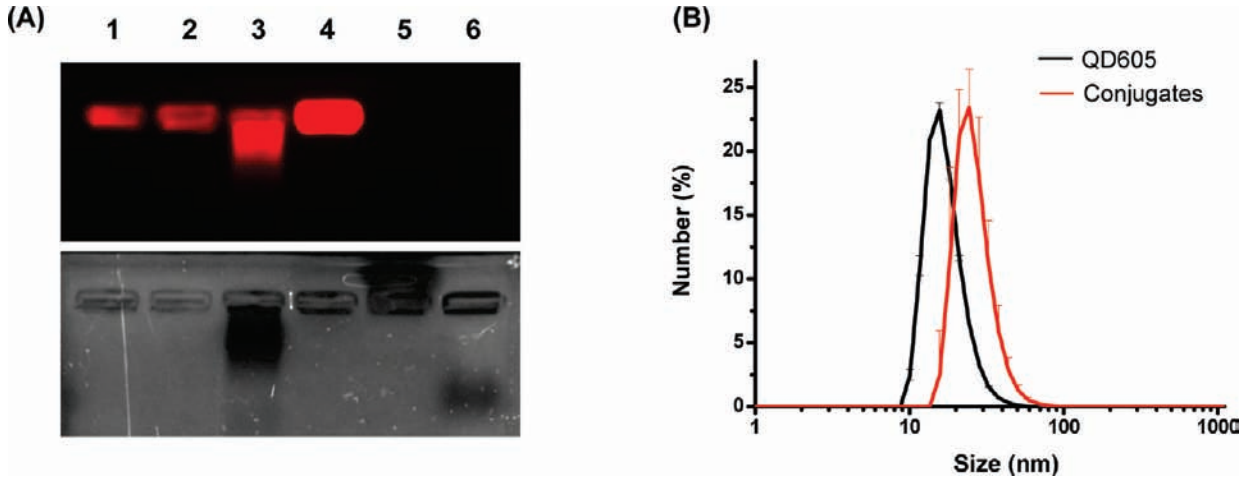


Figure 1. Confirmation of QD−cetuximab conjugates by agarose gel electrophoresis (A) and dynamic light scattering (DLS) measurement (B). (A) Fluorescence image of QD605 (up) and simultaneous protein staining with Colloidal Blue (down): 1, QD605 (control); 2, QD activated by sulfo-LC-SPDP; 3, QD−cetuximab conjugates (by LC-SPDP and SMCC linker); 4, QD−cetuximab conjugates (by EDC coupling); 5, Cetuximab antibody; 6, Cetuximab antibody activated by sulfo-SMCC (1% agarose gel 0.5× TBE buffer (pH 8.5), 50 V cm^{-1}, 40 min.

(A)

QD-cetuximab conjugates	Conc. of QD (μM)	Conc. of Cetuximab (μM)	Cetuximab/QD
EDC coupling	0.61	0.05 ± 0.19	0.08 ± 0.31
SMCC linker	2.43	11.76 ± 0.82	4.84 ± 0.34
LC-SPDP/SMCC linker	0.78	4.89 ± 0.48	6.27 ± 0.62

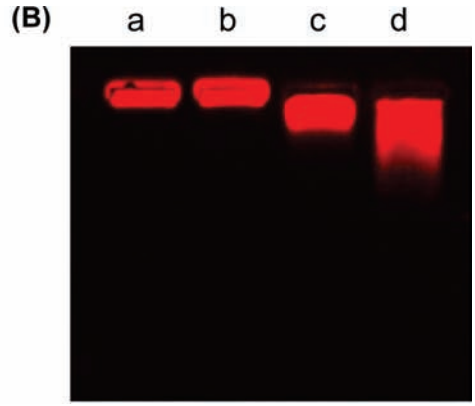


Figure 2. Molar ratio of cetuximab per QD (A) and gel electrophoresis (B): a, QD-PEG5000-NH_2; b, QD−cetuximab conjugates (EDC coupling); c, QD−cetuximab conjugates (SMCC linker), QD−cetuximab conjugates (LC-SPDP/SMCC linker).

the formation of aggregates. When the SMCC linker was used, the treatment of DTT generated the thiol groups of the cetuximab, which was then allowed to react with QD-SMCC conjugates. This approach yielded QD−cetuximab conjugate formation with 48% conjugation efficiency, which is much lower than that of the LC-SPDP-SMCC two-linker strategy. Also, these conjugates did not show any effective binding affinity to EGFR in A549 cells (see Supporting Information S3).

The low binding affinity of these conjugates can be explained by (i) the conjugation reaction by EDC resulted in extremely low conjugation efficiency, (ii) the sulfo-SMCC reaction requires the prereduction of the antibody to yield antibody fragment bearing free SH functionalities, which may reduce the original affinity of the antibody, and (iii) the steric hindrance induced by the nanoparticles can affect the affinity of the antibody by the use of short linker. The bifunctional linkers used in this study are composed of the freely rotatable sp^3 carbon (except heterocyclic ring), allowing to maximize the flexibility of the linker to diminish the steric hindrance. In this condition, the difference of the length of the linker should influence the accessibility of the QDs to antibodies.

The number of cetuximab per QD depending on the three different preparations was shown in Figure 2. While the reaction using EDC was unsuccessful, the reaction with the other two activated linkers resulted in QD−cetuximab conjugates with cetuximab molar ratio of 5−6 cetuximab/QD.

Specific Labeling of EGFR-Positive A549 Cells with QD−Cetuximab Conjugates. Cetuximab has been known to bind with EGFR-expressing cell lines such as A549 with high binding affinity (K_d = 4.54 nM) (*22*). To confirm the specificity of cetuximab toward the extracellular domain of EGFR, EGFR-positive A549 and EGFR-negative CT26.WT cells were incubated with QD−cetuximab conjugates. FACS analysis was carried out to see whether the targeting specificity of the QD−antibody conjugates toward EGFR is maintained (Figure 3A,B). QDs without cetuximab were used as a negative control. Fluorescence intensity of A549 cells incubated with QD−cetuximab conjugates **7** showed an increase of 2 orders of magnitude compared to the control CT26.WT cells. These results suggested the strong and selective binding of QD−cetuximab conjugates to EGFR expressing tumor cells. Furthermore, three types of conjugates, **7**, **8**, and **9**, were tested in EGFR-positive A549 cell solution (see Supporting Information S3).

The binding affinity of QD−cetuximab conjugates **7** was determined in A549 cells. Figure 3D shows the concentration-dependent saturation binding curve with the apparent dissociation constant (K_d) of 0.61 ± 0.28 nM. This result shows very high binding affinity of cetuximab on the QD toward A549 cells. On the other hand, that of the Cy5-labeled cetuximab was determined to be K_d = 0.22 ± 0.09 nM in identical experimental conditions (see Supporting Information S4). The slightly lower binding efficacy of the QD−cetuximab conjugate **7** than Cy5-labeled cetuximab was anticipated due to the large size of the

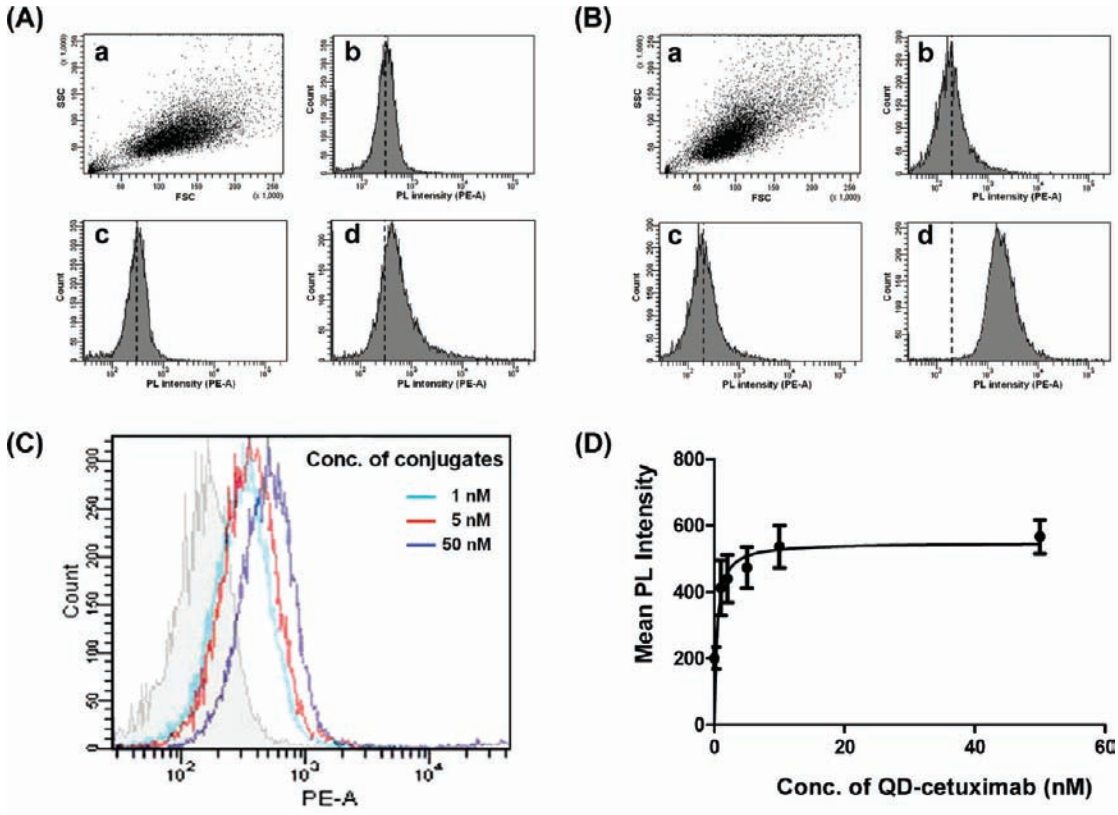


Figure 3. Specific binding of QD−cetuximab conjugates (A,B) and concentration-dependent binding (C,D) treated into the cells. Flow cytometry analysis of binding of QD605 labeled cetuximab to EGFR-negative CT26.wt cells (A) and EGFR-positive A549 cells (B): a, SSC vs FSC of the cells; b, threshold intensity of the cells; c, control QD (without cetuximab) treatment; and d, QD−cetuximab conjugates treatment. (C) PL signals depending on the concentration of QD−cetuximab conjugates treated into A549 cell and (D) a saturation binding curve obtained by the plot of mean fluorescence intensity as a function of the concentration of QD−cetuximab conjugates **7**.

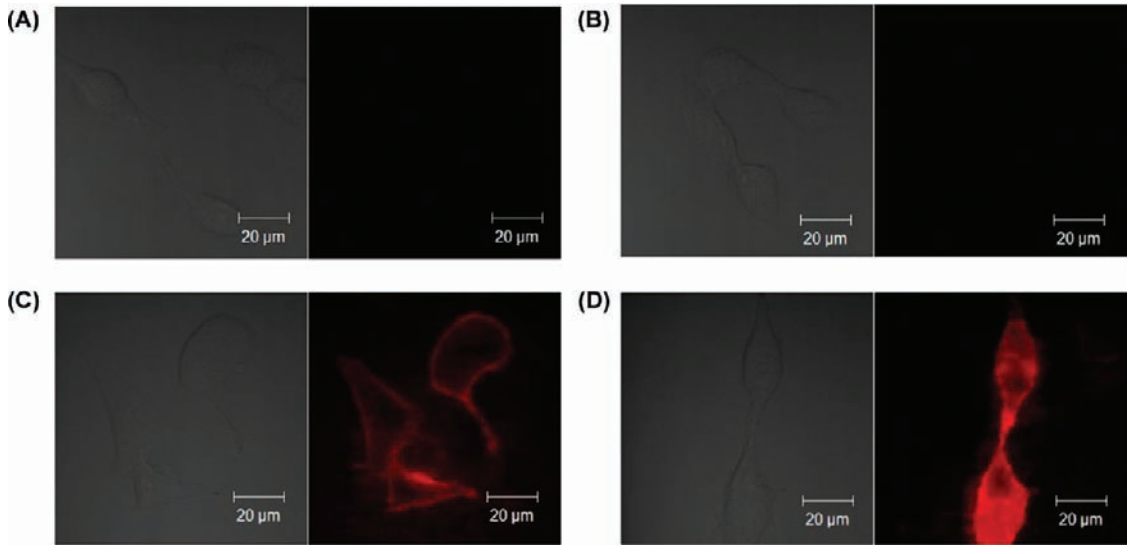


Figure 4. Competitive binding test of free cetuximab and QD−cetuximab conjugates: (A) A549 cell (control); (B) A549 cells incubated with QD−cetuximab conjugates after pretreatment of cetuximab (2 h incubation at 37 °C); (C) QD−cetuximab conjugates for 20 min; and (D) A549 cells incubated with QD−cetuximab conjugates for 1 h. Bright field image (left) and fluorescence image (right).

QDs. Wen et al. (*23*) also observed that DTPA(PEG)−cetuximab conjugate showed 66% of the binding affinity of original cetuximab. Our results represent the first quantitative analysis on the binding affinity of a nanoparticle-conjugated cetuximab for EGFR-positive cells. In our case, the specificity of QD−cetuximab conjugates **7** among the conjugates was not significantly altered after the chemical conjugation reactions. These results clearly suggested that the binding of the QD−cetuximab conjugates prepared by optimized conjugation protocol are mediated by EGFR, which leads us to implement specific detection and imaging of the EGFR overexpressed cancer cells taking advantage of the high luminescence and photostability of QD.

EGFR Imaging in Live Cell Using QD−Cetuximab Conjugates. The specific binding ability of the QD−cetuximab conjugates was tested in live cell experiments using a confocal microscope (Figure 4). The binding of QD−cetuximab conjugates to EGFR on the A549 cells occurred within 20 min (Figure

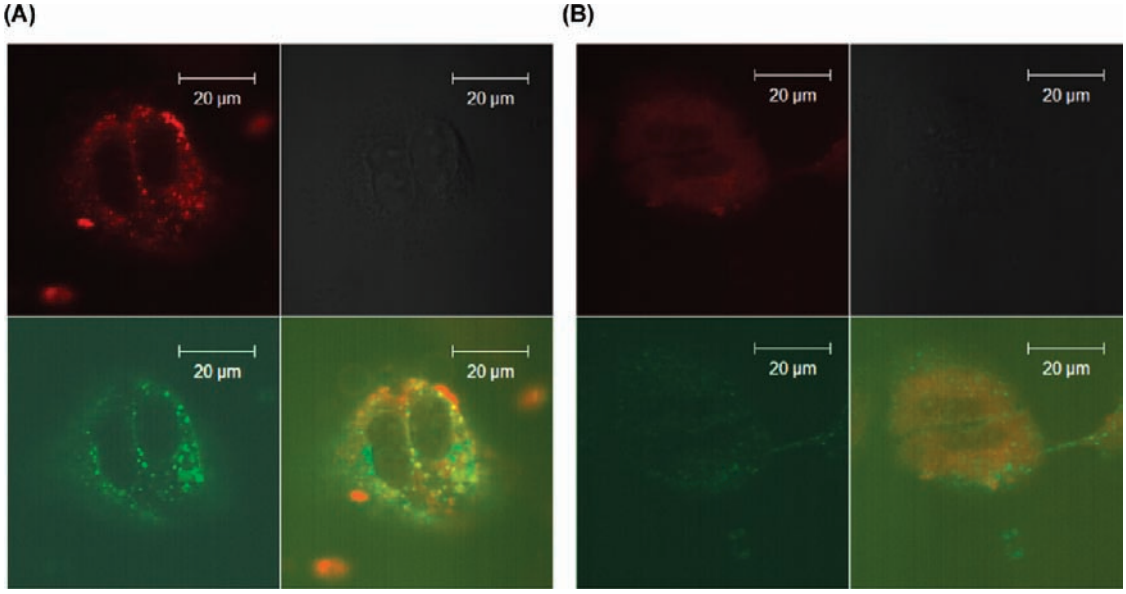


Figure 5. Fluorescence images of A549 cell treated with QD−cetuximab conjugates and Alexa633 conjugated transferrin. (A) QD−cetuximab conjugates treatment. (B) QD without cetuximab treatment. Images: QD fluorescence (up left), bright field image (up right), Alexa633 labeled transferrin (down left, pseudocolored), merge (down right).

4C). QD−cetuximab conjugate was found to bind competitively to the extracellular domain of EGFR showing exactly the same binding as cetuximab. Cetuximab binding has been known to inhibit the autophosphorylation of EGFR and induces its internalization. After 1 h incubation, most QD−cetuximab conjugates were internalized into the cytoplasm (Figure 4D). When the cells were pretreated with free cetuximab before adding the QD−cetuximab conjugates, the binding of QD−cetuximab conjugates to the cell membrane was completely blocked (Figure 4B).

The photostability of QD−cetuximab conjugates was also examined in the course of the cellular imaging (see the Supporting Information S5 and S6). QD−cetuximab conjugates clearly exhibited high photostability, of which the PL of Cy5−cetuximab decreased about 50% after 30 min of incubation. The high photostability of the QDs allowed us to observe the endocytotic pathway of QD−cetuximab conjugates in live A549 cells (Figure 5). The colocalized fluorescence images of A549 cells incubated with the QD−cetuximab conjugates and the Alexa633-labeled transferrin demonstrated that the internalization of QD−cetuximab conjugates occurred by well-known endocytosis and QD−cetuximab conjugates were trapped in endosome. Most QD−cetuximab conjugates were internalized via EGFR binding in 1 h 30 min. In a control experiment with the amine functionalized QDs without cetuximab, nonspecific binding was not observed; colocalization of QD and endosome was not detected either.

CONCLUSIONS

Successful conjugation of monoclonal anti-EGFR antibody (cetuximab) to QDs was achieved using PEG-conjugated polymer-coated QDs and two long-chain heterobifunctional linkers, sulfo-LC-SPDP and sulfo-SMCC. The dissociation constant of the QD−cetuximab conjugates to EGFR overexpressing A549 cancer cells was reproducibly determined to be 0.61 ± 0.28 nM. There was no significant nonspecific binding toward EGFR-negative CT26.WT cells. Competitive inhibition of the QD−cetuximab binding by free antibodies strongly suggested the binding specificity of the conjugates to EGFR-expressing cancer cells. As cetuximab has been known to induce internalization of EGFR, live cell imaging was performed to examine whether the QD−cetuximab conjugates were internalized by endocytosis. The cellular imaging experiments using the QD−cetuximab conjugates showed clear endocytosis pathway, which was evidenced by the colocalization of the QD−cetuximab conjugates with dye-labeled transferrin. These results suggest that the QD−cetuximab conjugates as an imaging modality for tumor EGFR overexpression can be expected to provide important information on the expression levels of EGFR on the cancer cells, including in vitro assay, cellular imaging, and in vivo imaging applications.

ACKNOWLEDGMENT

This work was supported by Ministry of Education and Science and Technology (MEST), and Korea Science and Engineering Foundation (KOSEF) through its National Nuclear Technology Program (No. 2009-0062234 and 2009-2006216) and National R&D Program (No. 2009-0082751).

Supporting Information Available: Additional information as described in the text. This material is available free of charge via the Internet at http://pubs.acs.org.

LITERATURE CITED

(1) Chan, W. C. W., and Nie, S. M. (1998) Quantum dot bioconjugates for ultrasensitive nonisotopic detection. *Science 281*, 2016–2018.
(2) Gao, X. H., Cui, Y. Y., Levenson, R. M., Chung, L. W. K., and Nie, S. M. (2004) In vivo cancer targeting and imaging with semiconductor quantum dots. *Nat. Biotechnol. 22*, 969–976.
(3) Michalet, X., Pinaud, F. F., Bentolila, L. A., Tsay, J. M., Doose, S., Li, J. J., Sundaresan, G., Wu, A. M., Gambhir, S. S., and Weiss, S. (2005) Quantum dots for live cells, in vivo imaging, and diagnostics. *Science 307*, 538–544.
(4) Bailey, R. E., Smith, A. M., and Nie, S. M. (2004) Quantum dots in biology and medicine. *Phys. E 25*, 1–12.
(5) Pathak, S., Cao, E., Davidson, M. C., Jin, S. H., and Silva, G. A. (2006) Quantum dot applications to neuroscience: New tools for probing neurons and glia. *J. Neurosci. 26*, 1893–1895.
(6) Hermanson, G. T. (2008) Zero-length crosslinkers. In *Bioconjugate Techniques*, pp 216−223, Elsevier Science, San Diego, CA.
(7) Mendelsohn, J. (2002) Targeting the epidermal growth factor receptor for cancer therapy. *J. Clin. Oncol. 20*, 1S–13S.

(8) Wong, S. F. (2005) Cetuximab: An epidermal growth factor receptor monoclonal antibody for the treatment of colorectal cancer. *Clinical Therapeutics 27*, 684–694.

(9) Saltz, L. B., Meropol, N. J., Loehrer, P. J., Needle, M. N., Kopit, J., and Mayer, R. J. (2004) Phase II trial of cetuximab in patients with refractory colorectal cancer that expresses the epidermal growth factor receptor. *J. Clin. Oncol. 22*, 1201–1208.

(10) Johnstone, P. A. S. (2002) The epidermal growth factor receptor: A new target for anticancer therapy - Introduction. *Curr. Prob. Cancer 26*, 114–164.

(11) Ritter, C. A., and Arteaga, C. L. (2003) The epidermal growth factor receptor-tyrosine kinase: A promising therapeutic target in solid tumors. *Semin. Oncol. 30*, 3–11.

(12) Li, W. P., Meyer, L. A., Capretto, D. A., Sherman, C. D., and Anderson, C. J. (2008) Receptor-binding, biodistribution, and metabolism studies of Cu-64-DOTA-cetuximab, a PET-imaging agent for epidermal growth-factor receptor-positive tumors. *Cancer Biother. Radiopharm. 23*, 158–171.

(13) Eiblmaier, M., Meyer, L. A., Watson, M. A., Fracassol, P. M., Pike, L. J., and Andersonl, C. J. (2008) Correlating EGFR expression with receptor-binding properties and internalization of Cu-64-DOTA-cetuximab in 5 cervical cancer cell lines. *J. Nucl. Med. 49*, 1472–1479.

(14) Wu, G., Barth, R. F., Yang, W. L., Chatterjee, M., Tjarks, W., Ciesielski, M. J., and Fenstermaker, R. A. (2004) Site-specific conjugation of boron-containing dendrimers to anti-EGF receptor monoclonal antibody cetuximab (IMC-C225) and its evaluation as a potential delivery agent for neutron capture therapy. *Bioconjugate Chem. 15*, 185–194.

(15) Yang, Y. A., Wu, H. M., Williams, K. R., and Cao, Y. C. (2005) Synthesis of CdSe and CdTe nanocrystals without precursor injection. *Angew. Chem., Int. Ed. 44*, 6712–6715.

(16) Peng, Z. A., and Peng, X. G. (2001) Formation of high-quality CdTe, CdSe, and CdS nanocrystals using CdO as precursor. *J. Am. Chem. Soc. 123*, 183–184.

(17) Yu, W. W., Qu, L. H., Guo, W. Z., and Peng, X. G. (2003) Experimental determination of the extinction coefficient of CdTe, CdSe, and CdS nanocrystals. *Chem. Mater. 15*, 2854–2860.

(18) Rosenthal, S. J., Tomlinson, A., Adkins, E. M., Schroeter, S., Adams, S., Swafford, L., McBride, J., Wang, Y. Q., DeFelice, L. J., and Blakely, R. D. (2002) Targeting cell surface receptors with ligand-conjugated nanocrystals. *J. Am. Chem. Soc. 124*, 4586–4594.

(19) Pathak, S., Davidson, M. C., and Silva, G. A. (2007) Characterization of the functional binding properties of antibody conjugated quantum dots. *Nano Lett. 7*, 1839–1845.

(20) Walther, C., Meyer, K., Rennert, R., and Neundorf, I. (2008) Quantum dot-carrier peptide conjugates suitable for imaging and delivery applications. *Bioconjugate Chem. 19*, 2346–2356.

(21) Liu, G., Lin, Y. Y., Wang, J., Wu, H., Wai, C. M., and Lin, Y. (2007) Disposable electrochemical immunosensor diagnosis device based on nanoparticle probe and immunochromatographic strip. *Anal. Chem. 79*, 7644–7653.

(22) Haeder, M., Rotsch, M., Bepler, G., Hennig, C., Havemann, K., Heimann, B., and Moelling, K. (1988) Epidermal growth factor receptor expression in human lung cancer cell lines. *Cancer Res. 48*, 1132–1136.

(23) Milenic, D. E., Wong, K. J., Baidoo, K. E., Ray, G. L., Garmestani, K., Williams, M., and Brechbiel, M. W. (2008) Cetuximab: preclinical evaluation of a monoclonal antibody targeting EGFR for radioimmunodiagnostic and radioimmunotherapeutic applications. *Cancer Biother. Radiopharm. 23*, 619–631.

BC9004975

Small-Animal PET Imaging of Human Epidermal Growth Factor Receptor Positive Tumor with a ^{64}Cu Labeled Affibody Protein

Zheng Miao,[†,‡,§] Gang Ren,[†,‡,§] Hongguang Liu,[†,‡,§] Lei Jiang,[†,‡,§] and Zhen Cheng*[,†,‡,§]

Molecular Imaging Program at Stanford (MIPS), Department of Radiology, and Bio-X Program, Stanford University, Stanford, California 94305-5344. Received November 20, 2009; Revised Manuscript Received February 25, 2010

Epidermal growth factor receptor (EGFR) has become an attractive target for cancer molecular imaging and therapy. Affibody proteins against EGFR have been reported, and thus, we were interested in evaluating their potential for positron emission tomography (PET) imaging of EGFR positive cancer. An Affibody analogue (Ac-Cys-$Z_{EGFR:1907}$) binding to EGFR was made through conventional solid phase peptide synthesis. The purified protein was site-specifically coupled with the 1,4,7,10-tetraazacyclododecane-1,4,7-tris-aceticacid-10-maleimidethylacetamide (maleimido-mono-amide-DOTA) to produce the bioconjugate, DOTA-$Z_{EGFR:1907}$. ^{64}Cu labeled probe ^{64}Cu-DOTA-$Z_{EGFR:1907}$ displayed a moderate specific activity (5−8 MBq/nmol, 22−35 μCi/μg). Cell uptake assays by pre-incubating without or with 300 times excess unlabeled Ac-Cys-$Z_{EGFR:1907}$ showed high EGFR-specific uptake (20% applied activity at 0.5 h) in A431 epidermoid carcinoma cancer cells. The affinity (K_D) of ^{64}Cu-DOTA-$Z_{EGFR:1907}$ as tested by cell saturation analysis was 20 nM. The serum stability test showed excellent stability of the probe with >95% intact after 4 h of incubation in mouse serum. In vivo small-animal PET imaging showed fast tumor targeting, high tumor accumulation (~10% ID/g at 1 h p.i.), and good tumor-to-normal tissue contrast of ^{64}Cu-DOTA-$Z_{EGFR:1907}$ spiked with a wide dose range of Ac-Cys-$Z_{EGFR:1907}$. Bio-distribution studies further demonstrated that the probe had high tumor, blood, liver, and kidney uptakes, while blood radioactivity concentration dropped dramatically at increased spiking doses. Co-injection of the probe with 500 μg of Ac-Cys-$Z_{EGFR:1907}$ for blocking significantly reduced the tumor uptake. Thus, ^{64}Cu-DOTA-$Z_{EGFR:1907}$ showed potential as a high tumor contrast EGFR PET imaging reagent. The probe spiked with 50 μg of Ac-Cys-$Z_{EGFR:1907}$ improved tumor imaging contrast which may have important clinical applications.

INTRODUCTION

Epidermal growth factor receptor 1 (EGFR) is a transmembrane protein belonging to the ErbB receptor kinase family. Overexpression of EGFR has been frequently detected in a wide range of human tumors, for example, small cell lung cancer, small cell carcinoma of the head and neck, esophageal cancer, gastric cancer, gliomas, colon cancer, pancreas cancer, breast cancer, ovarian cancer, bladder cancer, kidney cancer, prostate cancer, etc. (*1, 2*). Cetuximab, Lapatinib, Gefitinib, and Erlotinib have shown clinical benefits in lung, colorectal, pancreatic, and breast cancer patients by targeting over-expressed/activated EGFR (*3*−*5*). Furthermore, increasing evidence has demonstrated that there is a correlation between EGFR overexpression and tumor metastasis formation, therapy resistance, poor prognosis, and short survival for some cancer types. It has been found that EGFR expression level is a strong prognostic indicator for head and neck, ovarian, cervical, bladder, and esophageal cancer (*6, 7*). Therefore, EGFR has become an attractive target for cancer molecular imaging and therapy.

A variety of small molecules based upon EGFR substrates and EGF have been labeled with different radionuclides for molecular imaging of EGFR expression and activity. However, the small molecules and EGF based probes generally show rapid blood clearance and very low tumor uptake; thus, the imaging quality is poor (*8*−*10*). Radiolabeled monoclonal antibodies (MAbs) against EGFR demonstrate good tumor uptake, but the tumors can only be visualized at several hours or even days after the injection of probes because of both slow tumor targeting ability and slow clearance of the radiolabeled MAbs (*11, 12*). Recently, small protein scaffolds have shown great potential for recognizing a variety of biomarkers (*13*−*17*). Among them, Affibody molecules have demonstrated to be a promising universal platform for developing imaging or therapeutic agents for different molecular targets (*17*−*19*). Affibody molecules are small, engineered proteins with 58-amino acid residues and a three-helix bundle scaffold structure, yet at the same time they display a binding surface as large as that of antibodies. In our previous research, Affibody $Z_{HER2:477}$ site-specifically labeled with ^{18}F and ^{64}Cu has shown rapid human epidermal growth factor receptor 2 (HER2) positive tumor targeting ability and good tumor-to-normal tissue imaging contrast at even 1 h post-injection (p.i.) of the probe (*20, 21*). These results have encouraged us to further explore this type of protein scaffold for positron emission tomography (PET[2]) imaging of many other important tumor biomarkers including EGFR.

Several anti-EGFR Affibody proteins (Z_{EGFR}) with high affinities have been reported recently (*22, 23*). Some of them were radiolabeled with ^{111}In in a nonsite-specific manner and evaluated using EGFR-expressing A431 tumor xenografts. Biodistribution studies demonstrated that these Affibody molecules displayed specific and good tumor accumulation; especially, $Z_{EGFR:1907}$ was reported to show the best in vivo tumor

* To whom correspondence should be addressed. Molecular Imaging Program at Stanford, Department of Radiology and Bio-X Program, 1201 Welch Road, Lucas Expansion, P020A, Stanford University Stanford, CA 94305. Tel: 650-723-7866. Fax: 650-736-7925. E-mail: zcheng@stanford.edu.

† MIPS.

‡ Department of Radiology.

§ Bio-X Program.

[2]Abbreviations: DOTA, 1,4,7,10-tetraazacyclododecane-1,4,7,10-tetraacetic acid; PET, positron emission tomography; HPLC, high-performance liquid chromatography; p.i., postinjection.

10.1021/bc900515p © 2010 American Chemical Society
Published on Web 04/19/2010

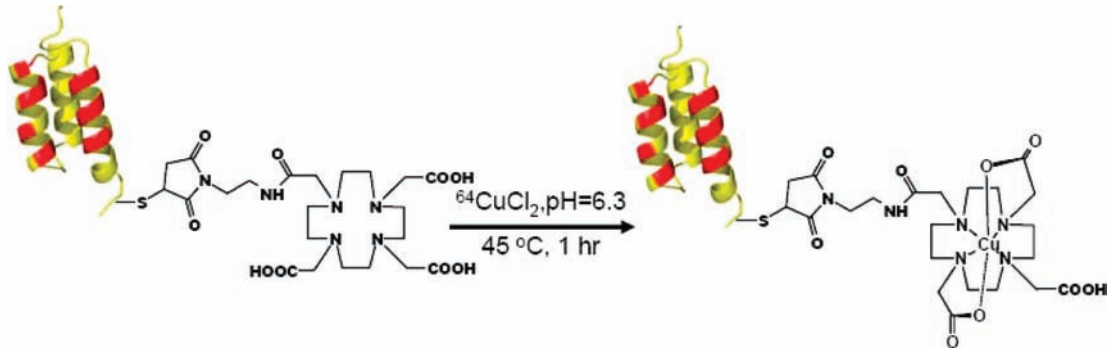


Figure 1. Anti-EGFR Affibody protein and ^{64}Cu radiolabeling of DOTA-$Z_{EGFR:1907}$ for EGFR imaging.

targeting properties. In this study, we aimed to develop an Affibody based PET probe for the imaging of an EGFR positive tumor. A $Z_{EGFR:1907}$ analogue, Ac-Cys-$Z_{EGFR:1907}$, was first synthesized so that the protein can be site-specifically conjugated with 1,4,7,10-tetraazacyclododecane-1,4,7-tris-aceticacid-10-maleimidethylacetamide (Malei mido-mono-amide-DOTA) through the cysteine residue (Figure 1). The resulting bioconjugate, Ac-Cys(DOTA)-$Z_{EGFR:1907}$ (abbreviated as DOTA-$Z_{EGFR:1907}$), was then radiolabeled with a positron emitter ^{64}Cu (half-life $t_{1/2}$ = 12.7 h, $E_\beta{}^+{}_{max}$ = 656 keV, and β^+ decay = 19%) because it can be produced in large quantities and high specific activity. The ability of ^{64}Cu-DOTA-$Z_{EGFR:1907}$ to image the EGFR positive tumor using small-animal-PET was then evaluated on the epidermoid carcinoma A431 tumor xenograft mice model.

MATERIALS AND METHODS

General. Maleimido-mono-amide-DOTA was purchased from Macrocyclics Inc. Dimethylsulfoxide (DMSO) and ethyl acetate were purchased from Fisher Scientific. Dichloromethane (DCM), trifluoroacetic acid (TFA), thioanisole (TIS), ethanedithiol (EDT), ethylene-diamine-tetra-acetic acid (EDTA), triethylamine, octanol, *N*-hydroxybenzotriazole hydrate (HOBT), 1-ethyl-3-[3-dimethylaminopropyl]carbodiimide (EDC), *N*,*N*-diisopropylethylamine (DIEA), ethyl acetate, dithiothriotol (DTT), and all other standard synthesis reagents were purchased from Sigma-Aldrich Chemical Co. The fluorescent dye 7-diethylamino-3-(4′-maleimidylphenyl)-4-methylcoumarin (CPM) was purchased from Molecular Probes Inc. All chemicals were used without further purification. The radionuclide, ^{64}Cu, was provided by the Department of Medical Physics, University of Wisconsin at Madison. Human epidermoid carcinoma cancer cell line A431 was obtained from the American Type Tissue Culture Collection. Analytical RP-HPLC columns (Dionex, Acclaim-120 C18, 4.6 mm ×250 mm) with a guard column were used for analysis of ^{64}Cu labeled protein and unlabeled protein. The mobile phase was solvent A, 0.1% trifluoroacetic acid (TFA)/H_2O, and solvent B, 0.1%TFA/acetonitrile. The flow rate was 1 mL/min, with the mobile phase starting from 95% solvent A and 5% solvent B (0−3 min) to 35% solvent A and 65% solvent B at 33 min, then going to 15% solvent A and 85% solvent B (33−36 min), maintaining this solvent composition for another 3 min (36−39 min) and returning to initial solvent composition by 42 min. All other general materials (e.g., mice) and instruments (e.g., radioactive dose calibrator and matrix-assisted laser desorption/ionization time of flight mass spectrometry (MALDI-TOF-MS), liquid chromatography electrospray ionization mass spectrometer (LC-ESI-MS), etc.) were the same as those previously reported (*20*).

Conjugation of DOTA-$Z_{EGFR:1907}$. Ac-Cys-$Z_{EGFR:1907}$ (Ac-CVDNKFNKEMWAAWEEIRNLPNLNGWQMTAFIA SLVD-DPSQSANLLAEAKKLNDAQAPK-NH_2) was synthesized on an automatic peptide synthesizer (CS Bio, CS 336X). Briefly, Rink Amide LS resin (200 mg, 40 μmol, Advanced ChemTech, 0.2 mmol/g loading) was swollen in *N*,*N*-dimethylformamide (DMF) for 30 min. Fmoc-protected amino acids were purchased from Novabiochem/EMD Chemicals Inc. Fmoc groups were removed with 20% piperidine in DMF. The aliquots of amino acids (0.20 mmol) were activated in a solution containing 0.20 mmol of HOBt and 0.5 M diisopropylcarbodiimide (DIC) in DMF. The small protein was N-terminal-acetylated by activation of acetic anhydride with HOBt/DIEA after deprotection of the Fmoc protection group of the last amino acid residue. Peptide cleavage and deprotection were carried out by a 3-h incubation in a mixture of TFA/TIS/EDT/H_2O (94:2:2:2). The mixture was filtered, and the peptide in solution was precipitated with anhydrous diethyl ether. The resulting peptide was washed four times with ice-cold anhydrous diethyl ether, dried, and dissolved in 1 mM DTT. The peptide was purified by RP-HPLC on a C-18 column. Fractions were collected and lyophilized. The target product was characterized by ESI-MS and was ready for use in the next step in the reaction.

The general procedure for the conjugation of maleimido-mono-amide-DOTA with Ac-Cys-$Z_{EGFR:1907}$ is as follows: Ac-Cys-$Z_{EGFR:1907}$ was dissolved with freshly degassed phosphate buffer (pH 7.4) at a concentration of 1 mg/mL. The bifunctional chelator maleimido-mono-amide-DOTA dissolved in DMSO (10 mM) was added at 20 equivalents per equivalent of the Affibody. After mixing by vortexing for 2 h, we purified the reaction mixture by a Dionex HPLC with a protein-and-peptide C4 column (Grace Vydac 214TP54). Characterization of the products was confirmed using MALDI-TOF-MS or LC-ESI-MS. The purity of the bioconjugate DOTA-$Z_{EGFR:1907}$ was confirmed by HPLC. The concentration of free cysteine side chains was determined with the fluorescent reagent CPM on both unconjugated and conjugated proteins. The method of Greiner et al. (*24*) was slightly modified as follows: β-mercaptoethanol standard solutions were prepared in MOPS buffer (1 mM MOPS, pH 7.9, 120 mM NaCl, 10 mM $MgCl_2$, and 1.0 mM EDTA) at concentrations of 30, 20, 10, 5, 3, 1, 0.3, and 0.1 μM. The protein concentration was determined by the micro-Bradford assay. A 15 μL aliquot of 0.4 mM CPM in DMF was added to 15 μL of each standard and each protein sample. After a 1-h incubation time at room temperature, triton X-100 (3 mL, 1%) was added to each reaction. The intensity of fluorescence emission was measured on 50 μL of samples on a NUNC plate, using a TECAN SAFIRE fluorescence plate reader. The excitation and emission wavelengths were 390 and 473 nm, respectively.

^{64}Cu Radiolabeling of DOTA-$Z_{EGFR:1907}$. The Affibody conjugate DOTA-$Z_{EGFR:1907}$ was radiolabeled with ^{64}Cu by the addition of 66.6−148 MBq (2−4 mCi) $^{64}CuCl_2$ (1 μg of DOTA-$Z_{EGFR:1907}$ per 2.96 MBq ^{64}Cu) in 0.1 N sodium acetate (NaOAc, pH 6.3) buffer followed by a 1-h incubation at 45 °C. EDTA

(5 μL, 10 mM) was then added to quench the free ^{64}Cu. The radiolabeled complex was purified by a PD-10 column (GE Healthcare). The product was washed out by phosphate-buffered saline (PBS, pH 7.4) and passed through a 0.22-μm Millipore filter into a sterile vial for in vitro and animal experiments. Radioanalytical HPLC was used to analyze the purified ^{64}Cu-DOTA-$Z_{EGFR:1907}$.

Octanol/Water Partition Coefficient. To determine the lipophilicity of ^{64}Cu-DOTA-$Z_{EGFR:1907}$, approximately 370 kBq of the probe in 500 μL of PBS (0.01 M, pH 7.4) was added to 500 μL of octanol in an Eppendorf microcentrifuge tube. The resulting biphasic system was mixed vigorously for 0.5 h and left at room temperature for another 0.5 h. The two phases were then separated by centrifugation at 3000*g* for 5 min (model 5415R Eppendorf microcentrifuge; Brinkman). From each layer, an aliquot of 100 μL was removed and counted in a γ-counter (Packard Instrument). The partition coefficient (log *P*) was then calculated as a ratio of counts in the octanol fraction to the counts in the water fraction. The experiment was repeated 3 times.

Serum Stability. ^{64}Cu-DOTA-$Z_{EGFR:1907}$ (6.7 MBq, 180 μCi) in 250 μL of PBS was added to 1 mL of mouse serum (Sigma). After incubation at 37 °C for 1 h, 4 h, and 23 h, 74 kBq−118 kBq (20−40 μCi) solution was precipitated with 300 μL of ethanol. After centrifugation, the supernatant was transferred to a new Eppendorf tube, and DMF (300 μL) was added to precipitate the residue of serum protein. After centrifugation, the supernatant was acidified with 300 μL of buffer A (water + 0.1% TFA) and filtered through a Spin-X centrifuge tube filter (0.22 μm nylon, COSTAR). The filtrate was then injected into the radio-HPLC under conditions identical to the ones used for analyzing the original ^{64}Cu-DOTA-$Z_{EGFR:1907}$.

In Vitro Cell Assays. The EGFR positive A431 cell line was cultured in high glucose DMEM supplemented with 10% fetal bovine serum (FBS) and 1% penicillin−streptomycin (Invitrogen Life Technologies). The cells were maintained in a humidified atmosphere of 5% CO_2 at 37 °C, with the medium changed every two days. A 70−80% confluent monolayer was detached by 0.1% trypsin and dissociated into a single cell suspension for further cell culture.

The in vitro cell uptake assays of the ^{64}Cu-DOTA-$Z_{EGFR:1907}$ were performed as previously described with minor modifications (*23*, *25*). Briefly, the A431 cells were washed three times with PBS and dissociated with 0.25% trypsin-EDTA. DMEM medium was then added to neutralize trypsin-EDTA. Cells were spun down and resuspended with serum free DMEM. 5×10^5 cells were incubated at 37 °C for 0.25 to 2 h with the radioactive probe (7.4 kBq, ∼7 ng of Affibody) in 0.5 mL of serum-free DMEM medium. The nonspecific binding of the probes with A431 cells was determined by coincubation with nonradiolabeled DOTA-$Z_{EGFR:1907}$ (final concentration 0.6 μM). The cells were washed three times with 0.01 M PBS (pH 7.4). Cells were then washed three times with chilled PBS and spun down at a speed of 7000−8000 rpm. The cell pellets at the bottom of the tube were spliced, and the radioactivity of the pellets was measured using a γ-counter (PerkinElmer 1470, Waltham, MA). The uptake (counts/min) was normalized to the percentage of binding for analysis using Excel (Microsoft).

The receptor saturation assay of ^{64}Cu-DOTA-$Z_{EGFR:1907}$ was conducted with the A431 cells, and 3×10^5 cells were plated on 6-well plates one day before the experiment. Cells were washed with PBS three times. Serum free DMEM (1 mL) was added to each well, and 8.9 kBq−532.8 kBq (0.24 μCi −14.4 μCi, 2 nM−120nM final concentration) of ^{64}Cu-DOTA-$Z_{EGFR:1907}$ with or without 100 times excess of Ac-Cys-$Z_{EGFR:1907}$ was added to the plates. The plates were incubated on ice for 2 h. Then cells were washed with cold PBS three times and detached with TrypLE-Express (Invitrogen, San Diego, CA). The radioactivity of the cells was measured in a γ-counter. The data was analyzed using GraphPad Prism (GraphPad Software, Inc., San Diego, CA, USA), and the K_D value of DOTA-$Z_{EGFR:1907}$ was calculated from a one-site fit binding curve.

Biodistribution Studies. All animal studies were carried out in compliance with federal and local institutional rules for the conduct of animal experimentation. The A431 cells (5×10^6) suspended in PBS were implanted subcutaneously in the right upper shoulders of nude mice. Tumors were allowed to grow to around 0.4−0.6 cm in diameter (1−2 weeks). The tumor bearing mice were subject to in vivo biodistribution and imaging studies.

For biodistribution studies, the A431 tumor-bearing mice ($n = 3$ for each group) were injected with ^{64}Cu-DOTA-$Z_{EGFR:1907}$ (1.11−1.85 MBq, 30−50 μCi, 1−2 μg) spiked with different doses of nonradioactive Ac-Cys-$Z_{EGFR:1907}$ (0, 5, 50, and 500 μg) through the tail vein and sacrificed at different time points (1, 4, and 24 h) p.i. Tumor and normal tissues of interest were removed and weighed, and their radioactivity was measured in a γ-counter. The radioactivity uptake in the tumor and normal tissues was expressed as a percentage of the injected radioactivity (decay corrected) per gram of tissue (% ID/g).

Small-Animal PET Imaging. PET imaging of tumor-bearing mice was performed on a microPET R4 rodent model scanner (Siemens Medical Solutions USA, Inc.). The mice bearing A431 were injected with ^{64}Cu-DOTA-$Z_{EGFR:1907}$ (1.11−1.85 MBq, 30−50 μCi, 1−2 μg) spiked with cold Ac-Cys-$Z_{EGFR:1907}$ (0, 5, 50, and 500 μg) via the tail vein. At different times after the injection, the mice were anesthetized with 2% isoflurane and placed in the prone position and near the center of the field of view of a microPET. The 3-min static scans were obtained, and the images were reconstructed by a two-dimensional ordered subsets expectation maximum (OSEM) algorithm. No background correction was performed. The method for quantification analysis of the images was the same as that reported previously (*20*).

EGFR Western Analysis of Tumor Cells and Tissues. Tumor, liver, and kidneys from A431 xenografted mice were harvested and immediately frozen in dry ice. Thawed tissues were sliced into pieces. RIPA cell lysis buffer (Sigma) supplemented with protease inhibitor cocktail was added to the sliced tissue samples and incubated for 10 min in ice. The supernatant was collected by centrifuging at 14,000 rpm for 10 min at 4 °C. The protein concentrations of the samples were measured using the Bradford assay (BioRad, Hercules, CA). An equal amount of protein from each sample was loaded onto a 10% NuPAGE Bis-Tris gel and electroblotted to a PVDF membrane. After blocking with Tris buffered saline (TBS) plus 0.05% Tween 20 containing 5% powdered milk, the membrane was divided into two pieces at the 60 kDa marker. The top and bottom membranes were incubated separately with a rabbit monoclonal anti-human EGFR antibody (Cell Signal Technology) (1:1000) or mouse monoclonal anti-actin (Sigma-Aldrich) (1:1000) overnight, followed by incubation with horseradish peroxidase (HRP)-conjugated goat anti-rabbit IgG (Invitrogen) (1:1,000) or HRP-conjugated goat anti-mouse IgG (1:1,000), respectively for 1 h. After extensive washing, the protein bands were visualized using ECL plus (Invitrogen).

Statistical Methods. Statistical analysis was performed using Student's two-tailed *t*-test for unpaired data. A 95% confidence level was chosen to determine the significance between groups, with $P < 0.05$ being significantly different.

RESULTS

Chemistry and Radiochemistry. Ac-Cys-$Z_{EGFR:1907}$ with a cysteine residue at the N-terminal was successfully synthesized

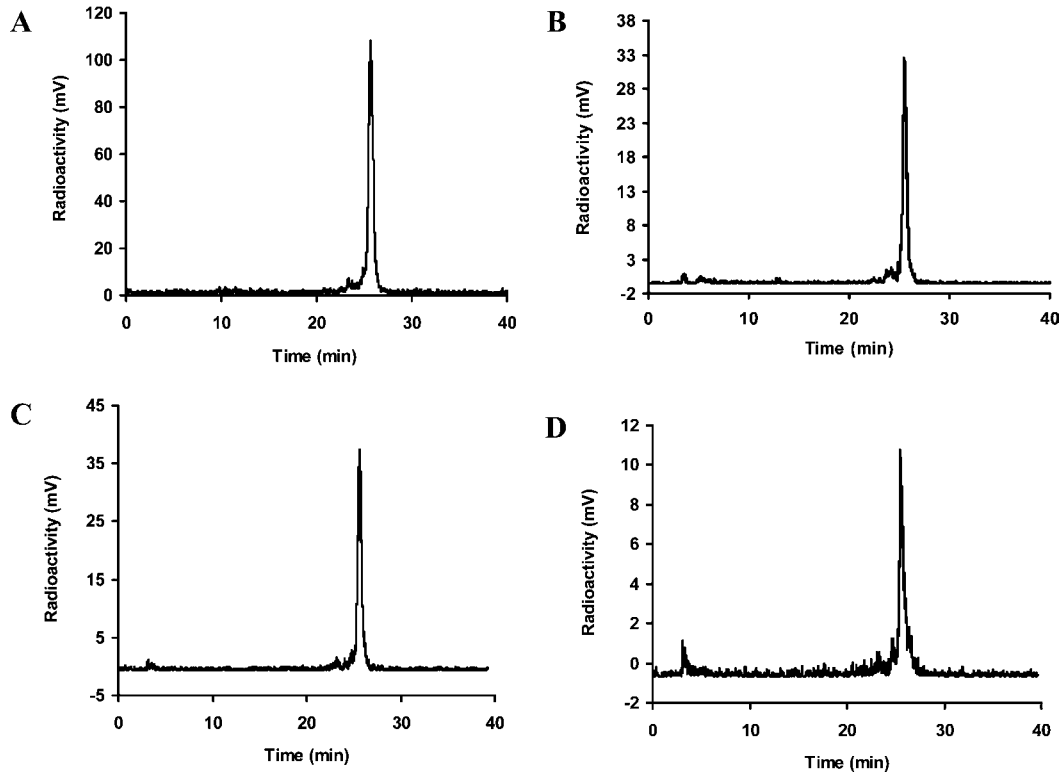


Figure 2. HPLC radiochromatograms of purified ^{64}Cu-DOTA-$Z_{EGFR:1907}$ (A) and radiolabeled probe after 1 h (B), 4 h (C), and 23 h (D) of incubation with mouse serum.

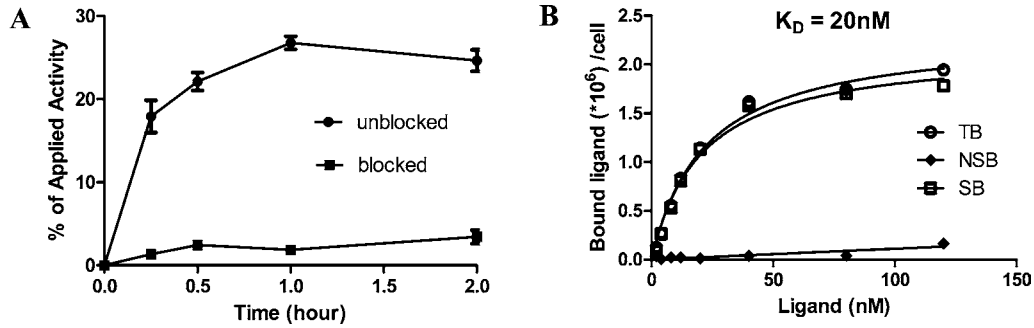


Figure 3. Characterization of EGFR-specific binding. (A) Cell uptakes of ^{64}Cu-DOTA- $Z_{EGFR:1907}$ in A431 cells over time at 37 °C with or without the presence of nonradioactive Affibody molecules DOTA-$Z_{EGFR:1907}$. All results are expressed as the mean of triplicate measurements ± standard deviation. (B) Saturation assay using SKOV3 cells plotted by concentration of total radioligands versus bound radioligand. NSB, nonspecific binding; TB, total binding; and SB, specific binding.

through conventional solid phase peptide synthesis and purified by semi-preparative HPLC. The purified peptide was generally obtained in about 10% yield. The retention time on analytical HPLC for Ac-Cys-$Z_{EGFR:1907}$ was found to be 26 min. The purified Ac-Cys-$Z_{EGFR:1907}$ was characterized by MALDI-TOF-MS. The measured molecular weight (MW) was consistent with the expected MW: m/z = 6690.0 for $[M + H]^+$ (calculated $MW_{[M+H]}^+ = 6689.6$). Ac-Cys-$Z_{EGFR:1907}$ was then conjugated with maleimido-mono-amide-DOTA and purified by C4 analytical HPLC. Analysis of free thiol of the DOTA-$Z_{EGFR:1907}$ confirmed the absence of unreacted Ac-Cys-$Z_{EGFR:1907}$ (data not shown). Furthermore, mass spectrometry analysis of the final product also only showed the expected mass peak for DOTA-$Z_{EGFR:1907}$. The measured MW was m/z = 7215 for $[M + H]^+$ (calculated $MW_{[M+H]}^+ = 7215.1$). The recovery yield was 47% after purification, and the purity for the final product was over 95% (retention time: 26 min).

DOTA-$Z_{EGFR:1907}$ was successfully labeled with ^{64}Cu at 45 °C for a 1-h incubation (Figure 1). The labeling yield with ^{64}Cu was generally over 50%. The purification of radiolabeling solution using a PD-10 column afforded ^{64}Cu-DOTA-$Z_{EGFR:1907}$ with >95% radiochemical purity (Figure 2A, retention time =26 min) with modest specific activity (5−8 MBq/nmol, 22−35 μCi/μg) at the end of synthesis (EOS). From the octanol−water partition coefficient measurements, the log P value of ^{64}Cu-DOTA- $Z_{EGFR:1907}$ was determined to be −1.01 ± 0.09, indicating a moderate hydrophilicity of the radiolabeled Affibody.

In Vitro Assay of ^{64}Cu-DOTA-$Z_{EGFR:1907}$. The serum stability study showed that ^{64}Cu-DOTA-$Z_{EGFR:1907}$ had excellent resistance to proteolysis and transchelation with >95% of the probe intact after a 4-h incubation in the serum, and there was ∼85% intact ^{64}Cu-DOTA-$Z_{EGFR:1907}$ after 24 h of incubation (Figure 2). The receptor-binding affinity study of ^{64}Cu -DOTA-$Z_{EGFR:1907}$ for EGFR was performed using A431 cells (Figure 3B). The K_D value of ^{64}Cu-DOTA-$Z_{EGFR:1907}$ was determined to be 20 nM from the saturation assay. Figure 3A shows the cell uptake of ^{64}Cu-DOTA- $Z_{EGFR:1907}$ in A431 cells at 37 °C over a 2-h incubation period. It was observed that the radiola-

Table 1. Biodistribution Results for ^{64}Cu-DOTA-$Z_{EGFR:1907}$ in Nude Mice Bearing Subcutaneously Xenotransplanted A431 Human Epidermoid Carcinoma Cancer[a]

organ (% ID/g) (spiked dose)	1 h	4 h				24 h
	5 μg	0 μg	5 μg	50 μg	500 μg (block)	5 μg
tumor	9.72 ± 4.89	11.71 ± 1.98	11.02 ± 1.41[f]	17.35 ± 4.48[e]	6.15 ± 0.49[e,f]	10.46 ± 2.11
blood	10.03 ± 3.80[b]	11.68 ± 1.39[c]	4.84 ± 0.26[c,d,f]	1.81 ± 0.44[d]	1.15 ± 0.05[f]	1.99 ± 0.59[b]
heart	2.55 ± 0.77	3.35 ± 0.43[c]	1.97 ± 0.09[c,d,f]	1.50 ± 0.14[d,e]	0.83 ± 0.08[e,f]	2.65 ± 0.48
liver	22.81 ± 5.70	18.99 ± 2.88	20.03 ± 3.03[d,f]	13.27 ± 2.02[d,e]	6.47 ± 1.52[e,f]	12.83 ± 3.27
lungs	5.54 ± 0.45	5.81 ± 0.36[c]	4.02 ± 0.65[c,f]	3.07 ± 0.63	2.38 ± 0.13[f]	5.78 ± 2.28
muscle	0.59 ± 0.12	0.74 ± 0.06[c]	0.53 ± 0.08[c,d]	0.35 ± 0.06[d]	0.31 ± 0.11	0.74 ± 0.18
kidney	86.86 ± 25.59	88.45 ± 14.72	126.51 ± 35.09	207.35 ± 101.16	151.41 ± 9.94	61.33 ± 18.67
spleen	2.57 ± 0.59	3.09 ± 0.81	1.86 ± 0.26	2.02 ± 0.30	1.41 ± 0.26	2.33 ± 0.74
brain	0.34 ± 0.15	0.31 ± 0.06	0.22 ± 0.07	0.14 ± 0.07	0.12 ± 0.04	0.35 ± 0.09
intestine	3.28 ± 0.74	3.49 ± 1.18	3.26 ± 0.22[f]	3.65 ± 0.41[e]	1.67 ± 0.12[e,f]	4.43 ± 0.91
skin	1.49 ± 0.44	1.56 ± 0.21	2.86 ± 0.83[f]	2.08 ± 0.09[e]	0.76 ± 0.08[e,f]	2.48 ± 1.05
stomach	3.85 ± 0.91	3.87 ± 0.66	3.33 ± 0.43	2.73 ± 0.50	2.74 ± 0.33	3.88 ± 0.90
pancreas	2.15 ± 1.22	1.72 ± 0.38	1.95 ± 0.05[d,f]	1.36 ± 0.21[d,e]	0.60 ± 0.05[e,f]	2.16 ± 0.72
bone	1.54 ± 0.10	1.08 ± 0.05	1.32 ± 0.54[f]	1.28 ± 0.54	0.43 ± 0.06[f]	1.33 ± 0.33
			Uptake Ratios			
T/blood	1.23 ± 1.07[b]	1.04 ± 0.01[c]	2.29 ± 0.43[c,f]	9.87 ± 2.99	5.84 ± 0.84[f]	5.39 ± 0.69[b]
T/muscle	16.29 ± 6.62	17.82 ± 3.66	20.98 ± 2.99	49.46 ± 11.43[e]	20.98 ± 2.99[e]	16.05 ± 4.00

[a] Data are expressed as the percentage of administered activity (injected probe) per gram of tissue (% ID/g) after intravenous injection of the probe (1.11−1.85 MBq, 30−50 μCi, 1−2 μg) spiked with 0, 5, 50, and 500 μg of Ac-Cys-$Z_{EGFR:1907}$ at 1, 4, or 24 h (n = 3). ^{64}Cu-DOTA-$Z_{EGFR:1907}$ demonstrates significantly higher uptake in A431 tumor mice than that of the blocked group (500 μg) at 4 h p.i. ($P < 0.05$). Student's unpaired two tailed t-test was conducted. $P < 0.05$ was considered significant. [b] $P < 0.05$, comparing 5 μg of spike tracer biodistribution 1 h and 24 h p.i. [c] $P < 0.05$, comparing 0 μg and 5 μg of spike tracer biodistribution at 4 h p.i. [d] $P < 0.05$, comparing 5 μg and 50 μg of spike tracer biodistribution at 4 h p.i. [e] $P < 0.05$, comparing 50 μg spike and 500 μg (block) of dose tracer biodistribution at 4 h p.i. [f] $>P < 0.05$, comparing 5 μg spike and 500 μg (block) of dose tracer biodistribution at 4 h p.i.

beled peptide steadily increased over the 2-h incubation time, and it reached an EGFR specific uptake of ~20% applied activity in 0.5 h. Pre-incubation with 300 time excess of DOTA-$Z_{EGFR:1907}$ significantly blocked ^{64}Cu-DOTA-$Z_{EGFR:1907}$ uptake ($P < 0.05$ at all time points), demonstrating the receptor binding specificity of the PET probe.

In Vivo Biodistribution Studies. The in vivo biodistribution studies of ^{64}Cu-DOTA-$Z_{EGFR:1907}$ were examined in a A431 xenograft mouse model, and the biodistribution data and statistical analysis results are presented in Table 1. For the probe spiked with 5 μg of Ac-Cys-$Z_{EGFR:1907}$, high activity accumulation in the tumor was observed at early time points, with 9.72 ± 4.89 and 11.02 ± 1.41% ID/g uptake at 1 and 4 h p.i., respectively. ^{64}Cu-DOTA-$Z_{EGFR:1907}$ also showed good tumor retention with uptake of 10.46 ± 2.11% ID/g at 24 h. Blood radioactivity concentration was high at early time with 10.03 ± 3.80% ID/g at 1 h and dropped to 4.84 ± 0.26% ID/g at 4 h and 1.99 ± 0.59% ID/g at 24 h. High liver uptake and retention were also found (20.03 ± 3.03 and 12.83 ± 3.27%ID/g at 4 and 24 h p.i., respectively). At later time points such as 24 h p.i., ^{64}Cu-DOTA-$Z_{EGFR:1907}$ displayed a good tumor to blood ratio of 5.39 ± 0.69 (Table 1, 5 μg spiking dose). Excellent tumor-to-muscle ratios (>16) were found for all the time points studied.

To study the spiking dose-dependent biodistribution of ^{64}Cu-DOTA-$Z_{EGFR:1907}$, ^{64}Cu-DOTA-$Z_{EGFR:1907}$ (1.11−1.85 MBq) was co-injected with 0, 5, and 50 μg of Ac-Cys-$Z_{EGFR:1907}$ into A431 tumor bearing mice (Table 1). Tumor uptakes were maintained over 10% ID/g at 4 h p.i. for all different spiking doses. However, the blood radioactivity concentration of ^{64}Cu-DOTA-$Z_{EGFR:1907}$ was very different with uptake values of 11.68 ± 1.39, 4.84 ± 0.26, and 1.81 ± 0.44% ID/g at 0, 5, and 50 μg spiking dose respectively (4 h p.i., $P < 0.05$). Thus, high specific activity of ^{64}Cu-DOTA-$Z_{EGFR:1907}$ could not increase the tumor uptake, and the tumor-to-blood ratios at 0 and 5 μg were low (Table 1). Liver uptakes were also relatively high (18.99 ± 2.88 and 20.03 ± 3.03% ID/g, 4 h) at 0 and 5 μg spiking doses. In contrast, at 50 μg spiking dose the liver uptake (13.87 ± 1.43% ID/g, 4 h) was significantly reduced ($P < 0.05$). Tumor-to-liver ratio at 4 h thus increased from 0.62 ± 0.07 (0 μg spiking dose) and 0.56 ± 0.09 (5 μg spiking dose) to 1.32 ± 0.37 (50 μg spiking dose) ($P < 0.05$). Moreover, tumor-to-blood ratios at 4 h also improved from 1.04 ± 0.01 (0 μg spiking dose) and 2.29 ± 0.43 (5 μg spiking dose) to 9.87 ± 2.99 (50 μg spiking dose) ($P < 0.05$) (Figure 4).

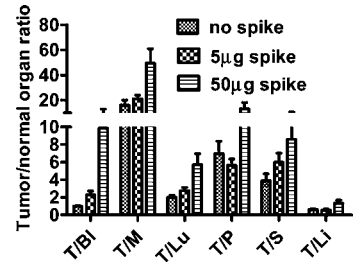


Figure 4. Tumor-to-normal organ ratios of ^{64}Cu-DOTA-$Z_{EGFR:1907}$ in mice bearing the A431 tumor at 4 h p.i. (n = 3).

The in vivo tumor targeting specificity was confirmed by co-injection of the probe with 500 μg of Ac-Cys-$Z_{EGFR:1907}$. It was found that the tumor had a significantly reduced uptake of 6.15 ± 0.49% ID/g, compared with 17.35 ± 4.48% ID/g at 50 μg spiking dose (4 h p.i., $P < 0.05$). Liver uptake was also significantly decreased (6.47 vs 13.27% ID/g at 50 μg spiking dose, 4 h, $P < 0.05$).

Small-Animal PET Imaging. Imaging studies were conducted at 1, 2, 4, and 24 h after tail vein injection of ^{64}Cu-DOTA-$Z_{EGFR:1907}$ with or without co-injection of 5, 50, and 500 μg (block) of cold Ac-Cys-$Z_{EGFR:1907}$. Decay-corrected coronal microPET images are shown in Figure 5. At 5 μg spiking dose, the tumor was clearly visible up to 24 h p.i. with good tumor-to-background contrast. Also, high activity accumulation in the kidneys and liver for ^{64}Cu-DOTA-$Z_{EGFR:1907}$ was observed (Figure 5E). At 0 and 50 μg spiking dose, tumors are both clearly visible at 4 h p.i., while much better tumor imaging contrast was obtained for 50 μg spiking dose at early time points (1 and 2 h p.i.) (Figure 5A and B). For the blocking group (500 μg), the tumor was barely visible on micro-PET images at all time points (Figure 5C). Quantification analysis of PET images

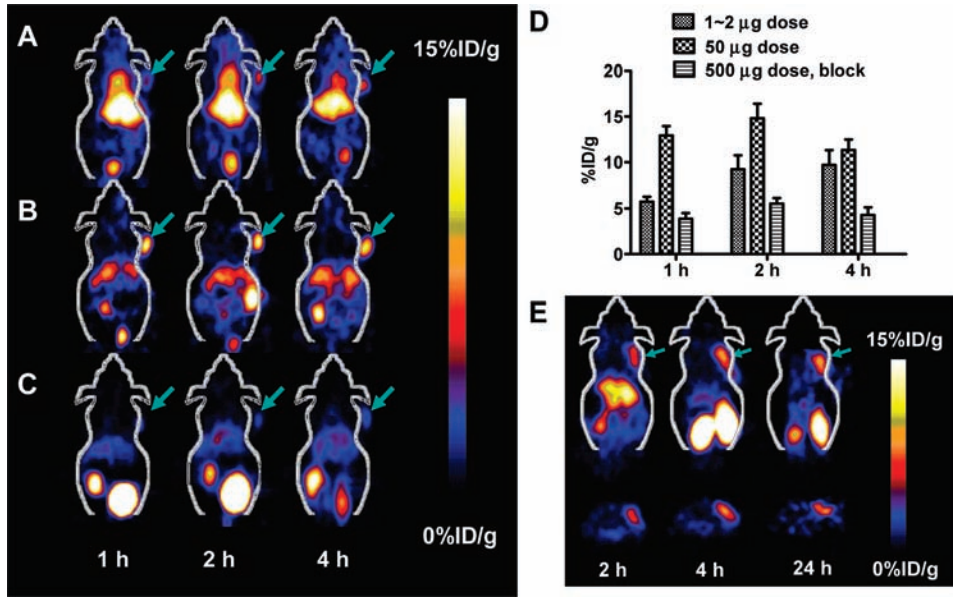


Figure 5. Representative images of decay corrected coronal microPET images of nude mice bearing the A431 tumor on the right shoulder at 1, 2, and 4 h after tail vein injection of ^{64}Cu-DOTA-$Z_{EGFR:1907}$ (1.11−1.85 MBq, 30−50 μCi) spiked with 0 μg (A), 50 μg (B), and 500 μg (C) of Ac-Cys-$Z_{EGFR:1907}$. Arrows indicate the location of tumors. Quantitative analysis of tumor uptakes at 1, 2, and 4 h p.i. (D) ROI was drawn on coronal images. Uptake was calculated with the mean uptake value (n = 3). (E) Representative images of decay corrected coronal (top) and transaxial (bottom) microPET images of nude mice bearing the A431 tumor on the right shoulder at 2, 4, and 24 h after tail vein injection of ^{64}Cu-DOTA-$Z_{EGFR:1907}$ (1.11−1.85 MBq, 30−50 μCi, spiked with 5 μg of Ac-Cys-$Z_{EGFR:1907}$). Arrows indicate the location of tumors.

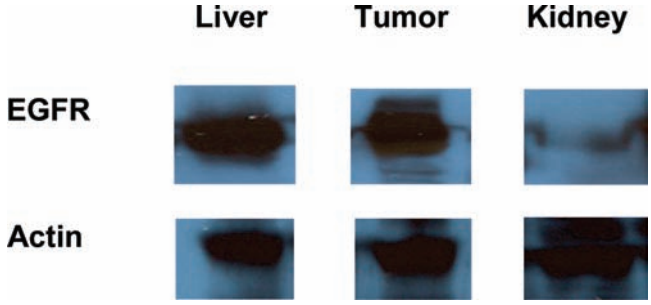


Figure 6. Representative western blot detection of EGFR expression in liver, tumor, and kidney tissue samples. Liver, A431 tumor, and kidney homogenates were prepared, and 50 μg of protein was detected with the rabbit antihuman EGFR monoclonal antibody.

showed much lower tumor uptake for mice injected with 500 μg spiking dose compared with 50 μg spiking dose ($P < 0.05$) at all time points (1−4 h p.i.) (Figure 5D). Western blot analysis is shown in Figure 6. High EGFR expression was detected for both liver and A431 tumor samples, which explained the blocking effects in the tumor and liver observed in microPET imaging studies.

DISCUSSION

Molecular imaging techniques have been demonstrated to be powerful noninvasive tools to address many important clinical questions. PET imaging is particularly useful because of its high sensitivity, high spatial resolution, strong quantification ability, and its great potential for clinical translation. The EGFR targeted PET molecular probes are expected to provide a real-time assay of EGFR expression in all tumor sites (primary and metastatic lesions) in living subjects. These imaging probes could potentially be used for early detection of EGFR positive tumor recurrence, stratification of cancer patients and optimization of the dose for EGFR targeted therapy, and monitoring the efficacy of EGFR based tumor treatment.

Affibody scaffold proteins are chemically robust like small molecules. They have good in vivo stability and bioavailability (*18*−*20*). In this study, we site-specifically conjugated an Affibody analogue Ac-Cys-$Z_{EGFR:1907}$ with a versatile chelator DOTA-monomaleimide and measured the binding specificity and affinity to EGFR. The conjugated DOTA-$Z_{EGFR:1907}$ has good binding affinity with a K_D of 20 nM. In vitro cell uptake experiments showed that ^{64}Cu-DOTA-$Z_{EGFR:1907}$ had rapid accumulation in the A431 cells. The uptake reached a plateau in 0.5 h. This accumulation is EGFR specific since blocking with cold DOTA-$Z_{EGFR:1907}$ significantly reduced cell uptake from 26.77% ± 1.35% to 1.86% ± 0.67% of applied activity (1 h) ($P < 0.05$). It is reported that in EGFR over expression tumors the concentration of EGFR is about 100 nM (*26*, *27*); thus, 20 nM affinity was considered efficient for the in vivo imaging application.

Site-specifically labeled ^{64}Cu-DOTA-$Z_{EGFR:1907}$ showed good in vivo pharmacokinetics for EGFR targeted PET imaging. Good contrast imaging of the EGFR positive A431 tumor xenograft model were obtained with optimized spiking doses (5−50 μg) at early time (1 h p.i.) after the injection of ^{64}Cu-DOTA-$Z_{EGFR:1907}$. High tumor uptake (~10% ID/g, 5 μg spiking dose) at 1 h p.i. confirmed the fast tumor targeting ability of the probe. The biodistribution study showed that optimal good tumor/blood ratio was obtained with partially blocking with 5−50 μg unlabeled Affibody (9.87 ± 2.99 at 4 h p.i., 50 μg spiking dose; 5.39 ± 0.69 at 24 h p.i., 5 μg spiking dose), which was consistent with reports that radioiodine labeled EGF with large (3 mg) spiking dose of cold EGF can give improved imaging quality in clinics (*11*).This observation may be attributed to the fact that the liver has high expression of EGFR (Figure 6) and could retain significant amount of the radiolabeled ligand (Figure 5). When spiked with an optimized amount of the cold ligand, the availability of the probe in the circulation would be increased. Because of the relatively small size of the scaffold protein, majority of the probe was quickly cleared through the kidney−urinary system. EGFR targeting specificity of ^{64}Cu-DOTA-$Z_{EGFR:1907}$ was also proven in vivo. When 500 μg of

Ac-Cys-$Z_{EGFR:1907}$ was co-injected, uptakes in high EGFR expression organs/tissues, such as the tumor and liver, were both significantly reduced at 4 h p.i. ($P < 0.05$).

High liver accumulation of radioactivity (>10% ID/g, 4 h p.i.) was also observed, which is mainly caused by the high EGFR expression in the liver, as well as nonspecific clearance of the probe through the hepatobiliary system and transchelation of ^{64}Cu in the liver. Recently, the Affibody $Z_{EGFR:1907}$ has been modified with a chelator Bz-DTPA through lysine residues and then labeled with ^{111}In (*28*). The resulting single photon emission computed tomography (SPECT) probe ^{111}In-Bz-DTPA-$Z_{EGFR:1907}$ showed much lower blood and liver uptakes (0.23 and 1.5% ID/g, repectively, at 4 h p.i., with 50 μg spiking dose). However, tumor uptake of ^{111}In-Bz-DTPA-$Z_{EGFR:1907}$ was also much lower (3−4% ID/g at 4 h p.i., with 50 μg spiking dose). This may be caused by the nonspecific labeling strategy used in the study, which could lead to reduced affinity of the probe and low tumor uptake. This is a disadvantage, especially because it may result in low sensitivity for the detection of the tumors with moderate or low EGFR expression, such as breast carcinoma (only about 3% of A431 EGFR expression level) (*2*). Further studies are required to compare these two EGFR imaging probes to conclude which one would be better for a specific application. ^{64}Cu-DOTA-$Z_{EGFR:1907}$ also showed extremely high kidney uptake (196 ± 4% ID/g vs 207.35 ± 101.16% ID/g at 4 h, with 50 μg spiking dose). Thus, radioactive coppers with higher fraction of positron emission and shorter half-life such as ^{60}Cu ($t_{1/2}$ = 24.5 min, 93% β^+) and ^{61}Cu ($t_{1/2}$ = 3.333 h, 60% β^+) will be more favorable for future clinical translation (*29*). ^{18}F ($t_{1/2}$ =109.8 min, 98% decay by positron emission) labeled Affibody could also have significantly reduced kidney radiation because of the nonresidualizing properties of radiohalogen (*30*).

On the basis of the biodistribution and microPET imaging results, it has been found that Affibody molecule based probe ^{64}Cu-DOTA-$Z_{EGFR:1907}$ shows much better properties for PET imaging than ^{64}Cu labeled monoclonal antibody Cetuximab. Affibody protein $Z_{EGFR:1907}$ is much smaller than Cetuximab (7 kDa vs 150 kDa). $Z_{EGFR:1907}$ site specifically modified with DOTA still has low-nanomolar affinity to EGFR (IC_{50} = 26.1 ± 8.8 nM). High tumor uptake (over 9% ID/g) could be obtained at as early as 1 h p.i. of the ^{64}Cu-DOTA-$Z_{EGFR:1907}$, while it takes ~24 h for ^{64}Cu labeled DOTA-Cetuximab to achieve over 10% ID/g tumor uptake (A431, U87MG, and PC-3 tumors) (*31*, *32*). In addition, blood clearance was much faster for ^{64}Cu-DOTA-$Z_{EGFR:1907}$ (1.96 ± 0.30% ID/g at 50 μg spiking dose, 4 h p.i. vs 9.4 ± 1.2, 5.7 ± 1.9% ID/g for ^{64}Cu-DOTA-cetuximab at 16 and 48 h p.i., respectively); thus, much better contrast was obtained for the Affibody based PET probe at early time. Compared with Affibody protein based probes, antibody based PET probes have poorer tumor penetration and higher nonspecific uptake because of their bulky size. Recently, in a quantitative PET imaging study of EGFR using a ^{64}Cu-labeled antibody, it was found that EGFR expression level measured in head and neck cancer cells was not correlated with the PET signal at all (*33*), suggesting that a bulky antibody based PET probe may not be suitable for quantitative imaging of EGFR. It is expected that an Affibody based PET probe such as ^{64}Cu-DOTA-$Z_{EGFR:1907}$ may overcome this problem. Further research is ongoing in our group to address this important question.

CONCLUSIONS

In conclusion, a novel Affibody based PET probe, ^{64}Cu-DOTA-$Z_{EGFR:1907}$, has been successfully developed for molecular imaging of EGFR in vivo. This probe provides high specificity, sensitivity, and excellent tumor contrast as early as 1 h p.i.. It may find important applications in cancer PET molecular imaging.

ACKNOWLEDGMENT

This work was supported, in part, by the California Breast Cancer Research Program 14IB-0091 and an SNM Pilot Research Grant.

LITERATURE CITED

(1) Real, F. X., Rettig, W. J., Chesa, P. G., Melamed, M. R., Old, L. J., and Mendelsohn, J. (1986) Expression of epidermal growth factor receptor in human cultured cells and tissues. *Cancer Res. 46*, 4726–4731.

(2) Kevin, W. R., Jonathon, R. R., Alison, K. L., James, J. G., Timothy, G., and Peter, D. S. (2002) Radioimmunohistochemistry of epidermal growth factor receptor in breast cancer. *Arch. Pathol. Lab. Med. 126*, 177–181.

(3) Burris, H. A. (2004) Dual kinase inhibition in the treatment of breast cancer: initial experience with the EGFR/ErbB-2 inhibitor lapatinib. *Oncologist 9*, 10–15.

(4) Geyer, C. E., Forster, J., Lindquist, D., Lindquist, D., Chan, S., Romieu, C. G., Pienkowski, T., Jagiello-Gruszfeld, A., Crown, J., Chan, A., Kaufman, B., Skarlos, D., Campone, M., Davidson, N., Berger, M., Oliva, C., Rubin, S. D., Stein, S., and Cameron, D. (2006) Lapatinib plus capecitabine for HER2-positive advanced breast cancer. *N. Engl. J. Med. 355*, 2733–2743.

(5) Jones, H., Goddard, L., Gee, J., Gee, J. M., Hiscox, S., Rubini, M., Barrow, D., Knowlden, J. M., Williams, S., Wakeling, A. E., and Nicholson, R. I. (2004) Insulin-like growth factor-I receptor signalling and acquired resistance to gefitinib (ZD1839; Iressa) in human breast and prostate cancer cells. *Endocr. Relat. Cancer 11*, 793–814.

(6) Nicholson, R. I., Gee, J. M., and Harper, M. E. (2001) EGFR and cancer prognosis. *Eur. J. Cancer 37*, 9–15.

(7) DiGiovanna, M. P., Stern, D. F., Edgerton, S. M., Whalen, S. G., Moore, D., and Thor, A. D. (2005) Relationship of epidermal growth factor receptor expression to ErbB-2 signaling activity and prognosis in breast cancer patients. *J. Clin. Oncol. 23*, 1152–1160.

(8) Pal, A., Glekas, A., Doubrovin, M., Balatoni, J., Namavari, M., Beresten, T., Maxwell, D., Soghomonyan, S., Shavrin, A., Ageyeva, L., Finn, R., Larson, S. M., Bornmann, W., and Gelovani, J. G. (2006) Molecular imaging of EGFR kinase activity in tumors with 124I-labeled small molecular tracer and positron emission tomography. *Mol. Imaging Biol. 8*, 262–277.

(9) Levashova, Z., Backer, M. V., Horng, G., Felsher, D., Backer, J. M., and Blankenberg, F. G. (2009) SPECT and PET imaging of EGF receptors with site-specifically labeled EGF and dimeric EGF. *Bioconjugate Chem. 20*, 742–749.

(10) Wang, H., Yu, J., Yang, G., Yang, G., Song, X., Sun, X., Zhao, S., and Mu, D. (2007) Assessment of 11C-labeled-4-N-(3-bromoanilino)-6,7-dimethoxyquinazoline as a positron emission tomography agent to monitor epidermal growth factor receptor expression. *Cancer Sci. 98*, 1413–1416.

(11) Divgi, C. R., Welt, S., Kris, M., Real, F. X., Yeh, S. D. J., Gralla, R., Merchant, B., Schweighart, S., Unger, M., Larson, S. M., and Mendelsohn, J. (1991) Phase I and imaging trial of indium-111-labeled anti-epidermal growth factor receptor monoclonal antibody 225 in patients with squamous cell lung carcinoma. *J. Natl. Cancer Inst. (Bethesda) 83*, 97–104.

(12) Ramos-Suzarte, M., Rodriguez, N., Oliva, J. P., Iznaga-Escobar, N., Perera, A., Morales, A., Gonzalez, N., Cordero, M., Torres, L., Pimentel, G., Borron, M., Gonzalez, J., Torres, O., Rodriguez, T., and Perez, R. (1999) 99mTc-labeled anti-human epidermal growth factor receptor antibody in patients with tumors of epithelial origin: Part III. Clinical trials safety and diagnostic efficacy. *J. Nucl. Med. 40*, 768–775.

(13) Hosse, R. J., Rothe, A., and Power, B. E. (2006) A new generation of protein display scaffolds for molecular recognition. *Protein Sci. 15*, 14–27.
(14) Nygren, P. A., and Skerra, A. (2004) Binding proteins from alternative scaffolds. *J. Immunol. Methods 290*, 3–28.
(15) Binz, H. K., Amstutz, P., and Pluckthun, A. (2005) Engineering novel binding proteins from nonimmunoglobulin domains. *Nat. Biotechnol. 23*, 1257–1268.
(16) Binz, H. K., and Pluckthun, A. (2005) Engineered proteins as specific binding reagents. *Curr. Opin. Biotechnol. 16*, 459–469.
(17) Nord, K., Gunneriusson, E., Ringdahl, J., Stahl, S., Uhlen, M., and Nygren, P. A. (1997) Binding proteins selected from combinatorial libraries of an alpha-helical bacterial receptor domain. *Nat. Biotechnol. 15*, 772–777.
(18) Wikman, M., Steffen, A. C., Gunneriusson, E., Tolmachev, V., Adams, G. P., Carlsson, J., and Stahl, S. (2004) Selection and characterization of HER2/neu-binding affibody ligands. *Protein Eng. Des. Sel. 17*, 455–462.
(19) Orlova, A., Magnusson, M., Eriksson, T. L., Nilsson, M., Larsson, B., Hoiden-Guthenberg, I., Widstrom, C., Carlsson, J., Tolmachev, V., Stahl, S., and Nilsson, F. Y. (2006) Tumor imaging using a picomolar affinity HER2 binding affibody molecule. *Cancer Res. 66*, 4339–4348.
(20) Cheng, Z., Padilla, De Jesus, O., Namavari, M., De, A., Levi, J., Webster, J. M., Zhang, R., Lee, B., Syud, F. A., and Gambhir, S. S. (2008) Small-animal PET imaging of human epidermal growth factor receptor type 2 expression with site-specific 18F-labeled protein scaffold molecules. *J. Nucl. Med. 49*, 804–813.
(21) Cheng, Z., De Jesus, O. P., Kramer, D. J., De, A., Webster, J. M., Gheysens, O., Levi, J., Namavari, M., Wang, S., Park, J. M., Zhang, R., Liu, H., Lee, B., Syud, F. A., and Gambhir, S. S. (2009) (64)Cu-Labeled affibody molecules for imaging of HER2 expressing tumors. *Mol. Imaging Biol.* [online early access], DOI: 10.1007/s11307-009-0256-6.
(22) Friedman, M., Nordberg, E., Hoiden-Guthenberg, I., Brismar, H., Adams, G. P., Nilsson, F. Y., Carlsson, J., and Stahl, S. (2007) Phage display selection of Affibody molecules with specific binding to the extracellular domain of the epidermal growth factor receptor. *Protein Eng. Des. Sel. 20*, 189–199.
(23) Friedman, M., Orlova, A., Johansson, E., Johansson, E., Eriksson, T. L., Hoiden-Guthenberg, I., Tolmachev, V., Nilsson, F. Y., and Stahl, S. (2008) Directed evolution to low nanomolar affinity of a tumor-targeting epidermal growth factor receptor-binding Affibody molecule. *J. Mol. Biol. 376*, 1388–1402.
(24) Greiner, D. P., Miyake, R., Moran, J. K., Moran, J. K., Jones, A. D., Negishi, T., Ishihama, A., and Meares, C. F. (1997) Synthesis of the protein cutting reagent iron (S)-1-(p-bromoacetamidobenzyl) ethylenediaminetetraacetate and conjugation to cysteine side chains. *Bioconjugate Chem. 8*, 44–48.
(25) Cheng, Z., Xiong, Z., Subbarayan, M., Chen, X., and Gambhir, S. S. (2007) ^{64}Cu-labeled alpha-melanocyte-stimulating hormone analog for microPET imaging of melanocortin 1 receptor expression. *Bioconjugate Chem. 18*, 765–772.
(26) Senekowitsch-Schmidtke, R., Steiner, K., Haunschild, J., Mollenstadt, S., and Truckenbrodt, R. (1996) In vivo evaluation of epidermal growth factor (EGF) receptor density on human tumor xenografts using radiolabeled EGF and anti-(EGF receptor) mAb 425. *Cancer Immunol. Immunother. 42*, 108–114.
(27) Su, H., Seimbille, Y., Ferl, G. Z., Ferl, G. Z., Bodenstein, C., Fueger, B., Kim, K. J., Hsu, Y. T., Dubinett, S. M., Phelps, M. E., Czernin, J., and Weber, W. A. (2008) Evaluation of [^{18}F]gefitinib as a molecular imaging probe for the assessment of the epidermal growth factor receptor status in malignant tumors. *Eur. J. Nucl. Med. Mol. Imaging 35*, 1089–1099.
(28) Tolmachev, V., Friedman, M., Sandstrom, M., Eriksson, T. L., Rosik, D., Hodik, M., Stahl, S., Frejd, F. Y., and Orlova, A. (2009) Affibody molecules for epidermal growth factor receptor targeting in vivo: aspects of dimerization and labeling chemistry. *J. Nucl. Med. 50*, 274–283.
(29) Laforest, R., Dehdashti, F., Lewis, J. S., and Schwarz, S. W. (2005) Dosimetry of 60/61/62/64Cu-ATSM: a hypoxia imaging agent for PET. *Eur. J. Nucl. Med. Mol. Imaging 32*, 764–770.
(30) Kramer-Marek, G., Kiesewetter, D. O., Martiniova, L., Jagoda, E., Lee, S. B., and Capala, J. (2008) [18F]FBEM-Z(HER2:342)-Affibody molecule-a new molecular tracer for in vivo monitoring of HER2 expression by positron emission tomography. *Eur. J. Nucl. Med. Mol. Imaging 35*, 1008–1018.
(31) Cai, W., Chen, K., He, L., Cao, Q., Koong, A., and Chen, X. (2007) Quantitative PET of EGFR expression in xenograft-bearing mice using ^{64}Cu-labeled cetuximab, a chimeric anti-EGFR monoclonal antibody. *Eur. J. Nucl. Med. Mol. Imaging 34*, 850–858.
(32) Li, W. P., Meyer, L. A., Capretto, D. A., Sherman, C. D., and Anderson, C. J. (2008) Receptor-binding, biodistribution, and metabolism studies of ^{64}Cu-DOTA-cetuximab, a PET-imaging agent for epidermal growth-factor receptor-positive tumors. *Cancer Biother. Radiopharm. 23*, 158–171.
(33) Niu, G., Li, Z., Xie, J., Le, Q. T., and Chen, X. (2009) PET of EGFR antibody distribution in head and neck squamous cell carcinoma models. *J. Nucl. Med. 50*, 1116–1123.

BC900515P

New Nanosized Biocompatible MR Contrast Agents Based on Lysine-Dendri-Graft Macromolecules

Mikako Ogawa, Celeste A. S. Regino, Bernardo Marcelino, Mark Williams, Nobuyuki Kosaka, L. Henry Bryant, Jr., Peter L. Choyke, and Hisataka Kobayashi*

Molecular Imaging Program, Center for Cancer Research, National Cancer Institute, National Institute of Health, Research Technology Program, SAIC-Frederick, Inc., NCI-Frederick, and Laboratory of Diagnostic Radiology Research, Radiology & Imaging Sciences, Clinical Center, National Institutes of Health. Received December 9, 2009; Revised Manuscript Received January 17, 2010

Paramagnetic nanomaterials for use as magnetic resonance imaging (MRI) contrast agents have higher relaxivity than conventional low molecular weight MRI agents. However, the biocompatibility and pharmacokinetics of such nanomaterials will strongly affect the likelihood of clinical approval. We synthesized MRI contrast agents based on biocompatible lysine-dendri-grafts: Gd-BzDTPA-lysineG2 and Gd-BzDTPA-lysineG3. The relaxivity of Gd-BzDTPA-lysineG2 and Gd-BzDTPA-lysineG3 increased with sample temperature, while the relaxivity of Gd-BzDTPA-PAMAMG4 decreased with increasing sample temperature. The increase in relaxivity with increasing temperature may be attributed to accessibility of water to the internal Gd chelates with lysine-dendri-grafts, which does not occur with PAMAM dendrimers. Gd-BzDTPA-lysineG3 had a long intravascular half-life but were largely excreted by the kidneys. Therefore, Gd-BzDTPA-lysineG3 enhanced the blood vessels for longer periods than Gd-BzDTPA-PAMAMG4, but was still excreted through the kidney. Because of their biocompatibility, desirable magneto-physical characteristics and favorable pharmacokinetics, which are derived from different interior structures rather than the physical size, lysine-dendri-graft MR contrast agents may be feasible for clinical use.

INTRODUCTION

There are distinct physical and chemical characteristics of nanosized macromolecules, such as size, charge, and hydrophobicity that greatly influence their behavior, in vivo (*1, 2*). Nanosized macromolecules can be finely tuned to have optimal characteristics for biological applications (*3*−*5*). Although in vivo behavior of nanosized macromolecules is not easy to predict (*6*), precise physical and biological characteristics of specific nanoparticles must be verified with animal studies.

Nanosized magnetic resonance imaging (MRI) contrast agents are attractive because they have numerous attachment sites for chelated gadolinium (or other chelated lanthanides) and favorable physical properties that lead to higher T1 relaxivity compared with conventional small molecular weight contrast agents. Lysine-dendri-graft is a new nanosized soft material that is thought to have favorable physicochemical features, which should increase relaxivity. However, the physicochemical characteristics, biocompatibility, and pharmacokinetics of such nanoparticles must be determined before clinical translation (*7, 8*).

In this paper, we synthesized two new MRI contrast agents based on generation-2 and -3 lysine-dendri-grafts, and studied their physical and biological characteristics in vitro and in vivo.

MATERIALS AND METHODS

Reagents. The poly(L-lysine) dendri-grafts (generation-2; G2 and generation-3; G3) were purchased from COLCOM SAS (Montpellier, France). The G2 and G3 dendri-grafts have 50 and 127 terminal primary amino groups, respectively. 2-(4-Isothiocyanatobenzyl)-diethylenetriamine pentaacetic acid (*p*-SCN-BzDTPA) was purchased from Macrocyclics (Dallas, TX). Carrier-free $^{111}InCl_3$ was purchased from Perkin-Elmer Health Sciences, Inc. (North Billerica, MA). All other chemicals used were of reagent grade. A generation-4 PAMAM dendrimer, which has 64 terminal primary amino groups, was purchased from Aldrich Chemical Co. (Milwaukee, WI).

Conjugation of Chelates to the Lysine-Dendri-Grafts. Synthetic scheme is shown in Figure 1. The poly(L-lysine) dendri-graft G2 (1.2 μmol, 1 equiv) was reacted with *p*-SCN-BzDTPA (55.8 μmol, 48 equiv) in a bicarbonate buffer (pH 9, 2 mL) at 40 °C. Following this, *p*-SCN-BzDTPA (55.8 μmol, 48 equiv) was added 48 h later to the reaction solution and maintained at pH 9. The reaction mixture was kept at 40 °C for 48 h. The resulting solution was purified by diafiltration using Centricon 10 (Millipore, Billerica, MA) to obtain BzDTPA conjugated poly(L-lysine) dendri-graft G2 (BzDTPA-lysineG2), and the buffer was changed to PBS. The number of chelates on a dendri-graft was determined using HPLC (column, TSKgel G2000SW (7.8 × 300 mm, Tosoh Bioscience LLC.); flow rate = 0.5 mL/min; eluent, PBS (pH 7.2)) by comparing the UV peak area of BzDTPA-lysineG2 and *p*-SCN-BzDTPA. An average of 20 BzDTPA chelates was conjugated to a dendri-graft.

After the buffer was changed to the 0.5 M ammonium citrate (pH 4.8), the BzDTPA-lysineG2 (23 μmol) was reacted with Gd(III) acetate (46 μmol) overnight at 37 °C. Excess Gd(III) was removed by diafiltration using Centricon 10, and the buffer was changed to PBS. The number of chelated Gd was measured by ICP-OES (Columbia Analytical Services, Tucson, AZ). The number of available chelates for binding Gd atom was 17.

Gd-BzDTPA-lysineG3 was prepared in a similar manner to Gd-BzDTPA-lysineG2, by treating G3 poly(L-lysine) dendri-graft (0.45 μmol, 1 equiv) with two separated additions of *p*-SCN-BzDTPA (55.8 μmol, 48 equiv). The resulting BzDTPA-lysineG3 (21 μmol) was treated with Gd(III) acetate (42 μmol)

* Corresponding author. Hisataka Kobayashi, M.D., Ph.D. Molecular Imaging Program, Center for Cancer Research, National Cancer Institute, NIH, Building 10, Room 1B40, MSC1088, Bethesda, MD 20892-1088. Phone: 301-451-4220; Fax: 301-402-3191; E-mail: kobayash@mail.nih.gov.

10.1021/bc9005442 © 2010 American Chemical Society
Published on Web 03/17/2010

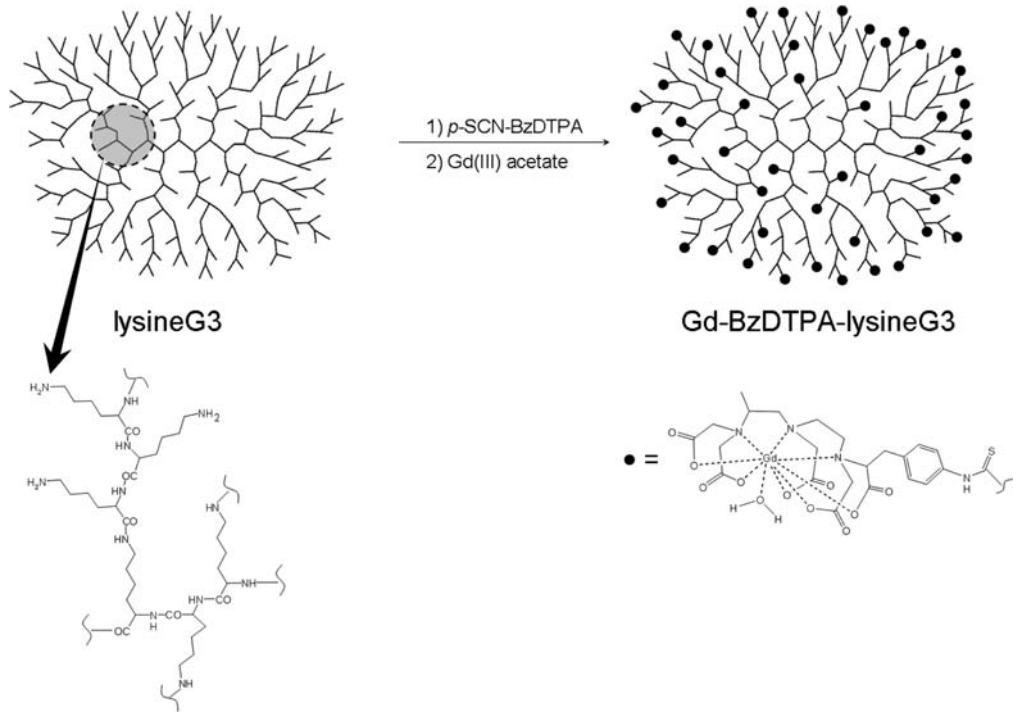


Figure 1. Synthetic scheme of Gd-BzDTPA-lysineG3.

to obtain Gd-BzDTPA-lysineG3. The number of chelates on the dendri-graft was 46, and the number of available chelates for binding Gd atom was 38.

Gd-BzDTPA-PAMAMG4 was also prepared as a control by treating PAMAM G4 dendrimer with *p*-SCN-BzDTPA as previously described (*1*). The number of chelates per dendrimer was 59, and number of available chelates for binding Gd atom was 57. Molecular weights of synthesized Gd-BzDTPA-lysineG2, Gd-BzDTPA-lysineG3 and Gd-BzDTPA-PAMAMG4 are 25.3, 40.4, and 64.5 kDa, respectively.

Size Measurement of Gd-BzDTPA-LysineG2 and Gd-BzDTPA-LysineG3. The sizes of Gd-BzDTPA-lysineG2, Gd-BzDTPA-lysineG3, and Gd-BzDTPA-PAMAMG4 were measured by dynamic light scattering (DLS) using Malvern Zeta Sizer Nano instrument (Malven Instruments Ltd., Malvern, UK) and by size exclusion HPLC (column, TSKgel G2000SW (7.8 × 300 mm, Tosoh Bioscience LLC.); flow rate = 0.5 mL/min; eluent, PBS (pH 7.2)).

Radiolabeling of Lysine-Dendri-Grafts. The Gd-BzDTPA-lysine dendri-grafts (~200 μg) were reacted with carrier-free ^{111}In in 0.15 M NH_4OAc pH 4.25 for 1 h at room temperature. To remove any non-incorporated free radiometal, 10 μL of 0.1 M EDTA was added and purified using an Amicon Ultra-4 centrifuge with Ultracel-10 (MWCO 10k) (Millipore, Billerica, MA) with an average radiolabeling yield of ~85%.

All radiolabeled [^{111}In]-Gd-BzDTPA dendri-grafts were analyzed by HPLC using TSK 2000SW (Toso Haas) size-exclusion columns connected to Flow-count radio-HPLC detector (Bioscan, Washington, DC, USA). Samples were eluted using 1× PBS (10 mM phosphate buffer at pH 7.4 in 0.15 M NaCl) at a flow rate of 0.5 mL/min. Radiochemical purity was also assessed using radio-ITLC and was found to be >98%.

Biodistribution of [^{111}In]BzDTPA-LysineG2 and [^{111}In]-BzDTPA-LysineG3. All procedures were carried out in compliance with the Guide for the Care and Use of Laboratory Animal Resources (1996), National Research Council, and approved by the NIH Animal Care and Use Committee. The carrier molecule, Gd-BzDTPA-lysineG2, Gd-BzDTPA-lysineG3, or Gd-BzDTPA-PAMAMG4, was added to the radiolabeled solution; and [^{111}In]Gd-BzDTPA-lysineG2 (185 kBq, 300 μg), [^{111}In]Gd-BzDTPA-lysineG3 (185 kBq, 300 μg), or [^{111}In]Gd-BzDTPA-PAMAMG4 (185 kBq, 300 μg) was injected intravenously into female nude mice (National Cancer Institute Animal Production Facility, Frederick, MD). The mice were sacrificed at 15 min, 1 h, 4 h, and 24 h, and the organs were weighed and counted in a gamma counter to calculate %ID/g.

Relaxivity. Relaxivity was measured by a custom-designed variable field T1-T2 analyzer (Southwest Research Institute, San Antonio, TX) and a 3T MR system (Signa LX, GE Healthcare, Waukesha, WI, USA).

For the variable field analyzer, the field strength was varied from 0.035 to 1.5 T (1.5−62 MHz) and the sample temperature was set at 23 °C. Solutions of Gd-BzDTPA-lysineG2, Gd-BzDTPA-lysineG3, Gd-BzDTPA-PAMAMG4, and Gd_DTPA (Magnevist, Berlex, Princeton, NJ) (1 mMGd, PBS, pH 7.4) were prepared, and T1 was measured using a saturation recovery pulse sequence with 32 incremental recovery times. T2 was measured using a Carr-Purcel-Meiboom-Gill pulse sequence of 500 echoes and an interecho time of 2 ms. To investigate the temperature dependency, additional measurements were performed at 0.8 T field strength by changing the temperature to 16, 23, and 37 °C.

We also measured the relaxivity at 22 °C using a 3.0T clinical scanner (Signa Excite, GE Healthcare, Waukesha, WI, USA) equipped with a rectangular single loop receiver coil (84 × 126 × 6 mm). Phantom solutions in 1× PBS consisting of 0, 0.1, 0.25, 0.5, 0.75, and 1 mM in Gd(III) together with Gd-DTPA as reference controls were prepared. A series of single-slice 2D inversion recovery (IR) fast spin−echo images of all solutions were obtained at an echo time (TE) of about 7.54 ms using different inversion recovery times (TI) of 50, 100, 350, 750, 1250, 2500, and 5000 ms for r1 calculation, an 8-echo 2D-SE sequence with a TR = 5000 ms and an echo time interval of 8.5 ms for r2 calculation. The r1 values for each dilution were determined by fitting ROI intensity values from variable IR images using Igor Pro (http://www.wavemetrics.com). r2 values were measured from ROI values from T2 maps, which were

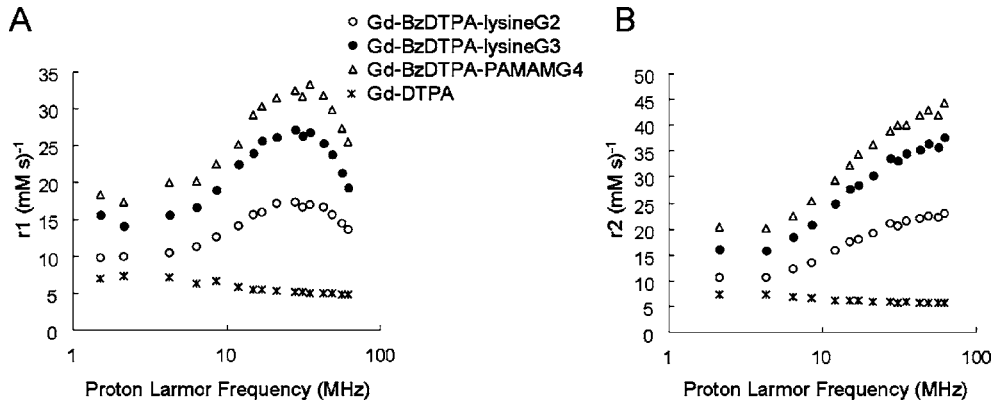


Figure 2. Frequency dependency of r1 (A) and r2 (B) profiles for each contrast agent at 23 °C.

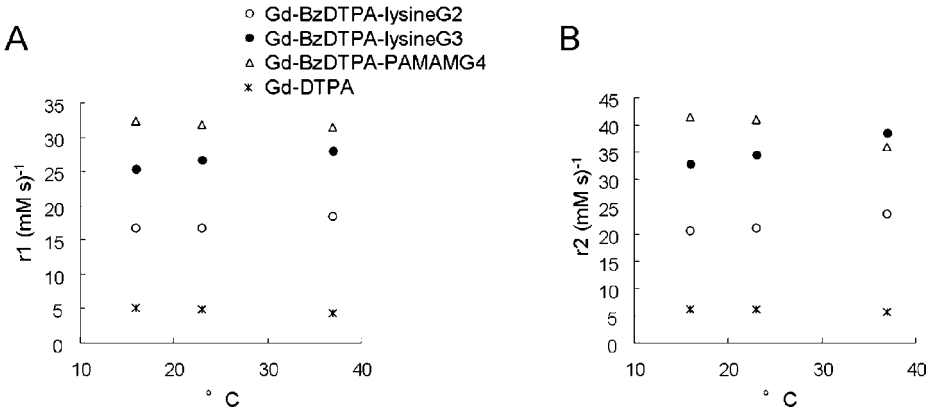


Figure 3. Temperature dependency r1 (A) and r2 (B) profiles for each contrast agent at 35 MHz.

calculated from the multiecho images in *ImageJ* (http://rsb.info.nih.gov/ij) using the MRI analysis plug-in (http://rsb.info.nih.gov/ij/plugins/mri-analysis.html). The molar relaxivities, r1 and r2, were obtained from the slope of 1/T1 or 1/T2 vs [Gd(III)] plots determined from region of interest measurements.

Contrast-Enhanced Dynamic 3D-Micro MRI of Mice. All dynamic micro-MRI images were obtained at 3 T with a 1 in round receive-only modified Alderman-Grant resonators. Mice were chemically restrained with 2% isoflurane (Abbott Laboratories, NJ) in O_2 delivered using a Summit Anesthesia Solutions vaporizer (Bend, OR) at a flow rate of 0.8 L/min. Respiration rate was maintained at 25−30 respirations per min and monitored using a Biopac System MP150 (Biopac Inc., Goleta, CA). The temperature of the mouse was maintained at 32 ± 1 °C using a Polyscience Model 210 heating recirculator with 3 M Fluorinert Electronic Liquid FC-77 with body temperature monitored using FOT-M fiberoptic sensors (Fiso Technologies Inc., San Jose, CA) and a UMI-8 multichannel instrument (Fiso Technologies Inc.). A tail vein cannula consisting of a 30-gauge needle attached to Tygon tubing (0.01 in i.d.) was then established. Prior to injection of the contrast agent, a T1 map was obtained by using a 3D-fast spoiled gradient echo image (3D-fSPGR) sequence at two different flip angles (repetition time/echo time 10.888/3.86 ms; flip angles 8° and 24°; bandwidth 31.25 kHz; matrix size 512 × 128 × 40; voxel resolution 156 × 156 × 600 μm; slice thickness 0.6 mm; two averages; scan time ~2 min). One hundred microliters (100 μL) of the Gd-BzDTPA-lysineG2, Gd-BzDTPA-lysineG3, or Gd-BzDTPA-PAMAMG4 was injected (0.03 mmol Gd/kg) from the tail vain. The region of interest was placed on the liver, the cortex and medulla of the kidney, the muscle at the femoral region, and the jugular vein, and the time−intensity curves were made. In addition, the slice data were processed into 3D images with the maximum intensity protection (MIP) method.

RESULTS

Size. The size of Gd-BzDTPA-lysineG2, Gd-BzDTPA-lysineG3, and Gd-BzDTPA-PAMAMG4, measured by dynamic light scattering (DLS), was 8.58, 14.59, and 9.28 nm, respectively. The retention time by size-exclusion HPLC was 15.2, 12.4, and 14.3 min for Gd-BzDTPA-lysineG2, Gd-BzDTPA-lysineG3, and Gd-BzDTPA-PAMAMG4, respectively, and the results were matched with the DLS results.

Relaxivity. The r1 profiles of the Gd-BzDTPA-lysineG2, Gd-BzDTPA-lysineG3, Gd-DTPA, and Gd-BzDTPA-PAMAMG4 at 23 °C are plotted in Figure 2. The profiles are similar for Gd-BzDTPA-lysineG2, Gd-BzDTPA-lysineG3, and Gd-BzDTPA-PAMAMG4 and exhibit an increase in peak relaxivity at about 35 MHz as observed previously for macromolecular MRI contrast agents. The low molecular weight contrast agent Gd-BzDTPA exhibits dispersion at around 10 MHz and slightly decreases over 10 MHz in this frequency range. All samples exhibited characteristic T1 and T2 profiles. Gd-BzDTPA-lysineG2, Gd-BzDTPA-lysineG3, and Gd-BzDTPA-PAMAMG4 had peak relaxivities around 35 MHz (0.8 T). The Gd-BzDTPA-lysineG2 and Gd-BzDTPA showed lowest r1 values. The r2 values of Gd-BzDTPA-lysineG2, Gd-BzDTPA-lysineG3, and Gd-BzDTPA-PAMAMG4 increased with frequency as expected.

The r1 values of Gd-BzDTPA-lysineG2 and Gd-BzDTPA-lysineG3 increased with sample temperature; in contrast, r1 decreased with temperature for Gd-BzDTPA-PAMAMG4 and Gd-DTPA. The similar tendency was observed for r2 values (Figure 3). However, the magnitude of r2 for the G3 lysine was greater than G4 PAMAM at 35 °C. This has been attributed to

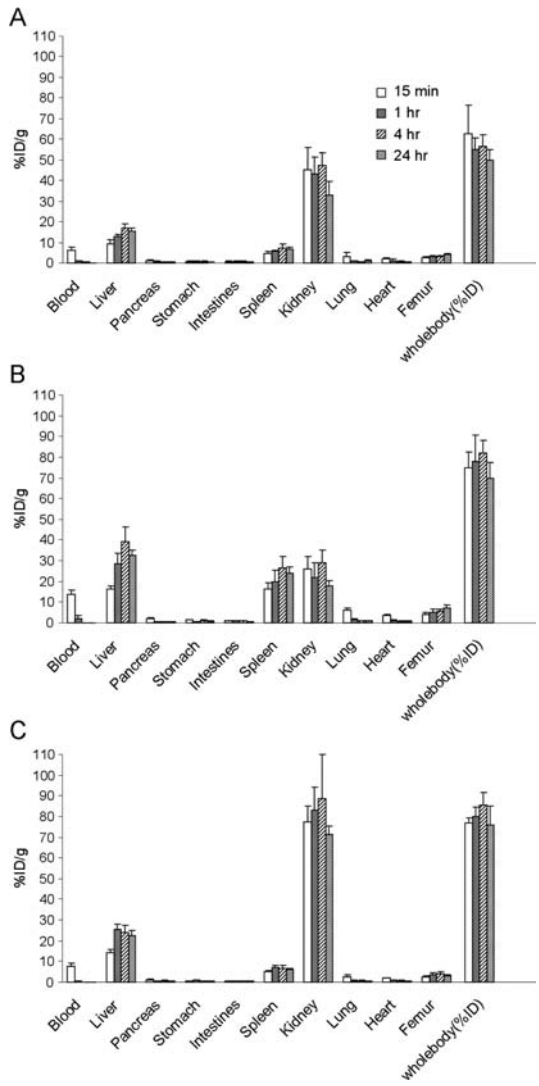


Figure 4. Biodistribution of [^{111}In]Gd-BzDTPA-lysineG2 (A), [^{111}In]Gd-BzDTPA-lysineG3 (B), and [^{111}In]Gd-BzDTPA-PAMAMG4 (C) in mice.

improved access of water to the interior Gd chelates in the lysine-dendri-graft. The r1 and r2 values of Gd-BzDTPA-lysineG2, Gd-BzDTPA-lysineG3, Gd-BzDTPA-PAMAMG4, and Gd-DTPA measured by 3T clinical scanner were 7.53, 6.86, 11.04, and 4.44 /s/mM for r1, and 25.72, 26.38, 30.64, and 5.46 /s/mM for r2, respectively.

Biodistribution of [^{111}In]Gd-BzDTPA-LysineG2, [^{111}In]Gd-BzDTPA-LysineG3, and [^{111}In]Gd-BzDTPA-PAMAMG4. The results of biodistribution experiments are summarized in Figure 4. High kidney activity for all agents, but was highest for [^{111}In]Gd-BzDTPA-PAMAMG4 and lowest for [^{111}In]Gd-BzDTPA-lysineG2. The liver accumulation was highest for [^{111}In]Gd-BzDTPA-lysineG3. [^{111}In]Gd-BzDTPA-lysineG3 also showed high splenic uptake. The blood clearance was slowest for [^{111}In]Gd-BzDTPA-lysineG3. The clearance from the body was fastest for [^{111}In]Gd-BzDTPA-lysineG2.

3D-Micro-MR. The time−intensity curve and MIP images are shown in Figures 5 and 6, respectively. The blood retention was greatest for Gd-BzDTPA-lysineG3. The profiles of signal intensity in blood were similar for Gd-BzDTPA-lysineG2 and Gd-BzDTPA-PAMAMG4. Relatively high signal intensity was detected in the cortex of the kidneys for Gd-BzDTPA-lysineG2. The signal intensities in the renal pelvis were high for both the G2 and G3 lysine-dendri-grafts, while it was lower for Gd-BzDTPA-PAMAMG4. Gd-BzDTPA-lysineG3 showed higher signal intensity than Gd-BzDTPA-lysineG2 and PAMAMG4 in the liver. The signal in muscle was low for all compounds.

DISCUSSION

An interesting physical characteristic of lysine-dendri-graft based MRI contrast agents is their relaxivity behavior relative to PAMAM-based dendrimers of similar sizes or small molecular weight chelates. Since the Gd-chelates are located on the surface of low-generation PAMAM-based dendrimer contrast agents, they constantly interact with water, the rotational correlation time of the chelated Gd ions increases as the temperature decreases leading to an increase in r1 for these contrast agents. Similar results were previously obtained by Jaszberenyi et al. (*9*) Low molecular weight gadolinium chelates behave similarly. Conversely, an increase in temperature results in a decrease in r1 because of the decrease in the rotational correlation time of the single Gd chelate or the Gd chelates on the surface of the low generation dendrimers. In contrast, lysine-dendri-grafts demonstrate higher r1's as the temperature increases, as has been previously observed for high-generation PAMAM dendrimers (*10*). In addition, the overall r1 of the lysine-dendri-graft based MRI contrast agents was lower than that of PAMAM-based dendrimer contrast agents with similar size especially at the low temperature. The lysine-dendri-grafts potentially have terminal amines in the interior structure. Therefore, some of the chelated Gd ions might not be fully accessible by water. As the temperature increases, however, water can access the internal chelates which lead to an increase in relaxivity. Furthermore, the increase in water exchange between the (interior) bound water and the exterior bulk water with rising temperature would also result in an increased relaxivity. However, it is difficult to know the exact extent of the interplay between water accessibility and the water exchange and additional studies are needed over a larger range of lysine-based dendri-graft generations. However, the exchange time of the water bound to the interior Gd chelates and in bulk solution also increases, because now, the water has to go inside the dendrimer and then back out. With PAMAM, it only has to go to the exterior and then back to the bulk water. So, this increases the water exchange time for the lysine-dendri-graft compared to the PAMAM dendrimer and increases even further with rising temperature. The effect on increasing the water exchange time is the same effect as increasing the rotational correlation time—an increase in relaxivity. As was observed for the high-generation PAMAM, if the water exchange time is increased too much, it actually will start to decrease the relaxivity. Therefore, this unique relaxivity behavior of the contrast agents based on the lysine-dendri-graft compared with the PAMAM-based contrast agent of the similar size could be derived from the less packed, therefore, better flexible interior of the lysine-dendri-grafts than that of PAMAM dendrimer (*9*−*11*). The relaxivity change of the macromolecular contrast agents was mostly focused on the size of the molecule because of the rotational correlation time; however, our findings suggested that the flexibility of the interior can also affect the relaxivity change. This theory can be useful for designing nanosized contrast agents with high relaxivity or chemical exchange saturation transfer (CEST) contrast using various soft nanomaterials.

Accelerated renal excretion is important to minimize the potential toxicity of Gd-chelated agents. It is known that excretion by glomerular filtration primarily depends on molecular size (*12*). The lysine-dendri-graft based MRI contrast agents are relatively larger in hydrodynamic physical size than the PAMAM-based dendrimer contrast agents. Nevertheless, lysine-dendri-grafts demonstrate renal excretion, an observation likely related to the flexibility of the molecule. In addition, it is known that lysine administration can block renal tubular reabsorption

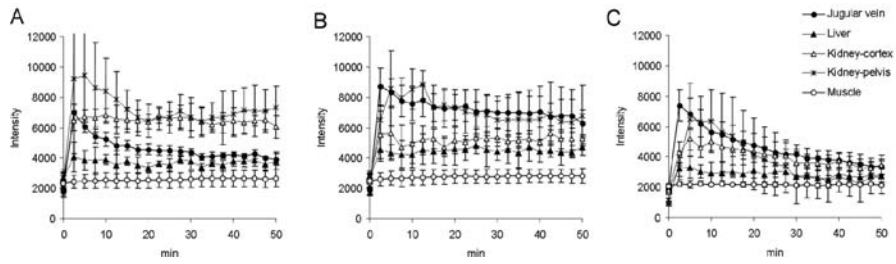


Figure 5. Plots of the signal intensity in the jugular vein, the liver, the cortex and medulla of the kidney, and the muscle at the femoral region obtained from the contrast enhanced dynamic MRI of mice: Gd-BzDTPA-lysineG2 (A), Gd-BzDTPA-lysineG3 (B), and Gd-BzDTPA-PAMAMG4 (C).

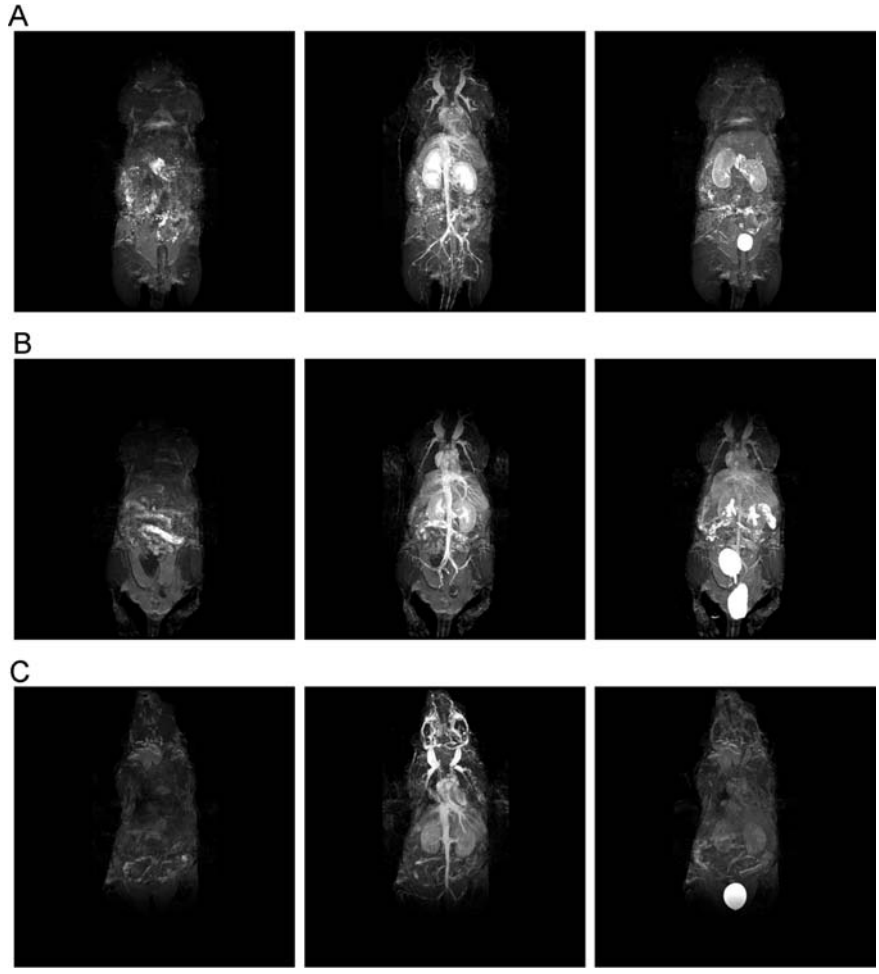


Figure 6. Whole body 3D MR images of mice, which were constructed with the MIP method with preinjection (left), immediately after (middle), and 50 min after (right) injection of Gd-BzDTPA-lysineG2 (A), Gd-BzDTPA-lysineG3 (B), or Gd-BzDTPA-PAMAMG4 (C).

of small-molecular-weight proteins (*13*, *14*), and Kobayashi et al. previously reported that lysine coinjection can accelerate the renal excretion of Gd-chelated PAMAMG4 (*15*). Therefore, Gd-BzDTPA-lysineG3 can visualize the blood vessels longer than Gd-BzDTPA-PAMAMG4, but still can be excreted through the kidney. Since the G8 PAMAM-based dendrimer contrast agent with similar size to Gd-BzDTPA-lysineG3 is not excreted from the kidney, this pharmacokinetic characteristic of lysine-dendri-graft based MRI contrast agents is potentially advantageous.

In conclusion, we have synthesized nanosized MRI contrast agents using lysine-dendri-graft platforms and compared their physical and pharmacological characteristics with those of a PAMAM-based dendrimer contrast agent of comparable size. Nanosized MRI contrast agents using lysine-dendri-graft platforms showed different relaxivity characteristics from the PAMAM-based agents of the similar size. In addition to its biocompatibility, preferable physical characteristics and pharmacokinetics of nano-sized MRI contrast agents with lysine-dendri-graft, which are derived from different interior structures rather than the physical size, might make these agents clinically feasible.

ACKNOWLEDGMENT

This research was supported by the Intramural Research Program of the NIH, National Cancer Institute, Center for Cancer Research.

LITERATURE CITED

(1) Kobayashi, H., and Brechbiel, M. W. (2005) Nano-sized MRI contrast agents with dendrimer cores. *Adv. Drug Delivery Rev. 57*, 2271–86.

(2) Kobayashi, H., and Brechbiel, M. W. (2003) Dendrimer-based macromolecular MRI contrast agents: characteristics and application. *Mol. Imaging 2*, 1–10.
(3) Bawarski, W. E., Chidlowsky, E., Bharali, D. J., and Mousa, S. A. (2008) Emerging nanopharmaceuticals. *Nanomedicine 4*, 273–82.
(4) Helms, B., and Meijer, E. W. (2006) Chemistry. Dendrimers at work. *Science 313*, 929–30.
(5) Thierry, B. (2009) Drug nanocarriers and functional nanoparticles: applications in cancer therapy. *Curr. Drug Delivery 6*, 391–403.
(6) Longmire, M., Choyke, P. L., and Kobayashi, H. (2008) Clearance properties of nano-sized particles and molecules as imaging agents: considerations and caveats. *Nanomedicine 3*, 703–17.
(7) Lu, Z. R., Mohs, A. M., Zong, Y., and Feng, Y. (2006) Polydisulfide Gd(III) chelates as biodegradable macromolecular magnetic resonance imaging contrast agents. *Int. J. Nanomed. 1*, 31–40.
(8) Lu, Z. R., Parker, D. L., Goodrich, K. C., Wang, X., Dalle, J. G., and Buswell, H. R. (2004) Extracellular biodegradable macromolecular gadolinium(III) complexes for MRI. *Magn. Reson. Med. 51*, 27–34.
(9) Jaszberenyi, Z., Moriggi, L., Schmidt, P., Weidensteiner, C., Kneuer, R., Merbach, A. E., Helm, L., and Toth, E. (2007) Physicochemical and MRI characterization of Gd3+-loaded polyamidoamine and hyperbranched dendrimers. *J. Biol. Inorg. Chem. 12*, 406–20.
(10) Bryant, L. H., Jr., Brechbiel, M. W., Wu, C., Bulte, J. W., Herynek, V., and Frank, J. A. (1999) Synthesis and relaxometry of high-generation (G = 5, 7, 9, and 10) PAMAM dendrimer-DOTA-gadolinium chelates. *J. Magn. Reson. Imaging 9*, 348–52.
(11) Wiener, E. C., Brechbiel, M. W., Brothers, H., Magin, R. L., Gansow, O. A., Tomalia, D. A., and Lauterbur, P. C. (1994) Dendrimer-based metal chelates: a new class of magnetic resonance imaging contrast agents. *Magn. Reson. Med. 31*, 1–8.
(12) Chang, R. L., Ueki, I. F., Troy, J. L., Deen, W. M., Robertson, C. R., and Brenner, B. M. (1975) Permselectivity of the glomerular capillary wall to macromolecules. II. Experimental studies in rats using neutral dextran. *Biophys. J. 15*, 887–906.
(13) Behr, T. M., Sharkey, R. M., Juweid, M. E., Blumenthal, R. D., Dunn, R. M., Griffiths, G. L., Bair, H. J., Wolf, F. G., Becker, W. S., and Goldenberg, D. M. (1995) Reduction of the renal uptake of radiolabeled monoclonal antibody fragments by cationic amino acids and their derivatives. *Cancer Res. 55*, 3825–34.
(14) Kobayashi, H., Yoo, T. M., Kim, I. S., Kim, M. K., Le, N., Webber, K. O., Pastan, I., Paik, C. H., Eckelman, W. C., and Carrasquillo, J. A. (1996) L-lysine effectively blocks renal uptake of 125I- or 99mTc-labeled anti-Tac disulfide-stabilized Fv fragment. *Cancer Res. 56*, 3788–95.
(15) Kobayashi, H., Sato, N., Kawamoto, S., Saga, T., Hiraga, A., Ishimori, T., Konishi, J., Togashi, K., and Brechbiel, M. W. (2001) Novel intravascular macromolecular MRI contrast agent with generation-4 polyamidoamine dendrimer core: accelerated renal excretion with coinjection of lysine. *Magn. Reson. Med. 46*, 457–64.

BC9005442

Folate-Immunoglobulin G as an Anticancer Therapeutic Antibody

Hong Li,[†,‡] Yanhui Lu,[†,‡] Longzhu Piao,[‡] Jun Wu,[‡] Xiaojuan Yang,[‡,§] Sri Vidya Kondadasula,[||,⊥] William E. Carson,[||,⊥,#] and Robert J. Lee*[,‡,§,⊥]

Division of Pharmaceutics, NSF Nanoscale Science and Engineering Center (NSEC), Department of Molecular Virology, Immunology, and Medical Genetics, OSU Comprehensive Cancer Center (OSUCCC), and Department of Surgery, The Ohio State University, Columbus, Ohio 43210. Received December 9, 2009; Revised Manuscript Received February 5, 2010

Folate receptor-α (FR) is a promising cellular marker for tumor-specific drug delivery. Conjugation of folic acid to therapeutic and imaging agents has been shown to enhance their delivery to FR (+) cancer cells in vitro and in tumor-bearing mice via an FR-mediated cellular uptake mechanism. In this study, immunoglobulin G (IgG) was conjugated to folate and evaluated as a therapeutic antibody against folate receptor (FR)-positive tumors. Murine IgG (mIgG) was conjugated to folate via an amide bond to yield folate-conjugated mIgG (f-mIgG) that contained an average of ∼2.6 folates per molecule. Selective uptake of f-IgG by FR (+) tumor cells was determined by fluorescence microscopy and by flow cytometry. Lysis of L1210JF cells by NK cells from murine donors was increased 1.4−9.0-fold at the effector:target (E:T) ratio of 25:1, relative to control mIgG. In mice bearing L1210JF tumors, f-mIgG was found to significantly inhibit tumor growth and to have prolonged the median survival time (MeST). Significantly, the antitumor efficacy of f-mIgG was greatly increased when combined with liposomal G3139, an 18-mer phosphorothioate oligonucleotide. In fact, the combination resulted in a 100% cure rate among the tumor-bearing mice. Injection of f-mIgG significantly increased serum INF-γ and IL-6 level in mice compared with mIgG and dramatically increased serum INF-γ and IL-6 level when combined with liposomal G3139. These results suggested that f-IgG, a novel immunotherapy agent, has potent activity as a therapeutic antibody to the FR-positive cancer, and the therapeutic activity is enhanced by immunomodulatory agents.

INTRODUCTION

Folate receptor-α (FR) is a promising cellular marker for tumor-specific drug delivery, because it is up-regulated in many types of human epithelial cancers. These include tumors arising in the ovary, lung, kidney, mesothelium, head and neck, and brain (*1*−*5*). Conjugation of folic acid to therapeutic and imaging agents has been shown to enhance their delivery to FR(+) cancer cells in vitro and in tumor-bearing mice via an FR-mediated cellular uptake mechanism (*6*−*8*) and are currently being developed in the clinic by Endocyte Inc. Some folate conjugates have shown significant antitumor activities as immunotherapeutic agents (*9*−*12*). For example, folate−fluorescein was shown to eliminate FR(+) tumors in fluorescein-immunized mice (*11, 12*). Moreover, co-administration of interleukin 2 (IL-2) and interferon-α (IFN-α) was shown to enhance the therapeutic efficiency of the folate−fluorescein conjugate (*11*). In other studies, anti-FR-α monoclonal antibodies such as Mov-18 (*13, 14*) and MORAb-003 (Farletuzumab) (*15*) have been reported to target ovarian cancer and have undergone clinical evaluation as therapeutic agents with promising initial results. In addition, a folate-conjugated anti-TCR antibody was shown to re-target cytotoxic T lymphocytes to FR(+) tumors resulting in significant therapeutic activity (*16*−*18*).

G3139 (oblimersen or Genasense) is an 18-mer phosphorothioate oligonucleotide that was designed as an antisense agent against antiapoptotic factor bcl-2 (*19*−*21*). G3139 contains 2 CpG dinucleotides (*22*−*24*) and has been shown to induce a potent cytokine response, presumably through activation of toll-like receptor 9 (TLR9) (*25, 26*). Liposomal encapsulation of G3139 has recently been shown by us to further enhance the immunomodulatory effect of G3139 (*27*).

The objective of this study was to evaluate the therapeutic efficacy of folate conjugated IgG (f-IgG) as a therapeutic antibody against FR(+) tumors. F-mIgG conjugates was synthesized and evaluated in vitro as well as in vivo. Furthermore, the combined effect of f-mIgG and liposomal G3139 was also examined.

EXPERIMENTAL SECTION

Materials. Murine IgG (mIgG) was purchased from Equitech-Bio Inc. (Kerrville, TX). Folic acid, fluorescein isothiocyanate (FITC isomer I), *N*,*N*′-dicyclohexylcarbodiimide (DCC), and *N*-hydroxysuccinimide (NHS) were purchased from Sigma Chemical Co. (St. Louis, MO, USA). G3139 was synthesized by Alpha DNA (Montreal, CA). Phosphatidylcholine from egg yolk (EPC), 3β-[*N*-(*N*′,*N*′-dimethylaminoethane)carbamoyl] cholesterol hydrochloride (DC-Chol), and methoxy-poly(ethylene glycol) (MW = 2000) distearoyl phosphatidylethanolamine (mPEG-DSPE) were purchased from Avanti Polar Lipids (Alabaster, AL). All chemicals used were of analytical or HPLC grade. Recombinant IL-2 with specific activity of 1×10^6 IU/mL was obtained from Hoffmann-La Roche Pharmaceuticals (Nutley, NJ).

Cell Lines. KB and K562 cells were purchased from American Type Culture Collection (Rockville, MD). L1210JF cells were provided by Dr. Manohar Ratnam at University of Toledo (Toledo, OH). KB, L1210JF cells were grown in folate-

* Address correspondence to: Dr. Robert J. Lee, College of Pharmacy, 500 West 12th Ave., Columbus, Ohio 43210. Phone: (614) 292-4172; Fax: (614) 292-7766; E-mail: lee.1339@osu.edu.

† These authors contributed equally to this work.

‡ Division of Pharmaceutics.

§ NSEC.

|| Department of Molecular Virology, Immunology, and Medical Genetics.

⊥ OSUCCC.

Department of Surgery.

10.1021/bc900545h © 2010 American Chemical Society
Published on Web 04/29/2010

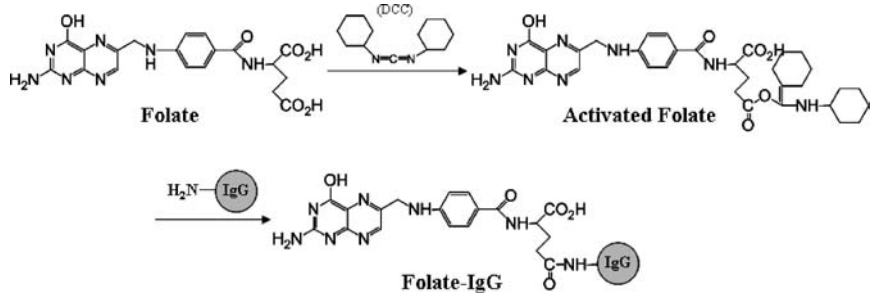


Figure 1. Synthesis of f-IgG conjugate. Conjugation to γ-carboxylic acid in folate is shown in this figure. However, the α-carboxylic acid group can also be conjugated.

free RPMI 1640 medium, and K562 cells were grown in RPMI1640 medium (Invitrogen Life Technologies Inc.). The media were supplemented with 10% heat-inactivated fetal bovine serum (FBS), 2 mM L-glutamine, 100 U/mL penicillin, and 100 mg/mL streptomycin. The cells were maintained in a humidified incubator at 37 °C in 5% CO_2.

Synthesis of Folate-Conjugated Antibodies. The f-IgG was synthesized as previously described (*28*) with minor modifications. Briefly, folate was reacted with *N*,*N*′-dicyclohexylcarbodiimide (DCC) and *N*-hydroxysuccinimide (NHS) in DMSO at molar ratios of folate/DCC/NHS = 1/1.5/1.1 for 3 h at room temperature. The product f-NHS was centrifuged to remove byproducts and then was added to IgG in a pH 8.0 PBS buffer solution at a folate-to-IgG molar ratio of 12:1 for 2 h at room temperature. For the preparation of FITC labeled f-IgG (f-IgG-FITC) or IgG (IgG-FITC), 5× FITC dissolved in a small volume of DMSO was added to the protein solution at pH 8. To purify the conjugates, the reaction mixture was passed through a PD-10 column equilibrated in PBS (pH 8.0) and the product was collected in the void volume fractions. Folate content of the product was determined by UV spectrometry at 371 nm, and the antibody protein concentration was determined using the Pierce BCA Protein Assay Kit. A synthetic scheme is described in Figure 1.

Uptake of f-IgG-FITC by Tumor Cells. The cellular uptake of f-IgG was determined in FR(+) KB, L1210JF, and FR(-) K562 cells. Approximately 1×10^6 cells were incubated with 200 nM FITC labeled IgG or f-IgG in 1 mL folate-free RPMI1640 at 37 °C for 30 min. The cells were then washed three times with cold PBS containing 1% BSA and examined by fluorescence microscopy or by flow cytometry. For receptor blocking studies, 200 μM of free folate was added to media during f-IgG-FITC exposure.

Antibody Dependent Cellular Cytotoxicity (ADCC) Mediated by f-IgG in L1210JF Cells. Murine NK cells were isolated from splenocytes of DBA/2 mice (Charles River, Wilmington, MA) via mechanical digestion followed by lysis of red blood cells. Spleenocytes were then incubated with phycoerythrin-labeled anti-DX5 antibody (BD PharMingen, San Diego, CA) for 30 min at 4 °C. Following this, the cells were washed and incubated with antiphycoerythrin antibody-coated magnetic microbeads (Miltenyi Biotech, Auburn, CA) for an additional 30 min at 4 °C according to the instructions of the manufacturer. NK cells were isolated via positive selection through an LS+ magnetic column (Miltenyi Biotech). Isolated murine NK cells were >90% $DX5^+$ by FACS analysis. Purified murine NK cells were plated in 96-well V-bottom plates in 10% HAB containing glutamine free, folate-free RPMI 1640 medium supplemented with a low dose of IL-2 (1 nM), and incubated overnight at 37 °C. For ADCC assays, mIgG or f-mIgG treated, ^{51}Cr-labeled L1210JF tumor cells were added to NK cells at effector:target (E:T) ratios of 25:1 and 12.5:1 and 6.25:1, and cytotoxic interactions were allowed to proceed for 4 h at 37 °C. Target cell lysis was determined by counting 100 μL of supernatant in a scintillation counter after removal of intact cells by centrifugation. Spontaneous and maximum lysis were determined by incubating radiolabeled target cells in the absence of effector cells or by adding 10% SDS to the radiolabeled target cells, respectively. The percentage of cell lysis was calculated by the following formula: Lysis (%) = 100 × (experimental release − spontaneous release)/(maximal release − spontaneous release).

Preparation of Liposomal G3139. Liposomes containing G3139 were prepared by the EtOH dilution/diafiltration method, as described previously (*27*). DC-Chol, egg PC, and mPEG-DSPE were dissolved in ethanol and mixed at a molar ratio of 30:65:5. The lipid mixture (20 mg/mL) was mixed with protamine solution in citrate buffer (pH 4.0, 20 mM) and then slowly added to G3139 solution in citrate buffer (pH 4.0, 20 mM) under vortex mixing to achieve a final ethanol concentration of 40% and a G3139, lipid, and protamine ratio of 1:12.5:0.3 (w/w/w). The preparation was then dialyzed against citrate buffer (pH 4.0, 20 mM) for 1 h and then against HEPES-buffered saline (HBS, pH 7.5) overnight to remove ethanol. Final product was stored at 4 °C before use. The mean particle size was determined by dynamic light scattering on a Nicomp model 370 Submicrometer Particle Sizer (Particle Sizing Systems, Santa Barbara, CA). Zeta potential (ζ) of liposomal G3139 was measured on a Brookhaven 90plus Particle Analyzer (Holtsville, NY).

Therapeutic Efficacy in Murine Leukemia Model. Therapeutic efficacy in murine leukemia model was evaluated in DBA/2 mice (Charles River, Wilmington, MA). Female mice (18−22 g) were injected subcutaneously on day 0 with 1×10^6 L1210JF cells and then randomized to different treatment groups to eliminate cage effects. Before leukemia cell inoculation, mice were placed on a folate-free diet (AIN-90G, Dyets, Bethlehem, PA) for 1 week. Normal rodent chow was not used because it contains approximately 3.19 mg/kg folic acid, which leads to supra-physiological serum folate concentration. When a tumor reached a volume of ~25 mm^3, the mice were treated with the desired immunotherapy regimens 4 times every 4 days (q4dx4). In the first treatment regimen, mice were given 100 mg/kg mIgG or f-mIgG intraperitoneally. In the second treatment regimen, mice were treated with 1 mg/kg free G3139 or liposomal G3139. In the third treatment regimen, mice were given 100 mg/kg f-mIgG combined with free G3139 or liposomal G3139. Tumor dimensions were determined by measuring with a caliper, and the tumor volume (in mm^3) was calculated by the formula 0.5 × (length × width × height). Mice were sacrificed once the tumor size reached greater than 1500 mm^3. Tumor inhibition ratio was calculated by $(C - T)/C \times 100\%$, where T and C represent the mean tumor volume of the treated and control animals, respectively. Animal survival was evaluated by Kaplan−Meier analysis and increase-in-

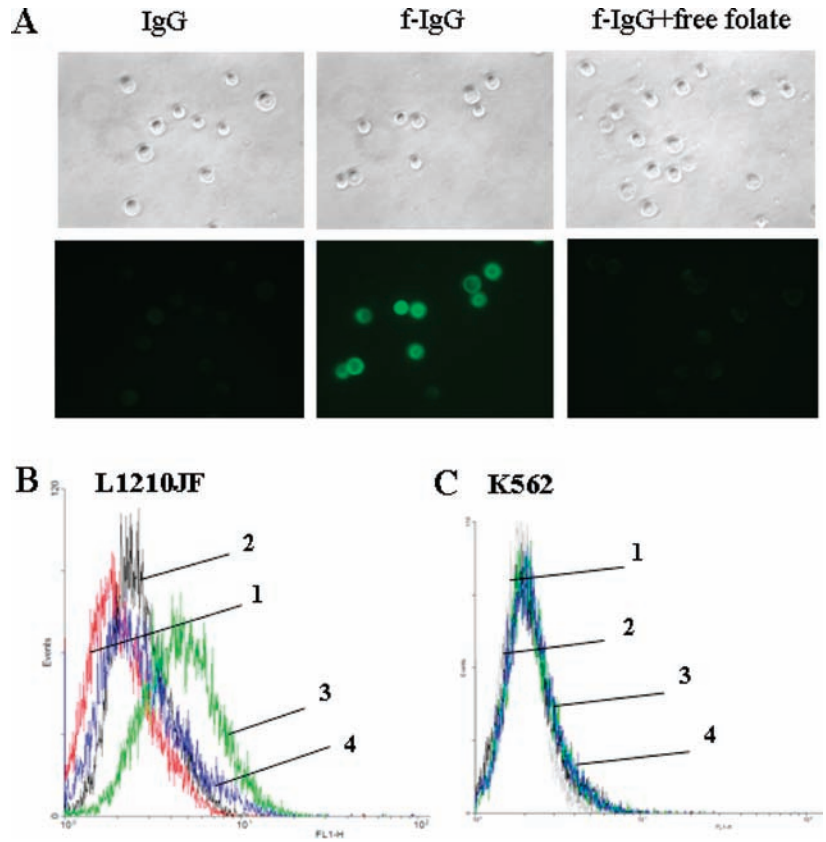


Figure 2. Uptake of f-IgG-FITC in KB (A), L1210JF (B), and K562 (C) cells. Cells were treated with 200 nM FITC labeled IgG or f-IgG in folate-free RPMI1640 at 37 °C for 30 min. For the receptor blocking study, 200 μM of free folate was added to media during f-IgG-FITC exposure. f-IgG-FITC binding in KB cells by fluorescence microscopy. After treatment, KB cells were photographed in both phase-contrast (upper panels) and fluorescence (lower panels) mode on a Nikon Eclipse 800 fluorescence microscopy. Uptake of f-IgG-FITC in L1210JF and K562 cells by flow cytometry. (1) Untreated cells. (2) Cells were treated with IgG-FITC. (3) Cells were treated with f-IgG-FITC. (4) Cells were treated with f-IgG-FITC and free folate.

lifespan (ILS, %) was calculated by ILS = (mean survival time of the treated mice/mean survival time of control mice − 1) × 100%.

Serum Cytokine Levels in Murine Leukemia Model. The serum cytokine levels were investigated in L1210JF tumor-bearing DBA/2 mice (Charles River, Wilmington, MA). Before leukemia cell inoculation, mice were placed on a folate-deficient diet (AIN-90G, Dyets, Bethlehem, PA) for at least 1 week. At 5 days after tumor cells inoculation, the mice were injected intraperitoneally with 100 mg/kg mIgG and f-mIgG. For the therapeutic combination study, f-mIgG was intraperitoneally administered with free G3139 or liposomal G3139. Blood samples were collected at 2, 6, and 24 h after injection. Serum was obtained by centrifugation of blood samples at 7000 × *g* for 10 min and stored −20 °C until the time of assay. IL-6 and INF-γ was determined by ELISA Ready-Set-Go kits.

Statistical Analysis. Statistical analysis of survival data was performed using the log-rank test. Comparisons between groups were made by Student's *t* tests using the MiniTAB software (Minitab Inc., State College, PA). Difference in survival or tumor growth were considered significant when the *p* value was <0.05.

RESULTS

Characterization of f-IgG Conjugates. The concentrations of IgG and folate were determined by BCA protein assay and UV spectrometry at 371 nm, respectively. Conjugation reactions performed at IgG-to-folate-NHS ratios of 12:1 and 100:1 yielded preparations containing an average molar ratio of 2.6 folates per IgG and 9.0 folates per IgG, respectively. Because excessive folate conjugation may adversely affect the effector function of the IgG, a lower conjugation level was desirable. Therefore, f-IgG with the lower conjugation level was selected for subsequent studies. The presence of folate on IgG was further confirmed by MALDI-TOF mass spectroscopy (data not shown).

To evaluate the FR targeting efficiency of f-IgG, tumor cell uptake of f-IgG-FITC was determined by fluorescence microscopy or by flow cytometry. In FR(+) KB cells, f-IgG-FITC was shown to be taken up much more compared to IgG-FITC (Figure 2A). The uptake of f-IgG-FITC was blocked by 200 μM free folate (Figure 2A). The results from flow cytometry were consistent with those obtained by fluorescence microscopy. In FR(+) murine L1210JF cells, incubation of f-IgG-FITC with cells resulted in greater fluorescence intensity compared with that of cells treated with IgG-FITC (Figure 2B). No increased fluorescence was observed when cells were incubated with f-IgG-FITC in the presence of 200 μM free folate (Figure 2B). In contrast, in FR(-) K562 cells, the uptake of f-IgG-FITC and of IgG-FITC were similar, and the uptake was not affected by 200 μM free folate (Figure 2C). These results indicated that f-IgG-FITC selectively targeted FR (+) tumor cells and was taken up via the FR.

F-IgG Enhanced NK Mediated ADCC against L1210JF Cells. The effects of f-IgG on NK cell lytic activity were examined in an ADCC assay using L1210JF tumor cells as targets. Murine NK cells were activated overnight in medium supplemented with IL-2 (1nM). These cells were then used as effectors against ^{51}Cr labeled target cells that were treated with either mIgG or f-mIgG. As shown in Figure 3A, f-IgG markedly enhanced the ADCC activity of NK cells at all E:T ratios

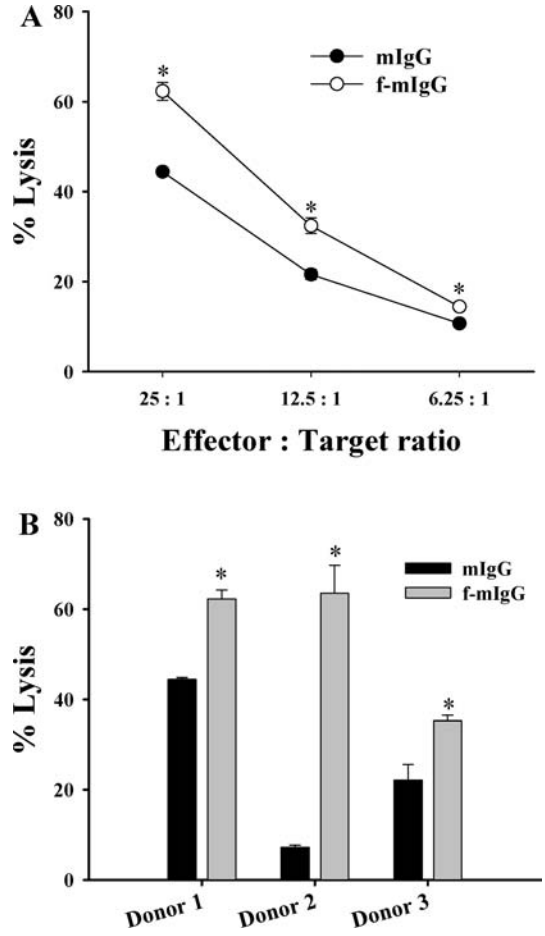


Figure 3. Effect of f-IgG on ADCC activity against FR-positive L1210JF cells at different effector:target ratio (A) and different donor from different mice (B). The NK cell lytic activity was assessed in a standard 4 h chromium release assay using f-mIgG-coated L1210JF cancer cells. The percentage of lysis was calculated as described in Experimental Section. Data represent the mean ± SD ($n = 3$).

examined compared with IgG (Figure 3A). Similar results was observed at E:T ratio of 25:1 for each of the three donors (Figure 3B). However, a relatively large variation was observed among different donors, presumably due to the variability in effector cell activities from different mice.

Characterization of Liposomal G3139. Liposomes containing G3139 was prepared by the EtOH dilution/diafiltration method. The G3139 liposomes showed mean diameter of 92.4 ± 43.6 nm, encapsulation efficiencies of >95%, and zeta potential of 5.02 ± 0.4 mV.

Therapeutic Activity of f-IgG in the Murine Leukemia Model. f-IgG was evaluated in the FR (+) L1210JF murine leukemia model. Mice bearing L1210JF tumors of ~25 mm^3 in size were treated with PBS, 100 mg/kg of mIgG, or 100 mg/kg of f-mIgG by intraperitoneal injection every 4 days for a total of 4 injections. The mice treated with f-mIgG had 59.6% reduction in tumor volume by day 24 after the engraftment of L1210JF cells compared with mIgG treated mice ($p < 0.05$) (Figure 4A). However, tumor-bearing mice treated with mIgG did not show any difference in tumor volume compared to the mice treated with PBS. The median survival time (MeST) for PBS, mIgG, or f-mIgG groups was 24, 27, and 39 days, respectively (Figure 4B, Table 1). Percentage ILS values are 62.5% for f-mIgG and 12.5% for mIgG. Moreover, 1 out of 5 mice was completely cured following treatment with f-mIgG (Figure 4B). The data indicated that f-IgG was more therapeutically effective than IgG or PBS in inhibiting tumor growth and prolonging animal survival ($p = 0.004\,01$; by log-rank test).

In order to investigate whether the anticancer activity was due to FR targeting, anticancer activity of f-mIgG was evaluated in the FR (-) L1210 murine leukemia model. As shown in Figure 4C, f -mIgG slightly decreased tumor volume by day 23 after the engraftment of L1210 cells compared with mIgG and PBS, although no significant differences were observed among f-mIgG, mIgG, and PBS. The median survival times (MeST) for PBS, mIgG, and f-mIgG were 25, 28, and 28, respectively. Similar to data on tumor inhibition, survival time was not significantly prolonged by treatment of f-mIgG compared with mIgG ($p = 0.535$; by log-rank test). Taken together, these results suggested that anticancer activity of f-mIgG in FR positive L1210JF tumor-bearing mice was likely due to the FR targeting.

Therapeutic Efficacy of Liposomal G3139 in Murine Leukemia Model. Previous studies have shown that the cellular uptake and the immunomodulatory effect of G3139 can be significantly enhanced when delivered in a liposomal form (*29*). In order to compare the antitumor efficacy of free G3139 and liposomal G3139, mice carrying L1210JF tumors were treated with 1 mg/kg of G3139 in free form or in liposomal form. As shown in Figure 5, tumor-bearing mice treated with liposomal G3139 had a 45.5% reduction in tumor volume compared with PBS-treated mice ($p < 0.05$). In contrast, free G3139 did not decrease tumor growth compared with PBS. The median survival times (MeST) for PBS, free G3139, or liposomal G3139 were 24, 36, and 36 days, respectively (Figure 5). However, there was no significant difference between free G3139 and liposomal G3139 ($p = 0.252$; by log-rank test). These data suggested that liposomal G3139 was more effective than free G3139 or PBS in mediating tumor regression but not in prolonging survival time of mice compared with free G3139.

Synergistic Effect of f-IgG Combined with Liposomal G3139. Loomis et al. (*30*) has shown that antitumor efficacy of G3139 significantly increased when combined with rituximab, a monoclonal antibody directed against CD20 in a SCID mouse xenograft model. Since f-IgG is being evaluated as a therapeutic antibody, we examined the antitumor efficacy of free and liposomal G3139 coadministered with mIgG or f-mIgG in the murine L1210JF leukemia model. Treatment of IgG combined with liposomal G3139 significantly increased MeST of the mice compared with the treatment of IgG combined with free G3139 (data not shown). With regard to tumor growth inhibition, liposomal G3139 further increased the antitumor efficacy of f-IgG (Figure 5A, Table 1). Importantly, all of the mice were rendered tumor-free after combined treatment with liposomal G3139 and f-IgG (Figure 5B). In comparison, less impressive 20% and 25% cure rates were observed following treatment with f-mIgG alone and following combined treatment with f-mIgG and free G3139, respectively (Figure 5B). These data indicate a strong synergistic effect between f-IgG and liposomal G3139.

Serum Cytokine Levels in Murine Leukemia Model. In order to investigate the effect of cytokine production on anticancer activity, the serum cytokine was determined in DBA/2 mice after administration of mIgG or f-mIgG and combined with free G3139 or liposomal G3139. As shown in Figure 6, levels of INF-γ peaked at 8 h, while levels of IL-6 peaked at 2 h. After 24 h, all cytokine levels were diminished. Compared with mIgG, f-mIgG showed significant cytokine (INF-γ and IL-6) production (Figure 6A,B). In combination with free G3139 and liposomal G3139, f-mIgG induced 2.3-fold and 6.1-fold higher INF-γ production than f-mIgG alone at 6 h postinjection, respectively. Similar results were observed from IL-6 induction in L1210JF murine leukemia model. These data suggested that increased uptake of f-mIgG might elevate the

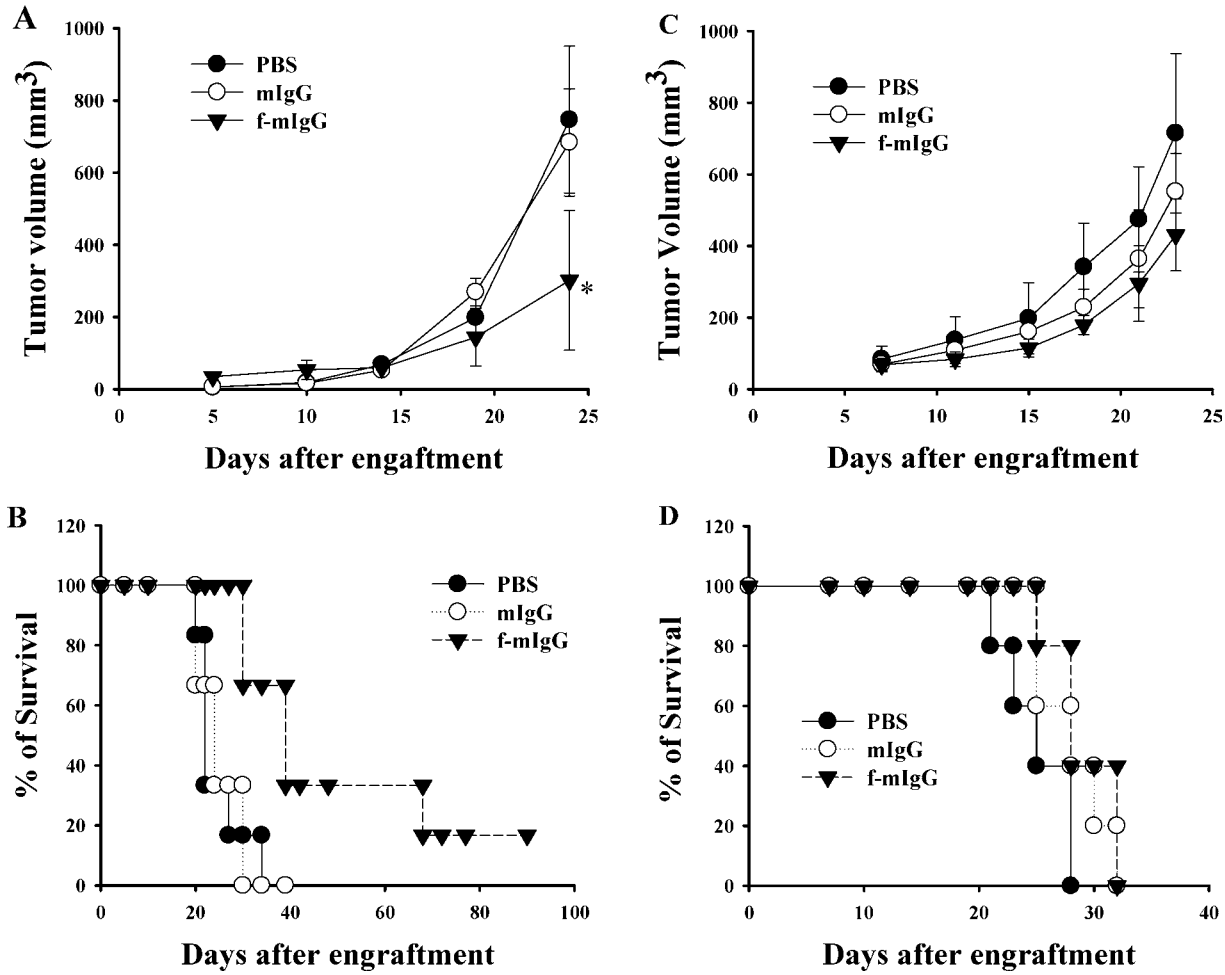


Figure 4. In vivo efficacy of folate receptor mediated immunotherapy in L1210JF (A,B) and L1210 (C,D) bearing DBA/2 mice. Mice (5−6 per group) were implanted subcutaneously on day 0 with 1×10^6 L1210JF cells. On day 5 or 7, animals were treated with 100 mg/kg of mIgG or f-mIgG. The treatment was continued every 4 days for four times. (A,C) Inhibition of tumor growth. Tumor dimensions were measured every 2 days using calipers. (B,D) Survival of L1210JF and L1210 tumor-bearing mice after treatment with mIgG or f-mIgG. PBS was injected as a vehicle control. (*, $P < 0.01$ compared with PBS group.)

Table 1. Survival of Mice after Treatment with mIgG and f-mIgG Alone or in Combination with Free or Liposomal G3139 (L-G3139) in L1210JF Tumor-Bearing Mice[a]

treatment	tumor inhibition ratio[b] (%)	MeST (days)	ILS[c] (%)	Log-rank *p* value
PBS	0	24	0	-
mIgG	8.4	27	12.5	0.901
f-mIgG	59.6	39	62.5	0.00401
G3139	5.6	36	50.0	0.0209
L-G3139	45.5	36	50.0	0.00804
f-mIgG+G3139	83.1	70	191.7	0.000495 (0.198)[d]
f-mIgG+L-G3139	100.0	∞	∞	0.000495 (0.00432)[d]

[a] $n = 6$ for each treatment group. [b] Tumor inhibition ratio was calculated by $(C - T)/C \times 100\%$, where T and C represent the mean tumor volume of the treated and control mice, respectively. [c] ILS(%) was calculated by (MeST of the treated mice/MeST of control mice − 1) × 100%, where MeST represents the mean survival time. [d] The *p* value was calculated in comparison to f-mIgG.

level of cytokines and combined with liposomal G3139 more potently increased the level of cytokines.

DISCUSSION

FR is a promising target for tumor-specific drug delivery. In this study, we describe a novel immunotherapy agent that combines the FR-targeting properties of folate and the effector functions of the IgG. Although folate−hapten's activities have been reported previously (*11*, *12*), that strategy involves preimmunization of the animal and in vivo coupling of the folate−hapten and the endogenous antihapten antibody, which may present an challenging issue. The f-IgG strategy is more analogous to FRα monoclonal antibodies such as MOv-18 (*13*, *14*) and Morab-003 (*15*) currently under clinical development. Compared with FRα monoclonal antibodies, f-IgG targets both FR subtypes, and the underlying IgG used is human and polyclonal, which may be less immunogenic.

f-IgG showed much stronger antitumor effect than IgG in the FR(+) L1210JF tumor-bearing mice (Figure 4A,B) but not in the FR(-) L1210 tumor-bearing mice (Figure 4C,D). These results presumably were due to FR-mediated tumor cell targeting. Tissue toxicity and splenomegaly was not founded by treatment of f-IgG in tumor-bearing mice. Selective folate receptor binding was also observed in the FR(+) L1210JF and KB cells in vitro (Figure 3). Besides folate receptor binding, Fc receptor (FcR) is critical in f-IgG mediated immunotherapy (*31*). FcR-expressing immune cells that recognize a constant (Fc) region of IgG and induce immune response such as ADCC, phagocytosis, neutrophil activation, and the paradoxical inhibition of B cell activation (*31*−*34*). The potential role of NK cell-mediated ADCC of f-IgG was examined. The results showed that lysis of L1210JF tumor cells by NK cells was increased 1.4−9.0-fold by treatment of f-IgG as compared with IgG (Figure 3). In contrast, f-IgG did not bind to FR(-) cell lines (e.g., A549 human alveolar basal epithelial) and did not enhance their lysis by NK cells (data not shown). These results suggested

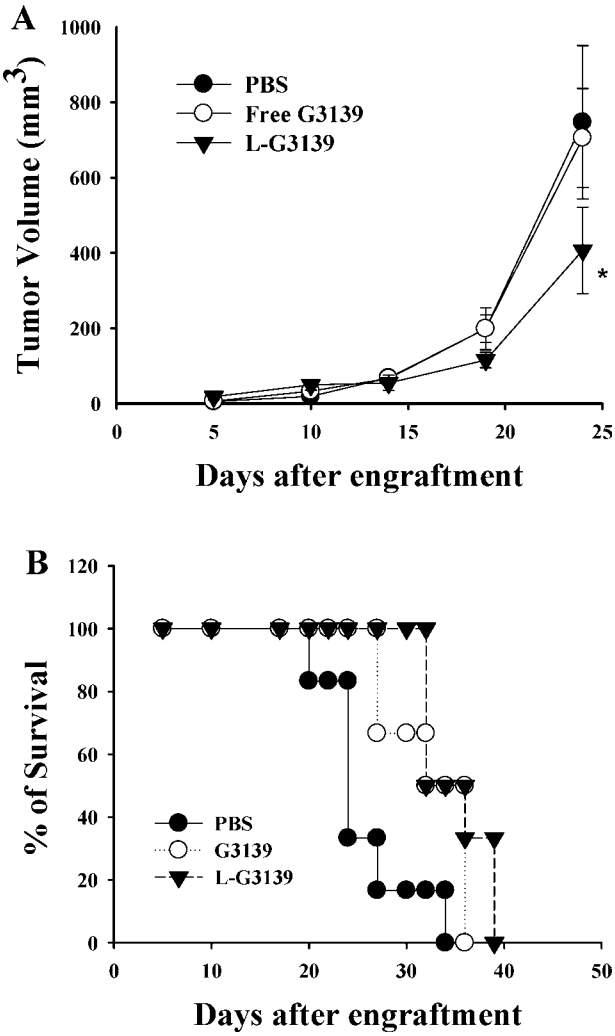


Figure 5. In vivo antitumor efficacy of G3139 in L1210JF bearing DBA/2 mice. Mice (6 per group) were implanted subcutaneously on day 0 with 1×10^6 L1210JF cells. On day 5, animals were treated with with 1 mg/kg of free G3139 or liposomal G3139. The treatment was continued every 4 days for four times. (A) Inhibition of tumor growth. Tumor dimensions were measured every 2 days using caliper. (B) Survival of L1210JF bearing mice after treatment with free G3139 or liposomal G3139. PBS was injected as a vehicle control. (*; $P < 0.05$ compared with PBS group.)

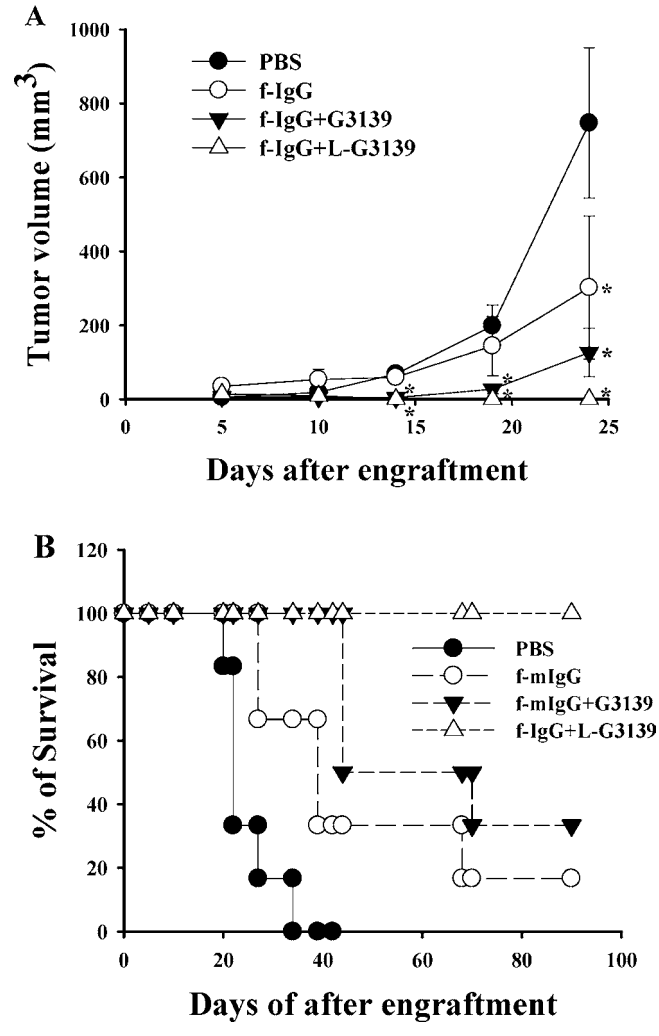


Figure 6. In vivo antitumor efficacy of f-mIgG combined with free G3139 or liposomal G3139 in L1210JF bearing DBA/2 mice. Mice (6 per group) were implanted subcutaneously on day 0 with 1×10^6 L1210JF cells. On day 5, animals were treated with 100 mg/kg of f-mIgG alone or combined with 1 mg/kg of free G3139 or liposomal G3139. The treatment was continued every 4 days for four times. (A) Inhibition of tumor growth. Tumor dimensions were measured every 2 days using caliper. (B) Survival of L1210JF bearing mice after treatment with free G3139 or liposomal G3139. PBS was injected as a vehicle control. (*; $P < 0.01$ compared with PBS group.)

that NK-mediated ADCC was FR-specific. Moreover, we demonstrated enhanced INF-γ production by NK cells when NK cells were co-cultured with f-IgG coated FR(+) tumor cells (*35*). Consistent with this, high levels of INF-γ and IL-6 were observed in the FR(+) tumor-bearing mice after administration of f-IgG compared with IgG (Figure 6), indicating that increased binding of f-IgG to tumor might elevate the level of cytokines. These results suggested that f-IgG might form a bispecific molecular bridge between the FR(+) tumor cells and immune effector cells that mediates tumor cell killing, through NK cell ADCC and cytokine production by NK cells, i.e., the same mechanism of a therapeutic antibody. A similar mechanism was reported by Lu et al. with a combination of a folate−hapten conjugate and endogenous antihapten antibody (*11, 12*). Therefore, the potent anticancer activity of f-IgG in FR(+) tumor-bearing mice observed was likely the result of FcR mediated ADCC and cytokine production, stimulated by f-IgG coated tumor cells via the bispecific molecular bridge. In addition, activated macrophages are known to express folate receptor (*36, 37*). Recently, Turk and Low showed that livers and spleens of tumor-bearing mice preferentially accumulated folate-targeted liposomes, presumably due to the FR-mediated targeting of agents to macrophages in livers and spleens (*38, 39*). Therefore, cytokine production by f-IgG accumulated macrophages in liver and spleen may also contribute to the anticancer activity of f-IgG in tumor-bearing mice. This mechanism remains to be investigated in the future studies.

G3139 was originally designed as a human bcl-2 mRNA antisense and has been investigated in phase I to III clinical trials as a monotherapy or combination with chemotherapy for treatment of chronic lymphocytic leukemia (CLL) (*40, 41*). Importantly, G3139 contains two CpG motifs, which have been shown to activate cytokine production via TLR9 (*25*). We therefore hypothesized that G3139 administration could enhance the antitumor effects of f-IgG. Free G3139 or liposomal G3139 have been shown to prolong animal survival. Compared to free G3139, liposomal G3139 was shown to be significantly more active in tumor inhibition (Figure 5). Recent studies in our lab have demonstrated that liposomal G3139 significantly increased plasma concentration of IFN-γ and IL-6 in mice, and increased proliferation of the DCs and NK cells (*27*). In contrast, no down-regulation of bcl-2 in murine L1210JF cells was observed, presumably due to sequence mismatches between G3139 and

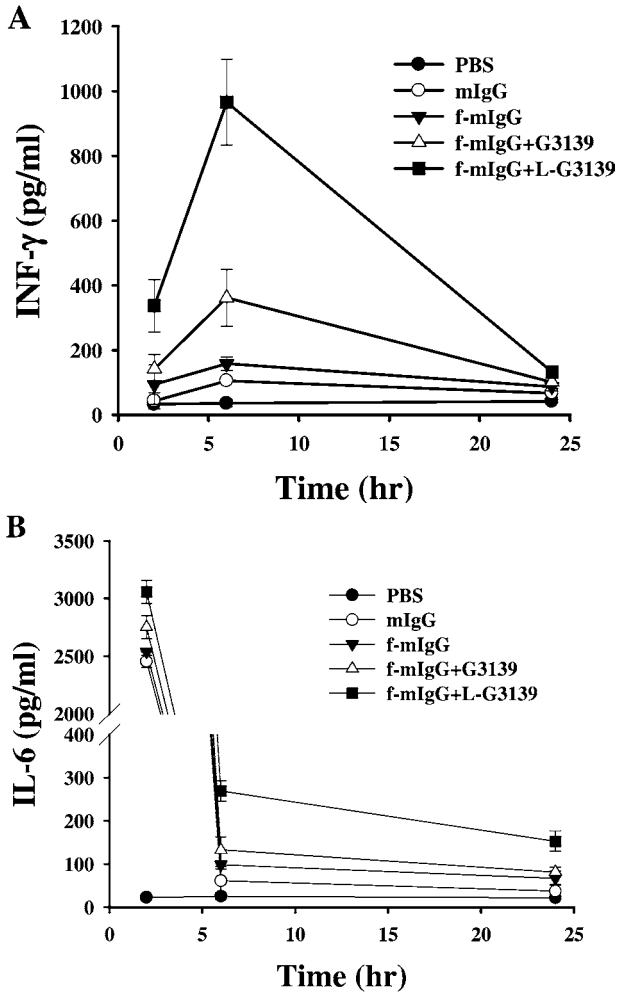


Figure 7. In vivo serum INF-γ (A) and IL-6 (B) production in L1210JF tumor-bearing mice. The tumor-bearing mice were treated with mIgG, f-mIgG alone or in combination with free or liposomal G3139. Blood samples were collected at 2, 6, and 24 h after injection. Serum was obtained by centrifugation and analyzed for INF-γ and IL-6 content by ELISA.

murine bcl-2 (*27*). These results suggested that the antitumor activity was not due to bcl-2 down-regulation but rather the immunomodulatory effect of G3139, which was amplified by liposomal delivery.

Moreover, a strong synergistic antitumor activity was observed when liposomal G3139 was used in combination with f-IgG (Figure 5). Consistent with this result, serum cytokine (INF-γ and IL-6) level was dramatically increased when f-IgG was combined with liposomal G3139 than combined with free G3139 (Figure 6). These results suggested that the synergic antitumor activity was due to the synergistically amplified cytokine (INF-α and IL-6) production in combination with liposomal G3139 and f-IgG. These results were consistent with previous reports (*11*), in which ADCC-activating cytokines such as interleukin 2 (IL-2) or interferon-alpha (IFN-α) have been shown to synergize with the folate receptor targeted immunotherapy.

CONCLUSIONS

F-IgG was shown to specifically target FR(+) tumor cells and be more effective against tumor compared to IgG in a murine tumor model. Moreover, the antitumor efficacy and the serum cytokine level were synergistically increased when co-administrated with liposomal G3139. A series of immunological assays indicated f-IgG's ability to mediate ADCC and cytokine production by immune cells. Therefore, f-IgG exhibits the characteristics of a therapeutic antibody. In addition, folate targeted f-IgG immunotherapy, combined with liposomal G3139, is a promising strategy for treatment of FR(+) cancers.

LITERATURE CITED

(1) Toffoli, G., Cernigoi, C., Russo, A., Gallo, A., Bagnoli, M., and Boiocchi, M. (1997) Overexpression of folate binding protein in ovarian cancers. *Int. J. Cancer 74*, 193–198.

(2) Bueno, R., Appasani, K., Mercer, H., Lester, S., and Sugarbaker, D. (2001) The alpha folate receptor is highly activated in malignant pleural mesothelioma. *J. Thorac. Cardiovasc. Surg. 121*, 225–233.

(3) Parker, N., Turk, E., Westrick, M. J., Lewis, J. D., Low, P. S., and Leamon, C. P. (2005) Folate receptor expression in carcinomas and normal tissues determined by a quantitative radioligand binding assay. *Anal. Biochem. 338*, 284–293.

(4) Ross, J. F., Chaudhuri, P. K., and Ratnam, M. (1994) Differential regulation of folate receptor isoforms in normal and malignant tissues in vivo and in established cell lines. Physiologic and clinical implications. *Cancer 73*, 2432–2443.

(5) Weitman, S. D., Frazier, K. M., and Kamen, B. A. (1994) The folate receptor in central nervous system malignancies of childhood. *J. Neurooncol. 21*, 107–112.

(6) Low, P. S., Henne, W. A., and Doorneweerd, D. D. (2008) Discovery and development of folic-acid-based receptor targeting for imaging and therapy of cancer and inflammatory diseases. *Acc. Chem. Res. 41*, 20–29.

(7) Ke, C. Y., Mathias, C. J., and Green, M. A. (2004) Folate-receptor-targeted radionuclide imaging agents. *Adv. Drug Delivery Rev. 56*, 1143–1160.

(8) Lu, Y., Sega, E., Leamon, C. P., and Low, P. S. (2004) Folate receptor targeted immunotherapy of cancer: mechanism and therapeutic potential. *Adv. Drug Delivery Rev. 56*, 1161–1176.

(9) Siegel, B. A., Dehdashti, F., Mutch, D. G., Podoloff, D. A., Wendt, R., Sutton, G. P., Burt, R. W., Ellis, P. R., Mathias, C. J., Green, M. A., and Gershenson, D. M. (2003) Evaluation of 111In-DTPA-folate as a receptor-targeted diagnostic agent for ovarian cancer: initial clinical results. *J. Nucl. Med. 44*, 700–707.

(10) Naveed, F., Fisher, R., Engel, J. S., Lu, J., Low, P., and Amato, R. J. (2004) Folate-scan in subjects with suspected metastatic renal cell carcinoma. *J. Clin. Oncol. ASCO Annu. Meet. Proc. 22*, 4751.

(11) Lu, Y., and Low, P. S. (2002) Folate targeting of haptens to cancer cell surfaces mediates immunotherapy of syngeneic murine tumors. *Cancer Immunol. Immunother. 51*, 153–162.

(12) Lu, Y., Sega, E., and Low, P. S. (2005) Folate receptor-targeted immunotherapy: induction of humoral and cellular immunity against hapten-decorated cancer cells. *Int. J. Cancer 116*, 710–719.

(13) van Zanten-Przybysz, I., Molthoff, C., Gebbinck, J. K., von Mensdorff-Pouilly, S., Verstraeten, R., Kenemans, P., and Verheijen, R. (2002) Cellular and humoral responses after multiple injections of unconjugated chimeric monoclonal antibody MOv18 in ovarian cancer patients: a pilot study. *J. Cancer Res. Clin. Oncol. 128*, 484–492.

(14) Buist, M. R., Kenemans, P., den Hollander, W., Vermorken, J. B., Molthoff, C. J., Burger, C. W., Helmerhorst, T. J., Baak, J. P., and Roos, J. C. (1993) Kinetics and tissue distribution of the radiolabeled chimeric monoclonal antibody MOv18 IgG and F(ab')2 fragments in ovarian carcinoma patients. *Cancer Res. 53*, 5413–5418.

(15) Ebel, W., Routhier, E. L., Foley, B., Jacob, S., McDonough, J. M., Patel, R. K., Turchin, H. A., Chao, Q., Kline, J. B., Old, L. J., Phillips, M. D., Nicolaides, N. C., Sass, P. M., and Grasso, L. (2007) Preclinical evaluation of MORAb-003, a humanized monoclonal antibody antagonizing folate receptor-alpha. *Cancer Immun. 7*, 6–13.

(16) Kranz, D. M., Patrick, T. A., Brigle, K. E., Spinella, M. J., and Roy, E. J. (1995) Conjugates of folate and anti-T-cell-receptor antibodies specifically target folate-receptor-positive tumor cells for lysis. *Proc. Natl. Acad. Sci. U.S.A. 92*, 9057–9061.

(17) Kranz, D. M., Manning, T. C., Rund, L. A., Cho, B. K., Gruber, M. M., and Roy, E. J. (1998) Targeting tumor cells with bispecific antibodies and T cells. *J. Controlled Release 53*, 77–84.

(18) Roy, E. J., Cho, B. K., Rund, L. A., Patrick, T. A., and Franz, D. M. (1998) Targeting T cells against brain tumors with a bispecific ligand-antibody conjugate. *Int. J. Cancer 76*, 761–766.

(19) Cotter, F. E. (1999) Antisense therapy of hematologic malignancies. *Semin. Hematol. 36*, 9–14.

(20) Tortora, G., Caputo, R., Damiano, V., Bianco, R., Fontanini, G., Cuccato, S., De Placido, S., Bianco, A. R., and Ciardiello, F. (2001) Combined blockade of protein kinase A and bcl-2 by antisense strategy induces apoptosis and inhibits tumor growth and angiogenesis. *Clin. Cancer Res. 7*, 2537–2544.

(21) Pepper, C., Thomas, A., Hoy, T., Cotter, F., and Bentley, P. (1999) Antisense-mediated suppression of Bcl-2 highlights its pivotal role in failed apoptosis in B-cell chronic lymphocytic leukaemia. *Br. J. Hamaetol. 107*, 611–615.

(22) Gekeler, V., Gimmnich, P., Hofmann, H. P., Grebe, C., Römmele, M., Leja, A., Baudler, M., Benimetskaya, L., Gonser, B., Pieles, U., Maier, T., Wagner, T., Sanders, K., Beck, J. F., Hanauer, G., and Stein, C. A. (2006) G3139 and other CpG-containing immunostimulatory phosphorothioate oligodeoxynucleotides are potent suppressors of the growth of human tumor xenografts in nude mice. *Oligonucleotides 16*, 83–93.

(23) Krieg, A. M. (2002) CpG motifs in bacterial DNA and their immune effects. *Annu. Rev. Immunol. 20*, 709–760.

(24) Uhlmann, E., and Vollmer, J. (2003) Recent advances in the development of immunostimulatory oligonucleotides. *Curr. Opin. Drug Discovery Dev. 6*, 204–217.

(25) Wacheck, V., Krepler, C., Strommer, S., Heere-Ress, E., Klem, R., Pehamberger, H., Eichler, H. G., and Jansen, B. (2002) Antitumor effect of G3139 Bcl-2 antisense oligonucleotide is independent of its immune stimulation by CpG motifs in SCID mice. *Antisense Nucleic Acid Drug Dev. 12*, 359–367.

(26) Badros, A. Z., Goloubeva, O., Rapoport, A. P., Ratterree, B., Gahres, N., Meisenberg, B., Takebe, N., Heyman, M., Zwiebel, J., Streicher, H., Gocke, C. D., Tomic, D., Flaws, J. A., Zhang, B., and Fenton, R. G. (2005) Phase II Study of G3139, a Bcl-2 Antisense oligonucleotide, in combination with dexamethasone and thalidomide in relapsed multiple myeloma patients. *J. Clin. Oncol. 23*, 4089–4099.

(27) Pan, X., Chen, L., Liu, S., Gao, J. X., Yang, X., and Lee, R. J. (2008) Antitumor activity of G3139 lipid nanoparticles (LNPs). *Mol. Pharm. 6*, 211–220.

(28) Guo, W., Hinkle, G. H., and Lee, R. J. (1999) 99mTc-HYNIC-folate: a novel receptor-based targeted radiopharmaceutical for tumor imaging. *J. Nucl. Med. 40*, 1563–1569.

(29) Dai, G., Chan, K. K., Liu, S., Hoyt, D., Whitman, S., Klisovic, M., Shen, T., Caligiuri, M. A., Byrd, J., Grever, M., and Marcucci, G. (2005) Cellular uptake and intracellular levels of the Bcl-2 antisense G3139 in cultured cells and treated patients with acute myeloid leukemia. *Clin. Cancer Res. 11*, 2998–3008.

(30) Loomis, R., Carbone, R., Reiss, M., and Lacy, J. (2003) Bcl-2 antisense (G3139, Genasense) enhances the in vitro and in vivo response of Epstein-Barr virus-associated lymphoproliferative disease to rituximab. *Clin. Cancer Res. 9*, 1931–1939.

(31) Ravetch, J. V., and Bolland, S. (2001) IgG Fc receptors. *Annu. Rev. Immunol. 19*, 275–90.

(32) Sliwkowski, M. X., Lofgren, J. A., Lewis, G. D., Hotaling, T. E., Fendly, B. M., and Fox, J. A. (1999) Nonclinical studies addressing the mechanism of action of trastuzumab (Herceptin). *Semin. Oncol. 26*, 60–70.

(33) Johnson, P., and Glennie, M. (2003) The mechanisms of action of rituximab in the elimination of tumor cells. *Semin. Oncol. 30*, 3–8.

(34) Manches, O., Lui, G., Chaperot, L., Gressin, R., Molens, J. P., Jacob, M. C., Sotto, J. J., Leroux, D., Bensa, J., and Plumas, C. J. (2003) In vitro mechanisms of action of rituximab on primary non-Hodgkin lymphomas. *Blood 101*, 949–954.

(35) Kondadasula, S. V., Mani, A., Jones, N., Roda, J., Lu, Y. H., Li, H., Zhang, X. L., Jarjoura, D., Lee, R. J., and Carson, W. E. (2008) Cytokines enhance the anti-tumor effects of folate conjugated immunoglobulin. *J. Immunol. 31*, 971–971.

(36) Hattori, Y., Sakaguchi, M., and Maitani, Y. (2006) Folate-linked lipid-based nanoparticles deliver a NFκ B decoy into activated murine macrophage-like RAW264.7 cells. *Biol. Pharm. Bull. 29*, 1516–1520.

(37) Paulos, C. M., Turk, M. J., Breur, G. J., and Low, P. S. (2004) Folate receptor-mediated targeting of therapeutic and imaging agents to activated macrophages in rheumatoid arthritis. *Adv. Drug Delivery Rev. 56*, 1205–1217.

(38) Turk, M. J., Breur, G. J., Widmer, W. R., Paulos, C. M., Xu, L. C., Grote, L. A., and Low, P. S. (2002) Folate-targeted imaging of activated macrophages in rats with adjuvant-induced arthritis. *Arthritis Rheum. 46*, 1947–1955.

(39) Turk, M. J., Waters, D. J., and Low, P. S. (2004) Folate-conjugated liposomes preferentially target macrophages associated with ovarian carcinoma. *Cancer Lett. 213*, 165–172.

(40) Marcucci, G., Byrd, J. C., Dai, G., Klisovic, M. I., Kourlas, P. J., Young, D. C., Cataland, S. R., Fisher, D. B., Lucas, D., Chan, K. K., Porcu, P., Lin, Z. P., Farag, S. F., Frankel, S. R., Zwiebel, J. A., Kraut, E. H., Balcerzak, S. P., Bloomfield, C. D., Grever, M. R., and Caligiuri, M. A. (2003) Phase 1 and pharmacodynamic studies of G3139, a Bcl-2 antisense oligonucleotide, in combination with chemotherapy in refractory or relapsed acute leukemia. *Blood 101*, 425–432.

(41) Morris, M. J., Tong, W. P., Cordon-Cardo, C., Drobnjak, M., Kelly, W. K., Slovin, S. F., Terry, K. L., Siedlecki, K., Swanson, P., Rafi, M., DiPaola, R. S., Rosen, N., and Scher, H. I. (2002) Phase I trial of BCL-2 antisense oligonucleotide (G3139) administered by continuous intravenous infusion in patients with advanced cancer. *Clin. Cancer Res. 8*, 679–683.

BC900545H

Evaluation of ^{111}In-Labeled Cyclic RGD Peptides: Tetrameric not Tetravalent

Sudipta Chakraborty,[†] Jiyun Shi,[†,‡] Young-Seung Kim,[†] Yang Zhou,[†] Bing Jia,[‡] Fan Wang,[‡] and Shuang Liu*[,†]

School of Health Sciences, Purdue University, Indiana 47907, and Medical Isotopes Research Center, Peking University, Beijing 100191, China. Received December 14, 2009; Revised Manuscript Received March 17, 2010

This report presents the synthesis and evaluation of ^{111}In(DOTA-6G-RGD$_4$) (DOTA = 1,4,7,10-tetraazacyclododecane-1,4,7,10-tetracetic acid; 6G-RGD$_4$ = E{G$_3$-E[G$_3$-c(RGDfK)]$_2$}$_2$ and G$_3$ = Gly-Gly-Gly), ^{111}In(DOTA-RGD$_4$) (RGD$_4$ = E{E[c(RGDfK)]$_2$}$_2$) and ^{111}In(DOTA-3G-RGD$_2$) (3G-RGD$_2$ = G$_3$-E[G$_3$-c(RGDfK)]$_2$) as new radiotracers for imaging integrin $\alpha_v\beta_3$-positive tumors. The IC$_{50}$ values of DOTA-6G-RGD$_4$, DOTA-RGD$_4$, and DOTA-3G-RGD$_2$ were determined to be 0.4 ± 0.1, 1.4 ± 0.1 and 1.1 ± 0.1 nM against ^{125}I-c(RGDyK) bound to integrin $\alpha_v\beta_3$-positive U87MG human glioma cells. ^{111}In(DOTA-6G-RGD$_4$), ^{111}In(DOTA-RGD$_4$), and ^{111}In(DOTA-3G-RGD$_2$) were prepared by reacting ^{111}InCl$_3$ with the respective DOTA conjugate in NH$_4$OAc buffer (100 mM, pH = 5.5). Radiolabeling could be completed by heating the reaction mixture at 100 °C for 15−20 min. The specific activity was ∼1850 MBq/μmol for ^{111}In(DOTA-3G-RGD$_2$) and ∼1480 MBq/μmol for ^{111}In(DOTA-6G-RGD$_4$). The athymic nude mice bearing U87MG human glioma xenografts were used to evaluate tumor uptake and excretion kinetics of ^{111}In(DOTA-6G-RGD$_4$), ^{111}In(DOTA-RGD$_4$), and ^{111}In(DOTA-3G-RGD$_2$). The results from both the integrin $\alpha_v\beta_3$ binding assay and biodistribution studies suggest that the tetrameric cyclic RGD peptides, such as RGD$_4$ and 6G-RGD$_4$, are most likely bivalent in binding to the integrin $\alpha_v\beta_3$. Both ^{111}In(DOTA-6G-RGD$_4$) and ^{111}In(DOTA-RGD$_4$) had significantly higher tumor uptake than ^{111}In(DOTA-3G-RGD$_2$) at 24−72 h postinjection due to the extra RGD motifs in RGD$_4$ and 6G-RGD$_4$. ^{111}In(DOTA-3G-RGD$_2$) had very little metabolism, while ^{111}In(DOTA-6G-RGD$_4$) had significant metabolism during its excretion via both renal and hepatobiliary routes over the 2 h period, probably due to its much larger size. The combination of high tumor uptake with long tumor retention suggests that their corresponding ^{90}Y and ^{177}Lu analogues M(DOTA-6G-RGD$_4$) (M = ^{90}Y and ^{177}Lu) might be useful as therapeutic radiotracers for treatment of integrin $\alpha_v\beta_3$-positive solid tumors.

INTRODUCTION

Radiolabeled cyclic RGD (Arg-Gly-Asp) peptides represent a new class of radiotracers that target the integrin $\alpha_v\beta_3$ overexpressed on both tumor cells and activated endothelial cells of the neovasculature during tumor growth, invasion, and metastasis (*1*−*9*). Over the past several years, many multimeric cyclic RGD peptides, such as E[c(RGDfK)]$_2$ (RGD$_2$) and E{E[c(RGDfK)]$_2$}$_2$ (RGD$_4$), have been used to maximize the integrin $\alpha_v\beta_3$ binding affinity and improve the radiotracer tumor uptake (*10*−*30*). The results from in vitro assays, ex vivo biodistribution, and in vivo imaging studies clearly demonstrated that radiolabeled (^{99m}Tc, ^{18}F, ^{64}Cu, and ^{68}Ga) cyclic RGD peptide tetramers, such as E{E[c(RGD*x*K)]$_2$}$_2$ (*x* = f and y), have better tumor targeting capability as evidenced by their higher tumor uptake and longer tumor retention times than their dimeric and monomeric counterparts (*25*, *26*, *29*, *30*). In our previous studies (*31*−*37*), we found that RGD$_2$ was monodentate while PEG$_4$-E[PEG$_4$-c(RGDfK)]$_2$ (3P-RGD$_2$: PEG$_4$ = 15-amino-4,7,10,13-tetraoxapentadecanoic acid) and (G$_3$-E[G$_3$-c(RGDfK)]$_2$ (3G-RGD$_2$: G$_3$ = Gly-Gly-Gly) were bivalent due to the longer distance between two RGD motifs. However, it remains unclear if the cyclic RGD tetramers, such as RGD$_4$, are tetravalent in binding to integrin $\alpha_v\beta_3$.

To answer this fundamental question, we prepared a new RGD tetramer conjugate, DOTA-E{G$_3$-E[G$_3$-c(RGDfK)]$_2$}$_2$ (Figure 1: DOTA-6G-RGD$_4$, DOTA = 1,4,7,10-tetraazacyclododecane-1,4,7,10-tetraacetic acid) and its ^{111}In complex ^{11}In(DOTA-6G-RGD$_4$). A competitive displacement assay was used to determine the integrin $\alpha_v\beta_3$ binding affinity of DOTA-3G-RGD$_2$, DOTA-RGD$_4$, and DOTA-6G-RGD$_4$ against ^{125}I-c(RGDyK) bound to the integrin $\alpha_v\beta_3$-positive U87MG glioma cells. Biodistribution and imaging studies were carried out in athymic nude mice bearing U87MG glioma xenografts. For comparison purposes, we also evaluated DOTA-RGD$_4$, DOTA-3G-RGD$_2$,^{111}In(DOTA-RGD$_4$), and ^{111}In(DOTA-3G-RGD$_2$) using the same assays. The comparison of IC$_{50}$ values of DOTA-3G-RGD$_2$, DOTA-RGD$_4$, and DOTA-6G-RGD$_4$ and tumor uptake of ^{111}In(DOTA-6G-RGD$_4$), ^{111}In(DOTA-RGD$_4$), and ^{111}In(DOTA-3G-RGD$_2$) will allow us to determine the valency of RGD$_4$ and 6G-RGD$_4$.

EXPERIMENTAL SECTION

Materials and Instruments. Chemicals were purchased from Sigma/Aldrich (St. Louis, MO). Cyclic RGD peptide 3G-RGD$_2$ was purchased from the Peptides International, Inc. (Louisville, KY). DOTA-OSu (1,4,7,10-tetraazacyclododecane-4,7,10-triacetic acid-1-acetate-(*N*-hydroxysuccinamide)) was purchased from Macrocyclics (Dallas, TX). DOTA-3G-RGD$_2$ and DOTA-RGD$_4$ were prepared according to the literature methods (*14*, *26*, *33*). MALDI (matrix assisted laser desorption ionization) mass spectral data were collected using an Applied Biosystems Voyager DE PRO mass spectrometer (Framingham, MA), Department of Chemistry, Purdue University. ^{111}InCl$_3$ was obtained from Perkin-Elmer Life and Analytical Sciences (North Billerica, MA). The NH$_4$OAc buffer for ^{111}In-labeling studies

* To whom correspondence should be addressed. School of Health Sciences, Purdue University, 550 Stadium Mall Drive, West Lafayette, IN 47907. Phone: 765-494-0236; Fax: 765-496-1377; Email: lius@pharmacy.purdue.edu.

[†] Purdue University.

[‡] Peking University.

10.1021/bc900555q © 2010 American Chemical Society
Published on Web 04/13/2010

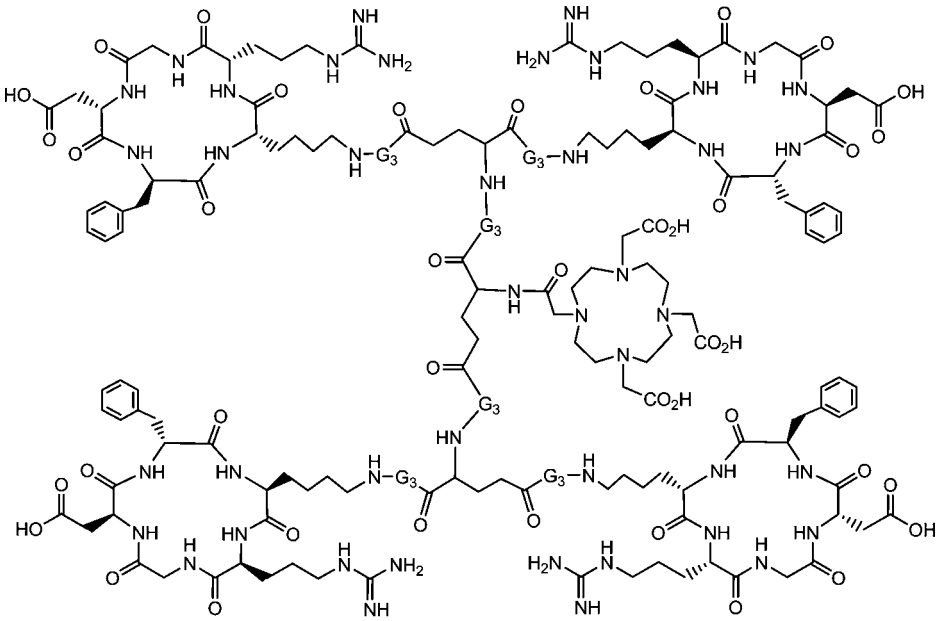


Figure 1. Structure of a new cyclic RGD tetramer conjugate: DOTA-6G-RGD_4.

was passed over a Chelex-100 column (1 × 15 cm) to minimize the trace metal contaminants.

HPLC Methods. Method 1 used a LabAlliance HPLC system equipped with a UV/vis detector ($\lambda = 254$ nm) and Zorbax C_{18} semiprep column (9.4 mm × 250 mm, 100 Å pore size; Agilent Technologies, Santa Clara, CA). The flow rate was 2.5 mL/min, and the mobile phase was isocratic with 90% A (0.1% TFA in water) and 10% B (0.1% TFA in acetonitrile) at 0−5 min, followed by a gradient mobile phase going from 10% B at 5 min to 40% B at 20 min. Method 2 used the LabAlliance HPLC system equipped with a β-ram IN/US detector (Tampa, FL) and Zorbax C_{18} column (4.6 mm × 250 mm, 300 Å pore size; Agilent Technologies, Santa Clara, CA). The flow rate was 1 mL/min. The mobile phase was isocratic with 90% A (25 mM NH_4OAc, pH = 6.8) and 10% B (acetonitrile) at 0−5 min, followed by a gradient mobile phase from 10% B at 5 min to 20% B at 15 min and to 50% B at 20 min.

Boc-E{G_3-E[G_3-c(RGDfK)]$_2$}$_2$ (Boc-6G-RGD_4). The succinimidyl ester of Boc-protected glutamic acid (Boc-E$(OSu)_2$) was prepared according to the literature method (*12*). To a solution of Boc-E$(OSu)_2$ (2.1 mg, 4.75 μmol) in DMF (2 mL) was added 3G-RGD_2 (21 mg, 11.5 μmol). After addition of DIEA (3 drops), the reaction mixture was stirred for 2 h at room temperature. The reaction was terminated by addition of 3 mL NH_4OAc buffer (100 mM, pH = 7.0). The product was isolated by HPLC (Method 1). Lyophilization of the collected fractions at 15.8 min afforded desired product Boc-6G-RGD_4. The yield was 7.6 mg (∼41%). MALDI-MS: $m/z = 3877$ for $[M + H]^+$ ($M = 3875$ calcd. for $[C_{164}H_{241}N_{57}O_{54}]^+$).

E{G_3-E[G_3-c(RGDfK)]$_2$}$_2$ (6G-RGD_4). Boc-6G-RGD_4 was dissolved in TFA (2 mL). After standing at room temperature for 5 min, excess TFA was removed. The residue was dissolved in 2 mL of 0.1 M NH_4OAc buffer (100 mM, pH = 7.0). The product was separated from the mixture by HPLC (Method 1). Lyophilization of the collected fractions at 14.2 min afforded 6G-RGD_4. The yield was 5.6 mg (∼76%). MALDI-MS: $m/z = 3777$ for $[M + H]^+$ ($M = 3775$ calcd. for $[C_{159}H_{233}N_{57}O_{52}]^+$).

DOTA-E{G_3-E[G_3-c(RGDfK)]$_2$}$_2$ (DOTA-6G-RGD_4). DOTA-OSu (5.0 mg, 10.0 μmol) and 6G-RGD_4 (3.8 mg, 1.0 μmol) were dissolved in anhydrous DMF (1 mL). After addition of excess DIEA (3 drops), the reaction mixture was stirred for 2 h at room temperature. Upon addition of 2 mL NH_4OAc buffer (100 mM, pH = 7.0), the product was separated by HPLC (Method 1). Lyophilization of the collected fractions at 14.5 min afforded DOTA-6G-RGD_4 with >95% purity. The yield was 3.2 mg (∼76%). MALDI-MS: $m/z = 4163$ for $[M + H]^+$ ($M = 4161$ calcd. for $[C_{175}H_{259}N_{61}O_{59}]^+$).

^{111}In-Labeling and Dose Preparation. To a clean Eppendorf tube were added 200−300 μL of the DOTA conjugate solution (0.1 mg/mL in 0.1 M NaOAc buffer, pH = 5.5) and 20 μL of $^{111}InCl_3$ solution (∼18.5 MBq in 0.05 M HCl). The vial was heated in a water bath at 100 °C for ∼15 min. After heating, the Eppendorf tube was allowed to stand at room temperature for ∼10 min. A sample of the resulting solution was analyzed by radio-HPLC (Method 2). For biodistribution studies, the ^{111}In radiotracer was purified by HPLC (Method 2). Volatiles in the mobile phase were removed under vacuum (∼5 mmHg) at room temperature. Doses were prepared by dissolving the purified radiotracer in saline to a concentration of ∼1.1 MBq/mL. For imaging studies, doses were prepared by dissolving the radiotracer in saline to ∼37 MBq/mL. The resulting solution was filtered with a 0.20 μm Millex-LG filter before being injected into animals. Each animal was injected with ∼0.1 mL of the dose solution.

Determination of Octanol/Water Partition Coefficients. The octanol/water partition coefficients were determined using the following procedure. In short, the ^{111}In radiotracer was purified by HPLC. Volatiles were removed completely under vacuum. The residue was dissolved in an equal volume (3 mL/3 mL) mixture of *n*-octanol and 25 mM phosphate buffer (pH = 7.4). After stirring vigorously for ∼20 min, the mixture was centrifuged at a speed of 8000 rpm for 5 min. Samples (in triplets) from both *n*-octanol and aqueous layers were counted in a Perkin-Elmer Wizard -1480 γ-counter (Shelton, CT). The partition coefficients were calculated. The log P values were measured three different times and reported as an average of three independent measurements plus the standard deviation.

In Vitro Whole-Cell Integrin $\alpha_v\beta_3$ Binding Assay. The in vitro integrin binding affinity and specificity of RGD peptides were assessed using ^{125}I-c(RGDyK) as the integrin-specific radioligand. Briefly, U87MG human glioma cells were grown in Gibco's Dulbecco's medium supplemented with 10% fetal

bovine serum (FBS), 100 IU/mL penicillin, and 100 μg/mL streptomycin (Invitrogen Co, Carlsbad, CA), at 37 °C in humidified atmosphere containing 5% CO_2. Filter multiscreen DV plates were seeded with 10^5 glioma cells in binding buffer and incubated with ^{125}I-c(RGDyK) in the presence of increasing concentrations of the RGD conjugate. After removing the unbound ^{125}I-c(RGDyK), hydrophilic PVDF filters were collected. The radioactivity was determined using a γ-counter (Packard, Meriden, CT). The IC_{50} values were calculated by fitting the data by nonlinear regression using GraphPad Prism (GraphPad Software, Inc., San Diego, CA). Experiments were carried out twice with triplicate samples. The IC_{50} values are reported as an average plus the standard deviation.

Animal Model. Biodistribution and imaging studies were performed using the athymic nude mice bearing U87MG human glioma xenografts in compliance with NIH animal experiment guidelines (*Principles of Laboratory Animal Care*, NIH Publication No. 86−23, revised 1985). The animal protocol was approved by the Purdue University Animal Care and Use Committee. U87MG cells were cultured in the Minimum Essential Medium, Eagle with Earle's Balanced Salt Solution (nonessential amino acids sodium pyruvate) (ATCC, Manassas, VA) in humidified atmosphere of 5% carbon dioxide, and were supplemented with 10% fetal bovine serum and 1% penicillin and streptomycin solution (GIBCO, Grand Island, NY). Female athymic nu/nu mice were purchased from Harlan (Indianapolis, IN) at 4−5 weeks of age. Each mouse was implanted subcutaneously with 5×10^6 tumor cells into the left and right upper flanks. In this way, one could assess the impact of tumor size on the radiotracer imaging quality in a single tumor-bearing mouse. All procedures will be performed in a laminar flow cabinet using aseptic technique. Three to four weeks after inoculation, the tumor size was 0.05−0.4 g, and animals were used for biodistribution and imaging studies.

Biodistribution Protocol. Twenty-five tumor-bearing mice (20−25 g) were randomly divided into five groups. Each tumor-bearing mouse was administered with ~111 KBq of the ^{111}In radiotracer by tail vein injection. Five animals were sacrificed by sodium pentobarbital overdose (~200 mg/kg) at 0.5, 1, 4, 24, and 72 h postinjection (p.i.). Blood samples were withdrawn from the heart of the tumor-bearing mice. Tumor and normal organs (brain, eyes, heart, spleen, lungs, liver, kidneys, muscle, and intestine) were harvested, washed with saline, dried with absorbent tissue, weighed, and counted on a γ-counter (Perkin-Elmer Wizard -1480, Shelton, CT). The organ uptake was calculated as the percentage of injected dose per gram of organ mass (%ID/g) or the percentage of injected dose per organ (%ID/organ). For the blocking experiment, five tumor-bearing athymic nude mice (20−25 g) were used, and each animal was administered with ~111 KBq of ^{111}In(DOTA-6G-RGD$_4$) along with ~350 μg (~14 mg/kg) of RGD_2. Such a high dose of blocking agent was used to make sure that the integrin $\alpha_v\beta_3$ binding was completely blocked. At 1 h p.i., all five tumor-bearing animals were sacrificed for organ biodistribution. Biodistribution data (%ID/g) and target-to-background (T/B) ratios are reported as an average plus the standard deviation based on the results from five tumor-bearing mice (10 tumors) at each time point. Comparison between two radiotracers was made using the two-way ANOVA test (GraphPad Prim 5.0, San Diego, CA). The level of significance was set at $p < 0.05$.

Planar Imaging. The athymic nude mice ($n = 3$) bearing U87MG glioma xenografts were used for imaging studies of ^{111}In(DOTA-6G-RGD$_4$) and ^{111}In(DOTA-3G-RGD$_2$). Each tumor-bearing mouse was administered with ~3.7 MBq of ^{111}In radiotracer via tail vein injection. Animals were anesthetized with intraperitoneal injection of ketamine (80 mg/kg) and xylazine (19 mg/kg), and were then placed supine on a single head mini γ-camera (Diagnostic Services Inc., NJ) equipped with a parallel-hole, medium-energy, and high-resolution collimator. Anterior images were acquired at 0.5, 1, 4, 24, and 72 h p.i. and stored digitally in a 128 × 128 matrix. The acquisition count limits were set at 200 K. After completion of imaging, animals were sacrificed by sodium pentobarbital overdose (~200 mg/kg).

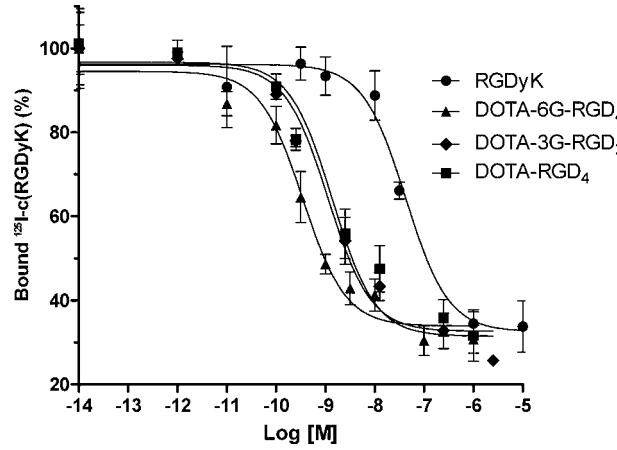


Figure 2. Competitive inhibition curves of ^{125}I-c(RGDyK) bound to the U87MG human glioma cells by c(RGDyK), DOTA-3G-RGD$_2$, DOTA-RGD$_4$, and DOTA-6G-RGD$_4$. Their IC_{50} values were calculated to be 42.2 ± 5.2, 1.1 ± 0.1, 1.4 ± 0.1 and 0.4 ± 0.1 nM, respectively.

Metabolism. Normal nude mice were used for metabolism studies. Each mouse was administered with ~3.7 MBq of ^{111}In(DOTA-3G-RGD$_2$) and ^{111}In(DOTA-6G-RGD$_4$) via tail vein. The urine samples were collected at 30 and 120 min p.i. by manual void and were mixed with equal volume of 50% acetonitrile aqueous solution. The mixture was centrifuged at 8000 rpm. The supernatant was collected and passed through a 0.20 μ Millex-LG filter unit. The filtrate was analyzed by HPLC (Method 2). Feces, liver, and kidney samples were collected at 120 min p.i. and suspended in 20% acetonitrile aqueous solution after homogenization. The resulting mixture was vortexed for 5−10 min. After centrifuging at 8000 rpm, the supernatant was collected and passed through a 0.20 μ Millex-LG filter unit. The filtrate was analyzed by radio-HPLC (Method 2). The percentage radioactivity recovery was >95% (by γ-counting) for both urine and feces samples.

RESULTS

DOTA-6G-RGD$_4$. Synthesis of DOTA-6G-RGD$_4$ was straightforward. The key step was the deprotection of Boc-6G-RGD$_4$. The excess TFA must be removed within 10 min of the reaction. Otherwise, the major product was the hydrolyzed product E-3G-RGD$_2$ (E-G$_3$-E[G$_3$-c(RGDfK)]$_2$), not 6G-RGD$_4$. Conjugation of 6G-RGD$_4$ with excess DOTA-OSu in DMF in the presence of excess DIEA afforded DOTA-6G-RGD$_4$ in high yield (76%). Its identity has been confirmed by MALDI-MS.

In Vitro Integrin $\alpha_v\beta_3$ Binding Affinity. The integrin $\alpha_v\beta_3$ binding affinities of c(RGDyK), DOTA-3G-RGD$_2$, DOTA-RGD$_4$, and DOTA-6G-RGD$_4$ were determined using the integrin $\alpha_v\beta_3$-positive U87MG human glioma cells. Figure 2 shows displacement curves of ^{125}I-c(RGDyK) by c(RGDyK), DOTA-3G-RGD$_2$, DOTA-RGD$_4$, and DOTA-6G-RGD$_4$. Their IC_{50} values were calculated to be 42.2 ± 5.2, 1.1 ± 0.1, 1.4 ± 0.1 and 0.4 ± 0.1 nM, respectively.

Radiochemistry. ^{111}In(DOTA-6G-RGD$_4$), ^{111}In(DOTA-RGD$_4$), and ^{111}In(DOTA-3G-RGD$_2$) were prepared by reacting $^{111}InCl_3$ with DOTA-6G-RGD$_4$, DOTA-RGD$_4$, and DOTA-3G-RGD$_2$, respectively, in NH_4OAc buffer (100 mM, pH = 5.5).

Table 1. Radiochemical Purity (RCP), HPLC Retention Time and Log P Values for ^{111}In-Labeled Cyclic RGD Peptides

compound	RCP (%)	retention time (min)	log P value
^{111}In(DOTA-3G-RGD$_2$)	>95	13.9	−4.13 ± 0.08
^{111}In(DOTA-6G-RGD$_4$)	>92	17.1	−4.40 ± 0.04
^{111}In(DOTA-RGD$_4$)	>92	19.1	−3.41 ± 0.13

Radiolabeling was completed by heating the reaction mixture at 100 °C for ∼15 min. The radiochemical purity was >92% for all three ^{111}In radiotracers. The specific activity was ∼925 MBq/mg (∼1850 MBq/μmol) for ^{111}In(DOTA-3G-RGD$_2$). They were analyzed using the same method (Method 2). Their HPLC retention times and log P values were listed in Table 1.

Biodistribution Characteristics. Selected biodistribution data are listed in Tables 2−4 for ^{111}In(DOTA-6G-RGD$_4$), ^{111}In-(DOTA-RGD$_4$), and ^{111}In(DOTA-3G-RGD$_2$). Figure 3 compares their uptake (%ID/g) in the tumor and intestine, as well as their tumor/kidney and tumor/liver ratios in the athymic nude mice bearing U87MG human glioma xenografts. The comparison of their tumor uptake in combination with the IC_{50} values of cyclic RGD peptide DOTA conjugates will allow us to determine if they are actually tetravalent in binding to the integrin $\alpha_v\beta_3$.

In general, ^{111}In(DOTA-6G-RGD$_4$) excreted predominantly via the renal route with >75% of the injected radioactivity recovered from urine and <10% of the injected radioactivity recovered from feces at 2 h p.i. ^{111}In(DOTA-6G-RGD$_4$) had a

Table 2. Selected Biodistribution Data of ^{111}In(DOTA-6G-RGD$_4$) in Athymic Nude Mice (n = 5) Bearing U87MG Human Glioma Xenografts

%ID/gram	0.5 h	1 h	4 h	24 h	72 h
Blood	0.97 ± 0.10	0.25 ± 0.04	0.05 ± 0.00	0.06 ± 0.02	0.03 ± 0.01
bone	2.26 ± 0.71	2.35 ± 0.64	1.99 ± 0.15	1.41 ± 0.29	0.90 ± 0.41
brain	0.13 ± 0.08	0.14 ± 0.03	0.13 ± 0.07	0.12 ± 0.07	0.10 ± 0.04
eyes	1.20 ± 0.60	1.54 ± 0.22	1.61 ± 1.38	0.83 ± 0.20	0.53 ± 0.12
heart	1.50 ± 0.76	1.49 ± 0.29	1.03 ± 0.23	0.80 ± 0.22	0.51 ± 0.16
intestine	7.15 ± 3.70	9.25 ± 1.27	8.79 ± 2.98	10.91 ± 1.94	8.31 ± 2.14
kidney	8.35 ± 0.52	8.42 ± 0.86	6.21 ± 0.65	4.44 ± 0.45	3.45 ± 0.90
liver	3.04 ± 1.38	3.77 ± 0.79	3.05 ± 0.14	2.46 ± 0.36	2.01 ± 0.45
lungs	3.65 ± 0.87	3.44 ± 1.86	2.72 ± 0.38	1.51 ± 0.22	0.91 ± 0.08
muscle	1.23 ± 0.42	1.14 ± 0.23	0.80 ± 0.11	0.93 ± 0.54	0.45 ± 0.06
spleen	2.63 ± 0.45	2.38 ± 0.49	2.35 ± 0.23	1.96 ± 0.31	2.07 ± 0.24
U87MG	12.66 ± 1.25	11.45 ± 2.46	8.99 ± 2.61	8.68 ± 1.42	5.59 ± 0.54
tumor/blood	13.06 ± 1.29	44.92 ± 9.66	198.34 ± 57.67	143.01 ± 23.40	152.37 ± 102.84
tumor/bone	5.60 ± 0.55	4.88 ± 1.05	4.53 ± 1.32	6.16 ± 1.01	4.67 ± 3.15
tumor/kidney	1.52 ± 0.15	1.36 ± 0.29	1.45 ± 0.42	1.95 ± 0.32	1.21 ± 0.82
tumor/liver	4.16 ± 0.41	3.04 ± 0.65	2.95 ± 0.86	3.53 ± 0.58	2.09 ± 1.41
tumor/lungs	3.46 ± 0.34	3.33 ± 0.72	3.30 ± 0.96	5.74 ± 0.94	4.59 ± 3.10
tumor/muscle	10.30 ± 1.02	10.08 ± 2.17	11.20 ± 3.26	9.30 ± 1.52	9.21 ± 6.22

Table 3. Selected Biodistribution Data of ^{111}In(DOTA-RGD$_4$) in Athymic Nude Mice (n = 5) Bearing U87MG Human Glioma Xenografts

%ID/gram	0.5 h	1 h	4 h	24 h	72 h
blood	0.80 ± 0.18	0.37 ± 0.08	0.12 ± 0.05	0.04 ± 0.01	0.07 ± 0.02
bone	1.64 ± 0.17	0.93 ± 0.13	0.86 ± 0.20	0.53 ± 0.27	0.75 ± 0.09
brain	0.15 ± 0.04	0.12 ± 0.01	0.10 ± 0.02	0.07 ± 0.02	0.14 ± 0.07
eyes	1.56 ± 0.15	1.23 ± 0.10	0.92 ± 0.46	0.64 ± 0.10	0.78 ± 0.46
heart	1.45 ± 0.53	1.23 ± 0.11	0.90 ± 0.18	0.54 ± 0.26	1.01 ± 0.76
intestine	10.79 ± 1.46	8.42 ± 1.65	9.19 ± 1.58	7.03 ± 2.06	3.37 ± 0.30
kidney	11.18 ± 1.22	7.28 ± 0.57	5.83 ± 0.70	5.11 ± 0.52	3.48 ± 1.10
liver	2.98 ± 0.51	2.67 ± 0.32	2.75 ± 0.29	2.15 ± 0.57	1.62 ± 0.40
lungs	4.29 ± 1.26	3.43 ± 0.54	2.06 ± 0.39	1.50 ± 0.39	0.62 ± 0.36
muscle	1.79 ± 0.38	1.22 ± 0.45	0.63 ± 0.11	0.78 ± 0.19	0.68 ± 0.31
spleen	2.65 ± 1.36	2.40 ± 0.51	1.40 ± 0.95	1.15 ± 0.84	1.16 ± 0.63
U87MG	8.97 ± 0.52	7.98 ± 2.36	7.32 ± 2.66	5.84 ± 1.09	3.16 ± 0.43
Tumor/Blood	10.61 ± 1.97	19.00 ± 3.60	42.74 ± 5.65	151.67 ± 57.32	31.78 ± 4.57
tumor/bone	5.35 ± 0.60	8.58 ± 1.46	9.22 ± 4.79	28.78 ± 16.18	4.49 ± 0.04
tumor/kidney	0.84 ± 0.05	1.09 ± 0.25	1.26 ± 0.36	1.15 ± 0.74	0.96 ± 0.22
tumor/liver	2.69 ± 0.29	2.85 ± 0.67	2.50 ± 0.60	2.91 ± 1.17	1.68 ± 0.23
tumor/lungs	2.32 ± 1.03	2.77 ± 1.14	4.06 ± 0.83	4.71 ± 1.79	5.45 ± 1.61
tumor/muscle	5.37 ± 0.20	6.50 ± 1.22	14.07 ± 5.93	9.31 ± 6.36	4.87 ± 2.24

Table 4. Biodistribution Data of ^{111}In(DOTA-3G-RGD$_2$) in Athymic Nude Mice (n = 5) Bearing U87MG Human Glioma Xenografts

%ID/gram	0.5 h	1 h	4 h	24 h	72 h
Blood	0.87 ± 0.13	0.30 ± 0.07	0.09 ± 0.00	0.03 ± 0.01	0.01 ± 0.00
brain	0.13 ± 0.03	0.09 ± 0.00	0.07 ± 0.00	0.05 ± 0.01	0.04 ± 0.00
eyes	1.20 ± 0.24	0.84 ± 0.13	0.51 ± 0.04	0.32 ± 0.05	0.16 ± 0.03
heart	1.03 ± 0.12	0.60 ± 0.12	0.44 ± 0.02	0.28 ± 0.04	0.15 ± 0.04
intestine	4.83 ± 1.15	4.81 ± 1.01	5.09 ± 1.75	3.77 ± 0.07	1.89 ± 0.19
kidney	6.74 ± 0.79	3.88 ± 0.48	2.69 ± 0.10	2.08 ± 0.16	1.48 ± 0.14
liver	2.45 ± 0.14	2.25 ± 0.04	2.23 ± 0.05	1.52 ± 0.15	0.85 ± 0.09
lungs	3.13 ± 0.47	1.71 ± 0.48	1.22 ± 0.08	0.75 ± 0.02	0.32 ± 0.06
muscle	1.33 ± 0.24	0.70 ± 0.03	0.39 ± 0.05	0.30 ± 0.09	0.20 ± 0.05
spleen	1.63 ± 0.08	1.36 ± 0.13	1.18 ± 0.20	0.91 ± 0.10	0.88 ± 0.17
U87MG	10.19 ± 3.61	10.69 ± 1.82	6.72 ± 2.06	4.83 ± 1.19	1.99 ± 0.39
tumor/blood	11.74 ± 3.82	36.93 ± 9.74	72.50 ± 23.09	300.15 ± 29.08	215.91 ± 56.80
tumor/kidney	1.51 ± 0.47	2.77 ± 0.51	2.49 ± 0.75	2.36 ± 0.69	1.86 ± 0.30
tumor/liver	4.16 ± 1.43	4.74 ± 0.81	3.01 ± 0.87	3.25 ± 1.01	2.35 ± 0.54
tumor/lungs	3.35 ± 1.36	6.59 ± 1.86	5.60 ± 1.93	6.38 ± 1.49	6.43 ± 1.66
tumor/muscle	8.03 ± 3.56	15.31 ± 2.44	17.61 ± 5.95	17.86 ± 7.44	10.79 ± 3.69

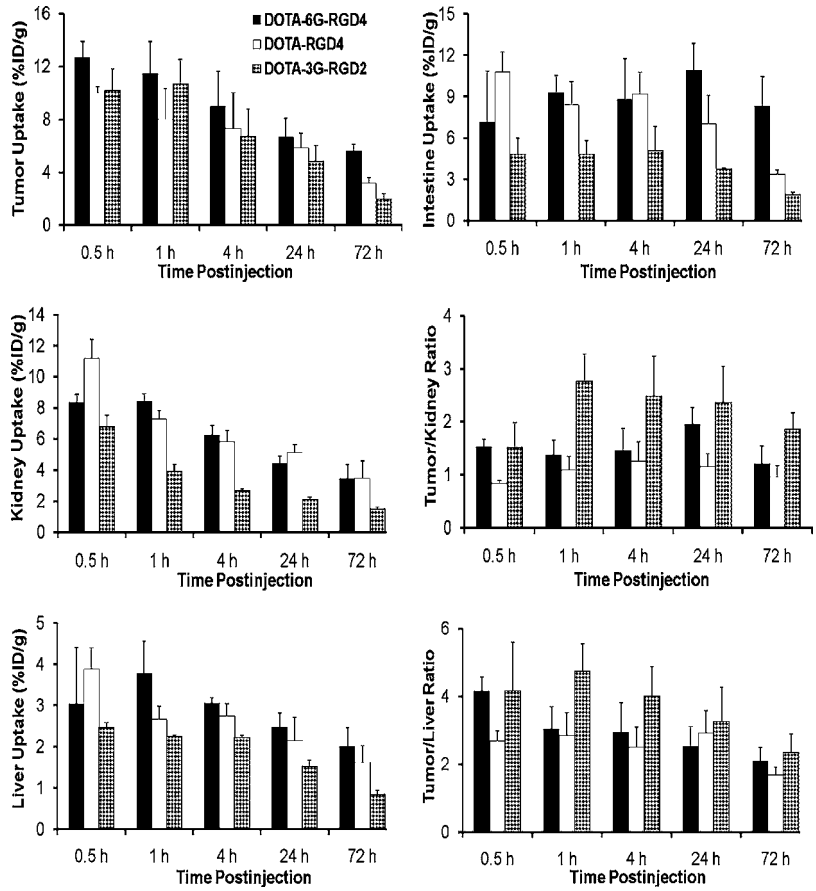


Figure 3. Direct comparison of the tumor and intestine uptake (%ID/g), tumor/kidney, and tumor/liver ratios between ^{111}In(DOTA-6G-RGD$_4$), ^{111}In(DOTA-RGD$_4$), and ^{111}In(DOTA-3G-RGD$_2$) in the athymic nude mice ($n = 5$) bearing U87MG human glioma xenografts.

rapid blood clearance with high tumor/blood ratios (Table 2). It had a high initial tumor uptake (12.66 ± 1.25%ID/g at 0.5 h p.i.) with a slow washout (11.45 ± 2.46, 8.99 ± 2.61, 6.68 ± 1.42, and 5.59 ± 0.54%ID/g at 1, 4, 24, and 72 h p.i., respectively). The liver uptake of ^{111}In(DOTA-6G-RGD$_4$) was low (3.04 ± 1.38, 3.77 ± 0.79, 3.05 ± 0.14, 2.46 ± 0.36, and 2.01 ± 0.45%ID/g at 0.5, 1, 4, 24, and 72 h p.i., respectively), and its tumor/liver ratios were high (4.16 ± 0.41, 3.04 ± 0.65, 2.95 ± 0.86, 3.53 ± 0.58, and 2.09 ± 1.41 at 0.5, 1, 4, 24, and 72 h p.i., respectively). The kidney and muscle uptake of ^{111}In(DOTA-6G-RGD$_4$) was also low with high tumor/kidney and tumor/muscle ratios (Table 2). The tumor uptake of ^{111}In(DOTA-RGD$_4$) was high (8.97 ± 0.52, 7.98 ± 2.36, 7.32 ± 2.66, 5.84 ± 1.09, and 3.16 ± 0.43%ID/g at 0.5, 1, 4, 24, and 72 h p.i., respectively), but its tumor retention time was not as long as that of ^{111}In(DOTA-6G-RGD4) (Figure 3). ^{111}In(DOTA-RGD$_4$) had a rapid blood clearance with high tumor/blood ratios over the 72 h period (Table 3). The initial kidney uptake (Figure 3) of ^{111}In(DOTA-RGD$_4$) was significantly higher than that of ^{111}In(DOTA-6G-RGD$_4$). However, there was no significant difference between ^{111}In(DOTA-RGD$_4$) and ^{111}In(DOTA-6G-RGD$_4$) in their kidney uptake at >1 h p.i. ^{111}In(DOTA-RGD$_4$) and ^{111}In(DOTA-6G-RGD$_4$) shared very similar liver uptake and tumor/liver ratio (Figure 3). ^{111}In-(DOTA-3G-RGD$_2$) also had a rapid blood clearance with high tumor/blood ratios (Table 4). Its initial tumor uptake (10.19 ± 3.61%ID/g at 0.5 h p.i.) was comparable to that of^{111}In(DOTA-RGD$_4$) and ^{111}In(DOTA-6G-RGD$_4$) within the experimental error, but its tumor uptake was significantly ($p < 0.01$) lower (Figure 3: tumor uptake = 5.59 ± 0.54%ID/g for ^{111}In(DOTA-6G-RGD4), 3.16 ± 0.43%ID/g for ^{111}In(DOTA-RGD$_4$), and 1.99 ± 0.39%ID/g for ^{111}In(DOTA-3G-RGD$_2$) at 72 h p.i.). The uptake of ^{111}In(DOTA-3G-RGD$_2$) in intestine, kidneys, and liver was also significantly ($p < 0.05$) lower than that of ^{111}In(DOTA-RGD$_4$) and ^{111}In(DOTA-6G-RGD$_4$). As a result, the tumor/kidney and tumor/liver ratios of ^{111}In(DOTA-3G-RGD$_2$) were higher than that of both ^{111}In(DOTA-RGD$_4$) and ^{111}In(DOTA-6G-RGD$_4$) (Figure 3).

Tumor Size vs Tumor Uptake. As illustrated in Figure 4A, there was a linear relationship between the %ID tumor uptake of ^{111}In(DOTA-3G-RGD$_2$) at 60 min p.i. and tumor size (0.03−0.60 g; $n = 12$) with $R^2 = 0.959$. As the tumor became larger, the total tumor uptake of ^{111}In(DOTA-3G-RGD$_2$) increased. In contrast, the %ID/g tumor uptake (Figure 4B) of ^{111}In(DOTA-3G-RGD$_2$) decreased as the tumor size increased. For example, ^{111}In(DOTA-3G-RGD$_2$) has tumor uptake in the range 8.0−15%ID/g with the tumor size 0.05−0.30 g. When the tumor size is in the range 0.5−0.6 g, the tumor uptake of ^{111}In(DOTA-3G-RGD$_2$) is only ∼6.0%ID/g.

Integrin $\alpha_v\beta_3$ Specificity. Figure 5 compares the 60 min organ uptake of ^{111}In(DOTA-6G-RGD$_4$) in the absence/presence of RGD$_2$. Clearly, coinjection of RGD$_2$ significantly blocked the tumor uptake of ^{111}In(DOTA-6G-RGD$_4$) (1.23 ± 0.26%ID/g with RGD$_2$ vs 11.45 ± 2.46%ID/g without RGD$_2$ at 1 h p.i.). Its uptake in normal organs was also significantly blocked by coinjection of excess RGD$_2$. For example, the uptake of ^{111}In(DOTA-6G-RGD$_4$) in eyes, heart, intestine, liver, lungs, and spleen was 1.54 ± 0.22, 1.49 ± 0.29, 9.25 ± 1.27, 3.77 ± 0.79, 3.44 ± 1.86, and 2.38 ± 0.49%ID/g, respectively, without RGD$_2$, while its uptake in the same organs was only 0.33 ± 0.06, 0.66 ± 0.18, 0.79 ± 0.10, 0.79 ± 0.20, 2.06 ± 1.12, and 0.54 ± 0.09%ID/g, respectively, in the presence of excess RGD$_2$.

Planar Imaging. Figure 6 illustrates the planar images of the glioma-bearing mice administered with ∼3.7 MBq of ^{111}In(DOTA-6G-RGD$_4$) (top), ^{111}In(DOTA-3G-RGD$_2$) (bottom) and at 1, 4, 24, and 72 h p.i. The tumors could be clearly

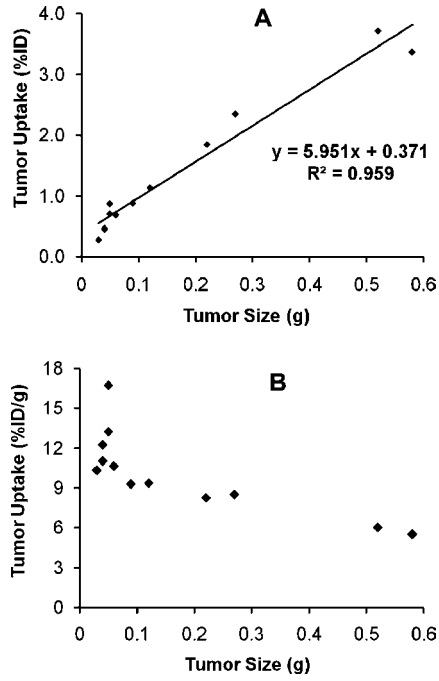


Figure 4. Relationship between the tumor size and tumor uptake of ^{111}In(DOTA-3G-RGD$_2$) at 60 min p.i. in the athymic nude mice (n = 12) bearing the U87MG glioma xenografts.

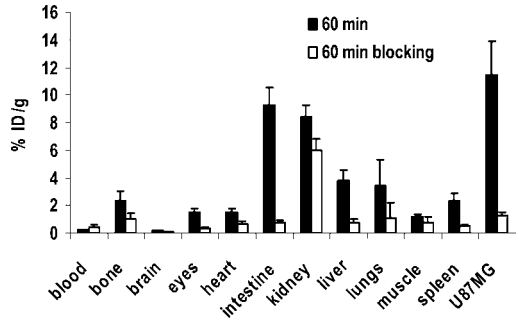


Figure 5. Comparison of the 60 min biodistribution data of ^{111}In(DOTA-6G-RGD$_4$) in athymic nude mice (n = 5) bearing U87MG glioma xenografts in the absence/presence of excess RGD$_2$ to demonstrate its integrin $\alpha_v\beta_3$-specificity.

visualized with excellent T/B contrast as early as 1 h p.i. in the glioma-bearing mice administered with ^{111}In(DOTA-6G-RGD$_4$) and ^{111}In(DOTA-3G-RGD$_2$). Both ^{111}In(DOTA-6G-RGD$_4$) and ^{111}In(DOTA-3G-RGD$_2$) had a very long tumor retention time ($t_{1/2}$ > 30 h), which was consistent with the results obtained from biodistribution studies (Tables 2 and 4). In addition, we also observed that the tumor distribution of ^{111}In(DOTA-3G-RGD$_2$) is quite heterogeneous most likely due to the heterogeneity of integrin $\alpha_v\beta_3$ overexpressed on tumor tissues.

Metabolism. Figure 7 shows representative radio-HPLC chromatograms of ^{111}In(DOTA-6G-RGD$_4$) and ^{111}In(DOTA-3G-RGD$_2$) in saline before injection, in urine at 30 and 120 min p.i., and in feces at 120 min p.i. The percentage radioactivity recovery from the urine and feces samples was >95% for both radiotracers. Attempts to extract radioactivity from the liver and kidneys were not successful due to limited radioactivity accumulation in both organs. There was very little metabolite detected in either urine or feces samples over the 2 h period for ^{111}In(DOTA-3G-RGD$_2$). For ^{111}In(DOTA-6G-RGD$_4$), however, there was significant metabolism during its excretion via both renal and hepatobiliary routes. Only ~25% of ^{111}In(DOTA-6G-RGD$_4$) remained intact in the feces sample.

DISCUSSION

In this study, we prepared ^{111}In complexes of DOTA-6G-RGD$_4$, DOTA-RGD$_4$, and DOTA-3G-RGD$_2$. It was found that the integrin $\alpha_v\beta_3$ binding affinity follows the order of DOTA-6G-RGD$_4$ > DOTA-RGD$_4$ ~ DOTA-3G-RGD$_2$ ≫ c(RGDyK). Two factors contribute to the higher integrin $\alpha_v\beta_3$ binding affinity of DOTA-6G-RGD$_4$, DOTA-RGD$_4$, and DOTA-3G-RGD$_2$ as compared to c(RGDyK). Previously, we have clearly demonstrated that 3G-RGD$_2$ binds to the integrin $\alpha_v\beta_3$ in a bivalent fashion while RGD$_2$ is only monovalent due to the short distance (6 bonds excluding K residues) between two RGD motifs (*31*, *33*, *37*). The fact that DOTA-RGD$_4$ (IC$_{50}$ = 1.5 ± 0.2 nM) and DOTA-3G-RGD$_2$ (IC$_{50}$ = 1.3 ± 0.2 nM) shared almost identical IC$_{50}$ values strongly suggests that DOTA-RGD$_4$ is bivalent in binding to integrin $\alpha_v\beta_3$. This conclusion is supported by their similar tumor uptake (Figure 3) and is completely consistent with the biodistribution data obtained for the ^{99m}Tc-labeled cyclic RGD peptides 3G-RGD$_2$ and RGD$_4$ (*31*, *37*). Were DOTA-RGD$_4$ tetravalent, it would have had significantly higher integrin $\alpha_v\beta_3$ binding affinity than DOTA-3G-RGD$_2$, whereas ^{111}In(DOTA-RGD$_4$) would have had higher initial tumor uptake than ^{111}In(DOTA-3G-RGD$_2$).

DOTA-6G-RGD$_4$ (IC$_{50}$ = 0.4 ± 0.1 nM) has higher integrin $\alpha_v\beta_3$ binding affinity than DOTA-RGD$_4$ (IC$_{50}$ = 1.5 ± 0.2 nM). As a result, ^{111}In(DOTA-6G-RGD$_4$) has slightly higher initial tumor uptake (Figure 3) than ^{111}In(DOTA-RGD$_4$). Previously, we found that both bivalency and the "locally enhanced RGD concentration" contribute to the higher integrin $\alpha_v\beta_3$ binding affinity of 3G-RGD$_2$ and 3P-RGD$_2$ as compared to that of c(RGDfK) (*31*−*37*). We also found that the contribution from the bivalency to integrin $\alpha_v\beta_3$ binding affinity and radiotracer tumor uptake are much more significant than that from the "locally enhanced RGD concentration" (*31*, *32*). For example, the tumor uptake of the ^{99m}Tc-labeled 3G-RGD$_2$ was almost 3× higher than that of the ^{99m}Tc-labeled c(RGDfK) in the same model (*31*). Thus, we believe that the differences in the integrin $\alpha_v\beta_3$ binding affinity of DOTA-6G-RGD$_4$ and DOTA-RGD$_4$ and the initial tumor uptake of ^{111}In(DOTA-6G-RGD$_4$) and ^{111}In(DOTA-RGD$_4$) are most likely caused by the number of possibilities to achieve simultaneous integrin $\alpha_v\beta_3$ binding for 6G-RGD$_4$ and RGD$_4$. The concentration factor exists in both DOTA-6G-RGD$_4$ and DOTA-RGD$_4$. The difference is that there are only two possibilities for DOTA-RGD$_4$ to achieve bivalency while any two of the four RGD motifs in DOTA-6G-RGD$_4$ can achieve bivalency due to the longer distance between RGD motifs. If DOTA-6G-RGD$_4$ were tetravalent or trivalent, it would have had much higher integrin $\alpha_v\beta_3$ binding affinity than DOTA-RGD$_4$, whereas ^{111}In(DOTA-6G-RGD$_4$) would have shown much higher initial tumor uptake than ^{111}In(DOTA-RGD$_4$). This conclusion is supported by the fact that ^{111}In(DOTA-6G-RGD$_4$) and ^{111}In(DOTA-3G-RGD$_2$) share a similar initial tumor uptake (Figure 3: 12.66 ± 1.25%ID/g and 10.19 ± 3.61%ID/g, respectively) at 0.5 h p.i. Even though DOTA-6G-RGD$_4$ and DOTA-RGD$_4$ may not be tetravalent, the extra cyclic RGD motifs in DOTA-6G-RGD$_4$ and DOTA-RGD$_4$ contribute significantly to the higher tumor uptake of ^{111}In(DOTA-6G-RGD$_4$) and ^{111}In(DOTA-RGD$_4$) than that of ^{111}In(DOTA-3G-RGD$_2$) at 24−72 h p.i. (Figure 3). The concentration factor might also explain why ^{111}In(DOTA-6G-RGD$_4$) and ^{111}In(DOTA-RGD$_4$) had higher uptake than ^{111}In(DOTA-3G-RGD$_2$) (Figure 3) in the intestine, liver, and kidneys, all of which are integrin $\alpha_v\beta_3$-positive (*15*, *16*). From this point of view, we believe that ^{111}In(DOTA-6G-RGD$_4$) is most likely bivalent in binding to the integrin $\alpha_v\beta_3$. However, the IC$_{50}$ values and ex

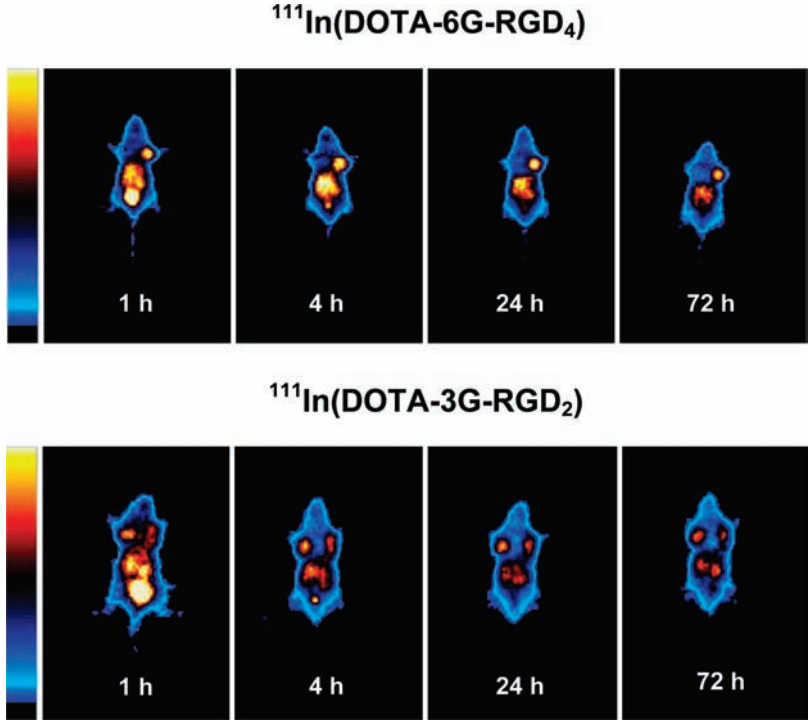


Figure 6. Whole-body planar images of the tumor-bearing mice administered with ~3.7 Mbq of ^{111}In(DOTA-6G-RGD$_4$) (top) and ^{111}In(DOTA-3G-RGD$_2$) (bottom) at 1, 4, 24, and 72 h p.i.

vivo biodistribution data cannot completely eliminate the possibility of trivalency or tetravalency for ^{111}In(DOTA-6G-RGD$_4$).

For diagnostic radiotracers, the tumor retention time may not be as critical as tumor uptake and T/B ratios. For the ^{90}Y and ^{177}Lu radiotracers, however, the longer tumor retention time will result in higher radiation dose to the integrin $\alpha_v\beta_3$-positive tumors during the same period of time. It must be noted that the ability of a multimeric RGD peptide to achieve bivalency also depends on the integrin $\alpha_v\beta_3$ density. If the tumor integrin $\alpha_v\beta_3$ density is high, the distance between two neighboring integrin $\alpha_v\beta_3$ sites will be short, and it is easier for the multimeric RGD peptide to achieve bivalency. If the integrin $\alpha_v\beta_3$ density is very low, the distance between two neighboring integrin $\alpha_v\beta_3$ sites will be long, and it might be more difficult for the same multimeric RGD peptide to achieve simultaneous integrin $\alpha_v\beta_3$ binding.

The integrin $\alpha_v\beta_3$-specificity of ^{111}In(DOTA-6G-RGD$_4$) is demonstrated by the "blocking experiment" (Figure 5). The blockage of radiotracer uptake strongly suggests that its glioma localization is indeed integrin $\alpha_v\beta_3$-mediated. The partial uptake blockage in the eyes, heart, intestine, lungs, liver, and spleen indicates that the accumulation of ^{111}In(DOTA-6G-RGD$_4$) in these organs is in large part integrin $\alpha_v\beta_3$-mediated. This conclusion is supported by the immunohistopathological studies (*15, 16*), which showed a strong positive staining of endothelial cells of small glomeruli vessels in kidneys and weak staining in branches of the hepatic portal vein. Similar results were also obtained for radiolabeled (^{99m}Tc and ^{64}Cu) cyclic RGD peptide dimers, such as 3G-RGD$_2$ and 3P-RGD$_2$ (*31*−*33, 36, 37*).

It is well-established that multimerization of cyclic RGD peptides can significantly improve the integrin $\alpha_v\beta_3$-targeting capability as evidenced by their higher integrin $\alpha_v\beta_3$ binding affinity and better tumor uptake with better tumor uptake than their monomeric counterparts (*26, 30*−*37*). However, this also leads to more radioactivity accumulation of radiolabeled multimeric cyclic RGD peptides in normal organs, as evidenced by the higher uptake of ^{111}In(DOTA-6G-RGD$_4$) and ^{111}In-(DOTA-RGD$_4$) than ^{111}In(DOTA-3G-RGD$_2$) in the intestine, liver, and kidneys. As a result, the tumor/liver and tumor/kidney ratios of ^{111}In(DOTA-6G-RGD$_4$) and ^{111}In(DOTA-RGD$_4$) are significantly ($p < 0.01$) lower than those of ^{111}In(DOTA-3G-RGD$_2$) at >1 h p.i. This is consistent with greater accumulation in the abdominal region of tumor-bearing mice administered with ^{111}In(DOTA-6G-RGD$_4$) (Figure 6: top) than that with ^{111}In(DOTA-3G-RGD$_2$) (Figure 6: bottom). Thus, ^{111}In(DOTA-3G-RGD$_2$) is a better radiotracer than ^{111}In(DOTA-6G-RGD$_4$) and ^{111}In(DOTA-RGD$_4$) for diagnostic purposes. For the integrin $\alpha_v\beta_3$-targeted therapeutic radiotracers, however, 6G-RGD$_4$ has advantages over RGD$_4$ and 3G-RGD$_2$, because ^{111}In(DOTA-6G-RGD$_4$) has a longer tumor retention time than both ^{111}In-(DOTA-3G-RGD$_2$) and ^{111}In(DOTA-RGD$_4$). At this moment, it is not clear why ^{111}In(DOTA-3G-RGD$_2$) is able to maintain its integrity during its excretion from both renal and hepatobiliary routes while ^{111}In(DOTA-6G-RGD$_4$) has significant degradation during its excretion from the hepatobiliary route (Figure 7). It is likely that the metabolic instability of ^{111}In-(DOTA-6G-RGD$_4$) during its hepatobiliary excretion is caused by its much larger size (MW = 4269 Da) than that of ^{111}In(DOTA-3G-RGD$_2$) (MW = 2326 Da).

The %ID tumor uptake reflects the total integrin $\alpha_v\beta_3$ expression level on tumor cells and tumor neovasculature, while the %ID/g tumor uptake reflects the integrin $\alpha_v\beta_3$ density. When tumor is small (<0.05 g or 50 mm^3), there is little tumor mass and angiogenesis. As a result, ^{111}In(DOTA-3G-RGD$_2$) has low %ID tumor uptake (Figure 4A). As tumor grows, the integrin $\alpha_v\beta_3$ level becomes higher, and the %ID tumor uptake of ^{111}In(DOTA-3G-RGD$_2$) increases (Figure 4A). However, the microvessel density decreases due to the maturation of blood vessels, and the integrin $\alpha_v\beta_3$ density also decreases due to larger interstitial space and higher collagen concentrations (*38*). In addition, parts of the tumor may become necrotic, leading to lower integrin $\alpha_v\beta_3$ density.

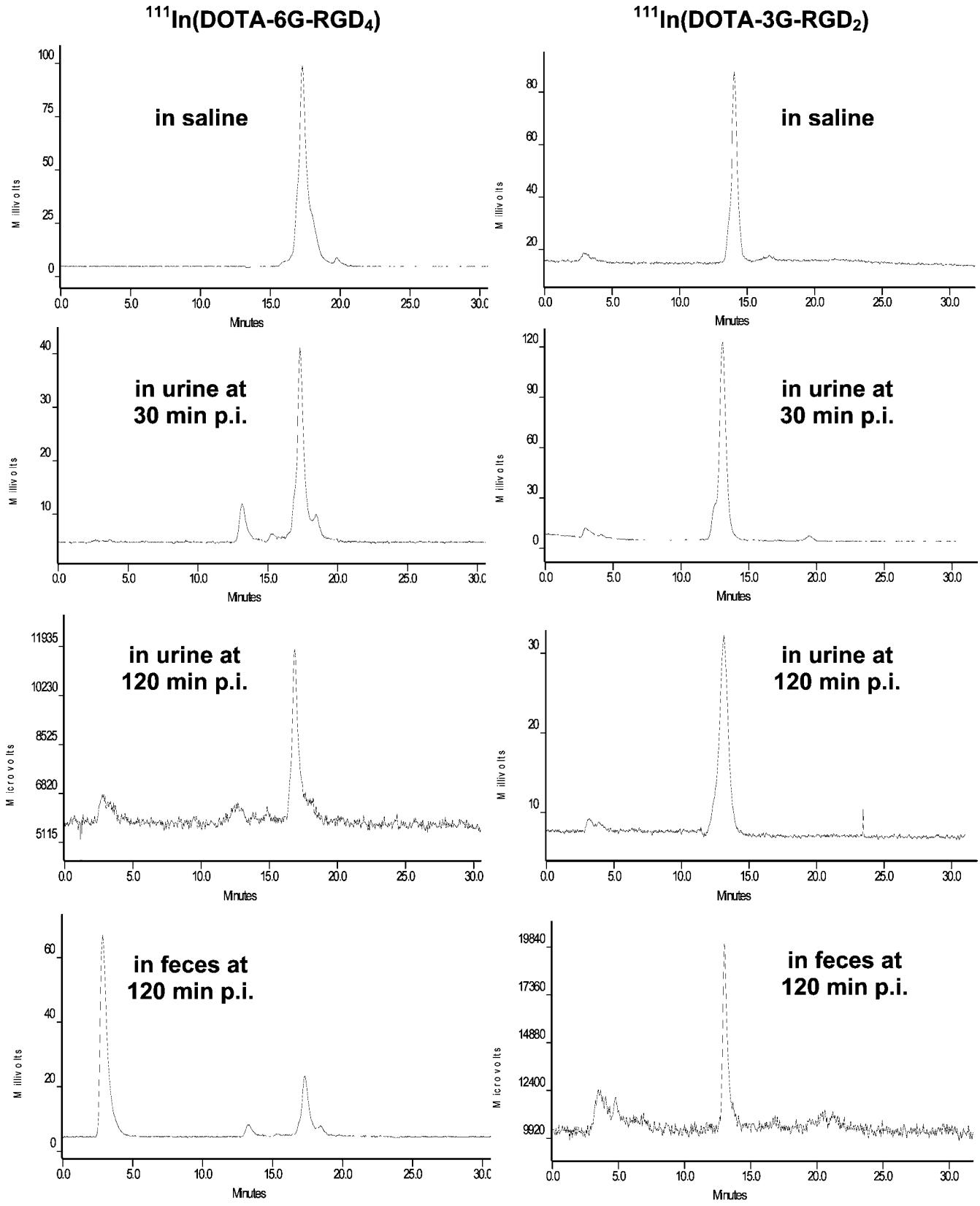


Figure 7. Typical radio-HPLC chromatograms of ^{111}In(DOTA-6G-RGD$_4$) (left) and ^{111}In(DOTA-3G-RGD$_2$) (right) in saline before injection, in urine at 30 and 120 min p.i., and in feces at 120 min p.i. Each mouse was administered with ~3.7 Mbq radiotracer.

It is not surprising that ^{111}In(DOTA-3G-RGD$_2$) had significantly less %ID/g uptake in larger tumors (Figure 4B). Similar results were also reported for ^{64}Cu(DOTA-3P-RGD$_2$) (*33*). The linear relationship between the tumor size and %ID tumor uptake suggests that ^{111}In(DOTA-3G-RGD$_2$) might have the potential for monitoring tumor growth or shrinkage. However, the relationship between the radiotracer uptake and integrin $\alpha_v\beta_3$ levels needs to be further established in our

future studies. The ability to noninvasively quantify integrin $\alpha_v\beta_3$ level will provide a useful tool to select the patients more appropriately for antiangiogenic therapy (*39, 40*).

CONCLUSION

In this study, we evaluated ^{111}In(DOTA-6G-RGD$_4$), ^{111}In(DOTA-RGD$_4$), and ^{111}In(DOTA-3G-RGD$_2$) for their potential as new integrin $\alpha_v\beta_3$-targeted radiotracers. On the basis of results from the integrin $\alpha_v\beta_3$ binding assay and biodistribution studies, it is concluded that (1) tetrameric RGD peptides 6G-RGD$_4$ and RGD$_4$ are not tetravalent; (2) 6G-RGD$_4$, RGD$_4$ and 3G-RGD$_2$ most likely bind to the integrin $\alpha_v\beta_3$ in a bivalent fashion; (3) two extra cyclic RGD motifs in 6G-RGD$_4$ and RGD$_4$ contribute significantly to the longer tumor retention times of ^{111}In(DOTA-6G-RGD$_4$) and ^{111}In(DOTA-RGD$_4$) than that of ^{111}In(DOTA-3G-RGD$_2$); (4) further increase of multiplicity from cyclic RGD dimers, such as 3G-RGD$_2$, has an adverse impact on T/B ratios due to the increased radioactivity accumulation in normal organs; and (5) the combination of high tumor uptake and prolonged tumor retention of ^{111}In(DOTA-6G-RGD$_4$) suggests that its ^{90}Y and ^{177}Lu analogues, M(DOTA-6G-RGD$_4$) (M = ^{90}Y and ^{177}Lu), might have potential for targeted radiotherapy of glioblastoma.

ACKNOWLEDGMENT

This work is supported, in part, by Purdue University and research grants: R01 CA115883-A2 from National Cancer Institute (NCI), R21 HL08396-01 from National Heart, Lung, and Blood Institute (NHLBI), and DE-FG02-08ER64684 from the Department of Energy.

LITERATURE CITED

(1) Weber, W. A., Haubner, R., Vabuliene, E., Kuhnast, B., Wester, H. J., and Schwaiger, M. (2001) Tumor angiogenesis targeting using imaging agents. *Q. J. Nucl. Med. 45*, 179–182.

(2) Costouros, N. G., Diehn, F. E., and Libutti, S. K. (2002) Molecular imaging of tumor angiogenesis. *J. Cell. Biochem. Suppl. 39*, 72–78.

(3) Liu, S., Robinson, S. P., and Edwards, D. S. (2003) Integrin $\alpha_v\beta_3$ directed radiopharmaceuticals for tumor imaging. *Drugs Future 28*, 551–564.

(4) Haubner, R., and Wester, H. J. (2004) Radiolabeled tracers for imaging of tumor angiogenesis and evaluation of antiantiogenic therapies. *Curr. Pharm. Des. 10*, 1439–1455.

(5) Liu, S. (2006) Radiolabeled multimeric cyclic RGD peptides as integrin $\alpha_v\beta_3$-targeted radiotracers for tumor imaging. *Mol. Pharm. 3*, 472–487.

(6) Chen, X. (2006) Multimodality imaging of tumor integrin $\alpha_v\beta_3$ expression. *Mini-Rev. Med. Chem. 6*, 227–234.

(7) Cai, W., and Chen, X. (2008) Multimodality molecular imaging of tumor angiogenesis. *J. Nucl. Med. 49*, 113S–128S.

(8) Cai, W., Niu, G., and Chen, X. (2008) Imaging of integrins as biomarkers for tumor angiogenesis. *Curr. Pharmaceut. Des. 14*, 2943–2973.

(9) Liu, S. (2009) Radiolabeled cyclic RGD peptides as integrin $\alpha_v\beta_3$-targeted radiotracers: maximizing binding affinity via bivalency. *Bioconjugate Chem.* [Online early access].

(10) Thumshirn, G., Hersel, U., Goodman, S. L., and Kessler, H. (2003) Multimeric cyclic RGD peptides as potential tools for tumor targeting: solid-phase peptide synthesis and chemoselective oxime ligation. *Chem.—Eur. J. 9*, 2717–2725.

(11) Poethko, T., Schottelius, M., Thumshirn, G., Herz, M., Haubner, R., Henriksen, G., Kessler, H., Schwaiger, M., and Wester, H. J. (2004) Chemoselective pre-conjugate radiohalogenation of unprotected mono- and multimeric peptides via oxime formation. *Radiochim. Acta 92*, 317–327.

(12) Chen, X., Liu, S., Hou, Y., Tohme, M., Park, R., Bading, J. R., and Conti, P. S. (2004) MicroPET imaging of breast cancer α_v-integrin expression with ^{64}Cu-labeled dimeric RGD peptides. *Mol. Imaging Biol. 6*, 350–359.

(13) Chen, X., Tohme, M., Park, R., Hou, Y., Bading, J. R., and Conti, P. S. (2004) MicroPET imaging of breast cancer α_v-integrin expression with ^{18}F-labeled dimeric RGD peptide. *Mol. Imaging 3*, 96–104.

(14) Wu, Y., Zhang, X., Xiong, Z., Cheng, Z., Fisher, D. R., Liu, S., Gambhir, S. S., and Chen, X. (2005) MicroPET imaging of glioma integrin $\alpha_v\beta_3$ expression using ^{64}Cu-labeled tetrameric RGD peptide. *J. Nucl. Med. 46*, 1707–1718.

(15) Zhang, X., Xiong, Z., Wu, Y., Cai, W., Tseng, J. R., Gambhir, S. S., and Chen, X. (2006) Quantitative PET imaging of tumor integrin $\alpha_v\beta_3$ expression with ^{18}F-FRGD2. *J. Nucl. Med. 47*, 113–121.

(16) Wu, Z., Li, Z., Chen, K., Cai, W., He, L., Chin, F. T., Li, F., and Chen, X. (2007) Micro-PET of tumor integrin $\alpha_v\beta_3$ expression using ^{18}F-labeled PEGylated tetrameric RGD peptide (^{18}F-FPRGD4). *J. Nucl. Med. 48*, 1536–1544.

(17) Li, Z. B., Chen, K., and Chen, X. (2008) ^{68}Ga-labeled multimeric RGD peptides for microPET imaging of integrin $\alpha_v\beta_3$ expression. *Eur. J. Nucl. Med. Mol. Imaging 35*, 1100–1108.

(18) Liu, S., Edwards, D. S., Ziegler, M. C., Harris, A. R., Hemingway, S. J., and Barrett, J. A. (2001) ^{99m}Tc-Labeling of a hydrazinonicotinamide-conjugated vitronectin receptor antagonist useful for imaging tumor. *Bioconjugate Chem. 12*, 624–629.

(19) Liu, S., Cheung, E., Ziegler, M. C., Rajopadhye, M., and Edwards, D. S. (2001) ^{90}Y- and ^{177}Lu-labeling of a DOTA-conjugated vitronectin receptor antagonist for tumor therapy. *Bioconjugate Chem. 12*, 559–568.

(20) Janssen, M., Oyen, W. J. G., Massuger, L. F. A. G., Frielink, C., Dijkgraaf, I., Edwards, D. S., Radjopadhye, M., Corstens, F. H., and Boerman, O. C. (2002) Comparison of a monomeric and dimeric radiolabeled RGD-peptide for tumor targeting. *Cancer Biother. Radiopharm. 17*, 641–646.

(21) Janssen, M., Oyen, W. J. G., Dijkgraaf, I., Massuger, L. F., Frielink, C., Edwards, D. S., Rajopadhye, M., Boonstra, H., Corstens, F. H., and Boerman, O. C. (2002) Tumor targeting with radiolabeled integrin $\alpha_v\beta_3$ binding peptides in a nude mice model. *Cancer Res. 62*, 6146–6151.

(22) Liu, S., Hsieh, W. Y., Kim, Y. S., and Mohammed, S. I. (2005) Effect of coligands on biodistribution characteristics of ternary ligand ^{99m}Tc complexes of a HYNIC-conjugated cyclic RGDfK dimer. *Bioconjugate Chem. 16*, 1580–1588.

(23) Jia, B., Shi, J., Yang, Z., Xu, B., Liu, Z., Zhao, H., Liu, S., and Wang, F. (2006) ^{99m}Tc-labeled cyclic RGDfK dimer: initial evaluation for SPECT imaging of glioma integrin $\alpha_v\beta_3$ expression. *Bioconjugate Chem. 17*, 1069–1076.

(24) Liu, S., He, Z. J., Hsieh, W. Y., Kim, Y. S., and Jiang, Y. (2006) Impact of PKM linkers on biodistribution characteristics of the ^{99m}Tc-labeled cyclic RGDfK dimer. *Bioconjugate Chem. 17*, 1499–1507.

(25) Liu, S., Hsieh, W. Y., Jiang, Y., Kim, Y. S., Sreerama, S. G., Chen, X., Jia, B., and Wang, F. (2007) Evaluation of a ^{99m}Tc-labeled cyclic RGD tetramer for noninvasive imaging integrin $\alpha_v\beta_3$-positive breast cancer. *Bioconjugate Chem. 18*, 438–446.

(26) Dijkgraaf, I., Kruijtzer, J. A. W., Liu, S., Soede, A., Oyen, W. J. G., Corstens, F. H. M., Liskamp, R. M. J., and Boerman, O. C. (2007) Improved targeting of the $\alpha_v\beta_3$ integrin by multimerization of RGD peptides. *Eur. J. Nucl. Med. Mol. Imaging 34*, 267–273.

(27) Dijkgraaf, I., Liu, S., Kruijtzer, J. A. W, Soede, A. C., Oyen, W. J. G., Liskamp, R. M. J., Corstens, F. H., and Boerman, O. C. (2007) Effect of linker variation on the in vitro and in vivo

characteristics of an ^{111}In-labeled RGD Peptide. *Nucl. Med. Biol. 34*, 29–35.

(28) Jia, B., Liu, Z., Shi, J., Yu, Z. L., Yang, Z., Zhao, H. Y., He, Z., Liu, S., and Wang, F. (2008) Linker effects on biological properties of ^{111}In-labeled DTPA conjugates of a cyclic RGDfK dimer. *Bioconjugate Chem. 19*, 201–210.

(29) Wang, J. J., Kim, Y. S., and Liu, S. (2008) ^{99m}Tc-labeling of HYNIC-conjugated cyclic RGDfK dimer and tetramer using EDDA as coligand. *Bioconjugate Chem. 19*, 634–642.

(30) Liu, S., Kim, Y. S., Hsieh, W. Y., and Sreerama, S. G. (2008) Coligand effects on solution stability, biodistribution and metabolism of ^{99m}Tc-labeled cyclic RGDfK tetramer. *Nucl. Med. Biol. 35*, 111–121.

(31) Shi, J., Wang, L., Kim, Y. S., Zhai, S., Liu, Z., Chen, X., and Liu, S. (2008) Improving tumor uptake and excretion kinetics of ^{99m}Tc-labeled cyclic Arginine-Glycine-Aspartic (RGD) dimers with triglycine linkers. *J. Med. Chem. 51*, 7980–7990.

(32) Wang, L., Shi, J., Kim, Y. S., Zhai, S., Jia, B., Liu, Z., Zhao, H., Liu, Z., Wang, F., Chen, X., and Liu, S. (2009) Improving tumor targeting capability and pharmacokinetics of ^{99m}Tc-labeled cyclic RGD dimers with PEG_4 linkers. *Mol. Pharm. 6*, 231–245.

(33) Shi, J., Kim, Y. S., Zhai, S., Liu, Z., Chen, X., and Liu, S. (2009) Improving tumor uptake and pharmacokinetics of ^{64}Cu-labeled cyclic RGD dimers with G_3 and PEG_4 Linkers. *Bioconjugate Chem. 20*, 750–759.

(34) Liu, Z., Niu, G., Shi, J., Liu, S. L., Wang, F., and Liu, S. (2009) ^{68}Ga-Labeled cyclic RGD dimers with Gly_3 and PEG_4 linkers: promising agents for tumor integrin $\alpha_v\beta_3$ PET imaging. *Eur. J. Nucl. Med. Mol. Imaging 36*, 947–957.

(35) Liu, Z., Liu, S., Wang, F., Liu, S., and Chen, X. (2009) Noninvasive imaging of tumor integrin expression using ^{18}F-labeled RGD dimer peptide with PEG_4 linkers. *Eur. J. Nucl. Med. Mol. Imaging 36*, 1296–1307.

(36) Shi, J., Kim, Y. S., Chakraborty, S., Jia, B., Wang, F., and Liu, S. (2009) 2-Mercaptoacetylglycylglycyl (MAG_2) as a bifunctional chelator for^{99m}Tc-labeling of cyclic RGD dimers: effects of technetium chelate on tumor uptake and pharmacokinetics. *Bioconjugate Chem. 20*, 1559–1568.

(37) Shi, J., Wang, L., Kim, Y. S., Zhai, S., Jia, B., Zhao, H., Wang, F., and Liu, S. (2009) ^{99m}TcO(MAG_2-$3G_3$-dimer): a new integrin $\alpha_v\beta_3$-targeted SPECT radiotracer with high tumor uptake and favorable pharmacokinetics. *Eur. J. Nucl. Med. Mol. Imaging 36*, 1874–1884.

(38) Jain, R. K. (1987) Transport of molecules in the tumor interstitium: a review. *Cancer Res. 47*, 3039–3051.

(39) Cai, W., Rao, J., Gambhir, S. S., and Chen, X. (2006) How molecular imaging is speeding up antiangiogenic drug development. *Mol. Cancer Ther. 5*, 2624–2633.

(40) Niu, G., and Chen, X. (2008) Has molecular and cellular imaging enhanced drug discovery and drug development? *Drugs R&D 9*, 351–368.

BC900555Q

Mechanism-Based Tumor-Targeting Drug Delivery System. Validation of Efficient Vitamin Receptor-Mediated Endocytosis and Drug Release

Shuyi Chen,[†] Xianrui Zhao,[†] Jingyi Chen,[‡] Jin Chen,[†] Larisa Kuznetsova,[†] Stanislaus S. Wong,[†,‡] and Iwao Ojima*[,†,§]

Department of Chemistry and Institute of Chemical Biology & Drug Discovery, State University of New York at Stony Brook, Stony Brook, New York 11794-3400, Condensed Matter Physics & Materials Science Department, Brookhaven National Laboratory, Upton, New York 11973. Received December 20, 2009; Revised Manuscript Received April 6, 2010

An efficient mechanism-based tumor-targeting drug delivery system, based on tumor-specific vitamin-receptor mediated endocytosis, has been developed. The tumor-targeting drug delivery system is a conjugate of a tumor-targeting molecule (biotin: vitamin H or vitamin B-7), a mechanism-based self-immolative linker and a second-generation taxoid (SB-T-1214) as the cytotoxic agent. This conjugate (**1**) is designed to be (i) specific to the vitamin receptors overexpressed on tumor cell surface and (ii) internalized efficiently through receptor-mediated endocytosis, followed by smooth drug release via glutathione-triggered self-immolation of the linker. In order to monitor and validate the sequence of events hypothesized, i.e., receptor-mediated endocytosis of the conjugate, drug release, and drug-binding to the target protein (microtubules), three fluorescent/fluorogenic molecular probes (**2**, **3**, and **4**) were designed and synthesized. The actual occurrence of these processes was unambiguously confirmed by means of confocal fluorescence microscopy (CFM) and flow cytometry using L1210FR leukemia cells, overexpressing biotin receptors. The molecular probe **4**, bearing the taxoid linked to fluorescein, was also used to examine the cell specificity (i.e., efficacy of receptor-based cell targeting) for three cell lines, L1210FR (biotin receptors overexpressed), L1210 (biotin receptors not overexpressed), and WI38 (normal human lung fibroblast, biotin receptor negative). As anticipated, the molecular probe **4** exhibited high specificity only to L1210FR. To confirm the direct correlation between the cell-specific drug delivery and anticancer activity of the probe **4**, its cytotoxicity against these three cell lines was also examined. The results clearly showed a good correlation between the two methods. In the same manner, excellent cell-specific cytotoxicity of the conjugate **1** (without fluorescein attachment to the taxoid) against the same three cell lines was confirmed. This mechanism-based tumor-targeting drug delivery system will find a range of applications.

INTRODUCTION

Cancer is the second leading cause of death (the number 1 cause of death under the age of 85) in the U.S. and remains one of the most challenging diseases to combat. Traditional cancer chemotherapy is based on the premise that tumor cells are more likely to be killed by anticancer drugs because of the faster proliferation of those cancer cells (*1*). However, in reality, the representative cytotoxic chemotherapeutic agents, such as paclitaxel, cisplatin, and doxorubicin, cannot distinguish cancer cells from normal cells. This lack of selectivity leads to undesirable side effects associated with these drugs (*2*), i.e., patients would be at risk of systemic cytotoxicity if exposed to the high doses of cytotoxic agents required to eradicate the tumor. Accordingly, the development of tumor-specific delivery systems for anticancer agents, recognizing the intrinsic differences between normal and tumor cells, is an urgent need for efficacious cancer chemotherapy, and has been receiving increasing attention in recent years (*3*).

In general, a tumor-targeting drug delivery system (DDS) consists of a tumor recognition moiety and a cytotoxic agent connected directly or through a suitable linker to form a conjugate (*4*). The tumor-targeting DDS should be systemically nontoxic. This means that the linker must be stable in blood circulation, but upon internalization into the tumor cells, the conjugate should be readily cleaved to regenerate the active cytotoxic agent.

Cancer cells overexpress many tumor-specific receptors, which can be used as targets to deliver cytotoxic agents into tumors (*3*). For example, monoclonal antibodies (*1, 2, 5*−*7*), polyunsaturated fatty acids (*8, 9*), folic acid (*10*−*12*), aptamers (*13, 14*), transferrin (*15*), oligopeptides (*16*), and hyaluronic acid (*17*) have been employed as tumor-specific "guiding modules" to construct tumor-targeting drug conjugates.

We have constructed efficacious tumor-targeting DDS based on highly potent new-generation taxoids, which were discovered and developed in our laboratory, in combination with monoclonal antibodies (mAb's: targeting epidermal growth factor receptor) as well as omega-3 polyunsaturated fatty acids (*2, 4, 9*). These tumor-targeting drug conjugates exhibited remarkable efficacy against tumor xenografts in mouse models (*2, 4, 9*), and the mAb-taxoid conjugates demonstrated exceptional tumor-targeting specificity (*2, 4*). However, mAb's are very large (ca. 150 kD) and expensive, containing modification sites that are difficult to pinpoint, and are potentially immunogenic, while drug conjugates with omega-3 fatty acids provide only passive tumor-targeting delivery, although efficacious in vivo. Accordingly, we turned our attention to explore small molecules as tumor-targeting molecules and found that vitamins would serve as excellent guiding molecules (*4, 18*).

* To whom correspondence should be addressed. E-mail: iojima@notes.cc.sunysb.edu.

[†] Department of Chemistry, State University of New York at Stony Brook.

[‡] Brookhaven National Laboratory.

[§] Institute of Chemical Biology & Drug Discovery, State University of New York at Stony Brook.

10.1021/bc9005656 © 2010 American Chemical Society
Published on Web 04/29/2010

Although all living cells require vitamins for their survival, rapidly dividing cancer cells, in particular, require certain vitamins to sustain their rapid growth (*19, 20*). Consequently, the receptors involved in uptake of the vitamins are overexpressed on the cancer cell surface. Therefore, those vitamin receptors serve as useful biomarkers for the imaging and identification of tumor cells as well as tumor-targeting drug delivery. Vitamin B12, folic acid, biotin, and riboflavin are essential vitamins for the division of all cells, but particularly for the growth of cancer cells. The folate receptors were recognized as potentially excellent biomarkers for targeted drug delivery, and significant advancement has been made to date (*10, 11, 21, 22*). In contrast, the biotin receptors were not investigated for this purpose until recently. Biotin (vitamin H or B-7) is a growth promoter at the cellular level, and its content in tumors is substantially higher than that in normal tissues (*19*). Recently, it has been shown that the biotin receptors are overexpressed more than the folate and/or vitamin B-12 receptors in many cancer cells, e.g., leukemia (L1210FR), ovarian (Ov2008, ID8), Colon (Colo-26), mastocytoma (P815), lung (M109), renal (RENCA, RD0995), and breast (4T1, JC, MMT06056) cancer cell lines (*19, 20*). Accordingly, we chose biotin as the tumor-targeting molecule for our tumor-targeting DDS bearing a self-immolative disulfide linker with a second-generation taxoid as the cytotoxic agent (*4, 18*).

We describe here a mechanistic study on the validation of tumor-targeting DDS by monitoring (i) the internalization through receptor-mediated endocytosis (RME), (ii) drug release triggered by an intracellular thiol, e.g., glutathione (GSH), and (iii) drug binding to the molecular target in cancer cells, using fluorescent and fluorogenic molecular probes of the biotin-linker-taxoid conjugate. The efficacy and cell-specificity of the biotin-linker-taxoid conjugate is also evaluated based on cytotoxicity of the conjugate against cells that overexpress the biotin receptor, as well as those do not express this vitamin receptor, including normal human cells.

EXPERIMENTAL SECTION

Chemical Syntheses, Procedures, and Characterization Data for Conjugates 1−4. See Supporting Information.

Cell Culture. L1210 (ATCC) and L1210FR (a gift from Dr. Gregory Russell-Jones, Access Pharmaceuticals Australia Pty Ltd., Australia) cell lines were grown as a suspension in the RPMI-1640 cell culture medium (Gibco) in the absence of folic acid (FA) but supplemented with 10% (v/v) heat-inactivated fetal bovine serum (FBS) as well as 1% (v/v) penicillin and streptomycin (P/S) at 37 °C in a humidified atmosphere with 5% CO_2. WI-38 human lung fibroblast cells (ATCC) were cultured as monolayers on 100 mm tissue culture dishes in a DMEM cell culture medium (Gibco) that was supplemented with 10% (v/v) heat-inactivated FBS and 1% (v/v) P/S at 37 °C in a humidified atmosphere with 5% CO_2. The cells were harvested, collected by centrifugation at 1000 rpm for 6 min, and finally resuspended in fresh cell culture medium containing different cell densities for subsequent biological experiments and analysis.

Incubation of Cells with the Biotin−FITC Conjugate 2. The cell suspension (1 mL) at 5×10^5 cells/mL was added to a 1.5 mL microcentrifuge tube first. The biotin−FITC conjugate **2** (10 μM) in DMSO (10 μL) was then injected into the microcentrifuge tube to provide the final concentration of 100 nM, and the resultant suspension was incubated at 37 °C for 3 h. For low-temperature experiments, the incubation of cells (L1210FR) with conjugate **2** was carried out in the cold room at 4 °C for 3 h. For the assessment of the effect of NaN_3 addition, the cells were initially preincubated at 37 °C for 0.5 h with 0.05% (w/v) of NaN_3, prior to the addition of conjugate **2**. For the assessment of the effect of excess biotin addition, the cells were treated with 2 mM of biotin (at the final concentration) at 37 °C for 1 h prior to incubation with conjugate **2**. After incubation, the cells were washed twice with PBS, collected by centrifugation, and resuspended in 100 μL PBS for imaging.

Incubation of Cells with the Biotin-Linker-Coumarin Conjugate 3. The cell suspension (1 mL: 5×10^5 cells/mL) was added to 1.5 mL microcentrifuge tube. The conjugate **3** (100 μM) in DMSO (10 μL) was added to the microcentrifuge tube at the final concentration of 1 μM. After incubation at 37 °C for 3 h, the cells were washed twice by PBS to remove excess conjugates and resuspended in the medium. To observe the release of coumarin in a short period of time, GSH-OEt (10 μL) was added to the L1210FR cell suspension at the final concentration of 2 mM and incubated for another 2 h. Excess GSH-OEt was removed by washing twice with PBS, and the cells were collected by centrifugation. Then, the cells were resuspended in 100 μL PBS prior to imaging. In the control experiment, DMSO (10 μL) was added to the suspension and incubated for another 2 h. After incubation, cells were washed with PBS twice, collected by centrifugation, and resuspended in 100 μL PBS prior to imaging.

Incubation of Cells with the Biotin-Linker-SB-T-1214-Fluorescein Conjugate 4. The cell suspension (1 mL: 5×10^5 cells/mL) was added to a 1.5 mL microcentrifuge tube. The biotin-linker-SB-T-1214-fluorescein conjugate **4** (2 mM) in DMSO (10 μL) was added to the microcentrifuge tube at the final concentration of 20 μM. After incubation at 37 °C for 2 h, the cells were washed twice with PBS to remove excess conjugates and resuspended in the medium. For observation of the release of taxoid in a short period of time, GSH-OEt (10 μL) was added to the L1210FR cell suspension at the final concentration of 2 mM and incubated for another 1 h. Excess GSH-OEt was removed by washing twice with PBS, and the cells were collected by centrifugation. Then, the cells were resuspended in 100 μL PBS prior to imaging. In the control experiment, DMSO (10 μL) was added to the suspension and incubated for another 1 h. After incubation, cells were washed with PBS twice, collected by centrifugation, and resuspended in 100 μL PBS prior to imaging.

Confocal Microscopy Imaging of the Treated Cells. Cells treated as described above were resuspended in 100 μL of PBS after each experiment, and dropped onto an uncoated glass dish (MatTek Corp.). Confocal fluorescence microscopy (CFM) experiments were performed using a Zeiss LSM 510 META NLO two-photon laser scanning confocal microscope system, operating at a 488 nm excitation wavelength and at 527 ± 23 nm detecting emission wavelength using a 505−550 nm bandpass filter. Images were captured using a C-Apochromat 63×/1.2 water (corr.) objective or a Plan-Apochromat 100×/1.45 oil objective. Acquired data were analyzed using LSM 510 META software.

Flow Cytometry Fluorescent Measurements of the Cells. Flow cytometry analysis of the treated cells was performed with a flow cytometer, FACSCalibur, operating at a 488 nm excitation wavelength and detecting emission wavelengths with a 530/30 nm bandpass filter. Cells treated as described above were resuspended in 0.5 mL of PBS. At least 10 000 cells were counted for each experiment using *CellQuest 3.3* software (Becton Dickinson) and the distribution of FITC fluorescence was analyzed using *WinMDI 2.8* freeware (Joseph Trotter, Scripps Research Institute). Propidium iodide staining was used in all experiments to rule out dead cell count in the analysis.

In Vitro Cytotoxicity Assay. The cytotoxicities of biotin-linker-SB-T-1214 (**1**), biotin-linker-SB-T-1214-fluorescein (**4**), SB-T-1214, SB-T-1214-fluorescein (**24**), and paclitaxel were evaluated in vitro against murine leukemia cell lines, L1210FR and L1210, as well as a human lung blastoma cell line, WI38, by means of a quantitative colorimetric assay using a tetrazolium

salt-based analysis ("MTT assay" (*23*); MTT = 3-(4,5-dimethylthiazol-2-yl)-2,5-diphenyltetrazolium bromide; Sigma Chemical Co.). The inhibitory activity of each compound is represented by the IC_{50} value, which is defined as the concentration required for inhibiting 50% of the cell growth. Cells were harvested, collected, and resuspended in 100 μL medium at a concentration of $\sim 2 \times 10^4$ cells per well over a 96-well plate. For the adhesive cell type, cells were allowed to descend to the bottom of the plates overnight and fresh medium was added to each well upon removal of the old medium. A conjugate (**1** or **4**), taxoid (SB-T-1214 or **24**), or paclitaxel in DMSO stock solution was diluted to a series of concentrations in the cell culture medium without FBS to prepare test solutions. These test solutions at different concentrations ranging from 0.1 to 100 nM (10 μL each) were added to the wells in the 96-well plate and cells were subsequently cultured for 72 h. After spinning down the cells and removing the old medium, the fresh medium containing MTT (e.g., 100 μL of 0.5 mg/mL) was added and incubated at 37 °C for 4 h. The resulting medium was then removed and as-produced insoluble violet formazan crystals were dissolved into 0.1 N HCl in isopropanol with 10% Triton X-100 to give a violet solution. The spectrophotometric absorbance measurement of each well in the 96-well plate was run at 570 nm. The IC_{50} values and their standard errors were calculated from the viability−concentration curve using the Four Parameter Logistic Model of *Sigmaplot*. The concentration of DMSO per well was ≤1% in all cases. The control experiment, i.e., adding 1% DMSO to the cells, indicated that 1% DMSO was not cytotoxic, and thus, all the cells treated remained virtually 100% positive.

RESULTS AND DISCUSSION

Design of an Efficient Tumor-Targeting DDS and Its Molecular Probes. Our tumor-targeting DDS consists of a tumor recognition moiety (biotin in the present study) and a cytotoxic agent connected through a self-immolative linker. The drug conjugate should be nontoxic systemically but release the cytotoxic agent upon internalization to cancer cells, as mentioned above.

Self-Immolative Disulfide Linker. In order to develop efficacious tumor-targeting DDS's, efficient mechanism-based linkers are critically important since the tumor-targeting DDS should be stable in blood circulation while readily cleavable in the tumor. These linkers should be bifunctional so that the cytotoxic agent can be connected to the linker at one end and the tumor-targeting module at the other end. Previously, we designed and examined mAb−taxoid conjugates as tumor-targeting DDS, which exhibited extremely promising results against human cancer xenografts in SCID mice (*2*). The results clearly demonstrated the tumor-specific delivery of a taxoid anticancer agent, curing all animals tested without any noticeable toxicity to the animals (*2*). As the linker for these mAb-taxoid DDS's, a simple disulfide linker was employed, which was stable in blood circulation but efficiently cleaved by intracellular reducing substances in the tumor. However, in this first-generation mAb-taxoid DDS, the original taxoid molecule was not released because of the compromised modification of the taxoid molecule to accommodate the disulfide linker. Thus, the cytotoxicity of the taxoid released (SB-T-12136-SH) was 8 times weaker than the parent taxoid (SB-T-1213) (*2*).

As a solution to this problem, we devised the second-generation mechanism-based bifunctional disulfide linkers, which can be connected to various cytotoxic agents and tumor-targeting molecules. We designed self-immolative disulfide linkers wherein the intracellular thiol-triggered cascade drug release should generate the original anticancer agent via thiolactone formation and ester bond cleavage (Figure 1) (*24*).

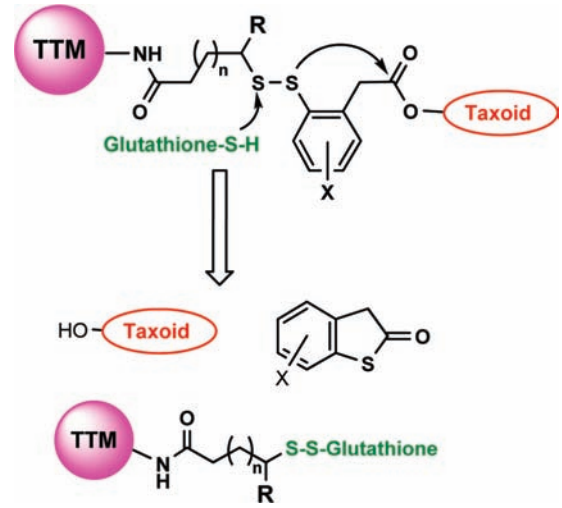


Figure 1. Second-generation self-immolative disulfide linkers (TTM = tumor-targeting module).

The designed mechanism-based drug release has been proven in a fluorine-labeled model system by monitoring the reaction with ^{19}F NMR (*24*). The strategic placement of a phenyl group attached to the disulfide linkage should direct the cleavage of this linkage by a thiol to generate the desirable thiophenolate or sulfhydrylphenyl species for thiolactonization. The disulfide linkage should be cleaved by endogenous thiols, e.g., GSH and thioredoxin. It has been shown that the GSH level in cancer cells is >1000 times higher than that in blood plasma (*25*−*29*). The resulting thiol undergoes an intramolecular nucleophilic substitution at the ester moiety, forming a 5-membered ring thiolactone and releasing the taxoid in its original form. This type of self-immolative disulfide linker can readily be applied to a variety of tumor-targeting drug conjugates. We chose a rather simple linker (R = X = H, $n = 0$) in the present study.

Cytotoxic Agent. Although paclitaxel and docetaxel have brought about significant impact on cancer chemotherapy, mainly because of their unique mechanism of action (*30*), these drugs seriously suffer from the lack of tumor specificity and multidrug resistance (MDR). These taxane drugs are effective against breast, ovary, and lung cancers, while they do not show efficacy against colon, pancreatic, melanoma, and renal cancers. As an example, human colon carcinoma is inherently multidrug-resistant due to the overexpression of P-glycoprotein (Pgp), which is an effective ATP-binding cassette (ABC) transporter and effluxes out hydrophobic anticancer agents, such as paclitaxel and docetaxel (*31*).

We have developed a series of highly potent second- and third-generation taxoids through structure−activity relationship study of taxoids (*32*−*37*). Most of these taxoids exhibited 2−3 orders of magnitude higher potency than those of paclitaxel and docetaxel against MDR cell lines expressing Pgp. Accordingly, these highly potent taxoids have been used as cytotoxic agents of our tumor-targeting DDS's. Among these new-generation taxoids, we chose SB-T-1214, a second-generation taxoid, as the warhead for the present study.

Molecular Probes of the Biotin-Linker-Taxoid Conjugate. The structure of a "guided molecular missile", biotin-linker-SB-T-1214 (**1**), is shown in Figure 2. In order to monitor the sequence of events involved in tumor-targeting drug delivery of conjugate **1**, it was necessary for us to design and synthesize three fluorescence-labeled biotin conjugates, i.e., biotin-fluorescein (**2**), biotin-linker-coumarin (**3**) (fluorogenic probe), and biotin-linker-taxoid-fluorescein (**4**) (Figure 3).

Conjugate **2** was designed to observe RME (Figure 4), while conjugate **3** was designed for confirming the internalization of

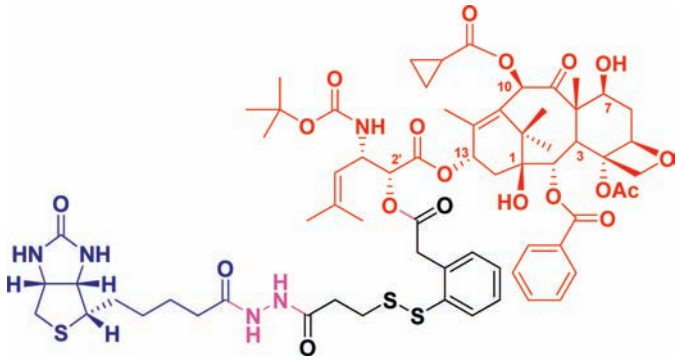


Figure 2. Biotin-linker-SB-T-1214 conjugate (**1**).

the conjugate via RME and the release of coumarin, which becomes fluorescent only when it is released as a free molecule via disulfide cleavage. Fluorogenic molecules, such as coumarin derivatives, have been widely utilized as model systems for probing drug release (*38*). Conjugate **4** was designed to validate the whole internalization by RME and drug release processes, wherein the released fluorescent taxoid should bind to the target protein, microtubules, in the cancer cells (Figure 4).

Figure 4 illustrates the internalization and drug release mechanism of a biotin-linker-taxoid conjugate. Once localized at the tumor site, the drug-conjugate binds to its complementary receptor on the tumor cell surface and is further internalized via RME. The disulfide linkage of the drug-conjugate is cleaved by endogenous reducing agents (e.g., GSH) to generate a thiol group. The resulting thiol group undergoes thiolactonization to release the taxoid warhead in its original form (i.e., SB-T-1214). When a fluorescent taxoid (i.e., SB-T-1214-fluorescein) is used, it should bind to microtubules, visualizing the fluorescent microtubule network.

Chemical Synthesis. The fluorescent probe, biotin-FITC **2**, was synthesized via coupling of fluorescein isothiocyanate (FITC) to biotin-$NHNH_2$ (**5**), which was readily prepared from biotin through esterification and subsequent reaction with hydrazine, as shown in Scheme 1.

The synthesis of the fluorogenic probe, biotin-linker-coumarin **3**, is illustrated in Scheme 2. First, triisopropylsilyl(TIPS) pyridine-2-yldisulfanylpropanoate (**8**) was prepared through thiol-disulfide exchange reaction of pyridine disulfide (**6**) with 3-sulfhydrylpropanoic acid, giving **7**, followed by TIPS protection of the carboxylic acid moiety of **7**. Second, 2-sulfhydrylphenylacetic acid (**11**) was prepared from benzothiophene-2-boronic acid (**9**) through hydrogen peroxide oxidation to benzothiophen-2-one (**10**), followed by hydrolysis with lithium hydroxide. The reaction of **8** with **11** via thiol-disulfide exchange reaction gave 2-(TIPSO-carbonylethyl)disulfanylphenylacetic acid (**12**). The coupling of **12** with 7-hydroxy-4-methylcoumarin (**13**) gave coumarin-linker (TIPS) conjugate (**14**), which was deprotected to afford coumarin-linker conjugate **15**. The DCC-coupling of **15** with *N*-hydroxysuccinimide (HOSu) afforded coumarin-linker-OSu active ester **16**. The amide coupling of **5** with **16** gave conjugate **3**.

The synthesis of biotin-linker-taxoid-fluorescein **4** is illustrated in Schemes 3−5. First, commercially available fluorescein was converted to the corresponding methyl ester **17** (*39*), while succinic acid mono-*tert*-butyl ester (**18**) was reduced to *tert*-butyl 4-hydroxybutanoate (**19**) (*40*). The Mitsunobu coupling of **17** with **19** afforded modified fluorescein diester **20** (*39*). Selective deprotection of the *tert*-butyl group of **20** with trifluoroacetic acid afforded 6-tethered fluorescein methyl ester **21** (Scheme 3). Next, the C2′ hydroxy group of taxoid SB-T-1214 was protected as *tert*-butyldimethylsilyl (TBS) ether to give **22**, which was coupled with **21** under DIC/DMAP conditions, followed by deprotection of the C2′-TBDMS group to afford 7-fluorescein-tethered taxoid **24** (Scheme 4). Subsequently, SB-T-1214-fluorescein **24** was coupled with disulfanylacetic acid **12** using DIC/DMAP to give **25**, which was deprotected with HF-pyridine to afford (SB-T-1214-fluorescein)-linker-CO_2H conjugate **26** (Scheme 5). The carboxylic acid moiety of **26** was converted to the corresponding activated ester **27** via esterification with HOSu in the presence of DIC. Finally, activated ester **27** was reacted with **5** to give biotin-linker-SB-T-1214-fluorescein conjugate **4** in high yield (Scheme 5).

Following the same synthetic protocol, biotin-linker-SB-T-1214 **1** was synthesized by using SB-T-1214 without the fluorescein tether, as shown in Scheme 6.

Probing Receptor-Mediated Endocytosis (RME), Drug Release, and Drug Binding to Target. Internalization of these fluorescent and fluorogenic probes **2**−**4** was monitored by confocal fluorescence microscopy (CFM) and the fluorescence was quantified by flow cytometry, using ca. 10 000 treated live cells. Results are shown in Figures 5−8.

Figure 5A shows the intense fluorescence observed when the L1210FR cell was incubated with the probe **2** (100 nM) at 37 °C for 3 h, followed by thorough washing of the cells by phosphate-buffered saline (PBS) and CFM analysis. The result clearly indicates the efficient internalization of the fluorescent probe **2** into the leukemia cells. It has been shown that endocytosis is an energy-dependent process and should be inhibited either at low temperature (4 °C) or in the presence of the metabolism inhibitor, typically NaN_3 (*41*−*43*). The CFM image of the probe **2**, incubated at 4 °C (100 nM, 3 h) showed dramatically diminished (ca. 6 times by flow cytometry) fluorescence in the cells (Figure 5B). When L1210FR cells were incubated with probe **2** (100 nM, 3 h) in the presence of 0.05% (w/v) NaN_3 at 37 °C, a substantial decrease (ca. 4 times) in fluorescence occurred inside the cells as well (Figure 5C). These results unambiguously show that probe **2** was internalized through endocytosis. To validate that this was a RME process, excess free biotin (2 mM) was preincubated for 1 h to saturate the biotin receptors on the cancer cell surface, and subsequently, probe **2** (100 nM, 37 °C, 3 h) was added. The CFM image revealed a substantial decrease (ca. 4.5 times) in fluorescence. The result confirms that this is indeed the receptor-mediated endocytosis (Figure 5D).

Next, the fluorogenic probe **3** (1 μM) was incubated with L1210FR cells at 37 °C for 3 h, and afterward, the cells were washed thoroughly with PBS. Then, glutathione ethyl ester (GSH-OEt, 2 mM) was added to the medium and cells were incubated for another 2 h at 37 °C. The addition of GSH-OEt was to ensure the cleavage of the self-immolative disulfide linker to release free coumarin, as designed. [Note: It has been shown that GSH-OEt is internalized into cells to generate GSH inside the cell (*44*). GSH-OEt also acts as a reducing agent.] As Figure 6A shows, fluorescent coumarin molecules (blue) are indeed released in L1210FR cells. The result unambiguously demonstrates that the intracellular release of coumarin (a drug surrogate) via cleavage of the disulfide linkage by GSH and the subsequent thiolactonization, took place as designed. In the absence of additional GSH (or GSH-OEt), the observed blue fluorescence was drastically weaker (Figure 6B). This means that the concentration of intracellular GSH in this leukemia L1210FR cell line is rather low, especially in the 3 h time frame, under the in vitro experimental conditions, which are significantly different from those in vivo where the GSH supply in tumor tissues is more than adequate (*26*, *27*). On the other hand, this experiment using additional GSH (as GSH-OEt) confirmed that the cleavage of the self-immolative disulfide linkage and subsequent drug release was caused by GSH.

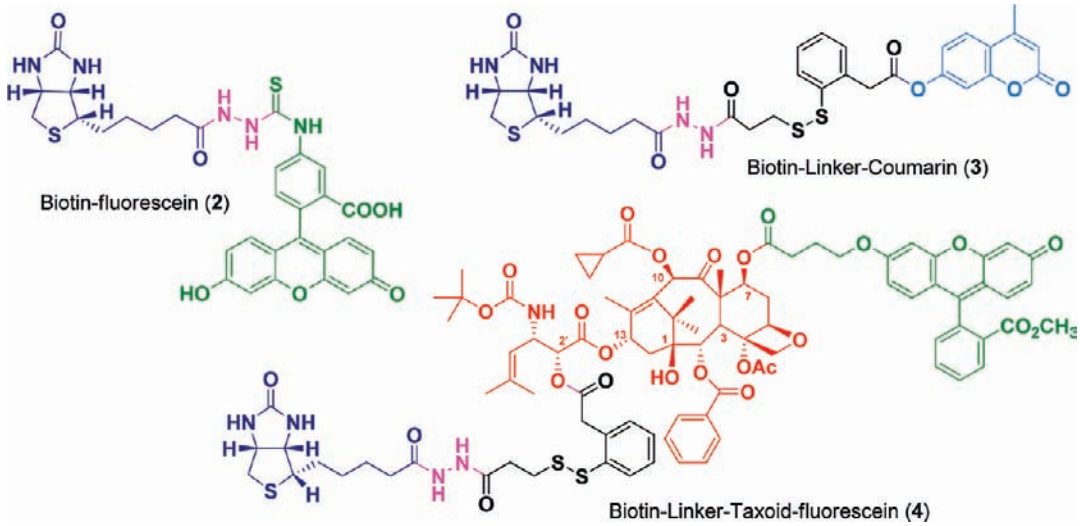


Figure 3. Fluorescent and fluorogenic probes for the internalization and drug-release.

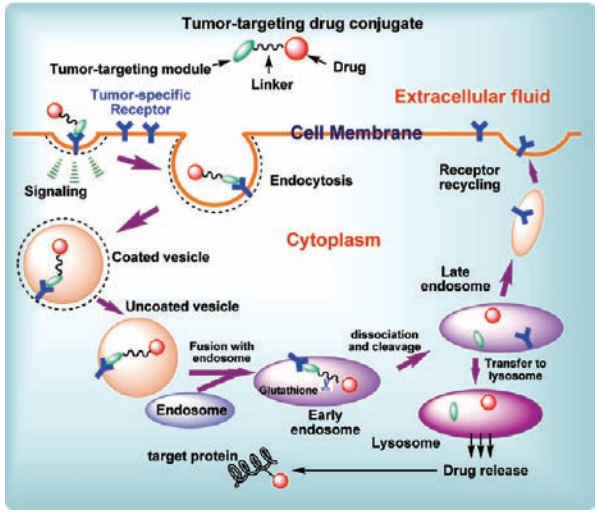
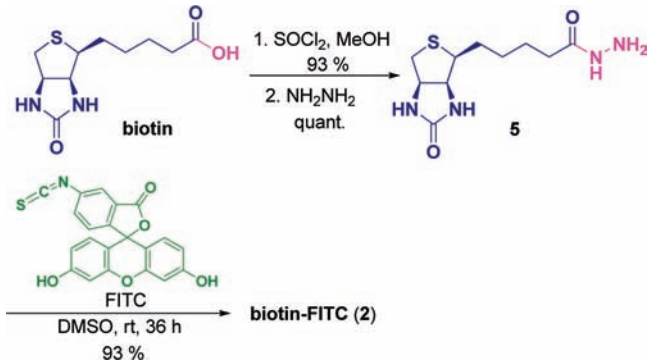


Figure 4. Schematic representation of the RME of a tumor-targeting drug conjugate, drug release, and drug-binding to the target protein.

Scheme 1. Synthesis of Biotin−FITC Conjugate 2



Finally, the internalization and drug release of probe **4** was examined. Probe **4** (20 μM) was incubated with L1210FR cells at 37 °C for 2 h and analyzed by CFM. As Figure 7A shows, the whole conjugate was internalized in the same manner as that described above for the probe **2** (see Figure 5A). Next, GSH-OEt (2 mM) was added to the medium, and the cells were incubated for another 1 h to ensure the drug release. As Figure 7B shows, the CFM image of this system is dramatically different from that shown in Figure 7A. The CFM image in Figure 7B indicates that the released fluorescent taxoid binds to the microtubules that are the drug target of the taxoid and highlights the fluorescence-labeled microtubule bundles. The result confirms that the release of the taxoid proceeded through the designed mechanism (see Figure 1) in the same manner as that observed for the fluorogenic probe **3**. To double-check the morphology of microtubules with the fluorescence-labeled taxoid, the CFM image of the L1210FR cells treated with SB-T-1214-fluorescein (**24**) was taken. As Figure 7C shows, the morphology of treated cells is indeed virtually identical to that treated with the conjugate **4**. This provides additional evidence of efficient release of **24** from the conjugate **4**.

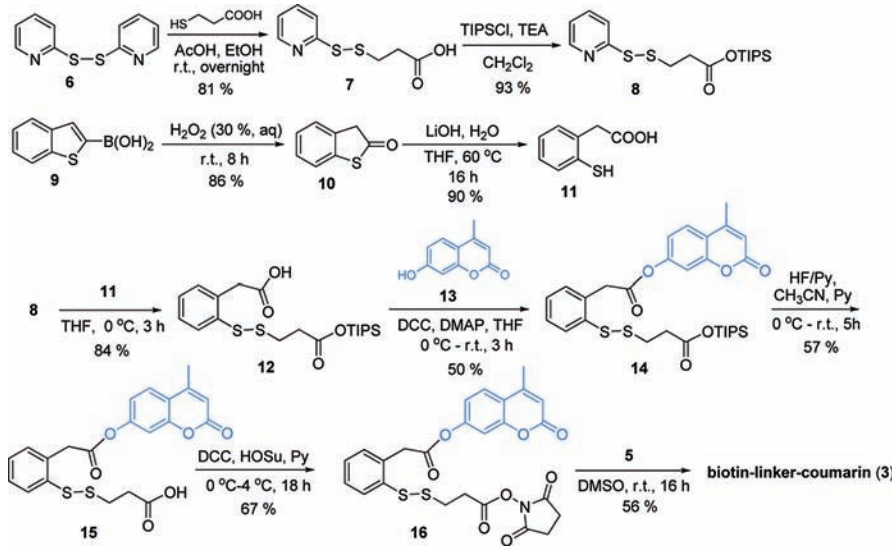
It should be noted that the intracellular GSH in L1210FR would also be able to cleave the disulfide linkage with longer incubation time (vide infra), but the endogenous GSH level in cancer cells varies due to the significant difference in the physiological conditions in the actual leukemia or solid tumors. Accordingly, the extracellular addition of excess GSH-OEt was beneficial for rapid visualization of the drug release inside the leukemia cells.

Consequently, we can safely conclude that the tumor-targeting DDS successfully delivered the active cytotoxic agent to the drug target, as designed, through RME and GSH-triggered intracellular drug release via cleavage of self-immolative disulfide linker and thiolactonization.

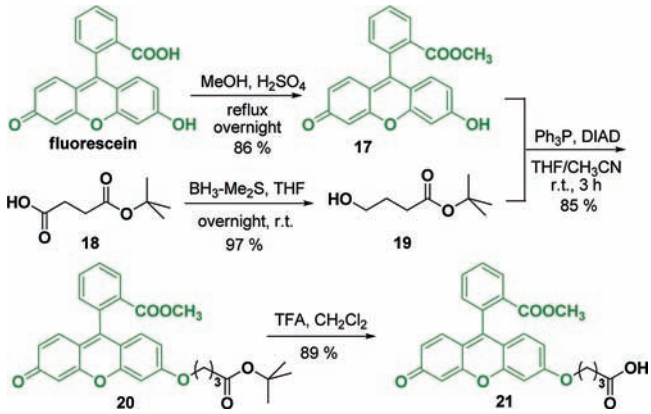
Evaluation of Tumor-Targeting Specificity of Biotin-Linker-Taxoid Conjugates by CFM and Cytotoxicity Assay. To evaluate the tumor specificity of the biotin-mediated RME, two other cell lines, i.e., L1210 murine leukemia cell line and WI38 noncancerous human lung fibroblast cell line, were chosen to compare results with that for L1210FR cell line. Both L1210 and WI38 cell lines do not overexpress biotin receptors on their cell surfaces. Accordingly, this comparison should provide a fair and definitive information about the efficacy of tumor-targeting using biotin as the "guiding" module for our "guided molecular missile".

As Figure 8 clearly shows, much stronger (ca. 12−13 times) fluorescence was indeed observed in L1210FR cells (Figure 8A) as compared to that in L1210 cells (Figure 8B) as well as WI38 cells (Figure 8C) upon incubation with the probe **4** under identical conditions (20 μM at 37 °C for 2 h) by CFM and flow cytometry analyses. Thus, the results confirm the validity of our tumor-targeting design based on this vitamin and its receptors, which can clearly distinguish cancer cells overexpressing the vitamin receptors from other cells which do not, including human normal cells.

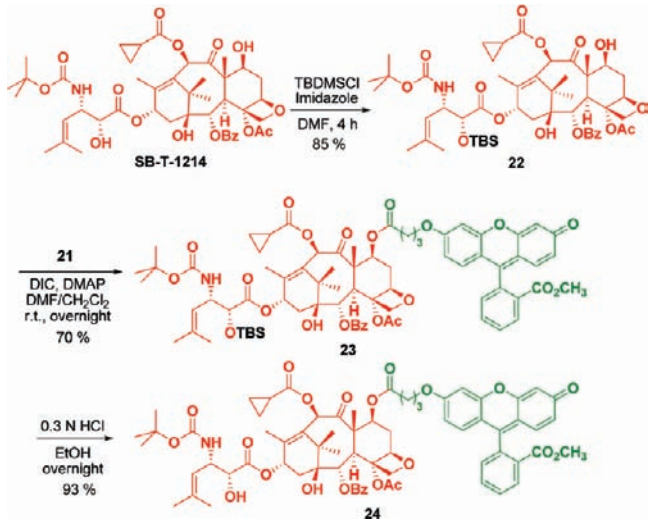
Scheme 2. Synthesis of Biotin-Linker-Coumarin Conjugate (3)



Scheme 3. Preparation of Fluorescein Derivative with Carboxylic Acid Tether

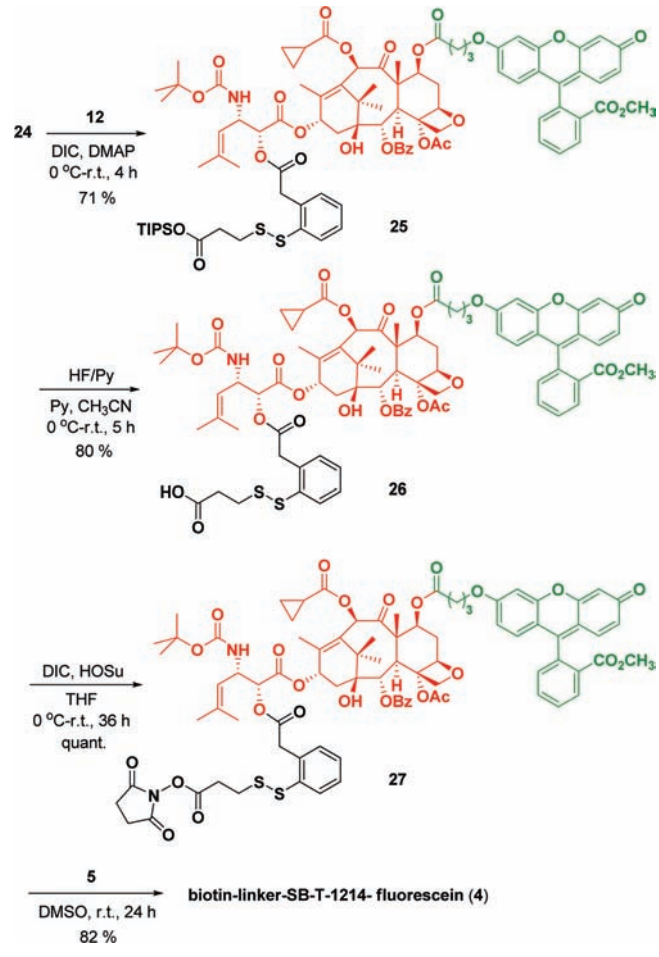


Scheme 4. Synthesis of SB-T-1214 Linked to Fluorescein (24)



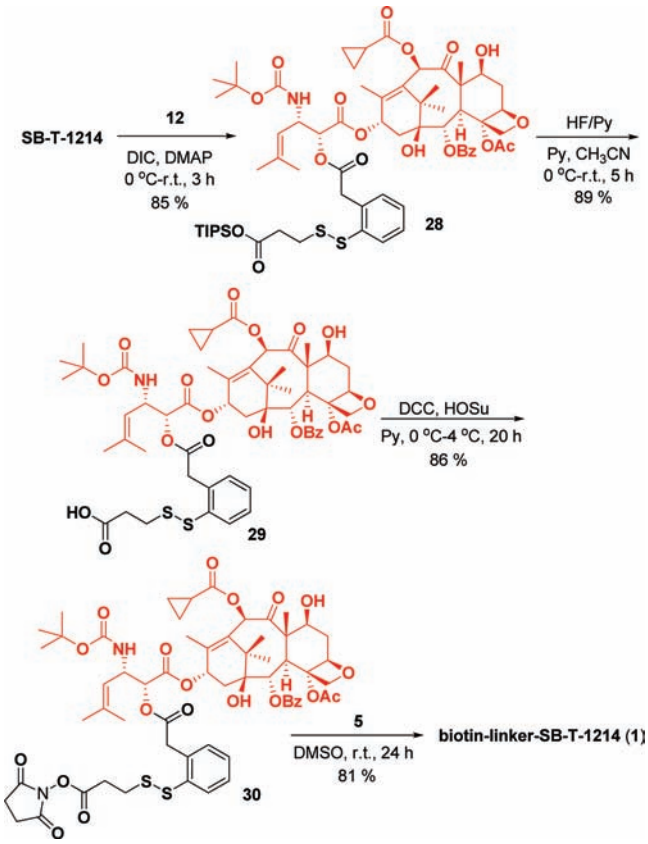
As described above, the mechanistic investigation into the cancer cell specificity, RME, drug release, and drug binding to the target protein with the use of fluorescent and fluorogenic molecular probes were successfully executed by means of CFM and flow cytometry. However, these observations should be correlated to the cancer cell specific cytotoxicity of the originally designed biotin-linker-taxoid conjugate **1** against three cell lines examined by CFM and flow cytometry.

Scheme 5. Synthesis Diagram of Biotin-Linker-SB-T-1214-Fluorescein Conjugate (4)



Accordingly, the cytotoxicity assays (MTT method (*23*)) of conjugate **1** against L1210FR, L1210, and WI38 cell lines were performed. For comparison purpose, the parent taxoid (SB-T-1214), its fluorescein conjugate **24**, and paclitaxel were assayed as well. It should be noted that, in these assays, no GSH-OEt was added to the medium, since the exposure time is much longer (72 h) than that for CFM and flow cytometry analyses

Scheme 6. Synthesis of Biotin-Linker-SB-T-1214 (1)



(2−3 h), and hence, the amount of endogenous GSH should be sufficient to release the taxoid warhead (SB-T-1214) from conjugate **1**. Results are summarized in Table 1.

As Table 1 shows, conjugate **1** exhibited high potency (IC_{50} 8.8 nM) against L1210FR, overexpressing biotin receptors, while those against L1210 (IC_{50} 522 nM) and WI38 (IC_{50} 570 nM) cell lines were 59 times and 65 times less. For comparison, the parent taxoid (SB-T-1214) was also assayed against those three cell lines. As anticipated, SB-T-1214 cannot distinguish these cell lines, resulting in very similar IC_{50} values, i.e., 9.5 nM for L1210FR, 9.7 nM for L1210, and 10.7 nM for WI38. The results clearly indicate that highly efficient vitamin-receptor specific drug delivery to cancer cells has been achieved by conjugate **1**, and also, the drug release by endogenous GSH (and possibly by some other thiols) is efficient as well in 72 h incubation.

As Table 1 shows, the IC_{50} values of SB-T-1214, SB-T-1214-fluorescein, (**24**) and paclitaxel against L1210FR are 9.5 nM, 87.6 nM, and 122 nM, respectively. Thus, SB-T-1214 is ca. 13 times more potent than paclitaxel, and fluorescently labeled **24** is ca. 9 times less potent than the parent SB-T-1214 against L1210FR. As mentioned above, SB-T-1214 exhibited very similar IC_{50} values against these three cell lines. SB-T-1214-fluorescein **24** and paclitaxel showed slight to small differences in their IC_{50} values against the three cell lines, but differences are less than 45% at most (see Table 1). Thus, it is safe to say that these two taxanes cannot distinguish targeted cancer cells from normal cells, as anticipated.

We also assayed the cytotoxicity of the probe **4** against the same three cell lines. As Table 1 shows, virtually the same differences in IC_{50} values were observed, i.e., 81.7 nM for L1210FR and >5 μM for L1210 as well as WI38 (>61 times difference), as those for the conjugate **1**. Thus, the drug delivery to L1210FR is highly specific through vitamin-receptor recognition and RME in this conjugate (probe **4**), as well. As mentioned above, the cell specificity of probe **4** quantified by flow

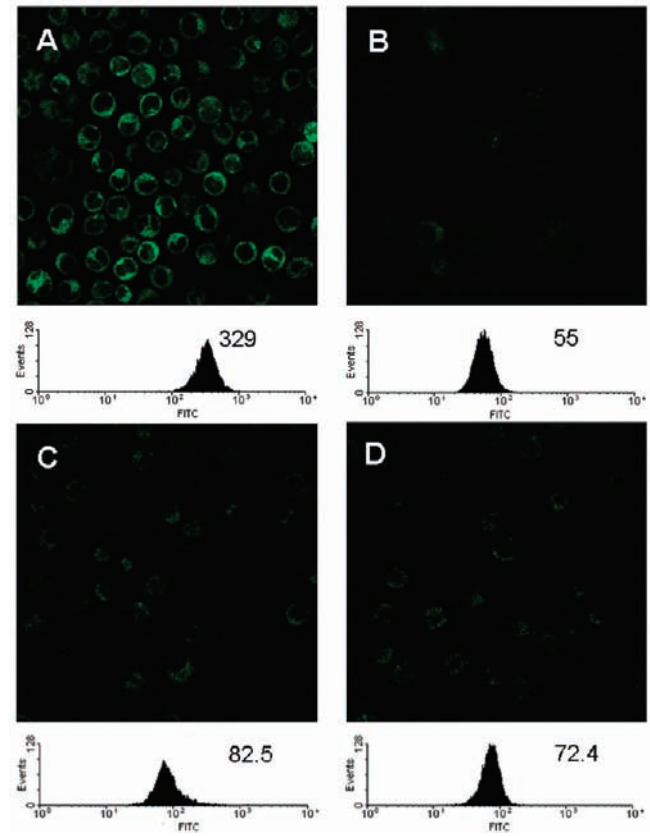


Figure 5. CFM images and flow cytometry analysis of L1210FR cells after incubation with the probe **2** under different conditions: (A) 100 nM, 37 °C, 3 h; (B) 100 nM, 4 °C, 3 h; (C) 100 nM, 37 °C, 0.05% NaN_3, 3 h; (D) 100 nM, 37 °C, 3 h, pretreated with excess biotin (2 mM).

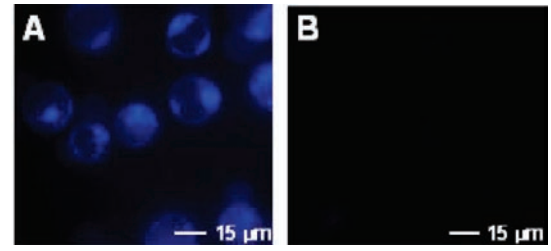


Figure 6. (A) Epifluorescence image of L1210FR cells that were initially incubated with the probe **3** (nonfluorescent form), followed by treatment with GSH-OEt to trigger the self-immolation of the linker. The released coumarin showed blue fluorescence. (B) Epifluorescence image of L1210FR cells after incubation with the probe **3** (nonfluorescent form).

cytometry was 11.7 for L1210FR/L1210 and 13.2 for L1210FR/WI38, which is more modest as compared to that based on cytotoxicity. It is most likely that this difference is attributed to the substantially shorter exposure time for the flow cytometry analysis (2 h) than that for the cytotoxicity assay (72 h), i.e., the internalization of the probe **4** has not been completed in 2 h. At any rate, the observation by CFM and flow cytometry corresponds well to the cytotoxicity assay results.

CONCLUSIONS

A highly efficient mechanism-based tumor-targeting DDS, consisting of a tumor-targeting molecule, self-immolative linker, and a cytotoxic agent, was designed and successfully developed. The proof of concept was obtained by using a drug conjugate, bearing biotin as the cell-targeting moiety, a mechanism-based

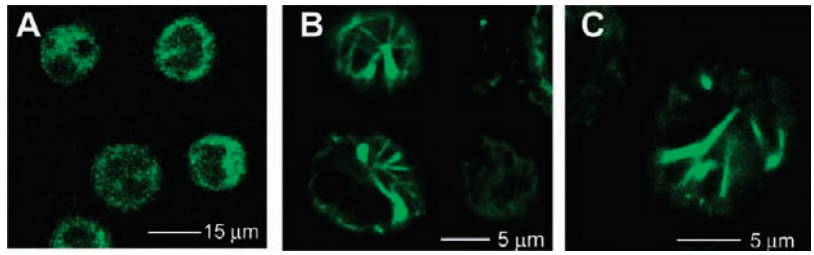


Figure 7. (A) CFM image of L1210FR cells after incubation with the probe **4**. (B) CFM image of L1210FR cells that were initially incubated with the probe **4**, followed by treatment with GSH-OEt to release the fluorescent taxoid **24**. Then, the microtubule network in the cells was fluorescently labeled by **24** and visualized. (C) CFM image of L1210FR cells after incubation with **24** as a control experiment.

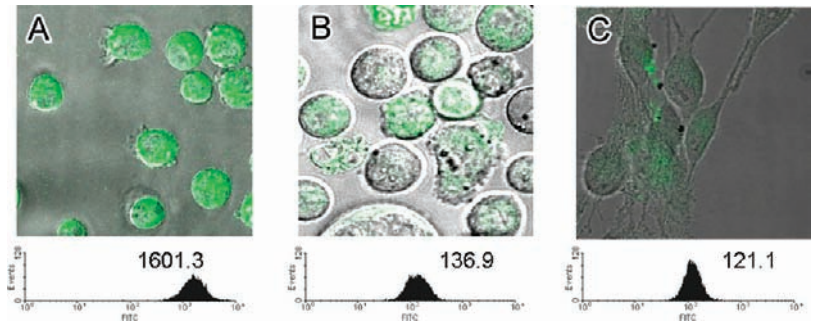


Figure 8. CFM images and flow cytometry analysis of different types of cells after incubation with the probe **4** at the final concentration of 20 μM at 37 °C for 2 h: (A) L1210FR that overexpressed biotin receptors; (B) L1210; and (C) WI38 human lung fibroblast cells.

Table 1. Cytotoxicities (IC_{50}, nM) of Paclitaxel, SB-T-1214, and Its Conjugates

	L1210FR	L1210	WI38
paclitaxel	121	151	157
SB-T-1214	9.50	9.72	10.7
24	87.6	107	127
1	8.80	522	570
4	81.7	>5000	>5000

disulfide linker, and a second-generation taxoid linked to fluorescein by means of CFM and flow cytometry. The result was confirmed by cytotoxicity assay using the drug conjugates with and without a link to fluorescein. Both conjugates exhibited excellent cell-specificity against three cell lines, L1210FR (biotin receptor +++), L1210 (biotin receptor ±), and WI38 (biotin receptor ±) based on the expression of biotin receptors on the cell surfaces. Efficient internalization of the drug conjugate into the targeted cancer cells via RME, smooth drug release via GSH-triggered self-immolation of disulfide linker, and drug binding to the target protein (microtubules) were monitored and validated by means of CFM using three fluorescent/fluorogenic molecular probes. This tumor-targeting DDS is applicable to a variety of drug conjugates consisting of various tumor-targeting molecules, e.g., monoclonal antibodies, aptamers, vitamins, peptides, and proteins, as well as cytotoxic agents. Further studies along this line are actively underway in these laboratories (*18*).

ACKNOWLEDGMENT

This work was supported by grants from the National Institutes of Health (GM427980 and CA 103314 to I.O.) and the National Science Foundation (CAREER DMR-0348239 to S.S.W.). J.C. thanks the Battelle Memorial Institute for support through CRADA #05-25, administered by Brookhaven National Laboratory (BNL). Work at BNL was also supported by the U.S. Department of Energy Office of Basic Energy Sciences under Contract DE-AC-02-98CH10886. The authors thank Dr. Gregory Russell-Jones (Access Pharmaceuticals Australia Pty Ltd.) for providing the L1210FR cell lines, Dr. Rebecca A. Rowehl for cell culture, and Dr. Guo-wei Tian for the assistance with confocal microscopy imaging.

Supporting Information Available: Chemical synthesis of conjugates **1**−**4** and intermediates, including procedures and characterization data. This material is available free of charge via the Internet at http://pubs.acs.org.

LITERATURE CITED

(1) Chari, R. V. J. (1998) Targeted delivery of chemotherapeutics: tumor-activated prodrug therapy. *Adv. Drug Delivery Rev. 31*, 89–104.

(2) Ojima, I., Geng, X., Wu, X., Qu, C., Borella, C. P., Xie, H., Wilhelm, S. D., Leece, B. A., Bartle, L. M., Goldmacher, V. S., and Chari, R. V. J. (2002) Tumor-specific novel taxoid-monoclonal antibody conjugates. *J. Med. Chem. 45*, 5620–5623.

(3) Jaracz, S., Chen, J., Kuznetsova, L. V., and Ojima, I. (2005) Recent advances in tumor-targeting anticancer drug conjugates. *Bioorg. Med. Chem. 13*, 5043–5054.

(4) Ojima, I. (2008) Guided molecular missiles for tumor-targeting chemotherapy-case studies using the second-generation taxoids as warheads. *Acc. Chem. Res. 41*, 108–119.

(5) Chen, J., Jaracz, S., Zhao, X., S., C., and Ojima, I. (2005) Antibody-based toxin conjugates for cancer therapy. *Exp. Opin. Drug Delivery 2*, 873–890.

(6) Wu, X., and Ojima, I. (2004) Tumor specific novel taxoid-monoclonal antibody conjugates. *Curr. Med. Chem. 11*, 429–438.

(7) Hamaan, P. R., Hinman, L. M., Hollander, I., Beyer, C. F., Lindh, D., Holcomb, R., Hallett, W., Tsou, H.-H., Upeslacis, J., Shochat, D., Mountain, A., Flowers, D. A., and Bernstein, I. (2002) Gemtuzumab Ozogamicin, a potent and selective anti-CD33 antibody-calicheamicin conjugate for treatment of acute myeloid leukemia. *Bioconjugate Chem. 13*, 47–58.

(8) Bradley, M. O., Webb, N. L., Anthony, F. H., Devanesan, P., Witman, P. A., Hemamalini, S., Chander, M. C., Baker, S. D., He, L., Horowitz, S. B., and Swindell, C. S. (2001) Tumor targeting by covalent conjugation of a natural fatty acid to taxol. *Clin. Cancer Res. 7*, 3229–3238.

(9) Kuznetsova, L., Chen, J., Sun, L., Wu, X., Pepe, A., Veith, J. M., Pera, P., Bernacki, R. J., and Ojima, I. (2006) Syntheses and evaluation of novel fatty acid-second-generation taxoid conjugates as promising anticancer agents. *Bioorg. Med. Chem. Lett. 16*, 974–977.

(10) Leamon, C. P., and Reddy, J. A. (2004) Folate-targeted chemotherapy. *Adv. Drug Delivery Rev. 56*, 1127–1141.
(11) Lu, Y., and Low, P. S. (2002) Folate-mediated delivery of macromolecular anticancer therapeutic agents. *Adv. Drug Delivery Rev. 54*, 675–693.
(12) Lee, J. W., Lu, J. Y., Low, P. S., and Fuchs, P. L. (2002) Synthesis and evaluation of taxol-folic acid conjugates as targeted antineoplastics. *Bioorg. Med. Chem. 10*, 2397–2414.
(13) Chu, T. C., Marks, J. W., III, Lavery, L. A., Faulkner, S., Rosenblum, M. G., Ellington, A. D., and Matthew Levy, M. (2006) Aptamer: toxin conjugates that specifically target prostate tumor cells. *Cancer Res. 66*, 5989–5992.
(14) Farokhzad, O. C., Cheng, J., Teply, B. A., Sherifi, I., Jon, S., Kantoff, P. W., Richie, J. P., and Langer, R. (2006) Targeted nanoparticle-aptamer bioconjugates for cancer chemotherapy in vivo. *Proc. Natl. Acad. Sci. U.S.A. 103*, 6315–6320.
(15) Wagner, E., Curiel, D., and Cotten, M. (1994) Delivery of drugs, proteins and genes into cells using transferrin as a ligand for receptor-mediated endocytosis. *Adv. Drug Delivery Rev. 14*, 113–135.
(16) Nagy, A., Schally, A. V., Halmos, G., Armatis, P., Cai, R.-Z., Csernus, V., Kovacs, M., Koppan, M., Szepeshazi, K., and Kahan, Z. (1998) Synthesis and biological evaluation of cytotoxic analogs of somatostatin containing doxorubicin or its intensely potent derivative, 2-pyrrolinodoxorubicin. *Proc. Natl. Acad. Sci. U.S.A. 95*, 1794–1799.
(17) Luo, Y., Bernshaw, N. J., Lu, Z.-R., Kopecek, J., and Prestwich, G. D. (2002) Targeted delivery of doxorubicin by HPMA copolymer-hyaluronan bioconjugates. *Pharm. Res. 19*, 396–402.
(18) Chen, J., Chen, S., Zhao, X., Kuznetsova, L. V., Wong, S. S., and Ojima, I. (2008) Functionalized single-walled carbon nanotubes as rationally designed vehicles for tumor-targeted drug delivery. *J. Am. Chem. Soc. 130*, 16778–16785.
(19) Russell-Jones, G., McTavish, K., McEwan, J., Rice, J., and Nowotnik, D. (2004) Vitamin-mediated targeting as a potential mechanism to increase drug uptake by tumors. *J. Inorg. Biochem. 98*, 1625–1633.
(20) Russell-Jones, G., and McEwan, J. (Access Pharmaceuticals Australia Pty. Ltd., Australia) (2004) *Amplification of biotin-mediated targeting*, PCT WO2004/045647.
(21) Reddy, J. A., Westrick, E., Vlahov, I., Howard, S. J., Santhapuram, H. K., and Leamon, C. P. (2006) Folate receptor specific anti-tumor activity of folate-mitomycin conjugates. *Cancer Chemother. Pharmacol. 58*, 229–236.
(22) Leamon, C. P., Reddy, J. A., Vlahov, I. R., Vetzel, M., Parker, N., Nicoson, J. S., Xu, L.-C., and Westrick, E. (2005) Synthesis and biological evaluation of EC72: a new folate-targeted chemotherapeutic. *Bioconjugate Chem. 16*, 803–811.
(23) Mosmann, T. (1983) Rapid colorimetric assay for cellular growth and survival: application to proliferation and cytotoxicity assays. *J. Immunol. Methods 65*, 55–63.
(24) Ojima, I. (2004) Use of fluorine in the medicinal chemistry and chemical biology of bioactive compounds—a case study on fluorinated taxane anticancer agents. *ChemBioChem 5*, 628–635.
(25) Zheng, Z.-B., Zhu, G., Tak, H., Joseph, E., Eiseman, J. L., and Creighton, D. J. (2005) N-(2-Hydroxypropyl)methacrylamide copolymers of a glutathione (GSH)-activated glyoxalase I inhibitor and DNA alkylating agent: synthesis, reaction kinetics with GSH, and in vitro antitumor activities. *Bioconjugate Chem. 16*, 598–607.
(26) Kosower, N. S., and Kosower, E. M. (1978) The glutathione status of cells. *Int. Rev. Cytol. 54*, 109–160.
(27) Meister, A. (1983) Metabolism and transport of glutathione and other γ-glutamyl compounds, In *Functions of Glutathione: Biochemical, Physiological, Toxicological, and Clinical Aspects* (Larsson, A., Ed.), pp 1−22, Raven Press, New York.
(28) Britten, R. A., and Green, J. A. (1992) Cellular glutathione and glutathione S-transferase activity in human ovarian tumor biopsies following exposure to alkylating agents. *Int. J. Radiat. Oncol. Biol. Phys. 24*, 527–531.
(29) Anderson, M. E. (1989) Enzymatic and chemical methods for determination of glutathione, In *Glutathione: Chemical, Biochemical, and Medical Aspects* (Dolphin, D., Avramovic, O., and Poulson, R., Eds.) pp 340−365, John Wiley and Sons, Toronto.
(30) Schiff, P. B., Fant, J., and Horwitz, S. B. (1979) Promotion of microtubule assembly *in vitro* by taxol. *Nature 277*, 665–667.
(31) Vredenburg, M. R., Ojima, I., Veith, J., Pera, P., Kee, K., Cabral, F., Sharma, A., Kanter, P., and Bernacki, R. J. (2001) Effects of orally active taxanes on P-glycoprotein modulation and colon and breast carcinoma drug resistance. *J. Natl. Cancer Inst. 93*, 1234–1245.
(32) Ojima, I., Slater, J. C., Michaud, E., Kuduk, S. D., Bounaud, P.-Y., Vrignaud, P., Bissery, M.-C., Veith, J., Pera, P., and Bernacki, R. J. (1996) Syntheses and structure-activity relationships of the second generation antitumor taxoids. exceptional activity against drug-resistant cancer cells. *J. Med. Chem. 39*, 3889–3896.
(33) Ojima, I., Slater, J. S., Kuduk, S. D., Takeuchi, C. S., Gimi, R. H., Sun, C.-M., Park, Y. H., Pera, P., Veith, J. M., and Bernacki, R. J. (1997) Syntheses and structure-activity relationships of taxoids derived from 14β-hydroxy-10-deacetylbaccatin III. *J. Med. Chem. 40*, 267–278.
(34) Ojima, I., Wang, T., Miller, M. L., Lin, S., Borella, C., Geng, X., Pera, P., and Bernacki, R. J. (1999) Syntheses and structure-activity relationships of new second-generation taxoids. *Bioorg. Med. Chem. Lett. 9*, 3423–3428.
(35) Ojima, I., Lin, S., and Wang, T. (1999) The recent advances in the medicinal chemistry of taxoids with novel β-amino acid side chains. in the chemistry and biology of β-amino acids. *Curr. Med. Chem. 6*, 927–954.
(36) Geney, R., Chen, J., and Ojima, I. (2005) Recent advance in the new generation taxane anticancer agents. *Med. Chem. 1*, 125–139.
(37) Ojima, I., Chen, J., Sun, L., Borella, C. P., Wang, W., Miller, M. L., Lin, S., Geng, X., Kuznetsova, L., Qu, C., Gallager, D., Zhao, X., Zanardi, I., Xia, S., Horwitz, S. B., Mallen-St, J., Guerriero, J. L., Bar-Sagi, D., Veith, J. M., Pera, P., and Bernacki, R. J. (2008) Design, synthesis, and biological evaluation of new-generation taxoids. *J. Med. Chem. 51*, 3203–3221.
(38) Pires, M. M., and Chmielewski, J. (2008) Fluorescence imaging of cellular glutathione using a latent rhodamine. *Org. Lett. 10*, 837–840.
(39) Adamczyk, M., Grote, J., and Moore, J. A. (1999) Chemoenzymic synthesis of 3′-O-(carboxyalkyl)fluorescein labels. *Bioconjugate Chem. 10*, 544–547.
(40) Liu, F., Zha, H.-Y., and Yao, Z.-J. (2003) Synthesis of a new conformation-constrained L-Tyrosine analogue as a potential scaffold for SH2 domain ligands. *J. Org. Chem. 68*, 6679–6684.
(41) Mukherjee, S., Ghosh, R. N., and Masfield, F. R. (1997) Endocytosis. *Physiol. Rev. 77*, 759–803.
(42) Silverstein, S. C., Steinman, R. M., and Cohn, Z. A. (1977) *Annu. Rev. Biochem. 46*, 669–722.
(43) Schmid, S. L., and Carter, L. L. (1990) ATP is required for receptor-mediated endocytosis in intact cells. *J. Cell Biol. 111*, 2307–2318.
(44) Hong, R., Han, G., Fernandez, J. M., Kim, B., Forbes, N. S., and Rotello, V. M. (2006) Glutathione-mediated delivery and release using monolayer protected nanoparticle carriers. *J. Am. Chem. Soc. 128*, 1078–1079.

BC9005656

The Effect of Charge-Reversal Amphiphile Spacer Composition on DNA and siRNA Delivery

Xiao-Xiang Zhang,[†] Carla A. H. Prata,[†] Thomas J. McIntosh,[‡] Philippe Barthélémy,[§] and Mark W. Grinstaff*,[†]

Departments of Biomedical Engineering and Chemistry, Boston University, Boston, Massachusetts 02215, Department of Cell Biology, Duke University Medical Center, Durham, North Carolina 27710, and Inserm, U-869, Université de Bordeaux, Bordeaux, F-33076, France. Received December 9, 2009; Revised Manuscript Received April 7, 2010

A series of charge-reversal amphiphiles with different spacers separating the headgroup from the hydrophobic chains are described for delivery of DNA and siRNA. Among them, the amphiphiles possessing a glycine spacer (e.g., **B-GlyGly**) showed effective DNA transfection in CHO and NIH 3T3 cells, as well as siRNA gene knockdown in HepG2 and UASMC cells. Ethidium bromide quenching assays revealed that DNA was released the fastest from the lipoplex of **B-GlyGly** in the presence of esterase. Also, X-ray diffraction results indicated that the DNA was located between the adjacent lipid bilayers in the lipoplex of **B-GlyGly**. These distinct features appear to be required for high transfection activity.

INTRODUCTION

Gene therapy has received significant attention in the past decade due to its advantages over traditional therapies. The two most common methods for gene delivery use either synthetic (*1*−*5*) or viral (*6*−*10*) vectors. Compared to viral vectors, nonviral vectors have lower toxicity and high load capacity and are easy to synthesize. Consequently, there has been a significant effort to develop and evaluate nonviral vectors, which include cationic amphiphiles and polymers (*11*−*15*) and, more recently, anionic amphiphiles (*16*). Yet, synthetic vectors also have a number of limitations including low transfection efficiencies both in vitro and in vivo, significant cytotoxicity, and inactivation in the presence of serum. To overcome these limitations, investigators are modifying the amphiphile structure, and for small cationic amphiphiles, this entails alternative cationic head groups, linkers, and hydrophobic moieties. Examples of different cationic head groups explored include choline (*17, 18*), spermine (*19*), di- and tripeptides (*20, 21*), carbohydrates (*22, 23*), and nucleosides (*24*−*32*). With regard to the hydrophobic moiety, long chain ester and ether linked hydrocarbons have been extensively studied. The fluorinated analogues of cationic lipids, like DOTMA, have also been explored, and these amphiphiles exhibited higher transfection activities in vitro (*33*) and in vivo compared to their hydrocarbon analogues (*34*). In addition, researchers have used combinatorial approaches to screen large libraries of amphiphiles in order to identify key structural components of the amphiphile responsible for high transfection activity (*35, 36*).

Although significant research has been conducted regarding the structure−property relationships of a wide range of cationic lipids, only a few studies can be found that systematically investigate the effect of spacers within the headgroup, and include cationic lipids derived from betaine glycine (*37*), cationic glycolipids (*38*), and cholesterol-based cationic lipids (*39*). These studies, along with others, have begun to provide design parameters for optimizing the chemical structure for efficient nucleic acid delivery with minimal cytotoxicity.

* Correspondence should be addressed to M.W.G. E-mail: mgrin@bu.edu.
[†] Boston University.
[‡] Duke University Medical Center.
[§] Inserm, U-869.

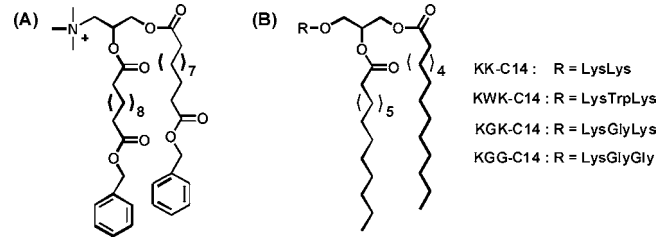


Figure 1. Amphiphiles previously studied.

In previous research in our lab, we found that a charge-reversal amphiphile (Figure 1A) which possesses benzyl esters at the end of alkyl chains showed high transfection activity (*40*). The total charge of this amphiphile was capable of switching from +1 to −1 when the benzyl esters are hydrolyzed. This charge-reversal effect was implemented to facilitate the release of DNA from the amphiphiles. In a separate study, we also found that spacing of the cationic charges within the headgroup in a series of peptide-based amphiphiles can afford improved transfection performance with amphiphiles **KWK-C14**, **KGK-C14**, and **KGG-C14** showing higher transfection compared to **KK-C14** (Figure 1B) (*21*). To take advantage of the charge-reversal effect, as well as to further understand how spacer length and composition affect transfection efficacy, here we present a study on a series of charge-reversal amphiphiles with different spacers separating the headgroup from the hydrophobic chains.

All the amphiphiles studied (Figure 2) possess a quaternary ammonium as a cationic headgroup (**B**) and the same alkyl chains ending with benzyl esters, but have spacers of different lengths: two, five, or seven atoms. The nature of the spacers is also varied: (1) the glycine and alanine spacers are relatively rigid, hydrophilic, and capable of hydrogen bonding (**B-Gly**, **B-GlyGly, B-AlaAla**; (2) the ethylene oxide spacers are flexible and hydrophilic (**B-EO**, **B-(EO)$_2$**); and (3) the alkyl chain spacers are flexible and hydrophobic (**B-(CH$_2$)$_4$**, **B-(CH$_2$)$_7$**).

RESULTS AND DISCUSSION

The synthetic routes to the different amphiphiles can be found in Scheme 1, and a detailed procedure can be found in the Supporting Information. In general, the different spacers

10.1021/bc9005464 © 2010 American Chemical Society
Published on Web 04/30/2010

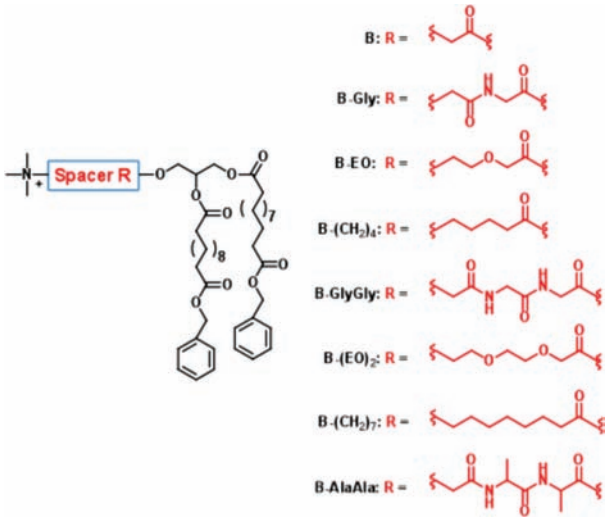
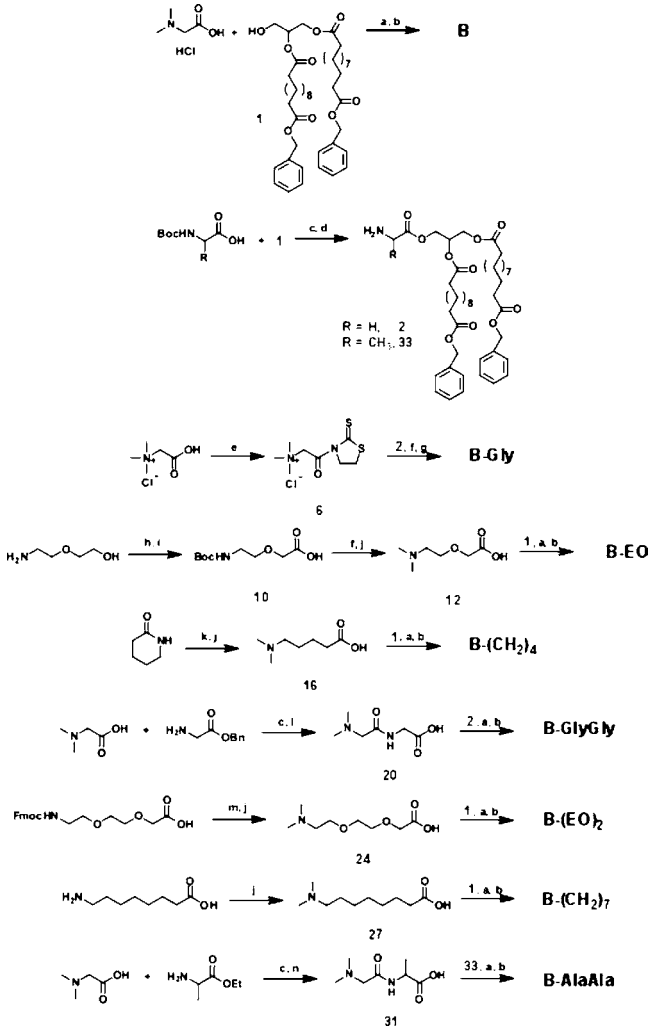


Figure 2. Amphiphiles with different spacers.

Scheme 1. Synthesis of the Cationic Amphiphiles



containing the headgroup were first synthesized and then coupled to **1** or **2** to afford the desired products. As a representative example, the synthesis of the **B-GlyGly** amphiphile is described next. *N*,*N*-Dimethylglycine hydrochloride and glycine benzyl ester hydrochloride were reacted in the presence of DCC and DMAP at RT for 16 h. Benzyl 2-(2-(dimethylamino)acetamido)acetate was purified as yellow oil (76%). The benzyl group

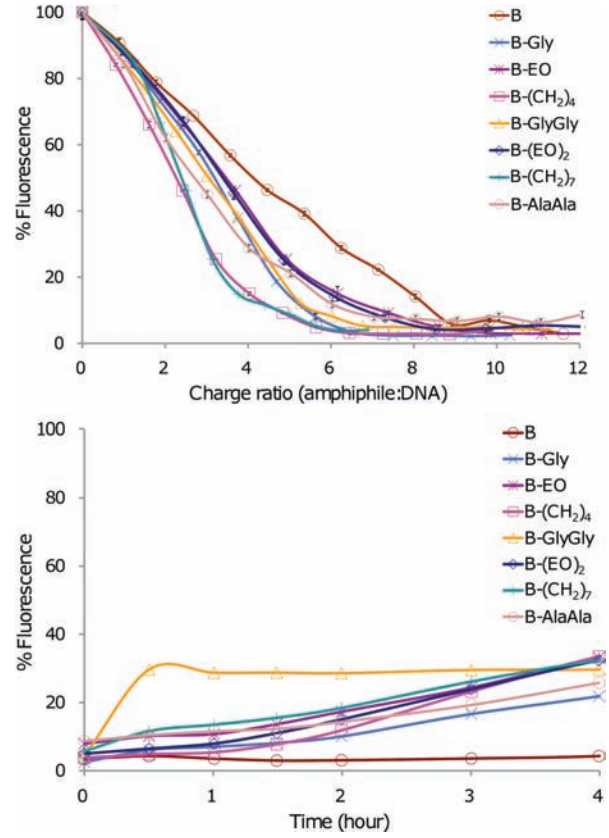


Figure 3. EtBr displacement assay showing the fluorescence intensity. Top: as a function of amphiphile/DNA charge ratio. Bottom: as a function of time in presence of porcine liver esterase (300 units/mL).

was removed in the presence of a catalytic amount of Pd(II) on carbon at RT under 50 psi H_2 for 16 h to afford the intermediate, in 84% yield. The deprotected 2-(2-(dimethylamino)acetamido)acetic acid was then coupled with **2** followed by reaction with CH_3I to afford the **B-GlyGly** amphiphile as a viscous oil in 80% yield. The characterization data for **B-GlyGly**, as well as all of the amphiphiles, can be found in the Supporting Information.

To determine whether the amphiphiles would bind DNA, a standard ethidium bromide (EtBr)-DNA fluorescence quenching assay was performed, as shown in Figure 3 (top). DNA binding was observed for all the amphiphiles with similar affinity. Among the amphiphiles, **B-$(CH_2)_4$** and **B-$(CH_2)_7$** showed the strongest binding affinity with a ± charge ratio of 6:1, and **B** bound the weakest with a charge ratio of 9:1. Next, the above DNA/EtBr/amphiphile solution was incubated with esterase at pH 7.4 (100 mM Tris, 100 mM NaCl buffer, 300 units/mL). The intensity of fluorescence, which reflects the dissociation of the amphiphile from the DNA as a consequence of the hydrolysis of the terminal benzyl esters, increased at slightly different rates for the amphiphiles, as shown in Figure 3 (bottom). DNA was released the fastest from the **B-GlyGly** complex with around 30% fluorescence recovered in the first 30 min, while less than 10% fluorescence recovery was observed for all the other complexes. During the 4 h period, fluorescence intensity increased slowly and reached ∼20−35% for all other complexes, except for **B** where the fluorescence did not change significantly.

Given their polar headgroup and long hydrophobic alkyl chains, these amphiphiles are likely to form bilayer vesicles in aqueous solution. Differential scanning calorimetry (DSC) traces of hydrated amphiphiles showed phase-transition temperatures between ∼−22 and −15 °C, except for **B**, which was 60.6 °C

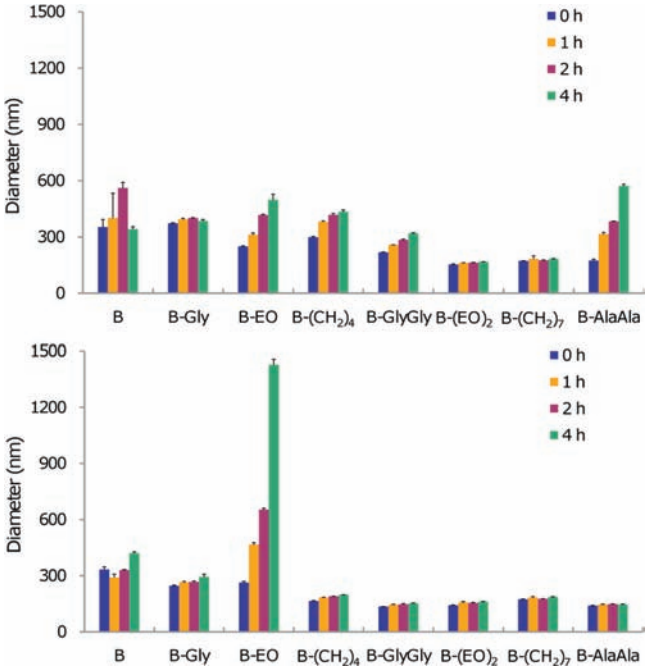


Figure 4. Sizes of lipoplexes (nm) at pH 7.4 (top) and pH 5 (bottom). $N = 3$, mean ± SD.

Table 1. Phase Transition Temperatures of the Amphiphiles and Repeat Periods without and with DNA

		repeating period (nm)	
amphiphiles	T_m (°C)	without DNA	with DNA
B	60.6	5.9	6.2
B-Gly	−15.4	5.4	5.6
B-EO	−22.2	5.7	6.7
B-$(CH_2)_4$	−17.3	7.6	7.8
B-GlyGly	−16.8	6.1	7.9
B-$(EO)_2$	−19.6	6.4	6.5
B-$(CH_2)_7$	−14.8	1.4	5.8
B-AlaAla	−19.3	6.4	7.0

(Table 1). We subsequently prepared liposome solutions of all the amphiphiles by sonicating a hydrated film of the amphiphile in an aqueous solution (see Supporting Information for details). Dynamic light scattering measurements revealed that the sizes of liposomes in the presence of DNA varied from 154 to 353 nm in pH 7.4 solution (100 mM NaCl, 100 mM Tris buffer). The stability of the liposomes over time was examined by measuring their sizes at 0, 1, 2, and 4 h (Figure 4 top). The size of liposomes formed from **B-Gly**, **B-$(EO)_2$**, and **B-$(CH_2)_7$** remained almost constant during the 4 h period, while those of other amphiphiles increased moderately. Given that these increasing rates are very small, all the liposomes appeared to be stable.

Since endocytosis is one of the major cell uptake pathways for internalization of nonviral vectors (*41*−*44*), liposomes were incubated in a solution (100 mM NaCl, 100 mM phosphate buffer) of pH 5, which resembles the pH of the endosome, and analyzed at 0, 1, 2, 4 h (Figure 4 bottom). Generally, the size of liposomes at pH 5 is slightly smaller than those at pH 7.4. During the 4 h period, all the liposomes were stable except for the liposome formed with **B-EO**, which quickly increased in size. The size increased from 264 to 468 nm in 1 h, and further to 655 and 1428 nm in 2 and 4 h. These findings demonstrated that the liposomes formed from the amphiphiles were stable under pH 7.4 and mildly acidic conditions, except those formed from **B-EO**.

Next, to characterize the supramolecular structures, X-ray diffraction experiments were performed at 22 °C on all of the

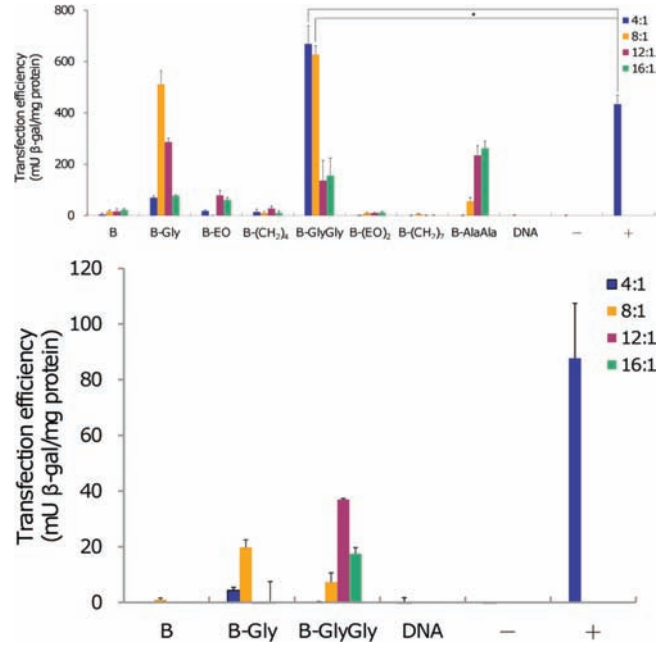


Figure 5. DNA transfection after 48 h in CHO (top) and NIH3T3 (bottom) cells as a function of amphiphiles and DNA molar ratio. Lipofectamine 2000 was used as positive control. $N = 3$, mean ± SD, * $p < 0.05$.

samples in the absence and presence of DNA. A hydrated vesicle pellet was obtained for all samples, and oriented multilayers were prepared for X-ray analysis by placing the pellets on a curved glass substrate and incubating at 66% relative humidity. All of the samples showed multiple reflection indexing as orders of lamellar repeat periods, characteristic of lipid bilayers (Table 1).

The repeat periods of all samples in the absence of DNA were between 5.4 and 7.6 nm, except for **B-$(CH_2)_7$**, which had a period of 1.4 nm. This period was abnormally small and could be a higher-order reflection from a larger repeat period. The addition of DNA increased the repeat period for all of the assemblies. A smaller increase between 0.1 and 0.6 nm was observed for **B**, **B-Gly**, **B-$(CH_2)_4$**, **B-$(EO)_2$**, and **B-AlaAla**, while for **B-GlyGly**, we observed an increase in the period of 1.8 nm. This larger change would be consistent with a structural model where a smectic phase was formed with the DNA chains located between the adjacent lipid bilayers within the multilamellar liposome. This structural model has been reported for complexes of DNA with DOTAP (*45*) and cationic triesters of phosphatidylcholine (*46*). For the other samples, the repeat periods did not change significantly, indicating that DNA was not located within the lipid multilayers.

Transfection experiments using reporter gene, β-galactosidase (β-gal, pVax-LacZ1, Invitrogen) were performed with CHO and NIH 3T3 cells (Figure 5). Gene transfection results were determined after 48 h as a function of cation/anion ratios (4:1, 8:1, 12:1, 16:1).

In CHO cells, amphiphiles **B-Gly** and **B-GlyGly** showed the highest transfection activity, amphiphile B-AlaAla exhibited moderate activity, and the other amphiphiles showed minimal transfection efficiency. **B-GlyGly** was significantly more active than the positive control, Lipofectamine 2000. However, both amphiphiles **B-Gly** and **B-GlyGly** were less active than Lipofectamine 2000 in NIH 3T3 cells, but still had higher transfection efficiency compared to the other amphiphiles we tested. These results showed that those amphiphiles containing spacers that are hydrophilic, relatively rigid, and capable of hydrogen bonding possessed the highest transfection activity. We also

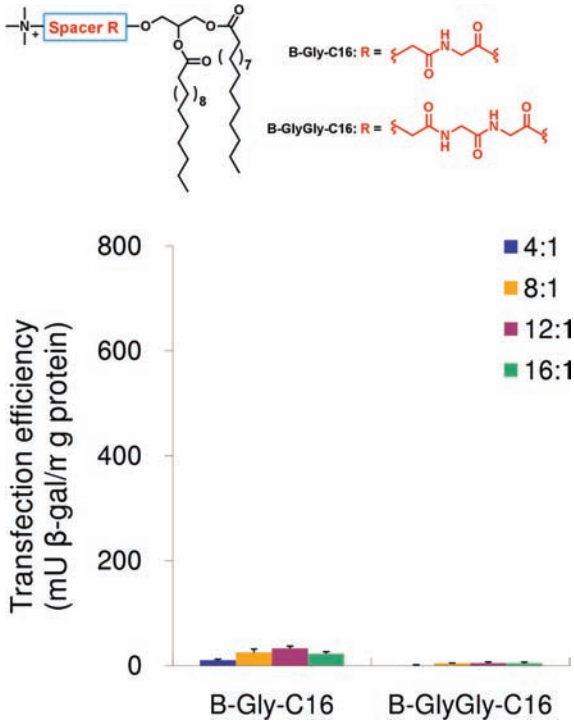


Figure 6. Structures of **B-Gly**-C16 and **B-GlyGly**-C16 and DNA transfection after 48 h in CHO cells as a function of amphiphiles and DNA molar ratio. Lipofectamine 2000 was used as positive control. $N = 3$, mean ± SD.

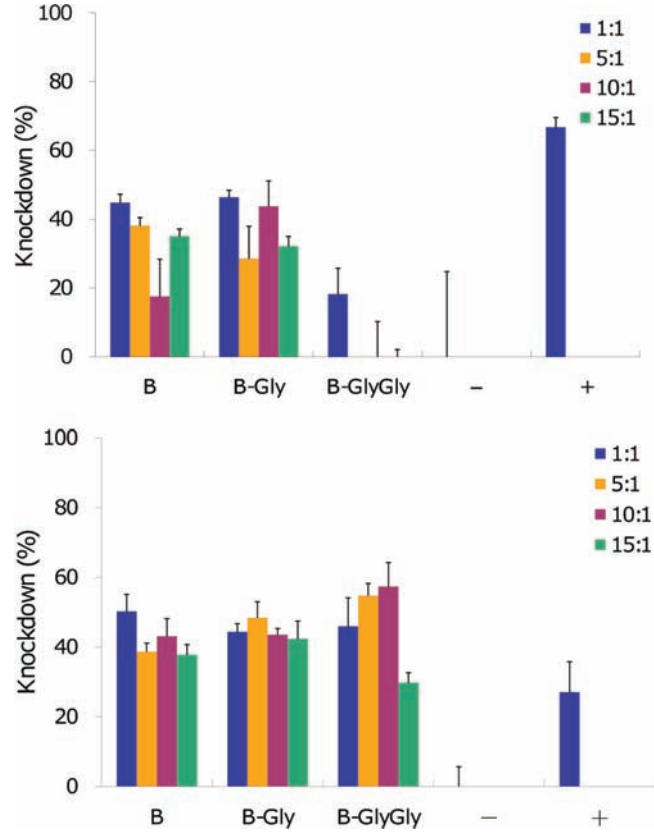


Figure 7. siRNA transfection after 48 h in HepG2 cells (top) and UASMC cells (bottom) as a function of amphiphiles and siRNA molar ratio, NeoFX was used as positive control. $N = 3$, mean ± SD.

prepared the **B-AlaAla** amphiphile, since this amphiphile is similar to the **B-GlyGly** amphiphile but the spacer is slightly more hydrophobic and rigid. The **B-AlaAla** amphiphile showed moderate transfection activity but less than that observed with the **B-GlyGly** amphiphile. To confirm that the benzyl ester linkages on the hydrophobic chains (and the resulting charge-reversal effect) were a contributing factor to the gene delivery efficiency of these amphiphiles, we synthesized two additional control amphiphiles with the Gly or GlyGly spacers, possessing saturated C16 chains instead of the benzyl ester terminated hydrophobic chains. As shown in Figure 6, both amphiphiles displayed minimum transfection activity in CHO cells. This result demonstrated the importance of the charge-reversal effect on the transfection. MTS assays performed with all the amphiphiles showed no significant cytotoxicity in the two cell lines (see Supporting Information).

Next, siRNA transfections were performed with the base amphiphiles **B** and the two best performing amphiphiles, **B-Gly** and **B-GlyGly**, using the KDalert GAPDH assay (Ambion) with HepG2 and UASMC cells (Figure 7) at four different cation/anion ratios (1:1, 5:1, 10:1, 15:1). NeoFX was used as the positive control. After 48 hrs of transfection, in HepG2 cells, **B** and **B-Gly** achieved 50% gene knockdown, while **B-GlyGly** only achieved 20% knockdown. In UASMC cells, **B** and **B-Gly** achieved 50% gene knockdown, while **B-GlyGly** reached 60% knockdown. These results were comparable to those obtained with NeoFX.

CONCLUSION

In summary, a series of amphiphiles with different spacers within the headgroup were evaluated for DNA and siRNA delivery. Among them, the amphiphiles possessing the relatively rigid and hydrophilic glycine or alaine spacers, capable of hydrogen bonding, showed effective DNA transfection in vitro. As for siRNA transfection, **B**, **B-Gly** and **B-GlyGly** showed gene knockdown. The binding affinity for the amphiphiles with the peptide spacers was similar to all the other amphiphiles, but DNA was released the fastest from **B-GlyGly** in the presence of esterase. Also, X-ray diffraction results indicate that DNA is located between the adjacent lipid bilayers in the complex formed with **B-GlyGly**. It is clear that many factors can influence transfection efficiency and that small perturbations in structure can have a significant effect. In this study, we found that the best performing amphiphile has a peptide linker separating the headgroup from the chains, complexes with DNA to afford a bilayer structure, and forms lipoplexes of 200 nm in diameter. This study highlights the importance and sensitivity of the spacer group in DNA/amphiphile assembly, liposome stability, and gene transfection activity. Continued studies with different amphiphile compositions will facilitate the development of a set of design requirements for efficient DNA and RNA delivery.

ACKNOWLEDGMENT

This work was supported by the National Institutes of Health (EB005658 to M.W.G. and GM27278 to T.J.M.).

Supporting Information Available: Detailed synthetic procedures, preparation of liposomes, lipoplexes, and DNA and siRNA transfection protocols, and statistical analysis. This material is available free of charge via the Internet at http://pubs.acs.org.

LITERATURE CITED

(1) Mintzer, M. A., and Simanek, E. E. (2009) Nonviral vectors for gene delivery. *Chem. Rev. 109*, 259–302.
(2) Ewert, K. K., Ahmad, A., Bouxsein, N. F., Evans, H. M., and Safinya, C. R. (2008) Non-viral gene delivery with cationic liposome-DNA complexes. *Methods Mol. Biol. 433*, 159–175.

(3) Christine, C. C., and Huang, L. (2005) Recent advances in non-viral gene delivery. *Adv. Genet. 53*, 3–18.
(4) Wolff, J. A., and Rozema, D. B. (2008) Breaking the bonds: Non-viral vectors become chemically dynamic. *Mol. Ther. 16*, 8–15.
(5) Reineke, T. M., and Grinstaff, M. W. (2005) Designer materials for nucleic acid delivery. *Mater. Res. Soc. Bull. 30*, 635–639.
(6) Deregowski, P., and Canalis, E. (2008) Gene delivery by retroviruses. *Methods Mol. Biol. 455*, 157–162.
(7) Ozawa, K. (2007) Gene therapy using aav vectors. *Drug Delivery System 22* (6), 643–650.
(8) Moroziewicz, D., and Kaufman, H. L. (2005) Gene therapy with poxvirus vectors. *Curr. Opin. Mol. Ther. 7* (4), 317–325.
(9) Lundstrom, K. (2004) Gene therapy applications of viral vectors. *Technol. Cancer Res. Treat. 3* (5), 467–477.
(10) Flotte, T. R. (2004) Gene therapy progress and prospects: Recombinant adeno-associated virus (raav) vectors. *Gene Ther. 11* (10), 805–810.
(11) Putnam, D. (2006) Polymers for gene delivery across length scales. *Nat. Mater. 5*, 439–451.
(12) Yan, W., and Huang, L. (2007) Recent advances in liposome-based nanoparticles for antigen delivery. *Polym. Rev. 47*, 329–344.
(13) Nicolazzi, C. l., Garinot, M., Mignet, N., Scherman, D., and Bessodes, M. (2003) Cationic lipids for transfection. *Curr. Med. Chem. 10*, 1263–1277.
(14) Luten, J., van Nostrum, C. F., De Smedt, S. C., and Hennink, W. E. (2008) Biodegradable polymers as non- viral carriers for plasmid DNA delivery. *J. Controlled Release 126* (2), 97–110.
(15) Green, J. J., Langer, R., and Anderson, D. G. (2008) A combinatorial polymer library approach yields insight into nonviral gene delivery. *Acc. Chem. Res. 41*, 749–759.
(16) Khiati, S., Pierre, N., Soahary, S., Grinstaff, M. W., Arazam, N., Nallet, F., Navailles, L., and Barthélémy, P. (2009) Anionic nucleotide-lipids for in vitro DNA transfection. *Bioconjugate Chem. 20*, 1765–1772.
(17) Miller, A. D. (1998) Cationic liposomes for gene therapy. *Angew. Chem., Int. Ed. 37*, 1768–1785.
(18) Felgner, P. L., Gadek, T. R., Holm, M., Roman, R., Chan, H. W., Wenz, M., Northrop, J. P., Ringgold, G. M., and Danielsen, M. (1987) Lipofectin: A highly efficient, lipid mediated DNA-transfection procedure. *Proc. Natl. Acad. Sci. U.S.A. 84*, 7413–7417.
(19) Behr, J. P., Demeneix, B., Loeffler, J. P., and Perez-Mutul, J. (1989) Efficient gene transfer into mammalian primary endocrine cells with lipopolyamine coated DNA. *Proc. Natl. Acad. Sci. U.S.A. 86*, 6982–6986.
(20) Chan, E., Amon, M., Marano, R. J., Wimmer, N., Kearns, P. S., Manolios, N., Rakoczy, P. E., and Toth, I. (2007) Novel cationic lipophilic peptides for oligodeoxynucleotide delivery. *Bioorg. Med. Chem. 15*, 4091–4097.
(21) Prata, C. A. H., Zhang, X., Luo, D., McIntosh, T. J., Barthélémy, P., and Grinstaff, M. W. (2008) Lipophilic peptides for gene delivery. *Bioconjugate Chem. 19*, 418–420.
(22) Bessodes, M., Dubertret, C., Jaslin, G., and Scherman, D. (2000) Synthesis and biological properties of new glycosidic cationic lipids for DNA delivery. *Bioorg. Med. Chem. Lett. 10*, 1393–1395.
(23) Herscovici, J., Egron, M. J., Quenot, A., Leclercq, F., Leforestier, N., Mignet, N., Wetzer, B., and Scherman, D. (2001) Synthesis of new cationic lipids from unsaturated glycoside scaffold. *Org. Lett. 3* (12), 1893–1896.
(24) Gissot, A., Camplo, M., Grinstaff, M. W., and Barthélémy, P. (2008) Nucleoside, nucleotide and oligonucleotide based amphiphiles: A successful marriage of nucleic acids with lipids. *Org. Biomol. Chem. 6*, 1324–1333.
(25) Moreau, L., Barthélémy, P., Maataoui, M. E., and Grinstaff, M. W. (2004) Supramolecular assemblies of nucleoside-based amphiphiles. *J. Am. Chem. Soc. 126*, 7533–7539.
(26) Moreau, L., Ziarelli, F., Grinstaff, M. W., and Barthélémy, P. (2006) Self-assembled microspheres from f-block elements and nucleoamphiphiles. *Chem. Commun. 15*, 1661–1663.
(27) Moreau, l., Campins, N., Grinstaff, M. W., and, Barth, 940 > eĺ, and emy, P. (2006) A fluorocarbon nucleoamphiphile for the construction of actinide loaded microspheres. *Tet. Lett. 47*, 7117–7120.
(28) Barthélémy, P., Prata, C. A. H., Filocamo, S. F., Immoos, C. E., Maynor, B. W., Hashmi, S. A. N., Lee, S. J., and Grinstaff, M. W. (2005) Supramolecular assemblies of DNA with neutral nucleoside amphiphiles. *Chem. Commun.* 1261–1263.
(29) Campins, N., Dieudonné, P., Grinstaff, M. W., and Barthélémy, P. (2007) Nanostructured assemblies from nucleotide based amphiphiles. *New. J. Chem. 31*, 1928–1934.
(30) Chabaud, P., Camplo, M., Payet, D., Serin, G., Moreau, L., Barthélémy, P., and Grinstaff, M. W. (2006) Cationic nucleoside lipids for gene delivery. *Bioconjugate Chem. 17*, 466–472.
(31) Moreau, L., Barthélémy, P., Li, Y., Luo, D., Prata, C. A. H., and Grinstaff, M. W. (2005) Nucleoside phosphocholine amphiphile for in vitro DNA transfection. *Mol. Biosyst. 1*, 260–264.
(32) Arigon, J., Prata, C. A. H., Grinstaff, M. W., and Barthélémy, P. (2005) Nucleic acid complexing glycosyl nucleoside-based amphiphile. *Bioconjugate Chem. 16*, 864–872.
(33) Gaucheron, J., Santaella, C., and Vierling, P. (2002) Transfection with fluorinated lipoplexes based on fluorinated analogues of dotma, dmrie and dppes. *Biochim. Biophys. Acta 1564*, 349–358.
(34) Boussif, O., Gaucheron, J., Boulanger, C., Santaella, C., Kolbe, H. V. J., and Vierling, P. (2001) Enhanced in vitro and in vivo cationic lipid-mediated gene delivery with a fluorinated glycerophosphoethanolamine helper lipid. *J. Gene Med. 3*, 109–114.
(35) Akinc, A., Zumbuehl, A., Goldberg, M., Leshchiner, E. S., Busini, V., Hossain, N., Bacallado, S. A., Nguyen, D. N., Fuller, J., Alvarez, R., Borodovsky, A., Borland, T., Constien, R., de Fougerolles, A., Dorkin, J. R., Jayaprakash, K. N., Jayaraman, M., John, M., Koteliansky, V., Manoharan, M., Nechev, L., Qin, J., Racie, T., Raitcheva, D., Rajeev, K. G., Sah, D. W. Y., Soutschek, J., Toudjarska, I., Vornlocher, H. P., Zimmermann, T. S., Langer, R., and Anderson, D. G. (2008) A combinatorial library of lipid-like materials for delivery of rnai therapeutics. *Nat. Biotechnol. 26*, 561–569.
(36) Akinc, A., Lynn, D. M., Anderson, D. G., and Langer, R. (2003) Parallel synthesis and biophysical characterization of a degradable polymer library for gene delivery. *J. Am. Chem. Soc. 125*, 5316–5323.
(37) Gilot, D., and Miramon, M.-L. (2002) Cationic lipids derived from glycine betaine promote efficient and non-toxic gene transfection in cultured hepatocytes. *J. Gene Med. 4*, 415–427.
(38) Mahidhar, Y. V., Rajesh, M., and Chaudhuri, A. (2004) Spacer-arm modulated gene delivery efficacy of novel cationic glycolipids: Design, synthesis, and in vitro transfection biology. *J. Med. Chem. 47*, 3938–3948.
(39) Reynier, P., Briane, D., Coudert, R., Fadda, G., Bouchemal, N., Bissieres, P., Taillandier, E., and Cao, A. (2004) Modifications in the head group and in the spacer of cholesterol-based cationic lipids promote transfection in melanoma b16-f10 cells and tumours. *J. Drug Targeting 12* (1), 25–38.
(40) Prata, C. A. H., Zhao, Y., Barthelemy, P., Li, Y., Luo, D., McIntosh, T. J., Lee, S. J., and Grinstaff, M. W. (2004) Charge-reversal amphiphiles for gene delivery. *J. Am. Chem. Soc. 126*, 12196–12197.
(41) Friend, D. S., Papahadjopoulos, D., and Debs, R. J. (1996) Endocytosis and intracellular processing accompanying transfection mediated by cationic liposomes. *Biochim. Biophys. Acta 1278*, 41–50.
(42) Labat-Moleur, F., Steffan, A. M., Brisson, C., Perron, H., Feugeas, O., Furstenberger, P., Oberling, F., Brambilla, E., and Behr, J. P. (1996) An electron microscopy study into the mechanism of gene transfer with lipopolyamines. *Gene Ther. 3*, 1010–1017.
(43) Zuhorn, I. S., Kalicharan, R., and Hoekstra, D. (2002) Lipoplex-mediated transfection of mammalian cells occurs through the cholesterol-dependent clathrin-mediated pathway of endocytosis. *J. Biol. Chem. 277*, 18021–18028.

(44) Wrobela, I., and Collins, D. (1995) Fusion of cationic liposomes with mammalian cells occurs after endocytosis. *Biochim. Biophys. Acta 1235* (2), 296–304.

(45) Rädler, J. O., Koltover, I., Salditt, T., and Safinya, C. R. (1997) Structure of DNA-cationic liposome complexes: DNA intercalation in multilamellar membranes in distinct interhelical packing regimes. *Science* 810–814.

(46) MacDonald, R. C., Ashley, G. W., Shida, M. M., Rakhmanova, V. A., Tarahovsky, Y. S., Kennedy, M. T., Pozharski, E. V., Baker, K. A., Jones, R. D., Rosenzweig, H. S., Choi, K. L., Qiu, R., and McIntosh, T. J. (1999) Physical and biological properties of cationic triesters of phosphatidylcholine. *Biophys. J. 77*, 2612–2629.

BC9005464

Proton Sponge Trick for pH-Sensitive Disassembly of Polyethylenimine-Based siRNA Delivery Systems

Gaelle Creusat,[†] Anne-Sophie Rinaldi,[‡] Etienne Weiss,[‡] Rkia Elbaghdadi,[†] Jean-Serge Remy,[†] Rita Mulherkar,[§] and Guy Zuber*[,†]

Laboratoire de Conception et Application de Molécules Bioactives, CNRS-Université de Strasbourg UMR 7199, Faculté de Pharmacie, 74, route du Rhin, 67400 Illkirch, France, ESBS - FRE 3211, Immunobiotechnologie Bld., Sébastien Brant BP, 10413 F-67412 Illkirch, France, and ACTREC, Tata Memorial Centre Kharghar, Navi Mumbai 410210, India. Received January 9, 2010; Revised Manuscript Received March 18, 2010

Small interfering RNAs offer novel opportunities to inhibit gene expression in a highly selective and efficient manner but depend on cytosolic translocation with synthetic delivery systems. The polyethylenimine (PEI) is widely used for plasmid DNA transfection. However, the water-soluble PEI does not form siRNA polyplexes stable enough in extracellular media for effective delivery. We previously showed that rendering PEI insoluble in physiological media, without modifying drastically its overall cationic charge density, by simple conjugation with natural hydrophobic α-amino acids, can lead to effective siRNA delivery in mammalian cells. In here, we comprehensively investigated the mechanism behind the excellent efficacy of the leading PEIY vector. Our data revealed that the underlining proton sponge property is key to the effectiveness of the tyrosine−polyethylenimine conjugate as it may allow both endosomal rupture and siRNA liberation via an optimal pH-sensitive dissolution of the PEIY self-aggregates. Altogether, these results should facilitate the development of novel and more sophisticated siRNA delivery systems.

INTRODUCTION

RNA interference (RNAi) is a sequence-specific and post-transcriptional gene silencing process present in animals and in plants and is mediated by 21−22nt long RNA duplexes, called small interfering RNA (siRNA) (*1*). This gene silencing mechanism appears to be particularly effective and holds great potential for decoding gene function and in gene-specific therapeutics (*2*). However, oligonucleotides do not diffuse freely across plasma membrane and imperiously depend on formulation within synthetic delivery systems (*3, 4*).

Nonviral delivery vehicles were initially developed for plasmid delivery (*5, 6*). They are generally cationic lipids or cationic polymers that interact electrostatically with the nucleic acid phosphate backbone to form stable complexes (*7, 8*). These cationic complexes in turn bind to anionic proteoglycans present on cell surfaces, enter cells within membrane-coated vesicles, and experience acidification on their road to degradative compartments. Escape from this pathway is required and relies on the incorporation of fusogenic lipids or endosomolytic functions within the complexes. Among the cationic polymers, PEI[1] is certainly the most used plasmid DNA transfection agent because its high buffering capacity in the pH range between 5.0 and 7.5 facilitates rupture of endosomal membranes via a "proton sponge" mechanism (*9, 10*). However, PEI was shown to be a poor siRNA delivery agent (*11*), especially in comparison to lipids (*12, 13*).

Numerous approaches and hypotheses have been investigated to create efficient polymer-based delivery vehicles dedicated to siRNA (*14*−*21*). While siRNA duplexes and genes share a similar anionic charge density, the reduced number of anionic charges of a siRNA duplex (40) in comparison to a plasmid DNA (average anionic charge of 7000) reduces the electrostatic cohesion of the soluble PEI with siRNA. Polyanionic proteoglycans present outside the cells and on the cell surfaces may then effectively displace PEI from the complexes, resulting in release of siRNA in the extracellular medium (*22*). No delivery and siRNA-mediated gene silencing can consequently occur.

Increased stability of oligonucleotide polyplexes may be performed by three means. siRNA duplexes could be artificially transformed into long structures, like plasmid DNA, by equipment with self-complementary and overhanging nucleotides (*22*). Oligonucleotides could be conjugated with cholesterol for enhanced anchorage to cationic micelles (*23*) or to cationic peptide so as to obtain an overall self-aggregating and cationic species (*24*). Finally, transformation of the water-soluble PEI into an insoluble molecule, similar to cationic lipids, could also favor overall siRNA delivery. We have previously reported that the latter approach was successful (*25*). Simple modification of the commercial branched 25 kDa PEI with various α-amino acids, at a modification degree of 30% per ethylenimine, maintains the proton sponge and siRNA binding properties of the vector, but confers self-aggregation and siRNA delivery aptitude to the polymers (Figure 1). The tyrosine-modified PEI (PEIY) appeared particularly effective relative to the other self-aggregating polymers as it led to more than 90% luciferase expression silencing versus only about 50% with the other ones. The effectiveness of the PEIY could not be explained by a molecular specificity of the tyrosine. Indeed, decreasing the content of the PEIY from 30% to 20% (PEIY20) diminishes the delivery potential, while an opposite trend is observed with

* Email: zuber@unistra.fr.
[†] CNRS-Université de Strasbourg UMR 7199.
[‡] ESBS - FRE 3211.
[§] ACTREC.

[1]Abbreviations: PEI, polyethylenimine; BSA, bovine serum albumin; RLU, relative light units; FBS, fetal bovine serum; PBS, phosphate buffer saline; α-aa, α-amino acid; Boc, *tert*-butyloxycarbonyl; DLS, dynamic light scattering; NR, Nile Red; CTAB, cetyl trimethylammonium bromide; siRNA, small interfering RNA; Y, tyrosine; W, tryptophan; R, arginine; F, phenylalanine; L, leucine; RPMI medium, Roswell Park Memorial Institute 1640 medium.

10.1021/bc100010k © 2010 American Chemical Society
Published on Web 04/16/2010

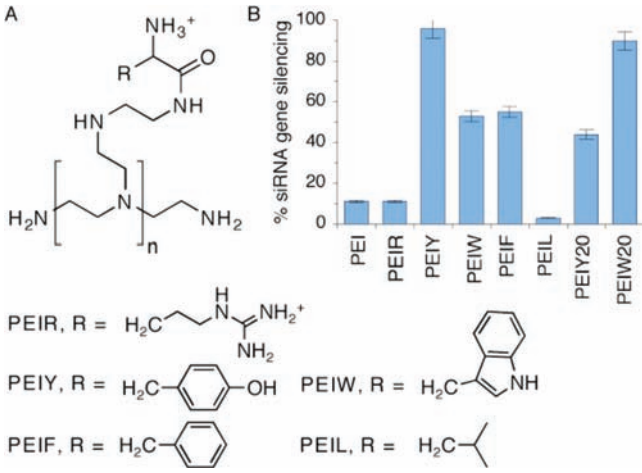


Figure 1. A. Chemical structure of the α-amino acid−polyethylenimine conjugates. B. siRNA delivery abilities of the various polymers in a model cell line, as judged by inhibition of a reporter gene expression. siRNA (10 nM) was delivered to A549Luc cells with 20 μM of the indicated polymer.

the tryptophan-modified PEI (PEIW) for which 20% amino acid content generated a polymer with almost the same efficiency as the PEIY.

In the present work, we comprehensively investigated the mechanism behind the excellent efficacy of the leading PEIY vector. We measured the hydrophobicity of several representative polymers using a fluorescent probe and evaluated their hemolytic, cytotoxic, self-aggregating, and siRNA delivery abilities. Results revealed that the acidic environment encountered in PEI-loaded endosomes can direct dissolution of tyrosine−polyethylenimine aggregates and mediate disassembly of siRNA polyplexes through protonation of the polymer.

EXPERIMENTAL PROCEDURES

Materials. The amino acid-modified PEIs were prepared as previously described (*25*). Succinimidyl ester of N-Boc protected α-amino acids were purchased from Novabiochem, Merck KgaA (Darmstadt, Germany). Branched PEI (40,872−7, batch 09529KD-466; 25 kDa) was from Aldrich (St. Quentin, France). Water was deionized on a Millipore Milli-Q apparatus. All other chemicals were at least of analytical grade and were used as supplied. NMR spectra were performed on Bruker DPX 300 or 200 MHz spectrometers. HiPerfect (Qiagen) was used according to manufacturer's protocol. Before use, dialysis membranes were soaked in Milli-Q water (200 mL, 3 times, 8 h each) to remove preservatives.

Synthesis of Fluorescently Labeled PEIY (Green-PEI). 6-Carboxyfluorescein *N*-hydroxysuccinimide ester (2.4 μmol), freshly dissolved in methanol (1 mL), was added at once to a solution of PEIY (0.2 M in ethylenimine, 1.0 mL), which was first buffered to pH 7.0 by addition of 0.6 equiv NaOH. The solution was stirred in the dark overnight at room temperature and the solution subjected to dialysis using a SpectraPor 12−14 kDa membrane against methanol/water 1/1 mixture (0.1 L, 2 changes over a 48 h period), aqueous 100 mM HCl (0.1 L, 24 h), followed by water (0.2 L, 2 changes over a 48 h period).

Size Measurement. The apparent sizes were determined via dynamic light scattering measurements using a NanoZS apparatus (Malvern instruments, Paris, France) with the following specifications: sampling time = 90 s; refractive index of medium = 1.3402; refractive index of particles = 1.47; medium viscosity = 1.145 cP; and temperature = 25 °C. Data were analyzed using the multimodal number distribution software included with the instrument.

Determination of the Polymer Hydrophobicity. A stock solution of Nile Red was prepared in DMSO at a concentration of 0.4 mM and stored at −20 °C. Stock solutions of polymer were in water at a 0.2 M concentration in ethylenimine. Each polymer (2 μL) was first added to 1 mL RPMI solution to final concentration of 400 μM. Increment (0.2 μL) of the Nile Red solution was then added between measurements. The excitation wavelength was set at 540 nm (bandpass: 5 nm) and emission was recorded from 580 to 700 nm (bandpass: 5 nm) using a fluorescent spectrophotometer. Representative emission spectra were extracted from experiments containing 0.56 μM Nile Red.

Determination of Polymer Aggregation pH. Self-aggregation was determined by turbidity. Each polymer (HCl salt) was first solubilized in water at a 20 mM concentration (0.5 mL volume). The solution was then titrated by addition of NaOH solution (0.25 M, 1 μL increment) until occurrence of aggregate as seen by turbidity. pH of the solution was then measured with a calibrated pH meter. The turbid solution was then titrated with HCl (0.1 M, 1 μL increment) up to full dissolution and the pH measured again. For all polymers, the transition was relatively narrow and within 0.2 pH unit.

Hemolysis Experiments. For recovery from washing steps, sheep red blood cells (RBC) (Eurobio, Courtaboeuf, France) were centrifuged at 400 RCF for 10 min. Before experiments, cells were washed three times with NaCl aqueous solution (150 mM). RBC were then resuspended in phosphate buffer (100 mM, pH 7.4), prepared to be isoosmotic to the inside of a RBC and caused negligible hemolysis, and plated in 96 well plates to obtain 15×10^6 cells in 50 μL. 50 μL aliquots of polymer solutions at different concentrations, also prepared in the same phosphate buffer, were added to the erythrocytes and incubated for 2 h at 37 °C and 5% CO_2. The release of hemoglobin was determined after centrifugation at 700 RCF for 10 min by spectrophotometric analysis of the supernatant at 550 nm (Bio-Rad model 550, Marnes-la-Coquette, France). Complete hemolysis was achieved using deionized water yielding the 100% control value. The negative control was obtained by suspension of RBC in phosphate buffer alone. The experiments were performed in triplicate.

siRNA Polyplexes Preparation. PAGE-purified siRNA were purchased from Eurogentec (Seraing, Belgique) and stored at −20 °C as a 20 μM solution in RNase-free water as indicated by the manufacturer. The luciferase gene originating from pGL3 plasmid was silenced with a RNA duplex of the sense sequence: 5′-CUUACGCUGAGUACUUCGA. Untargeted pGL2luc RNA duplex was of sequence 5′-C**G**UACGC**G**GA**A**UACUUCGA (bold marks showed mismatches by comparison to pGL3 sequence). Human papillomavirus 18 E6 oncoprotein from infected HeLa cells was silenced with a RNA duplex of sense sequence 5′-CUAACUAACACUGGGUUAU.

To prepare polyplexes, appropriate quantities of siRNA and polymer were separately diluted in RPMI medium (Eurobio, Courtaboeuf, France). After 10 min equilibration, the polymer solution was added to the siRNA solution. Then, the mixture was vortexed for 10 s and incubated at room temperature for 30 min.

Determination of Polyplex Stability. 50 pmol of siRNA and 100 nmol of polymer buffered to pH 6.0 were prepared either in RPMI (15 μL, final pH of 7.8) or in water (15 μL, final pH of 6.0). Complexes were then incubated for 30 min with increasing charge excess of heparin (Sigma-Aldrich, Saint-Quentin-Fallavier, France). The mixture was then loaded onto a 2% agarose gel containing 1 mM EDTA and 40 mM Tris acetate buffer pH 8.0, and subjected to electrophoresis for 30 min at 90 V. After staining with ethidium bromide solution (0.5 μg/mL) for 15 min, siRNA released from polyplexes by heparin

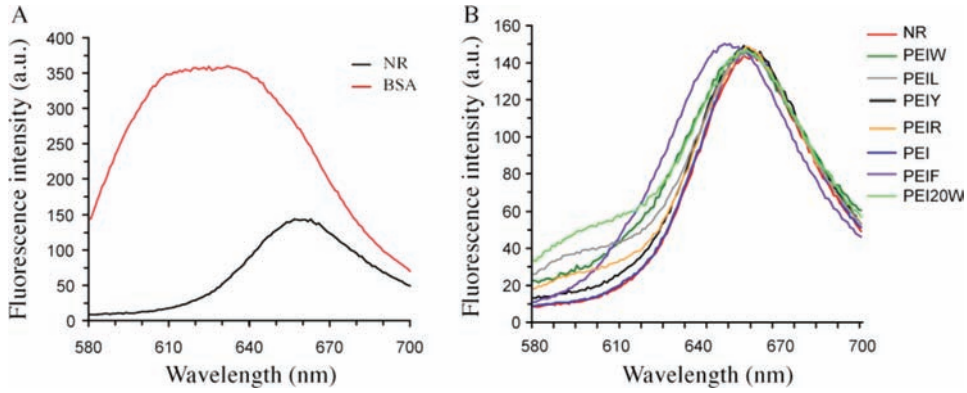


Figure 2. Determination of polymer hydophobicity using a fluorescent probe. Fluorescence emission spectra of Nile Red (0.56 μM) in the presence of bovine serum albumin (5 μM) (A) or with the indicated polymer (0.4 mM) (B). Excitation was at 540 nm and polymers were in RPMI medium.

was visualized with a UV transilluminator and quantified using picture analysis software (NIH *ImageJ*).

Cell Culture. All cell culture media were supplemented with 10% FBS (Perbio, Brebières, France), 100 units/mL penicillin, and 100 μg/mL streptomycin (Eurobio, Courtaboeuf, France). Cells were maintained at 37 °C in a 5% CO_2 humidified atmosphere.

A549 cells (human lung carcinoma; CCL-185; ATCC) were transformed to stably express the *Photinus pyralis* luciferase gene originating from the pGL3 plasmid (Clontech, Mountain View, CA) and selected on G418. The transfectants A549Luc were grown in RPMI 1640 medium containing 2 mM L-glutamine (Eurobio, Courtaboeuf, France) and 0.8 mg/mL G418 (Promega, Charbonnières, France). HeLa cells (human cervix epithelial adenocarcinoma; CCL-2; ATCC) were grown in Eagle's MEM medium.

Delivery Experiments. The procedure is for 24-well plates or 4-well-chambered cover glass experiments. The day before experiment, cells were plated at 25 000 cells per well for A549Luc cells and 50 000 cells per well for HeLa cells. 100 μL of polyplexes, prepared as described above, were added in each well by dilution with the cell medium containing serum (0.5 mL). To ensure optimal cell growth, 24 h after polyplex addition each well was filled with an optional addition of serum-containing growth medium (0.5 mL). In the case of experiments with high concentrations of serum, growth medium was added 4 h after polyplex addition to achieve 10% serum-containing medium. The gene expression profiles were analyzed 48 h after addition of the complexes.

Confocal Microscopy. A549Luc cells were cultured on 4-well-chambered cover glasses (Lab-Tek, Nunc). Complexes were prepared and added to cells as described above except that siRNA and PEIY were replaced with Cy-3-siRNA and carboxyfluorescein-PEIY, respectively. After 4 h of incubation, the cell culture medium was removed and replaced with complete growth medium containing no phenol red (Sigma-Aldrich, Saint-Quentin Fallavier, France). Living cells were analyzed with a Leica TCS SP2 AOBS confocal microscope coupled to the Leica Confocal Software (Leica Microsystems), using 63× oil-immersion objective and excitation at 488 and 543 nm. Confocal sections were taken every 1 μm. Images showing one section of the middle of cells were processed by Photoshop (Adobe Systems Incorporated).

Luciferase Profile Analysis. Luciferase gene expression was determined 48 h after delivery with a commercial kit using manufacturer's protocol (Promega, Charbonnières, France). The luminescence was measured from 1 μL of lysate during 1 s with a luminometer (Centro LB960 XS; Berthold, Thoiry, France). Luciferase activity was expressed as light units integrated over 10 s (RLU) and normalized per milligram of cell protein by using the BCA assay (Pierce, Brebières, France). The error bars represent standard deviation derived from triplicate experiments. Luciferase silencing efficiency of pGL3luc with siRNA was calculated relative to cells treated with a nonspecific siRNA (GL2luc).

Detection of p53 Level. For immunohistochemistry imaging, cells were washed with PBS and fixed with 4% paraformaldehyde solution 48 h after addition of the complexes. p53 was detected with anti-p53 rabbit polyclonal serum FL-393 (Santa Cruz Biotechnology) followed by Alexa Fluor 488 labeled goat antirabbit immunoglobulins (Molecular Probes). DAPI was used for counterstaining nuclei. For Western blot analysis, cells were washed with PBS and harvested by trypsination. Each cell pellet was lysed in 50 mM Tris-HCl buffer, pH 8, containing 150 mM NaCl, 0.1% SDS, 1% NP40, 1 mM DTT, and protease inhibitors (Complete, Roche). Protein levels were next quantified using a Bradford assay and 50 μg lysate from each sample was subjected to 12% SDS−polyacrylamide gel electrophoresis and electro-transferred to nitrocellulose membrane. p53 and actin polypeptides were revealed using monoclonal anti-p53 (DO-7, Santa Cruz Biotechnology) and rabbit polyclonal anti-actin (Sigma-Aldrich) antibodies, respectively, using enhanced chemiluminescence kit (ECL kit, Millipore).

RESULTS AND DISCUSSION

Hydrophobic Character of the Polymers. The hydrophobic character of each α-aa-PEI was evaluated using Nile Red (NR) as a fluorescent probe. Nile red is a zwitterionic fluorescent molecule that is sensitive to local polarity but pH-insensitive, and has been used to monitor hydrophobic surfaces of proteins (*26*). In a polar environment, Nile Red is weakly fluorescent. In a more hydrophobic environment, its quantum yield increases and its maximum emission is progressively blue-shifted. For example, interaction of Nile Red with hydrophobic surfaces of bovine serum protein (BSA) led to a 2.5-fold increase in its quantum yield as well as a remarkable blue shift of the emission maximum from 660 to 630 nm (Figure 2A). No modification of the NR emission spectrum was observed for PEI alone or for PEIs modified with the hydrosympathetic amino acids R or mixed Y (Figure 2B). The probe did not sense large hydrophobic domains on PEIL, even if this residue has a high hydropathy index, probably because the aliphatic chain is too short for formation of stable micelles/domains for NR insertion (*27*). A slight shoulder in the NR spectrum below 630 nm is seen and may be tentatively attributed to highly labile and weak interactions between the probe and solvated aliphatic chains. The impact of PEIW on the NR spectrum is a function of the modification degree. As previously seen with PEIL, interaction

Table 1. Self-Aggregation Abilities of α-Amino Acid Modified Polyethylenimines

polymer	PEI	PEIR	PEIY	PEIW	PEIF	PEIL	PEIY20[a]	PEIW20[a]
hydropathy index[b]		−4.5	−1.3	−0.9	2.8	3.8		
aggregation pH[c]	[d]	[d]	6.3	5.2	6.9	[d]	7.25	6.4
sizes of the polymer self-aggregates (nm)[e]	[d]	[d]	325 ± 28	475 ± 11	700 ± 34	[d]	160 ± 40	218 ± 2

[a] Polymer with a 20% degree of modification. [b] Obtained from ref 40. [c] Corresponds to the pH for which polymer goes for a soluble to an aggregated state. The value was estimated by turbidity upon titration of a 20 mM polymer HCl solution with NaOH. [d] No DLS signal detected. [e] Estimated in RPMI media, pH 7.8, from DLS data with 120 μM of the polymer.

of NR with the indoles of PEIW20 also leads to an NR spectrum with a similar shoulder but of higher intensity, presumably for the same reason as previously indicated. No shoulder is observed with the PEIW that was modified at a 30% content, indicating that the indoles of the PEIW are no longer accessible (not solvated) for interaction with the NR probe and they probably interact together in domains without affinity for the NR. Only PEIF (hydropathy index of 2.8) induces a modest 7 nm blue shift of the NR spectrum but without enhancement of the probe quantum yield. Overall, these results indicated that modification of PEI with the selected amino acids does not lead to extensive hydrophobic domains or pockets in which Nile Red can bind. With the notable exception of aliphatic leucine, this method did nonetheless make it possible to confirm the direct transfer of the hydropathy character from the individual amino acid to the modified PEIs.

Aggregation Properties of the Polymers. As hydrochloride salts, all polymers are fully soluble in water even at 0.5 M concentration and can be stored in solution for extensive periods at 0−4 °C or at −20 °C. However, the amino acid modified PEIs exist in a wide variety of protonation states, which can affect their solvation in aqueous media. For example, addition of these polymers in RMPI cell growth medium, pH 7.8, provokes self-aggregation of the polymers PEIY, PEIW, PEIF, PEIY20, and PEIW20 (Table 1). In the next experiment, we determined precisely the pH value where aggregation occurs. Each polymer−HCl salt (20 mM) was carefully deprotonated with NaOH until turbidity and the pH value was measured (Table 1). PEI, the hydrophilic PEIR, and the aliphatic PEIL do not aggregate up to pH 9.0. On the other hand, the aromatic amino acid modified PEIY, PEIW, and PEIF lead to aggregation at pH of 6.3, 5.2, and 6.9, respectively, and in a narrow range (transition from a limpid to a turbid solution occurred within 0.1 pH unit). Decreasing the tyrosine or tryptophane content from 30% to 20% is conducive to aggregation at higher pH (around 1 pH unit higher) and to a softer transition. These results indicate that the aggregation abilities of the modified PEIs vary as functions of the pH and of the nature of the amino acid.

Evaluation of the Membrane-Destabilizing Properties and Cytotoxicity of the Polymers. Technically, nucleic acid translocation into the cell must involve a rupture of the lipid membrane integrity. Some amino acid−PEI conjugates may induce direct membrane destabilization via interfacial activity of the amino acid side chains (*28*). We therefore evaluated the effect of the polymers on mammalian plasma cell membranes by monitoring the release of hemoglobin from sheep erythrocytes (Figure 3A). PEIF is the only polymer with important hemolytic activity at 1 mM concentration. At higher concentration (10 mM), PEIL shows partial hemolysis, whereas all other PEIs have no hemolytic activity. One important property that was unique to PEIW but not to PEIW20 was that it resulted in red cells becoming brownish at pH 7.4, without apparent release of heme in solution, suggesting interference with membrane stability.

In parallel, we evaluated the toxicity level of the polymers on A459Luc cells by measuring the mitochondrial activity using the MTT assay and reported the maximum polymer concentration for which cells remained 100% viable (Figure 3B).

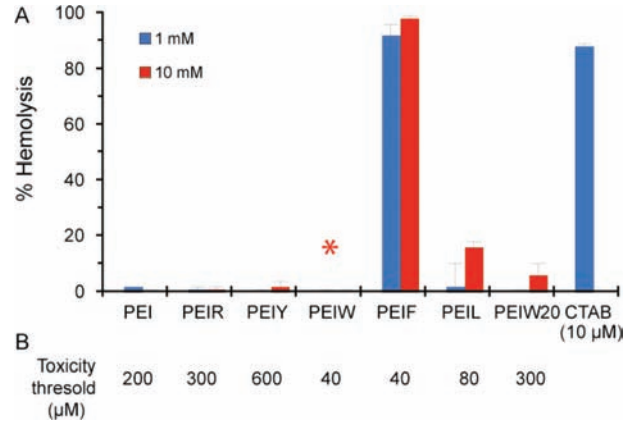


Figure 3. A. Permeation effect of polymers on mammalian cell membranes at extracellular pH. Sheep erythrocytes were incubated for 2 h at 37 °C with 1 and 10 mM of the various polymers in PBS, pH 7.4. Cells were then centrifuged and rupture of erythrocyte membranes was monitored by release of hemoglobin in the supernatant. Cationic detergent cetyl trimethylammonium bromide (CTAB) was used at 10 μM. [*] PEIW modifies the color of the cells from red to brown at pH 7.4 at both concentrations. B. Maximum concentration of polymer which did not provoke cell toxicity as measured by MTT assay on A549Luc cells.

Membrane-perturbing polymers PEIF, PEIL, and PEIW affect considerably the cell viability, while the others are friendlier to cells. In particular, PEIY offers an important cushion between its effective concentration (20 μM) and its toxicity threshold (600 μM). Altogether, these experiments show that PEIY does not possess any hemolytic activity and that the polymers with membrane-perturbing activity at extracellular pH rather lead to cell lethality.

Evaluation of siRNA/PEIY Polyplexes Suitability for Entry into the Cellular Degradative Endosomal/Lysosomal Compartment. The previous experiment showed that direct permeation of the plasma membrane is not an efficient translocation method. Translocation should rather be a consequence of a more localized rupture of lipid membranes surrounding endocytosed complexes. To take this route, most synthetic delivery systems use initial electrostatic anchorage to sulfated (polyanionic) proteoglycans present on membranes of adherent cells. While polyanions may effectively displace siRNA from polyplexes, we investigated the stability of the siRNA polyplexes in the presence of heparin, a natural polymer with high anionic density. siRNA polyplexes were prepared in RPMI medium (pH 7.8) at an N/P ratio of 50 to ensure full complexation and then incubated for 30 min with increasing quantities of heparin. The mixtures were then subjected to analysis by agarose gel electrophoresis. Release of siRNA was monitored after ethidium bromide staining and quantified (Figure 4). Heparin effectively displaces PEI from the weakly cohesive siRNA/PEI complexes and provokes a quantitative liberation of siRNA, even at a low heparin to ethylenimine ratio. According to the working hypothesis, transformation of the soluble PEI into cohesive species does indeed allow the stabilization of the polyplexes against electrostatic displacement, but to various extents. PEIY20 and PEIF, for which aggregation in water occurs at

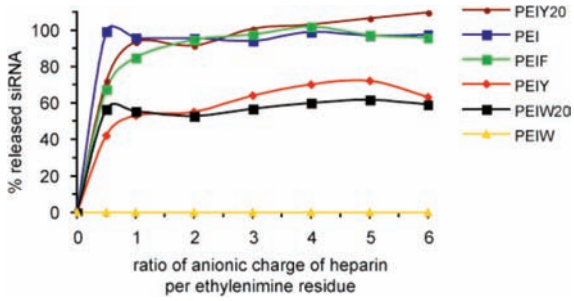


Figure 4. Evaluation of the electrostatic stability of the polyplexes. siRNA polyplexes (N/P 50, 0.7 μg siRNA) were incubated for 30 min with increasing amounts of heparin in RPMI medium, and release of siRNA was determined from agarose gel electrophoresis analyses.

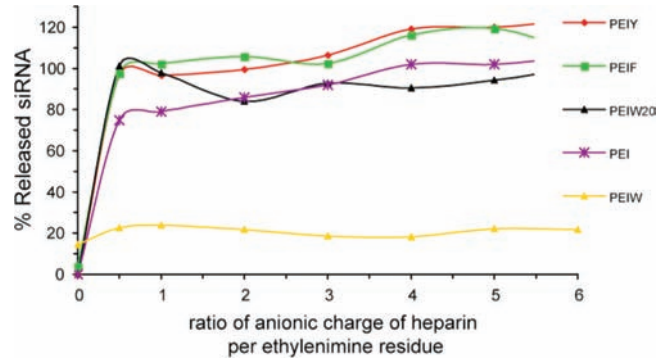


Figure 6. Evaluation of the electrostatic stability of the polyplexes at endosomal pH. siRNA polyplexes (N/P 50, 0.7 μg siRNA) were incubated for 30 min at pH 6.0 with increasing amounts of heparin. Release of siRNA was determined from agarose gel electrophoresis analyses.

pH 7.25 and 6.9, respectively, form moderately stable siRNA polyplexes against electrostatic displacement. On the other hand, PEIW assembles and entraps siRNA into an extremely resistant shell, as judged by the absence of siRNA liberation even at high heparin amount. An intermediate siRNA release profile is observed for the two most effective siRNA polyplexes made with PEIY or PEIW20. A fast siRNA release, obtained by displacement of superficially polyplex-bound siRNA, is followed by a plateau, for which about 40% of the RNA duplexes remained entrapped, presumably within the insoluble complex cores. These experiments suggest that the relatively low efficiency of PEIF and PEIY20 is due to instability of their self-assemblies, leading to impaired cell anchorage. Self-aggregation of PEIY, PEIW20, and PEIW is cohesive enough to protect siRNA from dissociation against electrostatic competition in an extracellular medium.

Intracellular Fate of siRNA/PEIY Complexes. We next followed delivery of the siRNA/PEIY complexes using Cy3-labeled fluorescent siRNA and fluorescein-labeled PEIY (green-PEIY). First, the delivery efficacy of the green-PEIY was compared to that of native PEIY using A549 cell line that stably express the pGL3 luciferase gene (A549Luc) (*22*). The polymer (12 nmol in ethylenimine residue) was mixed with siRNA (6 pmol in duplex of either targeting or untargeting sequence) in RPMI cell growth medium (100 μL) and the cationic complexes added to cells that were grown in 10% serum-containing RPMI medium. Cells were lysed 48 h later. Measured luciferase activity showed that the fluorescent tag does not significantly modify the delivery properties of PEIY (Figure 5A). Fluorescent polyplexes were then prepared and incubated under identical conditions. The fluorescent species were observed with a scanning fluorescent microscope 4 h later on living cells (Figure 5B,C). Tracking the siRNA/PEIY from the PEIY species (Figure 5B) provides images similar to those previously observed for PEI/DNA complexes (*29*). Indeed, PEIY appears as discrete spots located on the cell surfaces and in the cytoplasm in perinuclear areas, indicating that these complexes enter via the same degradative lysosomal pathway. The siRNA displays a different pattern (Figure 5C) with intracellular patches, corresponding to PEIY complexes, and a diffuse fluorescence in the cytosol. Observation of siRNA diffusion in the cytosol to that extent was quite surprising because siRNA delivered with a cationic lipid did not show such a diffuse pattern (*22*), even if the size of siRNA duplexes does not restrict cytosolic diffusion (*30*).

To explain this phenomenon, we hypothesized that acidity of the endosome may render the PEIY soluble and lose the siRNA/PEIY polyplexes. Sulfated proteoglycan receptors, which are concomitantly engulfed in endosomes, may play a favorable role here by favoring siRNA release from polyplexes. We therefore investigated once again the stability of the siRNA polyplexes in the presence of heparin but at an endosomal pH. Complexes that enter the degradative lysosomal trafficking pathway undergo progressive acidification (within 3 to 4 h) of their environments from pH 7.4 to as low as 4.5. The buffering capacity of PEI nonetheless blocks acidification of PEI-loaded endosomes at measured pHs of 5.9 (*31*) or 6.1 (*32*). siRNA polyplexes were hence incubated in the presence of increasing proportion of heparin at pH 6.0 and siRNA release reported in Figure 6. Even if low pH environments increase the cationic charge density of the PEI and strengthen the electrostatic polyplex cohesion (*33*), heparin effectively dissociates siRNA polyplexes made from the now soluble polymers PEIY and PEIW20. As previously observed at higher pH, still insoluble PEIW retains siRNA within its self-assemblies, explaining why this polymer leads to modest siRNA-mediated luciferase silencing. To complete this study, we evaluated the hemolytic activities of the polymers at pH 6.0. Results (Supporting Information, Figure S6) confirmed that PEIY has no hemolytic activity at 1 and 10 mM concentrations, suggesting that endo-

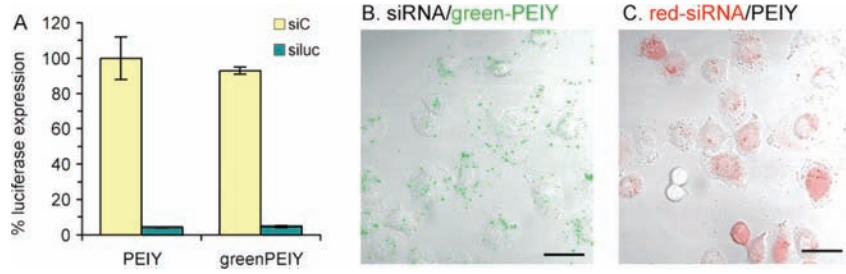


Figure 5. Evaluation of the PEIY delivery efficiency and intracellular fate of siRNA and PEIY following application of complexes onto cells. A. Targeting (siluc) or untargeting (siC) siRNA (10 nM) were delivered to A549Luc cells with 20 μM of PEIY or green-PEIY. Luciferase expression was measured 48 h later. For images A and B, complexes of fluorescently Cy3-labeled siRNA (red, 6 pmol) and fluorescein-labeled PEIY (green, 12 nmol) were applied to A549Luc cells grown in RPMI medium containing serum. The living cells were analyzed 4 h later by scanning fluorescence microscopy. The scale bars represent 40 μm.

somal membrane rupture for this polymer results purely from the PEI proton sponge mechanism.

Altogether, these experiments suggest that sticky PEIY and PEIW20 possess just the right hydrophobic/hydrophilic balance for carrying siRNA into endosomes and for directing siRNA release at endosomal pH values.

Impact of Self-Aggregation on siRNA-Mediated Delivery. Electrostatic condensation of a plasmid DNA with soluble polycations is a kinetically driven and almost irreversible process. When initial electrostatic stoichiometry between DNA phosphates and PEI is in favor of the latter, PEI molecules entangle in large excess with plasmid DNA molecules and form thermodynamically unstable cationic complexes. For the branched PEI, which is weakly protonated at pH 7.4, assembly at a PEI nitrogen amine (N) to DNA phosphate (P) ratio of 13 appeared to offer complexes with optimal gene transfection activities in vitro (*9*), presumably because this N/P ratio both permits an accurate cationic particle formation process (100% DNA condensation in cationic particles) and limits the occurrence of free PEI in solution.

The ability of PEIY to self-aggregate in extracellular medium implies that there is no free entity left in the solution. We therefore investigated the PEIY dose dependency of siRNA delivery by using three different siRNA concentrations (Figure 7). Regardless of the siRNA concentrations and of the N/P ratio, the histograms present a U-shape with an optimal gene silencing efficiency in a narrow quantity range of PEIY (7.6 to 12 nmol) for about 25 000 cells. This behavior emphasizes the importance of the dose of the active carrier for an effective endosomal rupture and subsequent siRNA activity (*34*−*37*). The U-shape is likely a combination of two opposite trends. A gradual decrease in luciferase activity with increasing PEIY quantity presumably corresponds to progressive titration of the particle's cell surface receptors up to full occupancy. The subsequent increase in PEIY to siRNA ratio in turn dilutes the siRNA within PEIY containing particles and diminishes the quantity of delivered siRNA into the cytosol. Decreased luciferase silencing activity is then observed and is amplified at low siRNA inputs. Although the mechanism of siRNA-mediated silencing also depends on the siRNA concentration, it is worth mentioning that 75% silencing efficiency was obtained with extracellular siRNA duplex concentration as low as 0.1 nM, reflecting nonetheless the effectiveness of such a mechanism.

PEIY versus a Cationic Lipid Formulation for siRNA-Mediated Silencing of a Viral Oncoprotein. To evaluate the potential of PEIY as a general siRNA delivery reagent, we next compare it to HiPerfect, a commercially available siRNA-optimized, "second-generation", cationic lipid formulation for the delivery of oncoprotein-targeting siRNAs. A majority of cervical cancers is caused by high-risk types of human papillomaviruses (HPV) and derives from genetic integration of viral E6 and E7 oncoproteins into infected cells. These two oncoproteins disrupt several cellular growth control mechanisms. Malignancy due to E6 is attributed to its ability to induce proteasomal degradation of the p53 tumor suppressor protein. The cervical cancer cells HeLa harbor copies of the HPV-18 genome, and in vitro studies showed that p53 levels can be restored by silencing E6 expression with an E6-selective siRNA (siE6) (*38*). siE6/PEIY complexes were prepared as described earlier, and the cationic lipid formulation was used according to the manufacturer's instructions. Complexes were simply added to the cells grown in complete MEM medium. The p53 level was monitored by immunohistochemistry and Western blot analysis (Figure 8). A siE6-mediated increase of nuclear p53 is observed in almost all cell nuclei to the same extent as the lipid formulation, although nonspecific antibody binding to PEIY aggregates is also seen (Figure 8A). Quantification of p53 level in the immunoblot after delivery with an untargeted siRNA (siC) or without carrier (Figure 8B) confirms that PEIY does not interfere with the cellular cascade leading to the p53 increase. These results suggest that PEIY represents an alternative siRNA delivery reagent to the lipidic ones and can be applied for silencing malignant gene expression.

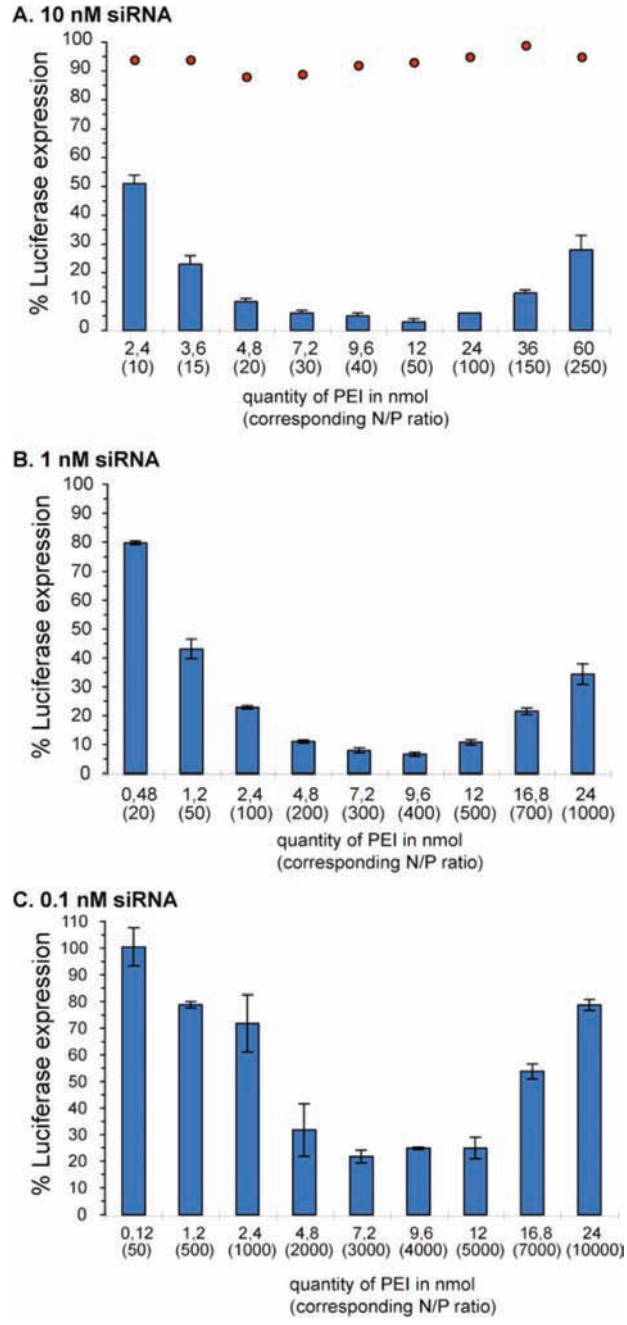


Figure 7. Evaluation of the siRNA delivery efficacy as a function of the PEIY quantity. The polymer at the indicated quantity was mixed with siRNA (6 pmol (A), 0.6 pmol (B), or 0.06 pmol (C)) in 0.1 mL RPMI and added to A549Luc cells grown in medium containing serum (0.5 mL). Luciferase expression was measured 48 h after addition of polyplexes. The bar represents the residual luciferase activity. The red points measured the percentage of cell protein levels relative to mock (same scale as luciferase expression).

Stability of siRNA/PEIY Complexes in High Serum Content. In this final experiment, we examined the stability of the siRNA/PEIY complexes in the presence of varying amounts of serum from luciferase silencing experiments.

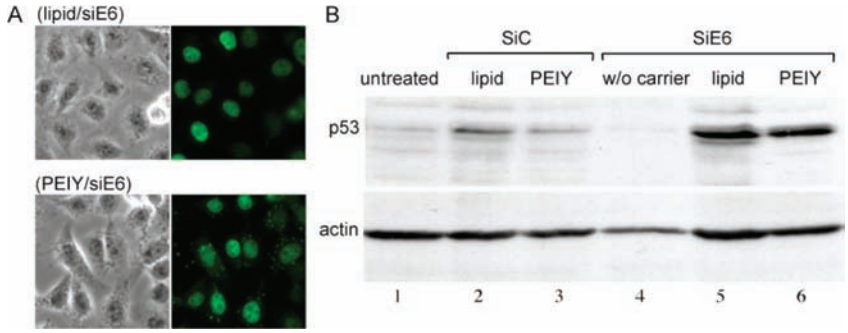


Figure 8. Inhibition of the HPV18 E6 oncoprotein in HeLa cells using siRNA (6 pmol) delivered with either PEIY (12 nmol) or a commercial cationic lipid (HiPerfect). The resulting increase of p53 was visualized by immunohistochemistry (A) and Western blotting (B). SiC: untargeted siRNA. siE6: E6 targeted siRNA.

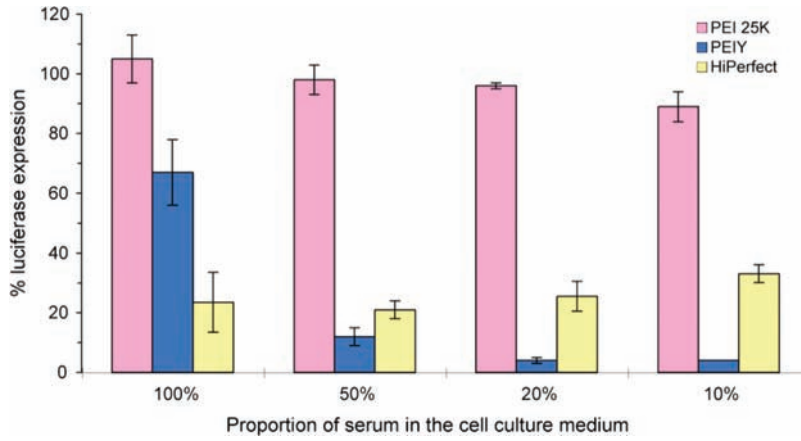


Figure 9. Evaluation of the PEIY delivery efficacy in the presence of high serum concentration. siRNA (10 nM) were delivered to A549Luc cells with PEI 25K (pink bars), PEIY (blue bars), or HiPerfect (yellow bars) in the presence of 100%, 50%, and 20% serum, respectively. After 4 h, the medium was replaced with the optimal cell growth medium (RPMI containing 10% serum) and luciferase expression was measured 48 h later. The results are relative to cells treated with nonspecific siRNA.

Indeed, extracellular serum contains many amphiphiles with hydrophobic surfaces, such as seric albumin, that can potentially interfere with the tyrosine-tyrosine interactions and hence diminish the cohesion of the polyplexes. Figure 9 shows that PEIY remains a remarkable siRNA delivery agent up to a 50% serum content (90% luciferase inhibition) but loses its efficiency in 100% serum. By comparison, HiPerfect-based lipoplexes appear less effective in delivering siRNA to A549 cells than to Hela cells but are fully insensitive to serum proportion in the cell culture media. These results, in combination with the absence of hemolytic activity, suggest that PEIY may be suitable for in vivo administration but is not tailored for intravenous delivery.

CONCLUSION

Our results show that tyrosine−polyethylenimine conjugate has a favorable efficiency/toxicity balance and is able to convey effectively low quantities of siRNA, even in the presence of high serum content. The success of tyrosine−polyethylenimine does not derive from membrane-perturbing activity but may originate from a disassembly sensitivity at pH 6.0, a pH value that is found in PEI-buffered endosomes. This property emanates from the PEI proton sponge ability and favors siRNA release from polyplexes at moments when PEI conducts osmotic pressure increase on endosomal membranes. Subsequent siRNA diffusion into the cytosol may hence not be restricted when endosome swelling/lysis events take place. Regardless of its mechanism, ease of preparation at low cost and high delivery efficacies should be appreciated for gene silencing experiments in cell culture. More experiments are currently underway to address usefulness of such modified PEIs in vivo for administration and pathologies for which cell surfaces are accessible to large delivery systems (*36*, *39*).

ACKNOWLEDGMENT

This work is dedicated to J.-P. Behr and was funded by the CEFIPRA and by a MRT fellowship to GC. We are grateful to Guy Duportail for assistance with the Nile Red assay and Jean-Luc Vonesh (IGMBC, Strasbourg) for access to the IGMBC imaging facilities. We also thank Dr. Coll and Giliane Coupin for kindly providing the A549Luc cells and red sheep erythrocytes, respectively.

Supporting Information Available: Detailed discussion on the synthetic design of the polymers, procedures for polymer synthesis and toxicity assay. Figure S1 shows NR spectra in presence of the various polymers in 150 mM NaCl. Figures S2−3 are the cell viability dose response to the polymers. Figure S4 shows the efficiency of PEIY to deliver siRNA following siRNA/PEIY polyplexes assembly in various media. Figure S5 shows confocal image analysis of A549Luc cells that were treated with Cy3-siRNA and its corresponding PEI polyplexes. Figure S6 is the hemolysis assay at pH 6.0. Figures S7 and S8 are the agarose gels used to plot the Figures 4 and 6. Figure S9 shows siRNA-mediated cyclinD1 silencing using PEIY as the delivery carrier. This material is available free of charge via the Internet at http://pubs.acs.org.

LITERATURE CITED

(1) Elbashir, S. M., Harborth, J., Lendeckel, W., Yalcin, A., Weber, K., and Tuschl, T. (2001) Duplexes of 21-nucleotide RNAs mediate RNA interference in cultured mammalian cells. *Nature 411*, 494–498.

(2) Kim, D. H., and Rossi, J. J. (2007) Strategies for silencing human disease using RNA interference. *Nat. Rev. Genet. 8*, 173–184.

(3) Wolfrum, C., Shi, S., Jayaprakash, K. N., Jayaraman, M., Wang, G., Pandey, R. K., Rajeev, K. G., Nakayama, T., Charrise, K., Ndungo, E. M., Zimmermann, T., Koteliansky, V., Manoharan, M., and Stoffel, M. (2007) Mechanisms and optimization of in vivo delivery of lipophilic siRNAs. *Nat. Biotechnol. 25*, 1149–1157.

(4) Juliano, R., Alam, M. R., Dixit, V., and Kang, H. (2008) Mechanisms and strategies for effective delivery of antisense and siRNA oligonucleotides. *Nucleic Acids Res. 36*, 4158–4171.

(5) Felgner, P. L. (1999) Prospects for synthetic self-assembling systems in gene delivery. *J. Gene Med. 1*, 290–292.

(6) Neu, M., Fischer, D., and Kissel, T. (2005) Recent advances in rational gene transfer vector design based on poly(ethylene imine) and its derivatives. *J. Gene Med. 7*, 992–1009.

(7) Lleres, D., Weibel, J. M., Heissler, D., Zuber, G., Duportail, G., and Mely, Y. (2004) Dependence of the cellular internalization and transfection efficiency on the structure and physicochemical properties of cationic detergent/DNA/liposomes. *J. Gene Med. 6*, 415–428.

(8) Itaka, K., and Kataoka, K. (2009) Recent development of nonviral gene delivery systems with virus-like structures and mechanisms. *Eur. J. Pharm. Biopharm. 71*, 475–483.

(9) Boussif, O., Lezoualch, F., Zanta, M. A., Mergny, M. D., Scherman, D., Demeneix, B., and Behr, J. P. (1995) A versatile vector for gene and oligonucleotide transfer into cells in culture and in vivo: Polyethylenimine. *Proc. Natl. Acad. Sci. U.S.A. 92*, 7297–7301.

(10) Kichler, A., Leborgne, C., Coeytaux, E., and Danos, O. (2001) Polyethylenimine-mediated gene delivery: a mechanistic study. *J. Gene Med. 3*, 135–44.

(11) Grayson, A. C., Doody, A. M., and Putnam, D. (2006) Biophysical and structural characterization of polyethylenimine-mediated siRNA delivery in vitro. *Pharm. Res. 23*, 1868–1876.

(12) Spagnou, S., Miller, A. D., and Keller, M. (2004) Lipidic carriers of siRNA: differences in the formulation, cellular uptake, and delivery with plasmid DNA. *Biochemistry 43*, 13348–13356.

(13) van der Gun, B. T., Monami, A., Laarmann, S., Rasko, T., Slaska-Kiss, K., Weinhold, E., Wasserkort, R., de Leij, L. F., Ruiters, M. H., Kiss, A., and McLaughlin, P. M. (2007) Serum insensitive, intranuclear protein delivery by the multipurpose cationic lipid SAINT-2. *J. Controlled Release 123*, 228–238.

(14) Meyer, M., Dohmen, C., Philipp, A., Kiener, D., Maiwald, G., Scheu, C., Ogris, M., and Wagner, E. (2009) Synthesis and biological evaluation of a bioresponsive and endosomolytic siRNA-polymer conjugate. *Mol. Pharm. 6*, 752–762.

(15) Baigude, H., McCarroll, J., Yang, C. S., Swain, P. M., and Rana, T. M. (2007) Design and creation of new nanomaterials for therapeutic RNAi. *ACS Chem. Biol. 2*, 237–41.

(16) Davis, M. E. (2009) The first targeted delivery of siRNA in humans via a self-assembling, cyclodextrin polymer-based nanoparticle: from concept to clinic. *Mol. Pharm. 6*, 659–668.

(17) Lim, Y. B., Lee, E., Yoon, Y. R., Lee, M. S., and Lee, M. (2008) Filamentous artificial virus from a self-assembled discrete nanoribbon. *Angew. Chem., Int. Ed. Engl. 47*, 4525–4528.

(18) Zintchenko, A., Philipp, A., Dehshahri, A., and Wagner, E. (2008) Simple modifications of branched PEI lead to highly efficient siRNA carriers with low toxicity. *Bioconjugate Chem. 19*, 1448–1455.

(19) Brus, C., Petersen, H., Aigner, A., Czubayko, F., and Kissel, T. (2004) Physicochemical and biological characterization of polyethylenimine-graft-poly(ethylene glycol) block copolymers as a delivery system for oligonucleotides and ribozymes. *Bioconjugate Chem. 15*, 677–684.

(20) Dufresne, M. H., Elsabahy, M., and Leroux, J. C. (2008) Characterization of polyion complex micelles designed to address the challenges of oligonucleotide delivery. *Pharm. Res. 25*, 2083–2093.

(21) Kim, Y., Tewari, M., Pajerowski, J. D., Cai, S., Sen, S., Williams, J., Sirsi, S., Lutz, G., and Discher, D. E. (2009) Polymersome delivery of siRNA and antisense oligonucleotides. *J. Controlled Release 134*, 132–140.

(22) Bolcato-Bellemin, A. L., Bonnet, M. E., Creusat, G., Erbacher, P., and Behr, J. P. (2007) Sticky overhangs enhance siRNA-mediated gene silencing. *Proc. Natl. Acad. Sci. U.S.A. 104*, 16050–16055.

(23) Zimmermann, T. S., Lee, A. C., Akinc, A., Bramlage, B., Bumcrot, D., Fedoruk, M. N., Harborth, J., Heyes, J. A., Jeffs, L. B., John, M., Judge, A. D., Lam, K., McClintock, K., Nechev, L. V., Palmer, L. R., Racie, T., Rohl, I., Seiffert, S., Shanmugam, S., Sood, V., Soutschek, J., Toudjarska, I., Wheat, A. J., Yaworski, E., Zedalis, W., Koteliansky, V., Manoharan, M., Vornlocher, H. P., and MacLachlan, I. (2006) RNAi-mediated gene silencing in non-human primates. *Nature 441*, 111–114.

(24) Fraley, A. W., Pons, B., Dalkara, D., Nullans, G., Behr, J. P., and Zuber, G. (2006) Cationic oligonucleotide-peptide conjugates with aggregating properties enter efficiently into cells while maintaining hybridization properties and enzymatic recognition. *J. Am. Chem. Soc. 128*, 10763–10771.

(25) Creusat, G., and Zuber, G. (2008) Self-assembling polyethylenimine derivatives mediate efficient siRNA delivery in mammalian cells. *ChemBioChem 9*, 2787–2789.

(26) Hendriks, J., Gensch, T., Hviid, L., van Der Horst, M. A., Hellingwerf, K. J., and van Thor, J. J. (2002) Transient exposure of hydrophobic surface in the photoactive yellow protein monitored with Nile Red. *Biophys. J. 82*, 1632–1643.

(27) Ercelen, S., Zhang, X., Duportail, G., Grandfils, C., Desbrieres, J., Karaeva, S., Tikhonov, V., Mely, Y., and Babak, V. (2006) Physicochemical properties of low molecular weight alkylated chitosans: a new class of potential nonviral vectors for gene delivery. *Colloids Surf., B: Biointerfaces 51*, 140–148.

(28) Rathinakumar, R., Walkenhorst, W. F., and Wimley, W. C. (2009) Broad-spectrum antimicrobial peptides by rational combinatorial design and high-throughput screening: the importance of interfacial activity. *J. Am. Chem. Soc. 131*, 7609–7617.

(29) Kopatz, I., Remy, J. S., and Behr, J. P. (2004) A model for non-viral gene delivery: through syndecan adhesion molecules and powered by actin. *J. Gene Med. 6*, 769–776.

(30) Verkman, A. S. (2002) Solute and macromolecule diffusion in cellular aqueous compartments. *Trends Biochem. Sci. 27*, 27–33.

(31) Sonawane, N. D., Szoka, F. C., Jr., and Verkman, A. S. (2003) Chloride accumulation and swelling in endosomes enhances DNA transfer by polyamine-DNA polyplexes. *J. Biol. Chem. 278*, 44826–44831.

(32) Akinc, A., Thomas, M., Klibanov, A. M., and Langer, R. (2005) Exploring polyethylenimine-mediated DNA transfection and the proton sponge hypothesis. *J. Gene Med. 7*, 657–663.

(33) Yang, S., and May, S. (2008) Release of cationic polymer-DNA complexes from the endosome: A theoretical investigation of the proton sponge hypothesis. *J. Chem. Phys. 129*, 185105.

(34) Wightman, L., Kircheis, R., Rossler, V., Carotta, S., Ruzicka, R., Kursa, M., and Wagner, E. (2001) Different behavior of branched and linear polyethylenimine for gene delivery in vitro and in vivo. *J. Gene Med. 3*, 362–372.

(35) Ogris, M., Steinlein, P., Kursa, M., Mechtler, K., Kircheis, R., and Wagner, E. (1998) The size of DNA/transferrin-PEI complexes is an important factor for gene expression in cultured cells. *Gene Ther. 5*, 1425–1433.

(36) Williams, J. H., Sirsi, S. R., Latta, D. R., and Lutz, G. J. (2006) Induction of dystrophin expression by exon skipping in mdx mice following intramuscular injection of antisense oligonucleotides complexed with PEG-PEI copolymers. *Mol. Ther. 14*, 88–96.

(37) Zuber, G., Dontenwill, M., and Behr, J. P. (2009) Synthetic viruslike particles for targeted gene delivery to alpha(v)beta(3) integrin-presenting endothelial cells. *Mol. Pharm. 6*, 1544–1552.

(38) Courtete, J., Sibler, A. P., Zeder-Lutz, G., Dalkara, D., Oulad-Abdelghani, M., Zuber, G., and Weiss, E. (2007) Suppression of cervical carcinoma cell growth by intracytoplasmic codelivery of anti-oncoprotein E6 antibody and small interfering RNA. *Mol. Cancer Ther. 6*, 1728–1735.

(39) Hobbs, S. K., Monsky, W. L., Yuan, F., Roberts, W. G., Griffith, L., Torchilin, V. P., and Jain, R. K. (1998) Regulation of transport pathways in tumor vessels: role of tumor type and microenvironment. *Proc. Natl. Acad. Sci. U.S.A. 95*, 4607–4612.

(40) Kyte, J., and Doolite, A. (1998) A simple method for displaying the hydropathy character of protein. *J. Mol. Biol. 157*, 105–132.

BC100010K

Hybrids of Nonviral Vectors for Gene Delivery

Shubiao Zhang,* Yinan Zhao, Budiao Zhao, and Bing Wang

SEAC-ME Key Laboratory of Biotechnology and Bioresources Utilization, College of Life Science, Dalian Nationalities University, Dalian 116600, Liaoning, China. Received June 12, 2009; Revised Manuscript Received December 27, 2009

Gene transfer has been a critical step for gene therapy. Viral vectors and nonviral vectors are commonly used for gene transfer. It has been shown that nonviral vectors have the advantage over viral ones, as they are nonimmunogenic, easy to produce, and not oncogenic. However, they have the major limitation of inefficient transfection; the hybridized usage of nonviral vectors may provide a partial solution. This article reviews the hybrids (different materials used in one delivery system) of nonviral vectors for gene delivery including hybrids between cationic lipids and helper lipids, conjugates of peptides or targeting moieties and lipids, and hybrids of cationic liposomes and polymers.

INTRODUCTION

Gene therapy has been developed for treatment of both acquired and inherited diseases such as severe combined immunodeficiency (*1*), cystic fibrosis (*2*), and Parkinson's disease (*3*), as well as an alternative method to traditional chemotherapy used in treating cancer (*4*). This approach is based on the principle of correcting the basis of diseases at their origin by delivery and subsequent expression of exogenous DNA, which encodes for a missing or defective gene product (*5*). Naked nucleic acids are easily degraded when used either *in vitro* or *in vivo*, so vectors are employed in many methods to protect nucleic acids and deliver them to targeted cells. These vectors can be generally divided into two categories, viral vectors and nonviral vectors.

After several accidents (*6–8*), nonviral vectors gained great attention for they are nonimmunogenic, not oncogenic, easy to produce in large scale, and capable of delivering large genetic material. However, unlike viral analogues that have evolved to overcome cellular barriers and immune defense mechanisms, nonviral gene carriers consistently exhibit significantly lower transfection efficiency compared with viral ones.

People have been designing and synthesizing a large number of new compounds (*9, 10*); at the same time, the hybridized utilization of nonviral vectors may provide a solution to the problem. We could combine cationic lipids and helper lipids, hybridize cationic lipsomes and polymers, and introduce peptides and targeting moieties into lipids to approach the requirements of gene therapy. Though many high-quality reviews have been published recently (*11–13*), we found it necessary to demonstrate the status of hybrids of nonviral vectors.

HYBRIDS BETWEEN CATIONIC LIPIDS AND HELPER LIPIDS

Though some cationic lipids show transfection ability when used alone in cationic liposomes, in many cases helper lipids are required to be incorporated into the formulations to yield high transfection efficiency. Among helper lipids, DOPE has been researched very extensively for it often presents a super synergistic effect when used in cationic liposomes. In early study, people have realized that DOPE destabilized lipid bilayers, and it was believed to be involved in endosomal disruption (*14*). Then, an endocytosis model of DNA delivery by cationic liposomes was proposed in which the principal function of the chase liposomes was to destabilize the endosome membrane and allow the release of DNA into the cytosol (*15*). When compared with other helper lipids, such as DOPC, DOPE shows superior activity. It has been proven that the replacement of DOPE with DOPC abolished most of the transfection activity of cationic liposomes (*16–19*). The difference in their head groups can be the reason, as DOPC contains a choline headgroup instead of the ethanolamine headgroup in DOPE (*14*). All the studies support DOPE as a strong destabilizer of lipid bilayers.

Recent studies disclosed by Safinya et al. (*20*) further gave the reason in the level of phase transition. They used synchrotron small-angle X-ray scattering (SAXS) and optical microscopy to find a completely different columnar inverted hexagonal H_{II}^C liquid-crystalline state in cationic liposome−DNA complexes. In this process, DOPE induced the phase transition from L_α^C to H_{II}^C by controlling the spontaneous curvature $C_o = 1/R_o$ of the lipid monolayer. It has been concluded that DOPE facilitates endosomal escape by forming an unstable inverted hexagonal phase at the endosomal pH that destabilizes both the complex and the endosomal membrane. Conversely, it would be expected that lipids such as dioleoylphosphatidylcholine (DOPC) would hinder the ability of cationic lipids to induce nonbilayer structure (*21*).

Another helper lipid, cholesterol, could also promote H_{II}^C organization as DOPE. Usage of cholesterol and its derivatives as helper lipids allowed one to attain higher transfection levels in vivo (*22, 23*). Reliably higher expression in many organs was revealed upon the application of cholesterol-containing liposomes (*24, 25*) as compared to other liposomes. Some studies indicated that in in vivo applications cholesterol was a more effective helper lipid than DOPE (*26*). Needless to say, the structure of cationic lipids plays a very important role in various phase structures. Safinya (*27*) also found that hexagonally arranged tubular lipid micelles (H_I^C) surrounded by DNA rods were formed though DOPC was used in the dendritic lipid-based cationic liposome. Helper lipid is indispensable for many cationic liposome formulations; the hybrids of helper lipids and cationic lipids would continue to be a research highlight.

CONJUGATES OF PEPTIDES AND LIPIDS

One of the most challenge things for gene delivery by cationic liposome method is the toxicity of cationic lipids originated in the cationic nature. The cationic lipids can become cytotoxic by interacting with critical enzymes such as PKC. It has been

* zsb@dlnu.edu.cn.

10.1021/bc900261c © 2010 American Chemical Society
Published on Web 03/05/2010

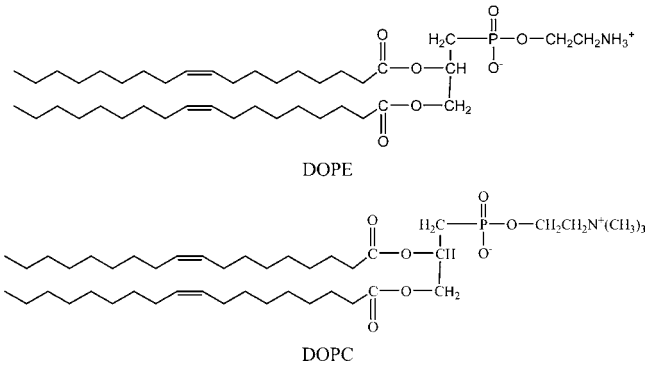


Figure 1. Chemical structures of DOPE and DOPC.

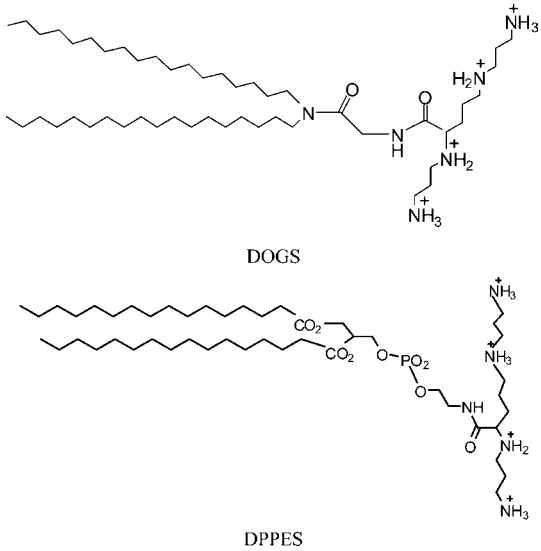


Figure 2. Chemical structures of DOGS and DPPES.

proven that many derivatives of cholesterol can inhibit PKC activity, which contained tertiary or quaternary nitrogen head groups (*28*). So, the replacement of cationic head groups has been a major trend with other more biocompatible groups, such as peptides, in recent years. The conjugates of peptides and lipids are much less toxic, while keeping the same transfection efficiency. The early examples (*29*) are DOGS (dioctadecylamidoglycylspermine) and DPPES (dipalmitoyl phosphatidylethanolamidospermine) in which spermine as headgroup was attached to lipids through peptide bonds. A variety of eukaryotic cell cultures also have been transfected with success for transient and stable expression. Even a single-tailed and ornithine-based cationic lipid, OLON (a cationic lipid-oleoyl ornithinate), has been proven to be less toxic and more than 10 times the transgene expression than other liposomes when used with DOPE (*30*).

Such a combination of peptides and lipids has been reported to produce superior transfection of genes. A compound which contained cholesterol and a dipeptide consisting of glycine and sterically protected arginine has been proven to be suitable for in vitro transfection in the presence of 10% serum more efficiently than other cholesterol derivatives (*31*). The structure−activity study has proven that a change in peptide groups would cause very different transfection efficiency. In a structure−activity investigation, cationic lipids with alanine and β-alanine headgroups were found to be remarkably more transfection efficient than their serine headgroup counterparts, and some of the conjugates in combination with cholesterol as auxiliary lipid were much more effective than Lipofectamine 2000 (*32*). In a later study, they studied three novel nontoxic cationic transfection amphiphiles containing mono-, di-, and trihistidine functionalities in their headgroup regions in multiple cultured cells for elucidating the structure−activity relationship (*33*). Yosuke Obata et al (*34*) have proven that the lysine- or arginine-type lipids exhibited higher gene expression efficiencies than Lipofectamine 2000, against COS-7 cells. The gene expression efficiency in relation to the cationic headgroup of the lipids was as follows: lysine > arginine > histidine. Peptide-based gemini surfactants GS (Figure 3) could lead to an increase in levels of gene expression in vitro compared to well-established nonviral reagents (*35*).

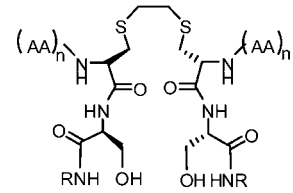


Figure 3. Chemical structure of GS.

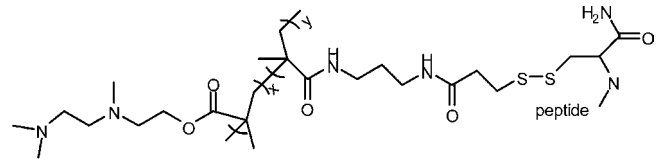


Figure 4. Chemical structure of INF7 peptide−polymer conjugates.

A series of new lipophilic peptides possessing a cationic tripeptide headgroup were effective nonviral vectors for gene delivery. Cytotoxity experiments performed with all the tripeptide lipophilic peptides showed no significant cytotoxicity, significantly better than Lipofectamine 2000 when exposed to chinese hamster ovarian (CHO) or NIH 3T3 cells (*36*). A subset of lipitoids with a repeated side chain trimer motif conjugated with dimyristoyl phosphatidyl-ethanolamine (DMPE) mediated DNA were also found to transfer cells with high efficiency (*37*).

Some peptide headgroups could endow additional functions to the lipids, such as membrane-disturbing ability. In a hybrid molecule, the covalent coupling of an amphipathic and membrane-disturbing peptide to a lipid moiety might create a stable and efficient peptide-based gene transfer system. The luciferase activity induced by the dioleoylmelittin/DNA complex was 5−500-fold higher than that induced by a cationic lipid/DNA complex, depending on the cationic lipid and the cell line (*38*). A membrane-disrupting peptide derived from the influenza virus was covalently linked to different polymethacrylates using *N*-succinimidyl 3-(2-pyridyldithio)propionate (SPDP) as a coupling agent to increase the transfection efficiency of polyplexes based on these polymers (Figure 4). In vitro transfection and toxicity were tested in COS-7 cells, and these experiments showed that the polyplexes with grafted peptides had a substantially higher transfection activity than the control polyplexes, while the toxicity remained unchanged (*39*).

Moreover, some peptide type cationic lipids are not serum-sensitive, which is crucial in in vivo applications (*40–42*). Dioleoylmelittin represented a new class of efficient peptide-based transfection reagents, especially suited for serum-sensitive cells, in which the presence of 10−50% fetal calf serum during dioleoylmelittin-mediated transfection enhanced 1.5−3-fold gene expression (*38*). The headgroups of asymmetric diether lipids have been varied by the coupling of the four naturally occurring amino acids with cationic side chains, sarginine, histidine, lysine, and tryptophan, and several formulations have

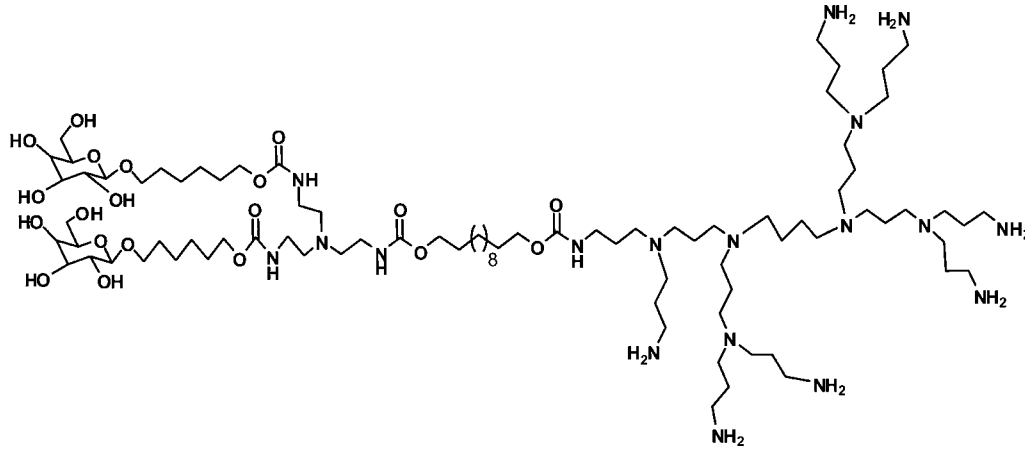


Figure 5. Chemical structure of DAB-dendr-$(NH_2)_8$.

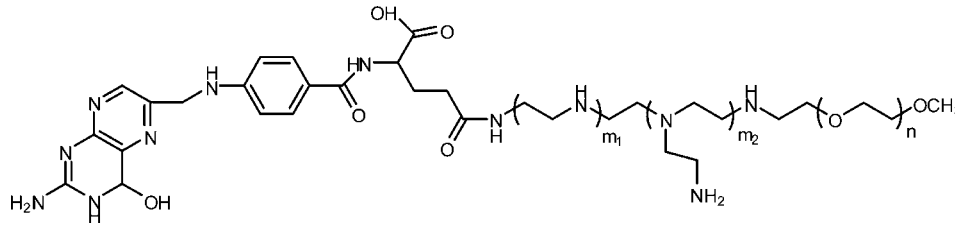


Figure 6. Chemical structure of FOL-PEI-b-PEG.

been shown to transfect different cell lines with up to 10 times the efficacy of the commonly used DC-Chol/DOPE formulation (*43*).

CONJUGATES OF TARGETING MOIETIES AND NONVIRAL VECTORS

The incorporation of targeting moieties into liposomes by direct formulation, with no covalent bond to any lipid (*44*); conjugated to helper lipid (*45, 46*), or connected directly to the cationic lipids (*47, 48*) can increase uptake and selectivity of liposomes for certain tissues. The targeting groups often used include folate (*45, 46*), galactose (*47, 48*), mannose (*49, 50*), and proteins such as antibodies (*51*) and transferrin (*44*).

The hepatic asialoglycoprotein receptor could recognize and bind to β-D-galactoside terminated glycoproteins (*52*). By using this physical and biological feature, asialoglycoprotein receptor has been studied as a target for gene delivery into hepatocytes. Hashida et al (*53*) synthesized novel galactosylated cholesterol derivatives, cholesten-5-yloxy-*N*-(4-((1-imino-c-β-D-thiogalactosylethyl)amino)alkylformamide, for gene delivery to hepatocytes. In HepG2 cells, the liposomes containing galactosylated cholesterol derivatives showed higher transfection activities than DC-Chol liposomes based on a receptor-mediated mechanism. Later, they used galactosylated cationic liposomes to target liver cells asialo-glycoprotein receptors in vivo (*48*). Liu et al (*54*) developed an efficient route toward the synthesis of bifunctional cationic compounds with DAB-dendr-$(NH_2)_8$ (Figure 5) as the DNA binding domain and galactose ligand for binding to the asialoglycoprotein receptor to prove that the galactosyl compounds Di-Gal and Tri-Gal could effectively deliver DNA into HepG2 cells.

The folate receptor (FR) is a tumor marker overexpressed in large numbers of cancer cells. As a low molecular weight ligand, folic acid has the advantages of being stable and nonimmunogenic compared to monoclonal antibodies (*55*), and still having a relatively high receptor affinity. Folate-targeted liposomes have been successfully used in the tumor cell specific delivery of anticancer drugs and antisense oligodeoxynucleotides in vitro (*56*). In a study, folate was connected to polyethylenimine-*block*-poly(ethylene glycol) to form a copolymer, FOL-PEI-b-PEG (Figure 6), which showed less toxicity in comparison with that of 25 kDa PEI and effective transfection efficiency (*57*). Huang et al (*58, 59*) developed vectors in which poly(lysine)-condensed DNA was entrapped into folate-targeted cationic liposomes (LPD). They found LPD vector to be more efficient and less cytotoxic compared to conventional cationic liposomal vectors.

The physical and biological features of mannosylated vectors offer them the opportunity to deliver plasmid DNA (pDNA) to the liver NPC via mannose receptor mediated endocytosis. The application of poly(lysine) linked to mannose with naked pDNA has been reported to enhance gene expression in macrophages (*60*). Hashida et al. (*61*) have developed a novel mannosylated cholesterol derivative, Man-C4-Chol, consisting of modified cationic liposomes with mannose moieties for NPC-selective gene delivery via mannose receptors on NPC. The mannosylated cationic liposomes can deliver pDNA to liver nonparenchymal cells (*61*) and splenic DCs and improve immune activation in DNA vaccines (*62*). They also proved that DOPE could improve gene expression of the mannosylated cationic liposomes after intraportal administration into mice, and DOPE complex was accumulated in the liver more efficiently through intravenous administration (*63*).

Targeting proteins such as antibodies or transferrin were conjugated to cationic polymers (e.g., poly(lysine) (*64*) or polyethylenimine *65–67*) to mediate uptake of plasmid DNA and antisense oligonucleotides. Since antibodies feature a highly selective binding to their antigen, they are of particular interest as targeting moieties. PEI was modified with G250 mAb to gain targeting effect and enhanced gene delivery to tumor cells that express G250 antigen. The conjugate showed targeted gene delivery to RCC and Hela cells, even in the presence of serum, but with restricted reactivity to G250 negative cells or normal cells (*51*). Transferrin was covalently linked to protamine to deliver functional plasmid DNA to erythroblasts (*68, 69*). Hormone receptors, such as the epidermal growth factor receptor family member ErbB2, expressed on the cell surface can serve

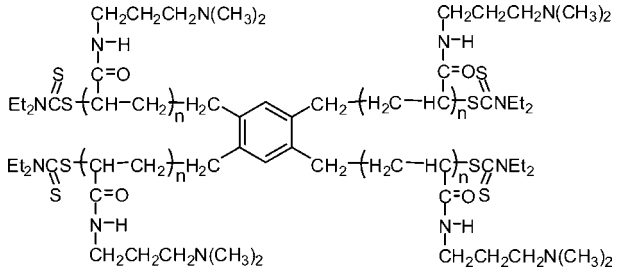


Figure 7. Chemical structure of PDMAPAAm-branched polymer.

as target structures for nucleic acid delivery. A recombinant fusion protein of an ErbB2-specific single-chain antibody fused to protamine successfully transported plasmid DNA to ErbB2 antigen expressing cells (*69, 70*).

Peptides containing the amino acid sequence Arg-Gly-Asp (RGD) can be used for specific targeting to integrin receptors, including the vitronectin receptor $\alpha v\beta 3$, which is known to be highly upregulated in certain tumors (*71*). Anderson et al. (*72*) used RGD containing peptide to coat nanoparticles; the noncovalent peptide coated nanoparticles were found to have favorable biophysical characteristics including small particle size, near-neutral ζ potential, and stability in serum. At appropriate formulation conditions, the coated nanoparticles enabled effective ligand-specific gene delivery to human primary endothelial cells in serum-containing media.

Nakayama (*73*) also proved the fact of RGD peptide enhancing gene expression of a cationic nonviral gene carrier, poly(*N*,*N*-dimethylaminopropylacrylamide) (Figure 7), in endothelial cells. The addition of the RGD-containing peptide to the polyplex solution led to a decrease in the ζ-potential and particle size, and an increase of transfection against endothelial cells and reduction of cellular cytotoxicity.

HYBRIDS OF CATIONIC LIPOSOMES AND POLYMERS

Cationic liposomes, cationic polymers, micelles, or nanoparticles are often researched for gene delivery, but none of them seem to meet the need of the theoretical study or clinical trials for gene therapy. The combination of them may provide a synergistic effect on the transfection efficiency and a promising solution to the problem frustrating us.

Serum is a major hurdle for nucleic delivery of cationic liposomes, as the binding of negatively charged serum components to positively charged DNA complexes can significantly decrease transfection efficiency (*74, 75*). To decrease or reverse the overall particle charge and hence reduce serum opsonization, anionic polymers have been employed as an additional component of the delivery vector (*76–78*). Roth (*79*) showed that the addition of a synthetic, pH-sensitive, membrane-disrupting polyanion, poly(propylacrylic acid) (PPAA), improved the in vitro efficiency of the cationic lipid, DOTAP, with regard to oligonucleotide delivery and antisense activity.

Low-molecular-weight PEIs and cationic liposomes can be combined resulting in a synergistic increase in transfection efficiency. PEI2K-DNA-Dosper complexes showed much more cellular uptake of DNA than PEI2K-DNA complexes and two times higher transfection than Dosper-DNA complexes. It has been hypothesized that Dosper improved the cellular uptake of PEI2K-DNA complexes and PEI2K improved a transfer of the complexes from lysosomes to nucleus (*80*). In a study, the combination of PEI and DOTAP-Chol caused more than 10-fold increase in the transfection efficiency in many cells compared with using polymer or liposome alone. Minimal toxicity was also shown in these cultured cells in vitro (*81*).

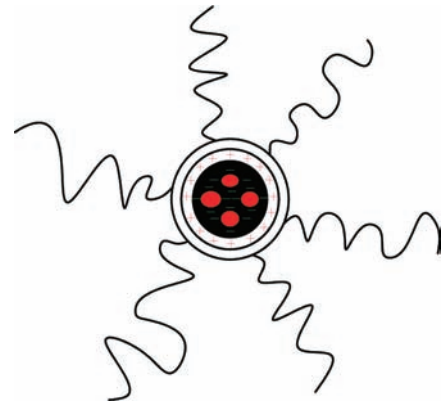


Figure 8. PEGylated LPD through the hybridization of polyplex, liposome and PEG based lipid (This figure was adapted from Huang et al's illustration in ref *84*).

It has been reported that liposome-mediated gene transfer could be improved by natural polycations such as protamine sulfate (PS), poly(L-lysine) (PLL), and spermine (*57, 82*). The addition of poly(L-lysine) and protamine dramatically reduced the particle size of the complex formed between DNA and cationic liposomes and rendered DNA resistant to the nuclease activity (*58*). As copolymers, they can markedly enhance the transfection efficiency of several types of cationic liposomes by 2−28-fold in a number of cell lines in vitro (*58*) and in vivo (*82*). These polycations are known to form a complex with DNA and condense DNA from extended conformation to highly compact structure into 30−100 nm in size. They exhibit a synergistic effect when combined with several different types of cationic LPs in delivering plasmid DNA into several different types of cells (*58*).

Moreover, three natural polycations, protamine sulfate (PS), poly(L-lysine), and spermine, were selected as DNA condensing active agents to enhance the in vitro and in vivo transfection activity of the cationic lipid emulsion (LE). The transfection activity of the ternary complex increased by at least 2.5−5-fold in vitro cell culture system in the presence of 80% serum, as well as in vivo mouse system, as compared with LE/DNA binary complexes. More importantly, after intravenous and intranasal administrations, the in vivo transfection efficiency of the LE/PS/DNA complex was ca. 30 and 50 times higher than that of the liposome (LP)/DNA complex in spleen and lung, respectively. On the other hand, cell toxicity of the ternary complex is lower than that of binary complex (*83*).

We have stated already that Huang et al (*58, 59*) developed vectors in which poly(lysine)-condensed DNA was entrapped into folate-targeted cationic liposomes (LPD). Later, they modified LPDs through different cationic liposomes wherein LPDS were used to deliver antisense oligodeoxynucleotide and siRNA (*84, 85*). Though they used DOTAP and *N*,*N*-distearyl-*N*-methyl-*N*-2[*N*-(*N*2-guanidino-L-lysinyl)] aminoethyl ammonium chloride (DSGLA), a novel non-glycerol-based cationic lipid, which contained both a guanidinium and a lysine residue as the cationic headgroup and downregulated pERK more efficiently in H460 cells than DOTAP as cationic liposomes in the process of LPD preparation, the procedure is very similar. Nucleic acids were mixed with a carrier DNA, calf thymus DNA, before complexing with protamine, a highly positively charged peptide. The resulting particles were coated with cationic liposomes to obtain LPD (liposome−polycation−DNA) nanoparticles. Ligand targeting and steric stabilization were then introduced by incubating preformed LPD nanoparticles with PEGylated ligand lipid (Figure 8).

Maitani et al (*86*) developed cell-penetrating peptide-based gene delivery vectors. A novel oligoarginine lipid ($(Arg)_n$-B, *n*

= 4, 10) conjugated to 3,5-bis(dodecyloxy)benzamide (BDB) lipid with a poly(ethylene glycol) (PEG) spacer was synthesized. Oligoarginine lipid-coated vector was prepared by the addition of $(Arg)_n$-B to DNA/protamine complex (PD) ($(Arg)_n$-B-PD). This result suggested that negatively charged tetraarginine conjugated-PEG lipid-coated PD is a promising gene delivery vector for intratumoral injection.

In another study (*87*), polyamidoamine (PAMAM) dendrimer/DNA complexes encapsulated in a water-soluble polymer, poly-α,β-[*N*-(2-hydroxyethyl)-L-aspartamide) (PHEA), were supported on a cholic acid functionalized star poly(DL-lactide) film with a fast degradation rate to mediate localized gene delivery. The star poly(DL-lactide) supported PHEA encapsulated PAMAM/DNA complexes could effectively mediate transfection to indicate that the existence of PHEA played an important role in the efficient transfection. pH-sensitive fusogenic polymer-modified liposomes exhibited higher transfection activity toward DC2.4 cells than some commercial reagents and hence may be useful as a gene vector for DCs (*88*).

Recently, hybrids of nonviral and viral carriers have been extended to deliver genes, though they have mainly been used for drug delivery systems (*89, 90*). Bionanocapsules (BNCs) consisting of hepatitis B virus (HBV) surface antigen (HBsAg) and lipid bilayer and displaying a human hepatocyte-recognizing molecule (pre-S1 peptide) were approximately 50 nm hollow particles which have been used as an HB vaccine (*91, 92*). BNCs could be produced efficiently in recombinant yeast and therefore were free of other components of HBV (*93*). On the basis of these studies, Kuroda et al (*94*) developed a new BNC conjugated with liposomes. The conjugate could deliver large materials (100 nm fluorescence-labeled polystyrene beads and N30 kbp plasmids) to human hepatocytes specifically in vitro and in vivo. The transfection efficiency of the BNC−liposome complex was significantly higher than that of the original BNC.

CONCLUDING REMARKS

Though the past decade has seen tremendous progress in the design and synthesis of nonviral vectors for gene delivery as well as application of a battery of techniques, the hybrids of nonviral vectors provide another route to overcome the low transfection efficiency of nonviral vectors. Cationic lipids themselves are rarely used, as they do not show effective transfection without the addition of helper lipids such as DOPE. The combination between cationic lipids and helper lipids represents the most successful formulations for gene delivery. However, this may not meet the requirements of in vivo transfection, because of the lack of targeting ability. To promote the uptake of vector−DNA complexes by specific cell types, vectors are usually conjugated with a number of cell targeting agents, particularly folate for cancer cell targeting and galactose for hepatic cell targeting. It has been proven that tertiary amine and quaternary ammonium containing vectors show toxicity to some extent; the conjugates of peptides and lipids are being explored to resolve this problem. They show relatively low toxicity, while retaining acceptable transfection efficiency. The combined utilization of cationic liposomes and other nonviral vectors may provide the most exciting solution for gene delivery, for many advantages could concentrate on the delivery systems. Besides the above-mentioned hybrids, other new formulations are being explored, such as the combination of nonviral and viral carriers.

ACKNOWLEDGMENT

The study was supported by Program for New Century Excellent Talents in University (NCET-08-0654) and the National Natural Science Foundation of China (20876027).

LITERATURE CITED

(1) Cavazzana-Calvo, M., Hacein-Bey, S., De.Saint Basile, G., Gross, F., Yvon, E., Nusbaum, P., Selz, F., Hue, C., Certain, S., Casanova, J. L., Bousso, P., Le Deist, F., and Fischer, A. (2000) Gene therapy of human severe combined immunodeficiency (SCID)-X1 disease. *Science 288*, 669–672.

(2) Boyd, A. C. (2006) *Gene and Stem Cell Therapy. Progress in Respiratory Research Volume 3: Cystic Fibrosis in the 21st Century* (Bush, A., Alton, E. W. F. W., Davies, J. C., Griesenbach, U., and Jaffe, A., Eds.) pp 221−231, Chapter *29*; Karger, New York.

(3) Kaplitt, M. G., Feigin, A., Tang, C., Fitzsimons, H. L., Mattis, P., Lawlor, P. A., Bland, R. J., Young, D., Strybing, K., Eidelberg, D., and During, M. J. (2007) Safety and tolerability of gene therapy with an adeno-associated virus (AAV) borne GAD gene for Parkinson's disease: an open label, phase I trial. *Lancet 369*, 2097–2105.

(4) Zhang, S. B., Xu, Y. M., Wang, B., Qiao, W. H., Liu, D. L., and Li, Z. S. (2004) Cationic compounds used in lipoplexes and polyplexes for gene delivery. *J. Controlled Release 100*, 165–180.

(5) Liu, F., and Huang, L. (2002) Development of non-viral vectors for systemic gene delivery. *J. Controlled Release 78*, 259–266.

(6) Ferber, D. (2001) Gene therapy: safer and virus-free. *Science 294*, 1638–1642.

(7) Hacein-Bey-Abina, S., von Kalle, C., Schmidt, M., Le Deist, F., Wulffraat, N., McIntyre, E., Radford, I., Villeval, J. L., Fraser, C. C., Cavazzana-Calvo, M., and Fischer, A. (2003) A serious adverse event after successful gene therapy for X linked severe combined immunodeficiency. *N. Engl. J. Med. 348*, 255–256.

(8) Woods, N. B., Bottero, V., Schmidt, M., von Kalle, C. I., and Verma, M. (2006) Gene therapy: therapeutic gene causing lymphoma. *Nature 440*, 1123.

(9) Arpicco, S., Canevari, S., Ceruti, M., Galmozzi, E., Rocco, F., and Cattel, L. (2004) Synthesis characterization and transfection activity of new saturated and unsaturated cationic lipids. *Il Farmaco 59*, 869–878.

(10) Bianco, A., Bonadies, F., Napolitano, R., and Ortaggi, G. (2005) A simple approach to DC-cholesterol, its analogues and vitamin D-based cationic lipids for gene therapy. *Lett. Org. Chem. 2*, 79–82.

(11) Woodle, M. C., and Scaria, P. (2001) Cationic liposomes and nucleic acids. *Curr. Opin. Colloid Interface Sci. 6*, 78–84.

(12) Zabner, J. (1997) Cationic lipids used in gene transfer. *Adv. Drug Delivery Rev. 27*, 17–28.

(13) Zhdanov, R. I., Podobed, O. V., and Vlassov, V. V. (2002) Cationic lipid-DNA complexes−lipoplexes for gene transfer and therapy. *Bioelectrochemistry 58*, 53–64.

(14) Litzinger, D., and Huang, L. (1992) Phosphatidylethanolamine liposomes: drug delivery, gene transfer and immunodiagnostic applications. *Biochim. Biophys. Acta 1113*, 201–227.

(15) Farhood, H., Serbina, N., and Huang, L. (1995) The role of dioleoyl phosphatidylethanolamine in cationic liposome mediated gene transfer. *Biochim. Biophys. Acta 1235*, 289–295.

(16) Farhood, H., Bottega, R., Epand, R. M., and Huang, L. (1992) Effect of cationic cholesterol derivatives on gene transfer and protein kinase C activity. *Biochim. Biophys. Acta 1111*, 239–246.

(17) Legendre, J. Y., Jr. (1992) Delivery of plasmid DNA into mammalian cell lines using pH-sensitive liposomes: comparison with cationic liposomes. *Pharm. Res. 9*, 1235–1242.

(18) Zhou, X., and Huang, L. (1994) DNA transfection mediated by cationic liposomes containing lipopolylysine: characterization and mechanism of action. *Biochim. Biophys. Acta 1189*, 195–203.

(19) Feigner, J. H., Kumar, R., Sridhar, C. N., Wheeler, C. J., Tsai, Y. J., Border, R., Ramsey, P., Martin, M., and Feigner, P. L. (1994) Enhanced gene delivery and mechanism studies with a novel series of cationic lipid formulations. *J. Biol. Chem. 269*, 2550–2561.

(20) Koltover, I., Salditt, T., Radler, J. O., and Safinya, C. R. (1998) An inverted hexagonal phase of cationic liposome-DNA complexes related to DNA release and delivery. *Science 281*, 78–81.

(21) Hafez, I. M., N., and Maurer, P. R. (2001) Cullis, On the mechanism whereby cationic lipids promote intracellular delivery of polynucleic acids. *Gene Ther. 8*, 1188–1196.

(22) Hong, K., Zheng, W., Baker, A., and Papahadjopoulos, D. (1997) Stabilisation of cationic liposome/DNA complexes by polyamines and polyethylenglycol-phospholipid conjugates for efficient *in vivo* gene delivery. *FEBS Lett. 414*, 187–192.

(23) Lasic, D. D. (1997) *Liposomes in Gene Delivery*, CRC Press, Inc., Boca Raton.

(24) Tempelton, N. S., Lasic, D. D., Frederik, P. M., Strey, H. H., Roberts, D. D., and Palvakis, G. N. (1997) Improved DNA: liposomes complexes for increased systemic delivery and gene expression. *Nat. Biotechnol. 15*, 647–652.

(25) Bennet, M. J., Nantz, M. H., Balasubramanian, R. P., Gruenert, D. C., and Malone, R. W. (1995) Cholesterol enhances cationic liposome-mediated DNA transfection of human respiratory ephitelial cells. *Biosci. Rep. 15*, 47–53.

(26) Lasic, D. D. (1997) Recent developments in medical applications of liposomes: sterically stabilized liposomes in cancer therapy and gene delivery *in vivo*. *J. Controlled Release 48*, 203–222.

(27) Ewert, K. K., Evans, H. M., Zidovska, A., Bouxsein, N. F., Ahmad, A., and Safinya, C. R. (2006) A columnar phase of dendritic lipid-based cationic liposome-DNA complexes for gene delivery: Hexagonally ordered cylindrical micelles embedded in a DNA honeycomb lattice. *J. Am. Chem. Soc. 128*, 3998–4006.

(28) Bottega, R., and Epand, R. M. (1992) Inhibition of protein kinase C by cationic amphiphiles. *Biochemistry 31*, 9025–30.

(29) Behr, J. P., Demeneix, B., Loerrler, J. P., and Perez-Mutul, J. (1989) Efficient gene transfer into mammalian primary endocrine cells with lipopolyamine-coated DNA. *Proc. Natl. Acad. Sci. U.S.A. 86*, 6982–6986.

(30) Tang, F. X., and Hughes, J. A. (1999) Synthesis of a single-tailed cationic lipid and investigation of its transfection. *J. Controlled Release 62*, 345–358.

(31) Sochanik, A., Kaida, I., Mitrus, I., Rajca, A., and Szala, S. (2000) A new cholesterol derivative suitable for transfecting certain type of cells in the presence of 10% serum. *Cancer Gene Ther. 7*, 513–520.

(32) Sen, J., and Chaudhuri, A. (2005) Gene transfer efficacies of novel cationic amphiphiles with alanine, β-alanine, and serine headgroups: a structure-activity investigation. *Bioconjugate Chem. 16*, 903–912.

(33) Karmali, P. P., Majeti, B. K., Sreedhar, B., and Chaudhuri, A. (2006) In vitro gene transfer efficacies and serum compatibility profiles of novel mono-, di-, and tri-histidinylated cationic transfection lipids: a structure-activity investigation. *Bioconjugate Chem. 17*, 159–171.

(34) Obata, Y., Suzuki, D., and Takeoka, S. (2008) Evaluation of cationic assemblies constructed with amino acid based lipids for plasmid DNA delivery. *Bioconjugate Chem. 19*, 1055–1063.

(35) McGregor, C., Perrin, C., Monck, M., Camilleri, P., and Kirby, A. J. (2001) Rational approaches to the design of cationic gemini surfactants for gene delivery. *J. Am. Chem. Soc. 123*, 6215–6220.

(36) Prata, Carla, A. H., Zhang, X. X., Luo, D., McIntosh, T. J., Barthelemy, P., and Grinstaff, M. W. (2008) Lipophilic peptides for gene delivery. *Bioconjugate Chem 19*, 418–420.

(37) Huang, C. Y., Uno, T., Murphy, J. E., Lee, S., Hamer, J. D., Escobedo, J. A., Cohen, F. E., Radhakrishnan, R., Dwarki, V., and Zuckermann, R. N. (1998) Lipitoids - novel cationic lipids for cellular delivery of plasmid DNA in vitro. *Chem. Biol. 5*, 345–354.

(38) Legendre, J. Y., Trzeciak, A., Bohrmann, B., Deuschle, U., Kitas, E., and Supersaxo, A. (1997) Dioleoylmelittin as a novel serum-insensitive reagent for efficient transfection of mammalian cells. *Bioconjugate Chem. 8*, 57–63.

(39) Funhoff, A. M., van Nostruma, C. F., Loka, M. C., Kruijtzerb, J. A. W., Crommelina, D. J. A., and Henninka, W. E. (2005) Cationic polymethacrylates with covalently linked membrane destabilizing peptides as gene delivery vectors. *J. Controlled Release 101*, 233–246.

(40) Nishikawa, M., Yamauchi, M., Morimoto, K., Ishida, E., Takakura, Y., and Hashida, M. (2000) Heptocyte-targeted *in vivo* gene expression by intraveneous injection of plasmid DNA complexed with synthetic multi-functional gene delivery system. *Gene Ther. 7*, 548–555.

(41) Schuster, M. J., Wu, G. Y., Walton, C. M., and Wu, C. H. (1999) Multicomponent DNA carrier with a vesicular stomatitis virus G-peptide greatly enhaances liver-targeted gene expression in mice. *Bioconjugate Chem. 10*, 1075–1083.

(42) McKenzie, D. L., Kwok, K. Y., and Rice, K. G. (2000) A potent new class of reductively activated peptide gene delivery agents. *J. Biol. Chem. 275*, 9970–9977.

(43) Heyes, J. A., Niculescu-Duvaz, D., Cooper, R. G., and Springer, C. J. (2002) Synthesis of novel cationic lipids: effect of structural modification on the efficiency of gene transfer. *J. Med. Chem. 45*, 99–114.

(44) Seol, J. G., Heo, D. S., Kim, H. K., Yoon, J.-H., Choi, B. I., Lee, H.-S., Kim, N. K., and Kim, C. Y. (2000) Selective gene expression in hepatic tumor with trans-arterial delivery of DNA/liposome/transferrin complex. *In Vivo 14*, 513–518.

(45) Hofland, H. E. J., Masson, C., Iginla, S., Osetinsky, I., Reddy, J. A., Leamon, C. P., Scherman, D., Bessodes, M., and Wils, P. (2002) Folate-targeted gene transfer in vivo. *Mol. Ther. 5*, 739–744.

(46) Dauty, E., Remy, J. S., Zuber, G., and Behr, J.-P. (2002) Intracellular delivery of nanometric DNA particles via the folate receptor. *Bioconjugate Chem. 13*, 831–839.

(47) Gaucheron, J., Santaella, C., and Vierling, P. (2001) In vitro gene transfer with a novel galactosylated spermine bolaamphiphile. *Bioconjugate Chem. 12*, 569–575.

(48) Kawakami, S., Fumoto, S., Nishikawa, M., Yamashita, F., and Hashida, M. (2000) In vivo gene delivery to the liver using novel galactosylated cationic liposomes. *Pharm. Res. 17*, 306–313.

(49) Kawakami, S., Sato, A., Nishikawa, M., Yamashita, F., and Hashida, M. (2000) Mannose receptor-mediated gene transfer into macrophages using novel mannosylated cationic liposomes. *Gene Ther. 7*, 292–299.

(50) Hattori, Y., Kawakami, S., Suzuki, S., Yamashita, F., and Hashida, M. (2004) Enhancement of immune responses by DNA vaccination through targeted gene delivery using mannosylated cationic liposome formulations following intravenous administration in mice. *Biochem. Biophys. Res. Commun. 317*, 992–999.

(51) Duan, Y. J., Zheng, J. N., Han, S. F., Wu, Y., Wang, Y. M., Li, D. J., Kong, D. L., and Yu, Y. T. (2008) A tumor targeted gene vector modified with G250 monoclonal antibody for gene therapy. *J. Controlled Release 127*, 173–179.

(52) Ashwell, G., and Harford, J. (1982) Carbohydrate-specific receptors of the liverAnnu. *Rev. Biochem. 51*, 531–554.

(53) Kawakami, S., Yamashita, F., Nishikawa, M., Takakura, Y., and Hashida, M. (1998) Asialoglycoprotein receptor-mediated gene transfer using novel galactosylated cationic liposomes. *Biochem. Biophys. Res. Commun. 252*, 78–83.

(54) Ren, T., Zhang, G. S., and Liu, D. X. (2001) Synthesis of Galactosyl compounds for targeted gene delivery. *Bioorg. Med. Chem. 9*, 2969–2978.

(55) Kane, M. A., Elwood, P. C., Portillo, R. M., Antony, A. C., and Kolhouse, J. F. (1986) The interrelationship of the soluble and membrane-associated folate-binding proteins in human KB cells. *J. Biol. Chem. 261*, 15625–15631.

(56) Wang, S., Lee, R. J., Cauchon, G., Gorenstein, D. G., and Low, P. S. (1995) Delivery of antisense oligodeoxyribonucleotides against the human epidermal growth factor receptor into cultured KB cells with liposomes conjugated to folate via polyethylene glycol. *Proc. Natl. Acad. Sci. U.S.A. 92*, 3318–3322.

(57) Cheng, H., Zhu, J. L., Zeng, X., Jing, Y., Zhang, X. Z., and Zhuo, R. X. (2009) Targeted gene delivery dediated by folate-polyethylenimine-block-poly(ethylene glycol) with receptor selectivity. *Bioconjugate Chem. 20*, 481–487.

(58) Gao, X., and Huang, L. (1996) Potentiation of cationic liposome-mediated gene delivery by polycations. *Biochemistry 35*, 1027–1036.

(59) Lee, R. J., and Huang, L. (1996) Folate-targeted, anionic liposome-entrapped polylysine-condensed DNA for tumor cell-specific gene transfer. *J. Biol. Chem. 271*, 8481–8487.
(60) Erbacher, P., Bousser, M. T., Raimond, J., Monsigny, M., Midoux, P., and Roche, A. C. (1996) Gene transfer by DNA/glycosylated polylysine complexes into human blood monocyte-derived macrophages. *Hum. Gene Ther. 7*, 721–729.
(61) Kawakami, S., Sato, A., Nishikawa, M., Yamashita, F., and Hashida, M. (2000) Mannose receptor-mediated gene transfer into macrophages using novel mannosylated cationic liposomes. *Gene Ther. 7*, 292–299.
(62) Hattori, Y., Kawakami, S., Suzuki, S., Yamashita, F., and Hashida, M. (2004) Enhancement of immune responses by DNA vaccination through targeted gene delivery using mannosylated cationic liposome formulations following intravenous administration in mice. *Biochem. Biophys. Res. Commun. 317*, 992–999.
(63) Hattori, Y., Sachiko, S., Kawakami, S., Yamashita, F., and Hashida, M. (2005) The role of dioleoylphosphatidylethanolamine (DOPE) in targeted gene delivery with mannosylated cationic liposomes via intravenous route. *J. Controlled Release 108*, 484–495.
(64) Citro, G., Perrotti, D., Cucco, C., D'Agnano, I., Sacchi, A., Zupi, G., and Calabretta, B. (1992) Inhibition of leukemia cell proliferation by receptor-mediated uptake of c-myb antisense oligodeoxynucleotides. *Proc. Natl. Acad. Sci. U.S.A. 89*, 7031–7035.
(65) Chiu, S. J., Ueno, N. T., and Lee, R. J. (2004) Tumor-targeted gene delivery via anti-HER2 antibody (trastuzumab, Herceptin) conjugated polyethylenimine. *J. Controlled Release 97*, 357–369.
(66) Guillem, V. M., Tormo, M., Revert, F., Benet, I., García-Conde, J., Crespo, A., and Aliño, S. F. (2002) Polyethyleneimine-based immunopolyplex for targeted gene transfer in human lymphoma cell lines. *J. Gene Med. 4*, 170–182.
(67) Li, S., Tan, Y., Viroonchatapan, E., Pitt, B. R., and Huang, L. (2000) Targeted gene delivery to pulmonary endothelium by anti-PECAM antibody. *Am. J. Physiol. Lung Cell Mol. Physiol. 278*, L504–L511.
(68) Wagner, E., Zenke, M., Cotten, M., Beug, H., and Birnstiel, M. L. (1990) Transferrin-polycation conjugates as carriers for DNA uptake into cells. *Proc. Natl. Acad. Sci. U.S.A. 87*, 3410–3414.
(69) Vornlocher, H. P. (2006) Antibody-directed cell-type-specific delivery of siRNA. *Trends Mol. Med. 12*, 1–3.
(70) Li, X. G., Stuckert, P., Bosch, I., Marks, J. D., and Marasco, W. A. (2001) Single-chain antibody-mediated gene delivery into ErbB2-positive human breast cancer cells. *Cancer Gene Ther. 8*, 555–565.
(71) Kunath, K., Merdan, T., Hegener, O., Haberlein, H., and Kissel, T. (2003) Integrin targeting using RGD-PEI conjugates for in vitro gene transfer. *J. Gene Med. 5*, 588–599.
(72) Green, J. J., Chiu, E., Leshchiner, E. S., Shi, J., Langer, R., and Anderson, D. G. (2007) Electrostatic ligand coatings of nanoparticles enable ligand-specific gene delivery to human primary cells. *Nano Lett. 7*, 874–879.
(73) Ishikawa, A., Zhou, Y. M., Kambe, N., and Nakayama, Y. (2008) Enhancement of star vector-based gene delivery to endothelial cells by addition of RGD-peptide. *Bioconjugate Chem. 19*, 558–561.
(74) Zelphati, O., Uyechi, L. S., Barron, L. G., and Szoka, F. C., Jr. (1998) Effect of serum components on the physico-chemical properties of cationic lipid/oligonucleotide complexes and their interactions with cells. *Biochim. Biophys. Acta 1390*, 119–133.
(75) Zhang, Y., and Anchordoquy, T. J. (2004) The role of lipid charge density in the serum stability of cationic lipid/DNA complexes. *Biochim. Biophys. Acta 1663*, 143–157.
(76) Trubetskoy, V. S., Loomis, A., Hagstrom, J. E., Budker, V. G., and Wolff, J. A. (1999) Layer-by-layer deposition of oppositely charged polyelectrolytes on the surface of condensed DNA particles. *Nucleic Acids Res. 27*, 3090–3095.
(77) Trubetskoy, V. S., Wong, S. C., Subbotin, V., Budker, V. G., Loomis, A., Hagstrom, J. E., and Wolff, J. A. (2003) Recharging cationic DNA complexes with highly charged polyanions for in vitro and in vivo gene delivery. *Gene Ther. 10*, 261–271.
(78) Finsinger, D., Remy, J. S., Erbacher, P., Koch, C., and Plank, C. (2000) Protective copolymers for nonviral gene vectors: synthesis, vector characterization and application in gene delivery. *Gene Ther. 7*, 1183–1192.
(79) Lee, L. K., Williams, C. L., Devore, D., and Roth, C. M. (2006) Poly(propylacrylic acid) enhances cationic lipid-mediated delivery of antisense oligonucleotides. *Biomacromolecules 7*, 1502–1508.
(80) Lampela, P., Elomaa, M., Ruponen, M., Urtti, A., Männistö, P. T., and Raasmaja, A. (2003) Different synergistic roles of small polyethylenimine and Dosper in gene delivery. *J. Controlled Release 88*, 173–183.
(81) Lee, C. H., Ni, Y. H., Chen, C. C., Chou, C. K., and Chang, F. H. (2003) Synergistic effect of polyethylenimine and cationic liposomes in nucleic acid delivery to human cancer cells. *Biochim. Biophy. Acta 1611*, 55–62.
(82) Li, S., and Huang, L. (1997) In vivo gene transfer via intravenous administration of cationic lipid-protamine-DNA (LPD) complexes. *Gene Ther. 4*, 891–900.
(83) Kima, T. W., Chung, H., Kwon, I. C., Sung, H. C., Shin, B. C., and Jeong, S. Y. (2005) Polycations enhance emulsion-mediated in vitro and in vivo transfection. *Int. J. Pharm. 295*, 35–45.
(84) Li, S. D., and Huang, L. (2006) Targeted delivery of antisense oligodeoxynucleotide and small interference RNA into lung cancer cells. *Mol. Pharmaceutics 3*, 579–588.
(85) Chen, Y. C., Sen, J., Bathula, S. R., Yang, Q., Fittipaldi, R., and Huang, L. (2009) Novel cationic lipid that delivers siRNA and enhances therapeutic effect in lung cancer cells. *Mol. Pharmaceutics 6*, 696–705.
(86) Fujita, T., Furuhata, M., Hattori, Y., Kawakami, H., Toma, K., and Maitani, Y. (2008) High gene delivery in tumor by intratumoral injection of tetraarginine-PEG lipid-coated protamine/DNA. *J. Controlled Release 129*, 124–127.
(87) Fu, H. L., Cheng, S. X., Zhang, X. Z., and Zhuo, R. X. (2007) Dendrimer/DNA complexes encapsulated in a water soluble polymer and supported on fast degrading star poly(DL-lactide) for localized gene delivery. *J. Controlled Release 124*, 181–188.
(88) Yuba, E., Kojima, C., Sakaguchi, N., Harada, A., Koiwai, K., and Kono, K. (2008) Gene delivery to dendritic cells mediated by complexes of lipoplexes and pH-sensitive fusogenic polymer-modified liposomes. *J. Controlled Release 130*, 77–83.
(89) Mima, H., Yamamoto, S., Ito, M., Tomoshige, R., Tabata, Y., Tamai, K., and Kaneda, Y. (2006) Targeted chemotherapy against intraperitoneally disseminated colon carcinoma using a cationized gelatin-conjugated HVJ envelope vector. *Mol. Cancer Ther. 5*, 1021–1028.
(90) Kunisawa, J., Masuda, T., Katayama, K., Yoshikawa, T., Tsutsumi, Y., Akashi, M., Mayumi, T., and Nakagawa, S. (2005) Fusogenic liposome delivers encapsulated nanoparticles for cytosolic controlled gene release. *J. Controlled Release 105*, 344–353.
(91) Yamada, T., Iwabuki, H., Kanno, T., Tanaka, H., Kawai, T., Fukuda, H., Kondo, A., Seno, M., Tanizawa, K., and Kuroda, S. (2001) Physicochemical and immunological characterization of hepatitis B virus envelope particles exclusively consisting of the entire L (pre-S1+pre-S2+S) protein. *Vaccine 19*, 3154–3163.
(92) Neurath, A. R., Kent, S. B., Strick, N., and Parker, K. (1986) Identification and chemical synthesis of a host cell receptor binding site on hepatitis B virus. *Cell 46*, 429–436.
(93) Kuroda, S., Otaka, S., Miyazaki, T., Nakao, M., and Fujisawa, Y. (1999) Hepatitis B virus envelope L protein particles. Synthesis and assembly in Saccharomyces cerevisiae, purification and characterization. *J. Biol. Chem. 267*, 1953–1961.
(94) Jung, J., Matsuzaki, T., Tatematsu, K., Okajima, T., Tanizawa, K., and Kuroda, S. (2008) Bio-nanocapsule conjugated with liposomes for in vivo pinpoint delivery of various materials. *J. Controlled Release 126*, 255–264.

BC900261C

Expedient Synthesis of a Modular Phosphate Affinity Reagent

Nicolas P. Tilmans, Casey J. Krusemark, and Pehr A. B. Harbury*

Department of Biochemistry, Stanford University School of Medicine, California. Received December 6, 2009; Revised Manuscript Received April 12, 2010

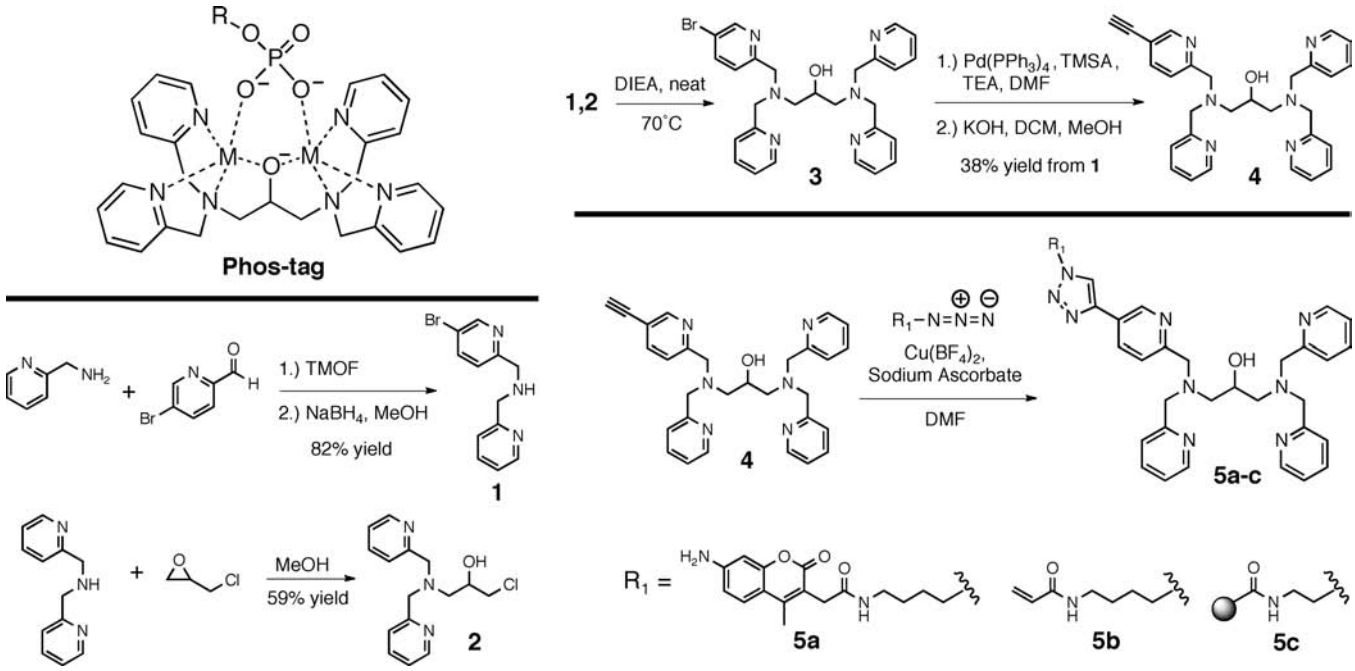
Isolation and identification of phosphorylated macromolecules is essential for the deconvolution of most biological regulatory networks. Koike and co-workers recently reported the application of a dinuclear zinc-(pyridylmethyl)-amine complex to phosphate-specific affinity purifications and gave it the shorthand name "phos-tag". This complex is valuable for studying phosphorylation because it binds selectively to phosphate dianion in the presence of acidic functional groups at physiological pH, and because the binding is largely independent of molecular context. These properties of phos-tag recommend it for applications in phosphoproteomics, metabolomics, and nucleic acid biology. The catch has been that the molecule is difficult to make and prohibitively expensive to buy. Here, we describe an efficient and inexpensive synthesis of a phos-tag derivative with a versatile alkyne handle. The alkyne handle allows for attachment of phos-tag to alkyl azides via the copper(I)-catalyzed azide−alkyne cycloaddition reaction ("click chemistry"). We characterize the phosphate binding behavior of the new phos-tag derivative in a variety of experimental assays, including its conjugation to a fluorescent reporter, to acrylamide gels, and to sepharose chromatography resin. The synthesis we report should enable a broader use of phos-tag for phosphate-related biochemistry, as both an analytical and a preparative reagent.

Phosphorylation plays a central regulatory role in many biological networks (*1*−*3*). Understanding such networks requires the detection and purification of different phospho-isoforms of proteins, nucleic acids, lipids, sugars, and small metabolites. Existing work has focused primarily on proteins, and multiple technologies for phospho-peptide enrichment exist (*4*). Importantly, however, most of these techniques require harsh acidic conditions to suppress polyvalent binding of carboxylic acids (*4*). The necessity for acidic pH, which can induce chemical decomposition or denaturation, limits the utility and generality of most known phosphate affinity reagents.

Phos-tag is a phosphate-binding metal chelate complex that operates under milder conditions (*4, 5*). It contains an organic core consisting of two bis(pyridylmethyl)amine moieties attached to the first and third carbon atoms of an isopropanol molecule (Scheme 1). The core chelates a pair of divalent metal

* Beckman Center, Room B400, 279 Campus Drive, Stanford, CA 94305-5307, Phone: 650-725-7989, Alt. Phone: 650-723-6289, Fax: 650-723-6783, E-mail: harbury@cmgm.stanford.edu.

Scheme 1. Synthesis of Modular Phos-Tag Ligand[a]



[a] Percentages describe representative yields of given reaction. M: 2+ metal ion. TMOF: trimethyl orthoformate. MeOH: methanol. DIEA: diisopropylethylamine. TMSA: (trimethylsilyl)acetylene. TEA: triethylamine. DMF: dimethylformamide. DCM: dichloromethane.

10.1021/bc900538b © 2010 American Chemical Society
Published on Web 05/21/2010

cations (Cd^{2+}, Co^{2+}, Cu^{2+}, Fe^{2+}, La^{2+}, Mn^{2+}, Ni^{2+}, and Zn^{2+} in literature reports) (*6*−*11*). Some of these metals in turn coordinate tightly to the nonbridging oxygen atoms of phosphate. At physiological pH and salt concentration, phosphate monoester dianion binds to phos-tag(Zn^{2+}) with nanomolar affinity, while sulfate dianion, acetate, chloride, and phosphate monoanion bind with dissociation constants that are 5000- to 800 000-fold weaker (*12*). Phos-tag has been used successfully to produce phospho-specific fluorescent dyes, to retard phosphorylated macromolecules in acrylamide gels, to tag or isolate phosphorylated compounds for mass spectrometry, and to enrich phosphorylated peptides and proteins by column chromatography (*11, 13*−*17*).

Currently, tethered phos-tag is available from a single commercial source in a limited number of formats at a cost of ~$50 000/g (*18*). A single synthesis of phos-tag with an immobilization handle is reported in the patent literature (*19*). The published synthesis proceeds from the cost-limiting reagent 6-methyl nicotinate ($371/g) in a 38% reported yield over four steps. The steps generate product mixtures, and four flash column purifications are required. This cumbersome synthetic scheme, and the expense of the commercially available material, practically limits the use of phos-tag for preparative applications and in novel experimental formats. Here, we present a simple, inexpensive, and convergent synthesis of a phos-tag ligand bearing a versatile alkyne handle for single-point attachment to solid supports and to reporter molecules.

An exploration of the literature for synthetic strategies to the unsubstituted phos-tag ligand (Scheme 1) yielded two prevalent synthetic routes: alkylation of 1,3-diamino-2-propanol with methylpyridines (*20*) and addition of one or two bis(pyridylmethyl)amine units to epichlorohydrin (*21, 22*). In our hands, the alkylation route generated a mixture of products that were difficult to separate. The epichlorohydrin route, on the other hand, promised greater synthetic control. It could be carried out in two steps with sequential addition of a first and second bis(pyridylmethyl)amine unit. Addition of unsubstituted bis(pyridylmethyl)amine followed by a singly functionalized bis(pyridylmethyl)amine would generate a single phos-tag product with a chemically accessible handle (Scheme 1).

A search of commercially available pyridylmethyl derivatives led to 2-formyl,5-bromopyridine (Scheme 1). Reductive amination of this compound with 2-aminomethylpyridine provides an asymmetric, singly brominated bis(pyridylmethyl)amine. Sequential addition of unsubstituted bis(pyridylmethyl)amine and then the brominated bis(pyridylmethyl)amine to epichlorohydrin produces a singly brominated phos-tag derivative. Finally, Sonogashira coupling to (trimethylsilyl)acetylene, followed by base-mediated deprotection, converts the bromine group to a terminal alkyne group (*23, 24*).

The synthesis proceeds in four steps from five commercially available reagents. The overall yield from the cost-limiting reagent, 2-formyl,5-bromo pyridine ($19/g), is 31%. Thus, the cost per gram of the product amounts to approximately $60. The alkyne handle is particularly useful because it can be linked chemoselectively to azide-containing partners by the copper-mediated alkyne−azide cycloaddition reaction (colloquially called the "click" reaction). The resulting linker consists of a triazole.

A first question is whether triazole-linked phos-tag binds to phosphate monoesters with the same affinity as the known amide-linked phos-tag. To address this question, we measured the dissociation constant (K_D) of phos-tag(Zn^{2+})-triazole-aminomethylcoumarin (**5a**) from fluorescein−phosphoethanolamine using a published fluorescence assay (Figure 1 and ref *25*). The fluorescence emission of the aminomethylcoumarin donor chromophore (emission maximum at 445 nm) is suppressed by

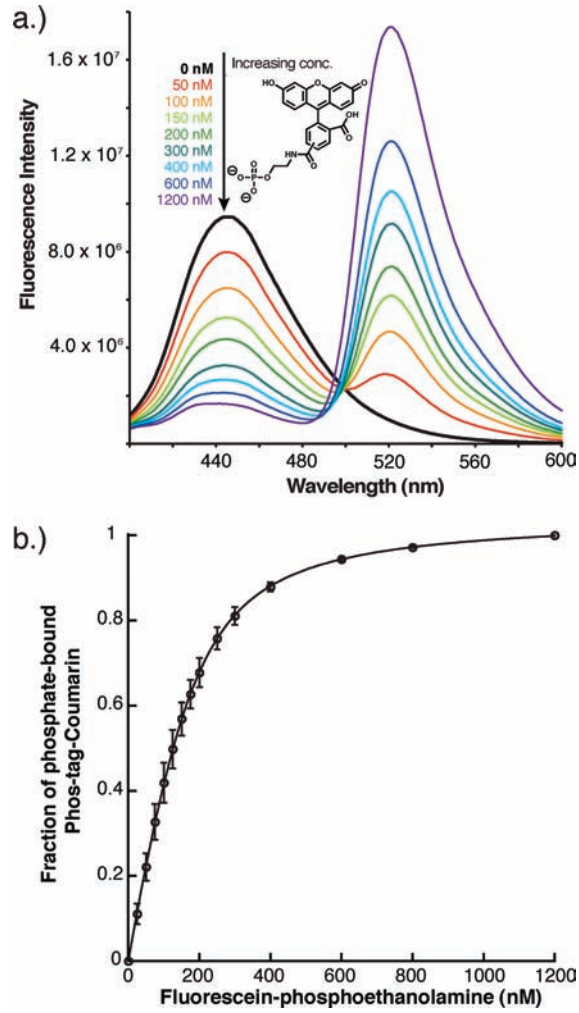


Figure 1. Triazole-linked phos-tag binds phosphate monoesters with an affinity comparable to amide-linked phos-tag. A. Overlaid emission spectra of phos-tag(Zn^{2+})-triazole-aminomethylcoumarin (**5a** at 170 nM concentration, λ_{ex} = 345 nm, 25 °C) with increasing concentrations of fluorescein−phosphoethanolamine. The aminomethylcoumarin fluorophore has an emission maximum at 445 nm, and the fluorescein has an emission maximum at 524 nm. B. Plot of triplicate FRET data with error bars indicating ±1 standard deviation. The fraction of bound phos-tag(Zn^{2+})-triazole-aminomethylcoumarin is plotted vs fluorescein−phosphoethanolamine concentration (0, 25, 50, 75, 100, 125, 150, 175, 200, 250, 300, 400, 600, 800, and 1200 nM). The calculated bimolecular dissociation curve with a K_D of 47 nM is shown as a solid line. Phos-tag(Zn^{2+})-amide-aminomethylcoumarin is reported to bind fluorescein−phosphoserine with a K_D of 70 nM (*25*).

increasing concentrations of the fluorescein acceptor (absorption maximum at 490 nm). The bimolecular dissociation curve that best fits the data has a K_D of 47 ± 10 nM, comparable to the 70 nM K_D measured for the dissociation of phos-tag(Zn^{2+})-amide-aminomethylcoumarin from fluorescein−phosphoserine (*25*). The data suggest that the binding properties of phos-tag are largely unperturbed by the triazole linker.

We next checked whether triazole-linked phos-tag is a practical phosphate-affinity reagent in standard electrophoretic and chromatographic applications. For electrophoresis experiments, the phos-tag alkyne was coupled to an azido-acrylamide moiety (**5b**) and incorporated into native 15% acrylamide gels supplemented with zinc. We compared the migration of two double-stranded PCR amplicons of 200 base-pair length that differed by a single 5′-phosphorylation (Figure 2A). Compound **5b** at 700 nM shifted the phosphorylated amplicon such that it migrated with an apparent size of 275 base pairs, while the amplicon lacking a terminal 5′-phosphate migrated as a 200mer.

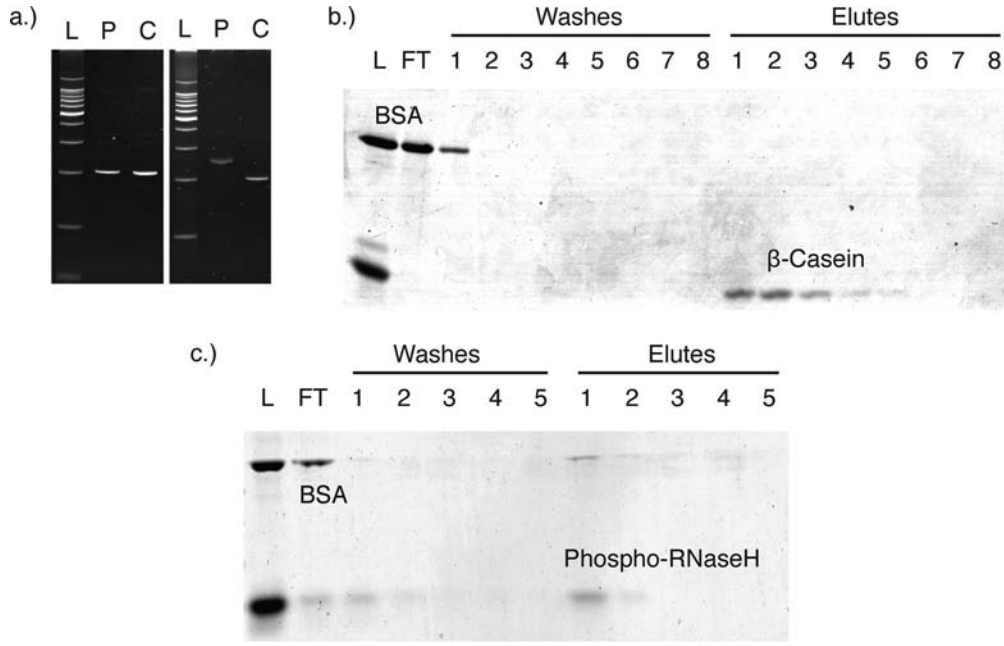


Figure 2. Detection and purification of phosphorylated macromolecules with the triazole-linked phos-tag. A. Phospho-specific DNA gel shift. A conventional 15% native DNA acrylamide gel (left) is compared with an identical gel containing 700 nM phos-tag acrylamide (right). Both gels were cast with 100 μM zinc nitrate. The samples include a 100 base-pair DNA ladder (L), a 200mer DNA with a single 5′-phosphate modification (P), and an identical 200mer DNA with two 5′-hydroxyl termini (C). The migration of the phosphorylated DNA is retarded in the phos-tag-containing gel. B. Phospho-specific protein purification. Load (L), flow-through (FT), wash and elute fractions from a phos-tag sepharose spin column were analyzed on 15% Laemmli gels stained with colloidal coomassie blue. β-casein (a polyphosphorylated protein) is separated away from bovine serum albumin (BSA, a non-phosphorylated acidic protein). The wash buffer was 100 mM citrate and 100 mM Tris-acetate pH 7.4. Elution was accomplished by addition of 100 mM sodium phosphate to the wash buffer. C. Laemmli gel as in **B** showing the partial separation of a monophosphorylated RNase H derivative (engineered to contain a single substrate recognition site for protein kinase A) away from BSA. The wash buffer was 1 M sodium acetate and 100 mM Tris-acetate pH 7.4. Elution was accomplished by addition of 10 mM sodium phosphate to the wash buffer.

The two amplicons migrated identically in a gel containing zinc but lacking compound **5b**.

For phosphate-affinity chromatography experiments, we coupled phos-tag alkyne to azide-derivatized NHS-sepharose at a final substitution level of 5 mM. The phos-tag sepharose resin (**5c**) was placed into 50 μL volume spin columns and loaded with Zn^{2+}. We compared the retention of the polyphosphorylated protein β-casein to the retention of the acidic protein bovine serum albumin (BSA). The use of the highly acidic protein BSA (net charge of -11 at the pH 7.4 used for the separations (*26*)) represents a challenging control. Acidic peptides and proteins are commonly co-purified in phospho-specific purifications, presumably through weak polyvalent interactions of carboxylic acids with the affinity reagent. Nevertheless, the triazole-linked phos-tag(Zn^{2+}) resin cleanly separated β-casein from BSA (Figure 2B), consistent with previous reports for amide-linked phos-tag(Zn^{2+}) (*17*). Thus, triazole-linked phos-tag works well for purification of polyphosphorylated proteins from mixtures.

Previously published phos-tag affinity separations of simple protein mixtures have all used polyphosphorylated proteins as the model phosphorylated species (*5, 17*). To explore the selectivity for monophosphorylated proteins, we measured the retention of a variant of RNase H engineered to include a single substrate recognition site for protein kinase A. The monophosphorylated RNase H bound to the resin but was eluted by citrate wash buffer. It remained bound during washes with 1 M NaCl and could then be eluted by addition of phosphate (Figure 2C). However, BSA was not fully cleared under these milder wash conditions, and some BSA eluted in a phosphate-dependent manner. Alternate wash solutions (1 M sodium acetate and 1 M ethylene diamine) and loading the phos-tag with an alternate metal (Mn^{2+} instead of Zn^{2+}) failed to abolish binding of BSA while retaining complete binding of monophosphorylated RNase H.

Although phos-tag(Zn^{2+}) binds to phosphate dianion 16 000-fold more tightly than it binds to acetate (*12*), in our hands phos-tag sepharose resin cannot cleanly separate a monophosphorylated protein from the acidic protein BSA. Additionally, the tricarboxylic acid citrate at 100 mM concentration competitively displaces monophosphorylated protein from phos-tag sepharose resin, whereas the monocarboxylic acid acetate at 1 M concentration does not. A possible explanation is that multiple weak interactions of carboxylates with the phos-tag sepharose resin are comparable in strength to the interaction with a single phosphate monoester. Increasing the mean distance between phos-tag ligands would suppress such multivalent binding and could be accomplished by reducing the phos-tag substitution level on the resin and by ensuring an even spatial distribution of the ligand. This remedy would presumably improve the specificity with which monophosphorylated proteins could be isolated, at the cost of decreased resin binding capacity. Notably, β-casein remains bound to phos-tag sepharose at high concentrations of citrate. Thus, isolation of polyphosphorylated proteins from complex mixtures is possible using highly substituted resins.

When synthesized as described, phos-tag alkyne is roughly 3 orders of magnitude less expensive than commercially available phosphate-affinity reagents or supports. It recapitulates the published properties of the amide-linked molecule. Our data suggest that phos-tag alkyne can be substituted directly for the commercially available phos-tag, with similar performance. The substantial cost reduction achieved by the new synthesis allows phos-tag to be considered as a practical reagent for preparative

protein purification. The versatility of the alkyne linkage handle should also facilitate new applications of the phos-tag chelate core.

ACKNOWLEDGMENT

This work was supported by National Institutes of Health grant DP OD000429-01 to P.ABH. The authors thank Rebecca Weisinger for constant, valuable advice and Kierstin Schmidt for the engineered *E. coli* RNase H protein.

Supporting Information Available: Materials, detailed synthetic procedures, characterization of synthesized molecules, and experimental protocols. This material is available free of charge via the Internet at http://pubs.acs.org.

LITERATURE CITED

(1) Davis, R. J. (1993) The mitogen-activated protein kinase signal transduction pathwayy. *J. Biol. Chem. 268*, 14553–14556.
(2) Kreegipuu, A., Blom, N., and Brunak, S. (1999) PhosphoBase, a database of phosphorylation sites: release 2.0. *Nucleic Acids Res. 27*, 237–239.
(3) Blume-Jensen, P., and Hunter, T. (2001) Oncogenic kinase signalling. *Nature 411*, 355–366.
(4) Schmidt, S. R., Schweikart, F., and Andersson, M. E. (2007) Current methods for phosphoprotein isolation and enrichment. *J. Chromatogr., B 849*, 154–162.
(5) Kinoshita-Kikuta, E., Kinoshita, E., Yamada, A., Endo, M., and Koike, T. (2006) Enrichment of phosphorylated proteins from cell lysate using a novel phosphate-affinity chromatography at physiological pH. *Proteomics 6*, 5088–5095.
(6) Yashiro, M., Hattori, M., Ishikubo, A., and Komiyama, M. (1996) Dinuclear Cd(II) complex for the efficient RNA hydrolysis. *Nucleic Acids Symp. Ser. 35*, 143–144.
(7) Feig, A. L., Becker, M., Schindler, S., van Eldik, R., and Lippard, S. J. (1996) Mechanistic studies of the formation and decay of diiron(III) peroxo complexes in the reaction of diiron(II) precursors with dioxygen. *Inorg. Chem. 35*, 2590–2601.
(8) Kamitani, J., Kawahara, R., Yashiro, M., and Komiyama, M. (1998) Design of a dinuclear metal center for RNA hydrolysis. *Nucleic Acids Symp. Ser. 39*, 139–140.
(9) Nishida, Y., Nishino, S., Guo, L. L., Matsushima, H., and Tokii, T. (1999) DNA promotes the activation of oxygen molecules by binuclear cobalt(II) compounds. *Inorg. Chem. Commun. 2*, 609–611.
(10) Marvey, B. B., Gultneh, Y., and Butcher, R. (2006) Synthesis and structure of a binuclear Cu(II) complex of 1,3-bis [N,N-bis(2-picolyl)amino]propan-2-ol. *Int. J. Mol. Sci. 7*, 179–185.
(11) Kinoshita, E., Kinoshita-Kikuta, E., Takiyama, K., and Koike, T. (2006) Phosphate-binding tag, a new tool to visualize phosphorylated proteins. *Mol. Cell. Proteomics 5*, 749–757.
(12) Kinoshita, E., Takahashi, M., Takeda, H., Shiro, M., and Koike, T. (2004) Recognition of phosphate monoester dianion by an alkoxide-bridged dinuclear zinc(II) complex. *Dalton Trans. 8*, 1189–1193.
(13) Lee, J., Alm, H., Shin, D., and Ahn, D. (2008) Label-free and real-time monitoring of phosphatase reactions using a phosphate-specific and fluorescent probe. *Bull. Korean Chem. Soc. 29*, 943–947.
(14) Kinoshita, E., Kinoshita-Kikuta, E., and Koike, T. (2009) Separation and detection of large phosphoproteins using Phos-tag SDS-PAGE. *Nat. Protoc. 4*, 1513–1521.
(15) Takeda, H A. K., Takahashi, M., Yamada, A., and Koike, T. (2003) Matrix-assisted laser desorption/ionization time-of-flight mass spectrometry of phosphorylated compounds using a novel phosphate capture molecule. *Rapid Commun. Mass Spectrom. 17*, 2075–2081.
(16) Nabetani, T Y. K., Watanabe, M., Ohashi, Y., Kamiguchi, H., and Hirabayashi, Y. (2009) Improved method of phosphopeptides enrichment using biphasic phosphate-binding tag/C18 tip for versatile analysis of phosphorylation dynamics. *Proteomics 9*, 5525–5533.
(17) Kinoshita, E., Yamada, A., Takeda, H., Kinoshita-Kikuta, E., and Koike, T. (2005) Novel immobilized zinc(II) affinity chromatography for phosphopeptides and phosphorylated proteins. *J. Sep. Sci. 28*, 155–162.
(18) Phostag Consortium. (2009) Phos-tag.com. URL: http://www.phos-tag.com/english/shouh/index.html. Accessed on: July 14, 2009. *Phostag consortium price list for Phostag compounds*.
(19) Koike, T., Kawasaki, A., Kobashi, T., and Takahagi, M., U.S. Patent 20040198712 A1, 2004; Chem. Abstr. 2004:732311.
(20) Sato, M. M., Y., and Iida, T. (1992) Convenient synthesis of N, N, N′, N′-Tetrakis(2-pyridylmethyl)-alpha, omega-alkanediamines using a phase-transfer catalyst. *Synthesis 6*, 539–540.
(21) Hayashi, Y., Kayatani, T., Sugimoto, H., Suzuki, M., Inomata, K., Uehara, A., Mizutani, Y., Kitagawa, T., and Maeda, Y. (1995) Synthesis, characterization, and reversible oxygenation of mu-alkoxo diiron(II) complexes with the dinucleating ligand N, N, N′, N′-Tetrakis((6-methyl-2-pyridyl)methyl)-1,3-diaminopropan-2-olate. *J. Am. Chem. Soc. 117*, 11220–11229.
(22) Rossi, L. M., Neves, A., Bortoluzzi, A. J., Horner, R., Szpoganicz, B., Terenzi, H., Mangrich, A. S., Pereira-Maia, E., Castellano, E. E., and Haase, W. (2005) Synthesis, structure and properties of unsymmetrical mu-alkoxo-dicopper(II) complexes: biological relevance to phosphodiester and DNA cleavage and cytotoxic activity. *Inorg. Chim. Acta 358*, 1807–1822.
(23) Lu, Y. F., and Fallis, A. G. (1993) An intramolecular diels-alder approach to tricyclic taxoid skeletons. *Tetrahedron Lett. 34*, 3367–3370.
(24) Chinchilla, R., and Najera, C. (2007) The Sonogashira reaction: a booming methodology in synthetic organic chemistry. *Chem. Rev. 107*, 874–922.
(25) Takiyama, K., Kinoshita, E., Kinoshita-Kikuta, E., Fujioka, Y., Kubo, Y., and Koike, T. (2009) A Phos-tag-based fluorescence resonance energy transfer system for the analysis of the dephosphorylation of phosphopeptides. *Anal. Biochem. 388*, 235–241.
(26) Tanford, C., Swanson, S., and Shore, W. (1955) Hydrogen ion equilibria of bovine serum albumin. *J. Am. Chem. Soc. 77*, 6414–6421.

BC900538B

Poly(amidoamine) Dendrimer Based MRI Contrast Agents Exhibiting Enhanced Relaxivities Derived via Metal Preligation Techniques

Kido Nwe,[†] L. Henry Bryant, Jr.,[‡] and Martin W. Brechbiel*,[†]

Radioimmune & Inorganic Chemistry Section, Radiation Oncology Branch, National Cancer Institute, 10 Center Drive, Bethesda, Maryland 20892, and Laboratory of Diagnostic Radiology Research (CC), National Institutes of Health, Bethesda, Maryland 20892. Received February 9, 2010; Revised Manuscript Received April 27, 2010

This report presents the preparation and characterization of three [Gd-*C*-DOTA]$^{-1}$−dendrimer assemblies by way of analysis, NMRD spectroscopy, and photon correlation spectroscopy (PCS). The metal−ligand chelates were preformed in alcohol media prior to conjugation to generation 4, 5, and 6 PAMAM dendrimers. The dendrimer-based agents were purified by Sephadex G-25 column chromatography. The combustion analysis, SE-HPLC, and UV−vis data indicated chelate to dendrimer ratios of 28:1, 61:1 and 115:1, respectively. Molar relaxivity measured at pH 7.4, 22 °C, and 3 T (29.6, 49.8, and 89.1 mM^{-1} s^{-1}) indicated the viability of conjugates as MRI contrast agents. $1/T_1$ NMRD profiles were measured at 23 °C and indicated that at 22 MHz the $1/T_1$ reached a plateau at 60, 85, and 140 mM^{-1} s^{-1} for the generation 4, 5, and 6 dendrimer conjugates, respectively. The PCS data showed the respective sizes of 5.2, 6.5, and 7.8 nm for G-4, 5, and 6 conjugates.

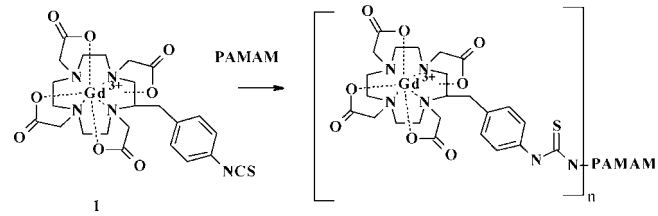
During the development of MRI, contrast agents have been employed to induce additional contrast and increase the sensitivity of MRI scans (*1, 2*). Increased usage of MRI, combined with the necessity for a contrast agent, prompts development of new, efficient agents. Clinically used low molecular weight extracellular contrast agents, e.g., [Gd(DTPA)(H_2O)]$^{-2}$ (Magnevist) suffer from rapid extravasation from blood vessels into interstitial space and fast decrease in concentration in blood vessels, combined with rapid whole body clearance.

In recent years, dendrimers have become an exciting class of polymeric platforms for assembly of multifunctional macromolecular nanomaterials undergoing preclinical development as diagnostics and therapeutic delivery vehicles. There have been reports indicating that dendrimers are applicable as carriers for site-specific delivery of drugs and that they do not alter the function of the molecules attached (*3*−*8*). It has also been discovered that dendrimers can act as drugs themselves (*9, 10*). In the MRI field, dendrimers have not only allowed molecules to retain their function, but also greatly enhanced the signal-to-noise ratio of various imaging modalities; however, this application has never reached its full potential.

The use of Gd(III) chelates conjugated to high molecular weight carriers such as a PAMAM dendrimer prolongs intravascular retention and circulation time, slows down molecular rotation, which results in a short relaxation time, and increases relaxivity (*11*−*13*). Polyamidoamine (PAMAM) dendrimers of different generations conjugated to acyclic diethylenetriamine pentaacetic acid (DTPA) derivatives, e.g., 2-(*p*-isothiocyanatobenzyl)-6-methyl-diethylenetriaminepentaacetic acid (1B4M-DTPA), are versatile in MRI applications due to their monodispersed nature and available range of molecular sizes (*14, 15*).

An acceptable contrast agent must be noncytotoxic and must have high water solubility, most preferably at physiological pH,

Scheme 1. Synthesis of Dendrimer Conjugates



1

and high relaxivity properties. The recent reports regarding nephrogenic systemic fibrosis (NSF) linked to the use of [Gd DTPA]$^{-2}$ derived MR contrast agents provided our laboratory with an impetus to re-evaluate the use of bifunctional DTPA agents for creation of macromolecular MR agents not only with regard to complex stability (*16*−*20*), but also with regard to their inherent extended in vivo residence time. [Gd(DOTA)]$^{-1}$ (1,4,7,10-tetraazacyclododecane-*N,N′,N″,N‴*-tetraacetic acid) is known to be a better contrast agent in terms of complex stability and thus potentially less toxicity as compared to [Gd(DTPA)]$^{-2}$ (*21, 22*). [Gd(DOTA)]$^{-1}$, DOTAREM, has been extensively evaluated in patients with pre-existing renal diseases and to date without clinical side effects (*23*). The higher relaxivity and kinetic stability of [Gd(DOTA)]$^{-1}$ makes it an alternative contrast agent for MRI (*24*). The formation and stability of the [Gd(DOTA)]$^{-1}$ complex has also been thoroughly studied; dissociation of the metal ion was exceedingly slow even at low pH (2−4), on the order of days (*25*), while its thermodynamic stability was comparable to [Gd(III)](DTPA) (*26*). [Gd(DOTA)]$^{-1}$ was previously shown to be 5 orders of magnitude higher in in vitro stability as compared to [Gd(DTPA)]$^{-2}$, which potentially translates to decreased in vivo toxicity (*21*).

Herein, we report the preparation and characterization of three contrast agents with different generation (4, 5, and 6) of dendrimers. The *C*-DOTA (2-(4-nitrobenzyl)-1,4,7,10-tetraazacyclododecane-*N,N′,N″,N‴*-tetraacetic acid) ligand is first used to sequester Gd(III) (Scheme 1), and thereafter, the formed metal complex is covalently attached to the terminal -NH_2 groups of the dendrimer. We have recently reported that premetalation method to be significantly advantageous over conventional

* Correspondence to Martin W. Brechbiel, Ph.D., Radioimmune & Inorganic Chemistry Section, Radiation Oncology Branch, NCI, NIH Building 10, Room B3B69, 10 Center Drive, Bethesda, MD 20892. Fax: (301) 402-1923. E-mail: martinwb@mail.nih.gov.

[†] National Cancer Institute.

[‡] National Institutes of Health.

10.1021/bc1000802 This article not subject to U.S. Copyright. Published 2010 by the American Chemical Society
Published on Web 05/12/2010

Table 1. Number of Chelates and Molar Relaxivity Values Measured for G4-(*C*-DOTA-Gd)$_{28}$, G5-(*C*-DOTA-Gd)$_{61}$, and G6-(*C*-DOTA-Gd)$_{115}$

agent	no. chelate (analysis)	no. chelate (UV)	r_1 (mM^{-1} s^{-1})
Magnevist	---	---	4.2
G4-(*C*-DOTA-Gd)$_{28}$	28	26	29.6
G5-(*C*-DOTA-Gd)$_{61}$	61	58	49.8
G6-(*C*-DOTA-Gd)$_{115}$	113	107	89.1

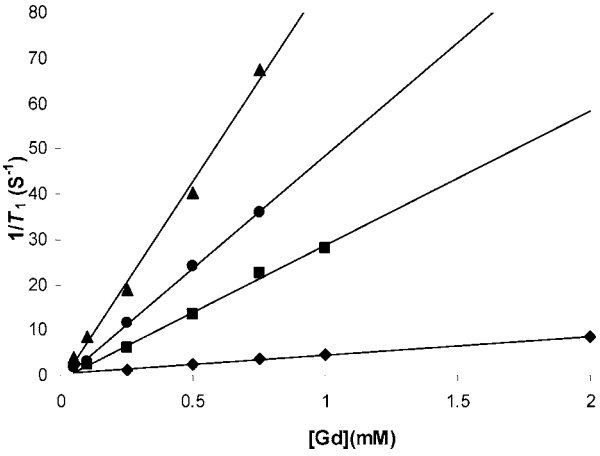


Figure 1. Molar relaxivity plots of G4-(*C*-DOTA-Gd)$_{28}$ (□; 29.6 mM^{-1} s^{-1}), G5-(*C*-DOTA-Gd)$_{61}$) (•; 49.8 mM^{-1} s^{-1}), G6-(*C*-DOTA-Gd)$_{115}$) (▲; 89.1 mM^{-1} s^{-1}), and Magnevist (♦; 4.2 mM^{-1} s^{-1}).

postmetalation methods, resulting in both a more directly characterizable product possessing an ~2-fold enhancement of molar relaxivity when using a bifunctional DTPA chelating agent while also decreasing the overall Gd(III) content by ~30% (*27*). We have also reported the applicability of a *C*-DOTA derivative applied to complex Gd(III) as an agent of choice to replace the use of bifunctional DTPA agents employed to sequester Gd(III) as a component of macromolecular MR contrast agents (*28*).

Table 1 summarizes the number of chelates per dendrimer obtained from analysis and SE-HPLC. For comparison, a UV−vis spectrophotometric titration method was developed. A standard curve using compound **2** (Figure 1 in Supporting Information), which represents a surrogate of the chelate conjugated to an amino surface on the dendrimer, was generated from this method and is shown in Supporting Information Figure 2. The results from assessing the number of chelates per dendrimer were collected in Table 1. Clearly, there is agreement between the two methods within experimental error indicating that spectrophotometric method also to be a viable method for the determination of the number of chelates conjugated to a dendrimer platform.

A plot of the inverse of longitudinal relaxation time ($1/T_1$) versus Gd(III) concentration for the three dendrimer conjugates and Magnevist is shown in Figure 1, while the relaxivity values obtained as a slope of this plot are summarized in Table 1. The data showed that the relaxivity of the three dendrimer based agents are 7−21 times higher than that of Magnevist. This indicates that G6-(*C*-DOTA-Gd)$_{115}$ might be applicable in the submicromolar range and thus also presents the highest potential to eliminate concerns regarding Gd(III) toxicity.

The relaxivity values (30, 50, and 90 mM^{-1} s^{-1}) reported here produced by macromolecules measured at 3 T field strength might seem high, but the reality is that these numbers are not uncommon. A relaxivity range of 139−237 mM^{-1} s^{-1} at 2.4 T field strength, which is close to our field strength, has been reported by Zhang et al. in their contemporary work with fullerene (*29*). The solutions prepared were based on the

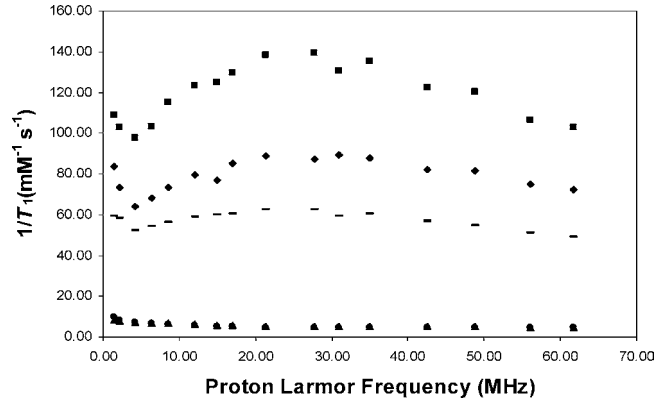


Figure 2. $1/T_1$ NMRD profiles of 1 mM solution of prohance (▲), Magnevist (•), G4-(*C*-DOTA-Gd)$_{28}$ (-), G5-(*C*-DOTA-Gd)$_{61}$ (♦), G6-(*C*-DOTA-Gd)$_{115}$ (□), as a function of frequencies at 23 °C.

Table 2. Values of Size and ζ Potential for Free and Conjugated Dendrimers

generation	predicted diameter[a] (nm)	measured diameter (nm)	ζ potential
G4	4.0	4.2	0.1
G4 Conjugate		5.2	−60
G5	5.3	5.1	7.6
G5 Conjugate		6.5	65
G6	6.7	6.4	17.4
G6 Conjugate		7.8	−69

[a] Predicted values by Tomalia (*41*).

gadolinium content from the ICP report of the purified dendrimer conjugate. We reported the efficiency of this macromolecular purification method earlier (*27*), which is also utilized by other researchers (*29*).

In general, conjugation of compound **1** [Gd(*C*-DOTA))$^{-1}$ (Scheme 1) to a higher generation dendrimer such as G6 would result in a more hydrophobic conjugate due to the replacement of exterior primary amines with the complexes. Hydrophobic interaction with solvent molecules is known to slow down the tumbling time (τ_R) which results in increase of the relaxivity (*30*−*32*). On the basis of the combustion analysis, SE-HPLC, and UV−vis data, the agent based on the G6 has the highest free amino sites (141), and thus it is expected to have the highest relaxivity. The experimental data (Table 1) support this position.

Consideration of the nuclear magnetic relaxation dispersion (NMRD) for a given contrast agent is essential, since the field strength of clinical MRI instrumentation ranges from 2 to 180 MHz. The $1/T_1$ NMRD profiles of the G4, G5, and G6 dendrimer conjugates at 23 °C are depicted in Figure 2, wherein the relaxivity for all three agents peaked at ~22 MHz. This behavior is similar to a previously reported measurement using G5, G7, G9, and G10 dendrimers in which the relaxivities peaked at ~22 MHz (*33, 34*). Henry et al. pointed out that the relaxivity of G7 conjugate is comparable to that of G6, which means G6 is the highest generation dendrimer where a significant increase in relaxivity can be observed based on the simple size and amine number of the dendrimers platform (*33, 34*). However, whether that result will hold true for the agents prepared employing the premetalation method presented here remains to be determined in future studies.

The sizes of conjugates determined here are based on 1 μM stock solution prepared in ambient water at pH = 6 to eliminate buffer interference (Table 2). As noted earlier, size measurement based on PCS is concentration dependent (*35*) and also buffer dependent (*36*). As expected, the G6 conjugate has the largest size (Table 2) and thus has the highest impact on the relaxivity (Table 1). This is the first time that our laboratory has measured

the size of PAMAM dendrimer conjugated to [Gd(*C*-DOTA)]$^{-1}$. Relaxivity was observed to be linearly correlated to the size of chelated dendrimer conjugate; the larger the size, the greater the relaxivity (Figure 5; Supporting Information). This is in agreement with a previous report utilizing a similar [Gd(DO3A)]-derivative by Margerum et al. (*36*), and other authors where subsequent increases in size and molecular weight results in increased relaxivity (*33, 34*). This is also a major benefit from attaching a small chelate to a large macromolecule in which the associated tumbling time of the molecule increases leading to increases in relaxation enhancement (*37*). Our NMRD data showed that the relaxivity of G = 6 dendrimer chelate is 140 mM^{-1} s^{-1} at 22 MHz, which is slightly lower than Gd(III)-glutamine synthetase (148 mM^{-1} s^{-1}) at 22.5 MHz (*38, 39*).

The measurement of zeta potential (ζ) reveals the accumulation of ions at the particle surface (*35*). The overall surface charge or ζ potential of the G6 agent is the highest due to the highest density of surface charge as expected. Also, high positive charge ζ potential is indicative of high electrostatic repulsion between particles and provides an energy barrier against aggregation (*35*). Since the differences in ζ potential of the agents is not significant based on the data obtained, one can assume a likelihood of each agent to aggregate to be low. This will be advantageous for in vivo applications where aggregation could interfere with glomerulal filtration clearance through kidney, which would be the preferred route (*40*), especially for larger G5 and G6 conjugates.

In summary, this study indicates that macromolecular-based MRI contrast agents prepared here are efficient and effective in modulating and relaxing water protons when compared to a single Gd(III) chelate. Our study also shows that appending the preformed Gd(III) complex to the dendrimer is far more convenient and significantly more advantageous in areas including species distribution, ease of characterization, stability, and solubility. As reported earlier, this premetalation strategy also produces a more hydrophobic agent that results in high relaxivity and faster blood clearance rate in vivo (*27*). The characterized data provide us with valuable information regarding the nature of the conjugates such as the size and the surface charge, and also enhance our understanding of how these parameters impact the relaxivity and to a certain degree what we can expect from these agents in vivo. These data strongly suggest that the G6-(*C*-DOTA-Gd)$_{115}$ is a superior agent based on its high relaxivity which will also enable use of a much lower injected dose for all future studies thereby facilitating also translation into clinical trial evaluation.

EXPERIMENTAL SECTION

See Supporting Information.

ACKNOWLEDGMENT

This research was supported by the Intramural Research Program of the National Institute of Health, National Cancer Institute, Center for Cancer Research, and the United States Department of Health and Human Services.

Supporting Information Available: Detailed description of syntheses, molar relaxivity measurements, relaxometry, photon correlation spectroscopy (PCS), and zeta (ζ) potential, UV−vis spectroscopy, and figures. This material is available free of charge via the Internet at http://pubs.acs.org..

LITERATURE CITED

(1) Caravan, P. (2006) Strategies for increasing the sensitivity of gadolinium based MRI contrast agents. *Chem. Soc. Rev. 35*, 512–523.

(2) Villaraza, A. J. L., Bumb, A., and Brechbiel, M. W. (2010) Macromolecules, dendrimers, and nanomaterials in magnetic resonance imaging: the interplay between size, function, and pharmacokinetics, *Chem. Rev.* in press.

(3) Koyama, Y., Talanov, V. S., Bernardo, M., Hama, Y., Regino, C. A. S., Brechbiel, M. W., Choyke, P. L., and Kobayashi, H. (2007) A dendrimer-based nanosized contrast agent dual-labeled for magnetic resonance and optical fluorescence imaging to localize the sentinel lymph node in mice. *J. Magn. Reson. Imaging 25*, 866–871.

(4) Lee, C. C., Gillies, E. R., Fox, M. E., Guillaudeu, S. J., Frechet, J. M. J., Dy, E. E., and Szoka, F. C. (2006) A single dose of doxorubicin-functionalized bow-tie dendrimer cures mice bearing C-26 colon carcinomas. *Proc. Nat. Acad. Sci. U.S.A. 103*, 16649–16654.

(5) Gillies, E. R., and Fréchet, J. M. J. (2005) Dendrimers and dendritic polymers in drug delivery. *Drug Discovery Today 10*, 35–43.

(6) Gurdag, S., Khandare, J., Stapels, S., Matherly, L. H., and Kannan, R. M. (2006) Activity of dendrimer-methotrexate conjugates on methotrexate-sensitive and -resistant cell lines. *Bioconjugate Chem. 17*, 275–283.

(7) Kukowska-Latallo, J. F, Candido, K. A, Cao, Z, Nigavekar, S. S, Majoros, I. J, Thomas, T. P, Balogh, L. P, Khan, M. K, and Baker, J. R., Jr. (2005) Nanoparticle targeting of anticancer drug improves therapeutic response in animal model of human epithelial cancer. *Cancer Res. 65*, 5317–5324.

(8) Kim, Y., Hechler, B. a., Gao, Z.-G., Gachet, C, and Jacobson, K. A. (2009) PEGylated dendritic unimolecular micelles as versatile carriers for ligands of G protein-coupled receptors. *Bioconjugate Chem 20*, 1888–1898.

(9) Lee, C. C., MacKay, J. A., Frechet, J. M. J., and Szoka, F. C. (2005) *Nat. Biotechnol. 23*, 1517–1526.

(10) Menjoge, A. R., Kannan, R. M., and Tomalia, D. A. (2010) Dendrimer-based drug and imaging conjugates: design considerations for nanomedical applications. *Drug Discovery Today 15*, 171–185.

(11) Wang, S. J., Brechbiel, M., and Wiener, E. C. (2003) Characteristics of a new MRI contrast agent prepared from polypropyleneimine dendrimers, generation 2. *Invest. Radiol. 38*, 662–668.

(12) Wiener, E., Brechbiel, M. W., Brothers, H., Magin, R. L., Gansow, O. A., Tomalia, D. A., and Lauterbur, P. C. (1994) Dendrimer-based metal chelates: A new class of magnetic resonance imaging contrast agents. *Magn. Reson. Med. 31*, 1–8.

(13) Tomalia, D. A., Reyna, L. A., and Svenson, S. (2007) Dendrimers as multi-purpose nanodevices for oncology drug delivery and diagnostic imaging. *Biochem. Soc. Trans. 035*, 61–67.

(14) Kobayashi, H., and Brechbiel, M. W. (2003) Dendrimer-based macromolecular MRI contrast agents:characteristic and application. *Mol. Imaging 2*, 1–10.

(15) Sato, N., Kobayashi, H., Hiraga, A., Saga, T., Togashi, K., Konishi, J., and Brechbiel, M. W. (2001) Pharmacokinetics and enhancement patterns of macromolecular MR contrast agents with various sizes of polyamidoamine dendrimer cores. *Magn. Reson. Med. 46*, 1169–1173.

(16) Sieber, M. A., Lengsfeld, P., Walter, J., Schirmer, H., Frenzel, T., Siegmund, F., Weinmann, H.-J., and Pietsch, H. (2008) Gadolinium-based contrast agents and their potential role in the pathogenesis of nephrogenic systemic fibrosis: The role of excess ligand. *J. Magn. Reson. Imaging 27*, 955–962.

(17) Thakral, C., Alhariri, J., and Abraham, J. L. (2007) Long-term retention of gadolinium in tissues from nephrogenic systemic fibrosis patient after multiple gadolinium-enhanced MRI scans: case report and implications. *Contr. Media Mol. Imaging 2*, 199–205.

(18) Stratta, P., Canavese, C., and Aime, S. (2008) Gadolinium-enhanced magnetic resonance imaging, renal failure and nephrogenic systemic fibrosis /nephrogenic fibrosing dermopathy. *Curr. Med. Chem. 15*, 1229–1235.

(19) Port, M., Idée, J.-M., Medina, C., Robic, C., Sabatou, M., and Corot, C. (2008) Efficiency, thermodynamic and kinetic stability of marketed gadolinium chelates and their possible clinical consequences: a critical review. *BioMetals 21*, 469–490.
(20) Abraham, J. L., Chandra, S., Thakral, C., and Abraham, J. M. (2008) SIMS imaging of gadolinium isotopes in tissue from nephrogenic systemic fibrosis patients: release of free Gd from magnetic resonance imaging (MRI) contrast agents. *Appl. Surf. Sci. 255*, 1181–1184.
(21) Bousquet, J. C., Saini, S., Stark, D. D., Hahn, P. F., Nigam, M., Wittenberg, J, and Ferrucci, J. T., Jr. (1988) Gd-DOTA: characterization of a new paramagnetic complex. *Radiology 166*, 693–698.
(22) Allard, M., Doucet, D., Kien, P., Bonnemain, B., and Caille, J. M. (1988) Experimental study of DOTA-Gadolinium pharmacokinetics and pharmacologic properties. *Invest. Radiol. 23* (suppl 1), S271–S274.
(23) Deray, G., Bellin, M. F., Baumelou, B., Rey, J.-P., Boulechfar, H., Grellet, J., and Jacobs, C. (1990) Renal tolerance of the paramagnetic contrast medium Gd-DOTA in patients with chronic renal failure. *Am. J. Nephrol. 10*, 522–523.
(24) Magerstädt, M., Gansow, O. A., Brechbiel, M. W., Colcher, D., Baltzer, L., Knop, R. H., Girton, M. E., and Naegele, M. (1986) Gd(DOTA): An alternative to Gd(DTPA) as a T1,2 relaxation agent for NMR imaging or spectroscopy. *Magn. Reson. Med. 3*, 808–812.
(25) Wang, X., Jin, T., Comblin, V., Lopez-Mut, A., Merciny, E., and Desreux, J. F. (1992) A kinetic investigation of the lanthanide DOTA chelates. Stability and rates of formation and of dissociation of a macrocyclic gadolinium(III) polyaza polycarboxylic MRI contrast agent. *Inorg. Chem. 31*, 1095–1099.
(26) Benazeth, S., Purans, J., Chalbot, M.-C., Nguyen-van-Duong, M. K., Nicolas, L., Keller, F., and Gaudemer, A. (1998) Temperature and pH dependence XAFS study of Gd(DOTA)- and Gd(DTPA)2- complexes: solid state and solution structures. *Inorg. Chem. 37*, 3667–3674.
(27) Nwe, K., Xu, H., Regino, C. A. S., Bernardo, M., Ileva, L., Riffle, L., Wong, K. J., and Brechbiel, M. W. (2009) A new approach in the preparation of dendrimer-based bifunctional diethylenetriaminepentaacetic acid MR contrast agent derivatives. *Bioconjugate Chem. 20*, 1412–1418.
(28) Nwe, K., Bernardo, M., Regino, C. A. S., Williams, M., Brechbiel, and M. W. (2010) Comparison of magnetic resonane imaging (MRI) properties between derivatized diethylenetriamine-N, N', N', N″, N″-pentaacetic acid (DTPA) and 1,4,7,10-tetraazacyclododecane-N, N', N″, N‴-tetraacetic acid (DOTA) gadolinium- dendrimer conjugates, Manuscript Submitted.
(29) Zhang, J., Fatouros, P. P., Shu, C., Reid, J., Owens, L. S., Cai, T., Gibson, H. W., Long, G. L., Corwin, F. D., Chen, Z.-J., and Dorn, H. C. High relaxivity trimetallic nitride (Gd3N) metallofullerene MRI contrast agents with optimized functionality, *Bioconjugate Chem.* ASAP.
(30) Wang, S. J., Brechbiel, M. W., and Weiner, E. C. (2003) Characteristics of a new MRI contrast agent prepared from polypropyleneimine dendrimers, generation 2. *Invest. Radiol. 38*, 662–668.
(31) Kellar, K. E., Henrichs, P. M., Hollister, R., Koenig, S. H., Eck, J., and Wei, D. (1997) High relaxivity linear Gd(DTPA)-polymer conjugates: the role of hydrophobic interactions. *Magn. Reson. Med. 38*, 712–716.
(32) Zech, S. G., Eldredge, H. B., Lowe, M. P., and Caravan, P. (2007) Protein binding to lanthanide(III) complexes can reduce the water exchange rate at the lanthanide. *Inorg. Chem. 46*, 3576–3584.
(33) Bryant, L. H., Jr., Martin, W. B., Wu, C., Bulte, J. W. M., Herynek, V., and Frank, J. A. (1999) Synthesis and relaxometry of high-generation (G = 5, 7, 9, and 10) PAMAM dendrimer-DOTA-gadolinium chelates. *J. Magn. Reson. Imaging 9*, 348–352.
(34) Weiner, E. C., and Brechbiel, M. W. (1994) Dendrimer-based metal chelates: a new class of magnetic resonance imaging contrast agents. *Magn. Reson. Med. 31*, 1–8.
(35) Suvarna, S., Espinasse, B., Qi, R., Lubica, R., Poncz, M., Cines, D. B., Wiesner, M. R., and Arepally, G. M. (2007) Determinants of PF4/heparin immunogenicity. *Blood 110*, 4253–4260.
(36) Margerum, L. D., Campion, B. K., Koo, M., Shargill, N., Lai, J.-J., Marumoto, A., and Christian Sontum, P. (1997) Gadolinium(III) DO3A macrocycles and polyethylene glycol coupled to dendrimers Effect of molecular weight on physical and biological properties of macromolecular magnetic resonance imaging contrast agents. *J. Alloys Compd. 249*, 185–190.
(37) Koenig, S. H., and Brown, R. D. (1984) Relaxation of solvent protons by paramagnetic ions and its dependence on magnetic field and chemical environment: implications for NMR imaging. *Magn. Reson. Med. 1*, 478–495.
(38) Eads, C. D., Mulqueen, P., Horrocks, W. D., and Villafranca, J. J. (1985) Comparative study of glutamine synthetase bound lanthanide(III) ions using NMR relaxation and lanthanide(III) luminescence techniques. *Biochemistry 24*, 1221–1226.
(39) Lauffer, R. B. (1987) Paramagnetic metal complexes as water proton relaxation agents for NMR imaging: theory and design. *Chem. Rev. 87*, 901–927.
(40) Vexler, V. S., Clément, O., Schmitt-Willich, H., and Brasch, R. C. (1994) Effect of varying the molecular weight of the MR contrast agent Gd-DTPA-polylysine on blood pharmacokinetics and enhancement patterns. *J. Magn. Reson. Imaging 4*, 381–388.
(41) Donald, A. T., Adel, M. N., and William, A. G., III (1990) Starburst Dendrimers: Molecular-Level Control of Size, Shape, Surface Chemistry, Topology, and Flexibility from Atoms to Macroscopic Matter. *Angew. Chem., Int. Ed. Engl. 29*, 138–175.

BC1000802

Conjugation to Nickel-Chelating Nanolipoprotein Particles Increases the Potency and Efficacy of Subunit Vaccines to Prevent West Nile Encephalitis

Nicholas O. Fischer,[†] Ernesto Infante,[‡] Tomohiro Ishikawa,[||,‡] Craig D. Blanchette,[†] Nigel Bourne,[‡] Paul D. Hoeprich,*[,†] and Peter W. Mason*[,⊥,‡]

Physical and Life Sciences Directorate, Lawrence Livermore National Laboratory, Livermore, California 94551, and Department of Pathology, Microbiology & Immunology, University of Texas Medical Branch, Galveston, Texas 77555. Received February 9, 2010; Revised Manuscript Received April 19, 2010

Subunit antigens are attractive candidates for vaccine development, as they are safe, cost-effective, and rapidly produced. Nevertheless, subunit antigens often need to be adjuvanted and/or formulated to produce products with acceptable potency and efficacy. Here, we describe a simple method for improving the potency and efficacy of a recombinant subunit antigen by its immobilization on nickel-chelating nanolipoprotein particles (NiNLPs). NiNLPs are membrane mimetic nanoparticles that provide a delivery and presentation platform amenable to binding any recombinant subunit immunogens featuring a polyhistidine tag. A His-tagged, soluble truncated form of the West Nile virus (WNV) envelope protein (trE-His) was immobilized on NiNLPs. Single inoculations of the NiNLP-trE-His produced superior anti-WNV immune responses and provided significantly improved protection against a live WNV challenge compared to mice inoculated with trE-His alone. These results have broad implications in vaccine development and optimization, as NiNLP technology is well-suited to many types of vaccines, providing a universal platform for enhancing the potency and efficacy of recombinant subunit immunogens.

Rational design of vaccines, made possible by an enhanced understanding of the mechanisms that trigger an effective immune response, includes the optimization of immunogen generation, addition of adjuvants, and improvement of delivery. Numerous vaccine formulations have been very successful, but no single technology covers the key requirements of the ideal vaccine, namely, impeccable safety, low cost, rapid preparation, and high potency (*1*). The three former characteristics are found with subunit antigens (i.e., purified protein components from pathogen candidates) (*2*), though these immunogens suffer from poor potency and thus often are formulated with adjuvants to improved their immunogenicity (*3, 4*). However, adjuvants themselves can have unwanted side effects, and few are approved for use in humans (*4*). The development of an adjuvant-free technology to improve potency through antigen presentation or delivery would accelerate the development of new subunit vaccines.

Multivalency and shape are likely important determinants of vaccine potency and efficacy, since valency may increase affinity and/or aggregate receptors, leading to activation (*5*), and the immune system has likely evolved to react more strongly to particles of the size of invading microorganisms. On the basis of these concepts, multiple investigators have developed multimeric, particulate antigens as vaccine candidates against hepatitis B virus and the human papilloma virus, respectively, produced in yeast and mammalian cells to form 10−20-nm-diameter particles (*6, 7*). While these approaches have been highly effective and widely utilized, their multimeric nature is dictated by the properties of the virus-encoded antigens and is not readily manipulated to produce vaccines for other agents.

* E-mail: hoeprich2@llnl.gov, peter.mason@novartis.com.
[†] Lawrence Livermore National Laboratory.
[‡] University of Texas Medical Branch.
[||] Current address: Department of International Health, Kobe University Graduate School of Health Sciences, Kobe, 654-0142 Japan.
[⊥] Current address: Novartis Vaccines and Diagnostics, Cambridge, Massachusetts 02139.

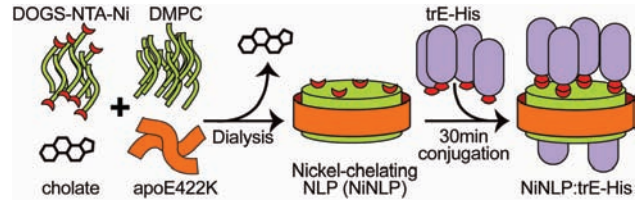


Figure 1. Schematic of NiNLP assembly and His-tagged antigen (trE-His) conjugation.

Other approaches utilizing particulate platforms (*8, 9*) to achieve multivalent presentation of antigens have shown promise, including liposomes (*10*), nanoscale microemulsions (*11*), and nanoparticles (*12*).

Here, we describe a simple method to improve the potency and efficacy of His-tagged recombinant subunit vaccines using nickel-functionalized nanolipoprotein particles (NiNLPs) as a versatile antigen presentation and delivery platform to improve immune response to subunit antigens without requiring adjuvants (Figure 1). To harness multivalent and particulate characteristics for a universal vaccine platform, NiNLPs represent a promising technology. NLPs, also referred to as reconstituted high- or low-density lipoproteins (rHDLs and rLDLs, respectively), are self-assembled, nanometer-sized discoidal particles comprising lipoproteins and phospholipids (*13*−*15*). The lipoproteins are amphipathic, α-helical bundles. Upon lipid binding, the hydrophobic faces of the helices bind the exposed hydrophobic core of the phospholipid bilayer, effectively protecting the lipid patches, producing discrete, soluble particles. The versatility of these biological nanoparticles is underscored by the ability to form NLPs with different apolipoproteins (*13, 16, 17*) and lipids (*13, 18, 19*), including functionalized lipids (*20*−*22*). Traditionally, NLPs have been used as model membrane mimetics for stabilizing and studying membrane proteins (*23*−*27*), although diagnostic (*21, 22, 28*) and drug delivery (*29*−*34*) applications have also been explored.

10.1021/bc100083d © 2010 American Chemical Society
Published on Web 05/28/2010

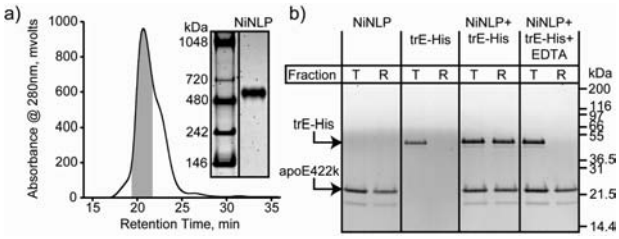


Figure 2. NiNLP characterization and trE-His immobilization. (a) NiNLPs were purified by SEC (shaded region) and analyzed for purity by native gel electrophoresis (inset). (b) Conjugation of WNV trE-His antigen to NiNLPs was verified by centrifugal filtration using a 100 kDa molecular weight cutoff membrane. Total sample (T) and retentate after filtration (R) were resolved by SDS-PAGE and developed using SyproRuby.

We recently reported the facile functionalization of NLPs by incorporating lipids featuring nickel-chelating headgroups during the assembly process (*20*). The resulting particles present a lipid bilayer surface decorated with chelated nickel ions capable of binding recombinant proteins incorporating a poly-His peptide (Figure 1). NiNLPs were prepared by incubating a human apolipoprotein (apoE422K) with a cholate-solubilized mixture of 1,2-dimyristoyl-*sn*-glycero-3-phosphocholine (DMPC) and the nickel-chelating lipid 1,2-dioleoyl-*sn*-glycero-3-{[*N*-(5-amino-1-carboxypentyl)iminodiacetic acid]succinyl} (nickel salt) (DOGS-NTA-Ni). A 9:1 molar ratio of DMPC to DOGS-NTA-Ni was used to ensure that 10% of the NiNLP bilayer lipids feature chelated nickel (*20*). After dialysis to remove excess cholate, the assembled NiNLPs were purified by size exclusion chromatography (SEC) (Figure 2a). SEC fractions were subsequently analyzed by nondenaturing gradient gel electrophoresis (NDGGE) to identify fractions containing homogeneous populations of NiNLPs, which were then pooled. This approach yields NiNLPs of high purity and homogeneity, as assessed by native gel electrophoresis (Figure 2a, inset). Atomic force microscopy (AFM) confirmed the discoidal nature of the NiNLPs and indicated an average diameter of 23.2 ± 2.3 nm (see Supporting Information). On the basis of previous modeling simulations of apoE422K-based NLPs, the molecular weight of 23.5 nm NLPs is estimated at 860 kDa (*35*), whereas the approximate molecular weight extrapolated from native gel mobility was ~500 kDa (Figure 2a, inset). This discrepancy is due in part to the effects of lipid composition on NLP native gel migration (unpublished observations) as well as the comparison of discoidal NLPs to globular molecular weight markers (*35*).

To determine the ability of NiNLP technology to enhance the antigenicity of recombinant protein immunogens, the envelope protein (E) of West Nile virus (WNV) was identified as a candidate immunogen. Flaviviruses are responsible for serious diseases, including encephalitis (caused by WNV and Japanese encephalitis virus) as well as hemorrhagic fevers (caused by yellow fever virus and dengue viruses) (*36*). Two types of vaccines are currently available against flaviviruses: live-attenuated vaccines (LAVs) and formalin inactivated vaccines (INVs). While effective, LAVs are not recommended for all individuals and have been associated with adverse side effects (*37*). INVs are considered to be a safer type of vaccine, although multiple doses are required to induce high and long-lasting immunity (*38*). Therefore, safer and more potent vaccines need to be developed.

Vaccine-induced immunity to flavivirus infection has been linked to the E protein (*36*). In particular, vaccines based on subviral particles, characterized as 25 nm-diameter cell-derived lipid bilayers coated with E, have been effective against live viral challenges (*39*−*44*). These studies have confirmed the potential of subviral particles as vaccine candidates, but they are currently limited to vaccine formulations against viral targets. Recombinantly expressed E protein has been shown to elicit immunity, however, only in the presence of various adjuvants (*45*−*48*). A broadly adaptable platform for the presentation of antigens from a wide range of pathogens (e.g., viruses, bacteria, and parasites) in the absence of adjuvants would therefore present an important complementary approach to vaccine delivery. To adapt the E protein as a model antigen for use with the NiNLP platforms, a truncated variant of E, in which the native C-terminal membrane-binding domains were substituted with a polyhistidine tag (trE-His), was used in this study (*49*).

We have previously shown that His-tagged proteins are readily immobilized on NiNLPs (*20*). To verify that WNV trE-His was successfully bound to the NiNLPs after 45 min incubation at room temperature, samples were isolated post-conjugation by centrifugal separation using a 100 kDa molecular weight cutoff filter. By this approach, all NiNLP constituents, including apoE422K and any immobilized proteins, are retained by the membrane, whereas unconjugated proteins are removed. Analyses of total (T) and retentate (R) samples by SDS polyacrylamide electrophoresis are shown in Figure 2b, documenting that (1) the NiNLP was retained by the filter, (2) trE-His alone freely passed through the filter, (3) trE-His incubated with NiNLP was retained by the filter, and (4) the presence of EDTA in the mixture disrupted the association of the NiNLP with trE-His, permitting the trE-His to pass through the filter. AFM was used to independently verify immobilization of trE-His on the NiNLPs. An increase in NiNLP height was measured only in the presence of trE-His. No height increase was observed between trE-His and NiNLPs in the presence of EDTA (see Supporting Information).

To determine whether NiNLP conjugation enhanced the immunogenicity of the trE-His to elicit WNV-specific immune responses, a pilot study was performed in 6-week-old mice. The groups of 5 mice were vaccinated once (i.e., no boost) with formulations containing 2.5 μg total trE-His protein, either as free protein (trE-His alone) or conjugated to the NiNLPs (NiNLP-trE-His). In addition, groups of animals were vaccinated with diluent or NiNLP alone. Figure 3a shows the results of the serological trE-His responses detected in the animals in these groups 3 weeks postvaccination. At this dose, only the sera from mice vaccinated with NiNLP-trE-His produced readily detectable IgG responses to trE (Figure 3a). The large standard deviations in the IgG responses are indicative of variable responses by individual mice, rather than experimental error of the ELISAs (see Supporting Information). No response against apoE422K was detected by ELISA assays (data not shown), suggesting either that apoE422K is not immunogenic in mice or that too little protein is used in NLP formation, so an immune response is not observed. To test the ability of NiNLP conjugation to increase the efficacy of trE-His, the animals in this pilot study were challenged with 1000 ffu of live WNV NY99 (corresponding to 10 LD_{50} in 8-week-old mice) two weeks after the collection of sera (5 weeks postvaccination, 11 weeks old), and observed daily for three weeks. The Kaplan−Meier survival curve shown in Figure 3c shows that all mice inoculated with the NiNLP-trE-His preparation survived to 21 days postchallenge when the experiment was terminated (at which time, none of these animals displayed any morbidity—including weight loss; Figure 3e). All of the animals in the other groups succumbed to infection with the exception of two animals that received trE-His, and one animal in each of the NiNLP or diluent groups.

To further assess the efficacy of NiNLP-trE-His, a larger trial using 5-week-old mice in groups of 10 animals was conducted. As with the pilot study, 2.5 μg total trE-His protein, either as free protein or as NiNLP-trE-His, were administered in a single dose. Serological responses were determined 4 weeks postvaccination,

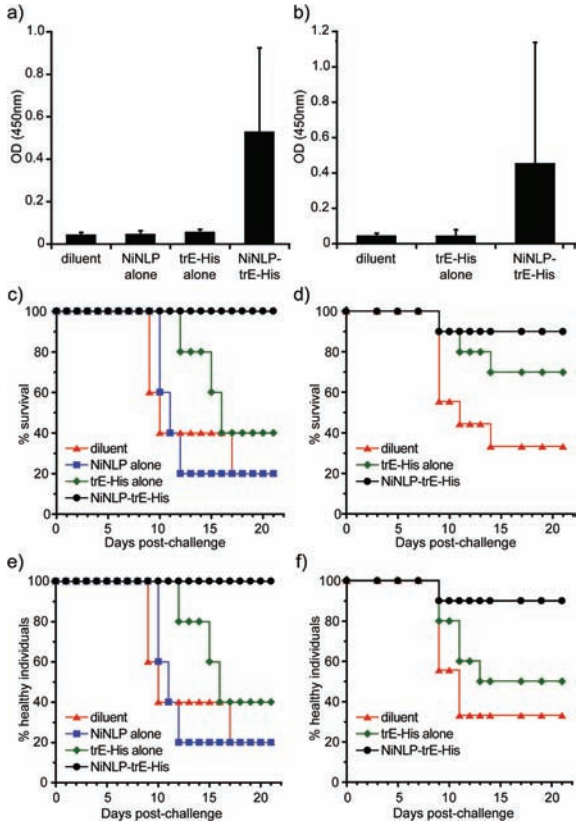


Figure 3. NiNLP conjugation increases the potency of WNV trE vaccines: (a), (c), and (e) first experiment, $n = 5$; (b), (d), and (f) second experiment, $n = 10$. (a) and (b) WNV trE-His ELISA reactivity of sera from mice collected 21 or 28 days postvaccination (first and second experiment, respectively) with various formulations, containing either 2.5 μg of trE-His or no trE-His antigen. Bars represent average OD values obtained from 1:100 dilutions of sera assayed for reactivity to trE-His using standard methods (*37*). Error bars represent s.d. determined from OD values for all animals in each group. (c) and (d) Kaplan−Meier survival curves demonstrating that NiNLP conjugation improved trE-His efficacy. Animals were challenged with 1000 ffu of WNV and observed daily for 21 days. Animals that needed to be euthanized due to disease signs predictive of death within 24 h were scored as dead the following day (*37*). (e) and (f) Morbidity curves reflecting the health of the challenged mice. Individuals were scored as unhealthy if indications of morbidity were observed (weight loss of more than 5%, paralysis, ruffled fur, or inactivity).

and the results mirrored those of the pilot experiment; only those animals receiving the NiNLP-trE-His constructs produced detectable IgG responses to trE (Figure 3b). In contrast to the pilot study, animals were challenged 4 weeks postvaccination. However, exactly the same challenge dose used in the pilot study (1000 ffu of live WNV) was administered. The animals were monitored for 21 days for signs of morbidity and mortality. Importantly, 90% of animals (9/10) receiving the NiNLP-trE-His inoculum survived (Figure 3d) with no indications of morbidity (weight loss of more than 5%, paralysis, ruffled fur, or inactivity) (Figure 3f). Among the animals receiving the unconjugated trE-His subunit in the second experiment, 70% (7/10) survived; however, two animals displayed signs of morbidity (Figure 3f). Of the animals receiving only diluent controls ($n = 9$), only three animals survived.

Taking the health of surviving individuals into account, the two experiments demonstrated a similar outcome. In the first experiment, 100% of NLP-trE-His treated mice survived and were healthy (5/5), whereas only 40% of those receiving trE-His alone (2/5) remained healthy. In the second experiment, 90% of mice receiving the NLP construct (9/10) were healthy following challenge, whereas only 50% of the trE-His vaccinated mice (5/10) remained healthy. Application of Fisher's exact test to the combined 21 day survival data from the two experiments showed a significant difference between the NiNLP-trE-His groups and diluent and a significant difference between the NiNLP-trE-His and trE-His alone (in both cases, $p < 0.01$).

In order for NLPs to gain general use in the preparation of vaccines, a number of items require further investigation, including stability, biodistribution, and elimination. Preliminary stability assessments have demonstrated the ability to lyophilize and rehydrate NiNLPs with no loss in the ability to conjugate His-tagged proteins (data not shown). In vivo applications of rHDLs suggest significant stability over the length of the experiments (*21*). The in vivo fate of NiNLPs will be an important factor in determining the potential of this delivery vehicle. NLPs are most likely eliminated through the same pathway as native HDLs, i.e., processing through the liver. However, toxicology and biodistribution studies are currently underway to address this issue, as are additional stability and storage analyses. Since this vaccine preparation does not require infectious agents, inactivation procedures as well as controlled containment system for infectious agents are avoided, reducing potential costs significantly. Furthermore, we estimate that the process of NLP formation is scalable and the eventual cost of NiNLP-based vaccine platforms will reflect benefits of manufacturing.

We have demonstrated that the immunogenicity of the trE-His antigen is markedly increased when conjugated to NiNLPs. This approach is representative of a more general strategy wherein any protein with a His-tag can be used to generate a NLP-based construct in a matter of a few hours and can be administered to afford protective immunity. Furthermore, NiNLPs offer the potential to codeliver immune stimulators similarly derivatized with a His-tag, providing for enhanced, specific, rapid immune stimulation at the site of delivery and uptake of the NiNLP-antigen construct.

ACKNOWLEDGMENT

The authors thank Dr. Karl Weisgraber for providing apoE422K. This work was performed under the auspices of the U.S. Department of Energy by Lawrence Livermore National Laboratory (LLNL-JRNL-420436) under Contract DE-AC52-07NA27344 with support from Lawrence Livermore National Laboratory (LDRD 06-SI-003 awarded to P.D.H and LDRD 09-LW-077 awarded to C.D.B.). P.W.M acknowledges support from NIAID through the Western Regional Center of Excellence for Biodefense and Emerging Infectious Disease Research (NIH grant number U54 AI057156) and R21 AI077077.

Supporting Information Available: Experimental details, Figure S1 showing NiNLP purification, Figure S2 showing AFM characterization of NiNLP, Figure S3 showing AFM analyses of trE-His binding, Figure S4 showing individual serological responses. This material is available free of charge via the Internet at http://pubs.acs.org.

LITERATURE CITED

(1) Bae, K., Choi, J., Jang, Y., Ahn, S., and Hur, B. (2009) Innovative vaccine production technologies: The evolution and value of vaccine production technologies. *Arch. Pharm. Res. 32*, 465–480.

(2) Toth, I., Simerska, P., and Fujita, Y. (2008) Recent advances in design and synthesis of self-adjuvanting lipopeptide vaccines. *Int. J. Pept. Res. Ther. 14*, 333–340.

(3) Kwissa, M., Kasturi, S. P., and Pulendran, B. (2007) The science of adjuvants. *Expert Rev. Vaccines 6*, 673–684.

(4) Vogel, F. R., and Hem, S. L. (2008) Immunologic Adjuvants, in *Vaccines* (Plotkin, S. A., Orenstein, W. A., and Offit, P. A., Eds.) pp 59−72, Saunders, London.

(5) Bachmann, M. F., and Zinkernagel, R. M. (1997) Neutralizing antiviral B cell responses. *15*, 235–270.
(6) Mast, E. E., and Ward, J. W. (2008) Immunologic Adjuvants, in *Vaccines* (Plotkin, S. A., Orenstein, W. A., and Offit, P. A., Eds.) pp 177−204, Saunders, London.
(7) Lenz, P., Day, P. M., Pang, Y. Y. S., Frye, S. A., Jensen, P. N., Lowy, D. R., and Schiller, J. T. (2001) Papillomavirus-like particles induce acute activation of dendritic cells. *J. Immunol. 166*, 5346–5355.
(8) Bramwell, V. W., and Perrie, Y. (2005) Particulate delivery systems for vaccines. *Crit. Rev. Ther. Drug Carr. Syst. 22*, 151–214.
(9) Peek, L. J., Middaugh, C. R., and Berkland, C. (2008) Nanotechnology in vaccine delivery. *Adv. Drug Delivery Rev. 60*, 915–928.
(10) Perrie, Y., Mohammed, A. R., Kirby, D. J., McNeil, S. E., and Bramwell, V. W. (2008) Vaccine adjuvant systems: Enhancing the efficacy of sub-unit protein antigens. *Int. J. Pharm. 364*, 272–280.
(11) Patel, J. D., O'Carra, R., Jones, J., Woodward, J. G., and Mumper, R. J. (2007) Preparation and characterization of nickel nanoparticles for binding to his-tag proteins and antigens. *Pharm. Res. 24*, 343–352.
(12) Reddy, S. T., van der Vlies, A. J., Simeoni, E., Angeli, V., Randolph, G. J., O'Neill, C. P., Lee, L. K., Swartz, M. A., and Hubbell, J. A. (2007) Exploiting lymphatic transport and complement activation in nanoparticle vaccines. *Nat. Biotechnol. 25*, 1159–1164.
(13) Chromy, B. A., Arroyo, E., Blanchette, C. D., Bench, G., Benner, H., Cappuccio, J. A., Coleman, M. A., Henderson, P. T., Hinz, A. K., Kuhn, E. A., Pesavento, J. B., Segelke, B. W., Sulchek, T. A., Tarasow, T., Walsworth, V. L., and Hoeprich, P. D. (2007) Different apolipoproteins impact nanolipoprotein particle formation. *J. Am. Chem. Soc. 129*, 14348–14354.
(14) Jonas, A., Kezdy, K. E., and Wald, J. H. (1989) Defined apolipoprotein A-I conformations in reconstituted high-density lipoprotein disks. *J. Biol. Chem. 264*, 4818–4824.
(15) Matz, C. E., and Jonas, A. (1982) Micellar complexes of human apolipoprotein A-I with phosphatidylcholines and cholesterol prepared from cholate-lipid dispersions. *J. Biol. Chem. 257*, 4535–4540.
(16) Fang, Y. L., Gursky, O., and Atkinson, D. (2003) Lipid-binding studies of human apolipoprotein A-I and its terminally truncated mutants. *Biochemistry 42*, 13260–13268.
(17) Weers, P. M. M., and Ryan, R. O. (2006) Apolipophorin III: Role model apolipoprotein. *Insect Biochem. Mol. Biol. 36*, 231–240.
(18) Bhat, S., Sorci-Thomas, M. G., Tuladhar, R., Samuel, M. P., and Thomas, M. J. (2007) Conformational adaptation of apolipoprotein A-I to discretely sized phospholipid complexes. *Biochemistry 46*, 7811–7821.
(19) Denisov, I. G., McLean, M. A., Shaw, A. W., Grinkova, Y. V., and Sligar, S. G. (2005) Thermotropic phase transition in soluble nanoscale lipid bilayers. *J. Phys. Chem. B 109*, 15580–15588.
(20) Fischer, N. O., Blanchette, C. D., Chromy, B. A., Kuhn, E. A., Segelke, B. W., Corzett, M., Bench, G., Mason, P. W., and Hoeprich, P. D. (2009) Immobilization of His-tagged proteins on nickel-chelating nanolipoprotein particles. *Bioconjugate Chem. 20*, 460–465.
(21) Frias, J. C., Ma, Y. Q., Williams, K. J., Fayad, Z. A., and Fisher, E. A. (2006) Properties of a versatile nanoparticle platform contrast agent to image and characterize atherosclerotic plaques by magnetic resonance imaging. *Nano Lett. 6*, 2220–2224.
(22) Li, H., Gray, B. D., Corbin, I., Lebherz, C., Choi, H., Lund-Katz, S., Wilson, J. M., Glickson, J. D., and Zhou, R. (2004) MR and fluorescent imaging of low-density lipoprotein receptors. *Acad. Radiol. 11*, 1251–1259.
(23) Baker, S. E., Hopkins, R. C., Blanchette, C. D., Walsworth, V. L., Sumbad, R., Fischer, N. O., Kuhn, E. A., Coleman, M., Chromy, B. A., Letant, S. E., Hoeprich, P. D., Adams, M. W. W., and Henderson, P. T. (2009) Hydrogen production by a hyperthermophilic membrane-bound hydrogenase in water-soluble nanolipoprotein particles. *J. Am. Chem. Soc. 131*, 7508–9.
(24) Cappuccio, J. A., Blanchette, C. D., Sulchek, T. A., Arroyo, E. S., Kralj, J. M., Hinz, A. K., Kuhn, E. A., Chromy, B. A., Segelke, B. W., Rothschild, K. J., Fletcher, J. E., Katzen, F., Peterson, T. C., Kudlicki, W. A., Bench, G., Hoeprich, P. D., and Coleman, M. A. (2008) Cell-free co-expression of functional membrane proteins and apolipoprotein, forming soluble nanolipoprotein particles. *Mol. Cell. Proteomics 7*, 2246–2253.
(25) Katzen, F., Fletcher, J. E., Yang, J. P., Kang, D., Peterson, T. C., Cappuccio, J. A., Blanchette, C. D., Sulchek, T., Chromy, B. A., Hoeprich, P. D., Coleman, M. A., and Kudlicki, W. (2008) Insertion of membrane proteins into discoidal membranes using a cell-free protein expression approach. *J. Proteome Res. 7*, 3535–3542.
(26) Lyukmanova, E. N., Shenkarev, Z. O., Paramonov, A. S., Sobol, A. G., Ovchinnikova, T. V., Chupin, V. V., Kirpichnikov, M. P., Blommers, M. J. J., and Arseniev, A. S. (2008) Lipid-protein nanoscale bilayers: A versatile medium for NMR investigations of membrane proteins and membrane-active peptides. *J. Am. Chem. Soc. 130*, 2140–2141.
(27) Nath, A., Atkins, W. M., and Sligar, S. G. (2007) Applications of phospholipid bilayer nanodiscs in the study of membranes and membrane proteins. *Biochemistry 46*, 2059–2069.
(28) Cormode, D. P., Chandrasekar, R., Delshad, A., Briley-Saebo, K. C., Calcagno, C., Barazza, A., Mulder, W. J. M., Fisher, E. A., and Fayad, Z. A. (2009) Comparison of synthetic high density lipoprotein (HDL) contrast agents for MR imaging of atherosclerosis. *Bioconjugate Chem. 20*, 937–943.
(29) Feng, M. Q., Cai, Q. S., Shi, X. L., Huang, H., Zhou, P., and Guo, X. (2008) Recombinant high-density lipoprotein complex as a targeting system of nosiheptide to liver cells. *J. Drug Targeting 16*, 502–508.
(30) Nguyen, T. S., Weers, P. M. M., Raussens, V., Wang, Z., Ren, G., Sulchek, T., Hoeprich, P. D., and Ryan, R. O. (2008) Amphotericin B induces interdigitation of apolipoprotein stabilized nanodisk bilayers. *Biochim. Biophys. Acta, Biomembr. 1778*, 303–312.
(31) Ryan, R. O. (2008) Nanodisks: hydrophobic drug delivery vehicles. *Expert Opin. Drug Delivery 5*, 343–351.
(32) Tufteland, M., Ren, G., and Ryan, R. (2008) Nanodisks derived from amphotericin B lipid complex. *J. Pharm. Sci. 97*, 4425–4432.
(33) McConathy, W. J., Nair, M. P., Paranjape, S., Mooberry, L., and Lacko, A. G. (2008) Evaluation of synthetic/reconstituted high-density lipoproteins as delivery vehicles for paclitaxel. *Anti-Cancer Drugs 19*, 183–188.
(34) Nikanjarn, M., Gibbs, A. R., Hunt, A., Budinger, T. F., and Forte, T. M. (2007) Synthetic nano-LDL with paclitaxel oleate as a targeted drug delivery vehicle for glioblastoma multiforme. *J. Controlled Release 124*, 163–171.
(35) Blanchette, C. D., Law, R., Benner, W. H., Pesavento, J. B., Cappuccio, J. A., Walsworth, V., Kuhn, E. A., Corzett, M., Chromy, B. A., Segelke, B. W., Coleman, M. A., Bench, G., Hoeprich, P. D., and Sulchek, T. A. (2008) Quantifying size distributions of nanolipoprotein particles with single-particle analysis and molecular dynamic simulations. *J. Lipid Res. 49*, 1420–1430.
(36) Gubler, D., Kuno, G., and Markoff, L. (2007) Flaviviruses, in *Fields Virology* (Knipe, D. M., and Howley, P. M., Eds.) Lippincott Williams & Wilkins, Philadelphia.
(37) Widman, D. G., Ishikawa, T., Fayzulin, R., Bourne, N., and Mason, P. W. (2008) Construction and characterization of a second-generation pseudoinfectious West Nile virus vaccine propagated using a new cultivation system. *Vaccine 26*, 2762–2771.
(38) Tsai, T. F. (1993) Inactivated Japanese encephalitis virus vaccine: recommendations of the advisory committee on immunization practices (ACIP). *M. M. W. R. Recomm. Rep. 42*, 1–15.
(39) Aberle, J. H., Aberle, S. W., Allison, S. L., Stiasny, K., Ecker, M., Mandl, C. W., Berger, R., and Heinz, F. X. (1999)

A DNA immunization model study with constructs expressing the tick-borne encephalitis virus envelope protein E in different physical forms. *J. Immunol. 163*, 6756–6761.

(40) Fonseca, B. A. L., Pincus, S., Shope, R. E., Paoletti, E., and Mason, P. W. (1994) Recombinant vaccinia viruses co-expressing dengue-1 glycoproteins prM and E induce neutralizing antibodies in mice. *Vaccine 12*, 279–285.

(41) Konishi, E., Pincus, S., Paoletti, E., Shope, R. E., Burrage, T., and Mason, P. W. (1992) Mice immunized with a subviral particle containing the japanese encephalitis virus prM/M and E proteins are protected from lethal JEV infection. *Virology 188*, 714–720.

(42) Mason, P. W., Pincus, S., Fournier, M. J., Mason, T. L., Shope, R. E., and Paoletti, E. (1991) Japanese encephalitis virus-vaccinia recombinants produce particulate forms of the structural membrane proteins and induce high levels of protection against lethal JEV infection. *Virology 180*, 294–305.

(43) Pincus, S., Mason, P. W., Konishi, E., Fonseca, B. A. L., Shope, R. E., Rice, C. M., and Paoletti, E. (1992) Recombinant vaccinia virus producing the prM and E proteins of yellow fever virus protects mice from lethal yellow fever encephalitis. *Virology 187*, 290–297.

(44) Qiao, M., Ashok, M., Bernard, K. A., Palacios, G., Zhou, Z. H., Lipkin, W. I., and Liang, T. J. (2004) Induction of sterilizing immunity against west nile virus (WNV), by immunization with WNV-like particles produced in insect cells. *J. Infect. Dis. 190*, 2104–2108.

(45) Chu, J. H. J., Chiang, C. C. S., and Ng, M. L. (2007) Immunization of flavivirus West Nile recombinant envelope domain III protein induced specific immune response and protection against West Nile virus infection. *J. Immunol. 178*, 2699–2705.

(46) Lieberman, M. M., Nerurkar, V. R., Luo, H. Y., Cropp, B., Carrion, R., de la Garza, M., Coller, B. A., Clements, D., Ogata, S., Wong, T., Martyak, T., and Weeks-Levy, C. (2009) Immunogenicity and protective efficacy of a recombinant subunit West Nile virus vaccine in rhesus monkeys. *Clin. Vaccine Immunol. 16*, 1332–1337.

(47) Martina, B. E., Koraka, P., van den Doel, P., van Amerongen, G., Rimmelzwaan, G. F., and Osterhaus, A. (2008) Immunization with West Nile virus envelope domain III protects mice against lethal infection with homologous and heterologous virus. *Vaccine 26*, 153–157.

(48) McDonald, W. F., Huleatt, J. W., Foellmer, H. G., Hewitt, D., Tang, J., Desai, P., Price, A., Jacobs, A., Takahashi, V. N., Huang, Y., Nakaar, V., Alexopoulou, L., Fikrig, E., and Powell, T. J. (2007) A West Nile virus recombinant protein vaccine that coactivates innate and adaptive immunity. *J. Infect. Dis. 195*, 1607–1617.

(49) Mason, P. W., Shustov, A. V., and Frolov, I. (2006) Production and characterization of vaccines based on flaviviruses defective in replication. *Virology 351*, 432–443.

BC100083D

Facile Synthesis of Advanced Photodynamic Molecular Beacon Architectures

Jonathan F. Lovell,[†] Juan Chen,[‡] Elizabeth Huynh,[‡] Mark T. Jarvi,[‡] Brian C. Wilson,[‡] and Gang Zheng*[,†,‡]

Institute of Biomaterials and Biomedical Engineering and Department of Medical Biophysics, Ontario Cancer Institute, University of Toronto, Toronto, Ontario. Received April 22, 2010; Revised Manuscript Received May 14, 2010

Nucleic acid photodynamic molecular beacons (PMBs) are a class of activatable photosensitizers that increase singlet oxygen generation upon binding a specific target sequence. Normally, PMBs are functionalized with multiple solution-phase labeling and purification steps. Here, we make use of a flexible solid-phase approach for completely automated synthesis of PMBs. This enabled the creation of a new type of molecular beacon that uses a linear superquencher architecture. The 3′ terminus was labeled with a photosensitizer by generating pyropheophorbide-labeled solid-phase support. The 5′ terminus was labeled with up to three consecutive additions of a dark quencher phosphoramidite. These photosensitizing and quenching moieties were stable in the harsh DNA synthesis environment and their hydrophobicity facilitated PMB purification by HPLC. Linear superquenchers exhibited highly efficient quenching. This fully automated synthesis method simplifies not only the synthesis and purification of PMBs, but also the creation of new activatable photosensitizer designs.

INTRODUCTION

Activatable photosensitizers modulate singlet oxygen production in response to interactions with a variety of target biomolecules (*1*). Nucleic acid-activatable photosensitizers are based on hybridization to specific nucleic acid target sequences. Nucleic acid photodynamic molecular beacons (PMBs) synthesized with porphyrin or phthalocyanine photosensitizers have recently been developed (*2, 3*). Molecular beacons are hairpin-loop structures that hold a quencher and fluorophore together, until the loop portion hybridizes to a target sequence, causing stem separation and unquenching. PMBs are an extension of prototypical molecular beacons that offer single base mismatch sensitivity and large fluorescence signal differences between the hybridized and nonhybridized states (*4, 5*). Excluding molecular beacons, alternative strategies for DNA control of singlet oxygen have also been proposed. Single-walled nanotubes that bound and quenched a chlorin-*e*6 conjugated aptamer were displaced when the aptamer bound its thrombin target, leading to photosensitizer activation (*6*). Another approach was based on the hybridization and displacement of pyropheophorbide-labeled oligonucleotides to another quenching DNA strand (*7*). These multicomponent systems make use of separate quenching and photosensitizing molecules, which simplifies the synthesis and purification of each individual component but adds a layer of uncertainty of how the subunits behave in diverse hybridization conditions. Here, we report a new synthesis method for PMBs that facilitates their synthesis and purification and also permits the development of novel photodynamic beacon architectures.

Although production of standard molecular beacons is routine, there have been few reports of synthesis and purification of PMBs. Normally, the nucleic acid portion is produced using standard DNA synthesis methods, and then one beacon terminus is labeled with a photosensitizer and the other is labeled with a quenching (or self-quenching) moiety. There are several approaches to the conjugation of these functional groups. To simplify the labeling procedure, previous efforts resulted in the development of a porphyrin phosphoramidite (*7*). While this phosphoramidite is ideal for labeling the 5′ terminus of an oligonucleotide in the final addition cycle of a solid-phase synthesis, no subsequent additions are possible. The most common approach is the incorporation of amine-modified functional groups with different protecting groups that permit sequential deprotection and labeling of each terminus using an activated ester or acid-modified labeling moiety. In the case of self-quenched beacons, only a single type of conjugatable group is required since the same labeling reaction may be repeated at both termini. In some cases, it may be challenging to find a suitable solvent for dissolving the hydrophobic photosensitizer with the hydrophilic nucleic acid. If the oligonucleotide is conjugated at the 3′ prior to synthesis, purification problems can arise using reverse-phase HPLC, because short degradation sequences labeled with a hydrophobic photosensitizer or quencher can elute at the same time as the ion-paired full-length product. Solid-phase synthesis approaches have been described for dual terminal oligonucleotide labeling (*8*) and are applied here to automate PMB synthesis and simplify purification.

RESULTS AND DISCUSSION

To generate a complete solid-phase synthesis approach for PMBs, we first labeled controlled pore glass (CPG) with a photosensitizer. Pyropheophorbide was a suitable choice, since this fluorescent photosensitizer was stable under the harsh conditions of multiple DNA synthesis cycles and oligonucleotide deprotection. The photosensitizer was conjugated to the CPG using a simple dehydration reaction after removing the CPG FMOC group (Figure 1A). After conjugation and washing, the statically charged CPG displayed a dark green color (Figure 1B). A solid-phase packing scheme was developed using a vacuum line, in which empty columns were two-thirds filled to ensure reproducible synthesizer reagent flowthrough during the synthesis (Figure 1C). For the quenching moiety on the opposing 5′ terminus, we employed a commercially available phosphoramidite quencher, BlackBerry quencher dT (BBQ-dT). This is nonterminating and so could be used for multiple additions. As

* Correspondence to Gang Zheng, TMDT 5-363; 101 College Street, Toronto ON M5G 1L7, Tel.: 416-581-7666; Fax: 416-581-7667; gang.zheng@uhnres.utoronto.ca.

[†] Institute of Biomaterials and Biomedical Engineering.

[‡] Department of Medical Biophysics.

10.1021/bc100178z © 2010 American Chemical Society
Published on Web 05/28/2010

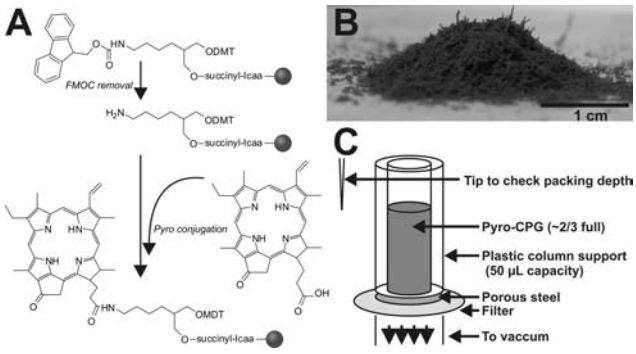


Figure 1. Solid-phase support for automated PMB synthesis. (A) Synthetic scheme for generation of pyropheophorbide solid-phase CPG support. (B) Photograph of pyropheophorbide CPG. (C) Packing method for achieving reproducible solid-phase synthesis.

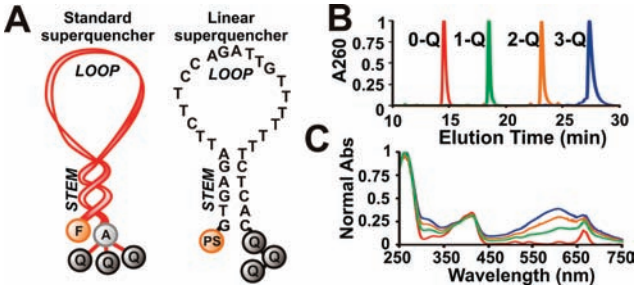


Figure 2. Solid-phase generation of new PMB architectures. (A) Standard (left) and linear (right) superquenchers. F represents the fluorophore, A represents an adapter phosphoramidite, and Q represents the quencher. The linear superquencher details the sequence used. PS represents pyropheophorbide. (B) HPLC retention times of the 0, 1, 2, or 3 quencher PMBs. (C) Absorption profiles of the molecular beacons: color scheme as in B.

an example of a useful application of this solid-phase synthesis approach, we generated a new class of PMBs that feature the first linear superquencher.

Superquenchers are assemblies of multiple quenchers that efficiently quench molecular beacon fluorescence when the beacon is in the inactive state (*9*). These have not been previously explored as singlet oxygen quenchers. Standard superquenchers use a trebler phosphoramidite that branches the oligonucleotide, permitting multiple quencher additions in the next addition cycle (Figure 2A, left). While this approach is effective, it requires the use of an additional specialty phosphoramidite (the trebler phosphoramidite, in addition to the quencher phosphoramidite). Instead, we used multiple additions of the BlackBerry quencher phosphoramidite at the 5′ terminus to achieve the first "linear superquencher" (Figure 2A, right) that has multiple quencher moieties attached sequentially (via phosphodiester bonds) in series rather than in parallel. The PMB included pyropheophorbide on the 3′ terminus, the oligonucleotide sequence indicated in the figure (which is a shared stem beacon (*10*) with one stem complementary to a portion the target sequence), and 0, 1, 2, or 3 BlackBerry quenchers linked on the 5′ terminus. After synthesis, the PMBs were deprotected with methylamine/ammonium hydroxide (1:1) for 15 min at 55 °C and were then purified by reverse-phase HPLC. This rapid protocol resulted in PMBs that could be synthesized and purified in a single day. The PMB identities were confirmed with mass spectroscopy. Figure 2B shows the reverse-phase HPLC elution profiles of the beacons. As expected, each additional quencher increased the hydrophobicity and retention times of the beacon. One advantage of the increased retention time was that the linear superquencher could be distinguished from pyropheophorbide-labeled degradation products that tend to elute near the full-length beacon with no quencher or a single quencher (note that Figure 2 shows traces for the purified beacons). The addition of 2 or 3 hydrophobic quenching moieties shifted the elution time so that HPLC purification of the full-length product was straightforward. The absorption profile of the 0, 1, 2, or 3-quencher beacons shown in Figure 2C confirmed that the oligonucleotide (260 nm) and pyropheophorbide (410 and 680 nm) ratios remained constant, while each additional quenching moiety contributed to the broad peak from 500 to 750 nm. The separate spectra of pyropheophorbide and BlackBerry quencher are shown in Supporting Information Figure 1.

The fluorescence response of the beacons was characterized to confirm the beacon activation. As shown in Figure 3A, all

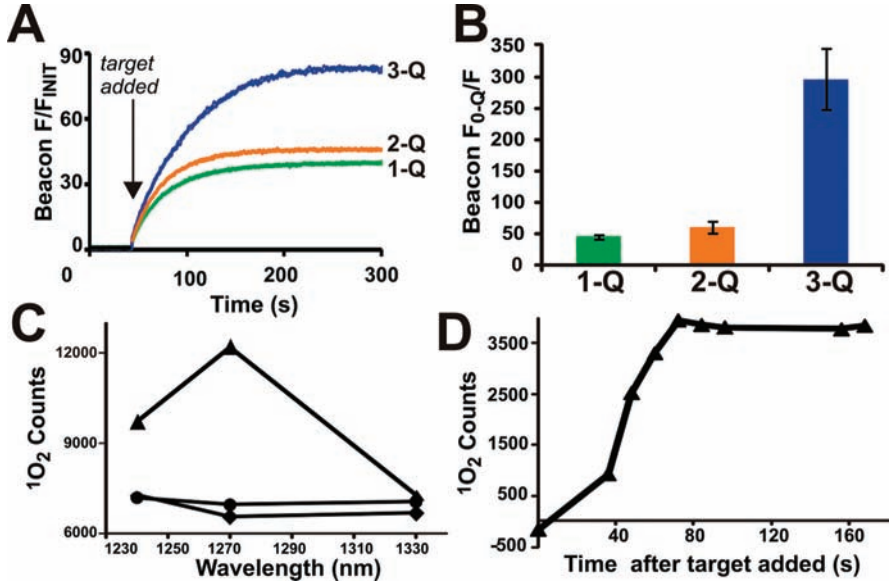


Figure 3. Characterization of linear superquencher (A) 50 nM PMB fluorescence response to addition of a 10-fold excess of target DNA in buffered saline. F is the beacon fluorescence and F_{INIT} is the beacon fluorescence at the initial time point. (B) Beacon fluorescence quenching compared to the 0-Q beacon. (C) Direct measurement of singlet oxygen luminescence for the 1-Q beacon. Triangles: beacon + target. Circles: buffer alone. Diamonds: beacon alone. (D) Singlet oxygen luminescence activation kinetics of the 1-Q beacon measured in buffered saline supplemented with 75% D_2O.

beacons rapidly hybridized to the target nucleic acid, resulting in increased fluorescence. While the single and double quencher were activated 30- and 40-fold, respectively, the triple quencher had a higher activation of approximately 90-fold. This activation is similar to the 100-fold activation observed using gold as a potent molecular beacon quencher (*11*), yet it is not as effective as the 300-fold activation observed with standard branched superquenchers (*9*). However, when the fluorescence intensity of the closed beacon was compared to the 0-Q beacon that lacked any quencher (as opposed to comparing the closed beacon to the target-activated beacon), 300-fold quenching was indeed observed (Figure 3B). This shows that the quenching of the triple quencher was extremely effective, but there was some residual intramolecular quenching in the activated state likely due to the extremely hydrophobic nature of the photosensitizer and quenchers. The singlet oxygen generation of the beacons was next examined. As shown in Figure 3C, in the closed state, the beacon with only 1 quencher generated lower singlet oxygen luminescence than that of the buffer alone. However, when the target was added, a clear singlet oxygen luminescence peak appeared at 1270 nm as expected. Maximum singlet oxygen activation occurred within 80 s of target addition (Figure 3D). Because the singlet oxygen luminescence of the closed-state beacon was below the instrument detection limits with even the 1-Q beacon, we could not accurately determine the activation of the 2-Q or 3-Q PMBs. It would be expected to be similar to the activation of fluorescence, since the degree of fluorescence quenching is highly correlated to the degree of singlet oxygen quenching (*12*).

In summary, the solid-phase approach was effective for generating PMBs that are more convenient to synthesize and purify. By using pyropheophorbide modified CPG, the entire PMB could be synthesized in one run on a standard DNA synthesizer using only one specialty quenching phosphoramidite. Purification was also facilitated by the change in HPLC retention time induced by the presence of multiple quenchers. This synthetic approach permitted the generation of a modified and powerful singlet oxygen superquencher, in which the quenchers were assembled linearly rather than in a branched configuration. The 3-Q PMB displayed favorable characteristics for purification and low-background activation. Fully automated DNA synthesis methods facilitate effective nucleic acid activatable photosensitizer design and implementation.

ACKNOWLEDGMENT

This work was supported by the Canadian Cancer Society (grants 18510 and 19484), the Canadian Institute of Health Research, the Ontario Institute for Cancer Research, the Natural Sciences & Engineering Research Council of Canada, the Joey and Toby Tanenbaum/Brazilian Ball Chair in Prostate Cancer Research.

Supporting Information Available: Experimental procedures and absorption spectra of BBQ and pyropheophorbide. This material is available free of charge via the Internet at http://pubs.acs.org.

LITERATURE CITED

(1) Lovell, J., Chen, J., Liu, T., and Zheng, G. (2010) Activatable photosensitizers for imaging and therapy. *Chem. Rev. 110*, 2839–2857.

(2) Chen, J., Lovell, J. F., Lo, P., Stefflova, K., Niedre, M., Wilson, B. C., and Zheng, G. (2008) A tumor mRNA-triggered photodynamic molecular beacon based on oligonucleotide hairpin control of singlet oxygen production. *Photochem. Photobiol. Sci. 7*, 775.

(3) Nesterova, I. V., Erdem, S. S., Pakhomov, S., Hammer, R. P., and Soper, S. A. (2009) Phthalocyanine dimerization-based molecular beacons using near-IR fluorescence. *J. Am. Chem. Soc. 131*, 2432–2433.

(4) Tyagi, S., and Kramer, F. R. (1996) Molecular beacons: probes that fluoresce upon hybridization. *Nat. Biotechnol. 14*, 303–308.

(5) Wang, K., Tang, Z., Yang, C., Kim, Y., Fang, X., Li, W., Wu, Y., Medley, C., Cao, Z., Li, J., Colon, P., Lin, H., and Tan, W. (2009) Molecular engineering of DNA: molecular beacons. *Angew. Chem., Int. Ed. 48*, 856–870.

(6) Zhu, Z., Tang, Z., Phillips, J. A., Yang, R., Wang, H., and Tan, W. (2008) Regulation of singlet oxygen generation using single-walled carbon nanotubes. *J. Am. Chem. Soc. 130*, 10856–10857.

(7) Clo, E., Snyder, J. W., Voigt, N. V., Ogilby, P. R., and Gothelf, K. V. (2006) DNA-programmed control of photosensitized singlet oxygen production. *J. Am. Chem. Soc. 128*, 4200–4201.

(8) Kuhn, H., Demidov, V. V., Coull, J. M., Fiandaca, M. J., Gildea, B. D., and Frank-Kamenetskii, M. D. (2002) Hybridization of DNA and PNA molecular beacons to single-stranded and double-stranded DNA targets. *J. Am. Chem. Soc. 124*, 1097–1103.

(9) Yang, C. J., Lin, H., and Tan, W. (2005) Molecular assembly of superquenchers in signaling molecular interactions. *J. Am. Chem. Soc. 127*, 12772–12773.

(10) Tsourkas, A., Behlke, M. A., and Bao, G. (2002) Structure-function relationships of shared-stem and conventional molecular beacons. *Nucleic Acids Res. 30*, 4208–4215.

(11) Dubertret, B., Calame, M., and Libchaber, A. J. (2001) Single-mismatch detection using gold-quenched fluorescent oligonucleotides. *Nat. Biotechnol. 19*, 365–370.

(12) Lovell, J. F., Chen, J., Jarvi, M. T., Cao, W., Allen, A. D., Liu, Y., Tidwell, T. T., Wilson, B. C., and Zheng, G. (2009) FRET quenching of photosensitizer singlet oxygen generation. *J. Phys. Chem. B 113*, 3203–3211.

BC100178Z

Simple PEG Conjugation of SPIO via an Au−S Bond Improves Its Tumor Targeting Potency as a Novel MR Tumor Imaging Agent

Hiroki Kojima,[†] Yohei Mukai,*[,†] Mai Yoshikawa,[†] Kazumasa Kamei,[†] Tomoaki Yoshikawa,[†] Masahito Morita,[‡,§] Toshiro Inubushi,[§] Takao A Yamamoto,[||] Yasuo Yoshioka,[†,⊥] Naoki Okada,[†] Satoshi Seino,[||] and Shinsaku Nakagawa*[,†,⊥]

Graduate School of Pharmaceutical Sciences and Center for Advanced Medical Engineering and Informatics, Osaka University, 1−6 Yamadaoka, Suita, Osaka 565−0871, Japan, Immunology Frontier Research Center, Osaka University, 1-3 Yamadaoka, Suita, Osaka 565−0871, Japan, Graduate School of Engineering, Osaka University, 2−1 Yamadaoka, Suita, Osaka 565−0871, Japan, and Biomedical MR Science Center, Shiga University of Medical Science, Tsukiwa-cho, Seta, Otsu, Shiga, 520-2192, Japan. Received November 10, 2009; Revised Manuscript Received April 11, 2010

Gold/iron oxide magnetic nanoparticles are hybrid nanoparticles containing a core of magnetic iron oxide and surface colloidal gold, which allows for various biomaterials to be immobilized on the surface of the iron oxide nanoparticles *via* colloidal gold. Here, we developed a novel magnetic resonance (MR) imaging agent to broaden the MR tumor-imaging spectrum of superparamagnetic iron oxide nanoparticles (SPIO), e.g., Feridex, a clinical MR imaging agent for diagnosing liver cancer. Au/Feridex was synthesized by electron beam irradiation, and thiol-modified poly(ethylene glycol) (PEG-SH) was easily conjugated to its surface via an Au−S bond without the need for any chemical reactions. PEG conjugation of Au/Feridex enhanced its accumulation in Meth-A tumor tissue and decreased its accumulation in normal liver tissue. In addition, MRI using PEG-Au/Feridex, in contrast to MRI using unmodified Au/Feridex and Feridex, detected B16BL6 and Meth-A tumor tissues *in vivo*. This finding indicates that PEG-Au/Feridex is useful for diagnosing various types of tumors. In addition, because the synthesis of PEG-Au/Feridex is simple and high yields are easily produced, PEG-modified SPIO for tumor diagnosis can be prepared on an industrial scale with low cost.

INTRODUCTION

Superparamagnetic iron oxide (SPIO) is a potent contrast agent for magnetic resonance imaging (MRI) (*1*−*4*), represented by Feridex (AMAG Pharmaceuticals, Inc., MA) and Resovist (Bayer Schering Pharma AG., Germany). These compounds contain a core iron oxide nanoparticle coated with a dextran polymer. SPIO decreases the signal intensity on T_2 (T_2*)-weighted MR images and is clinically used for diagnosing liver cancer (*5*−*7*). SPIO is expected to improve the accuracy and specificity of cancer diagnoses in combination with other diagnostic tools such as computed tomography and ultrasonography (*8*).

SPIO in the blood is rapidly taken up by the reticular endothelial system (RES) like the hepatic specialized macrophages and Kuppfer cells, resulting in a high accumulation in healthy liver tissue (*9, 10*). On the other hand, SPIO does not accumulate in liver tumor tissue lacking Kuppfer cells and does not decrease the signal intensity of tumors, which leads to an increased contrast between healthy liver tissue and tumor tissue (*8*−*10*). Because this mechanism inhibits the distribution of SPIO to other tissues, however, the application of SPIO is limited to the diagnosis of liver cancer. Therefore, many researchers have attempted to develop novel contrast agents for various types of tumors by improving the SPIO (*1, 11, 12*).

Surface modification of SPIO with various biomaterials to inhibit RES uptake is considered effective for targeting tumors (*1*). In particular, conjugation with a water-soluble polymer on the SPIO surface is an effective method of inhibiting RES uptake, subsequently prolonging the half-life of SPIO in the blood. A longer blood half-life of SPIO allows for specific accumulation in tumor tissue by an enhanced permeability and retention effect (EPR effect) (*1, 13*−*18*). Many methods of surface modification have been reported: encapsulation of SPIO into nanoimmunoliposomes (*13*), conjugation of SPIO with polymers such as poly(ethylene glycol) (PEG), poly(ethylene oxide), and dextran (*17, 19*). These approaches, however, require specially designed polymer molecules or complicated preparation methods (*20, 21*). There is therefore strong interest in developing a simple and easy method of conjugating functional molecules to the SPIO surface.

We developed gold/iron magnetic nanoparticles that are easily synthesized by electron beam irradiation of a mixture of iron oxide nanoparticles and Au solution (*22*). Using this method, gold/iron magnetic nanoparticles are obtained in extremely high yield (almost 100%). Colloidal gold forms a strong Au−S bond with a thiol group just by mixing, without any catalysts or linker molecules (*22*−*25*). This property is useful for conjugating various polymers or biomolecules on the nanoparticle surface. As one application, we previously reported that an adenovirus vector (Ad) could be easily immobilized on the gold/iron nanoparticle via the Au−S bond, allowing the Ad/nanoparticle

* Corresponding authors. Yohei Mukai, Ph.D., Department of Biotechnology and Therapeutics, Graduate School of Pharmaceutical Sciences, Osaka University, 1−6 Yamadaoka, Suita, Osaka 565−0871, Japan. Tel: +81-6-6879-8178, Fax: +81-6-6879-8179, E-mail: yohe@phs.osaka-u.ac.jp. Shinsaku Nakagawa, Ph.D., Department of Biotechnology and Therapeutics, Graduate School of Pharmaceutical Sciences, Osaka University, 1−6 Yamadaoka, Suita, Osaka 565−0871, Japan. Tel: +81-6-6879-8175, Fax: +81-6-6879-8179, E-mail: nakagawa@phs.osaka-u.ac.jp.

[†] Graduate School of Pharmaceutical Sciences, Osaka University.

[‡] Immunology Frontier Research Center, Osaka University.

[§] Shiga University of Medical Science.

[||] Graduate School of Engineering, Osaka University.

[⊥] Center for Advanced Medical Engineering and Informatics, Osaka University.

10.1021/bc900487p © 2010 American Chemical Society
Published on Web 05/06/2010

complex to be introduced into cells by magnetic force, resulting in great improvement in the gene transduction efficacy of the Ad (*23*). In the present study, we synthesized a gold/iron magnetic nanoparticle using Feridex, a clinically available SPIO for liver cancer diagnosis, as its core (Au/Feridex). We coated the surface of Au/Feridex using a thiol-modified PEG to inhibit its accumulation in the liver, thereby extending its half-life in the blood, and to target tumors by the EPR effect. We evaluated the efficacy of PEG-conjugated Au/Feridex (PEG-Au/Feridex) as a tumor contrast agent in tumor-bearing mice.

EXPERIMENTAL PROCEDURES

Au/Feridex Synthesis. Feridex (Advanced Magnetics, Inc.) was dispersed at a concentration of 0.1 g/L in an aqueous solution containing 0.5 mM $AuHCl_4$, 4.125 mM 2-propanol, and 10 g/L poly(vinyl alcohol) (PVA). The dispersion was poured into a glass vial and irradiated with an electron beam at a dose of 6 kGy. Au/Feridex was purified by high-speed centrifugation and redispersed in distilled water. The size was measured using a dynamic light scattering method with a Z-sizer 3000-HS (Malvern Instruments Ltd., UK).

Cell Line. Mouse melanoma cells (B16BL6) were kindly provided from Kobegakuin University. B16BL6 cells were cultured in Minimum Essential Medium (Sigma-Aldrich, St. Louis, MO) containing 7.5% fetal bovine serum (Invitrogen Corporation, Carlsbad, CA) and Antibiotic-Antimycotic Mixed Solution (Nacalai Tesque Inc., Japan). RAW264.7 cells were purchased from American Type Culture Collection. RAW264.7 cells were cultured in Dulbecco's Modified Eagle's Medium (Wako Pure Chemical Industries Ltd., Osaka, Japan) containing 10% fetal bovine serum and Antibiotic-Antimycotic Mixed Solution. Meth-A cells were kindly provided by the Institute of Development, Aging, and Cancer of Tohoku University. Meth-A cells were maintained by intraperitoneal passage in BALB/c mice.

Transmission Electron Microscopy (TEM) Observation of Feridex and Au/Feridex. The morphologies of the Feridex and Au/Feridex were observed by a TEM (H-8100T, Hitachi Ltd., Tokyo, Japan) operated at 200 kV. The typical image from several TEM micrographs is shown in this report.

Preparation of PEG-Conjugated Au/Feridex (PEG-Au/Feridex). Au/Feridex and thiol-modified PEG (PEG-SH, MW = 5000 Da; NOF Corporation, Japan) were mixed at a ratio of 1:1 (1 μmol PEG-SH/mg Fe) in Au/Feridex. The mixture was incubated at room temperature for 1 h and then purified by high-speed centrifugation (28 000 rpm, 30 min). The concentrations of Fe and Au were determined using an inductively coupled plasma (ICP) spectrometer ICPS-7500 (Shimadzu Corporation, Japan).

PVA Test—Cross-Linking of PEGylated Contrast Agents. Contrast agents (Feridex or Au/Feridex) and PEGs (PEG-SH or nonmodified PEG, MW = 5000 Da; Wako Pure Chemical Industries Ltd.) were mixed at a ratio of 1:1 (1 μmol PEGs/mg Fe). After 1 h incubation at room temperature, the mixtures were purified by high-speed centrifugation (100 000 × *g*, 30 min), and the pellet was resuspended with distilled water. An aliquot of 5 mg Fe/mL of these reactants was mixed with an equal volume of 30% PVA (Wako Pure Chemical Industries Ltd.) and incubated at room temperature for 1 h. Cross-linking between PVA and PEG resulted in a precipitate that contained the nanoparticles (*26*).

Quantification of PEG-SH Immobilized on Contrast Agents. Feridex and Au/Feridex were mixed with PEG-SH at a ratio of 1:1 (1 μmol PEGs/mg Fe). After 1 h incubation at room temperature, the mixtures were purified by high-speed centrifugation (100 000 × *g*, 30 min). The amount of sulfur contained in PEG-SH in each sample was then determined using an ICP spectrometer.

***In Vitro* MRI.** Feridex, Au/Feridex, and PEG-Au/Feridex were diluted with distilled water to contain the same iron concentration (50 μg/mL, 10 μg/mL, and 2 μg/mL). T_2-weighted images (multislice spin-echo coronal images; TR = 2000 ms, TE = 69 ms) of these solutions were obtained with a 1.5 T MRI (MRminiSA; DS Pharma Biomedical Co., Ltd., Japan).

***In Vivo* Blood Clearance.** BALB/c mice were intravenously injected with 1 mg Fe in contrast agents (Feridex, Au/Feridex, and PEG-Au/Feridex). Blood samples were collected at 2, 5, 10, 30, and 60 min postinjection. T_2-weighted images of these samples were obtained with a 1.5 T MRI (MRminiSA; DS Pharma Biomedical Co., Ltd., Japan). The signal intensity of each sample on the MR image was analyzed using *Image J* software (National Institutes of Health, USA). The iron concentration of the samples was calculated based on the correlation between the signal intensity and the iron concentration of Feridex. All studies involving animals were approved by the institute's animal care and use committee.

***In Vivo* Distribution.** Meth-A cells (5×10^5 cells/100 μL) were injected intradermally into the abdomen of 6-week-old BALB/c mice. When the tumor size reached 10 mm in diameter, 1 mg Fe/200 μL of each contrast agent (Au/Feridex, PEG-Au/Feridex) was injected intravenously into the mice ($n = 3$ mice per group). The mice were killed, and the tumor and liver were extracted at 1 or 24 h postinjection and immediately freeze-dried. Radiation was counted after irradiation of vials containing samples in a nuclear reactor (JRR-3 in Japan Atomic Energy Agency, Ibaragi, Japan) with a thermal neutron flux of 5.2×10^{17} neutrons/cm/s for 20 min. After a delay of 4 to 5 days, irradiated samples were counted by computer-based γ-ray spectrometry on a Ge detector for 2000 s, and then the peak area of 412 keV γ-rays from ^{198}Au elements was measured using a multichannel pulse height analyzer with automatic dead time (<10%) correction.

***In Vivo* MR Tumor Imaging.** C57BL/6 mice (6 weeks old) were injected intradermally in the abdomen with 5×10^5 cells/100 μL of B16BL6 cells. Meth-A tumor-bearing mice were prepared as described below. When the tumors were 10 mm in diameter, 1 mg Fe/200 μL of each contrast agent (Feridex, Au/Feridex, PEG-Au/Feridex) was injected into the mice ($n = 3$ mice per group). MRI studies were performed with MRminiSA (DS Pharma Biomedical Co., Ltd.). Tumor-bearing mice were anesthetized with a 1.5% isoflurane/air mixture and maintained at 37 °C inside the magnet. All images were obtained as T_2-weighted images (multislice spin-echo axial images; TR = 2000 ms, TE = 69 ms). MRI scans were performed before and 1 h after the injection.

Iron Staining of Tumor Sections. After *in vivo* MRI analysis, the tumor and liver were extracted and fixed with 4% paraformaldehyde followed by sequential immersion in 10%, 20%, and 30% sucrose solutions. Tissues were frozen in OCT compound (Sakura Finetek Inc., Torrance, CA) with liquid nitrogen and sectioned at 10 μm using a cryostat (CM1850; Leica Microsystems GmbH). Sections were stained with Prussian blue to detect the particles of Feridex, Au/Feridex, and PEG-Au/Feridex. Sections were stained with 1% potassium hexacyanoferrate (II)-trihydrate in 0.1 M HCl followed by counterstaining with 0.5% eosin Y ethanol solution.

RESULTS

Synthesis of PEG-Au/Feridex. Au/Feridex was synthesized by electron beam irradiation of the mixture of $AuHCl_4$ and the Feridex solution. Synthesis of Au/Feridex was confirmed by transmission electron microscopy (Figure 1). Au/Feridex was visualized as colloidal gold nanoparticles (black particles) on

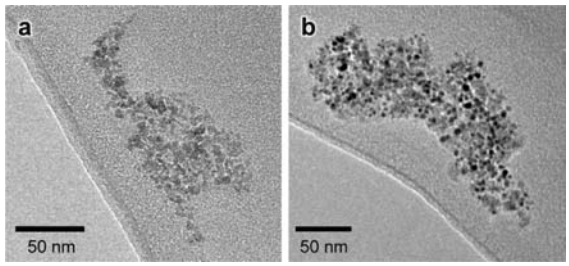


Figure 1. Transmission electron microscopy image of (a) Feridexand (b) Au/Feridex.

the surface of Feridex (gray particles; Figure 1b). Unreacted Feridex, i.e., without colloidal gold, was not observed in this solution. The ratio of Au/Fe was determined as 0.944 Au/Fe by weight using an ICP spectrometer.

PEG conjugation of Au/Feridex was performed by mixing PEG-SH (MW = 5000 Da) with Au/Feridex. PEG conjugation was confirmed by a PVA test, in which PEG-modified particles form a precipitate due to hydrogen bonding between PEG and PVA (*26*). Precipitation was observed only in the PEG-SH and Au/Feridex mixture, and there was no precipitate in the other mixtures (PEG-SH and Feridex, PEG and Au/Feridex, Au/Feridex alone; Figure 2). This findings indicated that PEG modification of Feridex was achieved by an Au−S bond.

Characterization of PEG-Au/Feridex. We measured the amount of PEG-SH immobilized on Au/Feridex using an ICP spectrometer. The amount of immobilized PEG-SH on Au/Feridex was 1.58 mg PEG-SH/mg Fe (1.74 mg PEG-SH/mg Au) and the amount immobilized on Feridex was 0.038 mg. This finding also suggests that PEG-SH was efficiently immobilized on Au/Feridex via Au−S bonds.

We measured the hydrodynamic size of these contrast agents (Feridex, Au/Feridex, and PEG-Au/Feridex) using a dynamic light scattering method. The hydrodynamic size of Feridex, Au/Feridex, and PEG-Au/Feridex was 69.4 nm, 163.9 nm, and 153.6 nm, respectively. Notably, the size of PEG-Au/Feridex (153.6 nm) was smaller than that of Au/Feridex (163.9 nm), suggesting that the state of dispersion was improved by PEG conjugation. The state of dispersion is an important factor in tumor targeting using the EPR effect (*27, 28*). Therefore, this result suggests that PEG-Au/Feridex may be able to effectively target tumors. PEG-Au/Feridex was not cytotoxic to RAW264.7 cells at a concentration of 300 μg Fe/mL (Supporting Information Figure S1). In fetal bovine serum at 37 °C, the Au−S bond remained unbroken after 1 h incubation (Supporting Information Figure S2). Moreover, PEG-Au/Feridex did not aggregate under this condition (data not shown). These results suggested that this conjugation method using the Au−S bond is suitable for *in vivo* applications.

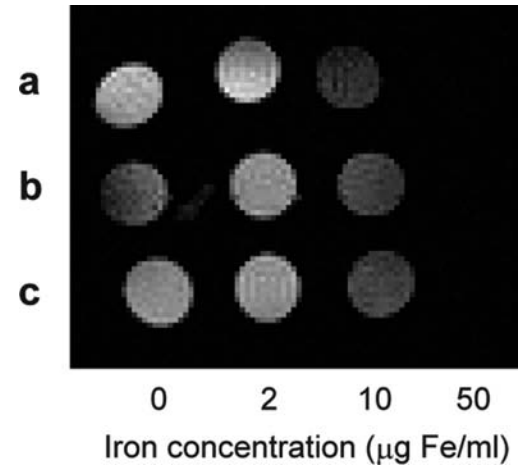


Figure 3. T_2-weighted images of each contrast agent. (a) Feridex, (b) Au/Feridex, and (c) PEG-Au/Feridex were diluted to the same iron concentration with distilled water. T_2-weighted images (spin-echo sequence: TR = 2000 ms, TE = 69 ms) were obtained using MRminiSA.

We then evaluated the transverse T_2 relaxation time of the three contrast agents using *in vitro* MRI images. All the contrast agents showed relaxation at an iron concentration of 10 μg/mL (Figure 3). These results indicate that the T_2 relaxation time was maintained after modification of colloidal gold and PEG-SH, suggesting that PEG-Au/Feridex and Feridex, a clinically used contrast agent, have a nearly equal T_2 relaxation.

Distribution of Each Contrast Agent. The efficacy of PEG modification was estimated by analyzing the blood clearance of Feridex, Au/Feridex, and PEG-Au/Freidex. Blood concentrations of each contrast agent were measured after intravenous injection into mice. The initial Fe concentration in the blood of mice injected with PEG-Au/Feridex was higher than in mice injected with Feridex and Au/Feridex (Figure 4). In addition, the clearance of PEG-Au/Feridex was moderate compared with that of Feridex and Au/Feridex (Figure 4). These findings suggest that the blood concentration of the imaging agent is increased by PEG modification.

We then evaluated the accumulation of the contrast agent in the liver and tumor. Au/Feridex and PEG-Au/Feridex were intravenously injected into Meth-A tumor-bearing BALB/c mice. At 1 h postinjection, the distribution in the liver and tumor tissues was determined by radiochemical neutron

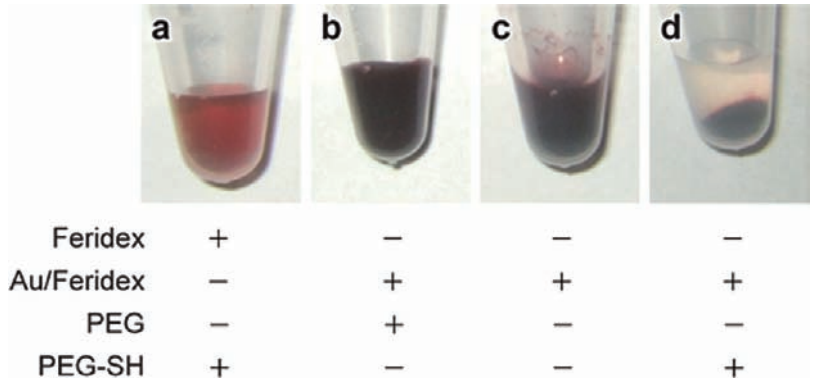


Figure 2. Confirmation of PEG-conjugation to Au/Feridex. PEGs (nonmodified PEG and thiol-modified PEG) were mixed with 5 mg Fe/mL of contrast agents (Feridex and Au/Feridex), as shown in the figure, and purified by high-speed centrifugation. The purified mixtures were mixed with PVA to a final concentration of 15% PVA and incubated overnight at room temperature.

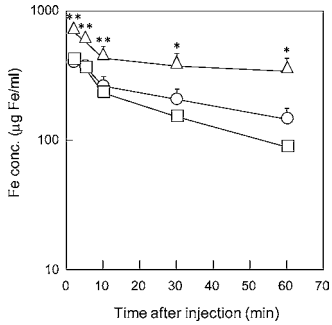


Figure 4. Fe concentration of contrast agents in blood. Fe concentrations were calculated from the intensities of T_2-weighed images (TR = 2000 ms, TE = 69 ms) of mouse blood samples. (o) Feridex, (□) Au/Feridex, and (Δ) PEG-Au/Feridex were intravenously administered and blood samples were collected at 2, 5, 10, 30, and 60 min. The error bars represent the SEM ($n = 5$). *$P < 0.001$, **$P < 0.000\,01$ by two-tailed t-test.

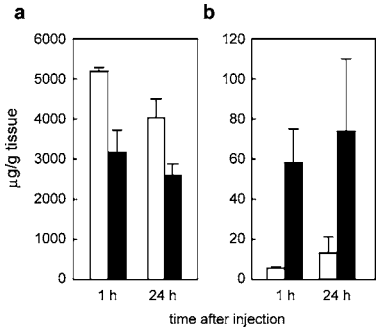


Figure 5. Accumulation of contrast agents in the liver and tumor. Au/Feridex and PEG-Au/Feridex were intravenously injected into tumor-bearing mice, and the livers and tumors were extracted 1 h postinjection. The quantity of (□) Au/Feridex and (■) PEG-Au/Feridex accumulated in the (a) liver or (b) tumor was measured by radiochemical neutron activation analysis of the Au element. Each bar represents SEM ($n = 3$).

activation analysis of the Au element (Figure 5). Liver accumulation of Au/Feridex was decreased by PEG conjugation (Figure 5a), suggesting that PEG conjugation inhibited uptake of the SPIO by the Kupffer cells in the liver. In the tumor, the accumulation of PEG-Au/Feridex was approximately 10-fold higher than that of Au/Feridex (Figure 5b). Accumulation of PEG-Au/Feridex in the tumor at 24 h was slightly increased compared with that at 1 h. The findings suggest that PEG conjugation efficiently enhanced the targeting of Feridex to the tumor.

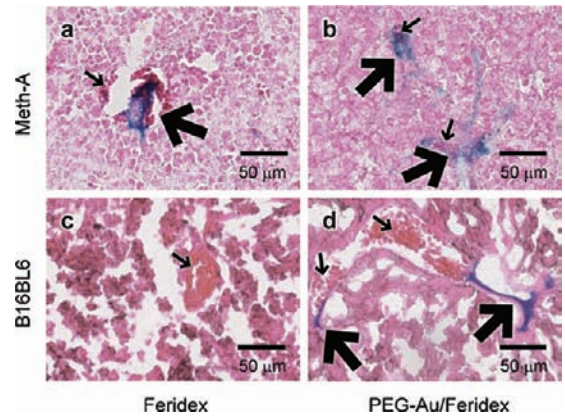


Figure 7. Analysis of tumor-accumulating mechanism of PEG-Au/Feridex. Ex vivo Prussian blue-stained images of tumor tissues extracted from tumor-bearing mice (a,b: Meth-A. c,d: B16BL6) at 1 h postinjection of 1 mg Fe of (a,c) Feridex or (b,d) PEG-Au/Feridex (counterstaining: eosin staining). Narrow arrowhead indicates tumor blood vessel in which erythrocytes are observed. Bold arrowhead indicates location of contrast agents.

PEG-Au/Feridex Enhances Tumor Contrast by an EPR Effect in MR Imaging. We used MR imaging to visualize the efficacy of PEG-conjugated Au/Feridex. MRI of Meth-A tumor-bearing mice was performed 1 h postinjection of Feridex, Au/Feridex, and PEG-Au/Feridex. T_2-weighted images showed that PEG-Au/Feridex decreased the signal intensity of the tumor, leading to the clear identification of a Meth-A tumor, whereas Feridex and Au/Feridex did not improve the tumor contrast (Figure 6a−f). Similar results were obtained using B16BL6 melanoma bearing mice (Figure 6g−l). These results suggested that our PEG-Au/Feridex was effective for identifying various tumor types.

We also tried to determine the mechanism of accumulation in the tumor by analyzing the location of these contrast agents in the tumor tissue. Tumor tissues were extracted from the same mice used to take the MR images, and then slices of the tissues were stained using the Prussian blue staining method to detect the Fe molecules. In both Meth-A and B16BL6-injected mice, PEG-Au/Feridex was distributed around the tumor blood vessels (Figure 7), suggesting that PEG-Au/Feridex leaked from the tumor blood vessels to the outside through the leaky tumor vascular walls. On the other hand, Feridex was not detected in the tumor sections (Figure 6). These results suggest that PEG-Au/Feridex has a decreased liver uptake and accumulated in the tumor by the EPR effect.

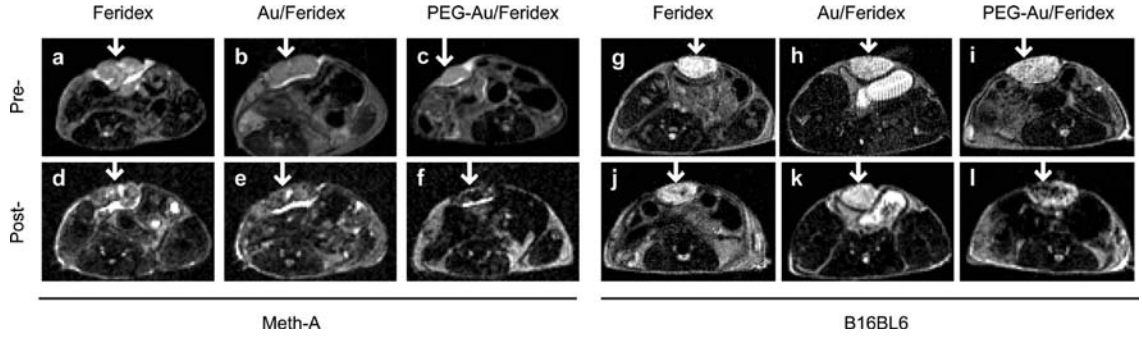


Figure 6. In vivo MRI tumor imaging. T_2-weighted images (1.5 T, spin-echo sequence: TR = 2000 ms, TE = 69 ms) of tumor-bearing mice (a−f, Meth-A; g−l, B16BL6) taken pre- and 1 h postinjection of 1 mg Fe of contrast agent (a,d,g,j: Feridex. b,e,h,k: Au/Feridex. c,f,i,l: PEG-Au/Feridex). Images a−c and g−i were obtained preinjection, and images d−f and j−l were obtained 1 h postinjection. Arrowhead indicates tumor. All images were obtained using MRminiSA.

DISCUSSION

Several studies have been performed in an effort to develop tumor-targeted SPIO (*1*). Most of the previously developed methods, however, require polymers containing special functional groups and some reaction steps that complicate the synthesis of surface-modified SPIO. Moreover, the low yield at each step of the reaction limits the usefulness (*19*). In the present study, these problems were overcome by the use of our original nanomaterial, an Au/Fe magnetic nanoparticle. We designed Au/Feridex from Feridex, a clinically used SPIO coated with dextran. Au immobilization on Feridex was achieved simply (an electron beam irradiation) and its efficiency was almost 100% based on TEM observation (Figure 1). This Au immobilization method is also successful for other iron oxide nanoparticles that do not contain surface dextran (*23*), suggesting that this technology is applicable to various types of SPIO. PEG conjugation via Au−S bonds proceeded under mild conditions at room temperature, without any catalysts or special chemical reactions. The number of PEG-SH molecules on PEG-Au/Feridex was estimated to be approximately 3000 molecules/particle (100 molecules/colloidal gold) based on the assumption that Au/Feridex is a 150-nm-diameter sphere and colloidal gold is a 3.4-nm diameter sphere, which was supported by TEM images (Figure 1). Moreover, the efficiency of PEG conjugation was also estimated to be almost 100%, supported by the clear supernatant in the PVA test (Figure 2). Therefore, this conjugation method is simpler, easier, and more efficient than previously described methods (*13, 14, 16*−*19, 29*). In this aspect, Au/Fe magnetic nanoparticles are an innovative tool that retains the activity of the conjugated molecules (*23*). The efficacy of PEG conjugation was demonstrated by the pharmacokinetics (Figure 4). The higher Fe concentration of PEG-Au/Feridex in the early phase suggests that the distribution volume was decreased and indicates that PEG conjugation inhibited uptake of Au/Feridex into liver (Figure 5). These results clearly show that Au immobilization and surface modification of SPIO is useful for creating a novel MRI tumor contrast agent.

On the other hand, the size of the PEG-conjugated contrast agents is important for tumor targeting (*27*). The size of the gold/iron magnetic nanoparticles can be easily altered by changing the core particle size (*23*). This feature might allow for better control of the pharmacokinetics of the contrast agent (*15, 27*). An effective tumor-targeting method may thus be developed by controlling two parameters: the particle size and the targeting agent. In the future, innovative methods to target various diseases may be developed by synthesizing smaller gold/iron magnetic nanoparticles to decrease the accumulation in the liver, and by applying various targeting agents to control the pharmacokinetics. Our novel MRI contrast agents have high potential for the diagnosis of various diseases.

CONCLUSION

The present paper reports a novel MRI tumor contrast agent (PEG-Au/Feridex) produced using a unique technique. Here, we showed that Au/Feridex can be simply and easily conjugated with PEG-SH. At each reaction step (synthesis of Au/Feridex and modification with PEG-SH), the yield was approximately 100%. PEG-Au/Feridex uptake was decreased in the liver and its accumulation in the tumor was approximately 10-fold greater than that of Au/Feridex, which led to clear identification of the tumor on T_2-weighted images that could not be achieved with Feridex alone. This newly developed contrast agent can be modified with various targeting agents containing a thiol group and will thus be potentially very useful for the diagnosis of various diseases.

ACKNOWLEDGMENT

This study was supported by Research for Promoting Technological Seeds from the Japan Science and Technology Agency (JST); in part by a Grant-in-Aid for Scientific Research and a Grant-in-Aid for Young Scientists (B) from the Ministry of Education, Culture, Sports, Science, and Technology of Japan (MEXT) and the Japan Society for the Promotion of Science (JSPS); in part by a Research Fund Project on Health Sciences focusing on Drug Innovation from the Japan Health Sciences Foundation; and in part by the Magnetic Health Science Foundation. Feridex was kindly provided by Eiken Chemical Co. Ltd. (Tokyo, Japan). Radiochemical neutron activity analysis of the Au element was performed by Dr. Norio Ito at the Osaka Prefecture University (Osaka, Japan).

Supporting Information Available: Additonal figures as described in the text. This material is available free of charge via the Internet at http://pubs.acs.org.

LITERATURE CITED

(1) Corot, C., Robert, P., Idee, J. M., and Port, M. (2006) Recent advances in iron oxide nanocrystal technology for medical imaging. *Adv. Drug Delivery Rev. 58*, 1471–1504.

(2) Ferrucci, J. T., and Stark, D. D. (1990) Iron oxide-enhanced MR imaging of the liver and spleen: review of the first 5 years. *Am. J. Roentgenol. 155*, 943–950.

(3) de Vries, I. J., Lesterhuis, W. J., Barentsz, J. O., Verdijk, P., van Krieken, J. H., Boerman, O. C., Oyen, W. J., Bonenkamp, J. J., Boezeman, J. B., Adema, G. J., Bulte, J. W., Scheenen, T. W., Punt, C. J., Heerschap, A., and Figdor, C. G. (2005) Magnetic resonance tracking of dendritic cells in melanoma patients for monitoring of cellular therapy. *Nat. Biotechnol. 23*, 1407–1413.

(4) Bulte, J. W., and Kraitchman, D. L. (2004) Iron oxide MR contrast agents for molecular and cellular imaging. *NMR Biomed. 17*, 484–499.

(5) Kopp, A. F., Laniado, M., Dammann, F., Stern, W., Gronewaller, E., Balzer, T., Schimpfky, C., and Claussen, C. D. (1997) MR imaging of the liver with Resovist: safety, efficacy, and pharmacodynamic properties. *Radiology 204*, 749–756.

(6) Reimer, P., and Tombach, B. (1998) Hepatic MRI with SPIO: detection and characterization of focal liver lesions. *Eur. Radiol. 8*, 1198–1204.

(7) Hahn, P. F., Stark, D. D., and Ferrucci, J. T. (1992) Accumulation of iron oxide particles around liver metastases during MR imaging. *Gastrointest. Radiol. 17*, 173–174.

(8) Tanimoto, A., and Kuribayashi, S. (2006) Application of superparamagnetic iron oxide to imaging of hepatocellular carcinoma. *Eur. J. Radiol. 58*, 200–216.

(9) Raynal, I., Prigent, P., Peyramaure, S., Najid, A., Rebuzzi, C., and Corot, C. (2004) Macrophage endocytosis of superparamagnetic iron oxide nanoparticles: mechanisms and comparison of ferumoxides and ferumoxtran-10. *Invest. Radiol. 39*, 56–63.

(10) Rogers, W. J., and Basu, P. (2005) Factors regulating macrophage endocytosis of nanoparticles: implications for targeted magnetic resonance plaque imaging. *Atherosclerosis 178*, 67–73.

(11) Peng, X. H., Qian, X., Mao, H., Wang, A. Y., Chen, Z. G., Nie, S., and Shin, D. M. (2008) Targeted magnetic iron oxide nanoparticles for tumor imaging and therapy. *Int. J. Nanomed. 3*, 311–321.

(12) Liu, S., Jia, B., Qiao, R., Yang, Z., Yu, Z., Liu, Z., Liu, K., Shi, J., Ouyang, H., Wang, F., and Gao, M. (2009) A novel type of dual-modality molecular probe for MR and nuclear imaging of tumor: preparation, characterization and in vivo application. *Mol. Pharmaceut. 6*, 1074–1082.

(13) Yang, C., Rait, A., Pirollo, K. F., Dagata, J. A., Farkas, N., and Chang, E. H. (2008) Nanoimmunoliposome delivery of superparamagnetic iron oxide markedly enhances targeting and uptake in human cancer cells in vitro and in vivo. *Nanomedicine 4*, 318–329.

(14) Kumagai, M., Imai, Y., Nakamura, T., Yamasaki, Y., Sekino, M., Ueno, S., Hanaoka, K., Kikuchi, K., Nagano, T., Kaneko, E., Shimokado, K., and Kataoka, K. (2007) Iron hydroxide nanoparticles coated with poly(ethylene glycol)-poly(aspartic acid) block copolymer as novel magnetic resonance contrast agents for in vivo cancer imaging. *Colloids Surf., B: Biointerfaces 56*, 174–181.

(15) Larsen, E. K., Nielsen, T., Wittenborn, T., Birkedal, H., Vorup-Jensen, T., Jakobsen, M. H., Ostergaard, L., Horsman, M. R., Besenbacher, F., Howard, K. A., and Kjems, J. (2009) Size-dependent accumulation of PEGylated silane-coated magnetic iron oxide nanoparticles in murine tumors. *ACS Nano 3*, 1947–1951.

(16) Lee, H., Lee, E., Kim do, K., Jang, N. K., Jeong, Y. Y., and Jon, S. (2006) Antibiofouling polymer-coated superparamagnetic iron oxide nanoparticles as potential magnetic resonance contrast agents for in vivo cancer imaging. *J. Am. Chem. Soc. 128*, 7383–7389.

(17) Zhang, Y., Kohler, N., and Zhang, M. (2002) Surface modification of superparamagnetic magnetite nanoparticles and their intracellular uptake. *Biomaterials 23*, 1553–1561.

(18) Chen, T. J., Cheng, T. H., Hung, Y. C., Lin, K. T., Liu, G. C., and Wang, Y. M. (2008) Targeted folic acid-PEG nanoparticles for noninvasive imaging of folate receptor by MRI. *J. Biomed. Mater. Res., Part A 87*, 165–175.

(19) Thunemann, A. F., Schutt, D., Kaufner, L., Pison, U., and Mohwald, H. (2006) Maghemite nanoparticles protectively coated with poly(ethylene imine) and poly(ethylene oxide)-block-poly(glutamic acid). *Langmuir 22*, 2351–2357.

(20) Moghimi, S. M., Hunter, A. C., and Murray, J. C. (2001) Long-circulating and target-specific nanoparticles: theory to practice. *Pharmacol. Rev. 53*, 283–318.

(21) Beduneau, A., Ma, Z., Grotepas, C. B., Kabanov, A., Rabinow, B. E., Gong, N., Mosley, R. L., Dou, H., Boska, M. D., and Gendelman, H. E. (2009) Facilitated monocyte-macrophage uptake and tissue distribution of superparmagnetic iron-oxide nanoparticles. *PLoS One 4*, e4343.

(22) Mizukoshi, Y., Seino, S., Okitsu, K., Kinoshita, T., Otome, Y., Nakagawa, T., and Yamamoto, T. A. (2005) Sonochemical preparation of composite nanoparticles of Au/gamma-Fe_2O_3 and magnetic separation of glutathione. *Ultrason. Sonochem. 12*, 191–195.

(23) Kamei, K., Mukai, Y., Kojima, H., Yoshikawa, T., Yoshikawa, M., Kiyohara, G., Yamamoto, T. A., Yoshioka, Y., Okada, N., Seino, S., and Nakagawa, S. (2009) Direct cell entry of gold/iron-oxide magnetic nanoparticles in adenovirus mediated gene delivery. *Biomaterials 30*, 1809–1814.

(24) Seino, S., Otome, T., Maki, Y., Nakagawa, T., Okitsu, T., Mizukoshi, K., Nakayama, Y., Sekino, T., Niihara, T., and Yamamoto, T. A. (2004) Gamma-ray synthesis of composite nanoparticles of noble metals and magnetic iron oxides. *Scr. Mater. 51*, 467–472.

(25) Seino, S., Nakagawa, T., Kojima, T., Taniguchi, T., Okuda, R., and Yamamoto, T. A. (2007) Radiation induced synthesis of gold/iron-oxide composite nanoparticles using high-energy electron beam. *J. Nanopart. Res. 10*, 1071–1076.

(26) Fujita, M. (2006) Patent No. JP 2006−327962A.

(27) Pouliquen, D., Le Jeune, J. J., Perdrisot, R., Ermias, A., and Jallet, P. (1991) Iron oxide nanoparticles for use as an MRI contrast agent: pharmacokinetics and metabolism. *Magn. Reson. Imaging 9*, 275–283.

(28) van Vlerken, L. E., Vyas, T. K., and Amiji, M. M. (2007) Poly(ethylene glycol)-modified nanocarriers for tumor-targeted and intracellular delivery. *Pharm. Res. 24*, 1405–1414.

(29) Larsen, E. K., Nielsen, T., Wittenborn, T., Birkedal, H., Vorup-Jensen, T., Jakobsen, M. H., Ostergaard, L., Horsman, M. R., Besenbacher, F., Howard, K. A., and Kjems, J. (2009) Size-dependent accumulation of PEGylated silane-coated magnetic iron oxide nanoparticles in murine tumors. *ACS Nano 3*, 1947–1951.

BC900487P

Novel Polar Single Amino Acid Chelates for Technetium-99m Tricarbonyl-Based Radiopharmaceuticals with Enhanced Renal Clearance: Application to Octreotide

Kevin P. Maresca, John C. Marquis, Shawn M. Hillier, Genliang Lu, Frank J. Femia, Craig N. Zimmerman, William C. Eckelman, John L. Joyal, and John W. Babich*

Molecular Insight Pharmaceuticals, Inc., 160 Second Street, Cambridge, Massachusetts 02142. Received November 23, 2009; Revised Manuscript Received March 10, 2010

Single amino acid chelate (SAAC) systems for the incorporation of the $M(CO)_3$ moiety (M = Tc/Re) have been successfully incorporated into novel synthetic strategies for radiopharmaceuticals and evaluated in a variety of biological applications. However, the lipophilicity of the first generation $Tc(CO)_3$-dipyridyl complexes has resulted in substantial hepatobiliary uptake when either examined as lysine derivatives or integrated into biologically active small molecules and peptides. Here we designed, synthesized, and evaluated novel SAAC systems that have been chemically modified to promote overall $Tc(CO)_3L_3$ complex hydrophilicity with the intent of enhancing renal clearance. A series of lysine derived SAAC systems containing functionalized polar imidazole rings and/or carboxylic acids were synthesized via reductive alkylation of the ε amino group of lysine. The SAAC systems were radiolabeled with ^{99m}Tc, purified, and evaluated for radiochemical stability, lipophilicity, and tissue distribution in rats. The log *P* values of the ^{99m}Tc complexes were determined experimentally and ranged from −0.91 to −2.33. The resulting complexes were stable (>90%) for at least 24 h. Tissue distribution in normal rats of the lead ^{99m}Tc complexes demonstrated decreased liver (<1 %ID/g) and gastrointestinal clearance (<1.5%ID/g) and increased kidney clearance (>15 %ID/g) at 2 h after injection compared to the dipyridyl lysine complex (DpK). One of the new SAAC ligands, [^{99m}Tc]bis-carboxymethylimidazole lysine, was conjugated to the N-terminus of Tyr-3 octreotide and evaluated for localization in nude mice bearing AR42J xenografts to examine tissue distribution, tumor uptake and retention, clearance, and route of excretion for comparison to ^{111}In-DOTA-Tyr-3-octreotide and ^{99m}Tc-DpK-Tyr-3-octreotide. ^{99m}Tc-bis-(carboxymethylimidazole)-lysine-Tyr-3-octreotide exhibited significantly less liver uptake and gastrointestinal clearance compared to ^{99m}Tc-DpK-Tyr-3-octreotide while maintaining tumor uptake in the same mouse model. These novel chelators demonstrate that lipophilicity can be controlled and organ distribution significantly altered, opening up broad application of these novel SAAC systems for radiopharmaceutical design.

INTRODUCTION

The potential to employ the radionuclide technetium-99m with its optimal decay characteristics into targeting molecules has been the foremost consideration in developing diagnostic radiopharmaceuticals (*1*−*3*). ^{99m}Tc-labeled radiopharmaceuticals are preferred over other isotopes because of the ideal nuclear properties of the isotope, as well as its widespread availability from commercial generator columns. ^{99m}Tc emits a 140 keV γ-ray with 89% abundance, which is ideal for imaging with commercial γ cameras. Furthermore, the combination of the medically useful radionuclides, ^{99m}Tc and rhenium-186/188 ($^{186/188}$Re), which have remarkably similar coordination chemistries in terms of the $\{M(CO)_3L_3\}^+$ core thereby yielding isostructural coordination complexes with favorable physical decay characteristics, is attractive for molecular imaging and radiotherapy, respectively (*4, 5*).

We previously described a technology known as the single amino acid chelate (SAAC) (*6*), a radiolabeling platform that has broad utility in radiochemical, fluorescent and dual modality (radio/fluorescent) molecular imaging. SAAC ligands are novel bifunctional chelates constructed from derivatized amino acids modified to provide three donor groups (L_3) for chelation to the $\{M(CO)_3\}^{1+}$ core (M = Tc or Re). SAAC derivatives demonstrate facile labeling with ^{99m}Tc and robust complex stability toward cysteine and histidine challenges, which present major in vivo competition for these ligands (*7*). SAAC avoids the many problems associated with using sulfhydryl containing radioligands and chelating agents that do not fully occupy the coordination sites of Tc and Re or form unstable complexes. In addition, SAAC may be incorporated into bioactive peptides via standard solid phase peptide synthesis and subsequently labeled with ^{99m}Tc and $^{186/188}$Re (*8, 9*).

During the past decade, the field of technetium coordination chemistry has seen both a rising interest in the Tc(I) core (*10*−*15*) and diminishing expectations for its utility, as the core and the subsequent chelators have demonstrated significant deficiencies (*16, 17*). These shortcomings, most notably the hydrophobicity of the metal complexes, are inherent characteristics of the core itself, which are exaggerated by the very nature of the chelators that form the robust complexes. Unfortunately, the lipophilicity of the chelators typically contributes to a poor pharmacokinetic profile of the radiotracer characterized by hepatic accumulation or hepatobiliary clearance. The ability to capitalize on the synthetic flexibility of incorporation, and the stability and inertness of the Tc(I) core, while decreasing the lipophilicity is key to the future success of the technology.

One potential solution to overcome the high hepatobiliary clearance of the complexes is to decrease the lipophilicity surrounding the metal center. Two possible ways to address this issue include (i) derivatizing the metal coordinating ligands with polar, nonlipophilic substituents to counterbalance the lipophilic metal-chelate core or (ii) decreasing the overall size of the ligands used to coordinate the metal core (*18, 19*). The former may be accomplished by modifying imidazole SAAC systems

* Corresponding author.

10.1021/bc900517x © 2010 American Chemical Society
Published on Web 04/19/2010

with polar, water-solubilizing functional groups such as ethers, alcohols, and carboxylic acids, which should alter the pharmacokinetic properties of the SAAC systems, and the biologically relevant molecules to which they are conjugated. In addition, these substitutions will result in metal complexes with neutral, cationic, or anionic charges of the metal complex, which may impact the pharmacokinetic profile. Alternatively, replacing one or more of the ligand donor heteroaromatic rings with a smaller, less hydrophobic donor, i.e., acetic acid, will reduce the size and lipophilicity of the complexes. For example, the nitrilotriacetic acid chelate (NTA) reported by Lipowska et al. (*20*) favored tubular transport rather than hepotobiliary excretion.

In an attempt to address the undesirable liver and gastrointestinal uptake and clearance characteristic of many of the SAAC systems previously designed and evaluated in our laboratory, we have investigated functionalized polar lysine imidazole derivatives with the potential to enhance renal clearance. These novel imidazole SAAC systems can be synthesized with a variety of hydrophilic R-groups via alkylation of imidazole-2-carboxaldehyde with available alkyl halides that contain the desired polar functionality (*21*). In previous work, we functionalized imidazole ligands with ether-containing moieties to investigate cardiac imaging (*22*) resulting in complexes with very low liver uptake and retention. These same principles, expanded to include various alcohols, ethers, and acids, were applied to the SAAC systems to shift the current pharmacokinetic profile from hepatobiliary uptake to higher renal clearance.

Here we describe the synthesis and evaluation of a series of lysine derived SAAC systems with a variety of metal donor ligand groups to form (2-amino-6-(bis((1-X-1*H*-imidazol-2-yl)methyl)amino)hexanoic acid) where X = methyl (**1**), 2,2-dimethoxyethyl (**2**), 2-ethoxyethyl (**3**), carboxymethyl (**4**), 2-hydroxyethyl (**5**), 3-(diethoxyphosphoryl)propyl (**6**), as well as (*S*)-2-amino-6-((carboxymethyl)(thiazol-2-ylmethyl)aminohexanoic acid (**7**), (*S*)-2-amino-6-((carboxymethyl)((1-methyl-1*H*-imidazol-2-yl)methyl)aminohexanoic acid (**8**), 2,2′-(5-amino-5-carboxypentylazanediyl)diacetic acid (**9**) and compared them to 2-amino-6-(bis(pyridin-2-ylmethyl)amino)hexanoic acid (DpK) and 2-amino-6-((carboxymethyl)(pyridin-2-ylmethyl)amino)hexanoic acid (PAMAK). Tissue distribution data obtained with these complexes in normal rats demonstrated greater kidney clearance and significantly less liver and gastrointestinal uptake than first generation SAAC ligands. Two SAAC ligands were subsequently incorporated using solid phase peptide synthesis into Tyr-3-octreotide yielding, ^{99m}Tc-**4**-Tyr-3-octreotide and ^{99m}Tc-DpK-Tyr-3-octreotide. These peptides were evaluated for localization in nude mice bearing AR42J xenografts to examine tissue distribution, tumor uptake and retention, clearance, and route of excretion for comparison to ^{111}In-DOTA-Tyr-3-octreotide, a well established radioimaging agent with excellent pharmacokinetic properties that targets the type 2 somatostatin receptor in neuroendocrine tumors (*23*−*25*).

EXPERIMENTAL SECTION

General Methods. All reactions were carried out in dry glassware under an atmosphere of argon unless otherwise noted. Reactions were purified by column chromatography under medium pressure using a Biotage SP4 or by preparative high pressure liquid chromatography using a Varian Prostar 210 preparative high pressure liquid chromatography (HPLC) system equipped with a semipreparative Vydac C18 reverse-phase column (250 mm ×10 mm × 5 μm) connected to a Varian Prostar model 320 UV−visible detector and monitored at a wavelength of 254 nm. The final technetium SAAC complexes were purified and analyzed using a binary solvent gradient of 5−95% buffer B over 21 min (buffer A = triethylammonium phosphate (TEAP), pH 3, buffer B = methanol). The final ^{99m}Tc-SAAC-peptide conjugates were purified and analyzed on Vydac C18 reverse-phase column (250 mm × 4.6 mm × 5 μm) employing a gradient method of 5−50% buffer B over 30 min (buffer A = water + 0.1% TFA, buffer B = acetonitrile + 0.1% TFA). ^{1}H NMR spectra were obtained on a Bruker 400 MHz instrument. Spectra are reported as ppm and are referenced to the solvent resonances in chloroform-*d* ($CDCl_3$), dimethyl sulfoxide-d_6 (DMSO-d_6), or methanol-d_4 (MeOD). Combustion analyses were performed by Prevalere Life Sciences, Inc. ^{99m}Tc was used as a solution of $Na^{99m}TcO_4$ in saline, as a commercial ^{99}Mo/^{99m}Tc generator eluant (Cardinal Health). The ^{99m}Tc-containing solutions were always kept behind sufficient lead shielding. The $[^{99m}Tc(CO)_3(H_2O)_3]^+$ was prepared from commercially available Isolink kits (Covidien). The ^{111}In was used as an $^{111}InCl_3$ solution commercially available from MDS Nordion. All solvents and reagents were purchased from Sigma Aldrich (St. Louis, MO), Bachem (Switzerland), Akaal (Long Beach, CA), or Anaspec (San Jose, CA). The following abbreviations are used: Fmoc = fluorenylmethyloxycarbonyl, DMAP = *N*,*N*-dimethylaminopyridine, DMF = *N*,*N*-dimethylformamide, DMSO = dimethyl sulfoxide, DCM = dichloromethane, DCE = 1,2-dichloroethane, NaOH = sodium hydroxide, (*S*)-2-(((9*H*-fluoren-9-yl)methoxy)carbonylamino)-6-aminohexanoic acid hydrochloride salt = L-Fmoc-lysine-OH hydrochloride salt, ID/g = injected dose per gram, NTA = nitrilotriacetic acid, PBS = phosphate buffered saline, RCP = radiochemical purity, RCY = radiochemical yield.

Syntheses. *General Procedure for the Alkylations.* To a solution of the imidazole-2-carboxaldehyde dissolved in DMF (1 mL) was added 1 mol equiv of the alkyl bromide, excess potassium carbonate, and a catalytic amount of potassium iodide. The mixture was heated at 110 °C for 18 h followed by evaporation to dryness and purified utilizing a Biotage SP4 with a gradient method of 5−50% methanol in DCM.

General Procedure for the Reductive Aminations. To a solution of L-Fmoc-lysine-OH hydrochloride salt (90 mg, 0.19 mmol) dissolved in DCE (2 mL) was added 2.1 equiv of the aldehyde. The mixture was heated at 50 °C for 1 h whereupon sodium triacetoxyborohydride (36 mg, 0.19 mmol) was added. The mixture was stirred at room temperature for 12 h and was subsequently evaporated to dryness and purified utilizing a Biotage SP4 with a gradient method of 5−50% methanol in DCM. The purified compound (24 mg, 0.034 mmol) was deprotected by treatment with piperidine/DMF 1:1 (1 mL), and the mixture was stirred at room temperature for 2 h. Following evaporation to residue, aqueous extraction and washing with excess DCM afforded the desired compounds as an off-white solid.

*(S)-2-Amino-6-(bis((1-methyl-1H-imidazol-2-yl)methyl)amino)-hexanoic Acid (**1**).* A solution of Fmoc-Lys-OH·HCl (1.8 g, 4.5 mmol) and 1-methyl-1*H*-imidazole-2-carbaldehyde (1.1 g, 10 mmol) in DCE (50 mL) was stirred at 75 °C for 30 min under nitrogen. The reaction mixture was cooled to 0 °C and treated with sodium triacetoxyborohydride (3.2 g, 15 mmol). The reaction mixture was stirred at room temperature overnight and was decomposed with water. The reaction mixture was extracted with DCM. The organic layer was dried and concentrated under reduced pressure. The residue was purified by flash chromatography over silica gel to afford (*S*)-2-(((9*H*-fluoren-9-yl)-methoxy)carbonylamino)-6-(bis((1-methyl-1*H*-imidazol-2-yl)-methyl)amino)hexanoic acid (2.3 g, 92%). MS (ESI), 557 (M + H)$^+$. To a solution of (*S*)-2-(((9*H*-fluoren-9-yl)methoxy)carbonyl-amino)-6-(bis((1-methyl-1*H*-imidazol-2-yl)methyl)amino)hexanoic acid (556 mg, 1.00 mmol) in DMF (4.0 mL) was added piperidine (0.80 mL). The mixture was stirred at room temperature for 2 h. Solvent was evaporated under reduce pressure to afford a residue, which was purified by Amberchrom column chromatography to afford (*S*)-2-

amino-6-(bis((1-methyl-1*H*-imidazol-2-yl)methyl)amino)hexanoic acid (320 mg, 0.958 mmol, 96% yield). ^{1}H NMR (400 MHz, DMSO-d_6) δ 7.94 (s, 1 H), 7.04 (d, J = 3, 1.2 Hz, 2H), 6.74 (d, J = 1.2 Hz, 2 H), 3.54 (s, 4 H), 3.98 (brs, 1 H), 2.88 (s, 3 H), 2.72 (s, 3 H), 2.35 (t, J = 6.8 Hz, 2 H), 1.60−1.54 (m, 1 H), 1.43−1.29 (m, 3 H), 1.16−1.11 (m, 2 H). MS (ESI): 335 $(M + H)^+$.

*1-(2,2-Dimethoxyethyl)-1H-imidazole-2-carbaldehyde (**2A**).* To a solution of the imidazole-2-carboxaldehyde (410 mg, 4.3 mmol) dissolved in DMF (1 mL) was added 1.1 equiv of 2-bromo-1,1-dimethoxyethane (800 mg, 4.7 mmol), potassium carbonate, and a catalytic amount of potassium iodide. The mixture was heated at 110 °C for 18 h followed by evaporation to dryness and purified utilizing a Biotage SP4 with a gradient method of 5−50% methanol in DCM to yield the desired compound (250 mg, 1.4 mmol, 32% yield). ^{1}H NMR (400 MHz, DMSO-d_6) δ 9.9 (s, H), 7.85 (s, H), 7.55 (s, H), 5.82 (m, H), 4.75 (d, 2H), 3.45 (s, 6H).

*(S)-2-Amino-6-(bis((1-(2,2-dimethoxyethyl)-1H-imidazol-2-yl)-methyl)amino)hexanoic Acid (**2**).* Following the same procedure as utilized in the preparation of **1** yielded the desired compound (93 mg, 0.132 mmol, 54% yield). ^{1}H NMR (400 MHz, DMSO-d_6) δ 7.90 (d, 2H), 7.72 (d, 2H), 7.41 (m, 2H), 7.30 (m, 2H), 7.05 (s, H), 6.75 (s, H), 4.45 (m, 3H), 4.2 (m, 4H), 3.95 (d, 2H), 3.80 (m, H), 3.55 (s, 2H), 3.2 (s, 6H), 2.3 (m, 2H), 1.60 (m, H), 1.35 (m, H) 1.15 (m, 2H). ESMS *m*/*z*: 705 $(M + H)^+$.

The purified compound was deprotected by treatment with piperidine/DMF 1:1 (1 mL), and the mixture was stirred at room temperature for 18 h. Following evaporation to residue, aqueous extraction from DCM afforded the desired product (44 mg, 0.093 mmol, 76% yield) as an off-white solid. ^{1}H NMR (400 MHz, DMSO-d_6) δ 7.98 (s, H), 7.05 (s, H), 6.85 (s, H), 4.45 (s, 2H), 3.95 (m, 4H), 3.55 (s, 2H), 3.2 (s, 6H), 2.85 (m, 2H), 2.15 (m, 2H), 1.40 (m, 2H). 1.15 (m, 2H). ESMS *m*/*z*: 483 $(M + H)^+$.

*1-(2-Ethoxyethyl)-1H-imidazole-2-carbaldehyde (**3A**).* Following the same procedure as utilized in the preparation of **2A**, the target compound was prepared from 1-bromo-2-ethoxyethane (3.51 g, 22 mmol) and imidazole-2-carboxaldehyde to yield the desired compound (580 mg, 3.56 mmol, 17% yield). ^{1}H NMR (400 MHz, DMSO-d_6) δ 9.63 (s, H), 7.6 (s, H), 7.21 (s, H), 4.45 (dd, 2H), 3.62 (dd, 2H), 3.38 (m, 2H), 1.05 (t, 3H).

*(S)-2-Amino-6-(bis((1-(2-ethoxyethyl)-1H-imidazol-2-yl)methyl)-amino)hexanoic Acid (**3**).* Following the same procedure as utilized in the preparation of **1** yielded the desired Fmoc-protected product (141 mg, 0.210 mmol, 44% yield). ^{1}H NMR (400 MHz, DMSO-d_6) δ 7.67 (d, 2H), 7.35 (m, 4H), 7.30 (m, 2H), 7.05 (s, H), 6.75 (s, H), 3.95 (m, 4H), 3.58 (d, 4H), 3.55 (s, 4H), 3.3 (s, 4H), 2.30 (m, 2H), 2.15 (m, 2H), 1.50 (m, 2H). 1.15 (s, 2H), 1.05 (t, 6H). ESMS *m*/*z*: 674 $(M + H)^+$. The purified compound was deprotected by treatment with piperidine/DMF 1:1 (1 mL), and the mixture was stirred at room temperature for 18 h. Following evaporation to residue, aqueous extraction from DCM afforded the desired product (31 mg, 0.069 mmol, 91% yield) as an off-white solid. ^{1}H NMR (400 MHz, DMSO-d_6) δ 8.35 (s, H), 7.98 (s, H), 7.05 (s, H), 6.75 (s, H), 3.95 (m, 4H), 3.58 (d, 4H), 3.55 (s, 4H), 3.3 (s, 4H), 2.30 (m, 2H), 2.15 (m, 2H), 1.50 (m, 2H). 1.15 (s, 2H), 1.05 (t, 6H). ESMS *m*/*z*: 451 $(M + H)^+$.

*tert-Butyl 2-(2-Formyl-1H-imidazol-1-yl)acetate (**4A**).* Following the same procedure as utilized in the preparation of **2A**, the target compound was prepared from *tert*-butyl 2-bromoacetate and imidazole-2-carboxaldehyde to yield the desired compound (850 mg, 4.03 mmol, 39% yield). ^{1}H NMR (400 MHz, DMSO-d_6) δ 7.6 (s, H), 7.23 (s, H), 5.15 (s, 2H), 1.40 (s, 9H).

*(S)-2,2′-(2,2′-(5-Amino-5-carboxypentylazanediyl)bis(methylene)-bis(1H-imidazole-2,1-diyl))diacetic Acid (**4**).* Following the same procedure as utilized in the preparation of **1** yielded the desired Fmoc-protected product (155 mg, 0.205 mmol, 42% yield). ^{1}H NMR (400 MHz, DMSO-d_6) δ 7.67 (d, 2H), 7.35 (m, 4H), 7.30 (m, 2H), 7.05 (s, H), 6.7 (s, H), 4.70 (s, 4H), 4.2 (m, 4H), 3.4 (d, 2H), 2.4 (m, 2H), 1.8 (s, 2H), 1.39 (s, 18H). 1.2 (m, 2H). ESMS *m*/*z*: 758 $(M + H)^+$. The purified compound was deprotected by treatment with piperidine/DMF 1:1 (1 mL), and the mixture was stirred at room temperature for 18 h. Following evaporation to a residue, aqueous extraction from DCM afforded the desired product (25 mg, 0.047 mmol, 25% yield) as an off-white solid. ^{1}H NMR (400 MHz, DMSO-d_6) δ 7.0 (s, 2H), 6.65 (s, H), 4.70 (s, 4H), 4.2 (m, 4H), 3.2 (d, 2H), 2.4 (m, 2H), 1.8 (s, 2H), 1.39 (s, 18H). 1.15 (m, 2H). ESMS *m*/*z*: 535 $(M + H)^+$.

*(S)-2-Amino-6-(bis((1-(2-hydroxyethyl)-1H-imidazol-2-yl)methyl)-amino)hexanoic Acid (**5**).* To a solution of **3** (25 mg, 0.055 mmol) dissolved in DCM (10 mL) was added 1.0 M boron tribromide in DCM (83 mg, 0.333 mmol) at −20 °C. The mixture was stirred at −20 °C for 2 h and was subsequently quenched with water and washed with excess DCM. The water portion was evaporated to dryness and purified as the product utilizing a Biotage SP4 with a gradient method of 5−50% methanol in DCM (15 mg, 0.038 mmol, 34% yield). ^{1}H NMR (400 MHz, DMSO-d_6) δ 8.40 (m, 2H), 8.16 (d, 2H), 7.70 (d, 2H), 5.50 (s, 2H), 4.20 (s, 2H), 4.05 (m, 4H), 3.68 (d, 2H), 3.15 (m, 5H), 2.46 (s, 2H), 1.70 (m, 2H), 1.65 (m, 2H). 1.21 (m, 2H). ESMS *m*/*z*: 395 $(M + H)^+$.

*Diethyl 3-(2-Formyl-1H-imidazol-1-yl)propylphosphonate (**6A**).* Following the same procedure as utilized in the preparation of **2A**, the target compound was prepared from diethyl (3-bromopropyl)phosphonate (2.96 g, 11.4 mmol) and imidazole-2-carboxaldehyde to yield the desired compound (466 mg, 1.69 mmol, 16% yield). ESMS *m*/*z*: 275 $(M + H)^+$.

*(S)-2-Amino-6-(bis((1-(3-(diethoxyphosphoryl)propyl)-1H-imidazol-2-yl)methyl)amino)hexanoic Acid (**6**).* Following the same procedure as utilized in the preparation of **1** yielded the desired Fmoc-protected product (63 mg, 0.071 mmol, 21% yield). ESMS *m*/*z*: 443 (M/2). The purified compound (53 mg, 0.060 mmol) was deprotected by treatment with piperidine/DMF 1:1 (1 mL), and the mixture was stirred at room temperature for 18 h. Following evaporation to a residue, aqueous extraction from DCM afforded the desired product (32 mg, 0.048 mmol, 80% yield) as an off-white solid. ^{1}H NMR (400 MHz, DMSO-d_6) δ 7.1 (s, 2H), 6.78 (s, 2H), 3.98 (m, 4H), 3.8 (m, 4H), 3.6 (s, 4H), 2.85 (m, 4H), 2.75 (s, H), 2.38 (s, 2H), 1.77 (m, 4H), 1.55 (m, 4H), 1.39 (s, 2H), 1.18 (t, 12H). ESMS *m*/*z*: 664 $(M + H)^+$.

*(S)-2-Amino-6-((carboxymethyl)(thiazol-2-ylmethyl)amino)hexanoic Acid (**7**).* A suspension of Fmoc-Lys-OH·HCl (6.1 g, 15 mmol) and thiazole-2-carbaldehyde (1.697 g, 15 mmol) in DCE (100 mL) was refluxed for 30 min under nitrogen. The reaction mixture was cooled to 0 °C and treated sequentially with sodium triacetoxyborohydride (7.9 g, 38 mmol) and crude *tert*-butyl glyoxalate (3.53 g, 27 mmol) as previously reported (*26*). The reaction mixture was stirred at room temperature overnight and decomposed with water. The reaction mixture was extracted with DCM. The organic layer was dried and concentrated under reduced pressure. The residue was purified by flash chromatography over silica gel to afford (*S*)-1-(9*H*-fluoren-9-yl)-14,14-dimethyl-3,12-dioxo-10-(thiazol-2-ylmethyl)-2,13-dioxa-4,10-diazapentadecane-5-carboxylic acid (1.85 g, 21%). MS (ESI), 580 $(M + H)^+$. To a solution of (*S*)-1-(9*H*-fluoren-9-yl)-14,14-dimethyl-3,12-dioxo-10-(thiazol-2-ylmethyl)-2,13-dioxa-4,10-diazapentadecane-5-carboxylic acid (72.5 mg, 0.125 mmol) in DMF (1.0 mL) was added piperidine (0.20 mL). The mixture was stirred at room temperature for 2 h. Solvent was evaporated under reduced pressure to afford a residue, which was purified by flash chromatography over silica eluting with 10% MeOH in DCM to afford (*S*)-2-amino-6-((2-*tert*-butoxy-2-oxoethyl)(thi-

azol-2-ylmethyl)amino)hexanoic acid (25 mg, 0.083 mmol, 66%). ^{1}H NMR (400 MHz, CD_3OD) δ 7.70 (d, $J = 3.6$ Hz, 1 H), 7.52 (d, $J = 3.6$ Hz, 1 H), 4.15 (s, 2 H), 3.52 (dd, $J = 7.2$, 5.2 Hz, 1 H), 3.39 (s, 2 H), 2.73 (t, $J = 7.2$ Hz, 2 H), 1.91−1.76 (m, 2 H), 1.60−1.57 (m, 2 H), 1.55−1.47 (m, 11 H). MS (ESI): 358 $(M + H)^+$.

*(S)-2-Amino-6-((2-tert-butoxy-2-oxoethyl)((1-methyl-1H-imidazol-2-yl)methyl)amino)hexanoic Acid (**8**).* The title compound was prepared by following the same procedure as described in the preparation of **7** except 1-methyl-1*H*-imidazole-2-carbaldehyde was used in place of thiazole-2-carbaldehyde. ^{1}H NMR (400 MHz, $CDCl_3$) δ 7.88 (d, $J = 7.2$ Hz, 2 H), 7.71 (dd, $J = 7.2$, 2.4 Hz, 2 H), 7.55 (d, $J = 8.0$ Hz, 1 H), 7.40 (t, $J = 7.6$ Hz, 2 H), 7.31 (t, $J = 7.6$ Hz, 4 H), 7.01 (s, 1 H), 6.71 (s, 1 H), 4.27−4.18 (m, 3 H), 3.88−3.83 (m, 1 H), 3.72 (s, 2 H), 3.14 (s, 2 H), 1.62−1.50 (m, 2 H), 1.38 (s, 9 H), 1.33−1.21 (m, 4 H). MS (ESI): 577 $(M + H)^+$. To a solution of (*S*)-1-(9*H*-fluoren-9-yl)-14,14-dimethyl-10-((1-methyl-1*H*-imidazol-2-yl)methyl)-3,12-dioxo-2,13-dioxa-4,10-diazapentadecane-5-carboxylic acid (190 mg, 0.33 mmol) in DMF (2 mL) was added piperidine (0.4 mL). The mixture was stirred at room temperature for 2 h. Solvent was evaporated under reduce pressure to afford a residue, which was purified by Amberchrom column chromatography to afford (*S*)-2-amino-6-((2-*tert*-butoxy-2-oxoethyl)((1-methyl-1*H*-imidazol-2-yl)methyl)amino)hexanoic acid (115 mg, 0.32 mmol, 97%). ^{1}H NMR (400 MHz, DMSO) δ 7.27 (brs, 1 H), 7.04 (s, 1 H), 6.72 (s, 1 H), 3.73 (s, 2 H), 3.64 (s, 3 H), 3.15 (s, 2 H), 3.04 (dd, $J = 6.8$, 5.2 Hz, 1 H), 2.47 (t, $J = 7.2$ Hz, 2 H), 1.65−1.46 (m, 2 H), 1.39 (s, 9 H), 1.30−1.21 (m, 4 H). MS (ESI): 355 $(M + H)^+$.

*(S)-2,2′-(5-Amino-5-carboxypentylazanediyl)diacetic Acid (**9**).* (*S*)-10-(2-*tert*-Butoxy-2-oxoethyl)-1-(9*H*-fluoren-9-yl)-14,14-dimethyl-3,12-dioxo-2,13-dioxa-4,10-diazapentadecane-5-carboxylic acid was prepared from a solution of Fmoc-Lys-OH (1.5 g, 4.0 mmol) and crude *tert*-butyl glyoxalate (3.6 g, 27.6 mmol) in DCE (50 mL), and the mixture was stirred at 75 °C for 30 min under nitrogen. The reaction mixture was cooled to 0 °C and treated with sodium triacetoxyborohydride (2.1 g, 10 mmol). The reaction mixture was stirred at room temperature for 3 h and decomposed with water. The reaction mixture was extracted with DCM. The organic layer was dried and concentrated under reduced pressure. The residue was purified by flash chromatography over silica gel to afford (*S*)-10-(2-*tert*-butoxy-2-oxoethyl)-1-(9*H*-fluoren-9-yl)-14,14-dimethyl-3,12-dioxo-2,13-dioxa-4,10-diazapentadecane-5-carboxylic acid (1.70 g, 3.51 mmol 71%). ^{1}H NMR (400 MHz, $CDCl_3$) δ 7.76 (d, $J = 7.2$ Hz, 2 H), 7.60 (d, $J = 7.2$ Hz, 2 H), 7.40 (t, $J = 7.2$ Hz, 2 H), 7.30 (t, $J = 7.2$ Hz, 2 H), 6.63 (d, $J = 7.6$ Hz, 1 H), 4.40−4.34 (m, 3 H), 4.22 (t, $J = 7.2$ Hz, 1 H), 3.49 (s, 4 H), 2.83−2.64 (m, 4 H), 1.96−1.77 (m, 4 H), 1.40 (s, 18 H). MS (ESI): 598 $(M + H)^+$. The purified compound (12 mg, 0.21 mmol) was deprotected by treatment with piperidine/DMF 1:1 (1 mL), and the mixture was stirred at room temperature for 18 h. Following evaporation to a residue, aqueous extraction from DCM afforded the desired product **9** (3 mg, 0.11 mmol, 55% yield) as an off-white solid. ^{1}H NMR (400 MHz, DMSO-d_6) δ 7.9 (s, 2H), 3.5 (m, H), 3.3 (d, 2H), 2.4 (m, 2H), 1.8 (s, 2H), 1.45 (m, 2H), 1.15 (m, 2H). ESMS *m/z*: 263 $(M + H)^+$.

General Preparation of ^{99m}Tc Complexes and Peptides. The $^{99m}Tc(I)(CO)_3^+$ radiolabeling of the SAAC systems to form the metal complexes was accomplished on either the free α-amino acids or the α-*N*-Fmoc protected lysine derivative utilizing similar methodology. The radiolabeling was accomplished in two steps using commercially available IsoLink kits (Covidien) to form the $[^{99m}Tc(CO)_3(H_2O)_3]^+$ intermediate, which was neutralized and reacted with the appropriate SAAC system (Figure 2) at 10^{-6}−10^{-4} M in an equal volume mixture of acetonitrile and water in a sealed vial. The sealed vial was heated at 100 °C for 30 min, and upon cooling, the mixture was analyzed for purity via reverse-phase HPLC. Purification by HPLC resulted in "carrier-free" products, and the RCP was determined via HPLC and shown to be consistently ≥95% pure. The radiolabeling can be achieved at concentrations as low as 10^{-6} M at 75 °C with RCY ≤ 80% and with RCY > 95% when conducted at 10^{-4} M at 75 °C.

The $^{99m}Tc(I)(CO)_3^+$ radiolabeling of the SAAC-conjugated peptides was achieved and purified in a similar manner with the exception of the heating temperature, which was reduced to 60 °C. The ^{111}In-DOTA-Tyr-3-octreotide was prepared from $^{111}InCl_3$ in an aqueous solution (10^{-4} M of the peptide) by heating at 100 °C for 30 min.

Determination of log *P* Values. The log *P* values of the $^{99m}Tc(I)$ complexes were determined using the following procedure: The ^{99m}Tc radiotracer was prepared and purified by reverse-phase HPLC. The collected mobile phase was evaporated and the residue dissolved in an equal volume mixture of *n*-octanol and 25 mM phosphate buffer (pH 7.4). The samples were extracted as follows: the samples were vortexed for 20 min and centrifuged at 8000 rpm for 5 min, and then aliquots were removed from both the aqueous phosphate buffer and the organic *n*-octanol layers and counted separately in a γ counter (LKB model 1282, Wallac Oy, Finland). The extraction was repeated twice for a total number of three extractions to ensure full extraction of all the organic components. The partition coefficients were then calculated using the equation $P =$ (activity concentration in *n*-octanol)/(activity concentration in aqueous layer). The samples were analyzed in triplicate and the log *P* values determined from the average of the three different measurements.

Rat Tissue Distribution of SAAC Complexes. Tissue distribution studies of the ^{99m}Tc SAAC systems were performed in separate groups of male Sprague−Dawley rats ($n = 5$/time point) administered as a bolus intravenous injection (approximately 10 μCi/rat) in a constant volume of 0.1 mL. Animals were euthanized by carbon dioxide at 5, 30, 60, and 120 min after injection. Blood, heart, lungs, liver, spleen, kidneys, adrenals, stomach (with contents), large and small intestines (with contents), testes, skeletal muscle, bone, brain, and adipose were excised, weighed wet, transferred to plastic tubes, and counted in an automated γ counter (LKB model 1282, Wallac Oy, Finland). Aliquots of the injected dose were also measured to convert the counts per minute in each tissue sample to percent-injected dose per organ. Tissue radioactivity levels, expressed as %ID/g, were determined by converting the decay corrected counts per minute to the percent dose and dividing by the weight of the tissue or organ sample.

Peptide Synthesis. Tyr-3-octreotide analogues {**4**-Tyr-3-octreotide} and {DpK-Tyr-3-octreotide} with the lysine SAAC incorporated at the amino terminus were synthesized by AnaSpec, Inc. (San Jose, CA) using solid phase peptide synthesis employing standard Fmoc coupling techniques with cleavage and deprotection using TFA. Following synthesis, all peptides were purified using reverse phase HPLC and were lyophilized with purity profiles of >90%.

Tumor Cell Lines. AR42J cells were obtained from American Type Culture Collection (Rockville, MD). The cells were grown in Kaighn's F-12 media supplemented with 20% fetal bovine serum, sodium pyruvate, and gentamicin in a humidified atmosphere of 5% CO_2/95% air at 37 °C.

Tissue Distribution in AR42J Bearing Mice. Uptake of radiolabeled peptides in rat tumor xenograft models were performed according to published methods. Briefly, AR42J cells were trypsinized, counted, and suspended in a solution containing 50% Dulbecco's PBS (D-PBS) (with 1 mg/mL D-glucose

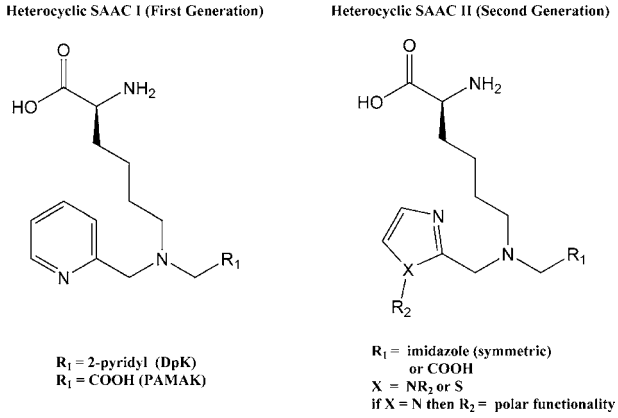


Figure 1. General structures of the first and second generation of heterocyclic SAAC systems.

and 36 μg/mL sodium pyruvate) and 50% Matrigel (BD Biosciences, Franklin Lakes, NJ). Male NCr$^{nu/nu}$ mice were anesthetized by intraperitoneal injection of 0.5 mL of Avertin (20 mg/mL) (Sigma-Aldrich, St. Louis, MO) and then inoculated subcutaneously into the hind flank with 2×10^6 cells in a 0.25 mL suspension volume. Studies of tumor uptake were conducted when the tumors reached a size of 600−800 mm^3. Tissue biodistribution studies were conducted by administering, via the tail vein, a bolus injection of 2 μCi/mouse in a constant volume of 0.05 mL of D-PBS containing 1 mg/mL bovine serum albumin. Groups of five animals were euthanized by asphyxiation with carbon dioxide at 1 and 4 h after injection. All tissues from Figure 4, including the tumor, were excised, weighed wet, and transferred to plastic tubes, and radioactivity present was counted in an automated γ-counter (LKB model 1282, Wallac Oy, Finland). Tissue time − radioactivity levels were expressed as % injected dose per gram tissue (%ID/g).

RESULTS AND DISCUSSION

We previously described a technology known as SAAC, a radiolabeling platform that has broad utility in radiochemical, fluorescent, and dual modality (radio/fluorescent) molecular imaging (*6, 9*) and is particularly convenient for developing radiolabeled peptides. One limitation of the $Tc(CO)_3$-dipyridyl complex, characteristic of the original SAAC systems, is the extremely hydrophobic nature of the radiolabeled complexes which has often lead to the liver accumulation and/or hepatobiliary clearance of the bioconjugates. This undesirable pharmacokinetic profile is not unique to the original SAAC systems but a characteristic shared by many bioconjugates (*27, 28*). The goal of this work was to develop a second generation series of hydrophilic lysine-based SAAC systems that have been modified to favor renal clearance of the ^{99m}Tc-SAAC complexes and thus facilitate the development of novel ^{99m}Tc-labeled radiopharmaceuticals that clear the body more readily. This was accomplished, as shown in Figure 1, by modifying the lysine core of SAAC systems in two ways to create novel tridentate chelators with reduced lipophilicity: the addition of polar substituents and the reduction of the ligand size. The N-protected lysine building block of the SAAC systems was derivatized at the ε amine with substituted heterocyclic rings (R_1) that contained distinct polar functional groups (R_2) in an attempt to reduce the lipophilicity of the resulting ^{99m}Tc complexes. The ε amine of lysine allows for the facile synthesis of large numbers of structural variants of SAAC systems with the potential of diverse physiochemical properties. The chemical synthesis of the bifunctional SAAC systems was accomplished via reductive alkylation of *N*-Fmoc protected lysine with the appropriate heterocyclic aldehyde. The availability of a diverse set of heterocyclic aldehydes coupled with the ease of synthesis has led to the preparation of several classes of polar SAAC systems that form cationic ^{99m}Tc complexes with enhanced renal clearance. In addition, incorporation of one acetic acid "arm" onto the ε amine of lysine (R_1) in lieu of the second heterocyclic ligand affords SAAC systems of reduced size with a neutral metal center.

Ligand Design. As illustrated in Figure 1, both first generation (SAAC I) and second generation (SAAC II) SAAC systems were derived from the amino acid lysine. First generation ligands incorporated either two pyridine rings or a pyridine and an acetic acid for R_1. The design of the novel second generation bifunctional chelates explored the concept of increasing the water solubility of the chelate ring systems through the modification of heterocyclic imidazole ring substituents for R_2. The effort focused on the SAAC ligands that form cationic homogeneous tridentate metal complexes as well as the smaller heterogeneous monoacetic acid derivatized compounds which form neutral metal complexes.

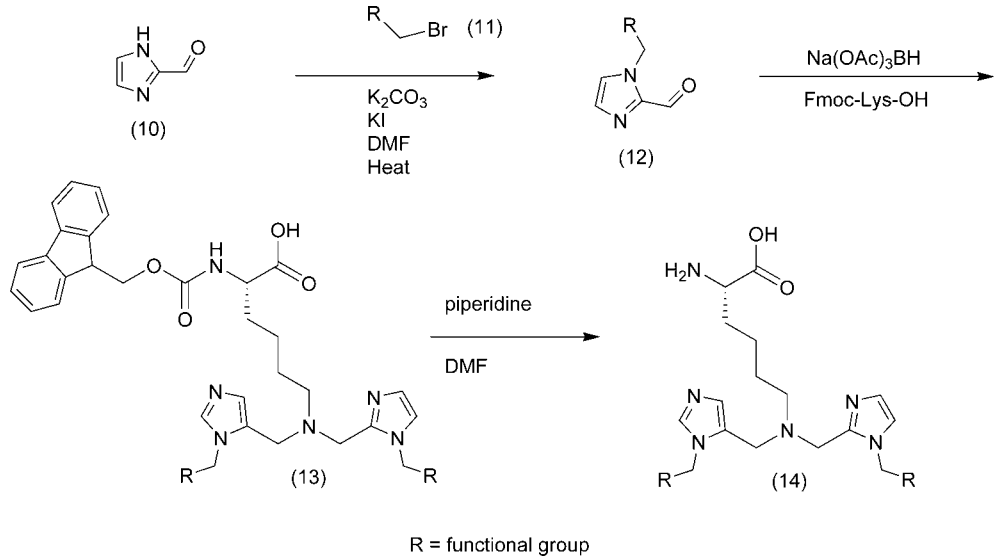
Preparation of Homogeneous Tridentate Ligands as Second Generation Lysine Imidazole Derivatived SAAC Systems. The derivatized imidazole SAAC systems were prepared via the alkylation of the commercially available imidazole-2-carboxaldehyde (**10**) with the desired alkyl halide (**11**) to afford the N-substituted imidazole-2-carboxaldehyde analogues (**12**). Reductive amination of *N*-Fmoc lysine with sodium triacetoxyborohydride produces the *N*-Fmoc protected SAAC system (**13**) which following deprotection with piperidine affords the desired SAAC systems (**14**) in good yields as illustrated in Scheme 1.

Preparation of Heterogeneous SAAC Systems: Monoacetic Acid Analogues. Several compounds from the homogeneous series described above which exhibited promising pharmacokinetic profiles were prepared as their corresponding monoacetic acid analogues, shown in Figure 2. These new heterogeneous ^{99m}Tc-SAAC complexes were smaller in size, were less hindered complexes, and were uncharged at the metal center, in contrast to the positive charged metal centers of the homogeneous complexes.

The compounds in this series were prepared using the double reductive alkylation sequence on Fmoc-lysine. Addition of the first aldehyde followed by reduction with sodium borohydride affords a monoalkylated intermediate as shown in Scheme 2. Subsequent treatment with *tert*-butyl glyoxalate followed by deprotections with piperidine and trifluoroacetic acid (TFA) afforded the desired series of heterogeneous neutral ligands (*26*).

Radiolabeling of ^{99m}Tc-SAAC. Radiolabeling of the SAAC systems was accomplished on either the free α-amino acids or as the appropriately N-protected amino acid derivative utilizing similar methodology to form ^{99m}Tc-**1**−**9**, demonstrating the flexibility of the radiolabeling and the ease of preparation of these novel SAAC metal complexes. The $^{99m}Tc(I)(CO)_3^+$ radiolabeling was accomplished in two steps using the commercially available IsoLink kits (Covidien) to form the $[^{99m}Tc(CO)_3(H_2O)_3]^+$ intermediate, which was reacted with the appropriate SAAC ligand (ligand concentration of 10^{-6}−10^{-4} M) in an equal volume mixture of 1:1 acetonitrile and phosphate buffer. The sealed vial was heated at 100 °C for 30 min, and upon cooling, the mixture was analyzed for purity via HPLC. The RCP after HPLC purification resulted in "carrier-free" products, with purity determined via HPLC to be consistently ≥95%. While possible to radiolabel at concentrations as low as 10^{-6} M, the RCY at 75 °C was ≤80%. To achieve RCY > 95% at 75 °C, the ligand concentration needed to be increased to 10^{-4} M. This was true for all of the compounds with the exception of 2,2′-(5-amino-5-carboxypentylazanediyl)diacetic acid (**9**) which required 10^{-3} M ligand to achieve >95% RCY.

Scheme 1. Preparation of Homogeneous Bifunctional Imidazole SAAC Systems



SAAC systems 2,2′-(2,2′-(5-amino-5-carboxypentylazanediyl)-bis(methylene)-bis(1*H*-imidazole-2,1-diyl))diacetic acid (**4**) and 2-amino-6-(bis((1-(2-hydroxyethyl)-1*H*-imidazol-2-yl)methyl)-amino)hexanoic acid (**5**) could be radiolabeled with the ester

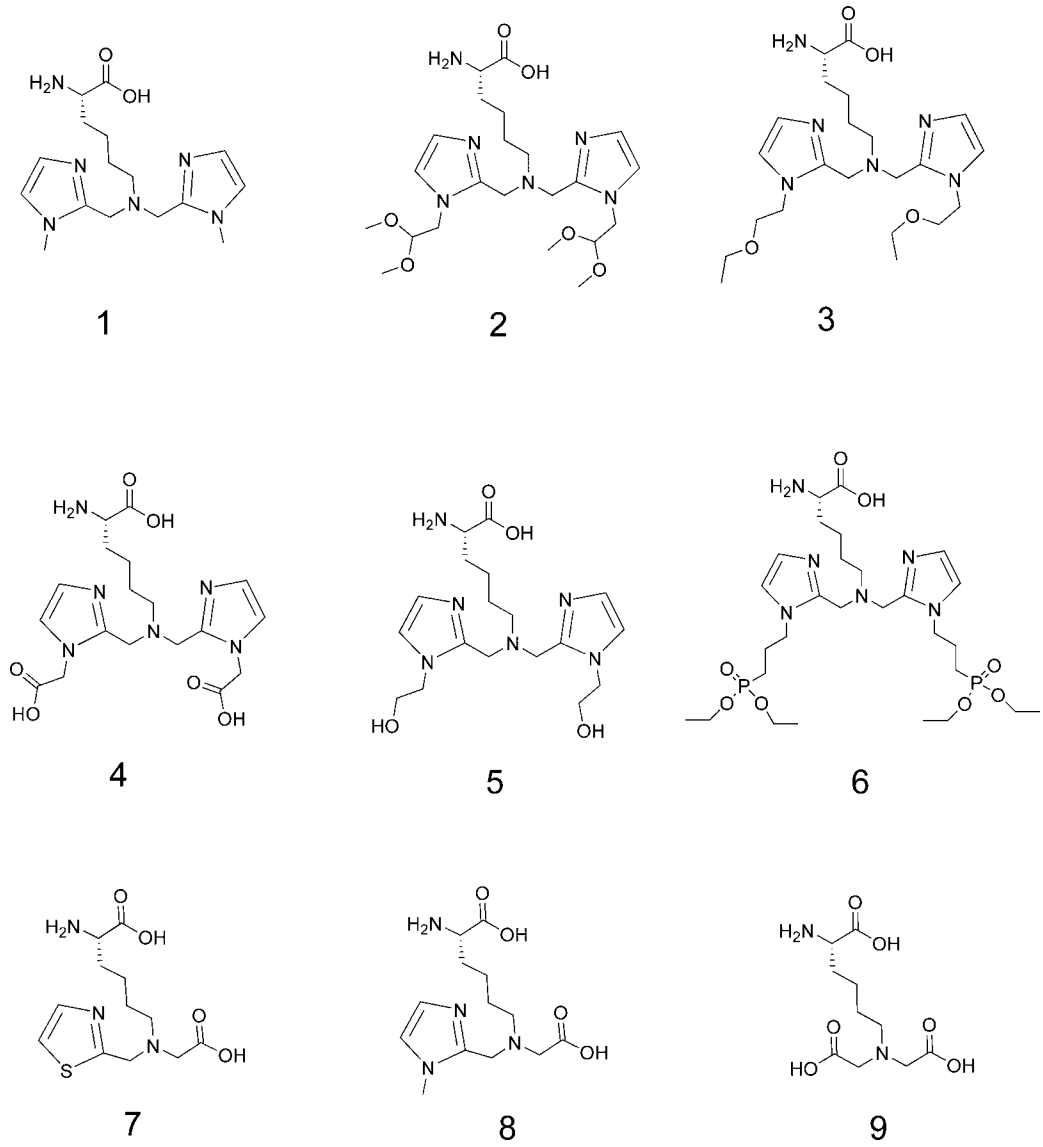
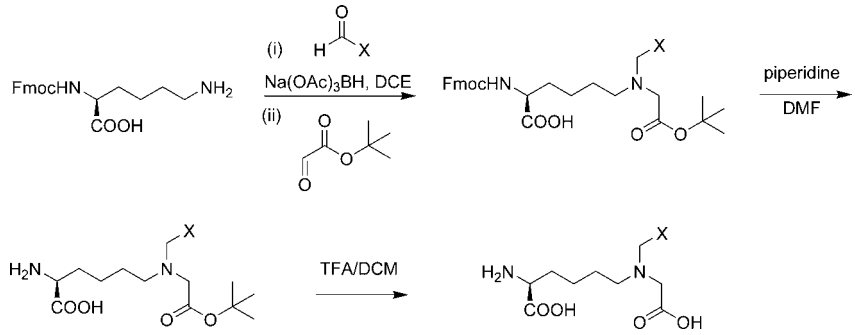


Figure 2. Structures of the novel lysine based SAAC systems.

Scheme 2. Preparation of the Heterogeneous SAAC Systems



protecting groups present on the bis-imidazole derivative or on the fully deprotected ligand. For example, the ^{99m}Tc complex of ligand **4** was prepared in 30 min followed by simple deprotection of the *tert*-butyl ester protecting groups using TFA at room temperature to produce ^{99m}Tc-**4**. The radiolabeling and subsequent deprotection could be followed by HPLC over time, as shown in Figure 3.

The ^{99m}Tc complex of 2-amino-6-(bis((1-(2-hydroxyethyl)-1*H*-imidazol-2-yl)methyl)amino)hexanoic acid (**5**) could be prepared by radiolabeling 2-amino-6-(bis((1-(2-ethoxyethyl)-1*H*-imidazol-2-yl)methyl)amino)hexanoic acid (**3**) followed by subsequent deprotection of the ethyl ethers using BBr_3 to afford the desired metal complex ^{99m}Tc-**5** (Scheme 3). Confirmation of the formation of the ^{99m}Tc-**5** complex was established by independent radiolabeling studies of the compounds **3** and **5** followed by the radiolabeling of **3** with conversion to the ^{99m}Tc-**5** complex.

Rat Tissue Distribution Studies of SAAC Complexes. Rat tissue distribution studies were performed with eight of the novel SAAC complexes, [^{99m}Tc(CO)$_3${η^3-((*S*)-2-amino-6-(bis((1-methyl-1*H*-imidazol-2-yl)methyl)amino)hexanoic acid)}] (^{99m}Tc-**1**), [^{99m}Tc(CO)$_3${η^3-(2-amino-6-(bis((1-(2,2-dimethoxyethyl)-1*H*-imidazol-2-yl)methyl)amino)hexanoic acid)}] (^{99m}Tc-**2**), [^{99m}Tc(CO)$_3${η^3-(2-amino-6-(bis((1-(2-ethoxyethyl)-1*H*-imidazol-2-yl)methyl)amino)hexanoic acid)}] (^{99m}Tc-**3**), [^{99m}Tc(CO)$_3${η^3-(2,2′-(2,2′-(5-amino-5-carboxypentylazanediyl)bis(methylene)-bis(1*H*-imidazole-2,1-diyl))diacetic acid)}] (^{99m}Tc-**4**), [^{99m}Tc(CO)$_3${η^3-(2-amino-6-(bis((1-(2-hydroxyethyl)-1*H*-imidazol-

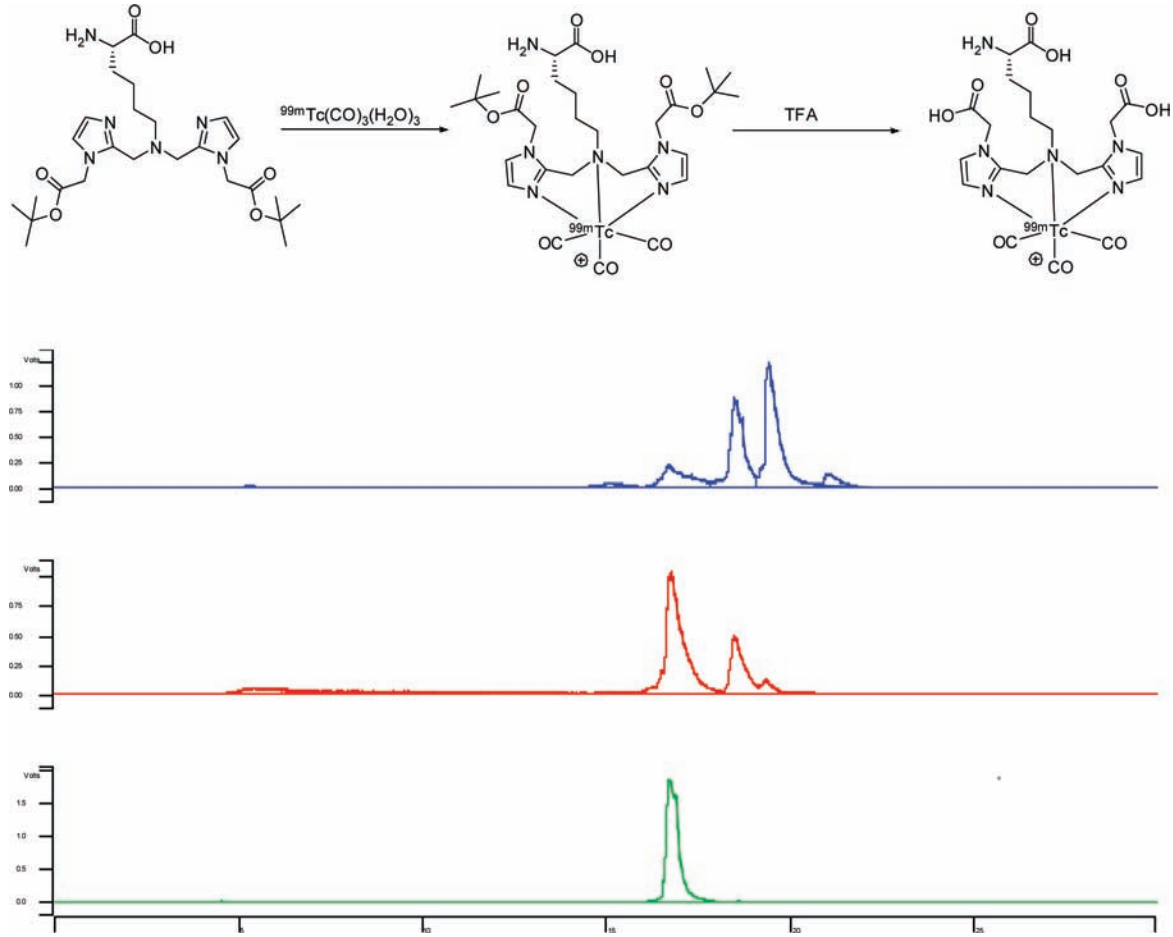
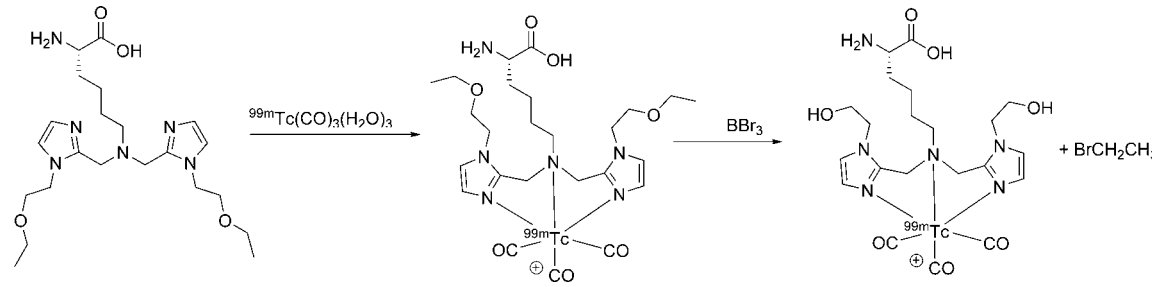


Figure 3. Radiochromatograms of ^{99m}Tc-**4**-di-*tert*-butyl ester: crude reaction after heating at 75 °C for 30 min (blue) showing multiple radioactive species; after TFA incubation (red) showing predominantly fully deprotected product (^{99m}Tc-**4**); after reverse phase HPLC purification (green) demonstrating ^{99m}*Tc*-**4** > 98% RCP.

Scheme 3. Radiolabeling of (2-Amino-6-(bis((1-(2-ethoxyethyl)-1*H*-imidazol-2-yl)methyl)amino)hexanoic acid (3) and Subsequent Deprotection To Form the Metal Complex ^{99m}Tc-5



2-yl)methyl)amino)hexanoic acid)}] (^{99m}Tc-**5**), [^{99m}Tc(CO)$_3$-{η^3-((*S*)-2-amino-6-((carboxymethyl)(thiazol-2-ylmethyl)amino)-hexanoic acid (^{99m}Tc-**7**), [^{99m}Tc(CO)$_3${η^3-((*S*)-2-amino-6-((2-*tert*-butoxy-2-oxoethyl)((1-methyl-1*H*-imidazol-2-yl)methylamino)hexanoic acid (^{99m}Tc-**8**), and [^{99m}Tc(CO)$_3${η^3-(2,2′-(5-amino-5-carboxypentylazanediyl)diacetic acid)}] (^{99m}Tc-**9**). Only [^{99m}Tc(CO)$_3${η^3-(2-amino-6-(bis((1-(3-(diethoxyphosphoryl)propyl)-1*H*-imidazol-2-yl)methyl)amino)hexanoic acid)}] (^{99m}Tc-**6**) was omitted because of the high lipophilicity of the complex. In addition, for comparison, rat tissue distribution studies were performed with previously published SAAC systems (*6*), the cationic bis-pyridine complex [^{99m}Tc(CO)$_3$(η^3-{2-amino-6-(bis(pyridin-2-ylmethyl)amino)hexanoic acid}] [^{99m}Tc-DpK] and the neutral pyridine amine monoacetic acid complex [^{99m}Tc(CO)$_3$(η^3-{2-amino-6-((carboxymethyl)(pyridin-2-ylmethyl)amino)hexanoic acid} [^{99m}Tc-PAMAK]. A summary of the uptake of all of the SAAC complexes examined in selected organs is shown in Table 1.

^{99m}Tc-SAAC imidazole complexes **1**, **2**, **3**, and **5** exhibited rapid clearance from the blood (maximum of 0.14 %ID/g at 2 h for ^{99m}Tc-**5**), relatively low liver uptake (maximum of 1.61 ± 0.32 %ID/g at 5 min for ^{99m}Tc-**3**), and low liver retention (maximum of 0.74 ± 0.14 %ID/g at 2 h for ^{99m}Tc-**1**). In addition, these complexes exhibited a shift from hepatobiliary clearance to a predominantly renal uptake pattern compared to ^{99m}Tc-DpK and ^{99m}Tc-PAMAK. However, the high renal accumulation was in the absence of substantial renal clearance over the 2 h time period of the study. The four complexes displayed >12 %ID/g in the kidneys at the earliest (0.5 h) and latest (2 h) time points tested, demonstrating very little clearance over time. It is not clear whether the undesirable kidney retention was due to nonspecific binding of the complexes in the kidneys or a result of amino acid recycling. Since the goal is to develop chelators that exhibit rapid clearance from all nontarget tissues, the extended retention in the kidneys can be viewed as a significant liability for the complexes and may mitigate their potential application to biologically relevant molecules.

^{99m}Tc-SAAC complex **4**, which contains carboxylic acid functionalized imidazole rings, also exhibited very low liver and gastrointestinal accumulation (0.39 ± 0.07 and 1.22 ± 0.27 %ID/g at 2 h) and high kidney uptake that did not clear over the time course of the study (10.7 ± 2.3 and 10.2 ± 2.5 %ID/g at 0.5 and 2 h, respectively). This complex exhibited the least initial liver uptake (0.52 ± 0.07 %ID/g at 5 min) of any chelate tested. Interestingly, **4** cleared the blood more slowly than any of the chelators examined, potentially because of increased binding to blood proteins.

The complexes of compounds **7** and **8**, the monothiazole and monomethylimidazole analogues, exhibited high kidney uptake, 9.07 ± 0.66 and 17.05 ± 3.17 %ID/g at 0.5 h, respectively, and rapid clearance of 1.63 ± 0.51 and 3.94 ± 0.43 %ID/g at 2 h, respectively. However, these complexes also demonstrated increased accumulation in the gastrointestinal tract (GI) (>2 %ID/g at 2 h) over the 2 h study period. Interestingly, these neutral complexes are similar in nature to ^{99m}Tc-PAMAK, with one heterocyclic chelating moiety and one acetic acid chelating moiety, and displayed a similar clearance pattern to ^{99m}Tc-PAMAK as well.

^{99m}Tc-SAAC complex **9**, the diacetic acid derivative, exhibited high initial kidney uptake with rapid renal clearance (5.68 ± 1.99 and 1.09 ± 0.17 %ID/g at 0.5 and 2 h, respectively) and the least liver and GI accumulation of any of the chelators tested after the initial time point (0.18 ± 0.03 and 0.69 ± 0.19 %ID/g at 2 h, respectively). This complex exhibited an ideal pharmacokinetic clearance profile for development into radiopharmaceuticals; however, this chelator was not studied further because of lower RCY.

Table 1. Comparison of the Rat Tissue Distribution Results of ^{99m}Tc-SAAC Complexes in Blood and Excretory Tissues[a]

		time (min)			
compd	tissue	5	30	60	120
DpK	blood	0.58 ± 0.05	0.07 ± 0.01	0.025 ± 0.005	0.013 ± 0.001
	liver	3.36 ± 0.44	2.75 ± 0.11	2.59 ± 0.08	2.12 ± 0.06
	kidney	6.05 ± 1.03	4.95 ± 0.11	4.93 ± 0.43	3.89 ± 0.42
	GI	0.49 ± 0.08	0.89 ± 0.07	1.46 ± 0.09	2.73 ± 0.57
PAMAK	blood	0.63 ± 0.06	0.19 ± 0.02	0.07 ± 0.002	0.03 ± 0.01
	liver	1.25 ± 0.14	1.34 ± 0.20	0.56 ± 0.05	0.20 ± 0.03
	kidney	6.38 ± 0.70	3.55 ± 0.35	1.14 ± 0.14	0.48 ± 0.05
	GI	0.18 ± 0.02	1.22 ± 0.24	1.80 ± 0.175	2.50 ± 0.59
1	blood	1.18 ± 0.18	0.28 ± 0.03	0.11 ± 0.02	0.03 ± 0.01
	liver	0.8 ± 0.28	1.03 ± 0.21	0.86 ± 0.16	0.74 ± 0.14
	kidney	6.65 ± 2.06	22.2 ± 0.3.9	25.4 ± 1.7	25.5 ± 3.4
	GI	0.15 ± 0.02	0.45 ± 0.11	0.84 ± 0.1	1.12 ± 0.37
2	blood	1.46 ± 0.21	0.47 ± 0.05	0.14 ± 0.04	0.04 ± 0.01
	liver	1.06 ± 0.34	0.45 ± 0.04	0.24 ± 0.04	0.16 ± 0.02
	kidney	13.82 ± 2.81	34.1 ± 5.59	40.25 ± 5.17	33.18 ± 2.75
	GI	0.34 ± 0.12	1.05 ± 0.2	1.39 ± 0.24	1.21 ± 0.27
3	blood	0.83 ± 0.09	0.09 ± 0.02	0.002 ± 0.001	0.01 ± 0.001
	liver	1.61 ± 0.32	0.35 ± 0.08	0.28 ± 0.07	0.14 ± 0.02
	kidney	6.86 ± 0.86	12.13 ± 2.36	12.54 ± 1.00	12.54 ± 0.81
	GI	0.57 ± 0.13	2.33 ± 0.61	3.62 ± 0.3	2.96 ± 0.44
4	blood	1.33 ± 0.2	1.14 ± 0.23	0.86 ± 0.17	0.72 ± 0.12
	liver	0.52 ± 0.07	0.55 ± 0.07	0.42 ± 0.08	0.39 ± 0.07
	kidney	6.58 ± 1.85	10.7 ± 2.3	16.8 ± 4.8	10.2 ± 2.5
	GI	0.15 ± 0.02	0.44 ± 0.08	0.76 ± 0.31	1.22 ± 0.27
5	blood	1.3 ± 0.25	0.52 ± 0.03	0.24 ± 0.03	0.14 ± 0.02
	liver	0.88 ± 0.24	0.95 ± 0.13	0.65 ± 0.13	0.46 ± 0.14
	kidney	8.55 ± 1.54	18.7 ± 1.2	22.1 ± 3.5	23.2 ± 5.0
	GI	0.19 ± 0.05	0.52 ± 0.09	0.76 ± 0.24	0.97 ± 0.37
7	blood	0.94 ± 0.19	0.22 ± 0.06	0.09 ± 0.001	0.03 ± 0.01
	liver	1.16 ± 0.09	1.06 ± 0.35	1.04 ± 0.18	0.72 ± 0.16
	kidney	10.84 ± 1.25	9.07 ± 0.66	4.19 ± 0.57	1.63 ± 0.51
	GI	0.16 ± 0.03	1.16 ± 0.4	1.93 ± 0.37	2.27 ± 0.59
8	blood	1.03 ± 0.14	0.45 ± 0.1	0.22 ± 0.02	0.09 ± 0.01
	liver	0.95 ± 0.14	3.02 ± 0.59	0.98 ± 0.22	0.44 ± 0.14
	kidney	10.79 ± 1.97	17.05 ± 3.17	9.52 ± 2.54	3.94 ± 0.43
	GI	0.16 ± 0.01	1.96 ± 0.49	1.64 ± 0.64	2.53 ± 0.70
9	blood	1.00 ± 0.14	0.35 ± 0.05	0.19 ± 0.03	0.14 ± 0.02
	liver	0.68 ± 0.06	0.5 ± 0.14	0.26 ± 0.04	0.18 ± 0.03
	kidney	12.8 ± 1.31	5.68 ± 1.99	2.38 ± 0.45	1.09 ± 0.17
	GI	0.12 ± 0.02	0.36 ± 0.11	0.72 ± 0.11	0.69 ± 0.19

[a] Data are %ID/g, expressed as mean ± SD.

Table 2. Comparisons of the Partition Coefficients (log *P*) for the ^{99m}Tc-SAAC Complexes

compd	log *P*
DpK	−1.89
PAMA-K	−1.80
1	−2.00
2	−1.72
3	−1.10
4	−2.33
5	−1.61
6	−0.91
7	−1.75
8	−1.84
9	−2.20
NTA control[a]	−2.88

[a] Lipowska et al. (*20*).

It is clear that despite the rapid clearance from the blood of the first generation of SAAC complexes, ^{99m}Tc-DpK and ^{99m}Tc-PAMAK, a significant portion of their excretion was via the hepatobiliary route, hindering the potential application of these chelators in the development of radiopharmaceuticals. These limitations are realized in the development of cancer imaging agents where the ability to visualize metastatic lesions in the abdominal cavity with a DpK containing chelator is confounded by the high background signal present in the liver and GI. Through the preparation of a variety of novel polar and/or hydrophilic SAAC systems that are inherently less lipophilic, the pharmacokinetic profiles have been successfully altered to favor renal clearance.

Determination of Partition Coefficients (log *P*) as a Measure of Lipophilicity. The log *P* values (Table 2) of the complexes were determined using the HPLC purified ^{99m}Tc-SAAC complexes by the shake flask method utilizing *n*-octanol and 25 mM phosphate buffer (pH 7.4) as the solvents. NTA was tested as a control based on the published results that the ^{99m}Tc-NTA complex undergoes rapid and efficient renal clearance (*20*).

The lipophilicity of the complexes as measured by the octanol/phosphate buffer (pH 7.4) extinction coefficients followed the general trend of the rat tissue distribution pharmacokinetic profiles whereby the complexes with more negative log *P* values displayed a more desirable pharmacokinetic profile (high kidney/low hepatobiliary clearance). For example, **4** with log *P* of −2.33 cleared primarily by renal excretion, while **7** with a less negative log *P* of −1.75 cleared by combined renal and hepatobiliary routes. However, the correlation between the log *P* measurements and renal uptake and clearance of the radioactive complexes was not perfect because complexes like **3** with a log *P* of −1.10 still have high kidney uptake. Therefore, the log *P* values should only be considered as one of many physiochemical properties of the complexes that govern the in vivo distribution, uptake, metabolism, and excretion.

Incorporation of ^{99m}Tc-SAAC Complexes into Tyr-3-octreotide. One of the most important applications for the SAAC technology is the incorporation of the SAAC ligands directly into clinically relevant peptides. This is readily accomplished using standard solid phase peptide synthesis strategies (*8, 29*). To that end, we have incorporated two SAAC ligands, DpK and **4**, at the N-terminus of Tyr-3-octreotide, a somatostatin receptor 2 (SSTR2) selective peptide agonist. Following complexation with ^{99m}Tc, we evaluated the tissue distribution for comparison to ^{111}In-DOTA-Tyr-3-octreotide, a well established peptide based radiopharmaceutical for the detection of carcinoid and neuroendocrine tumors (*30*−*33*). The SAAC ligand, **4**, was selected for evaluation based on the favorable pharmacokinetic profile in rats demonstrating kidney uptake and GI/liver clearance of the ^{99m}Tc-SAAC complex, high RCY, and prolonged

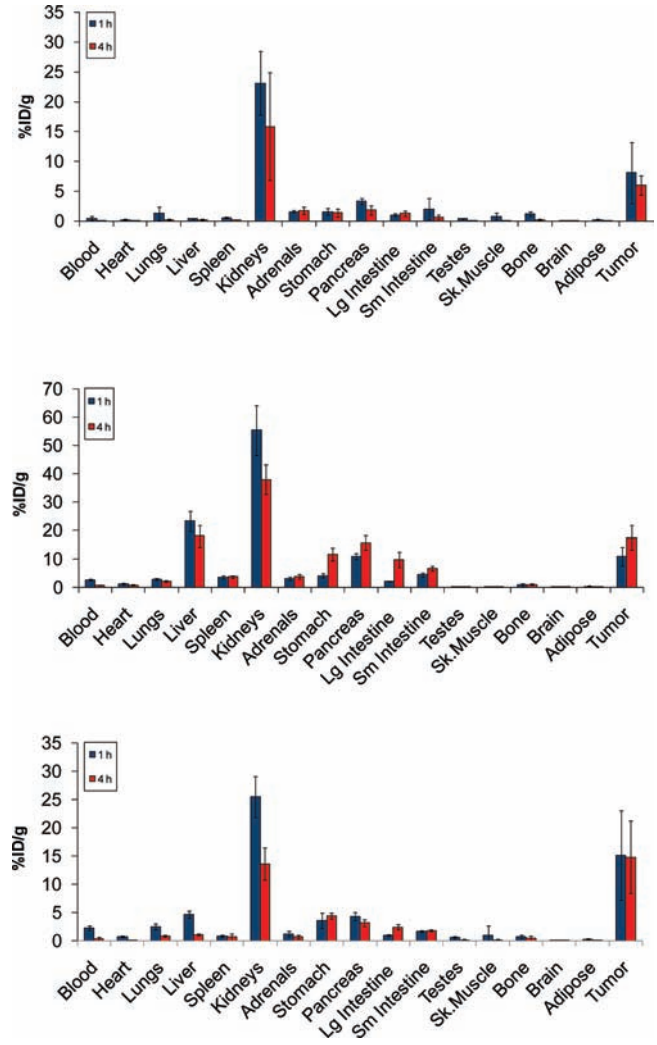


Figure 4. Tissue distribution of SSTR2 receptor mediated ^{111}In-DOTA-Tyr-3-octreotide (top) verses ^{99m}Tc-DpK-Tyr-3-octreotide (middle) and ^{99m}Tc-**4**-Tyr-3-octreotide (bottom) in AR42J mouse tumor model.

chemical stability. The incorporation of DpK was used for a direct comparison of a first generation SAAC with similar size. The results of the tissue distributions are shown in Figure 4. While both ^{99m}Tc-DpK-Tyr-3-octreotide and ^{111}In-DOTA-Tyr-3-octreotide demonstrate specific uptake and retention in target tissues, tumor and pancreas, the liver and GI uptake of ^{99m}Tc-DpK-Tyr-3-octreotide is significantly greater than that of ^{111}In-DOTA-Tyr-3-octreotide, thus highlighting the necessity of developing advanced SAAC ligands with a pharmacokinetic profile that favors renal clearance. In contrast, ^{99m}Tc-**4**-Tyr-3-octreotide exhibited a very similar tissue distribution to the ^{111}In-DOTA-Tyr-3-octreotide with high renal clearance and significantly reduced liver uptake of 4.63 ± 0.65 %ID/g at 1 h compared to 23.31 ± 3.5 %ID/g at 1 h for ^{99m}Tc-DpK-Tyr-3-octreotide ($p < 0.001$). Likewise, both the large and small intestines of the ^{99m}Tc-**4**-Tyr-3-octreotide showed reduced radioactivity at both time points examined compared to ^{99m}Tc-DpK-Tyr-3-octreotide. ^{99m}Tc-**4**-Tyr-3-octreotide also exhibited slightly higher tumor uptake at 1 h (15.15 ± 7.92 %ID/g) compared to the ^{111}In-DOTA-Tyr-3-octreotide (8.08 ± 5.17 %ID/g) and significantly higher tumor uptake at 4 h compared to ^{111}In-DOTA-Tyr-3-octreotide (14.85 ± 6.41 and 5.99 ± 1.65 %ID/g, respectively) ($p < 0.03$). The tumor-to-blood ratio of ^{99m}Tc-**4**-Tyr-3-octreotide was an encouraging 6.7:1 at 1 h and reached a maximum at 4 h with an impressive 35:1 ratio. Thus, the utility of this class of chelators is accentuated by the ability

to maintain high tumor uptake while driving preferential renal clearance of molecules, which would otherwise be dominated by hepatobiliary localization and excretion.

In summary, our ongoing research into the development of novel ^{99m}Tc chelators has led to significant improvements of a key characteristic of the already robust proprietary SAAC radiolabeling platform. The pharmacokinetic profile of the ^{99m}Tc-SAAC metal complex has been significantly altered through the design and synthesis of SAAC systems with the potential to enhance renal clearance and diminish hepatobiliary accumulation and/or clearance. The benefit of the second generation ^{99m}Tc-SAAC technology was realized upon incorporation of ^{99m}Tc-SAAC (**4**) into Tyr-3-octreotide, resulting in a significant decrease of the ^{99m}Tc-SAAC complex in nontarget and hepatobiliary tissues, thus affording the potential to design and develop a superior ^{99m}Tc-SAAC-Tyr-3-octreotide radioimaging agent with the potential to image cancer with improved whole body clearance. Future efforts will focus on applying the novel polar SAAC chelates to additional biologically relevant peptides and small molecules for the development of novel radiopharmaceuticals to image and potentially treat a variety of diseases.

ACKNOWLEDGMENT

This work was supported in part by grants (J.W.B.) from the Department of Energy (Grant D2-FG02-99ER62791) and the National Institutes of Health (Grant 1R41A1054080-01).

Supporting Information Available: Radiolabeling summary for ^{99m}Tc-**1**−**9** SAAC complexes as well as ^{99m}Tc-**4**-Tyr-3-octreotide, ^{99m}Tc-DpK-Tyr-3-octreotide, and ^{111}In-DOTA-Tyr-3-octreotide including representative radiochromatograms. This material is available free of charge via the Internet at http://pubs.acs.org.

LITERATURE CITED

(1) Mariani, G., Nicolini, M., Wagner, H. W., Eds. (1983) *Technetium in Chemistry and Nuclear Medicine* Vol. 1, Cortina International, Verona, Italy.

(2) Bartholomae, M., Valliant, J., Maresca, K. P., Babich, J. W., and Zubieta, J. (2009) Single amino acid chelates: a strategy for the design of technetium and rhenium radiopharmaceuticals. *Chem. Commun. 5*, 493–512.

(3) Jurisson, S. S., and Lyden, J. D. (1999) Potential technetium small molecule radiopharmaceuticals. *Chem. Rev. 99*, 2205.

(4) Heeg, M. J., and Jurisson, S. (1999) The role of inorganic chemistry in the development of radiometal agents for cancer therapy. *Acc. Chem. Res. 32* (12), 1053–1060.

(5) Nicolini, M., Bandoli, G., Mazzi, U., Eds. (2006) *Technetium, Rhenium and Other Metals in Chemistry and Nuclear Mediciine* Vol. 7, S. G. Editoriali, Padova, Italy.

(6) Maresca, K. P., Hillier, S. M., Femia, F. J., Zimmerman, C. N., Levadala, M. K., Banerjee, S. R., Hicks, J., Sundararajan, C., Valliant, J., Zubieta, J., Eckelman, W. C., Joyal, J. L., and Babich, J. W. (2009) Comprehensive radiolabeling, stability, and tissue distribution studies of technetium-99m single amino acid chelates (SAAC). *Bioconjugate Chem. 20* (8), 1625–1633.

(7) James, S., Maresca, K. P., Allis, D. G., Valliant, J. F., Eckelman, W., Babich, J. W., and Zubieta, J. (2006) Extension of the single amino acid chelate concept (SAAC) to bifunctional biotin analogues for complexation of the $M(CO)_3^{+1}$ core (M = Tc and Re): syntheses, characterization, biotinidase stability, and avidin binding. *Bioconjugate Chem. 17* (3), 579–589.

(8) Stephenson, K. A., Zubieta, J., Banerjee, S. R., Levadala, M. K., Taggart, L., Ryan, L., McFarlane, N., Boreham, D. R., Maresca, K. P., Babich, J. W., and Valliant, J. F. (2004) A new strategy for the preparation of peptide-targeted radiopharmaceuticals based on an Fmoc-lysine-derived single amino acid chelate (SAAC). Automated solid-phase synthesis, NMR characterization, and in vitro screening of fMLF(SAAC)G and fMLF[(SAAC-Re$(CO)_3)^+$]G. *Bioconjugate Chem. 15* (1), 128–136.

(9) Stephenson, K. A., Banerjee, S. R., Besanger, T., Sogbein, O. O., Levadala, M. K., McFarlane, N., Lemon, J. A., Boreham, D. R., Maresca, K. P., Brennan, J. D., Babich, J. W., Zubieta, J., and Valliant, J. F. (2004) Bridging the gap between in vitro and in vivo imaging: isostructural Re and ^{99m}Tc complexes for correlating fluorescence and radioimaging studies. *J. Am. Chem. Soc. 126* (28), 8598–8599.

(10) D'Andrea, L. D., Testa, I., Panico, M., Di Stasi, R., Caraco, C., Tarallo, L., Arra, C., Barbieri, A., Romanelli, A., and Aloj, L. (2008) In vivo and in vitro characterization of CCK8 bearing a histidine-based chelator labeled with ^{99m}Tc-tricarbonyl. *Biopolymers 90* (5), 707–712.

(11) Alberto, R., Schibli, R., Waibel, R., Abram, U., and Schubiger, A. P. (1999) Basic aqueous chemistry of $[M(OH_2)_3(CO)_3]^+$ (M=Re, Tc) directed towards radiopharmaceutical application. *Coord. Chem. Rev. 190*−*192*, 901–919.

(12) Schibil, R., La Bella, R., Alberto, R., Garcia-Garayoa, E., Ortner, K., Abram, U., and Schubiger, P. A. (2000) Influence of the denticity of ligand systems on the in vitro and in vivo behavior of ^{99m}Tc(I)-tricarbonyl complexes: a hint for the future functionalization of biomolecules. *Bioconjugate Chem. 11*, 345–351.

(13) Pietzsch, H.-J., Gupta, A., Reisgys, M., Drews, A., Seifert, S., Syhre, R., Spies, H., Alberto, R., Abram, U., and Schubiger, P. A. (2000) Chemical and biological characterization of technetium(I) and rhenium(I) tricarbonyl complexes with dithioether ligands serving as linkers for coupling the $Tc(CO)_3$ and $Re(CO)_3$ moieties to biologically active molecules. *Bioconjugate Chem. 11* (3), 414–424.

(14) Bourkoula, A., Paravatou-Petsotas, M., Papadopoulos, A., Santos, I., Pietzsch, H.-J., Livaniou, E., Pelecanou, M., Papadopoulos, M., and Pirmettis, I. (2009) Synthesis and characterization of rhenium and technetium-99m tricarbonyl complexes bearing the 4-[3-bromophenyl]quinazoline moiety as a biomarker for EGFR-TK imaging. *Eur. J. Med. Chem. 44* (10), 4021–4027.

(15) Maria, L., Fernandes, C., Garcia, R., Gano, L., Paulo, A., Santos, I. C., and Santos, I. (2009) Tris(pyrazolyl)methane ^{99m}Tc tricarbonyl complexes for myocardial imaging. *Dalton Trans.* (4), 603–606.

(16) Lu, G., Hillier, S. M., Maresca, K. P., Zimmerman, C. N., Wang, J., Shay, C., Marquis, J. C., Eckelman, W. C., Joyal, J. L., and Babich, J. W. (2009) Small molecule carbonic anhydrase IX inhibitors with Re/Tc for targeted molecular imaging of cancer. *Abstracts of Papers*, 238th National Meeting of the American Chemical Society, Washington, DC, August 16−20, American Chemical Society, Washington, DC.

(17) Femia, F. J., Maresca, K. P., Hillier, S. M., Zimmerman, C. N., Joyal, J. L., Barrett, J. A., Aras, O., Dilsizian, V., Eckelman, W. C., and Babich, J. W. (2008) Synthesis and evaluation of a series of $^{99m}Tc(CO)_3^+$ lisinopril complexes for in vivo imaging of angiotensin-converting enzyme expression. *J. Nucl. Med. 49* (6), 970–977.

(18) Lipowska, M., He, H., Malveaux, E., Xu, X., Marzilli, L. G., and Taylor, A. (2006) First evaluation of a ^{99m}Tc-tricarbonyl complex, ^{99m}Tc(CO)3(LAN), as a new renal radiopharmaceutical in humans. *J. Nucl. Med. 47* (6), 1032–1040.

(19) He, H., Lipowska, M., Christoforou, A., Marzilli, L. G., and Taylor, A. T. (2007) Initial evaluation of new $^{99m}Tc(CO)_3$ renal imaging agents having carboxyl-rich thioether ligands and chemical characterization of $Re(CO)_3$ analogues. *Nucl. Med. Biol. 34* (6), 709–716.

(20) Lipowska, M., Marzilli, L. G., and Taylor, A. T. (2009) $^{99m}Tc(CO)_3$-nitrilotriacetic acid: a new renal radiopharmaceutical showing pharmacokinetic properties in rats comparable to those of ^{131}I-OIH. *J. Nucl. Med. 50*, 454–460.

(21) Maresca, K. P., Kronauge, J. F., Zubieta, J., and Babich, J. W. (2007) Novel ether-containing ligands as potential ^{99m}technetium(I) heart agents. *Inorg. Chem. Commun. 10* (12), 1409–1412.

(22) Maresca, K. P., Keith, D., Femia, F. J., Graham-Coco, W. A., Kronauge, J. F., Sogbein, O. O., Valliant, J., Babich, J. W. (2006) SAR development of ether-containing ligand complexes of $Tc(CO)_3^+$ for cardiac imaging. In *Technetium in Chemistry and Nuclear Medicine*, 7th ed. (Mazzi, U., Ed.) pp 399−402, S. G. Editoriali, Padova, Italy.

(23) Shah, T., Kulakiene, I., Quigley, A., Warbey, V. S., Srirajaskanthan, R., Toumpanakis, C., Hochhauser, D., Buscombe, J., and Caplin, M. E. (2008) The role of ^{99m}Tc-depreotide in the management of neuroendocrine tumours. *Nucl. Med. Commun. 29* (5), 436–440.

(24) Quigley, A, Buscombe, J. R., Shah, T., Gnanasegaran, G., Roberts, D., Caplin, M. E., and Hilson, A. J. W. (2005) Intertumoural variability in functional imaging within patients suffering from neuroendocrine tumours. *Neuroendocrinology 82* (3−4), 215–220.

(25) Kowalski, J., Henze, M., Schuhmacher, J., Macke, H. R, Hofmann, M., and Haberkorn, U. (2003) Evaluation of positron emission tomography imaging using [^{68}Ga]-DOTA-D Phe(1)-Tyr(3)-octreotide in comparison to [^{111}In]-DTPAOC SPECT. First results in patients with neuroendocrine tumors. *Molecular Imaging Biol. 5* (1), 42–48.

(26) Yao, Z., Bhaumik, J., Dhanalekshmi, S., Ptaszek, M., Rodriguez, P. A., and Lindsey, J. S. (2007) Synthesis of porphyrins bearing 1−4 hydroxymethyl groups and other one-carbon oxygenic substituents in distinct patterns. *Tetrahedron 63*, 10657–10670.

(27) Schweinsberg, C., Maes, V., Brans, L., Blauenstein, P., Tourwe, D. A., Schubiger, P. A., Schibli, R., and Garayoa, E. G. (2008) Novel glycated [^{99m}Tc(CO)$_3$]-labeled bombesin analogues for improved targeting of gastrin-releasing peptide receptor-positive tumors. *Bioconjugate Chem. 19* (12), 2432–2439.

(28) Yang, C.-T., Kim, Y.-S., Wang, J., Wang, L., Shi, J., Li, Z.-B., Chen, X., Fan, M., Li, J.-J., and Liu, S. (2008) ^{64}Cu-labeled 2-(diphenylphosphoryl)ethyldiphenylphosphonium cations as highly selective tumor imaging agents: effects of linkers and chelates on radiotracer biodistribution characteristics. *Bioconjugate Chem. 19* (10), 2008–2022.

(29) Smith, C. J., Gali, H., Sieckman, G. L., Higginbotham, C., Volkert, W. A., and Hoffman, T. J. (2003) Radiochemical investigations of ^{99m}Tc-N3S-X-BBN[7−14]NH_2; an in vitro/in vivo structure−activity relationship study where X = 0, 3, 5, 8, and 11-carbon tethering moieties. *Bioconjugate Chem. 14*, 93–102.

(30) De Jong, M., Breeman, W. A. P., Kwekkeboom, D. J., Valkema, R., and Krenning, E. P. (2009) Tumor imaging and therapy using radiolabeled somatostatin analogues. *Acc. Chem. Res. 42* (7), 873–880.

(31) Oeberg, K. (2008) Molecular imaging of neuroendocrine tumors. *Expert Rev. Endocrinol. Metab. 3* (6), 739–749.

(32) Goldsmith, S. J. (2009) Update on nuclear medicine imaging of neuroendocrine tumors. *Future Oncol. 5* (1), 75–84.

(33) Reubi, J. C., and Maecke, H. R. (2008) Peptide-based probes for cancer imaging. *J. Nucl. Med. 49* (11), 1735–1738.

BC900517X

Fluorescent Labeling of (Oligo)Nucleotides by a New Fluoride Cleavable Linker Capable of Versatile Attachment Modes

Diana C. Knapp, Jennifer D'Onofrio, and Joachim W. Engels*

Institut für Organische Chemie und Chemische Biologie, Johann Wolfgang Goethe Universität, Max-von-Laue Strasse 7, 60438 Frankfurt am Main, Germany. Received December 9, 2009; Revised Manuscript Received March 31, 2010

The development of a fluoride cleavable linker **1** for reversibly labeling (oligo)nucleotides is described here. The linker allows different ways of chemical attachment of a reporter molecule, for example, click chemistry or amide formation. The versatile attachment modes of labels are demonstrated by derivatizations with pyrene and fluorescein. Besides the synthesis of the new linker, we also show the derivatization of iodobenzene as a model compound and a nucleoside to demonstrate the applicability. Further, cleavability studies in solution and on a solid-supported oligonucleotide are shown. The linker can be applied in the synthesis of reversible terminators, useful for new DNA sequencing technologies like cyclic reversibly terminating (CRT) sequencing.

INTRODUCTION

The fluorescent labeling of nucleotides is an important tool in biochemistry (*1, 2*). So far a very important application of fluorescently labeled nucleotides is the Sanger DNA-sequencing method (*3*). Novel sequencing approaches (*4, 5*) for future demands on "individualized" diagnostic genome analysis also require reversibly labeled nucleotides. This creates a need for cleavable linkers to reversibly attach a dye to a nucleotide.

These new sequencing techniques include methods for whole genome sequencing (*6*−*8*), as well as for the detection of mutations (mainly SNPs) in minisequencing approaches (*9, 10*). One of these new approaches is the array-based cyclic reversibly terminating (CRT) sequencing (*7, 11*). This technique does not need traditional gel electrophoretic separation but affords direct readout of the sequence by fluorescence detection. The labeled nucleotides are added sequentially to oligonucleotide templates that are immobilized on an array platform, thus sequencing can be performed in a highly parallel fashion. CRT sequencing is based on the use of so-called "reversible terminators" to achieve the defined sequential addition of one base after the other. The structural requirements for these reversible terminators include a reversibly terminating moiety at the 3′-position and a reporter molecule (i.e., a fluorescent dye) reversibly attached via a cleavable linker.

During development of such reversible terminators, one issue is to find a 3′-modification that meets the following demands: reliable termination of the polymerase reaction, quantitative and fast cleavage under reasonable conditions, and acceptance by a DNA polymerase. In a recent publication, we presented the fluoride cleavable 2-cyanoethyl (CE)[1] group as a very promising candidate for a 3′-reversibly terminating group (*12*). The next step is to develop a suitable cleavable linker to connect the nucleotides to the reporter moiety (fluorescent dye). This linker should be efficiently cleavable under the same conditions as the 3′-blocking group to allow the regeneration of the 3′-OH group and the removal of the linker−dye system in a single deprotection step. The dye will be attached to the base moiety of the nucleosides because Sanger sequencing has already demonstrated that modifications at the 7-position of purines and the 5-position of pyrimidines are well tolerated by DNA polymerases.

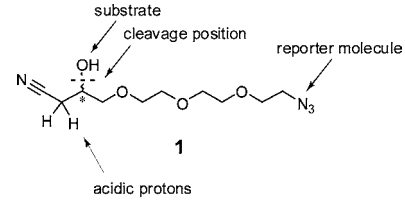


Figure 1. Core structure **1** of the new cleavable linker.

In this publication, we present the design, the synthesis, and the evaluation of a new fluoride cleavable linker for reversible labeling of (oligo)nucleotides. In Figure 1, the core structure **1** of the new linker is displayed.

The linker design was derived from the well-known acidity of protons vicinal to a nitrile function. This motif also plays a key role in the cleavage of other fluoride cleavable protecting groups that are not based on silicon, like the above-mentioned CE (*12, 13*), the 1-(2-cyanoethoxy)methyl (*14*), and the l-(2-cyanoethoxy)ethyl (*15*) protecting groups.

The connection of the substrate (nucleotide) is planned at the secondary alcohol function via a prop-2-ynylcarbamate moiety. The azide group at the end of the triglycol spacer then serves as a juncture for reporter molecules. These molecules can either be attached by click reactions to the existing azide moiety or via amide or carbamate bonds after reduction of the azide to the amine.

First the synthesis of the linker will be shown. For the evaluation of the cleavage properties, a simple model compound **9** was synthesized where the nucleotide moiety is replaced by a phenyl moiety. After defining the cleavage conditions of the model compound a 5-,3′-modified 2′-deoxyuridine derivative **17** was synthesized, bearing the 3′-*O*-(2-cyanoethyl) (CE) group and the cleavable linker at position 5 of the base moiety. Finally

* To whom correspondence should be addressed. Phone number: +49-69-79829150. Fax number: +49-69-79829148. E-mail address: joachim.engels@chemie.uni-frankfurt.de.

[1]Abbreviations: ACN, acetonitrile; Boc, *tert*-butoxycarbonyl; Bz, benzoyl; CE, 2-cyanoethyl; CPG, controlled pore glass; DIPEA, diisopropylethylamine; DMF, *N*,*N*-dimethylformamide; DMTr, 4,4′-dimethoxytrityl; EDTA, ethylenediaminetetraacetate; TBAF, tetrabutylammonium fluoride; TCA, trichloroacetic acid; TFA, trifluoroacetic acid; THF, tetrahydrofuran; TLC, thin layer chromatography; TMS(Cl), trimethylsilyl (chloride).

10.1021/bc900542f © 2010 American Chemical Society
Published on Web 05/28/2010

the optimized cleavage conditions were applied to a CPG-bound 8-mer bearing the fluorescently labeled and 3′-*O*-modified 2′-deoxyuridine at the 3′-end.

EXPERIMENTAL PROCEDURES

Materials and Methods. All reagents were of the highest commercially available quality and were used as received. Benzoyl chloride and acrylonitrile were distilled before use. Oligonucleotide synthesis was accomplished using an Expedite nucleic acid synthesis system from PerSeptive Biosystems. The 5′-*O*-(2-cyanoethyl)-*N*,*N*-diisopropylphosphoramidite-3′-(4,4′-dimethoxytrityl)-2′-deoxyribonucleosides building blocks were purchased from Pharmacia; the solid support (dT5′-CPG) was purchased from Glen Research. NMR spectra were recorded on Bruker AM, DPX, and AV instruments at 250, 300, and 400 MHz and 300 K. Chemical shifts (δ) are reported in ppm relative to the solvent signal. The fine structure of proton signals was specified with s (singlet), d (doublet), t (triplet), q (quartet), m (multiplet), dd (doublet of doublet), br (broad), and in quotations for pseudo-fine structure. Assignments were made by DEPT, COSY, HSQC, and HMBC experiments. Thin layer chromatograms (TLC) were recorded on Polygram Sil G/UV_{254} by Macherey Nagel & Co., Dueren (thickness of layer 0.2 mm) or 60 F_{254} by Merck KGaA, Darmstadt (thickness of layer 0.2 mm). Flash column chromatography was carried out on silica gel 60 (15−40 μm) by Merck KGaA, Darmstadt at a pressure of 2−3 bar. Reversed phase (RP) HPLC was performed on a Jasco LC-2000Plus HPLC system equipped with a Jasco UV 2075Plus detector (detection at 254 nm) and a Phenomenex Jupiter 4u Proteo 90A 4 μm column (250 mm × 4.6 mm). One molar triethylammonium acetate (TEAA) buffer, pH = 6.5, (A)/water (B)/acetonitrile (C) were used as eluents. Ion-exchange HPLC was performed on a Jasco LC-900 HPLC system equipped with a Jasco UV-970 detector (detection at 254 nm) and a Dionex BioLC DNAPac PA-100 column (250 mm × 9 mm) using water/0.25 M tris(hydroxymethyl)aminomethane hydrochloride (Tris-Cl) buffer, pH = 8/1 M sodium chloride solution as eluent. ESI mass spectrometry was performed on a Fisons instrument equipped with a VG platform II with quadrupole analyzer. MALDI mass spectrometry was performed on a VG TOFSpec from Fisons using 2,5-dihydroxybenzoic acid as matrix for single molecules and 6-aza-2-thiothymin as matrix for oligonucleotides. Fluorescence spectroscopy was performed on a Hitachi F4500 fluorescence spectrometer using 0.3 cm cuvettes. Elemental analyses were recorded on a Foss-Heraeus CHN-O Rapid instrument. The numbering of the atoms in the nucleoside parts is according to the common numbering convention of nucleosides.

2-{2-[2-(2-Azidoethoxy)ethoxy]ethoxymethyl}oxirane, 4. To a suspension of 151 mg of sodium hydride (6.28 mmol, 1.1 equiv) in 6 mL of dry THF, 1 g of compound **3** (5.7 mmol, 1.0 equiv) was added dropwise, and the resulting mixture was stirred for 2 h at room temperature. (±)-Epichlorohydrin (2.3 mL, 28.54 mmol, 5.0 equiv) was added dropwise, and the resulting mixture was stirred for 16 h at room temperature. The reaction mixture then was neutralized with 30% methanolic H_2SO_4 and poured into 40 mL of saturated NaCl solution. The aqueous layer was extracted two times with 30 mL of ethyl acetate and two times with 30 mL of methylene chloride. The combined organic layers were dried over Na_2SO_4 and concentrated under reduced pressure. The resulting oily residue was purified by flash column chromatography using a gradient from *n*-hexane/ether = 1:2 + 1% NH_3 to *n*-hexane/ether = 1:5 + 1% NH_3. Title compound **2** was obtained as colorless oil (884 mg, 67%). R_F = 0.13 (*n*-hexane/ether = 1:2 + 1% NH_3). ^{1}H NMR (400 MHz, DMSO-d_6, 300 K): δ = 2.540 (1H, dd, J = 2.7 and 5.1 Hz, CH_2 oxirane ring), 2.724 (1H, dd, J = 4.2 and 5.1 Hz, CH_2 oxirane ring), 3.07−3.11 (1H, m, C*H* oxirane ring), 3.268 (2H, dd, J = 6.4 and 11.6 Hz, CH_2 adjacent oxirane), 3.395 (2H, "t", N_3−CH_2), 3.52−3.63 (10H, m, 5 × CH_2 glycol), 3.714 (1H, dd, J = 2.8 and 11.6 Hz, CH_2 adjacent oxirane) ppm. ^{13}C-NMR (100 MHz, DMSO-d_6, 300 K): δ = 43.39 (*C*H_2 oxirane ring), 50.03 (N_3-*C*H_2), 50.29 (*C*H oxirane ring), 69.27, 69.72, 69.82, 69.84, 69.97 (5 × *C*H_2 glycol), 71.53 (*C*H_2 adjacent oxirane) ppm. FT-IR (NaCl): ν = 3050 (m, epoxide C−H), 2900 (s, >CH_2), 2120 (s, −N_3) cm^{-1}. ESI(+)-MS (*m/z*) Calcd: 231.2 [$C_9H_{17}N_3O_4$]. Found: 254.0 [M + Na]$^+$, 249.0 [M + H_2O]$^+$, 232.0 [M]$^+$. Anal. ($C_9H_{17}N_3O_4$) C, H, N.

4-{2-[2-(2-Azidoethoxy)ethoxy]ethoxy}-3-hydroxybutyronitrile, 1. To a solution of 500 mg of compound **4** (2.16 mmol, 1.0 equiv) in 2 mL of ethanol, 10 mL of water was added. After stirring for 5 min, 153 mg of sodium cyanide (3.03 mmol, 1.4 equiv) was added, and stirring was continued for 16 h at room temperature. The reaction mixture was then concentrated to about half the volume under reduced pressure, extracted two times with 20 mL of ethyl acetate and one time with 20 mL of methylene chloride, dried over Na_2SO_4 and concentrated. The oily residue was purified by flash-column-chromatography using CH_2Cl_2/MeOH = 97:3 as eluent. The desired compound **1** was obtained as colorless oil (498 mg, 89%). R_F = 0.37 (CH_2Cl_2/MeOH = 95:5). ^{1}H NMR (400 MHz, DMSO-d_6, 300 K): δ = 2.532 (1H, dd, J = 6.7 and 16.9 Hz, NC−CH_2), 2.655 (1H, dd, J = 4.4 and 16.8 Hz, NC−CH_2), 3.321 (1H, dd, J = 6.2 and 10.0 Hz, NC−CH_2−CH−CH_2), 3.382 (2H, "t", N_3−CH_2), 3.404 (1H, dd, J = 5.3 and 10.0 Hz, NC−CH_2−CH−CH_2), 3.52−3.62 (10H, m, 5 × CH_2 glycol), 3.872 (1H, m, NC−CH_2−C*H*), 5.455 (1H, d, J = 5.2 Hz, O*H*) ppm. ^{13}C-NMR (100 MHz, DMSO-d_6, 300 K): δ = 22.52 (NC-*C*H_2), 49.99 (N_3-*C*H_2), 65.24 (NC−CH_2-*C*H), 69.27, 69.70, 69.71, 69.83, 70.14 (5 × *C*H_2 glycol), 73.37 (NC−CH_2−CH-*C*H_2), 118.86 (N*C*) ppm. FT-IR (NaCl): ν = 3520−3300 (s, O−H), 2900 (s, >CH_2), 2250 (m, −C≡N), 2108 (s, −N_3) cm^{-1}. ESI(+)-MS (*m/z*) Calcd: 258.3 [$C_{10}H_{18}N_4O_4$]. Found: 280.9 [M + Na]$^+$, 275.9 [M + NH_4]$^+$, 299.9 [M + K]$^+$. Anal. ($C_{10}H_{18}N_4O_4$) C, H, N.

(2-{2-[2-(3-Cyano-2-hydroxypropoxy)ethoxy]ethoxy}ethyl)-carbamic Acid *tert*-Butyl Ester, 5. Compound **1** (5 g, 19.36 mmol, 1.0 equiv) was dissolved in dry dioxane, 10.47 g of triphenylphosphine (38.72 mmol, 2.0 equiv) was added, and the mixture was stirred at room temperature. After 8 h, TLC control indicated complete consumption of the starting material, and 100 mL of 25% aqueous ammonia was added. The reaction was left at room temperature for 12 h and subsequently dried in vacuum. The residue was dissolved in 100 mL of methylene chloride and extracted three times with 25 mL of 1 M HCl solution. The water phase was neutralized with solid $NaHCO_3$, and 40 mL of dioxane and another 2.4 g of $NaHCO_3$ (29.00 mmol, 1.5 equiv) were added. The mixture was cooled to 0 °C, and 8.7 g of Boc_2O (38.72 mmol, 2.00 equiv) was added in portions over 20 min. The reaction mixture was allowed to warm to room temperature and stirred for 10 h. After concentration in vacuum, the residue was divided between 100 mL of water and 100 mL of ethyl acetate. The aqueous layer was extracted two times with 70 mL of ethyl acetate. The combined organic layers were dried over Na_2SO_4, and the solvent was removed under reduced pressure. The oily residue was purified by flash column chromatography using CH_2Cl_2/MeOH = 99:1 + 1% $EtMe_2N$ as eluent. Compound **5** was obtained as a slightly yellow oil (6.45 g, 100%). R_F = 0.51 (CH_2Cl_2/MeOH/NH_3 = 90:10:1). ^{1}H NMR (300 MHz, DMSO-d_6, 300 K): δ = 1.368 (9H, s, 3 × CH_3), 2.518 (1H, dd, J = 6.6 and 18.6 Hz, NC−CH_2), 2.645 (1H, dd, J = 4.4 and 16.8 Hz, CN−CH_2), 3.058 (2H, q, J = 5.9 Hz, NH−CH_2), 3.27−3.45 (4H, m, NC−CH_2−CH−CH_2, NH−CH_2−CH_2), 3.48−3.56 (8H, m, 4 × CH_2 glycol), 3.864 (1H, m, NC−CH_2−C*H*), 5.443 (1H, d, J

= 5.2 Hz, O*H*), 6.703 (1H, m, N*H*) ppm. ^{13}C NMR (75 MHz, DMSO-d_6, 300 K): δ = 22.47 (NC−*C*H$_2$), 28.19 (3 × *C*H$_3$), 39.69 (NH−*C*H$_2$), 65.25 (NC−CH$_2$−*C*H), 69.18 (NH−CH−*C*H$_2$), 69.50, 69.67, 69.75, 70.14 (4 × *C*H$_2$ glycol), 73.37 (NC−CH$_2$−CH−*C*H$_2$), 77.56 ((CH$_3$)$_3$*C*), 118.71 (N*C*), 155.54 (*C*O) ppm. ESI(+)-MS (*m/z*) Calcd: 332.4 [$C_{15}H_{28}N_2O_6$]. Found: 355.2 [M + Na]$^+$, 333.1 [M + H]$^+$, 350.2 [M + NH$_4$]$^+$. Anal. ($C_{15}H_{28}N_2O_6$) C, H, N.

3-Hydroxy-4-(2-{2-[2-(4-phenyl-1,2,3-triazol-1-yl)ethoxy]ethoxy}ethoxy)butyronitrile, 6. Linker **1** (500 mg, 1.94 mmol, 1.0 equiv) was dissolved in 10 mL of methylene chloride and 5 mL of methanol. To the resulting solution, first 31 mg of $CuSO_4$ (0.19 mmol, 0.1 equiv) and then 775 mg of sodium ascorbate (3.87 mmol, 2 equiv) were added, followed by the addition of 1.5 equiv of phenylacetylene (329 mg, 2.90 mmol). The mixture was stirred at room temperature. After 18 h, another 0.5 equiv of phenylacetylene (110 mg, 0.97 mmol) was added, and the mixture was stirred at room temperature for additional 24 h. The reaction mixture then was concentrated under reduced pressure, and the residue was dissolved again in 50 mL of methylene chloride. The solution of the crude product was washed two times with 25 mL of 5% EDTA solution. The organic layer was dried over Na_2SO_4, and the solvent was evaporated in vacuum. The crude product was purified by flash column chromatography (CH_2Cl_2/MeOH = 98:2 to CH_2Cl_2/MeOH = 95:5), yielding 670 mg (96%) of the product **6** as colorless oil. R_F = 0.40 (CH_2Cl_2/MeOH = 90:10). ^{1}H NMR (400 MHz, DMSO-d_6, 300 K): δ = 2.498 (1H, dd, J = 7.0 and 16.9 Hz, NC−C*H*$_2$), 2.619 (1H, dd, J = 4.3 and 16.9 Hz, NC−C*H*$_2$), 3.271 (1H, dd, J = 6.2 and 9.8 Hz, NC−CH$_2$−CH−C*H*$_2$), 3.371 (1H, dd, J = 5.5 and 9.8 Hz, NC−CH$_2$−CH−C*H*$_2$), 3.46−3.58 (8H, m, 4 × C*H*$_2$ glycol), 3.79−3.90 (3H, m, NC−CH$_2$−C*H*, triazole−CH$_2$−C*H*$_2$), 4.571 (2H, t, J = 5.1 Hz, triazole−C*H*$_2$), 5.449 (1H, d, J = 5.1 Hz, O*H*), 7.30−7.36 (1H, m, phenyl C*H*$_p$), 7.42−7.49 (2H, m, 2 × phenyl C*H*$_m$), 7.81−7.87 (2H, m, 2 × phenyl C*H*$_o$), 8.522 (1H, s, triazole C*H*) ppm. ^{13}C NMR (100 MHz, DMSO-d_6, 300 K): δ = 22.47 (NC−*C*H$_2$), 49.58 (triazole−*C*H$_2$), 65.19 (NC−CH$_2$−*C*H), 68.64 (triazole-CH$_2$−*C*H$_2$), 69.61, 70.07 (4 × *C*H$_2$ glycol), 73.33 (NC−CH$_2$−CH−*C*H$_2$), 118.79 (N*C*), 121.71 (triazole *C*H), 125.07 (2 × phenyl *C*H$_o$), 127.76 (phenyl *C*H$_p$), 128.86 (2 × phenyl *C*H$_m$), 130.82 (triazole quaternary *C*), 146.16 (phenyl quaternary *C*) ppm. ESI(+)-MS (*m/z*) Calcd: 360.4 [$C_{18}H_{24}N_4O_4$]. Found: 361.3 [M + H]$^+$. Anal. ($C_{18}H_{24}N_4O_4$) C, H, N.

3-Hydroxy-4-(2-{2-[2-(4-pyren-1-yl-1,2,3-triazol-1-yl)ethoxy]ethoxy}ethoxy)butyronitrile, 7. *Method a.* Linker **1** (110 mg, 0.43 mmol, 1.0 equiv) was dissolved in 2 mL of methylene chloride and 1 mL of methanol. To the resulting solution, first 7 mg of $CuSO_4$ (0.04 mmol, 0.1 equiv) and then 170 mg of sodium ascorbate (0.85 mmol, 2 equiv) were added. In a separate flask, 146 mg of 1-ethynylpyrene (0.64 mmol, 1.5 equiv) was dissolved in 4 mL of methylene chloride and 2 mL of methanol. The pyrene solution was added to the linker solution via a syringe, and the resulting mixture was stirred for 20 h at room temperature. Because the reaction seemed to be quite slow, it was heated to 40 °C for another 24 h. Afterward the solvents were removed under reduced pressure, and the residue was dissolved in 20 mL of methylene chloride. The solution of the crude product was washed two times with 10 mL of 5% EDTA solution. The organic layer was dried over Na_2SO_4, and the solvent was evaporated in vacuum. The crude product was purified by flash column chromatography (CH_2Cl_2/MeOH = 99:1 to CH_2Cl_2/MeOH = 98:2), yielding 85 mg (41%) of the product **7** as a yellow oil.

Method b. Linker **1** (100 mg, 0.38 mmol, 1.0 equiv), DIPEA (130 μL, 0.77 mmol, 2.0 equiv), and CuI (7.2 mg, 0.038 mmol, 0.1 equiv) were mixed and irradiated for 30 min at 250 W in the microwave. Afterward, the residue was dissolved in methylene chloride and washed two times with 10 mL of 5% EDTA solution. The organic layer was dried over Na_2SO_4, and the solvent was evaporated in vacuum. The crude product was purified by flash column chromatography (CH_2Cl_2/MeOH = 99:1 to CH_2Cl_2/MeOH = 98:2), yielding 110 mg (60%) of the product **7** as yellow oil. R_F = 0.22 (CH_2Cl_2/MeOH = 95:5). ^{1}H NMR (400 MHz, DMSO-d_6, 300 K): δ = 2.459 (1H, dd, J = 6.7 and 16.8 Hz, NC−C*H*$_2$), 2.575 (1H, dd, J = 4.3 and 16.9 Hz, NC−C*H*$_2$), 3.226 (1H, dd, J = 6.3 and 10.1 Hz, NC−CH$_2$−CH−C*H*$_2$), 3.30−3.35 (1H, m, NC−CH$_2$−CH−C*H*$_2$), 3.45−3.66 (8H, m, 4 × C*H*$_2$ glycol), 3.807 ("sextet", NC−CH$_2$−C*H*), 3.992 (2H, t, J = 4.9 Hz, triazole−CH$_2$−C*H*$_2$), 4.728 (2H, t, J = 5.1 Hz, triazole−C*H*$_2$), 5.437 (1H, d, J = 5.4 Hz, O*H*), 8.115 (1H, t, J = 7.9 Hz, pyrene C*H*), 8.20−8.45 (7H, m, 7 × pyrene C*H*), 8.742 (1H, s, triazole C*H*), 8.884 (1H, d, J = 9.5 Hz, pyrene C*H*) ppm. ^{13}C-NMR (100 MHz, DMSO-d_6, 300 K): δ = 22.43 (NC−*C*H$_2$), 49.67 (triazole−*C*H$_2$), 65.17 (NC−CH$_2$−*C*H), 68.68 (triazole−CH$_2$−*C*H$_2$), 69.63, 69.64, 69.68, 70.06 (4 × *C*H$_2$ glycol), 73.32 (NC−CH$_2$−CH−*C*H$_2$), 118.77 (N*C*), 124.83, 124.87 (triazole *C*H, pyrene *C*H), 125.12, 125.15, 125.52, 126.46, 126.98, 127.33 127.64, 127.96 (8 × pyrene *C*H), 123.93, 1242.31, 125.46, 127.46, 130.36, 130.52, 130.94, 145.98 (triazole quaternary *C*, 7 × pyrene quaternary *C*) ppm. ESI(+)-MS (*m/z*) Calcd: 484.5 [$C_{28}H_{28}N_4O_4$]. Found: 485.5 [M + H]$^+$, 507.6 [M + Na]$^+$. HR-ESI(−)-MS (*m/z*) Calcd: 483.2038 [$C_{28}H_{27}N_4O_4$]$^-$. Found: 483.2043. Fluorescence: excitation 352 nm, emission 390 nm, 408 nm.

Carbonic Acid 1-{2-[2-(2-Azidoethoxy)ethoxy]ethoxymethyl}-2-cyanoethylester 2,5-dioxo-pyrrolidin-1-yl ester, 10. Compound **1** (750 mg, 2.90 mmol, 1.0 equiv) was dissolved in 25 mL of dry ACN and cooled to 0 °C. Then 223 mg of anhydrous K_2CO_3 (1.60 mmol, 0.55 equiv) was added, and the suspension was stirred at 0 °C for 1 h before 1.96 g of di(*N*-succinimidyl)-carbonate (7.26 mmol, 2.5 equiv) was added and the mixture was stirred for another 20 h at 0 °C. The solvent was removed in vacuum, and the residue was divided between 50 mL of ethyl acetate and 50 mL of saturated $NaHCO_3$ solution. The water phase was additionally extracted with 50 mL of ethyl acetate and 50 mL of methylene chloride. The combined organic layers were dried over Na_2SO_4 and concentrated under reduced pressure. The crude product was obtained as yellow oil **10** (1.15 g, 99%) and used without further purification. R_F = 0.35 (CH_2Cl_2/MeOH = 99:1). ^{1}H NMR (400 MHz, $CDCl_3$, 300 K): δ = 2.853 (4H, s, 2 × succinimidyl C*H*$_2$), 2.902 (1H, dd, J = 5.4 and 17.1 Hz, NC−C*H*$_2$), 2.968 (1H, dd, J = 6.0 and 17.0 Hz, NC−C*H*$_2$), 3.38−3.42 (2H, m, N$_3$−C*H*$_2$), 3.65−3.74 (10H, m, 5 × C*H*$_2$ glycol), 3.805 (1H, dd, J = 5.3 and 11.0 Hz, NC−CH$_2$−CH−CH$_2$−O), 3.851 (1H, dd, J = 4.7 and 11.0 Hz, NC−CH$_2$−CH−CH$_2$−O), 5.100 (1H, "quintet", NC−CH$_2$−C*H*) ppm. ^{13}C-NMR (100 MHz, DMSO-d_6, 300 K): δ = 19.77 (NC−*C*H$_2$), 25.50 (succinimidyl *C*H$_2$), 50.74 (N$_3$−*C*H$_2$), 69.36, 70.09, 70.62, 70.73, 70.74, 71.35 (NC−CH$_2$−CH−*C*H$_2$, 5 × *C*H$_2$ glycol), 74.91 (NC−CH$_2$−*C*H), 115.23 (N*C*), 150.86 (carbonate *C*O), 168.28 (succinimidyl *C*O) ppm. ESI(+)-MS (*m/z*) Calcd: 399.4 [$C_{15}H_{21}N_5O_8$]. Found: 417.00 [M + NH$_4$]$^+$, 422.00 [M + Na]$^+$, 372.00 [M − N$_2$+H]$^+$.

Carbonic Acid 1-{2-[2-(2-*tert*-Butoxycarbonylaminoethoxy)-ethoxy]ethoxymethyl}-2-cyano-ethylester 2,5-Dioxopyrrolidin-1-yl Ester, 11. Alcohol **5** (5.27 g, 15.86 mmol, 1.0 equiv) was dissolved in 150 mL of dry ACN and cooled to 0 °C. Anhydrous K_2CO_3 (1.11 g, 7.93 mmol, 0.5 equiv) was added, and the mixture was left at 0 °C for 2 h. Then 10.69 g of di(*N*-succinimidyl)carbonate (39.64 mmol, 2.5 equiv) was added, and stirring at 0 °C was continued for 24 h. The solvent was

evaporated, and the residue was divided between 75 mL of water and 75 mL of ethyl acetate. The aqueous layer was extracted two times with 50 mL of methylene chloride. The combined organic layers were dried over Na_2SO_4 and concentrated under reduced pressure. To the solid residue, first 30 mL of methylene chloride was added and the insoluble parts were filtered off, followed by the addition of 60 mL of ether. The resulting suspension was stored at 4 °C for 2 h and filtered again. The filtrate was concentrated in vacuum to give 6.73 g (90%) of the activated linker **11** as yellow oil. It was used as obtained, without further purification. $R_F = 0.03$ (CH_2Cl_2/MeOH/NH_3 = 90:10:1). ^{1}H NMR (400 MHz, DMSO-d_6, 300 K): δ = 1.372 (9H, s, 3 × CH_3), 2.817 (4H, s, 2 × succinimidyl CH_2), 3.01−3.11 (4H, m, NC−CH_2, NH−CH_2), 3.374 (2H, t, J = 6.1 Hz, NH−CH_2−CH_2), 3.47−3.61 (8H, m, 4 × CH_2 glycol), 3.654 (1H, dd, J = 6.4 and 11.7 Hz, NC−CH$_2$−CH−CH_2), 3.701 (1H, dd, J = 3.8 and 11.6 Hz, NC−CH$_2$−CH−CH_2), 5.16−5.23 (1H, m, NC−CH$_2$−CH), 6.68−6.77 (1H, m, NH) ppm. ^{13}C NMR (100 MHz, DMSO-d_6, 300 K): δ = 19.12 (NC−CH$_2$), 25.34 (succinimidyl CH$_2$), 28.19 (3 × CH$_3$), 39.65 (NH−CH$_2$), 69.21 (NH−CH$_2$−CH$_2$), 69.45, 69.57, 69.68, 69.74, 70.27 (5 × CH$_2$ glycol), 75.57 (NC−CH$_2$−CH), 77.55 ((CH$_3$)$_3C$), 116.79 (NC), 150.63 (carbonate CO), 155.54 (carbamate CO), 169.61 (succinimidyl CO) ppm. ESI(+)-MS (*m/z*) Calcd: 473.5 [$C_{20}H_{31}N_3O_{10}$]. Found: 491.0 [M + NH_4]$^+$, 496.2 [M + Na]$^+$, 474.1 [M]$^+$.

Prop-2-ynylcarbamic Acid 1-{2-[2-(2-Azidoethoxy)ethoxy]-ethoxymethyl}-2-cyanoethyl Ester, 8. Compound **1** (130 mg, 0.5 mmol, 1.0 equiv) was dissolved in 10 mL of dry ACN, and the solution was cooled to 0 °C before 70 mg of anhydrous K_2CO_3 (0.5 mmol, 1.0 equiv) was added and the suspension was stirred at 0 °C for 2 h. Afterward 190 mg of di(*N*-succinimidyl)carbonate (0.7 mmol, 1.4 equiv) was added together with another 5 mL of dry ACN. The suspension was stirred at 0 °C for 20 h. After the activation process, 100 mg of $NaHCO_3$ (1.0 mmol, 2.0 equiv) and 72 μL of propargylamine (1.1 mmol, 2.2 equiv) were added. The mixture was stirred at 0 °C for 1 h and at room temperature for 2 h. The solvent was removed under reduced pressure, and the residue was divided between 20 mL of saturated $NaHCO_3$ solution and 20 mL of methylene chloride. The organic layer was washed with 20 mL of saturated $NaHCO_3$ solution and 20 mL of saturated NH_4Cl solution. The combined aqueous layers were extracted two times with 20 mL of methylene chloride, and the combined organic layers were then dried over Na_2SO_4. The solvent was removed under reduced pressure, and the crude product was purified by flash column chromatography (*n*-hexane + 1% $EtMe_2N$ to *n*-hexane/ethyl acetate = 1:1 + 1% $EtMe_2N$). Compound **8** was obtained as slightly yellowish oil (129 mg, 76%). $R_F = 0.27$ (*n*-hexane/ethyl acetate = 1:2). ^{1}H NMR (400 MHz, DMSO-d_6, 300 K): δ = 2.832 (1H, dd, J = 6.3 and 17.2 Hz, NC−CH_2), 2.900 (1H, dd, J = 4.8 and 17.2 Hz, NC−CH_2), 3.120 (1H, t, J = 2.4 Hz, alkyne CH), 3.390 (2H, t, J = 5.2 Hz, N$_3$−CH_2), 3.50−3.62 (12H, m, NC−CH$_2$−CH−CH_2, 5 × CH_2 glycol), 3.782 (2H, dd, J = 2.4 and 5.8 Hz, NH−CH_2), 4.947 (1H, "quintet", NC−CH$_2$−CH), 7.891 (1H, t, J = 5.7 Hz, NH) ppm. ^{13}C-NMR (100 MHz, DMSO-d_6, 300 K): δ = 19.72 (NC−CH$_2$), 29.82 (NH−CH$_2$), 50.00 (N$_3$−CH$_2$), 67.89 (NC−CH$_2$−CH), 69.26, 69.67, 69.69, 69.83, 70.20, 70.32 (NC−CH$_2$−CH−CH$_2$, 5 × CH$_2$ glycol), 73.17 (alkyne CCH), 81.08 (alkyne CCH), 117.70 (NC), 154.88 (carbamate CO) ppm. FT-IR (NaCl): ν = 3297 (s br., >N−H, ≡C−H), 2900 (s br., >CH$_2$), 2252 (m, −C≡N), 2108 (s, −N$_3$), 1730 (s, −C═O) cm^{-1}. ESI(+)-MS (*m/z*) Calcd: 339.3 [$C_{14}H_{21}N_5O_5$]. Found: 362.0 [M + Na]$^+$, 357.0 [M + NH_4]$^+$, 340.0 [M]$^+$, 679.3 [2M]$^+$. Anal. ($C_{14}H_{21}N_5O_5$) C, H, N.

(3-Phenylprop-2-ynyl)carbamic Acid 1-{2-[2-(2-Azidoethoxy-ethoxy]ethoxymethyl}-2-cyanoethyl Ester, 9. Iodobenzene (300 mg, 1.44 mmol, 1.00 equiv) was dissolved in 7 mL of dry methylene chloride and degassed three times using the freeze−pump−thaw technique. Then 28 mg of CuI (0.14 mmol, 0.10 equiv) and 84 mg of $Pd(PPh_3)_4$ (0.07 mmol, 0.05 equiv) were added to the shaded flask. The alkyne **8** (572 mg, 11.69 mmol, 1.17 equiv) was added dropwise in two portions; one-half was added immediately and the other half after 1 h stirring at room temperature. After another 2 h stirring at room temperature, the reaction mixture was diluted by adding 20 mL of methylene chloride and washed two times with 50 mL of 5% EDTA solution and one time with 50 mL of saturated $NaHCO_3$ solution. The organic layer was dried over Na_2SO_4, filtered and the solvent was removed in vacuum. The crude product was purified by flash column chromatography (*n*-hexane + 1% $EtMe_2N$ to *n*-hexane/ethyl acetate = 1:1 + 1% $EtMe_2N$). Compound **9** was obtained as yellow oil (549 mg, 92%). R_F = 0.18 (*n*-hexane/ethyl acetate/$EtMe_2N$ = 1:1:0.02). ^{1}H NMR (300 MHz, DMSO-d_6, 300 K): δ = 2.80−2.96 (2H, m, NC−CH_2), 3.379 (2H, "t", N$_3$−CH_2), 3.51−3.62 (12H, m, NC−CH$_2$−CH−CH_2, 5 × CH_2 glycol), 4.064 (2H, d, J = 5.8 Hz, NH−CH_2), 4.988 (1H, "quintet", NC−CH$_2$−CH), 7.34−7.44 (5H, m, 5 × phenyl CH), 7.964 (1H, t, J = 5.7 Hz, NH) ppm. ^{13}C NMR (75 MHz, DMSO-d_6, 300 K): δ = 19.70 (NC−CH$_2$), 30.57 (NH−CH$_2$), 49.98 (N$_3$−CH$_2$), 67.88 (NC−CH$_2$−CH), 69.21, 69.65, 69.66, 69.79, 70.19, 70.33 (NC−CH$_2$−CH−CH$_2$, 5 × CH$_2$ glycol), 81.79 (alkyne CC−CH$_2$), 86.89 (alkyne CC−CH$_2$), 117.70 (NC), 122.22 (phenyl quaternary C), 128.47, 128.57, 131.28 (5 × phenyl CH), 154.90 (carbamate CO) ppm. FT-IR (NaCl): ν = 3332 (s br., >N−H), 3056 (m, C−H arom.), 2872 (s br., >CH$_2$), 2251 (m, −C≡N, −C≡C−), 2108 (s, −N$_3$), 1730 (s, −C═O) cm^{-1}. MALDI(+)-MS (*m/z*) Calcd: 415.44 [$C_{20}H_{25}N_5O_5$]. Found: 439.83 [M + Na + H]$^+$. Anal. ($C_{20}H_{25}N_5O_5$) C, H, N.

(*E*/*Z*)-4-{2-[2-(2-Azidoethoxy)ethoxy]ethoxy}but-2-enenitrile, 13. Model compound **9** (440 mg, 1.06 mmol, 1.0 equiv) was dissolved in 5 mL of dry THF, and 4.71 g of 1 M TBAF in THF (5 equiv) was added. The solution was stirred at room temperature for 10 min; then the solvents were evaporated in vacuum, and the residue was purified by flash column chromatography using a gradient from *n*-hexane/ethyl acetate = 3:1 to CH_2Cl_2/MeOH = 90:10 + 1% $EtMe_2N$. The elimination product **13** was obtained in quantitative yield (258 mg) in a 1:1 ratio of *E* and *Z* product (determined by ^{1}H NMR). Also cleavage product **12** was isolated in quantitative yield (145 mg); the analytical data for **12** correspond to literature values (*16*). R_F = 0.35 (CH_2Cl_2/MeOH = 99:1). ^{1}H NMR (300 MHz, $CDCl_3$, 300 K): δ = 3.395 (4H, t, J = 5.0 Hz, N$_3$−C$H_{2,E}$, N$_3$−C$H_{2,Z}$), 3.63−3.72 (20H, m, 5 × C$H_{2,E}$ glycol, 5 × C$H_{2,Z}$ glycol), 4.191 (2H, dd, J = 2.4 and 3.8 Hz, NC−CH═CH−C$H_{2,E}$), 4.373 (2H, dd, J = 1.7 and 6.0 Hz, NC−CH═CH−C$H_{2,Z}$), 5.461 (1H, dt, J = 1.7 and 11.3 Hz, NC−CH═CH_Z), 5.735 (1H, dt, J = 2.3 and 16.3 Hz, NC−CH═CH_E), 6.617 (1H, dt, J = 6.0 and 12.0 Hz, NC−CH_Z), 6.737 (1H, dt, J = 3.7 and 16.3 Hz, NC−CH_E) ppm. ^{13}C NMR (75 MHz, $CDCl_3$, 300 K): δ = 50.73 (N$_3$−CH$_{2,E/Z}$), 69.33, 69.58, 70.09, 70.13, 70.49, 70.59, 70.64, 70.71, 70.74, 70.76, 70.78 (2C) (NC−CH═CH−CH$_{2,E}$, NC−CH═CH−CH$_{2,Z}$, 5 × CH$_{2,E}$ glycol, 5 × CH$_{2,Z}$ glycol), 99.75 (NC−CH═CH$_E$), 100.60 (NC−CH═CH$_Z$), 115.15 (NC_Z), 117.31 (NC_E), 150.77 (NC−CH$_Z$), 150.87 (NC−CH$_E$) ppm. ESI(+)-MS (*m/z*) Calcd: 240.3 [$C_{10}H_{16}N_4O_3$]. Found: 258.0 [M + NH_4]$^+$, 262.9 [M + Na]$^+$, 240.9 [M + H]$^+$. Anal. ($C_{10}H_{16}N_4O_3$) C, H, N.

***N*^{3}-Benzoyl-5-iodo-5′-*O*-benzoyl-2′-deoxyuridine, 15.** To a solution of 1.5 g of compound **14** (3.27 mmol, 1.0 equiv) in 15 mL of dry pyridine were added dropwise 1.68 mL of DIPEA (9.82 mmol, 3.0 equiv) and 0.63 mL of TMSCl (4.91 mmol,

1.5 equiv). The reaction mixture was stirred 45 min at room temperature before 0.84 mL of benzoyl chloride (4.91 mmol, 1.5 equiv) was added. The red solution was stirred for another 15 min at room temperature and then poured into 100 mL of ice water and stirred for 10 min, and the organic layer was extracted two times with 40 mL of chloroform, dried over Na_2SO_4, and evaporated to dryness. The crude brown oil was dissolved in 60 mL of $CHCl_3$/MeOH = 1:1, and 75 μL portions of TFA were added every 20 min until the TMS group was cleaved quantitatively (TLC control). TFA (375 μL, 4.89 mmol, 1.5 equiv) was added within 2 h. The reaction mixture was diluted with 30 mL of chloroform and washed two times with 50 mL of 5% $NaHCO_3$ solution. The water phase was extracted three times with 30 mL of chloroform; the combined organic layers were dried over Na_2SO_4 and concentrated in vacuum. The crude product was filtered through silica gel and eluted with a gradient from pure CH_2Cl_2 to CH_2Cl_2/MeOH = 95:5. The product **15** was obtained as yellow foam (1.85 g, 98%). R_F = 0.43 (CH_2Cl_2/MeOH = 95:5). ^{1}H NMR (400 MHz, DMSO-d_6, 300 K): δ = 2.271 (1H, ddd, J = 3.7, 6.5, and 13.9 Hz, 2′-CH_2), 2.39−2.47 (1H, m, 2′-CH_2), 4.14−4.18 (1H, m, 4′-C*H*), 4.37−4.42 (1H, m, 3′-C*H*), 4.493 (1H, dd, J = 5.8 and 12.1 Hz, 5′-CH_2), 4.558 (1H, dd, J = 3.6 and 12.1 Hz, 5′-CH_2), 5.487 (1H, d, J = 4.4 Hz, 3′-O*H*), 6.114 (1H, t, J = 6.5 Hz, 1′-C*H*), 7.54−7.62 (4H, m, 2 × 5′-*O*-benzoyl CH_m, 2 × N^3-benzoyl CH_m), 7.67−7.72 (1H, m, N^3-benzoyl CH_p), 7.77−7.81 (1H, m, 5′-*O*-benzoyl CH_p), 8.01−8.05 (4H, m, 2 × 5′-*O*-benzoyl CH_o, 2 × N^3-benzoyl CH_o), 8.202 (1H, s, 6-C*H*) ppm. ^{13}C NMR (100 MHz, DMSO-d_6, 300 K): δ = 39.36 (2′-*C*H$_2$), 64.31 (5′-*C*H$_2$), 68.54 (5-*C*I), 70.04 (3′-*C*H), 84.43 (4′-*C*H), 86.06 (1′-*C*H), 128.88, 129.26, 129.45, 130.56 (5′-*O*-benzoyl *C*H$_o$, 5′-*O*-benzoyl *C*H$_m$, N^3-benzoyl *C*H$_o$, N^3-benzoyl *C*H$_m$), 130.64 (5′-*O*-benzoyl quaternary *C*, N^3-benzoyl quaternary *C*), 133.53 (N^3-benzoyl *C*H$_p$), 135.65 (5′-*O*-benzoyl *C*H$_p$), 145.28 (6-*C*H), 148.66 (2-*C*O), 159.18 (4-*C*O), 165.61 (N^3-benzoyl *C*O), 168.67 (5′-*O*-benzoyl *C*O) ppm. ESI(+)-MS (*m*/*z*) Calcd: 562.3 [$C_{23}H_{19}IN_2O_7$]. Found: 579.8 [M + NH_4]$^+$, 584.6 [M + Na]$^+$, 563.2 [M + H]$^+$, 601.1 [M + K]$^+$. Anal. ($C_{23}H_{19}IN_2O_7$) C, H, N.

5-Iodo-3′-*O*-(2-cyanoethyl)-2′-deoxyuridine, 16. Compound **15** (1.70 g, 3.02 mmol, 1.0 equiv) was dissolved in 4.5 mL of freshly distilled acrylonitrile (68.02 mmol, 22.5 equiv) in a dry 100 mL Erlenmeyer flask, equipped with a big triangle stirring bar and a septum connected to an argon line. The solution was stirred vigorously for 2 min before 9 mL of *t*-BuOH was added, and stirring continued for another 5 min; 990 mg of Cs_2CO_3 (3.02 mmol, 1.0 equiv) was added quickly, and the resulting suspension was stirred vigorously for 2.5 h. The reaction solution was separated from solid components by filtration over silica gel (CH_2Cl_2/MeOH = 95:5) and concentrated in vacuum. Because the purification of compound **16** is difficult because of loss of protecting groups on the column, only a small amount was purified by flash column chromatography for analysis of the fully protected compound N^3-benzoyl-5-iodo-3′-*O*-(2-cyanoethyl)-5′-*O*-benzoyl-2′-deoxyuridine (CH_2Cl_2/MeOH = 99.6:0.4 to CH_2Cl_2/MeOH = 99:1). The rest of the crude product (1.78 g) was directly used for the subsequent deprotection with ammonia. R_F = 0.27 (*n*-hexane/ethyl acetate/$EtMe_2N$ = 1:2:0.03). ^{1}H NMR (400 MHz, DMSO-d_6, 300 K): δ = 2.428 (1H, ddd, J = 2.6, 6.1, and 14.0 Hz, 2′-CH_2), 2.47−2.55 (1H, m, 2′-CH_2), 2.793 (2H, t, J = 6.0 Hz, NC−CH_2), 3.695 (2H, t, J = 6.0 Hz, NC−CH$_2$−CH_2), 4.33−4.38 (2H, m, 3′-C*H*, 4′-C*H*), 4.518 (1H, dd, J = 5.2 and 12.0 Hz, 5′-CH_2), 4.578 (1H, dd, J = 3.6 and 12.0 Hz, 5′-CH_2), 6.090 (1H, t, J = 6.8 Hz, 1′-C*H*), 7.54−7.62 (4H, m, 2 × 5′-*O*-benzoyl CH_m, 2 × N^3-benzoyl CH_m), 7.67−7.72 (1H, m, N^3-benzoyl CH_p), 7.76−7.82 (1H, m, 5′-*O*-benzoyl CH_p), 8.01−8.05 (4H, m, 2 × 5′-*O*-benzoyl CH_o, 2 × N^3-benzoyl CH_o), 8.219 (1H, s, 6-C*H*) ppm. ^{13}C NMR (100 MHz, DMSO-d_6, 300 K): δ = 18.19 (NC−*C*H$_2$), 36.66 (2′-*C*H$_2$), 63.77 (NC−CH$_2$−*C*H$_2$), 64.45 (5′-*C*H$_2$), 68.69 (5-*C*I), 78.68 (3′-*C*H), 81.97 (4′-*C*H), 86.13 (1′-*C*H), 119.56 (N*C*), 128.88, 129.28, 129.45, 130.56 (5′-*O*-benzoyl *C*H$_o$, 5′-*O*-benzoyl *C*H$_m$, N^3-benzoyl *C*H$_o$, N^3-benzoyl *C*H$_m$), 130.62 (5′-*O*-benzoyl quaternary *C*, N^3-benzoyl quaternary *C*), 133.56 (N^3-benzoyl *C*H$_p$), 135.67 (5′-*O*-benzoyl *C*H$_p$), 145.22 (6-*C*H), 148.66 (2-*C*O), 159.15 (4-*C*O), 165.56 (N^3-benzoyl *C*O), 168.61 (5′-*O*-benzoyl *C*O) ppm. ESI(+)-MS (*m*/*z*) Calcd: 615.4 [$C_{26}H_{22}IN_3O_7$]. Found: 633.2 [M + NH_4]$^+$, 616.1 [M + H]$^+$, 638.1 [M + Na]$^+$. Anal. ($C_{26}H_{22}IN_3O_7$) C, H, N.

The crude benzoyl-protected product N^3-benzoyl-5-iodo-3′-*O*-(2-cyanoethyl)-5′-*O*-benzoyl-2′-deoxyuridine (1.78 g) was dissolved in 150 mL of methanol, and 30 mL of concentrated (25%) aqueous ammonia was added. The mixture was left stirring for 20 h at room temperature, evaporated, and purified by flash column chromatography using a gradient from CH_2Cl_2 to CH_2Cl_2/MeOH = 98:2. 3′-Modified nucleoside **16** was obtained as colorless foam (765 mg, 65%, over two steps). R_F = 0.4 (CH_2Cl_2/MeOH = 90:10). ^{1}H NMR (400 MHz, DMSO-d_6, 300 K): δ = 2.18−2.30 (2H, m, 2′-CH_2), 2.773 (2H, t, J = 6.1 Hz, NC−CH_2), 3.634 (2H, t, J = 6.1 Hz, CN−CH$_2$−CH_2), 3.55−3.68 (2H, m, 5′-CH_2), 3.94−3.98 (1H, m, 4′-C*H*), 4.12−4.17 (1H, m, 3′-C*H*), 5.19−5.25 (1H, m, 5′-O*H*), 6.061 (1H, "t", 1′-C*H*), 8.359 (1H, s, 6-C*H*), 11.680 (1H, s, N^3*H*) ppm. ^{13}C-NMR (100 MHz, DMSO-d_6, 300 K): δ = 18.25 (NC−*C*H$_2$), 37.05 (2′-*C*H$_2$), 61.06 (5′-*C*H$_2$), 63.56 (NC−CH$_2$−*C*H$_2$), 69.51 (5-*C*I), 78.99 (3′-*C*H), 84.80 (1′-*C*H), 84.82 (4′-*C*H), 119.17 (N*C*), 144.88 (6-*C*H), 150.09 (2-*C*O), 160.44 (4-*C*O) ppm. ESI(−)-MS (*m*/*z*) Calcd: 407.2 [$C_{12}H_{14}IN_3O_5$]. Found: 406.1 [M − 1]$^-$. Anal. ($C_{12}H_{14}IN_3O_5$) C, H, N.

5-(3-Aminoprop-1-ynyl)-3′-*O*-(2-cyanoethyl)-2′-deoxyuridine, 17. Compound **16** (500 mg, 1.23 mmol, 1.0 equiv) was dissolved in 15 mL of dry DMF, and 855 μL of triethylamine (6.14 mmol, 5.0 equiv) was added. The solution was degassed three times by using the freeze−pump−thaw technique. After the solution warmed up, 48 mg of CuI (0.25 mmol, 0.2 equiv) and 143 mg of $Pd(PPh_3)_4$ (0.12 mmol, 0.1 equiv) were added. 2,2,2-Trifluor-*N*-(prop-2-ynyl)acetamid (371 mg, 2.46 mmol, 2.0 equiv) was added in two portions; one-half was injected directly, and the other half was added after stirring at room temperature for 1 h. The resulting mixture was stirred at room temperature in a shaded flask. After 5 h, the solvent was removed under reduced pressure, and the residue was dissolved in 25 mL of methylene chloride and washed two times with 25 mL of 5% EDTA solution. The organic layer was dried over Na_2SO_4 and filtered, and the solvent was removed in vacuum. The crude product, 5-[(2,2,2-trifluoro-acetylamino)-ethynyl]-3′-*O*-(2-cyanoethyl)2′-deoxyuridine, was filtered over silica gel (CH_2Cl_2/MeOH = 98:2), and 344 mg (65%) of the target compound was obtained as a yellow oil. R_F = 0.21 (CH_2Cl_2/MeOH = 90:10). ^{1}H NMR (250 MHz, DMSO-d_6, 300 K): δ = 2.15−2.34 (2H, m, 2′-CH_2), 2.777 (2H, t, J = 5.9 Hz, NC−CH_2), 3.52−3.68 (2H, m, 5′-CH_2), 3.632 (2H, t, J = 6.0 Hz, NC−CH$_2$−CH_2), 3.91−3.99 (1H, m, 4′-C*H*), 4.11−4.17 (1H, m, 3′-C*H*), 4.234 (1H, d, J = 5.5 Hz, NH−CH_2), 5.177 (1H, t, J = 5.0 Hz, 5′-O*H*), 6.068 (1H, t, J = 6.5 Hz, 1′-C*H*), 8.182 (1H, s, 6-C*H*), 10.067 (1H, t, J = 5.3 Hz, N*H*), 11.676 (1H, s, N^3*H*) ppm. ^{13}C NMR (63 MHz, DMSO-d_6, 300 K): δ = 18.22 (NC−*C*H$_2$), 29.42 (NH−*C*H$_2$), 36.93 (2′-*C*H$_2$), 61.08 (5′-*C*H$_2$), 63.54 (NC−CH$_2$−*C*H$_2$), 75.29 (alkyne *C*C−CH$_2$), 79.01 (3′-*C*H), 84.70 (1′-*C*H), 84.90 (4′-*C*H), 87.53 (alkyne C*C*−CH$_2$), 97.80 (5-C), 119.13 (N*C*), 144.00 (6-*C*H), 149.27 (2-*C*O), 161.47 (4-*C*O) ppm, the trifluoroacetate signals are not visible due to their low intensity (quartet structure). ESI(+)-MS (*m*/*z*) Calcd: 430.3 [$C_{17}H_{17}F_3N_4O_6$]. Found: 430.9 [M + H]$^+$.

5-[(2,2,2-Trifluoroacetylamino)ethynyl]-3′-*O*-(2-cyanoethyl)2′-*d*eoxyuridine (300 mg, 0.70 mmol, 1.0 equiv) was dissolved in 40 mL of methanol, and 8.5 mL of concentrated (25%) aqueous ammonia solution was added. The resulting mixture was stirred at room temperature for 12 h. Then the solvent was removed under reduced pressure, and 230 mg (99%) of compound **17** was obtained. The crude product was used without further purification. $R_F = 0.03$ (CH_2Cl_2/MeOH = 90:10). ^{1}H NMR (400 MHz, DMSO-d_6, 300 K): $\delta = 2.15-2.24$ (1H, m, 2′-CH_2), 2.278 (1H, ddd, $J = 2.7$, 8.7, and 13.6 Hz, 2′-CH_2), 2.776 (2H, t, $J = 5.8$ Hz, NC−CH_2), 3.547 (2H, s, NH_2−CH_2), 3.59−3.66 (4H, m, 5′-CH_2, NC−CH_2−CH_2), 3.94−3.99 (1H, m, 4′-CH), 4.13−4.18 (1H, m, 3′-CH), 5.04−6.50 (4H, br. s, 5′-OH, N^3H, NH_2), 6.079 (1H, dd, $J = 6.3$ and 7.5 Hz, 1′-CH), 8.153 (1H, s, 6-CH) ppm. ^{13}C NMR (100 MHz, DMSO-d_6, 300 K): $\delta =$ 18.22 (NC−*C*H_2), 30.63 (NH_2−*C*H_2), 37.02 (2′-*C*H_2), 61.13 (5′-*C*H_2), 63.52 (NC−CH_2−*C*H_2), 74.76 (alkyne *C*C−CH_2), 79.10 (3′-*C*H), 84.66 (1′-*C*H), 84.89 (4′-*C*H), 92.88 (alkyne C*C*−CH_2), 98.29 (5-C), 119.15 (N*C*), 143.43 (6-*C*H), 149.39 (2-*C*O), 161.50 (4-*C*O) ppm. HR-ESI(−)-MS (*m*/*z*) Calcd: 333.1204 [$C_{15}H_{17}N_4O_5$]$^-$. Found: 333.1204.

5-(Prop-2-ynyl)carbamic Acid 1-{2-[2-(2-Azidoethoxy)-ethoxy]ethoxymethyl}-2-cyanoethyl ester]-3′-*O*-(2-cyanoethyl)-2′-desoxyuridine, 18. Activated linker **10** (806 mg, 2.02 mmol, 2.5 equiv) was dissolved in 4.5 mL of dry ACN and cooled to 0 °C. After cooling, 162 mg of $KHCO_3$ (1.62 mmol, 2.0 equiv) was added. In a separate flask, 270 mg of compound **17** (0.81 mmol, 1.0 equiv) was dissolved in another 4 mL of dry ACN and added via a syringe dropwise to the solution of compound **10**. The resulting mixture was stirred at 0 °C for 30 min and at room temperature for 3.5 h. The solvent then was removed under reduced pressure, and the residue was divided between 25 mL of saturated NH_4Cl solution and 25 mL of methylene chloride. The organic layer was washed with 20 mL of saturated NaCl solution, and the combined aqueous layers were extracted two times with 30 mL of methylene chloride. The combined organic layers were dried over Na_2SO_4 and filtered, and the solvent was removed in vacuum. The crude product **18** was purified by flash column chromatography using a gradient from CH_2Cl_2/MeOH = 98:2 to CH_2Cl_2/MeOH = 95:5, yielding 328 mg (66%) of compound **18** as a yellow oil. $R_F = 0.39$ (CH_2Cl_2/MeOH = 90:10). ^{1}H NMR (400 MHz, DMSO-d_6, 300 K): $\delta = 2.17-2.31$ (2H, m, 2′-CH_2), 2.773 (2H, t, $J = 6.1$ Hz, nucleoside NC−CH_2), 2.839 (1H, dd, $J = 6.3$ and 17.3 Hz, linker NC−CH_2), 2.878 (1H, dd, $J = 5.0$ and 17.2 Hz, linker NC−CH_2), 3.387 (2H, t, $J = 5.0$ Hz, N_3−CH_2), 3.51−3.65 (16 H, m, 5′-CH_2, nucleoside NC−CH_2−CH_2, linker NC−CH_2−CH−CH_2, 5 × CH_2 glycol), 3.93−3.97 (1H, m, 4′-CH), 4.022 (2H, d, $J = 5.6$ Hz, NH−CH_2), 4.12−4.16 (1H, m, 3′-CH), 4.954 (1H, "quintet", linker NC−CH_2−CH), 5.169 (1H, t, $J = 5.0$ Hz, 5′-OH), 6.071 (1H, "t", 1′-CH), 7.934 (1H, t, $J = 5.5$ Hz, NH), 8.139 (1H, s, 6-CH), 11.642 (1H, s, N^3H) ppm. ^{13}C NMR (100 MHz, DMSO-d_6, 300 K): $\delta = 18.25$ (nucleoside NC−*C*H_2), 19.73 (linker NC−*C*H_2), 30.69 (NH−*C*H_2), 36.90 (2′-*C*H_2), 50.00 (N_3-*C*H_2), 61.14 (5′-*C*H_2), 63.55 (nucleoside NC−CH_2−*C*H_2), 67.91 (linker NC−CH_2−*C*H), 69.25, 69.66, 69.68, 69.82, 70.21 (5 × *C*H_2 glycol), 70.30 (linker NC−CH_2−CH−*C*H_2), 74.49 (alkyne *C*C−CH_2), 79.09 (3′-*C*H), 84.62 (1′-*C*H), 84.88 (4′-*C*H), 89.61 (alkyne C*C*−CH_2), 98.23 (5-C), 117.71 (linker N*C*), 119.17 (nucleoside N*C*), 143.60 (6-*C*H), 149.42 (2-*C*O), 154.88 (carbamate *C*O), 161.53 (4-*C*O) ppm. FT-IR (NaCl): $\nu = 3650-3120$ (m br., −O−H, >N−H), 3056 (m br., C−H arom.), 2874 (m br., >CH_2), 2252 (m, −C≡N, −C≡C−), 2103 (s, $-N_3$), 1780−1630 (m br., −C═O) cm^{-1}. ESI(+)-MS (*m*/*z*) Calcd: 618.6 [$C_{26}H_{34}N_8O_{10}$]. Found: 636.4 [M + NH_4]$^+$, 641.5 [M + Na]$^+$, 619.5 [M]$^+$. Anal. ($C_{26}H_{34}N_8O_{10}$) C, H, N.

5-(Prop-2-ynyl)carbamic Acid 1-{2-[2-(2-*tert*-Butoxycarbo-nylaminoethoxy)ethoxy]ethoxymethyl}-2-cyanoethyl Ester 3′-*O*-(2-Cyanoethyl)-2′-desoxyuridine, 19. Activated linker **11** (2.24 g, 4.74 mmol, 2.2 equiv) was dissolved in 15 mL of dry ACN and cooled to 0 °C. After cooling, 433 mg of $KHCO_3$ (4.31 mmol, 2.0 equiv) was added. In a separate flask, 1.0 g of compound **17** (2.15 mmol, 1.0 equiv) was dissolved in another 10 mL of dry ACN and added via a syringe dropwise to the solution of compound **11**. The resulting mixture was stirred at 0 °C for 1 h and at room temperature for 3.5 h. The solvent then was removed under reduced pressure, and the residue was divided between 75 mL of water and 100 mL of methylene chloride. The aqueous layer was extracted two times with 75 mL of methylene chloride. The combined organic layers were dried over Na_2SO_4 and filtered, and the solvent was removed in vacuum. The crude product **19** was purified by flash column chromatography using a gradient from CH_2Cl_2/MeOH = 99:1 to CH_2Cl_2/MeOH = 90:10, yielding 1.15 g (77%) of compound **19** as colorless foam. $R_F = 0.34$ (CH_2Cl_2/MeOH = 90:10). ^{1}H NMR (300 MHz, DMSO-d_6, 300 K): $\delta = 1.370$ (9H, s, 3 × CH_3), 2.16−2.31 (2H, m, 2′-CH_2), 2.774 (2H, t, $J = 5.9$ Hz, nucleoside NC−CH_2), 2.876 (2H, m, linker NC−CH_2), 3.055 (2H, q, $J = 6.0$ Hz, Boc-NH−CH_2), 3.370 (2H, t, $J = 6.1$ Hz, Boc-NH−CH_2−CH_2), 3.48−3.65 (14H, m, 5′-CH_2, nucleoside NC−CH_2−CH_2, linker NC−CH_2−CH−CH_2, 4 × CH_2 glycol), 3.93−3.97 (1H, m, 4′-CH), 4.022 (2H, d, $J = 5.9$ Hz, NH−CH_2), 4.138 (1H, quintet, $J = 2.7$ Hz, 3′-CH), 4.953 (1H, quintet, $J = 5.5$ Hz, linker NC−CH_2−CH), 5.13−5.19 (1H, m, 5′-OH), 6.071 (1H, t, $J = 7.3$ Hz, 1′-CH), 6.68−6.77 (1H, m, N^{Boc}H), 7.933 (1H, t, J = 5.7 Hz, NH), 8.137 (1H, s, 6-CH), 11.643 (1H, s, N^3H) ppm. ^{13}C NMR (75 MHz, DMSO-d_6, 300 K): $\delta = 18.23$ (nucleoside NC−*C*H_2), 19.72 (linker NC−*C*H_2), 28.21 (3 × *C*H_3), 30.68 (NH−*C*H_2), 36.90 (2′-*C*H_2), 39.69 (Boc-NH−*C*H_2), 61.14 (5′-*C*H_2), 63.56 (nucleoside NC−CH_2−*C*H_2), 67.91 (linker NC−CH_2−*C*H), 69.17 (Boc-NH−CH_2−*C*H_2), 69.49, 69.60, 69.73, 70.21, 70.30 (linker NC−CH_2−CH−*C*H_2, 4 × CH_2 glycol), 74.49 (alkyne *C*C−CH_2), 77.58 ((CH_3)$_3$*C*), 79.08 (3′-*C*H), 84.64 (1′-*C*H), 84.89 (4′-*C*H), 89.57 (alkyne C*C*−CH_2), 98.23 (5-C), 117.64 (linker N*C*), 119.26 (nucleoside N*C*), 143.40 (2-*C*O), 143.56 (6-*C*H), 154.84 (carbamate *C*O), 155.54 (Boc *C*O), 161.49 (4-*C*O) ppm. ESI(+)-MS (*m*/*z*) Calcd: 692.7 [$C_{31}H_{44}N_6O_{12}$]. Found: 710.5 [M + NH_4]$^+$, 715.4 [M + Na]$^+$. Anal. ($C_{31}H_{44}N_6O_{12}$) C, H, N.

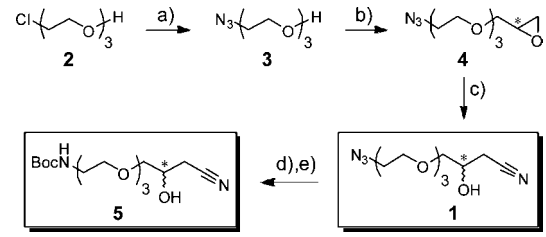
5-(Prop-2-ynyl)carbamic Acid 1-{2-[2-(2-Aminoethoxy)-ethoxy]ethoxymethyl}-2-cyanoethyl Ester 3′-*O*-(2-Cyanoethyl)-2′-deoxyuridine 5′-Phosphoramidite, 21. The well-dried nucleoside **19** (vacuum over 2 days) (200 mg, 0.29 mmol, 1.0 equiv) was dissolved in 5 mL of dry methylene chloride, 138 μL (0.44 mmol, 1.5 equiv) of *N*,*N*,*N*,*N*-tetraisopropyl-*O*-cyanoethyl-phosphoramidite and 40 mg (0.33 mmol, 1.15 equiv) of 4,5-dicyanoimidazole were added, and the reaction mixture was stirred at room temperature for 4 h. The mixture was diluted with methylene chloride to a volume of 25 mL and poured into 25 mL of saturated $NaHCO_3$ solution. After careful mixing, the phases were separated immediately, and the organic layer was washed quickly with saturated NaCl solution, dried over sodium sulfate for 5 min without stirring, filtered, and concentrated in vacuum. The crude product was purified over a short column by flash column chromatography (first CH_2Cl_2/EE/$EtMe_2N$ = 8:2:0.2 then CH_2Cl_2/MeOH/$EtMe_2N$ = 98:2:0.02). The phosphoramidite **21** was obtained as a slightly yellowish foam (260 mg, 100%). The two steroisomers caused by the chiral phosphorus atom (**21a** and **21b**) can be distinguished in the NMR spectra. $R_F = 0.17$ (CH_2Cl_2/MeOH/$EtMe_2N$ = 9:1:0.1). ^{1}H NMR (400 MHz, acetone-d_6, 300 K): $\delta = 1.24-1.31$ (24H, m, N−(CH−(CH_3)$_2$)$_{2,a}$, N−(CH−(CH_3)$_2$)$_{2,b}$), 1.45 (18H, s, Boc-C(CH_3)$_{3,a}$, Boc-C(CH_3)$_{3,b}$), 2.26−2.41 (2H, m, 2′-C$H_{2,a}$, 2′-

$CH_{2,b}$), 2.47−2.57 (2H, m, 2′-$CH_{2,a}$, 2′-$CH_{2,b}$), 2.82 (4H, t, J = 6.2 Hz, nucleoside NC−$CH_{2,a}$, nucleoside NC−$CH_{2,b}$), 2.85−2.99 (8H, m, linker NC−$CH_{2,a}$, linker NC−$CH_{2,b}$, phosphorus NC−$CH_{2,a}$, phosphorus NC−$CH_{2,b}$), 3.26 (4H, q, J = 5.7 Hz, Boc-NH−$CH_{2,a}$, Boc-NH−$CH_{2,b}$), 3.54 (4H, "t", Boc-NH−CH_2−$CH_{2,a}$, Boc-NH−CH_2−$CH_{2,b}$), 3.61−3.80 (24H, m, linker NC−CH_2−CH−$CH_{2,a}$, linker NC−CH_2−CH−$CH_{2,b}$, 4 × $CH_{2,a}$ glycol, 4 × $CH_{2,b}$ glycol, N-(CH)$_{2,a}$, N-(CH)$_{2,b}$), 3.82−3.88 (4H, m, nucleoside NC−CH_2−$CH_{2,a}$, nucleoside NC−CH_2−$CH_{2,b}$), 3.91−4.05 (8H, m, 5′-$CH_{2,a}$, 5′-$CH_{2,b}$, phosphorous NC−CH_2−$CH_{2,a}$, phosphorous NC−CH_2−$CH_{2,b}$), 4.17−4.24 (4H, m, NH−$CH_{2,a}$, NH−$CH_{2,b}$), 4.28/4.31 (each 1H, each "q", 4′-CH_a, 4′-CH_b), 4.34−4.38/4.39−4.43 (each 1H, each m, 3′-CH_a, 3′-CH_b), 5.09 (2H, quintet, J = 5.4 Hz, linker NC−CH_2−CH_a, linker NC−CH_2−CH_b), 5.92 (2H, br. s, Boc-NH_a, Boc-NH_b), 6.24/6.29 (each 1H, each dd, J = 5.7 and 8.6 Hz/J = 5.9 and 8.1 Hz, 1′-CH_a, 1′-CH_b), 7.04 (2H, m, carbamate NH_a, carbamate NH_b), 8.04/8.13 (each 1H, each s, 6-CH_a, 6-CH_b, 10.24 (2H, br. s, N^3H_a, N^3H_b) ppm. ^{13}C NMR (100 MHz, acetone-d_6, 300 K): δ = 19.18/19.20 (nucleoside NC−$CH_{2,a}$, nucleoside NC−$CH_{2,b}$), 20.54 (linker NC−$CH_{2,a}$, linker NC−$CH_{2,b}$), 20.84/20.87 (each d, J = 7.1 Hz/J = 7.1 Hz, phosphorus NC−$CH_{2,a}$, phosphorus NC−$CH_{2,b}$), 24.9−25.1 (4C, m, 2 × N−(CH−(CH_3)$_2$)$_{2,a}$, 2 × N−(CH−(CH_3)$_2$)$_{2,b}$), 28.65 (Boc-C(CH_3)$_{3,a}$, Boc-C(CH_3)$_{3,b}$), 31.87/31.93 (NH−$CH_{2,a}$, NH−$CH_{2,b}$), 38.32/38.47 (2′-$CH_{2,a}$, 2′-$CH_{2,b}$), 41.05 (Boc-NH−$CH_{2,a}$, Boc-NH−$CH_{2,b}$), 43.86 (d, J = 12.4 Hz, N−(CH)$_{2,a}$, N−(CH)$_{2,b}$), 59.63/59.77 (each d, J = 19.9 Hz/J = 19.9 Hz, phosphorus NC−CH_2−$CH_{2,a}$, phosphorus NC−CH_2−$CH_{2,b}$), 64.03/64.81 (each d, J = 8.3 Hz/J = 8.4 Hz, 5′-$CH_{2,a}$, 5′-$CH_{2,b}$), 64.99/65.04 (nucleoside NC−CH_2−$CH_{2,a}$, nucleoside NC−CH_2−$CH_{2,b}$), 69.30 (linker NC−CH_2−CH_a, linker NC−CH_2−CH_b), 70.63 (Boc-NH−CH_2−$CH_{2,a}$, Boc-NH−CH_2−$CH_{2,b}$), 70.91, 71.07, 71.18, 71.31, 71.65 (5 × $CH_{2,a}$ glycol, 5 × $CH_{2,b}$ glycol), 75.36/75.40 (alkyne CC−$CH_{2,a}$, alkyne CC−$CH_{2,b}$), 78.65 (C(CH_3)$_{3,a}$, C(CH_3)$_{3,b}$), 80.91/81.20 (3′-CH_a, 3′-CH_b), 85.09/85.11 (each d, J = 8.3 Hz/J = 8.4 Hz, 4′-CH_a, 4′-CH_b), 86.18/86.50 (1′-CH_a, 1′-CH_b), 90.06/90.20 (5-C_a, 5-C_b), 99.81/99.92 (alkyne CC−$CH_{2,a}$, alkyne CC−$CH_{2,b}$), 117.72 (linker NC_a, linker NC_b), 118.96/118.97 (nucleoside NC_a, nucleoside NC_b), 119.15/119.16 (phosphorus NC_a, phosphorus NC_b), 143.74/143.94 (6-CH_a, 6-CH_b), 150.22/150.29 (2-CO_a, 2-CO_b), 155.85/155.88 (carbamate CO_a, carbamate CO_b), 156.62 (Boc CO_a, Boc CO_b), 162.02 (4-CO_a, 4-CO_b) ppm. ^{31}P NMR (121 MHz, D_2O, 300 K): δ = 148.23, 148.43 (s, a-isomer, b-isomer) ppm. ESI(+)-MS (*m*/*z*) Calcd: 892.9 [$C_{40}H_{61}N_8O_{13}P$]. Found: 910.9 [M + NH_4]$^+$, 915.8 [M + Na]$^+$, 893.8 [M + H]$^+$.

Synthesis of Oligonucleotide 22. The oligonucleotide synthesis was carried out on an Expedite PerSeptive Biosystems DNA synthesizer, using commercially available 5′-*O*-(2-cyanoethyl)-*N*,*N*-diisopropylphosphoramidite 2′-deoxyribonucleosides and **21** as building blocks and dT5′-CPG as solid support. The protocol was a standard 1 μmol synthesis protocol with prolonged detritylation and coupling times. The sequence 5′-TATGACCT-3′ was assembled, observing in all cases coupling yields greater than 98% as evaluated by DMTr analysis.

Coupling with Fluorescein to Obtain Oligonucleotide 23. CPG-supported oligonucleotide **22** was treated several times with 3% TCA solution in methylene chloride to remove the Boc protecting group and afterward washed several times with ACN. After drying the support in vacuum, 10 equiv of fluorescein−NHS ester (5 mg, 10 μmol) and 15 equiv of DIPEA (2.6 μL, 15 μmol) in 400 μL of DMF were added to the support, and the reaction was left at room temperature for 20 h. After 20 h, the support was washed thoroughly with DMF, methylene chloride, methanol, and diethyl ether and dried in vacuum.

Scheme 1. Synthesis of the Core Structure 1 of the Cleavable Linker and Its Reduced, Boc-Protected Form 5[a]



[a] Reagents and conditions: (a) NaN_3, NaI, EtOH, reflux, 4 d, 94%; (b) (i) NaH, THF, rt, 2 h, (ii) (±)-epichlorohydrin, rt, 16 h, 70%; (c) NaCN, EtOH/H_2O = 5:1, rt, 16 h, 89%; (d) (i) triphenylphosphine, dry dioxane, rt, 8 h, (ii) 25% aqueous ammonia, rt, 12 h; (e) Boc_2O, $NaHCO_3$, water/dioxane, 0 °C to rt, 10 h, 100%.

Deprotection of the CPG-Supported Oligonucleotide 23. The CPG-support **23** was suspended in 6 mL of DMF and treated with 6 mL of 1 M TBAF/THF solution. The support was shaken for 15 min at 45 °C. Then the supernatant was collected, and its fluorescence was qualitatively analyzed under a UV lamp at 366 nm. The support was washed with methylene chloride and methanol.

Cleavage of Oligonucleotide 24 from the CPG Support. The support was treated with 2 mL of 25% aqueous ammonia at 50 °C for 18 h. The supernatant was filtered, and the support was washed with H_2O. The combined filtrates and washings were concentrated under reduced pressure, redissolved in H_2O, and analyzed and purified by ion exchange HPLC as described in the Materials and Methods using the gradient given below.

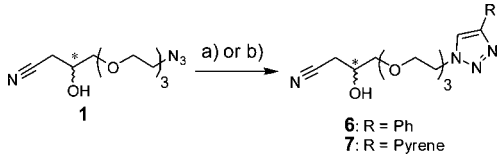
The collected fractions were evaporated. The detached oligonucleotide **25** was then dissolved in 1 mL of Millipore water and desalted on a PD-10 desalting column. The desalted oligonucleotide **25** was analyzed by ESI-MS. Ion exchange HPLC: flow rate 5 mL/min, gradient 0 min 85% A, 10% B, 5% C → 20 min 65% A, 10% B, 25% C → 23 min 0% A, 0% B, 100% C → 25 min 0% A, 0% B, 100% C → 27 min 85% A, 10% B, 5% C → 30 min 10% A, 90% B, 0% C; retention time 16.36 min (UV detection at 254 nm). ESI(−)-MS (*m*/*z*) Calcd: 2423.6. Found: 807.3 [M]$^{3-}$, 1211.2 [M]$^{2-}$, 814.5 [M + Na]$^{3-}$, 1222.3 [M + Na]$^{2-}$, 1233.4 [M + 2Na]$^{2-}$, 1244.5 [M + 3Na]$^{2-}$. Calculated masses: 2424.4 [M], 2446.4 [M + Na], 2468.8 [M + 2Na], 2490.8 [M + 3Na].

RESULTS AND DISCUSSION

Synthesis of the Core Structure 1 and the Reduced Form 5. The synthesis of the basic compound **1** and the reduced and Boc-protected form of the linker **5** are shown in Scheme 1. They can easily be synthesized with good to very good yields from inexpensive starting materials.

Starting from the commercially available triglycol monochloride **2**, the azido-modified triglycol **3** could be obtained with 94% yield following a literature procedure (*17*). In the next step, racemic epichlorohydrin was introduced using sodium hydride in dry THF yielding 70% of compound **4**. The epoxide was finally opened using sodium cyanide to build up the cleavage site, yielding 89% of compound **1**. Compound **1** was obtained with an overall yield of 58% over three steps. From the core structure **1**, the reduced linker **5** can easily be obtained in two additional steps. It was synthesized by applying the Staudinger reaction and subsequently protecting the free amino group as *tert*-butyl carbamate without intermediate purification of the free amine. A quantitative yield of compound **5** was obtained over these two steps. By the use of racemic epichlorohydrin, the linker is obtained as racemic mixture. This does not cause any problems as also in further derivatization where diasteroisomers

Scheme 2. Modification of the Linker 1 by the Use of Click Reactions[a]



[a] Reagents and conditions: (a) phenylacetylene (**6**) or 1-ethynylpyrene (**7**), $CuSO_4$, sodium ascorbate, CH_2Cl_2/MeOH = 2:1, for **6** rt, 42 h, 96%, for **7** rt, 20 h, 40 °C, 24 h, 41%; (b) 1-ethynylpyrene, CuI, DIPEA, 30 min, 250 W, 60%.

result, no difference in chemical or physical behavior (reactivity, on TLC, or in NMR spectra) was observed.

Click Reactions on the Azido-Modified Linker 1. The core linker **1** was coupled to phenylacetylene in a click reaction to evaluate the effectiveness of this method of attachment. The reaction is shown in Scheme 2. It was accomplished using catalytic amounts of copper(II)sulfate and L-ascorbic acid sodium salt in a 2:1 mixture of methylene chloride and methanol as solvents. The product **6** was obtained with 96% yield and thereby confirms the very good qualities of the linker in click reactions.

After this successful test reaction, we wanted to introduce a fluorescent label via a click reaction. Because often used dyes like fluorescein or TexasRed are not commercially available as their alkyne derivatives, we used 1-ethynylpyrene as a model dye (**7** in Scheme 2). The conversion was accomplished applying two different methods (a, b). Using very similar conditions as for derivative **6**, we observed that the reaction with pyrene went much slower. After stirring for 20 h at room temperature, there was still starting material left, so we heated it to 40 °C for another 24 h. We could isolate the labeled product **7** with a yield of 41%. An improved yield of 60% could be achieved by performing the reaction in the microwave (30 min, 250 W) without solvents according to a literature procedure (*18*). This demonstrates that the linker is useful for attaching labels by click reactions.

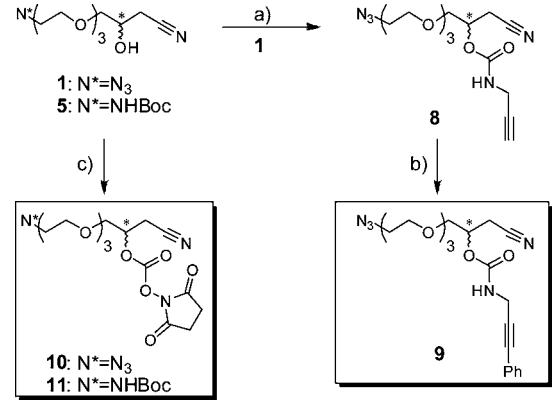
Synthesis and Cleavage of Model Compound 9. To prove the cleavability with fluoride and to investigate the cleavage mechanism, model compound **9** was synthesized where the nucleotide is replaced by a phenyl moiety. The cleavage mechanism is supposed to follow a β-elimination as is also suggested for the above-mentioned fluoride cleavable protecting groups. Fluoride therefore has to act as a base, not as a nucleophile. The synthesis of the model compound **9** is shown in Scheme 3.

Compound **1** was converted to the propargylamine carbamate **8** with 76% yield. In a one-pot procedure, compound **1** was first activated as *N*-succinimidyl carbonate at 0 °C with K_2CO_3 as base followed by the addition of propargylamine and $KHCO_3$ as additional base. The model compound **9** was then synthesized via Sonogashira coupling of the modified linker **8** to iodobenzene with a yield of 92%. From the starting materials **1** and **5**, the *N*-succinimidyl carbonates **10** and **11** were isolated as well by applying the same conditions as described for the transient activation of compound **1**, followed by an aqueous workup. They were used later on for derivatization of a nucleosidic compound (see Scheme 4).

The expected cleavage mechanism and products as well as several cleavage conditions examined using compound **9** are summarized in Table 1. The experiments were performed in a small scale (max. 30 mg of starting material) and analyzed by RP-HPLC where the UV visible compounds were detected (**9** and **12**).

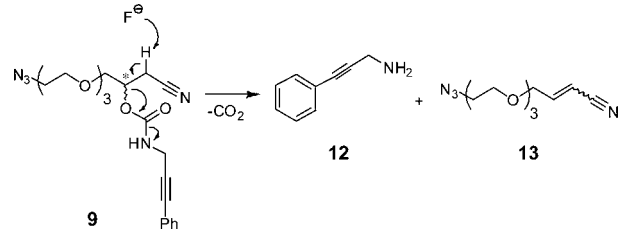
To make a comparison between the cleavage of the linker and our results found for the cleavage of the 3′-*O*-CE group,

Scheme 3. Synthesis of the Model Compound 9 and the Activated Compounds 10 and 11[a]



[a] Reagents and conditions: (a) (i) di-(*N*-succinimdyl)carbonate, anhydrous K_2CO_3, dry ACN, 0 °C, 20 h, (ii) propargylamine, $KHCO_3$, rt, 3 h, 76%; (b) iodobenzene, $Pd(PPh_3)_4$, CuI, Et_3N, dry CH_2Cl_2, rt, 3.5 h, 92%; (c) di(*N*-succinimidyl)carbonate, anhydrous K_2CO_3, dry ACN, 0 °C, **10**, 20 h, 99%; **11**, 24 h, 90%.

Table 1. Expected Cleavage Mechanism and Cleavage Experiments Using Model Compound 9 under Various Conditions[a]



exp. no.	reagent (equiv)/solvent	temp	cleavage/time [min]
1	1 M TBAF (50)[b]/dry THF	60 °C	quant/<1
2	1 M TBAF (50)[b]/dry THF	rt	quant/<1
3	1 M TBAF (5)[b]/dry THF	rt	quant/ca. 10
4	28% aq. NH_3 (100)[b]/MeOH	rt	ca. 60%/>1200
5	$Et_3N \cdot 3HF$ (5)[b]/dry THF	rt	no cleavage
6	aq. TFA/methanol	rt	no cleavage

[a] For following the reaction, 100 μL probes were taken out, diluted with 450 μL of methanol and 50 μL of Millipore water and applied to reversed-phase HPLC column. [b] Numbers in parentheses are the corresponding equivalents of TBAF used.

the first experiment was accomplished at elevated temperature because this is required for effective 3′-*O*-CE cleavage (*12*). A high excess of fluoride is chosen because this mimics the conditions on the chip in a CRT approach. The result for the designed linker was very good because it was cleaved in less than 1 min. Because of this very fast cleavage at 60 °C, the temperature was reduced to room temperature (experiment no. 2, Table 1). Comparing entries 1 and 2 demonstrates that no elevated temperature is needed for this ultrafast cleavage (see also Figure 2). Further the reduction of equivalents decelerated the reaction, but it was still complete in less than 10 min (experiment no. 3 in Table 1). One explanation for the ultrafast cleavage is the release of carbon dioxide.

The linker is also expected to be cleavable by other bases. So the cleavage with high excess of concentrated ammonia was investigated (entry 4, Table 1). The HPLC chromatogram in Figure 3 shows that there is a big difference in effectiveness between fluoride and ammonia. The linker is also cleavable with concentrated ammonia, but it is not complete after 20 h at room temperature (approximately 60% cleavage).

Entry 5 in Table 1 shows that the linker is stable against the slightly acidic fluoride reagent $Et_3N \cdot 3HF$ (Figure 3); no cleavage occurs during 18 h. We further found excellent stability even after 48 h under acidic conditions (TFA solution, entry 6

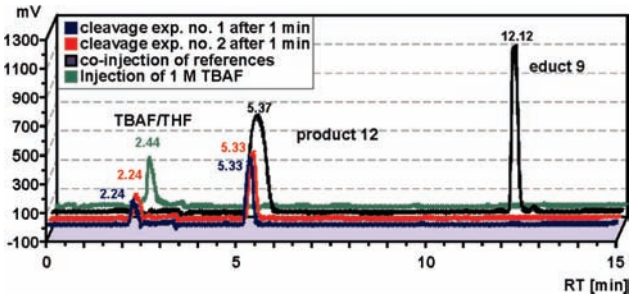


Figure 2. HPLC chromatogram of cleavage experiment nos. 1 and 2 in Table 1.Conditions: Phenomenex Jupiter 4u Proteo 90A 4 μm column 250 mm × 4.6 mm, flow rate 1 mL/min, gradient 0 min 10% A, 70% B, 20% C → 14 min 10% A, 15% B, 75% C → 20 min 10% A, 0% B, 90% C.

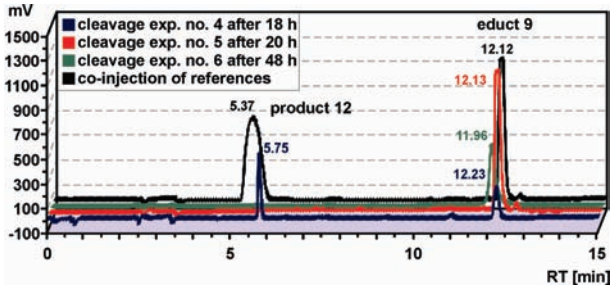


Figure 3. HPLC chromatograms of exp. no. 4, 5, and 6 in Table 1. Condition as described in Figure 2.

and Figure 3). This stability is important for the use of the Boc-protected linker because it has to be deprotected under acidic conditions after attachment to the nucleoside to enable the labeling.

The HPLC chromatograms provide a first hint of the expected cleavage mechanism because they show the appearance of cleavage product **12**. The glycol cleavage product is not UV-active and therefore not detectable by this HPLC system. Another indicator of the β-elimination mechanism is the stability of the linker against $Et_3N \cdot 3HF$. The final proof of the cleavage and its mechanism was achieved by repeating the reaction in a bigger scale to be able to isolate both cleavage products. The reaction was performed using an excess of 5 equiv of TBAF in dry THF at room temperature for 10 min. Both expected products **12** and **13** could be isolated in quantitative yields. The olefin is obtained in a 1:1 ratio of *cis* and *trans* isomers as determined by ^{1}H NMR.

These experiments show that the linker is extraordinarily effectively cleaved with 1 M TBAF in THF following a β-elimination mechanism and that it is completely stable under acidic conditions.

Synthesis and Cleavage of the 5-,3′-Modified 2′-Deoxyuridine Derivatives 18 and 19. To ensure that the cleavage works equally efficiently if the linker is attached to a nucleoside and to analyze the difference in cleavage rate between the 3′-*O*-CE group and the linker, the 5-,3′-modified compound **18** was synthesized (see Scheme 4). To enable the final cleavage experiment on a labeled, CPG-bound 8-mer, compound **19** was also synthesized, bearing the Boc-protected linker at the 5-position (see Scheme 4).

The introduction of the CE group to 5-iodo-2′-deoxyuridine **14** was accomplished in a similar way as described for the thymidine derivative (*12*). The only difference is that for the 5′-*O*-protection the benzoyl group was used instead of the MMTr group to just have one single deprotection step in the end. According to this, the first step was the selective introduction of the benzoyl group at the 5′-OH (*19*). By lowering the temperature to −18 °C we could improve the yield to 77% of 5′-mono protected product as compared with the yield reported in literature (70%). Following conditions described in the literature (*20*), the next step was the benzoyl protection of N^3 by transient TMS protection of the 3′-OH function in a one-pot procedure. The yield of 75% of completely protected nucleoside **15** suggests that two of the three steps mentioned were quantitative, including isolation and purification. The Michael addition was accomplished following the procedure described for the RNA 2′-position (*13*) using freshly distilled acrylonitrile and Cs_2CO_3 as base. The crude product of the Michael addition was directly deprotected and 65% of the 3′-*O*-modified nucleoside **16** was obtained after two steps. To enable the attachment of the cleavable linker, the propargylamine moiety was introduced by the well-known Sonogashira coupling with propargylamine-*N*-(1,1,1-trifluoro)acetate. After deprotection, compound **17** was obtained over the two steps in 65% yield. The coupling of the linker was readily accomplished by adding the activated linker moiety **10** to the modified nucleoside **17** in dry ACN with $KHCO_3$ as base giving 67% of the final compound **18**. Adding the corresponding activated linker **11** to compound **17** yields 77% of compound **19**.

The cleavage experiments using compound **18** were accomplished in the same manner as with model compound **9**. Approximately 30 mg of starting material was used, and the reactions were followed by RP-HPLC. In Table 2, the experiments are summarized.

With fluoride, the cleavage proceeds successively as shown in Table 2. For the linker, we observe a very fast cleavage according to the results obtained with the model compound **9**. For the 3′-*O*-CE group, we found a cleavage time of more than 1 h under the conditions applied in entry 1 of Table 2 (*12*). Estimated from these observed times, the linker is cleaved about 100 times faster than the 3′-modification. With ammonia, the cleavage of the linker occurs more slowly, and no cleavage is monitored for the 3′-*O*-CE group.

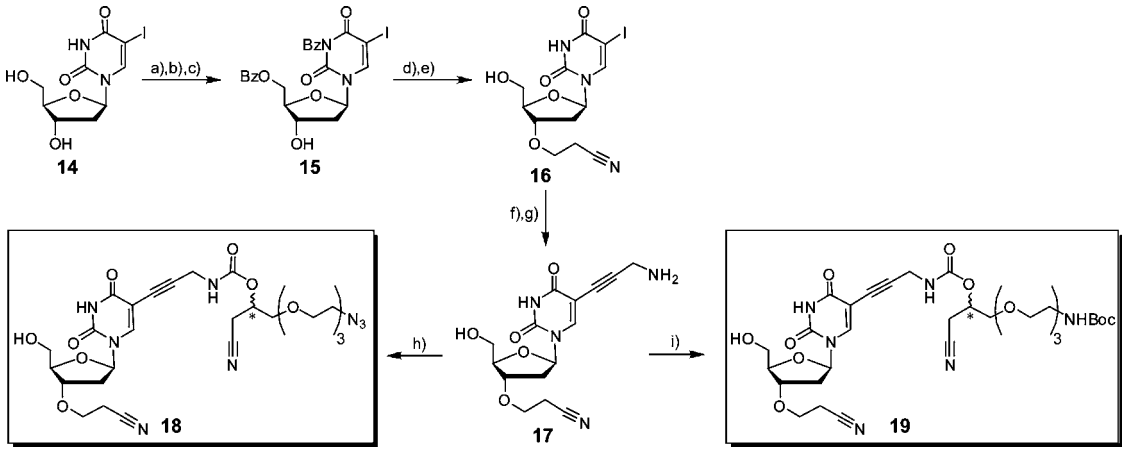
In Figure 4, the three reference compounds are shown. In Figures 5 and 6, the chromatograms of the two entries in Table 2 at different points of time are displayed.

The results of the HPLC analysis of experiment no. 1 are in accordance with the expectations. Figure 5 shows a very fast cleavage (less than 1 min) of the linker and a complete cleavage after 2 h of the 3′-*O*-CE group. Hence the cleavage is equally effective with the nucleoside compound **18** and the model compound **9**. The cleavage of the linker from the nucleoside **18** with ammonia (entry 2 in Table 2 and Figure 6) is faster than that from the model compound **9**. However it is not completely clear whether this is due to the nucleoside moiety because the conditions were not identical. In experiment no. 2 in Table 2, no additional solvent was used, and the excess was much higher compared with entry 4 in Table 1.

The fluoride cleavage experiment (exp. no. 1 in Table 2) shows that both parts are cleavable under the same conditions. For our future aim to use this combination of 3′-*O*-blocking group and cleavable linker as dye-labeled reversible terminator, it is important that both parts are efficiently cleaved within minutes. At room temperature, the speed of cleavage of the 3′-*O*-CE group does not meet the demands for CRT sequencing. However this problem we already solved and the optimal conditions for cleavage of the 3′-blocking group were found to be at 40 °C with DMF or DMSO as cosolvent (cleavage within 3 min) (*12*).

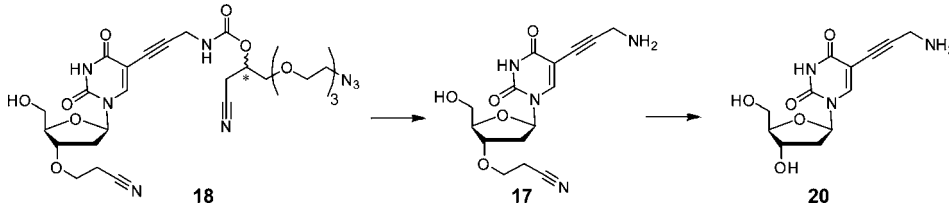
The future idea for the use of these reversible terminators is to elongate oligonucleotide templates, immobilized on a chip. To mimic these conditions and to show that both modifications can be cleaved in a reasonable time, a final deprotection experiment on a CPG-supported oligonucleotide was ac-

Scheme 4. Synthesis of the 5- and 3′-Modified Nucleosides 18 and 19[a]



[a] Reagents and conditions: (a) BzCl, dry CH_2Cl_2, dry pyridine, −18 °C, 3 h, 77%; (b) (i) TMSCl, DIPEA, dry pyridine, rt, 45 min, (ii) BzCl, rt, 15 min, 98%; (c) $CHCl_3$/MeOH = 1:1, TFA, rt, 2 h; (d) acrylonitrile, Cs_2CO_3, *t*-BuOH, rt, 2.5 h; (e) 25% aq. ammonia, rt, 20 h, 65% over two steps; (f) propargylamine-*N*-(1,1,1-trifluoro)acetate, $Pd(PPh_3)_4$, CuI, Et_3N, dry DMF, rt, 20 h, 65%; (g) 25% aq. ammonia, rt, 12 h, 99%; (h) **10**, $KHCO_3$, dry ACN, 0 °C, 30 min, rt, 3.5 h, 66%; (i) **11**, $KHCO_3$, dry ACN, dry DMF, 0 °C, 1 h, rt, 3.5 h, 77%.

Table 2. Cleavage Experiments Using the Modified Nucleoside 18[a]



exp. no.	reagent (equiv)/solvent	temp	cleavage/time [min]
1	1 M TBAF (55)[b]/dry THF	rt	linker: quant./<1 3′-*O*-CE: quant/>60
2	28% aq. NH_3 (450)[b]/no additional solvent	rt	linker: quant./120 3′-*O*-CE: no cleavage

[a] For following the reaction, 50 μL probes were taken out, diluted with 450 μL of methanol and 50 μL of Millipore water, and applied to reversed-phase HPLC column. [b] Numbers in parentheses are the corresponding equivalents of TBAF used.

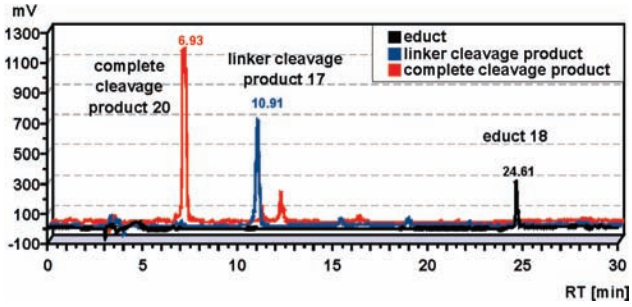


Figure 4. HPLC chromatogram of the reference products for the nucleoside cleavage experiments. Conditions: Phenomenex Jupiter 4u Proteo 90A 4 μm column 250 mm × 4.6 mm, flow rate 1 mL/min, gradient 0 min 10% A, 90% B, 0% C → 20 min 10% A, 60% B, 30% C → 25 min 10% A, 0% B, 90% C → 30 min 10% A, 90% B, 10% C.

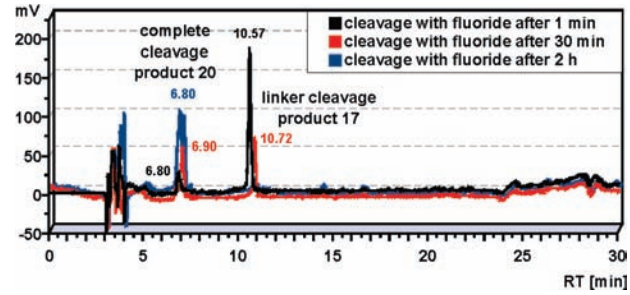


Figure 5. Chromatograms of the fluoride-mediated cleavage of compound **18**. Conditions as described in Figure 4.

complished. We chose an 8-mer bearing the complete 2′-deoxyuridine-derived reversible terminator at the 3′-end. To be able to detect the cleavage of the linker moiety from the oligonucleotide, the linker was labeled with fluorescein after assembly of the oligonucleotide. For this experiment, nucleoside **19** was used, and the dye was applied as its *N*-hydroxysuccinimidyl active ester.

In order to use the complete reversible terminator **19** in an automated oligonucleotide synthesis, the 5′-*O*-phosphoramidite was synthesized. In Scheme 5, the synthesis of the phosphoramidite **21** is shown. It was carried out using *N*,*N*,*N*,*N*-tetraisopropyl-*O*-cyanoethyl-phosphoramidite as phosphorylating reagent and 4,5-dicyanoimidazole as base. The 3′-modified 5′-phosphoramidite **21** was obtained in quantitative yield.

As a model oligonucleotide, we chose the following 8-mer: 5′-TCCAGTAT$_{mod}$-3′, **22**, where T_{mod} is the 5-,3′-*O*-modified nucleotide. The oligonucleotide synthesis had to be carried out in the inverse way (direction 5′ to 3′, instead of the conventional 3′ to 5′) with commercially available 5′-*O*-(2-cyanoethyl)-*N*,*N*-diisopropylphosphoramidite-2′-deoxyribonucleosides building blocks. After assembly, the oligonucleotide was left at the CPG support, and the amino group of the linker was deprotected by washing the column 10 times with deblock solution (3% TCA in methylene chloride). To this free amino group, fluorescein was coupled in order to be able to detect the cleavage product of the linker by fluorescence (Scheme 6). The solid phase bound labeled oligonucleotide **23** was washed and dried thoroughly before the treatment with 1 M TBAF in THF and dry DMF as cosolvent at 45 °C for 15 min. After this time, the supernatant

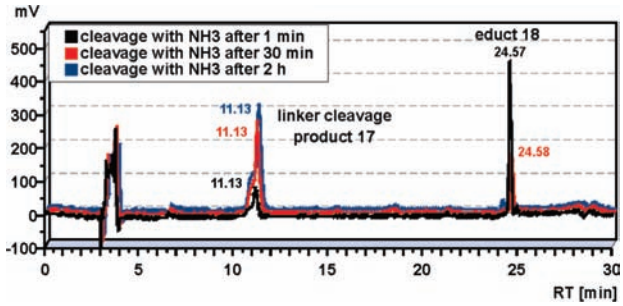
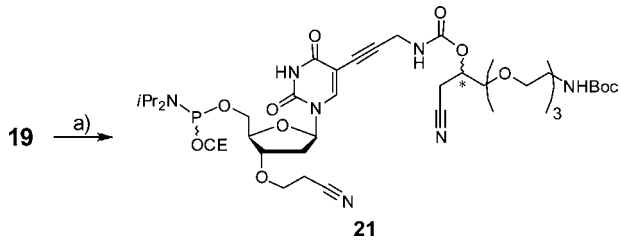


Figure 6. Chromatograms of the ammonia-mediated cleavage of compound **18**. Conditions as described in Figure 4.

Scheme 5. Synthesis of the 5′-Phosphoramidite 21[a]



[a] Reagents and conditions: (a) *N*,*N*,*N*,*N*-tetraisopropyl-*O*-cyanoethyl-phosphoramidite, 4,5-dicyanoimidazol, dry CH_2Cl_2, rt, 4 h, 100%.

was recovered, concentrated, redissolved in methanol, and irradiated under a UV lamp at 366 nm. At this wavelength, the solution showed a very strong fluorescence (small picture in Scheme 6). This demonstrates the cleavage of the linker−dye system during the fluoride treatment. To prove the cleavage of the 3′-*O*-CE group as well, the oligonucleotide was deprotected and detached from the solid support by treatment with concentrated aqueous ammonia at room temperature. After purification of the oligonucleotide **24** by ion exchange HPLC and desalting by gel filtration, the ESI-MS analysis indeed proved the presence of the completely deprotected oligonucleotide **24** (Scheme 6).

We designed a linker that is rapidly cleaved by fluoride through a β-elimination mechanism. The linker is useful for different modes of attachment, and therefore it is a versatile tool for reversibly labeling (oligo)nucleotides. We showed examples of successful attachment of labels by click reactions and by amide formation.

To prove the use of this linker for a reversible terminator, applicable in a DNA-sequencing approach, the modified nucleosides **18** and **19** were synthesized, and the cleavage properties were analyzed. Initial experiments were performed in solution but with the final cleavage experiment from the CPG-bound oligonucleotide, we could show that also under heterogeneous conditions TBAF efficiently removes the linker−dye system and the 3′-*O*-blocking group in one single step. Further this setup confirmed that oligonucleotides are stable under the applied chemical conditions. These results demonstrate that the developed linker, together with the 3′-*O*-blocking group meets the demands for a reversible terminator.

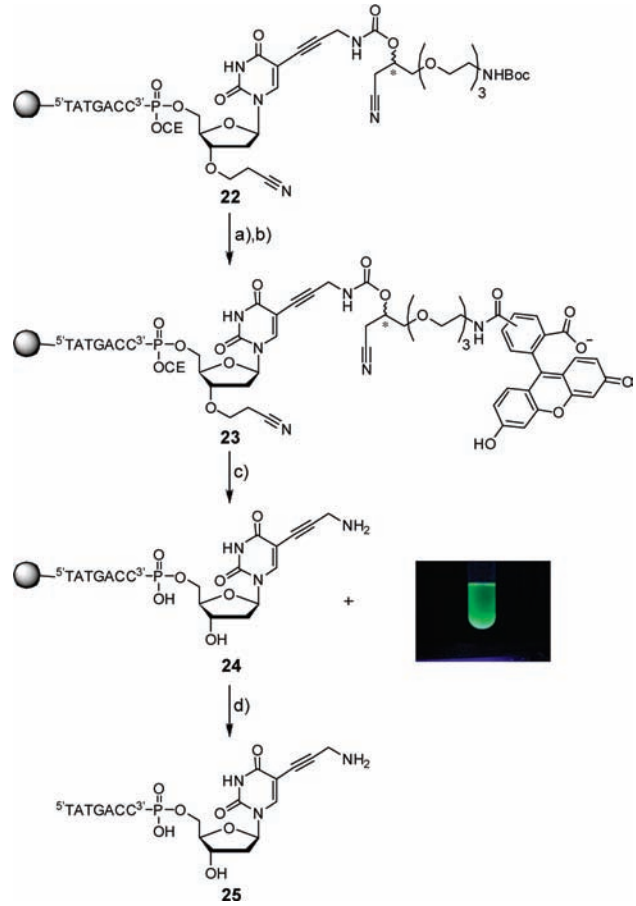
NUMERICAL RESULTS OF ELEMENTAL ANALYSES

2-{2-[2-(2-Azidoethoxy)ethoxy]ethoxymethyl}oxirane, 4. C: calcd, 46.74; found, 46.52. H: calcd, 7.41; found, 7.37. N: calcd, 18.17; found, 18.45.

4-{2-[2-(2-Azidoethoxy)ethoxy]ethoxy}-3-hydroxybutyronitrile, C: calcd, 46.26; found, 46.50. H: calcd, 7.18; found, 7.02. N: calcd, 21.81; found, 21.69.

(2-{2-[2-(3-Cyano-2-hydroxypropoxy)ethoxy]ethoxy}ethyl)-carbamic Acid *tert*-Butyl Ester, 5. C: calcd, 54.20; found, 54.19. H: calcd, 8.49; found, 8.57. N: calcd, 8.43; found, 8.25.

Scheme 6. Synthesis of the Labeled Oligonucleotide 23 and Cleavage of the 5- and 3′-Modifications from the CPG-Bound Oligonucleotide[a]



[a] Reagents and conditions: (a) TCA deblock solution; (b) 5(6)-carboxy-fluorescein−NHS ester, DIPEA, DMF, rt, 20 h; (c) 1 M TBAF/THF, dry DMF, 45 °C, 15 min; (d) conc. aq. NH_3, rt, 18 h.

3-Hydroxy-4-(2-{2-[2-(4-phenyl-1,2,3-triazol-1-yl)ethoxy]-ethoxy}ethoxy)butyronitrile, 6. C: calcd, 59.99; found, 59.89. H: calcd, 6.71; found, 6.68. N: calcd, 15.55; found, 15.28.

Prop-2-ynylcarbamic Acid 1-{2-[2-(2-Azidoethoxy)ethoxy]-ethoxymethyl}-2-cyanoethyl Ester, 8. C: calcd, 49.55; found, 49.68. H: calcd, 6.24; found, 6.30. N: calcd, 20.64; found, 20.78.

(3-Phenylprop-2-ynyl)carbamic Acid 1-{2-[2-(2-Azidoethoxy-ethoxy]ethoxymethyl}-2-cyanoethyl Ester, 9. C: calcd, 57.82; found, 58.04. H: calcd, 6.07; found, 6.01. N: calcd, 16.86; found, 16.92.

(*E*/*Z*)-4-{2-[2-(2-Azidoethoxy)ethoxy]ethoxy}but-2-enenitrile, 13. C: calcd, 49.99; found, 49.83. H: calcd, 6.71; found, 6.76. N: calcd, 23.32; found, 23.46.

***N*^{3}-Benzoyl-5-iodo-5′-*O*-benzoyl-2′-deoxyuridine, 15.** C: calcd, 49.13; found, 49.01. H: calcd, 3.41; found, 3.67. N: calcd, 4.98; found, 4.86.

5-Iodo-3′-*O*-(2-cyanoethyl)-2′-deoxyuridine, 16. C: calcd, 35.40; found, 35.51. H: calcd, 3.47; found, 3.62. N: calcd, 10.32; found, 10.29.

***N*^{3}-Benzoyl-5-iodo-3′-*O*-(2-cyanoethyl)-5′-*O*-benzoyl-2′-deoxyuridine.** C: calcd, 50.75; found, 50.94. H: calcd, 3.60; found, 3.82. N: calcd, 6.83; found, 6.67.

5-(Prop-2-ynyl)carbamic Acid 1-{2-[2-(2-Azidoethoxy)ethoxy]ethoxymethyl}-2-cyanoethyl ester]-3′-*O*-(2-cyanoethyl)-2′-desoxyuridine, 18. C: calcd, 50.48; found, 50.27. H: calcd, 5.54; found, 5.33. N: calcd, 18.11; found, 17.93.

5-(Prop-2-ynyl)carbamic Acid 1-{2-[2-(2-*tert*-Butoxycarbonylaminoethoxy)ethoxy]ethoxymethyl}-2-cyanoethyl Ester 3′-*O*-(2-Cyanoethyl)-2′-desoxyuridine, 19. C: calcd, 53.75; found, 53.53. H: calcd, 6.40; found, 6.51. N: calcd, 12.12; found, 11.88.

ACKNOWLEDGMENT

We would like to thank the EU FP6 CRAFT project "ArraySBS" for financial support.

LITERATURE CITED

(1) Kricka, L. J., and Fortina, P. (2009) Analytical ancestry: "Firsts" in fluorescent labeling of nucleosides, nucleotides, and nucleic acids. *Clin. Chem. 55*, 670–683.

(2) Wojczewski, C., Stolze, K., and Engels, J. W. (1999) Fluorescent oligonucleotides - Versatile tools as probes and primers for DNA and RNA analysis. *Synlett 10*, 1667–1678.

(3) Kumar, S., and Fuller, C. W. (2007) Advances in dye-nucleotide conjugate chemistry for DNA sequencing. *Perspect. Bioanal. 2*, 119–149.

(4) Metzker, M. L. (2008) Advances in next-generation DNA sequencing technologies. *Comparative Genomics basic and applied research* (Brown, J. R., Ed.), pp 13−28, Chapter 2, CRC Press Taylor & Francis Group, Boca Raton, FL.

(5) Shendure, J., and Ji, H. L. (2008) Next-generation DNA sequencing. *Nat. Biotechnol. 26*, 1135–1145.

(6) Eid, J., Fehr, A., Gray, J., Luong, K., Lyle, J., Otto, G., Peluso, P., Rank, D., Baybayan, P., Bettman, B., Bibillo, A., Bjornson, K., Chaudhuri, B., Christians, F., Cicero, R., Clark, S., Dalal, R., deWinter, A., Dixon, J., Foquet, M., Gaertner, A., Hardenbol, P., Heiner, C., Hester, K., Holden, D., Kearns, G., Kong, X., Kuse, R., Lacroix, Y., Lin, S., Lundquist, P., Ma, C., Marks, P., Maxham, M., Murphy, D., Park, I., Pham, T., Phillips, M., Roy, J., Sebra, R., Shen, G., Sorenson, J., Tomaney, A., Travers, K., Trulson, M., Vieceli, J., Wegener, J., Wu, D., Yang, A., Zaccarin, D., Zhao, P., Zhong, F., Korlach, J., and Turner, S. (2009) Real-time DNA sequencing from single polymerase molecules. *Science 323*, 133–138.

(7) Ju, J. Y., Kim, D. H., Bi, L. R., Meng, Q. L., Bai, X. P., Li, Z. M., Li, X. X., Marma, M. S., Shi, S., Wu, J., Edwards, J. R., Romu, A., and Turro, N. J. (2006) Four-color DNA sequencing by synthesis using cleavable fluorescent nucleotide reversible terminators. *Proc. Natl. Acad. Sci. U.S.A. 103*, 19635–19640.

(8) Margulies, M., Egholm, M., Altman, W. E., Attiya, S., Bader, J. S., Bemben, L. A., Berka, J., Braverman, M. S., Chen, Y.-J., Chen, Z., Dewell, S. B., Du, L., Fierro, J. M., Gomes, X. V., Godwin, B. C., He, W., Helgesen, S., Ho, C. H., Irzyk, G. P., Jando, S. C., Alenquer, M. L. I., Jarvie, T. P., Jirage, K. B., Kim, J.-B., Knight, J. R., Lanza, J. R., Leamon, J. H., Lefkowitz, S. M., Lei, M., Li, J., Lohman, K. L., Lu, H., Makhijani, V. B., McDade, K. E., McKenna, M. P., Myers, E. W., Nickerson, E., Nobile, J. R., Plant, R., Puc, B. P., Ronan, M. T., Roth, G. T., Sarkis, G. J., Simons, J. F., Simpson, J. W., Srinivasan, M., Tartaro, K. R., Tomasz, A., Vogt, K. A., Volkmer, G. A., Wang, S. H., Wang, Y., Weiner, M. P., Yu, P., Begley, R. F., and Rothberg, J. M. (2005) Genome sequencing in microfabricated high-density picolitre reactors. *Nature 437*, 376–380.

(9) Kurg, A., Tonisson, N., Georgiou, I., Shumaker, J., Tollett, J., and Metspalu, A. (2000) Arrayed primer extension: Solid-phase four-color DNA resequencing and mutation detection technology. *Genet. Test. 4*, 1–7.

(10) Syvanen, A. C. (2001) Accessing genetic variation: Genotyping single nucleotide polymorphisms. *Nat. Rev. Genet. 2*, 930–942.

(11) Bentley, D. R., Balasubramanian, S., Swerdlow, H. P., Smith, G. P., Milton, J., Brown, C. G., Hall, K. P., Evers, D. J., Barnes, C. L., Bignell, H. R., Boutell, J. M., Bryant, J., Carter, R. J., Cheetham, R. K., Cox, A. J., Ellis, D. J., Flatbush, M. R., Gormley, N. A., Humphray, S. J., Irving, L. J., Karbelashvili, M. S., Kirk, S. M., Li, H., Liu, X., Maisinger, K. S., Murray, L. J., Obradovic, B., Ost, T., Parkinson, M. L., Pratt, M. R., Rasolonjatovo, I. M. J., Reed, M. T., Rigatti, R., Rodighiero, C., Ross, M. T., Sabot, A., Sankar, S. V., Scally, A., Schroth, G. P., Smith, M. E., Smith, V. P., Spiridou, A., Torrance, P. E., Tzonev, S. S., Vermaas, E. H., Walter, K., Wu, X., Zhang, L., Alam, M. D., Anastasi, C., Aniebo, I. C., Bailey, D. M. D., Bancarz, I. R., Banerjee, S., Barbour, S. G., Baybayan, P. A., Benoit, V. A., Benson, K. F., Bevis, C., Black, P. J., Boodhun, A., Brennan, J. S., Bridgham, J. A., Brown, R. C., Brown, A. A., Buermann, D. H., Bundu, A. A., Burrows, J. C., Carter, N. P., Castillo, N., Catenazzi, M. C. E., Chang, S., Cooley, R. N., Crake, N. R., Dada, O. O., Diakoumakos, K. D., Dominguez-Fernandez, B., Earnshaw, D. J., Egbujor, U. C., Elmore, D. W., Etchin, S. S., Ewan, M. R., Fedurco, M., Fraser, L. J., Fuentes Fajardo, K. V., Furey, W. S., George, D., Gietzen, K. J., Goddard, C. P., Golda, G. S., Granieri, P. A., Green, D. E., Gustafson, D. L., Hansen, N. F., Harnish, K., Haudenschild, C. D., Heyer, N. I., Hims, M. M., Ho, J. T., Horgan, A. M., Hoschler, K., Hurwitz, S., Ivanov, D. V., Johnson, M. Q., James, T., Jones, T. A. H., Kang, G.-D., Kerelska, T. H., Kersey, A. D., Khrebtukova, I., Kindwall, A. P., Kingsbury, Z., Kokko-Gonzales, P. I., Kumar, A., Laurent, M. A., Lawley, C. T., Lee, S. E., Lee, X., Liao, A. K., Loch, J. A., Lok, M., Luo, S., Mammen, R. M., Martin, J. W., McCauley, P. G., McNitt, P., Mehta, P., Moon, K. W., Mullens, J. W., Newington, T., Ning, Z., Ng, B. L., Novo, S. M., O'Neill, M. J., Osborne, M. A., Osnowski, A., Ostadan, O., Paraschos, L. L., Pickering, L., Pike, A. C., Pike, A. C., Pinkard, D. C., Pliskin, D. P., Podhasky, J., Quijano, V. J., Raczy, C., Rae, V. H., Rawlings, S. R., Chiva Rodriguez, A., Roe, P. M., Rogers, J., Rogert Bacigalupo, M. C., Romanov, N., Romieu, A., Roth, R. K., Rourke, N. J., Ruediger, S. T., Rusman, E., Sanches-Kuiper, R. M., Schenker, M. R., Seoane, J. M., Shaw, R. J., Shiver, M. K., Short, S. W., Sizto, N. L., Sluis, J. P., Smith, M. A., Sohna Sohna, J.-E., Spence, E. J., Stevens, K., Sutton, N., Szajkowski, L., Tregidgo, C. L., Turcatti, G., vande Vondele, S., Verhovsky, Y., Virk, S. M., Wakelin, S., Walcott, G. C., Wang, J., Worsley, G. J., Yan, J., Yau, L., Zuerlein, M., Rogers, J., Mullikin, J. C., Hurles, M. E., McCooke, N. J., West, J. S., Oaks, F. L., Lundberg, P. L., Klenerman, D., Durbin, R., and Smith, A. J. (2008) Accurate whole human genome sequencing using reversible terminator chemistry. *Nature 456*, 53–59.

(12) Keller, A. C., Serva, S., Knapp, D. C., Kwiatkowski, M., and Engels, J. W. (2009) Synthesis of 3′-*O*-(2-cyanoethyl)-2′-deoxythymidine-5′-phosphate as a model compound for evaluation of cyanoethyl cleavage. *Collect. Czech. Chem. Commun. 74*, 515–534.

(13) Saneyoshi, H., Seio, K., and Sekine, M. (2005) A general method for the synthesis of 2′-*O*-cyanoethylated oligoribonucleotides having promising hybridization affinity for DNA and RNA and enhanced nuclease resistance. *J. Org. Chem. 70*, 10453–10460.

(14) Ohgi, T., Masutomi, Y., Ishiyama, K., Kitagawa, H., Shiba, Y., and Yano, J. (2005) A new RNA synthetic method with a 2′-*O*-(2-cyanoethoxymethyl) protecting group. *Org. Lett. 7*, 3477–3480.

(15) Matysiak, S., Fitznar, H.-P., Schnell, R., and Pfleiderer, W. (1998) Nucleosides. Part LXIII. Acetals as new 2′-*O*-protecting functions for the synthesis of oligoribonucleotides. Synthesis of uridine building blocks and evaluation of their relative acid stability. *Helv. Chim. Acta 81*, 1545–1566.

(16) Sakai, N., Kanada, R., Hirasawa, M., and Konakahara, T. (2005) Facile and convenient synthesis of functionalized propargylic alcohols and amines: An $InBr_3$-Et_3N reagent system promotes the alkynylation of aldehydes and *N*,*O*- or *N*,*S*-acetals. *Tetrahedron 61*, 9298–9304.

(17) Rensen, P. C. N., van Leeuwen, S. H., Sliedregt, L., van Berkel, T. J. C., and Biessen, E. A. L. (2004) Design and synthesis of novel *N*-acetylgalactosamine-terminated glycolipids for targeting of lipoproteins to the hepatic asialoglycoprotein receptor. *J. Med. Chem. 47*, 5798–5808.

(18) Krim, J., Sillahi, B., Taourirte, M., Rakib, E. M., and Engels, J. W. (2009) Microwave-assisted click chemistry: Synthesis of mono and bis-1,2,3-triazole acyclonucleoside analogues of Acyclovir via copper(I)-catalyzed cycloaddition. *ARKIVOC* 142–152.

(19) Yamashita, J., Matsumoto, H., Kobayashi, K., Noguchi, K., Yasumoto, M., and Ueda, T. (1989) Studies on antitumor agents. IX Synthesis of 3′-*O*-benzyl-2′-deoxy-5-trifluoromethyluridine. *Chem. Pharm. Bull. 37*, 2287–2292.

(20) Sekine, M., Fujii, M., Nagai, H., and Hata, T. (1987) An improved method for the synthesis of *N*3-benzoylthymidine. *Synthesis 12*, 1119–1121.

BC900542F

Optically Induced Linking of Protein and Nanoparticles to Gold Surfaces

Kasper Moth-Poulsen,[†,‡] Vesna Kofod-Hansen,[‡] Fadhil S. Kamounah,[||] Nikos S. Hatzakis,[†,§] Dimitrios Stamou,[†,§] Kjeld Schaumburg,*[,||] and Jørn B. Christensen*[,‡]

Nano-Science Center, Department of Chemistry, Bio-Nanotechnology Laboratory, and Department of Neuroscience and Pharmacology, University of Copenhagen, Universitetsparken 5, DK-2100 Copenhagen, Denmark, and Department of Science, Systems and Models, Roskilde University, P.O. Box 260, DK-4000 Roskilde, Denmark. Received January 4, 2010; Revised Manuscript Received May 11, 2010

Attachment of molecules and proteins to surfaces is of great interest for the development of a large variety of applications. We present herein a novel approach to efficiently couple a molecule of choice to biological building blocks. We synthesized and employed a new derivative of 5-bromo-7-nitroindoline to attach nucleophilic molecules and proteins to gold surfaces by photochemical activation. The reaction can be seen as a photoactivated alternative to the activated ester type chemistries that are commonly used to attach proteins or molecules to surfaces. We characterize the reaction by UV−vis and NMR spectroscopy, and as test of principle experiment, we show that we can attach proteins to surfaces and demonstrate that we can functionalize gold nanoparticles by this optically induced cross-linking reaction.

INTRODUCTION

Attachment of proteins and molecules to designated areas on surfaces is crucial for a large variety of biomedical applications such as drug screening platforms, microarrays, solid support protein synthesis, and single molecule experiments (*1*−*9*). Several methods have been developed to randomly or in a selective manner couple (bio)molecules on chemically modified surfaces. In random immobilization methods, the active residues of proteins, such as lysines, are coupled to surfaces containing N-hydroxysuccinimide (NHS) esters (*10*), epoxides (*11*), aldehydes (*8, 12*), oximes (*13*), semicarbazones (*14*), or isothiocyanate (*15*). Oriented immobilization can be obtained by reaction of the free solvent accessible thiols of proteins (*7*), by employing polyhistidine tags (His6)(16), AGT mediated methods (*17*), protein ligation (*18*−*20*), and splicing (*8, 21*). Alternatively, biomolecules can be positioned directly on surfaces by nonspecific adsorption (*22*). To avoid direct interactions with surfaces, enzymes have been coupled to bovine serum albumine (BSA) (*3*) or on streptavidin molecules (*4*) which are then immobilized on surfaces either randomly or by the use of microcontact printing techniques (*1, 2*). To increase coupling efficiency between a surface and a biomolecule, an attractive alternative is the Sharpless (*23, 24*) reaction where an alkyne species is reacting with an azide. Due to conveniently introducing an alkyne group on the amino acids of a protein and an azide group on the surface (or vise versa), this method has been widely employed to couple biomolecules together or covalently attach them on surfaces (*3, 23*−*27*). The advantage of the click-type chemistries is that the reactions are highly chemoselective and can be performed in aqueous media (*23*); a serious disadvantage is that copper and its salts are highly toxic to most living organisms, which can be circumvented by the use of Cu-free methods (*24*). Another shortcoming of the above-mentioned techniques is the limited stability of these reagents (NHS only 2 h (*10*)) or the use of additional proteins such as SAV that may limit or change the properties of the protein one wishes to attach to the surface. We herein present a new, attractive method to efficiently conjugate molecular entities using an in situ photoactivated type of chemistry.

The 5-bromo-7-nitroindolinyl (Bni) group was first reported as a light-sensitive protection group for carboxylic acids (*28*). Through the years, it as been used for a variety of applications, such as natural product synthesis (*29*), peptide synthesis (*30, 31*), and recently as a light sensitive protection group for amines and alcohols (*32*). To demonstrate the utility of the Bni-group for photoinduced cross-coupling reactions, the thiol-functionalized 5-bromo-7-nitroindolinyl molecule **1** was synthesized and explored as a photoactive linker to attach molecules or proteins to gold surfaces. To characterize the efficiency of this linker, we employed UV−vis and NMR techniques to monitor the photoinduced reaction of **1** with 1-aminohexane at various reaction times. To further show the versatility of this concept, we demonstrate that we can functionalize gold nanoparticles with **1** and link these by a photoinduced cross-linking reaction with 1,6- diaminohexane. In a final experiment, we exploited the potential of this method to link proteins through their solvent-accessible lysine groups on functionalized gold surfaces.

EXPERIMENTAL SECTION

^{1}H NMR (300 MHz) and ^{13}C NMR (75 MHz) NMR spectra were recorded on a Varian instrument. Fast atom bombardment (FAB^{+}) mass spectra were obtained on a Jeol JMS-HX 110 tandem mass spectrometer in the positive ion mode using 3-nitrobenzyl alcohol (NBA) as matrix. EI-MS spectra were recorded on a ZAB-EQ (VG-Analytical) instrument. Elemental analysis was performed by Mrs. Birgitta Kegel at the Microanalytical Laboratory at the Department of Chemistry, University of Copenhagen. Fluorescence micrographs were recorded on a Zeiss Axiocam microscope equipped with fluorescence filter filters. TEM images of AuNPs were obtained from transmission electron microscopes: JEOL JEM 2010F HRTEM (200 kV field emission gun).

***N*-(11-Mercaptoundecanoyl)-5-bromo-7-nitroindoline 1.** To a solution of *N*-(11-bromoundecanoyl)-5-bromo-7-nitroindoline **2** (1.00 g, 2.04 mmol) in dry ethanol (10 mL) was added

* E-mail: jbc@kiku.dk, ksch@ruc.dk.
† Nano-Science Center, University of Copenhagen.
‡ Department of Chemistry, University of Copenhagen.
§ Bio-Nanotechnology Laboratory and Department of Neuroscience and Pharmacology, University of Copenhagen.
|| Roskilde University.

10.1021/bc900561m © 2010 American Chemical Society
Published on Web 05/21/2010

$Na_2S_2O_3 \cdot 5H_2O$ (0.54 g, 2.19 mmol) dissolved in water (3 mL). The reaction was followed by TLC (THF/hexane 1:1). The mixture was refluxed for 62 h. The solvents were removed in vacuo and $CHCl_3$ (25 mL) and hydrochoric acid (1 M, 25 mL) was added. After the reaction was complete, the organic phase was separated and dried ($MgSO_4$), filtered, and concentrated in vacuo. The crude material was crystallized from 2-propanol. Yielding *N*-(11-mercaptoundecanoyl)-5-bromo-7-nitroindoline (**1**) as yellow crystals, 0.63 g (70%). Melting point: 82 °C. ^{1}H NMR ($CDCl_3$): δ 1.13−1.32 (b, 12H), 1.50−1.70 (b, 4H), 2.36−2.49 (b, 4H), 3.12−3.18 (t, J = 8.3 Hz, 2H), 4.18−4.20 (t, J = 8.0 Hz, 2H), 7.45−7.46 (b, 1H), 7.71−7.72 (b, 1H). ^{13}C NMR ($CDCl_3$): δ 24.54, 24.69, 28.23−29.59 (7 peaks), 33.92, 35.44, 115.95, 125.35, 131.40, 133.92, 138.31, 171.25. FAB^+ MS: m/z = 443.1 [MH^+] E.A. Calcd. for $C_{19}H_{27}BrN_2O_3S$ (%) C, 51.47; H, 6.14; N, 6.29; found C, 51.10; H, 6.06; N, 6.19.

***N*-(11-Bromoundecanoyl)-5-bromo-7-nitroindoline 2.** 11-Bromoundecanoic acid (1.00 g, 3,77 mmol) was dissolved in thionyl chloride (1 mL). The solution was stirred at room temperature under N_2 for 1 h. A solution of 5-bromo-7-nitroindoline (*33*) (0.30 g, 1.23 mmol) in dry toluene (7 mL) was added, and the reaction mixture was refluxed for 18 h in the dark. The mixture was cooled to room temperature, and CH_2Cl_2 (5 mL) was added. The organic phase was washed with aqueous Na_2CO_3 (10% w/w) until the remaining acids had been removed. The organic phase was dried over $MgSO_4$, filtered, and concentrated in vacuo. The remaining oil was crystallized from 2-propanol, yielding 0.46 g (76%) of the *N*-(11-bromoundecanoyl)-5-bromo-7-nitroindoline (**2**) as yellow crystals. Melting point: 95 °C. ^{1}H NMR ($CDCl_3$): δ (ppm) 1.23−1.49 (b, 12H), 1.59−1.70 (b, 2H), 1.72−1.83 (b, 2H), 2.36−2.42 (t, J = 7.3 Hz, 2H), 3.12−3.18 (t, J = 8.3 Hz, 2H), 3.31−3.37 (t, J = 6.9 Hz, 2H), 4.14−4.20 (t, J = 8.0 Hz, 2H), 7.45−7.46 (b,1H), 7.71−7.72 (b, 1H). ^{13}C NMR ($CDCl_3$): δ (ppm) 1.12, 24.68, 28.03, 28.60, 28.81, 28.99, 29.20, 32.70, 33.97, 35.42, 49.45, 56.81, 115.95, 125.33, 131.39, 138.31, 171.23. FAB^+ MS: m/z = 490.9 [MH^+] E.A. Calcd. for $C_{19}H_{26}Br_2N_2O_3$ (%) C, 46.6; H, 5.3; N, 5.7; found C, 46.9; H, 5.3; N, 5.7.

Photochemical Cross-Linking Followed by NMR. 1 (0.23 mg, 500 nmol) and aminohexane (0.044 mg, 500 nmol) were dissolved in deuterated chloroform (1.5 mL) and placed in an NMR tube. The NMR tube was then exposed to 380 nm light for 20 min intervals and the NMR spectra were recorded. The concentrations had to be low enough to result in satisfactorily high conversion within a reasonable time period, and just high enough to get reasonable NMR signals with 64 scans. Higher concentrations lead to longer reaction times due to internal filtering of the incoming light by the absorption from the reaction products. The full NMR spectra can be found in Supporting Information Figures S1 and S2.

Preparation of Fluorescently Labeled BSA. BSA was labeled with Alexa Fluor 488 (BSA^{488}) according to manufacturers protocol. Purification of BSA^{488} was performed on FPLC equipped with Superdex G75 size exclusion column. Collection of fractions permitted the isolation of BSA^{488} in HEPES pH = 8 buffer and concentration of ∼5 μM. On average, 4.5 alexa molecules were coupled to every BSA protein.

Attachment of Fluorescently Labeled Protein to the Gold Surface. Gold surfaces were prepared by UHV deposition of a thin layer of chromium (10 nm) followed by a layer of gold (100 nm) to a glass slide. The gold surface was removed from the evaporator and immediately exposed to a 0.1 mM solution of **1** in chloroform. The surface was left to react for 5 h to form a SAM of the nitroindoline on the surface. The surface was exposed to a 5 μM solution of BSA^{488} in HEPES pH = 8 and irradiated for 5 min with a 150 W Xe arc lamp equipped with a monochromator set to a wavelength of 380 nm. The gold surface was washed 3 times with HEPES buffer and 3 times with Milli-Q grade water to remove unreacted material and equilibrated with HEPES. The experiment was accompanied by control experiments where gold surfaces were exposed to BSA^{488} in the dark and experiments where the surface was covered with dodecanethiol and irradiated (Figure 7). Integrating the fluorescent intensity signal revealed a 6-fold increase in the binding of BSA^{488} compared to the control experiments. The relatively low increase in the fluorescent signal may originate from the depletion of the free solvent accessible lysines due to the labeling with Alexa Fluor 488.

Synthesis of Colloidal Gold Nanoparticles. The synthesis of the alkyl thiol stabilized gold nanoparticles (AuNPs) followed a slightly modified procedure from the one initially developed by Brust (*34*), which is a two-phase (toluene−water) reduction of $HAuCl_4$ in the presence of a stabilizing ligand. We used the thiol-functionalized **1** as the stabilizing thiol layer.

To a solution of $HAuCl_4 \cdot 3H_2O$ (0.10 g, 0.25 mmol) in water (8.50 mL) was added a solution of tetraoctyl ammonium bromide (0.35 g, 0.64 mmol) in toluene (25 mL). The reaction mixture was stirred vigorously under nitrogen atmosphere and compound **1** (0.11 g, 0.25 mmol) was added. The reaction mixture was stirred for 10 min and a solution of sodium borohydride (0.11 g, 2.74 mmol) in water (7.5 mL) was added dropwise. After the addition of sodium borohydride, the reaction mixture was left without stirring for 10 min, and the dark brown organic phase was separated and reduced in vacuo to a volume of approximately 5 mL. Ethanol (96%) was added and the reaction mixture was placed at −20 C overnight, allowing the black AuNPs to precipitate. The supernatant was filtered off, and the AuNPs were washed 4 times with ethanol (96%, 2 mL). Finally, the AuNPs was dried under a stream of nitrogen leaving the AuNPs as a black material (120 mg).

^{1}H NMR ($CDCl_3$): δ (ppm) 1.15−1.60 (b, 16 H), 2.36−2.41 (t, 1H, J = 7.18 Hz), 2.57−2.64 (t, 1H, J = 7.28 Hz), 3.12−3.18 (t, J = 8.20 Hz, 2H), 4.14−4.20 (t, J = 8.1 Hz, 2H), 7.45 (b, 1H), 7.70 (b, 1H). ^{13}C NMR ($CDCl_3$): δ (ppm) 13.95, 22.24, 22.47, 24.70, 26.34, 28.37−29.60 (5 peaks), 31.52, 35.44, 49.46, 59.22, 125.30, 131.40, 138.37, 171.26.

The **1** functionalized gold nanoparticles were further functionalized by adding a solution of 1,6-hexanediamine (45 mg, 0.39 mmol in chloroform (1 mL) to a solution of the gold nanoparticles (12 mg) in chloroform (1 mL). The gold nanoparticles were cooled in an ice/acetone bath and irradiated for 4 h with a 150 W Xe arc lamp equipped with a monochromator set to 380 nm. The nanoparticles precipitated leaving a clear solution with a black nanoparticle precipitate. The structure of the precipitate containing the nanoparticles was verified by TEM microscopy (Figure 4).

RESULTS AND DISCUSSION

The coupling reaction using Bni-based linkers does not require any auxiliary reactants such as metal catalysts or activated esters; it proceeds via a photoactivated, reversible transfer of the acyl group to the neighboring nitro group to form a very reactive acyl nitronate intermediate (*32, 35, 36*). If exposed to a nucleophile, the reaction will proceed as outlined in Figure 1. In the absence of nucleophile, the nitroindoline will revert to its initial form. This unique characteristics allows **1** to retain its functional form until the right criteria (nucleophile and light activation) are met (*28, 30*).

Compound **1** was synthesized from available 11-bromo undecanoic acid **3** via the reactive acid chloride **4** as outlined in Figure 2 and in the experimental section.

To test the coupling efficiency of **1**, we initially coupled it to 1-aminohexane in chloroform and monitored the reaction progress by UV−vis spectroscopy. As seen from Figure 3, the

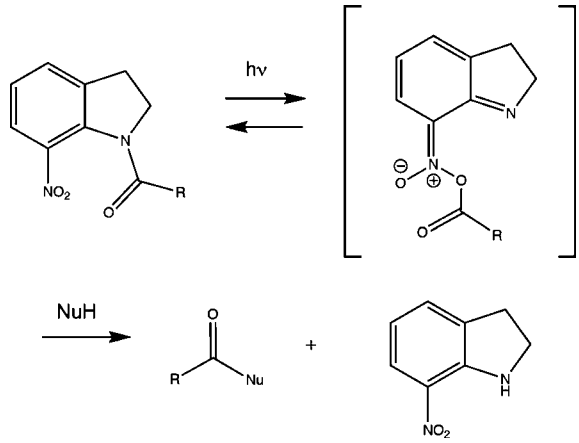


Figure 1. Mechanism for the photochemical activation of 7-nitroindolineamides (*32*).

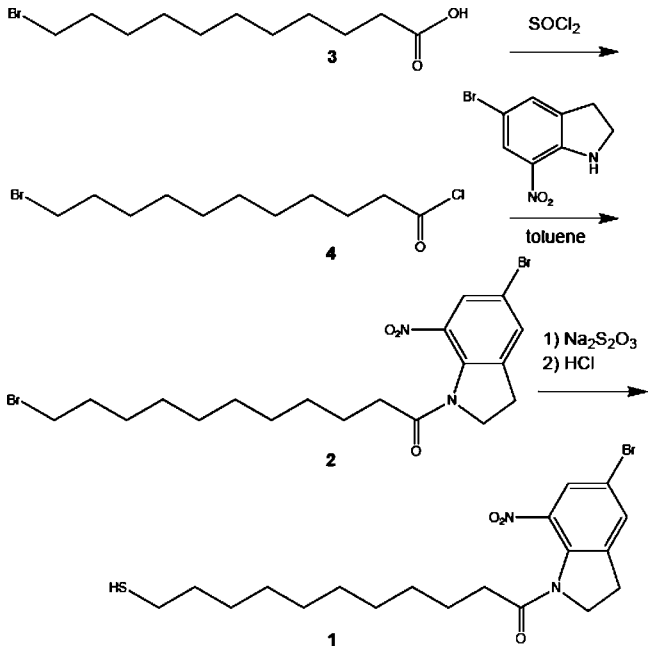


Figure 2. Synthesis of 1-(5-Bromo-7-nitro-2,3-dihydro-indol-1-yl)-11-mercapto-undecan-1-one (**1**).

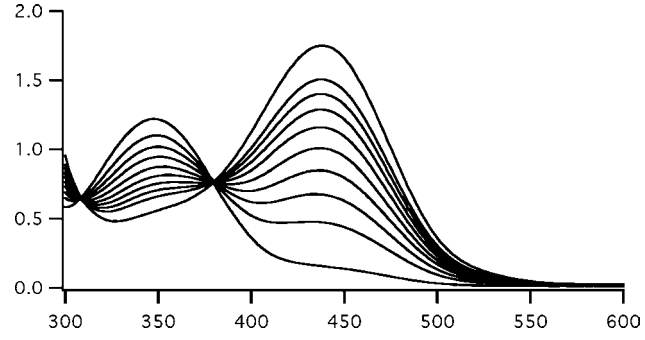


Figure 3. UV−vis spectra of the photoactivated reaction of 7-nitroindolineamide **1** with 1-hexaneamine in chloroform. The absorption band at 340 nm from the 7-nitroindolineamide **1** diminishes as the band at 440 nm from the free indoline rises during a period of 120 min.

absorption band at 340 nm from the 7-nitroindolineamide **1** diminishes as the band at 440 nm from the free indoline rises during a period of 120 min. A test reaction at the same reaction conditions, but without 1-aminohexane, showed no significant degradation of **1**. We further validated our initial observations

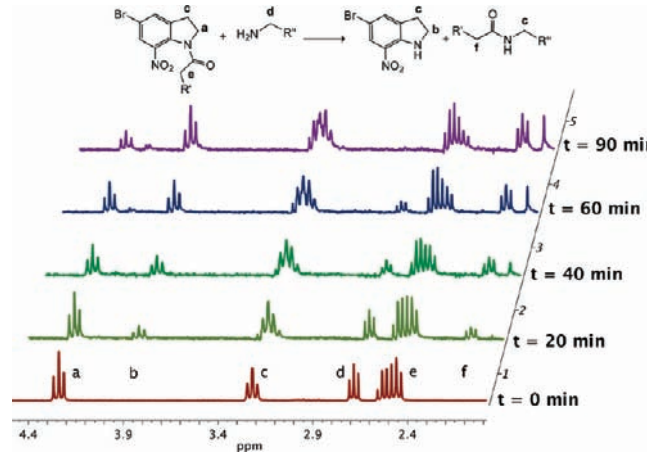


Figure 4. NMR spectra of the photoactivated reaction of 7-nitroindolineamide **1** with 1-aminohexane in chloroform.

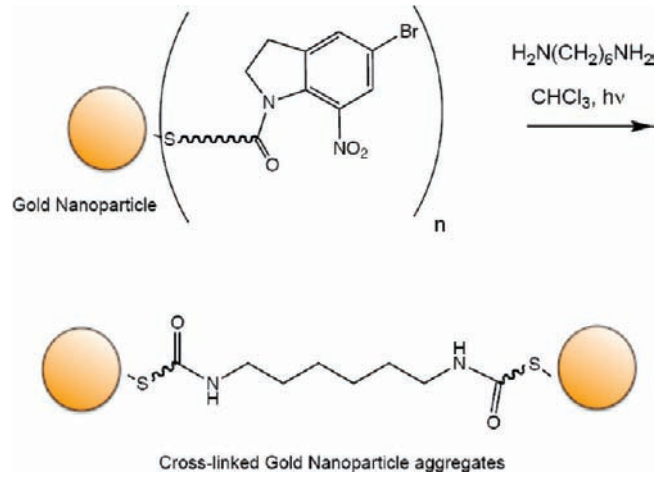


Figure 5. Mechanism for the photochemical cross-linking of the 7-nitroindolineamide-functionalized gold nanoparticles in the presence of 1,6-hexanediamine.

by monitoring the reaction by NMR spectroscopy (Figure 4). The figure represents a selected area (2.0−4.5 ppm) of the NMR spectrum of a mixture of 7-nitroindolineamide and 1-aminohexane at various exposure times (see Supporting Information S1 and S2 for full spectra). The reaction mixture was irradiated for 90 min, and NMR spectra were recorded at 0, 20, 40, 60, and 90 min of irradiation. During this period of time, the signal from the aliphatic protons on the indoline, **a** at 4.25 ppm, together with the α-protons on 1-aminohexane, **d**, were slowly disappearing, demonstrating that both reactants were consumed as the reaction progressed. The signal from the indoline protons **a** did not disappear completely, due to a slight excess of this reactant compared to the 1-aminohexane. Concurrently, new peaks for the aliphatic protons on the indoline product appeared at 3.9 ppm, **b**, together with a triplet at 2.1 ppm from the **f** protons on the newly formed amide, thus confirming the appearance of the two reaction products. The absence of any side products in combination with the quantitative reaction yield (based on NMR) illustrates the high efficiency of the photoactivated coupling reaction.

To test the reactivity of **1** once linked to a metal surface, we performed a simple test experiment: Photoinduced reaction of nanoparticles covered with **1** with a suitable α,ω-diamine should lead to clustering of the particles (Figure 5). Indeed, after exposure to light (380 nm) for 240 min the sample had changed from a dark solution to a clear solution with a dark precipitate. This precipitate was analyzed by TEM (Figure 6b). By

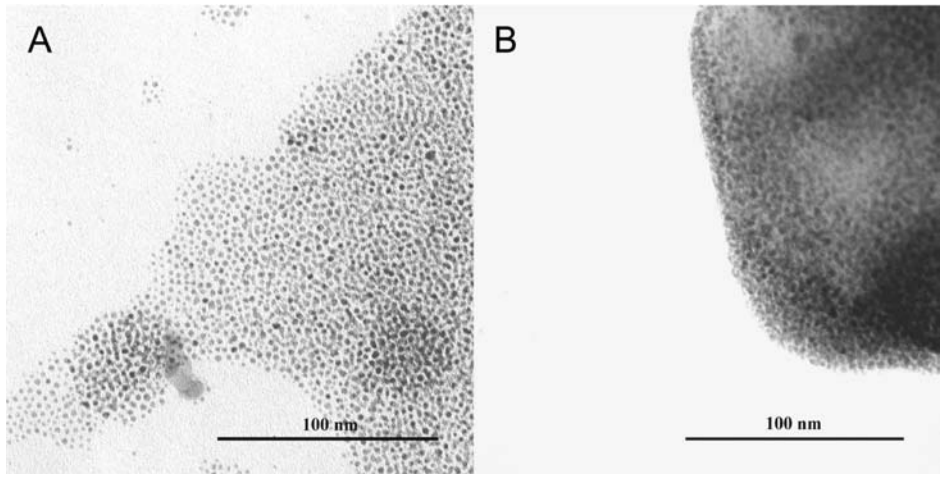


Figure 6. TEM micrographs of the nanoparticles. (A) The nanoparticles before irradiation. (B) One aggregate of gold nanoparticles after irradiation.

comparison of the two TEM pictures, it is evident that the nanoparticles (Figure 6a) were aggregated as a consequence of the reaction with the diamine, as seen in Figure 6b. To verify this result, three control experiments were carried out: (1) A solution of gold nanoparticles covered with **1** did not show any signs of reaction on exposure to light. (2) A mixture of a solution of gold nanoparticles covered with 1-dodecanethiol and 1,6-hexanediamine did not change upon irradiation, thus excluding light-induced ligand exchange, and (3) A solution of gold nanoparticles derivatized with **1** in $CHCl_3$ mixed with excess 1,6-diaminohexane did not change in the absence of light. A sample volume from the third test experiment was removed from the reaction mixture and analyzed by TEM (Figure 6a).

This observation together with the fact that both light and 1,6-diaminohexane are necessary for the precipitation to take place shows that postmodification of thiol-protected gold nanoparticles is possible utilizing **1**.

To further verify the versatility of the reaction, we successfully attached proteins to gold surfaces functionalized with SAMs of **1**. Bovine serum albumin (BSA) labeled with Alexa 488 NHS according to manufacturer's protocol (a fluorescence intensity trace of the FPLC purification is shown in the Supporting Information S3), and was exposed to the functionalized gold surface with and without exposure to a 380 nm wavelength light source. Fluorescence micrographs of the resulting surface are depicted in Figure 7.

Figure 7A shows the image of BSA^{488} coupled to SAM of **1** on gold using UV irradiation. To ensure the validity of our observations, we performed the following control experiments. First, we incubated BSA^{488} over the gold surface without UV activation. As shown in Figure 7B, limited nonspecific binding is obtained demonstrating that reaction only occurs after photoactivation. We then incubated BSA^{488} on a gold surface covered by a SAM of dodecane thiol with UV activation. In Figure 7C, we demonstrate that only limited binding takes place, thus illustrating that both compound **1** and light activation are necessary for the linking of the protein to the surface. To further quantify the degree of attachment of protein to the surfaces, we integrated the fluorescence intensity of a series of samples. The results of three independent experiments are shown in Figure 7D. The error bars represent the standard deviation of individual images. The integrated fluorescence signal form the functionalized surfaces revealed a ~6-fold increased binding of BSA^{488} compared to the controls, thus clearly demonstrating

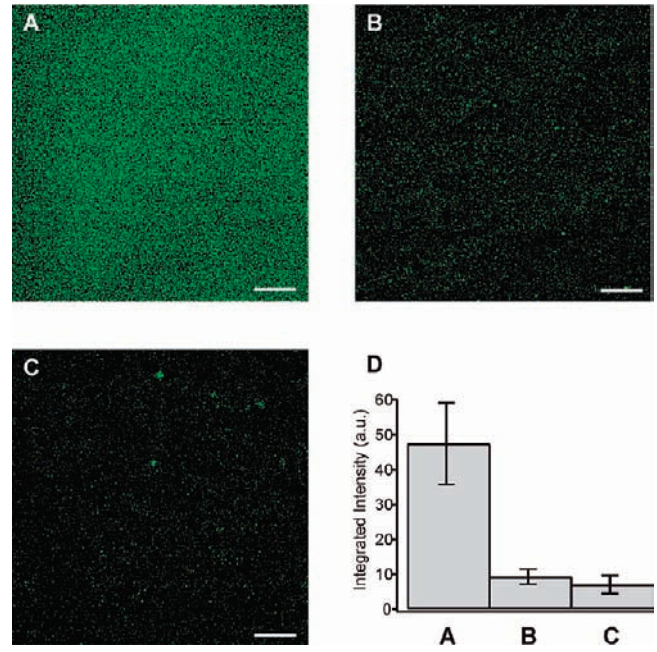


Figure 7. Quantification of the efficiency of **1** to immobilize BSA on gold surfaces using quantitative fluorescent microscopy. (A) Micrograph of Alexa 488 labeled BSA coupled ot SAM of **1** on gold using UV irradiation. (B) Nonspecific binding of BSA on SAMs of **1** in the absence of UV activation. (C) Nonspecific binding of BSA on SAMs of dodecane thiol after UV activation. (D) Integrated fluorescent intensity of the A−C micrographs, respectively. The error bars represent the s.d of individual images. Scale bar is 30 μm.

that the Bni SAMs can be used to link proteins to gold surfaces via photoactivation.

CONCLUSION

A versatile method for construction of protein conjugates using optically induced activation has been developed. We have tested the concept by showing that both light activation and a nucleophile are necessary for the reaction to proceed. As a proof of principle, we have used this chemistry to functionalize gold nanoparticles. The reaction has been investigated by the use of UV−vis spectroscopy and TEM imaging of the aggregated gold nanoparticles.

The method is simple to use, and involves only one light-induced reaction step to activate a surface for protein attachment. In contrast to Sharpless-type click chemistries (*23*−*25*), no

auxiliary reagents or heavy metal ions are needed, and in contrast to activated ester strategies such as NHS esters (*10*), the reactive species used here, the Bni group is stable for long periods of time (years of shelf-life time). As a proof of principle, we successfully coupled proteins to gold surfaces. By careful selection of the end group, Bni might also be employed to attach protein or other nucleophile-containing molecules on silicon surfaces or on polymers.

We foresee that this concept can, in a more general way, be used both for the attachment of nucleophiles to surfaces and for the subsequent release of active components by an external stimuli in the form of light. Also, we expect that this photoactive linker molecule will allow for a simple immobilization of arrays of DNA or proteins on surfaces integrated in advanced devices such as microfluidic channels.

ACKNOWLEDGMENT

D.S. would like to thank the Danish Councils for Independent and Strategic Research for funding. K.M.P. would like to thank The Danish Council for Independent Research for funding.

Supporting Information Available: Information on the purification of the protein conjugate and full NMR spectra of the irradiated mixtures. This material is available free of charge via the Internet at http://pubs.acs.org.

LITERATURE CITED

(1) Wong, S. L., Khan, F., and Micklefield, J. (2009) Selective covalent protein immobilization: strategies and applications. *Chem. Rev. 109*, 4025–4053.

(2) Camarero, J. A. (2008) Recent developments in the site-specific immobilization of proteins onto solid supports. *Biopolymers 90*, 450–458.

(3) Hatzakis, N. S., Engelkamp, H., Velonia, K., Hofkens, J., Christianen, P. C. M., Svendsen, A., Patkar, S. A., Vind, J., Maan, J. C., Rowan, A. E., and Nolte, R. J. M. (2006) Synthesis and single enzyme activity of a clicked lipase-BSA hetero-dimer. *Chem. Commun. 19*, 2012.

(4) English, B. P., Min, W., van Oijen, A. M., Lee, K. T., Luo, G. B., Sun, H. Y., Cherayil, B. J., Kou, S. C., and Xie, X. S. (2006) Ever-fluctuating single enzyme molecules: Michaelis-Menten equation revisited. *Nat. Chem. Biol. 2* (2), 87–94.

(5) Wu, G., Datar, R. H., Hansen, K. M., Thundat, T., Cote, R. J., and Majumdar, A. (2001) Bioassay of prostate-specific antigen (PSA) using microcantilevers. *Nat. Biotechnol. 19*, 856–860.

(6) MacBeath, G., and Schreiber, S. L. (2000) Printing proteins as microarrays for high-throughput function determination. *Science 289*, 54851760−1763.

(7) Kuznetsova, S., Zauner, G., Aartsma, T. J., Engelkamp, H., Hatzakis, N., Rowan, A. E., Nolte, R. J. M., Christianen, P. C. M., and Canters, G. W. (2008) The enzyme mechanism of nitrite reductase studied at single-molecule level. *Proc. Natl. Acad. Sci. U.S.A. 105*, 3250–3255.

(8) Camarero, J. A. (2008) Recent developments in the site-specific immobilization of proteins onto solid supports. *Biopolymers 90*, 450–458.

(9) Hermanson, G. T. (2008) *Bioconjugate Techniques*, 2nd ed., Academic Press, London.

(10) Tourniera, E. J. M., Wallach, J., and Blonda, P. (1998) Sulfosuccinimidyl 4-(N-maleimidomethyl)-1-cyclohexane carboxylate as a bifunctional immobilization agentOptimization of the coupling conditions. *Anal. Chim. Acta 361*, 33–44.

(11) Mateo, C., Torres, R., Fernandez-Lorente, G., Ortiz, C., Fuentes, M., Hidalgo, A., Lopez-Gallego, F., Abian, O., Palomo, J. M., Betancor, L., Pessela, B. C. C., Guisan, J. M., and Fernandez-Lafuente, R. (2003) Epoxy-amino groups: A new tool for improved immobilization of proteins by the epoxy method. *Biomacromolecules 4*, 772–777.

(12) Gemeiner, P., and Breier, A. (1982) Aldehydic derivatives of bead cellulose-relationships between the matrix structure and function in immobilization of enzymes catalyzing hydrolysis of high molecular substrates. *Biotechnol. Bioeng. 24*, 2573–82.

(13) Falsey, J. R., Renil, M., Park, S., Li, S. J., and Lam, K. S. (2001) Peptide and small molecule microarray for high throughput cell adhesion and functional assays. *Bioconjugate Chem 12*, 346–53.

(14) Olivier, C. (2003) Alpha-oxo semicarbazone peptide or oligodeoxynucleotide microarrays. *Bioconjugate Chem. 14*, 430–9.

(15) Groll, J., Amirgoulova, E. V., Ameringer, T., Heyes, C. D., Rocker, C., Nienhaus, G. U., and Moller, M. (2004) Biofunctionalized, ultrathin coatings of cross-linked star-shaped poly(ethylene oxide) allow reversible folding of immobilized proteins. *J. Am. Chem. Soc. 126*, 4234–4239.

(16) Schmid, E. L., Keller, T. A., Dienes, Z., and Vogel, H. (1997) Reversible oriented surface immobilization of functional proteins on oxide surfaces. *Anal. Chem. 69*, 1979–1985.

(17) Hodneland, C. D., Lee, Y. S., Min, D. H., and Mrksich, M. (2002) Selective immobilization of proteins to self-assembled monolayers presenting active site-directed capture ligands. *Proc. Natl. Acad. Sci. U.S.A. 99*, 5048–5052.

(18) Muir, T. W., Sondhi, D., and Cole, P. A. (1998) Expressed protein ligation: A general method for protein engineering. *Proc. Natl. Acad. Sci. U.S.A. 95*, 6705–6710.

(19) Camarero, J. A., Kwon, Y., and Coleman, M. A. (2004) Chemoselective attachment of biologically active proteins to surfaces by expressed protein ligation and its application for "protein chip" fabrication. *J. Am. Chem. Soc. 126*, 14730–14731.

(20) Mezzasoma, L., Bacarese-Hamilton, T., Di Cristina, M., Rossi, R., Bistoni, F., and Crisanti, A. (2002) Antigen microarrays for serodiagnosis of infectious diseases. *Clin. Chem. 48*, 121–130.

(21) Perler, F. B. (1999) A natural example of protein trans-splicing. *Trends Biochem. Sci. 26*, 209–211.

(22) Sigal, G. B., Mrksich, M., and Whitesides, G. M. (1998) Effect of surface wettability on the adsorption of proteins and detergents. *J. Am. Chem. Soc. 120*, 3464–3473.

(23) Kolb, H. C., Finn, M. G., and Sharpless, K. B. (2001) Click chemistry: Diverse chemical function from a few good reactions. *Angew. Chem., Int. Ed. 40*, 2004–2021.

(24) Baskin, J. M., Prescher, J. A., Laughlin, S. T., Agard, N. J., Chang, P. V., Miller, I. A., Anderson, L., Codelli, J. A., and Bertozzi, C. R. (2007) Copper-free click chemistry for dynamic in vivo imaging. *Proc. Natl. Acad. Sci. U.S.A. 104*, 16793–16797.

(25) Tornøe, C. W., Christensen, C., and Meldal, M. (2002) Peptidotriazoles on solid phase: [1,2,3]-triazoles by regiospecific copper(i)-catalyzed 1,3-dipolar cycloadditions of terminal alkynes to azides. *J. Org. Chem. 67*, 3057–3064.

(26) Brennan, J. L., Hatzakis, N. S., Tshikhudo, T. R., Dirvianskyte, N., Razumas, V., Patkar, S., Vind, J., Svendsen, A., Nolte, R. J. M., Rowan, A. E., and Brust, M. (2006) Bionanoconjugation via click chemistry: The creation of functional hybrids of lipases and gold nanoparticles. *Bioconjugate Chem. 17*, 1373–1375.

(27) Wang, Q., Chan, T. R., Hilgraf, R., Fokin, V. V., Sharpless, B. K., and Finn, M. G. (2003) Bioconjugation by copper(I)-catalyzed azide-alkyne [3 + 2] cycloaddition. *J. Am. Chem. Soc. 125*, 3192–3193.

(28) Amit, B., Ben-Efraim, D. A., and Patchornik, A. (1976) Light-sensitive amides. the photosolvolysis of substituted 1-acyl-7-nitroindolines. *J. Am. Chem. Soc. 98*, 843–844.

(29) Nicolaou, K. C., Safina, B. S., and Winssinger, N. (2001) A new photolabile linker for the photoactivation of carboxyl groups. *Synlett 2001*, 900.

(30) Pass, S., Amit, B., and Patchornik, A. (1981) Racemization-free photochemical coupling of peptide segments. *J. Am. Chem. Soc. 103*, 7674–7675.

(31) Papageorgiou, G., and Corrie, J. E. T. (2000) Effects of aromatic substituents on the photocleavage of 1-acyl-7-nitroindolines. *Tetrahedron 56*, 8197–8205.

(32) Hassner, A., Yagudayev, D., Pradhan, T. K., Nudelman, A., and Amit, B. (2007) Light-sensitive protecting groups for amines and alcohols: the photosolvolysis of N-substituted 7-nitroindolines. *Synlett. 15*, 2405–2409.

(33) Mortensen, M. B., Kamounah, F. S., and Christensen, J. B. (1996) Improved preparation of some nitroindolines. *Org. Prep. Proced. Int. 28*, 123–125.

(34) Brust, M., Fink, J., Bethell, D., Schriffrin, D. J., and Kiely, C. J. (1995) Synthesis and reactions of functionalized gold nanoparticles. *Chem. Commun. 1995*, 1655–1656.

(35) Cohen, A. D., Helgen, C., Bochet, C. G., and Toscano, J. G. (2005) The mechanism of photoinduced acylation of amines by *N*-acyl-5,7-dinitroindoline as determined by time-resolved infrared spectroscopy. *Org. Lett. 7*, 2845–2848.

(36) Papageorgiou, G., Ogden, D., Kelly, G., and Corrie, J. E. T. (2005) Synthetic and photochemical studies of substituted 1-acyl-7-nitroindolines. *Photochem. Photobiol. Sci. 4*, 887–896.

BC900561M

Cationic Nucleoside Lipids Derived from Universal Bases: A Rational Approach for siRNA Transfection

Claire Ceballos,[†] Salim Khiati,[‡] Carla A. H. Prata,[§] Xiao-Xiang Zhang,[§] Suzanne Giorgio,[†] Philippe Marsal,[†] Mark W. Grinstaff,[§] Philippe Barthélémy,*[,‡] and Michel Camplo*[,†]

Centre Interdisciplinaire de Nanoscience de Marseille CINaM, Upr-Cnrs 3118, Université Aix-Marseille II, Luminy, case 913, 13288 Marseille cedex 09, France, Inserm, U869, Université de Bordeaux, F-33076, Bordeaux, France, and Departments of Chemistry and Biomedical Engineering, Metcalf Center for Science and Engineering, Boston University, Boston, Massachusetts 02215. Received January 6, 2010; Revised Manuscript Received April 27, 2010

Cationic nucleoside lipids (CNLs) derived from 5-nitroindole and 4-nitroimidazole bases were prepared from D-ribose by using a straightforward chemical synthesis. TEM experiments indicate that these amphiphilic molecules self-assemble to form supramolecular organizations in aqueous solutions. Electrophoresis and standard ethidium bromide (EB) fluorescence displacement assay shows that CNLs are able to bind siRNA. We demonstrated that both the nature of the universal bases and the stereochemistry of the anomeric position (α, β) have an impact on the CNLs-siRNA complex formation. Correlations among chemical structure, stereochemistry, siRNA knockdown effect, and binding affinities for all the compounds were shown and analyzed with a simple molecular modeling study. The best binding affinities for siRNA were found for the β anomer of the 5-nitroindole CNL which exhibits protein knockdown activity similar to the standard siPORT NeoFX positive control. It is noteworthy that no significant cytotoxicity at the tested concentration was observed for the novel CNLs.

INTRODUCTION

Currently, there is substantial interest in the design of bioinspired molecules having a double functionality based on the combination of nucleic acids and lipid characteristics (*1*−*4*). Nucleoside lipids are emerging as tools for constructing both supramolecular assemblies and nucleic acid delivery applications. The 2′-deoxyribosyl derivatives of 3-nitropyrrole and 5-nitroindole represent a new class of compounds known as universal bases. When incorporated into oligonucleotides, they show little discrimination in their base-pairing properties, as they have no hydrogen bonding capability. Recently (*5*), we have described the synthesis and siRNA transfection activities of cationic nucleoside lipids (CNLs) **A** and **B** based on a 3-nitropyrrole universal base (Figure 1). The encouraging biological results with such derivatives prompt us to further investigate the potential of new CNL analogues containing the 5-nitroindole and 4-nitroimidazole universal bases (Figure 2). We hypothesized that the chemical structure of CNLs could have an impact on the siRNA/CNL stability and siRNA delivery. Indeed, puzzling questions are emerging from the siRNA/CNL complexes, for example, how can the structure and/or the stereochemistry of the universal base affect the formation siRNA/CNL or the transfection properties? To address these issues, the following two structural parameters were modulated: (i) the nature of the universal bases (5-nitroindole and 4-nitroimidazole) and (ii) the stereochemistry of the anomeric position.

The target CNLs shown in Figure 2 possess three key components: a quaternized amine at the 5 position, two oleic acid chains linked at the 2 and 3 positions, and a 5-nitroindole or a 4-nitroimidazole attached at the anomeric position. As for the 3-nitropyrrole derivatives **A** and **B** shown in Figure 1, the cationic charge of these new analogues is responsible for electrostatic binding to the nucleic acids, whereas the oleyl chains

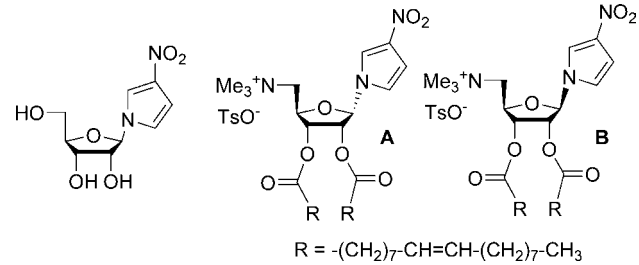


Figure 1. Chemical structures of the (β) universal nucleobase (left) and both CNLs (tosylate salts of 1′-(2′,3′-dioleyl-5′-trimethylammonium-α-D-ribofuranosyl)-3-nitropyrrole **A** and 1′-(2′,3′-dioleyl-5′-trimethylammonium-β-D-ribofuranosyl)-3-nitropyrrole **B** (*2*).

contribute to stabilization of the resulting nucleic acid−nucleolipid assembly through hydrophobic chain−chain interactions.

The 5-nitroindole universal base was selected because 1-(2′-deoxyribofuranosyl)-5-nitroindole has been shown to be generally less destabilizing than 1-(2′-deoxyribofuranosyl)-3-nitropyrrole analogue, with only a 2 °C decrease in melting temperature (T_m) value when incorporated toward the end of a 17mer duplex and 5 °C in the middle (*6*). It was suggested that this stabilization occurs because this nucleoside is sufficiently large to be able to intercalate into the opposite strand. The crystal structure of 1-(2′-deoxyribofuranosyl)-5-nitroindole shows that the base residues stack in columns, with overlap between each aromatic base (*7*). Also, 1-(2′-deoxyribofuranosyl)-5-nitroindole is nondiscriminating toward the natural DNA bases, with a T_m range of 3 °C, similar to that observed with the 3-nitropyrrole analogue.

Herein, we report the synthesis, physicochemical properties, and siRNA transfection efficiency of the universal-base nucleolipids, 2′,3′-dioleyl-5′-*O*-(α,β)-D-ribofuranosyl-5-nitroindole and 2′,3′-dioleyl-5′-*O*-(α-D-ribofuranosyl-4-nitroimidazole.

MATERIAL AND METHODS

Unless noted otherwise, all starting materials were purchased from Sigma-Aldrich, Acros, or Alfa Aesar and used as received.

* Corresponding author. camplo@univmed.fr.
[†] Upr-Cnrs 3118.
[‡] Inserm, U869.
[§] Boston University.

10.1021/bc100005k © 2010 American Chemical Society
Published on Web 05/19/2010

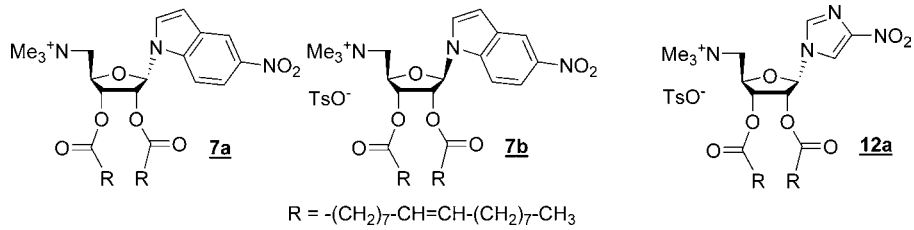


Figure 2. Chemical structures of the universal cationic nucleoside lipids (CNLs) used in this study. Tosylate salts of 1-(2,3-dioleyl-5-trimethylammonium-α-D-ribofuranosyl)-5-nitroindole and 1-(2,3-dioleyl-5-trimethylammonium-*β*-D-ribofuranosyl)-5-nitroindole, **7a** and **7b**, respectively. 1-(2,3-dioleyl-5-trimethylammonium-*β*-D-ribofuranosyl)-4-nitroimidazole) **12a**.

Some solvents were distilled under argon over appropriate drying agent: tetrahydrofuran and diethylether over sodium/benzophenone, dichloromethane over $CaCl_2$. Unless otherwise stated, the other solvents were used as commercially available. All compounds were characterized by ^1H NMR, ^{13}C NMR, and mass spectroscopy. 250 and 62.5 MHz ^{13}C nuclear magnetic resonance (NMR) spectra were recorded on a Bruker AC 250. The spectra were taken at 20 °C and referenced against residual proton-solvent signals (^1H, $CDCl_3$, 7.26 ppm; and ^{13}C, 77 ppm). The ^1H NMR coupling constants (*J*) are reported in hertz. ESI-MS and elemental analyses were performed at the spectropole of the Faculté des Sciences et Techniques de Saint Jerôme, Marseille, France. Electrospray ionization mass spectra (ESI-MS) were recorded with an API///Plus sciex triple quadripole spectrophotometer in the positive mode. Elemental analyses were recorded with a Thermo Finnigan EA 1112 elemental analysis apparatus driven by the Eager 300 software. TEM microscopy experiments were performed on a Philipps CM10 (negative staining with ammonium molybdate 1% in water, Cu/Pd carbon coated grids). Analytical thin layer chromatography (TLC) was performed on precoated glass plates with Kieselgel 60F254 neutral with aluminum support plate (0.25 mm layer thickness), SDS. The developed plates were air-dried and exposed to UV light and/or sprayed with a solution of cerium sulfate (1%) and molybdic acid (1.5%) in 10% aqueous sulfuric acid and heated at 150 °C. Preparative thin layer chromatography was performed on glass plates with Merck silica gel 60F-254 as the adsorbent (layer thickness 2 mm or 1 mm). Column chromatography was performed on Merck silica gel 60 (0.063−0.200 mm). Melting point (mp) were measured with an Electrothermal 9100. The synthesis of compounds **1**, **2**, and **2′** is described in the Supporting Information.

1-(5-*O*-*tert*-Butyldimethylsilyl-2,3-*O*-isopropylidene-D-ribofuranosyl)-5-nitroindole, 3. *Step 1.* Carbon tetrachloride (433 μL, 4.49 mmol) was added to a stirring solution of **2** (872 mg; 2.87 mmol) in anhydrous THF (10 mL). The solution was cooled to −70 °C and hexamethylphosphorous triamide (700 μL, 3.82 mmol) was added dropwise for 5 min, and the mixture was allowed to stir at the same temperature for 5 min. The resulting chewy compound was allowed to warm to room temperature and further stirred for 2 h. The solvent was evaporated and the residue dissolved in diethyl ether. The resulting insoluble material was removed by decantation and the organic layer was evaporated to give the crude compound **3** as an orange oil.

Step 2. To a cooled solution (0 °C) of 5-nitroindole (906 mg, 5.59 mmol) dissolved in anhydrous acetonitrile (9 mL) was added NaH (60%, 223 mg, 5.61 mmol); the solution was stirred at room temperature for 30 min. To the resulting bright yellow solution, the chlorosugar obtained from the first step was dissolved in anhydrous acetonitrile and transferred via canula. The reaction mixture was then warmed to room temperature and stirred for 40 h. The mixture was poured into H_2O (50 mL) and extracted with CH_2Cl_2 (3 × 50 mL). The organic layers were combined and successively washed with saturated aqueous NH_4Cl and saturated aqueous NaCl. The organic layer was dried over $MgSO_4$ and concentrated in vacuo. The residue was purified by flash column chromatography (90/10: cyclohexane/EtOAc) to give **3** (502 mg, 39%) as a yellow oil (anomeric mixture). ^1H NMR ($CDCl_3$): *δ* 8.57 (1H, d, $J = 2.14$ Hz, H_4); 8.11 (1H, dd, $J = 2.14$ Hz, $J = 9.12$ Hz, H_6); 7.60 (1H, d, $J = 3.43$ Hz, H_3); 7.30 (1H, d, $J = 9.12$ Hz, H_9); 6.71 (1H, d, $J = 3.43$ Hz, H_8); 6.48 (1Hα, d, $J = 4.11$ Hz, $H_{1'\alpha}$); 6.03 (1H*β*, d, $J = 3.38$ Hz, $H_{1'\beta}$); 4.96 (1H, d, $J = 6.06$ Hz, $H_{2'}$); 4.88 (1H, dd, $J = 4.15$ Hz, $J = 6.06$ Hz, $H_{3'}$); 4.45 (1H, m, $H_{4'}$); 3.95 (1H, dd, $J = 2.14$ Hz, $J = 11.05$ Hz, $H_{5'}$); 3.83 (1H, dd, $J = 2.14$ Hz, $J = 11.05$ Hz, $H_{5''}$); 1.43 (3H, s, CH_3−C); 1.30 (3H, s, CH_3−C); 1.00 (9H, s, $(CH_3)_3$−C); 0.15 (6H, s, $Si(CH_3)_2$). ^{13}C NMR ($CDCl_3$) *δ*: 138.34 (C_2); 129.81 (C_5); 128.14 (C_7); 118.08 (C_9); 117.30 (C_6); 113.29 (C_4); 109.24 (C_3); 104.16 (C−$(CH_3)_2$); 100.57 (C_8); 88.33 ($C_{1'}$); 82.76 ($C_{2'}$); 82.74 ($C_{4'}$); 80.53 ($C_{3'}$); 66.06 ($C_{5'}$); 29.69 (CH_3−C); 25.89 (CH_3−C); 25.71 ($(CH_3)_3$−C); 18.13 ($(CH_3)_3$−C); −5.46 ($Si(CH_3)_2$). MS (GT, FAB^+): 449 $[M+H]^+$. Rf (C_6H_{12}/EtOAc: 90/10): 0.54.

1-(2,3-*O*-Isopropylidene-D-ribofuranosyl)-5-nitroindole, 4a and 4b. To a solution of **3** (596 mg, 1.49 mmol) in dry THF (5 mL) was added TBAF (1 M in THF) (3 mL, 2.98 mmol) at room temperature, and the mixture was stirred for 30 min. The solution was evaporated under reduced pressure, diluted with CH_2Cl_2, and washed with brine. The organic layer was dried on $MgSO_4$ and evaporated under reduced pressure. The crude product was purified by flash column chromatography (cyclohexane/EtOAc: 70/30) to give the anomer α **4a** (198 mg, 54%) as a yellow oil and the anomer *β* **4b** (43 mg, 11%) as a yellow oil.

1-(2,3-*O*-Isopropylidene-α-D-ribofuranosyl)-5-nitroindole, 4a. ^1H NMR ($CDCl_3$): *δ* 8.57 (1H, d, $J = 2.16$ Hz, H_4); 8.10 (1H, dd, $J = 2.16$ Hz, $J = 9.10$ Hz, H_6); 7.60 (1H, d, $J = 3.43$ Hz, H_3); 7.41 (1H, d, $J = 9.10$ Hz, H_9); 6.72 (1H, d, $J = 3.43$ Hz, H_8); 6.45 (1H, d, $J = 3.93$ Hz, $H_{1'}$); 4.97 (2H, m, $H_{3'} + H_{2'}$); 4.50 (1H, t, $J = 2.75$ Hz, $H_{4'}$); 3.99 (1H, dd, $J = 2.75$ Hz, $J = 11.33$ Hz, $H_{5'}$); 3.88 (1H, dd, $J = 2.75$ Hz, $J = 11.33$ Hz, $H_{5''}$); 1.66 (1H, sl, OH); 1.40 (3H, s, CH_3−C); 1.30 (3H, s, CH_3−C). ^{13}C NMR ($CDCl_3$) *δ*: 141.79 (C_2); 138.39 (C_5); 129.78 (C_7); 128.08 (C_9); 118.04 (C_6); 117.23 (C_4); 113.59 (C_3); 109.59 ($(CH_3)_2$−C); 104.27 (C_8); 87.92 ($C_{1'}$); 82.75 ($C_{2'}$); 82.00 ($C_{4'}$); 80.45 ($C_{3'}$); 64.57 ($C_{5'}$); 25.67 (CH_3−C); 24.13 (CH_3−C). MS (GT, FAB^+): 335 $[M+H]^+$. HRMS (FAB^+): calculated for $[M+H]^+$ 335.1237, found 335.1243. Rf (C_6H_{12}/EtOAc: 50/50): 0.22.

1-(2,3-*O*-Isopropylidene-*β*-D-ribofuranosyl)-5-nitroindole, 4b. ^1H NMR ($CDCl_3$): *δ* 8.53 (1H, d, $J = 2.13$ Hz, H_4); 8.10 (1H, dd, $J = 2.13$ Hz, $J = 9.10$ Hz, H_6); 7.52 (1H, d, $J = 9.10$ Hz, H_3); 7.47 (1H, d, $J = 3.36$ Hz, H_9); 6.70 (1H, d, $J = 3.36$ Hz, H_8); 6.05 (1H, d, $J = 3.13$ Hz, $H_{1'}$); 4.94 (2H, m, $H_{3'} + H_{2'}$); 4.31 (1H, q, $J = 3.29$ Hz, $H_{4'}$); 3.92 (1H, dd, $J = 3.29$ Hz, $J = 12.00$ Hz, $H_{5'}$); 3.81 (1H, dd, $J = 3.29$ Hz, $J = 12.00$ Hz, $H_{5''}$); 2.32 (1H, sl, OH); 1.64 (3H, s, CH_3−C); 1.37 (3H, s, CH_3−C). ^{13}C NMR ($CDCl_3$) *δ*: 142.09 (C_2); 138.32 (C_5); 128.43 (C_7); 127.76 (C_9); 118.05 (C_6); 117.71 (C_4); 114.96 (C_3); 110.11 ($(CH_3)_2$−C); 105.42 (C_8); 91.76 ($C_{1'}$); 85.03 ($C_{2'}$); 84.42 ($C_{4'}$); 80.29 ($C_{3'}$); 62.29 ($C_{5'}$); 27.23 (CH_3−C); 25.22 (CH_3−C). SM

(GT, FAB^+): 335 $[M+H]^+$. HRMS (FAB^+): calculated for $[M+H]^+$ 335.1237, found 335.1244; Rf (C_6H_{12}/EtOAc: 50/50): 0.38.

1-(2,3-*O*-Isopropylidene-5-*O*-tosyl-α-D-ribofuranosyl)-5-nitroindole, 5a. Compound **4a** (100 mg, 0.30 mmol) was dissolved in dry dichloromethane (4 mL) and the solution was cooled to 0 °C. NEt_3 (168 μL, 1.20 mmol) was added, as well as tosyl chloride (171 mg, 0.90 mmol), in small portions. The solution was then allowed to warm to room temperature and stirred overnight. Dichloromethane was added and the solution was successively washed with brine and aqueous $NaHCO_3$ 5% w/v. The organic layer was dried on $MgSO_4$, filtered, and concentrated under reduced pressure. The residue was purified by preparative layer chromatography (cyclohexane/EtOAc: 60/40) to give **5a** (137 mg, 94%) as a yellow oil. ^1H NMR ($CDCl_3$) δ: 8.55 (1H, d, $J = 2.21$ Hz, H_4); 8.10 (1H, dd, $J = 2.21$ Hz, $J = 9.00$ Hz, H_6); 7.83 (2H, d, $J = 9.00$ Hz, H_{Ar}); 7.54 (1H, d, $J = 3.47$ Hz, H_3); 7.35 (3H, m, $H_{Ar} + H_9$); 6.70 (1H, d, $J = 3.47$ Hz, H_8); 6.26 (1H, d, $J = 2.37$ Hz, $H_{1'}$); 4.93 (2H, m, $H_{2'} + H_{3'}$); 4.55 (1H, t, $J = 2.37$ Hz, $H_{4'}$); 4.27 (2H, d, $J = 2.64$ Hz, $H_{5'} + H_{5''}$); 2.44 (3H, s, CH_3-C_{Ar}); 1.41 (3H, s, CH_3-C); 1.25 (3H, s, CH_3-C). ^{13}C NMR ($CDCl_3$) δ: 145.76 (C_{Ar}); 141.97 (C_2); 138.41 (C_5); 132.06 (C_{Ar}); 130.20 ($2 \times \underline{C}H_{Ar}$); 129.64 ($C_7$); 128.06 ($2 \times \underline{C}H_{Ar}$); 127.86 ($C_9$); 117.98($C_6$); 117.36($C_4$); 114.04 ($C_3$); 109.54 ($(CH_3)_2-\underline{C}$); 104.52 ($C_8$); 87.84 ($C_{1'}$); 81.67 ($C_{2'}$); 80.09 ($C_{3'}$); 79.81($C_{4'}$); 71.22 ($C_{5'}$); 25.65 ($\underline{C}H_3-C$); 24.09 ($\underline{C}H_3-C$); 21.67 ($\underline{C}H_3-C_{Ar}$). MS (GT, FAB^+): 489 $[M+H]^+$; 506 $[M+NH_4]^+$. Rf (C_6H_{12}/EtOAc: 70/30): 0.22.

1-(2,3-*O*-Isopropylidene-5-*O*-tosyl-β-D-ribofuranosyl)-3-nitroindole, 5b. Compound **5b** was obtained in 53% yield from compound **4b** by the procedure described above. Purification by preparative layer chromatography (cyclohexane/EtOAc: 60/40) gave a yellow oil. ^1H NMR ($CDCl_3$): δ 8.56 (1H, d, $J = 2.13$ Hz, H_4); 8.05 (1H, dd, $J = 2.13$ Hz, $J = 9.10$ Hz, H_6); 7.52 (2H, d, $J = 7.96$ Hz, H_{Ar}); 7.44 (1H, d, $J = 9.10$ Hz, H_3); 7.37 (1H, d, $J = 3.45$ Hz, H_9); 7.27 (2H, d, $J = 7.96$ Hz, H_{Ar}); 6.71 (1H, d, $J = 3.45$ Hz, H_8); 6.02 (1H, d, $J = 2.84$ Hz, $H_{1'}$); 4.91 (2H, m, $H_{3'} + H_{2'}$); 4.41 (1H, q, $J = 2.84$ Hz, $H_{4'}$); 4.30 (1H, dd, $J = 2.84$ Hz, $J = 10.90$ Hz, $H_{5'}$); 4.19 (1H, dd, $J = 2.84$ Hz, $J = 10.90$ Hz, $H_{5''}$); 2.41 (3H, s, CH_3-C_{Ar}); 1.63 (3H, s, CH_3-C); 1.36 (3H, s, CH_3-C). ^{13}C NMR ($CDCl_3$) δ: 154.49 (C_{Ar}); 142.22 C_2); 138.24(C_5); 131.97 (C_{Ar}); 129.98 ($2 \times \underline{C}H_{Ar}$); 128.51 ($C_7$); 127.89 ($2\times \underline{C}H_{Ar}$); 127.72 ($C_9$); 118.04 ($C_6$); 117.74 ($C_4$); 115.30 ($C_3$); 110.15 ($(CH_3)_2-\underline{C}$); 105.54 ($C_8$); 91.99 ($C_{1'}$); 84.08 ($C_{2'}$); 81.96 ($C_{3'}$); 80.12 ($C_{4'}$); 68.42 ($C_{5'}$); 27.17 ($\underline{C}H_3-C$); 25.19 ($\underline{C}H_3-C$); 21.62 ($\underline{C}H_3-C_{Ar}$). MS (GT, FAB^+): 489 $[M+H]^+$, 511 $[M+Na]^+$. Rf (C_6H_{12}/EtOAc: 70/30): 0.60.

1-(2,3-dioleyl-5-*O*-tosyl-α-D-ribofuranosyl)-5-nitroindole, 6a. At 0 °C, compound **5a** (40 mg, 0.08 mmol) was dissolved in 1 mL of an aqueous trifluoroacetic acid/H_2O (6/1) solution and stirred for 1 h at 0 °C. The solvents were coevaporated with methanol under reduced pressure, and the residue was dried in vacuo. The crude product was dissolved in dry CH_2Cl_2 (4 mL) and the solution was cooled to 0 °C. Dicyclohexylcarbodiimide (68 mg, 0.33 mmol), (dimethylamino)pyridine (40 mg, 0.33 mmol), and oleic acid (93 mg, 0.33 mmol) were added, and the mixture was stirred at room temperature overnight. DCU was then filtered, and the filtrate was successively washed with aqueous 2 N HCl and aqueous saturated $NaHCO_3$ solutions. The organic layer was dried on $MgSO_4$, filtered, and evaporated under reduced pressure. The crude product purified by flash column chromatography (cyclohexane/EtOAc: 70/30) gave **6a** (51 mg, 65%) as a yellow oil. ^1H NMR ($CDCl_3$): δ 8.55 (1H, d, $J = 2.21$ Hz, H_4); 8.11 (1H, dd, $J = 2.21$ Hz and $J = 9.16$ Hz, H_6); 7.84 (2H, d, $J = 8.27$ Hz, H_{Ar}); 7.46 (1H, d, $J = 2.21$ Hz, H_3); 7.43 (3H, m, $H_{Ar} + H_9$); 6.68 (1H, d, $J = 2.84$ Hz, $H_{1'}$); 6.33 (1H, d, $J = 5.37$ Hz, H_8); 5.62 (1H, t, $J = 5.69$ Hz, $H_{2'}$); 5.46 (1H, m, $H_{3'}$); 5.33 (4H, m, $2 \times C\underline{H}{=}C\underline{H}$); 4.56 (1H, q, $J = 2.84$ Hz, $H_{4'}$); 4.30 (2H, dd, $J = 2.84$ Hz, $J = 11.21$ Hz, $H_{5'} + H_{5''}$); 2.43 (3H, s, CH_3-C_{Ar}); 2.34 (2H, t, $J = 7.66$ Hz, $C\underline{H}_2-CO$); 2.25 (2H, t, $J = 7.33$ Hz, $C\underline{H}_2-CO$); 2.00 (8H, m, $2 \times C\underline{H}_2-CH{=}CH-C\underline{H}_2$); 1.60 (4H, m, $2 \times C\underline{H}_2-CH_2-CO$); 1.26 (40H, m, $2 \times 10\ CH_2$); 0.87 (6H, t, $J = 6.48$ Hz, $2 \times CH_3$). ^{13}C NMR ($CDCl_3$) δ: 172.15 (CO); 171.53 (CO); 145.50 (C_{Ar}); 142.12 (C_2); 138.70 (C_5); 132.06 (C_{Ar}); 130.01 ($2 \times \underline{C}H{=}\underline{C}H$); 129.53 ($2 \times CH_{Ar}$); 128.96 ($C_7$); 128.49 ($2 \times CH_{Ar}$); 127.97 ($C_9$); 125.85 ($C_6$); 125.19 ($C_4$); 104.31 ($C_3$); 100.78 ($C_8$); 79.82 ($C_{1'}$); 74.43 ($C_{4'}$); 73.80 ($C_{3'}$); 73.59 ($C_{2'}$); 65.57 ($C_{5'}$); 31.87 ($2 \times \underline{C}H_2-CO$); 29.78−28.67 ($2 \times 9\ CH_2$); 27.18 ($2 \times \underline{C}H_2-CH{=}CH-\underline{C}H_2$); 24.39 ($2 \times \underline{C}H_2-CH_2-CO$); 22.65 ($\underline{C}H_3-C_{Ar}$); 21.66 ($2 \times CH_3-\underline{C}H_2$); 14.09 ($2 \times CH_3$). MS (GT, FAB^+): 978 $[M+H]^+$; 1000 $[M+23]^+$. Rf (C_6H_{12}/EtOAc: 80/20): 0.39.

1-(2,3-Dioleyl-5-*O*-tosyl-β-D-ribofuranosyl)-5-nitroindole, 6b. Compound **6b** was obtained from **5b** with the same procedure described above. Purification by flash column chromatography (cyclohexane/EtOAc: 60/40) gave **6b** as a yellow oil in 73% yield. ^1H NMR ($CDCl_3$): δ 8.56 (1H, d, $J = 2.21$ Hz, H_4); 8.08 (1H, dd, $J = 2.21$ Hz, $J = 9.11$ Hz, H_6); 7.81 (2H, d, $J = 8.37$ Hz, H_{Ar}); 7.46 (2H, m, $H_3 + H_9$); 7.32 (2H, d, $J = 8.37$ Hz, H_{Ar}); 6.74 (1H, d, $J = 3.47$ Hz, $H_{1'}$); 6.13 (1H, d, $J = 6.63$ Hz, H_8); 5.45 (1H, t, $J = 6.00$ Hz, $H_{2'}$); 5.34 (6H, m, $2 \times C\underline{H}{=}C\underline{H} + H_{3'} + H_{4'}$); 4.34 (2H, m, $H_{5'} + H_{5''}$); 2.43 (3H, s, CH_3-C_{Ar}); 2.37 (2H, t, $J = 7.26$ Hz, CH_2-CO); 2.25 (2H, t, $J = 7.26$ Hz, CH_2-CO); 1.99 (8H, m, $2 \times C\underline{H}_2-CH{=}CH-C\underline{H}_2$); 1.63 (4H, m, $2 \times C\underline{H}_2-CH_2-CO$); 1.26 (40H, m, $2 \times 10\ CH_2$); 0.87 (6H, t, $J = 6.27$ Hz, $2 \times CH_3$). ^{13}C NMR ($CDCl_3$) δ: 172.44 (CO); 171.86 (CO); 145.50 (C_{Ar}); 142.34 (C_2); 138.91 (C_5); 132.04 (C_{Ar}); 130.07 ($2 \times \underline{C}H{=}\underline{C}H$); 130.08 ($2 \times CH_{Ar}$); 129.53 ($C_7$); 127.99 ($2 \times CH_{Ar}$); 127.25 ($C_9$); 118.12 ($C_6$); 117.82 ($C_4$); 109.62 ($C_3$); 99.69 ($C_8$); 86.90 ($C_{1'}$); 73.63 ($C_{4'}$); 73.02 ($C_{3'}$); 70.46 ($C_{2'}$); 64.07 ($C_{5'}$); 31.87 ($2 \times \underline{C}H_2-CO$); 29.72−28.89 ($2 \times 9\ CH_2$); 27.19 ($\underline{C}H_2-CH{=}CH-\underline{C}H_2$); 27.12 ($\underline{C}H_2-CH{=}CH-\underline{C}H_2$); 24.76 ($\underline{C}H_2-CH_2-CO$); 24.62 ($\underline{C}H_2-CH_2-CO$); 22.65 ($\underline{C}H_3-C_{Ar}$); 21.65 ($2 \times CH_3-\underline{C}H_2$); 14.09 ($2 \times CH_3$). MS (GT, FAB^+): 977 $[M+H]^+$; 999 $[M+23]^+$. Rf (C_6H_{12}/EtOAc: 60/40): 0.45.

Tosylate Salt of 1-(2,3-Dioleyl-5-trimethylammonium-α-D-ribofuranosyl)-5-nitroindole, 7a. Anhydrous triethylamine (1 mL) was transferred to a pressure tube cooled at −50 °C via canula. Next, anhydrous acetonitrile (2 mL) and a solution of **6a** (51 mg, 0.05 mmol) in dry THF (1 mL) were added. The tube was sealed and heated in an oil bath at 50 °C during 48 h, then cooled to −20 °C and opened. The solvents were evaporated under reduced pressure to give **7a** (54 mg, quantitative) as a yellow oil. ^1H NMR ($CDCl_3$): δ 8.48 (1H, d, $J = 2.05$ Hz, H_4); 7.88 (1H, dd, $J = 2.05$ Hz, $J = 9.07$ Hz, H_6); 7.74 (2H, d, $J = 8.05$ Hz, H_{Ar}); 7.49 (1H, d, $J = 2.05$ Hz, H_3); 7.35 (1H, d, $J = 6.48$ Hz, H_9); 7.11 (2H, d, $J = 8.05$ Hz, H_{Ar}); 6.66 (1H, d, $J = 3.50$ Hz, $H_{1'}$); 6.21 (1H, d, $J = 6.48$ Hz, H_8); 5.33 (4H, m, $2 \times C\underline{H}{=}C\underline{H}$); 4.70 (2H, m, $H_{2'} + H_{3'}$); 4.28 (1H, m, $H_{4'}$); 3.41 (9H, s, NCH_3^+); 3.33 (2H, m, $H_{5'} + H_{5''}$); 2.31 (3H, s, CH_3-C_{Ar}); 2.24 (4H, t, $J = 7.26$ Hz, $2 \times CH_2-CO$); 1.98 (8H, m, $2 \times C\underline{H}_2-CH{=}CH-C\underline{H}_2$); 1.53 (4H, m, $2 \times C\underline{H}_2-CH_2-CO$); 1.25 (40H, m, $2 \times 10\ CH_2$); 0.87 (6H, t, $J = 6.65$ Hz, $2 \times CH_3$). ^{13}C NMR ($CDCl_3$) δ: 172.65 (CO); 171.82 (CO); 145.50 (C_2); 143.39 (C_{Ar}); 142.29 (C_5); 139.63 (C_{Ar}); 130.03 ($2 \times \underline{C}H{=}\underline{C}H$); 130.00 ($2 \times CH_{Ar}$); 129.49 ($C_7$); 128.76 ($2 \times CH_{Ar}$); 127.16 ($C_9$); 125.91 ($C_6$); 125.73 ($C_4$); 101.20 ($C_3$); 96.05 ($C_8$); 83.17 ($C_{1'}$); 71.98 ($C_{3'}$); 66.55 ($C_{4'}$); 59.44 ($C_{2'}$); 66.93 ($C_{5'}$); 54.34 ($NCH_3^+$); 31.84 ($2 \times \underline{C}H_2-CO$); 30.23−28.90 ($2 \times 10\ CH_2$); 27.07 ($2 \times \underline{C}H_2-CH{=}CH-\underline{C}H_2$); 22.62 ($2 \times \underline{C}H_2-CH_2-CO$); 21.22 ($CH_3-C_{Ar}$); 21.22 ($2 \times CH_3-\underline{C}H_2$);

14.09 (2 × CH_3). MS (GT, FAB^+): 864 $[M-TsO^-]^+$. Anal. Calcd. C, 68.12; H, 9.00; N, 4.00; found C, 68.13; H, 8.97; N, 4.11.

Tosylate Salt of 1-(2,3-Dioleyl-5-trimethylammonium-β-D-ribofuranosyl)-5-nitroindole, 7b. This compound was prepared from **6b** with the same procedure described above to yield **7b** as a brown oil with quantitative yield. ^1H NMR ($CDCl_3$): δ 8.48 (1H, d, $J = 2.21$ Hz, H_6); 8.05 (1H, dd, $J = 2.21$ Hz, $J = 9.16$ Hz, H_4); 7.73 (3H, m, H_3 + H_{Ar}); 7.47 (1H, d, $J = 6.16$ Hz, H_9); 7.12 (2H, d, $J = 7.90$ Hz, H_{Ar}); 6.57 (1H, d, $J = 3.43$ Hz, $H_{1'}$); 6.21 (1H, d, $J = 6.16$ Hz, H_8); 5.32 (4H, m, 2 × C<u>H</u>═C<u>H</u>); 4.74 (1H, m, $H_{3'}$); 4.64 (1H, m, $H_{2'}$); 4.22 (1H, m, $H_{4'}$); 3.34 (9H, s, $N(CH_3)_3^+$); 3.27 (2H, m, $H_{5'}$ + $H_{5''}$); 2.32 (3H, s, CH_3-C_{Ar}); 2.26 (4H, t, $J = 7.42$ Hz, 2 × CH_2−CO); 1.98 (8H, m, 2 × C<u>H</u>$_2$−CH═CH−C<u>H</u>$_2$); 1.54 (4H, m, 2 × C<u>H</u>$_2$−CH_2−CO); 1.24 (40H, m, 2 × 10 CH_2); 0.86 (6H, t, $J = 6.32$ Hz, 2 × CH_3). ^{13}C NMR ($CDCl_3$) δ: 172.15 (CO); 171.86 (CO); 145.50 (C_2); 142.12 (2 × C_{Ar}); 138.70 (C_5); 132.06 (2 × C_{Ar}); 130.01 (2 × C<u>H</u>═C<u>H</u>); 129.53 (2 × CH_{Ar}); 128.96 (C_7); 128.49 (2 × CH_{Ar}); 127.97 (C_9); 125.85 (C_6); 125.19 (C_4); 104.31 (C_3); 100.78 (C_8); 79.82 ($C_{1'}$); 74.43 ($C_{3'}$); 73.80 ($C_{4'}$); 73.59 ($C_{2'}$); 65.57 ($C_{5'}$); 55.45 ($N(\underline{C}H_3)_3^+$); 31.87 (2 × <u>C</u>H_2−CO); 29.78−28.67 (2 × 9 CH_2); 27.18 (2 × <u>C</u>H_2−CH═CH−<u>C</u>H_2); 22.65 (2 × <u>C</u>H_2−CH_2−CO); 21.66 (<u>C</u>H_3−C_{Ar}); 21.65 (2 × CH_3−<u>C</u>H_2); 14.09 (2 × CH_3). MS (GT, FAB^+): 864 $[M-TsO^-]^+$. HMRS (FAB^+): calculated for $[M-TsO^-]^+$ 864.6460; found 864.6443. Anal. Calcd. C, 68.13; H, 9.01; N, 3.80; found C, 68.13; H, 8.97; N, 4.11.

1-(5-*O*-*tert*-Butyldiphenylsilyl-2,3-*O*-isopropylidene-D-ribofuranosyl)-4-nitroimidazole, 8. Compound **2′** (1.22 g, 2.85 mmol) was converted to **8** according to the procedure of glycosylation described for **3** and purified by flash column chromatography (cyclohexane/EtOAc: 90/10→80/20) to give **8a** (324 mg, 22%) and **8b** (170 mg, 11%).

1-(5-*O*-*tert*-Butyldiphenylsilyl-2,3-*O*-isopropylidene-α-D-ribofuranosyl)-4-nitroimidazole, 8a. ^1H NMR ($CDCl_3$) δ: 8.00 (1H, d, $J = 1.13$ Hz, H_5); 7.96 (1H, m, H_2); 7.66 (4H, m, H_{Ar}); 7.43 (6H, m, H_{Ar}); 6.69 (1H, d, $J = 4.99$ Hz, $H_{1'}$); 5.22 (1H, t, $J = 5.53$ Hz, $H_{2'}$); 4.78 (1H, d, $J = 5.53$ Hz, $H_{3'}$); 4.56 (1H, m, $H_{4'}$); 3.95 (1H, dd, $J = 2.10$ Hz, $J = 11.39$ Hz, $H_{5'}$); 3.73 (1H, dd, $J = 2.10$ Hz, $J = 11.39$ Hz, $H_{5''}$); 1.25 (3H, s, CH_3−C); 1.12 (9H, s, $(CH_3)_3$−C); 1.01 (3H, s, CH_3−C). ^{13}C NMR ($CDCl_3$): δ 138.55 (C_4); 135.52 (C_2); 133.06 (2 × C_{Ar}); 132.31 (2 × CH_{Ar}); 132.04 (2 × CH_{Ar}); 130.17 (2 × CH_{Ar}); 130.09 (4 × CH_{Ar}); 127.99 (C_5); 113.19 ($(CH_3)_2-\underline{C}$); 91.12 ($C_{1'}$); 84.11 ($C_{2'}$); 82.03 ($C_{4'}$); 81.11 ($C_{3'}$); 65.60 ($C_{5'}$); 26.81 (<u>C</u>H_3−C); 25.15 (<u>C</u>H_3−C); 24.37 ($(\underline{C}H_3)_3$−C); 19.04 ($(CH_3)_3-\underline{C}$). MS (GT, FAB^+): 524 $[M+H]^+$. Rf (C_6H_{12}/EtOAc: 90/10): 0.23.

1-(5-*O*-*tert*-Butyldiphenylsilyl-2,3-*O*-isopropylidene-β-D-ribofuranosyl)-4-nitroimidazole, 8b. ^1H NMR ($CDCl_3$) δ: 7.85 (1H, d, $J = 1.44$ Hz, H_5); 7.64 (4H, m, H_{Ar}); 7.52 (1H, d, $J = 1.46$ Hz, H_2); 7.44 (6H, m, H_{Ar}); 6.10 (1H, d, $J = 2.91$ Hz, $H_{1'}$); 4.91 (2H, m, $H_{2'}$ + $H_{3'}$); 4.44 (1H, t, $J = 2.10$ Hz, $H_{4'}$); 3.99 (1H, dd, $J = 2.10$ Hz, $J = 11.44$ Hz, $H_{5'}$); 3.79 (1H, dd, $J = 2.10$ Hz, $J = 11.44$ Hz, $H_{5''}$); 1.37 (3H, s, CH_3−C); 1.32 (3H, s, CH_3−C); 1.11 (9H, s, $(CH_3)_3$−C). ^{13}C NMR ($CDCl_3$) δ: 135.49 (C_4); 135.33 (C_2); 134.85 (2 × C_{Ar}); 132.11 (4 × CH_{Ar}); 130.34 (2 × CH_{Ar}); 130.26 (4 × CH_{Ar}); 128.07 (C_5); 113.98 ($(CH_3)_2-\underline{C}$); 89.41 ($C_{1'}$); 83.87 ($C_{2'}$); 82.32 ($C_{4'}$); 80.41 ($C_{3'}$); 66.13 ($C_{5'}$); 26.89 (2 × <u>C</u>H_3−C); 25.51 ($(\underline{C}H_3)_3$−C); 19.09 ($(CH_3)_3-\underline{C}$). MS (GT, FAB^+): 524 $[M+H]^+$. mp = 40 °C. Rf (C_6H_{12}/EtOAc: 90/10): 0.18.

1-(2,3-*O*-Isopropylidene-α-D-ribofuranosyl)-4-nitroimidazole, 9a. Compound **8a** (325 mg, 0.62 mmol) was converted to **9a** according to the procedure described for **4a** and purified by flash column chromatography (cyclohexane/EtOAc: 90/10→EtOAc) to give **9a** (80 mg, 46%). ^1H NMR ($CDCl_3$) δ: 7.99 (1H, d, $J = 1.13$ Hz, H_5); 7.93 (1H, m, H_2); 6.62 (1H, d, $J = 2.78$ Hz, $H_{1'}$); 5.15 (1H, t, $J = 5.93$ Hz, $H_{3'}$); 4.87 (1H, dd, $J = 2.78$ Hz, $J = 5.93$ Hz, $H_{2'}$); 4.63 (1H, t, $J = 2.78$ Hz, $H_{4'}$); 3.95 (1H, dd, $J = 2.78$ Hz, $J = 11.59$ Hz, $H_{5'}$); 3.81 (1H, dd, $J = 2.78$ Hz, $J = 11.59$ Hz, $H_{5''}$); 2.41 (1H, sl, O<u>H</u>); 1.27 (3H, s, CH_3−C); 0.98 (3H, s, CH_3−C). ^{13}C NMR ($CDCl_3$) δ: 139.31 (C_4); 135.00 (C_2); 118.72 (C_5); 113.96 ($(CH_3)_2-\underline{C}$); 89.30 ($C_{1'}$); 83.73 ($C_{2'}$); 82.13 ($C_{4'}$); 80.35 ($C_{3'}$); 64.39 ($C_{5'}$); 25.50 (<u>C</u>H_3−C); 24.15 (<u>C</u>H_3−C). MS (GT, FAB^+): 286 $[M+H]^+$; 308 $[M+Na]^+$. Rf (EtOAc): 0.43.

1-(2,3-*O*-Isopropylidene-β-D-ribofuranosyl)-4-nitroimidazole, 9b. Compound **8b** (166 mg, 0.32 mmol) was converted to **9b** according to the procedure described for **4b** and purified by flash column chromatography (cyclohexane/EtOAc: 70/30) to give **9b** (58 mg, 64%) as a white solid. mp = 142−144 °C. ^1H NMR ($CDCl_3$) δ: 7.91 (1H, d, $J = 1.37$ Hz, H_5); 7.61 (1H, d, $J = 1.37$ Hz, H_2); 6.11 (1H, d, $J = 2.51$ Hz, $H_{1'}$); 4.97 (1H, dd, $J = 2.51$ Hz, $J = 4.48$ Hz, $H_{3'}$); 4.90 (1H, dd, $J = 1.58$ Hz, $J = 4.48$ Hz, $H_{2'}$); 4.49 (1H, t, $J = 2.51$ Hz, $H_{4'}$); 3.98 (1H, dd, $J = 2.51$ Hz, $J = 11.47$ Hz, $H_{5'}$); 3.85 (1H, dd, $J = 2.51$ Hz, $J = 11.47$ Hz, $H_{5''}$); 1.38 (3H, s, CH_3−C); 1.33 (3H, s, CH_3−C). ^{13}C NMR ($CDCl_3$) δ: 138.32 (C_4); 137.85 (C_2); 132.85 (C_5); 113.49 ($(CH_3)_2-\underline{C}$); 90.93 ($C_{1'}$); 84.28 ($C_{2'}$); 81.73 ($C_{4'}$); 81.12 ($C_{3'}$); 63.74 ($C_{5'}$); 25.03 (<u>C</u>H_3−C); 24.40 (<u>C</u>H_3−C). MS (GT, FAB^+): 286 $[M+H]^+$; 308 $[M+Na]^+$. Rf (EtOAc): 0.72.

1-(2,3-*O*-Isopropylidene-5-*O*-tosyl-α-D-ribofuranosyl)-4-nitroimidazole, 10a. Compound **9a** (80 mg, 0.28 mmol) was converted to **10a** according to the procedure described for **5a** and purified by flash column chromatography (cyclohexane/EtOAc: 70/30) to give **10a** (50 mg, 46%) as an orange oil. ^1H NMR ($CDCl_3$) δ: 7.86 (1H, d, $J = 1.46$ Hz, H_5); 7.80 (2H, d, $J = 7.90$ Hz, H_{Ar}); 7.56 (1H, d, $J = 1.46$ Hz, H_2); 7.40 (2H, d, $J = 7.90$ Hz, H_{Ar}); 5.93 (1H, d, $J = 4.11$ Hz, $H_{1'}$); 4.89 (2H, m, $H_{4'}$ + $H_{2'}$); 4.56 (1H, t, $J = 1.74$ Hz, $H_{3'}$); 4.22 (2H, d, $J = 2.37$ Hz, $H_{5'}$ + $H_{5''}$); 2.47 (3H, s, CH_3-C_{Ar}); 1.36 (3H, s, CH_3−C); 1.30 (3H, s, CH_3−C). ^{13}C NMR ($CDCl_3$) δ: 145.93 (C_4); 138.81 (C_2); 134.85 (C_{Ar}); 131.83 (C_{Ar}); 130.25 (2 × CH_{Ar}); 127.87 (2 × CH_{Ar}); 118.43 (C_5); 114.59 ($(CH_3)_2-\underline{C}$); 89.12 ($C_{1'}$); 81.66 ($C_{2'}$); 81.07 ($C_{3'}$); 79.96 ($C_{4'}$); 70.90 ($C_{5'}$); 25.45 (<u>C</u>H_3−C); 24.15 (<u>C</u>H_3−C); 21.69 (<u>C</u>H_3-C_{Ar}). MS (GT, FAB^+): 440 $[M+H]^+$. Rf (C_6H_{12}/EtOAc: 70/30): 0.36.

1-(2,3-*O*-isopropylidene-5-*O*-tosyl-β-D-ribofuranosyl)-4-nitroimidazole, 10b. Compound **9b** (140 mg, 0.49 mmol) was converted to **10b** according to the procedure described for **5b** and purified by preparative layer chromatography (cyclohexane/EtOAc: 30/70) to give **10a** (90 mg, 42%) as a pale yellow oil. ^1H NMR ($CDCl_3$) δ: 7.98 (1H, d, $J = 1.43$ Hz, H_5); 7.82 (3H, d + m, $J = 8.53$ Hz, H_{Ar} + H_2); 7.38 (2H, d, $J = 8.53$ Hz, H_{Ar}); 6.34 (1H, d, $J = 2.84$ Hz, $H_{1'}$); 5.05 (1H, t, $J = 4.84$ Hz, $H_{4'}$); 4.77 (1H, d, $J = 2.84$ Hz, $H_{2'}$); 4.70 (1H, t, $J = 2.84$ Hz, $H_{3'}$); 4.26 (2H, m, $H_{5'}$ + $H_{5''}$); 2.46 (3H, s, CH_3-C_{Ar}); 1.23 (3H, s, CH_3−C); 0.96 (3H, s, CH_3−C). ^{13}C NMR ($CDCl_3$) δ: 145.77 (C_4); 134.02 (C_2); 132.37 (C_{Ar}); 131.31 (C_{Ar}); 130.19 (2 × CH_{Ar}); 127.84 (2 × CH_{Ar}); 121.95 (C_5); 114.07 ($(CH_3)_2-\underline{C}$); 81.35 ($C_{1'}$); 81.22 ($C_{2'}$); 80.73 ($C_{3'}$); 70.75 ($C_{4'}$); 69.87 ($C_{5'}$); 22.98 (<u>C</u>H_3−C); 24.36 (<u>C</u>H_3−C); 21.70 (<u>C</u>H_3-C_{Ar}). MS (GT, FAB^+): 440 $[M+H]^+$. Rf (C_6H_{12}/EtOAc: 90/10): 0.74.

1-(2,3-dioleyl-5-*O*-tosyl-α-D-ribofuranosyl)-4-nitroimidazole, 11a. Compound **10a** (80 mg, 0.28 mmol) was converted to **11a** according to the procedure described for **6a** and purified by flash column chromatography (cyclohexane/EtOAc: 70/30) to give **11a** (41 mg, 32%) as a yellow oil. ^1H NMR ($CDCl_3$): δ 7.88 (1H, d, $J = 1.46$ Hz, H_5); 7.82 (2H, d, $J = 8.06$ Hz, H_{Ar}); 7.51 (1H, d, $J = 1.46$ Hz, H_2); 7.39 (2H, d, $J = 8.06$ Hz, H_{Ar}); 6.09 (1H, d, $J = 5.49$ Hz, $H_{1'}$); 5.48 (2H, m, $H_{2'}$ + $H_{3'}$); 5.34 (4H, m, 2 × CH_2−C<u>H</u>═C<u>H</u>−CH_2); 4.58 (1H, m, $H_{4'}$); 4.34 (1H, dd, $J = 2.21$ Hz, $J = 11.26$ Hz, $H_{5'}$); 4.21 (1H, dd, $J = 2.21$

Hz, $J = 11.26$ Hz, $H_{5''}$); 2.47 (3H, s, CH_3-C_{Ar}); 2.32 (4H, m, $2 \times CH_2-CO$); 1.99 (8H, m, $2 \times CH_2-CH=CH-CH_2$); 1.56 (4H, m, $2 \times CH_2-CH_2-CO$); 1.26 (40H, m, 2×10 CH_2); 0.87 (6H, t, $J = 6.64$ Hz, $2 \times CH_3$). ^{13}C NMR ($CDCl_3$) δ: 173.01 (CO); 172.59 (CO); 149.54 (C_{Ar}); 147.69 (C_2); 143.42 (C_{Ar}); 140.11 (C_{Ar}); 133.65 ($2 \times CH=CH$); 131.27 ($2 \times CH_{Ar}$); 130.96 ($2 \times CH_{Ar}$); 118.88 (C_5); 87.71 ($C_{1'}$); 78.45 ($C_{4'}$); 76.23 ($C_{3'}$); 71.36 ($C_{2'}$); 65.67 ($C_{5'}$); 32.36 ($2 \times CH_2-CO$); 30.78 ($CH_2-CH=CH-CH_2$); 30.66 ($CH_2-CH=CH-CH_2$); 29.88−29.19 (2×9 CH_2); 26.76 (CH_2-CH_2-CO); 25.84 (CH_2-CH_2-CO); 23.05 (CH_3-C_{Ar}); 21.52 ($2 \times CH_3-CH_2$); 14.09 ($2 \times CH_3$). MS (GT, FAB^+): 929 $[M+H]^+$.

Tosylate Salt of 1-(2,3-Dioleyl-5-trimethylammonium-α-D-ribofuranosyl)-4-nitroimidazole, 12a. Compound **11a** (80 mg, 0.28 mmol) was converted to **12a** according to the procedure described for **7a** to give **11a** as a yellow oil with quantitative yield. ^1H NMR ($CDCl_3$): δ 7.95 (1H, d, $J = 1.46$ Hz, H_5); 7.68 (3H, d+m, $J = 7.90$ Hz, $H_{Ar} + H_2$); 7.15 (2H, d, $J = 7.90$ Hz, H_{Ar}); 5.76 (1H, d, $J = 5.50$ Hz, $H_{1'}$); 5.33 (4H, m, $2 \times CH_2-CH=CH-CH_2$); 4.91 (3H, m, $H_{2'} + H_{3'} + H_{4'}$); 3.37 (9H, s, NCH_3^+); 3.30 (2H, m, $H_{5'} + H_{5''}$); 2.33 (3H, s, CH_3-C_{Ar}); 2.15 (4H, m, CH_2-CO); 1.99 (8H, m, $2 \times CH_2-CH=CH-CH_2$); 1.50 (4H, m, $2 \times CH_2-CH_2-CO$); 1.26 (40H, m, 2×10 CH_2); 0.87 (6H, t, $J = 6.16$ Hz, $2 \times CH_3$). MS (GT, FAB^+): 815 $[M-TsO^-]^+$. Anal. Calcd. 65.63; H, 9.11; N, 5.62; Found C, 65.69; H, 9.19; N, 5.67.

Vesicle Preparation. 1 mg/mL of compounds **7a** or **7b** was dissolved in chloroform. The solution was evaporated and dried under vacuum for 2 h. 1 mL of DI water was added, and the solution was hydrated overnight at 4 °C. The resulting solution was sonicated for 20 min prior to any measurements.

Electrophoresis Studies. Electrophoresis studies were conducted in 2% agarose gels containing ethidium bromide in a 0.5 Tris-Borate-EDTA buffer. Cationic lipoplexes were prepared 10 min before use. 250 ng of siRNA (21 bp, Eurogentec SR-CL010−005) was mixed with lipids at different ratios (final volume is 20 μL). Then, 20 μL of each lipoplexes (samples) were mixed with 4 μL of loading buffer (glycerol 30%, v/v), bromophenol blue 0.25% (w/v), and xylene cyanol 0.25 (w/v) and subjected to agarose gel electrophoresis for 20 min at 100 V. The electrophoresis gel was visualized and digitally photographed using a G.BOX camera.

Exclusion Assay. Ten milliliters of EB (10 mg/mL) was diluted in 580 mL in deionized water. Ten microliters of 90 mg/mL solution of siRNA was added. A varying amount of lipid (depending on the siRNA/lipid ratio required) was added to the EB solution finally. The solutions were mixed on a benchtop vortex, and the fluorescence was measured ($\lambda_{exc} = 470$ nm, $\lambda_{em} = 600$ nm; 0.5 cm path length glass cuvette). The fluorescence was expressed as the percentage of the maximum fluorescence signal when EB was bound to the siRNA in the absence of lipid.

ζ Potential and Size Distribution of 7b CNLs (with and without siRNA). Experiments were realized with N/P ratio of 10 (CNLs/siRNA).

Transmission Electronic Microscopy (TEM). TEM experiments were performed on vesicle samples **7a**, **7b**, and **12a** using a Philips CM 10 (negative staining with ammonium molybdate 1% water, Cu/Pd carbon coated grids). Both (α) and (β) anomer nucleolipids formed small vesicles with diameters between 40 and 60 nm, respectively. Cationic lipoplexes were prepared as described above and were visualized by negative staining microscopy. Ten microliter aliquots of samples (either liposomes or lipoplexes) were transferred to a carbon-coated grid for 10 min. Then, the samples were dried and stained with 2.5% (w/w) of uranyl acetate for 30 s. The specimens were observed with a Hitachi H 7650 electron microscope. Both (α) and (β) anomer nucleolipids formed small vesicles with diameters between 40 and 60 nm, respectively.

siRNA Transfection. Trypsine adherent cells were diluted in normal growth medium to 1×10^5 cells per milliliter. The transfectant reagent was diluted in serum free medium and incubated at room temperature for 10 min before use. Next, siRNA (GAPDH siRNA or negative control siRNA, Ambion) was diluted in serum free medium. The siRNA and the tranfection reagent were mixed, incubated for 10 min at room temperature, and dispensed into a culture plate. Depending on the experimental design, the ratio of lipid, siRNA, and incubation time was varied. Cell suspension was overlayed onto the transfection mixture, then incubated at 37 °C and 5% CO_2. Assays for gene knockdown were assessed after 48 h depending on the experimental protocol.

The gene knockdown assay performed was KDalert GAPDH Assay (Ambion) following the manufacturer's protocol. Briefly, 48 h after siRNA transfection, the culture medium was aspirated from transfected cells; 200 μL KDalert Lysis Buffer was added to each sample well and the mixture incubated at 4 °C for 20 min to lyse the cells. The cell lysate was pipeted up and down 4−5 times to homogenize the lysate. 10 μL aliquots of each lysate or GAPDH enzyme dilution (including the GAPDH working stock) were transfered to the wells of a clean 96 well plate. 90 μL aliquots of KDalert master mix were added to each sample using a multichannel pipettor to dispense the KDalert master mix quickly. The increase in fluorescence of the samples was measured at room temperature.

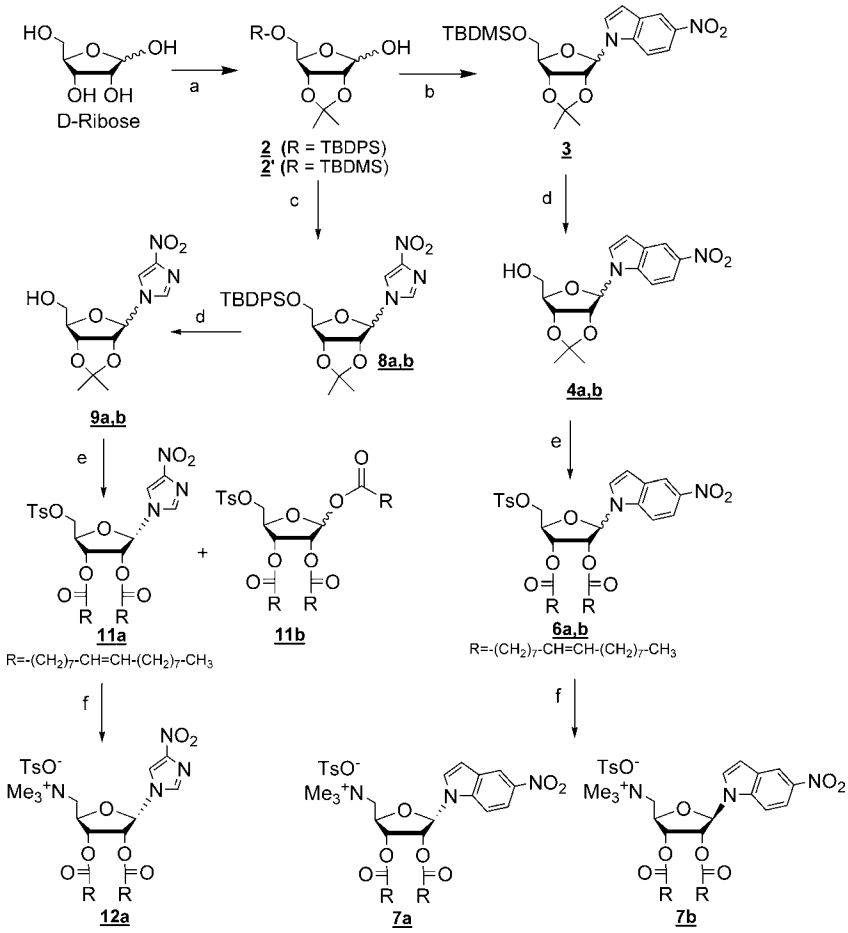
Cytotoxicity. Cytotoxicity was assessed using both a formazan-based proliferation assay (CellTiter 96 AQueous One Solution Cell Proliferation Assay kit, Promega) and a total protein-based assay (Pierce). Briefly, CHO cells were seeded onto a 24 well plate with an appropriate density of 1×10^6 cells per well. After 48 h, the MTS substrate was added to each well, and the plate was incubated for 4 h at 37 °C in a humidified, 5% CO_2 incubator. The amount of soluble formazan produced by cellular reduction of the substrate MTS was recorded at 490 nm using a multiwell plate reader. For the total protein based proliferation assay, cells were lysed at the same time as transfection efficiency was assayed. 10 μL aliquots of lysates were transferred to a separate multiwell plate. Total protein contents were assessed using the Coomassie Blue protein kit (Pierce, Rockford, IL) following the manufacturer protocol. Negative and positive controls were nontreated cells and commercial lipids treated cells, respectively. The proliferation results were expressed as percentages of nontreated cells.

Molecular Modeling. In order to obtain some information about the structure−activity of these universal base analogue nucleolipids, modelization of the five tested compounds was performed at the density functional theory (DFT) level (B3LYP) with a 6-31G* split-valence basis set (*8, 9*). Cavity surface area (CSA) and (polarized solute)-solvent (PSS) are determined within the same methodology in a solvent, water, using a PCM model (*10*). Briefly, cavity surface area (CSA) and (polarized solute)-solvent (PSS) were calculated for all the compounds as well as the quotient MC = |PSS/CSA|.

RESULTS AND DISCUSSION

Synthesis. The (α) and (β) anomers of 2′,3′-dioleyl-5′-*O*-D-ribofuranosyl-3-nitroindole, **7a** and **7b**, respectively, and the (α) anomer 2′,3′-dioleyl-5′-*O*-D-ribofuranosyl-4-nitroimidazole, **12a**, were synthesized from D-ribose as shown in Scheme 1. Accordingly, 5-*O*-*tert*-butyldimethylsilyl-2,3-*O*-isopropylidene-D-ribose **2** and 5-*O*-*tert*-butyldimethylsilyl-2,3-*O*-isopropylidene-D-ribose **2′** were prepared in two steps (see Supporting Information) from D-ribose following a published procedure (*11*). Next, the stereoselective chlorination of the protected

Scheme 1[a]



[a] Reaction conditions: (a) (i) acetone, $CuSO_4$, **1** (94%), (ii) TBDMSCl or TBDPSCl, DMAP, TEA; **2** (35%) and **2′** (46%); (b) (i) CCl_4, HMPT, (ii) 5-nitroindole, NaH, CH_3CN; **3** (40%); (c) (i) CCl_4, HMPT, (ii) 4-nitroimidazole, NaH, CH_3CN; **8a** (22%) and **8b** (11%); (d) TBAF dry THF; **4a/4b** (5/1; 65%); **9a** (46%), **9b** (64%); (e) (i) TsCl, TEA, DCM; **5a** (94%), **5b** (56%) and **10a** (42%), **10b** (46%), (ii) TFA/H_2O, quant., (iii) Oleic acid, DCC/DMAP; **6a** (65%), **6b** (73%), and **11a** (32%); (f) NMe_3, CH_3CN 60°C, 40 h, quantitative.

sugars **2** and **2′** with CCl_4 and hexamethylphosphorus triamide (HMPT) (*12*) was followed by coupling with the anions of 3-nitroindole pyrrole or 4-nitroimidazole. Deprotection of the resulting derivative **3** and **8** afforded the anomeric mixture of (α) **4a** (53%), (*β*) **4b** (18%), and (α) **9a** (53%), (*β*) **9b** (18%). As described previously for nitropyrrole derivatives, the (α) forms were found to be the major isolated polar isomers. The relative stereochemistry of these compounds was assigned by ^{1}H NMR when compared to the chemical shifts of the acetonide methyl group as well as those of the H-1′ (*13*). The anomeric pairs of compounds **4** and **9** were then separately tosylated with TsCl/TEA, deprotected with TFA/H_2O, and coupled with oleic acid using DCC/DMAP to afford the nucleolipids **6a**, **6b**, **11a**, and the side product **11b**. The latter was isolated and characterized by mass spectra. Unfortunately, we were unable to isolate the *β* anomer of **11a**. Indeed, the instability of the sulfonated intermediates has been demonstrated for adenosine analogues with intramolecular cyclization of the 5′-carbon and N3-position of the adenine ring (*14, 15*). It is likely that such an intermolecular cyclization occurs in the case of the nitroindole intermediate **11a**.

Finally, compounds **6a**,**b**, and **11a** were reacted with trimethylamine for two days in a sealed tube to afford the target nucleolipids **7a**, **7b**, and **12a**.

Complexation Studies. In order to determine whether the CNLs **7a**, **7b**, and **12a** bind nucleic acids, we performed (i) siRNA (21 bp) gel electrophoresis and (ii) standard ethidium bromide (EB) fluorescence displacement assays with siRNA (21 bp) as a model system (*16*). The siRNA gel electrophoresis was performed on compounds **7a** and **7b**; as shown in Figure 3, a full complexation occurs for a charge ratio **7b**/siRNA (*β* anomer) of 10/1 (Figure 3 column 6), whereas in the case of the **7a**/siRNA (α anomer), free siRNA is observed for all the ratios investigated (Figure 3 columns 8−12).

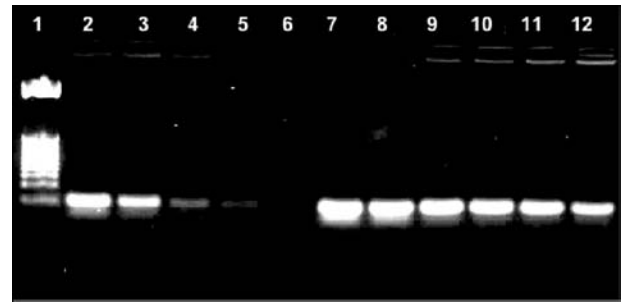


Figure 3. Electrophoretic mobility of **7b** (*β*) and **7a** (α). The lines represent the following (*1*): DNA stepladder 25 pb (*2*−*6*), siRNA with **7b** at different ratios N/P (2, 4, 6, 8, 10 respectively (*7*)), siRNA (*8*−*12*), siRNA with **7a** at different ratios N/P (2, 4, 6, 8, 10, respectively).

The binding affinity of siRNA by CNLs was also investigated by the fluorescence titration of EB with a premixed solution of siRNA and various concentrations of CNLs. In the presence of siRNA, the fluorescence emission of EB is enhanced relative to that in water as a result of EB intercalation between the RNA base pairs. The subsequent addition of CNLs to the siRNA−EB solution results in CNL binding to RNA and displacement of

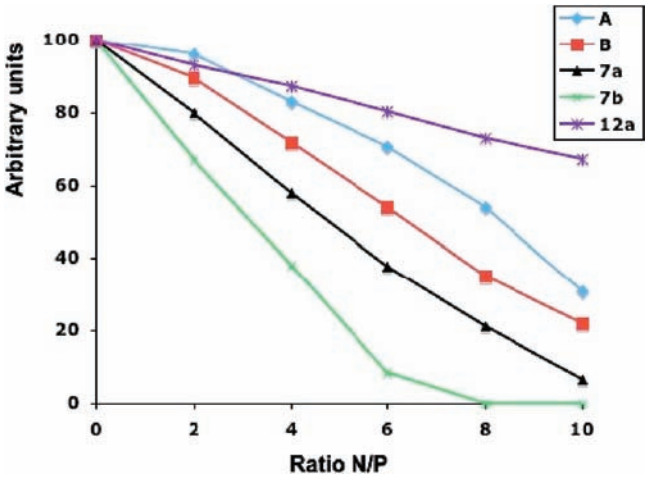


Figure 4. EB exclusion assays with **A**, **B**, **7a**, **7b**, and **12a** in the presence of siRNA (fluorescence intensity arbitrary units versus N/P charge ratio).

EB from the helix to water, which induces a decrease in fluorescence intensity. As shown in Figure 4, the fluorescence intensity decreases rapidly for all the CNLs investigated, including both 5-nitroindole derivatives **7b** (β), **7a** (α), the 4-nitroimidazole **12a**, and nitropyrrole CNLs previously reported (α,β anomers, compounds **A** and **B**, respectively). Interestingly, with a total decrease in fluorescence for N/P ratios higher than 8, the β anomer 5-nitroindole derivative **7b** exhibits the best binding affinity of the CNL series. The α anomer **7a**, which forms **7a**/siRNA complex at higher N/P ratios (higher than 10) compared to β analogue **7b**, shows a lower binding affinity indicating that stereochemistry of the anomeric position has an impact on the complexation with siRNA double helix. Likewise, a higher binding affinity is observed for nitropyrrole CNL **B** (β) compared to CNL **A** (α) confirming the importance of anomeric configuration in the complex formation. As expected, the nature of the CNL universal base has an impact on the formation of CNLs/siRNA complexes. With no residual EB fluorescence for ratio of 10/1, the 5-nitroindole derivatives **7b** (β) and **7a** (α) feature the best binding affinity, whereas 4-nitroimidazole **12a** is the least efficient of the CNLs. It is well-known that intermolecular overlapping of p-orbitals in π-conjugated systems causes $\pi-\pi$ interactions. Hence, these interactions become stronger as the number of π-electrons increases. Accordingly, the best binding affinity observed for the 5-nitroindole universal base can be explained by the 10 π electrons, whereas the 6 π electrons of both nitroindole and nitropyrrole induce fewer $\pi-\pi$ interactions.

Electronic Microscopy Studies, ζ Potential, and Size Distribution. TEM experiments were performed on vesicle samples **7a**, **7b**, and **12a** using a Hitachi H 7650 electron microscope (negative staining with 2.5% (w/w) of uranyl acetate). Both (α) and (β) anomer nucleolipids formed small vesicles with diameters between 40 and 60 nm, respectively (Supporting Information Figure S1). TEM experiments were also performed on samples prepared with siRNA. For these experiments, the CNL vesicles were incubated for 15 min in the presence of siRNA (21 bp). TEM micrographs (Figure 5) of the CNL-siRNA systems exhibited multilamellar vesicles (which are not observed in the case of CNL vesicles; see Supporting Information Figure S2) suggesting that the siRNA molecules are entrapped within the vesicular structures. ζ-potential and size distribution were determined for the CNL vesicles of **7b** with and without siRNA. As expected, the results show a significative decrease of ζ-potential (from 74 to 36.7 mV), as well as an increase of size distribution (from 108 to 360 nm) in the presence of siRNA suggesting its complexation with the CNL vesicles of **7b**.

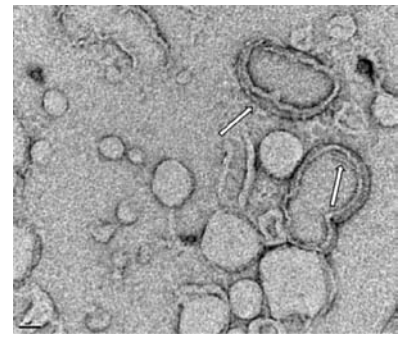


Figure 5. TEM image of CNL-siRNA systems obtained with **7b** (bar = 50 nm).

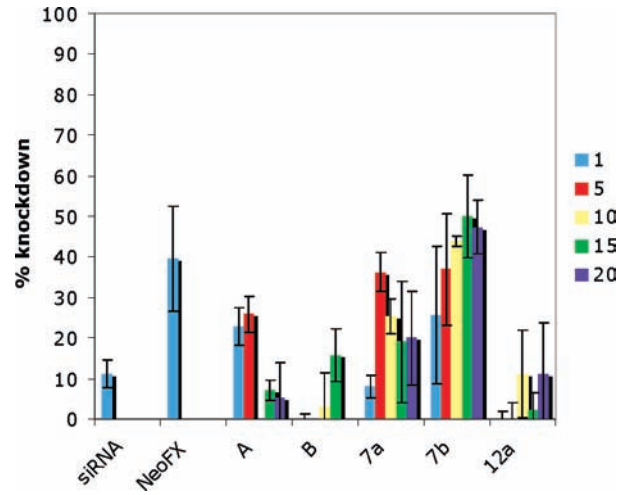


Figure 6. siRNA transfection results after 48 h in HepG2 as a function of nucleolipid (**A**, **B**, **7a**,**7b**, and **12a**) and N/P mole ratio. $n = 3$.

Transfection. The transfection of siRNA with **A**, **B**, **7a**, **7b**, and **12a** was next performed to evaluate the reduction in protein synthesis. Experiments used glyceraldehyde-3-phosphate dehydrogenase (GAPDH) siRNA (Ambion) on human liver (HepG2) cell line, and the complete details can be found in the Supporting Information. siRNA transfection results were accessed after 48 h as a function of both anomer and cation/anion (N/P) mole ratio. In each experiment, controls using GAPDH siRNA and negative control siRNA were used at 30 mM. siPORT NeoFX was used as the positive control, and the previously evaluated 3-nitropyrrole nucleolipids A and B (*2*) (Figure 1) were tested again in the experiment. As shown in Figure 6, siRNA knockdown was observed for most nucleolipids, with values similar to the positive control for compounds **7a** and **7b**. The transfection activity of **7a** was significant vs siRNA with N/P ratios of 5 and 10, whereas for **7b**, it was significant with N/P ratios of 5, 10, 15, and 20. Interestingly, the 5-nitroindole CNL **7b** (β), which features the best binding affinity for siRNA, is also globally the most efficient in term of transfection. In addition, none of the CNLs showed a significant cytotoxicity at these concentrations, similar to that to the negative control (Supporting Information Figure S3).

Molecular Modeling. A basic molecular modeling method described in the section above was used to calculate the MC quotient (MC = |PSS/CSA|). This quotient represents the stabilization in kilojoules per mole per surface unit; it reflects the system's capacity to maintain its cohesion, i.e., the smaller MC values reflect lower membrane cohesion. As shown in Table 1 with N/P ratios of >5, it can be seen that low MC values are correlated both to better transfection activity (Table 1, line 4)

Table 1. Relationship among MC Quotient, % Knockdown, and Fluorescence Intensity for Compounds A, B, 7a−b, and 12a−b[a]

compounds	**12a**	**A**	**B**	**7a**	**7b**
PSS (kJ.mol^{-1})	309.57	287.79	270.78	279.81	269.07
CSA (Å^2)	389.02	396.10	390.84	438.56	432.64
MC = |PSS/CSA| (kJ.mol^{-1} Å^{-2})	0.80	0.73	0.69	0.64	0.62
% knockdown (N/P ratios of 15)	3	8	15	18	50
fluorescence intensity (N/P ratios of 10, Figure 4)	70	30	20	5	0

[a] CSA: Cavity Surface Area. PSS: (Polarized Solute)-Solvent.

and to binding affinity (Figure 4). These results confirm that to a certain extent (N/P ratio >5) the lowest membrane cohesion of these series of CNLs vesicles are beneficial for the release and the activities of siRNA in the cytoplasm.

It is known that subtle change such as headgroup nature, headgroup charges, counterion nature, and so forth can dramatically affect the transfection properties (*17, 18*). However, for the first time to our knowledge, the results highlight the impact of both stereochemistry and base nature of these nucleoside amphiphiles, i.e., β anomeric configuration, as well as highly π conjugated bases, is likely to improve the transfection efficacy. These findings could provide a rationale for the design of universal base nucleoside amphiphiles for siRNA delivery.

CONCLUSION

In summary, we have synthesized and characterized several new universal base CNLs for siRNA delivery. The results obtained by gel electrophoresis and ethidium bromide exclusion assays clearly indicate that (i) the nature of the universal base (5-nitroindole and 4-nitroimidazole) and (ii) the stereochemistry of the anomeric position (α, β) have an impact on the CNLs-siRNA complex formation. We observed that the CNL featuring the nitroindole as universal base exhibits the best binding affinity for siRNA. We also demonstrated that higher binding affinities for siRNA are observed for β anomers of both nitroindole and nitropyrrole CNLs. Molecular modeling has shown that calculation of simple values (MC) reflecting the system's capacity to maintain its cohesion can be correlated to both binding affinities and transfection efficiencies. On the basis of this rational approach, work is in progress to synthesize and improve the efficacy of new, original cationic nucleoside amphiphiles for siRNA delivery.

ACKNOWLEDGMENT

The authors thank the CNRS and the "Ministère de l'enseignement supérieur et de la recherche" for financial support.

Supporting Information Available: Synthesis of compounds **1**, **2**, and **2′**; ζ potential and size distribution of **7b** CNLs; TEM images of **7a** and **12a**; cytotoxicities of CNLs on HepG2 cell; EB exclusion assays with **7a** and **7b**. This material is available free of charge via the Internet at http://pubs.acs.org.

LITERATURE CITED

(1) Chabaud, P., Camplo, M., Payet, D., Serin, G., Moreau, L., Barthélémy, P., and Grinstaff, M. (2006) Cationic nucleoside lipids derived for gene delivery. *Bioconjugate Chem. 17*, 466–472.

(2) Gissot, A., Camplo, M., Grinstaff, M. W., and Barthélémy, P. (2008) Nucleoside based amphiphiles: A Successful Marriage of nucleic acids with lipids. *Org. Biomol. Chem. Rev. 6*, 1324–1333.

(3) Moreau, L., Camplo, M., Wathier, M., Taib, N., Laguerre, M., Bestel, I., Grinstaff, M. W., and Barthélémy, P. (2008) Real time imaging of supramolecular assembly formation via programmed nucleolipid recognition. *J. Am. Chem. Soc. 130*, 14454–14455.

(4) Barthélémy, P. (2009) Nucleoside-based lipids at work: From supramolecular assemblies to biological applications. *C. R. Chim. 12*, 171–179.

(5) Ceballos, C., Prata, C. H., Giorgio, S., Payet, D., Barthélémy, P., Grinstaff, M. W., and Camplo, M. (2009) Cationic nucleoside lipids possessing a 3-nitropyrrole universal base for siRNA delivery. *Bioconjugate Chem. 20*, 193–196.

(6) Loakes, D. (2001) The applications of universal DNA base analogues. *Nucleic Acids Res. 29*, 2437–2447.

(7) Loakes, D., Hill, F., Brown, D. M., and Salisbury, S. A. (1997) Stability and structure of DNA oligonucleotides containing non-specific base analogues. *J. Mol. Biol. 270*, 426–435.

(8) Lee, C. T., Wang, W. T., and Parr, R. G. (1988) Development of the the colle-salvettu correlation-energy formula into a functional of the electron density. *Phys. Rev. B 37*, 785–789.

(9) Frisch, M. J., Trucks, G. W., Schlegel, H. B., Scuseria, G. E., Robb, M. A., Cheeseman, J. R., Montgomery, Jr., J. A. ,Vreven, T., Kudin, K. N., Burant, J. C., Millam, J. M., Iyengar, S. S., Tomasi, J., Barone, V., Mennucci, B., Cossi, M., Scalmani, G., Rega, N.,Petersson, G. A., Nakatsuji, H., Hada, M., Ehara, M., Toyota, K., Fukuda,R., Hasegawa, J., Ishida, M., Nakajima, T., Honda, Y., Kitao, O., Nakai, H., Klene, M., Li, X., Knox, J. E., Hratchian, H. P., Cross, J. B., Bakken, V., Adamo, C., Jaramillo, J., Gomperts, R., Stratmann, R. E., Yazyev, O., Austin, A. J., Cammi, R., Pomelli, C., Ochterski, J. W., Ayala, P. Y., Morokuma, K., Voth, G. A., Salvador, P., Dannenberg, J. J., Zakrzewski, V. G., Dapprich, S., Daniels, A. D., Strain, M. C., Farkas, O., Malick, D. K., Rabuck, A. D., Raghavachari, K., Foresman, J. B., Ortiz, J. V., Cui, Q., Baboul, A. G., Clifford, S., Cioslowski, J., Stefanov, B. B., Liu, G., Liashenko, A., Piskorz, P., Komaromi, I., Martin, R. L., Fox, D. J., Keith, T., Al-Laham, M. A., Peng, C. Y., Nanayakkara, A., Challacombe, M., Gill, P. M. W., Johnson, B., Chen, W., Wong, M. W., Gonzalez, C., Pople, J. A. (2004) *Gaussian 03, rev C.02*, Gaussian, Inc., Wallingford, CT.

(10) Cossi, M., Scalmani, G., Rega, N., and Barone, V. (2002) New developments in the polarizable continuum model for quantum mechanical and classical calculations on molecules in solution. *J. Chem. Phys. 117*, 43–54.

(11) Stewart, A. O., and Williams, R. M. (1985) C-glycosidation of pyridyl thioglycosides. *J. Am. Chem. Soc. 107*, 4289–4296.

(12) Harusawa, S., Imazu, T., Takashima, S., Araki, L., Ohishi, H., Kurihara, T., Sakamoto, Y., Yamamoto, Y., and Yamatodani, A. J. (1999) Synthesis of 4(5)-[5-(aminomethyl)tetrahydrofuran-2-yl- or 5-(aminomethyl)-2,5-dihydrofuran-2-yl]imidazoles by efficient use of a PHSe group: Application to novel histamine H3-ligands. *J. Org. Chem. 64*, 8608–8615.

(13) Imbach, J. L., Barascut, J. L., Kam, B. L., Rayner, B., Tamby, C., and Tapiero, C. (1973) Synthesis of nucleosides. III. New criterion determination of the anomer configuration of ribosidic nucleosides. *J. Heterocycl. Chem. 10* (6), 1069–70.

(14) Bakthavachalam, V., Lin, L. G., Cherian, X. M., and Czarnik, A. W. (1987) Synthesis, stereochemistry, intramolecular cyclization, and rates of hydrolysis of adenosine 2′,3′-acetals. *Carbohydr. Res. 170*, 124–135.

(15) Clark, V. M., Todd, A. R., and Zussman, J. (1951) Nucleotides. Part VIII cycloNucleoside salts. A novel rearrangement of some toluene-p-sulphonylnucleosides. *J. Chem. Soc.* 2952–2958.

(16) Geall, A. J., and Blasgbrough, I. S. (2000) Rapid and sensitive ethidium bromide fluorescence quenching assay of polyamine conjugate-DNA interactions for the analysis of lipoplex formation in gene therapy. *J. Pharm. Biomed. Anal. 22*, 849–859.

(17) Karmali, P. P., and Chaudhuri, A. (2006) Cationic liposomes as non-viral carriers of gene medicines: resolved issues, open questions, and future promises. *Med. Chem. Res. 27* (5), 696–722.

(18) Alberle, A. M., Bennet, M. J., Malone, R. W., and Nantz, M. H. (1996) The counterion influence of cationic lipid-mediated transfection of plasmid DNA. *Biochim. Biophys. Acta 1299*, 281–283.

BC100005K

Multifunctionalized Gold Nanoparticles with Peptides Targeted to Gastrin-Releasing Peptide Receptor of a Tumor Cell Line

Leticia Hosta-Rigau,[†] Ivonne Olmedo,[‡] Jordi Arbiol,[||] Luis J. Cruz,[†] Marcelo J. Kogan,*[,‡,§] and Fernando Albericio*[,†,⊥]

CIBER-BBN, Networking Centre on Bioengineering, Biomaterials and Nanomedicine, and Institute for Research in Biomedicine, Barcelona Science Park, Baldiri Reixac 10, 08028-barcelona, Spain, Division of Pharmacological and Toxicological Chemistry, School of Pharmacy and Chemistry, Casilla 233, University of Chile, Olivos 1007, Independencia, Santiago, Chile, Centre for Advanced Interdisciplinary Research in Material Sciences, Av. Blanco Encalada 2008, Santiago, Chile, Institucio Catalana de Recerca i Estudis Avançats (ICREA) and Institut de Ciencia de Materials de Barcelona, CSIC, Campus de la UAB, 08193 Bellaterra, CAT, Spain, and Department of Organic Chemistry, University of Barcelona, Martí i Franqués 1, 08028-barcelona, Spain. Received January 9, 2010; Revised Manuscript Received April 7, 2010

Functionalization of gold nanoparticles (AuNPs) with both a targeting peptide (an analogue of the peptide Bombesin) and a drug peptide ligand (an analogue of the RAF peptide) with the aim of improving selectivity in the delivery of the conjugates as well as the antitumor activity is described. Studies on the internalization mechanism of peptide−AuNP conjugates and viability of cells were carried out. An enhancement of the activity and selectivity of the peptide multifunctionalized conjugates was observed.

INTRODUCTION

Gold nanoparticles (AuNPs) have been extensively used in biological applications because of their biocompatibility, dimension, ease of characterization (*1, 2*), and rich history of surface chemistry. These features make these structures easily exploitable to meet the requirements of biomedical applications (*3*).

The size of AuNPs can be controlled from a few nanometers up to tens of nanometers, thereby placing them at dimensions that are smaller than or comparable to those of a cell (10−100 μm), a virus (20−450 nm), a protein (5−50 nm), or a gene (2 nm wide and 10−100 nm long). These sizes imply that they could get close to a biological target of interest (*4*). For example, AuNPs can be used to deliver a cargo, such as an anticancer drug, or a cohort of radionuclide atoms to a targeted region of the body, such as a tumor (*4*). On the other hand, AuNPs have been used in photothermal therapy for the destruction or molecular surgery of cancer cells or tumors. When irradiated with a focused laser in the near-infrared region (NIR) of suitable wavelength, targeted aggregates of AuNPs, nanorods, or nanoshells can kill bacteria (*5*) and cancer cells (*6*).

Thus, AuNPs provide an excellent intracellular targeting vector for two reasons: they can be synthesized routinely in appropriated sizes adequate for delivery varying from 0.8 to 200 nm with <10% size dispersity and can be modified with a large collection of small molecules, peptides, proteins, DNA, and polymers (*7*).

Surface modifications of AuNPs are often used to increase the functionality of nanoconjugates. These nanoparticle modifiers/conjugants include various peptides which can specifically recognize a target, thus improving cell type uptake (*8*) and ensuring that the AuNPs reach the desired target. Peptides attached to a single nanoparticle make the individual targeting signals more accessible to cell receptors (*9*), thus allowing them to participate in ligand−receptor interactions (*4, 10*).

The design and development of tumor-specific nanoparticles could significantly amplify the delivery capacity to a specific target of interest without affecting healthy cells. The target specificity of nanoparticles could be imparted by tagging with certain biovectors, which navigate them to particular organs or sites under in vivo conditions. The targeting vectors most commonly used are monoclonal antibodies and receptor-specific peptides. Monoclonal antibodies, due to their larger sizes, show poor in vivo mobility and thus delayed and reduced uptake over the desired target (*11–13*). Moreover, these antibodies are highly immunogenic and as such produce harmful side effects. In sharp contrast, peptides, which are smaller, offer various advantages, namely, rapid blood clearance, ease in the penetration of the tumor's vascular endothelium, increased diffusion rates in tissue, and low immunogenicity. Receptors for peptides are highly expressed on a variety of neoplastic and non-neoplastic cells. Furthermore, receptor-targeting peptides have shown a high level of internalization within tumor cells via receptor-mediated endocytosis. The capacity to internalize probes within tumor cells is crucial for delivering maximum payloads to tumor cells (*14–16*). These attractive physical properties coupled with their smaller size make peptides ideal candidates for developing new target-specific nanoparticles. In a recent paper, Chanda et al. conjugated a bombesin/gastrin-releasing peptide (BN/GRP) analogue to gold nanorods, which are internalized in cancer cells for the development of in vivo molecular imaging agents for cancer (*17*).

In the present study, we functionalized AuNPs with both a targeting peptide and a drug peptide ligand with the aim to improve not only the selectivity of the conjugates, but also their antitumor activity over the free drug. Since AuNPs conjugated to a targeting ligand have a higher capacity to enter cells, carrying the antitumor peptide and thus increasing its local concentration will, in turn, enhance the antitumor activity. BN was chosen as a targeting ligand for bombesin gastrin releasing

* To whom correspondence should be addressed. Phone: +34 934037088. Fax: +34 934037126. E-mail: albericio@pcb.ub.es, mkogan@ciq.uchile.cl.

[†] Barcelona Science Park.

[‡] University of Chile.

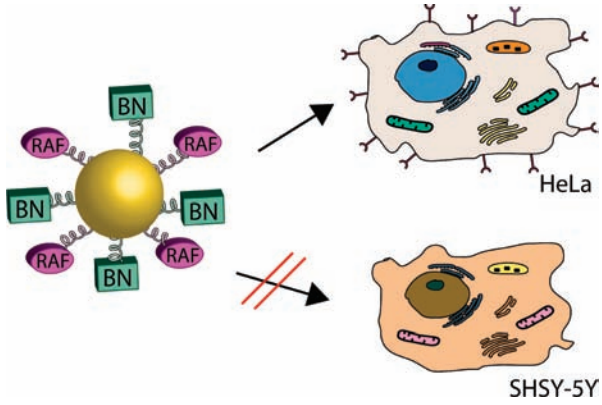
[§] Centre for Advanced Interdisciplinary Research in Material Sciences.

[||] ICREA and Institut de Ciencia de Materials de Barcelona.

[⊥] University of Barcelona.

10.1021/bc1000164 © 2010 American Chemical Society
Published on Web 05/18/2010

Scheme 1. Multifunctionalization of Gold Nanoparticles with a Targeting Peptide (BN) and an Antitumoral Peptide (RAF)[a]



[a] BN recognizes the GRP receptor overexpressed in HeLA cells and not in the neuroblastoma line SHSY-5Y. The recognition mediates the penetration into HeLa cells.

peptide receptor (GRPr), which has been found to be overexpressed in prostate, breast, small cell lung, and cervical cancer (*14–20*). Furthermore, AuNPs were functionalized with the drug peptide ligand RAF analogue which inhibits Rb-Raf-1 binding in vivo and therefore inhibits tumor growth and angiogenesis (*21*). In addition, AuNPs were multifunctionalized with a mixture of both peptides with the goal of implementing the targeting vehicle with antitumor activity.

The size of AuNPs may affect the cell permeability as well as toxicity. Taking into account these relevant points in this study, we chose 20-nm-diameter gold nanoparticles for three reasons: (i) they possess a widespread organ distribution (*22–24*) which is very relevant for future drug delivery applications, (ii) they have higher penetration in cells with respect to bigger AuNP (>70 nm) (*25*), and last (iii) AuNPs of this size were reported to pose no inherent toxicity to different cell lines (*26, 27*) and in zebrafish embryos (*28*), in contrast to AuNPs of 1−2 nm that were found to be highly toxic in cell lines (*29, 30*).

The multifunctionalized AuNPs with RAF peptide analogues (Ac-Cys-Ahx-RAF) and BN (Ac-Cys-Ahx-BN) (Scheme 1) were evaluated for their cell internalization properties and in vitro viability in HeLa cells, which overexpress GPRr, and in neuroblastoma SHSH-5Y cells, which do not overexpress these receptors.

RESULTS AND DISCUSSION

BN and RAF Peptide Analogues. A very promising group of small targeting ligands comprises a number of regulatory peptides. Among these, the BN peptide, originally isolated from the skin of a frog, has also shown antitumor activity (*31*). BN-like peptides are known to bind to GRPrs with high affinity and specificity. A high number of GRPrs are overexpressed in various human tumors (*32*) like glioblastoma, small cell lung, gastric, pancreatic, prostate, breast, cervical, and colon cancer (*16, 33–36*), as well as in premalignant cells in the case of prostate, gastric, and lung cancers (*37–39*). These receptors are therefore promising targets for targeted therapy of cancer because of their location on the plasma membrane, which promotes the internalization of the receptor−ligand complex upon binding of a ligand. These findings open up the possibility of applying BN-like peptides as vehicles to deliver cytotoxic drugs (*40, 41*) into tumor cells (*42*). On the basis of studies by Dasgupta et al. (*21*), we selected the RAF peptide as the drug antitumor ligand. The retinoblastoma tumor suppressor protein (Rb) plays a vital role in regulating mammalian cell cycle progression and inactivation of this protein is required for entry into the S phase. Rb is inactivated by phosphorylation upon growth factor stimulation of quiescent cells, thereby facilitating the transition from G_1 to S phase (*43*). Previous studies have shown that the signaling kinase c-Raf (Raf-1) physically and functionally interacts with Rb and contributes to its inactivation, thereby facilitating cell proliferation. Disruption of the Rb-Raf-1 interaction by the 9-amino-acid peptide significantly inhibits Rb phosphorylation and thus cell proliferation (*21*).

Table 1. Structures of the Two Peptides Complexed to Gold Nanoparticles (Ac-Cys-Ahx-BN and Ac-Cys-Ahx-RAF) and the Two Fluorescently Labeled Peptides (Ac-Cys-Ahx-Lys(CF)-BN and Ac-Cys-Ahx-Lys(CF)-RAF) Used in This Study[a]

name	sequence
Ac-Cys-Ahx-BN	Ac*-Cys-Ahx**-Gln-Trp-Ala-Val-Gly-His-Leu-Met-NH_2
Ac-Cys-Ahx-RAF	Ac*-Cys-Ahx**-Gly-Ile-Ser-Asn-Gly-Phe-Gly-Phe-Lys-NH_2
Ac-Cys-Ahx-Lys (CF)-BN	Ac*-Cys-Ahx**-Lys(CF)-Gln-Trp-Ala-Val-Gly-His-Leu-Met-NH_2
Ac-Cys-Ahx-Lys (CF)-RAF	Ac*-Cys-Ahx**-Lys(CF)-Gly-Ile-Ser-Asn-Gly-Phe-Gly-Phe-Lys-NH_2

[a] * The N-terminus has been acetylated, ** aminohexanoic acid.

The peptides were synthesized using a Fmoc/^{t}Bu solid-phase synthetic strategy (Materials and Methods section) and a free thiol containing Cys was introduced at the end of a spacer to facilitate attachment onto the gold surface (Table 1). As the *C*-terminus of BN is required for high-affinity binding (*44*), the *N*-terminus of the peptide was modified through an aliphatic linker to allow labeling with the cargo (*45*). The spacers have to position the gold conjugate sufficiently far from the GRPr-binding region of BN to prevent hindrance of the binding (affinity) of the BN motif with GRPr (*46, 47*). The optimal hydrocarbon spacer length should vary from 3 to 8 carbon atoms without adversely affecting the resultant binding affinity (*48*). As reported by Hoffman et al. (*49*), an increase in the hydrophobicity of the linker group to excessive levels reduces the receptor-binding affinity (*47, 49, 50*).

Thus, for conjugating both BN and the RAF peptides, a 6-carbon-atom spacer (aminohexanoic acid, Ahx) was selected to be attached to a free thiol containing Cys in order to facilitate anchoring onto the gold surface (Ac-Cys-Ahx-BN and Ac-Cys-Ahx-RAF) (Table 1). To check whether the free analogue peptides—unconjugated to AuNPs—BN and RAF have the capacity to penetrate the cell, we labeled peptides with a carboxyfluorescein (CF) fluorophore. The CF was introduced into the ε-amino of an additional residue of Lys, which was incorporated at the *N*-terminal of the peptide, before the incorporation of the Ahx residue. Peptides Ac-Cys-Ahx-Lys(CF)-BN and Ac-Cys-Ahx-Lys(CF)-RAF were also produced using a Fmoc/^{t}Bu/Alloc solid-phase strategy (Supporting Information Figure S1, Table S1). The Alloc group was used to block the Lys side chain and was removed once the elongation of the peptide sequence was done to incorporate the CF before the global deprotection and cleavage.

Conjugation of Ac-Cys-Ahx-BN and Ac-Cys-Ahx-RAF with AuNPs. Ac-Cys-Ahx-BN and Ac-Cys-Ahx-RAF were conjugated separately and also in an equimolar mixture with a 20 nM AuNP solution to obtain the following conjugates: Ac-Cys-Ahx-BN@AuNPs, Ac-Cys-Ahx-RAF@AuNPs, and Ac-Cys-Ahx-BN/Ac-Cys-Ahx-RAF@AuNPs (Note: From a peptide point of view, a more correct nomenclature should be Ac-Cys(AuNPs)-Ahx-BN, Ac-Cys(AuNPs)-Ahx-RAF, and Ac-Cys(AuNPs)-Ahx-BN/Ac-Cys(AuNPs)-Ahx-RAF) (Table 1). We then tested the influence of both the targeting and drug ligands on the cell penetration and antitumor activity of these conjugates. AuNPs were obtained via the sodium citrate reduction method (*51–55*), which allows the synthesis of clusters of particles between 6 and 60 nm by adding various amounts of the reducing agent. The AuNPs were characterized by UV−vis (Figure 1) and transmission electron microscopy (TEM)

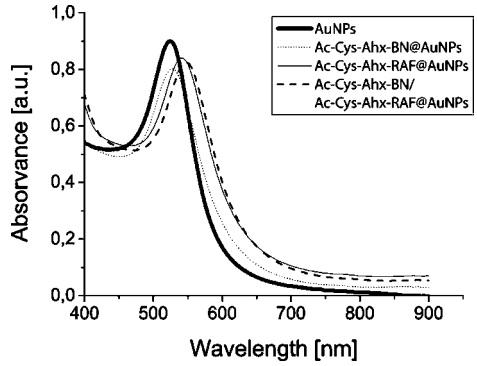


Figure 1. UV−vis spectra of AuNPs and their respective conjugates; a shift in the maximum is representative of the conjugation.

(Supporting Information Figure S3). The peptide-capped AuNPs were prepared by mixing a colloidal gold solution with an excess of peptide to obtain functionalized gold surfaces. The conjugates were characterized by using UV−vis spectroscopy, amino acid analysis (AAA), TEM, and electron energy loss spectroscopy (EELS).

Conjugation of Ac-Cys-Ahx-Lys(CF)-BN and Ac-Cys-Ahx-Lys(CF)-RAF with AuNPs. The same procedure described for the conjugation of Ac-Cys-Ahx-BN and Ac-Cys-Ahx-RAF to AuNPs was used to prepare Ac-Cys-Ahx-Lys(CF)-BN@AuNPs, Ac-Cys-Ahx-Lys(CF)-RAF@AuNPs, and Ac-Cys-Ahx-Lys(CF)-BN/Ac-Cys-Ahx-Lys(CF)-RAF@AuNPs.

Characterization of Conjugates. *UV−vis Spectroscopy.* The shift of the surface plasmon resonance band (SPR) to a longer wavelength (>522 nm with respect to the SPR of citrate AuNP, Figure 1), as a result of changes in the dielectric properties of the medium in which the AuNPs are found or the presence of materials adsorbed onto their surface, showed the capping of the AuNP surface with the peptide molecules (*4, 56*). The concentration of AuNPs was determined using the molar coefficient of extinction for the 20 nm AuNPs (5.41×10^8 M^{-1} cm^{-1}) as reported in the literature (*57*).

Electron Energy Loss Spectroscopy (EELS). To evaluate the presence of sulfur atoms and thus corroborate the functionalization of the AuNPs with the peptides, spectra between 140 and 220 eV were obtained on the AuNP surfaces for the conjugated and nonconjugated samples. An accurate analysis of the electron energy loss near the edge spectra (ELNES) at the S $L_{2,3}$ edge placed at around 165 eV was performed. All sample spectra show the S $L_{2,3}$ edge slope around 165 eV on the surface of the AuNPs, which is characteristic of peptide functionalization (Figure 2). Given that the nonconjugated sample was assumed to have a low number of S atoms, it was used to evaluate the signal-to-noise ratio in the S $L_{2,3}$ energy region. Table S2 (Supporting Information) shows a comparison of the maximum intensity obtained for the functionalized samples and the control. A slightly higher increment in intensity at 165 eV for the functionalized nanoparticles compared to the bare ones suggests that the thiol moiety of the peptides is attached to the AuNPs.

Determination of the Number of Peptide Molecules/Nanoparticle. To determine the number of peptide molecules per nanoparticle, the conjugates were centrifuged and the supernatants lyophilized, resuspended, and analyzed by HPLC to determine the amount of nonconjugated peptide by interpolation onto a calibration curve (Supporting Information Figure S2). Approximately 40% of the peptides used in the conjugation were attached to the AuNPs. In the case of the equimolar mixture of Ac-Cys-Ahx-BN and Ac-Cys-Ahx-RAF, 44% of the nonbounded peptide corresponds to Ac-Cys-Ahx-BN and 56% to Ac-Cys-Ahx-RAF. By subtracting the total amount of peptide used for the conjugation, the bounded peptide concentration was found to be about 50 μM and the AuNP solution was about 2 nM (determined spectrophotometrically), which results in a ratio of around 25 000 peptide molecules per AuNP. The large number of peptide molecules/nanoparticle could be attributed to a self-aggregation process that occurs in amphipathic peptides (*58*).

Amino Acid Analysis (AAA). The relationship among the concentrations of the amino acids His, Ile, and Phe give the relative concentration of these two peptides on the AuNPs. The relationship found, 1 for His/Ile and 2 for Phe/His, showed that both peptides were incorporated equimolarly onto the Ac-Cys-Ahx-BN/Ac-Cys-Ahx-RAF@AuNPs (Supporting Information Table S3).

Cellular Internalization of the Carboxyfluorescinated Peptides as Shown by Confocal Laser Scanning Microscopy (CLSM). Peptides Ac-Cys-Ahx-Lys(CF)-BN and Ac-Cys-Ahx-Lys(CF)-RAF were incubated with HeLa (cervical tumoral cell line which overexpresses GRP receptors) and SHSY-5Y cells for 24 h. As expected, Ac-Cys-Ahx-Lys(CF)-BN was efficiently internalized in HeLa cells and not in SHSY-5Y, while Ac-Cys-Ahx-Lys(CF)-RAF entered both HeLa and SHSY-5Y cell lines, hence showing its lack of specificity (Figure 3).

Accumulation of Peptide−AuNP Conjugates and AuNPs as Shown by CLSM. In order to prove whether the functionalization of AuNPs with BN and RAF—or with both together—favors selectivity in the delivery of the conjugates, the reflection of the nanoparticles was exploited. The red coloration of the nanoconjugates (*9*) of Ac-Cys-Ahx-BN and Ac-Cys-Ahx-RAF inside cells was observed due to the accumulation and reflection of the AuNP.

An internalization study of the conjugates after 24 h of incubation was performed in the tumoral cell line HeLa and in the SHSY-5Y cell line. The cell membrane was marked in green by WGA, and the nucleus was stained in blue with DRAQ5. The degree of accumulation inside the HeLa cells occurred in the following order Ac-Cys-Ahx-BN@AuNPs > Ac-Cys-Ahx-BN/Ac-Cys-Ahx-RAF@AuNPs > Ac-Cys-Ahx-RAF@AuNPs (Figure 4). Ac-Cys-Ahx-BN@AuNPs showed the greatest accumulation, suggesting a receptor-mediated internalization mechanism, most likely via endocytosis, as reported in the literature (*17*); however, in this paper we did not study the internalization mechanism. On the contrary, Ac-Cys-Ahx-RAF@AuNPs presented low internalization in HeLa cells due to the fact that the receptor-mediated internalization mechanism is not favored by target peptide. Finally, the conjugates Ac-Cys-Ahx-BN/Ac-Cys-Ahx-RAF@AuNPs showed an intermediate cell penetration capacity. As expected, gold conjugates did not accumulate in the SHSY-5Y cell line because of the low concentration of GRPr for this cell line.

These results provide an illustration of the power of our strategy. Thus, while the RAF conjugate internalizes poorly into HeLa cells, the AuNPs containing RAF and BN did because of the presence of the BN moiety, which has the capacity to bind to the GRPr of cells. Furthermore, the presence of the BN moiety provides selectivity for the drug−ligand conjugate as shown by the finding that none of the AuNPs penetrated the SHSY-5Y cells. This selectivity is potentially useful in the development of ligand-targeted therapeutics.

Colocalization of the Fluorescence and Gold Reflection Signal Caused by the Conjugate-Labeled Peptides as Shown by CLSM Imaging. The carboxyfluoresceinated conjugates, Ac-Cys-Ahx-Lys(CF)-BN@AuNPs, Ac-Cys-Ahx-Lys(CF)-RAF@AuNPs, and Ac-Cys-Ahx-Lys(CF)-BN/Ac-Cys-Ahx-Lys(CF)-RAF@AuNPs, were incubated with the tumor cell line HeLa for 24 h at 37 °C to colocalize the fluorescence signal caused by the peptide−AuNP conjugate and the reflection of the AuNP.

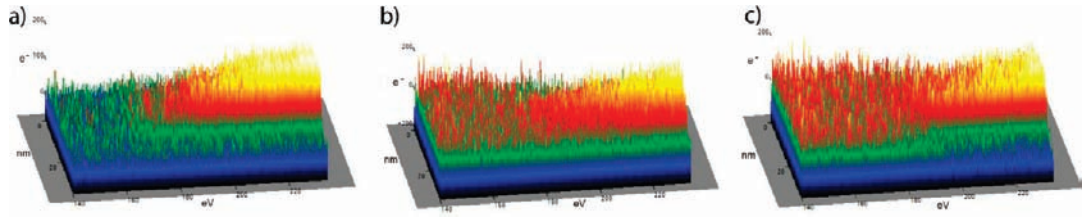


Figure 2. EELS spectrum obtained on the surface of (a) nonfunctionalized 20 nm AuNPs, (b) Ac-Cys-Ahx-BN functionalized AuNPs, and (c) Ac-Cys-Ahx-RAF functionalized AuNPs.

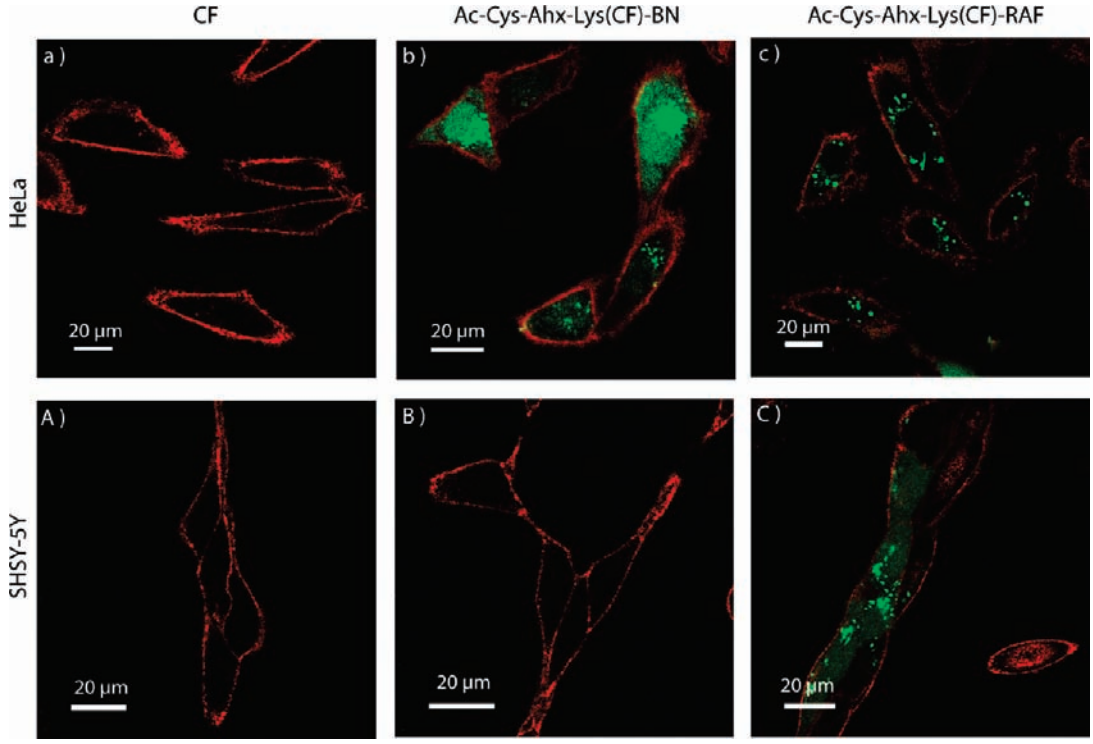


Figure 3. Localization of carboxyfluoresceinated peptides in HeLa cells (a−c) and in SHSY-5Y cells (A−D) incubated for 24 h. Control of CF (a, A), Ac-Cys-Ahx-Lys(CF)-BN (b, B), Ac-Cys-Ahx-Lys(CF)-RAF (c, C). Membranes (green) were stained with a fluorescence marker (WGA). The peptides were added at a final concentration of 1×10^{-5} M.

The membrane of the cells was stained green and the internalization of the fluorinated gold complexes was visualized using CLSM. These observations revealed that nearly all the AuNPs were complexed to the fluorescently labeled peptides (Figure 5) when overlapping the red reflection of the AuNPs with the blue fluorescence of the carboxyfluorinated peptides. These results indicate that the labeled peptides do not detach from the AuNP surface. However, a partial hydrolysis of the peptide in cells may occur. This possibility could not be discarded in the present study because the fluorescence label was found in the *N*-terminal extreme of the peptide, which was bound to the AuNPs surface.

Viability Studies. The degree of viability and effects of the free peptides (Ac-Cys-Ahx-BN and Ac-Cys-Ahx-RAF), gold conjugates Ac-Cys-Ahx-BN@AuNPs and Ac-Cys-Ahx-RAF@AuNPs, and the equimolar mixture Ac-Cys-Ahx-BN/Ac-Cys-Ahx-RAF@AuNPs and AuNPs on cell proliferation was determined by MTT assay in HeLa and SHSY-5Y cells following 24 h of incubation (Figure 6). AuNPs did not show any significant effects on HeLa cell viability, while Ac-Cys-Ahx-BN and Ac-Cys-Ahx-RAF at concentrations of 1×10^{-5} M reduced the viability of cells in 33% and 52%, respectively, with respect to the controls. As expected, the RAF peptide possesses a higher antitumor activity, since it is reported to suppress tumor growth and angiogenesis (*59, 60*). However, to the best of our knowledge, the antitumor activity of both peptides has never been compared in the same conditions. In the case of BN, the conjugation with AuNPs increases the toxicity in cells possibly due to a synergistic effect in the penetration between the AuNP and the peptide, which helps to increase the local concentration which in turn enhances the antitumor activity and is in accordance with the increased delivery of Ac-Cys-Ahx-BN-AuNP to HeLa cells. The conjugates Ac-Cys-Ahx-RAF-AuNP produce similar effects on cell viability with respect to the peptide Ac-Cys-Ahx-RAF-AuNP.

Interestingly, conjugates of the peptides with AuNPs did not show any effect on cell viability in neuroblastoma SHSY-5Y cells. The lack of toxicity could be attributed to the low penetration that the conjugates present in this cell line due to the low expression of GRPr receptors. Remarkably, Ac-Cys-Ahx-RAF is toxic against this cell line which evidences the low selectivity of this peptide against cells in general (as shown by the CLSM of the CF peptide, Figure 3); however, conjugation with AuNP results in increased selectivity (toxicity in HeLa cells but not in SHSY-5Y). The conjugation of this peptide with AuNPs could induce a change in the conformation of the peptide molecules that leads to a reduction of toxicity in neuroblastoma cells. This is an interesting point which we are currently studying.

CONCLUSIONS

In summary, we report herein a strategy to increase the activity and cell selectivity of AuNP−peptide conjugates by

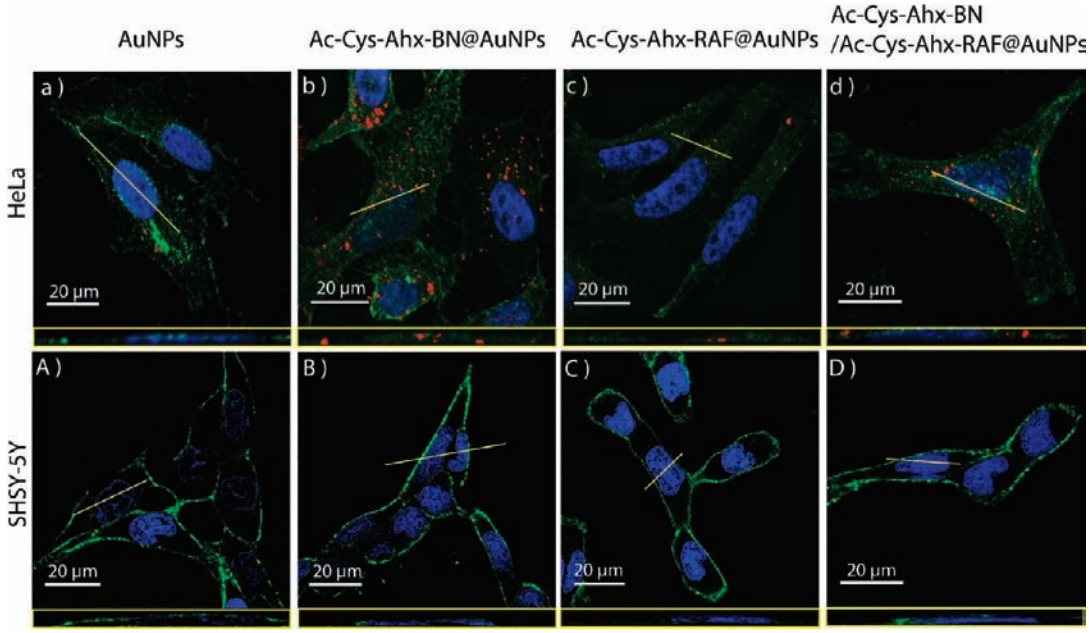


Figure 4. Localization of AuNPs and their conjugates in HeLa cells (a−d) and in SHSY-5Y cells (A−D) incubated for 24 h. AuNPs (a, A), Ac-Cys-Ahx-BN@AuNPs (b, B), Ac-Cys-Ahx-RAF@AuNPs (c, C), Ac-Cys-Ahx-BN/Ac-Cys-Ahx-RAF@AuNPs (d, D). The red dots represent reflections of groups of nanoparticles. Membranes (green) were stained with a fluorescence marker (WGA), and nuclei (blue) with a DNA marker (DRAQ5). The conjugated peptides were added at final concentrations of 1×10^{-5} M of peptides and 0.4 nM of AuNPs. The insets in yellow squares are the projection of the slides in the *z* axis to corroborate the localization of the gold nanoconjugates inside the cells and not onto the top of the cells.

means of the multifunctionalization of the AuNPs with a targeting peptide (BN) and an antitumor peptide (RAF). This work confirms that the conjugates in which BN is present penetrate cells that overexpress GRPr. However, a more detailed study of the internalization mechanism to confirm a receptor-mediated endocytosis mechanism in HeLa cells for the analogue of BN peptide is currently underway. The enhancement in activity and selectivity could contribute to a potential improvement of the efficacy of RAF for therapy by reducing the therapeutic index. Furthermore, this strategy will provide an opportunity for the controlled delivery of AuNPs used as cargoes for a localized (nanometrically) therapy like the so-called molecular surgery.

MATERIALS AND METHODS

Materials. Rink amide MBHA resin and Fmoc-N^{α}-protected amino acids were purchased from Iris Biotech GmbH (Marktredwitz, Germany). 7-Aza-1-hydroxy-1*H*-benzotriazole (HOAt) was obtained from GL Biochem (Shanghai, China); 1-benzotriazolyloxytris(pyrrolidino)-phosohonium hexafluorophosphate (PyBOP) was purchased from Novabiochem (Laüfelfelfingen, Switzerland); 7-azabenzotriazol-1-yloxytris(pyrrolidino)phosphonium hexafluorophosphate (PyAOP) from Applied Biosystems (Foster City, CA); *N,N*′-diisopropylethylamine (DIEA) from Albatros Chem. Inc. (Montreal, Canada); and *N,N*′-disopropylcarbodiimide (DIC) and triisopropylsilane (TIS) from Fluka Chemika (Buchs, Switzerland). 5(6)-Carboxyfluorescein (CF) was obtained from Acros (Somerville, NJ). Solvents for peptide synthesis and RP-HPLC were obtained from Scharlau (Barcelona, Spain). Trifluoroacetic (TFA) acid was supplied by KaliChemie (Bad Wimpfen, Germany). Dimethylformamide (DMF), dichoromethane (DCM), and acetonitrile (MeCN) were purchased from SDS (Peypin, France). Tetrakis(triphenylphosphine)palladium (0) [$Pd(PPh_3)_4$], phenyl silane ($PhSiH_3$), triisopropylsilane (TIS), and other chemicals used were obtained from Aldrich (Milwaukee, WI, USA) and were of the highest purity commercially available.

Peptide Synthesis and Chromatography. (All reported solvent ratios are expressed as v/v, unless otherwise stated). The four peptides were synthesized manually on Fmoc Rink amide MBHA resin (100 mg, 0.68 mmol/g) using a Fmoc/^{t}Bu strategy in polypropylene syringes, each fitted with a polyethylene porous disk. Solvents and soluble reagents were removed by suction. Washings between deprotection, couplings, and subsequent deprotection steps were carried out with DMF and DCM using around 10 mL solvent per gram of resin each time. The Fmoc group was removed by treatment with a mixture of piperidine−DMF (1:4 v/v) (2 × 10 min). After Fmoc removal, coupling reactions were carried out with Fmoc-amino acids (4 equiv), HOAt (4 equiv), and DIC (4 equiv) in DMF for 1.5 h. Couplings were monitored using the Kaiser test (*61*). When necessary, recouplings were done with PyBOP (4 equiv), HOAt (4 equiv), and DIEA (12 equiv) for 1.5 h. After completing the synthesis, we performed an acetylation step with a mixture of AcOH (10 equiv) and DIC (5 equiv) for 10 min. For fluorescently labeled peptides [Ac-Cys-Ahx-Lys(CF)-BN and Ac-Cys-Ahx-Lys(CF)-RAF], after completion of the peptide sequence, the Alloc (Allyloxycarbonyl) group was removed with $Pd(PPh_3)_4$ (0.1 equiv) in the presence of $PhSiH_3$ (10 equiv) (3 × 15 min) under Ar atmosphere followed by several washes (5 × 1 min) with sodium *N,N*′-diethyldithiocarbamate (0.02 M in DMF) and DMF. CF (5 equiv), PyAOP (5 equiv), HOAt (5 equiv), and DIEA (10 equiv) were dissolved in a mixture of DMF−DCM, preactivated for 10 min, and added to the peptidyl resin. The reaction mixture was stirred for 1.5 h. For the deprotection of side chain groups and concomitant cleavage of the peptides from the support, the resin was washed with DCM (3 × 1 min), dried, and treated with a TFA−H_2O−TIS (95:2.5:2.5) cocktail for 1 h. TFA was then removed by evaporation with a N_2 stream and peptides were precipitated with a mixture of cold anhydrous *tert*-butyl methyl ether (TBME) and hexane (2:1), dissolved in H_2O−MeCN (1:1) and freeze−dried. The crude peptides were purified using a semipreparative RP-HPLC [Waters 2487 Dual λ Absorbance Detector (Waters, MA, USA) equipped with a Waters 2700 Sample Manager, a Waters 600 controller, a Waters Fraction Collector, a Symmetry column (C_{18}, 5 μm, 30 × 100 mm), and Millenium software; flow rate = 10 mL/min, gradient = 0−20% B for 5 min, 20−40% B for 35 min, 40−100% B

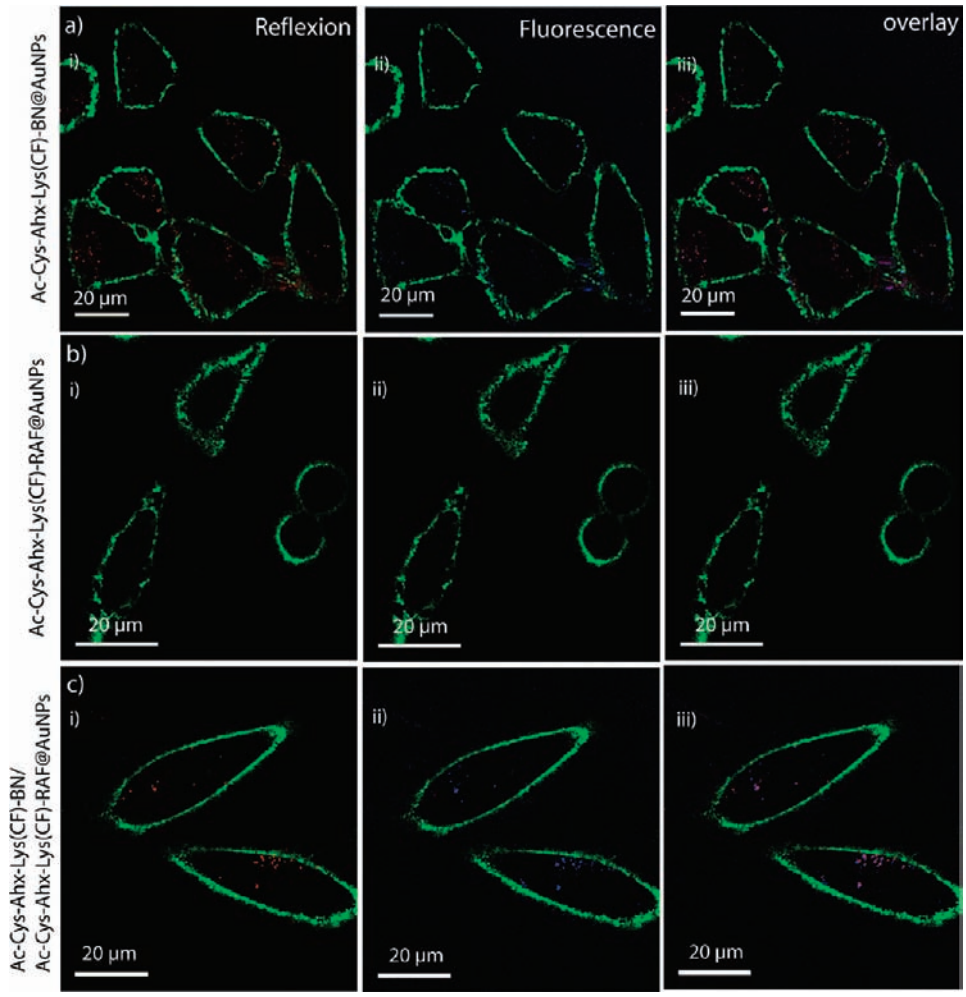


Figure 5. Localization of carboxyfluoresceinated peptides attached to AuNPs in HeLa cells incubated for 24 h. (a) Ac-Cys-Ahx-Lys(CF)-BN@AuNPs, (b) Ac-Cys-Ahx-Lys(CF)-RAF@AuNPs, (c) Ac-Cys-Ahx-Lys(CF)-BN/Ac-Cys-Ahx-Lys(CF)-RAF@AuNPs. Membranes (green) were stained with a fluorescence marker (WGA). Reflection of the AuNPs in red (i), carboxyfluorinated peptides in blue (ii), and the overlay of both channels in purple (iii). The conjugated peptides were added at a final concentration of 1×10^{-5} M of peptides and 0.4 nM of AuNPs.

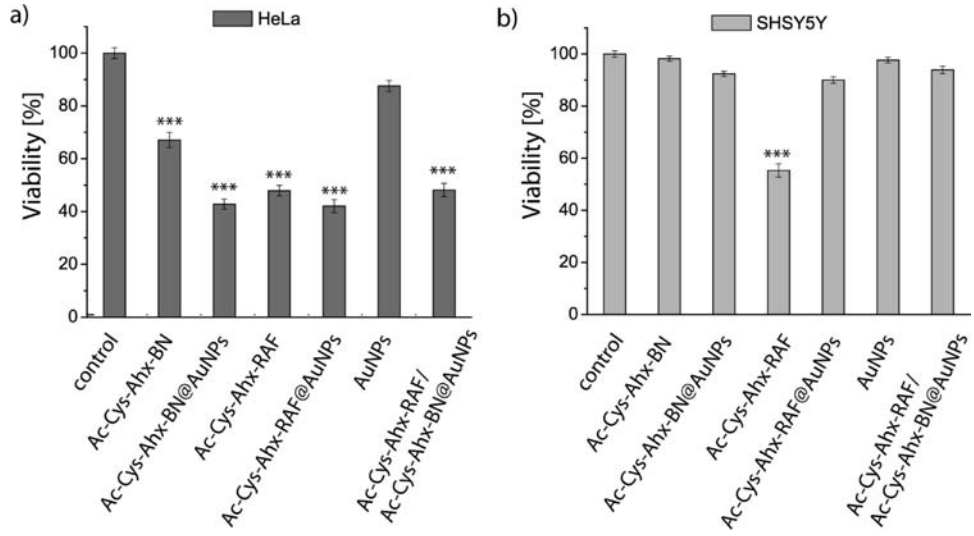


Figure 6. Cell viability assay after incubation of cells with Ac-Cys-Ahx-BN, Ac-Cys-Ahx-RAF, and their gold conjugates for 24 h: (a) HeLa cell line and (b) SHSY-5Y cell line. The conjugated and nonconjugated peptides were added at a final concentration of 1×10^{-5} M of peptides and 0.4 nM of AuNPs. The results are expressed as percentages compared to untreated cells and represent the mean ± standard deviation of three independent experiments (*** $P < 0.001$).

for 5 min (A = 0.1% TFA in H_2O, B = 0.05% TFA in MeCN)]. The purified peptides were identified (Supporting Information Figure S1 ai, bi, ci, di) at $\lambda = 220$ nm by analytical RP-HPLC [Waters 996 photodiode array detector equipped with Waters 2695 separation module, a Symmetry column (C_{18}, 5 μm, 4.6 × 150 mm) and Millennium software; flow rate = 1 mL/min, gradient = 20−40% D for 15 min for Ac-Cys-Ahx-BN, Ac-Cys-Ahx-RAF, Ac-Cys-Ahx-Lys(CF)-RAF, and 20−60% D for

15 min for Ac-Cys-Ahx-Lys(CF)-BN for 15 min (C = 0.045% TFA in H_2O, and D = 0.036% TFA in MeCN)]. Mass spectra were recorded on a MALDI Voyager DE RP time-of-flight (TOF) spectrometer (Applied Biosystems, Foster City, CA, USA) using ACH matrix (Supporting Information Figure S1 aii, bii, cii, dii).

Preparation of AuNPs. AuNPs were produced by reduction of $HAuCl_4 \times H_2O$ obtained from Aldrich (Milwaukee, WI, USA). $HAuCl_4 \times H_2O$ (8.7 mg) was added to a sodium citrate solution (100 mL, 2.2 mM) at reflux. The reducing agent was added rapidly, and the reaction was allowed to continue under uniform and vigorous stirring until a red wine color was observed (*58*).

Conjugation of Peptides with AuNPs. An excess of peptide was used for the conjugation (*62*). 1 mL of peptide solution (1 mg/mL in Milli-Q water) was added dropwise to 10 mL of AuNP solutions at room temperature with magnetic stirring, and the agitation was then maintained for 15 min. The conjugates were then purified by dialysis over three days in a Spectra/Por MWCO membrane: 6−8000 against 1 mM sodium citrate. The solution was refreshed six times to remove the excess peptide (Ac-Cys-Ahx-BN, Ac-Cys-Ahx-RAF, the equimolar mixture of Ac-Cys-Ahx-BN and Ac-Cys-Ahx-RAF or their fluorescently labeled counterparts).

UV−visible. UV−vis absorption spectra were recorded at room temperature with a 2501PC UV−vis recording spectrophotometer (Shimadzu Corporation, Kyoto, Japan).

Electron Energy Loss Spectroscopy (EELS). AuNP or AuNP-peptide (Ac-Cys-Ahx-BN@AuNPs, Ac-Cys-Ahx-RAF@AuNPs, Ac-Cys-Ahx-RAF/Ac-Cys-Ahx-BN@AuNPs) solutions (20 μL × 3) were placed on holley carbon Cu grids and allowed to dry at room temperature. Electron energy loss spectra were obtained in a Gatan Image Filter (GIF 2000) coupled to the JEOL 2010F microscope, with an energy resolution of 1.2 eV.

Amino Acid Analysis (AAA). Amino acid analysis was carried out by the AccQ. Tag method after acid hydrolysis with HCl (6N) for 24 h at 110 °C was used. The analysis was performed in a Waters Delta 600 RP-LC system with UV detection at 254 nm.

Determination of Conjugate Concentration. The number of peptides per particle was calculated by dividing the concentration of grafted peptide by the number of AuNPs in solution, which was determined spectrophotometrically considering the molar extinction coefficients detailed in the literature (*57*). The concentration of grafted peptide was determined by interpolation into a calibration curve (Supporting Information Figure S2) of the area of the HPLC peak of the solution resulting after centrifugation with an amicon filter (Amicon ultra-15, 3 kDa, MilliPore Corporation, Billerica, MA, USA) of a known volume of the conjugates at 13 500 rpm for 30 min. Once the AuNP pellet was removed, the free peptide containing solution was freeze−dried, dissolved again, and injected into the HPLC.

Cell Culture and Incubation with the Conjugates. HeLa and SHSY-5Y cell lines were obtained from ATCC no CCL-2 and ATCC no CRL-2266, respectively (Manasas, VA). Both cell lines were maintained in DMEM (low glucose medium for HeLa cell line and high glucose medium for SHSY-5Y) (Biological Industries) containing 10% fetal calf serum (FCS), 2 mM glutamine, 50 U/mL penicillin, and 0.05 g/mL streptomycin. For experiments, exponentially growing cells were detached from the culture flasks using a trypsin−0.25% ethylenediaminetetraacetic acid (EDTA) solution, and the cell suspensions were seeded at a concentration of 3.5×10^3 cells/cm^2 for the HeLa line and 1×10^3 cells/cm^2 for the SHSY-5Y line onto glass-bottom microwell dishes (35 mm Petri dish, 14 mm microwell, 1.5 mm cover glass) (Nalge Nunc International, Rochester, NY). Experiments were carried out 24 h later, when the confluence was approximately 70−80%. Nonadherent cells were washed away and attached cells were incubated at 37 °C in 5% CO_2 in DMEM with a known concentration of free AuNPs, peptide−AuNP conjugates, and carboxyfluorinated peptides. The conjugated and nonconjugated peptides were added in a 1:4 (conjugate/DMEM) ratio at a final concentration of 1×10^{-5} M of peptides and 0.4 nM of AuNPs.

MTT Assay. HeLa and SHSY-5Y viability in the presence of nonconjugated or conjugated nanoparticles and the free peptides was tested by the reduction of 3-[4,5-dimethylthiazol-2-yl]-2,5-diphenyltetrazolium bromide (MTT), including a control with no nanoparticles added. For each assay, 3.5×10^3 cells/cm^2 of the HeLa cell line and 1×10^3 cells/cm^2 of the SHSY-5Y cell line were seeded onto a 96-well plate (Nalge Nunc) and cultured for 24 h. The conjugates were added in a 1:4 (conjugate/DMEM) ratio, and the free peptides were added at the same concentration as the peptide−gold conjugates at a final concentration of 1×10^{-5} M of peptides and 0.4 nM of AuNPs. Cells were incubated for 22 h at 37 °C under a 5% CO_2 atmosphere. After incubation, the medium was removed and the cells were incubated with 200 μL fresh medium containing MTT (0.5 mg/mL) for 2 h. The resulting blue formazan was solubilized in 150 μL acidified isopropanol (0.04 M HCl) and the absorbance was measured at 560 nm using a plate reader (Multiskan Ascent, Thermo Scientific). The values of the untreated cells were taken as 100%, and cell viability was expressed as a percentage of the untreated cells. The data were obtained from three independent experiments performed in triplicate.

Confocal Laser Scanning Microscopy (CLSM). For the cellular localization of AuNP conjugates (Ac-Cys-Ahx-BN@AuNPS, Ac-Cys-Ahx-RAF@AuNPs, Ac-Cys-Ahx-BN/Ac-Cys-Ahx-RAF@AuNPs) and for the carboxyfluorinated peptides (Ac-Cys-Ahx-Lys(CF)-BN and Ac-Cys-Ahx-Lys(CF)-RAF), HeLa and SHSY-5Y cells were plated onto glass coverslips, grown to 60% confluence, and then incubated at 37 °C under a 5% CO_2 atmosphere with either Ac-Cys-Ahx-Lys(CF)-BN, Ac-Cys-Ahx-Lys(CF)-RAF or nanoparticle conjugates for 24 h. WGA as plasma membrane marker and DRAQ5 as a DNA dye were added just before recording the image. The samples were examined using an Olympus Fluoview 500 confocal microscope with a 60×/1.4 NA objective.

ACKNOWLEDGMENT

We gratefully acknowledge Tommaso Cupido for their helpful discussions. We thank Raquel Garcia Olivas, and Elisenda Coll (UB-SCT) for their assistance with CLSM and TEM, respectively. This work was partially supported by AECID, FONDECYT 1090143 CICYT (CTQ2009-07758), the Instituto de Salud Carlos III (CB06_01_0074), the Generalitat de Catalunya (2009SGR 1024), the Institute for Research in Biomedicine, and the Barcelona Science Park.

Supporting Information Available: Additional information as described in the text. This material is available free of charge via the Internet at http://pubs.acs.org.

LITERATURE CITED

(1) Sokolov, K., Follen, M., Aaron, J., Pavlova, I., Malpica, A., Lotan, R., and Richards-Kortum, R. (2003) Real-time vital optical imaging of precancer using anti-epidermal growth factor receptor antibodies conjugated to gold nanoparticles. *Cancer Res. 63*, 1999–2004.

(2) Elghanian, R., Storhoff, J. J., Mucic, R. C., Letsinger, R. L., and Mirkin, C. A. (1997) Selective colorimetric detection of polynucleotides based on the distance-dependent optical properties of gold nanoparticles. *Science 277*, 1078–1081.

(3) Bhattacharya, R., Mukherjee, P., Xiong, Z., Atala, A., Soker, S., and Mukhopadhyay, D. (2004) Gold nanoparticles inhibit VEGF165-induced proliferation of HUVEC cells. *Nano Lett. 4*, 2479–2481.

(4) Kogan, M. J., Olmedo, I., Hosta, L., Guerrero, A. R., Cruz, L. J., and Albericio, F. (2007) Peptides and metallic nanoparticles for biomedical applications. *Nanomedicine 2*, 287–306.

(5) Zharov, V. P., Mercer, K. E., Galitovskaya, E. N., and Smeltzer, M. S. (2006) Photothermal nanotherapeutics and nanodiagnostics for selective killing of bacteria targeted with gold nanoparticles. *Biophys. J. 90*, 619–627.

(6) Zharov, V. P., Galitovskaya, E. N., Johnson, C., and Kelly, T. (2005) Synergistic enhancement of selective nanophotothermolysis with gold nanoclusters: Potential for cancer therapy. *Lasers Surg. Med. 37*, 219–226.

(7) Tkachenko, A. G., Xie, H., Liu, Y. L., Coleman, D., Ryan, J., Glomm, W. R., Shipton, M. K., Franzen, S., and Feldheim, D. L. (2004) Cellular trajectories of peptide-modified gold particle complexes: Comparison of nuclear localization signals and peptide transduction domains. *Bioconjugate Chem. 15*, 482–490.

(8) Thurn, K. T., Brown, E. M. B., Wu, A., Vogt, S., Lai, B., Maser, J., Paunesku, T., and Woloschak, G. E. (2007) Nanoparticles for applications in cellular Imaging. *Nanoscale Res. Lett. 2*, 430–441.

(9) Tkachenko, A. G., Xie, H., Coleman, D., Glomm, W., Ryan, J., Anderson, M. F., Franzen, S., and Feldheim, D. L. (2003) Multifunctional gold nanoparticle-peptide complexes for nuclear targeting. *J. Am. Chem. Soc. 125*, 4700–4701.

(10) Efremov, R. G., Chugunov, A. O., Pyrkov, T. V., Priestle, J. P., Arseniev, A. S., and Jacoby, E. (2007) Molecular lipophilicity in protein modeling and drug design. *Curr. Med. Chem. 14*, 393–415.

(11) Pissuwan, D., Valenzuela, S. M., Miller, C. M., and Cortie, M. B. (2007) A golden bullet? Selective targeting of toxoplasma gondii tachyzoites using anti body-functionalized gold nanorods. *Nano Lett. 7*, 3808–3812.

(12) Souza, G. R., Christianson, D. R., Staquicini, F. I., Ozawa, M. G., Snyder, E. Y., Sidman, R. L., Miller, J. H., Arap, W., and Pasqualini, R. (2006) Networks of gold nanoparticles and bacteriophage as biological sensors and cell-targeting agents. *Proc. Natl. Acad. Sci. U.S.A. 103*, 1215–1220.

(13) Qian, X. M., Peng, X. H., Ansari, D. O., Yin-Goen, Q., Chen, G. Z., Shin, D. M., Yang, L., Young, A. N., Wang, M. D., and Nie, S. M. (2008) In vivo tumor targeting and spectroscopic detection with surface-enhanced Raman nanoparticle tags. *Nat. Biotechnol. 26*, 83–90.

(14) Scopinaro, F., De Vincentis, G., and Varvarigou, A. D. (2005) Use of radiolabeled bombesin in humans. *J. Clin. Oncol. 23*, 3170–3171.

(15) Bartholdi, M. F., Wu, J. M., Pu, H. F., Troncoso, P., Eden, P. A., and Feldman, R. I. (1998) In situ hybridization for gastrin-releasing peptide receptor (GRP receptor) expression in prostatic carcinoma. *Int. J. Cancer 79*, 82–90.

(16) Markwalder, R., and Reubi, J. C. (1999) Gastrin-releasing peptide receptors in the human prostate: Relation to neoplastic transformation. *Cancer Res. 59*, 1152–1159.

(17) Chanda, N., Shukla, R., Katti, K. V., and Kannan, R. (2009) Gastrin releasing protein receptor specific gold nanorods: breast and prostate tumor avid nanovectors for molecular imaging. *Nano Lett. 9*, 1798–1805.

(18) Schwartsmann, G., DiLeone, L. P., Horowitz, M., Schunemann, D., Cancella, A., Pereira, A. S., Richter, M., Souza, F., da Rocha, A. B., Souza, F. H., Pohlmann, P., and de Nucci, G. (2006) A phase I trial of the bombesin/gastrin-releasing peptide (BN/GRP) antagonist RC3095 in patients with advanced solid malignancies. *Invest. New Drugs 24*, 403–412.

(19) Varvarigou, A., Bouziotis, P., Zikos, C., Scopinaro, F., and De Vincentis, G. (2004) *Cancer Biother. Radiopharm. 19*, 219–229.

(20) Cornelio, D. B., Meurer, L., Roesler, R., and Schwartsmann, G. (2007) Gastrin-releasing peptide receptor expression in cervical cancer. *Oncology 73*, 340–345.

(21) Dasgupta, P., Sun, J. Z., Wang, S., Fusaro, G., Betts, V., Padmanabhan, J., Sebti, S. M., and Chellappan, S. P. (2004) Disruption of the Rb-Raf-1 interaction inhibits tumor growth and angiogenesis. *Mol. Cell. Biol. 24*, 9527–9541.

(22) Kim, J. H., Kim, K.-W., Kim, M. H., and Yu, Y. S. (2009) Intravenously administered gold nanoparticles pass through the blood-retinal barrier depending on the particle size, and induce no retinal toxicity. *Nanotechnology 20*, 505101–9.

(23) De Jong, W. H., Hagens, W. I., Krystek, P., Burger, M. C., Sips, A. J., and Geertsma, R. E. (2008) Particle size-dependent organ distribution of gold nanoparticles after intravenous administration. *Biomaterials 29* 1912–9.

(24) Sonavane, G., Tomoda, K., and Makino, K. (2008) Biodistribution of colloidal gold nanoparticles after intravenous administration: effect of particle size. *Colloids Surf., B 66*, 274–80.

(25) Chithrani, D. B., Ghazani, A. A., and Chan, W. C. W. (2006) Determining the size and shape dependence of gold nanoparticle uptake into mammalian cells. *Nano Lett. 6* (4), 662–668.

(26) Connor, E. E., Mwamuka, J., Gole, A., Murphy, C., and Wyatt, M. D. (2005) Gold nanoparticles are taken up by human cells but do not cause acute cytotoxicity. *Small 1* (3), 325–327.

(27) Kahn, J., Oillai, B., Das, T. K., Singh, Y., and Maiti, S. (2007) Molecular effects of uptake of gold nanoparticles in HeLa cell. *ChemBiochem 8*, 1237–1240.

(28) Bar-Ilan, O., Albrecht, R. M., Fako, V. E., and Furgeson, F. (2009) Toxicity assessments of multisized gold and silver nanoparticles in zebrafish embryos. *Small 5* (16), 1897–1910.

(29) H-Pan, Y., Neuss, S., Leifert, A., Fischler, M., Wen, F., and Simon, U. (2007) Size-dependent cytotoxicity of gold nanoparticles. *Small 3* (11), 1941–1949.

(30) Tsoli, M., Kuhn, H., Brandau, W., Esche, H., and Schmid, G. (2005) Cellular uptake and toxicity of Au55 clusters. *Small 1* (8−9), 841–844.

(31) Nagy, A., Armatis, P., Cai, R. Z., Szepeshazi, K., Halmos, G., and Schally, A. V. (1997) Design, synthesis, and in vitro evaluation of cytotoxic analogs of bombesin-like peptides containing doxorubicin or its intensely potent derivative, 2-pyrrolinodoxorubicin. *Proc. Natl. Acad. Sci. U.S.A. 94*, 652–656.

(32) Reubi, J. C. (1995) Neuropeptide receptors in health and disease - the molecular-basis for in-vivo imaging. *J. Nucl. Med. 36*, 1825–1835.

(33) Moody, T. W., Mahmoud, S., Staley, J., Naldini, L., Cirillo, D., South, V., Felder, S., and Kris, R. (1989) Human glioblastoma cell-lines have neuropeptide receptors for bombesin gastrin-releasing peptide. *J. Mol. Neurosci. 1*, 235–242.

(34) Moody, T. W., Carney, D. N., Cuttitta, F., Quattrocchi, K., and Minna, J. D. (1985) High-affinity receptors for bombesin GRP-like peptides on human small cell lung-cancer. *Life Sci. 37*, 105–113.

(35) Qin, Y. F., Ertl, T., Cai, R. Z., Halmos, G., and Schally, A. V. (1994) Inhibitory effect of bombesin receptor antagonistic RC-3095 on the growth of human pancreatic-cancer cells in-vivo and in-vitro. *Cancer Res. 54*, 1035–1041.

(36) Yano, T., Pinski, J., Groot, K., and Schally, A. V. (1992) Stimulation by bombesin and inhibition by bombesin gastrin-releasing peptide antagonist RC-3095 of growth of human breast-cancer cell-lines. *Cancer Res. 52*, 4545–4547.

(37) Preston, S. R., Woodhouse, L. F., Jonesblackett, S., Miller, G. V., and Primrose, J. N. (1995) High-affinity binding-sites for gastrin-releasing peptide on human colorectal-cancer tissue but not uninvolved mucosa. *Br. J. Cancer 71*, 1087–1089.

(38) Shriver, S. P., Bourdeau, H. A., Gubish, C. T., Tirpak, D. L., Davis, A. L. G., Luketich, J. D., and Siegfried, J. M. (2000) Sex-specific expression of gastrin-releasing peptide receptor: Relationship to smoking history and risk of lung cancer. *J. Natl. Cancer Inst. 92*, 24–33.

(39) Lin, K. S., Luu, A., Baidoo, K. E., Hashemzadeh-Gargari, H., Chen, M. K., Pili, R., Pomper, M., Carducci, M., and Wagner, H. N. (2004) A new high affinity technetium analogue of bombesin containing DTPA as a pharmacokinetic modifier. *Bioconjugate Chem. 15*, 1416–1423.

(40) Schally, A. V., and Nagy, A. (1999) Cancer chemotherapy based on targeting of cytotoxic peptide conjugates to their receptors on tumors. *Eur. J. End. 141*, 1–14.

(41) Szereday, Z., Schally, A. V., Nagy, A., Plonowski, A., Bajo, A. M., Halmos, G., Szepeshazi, K., and Groot, K. (2002) Effective treatment of experimental U-87MG human glioblastoma in nude mice with a targeted cytotoxic bombesin analogue, AN-215. *Br. J. Cancer 86*, 1322–1327.

(42) Zhang, H. W., Chen, J. H., Waldherr, C., Hinni, K., Waser, B., Reubi, J. C., and Maecke, H. R. (2004) Synthesis and evaluation of bombesin derivatives on the basis of pan-bombesin peptides labeled with indium-111, lutetium-177, and yttrium-90 for targeting bombesin receptor-expressing tumors. *Cancer Res. 64*, 6707–6715.

(43) Wang, S., Ghosh, R. N., and Chellappan, S. P. (1998) Raf-1 physically interacts with Rb and regulates its function: a link between mitogenic signaling and cell cycle regulation. *Mol. Cel. Biol. 18*, 7487–7498.

(44) Moody, T. W., Crawley, J. N., and Jensen, R. T. (1982) Pharmacology and neurochemistry of bombesin-like peptides. *Peptides 3*, 559–563.

(45) Hoehne, A., Mu, L., Honer, M., Schubiger, P. A., Ametamey, S. M., Graham, K., Stellfeld, T., Borkowski, S., Berndorff, D., Klar, U., Voigtmann, U., Cyr, J. E., Friebe, M., Dinkelborg, L., and Srinivasan, A. (2008) Synthesis, F-18-labeling, and in vitro and in vivo studies of bombesin peptides modified with silicon-based building blocks. *Bioconjugate Chem. 19*, 1871–1879.

(46) Hoffman, T. J., Quinn, T. P., and Volkert, W. A. (2001) Radiometallated receptor avid peptide conjugates for specific targeting of cancer cells. *J. Nucl. Med. 28*, 527–539.

(47) Hoffman, T. J., Gali, H., Smith, C. J., Sieckman, G. L., Hayes, D. L., Owen, N. K., and Volkert, W. A. (2003) Novel series of In-111-labeled bombesin analogs as potential radiopharmaceuticals for specific targeting of gastrin-releasing peptide receptors expressed on human prostate cancer cells. *J. Nucl. Med. 44*, 823–831.

(48) Abd-Elgaliel, W. R., Gallazzi, F., Garrison, J. C., Rold, T. L., Sieckman, G. L., Figueroa, S. D., Hoffman, T. J., and Lever, S. Z. (2008) Design, synthesis, and biological evaluation of an antagonist-bombesin analogue as targeting vector. *Bioconjugate Chem. 19*, 2040–2048.

(49) Hoffman, T. J., Simpson, S. D., Smith, C. J., Simmons, J., Siekman, G. L., Higginbotham, C., Eshima, D., Volkert, W., and Thornback, J. R. (1999) Accumulation and retention of Tc-99m RP591 by GRP receptor expressing tumours in SCID mice. *Eur. J. Nucl. Med. 26*, PS416.

(50) Hoffman, T. J., Smith, C. J., Simpson, S. D., Sieckman, G. L., Higginbotham, C., Jimenez, H., Eshima, D., Thornback, J. R., and Volkert, W. A. (2000) Optimizing pharmacokinetics of Tc-99m-GRP receptor targeting peptides using multi-amino acid linking groups. *J. Nucl. Med. 41*, 1013.

(51) Bauer, G., Hassmann, J., Walter, H., Haglmuller, J., Mayer, C., and Schalkhammer, T. (2003) Resonant nanocluster technology - from optical coding and high quality security features to biochips. *Nanotechnology 14*, 1289–1311.

(52) Hogemann, D., Ntziachristos, V., Josephson, L., and Weissleder, R. (2002) High throughput magnetic resonance imaging for evaluating targeted nanoparticle probes. *Bioconjugate Chem. 13*, 116–121.

(53) Liu, J. Q., Zhang, Q., Remsen, E. E., and Wooley, K. L. (2001) Nanostructured materials designed for cell binding and transduction. *Biomacromolecules 2*, 362–368.

(54) Marinakos, S. M., Anderson, M. F., Ryan, J. A., Martin, L. D., and Feldheim, D. L. (2001) Encapsulation, permeability, and cellular uptake characteristics of hollow nanometer-sized conductive polymer capsules. *J. Phys. Chem. B 105*, 8872–8876.

(55) West, J. L., and Halas, N. J. (2000) Applications of nanotechnology to biotechnology - Commentary. *Curr. Opin. Biotechnol. 11*, 215–217.

(56) McLean, J. A., Stumpo, K. A., and Russell, D. H. (2005) Size-selected (2−10 nm) gold nanoparticles for matrix assisted laser desorption ionization of peptides. *J. Am. Chem. Soc. 127*, 5304–5305.

(57) Haiss, W., Thanh, N. T. K., Aveyard, J., and Fernig, D. G. (2007) Determination of size and concentration of gold nanoparticles from UV-Vis spectra. *Anal. Chem. 79*, 4215–4221.

(58) Hosta, L., Pla-Roca, M., Arbiol, J., Lopez-Iglesias, C., Samitier, J., Cruz, L. J., Kogan, M. J., and Albericio, F. (2009) Conjugation of Kahalalide F with gold nanoparticles to enhance in vitro antitumoral activity. *Bioconjugate Chem. 20*, 138–146.

(59) Davis, R. K., and Chellappan, S. (2008) Disrupting the Rb-Raf−1 interaction: a potential therapeutic target for cancer. *Drug News Persp. 21*, 331–335.

(60) Ciuffreda, L., McCubrey, J. A., and Milella, M. (2009) Signaling intermediates (PI3K/PTEN/AKT/mTOR and RAF /MEK/ERK pathways) as therapeutic targets for anti-cancer and anti- angiogenesis treatments. *Curr. Signal Transduction Ther. 4*, 130–143.

(61) Kaiser, E., Colescott, R L., Bossinger, C. D., and Cook, P. I. (1970) Color test for detection of free terminal amino groups in the solid-phase synthesis of peptides. *Anal. Biochem. 34*, 595–598.

(62) Olmedo, I., Araya, E., Sanz, F., Medina, E., Arbiol, J., Toledo, P., Alvarez-Lueje, A., Giralt, E., and Kogan, M. J. (2008) How changes in the sequence of the peptide CLPFFD-NH2 can modify the conjugation and stability of gold nanoparticles and their affinity for β-amyloid fibrils. *Bioconjugate Chem. 19*, 1154–63.

BC1000164

Aggregation of Alzheimer Amyloid β Peptide (1−42) on the Multivalent Sulfonated Sugar Interface

Tomohiro Fukuda, Erino Matsumoto, Shunsuke Onogi, and Yoshiko Miura*

School of Materials Science, Japan Advanced Institute of Science and Technology, 1-1 Asahidai, Nomi, Ishikawa 923-1292, Japan. Received January 27, 2010; Revised Manuscript Received April 20, 2010

The mechanism of amyloidosis of amyloid β (1−42) (Aβ (1−42)) was investigated by the well-defined glycocluster interface. We prepared monovalent, divalent, and trivalent 6-sulfo-*N*-acetyl-D-glucosamine (6S-GlcNAc) immobilized substrates. The morphology and secondary structure of Aβ (1−42) aggregates on the substrates were investigated by dynamic-mode AFM and FTIR-RAS. Aβ (1−42) interactions with multivalent sugars were evaluated by surface plasmon resonance, and the cytotoxicity of Aβ (1−42) to HeLa cells was evaluated by MTT assay. Morphological images showed, interestingly, that Aβ (1−42) aggregates had a tendency to form globules rather than fibrils as the valency of 6S-GlcNAc on the substrate was increased. The SPR measurements indicated that this morphological change of Aβ (1−42) was related to the change of binding mode, and the binding mode was dependent on the multivalency of the sugar. Globular Aβ (1−42) was more toxic than fibrillar Aβ (1−42) to HeLa cells. These results suggested that the multivalency of sugars for the amyloidosis of Aβ (1−42) was significant in its morphology and aggregation effects at the surface of the cell membrane mimic.

INTRODUCTION

Alzheimer's disease (AD) is a serious dementia, accompanied by the presence of senile plaques (*1*). The main components of senile plaques are amyloid beta (Aβ) peptides of Aβ (1−40) and Aβ (1−42) (*2, 3*). Aβs are produced by cleavage of β- and γ-secretases into amyloid precursor protein (APP) and are present in the cerebral cortex. Since aggregates of Aβs exist in AD patients, it is believed that Aβ aggregates injure the neuron cells. The onset of AD is related to amyloidosis of Aβ (*3, 4*), and Aβ aggregates generally form insoluble fibrils. However, recent research indicated that the morphology of Aβ aggregates varied, and the cytotoxicity of Aβ has been reported to relate to the morphology and aggregation of Aβs as protofibrils, ADDLs, and amylospheroids (*5*−*9*). We were interested in the reason for the change in morphology of Aβ and the relationship of the morphological change to the cytotoxicity of Aβ. It has been reported that amyloidosis is induced by the interaction of Aβ with the cell surface. For example, various sugars on cell surfaces have been reported to be involved in the amyloidosis of Aβ (*10*−*13*). In particular, it is well-known that interactions of Aβ with glycosaminoglycans such as heparin and ganglioside GM1 clusters are also closely related to amyloidosis. Meanwhile, the recognitions where sugars were involved were impossible to regulate due to the clustering effect (*14*−*16*). Consequently, it is possible that the morphologies and biofunctionalities of Aβ are affected by the degree of sugar clustering. However, detailed analyses of amyloidosis with well-defined glyco-clusters have not been reported.

In this study, we investigated the influence of a sugar on the aggregation behavior and cytotoxicity of Aβ with well-ordered glyco-clusters at the surface of a cell membrane mimic. As the target, we selected Aβ (1−42) because it is a predominant biomolecule in the early pathological stage of senile plaque formation (*17*). We chose 6-sulfo-*N*-acetyl-D-glucosamine (6S-GlcNAc), which is the most abundant structure of heparin and has a similar structure to sialic acid, as a representative sugar for this study (*18*). Our group had reported that the linear polymer involving 6S-GlcNAc inhibited Aβ (1−40) (*19, 20*).

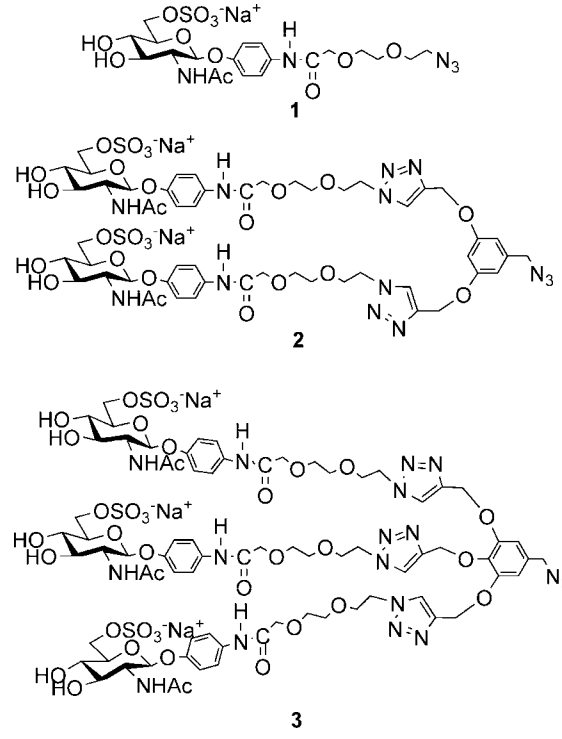


Figure 1. 6-Sulfo-*N*-acetyl-glucosamine dendritic compounds: monovalent (**1**), divalent (**2**), and trivalent (**3**) for immobilization.

We prepared functional self-assembled monolayers (SAMs) with glyco-clusters of mono (**1**)-, di (**2**)-, and tri (**3**)-valent 6S-GlcNAc (Figure 1) on a gold substrate via click chemistry (*21*).

* Corresponding author. Yoshiko Miura, School of Materials Science, Japan Advanced Institute of Science and Technology, 1-1 Asahidai, Nomi, Ishikawa 923-1292, Japan. E-mail: miuray@jaist.ac.jp. TEL: +81-761-51-1641. FAX: +81-761-51-1645.

10.1021/bc100053x © 2010 American Chemical Society
Published on Web 05/20/2010

We investigated the aggregation behavior, properties, and cytotoxicity of Aβ (1−42) on these SAMs.

EXPERIMENTAL SECTION

Materials. The following reagents were used as received. Dulbecco's modified Eagle's medium (DMEM), fetal bovine serum (FBS), penicillin−streptomycin solution (Invitrogen Co., GIBCO, Carlsbad, CA), chloroform ($CHCl_3$), copper (0) powder, copper(II) sulfate, *N*,*N*-dimethylformamide (DMF), 3-(4,5-dimethyl-2-thiazolyl)-2,5-diphenyltetrazolium bromide (MTT), ethanol (EtOH), ethyl acetate (EtOAc), *n*-hexane, methanol (MeOH), sodium L-ascorbate, sodium azide, tetrahydrofuran (THF) (Kanto Chemical Co., Inc., Tokyo, Japan), palladium/charcoal (Pd/C) (Merck & Co., Inc., Whitehouse Station, NJ), amyloid β protein (human, 1−42) (Aβ (1−42)), 2-(7-aza-1*H*-benzotriazole-1-yl)-1,1,3,3-tetramethyl uronium hexafluorophosphate (HATU) (Peptide Institute Inc., Osaka, Japan), and *N*,*N*-diisopropylethylamine (DIEPA) (Tokyo Chemical Industry Co., Ltd., Tokyo, Japan).

Other compounds such as multivalent compounds of 6S-GlcNAc (**1**−**3**) were synthesized. The detailed synthetic schemes and characterizations are described in the Supporting Information. NaOH-50 buffer was bought from GE Healthcare Bioscience (Chalfont St. Giles, U.K.), and 50 mM potassium phosphate buffer (pH 7.4) was prepared by the conventional method.

Measurements. The functional SAMs were prepared on gold-coated glass substrates. The substrate, purchased from Moritex Co. (Tokyo, Japan), was used for dynamic mode−atomic force microscope (D-AFM), FTIR-RAS, ellipsometry, X-ray photoelectron spectroscopy (XPS), and water contact angle goniometry, while Au-Kit, the substrate provided by GE Healthcare Bio-Science, was used for SPR analysis. Before the preparation, each gold substrate was prepared by exposure to UV/ozone (UV.TC.NA.003, Bioforce Nanoscience Inc., Ames, IA) and rinsing with EtOH. The surface functional groups were confirmed using an FTIR spectrometer (Perkin-Elmer Inc., Waltham, MA) equipped with an RAS attachment (Reflector 2, Harrick Scientific Products Inc., Pleasantville, NY). The surface was also investigated by XPS using an Ulvac Phi 5600 (Ulvac Inc., Kanagawa, Japan) instrument. Water contact angle was measured with a DropMaster300 (Kyowa Interface Science Co., Ltd., Saitama, Japan) instrument, and the thicknesses of the SAMs were estimated using an ellipsometer (PZ2000, Royal Philips Electronics, Eindhoven, Netherlands). Aβ (1−42) analyses were carried out using SPR, AFM, and FTIR-RAS. SPR binding analysis was performed using a BIACORE 3000 and Au-Kit as probe chip, all provided by GE Healthcare Bio-Sciences Co. D-AFM observation was accomplished using an SPI3800N instrument (Seiko Instruments Inc., Chiba, Japan) equipped with an SPA400 as a probe station, and a DF40P cantilever. The secondary structure of Aβ (1−42) was determined by FTIR-RAS, using the system that was utilized for SAM characterization. Ultracentrifugal separation for Aβ (1−42) preparation was carried out with a Himac CS120FX ultracentrifuge (Hitachi Koki Inc., Ltd., Tokyo, Japan). A microplate reader, Multiscan JX, purchased from ThermoFisher Scientific Inc. (Waltham, MA), was used in MTT assay. Discovery studio 2.0 (Accelrys Inc., San Diego, CA) software was used for molecular modeling.

Syntheses. Initially, *p*NP-6-sulfo-*N*-acetyl-D-glucosamine (*p*NP-6S-GlcNAc), [2-(2-azide-ethoxy)ethoxy]acetate, 3,5-bis(propagyloxy)benzyl chloride, and 3,4,5-tris(propagyloxy)benzyl chloride were synthesized: the synthetic schemes are described in detail in the Supporting Information.

*p-(N-(2-(2-Azide-ethoxy)ethoxy)amido)phenyl 6-sodium sulfo-N-acetyl-β-D-glucosamine (monovalent-6S-GlcNAc (**1**)).* *p*NP-6S-GlcNAc (775 mg, 1.91 mmol, 1.0 equiv) and Pd/C (100 mg) were added to MeOH (50 mL) and stirred under hydrogen at room temperature. After 1 h, the Pd/C was removed and the solution was evaporated to a brownish solid (717 mg). The product and [2-(2-azide-ethoxy) ethoxy]acetate (545 mg, 2.88 mmol, 1.5 equiv) were dissolved in DMF (50 mL) and stirred at 0 °C. Then, HATU (746 mg, 1.96 mmol, 1.0 equiv) and DIPEA (500 μL, 2.88 mmol, 1.5 equiv) were added to the solution. After 8 h, the presence of the product in the reaction mixture was confirmed by rev TLC ($MeOH/H_2O$ = 1:8) and the solution was evaporated to give crude product. A white powder was isolated (1.03 g, 99%) after purification of the crude product by reverse column chromatography (H_2O/MeOH = 10:1).

^{1}H NMR (300 MHz, D_2O, ppm): δ 7.27 (2H, d, J = 9.0 Hz, ArH, meta to 6S-GlcNAc), 6.98 (2H, d, J = 9.3 Hz, ArH, ortho to 6S-GlcNAc), 5.02 (1H, d, J = 8.1 Hz, H-1), 4.27 (1H, dd, J = 2.0 and 11.3 Hz, H-6_{proR}), 4.12 (1H, dd, J = 4.7 and 11.2 Hz, H-6_{proS}), 4.11 (2H, s, -NHCO-$\underline{CH_2}$-), 3.87 (1H, t, J = 9.5 Hz, H-2), 3.76−3.45 (7H, m, H-3, H-4, H-5 and -O$\underline{CH_2CH_2}$-O-), 3.04 (2H, t, J = 4.8 Hz, -O$\underline{CH_2}CH_2N_3$), 3.07 (2H, q, J = 7.4 Hz, $OCH_2\underline{CH_2}N_3$), 1.90 (3H, s, Ac). ^{13}C NMR (75 MHz, DMF-d_7, ppm): δ 169.9 (-NH$\underline{CO}CH_3$), 168.1 (-NHCO-), 154.4 (ArC, ipso to 6S-GlcNAc), 133.4 (ArC, para to 6S-GlcNAc), 121.1 (ArC, meta to 6S-GlcNAc), 116.9 (ArC, ortho to 6S-GlcNAc), 100.2 (C-1), 75.6 (C-5), 74.8 (C-4), 70.0 (-NHCO$\underline{CH_2}$O-, C-3), 69.8 (-$CH_2O\underline{CH_2}CH_2N_3$), 66.1 (C-6), 56.2 (C-2), 54.5 (-NHCOCH$_2$OCH$_2\underline{CH_2}$O-), 54.4 (-NHCOCH$_2$O$\underline{CH_2}$-CH$_2$O-), 50.6 (-$CH_2OCH_2\underline{CH_2}N_3$), 22.7 (-NHCO$\underline{CH_3}$). ESI-MS [negative]: 562.2 $[M-Na^+]^-$ (calculated), 562.3 $[M-Na^+]^-$ (observed).

*Divalent 6S-GlcNAc (**2**).* **1** (266 mg, 0.455 mmol, 3.4 equiv) and 3,5-bis(propargyloxy)benzyl chloride (31 mg, 0.133 mmol, 1.0 equiv) were dissolved in DMF, while sodium L-ascorbate (18 mg, 0.091 mmol, 0.7 equiv) and copper(II) sulfate pentahydrate (7 mg, 0.047 mmol, 0.3 equiv) were dissolved in distilled water. The reaction mixture was prepared by mixing the two solutions with the addition of copper (0) powder (0.4 mg), and stirred under nitrogen at room temperature for 1 day. The object product was confirmed by rev. TLC (H_2O/MeOH = 8:1). Residual copper was removed by centrifugation, and the water layer was removed under reduced pressure. The crude product was dissolved in DMF, and sodium azide (67 mg, 1.03 mmol, 7.7 equiv) was added. After stirring the reaction mixture at 70 °C for 1 day, the solution was evaporated and purified by rev. column chromatography (H_2O/MeOH = 8:1). A white powder was obtained (41 mg, 22%).

^{1}H NMR (300 MHz, D_2O, ppm): δ 7.91 (2H, s, cyclictriazole), 7.03 (2H, d, J = 8.7 Hz, ArH, meta to 6S-GlcNAc), 6.79 (2H, d, J = 9.0 Hz, ArH, ortho to 6S-GlcNAc), 6.39 (2H, s, ArH, cyclictriazole (ortho to benzylazide)), 6.24 (1H, s, ArH, cyclictriazole (para to benzylazide)), 4.92 (2H, d, J = 8.4 Hz, H-1), 4.87 (4H, s, -O$\underline{CH_2}$-cyclictriazole), 4.49 (4H, t, J = 4.6 Hz, -NHCO-$\underline{CH_2}$-), 4.22 (2H, dd, J = 1.7 and 11.3 Hz, H-6_{proR}), 4.10 (2H, s, -$ArCH_2N_3$), 4.08 (2H, dd, J = 5.4 and 11.4 Hz, H-6_{proS}), 3.90−3.81 (2H, m, H-2), 3.87 (4H, t, J = 5.1 Hz, -$CH_2\underline{CH_2}$-cyclictriazole-, 3.84 (4H, t, J = 4.5 Hz, -$\underline{CH_2}CH_2$-cyclictriazole-), 3.71−3.59 (2H, m, H-5), 3.56−3.37 (2H+2H+2H × 4, m, H-3, H-4 and -O$\underline{CH_2CH_2}$O-), 1.89 (3H × 2, s, Ac). ^{13}C NMR (75 MHz, DMF-d_7, ppm): δ 169.9 (-NH$\underline{CO}CH_3$), 168.1 (-NHCO-), 160.1 (ArC, meta to benzylazide), 154.3 (ArC, ipso to 6S-GlcNAc), 143.1 (-N(linker)-N═N-$\underline{C}$(CH_2O-benzylazide)═C-), 138.4 (ArC, ipso to benzylazide), 133.4 (ArC, para to 6S-GlcNAc), 125.2 (-N(linker)-N═N-C(CH_2O-benzylazide)═$\underline{C}$-), 121.1 (ArC, meta to 6S-GlcNAc), 116.9 (ArC, ortho to 6S-GlcNAc), 107.7 (ArC, ortho to benzylazide), 101.3 (C-1), 100.3 (ArC, para to benzylazide), 75.8 (C-5), 74.8 (C-4), 71.2

(-N(linker)-N═N-C(CH$_2$O-benzylazide)═C-), 70.7 (-NHCOCH$_2$-O-), 69.9 (C-3), 66.0 (C-6), 61.7 (-OCH$_2$CH$_2$-cyclictriazole), 56.2 (C-2), 53.8 (-OCH$_2$CH$_2$-cyclictriazole), 54.1 (ArCH$_2$N$_3$), 49.8 (-CH$_2$OCH$_2$CH$_2$-cyclictriazole), 22.7(-NHCOCH$_3$). MALDI-TOF-MS [negative]: 1388.4 [M−Na$^+$]$^-$ (calculated), 1388.5 [M−Na$^+$]$^-$ (observed).

*Trivalent 6S-GlcNAc (**3**).* **1** (420 mg, 0.718 mmol, 3.9 equiv) and 3,4,5-tris(propagyloxy)benzyl chloride (53 mg, 0.227 mmol, 1.0 equiv) were dissolved in DMF while sodium L-ascorbate (8.15 mg, 0.110 mmol, 0.6 equiv) and copper(II) sulfate pentahydrate (20.0 mg, 0.0700 mmol, 0.3 equiv) were dissolved in distilled water. The reaction mixture was prepared by mixing the two solutions with the addition of copper (0) powder (0.05 mg), and stirred under nitrogen at room temperature for 1 day. The object product was confirmed by rev. TLC (H$_2$O/MeOH/CH$_3$COOH = 8:1:1). The copper residue was removed by centrifugation, and the water layer was removed under reduced pressure. The crude compound was dissolved in DMF, and sodium azide (162 mg, 2.48 mmol, 5.8 equiv) was added. After stirring the reaction mixture at 70 °C for 1 day, the solution was evaporated and purified by rev. column chromatography (H$_2$O/MeOH = 8:1). A white powder was obtained (91 mg, 20%).

^{1}H NMR (300 MHz, D$_2$O, ppm): δ 7.91 (2H, s, cyclictriazole (meta to benzylazide)), 7.60 (1H, s, cyclictriazole (para to benzylazide), 7.11 (2H, s, cyclictriazole (ortho to benzylazide)), 7.02 (2H, d, J = 9.0 Hz, ArH, meta to 6S-GlcNAc (para to benzylazide)), 6.98 (4H, d, J = 8.7 Hz, ArH, meta to 6S-GlcNAc (meta to benzylazide)), 6.79 (2H, d, J = 9.0 Hz, ArH, ortho to 6S-GlcNAc (para to benzylazide)), 6.76 (4H, d, J = 8.7 Hz, ArH, ortho to 6S-GlcNAc (meta to benzylazide)), 4.92 (1H, d, J = 8.7 Hz, H-1 (para to benzylazide)), 4.89 (4H, s, -OCH$_2$-cyclictriazole (meta to benzylazide)), 4.89 (2H, d, J = 8.1 Hz, H-1 (meta to benzylazide)), 4.81 (2H, s, -OCH$_2$-cyclictriazole (para to benzylazide), 4.50 (4H, t, J = 4.7 Hz, -NHCOCH$_2$-(meta to benzylazide)), 4.37 (4H, t, J = 4.4 Hz, -NHCO-CH$_2$-(meta to benzylazide)), 4.22 (2H, dd, J = 2.2 and 13.3 Hz, H-6$_{proR}$), 4.21 (2H, m, H-6$_{proR}$ (meta and para to benzylazide)), 4.09 (2H, dd, J = 5.1 and 6.0 Hz, H-6$_{proS}$ (meta to benzylazide)), 4.07 (1H, dd, J = 5.0 and 6.6 Hz, H-6$_{proS}$ (para to benzylazide)), 3.85 (3H, t, J = 7.1 Hz, H-2), 3.88−3.74 (12H, m, -CH$_2$CH$_2$-cyclictriazole), 3.79 (2H, s, -ArCH$_2$N$_3$), 3.67−3.61 (3H, m, H-5), 3.53 (1H, t, J = 9.0 Hz, H-3 (para to benzylazide)), 3.52 (2H, t, J = 8.6 Hz, H-3 (meta to benzylazide)), 3.51 (1H, t, J = 8.6H z, H-4 (para to benzylazide)), 3.53−3.42 (2H+12H, t, J = 8.6 Hz, H-4 (para to benzylazide)) 1.88 (3H, s, Ac (para to benzylazide)), 1.87 (3H × 2, s, Ac (meta to benzylazide)). ^{13}C NMR (75 MHz, DMF-d_7, ppm): δ 169 0.9 (-NHCOCH$_3$), 168.1 (-NHCO-), 154.3 (ArC, ipso to 6S-GlcNAc), 152.4 (ArC, meta to benzylazide), 143.9 (-N(linker)-N═N-C(CH$_2$O-benzylazide)═C-), 143.1 (ArC, para to benzylazide), 133.4 (ArC, para to 6S-GlcNAc), 125.2 (-N(linker)-N═N-C(CH$_2$O-benzylazide)═C-), 125.1 (ArC, ipso to benzylazide), 121.1 (ArC, meta to 6S-GlcNAc), 117.0 (ArC, ortho to 6S-GlcNAc), 109.2 (ArC, ortho to benzylazide), 100.3 (C-1), 75.8 (C-5), 74.8 (C-4), 71.2 (-N(linker)-N═N-C(CH$_2$O-benzylazide)═C-), 70.7 (-NHCOCH$_2$O-), 69.9 (C-3), 66.0 (C-6), 62.9 (-NHCOCH$_2$OCH$_2$CH$_2$O-), 62.5 (-NHCOCH$_2$OCH$_2$CH$_2$O-), 56.2 (C-2), 52.0 (-OCH$_2$CH$_2$-cyclictriazole), 49.9 (ArCH$_2$N$_3$), 49.8 (-CH$_2$OCH$_2$CH$_2$-cyclictriazole), 22.7(-NHCOCH$_3$). ESI-MS [negative]: 1002.3 [M−2Na$^+$]$^{2-}$ and 660.5 [M−3Na$^+$]$^{3-}$ (calculated), 1003.9 [M−2Na$^+$]$^{2-}$ and 661.7 [M−3Na$^+$]$^{3-}$ (observed).

Preparation. *SAM Formation.* An acetylenyl group was attached to the gold substrate by formation of SAMs as described in the literature (*22, 23*); the SAMs comprised acetylenyl- and hydroxyl-terminated disulfides in molar ratio of 1:5. Subsequently, multivalent compounds of 6S-GlcNAc (**1**−**3**) were immobilized on the substrate by click reaction with acetylenyl-terminated SAM.

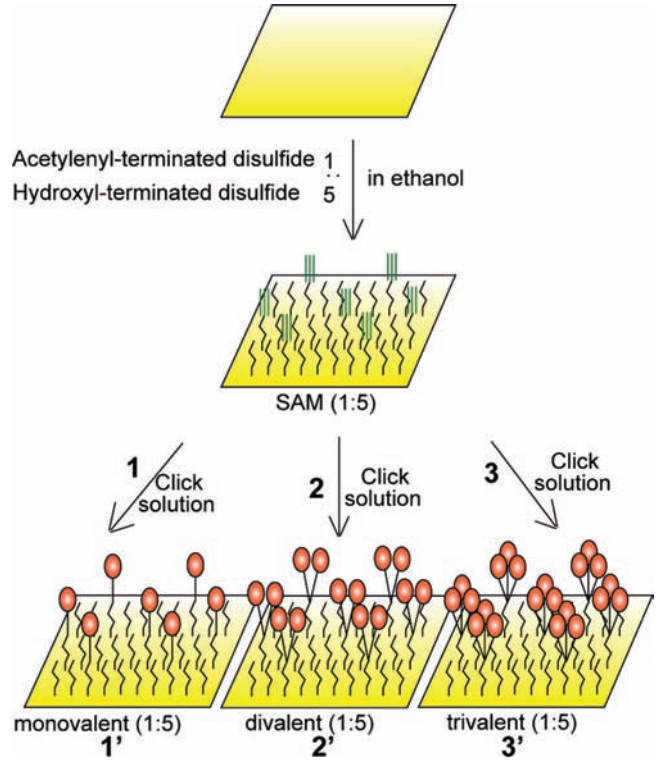


Figure 2. Schematic illustrations of the formation of glyco-clusters on the SAM (acetylenyl-terminated disulfide/hydroxyl-teminated disulfide = 1:5). The click solution was a mixed solution of DMF and water, which included CuSO$_4$, Cu (0) powder, and Na ascorbate.

Acetylenyl-functionalized layers were immobilized by the formation of a SAM. Disulfides with hydroxyl (**S1**) and acetylenyl (**S2**) terminals were dissolved in molar ratio **S1**:**S2** = 5:1 (total 10 mM) in EtOH (**S1** and **S2** were described in the Supporting Information). The gold substrate was immersed in the solution for 12 h and then rinsed several times with EtOH. Subsequently, azide-terminated 6S-GlcNAc derivatives (**1**−**3**) were reacted with acetylenyl-terminated SAM via click chemistry. Each reaction mixture was prepared from 5.0 mM 6S-GlcNAc, 0.10 mM CuSO$_4$, 0.50 mM sodium L-ascorbate, and 0.01 wt % copper (0) powder in an EtOH/H$_2$O = 1:2 (v/v) mixture, and dropped on the acetylenyl-terminated SAMs under N$_2$ gas. After 12 h, each substrate was washed with EtOH and H$_2$O repeatedly, SAMs were characterized by FTIR-RAS, ellipsometry, XPS, and water contact angle goniometry. The substrates with immobilized mono (**1**)-, di (**2**)-, and tri (**3**)-valent 6S-GlcNAc were designated **1′**, **2′**, and **3′**, respectively (Figure 2).

Aβ Sample Preparation. Aβ (1−42) (200 μM) was unfolded with 0.02% aqueous NH$_3$ solution and centrifuged at 4 × 10^4 rpm at 4 °C (*24*). The supernatant solution was separated into suitable volumes in plastic vials. After the vials were rapidly frozen in liquid N$_2$, they were stored at −20 °C. These frozen stock samples were diluted with appropriate buffer solutions just before use. Samples that were prepared from the same batch were used for assay between subsequent measurements.

Functional Analysis. *AFM Observation.* Ten micromolar sample solution was prepared by diluting the stock solution with an aqueous solution containing 0.1 M NaCl, 20 mM potassium phosphate buffer (pH 7.4), and 0.008% NH$_3$. The sample solution of Aβ (1−42) was incubated on **1′**−**3′** for 12 h at 25 °C in static conditions. After incubation, the surface was carefully rinsed several times with H$_2$O to remove excess Aβ

(1−42) and dried by N_2 gas. Images of the aggregates on each surface were collected by D-AFM. The operating parameters for the SI-DF40P-type cantilever were of resonant frequency ca. 330 kHz and spring constant 40 N m^{-1}. The applied voltage was 1.0 V and the scanning frequency was 1 Hz.

FTIR-RAS Measurement. The secondary structure of Aβ (1−42) on the substrates was investigated by Fourier transform−reflection adsorption spectroscopy (FTIR-RAS). To identify the conformation of Aβ (1−42), the sample substrate that was used for D-AFM analysis was also used for FTIR-RAS. Measurements were carried out using an MCT-N detector in dry air, at 4.0 cm^{-1} resolution.

SPR Evaluation. Binding analysis of Aβ (1−42) on multivalent 6S-GlcNAc immobilized surfaces was estimated kinetically by SPR. Flowing buffer solution (0.1 M NaCl, 20 mM potassium phosphate buffer (pH 7.4), 0.008% NH_3) was used for the measurement. The frozen stock sample solution was diluted with the same buffer solution just before measurement, to equalize the NH_{3aq} content for each measurement, and various concentrations of Aβ (1−42) (2.5, 5.0, 10, 20, and 40 μM) were prepared as sample solutions. Measurement was carried out at flow rate 5 μL min^{-1}. The sample solutions from 2.5 to 40 μM Aβ (1−42) were interacted with unmodified substrate and substrates with immobilized monovalent 6S-GlcNAc **1**, divalent 6S-GlcNAc **2,** and trivalent 6S-GlcNAc **3** for 3 or 25 min. The Aβ (1−42) deposited on the substrate was dissociated with three 15 μL aliquots of NaOH-50 solution before next measurement. Measurements were carried out in the order of increasing sample concentration.

MTT Assay. Viability of HeLa cells was evaluated by MTT assay. A cloning ring (d = 5 mm) was first fixed on the modified substrate, and the subsequent assays were carried out in the cloning ring. As a culture medium for HeLa cells, 10% FBS and 1% penicillin−streptomycin solution including DMEM solution were used. A 10 μM sample solution of Aβ (1−42) was incubated on the surface for 12 h at 25 °C. Then, 5×10^3 HeLa cells in the culture medium were added in the ratio of Aβ solution/culture medium of 1:9 and cultured at 37 °C under 5% CO_2 for 1 day. After cultivation, the culture medium was exchanged for 3 h with another assay medium solution which was a composite of 10% MTT (in PBS) and the culture medium solution. After removing the assay medium, the formazan resulting from reduction of MTT was dissolved in DMSO and the absorbance of the solution evaluated at 570 nm.

RESULTS

Preparation and Characterization of SAM. Substrates with mono (**1**)-, di (**2**)-, and tri (**3**)-valent 6S-GlcNAc, denoted **1′**, **2′**, and **3′**, respectively, were fabricated (Figure 2). To avoid reaction complexities due to the hydroxyl groups of the sugar, we synthesized and immobilized the compounds via click reaction (*21, 25*). Immobilization of the multivalent 6S-GlcNAc was confirmed by water contact angle goniometry, X-ray photoelectron spectroscopy (XPS), FTIR-RAS, and ellipsometry. The syntheses of compounds and the characterization of SAMs are described in the Supporting Information. The SAMs involving well-defined glyco-clusters on the substrate were regarded as a cell membrane mimic and used to determine how the multivalency of sugars contributes to amyloidosis of Aβ.

AFM Observation. The morphology of Aβ (1−42) aggregates on the substrate was observed by D-AFM. The shapes and the sizes of Aβ (1−42) on the substrates after preparation are summarized in Table 1 and shown in Figure 3. Interestingly, the morphology of Aβ was dependent on the type of glyco-cluster. When Aβ (1−42) was incubated on **1′**, fibril formation was observed; the fibrils were 4−6 nm high, 8−12 nm wide, and 1−2 μm long (Figure 3A). When incubated on **2′**, the morphology of Aβ (1−42) was changed; both fibrils (as on **1′**) and globular aggregates (7−9 nm high and 200−500 nm in diameter) were observed (Figure 3B). Incubation on **3′** dramatically changed the morphology of Aβ (1−42) aggregate to an exclusively globular form. The globular objects were 10−20 nm high and 500−600 nm in diameter (Figure 3C).

Table 1. Aggregate Patterns and Sizes of Aβ (1−42) on 1′, 2′ and 3′

		1′ (monovalent)	**2′** (divalent)	**3′** (trivalent)
aggregate pattern		fibril	fibril, globule	globule
fibril	width	8−12 nm	8−12 nm	
	length	1−2 μm	1−2 μm	
	height	4−6 nm	4−6 nm	
globule	height		7−9 nm	10−20 nm
	diameter		200−500 nm	500−600 nm

FTIR-RAS Measurement. The secondary structure of Aβ (1−42) aggregates on each substrate was elucidated by FTIR-RAS. The results for amide bands are shown in Figure 4. The amide I band (C═O stretching) at 1670 cm^{-1} was present in

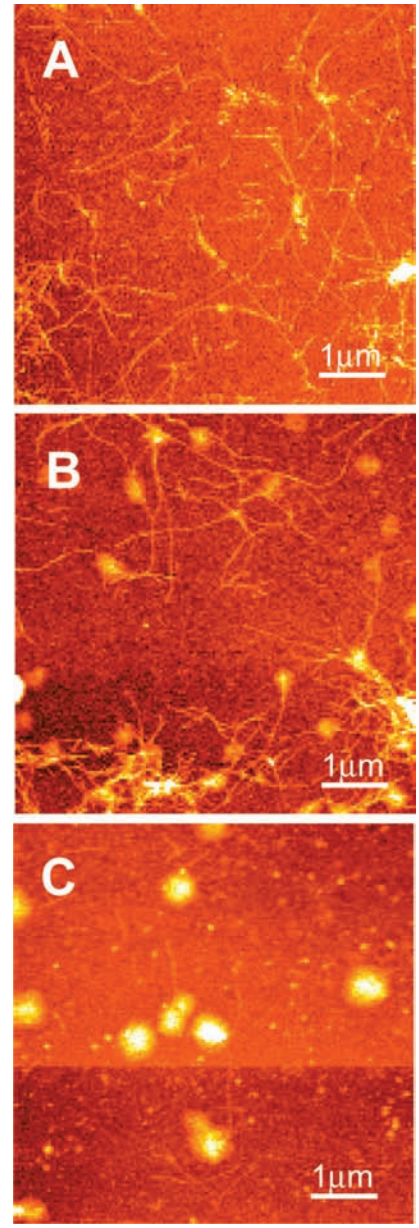


Figure 3. Morphologies observed by D-AFM (top) and aggregate model (bottom) on the (a) monovalent (**1′**), (b) divalent (**2′**), and (c) trivalent (**3′**).

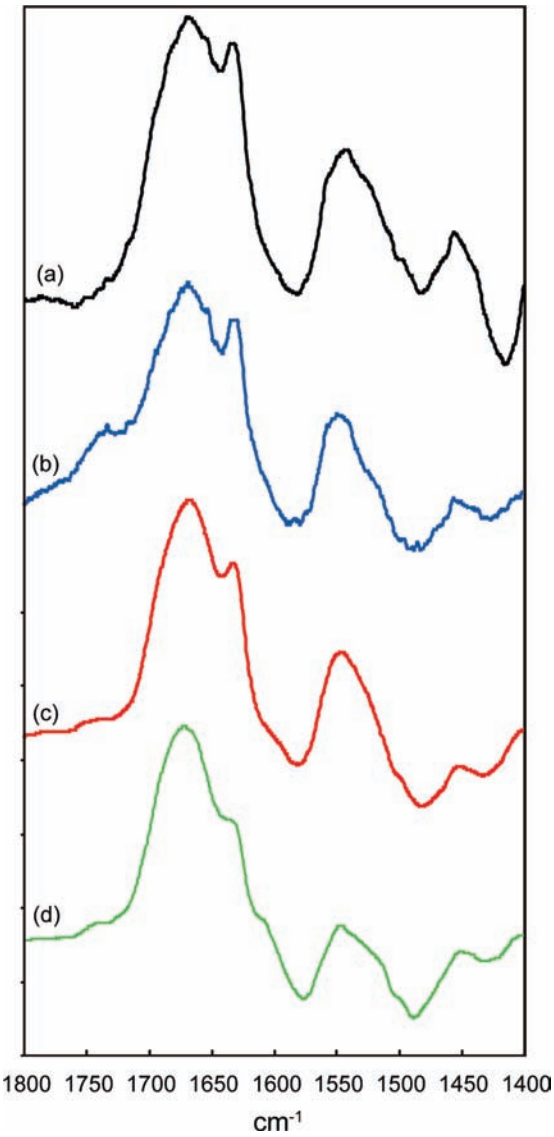


Figure 4. FTIR-RAS spectra of Aβ (1−42) on (a) no-sugar SAM, (b) **1′**, (c) **2′**, and (d) **3′**.

all cases, implying the β-turn structure (*26*). The band at 1632 cm^{-1} showed the existence of antiparallel β-sheet structure (*13, 27*). Remarkably, that band was least intense in the spectrum of the **3′** sample. With AFM observation taken into account, these results indicated that the fibrils on **1′** had predominantly β-sheet structure, and the globules on **3′** had little of the β-sheet structure. Although weak peaks at 1654 and 1648 cm^{-1}, correlated with α-helix and disorder, respectively, were observed on **1′** and on a 6S-GlcNAc-unmodified surface, these peaks disappeared from the spectra for the higher valencies. However, a peak at 1613 cm^{-1} in the β-sheet region was conspicuous in the spectra for the higher valencies.

Interaction Analysis with SPR. The SPR measurements were carried out for two different time schedules (1650 and 300 s), to investigate the initial Aβ (1−42) binding to sugars and the aggregation process of Aβ (1−42).

The interaction was monitored by the change of response unit (RU) on addition of 10 μM Aβ (1−42). The time course of RU change is shown in Figure 5 (A) and indicates responses of Aβ (1−42) in the order **2′** (913 RU) > **3′** (658 RU) ≫ **1′** (388 RU) in the 1650 s measurements, hence a nonlinear RU change with valency. The high level of interaction of **2′** and **3′** suggested the importance of glyco-clusters. The concentration dependence of RU for each substrate is shown in the Supporting Information.

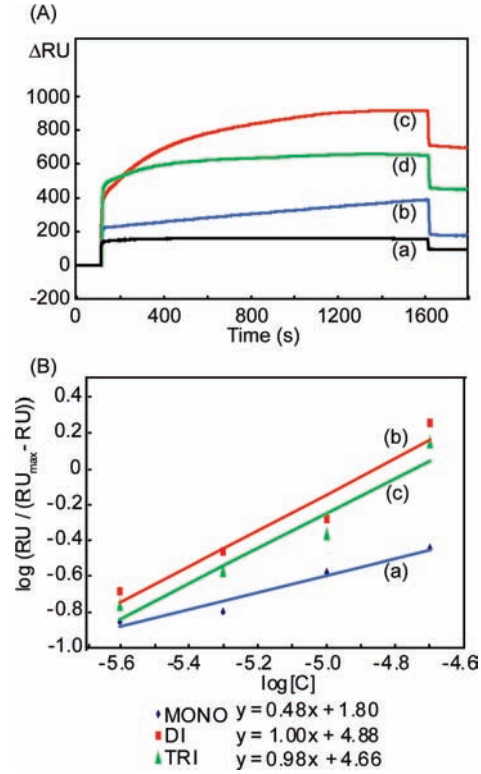


Figure 5. (A) Time courses of ΔRU on (a) no-sugar SAM, (b) **1′**, (c) **2′**, and (d) **3′** for 1800 s. (B) Hill plot analysis using the RU_{eqmax} at 1650 s on (a) no-sugar SAM, (b) **1′**, (c) **2′**, and (d) **3′**.

The interaction between 6S-GlcNAc and Aβ (1−42) was then remeasured for the shorter duration of 300 s; the results are shown in Figure 6. The values of RU_{eqmax} on **1′**, **2′**, and **3′** were 27, 386, and 416 RU, respectively, on the plateaus. Similar to the interaction for the longer time of 1650 s, the multivalent 6S-GlcNAc of **2′** and **3′** showed much stronger interaction than that of monovalent 6S-GlcNAc of **1′**. After 300 s, RU_{eqmax} on **3′** was larger than on **2′**, in contrast to the measurement at 1650 s.

MTT Assay. The cytotoxicity of Aβ (1−42) to HeLa cells was evaluated by MTT assay on the substrate. The results are shown in Figure 7, in which all data are mean values for three replicate experiments. The cell viabilities with Aβ (1−42) on **1′**, **2′**, and **3′** were 104 ± 11%, 84 ± 25%, and 76 ± 11%, respectively.

DISCUSSION

AFM observation of the substrate suggested that Aβ (1−42) had a tendency to form fibrils on the sugars (**1′** and **2′**) with lower valencies, and to form globular aggregates on substrates with higher sugar valencies (**2′** and **3′**). The densely packed sulfonated or acidic sugars strongly induced a morphological change in Aβ (1−42) aggregates. The morphological change of amyloid aggregate from fibrillar to globular objects is consistent with the report of Ban et al., who investigated the morphology of Aβ (1−40) on various sulfonated surfaces (*28*). In the present case, the well-defined nanostructure of multivalent 6S-GlcNAc encouraged Aβ (1−42) to aggregate in a globular morphology, indicating the significance of sugar multivalencies in amyloidosis.

The FTIR-RAS spectra showed that the multivalent sugars influenced not only the morphology of Aβ (1−42), but also its secondary structure. In particular, the band at 1632 cm^{-1} of the antiparallel β-sheet was much weaker in the spectrum of **3′** than that in **1′** and **2′**. The results indicated that Aβ fibrils contained

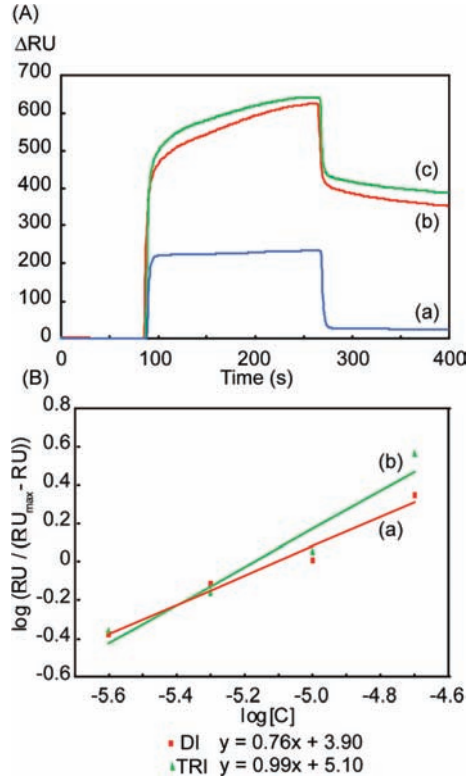


Figure 6. (A) Time courses of ΔRU (a) on no-sugar SAM, (b) **1′**, (c) **2′**, and (d) **3′** for 400 s. (B) Hill plot analysis using the RU_{eqmax} values at 300 s for (a) **2′** and (b) **3′**.

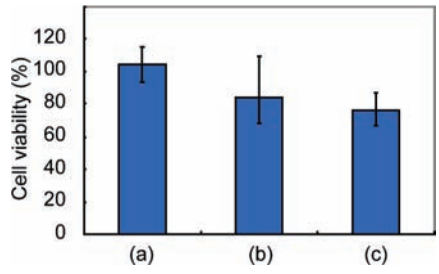


Figure 7. Cytotoxicity of Aβ (1−42) to HeLa cells on (a) **1′**, (b) **2′**, and (c) **3′** by MTT assay.

more antiparallel β-sheet structure than Aβ globular objects. On the other hand, the band at 1613 cm^{-1} appeared in the spectra for the high valencies (**3′**), but the origin of this band is not yet understood in detail. Goto et al. attributed the band at 1613 cm^{-1} to an unknown β-sheet structure (*29*). A similar band was observed by Zurdo et al. in spectra of amorphous aggregates of Aβ (*30*), and Daggett indicated that it was possible that this band implied α-sheet structure (*9*). The FTIR-RAS spectra also showed that the intensity ratio of amide I to amide II was much larger in the spectrum of **3′**. Since FTIR-RAS spectra reflected adsorption of Aβ (1−42) longitudinal to the substrate, the change of amide I to II ratio suggested the specific orientation of Aβ (1−42) to the substrate.

The SPR measurements indicated that the 6S-GlcNAc-immobilized surfaces recognized Aβ (1−42). The amount bound of Aβ (1−42) to the substrate (RU) changed with the valency, and the multivalent sugars were strongly bonded to Aβ (1−42). For the calculation of binding constants, RU_{eqmax} values at 1650 s were plotted against sample concentration (Figure 5B). Subsequently, Hill plots for the long time (1650s) were constructed as shown in Figure 5B, because the curves of RU_{eqmax} versus concentration were not correlated with Langmuir adsorption (*31*). The Hill equation is expressed by eq 1. The equilibrium

Table 2. Binding Mode of Aβ (1−42) to 1′, 2′, and 3′ on Each Time Scale

	binding mode (sugar/Aβ (1−42))		
time scale	**1′** (monovalent)	**2′** (divalent)	**3′** (trivalent)
long (1650s)	2:1	1:1	1:1
short (300s)	no data	2:1 and 1:1	1:1

dissociation constants (K_D) on **1′**, **2′**, and **3′** were 1.49×10^{-4}, 1.16×10^{-5}, and 1.89×10^{-5} [M], respectively. The slopes of the best-fit lines for **1′**, **2′**, and **3′** (i.e., the values of the Hill coefficient, n) were 0.48, 1.00, and 0.98 respectively, which implies that the binding modes between sugar and Aβ (1−42) can be represented as the ratios 2:1, 1:1, and 1:1 (sugar/Aβ (1−42)), respectively. Considering **2′** and **3′** displayed multivalent sugars, the multivalency of the sugars was a key component in binding mode definition.

$$\log\left(\frac{[RU_{eq\ max}]_{C[\mu M]}}{[RU_{eq\ max}]_{40[\mu M]} - [RU_{eq\ max}]_{C[\mu M]}}\right) = n \log[C[\mu M]] - \log K_D \quad (1)$$

The interaction analysis in the short term showed that RU_{eqmax} for **3′** was higher than for **2′**, which implies different trends for the short-time and long-time analyses. The equivalent values (RU_{eqmax}) were introduced into the Hill plot, and the equilibrium dissociation constants (K_D) on **2′** and **3′** were recalculated as 7.82×10^{-6} and 5.80×10^{-6} [M], respectively. The Hill plot for **1′** was not fitted due to the small number of RU_{eqmax} values.

The Hill coefficients for **2′** and **3′** in 300 s were calculated as 0.76 and 0.99, respectively. The different Hill coefficients for **2′** associated with the two time scales suggested that the binding mode changed between 300 and 1650 s, while the binding mode for **3′** was the same in both time scales. The Hill coefficient of 0.76 in the short time for **2′** corresponds to an intermediate value between 2:1 and 1:1 binding modes. The concerted binding mode of 2:1 and 1:1 in the early binding mode was changed into the 1:1 binding in the long-term measurement. The changes of the binding modes are summarized in Table 2. Taking account of the AFM observations, 2:1 binding reaction between sugar and Aβ (1−42) induced fibril formation of Aβ (1−42) on **1′**, and 1:1 binding reaction induced globule formation of Aβ (1−42) such as on **3′**. The mixture of 2:1 and 1:1 binding on **2′** represented both fibril and globule formations. Therefore, the binding mode and the affinities between sugar and Aβ were related to the morphology. The strong binding of **3′** (1:1) might induce the adhesion of Aβ, formation of nucleus, and subsequent globule aggregates.

The sugar intervals were different in the each compound. The multivalent sugars **2** and **3** had a divergence point at the phenyl ring with sugar interval of 5−10 Å, while the intervals of sugars were at least 22 Å on **1′** due to the composition of the SAMs (Figure 8A) (*32*). The net charge of Aβ (1−42) was slightly negative (*28*), but sulfonated sugars are known to interact through the basic residues of the HHQK region (*33*) (Figure 8B). His13, His14, and Lys16 are cationic to interact with Aβ by the electrostatic interaction. The distances between His13 and His14 units are 8−10 Å in the pleated sheet conformation, and the distances between His13 or His14 and Lys16 units are 10−20 Å. From the result of SPR evaluation, the interaction between sulfonated sugar and Aβ (1−42) was of two types (2:1 and 1:1 binding modes). In the 2:1 binding mode, two independent sugars interacted with Aβ (1−42), which indicates a long interaction distance between the sugars on **1′**. We surmised, therefore, that the amino acids that participate in 2:1 binding are His13-Lys16 rather than His13-His14. On the other hand, multivalent sugar clusters participated in 1:1 binding with the HHQK region, because the 1:1 binding mode is superior to

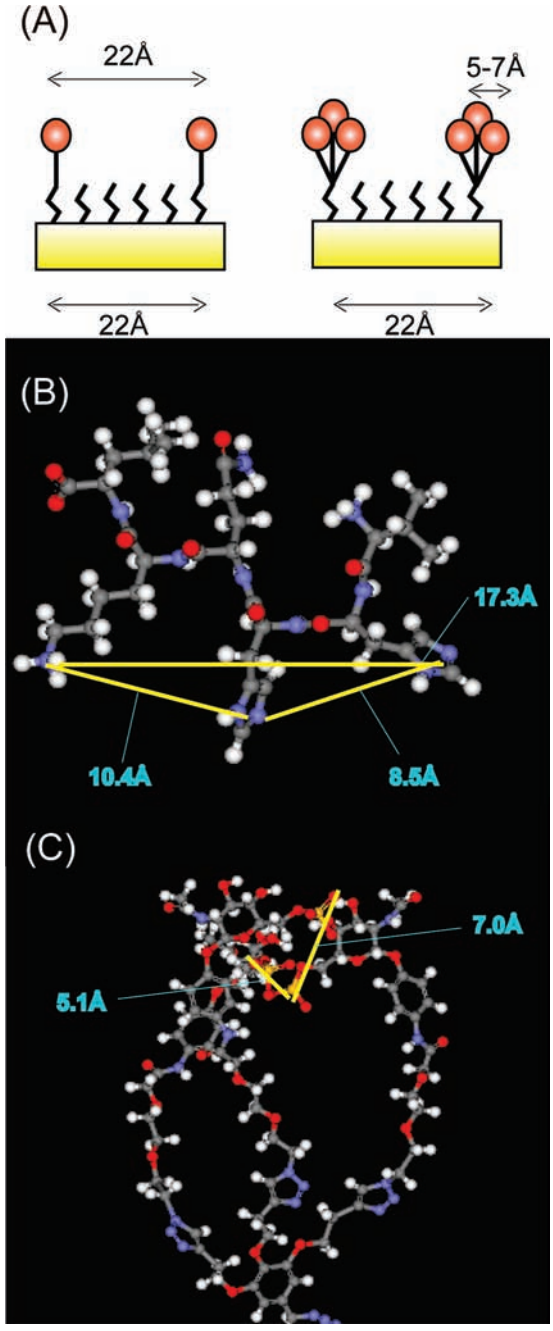


Figure 8. Illustration of sugar intervals on the surface (A). Graphical configurations of multivalent sugars (B) and 12−17 amino acid residues region (C).

the 2:1 binding mode. The sugar intervals of multivalent sugars **2** and **3** are comparable with that of His13-His14 (Figure 8C). Consequently, the multivalent cluster was considered to interact with the His-His region in 1:1 binding due to the steric effect. The change of binding mode allowed the peptide to form an alternative morphology and secondary structure, because peptides were reported to change their conformation in response to the ligand bindings (*34, 35*).

MTT assay showed that the cytotoxicity of Aβ (1−42) varied due to the aggregation process. Aggregation of Aβ (1−42) on **3′** which formed globules gave the highest cytotoxicity, followed by **2′**. By contrast, aggregation of Aβ (1−42) on **1′** formed fibrils and had no cytotoxicity. Lambert et al. reported that cytotoxicity of Aβ (1−42) was attributed to oligomeric, small globules of Aβ (1−42) (*36*), and Hoshi et al. also reported similar results (*8*). That result agreed with our observations in terms of the high cytotoxicity of Aβ (1−42) globules regardless of the difference of the size of Aβ (1−42). The FTIR spectrum of cytotoxic Aβ (1−42) had the characteristic of low-intensity bands at 1632 cm^{-1}, corresponding to β-sheet formation. Zako et al. reported that the insulin peptide with low cytotoxicity did not have the band around 1615 cm^{-1} (*37*). Our results in the band of 1613 cm^{-1} agreed the former results of FTIR spectra and cytotoxicity and suggested that the secondary structure change facilitated the morphological change to globules and cytotoxicity against HeLa cells. Moreover, the multivalency of sugar variously bound to Aβ (1−42) affected the secondary structure, which gives a correlation with the pathogenesis of AD.

FTIR-RAS, D-AFM, and SPR analyses suggested that the binding mode between sugar and Aβ (1−42) was highly affected by sugar valencies, and changed their secondary structure and morphology. Moreover, these changes were correlated to the cytotoxicity of Aβ (1−42). Each result showed that the amyloidosis of Aβ was controllable by the multivalency of sugars. Furthermore, we believe that the results suggest the importance of glyco-cluster formation on cell surfaces in AD.

CONCLUSION

This study revealed the role of sugars in amyloidosis using a well-ordered sugar display. The morphology of Aβ (1−42) was greatly influenced by the sugar valencies, and globular objects were induced to form in the presence of multivalent sugars. The secondary structure was also affected by the presence of multivalent sugars, and the affinity of Aβ (1−42) for sulfonated sugar was likewise highly affected by the valency. Moreover, the binding mode between sugar and Aβ (1−42) was also affected. The result of each D-AFM observation, SPR analysis, and IR evaluation suggested that the multivalency of sugars for the amyloidosis of Aβ had a significant effect on its morphology and aggregation at the surface of the cell membrane mimic. Cell viability assay implied that higher cytotoxicity to HeLa cells was induced by Aβ (1−42) which adsorbed on the multivalent sugars. These results correspond to the introduction of specific behavior of Aβ (1−42) with glycosaminoglycans and gangliosides. Various groups have tried in vain to identify the roles of glyco-clusters; artificial glyco-clusters with a well-defined surface provide a new means by which to clarify the roles of sugars in Alzheimer disease.

ACKNOWLEDGMENT

This work was supported by a Grant-in-Aid for Scientific Research on Innovative Areas (20106003). We thank Prof. Tooru Ooya (Kobe Univ.) and Prof. Shin-ichi Ikushiro (Toyama Pref. Univ.) for the SPR measurement. HeLa cell was kindly donated by Prof. Nobuhiko Yui (Japan Adv. Inst. Sci. Tech.).

Supporting Information Available: Detailed synthetic procedure of **1**−**3**, surface analysis data by FTIR-RAS, XPS, water contact angle, ellipsometry, and concentration-dependent RU curves of Aβ (1−42). This material is available free of charge via the Internet at http://pubs.acs.org.

LITERATURE CITED

(1) Laird, F. M., Cai, H., Savonenko, A. V., Farah, M. H., He, K., Melnikova, T., Wen, H., Chiang, H.-C., Xu, G., Koliatos, V. E., Borchelt, D. R., Prince, D. L., Lee, H.-K., and Wong, P. C. (2005) BACE1, a major determinant of selective vulnerability of the brain to amyloid-β amyloidogenesis, is essential for cognitive, emotional, and synaptic functions. *J. Neurosci. 25*, 11693–11709.

(2) Rak, M., Del Bigio, M. R., Mai, S., Westaway, D., and Gough, K. (2007) Dense-core and diffuse Aβ plaques in TgCRND8 mice studied with synchrotron FTIR microspectroscopy. *Biopolymers 87*, 207–217.
(3) Selkoe, D. J. (2001) Alzheimer's disease: Genes, proteins, and therapy. *Physiol. Rev. 81*, 741–766.
(4) Higuchi, M., Iwata, N., and Saido, T. C. (2005) Understanding molecular mechanisms of proteolysis in Alzheimer's disease: Progress toward therapeutic interventions. *Biochim. Biophys. Acta 1751*, 60–67.
(5) Glabe, C. G. (2008) Structural classification of toxic amyloid oligomers. *J. Biol. Chem. 283*, 29639–29643.
(6) Okada, T., Ikeda, K., Wakabayashi, M., Ogawa, M., and Matsuzaki, K. (2008) Formation of toxic Aβ(1−40) fibrils on GM1 ganglioside-containing membranes mimicking lipid rafts: Polymorphisms in Aβ(1−40) fibrils. *J. Mol. Biol. 382*, 1066–1074.
(7) Gong, Y., Chang, L., Viola, K. L., Lacor, P. N., Lambert, M. P., Finch, C. E., Krafft, G. A., and Klein, W. L. (2003) Alzheimer's disease-affected brain: Presence of oligomeric Aβ ligands (ADDLs) suggests a molecular basis for reversible memory loss. *Proc. Natl. Acad. Sci. U.S.A. 100*, 10417–10422.
(8) Hoshi, M., Sato, M., Matsumoto, S., Noguchi, A., Yasutake, K., Yoshida, N., and Sato, K. (2003) Spherical aggregates of β-amyloid (amylospheroid) show high neurotoxicity and activate tau protein kinase I/glycogen synthase kinase-3β. *Proc. Natl. Acad. Sci. U.S.A. 100*, 6370–6375.
(9) Daggett, V. (2006) α-Sheet: The toxic conformer in amyloid diseases? *Acc. Chem. Res. 39*, 594–602.
(10) McLaurin, J., Yang, D. S., Yip, C. M., and Fraser, P. E. (2000) Review: Modulating factors in amyloid-β fibril formation. *J. Struct. Biol. 130*, 259–270.
(11) Yanagisawa, K. (2007) Role of gangliosides in Alzheimer's disease. *Biochim. Biophys. Acta 1768*, 1943–1951.
(12) McLaurin, J., Franklin, T., Zhang, X., Deng, J., and Fraser, P. E. (1999) Interactions of Alzheimer amyloid-β peptides with glycosaminoglycans: Effects on fibril nucleation and growth. *Eur. J. Biochem. 266*, 1101–1110.
(13) Matsuzaki, K., and Horikiri, C. (1999) Interactions of amyloid β-peptide (1−40) with ganglioside-containing membranes. *Biochemistry 38*, 4137–4142.
(14) Lee, Y. C., and Lee, R. T. (1995) Carbohydrate-protein interactions: Basis of glycobiology. *Acc. Chem. Res. 28*, 321–327.
(15) Mammen, M., Choi, S.-K., and Whitesides, G. M. (1998) Polyvalent interactions in biological systems: Implications for design and use of multivalent ligands and inhibitors. *Angew. Chem., Int. Ed. 37*, 2754–2794.
(16) Mann, D. A., Kanai, M., Maly, D. J., and Kiessling, L. L. (1998) Probing low affinity and multivalent interactions with surface plasmon resonance: Ligands for concanavalin A. *J. Am. Chem. Soc. 120*, 10575–10582.
(17) Iwatsubo, T., Odaka, A., Suzuki, N., Mizusawa, H., Nukina, N., and Ihara, Y. (1994) Visualization of Aβ42(43) and Aβ40 in senile plaques with end-specific Aβ monoclonals: Evidence that an initially deposited species is Aβ42(43). *Neuron 13*, 45–53.
(18) Sasaki, K., Nishida, Y., Kambara, M., Uzawa, H., Takahashi, T., Suzuki, T., Suzuki, Y., and Kobayashi, K. (2004) Design of *N*-acetyl-6-sulfo-β-D-glucosaminide-based inhibitors of influenza virus sialidase. *Bioorg. Med. Chem. 12*, 1367–1375.
(19) Miura, Y., Yasuda, K., Yamamoto, K., Koike, M., Nishida, Y., and Kobayashi, K. (2007) Inhibition of Alzheimer amyloid aggregation with sulfated glycopolymers. *Biomacromolecules 8*, 2129–2134.
(20) Miura, Y., and Mizuno, H. (2009) Interaction of alzheimer amyloid β with glycosaminoglycan model polymer. *Polym. Prepr., Jpn. 58*, 17501.
(21) Kolb, H. C., Finn, M. G., and Sharpless, K. B. (2001) Click chemistry: Diverse chemical function from a few good reactions. *Angew. Chem., Int. Ed. 40*, 2004–2021.
(22) Lee, J. K., Chi, Y. S., and Choi, I. S. (2004) Reactivity of acetylenyl-terminated self-assembled monolayers on gold: Triazole formation. *Langmuir 20*, 3844–3847.
(23) Fukuda, T., Onogi, S., and Miura, Y. (2009) Dendritic sugar-microarrays by click chemistry. *Thin Solid Films 518*, 880–888.
(24) Matsumoto, E., Yamauchi, T., Fukuda, T., and Miura, Y. (2009) Sugar microarray via click chemistry: Molecular recognition with lectins and amyloid β (1−42). *Sci. Technol. Adv. Mater. 10*, 034605.
(25) Miura, Y., Yamauchi, T., Sato., H., and Fukuda, T. (2008) The self-assembled monolayer of saccharide via click chemistry: Formation and protein recognition. *Thin Solid Films 516*, 2443–2449.
(26) Hoos, M. D., Ahmed, M., Smith, S. O., and Van Nostrand, W. E. (2009) Myelin basic protein binds to and inhibits the fibrillar assembly of Aβ42 in vitro. *Biochemistry 48*, 4720–4727.
(27) Schmechel, A., Zentgraf, H., Scheuermann, S., Fritz, G., Pipkorn, R., Reed, J., Beyreuther, K., Bayer, T. A., and Multhaup, G. (2003) Alzheimer β-amyloid homodimers facilitate Aβ fibrillization and the generation of conformational antibodies. *J. Biol. Chem. 278*, 35317–35324.
(28) Ban., T., Morigaki, K., Yagi, H., Kawasaki, T., Kobayashi, A., Yuba, S., Naiki, H., and Goto, Y. (2006) Real-time and single fibril observation of the formation of amyloid β spherulitic structures. *J. Biol. Chem. 281*, 33677–33683.
(29) Hiramatsu, H., Goto, Y., Naiki, H., and Kitagawa, T. (2004) Core structure of amyloid fibril proposed from IR-microscope linear dichroism. *J. Am. Chem. Soc. 126*, 3008–3009.
(30) Zurdo, J., Guijarro, J. I., and Dobson, C. M. (2001) Preparation and characterization of purified amyloid fibrils. *J. Am. Chem. Soc. 123*, 8141–8142.
(31) Ingemarson, R., and Thelander, L. (1996) A kinetic study on the influence of nucleoside triphosphate effectors on subunit interaction in mouse ribonucleotide reductase. *Biochemistry 35*, 8603–8609.
(32) Ulman, A. (1996) Formation and structure of self-assembled monolayers. *Chem. Rev. 96*, 1533–1554.
(33) Giulian, D., Haverkamp, L. J., Yu, J., Karshin, W., Tom, D., Li, J., Kazanskaia, A., Kirkpatrick, J., and Roher, A. E. (1998) The HHQK domain of β-amyloid provides a structural basis for the immunopathology of Alzheimer's disease. *J. Biol. Chem. 273*, 29719–29726.
(34) Takahashi, T., and Mihara, H. (2008) Peptide and protein mimetics inhibiting amyloid β-peptide aggregation. *Acc. Chem. Res. 41*, 1309–1318.
(35) Schneider, J. P., and Kelly, J. W. (1995) Templates that induce α-helical, β-sheet, and loop conformations. *Chem. Rev. 95*, 2169–2187.
(36) Lambert, M. P., Barlow, A. K., Chromy, B. A., Edwards, C., Freed, E. C., Liosatos, M., Morgan, T. E., Rozovsky, I., Trommer, B., Viola, K. L., Wals, P., Zhang, C., Finch, C. E., Krafft, G. A., and Klein, W. L. (1998) Diffusible, nonfibrillar ligands derived from Aβ1−42 are potent central nervous system neurotoxins. *Proc. Natl. Acad. Sci. U.S.A. 95*, 6448–6453.
(37) Zako, T., Sakono, M., Hashimoto, N., Ihara, M., and Maeda, M. (2009) Bovine insulin filaments induced by reducing disulfide bonds show a different morphology, secondary structure, and cell toxicity from intact insulin amyloid fibrils. *Biophys. J. 96*, 3331–3340.

BC100053X

Efficient Gene Transfection by Histidine-Modified Chitosan through Enhancement of Endosomal Escape

Kai-Ling Chang,[†] Yuriko Higuchi,[†,‡] Shigeru Kawakami,[†] Fumiyoshi Yamashita,[†] and Mitsuru Hashida*[,†,§]

Department of Drug Delivery Research and Institute for Innovative NanoBio Drug Discovery and Development, Graduate School of Pharmaceutical Sciences, and Institute for the Integrated Cell-Material Sciences, Kyoto University, Japan. Received February 2, 2010; Revised Manuscript Received May 1, 2010

Chitosan has the potential to be a biocompatible gene carrier. However, the transfection efficiency of chitosan is low because of the slow endosomal escape rate. The buffering capacity of histidine in the endosomal pH range would help the escape of plasmid DNA (pDNA) from endosomes. In this study, histidine was introduced into chitosan to improve the transfection efficiency. Chitosan and histidine were linked by disulfide bonds provided by 2-iminothiolane and cysteine. The complexes were prepared by mixing chitosan or histidine-modified chitosan with plasmid DNA. A broader buffering range of histidine-modified chitosan was observed, and the cellular uptake of histidine-modified chitosan/pDNA complexes was higher than that of chitosan/pDNA complexes. Although chitosan/tetramethylrhodamine (TMR)-pDNA complexes were trapped in the vesicles in cytosol, TMR-pDNA carried by histidine-modified chitosan was more widely distributed in the cytosol. This result suggests that histidine can help pDNA escape from endosomes with the help of the high buffering capacity. The gene expression of histidine-modified chitosan/pDNA complexes was higher than that of chitosan/pDNA complexes. These results suggest that histidine modification improves the transfection efficiency of chitosan.

INTRODUCTION

Chitosan, which is a cationic polysaccharide, has played an important role in biomedicine for more than a decade, being used as a food additive (*1*) and a wound dressing to assist healing (*2*). It is also well-known that chitosan has the potential to act as a gene carrier (*3–6*). The amino groups in the structure of chitosan provide positive charges to form complexes with the negative charges of nucleic acids. The outstanding biocompatibility of chitosan is also an advantage for biomedical applications (*3*). A number of studies have proven that chitosan can be used in vivo with negligible side effects (*7, 8*). These advantages make chitosan a promising material for use as a gene carrier.

However, the gene transfection efficiency of chitosan as a carrier is very low compared with conventional nonviral gene carriers, including liposomes (*4, 9, 10*) and polyethyleneimines (*6, 11*). One reason for the low gene expression efficiency of chitosan is its slow endosomal escape rate (*6, 12*). In fact, chitosan effectively protects and introduces nucleic acids into cells. However, endosomes would be the next barrier to the gene delivery of chitosan. Köping-Höggård et al. showed that chitosan was trapped in endosomes over 24 h (*6*). Therefore, the enzymes in endosomes and lysosomes would gradually degrade the nucleic acids in endosomes or lysosomes over a long period. Other problems including low solubility under physiological conditions and complicated physicochemical properties are also major concerns for the efficient gene transfection of chitosan (*13*). These problems, especially the slow endosomal escape rate, need to be solved to enhance the transfection efficiency of chitosan prior to its application as a gene carrier.

There are several strategies to overcome the endosome barrier. For example, chloroquine, an endosomolytic reagent, can accumulate in lysosomes and disrupt them by increasing the pH (*14, 15*), and pH-sensitive liposomes can escape from endosomes due to membrane disturbance (*16, 17*). Histidine, a nonessential amino acid, contains an imidazole ring (pK_{a3} 6.04) which increases the buffering capacity in endosomes and lysosomes. Histidine and histidine-containing dipeptides, such as carosine and anserine, are known to act as endogenous buffers in skeletal muscle (*18, 19*). For this reason, histidine is commonly used as a modifying group to improve the endosomal escaping rate of several nonviral gene carriers, such as polylysine, liposomes, and poly(amino acid) derivatives (*20–24*). We have demonstrated that histidine can enhance the gene transfection efficiency of liposomes by increasing the buffering capacity (*21*). In addition, the conjugation site on the chitosan structure and the hydrophilicity of histidine itself may help the dissolution of chitosan.

The purpose of this study was to increase the gene transfection efficiency of chitosan/pDNA complexes by enhancing the endosomal escape rate. In this study, we introduced histidine to the amino groups of chitosan via disulfide bonds. The degree of substitution of histidine and the buffering capacity of histidine-modified chitosan were measured. The physicochemical properties of the complexes were evaluated by determination of the particle size and zeta potential, as well as agarose gel electrophoresis. The gene transfection process was examined by confocal microscopy, flow cytometry, and luciferase assay in order to prove the enhanced gene transfection of histidine-modified chitosan by increased cellular uptake and a buffering effect.

EXPERIMENTAL PROCEDURES

Materials. Highly purified chitosan (number-average molecular weight: 173 kDa, degree of deacetylation: 88%) was

* To whom correspondence should be addressed. Dr. Mitsuru Hashida, Department of Drug Delivery Research, Graduate School of Pharmaceutical Sciences, Kyoto University, 46-29 Yoshida-shimoadachi, Sakyo-ku, Kyoto 606-8501, Japan. Tel: +075-753-4525, Fax: +075-753-4575, E-mail: hashidam@pharm.kyoto-u.ac.jp.

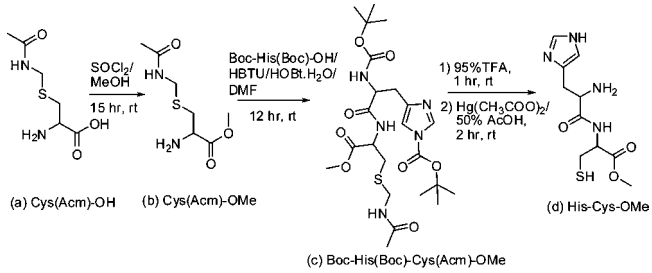
[†] Department of Drug Delivery Research.

[‡] Institute for Innovative NanoBio Drug Discovery and Development.

[§] Institute for the Integrated Cell-Material Sciences.

10.1021/bc1000609 © 2010 American Chemical Society
Published on Web 05/25/2010

Scheme 1. Histidine-Cysteine-OMe (His-Cys-OMe) Synthesis



purchased from SEIKAGAKU Biobusiness (Tokyo, Japan). Cys(Acm)−OH·HCl, Boc-His(Boc)−OH, and hydroxybenzotriazole·H_2O (HOBt·H_2O) were purchased from Watanabe Chemical Industries (Hiroshima, Japan). *O*-Benzotriazole-*N*,*N*,*N*′,*N*′-tetramethyl-uronium-hexafluorophosphate (HBTU) was purchased from Peptide Institute (Osaka, Japan). Thionyl chloride ($SOCl_2$), deuterium oxide (D_2O), sodium bicarbonate ($NaHCO_3$), citric acid monohydrate, sodium chloride, chloroform, methanol, ethanol, diethyl ether, trifluoroacetic acid (TFA), potassium diphosphate (KH_2PO_4), dimethyl sulfoxide (DMSO), sodium acetate·$3H_2O$, ninhydrin, hydrindantin·$2H_2O$, and sodium hydroxide (NaOH) were purchased from Nacalai Tesque (Kytoto, Japan). Dehydrated dimethylformamide (DMF), petroleum ether, L-histidine, glucose, magnesium chloride ($MgCl_2$), and 4% paraformaldehyde were purchased from Wako Pure Chemical Industries (Osaka, Japan). Mercury(II) acetate was purchased from Sigma-Aldrich Corporation (Saint Louis, MO). 2-iminothiolane·HCl was purchased from Pierce (Rockford, IL). Alexa Fluor 488 transferrin conjugate, LysoSensor Green DND-189, LysoTracker Green DND-26, Lipofectamine 2000, Opti-MEM I reduced serum medium, Trypan blue stain prepared in 0.85% NaCl, and SYBR Gold nucleic acid gel stain were purchased from Invitrogen (Carlsbad, CA). Agarose X and S were purchased from NIPPON GENE (Osaka, Japan). Label IT fluorescein nucleic acid labeling kit and Label IT TM-rhodamine nucleic acid labeling kit were purchased from Mirus Bio (Madison, WI). jetPEI was purchased from Polyplus-Transfection Inc. (New York, NY). PicaGene luciferase assay kit was purchased from Toyo Corporation (Tokyo, Japan). All solvent and reagents were ACS grade and used directly without further treatment.

His-Cys-OMe Synthesis (Scheme 1). Cys(Acm)−OH·HCl was reacted with $SOCl_2$ to form the methyl ester. Twenty milliliters of methanol was cooled to −30 °C, and then $SOCl_2$ was added to the methanol dropwise. After cooling on ice, the mixture was added with 1 g Cys(Acm)−OH and then stirred at room temperature for 15 h. The methanol in the mixture was removed in an evaporator, and the product, Cys(Acm)-OMe, was recrystallized from ethanol and cold diethyl ether. The coupling reaction of Cys(Acm)-OMe and Boc-His(Boc)−OH was conducted with HBTU and HOBt·H_2O in DMF for 12 h at room temperature. DMF was removed in an evaporator, and the residue was dissolved in chloroform and washed twice with 5% sodium bicarbonate, 10% citric acid, and saturated sodium chloride. Chloroform was removed in an evaporator and the Boc and Acm-protected product was recrystallized using a mixture of ethanol, petroleum ether, and diethyl ether. The deprotection of the Boc groups and Acm groups was carried out by 95% TFA and mercury(II) acetate treatment, respectively. The obtained His-Cys-OMe was confirmed by ESI-MS (Mariner ESI TOF Biospectrometry Workstation, PerSeptive Biosystems, Inc., Framingham, MA).

Synthesis of Histidine-Modified Chitosan (Chi-CH, Scheme 2). The conjugation of chitosan and His-Cys-OMe was carried out according to Masuko et al. (*25*) with slight modification. Chitosan was dissolved in 1% acetic acid (pH 2.0) and potassium phosphate buffer (50 mM KH_2PO_4, 2 mM EDTA·2Na, and 150 mM NaCl, pH 8.0) was mixed with this chitosan solution in the volume ratio of 1:1. Traut's reagent (2-iminothiolane·HCl) was added to the solution directly, and the reaction mixture was stirred for 4 h at room temperature. After purification by dialysis (1000 molecular weight cutoff) for 48 h, the reaction product was immediately reacted with His-Cys-OMe in different weight ratios to 2-iminothiolane·HCl (Table 1). DMSO was added to the reaction mixture in a volume ratio of 10:1 (reaction mixture/DMSO). The reaction mixture was stirred for 12 h, and then purified by dialysis (1000

Scheme 2. Chitosan-Cysteine-Histidine (Chi-CH) synthesis

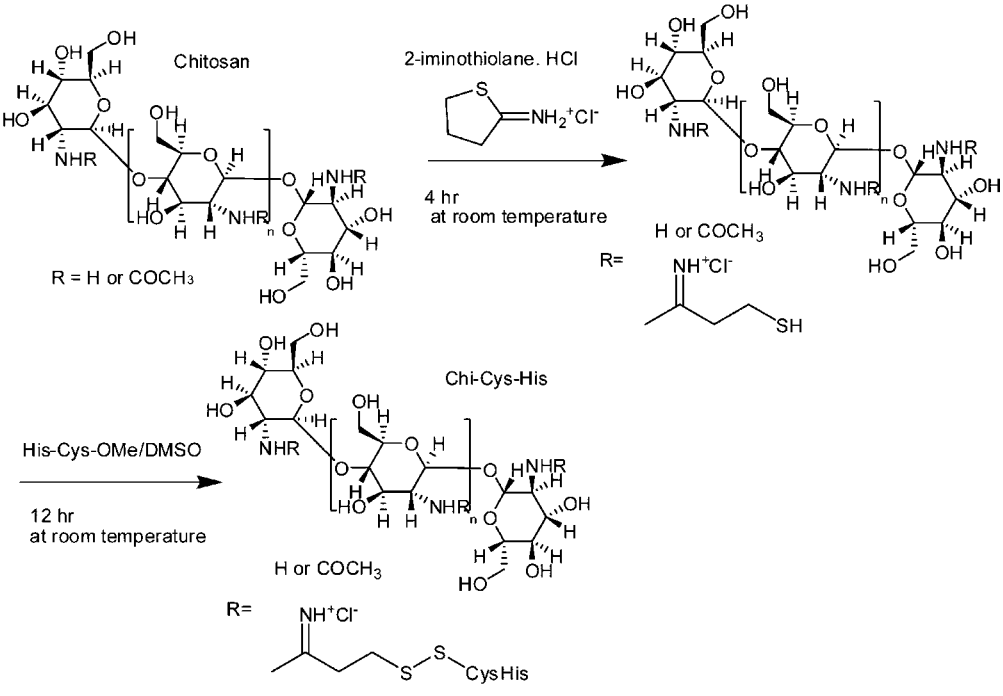


Table 1. Reaction Conditions for Chi-CH Synthesis and the Degree of Substitution of His-Cys-OMe in Chitosan

	reactant						product
	chitosan		2-iminothiolane·HCl		His-Cys-OMe		
material	(mg)	(mmol)	(mg)	(mmol)	(mg)	(mmol)	degree of substition (%)
Chi-CH A	100	0.0006	15	0.1090	200	0.7353	2.72
Chi-CH B	100	0.0006	35	0.2543	200	0.7353	3.41
Chi-CH C	100	0.0006	100	0.7266	400	1.4706	4.32

molecular weight cutoff) for 48 h. The reaction mixture after dialysis was freeze−dried.

Histidine Quantification. The amount of His-Cys-OMe conjugated to chitosan was measured by the ninhydrin test established by S−W Sun et al. (*26*). In brief, Chi-CH was dissolved in sodium acetate buffer (100 mM sodium acetate and 100 mM sodium chloride solution, pH 4.5), and the disulfide bonds were reduced using 75 mM dithiothreitol. The reduction reaction was carried out at room temperature for 1 h, and then the chitosan was removed by Microcon centrifugal filters (3000 molecular weight cutoff). The dipeptide solution in Chi-CH was analyzed by the ninhydrin test. Ninhydrin solution was prepared using 20 mg ninhydrin and 33.35 mg hydrindantin·$2H_2O$ dissolved in DMSO/4 N sodium acetate buffer (7.5 mL/2.5 mL) under nitrogen gas. Histidine standard solution (10−100 μg/mL) was prepared in distilled water. The histidine standard solution and the dipeptide solution were mixed with ninhydrin solution in a volume ratio of 1:1, and then heated at 100 °C for 10 min. After heating, the histidine standard solution and the dipeptide solution were placed on ice for 10 min. Fifty milliliters of the dipeptide solution was added to each well of a 96-well plate, followed by 125 μL 50% ethanol. The absorbance of the solution was determined using a microplate reader (Bio-Rad 550 microplate reader, Foster City, CA) at 570 nm. The degree of substitution was calculated based on a histidine standard curve.

Measurement of Buffering Capacity. Four micromolar chitosan and Chi-CH solutions were prepared in sodium acetate buffer (pH 5.5). The chitosan and Chi-CH solutions were titrated with 0.1 N NaOH. The pH was recorded using a pH meter (Twin pH AS-212, As one, Osaka, Japan), and the buffering capacity was compared.

Preparation and Purification of pCMV-Luc. pCMV-Luc was constructed by subcloning the *Hin*dIII/XbaI firefly luciferase cDNA fragment from a pGL3-control vector (Promega, Madison, WI) into the polylinker of a pcDNA3 vector (Invitrogen, Carlsbad, CA). pDNA was amplified in the *Escherichia coli* strain DH5α, isolated, and purified using a JETSTAR Plasmid Purification Giga Kit (GENOMED GmbH, Löhne, Germany). The concentration of pDNA was measured using a Shimadzu UV−vis spectrometer (Shimadzu, Kyoto, Japan) at 260 nm.

Measurement of Particle Size and Zeta Potential. Chitosan or Chi-CH was dissolved into sodium acetate buffer (pH 5.5) at a concentration of 5 mg/mL, and pDNA was dissolved in 5% glucose at a concentration of 1 mg/mL for use as stock solutions. Chitosan or Chi-CH and pDNA solutions were mixed in the same volume ratio with different concentrations based on the A/P ratio (A: amino groups in chitosan structure; P: phosphate groups in pDNA structure). The size and zeta potential of the complexes were measured using a ZetaNano-Sizer (Malvern ZetaNanoSizer Nano-ZS, Worcestershire, UK).

Evaluation of Complex Stability. The stability of the complexes was evaluated by agarose gel electrophoresis. One microgram of pDNA was mixed with chitosan or Chi-CH at different A/P ratios. The complexes were loaded onto 1% Agarose S gel. For the enzymatic stability assay, the complexes were incubated with 10 U DNase I (Roche, Manheim, Germany) in 5 mM $MgCl_2$ solution for 3 h at 37 °C. DNase I was quenched by TE buffer after a 3 h incubation, then DNA was extracted using phenol/chloroform/isoamyl alcohol (Nacalai Tesque, Kyoto, Japan). The extracted DNA was loaded onto 5% Agarose X gel. The pDNA on the gel was stained using a SYBR Gold nucleic acid gel stain.

pCMV-Luc Labeling. The pDNA was labeled with fluorescein and tetramethylrhodamine (TMR) using a Label IT fluorescein nucleic acid labeling kit or a Label IT TM-rhodamine nucleic acid labeling kit, respectively. The labeling procedure followed the manufacturer's instructions. Briefly, pDNA was incubated with labeling reagents at 37 °C for 2 h. Then, pDNA was precipitated with 100% ethanol and washed with 70% ethanol. The concentration of fluorescence-labeled pDNA was measured by UV absorbance at 260 nm.

Cell Culture and Cellular Uptake. For the uptake study, human embryonic kidney (HEK293) cells (RIKEN Cell Bank, Tsukuba, Japan) were incubated in Dulbecco's modified Eagle's medium (DMEM; Nissui Co., Tokyo, Japan) supplemented with 10% fetal bovine serum (FBS; Invitrogen, Carlsbad, CA), 100 U/mL penicillin, 100 μg/mL streptomycin, and 2 mM L-glutamine (Invitrogen, Carlsbad, CA). HEK293 cells were seeded onto 12 well plates at a density of 3×10^5 cell/mL. After a 24 h incubation, the medium was changed to Opti-MEM I for complex administration. One microgram per milliliter of fluorescein-labeled pDNA complexed with chitosan, Chi-CH, or Lipofectamine 2000 was added to each well. At 2, 6, and 12 h after incubation, Opti-MEM I containing complexes was removed, and the cells were collected in phosphate buffer and centrifuged at 5000 rpm for 10 min. The cell pellets were fixed and resuspended in 70% ethanol and incubated with Trypan blue for the quenching of the extracellular fluorescein. The resuspended cells were repeatedly centrifuged at 5000 rpm for 10 min and resuspended in phosphate buffer for flow cytometry analysis (Becton Dickinson FACSCalibur, Franklin Lakes, NJ).

Intracellular Distribution of pDNA. HEK293 cells were used as the cell model to monitor the endosomal escape of the complexes. HEK293 cells were seeded on 12 well plates at a cell density of 2×10^5 cells/mL. After a 24 h incubation, HEK293 cells were incubated with 100 μg/mL Alexa Fluor 488 transferrin conjugate for 20 min in Opti-MEM I medium before addition of the complexes. Lysosomes were labeled with 1 μM LysoSensor Green DND-189 and 1 μM LysoTracker Green DND-26 for 30 min in Opti-MEM I medium before addition of the complexes. The complexes containing 2 μg/mL TMR-labeled pDNA were then added to the cells. After a 6 h incubation, HEK293 cells were washed with phosphate buffer and fixed with 4% paraformaldehyde. The endosomal escape was observed using a Nikon Eclipse Ti inverted confocal microscope equipped with a Nikon EZ-C1 observation system (Nikon, Tokyo, Japan). The images were processed using *ImageJ* software. The objective was a 60× water immersion objective.

Proton Pump Inhibition. HEK293 cells were seeded in 12 well plates at a density of 1.5×10^5 cells/mL and incubated at 37 °C, 5% CO_2 for 24 h. Before addition of the complexes, the cells were incubated with 100 nM bafilomycin

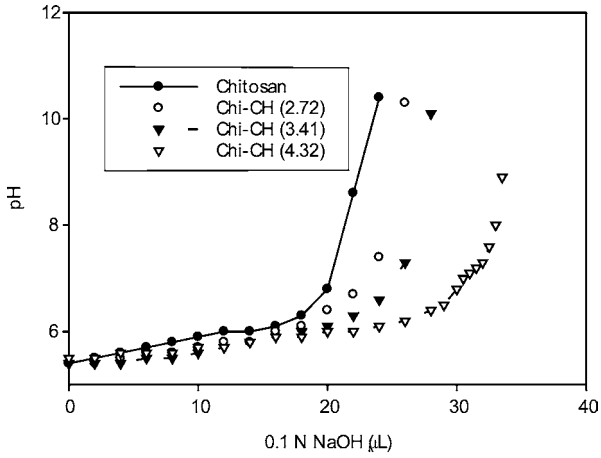


Figure 1. Buffering capacity of chitosan and Chi-CH. Chitosan and Chi-CH were determined after dissolution in sodium acetate buffer at pH 5.5 and then titration with 0.1 N NaOH. The pH was plotted to compare the differences in buffering capacity after treatment with different molar ratios of reactants.

A_1 in Opti-MEM I for 10 min. Then, 6 μg/mL pDNA complexed with chitosan or Chi-CH was added to each well. Lipofectamine 2000 containing 2 μg/mL pDNA was prepared according to the protocol provided by the manufacturer. The dose of pDNA of jetPEI was reduced to half the dose suggested by the protocol, 1 μg/mL, because of concerns about the toxicity of bafilomycin A_1 and polyethylenimine (PEI). The medium was changed to DMEM after a 6 h incubation. The cells were harvested after a 24 h incubation and then lysed. The amount of luciferase was measured using a PicaGene Luciferase Assay Kit.

Measurement of Gene Transfection Efficiency. HEK293 cells were seeded in 12-well plates at a density of 1×10^5 cells/mL. After a 24 h incubation, cells were incubated with complexes containing 6 μg/mL pDNA in Opti-MEM I for 6 h. The medium was changed to DMEM after a 6 h incubation. The cells were harvested at 72 h and then lysed for the measurement of luciferase activity as described previously. The relative luminescence unit (RLU) was measured by luminometer (Lumat Single Tube Luminometers LB 9507, Berthold Technologies GmbH & Co. KG, Wildbad, Germany) and normalized by the protein content, which was measured by Bradford assay.

RESULTS

Synthesis of Chi-CH. Liquid-phase synthesis was used in this study because a greater amount of dipeptide can be produced by liquid-phase synthesis than solid-phase synthesis. Mass calculated for $C_{10}H_{16}N_4O_3S$ (His-Cys-OMe): 272.32. Found by ESI-MS: 273.4 ($M+H^+$). The yields of Cys(Acm)-OMe, Boc-His(Boc)-Cys(Acm)-OMe, and His-Cys-OMe were 99%, 46%, and 90%, respectively, and confirmed by ESI-MS as 204.4 [$M+H^+$], 544.4 [$M+H^+$], and 273.4 [$M+H^+$]. Three different molar ratios of cross-linker and chitosan were designed to produce three types of Chi-CH: Chi-CH A, Chi-CH B, and Chi-CH C (Table 1). The ninhydrin results are shown in Table 1 demonstrating the degree of substitution of dipeptide. Chitosan was also measured in the same process as the control group. The data of the degree of substitution of chitosan were subtracted from that of Chi-CH A, B, and C groups. Chi-CH C showed the highest degree of substitution, 4.32%, compared with Chi-CH A and Chi-CH B, with a substitution of 2.72% and 3.41%, respectively.

Improvement of Buffering Capacity. The titration curve (Figure 1) showed that the Chi-CH C (4.32%) group tolerated more OH^- ions than the other two groups. Chitosan also had some buffering capacity between pH 5 and 6; however, the buffering range of chitosan was narrower than that of the histidine-modified chitosan groups. Therefore, Chi-CH C (4.32%) was chosen for use as a gene carrier for the subsequent experiments.

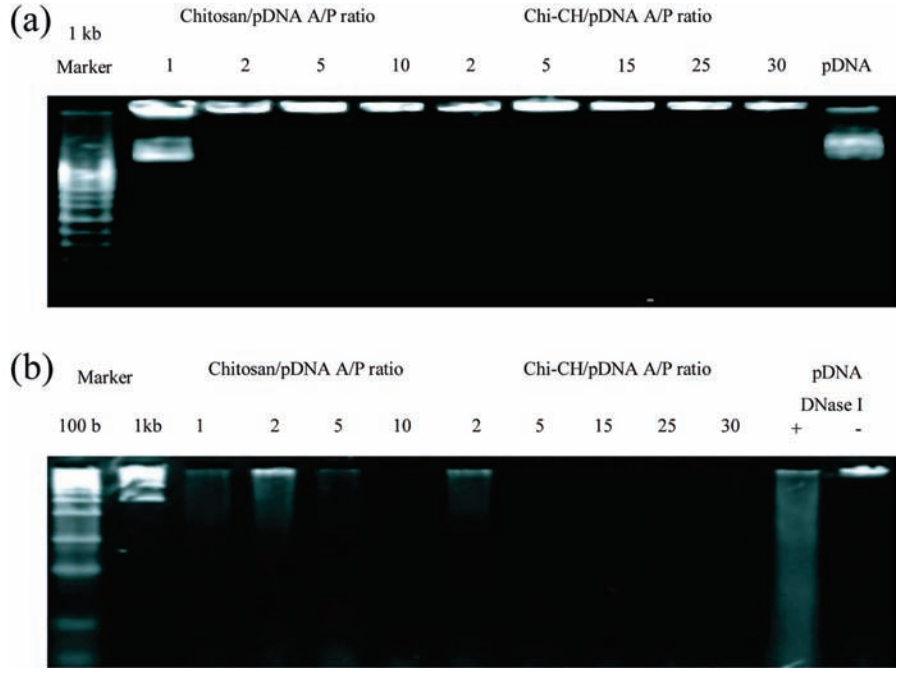


Figure 2. Physical and enzmatic stability of complexes. (a) Chitosan and Chi-CH were dissolved in sodium acetate buffer, pH 5.5, respectively, and mixed with pDNA solution at different A/P ratios.The mixed solutions were incubated at room temperature for 30 min and loaded into the wells of a 1% agarose gel. The gel was stained with SYBR Gold to detect DNA. (b) The complexes prepared at different A/P ratios were incubated with 10 U DNase I at 37 °C for 3 h. The DNA after incubation was extracted using phenol/chloroform/isoamyl alcohol (Nacalai Tesque Inc.) and loaded into the wells of a 1% agarose gel. The gel was stained with SYBR Gold.

Table 2. Particle Size and Zeta Potential of Chitosan/pDNA and Chi-CH/pDNA[a]

Particle Size (unit: nm)				
	pH 5.5		pH 7.4	
A/P ratio	Chitosan/pDNA	Chi-D/pDNA	Chitosan/pDNA	Chi-D/pDNA
0.5/1.0	37.53 ± 3.82	24.12 ± 3.31	42.52 ± 4.24	30.78 ± 10.78
1.0/1.0	66.74 ± 7.67	39.51 ± 4.15	74.72 ± 9.01	44.75 ± 4.33
2.0/1.0	68.42 ± 4.01	56.74 ± 7.61	225.95 ± 62.57	561.96 ± 305.97
4.0/1.0	51.85 ± 25.85	43.49 ± 32.92	264.47 ± 55.01	30.81 ± 28.31
5.0/1.0	45.11 ± 26.69	46.55 ± 30.14	122.8 ± 166.30	159.57 ± 10.56
10.0/1.0	70.26 ± 23.38	112.77 ± 3.46	135.12 ± 51.29	237.50 ± 11.95
15.0/1.0	74.44 ± 19.58	133.00 ± 46.88	358.23 ± 229.33	91.59 ± 9.48
25.0/1.0	55.28 ± 33.17	144.97 ± 6.48	N.D.	158.23 ± 32.28
Zeta Potential (unit: mV)				
	pH 5.5		pH 7.4	
A/P ratio	Chitosan/pDNA	Chi-D/pDNA	Chitosan/pDNA	Chi-D/pDNA
0.5/1.0	−33.6 ± 1.2	−36.0 ± 1.8	−33.6 ± 0.9	−36.5 ± 1.3
1.0/1.0	−19.3 ± 0.4	−29.1 ± 0.9	−26.6 ± 1.3	−35.3 ± 0.1
2.0/1.0	31.1 ± 1.2	−28.8 ± 0.6	−0.7 ± 0.1	−8.1 ± 0.4
4.0/1.0	36.3 ± 0.6	36.0 ± 1.1	12.50.3	5.1 ± 0.3
5.0/1.0	36.9 ± 1.6	36.7 ± 1.6	9.0 ± 0.5	13.0 ± 2.1
10.0/1.0	33.2 ± 0.6	35.3 ± 0.6	15.0 ± 0.8	14.0 ± 0.3
15.0/1.0	0.1 ± 0.0	35.3 ± 2.5	5.2 ± 0.6	16.2 ± 4.4
25.0/1.0	0.7 ± 2.9	32.0 ± 5.9	N.D.	7.6 ± 0.5

[a] Chitosan and Chi-CH were dissolved in sodium acetate buffer and mixed with pDNA solution at different A/P ratios. After 30 minutes incubation at room temperature, the particle size was measured by ZetaNanoSizer at pH 5.5 and pH 7.4 ($n = 3$).

Physicochemical Characterization of Complexes. The particle size of the complexes (Table 2a) was measured at pH 5.5 and 7.4 in order to evaluate the influence of pH on the dispersion of the complexes. At pH 5.5, both chitosan/pDNA and Chi-CH/pDNA had a particle size lower than 200 nm. At pH 7.4, chitosan/pDNA complexes had a small particle size at an A/P ratio less than 10. However, larger chitosan/pDNA complexes were observed at 15 and 25 A/P ratios, respectively, in contrast to the smaller size of the Chi-CH/pDNA complexes at the same A/P ratio. At A/P 25, ZetaNanoSizer could not measure the particle size of chitosan/pDNA complexes due to the aggregation that occurred at a high A/P ratio, which was beyond the detection limit of the instrument. The zeta potential is shown in Table 2b. At both pH 5.5 and 7.4, chitosan/pDNA and Chi-CH/pDNA complexes had the same zeta potential profile at a A/P ratio less than 10. However, the zeta potential of chitosan/pDNA complexes decreased from A/P 15, while that of Chi-CH/pDNA complexes was constant at A/P 15 and 25. The zeta potential of chitosan/pDNA at A/P 25 in pH 7.4 medium could not be measured due to aggregation.

Physical and Enzymatic Stability of Complexes. The physical stability of complexes evaluated by agarose gel electrophoresis (Figure 2a) demonstrated the high stability of both chitosan/pDNA and Chi-CH/pDNA groups, except for chitosan/pDNA at A/P 1. The ability to protect pDNA from enzyme degradation was also evaluated (Figure 2b). Chitosan/pDNA showed some degradation fragments at A/P 1, 2, and 5, while Chi-CH/pDNA showed degradation fragments only at A/P 2.

Enhancement of Cellular Uptake. The uptake of fluorescein-labeled pDNA by HEK293 was measured by flow cytometry at 2, 6, and 12 h (Figure 3). Chitosan/pDNA uptake was low at three time points. Chi-CH/pDNA demonstrated gradually increasing uptake from 2 to 6 h and reached an uptake plateau at 6 h in contrast to the negligible uptake of chitosan/pDNA.

Endosomal Escape. Endosomes (pH 5.0−6.0) and lysosomes (pH 5.0−5.5) in HEK293 cells were labeled with Alexa Fluor 488 transferrin conjugate (Figure 4a), LysoTracker Green DND-26 (Figure 4b), and LysoSensor Green DND-189 (Figure 4c), respectively. Chitosan/pDNA and Chi-CH/pDNA at A/P 2 and 25 were both examined first in endosome-labeling HEK293 cells

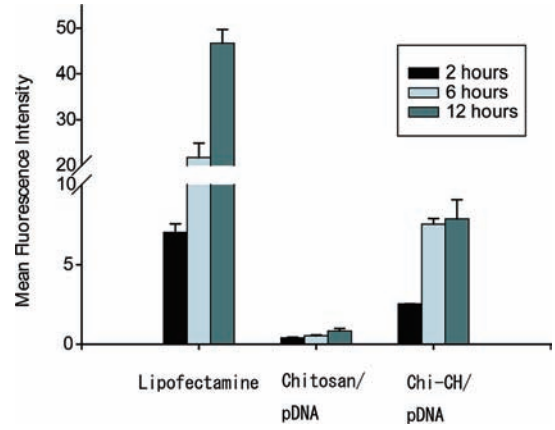


Figure 3. Cellular uptake of complexes. Fluorescein-labeled pDNA (1 μg/mL) complexes prepared by Lipofectamine 2000, chitosan, and Chi-CH were incubated with HEK 293 cells in Opti-MEMI at fixed time points. The extracellular fluorescence was quenched by Trypan blue, and the intracellular fluorescence was measured by flow cytometry. Lipofectamine 2000 was used as a positive control ($n = 3$).

(Figure 4a). We found that chitosan/pDNA at A/P 25 and Chi-CH/pDNA at A/P 2 did not show obvious intracellular distribution of TMR-labeled pDNA. Therefore, we chose chitosan/pDNA at A/P 2 and Chi-CH/pDNA at A/P 25 for the following lysosomal escape (Figure 4b,c). Chi-CH/pDNA showed a wide intracellular distribution of TMR-labeled pDNA at A/P 25 compared with a limited and overlapped intracellular distribution of chitosan/pDNA at A/P 2. These results suggested that chitosan/pDNA complexes may be trapped in the endosomes and lysosomes where the pH is lower than 5.5.

Effect of Proton Pump Inhibitor on Gene Transfection. Bafilomycin A_1 is an H^+-ATPase inhibitor, which inhibits acidification in endosomes and lysosomes (*27*). Generally, bafilomycin A_1 is used to indirectly prove that the buffering capacity of PEI increases the endosomal escape rate. This is because bafilomycin A_1 treatment inhibits the flow of hydrogen ions from cytosol into vesicles and then inhibits the increase of

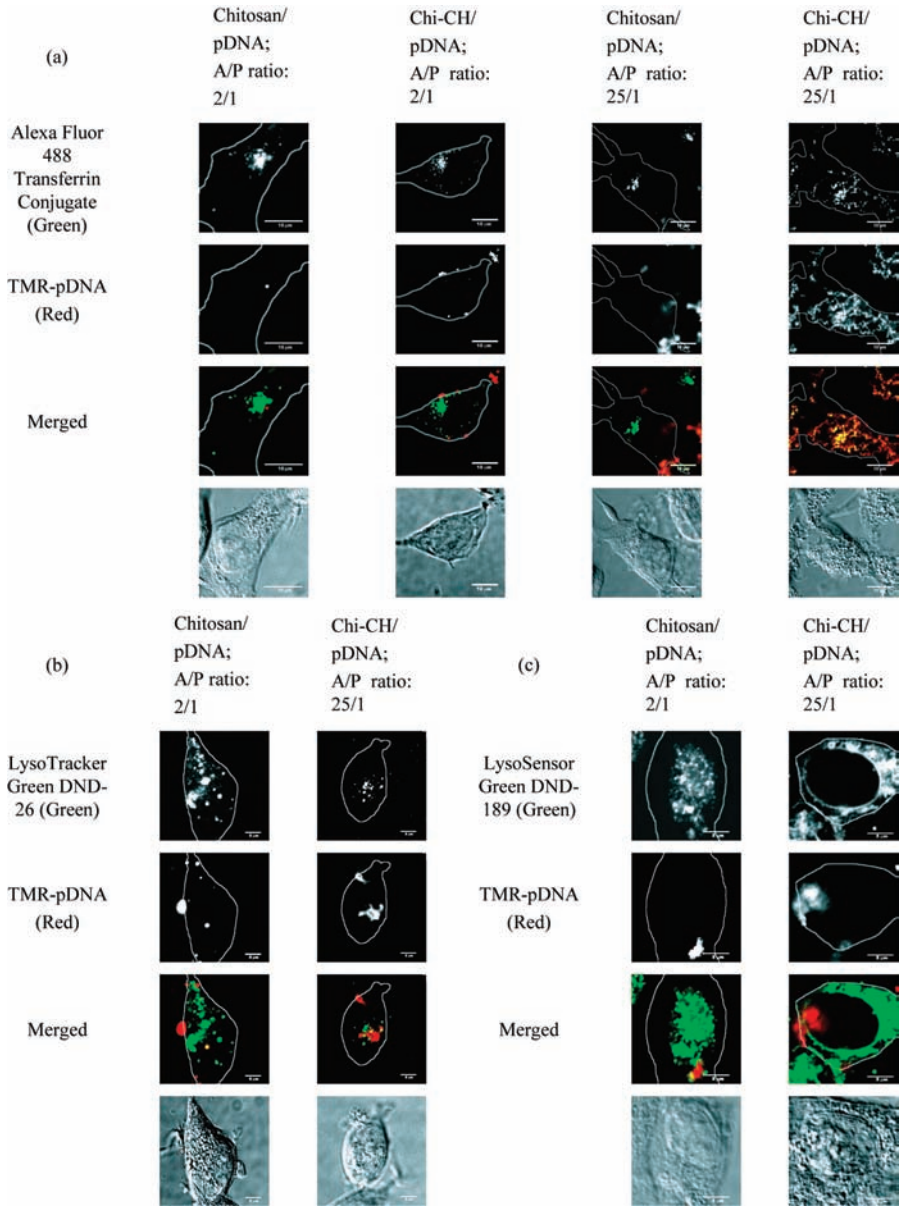


Figure 4. Confocal microscopy of complexes. Chitosan and Chi-CH formed complexes with TMRpDNA in A/P ratios of 2/1 and 25/1. HEK 293 cells were used as models to observe the endosomal escape. Cells were seeded into 12 well plates at 70% confluence. After 24 h incubation, medium of 100 mg/mL Alexa Fluor 488 transferrin conjugate (a), 1 μM LysoTracker Green DND-189 (b), or 1 μM LysoSenser Green DND-26 (c) was added to each well before complex administration. After a 20 to 30 min incubation, chitosan/TMR-pDNA and Chi-CH/TMR-pDNA were added to each well. After a 6 h incubation, the cells were washed by PBS and fixed with 4% paraformaldehyde. The distribution of fluorescence was observed by Nikon confocal microscopy (60× water immersion lens).

osmotic pressure caused by PEI (*28*). The inhibition of gene expression after bafilomycin A_1 treatment (Figure 5) may prove that the hydrogen ion concentration gradient plays an important role in the gene transfection process of Chi-CH/pDNA. After 100 nM bafilomycin A_1 treatment, a significant decrease in gene expression was observed in Chi-CH/pDNA and commercially available jetPEI (data not shown), while a slight but insignificant decrease in gene expression could also be recognized in chitosan/pDNA.

Evaluation of Gene Transfection Efficiency. Chitosan/pDNA and Chi-CH/pDNA complexes at different A/P ratios were prepared and transfected in HEK293 cells for gene expression screening (Figure 6). In the chitosan/pDNA groups, the A/P 2 group showed the highest gene expression after a 72 h incubation. The A/P 25 group of Chi-CH/pDNA showed the highest gene expression compared with other A/P ratios.

DISCUSSION

In this study, we designed His-Cys-OMe after considering three factors. First, the primary amine group in histidine was retained in order to prevent a reduction in nucleic acid binding strength. The positive charge of the primary amino group in histidine could bind to nucleic acids, which would help the formation of chitosan/pDNA complexes. Second, the direct linkage of the amine groups on the chitosan chain and the carboxylic acid group on histidine may reduce the buffering capacity of the histidyl imidazole group. A previous report demonstrated that the buffering range of histidine increased from pH 5−7 to pH 6−8 following conjugation with the acidic group

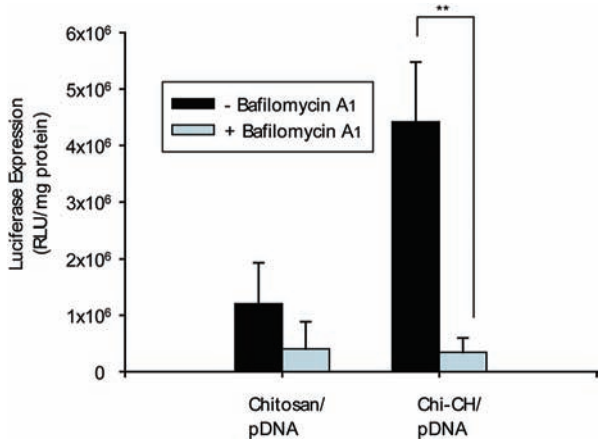


Figure 5. Proton pump inhibition. One hundred nanomolar bafilomycin A1 was added to HEK 293 cells seeded before 24 h into 12-well plates at a density of 1.5×10^4 cells/mL 10 min before complex administration. Complexes and bafilomycin A1 were incubated with the cells for 6 h, and then the medium changed from Opti-MEM I to DMEM(+) and the cells were incubated for another 66 h. The relative light units (RLU) were evaluated by luminometer and calibrated by Bradford protein assay. $^{**}p < 0.01$ ($n = 3$, +Bafilomycin A1 vs −Bafilomycin A1, Student's t test).

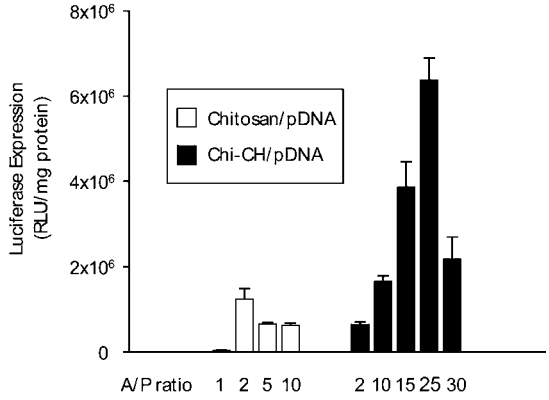


Figure 6. Gene expression of complexes. The gene transfection efficiency of different A/P ratios of chitosan/pDNA and Chi-CH/pDNA was screened by luciferase assay in HEK 293 cells. The RLU were calibrated by Bradford protein assay to obtain an accurate luciferase intensity per milligram protein ($n = 3$).

(*18*). Therefore, chitosan conjugated directly to histidine may increase the pK_a of histidine and then decrease the buffering capacity around the pH range of endosomes and lysosomes. Third, the disulfide bond formed between a cross-linker, 2-iminothiolane, conjugated to chitosan and cysteine linked to histidine can be formed at room temperature and in 10% DMSO. This process did not need any other organic solvent or further reagent treatment. No other side product which could disturb the biocompatibility was produced during the synthesis. This reaction could be performed under mild conditions without influencing the biocompatibility of chitosan (*25, 29*).

Materials with a high buffering capacity in endosomes and lysosomes, such as PEI, polylysine, and polyamidoamine, can trap hydrogen ions in endosomes and lysosomes; then, the H^+-ATPase pump on the membrane of endosomes and lysosomes would introduce more hydrogen ions inside and, finally, disrupt the endosomes and lysosomes because of the high osmotic pressure (*30*). Endosomal escape can be achieved by the high buffering capacity in the pH range of endosomes and lysosomes. In this study, Chi-CH (4.32%) exhibited the highest degree of substitution of the Chi-CH derivatives (Table 1) and have more buffering capacity than chitosan alone in solution (Figure 1). Therefore, Chi-CH (4.32%) was selected for the subsequent analysis and complex preparation. The buffering capacity of Chi-CH was also evaluated in cells by microscopic imaging. LysoSensor Green DND-189 emits a green color when the pH of the vesicles is lower than its pK_a (pK_a 5.2) corresponding to the lysosomal pH (Figure 4c). This result suggests that the TMR-labeled pDNA carried by Chi-CH was not surrounded by a low pH environment. This might be due to the buffering capacity of Chi-CH neutralizing the low pH in late endosomes or lysosomes and then improving the endosomal escape. In order to evaluate this endosomal escape, we examined the intracellular distribution of pDNA from chitosan/pDNA and Chi-CH/pDNA. Chi-CH/pDNA shows independent scattered red spots (TMR-labeled pDNA) without any overlapping green fluorescence (Alexa Fluor 488 transferrin conjugate in Figure 4a or LysoTracker Green DND-26 in Figure 4b), while chitosan/pDNA at an A/P ratio of 2/1 and 25/1 shows overlapping red and green fluorescence and aggregation of red fluorescence on the cell membrane, respectively. This result suggests that Chi-CH/pDNA escaped from endosomes or lysosomes more efficiently than chitosan/pDNA. The endosomal escape ability of Chi-CH/pDNA would be due to the buffering capacity provided by histidine. In addition, the gene expression of Chi-CH/pDNA with bafilomycin A_1 treatment was lower than that without bafilomycin A_1 treatment. This phenomenon could be explained by the higher buffering capacity of Chi-CH compared with chitosan. With these results taken into consideration, histidine modification could increase the endosomal escape of chitosan complexes efficiently by increasing the buffering capacity of chitosan.

The high cellular uptake was also an important factor for improving the gene transfection efficiency of Chi-CH/pDNA. Chitosan/pDNA shows negligible mean fluorescence intensity in cells even after a 12 h incubation (Figure 3). In combination with the result in Figure 4, which showed aggregation on the cell membrane, these results suggest that the low gene expression of chitosan/pDNA was mainly due to the slow pDNA release from the aggregates on the cell membrane. Moreover, the particle size of Chi-CH/pDNA was smaller than that of chitosan/pDNA at A/P ratios higher than 15 under neutral conditions (Table 2). The zeta potential of chitosan/pDNA also indicated a decreasing trend of chitosan/pDNA at a A/P ratio of 15 under neutral conditions (Table 2). These results suggest that chitosan/pDNA may encourage aggregation under neutral conditions. At pH 5.5, although the particle size of chitosan/pDNA did not increase at A/P ratios higher than 15, the zeta potential also shows the decreasing trend. Zeta potential is related to the electrophoretic mobility which was determined by ZetaNanoSizer. At A/P ratio higher than 15, the increasing viscosity of chitosan (*31*) and partial aggregation of chitosan/pDNA may affect the decrease of zeta potential. As far as cellular uptake is concerned, Chi-CH/pDNA shows nearly an 8-fold higher cellular uptake than chitosan/pDNA (Figure 3). The increase in the solubility after histidine conjugation, from nearly 0 mg/mL to 10 mg/mL under neutral conditions (data not shown), also provided a possible explanation for the higher cellular uptake. In several reports, the degree of aggregation of chitosan/pDNA has been shown to be reduced by increasing the water solubility of chitosan, such as modification by hydrophilic groups (*13*) and adjusting the molecular weight of chitosan (*6, 9, 32*). Therefore, the improvement in the cellular uptake of Chi-CH/pDNA might be partly attributed to the higher solubility of Chi-CH compared with chitosan.

In order to solve the problem of the slow endosomal escape rate during the process of drug or gene delivery, other reports have described how chitosan could also be modified with moieties which have a buffering capacity, including imidazole

(*33*) and *N*-α-acetyl-L-histidine (*34*). Our results are in agreement with these reports. The modification of imidazole proved that the increase in buffering capacity can increase the gene transfection efficiency of chitosan (*33*). The modification of *N*-α-acetyl-L-histidine on glycol chitosan also allowed the endosomal escape of paclitaxel (*34*). However, the acetylation on the N terminal end of histidine may increase the pK_a of the imidazole ring and then shift the buffering range of histidine to a higher pH. For example, the pK_a of histidine increases to 7−8 adjacent to an acidic amino acid (*18*), and the pK_a of *N*-α-acetyl-L-histidine is 7.2 (*35*). The shift of buffering range may reduce the buffering capacity of histidine in endosomes and lysosomes. In our design, the primary amino group (pK_a 9.2) and the imidazole ring (pK_a 6.0) could be prevented from basic shift of pK_a because we avoid chemical modification at the N terminal end of histidine.

CONCLUSION

We conjugated histidine to chitosan and increased the gene transfection efficiency of chitosan successfully by increasing the buffering capacity in the pH range of endosomes and lysosomes without affecting the integrity of the complexes. These results suggest that histidine helped the uptake of pDNA by cells and increased the efficiency of escape from endosomes and lysosomes.

ACKNOWLEDGMENT

This work was supported in part by Grants-in-Aid for Scientific Research from the Ministry of Education, Culture, Sports, Science, and by Research on Publicly Essential Drugs and Medical Devices in Japan Health Sciences Foundation.

LITERATURE CITED

(1) Shahidi, F., Arachchi, J. K. V., and Jeon, Y.-J. (1999) Food applications of chitin and chitosans. *Trends Food Sci. Technol. 10*, 37–51.

(2) Ueno, H., Mori, T., and Fujinaga, T. (2001) Topical formulations and wound healing applications of chitosan. *Adv. Drug Delivery Rev. 52*, 105–115.

(3) Richardson, S. C. W., Kolbe, H. V. J., and Duncan, R. (1999) Potential of low molecular mass chitosan as a DNA delivery system: biocompatibility, body distribution and ability to complex and protect DNA. *Int. J. Pharm. 178*, 231–243.

(4) MacLaughlin, F. C., Mumper, R. J., Wang, J., Tagliaferri, J. M., Gill, I., Hinchcliffe, M., and Rolland, A. P. (1998) Chitosan and depolymerized chitosan oligomers as condensing carriers for in vivo plasmid delivery. *J. Controlled Release 56*, 259–272.

(5) Sato, T., Ishii, T., and Okahata, Y. (2001) In vitro gene delivery mediated by chitosan.Effect of pH, serum, and molecular mass of chitosan on the transfection efficiency. *Biomaterials 22*, 2075–2080.

(6) Köping-Höggård, M., Tubulekas, I., Guan, H., Edwards, K., Nilsson, M., Vårum, K. M., and Artursson, P. (2001) Chitosan as a nonviral gene delivery system. Structure-property relationships and characteristics compared with polyethylenimine in vitro and after lung administration in vivo. *Gene Ther. 8*, 1108.

(7) Zaharoff, D. A., Rogers, C. J., Hance, K. W., Schlom, J., and Greiner, J. W. (2007) Chitosan solution enhances both humoral and cell-mediated immune responses to subcutaneous vaccination. *Vaccine 25*, 2085–2094.

(8) Aspden, T. J., Manson, D. T., Jones, N. S., Lowe, J., Skaugrud, W., and Illum, L. (1997) Chitosan as a nasal delivery system: The effect of chitosan solutions on *in vitro* and *in vivo* mucociliary transport rates in human turbinates and volunteers. *J. Pharm. Sci. 86*, 509–513.

(9) Ishii, T., Okahata, Y., and Sato, T. (2001) Mechanism of cell transfection with plasmid/chitosan complexes. *Biochim. Biophys. Acta, Biomembr. 1514*, 51–64.

(10) Corsi, K., Chellat, F., Yahia, L., and Fernandes, J. C. (2003) Mesenchymal stem cells, MG63 and HEK293 transfection using chitosan-DNA nanoparticles. *Biomaterials 24*, 1255–1264.

(11) Jiang, H.-L., Kim, Y.-K., Arote, R., Nah, J.-W., Cho, M.-H., Choi, Y.-J., Akaike, T., and Cho, C.-S. (2007) Chitosan-graft-polyethylenimine as a gene carrier. *J. Controlled Release 117*, 273–280.

(12) Chen, H. H., Ho, Y.-P., Jiang, X., Mao, H.-Q., Wang, T.-H., and Leong, K. W. (2008) Quantitative comparison of intracellular unpacking kinetics of polyplexes by a model constructed from quantum dot-FRET. *Mol. Ther. 16*, 324–332.

(13) Jiang, X., Dai, H., Leong, K. W., Goh, S.-H., Mao, H.-Q., and Yang, Y.-Y. (2006) Chitosan-*g*-PEG/DNA complexes deliver gene to the rat liver via intrabiliary and intraportal infusions. *J. Gene Med. 8*, 477–487.

(14) Mao, H.-Q., Roy, K., Troung-Le, V. L., Janes, K. A., Lin, K. Y., Wang, Y., August, J. T., and Leong, K. W. (2001) Chitosan-DNA nanoparticles as gene carriers: synthesis, characterization and transfection efficiency. *J. Controlled Release 70*, 399–421.

(15) Gonzalez-Noriega, A., Grubb, J. H., Talkad, V., and Sly, W. S. (1980) Chloroquine inhibits lysosomal enzyme pinocytosis and enhances lysosomal enzyme secretion by impairing receptor recycling. *J. Cell Biol. 85*, 839–852.

(16) Zuhorn, I. S., and Hoekstra, D. (2002) On the mechanism of cationic amphiphile-mediated transfection. To fuse or not to fuse: Is that the question? *J. Membr. Sci. 189*, 167–179.

(17) Elouahabi, A., and Ruysschaert, J.-M. (2005) Formation and Intracellular trafficking of lipoplexes and polyplexes. *Mol. Ther. 11*, 336–347.

(18) Abe, H. (2000) Role of histidine-related compounds as intracellular proton buffering constituents in vertebrate muscle. *Biochemistry (Mosc.) 65*, 757–765.

(19) Abe, H., Dobson, G. P., Hoeger, U., and Parkhouse, W. S. (1985) Role of histidine-related compounds to intracellular buffering in fish skeletal muscle. *Am. J. Physiol. 249*, R449–454.

(20) Midoux, P., and Monsigny, M. (1999) Efficient gene transfer by histidylated polylysine/pDNA complexes. *Bioconjugate Chem. 10*, 406–411.

(21) Shigeta, K., Kawakami, S., Higuchi, Y., Okuda, T., Yagi, H., Yamashita, F., and Hashida, M. (2007) Novel histidine-conjugated galactosylated cationic liposomes for efficient hepatocyte-selective gene transfer in human hepatoma HepG2 cells. *J. Controlled Release 118*, 262–270.

(22) Yang, S. R., Lee, H. J., and Kim, J.-D. (2006) Histidine-conjugated poly(amino acid) derivatives for the novel endosomolytic delivery carrier of doxorubicin. *J. Controlled Release 114*, 60–68.

(23) Leng, Q., and Mixson, A. J. (2005) Modified branched peptides with a histidine-rich tail enhance in vitro gene transfection. *Nucleic Acids Res. 33*, e40.

(24) Pichon, C., Gonçalves, C., and Midoux, P. (2001) Histidine-rich peptides and polymers for nucleic acids delivery. *Adv. Drug Delivery Rev. 53*, 75–94.

(25) Masuko, T., Iwasaki, N., Yamane, S., Funakoshi, T., Majima, T., Minami, A., Ohsuga, N., Ohta, T., and Nishimura, S.-I. (2005) Chitosan-RGDSGGC conjugate as a scaffold material for musculoskeletal tissue engineering. *Biomaterials 26*, 5339–5347.

(26) Sun, S.-W., Lin, Y.-C., Weng, Y.-M., and Chen, M.-J. (2007) Efficiency improvements on ninhydrin method for amino acid quantification. *J. Food Compost Anal. 19*, 112–117.

(27) Yoshimori, T., Yamamoto, A., Moriyama, Y., Futai, M., and Tashiro, Y. (1991) Bafilomycin A1, a specific inhibitor of vacuolar-type H(+)-ATPase, inhibits acidification and protein degradation in lysosomes of cultured cells. *J. Biol. Chem. 266*, 17707–17712.

(28) Antoine, K., Christian, L., Emmanuel, C., and Olivier, D. (2001) Polyethylenimine-mediated gene delivery: a mechanistic study. *J. Gene Med. 3*, 135–144.

(29) Bernkop-Schnürch, A., Hornof, M., and Zoidl, T. (2003) Thiolated polymers--thiomers: synthesis and in vitro evaluation of chitosan-2-iminothiolane conjugates. *Int. J. Pharm. 260*, 229–237.

(30) Sonawane, N. D., Szoka, F. C., and Verkman, A. S. (2003) Chloride accumulation and swelling in endosomes enhances DNA transfer by polyamine-DNA polyplexes. *J. Biol. Chem. 278*, 44826–44831.

(31) Shepherd, R., Reader, S., and Falshaw, a. (1997) Chitosan functional properties. *Glycoconj. J. 14*, 535–42.

(32) Lavertu, M., Mèthot, S., Tran-Khanh, N., and Buschmann, M. D. (2006) High efficiency gene transfer using chitosan/DNA nanoparticles with specific combinations of molecular weight and degree of deacetylation. *Biomaterials 27*, 4815–4824.

(33) Moreira, C., Oliveira, H., Pires, L. R., Simões, S., Barbosa, M. A., and Pêgo, A. P. (2009) Improving chitosan-mediated gene transfer by the introduction of intracellular buffering moieties into the chitosan backbone. *Acta Biomater. 5*, 2995–3006.

(34) Park, J. S., Han, T. H., Lee, K. Y., Han, S. S., Hwang, J. J., Moon, D. H., Kim, S. Y., and Cho, Y. W. (2006) N-acetyl histidine-conjugated glycol chitosan self-assembled nanoparticles for intracytoplasmic delivery of drugs: Endocytosis, exocytosis and drug release. *J. Controlled Release 115*, 37–45.

(35) Rauen, U., Klempt, S., and de Groot, H. (2007) Histidine-induced injury to cultured liver cells, effects of histidine derivatives and of iron chelators. *Cell. Mol. Life Sci. 64*, 192–205.

BC1000609

Development of [F-18]Fluorine-Substituted Tanaproget as a Progesterone Receptor Imaging Agent for Positron Emission Tomography

Jae Hak Lee,[‡] Hai-bing Zhou,[†,‡] Carmen S. Dence,[§] Kathryn E. Carlson,[‡] Michael J. Welch,[§] and John A. Katzenellenbogen*[,‡]

Department of Chemistry, University of Illinois at Urbana−Champaign, 600 South Matthews Avenue, Urbana, Illinois 61801, and Mallinckrodt Institute of Radiology, Washington University School of Medicine, 510 South Kingshighway, St. Louis, Missouri 63110. Received February 24, 2010; Revised Manuscript Received March 29, 2010

The level of progesterone receptors (PRs) in breast tumors can be used to guide the selection of endocrine therapies for breast cancer patients. To this end, we have prepared a fluorine-18 labeled analogue of Tanaproget, a nonsteroidal progestin with very high PR binding affinity and low affinity for androgen and glucocorticoid receptors, and have studied its tissue distribution in estrogen-primed rats to evaluate its potential for imaging PR levels by positron emission tomography. 4-[^{18}F]Fluoropropyl-Tanaproget ([^{18}F]**9**, **FPTP**) was prepared in three steps, within 140 min at an overall decay-corrected yield of 5% and effective specific activity of >550 Ci/mmol. In biodistribution studies, [^{18}F]**9** uptake was high in target tissues at both 1 and 3 h (uterus, 4.55 and 5.26%ID/g; ovary, 2.32 and 2.20%ID/g, respectively) and was cleanly blocked by coinjection of excess unlabeled compound. Uterus to blood and muscle activity ratios were 9.2 and 5.2 at 1 h and 32 and 26 at 3 h, respectively. The biodistribution of [^{18}F]**9** compares favorably to that of previously prepared F-18 labeled steroidal progestins, FENP and FFNP. Its high target tissue uptake efficiency and selectivity, and prolonged retention, suggest that it has excellent promise as a PET imaging agent for PR-positive breast tumors.

INTRODUCTION

Receptor-targeted radiopharmaceuticals are designed to image specific molecular targets and thereby obtain quantitative information about important metabolic, physiological, and pathological processes in living systems. Steroid receptors, members of the nuclear hormone receptor superfamily, are key regulators of gene expression and cellular function, and have emerged as very attractive targets for imaging (*1*). The activity of certain steroid receptors drives the growth of hormone-responsive cancers, both the estrogen receptor (ER) and the progesterone receptor (PR) in breast cancer, and the androgen receptor (AR) in prostate cancer. Consequently, these receptors are both biomarkers for diagnosis and targets for cancer endocrine therapies (*1*).

Currently, measurements of tumor ER, PR, or AR levels are done in vitro by immunohistochemical assays (*2*−*4*), but there is great interest in developing methods to determine receptor levels by in vivo imaging using positron emission tomography (PET), which could potentially measure receptor levels at all tumor sites, simultaneously and noninvasively (*1, 5*−*8*). This information could be used to select patients most likely to benefit from endocrine therapies, thereby sparing some the morbidity of radiation and chemotherapy. Clinical PET imaging of ER in breast cancer using 16α-[^{18}F]fluoroestradiol (FES) (*9*−*14*) and AR in prostate cancer using 16β-[^{18}F]fluoro-5α-dihydrotestosterone (FDHT) (*15*−*18*) is quite advanced, but thus far, only limited progress has been made with PET imaging of PR (*19*−*22*).

Because PR levels are regulated through ER, breast tumor PR levels have been used, together with ER levels, to predict patient response to ER-targeted therapies (either antiestrogens or aromatase inhibitors) (*2*). In fact, because PR levels are increased by estrogen treatment, measurement of an increase in PR levels in breast tumors by PET, after a brief exposure to estrogen, might be useful in assessing whether the ER is functional and thus capable of mediating endocrine therapies (*19, 23*). PR itself is also a target for endocrine therapy in breast cancer using antiprogestins (*24*).

Currently, most PR ligands are steroidal compounds having similar core structures (Figure 1) (*25, 26*). In the search for diagnostic PR tumor imaging agents, some of these have been labeled with radionuclides such as F-18, I-123, and Br-76 (*1, 21, 27*−*29*). Because fluorine-18 ($t_{1/2}$ = 110 min, β^+ emitting) has the most favorable nuclear and physical properties for PET imaging, we and others have investigated the in vivo behavior of two F-18 labeled steroidal progestins, 21-[^{18}F]fluoro-16α-ethyl-norprogesterone (**[^{18}F]FENP**, **2**) and 21-[^{18}F]fluoro-furanyl-norprogesterone (**[^{18}F]FFNP**, **5**). FENP, based on the well-known, potent Organon progestin, ORG2058 (**1**), has very high binding affinity and showed excellent target tissue uptake efficiency and selectivity in estrogen-primed rats, but surprisingly failed to image PR in humans (*20*). This species difference was traced to 20-hydroxysteroid dehydrogenase (20-HSD) activity, present in the blood of humans but not rodents, that rapidly converts **FENP** into the inactive 20-hydroxy analogue (*27*). **FFNP** (*19*), on the other hand, appears resistant to this dehydrogenase and is currently being evaluated as a PET PR imaging agent in humans.

Despite the continuing promise of **FFNP**, there are potential liabilities in using 20-keto steroids as PR PET imaging agents, because steroidal progestins often show cross reactivity with other steroid receptors, notably the glucocorticoid receptor (GR)

* To whom correspondence should be addressed: Prof. John A. Katzenellenbogen, Department of Chemistry, University of Illinois at Urbana−Champaign, 600 South Mathews Avenue, Urbana, IL, 61801. Telephone: +1-217-333-6310, Fax: +1-217-333-7325, E-mail: jkatzene@uiuc.edu.

† Current address: College of Pharmacy, Wuhan University, Wuhan, 430072 China.

‡ University of Illinois at Urbana−Champaign.

§ Washington University School of Medicine.

10.1021/bc1001054 © 2010 American Chemical Society
Published on Web 05/24/2010

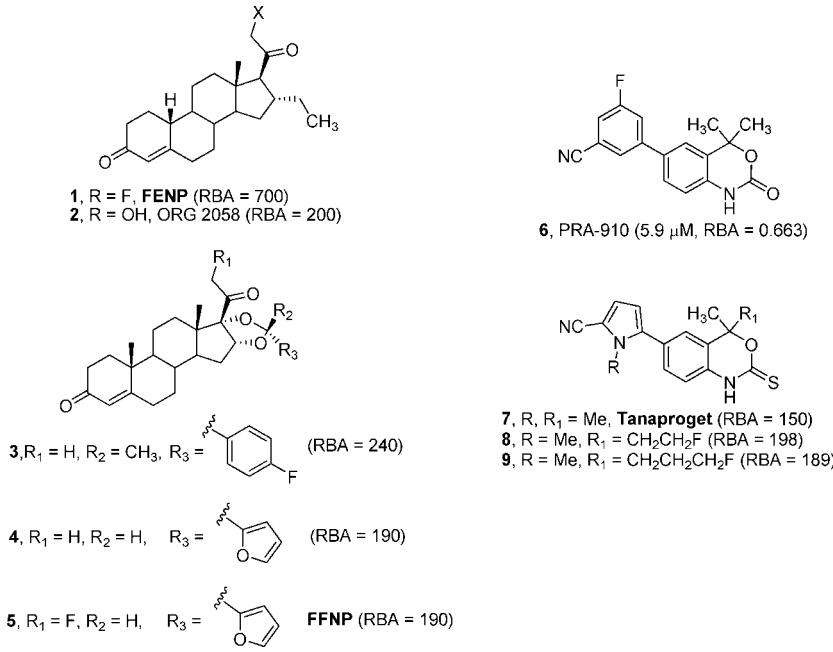


Figure 1. Structure and PR binding affinity of some steroidal (**1**−**5**) and nonsteroidal (**6**−**9**) progestins in the series leading to the F-18 labeled analogues, **FENP** (**2**), **FFNP** (**5**), and **FPTP** (**9**).

and AR (*30*), and the inactivating metabolism by the 20-HSD is still possible (*27*). Additionally, steroids generally have high lipophilicity, which could increase nonspecific binding.

A number of pharmaceutical companies have reported nonsteroidal progestins with high PR binding affinity and excellent selectivity (*26, 31*−*33*). We were particularly attracted to Tanaproget (**7**), a nonsteroidal progestin developed by Wyeth, that is based on a dihydrobenzoxazinethione core structure. Its PR binding affinity is very high, nearly twice that of the potent steroidal progestin R5020, giving it an estimated K_D of ∼0.2 nM (*34, 35*); its affinity for GR and AR is also very low. Thus, if the F-18 radionuclide could be introduced into Tanaproget or a high-affinity analogue, it might be an effective PET imaging agent for PR-positive tumors.

We recently reported the syntheses and binding affinity of several Tanaproget derivatives containing fluoroethyl or fluoropropyl substituents as potential PET PR imaging agents, including ones having affinities higher than Tanaproget itself (*36*). In this report, we describe synthesis of [^{18}F]fluoropropyl-Tanaproget (**FPTP**, **9**), and we evaluate its tissue distribution in estrogen-primed immature female rats. Its target tissue uptake efficiency, selectivity, and specificity are excellent, and compare favorably with those of **FENP** and **FFNP**. Therefore, it appears to be an excellent prospect for further evaluation as an agent for PET imaging of PR in breast tumors.

RESULTS

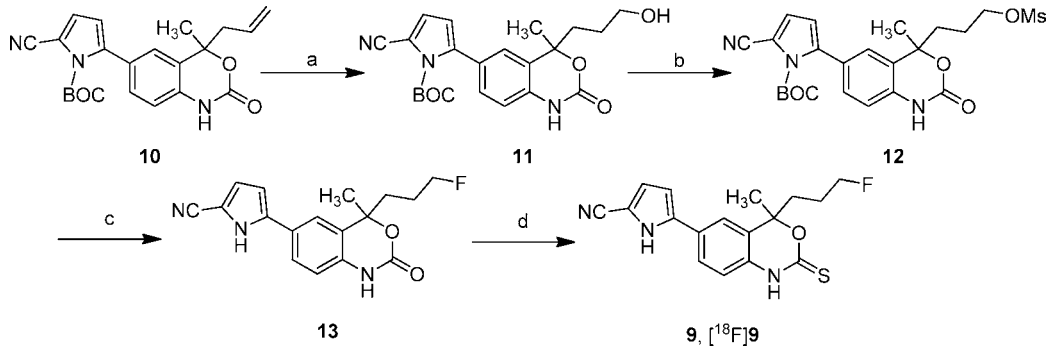
Chemistry. *Synthesis of Fluoropropyl Tanaproget Derivatives.* Guided by the structure−affinity relationships in the Tanaproget series, available in the literature, we synthesized a number of Tanaproget analogues containing 2-fluoroethyl and 3-fluoropropyl groups. These are described in our recent publication (*36*). Substitution on the pyrrole nitrogen gave lower-affinity analogues, but replacement of one of the methyl groups on the dihydrobenzoxazinethione core with a 2-fluoroethyl or a 3-fluoropropyl group gave very high affinity Tanaproget analogues (Figure 1). We chose one of these, 3-fluoropropyl-Tanaproget (**FPTP**, **9**), to evaluate further. In competitive radiometric PR binding assays, where the standard progestin, R5020, is given a relative binding affinity (RBA) value of 100, Tanaproget has an RBA value of 150 and **FTPT** of 189 (*36*).

Our original route to unlabeled **FTPT** was not well suited for F-18 labeling, because fluoride ion was introduced early in the sequence, and three subsequent steps were required to produce the final product. In our first approach to develop an alternative synthesis more amenable to F-18 labeling, we tried to prepare a precursor in which F-18 could be introduced in the last step by fluoride ion displacement of a methanesulfonate analogue of **FTPT** itself (or a BOC-protected version). However, the alcohol in the hydroxypropyl group was not stable under the harsh conditions required to convert the carbamate to the thiocarbamate with Lawesson's reagent. It was also very unlikely that the electrophilic methanesulfonate group would have been compatible with the nucleophilic thiocarbamate function under the conditions required for fluoride ion substitution. We therefore turned to the use of the methanesulfonate of the corresponding carbamate (**12**), thinking that the oxygen would be less nucleophilic than the sulfur. As shown in Scheme 1, synthesis of this precursor began with allylcarbmate **10**, which was hydroborated and oxidized to give corresponding hydroxyl compound **11** in good yield (74%). Subsequent treatment with methansulfonyl chloride and triethylamine furnished the desired labeling precursor **12** in good yield (79%).

In model reactions for F-18 labeling, and to prepare authentic samples of the unlabeled compounds, mesylate **12** was treated with tetrabutylammonium fluoride (TBAF) in *tert*-butyl alcohol at 90 °C for 2 h, followed after solvent removal by heating at 160 °C neat for 20 min to remove the BOC protecting group on the pyrrole. This one-pot/two-step sequence provided the fluorinated carbamate **13** in a high yield (81%). As has been observed in other systems (*37*−*41*), use of this protic solvent protocol for the fluoride substitution step was effective in reducing the formation of side products through elimination or hydrolysis, and gave high yields of the fluorinated product. **FPTP** (**9**) itself was then obtained in good yield (70%) by treatment with Lawesson's reagent, which converted the carbamate to the thiocarbamate. However, the reaction required heating in toluene at 100 °C for 2 h, conditions that were subsequently modified to be more suitable for labeling with the short-lived F-18 radionuclide ($t_{1/2}$ = 110 min) (see below).

Synthesis of [^{18}F]Fluoropropyl-Tanaproget. 4-[^{18}F]Fluoropropyl-Tanaproget **9** (**FPTP**) was prepared by the same

Scheme 1[a]



[a] Reagents and conditions: (a) (i) BH_3·THF, THF, −10 °C, N_2, 90 min; (ii) 4 N NaOH, 10 min; (iii) H_2O_2, 2 h, 74%; (b) MsCl, CH_2Cl_2, 0 °C, 2 h, 79%; (c) (i) *n*-Bu_4NF, *tert*-BuOH, 90 °C, 2 h; (ii) neat, 160 °C, 20 min, 81%; (d) Lawesson's reagent, toluene, 100 °C, 2 h, 70%. Radiolabeling conditions: (c) (i) *n*-$Bu_4N[^{18}F]F$, *tert*-amyl alcohol. 130 °C, 20 min, (ii) 160 °C, 10 min; (d) Lawesson's reagent, toluene, 130 °C, 30 min.

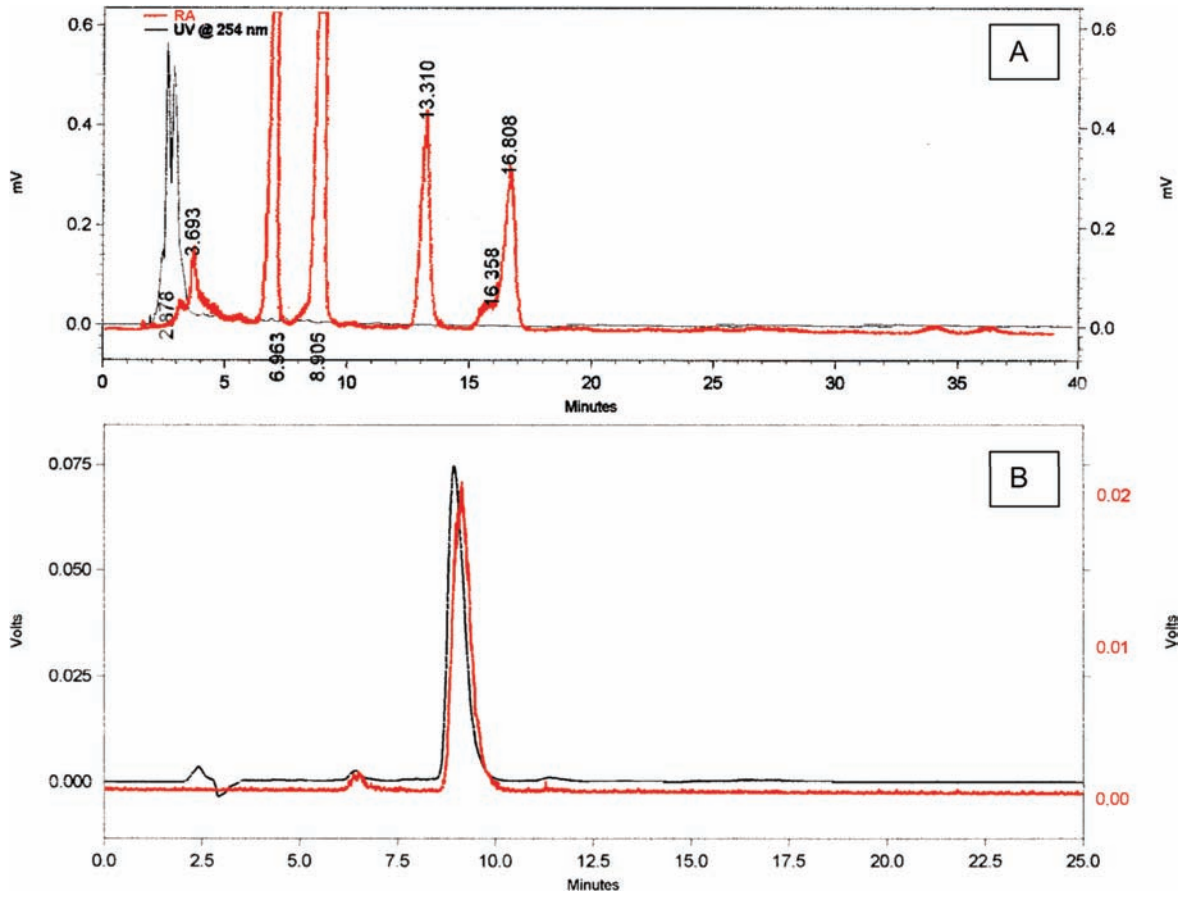


Figure 2. HPLC Profile of reaction mixture from the production of [^{18}F]**9** (Panel A), and purified [^{18}F]**9** coinjected with unlabeled **9** (Panel B). HPLC conditions (Panel A): Altima, C18, 10 μm, 250 × 10 mm, MeOH/water = 65:35, 3.5 mL/min, R_t = 16.8 min; (Panel B): co-injection with standard **9** and [^{18}F]**9**: Econosil, C18, 10 μm, 250 × 4.6 mm, CH_3CN/water = 50:50, 0.8 mL/min, 254 nm.

sequence from methanesulfonate precursor **12**. Treatment with *n*-$Bu_4N[^{18}F]F$ in *tert*-amyl alcohol at 130 °C for 20 min gave the F-18 labeled intermediate, which on further heating in the same vessel after solvent removal (160 °C for 10 min) underwent deprotection to give the penultimate precursor, **13**. Conversion of the carbamate group to the thiocarbamate was achieved by heating with Lawesson's reagent in toluene at 130 °C for 30 min. The final step, producing [^{18}F]**9**, proceeded in 5% yield (decay corrected), after purification by reversed-phase HPLC (see Figure 2).

To accelerate the last step and increase conversion yield, we used 3.0 equiv of Lawesson's reagent, rather than 0.6 equiv, which was sufficient in preparative scale reactions. We also increased the reaction temperature to 130 °C and reduced the reaction volume to 300 μL. Under our original conditions for synthesizing the unlabeled compound (1.2 equiv and 100 °C for 2 h), the carbamate to thiocarbamate conversion proceeded in an overall yield of less than 10%, whereas the modified conditions gave a 40% yield.

With these modifications, the overall radiochemical yield of desired F-18 labeled compound [^{18}F]**8** was 5% (decay-corrected), within a total synthesis time of 140 min from end of bombardment (EOB). The radiochemical purity of [^{18}F]**9** was determined to be >95% by reversed-phase HPLC. The effective specific activity of [^{18}F]**9** was >550 Ci/mmol, determined by a competitive receptor binding assay (*42*).

*Tissue Distribution Studies with [^{18}F]**9** (FPTP).* Purified F-18 fluoropropyl-Tanaproget ([^{18}F]**9**) was reconstituted in 10%

Table 1. Tissue Biodistribution of 3-[18F]Fluoropropyl-Tanaparoget Derivative [18F]9 in Immature Estrogen-Primed Female Rats

	percentage injected dose/gram ± SD[a] ($n = 5$)			
	1 h	1 h blocked	3 h	3 h blocked
blood	0.49 ± 0.08	0.48 ± 0.05	0.16 ± 0.02	0.17 ± 0.02
liver	3.52 ± 0.35	3.37 ± 0.41	1.40 ± 0.18	1.47 ± 0.15
spleen	0.88 ± 0.08	0.85 ± 0.15	0.28 ± 0.05	0.27 ± 0.04
kidney	2.56 ± 0.30	2.46 ± 0.41	0.76 ± 0.08	0.76 ± 0.07
muscle	0.87 ± 0.09	0.89 ± 0.09	0.20 ± 0.03	0.20 ± 0.03
bone	0.93 ± 0.11	0.90 ± 0.18	0.60 ± 0.04	0.56 ± 0.09
uterus	4.55 ± 1.08	0.98 ± 0.11	5.26 ± 0.50	0.37 ± 0.07
ovaries	2.32 ± 0.23	1.27 ± 0.11	2.20 ± 0.42	0.37 ± 0.06
uterus/blood	9.19 ± 1.52	2.06 ± 0.36	32.22 ± 1.57	2.20 ± 0.37
uterus/muscle	5.16 ± 0.77	1.12 ± 0.16	26.54 ± 2.84	1.87 ± 0.13
ovaries/blood	4.84 ± 0.37	2.67 ± 0.48	13.39 ± 1.65	2.20 ± 0.41
ovaries/muscle	3.95 ± 1.26	1.45 ± 0.24	11.04 ± 1.90	1.90 ± 0.21

[a] SD is standard deviation.

EtOH/saline. This solution was injected (i.v., veil tail) into immature female rats that had been estrogen pretreated to induce the levels of PR in the uterus (*19, 21*). Doses employed were 26 μCi/rat. The tissue distribution was determined at 1 and 3 h postinjection, and tissue activity, as percent injected dose/gram, and target tissue to blood and muscle ratios are given in Table 1. To confirm that the uptake was mediated by a high-affinity, limited-capacity system, one set of rats in each time study was coinjected with the [18F]**9** and 33.3 μg/rat of unlabeled **9**, to saturate the PR (Table 1, 1 and 3 h "blocked").

Labeled **FPTP** ([18F]**9**) showed target tissue uptake that was efficient, selective, and persistent. At 1 h, the %ID/g was 4.55% in the uterus and 2.32% in the ovary; this level of target tissue uptake persisted at 3 h without diminution. While initial uptake in certain nontarget tissues was high (liver, 3.52% ID/g; kidney, 2.56% ID/g), these levels cleared considerably at the later time. Consequently, the ratio of activity in uterus to blood and muscle increased markedly with time, so that at 3 h, the ratios were 32 for uterus/blood and 26 for uterus/muscle; these ratios for the ovary were 13 and 11, respectively.

The selectivity of target tissue uptake was evident from the marked displacement that occurred in uterus and ovary when the unlabeled compound (**9**) was coinjected. At 3 h, uterine activity was blocked by 93% and ovary activity by 86%; no block was observed in nontarget tissues. The uptake in the bone, which, if high and persistent, can be an indicator of in vivo defluorination, was relatively low, 0.93% ID/g at 1 h, and declined at 3 h (0.6% ID/g).

DISCUSSION

In a quest for effective agents for imaging progesterone receptor (PR) in breast tumors by PET, we have synthesized a fluoropropyl analogue of the high affinity, nonsteroidal progestin, Tanaproget (**7**), that we term fluoropropyl-Tanaproget (**FPTP**, **9**) (*36*). We developed a method to label this compound with F-18 at high specific activity ([18F]**FPTP**, **9**), and in an estrogen-primed immature rat animal model, we demonstrated that **[18F]FPTP** (**9**) shows target tissue uptake that is efficient, selective, and persistent. The synthesis of [18F]**9** required two steps after F-18 incorporation, the most challenging of which involved conversion of a carbamate to a thiocarbamate function. The overall process of F-18 labeling and subsequent transformations and purifications took 140 min and gave the final material in 5% radiochemical yield (RCY) with an effective specific activity of >500 Ci/mmol.

It is instructive to compare the biodistribution of [18F]**FPTP** (**9**) with that of two other F-18 labeled progestins that we have studied, 21-[18F]fluoro-16α-ethyl-norprogesterone (**FENP**, **2**) and 21-[18F]fluoro-furanyl-norprogesterone (**FFNP**, **5**) (Figure 3). The ovarian and uterine uptake of [18F]**FPTP** (**9**) at 1 h postinjection was comparable with that of the other progestins, [18F]**FENP** and [18F]**FFNP**; kidney and, in one case, liver uptake of [18F]**FPTP**, however, was somewhat higher. All three compounds showed very good retention in target tissues, so that at 3 h postinjection, activity in the ovaries and uterus is essentially the same as at 1 h, but activity in nontarget tissues (liver, kidney, muscle, and blood) has decreased. Of the three compounds, bone uptake is the least with [18F]**FPTP**, indicating that metabolic defluorination of this compound is minimal. Bone uptake with [18F]**FFNP** is considerable, but some F-18 labeled compounds that show high bone uptake in rats show little bone uptake in primates and humans (*43*).

In previous work, we sometimes compared the biophysical properties of potential PET receptor imaging agents not just in terms of their binding affinities (expressed as relative binding affinity or RBA values), but also in terms of their nonspecific binding (NSB), which we estimated from their lipophilicity, as expressed by their calculated or measured octanol−water partition coefficients (log $P_{o/w}$) (*1, 22*). We also calculated the ratio of these two values, RBA/NSB, which we termed the binding selectivity index (BSI) of the compound. Often, the BSI of a compound proved to be a more accurate predictor of the target tissue uptake characteristics of the compound than its RBA value (*1, 22*). This was true with both estrogens (*44, 45*) and progestins (*19*). Table 2 (left) summarizes these PR biophysical characteristics of the three F-18 labeled progestins and the standard progestin R5020 and (right) gives their GR and AR binding affinities.

The PR binding affinities of all three progestins are greater than that of the standard progestin, R5020, with **FENP** being the highest. The BSI values for all three progestins, however, are very similar, because both **FFNP** and **FPTP** have lower NSB values than **FENP** and R5020. Thus, in terms of these biophysical properties, all three F-18 labeled progestins appear quite comparable.

Although **FPTP** does not have biodistribution characteristics in estrogen-primed immature rat model that are significantly better than those of **FENP** and **FFNP**, it has other very favorable attributes that make it a compound that should be strongly considered for further development: First, **FPTP** is a nonsteroidal progestin and thus would not be a substrate for the 20-hydroxysteroid dehydrogenase found in human blood (*27*); this dehydrogenase led to the failure of **FENP** in humans (*27*), despite the excellent biodistribution of this compound in the rat model (*19* cf., Figure 3). **FFNP** shares a 20-keto group with **FENP**, but although the bulky acetal function fused to the D-ring in **FFNP** is thought to retard or block this inactivating metabolism, this is not certain. Second, **FPTP**, again being a nonsteroidal compound, has very low affinity for other receptors in the same receptor subfamily, namely, AR and GR; **FFNP**, by contrast, binds to GR avidly (Table 2, right). Whether this proves to be an important matter in breast tumor imaging needs to await further studies. Finally, **FPTP** is a chiral compound and thus far has been prepared and studied only as a racemate. Because it is likely that one **FPTP** enantiomer will have higher binding affinity than the other, the high-affinity isomer might have yet more favorable biodistribution properties. We are currently developing methods to separate and/or prepare selectively the **FPTP** enantiomers, and if they have different affinities, we will prepare them in F-18 labeled form for further study.

CONCLUSION

We have prepared a fluoropropyl-Tanaproget derivative, **FPTP** ([18F]**9**), as a potential agent for PET imaging of PR in breast cancer. This nonsteroidal compound has very high PR binding affinity and low affinity for AR and GR and would be

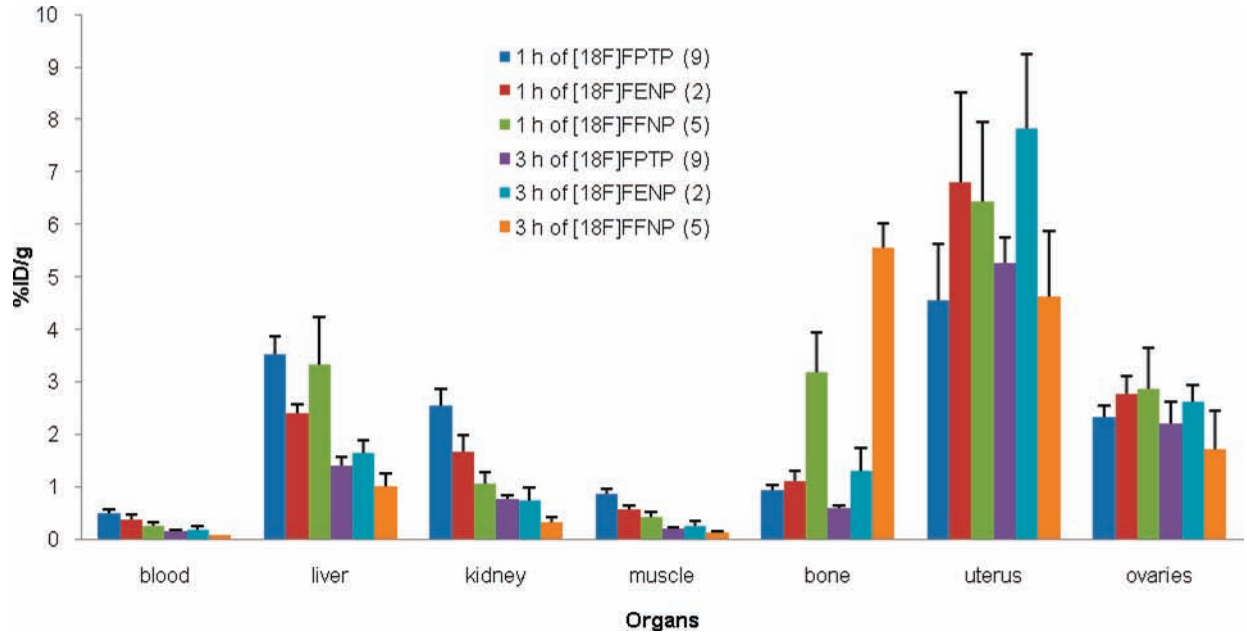


Figure 3. Comparison of tissue biodistribution data of [^{18}F]**FPTP** (**9**), [^{18}F]**FENP** (**2**), and [^{18}F]**FFNP** (**5**) in immature estrogen-primed female rats.

Table 2. Comparison of Receptor Binding Affinities and Biophysical Properties of Three F-18 Labeled Progestins

compd	PR-RBA[a]	cLogP[b]	PR-NSB[c]	PR-BSI[d]	GR-RBA[f]	AR-RBA[g]
FPTP (**9**)	189	3.03	0.400	472	0.9	0.04
FENP (**2**)	700	3.98	1.06	660[e]	1.3	0.11
FFNP (**5**)	190	2.94	0.364	521[e]	365	0.53
R5020	[100]	3.92	[1]	[100]	2.6	0.26

[a] RBA is relative binding affinity value, relative to the standard, R5020 (K_D [R5020] is 0.4 nM). [b] Calculated log $P_{o/w}$ from *ChemDraw*. [c] For calculation of NSB, see ref *46*. [d] BSI = RBA/NSB. [e] These BSI values differ somewhat from those reported earlier (*19*), which were based on experimentally measured log $P_{o/w}$ values. [f] GR-RBA values are relative to the standard, dexamethasone (K_D [dexamethasone] is 20 nM). [g] AR-RBA values are relative to the standard, R1881 (K_D [R1881] is 0.6 nM).

resistant to 20-hydroxysteroid dehydrogenase inactivation. It also shows very favorable target tissue distribution in an estrogen-primed immature rat model. Further studies are planned on this compound and its constituent enantiomers in other animal models.

EXPERIMENTAL SECTION

All chemical was commercially purchased from Sigma-Aldrich Chemical Co. and TCI and used without further purification. Anhydrous THF solvent was obtained from an anhydrous solvent dispensing system (*47*). Flash column chromatography was performed with silica gel (Merck, 230−400 mesh ASTM). Analytical thin layer chromatography (TLC) was performed with Merck silica gel F-254 glass-backed plates. Visualization on TLC was monitored by UV light. ^{1}H and ^{13}C NMR spectra were obtained on Varian Unity 400 (400 MHz) and 500 (500 MHz) and are reported in parts per million downfield from internal tetramethylsilane. Mass spectra were obtained on 70 eV using the micromass 70-VSE mass spectrometer, and ESI mass spectra were achieved using the Quattro mass spectrometer. Melting points obtained using a Thomas-Hoover Uni-Melt capillary melting point apparatus and are uncorrected. High-performance liquid chromatography (HPLC) was carried out on a Thermo Co. system with a semipreparative column. $H_2{}^{18}O$ was purchased from Rotem Industries. The screwcap test tubes used for fluoride incorporation were purchased from Fisher Scientific (Pyrex no. 9825). Oasis HLB-6 cm^3 cartridges (500 mg) as ion exchange cartridge were purchased from Waters Corp. (part no. 186000115). [^{18}F]Fluoride ion was produced at Washington University by ^{18}O(p,n)^{18}F reaction through irradiation of 95% enriched [^{18}O]water, using either the JSW BC16/8 cyclotron (The Japan Steel Works Ltd.) or the CS15 cyclotron (The Cyclotron Corp.). Radiochemical purification of [^{18}F]**9** utilized a reversed-phase semipreparative HPLC column (Alltima C18, 250 × 10 mm, 10 μm, 254 nm, MeOH/water = 65:35, 3.5 mL/min). For quality control, the radiochemical purity of [^{18}F]**9** was determined by analytical HPLC (Econosil C18, 250 × 4.6 mm, 10 μm, 254 nm, CH_3CN/water = 50:50, 0.8 mL/min). TLC plates were analyzed using a Bioscan, Inc., System 200 imaging scanner. Radioactivity was determined with a dose calibrator. Radiochemical yields are decay-corrected to the beginning of synthesis time. *N-tert*-Butoxycarbonylpyrrole-2-boronic acid is commercially available (CAS no 135884−31−0).

Synthesis of 5-(4-(3-Hydroxy)-4-methyl-2-oxo-2,4-dihydro-1*H*-benzo[*d*][1,3]oxazin-6-yl)-*N*-*tert*-buthoxycarbonyl-pyrrole-2-carbonitrile (11). To a solution of 2-(4-allyl-4-methyl-2-oxo-1,4-dihydro-2*H*-benzo[*d*][1,3]oxazin-6-yl)-5-cyano-pyrrole-1-carboxylic acid *tert*-butyl ester (**10**) (*36*) (200 mg, 681.849 μmol) in dried THF (10 mL) was added BH_3·THF (1.0 M, 3.41 mL, 3.409 mmol) at −10 °C and stirred for 90 min. The reaction mixture was added aq. NaOH (4.0 M, 852 μL, 3.409 mmol) and stirred for 10 min, followed by addition of H_2O_2 (30%, 386 μL, 3.409 mmol) and further stirring for 2 h. The reaction mixture was added to water (200 mL) and extracted with EtOAc (20 mL × 3). The combined organic layer was dried over Na_2SO_4 and concentrated under reduced pressure. The residue was purified by flash column chromatography on silica gel to give 3-hydroxypropyl benzo[*d*]oxazines **11** (170 mg, 81%) as a bright yellow oil. ^{1}H NMR (500 MHz, $CDCl_3$) δ 9.61 (s, 1H), 7.20 (dd, J = 8.5 Hz, 2.0 Hz, 1H), 7.07 (d, J = 1.5 Hz, 1H), 6.96 (d, J = 3.5 Hz, 1H), 6.93 (d, J = 8.5 Hz, 1H), 6.23 (d, J = 3.5 Hz, 1H), 3.62 (td, J = 6.2 Hz, 1.2 Hz, 2H), 2,23 (br s, 1H), 2.17−2.01 (m, 2H), 1.71 (s, 3H), 1.69−1.62 (m, 2H), 1.52 (s, 9H); ^{13}C NMR (125 MHz, $CDCl_3$) δ 152.7, 147.1, 139.6, 134.4, 129.5, 127.3, 124.6, 124.4, 124.2, 114.3, 113.9, 113.3, 105.4, 87.2, 85.5, 62.1, 37.2, 27.5, 27.1, 26.7; MS (FAB): *m/z*

412.2 $(M+H)^+$, 356.1, 311.1, 289.1, 269.1, 154.2 (100), 136.1, 106.7. HRMS (FAB) calcd for $C_{22}H_{26}N_3O_5$ 412.1872, found 412.1873.

Synthesis of 5-(4-(3-Methylsulfonyloxy)-4-methyl-2-oxo-2,4-dihydro-1*H*-benzo[*d*][1,3]oxazin-6-yl)-*N*-*tert*-buthoxycarbonyl-pyrrole-2-carbonitrile (12). To a solution of 3-hydroxypropyl benzo[*d*]oxazines **11** (170 mg, 413.173 μmol) in CH_2Cl_2 (50 mL) was added triethylamine (173 μL, 1.240 mmol), and the mixture was cooled to 0 °C. Methanesulfonyl chloride (48 μL, 619.759 μmol) was added, and stirring continued for 2 h. The mixture was added to water (100 mL). The organic layer was separated, and aqueous layer was extracted with CH_2Cl_2 (20 mL × 2). The combined organic layer was dried over Na_2SO_4 and concentrated by rotary evaporation. The residue was purified by flash column chromatography on silica gel (70% EtOAc/hexane) to obtain mesylated benzo[*d*]oxazines **12** (136 mg, 67%) as a bright yellow oil. ^{1}H NMR (500 MHz, $CDCl_3$) δ 9.54 (s, 1H), 7.23 (dd, J = 8.5 Hz, 2.0 Hz, 1H), 7.06 (d, J = 1.5 Hz, 1H), 6.97 (d, J = 3.5 Hz, 1H), 6.92 (d, J = 8.0 Hz, 1H), 6.25 (d, J = 4.0 Hz, 1H), 4.23 (t, J = 6.0 Hz, 2H), 2.98 (s, 3H), 2.21−2.06 (m, 2H), 1.94−1.83 (m, 2H), 1.71 (s, 3H), 1.51 (s, 9H); ^{13}C NMR (125 MHz, $CDCl_3$) δ 152.4, 147.1, 139.4, 134.3, 129.8, 127.6, 124.45, 124.43, 123.6, 114.4, 114.0, 113.3, 105.5, 87.2, 84.9, 69.4, 37.3, 36.6, 27.5, 27.3, 23.7; MS (FAB): *m*/*z* 490.1 $(M+H)^+$, 460.1, 389.1, 307.1, 289.1, 273.1, 154.2 (100), 136.1, 119.9, 106.7. HRMS (FAB) calcd for $C_{23}H_{28}N_3O_7S$ 490.1648, found 490.1648.

Synthesis of 5-(4-(3-Fluoropropyl)-4-methyl-2-oxo-2,4-dihydro-1*H*-benzo[*d*][1,3]oxazin-6-yl)-1*H*-pyrrole-2-carbonitrile (13). To a solution of mesylated benzo[*d*]oxazines **12** (680 mg, 1.390 mmol) in *tert*-BuOH (100 mL) was added n-$Bu_4NF\cdot 3H_2O$ (658 mg, 2.085 mmol) at room temperature. The reaction mixture was stirred at 90 °C for 2 h. The reaction mixture was heated to 160 °C for 20 min under N_2 gentle stream. The vial was cooled to room temperature, dissolved with EtOAc (50 mL), and absorbed onto a small amount of silica gel. Purification by flash column chromatography on silica gel (60% EtOAc/hexane) gave compound **13** (350 mg, 81%) as a bright yellow oil. ^{1}H NMR (500 MHz, $CDCl_3$) δ 10.42 (s, H), 9.14 (s, 1H), 7.44 (dd, J = 8.2 Hz, 1.8 Hz, 1H), 7.35 (d, J = 2.0 Hz, 1H), 6.92−6.90 (m, 2H), 6.46 (dd, J = 4.0 Hz, 2.5 Hz, 1H), 4.47 (dt, J = 47.0 Hz, 5.8 Hz, 2H), 2.89−2.11 (m, 2H). 1.87−1.77 (m, 2H), 1.74 (s, 3H); ^{13}C NMR (125 MHz, $CDCl_3$) δ 152.5, 136.9, 133.8, 126.7, 125.9, 125.0, 121.5, 120.4, 115.43, 115.36, 107.0, 100.9, 85.5, 83.8 (d, J = 164.0 Hz, 1C), 36.5 (d, J = 3.75 Hz, 1C), 27.5, 24.9 (d, J = 20.1 Hz, 1C); MS (FAB): *m*/*z* 314.1 $(M+H)^+$, 307.1, 289.1, 273.1, 258.1, 235.2, 219.3, 195.2, 165.2, 154.1 (100), 136.1, 119.9, 106.7. HRMS (FAB) calcd for $C_{17}H_{17}FN_3O_2$ 314.1305, found 314.1305.

Synthesis of 5-(4-(3-Fluoropropyl)-4-methyl-2-thioxo-2,4-dihydro-1*H*-benzo[*d*][1,3]oxazin-6-yl)-1*H*-pyrrole-2-carbonitrile (9). The mixture of compound **13** (20.0 mg, 63.830 μmol) and Lawesson's reagent (28.4 mg, 70.214 μmol) in toluene was heated at 100 °C for 2 h. The reaction mixture was added to water (10 mL) and extracted with EtOAc (5 mL × 3). The combined organic layer was dried over Na_2SO_4 and concentrated in vacuo. The residue was purified by flash column chromatography on silica gel (30% EtOAc/hexane) to give 3-fluoropropyl benzo[*d*]thiazines **9** (14.7 mg, 70%) as a yellow oil. ^{1}H NMR (500 MHz, $CDCl_3$) δ 9.23 (s, 1H), 9.12 (s, 1H), 7.46 (dd, J = 8.5 Hz, 1.5 Hz, 1H), 7.29 (s, 1H), 6.93 (t, J = 3.0 Hz, 1H), 6.89 (d, J = 8.5 Hz, 1H), 6.51 (t, J = 3.0 Hz, 1H), 3.62−3.54 (m, 2H), 2.36−2.30 (m, 1H), 2.22−2.16 (m, 1H), 2.03−1.96 (m, 1H), 1.92−1.84 (m, 1H), 1.78 (s, 3H); ^{13}C NMR (125 MHz, $CDCl_3$) δ 25.1 (d, J = 20.3 Hz, 1C), 26.0, 36.3 (d, J = 4.0 Hz, 1C), 83.6 (d, J = 162.3 Hz, 1C), 85.8, 107.5, 114.7, 115.1, 120.8, 121.0, 126.0, 126.2, 127.9, 132.2, 135.2, 136.9, 160.6. MS *m*/*z* 329 ($[M]^+$, 15%), HRMS (EI) calcd for $C_{17}H_{16}ON_3SF$ 329.0998, found 329.0998.

General Radiochemical Synthesis of 5-(4-(3-[^{18}F]fluoropropyl)-4-methyl-2-thioxo-2,4-dihydro-1*H*-benzo[*d*][1,3]oxazin-6-yl)-1*H*-pyrrole-2-carbonitrile ([^{18}F]9). The fluorine-18 radionuclide was produced by the ^{18}O(p,n)^{18}F reaction on an enriched water target. Oxygen-18 water containing the [^{18}F]fluoride anion was transferred to a reaction vessel containing tetrabutylammonium bicarbonate ($TBAHCO_3$) (40% in water, 2 μL), and CH_3CN was added. The water in the reaction vessel was removed by azeotropic distillation with CH_3CN under an N_2 stream at 110 °C. The reaction vessel was cooled to room temperature, and the remaining solvent was removed under a gentle N_2 stream at room temperature. The 3-mesylated Tanaproget substrate **12** was added to reaction vessel followed by adding *tert*-amyl alcohol (500 μL). The capped reaction vessel was heated at 130 °C for 20 min and then cooled to room temperature. After radio-TLC analysis to confirm incorporation of the radionuclide, the reaction solvent was removed completely under a stream of N_2 at 110 °C, and the residue in the vessel was heated to 160 °C for 10 min. The reaction mixture was allowed to reach room temperature and dissolved with EtOAc; water (2 mL) and brine (500 μL) were added. The resulting solution was extracted with EtOAc (1 mL × 2). The combined organic layer was evaporated completely under a gentle N_2 stream at 110 °C. The residue was treated with Lawesson's reagent followed by addition of toluene and then heated to 130 °C for 30 min. The solvent removed under N_2 stream at 110 °C. After being cooled to room temperature, the residue was dissolved with CH_3CN followed by passage through an activated silica Sep-Pak. The resulting solution was added to an equal volume of deionized water and purified by reversed-phase semipreparative HPLC (MeOH/water = 65:35, 3.5 mL/min) to give the desired product [^{18}F]**9**, which eluted at 19−21 min (5% decay-corrected radiochemical yield from end of bombardment; a total synthesis time of approximately 140 min). The fractions were collected and diluted with deionized water (50 mL) and passed through an activated C18 Sep-Pak. The radioactivity on C18 Sep-Pak was eluted with EtOH (1.5 mL). The solution was removed under a N_2 stream at room temperature, and the residue was dissolved in 10% EtOH/saline (1.5 mL) for the tissue distribution studies. The radiochemical purity, determined by analytical reversed-phase HPLC, was in all cases greater than 95%. The effective specific activity, determined by a competitive radiometric ligand binding assay (*42*) was >550 mCi/mmol. The identity of the desired product was also confirmed by reversed-phase analytical HPLC (CH_3CN/water = 50:50, 0.8 mL/min, 254 nm), by coinjecting with an authentic sample of compound **9** with [^{18}F]**9**.

Biological Procedures for Relative Binding Affinity (RBA) and Specific Activity Determinations. Relative binding affinities of the progestins were determined in several receptor systems using competitive radiometric binding assays. Measurements were carried out using procedures reported in previous publications for progesterone receptor (*28, 48*), glucocorticoid receptor (*49, 50*), and androgen receptor (*48, 51*). The PR assay used purified recombinant full-length PR B (Invitrogen, Carlsbad, CA) and R5020 as the standard and ^{3}H tracer (Perkin-Elmer, Boston, MA) (K_d = 0.4 nM); GR used adrenalectomized rat liver cytosol and dexamethasone as the standard and ^{3}H tracer (Amersham Biosciences, Piscataway, NJ) (K_d = 20 nM), and for AR, purified recombinant AR ligand binding domain (Invitrogen, Carlsbad, CA) and as the standard and ^{3}H tracer R1881 (Perkin-Elmer, Boston, MA) (K_d = 0.6 nM) for AR. By definition, the standards have RBA values of 100%. Effective specific activities of the ^{18}F-labeled progestins were measured

by in vitro competitive binding assays performed on fully decayed samples (*42*).

Tissue Distribution Studies. The progesterone receptor levels in the uteri of immature Sprague−Dawley rats (21 days old, 40−50 g, five rats per time point) were induced by daily subcutaneous injections for 2 days of 5 μg of estradiol in 0.2 mL of 20% ethanol/sunflower seed oil (*19*). The experiments were begun 24 h after the last injection. The ^{18}F-labeled Tanaproget derivative [^{18}F]**9**, purified by reversed-phase HPLC, concentrated in vacuo, and redissolved in 10% EtOH/isotonic saline, was passed through a filter. Anesthetized rats were injected in the tail vein with 26 μCi/100 μL of the ^{18}F-labeled compound [^{18}F]**9**. At specified time points postinjection, the rats were sacrificed by decapitation, and blood and organs were removed, weighed, and counted in a Beckman Gamma 6000 counter. To determine whether the uptake was mediated by a high-affinity, limited-capacity system, one set of animals was coinjected with the ^{18}F-labeled fluoropropyl-Tanaproget derivative [^{18}F]**9** together with 33.3 μg of unlabeled fluoropropyl-Tanaproget derivative **9** in 14% ethanol/∼30% 2-hydroxypropyl-β-cyclodextrin in saline as standard compound to fully occupy the progesterone receptors.

ACKNOWLEDGMENT

This work has been presented at the 18th International Symposium on Radiopharmaceutical Sciences, S218, Edmonton, Canada, 12−17 July 2009. Supported by grants from the NIH (PHS R01 CA025836 to JAK; R24 CA086307 to MJW). Funding for NMR and MS instrumentation at the University of Illinois is from the Keck Foundation, NIH, and NSF. We are grateful to Terry Sharp, Nicole Fettig, Margaret Morris, Paul Eisenbeis, and Amanda Roth for help with the animal experiments.

LITERATURE CITED

(1) Katzenellenbogen, J. A. (2003) Receptor Imaging of Tumors (Non-Peptide), in *Handbook of Radiopharmaceuticals: Radiochemistry and Applications* (Welch, M. J., and Redvanly, C., Eds.) pp 715−750, John Wiley & Sons, Ltd, London.

(2) Allred, D. C., Carlson, R. W., Berry, D. A., Burstein, H. J., Edge, S. B., Goldstein, L. J., Gown, A., Hammond, M. E., Iglehart, J. D., Moench, S., Pierce, L. J., Ravdin, P., Schnitt, S. J., and Wolff, A. C. (2009) NCCN task force report: estrogen receptor and progesterone receptor testing in breast cancer by immunohistochemistry. *J. Natl. Compr. Canc. Netw. 7 Suppl. 6*, S1-S21; quiz S22−23.

(3) Dowsett, M., and Dunbier, A. K. (2008) Emerging biomarkers and new understanding of traditional markers in personalized therapy for breast cancer. *Clin. Cancer Res. 14*, 8019–8026.

(4) Pavone-Macaluso, M., Carruba, G., and Castagnetta, L. (1994) Steroid receptors in prostate cancer tissues and cells: pathophysiology, problems in methodology, clinical value and controversial questions. *Arch. Esp. Urol. 47*, 189–201.

(5) Almubarak, M., Osman, S., Marano, G., and Abraham, J. (2009) Role of positron-emission tomography scan in the diagnosis and management of breast cancer. *Oncology (Williston Park) 23*, 255–261.

(6) Hospers, G. A., Helmond, F. A., de Vries, E. G., Dierckx, R. A., and de Vries, E. F. (2008) PET imaging of steroid receptor expression in breast and prostate cancer. *Curr. Pharm. Des. 14*, 3020–3032.

(7) Jadvar, H., Alavi, A., and Gambhir, S. S. (2009) 18F-FDG uptake in lung, breast, and colon cancers: molecular biology correlates and disease characterization. *J. Nucl. Med. 50*, 1820–1827.

(8) Podoloff, D. A., Ball, D. W., Ben-Josef, E., Benson, A. B., Cohen, S. J., Coleman, R. E., Delbeke, D., Ho, M., Ilson, D. H., Kalemkerian, G. P., Lee, R. J., Loeffler, J. S., Macapinlac, H. A., Morgan, R. J., Jr., Siegel, B. A., Singhal, S., Tyler, D. S., and Wong, R. J. (2009) NCCN task force: clinical utility of PET in a variety of tumor types. *J. Natl. Compr. Canc. Netw. 7*, S1–26, Suppl 2.

(9) McGuire, A. H., Dehdashti, F., Siegel, B. A., Lyss, A. P., Brodack, J. W., Mathias, C. J., Mintun, M. A., Katzenellenbogen, J. A., and Welch, M. J. (1991) Positron tomographic assessment of 16 alpha-[18F] fluoro-17 beta-estradiol uptake in metastatic breast carcinoma. *J. Nucl. Med. 32*, 1526–1531.

(10) Mintun, M. A., Welch, M. J., Siegel, B. A., Mathias, C. J., Brodack, J. W., McGuire, A. H., and Katzenellenbogen, J. A. (1988) Breast cancer: PET imaging of estrogen receptors. *Radiology 169*, 45–48.

(11) Mortimer, J. E., Dehdashti, F., Siegel, B. A., Katzenellenbogen, J. A., Fracasso, P., and Welch, M. J. (1996) Positron emission tomography with 2-[18F]Fluoro-2-deoxy-D-glucose and 16alpha-[18F]fluoro-17beta-estradiol in breast cancer: correlation with estrogen receptor status and response to systemic therapy. *Clin. Cancer Res. 2*, 933–939.

(12) Mortimer, J. E., Dehdashti, F., Siegel, B. A., Trinkaus, K., Katzenellenbogen, J. A., and Welch, M. J. (2001) Metabolic flare: indicator of hormone responsiveness in advanced breast cancer. *J. Clin. Oncol. 19*, 2797–2803.

(13) Dehdashti, F., Flanagan, F. L., Mortimer, J. E., Katzenellenbogen, J. A., Welch, M. J., and Siegel, B. A. (1999) Positron emission tomographic assessment of "metabolic flare" to predict response of metastatic breast cancer to antiestrogen therapy. *Eur. J. Nucl. Med. 26*, 51–56.

(14) Dehdashti, F., Mortimer, J. E., Trinkaus, K., Naughton, M. J., Ellis, M., Katzenellenbogen, J. A., Welch, M. J., and Siegel, B. A. (2009) PET-based estradiol challenge as a predictive biomarker of response to endocrine therapy in women with estrogen-receptor-positive breast cancer. *Breast Cancer Res. Treat. 113*, 509–517.

(15) Beattie, B. J., Smith-Jones, P. M., Jhanwar, Y. S., Schoder, H., Schmidtlein, C. R., Morris, M. J., Zanzonico, P., Squire, O., Meirelles, G. S., Finn, R., Namavari, M., Cai, S., Scher, H. I., Larson, S. M., and Humm, J. L. (2010) Pharmacokinetic assessment of the uptake of 16{beta}-18F-fluoro-5{alpha}-dihydrotestosterone (FDHT) in prostate tumors as measured by PET. *J. Nucl. Med. 51*, 183–192.

(16) Dehdashti, F., Picus, J., Michalski, J. M., Dence, C. S., Siegel, B. A., Katzenellenbogen, J. A., and Welch, M. J. (2005) Positron tomographic assessment of androgen receptors in prostatic carcinoma. *Eur. J. Nucl. Med. Mol. Imaging 32*, 344–350.

(17) Larson, S. M., Morris, M., Gunther, I., Beattie, B., Humm, J. L., Akhurst, T. A., Finn, R. D., Erdi, Y., Pentlow, K., Dyke, J., Squire, O., Bornmann, W., McCarthy, T., Welch, M., and Scher, H. (2004) Tumor localization of 16beta-18F-fluoro-5alpha-dihydrotestosterone versus 18F-FDG in patients with progressive, metastatic prostate cancer. *J. Nucl. Med. 45*, 366–373.

(18) Zanzonico, P. B., Finn, R., Pentlow, K. S., Erdi, Y., Beattie, B., Akhurst, T., Squire, O., Morris, M., Scher, H., McCarthy, T., Welch, M., Larson, S. M., and Humm, J. L. (2004) PET-based radiation dosimetry in man of 18F-fluorodihydrotestosterone, a new radiotracer for imaging prostate cancer. *J. Nucl. Med. 45*, 1966–1971.

(19) Buckman, B. O., Bonasera, T. A., Kirschbaum, K. S., Welch, M. J., and Katzenellenbogen, J. A. (1995) Fluorine-18-labeled progestin 16 alpha, 17 alpha-dioxolanes: development of high-affinity ligands for the progesterone receptor with high in vivo target site selectivity. *J. Med. Chem. 38*, 328–337.

(20) Dehdashti, F., McGuire, A. H., Van Brocklin, H. F., Siegel, B. A., Andriole, D. P., Griffeth, L. K., Pomper, M. G., Katzenellenbogen, J. A., and Welch, M. J. (1991) Assessment of 21-[18F]fluoro-16 alpha-ethyl-19-norprogesterone as a positron-emitting radiopharmaceutical for the detection of progestin receptors in human breast carcinomas. *J. Nucl. Med. 32*, 1532–1537.

(21) Kochanny, M. J., VanBrocklin, H. F., Kym, P. R., Carlson, K. E., O'Neil, J. P., Bonasera, T. A., Welch, M. J., and

Katzenellenbogen, J. A. (1993) Fluorine-18-labeled progestin ketals: synthesis and target tissue uptake selectivity of potential imaging agents for receptor-positive breast tumors. *J. Med. Chem. 36*, 1120–1127.

(22) Katzenellenbogen, J. A. (1996) Estrogen and Progestin Radiopharmaceuticals for Imaging Breast Cancer, in *Estrogens, Progestins, and Their Antagonists* (Pavlik, E. J., Ed.) pp 197−242, Birkhäuser, Boston.

(23) Pomper, M. G., Katzenellenbogen, J. A., Welch, M. J., Brodack, J. W., and Mathias, C. J. (1988) 21-[18F]fluoro-16 alpha-ethyl-19-norprogesterone: synthesis and target tissue selective uptake of a progestin receptor based radiotracer for positron emission tomography. *J. Med. Chem. 31*, 1360–1363.

(24) Giersig, C. (2008) Progestin and breast cancer. The missing pieces of a puzzle. *Bundesgesundheitsblatt Gesundheitsforschung Gesundheitsschutz 51*, 782–786.

(25) Mangelsdorf, D. J., Thummel, C., Beato, M., Herrlich, P., Schutz, G., Umesono, K., Blumberg, B., Kastner, P., Mark, M., Chambon, P., and Evans, R. M. (1995) The nuclear receptor superfamily: the second decade. *Cell 83*, 835–839.

(26) Winneker, R. C., Fensome, A., Zhang, P., Yudt, M. R., McComas, C. C., and Unwalla, R. J. (2008) A new generation of progesterone receptor modulators. *Steroids 73*, 689–701.

(27) Verhagen, A., Studeny, M., Luurtsema, G., Visser, G. M., De Goeij, C. C., Sluyser, M., Nieweg, O. E., Van der Ploeg, E., Go, K. G., and Vaalburg, W. (1994) Metabolism of a [18F]fluorine labeled progestin (21-[18F]fluoro-16 alpha-ethyl-19-norprogesterone) in humans: a clue for future investigations. *Nucl. Med. Biol. 21*, 941–952.

(28) Zhou, D., Carlson, K. E., Katzenellenbogen, J. A., and Welch, M. J. (2006) Bromine- and iodine-substituted 16alpha,17alpha-dioxolane progestins for breast tumor imaging and radiotherapy: synthesis and receptor binding affinity. *J. Med. Chem. 49*, 4737–4744.

(29) Zhou, D., Sharp, T. L., Fettig, N. M., Lee, H., Lewis, J. S., Katzenellenbogen, J. A., and Welch, M. J. (2008) Evaluation of a bromine-76-labeled progestin 16alpha,17alpha-dioxolane for breast tumor imaging and radiotherapy: in vivo biodistribution and metabolic stability studies. *Nucl. Med. Biol. 35*, 655–663.

(30) Ojasoo, T., Dore, J. C., Gilbert, J., and Raynaud, J. P. (1988) Binding of steroids to the progestin and glucocorticoid receptors analyzed by correspondence analysis. *J. Med. Chem. 31*, 1160–1169.

(31) Fensome, A., Adams, W. R., Adams, A. L., Berrodin, T. J., Cohen, J., Huselton, C., Illenberger, A., Kern, J. C., Hudak, V. A., Marella, M. A., Melenski, E. G., McComas, C. C., Mugford, C. A., Slayden, O. D., Yudt, M., Zhang, Z., Zhang, P., Zhu, Y., Winneker, R. C., and Wrobel, J. E. (2008) Design, synthesis, and SAR of new pyrrole-oxindole progesterone receptor modulators leading to 5-(7-fluoro-3,3-dimethyl-2-oxo-2,3-dihydro-1H-indol-5-yl)-1-methyl-1H-pyrrole-2-carbonitrile (WAY-255348). *J. Med. Chem. 51*, 1861–1873.

(32) Pedram, B., van Oeveren, A., Mais, D. E., Marschke, K. B., Verbost, P. M., Groen, M. B., and Zhi, L. (2008) A tissue-selective nonsteroidal progesterone receptor modulator: 7,9-difluoro-5-(3-methylcyclohex-2-enyl)-2,2,4-trimethyl-1,2-dihydrochrome no[3,4-f]quinoline. *J. Med. Chem. 51*, 3696–3699.

(33) Zhang, P., Terefenko, E. A., Fensome, A., Wrobel, J., Winneker, R., Lundeen, S., Marschke, K. B., and Zhang, Z. (2002) 6-Aryl-1,4-dihydro-benzo[d][1,3]oxazin-2-ones: a novel class of potent, selective, and orally active nonsteroidal progesterone receptor antagonists. *J. Med. Chem. 45*, 4379–4382.

(34) Fensome, A., Bender, R., Chopra, R., Cohen, J., Collins, M. A., Hudak, V., Malakian, K., Lockhead, S., Olland, A., Svenson, K., Terefenko, E. A., Unwalla, R. J., Wilhelm, J. M., Wolfrom, S., Zhu, Y., Zhang, Z., Zhang, P., Winneker, R. C., and Wrobel, J. (2005) Synthesis and structure-activity relationship of novel 6-aryl-1,4-dihydrobenzo[d][1,3]oxazine-2-thiones as progesterone receptor modulators leading to the potent and selective nonsteroidal progesterone receptor agonist tanaproget. *J. Med. Chem. 48*, 5092–5095.

(35) Zhang, Z., Olland, A. M., Zhu, Y., Cohen, J., Berrodin, T., Chippari, S., Appavu, C., Li, S., Wilhem, J., Chopra, R., Fensome, A., Zhang, P., Wrobel, J., Unwalla, R. J., Lyttle, C. R., and Winneker, R. C. (2005) Molecular and pharmacological properties of a potent and selective novel nonsteroidal progesterone receptor agonist tanaproget. *J. Biol. Chem. 280*, 28468–28475.

(36) Zhou, H., Lee, J. H., Mayne, C. G., Carlson, K. E., and Katzenellenbogen, J. A. (2010) Imaging progesterone receptor in breast tumors: Synthesis and receptor binding affinity of fluoroalkyl-substituted analogs of Tanaproget. *J. Med. Chem.*, *53*, 3349−3360.

(37) Kim, D. W., Ahn, D. S., Oh, Y. H., Lee, S., Kil, H. S., Oh, S. J., Lee, S. J., Kim, J. S., Ryu, J. S., Moon, D. H., and Chi, D. Y. (2006) A new class of SN2 reactions catalyzed by protic solvents: Facile fluorination for isotopic labeling of diagnostic molecules. *J. Am. Chem. Soc. 128*, 16394–16397.

(38) Kim, D. W., Choe, Y. S., and Chi, D. Y. (2003) A new nucleophilic fluorine-18 labeling method for aliphatic mesylates: reaction in ionic liquids shows tolerance for water. *Nucl. Med. Biol. 30*, 345–350.

(39) Kim, D. W., Jeong, H. J., Lim, S. T., Sohn, M. H., Katzenellenbogen, J. A., and Chi, D. Y. (2008) Facile nucleophilic fluorination reactions using tert-alcohols as a reaction medium: significantly enhanced reactivity of alkali metal fluorides and improved selectivity. *J. Org. Chem. 73*, 957–962.

(40) Kim, D. W., Song, C. E., and Chi, D. Y. (2002) New method of fluorination using potassium fluoride in ionic liquid: significantly enhanced reactivity of fluoride and improved selectivity. *J. Am. Chem. Soc. 124*, 10278–10279.

(41) Kim, D. W., Song, C. E., and Chi, D. Y. (2003) Significantly enhanced reactivities of the nucleophilic substitution reactions in ionic liquid. *J. Org. Chem. 68*, 4281–4285.

(42) Senderoff, S. G., McElvany, K. D., Carlson, K. E., Heiman, D. F., Katzenellenbogen, J. A., and Welch, M. J. (1982) Methodology for the synthesis and specific activity determination of 16 alpha-[77Br]-bromoestradiol-17 beta and 16 alpha-[77Br]-11 beta-methoxyestradiol-17 beta, two estrogen receptor-binding radiopharmaceuticals. *Int. J. Appl. Radiat. Isot. 33*, 545–551.

(43) Bonasera, T. A., O'Neil, J. P., Xu, M., Dobkin, J. A., Cutler, P. D., Lich, L. L., Choe, Y. S., Katzenellenbogen, J. A., and Welch, M. J. (1996) Preclinical evaluation of fluorine-18-labeled androgen receptor ligands in baboons. *J. Nucl. Med. 37*, 1009–1015.

(44) VanBrocklin, H. F., Carlson, K. E., Katzenellenbogen, J. A., and Welch, M. J. (1993) 16 beta-([18F]fluoro)estrogens: systematic investigation of a new series of fluorine-18-labeled estrogens as potential imaging agents for estrogen-receptor-positive breast tumors. *J. Med. Chem. 36*, 1619–1629.

(45) VanBrocklin, H. F., Liu, A., Welch, M. J., O'Neil, J. P., and Katzenellenbogen, J. A. (1994) The synthesis of 7 alpha-methyl-substituted estrogens labeled with fluorine-18: potential breast tumor imaging agents. *Steroids 59*, 34–45.

(46) Katzenellenbogen, J. A., Heiman, D. F., Carlson, K. E., and Lloyd, J. E. (1982) In Vivo and In Vitro Steroid Receptor Assays in the Design of Estrogen Pharmaceuticals, in *Receptor Binding Radiotracers* (Eckelman, W. C., Ed.) pp 93−126, CRC Press, Boca Raton, FL.

(47) Pangborn, A. B., Giardello, M. A., Grubbs, R. H., Rosen, R. K., and Timmers, F. J. (1996) Safe and convenient procedure for solvent purification. *Organometallics 15*, 1518−1520.

(48) Brandes, S. J., and Katzenellenbogen, J. A. (1987) Fluorinated androgens and progestins: molecular probes for androgen and progesterone receptors with potential use in positron emission tomography. *Mol. Pharmacol. 32*, 391–403.

(49) Pinney, K. G., Carlson, K. E., and Katzenellenbogen, J. A. (1990) [3H]DU41165: a high affinity ligand and novel photoaffinity labeling reagent for the progesterone receptor. *J. Steroid Biochem. 35*, 179–189.

(50) Wust, F., Carlson, K. E., and Katzenellenbogen, J. A. (2003) Synthesis of novel arylpyrazolo corticosteroids as potential ligands for imaging brain glucocorticoid receptors. *Steroids 68*, 177–191.

(51) Parent, E. E., Dence, C. S., Jenks, C., Sharp, T. L., Welch, M. J., and Katzenellenbogen, J. A. (2007) Synthesis and biological evaluation of [18F]bicalutamide, 4-[76Br]bromobicalutamide, and 4-[76Br]bromo-thiobicalutamide as non-steroidal androgens for prostate cancer imaging. *J. Med. Chem. 50*, 1028–1040.

BC1001054

Spectroscopic and Calorimetric Studies on the Triplex Formation with Oligonucleotide−Ligand Conjugates

Andrea Eick, Fanny Riechert-Krause, and Klaus Weisz*

Institute of Biochemistry, Ernst-Moritz-Arndt University Greifswald, Felix-Hausdorff-Str. 4, D-17487 Greifswald, Germany.
Received February 25, 2010; Revised Manuscript Received April 13, 2010

Several triplex-forming 9-mer oligonucleotide (TFO) conjugates with a methyl- or methoxy-substituted 5-phenyl-6*H*-indolo[3,2-*b*]quinoline (PIQ) attached at the 5′-terminus or 3′-terminus or at an internal C5 thymine position were synthesized and tested for their ability to form and stabilize a triple helix with a double-helical DNA target employing UV melting experiments, fluorescence titrations, and isothermal titration calorimetry (ITC). A considerable thermal stabilization by up to 14 °C at pH 6.0 was observed for the 5′- and 3′-conjugates with little influence on the type of substituent but also for a conjugate with the ligand tethered by a short linker to the interior of the 9-mer TFO. A detailed thermodynamic characterization of the unmodified TFO and its 5′-conjugate with a methyl-substituted ligand by ITC experiments yielded a $\Delta\Delta G^\circ$ of -1.8 kcal mol^{-1} at pH 6.0 for the TFO-attached PIQ−triplex interaction and also revealed a favorable entropic contribution as the major determinant for the free energy of PIQ binding in the conjugate. The pH dependence of triplex thermal stability highlights the importance of ring protonation of the triplex-bound ligand for its effective interaction and triplex stabilization near physiological conditions.

INTRODUCTION

DNA triple helices formed through the sequence-specific recognition of a DNA duplex by a third-strand oligonucleotide constitute an alternative nucleic acid secondary structure with potential biological relevance (*1, 2*). The formation of a triple-stranded DNA is based on Hoogsteen hydrogen bond interactions between bases of the triplex-forming oligonucleotide (TFO) and available hydrogen bond donor and acceptor groups of purine bases in the double-helical DNA target directed toward its major groove (*3*). The ability of TFOs to bind complementary duplex DNA with a defined base−base recognition code places them among the most specific DNA binding ligands. Currently, TFO-based strategies in biotechnological and gene therapeutic applications focus on the specific regulation of gene expression known as antigene strategy (*4, 5*) and may also include interference with DNA transcription factors (*6, 7*) or site-directed mutagenesis (*8, 9*). However, the exclusive TFO binding to purine bases of the duplex limits effective triplex formation to the presence of oligopyrimidine•oligopurine sequences which are found to be overrepresented especially in promoter regions of the human genome (*10*).

From the two standard types of triplexes, the more extensively studied pyrimidine motif consists of a pyrimidine third strand oriented parallel to the oligopurine strand of the cognate duplex forming isomorphous T•AT and C^+•GC base triplets (*3*). Here, the formation of two Hoogsteen hydrogen bonds requires the protonation of third-strand cytosines resulting in a considerable pH dependence of triplex stability. Given their relatively low stability under physiological conditions, attempts to increase the thermodynamic stability of triple helices in the past have employed various strategies including the addition of triplex binding ligands and multivalent cations to compensate for the charge repulsion between strands, synthetic modification of the nucleobases, deoxyribose sugars or the phosphodiester backbone, (*11, 12*) as well as the covalent attachment of DNA intercalators to the third strand (*13−15*).

On the basis of the latter approach, we have recently designed a TFO conjugated with the benzo-annulated δ-carboline 5-phenyl-6*H*-indolo[3,2-*b*]quinoline (PIQ) that is able to form and to significantly stabilize triple helical structures with a DNA duplex and suggested an intercalative mode of binding at the triplex−duplex junction of this polyaromatic compound (*16*). In the present study, we have covalently tethered methyl- or methoxy-substituted indoloquinoline derivatives to 5′-, 3′-, or internal positions of the TFO with different linkers and examined the ability of the various TFO conjugates to form and stabilize triplexes with a 15-mer target duplex combining different spectroscopic and calorimetric techniques. The results obtained from a detailed thermodynamic characterization of a 5′-conjugate provide for important information on the major driving forces for triplex binding of the indoloquinolines when attached to the TFO and are discussed with respect to the thermodynamics reported for other triplex selective ligands.

EXPERIMENTAL PROCEDURES

Materials. Unmodified and amino-functionalized oligonucleotides were purchased from TIB MOLBIOL (Berlin, Germany) and Eurofins MWG Operon (Ebersberg, Germany). The two phenyl-substituted indolo[3,2-*b*]quinoline derivatives 1,7-dimethyl- and 1,7-dimethoxy-5-(4-succinimido-carboxyphenyl)-6*H*-indolo[3,2-*b*]quinoline were prepared according to previously published procedures (*16*).

The concentration of the oligonucleotides was calculated using molar extinction coefficients at 260 nm derived from the nearest-neighbor model of Tataurov et al. (*17*). The concentration of the TFO-PIQ conjugates was approximated by adding the determined molar extinction coefficient of the free carboxy derivatives of PIQa ($\varepsilon_{260\ nm} = 26\ 818$ M^{-1} cm^{-1}) and PIQb ($\varepsilon_{260\ nm} = 23\ 920$ M^{-1} cm^{-1}) dissolved in a DMSO−water mixture with ≤6% DMSO to the calculated extinction coefficient of the oligonucleotide ($\varepsilon_{260\ nm} = 70\ 800$ M^{-1} cm^{-1}).

Solvents were distilled prior to use. Buffer solutions were prepared using deionized water (Millipore Simplicity 185). All reactions were monitored by TLC using Merck silica gel plates

* Corresponding author. Tel. +49 (0)3834 864426; fax +49 (0)3834 864427; e-mail address: weisz@uni-greifswald.de.

10.1021/bc100107n © 2010 American Chemical Society
Published on Web 05/19/2010

$60F_{254}$. HPLC separations were carried out with a Hitachi/Knauer system. The purification was performed on a reverse column (Kromasil 100 Å C18 5 μm, 4.6 × 250 mm, Wicom GmbH, Heppenheim, Germany). A gradient was applied using buffer A (0.1 M triethylammonium acetate/CH_3CN = 1:1, pH 6.8) and buffer B (0.1 M triethylammonium acetate/CH_3CN = 98:2, pH 6.8) as eluent. A flow rate of 1.2 mL/min was used and the fractions detected simultaneously at 260, 281, 347, and 406 nm.

Synthesis of the TFO Conjugates. The amino-modified oligonucleotide (5.0 OD, 0.07 μmol) was dissolved in water (150 μL), and 0.1 M sodium phosphate buffer (pH 8.2, 65 μL) containing 50 mM lithium chloride was added. The NHS-ester functionalized phenyl-indoloquinoline PIQa or PIQb (1 mg/100 μL, 2.1 μmol PIQa and 2.0 μmol PIQb, respectively) dissolved in DMF was added. The solution was stirred for 6−8 days at 50 °C and checked by TLC (propanol/H_2O 5:3). Reaction batches showing only modest product formation after 3−4 days (especially reactions with the PIQb analogue as a result of increased NHS−ester hydrolysis) were additionally combined with another portion of NHS−ester (0.5 mg/50 μL, 1 μmol). The final product mixtures were dried in vacuo and the residue dissolved in water. Excessive NHS−ester of PIQa and PIQb was extracted three times by dichloromethane. The TFO−indoloquinoline conjugates were finally purified by HPLC and desalted by using Sep-Pak C18-Cartridges (Waters Corporation, Milford, USA). Final products were characterized by MALDI-TOF mass spectrometry.

Mass Spectrometry. Mass data were recorded on a Bruker Microflex Maldi-TOF with Flexcontrol and Flexanalysis software. A linear detection method and negative ion mode was chosen. The measurements were performed with 400 shots. The HPLC-purified conjugates and the matrix solution (saturated 3-hydroxypicolinic acid in water) were desalted via ammonium-activated cation-exchange resin beads (Dowex 50 W × 8 100−200 mesh; Fluka) and applied on a target plate. The main peak is equivalent to *m/z* M-1.

UV−vis Spectroscopy. All UV measurements were performed on a Cary 100 spectrophotometer equipped with a temperature control unit (Varian Deutschland, Darmstadt). Melting curves were recorded with 1 data point/°C at 260 nm in a temperature interval from 1 to 90 °C. To prevent water condensation at temperatures below 25 °C on the 1 cm cuvettes, the sample chamber was constantly flushed with nitrogen gas. The lyophilized unmodified or conjugated TFO (1.7 μM) and target duplex (1.45 μM) were dissolved in cacodylate buffer pH 6.0 (0.1 M NaCl, 0.02 M cacodylate, 1 mM spermine) and annealed prior to each melting experiment by heating to 90 °C followed by slow cooling to room temperature. For pH-dependent melting experiments, the cacodylate buffer was adjusted with HCl or NaOH within the pH range 5.5−6.5. Measurements included one heating ramp (1 °C/min), followed by one cooling (1 °C/min) and a second heating period (1 °C/min). Heating and cooling curves showed small hysteresis effects due to slow kinetics of 0.5−3 °C depending on the particular TFO conjugate. The melting temperature was determined by the maximum of the first derivative plot of the second heating curve after appropriate smoothing.

The relative hyperchromicity H for the triplex-to-duplex transition is calculated from the melting curve and given as percentage according to $H = (\Delta A_{t\rightarrow d} \times 100)/(\Delta A_{t\rightarrow ss})$.

Fluorescence Measurements. Fluorescence measurements were performed with a Jasco FP-6500 spectrofluorometer (Jasco, Tokyo, Japan). Using an excitation wavelength of 350 nm, emission spectra were acquired from 360 to 650 nm with a scanning speed of 50 nm/min, emission and excitation bandwidths of 5 nm, and a response time of 1 s. The sensitivity was manually adjusted by setting the photomultiplier tube voltage (PMT) to 350 V (400 V for conjugate **S16b**). Fluorescence measurements were carried out with a conjugate concentration between 0.7 and 1.7 μM in cacodylate buffer pH 6.0 (0.1 M NaCl, 0.02 M cacodylate, 1 mM spermine). Relative fluorescence intensities were followed during the addition of the duplex solution (100 μM) in 20 steps to the conjugate to reach a final duplex-to-TFO molar ratio of 2:1. All data were blank and volume corrected.

Binding curves of conjugate **S16a** were constructed by recording the fluorescence emission at 466 or 463 nm after each titration step and fit to a single-site binding model. The mathematical description of this model is represented by

$$\frac{F}{[M_0] \times f_0} = \frac{F_{ML} \times K_a \times [L] + 1}{K_a \times [L] + 1} \quad (1)$$

$$[L]^2 + \left([M_0] - [L_0] + \frac{1}{K_a}\right) \times [L] - \frac{[L_0]}{K_a} = 0 \quad (2)$$

where F is the fluorescence intensity at each titration point, $[M_0]$ and $[L]$ are the total concentration of the conjugate and the concentration of free duplex DNA, respectively, F_{ML} is the fluorescence enhancement factor, f_0 the molar fluorescence of the TFO-PIQ conjugate, and K_a the binding constant. Solving the quadratic eq 2 with the total DNA concentration $[L_0]$ gives the free duplex concentration $[L]$ (*18*).

Isothermal Titration Calorimetry. ITC experiments were performed with a MicroCal VP-ITC instrument (MicroCal, Northampton, USA), and the final data were analyzed with the *Origin* software. All samples were dissolved in cacodylate buffer pH 6.0 (0.1 M NaCl, 0.02 M cacodylate, 1 mM spermine). The smaller first injection volume (4−5 μL) was rejected before data analysis. Subsequent titration steps involved injections with 7−10 μL each and a delay between injections of 4 min. All ITC titrations were performed in triplicate with a reference power of 8 μcal/s at 10 °C. For the ITC experiments on the reference triplex, concentrations of 11−12 μM for the duplex and 140−150 μM for the third-strand oligonucleotide were employed. For the direct determination of binding enthalpies by the excess-site method with modified and unmodified third-strand oligonucleotides, buffer solutions of 130 μM duplex and 136 μM TFO conjugate as well as 130 μM third-strand oligonucleotide were employed, respectively.

Blank titrations were conducted by injecting the TFO into buffer under otherwise identical experimental conditions. The blank-corrected titration curves of the reference triplex were fitted to a model with a single binding site yielding the binding constant K_a and the molar binding enthalpy $\Delta H°$. In the case of the model-independent protocol, the final binding enthalpy was directly determined by peak integration of the power output following each injection, normalization by the number of moles of added ligand, and averaging from three independent experiments with 10 titration steps each. The Gibbs free energy $\Delta G°$ was calculated according to the relationship

$$\Delta G^\circ = -RT \ln K_a \quad (3)$$

The entropic contribution $T\Delta S°$ was calculated from the free energy of binding and the binding enthalpy as determined by the ITC measurements according to the standard thermodynamic relationship

$$\Delta G^\circ = \Delta H^\circ - T\Delta S^\circ \quad (4)$$

RESULTS AND DISCUSSION

Design of the Triple-Helical Construct. In an attempt to limit the size of the triplex construct but nevertheless allow the

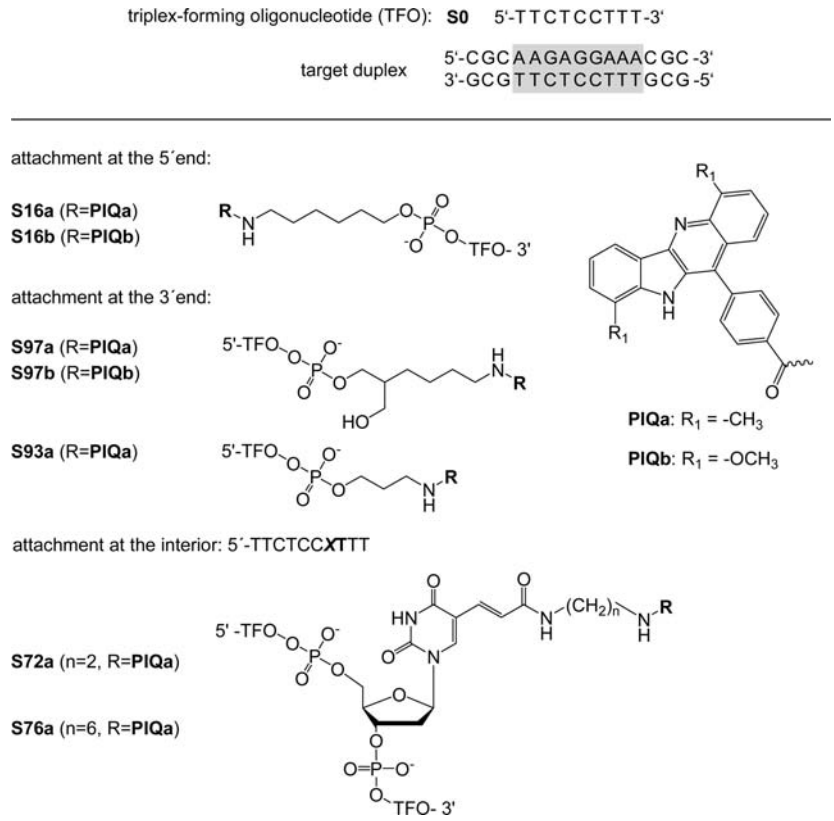


Figure 1. Triple-helical construct formed through the binding of the TFO **S0** to the target duplex (top) and structures of the conjugates with the indoloquinolines PIQa and PIQb.

formation of a stable pyrimidine triplex at pH 6.0 close to physiological conditions, we chose to employ a 9-mer TFO sequence 5′-TTCTCCTTT targeted against a 15-mer duplex as shown in Figure 1. As an added benefit of using shorter oligonucleotides, fewer side reactions occurred during the coupling reaction associated with higher yields of conjugated product. The homopyrimidine TFO binds the homopurine tract of the duplex target in a parallel orientation with the formation of T·AT and C^+·GC triplets. The two all-CG duplex overhangs on either side of the formed triplex strongly stabilize the underlying duplex and clearly separate the onset of triplex and high-temperature duplex denaturation. In addition to their effects on the triplex stability (*19*), 3′- and 5′-overhang sequences provide for triplex−duplex junctions known to constitute a strong binding site for many intercalators (*20, 21*).

Synthesis of the TFO Conjugates. All conjugates (see Figure 1) were synthesized through the coupling of two NHS-activated indoloquinoline (PIQ) derivatives to the various aminoalkyl-functionalized triplex-forming oligonucleotides according to previously published protocols (*16, 22*). For the attachment of the PIQ ligands, amino linkers with various lengths at the 5′- and 3′-ends as well as at the C5-position of a central thymidine within the triplex-forming oligonucleotide were employed. The two derivatives designated in the following as PIQa and PIQb contain either two methyl or two methoxy substituents at the indole and the quinoline moiety. Small modifications for the coupling reaction with derivative PIQb were necessary as a result of increased water solubility and fast NHS−ester hydrolysis. All conjugates were purified by HPLC and characterized by MALDI mass spectrometry. Excellent yields were obtained for the 5′-conjugates, whereas lower yields were generally obtained with 3′-conjugates and conjugates with the ligand attached to an internal position (Table 1).

Thermal Denaturation Studies. Upon third-strand dissociation from the triplex, hyperchromicity is observed at 260 nm in temperature-dependent UV measurements. The melting temperature of the triplex T_m defined by the midpoint of this transition is a measure of the thermal stability of the triple helix. To study the ability of the different TFO-PIQ conjugates to stabilize triplexes, UV thermal melting studies were performed with the 15-mer duplex target and each of the conjugates. Typical UV melting curves are shown in Figure 2 for triple helix formation of the duplex with conjugate **S16a** as well as with unmodified third strand **S0** used as a reference. The results of all measurements are summarized in Table 2.

Table 1. Synthesis and Characterization of the Oligonucleotide−PIQ Conjugates

		MS (*m*/*z*)	
TFO	average yield (%)	found	calcd
S16a	70.8	3158.7	3156.6
S16b	54.6	3188.8	3188.6
S97a	44.3	3188.8	3186.6
S97b	36.9	3218.2	3218.6
S93a	22.8	3116.2	3114.6
S72a	19.9	3077.2	3077.6
S76a	36.7	3132.2	3131.8

Ionic strengths and additives are known to potentially have significant effects on the stability of triple helical structures. Thus, the polyvalent cation spermine present under physiological conditions has been shown to considerably stabilize triplexes. To probe its effect on the conjugate binding, two different cacodylate buffers with and without the addition of 1 mM spermine were prepared and used in initial UV melting experiments. As expected, T_m values for triplexes with the unmodified TFO **S0** and conjugate **S16a** increased by 8 and 11 °C in the presence of spermine, respectively. Interestingly, however, as shown by the difference in ΔT_m of 3 °C, triplex thermal stabilization by the PIQ ligand in **S16a** was further promoted by spermine. For all subsequent measurements, a

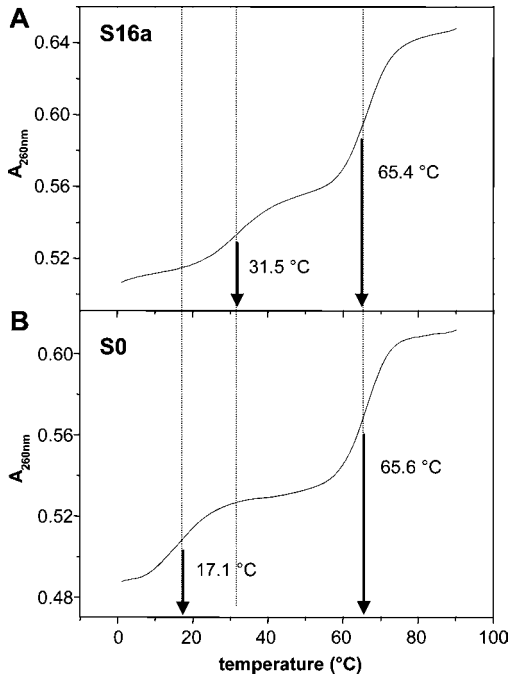


Figure 2. UV melting curves showing a low-temperature triplex−duplex and high-temperature duplex−single strand transition for the cognate duplex in the presence of conjugate **S16a** (A) and the unmodified TFO **S0** (B) in 0.1 M NaCl, 0.02 M cacodylate, 1 mM spermine, pH 6.0.

Table 2. Thermal Melting Data of Triplex-to-Duplex Transitions[a]

TFO	T_m (°C)	ΔT_m	H (%)[c]
S0	8.9 ± 0.4[b]	---	n.d.[d]
	17.1 ± 0.7	---	34
	5′-attachment to the TFO		
S16a	20.6 ± 0.3[b]	11.7[b]	n.d.[d]
	31.5 ± 0.6	14.4	37
S16b	30.9 ± 0.3	13.8	37
	3′-attachment to the TFO		
S97a	31.5 ± 0.2	14.4	31
S97b	29.4 ± 0.1	12.3	29
S93a	29.5 ± 1.2	12.4	20
	Internal Linkage 5′-TTCTCCXTTT		
S72a	28.5 ± 1.2	11.4	24
S76a	18.5 ± 1.8	1.4	20

[a] All T_m values are given as averages with standard deviations from three independent measurements on a mixture of TFO (1.7 μM) and duplex (1.45 μM) in a 1.2:1 molar ratio. [b] Without spermine in 0.1 M NaCl, 0.02 M cacodylate, pH 6.0. [c] For definition and calculation, see Experimental Procedures. [d] Not determined.

buffer with 1 mM spermine was therefore employed for its triplex stabilizing effect facilitating the analysis of melting profiles with lower transition temperatures.

All conjugates formed more stable triplexes compared to the unmodified third strand. At the same time, the second high-temperature melting transition at 65.5 ± 0.5 °C is independent of the type of third-strand conjugate as expected from duplex melting into single strands. The highest triplex thermal stabilization was observed in the presence of third-strand oligonucleotides with the ligand attached to either the 5′- or 3′-end. Thus, TFO **S16a**, **S16b**, and **S97a** form triplexes with melting temperatures of ~31 °C increasing T_m by 14 °C compared to the unmodified reference triplex. The other two 3′-modified conjugates **S97b** and **S93a** only show a slightly reduced stability with a ΔT_m value of ~12 °C. Most noticeably, however, oligonucleotide **S72a** with the ligand attached to the interior also exhibits substantial stabilizing effects on the triplex with a melting temperature of 28 °C and a ΔT_m of 11 °C. However, whereas a shortening of the linker length in the conjugate in the case of a 3′-attachment has only small effects on the thermal stabilization (compare **S97a** and **S93a** with a C6 and C3 linker, respectively), extending the linker for the internal attachment to thymine C5 by $(CH_2)_4$ has a dramatic effect on the ligand-induced triplex stabilization, and the increase in T_m nearly vanishes for conjugate **S76a** when compared to the unmodified triplex. Thus, a potential intercalation of the thymine C5 tethered ligand within the triplex interior seems to be disfavored by an elongated linker with its increased flexibility. It has to be noted, however, that, in addition to the typical signature of a triple-stranded structure found in circular dichroism (CD) spectra on mixtures of the target duplex with the various conjugates at 10 °C, another negative albeit weak induced CD band centered at the long-wavelength absorbance maximum of the indoloquinoline at about 380 nm is observed for both internally modified conjugates (see Supporting Information). Such induced CD effects are indicative of ligand binding in an asymmetric environment and based on their negative sign together with their low intensity suggest a partial intercalative mode of binding even for conjugate **S76a** (*16, 23*). Consequently, differences in triplex thermal stabilizations may not only reflect variable stacking interactions within the triplex, but also at least partially arise from a variable extent of ligand stacking with bases in the dissociated TFO.

The effect of substituents on the triplex stability can be examined by melting data for PIQa and PIQb. Surprisingly, substituting methyl by methoxy groups has no or only a small effect on triplex stabilization in the case of ligand attachment at the 5′- and 3′-end, respectively. The two substituents differ in hydrophobicity, and theoretical calculations on the HF-6-31G* optimized geometries of the two indoloquinoline chromophores also indicate different dipole moments (3.0 vs 2.5 D for PIQa and PIQb, respectively). In the case of intercalation, stacking interactions with nucleic acid bases are expected to be modulated by the different charge distribution. Also, a different degree of the ring nitrogen protonation in the indoloquinoline structure is likely to have an impact on the binding affinity for the two ligands. Consequently, the lack of a noticeable influence of the substituent on binding may also result from partial compensation of different effects.

There have been few comparative studies on the relative triplex stabilization of intercalators coupled to either a terminal or internal position of the TFO. Except for a strongly triplex stabilizing benzo[*e*]pyridoindole (*14*) and a benzo[*f*]pyridoquinoxaline (*24*) attached through an internucleotide pentamethylene and tetramethylene containing linker in the interior of the TFO, respectively, conjugates with a centrally positioned ligand seem generally less effective in triplex stabilization compared to conjugates with terminal modifications (*25, 26*). In addition to the ligand structure, favorable interactions of internally attached intercalators have also been found to be particularly sensitive to the type and length of the linker in line with the present data. Clearly, ligand orientation and thus steric requirements greatly differ in the case of an internucleotide linkage or a direct coupling to a nucleobase. However, unlike the considerable triplex stabilizing effects of the internally modified **S72a**, UV melting studies reported on benzo[*e*] and benzo[*g*]pyridoindoles similarly tethered via a flexible linker to the 5-position of a modified 2′-deoxyuridine indicate enhanced third-strand binding to a target duplex only when located at the 5′-end of the TFO, but no stabilization was observed with ligands fixed at internal positions (*25*).

In contrast to previous reports that the highest affinity is obtained by intercalators attached to the 5′-end of the triplex-

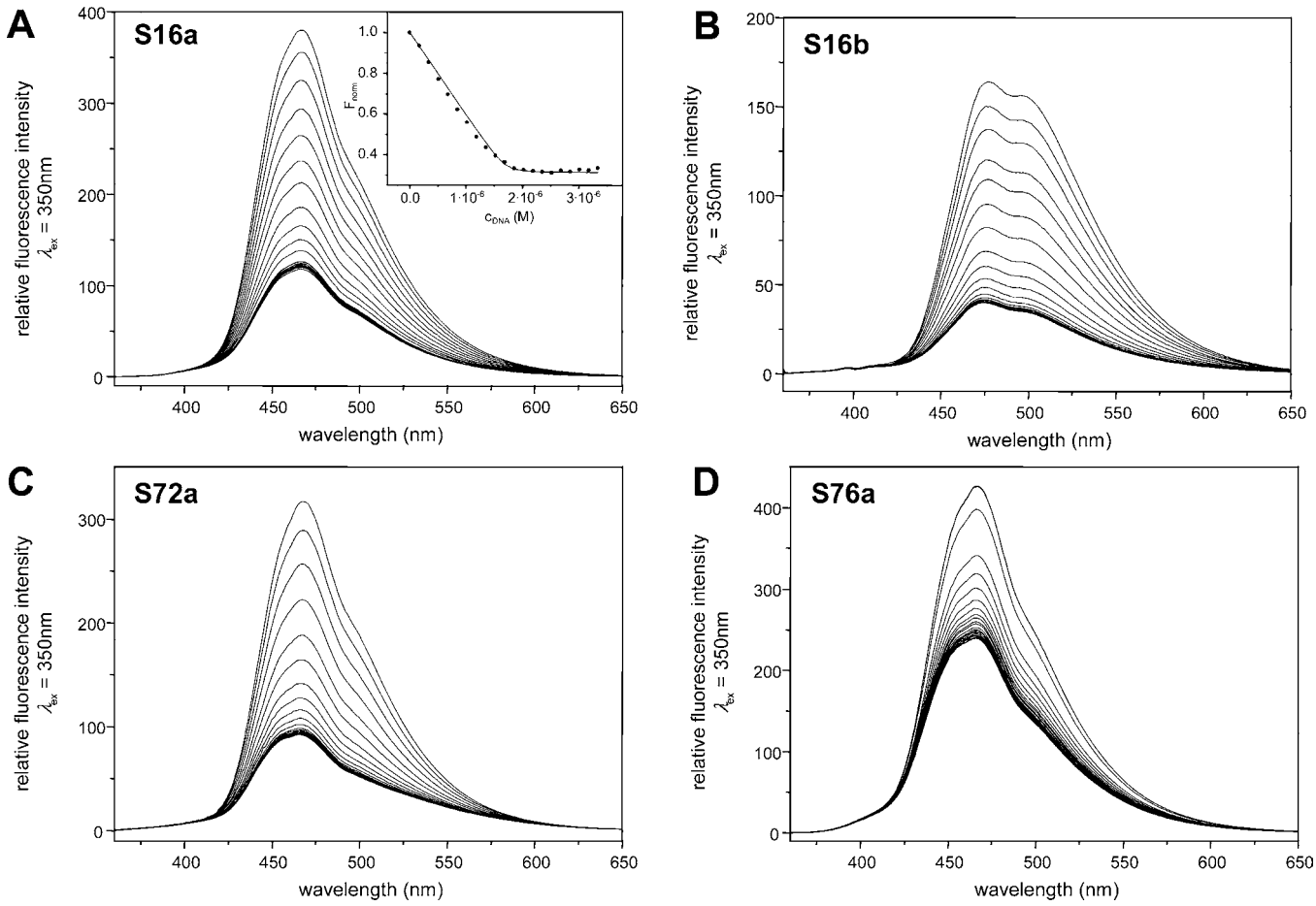


Figure 3. Fluorescence emission spectra of δ-carboline-TFO conjugate **S16a** (A), **S16b** (B), **S72a** (C), and **S76a** (D) titrated with the target duplex at 10 °C; addition of duplex to the conjugate (1.7 μM) results in progressively decreased fluorescence. The inset in (A) shows a linear least-squares fit for the fluorescence intensity at 466 nm. Twenty titration steps up to a 2:1 duplex-to-conjugate molar ratio were performed.

forming oligonucleotide (*27*), the present data show only minor effects on the thermal stabilization from the ligand attachment to either the 5′- or 3′-terminus of the TFO. More significant differences are revealed by looking at hyperchromicities for the triplex-to-duplex transition mainly arising from base stacking interactions also including the ligand chromophore. With the TFO in excess, a relative triplex hyperchromicity was defined with respect to the sum of triplex-to-duplex and duplex-to-single strand hyperchromicities to eliminate any additional influence of concentration (Table 2). Note that in all cases triplex and duplex melting transitions are well-separated, but due to baseline effects a considerable uncertainty has to be taken into account. Nevertheless, the calculated relative triplex hyperchromicities enable the arrangement of the conjugates into three clearly defined groups: **S16a,b** > **S97a,b** > **S93a**, **S72a**, **S76a**. With exclusion of any noticeable effects of the different linker moieties on the hyperchromicity, these data are consistent with enhanced stacking interactions for a 5′-conjugate compared to 3′-conjugates as a result of the structurally different 5′- and 3′-triplex−duplex junctions (*28*) and also with more noticeable structural distortions in the case of a shorter or internal linker. However, persisting stacking of the ligand especially at an internal position with the bases of the dissociated TFO may again contribute to the considerable variation in hyperchromicity upon triplex melting.

Fluorescence Emission. Because a triplex bound benzo-annulated δ-carboline has previously been shown to exhibit a strong fluorescence enhancement upon triplex melting (*16*), changes in fluorescence properties of the PIQ fluorophore were used to monitor DNA−ligand interactions with the conjugates **S16a**, **S16b**, **S72a**, and **S76a**. With an excitation wavelength set to 350 nm for maximum fluorescence emission of all conjugates, fluorescence of free methoxy-substituted PIQb conjugate **S16b** was found to be noticeably weaker compared to the intensities observed with methyl-substituted PIQa conjugates **S16a**, **S72a**, and **S76a** under the same conditions. In contrast, the methyl-substituted ligands in the free conjugate exhibit only small differences in their fluorescence quantum yields as expected (Figure 3).

Addition of the target duplex with concomitant triplex formation induced a modest shift in the emission wavelength but a significant degree of fluorescence quenching for all conjugates. Thus, a small hypsochromic shift in the emission maximum from 467 to 466 nm for PIQa and 477 to 473 nm for PIQb must be attributed to the change in the local environment of the ligand upon triplex formation. Most noticeably, however, **S16a**, **S16b**, **S72a**, and **S76a** conjugates were quenched by 67%, 75%, 71%, and 44% upon saturation with duplex, respectively. The fluorescence emission intensity of the indoloquinolines is expected to be influenced by neighboring bases and their solvent accessibility and may thus be taken as indicator for base−ligand interactions within a formed triple-helical complex. Correspondingly, indoloquinoline fluorophores in conjugates **S16a**, **S16b**, and **S72a** displaying a high degree of quenching (~70%) are likely to be in close contact to DNA bases and efficiently screened from the aqueous solvent in the triple-helical DNA. In contrast, conjugate **S76a** experiencing a considerably smaller degree of quenching (44%) suggests weaker DNA−ligand interactions within the triple helix, possibly resulting from hindered intercalation of the indoloquinoline between base triads

Table 3. Thermodynamic Parameters for the Binding of Conjugate S16a and the Unmodified TFO S0 to the Target Duplex at 10 °C[a]

TFO	method	n	K_a (M^{-1})	$\Delta H°$ (kcal mol^{-1})	$T\Delta S°$ (kcal mol^{-1})	$\Delta G°$ (kcal mol^{-1})
S0	UV melting	---	6.8×10^6 [b]	−		−8.8
	ITC	1.02 ± 0.05	$2.8 \times 10^6 \pm 0.75 \times 10^6$	-43.3 ± 2.6		−8.3
	model-free ITC	---	−	-44.2 ± 1.3	−35.9[c]	
S16a	UV melting	---	2.7×10^8 [b]	−		−10.9
	fluorescence titration	---	$6.2 \times 10^7 \pm 2.4 \times 10^7$	−		−10.1
	model-free ITC	---	−	-44.9 ± 0.1	−34.8[c]	
				$\Delta\Delta H°$	$\Delta(T\Delta S°)$	$\Delta\Delta G°$
				−0.7[d]	1.1	−1.8[c]

[a] Average values with standard deviations from three or five (fluorescence titrations) independent experiments at 283 K. [b] Calculated for 283 K with a constant $\Delta H°$ obtained from "model-free" ITC titrations. [c] Calculated with $\Delta G°$ as obtained from ITC or fluorescence titrations. [d] Calculated with $\Delta H°$ obtained from "model-free" ITC titrations.

in line with the UV melting experiments (vide supra). However, without detailed knowledge of the quenching mechanism for these ligands, fluorescence data do not provide further information in support of a particular binding mode.

We also plotted the relative fluorescence intensity for **S16a** at 466 nm taken from the corresponding emission spectra against the duplex concentration (inset Figure 3A). By using a 1:1 binding model for the triplex formation (*18*), a fit of the titration data from five independent experiments yielded an average binding constant of $K_a = 6.2 \times 10^7$ M^{-1} at 10 °C.

Isothermal Titration Calorimetry. Isothermal titration calorimetry (ITC) allows for an almost complete thermodynamic profile for a binding interaction in a single experiment enabling the direct determination of the molar binding enthalpy (*29, 30*). Although ITC has become increasingly popular for the thermodynamic analysis of biomolecular interactions in general and drug−DNA interactions in particular, binding of triplex selective ligands to a duplex target has only rarely been scrutinized by direct calorimetric methods. This is particularly true for ligands covalently attached to the TFO and known to result in more efficient triplex stabilization compared to free ligand apparently due to more favorable entropic contributions on binding. Whereas the formation of a regular triplex of the pyrimidine motif has been thermodynamically characterized by ITC titrations in the past (*31, 32*), no detailed quantitation of enthalpic and entropic effects of bound ligands in a TFO conjugate through direct calorimetric measurements has been reported so far to the best of our knowledge. Clearly, problems with such studies are associated with the significantly varied stability of triplexes under specific conditions and with the rather high accuracy required to reliably quantify the mostly small contribution of the bound ligand on the overall free energy of conjugate binding in particular.

We focused on the ITC thermodynamic analysis of the unmodified reference triplex and of the triplex formation with conjugate **S16a** available in sufficient quantities by its efficient coupling to the 5′-end of the TFO. To ensure an intact duplex target and TFO binding with a free energy of association suitable for accurate ITC measurements, we chose a temperature of 10 °C for all titration experiments based on the UV melting temperatures. All thermodynamic parameters obtained from initial ITC experiments on the triplex formation with unmodified TFO are given in Table 3.

Binding isotherms are constructed by integration of the power output for each injection with respect to time and corrected for the heats of dilution. Through a fit of the observed binding isotherms based on a model with a single set of identical binding sites, the equilibrium binding constant K_a, the binding stoichiometry n, and the molar binding enthalpy $\Delta H°$ were determined to be 2.8×10^6 M^{-1}, 1.02, and −43.3 kcal mol^{-1}, respectively (Figure 4A). Note that triplex formation involves binding of the 9-mer TFO within the major groove of the 15-mer duplex target and should result in a well-defined 1:1 complex in line with the ITC data. In an attempt to further increase its accuracy, the binding enthalpy was directly measured in a model-independent fashion through the excess-site method (*33, 34*). In this protocol, a high concentration of the duplex DNA is placed in the cell and titrated with very low amounts of ligand to ensure complete ligand binding to the target duplex after each injection. Under such excess duplex conditions, the integration of each injection peak yields the heat released per injection and its normalization per mole of added ligand directly results in the molar binding enthalpy without the requirement to resort to specific binding models or fitting procedures (Figure 4B). As shown in Table 3, the determined enthalpy value of −44.2 kcal mol^{-1} for the unmodified triplex is in good agreement with the value determined by the standard ITC titration protocol. Moreover, the high accuracy and good reproducibility of $\Delta H°$ is indicated by its rather small standard deviation calculated for different independent experiments.

The model-free excess-site method was also employed for a direct determination of binding enthalpies for the TFO conjugate **S16a** (Figure 4C). Here, a similar and highly reproducible enthalpy value of −44.9 kcal mol^{-1} is obtained for binding (Table 3). As seen from Figure 4C (**S16a**) and B (**S0**) in the upper panel, the blank titration with the conjugate sample shows larger effects in the endothermic heat of dilution compared to the unmodified TFO at equal concentrations as a consequence of the attached hydrophobic ligand. With an association constant close to 10^8 M^{-1} already determined by fluorescence titrations and the limitations imposed by the ITC method, a standard ITC titration protocol is expected to yield less reliable binding constants in the case of the conjugate, and these were therefore not employed for a subsequent evaluation. In addition, corresponding experiments highlight another potential source of error arising from slow kinetics of triplex formation with the conjugate especially toward the equivalence point under the low-temperature and small concentration conditions required for the experimental setup. Thus, fitting of the isotherms for the conjugate binding consistently underestimated binding enthalpies and association constants. In fact, raw ITC data reveal the influence of slow conjugate association on closer inspection, e.g., through baseline distortions, and it also becomes apparent in corresponding fluorescence titrations requiring delay times between titration steps of up to 30 min in some cases for full equilibration.

In addition to the association constants as determined by fluorescence titrations and ITC titrations, K_a was calculated at 283 K from the UV melting data (Table 2) and is also given in Table 3 for ligand-modified and unmodified triplex. Neglecting any temperature dependence of $\Delta H°$, the van't Hoff equation was solved with the calorimetric binding enthalpy from "model-free" ITC measurements and applied to the association constant given at the melting temperature to

$$K_a(T_m) = \frac{1}{c_{TFO}} \quad (5)$$

$$c_{TFO}(T_m) = c^o_{TFO} - \frac{1}{2} c^o_{duplex} \quad (6)$$

with the concentration of free TFO c_{TFO} and the total TFO and duplex concentration c^o_{TFO} and c^o_{duplex}, respectively. As shown by Table 3, these calculated binding constants K_a deviate by a factor of about 2 and 4 in the case of unmodified and modified TFO and translate to differences in the free energy of association of 0.5 and 0.8 kcal mol^{-1}, respectively. Discrepancies between calorimetric enthalpy changes and thermodynamic analyses based on the van't Hoff relationship have been extensively discussed and may involve coupled processes during association (*31*). In particular, stacking interactions within the unbound single-stranded TFO, especially involving stacking of the polycyclic ligand with the nucleobases, may contribute to a significant temperature dependence of the overall binding enthalpy. Nevertheless, the data as obtained from the different methods are in good agreement given the various approximations and confirm the consistency and reliability of the thermodynamic parameters.

Effect of pH on Triplex Stabilization. In vivo applications of triplex-forming oligonucleotides directed against double-helical target sequences require strong and selective binding at physiological pH and temperature. The effect of pH on the triplex stabilization by the attached ligand has been examined by additional UV melting experiments for the two 5′-conjugates **S16a** and **S16b** and is shown in Figure 5. Clearly, while duplex melting is essentially unaffected triplex melting temperatures increase for the unmodified reference triplex from 12 to 33 °C upon lowering the pH from 6.5 to 5.5 due to a larger extent of third-strand cytosine protonation required for a stable Hoogsteen base pair within the pyrimidine triplex motif (Figure 5A). Again, the PIQ ligands lead to additional stabilization and form stronger triplexes compared to the nonconjugated TFO at all pH values. However, as shown by Figure 5B ligand stabilization strongly depends on the particular pH of the solution ranging from a ΔT_m of about 17 °C at pH 5.75 to only 9 °C at pH 6.5 for conjugate **S16a** and is expected to further decrease above neutral pH.

If protonation equilibria were excluded as major determinants of ligand stabilization, the temperature dependence of ligand binding, i.e., $\Delta H°$, must be responsible for the varying ΔT_m values. Note that changes in melting temperatures reflect triplex stabilizing effects at T_m, and these are strongly dependent on pH (Figure 5A). However, with an experimentally determined $\Delta H°$ of −0.7 kcal mol^{-1} attributed to the DNA interactions with the covalently attached ligand (vide supra) no significant change or even a decrease in ligand binding affinity is expected from the van't Hoff relationship when increasing the overall triplex stability by lowering the pH. Consequently, protonation of the ligand and/or third-strand cytosines must play a major role in the ligand-induced triplex stabilization. With the 5′-attached ligand separated from the nearest cytosine by two thymine bases, any influence of ligand interactions through cytosine protonation is anticipated to only result from long-range effects. This suggests a direct protonation of the ligand as the major contributor to triplex specific binding. In fact, a large increase

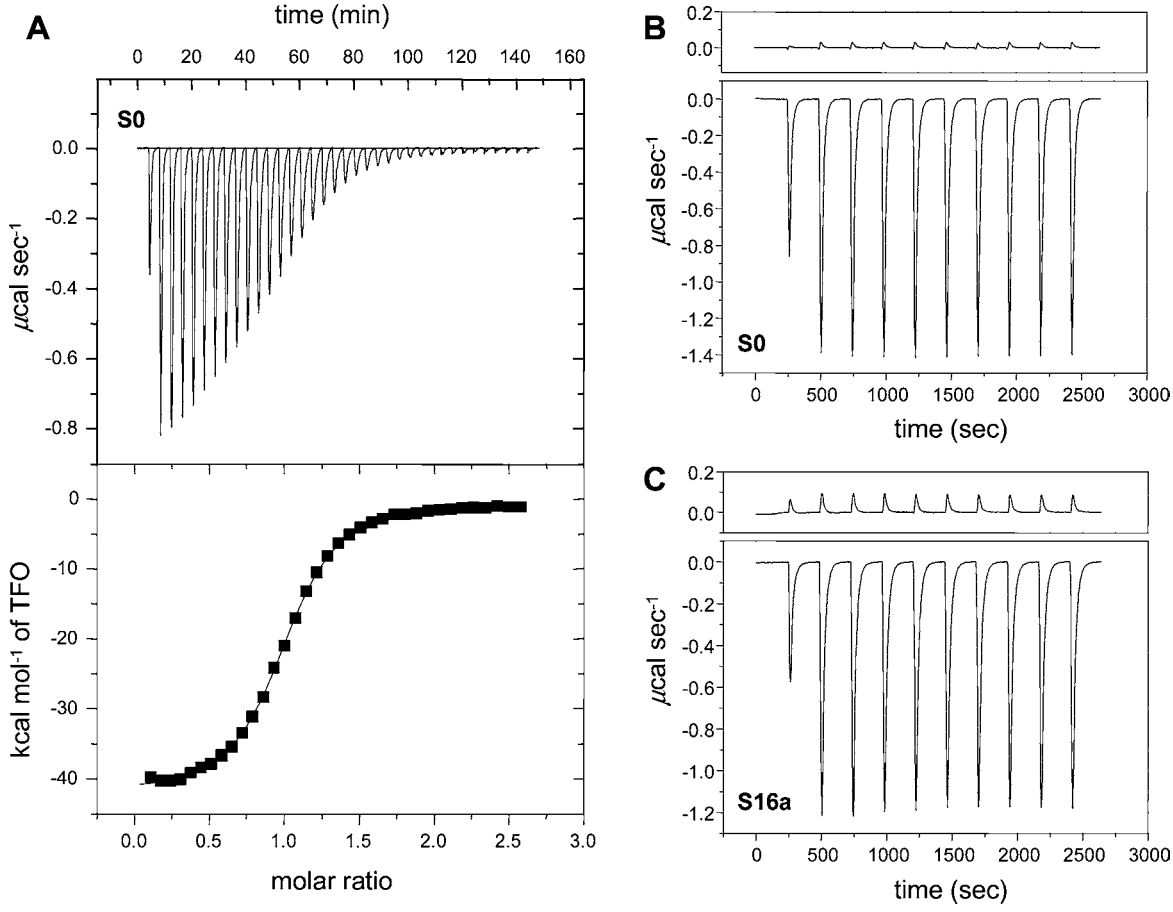


Figure 4. (A) ITC binding isotherm of the triplex formation with unmodified TFO **S0**. The upper panel shows the heat burst for every injection step, and the lower panel represents the corresponding normalized heat signals versus molar ratio. The data points reflect the experimental data, while the solid line represents the calculated fit. (B) The model-independent ITC titration with unmodified TFO **S0** and (C) with conjugate **S16a** representing the blank titration in the upper panel and the blank-corrected ITC data used for the calculation in the lower panel.

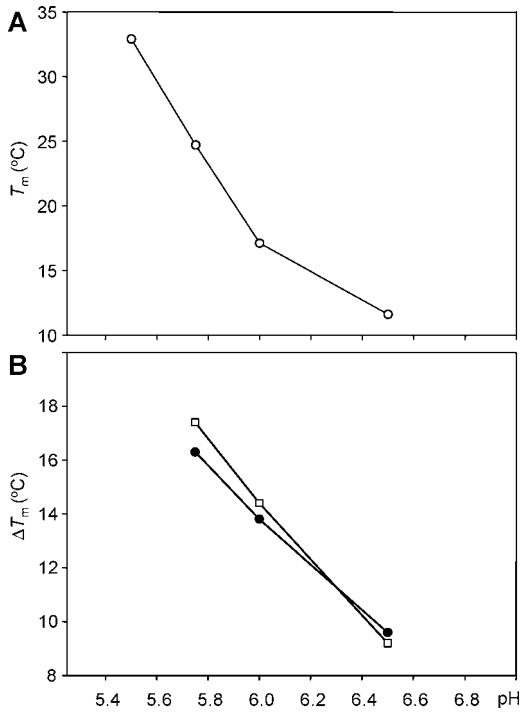


Figure 5. (A) Triplex melting temperatures for the unmodified reference triplex and (B) ΔT_m for the triplex transition with 5′-conjugates **S16a** (open squares) and **S16b** (filled circles) as a function of pH (0.1 M NaCl, 0.02 M cacodylate, 1 mM spermine). Below pH 5.75, no accurate ΔT_m could be obtained due to partially overlapping triplex and duplex melting transitions for the conjugates.

in pK_a values of about two pH units has been observed for two nonconjugated and soluble derivatives of PIQa and PIQb when bound to triplex DNA pointing to enhanced binding energetics for the protonated ligands (see Supporting Information). With apparent pK_a values of 6.2 and 6.7 determined for the methyl- and methoxy-substituted indoloquinolines in the presence of excess triplex DNA, respectively, protonation must be coupled to ligand binding, and a strongly pH dependent but different degree of protonation is expected for the ligand in **S16a** and **S16b** within the experimentally accessed pH range of 6.0 ± 0.5. With its higher pK_a value, the methoxy-substituted ligand of conjugate **S16b** being slightly less stabilizing at pH 5.75 compared to **S16a** becomes more stabilizing at pH 6.5 in line with its significantly higher degree of protonation at this pH. Apparently, triplex binding is only modest under physiological conditions for the present indoloquinolines being mostly deprotonated and uncharged. However, introduction of suitable substituents are expected to considerably increase the pK_a of the indoloquinoline structure beyond 7 when bound to a triplex resulting in compounds with the propensity to strongly bind triplexes even at higher pH.

Thermodynamics of Conjugate Binding. As found previously for different triple helices under various conditions, triplex formation is driven by a large negative enthalpy change and partly balanced by an unfavorable entropy of association for both unmodified and modified TFO. With a molar binding enthalpy for the unmodified third strand of −44.2 kcal mol^{-1}, the calorimetric enthalpy change upon triplex formation amounts to −4.9 kcal mol^{-1} per base being within the range typically observed for a pyrimidine-type triplex (*31, 35*). Thus, a value of −4.9 kcal mol^{-1} per base has also been reported for a similar 15-mer triplex construct of the pyrimidine motif at 15 °C and pH 4.8 (*31*). As a result of their higher apparent pK_a value in a triplex (*36*), cytosine bases as well as the ligand of the TFO are expected to become partly protonated at pH 6 upon

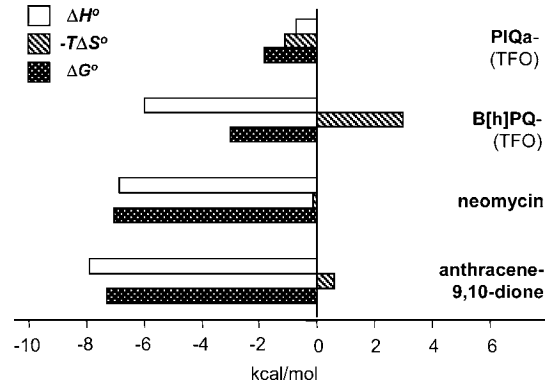


Figure 6. Thermodynamic profiles with enthalpic and entropic contributions $\Delta H°$ and $-T\Delta S°$ to the overall free energy $\Delta G°$ for the triplex interaction of 5′-TFO attached PIQa (see Table 3) and B[*h*]PQ (*24*), as well as of the nonconjugated triplex selective 2,6-bis(ω-aminopropionamido)-substituted anthracene-9,10-dione (*37*) and neomycin (*38*). For comparison, all parameters were calculated for 25 °C if determined at different temperatures assuming temperature-independent binding enthalpies and entropies.

association and the measured $\Delta H°$ involves contributions from the deprotonation of buffer and from the protonation of cytosines, as well as ligand in the conjugate.

Contributions to triplex stability from the tethered indoloquinolines can be evaluated by the differences in enthalpy and entropy changes as determined for the binding of unmodified TFO and ligand-bearing conjugate. These are also given in Table 3. It has to be noted that these values do not exclusively reflect direct ligand−DNA interactions but may also include indirect effects through structural distortions even at distant triple- or double-helical regions caused by the accommodation of the chromophore. Most noticeably, the attached ligand only adds a very small amount of −0.7 kcal mol^{-1} to the overall negative binding enthalpy. This may be partly attributed to the covalent attachment that hampers maximization of interactions within the triplex. On the other hand, tethering the indoloquinolines to the TFO considerably reduces entropic penalties upon binding resulting in a positive entropy change that mostly contributes to the ligand binding affinity. Clearly, even taking into account experimental uncertainties as expressed by the standard deviations, both enthalpy and entropy contributions are small but add to an overall free energy of −1.8 kcal mol^{-1} at 10 °C for the ligand interactions comprising almost 20% of the total standard free energy of triplex formation.

To better assess the triplex affinity of the 5′-attached ligand within the conjugate **S16a**, its thermodynamic profile for triplex binding was compared with corresponding profiles previously reported for a strongly triplex stabilizing and intercalating benzopyridoquinoxaline B[*h*]PQ covalently attached to the 5′-end of a 15-mer TFO (*24*). Note that in contrast to the calorimetric enthalpies for PIQa the thermodynamic parameters for the B[*h*]PQ ligand have been derived from UV melting curves by a van't Hoff analysis. Also included for comparison are thermodynamic parameters on triplex binding that have been reported for two nonconjugated triplex selective ligands through calorimetric measurements, namely, an intercalating 2,6-disubstituted anthracene-9,10-dione (*37*) and the groove binding aminoglycoside neomycin (*38*). After the varied experimental conditions on data collection are disregarded, the profiles as shown in Figure 6 reveal significant differences for the triplex stabilizing contributions at 298 K. Triplex binding for conjugated B[*h*]PQ and the two free anthracene and neomycin ligands is largely enthalpy-driven associated with a significant negative binding enthalpy. In contrast, with only a small change in enthalpy but favorable changes in entropy, binding of the TFO-

attached PIQ is essentially entropy-driven. This suggests rather weak DNA−ligand interactions but significant hydrophobic contributions to the binding free energy for the latter.

The binding affinity toward triple-helical DNA as reflected by the free energy of binding ΔG° is found to be significantly more exergonic for the nonconjugated free ligands compared to the TFO-attached intercalators. It has to be noted, however, that weaker triplex binding is compensated by a much better discrimination of triplex against duplex for the TFO-conjugated ligands making these generally more effective for a triplex thermal stabilization. In fact, they may be considered truly triplex specific in line with spectroscopic data suggesting a one-step dissociation of the TFO conjugate from the triplex upon melting (*16*).

CONCLUSIONS

Novel TFO conjugates with triplex binding indolo[3,2-*b*]-quinoline derivatives attached at the oligonucleotide termini or at an internal thymine position with different linkers were synthesized and tested for their triplex formation. In general, 5′- and 3′-conjugates form triplexes with the highest stability but for maximum thermal stabilization the attachment site, and the type of linker needs to be optimized. The detailed thermodynamic profile and pH dependence of triplex formation points to the importance of ring protonation for the ligands to achieve efficient triplex binding. The present structures still suffer from a relatively low pK_a when employed under neutral solution conditions. However, modified phenyl-indoloquinolines with ring substituents like amino groups should allow for a higher basicity accompanied with apparent pK_a values above 7 and will be promising future candidates for triplex recognition and triplex formation even under physiological conditions.

ACKNOWLEDGMENT

We thank Mrs. R. Schröder for her help in the synthesis of the 5-phenyl-6*H*-indolo[3,2-*b*]quinolines.

Supporting Information Available: CD spectra of triplexes with unmodified and internally modified TFOs as well as details of pK_a determinations including pH dependent UV−vis spectra and absorbances for the free and triplex bound PIQa and PIQb ligands. This material is available free of charge via the Internet at http://pubs.acs.org.

LITERATURE CITED

(1) Jain, A., Wang, G., and Vasquez, K. M. (2008) DNA triple helices: Biological consequences and therapeutic potential. *Biochimie 90*, 1117–1130.

(2) Mirkin, S. M. (2008) Discovery of alternative DNA structures: A heroic decade (1979−1989). *Front. Biosci. 13*, 1064–1071.

(3) Thuong, N. T., and Hélène, C. (1993) Sequence-specific recognition and modification of double-helical DNA by oligonucleotides. *Angew. Chem., Int. Ed. Engl. 32*, 666–690.

(4) Hélène, C., Thuong, N. T., and Harel-Bellan, A. (1992) Control of gene expression by triple helix-forming oligonucleotides. The antigene strategy. *Ann. N.Y. Acad. Sci. 660*, 27–36.

(5) Knauert, M. P., and Glazer, P. M. (2001) Triplex forming oligonucleotides: Sequence-specific tools for gene targeting. *Hum. Mol. Genet. 10*, 2243–2251.

(6) Belotserkovskii, B. P., De Silva, E., Tornaletti, S., Wang, G., Vasquez, K. M., and Hanawalt, P. C. (2007) A triplex-forming sequence from the human c-*MYC* promoter interferes with DNA transcription. *J. Biol. Chem. 282*, 32433–32441.

(7) Giovannangeli, C., and Hélène, C. (2000) Triplex technology takes off. *Nat. Biotechnol. 18*, 1245–1246.

(8) Povsic, T. J., Strobel, S. A., and Dervan, P. B. (1992) Sequence-specific double-strand alkylation and cleavage of DNA mediated by triple-helix formation. *J. Am. Chem. Soc. 114*, 5934–5941.

(9) Vasquez, K. M., Narayanan, L., and Glazer, P. M. (2000) Specific mutations induced by triplex-forming oligonucleotides in mice. *Science 290*, 530–533.

(10) Gonñi, J. R., Vaquerizas, J. M., Dopazo, J., and Orozco, M. (2006) Exploring the reasons for the large density of triplex-forming oligonucleotide target sequences in the human regulatory regions. *BMC Genomics 7*, 63–72.

(11) Duca, M., Vekhoff, P., Oussedik, K., Halby, L., and Arimondo, P. B. (2008) The triple helix: 50 years later, the outcome. *Nucleic Acids Res. 36*, 5123–5138.

(12) Fox, K. R. (2000) Targeting DNA with triplexes. *Curr. Med. Chem. 7*, 17–37.

(13) Gianolio, D. A., Segismundo, J. M., and McLaughlin, L. W. (2000) Tethered naphthalene diimide-based intercalators for DNA triplex stabilization. *Nucleic Acids Res. 28*, 2128–2134.

(14) Silver, G. C., Sun, J.-S., Nguyen, C. H., Boutorine, A. S., Bisagni, E., and Hélène, C. (1997) Stable triple-helical DNA complexes formed by benzopyridoindole- and benzopyridoquinoxaline-oligonucleotide conjugates. *J. Am. Chem. Soc. 119*, 263–268.

(15) Gaied, N. B., Zhao, Z., Gerrard, S. R., Fox, K. R., and Brown, T. (2009) Potent triple helix stabilization by 5′,3′-modified triplex-forming oligonucleotides. *ChemBioChem 10*, 1839–1851.

(16) Eick, A., Xiao, Z., Langer, P., and Weisz, K. (2008) Spectroscopic studies on the formation and thermal stability of DNA triplexes with a benzoannulated δ-carboline-oligonucleotide conjugate. *Bioorg. Med. Chem. 16*, 9106–9112.

(17) Tataurov, A. V., You, Y., and Owczarzy, R. (2008) Predicting ultraviolet spectrum of single stranded and double stranded deoxyribonucleic acids. *Biophys. Chem. 133*, 66–70.

(18) Eftink, M. R. (1997) Fluorescence methods for studying equilibrium macromolecule-ligand interactions. *Methods Enzymol. 278*, 221–257.

(19) Rusling, D. A., Rachwal, P. A., Brown, T., and Fox, K. R. (2009) The stability of triplex DNA is affected by the stability of the underlying duplex. *Biophys. Chem. 145*, 105–110.

(20) Asensio, J. L., Dosanjh, H. S., Jenkins, T. C., and Lane, A. N. (1998) Thermodynamic, kinetic, and conformational properties of a parallel intermolecular DNA triplex containing 5′ and 3′ junctions. *Biochemistry 37*, 15188–15198.

(21) Collier, D. A., Mergny, J.-L., Thuong, N. T., and Hélène, C. (1991) Site-specific intercalation at the triplex-duplex junction induces a conformational change which is detectable by hypersensitivity to diethylpyrocarbonate. *Nucleic Acids Res. 19*, 4219–4224.

(22) Todorović, N., Thi Bich Phuong, N., Langer, P., and Weisz, K. (2006) DNA triplex stabilization by a δ-carboline derivative tethered to third strand oligonucleotides. *Bioorg. Med. Chem. Lett. 16*, 1647–1650.

(23) Tuite, E., and Nordén, B. (1994) Sequence-specific interactions of methylene blue with polynucleotides and DNA: A spectroscopic study. *J. Am. Chem. Soc. 116*, 7548–7556.

(24) Silver, G. C., Nguyen, C. H., Boutorine, A. S., Bisagni, E., Garestier, T., and Hélène, C. (1997) Conjugates of oligonucleotides with triplex-specific intercalating agents. Stabilization of triple-helical DNA in the promoter region of the gene for the α-subunit of interleukin 2 (IL-2Rα). *Bioconjugate Chem. 8*, 15–22.

(25) Vinogradov, S., Roig, V., Sergueeva, Z., Nguyen, C. H., Arimondo, P., Thuong, N. T., Bisagni, E., Sun, J.-S., Hélène, C., and Asseline, U. (2003) Synthesis and binding properties of oligo-2′-deoxyribonucleotides conjugated with triple-helix-specific intercalators: benzo[*e*] and benzo[*g*] pyridoindoles. *Bioconjugate Chem. 14*, 120–135.

(26) Ossipov, D., Zamaratski, E., and Chattopadhyaya, J. (1999) Dipyrido[3,2-a:2′,3′-*c*]phenazine-tethered oligo-DNA: synthesis and thermal stability of their DNA·DNA and DNA·RNA duplexes and DNA·DNA·DNA triplexes. *Helv. Chim. Acta 82*, 2186–2200.

(27) Sun, J.-S., François, J. C., Montenay-Garestier, T., Saison-Behmoaras, T., Roig, V., Thuong, N. T., and Hélène, C. (1989) Sequence-specific intercalating agents: Intercalation at specific sequences on duplex DNA via major groove recognition by oligonucleotide-intercalator conjugates. *Proc. Natl. Acad. Sci. U.S.A. 86*, 9198–9202.

(28) Chomilier, J., Sun, J.-S., Collier, D. A., Garestier, T., Hélène, C., and Lavery, R. (1992) A computational and experimental study of the bending induced at a double-triple helix junction. *Biophys. Chem. 45*, 143–152.

(29) Chaires, J. B. (2008) Calorimetry and thermodynamics in drug design. *Annu. Rev. Biophys. 37*, 135–151.

(30) Haq, I. (2002) Thermodynamics of drug-DNA interactions. *Arch. Biochem. Biophys. 403*, 1–15.

(31) Kamiya, M., Torigoe, H., Shindo, H., and Sarai, A. (1996) Temperature dependence and sequence specificity of DNA triplex formation: An analysis using isothermal titration calorimetry. *J. Am. Chem. Soc. 118*, 4532–4538.

(32) Torigoe, H., Shimizume, R., Akinori, S., and Shindo, H. (1999) Triplex formation of chemically modified homopyrimidine oligonucleotides: Thermodynamic and kinetic studies. *Biochemistry 38*, 14653–14659.

(33) Haq, I., Chowdhry, B. Z., and Jenkins, T. C. (2001) Calorimetric techniques in the study of high-order DNA-drug interactions. *Methods Enzymol. 340*, 109–149.

(34) Ren, J., Jenkins, T. C., and Chaires, J. B. (2000) Energetics of DNA intercalation reactions. *Biochemistry 39*, 8439–8447.

(35) Wachowius, F., Rettig, M., Palm, G., and Weisz, K. (2008) Synthesis and DNA duplex recognition of a triplex-forming oligonucleotide with an ureido-substituted 4-phenylimidazole nucleoside. *Tetrahedron Lett. 49*, 7264–7267.

(36) Leitner, D., Schröder, W., and Weisz, K. (1998) Direct monitoring of cytosine protonation in an intramolecular DNA triple helix. *J. Am. Chem. Soc. 120*, 7123–7124.

(37) Haq, I., Ladbury, J. E., Chowdhry, B. Z., and Jenkins, T. C. (1996) Molecular anchoring of duplex and triplex DNA by disubstituted anthracene-9,10-diones: Calorimetric, UV melting, and competition dialysis studies. *J. Am. Chem. Soc. 118*, 10693–10701.

(38) Arya, D. P., Micovic, L., Charles, I., Coffee, R. L., Jr., Willis, B., and Xue, L. (2003) Neomycin binding to Watson-Hoogsteen (W-H) DNA triplex groove: A model. *J. Am. Chem. Soc. 125*, 3733–3744.

BC100107N

Double Displacement: An Improved Bioorthogonal Reaction Strategy for Templated Nucleic Acid Detection

Daniel J. Kleinbaum, Gregory P. Miller, and Eric T. Kool*

Department of Chemistry, Stanford University, Stanford, California 94305-5080. Received April 3, 2010; Revised Manuscript Received April 26, 2010

Quenched autoligation probes have been employed previously in a target-templated nonenzymatic ligation strategy for detecting nucleic acids in cells by fluorescence. A common source of background signal in such probes is the undesired reaction with water and other cellular nucleophiles. Here, we describe a new class of self-ligating probes, double displacement (DD) probes, that rely on two displacement reactions to fully unquench a nearby fluorophore. Three potential double displacement architectures, all possessing two fluorescence quencher/leaving groups (dabsylate groups), were synthesized and evaluated for templated reaction with nucleophile (phosphorothioate) probes both in vitro and in intact bacterial cells. All three DD probe designs provided substantially better initial quenching than a single-Dabsyl control. In isothermal templated reactions in vitro, double displacement probes yielded considerably lower background signal than previous single displacement probes; investigation into the mechanism revealed that one dabsylate acts as a sacrificial leaving group, reacting nonspecifically with water, but yielding little signal because another quencher group remains. Templated reaction with the specific nucleophile probe is required to activate a signal. The double displacement probes provided a ca. 80-fold turn-on signal and yielded a 2−4-fold improvement in signal/background over single Dabsyl probes. The best-performing probe architecture was demonstrated in a two-color, FRET-based two-allele discrimination system in vitro and was shown to be capable of discriminating between two closely related species of bacteria differing by a single nucleotide at an rRNA target site.

INTRODUCTION

Nucleic acid templated chemistry is a versatile approach to a growing number of applications in chemistry, biology, and medicine. These reactions have been used to ligate short oligonucleotides (*1*−*3*), catalyze prodrug release (*4*) or cytotoxic drug generation (*5*), synthesize small molecules (*6*−*9*), and evolve modified nucleic acids (*10*). Templated reactions have also been used to detect nucleic acid sequences both in vitro and in cells (*11*). Unlike more conventional methods for nucleic acid detection such as polymerase chain reaction (PCR) (*12*) and fluorescence in situ hybridization (FISH) (*13, 14*), templated reactive probes can in some cases be employed for cellular RNA/DNA identification without lysing or fixing the cells, and do not require washing steps. This makes probing operationally easier to perform and the results straightforward to interpret. It also allows for the analysis of heterogeneous samples of cells and for sorting cells based on their genetics (*15*). In addition to templated reactive probes, other classes of fluorogenic nucleic acid probes, including molecular beacons and nanoparticle-based systems, are also under investigation for such applications (*16*−*20*).

Several fluorogenic reaction strategies have been investigated for templated nucleic acid detection, including fluorophore uncaging (*21*−*27*), quencher release (*28*), fluorophore synthesis (*29, 30*), fluorophore release (*31*), and quencher transfer (*32, 33*). Our laboratory has described quenched autoligation (QUAL) probes that rely on an S_N2 reaction to displace a fluorescence quencher, unquenching a nearby fluorophore (*34*−*36*). While these probes have been used to discriminate among different strains of bacteria based on small differences in rRNA sequences and to detect high-copy-number mRNAs in mammalian cells, the reported designs can be limited by a significant background signal; a low background would ultimately be needed to detect rarer RNAs. The background signal from the probes arose largely from nontemplated displacement of the quencher by cellular nucleophiles such as water and thiols. Thus, we have pursued new strategies that increase specific signals and decrease such background signals. In this light, we describe here double displacement (DD) probes, which require two displacement events to fully unquench a fluorophore.

Double displacement probes were designed to have two fluorescence quenchers as leaving groups on the terminus of a DNA probe. The nonspecific displacement of only one of these quenchers (by water, for example) should not produce a large increase in fluorescence, since another quencher remains. However, the binding of a DD probe adjacent to a nucleophile probe on a target sequence markedly increases the rate at which the quenchers are displaced, leading to signal generation. Herein, we describe the synthesis and evaluation of three architectures for double displacement. These new probes are shown to provide enhanced initial quenching and also yield considerably lower background signal during in vitro and cellular nucleic acid detection. Two-color DD probes are further shown to discriminate among bacterial cell types in a heterogeneous mixture based on a single-nucleotide polymorphism.

EXPERIMENTAL PROCEDURES

Double Displacement Oligonucleotide Probe Synthesis. Pac-dA, iPr-dG, and Ac-dC phosphoramidites for UltraMild synthesis (Glen Research) were employed in synthesizing oligonucleotides containing the double displacement linker. The fluorescein label was introduced with fluorescein-dT phosphoramidite (Glen Research). The TAMRA label was introduced using a 3′-TAMRA CPG (Glen Research). Deprotection and cleavage from the CPG support was carried out by incubation in 0.05 M K_2CO_3 in CH_3OH (Glen Research) for 4 h at room temperature. The oligonucleotides were purified by reverse-

* E-mail: kool@stanford.edu.

10.1021/bc100165h © 2010 American Chemical Society
Published on Web 05/28/2010

phase HPLC (Prosphere C18 300 Å 10u 250 mm, eluting with 0.1 M triethylammonium acetate, pH 7.0 and acetonitrile). Probe structure was confirmed by MALDI-TOF mass spectrometry (see Supporting Information).

Preparation of Single-Dabsyl Probes. Single-Dabsyl (butyl linker) probes were prepared and purified as previously described (*36*).

Templated Double Displacement Reactions. Reactions were performed in 70 mM PIPES buffer (pH 7.0) containing 10 mM $MgCl_2$ and 50 μM dithiothreitol in a Flexstation II 384 microplate reader. Reaction mixtures contained 100 nM each of quencher probe and template and 120 nM of nucleophile DNA. Reactions were initiated by addition of the nucleophile DNA to wells containing the quencher probe and template DNA. The emission was measured in 2 min intervals at 525 nm with excitation at 494 nm over 8 h. The control reactions were performed with the template omitted from the reaction mixture.

Monitoring Dabsylate Release by HPLC. Reactions were performed in 70 mM PIPES buffer (pH 7.0) containing 10 mM $MgCl_2$ and 50 μM dithiothreitol at 25 °C. At the specified time points, aliquots of the reaction were taken and injected onto an analytical RP-HPLC column (Alltech Platinum C18 100 Å 5u 250 mm), eluting with 0.1 M triethylammonium acetate, pH 7.0, and acetonitrile. The integration of the dabsylate peak was taken and converted to a measure of the number of equivalents of dabsylate based on a standard curve prepared separately with known concentrations.

Testing Intracellular RNA Detection. *E. coli* K12 and *S. enterica* cells were grown to log phase (OD600 = 0.4−0.6) in Luria−Bertani (LB) media at 37 °C with rapid shaking. Aliquots of media were centrifuged for 5 min. The supernatant was removed and pellets were resuspended in 0.1 mL phosphate-buffered saline solution (pH 7.4). The cells were centrifuged again for 5 min and the supernatant was removed. The pellets were resuspended in 0.1 mL hybridization buffer: 0.9 M sodium chloride and 90 mM sodium citrate (6× SSC) and 0.05% SDS. Aliquots of bacteria suspended in the buffer were treated with quencher probe (200 nM), nucleophile probe (2 μM), and helper probes (3 μM each). The reaction mixtures were incubated in the dark at 37 °C. Aliquots of incubated bacteria were mixed 1:1 with a 1% agarose solution and spotted on a glass slide without washing or fixation steps. Imaging was performed on a Nikon Eclipse E800 epifluorescence microscope equipped with a Nikon Plan AP 100×/1.40 oil immersion objective and a SPOT RT digital camera.

RESULTS

Design and Synthesis of Double Displacement Probes. Three potential double displacement probe scaffolds were designed to improve the signal/background ratio of the original single displacement probe structure (Figure 1). As with the prior design, the leaving group in this approach (called dabsylate in analogy to tosylate) serves both to activate the substrate for electrophilic attack and to quench a nearby fluorophore.

The first two linkers designed are structural isomers based on a 1,3,5-pentanetriol scaffold. The first (1,5-Pentyl) has the quenchers on the two primary positions, which should make both reactive S_N2 substrates. The second (1,3-Pentyl) has the quenchers at a primary and a secondary position. Since S_N2 reactions are approximately 1 order of magnitude slower at secondary carbons than at terminal alkyl positions (*37*), we hypothesized that this scaffold would be less prone to multiple nontemplated reactions. The third new scaffold (Isobutyl) was designed with both quenchers at more hindered positions by using a branched scaffold. Isobutyl electrophiles are expected to react with rates around the same order of magnitude as secondary positions (*37*), which was expected to make this linker the most challenging S_N2 substrate of the three and therefore allow fewer untemplated reactions and an even lower background signal.

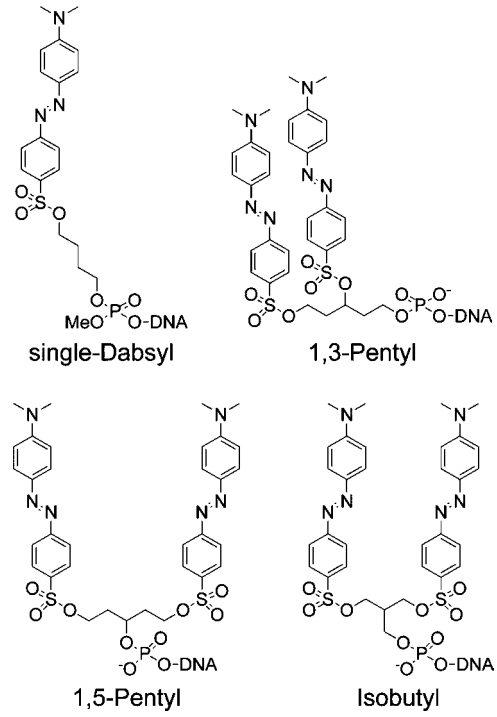


Figure 1. Structures of the reactive parts of double displacement and control (single displacement) probes.

The synthesis of all three new reactive linkers was straightforward, with phosphoramidite analogues prepared on the third alcohol group. The synthesis of the 1,3-Pentyl linker did require extra steps to allow for installation of a quencher at the secondary position instead of one of the primary positions, but it was still synthetically accessible. For the initial studies, we prepared identical 18mer DNA probes having the DD reactive linkers at the 5′ end, along with a fluorescein moiety at the third position. The syntheses of all three DD linker phosphoramidites and their subsequent oligonucleotide conjugation are described in the Supporting Information and Experimental Procedures, respectively.

Initial Quenching Efficiency. The initial quenching efficiencies of the three double displacement probes were measured and compared to the initial degree of quenching of the single-Dabsyl control probe. All three double displacement scaffolds demonstrated superior quenching of the nearby fluorescein moiety, yielding lower initial fluorescence of the unreacted probe (Supporting Information, Figure S1) by a factor of at least four. Such an effect has been demonstrated with molecular beacons, where adding multiple quenchers improved the quenching efficiency (*38*). It is unclear why both the 1,3-Pentyl and Isobutyl probes produce more efficient initial quenching than the 1,5-Pentyl probe, as all three have two quenchers approximately equidistant from the fluorophore. Differences in the structure and flexibility of the linkers may account for these small differences in quenching, by allowing different degrees of contact between quencher and fluorophore.

Templated Unquenching of Double Displacement Probes. We tested the reactivity of the probes in the presence of a DNA template. The fluorescence was monitored over 8 h at 37 °C with 100 nM probes in a pH 7.0 buffer containing 70 mM PIPES, 10 mM $MgCl_2$, and 50 μM dithiothreitol (Figure 2). As a control to evaluate background (off-template) signal levels, the template DNA was omitted in separate reactions for each

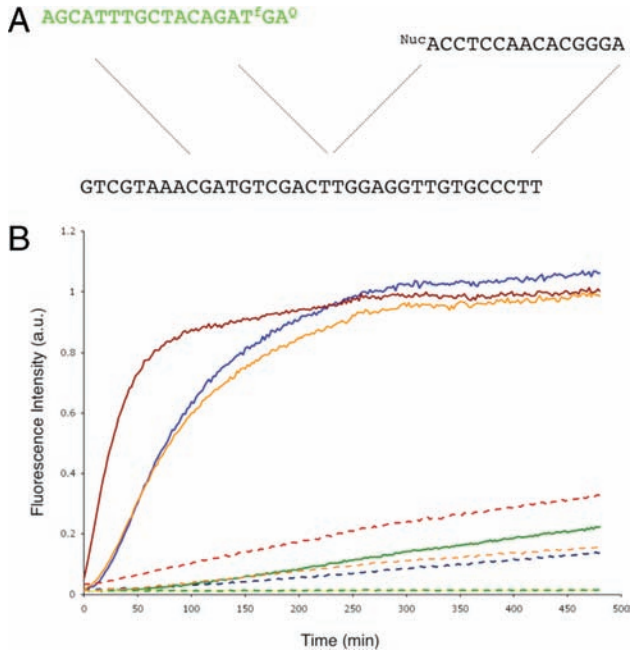


Figure 2. Fluorescence time course of double displacement and single Dabsyl ligation reactions at 37 °C. (A) Sequences of DNA probes and targets (T^f = fluorescein dT; Q = single-Dabsyl or double displacement linker; Nuc = phosphorothioate). (B) 100 nM of 1,3-Pentyl (blue), Isobutyl (green), 1,5-Pentyl (yellow), or single-Dabsyl (red) probe and 120 nM phosphorothioate probe were incubated with or without 100 nM template DNA at 37 °C in pH 7.0 buffer containing 70 mM PIPES, 10 mM $MgCl_2$, 50 μM dithiothreitol. The background (no template) reactions for each probe are shown as broken lines. The fluorescence was measured every 120 s with 494 nm excitation and 525 nm emission. Reactions were repeated in triplicate; representative traces are shown.

probe type. 15mer DNAs with 3′-phosphorothioate groups were used as the nucleophile probe in this and all subsequent experiments. In initial experiments, we also tested 3′-phosphorodithioate nucleophile DNAs; the dithioate moiety is a stronger nucleophile and produces faster displacement reactions (*39*). However, we found that stability issues at 37 °C made them less well suited for these experiments. Reactions and stability of phosphorodithioate nucleophiles in double displacement reactions are described in the Supporting Information.

In templated reactions with the phosphorothioate nucleophile DNA, results showed that two of the three DD probes yielded a substantial fluorescence turn-on signal. The 1,5-Pentyl and 1,3-Pentyl probes showed very similar fluorescence turn-on kinetics, somewhat slower than the rate of the single-Dabsyl control but reaching the same ultimate fluorescence level (Figure 2). The Isobutyl probe, which has both quenchers linked at hindered positions, gave a significantly slower reaction, reaching only ~30% conversion after 8 h. Importantly, background signals for all three DD probes were substantially lower than that of the single-Dabsyl control. Indeed, the background of the slower-reacting Isobutyl probe did not seem to increase at all over the time of the experiment.

From the kinetic data, we plotted the signal/background versus time for each reaction (Figure 3). The 1,3-Pentyl probe showed a higher signal/background at its peak than either the single-Dabsyl or 1,5-Pentyl probe, although the latter had a better ratio over the first hour of reaction. The signal/background ratio for the Isobutyl probe rose more slowly due to its lower reaction rate. However, at long reaction times the value approached that of the best probes. We also evaluated the different probes based on the fold change in fluorescence intensity over time (Figure 4). This metric takes into account the starting fluorescence level

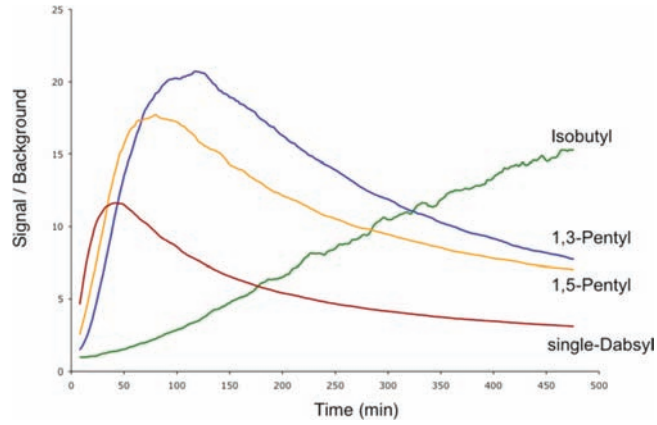


Figure 3. Change in signal/background for double displacement and single Dabsyl probes over time. The signal/background ratios for the 1,3-Pentyl (blue), Isobutyl (green), 1,5-Pentyl (yellow), and single Dabsyl (red) reactions over an 8 h time period. The reactions were run at 37 °C. 100 nM quencher probe and 120 nM phosphorothioate probe were incubated with or without 100 nM template DNA at 25 °C in pH 7.0 buffer containing 70 mM PIPES, 10 mM $MgCl_2$, and 50 μM dithiothreitol. The fluorescence was measured every 120 s with 494 nm excitation and 525 nm emission. The data were smoothed using a 7 point running average.

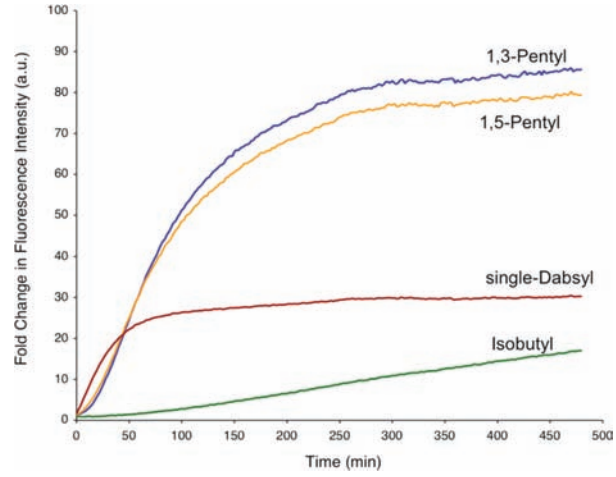


Figure 4. Fold change in fluorescence intensity over time. 100 nM of 1,3-Pentyl (blue), Isobutyl (green), 1,5-Pentyl (yellow), or single Dabsyl (red) probe and 120 nM phosphorothioate probe was incubated with 100 nM template DNA at 37 °C in pH 7.0 buffer containing 70 mM PIPES, 10 mM $MgCl_2$, and 50 μM dithiothreitol. The initial quenching was calculated before the phosphorothioate DNA was added to initiate the reaction. The fluorescence was measured every 120 s with 494 nm excitation and 525 nm emission. Reactions were repeated in triplicate, and the traces shown represent the average fold change in fluorescence at each time point.

of the probes, providing the relative magnitudes of fluorescence turn-on. This is particularly pertinent if the probes will be used for visual evaluations, because the probes with the highest amount of change over time will be the easiest to identify by eye. By this measure, the 1,3-Pentyl and 1,5-Pentyl probes produced similar 75- to 85-fold turn-on, both of which represent a significant improvement over the single-Dabsyl probe (30-fold). These fluorescence enhancements are similar in magnitude to those of the best turn-on values for other templated probes in the literature (*23, 24, 26*−*28*).

Determining Double Displacement Reaction Mechanism. In order to gain insight into the mechanism of reaction of the double displacement probes, the displacement of the quencher leaving group was monitored quantitatively by following the increase in dabsylate concentration in solution over time by RP-

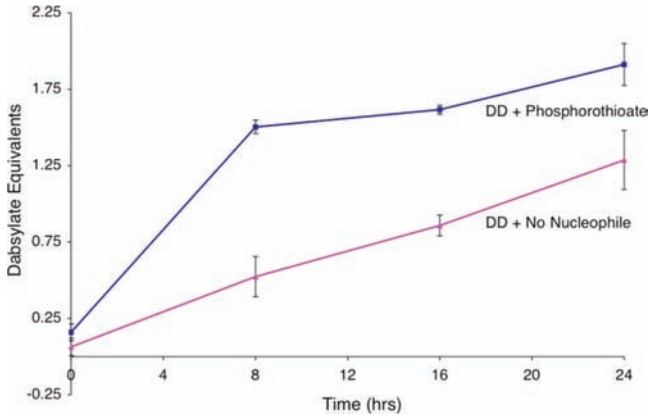


Figure 5. Monitoring dabsylate release in double displacement reaction. The amount of free dabsylate released in solution, as monitored by HPLC from reactions containing 1 μM DD probe, 1 μM template strand, and 1.2 μM phosphorothioate probe (blue) at 25 °C. The DD probe and template with no nucleophile probe present is shown in pink.

HPLC. The 1,5-Pentyl linker was chosen as a representative double displacement scaffold for these experiments. The data show that the rates of dabsylate appearance for reactions with and without a nucleophile probe primarily differ in the first few hours of the reaction (Figure 5). At 8 h, the reaction with the nucleophile had lost 1.5 equiv of dabsylate and the reaction without the nucleophile had lost 0.5 equiv. From then on, the rates of dabsylate appearance are very similar. By the time the reactions with the nucleophile displace 2 equiv of dabsylate, the reaction with no nucleophile present had displaced 1 equiv. This supports the intention of the probe design: while background (water) displacement of one of the quenchers does occur, there is a negligible change in signal until a templated nucleophile can react to displace the second one.

Detection of rRNA in Intact Bacterial Cells. In order to determine if the results we obtained in vitro translated to cellular conditions, all four probes were used to detect a previously targeted rRNA sequence in *Escherichia coli* cells (*39, 40*). Aliquots of bacteria in log phase growth were treated with 0.9 M sodium chloride and 90 mM sodium citrate (6× SSC) + 0.05% SDS, unlabeled helper DNAs, 3′-phosphorothioate probes, and the single Dabsyl or double displacement probes and incubated at 37 °C for 3 h. The purpose of the helper oligonucleotides was to disrupt the secondary structure of the rRNA and increase accessibility for the probes (*41*). The background fluorescence was determined by omitting the 3′-phosphorothioate oligonucleotides from the reaction. No washing or cell preparation steps were taken; the result was simply imaged after 3 h. Figure 6 shows representative images of cells for the foreground and background of each probe. Gratifyingly, the 1,3-Pentyl and 1,5-Pentyl probe give the best contrast between the templated and untemplated reactions in the intact bacteria, fully consistent with the results of the in vitro experiments.

Two-Color Probes for Discrimination Between Bacterial Species. Next, we tested whether double displacement linkers could be adapted to a two-color system of probes that allows one to visually distinguish between different types of cells in a heterogeneous mixture. To this end, we synthesized two new probes, both with a 1,3-Pentyl double displacement linker. Both probes are fluorophore-labeled 10mer oligonucleotides that differ only by a single base pair to render them complementary to a known site in *E. coli* and *Salmonella enterica* rRNA that differs by a single base (G for *E. coli*; U for *S. enterica*). The EC (green) probe has only a fluorescein-labeled dT, while the SE (red) probe was designed to have a FRET pair with a fluorescein-labeled dT as the donor and a 3′-TAMRA fluorophore as the acceptor (Figure 7a). Our laboratory has previously used a similar design for QUAL and Q-STAR probes (*15, 28, 42*).

This set of probes was first tested in vitro to validate the two-color system. Both the EC and SE probes were incubated with the 3′-phosphorothioate strand and either the EC or SE template in pH 7.0 buffer containing 70 mM PIPES, 10 mM $MgCl_2$, and 50 μM dithiothreitol at 37 °C for 1 h. The emission spectra of the individual reactions were measured from 500 to 650 nm with a 494 nm (fluorescein) excitation. When the template containing the complementary sequence for the *E. coli* probe was used, the experiment showed a strong signal at 520 nm, consistent with fluorescein emission. When the *S. enterica* template was used, the probes showed a clear FRET signal, with emission peaks at both 520 and 580 nm (Figure 7b). The kinetics of these reactions were also measured at 37 °C over 8 h with and without the template strands (Supporting Information, Figure S7).

After verifying that these probes performed correctly in vitro, their specificity to the desired cell type was tested. Each probe, along with the 3′-phosphorothioate and the appropriate helper probes, was used to treat *E. coli* and *S. enterica* cells in 6× SSC + 0.05% SDS. The intact cells were imaged under an epifluorescence microscope. The results clearly show that the probes were selectively unquenched with the appropriate cell type, as the images of the probes in the incorrect cells showed fluorescence levels that are equivalent to the fluorescence when

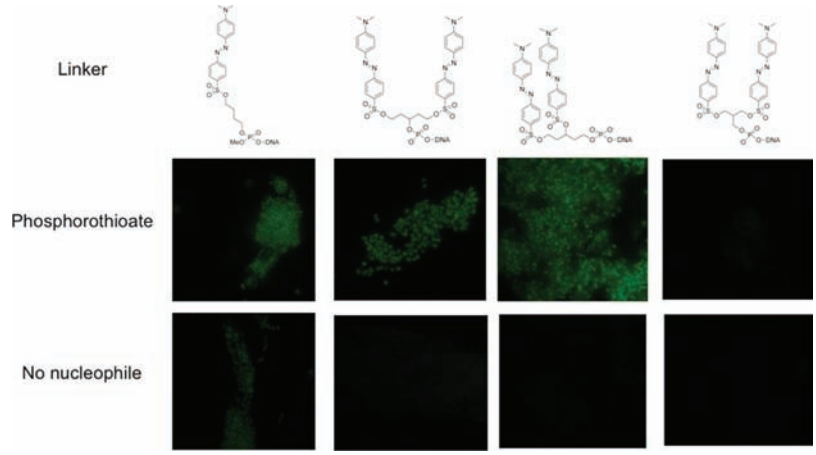


Figure 6. Comparison of double displacement and single Dabsyl probes for detecting cellular 16S rRNA The indicated double displacement or single Dabsyl probe (200 nM), helper DNAs (3 μM), and 3′-phosphorothioate probes (2 μM) were incubated with *E. coli* cells in 6× SSC buffer with 0.05% SDS at 37 °C for 3 h. Images were taken with a black/white camera and false-colored green.

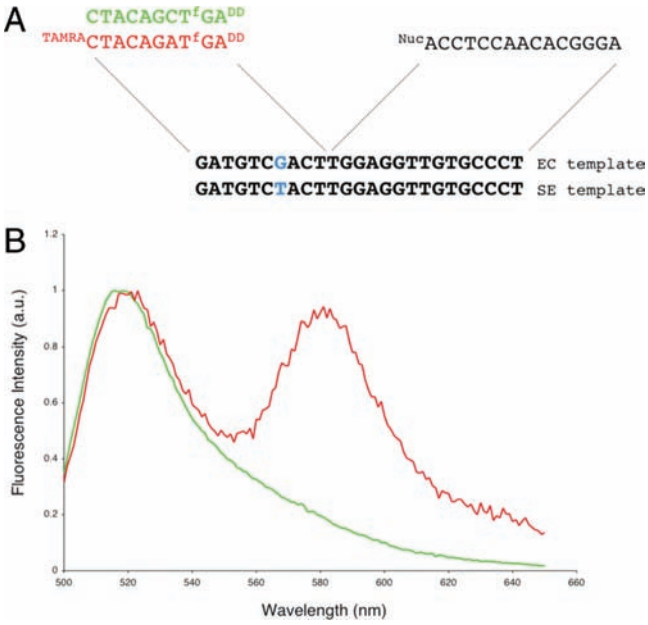


Figure 7. FRET probes for two-color detection scheme. (A) Sequences of DNA probes and targets (T^f = fluorescein dT; DD = 1,3-pentyl linker; Nuc = phosphorothioate). (B) Normalized fluorescence emission spectra of a mixture of EC and SE probes incubated with 3′-phosphorothioate probe and either EC DNA or SE DNA. Conditions: 200 nM EC probe, 200 nM SE probe, 600 nM phosphorothioate DNA, and 200 nM EC (green) or SE DNA (red). The reactions were incubated for 1 h at 37 °C in pH 7.0 buffer containing 70 mM PIPES, 10 mM $MgCl_2$, and 50 μM dithiothreitol. The excitation wavelength was 494 nm.

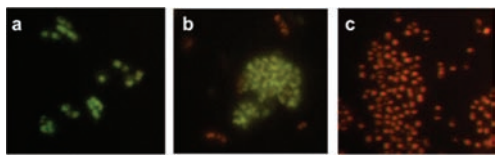


Figure 8. Two-color discrimination of *E. coli* and *S. enterica* based on a single nucleotide polymorphism in the 16S rRNA. EC and SE double displacement probes (200 nM each), helper probes (3 μM), and 3′-phosphorothioate probes (2 μM) in 6× SSC + 0.05% SDS buffer were incubated in the indicated cell type or mixture of cells at 37 °C for 5 h. A B-2A filter was used for imaging. (a) *E. coli* cells. (b) *E. coli* and *S. enterica* cells. (c) *S. enterica* cells.

no nucleophile probe is added (Supporting Information, Figure S8). This study was extended further to show cell-type analysis of a heterogeneous mixture. Both probes were simultaneously added with the same nucleophile and helper strands to a mixture of *E. coli* and *S. enterica* cells. After incubation, the mixture of cells was imaged under a fluorescence microscope, clearly showing two differently colored populations of cells (Figure 8), demonstrating that these probes can be used to distinguish between two cell lines with single nucleotide discrimination.

DISCUSSION

The experiments presented here expand on the previously described quenched autoligation reactions as a viable approach to the detection of nucleic acids. Previous work with this class of reactions showed that nonspecific displacement of the quencher was the primary source of background (*36, 41*). Therefore, in designing the double displacement linkers we sought to use scaffolds that would necessitate two reactions to produce a fully unquenched fluorophore, hoping that this would increase the likelihood that a full unquenching of the probe would include a templated reaction. The results with the three new double displacement probes clearly confirmed this, showing strongly enhanced signal/background as a result of the dual reactive groups. The faster-reacting Pentyl probes also showed improved signal/background in a cellular context. An added benefit of the dual-quencher design was the enhancement of the initial quenching of the probes. For two of the new probes, this produced a much larger increase in fluorescence intensity over time as compared to the previous probes with a single-leaving quencher/leaving group.

The third new probe, based on an isobutyl scaffold, reacted more slowly than expected. Although both leaving groups are at primary positions, the linker appears to be too sterically demanding for the S_N2 reactions necessary for unquenching to occur on a useful time scale. This gives these probes very low background levels, but also a very slow turn-on rate. While these properties may make the Isobutyl probes appropriate for other applications (for example, at higher temperature), they do not lend themselves well to cell-based diagnostics at 37 °C.

Our experiments in single-color detection of rRNA in *E. coli* showed similar trends in signal/background as were observed in vitro. The 1,3-Pentyl and 1,5-Pentyl probes showed a clearer visual difference between the probes with and without the nucleophile strand than did the Isobutyl or single Dabsyl probes. The slow-reacting Isobutyl probes yielded cell images that were hardly fluorescent at all, regardless of whether or not the nucleophile was present. In two-color mixed probe experiments, probes were capable of clearly differentiating between these two cell types based on their genetics in a heterogeneous sample. Thus, the Pentyl probe designs are potentially very applicable in bacterial discrimination in clinical microbiology laboratories, offering clearer signal and less background than previous designs (*42*). Although both the 1,3-Pentyl and 1,5-Pentyl probes performed with similar kinetics and signal/background, from a functional perspective we currently favor the 1,3-Pentyl probes because they appear to give slightly better signal/background in our cellular experiments. However, the 1,5-Pentyl probes do offer a practical advantage, as the synthesis of the phosphoramidite is several steps shorter.

The two-color cellular demonstration of DD probes illustrates one of a number of possible applications of templated chemistry, particularly for single nucleotide discrimination, which is difficult to achieve with classical FISH probes. Continued development of these reactive probes and tests of their application in mammalian cells are underway.

ACKNOWLEDGMENT

The authors thank the U.S. National Institutes of Health (GM068122) for support, the Stanford High-Throughput Bioscience Center for assistance with microplate reader experiments, and R. Franzini, A. Madsen, and A. Silverman for helpful discussions.

Supporting Information Available: Experimental details, additional data, and characterization of synthetic intermediates. This material is available free of charge via the Internet at http://pubs.acs.org.

LITERATURE CITED

(1) Gryaznov, S. M., and Letsinger, R. L. (1993) Template controlled coupling and recombination of oligonucleotide blocks containing thiophosphoryl groups. *Nucleic Acids Res. 21*, 1403–8.
(2) Gryaznov, S. M., Schultz, R., Chaturvedi, S. K., and Letsinger, R. L. (1994) Enhancement of selectivity in recognition of nucleic acids via chemical autoligation. *Nucleic Acids Res. 22*, 2366–9.
(3) Herrlein, M. K., and Letsinger, R. L. (1994) Selective chemical autoligation on a double-stranded DNA template. *Nucleic Acids Res. 22*, 5076–8.

(4) Jacobsen, M. F., Clo, E., Mokhir, A., and Gothelf, K. V. (2007) Model systems for activation of nucleic acid encoded prodrugs. *ChemMedChem 2*, 793–9.
(5) Arian, D., Clo, E., Gothelf, K. V., and Mokhir, A. A nucleic acid dependent chemical photocatalysis in live human cells. *Chemistry 16*, 288–95.
(6) Gartner, Z. J., Kanan, M. W., and Liu, D. R. (2002) Multistep small-molecule synthesis programmed by DNA templates. *J. Am. Chem. Soc. 124*, 10304–6.
(7) Gartner, Z. J., Tse, B. N., Grubina, R., Doyon, J. B., Snyder, T. M., and Liu, D. R. (2004) DNA-templated organic synthesis and selection of a library of macrocycles. *Science 305*, 1601–5.
(8) Liu, D. R. (2004) Translating DNA into synthetic molecules. *PLoS Biol. 2*, E223.
(9) Snyder, T. M., and Liu, D. R. (2005) Ordered multistep synthesis in a single solution directed by DNA templates. *Angew. Chem., Int. Ed. Engl. 44*, 7379–82.
(10) Brudno, Y., Birnbaum, M. E., Kleiner, R. E., and Liu, D. R. An in vitro translation, selection and amplification system for peptide nucleic acids. *Nat. Chem. Biol. 6*, 148–55.
(11) Silverman, A. P., and Kool, E. T. (2006) Detecting RNA and DNA with templated chemical reactions. *Chem. Rev. 106*, 3775–89.
(12) Fey, A., Eichler, S., Flavier, S., Christen, R., Hofle, M. G., and Guzman, C. A. (2004) Establishment of a real-time PCR-based approach for accurate quantification of bacterial RNA targets in water, using Salmonella as a model organism. *Appl. Environ. Microbiol. 70*, 3618–23.
(13) Paillasson, S., Van De Corput, M., Dirks, R. W., Tanke, H. J., Robert-Nicoud, M., and Ronot, X. (1997) In situ hybridization in living cells: detection of RNA molecules. *Exp. Cell Res. 231*, 226–33.
(14) Amann, R., Fuchs, B. M., and Behrens, S. (2001) The identification of microorganisms by fluorescence in situ hybridisation. *Curr. Opin. Biotechnol. 12*, 231–6.
(15) Abe, H., and Kool, E. T. (2006) Flow cytometric detection of specific RNAs in native human cells with quenched autoligating FRET probes. *Proc. Natl. Acad. Sci. U.S.A. 103*, 263–8.
(16) Nitin, N., Santangelo, P. J., Kim, G., Nie, S., and Bao, G. (2004) Peptide-linked molecular beacons for efficient delivery and rapid mRNA detection in living cells. *Nucleic Acids Res. 32*, e58.
(17) Santangelo, P. J., Nitin, N., and Bao, G. (2005) Direct visualization of mRNA colocalization with mitochondria in living cells using molecular beacons. *J. Biomed. Opt. 10*, 44025.
(18) Santangelo, P. J., Nix, B., Tsourkas, A., and Bao, G. (2004) Dual FRET molecular beacons for mRNA detection in living cells. *Nucleic Acids Res. 32*, e57.
(19) Nitin, N., and Bao, G. (2008) NLS peptide conjugated molecular beacons for visualizing nuclear RNA in living cells. *Bioconjugate Chem. 19*, 2205–11.
(20) Seferos, D. S., Giljohann, D. A., Hill, H. D., Prigodich, A. E., and Mirkin, C. A. (2007) Nano-flares: probes for transfection and mRNA detection in living cells. *J. Am. Chem. Soc. 129*, 15477–9.
(21) Cai, J., Li, X., Yue, X., and Taylor, J. S. (2004) Nucleic acid-triggered fluorescent probe activation by the Staudinger reaction. *J. Am. Chem. Soc. 126*, 16324–5.
(22) Pianowski, Z. L., and Winssinger, N. (2007) Fluorescence-based detection of single nucleotide permutation in DNA via catalytically templated reaction. *Chem. Commun. (Camb.)* 3820–2.
(23) Abe, H., Wang, J., Furukawa, K., Oki, K., Uda, M., Tsuneda, S., and Ito, Y. (2008) A reduction-triggered fluorescence probe for sensing nucleic acids. *Bioconjugate Chem. 19*, 1219–26.
(24) Franzini, R. M., and Kool, E. T. (2008) 7-Azidomethoxycoumarins as profluorophores for templated nucleic acid detection. *ChemBioChem 9*, 2981–8.
(25) Furukawa, K., Abe, H., Hibino, K., Sako, Y., Tsuneda, S., and Ito, Y. (2009) Reduction-triggered fluorescent amplification probe for the detection of endogenous RNAs in living human cells. *Bioconjugate Chem.* .
(26) Furukawa, K., Abe, H., Wang, J., Uda, M., Koshino, H., Tsuneda, S., and Ito, Y. (2009) Reduction-triggered red fluorescent probes for dual-color detection of oligonucleotide sequences. *Org. Biomol. Chem. 7*, 671–7.
(27) Pianowski, Z., Gorska, K., Oswald, L., Merten, C. A., and Winssinger, N. (2009) Imaging of mRNA in live cells using nucleic acid-templated reduction of azidorhodamine probes. *J. Am. Chem. Soc.* .
(28) Franzini, R. M., and Kool, E. T. (2009) Efficient nucleic acid detection by templated reductive quencher release. *J. Am. Chem. Soc. 131*, 16021–3.
(29) Huang, Y., and Coull, J. M. (2008) Diamine catalyzed hemicyanine dye formation from nonfluorescent precursors through DNA programmed chemistry. *J. Am. Chem. Soc. 130*, 3238–9.
(30) Jentzsch, E., and Mokhir, A. (2009) A fluorogenic, nucleic acid directed "click" reaction. *Inorg. Chem. 48*, 9593–5.
(31) Cai, J., Li, X., and Taylor, J. S. (2005) Improved nucleic acid triggered probe activation through the use of a 5-thiomethyluracil peptide nucleic acid building block. *Org. Lett. 7*, 751–4.
(32) Grossmann, T. N., Roglin, L., and Seitz, O. (2008) Target-catalyzed transfer reactions for the amplified detection of RNA. *Angew. Chem., Int. Ed. Engl. 47*, 7119–22.
(33) Grossmann, T. N., Strohbach, A., and Seitz, O. (2008) Achieving turnover in DNA-templated reactions. *ChemBioChem 9*, 2185–92.
(34) Sando, S., and Kool, E. T. (2002) Quencher as leaving group: efficient detection of DNA-joining reactions. *J. Am. Chem. Soc. 124*, 2096–7.
(35) Sando, S., Abe, H., and Kool, E. T. (2004) Quenched autoligating DNAs: multicolor identification of nucleic acids at single nucleotide resolution. *J. Am. Chem. Soc. 126*, 1081–7.
(36) Abe, H., and Kool, E. T. (2004) Destabilizing universal linkers for signal amplification in self-ligating probes for RNA. *J. Am. Chem. Soc. 126*, 13980–6.
(37) March, S. A. (2007) *March's Advanced Organic Chemistry*, p 479, John Wiley & Sons, Inc., New York.
(38) Yang, C. J., Lin, H., and Tan, W. (2005) Molecular assembly of superquenchers in signaling molecular interactions. *J. Am. Chem. Soc. 127*, 12772–3.
(39) Miller, G. P., Silverman, A. P., and Kool, E. T. (2008) New, stronger nucleophiles for nucleic acid-templated chemistry: Synthesis and application in fluorescence detection of cellular RNA. *Bioorg. Med. Chem. 16*, 56–64.
(40) Silverman, A. P., and Kool, E. T. (2005) Quenched autoligation probes allow discrimination of live bacterial species by single nucleotide differences in rRNA. *Nucleic Acids Res. 33*, 4978–86.
(41) Fuchs, B. M., Glockner, F. O., Wulf, J., and Amann, R. (2000) Unlabeled helper oligonucleotides increase the in situ accessibility to 16S rRNA of fluorescently labeled oligonucleotide probes. *Appl. Environ. Microbiol. 66*, 3603–7.
(42) Silverman, A. P., Baron, E. J., and Kool, E. T. (2006) RNA-templated chemistry in cells: discrimination of Escherichia, Shigella and Salmonella bacterial strains with a new two-color FRET strategy. *ChemBioChem 7*, 1890–4.

BC100165H